Russian Journal of Applied Chemistry, Vol. 75, No. 1, 2002, pp. 1–4. Translated from Zhurnal Prikladnoi Khimii, Vol. 75, No. 1, 2002, pp. 3–6.
Original Russian Text Copyright © 2002 by Grebenshchikov, Shitova, Mikirticheva, Petrov, Grabovenko, Kuchaeva.

INORGANIC SYNTHESIS AND INDUSTRIAL INORGANIC CHEMISTRY

Isomorphism and Phase Relationships in the Systems of Metagermanosilicates of Alkaline-Earth Metals

R. G. Grebenshchikov, V. I. Shitova, G. A. Mikirticheva, S. A. Petrov, L. Yu. Grabovenko, and S. K. Kuchaeva

Institute of Silicate Chemistry, Russian Academy of Sciences, St. Petersburg, Russia

Received June 4, 2001

Abstract—A comparative analysis of the phase relationships in the ternary mutual systems CaO,SrO‖SiO_2, GeO_2; CaO,BaO‖SiO_2,GeO_2; and SrO,BaO‖SiO_2,GeO_2 was performed and the crystal-chemical properties of the phases crystallizing in them were determined.

Study of the phase equilibria in silicate-based and related systems is one of the central problems in chemical materials science. This work completes our series of studies of the phase relationships in the systems of metagermanosilicates of alkaline-earth metals (Ca, Sr, Ba). The chemical composition of the simplest pyroxenoids is expressed by the general formula $M_n[SiO_3]_n$, where M is a group of double-charged cations with the large ionic radii presented in various integral and fractional ratios [1–4]. Systematic study of the ternary mutual germanosilicate systems CaO, SrO‖SiO_2,GeO_2; CaO,BaO‖SiO_2,GeO_2; and SrO, BaO‖SiO_2,GeO_2 is of undoubted theoretical and practical importance. Extending the chemical composition of pyroxenoids, studying the phase relationships among them, and establishing the concentration regions of homogeneity in these systems is one of the necessary stages in the development of new materials (enamels, electroceramics, etc.). Extended isomorphism of the end members of the systems considered is a prerequisite for the preparation of technical materials based on them.

Figure 1a–1c shows the phase diagrams of the edge sections of the three concentration quadrangles, $CaSiO_3$–$CaGeO_3$–$SrGeO_3$–$SrSiO_3$, $CaSiO_3$–$GaGeO_3$–$BaGeO_3$–$BaSiO_3$, and $SrSiO_3$–$SrGeO_3$–$BaGeO_3$–$BaSiO_3$. The limiting boundaries of solubility in the solid solution systems at 1200°C are shown schematically in their central parts. The concentration limits of stability are plotted on the basis of studying the phase relationships on the edges and in the diagonal sections of the quadrangles considered [5–18]. In these works the characteristic of the end members of all the sections is given in detail, along with the experimental technique. Let us briefly consider the structural properties of the phases crystallizing in the system. All end members of the systems studied can be ranked as one of two structural types of anionic sublattices: chain-like pyroxenoid (β-$CaSiO_3$, $CaGeO_3$, β-$BaSiO_3$, β-$BaGeO_3$) and ring-like pseudowollastonite (α-$CaSiO_3$, α-$SrSiO_3$, α-$SrGeO_3$, α-$BaSiO_3$, α-$BaGeO_3$).

In all the three concentration quadrangles the homogeneity fields were revealed for the phase of variable composition isostructural with walstromite $Ca_2BaSi_3O_9$ (W). This compound has a distorted ring-like pseudowollastonite structure [19, 20].

The phase diagrams show the temperature and concentration limits of feasible variations of the chemical composition of each phase in the series of the systems considered (Figs. 1a–1c). The experiment has shown that more complex chemical composition due to isomorphous transitions and the considerable dissimilarity in sizes of replaced cationic pairs $Ca^{2+}Si^{4+} \rightleftarrows Sr^{2+}Si^{4+}$, $Ca^{2+}Si^{4+} \rightleftarrows Sr^{2+}Ge^{4+}$, $Sr^{2+}Si^{4+} \rightleftarrows Ba^{2+}Si^{4+}$ result in the formation of a wide homogeneity region based on the berthollide phases crystallizing in the walstromite structure. Passing from one structural type to another in each system is realized either via gradual isomorphous transitions or via discrete-stoichiometric variations of the chemical composition.

Let us consider the specific features of phase relationships in the systems studied. For the ternary mutual system CaO,SrO‖SiO_2,GeO_2 the α-$CaSiO_3$ lattice (pseudowollastonite structure) allows extended isomorphism in both the cationic ($CaSiO_3$‖$SrSiO_3$) and anionic ($SrSiO_3$‖$SrGeO_3$) sublattices (Fig. 1a). Replacement of silicon(IV) by germanium(IV) in the

1070-4272/02/7501-0001$27.00 © 2002 MAIK "Nauka/Interperiodica"

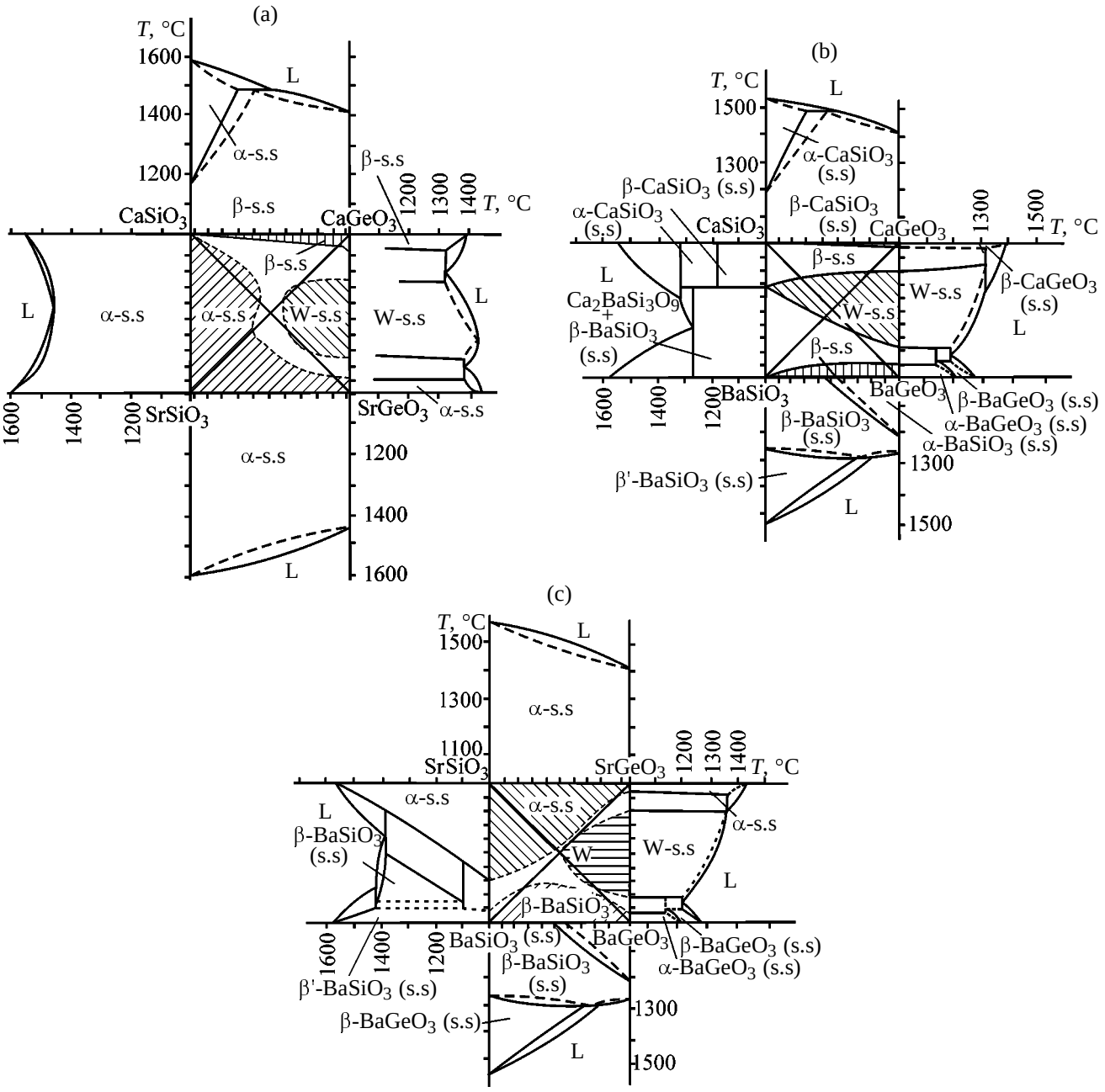

Fig. 1. Phase relationships in the ternary mutual systems. (*T*) Temperature. System: (a) CaO,SrO‖SiO_2,GeO_2; (b) CaO, BaO‖SiO_2,GeO_2; and (c) SrO,BaO‖SiO_2,GeO_2.

$CaSiO_3$ lattice results in the stabilization of the β-wollastonite structure. However, introduction of the strontium(II) ion into the cationic sublattice of β-$CaGeO_3$ drastically limits the concentration boundaries of stability of this structural form (up to 10 mol % $SrGeO_3$) and results in the morphotropic transition β-$CaGeO_3$ → walstromite → α-$SrGeO_3$. The walstromite-like solid solution mainly exists in the region of germanium(IV)-rich compositions.

The phase relationships in the ternary mutual system CaO,SrO‖SiO_2,GeO_2, where calcium is replaced by the larger (compared to strontium) barium ion, drastically differs from the systems considered above. Actually, the concentrational field of the walstromite solid solution is the largest as compared to the other solid solutions (Fig. 1b). In the section $CaSiO_3$‖$BaSiO_3$ this phase is realized solely as incongruently melting compound $Ca_2BaSi_3O_9$. In the

case of conjugate isomorphism $Ca^{2+}Si^{4+} \rightleftarrows Ba^{2+}Ge^{4+}$, $Ca^{2+}Ge^{4+} \rightleftarrows Ba^{2+}Si^{4+}$, the walstromite solid solutions with a reasonably wide homogeneity region exist in the diagonal sections of the concentration quadrangle. In the germanate section $CaGeO_3$–$BaGeO_3$ the solid solution concentration range is even wider. The isothermal section has no field of the α-solid solution and the limited homogeneity regions of the β-$CaSiO_3$ and β-$BaSiO_3$ solid solutions (Fig. 1b).

The isothermal section of the ternary mutual system SrO, $BaO\|SiO_2$, GeO_2 has three homogeneity regions: α-$SrSiO_3$ solid solutions, walstromite-like solid solution, and solid solution based on pyroxenoid $BaSiO_3$. Similar to the $CaO,SrO\|SiO_2,GeO_2$ system, the main phase is the hexagonal α-solid solution. The two other solid solutions have the narrower homogeneity fields.

The performed comparison of the phase relationships in the three mutual systems studied revealed the criteria determining the stability of a given phase and regular trends of physicochemical properties in the similar systems. The obtained data show that the temperature affects to a considerably lesser extent the mutual solubility of the components than the physicochemical nature of the cations occupying the octahedral and tetrahedral positions. It was found that the α-$CaSiO_3$ lattice in which the three-unit ring $[Si_3O_9]^{6-}$ is the main structural element allows the most extended isomorphism. For example, in the pure silicate systems considered, $CaSiO_3\|SrSiO_3$ and $SrSiO_3\|BaSiO_3$, the cationic radii differ considerably (r_{Ca} = 1.00 Å , r_{Sr} = 1.18 Å, and r_{Ba} = 1.35 Å). At the same time, the miscibility of the edge members is higher than in the analogous germanate systems.

Replacement of the silicon ion by the larger germanium ion (r_{Si} = 0.26, r_{Ge} = 0.39 Å) in the anionic sublattices of $CaSiO_3$, $SrSiO_3$, and $BaSiO_3$ results in the stabilization of the corresponding solid solutions. Probably, the condition that the same cation occupies the cationic sublattice plays the decisive role in these cases. Passing to more complex chemical composition in the germanate systems ($CaGeO_3\|SrGeO_3$, $CaGeO_3\|BaGeO_3$, $SrGeO_3\|BaGeO_3$) and in the diagonal sections (conjugate isomorphism) results in the appearance of the discrete intermediate berthollide phases crystallizing in the walstromite structure. Probably, the isomorphous transitions in these systems give rise to size mismatch in the structure of the solid solutions based on the edge members. As a result, the miscibility is broken, and the walstromite-like phases with the distorted pseudowollastonite structure are formed. Apparently, the latter structure allows more considerable variation of the sizes of the large cations occupying the corresponding sublattice. This process is also facilitated by the arrangement of the germanium ions in the anionic sublattice of these phases. Compared to the Si–O bond, the chemical bond Ge–O is less rigid, ensuring greater tolerance of the ring geramanate–silicate systems to the isomorphous replacements in the cationic sublattice. Probably, this fact can explain formation of the walstromite phases in the given systems. The relative size mismatch occurring upon replacements in the cationic and anionic sublattices of this structure is compensated by the partial distortion of the anionic skeleton owing to the possible deformation of the Ge–O bonds in the tetrahedra.

To conclude, the extended isomorphism of the crystalline phases in the germanate–silicate systems studied is largely determined by the stoichiometric and energy compatibility of the structural elements and by the similarity in the sizes of atoms and groups involved in the replacement. The extended isomorphism, generally found in the multicomponent systems studied, makes a quite encouraging experimental basis for development of novel materials.

CONCLUSIONS

(1) The phase relationships in the ternary mutual germanosilicate systems $CaO,SrO\|SiO_2,GeO_2$; $CaO,BaO\|SiO_2,GeO_2$; and $SrO,BaO\|SiO_2,GeO_2$ were compared.

(2) In the systems studied, the temperature and concentration fields of homogeneity based on the different crystalline structures were revealed. The correlation between the chemical composition of the crystallizing phases and the limits of their isomorphous capacity were established.

(3) The conditions of formation of the berthollide phases crystallizing in the walstromite structure were determined.

REFERENCES

1. Zussman, J., *Earth Sci. Rev*., 1968, vol. 4, no. 1, pp. 39–67.
2. Takenchi, Y. and Koto K., *Mineral. J*., 1977, vol. 8, no. 5, pp. 272–285.
3. Papike, J.J. and Cameron, M., *Rev. Geophys. Space Phys*., 1976, vol. 14, no. 1, pp. 37–80.
4. Deer, W.A., Howie, R.A., and Zussman, J., *Rock-Forming Minerals*, vol. 2a: *Single-Chain Silicates*, London: Longman, 1978.

5. Moir, G.K., Gard, J.A., and Glasser, F.P., *Z. Kristallogr*., 1975, vol. 141, nos. 5–6, pp. 437–450.
6. DeVries, R.S., *J. Am. Ceram. Soc*., 1988, vol. 71, no. 10, pp. 416–417.
7. Petrov, S.A., Grabovenko, L.Yu., Kuchaeva, S.K., *et al*., *Zh. Prikl. Khim*., 2000, vol. 73, no. 2, pp. 177–180.
8. Petrov, S.A., Mikirticheva, G.A., Shitova, V.I., *et al*., *Zh. Prikl. Khim*., 2000, vol. 73, no. 11, pp. 1758–1760.
9. Grebenshchikov, R.G., Shitova, V.I., Mikirticheva, G.A., *et al*., *Zh. Prikl. Khim*., 2000, vol. 73, no. 11, pp. 1763–1766.
10. Grebenshchikov, R.G., Shirvinskaya, A.K., and Parfenenkov, V.N., *Izv. Akad. Nauk SSSR, Neorg. Mater*., 1970, vol. 6, no. 2, pp. 323–326.
11. Grebenshchikov, R.G. and Shitova, V.I., *Izv. Akad. Nauk SSSR, Neorg. Mater*., 1976, vol. 12, no 4, pp. 674–678.
12. Mikirticheva, G.A., Shitova, V.I., Petrov, S.A., *et al*., *Zh. Prikl. Khim*., 2001, vol. 74, no. 8, pp. 1235–1239.
13. Shteinberg, Yu.G., *Strontsievye glazuri* (Strontium Glazes), Leningrad: Stroizdat, 1967.
14. Fields, J.M., Dear, P.S., and Brown, J.J., *J. Am. Ceram. Soc*., 1972, vol. 55, no. 12, pp. 585–588.
15. Huntelaar, M.E. and Cordfunke, H.P., Abstracts of Papers, *12th IUPAC Conf. on Chemical Thermodynamics*, Snowbird, Utah, August 16–21, 1992, pp. 318–319.
16. Grebenshchikov, R.G., Shirvinskaya, A.K., and Popova, V.F., *Zh. Prikl. Khim*., 2000, vol. 73, no. 10, pp. 1577–1581.
17. Grebenshchikov, R.G., Shitova, V.I., and Dmitrieva, L.Yu., *Zh. Neorg. Khim*., 1981, vol. 26, no. 1, pp. 226–231.
18. Grebenshchikov, R.G., Shitova, V.I., Grabovenko, L.Yu., and Romanov, D.P., *Zh. Neorg. Khim*., 1985, vol. 30, no. 3, pp. 757–762.
19. Belov, N.V., *Ocherki po strukturnoi mineralogii* (Essays on Structural Mineralogy), Moscow: Nedra, 1976.
20. Glasser, L.S. and Glasser, F.P., *Am. Mineral*., 1968, vol. 53, no. 1, pp. 9–13.

Russian Journal of Applied Chemistry, Vol. 75, No. 1, 2002, pp. 5–8. Translated from Zhurnal Prikladnoi Khimii, Vol. 75, No. 1, 2002, pp. 6–9.
Original Russian Text Copyright © 2002 by Kurzina, Galanov, Kurina.

INORGANIC SYNTHESIS AND INDUSTRIAL INORGANIC CHEMISTRY

Phase Composition of the Lead–Tin Oxide System

I. A. Kurzina, S. I. Galanov, and L. N. Kurina

Tomsk State University, Tomsk, Russia

Received May 15, 2001

Abstract—The influence of the component ratio, support type, and preparation procedure on the phase composition of the lead–tin oxide catalysts was studied.

Oxide systems containing SnO_2 are catalytically active in oxidative dehydrodimerization of hydrocarbons [1–3]. The lead–tin oxide systems are active in oxidative dehydrodimerization of propylene [4] and methane [5]. The supported catalysts exhibit enhanced thermal stability. To reveal the correlation between the activity and physicochemical properties of catalytic systems, it is necessary to know their phase composition.

In this work, we studied the influence of the composition, preparation procedure, and support type on the phase composition of the Pb–Sn–O catalysts.

EXPERIMENTAL

The lead–tin oxide catalysts (neat and supported) were used. The monolithic lead–tin samples were prepared by calcination at 800°C for 10 h in air of a mixture of tin(II) and lead(II) hydroxides. Supported samples were prepared by alternate impregnation of the support with solutions of $Pb(NO_3)_2$ and $SnSO_4$, and also by applying a wet paste of a mixture of tin(II) or tin(IV) and lead(II) hydroxides with subsequent drying at 200°C for 2 h and calcination at 800°C for 10 h. Supports were corundum α-Al_2O_3, aluminosilicate (40 wt % SiO_2), and commercial pumice sample. The support surface was preliminarily treated with a $Ca(OH)_2$ saturated solution at 200°C for 20 min, and then the samples were calcined at 800°C for 6 h. The amount of the lead–tin oxide composition applied to the support was 20 wt %.

The thermogravimetric curves of the hydroxide mixtures dried at 150°C and heated in air at a rate of 10 deg min^{-1} were taken on an MOM derivatograph (Hungary). The phase composition of the lead–tin samples was studied by X-ray phase analysis (DRON-0.5 diffractometer, CuK_α radiation). The specific surface area S_{sp} of the samples was determined chromatographically by thermal desorption of argon (S_{sp} = 2.1–2.5 $m^2\ g^{-1}$).

The X-ray phase analysis of the initial Pb–Sn–O compositions differing in the component ratios revealed tetragonal SnO_2 and rhombic PbO (Fig. 1a). The lead ortho- and metastannates are formed in the system at higher PbO content. The samples with 40–80 wt % PbO contain small amounts of lead metastannate $PbSnO_3$. The reflections assigned to lead orthostannate Pb_2SnO_4 are observed in the diffraction patterns of all the mixed Pb–Sn–O systems. Increasing lead oxide content in the samples increases the Pb_2SnO_4 content.

The thermogravimetric curves of the Pb–Sn–O samples of different compositions are shown in Fig. 1b. The DTA curves show several maxima corresponding to the different stages of phase formation in the system. The endothermic effects at 195 and 860°C, which correspond to dehydration of $Pb(OH)_2$ to PbO and to the melting of PbO, respectively [6], were observed with lead hydroxide. The diffuse exothermic effect at 360°C is assigned to the formation of nonstoichiometric lead oxides, Pb_3O_4 and Pb_2O_3. Further decomposition of these oxides to PbO and the phase transitions $PbO_{tetr} \rightleftarrows PbO_{rh}$ are accompanied by the endothermic effects at 450 and 510°C [6, 7]. On heating $Sn(OH)_2$ in air, two processes occur simultaneously: dehydration of tin hydroxide to SnO and its oxidation to SnO_2, which is revealed as two typical effects at 240 and 330°C. The TG curve shows weight loss (up to 240°C) followed by weight gain (up to 380°C) due to the SnO oxidation to SnO_2.

The DTA curves of the lead–tin systems containing 20, 40, and 60 wt % lead oxide (Fig. 1b) show, apart from the above thermal effects, also the exothermic peaks at 415–480°C attributable to the formation of

1070-4272/02/7501-0005$27.00 © 2002 MAIK "Nauka/Interperiodica"

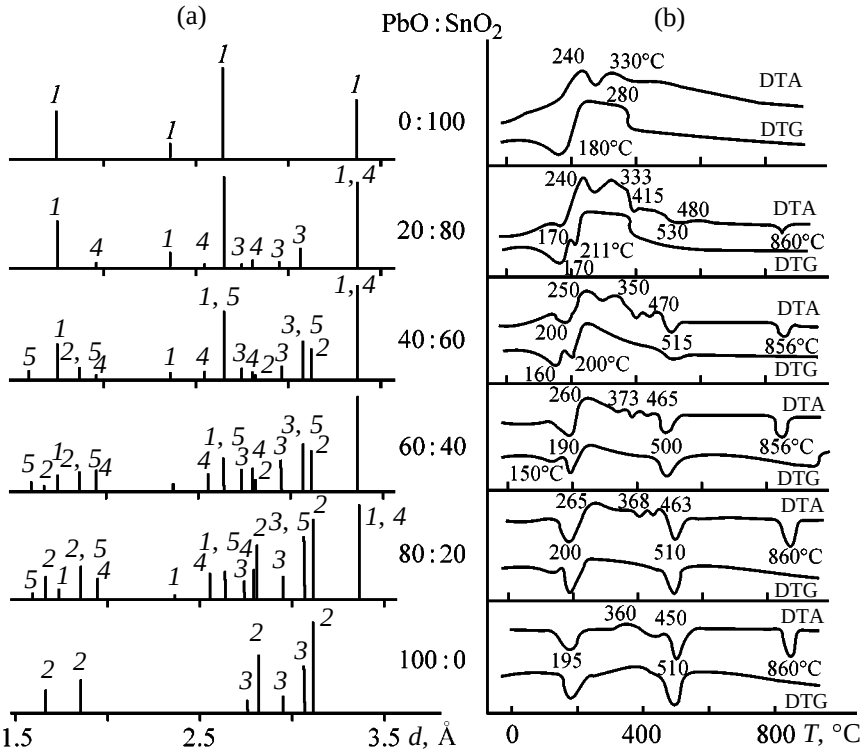

Fig. 1. (a) X-ray diffraction patterns and (b) thermograms of the Pb–Sn–O oxide systems. (*d*) Interplanar spacing and (*T*) temperature. Phase: (*1*) SnO_2, (*2*) PbO_{rh}, (*3*) PbO_{tetr}, (*4*) Pb_2SnO_4, and (*5*) $PbSnO_3$.

lead meta- and orthostannates [4, 6]. As seen, the lead orthostannate phase is formed even at 20 wt % PbO. Increasing lead oxide content increases the amount of this phase.

Thus, over the entire range of the component ratios, tin and lead oxides interact with the formation of multiphase systems, which alters the bulk and surface properties of the samples. Study of the catalytic properties of SnO_2 and of mixed Pb–Sn–O samples of different compositions in oxidative dehydrodimerization of methane (ODM) has shown that the increase in the PbO content in the samples increases the yield of ethane and ethylene. The sample of the composition (wt %) $PbO : SnO_2 = 80 : 20$ has the highest activity in ODM [5]. The results of [5] show that the yield of ethane and ethylene correlates with the total concentration of lead oxide and chemical compounds Pb_2SnO_4 and $PbSnO_3$. The multiphase composition of the systems enhances the catalytic properties of the samples [8].

To increase the thermal stability of the lead–tin samples in ODM, the most selective system of composition (wt %) $PbO : SnO_2 = 80 : 20$ was applied to a number of supports. In view of the fact that the most used supports for ODM catalysts are silicon and aluminum oxides [9, 10], the supports chosen in this study contained oxides SiO_2 and Al_2O_3 in different concentrations and had the close specific surface areas. To enhance the selectivity of ODM catalysts, it is proposed to decrease the acidity of the supports by treating them with NaOH, $Ca(OH)_2$, $Mg(OH)_2$, and other hydroxides. In this work, pumice, aluminosilicate (40% SiO_2), and corundum, pretreated with the saturated solution of $Ca(OH)_2$ and calcined at 800°C for 6 h, were used as supports. The supports show low activity in methane oxidation. The reaction products contain insignificant amounts of carbon monoxide.

It was found that the phase formation of the supported lead–tin samples significantly depends on the support type and application procedure. The phase composition of the Pb–Sn–O system prepared by applying a wet paste of a mixture of $Pb(OH)_2$ and $Sn(OH)_2$, with subsequent drying at 200°C for 2 h and calcination at 800°C for 10 h, is presented in Table 1 and Fig. 2. Use of the SiO_2-containing supports results in the formation of lead aluminosilicates, $Pb_3Al_2Si_4O_{14}$ and $Pb_4Al_2Si_2O_{11}$.

The X-ray analysis showed that in the case of the Pb–Sn–O/α-Al_2O_3 system the active component does

Table 1. Influence of support on phase composition of the Pb–Sn–O samples with the weight ratio PbO : SnO_2 = 80 : 20

Sample	S_{sp}, $m^2\ g^{-1}$	SiO_2 content in support, wt %	Phase composition
Sn–Pb–O/pumice	1.1	60–70	$Al_2Si_4O_{11}$, SiO_2, SnO_2, PbO_{rh}, $Pb_4Al_2Si_2O_{11}$
Sn–Pb–O/Al_2O_3–SiO_2	2.0	40	SnO_2, PbO_{rh}, Al_2SiO_5 (sillimanite), Al_2SiO_5 (kyanite), $PbAl_2O_4$, $Pb_3Al_2Si_4O_{14}$
Sn–Pb–O/α-Al_2O_3	2.2	–	α-Al_2O_3, SnO_2, PbO_{rh}, PbO_{tetr}, Pb_2SnO_4

Table 2. Influence of the preparation procedure of Pb–Sn–O/α-Al_2O_3 on the phase composition of the sample. PbO : SnO_2 = 80 : 20, T_{cal} = 800°C, 10 h

Sample	Preparation procedure	Phase composition
I	Application of a wet paste of a mixture of $Pb(OH)_2$ and $Sn(OH)_2$	α-Al_2O_3, SnO_2, PbO_{rh}, PbO_{tet}, Pb_2SnO_4
II	Impregnation with $Pb(NO_3)_2$, calcination at 800°C for 6 h, and impregnation with $SnSO_4$	"
III	Impregnation with $SnSO_4$, calcination at 800°C for 6 h, and impregnation with $Pb(NO_3)_2$	"
IV	Application of H_2SnO_4 and subsequent impregnation with $Pb(NO_3)_2$	α-Al_2O_3, SnO_2, $PbO_{rh,}$ PbO_{tetr}
V	Application of a mixture of $Pb(OH)_2$ and H_4SnO_4	α-Al_2O_3, SnO_2, PbO_{rh}, PbO_{tetr}, $PbSnO_3$

not interact with the support. Evidently, it is a result not only of the α-Al_2O_3 stability, but of its compact structure as well [11]. The latter impedes diffusion of metal ions and facilitates the uniform distribution throughout the surface of active phase.

The X-ray phase analysis revealed lead orthostannate and tin and lead oxides in the Pb–Sn–O/α-Al_2O_3 system. However, the phase ratio and the sequence of phase formation depend on the preparation procedure (Fig. 3, Table 2).

The samples based on the tin(II) compounds (samples *I*–*III*) contain lead orthostannate, in addition to tin and lead oxides. The comparison of the reflection intensities with d = 2.75 Å revealed the highest content of Pb_2SnO_4 in sample *I* (Fig. 3). Sample *V* prepared by applying to α-Al_2O_3 a mixture of $Pb(OH)_2$ and H_4SnO_4 contains trace amounts of lead metastannate.

The study of the influence of the support type and preparation procedure showed that the optimal support for the Pb–Sn–O composition is α-Al_2O_3, because it does not react chemically with the active phase. The lead–tin catalysts of the composition (wt %) Pb : Sn =

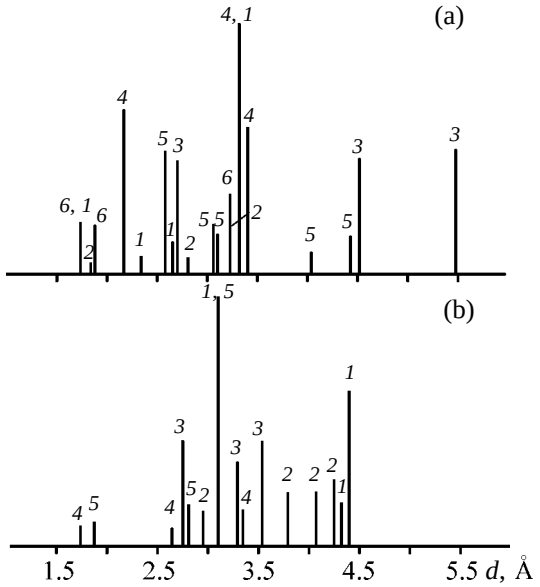

Fig. 2. X-ray diffraction patterns of the systems (a) Pb–Sn–O/Al–Si–O and (b) Pb–Sn–O/pumice. (*d*) Interplanar spacing; the same for Fig. 3. Phase: (a) (*1*) SnO_2, (*2*) PbO_{rh}, (*3*) Al_2SiO_5 (sillimanite), (*4*) Al_2SiO_5 (kyanite), (*5*) $PbAl_2O_4$, and (*6*) $Pb_3Al_2Si_4O_{14}$; (b) (*1*) $Al_2Si_4O_{11}$, (*2*) SiO_2, (*3*) $Pb_4Al_2Si_2O_{11}$, (*4*) SnO_2, and (*5*) PbO_{rh}.

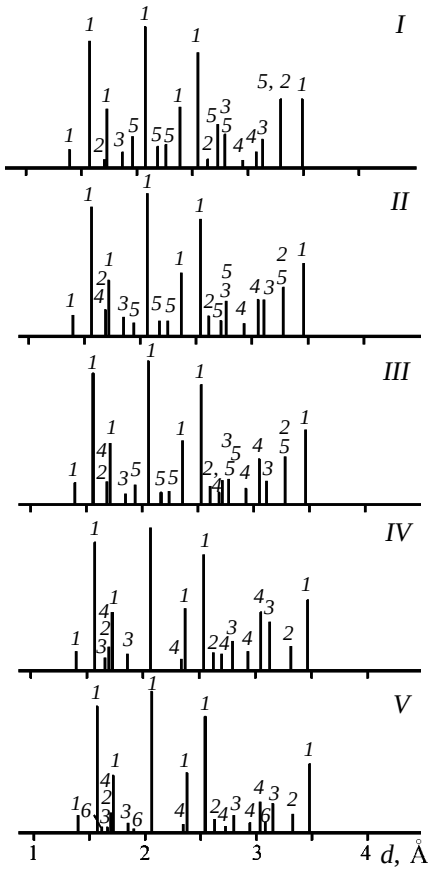

Fig. 3. X-ray diffraction patterns of the Pb–Sn–O/α-Al_2O_3 sample prepared by different procedures. Phase: (*1*) α-Al_2O_3, (*2*) SnO_2, (*3*) PbO_{rh}, (*4*) PbO_{tetr}, (*5*) Pb_2SnO_4, and (*6*) $PbSnO_3$. (*I*–*V*) Sample nos. in Table 2.

80 : 20, prepared by application to α-Al_2O_3 of a mixture of $Sn(OH)_2$ and $Pb(OH)_2$, exhibit thermal stability and stable activity in oxidative dehydrodimerization of methane [5].

CONCLUSION

The X-ray phase and thermal analyses showed formation of $PbSnO_3$ and $PbSnO_4$. The lead orthostannate phase, Pb_2SnO_4, affects the activity of the Pb–Sn–O systems. Use of SiO_2-containing supports results in the formation of the compounds $Pb_4Al_2 \cdot Si_2O_{11}$ and $Pb_3Al_2Si_4O_{14}$.

REFERENCES

1. Mamedov, E.A., and Sokolovskii, V.D., *Okislitel'naya degidrodimerizatsiya uglevodorodov* (Oxidative Dehydrodimerization of Hydrocarbons), Novosibirsk: Nauka, 1992.
2. Kurzina, I.A., Galanov, S.I., Kurina, L.N., *et al*., *Zh. Fiz. Khim*., 1998, vol. 72, no. 12, pp. 2189–2191.
3. Galanov, S.I., Shabalin, E.Yu., and Kurina, L.N., *Khim. Tverd. Topl*., 1993, no. 2, pp. 76–77.
4. Vislovskii, V.P., Mamedov, E.A., Mekhtiev, K.M., and Rizaev, R.G., *Neftekhimiya*, 1982, vol. 22, no. 3, pp. 329–334.
5. Kurzina, I.A., Galanov, S.I., Kurina, L.N., and Belousova, V.N., *Zh. Prikl. Khim*., 1999, vol. 72, no. 2, pp. 242–245.
6. *Fiziko-khimicheskie svoista oksidov: Spravochnik* (Physicochemical Properties of Oxides: Reference Book), Samsonov, G.V., Ed., Moscow: Metallurgiya, 1969, p. 456.
7. Nekrasov, B.V., *Osnovy obshchei khimii* (Fundamentals of General Chemistry), Moscow: Khimiya, 1973, vol. 2.
8. Krylov, O.V., *Kinet. Katal*., 1999, vol. 40, no. 5, pp. 752–758.
9. Sinev, M.Yu., Vorob'eva, G.A., and Korchak, V.N., *Kinet. Katal*., 1986, vol. 27, no. 5, pp. 1164–1169.
10. Jones, C.A., Leonard, J.J., and Sofranko, J.A., *J. Catal*., 1987, vol. 103, no. 2, pp. 311–319.
11. Putanov, P., *Mekhanizm kataliza* (Catalysis Mechanism), Novosibirsk: Nauka, 1984, part 1, pp. 210–215.

Russian Journal of Applied Chemistry, Vol. 75, No. 1, 2002, pp. 9–13. Translated from Zhurnal Prikladnoi Khimii, Vol. 75, No. 1, 2002, pp. 10–14.
Original Russian Text Copyright © 2002 by D'yachkov.

INORGANIC SYNTHESIS AND INDUSTRIAL INORGANIC CHEMISTRY

Temperature Dependence of Oxidation Rate Constants for Titanium–Iron Alloys

V. I. D'yachkov

St. Petersburg State University, St. Petersburg, Russia

Received July 27, 2001

Abstract—The influence of titanium alloying with iron on the temperature dependence of the rate constants and activation energy of oxidation in air at 973–1473 K was studied.

In the previous communication [1], I reported on the kinetics of oxidation of titanium–iron alloys in air of controlled humidity at 1023–1473 K. It was found, in particular, that the rate of this process (up to 30 h) for Ti–Fe alloys (C_{Fe} = 1.5, 5.0, 10.0 wt %) is for the most part described by the Evans equation

$$K_l q^2 + K_p q = K_l K_p \tau + C',$$

where q is the mass of the gases taken up, τ is time, C' is a constant, and K_l and K_p are the rate constants of oxidation by the linear and parabolic laws, respectively.

As known [2], the fulfillment of this equation indicates that the oxidation process is nonstationary and, consequently, its rate is controlled to comparable extents by diffusion and interphase reaction. As for the question of how the iron concentration affects the temperature dependence of the rate constants of alloy oxidation and its activation energy, which are the most important characteristics of the process, it remains open. An attempt to find an answer to it is the subject of the present study performed in air at 973–1473 K.

The procedure used in the experiments with alloys of the above composition and refined titanium was described in [1].

According to the results obtained in [1], two, and occasionally more forms of the Evans equation are observed in isothermal oxidation of alloys (3 h) at above 1023 K. These forms, successively replacing one another, have different rate constants K_l and K_p. The time during which the initial form of this equation is operative may vary in the range from 15 to 30 min and more. Figure 1 shows as an example the temperature dependence of K_l and K_p for the initial and subsequent periods of oxidation of the Ti–5.0 wt % Fe alloy. Being similar in shape, these dependences are, naturally, not identical. This is mainly due to the difference in the constants K_l and K_p themselves for the mentioned stages of testing. In addition, the boundaries of some temperature zones (Fig. 1a) and also the slopes of the respective plots may be different for K_l and K_p, which points to different oxidation mechanisms in the initial and subsequent periods. In the case of pure titanium, such differences in the temperature dependences of K_l and K_p for these stages of oxidation are less significant. This fact makes difficult unambiguous interpretation of the effect of titanium alloying with iron on the temperature dependence of K_l and K_p and on the activation energy of oxidation. In principle, this effect can be assessed using data for both periods of the process, or even on the basis of averaged values of K_l and K_p. However, by virtue of the above circumstances, and also because of the discrepancy between the times of transition of the oxidation process to the second stage for different alloys and for parallel runs, it seems appropriate to use the results obtained during the initial stage of the test.

The data obtained (Fig. 2) indicate that the temperature dependence of K_l and K_p is complex and is affected by the content of iron in the alloys. This is manifested in an abrupt change in the slope of these dependences at certain temperatures. For pure titanium, this change in slope is observed for $\log K_l = f(1/T)$ at around 1173 K, and for Ti–Fe alloys this occurs twice: near 1173 (C_{Fe} = 1.5 wt %) and 1123 K (C_{Fe} = 5.0, 10.0 wt %) for the first time, and at around 1223 (C_{Fe} = 1.5, 5.0 wt %) and 1173 K (C_{Fe} = 10.0 wt %) for the second. As seen, the temperature of the first change in the slope of this dependence tends

1070-4272/02/7501-0009$27.00 © 2002 MAIK "Nauka/Interperiodica"

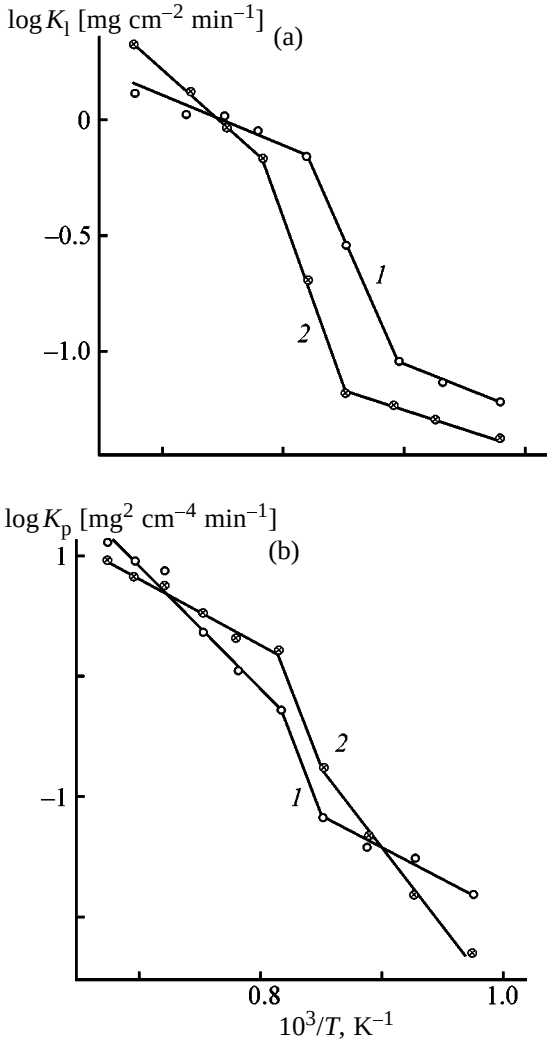

Fig. 1. Temperature dependences of (a) K_l and (b) K_p for the (*1*) initial and (*2*) supsequent oxidation periods of the Ti– 5.0 wt % Fe alloy.

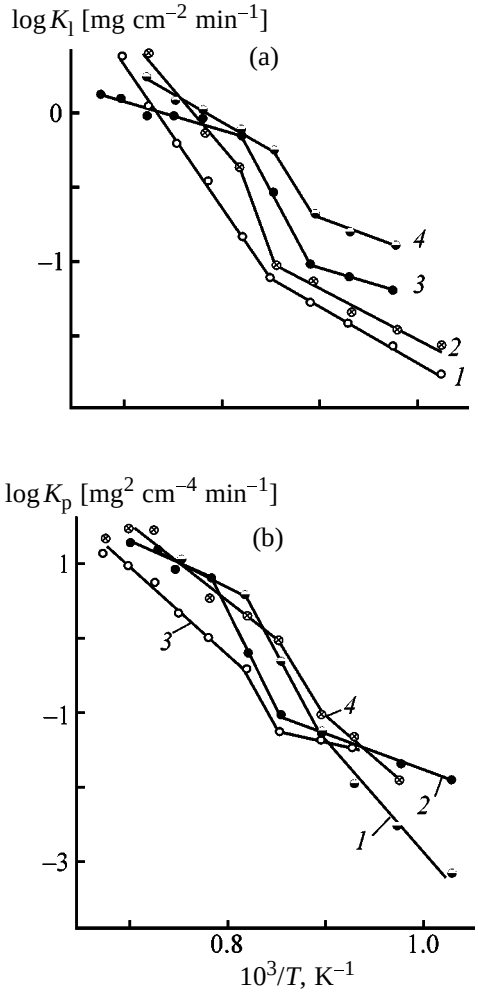

Fig. 2. Temperature dependences of (a) K_l and (b) K_p for the initial stage of oxidation of (*1*) titanium and (*2*–*4*) Ti–Fe alloys. Content of iron in alloy (wt %): (*2*) 1.5, (*3*) 5.0, and (*4*) 10.0.

to decrease with increasing C_{Fe} in the alloys. Thus, in contrast to pure titanium, alloys are characterized by the existence of a transition temperature zone 1123(1173)–1223 K, in which the temperature coefficient K_l markedly decreases with increasing C_{Fe}. In the adjacent temperature zone, the dependence of K_l on C_{Fe} is more complex.

In the interval 973–1473 K, the temperature dependence of K_p (Fig. 2b), similarly to $\log K_l = f(1/T)$, exhibits two changes in slope: at 1123 and 1223 K for titanium; and at around 1173 and 1273, 1173 and 1223, and 1123 and 1173 K for alloys with 1.5, 5.0, and 10.0 wt % Fe, respectively. In going from titanium to alloys and with increasing C_{Fe} in the alloys, the transition temperature zone shows a tendency toward narrowing. With increasing C_{Fe}, the temperature of the first change in the slope of the dependence $\log K_p = f(1/T)$ decreases, and for the second change in the slope this decrease is more pronounced. In all cases, the temperature coefficients of K_l and K_p increase at 1123 (1173) K and decrease markedly above 1223 K (Fig. 2).

Table 1 presents the apparent activation energies E (kJ mol^{-1}) of oxidation of titanium and Ti–Fe alloys by the linear (E_l) and parabolic (E_p) laws for the initial ($E_l^{(1)}$, $E_p^{(1)}$) and subsequent ($E_l^{(2)}$, $E_p^{(2)}$) periods of testing, calculated from the linear portions of the temperature dependences of K_l and K_p. The temperature intervals for each E value are given in parentheses. The errors in determining E for titanium and Ti–Fe alloys are, respectively, ±(3–5) and ±(3–7)%, respectively. Approximate values are given for the temperature zone 1123 (1173)–1223 K because of its narrow

Table 1. Effect of various factors on the apparent activation energy E of oxidation in air of titanium and its alloys with iron

E	E, kJ mol^{-1} (temperature, K)			
	refined titanium	Ti–1.5 wt % Fe	Ti–5.0 wt % Fe	Ti–10.0 wt % Fe
$E_l^{(1)}$	71 (973–1173) 199 (1173–1423)	64 (973–1173) 350 (1173–1223) 152 (1223–1373)	40 (1023–1123) 240 (1123–1233) 45 (1223–1473)	54 (1023–1123) 190 (1123–1173) 85 (1173–1373)
$E_l^{(2)}$	65 (973–1173) 180 (1173–1373)	30 (1023–1173) 330 (1173–1223) 102 (1223–1373)	31 (1023–1173) 292 (1173–1273) 97 (1273–1473)	52 (1023–1173) 141 (1173–1373)
$E_p^{(1)}$	235 (973–1123) 510 (1123–1223) 158 (1223–1373)	96 (973–1173) 610 (1173–1273) 129 (1273–1423)	95 (1023–1173) 550 (1173–1223) 225 (1223–1473)	189 (1023–1123) 460 (1123–1173) 215 (1173–1373)
$E_p^{(2)}$	203 (973–1073) 530 (1073–1173) 159 (1223–1373)	213 (1023–1173) 780 (1173–1223) 153 (1223–1473)	223 (1023–1173) 630 (1173–1223) 117 (1223–1473)	302 (1023–1123) 500 (1123–1173) 189 (1173–1373)

Table 2. Effect of iron content in alloys and temperature on the K_l/K_p ratio in the initial stage of oxidation

Material	K_l/K_p ratio at indicated temperature, K								
	1023	1073	1123	1173	1223	1273	1323	1373	1423
Titanium	9	4.3	1.0	0.3	0.04	0.06	0.06	0.07	–
Ti–1.5 wt % Fe	2	1.4	1.5	1.3	0.80	0.15	0.16	0.20	0.25
Ti–5.0 wt % Fe	3	2.8	2.5	4.5	1.55	0.82	0.53	0.16	0.13
Ti–10.0 wt % Fe	6	3.2	2.2	0.6	0.32	0.28	0.11	0.08	0.06

width (50–100 K). The data of Tables 1 and 2 make it possible to assess the effect of temperature, titanium alloying with iron, and C_{Fe} in the alloys on E_l and E_p, and also to determine their change in going from the initial to the subsequent stage of oxidation.

The changes in the slopes of the temperature dependences of K_l and K_p (Fig. 2) and in the E_l and E_p values (Table 1) are due to changes in the mechanism of oxidation, remaining, however, nonstationary. It follows from Table 1 and Fig. 2 and from the equilibrium phase diagrams of the corresponding systems [3, 4] that the interval 1123 (1173)–1223 K with high E_l and E_p includes, or is close to, the temperature of allotropic ($\alpha \rightleftarrows \beta$) transition in the metal phase, equal to 1155 K for pure titanium. It is the ($\alpha \rightleftarrows \beta$) transition, accompanied by weakening of the interatomic bonding in the metal lattice, excitation of atoms, and acceleration of diffusion processes,

that is, presumably, the main reason for a dramatic increase in E_l and E_p at 1123 (1173) K. In the case of alloys with iron, which stabilizes the β phase, a decrease in the temperature at which the ($\alpha \rightleftarrows \beta$) transition starts to affect the oxidation process would be expected, which does not contradict the data obtained (Table 1, Fig. 2). However, the actual course of the process is complicated by the following two factors. On the one hand, absorption of oxygen, which stabilizes the α phase, by the metal exerts the opposite influence on the temperature of the ($\alpha \rightleftarrows \beta$) transition. On the other hand, the process is affected by specific features of redistribution in the metal of iron, which changes conditions and rate of the growth of the oxygen diffusion layer.

As seen from Table 2, the K_l/K_p ratio decreases with increasing temperature, at least to a certain extent, for all formulations. This indicates the increasing part played by interphase reactions in the control over the rate of nonstationary oxidation and does not contradict the existing general theories. Comparison of the data of Tables 1 and 2 and Fig. 2 shows that the zones of abrupt changes in K_l/K_p values, on the one hand, and temperature coefficients of K_l and K_p (E_l and E_p), on the other, virtually coincide. This means that the contribution of interphase reactions to the control over the oxidation rate increases to the greatest extent in the temperature interval 1123–1223 K. The reason is that the rate of diffusion processes grows in this range most abruptly, which is due, in particular, to the above-mentioned influence of the ($\alpha \rightleftarrows \beta$) transition formation in the metal phase.

In the temperature range above 1223 K, in which the second change in the temperature coefficients K_l and K_p (E_l and E_p) is observed, with the single-phase β structure being the same for all the compositions, the part played by the allotropic ($\alpha \rightleftarrows \beta$) transition in the oxidation process is, presumably, markedly diminished.

According to Table 1, the E_l and E_p values for both oxidation stages markedly increase in the interval 1123–1223 K upon alloying of titanium with 1.5 wt % iron, and steadily decrease with increasing C_{Fe} in the alloys. Outside this temperature zone, the E_l values for titanium for the initial and subsequent stages of tests ($E_l^{(1)}$, $E_l^{(2)}$) are higher than those for the alloys. The E_l value, as a rule, decreases (or remains unchanged) with C_{Fe} increasing from 1.5 to 5.0 wt %, and increases noticeably on passing to C_{Fe} = 10.0 wt %. A decrease in $E_p^{(1)}$ upon alloying of titanium with iron is only observed in the interval 973–1173 K, whereas at 1223–1373 (1473) K the trend is opposite. At the same time, the dependence of $E_p^{(1)}$ and $E_p^{(2)}$ on C_{Fe} in allows shows no regular behavior, in contrast to E_l. In the interval 973–1173 K, alloys with 1.5 and 5.0 wt % iron have virtually coinciding values of $E_p^{(1)}$ and $E_p^{(2)}$.

Thus, according to Table 1, E_l and E_p are the highest in the intermediate temperature zone 1123 (1173)–1223 K. At higher temperatures, the E_l value much exceeds that in the interval 973 (1023)–1123 (1173) K for all the formulations. In the case of alloys, the temperature dependence of $E_p^{(1)}$ is similar, in contrast to $E_p^{(1)}$ for titanium, which is much lower above 123 K than that in the interval 973–1173 K. At the same time, the $E_p^{(2)}$ value markedly decreases in going from 973 (1023)–1173 K to temperatures higher than 1223 K.

The change in the activation energy of oxidation in going from titanium to Ti–Fe alloys and with increasing C_{Fe} in the corresponding temperature zones is presumably accounted for, among other factors, by a decrease in the chemical bonding strength in the titanium lattice upon its alloying with iron [5], which stabilizes the β phase, and by an increase in the role of cation diffusion in scale formation as a result of incorporation into the rutile lattice of iron ions having lower charge than titanium ions. With increasing C_{Fe}, the composition and structure of the oxide film and the gas-saturated zone of the metal change as a result of metal redistribution in oxidation under the action of absorbed oxygen stabilizing the α phase with exceedingly low solubility of iron. This leads to an increase in the iron concentration in the β phase and enrichment with iron of the metal–scale interface [1, 6, 7], which markedly changes the conditions of titanium and oxygen transport across the interface.

The established dependence of $E_l^{(1)}$ on temperature and material composition may be due, in particular, to a change in the degree of delocalization of the chemical reaction front, e.g., by an increase in the part played by processes occurring by a different mechanism at the oxide–gas interface as a result of increasing concentration of cationic defects in the scale under the action of temperature rise and iron dissolution in the rutile lattice. The results obtained for the initial stage of alloy oxidation (Table 1) do not contradict the concept that the part played in scale formation by bulk diffusion characterized by high energy consumption, compared with intercrystallite diffusion, becomes more important with increasing temperature. The disagreement with this concept of the data for titanium and, during the second stage of oxidation, for all

formulations indicates the existence of other factors of opposite action. To these can be assigned, e.g., increasing total, or fraction of open, porosity of the oxide film with growing temperature, resulting in more important role of surface and, possibly, even gas diffusion.

According to Table 1, transition from the initial to the subsequent stage of oxidation for all formulations in the interval 973 (1023)–1373 (1473) K is accompanied in most cases by a decrease in E_l, even though differences in its values are frequently within the experimental error, i.e., $E_l^{(1)} \geq E_l^{(2)}$. In the case of a parabolic law of titanium oxidation, the E_p value markedly decreases in going from the initial to the second stage at 973–1073 K, and remains virtually unchanged above 1123 K. It was found in tests with Ti–Fe alloys in the temperature range 973–1373 (1473) K that, with few exceptions, $E_p^{(1)} < E_p^{(2)}$.

Since the decrease in K_l/K_p in going from the initial to subsequent stage of oxidation occurs through decrease in K_l and increase in K_p [1], it may be assumed that one of the reasons for this transition is the increase in the diffusion permeability of the oxide film as a result of, e.g., local disruptions of its continuity. This presumably causes the corresponding change in the mechanisms of the interphase reaction and diffusion processes and, consequently, in their activation energy.

Because of the lack of the necessary data, it is hardly appropriate to attempt to make any deeper interpretation of the obtained results concerning the dependence of E_l and E_p on various factors. Solving this problem requires additional special-purpose investigations.

CONCLUSIONS

(1) The temperature dependence of the linear and parabolic rate constants of nonstationary oxidation in air of Ti–Fe (1.5, 5.0, 10.0 wt %) alloys in the temperature interval 973–1473 K changes its slope twice: at around 1123 (1173) and at 1223 K, with the temperature of the first change becoming lower with increasing C_{Fe}. In titanium oxidation, a similar behavior is observed for $\log K_p = f(1/T)$, with a single change in the temperature coefficient K_l at around 1173 K.

(2) In titanium alloying with iron up to 5.0 wt %, the activation energy of oxidation in the interval 1123 (1173)–1223 K increases, and at C_{Fe} = 10.0 wt % decreases somewhat or remains virtually unchanged. Outside this temperature zone, E_l and E_p for the initial stage of oxidation decrease upon introduction into titanium of 1.5–10.0 wt % iron, with the exception of $E_p^{(1)}$ at 1223–1373 K.

(3) With C_{Fe} increasing from 1.5 to 10.0 wt %, the E_l and E_p values for both stages of oxidation decrease steadily in the interval 1123 (1173)–1223 K. Outside this region, E_l decreases or remains constant in going from 1.5 to 5.0 wt % iron, and, with C_{Fe} increasing to 10.0 wt %, grows. The dependence of E_p on C_{Fe} is more complex.

(4) The E_l and E_p values are the highest for all the formulations in the temperature interval 1123 (1173)–1223 K. At T > 1223 K, the E_l value for the initial stage of oxidation for titanium and the alloys, and E_p only for the alloys, are much higher than those in the region below 1123 (1173) K, whereas in the case of titanium, an inverse dependence is observed for E_p.

(5) In the interval 973 (1023)–1373 (1473) K, in a transition from the initial to the subsequent stage of oxidation, $E_l^{(1)} \geq E_l^{(2)}$ for most of formulations, and $E_p^{(1)} < E_p^{(2)}$ for alloys and $E_p^{(1)} \geq E_p^{(2)}$ for titanium.

REFERENCES

1. D'yachkov, V.I., *Zh. Prikl. Khim.*, 1991, vol. 64, no. 3, pp. 473–479.
2. Evans, U.R., *Trans. Electrochem. Soc.*, 1924, vol. 46, no. 1, pp. 247–274.
3. Kornilov, I.I., *Titan* (Titanium), Moscow: Nauka, 1975.
4. Molchanova, E.K., *Atlas diagramm sostoyaniya titanovykh splavov* (Atlas of Phase Diagrams of Titanium Alloys), Moscow: Mashinostroenie, 1964.
5. Glazova, V.V., *Legirovanie titana* (Alloying of Titanium), Moscow: Metallurgiya, 1966.
6. Voitovich, R.F. and Golovko, E.I., *Vysokotemperaturnoe okislenie titana i ego splavov* (High-Temperature Oxidation of Titanium and Its Alloys), Kiev: Naukova Dumka, 1984.
7. D'yachkov, V.I., *Zh. Prikl. Khim.*, 1998, vol. 71, no. 11, pp. 1761–1766.

Russian Journal of Applied Chemistry, Vol. 75, No. 1, 2002, pp. 14–17. Translated from Zhurnal Prikladnoi Khimii, Vol. 75, No. 1, 2002, pp. 15–18.
Original Russian Text Copyright © 2002 by Malysh, Gaisin, Volkova, Prokhorov, Tkachev.

INORGANIC SYNTHESIS AND INDUSTRIAL INORGANIC CHEMISTRY

Reduction of Recycled Barium Sulfate

L. A. Malysh, L. G. Gaisin, M. F. Volkova, A. G. Prokhorov, and K. V. Tkachev

Ural Research Chemical Institute with Experimental Plant, State Unitary Enterprise, Yekaterinburg, Russia
Karpov Chemical Plant, Joint-Stock Company, Mendeleevsk, Tatarstan, Russia

Received May 20, 2001

Abstract—Barium sulfate, which is recycled according to a new flowsheet of sodium sulfide production, was reduced by various carbon-containing materials (oil and furnace coke and Zh-grade coal). The reduction process was studied in comparison with the reduction of natural barite concentrate.

Sodium sulfide used in concentration of nonferrous metal ores, dyeing of fabrics, dressing of leather, and also in production of dyes, soda products, cellulose, and glass is presently produced in Russia by the reduction of packaged sodium sulfate by furnace coke in shaft furnaces [1]. This process is now out of date; it does not meet modern requirements to the environmental protection and to the product quality and is characterized by low utilization of the raw material.

A new low-waste technology is based on obtaining sodium sulfide by the reaction [2, 3]

$$BaS + Na_2SO_4 = BaSO_4 + Na_2S. \quad (1)$$

Barium sulfide is regenerated by reductive roasting of the forming barium sulfate, and, therefore, a barium raw material theoretically is not consumed, and only its loss should be replenished. The reductive roasting of natural barite raw material is widely used in industrial production of barium salts.

The regeneration of barium sulfide is a key stage of the new process; therefore, we have carried out laboratory studies with the aim to reveal features of the reduction of barium sulfate formed by reaction (1) with various reducing agents (oil and furnace coke and Zh-grade coal).

The reduction of barium sulfate with carbon has been described in sufficient detail [4–8]. According to modern views, this process involves stages of solid carbon gasification (2) and barium sulfate reduction (3)

$$C + CO_2 = 2CO, \quad (2)$$

$$BaSO_4 + 4CO = BaS + 4CO_2. \quad (3)$$

The overall process is expressed by the total reaction

$$BaSO_4 + 2C = BaS + 2CO_2. \quad (4)$$

The following reactions yielding acid-soluble barium compounds occur concurrently:

$$BaSO_4 + SiO_2 + C = BaSiO_3 + SO_2 + CO, \quad (5)$$

$$BaS + CO_2 + H_2O = BaCO_3 + H_2S. \quad (6)$$

It is noted [9] that the reduction of barium sulfate is intensified as soon as the first particles of barium sulfide are formed, as they catalyze the process similarly to calcium and sodium sulfides in the case of the reduction of sulfates of these metals.

EXPERIMENTAL

To obtain a comparative pattern, we have carried out experiments with charges containing either barite concentrate (BC) or recycled barium sulfate, with reducing agent dosages being 125 and 155% of the stoichiometric amount according to Eq. (4).

The chemical compositions of the raw materials are given in Table 1. The dispersity of all the components was 0.25 mm.

Reductive roasting of charges was carried out under static conditions in a muffle at 1000°C for 30 min in alundum crucibles closed by lids. These conditions suppress the secondary reactions of barium sulfide carbonation and oxidation, and also prevent burning-out of carbon-containing materials. The resulting melt was cooled in a desiccator and analyzed. We determined the content of BaS and BaS_2O_3 by iodometric titration, of water-soluble (ws) and acid-

1070-4272/02/7501-0014$27.00 © 2002 MAIK "Nauka/Interperiodica"

Table 1. Chemical composition of charge components

Parameter	Barite concentrate	Recycled barium sulfate		Metallurgical coke	Zh-grade coal	Petroleum coke
		R_1	R_2			
Content, wt %:						
$BaSO_4$	91.51	87.73	91.91			
$BaCO_3$	3.61	1.85	1.66			
H_2O	0.63	0.01	0.01	2.07	1.65	1.12
Na_2S		0.05	0.12			
$Na_2S_2O_3$		1.23	1.10			
Na_2SO_3		2.70	0.62			
Na_2SO_4		3.38	2.85			
Na_2CO_3		1.81	1.26			
carbon				85.50	62.11	87.84
Yield of volatile compounds				1.53	29.10	7.03
Ash residue, %				10.30	6.94	0.21
Sulfur, wt %				0.60	0.20	3.80

Table 2. Reductive roasting of barite concentrate and recycled barium sulfate (R_1 and R_2) with various reducing agents

Run no.	Charge component			Fused product composition, wt %			η_1	η_2
	reducing agent	dose, %	BC, R_1, R_2	BaS (by I_2)	BaS_{ws}	$BaSO_4$	%	
1	Petroleum coke	125	BC	77.58	82.28	0.63	99.48	87.76
2	″	155	BC	76.48	81.81	0.52	99.56	88.17
3	Furnace coke	125	BC	70.11	75.70	5.67	95.09	83.66
4	″	155	BC	56.93	62.04	16.99	85.19	68.39
5	Zh-grade coal	125	BC	75.02	80.94	1.23	98.98	85.67
6	″	155	BC	58.91	63.63	15.65	85.86	73.31
7	Petroleum coke	125	R_1	78.82	82.67	0.45	99.91	89.50
8	″	155	R_1	80.10	83.64	0.05	99.96	92.04
9	Furnace coke	125	R_2	77.92	86.00	–	100.00	85.87
10	″	155	R_2	77.99	83.64	–	100.00	88.87
11	Zh-grade coal	125	R_2	80.08	87.11	0.41	99.67	87.62
12	″	155	R_2	80.21	85.66	–	100.00	90.54

soluble (as) barium and calcium compounds (in terms of BaS_{ws}, CaS_{ws} and BaS_{cr}, CaS_{cr}, respectively) by complexometric titration, and of the water-insoluble residue (carbon), gravimetrically.

From the chemical analysis data we calculated the degree of $BaSO_4$ reduction η_1 and the degree of $BaSO_4$ conversion to BaS η_2 by the formulas

$$\eta_1 = \frac{(m_{ch}BaSO_{4ch} - m_f BaSO_{4f}) \times 100}{m_{ch}BaSO_{4ch}},$$

$$\eta_2 = \frac{1.3778 m_{ch}BaS_{ch} \times 100}{m_{ch}BaSO_{4ch}},$$

where m_{ch} is the charge weight (g); m_f is the weight of the fused barium sulfide product (g); $BaSO_{4ch}$, $BaSO_{4f}$, and BaS_f are contents of barium sulfate in the charge and in the fused product and of barium sulfide in the fused product, respectively (wt %); 1.3778 is the scaling ratio for the conversion from BaS to $BaSO_4$.

The experimental data are given in Table 2, each result being an average of two parallel experiments.

A criterion for estimating the optimal dosage of the reducing agent was the quality of the resulting fused barium sulfide product. We found that a better quality of the fused product was reached with barite concen-

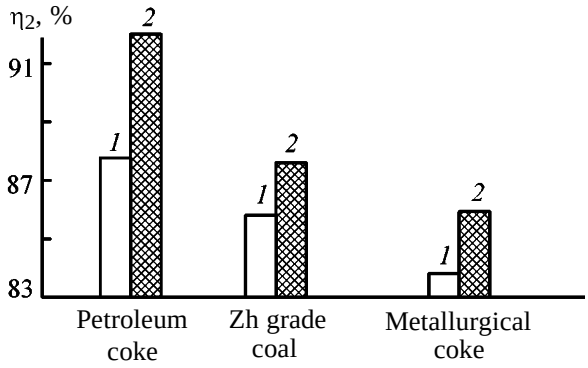

Degree of $BaSO_4$ conversion to BaS η_2 at 125% dosage of the reducing agent in the charge. (*1*) Barium concentrate and (*2*) recycled $BaSO_4$.

trate (run nos. 1, 3, 5) and with recycled barium sulfate (run nos. 7, 9, 11) at a 125% dosage (against the stoichiometry) of any of the tested reducing agents. Therefore, this dosage is preferential for the stationary roasting conditions.

Comparing the activity of the reducing agents at their optimal dosage in the chage, we see that all the tested carbon-containing materials are highly reactive, as the degree of the $BaSO_4$ reduction is 95.09–100.00% (Table 2). A low degree of the $BaSO_4$ reduction (85.19 and 85.86%) at an elevated dosage of furnace coke and Zh-grade coal (155%) is attributable to the fact that, as carbon is gasified, the surface of barium sulfate grains is screened to a greater degree by the ash residue of the reducing agent, which hampers the contact of $BaSO_4$ with carbon(II) oxide. However, of practical interest for the new procedure of sodium sulfide production is the degree η_2 of the $BaSO_4$ conversion to BaS, as barium sulfide is the supplier of S^{2-} ions into the final product Na_2S; therefore, it makes sense to estimate the activity of the reducing agent by η_2. As seen from the figure, petroleum coke is the best reducing agent for both the barite concentrate and recycled barium sulfate, probably owing to sulfiding action of sulfur contained in petroleum coke, for example, by the reaction

$$2BaCO_3 + 2S + C = 2BaS + 3CO_2. \quad (7)$$

Furthermore, petroleum coke belongs to low-ash reducing agents, so that the contents of water-insoluble impurities in the fused barium sulfide product is less than 0.7%, i.e., four times less than in the fused product obtained by the reduction with furnace coke and Zh-grade coal and almost ten times less than in the fused product obtained from the barite concentrate reduced with petroleum coke. Such a product does not require additional labor-consuming operations for removing water-insoluble impurities, which considerably simplifies the flowsheet of sodium sulfide production.

Examination of the data obtained shows that recycled barium sulfate is more effectively reduced than the barite concentrate, which may be due to the fact that freshly precipitated barium sulfate, owing to its high dispersity, is more active than natural barium sulfate. Thus, we have found experimentally that with petroleum coke used for the reduction of barium sulfate it is possible to obtain high-quality fusedf barium sulfide product at rather high utilization of the raw material and a high degree of conversion of barium sulfate to sulfide.

The data of laboratory experiments on the reductive roasting of a charge with petroleum coke as a reducing agent were confirmed by semicommercial tests. A charge (16.4 t) was reduced in a rotary kiln with a volume of 14 m^3 at a specific charge load of 35 kg m^{-3} h^{-1}. The content of BaS_{ws} in the fused product reached 63.4–64.6% at 96.20% conversion of $BaSO_4$ to BaS_{ws}, which is at a level of parameters of industrial production of barium salts.

It should be noted that unchanged reducing agent is recycled together with barium sulfate, which provides its full utilization.

The use of petroleum coke as a reducing agent simultaneously solves the problem of the utilization of coal breakage, which is formed as a waste of the production of lump electrode petroleum coke, and owing to its low ash residue the sodium sulfide production becomes virtually wasteless.

CONCLUSIONS

(1) All the tested carbon-containing reducing agents (petroleum coke, Zh-grade coal, and furnace coke) have a high reducing power with respect to barium sulfate. The reducing agent is taken in an amount of 125% relative to the stoichiometry of Eq. (4). The best reducing agent for barium sulfate is petroleum coke, as proved by semicommercial tests.

(2) The reductive roasting of recycled barium sulfate has no principal differences from the industrial roasting of barite concentrate with petroleum coke as reducing agent. Therefore, its flowsheet and equipment can be utilized without changes in the new procedure for producing sodium sulfide, which ensures its high reliability.

REFERENCES

1. Prokhorov, A.G., Nevyazhskaya, E.A., and Svirskaya, M.I., *Tr. Ural. Nauchno-Issled. Khim. Inst.* (Sverdlovsk), 1973, issue 24, pp. 29–32.
2. RF Patent 2142907.
3. Busygin, V.M., Gaisin, L.G., Tkachev, K.V., and Prokhorov, A.G., Abstracts of Papers, *XVI Mendeleevskii s"ezd po obshchei i prikladnoi khimii* (XVI Mendeleev Congr. on General and Applied Chemistry), St. Petersburg, 1998, vol. 2, pp. 253–254.
4. Safiullin, N.Sh., Strigunov, F.I., and Gavrilova, Z.F., *Tr. NIOKhIM* (Kharkov), 1969, vol. 19, pp. 123–128.
5. Pozin, M.E., *Tekhnologiya mineral'nykh solei (udobrenii, pestitsidov, promyshlennykh solei, okislov i kislot)* (Technology of Mineral Salts (Fertilizers, Pesticides, Industrial Salts, Oxides, and Acids)), Leningrad: Khimiya, 1974, part 1.
6. Akhmetov, V.I., Studies in the Field of Technology of Barium Salts, *Doctoral Dissertation*, Moscow, 1976.
7. Alekseev, V.I., Reductive Roasting of Barite Concentrates, *Cand. Sci. Dissertation*, Kharkov, 1977.
8. Akhmetov, V.I., Busygin, V.M., Gaisin, L.G., and Porfir'eva, R.T., *Khimicheskaya tekhnologiya neorganicheskikh veshchestv* (Chemical Technology of Inorganic Substances), Moscow: Khimiya, 1998.
9. Alekseev, V.I., Strigunov, F.I., and Dobrovol'skaya, M.F., *Tr. Nauchno-Issled. Proektn. Inst. Osn. Khim.* (Kharkov), 1969, vol. 51, pp. 43–47.

Russian Journal of Applied Chemistry, Vol. 75, No. 1, 2002, pp. 18–21. Translated from Zhurnal Prikladnoi Khimii, Vol. 75, No. 1, 2002, pp. 19–22.
Original Russian Text Copyright © 2002 by Akhrimenko.

INORGANIC SYNTHESIS AND INDUSTRIAL INORGANIC CHEMISTRY

Effect of Additions of Silica Gel and Certain Salts of Inorganic Acids on Corrosion Resistance of Cement Stone

V. E. Akhrimenko

Kuban State Agricultural University, Krasnodar, Russia

Received April 28, 2001

Abstract—Effect of additions of silica gel and certain salts on the rheological parameters of cement mortar and corrosion resistance of cement stone was considered.

Building of ports, docks, and breakwaters and also of oil and gas wells requires cement mortars forming corrosion-resistant cement stone on hardening.

The aim of this work was to study the effect of additions of silica gel and salts of inorganic acids on the corrosion resistance of cement stones. We used oil-well portland cement for cold wells produced by Oktyabr' Plant (Novorossiisk) and silica gel produced by Azot Production Association (Nevinnomyssk) [1].

As the chemical treatment of grouting mortars is the main means of the control over their process parameters (flowing, setting time, and sedimentation stability), we determined the properties of cement mortars along with the corrosion resistance of cement stones.

EXPERIMENTAL

We studied cement stone corrosion by keeping stone samples in the chosen aggressive solutions under conditions the most closely simulating the actual operation conditions of a cement stone in a well.

As aggressive media we used 50 g l^{-1} solutions of sodium and magnesium chlorides and sulfates, which corresponds to highly mineralized stratal waters. In tempering liquids for cementing agents under study the salt content was the same.

Cement mortars were prepared by thorough mixing of cement with silica gel and by tempering this mixture with drinking water or salt solutions. The resulting cement mortars were tested according to the procedure in [2] and GOST (State Standard) 26798.2–85.

We molded cement beams from cement mortars. For this purpose we filled with cement mortar metallic molds ($20 \times 20 \times 100$ mm), placed them in a desiccator with drinking water, and left to harden at $20 \pm 2°C$.

After hardening for two days, cement beams were taken from the molds, marked, and placed in a bath with drinking water or salt solutions for 7, 14, 28, and 90 days. On completion of hardening terms, the cement samples were taken from the baths, and their compression strength was determined. The results (average of three experiments) are given in Table 1.

These experiments have shown (Table 1) that a cement with silica gel added is more sedimentation-stable; the water separation of such a solution is four times less than that of a mortar solution without silica gel.

As fluid-conducting channels, which are responsible for interstratal crossflows, arise in the cement stone structure in the course of hardening of a sedimentation-unstable cement mortar, it was necessary first of all to obtain a sedimentation-stable cement mortar.

It follows from Table 1 that the addition of silica gel to a cement mortar considerably accelerates structure formation, which reduces the setting time of the cement mortar. The cement mortar with sodium sulfate as a tempering liquid starts to set in 8 h 50 min, whereas the same cement mortar containing silica gel starts to set in 3 h 20 min.

The capacity of silica gel to accelerate the hydration is probably due to taking up a considerable part of a free tempering liquid, so that the fluid phase becomes oversaturated with respect to calcium hydrosilicates, which accelerates their separation from the solution. The precipitated calcium hydrosilicates act

1070-4272/02/7501-0018$27.00 © 2002 MAIK "Nauka/Interperiodica"

Table 1. Physicochemical properties of samples of cement mortar and cement stone obtained from oil-well portland cement without addition (system I) and with addition of 5% silica gel (system II)*

Tempering solution	Water separation, %	Setting times		Compression strength, MPa, after storage for indicated time, days				
		onset	end	2	7	14	28	90
System I, water/cement = 0.5								
H_2O	2.5	9–0	12–40	9.99	20.96	25.19	40.00	49.99
NaCl	3.2	8–40	11–50	15.54	23.72	32.01	42.34	54.57
Na_2SO_4	2.8	8–50	11–30	13.38	21.22	30.06	39.96	51.95
$MgCl_2$	2.5	6–40	10–20	11.75	22.95	31.06	39.95	51.86
$MgSO_4$	2.5	6–30	11–20	13.55	21.54	28.41	40.98	51.96
System I, water/cement = 0.6								
H_2O	0.6	5–40	8–20	7.46	18.06	22.96	36.96	46.88
NaCl	0.5	5–30	7–40	12.45	20.90	28.32	38.97	42.96
Na_2SO_4	0.2	3–20	5–40	14.58	23.38	31.52	36.96	49.27
$MgCl_2$	0.5	4–50	6–20	9.11	20.85	26.77	36.66	47.03
$MgSO_4$	0.3	3–35	5–35	12.64	17.49	23.90	37.26	48.54

* Hardening in drinking water at 20±2°C.

as crystallization nuclei for new hydrate formations, intensifying structure formation in cementing systems.

To make more descriptive the effect of salts on the corrosion resistance of the cement stone, we determined the factor of cement corrosion resistance (CR), which represents the ratio of the average ultimate compression strength of the cement stone C_1 after keeping samples in an aggressive medium for 3 month to the average ultimate compression strength C_2 of cement beams made of the same cement after hardening for 3 months in drinking water.

Our experiments have shown that in all cases the additions of salts to a cement increase the strength of the cement stone both at the beginning of hardening and after three-month aging. It follows from Table 1 that the additions enhance the corrosion resistance of the cement stones obtained from both pure portland cement and from portland cement with silica gel added.

Table 1 shows that from the beginning of hardening up to 28 days the strength of the cement stone obtained from oil-well portland cement increases most intensively. The strength of the cement stone of portland cement with silica gel added increases slowly at the beginning of hardening and more actively after 14-day hardening.

Our data indicate that the strength of the cement stone of portland cement and of portland cement with silica gel added increases in the medium of sodium chloride and sodium sulfate, respectively. The experiments show that within the 90-day observation period the strength of the cement stone is not affected by leaching corrosion, and the addition of sodium chloride further enhances the cement stone resistance against this kind of corrosion. The strength of cement stone samples hardened in water and tempered with water was 50.0 MPa after 3 months. The cement stone strength reached 51.27 MPa for cement stone samples tempered and hardened in a sodium chloride solution.

As for sodium sulfate, hardening of a cement stone without additions in its solution is accompanied by a decrease in the corrosion resistance factor (CR = 0.87) as compared to control samples hardened in drinking water (CR = 0.96).

The main reason for the degradation of cement stone in a solution of sodium sulfate is the reaction of Na_2SO_4 with unchanged calcium aluminate $3CaO \cdot Al_2O_3$ and calcium hydroxide $Ca(OH)_2$ with the formation of ettringite $3CaO \cdot Al_2O_3 \cdot 3CaSO_4 \cdot 31H_2O$, which increases in volume by a factor of 2.5 on crystallization and destroys the cement stone.

When sodium sulfate is added to tempering water, a reverse pattern (CR = 0.94) is observed. This may be due to the fact that the main amount of gypsum contained in the cement was bonded in ettringite in the beginning of hardening before a rigid inductile structure of the cement grout is formed, which is of importance for the subsequent formation of stable cement stone in sulfate solutions.

Table 2. Effect of salt additions on the corrosion resistance of cement stone after hardening for 3 months

Cementing agent	Series no.	Tempering solution	Hardening medium	Ultimate compressing strength, MPa		CR
				in aggressive medium	in drinking water	
Portland cement	1.1	H_2O	NaCl	48.04	50.0	0.96
	1.2	NaCl	NaCl	51.27	54.57	0.939
	1.3	H_2O	Na_2SO_4	43.52	50.0	0.87
	1.4	Na_2SO_4	Na_2SO_4	48.87	51.95	0.94
	1.5	H_2O	$MgCl_2$	37.68	50.0	0.753
	1.6	$MgCl_2$	$MgCl_2$	40.74	51.86	0.785
	1.7	H_2O	$MgSO_4$	36.73	50.0	0.734
	1.8	$MgSO_4$	$MgSO_4$	46.52	51.96	0.895
Portland cement + 5% silica gel	2.1	H_2O	NaCl	46.41	46.88	0.989
	2.2	NaCl	NaCl	48.27	42.96	1.123
	2.3	H_2O	Na_2SO_4	43.52	46.88	0.928
	2.4	Na_2SO_4	Na_2SO_4	51.35	49.27	1.04
	2.5	H_2O	$MgCl_2$	40.15	46.88	0.856
	2.6	$MgCl_2$	$MgCl_2$	41.73	47.03	0.887
	2.7	H_2O	$MgSO_4$	45.83	46.88	0.977
	2.8	$MgSO_4$	$MgSO_4$	46.27	46.54	0.953

The greater fraction of the initially present aluminates will be chemically bound in the initial hardening stage, the more resistant will be the cement stone later on. Furthermore, the addition of sodium sulfate increases the solubility and hydrolysis of cement silicate components by binding the hydrolysis product [$Ca(OH)_2$] in a sparingly soluble compound and thus accelerates the formation of low-basic silicates, which are mainly responsible for the cement stone strength. The introduction of sodium sulfate in tempering water for a portland cement with a silica gel addition increases the corrosion resistance of the cement stone: in the first case CR = 0.96 and in second, 1.04 (Table 2).

Our experiments have shown that the portland cement with an addition of silica gel forms a cement stone more resistant against sulfates than the portland cement stone without silica gel, which agrees with the data of [3]. The added silica gel reacts with portland cement lime and converts it to difficultly soluble calcium silicates.

The effect of added magnesium salts on the hardening rate of cement stones prepared from cements with and without silica gel can be seen in Table 1, which shows that the addition of magnesium salts to a cement mortar considerably reduces its setting time. Pure portland cement and the cement with silica gel added, both tempered with water, start to set in 9 h and in 5 h 40 min, whereas the same cements tempered with an $MgSO_4$ solution start to set in 6 h 30 min and 3 h 35 min, respectively.

The reduction in the setting time of cement mortars also affects the early strength of the cement stone, which somewhat increases in the case of the cement stone containing magnesium salts. Later on the strength parameters of the cement stone decrease owing to magnesia corrosion.

Magnesium hydroxide formed in the reaction of $MgCl_2$ with cement $Ca(OH)_2$ precipitates in the initial stage of the hardening, fills vug holes in the pore space of a cement stone, and thus compacts its structure, which enhances its corrosion resistance.

In time the amount of soluble lime becomes insufficient to neutralize $MgCl_2$, which arrives from a storage medium to the cement stone surface and diffuses into the depth of its structure. Then $MgCl_2$ destroys the cement stone structure by reacting with calcium silicate and other hydrates that form this structure.

In solutions of magnesium chloride and sulfate the cement stone of pure portland cement is destroyed faster (CR = 0.753) than the cement stone of oil-well cement with silica gel added (CR = 0.856), which is probably due to the mudding action of finely dispersed silica gel on the pore space and thus to general compaction of the cement stone structure.

The introduction of magnesium salts in a tempering solution increases the corrosion resistance of the

cement stone for both portland cement (CR = 0.785) and portland cement with silica gel added (CR = 0.887), apparently at the expense of the equalization of salt concentrations in the pore space of the cement stone and in stratal water. This results in suppression of osmotic processes and consequently in decreased permeability of the cement stone, which suppresses the destructive processes.

Thus, we showed that salts contained in stratal waters or silica gel should be added to a cement mortar to increase the corrosion resistance of the cement stone when wells drilled in saline horizons are cemented.

CONCLUSIONS

(1) The effect of silica gel and certain salts of mineral acids on the corrosion resistance of cement stone was studied.

(2) Silica gel affects the sedimentation stability of cement mortar and the kinetics of its hardening.

(3) Addition of silica gel to a cement mortar increases the corrosion resistance of the cement stone.

ACKNOWLEDGMENTS

This work was financially supported by the Russian Foundation for Basic Research (project no. 00-05-96017).

REFERENCES

1. Palii, L.V., Akhrimenko, V.E., Gagai, G.I., and Levshina, Z.P., *Zh. Prikl. Khim.*, 1989, vol. 62, no. 8, pp. 1779–1784.
2. Akhrimenko, V.E., Akhrimenko, Z.M., and Korol', O.E., in *Stroitel'stvo neftyanykh i gazovykh skvazhin na sushe i na more* (Building Oil and Gas Wells Overland and on the Sea), Moscow: VNIIOENG, 1999, no. 1.2, p. 34.
3. Andreeva, E.P., Porodenko, E.V., and Stukalova, N.P., *Zh. Prikl. Khim.*, 1991, vol. 64, no. 5, pp. 1033–1038.

Russian Journal of Applied Chemistry, Vol. 75, No. 1, 2002, pp. 22–24. Translated from Zhurnal Prikladnoi Khimii, Vol. 75, No. 1, 2002, pp. 23–25.
Original Russian Text Copyright © 2002 by Ryabova, Voloshenko, Maiorov, Osipova.

PHYSICOCHEMICAL STUDIES OF SYSTEMS AND PROCESSES

Equilibrium Composition of Formaldehyde Oligomers in Aqueous Solutions from IR Data

R. S. Ryabova, G. I. Voloshenko, V. D. Maiorov, and G. F. Osipova

Semenov Institute of Chemical Physics, Russian Academy of Sciences, Moscow, Russia

Received April 16, 2001

Abstract—The complex band of formaldehyde at 950–1150 cm^{-1} in the IR spectrum of its aqueous solutions was resolved into individual bands by computer analysis. The calculated band intensities were compared with known concentrations of monomeric, dimeric, and trimeric formaldehyde species. The IR data are consistent with the published NMR data.

To establish the mechanism of the reaction of formaldehyde (FA) with various reagents in aqueous solutions, it is necessary to know the equilibrium composition of its oligomers. When dissolved in water, gaseous FA forms methylene glycol (MG), $HOCH_2OH$ [1]. The ^{13}C NMR study of FA aqueous solutions at various FA concentrations [2, 3] showed that MG easily oligomerizes to form hydrated FA polymers $HO(CH_2O)_nH$. Botlan *et al*. [2] determined the per cent content of oligomers in formaldehyde units within a fairly wide interval of FA concentrations (0.5–50 wt %) at 30°C. Data of [2, 3] on the equilibrium composition of oligomers show that the concentration of the monomer $HOCH_2OH$ decreases and the concentrations of oligomers $HO(CH_2O)_nH$ with n = 2–6 increase, as the FA content in the solution is increased.

The goal of this work is to analyze the IR spectra of the FA aqueous solutions and to assign the bands to the individual FA oligomers.

EXPERIMENTAL

Aqueous solutions of FA were prepared by the method in [3]. The data of [2, 3] were used to calculate the molar composition of oligomers (Table 1).

The IR spectra were recorded in the 900–1200 cm^{-1} range on a UR-20 spectrophotometer equipped with a multiple attenuated total internal reflection (MATIR) device [4]. The Ge prism with a 30° incidence angle and 8 reflections was used. The solution was placed into Teflon cavities adjoining to prism facets. The effective thickness of the absorption layer at 2000 cm^{-1} was 3.72 μm. The spectra of 6–25 wt % FA solutions were obtained at 30°C.

The IR spectra were treated by a universal program for treatment of spectra (UPTS) [5] based on the method of differential moments. To determine the number of bands, plots of the second derivatives for the complete series of the spectra were analyzed. The peak was assumed to be existing when the corresponding minimum occurred in all the plots. Then the number of bands was fixed and their position, width, and shape characteristics were varied [5]. When any parameter was the same for all the series of the spectra, its average value was used. When the band width and location varied noticeably (> 5% for width) and monotonically, it was assumed that the band consists of two peaks with parameters differently depending of the solution composition, and, correspondingly, one more band was considered. To describe the contours of spectra of eight solutions, the minimum possible number of bands was 5. It is impossible to describe the spectra of the series considered using the smaller number of bands under the condition of the constancy of the band parameters [spectral location, width, and contour (Gaussian, Lorentzian, or mixed)].

The final treatment of the series of spectra included only variation of the band optical density D. The solution becomes stable when independent calculations for each of eight solutions at the constant number of bands give the set of the constant parameters. Therewith, the calculated optical densities form smooth curves, and the calculation results are independent of the initial values of the optical densities assigned. The accuracy of the results was checked both by the root-mean-square deviations for the experimental and

1070-4272/02/7501-0022$27.00 © 2002 MAIK "Nauka/Interperiodica"

Table 1. Equilibrium composition of FA olygomers in aqueous solutions*

c^0_{FA}		[M]	[D]	[T_3]	[T_4]
wt %	M	M			
5.97	2.07	1.4	0.2	0.05	–
9.2	3.2	1.8	0.4	0.10	0.01
11.9	4.2	2.2	0.6	0.14	0.03
14.7	5.0	2.4	0.8	0.18	0.05
17.8	6.4	2.8	1.1	0.26	0.07
20.8	7.5	2.95	1.3	0.34	0.11
21.8	7.8	2.95	1.35 (1.5 ± 0.2)**	0.39	0.12
25.0	9.1	2.9 (3.4 ± 0.3)	1.5 (1.7 ± 0.2)	0.48 (0.43 ± 0.03)	0.17

* M, D, T_3, and T_4 are monomer, dimer, trimer, and tetramer of FA, respectively.
** The concentrations of oligomers determined in this work are given in parentheses.

simulated spectra and directly by the difference between these spectra, which was plotted. As a rule, deviations were no more than 5%.

The result of the computer analysis of one of the spectra studied is shown in Fig. 1. The following set of bands was obtained: 992, 1026, 1050, 1072, and 1100 cm^{-1}. The band intensities are listed in Table 2.

According to [2, 3], FA exists in aqueous solutions as a mixture of monomer (n = 1) and polymers (n > 2).

The bands observed in the examined 900–1200 cm^{-1} range correspond to the stretching vibrations of the C–O bonds in the C–O–H groups of the monomer and polymers and in C–O–C bridges of polymers [6]. The experimental spectrum is the contour consisting of several overlapped bands. This contour changes as the FA content in the solution is varied. This reveals the bands belonging to different oligomers.

The intensity of the strongest band at 1026 cm^{-1} is proportional to the FA concentration up to 7.8 M (Fig. 2), i.e., this band is the sum of bands of FA oligomers. The band at 1050 cm^{-1} can be assigned to the FA monomer. Its intensity is proportional to the monomer concentration determined in [2] up to 7.8 M FA (Fig. 3). At an FA concentration of 9.1 M, the intensity of this band increases in spite of decrease in the monomer concentration [2] (Table 1). Deviation from the linearity of the plot of I_{1050} vs. monomer concentration can be caused by inaccurate determination of the latter in [2]. It follows from Fig. 3 that the monomer concentration in the most concentrated solution of FA is underestimated by about 0.5 M. At c^0_{FA} = 25 wt %, it should be 3.4 ± 0.3 M.

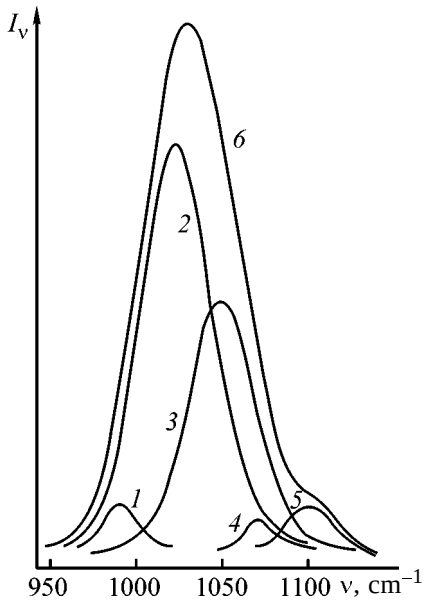

Fig. 1. IR spectrum of FA aqueous solution (c_{FA} = 14.47 wt %) resolved into individual bands: (*1*) intensity and (ν) frequency. ν (cm^{-1}): (*1*) 992, (*2*) 1026, (*3*) 1050, (*4*) 1072, and (*5*) 1100; (*6*) initial experimental spectrum.

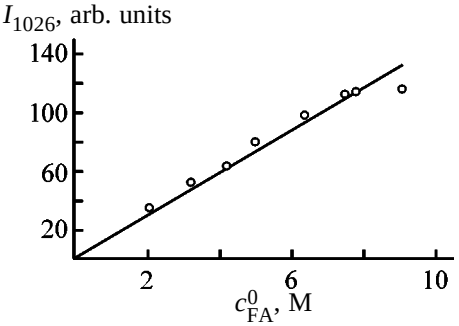

Fig. 2. Intensity of the band at 1026 cm^{-1}, I_{1026} as a function of the initial FA concentration, c^0_{FA}.

Table 2. Intensities I_ν of constituent bands in the IR spectra, calculated by computer analysis

c^0_{FA}, M	I_ν, arb. units, for indicated ν, cm^{-1}				
	992	1026	1050	1072	1100
2.07	1.6	35.0	12.0	2.0	3.7
3.2	2.0	52.0	37.0	2.0	4.4
4.2	3.5	64.0	41.0	6.7	6.0
5.0	9.4	80.0	50.0	7.0	7.9
6.4	11.6	98.0	53.0	12.0	8.7
7.5	18.2	112.0	60.0	12.0	11.4
7.8	25.2	114.0	62.0	17.9	14.0
9.1	26.3	115.9	66.0	17.3	16.0

The band at 1072 cm^{-1} was assigned to the dimer (Fig. 4). The intensity of this band well correlates with the dimer concentration determined in [2]. However, the intensity of this band increases faster than the dimer concentration. The refined values of the dimer concentration are listed in Table 1.

The intensity of the band at 1100 cm^{-1} well correlates with the concentration of the trimer (T_3)

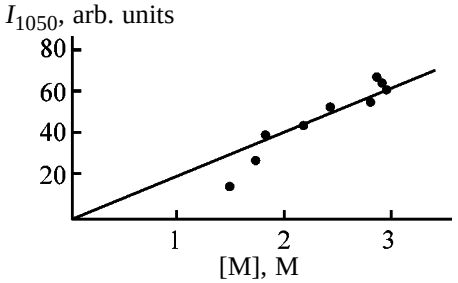

Fig. 3. Intensity of the band at 1050 cm^{-1}, I_{1050} as a function of the FA monomer concentration, [M].

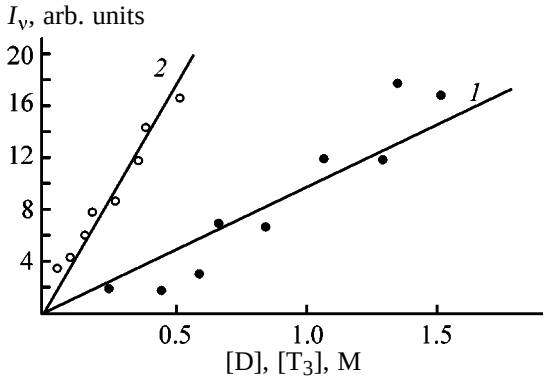

Fig. 4. Intensities of the absorption bands I_ν as functions of concentrations of (*1*) dimer, [D] and (*2*) trimer, [T_3]. ν (cm^{-1}): (*1*) 1072 and (*2*) 1100.

(Fig. 4). It follows from Table 1 that the trimer content in the 9.1 M FA solution is overestimated by about 0.05 M (Table 1). The band belonging to the tetramer was not found, probably because of its low concentration within the FA concentration range studied.

The intensity of the band at 992 cm^{-1} rapidly increases in concentrated FA solutions. This shows that it belongs to FA polymers. However, the variation of the band intensity shows no correlation with the concentration of any of the above oligomers. Probably this band reflects the existence of dimers, trimers, and other polymers with different absorption coefficients.

CONCLUSIONS

(1) The IR spectra of aqueous solutions of formaldehyde (6–25 wt %, 30°C) within the 900–1200 cm^{-1} range were resolved into the individual components.

(2) The component bands were assigned to separate formaldehyde oligomers.

(3) The oligomer concentrations measured using ^{13}C NMR agree with the intensities of the bands assigned to separate oligomers. The concentrations of formaldehyde oligomers were refined on the basis of the IR spectroscopic data obtained.

ACKNOWLEDGMENTS

The authors are indebted to A.P. Kucherov for submitting the UPTS program for treatment of the complex spectra.

REFERENCES

1. Walker, J.F., *Formaldehyde*, New York: Am. Chem. Soc., 1953, 2nd ed.
2. Botlan, D.J., Mechin, B.C., and Martin, J.J., *Anal. Chem.*, 1983, vol. 55, no. 3, pp. 587–589.
3. Ryabova, R.S. and Osipova, G.F., *Zh. Prikl. Khim.*, 2000, vol. 73, no. 7, pp. 1214–1216.
4. Harrick, N.J., *Internal Reflection Spectroscopy*, New York: Interscience, 1964.
5. Kucherov, A.P., *Zh. Prikl. Spektrosk.*, 1984, vol. 41, no. 1, pp. 79–82.
6. Bellamy, L.J., *The Infra-Red Spectra of Complex Molecules*, London: Methuen, 1954.

Russian Journal of Applied Chemistry, Vol. 75, No. 1, 2002, pp. 25–28. Translated from Zhurnal Prikladnoi Khimii, Vol. 75, No. 1, 2002, pp. 26–29.
Original Russian Text Copyright © 2002 by Baev, Shishko.

PHYSICOCHEMICAL STUDIES OF SYSTEMS AND PROCESSES

Thermal Behavior of Aluminum Trialkyls

A. K. Baev and M. A. Shishko

Belarussian State Technological University, Minsk, Belarus

Received September 19, 2000; in final form, October 2001

Abstract—Thermal behavior of tributylaluminum at 273–475 K under static conditions was studied. The composition of the gaseous thermolysis products was determined.

Aluminum trialkyls are used in organic synthesis as catalysts or alkylating agents. To optimize conditions of their industrial production, thermodynamic parameters of these compounds should be determined. Among all aluminum trialkyls used in practice, reliable thermodynamic parameters were obtained only for $AlMe_3$ and $AlEt_3$ [1, 2]. The thermodynamic data for other aluminum trialkyls [3–7] are contradictory. The vaporization parameters of $AlBu_3$ are confined to the ethalpy of vaporization (66.6 kJ mol^{-1}) referred to the boiling point under normal conditions [8]. The determination method is not reported. Spontaneous reversible dissociation of aluminum trialkyls [9] and exchange of their alkyl groups are frequently ignored when these compounds are used for synthetic purposes. However, the following reaction is possible [9]:

$$AlAlk_3 \rightleftarrows AlHAlk_2 + C_nH_{2n}.$$

This reaction of $AlEt_3$ was studied for the first time in our previous work [10]. The thermodynamic parameters of the components and of the process as a whole were determined. The equilibrium also involves condensation processes such as

$$(AlAlk_3)_2(l) \rightleftarrows Alk_2AlHAlAlk_3(l) + C_nH_{2n}.$$

At 453 K, 85.6% of $AlBu_3$ is decomposed [11]. The sample contains the following compounds (mol %): $AlBu_2H$ (38.4), $AlBu_3$ (13.4), $AlBu_2$(*i*-Oct) (13.7), hydrocarbons (34.5) including *n*-C_4H_8 (25.5), *i*-C_8H_{16} (4.9), *n*-C_8H_{18} (2.0), and also H_2 (2.5).

The discrepancy in the thermodynamic parameters of aluminum trialkyls, obtained by different authors, is due to the above processes. In this work we studied equilibrium vaporization, dissociation, and thermolysis of $AlBu_3$, $AlPr_3$, and $AlEt_3$.

EXPERIMENTAL

Thermal behavior of tributylaluminum under static conditions was studied with a membrane zero gage [10]. The $p = f(T)$ dependence for three $AlBu_3$ samples with different volume concentrations is shown in the figure. The slope of the *p*–*T* curve and the total pressure depend on the initial amount of the sample.

The dependence of the slope on the $AlBu_3$ concentration in the chamber confirms dissociation of the compound. Since the reverse process is hindered, the heating and cooling curves differ (curves *1*, *2*). However, after cooling of the system with liquid nitrogen and prolonged keeping at a definite temperature the vapor pressure is reproduced, which indicates that the $AlBu_3$ dissociation is reversible. A large difference in the vapor pressures of a freshly prepared sample and a sample distilled into the gage chamber at a high

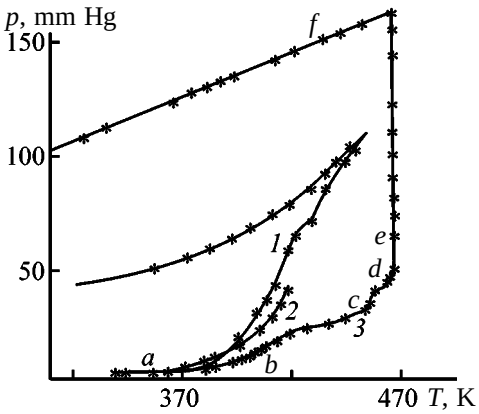

p–*T* diagram of tributylaluminum at 320–471 K with formation of unsaturated vapor. (*1*–*3*) samples differ in the volume concentration: $m_1v_1 > m_2v_2 > m_3v_3$: (*a*) Equilibrium vaporization; (*b*) vaporization with decomposition; (*c*) reversible thermolysis; (*d*, *e*) irreversible thermolysis of $AlHBu_2$; and (*f*) gas expansion.

1070-4272/02/7501-0025$27.00 © 2002 MAIK "Nauka/Interperiodica"

volume concentration indicates partial dissociation of $AlBu_3$ during distillation to form more volatile products. On the contrary, the equilibrium vapor pressures of the samples kept for a prolonged period at a definite temperature in the range 340–390 K (curves *1–3*) are similar. However, at higher temperatures the reproducibility of the *p–T* curve on heating and on cooling, on the one hand, and the dependence of the slope of these curves on the concentration of the sample in the chamber, on the other hand, confirm equilibrium dissociation of $AlBu_3$. The temperature dependence of the vapor pressure of $AlBu_3$ up to the onset of its thermal dissociation (383 K, section *a*) [8] is reversible and reproducible within the limits of the experimental error. The vapor pressure in the chamber does not exceed 5 mm Hg. The processes occurring at 383–458 K (section *b*) are also reversible. At temperatures higher than 471 K $AlBu_3$ decomposes irreversibly (sections *d, e*) to form a gray deposit (probably metallic aluminum) on the chamber walls. Chromatographic analysis showed that the main gaseous thermolysis products are (mol %) unsaturated hydrocarbons 1-butene (32.8), *trans*-2-butene (23.4), *cis*-2-butene (11.2), and hydrogen (30.9). Methane (0.9 mol %), ethane and ethylene (0.4 mol %), and propane and propylene (0.2 mol %) were also detected.

Based on these results and the concept of equilibrium decomposition of $AlAlk_3$ [9], $AlBu_3$ dissociation can be described by a series of consecutive or consecutive-parallel steps. Up to the onset of the decomposition (320 K, section *a*) dimeric and monomeric $AlBu_3$ molecules vaporize. At 320–433 K (section *b*) vaporization is accompanied by $AlBu_3$ dissociation. The reproducibility of the *p–T* curves obtained on heating and on cooling indicates that these processes are reversible. Occurrence of all these processes is indicated by the dependence of the slope of the *p–T* curves on the $AlBu_3$ concentration in the chamber. A change in the initial concentration affects mainly the dissociation

$$AlBu_3 \rightleftarrows AlHBu_2 + C_4H_8.$$

On heating above 433 K (curve *3*), all liquid components of the system completely vaporize. Section *c* corresponds to formation of unsaturated vapor. At these temperatures $AlBu_3$ and $AlHBu_2$ dimers dissociate, which is indicated by the reproducibility of the *p–T* dependence and the fact that the vapor pressure in the system is higher than that determined by the Gay–Lussac law.

The average molecular weights of the system calculated from the experimental results (433–440 K) and from the above equilibrium are similar and equal to 264. This value does not contradict the existence of this equilibrium in the gas phase. At 440–458 K the processes occurring in the system remain reversible, but the course of the *p–T* dependence differs from the gas expansion line. This indicates that process increasing the number of moles of gases in the system occurs to a significant extent. Proportional increase in the vapor pressure and the fact that experimental and calculated molecular weights are close (198 and 203, respectively) are consistent with the assumed dissociation of the dimeric species and intense dissociation of $AlBu_3$.

The pressure jump at 459 K and the discrepancy between the *p–T* curves (section *d*) measured on heating and cooling indicate that thermolysis of $AlBu_3$ and $AlHBu_2$ becomes irreversible.

The average molecular weight of the gaseous products, determined by chromatography, is 38.4. The vapor pressure in the system, calculated from this molecular weight, is 142 mm Hg, which agrees, within the limits of the determination error, with the experimental value (150 mm Hg). On cooling (curve *f*) down to hydrogen condensation temperature, the *p–T* dependence obeys the Gay–Lussac law. Thus, gas-phase thermal dissociation of $AlBu_3$ occurs in two steps by the olefin–hydride mechanism. The first step is reversible dissociation to form $AlHBu_2$, the olefin, and the mixed dimer $Bu_2AlBuAlHBu_2$. The second step is irreversible thermolysis of $AlHBu_2$ to form hydrogen, 1(2)-butene, and probably aluminum. Calculation of the mass balance by the procedure in [12] showed slightly overestimated content of carbon and hydrogen.

The fact that the vaporization parameters are irreproducible can be explained in terms of the proposed scheme by the reversible dissociation. The enthalpy of vaporization (66.6 kJ mol^{-1}) reported in [11] cannot be taken into account since the $AlBu_3$ pressure should be measured below 380 K. However, this procedure cannot be used because of the low vapor pressure (5 mm Hg) and noticeable determination error. It should also be noted that the enthalpy (65.8 kJ mol^{-1}) and entropy (131 J $mol^{-1}K^{-1}$) of vaporization calculated form the total vapor pressure (Fig. 1, curves *1*, *2*) agree well with the data presented in [11], which indicates that these parameters are doubtful. Since thermal transformation of $AlBu_3$ to $AlHBu_2$ is almost quantitative, small amount of methane, ethane, ethylene, and propane, determined by chromatography, can originate from thermolysis of the possible oligomer

$Al(C_4H_8)_n$:

$$Al(C_4H_8)_n \rightarrow aCH_4 + bC_2H_4 + cC_2H_6 + dC_3H_8 + Al(C_2H_4)_n.$$

Taking into account the nature of the gaseous products, generation and termination of radicals involve a sequence of free-radical reactions but are not the chain processes. Thermolysis of $AlHBu_2$ occurs by radical and olefin–hydride mechanism. By the analogy with hydrocarbon thermolysis [13], autoinhibition of $AlBu_3$ thermal degradation is probably due to recombination of butyl radical and its reaction with atomic hydrogen:

$$\dot{C}_4H_9 + \dot{C}_4H_9 \rightarrow C_4H_8 + C_4H_{10},$$

$$\dot{C}_4H_9 + \dot{H} \rightarrow C_4H_{10}.$$

The study of the gas-phase thermolysis of $AlHEt_2$ showed that its rate is almost independent of the initial $AlHEt_2$ concentration and hence is described by the first-order kinetic equation. At definite initial $AlEt_3$ concentrations the kinetic curves of $AlEt_3$ thermolysis do not pass through the origin of the coordinates because of partial decomposition of the sample during heating to the experimental temperature. These curves were approximated by equations of different orders. The degree of thermolysis of a sample by a definite time was calculated as $\Delta p/p_{tot}$, where Δp is the pressure increment and p_{tot} is the total pressure of $AlEt_3$. The experimental results are described well by the first-order kinetic equation. The rate constants at 469.3 and 503.3 K, calculated by the least-squares treatment of the kinetic data by the first-order equation, are 1.04×10^{-5} and 10.96×10^{-5} s^{-1}, respectively.

The chromatographic analysis of the gaseous products of $AlEt_3$ thermolysis showed the presence of the following components (mol %): hydrogen (28.6), CH_4 (28), C_2H_6 (21.0), C_2H_4 (12.0), C_3H_8 (20.2), C_4H_{10} (0.9), *n*-C_4H_8 (0.07), C_4H_6 (0.03), the total of C_5 (1.8), and the total of C_6 (12.6). The walls of the reaction chamber were coated with a gray nontransparent nonuniform film. The main gaseous products were hydrogen, ethane, ethylene, propane, and C_6 hydrocarbons. As in the case of $AlBu_3$ thermolysis, the high content of hydrogen and ethylene suggests the olefin–hydride mechanism of the thermolysis. However, high content of saturated hydrocarbons suggests occurrence of radical reactions, and high propane yield is due to the following transformations of the C_2H_5 radical:

$$AlHC_2H_4 + C_2H_5 \rightarrow 1/2H_2 + C_4H_9 + Al,$$

$$\dot{A}lC_2H_4 + \dot{C}_2H_5 \rightarrow \dot{A}lCH + \dot{C}_3H_6.$$

The products of these reactions form nonuniform film on the membrane surface. Propane formation suggests formation of the AlC_2H_4 radical. It probably decomposes to form CH_3 radical which reacts with C_4H_9 and C_2H_5 radicals to form small amounts of methane and C_5 hydrocarbons. The high yield of C_6 hydrocarbons indicates appreciable contribution of the following reactions:

$$\dot{A}lHC_2H_4 + \dot{C}_2H_5 \rightarrow \dot{A}lHC_4H_9,$$

$$\dot{A}lHC_4H_9 \rightarrow AlH + \dot{C}_4H_9.$$

Butyl radical C_4H_9 reacts with ethyl radical

$$\dot{C}_4H_9 + \dot{C}_2H_5 \rightarrow C_6H_{14},$$

$$\dot{C}_4H_9 + \dot{C}_2H_5 \rightarrow C_4H_8 + C_2H_6$$

to form small amounts of 1(2)-butenes. Autoinhibition of the thermolysis is probably due to these reactions and recombination of ethyl radicals:

$$\dot{C}_2H_5 + \dot{C}_2H_5 \rightarrow C_4H_{10}.$$

Reactions of radical formation and chain termination in the course of $AlEt_3$ thermolysis involve a sequence of nonchain free-radical processes. Thus, $AlEt_3$ thermolysis occurs by the radical and olefin–hydride mechanism. Based on the results of this work and the data on thermal behavior of $AlOct_3$ [10], the reactivity of aluminum tri-*n*-alkyls with respect to olefin-hydride thermolysis increases with an increase in the length of the carbon chain in the following order: $AlMe_3 < AlEt_3 < AlPr_3 < AlBu_3 < AlOct_3$. This agrees with data of [11].

These results show that $AlPr_3$ vaporization should be studied at low temperatures. The vapor pressures determined in separate experiments agree well with each other. The molecular weight of this compound in the gas phase, calculated from the unsaturated vapor pressure produced by a definite weighed portion of the sample in the volume of the membrane chamber, is 165.0. The formular weight is 156.0.

The overestimation of the molecular weight by 11.0 is due to the presence of gaseous dimers whose contribution to the vapor pressure does not exceed

3%. The low polymerization degree of gaseous $AlPr_3$ is consistent with the decrease in the tendency to polymerization in the series Al_2Me_6 > Al_2Et_6 > Al_2Pr_6. The onset temperature of thermal degradation of $AlPr_3$ (465 K) was determined by heating with a 1 K increment and subsequent thermostatic control. However, when the system was thermostatically controlled for several days, the onset temperature was determined to be 413 K. Up to this temperature no additional increase in the unsaturated vapor pressure was observed. The treatment of the temperature dependence of the saturated vapor pressure by various equations gave the following equation:

$$\log p = 7.28 - 2246/T.$$

The enthalpy and entropy of vaporization of tripropylaluminum are 43 ± 2.0 kJ mol^{-1} and 88 ± 6 J mol^{-1} k^{-1}, respectively. These low values are due to weaker association of $AlPr_3$ as compared to $AlEt_3$.

CONCLUSION

Conditions of equilibrium dissociation of tributylaluminum, irreversible thermolysis of dibutylaluminum hydride, and vaporization of tripropylaluminum were determined. These data can be used for optimizing the preparation of these compounds and their application as catalysts and alkylating agents.

REFERENCES

1. Vitalev, S.E. and Baev, A.K., *Izv. Vyssh. Uchebn. Zaved., Khim. Khim. Tekhnol*., 1988, vol. 31, no. 11, pp. 46–49.
2. Baev, A.K. and Vitalev, S.E., *Izv. Vyssh. Uchebn. Zaved., Khim. Khim. Tekhnol*., 1993, vol. 36, no. 6, pp. 36–40.
3. Lanbengayer, W.S. and Gilliam, W.F., *J. Am. Chem. Soc*., 1941, vol. 63, no. 3, p. 477.
4. Bamford, G.H., Levi, D.L., and Newitt, B.M., *J. Am. Chem. Soc*., 1946, vol. 68, no. 3, pp. 468–471.
5. Cox, J.D. and Pilcher, G., *Thermochemistry of Organic and Organometallic Compounds*, London: Academic Press, 1970.
6. McCullough, J.P., Messerly, J.F., Moore R.T., *et al*., *J. Phys. Chem*., 1963, vol. 67, no. 3, pp. 677–679.
7. Shmyreva, G.O., Sakharovskaya, G.B., Popov, A.F., *et al*., *Zh. Fiz. Khim*., 1971, vol. 45, no. 2, p. 467.
8. Korneev, N.N., Govorov, N.N., and Tomashevskii, M.V., *Alyuminiiorganicheskie soedineniya: Obzornaya informatsiya, Seriya "Elemetoorganicheskie soedineniya i ikh primenenie"* (Oranoaluminium Compounds: Review, Ser.: Organoelement Compounds and Their Application), Moscow: NIITEKhIM, 1988.
9. *Alyuminiiorganicheskie soedineniya* (Organoaluminum Compounds), Zhigach, A.F., Ed., Moscow: Inostrannaya Literatura, 1962.
10. Baev, A.K. and Shishko, M.A., *Zh. Org. Khim*., 1999, vol. 35, no. 8, pp. 1157–1160.
11. Korneev, N.N., *Khimiya i tekhnologiya alyuminiiorganicheskikh soedinenii* (Chemistry and Technology of Organoaluminum Compounds), Moscow: Khimiya, 1979.
12. Sokolovskii, A.E. and Baev, A.K., *Izv. Vyssh. Uchebn. Zaved., Khim. Khim. Tekhnol*., 1985, vol. 28, no. 2, pp. 30–31.
13. Stepukhovich, A.D., *Kinetika i mekhanizm termicheskogo krekinga alkilov* (Kinetics and Mechanism of Thermal Cracking of Alkyls), Saratov: Saratov. Gos. Univ., 1965, part 1, pp. 106–159.

Russian Journal of Applied Chemistry, Vol. 75, No. 1, 2002, pp. 29–33. Translated from Zhurnal Prikladnoi Khimii, Vol. 75, No. 1, 2002, pp. 30–33.
Original Russian Text Copyright © 2002 by Tikhomirov, Lavrenyuk, Orlov, Vidyaev.

PHYSICOCHEMICAL STUDIES OF SYSTEMS AND PROCESSES

Decomposition Kinetics of Alkali Metal Gallams in Hydroxide Aqueous Solutions

I. A. Tikhomirov, P. I. Lavrenyuk, A. A. Orlov, and D. G. Vidyaev

Tomsk Polytechnic University, Tomsk, Russia

Received May 18, 2001

Abstract—The decomposition kinetics of alkali metal gallams in LiGa–LiOH, NaGa–NaOH, KGa–KOH, LiGa–NaOH, LiGa–KOH, and KGa–NaOH systems in the 40–80°C range was studied. The rate constant and current density of decomposition were determined. The rate equation of gallam decomposition under the given experimental conditions was obtained.

Thanks to the high environmental safety and valuable properties of gallium and its compounds, the areas of their practical use are steadily expanding. In particular, in the exchange separation and purification of alkali metals to prepare alkali metal hydroxides [1] the substitution of highly toxic amalgams by gallium compounds (gallams) [2, 3] is of particular importance. The efficiency of the exchange reaction depends on the decomposition kinetics of the intermetallic compound (gallam) at contact with aqueous solution of alkali metal hydroxide, because at its decomposition alkali metal partially passes into solution. If the rate of gallam decomposition is higher than or equal to the rate of element exchange in the system studied, the separation of alkali metals is impossible. Thus, analysis of the kinetics and mechanism of the above processes is urgent. In this work we studied the kinetic parameters of decomposition of gallams upon their contact with aqueous alkali solutions in the LiGa–LiOH, NaGa–NaOH, KGa–KOH, LiGa–NaOH, LiGa–KOH, and KGa–NaOH systems.

EXPERIMENTAL

Lithium, sodium, and potassium gallams were prepared by direct dissolution of the corresponding alkali metal in gallium. In our work we used LE-1 brand lithium, chemically pure grade (99.9%) gallium, and pure grade sodium and potassium. The aqueous solutions of lithium, sodium, and potassium hydroxides were prepared by dissolving the corresponding chemically pure grade hydroxide in distilled water. The experiments were performed at 40–80°C, because gallam solidified at the concentration more than 1.5 M and temperature lower than 40°C [4], whereas at temperatures higher than 80°C the aqueous solution of alkali metal hydroxide strongly evaporates, which is unacceptable for the separation processes.

The scheme of the experimental unit is shown in Fig. 1. The experiments were carried out in a cylindrical cell *1* (30 mm in diameter) equipped with a water jacket, which was heated to a required temperature with a thermostat *2*. In the course of experiments the cell was first charged with hydroxide solution *3*,

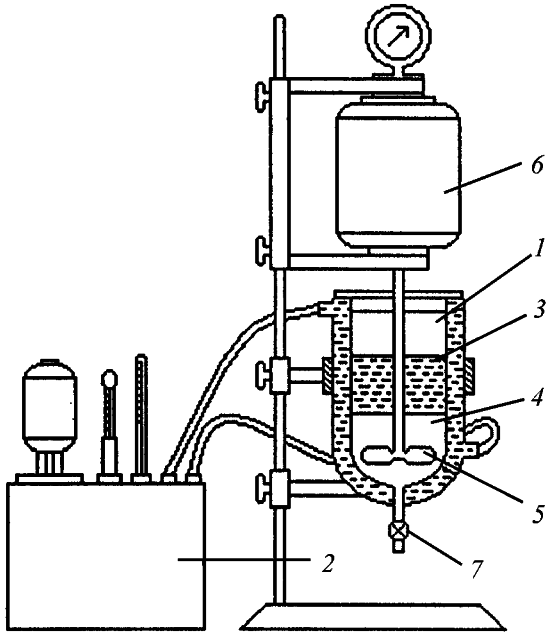

Fig. 1. Scheme of experimental laboratory unit: (*1*) cylindrical cell with a water jacket, (*2*) thermostat, (*3*) aqueous hydroxide solution, (*4*) gallam, (*5*) propeller stirrer, (*6*) electrical motor, and (*7*) valve.

1070-4272/02/7501-0029$27.00 © 2002 MAIK "Nauka/Interperiodica"

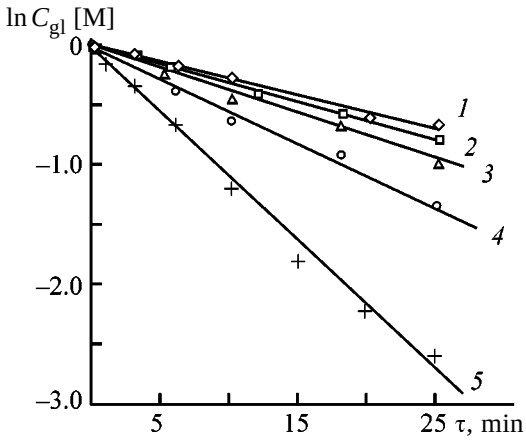

Fig. 2. Variations with time τ of the lithium gallam concentration upon contact with lithium hydroxide solution. (C_{gl}) Concentration of lithium ions in gallam. Temperature, °C: (*1*) 80, (*2*) 70, (*3*) 60, (*4*) 50, and (*5*) 40; the same for Fig. 4.

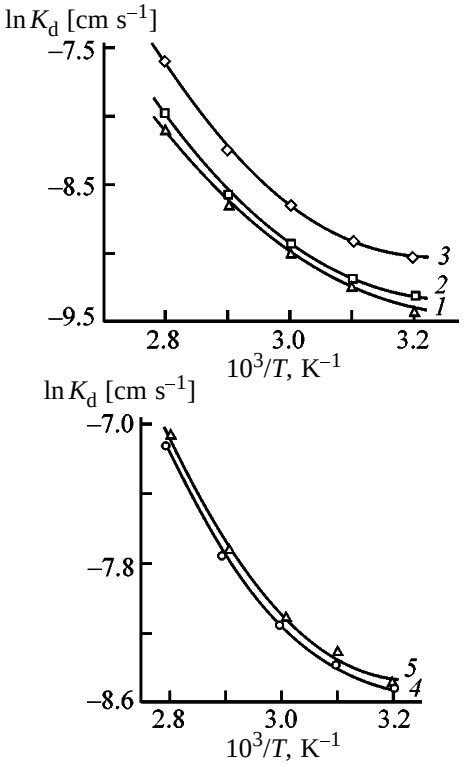

Fig. 3. Rate constant of gallam decomposition K_d as a function of temperature *T*. System: (*1*) KGa–KOH, (*2*) NaGa–NaOH, (*3*) LiGa–LiOH, (*4*) LiGa–NaOH, and (*5*) LiGa–KOH.

and then, when the required temperature was attained, a gallam *4* was charged directly to the cell bottom using a funnel with a long tip. The phases were mixed with a propeller stirrer *5* using an electrical motor *6* (750–800 rpm). No dispersion of gallam on stirring was observed. The area of the phase contact was calculated as the area of the cone formed at the gallam–solution boundary upon stirring. After experiments the hydroxide solution was removed from the top of the exchange cell, whereas the gallam was removed through a valve *7*. When the decomposition kinetics of alkali metal gallams in the LiGa–LiOH, NaGa–NaOH, and KGa–KOH systems were studied, aliquots of hydroxide solutions were sampled from the cell at certain intervals and the gallam concentration was determined by their titration. In the case of LiGa–NaOH, LiGa–KOH, and KGa–NaOH systems aliquots of the hydroxide solution and gallam were taken. The gallam samples were decomposed with freshly distilled hydrochloric acid. Then the resulting salt solutions and the hydroxide solutions sampled directly from the exchange cell were analyzed by flame photometry [5]. The measurement errors were calculated by the standard procedure [6]. The kinetic parameters of decomposition of lithium, sodium, and potassium gallams in the systems of the Me_1Ga–Me_1OH and Me_1Ga–Me_2–OH types were evaluated by the procedures given elsewhere [7, 8].

The decomposition kinetics of lithium, sodium, and potassium gallams in aqueous solutions of the respective alkali metal hydroxides was studied in the 40–80°C range using the following concentrations of the reacting phases, M: lithium (sodium) gallam 0.95, potassium gallam 0.92, and sodium and potassium hydroxides 4.00. In all the cases the experimental kinetic dependences of the gallam concentration plotted in the semilog coordinates are straight lines (Fig. 2). Thus, the reaction order of lithium (sodium, potassium) oxidation is 1. From the slopes of these straight lines we determined the apparent rate constants of decomposition depending on the temperature and hydroxide concentration. The resulting kinetic parameters of gallam decomposition in the LiGa–LiOH, NaGa–NaOH, and KGa–KOH systems are given in the table. The experimental error in K_d measurements was ±15%.

To study the influence of temperature on the decomposition rate constant in the systems in question, we plotted the dependences in the $\log K_d$–$10^3/T$ coordinates (*T* is the absolute temperature) (Fig. 3, curves *1–3*). As seen, with increasing temperature the rate of decomposition significantly increases, whereas with increasing hydroxide concentration it decreases (Fig. 4). Moreover, the shape of these curves suggests that the oxidation of alkali metals (lithium, sodium, and potassium) and reduction of hydrogen proceed simultaneously. The gallams of lithium, sodium, and potassium were used in experiments without purification. This suggests that, similarly to the case of decomposition of lithium (sodium, potassium) amalgam

under the industrial conditions, in this case two mechanisms operate simultaneously: electrochemical decomposition of gallam with separation of the anodic (on gallium) and cathodic (on the impurities) processes and its chemical decomposition. At low temperature (40–50°C), the diffusion processes control the decomposition rate of gallams, and with increasing temperature their effect decreases.

To determine the reaction order with respect to hydroxide, we plotted the dependences in the $\log K_d$–$\log C_{OH^-}$ coordinates (C_{OH^-} is the hydroxide ion concentration). These dependences are straight lines with different slopes; the typical dependence determined in the LiGa–LiOH system [9] is shown in Fig. 4. The slopes are different; hence, the reaction order depends on the hydroxide ion concentration, and the temperature dependence of the decomposition rate cannot be described by the Arrhenius equation. The decomposition rate of lithium, sodium, and potassium gallams can be described as follows:

$$W = -dC_{gl}/d\tau = -KC_{gl} = KC'_{gl}e^{-K\tau}, \quad (1)$$

where

$$K = (K_1 + K_2)/C_{OH^-}, \quad (2)$$

W is the rate of the gallam decomposition, K is the decomposition rate constant (s^{-1}), C_{gl} and C'_{gl} are, respectively, the current and initial gallam concentrations (M), τ is the time (s), and K_1 and K_2 are two components of the decomposition rate constant.

In this case we assumed that the rate of the reverse reaction can be neglected. The K_1 and K_2 values were determined as the limits in the $\log K_d$–$10^3/T$ dependence with an inflection point; at low temperatures $K_1 > K_2$, whereas at high temperatures $K_1 < K_2$. The expressions for K_1 and K_2 in the final form are given below:

$$K_1 = K_{01}e^{-96\,500/(RT)}, \quad (3)$$

$$K_2 = K_{02}e^{-10\,000/(RT)}, \quad (4)$$

where T is the absolute temperature (K) and R is the universal gas constant (J mol^{-1} K^{-1}).

For K_{01} and K_{02} we obtained the following expressions:

$$K_{01} = ae^b, \quad (5)$$

$$K_{02} = cC_{OH^-}/(1 + C_{OH^-})e^d. \quad (6)$$

The a, b, c, and d parameters for the systems in question are listed below:

System	a	b	c	d
LiGa–LiOH	0.732	32.5	0.32	3.37
NaGa–NaOH	0.725	31.2	0.317	2.1
KGa–KOH	0.677	31.4	0.31	2.2

Kinetic parameters of gallam decomposition

Parameter*	Temperature, °C				
	40	50	60	70	80
LiGa–LiOH					
$I_d \times 10$, kA m^{-2}	1.09	1.24	1.61	2.43	4.59
$K_d \times 10^4$, cm s^{-1}:					
experimental	1.19	1.36	1.75	2.65	5.00
calculated	1.17	1.34	1.94	3.04	5.07
NaGa–NaOH					
$I_d \times 10$, kA m^{-2}	0.74	0.90	1.13	1.62	2.78
$K_d \times 10^4$, cm s^{-1}:					
experimental	0.81	0.98	1.23	1.76	3.04
calculated	0.81	0.85	1.12	1.71	3.05
KGa–KOH					
$I_d \times 10$, kA m^{-2}	0.79	0.90	1.18	1.68	3.04
$K_d \times 10^4$, cm s^{-1}:					
experimental	0.88	1.01	1.33	1.89	3.42
calculated	0.88	0.92	1.23	1.89	3.42
LiGa–NaOH					
$I_d \times 10$, kA m^{-2}	1.78	2.11	2.63	3.97	7.28
$K_d \times 10^4$, cm s^{-1}:					
experimental	1.94	2.30	2.87	4.33	7.94
calculated	1.95	2.05	2.76	4.33	7.95
LiGa–KOH					
$I_d \times 10$, kA m^{-2}	1.87	2.27	2.73	4.11	7.80
$K_d \times 10^4$, cm s^{-1}:					
experimental	2.04	2.48	2.98	4.49	8.51
calculated	2.04	2.15	2.92	4.60	8.51

* (I_d) Decomposition current density and (K_d) decomposition rate constant.

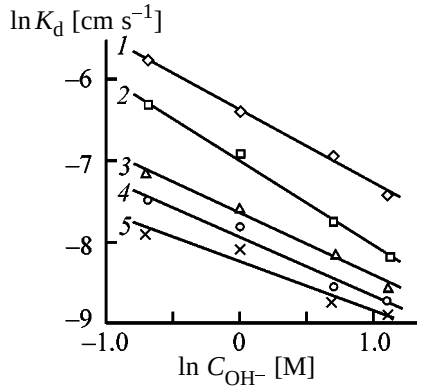

Fig. 4. Rate constant of lithium gallam decomposition K_d as a function of concentration of lithium hydroxide C_{OH^-}.

For comparison of our data with the published values, the decomposition rate constants (s^{-1}) were converted to the cm s^{-1} dimension. The resulting rate constants are given in the table. As seen, the agreement between the experimental and calculated K_d is quite satisfactory. The maximal deviation in the LiGa–LiOH, NaGa–NaOH, and KGa–KOH systems does not exceed 15, 13, and 9%, respectively.

Our study showed that with increasing temperature the decomposition rate of alkali metal (lithium, sodium, and potassium) gallams in the systems in question increases, and thus it is advisable to perform exchange at 40°C. Data on the decomposition kinetics suggest that the rate of gallam decomposition increases in the following order: sodium < potassium < lithium. The kinetic parameters of decomposition of lithium, sodium, and potassium gallams in the aqueous solutions of the respective alkali metal hydroxides were evaluated. Comparison of the kinetic parameters in the gallam systems studied with the data characterizing decomposition in the analogous amalgam systems [10] shows that the rate of gallam decomposition at 40°C is two times higher than the decomposition rate of the corresponding amalgams at 20°C. This is probably due to the lower hydrogen overvoltage at gallium. The hydrogen evolution is the slowest stage and thus it determines the overall rate of gallam decomposition.

Under the real exchange conditions the mixed alkali metal gallams decompose in aqueous solutions containing a mixture of hydroxides of these metals. It was of interest to study decomposition of the mixed gallams. Gallam decomposition was performed in the LiGa–NaOH and LiGa–KOH systems at 40–80°C using the following concentrations of the reacting phases, M: lithium gallam 0.95 and sodium and potassium hydroxides 4.00. Because of high fire risk of the potassium gallam–aqueous potassium hydroxide system, due to the high reactivity of potassium toward water and its vapor, the tests were performed under the following experimental conditions: 40°C, concentrations of gallam and hydroxide 0.92 and 4.00 M, respectively.

In the LiGa–NaOH and LiGa–KOH systems the experimental kinetic dependences of the gallam concentration are also linear, and thus the reaction order of lithium (potassium) oxidation is 1. The experimental kinetic characteristics of the gallam decomposition in the Li–Na and Li–K systems are listed in the table along with the theoretical decomposition rate constants calculated from Eqs. (2)–(6) using the following parameters *a*, *b*, *c*, and *d*:

System	*a*	*b*	*c*	*d*
LiGa–NaOH	0.655	32.3	0.278	3.1
LiGa–KOH	0.708	32.3	0.291	3.1

The measurement error of K_d was 15%.

As seen from the table, the agreement between the experimental and calculated K_d is quite satisfactory. The maximal divergence in the LiGa–NaOH and LiGa–KOH systems does not exceed 11 and 13%, respectively. For potassium gallam–sodium hydroxide aqueous solution we obtained the following kinetic characteristics: I_d = 0.16 kA m^{-2} and K_d = 1.81×10^{-4} cm s^{-1}. The experimental dependences of the decomposition rate constants on reciprocal temperature are shown in Fig. 3 (curves *4, 5*). As seen, in the LiGa–NaOH and LiGa–KOH systems the rate of gallam decomposition increases with temperature. On the average, the decomposition rate of mixed gallams at 40°C is two times greater than that of the corresponding amalgams at 20°C [10].

CONCLUSIONS

(1) At gallam decomposition, oxidation of lithium, sodium, and potassium proceeds simultaneously with reduction of hydrogen. With increasing temperature the rate of gallam decomposition increases, whereas with increasing hydroxide concentration it decreases.

(2) Similarly to decomposition of alkali metal amalgams, two processes probably occur simultaneously in the course of decomposition of the alkali metal gallams: chemical decomposition and electrochemical decomposition with separation of the anodic (on gallam) and cathodic (on the impurities) processes.

(3) The decomposition rate of the alkali metal gallams at 40°C is, on the average, two times higher than the decomposition rate of the corresponding amalgams at 20°C.

ACKNOWLEDGMENTS

This work was financially supported by the Ministry of Education of the Russian Federation (project no. TOO-7.4-897).

REFERENCES

1. RF Patent Application no. 93 008 155.
2. Tikhomirov, I.A. and Orlov, A.A., *Izv. Vyssh. Uchebn. Zaved., Fiz.*, 2000, vol. 43, no. 5, pp. 111–115.

3. Tikhomirov, I.A., Lavrenuk, P.I., Orlov, A.A., and Vidyaev, D.G., Abstracts of Papers, *Seventh Workshop on Separation Phenomena in Liquids and Gases*, Moscow, July 24–28, 2000, p. 30.
4. Tikhomirov, I.A., Orlov, A.A., Bogoslovskii, A.V., and Poluektov, M.A., *Vyazkost' binarnoi sistemy gallii–litii* (Viscosity of the Gallium–Lithium Binary System), Available from VINITI, 1989, Tomsk, no. 6345-V89.
5. Poluektov, N.S., *Metody analiza po fotometrii plameni* (Analytical Methods Based on Flame Photometry), Moscow: Khimiya, 1967.
6. Zaidel', A.N., *Oshibki izmerenii fizicheskikh velichin* (Measurement Errors of Physical Quantities), Leningrad: Nauka, 1974.
7. Tsivadze, A.Yu., Levkin, A.V., Knyazev, D.A., and Klinskii, G.D., *Zh. Neorg. Khim.*, 1987, vol. 32, no. 7, pp. 1757–1758.
8. Konstantinov, B.P., Kiselev, B.P., and Skrebtsov, G.P., *Radiokhimiya*, 1960, vol. 2, no. 1, pp. 44–49.
9. Tikhomirov I.A. and Orlov, A.A., *Zh. Prikl. Khim.*, 1993, vol. 66, no. 1, pp. 23–26.
10. Korshunov, V.N. and Iofa, Z.A., *Dokl. Akad. Nauk SSSR*, 1961, vol. 141, no. 1, pp. 143–146.

Russian Journal of Applied Chemistry, Vol. 75, No. 1, 2002, pp. 34–38. Translated from Zhurnal Prikladnoi Khimii, Vol. 75, No. 1, 2002, pp. 34–38.
Original Russian Text Copyright © 2002 by Egiazarov, Kravchuk, Radkevich, Ivko, Bogushevich.

SORPTION AND ION-EXCHANGE PROCESSES

Influence of Exchangeable Cation on Dehydration and Thermal Stability of FIBAN K-1 Fibrous Sulfonic Cation Exchanger

Yu. G. Egiazarov, L. S. Kravchuk, V. Z. Radkevich, A. A. Ivko, and S. E. Bogushevich

Institute of Physical Organical Chemistry, Belarussian National Academy of Sciences, Minsk, Belarus

Received January 16, 2001

Abstract—The influence of exchangeable cation on dehydration, desulfonation, and thermal oxidative degradation of FIBAN K-1 fibrous sulfonic cation exchanger in the hydrogen, alkali metal, and alkaline-earth metal forms was studied.

FIBAN K-1 gel-like fibrous sulfonic cation exchanger in the H form is the efficient catalyst of methyl *tert*-butyl ether synthesis [1] and alcohol dehydration [2]. It was reported also [3, 4] that palladium applied to this ion exchanger in the Ba form actively catalyzes hydrogen oxidation [3, 4].

In catalysis at elevated temperatures, ion-exchange resins are dehydrated to some extent, which results in deterioration of their physicochemical characteristics, in particular, of the thermal stability. This fact is important for industrial catalytic processes with catalysts based on ion-exchange resins.

Published data show that at present there is no generally accepted approach to evaluation of the ion exchanger thermal stability. The thermal stability of resins is characterized by several factors: weight loss, change of the exchange capacity (EC) and moisture capacity, and also the amount and composition of volatile thermal degradation products. It is evident that all these factors specifically reflect the degradation of functional groups. Therefore, to characterize the thermal stability of an ion exchanger, the temperature of the onset of functional group degradation should be determined. For catalysts based on sulfonic cation exchangers, this temperature should be established for sulfonic groups.

The state of water in KU-2 granular sulfonic cation exchanger in various cationic forms and its influence on desulfonation of these resins was studied in [5–7]. It was found that desulfonation of this cation exchanger in the presence of excess water involves not only associated but also dissociated sulfonic groups. The water molecules bound in the first hydration shell are not involved in the limiting stage of desulfonation.

The influence of exchangeable cation nature on the heat resistance of granular sulfonic cation exchangers in air was studied in [8–10]. It was found that cation exchangers in the metal cationic form exhibit higher thermal stability than those in the H form. It is difficult to exhaustively explain this effect, because along with thermal degradation, various reactions of resin oxidation with atmospheric oxygen occur, among them the thermal oxidative degradation of the polymeric matrix.

In this work we studied the effect of exchangeable cation on dehydration of FIBAN K-1 fibrous sulfonic cation exchanger and also on its thermal and thermal oxidative degradation. To prevent the reactions of the resin with atmospheric oxygen and ensure high precision of the results, the temperature of the onset of the functional group degradation was determined by mass spectrometry.

Mass spectrometry is widely used in studying macromolecular compounds, in particular, for determination of their composition [11, 12]. However, we found no available data on mass-spectrometric characterization of the thermal stability of sulfonic cation exchangers.

EXPERIMENTAL

FIBAN K-1 fibrous sulfonic cation exchanger was prepared by radiation grafting of copolymer of styrene (98%) and divinyl benzene (2%) to a polypropylene staple fiber, followed by sulfonation of poly(styrene–divinylbenzene) matrix with concentrated sulfuric acid [13]. In experiments we used samples of the cation exchanger in the H form with EC 0.6, 1.3, 2.2, 2.6, and 3.2 mg-equiv g^{-1}. The samples of completely sub-

1070-4272/02/7501-0034$27.00 © 2002 MAIK "Nauka/Interperiodica"

stituted ion exchangers in the Li, Na, Cs, Mg, Ca, and Ba forms were prepared by passing an excess of I N solution of the corresponding metal chloride through a column packed with the ion exchanger in the H form (EC 3.2 mg-equiv g^{-1}) to the neutral reaction of the filtrate. Thereafter the resin was washed with distilled water to complete removal of chloride anions and dried in air at room temperature.

Mass-spectrometric analysis of the volatile products of the ion exchanger degradation was carried out on an MKh-1320 mass spectrometer. In these experiments a portion of ion exchanger placed into a standard test tube was inserted into the inlet unit of the mass spectrometer. This sample was electrically heated with platinum coil, simultaneously functioning as a temperature-sensitive element. The mass spectra of the products of thermal desorption and thermal degradation of the ion exchanger were recorded at the ionizing voltage of 50 V and accelerating voltage of 2.5 kV.

Thermogravimetric study of sulfonic cation exchangers was carried out on an MOM (Hungary) derivatograph. In the first experimental series the weight loss was measured for ion exchanger samples in the H form with the different exchange capacities on heating from 20 to 200°C at a heating rate of 5 deg min^{-1}. In the second experimental series the resin resistance to thermal oxidative degradation was studied for samples with similar exchange capacity but containing different exchangeable cations. The samples were heated from 20 to 250°C at a heating rate of 5 deg min^{-1} and then kept at the maximal temperature for 5 min. The extent of thermal oxidative degradation of the poly(styrene–divinylbenzene) matrix was evaluated by measuring the concentration of paramagnetic centers (PCs).

The ESR spectra of heat-treated sulfonic cation exchangers were registered on a small-scale ESR spectrometer with sensitivity of 10^{10} spin g^{-1}, equipped with a software ensuring the multiple scan mode and fast data processing. MgO doped with Mn^{2+} ions was used as external reference.

Figure 1 illustrates the temperature dependence of the weight loss for resins with different exchange capacities. The water loss starts at a temperature lower than 50°C. On heating from 100 to 200°C (especially in the temperature range 100–150°C) the plot of the weight loss vs. *T* is steeper for ion exchangers with higher EC.

According to [14], ion exchangers contain two types of water molecules: those bound in the first

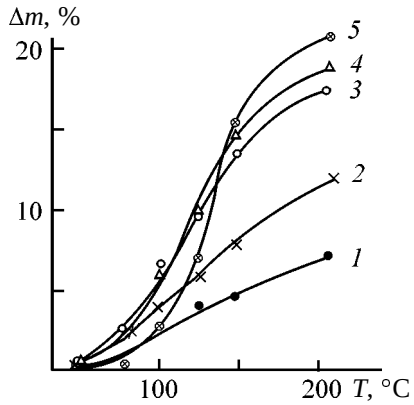

Fig. 1. Weight loss Δm of cation exchangers in the H form as a function of temperature *T*. Exchange capacity (mg-equiv g^{-1}): (*1*) 0.6, (*2*) 1.3, (*3*) 2.2, (*4*) 2.6, and (*5*) 3.2.

hydration shell and "free" (unbound) water molecules. The water state in cation exchangers was analyzed in more detail by Selemenev *et al*. [15]. They believe that water molecules in KU-2 granular sulfonic cation exchanger occur in three energetically different forms. The first form, so-called freely bound water, is mainly localized in the external (third) hydration shell and is bound by intermolecular dipole–dipole interactions. This water is removed from the cation exchanger in the first dehydration stage in the temperature range 50–80°C. In the second dehydration stage (80–115°C), water of the second hydration shell is removed. These water molecules form associates localized near hydrophilic sites of the ion exchanger. In the third dehydration stage, at temperatures higher than 115°C, water molecules of the first hydration shell bound to the metal ions by ion–dipole interaction are removed. In the DTA curves the endothermic peaks of different intensity appear in the temperature ranges 90–120 and 150–180 °C. The low-temperature peak can be assigned to intensive dehydration of the cation exchanger. The high-temperature peak is probably due to structural transformations of the functional groups.

It is known [16, 17] that in deep dehydration of sulfonic cation exchangers in the H form the functional groups are transformed from the dissociated to the nondissociated state. The oxygen atoms of the nondissociated sulfonic groups are stronger electron acceptors than those of the dissociated groups. Therefore, the protons of the SO_3H groups are bound to oxygen atoms of the adjacent sulfonic groups to form associates containing two and more sulfonic groups bound with hydrogen bonds. We believe that the high-temperature endothermic effect (150–180 °C) is due to breakdown of these associates.

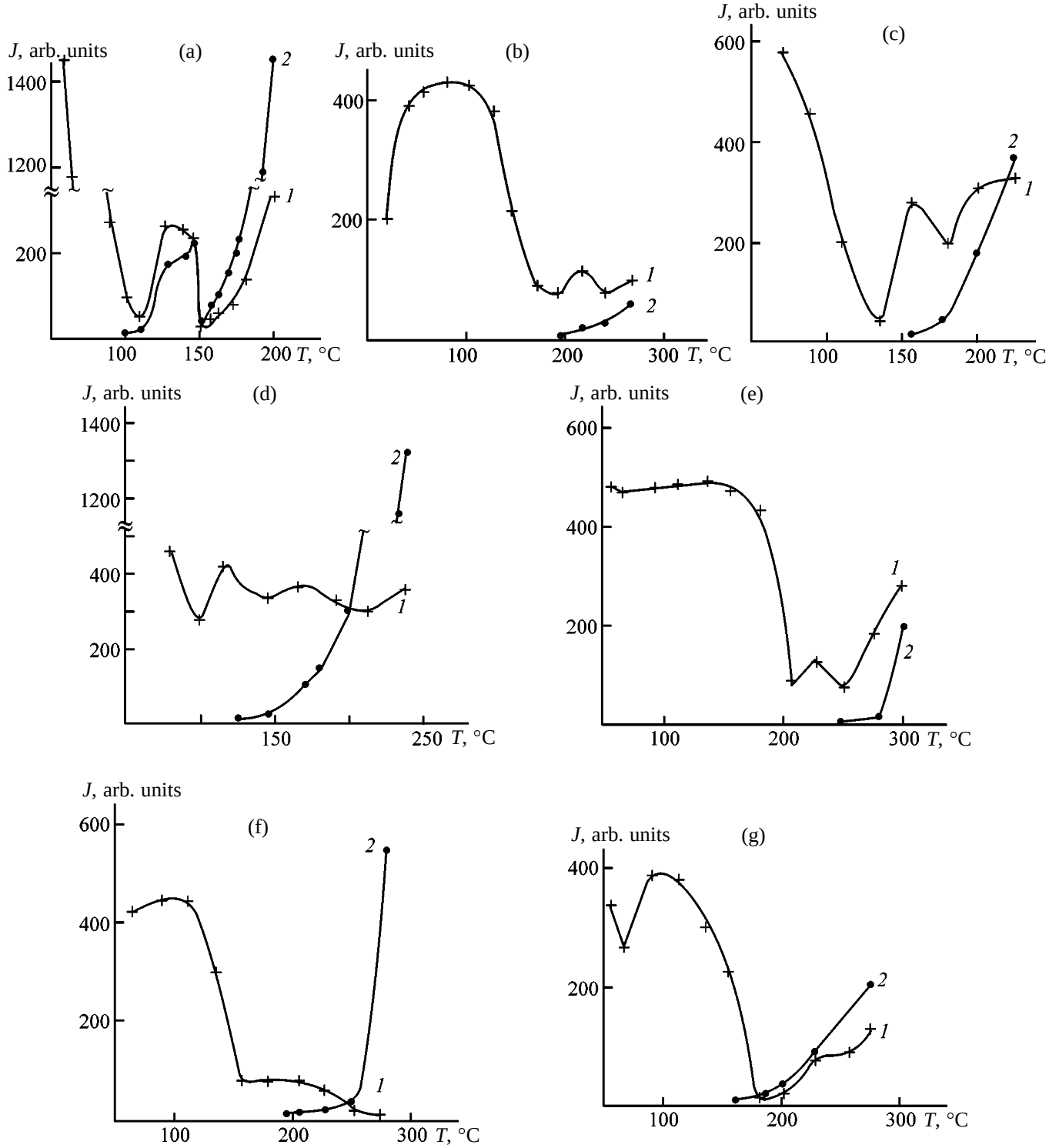

Fig. 2. Temperature dependence of the relative content J of (*1*) H_2O^+ and (*2*) SO_2^+ ions in the mass spectra. Cation exchanger form: (a) H, (b) Li, (c) Na, (d) Cs, (e) Mg, (f) Ca, and (g) Ba.

Figure 1 shows that the weight loss for the samples with EC 0.6, 1.3, 2.2, 2.6, and 3.2 mg-equiv g^{-1} in the temperature range 115–200°C is 3.9, 7.0, 9.5, 11.1, and 16.0%, respectively. This weight loss is due not only to dehydration of ion exchangers but also to breakdown of the functional groups. Figure 2 illustrates the temperature dependence of the relative content in the mass spectra of H_2O^+ and SO_2^+ ions

with *m*/*z* 18 and 64, respectively. Curve *I* shows that the temperature dependence of water evolution has three portions at 20–110, 110–150, and 150–200°C separated by sharp minima at 110 and 150°C. We believe that in the temperature range 20–110°C the free and weakly bound hydration water is removed from the cation exchanger. In the range 110–150°C relatively small amount of water and sulfur dioxide is evolved into gas phase, apparently originating from dehydration and degradation of dissociated sulfonic groups. Increase in the content of H_2O^+ and SO_2^+ in the mass spectra at temperatures higher than 150°C is apparently due to breakdown of both nondissociated and associated sulfonic groups.

The thermogravimetric and chemical analyses showed [8, 18–20] that heating of sulfonic cation exchangers in air in the temperature range 150–220°C results in their desulfonation by hydrolytic cleavage of the C–S bonds to form sulfuric acid. Further heating is accompanied by the matrix resulfonation and reaction between sulfuric acid and reducible matrix groups. The latter reaction yields sulfurous acid which decomposes into water and sulfur dioxide. In the first stage of desulfonation of anhydrous sulfopolystyrene in a vacuum (residual pressure ≤0.1 torr), the sulfonic groups react with the polymeric matrix at 200–230°C to form sulfones and water [21]. At higher temperature the reaction involves two sulfonic groups and yields sulfuric acid.

We found that the course of sulfonic cation exchanger desulfonation in the mass-spectrometric experiments somewhat differs from that determined by thermogravimetric analysis. Namely, in the mass-spectrometric experiment sulfur dioxide is evolved from the cation exchanger at lower temperatures starting from 90°C. This effect is apparently due to both higher sensitivity of the mass-spectrometric technique and considerable influence of a high vacuum (10^{-7} torr) on the mechanism and rate of desulfonation. Under high vacuum the reactions in question can occur at lower temperature, and, along with hydrolytic cleavage of the C–S bonds, their heterolytic cleavage is possible.

Figures 2b–2d show that temperature dependences of water and sulfur dioxide evolution from the cation exchanger in the Li, Na, and Cs forms differ substantially from those for the cation exchanger in the H form.

The water molecules tightly bound to the counterions are removed at 240, 180, and 150°C for cation exchanger in the Li, Na, and Cs forms, respectively. These results correlate with decrease in the ionic potential z/r^2 in the series Li^+, Na^+, and Cs^+ (1.47, 1.02, and 0.61, respectively).

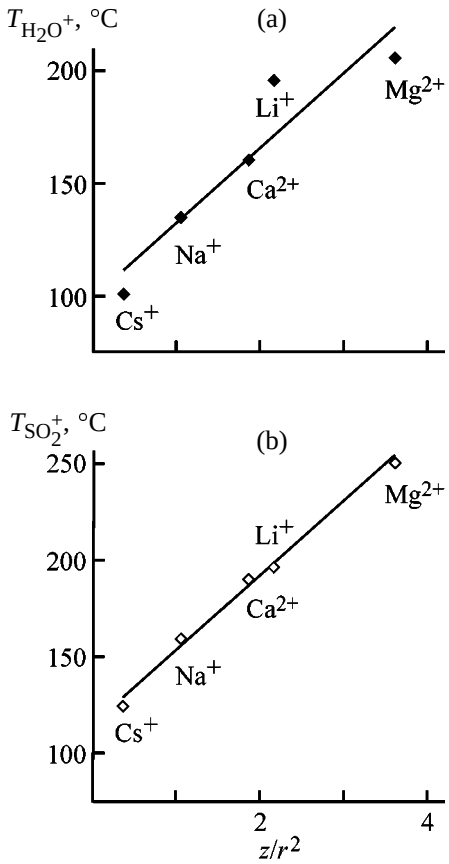

Fig. 3. Temperature (°C) of the onset of (a) water evolution from the first hydration shell $T_{H_2O^+}$ and (b) desulfonation $T_{SO_2^+}$ as a function of the ionic potential z/r^2.

The functional groups of sulfonic cation exchangers in the Li and Na forms decompose to form SO_2^+ ions at temperatures close to those of evolution of the water molecules bound to the counterions. As seen from Figs. 2b–2d (curves *2*), by contrast to the cation exchanger in the H form, for the cation exchanger in the metal cation form there is no correlation between SO_2^+ and H_2O^+ peak intensities because the SO_2^+ content continuously increases with temperature. This is apparently due to the fact that the sulfonic groups of the cation exchanger in the metal cation forms are incapable of association. The temperature of the onset of desulfonation of the cation exchanger in the Li, Na, and Cs forms is 190, 160, and 125°C, respectively.

Comparison of Figs. 2e–2g shows that decomposition of the sulfonic cation exchanger in the alkali and alkaline-earth metal forms occurs similary. The temperature of the onset of SO_2^+ evolution from the sulfonic cation exchanger in the Mg, Ca, and Ba forms is 250, 190, and 150°C, respectively.

As seen from Figs. 3a and 3b, the temperature of the onset of water evolution from the first hydration shell and formation of SO_2^+ ions varies in direct proportion with the ionic potential z/r^2 of the exchangeable cations. These results suggest that desulfonation of the fibrous sulfonic cation exchanger involves breakdown of the cation hydration shell.

Along with H_2O^+ and SO_2^+, heavier ions were detected, originating from thermal degradation of the polymeric matrix. We found that on heating of the sulfonic cation exchanger in the H form, organic fragments appear in the gas phase even at 90–120°C. The polymeric matrix of the cation exchanger in the alkali and alkaline-earth metal forms is more heat-resistant, and therefore the gaseous organic fragments are generated at 130–220°C. The most heat-resistant are the cation exchangers in the Mg and Ca forms.

We studied also thermal oxidative degradation of fibrous cation exchanger in various cationic forms in air by thermogravimetric analysis. The following concentrations of paramagnetic centers were determined (spin g^{-1}) for the respective forms: H 1995, Li 11, Na 21, Cs 8, Mg 10, Ca 14, and Ba 15.

These results show that the concentration of PCs generated by thermal oxidative degradation of the ion exchanger in the H form is higher by two order of magnitude than that for the cation exchanger in the alkali and alkaline-earth metal forms. It is possible that intermediate compounds of alkali and alkaline-earth metals formed in oxidative degradation of the ion exchanger inhibit the resin oxidation with atmospheric oxygen.

CONCLUSIONS

(1) The thermal stability of FIBAN K-1 fibrous sulfonic cation exchanger is sensitive to the nature of the exchangeable cation. Substitution of protons by alkali, and to a still greater extent, by alkaline-earth metal cations significantly increases the resistance of the cation exchanger to thermal and thermal oxidative degradation.

(2) Decomposition of sulfonic groups is associated with breakdown of the hydration shells of the cations. With increasing ionic potential of the exchangeable cation, the resistance of sulfonic group to thermal degradation increases.

REFERENCES

1. Cherches, B.Kh., Shunkevich, A.A., Belotserkovskaya, T.N., and Egiazarov, Yu.G., *Zh. Prikl. Khim.*, 1999, vol. 72, no. 4, pp. 623–627.
2. Petkevich, T.S., Berezovik, G.K., Sen'ko, T.L., and Egiazarov, Yu.G., *Vestsi Nats. Akad. Navuk Bel., Ser. Khim. Navuk*, 1999, no. 1, pp. 56–61.
3. Egiazarov, Yu.G., Soldatov, V.S., Radkevich, V.Z., *et al.*, Abstracts of Papers, *XVI Mendeleevskii S"ezd po obshchei i prikladnoi khimii, Sankt-Peterburg, 1998* (XVI Mendeleev Congr. on General and Applied Chemistry, St. Petersburg, 1998), Moscow, 1998, vol. 2, p. 292.
4. Yegiazarov, Yu.G., Radkevich, V.Z., Johann, J., *et al.*, *React. Funct. Polym.*, 2000, vol. 44, pp. 145–152.
5. Bogatyrev, V.L., Yur'ev, G.S., and Yakhin, V.S., *Rentgenografiya ionitov* (X-ray Diffractometry of Ion Exchangers), Novosibirsk: Nauka, 1982.
6. Gantman, A.I., *Zh. Fiz. Khim.*, 1986, vol. 60, no. 2, pp. 454–460.
7. Tulupov, P.E. and Gantman, A.I., *Zh. Fiz. Khim.*, 1986, vol. 60, no. 6, pp. 1404–1408.
8. Karpov, O.N., Tulupov, P.E., and Volkov, V.I., *Zh. Fiz. Khim.*, 1971, vol. 45, no. 7, pp. 1750–1763.
9. Uglyanskaya, V.A., Zav'yalova, T.A., Romanenko, E.F., *et al.*, *Zh. Fiz. Khim.*, 1981, vol. 35, no. 11, pp. 2868–2871.
10. Kurenkov, V.F. and Safin, A.G., *Zh. Prikl. Khim.*, 1998, vol. 71, no. 11, pp. 1927–1929.
11. Gal', A.E., Perepelkin, K.E., Pozdnyakov, O.F., *et al.*, *Khim. Volokna*, 1985, no. 4, pp. 14–17.
12. Kalashnik, A.T., Efremov, V.Ya., and Glazunov, V.B., *Khim. Volokna*, 1999, no. 1, pp. 50–51.
13. Soldatov, V.S., Pokrovskaya, A.I., and Martsinkevich, R.V., *Zh. Prikl. Khim.*, 1984, vol. 57, no. 9, pp. 2030–2034.
14. Helfferich, F., *Ionenaustauscher*, Weinheim: Chemie, 1959, vol. 1.
15. Selemenev, V.F., Kotova, D.L., Korenman, N.Ya., and Oros, G.Yu., *Zh. Fiz. Khim.*, 1991, vol. 65, no. 9, pp. 2579–2582.
16. Zundel, G., *Hydration and Intermolecular Interaction. Infrared Investigations with Polyelectrolyte Membranes*, New York: Academic, 1969.
17. Gates, B.C., Wisnouskas, J.S., and Heath, H.W., *J. Catal.*, 1972, vol. 24, p. 320.
18. Polyanskii, N.G., Tulupov, P.E., Sadovskaya, G.K., and Slovokhotov, N.A., *Zh. Prikl. Khim.*, 1965, vol. 38, no. 4, pp. 910–918.
19. Saldadze, K.M., Polyanskii, N.G., and Pashkov, A.B., *Khromatografiya, ee teoriya i primenenie* (Chromatography. Theory and Application), Moscow: Akad. Nauk SSSR, 1960, pp. 77–82.
20. Tulupov, P.E., *Stoikost' ionoobmennykh materialov* (Stability of Ion-Exchange Materials), Moscow: Khimiya, 1984.
21. Babkin, I.Yu., Gordeev, Yu.M., Krasnogorov, A.I., *et al.*, *Kolloidn. Zh.*, 1972, no. 5, pp. 659–664.

Russian Journal of Applied Chemistry, Vol. 75, No. 1, 2002, pp. 39–46. Translated from Zhurnal Prikladnoi Khimii, Vol. 75, No. 1, 2002, pp. 39–46.
Original Russian Text Copyright © 2002 by Vitenberg, Efremova, Kotov.

SORPTION AND ION-EXCHANGE PROCESSES

Methods for Preparation of Stable Gas–Vapor Mixtures with Fixed Concentration of Volatile Components on the Basis of Buffer Effect of Heterogeneous Systems

A. G. Vitenberg, O. V. Efremova, and G. N. Kotov

St. Petersburg State University, St. Petersburg, Russia
Mendeleev Russian Research Institute of Metrology, State Unitary Enterprise, St. Petersburg, Russia

Received April 5, 2001

Abstract—Theoretical concepts of multiple gas extraction are checked experimentally. The possibility is studied of preparing stable gas–vapor mixtures with fixed concentrations of styrene, acrolein, and other volatile organic compounds.

The measurement assurance demand [1] and rapidly growing topicality of determining traces of toxic compounds in the environment, medico-biological objects, food, agricultural, and industrial products necessitate unification and metrological control of trace analyses. Among the most important measures directed at increasing quality of gas analysis is perfection of the existing methods and development of new advanced methods for preparation of reference vapor mixtures with precisely fixed microconcentrations of components. The methods now employed in analytical practice do not solve to full measure the problem of preparing reference vapor mixtures containing concentrations of volatile components at a level of milligram per liter and lower [2]. The major cause is that such mixtures appear to be unstable as a result of loss through sorption and chemical interactions. Furthermore, reliable methods of preparing reference vapor mixtures containing unstable and reactive compounds are practically lacking at all.

Dynamic and static methods differ in the vapor mixture preparation technique. Dynamic methods produce gas streams used immediately. Although these methods are time-consuming and require sophisticated instrumentation, they are more frequently used as compared to static methods, which, even being simpler, appear to be hardly suitable for preparing stable gaseous mixtures with low component concentrations, based on homogeneous systems.

The levels of theoretical and technical development of these methods differ considerably [2], the less known and frequently employed being those based on phase equilibria [3–6]. However, it is such methods utilizing the headspace analysis (HSA) principles [7–9] that appear to be the most effective in many cases. In principle, is appropriate to use the equilibrium between the gas and condensed phases in all variations of HSA techniques, including static and dynamic modes with constant or regularly varying component concentration in a gas flow.

The idea of using the partition law in the liquid–vapor systems for preparing gas mixtures with fixed concentrations of volatiles dates as far back as the beginning of the 1960s. In the first publication on this problem a static method for calibration of an Ar ionization detector with aqueous acetone and ethanol was reported [10]. Nearly at the same time dynamic variations of HSA, continuous gas extraction of volatile hydrocarbons from squalane solutions with a nitrogen gas flow, was recommended for calibration of gas chromatographic detectors over a wide concentration range [11–13].

However, the lack of precise data on the partition coefficients in the system liquid–gas limited the use of this promising method. Later publications on the dynamic headspace method of preparing standard gas mixtures dealt with the problem of obtaining mixtures of constant compositions only [14–18]. The gas–liquid equilibrium under static conditions also was employed on a very limited scale. The available information refers to calibration of flame ionization detectors with mercaptans [19] and of flame photometric detectors with sulfurous compounds [20].

Wider application of the static method has been limited by the lack of sufficiently simple and precise techniques of measuring the partition coefficients needed for estimating the equilibrium vapor composi-

1070-4272/02/7501-0039$27.00 © 2002 MAIK "Nauka/Interperiodica"

tion. The optimum conditions for the use of heterogeneous systems as concentration standards likewise remained obscure.

The above-indicated and other problems of application of HSA principles to gas analysis are considered in [3–5]. There was introduced the concept of buffer effect of heterogeneous systems as well as parameters for its quantitative characterization. In these works were eliminated the divergences found in the literature on the theory of gas extraction. Finally, in these works methods for preparing gas mixtures with constant or regularly changing in time microcomponent concentrations were proposed, not requiring *a priori* knowledge of the partition coefficients.

The distinguished features of this approach are as follows. Gas mixtures can be prepared over wide ranges of micro- and ultramicroconcentrations of volatile compounds not only by dynamic, but also by static methods; both static and dynamic methods can produce gas mixtures not only with constant concentration, but also with concentration regularly changing with time, which allows detector calibration with one sample over a range covering several orders of magnitude; in principle, new solutions can be obtained on the basis of discrete and multiple gas extraction and also with systems in which the phase equilibrium liquid–vapor is combined with chemical (acid–base or complexation) equilibria in the solution. Even having certain advantages, allowing elimination of a series of certain limitations characteristic of the existing, among them official methods, such methods are not practically employed in analytical work. The major cause is that no simple technique is developed that would demonstrate indisputable advantages over the existing methods not only in the accuracy, but also in the analysis time, labor-intensiveness, and cost.

Therefore, the main goal of the work was to experimentally confirm the possibility of using HSA principles for preparation of gas mixtures with constant microconcentrations of volatile components by the dynamic method. An integral part of the work was also development of simple engineering solutions best suited for practical realization in research and plant laboratories. Of particular interest was preparation of mixtures containing vapors of unstable compounds.

THEORY

Buffer Effect of Heterogeneous Systems

By analogy with the well-known concept of the buffer capacity of solutions [21], we introduced the concept of the buffer effect of heterogeneous systems manifested in the resistance of one (gas) phase to changing component concentration due to its equilibrium with the other (condensed) phase. If, as a result of sorption or interaction with parts of the equipment or with compounds sorbed on its walls, an amount of a microcomponent q is absorbed, then, according to the material balance equation, the decrease in its concentration in the isolated gas phase $\Delta c'_G$ is written as

$$\Delta c'_G = q/V_G. \quad (1)$$

where V_G is the gas volume.

If the gas (V_G) and liquid volumes (V_L) are in equilibrium, the same loss in the amount of the component in the gas phase will result in a smaller change in its concentration in this phase, which is given by Eq. (2).

$$\Delta c_G = \frac{q}{KV_L + V'_G}, \quad (2)$$

where K is the partition coefficient expressed as a ratio of the equilibrium concentrations of the volatile component in liquid (c_L) and gas phases (c_G):

$$K = c_L/c_G. \quad (3)$$

As a measure of the buffer effect of the heterogeneous system can serve the relative concentration difference which may be expressed via K and the phase volume ratio $r = V_G/V_L$ by Eq. (4)

$$\frac{\Delta c'_G - \Delta c_G}{\Delta c'_G} = \frac{K}{K + r} = B, \quad (4)$$

where B is the buffering factor numerically equal to the fraction of the component in the condensed phase.

By definition, B can change from zero to unity. At $B \to 0$ the buffer effect in the system is practically lacking because of a nearly zero partition coefficient or liquid phase volume. At another limit ($B \to 1$) the buffer effect is the maximal, i.e., the preset component concentration is stable ($\Delta c_G \sim 0$) even at large loss of the component in the gas phase. Therefore, the composition of the gas mixture in equilibrium with a sufficiently large volume of the solution containing the given volatile component characterized by high K, in principle, may be stabilized arbitrarily exactly.

Backgrounds of Dynamic Headspace Analysis

Single-stage continuous gas extraction. This dynamic procedure of standard mixture preparation is

based on continuous gas extraction (CGE) realized by bubbling of pure gas through a fixed volume V_L of a liquid contained in a vessel with a gas volume V_G above it. Regularly changing concentration of a volatile component in the gas flow at the outlet was treated by several authors [7–9], and considerably different final expressions were obtained. When analyzing the CGE theory, we demonstrated [22] that it is preferable to avoid considerable "dead" gas volumes above the solution and to perform extraction in vessels with negligibly small V_G. In this case a rather simple approximation holds true at a sufficient accuracy:

$$c_G = (c_L^0/K)\exp(-V_g/KV_L) = (c_L^0/K)\exp(-X), \quad (5)$$

where c_L^0 is the fixed initial concentration of the volatile component in the liquid phase, V_g is the volume of the gaseous extractant passed through, and X is the extraction coefficient expressed as

$$X = \frac{V_g V_L^{-1}}{K}. \quad (6)$$

The applicability of Eq. (5), i.e., the maximal dead volume of the gas in a vessel for CGE which can be neglected in calculations, is controlled by the maximal permissible error of setting the volatile component concentration in the gas flow δ (fraction), partition coefficient, and the solution volume:

$$V_G \le \delta K V_L. \quad (7)$$

Multiple continuous gas extraction involves extraction of volatile compounds with an extractant gas flow successively from several vessels with the initial liquid mixture. This procedure allows an abrupt increase in the CGE efficiency, particularly in the systems with insufficient buffer effect, when B is much below unity.

The theory of multiple CGE was considered in [23, 24]. It was demonstrated that if the solution volume V_L with the initial concentration of the volatile component c_L^0 is divided into N equal portions, each portion is placed in a separate vessel, and a gas flow of a volume V_g is passed successively through i vessels with assurance of the equilibrium condition of CGE or the constancy of K, then the volatile component concentration in the gas phase at the outlet from the Nth vessel c_G^N can be written as

$$c_G^N = \frac{c_L}{K}\sum_{i=1}^{N}\frac{X^{i-1}}{(i-1)!}\exp(-X). \quad (8)$$

Finally, the relationships derived for single-stage and multiple CGE techniques allow estimation of the stabilization effect of the condensed phase on the volatile component concentration in the gas flow, depending on the characteristics of the heterogeneous system and its buffering action.

EXPERIMENTAL

Measurements were carried out on a Tsvet-500 chromatograph with a flame ionization detector interfaced with a Multikhrom v. 1.39 data processing system. A mixture of aromatic hydrocarbons (benzene, *p*-xylene, and styrene) and acrolein was analyzed with a 200 × 0.3 cm steel column packed with Chromaton N-AW-DMWS (grain size 0.250–0.315 mm) containing 5% Carbowax 20 M. Gas mixtures containing organic compounds at concentrations below 10 mg m^{-3} were analyzed on a 50 m × 0.32 mm quartz capillary column coated with OV-101 liquid phase (film thickness 1 μm).

Chromatographic conditions were as follows. The packed column: column temperature 90°C, carrier gas (He) flow rate 30 ml min^{-1}; gas–vapor mixtures were injected into the column using a six-way on–off gas valve (Valco Model W) thermostated at 150°C. The capillary column: column temperature 120°C, carrier gas (nitrogen) flow rate 5.5 ml min^{-1}; gas–vapor mixtures with an aromatic hydrocarbon concentration below 1 mg m^{-3} were injected with preliminary cryofocusing of the components to be determined in the initial section of the column at the liquid nitrogen temperature.

In the work we used benzene and *p*-xylene (chemically pure grade) and styrene and acrolein (chemically pure grade) stabilized with hydroquinone. As practically nonvolatile solvents for aromatic hydrocarbons we used transformer oil [GOST (State Standard) 10121–76], VM-1 vacuum oil (GOST 5.671–70) and for acrolein, dibutyl phthalate (extra grade). The solvents were purified prior to use to remove volatile impurities by bubbling an inert gas (continuous gas extraction) at 70°C for 24 h (gas flow rate 50 ml min^{-1}). The quality of the solvents was controlled by GC. For all the solvents used the noise level was below 50 μV (charge amplifier scale 2×10^{-12} A).

The procedure for preparing gas–vapor mixture by dynamic single-stage gas extraction was as follows. An inert gas (nitrogen or helium) flow was passed through a thermostated saturator (220-ml Drechsel bottle equipped with a glass filter to obtain a finely dispersed jet) containing 200 ml of the liquid phase

Table 1. Partition coefficients in systems low-volatile solvent–helium at 25°C

Component	Solvent	K*
Benzene	Transformer oil	710
Benzene	Vacuum oil	490
p-Xylene	Transformer oil	7660
Styrene	″	9470
Acrolein	Dibutyl phthalate	320

* Determined to within 5%.

at 25 ± 0.1°C. The gas flow rate (50–150 ml min^{-1}) was set and maintained constant to within 1% with a BPG-167 standard gas flow controller of the chromatograph and measured with an IRG-100 digital gas flow meter. The gas volume passed through was estimated from its flow rate and the extraction time (in the case of constant flow rate) or measured by an electromechanical counter (at variable gas flow rate). The multiple gas extraction was realized using series-connected 30-ml glass vials and a bubbler with a tip drawn into a capillary.

Let us consider the potentialities of the method and the techniques developed for static and dynamic headspace analysis with examples of preparation of gas–vapor flows with constant concentrations of quite reactive and unstable components. In the single-stage extraction procedure, as such components we selected aromatic hydrocarbons (benzene, *p*-xylene, and styrene); and in the multiple extraction, acrolein. Selection of these compounds, first of all styrene and acrolein, which are very reactive, was dictated also by the topicality of the problem of developing sufficiently simple techniques for preparing stable gas–vapor flows with constant microconcentrations of labile compounds. Such systems are needed for calibration and check resting of gas analyzers and also for quality assurance testing of techniques for determination of trace amounts of volatile compounds in gaseous media.

The best suited low-volatile solvent for continuous gas extraction of the indicated aromatic hydrocarbons (with respect to physicochemical properties, possibility of being purified to remove interfering impurities, availability, and cost) appeared to be transformer and vacuum oils, and for acrolein, dibutyl phthalate.

Single-stage procedure of continuous gas extraction. To prepare a gas–vapor flow with a fixed concentrations of volatile compounds by the dynamic HSA technique, it is necessary to preset the corresponding concentration of the compound in the liquid phase, which, in turn, requires knowledge on the partition coefficient K.

The partition coefficients of the above-indicated aromatic hydrocarbons in the system transformer oil–helium were determined by comparison of the results of GC determination of the volatile component concentrations c_G^* and c_G in the gas flows obtained with a Mikrogaz standard system and by continuous gas extraction from a solution with a precisely set concentration of the hydrocarbon to be determined c_L, respectively. The partition coefficients were estimated by Eq. (9) with allowance for the chromatographic peak areas of the aromatic hydrocarbons in the gas flow from the Mikrogaz system (A_G^*) and in that obtained by CGE from the solution (A_G):

$$K = \frac{c_L}{c_G}\frac{A_G^*}{c_G}. \quad (9)$$

The partition coefficients at 25°C of the investigated hydrocarbons are given in Table 1. The error of determination was estimated as a sum of the relative errors of presetting c_G^* and c_G and of measuring A_G^* and A_G to be no more than 5–7%.

The features of continuous gas extraction along with experimental data obtained on the partition coefficients allows optimization of the preparation procedure of gas–vapor mixtures with constant concentrations of volatile components, as well as estimation of the major parameters of the systems used. The concentration in the gas flow c_G at a given temperature is estimated from the base relationship of the partition law (3) with known K and fixed c_L. The maximal volume of the gas–vapor mixture V_g^{lim} which can be obtained with constant volatile component concentration is controlled primarily by the buffer capacity of the system and limited by the admissible deviation of the actual concentration c_G from the preset value. This deviation, in its turn, is controlled by the difference from zero of the extraction factor X. The vapor flow volume in which the volatile component concentration differs from the preset value by no more than the admissible value δ can be estimated by Eq. (10):

$$V_g^{lim} = KV_L \ln(1 + \delta). \quad (10)$$

Therefore, setting the tolerable decrease in the component concentration in the gas flow δ (fraction) and knowing V_L and K, one may always estimate the volume of the gas that can be passed through at practically constant concentration. For example, if 1 l of a solution of a volatile compound with $K = 5 \times 10^3$

and c_L = 50 mg l^{-1} (~0.005%) in a practically nonvolatile solvent is used for preparation of a gas–vapor mixture, with presetting c_G to within δ = 2% one may obtain 99 l of a gas–vapor mixture with a concentration of 10 mg m^{-3}. With increasing δ to 10%, all other parameters being unchanged, the volume will increase to 476 l. The estimated maximal volume of gas flow with practically constant benzene concentration is given in Table 2. The values estimated by Eq. (10) for various δ are well consistent with those obtained experimentally.

The measured current concentrations of benzene, *p*-xylene, and styrene in the gas flow in the course of their continuous gas extraction from 200 ml of the solution in transformer oil at the initial concentration c_L^0 of 96.7, 889.7, and 1864 mg l^{-1}, respectively, are in a good agreement with the theoretical results (Fig. 1). The differences between the c_G values estimated by Eq. (5) and those obtained experimentally were within 10%. Evidently, the major contribution to this difference is due to the errors of GC determination of such low concentrations of the organic compounds in the gas–vapor mixtures.

The stability of the volatile component concentration at the outlet from the vessel with the stabilizing solution depends on the quality of the solvent, degree of linearity of the partition isotherm, and *K* of volatile components. The maximal concentrations of volatile compounds in the gas flow are limited primarily by their saturated vapor pressures, being 20, 50, and 320 g m^{-3} for styrene, *p*-xylene, and benzene, respectively. However, the maximal concentrations corresponding to the ends of the linear section of the partition isotherms, i.e., of the region of infinitely dilute solutions characterized by constant *K*, are lower by approximately an order of magnitude. When dealing with such concentrations one should take into account that *K* may change on passing to the nonlinear section of the partition isotherm of volatile compounds between the stabilizing solution and the gas phase.

The lower limit of the preset component concentration is controlled by the desired signal/noise ratio, i.e., by the impurity level in the low-volatile solvent. At a signal/noise ratio of 10 : 1 the solvents used in this work allowed preparation of gas–vapor mixtures with the minimal concentration of about 5 and 1 mg m^{-3} for transformer and vacuum oils, respectively (the quality of vacuum oil was higher). Further decrease in the volatile compound concentration can be realized by either increasing quality of the low-volatile solvent or diluting the gas flow at the outlet from the vessel with the stabilizing solution.

Table 2. Maximal volume of gas flow with constant target component concentration as a function of δ*

δ, %	V_g^{lim}, l		
	benzene	*p*-xylene	styrene
1	1.5	15	19
3	4	47	58
5	7	72	97
10	15	160	200

* Estimated by Eq. (10) at V_L = 200 ml with *K* taken from Table 1.

The temperature of CGS and its stability in the vessel with the stabilizing solution throughout the process strongly affect the concentration of interested volatile components in the gas flow. For the most of organic compounds changing temperature by 1°C results in change in *K* and therefore c_G within 3–8% [7]. Therefore, the lesser the accepted error in setting c_G, the more stable should be the temperature throughout continuous gas extraction. The experimental temperature dependence of *K*, obtained for the infinite dilution region of the partition isotherms of *p*-xylene and styrene ($c_L \le 0.03\%$) in the system transformer oil–nitrogen at 15–30°C, demonstrates practically ideal linearity when plotted as $\ln K$ vs. T^{-1} (Fig. 2), allowing estimation of the required degree of temperature stabilization.

For example, in the cases of *p*-xylene and styrene, when $\delta \le 0.02$ is fixed, the temperature should be stable to within 0.4°C. To attain a reproducibility of the analytical signal within 1%, the temperature stability should be within 0.2°C, and with changing temperature of the stabilizing solution by 1°C the analytical signal variation should be within 5%. The estab-

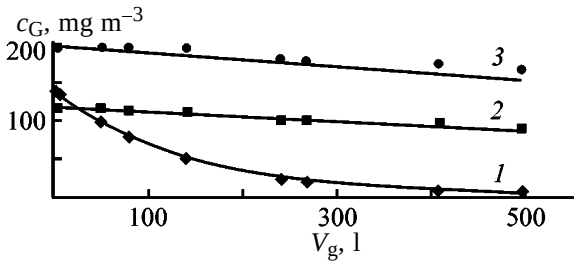

Fig. 1. Theoretical and experimental dependences of the aromatic hydrocarbon concentration in the mixture on the gas volume passed through V_g. (c_G) Interested component concentration in the vapor phase: (*1*) benzene, (*2*) *p*-xylene, and (*3*) styrene. Solid lines show the theoretical dependences, and points, experimental data; the same for Fig. 4.

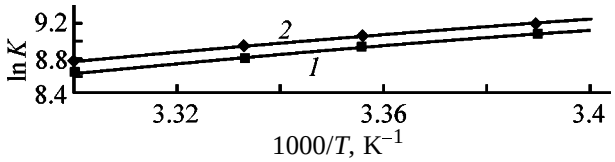

Fig. 2. Partition coefficient K as a function of the temperature T: (*1*) *p*-xylene and (*2*) styrene.

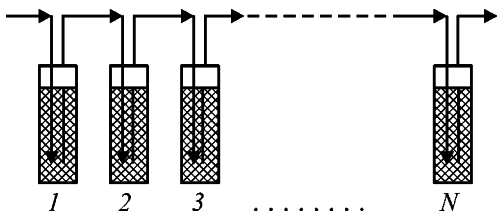

Fig. 3. Schematic flowsheet of multiple continuous gas extraction. (*N*) Number of steps.

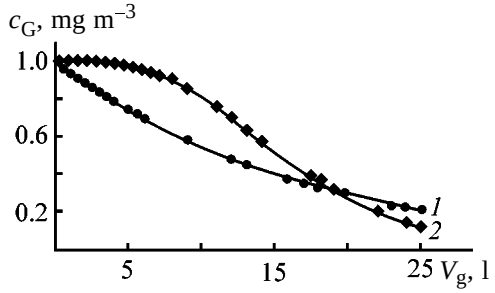

Fig. 4. Acrolein concentration in the gas flow at the outlet from the last vial c_G as a function of the volume of the gas extractant V_G for (*1*) single-step and (*2*) five-step continuous gas extraction at the same total volume of the liquid phase.

lishment of equilibrium, which is the necessary condition of successful use of the CGE method, was controlled by measuring the volatile component concentrations (chromatographic peak areas) at various gas flow rates. It was demonstrated that with the quite viscous solvents used, solution column of no less than 10 cm, and finely dispersed jet of the gas extractant (0.3-mm orifices) this condition is realized at the flow rate from 10 to 400 ml min^{-1}.

The stability in time of solutions of the volatile compounds in the low-volatile solvents, which were used for preparing gas–vapor flows with preset *p*-xylene and styrene concentrations of about 30–35 mg m^{-3}, was monitored for a year by measuring c_G of each component with allowance for possible change in the sensitivity of the detectors. The correction factor was determined as the peak area ratio of the interested component and an external reference (propane). The results showed that the differences from the preset styrene and *p*-xylene concentrations in the gas flow at the outlet from the vessel were within 3%.

Multistep procedure of continuous gas extraction. The expedience of using this somewhat more complicated procedure of gas extraction is caused primarily by the possibility of considerable increase in the volume of the gas flow with practically constant concentration of volatile components, all other conditions being equal. The schematic flowsheet of multiple continuous gas extraction is presented in Fig. 3.

The major trends of multiple CGE were experimentally checked by studying the distribution of acrolein between dibutyl phthalate and nitrogen. The partition coefficient of acrolein in this system was measured previously by the CGE method [7] to be 320 (Table 1). It is easy to demonstrate that in the single-stage procedure, 600 ml of the solution is needed to obtain 10 l of the gas flow with a stable concentration of acrolein (δ = ±5%, 25°C). In the five-step procedure this may be realized with only 80 ml of the solution.

The dependence of the acrolein vapor concentration in the gas flow on the gas extractant volume passed through 50 ml of an acrolein solution in dibutyl phthalate (c_L = 190 mg l^{-1}) is presented in Fig. 4, demonstrating a satisfactory agreement of the theoretical and experimental data and an abrupt increase (by a factor of about 7) in the volume of the gas flow with practically constant acrolein concentration V_g^{lim} on passing from a single-step to a five-step extractor. The process was theoretically treated using Eq. (8) at K = 320.

Such a considerable increase in V_g^{lim} in multiple CGE is provided by progressive saturation of the gas-extractant in the first extraction steps. In this case the volatile component concentration in the solution in the last steps remains practically unchanged. As the solution in the initial steps is exhausted, the next steps start to take the stabilizing function, which is clearly demonstrated by the dynamics of variation of the acrolein concentration in the gas flow at the outlet of each cell, estimated by Eq. (8) and given in Fig. 5.

Similar effect providing considerable increase in V_g^{lim} in multistep extractors as compared to single-step devices was experimentally demonstrated also for the case of benzene distribution between vacuum oil and nitrogen. Passing from a single-step extractor to a three-step one at a fixed volume of the liquid phase V_L increases V_g^{lim} by a factor of about 5, and in the case of a ten-step extractor, by a factor of almost 10. Further increase in N appeared to be inexpedient, as

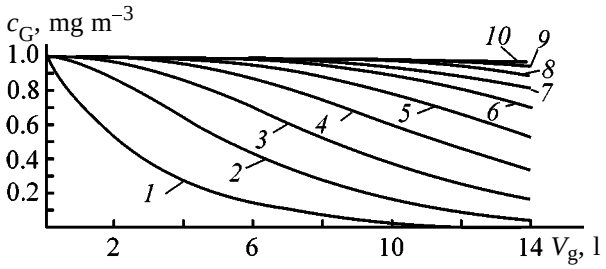

Fig. 5. Acrolein concentration in the gas flow at the outlet from each of ten cells c_G as a function of the volume of the gas-extractant V_g. The figures at the curves correspond to the cell number.

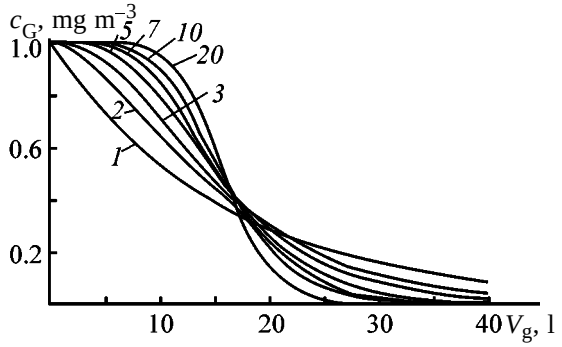

Fig. 6. Benzene concentration in the gas flow at the outlet from the last cell c_G as a function of the volume of the gas-extractant V_g at the same total volume of the liquid phase (0.05 l) and various cell numbers (from 1 to 20). The figures at the curves correspond to the total number of the cells.

only slightly increasing V_g^{lim}. Figure 6 shows the theoretical data on benzene distribution between vacuum oil and nitrogen (V_L = 50 ml, K = 490) for N 1–20. The optimal number of steps with the same solution volume can be determined from the dependence of V_g^{lim} on N.

To conclude, the potentialities of the method for preparing gas–vapor flows with a preset microconcentration of volatile components are not restricted to only the compounds studied in this work (aromatic hydrocarbons and acrolein). Basing on the headspace analysis principles and using heterogeneous systems having sufficient buffer capacity ($B \le 0.5$), it is possible to prepare stable gas–vapor mixtures with volatile component concentration varying over the range covering up to seven orders of magnitude (from several μg m^{-3} to tens g m^{-3}). The spectrum of compounds suitable in this method is limited by their saturated vapor pressure, which should fall in the range 10^{-2}–10^2 mm Hg at normal conditions.

CONCLUSIONS

(1) Stable gas–vapor mixtures with a fixed volatile compound concentration ranging from several μg m^{-3} to tens g m^{-3} can be prepared by dynamic headspace analysis technique.

(2) Appropriate liquid–gas systems are proposed for preparing stable gas–vapor mixtures of such reactive compounds as styrene and acrolein.

(3) The theoretically derived features of multiple continuous gas extraction are checked experimentally. Use of the multistep procedure allows considerable improvement of the performance of continuous gas extraction, particularly, increase in the volume of the gas flow with practically constant concentration of a target compound.

ACKNOWLEDGMENTS

The authors are grateful to L.A. Konopel'ko (Mendeleev Russian Research Institute of Metrology, State Unitary Enterprise) for support of this work.

REFERENCES

1. *Rekomendatsii po mezhgosudarstvennoi standartizatsii. Metrologiya. Osnovnye terminy i opredeleniya* (Recommendations on Intergovernmental Standardization. Metrology. Basic Terms and Definitions), RMG 29–99.
2. McKinley, J. and Majors, R.E., *LC–GC Eur.*, 2000, December, pp. 892–901.
3. Vitenberg, A.G. and Kostkina, M.I., *Zh. Anal. Khim.*, 1980, vol. 35, no. 3, pp. 539–546.
4. Vitenberg, A.G., Kostkina, M.I., and Ioffe, B.V., *Anal. Chem.*, 1984, vol. 56, no. 13, pp. 2496–2500.
5. Vitenberg, A.G., Kostkina, M.I., and Ioffe, B.V., *Anal. Chem.*, 1984, vol. 56, no. 13, pp. 2500–2503.
6. Vitenberg, A.G., in *Pamyati professora Sankt-Peterburgskogo universiteta B.V. Ioffe* (In Memory of Prof. B.V. Ioffe, St. Petersburg State University), Nauchno-Issled. Inst. Khim., Sankt-Peterb. Gos. Univ., 1998, pp. 45–51.
7. Vitenberg, A.G. and Ioffe, B.V., *Gazovaya ekstraktsiya v khromatograficheskom analize* (Headspace Analysis in Gas Chromatography), Leningrad: Khimiya, 1982.
8. Ioffe, B.V. and Vitenberg, A.G., *Headspace Analysis and Related Methods in Gas Chromatography*, New York: Wiley, 1984.
9. Kolb, B. and Ettre, L.S., *Static Headspace Gas Chromatography*, New York: Wiley, 1997.

10. Burnett, M.G. and Swoboda, P.A.T., *Anal. Chem.*, 1962, vol. 34, no. 9, pp. 1162–1163.
11. Fowlis, I.A. and Scott, R.P.W., *J. Chromatogr.*, 1963, vol. 11, no. 1, pp. 1–10.
12. Fowlis, I.A., Maggs, R.S., and Scott, R.P.W., *J. Chromatogr.*, 1964, vol. 15, no. 2, pp. 471–481.
13. Burnett, M.G., *Anal. Chem.*, 1963, vol. 35, no. 11, pp. 1567–1570.
14. Scarano, E., Forina, M., and Gay, G., *Anal. Chem.*, 1971, vol. 43, no. 10, pp. 1310–1312.
15. Scarano, E., Forina, M., and Calcagno, C., *Anal. Chem.*, 1973, vol. 45, no. 3, pp. 557–562.
16. Forina, M., *Ann. Chim.*, 1975, vol. 65, no. 4, pp. 491–508.
17. Vejrosta, J. and Novak, J., *J. Chromatogr.*, 1979, vol. 175, no. 1, pp. 261–267.
18. Berezkin, V.G., Budantseva, M.N., Bannikov, V.N., and Mal'tsev, V.V., Abstracts of Papers, *Chetvertaya Vsesoyuznaya konferentsiya po analiticheskoi khimii organicheskikh soedinenii* (Fourth All-Union Conf. on Analytical Chemistry of Organic Compounds), Moscow, January 7–8, 1980, p. 56.
19. Field, T.G. and Gulbert, J.B., *Anal. Chem.*, 1966, vol. 38, no. 4, pp. 628–629.
20. Ronkainen, P., Denslow, J., and Leppanen, O., *J. Chromatogr. Sci.*, 1973, vol. 11, no. 3, pp. 384–390.
21. Ioffe, B.V. and Reznik, T.L., *Zh. Anal. Khim.*, 1981, vol. 36, no. 10, pp. 2191–2198.
22. Vitenberg, A.G. and Kostkina, M.I., *Zh. Anal. Khim.*, 1979, vol. 34, no. 9, pp. 1800–1808.
23. Marinichev, A.N. and Vitenberg, A.G., *Zh. Prikl. Khim.*, 1990, vol. 63, no. 10, pp. 2385–2388.
24. Marinichev, A.N. and Vitenberg, A.G., *J. Chromatogr.*, 1992, vol. 600, no. 2, pp. 251–256.

Russian Journal of Applied Chemistry, Vol. 75, No. 1, 2002, pp. 47–49. Translated from Zhurnal Prikladnoi Khimii, Vol. 75, No. 1, 2002, pp. 47–49.
Original Russian Text Copyright © 2002 by Kaverin, Pisarevskii, Sapogova.

APPLIED ELECTROCHEMISTRY AND CORROSION PROTECTION OF METALS

Coulometric Generation of Molecular Iodine

A. V. Kaverin, A. M. Pisarevskii, and S. B. Sapogova

Research Institute of Chemistry, St. Petersburg State University, St. Petersburg, Russia

Received September 17, 2001

Abstract—Coulometric generation of molecular iodine at the Pt anode in acid 0.2 M KI solutions was investigated in a cell without diaphragm. The current efficiency by iodine was studied in a wide range of anode current densities (3–100 mA cm^{-2}).

Iodometric titration has gained such a strong position in quantitative chemical analysis that it is perceived as standard technique in comparison and certification of various analytical methods [1, 2]. In this connection, the iodometric equipment is being constantly improved and electrochemical methods (ammetric [3], potentiometric [4], and coulometric [5, 6] titration) have become customary, together with the classical titration.

It has been shown, on the basis of electrochemical studies of redox system iodine–iodide on a platinum electrode, that the components of this redox system are chemisorbed to modify the electrode surface [4, 7]. As a result, the exchange current in the system iodine–iodide decreases only 2–3-fold, whereas the exchange currents in a great number of redox systems decrease by 3 to 4 orders of magnitude [4]. Such a dramatic decrease in the rate of electrode processes in "competing" redox systems, including O_2/H_2O and H^+/H_2, leads to important practical results.

(1) It is possible to perform equilibrium redox measurements in solutions of the system iodine–iodide down to as low concentrations of molecular iodine as about 10^{-6} [8] or even 3×10^{-7} M [9], although measurements at these concentrations are markedly affected by the solution agitation mode and concentration of dissolved oxygen.

(2) Electrochemical oxidation of iodide ions to molecular iodine at the Pt anode occurs with 100% current efficiency.

(3) It is convenient to use a Pt electrode with point surface, at which only molecular hydrogen is evolved during electrolysis [10], and low rate of homogeneous reaction between H_2 and I_2 allows coulometric generation of iodine without separation of the cathode and anode spaces. The competing process of anodic oxidation of H_2 can be disregarded in the given case because of the low exchange current in the system H^+/H_2 at a modified platinum electrode [4].

An important issue in iodometric techniques relying upon coulometric generation of molecular iodine is the choice of the generation current. If relatively large amounts of iodine are to be obtained, it is advantageous to make the generation time shorter by raising the anode current density, with 100% current efficiency by iodine preserved. As a rule, the choice of the generation current is limited from theoretical considerations to the region of small deviations of the anode potential from the equilibrium value. Below are presented data on the generation currents used in a number of experimental studies:

KI, M	i, mA cm^{-2}	References
0.005	0.6	[11]
0.2	3–20	[8, 10]
0.1–1.0	16.7	[12]

It is seen that in [10, 12] anodic oxidation with 100% current efficiency was performed at relatively large overvoltages; however, in these cases too, as judged from the descriptions of the experiments, the limiting diffusion current was not reached. It is known that, in 1 M salt solutions that were not stirred intentionally, the limiting diffusion current is about 25 mA cm^{-2} [13]. Use of a magnetic stirrer does not specify the agitation mode strictly; however, the limiting diffusion current increases by an order of magnitude even under weak stirring [14]. Unfortunately, no data concerning the upper limit of 100% current efficiency ω in electrochemical production of iodine from KI solutions were reported in the papers cited.

The aim of this study was to analyze the region in which 100% current efficiency is preserved in a cell

1070-4272/02/7501-0047$27.00 © 2002 MAIK "Nauka/Interperiodica"

Results of titrimetric determinations

i, mA cm^{-2}	ω, %	S, %	n*	t, s
3.2	101.9	1.1	7	360–400
10.1	100.0	0.1	4	180
10.1**	99.9	1.4	11	250
21.2	99.4	1.5	10	120
20.0 [10]	100.4	0.8	4	100–800
31.4	99.6	0.5	8	120
29.9	98.9	0.7	5	400
41.4	100.1	0.3	8	68
42.0	98.4	2.6	22	120
51.6	97.2	4.6	15	120
61.6	100.3	2.8	6	30
60.5	100.1	1.6	10	45
61.6	96.9	1.0	7	70
61.6	84.6	2.1	7	120
71.6	100.7	1.2	7	35
79.6	101.3	0.8	8	30
92.7	98.6	1.0	7	25
101.6	100.3	2.8	6	20
100.7	62.3	1.2	6	100

* n is the number of runs.

** Solution composition (M): KI 0.2, H_2SO_4 0.0016, and KSCN 0.002.

without diaphragm in a wide range of anode current densities.

EXPERIMENTAL

As anode served smooth Pt electrode with electrode surface in the form of a plate ($S \approx 1$ cm^2), as cathode was used Pt electrode of the EPV-1 type ($S < 1$ mm^2). Between measurements the electrodes were kept in an acid solution of the system iodine–iodide. The current was set in electrolysis with a B5-50 dc power source and monitored with a V7-21 milliammeter with resolution down to 0.01 mA. During electrolysis, the KI solution was stirred with an MM-5 magnetic rabble (speed of rotation of about 500 rpm). The generated amount of iodine was titrated with 0.01 M sodium thiosulfate solution with a microburette with scale-division value of 0.02 ml. As indicator of the process completion was used starch solution.

The current efficiency ω by iodine was studied in acid 0.2 M solutions of potassium iodide, containing 0.0016 M of H_2SO_4. The results of titrimetric determination of iodine generated at a current density under study are presented in the table.

In discussing the presented results, mention should be made of the fact that a current efficiency by iodine, equal to 100% within the natural error of titrimetry (1%), is obtained at $i \le 30$ mA cm^{-2}, in full agreement with published data [8, 10–12]. At the same time, in experiments performed at generation currents exceeding 50 mA m^{-2}, it was found that the current efficiency by iodine approaches 100% with decreasing time of electrolysis. In the case of electrolysis durations of 20–30 s, the 100% current efficiency is preserved over nearly entire range of current densities studied; however, obviously understated values were observed with the time of electrolysis increasing to 100 s and longer, and even more so at 100 mA cm^{-2}. These observations could be explained after analysis of the state of the anode surface during electrolysis. The entire range of anode current densities studied can be divided into three parts.

(1) Range $i \le 30$ mA cm^{-2} (Fig. 1a). In this range, the whole amount of iodine generated on the electrode is instantaneously washed away into the solution. As expected, stable 100% current efficiencies were obtained in this set of experiments.

(2) Range $30 < i < 50$ mA cm^{-2} (Fig. 1b). In this range of currents the current efficiency by iodine is more strongly affected by hydrodynamic conditions. In this case, the generated iodine already has no time to diffuse entirely into the solution bulk, and the appearance of a thin layer of concentrated iodine solution was observed in the near-electrode space. Even minor changes in the solution flow rate lead either to electrode "baring" or to formation of a crust of crystalline iodine on the electrode surface. Actually, this range is intermediate between the first and third, and the current efficiency by iodine is unstable in this range and is accompanied by abrupt changes in anode potential during electrolysis.

(3) Range $i > 50$ mA cm^{-2}. At these currents the 100% efficiency can only be observed in the initial stage of electrolysis (20–30 s). Later on, the formation of a crust of deposited iodine is visually observed. Also, it is noticed that a parallel process of molecular oxygen evolution sets in on that part of the surface which is still free of undissolved iodine, and the potential shifts to anodic values.

CONCLUSION

The choice of the anode current for reliable generation of iodine with 100% current efficiency is governed by a number of factors: electrode geometry, position of the electrode surface with respect to the solution flow, stirring intensity, and KI concentration.

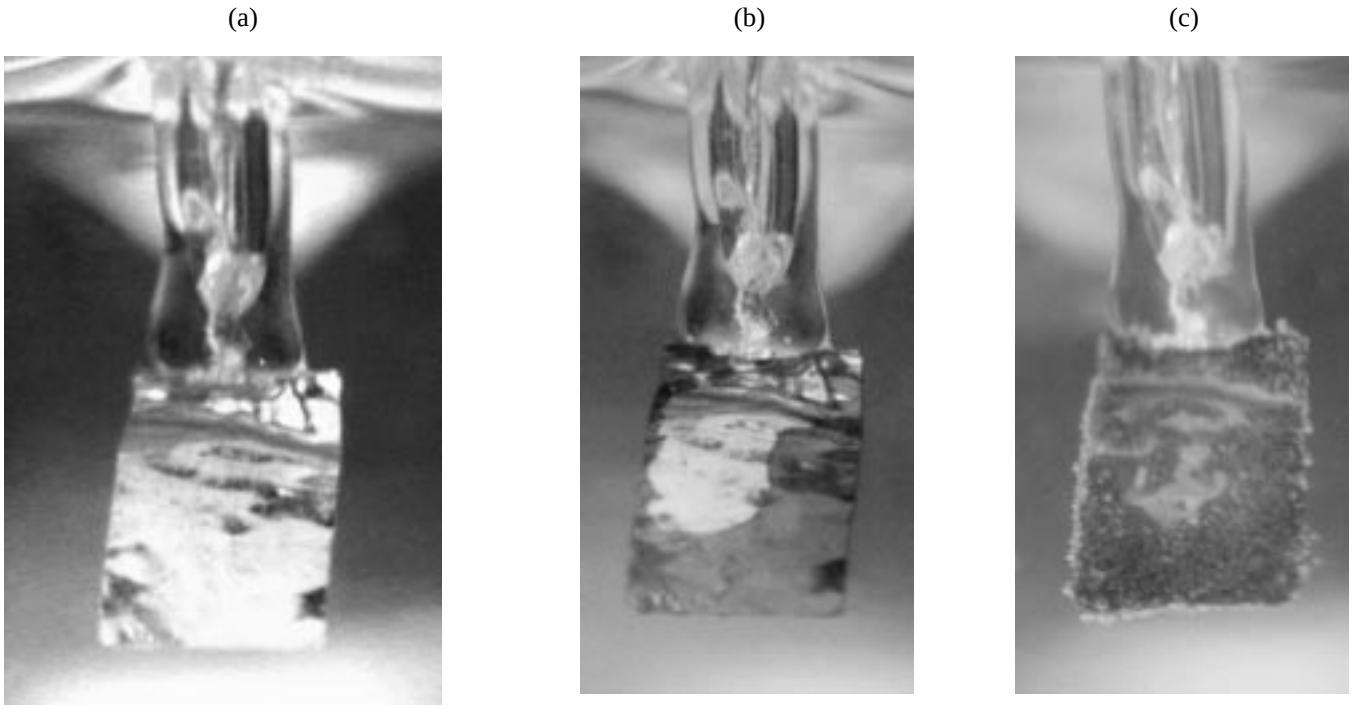

Fig. 1. State of the anode surface at (a) $i < 30$, (b) $30 < i < 50$, and (c) $i > 50$ mA cm^{-2}.

It was shown experimentally that a 100% current efficiency by iodine is preserved in 0.2 M KI solutions stirred with a magnetic rabble at current densities equal to, or less than 30 mA cm^{-2}.

ACKNOWLEDGMENTS

The study was supported financially by the Federal Target Program "Universities of Russia. Basic Research" (project no. 992663).

REFERENCES

1. Laitinen, G.A. and Harris, W.E., *Chemical Analysis*, New York: McGraw-Hill, 1975, 2nd ed.
2. *GSO* (State Reference Sample) *7104–94–7106–94: Composition of Aqueous Potassium Iodate Solutions* (kit no. 29k).
3. Songina, O.A. and Zakharov, V.A., *Amperometricheskoe titrovanie* (Ammetric Titration), Moscow: Khimiya, 1979.
4. Shul'ts, M.M., Pisarevskii, A.M., and Polozova, I.P., *Okislitel'nyi potentsial* (Oxidation Potential), Leningrad: Khimiya, 1984.
5. Lingane, J.J., *Electroanalytical Chemistry*, New York: Interscience, 1958.
6. Rowley, K. and Swift, E.H., *Anal. Chem.*, 1954, vol. 26, no. 2, pp. 373–375.
7. Zakharov, V.A. and Songina, O.A., *Zh. Fiz. Khim.*, 1962, vol. 36, no. 6, pp. 1226–1231.
8. Pisarevskii, A.M. and Kaverin, A.V., *Zh. Prikl. Khim.*, 1999, vol. 72, no. 10, pp. 1658–1662.
9. Rigdon, L.P., Moody, G.J., and Frazer, J.W., *Anal. Chem.*, 1978, vol. 50, no. 3, pp. 465–469.
10. Tur'yan, Ya.I., Pokhodzei, V.F., Markova, T.R., *et al.*, *Elektrokhimiya*, 1987, vol. 23, no. 3, pp. 423–424.
11. Pisarevskii, A.M., Serikov, Yu.A., Shigaeva, T.D., *et al.*, *Zh. Prikl. Khim.*, 1986, vol. 59, no. 8, pp. 1737–1743.
12. Van der Hulst, A.J., *Anal. Chem.*, 1969, vol. 41, no. 1, pp. 207–209.
13. Kravtsov, V.I., *Elektrodnye protsessy v rastvorakh kompleksov metallov* (Electrode Processes in Metal Complex Solutions), Leningrad: Leningr. Gos. Univ., 1969.
14. Bockris, J. and Reddy, A.K., *Modern Electrochemistry*, New York: Plenum, 1973, vol. 2.

Russian Journal of Applied Chemistry, Vol. 75, No. 1, 2002, pp. 50–53. Translated from Zhurnal Prikladnoi Khimii, Vol. 75, No. 1, 2002, pp. 50–53.
Original Russian Text Copyright © 2002 by Aliev, Vladimirova, Kharlamova, Malofeeva.

APPLIED ELECTROCHEMISTRY AND CORROSION PROTECTION OF METALS

Synthesis of Zinc and Nickel Carbonates by Anodic Dissolution of Metals in Electrolyte Solutions under Elevated Carbon Dioxide Pressure

Z. M. Aliev, M. V. Vladimirova, T. A. Kharlamova, and L. S. Malofeeva

Moscow State University of Food Industry, Moscow, Russia

Received April 25, 2001

Abstract— The process of single-stage electrochemical preparation of pure zinc and nickel carbonates in solutions saturated with carbon dioxide under elevated pressure was studied.

Special-purity zinc and nickel carbonates find use in medicine, semiconductor technology, and manufacture of various sorbents and catalysts. Purification of carbonates to remove impurities is a labor-consuming process, and, therefore, it is advisable to obtain pure products directly, by anodic dissolution of the corresponding metals.

Electrochemical methods for carbonate preparation have been described in the literature. For example, an electrochemical method for production of basic zinc carbonate is known [1], according to which zinc is anodically dissolved in an electrolyte containing 15–20 g l^{-1} of sodium hydroxide and 90–100 g l^{-1} of sodium nitrate. The process is carried out at a current density of 0.09–0.10 A cm^{-2}.

In order to obtain carbonates of various metals, the authors of [2] subjected a metal (Pb, Ni, Zn, etc.) to anodic dissolution in an ammonium carbonate solution at high current density with simultaneous continuous bubbling-through of ammonia and carbon dioxide. The method yields target products with high current efficiency.

An electrochemical method has been described for obtaining metal carbonates by anodic dissolution of the corresponding metal in an aqueous ammonium carbonate solution with bubbling of carbon dioxide through the aqueous solution at a current density of 0.10–0.15 A cm^{-2} and constant carbon dioxide pressure in the autoclave of 0.5–1.0 MPa [3].

The study [4] was also concerned with preparation of basic lead and copper carbonates in anodic dissolution of the corresponding metal in a diaphragm electrolyzer with the use of multicomponent electrolytes.

The common disadvantage of all the proposed methods consists in use of concentrated solutions of various electrolytes, from which it is difficult to isolate pure carbonates. In order to lower to the maximum possible extent the electrolyte concentration and obtain sufficiently pure zinc and nickel carbonates in a single stage, we studied the process of their electrochemical preparation in solutions saturated with carbon dioxide under elevated pressure.

EXPERIMENTAL

Measurements under elevated pressure were done in a specially designed autoclave made of a corrosion-resistant titanium alloy [5]. Valves for gas supply, pressure gage, and current leads for the electrodes were built in the autoclave cover.

The electrical conductivity of carbon dioxide saturated water and aqueous electrolyte solutions was determined using a versatile bridge with thermostating at a prescribed temperature. Potentiostatic measurements were carried out with a P-5827 M potentiostat. Zinc and nickel plates were used as working electrodes; platinum foil, as auxiliary electrode; and saturated silver chloride electrode, as reference.

The effect of carbon dioxide pressure on electrochemical synthesis of zinc and nickel carbonates was studied in distilled water and dilute aqueous solutions of potassium carbonate (0.01 M) and sodium chloride (0.05 M) in the same autoclave, with zinc and nickel of, respectively, TsV and N1 U brands of 99% purity used as anode materials. The current efficiencies (CE) by carbonates were determined gravimetrically after drying a deposit to constant weight.

1070-4272/02/7501-0050$27.00 © 2002 MAIK "Nauka/Interperiodica"

One of the main parameters of the economic feasibility of the proposed way to obtain pure carbonates is the electrical conductivity of solutions subjected to electrolysis. Calculations of the volume of carbon dioxide dissolved in water and its solubility in relation to temperature T and pressure P by means of Rolf–Stinhof and Sechenov formulas [6] show that the solubility of CO_2 in water and dilute NaCl and K_2CO_3 solutions increases approximately 10-fold in the pressure range 0.2–2.0 MPa.

Also, we studied the effect of CO_2 pressure on the electrical conductivity χ of water in the temperature interval 20–90°C (Fig. 1). At low pressures, its electrical conductivity grows somewhat with increasing CO_2 pressure, irrespective of water temperature. At CO_2 pressure exceeding 2.0 MPa, the situation changes significantly: the electrical conductivity grows more steeply, and the more so, the higher the water temperature. The conductivity grows particularly strongly with increasing pressure at a temperature close to the boiling point.

Analysis of the experimental dependence of the electrical conductivity on the CO_2 pressure at various temperatures yields the following relations:

$$1/\chi = -2.07\log P + 4.4,\ 40°C,$$

$$1/\chi = -2.30\log P + 4.7,\ 60°C,$$

$$1/\chi = -2.10\log P + 4.5,\ 70°C,$$

$$1/\chi = -2.34\log P + 4.8,\ 80°C,$$

$$1/\chi = -2.75\log P + 2.7,\ 90°C,$$

where χ is the electrical conductivity (Ω^{-1} cm^{-1}), and P is pressure (MPa).

The measurements demonstrated that it is advisable to carry out investigations in aqueous SO_2 solutions at elevated pressures and temperatures.

Polarization curves of anodic dissolution of zinc in an atmosphere of pure CO_2 were measured at pressures of 0.05 to 0.9 MPa (Fig. 2). At gas pressures of up to 0.2 MPa two regions are observed in which the anodic process is inhibited (Fig. 2, curve *1*). The onset potential of the first passivation region is approximately –0.64 V, and that of the second, –0.35 V. At gas pressure exceeding 0.4 MPa the polarization curves have no bends (Fig. 2, curve *2*) corresponding to a transition into the passive state, which may be due to a pronounced decrease in the solution pH, promoting intensive dissolution of zinc [7].

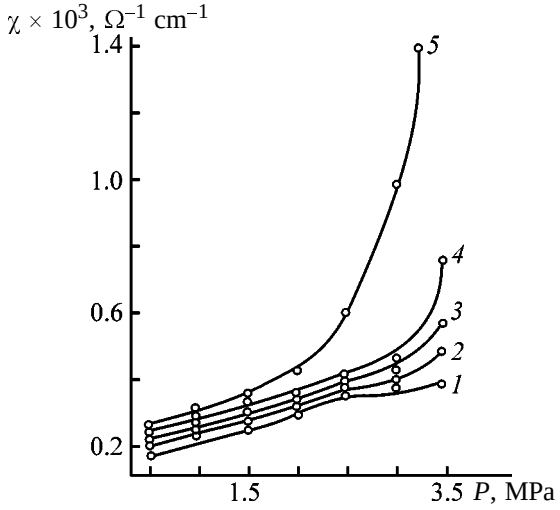

Fig. 1. Electrical conductivity χ of water vs. carbon dioxide pressure P at different temperatures. Temperature (°C): (*1*) 20, (*2*) 40, (*3*) 60, (*4*) 80, and (*5*) 90.

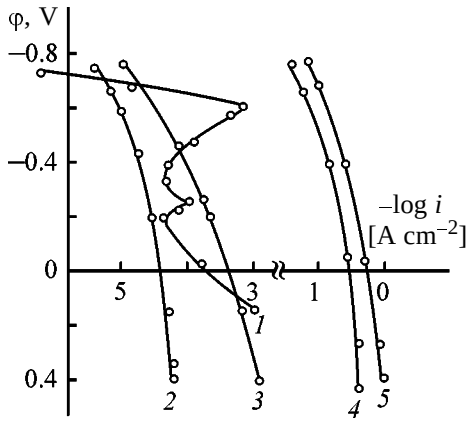

Fig. 2. Polarization curves for Zn electrode in water. (φ) Potential and (*i*) current density; the same for Figs. 3 and 4. CO_2 pressure (MPa): (*1*) 0.2, (*2, 4*) 0.4, and (*3, 5*) 0.9. (*4, 5*) NaCl concentration 0.05 M.

The time dependence of the anode current was studied for zinc electrode passivation regions at negative potentials of –0.4, –0.2, and –0.1 V at CO_2 pressure of 0.05 MPa. At a potential of –0.4 V the corrosion current density is virtually time-independent. At potentials of –0.1 and –0.2 V the corrosion current density decreases with time in accordance with the relation

$$i = K/\tau,$$

where i is the corrosion current density (A cm^{-2}), τ is time (min), and K is a coefficient equal to 0.20 and 0.24 A min cm^{-2} at potentials of –0.1 and –0.2 V, respectively. This behavior is preserved for 2 h.

It is inexpedient to perform electrolysis in pure

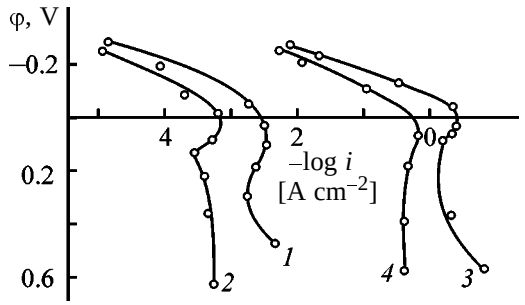

Fig. 3. Polarization curves for Ni electrode in water. CO_2 pressure (MPa): (*1, 3*) 0.1 and (*2, 4*) 0.9. (*3, 4*) K_2CO_3 concentration 0.01 M.

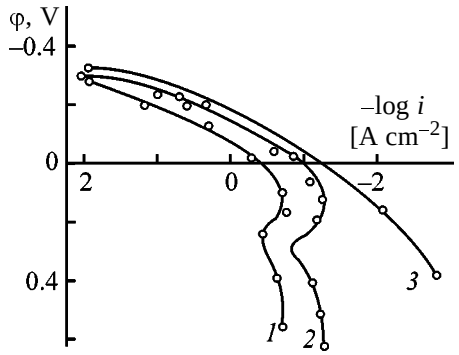

Fig. 4. Polarization curves for Ni electrode in 0.05 M NaCl solution. CO_2 pressure (MPa): (*1*) 0.1, (*2*) 0.4, and (*3*) 0.9.

water because of its low electrical conductivity. In this connection, the anodic dissolution of zinc was studied in electrolyte solutions of K_2CO_3 and NaCl under elevated pressure of CO_2.

Addition of 0.01 M of K_2CO_3 to a solution being analyzed raises the zinc dissolution rate at pressures of 0.1, 0.4, and 0.9 MPa by nearly three orders of magnitude. However, a peak appears in the polarization curves, which is not observed in water in an atmosphere of pure CO_2 at the same pressures. The region of intensive metal dissolution is observed at potentials ranging from –0.6 to +0.2 V. With the potential increasing further, the rise in the current density slows down (prepassivation region) and, at a potential of –0.05 V, the metal becomes passive.

The behavior of zinc does not change significantly upon addition of NaCl. The polarization curves measured in a 0.05 M NaCl solution at CO_2 pressure of 0.1 to 0.9 MPa show no portions of passive film formation at potential in the range from –0.9 to +0.6 V (Fig. 2, curves *4* and *5*). Noteworthy is the pronounced increase in the anode current, compared with that in water and K_2CO_3 solution. The value of $\log i$ also grows with increasing CO_2 pressure. For example, $\log i$ equals –0.88 (0.1 MPa), –0.64 (0.4 MPa), and –0.52 (0.9 MPa) at a potential of –0.3 V.

The polarization curves for nickel in water at a CO_2 pressure of 0.1–0.9 MPa have a single peak (Fig. 3, curve *1*). At potentials of –0.3 to –0.1 V, the metal dissolves intensively. Then the current density passes through a maximum at potentials close to +0.05 V and then falls. A passive region is observed at potentials in the range from +0.05 to +0.25 V, ending in current rise. Raising the CO_2 pressure exerts the same influence on the region of intensive dissolution of the metal: the rate of nickel dissolution decreases with increasing CO_2 pressure. For example, the maximum values of $\log i$ are –2.40, –2.63, and –3.05 at CO_2 pressures of, respectively, 0.1, 0.4, and 0.9 MPa. The passivation region begins at a pressure of 0.9 MPa approximately 0.04 V earlier, compared with that at 0.1 MPa.

The polarization curves measured upon addition of K_2CO_3 to the solution differ only slightly from those obtained in an aqueous solution of CO_2; however, the rate of metal dissolution increases noticeably. The pattern in which the current density decreases with increasing CO_2 pressure in the region of intensive metal dissolution is preserved (Fig. 3, curves *3* and *4*). The maximum $\log i$ values are +0.4, +0.25, and –0.20 at CO_2 pressures of, respectively, 0.1, 0.4, and 0.9 MPa.

The presence of chloride ions in solution strongly affects the run of the polarization curves and the rate of dissolution of the nickel anode (Fig. 4). At NaCl concentration of 0.05 M and CO_2 pressure of 0.1 and 0.4 MPa the peak potential (Fig. 4, curves *1* and *2*) shifts to the positive region, and the passive state of nickel is disrupted already at potentials close to +0.25 V, which is manifested in abrupt change from decrease in the current to an increase in the metal dissolution rate. No inhibition of the electrode process is observed at potentials in the range from –0.3 to +0.6 V at a CO_2 pressure of 0.9 MPa (Fig. 4, curve *3*), which indicates the absence of passivation of the nickel anode.

The polarization measurements performed demonstrated that the anodes are passivated in anodic dissolution of zinc and nickel aqueous solutions of both CO_2 and potassium carbonate, which is presumably due to formation on the electrode surface of a film of metal carbonates and oxides. The passivation phenomenon is completely eliminated in a sodium chloride solution. Here it is important to note that this occurs even at sodium chloride concentration of 0.05 M. Electrolysis in chloride solutions was carried out with account of these data.

To choose the optimal conditions, carbonates were synthesized with pressure and temperature varied within 0.2–1.0 MPa and 20–100°C. An analysis of the data obtained demonstrated that raising both pressure and temperature results in a certain increase in CE by carbonates, with pressure exerting stronger influence than temperature. For example, the increase in CE was about 20% on raising the CO_2 pressure from 0.2 to 1.0 MPa, and only about 6% on elevating temperature from 20 to 100°C.

Syntheses of carbonates with the use of various cathode materials demonstrated that, under the same conditions, the CE depends on the nature of the cathode material (0.05 M NaCl solution):

Cathode	Anode	CE, %
Copper	Nickel	90.8
Platinum	Nickel	98.2
Copper	Zinc	94.1
Platinum	Zinc	96.8

The effect of the cathode material on the CE can be accounted for by reduction of metal ions at the cathode, which makes lower the CE of the target product. The maximum CE values in NaCl solution are observed with platinum as the cathode.

The rate of anodic dissolution of zinc in water and aqueous solutions of K_2CO_3 and NaCl grows with increasing pressure at any preset potential (from –0.6 to +0.4 V). However, nickel dissolves anodically only up to potential of 0.0 V. Further, its potential remains constant to high current densities, which can be attributed to shielding of the electrode surface by firmly adsorbed insoluble compounds of zinc with ions formed in the system in CO_2 dissolution.

The table presents the results obtained in studying the effect of CO_2 pressure on the current density at two fixed potentials of –0.2 and 0.0 V in anodic dissolution of Zn and Ni in water and aqueous solutions of K_2CO_3 and NaCl.

It can be seen that the rate of anodic dissolution of Zn and Ni in an NaCl solution is higher as a result of the depolarizing action of chloride ions. Under the chosen optimal conditions, nickel and zinc carbonates are obtained at current densities of up to 0.35 A cm^{-2} in nearly quantitative yields.

Effect of CO_2 pressure on the current density at constant potential in anodic dissolution of zinc and nickel

φ, V	*P*, MPa	–log *i* in indicated solution, M					
		H_2O		K_2CO_3, 0.01		NaCl, 0.05	
		Zn	Ni	Zn	Ni	Zn	Ni
–0.2	0.1	4.3	3.7	1.3	1.4	0.81	1.3
	0.4	4.6	4.1	1.8	1.6	0.65	0.7
	0.9	3.6	4.5	1.1	1.7	0.48	0.4
0.0	0.1	4.8	2.6	1.4	–	0.7	0.9
	0.4	4.4	2.8	1.3	0.0	0.55	0.65
	0.9	3.4	3.1	0.7	0.2	0.35	0.38

CONCLUSION

The preparation of pure Zn and Ni carbonates can be intensified by performing electrolysis in solutions saturated with CO_2 under elevated pressure.

ACKNOWLEDGMENTS

The authors are grateful to A.P. Tomilov for helpful discussions.

REFERENCES

1. USSR Inventor's Certificate no. 447366.
2. USSR Inventor's Certificate no. 544715.
3. RF Patent 2096527.
4. Aksenov, N.N., Investigation and Development of Technology of Basic Copper and Zinc Carbonates as Raw Materials for Manufacture of Catalysts and Sorbents, *Cand. Sci. Dissertation*, Ivanovo, 1979.
5. Vladimirova, M.V., Fundamental Aspects of Electrode Reactions in Synthesis of Carbonate Salts of Metals in Aqueous Electrolyte Solutions under Elevated Carbon Dioxide Pressures, *Cand. Sci. Dissertation*, Makhachkala, 1999.
6. Serbezov, D.M. and Furnadzhiev, M.K., *Proizvodstvo bezalkogol'nykh napitkov* (Manufacture of Soft Drinks), Moscow: Pishchevaya Prom–st., 1974.
7. *Korroziya: Spravochnoe izdanie* (Corrosion: Reference Book), Shraier, L.L., Ed., Moscow: Metallurgiya, 1981.

Russian Journal of Applied Chemistry, Vol. 75, No. 1, 2002, pp. 54–59. Translated from Zhurnal Prikladnoi Khimii, Vol. 75, No. 1, 2002, pp. 54–59.
Original Russian Text Copyright © 2002 by Vigdorovich, Sinyutina, Chivilev.

APPLIED ELECTROCHEMISTRY AND CORROSION PROTECTION OF METALS

Effect of External Polarization on Hydrogen Diffusion across Steel Membrane in Dilute HCl Solutions Containing a Number of Aromatic Amines

V. I. Vigdorovich, S. E. Sinyutina, and L. V. Chivilev

Derzhavin State University, Tambov, Russia

Received September 4, 2001

Abstract—The effect of a number of aromatic amines on the hydrogen diffusion flux across a steel (St.3 brand) membrane under conditions of anodic and cathodic polarization in weakly acidic solutions, including media containing hydrogen sulfide, was studied. The experimentally observed dependences are interpreted in terms of the Horiuti approach.

Hydrogenation of metalware under industrial conditions in acid media [1] and highly mineralized nearly neutral media containing hydrogen sulfide [2] and carbon dioxide [3] is one of the most dangerous kinds of corrosive destruction. The hydrogen embrittlement of metallic structural materials, impairing their strength characteristics, causes huge direct and indirect losses. Despite numerous studies [4–7], the mechanism of the process remains nearly totally unclear, which markedly hinders a theoretically substantiated search for inhibitors of hydrogenation in various media. In acids, the build-up of cathodic polarization within certain limits raises the rate of hydrogen diffusion across a steel membrane, i_H; then a region with $i_H \neq F(i_c)$ is observed, where i_c is the cathode current density; and then a transition occurs from the first stage

$$H_3O^+ + e \xrightarrow{i_1} H_{ads} + H_2O \qquad (1)$$

to water discharge

$$H_2O + e \rightarrow H_{ads} + OH^-$$

and to an increase in pH in the near-electrode layer [8]. Various additives may change substantially the type of the $i_H = F(i_c)$ dependence [6].

In the case of cathodic polarization, the function $i_H = F(\Delta E_c)$, where $\Delta E_c = E_{cor} - E_c$, and E_c and E_{cor} are the potentials of the working side of the membrane under the conditions of a flowing external cathode current and under self-dissolution conditions, has a maximum in a wide range of pH values [9].

A similar maximum is observed at small shifts of the potentials to the anodic region. The type of the $i_H = F(\Delta E_a)$ dependence [10] is accounted for by the negative difference effect as a result of emergence into solution of low-charge species inducing chemical decomposition of water and giving rise to H_{ads}. Hydrogenation in a weakly alkaline borate buffer solution also occurs at potentials that are more positive than that of the equilibrium hydrogen electrode, E_r [11]. The authors attribute the observed experimental facts to H_3O^+ accumulation as a result of anodic ionization of iron in accordance with the scheme [12]

$$Fe + 2H_2O \rightleftarrows Fe(OH)_{ads} + H_3O^+ + e, \qquad (2)$$

$$Fe(OH)_{ads} \rightarrow Fe(OH)_{solv} + e,$$

$$Fe(OH)_{solv} \rightleftarrows Fe^{2+} + OH^-.$$

The forming hydroxonium ions can be reduced by reaction (1), and it is this factor that is responsible for metal hydrogenation.

Marshakov *et al.* [4] developed this approach [11] using a modified Bokris scheme for the mechanism of iron ionization in weakly acidic sulfate solutions, having replaced in this scheme the reactive OH^- ions (because of their low concentration) with H_2O. However, the questions remain as to whether reaction (1) at $E > E_r$ and H_3O^+ accumulation are possible if proton donor is formed in the quasi-equilibrium reaction (2) and consumed in the reaction

$$Fe(OH)^+ + H_3O^+ \rightleftarrows Fe^{2+} + 2H_2O \qquad (3)$$

1070-4272/02/7501-0054$27.00 © 2002 MAIK "Nauka/Interperiodica"

in stoichiometric amounts. According to [13], the effect occurs if reaction (3) proceeds by the Kolotyrkin–Florianovich mechanism

$$Fe(OH)_{ads} + HSO_4^- \rightleftarrows FeSO_4 + H_2O + e,$$

in which the hydrosulfate ion acts as a source of H_3O^+. However, in chloride media, in which iron ionization proceeds by the scheme [14]

$$Fe + 2H_2O + Cl^- \rightleftarrows (FeClOH^-) + H_3O^+ + e,$$

$$(FeClOH^-) \rightarrow FeClOH + e,$$

$$FeClOH + H_3O^+ \rightleftarrows Fe^{2+} + Cl^- + H_2O,$$

H_3O^+ ions are not accumulated and i_H must not grow in anodic polarization, in contradiction with experimental data.

The rise in i_H is possible through an increase in the concentration of adsorption centers for hydrogen atom as a result of anodic activation of passivated parts of the metal surface, existing at $E \le E_{cor}$ [5]. However, a situation of this kind is also observed in ethylene glycol solutions of HCl [15], in which, according to photoelectric polarization data, there are no passive regions on the iron surface. Thus, many fundamental aspects of steel hydrogenation have no satisfactory theoretical interpretation.

In the presence of inhibiting additives, the situation becomes even more complicated [16]. Therefore, in continuation of [16], the present study employs an approach [17, 18] according to which two H_{ads} species exist on the iron surface. One of these determines, all other conditions being the same, the flux of the solid-phase diffusion of hydrogen [15]. With account of these results, the present study analyzes and gives an interpretation of the influence exerted by a number of aliphatic amines on i_H under conditions of anodic and cathodic polarization.

EXPERIMENTAL

The studies were carried out in a two-chamber Pyrex glass cell of the Devanathan type, with a partition in the form of vertical steel membrane (St.3 steel) 0.3 mm thick with area of 3.63 cm^2, using the procedure described in [19]. The working solution was introduced into the polarization part of the cell, and a precisely measured amount of titrated 0.01 N potassium permanganate solution, into the diffusion part. According to the theory of the method, hydrogen diffusing across the membrane reacts on its diffusion side with $KMnO_4$, converting it into manganese dioxide on the electrode surface:

$$3H_{ads} + MnO_4^- = MnO_2 + H_2O + OH^-.$$

The amount of hydrogen that passed across the membrane was determined from the change in the concentration of the $KMnO_4$ solution by its titration with an oxalic acid solution in accordance with the equation

$$5H_2C_2O_4 + 2KMnO_4 + 3H_2SO_4 \rightarrow 2MnSO_4 + K_2SO_4 + 8H_2O + 10CO_2.$$

The amount of potassium permanganate consumed for passivation of the membrane surface was determined in a blank run without filling the polarization compartment of the cell. The amount of hydrogen diffused across the membrane, expressed in current density units, was calculated as follows. The amount of reacted potassium permanganate is given by

$$n(KMnO_4) = \Delta C(KMnO_4)V_{cell}/(5 \times 1000),$$

where C is the equivalent concentration of $KMnO_4$.

The amount of atomic hydrogen that reacted with potassium permanganate was calculated using the relation

$$n(H) = 3n(KMnO_4).$$

Since $M(H) = 1$ g mol^{-1}, then $n(H)$ and $m(H)$ are numerically equal. In this case, the current density of hydrogen diffusion across the membrane, i_H (A m^{-2}), can be calculated by the formula

$$i_H = mF/E_H S\tau = 0.016\Delta CV_{cell}/S\tau,$$

where E_H is the molar mass of the chemical equivalent of hydrogen, τ is the experiment duration (h), and S is the membrane area (m^2).

The polarization was done with a P5827m potentiostat, silver chloride electrode served as reference, and Pt was used as auxiliary electrode. The working solution was prepared by saturation of distilled water with dry hydrogen chloride and subsequent adjustment to the prescribed concentration.

Hydrogen sulfide was introduced by saturation of hydrochloric acid solutions with gaseous H_2S and subsequent dilution with the working solution. All experiments were carried out at room temperature in the course of 2 h. The aromatic amines listed in the table were used.

Physicochemical constants of compounds

Compound	Empirical formula	Hammett constant σ_H [20]	pK_b [20]	Dipole moment $\mu \times 10^{30}$, C m [20]
p-Anisidine (**I**)	$CH_3O–C_6H_4–NH_2$	–0.268	5.29	6.11
p-Toluidine (**II**)	$CH_3–C_6H_4–NH_2$	–0.170	5.12	4.49
Aniline (**III**)	$H–C_6H_4–NH_2$	0.000	4.58	5.28
p-Bromoaniline (**IV**)	$Br–C_6H_4–NH_2$	0.232	3.91	9.87

In uninhibited 5 M HCl solutions, the diffusion flux grows with ΔE_c increasing within the limits $0 < \Delta E_c < 0.1$ V. Further, i_H is virtually independent of ΔE_c (Fig. 1Ia, curve *1*). Introduction of 1 mM of *p*-anisidine (**I**), *p*-toluidine (**II**), and aniline (**III**) leads to an $i_H = F(\Delta E_c)$ dependence with a maximum at ΔE_c equal to 0.05 (**I**, **III**) or 0.1 V (**II**). Introduction of *p*-bromoaniline (**IV**) diminishes i_H to virtually zero, with no extremum observed in the corresponding dependence (Fig. 1Ia, curve *5*).

In the presence of hydrogen sulfide (6 mM) in a buffer solution without addition of aromatic amines, a maximum appears in the $i_H = F(\Delta E_c)$ dependence (Fig. 1Ib, curve *1*) and the absolute value of i_H (ΔE_c = const) markedly increases. The nature of the relationship between i_H and ΔE_c upon introduction of aniline and its derivatives depends on a substituent. In the presence of aniline, an increase in ΔE_c to 0.05 V makes i_H lower; further, the diffusion flux remains virtually unchanged (Fig. 1Ib, curve *4*). The compound $C_6H_5NH_2$ strongly diminishes the absolute value of i_H under conditions of cathodic polarization. A similar situation is observed in the presence of **I**. Introduction of *p*-toluidine (**II**) leads to a dependence of i_H on ΔE_c with a clearly pronounced maximum. Finally, 1 mM of *p*-bromoaniline (**IV**) in a weakly

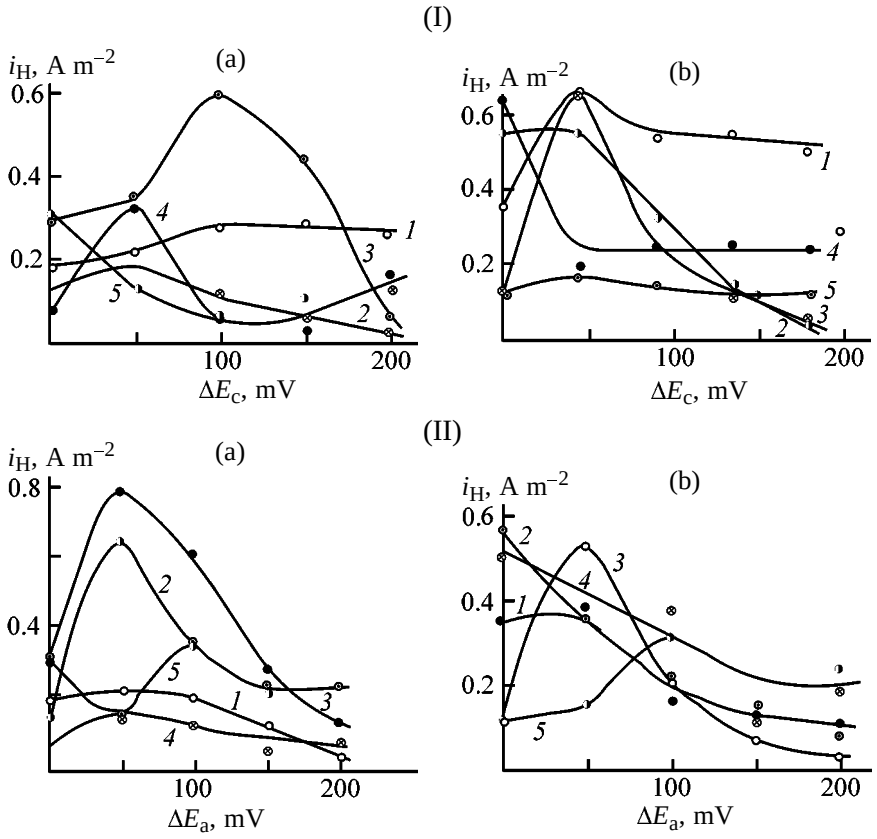

Fig. 1. Current of hydrogen penetration vs. (I) cathodic and (II) anodic polarization ΔE of a steel membrane in 5 mM HCl solutions containing 1 mM of aromatic amines. Temperature 20°C, test duration 2 h. (*1*) No additive; amine added: (*2*) **I**, (*3*) **II**, (*4*) **III**, and (*5*) **IV**. H_2S concentration (mM): (a) 0 and (b) 6.

acidic H_2S-containing medium markedly lowers i_H (ΔE_c = const). At the same time, i_H is virtually independent of ΔE_c.

In the case of anodic polarization ($\Delta E_a = E_a - E_{cor}$, where E_a is the potential of the working side of the membrane on applying an external anodic current) in uninhibited buffer solution, the dependence $i_H = F(\Delta E_a)$ has a maximum (Fig. 1IIa, ΔE_a = 0.05 V). Upon introduction of 1 mM of **I**–**III**, this maximum is reproduced, and in the presence of **I** and **II** the maximum is more clearly pronounced, with the last two additives acting as hydrogenation stimulants.

The presence of 6 mM of hydrogen sulfide in an uninhibited buffer solution leads to narrowing of the peak in the $i_H = F(\Delta E_a)$ curve, without changing its coordinate along the ΔE_a axis (Fig. 1IIb). i_H grows in absolute value (ΔE_a = const), especially so at small ΔE_a.

In solutions of **I** and **III** there is no maximum, whereas upon introduction of **II** or **IV** it is rather clearly pronounced at E_a of, respectively, 0.05 and 0.10 V.

Thus, the presence of an extremum in the $i_H = F(\Delta E_a)$ dependence occurs rather frequently.

Other conditions being the same, the diffusion flux is governed by at least two factors: first, by decreasing surface coverage by atomic hydrogen whose adsorption in buffer solution is determined by stage (1); in the presence of hydrogen sulfide, a concurrent reaction appears

$$H_2S + e \xrightarrow{i_4} H_{ads} + HS^-. \quad (4)$$

On introduction of aromatic amines, the following processes become possible:

$$R\text{–}NH_3^+ + e \xrightarrow{i_5} H_{ads} + R\text{–}NH_2. \quad (5)$$

Second, it may be determined by pathways of H_{ads} removal, which may occur via the concurrent stages

$$H_{ads} + H_{ads} \xrightarrow{i_6} H_2, \quad (6)$$

$$H_{ads} + H_3O^+ + e \xrightarrow{i_7} H_2 + H_2O, \quad (7)$$

$$H_{ads} + H_2S + e \xrightarrow{i_8} H_2 + HS^-, \quad (8)$$

$$H_{ads} + R\text{–}NH_3^+ + e \xrightarrow{i_9} H_2 + R\text{–}NH_2, \quad (9)$$

$$H_{ads} \xrightarrow{i_{10}} H_{ads}, \quad (10)$$

where i_j are the rates of the respective reactions.

The predominant rise in i_{10} in the case of valid inequality

$$\Delta i_{10} > \Delta(i_6 + i_7 + i_8 + i_9) \quad (11)$$

stimulates hydrogenation, whereas reversal of (11) reduces the diffusion of hydrogen into the metal. The occurrence of a maximum in the $i_H = F(\Delta E_a, \Delta E_c)$ curves is determined by the existence of at least two oppositely acting factors. Actually, the number of these factors is probably larger.

It is noteworthy that two adsorbed atomic hydrogen species are present on the metal surface [17, 18]: oversurface H^r and subsurface H^s, whose two-dimensional concentrations are determined by the equilibrium

$$H^r \rightleftarrows H^s. \quad (12)$$

The corresponding coverage factors are denoted by θ^r and θ^s. The H^r species are bound to individual atoms of the metal crystal lattice and, owing to difference between the electronegativities of hydrogen and iron [21], have a dipole moment μ of 0.53×10^{-30} C m.

The $\mu(H^4)$ value is nearly 3 times lower (0.2×10^{-30} C m). It is believed that H^r atoms are responsible for stages (6)–(9), and H^s atoms, for stage (10) [15].

In addition, the dependence $i_H = F(\Delta E_a, \Delta E_c)$ is determined by the nature of successive discharge–molization stages and that of inequality (11). If the mechanism of proton donor discharge is determined by the successive occurrence of reactions (1) and (7), then, according to [22],

$$\theta = K_1/(K_1 + K_2).$$

The index of a rate constant characterizes the number of the corresponding reaction. At $K_7 \gg K_1$ stage (1) is rate-determining and, therefore, θ_H and i_H are small. Moreover, K_1 and K_7 are independent of the proton donor concentration, but are functions of the potential

$$K_i = K_i^{\dagger} \exp(-\alpha EF/RT)$$

(E is potential, α is the Brønsted coefficient, other designations are conventional). Therefore, to a first approximation, i_H depends on the electrode potential only slightly in a wide range of E.

At $K_1 \gg K_7$ the state of the surface is close to saturation [22], and, consequently, the i_H value changes only slightly, or not at all, with increasing ΔE_c ($\theta_H \to 1$).

In the case of a mechanism with successive stages (1) and (6), of which the first is rate-determining, $K_1 \gg K_{-1}$ and $K_1(1 - \theta_H) \gg K_{-1}\theta_H$ [17]. At $i_6 \gg i$ and $i_6 \gg i_{-6}$, θ_H is equal to the equilibrium value θ_H^0. Then [22]

$$\theta_H^0 = \frac{K_1^0/K_{-1}^0}{K_1^0/K_{-1}^0 + 1} = \frac{(K_{-6}^0/K_6^0)^{1/2}}{(K_{-6}^0/K_6^0)^{1/2} - 1}.$$

Using the approach of [23] and setting the ratio K_1^0/K_{-1}^0, one can readily demonstrate how fast θ_H^0 grows under the specified conditions.

K_1^0/K_{-1}^0	1	2	5	10	20	100
K_{-6}/K_6	1	1.42	2.21	3.62	4.36	7.00
θ_H^0	0.50	0.67	0.83	0.91	0.95	~1.00

In terms of the classical recombination theory, when stage (4) is rate-determining, θ_H is related to K_i by

$$K_1/K_6 = 1/(1 - \theta_H).$$

The relationship between the ratio K_1/K_6 and θ_H in the case of Tafel reaction limiting the discharge of proton donors is characterized below:

K_1/K_6	2	3	6	11	20	100
θ_H	0.50	0.67	0.83	0.91	0.95	0.98

Since K_1 is a function of the electrode potential, and K_6, being the chemical reaction constant, is independent of this potential, it can be readily seen at what values of the K_1/K_6 ratio the rise in cathodic polarization ceases to affect i_H at invariable process mechanism. For example, if already under free-corrosion conditions ($E = E_{cor}$) $K_1/K_6 \to 100$, then $\theta_H \to 1$ and $i \neq F(\Delta E_c)$. Simultaneously, the cathodic process may occur at the limiting current of the lateral diffusion. Contrariwise, at $K_1/K_6 \ll 100$, an increase in ΔE_c makes the ratio of these K_i higher and θ_H grows. Independent investigations with the use of Armco ion demonstrated that, according to the criterial quantities $dE/d\log i_c$, $(d\log i_c/d\log C_{H^+})E$, $dE/d\log C_{H^+}$, $d\eta/d\log i_c$ $(d\log i_c/d\log C_{H^+})_\eta$, $d\eta/d\log C_{H^+}$, the hindered stage on Armco iron in acid chloride solutions with 0.99–0.01 M H_3O^+ (constant ionic strength equal to unity) is the discharge reaction (1). The weak dependence of i_H on ΔE_c (Fig. 1Ia, curve 1) satisfactorily correlates with this conclusion.

The presence of hydrogen sulfide makes i_H higher in the region of small cathodic polarizations (Fig. 1, Ib, rising portion of curve *1*). Probably, partly hindered discharge gives way to hindered recombination (6) or electrochemical desorption (7) or (8), which leads to rise in i_H. The possibility of parallel discharge of proton donors with different hindered stages was indicated in [24]. With the subsequent increase in ΔE_c, the effective adsorption energy of H_{ads}^r decreases because of the shift of the surface charge to negative values. Simultaneously, in accordance with the dependence [25]

$$\Delta H_{ads}/E_m \geq 5$$

the activation energy of migration, E_m, also decreases, which makes higher the rate of stage (6) and lowers the contribution of (11) to H_{ads} drain and diffusion flux into the metal. The subsequent independence of i_H from ΔE_c is presumably due to the constancy of θ_H as a result of a simultaneous increase in adsorption of H_{ads} atoms and their removal via molization and evolution into the gas phase.

In the presence of aromatic amines **I**–**III** (Fig. 1I, buffer solution), the experimental dependence $i_H = F(\Delta E_c)$ can be accounted for by the same factors. Introduction of **IV** presumably shifts the equilibrium (12) virtually entirely to the left, and $i_{10} \to 0$ with increasing ΔE_c. The presence of H_2S together with $R–NH_2$ leads to possible parallel adsorption of H_{ads} by schemes (1)–(5) and removal in accordance with stages (6)–(10), which determines the existence of additional secondary factors. In particular, cathodic polarization affects differently the adsorption energies of H_2S molecules and $R–NH_3^+$ cations. Blocking certain active centers under conditions of energy nonuniformity of the steel surface, they change markedly ΔH_{ads} and the conditions of surface diffusion of H^r atoms, and also the contribution of stage (10) to the removal of atomic hydrogen and the i_H value.

In the case of anodic polarization of the working side of the membrane in a buffer sulfuric acid solution, one more factor should be taken into account. With increasing ΔE_a, proton donor reduction slows down, which, in principle, must only make i_H lower. However, the build-up of positive charge on the surface changes in different ways the energies of binding to the surface for H^r and H^s atoms carrying different amounts of negative charge. If the binding energy of H^r to the surface grows faster, then the contribution from reaction (10) and i_H value increase. The descending portion of curve *1* in Fig. 1IIb is determined by the effect of decreasing rate of proton donor reduction under conditions of anodic polarization, irrespective of the nature of the rate-determining stage. In a similar way can be interpreted the dependence $i_H = F(\Delta E_a)$ in a hydrochloric acid solution containing H_2S (Fig. 1IIb, curve *1*) and also the extrema in the curves measured in the presence of aromatic amines. The absence of an extremum and the descending run of the dependence

of i_H in the interval $0 < \Delta E_a \le 0.2$ V are related to the key influence exerted by θ_H decreasing with anodic shift of the potential of the working side of the membrane. At the same time, the performance of aromatic amines as potential inhibitors in the multifactor phenomenon of steel hydrogenation from weakly acidic solutions, including those containing process stimulants (H_2S), cannot be unambiguously related to the physicochemical parameters of their molecules (σ_H, pK_b, and μ). Presumably, the complexity of the observed kinetics of the process is determined not only by the nature of the occurring reactions, but also by the concomitant, and rather important, factors: competitive adsorption of atomic hydrogen, H_2S, amines, and solvent molecules and the energy nonuniformity of the steel surface. The last factor results in that the adsorbabilities of the competing species in different θ regions are strongly dissimilar. As a result, the functional dependences $\theta_i = F(\Delta H^i_{ads})$ of the competing *i*th species may intersect. Then, the contributions from the reactions of molization, (8) and (9), with H_2 evolution into the gas phase, on the one hand, and adsorption by metal, (10), on the other, must change substantially.

CONCLUSIONS

(1) As a rule, the dependence $i_H = F(\Delta E_a, \Delta E_c)$ in weakly acid chloride solutions in the presence of hydrogen sulfide and aromatic amines has a maximum whose position is determined by the nature of R_i–NH_2.

(2) The quantitative characteristics of the dependence of i_H on the anodic and cathodic polarization are in the first place determined by the nature of successive discharge–molization stages and by the relative contributions of the corresponding reactions to the total removal of adsorbed hydrogen.

(3) The effect of aromatic amines on the hydrogenation cannot be unambiguously related to physicochemical parameters of their molecules.

REFERENCES

1. Kuznetsov, V.V., Khaldeev, G.V., and Kichigin, V.I., *Navodorozhivanie metallov v elektrolitakh* (Hydrogenation of Metals in Electrolytes), Moscow: Mashinostroenie, 1993.
2. Getmanskii, M.D., Khudyakova, L.P., Gershova, A.I., *et al*., *Zashch. Met*., 1988, vol. 24, no. 2, pp. 333–335.
3. Markin, A.N., *Zashch. Met.*, 1994, vol. 30, no. 1, pp. 452–457.
4. Marshakov, A.I., Maksaeva, L.B., and Mikhailovskii, Yu.N., *Zashch. Met.*, 1993, vol. 29, no. 6, pp. 857–868.
5. Marshakov, A.I., Maksaeva, L.B., and Mikhailovskii, Yu.N., *Zashch. Met*., 1993, vol. 29, no. 6, pp. 869–873.
6. Nazarov, A.P., Lisovskii, A.P., and Mikhailovskii, Yu.N., *Zashch. Met*., 1996, vol. 32, no. 6, pp. 602–606.
7. Marshakov, A.I., Maksaeva, L.B., and Mikhailovskii, Yu.N., *Zashch. Met*., 1997, vol. 33, no. 3, pp. 278–280.
8. Antropov, L.I. and Savgira, Yu.A., *Trudy III Mezhdunarodnogo kongressa po korrozii metallov* (Proc. III Int. Congr. on Metal Corrosion), Moscow: Mir, 1968, vol. 2, pp. 54–62.
9. Marshakov, A.I., Batishcheva, O.V., and Maksaeva, L.B., *Zashch. Met*., 1991, vol. 27, no. 5, pp. 713–718.
10. Fokin, M.N., Bulygin, E.V., and Oshe, E.K., *Khim. Khim. Tekhnol*., 1986, vol. 29, no. 3, pp. 117–119.
11. Marichev, V.A. and Molokanov, V.V., *Zashch. Met*., 1991, vol. 27, no. 5, pp. 810–814.
12. Bocris, J.O.M., Genshaw, M.A., Brusic, V., *et al*., *Electrochim. Acta*, 1971, vol. 16, no. 11, pp. 1859–1869.
13. Nazarov, A.P., Lisovskii, A.P., and Mikhailovskii, Yu.N., *Zashch. Met*., 1996, vol. 32, no. 5, pp. 478–483.
14. Chin, R. and Nobe, K., *J. Electrochem. Soc*., 1972, vol. 119, no. 11, pp. 1457–1461.
15. Vigdorovich, V.I., Tsygankova, L.E., D'yachkova, T.P., *et al*., *Khim. Khim. Tekhnol*., 2000, vol. 43, no. 2, pp. 63–70.
16. Vigdorovich, V.I., Tsygankova, L.E., Sinyutina, S.E., and Boldyrev, A.V., *Zh. Prikl. Khim*., 2000, vol. 73, no. 10, pp. 1664–1669.
17. *Solid State Surface Science*, Green, M., Ed., New York: Marcel Dekker, 1969. Translated under the title *Poverkhnostnye svoistva tverdykh tel*, Moscow: Mir, 1972, pp. 1–13.
18. Toya, T., Ito, T., and Ishi, I., *Elektrokhimiya*, 1978, vol. 14, no. 5, pp. 703–714.
19. Kardash, N.V. and Batrakov, V.V., *Zashch. Met*., 1995, vol. 31, no. 4, pp. 441–444.
20. Grigor'ev, V.P. and Ekilik, V.V., *Zashch. Met*., 1968, vol. 4, no. 1, pp. 31–36.
21. Cotton, F.A. and Wilkinson, G., *Advanced Inorganic Chemistry*, New York: Interscience, 1966.
22. Frumkin, A.N., *Zh. Fiz. Khim*., 1937, vol. 10, no. 4, pp. 568–574.
23. Frumkin, A.N., *Zh. Fiz. Khim*., 1957, vol. 31, no. 8, pp. 1875–1890.
24. Antropov, L.I., *Teoreticheskaya elektrokhimiya* (Theoretical Electrochemistry), Moscow: Vysshaya Shkola, 1984.
25. Kislyuk, U.M., *Itogi Nauki Tekh., Ser.: Kinet. Katal*., 1991, vol. 25, pp. 13–28.

Russian Journal of Applied Chemistry, Vol. 75, No. 1, 2002, pp. 60–62. Translated from Zhurnal Prikladnoi Khimii, Vol. 75, No. 1, 2002, pp. 60–62.
Original Russian Text Copyright © 2002 by Varentsov, Varentsova, Renard.

APPLIED ELECTROCHEMISTRY AND CORROSION PROTECTION OF METALS

Stability of Fibrous Carbon Materials in Cathodic Polarization in Nitric Acid Solutions

V. K. Varentsov, V. I. Varentsova, and E. V. Renard

Institute of Solid-State Chemistry and Mineral Raw Material Processing, Siberian Division, Russian Academy of Sciences, Novosibirsk, Russia

Received November 23, 2000; in final form, October 2001

Abstract—Stability and electrical conductivity of graphitized and carbonized fibrous carbon materials are studied in cathodic polarization in nitric acid solutions.

Fibrous carbon materials (FCMs) are widely used as electrode materials for intensification of redox reactions in aqueous solutions in hydrometallurgy, electroplating, and other branches of industry [1–4] and also in fuel elements. In all these cases the problems necessarily arise associated with the stability of FCMs in aqueous solutions and also with variation of their properties in the course of electrolysis, since it is well known that under polarization the surface of carbon materials can change as a result of formation of various kinds of surface compounds [5, 6].

Nitric acid solutions are widely used in electrosynthesis of a number of compounds, for example, for preparation of graphite intercalates [7, 8], as active components in chemical power sources [8], for dissolution of spent fuel of nuclear power plants [9], etc. Previously it was demonstrated that FCMs are corrosion-resistant in sulfuric acid solutions. Even at high current density cathodic treatment resulted in longitudinal fracturing of fibers and their partial degradation due to hydrogen gas liberation [10]. Altered surface condition of a carbon fiber is reflected in FCM weight loss and shift of the electrode potential in the negative direction. However, changes in the stationary potential are reversible, and the initial value is restored in 24–48 h.

The goal of this work was to study the stability of fibrous graphitized carbon materials upon cathodic polarization in nitric acid solutions. For comparison are reported the results obtained in sulfuric acid solutions.

EXPERIMENTAL

The effect of cathodic polarization on FCM characteristics was monitored by the weight loss and electrical conductivity, i.e., by the properties determining the performance of FCM in electrochemical processes [1].

For the study we selected carbonized (NT-1) and graphitized carbon materials (VINN-250) with a graphite content of 85 and 99.8 wt %, respectively. A laboratory setup for studying the effect of polarization was described elsewhere [10]. Cathodic polarization was carried out in 0.25 M sulfuric acid and 1.5 or 3.5 M nitric acid solutions for 1–3 h using a TES-41 dc source. Circulation of the solution throughout the bulk of the electrode was provided by a PP-2-15 peristaltic pump. The acids used were of chemically pure grade. Cathodic treatment experiments were conducted without or with separation of the electrode spaces with an MK-40 ion-exchange membrane. The area of the fibrous carbon cathode was 2 cm^2. The cell includes a Pt anode and a perforated current lead. The electrode after treatment was thoroughly washed with distilled water to constant pH and dried at 80°C. The electrical conductivity of the test materials was measured with a VM-509 ac bridge [11]. The redox potential E was measured with a V7-22A high-resistance voltmeter using a Pt electrode relative to a silver chloride electrode. The Pt electrode was immersed in an intermediate vessel through which the working solution circulated.

Data on the FCM weight loss after cathodic polarization in nitric and sulfuric acid solutions under various process conditions are given in the table.

The results show that the nature and concentration of an acid used as well as the process conditions (current density and treating time) affect the stability of FCMs. In sulfuric acid solutions cathodic treatment does not appreciably change the weight of the graph-

1070-4272/02/7501-0060$27.00 © 2002 MAIK "Nauka/Interperiodica"

Variations in FCM weight loss Δm and electrical conductivity χ after cathodic polarization*

Material	Concentration, M		Δm, %/χ, S cm^{-1}, at indicated current density, A m^{-2}					
			0		500		1000	
	HNO_3	H_2SO_4	treatment time, h					
			1	3	1	3	1	3
No separation of electrode spaces								
VINN-250	0	0.25	0/0.17	–	0/0.19	–0.5/0.18	–1.3/0.15	–0.5/0.17
NT-1	0	0.25	–2.6/0.04	–	–5.3/0.07	–4.7/0.5	–6.0/0.05	–5.0/0.04
VINN-250	3.5	0	–1.4/0.14	–0.6/0.14	–	–	–1.5/0.15	–3.1/0.155
NT-1	3.5	0	1.1/0.014	3.4/0.011	–	–	–5.5/0.02	–5.6/0.03
Separated electrode spaces								
VINN-250	1.5	0	–	–	–2.7/0.15	–2.3/0.1	–2.8/0.12	–3.7/0.1
NT-1	1.5	0	–	–	–0.3/0.01	–0.3/0.01	–1.9/0.01	–1.3/0.01
VINN-250	3.5	0	–	–	–2.7/0.14	–3.6/0.1	–1.8/0.13	–2.6/0.1
NT-1	3.5	0	–	–	–3.0/0.03	1.6/0.02	–2.4/0.02	1.8/0.02

* χ of FCMs before treatment (S cm^{-1}): VINN-250 0.155 and NT-1 0.041.

itized FCM (loss is within 1.3%). The carbonized material is less stable, and the weight of NT-1 decreased by 5–6% regardless of the process conditions.

Different trends are observed in nitric acid solutions. In this case the treatment conditions considerably influence the stability of FCMs. Upon polarization in 3.5 M HNO_3 (no separation of the cathode and anode spaces), the weight loss in the carbonized FCM is nearly the same as in polarization in the sulfuric acid solution; in the case of the graphitized material the weight loss is somewhat larger (up to 2–3%), which is probably due to degradation of the FCM fibers by liberated hydrogen gas in more concentrated HNO_3 solutions.

Cathodic treatment of graphitized FCMs in the cell with separated electrode spaces has no effect on the material weight loss. For the carbonized FCM the weight loss in 1.5 M HNO_3 is 0.3–1.9%, depending on the treatment conditions. In 3.5 M HNO_3 the material weight even increases under certain treatment conditions or without treatment (see table). The results obtained can be interpreted as follows. It is known that in nitric acid solutions oxidized layers of a complex composition are formed on the surface of carbonaceous materials [5]. This is primarily due to complex redox behavior of nitric acid solutions. Among possible nitric acid reduction products are NO, NO_2, N_2O_4, HNO_2, N_2O_3 [13], hydroxylamine, and ammonia [8, 14]. Upon cathodic polarization various redox reactions can proceed in parallel, as having close standard potentials. The resulting nitrous acid can also be reduced to various nitrogen oxides and other compounds [8]. Finally, under the experimental cathodic treatment conditions hydrogen ions can be reduced.

In the absence of a membrane separator in the cell, nitric acid reduction products can be partially oxidized on the anode in parallel with oxidation of water. In the presence of the separator these products can be accumulated in the solution, shifting the equilibrium and changing the redox potential E [12]. Without polarization the redox potentials realized on Pt in 1.5 and 3.5 M HNO_3 are +0.70 and +0.81 V, respectively. Variation of E in time in 3.5 M HNO_3 under cathodic treatment of FCMs with and without a membrane separator in the cell is illustrated in the figure.

In cathodic treatment in the cell without a separator, E initially abruptly decreases (curve *1*) and then turns back to the initial value. Similar result was obtained in sulfuric acid solutions. In the cell with a separator, accumulation of nitric acid reduction products shifts E in the negative direction (curve *2*). In this case the condition of the carbon fiber surface can change as a result of interaction with the solution components. In the table are given the changes in the electrical conductivity of FCMs, resulting from their cathodic treatment in sulfuric and nitric acid solutions. For the both types of FCMs the conductivity increases

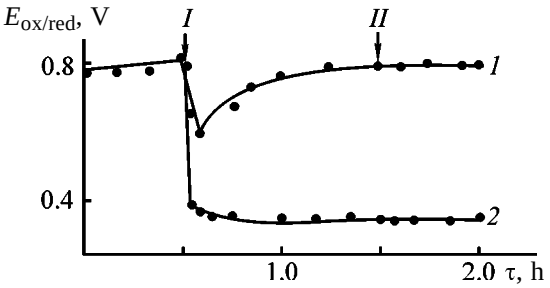

Redox potential E of VINN-250 in 3.5 M HNO_3 as a function of cathodic treatment time τ at a current density of 1000 A m^{-2}: (*1*) no separation of electrode spaces and (*2*) separated electrode spaces. (*I*) Switch on and (*II*) switch off.

after cathodic treatment, which is consistent with data of [10] and can be attributed to desorption of chemisorbed oxygen from the fiber surface.

Upon cathodic treatment in nitric acid solutions, the conductivity trend depends on the experimental conditions. In the cell without a separator the conductivity of the graphitized FCM does not change, and that of the carbonized FCM decreases by a factor of 1.25–1.27. In the cell with a separator the conductivity of VINN-250 decreases by 12–30%, and that of NT-1, by a factor of 2–4, depending on the nitric acid concentration and polarization parameters. The observed decrease in the conductivity of the tested FCMs is due to formation of low-conducting layers on the fiber surface [5, 6, 15].

Finally, the graphitized FCM demonstrates a high stability upon cathodic treatment in nitric and sulfuric acid solutions under various polarization conditions. The stability of the carbonized FCM depends on the acid nature and cathodic polarization conditions, which should be taken into account in evaluating its suitability for the use as a cathode material in aqueous solutions, for example, in electroplating and hydrometallurgy, particularly, in recovery of small amounts of fission platinoids from nitric acid solutions.

CONCLUSIONS

(1) Stability of the tested fibrous carbon materials upon cathodic treatment in nitric acid solutions considerably depends on the polarization conditions. Separation of the cathode and anode spaces by an ion-exchange membrane reduces the weight of the graphitized FCM by 5–6%. Also this reduces the electrical conductivity of the graphitized and carbonized fibrous carbon materials by 12–40% and by a factor of 2–4, respectively.

(2) The differences in the stability of the tested fibrous carbon materials upon cathodic treatment in nitric acid solutions, observed in the cell with a membrane separator, are associated with changing redox potentials of the systems due to accumulation of nitric acid reduction products.

REFERENCES

1. Varentsov, V.K., in *Intensifikatsiya elektrokhimicheskikh protsessov* (Intensification of Electrochemical Processes), Tomilov, A.P., Ed., Moscow: Nauka, 1988.
2. Varentsov, V.K., *Khim. Inter. Ustoich. Razv.*, 1997, vol. 5, no. 2, pp. 147–156.
3. Varentsov, V.K., *Zh. Ekol. Khim.*, 1993, vol. 14, no. 3, pp. 335–341.
4. Igumnov, M.S., Belov, S.F., and Drobot, D.V., *Ross. Khim. Zh.*, 1998, no. 6, pp. 135–142.
5. Tarkovskaya, I.A., *Okislennyi ugol'* (Oxidized Coal), Kiev: Naukova Dumka, 1981.
6. Tarasevich, M.P., *Elektrokhimiya uglerodnykh materialov* (Electrochemistry of Carbon Materials), Moscow: Nauka, 1984.
7. Yaroshenko, A.P., Popov, A.F., and Shapranov, V.V., *Zh. Prikl. Khim.*, 1994, vol. 67, no. 2, pp. 204–211.
8. Yakovlev, A.V., Finaenov, A.I., Nikitina, L.E., and Apostolov, S.P., *Zh. Prikl. Khim.*, 1999, vol. 72, no. 4, pp. 582–593.
9. Arseenkov, L.V., Zakharkin, B.S., Lunichkina, K.P., *et al.*, *At. Energ.*, 1999, vol. 72, no. 5, pp. 462–473.
10. Varentsov, V.K. and Varentsova, V.I., *Zh. Prikl. Khim.*, 1999, vol. 72, no. 4, pp. 605–609.
11. Varentsov, V.K., Zherebilov, A.F., and Malei, M.D., *Izv. Sib. Otd. Akad. Nauk SSSR, Ser. Khim. Nauk*, 1984, no. 6, pp. 120–127.
12. Zakhar'evskii, M.S., *Oksredmetriya* (Redoxmetry), Leningrad: Khimiya, 1967.
13. Vetter, K.J., *Elektrochemische Kinetik*, Berlin: Springer, 1961.
14. Fioshin, M.Ya., *Itogi Nauki Tekh., Ser.: Elektrokhimiya*, 1971, vol. 7, pp. 150–213.
15. Varentsov, V.K. and Varentsova, V.I., *Zh. Prikl. Khim.*, 1999, vol. 72, no. 4, pp. 605–609.

Russian Journal of Applied Chemistry, Vol. 75, No. 1, 2002, pp. 63–67. Translated from Zhurnal Prikladnoi Khimii, Vol. 75, No. 1, 2002, pp. 63–66.
Original Russian Text Copyright © 2002 by Khitrin, Fuks, Devyaterikova.

APPLIED ELECTROCHEMISTRY AND CORROSION PROTECTION OF METALS

Properties and Composition of the Wastes of Monoethanolamine Treatment of Hydrogen to Remove Carbon Dioxide

S. V. Khitrin, S. L. Fuks, and S. V. Devyaterikova

Vyatka State University, Kirov, Russia

Received June 14, 2001

Abstract—The properties and composition of the wastes of monoethanolamine treatment of pyrolysis hydrogen to remove carbon dioxide and their effect on corrosion of ferrous and non-ferrous metals in various media were studied.

At present, pyrolysis hydrogen is treated to remove carbon dioxide with monoethanolamine (MEA) solution; this solution in the course of prolonged operation accumulates impurities, which form a gummy fraction consisting of various organic compounds and products of apparatus corrosion [1]. The bottoms of the absorption procedure are often burned out, but their components can be valuable raw materials. The data on the bottoms composition determined by various authors [1–5] are ambiguous. For example, in [1, 4] it was suggested that the reaction of MEA with carbon dioxide yields oxazolidone-2, which then converts successively into imidazolidone-2 and *N*-(2-hydroxyethyl)ethylenediamine, whereas in [5] it was found that the main reaction product was *N*,*N*-diethylolurea. As seen from the published data [1–3], the bottoms can contain various amine-containing components. In this work we studied the composition of bottoms and the feasibility of using them or their components to inhibit corrosion of ferrous and non-ferrous metals in various media.

EXPERIMENTAL

The bottoms composition was studied by gas chromatography–mass spectrometry at programmed heating in the 50–250°C range using a Hewlett–Packard MD-800 Fisous Instruments GS 8000 unit equipped with a mass-selective detector and a PC for identification of the experimental mass spectra (Masslab software). The mixtures were separated on a standard glass column (30 m long, 0.32 mm in diameter) coated with the DB-Sms stationary phase (0.25-μm layer); the flow rate of the carrier gas (He) was 4 ml min^{-1}.

Our analytical results showed that the bottoms contained more than 50 organic compounds. The main components, along with residual MEA, are nitrogen- and oxygen-containing linear and cyclic compounds given in Table 1. The presence of carbonyl compounds suggests occurrence of oxidation and hydrogenation with subsequent nucleophilic addition and condensation, which can explain formation of some main and trace component of the bottoms.

Our calculations showed that the composition of the bottoms was as follows, %: *N*-ethylolethylenediamine 37.9, MEA 20, piperazine and its derivatives 20, 2-aminoheptane 5, DEA 4, saturated hydrocarbons 1, and esters of fatty acids 1.

To determine the properties of the bottoms components and the possibility of their utilization, we performed the vacuum distillation of the bottoms at 4 mm Hg. The content of primary, secondary, and tertiary amines in the fractions after distillation is given in Table 2.

It is known [6] that amines are used as inhibitors of the metal corrosion. Therefore, we studied the effect of bottoms in question on the corrosion processes. In our tests we used 65G, 60S2A, and 65S2VA spring steels after their thermal treatment. The content of the inhibitor was selected using published data [7–10] and was varied within 10–75 ml l^{-1}. The corrosion tests were performed in the solutions of hydrochloric acid (210 g l^{-1}), off-gas hydrochloric acid (150 g l^{-1}), sodium chloride (3%), and sodium sulfate (3%). The corrosion rate was evaluated using the weight corrosion parameter $K_w = \Delta m/(S\tau)$ (g cm^{-2} h^{-1}, Δm is the weight loss in the course of corrosion, S is the sample area, and τ is the corrosion time), the depth corrosion parameter $K_d = K_w \times 8.76/\rho_M$ (mm per year, ρ_M is

1070-4272/02/7501-0063$27.00 © 2002 MAIK "Nauka/Interperiodica"

Table 1. Bottoms components and their retention times

Compound	Retention time, min	
	sample no. 1	sample no. 2
MEA	1.826	1.465
N-Ethylolpiperazine	6.566	4.936
1-(3-Aminopropyl)-4-methylpiperazine	6.916	5.176
Butanal dimethylhydrazone	7.406	5.576
1,4-Dimethylpiperazine	7.747	5.826
N-Ethyl-*N*-cyclohexylacetamide	7.957	5.336
2-Aminoheptane	8.417	1.075
3,5-Dimethyl-2-pyrazolecarboxamide	9.337	6.846
2-Amino-4,6-dihydroxypyrimidine	10.427	7.627
2,4-Dimethyl-3-pentanone	2.516	–
2-Azacyclooctanone	–	7.797
N-(3-Aminopropyl)morpholine	8.727	–
1-Piperazinoethylamine	–	9.680
N-Ethylolethylenediamine	9.817	–
Diethanolamine (DEA)	–	4.376
2,3-Dimethylperhydro-1,3-oxazine	10.297	–
2,6-Dimethylpiperazine	–	6.206
N,*N*-(3-Aminopropyl)piperazine	10.637	–
N,*N*-Diethylolpiperazine	–	7.186
N-{2-[Bis(methoxycarbonyl)amino]ethyl}-*N*-ethylolglycine	14.438	–
N-Methoxy-*N*-nitrosomethylamine	–	3.526

Table 2. Content of amines in experimental solutions

Solution	Content of amines, g-equiv l^{-1}		
	primary	secondary	tertiary
MEA from the absorber	1.34	0.39	0.09
Bottoms from the tank under the absorber	1.49	1.21	0.77
Bottoms distillation:			
fraction no. 1	4.17	0.42	0.42
fraction no. 2	2.65	1.71	0.26
fraction no. 3	1.46	1.96	0.87

Table 3. Effect of bottoms on the steel corrosion in hydrochloric acid solution

C_B, ml l^{-1}	$K_w \times 10^4$, g cm^{-2} h^{-1}	Z, %	Sample and its appearance
0	4.62	–	no. 1, pitting, cracks
10	2.64	44	
50	1.83	60	
10	2.62	46	no. 2 (contains
50	2.50	49	NaOH), pitting

the metal density), and the protection degree $Z = 1 - (K_w/K_w^0) \times 100$ (%, K_w^0 is the weight corrosion parameter in the individual solution) [6].

The corrosion parameters for the steel treated for 164 h in hydrochloric acid solution containing bottoms are listed in Table 3.

As seen from Table 3, the bottoms in question inhibit corrosion in the acidic media, but the protection degree is rather low, 44–60%, i.e., 9 points according to the scale of protection efficiency, and this inhibitor belongs to class V [6]. Thus, this bottoms can be used as corrosion inhibitors only at short contacts of metals with acid solutions.

We also studied the inhibiting effect of the bottoms on the steel corrosion in off-gas hydrochloric acid (150 ml l^{-1}). The results of our tests (330 h) are listed in Table 4.

As seen from Table 4, the bottoms at the 75 ml l^{-1} content strongly decelerate the corrosion rate of the steel in off-gas hydrochloric acid solution and decrease the depth corrosion parameter; the deceleration coefficient reaches 78.7% at 330-h contact.

The effect of bottoms in sodium chloride solution

is almost independent of the test time, and certain decrease in the corrosion rate is observed (Fig. 1). At 75 ml l^{-1} content of the bottoms the protection degree is satisfactory (7 points [6]).

Our visual tests showed that the corrosion pitting on the sample surface appeared in acid solutions after 164-h contact, whereas in neutral solutions the evidences of corrosion were observed only after 900 h.

During vacuum distillation of the bottoms some volatile fractions were separated. In this connection we studied the effect of bottoms on the rate of atmospheric corrosion. Steel samples were stored in a sealed vessel at room temperature over the sodium chloride solution containing bottoms (10–75 ml l^{-1}).

As seen from Fig. 2, the corrosion rate is the highest at the bottoms content of 10 ml l^{-1}. At the bottoms content increased to 75 ml l^{-1} the rate of atmospheric corrosion is several times lower. Visual examination showed that pitting appeared on the sample surface at bottoms content of 10 ml l^{-1} after 900 h.

We also studied the effect of bottoms on the corrosion of non-ferrous metals and alloys, in particular, M06 copper, L85 brass, and AD31 aluminum in 3% sodium chloride and sodium sulfate solutions. As seen, at bottoms content of 35 ml l^{-1} the rate of metal dissolution increases. The dependence of the catalytic effect $G = K_w/K_w^0$ of the additive on the time of copper and brass treatment in sodium chloride solution (Fig. 3a) shows that the catalytic effect of bottoms increases with time, and the most pronounced catalytic effect is observed in the case of brass corrosion (Fig. 3a, curve *2*).

Our visual observation showed that both in the absence and in the presence of bottoms the sample surface is coated with a dense smooth film, whose main component is CuOHCl, which is consistent with the data given in [9]. In solution containing bottoms this film appears after a longer period, the surface becomes glossy and retains the decorative properties for a long time.

The brass is coated with the oxide film after a longer time as compared to copper, and its decorative properties are higher.

As seen from the kinetic dependences of the catalytic effect of bottoms on copper and brass dissolution in sodium sulfate solutions (Fig. 3b), the catalytic effect on the copper corrosion is higher (curve *1*) as compared to brass (curve *2*). It should be noted that in the solution containing bottoms the sample surface after prolonged treatment remained clean and lustrous without any visual evidence of corrosion. Thus, the bottoms in question can be recommended as a polish-

Table 4. Effect of bottoms on the steel corrosion in hydrochloric acid solution

C_B (sample no. 3), ml l^{-1}	Steel brand	$K_w \times 10^4$, g cm^{-2} h^{-1}	$K_d \times 10^4$, mm per year	Z, %
0	65G	3.07	3.45	
	60S2A	1.04	1.17	
	65S2VA	1.36	1.53	
75	65G	0.61	0.69	78.7
	60S2A	0.34	0.38	64.2
	65S2VA	0.52	0.58	57.7

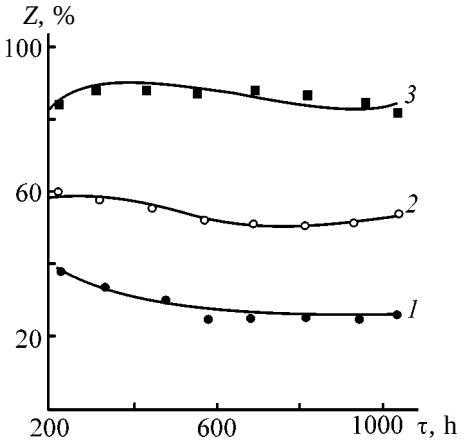

Fig. 1. Corrosion protection Z of 60S2A steel in NaCl (3%) + bottoms solution as a function of the contact time τ. Bottoms content, ml l^{-1}: (*1*) 10, (*2*) 15, and (*3*) 75.

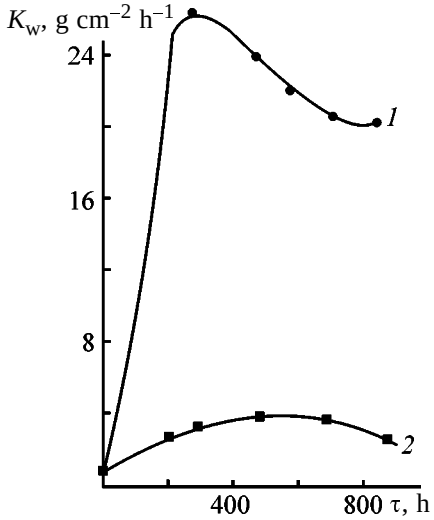

Fig. 2. Corrosion rate of steel in the atmosphere containing bottoms components and chloride ions as a function of time τ. (K_w) Weight corrosion parameter. Bottoms, ml l^{-1}: (*1*) 10 and (*2*) 75.

Table 5. Variation in the amine content in solutions in the course of corrosion tests for 900 h

Metal or alloy	Aggressive medium	C_B, ml l^{-1}	Content of amines, g-equiv l^{-1}		
			$[NH_2]$	[NH]	[N]
Steel	NaCl	10	0.015*/0.060	0.012/0.070	0.001/0.100
		75	0.113/0.330	0.090/0.170	0.008/0.510
Aluminum	NaCl	35	0.060/0.190	0.050/0.220	0.050/0.380
Copper	NaCl	35	0.060/0.050	0.050/0.040	0.050/0.110
Brass	Na_2SO_4	35	0.060/0.240	0.040/0.100	0.080/0.380

* The content of amines before and after the tests is given in the numerator and denominator, respectively.

ing agent for copper and its alloys with prolonged preservation of the decorative properties.

The bottoms in the chloride-containing solution catalyze the corrosion of aluminum, and the corrosion rate of aluminum is more than two orders of magnitude higher than in the bottoms-free solution. The aluminum sample in the bottoms-containing solution was coated with the corrosion products in several hours, and the corrosion rate was high throughout the period of visual observations.

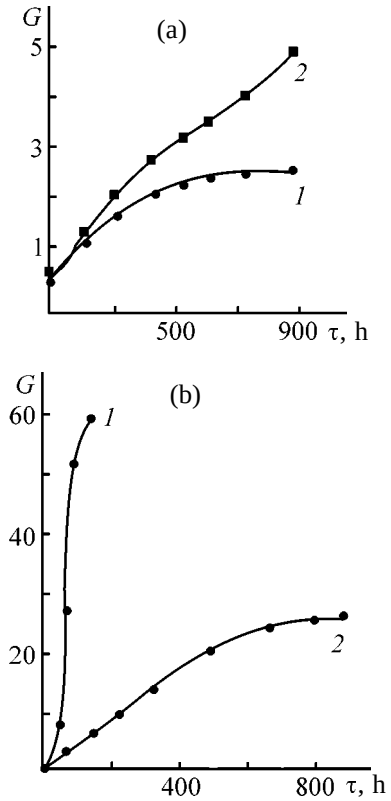

Fig. 3. Catalytic effect of bottoms *G* as a function of time τ in solutions of (a) sodium chloride and (b) sodium sulfate; (*1*) copper and (*2*) brass.

We also studied changes in the composition of corrosion-active media after corrosion of various alloys. In this case, the content of amines before and after the tests was determined by potentiometric titration; the results are listed in Table 5.

The increase in the amine content observed in most cases is probably due to the decomposition of amine compounds. The decrease in the content of primary and secondary amines in the tests with copper is probably caused by their conversion under the influence of corrosion products.

CONCLUSIONS

(1) The composition of the large-scale wastes from monoethanolamine treatment of pyrolysis hydrogen to remove carbon dioxide was studied.

(2) The bottoms after monoethanolamine treatment inhibit corrosion of steel with relatively poor and satisfactory protective power in acidic and neutral solutions, respectively, whereas in the case of nonferrous metals they catalyze corrosion and can be used as polishing agent for copper and brass.

(3) The bottoms inhibit the atmospheric corrosion of steel at their content in solution of 75 ml l^{-1}.

(4) In the course of corrosion tests the content of primary and secondary amines increases (or slightly decreases) in the case of copper.

REFERENCES

1. Koul', A.L. and Rizenfel'd, F.S., *Ochistka gaza* (Gas Purification), Moscow: Nedra, 1968.
2. Ferber, M.B., Metsik, R.E., and Rokhumyagin, E.I.,

Korroz. Zashch. Neftegaz. Prom–sti., 1979, no. 11, pp. 3–5.

3. Levkovich, M.I. and Kolesnikova, G.V., *Khim. Prom–st.*, 1972, no. 11, pp. 830–834.
4. Yazvikova, N.V., Zelenskaya, L.G., and Balyasnikova, L.V., *Zh. Prikl. Khim.*, 1975, vol. 48, no. 3, pp. 674–680.
5. Polderman, L.D., Dillon, C.P., and Steel, A.F., *Oil Gas J.*, 1967, vol. 65, no. 44, pp. 180–184.
6. Ivanov, E.S., *Ingibitory korrozii metallov v kislykh sredakh* (Inhibitors of Metal Corrosion in Acid Solutions), Moscow: Metallurgiya, 1986.
7. US Patent 4504279.
8. Munyaev, V.M., Brintsev, A.I., and Khachaturov, I.E., *Tr. Severo-Kavkaz. Naucho-Issled. Proektn. Inst. Neft. Prom–sti*., 1985, no. 43, pp. 20–25.
9. Romanian Patent 84773.
10. FRG Patent 3501180.

Russian Journal of Applied Chemistry, Vol. 75, No. 1, 2002, pp. 68–70. Translated from Zhurnal Prikladnoi Khimii, Vol. 75, No. 1, 2002, pp. 67–70.
Original Russian Text Copyright © 2002 by Aleksandrov, Shekunova, Kolmakov, Tarasov.

CATALYSIS

Carbonylation of Methanol with Carbon Monoxide in the Presence of Sulfur-containing Catalysts

Yu. A. Aleksandrov, V. M. Shekunova, A. O. Kolmakov, and E. H. Tarasov

Research Institute of Chemistry, Lobachevskii Nizhni Novgorod State University, Nizhni Novgorod, Russia

Received June 25, 2001

Abstract—Physicochemical features of methanol carbonylation with carbon monoxide catalyzed with sodium sulfides Na_2S_x (x = 1, 2, 4) were studied. The effect of admixtures of sulfur dioxide in the gas phase on the yield of the target product (methyl formate) was revealed.

Methanol is a versatile intermediate, which can be used in syntheses of various chemical substances by the reaction with carbon monoxide or synthesis gas [1]. Some of such syntheses are performed on the commercial scale, e.g., production of acetic acid by catalytic carbonylation of methanol using complex rhodium homogeneous catalyst. It is well known [2] that base catalysts effect formation of methyl formate by reaction of carbon monoxide with methanol at elevated pressure:

$$CH_3OH + CO \xrightarrow{\text{Cat.}} HCO_2CH_3. \quad (1)$$

Methyl formate is formed in a high yield with sodium methylate as catalyst. However, metallic sodium is required for the synthesis of this catalyst, which restricts its use.

It was shown previously [3, 4] that sulfur-containing catalysts can be used for the synthesis of urethanes by carbonylation of aromatic nitro compounds with carbon monoxide in methanol.

The goal of this work was to study carbonylation of methanol with carbon monoxide in the presence of sulfur-containing catalysts.

Sodium sulfides Na_2S_x with x = 1, 2, 4, which are relatively available and cheap commercial products, were used as catalysts.

As seen from Table 1, anhydrous sodium monosulfide is the most active catalyst. With increasing its concentration within the 0.3–1.2 M range, the yield of the target product (methyl formate) increases to 95%. As opposed to nitrobenzene carbonylation [5], V(V) compounds, pyridine, or polyethylene glycol added as activators of sulfur-containing catalysts did not increase the methyl formate yield.

The catalytic activity of sodium sulfide in carbonylation of methanol with carbon monoxide depends on the solvent (Table 2). This reaction proceeds most easily in neat methanol or in aromatic hydrocarbons (benzene, toluene). The yield of methyl formate at the constant Na_2S : methanol ratio increases with increasing methanol concentration in benzene from 1.3 to 5.0 M. The further growth of the methanol concentration up to pure methanol does not increase the methyl formate yield. The above results can be explained by variation of the solvent polarity and CO solubility in the solvent.

Water added to methanol even in small amounts (0.2–0.4 M) noticeably inhibits the reaction and practically stops it at concentrations higher than 0.9 M (Table 3). This effect is probably caused by deactivation of the catalyst due to its shielding by the hydrate shell.

Table 1. Activity of sulfur-containing catalysts in carbonylation of methanol with carbon monoxide* (1 h, temperature 80°C, CO pressure 15 MPa)

Catalyst	C_c, M	Y_{mf}, %	P_c, g l^{-1} h^{-1}
Na_2S	0.3	80	1190
	0.6	90	1338
	1.2	95	1396
Na_2S_2	0.6	10	146
Na_2S_4	0.6	8	117
Na_2S : KVO_3	0.6 : 0.06	89	1323
Na_2S : pyridine	0.6 : 0.6	85	1260
Na_2S : polyethylene glycol	0.6 : 0.6	85	1266

* Y_{mf} is the yield of methyl formate; P_c is the catalyst performance.

1070-4272/02/7501-0068$27.00 © 2002 MAIK "Nauka/Interperiodica"

Table 2. Effect of solvent on carbonylation of methanol with carbon monoxide in the presence of sodium sulfide* (1 h, temperature 80°C, CO pressure 10 MPa)

Solvent	C_{CH_3OH}, M	K_{CH_3OH},** %	S,** %	Y_{mf}, %	P_c, g l^{-1} h^{-1}
–	24.8	94	90	85	1266
CCl_4	5.0	0	0	0	0
Dioxane	5.0	1	80	1	3
Ethyl acetate	5.0	94	29	27	79
Chlorobenzene	5.0	96	80	77	227
THF	5.0	86	90	77	227
Toluene	5.0	97	85	82	241
Benzene	1.3	71	69	49	34
	2.5	80	77	62	91
	5.0	96	89	86	251
	9.9	94	88	84	466

* Molar ratio Na_2S : methanol = 0.024; the same for Tables 4 and 5.
** K_{CH_3OH} is the methanol conversion; S is the selectivity with respect to methyl formate.

The effect of the CO pressure on the methanol carbonylation in benzene in the presence of sodium sulfide was also studied (Table 4). As the CO pressure is increased from 3 to 7 Mpa, the methyl formate yield grows substantially, but it does not appreciable grow further at the pressure of about 15 MPa.

The carbonylation rate noticeably increases with the CO pressure. For instance, at the CO pressure of 10 MPa the methyl formate yield in 10 min is the same as in 60 min at 7 MPa; in 10 min at 7 MPa the yield is lower by half.

The temperature also affects the methanol carbonylation with CO (Table 5). The maximal yield is observed at 80°C. At lower temperatures, the reaction is too slow. At higher temperatures, the methyl formate yield also decreases probably because of low thermal stability of the intermediate participating in the catalytic step; both methanol conversion and reaction selectivity with respect to methanol decrease.

The above results suggest the following scheme of the catalytic carbonylation of methanol with CO:

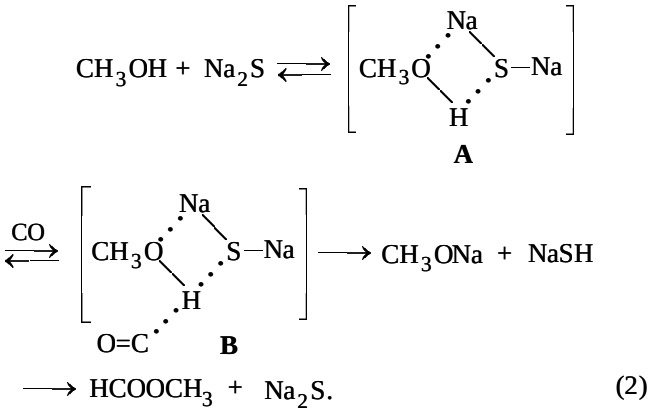

(2)

Table 3. Effect of water on carbonylation of methanol with carbon monoxide in the presence of sodium sulfide* (1 h, temperature 80°C, CO pressure 10 MPa)

C_{H_2O}, M	Y_{mf}, %	P_c, g l^{-1} h^{-1}
0.2	85	1266
0.4	69	1024
0.9	1	14
1.8	Traces	Not determined
7.4	0	0

* Initial concentration of Na_2S 0.6 M.

Table 4. Catalytic carbonylation of methanol in benzene at various CO pressures and 80°C

P_{CO}, MPa	τ, min	K_{CH_3OH}, %	S, %	Y_{mf}, %	P_c, g l^{-1} h^{-1}
3	60	65	76	49	144
5	60	89	86	77	226
7	60	95	88	84	247
10	60	96	89	86	251
15	60	98	92	90	263
7	10	59	80	42	735
10	10	96	86	82	1442

Table 5. Catalytic carbonylation of methanol with carbon monoxide in benzene (1 h, CO pressure 10 MPa)

T, °C	Y_{mf}, %	P_c, g l^{-1} h^{-1}
60	62	183
80	85	251
100	71	209
180	21	62

Table 6. Effect of SO_2 on methanol carbonylation with carbon monoxide in the presence of sodium sulfide* (0.5 h, 80°C, CO pressure 10 MPa)

C_{SO_2}, vol %	P_{SO_2}, MPa	Y_{mf}, %
0	0	97
0.72	0.06	97
1.05	0.09	50
1.30	0.11	25
5.61	0.49	Traces

* Initial Na_2S concentration 1.2 M.

Methanol forms hydrogen-bonded intermediate **A** with sodium sulfide and then **A** reacts with CO to form intermediate **B**. The latter rearranges through sodium methylate and hydrosulfide and converts into methyl formate with regeneration of sodium sulfide. In addition, **A** can decompose with formation of sodium methylate and sodium hydrosulfide.

Saturation observed with increasing the methanol concentration in the solvent (Table 2) and the effect of the temperature on the target product yield (Table 5) confirm formation of intermediate **B**. Inhibition of the reaction by water is explained by blocking of the active centers of the catalyst by the hydrate shell. It is well known [6] that small admixtures of sulfur compounds in exhaust gases deactivate many catalytic systems. Therefore, we studied the effect of acidic gaseous admixtures, in particular, sulfur dioxide, which are present together with CO in exhaust gases of metallurgic, heat and power, and other plants and can affect carbonylation of methanol with carbon monoxide.

The initial SO_2 concentration in the gas mixture was varied within the 0–5.61 vol % range (Table 6). As seen, at an SO_2 content from 0.72 to 1.30 vol % carbonylation of methanol is inhibited, and at 5.61 vol % it completely stops.

EXPERIMENTAL

Anhydrous Na_2S was prepared by dehydration of $Na_2S \cdot 9H_2O$ [7]. Na_2S_2 and Na_2S_4 were synthesized by fusion of anhydrous Na_2S with stoichiometric amounts of chemically pure grade sulfur [8].

CO and SO_2 were used without additional purification. Methanol, benzene, toluene, dioxane, tetrahydrofuran, chlorobenzene, ethyl acetate, and carbon tetrachloride were purified by common procedures [9].

Carbonylation of methanol was performed in a stainless steel (KhM-18) 50 cm^3 autoclave charged with the calculated amounts of methanol and catalysts. The autoclave was purged with carbon monoxide at continuous agitation of the reaction mixture. After that CO was pumped to a pressure of 6–10 MPa. Then the temperature of the experiment, which was monitored with a thermometer inserted into the body of the autoclave, and the required pressure were set. This instant was taken as the reaction start. The reaction process was monitored by the pressure decrease. After the reaction completion, the autoclave was cooled, and the pressure was relieved. Liquid reaction products were analyzed by GLC on a Tsvet-101 chromatograph with a thermal conductivity detector. Helium was used as a carrier gas (flow rate 30 $cm^3\ min^{-1}$); 3000×3 mm glass column was used; stationary phase PEG 1500, temperature 60°C.

CONCLUSION

Anhydrous sodium sulfide is the effective catalyst of carbonylation of methanol with carbon monoxide. Sulfur dioxide as an admixture in CO deactivates the reaction.

REFERENCES

1. Sheldon, R.A., *Chemicals from Synthesis Gas: Catalytic Reactions of CO and H_2*, Dordrecht: Reidel, 1983.
2. Tagaev, O.A., Gashchuk, M.D., Padzerskii, Yu.A., and Moiseev, I.I., *Izv. Akad. Nauk SSSR, Ser. Khim.*, 1982, no. 11, p. 2638.
3. Bordzilovskii, V.Ya., Redoshkin, B.A., Gerega, V.F., *et al.*, *Zh. Prikl. Khim.*, 1984, vol. 57, no. 2, pp. 360–363.
4. Redoshkin, B.A., Bordzilovskii, V.Ya., Gerega, V.F., *et al.*, *Zh. Prikl. Khim.*, 1984, vol. 57, no.3, pp. 600–602.
5. Kolmakov, A.O., Shekunova, V.M., and Aleksandrov, Yu.A., *Zh. Obshch. Khim.*, 1998, vol. 68, no. 8, p. 1405.
6. Sokolovskii, V.D., Yur'eva, T.M., Matros, Yu.Sh., *et al.*, *Usp. Khim.*, 1989, vol. 18, no. 1, pp. 5–37.
7. Klyuchnikov, N.G., *Neorganicheskii sintez* (Inorganic Synthesis), Moscow: Prosveshchenie, 1983.
8. *Handbuch der präparativen anorganischen Chemie*, Brauer, G. von, Ed., Stuttgart: Enke, 1978.
9. *Organic Solvents. Physical Properties and Methods of Purification*, Weissberger, A., Proskauer, E.S., Riddick, J.A., and Toops, E.E., Eds., New York: Interscience, 1955.

Russian Journal of Applied Chemistry, Vol. 75, No. 1, 2002, pp. 71–74. Translated from Zhurnal Prikladnoi Khimii, Vol. 75, No. 1, 2002, pp. 71–74.
Original Russian Text Copyright © 2002 by Gafurova, Khakimzhanov, Mukhamediev, Musaev.

ENVIRONMENTAL PROBLEMS OF CHEMISTRY AND TECHNOLOGY

Sorption of Cr(VI) on the Anion-Exchange Fibrous Material Based on Nitron

D. A. Gafurova, B. Sh. Khakimzhanov, M. G. Mukhamediev, and U. N. Musaev

Ulugbek National University, Tashkent, Uzbekistan

Received April 27, 2000; in final form, October 2001

Abstract—The kinetics and thermodynamics of Cr(VI) sorption under the static and dynamic conditions on the fibrous sorbent SMA-1 prepared by chemical modification of polyacrylonitrile were studied.

One of the main environmental problems is treatment of industrial wastewaters and sources of drinking water to remove ions of toxic metals (e.g., Zn, Cr, Cu, etc.) [1]. Among them the removal of chromium is the most urgent, because its compounds, being strong oxidants, negatively affect the human vital organs such as kidneys, liver, and brain. The removal of Cr(VI) from aqueous (especially acidic) solutions by sorption is rather difficult, because it oxidizes functional groups of the sorbent and causes its degradation. In the literature, major attention has been concentrated on the treatment of industrial wastewaters using granular anionic AV-17 × 8 [2] and EDE-10P [3] and some amphoteric ion exchangers [4]. The highest sorption of Cr(VI) on the AV-17 × 8 anion exchangers is observed at pH 1–4, and with increasing pH it gradually decreases. The EDE-10P anion exchanger is readily oxidized by dichromate ions, and thus is unsuitable for removing chromium from industrial wastewaters.

The advantage of fibrous anion exchangers as compared to granular sorbents is their strongly developed active surface providing high rates of sorption and desorption.

The sorption properties of the VION-AN-1 modified polyacrylonitrile ion-exchange fiber in removal of Cr(VI) from electroplating production wastewaters were studied in [5]. This fiber contains basic vinylpyridine groups with the static exchange capacity (SEC) of 1.1–1.2 mg-equiv g^{-1}, but the capacity of such sorbents for chromium is as low as 15 mg g^{-1} sorbent. Moreover, in the course of regeneration, due to the opening of pyridine rings with alkali, the above sorbents undergo strong degradation.

The anion-exchange fibrous sorbents were prepared by chemical modification of the Nitron fiber using nitrogen-containing bases such as hydroxylamine, hydrazine, ethylenediamine, and hexamethylenediamine (HMD) [6]. It was found that, among the ion exchangers prepared, the SMA-1 sorbent prepared by modification of Nitron fiber with HMD is the best suited for sorption removal of Cr(VI) from aqueous solutions.

The sorption of Cr(VI) was studied at pH 1–10 under the static conditions. A sorbent sample (1 g) in the chloride form was placed into an aqueous solution (200 ml) of potassium dichromate whose concentration was varied a wide range. The content of $Cr_2O_7^{2-}$ ions before and after sorption was analyzed by photocolorimetry using the calibration plot of the optical density of solutions on the concentration of dichromate ions at λ = 364 nm. The specific sorption $\Delta X/m$ was calculated from the following equation:

$$\Delta X/m = (C_0 - C_\tau)V/Mm,$$

where ΔX is the amount of sorbed anions (M), m is the sorbent weight (g), C_0 and C_τ are the concentrations of dichromate ions in solution before and after sorption (g l^{-1}), V is the solution volume (l), and M is the molecular weight of the ions (g mol^{-1}).

The sorption of dichromate anions by SMA-1 sorbent was studied as influenced by the time, temperature, and concentration of $Cr_2O_7^{2-}$ ions in the initial solution. As seen from Figs. 1 and 2, in all the cases the sorption equilibrium between the fiber and solution is attained in 3–5 min. With increasing temperature the specific sorption slightly decreases.

The sorption isotherms of $Cr_2O_7^{2-}$ ions on the SMA-1 sorbent at various temperatures are shown in Fig. 3. As seen, with increasing concentration of dichromate ions in the initial solution their sorption in-

1070-4272/02/7501-0071$27.00 © 2002 MAIK "Nauka/Interperiodica"

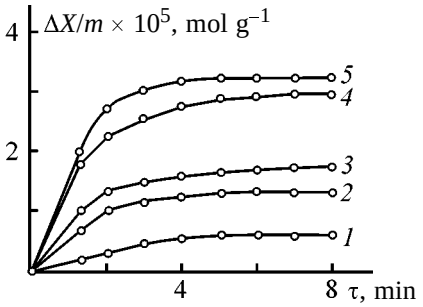

Fig. 1. Kinetics of dichromate ion sorption on the SMA-1 anion-exchange fiber at 20°C and various $Cr_2O_7^{2-}$ ion concentrations. ($\Delta X/m$) Specific sorption and (τ) sorption time; the same for Fig. 2. Solution concentration, mg l^{-1}: (*1*) 100, (*2*) 200, (*3*) 300, (*4*) 400, and (*5*) 500.

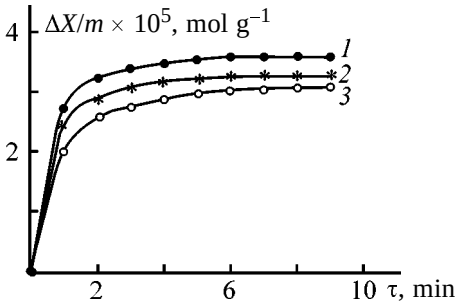

Fig. 2. Kinetics of dichromate ion sorption on the SMA-1 anion-exchange fiber at the initial $Cr_2O_7^{2-}$ ion concentration of 500 mg l^{-1} and various temperatures. Temperature, °C: (*1*) 20, (*2*) 30, and (*3*) 40; the same for Figs. 3 and 4.

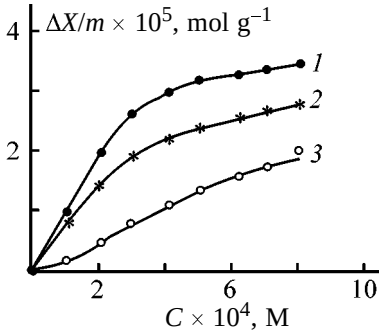

Fig. 3. Sorption isotherms of dichromate ions on the SMA-1 anion-exchange fiber: specific sorption $\Delta X/m$ vs. initial concentration of $Cr_2O_7^{2-}$ ions *C*.

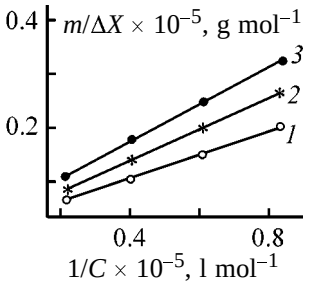

Fig. 4. Plot of $1/\Gamma$ vs. $1/C$.

creases, whereas with increasing temperature it decreases.

It is known that, in terms of the law of mass action, heterogeneous processes of addition and substitution involving the constant number of functional groups can be described by the Langmuir equations [7], and thus the sorption isotherms are presented as follows:

$$\Gamma = \Gamma_\infty KC/(1 + KC),$$

where K is the adsorption equilibrium constant, C is the current solution concentration (M), and Γ_∞ is the maximal sorption for the given temperature.

To determine K and Γ_∞, the Langmuir equation is often brought to the form

$$1/\Gamma = 1/\Gamma_\infty + (B/\Gamma_\infty)(1/C),$$

where $B = 1/K$.

Then, the $1/\Gamma$–$1/C$ dependences are plotted; the slope and the section cut off on the ordinate axis give the B/Γ_∞ and $1/\Gamma_\infty$ values, respectively. Such typical dependences for sorption of $Cr_2O_7^{2-}$ ions with SMA-1 sorbent at various temperatures are shown in Fig. 4.

The thermodynamic functions were calculated from the temperature dependence of the equilibrium constant. For this purpose the $R\ln K$–$1/T$ dependence was plotted, and then ΔH was calculated from the slope of this dependence. The ΔS value was calculated from the equation

$$\Delta S = (\Delta H - \Delta G)/T.$$

As seen from Table 1, the equilibrium sorption constants are significantly greater that 1, which suggests the selectivity of dichromate ion sorption on the SMA-1 sorbent; sorption proceeds with decrease in the free energy, enthalpy, and entropy of the system. The decrease in the two latter parameters indicates very strong binding of Cr(VI) with the sorbent.

Table 1. Thermodynamic functions of dichromate ion sorption on the SMA-1 sorbent*

T, K	Γ_∞, mol g^{-1}	*K*	ΔG, J mol^{-1}	ΔS, J mol^{-1} K^{-1}
293	0.04	609.7	–15617	–168.54
303	0.03	250.0	–13908	–168.62
313	0.02	97.7	–11925	–169.57

* ΔH = 65000 J mol^{-1}.

Table 2. Dynamic exchange capacity of SMA-1 sorbent for dichromate ions as influenced by solution pH

pH	DEC, mg g^{-1}		pH	DEC, mg g^{-1}	
	for $Cr_2O_7^{2-}$	recalculated to Cr		for $Cr_2O_7^{2-}$	recalculated to Cr
1.0	303	106	7.3	187.3	66
4.2	390	137	8.0	208	73
4.8	239	84	8.2	191	67
5.3	178.6	63	10	156	55
6.5	160	56			

Table 3. DEC of the SMA-1 sorbent for $Cr_2O_7^{2-}$ ion as influenced by the number of regeneration cycles with 5% potassium hydroxide solution

Cycle no.	DEC, mg g^{-1}		Cycle no.	DEC, mg g^{-1}	
	for $Cr_2O_7^{2-}$	recalculated to Cr		for $Cr_2O_7^{2-}$	recalculated to Cr
Before regeneration	303	106	6	230	81
1	250	88	7	225	79
2	230	81	8	200	70
3	240	84	9	200	70
4	245	86	10	200	70
5	237.5	83			

Table 4. DEC of the SMA-1 sorbent (SEC for HCl 2.5 mg-equiv g^{-1}) for $Cr_2O_7^{2-}$ ion as influenced by the concentration and flow rate of potassium dichromate solution

$[K_2Cr_2O_7]$, g l^{-1}	*v*, ml min^{-1}	DEC, mg g^{-1}		pH	
		for $Cr_2O_7^{2-}$	recalculated to Cr	before sorption	after sorption
1.0	50	279	98	4.0	5.8
0.5	50	255	90	4.1	5.8
0.1	50	245	86	4.2	5.8
0.01	50	235	82	4.5	5.8
0.001	50	231	81	4.9	5.8
0.5	50	255	90	4.1	5.8
0.5	100	175	62	4.1	5.8
0.5	300	165	58	4.1	5.8
0.5	375	160	56	4.1	5.8

To evaluate the performance of SMA-1 sorbent in treatment of industrial wastewaters to remove chromium(VI) compounds, the dynamic sorption mode was developed using model solutions. The sorbent prepared by modification of polyacrylonitrile with HMD (SMA-1) was packed into a column (0.2 g cm^{-3} bulk density) and activated with 0.1 M hydrochloric acid solution, after which a potassium dichromate solution (1 g l^{-1}) was passed. The dynamic exchange capacity (DEC) of the sorbent for chromium(VI) reached 390 mg g^{-1} at pH 4.2 (Table 2). As seen from these data, the sorption of Cr(VI) compounds depends on pH influencing the speciation of chromium ions.

It is known that at pH < 7 the solution contains $HCrO_4^-$ and $Cr_2O_7^{2-}$ ions, whereas at pH > 7 $HCrO_4^-$ and CrO_4^{2-} prevail [8]. Owing to the presence of highly basic groups in the sorbent, the sorption of Cr(VI) at pH 8–10 is sufficiently strong.

The sorbent was regenerated with 5% aqueous solution of potassium hydroxide. We found that the sorbent exhibits high chemical stability and can be reused. As seen from Table 3, after ten sorption–desorption cycles DEC remains rather constant. The data on DEC as influenced by the $K_2Cr_2O_7$ concentration in solution and flow rate of the solutions through the sorbent bed are listed in Table 4. In the pH range

studied our sorbents efficiently recover chromium(VI) compounds from solution even at concentrations of the order of 1 mg l^{-1} (Table 2).

At a 3–4-fold increase in the flow rate of the model solution through the sorbent bed, the sorption capacity of the SMA-1 sorbent remains high and can meet the requirements of the water treatment process.

CONCLUSION

(1) The sorption properties of the SMA-1 sorbent prepared by chemical modification of Nitron fiber with hexamethylenediamine exceed the properties of all the known ion exchangers based on acrylonitrile.

(2) Sorption proceeds without diffusion hindrance, and the sorption capacity of the sorbent for chromium reaches 137 mg g^{-1}. The sorbent developed can be used in the treatment of electroplating production wastewaters to remove chromium(VI) compounds and in concentration of process solutions.

REFERENCES

1. Zakharov, S.V. and Zverev, M.P., *Ekol. Prom–st. Ross*., 1997, November, pp. 18–20.
2. Antipova, V.P., *Ochistka Stochn. Vod*, 1969, no. 3, pp. 39–49.
3. Gutsanu, V.L. and Muntyap, S.A., *Zh. Prikl. Khim*., 1985, vol. 58, no. 9, pp. 1981–1986.
4. Uzb. Patent no. 3793, *Byull. Izobret*., 1996, no. 3.
5. Zhukov, N.A., Zholobova, L.V., Kuznetsov, N.P., *et al*., *Ekol. Prom–st. Ross.*, 1998, January, pp. 17–19.
6. Gafurova, D.A., Musaev, U.N., Khakimzhanov, B.Sh., and Mukhamediev, M.G., *Vestn. Tashkent. Gos. Univ*., 1999, no. 2, pp. 27–29.
7. Kokotov, Yu.A. and Pasechnik, V.A., *Ravnovesiya i kinetika ionnogo obmena* (Equilibria and Kinetics of Ion Exchange), Leningrad: Khimiya, 1970.
8. Tolstikov, V.P., *Zh. Obshch. Khim*., 1969, vol. 39, no. 2, pp. 240–247.

Russian Journal of Applied Chemistry, Vol. 75, No. 1, 2002, pp. 75–79. Translated from Zhurnal Prikladnoi Khimii, Vol. 75, No. 1, 2002, pp. 75–79.
Original Russian Text Copyright © 2002 by Ostroukhova, Zenkevich, Yuzikhin, Dolzhenko.

ENVIRONMENTAL PROBLEMS OF CHEMISTRY AND TECHNOLOGY

Specific Features of Reversed-Phase High-Performance Liquid Chromatography as Applied to Determining the Distribution Coefficients of Pesticides in the Hexane–Acetonitrile System

O. K. Ostroukhova, I. G. Zenkevich, O. S. Yuzikhin, and V. I. Dolzhenko

Research Institute of Chemistry, St. Petersburg State University, St. Petersburg, Russia
Russian Institute of Plant Protection, St. Petersburg, Russia

Received May 10, 2001

Abstract—The suitability of reversed-phase high-performance liquid chromatography for determining the distribution coefficients of organic compounds in the hexane–acetonitrile system was considered. A version of the necessary additional step in the sample preparation procedure was proposed, namely, changing from nonpolar hexane to a solvent unlimitedly miscible with the eluent. The distribution coefficients were determined for 20 pesticides by the proposed method and compared with those determined by gas chromatography.

Extensive use of chemical agents for plant protection (pesticides) requires efficient methods of their identification and determination of the residual amounts of them in agricultural products and environmental objects [1]. This problem can be solved by taking new approaches to development of the procedures for determining the residual amounts of pesticides. Many of these approaches are based on such characteristic of pesticides as their distribution coefficient K_d in heterophase systems of organic solvents.

The distribution coefficients K_d can be regarded as a characteristic of organic compounds like boiling point, refractive index, gas-chromatographic retention index, etc. Reference books usually cite, e.g., for pesticides, along with other physicochemical constants, the logarithms of their distribution coefficients in the octanol–water system ($\log P$) characterizing the lipophilic properties of these compounds [2] and their sorption and bioaccumulation abilities [3–5]. Thus, $\log P$ is an important parameter indirectly characterizing the behavior of toxicants in the environmental objects [3, 4]. But this characteristic is of little use for analytical purposes because of unsatisfactory rheological (high viscosity) and chromatographic (aqueous solution dosing is undesirable) properties of the system components. It is more convenient to use systems of low-boiling organic solvents, e.g., hexane–acetonitrile, as these solvents are most widely used as extracting agents for determining the residual amounts of pesticides in various objects [6]. Also, this system was suggested for identification of pesticides based on the K_d parameters [6].

Up to now, K_d has been mostly determined by three methods: titrimetric, photometric, and gas-chromatographic. The two first-named methods are typically used for aqueous–organic systems, in particular, for measuring $\log P$. The third, gas-chromatographic method, which received the independent name of partition chromatography [7, 8], is preferable for heterophase systems comprised of organic solvents exhibiting limited miscibility with respect to each other. However, this method is unsuitable for thermally unstable and low-volatile substances. Liquid chromatography virtually was not used for determining K_d of this kind of substances (in particular, pesticides), though such possibility was mentioned in the monograph [8].

The aim of this work was to study the specific features of reversed-phase high-performance liquid chromatography (HPLC) as applied to determining K_d of pesticides extensively used now in the Russian Federation.

EXPERIMENTAL

For determining K_d we selected 20 pesticides belonging, for the most part, to three chemical groups (organophosphorus compounds, heterocyclic compounds, namely, derivatives of pyridine, triazole, and tetrazole, and pyretroids, that is, derivatives of cyclopropanecarboxylic acid). They were dissolved (1 mg ml^{-1}) in acetonitrile (ultrapure grade) saturated with hexane (as recommended in [9], in K_d determina-

1070-4272/02/7501-0075$27.00 © 2002 MAIK "Nauka/Interperiodica"

tion the sum of the concentrations of the substances being characterized should not exceed 3 wt % as calculated for the total volume of the two phases).

To determine K_d of the pesticides by gas chromatography (reference method) we placed 3 ml of the solution of pesticide in acetonitrile into standard 10-ml test tubes. Next, an equal volume of hexane (chemically pure grade) saturated with acetonitrile was added. After shaking for 1 min, the test tubes were kept for 5–10 min at room temperature (21 ± 2°C). Each layer was analyzed chromatographically on a Mega (Carlo Erba, Italy) gas chromatograph with a flame-ionization detector and a 10 m × 0.53 mm capillary column (HP-1 stationary phase as 2.65-μm-thick film; temperature programming within 120–280°C, 10 deg min^{-1}). The flow division ratio was 1 : 5. The vaporizer temperature was 280°C. Equal volumes of each layer of the heterophase system (1 μl) were dosed with a Hamilton microsyringe. To prevent contamination of the lower-layer sample (acetonitrile) during passing of the syringe needle through the upper layer (hexane), the sample volume taken was increased to 5 μl and brought to the desired volume (1 μl) immediately before introduction into the chromatograph. The peak area was determined using Multichrom software. The parameter K_d for the pesticides was calculated by the formula

$$K_d = S_1/S_2. \quad (1)$$

Here, S_1 and S_2 are the peak areas of the analyzed substance in the hexane and acetonitrile phases, respectively.

In reversed-phase HPLC experiments we placed into standard 15-ml test tubes 5 ml of the solution of pesticide in acetonitrile, to which equal volume of hexane saturated with acetonitrile was added. After shaking for 1 min the test tubes were kept for 5–10 min at 16°C. Next, the heterophase system was transferred to a separatory funnel, and the lower acetonitrile layer was separated from the hexane layer. The hexane solution was placed into a weighing bottle, and the solvent was evaporated in a vent hood at room temperature. Acetonitrile (1 ml) was added to the dry residue, and the weighing bottle was placed into an ultrasonic bath for 5 min (for exhaustive dissolution of dry residue). Each layer was analyzed on a Waters liquid chromatograph with a Nova-Pak C18 (3.9 × 150 mm) column and UV detector. The detection wavelengths were 220 and 254 nm.

As mobile phase for compound nos. 1–16 (Table 1) in isocratic mode we used 50% aqueous acetonitrile and for compound nos. 17–20, 80% aqueous acetonitrile. The eluent flow rate was 1 ml min^{-1}.

The samples were dosed (5 μl) and injected automatically. The peak areas were determined using the Millenium software. The K_d parameters for the pesticides were calculated by the equation

$$K_d = S_1/(S_2 k). \quad (2)$$

Here, $k = V_1/V_2$ is the degree of concentration, i.e., the ratio of the hexane phase volume V_1 to that of the resulting solution in acetonitrile V_2 after changing to another solvent (k = 5 or 8).

The reproducibility of the K_d values was judged from attaining relative standard deviations under 0.15 for 3–5 measurements [9].

The distribution coefficient is essentially the ratio of the equilibrium concentrations of a substance in the coexisting layers of the heterophase system of solvents [8, 10]. Also, the distribution coefficient can be calculated using the parameter $\bar{P}$, as suggested by Beroza and Bowman [7]. This parameter is defined as the ratio of the concentrations of the analyzed substance in the nonpolar phase before and after adding the polar phase. The parameters K_d and $\bar{P}$ are interrelated as

$$K_d = \frac{\bar{P}}{\alpha(1 - \bar{P})}, \quad (3)$$

Here, α is the volume ratio of two immiscible phases (typically α = 1).

By contrast to direct methods of determining K_d, that is, from the ratio of the intensities of the analytical signals for the coexisting phases with arbitrary volume [formula (1)], the inaccuracies in calculating K_d by formula (3) depend not only on those of determining the chromatographic peak areas but also on those of measuring the phase volume ratio α.

Direct determination of K_d (titrimetrically and photometrically), as well as determination of the parameters $\bar{P}$, typically involves analysis of only one of the two phases of the heterophase system before and after mixing. Based on the difference, one determines the concentration of the substance in the other phase, which makes it possible to calculate K_d. The main sources of inaccuracy in determining K_d are unequal phase volumes analyzed before and after mixing, the inaccuracy of determining the equivalent point (in the case of titrimetric analysis), and falling of the optical density of the samples beyond the range

Table 1. Distribution coefficients of pesticides in the hexane–acetonitrile system (the degree of concentration after changing to another solvent $k = 5$)

Compound no.	Compound	$[K_d(\text{GLC}) \pm \bar{S}_k] \times 10^{-2}$	$[K_d(\text{HPLC}) \pm \bar{S}_k] \times 10^{-2}$		$[K_d(\text{HPLC}) - K_d(\text{GLC})]/K_d(\text{GLC})$, %
			$\lambda = 220$ nm	$\lambda = 254$ nm	
1	Metribusin	1.6 ± 0.2	1.9 ± 0.3	1.9 ± 0.3	+19
2	Dimethoate	0.60 ± 0.05	0.60 ± 0.05	0.50 ± 0.05	0
3	Pirimicarb	6.1 ± 0.7	8.6 ± 0.8	8.5 ± 0.8	+41
4	Methyl parathion	1.5 ± 0.2	2.3 ± 0.3	2.3 ± 0.3	+53
5	Acetochlor	15 ± 2	12 ± 2	12 ± 2	–20
6	Fenitrothion	3.4 ± 0.5	2.8 ± 0.3	2.8 ± 0.3	–18
7	Fenthion	14 ± 2	7.0 ± 0.7	6.9 ± 0.8	–50
8	Triadimefon	6.3 ± 0.7	3.4 ± 0.4	3.3 ± 0.4	–46
9	Diazinone	41 ± 5	30 ± 5	30 ± 5	–27
10	Tebuconazole	2.8 ± 0.3	3.6 ± 0.5	3.6 ± 0.5	+9
11	Diniconazole	6.4 ± 0.5	7.0 ± 0.8	7.0 ± 0.7	+29
12	Malathion	2.5 ± 0.2	2.8 ± 0.3	2.6 ± 0.3	+12
13	Propiconazole	6.2 ± 0.6	6.1 ± 0.6	6.7 ± 0.9	–6
14	Chlorpyrifos	33 ± 3	31 ± 4	32 ± 4	–2
15	Tetraconazole**	1.0 ± 0.1	–	–	–
16	Prochloraz	0.9 ± 0.1	3.5 ± 0.4	3.6 ± 0.3	+289***
17	β-Cypermethrin	7.2 ± 0.8	5.5 ± 0.6	5.6 ± 0.6	–24
18	Esfenvalerate	6.2 ± 0.8	6.1 ± 0.2	6.2 ± 0.3	–2
19	Biphentrin	59 ± 4	58 ± 3	58 ± 3	–2
20	Deltamethrin	5.4 ± 0.6	6.9 ± 0.3	7.0 ± 0.4	+28
Average relative deviation with the sign taken into account (minus Prochloraz), %					–0.3 ± 28

* According to the data for the detection wavelength of 220 nm.
** The outlier revealed after the concentration degree was increased.
*** The only example of abnormal differences in the K_d values determined by different methods.

of validity of the Bouguer–Lambert–Beer law (photometric analysis) [11].

When applied to the system of limitedly miscible low-boiling organic solvents, gas chromatography allows direct analysis of each phase of the heterophase system. Therefore, the main sources of inaccuracy in measuring K_d are those in measuring the peak areas and the possible variability of the concentration ratio of the substances being characterized at variations of their concentrations (deviations from Henry's law).

Analysis of each phase of the heterophase hexane–acetonitrile system by reversed-phase HPLC (by contrast to GLC) requires additional sample preparation procedure so as to exclude dosing into chromatograph of solutions of the samples in nonpolar solvents (especially with organic solvent–water mixtures as eluents). For such samples, hydrophobic solvents should be replaced by hydrophilic solvents. The procedure proposed in this work consists in the following. Hexane solutions are evaporated, whereupon the pesticides to be characterized are redissolved in acetonitrile or other suitable solvent. At the same time, this procedure increases the concentrations of compounds relative to those in the initial nonpolar phase, which decreases the inaccuracy in determining small K_d values, especially for $K_d < 0.01$. The amount of the substances under study can also be increased by varying the volumes of the samples dosed into chromatograph (5–100 μl), which is equivalent to additional 20-fold concentration. Further sources of inaccuracy in determining K_d for the sample preparation procedure considered are relatively high volatility at room temperature and irreversible sorption of the pesticides on the glass surface [12] during evaporation.

Table 1 presents the K_d parameters for the pesticides studied in this work (these are arranged in accordance with increasing molecular weight). These parameters were determined by GLC and HPLC (at UV detection wavelengths of 220 and 254 nm and the degree of concentration after changing to another solvent $k = 5$). Also, by taking GLC conventionally as

Table 2. Distribution coefficients for selected pesticides in the hexane–acetonitrile system at the degree of concentration $k = 8$

Compound	K_d(HPLC) × 10^{-2} ($\lambda = 254$ nm)	$\frac{K_d(\text{HPLC}) - K_d(\text{GLC})}{K_d(\text{GLC})}$, %
Pirimicarb	6.9 ± 0.6	+13
Methyl parathion	2.1 ± 0.3	+40
Fenthion	6.7 ± 0.3	–52
Triadimefon	3.6 ± 0.5	–43
Tetraconazole	1.2 ± 0.2	+20
Prochloraz	3.1 ± 0.3	+244
Average relative deviation with the sign taken into account (minus Prochloraz)		–4 ± 41

Table 3. Comparison of the distribution coefficients obtained in this work with the published data

Compound	K_d(GLC) × 10^{-2}	K_d(HPLC) × 10^{-2} (λ = 220 nm)	$K_d^*(p)$ × 10^{-2} [13]
Dimethoate	0.6	0.6	< 1
Diazinone	41	30	39, 43
Methyl parathion	1.5	2.3	2.2, 3.0
Malathion	2.5	2.8	4.4

* Recalculated using the p values by formula (3).

the standard method, it is possible to estimate the relative deviations from the standard of the K_d values determined by different methods. Table 1 shows that for 12 of the 20 pesticides studied the K_d values determined by the two chromatographic methods exhibit a good convergence (accurately to within the absolute measurement errors). The relative deviations of K_d (except for those of Tetraconazole and Prochloraz) vary from –46 to +53%. Nevertheless, our data suggest random scatter of the K_d values of the pesticides, as the average value of the relative deviations calculated with the sign taken into account is only –0.3%, the standard deviation being 28%. This proves the lack of any systematic errors in determining K_d by the two methods considered.

The K_d(HPLC) values listed in Table 1 for different wavelengths, namely, 220 and 254 nm, show that K_d is virtually unaffected by variation of the detection wavelength. Therefore, K_d(HPLC) of substances can be determined at any wavelength.

For the six pesticides whose relative divergences between the K_d(GLC) and K_d(HPLC) values are over 30% (Table 1), we repeatedly determined K_d(HPLC), now at the degree of concentration increased to $k = 8$ (Table 2). The results proved once again the random character of the divergences between the K_d(GLC) and K_d(HPLC) values for all the compounds except for Prochloraz. The relative divergences varying from –52 to +40% at $K_d < 0.1$ do not exceed the scatter in K_d revealed by such comparison for other methods. The average relative deviation for repeatedly determined K_d(HPLC) is –4%, which, similar to the previous run, is smaller than its standard deviation (±41%).

In the case of Prochloraz, a large difference in the K_d(GLC) and K_d(HPLC) values can be due to both unaccounted sorption effects and to instability of the compound itself during chromatographic analysis. It should be noted that for Tetraconazole [K_d(GLC) = 0.01] we succeeded in decreasing the relative differences in these values from +220 to +20% by increasing the degree of concentration (from 5 to 8), which suggests a typical outlier in the former case.

To test independently the method for determining K_d proposed in this work, it is reasonable to compare the K_d(HPLC) values for the pesticides obtained by us with the published data [13] (Table 3). Interestingly, $K_d < 1 \times 10^{-2}$ for dimethoate reported in [13] suggests that, by contrast to the method proposed by us, it is in principle impossible to precisely determine indirectly small K_d values (<0.01) using the P value. Comparison of the data obtained by us with those reported by other authors shows that their agreement does not contradict the modern views on interlaboratory reproducibility of the distribution coefficients in the octanol–water [14] and hexane–acetonitrile systems (in the form of the P value) [15].

Thus, we demonstrated the suitability of reversed-phase HPLC as an alternative chromatographic procedure for determining the distribution coefficients of a series of pesticides as an example. The inaccuracies in measuring K_d of the pesticides by different chromatographic methods are random. Moreover, it can be supposed that more reliable K_d values can be obtained by combining these methods.

CONCLUSION

A new method was proposed for determining the distribution coefficients of thermally unstable and low-volatile compounds, containing chromophore groups, in the heterophase hexane–acetonitrile system by reversed-phase high-performance liquid chroma-

tography. This method involves changing from a hydrocarbon to another solvent and additionally concentrating the samples. This method affords more reliable determination of small distribution coefficients typical for the majority of currently used pesticides.

REFERENCES

1. Zakharenko, V.A., *Agrokhimiya*, 2000, no. 4, pp. 75–92.
2. *The Pesticide Manual*, Tomlin, C., Ed., Surrey: Brit. Crop Prot. Council, 1997 (World Compendium).
3. Geyer, H., Politzki, G., and Freitag, D., *Chemosphere*, 1984, vol. 13, no. 2, pp. 37–53.
4. Brooke, D.N., Dobbs, A.J., and Williams, N., *Ecotoxicol. Environ. Saf.*, 1986, vol. 11, no. 3, pp. 251–260.
5. Karickhof, S.W., *Chemosphere*, 1981, vol. 10, no. 8, pp. 833–846.
6. Klisenko, M.A., Kalinina, A.A., Novikova, K.F., *et al.*, *Metody opredeleniya mikrokolichestv pestitsidov v produktakh pitaniya, kormakh i vneshnei srede: Spravochnik* (Methods of Determining Microamounts of Pesticides in Foodstuffs, Forage, and Environment: Reference Book), Moscow: Kolos, 1992, vols. 1, 2.
7. Beroza, M. and Bowman, M.C., *Anal. Chem.*, 1965, vol. 37, no. 2, pp. 291–292.
8. Berezkin, V.G., Loshchilova, V.D., Pankov, A.G., and Yagodovskii, V.D., *Khromatorasperdelitel'nyi method* (Partition Chromatographic Method), Moscow: Nauka, 1976.
9. Zenkevich, I.G. and Vasil'ev, A.V., *Zh. Anal. Khim.*, 1993, vol. 48, no. 3, pp. 473–486.
10. Korenman, I.M., *Ekstraktsiya v analize organicheskikh veshchestv* (Extraction in Analysis of Organic Substances), Moscow: Khimiya, 1977.
11. Fujita, T., Isawa, J., and Hansch, C., *J. Am. Chem. Soc.*, 1964, vol. 86, no. 23, pp. 5175–5180.
12. Magdic, S. and Pawliszyn, J., *J. Chromatogr., Ser. A*, 1996, vol. 723, no. 1, pp. 111–122.
13. Kim, Y.-H., Wodrow, J., and Seiber, J.H., *J. Chromatogr., Ser. A*, 1984, vol. 314, pp. 37–53.
14. Harnnisch, M., Mockel, H.J., and Schulze, G., *J. Chromatogr., Ser. A*, 1983, vol. 282, pp. 315–332.
15. Di Muccio, A., Ausili, A., Dommarco, R., *et al.*, *J. Chromatogr., Ser. A.*, 1991, vol. 552, pp. 241–247.

Russian Journal of Applied Chemistry, Vol. 75, No. 1, 2002, pp. 80–85. Translated from Zhurnal Prikladnoi Khimii, Vol. 75, No. 1, 2002, pp. 80–85.
Original Russian Text Copyright © 2002 by Talzi, Ignashin.

ENVIRONMENTAL PROBLEMS OF CHEMISTRY AND TECHNOLOGY

NMR Study of Decomposition of Monoethanolamine under Conditions of Industrial Gas Treatment

V. P. Talzi and S. V. Ignashin

Omsk Branch, Boreskov Institute of Catalysis, Siberian Division, Russian Academy of Sciences, Omsk, Russia

Received July 18, 2000; in final form, January 2001

Abstract—The main impurities in aqueous solution of monoethanolamine used in various stages of gas treatment at the Omsk Oil Refinery Joint-Stock Company were identified by ^{1}H and ^{13}C NMR spectroscopy. A mechanism of their formation was proposed. A probable dependence of service characteristics of the absorbent on its composition was considered.

Process gases are commonly treated in industry to remove acidic impurities (CO_2, H_2S, CS_2, and COS) using aqueous solutions of amino alcohols, among which monoethanolamine (MEA) is the most frequently used. For decades of industrial exploitation of gas treatment equipment, the optimum process parameters were selected, the main process problems were revealed, and measures intended to solve these problems were developed. Nevertheless, data on variation of the absorbent composition during its operation and the effect of the arising impurities on the efficiency of gas treatment are difficultly accessible, though it is well known that it is these impurities, unremovable in regeneration, that are often responsible for significant increase in the corrosion rate of the equipment, unwanted foaming, and the loss of absorption ability of the absorbent [1–5].

Under the conditions of industrial gas treatment the compounds formed in the reaction of MEA with CO_2, COS, and CS_2, are mainly carbamate $[HOCH_2CH_2 \cdot NHCO_2^-][H_3N^+CH_2CH_2OH]$ (**I**), thiocarbamate $[HOCH_2CH_2NHCOS^-][H_3N^+CH_2CH_2OH]$ (**II**), and dithiocarbamate $[HOCH_2CH_2NHCSS^-][H_3N^+CH_2 \cdot CH_2OH]$ (**III**) [1, 2].

The reversible formation and decomposition of **I**–**III** and also of monoethanolamine sulfide are the main reactions governing the process of amine gas treatment. Thio analogs of carbamate **I** are considerably more stable with respect to decomposition to COS or CS_2 and MEA [6]. Theoretical considerations suggest that specifically thiocarbamate (**II**) as a result of further transformations can give most likely the impurities unremovable by regeneration of the absorbent [2]. Isoxazolidone-5 (**IV**), 5-amino-3-aza-1-pentanol (**V**), *N*,*N*'-di(2-hydroxyethyl)urea (**VI**), and 1-(2-hydroxyethyl)imidazolidone-2 (**VII**) were described as these impurities [2]:

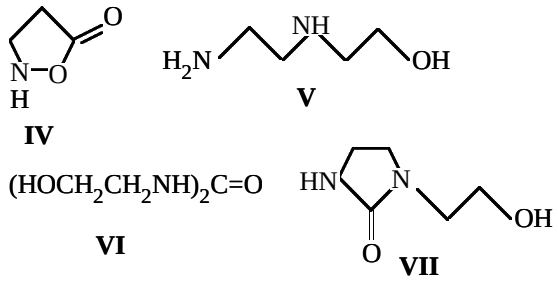

By NMR analysis of the absorbent samples (the samples were withdrawn from various installation units and stages of gas treatment at the Omsk Oil Refinery), we refined their composition and the mechanism of formation of impurities.

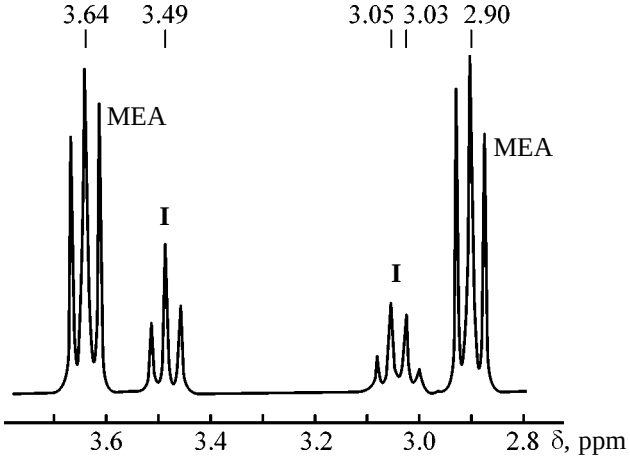

Fig. 1. Fragment of the ^{1}H NMR spectrum of aqueous solution of MEA before regeneration (ISP). (δ) Chemical shift.

1070-4272/02/7501-0080$27.00 © 2002 MAIK "Nauka/Interperiodica"

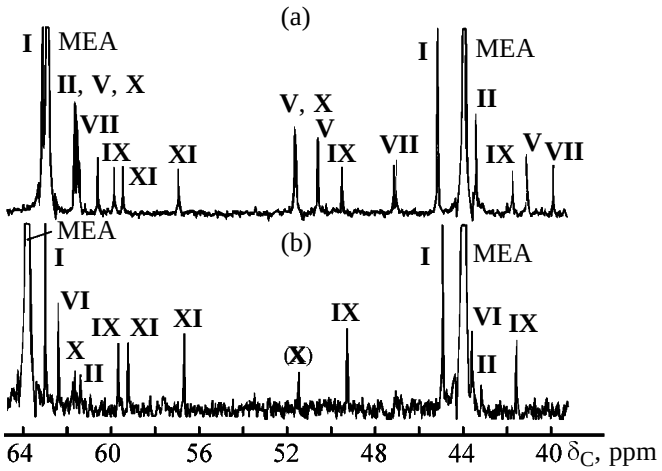

Fig. 2. Fragment of the ^{13}C NMR spectrum of (a) regenerated absorber (gas-fractionation setup, GFI) and (b) aqueous solution of MEA after regeneration (ISP). (δ_C) Chemical shift, ppm; the same for Fig. 3.

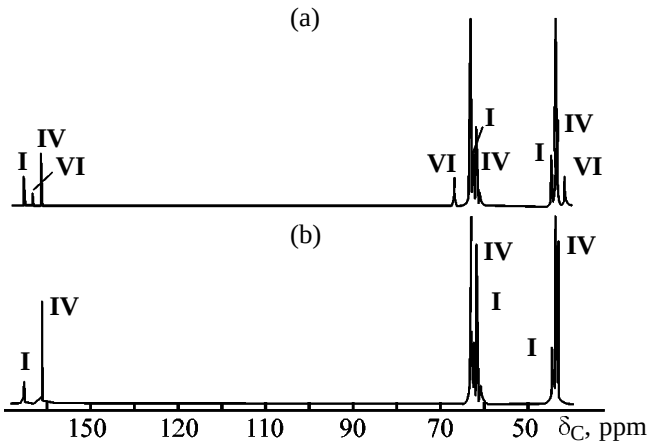

Fig. 3. ^{13}C NMR spectrum of COS solutions in aqueous MEA (20%) after boiling for (a) 10 and (b) 30 min.

The ^{1}H NMR spectrum of one of MEA solutions, saturated with acidic gases, before its regeneration (installation for sulfur production, ISP) is shown in Fig. 1. This solution contains approximately 4% of carbamate **I**. The spectrum of **I** contains a triplet at δ 3.49 ppm and two overlapped triplets at δ 3.03 and 3.05 ppm, corresponding to methylene protons in the α-position to oxygen atoms and nitrogen atoms of the anionic part of its molecule. The corresponding cation gives the signal overlapping with the MEA signal [6]. The identification of **I** was proved by independent synthesis (passing of carbon dioxide through aqueous solution of MEA).

After regeneration, the main impurity in the absorbent is usually carbamate **I** (approximately 0.5%). Along with carbamate **I**, we attempted to find thiocarbamates **I** and **III** considering the ^{13}C NMR spectra of the individual compounds formed by dissolving COS and CS_2 in aqueous MEA (see table). However, in the ^{13}C NMR spectra of samples withdrawn from the ISP the corresponding signals are lacking (Fig. 2b).

At the same time, ^{13}C NMR analysis of solutions obtained by bubbling of COS through 15–20% aqueous solutions of MEA under laboratory conditions showed that compounds **IV** and **VI**, giving the characteristic ^{1}H and ^{13}C NMR spectra (see table; Fig. 3a), are formed only on heating (70–100°C) or prolonged storage of the solutions obtained by this procedure and containing a mixture of carbamate **I** and thiocarbamate **II**.

Formation of **IV** and **VI** in saturated solutions of CO_2 in MEA was not observed. On heating of these solutions (≤120°C) only signals of MEA and carbamate **I** are present in their NMR spectra.

In the ^{13}C NMR spectra of the samples withdrawn from the ISP the signals at δ_C 62.4 and 43.8 ppm are the most intense (see table; Figs. 2b, 3a). These signals correspond to urea **VI**, suggested previously as an intermediate [5]. The signal of carbonyl carbon δ_C 162 ppm corresponding to **VI** has low intensity and is not always observed in the ^{13}C NMR spectra of the industrial absorbents.

Assignment of the signals in the ^{13}C NMR spectra of model compounds and samples of industrial absorbents (aqueous solutions of MEA)

Compound	Assignment of the ^{13}C NMR signals, δ_C, ppm		
	NCH_2	CH_2OH	C=O
MEA	43.89	63.57	
I	44.93	63.00	166.1
II	43.00	60.41	182.3
III	51.34	60.21	213.2
IV	40.52	66.71	163.3
V	50.75, 51.23, 39.05	60.30	
VI	43.59	62.41	161.8
VII	38.34, 46.82, 47.03	60.02	165.9
VIII		64.13	159.2
IX	49.20, 39.52	58.93*	**
X	51.24	60.32	
XI	56.48**	59.13	

* The signal is overlapped with the MEA signal.
** Signals were not registered owing to low intensity.

The signals of **IV** are lacking in the spectra of the industrial samples, while, as mentioned above, the signals of this compound along with the signals of urea **VI** are the most intense in the spectra of the laboratory samples obtained by absorption of COS with aqueous MEA (Fig. 3a). It turned out that the intensity of signals of **IV** initially increased and then decreased and became equal to zero in boiling of the saturated solutions for 0.5 h (Fig. 3b).

As known, **IV** and **VI** are formed by the well-known transformations of thiocarbamate **II** [reactions (1) and (2)] [2]:

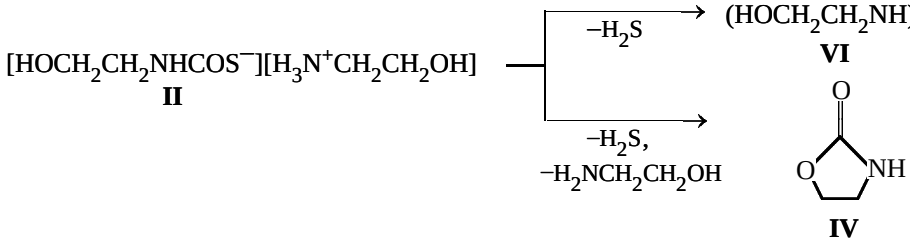

(1)

(2)

The formation of impurities **V** and **VII**, identified previously in the absorbent, can be due to the reactions of **IV**. In our opinion, there are at least three pathways [Eqs. (3)–(5)] for conversion of **IV**, which are well-known amidation and hydrolysis reactions [7]:

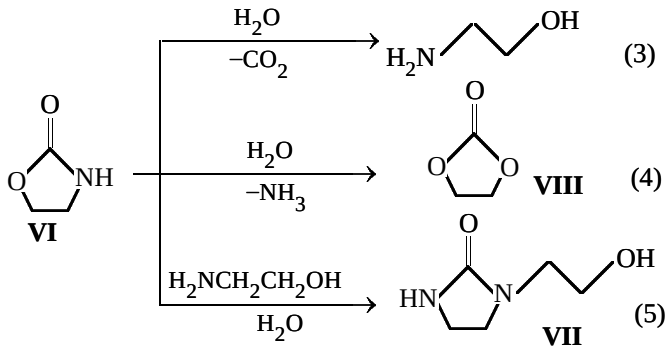

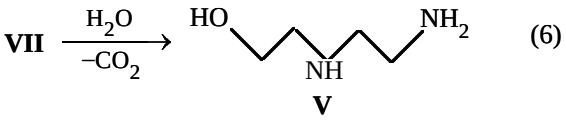

Reaction (3) results in the above-noted disappearance of the signals of **IV** from the ^{1}H and ^{13}C NMR spectra of laboratory samples of the absorbent during boiling (Fig. 3b) and causes the absence of **IV** in process solutions. In some cases the laboratory solution of COS in aqueous MEA after boiling or prolonged storage gives a mixture with the ^{13}C NMR spectrum in which, according to calculated and reference data, the strongest signals are the characteristic signals of methylene and carbonyl carbon atoms of compound **VII** described previously (see table) [8]. More frequently, in such experiments in ^{13}C NMR spectrum we observed, instead of the signals of **VII**, the signals of diamine **V**, which are also sufficiently characteristic to allow identification based on the reference data (see table). The above reaction (6) was proposed to explain formation of diamine **V** in the course of gas treatment [5].

Formation of **VII** by dehydration of urea **VI** [5] is unlikely, since **VI** remains the main impurity in the absorbent after its prolonged boiling (Fig. 3b).

Reaction (4) was not described previously in the publications devoted to absorption treatment of process gases; however, in the ^{13}C NMR spectra of laboratory and many of the industrial samples there is a weak characteristic signal at δ_C 64 ppm corresponding precisely to **VIII** [8]. The signal of the carbonyl carbon atom of carbonate **VIII** appears at δ_C of approximately 159 ppm (see table).

As was shown by laboratory experiments simulating treatment of gases to remove CO_2 and COS, specifically thiocarbamate **II** gives many of impurities accumulated in the industrial sorbents under operating conditions. There are no published data on the pathway of formation of thiocarbamate **II** under conditions of gas treatment, namely, whether it is formed exclusively owing to the presence of COS in the gases to be treated or also by the reaction of H_2S with carbamate **I**, reverse to hydrolysis of thiocarbamates [9] (see below).

To elucidate this problem, 20% aqueous solutions of MEA were saturated with CO_2 and H_2S under laboratory conditions, but neither signals of thiocarbamate **II** nor signals of urea **VI** formed from **II** in the stage of solution regeneration were registered in the

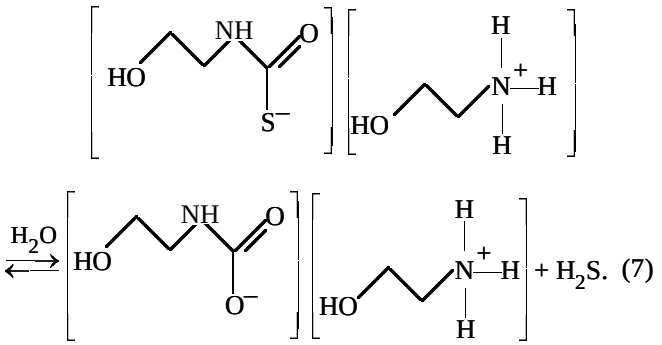

(7)

^{13}C NMR spectra. Thus, thiocarbamate **II** is formed exclusively by uptake of carbonyl sulfide (COS), apparently formed by the well-known reaction of CO with sulfur vapor (350°C) in the particular installation.

It was established that, along with the presence of oxidizing agent (dissolved oxygen), the ability of one of the components of the liquid medium to form complexes with metal ions is the most important factor of corrosion activity [10]. This causes the corrosion activity of MEA and diethanolamine. Previously [2] it was proposed that the corrosion activity of aqueous solution of MEA increases with increasing content of impurity of diamine **V** giving stable complexes with iron. Thus, evidently, the corrosion activity of absorbents increases with increasing probabilty of formation of thiocarbamate **II**, which is active complexing agent itself and gives diamine **V** by reactions (2), (5), and (6). It is well known [1–5] that decreased concentration of MEA solutions results in decreased probability of side reactions giving the impurities in hand, which is caused, in our opinion, by increased probability of hydrolysis of thiocarbamate **II** by reaction (7).

Turning back to the absorbent composition in the ISP, it should be noted that along with the signals of MEA, **I**, and **VI**, the ^{13}C NMR spectra (Fig. 2b) contain five more or less strong signals at δ_C 39, 49, 56, 58, and 59 ppm, which occur simultaneously in the majority of several tens of the studied samples withdrawn from various installations and have the same ratio of intensities as in Figs. 2a and 2b. It is significant that these signals were registered in the spectra of some aqueous MEA solutions saturated and regenerated under laboratory conditions only after absorption of COS but not CO_2. Considering characteristic reference and calculated data [8], three of five signals belong to compound **IX**, which has not been described as a component of the absorbents in hand and is the analog of **VII** formed by its hydrolysis [reaction (8)]. Compound **VII** is absent in the ISP absorbents. The fourth signal of **IX** is not observed owing to overlap with the signals of other components (see table). One further pathway of formation of **IX** is probably amidation of carbonate **VIII** [reaction (9)]:

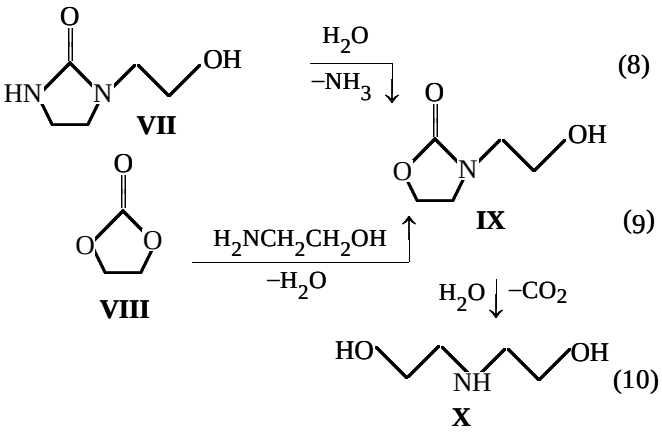

(8)

(9)

(10)

In accordance with reaction (5), diethanolamine **X** is formed by hydrolysis of **IX** [reaction (10)]. The characteristic signal of amine **X** is observed in the spectra of various samples of absorbents (Figs. 2a, 2b). This fact was established using an authentic sample of **X**. Amine **X** gives the NMR signal in the range close to that of dithiocarbamate **III**, so that special experiments using appropriate model systems were required for correct identification.

The other pathway of synthesis of amine **X** by the reaction of MEA with ethylene oxide formed by decomposition of MEA to give components used for its industrial production (NH_3 + CH_2CH_2O) can be ruled out because of the total absence of signals of ethylene glycol in all the samples studied. Thus, the presence of amine **X** in the absorbents additionally proves the indentification of **IX**.

The remaining two of the five considered signals in the ^{13}C NMR spectra at δ_C approximately 56 and 59 ppm are close to the characteristic signal of triethanolamine. Addition of triethanolamine to the absorbents gives the other pair of signals in the ^{13}C NMR spectrum, noticeably shifted downfield relative to the first two signals. These signals were tentatively assigned to azirine **XI** taking into account that it always accompanies **IX**, forming by its cleavage:

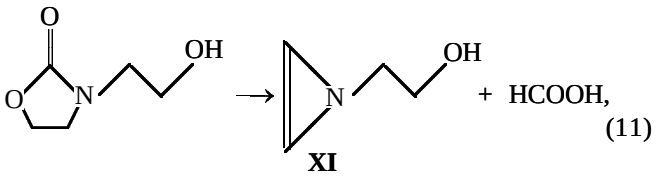

(11)

Attempts to register the signals of methine carbon atoms of **XI** failed. However, we have no other as-

sumptions concerning the structure of this component of commercial absorbents.

Formic acid presumably formed in synthesis of **XI** [reaction (11)] was registered in the industrial absorbents and is usually believed to originate from oxidative thermal degradation of MEA. Formic acid gives a peak in the ^{13}C NMR spectra at δ_C 172 ppm, observed in the spectra of industrial absorbents in the range corresponding to signals of carbonyl carbon atoms. In the same range, the signal of oxalic acid formed by oxidation of MEA is observed (δ_C 174 ppm) [2].

Along with the signals of MEA, **VI**, **IX**, and **XI**, in the spectra of samples withdrawn from the ISP there are some weaker signals. Two of these signals were assigned to amine **X**, and two other signals, to thiocarbamate **II** (see table).

Compound **II** detected in the absorbents withdrawn from the ISP was identified on the basis of the ^{13}C NMR spectra of the samples withdrawn from the GFI. In the GFI the content of thiocarbamate **II** is higher than that in the ISP. In some samples of regenerated absorbent withdrawn from the GFI only MEA has a higher concentration (Fig. 3a). Thus, we were able to find that two signals of methylene carbon atoms assigned to **II** correspond to the characteristic signal of the carbonyl carbon atom at δ_C of approximately 182 ppm, assigned to the NCOS fragment (see table).

The absorbent withdrawn from the GFI (approximately 20% MEA) has a more complicated composition than that withdrawn from the ISP. The strongest signals (excluding signals of MEA) in the ^{13}C NMR spectrum of the absorbent after regeneration are the signals of thiocarbamate **II**; in this case, the signals of carbamate **I** and urea **VI** are extremely weak.

The spectrum, whose fragment is shown in Fig. 2a, contains additional relatively strong signals of **V** and **VII**, which are absent in the spectra of the absorbents withdrawn from the ISP.

In addition, the spectrum of the absorbents withdrawn from the GFI contains the signals of two methyl carbon atoms (δ_C 23 and 24 ppm) of unidentified compound or compounds, to which correspond two singlets in the ^1H NMR spectrum in the region of δ 1.8 ppm.

According to process data, this absorbent has low absorption power with respect to CO_2 and H_2S, which is apparently caused by the fact that acidic salt **II**, whose content is higher in the GFI than in ISP, induces decomposition of carbamate **I** and MEA sulfide by the mechanism of general acid catalysis observed for carbamates of low-basic amines such as MEA [11]. Impurities of formic and oxalic acids exert the similar effect.

EXPERIMENTAL

The ^{13}C and ^1H NMR spectra of the absorbent samples were recorded on a Bruker ACP-200P spectrometer using standard procedures.

Under laboratory conditions the gas treatment process was simulated on a setup consisting of a flask for production of gases and absorption flasks. CO_2 and COS were produced in this setup by the reaction of sulfuric acid with sodium bicarbonate and potassium (ammonium) thiocyanate, respectively. H_2S, CS_2, diethanolamine, and triethanolamine were commercial chemicals of chemically pure grade.

Regeneration of absorbents was simulated by either heating on a water bath or boiling.

CONCLUSIONS

(1) Salts of ethanolamine with (2-hydroxyethyl)carbamic and (2-hydroxyethyl)thiocarbamic acids, 5-amino-3-aza-1-pentanol, *N*,*N*'-di(2-hydroxyethyl)urea, 1-(2-hydroxyethyl)imidazolidone-2, 1,3-dioxolanone-2, 3-(2-hydroxyethyl)-1,3-oxazolidone-2, and 3-aza-1,5-pentanediol were identified by ^{13}C NMR in the industrial absorbent based on aqueous solution of monoethanolamine. Among these compounds, isoxazolidone-2 is absent.

(2) The increase in the corrosion activity of the absorbent is apparently caused by the presence of active complexing impurities, such as monoethanolammonium (2-hydroxyethyl)thiocarbamate and 5-amino-3-aza-1-pentanol.

(3) The decrease in the absorption power of the absorbent with respect to CO_2 and H_2S is due to the presence of thiocarbamate and also oxalic and formic acids, inducing decomposition of (2-hydroxyethyl)carbamate and monoethanolamine by the mechanism of the general acid catalysis.

(4) Large amount of impurities unremovable by regeneration of the absorbent originate from transformations of thiocarbamate formed in absorption of COS.

ACKNOWLEDGMENTS

We are grateful to A.A. Ferber and M.A. Plekhanov (Omsk Oil Refinery) for submitting the samples of the industrial absorbent and process data.

REFERENCES

1. *Ochistka tekhnologicheskikh gazov* (Treatment of Process Gases), Semenova, T.A., Ed., Moscow: Khimiya, 1977.
2. Lupart, M.S., Bacon, T.R., and Edwards, D.J., *Neft', Gas Neftekhim. Rubezhom*, 1993, no. 12, pp. 975–977.
3. Khabibullin, R.R., Rogozin, V.I., and Vashnislavtsev, Yu.F., *Sovremennye metody ochistki gazov ot kislykh komponentov* (Modern Procedures of Gas Treatment to Remove Acidic Components), Moscow: TsNIITEneftekhim, 1988, issue 3, pp. 27–35.
4. Sobina, N.A., Marakhovskii, L.F., Kuznetsov, V.D., *et al*., *Khim. Koks*, 1989, no. 6, pp. 345–349.
5. Dmitrikov, V.P. and Nabivach, V.M., *Khim. Koks*, 1999, no. 10, pp. 21–25.
6. Savin, V.P., Talzi, V.P., and Bek, N.O., *Zh. Org. Khim*., 1984, vol. 20, no. 9, pp. 1824–1851.
7. Lebedev, N.N., *Khimiya i tekhnologiya osnovnogo organicheskogo i neftekhimicheskogo sinteza* (Chemistry and Technology of Basic Organic and Petrochemical Synthesis), Moscow: Khimiya, 1988.
8. Levy, G.C. and Nelson, G.L., *Carbon-13 Nuclear Magnetic Resonancs for Organic Chemists*, New York: Wiley, 1972.
9. Glazyrin, A.B., Talzi, V.P., Denisov, E.N., *et al*., *Zh. Prikl. Khim*., 1985, vol. 58, no. 10, pp. 2300–2304.
10. Lavrent'ev, I.P. and Khidekel', M.L., *Usp. Khim*., 1983, vol. 52, no. 4, pp. 596–618.
11. Ewig, Sh.P., Lockson, D., and Jencks, W.P., *J. Am. Chem. Soc*., 1980, vol. 102, no. 9, pp. 3072–3079.

Russian Journal of Applied Chemistry, Vol. 75, No. 1, 2002, pp. 86–89. Translated from Zhurnal Prikladnoi Khimii, Vol. 75, No. 1, 2002, pp. 86–89.
Original Russian Text Copyright © 2002 by Aristova, Piskarev.

ENVIRONMENTAL PROBLEMS OF CHEMISTRY AND TECHNOLOGY

Kinetics of Phenol Oxidation under Flash Corona Electric Discharge

N. A. Aristova and I. M. Piskarev

Nizhni Tagil Institute, Ural State Technical University, Nizhni Tagil, Sverdlovsk oblast, Russia
Research Institute of Nuclear Physics, Moscow State University, Moscow, Russia

Received March 6, 2001

Abstract—A study was made of the kinetics of phenol oxidation in a 3.5-l (liquid) tank at the initial chemical oxygen demand of the solution of 200–6000 mg O l^{-1}. The total current of flash corona electric discharge from 50 electrodes was 3 mA.

The technical and economic requirements to the quality and cost of wastewater treatment are now so stringent that neither of the known treatment methods fully satisfies them. Solving this problem requires the use of different methods. The place and role of each method are assessed in the development stage by mathematical simulation.

Phenol-containing wastewaters are widespread; therefore, it is of interest to develop new processes for their oxidation. In [1], we considered specific reactions induced by electric discharge, namely, by flash corona electric discharge generating a small volume concentration of active particles, extremely high electric field intensity in the discharge space, and pulse electric current. Also, we formulated the main features of the electric discharge utilized for initiating the reactions [1], described the reaction kinetics [2], and showed that under certain conditions this reaction has advantages over ozonation [3]. In this work, we analyzed the kinetics of phenol oxidation in a tank of a sufficiently large volume and compared the results with the characteristics of the known processes.

EXPERIMENTAL

The liquid was treated in a 35×60 cm^2 tank with a polyethylene bottom and 25-cm-high glass walls. The tank volume was 50 l. Along the bottom perimeter and in the central area longitudinally, a contact electrode made of aluminum wire, 3 mm in diameter, was mounted. The tank was filled with 3.5 l of liquid. Fifty discharge electrodes were placed at a distance of 5 mm from the liquid surface. Each discharge electrode was 12 cm long. The electrodes were mounted on a Teflon sheet arranged under the tank cover. The electrodes were separated from one another by 5 cm. The 10-kV negative-polarity voltage was applied to each electrode via the untying resistance of 10 MΩ. The total discharge current from all the electrodes was 3 mA. In the case of measurements in an oxygen medium, before the voltage was switched on, the tank was purged with oxygen at a rate of 3 l h^{-1} for 24 h. During the experiments, oxygen was supplied at the same rate. Oxygen was fed through the holes in the tank bottom (through the liquid), and gases were removed through the holes in the tank cover. During experiments in air, the ventilation holes were additionally opened at the tank cover, and oxygen purge was stopped. During treatment the liquid was mixed by ion movement and by "electric wind", which is a specific feature of the electric discharge mode chosen [1]. As working liquids served phenol and KI solutions of different concentrations in distilled water. The reagents were of chemically pure grade. The phenol concentration was 84 (COD 200 mg O l^{-1}, 840 (COD 2000 mg O l^{-1}), and 2520 mg l^{-1} (COD 6000 mg O l^{-1}). The phenol concentration in the initial and treated solutions was determined by extraction followed by spectrophotometry.

The active species yield Y was estimated by us previously for the treated liquid volumes of 20–100 ml at the discharge current of 0.1 mA [2, 4]. These yields were as follows: $Y(OH^{\bullet})$ = 14.4, $Y(H)$ = 18.0, and $Y(O)$ = 2.5 mol mol^{-1} electrons (or molecules per electron passed in the circuit). In [2] we showed that in the presence of ozone the H atoms are transformed into $OH^{\bullet}$ radicals, and their total yield $Y(OH^{\bullet})$ is about 32 mol mol^{-1} electrons, or 32 $OH^{\bullet}$

1070-4272/02/7501-0086$27.00 © 2002 MAIK "Nauka/Interperiodica"

radicals per electron passed in the circuit. The voltage on the electrode relative to the liquid surface is 10 kV, which means that the energy spent for transfer of this electron is equal to 10 keV. Then the average energy cost of formation of one $OH^{\bullet}$ radical will be 312 eV, or 0.32 $(100\ eV)^{-1}$. Additionally, the yield of ozone under the actual experimental conditions was determined. To this end, the tank was filled with 3.5 l of 0.1 M KI solution, and the iodine oxidation yield was measured. The oxidation of I^- and the accumulation in solution of $1/2I_2$ were calculated in terms of the process model considered previously [2]. In the calculation we used the above-cited yields of active species, the liquid volume V_l = 3.5 l, the gas phase volume V_g = 46.5 l, the liquid surface area $S_l = 2.1 \times 10^3$ cm^2, and the discharge current I = 3 mA. The ozone yield was treated as a free parameter. The calculated and experimental data proved to be consistent at the ozone yield of 135 mol mol^{-1} electrons. This value is somewhat lower than that obtained in [2], namely, 180 mol mol^{-1} electrons for one electrode. A decrease in the ozone yield on changing from one to a system of 50 electrodes is probably due to inaccurate arrangement of the electrodes and to the scatter in the distance between the electrodes and the surface. Namely, for a significant number of electrodes the distance from the liquid surface is not optimal.

We studied the decrease in the chemical oxygen demand (COD) for the phenol solution contained in the tank under the following conditions: experiment no. 1, under oxygen; during the discharge treatment, alkali (NaOH) was added to maintain pH within 6–7; experiment no. 2, under oxygen in the absence of alkali; and experiment no. 3, in air without alkali. For all the solutions the initial COD was 2000 mg O l^{-1}. The results are shown in Fig. 1. The concentration of phenol itself was monitored in experiment no. 1. The amount of the alkali utilized for maintaining pH in experiment no. 1 was 14 mol of NaOH per mole of electrons.

Figure 1 shows that within about 60 h the COD decreases by on order of magnitude, whereas the content of phenol itself decreases 1000-fold within about 5 h. Rapid consumption of phenol proper in the reaction under study is confirmed by our previous experiments [4]. Among intermediate reaction products, the most easily identifiable is benzoquinone. Its presence is confirmed by the fact that the initially colorless solution turns reddish-yellow within several hours of treatment, and this color is retained virtually until the experiment is complete. Within 45 h of treatment the solution turns colorless again.

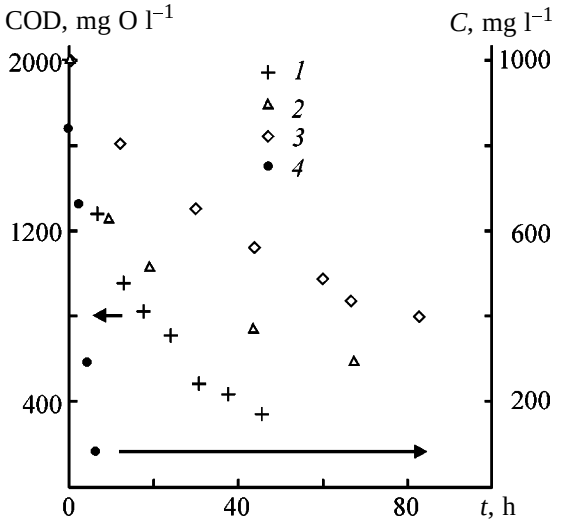

Fig. 1. Variation of the COD of the 840 mg l^{-1} phenol solution (COD_0 = 2000 mg O l^{-1}) with time t of treatment in the tank at the discharge current of 3 mA. Experiment no.: (*1*) 1, (*2*) 2, and (*3*) 3; (*4*) variation of the phenol concentration C, mg l^{-1}, in experiment no. 1.

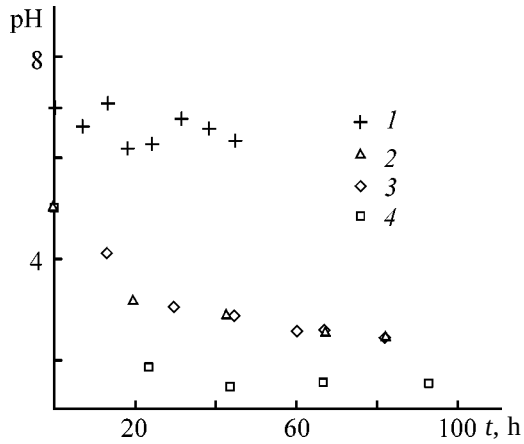

Fig. 2. Variation with treatment time t of the pH of the phenol solutions with the initial COD of (*1–3*) 2000 and (*4*) 6000 mg O l^{-1}. Medium: (*1, 3*) oxygen and (*2, 4*) air.

In the case of oxidation under oxygen without adding alkali (Fig. 1, experiment no. 2), within the first 10–12 h the oxidation rate is identical to that in the case of adding alkali (experiment no. 1), but then the oxidation rate tends to decrease with decreasing pH. Figure 2 shows how pH varies with the treatment time in experiment nos. 1–3. It is seen that within 15–20 h in experiment nos. 2 and 3 pH decreases from 5 to 3–4. The patterns of variation of pH with the time of treatment under oxygen and in air (experiment nos. 2 and 3) are virtually identical. This suggests a little significance of nitric acid formation under discharge in air. Accumulation of nitric acid under the same

Table 1. Experimental rates of oxygen uptake (COD decrease) for phenol solutions (COD_0 2000 mg O l^{-1}, total discharge current 3 mA, 50 electrodes)

Experiment no.	Oxygen uptake rate			
	oxidation beginning		oxidation end	
	mol O : mol electrons	$(100\ eV)^{-1}$	mol O : mol electrons	$(100\ eV)^{-1}$
1	210 ± 20	2.1 ± 0.2	20 ± 5	0.2 ± 0.05
2	190 ± 20	1.9 ± 0.2	12 ± 3	0.12 ± 0.03
3	80 ± 10	0.8 ± 0.1	13 ± 3	0.13 ± 0.03

Table 2. Comparison of the oxidation yields of phenol and organic substances, obtained in this work for discharge under oxygen in the aqueous solution with COD_0 2000 mg O l^{-1}, with those in [7, 12, 13] at the phenol concentration of 1 mM and COD_0 30 mg O l^{-1}

Yield	This work	Pulse corona [12]	Ozonation [13]*	Catalytic ozonation*
Organic substances:				
$(100\ eV)^{-1}$	0.14	–	–	–
g kW^{-1} h^{-1}	5	–	–	–
Phenol:				1
$(100\ eV)^{-1}$	1.5 (0.8)**	0.2	0.5	1
g kW^{-1} h^{-1}	~50 (27)	7.1	18	39
Ozone, $(100\ eV)^{-1}$	1.35–1.8	1.8	~6	~6
$OH^{\bullet}$ radicals $(100\ eV)^{-1}$	0.32	0.06–0.29	–	Up to 6

* Under assumption that 1 kW h goes for production of 100 g of ozone
** Given in parentheses are the data for the solution with COD_0 200 mg O l^{-1}.

type of discharge over the distilled water surface is about 5 mol mol^{-1} of electrons [5], and the rate constants of oxidation of atomic nitrogen and phenol are of the same order of magnitude [6]. However, the concentration of the oxidizable impurities in water at COD > 2000 mg O l^{-1} is much greater than that of atomic nitrogen forming under electric discharge. Therefore, at a high concentration of the impurities the active species are consumed, above all, for oxidation of these impurities, and nitric acid virtually does not form under discharge in air. Nitric acid can be accumulated in noticeable amounts in later stages, when slowly oxidizable products remain in solution and their concentration is low.

Experiment no. 4 for the phenol solution with the initial COD 6000 demonstrates how the pH is influenced by the phenol oxidation products (Fig. 2). It is seen that in this case the decrease in pH of solution is more pronounced than in the case of COD 2000. This is due to accumulation in solution of a large amount of organic acids. Table 1 presents the experimental rates of oxygen uptake (COD decrease) in the different stages of phenol oxidation. At the beginning of oxidation under discharge in oxygen COD decreases at a rate of 190–210 mol O mol^{-1} electrons, irrespective of adding the alkali.

In the case of discharge in air (experiment no. 3) the oxidation rate is lower owing to a decrease in the ozone yield with decreasing oxygen concentration. At the end of all the experiments the oxidation rate decreases by an order of magnitude. The reason is twofold: accumulation in the solution of products oxidized at a lower rate by both ozone and $OH^{\bullet}$ radicals and decrease in the concentration of the oxidizable substances. At the end of the experiment, the yields for discharges under oxygen and in air in the absence of alkali (experiment nos. 2 and 3) are approximately the same, namely, 12–13 mol O mol^{-1} electrons. This suggests that in this stage the major role belongs to $OH^{\bullet}$ radicals whose yield is determined by the partial pressure of the water vapor [4].

Let us compare the oxidation rates for organic impurities obtained in different works (Table 2). The

yield of oxygen uptake (decrease in COD at COD_0 2000 mg O l^{-1}) obtained in this work, i.e., approximately 2 $(100\ eV)^{-1}$, corresponds to the uptake of 11.9 g of oxygen per 1 kW h. The COD for phenol is 2.38 g O g^{-1} phenol. Therefore, when recalculated for phenol, the yield of oxidation of organic substances will be equal to 5 g $kW^{-1}\ h^{-1}$, or 0.14 $(100\ eV)^{-1}$. In many works, the CODs of phenol solutions during treatment are not given; presented is the content of phenol proper and of selected compounds, namely, its oxidation products. As phenol proper is oxidized in the reaction under study at an approximately 10-fold higher rate than its degradation products, the yield of oxidation of phenol proper at COD_0 2000 mg O l^{-1} will be equal to 50 g $kW^{-1}\ h^{-1}$, or 1.5 $(100\ eV)^{-1}$. At lower phenol concentrations, COD_0 200 mg O l^{-1}, the initial yield of oxidation determined in an additional experiment was about 27 g phenol $(kW\ h)^{-1}$, or 0.8 $(100\ eV)^{-1}$. It should be emphasized that the initial yield of oxidation is connected with consumption of phenol proper.

The phenol oxidation products were identified in [7–11]. For oxidation of phenol to hydroquinone, benzoquinone, and muconic acid the COD recalculated for one molecule decreases by 7.5, 17, and 28%, respectively. Further oxidation of these compounds is a slower process, and the total oxidation rate decreases. The data presented in other works for the phenol concentration of 1 mM (COD_0 ~230 mg O l^{-1}) are listed in Table 2. It is seen that among the works cited, the highest yield of phenol oxidation was achieved by catalytic ozonation [7]: 5 mol of ozone per mol of phenol. It should be noted, however, that the use of catalysts (e.g., Fe in that work) poses additional problems connected with contamination of the water with the catalyst itself. The yield achieved in electrode-free reaction is of the same order of magnitude as in catalytic ozonation, though the yield of ozone in the process under study per unit energy consumed is approximately 3 times lower than in conventional ozonizers [2].

CONCLUSION

The yield of phenol oxidation under flash corona electric discharge at the maximal electric field intensity in the discharge space and small density of generated active species is of the same order of magnitude as in the case of catalytic ozonation and exceeds that achieved by conventional ozonation.

REFERENCES

1. Piskarev, I.M., *Zh. Fiz. Khim.*, 1998, vol. 72, no. 11, pp. 1976–1983.
2. Piskarev, I.M., *Zh. Fiz. Khim.*, 2000, vol. 74, no. 3, pp. 546–551.
3. Piskarev, I.M., *Teor. Osn. Khim. Tekhnol.*, 2000, vol. 34, no. 3, pp. 333–336.
4. Piskarev, I.M., *Kinet. Katal.*, 1999, vol. 40, no. 4, pp. 505–511.
5. Piskarev, I.M., *Khim. Vys. Energ.*, 2000, vol. 34, no. 6, pp. 475–476.
6. Pikaev, A.K. and Kabakchi, S.A., *Reaktsionnaya sposobnost' pervichnykh produktov radioliza vody: Spravochnik* (Reactivity of the Primary Products of Water Radiolysis: Reference Book), Moscow: Energoatomizdat, 1982.
7. Al-Hayek, N., Legube, B., and Dore, M., *Environ. Technol. Lett.*, 1989, vol. 10, pp. 415–426.
8. Fajerwerg, K., Foussard, J.N., Perrard, A., and Debellefontaine, H., *Water Sci. Technol.*, 1997, vol. 35, no. 4, pp. 103–110.
9. Singer, P.C. and Gurol, M.D., *Water Res.*, 1983, vol. 17, no. 9, pp. 1163–1171.
10. Gurol, M.D. and Singer, P.C., *Water Res.*, 1983, vol. 17, no. 9, pp. 1173–1183.
11. Hoigne, J. and Bader, H., *Water Res.*, 1983, vol. 17, no. 1, pp. 185–194.
12. Hoeben, W.F.L.M., Van Veldhuizen, E.M., Rutgers, W.R., and Kroesen, G.M.W., *J. Phys. D.: Appl. Phys.*, 1999, vol. 32, pp. L133–L137.
13. Gurol, M.D. and Vatistas, R., *Water Res.*, 1987, vol. 21, no. 8, pp. 895–900.

Russian Journal of Applied Chemistry, Vol. 75, No. 1, 2002, pp. 90–94. Translated from Zhurnal Prikladnoi Khimii, Vol. 75, No. 1, 2002, pp. 90–94.
Original Russian Text Copyright © 2002 by Plesovskikh, Bezdenezhnykh, Polosin.

PROCESSES AND EQUIPMENT OF CHEMICAL INDUSTRY

Simulation of Steam Distillation of Multicomponent Mixtures of Higher Aliphatic Acids

V. A. Plesovskikh, A. A. Bezdenezhnykh, and A. N. Polosin

Nevskaya Kosmetika Private Company, St. Petersburg, Russia
St. Petersburg State Technological Institute, St. Petersburg, Russia

Received March 19, 2001

Abstract—A mathematical model of steam distillation of multicomponent mixtures of higher aliphatic acids is proposed, based on solving the equation of equilibrium states for closed systems with account of the nonideal behavior of a solution.

Higher aliphatic acids obtained from oils and fats of vegetable and animal origin are open-chain monobasic aliphatic (fatty) carboxylic acids, which are saturated and unsaturated compounds with the number of carbon atoms from C_{10} to C_{22} and boiling point in the range 300–370°C. In the industry, the acids are purified to remove various substances determining the color, odor, and other quality characteristics of target products (soaps, perfumes, cosmetics, detergents, etc.), with wide use of steam distillation.

In designing practice, distillation of multicomponent mixtures of fatty acids with and without steam is commonly calculated using the scheme for binary systems. In doing so, the properties of a multicomponent mixture are assessed with regard to its most difficultly volatile (highest-boiling) component. For most mixtures of higher aliphatic acids this is stearic acid. It is adopted *a priori* that the vapor phase obeys ideal gas laws, and the liquid phase, the laws of ideal solutions. However, this way to calculate the distillation of mixtures of aliphatic acids allows only approximate evaluation of the mode parameters (pressure, temperature, consumption rates, etc.) since the physicochemical properties of a multicomponent system and its equilibrium states markedly differ from the properties and states of stearic and other acids.

Here we propose to use equations of equilibrium states for closed systems, with account of the nonideality of the liquid phase, for calculating distillation of fatty acids in both batch and continuous modes.

The mathematical model of equilibrium states is based on the condition for thermodynamic equilibrium vapor–liquid, governed by the equality of volatilities or fugacities for, respectively, the vapor and liquid phases $f_{vi} = f_{li}$, with

$$f_{vi} = \nu_i y_i P_{mix}, \quad (1)$$

$$f_{li} = \gamma_i x_i P_i, \quad (2)$$

where y_i and x_i are the mole fractions of the ith component in the vapor and liquid phases; P_{mix} and P_i are the total saturated vapor pressure over solution and saturated vapor pressure of a pure component (mm Hg); ν_i and γ_i are the fugacity and activity coefficients of the ith component.

For the vapor phase, the fugacity coefficient ν_i characterizes the extent to which the gas (vapor) departs from the ideal state. At $P_{mix} \to 0$, $\nu_i \to 1$ for all the i components [1]. For higher fatty acids distilled under reduced pressure (5–30 mm Hg), it may be considered, to a first approximation, that $\nu_i = 1$, and the following assumption can be made: the multicomponent mixture of vapors of higher fatty acids is a mixture of ideal gases and is described by the equation of state for ideal gases with fugacity

$$f_{vi} = y_i P_{mix}. \quad (3)$$

For the liquid phase, the activity coefficient γ_i is a measure of solution nonideality and depends on solution composition, pressure, and temperature. Experimental studies of the equilibrium compositions of the liquid and vapor of binary mixtures of higher fatty acids [2] (selected results are presented in Table 1) demonstrated that the activity coefficient $\gamma_i = 0.9$–1.0 for the concentration x_i of ith component varying between 0 and 1. This means that, with the ideal solution model adopted for the liquid phase, the relative

1070-4272/02/7501-0090$27.00 © 2002 MAIK "Nauka/Interperiodica"

error in calculations of the component concentration in the vapor phase may be as high as +10 mol %.

In the general case, the solution nonideality, as a rule, originates from differences between characteristics of equitype and mixed interactions in the solution [3]. In the opinion of the majority of researchers, the nonideality of solutions of higher fatty acids is due to association between molecules of the acids

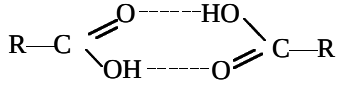

caused by rather strong polarity of the carboxy group COOH, resulting from the presence of dipole moments of the polar bonds C=O and O–H.

Thus, on the assumption that the vapor phase is ideal and the liquid phase shows nonideal behavior, the equation of the vapor–liquid equilibrium in a multicomponent mixture of higher aliphatic acids can be written as

$$y_i P_{\text{mix}} = \gamma_i x_i P_i, \quad (4)$$

$$y_i = \gamma_i x_i P_i / P_{\text{mix}}. \quad (5)$$

Equation (5) provides a basis for constructing a mathematical model of equilibrium states and completely determines its adequacy to the real process. In the presence of steam in the vapor phase, the total pressure P in the closed system at the equilibrium temperature is given by

$$P_0 = P_{\text{mix}} + P_{\text{v}} = \sum_{i=1}^{N} P_{ci} + P_{\text{s}}, \quad (6)$$

where P_{ci} and P_{s} are the partial pressures of the vapor of ith component and steam (mm Hg).

The mixture will start boiling when the pressure of its saturated vapor reaches the value $P_{\text{mix}} = P - P_{\text{s}}$. As a result, the boiling point of a mixture of acids decreases upon introduction of steam, compared with the boiling point without steam.

In the course of distillation, the initial molar flow rate of the initial mixture of acids is divided into the liquid and vapor phases (bottoms and distillate). The overall and partial material balance equations of the process will be, correspondingly, written as

$$G_0 = G_x + G_y, \quad (7)$$

$$G_{0i} = G_0 x_{0i} = G_{xi} + G_{yi} = G_x x_i + G_y y_i, \quad (8)$$

where G_0 is the molar flow rate of the starting mixture in the system (kmol h^{-1}); G_x, G_y are the molar flow rates of the liquid and vapor phases (kmol h^{-1}); and G_{0i}, G_{xi}, G_{yi} are the molar flow rates of ith component in, respectively, the starting mixture and liquid and vapor phases (kmol h^{-1}).

Table 1. Experimental activity coefficients of fatty acids at P_{mix} = 5 mm Hg

T, °C	x_1	y_1	γ_1	γ_2
		Palmitic–oleic		
207.2	0.084	0.176	0.954	0.999
205.0	0.167	0.315	0.973	0.998
201.5	0.303	0.514	0.984	0.996
200.4	0.350	0.576	0.985	0.991
196.6	0.535	0.750	0.991	0.989
193.8	0.676	0.844	0.994	0.981
190.7	0.833	0.934	0.996	0.972
189.0	0.931	0.980	0.998	0.964
207.4	0.101	0.201	0.925	0.999
205.9	0.140	0.268	0.941	0.990
205.0	0.183	0.346	0.952	0.987
203.4	0.250	0.440	0.960	0.983
201.7	0.316	0.524	0.967	0.980
198.0	0.473	0.696	0.973	0.975
196.9	0.530	0.743	0.981	0.968
193.3	0.692	0.857	0.995	0.959
188.9	0.916	0.970	0.999	0.940

Expressing x_i and y_i in terms of the molar flow rates, $x_i = G_{xi}/G_x$ and $y = G_{yi}/G_y$ and substituting the result in Eq. (5), we obtain

$$G_{yi}/G_y = \gamma_i P_i (G_{xi}/G_x)/P_{\text{mix}} = \gamma_i P_{ci}/P_{\text{mix}}.$$

Whence

$$P_{ci} = P_i (G_{xi}/G_x). \quad (9)$$

Substituting the expression for P_{ci} from (9) into (6), we have

$$\sum_{i=1}^{N} [P_i (G_{xi}/G_x)] + P_{\text{v}} = P. \quad (10)$$

Solving Eqs. (7) and (8) for G_{yi} and G_{xi} with account of the vapor–liquid equilibrium equation (5), we find

$$G_{yi} = \gamma_i (P_i/P_{\text{mix}})(G_{xi}/G_x)(G_0 - G_x), \quad (11)$$

$$G_{yi} = \frac{G_{0i}}{1 + \gamma_i (P_i/P_{\text{mix}})[(G_0/G_x) - 1]}. \quad (12)$$

Substituting the expressions for the flow rate G_{xi} from

(12) in (10), we obtain an equation of equilibrium states for the flow rate and composition of the liquid and vapor phases of a multicomponent mixture of higher fatty acids in steam distillation

$$\sum_{i=1}^{N} \frac{G_{0i}(P_i/P)}{G_0\gamma_i(P_i/P_{\text{mix}}) - G_x[\gamma_i(P_i/P_{\text{mix}}) - 1]} + P_s/P = 1. \quad (13)$$

In the general case, the partial pressure P_s of steam in Eq. (13) may correspond to the pressure of both saturated and superheated steam. This is due to the fact that, in practice, steam distillation of fatty acids is done both with saturated and with superheated steam.

In saturated-steam distillation, the vapor–liquid system is characterized by the following parameters: number of phases $\Phi = 3$ (steam, water, and multicomponent mutually soluble mixture of acids, fixed in a single phase); number of independent components $N + 1$; number of external factors affecting the equilibrium in the system, $n = 2$ (temperature, pressure); number of constraints on the concentration variables specifying the composition of the mixture of acids, $m = N - 1$. According to the Gibbs phase law, the number of degrees of freedom of the system, $C = (N + 1) - 3 + 2 - (N - 1) = 1$; in superheated-steam distillation, the water phase is absent and the number of degrees of freedom of the system $C = (N + 1) - 2 + 2 - (N - 1) = 2$. This means that, in superheated-steam distillation, the P_v value is determined by the distillation temperature and cannot be chosen or set arbitrarily, without taking into account the equilibrium conditions (13). In superheated-steam distillation, $C = 2$ and, consequently, at a given total pressure in the system, the partial pressure P_s of steam is not stringently related to the distillation temperature and can be varied irrespective of the equilibrium state. Since distillation of fatty acids is commonly done with superheated steam, such an independent choice of the pressure P_s makes markedly simpler the use of Eq. (13) and, in particular, enables the close system to attain equilibrium via change in the distillation temperature at a given pressure in the system.

According to the Clapeyron equation for a mixture of steam and a mixture of acid vapors, it can be written

$$P_sV = G_sRT = (G_s''/M_s)RT,$$

$$P_{\text{mix}}V = G_yRT = (G_y''/M_y)RT,$$

where G_s is the molar flow rate of steam (kmol h^{-1}); G_s'', G_y'' are the gravimetric flow rates of steam and mixture of acid vapors (kg h^{-1}); M_s, M_y are the molecular weights of steam and mixture of acid vapors (kg $kmol^{-1}$); V is the volume of the system (m^3); R is the universal gas constant (J mol^{-1} K^{-1}); and T is temperature (K).

Dividing the equalities one by another, we obtain

$$G_s = G_y''\frac{M_s}{M_y}\frac{P_s}{P_{\text{mix}}}. \quad (14)$$

In Eq. (14), P_{mix} corresponds to the saturated vapor pressure of a mixture of fatty acids. The saturation is reached at well-developed interface between the bubbling steam and liquid being evaporated and their prolonged contact. However, it is impossible in most cases to create such conditions in the still, and the pressure P_{mix} is lower than the saturated vapor pressure corresponding to the boiling point of the mixture. To correct P_{mix}, the coefficient of steam saturation with the vapor of a substance being distilled, $\varphi = 0.3$–0.8, is introduced and Eq. (14) is written as

$$G_s'' = G_y''\frac{M_s}{M_y}\frac{P_s}{\varphi P_{\text{mix}}} = G_y''\frac{M_s}{M_y}\frac{P_s}{\varphi(P - P_s)}. \quad (15)$$

For superheated-steam distillation of fatty acids, the saturation coefficient is taken to be $\varphi = 0.7$ in design calculations [5].

Equation (15) makes it possible to determine the gravimetric flow rate of steam from the flow rate of the vapor phase (evaporated mixture of acids) at given P and P_{mix} (or P_s) values or vice versa.

As practice shows [5], depression of the boiling point of fatty acids and their agitation with bubbling steam, close to ideal mixing, are achieved in continuous steam distillation of fatty acids at steam feed equal to 7–10 wt % relative to the amount of the liquid mixture of acids being evaporated, i.e., $G_s'' = (0.07–0.1)G_y''$. Hence, the specific consumption of steam per 1 kg of acids being distilled is given by

$$d = \frac{G_s''}{G_y''} = \frac{M_s}{M_y}\frac{P_s}{\varphi P_{\text{mix}}} = \frac{M_s}{M_y}\frac{P_s}{\varphi(P - P_s)} = 0.07–0.1. \quad (16)$$

The use of the equation of equilibrium states (13) is predetermined by the availability of data on the saturated vapor pressure P_i of a pure component and its activity coefficient γ_i.

The vapor pressure P_i was found using equations

Table 2. Parameters of Eq. (17)

i	Acid	$P_i \times 10^{-5}$, mm Hg	A_i	B_i	C_i
1	Lauric $C_{12}H_{24}O_2$	5.723	1.657	2609.448	1 286 435.259
2	Myristic $C_{14}H_{28}O_2$	5.727	1.530	2460.656	1 545 870.088
3	Palmitic $C_{16}H_{32}O_2$	5.728	1.445	2344.222	1 721 921.513
4	Linoleic $C_{18}H_{32}O_2$	5.730	1.386	2281.618	1 888 405.122
5	Oleic $C_{18}H_{34}O_2$	5.730	1.340	2184.896	1 942 904.898
6	Stearic $C_{18}H_{36}O_2$	5.731	1.328	2164.548	1 970 018.986

Table 3. Results of calculation of the first section of the distiller

i	Acid	Feed G_{0i}, kmol h^{-1}	P_i, mm Hg	γ_i	Distillate, kmol h^{-1}		Bottoms, kmol h^{-1}	
					G_y, expt.	G_{yi}, calc.	G_x, expt.	G_{xi}, calc.
1	Lauric	0.0067	9.97	0.948	0.3324	0.0047	2.923	0.0032
2	Myristic	0.1229	3.28	0.980	0.3324	0.0369	2.923	0.0903
3	Palmitic	0.9381	1.54	0.993	0.3324	0.1490	2.923	0.7988
4	Linoleic	0.0540	0.70	0.947	0.3324	0.0039	2.923	0.0502
5	Oleic	1.3090	0.63	0.994	0.3324	0.0900	2.923	1.2213
6	Stearic	0.7203	0.57	0.991	0.3324	0.0446	2.923	0.6767
7	Tar	0.1039	0.12	0.970	0.3324	0.0135	2.923	0.0917
$G_0 = \sum_{i=1}^{7} G_{0i} = 3.255$ kmol h^{-1} Pressure in still P = 5 mm Hg Steam pressure P_s = 2.133 mm Hg Mixture vapor pressure P_{mix} = 2.867 mm Hg Mixture boiling point T = 166.1°C					$G_{ycalc} = \sum_{i=1}^{7} G_{yi} = 3.426$ kmol h^{-1} Relative error –3.06%		$G_{xcalc} = \sum_{i=1}^{7} G_{xi} = 3.255$ kmol h^{-1} Relative error +0.003%	

derived in terms of Prigogine's molecular-statistic theory [6]:

$$\ln(P_i/P_i^*) = A_i - B_i/T - C_i/T^2, \quad (17)$$

where T is the boiling point of the mixture of acids (K); P_i^* is the characteristic pressure (in Prigogine's terms, mm Hg); A_i, C_i, B_i are constants functionally dependent on the number of carbon atoms in acid molecule.

The P_i, A_i, C_i, and B_i values for higher fatty acids are presented in Table 2.

The activity coefficient γ_i was determined using the equations of the ASOG model, method of group constituents.

On the whole, Eqs. (11)–(13), (16), and (17) and the equations of the ASOG model allow calculation of the equilibrium states of the composition of the liquid and vapor phases in a multicomponent mixture of fatty acids in steam distillation and quantitative determination of their material flows. One of the possible procedures for design calculations is as follows.

(1) Input data are taken: G_0'', G_x'', G_y'', x_{0i}'' (i = 1, 2, ..., N), M_i (molecular weights of individual acids), M_s, P, d, φ.

(2) Using formulas for recalculation of weight concentrations into molar concentrations, x_{0i} (i = 1, 2, ..., N) and M_0 (average molecular weigth of fatty acids) are found and the flow rates G_0, G_x, G_y, and G_{0i} (i = 1, 2, ..., N) are determined on the assumption that $M_x = M_y = M_0$.

(3) The partial pressure P_s of steam is calculated using formula (16).

(4) For a given temperature T the vapor pressures P_i (i = 1, 2, ..., N) of fatty acids are found using Eq. (17), and the activity coefficients γ_i, by the equations of the ASOG model.

(5) It is found whether or not the left-hand side of the equation of equilibrium states (13) is identically equal to unity (with prescribed precision). If the identity is not valid, the temperature is raised (left-hand

side less than unity) or lowered (left-hand side exceeding unity) and the calculations according to items 4 and 5 are repeated. The iterative search is continued until the identity (13) is satisfied.

(6) The molar flow rates of individual fatty acids in the liquid and vapor phases, G_{xi} and G_{yi}, and also the compositions of the liquid residue (bottoms) x_i and distillate y_i are calculated using formulas (11) and (12) for $i = 1, 2, .., N$.

(7) The average molecular weights of the liquid and vapor phases, M_x and M_y, are determined.

(8) The calculation according to items 3–7 is repeated.

The efficiency of the proposed algorithm for determining the equilibrium compositions and material flows was verified for the example of calculation of a sectioned industrial fatty acid distiller. The results obtained in calculating the first section of the distiller are presented in Table 3.

It can be seen that the relative discrepancy between the calculated and experimental values is 0.003% for distillate and 3.06% for still bottoms, which may serve as a proof of the adequacy of the developed model to the real process.

CONCLUSIONS

(1) A model of equilibrium states of multicomponent mixtures of higher aliphatic acids in steam distillation is proposed.

(2) An algorithm for calculation of single- and multiple-section distillers for both batch and continuous distillation was developed.

(3) The calculation algorithm can serve as a basis for creating systems for automated design of higher fatty acid distillation processes.

REFERENCES

1. Reid, R.G., Prausnitz, J.M., and Sherwood, T.K., *The Properties of Gases and Liquids*, New York: McGraw-Hill, 1977.
2. Hollo, J. and Lengyel, T., *Fette, Seifen, Anstrichm.*, 1960, vol. 62, no. 10, pp. 913–918.
3. *Termodinamika ravnovesiya zhidkost'–par* (Thermodynamics of the Liquid–Vapor Equilibrium), Morachevskii, A.G., Ed., Leningrad: Khimiya, 1989, pp. 239–285.
4. Szabo Sarkadi, D., *J. Am. Oil Chem. Soc.*, 1958, vol. 35, no. 9, pp. 479–481.
5. *Rukovodstvo po tekhnologii polucheniya i pererabotki rastitel'nykh masel i zhirov* (Manual of the Technology of Production and Processing of Vegetable Oils and Fats), vol. 4: *Proizvodstvo glitserina, zhirnykh kislot, tualetnogo i khozyaistvennogo myla i sinteticheskikh moyushchikh sredstv* (Manufacture of Glycerol, Fatty Acids, Toilet and Laundry Soaps, and Synthetic Detergents), Sergeev, A.G., Ed., Leningrad: Vses. Nauchno-Issled. Inst. Zhirov, 1975.
6. Plesovskikh, V.A., Bezdenezhnykh, A.A., and Kozlov, A.V., *Teor. Osn. Khim. Tekhnol.*, 2001, vol. 35, no. 3, pp. 1–4.

Russian Journal of Applied Chemistry, Vol. 75, No. 1, 2002, pp. 95–97. Translated from Zhurnal Prikladnoi Khimii, Vol. 75, No. 1, 2002, pp. 95–97.
Original Russian Text Copyright © 2002 by Gataullin, Minnigulov, Kudashev, Nurushev, Abdrakhmanov.

ORGANIC SYNTHESIS AND INDUSTRIAL ORGANIC CHEMISTRY

Synthesis of Alkenyl Derivatives of Difluoro-, Trifluoro, and Nitroanilines

R. R. Gataullin, F. F. Minnigulov, A. R. Kudashev, R. A. Nurushev, and I. B. Abdrakhmanov

Institute of Organic Chemistry, Ufa Scientific Center, Russian Academy of Sciences, Ufa, Bashkortostan, Russia
Bashkir State Agricultural University, Ufa, Bashkortostan, Russia

Received April 16, 2001

Abstract—*N*-Alkenyl derivatives of di- and trifluoroanilines were prepared by their reaction with 2-chloro-3-pentene. Their transformations under conditions of the Claisen rearrangement were studied. *C*-Alkenylnitroanilines were prepared by reaction of piperylene with *o*- and *p*-nitroanilines in the presence of $AlCl_3$.

Commercially available piperylene and 2-chloro-3-pentene, which can be readily prepared from piperylene, are widely used in syntheses of alkylarylamines [1–3]. At present, the best studied and most convenient route to these derivatives is rearrangement of *N*-(2-methyl-1-butenyl) derivatives into the *o*- and *p*-substituted products, occurring on heating in the presence of acids. The ratio of the *ortho* and *para* isomers is largely influenced by substituents in the aromatic ring. The aromatic amino-Claisen rearrangement has been well studied for *N*-alkylanilines and alkylnaphthalenes, but examples of this rearrangement with *N*-alkylanilines containing electron-withdrawing substituents in the aromatic ring are few [4, 5] and concern *N*-alkyl-3,4-difluoroanilines.

In this work we prepared *N*-substituted derivatives of di- and trifluoroanilines and studied their rearrangement at 140°C under the action of HCl or $ZnCl_2$. 2-Chloro-3-pentene readily reacts with fluorinated anilines **I**–**III** in triethanolamine to give *N*-alkenyl derivatives **IV**–**VI**. Heating of hydrochloride of **IV** in *o*-xylene at 140°C yields compound **VII** as major product. Hydrochlorides of **V** and **VI** remain unchanged under these conditions. The yield of **VII** and **VIII** under conditions of vacuum distillation could be higher, but the available amounts of **I**–**III** were insufficient to prepare compounds **IV**–**VI** in amounts required for these experiments. Heating of **V** with $ZnCl_2$ in *o*-xylene yields aniline **VIII**, whereas amine **VI** undergoes virtually no rearrangement under these conditions. This is probably due to the presence of the fluorine atom at C^2, whose strong –*I* effect deactivates the 6-position of the aromatic ring. Experiments on alkenylation of nitroanilines **IX** and **X** confirm this assumption:

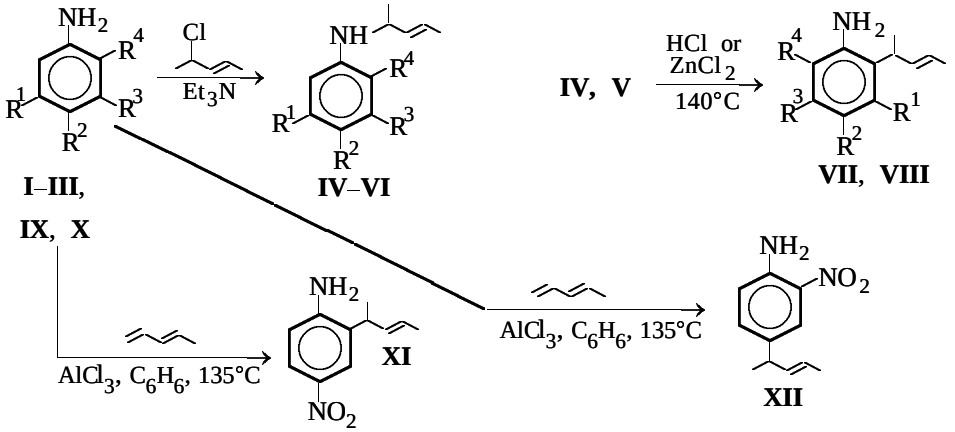

where $R^1 = R^3 = F$, $R^2 = R^4 = H$ (**I**, **IV**, **VII**); $R^1 = R^2 = R^3 = F$, $R^4 = H$ (**II**, **V**, **VIII**); $R^1 = R^2 = R^4 = F$, $R^3 = H$ (**III**, **VI**); $R^1 = R^3 = R^4 = H$, $R^2 = NO_2$ (**IX**); $R^1 = R^2 = R^3 = H$, $R^4 = NO_2$ (**X**).

1070-4272/02/7501-0095$27.00 © 2002 MAIK "Nauka/Interperiodica"

Reactions of nitroanilines **IX** and **X** with piperylene in autoclave in the presence of $AlCl_3$ yield a mixture of products from which we isolated and identified compounds **XI** and **XII**.

Thus, increase in the number of electron-withdrawing substituents in the aromatic ring prevents aromatic amino-Claisen rearrangement of fluorinated *N*-alkenylanilines.

The composition and structure of the synthesized compounds were determined by elemental analysis and spectroscopy. The ^1H NMR spectra allow reliable identification of all the anilines. The ^1H NMR spectrum of **VII** in the region of aromatic protons contains two one-proton signals of H^4 (d.t) and H^6 (d.d). The ^1H NMR spectrum of **VIII** in this range contains only the one-proton signal of H^6 (d.d.d). The location of H^4 between the fluorine atoms is confirmed by the fact that its signal is a triplet with large coupling constants *J*. Alkenylation of nitroanilines at the *o*- and *p*-positions was confirmed by the ^1H and ^{13}C NMR spectra. In both cases, in the region of aromatic protons there are two doublets and one singlet, which is possible only for the presumed structures. The H^3 signals in the spectra of both compounds are characterized by low remote coupling constant *J* with H^5 (1.9–2.2 Hz).

EXPERIMENTAL

The ^1H and ^{13}C NMR spectra were recorded on a Bruker AM-200 spectrometer (300 and 75 MHz, respectively, $CDCl_3$, internal reference TMS). The IR spectra were recorded on a UR-20 spectrometer (mulls in mineral oil). The reaction progress was monitored by GLC (Chrom-5 chromatograph, carrier gas helium, linear heating rate 12 deg min^{-1}) and TLC (Silufol UV-254 plates, benzene).

N-Alkenylation of fluoroanilines **I**–**III** was performed as follows: 2.2 mmol of 2-chloro-3-pentene was added to a solution of 2 mmol of **I**–**III** in 5 ml of triethylamine, and the mixture was refluxed for 3 h. After cooling to room temperature, 30 ml of CH_2Cl_2 was added, and the mixture was treated with 10 ml of 20% aqueous NaOH. The organic phase was separated, dried over KOH, and filtered; the solvent was evaporated in a water-jet-pump vacuum. The resulting amines **IV**–**VI** were purified by column chromatography (silica gel 100/40 μm, hexane).

***N*-(3-Penten-2-yl)-3,5-difluoroaniline IV.** Yield 85%, R_f 0.53 (CCl_4). IR spectrum, ν, cm^{-1}: 3432 (NH). ^1H NMR spectrum ($CDCl_3$), δ, ppm: 1.27 d (3H, CH_3, *J* 6.30 Hz), 1.69 d (3H, CH_3, *J* 6.23 Hz), 3.82 m (1H, C*H*CH_3), 3.90 br.s (1H, NH), 5.30–5.70 m (2H, HC=CH), 6.07 d.d (2H, H^2, H^6, J_1 1.93, J_2 7.95 Hz), 6.11 m (1H, H^4). ^{13}C NMR spectrum ($CDCl_3$), δ_C, ppm: 17.53 (CH*C*H_3), 21.70 (=CH*C*H_3), 50.52 (*C*HCH_3), 91.77 t (C^4, *J* 26.03 Hz), 95.70 d.d (C^2, C^6, J_1 9.15, J_2 19.50 Hz), 125.65 (*C*H=$CHCH_3$), 133.22 (CH=*C*HCH_3), 150.00 t (C^1, *J* 9.1 Hz), 163.94 d.d (C^3, C^5, J_1 16.88, J_2 242.55 Hz).

Found, %: C 66.72, H 6.33, F 18.88, N 6.73.
$C_{11}H_{13}F_2N$.
Calculated, %: C 66.99, H 6.64, F 19.27, N 7.10.

***N*-(3-Penten-2-yl)-3,4,5-trifluoroaniline V.** Yield 87%, R_f 0.8 (CCl_4). IR spectrum, ν, cm^{-1}: 3448 (NH). ^1H NMR spectrum ($CDCl_3$), δ, ppm: 1.26 d (3H, CH_3, *J* 6.67 Hz), 1.68 d (3H, CH_3, *J* 6.36 Hz), 3.77 m (2H, C*H*CH_3, NH), 5.30–5.75 m (2H, HC=CH), 6.14 d.d (2H, H^2, H^6, J_1 5.71, J_2 10.28 Hz). ^{13}C NMR spectrum ($CDCl_3$), δ_C, ppm: 17.54 (CH*C*H_3), 21.74 (=CH*C*H_3), 50.87 (*C*HCH_3), 96.56 d (C^2, C^6, *J* 23.7 Hz), 125.90 (*C*H=$CHCH_3$), 133.19 (CH=*C*H–CH_3), 143.66 t (C^1, *J* 10.65 Hz), 151.85 d.d.d.d (C^3, C^4, C^5, J_1 6.52, J_2 10.72, J_3 16.95, J_4 242.63 Hz).

Found, %: C 60.94, H 5.41, F 26.01, N 6.19.
$C_{11}H_{12}F_3N$.
Calculated, %: C 61.39, H 5.62, F 26.48, N 6.51.

***N*-(3-Penten-2-yl)-2,4,5-trifluoroaniline VI.** Yield 85%, R_f 0.75 (CCl_4). IR spectrum, ν, cm^{-1}: 3450 (NH). ^1H NMR spectrum ($CDCl_3$), δ, ppm: 1.27 d (3H, CH_3, *J* 6.34 Hz), 1.65 d (3H, CH_3, *J* 6.34 Hz), 3.76 m (2H, C*H*CH_3, NH), 5.30–5.70 m (2H, HC=CH), 6.46 d.d.d (1H, H^6, J_1 8.0, J_2 12.55, J_3 16.03 Hz), 6.82 d.d.d (1H, H^3, J_1 9.33, J_2 12.13, J_3 21.42 Hz). ^{13}C NMR spectrum ($CDCl_3$), δ_C, ppm: 17.50 (CH*C*H_3), 21.88 (=CH*C*H_3), 50.84 (*C*HCH_3), 101.39 d.d (C^6, J_1 4.12, J_2 23.77 Hz), 104.37 t (C^3, *J* 23.4 Hz), 125.86 (*C*H=$CHCH_3$), 133.24 (CH=*C*H–CH_3).

Found, %: C 61.31, H 5.58, F 26.45, N 6.52.
$C_{11}H_{12}F_3N$.
Calculated, %: C 61.39, H 5.62, F 26.48, N 6.51.

2-(3-Penten-2-yl)-3,5-difluoroaniline VII. A solution of 0.2 g of **IV** in 3 ml of *o*-xylene was saturated with gaseous HCl for 1 min. The resulting mixture was heated to 140°C for 6 h. After cooling to room temperature, 30 ml of benzene and 5 ml of 20% aqueous NaOH were added, the organic layer was separated and dried over KOH, and the solvent was vacuum-evaporated. The residue was chromatographed

on a column (0.5 × 30 cm) packed with silica gel (100/40 μm); eluent heptane. Compound **VII** was obtained; yield 0.08 g (40%), R_f 0.33 (benzene). IR spectrum, ν, cm^{-1}: 3472, 3384 (NH_2). ^1H NMR spectrum ($CDCl_3$), δ, ppm: 1.39 d (3H, CH_3, *J* 7.11 Hz), 1.73 d (3H, CH_3, *J* 6.05 Hz), 3.84 m (1H, C*H*CH_3), 4.02 br.s (2H, NH_2), 5.50–5.80 m (2H, HC=CH), 6.14 d.d (1H, H^6, *J* 1.63, J_2 8.78 Hz), 6.21 d.t (1H, H^4, J_1 1.63, J_2 11.32 Hz). ^{13}C NMR spectrum ($CDCl_3$), δ_C, ppm: 16.82 (CH*C*H_3), 17.89 (=CH*C*H_3), 31.52 (*C*HCH_3), 93.67 d.d (C^4, J_1 26.23, J_2 29.93 Hz), 98.64 d.d (C^6, J_1 3.90, *J* 23.93 Hz), 113.00 d.d (C^2, J_1 3.87, J_2 24.00 Hz), 124.90 (CH=*C*HCH_3), 133.67 (*C*H=$CHCH_3$), 147.43 d.d (C^1, *J* 8.78, J_2 12.75 Hz), 160.06–163.49 m (C^3, C^5).

Found, %: C 66.99, H 6.64, F 19.27, N 7.10.
$C_{11}H_{13}F_2N$.
Calculated, %: C 66.99, H 6.64, F 19.27, N 7.10.

2-(3-Penten-2-yl)-3,4,5-trifluoroaniline VIII. To a solution of 0.22 g of **V** in 3 ml of *o*-xylene, 0.02 g of $ZnCl_2$ was added, and the mixture was refluxed for 10 h. The reaction progress was monitored by GLC. After disappearance of the initial compound **V**, the mixture was cooled to room temperature, 30 ml of benzene was added, and the mixture was treated with 5 ml of 20% aqueous NaOH. The organic phase was separated and dried over KOH. The solvent was vacuum-evaporated, and the residue was chromatographed on a column (0.5 × 30 cm) packed with silica gel (100/40 μm); eluent heptane. Yield 0.09 g (41%), R_f 0.2 (benzene). IR spectrum, ν, cm^{-1}: 3472, 3384 (NH_2). ^1H NMR spectrum ($CDCl_3$), δ, ppm: 1.39 d (3H, CH_3, *J* 7.25 Hz), 1.72 d.d (3H, CH_3, J_1 1.09, J_2 5.05 Hz), 3.80 br.s (3H, CH, NH_2), 5.50–5.70 m (2H, HC=CH), 6.21 d.d.d (1H, H^6, J_{H^6,F^3} 2.12, J_{H^6,F^4} 6.30, J_{H^6,F^5} 8.56 Hz). ^{13}C NMR spectrum ($CDCl_3$), δ, ppm: 16.60 (CH*C*H_3), 17.69 (CH=CH*C*H_3), 31.99 (*C*H–CH_3), 99.20 d (C^6, *J* 19.35 Hz), 113.58 d (C^2), 125.45 (CH=*C*HCH_3), 132.90 (*C*H=$CHCH_3$), 140.83–151.68 m (C^3, C^5, C^1).

Found, %: C 61.02, H 5.12, F 26.00, N 6.14.
$C_{11}H_{12}F_3N$.
Calculated, %: C 61.39, H 5.62, F 26.48, N 6.51.

To alkylate nitroanilines **IX** and **X**, a 100-ml autoclave was charged with 1.38 g of nitroaniline **IX** or **X**, 60 ml of benzene, 0.65 g of $AlCl_3$, and 0.82 g of piperylene. The mixture was heated at 135°C for 4 h. After cooling to room temperature, 30 ml of 20% aqueous NaOH was added. The mixture was stirred, and the organic phase was separated and dried over KOH. The solvent was vacuum-evaporated, and the residue was chromatographed in a column (0.5 × 30 cm) packed with silica gel (100/40 μm); eluent hexane and then hexane–methanol (99 : 1).

2-(3-Penten-2-yl)-4-nitroaniline XI. Yield 0.85 g (41%), R_f 0.2 (benzene). IR spectrum, ν, cm^{-1}: 3470, 3455 (NH_2). ^1H NMR spectrum ($CDCl_3$), δ, ppm: 1.40 d (1H, CH_3, *J* 7.02 Hz), 1.72 d (3H, CH_3, *J* 4.95 Hz), 3.41 m (1H, C*H*CH_3), 4.60 br.s (2H, NH_2), 5.50–5.70 m (2H, HC=CH), 6.6 d (1H, H^6, *J* 8.37 Hz), 7.9 d.d (1H, H^5, J_1 2.21, J_2 8.37 Hz), 8.0 d (1H, H^3, *J* 2.21 Hz). ^{13}C NMR spectrum ($CDCl_3$), δ_C, ppm: 17.81, 19.32 ($2CH_3$), 37.11 (*C*HCH_3), 114.42 (C^6), 123.73 (C^5), 124.05 (C^7), 126.03 (*C*H=$CHCH_3$), 128.33 (C^2), 133.34 (CH=*C*HCH_3), 139.02 (C^4), 151.14 (C^1).

Found, %: C 63.72, H 6.42, N 13.14.
$C_{11}H_{14}N_2O_2$.
Calculated, %: C 64.06, H 6.86, N 13.58.

4-(3-Penten-2-yl)-2-nitroaniline XII. Yield 0.58 g (28%), R_f 0.3 (benzene). IR spectrum, ν, cm^{-1}: 3400, 3460 (NH_2). ^1H NMR spectrum ($CDCl_3$), δ, ppm: 1.20 d (3H, CH_3, *J* 7.07 Hz), 1.63 d (3H, CH_3, *J* 5.35 Hz), 3.32 d.q (1H, C*H*CH_3, J_1 3.0, J_2 7.07 Hz), 5.30–5.50 m (2H, HC=CH), 5.90 br.s (2H, NH_2), 6.7 d (1H, H^6, *J* 8.60 Hz), 7.1 d.d (1H, H^5, J_1 1.91, J_2 8.60 Hz), 7.9 d (1H, H^3, *J* 1.91 Hz). ^{13}C NMR spectrum ($CDCl_3$), δ_C, ppm: 17.91, 21.12 ($2CH_3$), 41.01 (*C*HCH_3), 116.92 (C^6), 123.83 (C^3), 124.53 (C^2), 126.24 (HC=*C*HCH_3), 128.41 (H*C*=$CHCH_3$), 132.04 (C^5), 135.52 (C^4), 143.24 (C^1).

Found, %: C 63.67, H 6.51, N 13.16.
$C_{11}H_{14}N_2O_2$.
Calculated, %: C 64.06, H 6.86, N 13.58.

REFERENCES

1. Abdrakhmanov, I.B., Sharafutdinov, V.M., and Tolstikov, G.A., *Zh. Org. Khim.*, 1984, vol. 20, no. 2, pp. 620–622.
2. Abdrakhmanov, I.B., Sharafutdinov, V.M., Nigmatullin, N.G., *et al.*, *Zh. Org. Khim.*, 1982, vol. 18, no. 7, pp. 1466–1471.
3. Abdrakhmanov, I.B., Saraeva, Z.I., Nigmatullin, N.G., *et al.*, *Izv. Akad. Nauk SSSR, Ser. Khim.*, 1989, no. 10, pp. 2303–2308.
4. Mustafin, A.G., Gimadieva, A.R., Khalilov, I.N., *et al.*, *Izv. Ross. Akad. Nauk, Ser. Khim.*, 1988, no. 1, pp. 188–190.
5. Gataullin, R.R., Kazhanova, T.V., Davydova, V.A., *et al.*, *Khim.-Farm. Zh.*, 1999, vol. 33, no. 5, pp. 29–32.

Russian Journal of Applied Chemistry, Vol. 75, No. 1, 2002, pp. 98–101. Translated from Zhurnal Prikladnoi Khimii, Vol. 75, No. 1, 2002, pp. 98–102.
Original Russian Text Copyright © 2002 by Sazanov.

MACROMOLECULAR CHEMISTRY AND POLYMERIC MATERIALS

"Relay" Stabilization of Polyimides

Yu. N. Sazanov

Institute of Macromolecular Compounds, Russian Academy of Sciences, St. Petersburg, Russia

Received May 8, 2001

Abstract—With triphenyl phosphate as example, thermal stabilization of polyimides was studied in a wide temperature range, and the step mechanism of the process, termed "relay" stabilization, was suggested.

By now, a large experience has been gained in synthesis of heterocyclic heat-resistant polymers. Some of these compounds (polyimides, polybenzimidazoles, polybenzoxazoles, and other compounds based on nitrogen-containing heterocycles) are produced on the commercial scale and are widely used in modern engineering. Initially these polymers in the form of various articles, preserving their service characteristics at considerably higher temperatures as compared to the previous generation of heat-resistant polymers, met the specialists' requirements. However, the requirements to articles operating under extreme conditions grew, and it became necessary to further enhance the heat resistance. Attempts to prepare new organic polynuclear heterocyclic structures have not led to appreciable success. In this connection, the necessity again arose in stabilization of polymers, but now this concerned cyclochain aromatic and heterocyclic polymers. Furthermore, the requirements to stabilizers sharply increased also, as these stabilizers should be effective at considerably higher temperatures (300–500°C and higher) than in the previously used systems. Only a narrow range of potential stabilizing agents, especially organic, meet this requirement.

In the course of the search for new thermal stabilizers for heat-resistant polymers, the main requirements to these agents were formulated. We believe that the main feature of such agents is their polyfunctional performance. Namely, a stabilizer should suppress the degradation of polymers at high temperatures and facilitate processes improving the service characteristics of a polymeric article under such conditions. At approximately 500°C, cardinal changes are observed in the kinetics and pathways of thermochemical processes in polymers. Apparently, stabilizers of the new type should be versatile, and their polyfunctional performance should cover the whole working range of the polymer.

This reasoning leads to the concept of "relay" stabilization of heat-resistant polymers, when a stabilizer in a ready polymer or prepolymer in the course of heating or service undergoes successive transformations in which it or its transformation products suppress undesirable processes. For polyimides, in the stage of synthesis of the prepolymer (polyamido acid, PAA) such a stabilizer should behave as catalyst. In the course of transformation of PAA into the polyimide, the stabilizer should protect intermediates and oligomers from reverse reactions (hydrolysis, acidolysis, etc.) and control the molecular weight of the polymer. At higher temperatures, it should suppress oxidative and secondary oxidative thermal hydrolytic reactions characteristic of intramolecular cyclization of heterochain polymers. Transforming into intermediate products of thermal oxidation and thermal hydrolysis, such a stabilizer protects the polymer from the attack of oxygen and hydroxide ions. Suppression of these degradation processes provides favorable conditions for high-temperature carbonization of the polymer, with a high yield of the carbon polymer. Thus, the "relay" stabilization of a polyimide, involving appropriate transformations of the stabilizer and its thermolysis products with increasing temperature, enhances the heat resistance of polymers at elevated temperatures.

It is well known that organic derivatives of P, Sb, B, and V were used as stabilizers of various heat-resistant polymers [1]. One of the first heterocyclic compounds with which such stabilizers (organophosphorus compounds, in particular, triphenyl phosphate, TPP) were tested was PM polyimide [1–6].

Triphenyl phosphate is used for a long time as plasticizer in production of many polymeric articles. A question arises: To what extent does TPP exert the plasticizing effect in synthesis of polyimides and how does it affect the heat resistance of the final product? Usually TPP is added to a PAA solution. Cyclodehydration of a film cast from such a solution occurs in the presence of TPP. Without TPP, degradation of PAA and incomplete cyclodehydration result in ac-

1070-4272/01/7501-0098$27.00 © 2002 MAIK "Nauka/Interperiodica"

cumulation in the polyimide macromolecules of "defective" structures: terminal groups and amido acid residues considerably reducing the heat resistance of the final product [5].

Using MTA, TG, and DTA, we examined the effect of TPP on transformation of PAA into the polyimide. Figure 1 shows the MTA curves for PAA derived from pyromellitic acid and diaminodiphenyl ether (PM PAA) without and with addition of TPP. It is seen that TPP remains in the film until the cyclodehydration is virtually complete, after which its loss starts. The temperature range in which PAA undergoes cyclodehydration in the presence of TPP is by 50°C narrower than in the absence of TPP. The activation energy of this process, calculated from the water release curve, decreases on approaching the curve maximum from 113 to 76 kJ mol^{-1} in the presence of TPP and from 80 to 58 kJ mol^{-1} without TPP.

Acceleration of cyclodehydration as a result of the plasticizing effect of TPP results in that the degree of intramolecular decomposition of PAA decreases, and the imidization becomes more complete as compared to the sample without TPP; as a result, the heat resistance of the polyimide is enhanced, and its deformation and strength properties are improved [7].

It should be noted that the effect of TPP on cyclodehydration cannot be reduced merely to its plasticizing effect. When PAA contans TPP, water released in the course of imidization can induce partial hydrolysis of TPP to form the acidic ester, which exerts approximately the same catalytic effect as phosphoric acid, the known catalyst of many polycondensations:

$$(PhO)_3P{=}O + H_2O \rightarrow PhOH + (PhO)_2P(O)OH. \quad (1)$$

Another probable mechanism of reaction of TPP with PAA, accelerating imidization, can be ring closure with intermediate formation of the mixed anhydride:

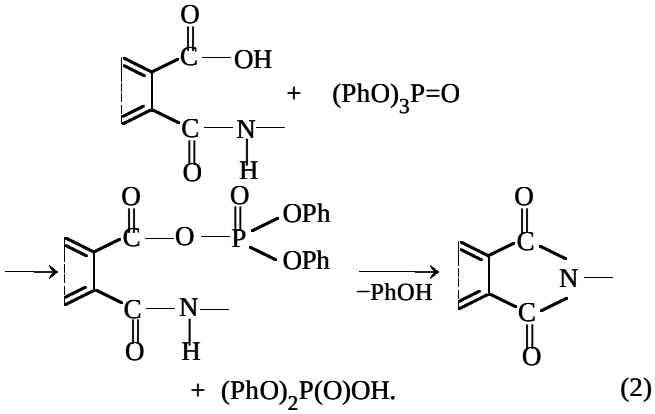

+ $(PhO)_2P(O)OH$. (2)

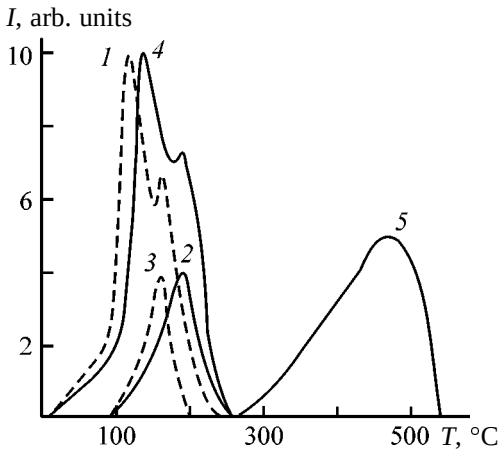

Fig. 1. Mass thermograms of cyclodehydration of a PM PAA film: (*I*) intensity and (*T*) temperature. (*1*) DMF and (*2*) H_2O from straight PAA; (*3*) DMF and (*4*) H_2O from the mixture PAA + 10% TPP; (5) TPP.

As a rule, thermal dehydration of PAA is accompanied by intramolecular decomposition. Water present in the system can hydrolyze the terminal anhydride groups arising in the course of decomposition, giving carboxylic acids which are inactive in acylation. Triphenyl phosphate, reacting with acids by the mechanism similar to that shown in scheme (2), facilitates the back synthesis of PAA, which increases the molecular weight of the polyimide and makes the structure less defective.

The question as to whether phosphorus-containing compounds remain in the polyimide becomes of principal importance. To answer this question, we analyzed by mass spectrometry the gaseous products released from the polyimide on heating. Figure 1, curve *5* shows that, along with degradation products, TPP is released from the film on heating to 500°C, and its content can be estimated gravimetrically. Apparently, even in a high vacuum the polyimide film retains a certain amount (1–3%) of TPP at temperatures of up to 500°C and higher, when degradation becomes appreciable. Naturally, under actual service conditions (atmospheric pressure, presence of moisture, oxygen, etc.) the degradation can start at lower temperature, and the amount of TPP remaining in the film can be higher than in our experiment; hence, the effect of TPP on degradation is beyond question. To elucidate the mechanisms by which TPP affects degradation of polyimides, we used data obtained for polyimides and model compounds using comparative thermal analysis [8] consisting essentially in quantitative determination of carbon oxides released during isothermal heating of samples in sealed ampules.

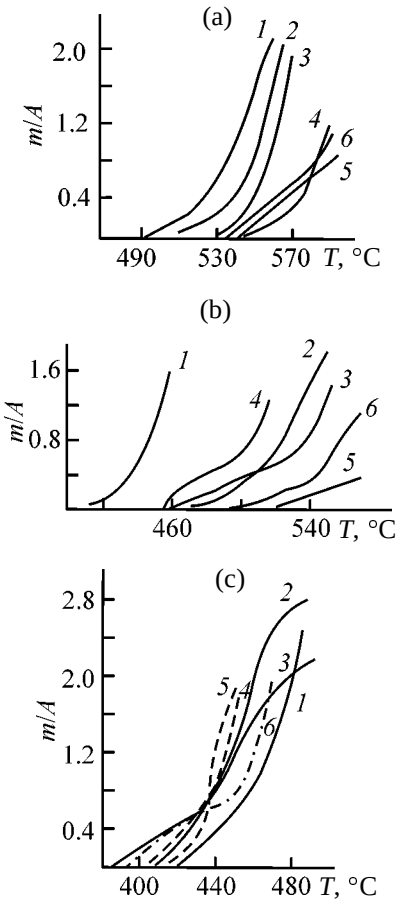

Fig. 2. Comparison of high-temperature degradation curves, as monitored by release of carbon oxides. (*m*/*A*) Number of moles of released CO and CO_2 per structural unit of the polymer and model; (*T*) temperature. (*1*–*3*) PM polyimide film and (*4*–*6*) PPI film. Stabilizer (5 wt %): (*1*, *4*) none, (*2*, *5*) B_2O_3, and (*3*, *6*) TPP. (a) Thermal degradation in a vacuum, (b) thermal hydrolysis, and (c) thermal oxidative degradation.

Figure 2 shows the total curves of gas release from polyimide and *N*-phenylphthalimide (PPI) films in the course of thermal degradation in a vacuum with and without addition of TPP and boric anhydride (5 wt %) [9]. For PPI the effect is insignificant, whereas polyimide is stabilized with the above compounds. It is noteworthy that, despite different chemical nature, both additives act similarly. Apparently, defective structures present in polyimide degrade at lower temperatures than regular fragments; the substances (in particular, water) released in the course of their degradation can promote degradation of the main structure.

Water can react with TPP and B_2O_3 to form in both cases a relatively strong acid. In this connection, several possible mechanisms of stabilization of the imide structure can be considered. It was repeatedly noted that TPP and B_2O_3 exert a stabilizing effect in thermal hydrolysis of polyimides and model imides [10, 11]. The examples are curves of gas release in the course of thermal hydrolysis of polyimides and PPI (Fig. 2). The stabilizing effect is appriximately equal for TPP and B_2O_3.

It is commonly believed that hydrolysis of imides starts with the nucleophilic attack of the carbonyl carbon atom by the H_2O molecule or by the stronger nucleophile, hydroxide ion:

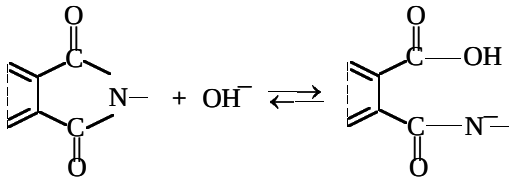

(3)

The concentration of hydroxide ions and hence the rate of polyimide hydrolysis increase with temperature. Appearance of strong acids in the system results in considerably increased concentration of protons and decreased concentration of hydroxide ions, which is one of the factors responsible for suppressed hydrolysis of imides.

However, the stabilizing effect of TPP is not limited to this factor. Because at high temperatures the imide ring should be noticeably hydrolyzed with water, amido acid fragments will arise in the system. Their further transformations can occur by several pathways:

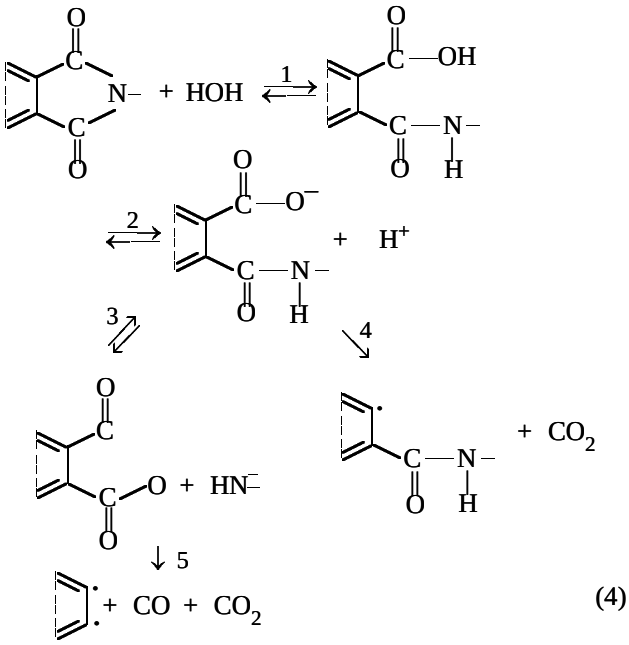

(4)

It is known that *o*-amido acid tends to form the imide ring, whereas dissociation of the acid group

facilitates the intramolecular cleavage of the amido acid group to form the anhydride and amine [reaction (3)]. In the temperature range under consideration (>400°C), the anhydride groups actively decompose with release of gaseous products [reaction (5)]. Furthermore, the acid undergoes decarboxylation [reaction (4)].

Thus, the stabilizing effect of TPP derivatives (and also of other acid additives) is due to suppression of dissociation of carboxyl in the amido acid group. Considering scheme (4), we can note the following positive aspects of such effect: stabilization of the imide ring due to the shift of equilibrium (1) toward cyclodehydration, stabilization of amido acid fragments due to decreased contribution of depolycondensation by reaction (3), and suppression of the dissociation of carboxy groups by itself.

The first two effects were discussed above, and the third effect is confirmed by observations of a strong thermostabilizing effect of TPP and B_2O_3 [10, 11]. This fact confirms once again that the mechanism of the stabilizing effect of these additives is similar. It can be shown that thermal oxidation and hydrolysis of polyimides and model imides promote each other (Fig. 2c). Because thermal oxidation is accompanied by release (accumulation in a closed system) of water, in a certain stage thermal oxidation and hydrolysis are superimposed. Naturally, beginning specifically from this moment, the protective effect of TPP on thermal hydrolysis of the imide structure should become operative. Comparison of Figs. 2b and 2c shows that, indeed, in the initial period of thermal oxidation TPP exerts no stabilizing effect, and only above 450°C the stabilizing effect becomes noticeable.

Comparison of the resistance to thermal oxidative degradation of polyimide films modified with various phosphorus compounds (Fig. 3) shows that the strongest effect is exerted by TPP and hexamethylphosphoramide. Organic derivatives of trivalent phosphorus do not inhibit thermal oxidation of polyimides. There are certain grounds to believe that some Sb and V compounds participate in "relay" stabilization of polyimides and polybenzimidazoles. However, in preliminary experiments with these compounds we observed only separate cases of stabilization, requiring more detailed study.

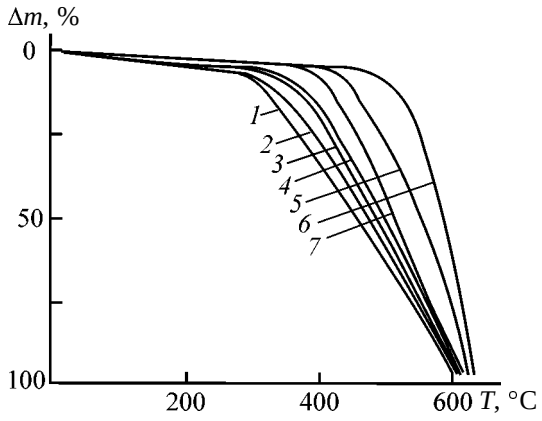

Fig. 3. TGA curves of a PM polyimide film in the presence of (*1–4*) P(III) acid esters, (*5*) hexamethylphosphoramide, and (*6*) TPP; (*7*) no additives. (Δ*m*) Weight loss and (*T*) temperature.

CONCLUSIONS

Stabilization of polyimides in the temperature range 20–500°C with triphenyl phosphate involves several stages. Participation of triphenyl phosphate and its derivatives in reactions with polyimide and its intermediate decomposition products is associated with the "relay" transfer of the stabilizing effect from one reaction to another, which results in suppression of the destructive effects of the environment and improvement of the quality of the polymeric materials.

REFERENCES

1. Kovarskaya, B.M., Byumel'fel'd, A.B., and Levantovskaya, I.I., *Termicheskaya stabil'nost' geterotsepnykh polimerov* (Heat Resistance of Heterochain Polymers), Moscow: Khimiya, 1977.
2. Annenkova, N.G., Kovarskaya, B.M., Dobrokhotova, M.L., *et al.*, *Plast. Massy*, 1976, no. 2, pp. 41–42.
3. Gur'yanova, N.G., Annenkova, N.G., and Novotvortseva, M.L., *Vysokomol. Soedin., Ser. A*, 1978, vol. 20, no. 1, pp. 207–214.
4. Koton, M.M., Sazanov, Yu.N., and Shibaev, L.A., *Dokl. Akad. Nauk SSSR*, 1978, vol. 241, no. 1, pp. 99–102.
5. Bessonov, M.I., Koton, M.M., Kudryavtsev, V.V., and Laius, L.A., *Poliimidy – klass termostoikikh polimerov* (Polyimides: A Class of Heat-Resistant Polymers), Leningrad: Nauka, 1983.
6. Koton, M.M., Sazanov, Yu.N., Shibaev, L.A., *et al.*, *Zh. Prikl. Khim.*, 1983, vol. 56, no. 3, pp. 617–624.
7. Mikhailov, G.M., Bel'nikevich, N.G., Shibaev, L.A., *et al.*, *Zh. Prikl. Khim.*, 1993, vol. 66, no. 6, pp. 1369–1375.
8. Sazanov, Yu.N., Stepanov, N.G., Shibaev, L.A., *et al.*, *Acta Polym.*, 1988, vol. 39, no. 8, pp. 422–424.
9. Sazanov, Yu.N., Antonova, T.A., Stepanov, N.G., *et al.*, *Acta Polym.*, 1991, vol. 42, no. 13, pp. 65–75.
10. Sazanov, Yu.N., Shibaev, L.A., and Antonova, T.A., *J. Therm. Anal.*, 1980, vol. 18, no. 1, pp. 65–75.
11. Sazanov, Yu.N. and Shibaev, L.A., *Acta Polym.*, 1980, vol. 31, no. 1, pp. 1–10.

Russian Journal of Applied Chemistry, Vol. 75, No. 1, 2002, pp. 102–105. Translated from Zhurnal Prikladnoi Khimii, Vol. 75, No. 1, 2002, pp. 103–106.
Original Russian Text Copyright © 2002 by Ergozhin, Chalov, Iskakova, Klepikova, Solomin.

MACROMOLECULAR CHEMISTRY AND POLYMERIC MATERIALS

^{13}C NMR Study of Polycondensation of Allyl Bromide, Diglycidyl Resorcinol Ether, and Polyethylenepolyamine

E. E. Ergozhin, A. K. Chalov, R. A. Iskakova, S. G. Klepikova, and V. A. Solomin

Bekturov Institute of Chemical Sciences, Ministry of Science and Higher Education of Kazakhstan Republic, Almaty, Kazakhstan

Received October 10, 2001

Abstract—The features of polycondensation of allyl bromide, diglycidyl resorcinol ether, and polyethylenepolyamine were studied by ^{13}C NMR.

Curing of polymer–polymer systems formed on the basis of epoxy and allyl oligomers was studied by NMR spectroscopy [1]. The structures of copolymers of *N*,*N*-dimethyl-*N*,*N*-diallylammonium chloride with *N*-vinylpyrrolidone [2], polymers based on glycidyl methacrylate, and its copolymers with methyl methacrylate [3] were studied.

The aim of this work is to study the features of polycondensation of allyl bromide (AB), diglycidyl resorcinol ether (DRE), and polyethylenepolyamine (PEPA) in the precondensation stage by ^{13}C NMR.

EXPERIMENTAL

Anion exchangers were synthesized in dimethylformamide (DMF) at 24°C with subsequent curing of the resulting gel at 80°C [4].

The ^{13}C NMR spectra of the initial compounds and reaction products were recorded at room temperature on a Bruker WP-80 spectrometer operating at 20.13 MHz.

Because aliphatic di- and polyamines are polyfunctional, three-dimensional polycondensation can be performed in two stages. At first precondensation was carried out in the presence of a solvent and then the precondensate was cured to form the maximum cross-linked polymer.

Cross-linked anion exchangers were synthesized by polycondensation of AB, DRE, and PEPA in DMF, since the initial products are readily soluble in DMF and the final products and intermediates readily swell in DMF. Polycondensation was carried out in a solution since in the absence of a solvent, owing to a high reactivity of the initial compounds and accessibility of the reaction centers of the reacting molecules, the process occurs at a high rate with formation of a heterogeneous gel. The use of a solvent allowed control of the process rate and excluded local over-heating resulting from the exothermic effect.

The signals in the ^{13}C NMR spectrum were assigned considering data obtained from the spectra of the initial compounds.

It is seen from the ^{13}C NMR spectrum of DRE that the carbon atom of the methylene group of the epoxy ring gives the signal at higher field (44.4 ppm) as compared to the exocyclic methylene group (70.0 ppm). Abnormally large difference in the chemical shifts can be attributed to the shielding effect of the three-membered ring. For the same reason, the signal of the methine group is shifted upfield and is observed at 50.5 ppm. The signals observed in the range 100–165 ppm belong to the carbon atoms of the aromatic ring. They were assigned using the shielding constants of substituents and the additive equation used for evaluating chemical shifts [5]. The calculated chemical shifts of carbon atoms C_1, $C_{2,6}$, $C_{3,5}$, and C_4 are 100.2, 161.4, 106.9, and 131.1 ppm, respectively, and are consistent with the experimental values of 102.5, 160.7, 108.0, and 130.7 ppm:

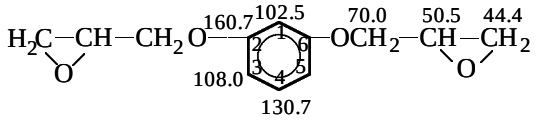

In the ^{13}C NMR spectrum of AB, there are three signals, two of which (119.4 and 135.1 ppm) correspond to the terminal methylene and methine groups of the olefin fragment, and the third signal (33.3 ppm) corresponds to the methylene group adjacent to

^{13}C chemical shifts of PEPA and its composition

Structure fragment	Chemical shift, ppm		Fraction of CH_2 groups in the structure fragment	Fraction of the fragment
	found	published data [2]		
$NH_2CH_2CH_2NH$–	42.0, 52.7	41.9, 52.7	0.68	0.82
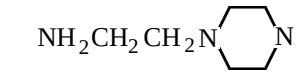	39.0, 62.1, 55.0, 46.2	38.8, 61.9, 54.9, 42.6	0.24	0.10
–$NHCH_2CH_2NH$–	49.6	49.6	0.05	0.06
$NH_2CH_2CH_2N<$	40.2, 58.0	40.2, 58.3	0.01	0.01
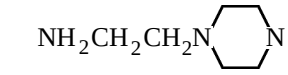	39.0, 61.4, 53.3	39.0, 61.3, 53.8	0.01	0.00
–$NHCH_2CH_2N<$	47.7, 54.8	47.9, 54.9	0.01	0.01

bromine atom:

$$\overset{119.4}{CH_2}=\overset{135.1}{CH}-\overset{33.3}{CH_2}Br$$

In the ^{13}C NMR spectrum of PEPA, there are seven strong and a series of weak signals. The signals were assigned on the basis of the ^{13}C NMR data obtained previously in studying the structure of commercial PEPA of the A grade [6] and macromolecular polyethylenimines [7]. It is well known that PEPA is a mixture of polyfunctional ethylenamines of various structures and various molecular weights. The dependence of the PEPA reactivity as cross-linking agent on its composition and content of amino groups of various basicities was clearly shown in [8]. Therefore, it was appropriate to determine the composition and structure of PEPA in hand as a component for production of the ion-exchange polymer.

According to chemical shifts evaluated by the additive scheme and found in the experiments for a series of model compounds [6, 7], the two strongest signals at 42.0 and 52.7 ppm were assigned to the methylene groups of $NH_2CH_2CH_2NH$– fragment. Four other signals at 39.0, 46.2, 55.0, and 62.1 ppm belong to *N*-2-aminoethylpiperazine. The signal at 49.6 ppm corresponds to the symmetrical fragment –$NHCH_2$–CH_2NH–. It should be noted that the observed values of chemical shifts do not noticeably differ from published data. The fraction of methylene groups in the structure fragments was evaluated from the ratio of the integral intensities, and then the relative content of these fragments was determined.

The assignment of the signals in the ^{13}C NMR spectrum of PEPA and its composition are presented in the table. The results obtained suggest predominance of three fragments, two of which are terminal (92%) and the third is middle (6%). The fraction of the other fragments is as low as 3%. Thus, PEPA in hand mainly consists of low-molecular-weight ethylenamines of linear and cyclic structure: diethylenetriamine, triethylenetetramine, and *N*-2-aminoethylpiperazine. Small amounts of ethylenamines of branched structure and also ethylenamines with the piperazine ring incorporated in the middle of the polymer chain were detected. It was found [8] that both low- and high-molecular-weight fractions containing components of the linear structure are highly reactive. In the first case, this is caused by a great number of primary amino groups, and in the second case, by increased functionality. It was noted that the presence of tertiary amino groups and piperazine ring decreases the reactivity of PEPA.

The ^{13}C NMR data obtained show that the quantitative and qualitative composition of PEPA differs dramatically from the composition of the commercial PEPA of the A grade [6]. The studied PEPA sample consists of considerably fewer components but contains a large amount of linear terminal fragments with the primary nitrogen atom, and hence it should be very reactive.

In the spectrum of the sample withdrawn 1 h after mixing of AB, DRE, and PEPA taken in the 2 : 1 : 1 ratio, the signal of the methylene group adjacent to the bromine atom disappears, and the signals characteristic of epoxy ring are lacking. In this case, the intensity of the signal of the methylene groups of $NH_2CH_2CH_2NH$– fragment abruptly decreases, and that of the signal of the methylene groups in the middle fragment of the linear structure increases. The signals of carbon atoms of the aromatic ring do not vary, whereas the signal of the OCH_2 groups adjacent to the aromatic ring is broadened and insignificantly

shifted downfield. The signals of olefin carbon atoms are also broadened and somewhat shifted downfield. Simultaneously, new signals appear, assigned to the methine carbon atom at the hydroxy group (69.0 ppm) and methylene group located between the olefin substituent and secondary (53.0 ppm) or tertiary (58.1 ppm) nitrogen atom. The intensities of the signals corresponding to the linear-branched structures $-NHCH_2CH_2N<$ (47.2 and 54.5 ppm) and $>NCH_2CH_2N<$ (53.7 ppm) increase.

The signals of piperazine fragments remain in the spectrum. Disappearance of the signals of the initial compounds and appearance of new signals primarily suggest occurrence of condensation of AB with PEPA, proceeding by nucleophilic attack of the unsaturated carbon atom of the allyl monomer by the nitrogen atom [9]. In this case, the electron density of the double bond is shifted and halide ion is eliminated. The second cause of spectrum changes is nucleophilic attack of the carbon atom of the terminal methylene group of the DRE epoxy ring by the nitrogen atom of PEPA, which results in ring opening and addition of PEPA with formation of zwitterionic structures [10] transforming then into the neutral adduct. As a result of these processes, as would be expected, the content of linear-branched fragments with secondary and tertiary amino groups increases.

Thus, in the initial stage molecules of AB and bifunctional DRE are completely consumed for formation of dimers and small branched oligomers. Owing to the presence of active centers of various basicities, these oligomers react with each other to form macromolecules with a high molecular weight.

Actually, the spectrum of the precondensate withdrawn in 24 h differs from the spectrum of the reaction products in the early stage. All signals are broadened, excluding the signals of the carbon atoms of the aromatic ring and methylene group (40.3 ppm) directly adjacent to the primary amino group in the terminal branched fragment $NH_2CH_2CH_2N<$ whose concentration is low in comparison with the other fragments. This is caused by growth of the polymer chains owing to increase in the size of the initially formed oligomer molecules. The signals observed can be divided into three groups. The first group includes three signals at 48.7, 53.6, and 58.2 ppm, assigned to methylene groups adjacent to the nitrogen atoms in the intermediate fragments. The second group is presented by two signals at 68.7 and 71.5 ppm, corresponding to methine groups adjacent to the hydroxy group and ether oxygen. The third group includes two broadened signals of the olefin carbon atoms at 117.8 and 133.6 ppm. These signals suggest that the reaction in the precondensation stage does not involve complete cleavage of double bonds.

The signals in the ^{13}C NMR spectrum of the anion exchanger based on AB, DRE, and PEPA (before additional curing) in DMF were assigned with the aid of the spectra of the unitial compounds using the additive scheme and model compounds for evaluation of chemical shifts:

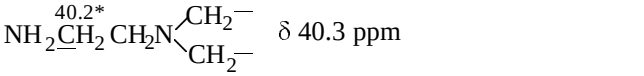
δ 40.3 ppm

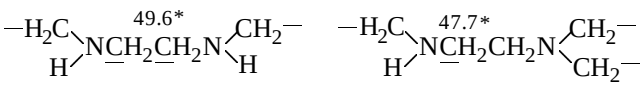
δ 48.7 ppm (br.)

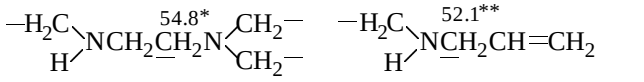

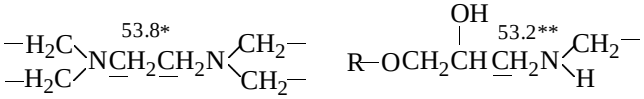

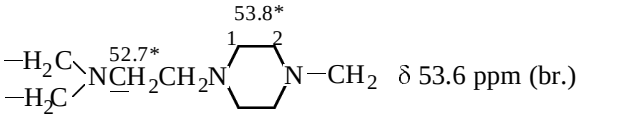
δ 53.6 ppm (br.)

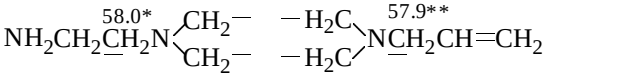

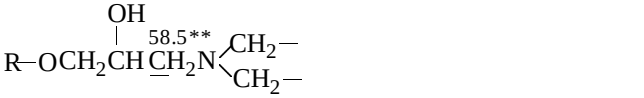
δ 58.2 ppm (br.)

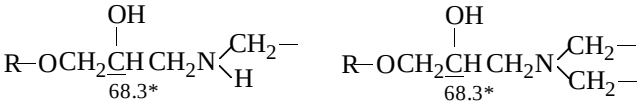
δ 68.7 ppm (br.)

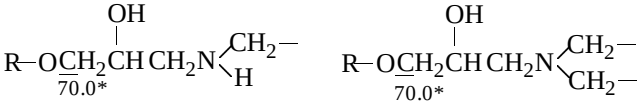
δ 71.5 ppm (br.)

where R = 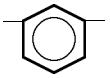

* Experimental, ** calculated.

Thus, the ^{13}C NMR study of polycondensation of AB, DRE, and PEPA before additional curing showed that short oligomers with linear and branched structures are formed in the early stage by nucleophilic attack of the unsaturated carbon atom of the allyl compound and terminal carbon atoms of the epoxy rings of DRE by the nitrogen atom of PEPA. In turn, the intermediate oligomers further react through unchanged functional groups to form macromolecules with a high degree of branching.

REFERENCES

1. Mikhal'chuk, V.M., Stroganov, V.F., and Lipatov, Yu.S., *Vysokomol. Soedin., Ser. A–B*, 1995, vol. 37, no. 10, pp. 1672–1679.
2. Topchiev, D.A., Martynenko, A.I., Kabanova, E.Yu., *et al*., *Vysokomol. Soedin., Ser. A–B*, 1994, vol. 36, no. 8, pp. 1242–1253.
3. Chopabaeva, N.N., Klepikova, S.G., Bektenev, N.A., *et al*., *Izv. Min. Obraz. Nauki Resp. Kazakhstan, Nats. Akad. Nauk Resp. Kazakhstan, Ser. Khim*., 2000, no. 5, pp. 122–129.
4. Ergozhin, E.E., Chalov, A.K., Iskakova, R.A., and Nikitina, A.I., *Zh. Prikl. Khim*., 2001, vol. 74, no. 4, pp. 629–633.
5. Ionin, B.I., Ershov, B.A., and Kol'tsov, A.I., *YaMR-spektroskopiya v organicheskoi khimii* (NMR Spectroscopy in Organic Chemistry), Leningrad: Khimiya, 1983.
6. Chetverikova, A.T., Chetverikov, A.F., Vakulenko, V.A., *et al*., *Plast. Massy*, 1979, no. 5, pp. 6–8.
7. Bulai, A.Kh., Slonim, I.Ya., Urman, Ya.G., *et al*., *Vysokomol. Soedin., Ser. A*, 1986, vol. 28, pp. 1665–1668.
8. Lukovkin, G.M. and Pshezhetskii, V.S., in *Sintez, svoistva i prakticheskoe ispol'zovanie polietilenimina* (Synthesis, Characteristics, and Use of Polyethylenimine), Moscow: Inst. Neftekhim. Sinteza, Akad. Nauk SSSR, 1974, pp. 19–26.
9. Roberts, J. and Caserio, M., *Basic Principles of Organic Chemistry*, New York: Benjamin, 1964, vol. 1.
10. Sojka, S.A. and Moniz, W.B., *J. Appl. Polym. Sci*., 1975, vol. 20, no. 7, pp. 1977–1982.

Russian Journal of Applied Chemistry, Vol. 75, No. 1, 2002, pp. 106–111. Translated from Zhurnal Prikladnoi Khimii, Vol. 75, No. 1, 2002, pp. 107–112.
Original Russian Text Copyright © 2002 by Mikhailova, Nazarova, Khizhnyak, Anan'eva, Pakhomov.

MACROMOLECULAR CHEMISTRY AND POLYMERIC MATERIALS

Structure and Properties of Filled Film Materials Based on Ultra-High-Molecular-Weight Polyethylene

Yu. N. Mikhailova, E. V. Nazarova, S. D. Khizhnyak, T. A. Anan'eva, and P. M. Pakhomov

Tver State University, Tver, Russia
St. Petersburg State University of Technology and Design, St. Peterburg, Russia

Received July 10, 2001

Abstract—The pore structure of filled films of ultra-high-molecular-weight polyethylene prepared by the gel process was studied by IR spectroscopy and optical microscopy. The moisture and water absorption and the maximal sorption capacity of the material were determined gravimetrically and examined in relation to the degree of filling of films with peat and to the molecular weight of the polymer.

Considerable researchers' efforts in the polymer technology are aimed at development and promotion of new materials with valuable properties, in particular, of porous materials. The most widely used procedure for preparing porous materials involves condensation cross-linking based on spontaneous physicochemical processes in polymer solutions [1, 2]. Polymers can also be processed into porous materials by extrusion of a polymer melt at a high flow velocity, followed by annealing of samples crystallized at room temperature, uniaxial drawing of the annealed samples, and thermal fixation [3].

One of promising processes in polymer technology is the sol–gel process. Interest in this process arose in mid-1970s and was due to the possibility of preparing ultra-high-strength fibers from solutions and gels of flexible-chain polymers [4, 5]. Researchers' efforts [6–8] were aimed at production of highly porous polymeric materials by the sol–gel process and at their structural study. In this connection, structural study of polymeric xerogels (dry gel without solvent), which are highly porous materials, becomes topical. It is also interesting to examine the effect of fillers on the gelation process and structure of the resulting filled porous materials, which can be used as sorbents for petroleum and other products.

The goal of this study was to reveal the effect of a disperse filler (peat) on the properties and structure of filled film materials prepared from ultra-high-molecular-weight polyethylene (UHMWPE) by the gel process.

EXPERIMENTAL

UHMWPE (M_w 1.5×10^6 and 4.0×10^6) was purchased from Hoechst. Films were prepared from a 2 wt % solution of UHMWPE in solid paraffin C_{24}–C_{40} [8]. As compared to traditionally used UHMWPE solvents such as xylene or decalin, paraffin is less active. In such a solvent, conditions for interaction of the polymer molecules and hence for formation of the three-dimensional polymer network are more favorable. Less active solvents are also preferable in production of filled materials [9].

As a UHMWPE filler we used peat. Peat was finely divided without preliminary drying and sieved through a standard set of sieves; the fraction with the grain size of 0.15–0.25 mm was collected. Among natural environmentally clean and cheap sorption-active materials, peat occupies a particular place. In the air-dry state it has low density, high porosity, high hygroscopicity, and high moisture- and gas-absorption power. In practice, peat sorbents are used as compacted briquettes, granules, and finely divided peat. However, studies showed that the impact of high temperatures in the course of briquetting appreciably impairs the sorption power of peat. Furthermore, in water peat briquettes swell and break down. The direct use of finely divided peat as a sorbent requires additional water treatment because of washing out of humic acids in the course of service [10, 11].

Filled film materials were prepared as follows. UHMWPE was dissolved in two stages. The first stage (swelling) was performed at vigorous stirring

1070-4272/01/7501-0106$27.00 © 2002 MAIK "Nauka/Interperiodica"

of a mixture of UHMWPE powder with the solvent at heating to 120°C at a rate of 2.7 deg min^{-1}. In the second stage, stirring was stopped, and the temperature was increased to 160–170°C. Within the subsequent 50–60 min, the solution became homogeneous. After complete dissolution of the polymer, the temperature was decreased to 140°C to avoid oxidative degradation of the polymer. The filler, preliminarily finely divided and fractionated, was charged in portions to the homogeneous UHMWPE solution at 140°C. The mixture was stiired for 10 min and poured onto a metallic table heated to 160°C, after which it was covered with a metallic lid, also heated to 160°C.

The table was cooled to room temperature at a rate of 1.6 deg min^{-1}. To remove the solvent, the films were extracted with heptane in the fixed state in a Soxhlet apparatus at 70–75°C. After extraction, the films were dried at room temperature to constant weight.

The moisture and water absorption and the maximal sorption capacity were determined gravimetrically. To determine the moisture absorption, a weighed portion of the sample was placed in a weighing bottle and dried to constant weight at 50°C in a thermostat. The dried sample was allowed to stand in air at room temperature for 1 h. The moisture absorption B was determined by the formula

$$B = \frac{b - a}{a} \times 100\%, \quad (1)$$

where a is the weight of the absolutely dry sample (immediately after weighing) and b is the weight of the sample after standing for 1 h under ambient conditions.

To determine the water absorption, samples were placed in a vessel under a layer of distilled water for no less than 24 h. The water absorption W was determined by the formula

$$W = \frac{p_2 - p_1}{p_1} \times 100\%, \quad (1)$$

where p_1 is the sample weight under ambient conditions, and p_2 is the weight of the wet sample.

To determine the sorption capacity for petroleum products, samples were placed in a vessel with machine oil for 1 h. The sorption capacity was calculated from the weight gain of the sample after sorption, related to 1 kg of the sorbent.

The apparent density of the sample was determined as the ratio of the sample weight to its volume.

The porosity of UHMWPE films filled with peat was studied by IR spectroscopy, and the sizes of scattering areas (peat particles and pores) were determined. The IR spectra of the films were taken on a Specord IR-75 spectrophotometer equipped with an attachment for taking attenuated total internal reflection (ATIR) spectra. The porosity on the surface and in the bulk of samples was determined according to [7]. In the IR spectrum of the polymer, we chose the most intense absorption band, as weakly sensitive to structural changes as possible. In UHMWPE, this was the band at 720 cm^{-1} originating from the rocking vibrations of the CH_2 groups in the crystalline phase of the polymer. The sample porosity (in relative units) was calculated by the formula

$$\varepsilon = D/d, \quad (3)$$

where ε is the extinction coefficient, which is the measure of the total porosity; D is the optical density in the maximum of the IR absorption band; and d is the film thickness.

The maximal pore diameter was determined from the limiting frequency (wave number) ν_m at which the scattering areas cease to affect the IR spectrum. The wave number and the corresponding wavelength determining the pore size were found at the IR transmission $T = 50\%$ [7, 12].

The surface of filled porous films was also examined by optical microscopy on an MIM-8 horizontal metallographic microscope equipped with a transmitting light attachment and a Sharp-135 video camera. The image was transmitted through the optical channel to the video camera and then, through a video amplifier, to the computer interface.

The influence of the degree of filling on the properties of UHMWPE-based film materials is illustrated by Table 1. It is seen that introduction of a disperse filler into the porous UHMWPE matrix significantly affects the apparent density ρ of the film materials, which is an indirect characteristic of the porosity. Introduction of 1 wt % disperse filler sharply increases the apparent density as compared to the unfilled sample. At the filler content increased further, the apparent density of the film decreases, reaching a minimum at 50% filling. This may be due to the fact that interaction of the polymeric chains of the crystallizing polymer with the filler particle affects the molecular mobility of the chains, which, in turn, affects the UHMWPE crystallization kinetics. The polymer crys-

Table 1. Influence of the degree of filling *n* on the properties of composite film materials

n, %	ρ, kg m^{-3}	*B*, %	*W*, %	SC,* g g^{-1}
0	270/262	1.5/1.5	8.9/7.2	3.8/4.0
1	462/404	1.0/0.7	9.1/10.7	0.8/0.7
5	383/348	1.5/1.7	10.3/12.6	1.1/0.8
7	356/340	1.6/1.9	15.8/15.2	1.1/0.8
10	268/278	1.6/2.2	23.7/18.5	3.9/4.1
20	229/235	1.9/2.6	24.5/38.7	4.2/4.5
30	227/217	2.2/2.9	56.9/40.2	4.5/4.7
40	229/189	3.1/3.2	88.4/73.3	4.7/5.3
50	199/186	4.0/4.5	104.8/99.3	6.5/7.0
60	209/210	4.9/5.0	143.1/106.4	5.2/5.8
70	223/210	5.4/5.9	149.4/171.2	5.0/5.4
80	225/216	6.0/5.9	174.8/179.5	4.2/4.8
85	239/221	6.4/7.4	177.7/182.2	4.1/4.7

* (SC) Sorption capacity.
** The values for M_w 1.5×10^6 and 4.0×10^6 are given in the numerator and denominator, respectively.

tallization in the presence of a filler is influenced by two factors: (i) interaction of a polymer with a filler, resulting in appearance on the polymer–filler interface of adsorbed chain sections promoting crystallization; (ii) increase in the viscosity owing to the presence of a filler, which should prevent crystallization. These factors are determined by the nature of the filler surface and by the filler concentration [13]. Apparently, at a low filler content (1–10%) the crystallization rate increases, with the filler particles acting as crystallization nuclei. This results in formation of a denser structure and hence in decreased porosity of film materials. As the filler concentration is increased from 10 to 50%, crystallization is inhibited, and a more porous structure is formed, with the porosity reaching a minimum at 50% filling. At the degree of filling exceeding 50%, the filler particles form areas separated by very thin UHMWPE layers. The film porosity therewith decreases, and the apparent density correspondingly increases (Table 1).

Figures 1 and 2 confirm the assumption that the porosity decreases at a low degree of filling and increases at a higher filler content. Figure 1 demonstrates the influence of the porous structure on the IR spectrum of filled films of UHMWPE of two molecular weights.

The scattering in the samples can be caused by areas of both increased (crystallites) and decreased (pores, cracks, disperse phase particles) density. The higher the total porosity of a sample, the more significant is its influence on the IR transmission due to the scattering effect. Figure 1 shows that, as the filler content increases, the transmission at 730 cm^{-1} decreases. This is due to scattering of the incident IR radiation on the filler particles themselves. The increased transmission of filled films with a low filler content (up to 10%), as compared to unfilled polyethylene films, is probably due to the fact that intro-

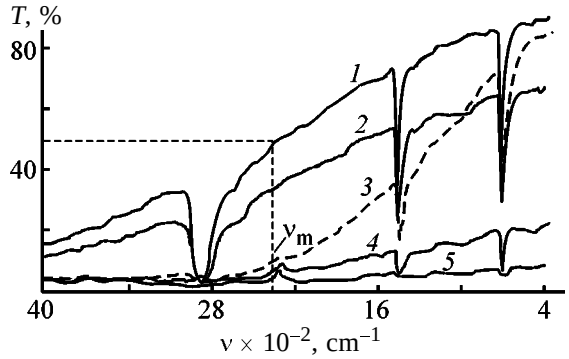

Fig. 1. IR transmission spectra of UHMWPE films (M_w 4.0×10^6) at degree of filling (%): (*1*) 1, (*2*) 10, (*3*) 0, (*4*) 30, and (*5*) 50. (*T*) Transmission and (ν) wave number.

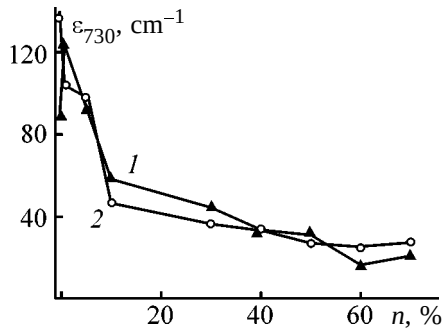

Fig. 2. Extinction coefficient at 730 cm^{-1} ε_{730} of UHMWPE films as a function of the degree of their filling *n*. $M_w \times 10^{-6}$: (*1*) 1.5 and (*2*) 4.0; the same for Fig. 3.

duction of low concentrations of filler particles favors more uniform distribution of the polymer in the bulk of the sample and hence formation of thinner films.

Figure 2 illustrates the influence of the filler concentration on the extinction coefficient of the film at 730 cm^{-1}. It is seen that, as the filler concentration is increased, the absorption decreases, indicating considerable increase in the total porosity. The observed slight increase in the total porosity with increasing M_w of the polymer is probably associated with the looser structure of the sample and with increased viscosity of the three-component system at increased filler concentration. This may be due to the lower mobility (larger length) of the macrochains in the high polymer, which affects the structure of the resulting films. As the filler content in the solution is increased, the film thickness increases, and simultaneously grows the pore size. These two factors (thickness and high porosity) significantly complicate recording of the IR spectra of such samples in the transmission mode at the degree of filling exceeding 50%.

The maximal pore diameter in samples with different M_w virtually coincides (Table 2), despite different total porosity, and slightly increases with increasing filler content. The larger d_p in unfilled samples is due to their loose structure.

However, some of the pores are open. The open porosity significantly affects the sorption and diffusion. The ATIR spectroscopy furnishes information on the structure of the sample surface layers. Figure 3 shows the extinction coefficient at 730 cm^{-1}, calculated from the ATIR spectra, of the film surface contacting the metallic table as a function of the filler concentration. The dependence is similar to those in Fig. 2; it shows that the porosity decreases with increasing filler concentration. The porosities of the polymer samples of different molecular weights virtually coincide, suggesting identical structure of the surface layers. The surface porosity of the films from the side of the metallic table was lower than the bulk porosity, whereas the surface porosity of the films from the opposite side (contacting air) was higher. Visual examination also confirmed that the film surface contacting the metallic table was smoother and less porous.

Figure 4 shows the photomicrographs of films of UHMWPE xerogels filled to 0, 50, and 85%. It is seen that the unfilled xerogel has a network skeleton structure reflecting the structure of the gel. The pore structure parameters of xerogels significantly differ depending on the filler concentration. The estimates

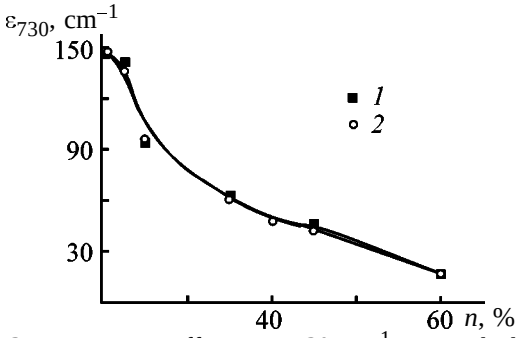

Fig. 3. Extinction coefficient at 730 cm^{-1} ε_{730}, calculated from the ATIR spectrum, of the surface of the UHMWPE film contacting the metallic table, as a function of the degree of filling *n*.

of the xerogel pore size, made by IR spectroscopy, are consistent with the results of optical microscopic examination. Figure 4 shows that the film surface is rough, but there are no coarse pores. Comparison of the pore size (Table 2) shows that the filled xerogels prepared in this work mainly preserve the morphology of the initial gels. The porosity of the unfilled sample is higher than that of the samples filled to 50 and 85%. This is due to its looser structure and to the fact that at an 85% filling the filler forms a layer on which a very thin polymer film is distributed; as a result, the total porosity decreases. Thus, by taking a filler for gel preparation in different concentrations, it is possible to vary in a wide range the morphology and hence the mechanical and sorption properties of xerogel films.

The moisture absorption increases with increasing content of the hydrophilic filler, except the films with the lowest filling, which is due to their increased apparent density, i.e., to the character of the porous structure formed at a 1% filling. The water absorption also increases with increasing degree of filling with the hydrophilic filler, but it remains considerably lower than that of peat (950–1780%).

Study of the sorption capacity of filled film materials for petroleum products based on Mobil Suns S oil

Table 2. Values of ν_m and d_p of UHMWPE films differing in the degree of filling with peat *n*

n, %	$M_w = 1.5 \times 10^6$		$M_w = 4.0 \times 10^6$	
	ν_m, cm^{-1}	d_p, μm	ν_m, cm^{-1}	d_p, μm
0	1300	8.0	1190	8.4
1	2200	4.67	2340	4.3
5	2199	4.55	2200	4.54
10	1830	5.5	1740	5.7

(a)

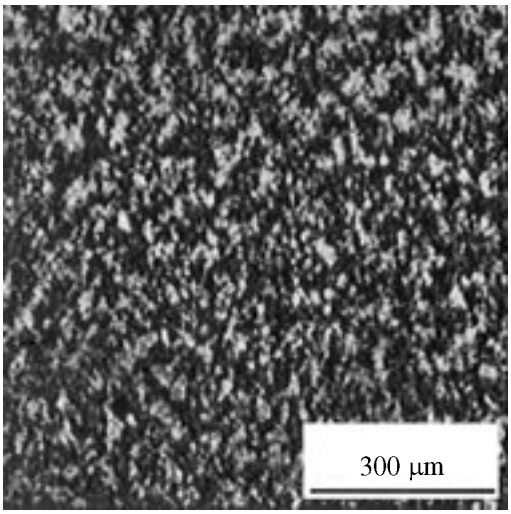

(b)

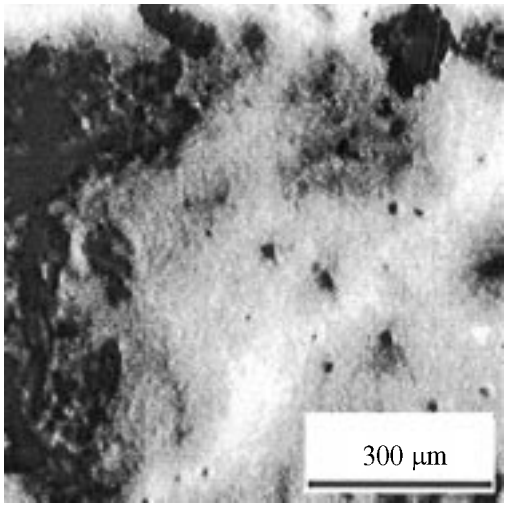

(c)

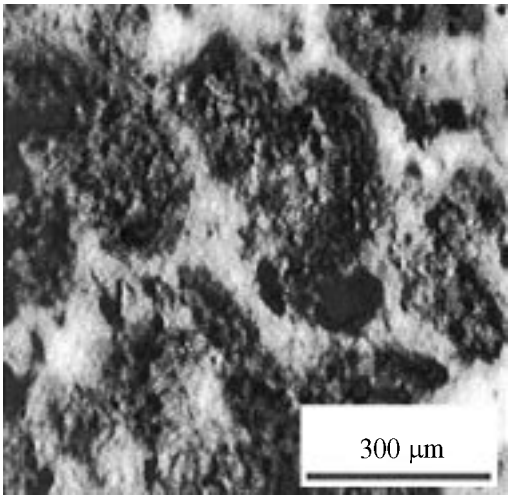

Fig. 4. Photomicrographs of UHMWPE films (M_w 1.5 × 10^6) filled with peat to (a) 0, (b) 50, and (c) 85%.

showed (Table 1) that the lowest sorption capacity is exhibited by the samples filled to 1–10%, and the highest sorption capacity, by the samples filled to 50%, which is consistent with variation of the apparent density. As the degree of filling is increased from 50 to 85%, the sorption capacity of the filled film materials decreases, because the porosity of the polymeric matrix decreases and the matrix itself ceases to participate in sorption.

Thus, our studies showed that the use of the sol–gel process for producing porous materials eliminates the main drawback of peat (high water absorption) with preservation of the high sorption power, which is realized at appropriate ratio of the filler and polymer in the polymeric xerogel.

CONCLUSIONS

(1) Ultra-high-molecular-weight polyethylene films with the degree of filling with peat of up to 85% were prepared by the gel process.

(2) The influence of filler (peat) and molecular weight of the polymer on the character of pore formation both in the bulk and on the surface of the film was studied. At a low filler content (1.0–10%), the film porosity is low. As the filler content is increased from 10 to 50%, the film porosity increases, but at a still higher filler content the porosity decreases.

(3) The optimal peat content in an ultra-high-molecular-weight film, required for efficient sorption of water and petroleum products, was determined.

ACKNOWLEDGMENTS

The authors are grateful to R.M. Grechishkin for microscopic measurements.

The study was financially supported by the Integration Federal Target Program (project no. A 0117) and NATO grant SfP N 973925.

REFERENCES

1. Kesting, R.E. *Synthetic Polymeric Membranes. A Structural Perspective*, New York: Wiley, 1991.
2. Volkov, F.V., Abstracts of Papers, *4-ya Assambleya molodykh uchenykh i spetsialistov* (4th Assembly of Young Scientists and Specialists), St. Petersburg, 1999, p. 25.
3. Kudasheva, O.V., Rozova, E.Yu., Karpov, E.A., and El'yashevich, G.K., *Vysokomol. Soedin., Ser. A*, 1997, vol. 39, no. 10, pp. 1635–1640.

4. Smith, P., Lemstra, P.J., and Kalb, B., *Polym. Bull.*, 1979, vol. 1, pp. 733–738.
5. Kalb, B. and Pennings, A.J., *Polymer*, 1980, vol. 21, pp. 3–12.
6. Pakhomov, P.M., Larionova, N.V., and Alekseev, V.G., *Vysokomol. Soedin., Ser. B*, 1995, vol. 37, no. 5, pp. 892–895.
7. Pakhomov, P.M., Kruglova, E.V., and Khizhnyak, S.D., *Vysokomol. Soedin., Ser. B*, 2000, vol. 42, no. 6, pp. 1081–1088.
8. Volkov, F.V., Anan'eva, T.A., and Nachinkin, O.I., in *Fizikokhimiya polimerov* (Physical Chemistry of Polymers), Tver: Tver. Gos. Univ., 1996, issue 2, pp. 26–31.
9. Nazarova, E.V., Volkov, F.V., and Anan'eva, T.A., in *Materialy nauchno-tekhnicheskoi konferentsii SPGUTD* (Proc. Scientific and Technical Conf. of the St. Petersburg State Univ. of Technology and Design), St. Petersburg, 2000, part 2, pp. 32–34.
10. *Torfyanoi fond RSFSR: Torfopodstilochnye i torfoizolyatsionnye syr'evye resursy* (Peat Resources of the Russian Sovient Federative Socialist Republic: Peat-Underlayer and Peat-Insulation Resources), Moscow: Glavnoe Upravlenie Torfyanogo Fonda pri Sovete Ministrov RSFSR, 1964.
11. Bel'kevich, P.I., Chistyakova, L.R., Rogach, L.M., *et al.*, *Torf. Prom–st.*, 1983, no. 4, pp. 29–32.
12. Kruglova, E.V., Pakhomov, P.M., Volkov, F.V., *et al.*, in *Fizikokhimiya polimerov* (Physical Chemistry of Polymers), Tver: Tver. Gos. Univ., 1999, issue 5, pp. 77–82.
13. Lipatov, Yu.S., *Fiziko-khimicheskie osnovy napolneniya polimerov* (Physicochemical Principles of Polymer Filling), Moscow: Khimiya, 1991.

Russian Journal of Applied Chemistry, Vol. 75, No. 1, 2002, pp. 112–118. Translated from Zhurnal Prikladnoi Khimii, Vol. 75, No. 1, 2002, pp. 113–119.
Original Russian Text Copyright © 2002 by Smirnov, Magomedov, Dzhamaeva.

MACROMOLECULAR CHEMISTRY AND POLYMERIC MATERIALS

Structural and Kinetic Features of Formation of Elastic, Relaxation, Dissipative, and Mechanical Properties of Carbon-Fiber-Reinforced Epoxy-Phenolic Plastic Materials Based on Binary Prepregs

Yu. N. Smirnov, G. M. Magomedov, and N. M. Dzhamaeva

Institute for Problems of Chemical Physics, Russian Academy of Sciences, Chernogolovka, Moscow oblast, Russia

Dagestan State Pedagogical University, Makhachkala, Dagestan, Russia

Received October 10, 2001

Abstract—The static bending strength and dynamic elastic, relaxation, and dissipative properties of two types of unidirectional carbon-fiber-reinforced plastic materials based on blend and binary prepregs were studied by the bending resonance vibration method in various directions in the course of curing (pressing).

Separate application of binder components (SCA) is one of the most efficient techniques for increasing the pot life of prepregs [1, 2]. In this method mixing of components goes directly in course of curing. The mixing proceeds through two physical processes. The first, rapid process, dominant in the initial curing steps, is initiated by the action of the mechanical field and involves mechanical mixing of binder components in the vertical and horizontal directions against the prepreg layers. The second process dominating in later curing steps involves mutual diffusion of binder components at the background of chemical cross-linking [3]. Evidently, the intensity of the indicated processes will depend on the nature and structure of binder components and also on the curing mode which should be optimized taking into account all specific structural and kinetic features of the binary technique. Transformations in the polymer matrix (PM) structure occurring with this technique and the corresponding evolution of the mechanical and relaxation properties of the resulting fiber glass plastic materials are considered in [1, 2, 4, 5]. In contrast to fiber glass plastic materials, carbon fibers (CF) are characterized by a considerable porosity and, as a result, a higher sorption capacity [6], affecting the curing kinetics and, correspondingly, the structure [7] and relaxation properties of unidirectional carbon-fiber-reinforced plastics (CFRPs) based on conventional blend carbon fiber woven prepregs.

In this work we studied the features of formation of the structure and mechanical, elastic, relaxation, and dissipative properties of carbon-fiber-reinforced plastic materials based on a binary prepreg (CFRP-II) in comparison with those of the composites based on a blend prepreg (CFRP-I).

EXPERIMENTAL

In the work we used an epoxy system containing 0.9 g-equiv of EN-6 polyglycidyl ether of novolac phenol–formaldehyde resin, 0.1 g-equiv of EKhD tetraglycidyl derivative of 3,3'-dichloro-4,4'-diaminodiphenylmethane, and 1 g-equiv of SF-0113 novolac phenol–formaldehyde resin.

As a reinforcement we used LU-P-0.1 carbon fiber band. Prepregs were prepared by impregnation of the carbon fiber band with alcohol–acetone solutions of the starting epoxy system and separate components using a laboratory-scale impregnator. Samples of CFRPs were prepared by pressing of the prepregs at 180°C under a pressure load of 5.5–6 MPa, followed by cooling under an asbestos cloth and weight (0.1 MPa; native samples). The binder content in CFRP-I varied from 23 to 25 wt % and the density, from 1410 to 1430 kg m^{-3}; those for CFRP-II were 20–22 wt % and 1390–1540 kg m^{-3}, respectively. Note that higher binder content in CFRP-I is realized by virtue of its lower fluidity upon pressing as a result of more rapid hardening and binder viscosity growth with blend prepregs.

The bending strength σ_b was determined following ISOR61/S11 regulations.

1070-4272/01/7501-0112$27.00 © 2002 MAIK "Nauka/Interperiodica"

Dynamic mechanical properties, the real part of the dynamic modulus of elasticity E' and mechanical loss tangent $\tan\delta$, were determined by the resonance bending vibration method with dead-ended samples over the frequency range 10–100 Hz on a setup described elsewhere [9].

The structural and kinetic studies in the course of curing of CFRPs obtained on the basis of various prepreg techniques revealed specific features of formation of their properties in the case of carbon fiber binary prepregs, particularly in the dynamics of evolution of the mechanical characteristics including the elastic, relaxation, and dissipative properties.

Mechanical properties of CFRPs. Figure 1 shows the bending strength as a function of the pressing time, i.e., the degree of conversion of functional groups of unidirectional CFRP-I and CFRP-II. The strength was determined in the longitudinal direction (along reinforcing fibers). The results show that starting from a curing time of 0.5 h (degree of conversion of the binder by this time is 55% [8]) σ_b of CFRP-I considerably decreases, whereas that of CFRP-II remains practically unchanged. To gain a better insight into the observed behavior of the static mechanical properties of the tested CFRPs in the course of curing, we studied their dynamic elastic, relaxation, and dissipative properties as determined in the longitudinal and transverse directions (relative to the reinforcement) by the resonance bending vibration technique. Previously it was demonstrated that this method is highly sensitive to structural transformations in polymeric [10] and composite materials [11–13].

Elastic properties of CFRPs. The real part of the dynamic modulus of elasticity at room temperature E'_{25} of unidirectional CFRP-I and CFRP-II is plotted in Fig. 2 against the time of pressing in the longitudinal and transverse directions (relative to the reinforcement).

In the transverse direction the properties of CFRPs are governed essentially by the contribution of the binder [8]: E'_{25} of CFRP-I after 0.5 h of pressing considerably decreases, whereas that of CFRP-II remains practically unchanged throughout pressing. For CFRP-I, E'_{25}, initially being considerably higher, to the end of curing becomes markedly lower than that of CFRP-II. Note that in the course of curing the trends of the transverse elastic properties of CFRPs are similar to the evolution of their structural behavior under bending stress. In the longitudinal direction the properties of CFRPs are controlled by the contribution of the reinforcement. Therefore, E'_{25} of the both materials in the longitudinal direction is markedly

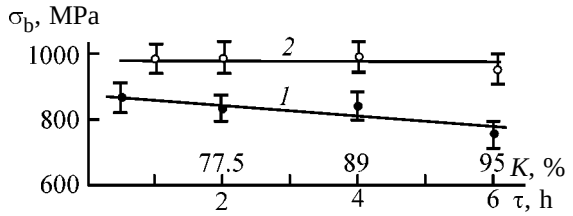

Fig. 1. Bending strength σ_b as a function of the pressing time τ: (*1*) CFRP-I and (*2*) CFRP-II. (*K*) Conversion.

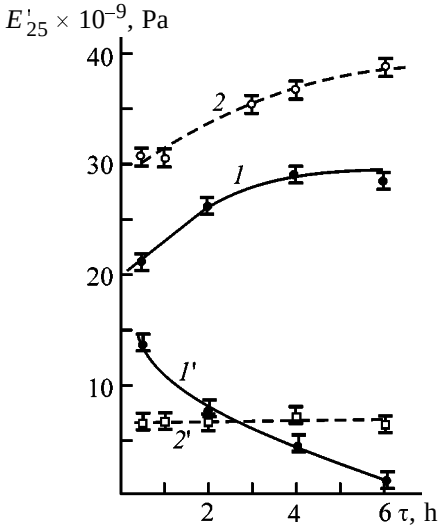

Fig. 2. Real part of the dynamic modulus of elasticity at room temperature E'_{25} as a function of the pressing time τ: (*1*, *1'*) CFRP-I and (*2*, *2'*) CFRP-II. Pressing direction: (*1*, *2*) longitudinal and (*1'*, *2'*) transverse.

higher as compared to that in the transverse direction. The higher modulus of elasticity of CFRP-II is probably due to higher degree of reinforcement as a result of higher fluidity of the binder in pressing of the binary prepreg. Note also that the trends of the elastic characteristics of CFRPs in the longitudinal direction do not correlate with evolution of their mechanical properties.

Relaxation properties. It was demonstrated previously [9, 13–17] that the relaxation properties of unidirectional CFRPs and organoplastics are strongly different, depending on the direction of testing. The nature of differences in properties of CFRP-I in the transverse and longitudinal directions in the course of curing was analyzed in [8]. It was demonstrated that the relaxation spectrum of CFRPs in the transverse direction is characterized by a single α-peak, which is practically identical to that of the starting binder. In the longitudinal direction the spectrum consists of two peaks (α_1 and α_2) of considerably lower intensity, which are strongly shifted to the high-temperature range.

This phenomenon was attributed to the effect of

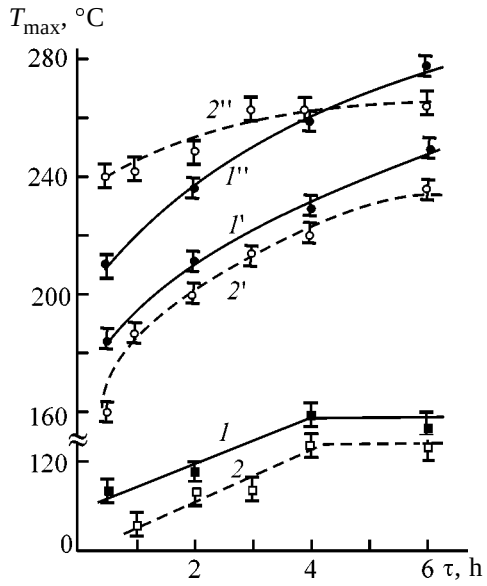

Fig. 3. Peak temperatures of α processes T_{max} as functions of the pressing time τ: (*1*, *1*', *1*") CFRP-I and (*2*, *2*', *2*") CFRP-II. Pressing direction: (*1*, *2*) transverse and (*1*', *1*", *2*', *2*") longitudinal.

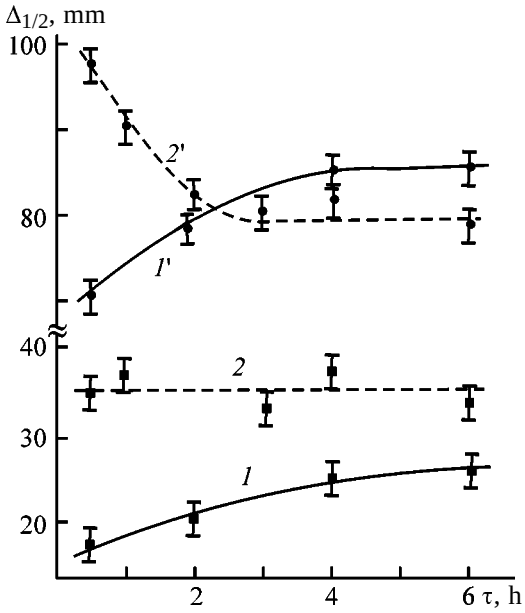

Fig. 4. Half-width of α peak $\Delta_{1/2}$ as a function of the pressing time τ: (*1*, *1*') CFRP-I and (*2*, *2*') CFRP-II. Pressing direction: (*1*, *2*) transverse and (*1*', *2*') longitudinal.

strong residual internal strain (RIS) of the thermal nature, localized at the PM–CF boundary. Splitting of the α peak is interpreted in terms of manifestation of different effect of bending stress on different (by the cross-linking density) microvolumes in structurally nonuniform polymer matrix.

From this standpoint we analyzed the differences in relaxation characteristics of the two CFRPs in the course of curing. As the basic parameters in analysis of the relaxation spectra we selected T_{max} (position of α peak) and $\Delta_{1/2}$ (half-width of α peak).

Evolution in time of T_{max} of the corresponding relaxation peaks is shown in Fig. 3 for CFRP-I and CFRP-II in the transverse and longitudinal directions. As seen, in the both directions the mechanical vitrification temperatures increase until completion of hardening of the polymer matrix. In the transverse direction T_{max} of CFRP-I (curve *1*) increases over the range 0.5–6 h from 115 to 130°C, which is practically identical to T_{max} of the starting binder [8]. For CFRP-II T_{max} (curve *2*) is noticeably lower, though the trend of variation is similar to that of curve *1*. In the longitudinal direction the initial values of T_{max} as well as their increase in the course of curing are higher for the both CFRPs as compared to the corresponding transverse values. For CFRP-II T_{max} of α_1 peak (curve *2*') is slightly lower, and T_{max} of α_2 peak, somewhat higher (curve *2*") than for CFRP-I.

The time dependences of $\Delta_{1/2}$, characterizing the relaxation homogeneity of PM in CFRPs, are presented in Fig. 4. The transverse $\Delta_{1/2}$ of CFRP-I increases in the course of curing, whereas that of the starting binder decreases [8]. For CFRP-II the initial $\Delta_{1/2}$ is considerably higher, remaining, however, practically unchanged in the course of curing. The initial longitudinal $\Delta_{1/2}$ of CFRP-I is much higher than that in the transverse direction, and its increase in the course of curing is higher also. CFRP-II demonstrates higher initial $\Delta_{1/2}$ values, which considerably decrease then, becoming lower than the corresponding values of CFRP-I to the end of curing.

Dissipative properties. The dissipative properties of CFRPs were analyzed on the basis of the relaxation spectra using two parameters. The first parameter, the internal friction background (IFB), was determined as the mechanical loss tangent at room temperature $\tan\delta_{25}$, i.e., at the CFRP testing temperature. Note that IFB can serve as a parameter characterizing the structural organization and intermolecular interaction in the polymer matrix itself [17] and also the internal friction (adhesion interaction) at the PM–CF boundary [18]. The second parameter, the energy dissipation in the α process, was determined as the α peak area or, approximately, the product of the α peak height ($\tan\delta_{max}$) by the α peak half-width $\Delta_{1/2}$. It should be pointed out that the energy dissipation in the α process can affect the binder strength at room temperature [19].

Figure 5a demonstrates the effect of the time of pressing in the transverse and longitudinal directions on $\tan\delta_{25}$ of CFRP-I and CFRP-II. For CFRP-I the transverse $\tan\delta_{25}$ slightly decreases in the course of curing (curve *1*), and for CFRP-II it is somewhat higher, remaining practically unchanged. The trend of evolution of the transverse IFB is similar to that of the structural behavior. The longitudinal IFB is considerably higher than the transverse IFB. For CFRP-I $\tan\delta_{25}$ slightly increases in the course of curing (curve *1*'). For CFRPII $\tan\delta_{25}$ passes through a maximum at τ of about 3 h (curve *2*'), generally being higher as compared to CFRP-I. Note that we found no correlation between IFB and the longitudinal structural behavior.

The dependences of $\tan\delta_{max}$ on the pressing time are shown in Fig. 5b. In the transverse direction, where the contribution of the polymer matrix dominates, $\tan\delta_{max}$ of CFRP-I (curve *1*), initially high, decreases considerably to the end of curing. For CFRP-II (curve *2*) $\tan\delta_{max}$ decreases for about 2 h and then remains unchanged until the end of curing. The longitudinal $\tan\delta_{max}$ regularly decreases for CFRP-I and remains unchanged for CFRP-II; in the end of curing $\tan\delta_{max}$ of the latter being higher. It should be pointed out that in the longitudinal direction this parameter, characterizing the dissipative properties of the α process, correlates with the structural behavior for the both tested CFRPs.

In Fig. 6 are presented the time dependences of the generalized dissipation factor of the α process in CFRPs, i.e., of the $\delta_{max}\Delta_{1/2}$ product. In all cases this factor decreases in the course of curing, reflecting, evidently, the general trend of the molecular segmental mobility in polymer matrices to decrease (increase in the averaged relaxation time). The most pronounced decrease in $\tan\delta_{max}\Delta_{1/2}$ was observed for CFRP-I in the longitudinal direction (curve *1*) and for CFRP-II in the transverse direction (curve *2*'). In the first case the decline is linear until the end point of curing. In the second case the dissipation factor abruptly decreases for about 2 h and then remains practically unchanged. Similar trends of $\tan\delta_{max}\Delta_{1/2}$ are observed for CFRP-II in the longitudinal direction (curve *1*') and for CFRP-I in the transverse direction (curve *2*).

To interpret the observed anisotropy of properties of the CFRPs under study in the course of curing, the following findings and considerations should be taken into account.

(1) The observed evolution in the properties of CFRPs in the course of curing is a resultant of the

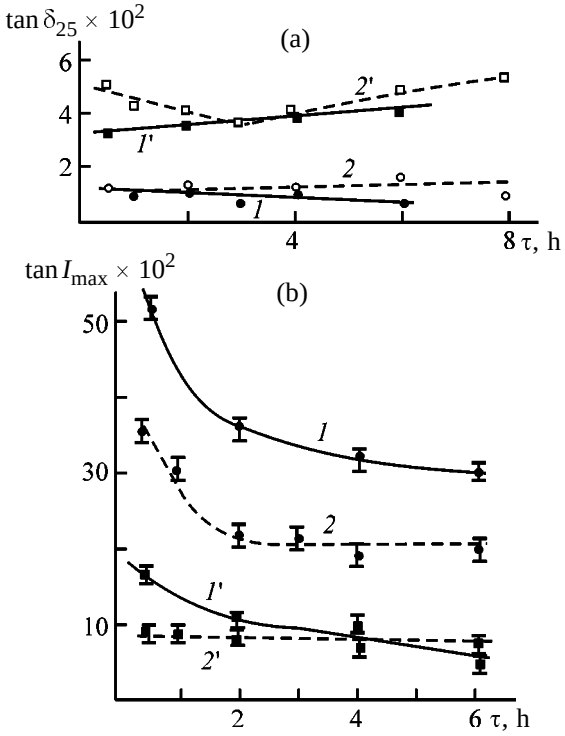

Fig. 5. (a) Internal friction background and (b) α peak intensity I_{max} as functions of the pressing time τ: (*1*, *1*') CFRP-I and (*2*, *2*') CFRP-II. Pressing direction: (*1*, *2*) transverse and (*1*', *2*') longitudinal.

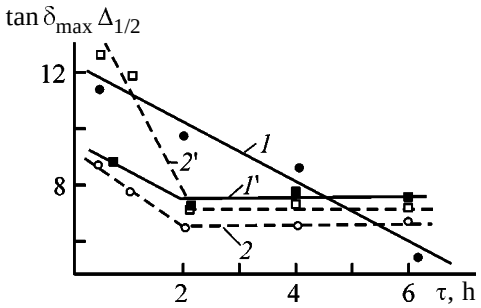

Fig. 6. Dissipation factor $\tan\delta_{max}\Delta_{1/2}$ as a function of the pressing time τ: (*1*, *1*') CFRP-I and (*2*, *2*') CFRP-II. Pressing direction: (*1*, *2*) transverse and (*1*', *2*') longitudinal.

effect of the structural and deformation factors [8, 20]. The structural factor is considered to mean the topological effects in the structure of the polymer matrix, which are associated with growing number of cross-links and functionality. By the deformation factor is meant the effect of residual internal strains, which are different in their value and action. Note that in unidirectional CFRPs the polymer matrix is subject to shrinkage stress in the transverse direction and to more strongly pronounced stretching effects due to thermal RIS in the longitudinal direction [8]. In the initial stages of curing (τ 2–3 h) the structural factor dominates. According to NMR data [7], in the initial

period the volume fraction of faulted microvolumes in the polymer matrix of CFRP-I approaches the minimum. In the subsequent stages of curing the deformation factor dominates.

(2) When analyzing the evolution of properties of CFRPs in the course of curing, it is necessary to take into account the specific features of dynamic mechanical spectrometry methods: under transverse load the entire bulk of PM contributes to the mechanical response, while under longitudinal load, only its small fraction, specifically, the layers directly contacting the CF surface [8, 20, 21]. It may be suggested that these layers concentrate the most faulted microvolumes of PM. In the case of CFRP-I they contain components which are specifically sorbed (immobilized) in CF pores [7, 8], and in the case of CFRP-II, not mechanically mixed binder components [20]. Evidently, for CFRP-II the initial structural inhomogeneity and, correspondingly, the molecular mobility in PM should be more pronounced, more so in the boundary layers.

(3) The initial inhomogeneity is responsible for the subsequent transformations in the PM structure. Thus, in the case of CFRP-II, the total number of chemical cross-links in the bulk of PM increases irregularly in the course of curing: the dominating process is local aftercure in topologically faulted low-cross-linked microvolumes of PM by virtue of diffusion-controlled reactions of functional groups [8]. Subsequently this should result in leveling of the structural parameters and, therefore, of various characteristics throughout the PM volume.

(4) The trends in variation of the relaxation characteristics of PM in CFRPs can be influenced by chemical relaxation (chemical debonding in locally overstrained PM microvolumes [22], for example, at the PM–CF boundary [2]).

Generally, the above considerations are sufficient to interpret the observed trends of the structural, elastic, relaxation, and dissipative properties of the tested CFRPs in the course of curing of different prepregs. However, a series of experimental results needs more detailed analysis. For example, we observed unexpected decrease in the transverse E'_{25} for CFRP-I and its constancy for CFRP-II , i.e., in the case when the contribution of the binder should dominate. It seems more likely that with further curing after a 55% conversion of functional groups (τ 0.5 h) the modulus of elasticity should necessarily increase. The observed behavior can be interpreted in terms of the Perepechko's effect [23], whose essence is that the growth in the number of chemical cross-links in the binder results in decreasing number of intermolecular contacts (bonds) providing the major contribution to the dynamic modulus of elasticity of the binder in the glassy state. The constancy in E'_{25} for CFRP-II can be attributed to the specific features of formation of the PM structure with binary prepregs [4, 5, 20]. In this case the total number of chemical cross-links in the bulk of PM increases irregularly in the course of curing: the dominating process is local aftercure in topologically faulted low-cross-linked microvolumes of PM by virtue of diffusion-controlled reactions of functional groups [8], which should result in leveling of the elastic characteristics throughout the PM volume. For the both CFRPs the growth in the longitudinal E'_{25} in the course of curing is caused by simultaneous effect of the structural and deformation factors. Taking into account the above-mentioned specific features of CF prepregs in PM boundary layers contributing to the mechanical response in the longitudinal direction, low-cross-linked, faulted microvolumes can be formed, where the Perepechko's effect is not pronounced yet. Therefore, the dynamic modulus of elasticity in this direction keeps on to increase. Furthermore, the increase in E'_{25} in this direction may be caused by strong stretching action due to residual internal strains of the thermal origin. As we suggested in [8], it is the effect of these strains that is responsible for considerable increase in the temperature of mechanical vitrification in the longitudinal direction. Decrease in the segmental mobility in PM in the longitudinal direction under the action of the stretching force due to residual internal strains should be reflected also in the elastic characteristics of CFRPs. This suggestion is supported by data given in [24–26] that the surface of the reinforcing agent in CFRPs and organoplastics favors formation of some ordered (consolidated) cluster structures in polymer matrices. These structures are oriented along the fibers, having a high degree of the cooperativity (hindrance) of segmental motion [24]. Evidently, they are realized under the effect of strong stretching thermal RIS directed along the fiber in the surface layer of PM. Note that in organic and carbon fibers the thermal expansivity coefficient in the longitudinal direction is negative, being $(-1 \div 6) \times 10^{-6}$, and that for epoxy binders, $(40 - 60) \times 10^{-6}$ K^{-1} [27].

Let us also discuss significant differences in the relaxation properties of the investigated CFRPs with an example of the α-peak half-width $\Delta_{1/2}$ characterizing the relaxation homogeneity of the spectrum. According to data reported in [8, 20], this parameter allows adequate evaluation of the effects of the structural and deformation factors on the polymer matrix in the course of curing. Increase in the transverse

$\Delta_{1/2}$ of CFRP-I with this parameter being decreased in the initial binder means that the observed broadening of α peak is caused essentially by the effect of the deformation factor, i.e., by increasing shrinking RIS. Higher $\Delta_{1/2}$ in this direction in CFRP-II, which remains unchanged in the course of curing, signifies that the structural heterogeneity in PM is higher in this case, but occurrence of low-cross-linked (having shorter relaxation time) microvolumes of microheterogeneous PM favors more efficient relaxation of residual internal strains in CFRP-II in the course of curing. The higher initial half-width of α peak in the longitudinal direction for the both CFRPs as compared to that in the transverse direction is caused by the effect of the structural factor, i.e., by more pronounced topological microheterogeneity of PM in the surface layers. At the same time, stronger increase in $\Delta_{1/2}$ for CFRP-I in the course of curing is due to a stronger effect of the deformation factor, i.e., the stretching effect of heavy thermal RIS. High initial $\Delta_{1/2}$ in CFRP-II and its subsequent decrease, in principle, would be attributed to the effect of the structural factor. More intense reaction in the deepest stages of curing in less cross-linked, topologically faulted microvolumes [5] should increase the homogeneity of the PM structure and decrease the half-width of α peak. However, if this were the case, similar effect should be observed in the transverse direction also. Therefore, taking into account stronger RIS in the longitudinal direction, the observed decrease in $\Delta_{1/2}$ as well as initial decrease in $\tan\delta_{25}$ and increase in IFB, evidently, are due to chemical relaxation (debonding) of overstrained bonds [2, 22].

Finally, study of the curing kinetics allows comparative analysis of the behavior of the bending strength for the both CFRPs and evolution in the elastic and dissipative properties and also the intensity of stress of PM in the longitudinal and transverse directions. The constancy of σ_b in CFRP-II and its decrease in the course of curing are well consistent with the trends of the dynamic modulus of elasticity, $\Delta_{1/2}$, and $\tan\delta_{25}$ in the transverse direction, and also of the $\tan\delta_{max}$ and, in part, $\tan\delta_{max}\Delta_{1/2}$ in the longitudinal direction. These results suggest that the bending strength of unidirectional carbon-fiber-reinforced plastics in the longitudinal direction is governed by three major factors: (1) relaxation characteristics of the polymer matrix, especially in the surface layers responsible for relaxation of the most harmful stretching residual internal stresses acting along the fiber–polymer matrix boundary; (2) elastic properties of the polymer matrix in the transverse direction, which provide efficient propagation of strains between carbon fibers and, therefore, a higher degree of cooperativity of their degradation; and (3) adhesion preventing peeling of the polymer matrix from carbon fibers due to tensile stress caused by residual internal strains originating from shrinkage.

CONCLUSION

Carbon-fiber-reinforced plastic materials prepared by the binary prepreg technique may surpass plastics based on the conventional blend prepregs by all the three mechanical parameters (elasticity, dissipation, and stress–strain behavior) in certain directions, which is caused primarily by the mosaic, partly gradient structure of the polymer matrix realized with the binary prepregs. This structure is characterized by an increased content of topologically faulted microvolumes, especially in its surface layers. The faulted microvolumes originating from incomplete mixing of the binder components favor efficient relaxation of various internal residual stresses, especially along the fibers.

REFERENCES

1. Smirnov, Yu.N., Shatskaya, T.E., Natrusov, V.I., *et al.*, *Plast. Massy*, 1985, no. 11, pp. 41–43.
2. Natrusov, V.I., Shatskaya, T.E., Lapitskii, V.A., *et al.*, *Mekh. Kompozit. Mater.*, 1987, no. 2, pp. 315–319.
3. Nakonechnyi, V.P., Red'kina, N.K., Dzhavadyan, E.A., *et al.*, *Vysokomol. Soedin., Ser. A*, 1986, vol. 28, no. 7, pp. 1512–1515.
4. Tarasov, V.P., Smirnov, Yu.N., Shatskaya, T.E., *et al.*, *Vysokomol. Soedin., Ser. B*, 1990, vol. 32, no. 6, pp. 428–431.
5. Smirnov, Yu.N., Magomedov, G.M., Shatskaya, T.E., and Natrusov, V.I., *Vysokomol. Soedin., Ser. A*, 1996, vol. 38, no. 10, pp. 1717–1721.
6. *Carbon Fibers and Their Composites*, Fitzer, E., Ed., Berlin: Springer, 1985.
7. Smirnov, Yu.N., Dzhamaeva, N.M., and Tarasov, V.P., *Plast. Massy*, 1998, no. 7, pp. 14–16.
8. Smirnov, Yu.N., Magomedov, G.M., and Dzhamaeva, N.M., *Plast. Massy*, 1999, no. 7, pp. 28–34.
9. Perepechko, I.I., *Akusticheskie metody issledovaniya polimerov* (Acoustic Methods in Polymer Research), Moscow: Khimiya, 1973.
10. Smirnov, Yu.N., Rozenberg, B.A., Mileiko, S.T., *et al.*, *Plast. Massy*, 1984, no. 4, pp. 17–20.
11. Belyakov, V.P., Danilov, V.A., Makushkin, A.P., and Perepechko, I.I., *Mekh. Kompozit. Mater.*, 1986, no. 6, pp. 969–972.

12. Magomedov, G.M., Ul'yanenko, S.N., Lebedev, L.B., *et al*., *Mekh. Kompozit. Mater*., 1984, no. 5, pp. 832–836.
13. Ul'yanenko, S.N., Magomedov, G.M., Lebedev, L.B., *et al*., *Mekh. Kompozit. Mater*., 1987, no. 3, pp. 414–417.
14. Rogers, K.F., Phillips, L.N., Kingstone-Lee, D.N., *et al*., *J. Mater. Sci*., 1977, vol. 12, no. 4, pp. 718–722.
15. Magomedov, G.M. and Zadorina, E.N., *Dokl. Akad. Nauk SSSR*, 1986, vol. 286, no. 3, pp. 630–632.
16. Kudryachova, G.M., Chinchenko, I.I., Bakulina, G.P., *et al*., *Mekh. Kompozit. Mater*., 1989, no. 5, pp. 776–778.
17. Bartenev, G.M. and Zelenev, Yu.V., *Vysokomol. Soedin., Ser. A*, 1972, vol. 14, no. 5, pp. 998–1009.
18. Gunyaev, G.M., Rumyantsev, A.F., Fedorenko, A.G., *et al*., *Mekh. Polim*., 1974, no. 2, pp. 358–360.
19. Smirnov, Yu.N., Irzhak, V.I., and Rozenberg, B.A., *Vysokomol. Soedin., Ser. B*, 1983, vol. 25, no. 12, pp. 914–916.
20. Smirnov, Yu.N., Magomedov, G.M., and Dzhamaeva, N.M., *Plast. Massy*, 1999, no. 9, pp. 9–12.
21. Yudin, V.E., Volodin, V.P., and Kenunen, I.V., *Mekh. Kompozit. Mater*., 1991, no. 3, pp. 542–545.
22. Glotova, Yu.K., Irzhak, V.I., and Rozenberg, B.A., *Vysokomol. Soedin., Ser. A*, 1982, vol. 24, no. 4, pp. 339–341.
23. Perepechko, I.I. and Kvacheva, L.A., *Vysokomol. Soedin., Ser. A*, 1971, vol. 13, no. 1, pp. 124–127.
24. Startsev, O.V. and Perepechko, I.I., *Mekh. Kompozit. Mater*., 1984, no. 3, pp. 387–389.
25. Perov, B.V., Kobets, L.P., Deev, I.S., *et al*., *Mekh. Kompozit. Mater*., 1988, no. 1, pp. 81–85.
26. Kregers, A.F., *Mekh. Kompozit. Mater*., 1983, no. 3, pp. 433–436.

Russian Journal of Applied Chemistry, Vol. 75, No. 1, 2002, pp. 119–123. Translated from Zhurnal Prikladnoi Khimii, Vol. 75, No. 1, 2002, pp. 120–124.
Original Russian Text Copyright © 2002 by Filimonova, Nikulin, Lychkin.

MACROMOLECULAR CHEMISTRY AND POLYMERIC MATERIALS

Copolymerization of Maleic Acid with Acetophenone-Containing Bottoms from Styrene Distillation

O. N. Filimonova, S. S. Nikulin, and I. P. Lychkin

Voronezh State Forestry Engineering Academy, Voronezh, Russia
Voronezh State Technological Academy, Voronezh, Russia

Received June 14, 2001

Abstract—The feasibility was studied for producing polymeric materials by high-temperature copolymerization of maleic acid with styrene distilation bottoms from joint production of styrene and propylene oxide. Regression equations were derived to predict the conditions for preparing the copolymer with the required properties. The structure, properties, and fields of possible application of the copolymer were studied.

A major problem of petrochemical industry is utilization of bottoms from production of vinylaromatic monomers. These bottoms are large-tonnage wastes. There are two main procedures for commercial production of styrene: dehydrogenation of ethylbenzene and dehydration of methylphenylcarbinol (MPC) formed in joint production of styrene and propylene oxide. Whereas synthesis of polymeric materials from styrene distillation bottoms (SDB) from the former process has been studied comprehensively, and the application fields of the resulting polymers are well examined, SDB from the latter process are studied poorly [1]. At the same time, maximal utilization of the whole amount of SDB with production of nontoxic polymeric products containing no styrene or other hazardous compounds is an urgent problem [2].

Reaction of styrene with maleic acid in the presence of MPC and acetophenone, which are the main components of SDB from joint production of styrene and propylene oxide, yields a polymeric product which can show the film-forming properties. The process is multistage and depends on many factors. Study of separate stages will give insight into the process mechanism and reveal the major factors affecting the yield and quality of the copolymer.

In this work we studied how the copolymer yield depends on the temperature, weight ratio of acetophenone-containing SDB and maleic acid, content of styrene in acetophenone-containing SDB, and process time. However, experimental assessment of the joint effect of these factors on production of the target product is time-consuming, which makes it particularly important to use simulation procedures. Study and construction of mathematical models requires thorough design of the experiment.

The experimental design was based on the fourth-order Greek–Latin square. With this design, the volume of experiments necessary to reveal separate significant factors, evaluate their effect, and obtain regression equation is considerably reduced. It becomes possible to evaulate simultaneously the effect of all the factors and to determine the factor values (within their variation range) providing the best result with respect to one or another criterion characterizing either the product quality or the process efficiency. This is particularly important when interaction between the factors is absent or can be neglected. The structure of the square [3] follows from the theory of experimental design.

Experimental study of the copolymer preparation involved (1) choice of the process temperature and time, reactant ratio, and content of styrene in the initial acetophenone-containing SDB as the main parameters affecting copolymerization; (2) estimation of the main copolymerization parameters, within the preset limits of their variation, ensuring the highest yield of the copolymer of the required quality; and (3) elucidation of the dependence of parameters characterizing the copolymer on the preparation conditions.

Under laboratory conditions, the copolymer was prepared in a glass reactor equipped with a reflux condenser, a Dean–Stark trap, and a stirrer; the reactor was placed in a thermostat to maintain the prescribed temperature. The major components of acetophenone-containing SDB were acetophenone (~35 wt %) and

1070-4272/01/7501-0119$27.00 © 2002 MAIK "Nauka/Interperiodica"

Table 1. Plan of the experiment*

T_p, °C	*c* and *d*, wt %, at indicated τ_p, h			
	τ_1 2, 3, 5 (10)	τ_2 2, 4, 6 (12)	τ_3 3, 4, 7 (14)	τ_4 3, 5, 8 (16)
T_1 115, 140, 165	c_1 15, d_1 1	c_2 25, d_2 4	c_3 35, d_3 7	c_4 45, d_4 10
T_2 120, 145, 170	c_2 25, d_3 7	c_1 15, d_4 10	c_4 45, d_1 1	c_3 35, d_2 4
T_3 125, 150, 175	c_3 35, c_4 10	c_4 45, d_3 7	c_1 15, d_2 4	c_2 25, d_1 1
T_4 130, 155, 180	c_4 45, d_2 4	c_3 35, d_1 1	c_2 25, d_4 10	c_1 15, d_3 7

* The synthesis temperature and time are given; the total synthesis time is given in parentheses.

MPC (~14 wt %); the styrene content, according to the experimental plan, was varied from 15 to 45 wt %. The remainder was tar containing polystyrene and other high-boiling compounds. Acetophenone-containing SDB and maleic acid in a prescribed ratio were simultaneously charged to the reactor and gradually heated with continuous stirring to the prescribed temperature, maintained to within ±2.5°C. The reaction progress was monitored chromatographically and viscometrically. After synthesis completion, acetophenone and nonpolymerized substances were distilled off in a vacuum (5–8 mm Hg, 165–170°C).

As factors affecting the process we chose the process temperature and time, the styrene content in the initial bottoms, and the amount of maleic acid added *d*. The plan of the experiment is given in Table 1. According to the plan, copolymerization is a three-stage process, with the stages differing in the temperature and time. As response functions we chose the copolymer yield and such its characteristics as molecular weight, acid number, and ester number, determining the main properties of the copolmer and its application fields.

To estimate the target functions and predict their values, the experimental results were processed to obtain the regression equations

$$Y = SF_1(t)F_2(\tau)F_4(d), \quad (1)$$

where Y is the target function; S is the coefficient; $T = T_2T_3/T_1 - (T_2T_3/T_1)_{min}$, T_1, T_2, T_3 are the temperatures of the first, second, and third reaction stages (°C); $\tau = \tau_2\tau_3/\tau_1 - (\tau_2\tau_3/\tau_1)_{min}$, τ_1, τ_2, and τ_3 are the times of the first, second, and third reaction stages (h); the subscript min means that the smallest of the possible values of T_2T_3/T_1 and $\tau_2\tau_3/\tau_1$ is taken; c is the concentration of styrene in acetophenone-containing SDB (wt %); d is the amount of maleic acid added (wt %); F_n is the function of single variable: $F_1 = F_1(T)$, $F_2 = F_2(\tau)$, $F_3 = F_3(c)$, $F_4 = F_4(d)$ characterize the influence of the process temperature and time, styrene concentration, and maleic acid content, respectively, on the value of the target function.

Table 2. Initial data for regression equations

Variable	Variation range
Temperature, °C:	
in first stage, T_1	115–130
in second stage, T_2	140–155
in third stage, T_3	165–180
Time, h:	
in first stage, τ_1	2–3
in second stage, τ_2	3–5
in third stage, τ_3	5–8
Temperature parameter T	0, 4.54, 9.11, 13.80
Time parameter τ	0, 4.50, 1.83, 5.83
Styrene concentration c, wt %	15–45
Maleic acid content d, wt %	1–10

In formula (1), the functions $F_1(T)$ and $F_2(\tau)$ are discrete and defined only for the T and τ values listed in Table 2. The T and τ values were chosen so as make convenient calculation of $F_1(T)$ and $F_2(\tau)$, approximated by third-degree polynomials. Because the levels of the temperature and time factors A and B are presented by sets of three numbers, it is insufficient to characterize their effect by a single number. The functions $F_1(T)$ and $F_2(\tau)$ in this model are discrete and only reproduce the experimental results.

The functions $F_3(c)$ and $F_4(d)$ are continuous, the possible experimental errors are smoothed assuming that the dependence has the form of a quadratic polynomial. Regression equations (1) for calculating the copolymer yield Y_y, molecular weight $Y_{\bar{M}_v}$, acid number Y_{an}, and ester number Y_{en}, after processing of the experimental data, have the form

$$Y_y = 2.14 \times 10^{-6}(75.3 + 0.3355T - 7.69 \times 10^{-2}T^2 + 6.24 \times 10^{-3}T^3)(76.8 + 7.47\tau - 3.40\tau^2 + 0.375\tau^3) \times (42.0 + 2.05c - 0.0251c^2)(69.1 + 2.91d - 0.187d^2),$$

$$Y_{\bar{M}_v} = 8.15 \times 10^{-5}(17.4 + 4.53T - 0.542T^2 + 1.63 \times 10^{-2}T^3)$$
$$\times (22.5 - 0.108\tau - 0.775\tau^2 + 0.162\tau^3)(29.3 - 0.449c$$
$$+ 6.80 \times 10^{-3}c^2)(19.4 + 1.174d - 6.44 \times 10^{-2}d^2),$$

$$Y_{an} = 6.84 \times 10^{-4}(12.6 - 0.571T + 8.06 \times 10^{-2}T^2$$
$$- 3.72 \times 10^{-3}T^3)(10.5 + 1.77\tau - 0.239\tau^2 - 1.39 \times 10^{-2}\tau^3)$$
$$\times (5.92 + 0.287c - 3.03 \times 10^{-3}c^{-2})(5.73 + 0.148d + 0.151d^2),$$

$$Y_{en} = 4.16 \times 10^{-5}(37.9 - 5.22T + 0.691T^2 - 2.72 \times 10^{-2}T^3)$$
$$\times (2.2 + 13.2\tau - 3.83\tau^2 + 0.299\tau^3)(18.6 + 0.517c$$
$$- 4.95 \times 10^{-3}c^2)(11.8 + 2.78d + 0.122d^2).$$

The ranges of variation of the response functions obtained with this experimental plan are given below:

Copolymer yield, wt %	69–90
Molecular weight of copolymer $\bar{M}_v$	12 120–42 660
Acid number, mg KOH g^{-1}	5–25
Ester number, mg KOH g^{-1}	11–81

The mean deviation of the calculated data from the experiment (by the absolute value, %) is as follows: for copolymer yield, 5.0; for average molecular weight, 16.4; for acid number, 3.6; and for ester number, 8.6.

The regression equation obtained allows presentation of the experimental results in the general form and calculation of the response functions for the conditions that differ from the tested conditions (Table 1) but fall within the variation range of the corresponding factors. The equations fairly reliably predict the possble results under conditions differing from those realized according to the fourth-order Greek–Latin square plan, allowing adjustment of process parameters and copolymer composition depending on the conditions of using the copolymer in composite materials.

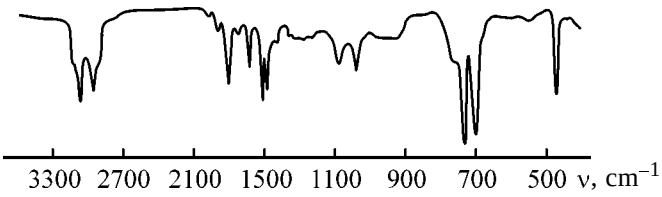

Fig. 1. IR spectrum of copolymer based on acetophenone-containing SDBs. (ν) Wave number.

The experimental results allow us to suggest the composition of the copolymer chain containing carboxy, anhydride, and ester groups. In all cases the ester number, determining the content of ester groups, is higher than the acid number. This fact suggests that the ester group is formed both by reaction of maleic acid with MPC and, possibly, by reaction of MPC with the carboxy groups of the copolymer chain. The presence of all the three kinds of groups in the copolymer chain is confirmed by IR spectroscopy.

Figure 1 shows a typical IR spectrum of the copolymer, taken on an IKS-29 spectrometer in the range 600–3200 cm^{-1}. The polystyrene base is confirmed by bands at 1640, 1030, 906, 750, and 700 cm^{-1}. Strong absorption at about 1820 and 1770 cm^{-1} is characteristic of anhydride groups (styrene–anhydride combination in the polystyrene chain and maleic anhydride). A band at 1710 cm^{-1} characterizes free maleic acid (dimer), with a shoulder at 1710–1660 cm^{-1} confirming the presence of the C=C bond with the *cis* geometry. The band at 1800–1850 cm^{-1} belongs to the anhydride group, and at 1740 cm^{-1}, to the ester group [4].

The structure of the synthesized copolymer can be represented as follows:

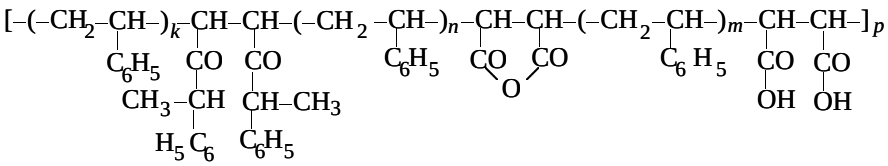

Thus, the experimental results allow us to propose conditions for joint processing of acetophenone-containing SDB and maleic acid to obtain the copolymer of required quality with the maximal yield.

At present, major attention is given to treatment of wood materials with the aim of enhancement of their water and moisture resistance, protection from biological degradation, prolongation of the service life, etc.

[5–9]. The structure and properties of the SDB copolymer obtained suggest that one of the promising fields of its application can be treatment of wood-fiber boards (WFBs) to enhance their water and moisture resistance and strength. The high content of functional groups suggests that this copolymer will interact with polymeric components of wood and bind with them chemically. The product, with cellulose as example, can be represented as follows:

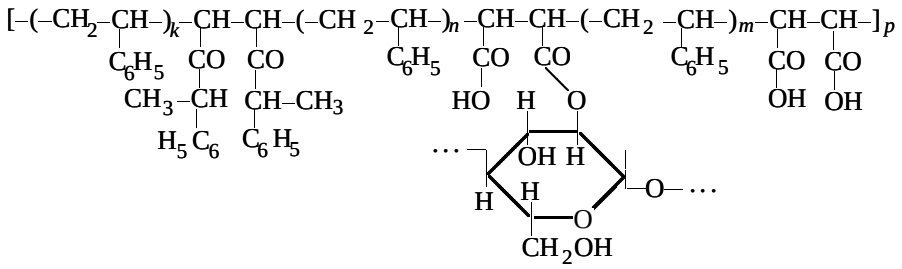

It should be assumed that grafting of low-molecular-weight SDB copolymer to cellulose macromolecules will eliminate such drawback of impregnating agents as their washout from articles in the course of their service.

The impregnating solution based on SDB copolymer was prepared by its dissolution in a mixed solvent widely used in production of paint-and-varnish materials: a 4 : 1 mixture of xylene with acetone. Experiments were performed according to the plan of a 4 × 4 Greek–Latin square. As the main factors exerting the strongest effect on the water resistance and strength of WFBs we chose the impregnation time (30, 60, 90, and 120 s, factor *A*), heat treatment temperature (120, 140, 160, and 180°C, factor *B*), heat treatment time (1.5, 3.0, 4.5, and 6.0 h, factor *C*), and copolymer concentration in solution (29, 42, 55, and 68 wt %, factor *D*). The polymer content in WFBs was determined gravimetrically from the weight gain. The modified boards were cooled in air to room temperature. After conditioning, the boards were tested according to GOST (State Standard) 19592–80. The content of the SDB copolymer in modified WFBs varied from 3.5 to 16.2 wt % depending on process conditions.

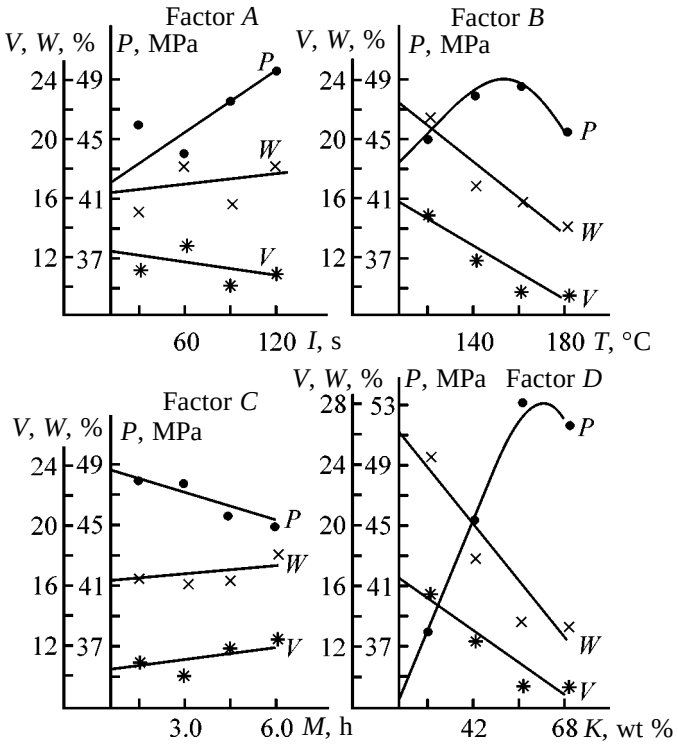

Fig. 2. Swelling with respect to thickness *V*, water absorption *W*, and bending strength *P* as functions of the impregnation time *I* (factor *A*), heat treatment temperature *T* (factor *B*), heat treatment time *M* (factor *C*), and impregnating solution concentration *K* (factor *D*).

Data on the strength and water resistance of WFBs are given in Table 2. Analysis of the dependences shows that the most significant effect on the properties of modified WFBs is exerted by the heat treatment temperature and concentration of the impregnating solution and, to a lesser extent, by the time of impregnation and heat treatment.

By processing the experimental results, we obtained the regression equations describing the effect of the chosen process parameters on the strength and water resistance of WFBs. The regression equations for the response functions are as follows: for the ultimate bending strength (MPa),

$$Y_{str} = 9.8 \times 10^{-6}(43.2 + 0.048a)(-41.9 + 1.2b - 3.98 \times 10^{-3}b^2)(49.6 - 0.76c)(1.04 + 1.64d - 1.3 \times 10^{-2}d^2),$$

Table 3. Experimental and calculated data on the strength and water resistance of WFBs

Parameter	Calculation	Experiment	Control
Ultimate bending strength, MPa	59.0	58.5–60.3	48.1–50.7
Swelling with respect to thickness in 24 h, %	7.9	6.6–7.1	10.2–11.8
Water absorption in 24 h, %	13.4	10.9–12.4	14.4–15.2

* Control boards were impregnated with tall oil used in production of enhanced-strength hard boards [10].

for swelling with respect to thickness (%),

$$Y_{sw} = 6.92 \times 10^{-4}(12.3 - 1.24 \times 10^{-2}a)(24.9 - 8.94 \times 10^{-2}b) \times (9.66 + 0.447c)(19.9 - 0.171d),$$

and for water absorption (%),

$$Y_{w} = 2.13 \times 10^{-4}(15.06 - 2.33 \times 10^{-2}a)(34.3 - 0.11b) \times (15.6 + 0.304c)(31.4 - 0.291d).$$

The optimal conditions for WFB modification with SDB copolymer are as follows: impregnation time 120 s, heat treatment temperature 160°C, heat treatment time 1.5 h, and concentration of SDB copolymer in solution about 60 wt %. The strength and water resistance of modified WFBs, calculated for these process parameters, and given in Table 3 in comparison with the experimental data. The calculation results reasonably agree with the experiment.

CONCLUSIONS

(1) Optimal conditions for production of polymeric materials based on styrene distillation bottoms from joint production of styrene and propylene oxide were determined by mathematical experimental design.

(2) The structure and properties of the copolymers were determined.

(3) One of the promising application fields of the resulting copolymers is modification of wood-fiber boards, enhancing their water and moisture resistance and strength.

REFERENCES

1. Petykhin, Yu.M. and Kontsova, L.V., *Otkhody neftekhimicheskikh proizvodstv – syr'e dlya sinteticheskikh produktov* (Petrochemical Production Wastes as a Raw Material for Synthetic Products), Moscow: TsNIITEneftekhim, 1991.
2. Nikulin, S.S., Butenko, T.R., Ryl'kov, A.A., *et al.*, *Perspektivy ispol'zovaniya kubovykh ostatkov proizvodstva vinilaromaticheskikh monomerov* (Prospects of Utilization of Bottoms from Production of Vinylaromatic Monomers), Moscow: TsNIITEneftekhim, 1996.
3. Akhnazarova, S.L. and Kafarov, V.V., *Optimizatsiya eksperimenta v khimii i khimicheskoi tekhnologii* (Optimization of Experiment in Chemistry and Chemical Technology), Moscow: Vysshaya Shkola, 1978.
4. Cross, A.D., *An Introduction to Practical Infra-Red Spectroscopy*, London: Butterworths, 1960.
5. Gorshin, S.N., *Konservirovanie drevesiny* (Preservation of Wood), Moscow: Lesnaya Prom–st., 1977.
6. Khrulev, V.M., Mashkin, N.A., and Dorofeev, N.S., *Modifitsirovannaya drevesina i ee primenenie* (Modified Wood and Its Use), Kemerovo: Knizhnoe, 1988.
7. Khrulev, V.M., *Proizvodstvo konstruktsii iz dereva i plastmass* (Production of Structures from Wood and Plastics), Moscow: Vysshaya Shkola, 1982.
8. Shamaev, V.A., *Modifikatsiya drevesiny* (Modification of Wood), Moscow: Ekologiya, 1991.
9. Bogomolov, B.D., *Khimiya drevesiny i osnovy khimii vysokomolekulyarnykh soedinenii* (Wood Chemistry and Principles of Macromolecular Chemistry), Moscow: Lesnaya Prom–st., 1973.
10. Mersov, E.D., *Proizvodstvo drevesnovoloknistykh plit* (Production of Wood-Fiber Boards), Moscow: Vysshaya Shkola, 1989.

Russian Journal of Applied Chemistry, Vol. 75, No. 1, 2002, pp. 124–126. Translated from Zhurnal Prikladnoi Khimii, Vol. 75, No. 1, 2002, pp. 125–127.
Original Russian Text Copyright © 2002 by Egorova, Migunova, Mukhina, Girbasova, Bilibin.

MACROMOLECULAR CHEMISTRY AND POLYMERIC MATERIALS

Photoinitiated Polymerization of Acryloyl Chloride

G. G. Egorova, I. I. Migunova, I. V. Mukhina, N. V. Girbasova, and A. Yu. Bilibin

St. Petersburg State University, St. Petersburg, Russia

Received December 27, 2000; in final form, April 2001

Abstract—Polymerization of acryloyl chloride in the bulk and in solution, induced by 300-nm UV radiation, was performed. The conditions were determined under which the polymer does not precipitate from the solution and is formed in a nearly quantitative yield, which allows its use in polymer-analogous transformations without isolation.

Thanks to high reactivity, poly(acryloyl chloride) (PAC) is used for preparing new polymers by polymer-analogous transformations in cases when polymerization of the corresponding monomers is difficult. In particular, such a procedure is used for incorporating complex structural fragments into the polymeric chain, including biologically active substances and drugs [1, 2].

A procedure was described for preparing PAC by radical polymerization of acryloyl chloride (AC) at 50°C in dioxane in the presence of azobis(isobutyronitrile) (AIBN) for 48 h. The degree of polymerization of the resulting product is 140–400 [3]. The reactants used in the experiment should be thoroughly purified and dried. Experiments on synthesis of PAC by the procedure described in [3] showed that the polymerization results are poorly reproducible; in some experiments the polymer did not form at all. It is known that homopolymerization of AC is difficult [4]. Therefore, in some studies, including recent papers, polymerization of AC was examined in detail [5, 6]. The best results were obtained when the reaction was performed in benzene or cyclohexane. However, the forming PAC precipitates from solution as a separate phase, which is unfavorable for its subsequent use in polymer-analogous transformations. Introduction of the isolation, drying, and redissolution stages increases the probability of PAC hydrolysis, which results in partial loss of the acyl chloride functional groups.

Thus, development of a simple and reproducible route to PAC allowing preparation of the polymer of a sufficiently high molecular weight in a high yield in solution remains urgent. Solution of this problem was the goal of our study.

To effect polymerization of AC, we chose photochemical initiation, allowing the process to be performed under mild conditions with a high efficiency. Because published data on photoinitiated polymerization of AC are scarce [7], it was appropriate to study this process both in the bulk and in solution. As solvent we used thoroughly dried dioxane, and as UV source, a PRK-2 continuous-spectrum lamp. The photoinitiator was AIBN (λ_{max} 340 nm). Initially the reaction was performed in quartz test tubes to use the whole spectrum of the UV radiation of the lamp. We found that under these conditions the polymer undergoes cross-linking, which may be due to photolysis of AC [8]:

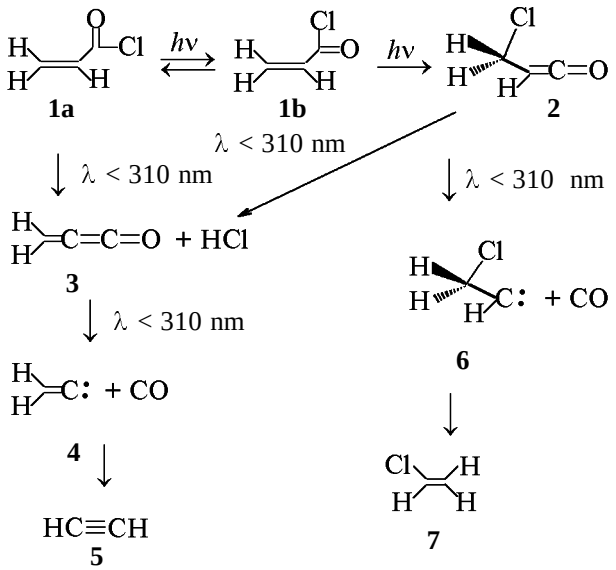

According to the above scheme, under broad-spectrum UV irradiation AC **1** undergoes isomerization and transformation into chloromethylketene **2**. This is followed by a series of transformations of **1** and **2**, yielding biradicals **4** and **6** causing cross-linking of

1070-4272/01/7501-0124$27.00 © 2002 MAIK "Nauka/Interperiodica"

PAC in the course of polymerization. According to the scheme, these species are mainly generated by the light with $\lambda < 310$ nm. Hence, by cutting off short-wave UV radiation, it is possible to prevent formation of **4** and **6** and thus to exclude cross-linking.

In subsequent experiments the AC polymerization was performed in glass test tubes transmitting radiation with $\lambda \geq 300$ nm. The process was performed in the bulk and in solution; the reaction time and the content of the initiator were varied. To determine the yield of the polymer and its molecular weight, PAC was converted to poly(methyl methacrylate) (PMA) by adding excess methanol. From the amount of the PMA formed, we calculated the yield of PAC in polymerization, and from the viscosity-average molecular weight of PMA calculated by the Mark–Kuhn–Houwink equation (30°C, chloroform [9])

$$[\eta] = 3.221 \times 10^{-4} M^{0.678}$$

we estimated its molecular weight.

Table 1 shows that the yield of the polymer increases with time and with increasing initiator concentration. This is accompanied by the growth of the viscosity, up to a full loss of the fluidity (run no. 5). The product dissolves in dioxane very slowly, and removal of the unchanged monomer is necessary. As a result, the probability of hydrolysis of acyl chloride groups sharply increases, which makes the polymer unsuitable for polymer-analogous transformations.

Our results show that, to preserve reactive acyl chloride groups in PAC, it is appropriate to perform polymerization of AC in solution using the solvent in which the polymer is soluble. For this purpose, we studied polymerization of AC in dioxane. The results are listed in Table 2.

Table 2 shows that the molecular weight of the polymer only slightly depends on the initiator concentration. The polymer yield reaches a maximum at 1.8 mol % AIBN. In all cases, the polymers fully soluble in dioxane were obtained.

The assumption that the use of PAC solution without preliminary isolation of the polymer allows the loss of acyl chloride groups to be fully avoided was confirmed by the reaction with methanol followed by examination of the resultng PMA. The solution of PAC in dioxane was obtained under conditions of run no. 4 (Table 2).

It should be noted that the PMA sample in hand contained no residual chlorine, which shows that the conversion of the acyl chloride groups was complete. The analytical data, within determination error, are consistent with the calculations made for the PMA unit. The structure was also confirmed by ^{1}H NMR.

Table 1. Photoinitiated polymerization of AC in the bulk (30°C, distance from the source 25 cm)

Run no.	[I], mol %	τ, h	Yield, wt %	$\overline{M}_\eta$ of PMA
1	0.3	0.5	Traces	–
2	0.3	1	9	75 000
3	0.3	1.5	27	62 000
4	0.6	1.5	48	42 000
5	1.8	1	60	42 000

Table 2. Photoinitiated polymerization of AC in dioxane (AC concentration 50 vol %, 40°C, 2 h, distance from the source 15 cm)

Run no.	[I], mol %	Yield, wt %	$\overline{M}_\eta$ of PMA
1	0.3	63	15 000
2	0.6	58	10 000
3	1.2	83	16 000
4	1.8	99	16 000
5	2.4	90	13 000

It is known that PAC readily reacts with primary amines, including amino acids [10], to form the corresponding substituted polyacrylamides. For example, the reaction with leucine at room temperature occurs with a 94–100% yield in 48 h [10]. We performed the reaction between PAC prepared under conditions of run no. 4 (Table 2) with dimethyl aspartate:

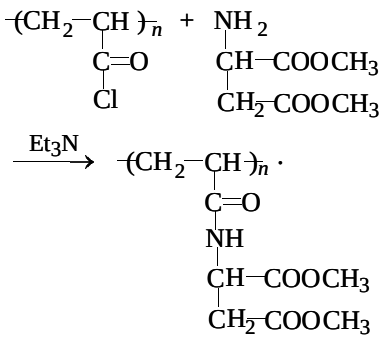

According to the ^{1}H NMR spectra and results of analysis for nitrogen, the conversion in 24 h at room temperature was as high as 96 mol %.

EXPERIMENTAL

The ^{1}H NMR spectra were taken on a Bruker DPX-300 spectrometer.

Acryloyl chloride was prepared as described in [11]. Polymerization was performed in a glass test tube, which was charged with 1 ml of AC, 1 ml of dry dioxane, and the calculated amount of AIBN. The mixture was irradiated for the prescribed period. In experiments on bulk polymerization, 4 ml of dioxane was added after reaction completion to dissolve the polymer.

To prepare PMA, a solution of PAC in dioxane was transferred into a 50-ml flask, 2.5 ml of absolute methanol was added, and the mixture was allowed to stand for 24 h. Then the solvent was removed in a vacuum, and the polymer was reprecipitated from chloroform into absolute diethyl ether. Yield 98%.

Found, %: C 55.76, H 7.27.
$C_4H_6O_2$. Calculated, %: C 55.81, H 6.98.

Molecular weight $\overline{M}_\eta$ 17000. ^{1}H NMR spectrum ($CDCl_3$, δ, ppm): 1.40–2.00 (2H, CH_2), 2.35 (1H, CH), 3.60–3.80 (3H, OCH_3).

Dimethyl aspartate was prepared as described in [12].

The reaction of PAC solution with dimethyl aspartate was performed as follows. Dimethyl aspartate hydrochloride (2.56 g, 0.013 mol) was placed in a flat-bottomed flask equipped with a dropping funnel and a $CaCl_2$ tube. Chloroform (30 ml) and triethylamine (3.13 ml, 0.022 mol) were added. The mixture was stirred with a magnetic stirrer. Then, a solution of PAC (0.84 g, 0.0093 mol) in dioxane was added dropwise with cooling (–10°C). The mixture was stirred for 1 h and then allowed to stand for a day at room temperature. The mixture was washed twice with water, the chloroform layer was dried over sodium sulfate and filtered, and the solvent was vacuum-evaporated. The polymer was reprecipitated from chloroform into diethyl ether. Yield 82% (1.4 g).

Found, %: C 49.67, H 6.07, N 6.43.
$C_9H_{13}NO_3$. Calculated, %: C 50.23, H 6.04, N 6.51.

^{1}H NMR spectrum ($CDCl_3$, δ, ppm): 1.30–2.70 (3H, CH_2CH), 2.70–3.30 (2H, CH_2), 3.40–4.30 (6H, OCH_3), 4.35–5.20 (1H, CH), 7.55–8.5 (1H, NH).

CONCLUSIONS

(1) Acryloyl chloride readily polymerizes in dioxane under UV irradiation ($\lambda \geq 300$ nm) to give soluble poly(acryloyl chloride) in up to 99% yield.

(2) Reactions of polyacryloyl chloride solutions with methanol and dimethyl aspartate yield products structurally similar to the corresponding homopolymers.

ACKNOWLEDGMENTS

The study was financially supported by the Russian Foundation for Basic Research (project no. 00-03-33199).

REFERENCES

1. Gavodore, G.C., *Biochimie*, 1978, vol. 60, no. 2, pp. 203–207.
2. Voronkov, M.G. and Zhdanovich, E.A., *Dokl. Ross. Akad. Nauk*, 1993, vol. 333, no. 6, pp. 730–731.
3. Schulz, P. and Elzer, W.K., *Macromol. Chem.*, 1961, vol. 42, no. 3, pp. 189–196.
4. Serenson, W.R. and Campbell, T.W., *Preparative Methods of Polymer Chemistry*, New York: Interscience, 1961.
5. Yang, Y.S., Qi, G.R., and Qian, J.W., *J. Appl. Polym. Sci.*, 1998, vol. 68, no. 4, pp. 665–670.
6. Tajima, T. and Otsu, T., *Mem. Fac. Eng. Osaka City Univ.*, 1977, vol. 18, pp. 107–110.
7. Boyer, S. and Rondeau, A., *Bull. Soc. Chim. Fr.*, 1958, no. 2, pp. 240–244.
8. Pietri, N., Monnier, M., and Aycard, J.P., *J. Org. Chem.*, 1998, vol. 63, no. 8, pp. 2462–2468.
9. Toroptseva, A.M., Belogorodskaya, K.V., and Bondarenko, V.M., *Laboratornyi praktikum po khimii i tekhnologii vysokomolekulyarnykh soedinenii* (Practical Laboratory Course of Chemistry and Technology of Macromolecular Compounds), Nikolaev, A.F., Ed., Leningrad: Khimiya, 1972.
10. Schulz, P., Elzer, W.K., and Kern, W., *Macromol. Chem.*, 1961, vol. 42, no. 3, pp. 197–204.
11. Srempel, H., Cross, R.P., and Mariella, R.P., *J. Am. Chem. Soc.*, 1950, vol. 72, no. 5, pp. 2299–2300.
12. Gershkovich, A.A. and Kibirev, V.K., *Sintez polipeptidov: Reagenty i metody* (Synthesis of Polypeptides: Chemicals and Procedures), Kiev: Naukova Dumka, 1987.

Russian Journal of Applied Chemistry, Vol. 75, No. 1, 2002, pp. 127–134. Translated from Zhurnal Prikladnoi Khimii, Vol. 75, No. 1, 2002, pp. 128–134.
Original Russian Text Copyright © 2002 by Semenov, Ladilina, Cherepennikova, Chesnokova.

MACROMOLECULAR CHEMISTRY AND POLYMERIC MATERIALS

Oligodimethylsilane Initiators for Photochemical Vulcanization of Siloxane Rubber

V. V. Semenov, E. Yu. Ladilina, N. F. Cherepennikova, and T. A. Chesnokova

Razuvaev Institute of Organometallic Chemistry, Russian Academy of Sciences, Nizhni Novgorod, Russia

Receibed May 3, 2001

Abstract—Photolytic vulcanization of siloxane rubber films in the presence of trimethylsiloxy-substituted di- and trisilanes, oligodimethylsilanosiloxanes $(Me_2SiO)_m(SiMe_2)_n$, $Me(Me_2SiO)_m(SiMe_2)_nMe$, oligodimethylsilanes $Me(Me_2Si)_nMe$, and volatile pyrolysis products of polydimethylsilane was studied.

Oligoorganosilanes are suggested as vulcanizing agents for photolytic curing of silicone rubber [1]. Methyl and phenyl derivatives of linear and cyclic structure, containing chains of 3–6 silicon atoms, were tested. Trisilanes containing, along with methyl groups, also one or two phenyl groups exhibit a good or satisfactory initiating activity [2, 3]. Octamethyltrisilane is considerably less effective than phenyl-containing trisilanes [2]. In this work we studied vulcanization of rubber in the presence of trisilanes with Me_3SiO substituents and of oligomers containing both Me_2Si and Me_2SiO units. Such compounds, in contrast to phenyl-substituted oligosilanes, are readily soluble in polydimethylsiloxanes. Also tested were curing agents prepared by the Wurtz reaction from dimethyldichlorosilane and by thermal decomposition of polydimethylsilane. The synthesis of the oligomeric initiators, their electronic absorption spectra, and photolysis pathways are reported. Transparent silicones cured by UV radiation exhibit high thermal and radiation resistance and biological inertness; they are used as protective sheaths for quartz fiber light guides [4], in microelectronics [5], and in production of antiadhesion paper [6] and of artificial crystalline lenses and irises of human eyes [7, 8].

To evaluate the curing activity of compounds, we used as substrate liquid siloxane rubber (polymethylvinylsiloxane PMVS-2) containing 2% randomly distributed vinyl groups and terminal hydroxy groups [9]. In the table we present the absorption maxima and extinction coefficients in the UV spectra, and also the curing times for two series of permethylated oligosilanes [10–15]. Compounds **I**–**XI** were prepared by us previously [11, 15]. Syntheses of **XII**–**XV** were performed after analyzing the dependence of the curing time on the structure of **I**–**XI**. It is seen from the table that only compounds containing a chain of no less than three Si atoms are effective as vulcanizing agents. Disilanosiloxanes **IV**–**VII** and hexamethyldisilane **I** are inactive. Replacement of one to four methyl groups in Me_6Si_2 by trimethylsiloxy groups (compounds **IV**–**VII**) does not enhance the activity. At the same time, introduction of the same substituent into octamethyltrisilane **II** (position 1, compound **VIII**, or 2, compound **IX**) considerably shortens the vulcanization time. 1-Methylsiloxyheptamethyltrisilane **VIII** is by a factor of 2 more active than its isomer **IX**. Replacement of one more methyl radical in position 2 by the Me_3SiO group (compound **X**) decreases the initiating power. Compound **XI** containing two trisilanyl fragments is even less active than the related trisilanosiloxanes **IX** and **X**. Analysis of the UV spectra of **I**–**XI** shows that introduction of the Me_3SiO group into both hexamethyldisilane and octamethyltrisilane molecules shifts the absorption maximum toward longer waves by 2 (**I**, **IV**) and 5 nm (**II**, **VIII**), respectively, with the decrease in the extinction coefficients by factors of 1.3 and 3.9, respectively. Introduction of the trimethylsiloxy group into position 2 (compound **IX**) causes more complex changes, as compared to position 1 (compound **VIII**). Two maxima at 224 and 238 nm are shifted toward longer waves, but both have higher extinction coefficients compared to **VIII**. Compounds **X** and **XI** exhibit a single maximum, and it exhibits a still larger bathochromic shift than in **IX**.

Thus, introduction of one or two oxygen-containing substituents into octamethyltrisilane causes a bathochromic shift, but the vulcanizing activity of the compound increases only if the oxygen atom is lo-

1070-4272/01/7501-0127$27.00 © 2002 MAIK "Nauka/Interperiodica"

UV spectra of oligosiloxanes (hexane) and the rubber curing time τ

Compound	Formula	λ,* nm	ε, l mol^{-1} cm^{-1}	τ, min
I	$Me_3SiSiMe_3$	194	10 800	No curing
II	$Me_3SiSiMe_2SiMe_3$	215	9000	30.0
III	$Me_3Si(SiMe_2)_2SiMe_3$	235	14 700	2.2
IV	$Me_3SiSiMe_2OSiMe_3$	196	8600	No curing
V	$Me_3SiOSiMe_2SiMe_2OSiMe_3$	233**	60	″
VI	$Me_3SiOSiMe_2SiMe(OSiMe_3)_2$	215	1200	″
VII	$(Me_3SiO)_2SiMeSiMe(OSiMe_3)_2$	211	1900	″
VIII	$Me_3SiSiMe_2SiMe_2OSiMe_3$	220	2300	3.4
IX	$(Me_3Si)_2SiMe(OSiMe_3)$	224	5800	6.5
		238	3000	
X	$(Me_3Si)_2Si(OSiMe_3)_2$	242	3700	7.3
XI	$[(Me_3SiO)(Me_3Si)_2Si]_2O$	243	12 000	12.0
XIIb	$(Me_2SiO)_m(SiMe_2)_n$	216	3500	2.3
		255	2400	
XIIIb	$Me(Me_2SiO)_m(SiMe_2)_nMe$	215	2100	2.0
		237	–	
		265	12 200	
		278	–	
XIVc	$Me(Me_2Si)_nMe$***			1.0
XIVd	$Me(Me_2Si)_nMe$	220	6600	1.5
		255	6100	
		262	4400	
XVb		223	2000	1.5
		238	1100	

* For **I**–**III**, λ and ε were taken from [10].
** In methylene chloride.
*** The UV spectrum was not measured, because the hexane solution became turbid.

cated at the end of the Si–Si–Si triad. Hence, for fast curing it is appropriate to use linear oligomers with $–(SiMe_2)_n–$ chains ($n \geq 3$) containing siloxy substituents at the ends of the blocks but not in their middle. Such derivatives, oligosilanosiloxanes [10, 16–19], can be prepared by the Wurtz reaction from α,ω-dichlorooligodimethylsiloxanes, dimethyldichlorosilane, and lithium [18] or sodium [19]. In our study we used a siloxane tetramer containing minor amounts of the trimer (7%) and pentamer (4%). The reactions were performed in nonane in the presence of trimethylchlorosilane as endcapping agent, or without it. It is known [19] that in such processes the siloxane fragments are redistributed; therefore, the final product should contain not only tetrameric siloxane blocks but also shorter and longer sequences:

$$ClMe_2Si(OSiMe_2)_2OSiMe_2Cl + Me_2SiCl_2$$

$$\xrightarrow[-NaCl]{Na} (Me_2SiO)_m(SiMe_2)_n,$$

XII

$$ClMe_2Si(OSiMe_2)_2OSiMe_2Cl + Me_2SiCl_2 + Me_3SiCl$$

$$\xrightarrow[-NaCl]{Na} Me(Me_2SiO)_m(SiMe_2)_nMe.$$

XIII

The resulting products are colorless viscous liquids readily soluble in polydimethylsiloxanes. The yields of **XII** and **XIII** are, respectively, 0.23 and 0.37 g per gram of the mixture of the chlorides. When heated in a vacuum, compounds **XII** and **XIII** release, respectively, 29 and 17 wt % of volatile oligomers. Both volatile (**XIIa**, **XIIIa**) and nondistillable (**XIIb**, **XIIIb**) fractions exhibit a high initiating activity. In the presence of **XIIIb** vulcanization occurs somewhat faster. The nondistillable oligomers, according to GPC, have the following molecular-weight characteristics: **XIIb**, M_w 1860, M_n 990, M_w/M_n 1.88; **XIIIb**, M_w 2150, M_n 1180, M_w/M_n 1.82. It is seen that in the presence of the endcapping agent compounds with somewhat higher M are obtained. This is probably due to the fact that the system α,ω-dichlorooligosiloxane–dimethyl-

dichlorosilane shows a greater tendency to form rings, and Me_3SiCl to a certain extent suppresses the ring formation. The gel chromatograms of **XIIb** and **XIIIb** (Fig. 1) show a low-molecular-weight maximum at about M 400.

The number of $SiMe_2$ units in the $–(SiMe_2)_n–$ chains was calculated from the results of bromine cleavage of the oligomers according to Stolberg's procedure [20]. It was found that compounds **XIIb** and **XIIIb** contain 42.73 and 37.45% Me_2Si groups, respectively. Knowing the molecular weights of the oligomers, it is possible to find the mean values of m and n: $(Me_2SiO)_{15}(SiMe_2)_{15}$ (**XIIb**), $(Me_2SiO)_{19}\cdot(SiMe_2)_{15}$ (**XIIIb**). It is seen from these formulas that somewhat higher M of **XIIIb** is due to the larger number of siloxane groups, whereas the number of dimethylsilanediyl fragments in the oligomer molecules is, on the average, the same. It should be noted that the $–(SiMe_2)–$ units do not form a single block with n = 15 but form several shorter blocks separated by siloxane groups. The sets of Si_n blocks in **XIIb** and **XIIIb** can be estimated from the UV spectra. These spectra reflect the complex structure of the copolymers and show that they consist of blocks of different lengths. For example, the spectrum of **XIIIb**, along with two major bands at 215 and 265 nm, shows weaker absorption at about 237 and 278 nm (Fig. 2). The UV spectrum of **XIIb** contains two bands at 216 and 255 nm. Oligodimethylsilanes $Me(Me_2Si)_nMe$ absorb in the following regions (nm): octamethyltrisilane (n = 3) and oligomer with n = 8, at 215; oligomers with n = 5 and 6, at 250–260; and oligomers with n = 7 and 8, at 270 [21]. In view of the fact that the oxygen atoms in the $SiOSi_n$ and $SiOSi_nOSi$ groups shift the absorption toward longer waves by approximately 5 nm, the spectra suggest that compound **XIIb** contains $Si_3–Si_6$ blocks, and compound **XIIIb**, $Si_3–Si_8$ blocks.

Figure 2 shows the UV spectra of the photoinitiators, and Fig. 3 illustrates the decay of UV absorption under irradiation for compound **XIIIb** dissolved in the rubber and in the free state. The main changes in the spectrum occur within 2 min of exposure. In the course of irradiation, the intensity of the long-wave absorption bands decreases rapidly, and that of the short-wave bands, more slowly. A pronounced hypsochromic shift is observed, suggesting degradation of longer Si_n chains (n = 6–8) and their transformation into shorter chains (n = 3–4). After a 3-min exposure, only the band at 218 nm remains, belonging to di- and trisilanyl groups SiOSiSiOSi and SiOSiSiSiOSi, which are the most stable to UV radiation. Irradiation

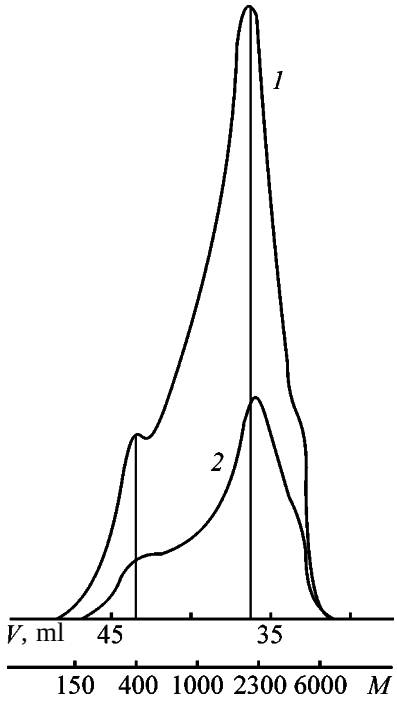

Fig. 1. Gel chromatograms of copolymers (*1*) **XIIb** and (*2*) **XIIIb**. (*V*) Retention volume and (*M*) molecular weight.

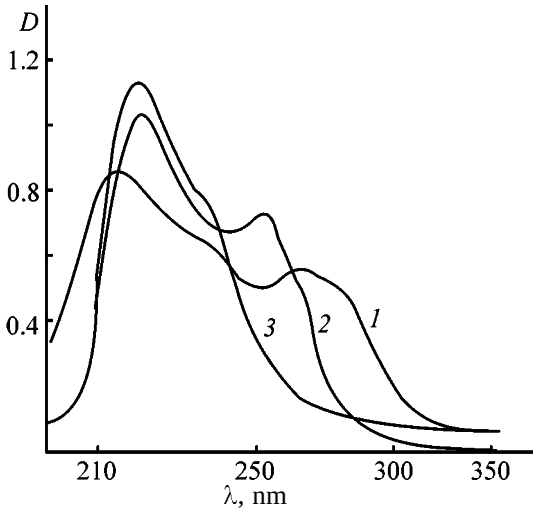

Fig. 2. UV spectra of photoinitiators (*1*) **XIIIb**, (*2*) **XIVd**, and (*3*) **XVb**. (*D*) Optical density and (λ) wavelength; the same for Fig. 3.

of **XIIIb** in the rubber causes vulcanization of the rubber, whereas a thin film of the neat oligomer remains visually unchanged (liquid) upon exposure.

Photochemical decomposition of **XIIIb** in the rubber follows the linear law $-c_\tau/c_0 = k\tau$ to 80% conversion (Fig. 4). The initial decomposition rate of the neat photoinitiator (2.2×10^{-2} s^{-1}) is higher than that of the photoinitiator diluted with the rubber ($9.1 \times$

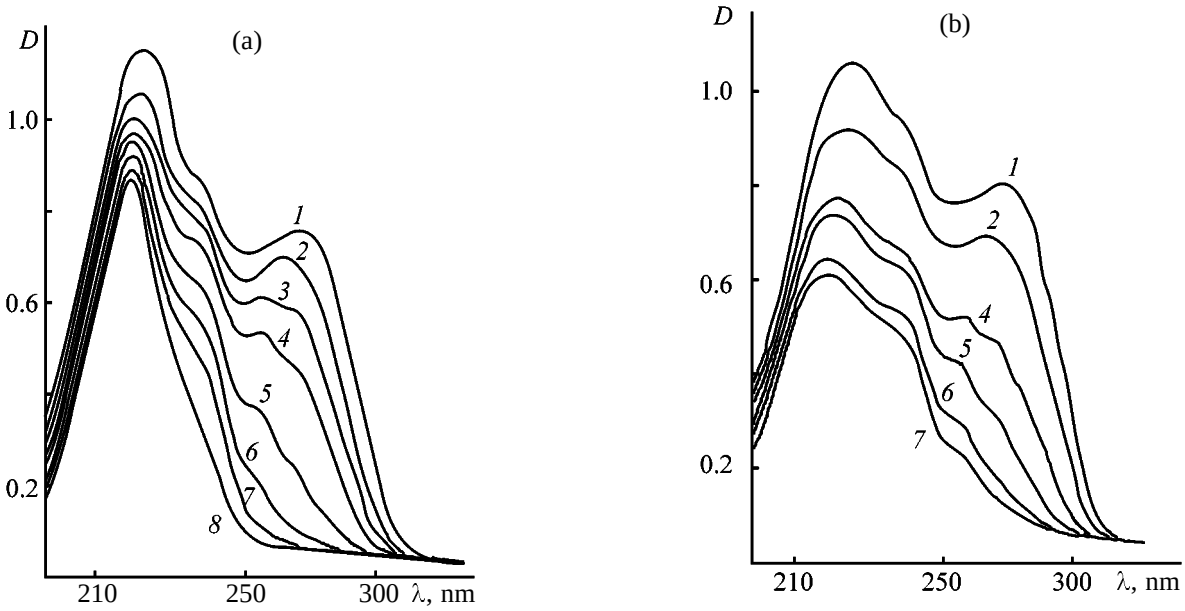

Fig. 3. Decay of UV absorption of **XIIIb** under irradiation: (a) film of solution in a rubber and (b) neat substance film. Exposure time, s: (*1*) 0, (*2*) 10, (*3*) 20, (*4*) 30, (*5*) 60, (*6*) 90, (*7*) 120, and (*8*) 180.

10^{-3} s^{-1}), but then the decomposition rate decreases. The conversion of **XIIIb** in 2 min is 92% in the rubber and 75% in the neat form. The reaction deceleration is probably due to accumulation in the neat oligomer film of the decomposition products absorbing at 254 nm. The observed transformation of the spectrum under UV irradiation is typical of oligoorganosilanes.

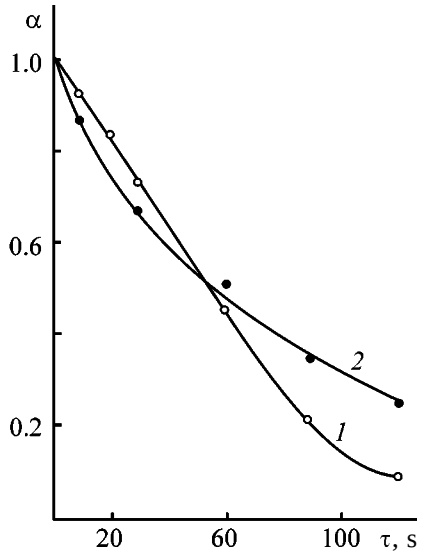

Fig. 4. Kinetic curves of photochemical decomposition of **XIIIb**: (*1*) film of solution in a rubber and (*2*) neat substance film. (α) Relative optical density of the film and (τ) irradiation time.

Such processes make shorter the Si_n lengths; they are accompanied by elimination of silylenes and formation of silyl radicals [22]. Such species cause crosslinking of the polysiloxane molecules.

Oligodimethylsilanes $Me(Me_2Si)_nMe$ (n = 4–6) showed high initiating activity [2, 3]. It was interesting to examine the vulcanizing power of methyl oligomers with n > 6. It is known [23] that, as n is increased, the absorption maximum of the polysilane is shifted toward longer waves, and the extinction coefficient per disilanediyl fragment increases. Therefore, for long-chain silanes we can expect enhanced initiating activity. Oligo- and polydimethylsilanes were prepared by the Wurtz reaction from dimethyldichlorosilane and sodium, with trimethylchlorosilane as endcapping agent. From 194 g of Me_2SiCl_2, 54 g of Me_3SiCl, and 90 g of Na we obtained 51.5 g of solid polydimethylsilane **XIVa** insoluble in silicones, 5 g of waxy polymer **XIVb**, 7.2 g of oligomers **XIVc** in the form of a light yellow transparent viscous mass, and 11.9 g of oligomers **XIVd** in the form of a transparent liquid distillable in a vacuum (the UV spectrum is shown in Fig. 2). The two latter types of oligosilanes are compatible with liquid rubber and initiate its curing. Fraction **XIVc** containing oligomers with n > 8 shows a higher initiating activity as compared to decamethyltetrasilane **III** (n = 4) and fraction **XIVd** (n = 4–8). However, its mixture with PMVS-2 is turbid, which suggests incomplete dissolution of oli-

godimethylsilanes. Fractions **XIVa** and **XIVb** are insoluble in the rubber and cannot be used as vulcanizing agents.

Our results show that, despite a fairly high content of the endcapping agent, trimethylchlorosilane, the yield of the soluble oligodimethylsilanes is low. The major product is solid insoluble polydimethylsilane. It is isolated from the reaction mixture when unreacted sodium is decomposed with alcohol and water; this product is a colorless coarse powder. After washing with water and drying, its solubility in organic solvents becomes incomplete. In chloroform and toluene, the polymer swells with insignificant dissolution. The product resembles the known polydimethylsilane [24, 25] used as the initial substance in production of silicon carbide ceramics [26]. It is known from the published data [27] that thermal decomposition of this polymer yields linear and cyclic silanes $Me(Me_2Si)_6 \cdot Me$, $Me(Me_2Si)_nH$ (n = 2, 3, 5, 6), $H(Me_2Si)_nH$ (n = 2–4), and $(Me_2Si)_n$ (n = 5–8). Tests of their initiating activity showed that volatile products formed by heating **XIVa** to 320–340°C are very effective in photochemical vulcanization. The curing time is 1.5 min. The primary distillate (compound **XVa**) is a viscous turbid liquid. Addition of this initiator (2 wt %) to transparent liquid rubber causes its turbidization, which, however, does not prevent vulcanization of up to 70 μm thick films. Transparent colorless photoinitiators **XVb** and **XVc** are obtained after repeated distillation of the initial distillate **XVa** or its successive treatment with CCl_4, aqueous NaOH, and Me_3SiCl in the presence of triethylamine (the UV spectrum of transparent photoinitiator **XVb** prepared by distillation of **XVa** is shown in Fig. 2). Such a sequence of treatments results in transformation of SiH groups into $SiOSiMe_3$ groups. It is known [28] that polymethylhydrosilanes quantitatively transform into polymethylchlorosilanes on dissolution in CCl_4. No catalyst is required. Fraction **XVa** was dissolved in CCl_4, heated, and hydrolyzed with aqueous NaOH, after which it was treated with trimethylchlorosilane in the presence of triethylamine. A mixture of colorless transparent trimethylsiloxy-substituted oligosilanes **XVc**, readily soluble in the siloxane rubber, was obtained. After such treatment, the bands at 2080 [ν(Si–H)] and 880 cm^{-1} [δ(Si–H)] virtually disappeared, and the intensity of the band at 1030 cm^{-1} [ν(Si–O)] increased considerably.

EXPERIMENTAL

The UV spectra were recorded on a Specord M-40 spectrophotometer (solutions on hexane or methylene chloride and films on quartz glass), and the IR spectra, on a Perkin–Elmer-577 spectrophotometer. The molecular-weight distribution of the oligomers was determined by gel-permeation chromatography on an installation consisting of three Styrogel columns (porosity 25, 25, and 8 nm), with THF as eluent and an RIDK-101 differential refractometer as detector. The calibration was performed with reference poly(propylene glycol) samples. Gas-chromatographic analysis of organosilicon compounds was performed with a Tsvet-530 chromatograph (0.3 × 200-cm stainless steel column, 5% SE-30 on Chromaton N-AW-DMCS, thermal conductivity detector, carrier gas helium).

PMVS-2 rubber was prepared by the procedure described in [9]. The photoinitiator was added in an amount of 2 wt %. Films, 30–70 μm thick, were formed on quartz glass supports from solutions in hexane. Irradiation was performed with a total spectrum of a PRK-4 medium-pressure mercury lamp (220 W), placed at a distance of 14 cm. The vulcanization time was determined and the kinetic curves of oligosilane decomposition were calculated by the procedure described in [3]. The relative optical density of the layer α, proportional to the relative photoinitiator concentration $c_\tau c_0^{-1}$, was expressed as $\alpha = (D_\tau - D_\infty)/(D_0 - D_\infty)$, where D_0, D_τ, and D_∞ are, respectively, the optical densities of the layer at λ = 265 nm before exposure, after exposure for time τ, and after prolonged exposure (until the absorption decreased to a constant limit). Compounds **I**–**III** [10], **IV** [11], **V** and **VIII** [12], **VI** and **VII** [13], **IX** [14], and **X** and **XI** [15] were prepared by known procedures.

Oligodimethylsilanosiloxane XII. A solution of 15.9 g of dichlorooctamethyltetrasiloxane and 5.85 g of dimethyldichlorosilane in 20 ml of nonane was added with vigorous stirring and heating (120°C) to a suspension of 4.7 g of Na in 200 ml of nonane. The reaction mixture was heated for 25 h at 130–140°C; after cooling, a mixture of 10 ml of methanol and 10 ml of glacial acetic acid and then 100 ml of distilled water were added. The organic layer was separated, washed with water, and dried over $CaCl_2$; the solvent was distilled off. From the residue, 1.51 g of a colorless transparent liquid was isolated, bp 100–105°C (0.1 mm Hg), fraction **XIIa**, n_D^{20} 1.4240. The nondistillable residue **XIIb** (3.54 g) was a viscous liquid. UV spectrum (hexane), λ_{max}, nm (ε, l mol^{-1} cm^{-1}): 216 (3500), 255 (2400).

Found, %: Me_2Si 42.73.
$(Me_2SiO)_{15}(SiMe_2)_{15}$. Calculated, %: Me_2Si 43.95.

Oligodimethylsilanosiloxane XIII was prepared similarly from 6.2 g of Na, 18.1 g of 1,7-dichlorooctamethyltetrasiloxane, 6.7 g of dimethyldichlorosilane, and 3.76 g of trimethylchlorosilane. Compound **XIIIa**: yield 1.8 g, bp 100–140°C (0.1 mm Hg), n_D^{20} 1.4310; **XIIIb**: 8.74 g. UV spectrum (hexane), λ_{max} (ε, l mol^{-1} cm^{-1}): 215 (2100), 265 (12 800). IR spectrum, ν, cm^{-1}: 2940, 2880, 2840, 1400, 1255, 1245, 1085, 1030, 850, 800, 760, 680; n_D^{20} 1.4475.

	Found, %:	Me_2Si 37.45.
$(Me_2SiO)_{19}(SiMe_2)_{15}$.	Calculated, %:	Me_2Si 38.24.

Oligo- and polydimethylsilanes XIV. To a suspension of 90 g of Na in 700 ml of toluene, prepared at 110°C and cooled to 90°C, we added dropwise with vigorous stirring 194 g of dimethyldichlorosilane and 54 g of trimethylchlorosilane. The mixture spontaneously warmed up to reflux. The stirring was continued for 25 h at 110°C until the mixture of chlorides was completely consumed (monitored by acid–base titration). The mixture was cooled with ice-cold water, and 150 ml of isopropyl alcohol and then 150 ml of distilled water were added. After addition of water, an abundant white precipitate formed. The solid polymer was filtered off, washed with water to neutral reaction, and dried, first in air at 20–25°C and then in a vacuum at 90–110°C. Polydimethylsilane **XIVa** (51.5 g) was obtained as white coarse powder. IR spectrum, ν, cm^{-1}: 1240, 830, 740, 725, 685, 625. The organic layer was washed with distilled water to neutral reaction and dried over $CaCl_2$, and the solvent was distilled off under argon. Vacuum distillation of the residue gave 11.9 g of liquid oligodimethylsilanes **XIVd**, bp 125–130°C (10 mm Hg), n_D^{20} 1.4880. UV spectrum (hexane), λ_{max}, nm (ε, l mol^{-1} cm^{-1}): 225 (6600), 255 (6100), 262 (4400). IR spectrum, ν, cm^{-1}: 2940, 2880, 1390, 1240, 1040, 830, 795, 765, 725, 685, 645. The residue was dissolved in 150 ml of hexane and filtered. To the filtrate 5 g of AG-3 activated carbon was added, and the mixture was stirred for 5 h at 25°C. After filtration and removal of hexane, 7.2 g of oligodimethylsilanes **XIVc** was obtained as a pale yellow viscous mass. IR spectrum, ν, cm^{-1}: 2940, 2920, 2880, 2840, 1395, 1240, 1045, 830, 800, 760, 730, 685, 625. When stored in air, the product turns dark. The hexane-insoluble fraction **XIVb** (5.3 g) is a waxy mass insoluble in polysiloxanes.

Pyrolysis of polydimethylsilane **XIVa** with simultaneous distillation of volatile oligodimethylsilanes was performed in an evacuated round-bottomed flask connected to a received for liquid products through an air-cooled condenser. The flask containing 100 g of the polymer was heated on an electric hot plate to 320°C. At this temperature slow distillation of liquid products started. For 12 h, the temperature was kept within 320–340°C, and the residual pressure, within 0.05–0.10 mm Hg. In the course of pyrolysis, 40.3 g of a viscous turbid liquid (fraction **XVa**) was collected in the receiver. This liquid was subjected to repeated vacuum distillation. The fraction boiling in the range 55–120°C (2 mm Hg) was collected. A mixture of oligodimethylsilanes (fraction **XVb**, 10.3 g) was obtained as a colorless transparent liquid; yield 10.3 g, n_D^{20} 1.4810. IR spectrum, ν, cm^{-1}: 2940, 2980, 1394, 1255, 1240, 800 ($SiCH_3$), 2080, 880 (SiH), 1075, 1020 (SiO). A 20-g portion of fraction **XVa** was dissolved in 100 ml of CCl_4 and refluxed for 5 h; after cooling, 100 ml of 1 N aqueous NaOH was added. The mixture was stirred at 25°C for 5 h; the organic layer was separated, washed with distilled water, and dried over $CaCl_2$. To the resulting solution, 20 g of trimethylchlorosilane and 20 g of triethylamine were added. The mixture was heated with stirring for 7 h and filtered; the filtrate was washed with distilled water, dried over $CaCl_2$, and vacuum-evaporated. A colorless transparent viscous liquid was obtained (**XVc**, 12.6 g); n_D^{20} 1.4840. IR spectrum, ν, cm^{-1}: 2940, 2910, 2880, 2840, 1390, 1250, 1245, 830, 795, 755 ($SiCH_3$), 1030 (SiO).

ACKNOWLEDGMENTS

The study was supported by INTAS (grant 97-1785) and Russian Foundation for Basic Research (project nos. 99-03-3211, 00-02-81 206 Bel 2000).

The analyses were performed in the Analytical Center, Razuvaev Institute of Organometallic Chemistry, Russian Academy of Sciences with the financial support of the Russian Foundation for Basic Research (project no. 96-03-40-042).

CONCLUSIONS

(1) Tests of the initiating activity of a series of trimethylsiloxy-substituted di- and trisilanes in photolytic curing of liquid polydimethylsiloxane rubber containing 2 wt % of randomly distributed vinyl groups showed that the most active are trisilanes containing Me_3SiO terminal groups.

(2) Effective photoinitiators, oligodimethylsilanosiloxanes, readily soluble in rubber, were prepared by

the Wurtz reaction from dimethyldichlorosilane, 1,7-dichlorooctamethyltrisiloxane, and sodium in the presence of trimethylchlorosilane as endcapping agent or without it.

(3) A series of liquid and solid oligo- and polydimethylsilanes were prepared similarly from dimethyldichlorosilane, trimethylchlorosilane, and sodium. The liquid oligomers are effective vulcanizing agents compatible with the rubber. Thermal decomposition of solid polydimethylsilane yields liquid soluible photoinitiators.

REFERENCES

1. Semenov, V.V. and Cherepennikova, N.F., *Dokl. Akad. Nauk SSSR*, 1989, vol. 309, no. 1. pp. 119–122.
2. Semenov, V.V., Cherepennikova, N.F., Artemicheva, S.B., and Razuvaev, G.A., *Appl. Organometal. Chem.*, 1990, vol. 4, no. 2, pp. 163–172.
3. Semenov, V.V., Cherepennikova, N.F., Treushnikov, V.M., *et al.*, *Vysokomol. Soedin., Ser. A*, 1994, vol. 36, no. 1, pp. 46–53.
4. Alekseeva, E.I., Nanush'yan, S.R., Milyavskii, Yu.S., *et al.*, Abstracts of Papers, *Vsesoyuznaya konferentsiya "Proizvodstvo kremniiorganicheskikh produktov i primenenie ikh dlya povysheniya dolgovechnosti i kachestva materialov i izdelii otraslei narodnogo khozyaistva"* (All-Union Conf. "Production of Organosilicon Substances and Their Use for Improving the Durability and Quality of Materials and Articles Used in the National Economy"), Novocheboksarsk, October 11–13, 1988, Moscow, 1988, p. 198.
5. Nanush'yan, S.R., Alekseeva, E.I., Polees, A.B., *et al.*, Abstracts of Papers, *Vsesoyuznaya konferentsiya "Proizvodstvo kremniiorganicheskikh produktov i primenenie ikh dlya povysheniya dolgovechnosti i kachestva materialov i izdelii otraslei narodnogo khozyaistva"* (All-Union Conf. "Production of Organosilicon Substances and Their Use for Improving the Durability and Quality of Materials and Articles Used in the National Economy"), Novocheboksarsk, October 11–13, 1988, Moscow, 1988, p. 74.
6. Fedorova, E.M. and Gaduashvili, V.M., Abstracts of Papers, *Vsesoyuznaya konferentsiya "Proizvodstvo kremniiorganicheskikh produktov i primenenie ikh dlya povysheniya dolgovechnosti i kachestva materialov i izdelii otraslei narodnogo khozyaistva"* (All-Union Conf. "Production of Organosilicon Substances and Their Use for Improving the Durability and Quality of Materials and Articles Used in the National Economy"), Novocheboksarsk, October 11–13, 1988, Moscow, 1988, p. 175.
7. Myakov, V.N. and Chuprov, A.D., Abstracts of Papers, *Andrianovskie chteniya* (Andrianov Readings), Moscow, January 17–19, 1995, p. 74.
8. Myakov, V.N., Makhrova, T.V., Chudakova, V.A., *et al.*, Abstracts of Papers, *Vserossiiskaya konferentsiya "Kremniiorganicheskie soedineniya: sintez, svoistva, primenenie"* (Russian Conf. "Organosilicon Compounds: Synthesis, Properties, and Use"), Moscow: February 1–3, 2000, p. S119.
9. Brevnova, T.N., Tikhonova, Z.A., Konov, A.S., *et al.*, in *Fiziko-khimicheskie osnovy sinteza i pererabotki polimerov* (Physicochemical Principles of Polymer Synthesis and Processing), Gor'kii: Gor'k. Gos. Univ., 1984, pp. 45–49.
10. Kumada, M. and Tamao, K., *Adv. Organomet. Chem.*, 1968, vol. 6, pp. 19–117.
11. Razuvaev, G.A., Brevnova, T.N., Semenov, V.V., *et al.*, *Zh. Obshch. Khim.*, 1987, vol. 57, no. 2, pp. 375–382.
12. Razuvaev, G.A., Brevnova, T.N., Semenov, V.V., *et al.*, *Zh. Obshch. Khim.*, 1986, vol. 56, no. 4, pp. 884–891.
13. Semenov, V.V. and Chesnokova, T.A., *Zh. Obshch. Khim.*, 1990, vol. 60, no. 1, pp. 150–159.
14. Semenov, V.V., Ladilina, E.Yu., Chesnokova, T.A., *et al.*, *Zh. Obshch. Khim.*, 1991, vol. 61, no. 5, pp. 1184–1195.
15. Semenov, V.V., Ladilina, E.Yu., Khorshev, S.Ya., *et al.*, *Zh. Obshch. Khim.*, 1994, vol. 64, no. 10, pp. 1652–1656.
16. Chajnowski, J., Kurjata, J., and Rubinstain, S., *Macromol. Chem. Rapid Commun.*, 1988, vol. 9, no. 7, pp. 469–473.
17. Chajnowski, J., Gladkova, N., Pluta, M., *et al.*, Abstracts of Papers, *10th Int. Symp. on Organosilicon Chemistry*, Poznan, August 15–20, 1993, p. 253.
18. US Patent 4626583.
19. Tchernyavski, A.J. and Zavin, B.G., Abstracts of Papers, *10th Int. Symp. on Organosilicon Chemistry*, Poznan, August 15–20, 1993, p. 273.
20. Stolberg, U.G., *Chem. Ber.*, 1963, vol. 96, no. 10, pp. 2798–2803.
21. *Homoatomic Rings, Chains and Macromolecules of Main-Group Elements*, Rheingold, A.L., Ed., Amsterdam: Elsevier, 1977, pp. 203–234.
22. Michl, J., Downing, J.W., Karatsu, T., *et al.*, *Pure Appl. Chem.*, 1988, vol. 60, no. 7, pp. 959–972.
23. Miller, R.D. and Michl, J., *Chem. Rev.*, 1989, no. 6, pp. 1359–1410.
24. Yajima, S., Hasegawa, Y., and Hayashi, I., *J. Mater.*

Sci., 1978, vol. 13, no. 12, pp. 2569–2576.

25. Wesson, J.P. and Williams, T.C., *J. Polym. Sci., Polym. Chem. Ed.*, 1979, vol. 17, no. 9, pp. 2833–2843.
26. Tsirlin, A.M. and Popova, N.A., *Keramikoobrazuyushchie kremniiorganicheskie polimery – polikarbosilany: Obzornaya informatsiya NIITEKhIM. Elementoorganicheskie soedineniya i ikh primenenie* (Polycarbosilanes as Ceramics-Forming Organosilicon Polymers: Review of the Research Institute of Feasibility Studies in Chemistry, Ser.: Organoelement Compounds and Their Use), Moscow: NIITEKhIM, 1990.
27. Popova, N.A., Lavrukhin, B.D., Zagorevskii, D.V., *et al.*, *Metalloorg. Khim.*, 1991, vol. 4, no. 5, pp. 984–991.
28. Sakurai, H., Yamagata, M., and Murakami, M., *Bull. Chem. Soc. Jpn.*, 1972, vol. 45, no. 8, pp. 2658–2659.

Russian Journal of Applied Chemistry, Vol. 75, No. 1, 2002, pp. 135–137. Translated from Zhurnal Prikladnoi Khimii, Vol. 75, No. 1, 2002, pp. 135–137.
Original Russian Text Copyright © 2002 by Loginova, Panova, Gun'kin.

MACROMOLECULAR CHEMISTRY AND POLYMERIC MATERIALS

Use of Fullerite (C_{60}/C_{70}) as Modifier of Epoxy–4,4'-Isopropylidenediphenol Oligomers

N. Yu. Loginova, L. G. Panova, and I. F. Gun'kin

Technological Institute, Saratov State Technical University, Engels, Saratov oblast, Russia

Received May 11, 2001

Abstract—The use of fullerite as modifier of ED-20 epoxy–4,4'-isopropylidenediphenol oligomer cured with polyethylenepolyamine was considered. Interaction of fullerite with the polymer was evaluated. The effect of fullerite on combustion and heat resistance of the epoxy compound and on formation of the three-dimensional network structure was determined.

Fullerenes as a new form of elemental carbon attract a particular researchers' interest. Fullerenes are highly symmetrical carbon clusters in which the carbon atoms are arranged in the vertices of regular penta- and hexagons on the sphere surface.

Fullerite was prepared as described in [1]. Fullerenes C_{60} and C_{70} were recovered from carbon black by extraction with toluene. Usually this procedure yields a dark brown solution; after distillation of toluene under argon, a mixture containing 85% C_{60}, 14% C_{70}, and 1% higher fullerenes (fullerite) is obtained. To separate low-molecular-weight and cumulene structures, fullerite was washed with CCl_4 and ether. After repeated washing with these solvents, the solid extract contained 99% C_{60} + C_{70} in the ratio $C_{60} : C_{70}$ = 84 : 15. This was confirmed by chromatography–mass spectrometry.

Despite major attention given to fullerenes and fullerene-containing materials, interaction of fullerenes with polymers was studied considerably less extensively.

To evaluate interaction of fullerite with polymers, it was added to ED-20 epoxy–4,4'-isopropylidenediphenol oligomer curable with polyethylenepolyamine (PEPA).

It is known that fullerene is an acceptor and reacts with nucleophilic agents [2]. The PEPA molecule contains an NH_2 group via which it bind with the C_{60} molecule. Such binding was confirmed by IR spectroscopy.

The IR spectra were recorded on a Specord M80 spectrophotometer in the range 400 – 4000 cm^{-1}. The IR spectra of the fullerite-containing epoxy compounds exhibit absorption assignable to C_{60} and to ED-20 + PEPA compound. The C_{60} molecule has four IR absorption bands: 528, 576, 1180, and 1428 cm^{-1}. In the spectra of the compound, the band at 1428 cm^{-1} disappears, and the bands at 528, 576, and 1180 cm^{-1} decrease in intensity. Furthermore, absorption bands appear in the range 1380–1248 cm^{-1}. These bands can be assigned to vibrations of the C–N bond formed between the C_{60} molecule and the NH_2 group of PEPA. The reaction apparently follows the scheme

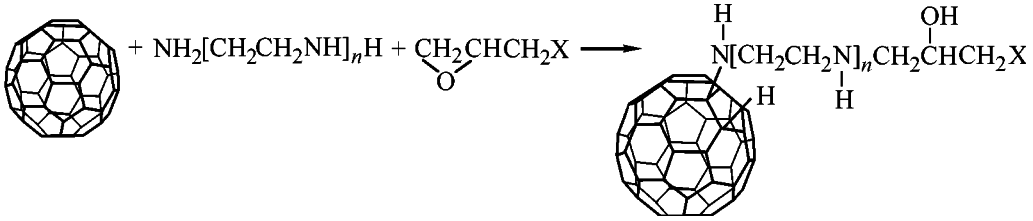

where X = [—O—C$_6$H$_4$—C(CH$_3$)$_2$—C$_6$H$_4$—O—CH$_2$—CH(OH)—CH$_2$—]$_n$—O—C$_6$H$_4$—C(CH$_3$)$_2$—C$_6$H$_4$—O—CH$_2$—CH(O)—CH$_2$·

1070-4272/01/7501-0135$27.00 © 2002 MAIK "Nauka/Interperiodica"

TGA data for ED-20 + 10 PEPA + additive (wt %) compounds*

Additive, wt %	Main degradation stage		Weight loss, %, at indicated temperature, °C				
	T_o–T_e/T_{max} [°C]	CR_o–CR_e/CR_{max} [%]	200	300	400	500	600
None	220–350/300	90–60/72.5	7	27.5	45	64	94
30 FOM-2	140–350/250	99–59.5/87.5	5	30	46	62	74
30 TCEP	150–350/210	99–49/86	5	30	46	62	74
			10	43	54	66	84
40 TCEP	150–310/240	98–50/77	15	46	56	68	85
50 TCEP	150–290/210	95–45/73	15	45	57	66	82
10 F	200–340/290	96–66/80	5	20	41	57	80
10 F + 30 FOM-2	180–320/260	96–64/78.5	5	31	47	65	87
10 F + 30 TCEP	200–330/250	90.5–57/78	9	36	48	63	85
10 F + 40 TCEP	220–330/260	99–58/71	13	43	52	64	83
10 F + 50 TCEP	220–330/240	98.5–53/72	17	45	53	64	85

* (F) Fullerite; (T_o, T_e, T_{max}) temperatures of the onset, end, and maximal rate of weight loss; (CR_o, CR_e, CR_{max}) yields of the carbonized residue at T_o, T_e, and T_{max}.

The thermal behavior of the compound was studied by TGA on an MOM Q-1500D derivatograph (Hungary). Samples (0.2 g) were heated in air from 20 to 1000°C at a constant rate of 10 deg min^{-1}. The sensitivity was 1/3 for DTA and 1/10 for DTG. The measurement accuracy was 0.1%. Addition of fullerite to the epoxy compound, according to TGA, decreases the thermolysis onset temperature by 20°C, increases the yield of the carbonized residue after completion of the main degradation stage, and shifts the weight loss maximu toward higher temperatures (see table; Fig. 1a, curve *6*).

One of the major problems of polymer science is enhancement of the fire and heat resistance of polymeric materials. In [3, 4] it is suggested to use for this purpose fullerenes and related compounds. However, their effect is significant only at a high degree of filling. Introduction of more than 10 wt % fullerite is impossible because of the high viscosity of the formulation and nonuniform filler distribution. Therefore, fullerite was added to the epoxy–4,4'-isopropylidenediphenol oligomer together with compounds decreasing simultaneously the viscosity and combustibility: β-trichloroethyl phosphate $(ClCH_2CH_2O)_3PO$ (TCEP) or the product of reaction of methylphosphonic dichloride with glycidyl methacrylate $[CH_2=C(CH_3)\cdot C(O)OCH_2–CH(CH_2Cl)O]_2P(O)CH_3$ (FOM-2). These compounds were added at simple mechanical stirring

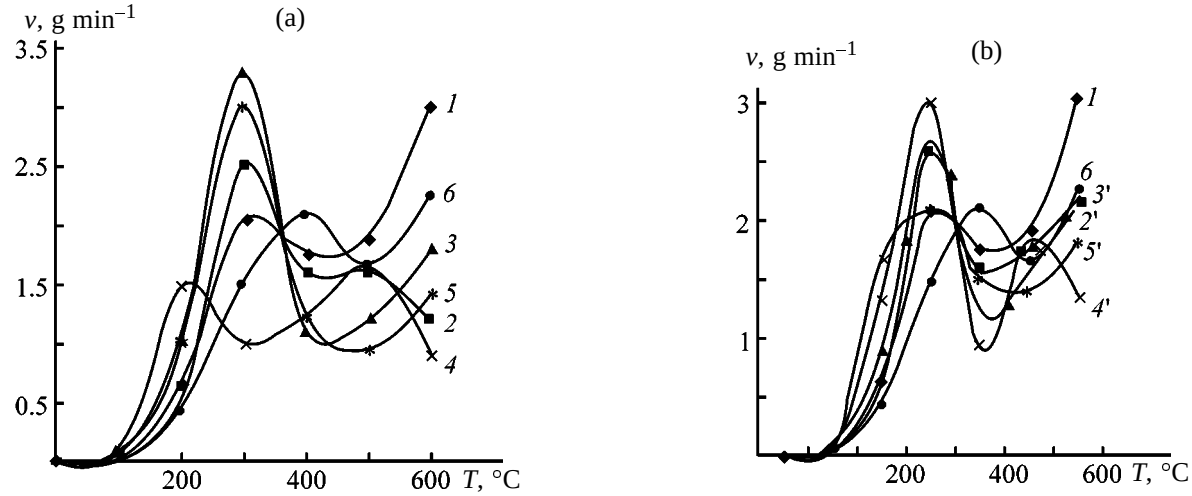

Fig. 1. Rate of weight loss v of compounds based on ED-20 + 10% PEPA with various additives. (a) Additives taken separately and (b) additives in combination with fullerite. (*T*) Temperature. Additive, %: (*1*) none, (*2*) 30 FOM-2, (*3*) 30 TCEP, (*4*) 40 TCEP, (*5*) 50 TCEP, and (*6*) 10 F; (*2'*–*5'*) the same as (*2*–*5*) but with addition of 10 F.

in amounts of 10, 15, 30, 40, and 50 wt %. Addition of only FOM-2 or TCEP decreases the onset temperature of thermal oxidative degradation, increases the rate of the weight loss (Fig. 1a, curves *2*–*5*), and decreases the yield of the carbonized residue after completion of the main stage. However, the oxygen index [GOST (State Standard) 12.1.044–89] characterizing the inflammability of the material increases from 19.8 to 24–25 vol %. This means that the combustion inhibitors present in TCEP and FOM-2 (P and Cl) affect mainly the gas-phase physicochemical transformations of the polymer.

According to TGA data for formulations containing TCEP and fullerite, the additives increase the degradation onset temperature and the yield of the carbonized residue (see table) and decrease the weight loss rate (Fig. 1b) after completion of the main degradation stage, as compared to the formulations containing TCEP only (Fig. 1a).

To evaluate the effect of components on formation of the three-dimensional network structure in the course of curing of the epoxy oligomer, we analyzed the kinetics of heat release. Curing of the epoxy oligomer with PEPA is exothermic (Fig. 2, curve *1*), the gelation time is 35–40 min, and the maximal temperature is 122°C. Modifiers decrease the maximal self-heating temperature from 120 to 27°C, and, with fullerite added, even to 21°C, which also confirms the chemical reaction of the additives with the epoxy oligomer and curing agent. The degree of conversion increases from 86 to 88%. The materials containing fullerite have a lower density (1181 kg m^{-3}) as compared to the initial materials (1562 kg m^{-3}).

CONCLUSIONS

The NH_2 groups of the curing agent react chemically with the C_{60} molecules. Fullerite alters the degradation mechanism of the polymeric matrix, enhancing its heat resistance, increasing the yield of the carbonized residue, and decreasing the combustibility. Fullerite affects formation of the three-dimensional network structure in the course of curing, decreasing the maximal temperature of the process from 120 to 21°C.

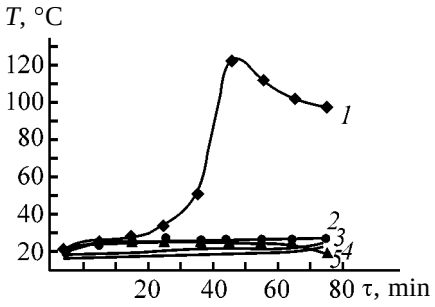

Fig. 2. Kinetic curves of curing of compounds based on ED-20 + 10% PEPA with various additives. (*T*) Temperature and (τ) time. Additive, %: (*1*) none, (*2*) 30 FOM-2, (*3*) 10 F + 30 FOM-2, (*4*) 10 F + 30 TCEP, and (*5*) 30 TCEP.

REFERENCES

1. Bubnov, V.P., Krainskii, I.S., Laukhina, E.E., and Yagubskii, E.B., *Izv. Ross. Akad. Nauk, Ser. Khim.*, 1994, no. 5, pp. 805–809.
4. Vol'pin, M.E., Parnes, Z.N., and Romanova, V.S., *Izv. Ross. Akad. Nauk, Ser. Khim.*, 1998, no. 5, pp. 1050–1054.
3. Shibaev, L.A., Antonova, T.A., Vinogradova, L.V., *et al.*, *Zh. Prikl. Khim.*, 1998, vol. 71, no. 5, pp. 835–842.
4. Sirotkin, N.V., Yatsenko, S.V., Somov, V.I., *et al.*, *Zh. Prikl. Khim.*, 2000, vol. 73, no. 10, pp. 1709–1712.

Russian Journal of Applied Chemistry, Vol. 75, No. 1, 2002, pp. 138–141. Translated from Zhurnal Prikladnoi Khimii, Vol. 75, No. 1, 2002, pp. 138–141.
Original Russian Text Copyright © 2002 by Starokadomskii, Solov'eva.

MACROMOLECULAR CHEMISTRY AND POLYMERIC MATERIALS

Effect of Silicon Oxide Fillers on Photochemical Curing of Compounds Based on Acrylic Monomers and Oligomers

D. L. Starokadomskii and T. N. Solov'eva

Institute of Surface Chemistry, National Academy of Sciences of Ukraine, Kiev, Ukraine

Received February 22, 2001

Abstract—The course of curing of photocurable compounds was studied as influenced by filling with disperse silicon oxide substances. The effect of the filler concentration on the conversion and rate of photopolymerization was examined.

The effect of inorganic fillers on polymerization attracts steady interest of researchers working in the field of development of new polymers. At the same time, photoinitiated polymerization of compounds filled with silicon oxide fillers is studied insufficiently, despite wide use of these materials in stomatology [1, 2]. By now, the number of publications concerning cationic, thermal, or radiation polymerization [3–9] considerably exceeds the number of papers on the effect of inorganic fillers on photoinitiated polymerization [10, 11–13]. Therefore, obtaining new data on the effect of fillers on photopolymerization (PP) is an urgent problem.

Addition of silicon oxide fillers transforms a compound into a colloidal disperse system with specific light scattering, reflection, refraction, and absorption properties. For example, the size of primary silica particles (10–50 nm) is smaller than the light wavelength, whereas the sizes of their aggregates (up to 300 nm [14]) and agglomerates (more than 1 μm [14]), and also the particle sizes of macrofillers (dispersed quartz, glass) are comparable to, or exceed the UV wavelength.

When studying photocurable polymers filled with the systems Aerosil–quartz, Aerosil–glass, Aerosil–Aerosil, and glass–quartz (to be used in production of stomatological materials), we found that the curing of compounds filled with silicon-containing fillers conforms to the generally accepted views on layer-by-layer PP of liquid unfilled compounds, described and theoretically substantiated in [15].

EXPERIMENTAL

The formulations contained the following components (chemically pure grade) in various ratios: bisphenol A glycidyl methacrylate (bis-GMA), oligomer of α,ω-bis(methacryloyloxyethyleneoxycarbonyloxy)-ethyleneoxyethylene (OCM-2), triethylene glycol dimethacrylate (TGM-3), methacrylic acid, and photoinitiator, benzil dimethyl ketal (BDK, λ_{max} = 340 nm, 0.3 wt %). The content of the monomer–oligomer base (matrix) was 30–85%, and that of the filler (Aerosil, Aerosil + dispersed glass + quartz), 15–70 wt %.

Aerosils A-175, A-300, and DK-100 [GOST (State Standard) 14922–77, TU (Technical Specifications) 6-18–78, Kalush Plant, Ukraine] were used; their specific surface area was 175, 300, and 100 $m^2 g^{-1}$, respectively (±30). Modification of Aerosils with methylvinyldichlorosilane was performed in the gas phase at 200–300°C for 2 h (1 h evacuation and 1 h reaction), with subsequent evacuation at 100–200°C for 1 h.

The degree of conversion α (measured as the percent ratio of the number of converted double bonds to their initial number) of compounds filled to less than 20 wt % was determined by IR spectroscopy. The decrease in the intensity of the band at 1635 cm^{-1} belonging to the vinyl groups of the oligomers was monitored. The degree of conversion of highly filled (>20 wt %) composites was measured by IR MATIR at 1635 cm^{-1} using a UR-20 device with a KRS-5 prism. The photopolymerization rate was determined from the slope of the curve of conversion α vs. irradiation time τ. The curing of highly filled composites was considered to be limiting if on further irradiation the intensity of the monitored absorption band and the strength of the cured photopolymer remained constant within measurement error. The enthalpy of polymerization was determined with a UIK-2101 microcalorimeter in a vacuum at 20°C. Sensitometric measure-

1070-4272/01/7501-0138$27.00 © 2002 MAIK "Nauka/Interperiodica"

ments were performed in UV-transparent (glass) or black (rubber, polyethylene) tubes of various heights (5–20 mm) and diameters (5–10 mm); curing of filled (thick) compounds in some experiments was performed in the open form. Curing was effected by UV irradiation from a Sakura photopolymerizing device (λ 340–500 nm).

Experiments show some differences in the photocuring of liquid unfilled monomeric formulations and their highly filled analogs.

Qualitative study of the effect of filling on photocuring of compounds revealed the following fact: On the whole, the curing of filled compounds occurs in the layer-by-layer fashion, which is consistent with the concept presented in [15], i.e., in a certain time after the start of irradiation a PP front (a boundary between the cured and liquid uncured mass) is formed, gradually moving into the depth of the compound.

In photopolymerization in transparent tubes and in the open form, the curing front moves in the perpendicular direction from the surface to the bulk of the material, until the whole volume is polymerized. However, a certain area in the bulk of the material can remain nonpolymerized (NPA), if the irradiation time is insufficient or the height and diameter of the sample are too large. As a result, when the sample is irradiated from all the sides, a cakelike structure is formed, with the outer well-cured "crust" and inner NPA. With a mirror support, curing occurs from the rear side also, whereas with a black support NPA outcrops to the rear surface of the sample.

When curing is performed in black tubes, i.e., when the light penetrates only through the upper surface of the sample, the upper polymerized layer is formed. However, in unfilled and filled samples the polymerized areas significantly differ in shape: In filled samples the cured area is a trunkated cone immersed in the nonpolymerized mass and narrowing in the direction from the surface to the bulk; in unfilled samples the conicity is manifested very weakly (e.g., in OCM-2 + 0.6 wt % BDK) or is not manifested at all (e.g., in bis-GMA + 0.6 wt % BDK), and the cured area only weakly differs from a cylinder.

The conical shape of the filled samples cured in black tubes may be due to absorption by black tube walls of the light escaping from the sample (primarily scattered light, and also reflected and refracted light). As a result, in the near-wall areas there is a deficiency of light, and no polymerization occurs. Furthermore, the polymerized area narrowing in the direction to the bulk will act as a lens promoting further narrowing of the cone. In unfilled compounds there is virtually no light scattering, and the conicity is not manifested to a significant extent.

Each photopolymer is characterized by a certain limiting curing thickness h_{lim} attained at a certain limiting irradiation time τ_{lim}; at $\tau > \tau_{lim}$, the thickness of the cured area does not increase further.

For example, in curing in transparent tubes, unfilled compounds OCM-2 + BDK and bis-GMA + DBK are cured to a depth of 15 mm within 30 s. We could not determine for the unfilled compounds the limiting thickness and limiting time; they exceed 20 mm and 45 min, respectively. Addition of 15 wt % Aerosil A-300 to these compounds makes h_{lim} measurable: 5 mm for OCM-2 + BDK and 3 mm for bis-GMA + BDK (τ_{lim} 20 min). Upon further irradiation, this thickness did not change. This example shows that addition of a filler causes a sharp decrease in h_{lim} and a noticeable increase in the time required to cure a layer of a given thickness. In curing filled samples (height >3 mm, diameter >5 mm) in transparent tubes or in the open form, a nonpolymerized area remains, which cannot be eliminated upon longer irradiation ($\tau > \tau_{lim}$).

A sharp decrease in h_{lim} (or increase in the time required for curing of a layer of a given thickness) after filling is due to the fact that in high concentrations (>15 wt %) the filler significantly shields the active radiation and acts as a light filter (absorption, reflection, and refraction effects).

The parameters h_{lim}, τ_{lim}, and the conicity angle are convenient characteristic parameters of individual filled photopolymeric composites.

Note that, when a sample is colored with dark pigments (umber, black iron oxide pigment, 0.01–0.1 wt %), the internal NPA increases as the content of the dark filler is increased, until an uncured vein cropping out at the rear surface is formed; correspondingly decreases the thickness of the completely cured layer.

The optical properties of a filled composite as a colloidal disperse system significantly affect the photocuring intensity [11]. At a 10–12 wt % content of Aerosil A-175, the parameter α considerably decreases as compared to the unfilled formulation (Fig. 1). This effect, as regards PP rate, has already been described [4] for radical (probably thermoinitiated) polymerization. However, as the filler concentration is increased further, α decreases. The same is true for Aerosil modified with methylvinyldichlorosilane, except that at any concentration with modified A-175

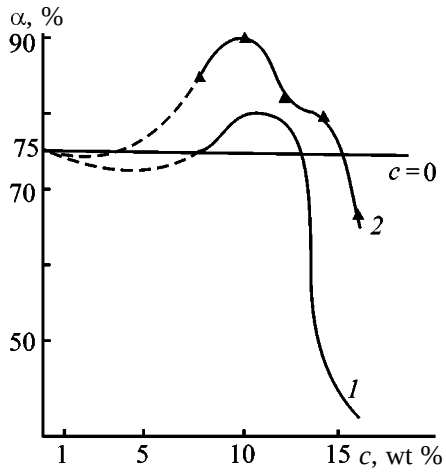

Fig. 1. Degree of photopolymerization (conversion) α as a function of concentration *c* of Aerosil A-175: (*1*) nonmodified and (*2*) modified with methylvinyldichlorosilane.

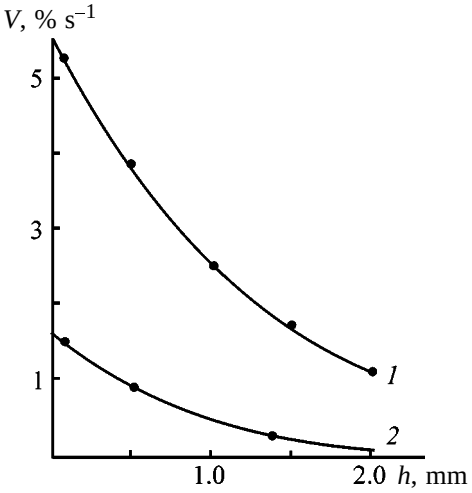

Fig. 2. Photopolymerization rate *V* as a function of the layer thickness *h* for (*1*) filled and (*2*) unfilled compounds.

α is higher than with the nonmodified Aerosil (Fig. 1, curve *2* lies above curve *1*).

Figure 2 shows that, as the filler concentration is increased, the deactivating effect of the layer thickness grows. As seen from Fig. 2, for an unfilled compound (composition, wt %: 55.4 OCM-2, 34 OUA2000T, 10 methacrylic acid, and 0.6 BDK) the photopolymerization rate V_0 (curve *1*) considerably exceeds *V* for the filled compound (25 wt % Aerosil DK-100 modified with methylvinyldichlorosilane; curve *2*). The V_0/V ratio increases with increasing *h*, i.e., from the surface to the depth of the compound. For example, at $h = 0.2$ mm $V_0/V = 3.5$, at $h = 2$ mm $V_0/V = 9$, and at larger *h* this ratio steadily grows. Thus, for the filled compound, as compared to the unfilled formulation, the photopolymerization rate in going from the surface to the depth of the compound decreases to a considerably greater extent.

The enthalpy of polymerization *H* of the compound 99.4 wt % OCM-2 + 0.6 wt % BDK at various concentrations of the filler (Aerosil A-175) is given below [data for the nonmodified and modified (with methylvinyldichlorosilane) Aerosil are given in the numerator and denominator, respectively]:

c, wt %	0	10	12	14	16
H, J g^{-1}	246.6 / 246.6	260.0 / 320.1	269.7 / 343.5	245.0 / 302.0	181.3 / 292.8

It is seen that filling to 10–12 wt % increases the enthalpy of photopolymerization. After modification, it increases by 20–30% at moderate fillings (up to 14 wt %) and to a still greater extent, at higher fillings. This fact suggests that grafted modifier molecules actively participate in photopolymerization, promoting the process.

The effect of Aerosil on the curing quality can be explained as follows. More complete curing after adding certain amounts of Aerosil (10–12 wt % in our case) is due to the fact that the light scattering, reflection, and refraction on particles of the disperse phase (Aerosil and its aggregates, quartz, etc.) become more active, enhancing the light intensity in the bulk of the compound; to cross-linking of the polymeric base [4] and increase in the viscosity; to immobilization by the silica surface of oligomer molecules and growing polymer chains, which increases their lifetime [6, 15, 16]; and to increase in the content of conformations favorable for polymerization [15].

Promotion of polymerization processes after modification with vinylsilane is due to replacement of the surface hydroxy groups of silica by organophilic groups, which activates immobilization processes and favors participation of grafted modifier molecules in photopolymerization [17]. Another significant factor is decrease in the amount of water physically adsorbed on the silica surface and negatively affecting the polymerization activity of the system [18]. Apparently, in the course of photopolymerization water adsorbed on the surface of silica particles acts as impurity ("process") water. Obviously, surface water also prevents compatibility of the phases. Therefore, hydrophobization of silica by chemical modification favors PP.

As the silica concentration is gradually increased (in our case, above 12 wt %), it starts to hinder photopolymerization, which is due to significant enhancement of the filtering (shielding) effect of the cured

layer, to the cage effect (sticking of active species in a cage of polymer chains and increase in the steric hindrance), to deactivation of primary radicals at the filler surface, and to the loss of the molecular mobility as a result of stronger physical interactions with the solid surface and between the macromolecules [4].

CONCLUSIONS

(1) Curing of oligoether compounds after filling with disperse silicon oxide substances, similar to that of unfilled compounds, occurs in the layer-by-layer fashion, with increased deactivating effect of the compound layer on the polymerization activity in the bulk.

(2) Curing of filled compounds in black tubes (illumination from the top) yields a polymer layer in the form of a cone narrowing to the depth; unfilled compounds of similar composition show practically no conicity of the polymer phase.

(3) When filled compounds are cured with illumination from the sides, a nonpolymerized area can remain, which can crop out at the rear surface; the nonpolymerized area is larger in pigmented samples.

(4) The limiting curing thickness h_{lim}, limiting curing time τ_{lim}, and conicity angle are convenient characteristic parameters of individual filled photopolymeric composites.

ACKNOWLEDGMENTS

The study was financially supported by Oksomat AN Research and Production Association. Calorimetric analysis and measurement of a part of IR spectra were performed by staffmembers of the Institute of Macromolecular Chemistry, National Academy of Sciences of Ukraine, under the guidance of G.M. Semenovich.

REFERENCES

1. Ugoleva, S., *Nov. Stomatol.*, 1995, no. 1(31), pp. 11–18.
2. Makeev, V.F. and Starokadomskii, D.L., *Nov. Stomatol.* (Ukraine), 1996, no. 1(6), pp. 40–44.
3. Menzheres, G.Ya., Simonenko, V.V., Chaiko, A.K., *et al.*, *Kompoz. Polim. Mater.*, 1989, no. 41, pp. 58–61.
4. Lipatova, T.E., *Kataliticheskaya polimerizatsiya oligomerov i formirovanie polimernykh setok* (Catalytic Polymerization of Oligomers and Formation of Polymer Networks), Kiev: Naukova Dumka, 1974.
5. Lipatov, Yu.S., *Fiziko-khimicheskie svoistva i osnovy napolneniya polimerov* (Physicochemical Properties and Principles of Polymer Filling), Moscow: Khimiya, 1991.
6. Mund, S.L., Bruk, M.A., and Abkin, A.D., *Vysokomol. Soedin., Ser. A*, 1976, vol. 18, no. 12, pp. 2631–2638.
7. Sidorenko, A., Minko, S., Meuser, K.S., *et al.*, *Langmuir*, 1999, vol. 15, pp. 8349–8355.
8. Aslamazova, T.R., Morozova, E.M., and Eliseeva, V.I., *Kompoz. Polim. Mater.*, 1985, no. 24, pp. 61–65.
9. Paeglitis, D.O. and Zoldners, Yu.A., *Kompoz. Polim. Mater.*, 1984, no. 23, pp. 40–45.
10. Grishchenko, V.K., Maslyuk, A.F., and Gudzera, S.S., *Zhidkie fotopolimerizuyushchiesya kompozitsii* (Liquid Photopolymerizable Compounds), Kiev: Naukova Dumka, 1985.
11. Starokadomskii, D.L. and Solov'eva, T.N., *Zh. Prikl. Spektrosk.*, 1999, vol. 66, no. 1, pp. 119–124.
12. Zubov, V.P., Andrianov, A.K., Olenin, A.V., *et al.*, Abstracts of Papers, *5-ya Respublikanskaya konferentsiya po vysokomolekulyarnym soedineniyam* (5th Republican Conf. on Macromolecular Compounds), Kiev, 1984, p. 207.
13. Zubov, V.P., Stepanyan, A.O., and Olenin, A.V., *5-ya Respublikanskaya konferentsiya po vysokomolekulyarnym soedineniyam* (5th Republican Conf. on Macromolecular Compounds), Kiev, 1984, p. 208.
14. *Khimiya poverkhnosti kremnezema* (Chemistry of Silica Surface), Chuiko, A.A., Ed., Kiev: Naukova Dumka, 2001, part 2.
15. Maslyuk, A.F. and Khranovskii, V.A., *Fotokhimiya polimerizatsionnosposobnykh oligomerov* (Photochemistry of Polymerizable Oligomers), Kiev: Naukova Dumka, 1989.
16. *Akrilovye oligomery i materialy na ikh osnove* (Acrylic Oligomers and Materials Based on Them), Berlin, A.A., Korolev, G.V., Kefeli, T.Ya., *et al.*, Moscow: Khimiya, 1983.
17. Solomko, V.P., *Napolnennye kristallizuyushchiesya polimery* (Filled Crystallizing Polymers), Kiev: Naukova Dumka, 1980.
18. El'tsov, A.V., *Svetochuvstvitel'nye polimernye materialy* (Photosensitive Polymeric Materials), Leningrad: Khimiya, 1976.

Russian Journal of Applied Chemistry, Vol. 75, No. 1, 2002, pp. 142–145. Translated from Zhurnal Prikladnoi Khimii, Vol. 75, No. 1, 2002, pp. 142–145.
Original Russian Text Copyright © 2002 by Sokolov, Voznyakovskii.

MACROMOLECULAR CHEMISTRY AND POLYMERIC MATERIALS

Distribution of Perfluoro(propyl Vinyl Ether) between the Latex Based on Tetrafluoroethylene Copolymer and the Gas Phase

Yu. P. Sokolov and A. P. Voznyakovskii

Lebedev Research Institute of Synthetic Rubber, St. Petersburg, Russia

Received June 20, 2000; in final form, September 2001

Abstract—The distribution factors of perfluoro(propyl vinyl ether) between the tetrafluoroethylene–perfluoro(propyl vinyl ether) copolymer and the gas phase in the temperature range 20–60°C were determined by gas chromatography. From the temperature dependence of the distribution factors, the integral heats of melting and vaporization and the partial molar excess enthalpy of solution of perfluoro(propyl vinyl ether) were calculated.

Despite numerous studies, determination of the solubility of monomers and polymers and the closely related problem of determination of residual monomers in latexes remain urgent. Data on the influence of temperature, pressure, and other factors on the solubility of monomers in polymers are important for mathematical description of polymerization and calculation of its kinetics. The content of residual monomers dissolved in latexes largely determines the industrial and environmental safety of polymer production by emulsion polymerization.

The procedures used to determine the solubility of monomers in polymers, as a rule, require either time-consuming sample preparation or the use of sophisticated and difficultly available equipment, which prevents their wide use in industry. As example we can mention a gas-chromatographic procedure [1] in which a polymer being tested is used as a stationary phase. This method allows calculation of the distribution factors of the monomers between the liquid and gas phases and of a number of thermodynamic parameters, but application of the polymer to a chromatographic support takes several days. A headspace analysis procedure was also described [2], allowing calculation of the content of volatile substances in the liquid and gas phases and of the distribution factor from the composition of the equilibrium gas phase, using a special attachment to a chromatograph.

Development of a procedure for determination of residual monomers in latexes that would not require sophisticated and difficultly available equipment, on the one hand, and would allow sampling directly from the polymerization reactor, on the other hand, will be very useful for both researchers and technologists.

Calculation of the distribution factors of volatile monomers between the liquid and gas phases in relation to temperature allows determination of the content of residual monomers in the latex and calculation of the monomer conversion from the concentration of the monomer vapor in the equilibrium gas phase over the latex.

The goal of this work was to determine the distribution factors of perfluoro(propyl vinyl ether) (PPVE) between the latex based on perfluorinated tetrafluoroethylene and PPVE (trade name Ftorelast A-2400) and the gas phase at various temperatures.

EXPERIMENTAL

Ftorelast A-2400, a copolymer exhibiting high resistance to high temperatures, corrosive media, and frost, was prepared by emulsion copolymerization of tetrafluoroethylene and PPVE. According to ^{19}F NMR, the copolymer contained 59 mol % tetrafluoroethylene units and 41 mol % PPVE units.

The copolymer content in the latex was 250 g l^{-1}. To determine the copolymer content, a 5–10-g latex sample was taken and vacuum-dried at 60°C to constant weight. The copolymer content in the latex was calculated taking into account the weight of the emulsifier in the sample.

To remove traces of PPVE from the latex, it was purged with argon at 60°C for 1 h, with addition of distilled water to compensate for its evaporation. The completeness of PPVE removal from the latex was checked by GLC. A 10-μl latex sample was taken with a Hamilton microsyringe and introduced into the

1070-4272/01/7501-0142$27.00 © 2002 MAIK "Nauka/Interperiodica"

chromatograph vaporizer heated to 300°C.[1] The chromatographing conditions are given below.

The distribution of PPVE between the Ftorelast A-2400 latex and the gas phase was studied with a setup described in Fig. 1. A preliminarily evacuated 250-ml autoclave *1* equipped with a stirrer, a manometer, and a temperature-control jacket was charged with 150 ml of Ftorelast A-2400 latex and evacuated for 5 min at ambient temperature to remove air. Then a definite amount of PPVE was introduced through the upper valve, the required temperature was adjusted, and the autoclave was stirred with intermittent determination of the PPVE vapor content in the gas phase by the following procedure.

To the upper valve of the autoclave, we connected a 20-ml glass vessel *2*, preliminarily evacuated and kept at the same temperature. The upper valve was opened for 3–5 s, and a sample of the gas phase was taken. Then the valve was closed, vessel *2* was connected to an evacuated vessel *3*, and vessel *3* was filled with the carrier gas (helium) to excess pressure of 100 mm Hg, after which the gas mixture was introduced into a chromatograph through a gas dosing cock.

The PPVE vapor content in the gas phase in the course of stirring started to gradually decrease and reached a constant value within 30–40 min. Probably, within this time the introduced PPVE fully dissolved in the latex, and the PPVE concentration in latex particles became equal throughout their volume.

For calibration, vessel *2* was filled with air under normal conditions (273 K, 101.3 Pa), and the air peak area was determined by a similar procedure.

Chromatographing conditions: LKhM-80 gas chromatograph; carrier gas helium; flow rate 20 ml min^{-1}; catharometer; bridge current 100 mA; 1000 × 4-mm column; sorbent Polysorb-1 (a styrene–divinylbenzene copolymer, analog of Porapak Q), grain size 0.25–0.315 mm; column temperature 100°C; detector temperature 150°C. The peak area was determined with an I-02 electronic integrator.

The PPVE vapor concentration in the gas phase was calculated by the formula

$$C_{PPVE} = (S_{PPVE}/S_{air})K_{cor}C_{air}, \quad (1)$$

where S_{PPVE} is the PPVE peak area, S_{air} is the air peak area under normal conditions, K_{cor} is the molar correction coefficient (0.35 for PPVE [3]; taken as 1.00 for air), and C_{air} is the amount of air (moles) in 1000 cm^3 under normal conditions.

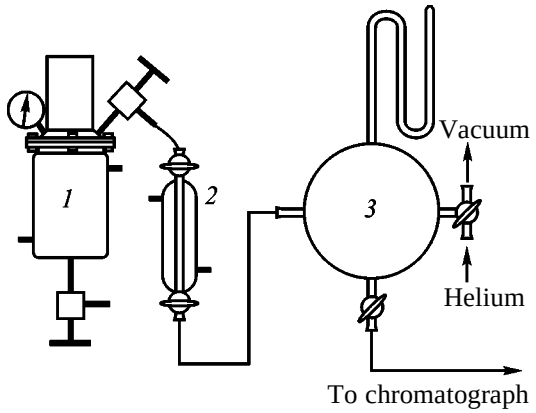

Fig. 1. Setup for analysis of gas–liquid samples under pressure: (*1*) stainless steel autoclave equipped with a stirrer with a packless gear, a manometer, and a temperature-control jacket; (*2*) calibrated glass vessel with a temperature-control jacket; and (*3*) glass vessel equipped with a mercury manometer and a three-way stopcock.

The PPVE distribution coefficients were calculated by the formula

$$K_d = C_2/C_1, \quad (2)$$

The concentration of PPVE dissolved in the polymer was calculated by the formula

$$C_2 = N_{PPVE}\,d_{pol}/(C_{pol}\,V), \quad (3)$$

where N_{PPVE} is the amount of PPVE (moles) added to the latex; C_{pol} is the polymer concentration in the latex; V is the latex volume; d_{pol} is the polymer density (the density of Ftorelast A-2400, measured by known procedures, was 1.95 g cm^{-3}).

The results of measuring the concentration of PPVE vapor in the gas phase at various temperatures and PPVE concentrations in the latex are listed in the table. In view of low solubility of PPVE in water (less than 0.001 wt %, according to [4]), it can be assumed that the whole amount of PPVE in the liquid phase is dissolved in the copolymer. Therefore, the PPVE concentration in the liquid phase is calculated for the volume of the copolymer in the latex and not for the whole latex volume.

In the case of incomplete PPVE dissolution, its undissolved part will form a separate phase (drops and/or micelles). Then the PPVE concentration in the

[1] It should be noted that this method can be recommended only for semiquantitative analysis, since for determination of traces of residual monomers large samples should be introduced, lying beyond the linear range of the catharometer response.

Concentration of PPVE vapor in the gas phase at various temperatures and PPVE concentrations in the polymer phase C_2

T, K	PPVE vapor concentration, M, in the PPVE–latex system at indicated C_2, M				
	0.08	0.28	0.48	0.84	PPVE–water
293	0.0019	0.0084	0.0119	0.0204	0.0274
303	0.0024	0.0106	0.0144	0.0267	0.0328
313	0.0035	0.0136	0.0209	0.0353	0.0454
323	0.0058	0.0199	0.0332	0.0461	0.0614
333	0.0085	0.0229	0.0501	0.0671	–

gas phase will be primarily determined by the saturated vapor pressure of PPVE occurring in the system as a separate liquid phase. To check whether dissolution of PPVE in the copolymer contained in the latex is complete, we performed similar measurements of the PPVE vapor concentration in the gas phase over the PPVE–water system in which PPVE is present as a separate phase.

Data on the PPVE concentration in the gas phase over the system PPVE–water are listed in the table. According to Raoult's law, with increasing concentration of PPVE dissolved in the polymer the PPVE vapor pressure at the same temperature should asymptotically approach the vapor pressure over neat PPVE. As seen from the table, the concentrations of PPVE vapor in the gas phases over the systems PPVE–latex and PPVE–water under similar conditions differ considerably (at least by 30–40%), which suggests the absence of PPVE undissolved in the latex.

According to the classical Yurzhenko–Harkins theory of emulsion polymerization [5], the polymer is formed in polymer–monomer particles. The main part

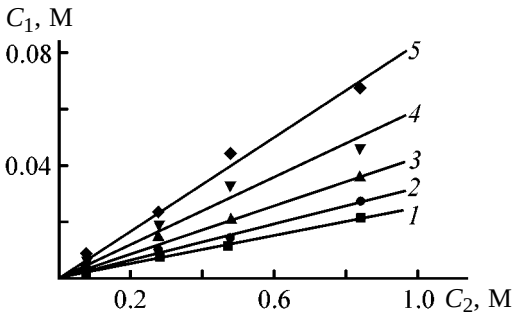

Fig. 2. PPVE concentration C_1 in the gas phase over the latex as a function of PPVE concentration C_2 in the polymer phase at various temperatures. Temperature, °C: (*1*) 20, (*2*) 30, (*3*) 40, (*4*) 50, and (*5*) 60.

of the monomer in the polymerizing system occurs as a separate phase (drops), from which it passes to polymer–monomer particles owing to diffusion. Hence, with intermittent analysis of the gas phase in the course of polymerization, it is possible to detect the beginning of the final stage of emulsion polymerization (disappearance of liquid monomer drops) as the moment at which the partial pressure of PPVE vapor starts to decrease.

With increasing temperature, the PPVE vapor concentration noticeably increases. Figure 2 shows the dependence of the PPVE vapor concentration in the gas phase on the concentration of PPVE solution in the copolymer at various temperatures. Statistical treatment of the data obtained showed that in the examined temperature and concentration range the dependence is described by Henry's law and is practically linear (the correlation coefficient in all cases is 0.965–0.995, relative deviation does not exceed 8%).

The distribution factors of PPVE between the polymer and gas phases are given below:

T, K	K_d
293	40.0 ± 1.5
303	31.3 ± 1.5
313	23.3 ± 1.5
323	16.9 ± 3.8
333	12.0 ± 3.6

To calculate the thermodynamic characteristics of distribution, let us pass from the distribution coefficient to the Henry constant, replacing the concentration ratio in Eq. (2) by the activity ratio

$$K = a_2/a_1 = C_2\gamma_2/(C_1\gamma_1), \quad (4)$$

where a_2 and a_1 are the activities, and γ_2 and γ_1 are the activity coefficients of PPVE in the corresponding phases. Let us take as the standard state for the gas phase the ideal gas at a pressure of 1.013×10^5 Pa and temperature of the system, and for the liquid phase, pure liquid PPVE (thus, the mole fraction $n_2 = 1$ and $\gamma_2 = 1$). Note that attainment of the equilibrium between the liquid and gas phases implies equal partial molar energies: $G_2 = G_1$. Taking into account that $G_1 = G_1^0 + RT\ln n_1$ and $G_2 = G_2^0 + RT\ln n_2$, where G_1^0 and G_2^0 are the energies in the gas and polymer zones, we obtain

$$\Delta G^0 = G_1^0 - C_2^0 = -RT\ln K. \quad (5)$$

The correlation between ΔG^0 and the enthalpy of

solution ΔH_s is given by

$$\Delta H_s/R = \mathrm{d}(\Delta G^0/T)/\mathrm{d}(1/T). \quad (6)$$

Combination of Eqs. (5) and (6) gives the final expression for calculating ΔH_s:

$$\Delta H_s/RT^2 = \mathrm{d}\ln K/\mathrm{d}T. \quad (7)$$

From the data in the table, using the dependences $\ln K = f(1/T)$ in the examined temperature and concentration range, we calculated the enthalpy of PPVE solution in Ftorelast A-2400 copolymer (ΔH_s = -24.6 ± 1.3 kJ mol^{-1}). From the dependence of the logarithm of the PPVE vapor concentration on $1/T$ for the system PPVE–water, we calculated the enthalpy of vaporization of PPVE (ΔH_v = -21.1 ± 1.2 kJ mol^{-1}), i.e., the dissolution of PPVE in the copolymer is exothermic.

It was interesting to determine the excess partial molar enthalpy of mixing. The quantity $\Delta H^{E\infty}$ was calculated by the equation $\Delta H^{E\infty} = \Delta H_s - \Delta H_v$ as -3.5 kJ mol^{-1}. The negative value of $\Delta H^{E\infty}$ shows that PPVE is a thermodynamically good solvent for Ftorelast A-2400.

CONCLUSIONS

(1) The distribution coefficients of perfluoro(propyl vinyl ether) between the latex of the tetrafluoroethylene–perfluoro(propyl vinyl ether) copolymer (Ftorelast A-2400) and the gas phase in the range 20–60°C were determined.

(2) From the temperature dependence of the distribution coefficients, the enthalpy of solution, enthalpy of vaporization, and excess partial molar enthalpy of solution of perfluoro(propyl vinyl ether) were calculated.

(3) Perfluoro(propyl vinyl ether) dissolves in Ftorelast A-2400 latex with heat release. Perfluoro(propyl vinyl ether) is a thermodynamically good solvent for Ftorelast A-2400.

(4) The suggested analytical procedure allows determination of residual monomers in the latex directly in the polymerization reactor, from the composition of the gas phase.

REFERENCES

1. Voznyakovskii, A.P., Genkin, A.N., Chechik, O.S., *et al.*, *Vysokomol. Soedin., Ser. A*, 1991, vol. 33, no. 6, pp. 1281–1288.
2. Stolyarov, B.V., Savinov, I.M., and Vitenberg, A.G., *Rukovodstvo k prakticheskim rabotam po gazovoi khromatografii* (Manual on Gas Chromatography), Leningrad: Khimiya, 1988.
3. Sokolov, Yu.P. and Konshin, A.I., *Zh. Prikl. Khim.*, 1990, vol. 63, no. 3, pp. 710–713.
4. Veretennikov, N.V., Reshetova, L.I., and Fil'chakova, T.I., *Vestn. Leningr. Gos. Univ.*, 1984, no. 4, pp. 112–114.
5. Yurzhenko, A.I. and Kolechkova, M., *Dokl. Akad. Nauk SSSR*, 1945, vol. 47, no. 5, pp. 354–356.

Russian Journal of Applied Chemistry, Vol. 75, No. 1, 2002, pp. 146–148. Translated from Zhurnal Prikladnoi Khimii, Vol. 75, No. 1, 2002, pp. 146–148.
Original Russian Text Copyright © 2002 by Novoselov, Sashina, Don'shina.

MACROMOLECULAR CHEMISTRY AND POLYMERIC MATERIALS

Effect of Aprotic Solvents on Intermolecular Interaction of Cellulose Macromolecule with *N*-Methylmorpholine *N*-Oxide Monohydrate

N. P. Novoselov, E. S. Sashina, and E. V. Don'shina

St. Petersburg State University of Technology and Design, St. Petersburg, Russia

Received April 10, 2001

Abstract—The influence of aprotic cosolvents dimethyl sulfoxide, dimethylformamide, and dimethylacetamide on interaction of *N*-methylmorpholine *N*-oxide with cellulose was studied.

Binary systems *N*-methylmorpholine *N*-oxide (NMMO)–cosolvent were suggested as cellulose solvents [1]. As cosolvents can be used organic liquids with the dipole moment no less than 3.5 D that, when taken separately, do not dissolve cellulose and do not react chemically with NMMO [2]. Cosolvents are added to decrease the solution viscosity and the consumption of expensive NMMO monohydrate. It is assumed [3] that the cosolvent behaves in the system as an inert component; however, our preliminary data [4] show that this is not the case.

EXPERIMENTAL

In this work we studied the effect of aprotic cosolvents dimethyl sulfoxide (DMSO), dimethylformamide (DMF), and dimethylacetamide (DMAA) (dipole moments 4.30, 3.86, and 3.80 D, respectively) on dissolution and phase separation of cellulose solutions in binary systems. In our studies we used NMMO monohydrate (mp 343–345 K) and chemically pure grade cosolvents.

Using a Calvet calorimeter equipped with a 100-ml calorimetric vessel, we measured the enthalpies of solution of cellulose in the binary systems at various ratios of the solvent components, and also the enthalpies of cellulose transfer from NMMO monohydrate into the mixed solvent (Table 1). It is seen that addition of 10–50% DMSO to NMMO monohydrate makes the cellulose dissolution more exothermic as compared to pure NMMO. In the presence of the two other tested cosolvents (DMF, DMAA), there is no noticeable increase in the exothermicity of the interaction with cellulose. The exothermicity passes through a maximum at the NMMO : DMSO ratio of 2 : 1. Presumably, at this component ratio the solvating power of the binary solvent increases [5].

Complexation in cellulose solutions in NMMO·H_2O–DMSO mixtures can be monitored by variation of the crystallization temperature of 7% cellulose solutions depending on the component ratio; this temperature was determined from the change in turbidity (light transmission coefficient at λ 540 nm), using a KFK-2MP photoelectric colorimeter and a 20-mm

Table 1. Enthalpies of solution ΔH_s and transfer ΔH_t of cellulose in binary systems NMMO·H_2O–aprotic solvent at 348 K

Cosolvent, wt %	$-\Delta H_s$	ΔH_t
	J g^{-1} cellulose	
DMSO:		
10.8	155.0	12.2
14.5	171.2	28.4
21.6	243.9	101.1
41.5	159.6	16.8
52.4	145.7	2.9
DMF:		
9.6	151.7	8.9
19.0	136.7	–6.1
47.2	136.4	–6.4
DMA:		
7.6	121.6	–21.2
20.5	134.7	–8.1
28.7	138.1	–3.7
48.3	137.1	–4.7

* (ΔH_t) Thermal effect in transfer of 1 g of cellulose from NMMO to the binary solvent.

1070-4272/01/7501-0146$27.00 © 2002 MAIK "Nauka/Interperiodica"

cell. As the crystallization onset temperature we took the temperature at which the light transmission of the sample gradually cooled from the initial temperature of 363 K abruptly decreases. As the DMSO content in the binary mixture is increased from 0 to 50 wt %, the crystallization onset temperature decreases from 333 to 310 K, but with further increase in the DMSO content the crystallization temperature starts to grow again, reaching 322 K. This value is attained at a DMSO content in the binary mixture of 67 wt %, which correlates with our data on the decrease in the system solvency [4]. In contrast to the system NMMO–DMSO–cellulose, in solutions of cellulose in $NMMO \cdot H_2O$–DMF and $NMMO \cdot H_2O$–DMA formation of crystallization centers is hindered. This is due to the tendency of these solutions to supercooling (the solutions do not crystallize for several hours at room temperature).

The effect of cosolvents on intermolecular interaction in cellulose solutions in NMMO can also be revealed by monitoring the phase separation of cellulose solutions in binary solvents. We studied the resistance of solutions to phase separation on adding water as a liquid that does not dissolve cellulose. The relative resistance to phase separation is proportional to the precipitation number PN and inversely proportional to the solvation number SN calculated as the molar ratio of the solvent and precipitant. To determine PN, we added the precipitant to the temperature-controlled cellulose solution, visually monitoring the solution transparency. After turbidization, corresponding to the onset of phase separation, we determined the precipitant consumption. The results are listed in Table 2.

Table 2. Precipitation (PN) and solvation (SN) numbers for 2% cellulose solutions in binary systems at precipitation with water

Cosolvent, wt %	*T*, K	PN, $\frac{\text{g precipitant}}{\text{g solution}}$	SN
–	358	0.15	0.87
DMSO:			
20	358	0.17	0.88
33	358	0.16	1.01
33	343	0.10	1.61
33	328	0.10	1.61
50	358	0.14	1.27
50	343	0.10	1.78
50	328	0.08	2.23
DMF:			
33	358	0.07	2.39
33	343	0.06	2.79
33	328	0.06	2.79
50	358	0.03	6.18
50	343	0.03	6.18
50	328	0.03	6.18
DMA:			
33	358	0.11	1.42
33	343	0.07	2.23
33	328	0.06	2.61
50	358	0.05	3.31
50	343	0.04	4.14
50	328	0.03	5.52

Table 2 shows that on adding DMSO to NMMO monohydrate the resistance to phase separation, proportional to the precipitation number, increases and starts to decrease only at a DMSO content in the solvent exceeding 50 wt %. This result correlates with the above-given data on the enthalpies of solution of cellulose in the binary mixtures. With decreasing temperature, the resistance of the system to phase separation decreases.

Knowing the features of phase transitions in cellulose solutions in $NMMO \cdot H_2O$ and binary mixtures is important for production of hydrated cellulose fibers by precipitation into an aqueous or aqueous-organic bath. The conditions of phase separation can be varied (to obtain cellulose particles of desired size) by adding into the precipitation bath a solvent or cosolvent. The nature and amount of the solvent in the precipitation bath determine the kinetics of cellulose coagulation, the resistance of the solution to the effect of the precipitant, and the "rigidity" of the precipitation conditions. Therefore, we studied the resistance of 2% solutions of cellulose in mixtures $NMMO \cdot H_2O$–aprotic solvent to the coagulating effect of a mixed precipitant, H_2O–NMMO. The results are shown in Figs. 1a–1c. The resistance of solutions to the coagulating effect of the precipitant was characterized by PN, determined as described above. Apparently, PN is the lower, and the precipitation conditions are the more rigorous, the less the precipitant consumption. Under rigorous precipitation conditions, cellulose readily coagulates from solution in the form of a flaky precipitate. Under milder conditions (PN $\geq$0.8), the precipitate becomes more finely dispersed, and precipitation is preceded by formation of a gelatinuous mass. At an $NMMO \cdot H_2O$ content in the precipitation bath above 60–65 wt %, a transition occurs from the rigorous to mild precipitation conditions, and the resistance of cellulose solutions to phase separation abruptly increases.

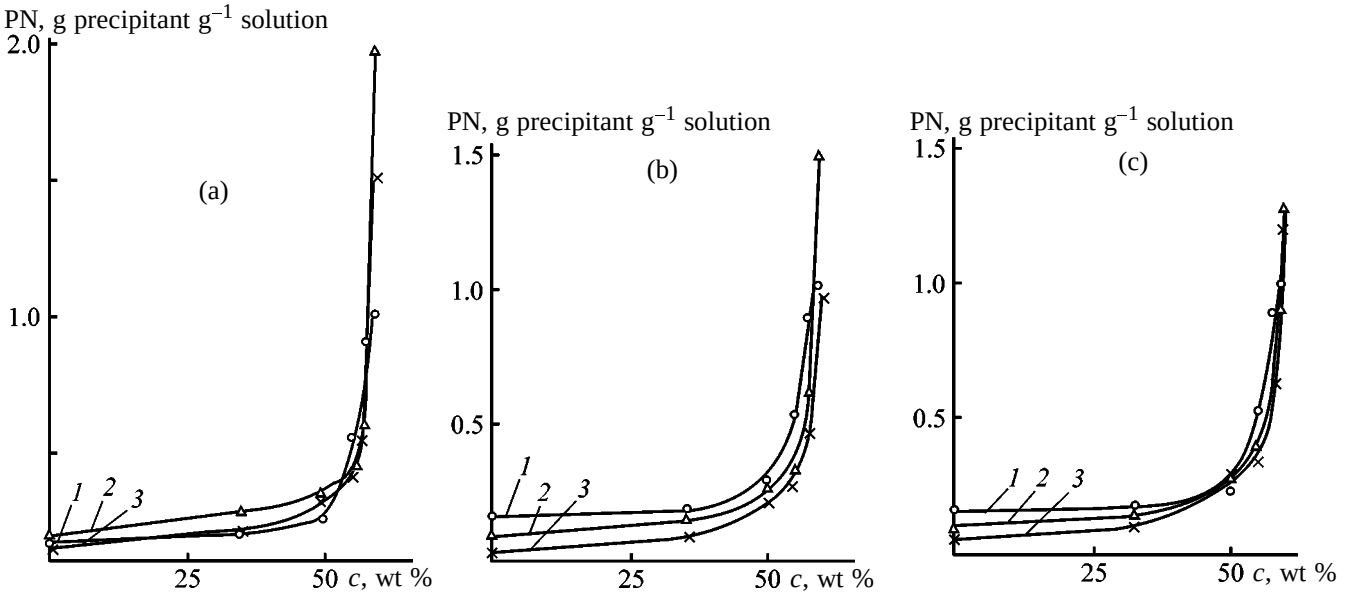

Fig. 1. Stability of 2% cellulose solutions in (*1*) NMMO monohydrate and in binary systems NMMO–cosolvent, (*2*) 2 : 1 and (*3*) 1 : 1, as a function of the NMMO content in the aqueous precipitation bath *c*. (PN) Precipitation number. Cosolvent: (a) DMSO, (b) DMF, and (c) DMA.

CONCLUSIONS

The tested aprotic cosolvents exert different effect on the intermolecular interaction in the binary system *N*-methylmorpholine *N*-oxide–cellulose. Addition of dimethyl sulfoxide makes the cellulose dissolution more exothermic, whereas with dimethylformamide and dimethylacetamide this trend is not observed. The presence of dimethylformamide and dimethylacetamide cosolvents in cellulose solutions decreases, and the presence of dimethyl sulfoxide increases the resistance of solutions to phase separation. Addition of *N*-methylmorpholine *N*-oxide to the aqueous precipitation bath enhances the resistance of cellulose solutions to phase separation.

REFERENCES

1. Humbert, H., Walker, M., Whitcombe, G., and Zimmerman, R., Abstracts of Papers, *2nd Int. Symp. "Alternative Cellulose—Herstellen, Verformen, Eigenschaften,"* Rudolstadt, September 2–4, 1996. pp. 32–37.
2. US Patent 4 196 282.
3. Berger, W., Kabrelian, V., and Keck, M., *Acta Polym.*, 1990, vol. 41, no. 2, pp. 81–86.
4. Novoselov, N.P. and Sashina, E.S., *Izv. Vyssh. Uchebn. Zaved., Khim. Khim. Tekhnol.*, 1999, vol. 42, no. 4, pp. 91–98.
5. Rozhkova, O.V., Myasoedova, V.V., and Krestov, G.A., *Khim. Drev.*, 1985, no. 2, pp. 26–31.

Russian Journal of Applied Chemistry, Vol. 75, No. 1, 2002, pp. 149–151. Translated from Zhurnal Prikladnoi Khimii, Vol. 75, No. 1, 2002, pp. 149–151.
Original Russian Text Copyright © 2002 by Dem'yantseva, Lysogorskaya, Klyubin, Zaitseva.

MACROMOLECULAR CHEMISTRY AND POLYMERIC MATERIALS

A Dynamic Light Scattering Study of the Temperature Dependence of the Size-Distribution Pattern and Aggregation Stability of Sulfate Lignin and Wood Resin in Aqueous Alkali Solution

E. Yu. Dem'yantseva, N. P. Lysogorskaya, V. V. Klyubin, and S. V. Zaitseva

St. Petersburg State Technological University of Plant Polymers, St. Petersburg, Russia
Lebedev Research Institute of Synthetic Rubber, St. Petersburg, Russia

Received May 8, 2001

Abstract—A dynamic light scattering study in the temperature range 293–333 K was made for solutions of sulfate lignin and resinous wood components, which are limitedly soluble in water, as well as for their mixture in an alkaline medium (pH 12.7) of sulfate cooking lye. This study proved the heterogeneous nature of these systems.

Up to now, there have been no systematic colloid-chemical studies of the cooking process which is one of the most important processes in pulp and paper production. No systematic studies have also been made on the nature of solutions of organic wood components in sulfate cooking lyes. The exception are works on studying the dispersion of resinous components in neutral, acid, or weakly basic medium (up to pH 8), but these do not cover a higher pH range [1–3]. Recently, the aggregation and sedimentation stability was studied for aqueous solutions of sulfate lignin over a wide pH range, up to pH 12–13 [4, 5]. However, these works casted doubt on the possibility of aggregation of lignin macromolecules and formation of heterogeneous systems in alkaline media, while these phenomena were revealed in media with pH < 8 [5]. In this connection, it was of interest to study the nature of solutions of organic wood components (resinous substances, sulfate lignin, carbohydrate fraction, and their mixture) in sulfate cooking lyes (pH 12.7) and to elucidate whether they are homogeneous or heterogeneous, especially after cooking is complete and the cooking solution is cooled. Our previous studies [4] by indirect analytical methods (sedimentation and other) suggested the heterogeneous nature of the systems mentioned. This assumption needed confirmation by a direct independent method of dynamic light scattering. For this study, we chose pH of the medium of 12.7 and the temperature range 333–293 K, which correspond to the stage of sulfate cooking completion and discharge of cellulose from the boiler, as specifically this cooking stage is the most seriously responsible for the appearance of resinous hindrances [3]. At the same time, the knowledge of the particle-size distribution pattern of organic wood substances in the sulfate cooking lye will make it possible to develop scientific principles of improving the production processes for secondary products of cellulose cooking. This concerns preparation of purer tallic products, increase of the coefficient of extraction of sulfate soap and lignin from cooking lyes, and simultaneous reduction of the energy consumed and the time required for conducting processes involved in lye concentration by evaporation and settling.

The samples of sulfate lignin and resinous components were prepared by extraction from the birch chips with dioxane and diethyl ether, respectively. After drying to a constant weight, dioxane lignin and resin were subjected to a procedure identical to the conventional sulfate cooking of cellulose [4]. After the cooking was complete, sulfate lignin was isolated from the solution with sulfuric acid, and the resin was extracted with dichloroethane. The preparations were again dried to constant weight in a vacuum at 323 K and dissolved in aqueous solutions of sodium hydroxide (pH 12.7) at 363 K. The birch resin and sulfate lignin concentrations were 0.27 and 2.5%, respectively.

The particle-size distribution pattern of the solution was studied by dynamic light scattering which allows recording particles with sizes within 0.001–10 μm.

1070-4272/01/7501-0149$27.00 © 2002 MAIK "Nauka/Interperiodica"

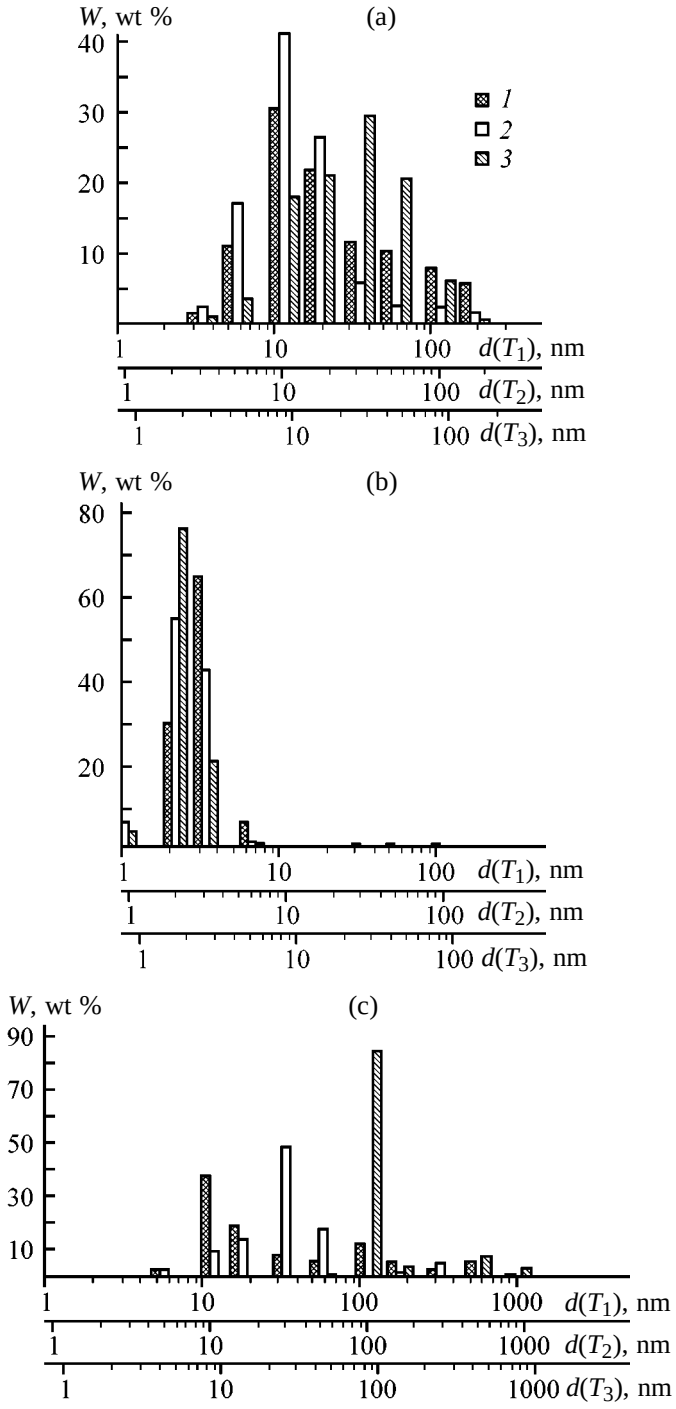

Fig. 1. Particle-size distribution pattern *W* for (a) sulfate lignin, (b) resin, and (c) sulfate lignin–resin mixture in an aqueous alkali solution (pH 12.7) at different temperatures. (*d*) Particle size; the same for Fig. 2. Temperature *T*, K: (*1*) 293, (*2*) 313, and (*3*) 333; the same for Fig. 2.

The measurements were carried out with a Coulter N 4 (Coultronics, France) dynamic light scattering correlator. The data obtained were processed by the previously developed routines [6]. The particle-size distribution patterns of the solutions are presented as histograms.

Figure 1a shows the particle-size distribution pattern for sulfate lignin at different temperatures. It is seen that the modal size of the particles of sulfate lignin dispersed at 293 and 313 K is 10 nm; at 333 K it increases to 30 nm. Clearly, rising temperature increases the aggregation instability of the sulfate lignin solution, as evidenced by increase in the particle size. Thus, we revealed thermal coagulation of sulfate lignin in the temperature range 313–333 K. This is evidently due to a decrease in the degree of hydration of sulfate lignin with rising temperature. Figure 1b shows that the birch resin particles dispersed at 333 K are much smaller than those of sulfate lignin (most of them are 2 nm in size). The aggregation stability of the resin solutions slightly decreases with cooling, by contrast to the sulfate lignin solutions (at 293 K the modal size of the particles is 3 nm); also, a minor amount of relatively large resin particles (316 and 562 nm) appears. Thus, the major part of the sulfate lignin and resin particles in the solutions under study are colloidal. From our data, we estimated the degree of aggregation of the molecules in the particles using the molecular weights of the substances determined by light scattering in organic solvents [7]. The degree of aggregation for the major part of the sulfate lignin and resin particles at 293 K was 55 and 27%, respectively. Thus, direct optical studies confirmed the heterogeneous nature of the systems, which was presumed earlier [3, 4].

We studied the particle-size distribution pattern for a 9 : 1 sulfate lignin–resin mixture corresponding to the real lye (Fig. 1c). It was found that the size of the revealed mixed particles also allows them to be classed with colloidal particles. The modal size of these particles tends to increase in the 293–333 K range from 10 to 100 nm, and at 333 K the fraction of small particles is completely absent. This may be due to the predominance in the mixture of sulfate lignin which exhibits aggregation instability at elevated temperatures. At 333 K, the modal size of the mixed particles is three times that of sulfate lignin and 50 times that of resin, as demonstrated by experiments on separate dispersion of the mixture components. Thus, dissolution of the sulfate lignin–resin mixture involves intensive heterocoagulation.

In view of the practical importance of this study we examined the particle-size distribution pattern for the real sulfate cooking lye comprising, along with the above-listed components, derivatives of wood carbohydrate fraction (primarily, sodium salts of α- and β-glucoisosaccharinic acid). These latter made with

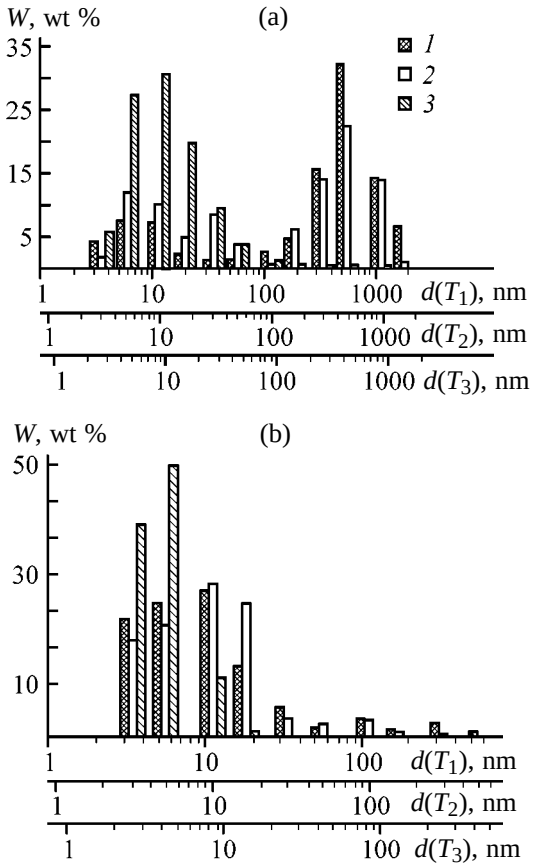

Fig. 2. Particle-size distribution pattern *W* at different temperatures for a mixture of organic substances (a) in sulfate solution, pH 12.7, and (b) in the presence of surfactant.

resin and sulfate lignin a 10 : 1 : 10 mixture. Figure 2a presents the results obtained. Studies of this mixture revealed particles from ultramicroheterogeneous (3–17 nm at 333 K) to finely and coarsely dispersed (300–1690 nm at 293 K). Pronounced heterocoagulation in the solution is observed upon cooling. In this dispersion, mixed particles are coarser than in the above-considered solutions. This is probably due to the presence in the mixture of a significant proportion of the wood carbohydrate fraction. Thus, during cooling the large particles revealed can precipitate onto the cellulose fiber, thus deteriorating the cellulose quality and causing resinous hindrances in fiber processing.

As known, these undesirable phenomena can be prevented by using a surfactant, Neonol AF 9–12, which is most suitable for alkaline medium [3, 8]. Figure 2b shows that Neonol additive decreases the size of the dispersed particles and increases their aggregation stability with lowering the solution temperature. The majority of the mixed particles are 10 nm in size at 293 K, which is comparable with the Neonol micelle size at pH 12.7 as determined previously [3]. Thus, adding Neonol to the cooking acid during cellulose cooking prevents enlargement and precipitation of the particles onto cellulose fiber, thus increasing the stability of these solutions and facilitating passing of the substances mentioned into solution. These factors govern the cellulose quality and the efficiency of using the secondary cooking products (sulfate lignin, sulfate soap, tall oil).

CONCLUSIONS

(1) Direct optical study by dynamic light scattering proved that aqueous solutions of sulfate lignin and resinous wood substances at pH 12.7 are dispersed systems, with nanoparticles dominating.

(2) The temperature dependence of the aggregation stability of dispersions of these substances is studied for the 293–333 K range.

(3) Joint dissolution of sulfate lignin, resinous substances, and wood carbohydrate fraction derivatives yields larger, compared to separate dispersion of the components, mixed particles forming by heterocoagulation.

(4) Adding Neonol decreases the size of the mixed particles and increases their aggregation stability.

ACKNOWLEDGMENTS

This work was financially supported by the Ministry of Education of the Russian Federation.

REFERENCES

1. Talmud, S.L., Shpenzer, N.P., and Ridiger, V.K., *Dokl. Akad. Nauk SSSR*, 1968, vol. 180, no. 3, pp. 668–671.
2. Ramm, K.S. and Shpenzer, N.P., *Kolloidn. Zh.*, 1971, vol. 33, no. 3, pp. 433–435.
3. Lysogorskaya, N.P., Scientific Principles of Cellulose Deresination by Surfactants, *Doctoral Dissertation*, St. Petersburg, 1993.
4. Dem'yantseva, E.Yu., Lysogorskaya, N.P., Halopenen, I.Yu., and Jaakkola, P., *Zh. Prikl. Khim.*, 1999, vol. 72, no. 9, pp. 1546–1548.
5. Chernoberezhskii, Yu.M., Lorentsson, A.V., and Dyagileva, A.B., *Zh. Prikl. Khim.*, 1999, vol. 72, no. 9, pp. 1496–1498.
6. Klyubin, V.V., *Vysokomol. Soedin., Ser. A.*, 1995, vol. 37, no. 4, pp. 670–675.
7. Lindberg, I., *Doklady Sovetsko-Finskogo Simpoziuma* (Proc. Soviet-Finnish Symp.), Leningrad: Lesotekh. Akad. im. S.M.Kirova, June 12–14, 1968, pp. 3–8.
8. Shpenzer, N.P., Frantsuzova, N.E., Lyubanskii, B.P., and Talmud, S.L., *Zh. Prikl. Khim.*, 1973, vol. 46, no. 2, pp. 479–480.

Russian Journal of Applied Chemistry, Vol. 75, No. 1, 2002, pp. 152–155. Translated from Zhurnal Prikladnoi Khimii, Vol. 75, No. 1, 2002, pp. 152–155.
Original Russian Text Copyright © 2002 by Egorov, Sukhorukov, Plotnikova, Khaliullin.

MACROMOLECULAR CHEMISTRY AND POLYMERIC MATERIALS

Fireproofing Coatings Based on Urea Resins for Metallic Structures

A. N. Egorov, Yu. I. Sukhorukov, G. V. Plotnikova, and A. K. Khaliullin

East-Siberian Institute, Ministry of Home Affairs of the Russian Federation, Irkutsk, Russia
Favorskii Irkutsk Institute of Chemistry, Siberian Division, Russian Academy of Sciences, Irkutsk, Russia

Received April 16, 2001

Abstract—A formulation was developed of a fireproofing compound for coating metallic structures, based on urea–formaldehyde resins and mineral fillers. The component ratio in the compound was optimized.

Progress of mining in Siberia and development of new regions with rich resources involves wide use of metallic structures. In this connection, an important problem is their fire protection [1], because metallic structures exhibit a poor resistance to high temperatures and, when rapidly heated, lose their strength.

A possible way to solve this problem is the use of inflating fire-proofing coatings. Such coatings exhibit a high heat-insulating power under conditions of a fire. When subjected to impact of high temperatures, they decompose and considerably increase in volume, forming a porous protective layer.

The goal of this study was to develop the formulation of a fireproofing compound for coating of metallic structures, based on urea–formaldehyde resin and mineral fillers.

EXPERIMENTAL

Urea–formaldehyde resin {KF-Zh, GOST (State Standard) 14231–78 [2]} was used as binder. The combustibility of the resin was reduced by adding fireproofing agents: ammonium hydrophosphate $(NH_4)_2HPO_4$ and sodium tetraborate $Na_2B_4O_7$. The same additives were expected to act as inflating agents. As fillers we used vermiculite, phlogopite, clay, chopped fiber glass, and loose asbestos fiber. Initially we examined the effect of fillers with the formulation varied in a wide range (Table 1). To find the optimal composition, the best formulation was optimized by varying the component ratio in narrower limits (Table 2).

The performance of a fireproofing conating was evaluated according to GOST 30.247.0–94 [3] as the time required for heating the inner surface of the coating to 500°C; no less than three samples were tested, and the arithmetic mean was calculated. This time was considered as the refractoriness limit, and, after reaching 500°C, the tests were terminated.

The tests of coatings presented in Table 1 for the fireproofing performance showed that for the formulations containing inflated vermiculite (nos. 1, 2) the refractoriness limit does not exceed 0.5 h. A similar result was obtained for the formulation containing phlogopite (no. 3).

Introduction of clay in addition to vermiculite or phlogopite decreases the refractoriness limit to 0.4 and 0.5 h, respectively. The decreased performance is due to increased density of the carbon residue.

The presence of an additional fireproofing agent

Table 1. Properties of fireproofing coatings*

Compound no.	Component content, wt %		
	KF-Zh resin	ammonium hydrophosphate	inflated vermiculite
1	65	13	22
2	58	23	14
3	51	15	–
4	45	14	–
5	46	26	15
6	53	15	18
7	68	18	10
8	60	18	11

* Other components, wt %: phlogopite 24 (no. 3), 31 (no. 4); clay 11 (no. 4), 13 (no. 6); sodium tetraborate 12 (no. 5); loose asbestos fiber 5 (no. 7); chopped fiber glass 11 (no. 8).

1070-4272/01/7501-0152$27.00 © 2002 MAIK "Nauka/Interperiodica"

Table 2. Component content in samples

Component	Content, wt %, in indicated compound					
	no. 9	no. 10	no. 11	no. 12	no. 13	no. 14
KF-Zh resin	64	61	60	59	58	57
Ammonium hydrophosphate	19	18	18	18	17	17
Inflated vermiculite (0.25 mm)	8	10	11	12	12	13
Chopped fiber glass	8	10	11	12	12	13

(sodium tetraborate) decreases the refratrotiness limit from 0.4 to 0.2 h. The best results were obtained with formulation nos. 7 and 8 containing, along with inflated vermiculite, also aspestos or chopped fiber glass: The refractoriness limit was 0.6 and 0.7 h, respectively. For the latter coating, the inflation factor ranges from 1.5 to 2.0. The carbon residue is porous and shows a high adhesion to metal.

Figure 1 shows how the sample temperature varies with time. Three stages can be distinguished in the course of reaching the critical temperature of 500°C. In the initial stage (up to 5 min) the sample temperature reaches 30–80°C, and this is not accompanied by any changes in the state of the coating. In the second stage the coating decomposes with inflation and formation of a heat-insulating surface layer.

The loss of thermal energy for endothermic processes of water evaporation, binder decomposition, and evaporation of degradation products and the increased heat-insulating power of the inflated coating prevent the temperature growth under the protective layer.

In the final stage, the porous system is broken down, and the temperature rapidly grows to 500°C.

Our results (Fig. 1) show that formation of a porous protective layer on the surface of metallic structures is determined by the binder content, resin-to-filler weight ratio, and nature of the filler.

The results obtained with formulation nos. 4 and 5 show that the 46% resin content is insufficient to form a porous protective layer. In such coatings the second stage is virtually lacking. In the other samples (binder content >51%), the second stage is clearly pronounced. The time before the onset of the third stage ranges from 22 to 30 min. The major role in preservation of the protective layer is played by addition of a small amount of the reinforcing filler (asbestos and chopped fiber glass, formulation nos. 7 and 8). Without these additives the breakdown of the inflated layer starts within 22–23 min (formulation nos. 1–3, 6).

The rate of the temperature rise in the third stage largely depends on the resin content in the initial formulation and on the thermal conductivity of the filler. The samples protected with compound nos. 1 and 7 containing more than 65% binder show the most rapid temperature rise in the final stage. Replacement of inflated vermiculite by more heat-conducting phlogopite and clay also favors rapid temperature growth in the third stage.

The best result was obtained with formulation no. 8, which well competes with many commercially used [4] compounds in the fireproofing performance. For example, the fireproofing coating based on OPV-1 vermiculite ensures the refractoriness limit of 0.7 h at a protective layer thickness on a metallic structure of 22 mm [5]. At the same time, formulation no. 8 ensures the same refractoriness limit at a considerably smaller layer thickness (10 mm).

To attain the highest performance of the fireproofing coating and determine the optimal component content in formulation no. 8, we performed additional experiments with the content of the binder, fireproofing agent $(NH_4)_2HPO_4$, and filler being varied. The filler content (inflated vermiculite and fiber glass in equal amounts) was varied in the range ensuring the optimal fluidity. The compositions are listed in Table 2.

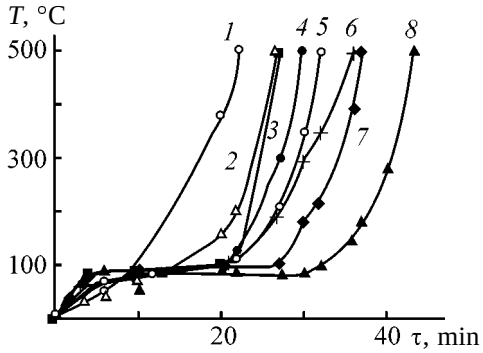

Fig. 1. Heating curves of fireproofing coatings of various compositions. Formulation no.: (*1*) 5, (*2*) 4, (*3*) 1, (*4*) 6, (*5*) 3, (*6*) 2, (*7*) 7, and (*8*) 8. (*T*) Temperature and (τ) time.

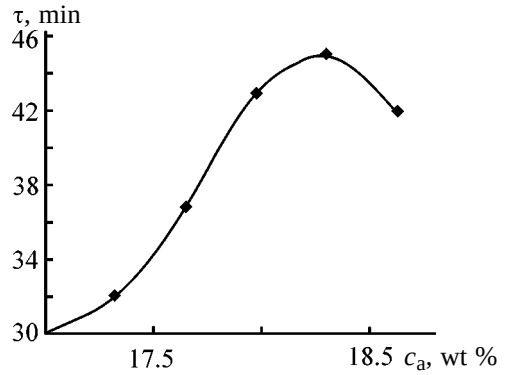

Fig. 2. Influence of the content of ammonium hydrophosphate (fireproofing agent) c_a on the coating refractoriness. (τ) Time; the same for Fig. 3.

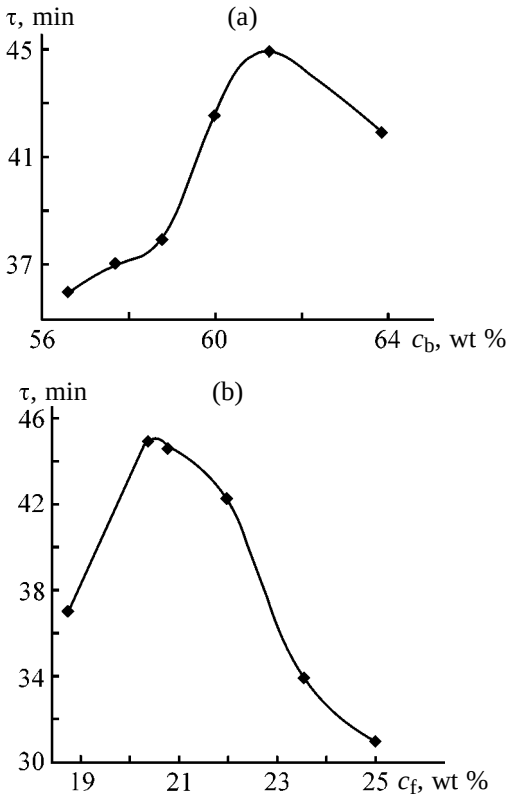

Fig. 3. Coating performance as a function of the content of (a) binder (KF-Zh resin) c_b and (b) filler (fiber glass, vermiculite) c_f.

Figure 2 shows how the refractoriness limit of the coating depends on the fireproofing agent content (at a constant weight ratio of fireproofing agent and resin, equal to 0.3). Formulation no. 10 shows the highest performance (refractoriness limit 0.8 h). It contains 61% KF-Zh urea–formaldehyde resin and 18% ammonium hydrophosphate.

The dependence of the coating refractoriness on the binder content is shown in Fig. 3a. It is seen that variation of the KF-Zh resin content affects the refractoriness limit to a lesser extent than variation of the $(NH_4)_2HPO_4$ content. The highest refractoriness limit (0.8 h) is exhibited by formulation no. 10 containing 61% resin. Apparently, at a lower resin content the heat-insulating performance of the inflated layer is lower, whereas at a higher resin content this layer is broken down faster, and the rate of temperature rise in the final stage increases.

Figure 3b shows how the performance of the fireproofing compounds depends on the filler content (fiber glass, vermiculite). It is seen that the vermiculite and fiber glass content lower than 19% does not ensure formation of a strong inflated layer with a low thermal conductivity. However, at a too high filler content (>23%) the fireproofing performance of the coating decreases, probably because of the increased thermal conductivity.

Thus, the highest performance (refractoriness limit 0.8 h) is shown by formulation no. 10 containing 61% resin, 18% fireproofing agent, 10% inflated vermiculite, and 10% chopped fiber glass. It should be noted that coatings of this compound surpass in the fireproofing performance those of OPV-1 and can have a considerably smaller thickness; thus, the load on the metallic structures being protected can be decreased.

Our results show thart the performance of a fireproofing coating is determined both by the nature of the binder and by the component ratio.

It is known that the decreased combustibility of the urea–formaldehyde resin is due to vigorous evolution of incombustible volatile products into the gas phase in the course of degradation and to accelerated coking. Decomposition of the urea–formaldehyde resin occurs with heat absorption and, owing to release of a large amount of gases, with formation of a protective layer with a porous, very pitted structure of the surface [6, 7]. However, the resin taken separately does not ensure the required fireproofing performance because of the low strength of this porous layer and strong tendency toward further degradation.

The walls of internal channels and pores of the protective layer formed by heating of a filled coating consist of partially degraded and sintered filler fibers, ensuring the required strength of the protective layer. Solid particles of coke, the final product of thermal degradation of the organic binder, are arranged between these fibers.

As the fireproofing coating is a composite material,

the major role is played by the nature of the filler, rather than by high-temperature cross-linking of the resin. Usually introduction of a mineral filler into polymers increases their thermal conductivity [8], which negatively affects the fireproofing performance. However, this effect is eliminated to certain extent by introducing inflated vermiculite. Fiber glass acts as a reinforcing filler, enhancing the strength of the inflated protective layer and thus increasing the refractoriness limit.

CONCLUSIONS

(1) The performance of compounds based on urea–formaldehyde resin as fireproofing agents for metallic structures was studied in relation to the nature and content of mineral fillers.

(2) The main stages of degradation of the fireproofing coating at high temperatures were revealed, and the effect of the coating components on this process was examined.

(3) Formulations were suggested for fireproofing coating, ensuring higher fireproofing power as compared to the commercially used compounds at a smaller thickness of the protective layer.

REFERENCES

1. Fedorov, V.V. and Mikhailov, D.N., in *Problemy obespecheniya pozharnoi bezopasnosti zdanii i sooruzhenii* (Problems of Fire Safety of Buildings), Moscow: Mosk. Dom Nauchno-Tekh. Propagandy, 1989, pp. 25–31.
2. *GOST* (State Standard) *14231–88: Urea–Formaldehyde Resins.*
3. *GOST* (State Standard) *30247–94: Building Structures. Refractoriness Testing Procedures. General Requirements.*
4. Trushin, V.A., Matlis, V.S., and Kuzmichev, N.N., in *Pozharnaya profilaktika* (Fire Prevention), Moscow: Vses. Nauchno-Issled. Inst. Pozharnoi Okhrany, 1982, pp. 142–151.
5. *TU* (Technical Specifications) *21-25-322–90: Fireproofing Coatings Based on OPV-1 Vermiculite.*
6. Shcheglov, P.P. and Ivannikov, V.A., *Pozharoopasnost' polimernykh materialov* (Inflammability of Polymeric Materials), Moscow: Stroiizdat, 1992.
7. Kodolov, V.I., *Goryuchest' i ognestoikost' polimernykh materialov* (Combustibility and Refractoriness of Polymeric Materials), Moscow: Khimiya. 1976.
8. *Napolniteli dlya polimernykh kompozitsionnykh materialov: Spravochnoe posobie* (Fillers for Polymeric Composite Materials: Handbook), Kats, G.S. and Milevski, D.V., Eds., Moscow: Khimiya, 1981.

Russian Journal of Applied Chemistry, Vol. 75, No. 1, 2002, pp. 156–158. Translated from Zhurnal Prikladnoi Khimii, Vol. 75, No. 1, 2002, pp. 156–158.
Original Russian Text Copyright © 2002 by Baev, Shishko.

BRIEF COMMUNICATIONS

Thermal Behavior of Titanium Tetrabutylate and Niobium Pentapropylate

A. K. Baev and M. A. Shishko

Belarussian State Technological University, Minsk, Belarus

Received May 10, 2001

Abstract—Thermal behavior of titanium tetrabutylate and niobium pentapropylate in a wide temperature range under static conditions was studied with a membrane zero-gage. The vapor pressure under conditions when vaporization is not complicated by other processes was determined. The enthalpy and entropy of vaporization were calculated. The mechanism of thermolysis of $Ti(OBu)_4$ and $Nb(OPr)_5$ was studied.

Metal alcoholates show promise for preparing submicron metal oxide epitaxial films by metal-organic chemical vapor deposition. To optimize this process, the stability and conditions of preparation and thermolysis of these compounds should be determined. Thermal behavior of $Ti(OBu)_4$ was studied by DTA, mass spectrometry, and gas–liquid chromatography [1, 2]. Two forms of this compound, monomeric and polymeric, were detected [2–4]. The monomer is unstable and irreversibly degrades in the range $373 < T < 473$ K, whereas the polymer is stable up to 473 K. The main thermolysis products are 1(2)-butene, propene, butane, and propane. The thermodynamic data on vaporization and parameters of vaporization of $Nb(OPr)_5$ as well as the dissociation energy $D_{M–OR}$ are reported in our previous works [5, 6].

The $p = f(T)$ dependence for saturated and unsaturated vapor was measured on heating and on cooling (Fig. 1). At 323–418 K the pressure is reproduced with the limits of the determination error and the shape of the $p = f(T)$ curve is independent of the time of thermostatic control. The vapor pressure in this temperature range is described by the equation

$$\log p = (7.5 \pm 0.1) - (248 \pm 39)/T.$$

The calculated enthalpy and entropy of $Ti(OBu)_4$ vaporization are 47.6 ± 0.7 kJ mol^{-1} and $88.5 + 1.9$ J mol^{-1} K^{-1}, respectively. Unsaturated vapor pressure obeys the Gay–Lussac law; the molecular weight determined in two independent experiments (332 and 345) is close to the calculated value (339.9). Above 423 K $Ti(OBu)_4$ appreciably decomposes. In the range 443–449 K the pressure is higher by a factor of 5/4 than the unsaturated vapor pressure measured below 423 K, i.e., every fourth molecule of $Ti(OBu)_4$ decomposes:

$$4Ti(OBu)_4 \rightarrow 3Ti(OBu)_4 + Ti(OH)(BuO)_3 + C_4H_8. \quad (1)$$

In accordance with Eq. (1) the average molecular weight of the gaseous species should be 272. The experimental molecular weight ranges from 279 to 267 and agrees well with the calculated value. The molecular weight determined at 443–449 K is 151–147 owing to strong increase in the vapor pressure. The molecular weight calculated from the equation

$$4Ti(OBu)_4 \rightarrow 3Ti(OH)(BuO_3)_3 + Ti(OH)_2(BuO)_2 + 5C_4H_8 \quad (2)$$

is 150.

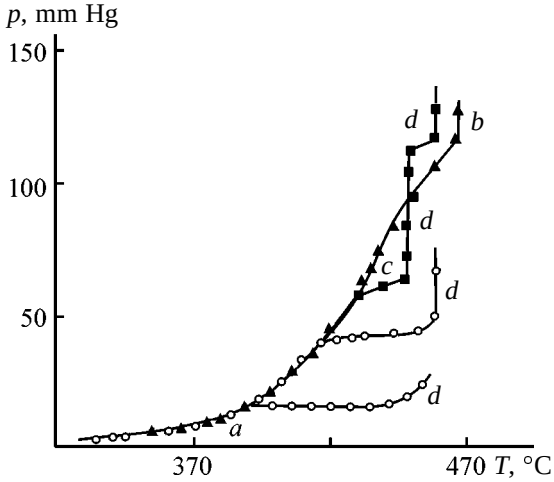

Fig. 1. p–T dependence for $Ti(OBu)_4$: (*a*) saturated vapor, (*b*) unsaturated vapor, (*c*) onset of thermolysis, and (*d*) intense thermolysis.

1070-4272/02/7501-0156$27.00 © 2002 MAIK "Nauka/Interperiodica"

Subsequent olefin elimination at these temperatures leads to formation of hydrated titanium oxide $TiO_2 \cdot nH_2O$.

Generally, $Ti(OBu)_4$ thermolysis occurs by the molecular mechanism and is described by the following scheme:

$$4Ti(OBu)_4 \xrightarrow[-C_4H_8]{} Ti(OH)(OBu)_3 \xrightarrow[-C_4H_8]{} Ti(OH)_2(OBu)_2 \xrightarrow[-2C_4H_8]{} TiO_2 \cdot H_2O \xrightarrow[-H_2O]{} TiO_2. \quad (3)$$

The formation of other unsaturated (propene) and saturated (prepane, butane) hydrocarbons in the $Ti(OBu)_4$ thermolysis is due to secondary radical reactions.

The $p = f(T)$ dependence for $Nb(OBu)_5$ was measured on heating and cooling (Fig. 2). Curve *1* contains the sections of $Nb(OBu)_5$ vaporization (up to 343 K) and its irreversible thermal dissociation (343–513 K). At 503 K $Nb(OBu)_5$ intensively decomposes. Since the vapor pressure of $Nb(OBu)_5$ below the temperature of its appreciable decomposition (358 K) is low (3 mm Hg), we cannot determine the thermodynamic parameters of vaporization of this compound. Our results suggest that the $\log p = f(T)$ dependence and parameters of $Nb(OBu)_5$ vaporization determined in the 383–434 K temperature range in our previous work [6] are doubtful. Above 503 K (Fig. 2, section *d*) the thermolysis is completed and the pressures increases owing to the gas expansion. On cooling (Fig. 2, curve *2*) the pressure decreases by the Gay–Lussac low (Fig. 2, section *e*), which is followed by stepwise condensation of thethermolysis products. The saturated vapor pressure of water (Fig. 2, section *f*), propanol (Fig. 2, section *g*), and propene (Fig. 2, section *h*) was determined from the total vapor pressure at different temperatures. The presence of propane and propene was confirmed by chromatography. Traces (~1%) of butane, 1(2)-butene, and methane were also detected. Based on these data and results of [2, 7], the mechanism of $Nb(OBu)_5$ thermolysis can be proposed.

The final thermolysis product of $Nb(OBu)_5$ was Nb_2O_5 [2, 7]. In the crystal structure of $[(RO)_5Nb]_2$ both terminal and bridging alkoxy groups are present, with the bridging M–OR bonds being considerably longer than the terminal bonds (2.3 and 1.9 Å, respectively). This difference and large bond angles at oxygen atoms of the terminal groups (135–160°) indicate strong $p_\pi d_\pi$ interaction in the $M–OR_t$ fragment. As a result, the multiplicity of these bonds increases and they become stronger. The p_π-donor power of the

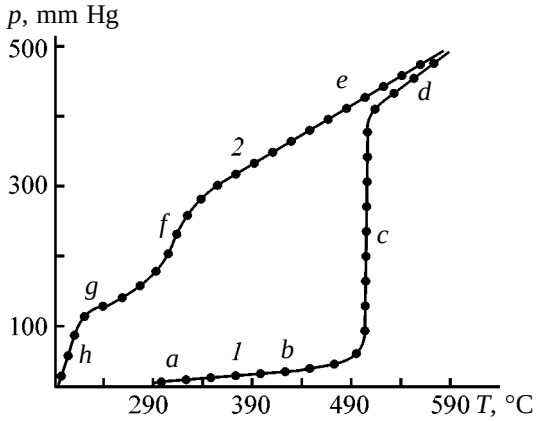

Fig. 2. p–T dependence for $Nb(OBu)_5$ (*1*) on heating and (*2*) on cooling: (a) $Nb(OBu)_5$ vaporization, (b) vaporization with partial decomposition of $Nb(OBu)_5$, (c) thermolysis, (d) thermolysis of the residue, (e) range of Gay–Lussac dependence; condensation of (f) water and isorpropanol, (g) propanol, and (h) propane and propylene.

bridging oxygen atoms is lower than that of the oxygen atoms of the terminal groups. Hence, dissociation of the bridging bonds is more energetically favorable. The presence of propanol and propene among the thermolysis products indicates elimination of these compounds at temperatures higher than 358 K by the following reactions:

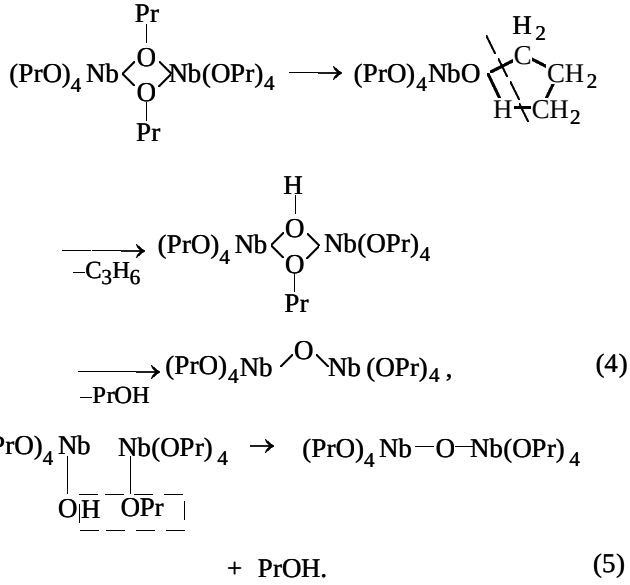

The volatility of $Nb(OPr)_5$ is low, and total pressure in the system is determined by the partial pressures of the alcohol and olefin. Niobium oxide Nb_2O_5 is formed with elimination of oxygen-containing compounds (the alcohol, ether, or H_2O). The ether content can be neglected since its yield in thermolysis of metal alkoxides decreases with an increase in the

length of the hydrocarbon chain of the alkoxy group and the ether yield in thermolysis of niobium ethylate is 0.1 mol. Propanol is formed only in the first step of thermal dissociation of $Nb(OPr)_5$.

Since all the other Nb–OR bonds are equivalent, we suggest that the mechanism of their cleavage is similar. Chromatographic analysis of the thermolysis products showed that the gas phase consists mainly of propene and propane in the 6 : 1 ratio. Thus, the next step of $Nb(OPr)_5$ dissociation is the olefin elimination to form hydrated niobium(V) oxide which at temperatures higher than 623 K is dehydrated to Nb_2O_5 [scheme (6)], i.e., five $[Nb(OPr)_5]_2$ molecules release five oxygen atoms in the form of single propanol molecule and four water molecules:

$$(PrO)_4Nb{-}O{-}Nb(OPr)_4$$

$$\xrightarrow[-C_2H_6]{} (PrO)_{4-x}(OH)_xNb{-}O{-}Nb(OH)_x(OPr)_{4-x}$$

$$\xrightarrow[-C_3H_6]{} Nb_2O_5\cdot 4H_2O \xrightarrow[-4H_2O]{} Nb_2O_5. \qquad (6)$$

The presence of ethylene and traces of methane, ethane, butane, and 1(2)-butene is due to the secondary free-radical processes occurring in the system. Thus, $Nb(OPr)_5$ thermally decomposes by the molecular mechanism. In accordance with the thermolysis scheme (3)–(5), 0.5 mol of isopropanol, 2 mol of water, and 4.5 mol of hydrocarbons are formed per mole of the initial substance.

EXPERIMENTAL

Thermal behavior of titanium tetrabutylate and niobium isopropylate under static conditions was studied with a membrane zero-gage. The temperature was measured with an accuracy of ± 0.1 K. The pressure was measured with an MChR-3 gage accurate to 0.1 mm Hg. The *p*–*T* dependence was measured on heating and on cooling. The initial compounds were purified by repeated vacuum distillation. As determined by elemental analysis, the purity of the initial samples was no less that 99.9%. The metal alcoholates were distilled into the gage chamber via an all-soldered glass system. Moisture traces were preliminarily removed from the system with the aid of a zeolite pump. The volatile thermolysis products were analyzed on an LKhM-72 chromatograph equipped with a 7-m column. The column was packed with 18% dinonyl phthalate on Chromaton-N (5 m) and a 20% ethylene glycol solution of $AgNO_3$ on Chromaton-N-AB (2 m).

REFERENCES

1. Razuvaev, G.A., Gribov, B.G., Domrachev, G.A., *et al*., *Metalloorganicheskie soedineniya v elektronike* (Organometallic Compounds in Electronics), Moscow: Nauka, 1972.
2. Bradley, D.C., Mehrotra, R.C., and Gaur, D.P., *Metal Alkoxides*, London: Pergamon, 1978.
3. Duffy, M.T., Wang, C.C., and Waxman, Q., *J. Electrochem. Soc*., 1969, no. 1, pp. 116–234.
4. Sakurai, S., Watable, S., and Mario, Q., *Rev. Electrochem. Commun. Lab*., 1963, vol. 178, no. 11, p. 178.
5. Klinchinova, S.A., Salomatin, B.A., and Gribov, B.G., *Izv. Vyssh. Uchebn. Zaved., Khim. Khim. Tekhnol*., 1976, vol. 19, no. 4, pp. 585–590.
6. Tel'noi, V.I. and Rabinovich, I.B., *Usp. Khim*., 1977, vol. 46, no. 8, pp. 1337–1367.
7. Gribov, B.G., Domrachev, G.A., Zhuk, B.V., *et al*., *Osazhdenie plenok i pokrytii razlozheniem metalloorganicheskikh soedinenii* (Preparation of Films and Coatings by Metal-Organic Chemical Vapor Deposition), Moscow: Nauka, 1981.

Russian Journal of Applied Chemistry, Vol. 75, No. 1, 2002, pp. 159–161. Translated from Zhurnal Prikladnoi Khimii, Vol. 75, No. 1, 2002, pp. 159–161.
Original Russian Text Copyright © 2002 by Baev.

BRIEF COMMUNICATIONS

Thermolysis of Dimethyltellurium and Its Mixture with Dimethylcadmium

A. K. Baev

Belarussian State Technological University, Minsk, Belarus

Received September 19, 2000; in final form, October 2001

Abstract—Thermolysis of dimethyltellurium and its mixture with dimethylcadmium (1:1) was studied. The composition of the thermolysis products was determined. The thermolysis mechanism was proposed.

The kinetic data on thermolysis of organometallic compounds are used to optimize the conditions of production of semiconductors and their low-temperature doping. However, the thermolysis mechanisms of practically important organometallic compounds and especially of binary mixtures [1] are studied insufficiently.

In this work we studied thermolysis of dimethyltellurium and its mixture with dimethylcadmium.

Thermal degradation of $Te(CH_3)_2$ to metallic tellurium at 623–773 K under static conditions was examined in [2]. The content of the main gaseous product, CH_4, decreases with increasing temperature. The process involves intramolecular disproportionation of CH_3 groups with intermediate formation of organotellurium polymer which degrades further to metallic tellurium:

$$n\mathrm{Te(CH_3)} \rightarrow n\mathrm{CH_4} + (\mathrm{TeCH_2})_n, \quad (1)$$

$$(\mathrm{TeCH_2})_n \rightarrow n\mathrm{Te} + n/2\mathrm{CH_4} + n/2\mathrm{C}. \quad (2)$$

In the condensed product CH_2 and CH groups were detected. The carbon content in metallic tellurium was 2.5%. Yablokov *et al*. studied thermolysis of $Te(CH_3)_2$ under static conditions [3]. The following temperature dependence of the rate constant was derived:

$$\ln k = (28.0 \pm 2.5) - (43\,200 \pm 3100)/RT.$$

In preliminary experiments the process was performed to a constant pressure in the system (~20 h). It was found that the degree of thermolysis at temperatures higher than 610 K is almost independent of temperature. The ratio of the attained constant pressure p_{const} and the initial pressure p_{in} at 603, 606, 617, 622, 633, and 641 K is 1.49, 1.50, 1.31, 1.33, 1.30, and 1.35, respectively.

Needle crystals and a translucent dark brown film were formed on the walls of the gage chamber. This agrees with data of Galliulina *et al*. [2] and indicates gas-phase thermolysis of the sample with subsequent condensation of the products on the walls of the gage chamber. At $\tau = 0$ the α–τ kinetic curves (Fig. 1) obtained at the initial $Te(CH_3)_2$ concentration of 3.8×10^{-4} M intercept different lengths on the ordinate, which is due to certain decomposition of the initial sample in the course of attaining the required temperature. Therefore, when treating the kinetic curves, we took as the start of the process the moment at which the constant temperature was attained. The kinetic data were approximated by equations of different orders. Up to the degree of decomposition of 0.8–0.9 the best fit was obtained with the first-order equation.

The experimental results are described well by the linear anamorphosis of the kinetic equation. The rate constants $k \times 10^5$ at 559.6, 577.2, 595.2, 603, 613,

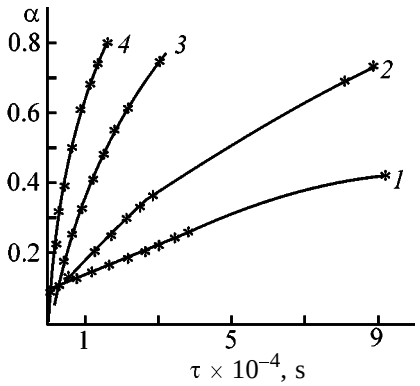

Fig. 1. Thermolysis of dimethyltellurium at (*1*) 548.6, (*2*) 559.6, (*3*) 577.2, and (*4*) 595.2 K. (α) Degree of substrate decomposition and (τ) time.

1070-4272/02/7501-0159$27.00 © 2002 MAIK "Nauka/Interperiodica"

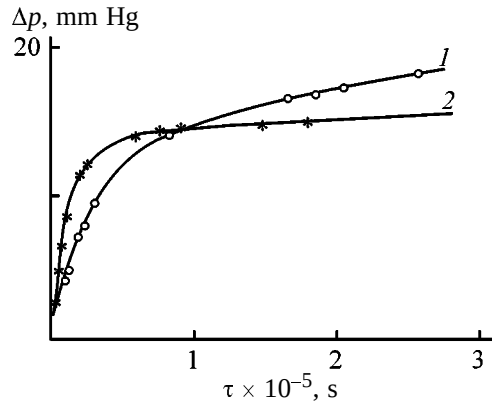

Fig. 2. Thermolysis of dimethyltellurium–dimethylcadmium mixture (molar ratio 1 : 1) at (*1*) 519.7 and (*2*) 536.2 K. (Δp) pressure change and (τ) time.

623, 633, 641, and 651 K, calculated by the least-squares treatment of the first-order equation, are 0.55, 1.48, 4.87, 10.6, 33.2, 68.4, 85.6, 177.6, 338.6, and 448 s^{-1}, respectively.

The first four values of k were calculated from our data and the other were taken from [3]. All these constants fall on the $\log k = (1/T)$ line. Least-squares treatment of the temperature dependence of the rate constant gave the Arrhenius equation

$$\log k = (13.45 \pm 0.56) - (10\,266 \pm 430)/T.$$

The calculated activation energy and pre-exponential factor are $196.7 + 6.1$ kJ mol^{-1} and $10^{13.45 \pm 0.7}$ s^{-1}, respectively.

Cooling of the zero gage to the liquid nitrogen temperature showed that the pressure in the system is produced by the saturated vapor of CH_4, and H_2 is absent in the thermolysis products. The composition of gaseous thermolysis products of $Te(CH_3)_2$ is independent of temperature. The main product (95.3–97.9%) formed at 548.6–565.2 K is methane. The content of unsaturated hydrocarbons is negligible. The mass-balance calculations performed by the procedure in [4] showed that 28–29% C and 6–8% H are present in the condensed phase.

Since the kinetics of $Te(CH_3)_2$ thermolysis obeys a simple law, the chain initiation is an elementary step of the process [5]. The high methane yield is due to reaction of CH_3 radicals with $Te(CH_3)_2$. The rate constants of recombination of CH_3CH_2 radicals and of CH_3 and CH_3CH_2 radicals are higher than those of the other reactions. However, the radical concentration is low and the recombination rate is usually comparable with those of other reactions. Low yield of C_2–C_4 hydrocarbons indicates negligible contribution of these reactions to the overall process. Analysis of thermolysis products showed that the hydrocarbon yield monotonically decreases with an increase in the length of the hydrocarbon chain. Based on these results, the thermolysis scheme was proposed. It should be noted that the composition of the tellurium film, estimated from the mass balance of the process, differs from $TeCH_2$ since these species reacts with CH_3 radicals [scheme (3)]. The products of this reaction are condensed on the wall of the gage chamber to form polymers degrading further with increasing temperature [scheme (4)]:

$$\dot{C}H_2Te + \dot{C}H_3 \rightarrow (CHTe)_n + CH_4, \quad (3)$$

$$(HCTe)_n \rightarrow nTe + n/4CH_4. \quad (4)$$

The occurrence of these reactions is confirmed by the presence of CH_2 and CH groups in the condensed product [3] and C : H = 0.65–0.90.

Methane formation is the major pathway of $Te(CH_3)_2$ thermolysis. The rate constant of the overall thermolysis process is about 1–3 orders of magnitude higher than that of generation of CH_3 radicals [6]. This fact and autoinhibition of the thermolysis [7] suggest its radical mechanism which agrees with the results of [4].

Dimethylcadmium appreciably decomposes at 423 K [8]. Based on the results of preliminary experiments, the temperature range for the study of thermolysis of the $Te(CH_3)_2$–$Cd(CH_3)_2$ mixture (1 : 1) was chosen to be 484–564 K. The experiments were performed at the total initial concentration of these compounds of 1×10^{-3} M. The kinetic curves are shown in Fig. 2. Analysis of these curves showed that at low temperatures the process is described by the first-order equation, but at higher temperatures the process kinetics is inconsistent with the orders of thermolysis of $Te(CH_3)_2$ and $Cd(CH_3)_2$ [8] (1 and 0.5, respectively). After cooling of the system with liquid nitrogen, no H_2 was detected in the gas phase. The gaseous thermolysis products were analyzed by chromatography. The main products formed at 484.0–564.2 K are CH_4 (53.8–86.2%) and C_2H_6 (8.3–35.7%). The yield of other alkanes is lower than 5%. The yield of methane decreases, the yield of C_2H_6, C_3H_8, and C_4H_{10} increases, and the yield of *iso*-C_4H_{12} and other thermolysis products remains virtually the same with increasing temperature.

Mass balance calculation of the composition of the condensation products showed that the H content in

this phase is maximal and the C : H ratio remains constant at 500–565 K. We suggest that, as compared to $Te(CH_3)_2$ thermolsysis, the decrease in the carbon and hydrogen content in the condensed phase and considerable increase in the C_2H_6 yield with increasing temperature are due to different thermolysis mechanism of these compounds. Since the activation energy of $Te(CH_3)_2$ thermolysis (196.2 kJ mol^{-1}) is higher than that of $Cd(CH_3)_2$ (129.2 kJ mol^{-1}), the rate constant of $Cd(CH_3)_2$ thermolysis is higher. Hence, in a $Te(CH_3)_2$–$Cd(CH_3)_2$ mixture $Cd(CH_3)_2$ starts to decompose at lower temperatures. The mechanism of $Cd(CH_3)_2$ thermolysis proposed in our previous work is confirmed by the experimental yield of C_2H_6 (18.95–20.9 %) at 521–536 K.

The C_2H_6 content in the products of thermolysis of a $Cd(CH_3)_2$–$Te(CH_3)_2$ mixture at 484 K is 8.3%, whereas in the case of $Te(CH_3)_2$ thermolysis it is 2.1–2.3%. This indicates that CH_3 radicals formed in the course of the thermal degradation react with $Te(CH_3)_2$. The reaction of CH_3 radical with $Cd(CH_3)_2$ and $Te(CH_3)_2$ increases the CH_4 yield in thermolysis of $Cd(CH_3)_2$–$Te(CH_3)_2$ mixture as compared to that in thermolysis of pure $Cd(CH_3)_2$. The corresponding decrease in the yield of the other products indicates greater contribution of reaction (5) owing to reaction of CH_2 radical with CH_4 [reaction (6)]:

$$Te(CH_3)_2 + \dot{C}H_3 \rightarrow \dot{C}H_2TeCH_3 + CH_4, \quad (5)$$

$$CH_4 + \ddot{C}H_2 \rightarrow C_2H_6. \quad (6)$$

These processes decrease the carbon content in a semiconductor. In this connection the temperature effect is of special importance, since the rate constant of radical initiation, especially of the reaction

$$\dot{C}H_2CdCH_3 \rightarrow \ddot{C}H_2 + \dot{C}H_3 + Cd, \quad (7)$$

increases [8] with temperature. It is the sharp increase in the C_2H_6 yield that indicates growing contribution of reaction (7). As the concentration of CH_2 radicals increases, the contribution of reaction (6) increases and hence the C_2H_6 yield increases and the CH_4 yield decreases. As a result, the total content of CH_4 and C_2H_6 remains virtually constant in the examined temperature range (94.92, 90.99, 92.28, 98.22, 88.84, 89.55%). The yield of other saturated hydrocarbons is almost equal to that in $Cd(CH_3)_2$ thermolysis. The increase in the content of unsaturated hydrocarbons C_5H_{10} and C_3H_6 by 2 and 1–1.5%, respectively, is due to reaction of $\ddot{C}H_2$ radical with C_nH_{2n+2}.

The most probable reactions of chain propagation and termination in thermolysis of a $Cd(CH_3)_2$–$Te(CH_3)_2$ mixture are similar to those occurring in thermolysis of the components. The CH_2 radical is involved not only in the above reactions but also in reaction (8)

$$Te(CH_3)_2 + \ddot{C}H_2 \rightarrow C_2H_5TeCH_3, \quad (8)$$

which decreases the C and H content in the condensed phase. With increasing temperature reactions of CH_2 radical decrease the CH_4 yield and the C : H ratio in the solid product. Thus, formation of $\ddot{C}H_2$ radical in thermolysis of $Cd(CH_3)_2$, which, in its turn, participates in thermolysis of $Te(CH_3)_2$, decreases the carbon content in the final product. Hence, the purity of the solid thermolysis product can be increased by increasing thermolysis temperature.

CONCLUSION

The data on thermolysis of dimethyltellurium, dimethylcadmium, and their mixture can be used to optimize the conditions of preparation of CdTe semiconductor and doping of other semiconductors with cadmium and tellurium by metal–organic chemical vapor deposition.

REFERENCES

1. Mashita, M., *Jpn. J. Appl. Phys., Part 1*, 1990, vol. 29, no. 5, pp. 2538–2540.
2. Galliulina, R.F., Pavlenko, E.A., Druzhkov, O.N., *et al*., *Tr. Khim. Khim. Tekhnol*. (Gor'kii), 1975, no. 5, pp. 82–83.
3. Yablokov, V.A., Dogovorov, A.V., Zorin, A.D., *et al*., *Zh. Obshch. Khim*., 1986, vol. 56, no. 7, pp. 1517–1574.
4. Emanuel', N.M. and Knorre, D.G., *Kurs khimicheskoi kinetiki* (Course of Chemical Kinetics), Moscow, Vysshaya Shkola, 1984.
5. Sokolovskii, A.E. and Baev, A.K., *Izv. Vyssh. Uchebn. Zaved., Khim. Khim. Tekhnol*., 1985, vol. 28, no. 2, pp. 30–37.
6. Sokolovskii, A.E. and Baev, A.K., *Zh. Obshch. Khim*., 1984, vol. 54, no. 11, pp. 2559–2566.
7. Magaril, R.O., *Mekhanizm i kinetika gomogennykh termicheskikh prevrashchenii uglevodorodov* (Mechanism and Kinetics of Homogeneous Thermal Transformations of Hydrocarbons), Moscow: Khimiya, 1970.
8. Sokolovskii, A.E. and Baev, A.K., *Izv. Vyssh. Uchebn. Zaved., Khim. Khim. Tekhnol*., 1993, vol. 36, no. 6, pp. 31–36.

Russian Journal of Applied Chemistry, Vol. 75, No. 1, 2002, pp. 162–163. Translated from Zhurnal Prikladnoi Khimii, Vol. 75, No. 1, 2002, pp. 162–163.
Original Russian Text Copyright © 2002 by Khalizov, Bayunov, Kolikova.

BRIEF COMMUNICATIONS

Resistance of Electrolyte in Pores of Lead Battery Electrodes

I. F. Khalizov, V. V. Bayunov, and G. A. Kolikova

Istochnik Battery Research Institute, Open Joint-Stock Company, St. Petersburg, Russia

Received June 13, 2001

Abstract—Relations for calculating the active resistance of electrolyte in pores of lead battery electrodes are proposed, and necessity for taking it into account in determining the active resistance of batteries is demonstrated.

Of particular interest in designing high-capacity lead batteries is determination of their electrical characteristics: dependence of the voltage U on the discharged capacity Q or time τ in various discharge modes at constant current I or power P:

$$U = f(Q),\ U = f(\tau) \text{ at } I = \text{const},\ P = \text{const}. \quad (1)$$

These calculations require that the internal resistance of a battery should be known. It is known that the internal resistance R of a battery is constituted by the active resistance R_a and polarization resistance R_p:

$$R = R_a + R_p. \quad (2)$$

The polarization resistance of a high-capacity battery can be found from service characteristics of a small battery using simulation. The components of the active resistance [resistances of positive and negative electrodes (R_+ and R_-), electrolyte with separator (R_e), and terminals (R_t)] are found by calculation:

$$R_a = R_+ + R_- + R_e + R_t. \quad (3)$$

The electrode resistance includes the resistances of current leads, active paste (as a conductor), contact resistance between the active paste and current lead, and resistance of active paste within cells.

From dependence (3) follows that the active resistance of the electrolyte in electrode pores is disregarded, and, therefore, it is included in calculations in the polarization resistance, which is not described by the Ohm law and depends on current. That is why an error is made in calculating the polarization resistance of small and large batteries. Let us evaluate this error.

In [1, 2], data on the porosity of the active paste, pore tortuosity, and relative resistance of electrolyte in pores of lead battery electrodes were reported. It is proposed to use these data to calculate the resistance of electrolyte in pores of positive and negative electrodes, R_{ep}, using the relations

$$R_{ep} = \frac{0.335\,\beta\, b/2}{SnP}\rho, \quad (4)$$

$$R_{ep} = \frac{0.335\,\rho_{rel}\, b/2}{Sn}\rho, \quad (4)$$

where b is the electrode thickness, S is the geometric surface area of the electrode, n is the number of positive or negative electrodes in a unit, β is the coefficient of pore tortuosity in the active paste, P is the porosity of the active paste, ρ_{rel} is the relative resistance of electrolyte in the electrode pores, ρ is the resistivity of electrolyte in the pores, and 0.335 is the coefficient of equivalence of the resistance of electrolyte in the electrode pores for the case of a uniform distribution of current density in the pores.

The resistances of electrolyte in pores of the positive and negative electrodes of a unit, calculated using relations (4) and (5), add up.

The resistances of electrolyte in the electrode pores, found using relations (4) and (5) for a stationary lead battery with capacity of 600 A h, differed by 23%. It is preferable to perform calculations with relation (5), since the error is diminished in this case because the relative resistance of the electrolyte in pores accounts for the pore tortuosity coefficient and the porosity of the active paste.

A calculation demonstrated that the active resistance R_a of the battery is, respectively, 1.69×10^{-4} and 1.768×10^{-4} Ω after 3–10 and 0.25–1 h of discharge,

1070-4272/02/7501-0162$27.00 © 2002 MAIK "Nauka/Interperiodica"

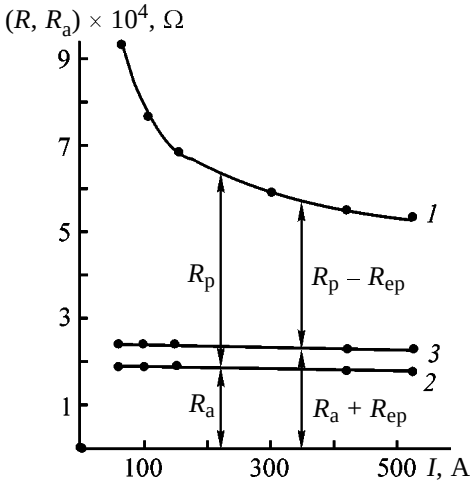

(*1*) Total (R) and (*2*, *3*) active (R_a) resistances of battery vs. discharge current I (*2*) without and (*3*) with account of the electrolyte resistance in pores.

and, with account of R_{ep}, 2.402×10^{-4} and 2.301×10^{-4} Ω for the same discharge modes. Thus, the active resistance R_a increased, with account of R_{ep}, by 28.5 and 30% after discharge for, respectively, 3–10 and 0.25–1 h.

The changes in the total battery resistance R, active resistance R_a, and polarization resistance R_p after 0.25–10 h of discharge, found with and without account of the electrolyte resistance in electrode pores, are presented in the figure. In calculations, the electrolyte densities in electrode pores and box of a charged battery were taken to be equal. The polarization resistance R_p decreased after 0.25 and 10 h of discharge by, respectively, 15 and 7%. These data point to the necessity for taking into account the resistance of electrolyte in the electrode pores, R_{ep} [relation (5)], in determining the active resistance of large and small batteries with the use of relation (3).

REFERENCES

1. Bessonova, T.M., Bol'shakova, N.V., and Zhivotinskii, P.B., in *Sbornik rabot po khimicheskim istochnikam toka* (Coll. of Works on Chemical Power Cells), Leningrad: Energiya, 1971, issue 6, pp. 28–34.
2. Bessonova, T.M., Zhivotinskii, P.B., and Marasanova, A.N., in *Sbornik rabot po khimicheskim istochnikam toka* (Coll. of Works on Chemical Power Cells), Leningrad: Energiya, 1975, issue 10, pp. 140–144.

Russian Journal of Applied Chemistry, Vol. 75, No. 1, 2002, pp. 164–165. Translated from Zhurnal Prikladnoi Khimii, Vol. 75, No. 1, 2002, pp. 164–165.
Original Russian Text Copyright © 2002 by Aronova, Ginak.

BRIEF COMMUNICATIONS

Efficient Synthesis of 3-Acyl-5-arylmethylene-4-oxothiazolidine-2-thiones

E. B. Aronova and A. I. Ginak

St. Petersburg State Technological Institute, St. Petersburg, Russia

Received June 27, 2001

Abstract—An efficient procedure was suggested for preparing 3-acyl-5-arylmethylene-4-oxothiazolidine-2-thiones.

3-Acyl-5-arylmethylene-4-oxothiazolidine-2-thiones are intermediates in synthesis of practically important substances: pesticides, drugs, dyes, vulcanizing agents, antioxidants, etc. [1]. These compounds are prepared in solutions by reactions of appropriate acyl chlorides with 5-arylmethylene-4-oxothiazolidine-2-thiones in the presence of bases [2, 3]. The reactions are accompanied by hydrolysis with ring cleavage, which decreases the yield of the target products by 25–40% and complicates their isolation from reaction mixtures. Synthesis of 3-acyl-5-arylmethylene-4-oxothiazolidine-2-thiones by cyclization from appropriate amides and carbon disulfide [4] is multistage and gives poor yields. Therefore, we suggest in this paper a procedure for preparing 3-acyl-5-arylmethylene-4-oxothiazolidine-2-thiones by direct acylation of solid alkali metal salts of 5-arylmethylene-4-oxothiazolidine-2-thiones with vapors of appropriate acyl chlorides (see table). It is known [5] that nucleophilic substitution reactions of solid ambident substrates with gaseous electrophiles are selective and are not complicated by degradation.

The reaction was performed in a tubular reactor (1 cm in diameter, 10 cm high) equipped with controllable (70–250°C) electric heating. Acyl chloride vapor mixed with an inert gas (nitrogen, argon) was passed through a substrate bed. The reaction progress was monitored by TLC. After reaction completion, excess acyl chloride was removed in a vacuum.

The acylation pathway was judged from the hydrolysis products. Addition of the acyl group to the nitrogen atom in the heterocycle follows from formation of the initial 5-arylmethylene-4-oxothiazolidine-2-thione in hydrolysis, according to the scheme

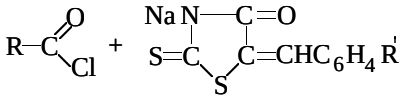

Yields after recrystallization *Y*, decomposition points T_{dec}, and elemental analyses of oxothiazolidinethiones **Ia**–**Ij**

Compound	*Y*, %	T_{dec}, °C	Found, %/Calculated, %		Formula
			N	S	
Ia	66.2	132–132.5	5.40/5.32	23.24/24.35	$C_{12}H_9NO_2S_2$
Ib	74.5	154–155	4.31/4.35	19.99/19.71	$C_{17}H_{11}NO_2S_2$
Ic	71.1	147–148	3.88/3.94	18.47/18.04	$C_{18}H_{13}NO_3S_2$
Id	72.8	137–138	4.04/4.08	19.48/18.68	$C_{17}H_{10}NO_2S_2F$
Ie	73.6	176–177	4.36/4.13	18.13/18.89	$C_{18}H_{13}NO_2S_2$
If	76.7	155–156	3.83/4.13	18.15/18.89	$C_{18}H_{13}NO_2S_2$
Ig	69.2	184–185	4.16/3.94	18.02/18.04	$C_{18}H_{13}NO_3S_2$
Ih	74.5	211–212	4.05/3.89	16.92/17.82	$C_{16}H_{10}NO_2S_2Cl$
Ii	67.2	219–220	7.97/7.60	17.97/17.40	$C_{19}H_{16}N_2O_2S_2$
Ij	68.1	215–216	7.12/7.56	17.01/17.31	$C_{17}H_{10}N_2O_4S_2$

1070-4272/02/7501-0164$27.00 © 2002 MAIK "Nauka/Interperiodica"

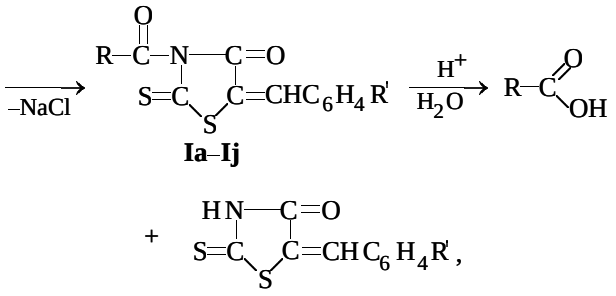

Ia–**Ij**

where R = Me, R' = H (**a**); R = Ph, R' = H (**b**); R = *p*-$CH_3OC_6H_4$, R' = H (**c**); R = *p*-FC_6H_4, R' = H (**d**); R = *p*-$CH_3C_6H_4$, R' = H (**e**); R = Ph, R' = *p*-CH_3 (**f**); R = Ph, R' = *p*-CH_3O (**g**); R = Ph, R' = *p*-Cl (**h**); R = Ph, R' = *p*-$N(CH_3)_2$ (**i**); and R = Ph, R' = *p*-NO_2 (**j**).

The structure of hydrolysis products was confirmed by independent synthesis [6] and TLC (Silufol UV-254, acetone–hexane–acetic acid, 1 : 2 : 0.01 [7]), and the structure of **Ia**–**Ij**, by coincidence of their UV and IR spectra with those of the known compounds [8].

REFERENCES

1. Brown, T.S., *Chem. Rev.*, 1961, vol. 61, no. 5, pp. 463–521.
2. Granacher, C., *Helv. Chim. Acta*, 1920, vol. 3, no. 2, pp. 150–158.
3. Sytnik, Z.P., Natanson, S.V., Deichmeister, M.V., and Zhilina, L.D., *Zh. Obshch. Khim.*, 1952, vol. 22, no. 4, pp. 705–711.
4. Campbell, N. and McKail, J.E., *J. Chem. Soc.*, 1948, no. 10, pp. 1248–1255.
5. Ginak, A.I., V'yunov, K.A., and Ramsh, S.M., *Zh. Org. Khim.*, 1983, vol. 19, no. 1, pp. 209–212.
6. Ginak, A.I., V'yunov, K.A., and Sochilin, E.G., *Khim. Geterotsikl. Soedin.*, 1971, no. 3, p. 858.
7. Bolliger, H.R., Brenner, M., and Gänshirt, H., *Dünnschicht Chromatographie. Ein Laboratoriumshandbuch*, Stahl, E., Ed., Berlin: Springer, 1962.
8. V'yunov, K.A., Ginak, A.I., and Sochilin, E.G., *Zh. Prikl. Spektrosk.*, 1972, vol. 16, no. 6, pp. 1037–1042.

Russian Journal of Applied Chemistry, Vol. 75, No. 1, 2002, pp. 166–167. Translated from Zhurnal Prikladnoi Khimii, Vol. 75, No. 1, 2002, pp. 166–167.
Original Russian Text Copyright © 2002 by Altunina, Gossen, Tikhonova, Yarmukhametova.

MACROMOLECULAR CHEMISTRY AND POLYMERIC MATERIALS

Structural Changes in Cellulose-Containing Materials in the Course of Mechanical Activation

L. K. Altunina, L. P. Gossen, L. D. Tikhonova, and E. G. Yarmukhametova

Institute of Petroleum Chemistry, Siberian Division, Russian Academy of Sciences, Tomsk, Russia

Received February 22, 2001

Abstract—The structure of cellulose-containing materials (powdered cellulose and rice husk) subjected to mechanochemical treatment was studied.

Mechanical treatment is known to affect the reactivity of a solid and cause distortions in its structure [1, 2]. Because IR spectroscopy is widely used for monitoring various structural transformations of cellulose [3, 4], we chose this method for studying structural changes in mechanically treated cellulose samples. Experiments were performed with rice husk as a vegetable material containing about 40% cellulose; powdered cellulose was used as reference.

EXPERIMENTAL

The IR spectra were recorded on a Specord spectrophotometer in the range 400–4000 cm^{-1}. Samples were prepared as KBr pellets (1 mg of substance per 300 mg of KBr). The band at 900 cm^{-1} was resolved graphically. The IR spectral coefficients of the analytical absorption bands were calculated from the corresponding optical densities.

The mechanical activation of cellulose and rice husk samples was performed with an MA-1 laboratory planetary activator. The microstructure of the mechanically treated samples was studied with a Neophot-2 optical microscope equipped with a scanning attachment for transferring the image to a computer. The ESR spectra of mechanically treated samples were recorded with a Radiopan SE/X 2544 spectrometer operating at 9.1 GHz.

Cellulose and rice husk samples were mechanically activated for various times. Samples placed in an activator are subject to loads causing dispersion and plastic deformations; these processes affect the bond lengths in the molecules of sample components. The shearing component of the mechanical force field alters the bond angles. As a result, the band of the CH_2 rocking vibrations at 900 cm^{-1} grows in intensity. This effect is directly related to changes in the conformation of pyranose units, associated with the loss of the sample crystallinity in the course of crushing. The increased intensity of the band at 900 cm^{-1} in the spectra of samples with the lost crystallinity was noted in numerous papers [5, 6]. The IR examination of mechanically treated samples of rice husk and powdered cellulose also revealed broadening of the band at 1066 cm^{-1}. This effect depended on the time of mechanical treatment and for rice husk was noticeable from the first minutes of the treatment (the half-width increased by 20 cm^{-1}). For cellulose, this effect was more pronounced in samples activated for 10–30 min; the half-width increased by 10 cm^{-1}. The vegetable raw materials contain pectin substances, hemicelluloses, lignin, and low-molecular-weight components capable of generating radicals in the course of mechanical treatment. Tasking into account the ESR data, we can suggest that the radicals generated from the low-molecular-weight components of mechanically treated rice husk samples owing to self-heating in the activator recombine to form new C–C bonds (including rings) and C–O bonds whose vibrations overlap with the similar vibrations of the cellulose moiety, causing the band broadening. As a result, the intensity of the band at 900 cm^{-1} increases at the expense of increased absorption at the wing of the broad strong band at 1066 cm^{-1}. Variation of the spectral coefficients calculated for the graphically resolved band at 900 cm^{-1} (Fig. 1a) reflects the fact that the crystallinity of powdered cellulose and rice husk in the course of mechanical treatment passes through several extrema.

Variation of the spectral coefficients calculated for the band at 1430 cm^{-1}, originating from the in-plane bending vibrations of the C–H bonds in the CH_2OH group and characterizing the level of the supramolec-

1070-4272/01/7501-0166$27.00 © 2002 MAIK "Nauka/Interperiodica"

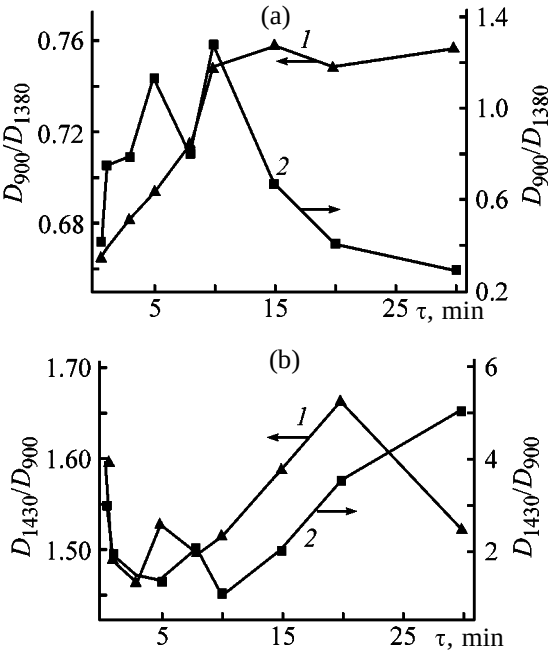

Fig. 1. Variation with the mechanical treatment time τ of the IR spectral coefficients (a) D_{900}/D_{1380} and (b) D_{1430}/D_{900} characterizing the crystallinity and supramolecular structure of the samples, respectively. (*1*) Powdered cellulose and (*2*) rice husk.

ular ordering of the polymer [5, 6], shows that at mechanical treatment of both rice husk and powdered cellulose samples the loss of the crystallinity is accompanied by formation of supramolecular structures (Fig. 1b). Hence, increase in the crystallinity of the samples involves the recrystallization stage, which is characteristic of crystalline polymers subjected to mechanical loads. Apparently, in mechanically treated rice husk samples containing radicals, the condensation products appearing after 10-min activation become centers of new enlarged formations, and the degree of supramolecular ordering increases (Fig. 1b, curve *2*). Simultaneously increases the degree of crystallinity (Fig. 1a, curve *2*). These data show that free radicals also participate in processes related to the loss of the total crystallinity of the samples.

In the samples of mechanically treated cellulose, in which the content of radicals is insignificant, the crystallinity and supramolecular structure vary to a lesser extent. After 20-min treatment, the crystallinity of the cellulose samples increases (Fig. 1a, curve *1*) owing to recrystallization, but the new formations with the more ordered supramolecular structure are not retained by exchange interaction forces because of the low content of radicals and are broken down under the action of mechanical forces, so that both the supramolecular ordering and the crystallinity decrease after treatment for 30 min (Figs. 1a, 1b, curves *1*). The observed rearrangement of the supramolecular structure of the samples is well consistent with variation in the course of mechanical treatment of the shape of some narrow bands in the range 1300–1500 cm^{-1}, sensitive to chemical and structural changes [7].

Photomicrographic analysis allows monitoring of changes occurring on the supramolecular level in cellulose and in cellulose components of rice husk in the course of mechanical treatment, namely, of the initial ordered structure of cellulose and of its breakdown under the action of mechanical forces. Changes in the relative intensity of the band at 1430 cm^{-1} also correspond to changes in the structure of rice husk and cellulose. The repeating processes of breakdown and formation of various crystalline modifications in the samples subjected to mechanical treatment give rise to several extrema in the curves of the relative optical densities, characterizing the changes in the crystallinity and supramolecular ordering, vs. activation time.

Our results can be used for studying the reactivity of cellulose-containing products subjected to mechanical and mechanochemical activation and developing procedures, based on mechanochemical treatment, for preparing new cellulose-containing polymeric compounds.

CONCLUSIONS

IR spectroscopic and optical microscopic study of the structure of powdered cellulose and rice husk subjected to mechanochemical activation revealed a complex (with several extrema) pattern of variation of their crystallinity and supramolecular ordering.

REFERENCES

1. Klenkova, N.I., *Struktura i reaktsionnaya sposobnost' tsellyulozy* (Structure and Reactivity of Cellulose), Leningrad: Nauka, 1976.
2. Lomovskii, O.I., *Khim. Inter. Ustoich. Razv.*, 1994, no. 1, pp. 473–482.
3. Higgins, H.G. and McKenrie, A.W., *Aust. J. Appl. Sci.*, 1958, vol. 9, no. 2, pp. 167–182.
4. Levitsky, H. and Norwits, G., *Anal. Chem.*, 1962, vol. 34, no. 9, pp. 1167–1169.
5. French, R.O., Wadsworth, M.E., Cook, M.A., and Gutler, I.B., *J. Phys. Chem.*, 1954, vol. 58, no. 10, pp. 805–816.
6. Beker, A.W., *J. Phys. Chem.*, 1957, vol. 61, no. 4, pp. 450–458.
7. Zhbankov, R.G., *Infrakrasnye spektry tsellyulozy i ee proizvodnykh* (Infrared Spectra of Cellulose and Its Derivatives), Minsk: Nauka i Tekhnika, 1964.

Russian Journal of Applied Chemistry, Vol. 75, No. 1, 2002, pp. 168–169. Translated from Zhurnal Prikladnoi Khimii, Vol. 75, No. 1, 2002, pp. 168–169.
Original Russian Text Copyright © 2002 by G. Zaikov, V. Zaikov.

INFORMATION

222nd ACS National Meeting. International Symposium on PVC and Related Polymers (Chemistry and Applications)

The 222nd American Chemical Society National Meeting was held from August 26 to 30, 2001, in Chicago, IL (the United States). Generally, such meetings are held twice a year (Fall and Spring meetings), and the next meeting will be held in April 2002 in Orlando, FL. More than 15000 scientists primarily from the United States and also from practically all the industrial countries participated in this Fall Meeting. The Meeting included various sessions, theoretical and practical symposia, seminars, and exhibitions.

Let us focus on the symposium *"PVC and Related Polymers: Chemistry and Applications,"* which was held in the framework of the ACS Meeting from August 28 to 30, 2001. The symposium organizers were W.H. Starnes, Jr. (Williamsburg, the United States) and D.E. Witenhafer (Dublin, the United States). Note that it was the first symposium on PVC in recent two decades. The symposium covered the topical theoretical and applied aspects of PVC chemistry and technology. The symposium participants were about 150 scientists from Canada, China, Czech Republic, Egypt, France, Germany, Hungary, India, Italy, Japan, Poland, Russia, Singapore, Spain, Sweden, Switzerland, the United Kingdom, and the United States, representing more than 50 research centers all over the world.

More than 30 plenary lectures were presented, and a great body of information was given in the poster session that preceded the main program of the symposium. In the opening ceremony, Prof. W.H. Starnes outlined the topicality of the problems to be discussed and their importance from the theoretical and practical standpoints. The major attention was paid to such topics concerning PVC as polymerization, physical properties, structure, chemical modification, additives, PVC modifiers including stabilizers and plasticizers, PVC degradation and stabilization, and PVC flammability and fire retardance.

Four sessions were held. The topic of the first session was *Polymerization and Structural Modification.* The first lecture entitled *PVC: Origin, Growth, and Future* was given by D. Braun (Darmstadt, Germany). Particularly, he said that in 2001 the humanity commemorated the 70th anniversary of PVC industrial use, and presently PVC is a large-tonnage polymer, whose production steadily grows and application area expands. The next three lectures were devoted to efforts aimed at PVC manufacture by nonradical pathways. K. Endo, N. Kaneda, H. Waku, M. Saitoh, and N. Emori (Osaka, Japan) gave a lecture on controlled polymerization of vinyl chloride with butyllithium and metallocene catalysts. R.F. Jordan (Chicago, the United States) reported on the attempts to apply single site olefin polymerization catalysts to vinyl chloride. The third lecture of this series [H.W. Boone, M.J. Mullins, P.S. Athey, and R.V. Snelgrove (Freeport, the United States)] was devoted to the possibility of using transition-metal catalysts for polymerization of vinyl chloride and also to new approaches to effective employment of these catalytic systems. The next series of contributions concerned chemical modification of PVC and development of new materials on its basis. The first lecture of this series entitled *New Polymers by Living Radical Graft Copolymerization Initiated from the Structural Defects of Poly(vinyl chloride) and by Living Radical Polymerization of Vinyl Chloride* was given by V. Percec, A.D. Asandei, F. Asgarzadeh, E. Ramirez, and A. Capotto (Philadelphia, the United States). Z. Pi and J.P. Kennedy (Akron, the United States) reported on new PVC derivatives obtained by carbocationic techniques. M.N. Guarrotxena (Madrid, Spain) focused in his lecture on stereochemical microstructure dependence of physical properties of PVC. Finally, the last lecture of the first session given by T. Szakacs, B. Ivan, and F. Pollreisz (Budapest, Hungary) was devoted to degradative transformations of poly(vinyl chloride) to new potentially useful products. The topic of the second session was *Physical Properties and Blends*. The questions concerning cross-linking and orientation of PVC were considered in the lecture given by M. Gilbert and D.J. Hitt (Loughborough, the United Kingdom). Considerable interest was expressed by the participants in the results reported by D. Wang, D. Parlow, and C.A. Wilkie (Milwaukee, the United States) in their lecture entitled *PVC–Clay Nanocomposites: Preparation, Thermal, and Mechanical Properties.* The questions of retrostructural analysis of PVC particles were considered by R.E. Lukas (Prague, Czech Republic). G.R. Mitchell, T. Gkourmpis, Y.-S. Chiou,

1070-4272/02/7501-0168$27.00 © 2002 MAIK "Nauka/Interperiodica"

W.H. Starnes, and V.G. Zaikov (Williamsburg, the United States; Reading, the United Kingdom) reported on X-ray and neutron scattering study of the local structure of PVC. The lecture given by E.M. Pearce (New York, the United States) and K. Pielichowski (Krakow, Poland) was devoted to preparation and properties of PVC blends with conducting polymers. Compatibilization of blends containing poly(vinyl chloride) and a polyolefin elastomer by block chlorinated polyethylenes was reported by E.A. Eastwood, M.D. Dadmun, N. Pourahmady, and C. Lepilleur (Knoxville, the United States). The next lecture given by D. Garcia, F. Borden, and E. Bouveresse (Pennsylvania, the United States) concerned the problems of identification, quantitation, and qualification of PVC multifunctional additive systems with near-IR spectroscopy and chemometrics.

The topic of the third session was *PVC Degradation and Weathering.* The first lecture given by G.E. Zaikov (Moscow, Russia) and K.S. Minsker (Ufa, Bashkortostan, Russia) reviewed the works conducted in Russia on studying PVC degradation and searching for methods for its stabilization. Results on prediction of pinking of PVC profiles in mild climatic conditions were reported in the lecture given by J.E. Lemaire (Aubiere, France). C. Decker (Mulhous, France) spoke about photostabilization of PVC by protective coatings. The lecture given by J.W. Summers and E.B. Rabinovitch (Cleveland, the United States) was devoted to weatherability of PVC plastics, changing of their mechanical characteristics, and possible stabilization methods. The problems of environmental pollution with PVC wastes and possible protection measures were considered in the lecture entitled *Fate of PVC Polymer and Plasticizers in Landfills* given by I. Mersiowsky, M. Weller (Stuttgart, Germany), and J. Ejlertsson (Stockholm, Sweden).

The last two lectures of this session were devoted to chemiluminescence study of medical PVC degradation and comparison with other techniques [L. Woo, S.Y. Ding, and C.L. Sandford (Stanford, the United States)] and radiation-induced degradation of vinyl chloride/vinylidene chloride copolymers [B.A. Howell, S.I. Ahmed, and D.E. Beyer (Michigan, the United States)]. Finally, the topic of the fourth session was *Thermal Degradation and Stabilization*. I.W. Parsons and R.S. Lehrle (Birmingham, the United Kingdom) reported on HCl quantification in pyrolysis-gas chromatography studies of hydrochlorocarbon polymers. B. Ivan (Hungary) gave in his lecture a critical overview of PVC stabilization mechanisms in the light of recent experimental results. Considerable interest among the participants was generated by a lecture given by M. Edge, H. Chaudhry, and N.S. Allen (Manchester, the United Kingdom), which was entitled *Mechanistic Action of Costabilizers for PVC* and devoted to the mechanism of action of costabilizers including the synergistic and antagonistic effects. In the next lecture, S. Kodali, W. Hood, T. Jennings, and M. Fender (Dower, the United States) reported on highly basic calcium stearate compositions for rigid PVC.

The last three lectures in this session were devoted to the use of phosphite ester compositions for PVC stabilization [D.R. Stevenson, M.E. Harr, and M.R. Jakupca (Dower, the United States)], stabilization of vinyl chloride/vinylidene chloride copolymers using *N*-substituted maleimides [B.A. Howell and J. Zhang (Michigan, the United States)], and, finally, development of a remarkable new class of nonmetallic additives for PVC , "plasticizer thiols," which are simultaneously stabilizers and plasticizers [W.H. Starnes, B. Du, and V.G. Zaikov (Williamsburg, the United States)].

Finally, it follows from the contributions presented at the symposium that, regardless of anything, for example, of well-known environmental problems, the interest in PVC is steadily high, owing to its low cost and unique physicochemical characteristics (note that the annual world output of PVC is about 22 mln tons). Symposium contributions will be published in 2002 in *J. Vinyl Additive Technol*. (the United States).

The titles of all reports presented at the 222nd ACS National Meeting and presenters' names are available from the library of the Institute of Chemical Physics, Russian Academy of Sciences (Moscow, Russia).

G. E. Zaikov and V. G. Zaikov

Russian Journal of Applied Chemistry, Vol. 75, No. 2, 2002, pp. 171–176. Translated from Zhurnal Prikladnoi Khimii, Vol. 75, No. 2, 2002, pp. 177–182.
Original Russian Text Copyright © 2002 by Kuznetsov, Zhizhaev, Kuznetsova.

INORGANIC SYNTHESIS AND INDUSTRIAL INORGANIC CHEMISTRY

Mechanochemical Synthesis of Nanosize Metastable Zirconium Oxide

P. N. Kuznetsov, A. M. Zhizhaev, and L. I. Kuznetsova

Institute of Chemistry and Chemical Engineering, Siberian Division, Russian Academy of Sciences, Krasnoyarsk, Russia

Received June 26, 2001

Abstract—The formation of oxide phases in the course of mechanical activation of amorphous zirconium hydroxide was studied.

Zirconium(IV) oxide–based catalysts for low-temperature isomerization of alkanes are prepared in several prolonged stages including deposition of a precursor and its crystallization, sulfonation, and thermal activation. The catalyst activity is governed by the superacidic properties of the sulfonated surface [1, 2]. An important part is played by the phase composition of zirconium(IV) oxide, which can exist in several crystalline modifications: monoclinic, stable at temperatures of up to 1172°C; tetragonal, stable in the range 1172–2347°C; and cubic, stable above 2347°C. The monoclinic ZrO_2 has low catalytic activity in isomerization and alkylation and has no practical importance as catalyst for these processes, irrespective of the activation temperature [1]. The highest efficiency is exhibited by catalysts based on tetragonal ZrO_2 [1–3].

The tetragonal modification of zirconium(IV) oxide can coexist as a metastable phase with the monoclinic form at low temperatures, if it consists of fine crystallites ($D \le$ ~30 nm [1] or $D \le$ ~10–15 nm [2]). Small particles are stabilized by addition of ~2–3 mol % oxides in the lowest oxidation state (Y_2O_3, Fe_2O_3, Mn_2O_3, and CaO), which form a solid solution on the surface [1, 3–5]. Fine particles can also be stabilized by sulfonation of amorphous zirconium(IV) hydroxide [1–5]. This results in the formation and stabilization of the tetragonal phase upon crystallization in the presence of doping additives. At higher concentrations of dopants (~5 mol %) [5, 6], the cubic modification of zirconium dioxide is stabilized.

Crystallization of the tetragonal zirconium(IV) oxide is a necessary, but insufficient condition for the existence of its catalytic activity. The catalytic activity is exhibited by acidic centers on the catalyst surface. This factor is the most pronounced when Lewis and Brønsted acids are present on the surface simultaneously [5, 7]. The acidity creates a covalent sulfate localized at crystallographic defects of the ZrO_2 tetragonal phase. It has been established in a number of studies that it is the amorphous zirconium(IV) hydroxide that should be sulfonated [1, 3–5]. Samples prepared by direct sulfonation of any crystalline phase of ZrO_2 are virtually inactive [1, 3]. The presence of sulfate ions in crystallization initiates formation of a great number of defects, but no new defects appear in sulfonation in the already formed rigid structures. At the same time, a catalyst can be obtained on the basis of calcined crystalline samples, if they retain a sufficient number of OH groups [4, 7]. High-temperature methods are known to yield a material with very low content of OH^- groups, and, therefore, the activity of such catalysts is poor. Lowering the temperature of sol–gel synthesis allows preparation of a crystalline phase with high concentration of hydroxide ions, the most appropriate for sulfonation and formation of the catalytic activity [4, 6, 7].

It is known that preliminary high-energy mechanical treatment makes it possible to lower the temperature of subsequent chemical processes [8], including solid-phase synthesis of high-temperature oxide catalysts from a reagent mixture [9]. This method enables generation of new kinds of defects and formation of a strongly distorted crystal lattice, which is important for structure-sensitive catalytic reactions [9, 10]. Mechanical activation of hydroxides results in a redistribution of bulk hydroxide groups in favor of single surface groups and closely spaced terminal

1070-4272/02/7502-0171 $27.00 © 2002 MAIK "Nauka/Interperiodica"

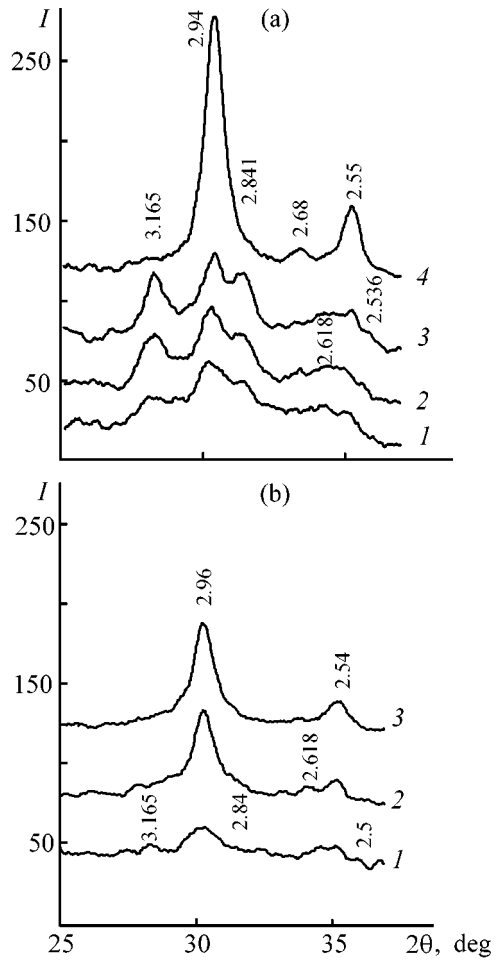

Fig. 1. Diffraction patterns of the fractions of the amorphous zirconium hydroxide mechanically activated in (a) dry and (b) wet regime. (*I*) Intensity and (2θ) Bragg angle; the same for Fig. 3. Treatment time τ (min): (*1*) 0.5, (*2*) 2, (*3*) 5, and (*4*) 15.

groups [10, 11]. A hydroxide "fringe" is formed around particles of oxide minerals, which facilitates sulfonation and formation of superacidic Lewis centers [4, 11] and acid Brønsted protons [5, 10]. Even when the required product is not formed in the course of activation of precursors (oxides or carbonates), the generated defects accelerate the diffusion and interaction of the reagents in the subsequent calcination [9, 12–14]. This makes it possible to lower the synthesis temperature and obtain mechanically activated crystalline products competitive with those produced with precursors prepared by sol–gel technology [11, 14–16].

Thus, there arises practical interest in use of mechanical activation of precursors of zirconium catalysts for lowering the synthesis temperature and enhancing the catalytic activity.

In this study, mechanochemical synthesis of a tetragonal modification of ZrO_2 was performed and the specific features of this process were analyzed.

EXPERIMENTAL

Highly dispersed amorphous zirconium hydroxide was obtained by precipitation from a 15% aqueous solution of $ZrOCl_2$ with 12% aqueous ammonia at room temperature and vigorous agitation. The gels prepared were kept for 3 h and then washed by decantation and on a filter with distilled water to negative reaction for Cl^- ions. The precipitate was dried in air at room temperature and then in a desiccator at 11°C for 15 h. Also, commercial reactive zirconium oxide of pure grade was used.

The mechanochemical activation was performed in an AGO-2 centrifugal-planetary mill for 0.5–22 min. The volume of the steel drums was 150 ml; weighed portion of a material, 3 g; mass of steel milling bodies 3 mm in diameter, 106 g; and load, 60 g. In the "wet" mode of activation, distilled water (3 ml) was poured into each drum. The drums were cooled with water in the course of the operation. Simultaneous grinding in dry mode was performed on an KM-1 lab vibration mill for 0.5–10 h (agate mortar, agate ball 3 cm in diameter, and 3-g weighed portion).

X-ray diffraction patterns were recorded on a DRON-3 diffractometer (Cu_{K_α} radiation, scan rate 1 deg min^{-1}).

An electron-microscopic study was done on a REMMA-202M scanning microscope. The statistical-average size of particles of the material studied was calculated from the specific surface area, as determined by thermal desorption of argon (BET).

The starting zirconium hydroxide prepared by precipitation is virtually completely X-ray-amorphous. Very weak reflections attributable to a monoclinic modification of zirconium dioxide are present in diffraction patterns in some cases. Zirconium hydroxide, having no regular crystal structure, is a mixture of compounds of variable composition $ZrO_n(OH)_{4-2n} \cdot xH_2O$, where $n = 0–2$. The presence of nuclei of the monoclinic phase, which starts crystallizing on heating the given sample even to 250–300°C, is rather probable. Dehydration in subsequent heating in the range 300–500°C leads to the formation of a monoclinic modification of the oxide phase (mainly) and its tetragonal modification (in minor amounts). At higher temperatures, the metastable tetragonal form transforms into a monoclinic oxide form. Calcination at 600–700°C yields virtually pure monoclinic zirconium dioxide.

The mechanical activation initiates fast crystallization of zirconium dioxide at room temperature. Weak diffuse reflections associated with this phase were recorded in diffraction patterns even after 30 s of treatment in a planetary mill (Fig. 1a, curve *1*). Further activation leads to recrystallization of the amorphous sample. Two crystalline modifications of ZrO_2 are formed, with the amount of the monoclinic phase growing faster (Fig. 1a, curves *1*–*3*). A sample treated for 5 min is a mixture of the monoclinic (d = 3.165, 2.841 Å, ICDPS, 24-1165) and tetragonal (d = 2.94 Å, ICDPS, 17-923) forms in 70 : 30 percentage ratio (Fig. 1a, curve *3*). The nearly equal intensities of the main reflections are a consequence of the higher symmetry of the tetragonal phase.

Figure 2 shows, according to the electron-microscopy data, the fractional composition of the samples studied. The differential characteristic of the starting amorphous zirconium hydroxide peaks around 3–5 μm. Its calcination in the range 600°C yields coarse particles of monoclinic ZrO_2 (with the peak in the differential characteristic shifted to 8–10 μm). The mechanical activation shifts the distribution maximum to the nanosize region, with mainly tetragonal zirconium dioxide formed.

Diffuse, but strong reflections, attributable solely to the tetragonal modification, are present in the diffraction pattern of the fraction treated for 15 min (Fig. 1a, curve *4*, main peak with d = 2.96 Å). The monoclinic phase is virtually absent. This means that further crystallization of the amorphous phase and recrystallization of the already formed monoclinic zirconium dioxide into the tetragonal form take place. The crystallite size of the tetragonal phase in this sample, calculated from the reflection broadening by the Debye–Scherrer formula, does not exceed 16 nm (see the table). It is interesting to note that the specific surface area of the samples decreases with increasing activation time, i.e., in this case the growth rate of the crystals is higher than their grinding rate.

The obtained result can be accounted for by the removal of "hydroxyl" water via local heating caused by collisions of milling bodies. However, the estimate using indirect data and the results of a calorimetric study shows that the local temperatures occurring in planetary mill treatment are low (not higher than 400–650°C [14]). For a monoclinic–tetragonal zirconium dioxide phase transition to occur, a temperature higher than 1172°C is necessary. The occurrence of that high local temperatures would cause a considerable warming-up of the material and grinding bodies. However, the temperature of the sample increases in the course of treatment only slightly.

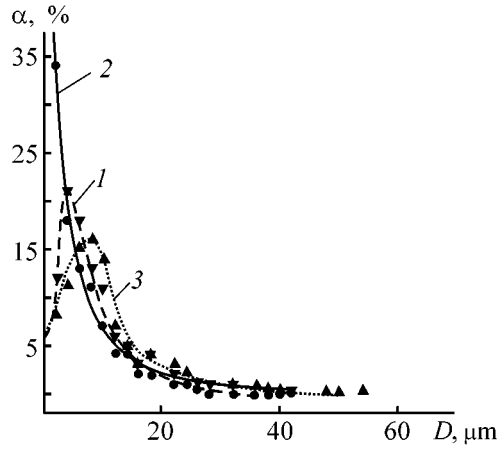

Fig. 2. The fractional composition of the samples studied (according to electron-microscopic data). (α) Particle fraction and (*D*) particle size. Hydroxide: (*1*) starting; (*2*) mechanically treated for 5 min, and (*3*) calcined at 600°C.

Figure 1b shows diffraction patterns of zirconium hydroxide samples mechanochemically activated in wet mode. A more condensed medium favors better removal of heat from the local points of impact interaction, which must lead to weaker crystallization and recrystallization of zirconium dioxide, if these processes are caused by local heating of the material. Nonetheless, the peaks associated with monoclinic (d = 3.165 Å) and tetragonal (d = 2.96 Å) zirconium dioxide are clearly seen in the diffraction patterns even after 2 min of treatment (Fig. 1b, curve *1*). Evidently, the tetragonal phase dominates, although its reflections are considerably broadened. Only trace amounts of monoclinic modification are recorded after 5 min of mechanical activation. At the same time, the reflec-

Dispersity of products obtained upon mechanical activation of amorphous zirconium dioxide*

τ, min	Activation mode	S_{sp}, $m^2\ g^{-1}$	D	D_{tet}
			nm	
–	–	198	5	–
2	Dry	25	32	–
5	〃	19	43	–
15	〃	20	42	16
2	Wet	–	–	9
5	〃	72	12	12
15	〃	–	–	14

* S_{sp} is the specific surface area, D the statistical-average crystallite size, and D_{tet} the crystallite size of the tetragonal phase of ZrO_2.

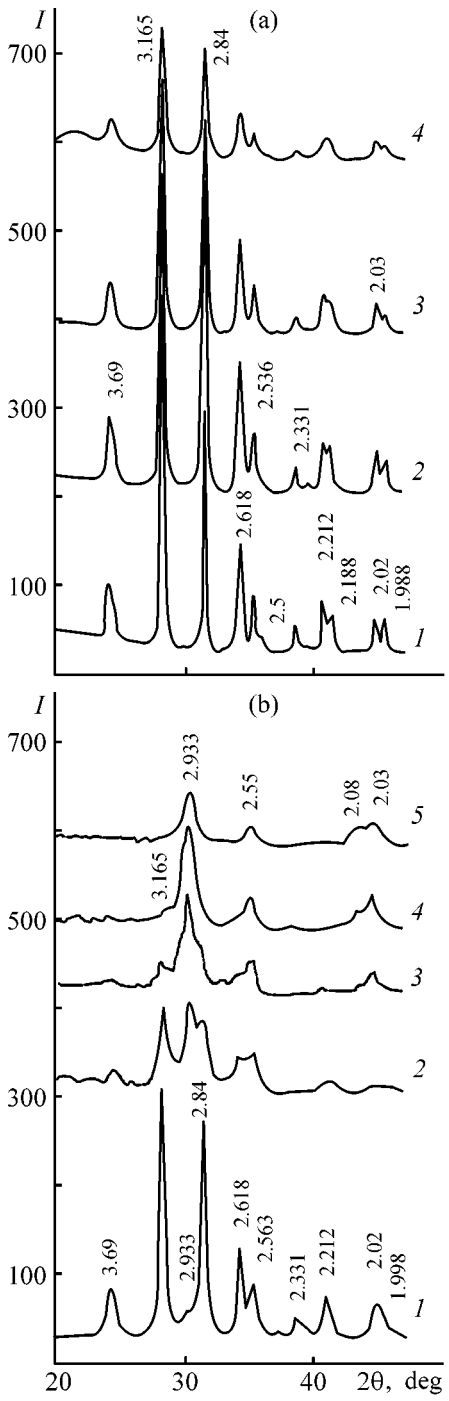

Fig. 3. Diffraction patterns of the fractions of the reactive zirconium dioxide treated in dry regime in (a) vibrational and (b) centrifugal-planetary mill. Treatment time (τ): (a) (*1*) 0.2, (*2*) 2, (*3*) 4, and (*4*) 9 h; (b) (*1*) 0.5, (*2*) 2, (*3*) 5, (*4*) 15, and (*5*) 22 min.

tions of the tetragonal modification are markedly intensified (d = 2.96 Å; Fig. 1b, curve *2*). After 15 min of treatment, the fraction consists of virtually pure zirconium dioxide of the tetragonal modification (Fig. 1b, curve *3*).

Taking into account the physical broadening of diffraction peaks shows that in the course of wet grinding of amorphous hydroxide the crystallite size of the tetragonal oxide phase increases from 7–9 to 14–15 nm (see table).

Thus, mechanical activation in wet mode, compared with the dry method, does not inhibit formation of crystalline phases essentially. Only the yield of the monoclinic zirconium dioxide is diminished (Fig. 1a, curve *3*; Fig. 1b, curve *2*). It may be concluded that it is this modification that is formed owing to the local rise in temperature upon collisions. By contrast, the tetragonal modification is formed under the action of impact pulses, as energy-favorable more closely packed lattice, and is stabilized as a result of the decreasing crystallite size. In the wet mode, grinding is facilitated, since the disjoining effect of a polar solvent impairs the crystallite strength. Brittle fracture dominates over plastic deformations, thus allowing preparation of more dispersed materials. The statistical-average size of the particles, as calculated from the specific surface area, virtually coincides with the value obtained from X-ray diffractometry (see table).

Of interest is the fact that the monoclinic modification of zirconium dioxide, formed in earlier stages, recrystallizes upon mechanical activation to give a tetragonal form. To confirm the occurrence of this process under the given conditions, reactive zirconium dioxide preliminarily calcined at 1000°C was taken as a starting material. The initial phase is represented solely by the monoclinic modification of ZrO_2 (Fig. 3a, curve *1*). All the reference peaks (down to 2% intensity) are excellently recorded. Already after 30 s of mechanical treatment, the intensity of the reflections of the starting oxide of this phase decreases and their broadening increases sharply. After only 2 min of mechanical activation, the diffraction pattern changes dramatically (Fig. 3b, curve *2*). The reflection intensities of the monoclinic phase diminish by more than an order of magnitude. The reflections are substantially broadened, which is indicative of more finely crystalline and(or) more defective structure, and a weak reflection associated with the new phase is observed in the range 2θ = 30–31° (Fig. 3b, curve *1*). A strong reflection with d = 2.933 Å, belonging to the cubic modification of zirconium dioxide, is revealed. The peak asymmetry points to the presence of the tetragonal phase, even if in minor amounts as compared with the cubic phase. The new phase exists in an amount of up to 40% relative to the main phase. After more prolonged activation, the presence of the monoclinic modification decreases to trace amounts

(Fig. 3b, curves *3* and *4*). After 15 min of treatment, the phase transition of the stable monoclinic oxide to the metastable cubic ZrO_2 is virtually complete. The cubic crystal system is even more closely packed lattice than the tetragonal and, especially, monoclinic lattices. Its formation under intensive energy supply to the system is reasonable. Further mechanical treatment (for 22 min) results in decreasing intensity and broadening of the reflections, which is a common result of mechanical activation of solids [8] (Fig. 3b, curve *5*).

Grinding of zirconium dioxide in a KM-1 mill for several hours leads to a significant decrease in the intensity of reflections in the diffraction patterns of the corresponding fractions (Fig. 3a, curves *2*–*4*). After 9 h of treatment the size of the coherent domains decreases from 1 μm to 25–30 nm. Further treatment yields even finer crystallites; however, no new phase is recorded in the process. Apparently, the rate of energy supply is insufficient for recrystallization of the monoclinic oxide.

In [10], the previously noted formation of a metastable cubic structure in the course of mechanical activation of hematite and lanthanum manganite was interpreted from the standpoint of a cooperative distortion of the sublattice of oxygen octahedra as a result of a change in the oxidation state of cations. In our case, the high abrasiveness of the starting material leads to the presence of a noticeable admixture of metallic iron ($d = 2.03$ Å, ICDPS, 6-696) and austenite (d = 2.08 Å, ICDPS, 31-619), originating from the walls of drums and stainless-steel milling bodies (Fig. 3b, curve *5*). This may lead both to partial reduction of cations Zr and to incorporation of iron into the crystal lattice of zirconium dioxide. However, an explanation in terms of the scaling factor seems to be preferable.

The known methods for stabilization of tetragonal zirconium dioxide at temperatures below the enantiotropic transition point involve introduction of doubly and triply charged metal cations or anions (SO_4^{2-} and WO_4^{2-}) into a precursor before crystallization [1–7]. In calcination, these additives hinder crystal growth owing to the formation of a solid solution on the particle surface or to blocking of the surface active centers. Under these conditions, the tetragonal phase exists as a metastable phase, if the size of its crystallites does not exceed 30 nm [1–3, 5, 6]. Consequently, a polymorphism of zirconium oxide, caused by the scaling factor, can be suggested. Sufficient energy supply (heating) results in the formation of nuclei of a new phase and isometric growth of crystallites. The particles are small in size and possess high surface energy. Under these conditions, the more energy-favorable crystals of higher symmetry (cubic) are preferentially formed.

With increasing crystallite size, the free surface energy decreases and the crystal growth directions become differentiated. Accelerated crystal growth occurs along the principal planes. The tetragonal modification becomes more energy favorable, and the cubic structure is replaced by the tetragonal structure.

Further increase in the crystallite size and decrease in the free surface energy in the course of crystallization allow formation of tabular crystals of the monoclinic crystal system, which are stable up to 1172°C. The process is monotropic at low temperatures.

The mechanical activation allows initiation of zirconium oxide crystallization from amorphous hydroxide at low temperatures and, at the same time, impedes growth of crystals exceeding a certain size. Two processes occur in the opposite directions. Their competition is responsible for the phase composition of the forming oxide phase. In the same way, the enantiotropic transition of monoclinic into tetragonal modification can be achieved without introduction of any doping additives at low temperature. The ΔH values of the polymorphous transition cubic $\rightarrow$ tetragonal $\rightarrow$ monoclinic zirconium dioxide are –13 and –8.4 kJ mol^{-1}, respectively. The energy supply of 10–60 W g^{-1}, provided in mechanical activation, gives the necessary energy for a reversible phase transition [14]. After the treatment is complete, the crystal growth at low temperature is impossible, and the given state is frozen in the form of a metastable phase.

CONCLUSION

Nanosize tetragonal zirconium hydroxide (metastable below 1172°C) was obtained by mechanical activation of amorphous zirconium hydroxide in a centrifugal-planetary mill at room temperature. The tetragonal ZrO_2, metastable at low temperatures, undergoes fast crystallization with the formation of an intermediate monoclinic modification. The possibility of recrystallization of the monoclinic phase into the cubic and tetragonal phases in the course of mechanical treatment is demonstrated. The phase stabilization is due to competition of crystallization and grinding. The size of the forming crystallites does not exceed 16 nm.

ACKNOWLEDGMENTS

The work was financially supported by the Krasnoyarsk Regional Research Foundation (grant 9F0112).

REFERENCES

1. Morterra, C., Cerrato, G., Pinna, F., and Signoretto, M., *J. Catal.*, 1995, no. 157, pp. 109–123.
2. Comelli, R.A., Vera, C.R., and Parera, J.M., *J. Catal.*, 1995, no. 151, pp. 96–101.
3. Morterra, C., Cerrato, G., Ferroni, L., and Montanaro, L., *Mater. Chem. Phys.*, 1994, no. 37, pp. 243–248.
4. Ward, D.A., and Ko, E.I., *J. Catal.*, 1995, no. 157, pp. 321–333.
5. Jentoft, F.C., Hahn, A.H.P., Jentoft, R.E., and Ressler, T., *12th Int. Congr. on Catalysis (12thICC)*, Granada (Spain), July 9–14, 2000, CD R076.
6. Scheithauer, M., Bosch, E., Schubert, U.A., *et al.*, *J. Catal.*, 1998, no. 177, pp. 137–144.
7. Ward, D.A. and Ko, E.I., *J. Catal.*, 1994, no. 150, pp. 18–33.
8. Avvakumov, E. G., *Mekhanicheskie metody aktivatsii khimicheskikh protsessov* (Mechanical Methods for Activation of Chemical Processes), Novosibirsk: Nauka, 1986.
9. Isupova, L.A., Sadykov, V.A., Avvakumov, E.G., and Kosova, N.V., *Khim. Inter. Ustoich. Razv.*, 1998, no. 6, pp. 207–210.
10. Sadykov, V.A., Isupova, L.A., Tsybulya, S.V., *et al.*, *J. Solid State Chem.*, 1996, no. 123, pp. 191–195.
11. Sadykova, V.A., Isupova, L.A., and Bulgakov, N.N., *Khim. Inter. Ustoich. Razv.*, 1998, no. 6, pp. 215–222.
12. Kustova, G.N., Burgina, E.B., Sadykov, V.A., and Poryvaev, S.G., *Phys. Chem. Minerals*, 1992, no. 18, pp. 379–387.
13. Kosova, N.V., Devyatkina, E.T., Avvakumov, E.G., *et al., Khim. Inter. Ustoich. Razv.*, 1998. no. 6, pp. 125–130.
14. Avvakumov, E.G., *Khim. Inter. Ustoich. Razv.*, 1994, vol. 2, nos. 2–3, pp. 541–558.
15. Karakcheev, L.G., Avvakumov, E.G., Vinokurova, O.B., *et al., Khim. Inter. Ustoich. Razv.*, 2001, no. 1, pp. 27–37.
16. Avvakumov, E.G., Chizhevskaya, S.V., Stoyanov, E.S., *et al., Zh. Prikl. Khim.*, 1999, vol.72, no. 9, pp. 1420–1424.

Russian Journal of Applied Chemistry, Vol. 75, No. 2, 2002, pp. 177–181. Translated from Zhurnal Prikladnoi Khimii, Vol. 75, No. 2, 2002, pp. 183–187.
Original Russian Text Copyright © 2002 by Mozheiko, Dikhtievskaya, Korshuk, Potkina, Kirilenko.

INORGANIC SYNTHESIS AND INDUSTRIAL INORGANIC CHEMISTRY

Effect of Modifying Surfactants on Physical and Mechanical Properties of Granulated Potash Fertilizers

F. F. Mozheiko, L. V. Dikhtievskaya, E. F. Korshuk, T. N. Potkina, and O. I. Kirilenko

Institute of General and Inorganic Chemistry, National Academy of Sciences of Belarus, Minsk, Belarus

Received August 31, 1999

Abstract—The modifying action of various nonpolar reagents and their mixtures with surfactants on physical and mechanical properties (humidity resistance, degree of hydrophobization, and dynamic strength) of granulated potash fertilizers was studied.

In order to extend the assortment of new effective modifying agents for granulated potassium chloride, having high adhesion and well protecting potash fertilizers to increase their humidity resistance and strength and make longer the preservation of their granulometric composition, the modifying action of nonpolar water-repellent reagents of various types and their formulations with surfactants on granulated potash fertilizers was studied.[1]

As nonpolar reagents were used intermediate and by-products and wastes of chemical industry, containing various hydrocarbons: paraffin-naphthenes—low-molecular polyethylene, paraffin slack wax, slop wax fraction, petrolatum, and oily fractions I–III; terpenes—neutral rosin oil; and aromatic hydrocarbons—extract of phenolic oil purification. As surfactants were used higher aliphatic amines and carboxylic acids [1, 2].

We determined physicochemical characteristics of granulated potash fertilizers as it was done previously [1]: degree of hydrophobization, from moisture sorption; dynamic strength, from abradability; induction period of dissolution, from electrical conductivity; and hygroscopicity, after Pestov [3].

Nonpolar reagents are organic compounds that contain no functional groups, cannot dissociate, and are rather difficultly soluble in water [4]. According to their chemical composition, they are mainly paraffins, naphthenes, terpenes, and aromatic hydrocarbons with weak intermolecular interaction and low free surface energy. For example, the surface tension at the interface with air is 18–23, 24–29, and 30–36 mJ m^{-2} for paraffin, naphthene, and aromatic hydrocarbons, respectively. Such substances with low cohesion energy can spread over surfaces with higher energy (e.g., granulated potash fertilizers), thus imparting hydrophobic properties to a product under treatment.

As evident from Table 1, the use of nonpolar reagents makes it possible to reach almost the same parameters (50% degree of hydrophobization and less than 10% abradability of KCl) as in the case when a granulated fertilizer is conditioned with such a typical water-repellent agent as amine [1]; however, the expenditure of the reagent is high (3000 – 4000 g ton^{-1}). Further increase in the expenditure does not improve the physical and mechanical characteristics of a granulated fertilizer any more.

Paraffin-naphthene hydrocarbons are most effective with respect to modifying action, followed by terpenes and aromatic hydrocarbons. In view of the absence of solidophilic groups in molecules of nonpolar compounds, they cannot be strongly attached to the potassium chloride surface. Their adsorption is due to weak Van der Waals forces and has only physical nature. Therefore, hydrocarbons create on a KCl surface a sorption coating, which is, as the practice demonstrates, not strong under dynamic conditions, and has a number of defects and cracks of the hydrocarbon layer, mainly formed in transportation and transshipping of fertilizers.

We demonstrated that the strength of hydrocarbon attachment considerably increases in the presence of such surfactants as amines or carboxylic acids. The method of IR spectroscopy was applied to determine

[1] Manufactured by Belaruskalii production association.

1070-4272/02/7502-0177 $27.00 © 2002 MAIK "Nauka/Interperiodica"

Table 1. Effect of nonpolar reagents on physical and mechanical characteristics of granulated potash fertilizer* (W_a = 82.1 %, τ = 6 h, T = 20°C)

Nonpolar solvent	Expenditure, g ton^{-1}	W, g H_2O/100 g KCl	H	I	P	τ, s	Nonpolar solvent	Expenditure, g ton^{-1}	W, g H_2O/100 g KCl	H	I	P	τ, s
			%							%			
Low-molecular polyethylene	1000	0.067	18				Gatch	1500	0.060	27			
	2000	0.056	32	8.3	91.7			2000	0.058	29			
	3000	0.049	40	7.5	92.5	25	Neutral rosin oil	1000	0.074	10			
	5000	0.045	45	7.0	93.0			2000	0.068	17			
Oily cut fraction II	1000	0.060	27	6.5	93.5			3000	0.061	25	9.0	91.0	20
	2000	0.052	36	6.3	93.7			5000	0.055	32			
	3000	0.045	45	6.0	94.0	22	Extract of phenolic oil purification	1000	0.075	8			
	4000	0.041	50	5.2	94.8			2000	0.070	15			
Slop wax fraction	1500	0.057	30					3000	0.065	21	8.7	91.3	20
	2000	0.055	32	5.2	94.8			5000	0.058	29			
	3000	0.047	42			27	–	0	0.082	0			1
	4000	0.039	52	4.7	95.3								

* W_a is air humidity, W moisture absorption, H hydrophobicity, I abradability, P dynamic strength, and τ induction period of dissolution.

Table 2. Effect of compositions based on paraffin-naphthene hydrocarbons, amine (AM), and acids of light vegetable oils (OA) on physical and mechanical properties of a floatation granulated potash fertilizer (W_a = 82%, τ = 6 h, expenditure of modifying formulation 1500 g ton^{-1})

Modifying formulation	W, g H_2O/100 g KCl	H, %	W, g H_2O/100 g KCl	H, %	I	P	τ, s
	at temperature, °C				%		
	25		35				
–	0.110	0	0.135	0	16.5	83.5	1
Fraction I	0.088	20	0.137	0	–	–	–
Fraction I : AM = 15 : 1	0.055	50	0.128	5	–	–	–
Fraction I : AM : OA = 15 : 0.5 : 0.5	0.050	55	0.109	19	–	–	–
Fraction II	0.077	30	0.128	5	2.3	97.7	15
Fraction II : AM = 15 : 1	0.041	64	0.107	21	2.0	98.0	26
Fraction II : OA = 10 : 1	0.069	37	–	–	–	–	–
Fraction II : AM : OA = 15 : 0.5 : 0.5	0.034	69	0.093	31	1.6	98.4	30
Fraction III	0.079	28	0.124	8	2.2	97.8	–
Fraction III : AM = 15 : 1	0.043	62	0.095	30	2.0	98.0	–
Fraction III : AM : OA = 15 : 0.5 : 0.5	0.035	68	0.103	34	1.8	98.2	–
Slop wax fraction	0.075	32	–	–	2.0	98.0	–
Slop wax fraction : AM	0.044	60	–	–	2.1	97.9	–
Slop wax fraction : AM : OA	0.033	70	–	–	–	–	33

the strength of hydrocarbon attachment to the surface of KCl granules. The spectra of hydrocarbons (with paraffin slack wax as an example) contain absorption bands at 3000–2800 cm^{-1}, associated with stretching vibrations of the CH bond, and also at 1400–1300 and 700 cm^{-1}, related to bending vibrations of CH bonds, which additionally confirms the composition of paraffin slack wax as a mixture of hydrocarbons [5]. To determine hydrocarbons quantitatively, we used the area of a composite absorption band in the range 3000–2800 cm^{-1}. This range includes peaks of stretching vibrations of methyl groups at 2962 and 2872 cm^{-1} and peaks of stretching vibrations of methylene groups at 2926 and 2853 cm^{-1}. We dem-

Table 3. Waterproofing action of formulations with various modifying agents on a halurgic granulated fertilizer (W_a = 82%, τ = 6 h, T = 25°C)

Modifying agent	*H*, %, at indicated expenditure of modifying agent, g g^{-1}					
	1000	1500	2000	3000	4000	3000
Fraction II	–	8	–	12	–	–
Fraction II : AM = = 15 : 1	10	14	27	31	38	7*
Fraction II : AM : OA = 15 : 0.5 : 0.5	12	16	333	37	43	11*

* Ambient temperature 35°C.

onstrated that approximately 30% of the total amount of hydrocarbon is removed from KCl granules treated with paraffin slack wax even after the first washing with hexane, whereas in the presence of amine, hydrocarbons almost completely remain on the surface of potassium chloride. Thus, the presence of a surfactant results in higher strength and elasticity of a hydrophobic coating. In this case, a feedback also exists: not only surfactants affect the creation of a strong hydrophobic amine-hydrocarbon film, but also nonpolar compounds promote amine adsorption onto the surface of potassium chloride [4]. For example, the adsorption of amine on KCl grains of size –1.6 + 1 mm increases by a factor of 1.1–1.8 in the presence of hydrocarbon, and the amount of firmly fixed amine, by more than a factor of 2.

The role of a surfactant consists in the creation of a preliminary hydrophobic base layer, with its hydrocarbon part facing outwards, on the mineral surface by means of electrostatic or chemical forces. Hydrocarbons further interact with this layer to cover granules with an additional hydrophobic film of a nonpolar modifying agent. Naturally, this enhances the water-repellent effect owing to the concentration of the nonpolar reagent in the zone where the adsorbed layer of a modifying surfactant is situated (Tables 2 and 3).

The above data show that it is sufficient to add a minor quantity of a surfactant to a formulation in order to achieve a reliable protection of the surface of granulated potash fertilizers from sorption of moisture. When amine is used as a surfactant, the optimal amine : hydrocarbon and acid : hydrocarbon ratios are 1 : (10–20) and 1 : (5–10), respectively. Ternary mixtures containing a hydrocarbon, amine, and an acid in (15–40) : 1 : 1 ratio have the greatest water-repellent capacity (Table 2). Thus, at a total expenditure of such a formulation of 1500 g ton^{-1} and the 30 : 1 : 1 ratio of the components, or, in other words, at an expenditure of 1400 g of hydrocarbon per 1 ton of a granulate potash fertilizer (oily fraction II, in particular), and 50 g of amine and acid each, it is possible to achieve an approximately 70% degree of hydrophobization of the surface of floatation KCl and a decrease in its abradability to 3–4% against 22% for untreated samples. Further increase in the surfactant expenditure is unprofitable, as this does not improve noticeably the physical and mechanical properties of the granulated fertilizer. To provide a noticeable hydrophobization of a halurgic granulated fertilizer, a higher expenditure of modifying formulations is required (Table 3).

We found that carboxylic acids partially replace amine and thus reduce its expenditure. Furthermore, addition of the acids raises the solubility of amines owing to the formation of ionized complexes [2], and, consequently, makes more dilute amine–hydrocarbon formulations and extends their flowability ranges, which ensures a more even distribution of surfactants in the bulk of solutions and their stronger attachment to the fertilizer surface. The hygroscopicity of a granulated potash fertilizer is largely determined by the presence of readily soluble magnesium and calcium chlorides, and carboxylic acids transform these ions into insoluble forms. All this intensifies the hydrophobization of granulated potash fertilizers in the presence of carboxylic acids.

The efficiency of a protective hydrophobic film based on hydrocarbons and surfactants is reflected upon not only the moisture sorption, but also the solubility of granules in water. For example, the induction period of dissolution of modified granules is 20–30 s, in contrast to untreated samples, which are dissolved instantaneously.

The physical and mechanical parameters of potash granules strongly depend on the hygroscopicity of a product. Potash fertilizers are known to be hygroscopic substances [3]. Strong condensation of moisture on fertilizer grains starts above the hygroscopic point, and a layer of saturated solution (external diffusion) is formed on the surface of crystals. Initially, only layers directly bordering moist air participate

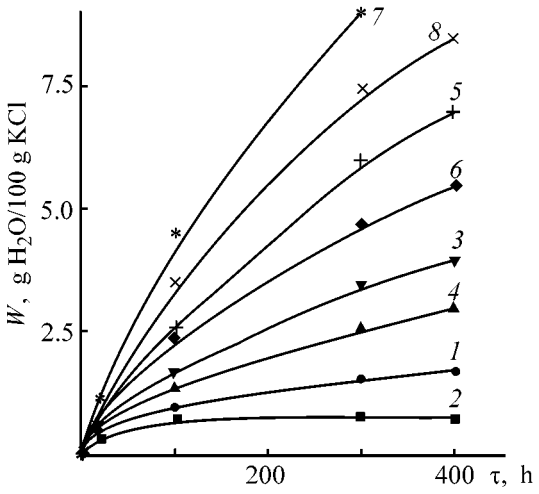

Moisture absorption W of KCl samples vs. time τ. KCl sample: (*1*), (*3*), (*5*), and (*7*) initial; (*2*), (*4*), (*6*), and (*8*) modified with a mixture fraction II : AM = 20 : 1. Air humidity (%): (*1*) and (*2*) 76; (*3*) and (*4*) 84.5; (*5*) and (*6*) 88.5; (*7*) and (*8*) 100.

in the moisture sorption. In this case, the absorbed moisture is not localized, but spreads over the bulk of the fertilizer under the action of capillary-diffusion forces, penetrating in pores of potassium chloride granules (internal diffusion) and acting as a propping agent inside them, which impairs the mechanical strength of granules and leads to their crushing into minute fragments. A change in the temperature mode of storage promotes crystallization processes with the formation of an external crystalline skeleton with high salt adhesion between fragments. It is the crystallization processes with the formation of salt bridges between fragments that give rise to strong phase contacts, which cement mineral fragments and lead to caking of the product and its transformation into a monolith. Therefore, moisture and temperature should be considered key factors, which strongly affect the properties of granulated fertilizers.

Table 4. Effect of various modifying agents on hygroscopicity parameters of granulated potash fertilizers (initial humidity of samples 0.5%)

System	Expenditure of modifying agent, g g^{-1}	h_0, %	Q, mg g^{-1} h^{-1}	K
KCl	–	70.5	0.66	2.24
KCl + addition:				
AM	500	72.0	0.60	2.06
OA	1000	71.0	0.63	2.16
AM + OA	1000	71.0	0.63	2.00
fraction II	2000	73.0	0.58	1.90
fraction II + AM	1500	74.0	0.51	1.36
fraction II + AM + OA	1500	74.0	0.51	1.36

The time dependence of the moisture absorption for modified samples at varied relative air humidity is shown in the figure in comparison with that of the initial samples. It is evident that, with increasing air humidity, the moisture absorption markedly grows for all KCl samples, which is especially pronounced at long exposures of the samples. For example, a change in humidity from 76 to 100% results in a threefold increase in the moisture absorption within a day (from 0.3 to 0.9 g H_2O per 100 g KCl), and an increase by a factor of 8 within 12 days (from 0.8 up to 6.5 g H_2O). However, a hydrophobic coating based on a surfactant and hydrocarbons is stable at any air humidity, 100% included, i.e., samples conditioned by the formulations absorb much lesser amount of moisture than untreated samples, and this difference becomes even greater with time.

The same refers to the effect of the ambient temperature on the moisture absorption by granulated potash fertilizers (Tables 2 and 3). For example, a 10°C increase in temperature (from 25 to 35°C) results in a decrease in the waterproofing effect by a factor of 3–10 for both floatation and halurgic granulated fertilizers. However, the negative temperature effect is greater for the halurgic granulated fertilizer, which requires a higher expenditure of modifying formulation to achieve a waterproofing effect at elevated temperatures. At 25°C, 1500 g ton^{-1} of a formulation based on oily fraction II and a surfactant ensures a 10% degree of hydrophobization, whereas at 35°C this effect is achieved at higher (3000 g ton^{-1}) expenditure of the formulation (Table 3).

Let us consider how the hygroscopicity of granulated potash fertilizers changes under the action of various modifying agents. The sample hygroscopicity is usually characterized by the hygroscopic point h_0 (relative air humidity at which a substance neither loses nor absorbs moisture); coefficient of moisture absorption rate, K (amount of moisture absorbed by unit surface area within unit time at 1% difference between the relative humidity of air and the hygroscopic point of a substance); and moisture absorption rate at 100% relative air humidity, Q. These parameters of granulated potash fertilizers, as determined by the "desiccator" technique after Pestov [3], are shown in Table 4. The expenditure of modifying formulations was selected so as to ensure, whenever possible, equal degrees of hydrophobization of granulated potash fertilizers. As seen, the modifying formulations

under consideration to a greater or lesser extent promote an increase in the hygroscopic point of KCl and slow down the moisture absorption. However, waterproofing formulations based on hydrocarbons and surfactants provide the greatest change in the indicated parameters. For example, a mixture of oily fraction II with amine and acid ensures a 4% increase in the hygroscopic point of a granulated potash fertilizer and a decrease in the coefficient of moisture absorption rate to 1.36 against 2.24 for untreated samples. In this case, the moisture absorption at 100% humidity decreases to 0.51 mg g^{-1} h^{-1} against 0.66 mg g^{-1} h^{-1} for untreated samples.

CONCLUSION

Treatment of both potash floatation and halurgic granulated fertilizers with anhydrous modifying formulations based on surfactants (higher aliphatic amines and carboxylic acids) and nonpolar reagents of predominantly paraffin-naphthene series results in a decrease in KCl hygroscopicity, which makes it possible to prolong the useful life of granulated potash fertilizers under conditions of temperature changes and high relative air humidity.

REFERENCES

1. Korshuk, E.F., Dikhtievskaya, L.V., Kirilenko, O.I., *et al.*, *Zh. Prikl. Khim.*, 1999, vol. 72, no. 4, pp. 559–564.
2. Korshuk, E.F., Dikhtievskaya, L.V., Kirilenko, O.I., *et al.*, *Zh. Prikl. Khim.*, 1999, vol. 72, no. 2, pp. 195–198.
3. Pestov, N.E., *Fiziko-khimicheskie svoistva zernistykh i poroshkoobraznykh khimicheskikh produktov* (Physicochemical Properties of Granular and Powder Chemical Products), Leningrad: Akad. Nauk SSSR, 1947.
4. Glembotskii, V.A., Dmitrieva, G.M., and Sorokin, M.M., *Apolyarnye reagenty i ikh deistvie pri flotatsii* (Nonpolar Reagents and their Action in Flotation), Moscow: Nauka, 1968.
5. Bellamy, L.J., *Advances in Infrared Group Frequencies*, London: Methuen, 1968.

Russian Journal of Applied Chemistry, Vol. 75, No. 2, 2002, pp. 182–185. Translated from Zhurnal Prikladnoi Khimii, Vol. 75, No. 2, 2002, pp. 188–191.
Original Russian Text Copyright © 2002 by Rakov, Grunskii.

PHYSICOCHEMICAL STUDIES OF SYSTEMS AND PROCESSES

Thermodynamic Analysis of Manufacture and Processing of Titanium Tetrafluoride

E. G. Rakov and A. V. Grunskii

Mendeleev Russian University of Chemical Technology, Moscow, Russia

Received February, 15, 2001

Abstract—Combustion temperatures in fluorination of titanium dioxide and pyrohydrolysis of titanium tetrafluoride and tetrachloride in H_2–air, H_2–O_2, oxygen–hydrocarbon, and NH_3–HF–O_2 flames were calculated using the "Chemical workbench" software. Dependences of the temperatures on reagent ratios were determined.

Sulfuric acid and chloride methods for ilmenite ore processing are widely used on a global scale [1]. In order to produce titanium and its compounds, a method for fluorination of titanium-containing ores (with ammonium hydrofluoride, in particular) has been proposed recently [2–4].

The processes occurring in a self-sustaining flame combustion mode are known to be widely used in the technology of uranium fluorides [5–9]. Vacant facilities released in the conversion of the uranium industry can be used for production of rare metals by the fluorination method [10, 11]. Therefore, titanium-containing ores could be treated in a flame. Thus, a thermodynamic analysis of flame processes involving rare metals is topical. Comparison of such quantities as combustion temperatures of, e.g., uranium tetrafluoride and titanium oxide, suggests that industrial flame reactors can be used for manufacture of titanium tetrafluoride. A comparison of temperatures developed in reduction or pyrohydrolysis of uranium hexafluoride with the corresponding temperatures for titanium hexafluoride will allow us to evaluate the possibility of utilization of apparatus and processes created for uranium compounds in manufacture of titanium dioxide.

As found previously, flame reactors similar to those used in the uranium technology can be applied to fluorination of substances with combustion temperatures not lower than 1200–1300K [12].

The aim of this study was to calculate the adiabatic combustion temperatures for the reactions of production and processing of titanium compounds. The "Chemical workbench" software[1] was used in these calculations.

The calculated adiabatic temperatures of TiO_2 combustion for the initial temperature of 300K and various starting $F_2 : TiO_2$ N molar ratios in F_2 atmosphere are given below:

N	T_c, K	N	T_c, K	N	T_c, K
2.0	2305	2.8	2306	3.6	2218
2.2	2306	3.0	2306	3.8	2025
2.4	2306	3.2	2306	4.0	1837
2.6	2306	3.4	2306		

It is seen that high combustion temperatures are developed, with 100% titanium dioxide conversion being attainable even at 300 K.

The reaction of TiO_2 and HF is unusable for production of TiF_4, since the product yield is very low even in an excess of HF (3.6% at $HF : TiO_2 = 6.0$). Furthermore, this reaction is reversible and a decrease in the temperature of the reaction gases results in hydrolysis of the forming TiF_4.

Fluorination with NH_4HF_2 is more efficient since it can be carried out in such a way that H_2O vapors will be removed in the stage of NH_4TiF_5 or $(NH_4)_2TiF_6$ formation. However, it is difficult to calculate the equilibrium of the process since the required data are unavailable. Tentative calculations show that flame processes are unusable in this process.

[1] Developed by Russian Scientific Centre Kurchatov Institute.

1070-4272/02/7502-0182 $27.00 © 2002 MAIK "Nauka/Interperiodica"

Natural titanium raw materials are $FeTiO_3$ and $CaTiO_3$. The combustion temperatures of these compounds cannot be calculated owing to the lack of the required data. However, evaluations indicate a high conversion in the F_2 atmosphere, with the adiabatic combustion temperatures falling within the same range as those for TiO_2 fluorination. Calcium and iron fluorides are nonvolatile and, consequently, they would not contaminate TiF_4 to any appreciable degree.

Fluorination is only the initial stage of processing of titanium raw materials. A major part of TiF_4 or ammonium fluorotitanates must be converted to TiO_2, which can be done using pyrohydrolysis reactions. For comparison, we considered similar processes of titanium dioxide production from titanium tetrachloride, which is widely used in industry [13–16].

The temperatures developed in pyrohydrolysis of $TiCl_4$ (curve *1*) and TiF_4 (curve *2*) to TiO_2 in the flame of a burning stoichiometric H_2–O_2 mixture can be judged from Fig. 1a. It is evident that, at TiX_4 concentrations below 24%, the combustion temperature is 2304 K (melting point of TiO_2). Only further increase in the TiX_4 concentration results in a decrease in the combustion temperature. The linear part seems to correspond to the formation of a mixture of solid and melted TiO_2. The combustion in a hydrogen–air mixture (curves *3* and *4*) involves appreciably lower combustion temperatures.

According to our calculations (Fig. 2), complete conversion of TiF_4 in TiO_2 is achieved at the combustion temperatures if the $H_2 : O_2$ ratio is 2 : 1 and TiF_4 content in gaseous mixture is not greater than 10%. However, for greater $H_2 : O_2$ ratios, curves of TiO_2 yield against TiF_4 concentration have maximums attributable to the formation of additional products, TiF_3 in particular.

As follows from the calculations, the yield of TiO_2 decreases when $TiCl_4$–H_2–O_2 is diluted with hydrogen, because of the increasing $TiCl_3$ fraction.

With the TiF_4–N_2–O_2–H_2 mixture diluted with hydrogen, maximums appear in dependence of the TiO_2 yield on TiF_4 concentration, and, therefore, the composition of products changes: TiF_3 yield grows with increasing H_2 content.

Since the processes of TiF_4 and $TiCl_4$ pyrohydrolysis are rather similar, we might expect that the known features of the latter process can be extended to the pyrohydrolysis of TiF_4.

The pyrohydrolysis of the products of fluorination of titanium-containing raw materials with NH_4HF_2 is complicated by the presence of NH_3 and HF in the starting mixture. Nevertheless, high temperatures are developed in the nO_2 : (HF + NH_3) flame (HF : NH_3 = 1 : 1). The maximum combustion temperature of 2594 K is reached at n = 0.78. Introduction of TiX_4

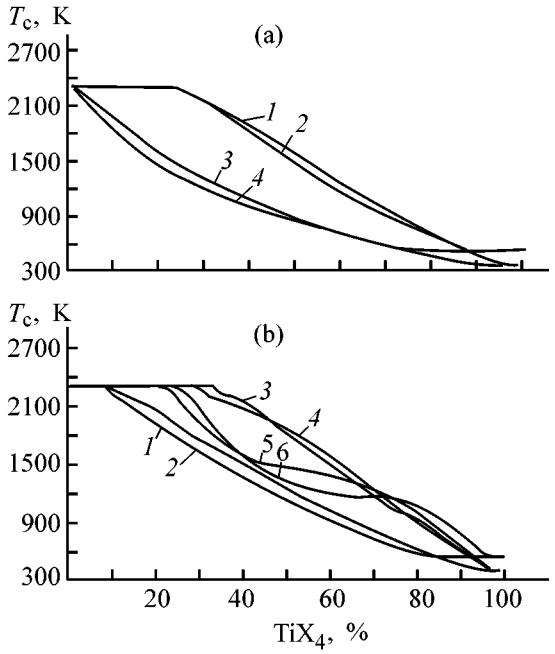

Fig. 1. Pyrohydrolysis combustion temperature T_c vs. [TiX_4] concentration in starting gas mixture. Mixture composition: (a) (*1*) $TiCl_4 + H_2 + O_2$ ($H_2 : O_2$ = 2.05), (*2*) $TiF_4 + H_2 + O_2$ ($H_2 : O_2$ = 2.05), (*3*) $TiCl_4 + N_2 + O_2 + H_2$ ($N_2 : O_2 : H_2$ = 4 : 1 : 2.12), (*4*) $TiF_4 + N_2 + O_2 + H_2$ ($N_2 : O_2 : H_2$ = 4 : 1 : 2.12); (b) (*1*) $TiF_4 + NH_3 + HF + O_2$ ($NH_3 : HF : O_2$ = 1 : 1 : 0.78), (*2*) $TiCl_4 + NH_3 + HF + O_2$ ($NH_3 : HF : O_2$ = 1 : 1 : 0.78), (*3*) $TiF_4 + CH_4 + O_2$ ($CH_4 : O_2$ = 0.55), (*4*) $TiCl_4 + CH_4 + O_2$ ($CH_4 : O_2$ = 0.55), (*5*) $TiCl_4 + C_2H_2 + O_2$ ($C_2H_2 : O_2$ = 0.7), (*6*) $TiF_4 + C_2H_2 + O_2$ ($C_2H_2 : O_2$ = 0.7).

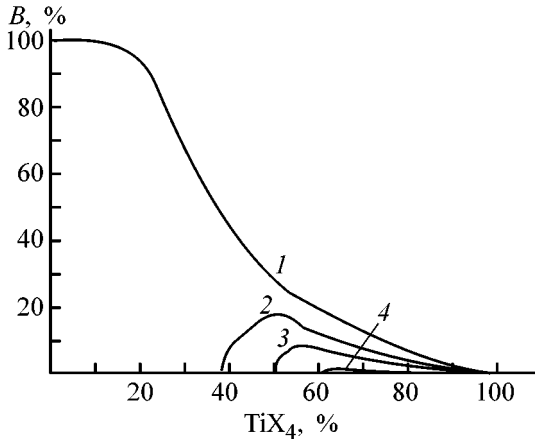

Fig. 2. TiO_2 yield B vs. TiF_4 concentration in starting H_2–O_2 gas mixture at the combustion temperature. $H_2 : O_2$ ratio: (*1*) 2 : 1, (*2*) 10 : 3, (*3*) 5 : 1, and (*4*) 10 : 1.

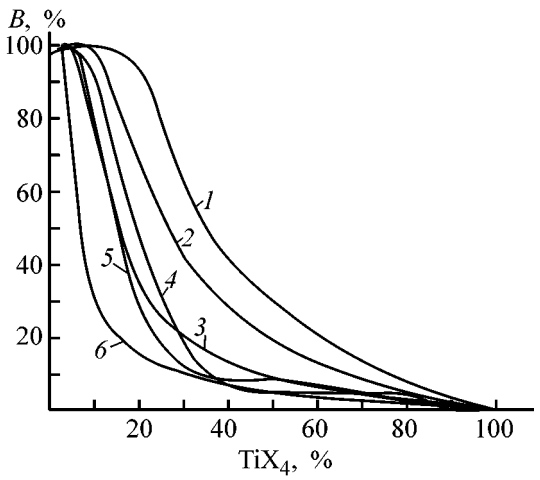

Fig. 3. TiO_2 yield B vs. TlF_4 concentration in starting gas mixtures at combustion temperature. Mixture composition: (*1*) $TiF_4 + CH_4 + 2O_2$, (*2*) $TiF_4 + CH_4 + 4O_2$, (*3*) $TiF_4 + CH_4 + 10O_2$, (*4*) $TiF_4 + C_2H_2 + 2O_2$, (*5*) $TiF_4 + C_2H_2 + 4O_2$, and (*6*) $TiF_4 + C_2H_2 + 10O_2$.

lowers the combustion temperature (Fig. 1b, curves *1* and *2*). In this case, a sharp decrease in temperature to 2304K occurs in the TiX_4 concentration range 0.001–0.005%. Further, the temperature remains unchanged up to addition of 8 vol % TiX_4 to the gaseous combustion mixture.

According to our calculations, the oxygen content in an NH_3–HF–O_2 mixture appreciably affects the TiO_2 yield B at a 20% TiF_4 concentration in this mixture:

n	1	2	4	10
T_c, K	1851	1531	1167	767
B, %	84.2	67.8	46.9	24.1

It is seen that TiO_2 yield decreases with increasing O_2 content in the NH_3–HF–O_2 mixture, because the reaction is not completed and a noticeable amount of titanium remains in the form of a tetrafluoride.

It is of interest to find out whether H_2 can be replaced with cheaper hydrocarbons. The results obtained in a study of TiX_4 in CH_4–O_2 and C_2H_2–O_2 mixtures are shown in Fig. 1b (curves *3*, *4*, and *5*, *6*, respectively). In these systems, as in the preceding cases, an increase in the TiX_4 concentration in hydrocarbon–O_2–TiX_4 mixtures results in a decrease in the combustion temperature.

The dependence of TiO_2 yield on TlF_4 concentration in hydrocarbon–O_2 mixtures is shown in Fig. 3 for various O_2 contents. It is seen that the TiO_2 yield decreases with increasing O_2 content because of the TiF_3 formation. The yield of TiO_2 reaches 100% if no more than 17 vol % TiF_4 is added to a CH_4–nO_2 (n = 2) mixture.

For comparison, we again consider the system containing $TiCl_4$. The calculated TiO_2 yields in hydrocarbon–O_2–50% $TiCl_4$ mixtures are shown below:

$C_2O_2 : O_2$	1 : 2	1 : 4	1 : 10
T_c, K	2044	1926	1681
B, %	16.1	40.1	71.4
$CH_4 : O_2$	1 : 2	1 : 4	1 : 10
T_c, K	1711	1898	1576
B, %	36.3	59.6	80.7

It is evident that TiO_2 yield grows with increasing O_2 content in the mixtures. In this case, $TiCl_4$ is converted incompletely to TiO_2 owing to the lack of oxygen, and a substantial amount of titanium remains in the tetrachloride.

Therefore, the calculations show that flame processes can be used, in principle, in fluorination of titanium raw materials with F_2 and also in pyrohydrolysis of TiF_4 or ammonium fluorotitanates to TiO_2. In these processes, apparatus similar to those employed in the uranium technology can be used. This conclusion was confirmed by an experimental study [17].

CONCLUSIONS

(1) Adiabatic temperatures of TiO_2 combustion in the F_2 atmosphere were determined for various ratios of these components.

(2) The combustion temperatures and yield of TiO_2 in TiF_4 pyrohydrolysis in a H_2–O_2 flame were calculated. It is shown that titanium dioxide is not virtually formed in a great excess of H_2, and the process yields TiF_3.

(3) The combustion temperatures and TiO_2 yield were calculated for TiF_4 pyrohydrolysis in the H_2–air flame. It is shown that the yield of TiF_3 grows with increasing hydrogen concentration in the TiF_4–N_2–O_2–H_2 system, and TiO_2 is scarcely formed under a great excess of hydrogen.

(4) The combustion temperatures and TiO_2 yield for the case of TiF_4 combustion in NH_3–HF–O_2 and also in hydrocarbon–O_2 flames were calculated. It was concluded that the greater the oxygen content in TiF_4–NH_3–HF–O_2 system, the larger the residual amount of titanium in the tetrafluoride. Introduction of a moderate amount of TiF_4 into the hydrocarbon–O_2

flame results in complete conversion of titanium tetrafluoride to TiO_2.

REFERENCES

1. Skrypnyuk, V.M., *Proizvodstvo titana. Metallurgiya tsvetnykh i redkikh metallov: Itogi nauki i tekhniki* (Titanium Production. Metallurgy of Nonferrous and Rare Metals. Advances of Science and Technology), Available from VINITI AN SSSR, 1980, Moscow, vol. 12, pp. 67–114.
2. Pong, T.K., O'Donnell, T.A., and Wood, D.G., *Ind. Eng. Chem. Res.*, 1995, vol. 34, no. 1, pp. 308–313.
3. Gabeldu, N.C., Moss, J.H., and Wright A., *Proc. Conf. High. Temperature Chemistry of Inorganic and Ceramic Materials*, Keele, 1976, London, 1977, p. 154.
4. Mel'nichenko, E.I., Maslennikova, I.G., Epov, D.G., and Bulanova, S.B., *Zh. Prikl. Khim.*, 1999, vol. 72, no. 3, pp. 362–366.
5. Galkin, N.P., Maiorov, A.A., Veryatin, U.L., *et al.*, *Khimiya i tekhnologiya ftoristykh soedinenii urana* (Chemistry and Technology of Fluoric Uranium Compounds), Moscow: Gosatomizdat, 1961.
6. Sudarikov, B.N. and Rakov, E.G., *Protsessy i apparaty uranovykh proizvodstv* (Processes and Apparatus of Uranium Plants), Moscow: Mashinostroenie, 1968.
7. Rakov, E.G. and Teslenko, V.V., *Pirogidroliz neorganicheskikh ftoridov* (Pyrohydrolysis of Inorganic Fluorides), Moscow: Energoatomizdat, 1987.
8. Heestand, R.L. and Leitten, C.F., *Nucl. Applic.*, 1965, vol. 1, no. 6, pp. 584–588.
9. Federer, J.I., Robinson, W.C., and Patterson F.H., *Nucl. Applic.*, 1969, vol. 4, no. 1, pp. 298–396.
10. Rakov, E.G., *Tsvetn. Met.*, 1999, no. 11, pp. 55–58.
11. Karelin, A.I., Rakov, E.G., Karelin, V.A., *Metally Evrazii*, 1999, no 1, pp. 66–67.
12. Rakov, E.G. and Grunskii, A.V., *Zh. Prikl. Khim.*, 2000, vol. 73, no. 12, pp. 1933–1936.
13. Khazin, L.G., *Dvuokis' titana* (Titanium Dioxide), 1970, 2nd ed.
14. Baitenev, N.A., Rubin, N.N., Suleimenov, E.N., *et al.*, *Proizvodstvo tetrakhlorida i dvuoikisi titana* (Production of Titanium Tetrachloride and Titanium Dioxide), Alma-Ata: Nauka, 1974.
15. Gvozdeva, O.M., Masterova, A.P., and Kabyshev, A.S., *Sbornik trudov Giredmeta* [Coll. of Sci. Works of Giredmet (State Institute of Rare Metals)], 1959, no. 1, pp. 59–62.
16. Berengart, A.S. and Vil'nomirskii, I.E., *Tsvetn. Met.*, 1987, no. 4, pp. 96–98.
17. Karelin, A.I., Karelin, V.A., and Rakov, E.G., Abstracts of Papers, *10 Simpozium po khimii neorganicheskikh ftoridov* (10 Symposium on the Chemistry of Inorganic Fluorides), Moscow: Dialog–MGU, 1998, p. 78.

Russian Journal of Applied Chemistry, Vol. 75, No. 2, 2002, pp. 186–190. Translated from Zhurnal Prikladnoi Khimii, Vol. 75, No. 2, 2002, pp. 192–196.
Original Russian Text Copyright © 2002 by Tsemekhman, Burylev, Golov, Miroevskii.

PHYSICOCHEMICAL STUDIES OF SYSTEMS AND PROCESSES

Modeling of Thermodynamic Properties and Fusion Diagrams of Ternary Oxosulfide Systems

L. Sh. Tsemekhman, B. P. Burylev, A. N. Golov, and G. P. Miroevskii

AO Institut Gipronikel', St. Petersburg, Russia

Received August 23, 2001

Abstract—Three different approximations are used to determine the thermodynamic properties of components and fusion diagrams of ternary oxosulfide systems FeS–FeO–Cu_2S and FeS–FeO–Ni_3S_2. The coordinates of eutectic points and eutectic temperatures are obtained, and equations for calculating the thermodynamic activities of the components are derived for the system FeS–FeO–Cu_2S.

Oxosulfide systems are widely used to manufacture copper and nickel. Data on ternary systems can be, in principle, obtained on the basis of those on binary systems. Examples of successful solution of this problem were given in [1, 2]. Results of calculations of fusion diagrams were reported in [3, 4], where a good agreement between the calculated and experimental melting points and compositions was obtained for eutectic systems. Following the same procedure, but using more complex model concepts, we obtain data on thermodynamic properties and fusion diagrams of ternary systems. The principal difficulty of analysis consists in that the available experimental data for binary systems are frequently unreliable and contradictory, and lacking at all for many systems [5, 6].

System FeS–FeO–Cu_2S. Let us consider, as a first approximation, calculations for ideal systems. We denote the components of the system FeS–FeO–Cu_2S by numbers 1, 2, and 3, respectively. For a binary ideal system

$$RT\ln x_i = T\Delta S_i^{\mathrm{m}} - \Delta H_i^{\mathrm{m}}, \quad (1)$$

where ΔH_i^{m} and ΔS_i^{m} are the enthalpy and entropy of melting of i-th component, x_i its solubility at temperature T (K), and R the universal gas constant.

For a binary system, the eutectic temperature can be calculated by equating the expressions for the two liquidus lines in the eutectic system:

$$T^{\mathrm{eut}} = \frac{\Delta H_1^{\mathrm{m}}}{\Delta S_1^{\mathrm{m}} - 19.14\log x_1} = \frac{\Delta H_2^{\mathrm{m}}}{\Delta S_2^{\mathrm{m}} - 19.14\log x_2}, \quad (2)$$

where $x_1 + x_2 = 1$ (x_i is the molar fraction of a component).

The results of calculations performed for binary systems entering into the composition of the ternary systems FeS–FeO–Cu_2S and FeS–FeO–Ni_3S_2 with the use of the Schroeder's equation and reference values of enthalpies of melting and melting points [7] are presented below:

System	FeS–FeO	FeS–FeO	FeO–Cu_2S
T^{eut}, K	1210	1105	1310
x_2^{eut}, mole fraction	0.428	0.325	0.455
System	FeS–Cu_2S	FeO–Ni_3S_2	FeS–Ni_3S_2
T^{eut}, K	1015	985	965
x_2^{eut}, mole fraction	0.310	0.793	0.748

The second eutectic temperature and eutectic concentration in the system FeS–FeO were obtained in studies of iron sulfide "FeS" + 3.5% Fe, which melts at 1247 K. Comparison with experimental data [8–10] characterizing the system FeS–FeO as a eutectic system shows that the eutectic temperatures are 1181 [8], 1181 [9], and 1213 K [10], and the respective eutectic concentrations $x_{\mathrm{FeO}}^{\mathrm{eut}}$, 0.315 [8], 0.360 [9], and 0.42 [10].

For the ternary eutectic we use the same property of the system—intersection of the equilibrium lines of binary eutectics at the same point for all the three constituent binary systems. Then we have for the triple eutectic point

$$T^{\mathrm{eut}} = \frac{\Delta H_1^{\mathrm{m}}}{\Delta S_1^{\mathrm{m}} - R\ln x_1} = \frac{\Delta H_2^{\mathrm{m}}}{\Delta S_2^{\mathrm{m}} - R\ln x_2} = \frac{\Delta H_3^{\mathrm{m}}}{\Delta S_3^{\mathrm{m}} - R\ln x_3}, \quad (3)$$

where $x_1 + x_2 + x_3 = 1$.

1070-4272/02/7502-0186 $27.00 © 2002 MAIK "Nauka/Interperiodica"

For the system FeS–FeO–Cu_2S, Eq. (3) is written in the form

$$T^{eut} = \frac{32\,340}{22.09 - 19.14\log x_{FeS}} = \frac{32\,170}{19.54 - 19.14\log x_{FeO}} = \frac{11\,300}{8.08 - 19.14\log x_{Cu_2S}}, \quad (4)$$

where the enthalpies and entropies of melting are taken to be equal to their reference values [7].

Equation (4) was solved by the method of successive approximation, with the dependence of T on x plotted for each of the three systems on the assumption that $x_{Cu_2S} = 1 - x_{FeS} - x_{FeO}$. The calculation gave the following results: eutectic temperature 930 K (657°C, eutectic composition $x_{FeS} = 0.218$, $x_{FeO} = 0.171$, and $x_{Cu_2S} = 0.611$.

In view of the fact that the boundary systems FeS–Cu_2S and FeO–Cu_2S are nonideal, account should be taken of deviations from ideality. For regular binary solutions

$$T^{eut} = \frac{\Delta H_1^m + Q(1 - x_1)^2}{\Delta S_1^m - R\ln x_1} = \frac{\Delta H_2^m + Q(1 - x_2)^2}{\Delta S_2^m - R\ln x_2}. \quad (5)$$

The system FeS–Cu_2S cannot be described by regular solution equations on the basis of studies of the fusion diagram [11]. Therefore, we take into account the asymmetry of the thermodynamic properties in this system with the use of equations derived in [12]. The expression takes the form

$$T^{eut} = \frac{\Delta H_1^m + (Q_1 - Q_2)(1 - x_1)^2 + 2Q_2(1 - x_1)^3}{\Delta S_1^m - R\ln x_1} = \frac{\Delta H_2^m + (Q_1 + 2Q_2)(1 - x_2)^2 - 2Q_2(1 - x_2)^3}{\Delta S_2^m - R\ln x_2}. \quad (6)$$

For a ternary system with nonadditive energies of the components, we obtain for the excess Gibbs energy

$$\Delta G^{ex} = x_1x_2Q'_{12} + x_1x_2^2Q''_{12} + x_1x_3Q'_{13} + x_1x_3^2Q''_{13} + x_2x_3Q'_{23} + x_2x_3^2Q''_{23}. \quad (7)$$

We have in Eq. (7) the excess Gibbs energy related to one mole of solution. Therefore, to obtain the total energy of a ternary solution containing n_1, n_2, and n_3 moles of components 1, 2, and 3, it is necessary to multiply the molar value by the total number of moles:

$$\Delta G_\Sigma^{ex} = \Delta G^{ex}(n_1 + n_2 + n_3).$$

The chemical potentials of the components can be defined by the expressions

$$\mu_1^{ex} = \frac{\partial\Delta G^{ex}(n_1 + n_2 + n_3)}{\partial n_1},$$

$$\mu_2^{ex} = \frac{\partial\Delta G^{ex}(n_1 + n_2 + n_3)}{\partial n_2},$$

$$\mu_3^{ex} = \frac{\partial\Delta G^{ex}(n_1 + n_2 + n_3)}{\partial n_3},$$

Since $\mu_{1_k}^{ex} = RT\ln f_i$, then we obtain, with account of $x_i = n_i/\sum_{i=1} n_i$, equations for the component activity coefficients for the system FeS–FeO–Cu_2S, for which $Q'_{12} = Q''_{12} = Q''_{23} = 0$:

$$RT\ln f_1 = (x_3^2 + x_2x_3)Q'_{13} + (x_3^3 + x_3^2x_2 - x_1x_3^2)Q''_{13} - x_2x_3Q'_{23}, \quad (8)$$

$$RT\ln f_2 = -x_1x_3Q'_{13} - 2x_1x_3^2Q''_{13} + (x_1x_3 - x_3^2)Q'_{23}, \quad (9)$$

$$RT\ln f_3 = (x_1^2 + x_1x_2)Q'_{13} + 2(x_1x_2x_3 - x_1^2x_3)Q''_{13} + (x_1x_2 - x_2^2)Q'_{23}. \quad (10)$$

From the position of the eutectic point of the system FeS–Cu_2S ($T^{eut} = 1193$ K, $x_{FeS} = 0.71$, $x_{Cu_2S} = 0.29$) we find $Q'_{12} = -9200$, $Q''_{12} = 52\,500$ J mol^{-1}.

Using the same method and approximate data of [13]: $T^{eut} \cong 13\,500$ K, $x_{FeO} = 0.05$, $x_{Cu_2S} = 0.95$, we obtain for the system FeO–Cu_2S $Q'_{12} = 25\,100$ J mol^{-1} and $Q''_{12} = 0$.

With account of equations for ternary asymmetric systems, we obtain for FeS–FeO–Cu_2S ($Q'_{12} = Q''_{12} = 0$, $Q'_{13} = -9200$, $Q''_{13} = 52\,500$, $Q'_{23} = 25\,000$ J mol^{-1}):

$$\Delta T^{eut} = \frac{32\,340 - 9200(x_{FeO}x_{Cu_2S} + x_{Cu_2S}^2) + 52\,500(x_{FeO}x_{Cu_2S}^2 + x_{Cu_2S}^3 - x_{FeS}x_{Cu_2S}^2) + 25\,100x_{FeO}x_{Cu_2S}}{22.09 - 19.14\log x_{FeS}}$$

$$= \frac{32\,170 - 9200\,x_{FeS}x_{Cu_2S} - 105\,000\,x_{FeS}x_{Cu_2S}^2 + 25\,100(x_{FeS}x_{Cu_2S} + x_{Cu_2S}^2)}{19.54 - 19.14\log x_{FeO}}$$

$$= \frac{11\,300 - 9200(x_{FeS}^2 + x_{FeS}x_{FeO}) + 105\,000(x_{FeS}^2x_{Cu_2S} + x_{FeS}x_{FeO}x_{Cu_2S}) + 25\,100(x_{FeS}x_{FeO} + x_{FeO}^2)}{8.08 - 19.14\log x_{Cu_2S}}. \quad (11)$$

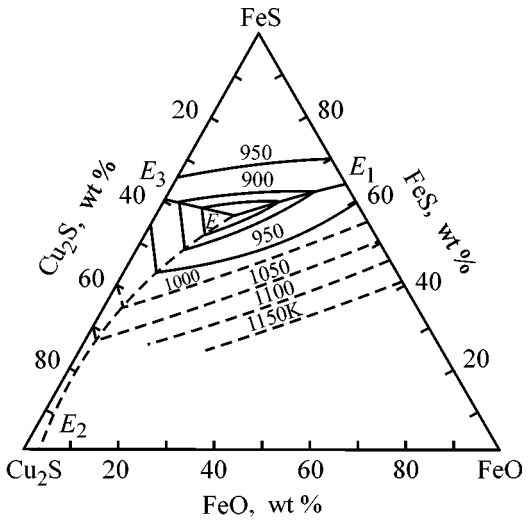

Fig. 1. Fusion diagram of the FeS–FeO–Cu_2S system [13].

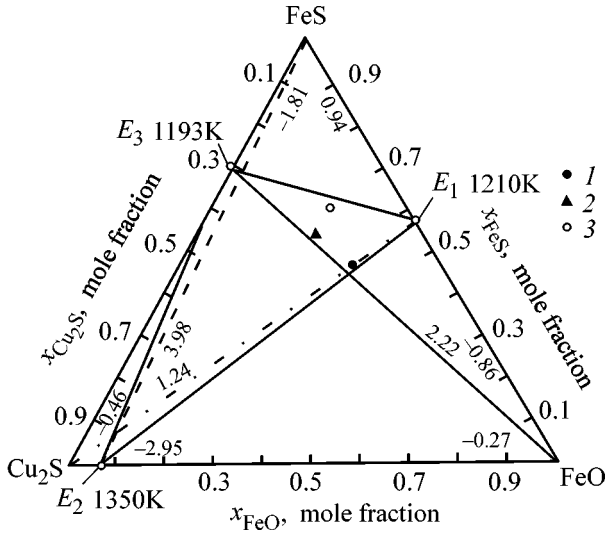

Fig. 2. Concentration triangle for the system FeS–FeO–Cu_2S. Ternary eutectic: (*1*) [13], (*2*) calculation by the method of successive approximations, and (*3*) calculation by the method proposed in [14].

The results of calculations give T^{eut} = 1085 K, x_{FeS} = 0.55, x_{FeO} = 0.22, x_{Cu_2S} = 0.23.

These values are in rather good agreement with the experimental data reported in [13], which can be seen in Fig. 1 presenting the concentration triangle for the system FeS–FeO–Cu_2S, with triple eutectic points found by different methods plotted in the figure.

Comparison of experimental and calculated values for an ideal system shows a significant shift of the triple eutectic to the iron sulfide–rich vertex of the diagram.

The composition and melting point of the ternary eutectic were calculated using the procedure proposed in [14] on the basis of data on binary systems. Data on the melting points of pure components and binary eutectics and on their compositions made it possible to calculate the relative changes in "reciprocal partial temperatures" of components A_i upon their transformation into eutectics:

$$A_i = \frac{2.303}{x_3^{i-3}} \log \frac{T_i^0 x_i^{i-3}}{T_{eut}^{i-3}}, \qquad (12)$$

where T_i^0 and T_{eut}^{i-3} are the melting points of pure *i*-th component and binary eutectic formed by this and the third components; x_3^{i-3} and x_i^{i-3} are the contents of 3rd and *i*-th component (i = 1 or 2) in the $i-3$ binary eutectic (mole fraction).

In Fig. 2, the A_i values are given at sides of the concentration triangle (e.g., $A_{Cu_2S}^{Cu_2S–FeS} = -0.48$, $A_{FeO}^{FeO–FeS} = -0.884$, $A_{FeO}^{FeO–Cu_2S} = -0.929$). With account of the results we obtained and the fact that the ternary eutectic lies in a field delimited by straight lines connecting the points corresponding to the compositions of the binary eutectics, we found the probable concentration region in which the ternary eutectic lies (delimited in Fig. 2 by the line E_1E_3 and the cut line originating from the binary eutectic E_3 and running toward the FeO vertex).

The quantities A_i were also used for evaluating the stability of the temperature surface folds. It was shown in [15] that, in ternary systems of eutectic type, ternary eutectics lie near intersection points of two the most stable folds. In the given case, these are the folds originating in binary systems Cu_2S–FeS and FeS–FeO. The corresponding cut lines in Fig. 2 are represented by solid lines.

The composition of the ternary eutectic of the system was found as the intersection point of these cut lines by solving the system of equations

$$x_{FeO}^{FeS–FeO–Cu_2S} : x_{FeS}^{FeS–FeO–Cu_2S} = x_{FeO}^{FeS–FeO} : x_{FeS}^{FeS–FeO},$$
$$x_{Cu_2S}^{FeS–FeO–Cu_2S} : x_{FeS}^{FeS–FeO–Cu_2S} = x_{Cu_2S}^{Cu_2S–FeS} : x_{FeS}^{Cu_2S–FeS},$$
$$x_{FeS}^{FeS–FeO–Cu_2S} + x_{FeO}^{FeS–FeO–Cu_2S} + x_{Cu_2S}^{FeS–FeO–Cu_2S} = 1. \qquad (13)$$

The obtained values are as follows: x_{FeS} = 0.46, x_{FeO} = 0.35, x_{Cu_2S} = 0.19.

The composition of the ternary eutectic was used to calculate its melting point by the formula

$$T_i^0 = \frac{1 - x_i^{1-2-3}}{1 - x_i^{j-k}} (T_i^0 - T_{eut}^{j-k}), \qquad (14)$$

where $j - k$ is the most readily fusible binary eutectic formed by i-th component.

The thus calculated melting point of the ternary eutectic was 1164 K.

The results obtained [Eqs. (8)–(10)] allow calculation of the component activity in this ternary system. The equations used have the form

$$RT\ln a_{FeS} = RT\ln x_{FeS} - 9200(x_{FeO}\,x_{Cu_2S} + x^2_{Cu_2S}) + 52\,500(x_{FeO}\,x^2_{Cu_2S} + x^3_{Cu_2S} - x_{FeS}\,x^2_{Cu_2S}) - 25\,100x_{FeO}\,x_{Cu_2S}, \quad (15)$$

$$RT\ln a_{FeO} = RT\ln x_{FeO} + 9200\,x_{FeS}\,x_{Cu_2S} - 105\,000\,x_{FeS}\,x_{Cu_2S} + 25\,100(x_{FeS}\,x_{Cu_2S} + x^2_{Cu_2S}), \quad (16)$$

$$RT\ln a_{Cu_2S} = RT\ln x_{Cu_2S} - 9200(x^2_{FeS} + x_{FeS}\,x_{FeO}) + 105\,000(x^2_{FeS}\,x_{Cu_2S} + x_{FeS}\,x_{FeO}\,x_{Cu_2S}) + 25\,100(x_{FeS}\,x_{FeO} + x^2_{FeO}). \quad (17)$$

Finally, the excess molar Gibbs energy of the ternary system can be calculated using the equations reported in [16].

FeS–FeO–Ni_3S_2 system. Data on boundary binary systems are lacking (FeO–Ni_3S_2 system) or contradictory (FeS–Ni_3S_2 system): deviations from ideality are positive and negative according to, respectively, viscosity or density measurements. In this connection, it is difficult as yet to construct the phase diagram of the ternary system FeS–FeO–Ni_3S_2 with account of deviations from ideality.

For the ideal system, the ternary eutectic is found from the equation

$$T^{eut} = \frac{32\,340}{22.09 - 19.14\log x_{FeS}} = \frac{32\,170}{19.54 - 19.14\log x_{FeO}} = \frac{24\,270}{21.01 - 19.14\log x_{Ni_3S_2}}. \quad (18)$$

Calculation by the method of successive approximations gives the value T^{eut} = 912 K (639°C) and eutectic composition x_{FeS} = 0.20, x_{FeO} = 0.15, $x_{Ni_3S_2}$ = 0.65. The concentration triangle for the ternary system FeS–FeO–Ni_3S_2 is presented schematically in Fig. 3. A calculation by the method proposed in [14] gives the eutectic composition x_{FeS} = 0.21, x_{FeO} = 0.16, $x_{Ni_3S_2}$ = 0.63, and eutectic temperature T^{eut} = 925 K. The results obtained using these calculation techniques are in good agreement.

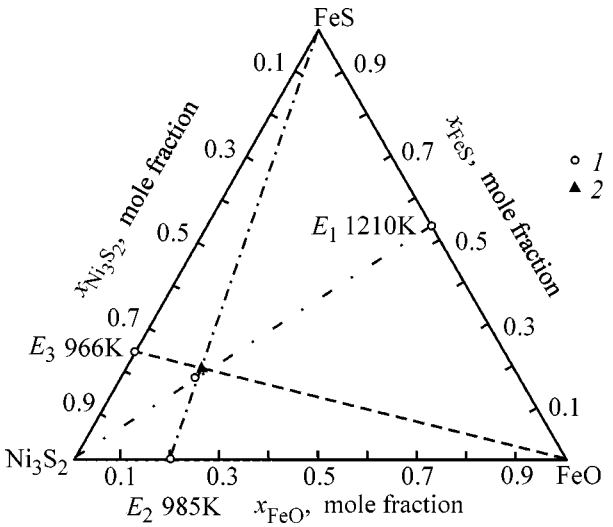

Fig. 3. Concentration triangle for the system FeS–FeO–Ni_3S_2. Ternary eutectic: (*1*) calculation by the method of successive approximations and (*2*) calculation by the method proposed in [14].

CONCLUSIONS

(1) Three calculation procedures were used for ternary oxosulfide systems FeS–FeO–Cu_2S and FeS–FeO–Ni_3S_2: (I) that relying upon the ideality approximation, (II) that based on reciprocal partial temperatures, and (III) that taking into account the interaction of the components. The following results were obtained for the ternary eutectic in the system FeS–FeO–Cu_2S: ideality approximation: T^{eut} = 930 K, x_{FeS} = 0.218, x_{FeO} = 0.171, x_{Cu_2S} = 0.611; procedure based on reciprocal partial temperatures: T^{eut} = 1164 K, x_{FeS} = 0.46, x_{FeO} = 0.35, x_{Cu_2S} = 0.19; equations taking into account the nonadditivity of the components: T^{eut} = 1085 K, x_{FeS} = 0.55, x_{FeO} = 0.22, x_{Cu_2S} = 0.23. The last set of values is in the best agreement with the available experimental data.

(2) Equations describing the component activity in the ternary system FeS–FeO–Cu_2S at various temperatures and melt compositions were derived for the first time.

(3) For the system FeS–FeO–Ni_3S_2, a calculation by the method of successive approximations gives T^{eut} = 912 K, x_{FeS} = 0.20, x_{FeO} = 0.15, $x_{Ni_3S_2}$ = 0.65; and that by the method of reciprocal partial temperatures, T^{eut} = 925 K, x_{FeS} = 0.21, x_{FeO} = 0.16, $x_{Ni_3S_2}$ = 0.63. The good agreement of the results obtained using these two methods gives reason to consider these results reliable.

REFERENCES

1. Burylev, B.P., Sryvalin, I.T., and Korpachev, V.G., *Primenenie priblizhennykh metodov dlya rascheta termodinamicheskikh svoistv galogenidnykh, oksidnykh i metallicheskikh sistem* (Use of Approximate Methods for Calculating the Thermodynamic Properties of Halide, Oxide, and Metallic Systems), Available from ONIITEKhIM, 1986, Krasnodar, no. 486-khp-86.
2. Morachevskii, A.G., *Termodinamika rasplavlennykh metallicheskikh i solevykh sistem* (Thermodynamics of Molten Metallic and Salt Systems), Moscow: Metallurgiya, 1987.
3. Storonkin, A.V., Vasil'kova, I.V., and Potelin, A.M., *Vestn. Len. Gos. Univ.*, 1974, no. 16, p. 74.
4. Saboungi, M. and Cerisier, P., *J. Electrochem. Soc.*, 1974, vol. 121, no. 10, pp. 1258–1263.
5. Isakova, R.A., *Davlenie para i dissotsiatsiya sul'fidov metallov* (Vapor Pressure and Dissociation of Metal Sulfides), Alma-Ata: Nauka, 1968.
6. Kopylov, N.I. and Toguzov, M.Z., *Diagrammy sostoyaniya sul'fidnykh sistem tyazhelykh tsvetnykh metallov, kharakterizuyushchie termicheskie svoistva vysokotsinkovykh kontsentratov* (Phase Diagrams of Sulfide Systems with Heavy Metals, Characterizing Thermal Properties of High-Zinc Concentrates), Novosibirsk: Gidrotsvetmet, 1981.
7. *Termodinamicheskie svoistva neorganicheskikh veshchestv: Spravochnik* (Thermodynamic Properties of Inorganic Substances: Reference Book), Zefirov, A.P., Ed., Moscow: Atomizdat, 1965.
8. Turkdogan, E.T., *BOF (Basic Oxygen Furnace) Steelmaking*, vol. 2, *Process Technology Division*, New York: Iron Steel Soc. Amer. Instit. Mining, Metallurgical and Petroleum Eng., 1978.
9. Mechev, V.V., Burylev, B.P., Vasil'ev, M.G., and Shkuridin, I.S., *Izv. Akad. Nauk SSSR, Ser. Met.*, 1976, no. 6, pp. 57–60.
10. Hilty, D.C. and Crafts, W., *J. Metals*, 1952, vol. 4, no. 12, pp. 1307–1312.
11. Kopylov, N.I. and Toguzov, M.Z., *Zh. Neorg. Khim.*, 1975, vol. 20, no. 9, pp. 2562–2565.
12. Burylev, B.P., *Izv. Vyssh. Uchebn. Zaved., Tsvetn. Metall.*, 1964, no. 4, pp. 65–72.
13. Schmiedl, I. and Repčák, V., *Hutnicke lisly*, 1969, no. 7, pp. 510–513.
14. Susarev, M.P. and Martynova, N.S., *Zh. Prikl. Khim.*, 1974, vol. 47, no. 3, pp. 526–528.
15. Susarev, M.P., Martynova, N.S., and Stulova, M.I., *Zh. Prikl. Khim.*, 1974, vol. 47, no. 7, pp.1658–1661.
16. Sryvalin, I.T., Burylev, B.P., Korpachev, V.G., *et al.*, *Izv. Vyssh. Uchebn. Zaved., Chern. Metall.*, 1970, no. 10, pp. 5–9.

Russian Journal of Applied Chemistry, Vol. 75, No. 2, 2002, pp. 191–194. Translated from Zhurnal Prikladnoi Khimii, Vol. 75, No. 2, 2002, pp. 197–201.
Original Russian Text Copyright © 2002 by Dibrov, Chirkst, Litvinova.

SORPTION AND ION-EXCHANGE PROCESSES

Thermodynamic Analysis of Cerium(III) Extraction from Sulfate Solutions with Salts of Quaternary Ammonium Bases

I. A. Dibrov, D. E. Chirkst, and T. E. Litvinova

Plekhanov State Mining Institute, St. Petersburg, Russia

Received August 31, 2000; in final form, April 2001

Abstract—Cerium(III) distribution between an aqueous sulfate solution and a solution of trialkylbenzylammonium sulfate in xylene was studied. The Ce(III) distribution coefficient grows with increasing pH. The extraction is provided by the formation of cerium mono- and disulfate complexes in the aqueous phase. Schemes of extraction equilibria are proposed and Gibbs energies and equilibrium constants are found.

Russia has no domestic resources of purely rare-earth ores, such as bastnäsite, monazite, and xenotime, widely used in the rare-earth industry abroad. The rare-earth metals (REMs) are produced as coproducts with other less-common metals (niobium, uranium, etc.) in smaller amounts than it is necessary for the industry. Therefore, a search for new raw materials containing REMs, development and improvement of flow-sheets for their recovery and separation are topical tasks. Extraction recovery of REM from sulfate media is expedient when poor ores, e.g., eudialyte ores of the Alluive bed [1] or by-products of the chemical and metallurgical productions are processed. Published data on extraction recovery of REM sulfates are scarce. In particular, it is known that REM sulfates are poorly extracted with neutral organophosphorus compounds, e.g., tributyl phosphate (TBP) [2]. Other widely used extractants are salts of quaternary ammonium bases [3, 4].

The main features of the cerium extraction were studied in sulfuric acid (0.37–4.37 mol kg^{-1}) solutions of cerium sulfate at pH 0–4 and constant concentration of sulfate ion, 2.55 mol kg^{-1}, provided by adding a required amount of chemically pure grade magnesium sulfate. This concentration of sulfate ion corresponds to that used in the experiments on sulfuric acid leaching of eudialyte concentrate [5]. A 0.5 M solution of trialkylbenzylammonium sulfate with C_4–C_{10} alkyl radicals (TABAS) in xylene was used. The volume ratio of the organic and aqueous phases was 1 : 2. The Ce(III) molality in the organic phase C_{org} was found as the difference of metal molalities in the initial C_0 and equilibrium aqueous C_{aq} phases with regard to mass ratio of aqueous m_{H_2O} and organic m_{org} phases (m_{H_2O}/m_{org} = 2.4 under conditions of the experiment):

$$C_{org} = (C_0 - C_{aq})\frac{m_{H_2O}}{m_{org}}. \quad (1)$$

The Ce(III) content in the aqueous phase was monitored spectrophotometrically with arsenazo III [6].

The experimental distribution coefficient D was found by the formula

$$D_{Ce} = C_{org}/C_{aq}. \quad (2)$$

Phases were mixed with a magnetic stirrer and separated in a separatory funnel; the phase separation time was 15–20 min. Experiments were performed at room temperature without thermostatic control, since small variations of temperature (±5°C) do not affect substantially the distribution coefficient [7].

It is accepted that the photometric measurements are performed with 5% relative error at 95% confidence probability. Therefore, the distribution coefficients D were determined with ±7% relative error. The theoretical error of the calculated equilibrium constants and Gibbs energies of extraction was not determined because of the difficulty of its calculation. The arithmetic mean values of these parameters were found, and the root-mean-square deviation from the average with regard to Student's coefficient was taken as an error.

1070-4272/02/7502-0191 $27.00 © 2002 MAIK "Nauka/Interperiodica"

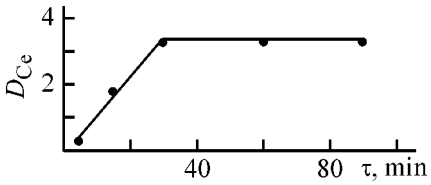

Fig. 1. Cerium(III) distribution coefficient D_{Ce} in the TABAS–$Ce_2(SO_4)_{3\,(aq)}$–$MgSO_4$–H_2SO_4 system vs. phase contact time, τ at pH 1.

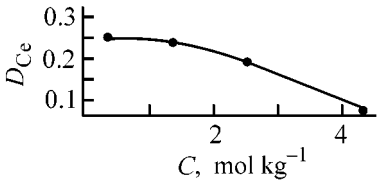

Fig. 2. Cerium(III) distribution coefficient D_{Ce} vs. H_2SO_4 concentration C.

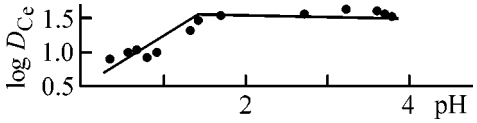

Fig. 3. Cerium(III) distribution coefficient D_{Ce} vs. pH.

To determine the time in which the thermodynamic equilibrium of extraction, we took at equal time intervals samples of phases and analyzed them for the Ce(III) content. The results are shown in Fig. 1. As seen, the equilibrium is attained within 30 min.

The dependence of D_{Ce} on sulfuric acid concentration was determined within the 0.05–4.37 mol kg^{-1} H_2SO_4 range at constant concentration of sulfate ion, 4.37 mol kg^{-1} (Fig. 2). As seen, the Ce(III) recovery from the concentrated acid solutions is very low, and the error in determination of D is high, since C_{org} is found as the difference of two close values.

The Ce(III) recovery becomes noticeable only at sulfuric acid concentrations of 0.1 mol kg^{-1} and lower. The dependence of the Ce(III) extraction on the equilibrium pH is presented in Table 1. The log D_{Ce}–pH plot is presented in Fig. 3. As seen, log D_{Ce} linearly increases in the range pH 0.4–1.65 and then becomes constant at higher pH in accordance with the following empirical equations:

$$\log D = 0.64 + 0.5\ \text{pH}\ (0.4 < \text{pH} < 1.65), \quad (3)$$

$$D = 35 \pm 4\ (1.65 < \text{pH} < 4.0). \quad (4)$$

To explain these dependences, we performed a thermodynamic calculation of the ionic composition of equilibrium aqueous phases, using the GIBBS program [8] based on minimization of the Gibbs energy of a multicomponent system. The equilibrium gross composition of the system and standard Gibbs energies of formation of the ions in aqueous solutions were used as input data for calculations [9, 10]:

Ion	HSO_4^-	SO_4^{2-}	H_2O	Ce^{3+}	$CeSO_4^+$	$Ce(SO_4)_2^-$
$-\Delta_f G^0_{298}$, kJ mol^{-1}	756.97	745.65	237.18	657.38	1440.97	2197.02

The GIBBS program allows calculation of the activity coefficients of ions in a second approximation of the Debye–Hückel theory. The following parameters were used: A = 0.509, B = 0.3284, a = 3 at the ion charge z = ±1, a = 4 at z = ±2, and a = 4.5 at z = ±3. The activity coefficients 0.43 for single-charged ions and 0.066 for double-charged ions at ionic strength of 10 were obtained. The results of the calculations are listed in Table 2.

Table 1. Distribution coefficient D_{Ce} at various equilibrium pH

pH	$C_0 \times 10^3$	$C_{aq} \times 10^3$	$C_{org} \times 10^3$	D_{Ce}
	mol kg^{-1}			
0.38	7.48	1.89	13.58	7.19
0.61	7.39	1.51	14.29	9.46
0.71	7.86	1.51	15.43	10.22
0.80	5.89	1.33	11.08	8.33
0.94	6.72	1.34	13.07	9.75
1.33	6.82	0.71	14.85	20.92
1.43	7.01	0.54	15.72	29.11
1.75	7.16	0.49	16.21	33.08
2.74	7.10	0.44	16.18	36.77
3.24	7.39	0.42	16.94	40.33
3.65	7.26	0.41	16.65	40.61
3.76	7.40	0.47	16.84	35.83
3.81	6.74	0.46	15.26	33.17

Table 2. Calculated ionic composition of solution in relation to pH of the equilibrium aqueous phase

pH	Concentration $C \times 10^3$, mol kg^{-1}				
	HSO_4^-	SO_4^{2-}	Ce^{3+}	$CeSO_4^+$	$Ce(SO_4)_2^-$
0.38	1.72	0.28	0.46	0.44	0.96
0.61	1.54	0.46	0.26	0.30	0.95
0.71	1.48	0.52	0.21	0.29	1.01
0.80	1.38	0.62	0.16	0.24	0.93
0.94	1.24	0.76	0.13	0.23	0.98
1.33	0.78	1.22	0.05	0.09	0.57
1.43	0.68	1.32	0.03	0.07	0.44
1.75	0.46	1.54	0.02	0.06	0.4
2.74	0.06	1.94	0.02	0.05	0.37
3.24	0.04	1.96	0.02	0.05	0.35
3.65	0.02	1.98	0.016	0.05	0.34
3.76	0.02	1.98	0.019	0.06	0.39
3.81	0.02	1.98	0.018	0.06	0.38

As seen, the Ce species and the ratio of sulfate to hydrosulfate ions in the aqueous phase change with increasing pH. Before the break point of the $\log D_{Ce} = f(pH)$ dependence (Fig. 3), HSO_4^- ions, and after it, SO_4^{2-} ions prevail in the solution.

Before the break point (pH < 1.3–1.6), three cerium species coexist in the solution in comparable amounts: Ce^{3+}, $CeSO_4^+$, and $Ce(SO_4)_2^-$; at higher pH the Ce^{3+} and $CeSO_4^+$ contents decrease relative to the disulfate species.

After the break point, the disulfate species content is independent of pH and, on the average, amounts to 3.83×10^{-4} mol kg^{-1} at a total cerium(III) content of 4.5×10^{-4} mol kg^{-1}, which exceeds by a factor of 10 the content of the sum of Ce^{3+} and monosulfate complex (Table 2).

Thus, the change of the mechanism of Ce(III) extraction at pH 1.3–1.65 is caused by conversion of hydrosulfate into sulfate and by changes in the Ce(III) speciation in the aqueous phase.

To calculate the extraction constants and Gibbs energies of the Ce(III) extraction, we wrote extraction equations based on the following assumptions.

(1) Only prevailing ionic species of the equilibrium aqueous phase were taken into consideration; species, whose content is a factor 10 smaller were disregarded.

(2) TABAS cations interact only with anionic cerium species.

(3) The composition of extraction complexes was chosen based on the electroneutrality principle and data of [11, 12] on probable number of extractant molecules in the extraction complex.

The extraction constants were calculated with regard to activity coefficients. Taking into consideration that at pH <1.3–1.65 cerium occurs mainly as $CeSO_4^+$ and $Ce(SO_4)_2^-$, we can suggest occurrence of the following equilibria in the extraction systems:

$$Ce(SO_4)_{2(aq)}^- + R_4NHSO_{4(org)} \rightarrow R_4N[Ce(SO_4)_2]_{(org)} + HSO_{4(aq)}^-, \quad (5)$$

$$CeSO_{4(aq)}^+ + R_4NHSO_{4(org)} \rightarrow R_4N[Ce(SO_4)_2]_{(org)} + H_{(aq)}^+. \quad (6)$$

Each of them contributes to the Ce(III) extraction into the organic phase. The generalized equation of extraction involving both the extractable Ce species is as follows

$$[Ce(SO_4)_x]_{(aq)}^{3-2x} + R_4NHSO_{4(org)} \rightarrow R_4N[Ce(SO_4)_2]_{(org)} + (x-1)HSO_{4(aq)}^- + (2-x)H_{(aq)}^+, \quad (7)$$

where x is the number of the sulfate groups in the cerium aqueous complex, $1 \le x \le 2$.

Table 3. Calculated equilibrium constants and Gibbs energies of extraction of cerium(III) sulfate complexes

pH	$K_{(5)}$	$-\Delta_{solv}G^0_{298(5)}$, kJ mol^{-1}	$K_{(6)}$	$-\Delta_{solv}G^0_{298(6)}$, kJ mol^{-1}
	reaction (5)		reaction (6)	
0.38	66.8	10.4	53.1	9.6
0.61	58.7	10.1	49.4	9.7
0.71	49.4	9.7	46.9	9.5
0.80	35.1	8.8	33.6	8.7
0.94	29.7	8.4	33.5	8.7
1.33	38.1	9.0	40.3	9.2
1.43	40.9	9.2	45.5	9.6

For equilibria (5) and (6), the equilibrium constants are as follows:

$$K_{(5)} = \frac{a_{HSO_4^-} C_{org}}{a_{Ce(SO_4)_2^-} C_{TABAS}}, \quad (8)$$

$$K_{(6)} = \frac{a_{H^+} C_{org}}{a_{CeSO_4^+} C_{TABAS}}. \quad (9)$$

These constants and Gibbs energies of extraction calculated at various pH are listed in Table 3. a_H^+, C_{org}, and C_{TABAS} are experimental, while the activities of cerium sulfate complexes were calculated from data of Table 2 and from the activity coefficients calculated by the GIBBS program.

Calculations showed that the transfer of both cerium complexes into the organic phase is characterized by close equilibrium constants and Gibbs energies ($K_{(5)} = 46 \pm 12$, $\Delta_{solv}G^0_{298(5)} = -9 \pm 1$ kJ mol^{-1}; $K_{(6)} = 43 \pm 7$, $\Delta_{solv}G^0_{298(6)} = -9.3 \pm 0.4$ kJ mol^{-1}). The root-mean-square errors were calculated for the expected probability 0.95 at a number of experiments equal to 7.

Extraction reactions (5) and (6) are characterized by different coefficients at H^+, but none of them corresponds to the experimental slope of the $\log D_{Ce} = f(pH)$ dependence [Eqs. (3), (4) and (8), (9)].

Probably both complexes participate in Ce(III) extraction. Taking into consideration the experimental slope of 0.5 in Eq. (3) and close values of $K_{(5)}$ and $K_{(6)}$, we can propose the following equation of the overall extraction equilibrium:

$$0.5Ce(SO_4)_{(aq)}^+ + 0.5Ce(SO_4)_{2(aq)}^- + (R_4N)HSO_{4(org)} \rightarrow (R_4N)[Ce(SO_4)_2]_{(org)} + 0.5H_{(aq)}^+ + 0.5HSO_{4(aq)}^-, \quad (10)$$

for which the equilibrium constant can be calculated as geometric mean of $K_{(5)}$ and $K_{(6)}$:

$$K_{(10)} = \sqrt{K_{(5)}K_{(6)}}. \quad (11)$$

Table 4. Calculated equilibrium constants and Gibbs energies of extraction of cerium(III) from sulfate solutions

pH	K	$-\Delta_{solv}G^0_{298}$, kJ mol^{-1}
0.38	59.3	10.1
0.61	53.9	9.9
0.71	48.1	9.6
0.80	34.4	8.8
0.94	31.5	8.5
1.33	39.2	9.1
1.43	44.1	9.4
$\overline{K} = 44 \pm 9$		$-\Delta_{solv}\overline{G}^0_{298} = 9.3 \pm 0.5$
1.75	42.2	9.3
2.74	35.9	8.9
3.24	39.9	9.1
3.65	40.6	9.2
3.76	35.3	8.8
3.81	32.8	8.6
$\overline{K} = 38 \pm 3$		$\overline{G}^0_{298} = 8.9 \pm 0.3$

The results of the calculation are listed in Table 4. At pH > 1.65, the Ce(III) disulfate complex prevails in the equilibrium aqueous phase, and its extraction can be approximated by the scheme

$$Ce(SO_4)_{2\,(aq)}^- + 0.5(R_4N)_2SO_{4\,(org)} \rightarrow (R_4N)[Ce(SO_4)_2]_{(org)} + 0.5SO^{2-}_{4\,(aq)}. \quad (12)$$

This extraction mechanism is confirmed by the independence of the Ce(III) distribution coefficient from pH [Table 1, Eq. (4)]. The equilibrium constant of reaction (12) is

$$K_{(12)} = \frac{C_{org}a^{0.5}_{SO_4^{2-}}}{a_{Ce(SO_4)_2^-}\,0.5C^{0.5}_{TABAS}}. \quad (13)$$

The calculated equilibrium constants and the corresponding Gibbs energies are listed in Table 4.

The close values the equilibrium constants and Gibbs energies at various pH within any branch of the log $D = f$(pH) dependence indicate the validity of the proposed mechanisms of extraction equilibria.

CONCLUSIONS

(1) The distribution of Ce(III) between the sulfuric acid solution and trialkylbenzylammonium sulfate in dodecane was studied. The cerium distribution coefficient grows with increasing pH and at pH 1.65 reaches the maximal value D = 35. Extraction is provided by transition into the organic phase of cerium mono- and disulfate complexes. The content of the latter grows with increasing pH.

(2) Two schemes of extraction equilibria at pH < 1.65 and pH > 1.65 were proposed, based on coordination of two sulfate ions with the metal ion in the sulfate complexes and on thermodynamic calculations of the compositions of aqueous solutions at known pH and total cerium content.

(3) The invariability of the equilibrium constants and standard Gibbs energies in both pH ranges (0–1.65 and > 1.65) confirms the adequacy of the proposed schemes of the extraction equilibria.

ACKNOWLEDGMENTS

The work was financially supported by Ministry of Education of the Russian Federation (project no. TOO.4.2.103).

REFERENCES

1. Lebedev, V.N., Lokshin, E.P., Masloboev, V.A., *et al.*, *Tsvetn. Met.*, 1997, no. 8, pp. 46–50.
2. Mikhalichenko, A.I., Mikhlin, E.B., and Patrikeev, Yu.V., *Redkozemel'nye metally* (Rare-Earth Metals), Moscow: Metallurgiya, 1987.
3. Smidt, V.S., *Ekstraktsiya aminami* (Extraction with Amines), Moscow: Atomizdat, 1970.
4. Danilov, N.A., El'-Farad, S., and Korpusov, G.V., *Radiokhimiya*, 1992, vol. 34, no. 2 pp. 72–81.
5. Dibrov, I.A., Chirkst, D.E., and Litvinova, T.E., *Zh. Prikl. Khim.*, 1996, vol. 69, no. 5, pp. 727–730.
6. Barkovskii, V.D. and Ganopol'skii, A.S., *Differentsial'naya spectrofotometriya* (Differential Spectrophotometry), Moscow: Khimiya, 1969.
7. Bral', V.V., Kopyrin, A.A., and Shokin, V.V., *Radiokhimiya*, 1983, vol. 25, no. 1, pp. 12–15.
8. Shvarov, Yu.V., *Dokl. Akad. Nauk SSSR*, 1981, vol. 257, no. 5, pp, 1221–1225.
9. *Termicheskie konstanty veshchestv: Spravochnik* (Thermal Constants of Substances: Handbook), Glushko, V.P., Ed., Moscow: Akad. Nauk SSSR, 1965–1976, vols. 1–7.
10. Robie, R.A., Hemingway, B.S., and Fisher, I.R., *Geol. Survey Bull.*, Washington, 1978, p. 1452.
11. Pyartman, A.K., Kovalev, S.V., Keskinov, V.A., and Kopyrin, A.A., *Radiokhimiya*, 1997, vol. 39, no. 2, pp. 141–144.
12. Mikhalichenko, A.I., Goryacheva, E.G., Dozhdeva, N.M., and Vakulenko, A.G., *Radiokhimiya*, 1977, vol. 19, no. 6, pp. 764–768.

Russian Journal of Applied Chemistry, Vol. 75, No. 2, 2002, pp. 195–199. Translated from Zhurnal Prikladnoi Khimii, Vol. 75, No. 2, 2002, pp. 202–207.
Original Russian Text Copyright © 2002 by Dibrov, Chirkst, Litvinova.

SORPTION AND ION-EXCHANGE PROCESSES

Experimental Study of Zirconium(IV) Extraction from Fluoride-Containing Acid Solutions

I. A. Dibrov, D. E. Chirkst, and T. E. Litvinova

Plekhanov State Mining Institute, St. Petersburg, Russia

Received August 31, 2000; in final form, April 2001

Abstract—Zirconium(IV) extraction from acid solutions was studied, and the optimal parameters of the process were found. Extractants for zirconium(IV) recovery from nitric and sulfuric acid solutions in the presence of fluoride ions were selected. The distribution coefficients of zirconium(IV) and fluoride ion were determined.

Eudialyte is a promising source of rare-earth metals and zirconium. It is readily decomposed with acids, which allows its comparatively simple processing. A number of works devoted to processing of eudialyte ores and concentrates have been published [1, 2]. The main problem in this field is the formation during acid leaching of difficultly filterable silica gel precipitates, with incomplete transfer of target components and in particular, zirconium into the solution. Earlier, it has been shown that introduction into the pulp of small amounts of fluoride ions at the instant of ore breakdown eliminates the above disadvantage [3]. The use of sulfuric acid instead of nitric acid makes eudialyte processing more efficient.

Nitric acid solutions obtained from ore breakdown are traditionally treated by extraction. Extraction of zirconium from sulfuric acid solutions, especially in the presence of fluoride ions, has not been studied.

In this work, we studied the zirconium(IV) distribution between the organic and aqueous phases, using the model solutions with the zirconium content of 5–15 g l^{-1}. This concentration range allowed determination of the effect of the zirconium(IV) content in the aqueous phase on its distribution coefficient, taking into consideration fluctuations in the zirconium concentration during eudialyte breakdown. The F : Zr molar ratio was varied from 0 to 6. The required fluoride content was provided by addition of chemically pure sodium fluoride. Zirconium was extracted from 10–40% sulfuric or nitric acid solutions with the following extractants: (1) 0.5 M solutions of trialkylbenzylammonium sulfate or nitrate in xylene (TABAS, TABAN, respectively; alkyl = C_4–C_{10}) and (2) 20 vol % solution of tributyl phosphate (TBP) in dodecane. The volume ratio of the organic to aqueous phase was 1 : 2.

The extractants were chosen taking into account their opposite mechanisms of extraction. Extraction with TBP proceeds by the donor–acceptor mechanism, while extraction with amines and, in particular, salts of quaternary ammonium bases is due to the ion exchange.

The Zr(IV) concentration was monitored spectrophotometrically with arsenazo III in 2 M HCl [4], and the fluoride ion concentration, potentiometrically with a fluoride-selective electrode [5].

The content of zirconium and fluoride ion in the organic phase C_{org} was found as the difference between their concentrations in the initial C_0 and equilibrium C_{aq} aqueous phases with regard to the weight ratio of water and the organic phase m_{H_2O}/m_{org}:

$$C_{org} = (C_0 - C_{aq})\frac{m_{H_2O}}{m_{org}}, \quad (1)$$

which was 2.43 in our experiment.

The Zr(IV) distribution coefficient D was determined as

$$D = C_{org}/C_{aq}. \quad (2)$$

Usually, the quantitative analysis performed by physicochemical methods is characterized by relative error of 5% at confidence probability of 95%. Therefore, the relative error of determination of dis-

1070-4272/02/7502-0195 $27.00 © 2002 MAIK "Nauka/Interperiodica"

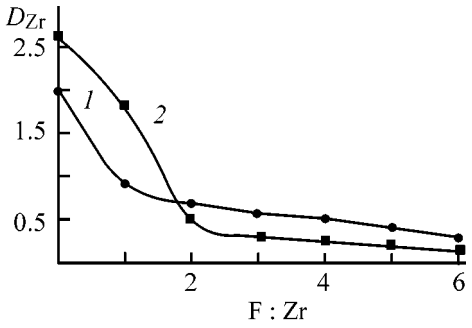

Fig. 1. Zirconium(IV) distribution coefficient vs. the F : Zr molar ratio in extraction with TBP (20% solution in dodecane). Acid (wt %): (*1*) H_2SO_4, 30; (*2*) HNO_3, 40 [7].

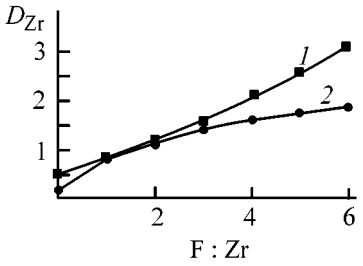

Fig. 2. Zirconium(IV) distribution coefficient vs. the F : Zr molar ratio in extraction with quaternary ammonium bases: (*1*) Extraction with TABAS (0.5 M solution in xylene) from 30% H_2SO_4 and (*2*) extraction with TABAN (0.5 M solution in xylene) from 40% HNO_3.

tribution coefficients D was estimated in this work to be ±7%.

The Zr(IV) extraction from fluoride-containing aqueous phases, and solution preparation were performed in Teflon vessels with mixing by means of a magnetic stirrer. The time of equilibrium attainment was determined experimentally and to be 30 min. Phases were separated in a separatory funnel at room temperature without thermostatic control, since small variations of temperature (±5°C) does not affect substantially the distribution coefficient [6]. The time of phase separation was 15–20 min.

In extraction with TBP, D decreases with increasing F to Zr molar ratio for systems containing sulfuric or nitric acid; at F : Zr > 2 the extraction from the sulfuric acid solution becomes more efficient than that from nitric acid solutions (Fig. 1).

In extraction with trialkylbenzylammonium salts, D grows with increasing F : Zr ratio, and extraction from sulfuric acid solutions is more efficient than that from nitric acid solutions at any F : Zr ratio (Fig. 2). The concentration of sulfuric and nitric acids in the aqueous phase was 30 and 20 wt %, respectively, which corresponds to the same equivalent concentration of 7.3 g-equiv l^{-1}.

The Zr(IV) distribution coefficients are presented in Table 1 in relation to the acid concentration in the aqueous phase within the 10–40 wt % range at F : Zr = 0 for TBP and 6 for TABAS and TABAN. As seen, the sulfuric acid concentration weakly affects the Zr(IV) extraction, while raising the nitric acid concentration leads to substantial increase in D.

To explain the above dependences, we performed thermodynamic analysis of the ionic composition of the equilibrium aqueous phases, using the GIBBS program [8]. This program is based on minimization of the Gibbs free energy of a multicomponent system. The equilibrium gross composition of the system and standard free energies of formation of ions studied in aqueous solutions [9] (Table 2) served as input parameters of the calculation. The results of the calculation are presented in Table 3.

Table 1. Zirconium(IV) distribution coefficient D_{Zr} at various concentrations of the acid

$C(HNO_3)$, wt %	D_{Zr}(TBP)	D_{Zr}(TABAN)	$C(H_2SO_4)$, wt %	D_{Zr}(TBP)	D_{Zr}(TABAS)
10	0.23	0.38	10	2.0	3.15
20	1.08	0.70	20	1.97	3.17
30	2.60	1.33	30	2.15	3.18
40	4.25	2.25	40	1.91	3.0

Table 2. Thermodynamic data for calculation of the ionic composition of the equilibrium aqueous phase

Ion	$-\Delta_f G^0_{298}$, kJ mol^{-1}	Ion	$-\Delta_f G^0_{298}$, kJ mol^{-1}	Ion	$-\Delta_f G^0_{298}$, kJ mol^{-1}	Ion	$-\Delta_f G^0_{298}$, kJ mol^{-1}	Ion	$-\Delta_f G^0_{298}$, kJ mol^{-1}
$Zr(NO_3)^{3+}$	640.57	$ZrSO_4^{2+}$	1304.15	ZrF^{3+}	860.05	ZrF_3^+	1506.13	ZrF_5^-	2123.33
$Zr(NO_3)_2^{2+}$	753.96	$Zr(SO_4)_2^0$	2074.00	ZrF_2^{2+}	1188.32	ZrF_4^0	1816.82	ZrF_6^{2-}	2419.41

Table 3. Content of major Zr(IV) species in the equilibrium aqueous phase (thermodynamic calculation)

Species	Concentration, mmol kg^{-1} at F : Zr molar ratio						
	0	1	2	3	4	5	6
				40% HNO_3			
$Zr(NO_3)^{3+}$	4.2	2.10	1.24	0.38	0.30	0.15	0.01
$Zr(NO_3)_2^{2+}$	46.6	23.6	12.0	4.24	1.87	0.59	0.08
ZrF^{3+}	–	3.97	2.8	1.81	1.22	0.71	0.25
ZrF_2^{2+}	–	9.21	15.9	18.0	15.0	11.6	7.69
ZrF_3^{+}	–	8.61	4.32	7.26	9.18	11.3	13.2
ZrF_4^{0}	–	0.02	0.18	0.55	1.84	3.06	4.28
ZrF_5^{-}	–	–	0.02	0.08	0.97	1.84	2.66
ZrF_6^{2-}	–	–	–	–	0.18	0.39	0.53
				30% H_2SO_4			
$ZrSO_4^{2+}$	3.67	1.22	0.1	0.01	–	–	–
$Zr(SO_4)_2^{0}$	37.0	17.0	3.37	0.27	0.2	–	–
ZrF^{3+}	–	3.62	1.93	0.44	0.15	0.06	0.01
ZrF_2^{2+}	–	13.5	20.2	12.9	6.48	3.66	1.61
ZrF_3^{+}	–	2.01	8.4	11.8	12.9	12.2	7.8
ZrF_4^{0}	–	4.75	0.57	2.71	3.88	5.82	6.04
ZrF_5^{-}	–	–	–	0.49	0.91	3.28	4.63
ZrF_6^{2-}	–	–	–	–	–	0.71	1.86

As seen, the dominating Zr(IV) species is $Zr(NO_3)_2^{2+}$ and $Zr(SO_4)_2^{0}$ in the fluoride-free nitric acid and sulfuric acid solutions, respectively.

Extraction of zirconium with TBP, TABAS, and TABAN from fluoride-free sulfuric and nitric acid solutions can be represented as extraction reactions written on the basis of a thermodynamic calculation (Table 3) and reference data indicating that the zirconium(IV) coordination number is 6 and the probable number of extractant molecules in the extraction complex is 2 [10, 11].

$$Zr(NO_3)_{2(aq)}^{2+} + 2NO_{3(aq)}^{-} + 2TBP_{(org)} \rightarrow Zr(NO_3)_4 \cdot 2TBP_{(org)}, \quad (3)$$

$$Zr(SO_4)_{2(aq)}^{0} + 2TBP_{(org)} \rightarrow Zr(SO_4)_2 \cdot 2TBP_{(org)}, \quad (4)$$

$$Zr(NO_3)_{2(aq)}^{2+} + 2NO_{3(aq)}^{-} + 2R_4N(NO_3)_{(org)} \rightarrow (R_4N)_2[Zr(NO_3)_6]_{(org)}, \quad (5)$$

$$Zr(SO_4)_{2(aq)}^{0} + 2R_4N(SO_4)_{(org)} \rightarrow (RN_4)_2[Zr(SO_4)_3]_{(org)} + H_{(aq)}^{+} + HSO_{4(aq)}^{-}. \quad (6)$$

Extraction from nitric acid solution involves nitrate ions. This accounts for the salting-out effect of nitric acid (D_{Zr} growing with increasing acid concentration). Sulfuric acid shows no salting-out effect because it is not involved in the corresponding extraction reaction.

The dependence of D_{Zr} on the initial zirconium content in 30% H_2SO_4 at F : Zr ratio of 0 for TBP and 6 for TABAS is presented in Table 4. As seen, the degree of Zr recovery with both extractants is independent of the initial metal concentration within the concentration range indicated above.

In the process developed for eudialyte concentrate breakdown [3], fluoride ions with molar ratio F : Zr > 3 always occur in solution after the ore breakdown. For such solutions, TBP is in efficient as extractant for both sulfuric and nitric acid solu-

Table 4. Effect of the initial Zr(IV) content on D_{Zr}

C_0[Zr(IV)], g l^{-1}	D_{Zr}	
	TBP	TABAS
5	2.07	2.89
10	2.08	3.02
15	1.73	2.91

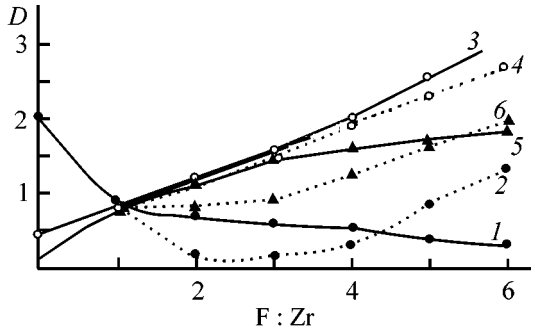

Fig. 3. (*1, 3, 5*) Zr(IV) and (*2, 4, 6*) F^- distribution coefficients D vs. the F : Zr molar ratio. Extraction: (*1, 2*) with TBP, data of [7]; (*3, 4*) with TABAS from 30% H_2SO_4; and (*5, 6*) with TABAN from 40% HNO_3.

tions (Figs. 1, 2). In addition, in extraction from sulfuric acid solution, the Zr(IV) distribution coefficient is independent of the acid concentration, which makes the extraction process more stable.

Further, we studied the distribution of the fluoride ion between the organic and aqueous phases in extraction with TABAS and TABAN. In these experiments, the initial zirconium concentration was 0.055 M. The results are listed in Table 5 and Fig. 3.

A comparison of the distribution coefficients of zirconium and fluoride ion showed that in extraction with TBP, when zirconium is absent, the distribution coefficient of fluoride ion is independent of its concentration within the concentration range studied and is equal to 1.2. In the presence of zirconium, the dependence of D_F on the F : Zr molar ratio has a minimum at F : Zr = 2–3 [7] (Fig. 3). It follows from Table 5 and Fig. 3 that the content of fluoride ion in the organic phase changes with its increasing content in the system, which indicates the change in the composition of the extractable complex. This change is nonmonotonic for the system with TBP (Fig. 5, curve *2*): the number of fluoride ions bonded with zirconium decreases to F : Zr = 2–3 and then increases again. The change in fluoride ion content and F : Zr ratio in the organic phase correlates with changes in the fluoride ion distribution coefficient. An analysis of the fluoride ion extraction with trialkylbenzylammonium salt showed that the given F : Zr molar ratio is virtually the same in both aqueous and organic phases within the entire range studied. In the organic phase, the F : Zr molar ratio is slightly lower than the initial one, which can be attributed to simultaneous extraction, along with $[ZrF_6]^{2-}$, of the other zirconium(IV) com-

Table 5. Distribution of Zr(IV) and F^- between the organic and aqueous phases in extraction with TABAS and TABAN from sulfuric and nitric acid solutions, respectively, with the same equivalent concentration

Initial F : Zr molar ratio	Distribution of Zr(IV)			Distribution of F^-			F : Zr molar ratio in the organic phase
	$C_{aq} \times 10^2$	$C_{org} \times 10^2$	D_{Zr}	$C_{aq} \times 10^2$	$C_{org} \times 10^2$	D_F	
	M			M			
			30% H_2SO_4				
0	4.07	1.79	0.44	–	–	–	–
1	3.78	3.06	0.81	3.85	2.89	0.75	0.94
2	3.44	4.12	1.20	7.07	7.85	1.11	1.90
3	3.17	4.94	1.56	9.63	14.35	1.49	2.90
4	2.47	5.00	2.02	10.19	19.36	1.90	3.87
5	2.57	6.46	2.54	13.49	31.03	2.30	4.80
6	2.17	6.66	3.07	14.04	37.91	2.70	5.70
			40% HNO_3				
0	5.11	0.77	0.15	–	–	–	–
1	3.97	3.03	0.77	3.40	2.60	0.76	0.86
2	3.54	3.93	1.11	7.75	6.51	0.84	1.66
3	3.24	4.54	1.42	11.20	10.42	0.93	2.30
4	3.06	4.90	1.60	13.41	17.17	1.28	3.50
5	2.97	5.05	1.69	15.11	24.78	1.64	4.91
6	2.86	5.26	1.84	14.73	29.46	2.00	5.60

plexes $[ZrF_n]^{4-n}$ with n = 1–5. In general, we can suggest the following reaction:

$$[ZrF_x]^{4-x}_{(aq)} + 2(R_4N)An_{(org)} \rightarrow (R_4N)_2[ZrF_xAn_{6-x}]_{(org)} + (x - 4)An^-_{(aq)}, \quad (7)$$

where An is NO_3^- or HSO_4^- ($1/2SO_4^{2-}$), and x = 1–6.

For the most part x = 6. This well conforms to data of Shmidt [11] who proposed the following scheme of extraction of Zr(IV) chloride complexes with trioctylamine from sulfuric acid solutions:

$$[ZrCl_6]^{2-} + 2(R_3NH)HSO_4 \rightarrow (R_3NH)_2[ZrCl_6] + 2HSO_4^-. \quad (8)$$

Thus, we found the optimal conditions of Zr(IV) extraction from fluoride-containing sulfuric acid solutions: 0.5 M TABAS in xylene, molar ratio F : Zr = 6 at sulfuric acid concentration from 10 to 30 wt % and Zr(IV) initial concentration in the aqueous solution from 5 to 15 g l^{-1}; volume ratio of the organic to aqueous phase 1 : 2.

Further, we studied the Zr(IV) backwashing from the organic phase containing the $[ZrF_6]^{2-}$ complex. The following backwashing agents were tested: water, 1 M HCl, 1 M H_2SO_4, and HCl + KCl mixture at pH 1 and chloride ion concentration of 1 M. The ratio of aqueous to organic phase in backwashing was 1 : 2. The backwashing efficiency was estimated as the Zr(IV) concentration in the equilibrium aqueous phase. The initial Zr(IV) concentration in the organic phase was known beforehand from extraction experiments. The best backwashing agent for Zr(IV) is 1 M HCl: up to 98% of zirconium passes into the aqueous phase. Water strips about 40% of zirconium, and sulfuric acid (1 M), about 10%.

Then the extraction power of TABAS after treatment with HCl was evaluated to assess the possibility of repeated use of the extractant. The Zr(IV) recovery was compared in extraction with the fresh solution of TABAS in xylene and with TABAS solution treated with HCl after Zr(IV) backwashing. The virtually the same values of the Zr(IV) distribution coefficient in both experiments show that treatment with HCl weakly affects the TABAS extraction power.

We also found that, in the extraction-backwashing cycle, all fluoride ions pass, together with zirconium, into the aqueous phase on contact with HCl. This follows from the constancy of the F : Zr molar ratio in the initial aqueous solution, extract, and backwash, which allows repeated use of the extractant without its additional purification.

CONCLUSIONS

(1) Extractants for Zr(IV) extraction from nitric and sulfuric acid solutions were selected. TBP is inefficient when fluoride ions are present in the system, and in this case trialkylbenzylammonium sulfate can be recommended.

(2) The distribution coefficients of Zr(IV) and F^- were determined. Fluoride ions are coextracted with Zr(IV); the F : Zr molar ratio remains constant in both organic and aqueous solutions. D_{Zr} is about 3 at F : Zr = 6.

(3) The most complete Zr(IV) backwashing is ensured by 1 M HCl at a 1 : 2 volume ratio of the organic to aqueous phase.

ACKNOWLEDGMENTS

The work was financially supported by the Ministry of Education of the Russian Federation (project no. TOO.4.2.103).

REFERENCES

1. Masloboev, V.A. and Lebedev, V.N., *Redkozemel'noe syr'e Kol'skogo poluostrova i problemy ego kompleksnoi pererabotki* (Rare-Earth Raw Materials of the Kola Peninsula and Problems of Their Integrated Processing), Apatity: Akad. Nauk SSSR, 1991.
2. Chekmarev, A.M., Chizhevskaya, S.V., Masloboev, V.A., *et al.*, in *Khimiya i tekhnologiya redkikh i rasseyannykh elementov* (Chemistry and Technology of Less-Common and Trace Elements), Leningrad: Leningr. Tekhnol. Inst. im. Lensoveta, 1989, pp. 65–74.
3. Dibrov, I.A., Chirkst, D.E., and Litvinova, T.E., *Zh. Prikl. Khim.*, 1996, vol. 69, no. 5, pp. 727–730.
4. Elinson, S.V. and Petrov, K.I., *Analiticheskaya khimiya zirkoniya i gafniya* (Analytical Chemistry of Zirconium and Hafnium), Moscow: Nauka, 1965.
5. Polyak, E.A. and Matusevich, V.S., *Zh. Anal. Khim.*, 1984, vol. 39, no. 6, pp. 1090–1093.
6. Danilov, N.A., El-Farad, S., and Korpusov, G.V., *Radiokhimiya*, 1992, vol. 34, no. 2, pp. 72–81.
7. Dibrov, I.A., Chirkst, D.E., and Litvinova, T.E., *Zh. Prikl. Khim.*, 1996, vol. 69, no. 3, pp. 397–403.
8. Shvarov, Yu.V., *Dokl. Akad. Nauk SSSR*, 1981, vol. 257, no. 5, pp, 1221–1225.
9. *Termicheskie konstanty veshchestv: Spravochnik* (Thermal Constants of Substances: Handbook), Glushko, V.P., Ed., Moscow: Akad. Nauk SSSR, 1965–1976, vol. 1–7.
10. Yagodin, G.A., Kaplan, G.E., Mostovaya, O.A., *et al.*, *Zh. Neorg. Khim.*, 1963, vol. 8, no. 8, pp. 1973–1979.
11. Shmidt, V.S., *Ekstraktsiya aminami* (Extraction with Amines), Moscow: Atomizdat, 1970.

Russian Journal of Applied Chemistry, Vol. 75, No. 2, 2002, pp. 200–202. Translated from Zhurnal Prikladnoi Khimii, Vol. 75, No. 2, 2002, pp. 208–210.
Original Russian Text Copyright © 2002 by Poleshchuk, Pimneva.

SORPTION AND ION-EXCHANGE PROCESSES

Sorption Kinetics of Ba^2+, Cu^2+, and Y^3+ on KRF-10p Complexing Cation Exchanger

I. N. Poleshchuk and L. A. Pimneva

Tyumen State Architectural and Building Academy, Tyumen, Russia

Received 14 December, 2000; in final form, June 2001

Abstract—The ion-exchange sorption kinetics of barium, copper, and yttrium on KRF-10p cation exchanger from $BaCl_2$, $CuCl_2$, and $Y(NO_3)_3$ aqueous solutions was studied. The ionic diffusion coefficients were determined as a function of temperature and concentration.

The ion exchange rate is one of the important factors influencing the sorption efficiency of ion exchangers. A study of ion-exchange sorption kinetics gives better insight into the mechanism of the sorption process as a whole. Kinetic curves allow determination of such principal parameters influencing the sorption as the rate of sorption equilibrium attainment and the maximal operating sorption capacity of an ion exchanger at a given solution composition and temperature. These kinetic data are useful in analysis of cation–resin interactions and can be used to determine the diffusion coefficients controlling the internal and external mass transfer of the cations and the limiting stage of sorption.

The aim of this work was to study the sorption kinetics of Ba^{2+}, Cu^{2+}, and Y^{3+} on KRF-10p cation exchanger in the H^+ form from chloride and nitrate solutions containing various amounts of hydrochloric and nitric acids.

EXPERIMENTAL

Prior to experiment, the cation exchanger was treated by the procedures described in [1]. The ion exchange in the H^+–Ba^{2+}, H^+–Cu^{2+}, and H^+–Y^{3+} systems was studied by the technique reported in [2].

The initial salt solution (500 ml) was poured in a vessel and placed in a thermostat. After the required temperature was reached (25, 45, and 60°C), a weighed portion of swollen KRF-10p cation exchanger in the H^+ form (1 g dry weight) was placed in vigorously stirred solution, and simultaneously the process timing was started. The solution was sampled at regular intervals with 5-ml portions taken, and the metal content was determined. The total solution volume sampled in the course of the experiment was no more than 2% of the initial solution volume. The cation concentration was determined complexometrically [3, 4].

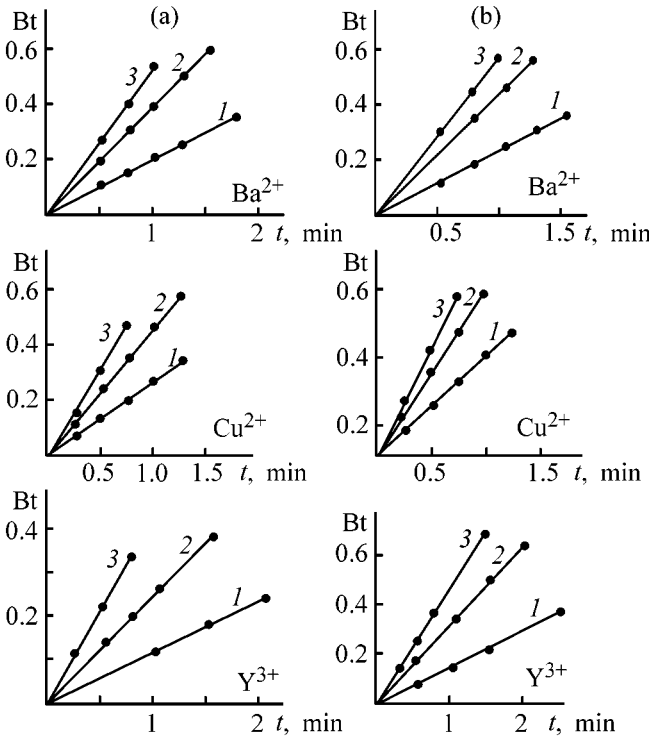

Fig. 1. The Bt parameter vs. time *t* for cation sorption from (a) starting 0.1 M $BaCl_2$, $CuCl_2$, and $Y(NO_3)_3$ solutions and (b) 0.1 M $BaCl_2$, $CuCl_2$, and $Y(NO_3)_3$ solutions containing 0.1M HCl (HNO_3) on KRF-10p cation exchanger in the H^+ form. Temperature (°C): (*1*) 25, (*2*) 45, and (*3*) 60.

1070-4272/02/7502-0200 $27.00 © 2002 MAIK "Nauka/Interperiodica"

The kinetics of cation-exchange sorption on KRF-10p is shown in Figs. 1–3 and table. The original experimental kinetic curves were processed using the Boyd–Adamson equation for pore diffusion [5, 6]

$$F = Q_t/Q_\infty = 1 - 6/\pi^2 \sum_{n=1}^{\infty} 1/n^2 \exp(-\mathrm{Bt}\, n^2), \qquad (1)$$

where F is the degree of ion exchange; Q_t and Q_∞ are the amounts of ions sorbed by the time of sampling t (s) and by the time of equilibrium attainment, respectively; $\mathrm{Bt} = (\bar{D}\pi^2 t)/r^2$ is the dimensionless parameter (Fourier homochronism criterium), and r is the ion-exchanger grain radius (mm).

The Bt parameters for different F were reported in [7].

The adequacy of Eq. (1) was confirmed in a set of sorption experiments with intermittent separation of the cation exchanger and aqueous phases [8]. It was found that the sorption rate increases after repeated contact of the cation exchanger and solution. This shows that the cation pore diffusion is the limiting stage of sorption. As seen from Fig. 3, this mechanism determines the sorption kinetics of Cu^{2+} on KRF-10p cation exchanger. Sorption of the other cations under consideration is characterized by similar kinetic curves. Our experimental results are satisfactorily fitted by Eq. (1), which is confirmed by the linear run of the plot of Bt vs. t for the systems under consideration at F ranging from 0 to 0.5–0.7 (Figs. 1a, 1b). These linear dependences also suggest that the pore diffusion within the resin grains is the limiting stage of mass transfer in cation sorption.

The diffusion coefficients were calculated by the equation

$$D = \frac{\mathrm{Bt}\, r^2}{\pi^2 t}.$$

Data in the table show that the cation diffusion coefficient grows with increasing acid concentration in the initial solution. Apparently, this trend is mainly caused by an increase in the concentration of the protonated ion-exchange groups on the surface and within ion exchanger grains, a decrease in the degree of cation hydration, an increase in the ionic strength of solution, and, as a result, an increase in the degree of ionization of the cation exchanger. The rate of cation exchange between the solution and cation exchanger is determined by the charge and radius of the cation and the strength of the bond between the cation and the sorbing site. The radii of cations under consideration increase in the following order: $Y^{3+} < Cu^{2+} < Ba^{2+}$.

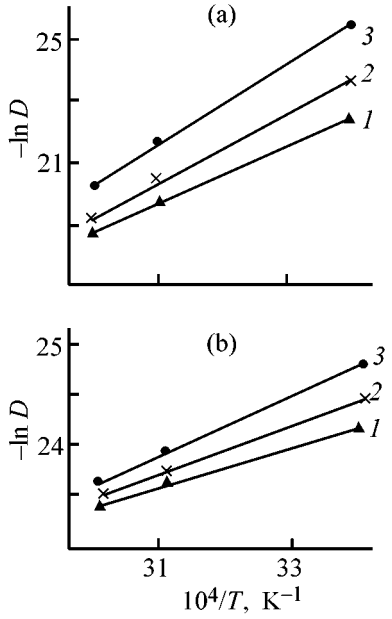

Fig. 2. Influence of temperature T on the diffusion coefficients D of (*1*) Cu^{2+}, (*2*) Ba^{2+}, and (*3*) Y^{3+} in their sorption from (a) starting $CuCl_2$, $BaCl_2$, and $Y(NO_3)_3$ solutions and (b) those containing 0.1 M HCl (HNO_3) on KRF-10p cation exchanger in the H^+ form.

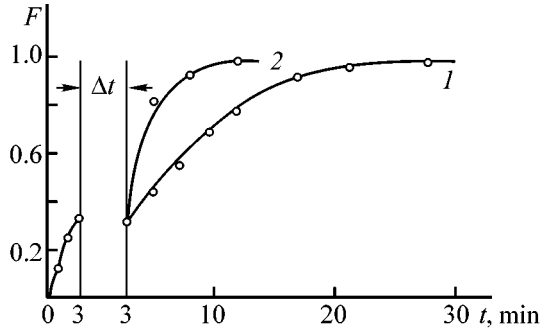

Fig. 3. Kinetic curves of copper sorption from 0.1 N $CuCl_2$ solution on KRF-10p cation exchanger. (F) Degree of exchange and (t) time; (*1*) at continuous contact between the liquid and cation exchanger phases and (*2*) with intermittent separation of the liquid and cation exchanger phases.

The ionic radii of these cations, reported in [8], are 0.93, 0.96, and 1.35 Å, respectively.

The diffusion coefficients increase in the following order: $Y^{3+} < Ba^{2+} < Cu^{2+}$.

The abnormally low yttrium diffusion coefficient in this series is due to its larger electrical charge. It is known [5] that the diffusion coefficients sharply decrease in passing to multicharged cations.

Kinetic parameters of Ba^{2+}, Cu^{2+}, and Y^{3+} diffusion transfer from 1 M $BaCl_2$, $CuCl_2$, and $Y(NO_3)_3$ solutions into grains of KRF-10p cation exchanger in the H^+ form

Cation	T, °C	$D \times 10^{12}$, $cm^2\ s^{-1}$		ΔE, kJ mol^{-1}	
		at indicated acid concentration, M			
		0	0.1	0	0.1
Ba^{2+}	25	20.08	23.12	22.53	20.52
	45	40.16	47.06		
	60	58.83	62.88		
Cu^{2+}	25	27.79	30.43	17.16	15.92
	45	48.89	52.33		
	60	63.29	65.93		
Y^{3+}	25	12.58	16.23	26.53	25.67
	45	30.43	39.15		
	60	46.25	54.77		

The activation energy of diffusion was calculated by the least-squares method by graphically solving the equation

$$\overline{D} = D_0 \exp(-E/RT). \quad (3)$$

The dependence $\ln \overline{D} = f(1/T)$ is plotted in Fig. 2.

The low activation energy of diffusion, obtained in our experiments, is typical of pore diffusion. These results show that cation exchange makes the major contribution to sorption. Therefore, we can assume that metals under consideration are mainly transferred within cation-exchanger grains in the cationic form. Our results on sorption kinetics can be used in designing sorption installations, solving problems of the ion-exchange dynamics, and optimizing the cation concentration and separation with KRF-10p phosphonic cation exchanger.

CONCLUSIONS

(1) The limiting stage of Ba^{2+}, Cu^{2+}, and Y^{3+} sorption is the pore diffusion of these cations within cation exchanger grains. The diffusion coefficients of these cations and the apparent activation energy were calculated by the pore-diffusion equation.

(2) The cation sorption is accelerated with increasing acid concentration in solution.

REFERENCES

1. Saldadze, K.M., Pashkov, A.B., and Titov, V.S., *Ionoobmennye vysokomolekulyarnye soedineniya* (Ion-Exchange Macromolecular Compounds), Moscow: Goskhimizdat, 1960.
2. Karnelli, M.E. and Legenchenko, I.A., *Issledovanie svoistv ionoobmennykh materialov* (Study of Ion-Exchange Material Properties), Moscow: Nauka, 1964.
3. Pribil, R., *Komplexometrie*, Prague: Chemapol, 1955.
4. Schwanzerbach G. And Flaschka, H., *Die Komplexometrische Titration*, Stuttgardt: Enke, 1965.
5. Kokotov, Yu.A. and Pasechnik, V.A., *Ravnovesie i kinetika ionnogo obmena* (Equilibrium and Kinetics of Ion Exchange), Leningrad: Khimiya, 1960.
6. Boyd, I., Adamson, A., and Meyers, L., *Khromatograficheskie metody razdeleniya ionov* (Chromatographic Technique for Ion Separation), Moscow: Inostrannaya Literatura, 1969.
7. Boyd. G.E., Adamson, A.W., and Meyers, L.S., *J. Am. Chem, Soc.*, 1947, vol. 69, p. 2836.
8. Helfferich, F., *Ionenaustaucher*, Weinheim: Chemie, 1959, vol. 1.

Russian Journal of Applied Chemistry, Vol. 75, No. 2, 2002, pp. 203–208. Translated from Zhurnal Prikladnoi Khimii, Vol. 75, No. 2, 2002, pp. 211–216.
Original Russian Text Copyright © 2002 by Kitikova, Shashkova, D'yachenko.

SORPTION AND ION-EXCHANGE PROCESSES

Effect of Thermal Treatment on Sorption Activity of Calcium and Magnesium Phosphates

N. V. Kitikova, I. L. Shashkova, and A. G. D'yachenko

Institute of General and Inorganic Chemistry, National Belarussian Academy of Sciences, Minsk, Belarus

Received April 11, 2000; in final form, March 2001

Abstract—The effect of thermal treatment in the range 20–800°C on the activity of hydrated calcium and magnesium phosphates in recovery of heavy metal ions from aqueous solutions was studied. The composition and sorption properties of materials obtained in all stages of thermal treatment of hydrophosphates and phosphates are considered. The manner in which the sorption activity of phosphates changes upon thermal treatment is interpreted.

Hydrated calcium and magnesium phosphates, precipitated from solutions of chlorides or nitrates of these metals with a solution of ammonium phosphate, are known as materials demonstrating high efficiency in recovery of ions of heavy and nonferrous metals M^{n+} (n = 2, 3) from aqueous solutions. In the case of a basic salt (calcium hydroxo apatite), the recovery of multicharged metal ions is due to the occurrence of ion-exchange processes [1–4], with capacity 1–3 mg-equiv g^{-1}. In the case of calcium and magnesium phosphates and hydrophosphates, the absorption of double- and triple-charged metal ions is a result of the occurrence of a chemical reaction between solid phosphates and M^{n+} ions [5–9], with the absorption of metal ions in these processes being as high as 25 mg-equiv g^{-1}. Compounds with such a capacity for absorption of ions of heavy and nonferrous metals are of indubitable practical interest.

Practical use of sorption-active materials assumes that data on their thermal stability must be available. Thermal treatment is a necessary operation in obtaining a granulated form of a sorbent and a widely adopted way of sorbent modification to unify or improve their properties.

Published data on the effect of temperature on the chemical activity of calcium and magnesium phosphates are lacking [10].

The present communication reports the results obtained in studying the effect of thermal treatment in the range 20–800°C on the sorption properties of calcium and magnesium phosphates and hydrophosphates precipitated from aqueous solutions.

EXPERIMENTAL

Phosphates $Mg_3(PO_4)_2 \cdot 22H_2O$ and $Ca_3(PO_4)_2 \cdot 3.45H_2O$; hydrophosphates $CaHPO_4 \cdot 2H_2O$, $MgHPO_4 \cdot 3H_2O$, and also a 1 : 1 mixture of $CaHPO_4 \cdot 2H_2O$ + $MgHPO_4 \cdot 3H_2O$ were studied. The salts $Mg_3(PO_4)_2 \cdot 22H_2O$, $CaHPO_4 \cdot 2H_2O$, and $MgHPO_4 \cdot 3H_2O$ were crystalline, and $Ca_3(PO_4)_2 \cdot 3.45H_2O$ was an amorphous substance.

The compounds studied were synthesized as follows. Crystal hydrates of the hydrophosphates and phosphates were precipitated from aqueous solutions of calcium or magnesium nitrates and ammonium phosphate at pH 5 and 10, respectively [10]. A sorption-active mixture of calcium and magnesium hydrophosphates was synthesized as described in [11], with natural dolomite used as raw material. A weighed portion of dolomite was placed in a 10% phosphoric acid solution (M_s : M_l = 1 : 6) and kept for a week with periodic stirring. Then the solution was decanted and the obtained precipitate of calcium and magnesium hydrophosphates was washed with water and dried in air.

The specific surface area of the synthesized compounds was determined from the low-temperature adsorption of nitrogen.

The thermal treatment of the phosphates was done stepwise in the temperature range 20–800°C in a muffle furnace. After 4 h of treatment at 200°C a specimen was cooled and sampled for determining its sorption activity, ground, and again placed in the furnace at higher temperature of 300°C, etc.

1070-4272/02/7502-0203 $27.00 © 2002 MAIK "Nauka/Interperiodica"

Table 1. Results of chemical analysis of synthesized calcium and magnesium phosphates and hydrophosphates

Phosphate	Content, %				M^*/P
	CaO	MgO	P_2O_5	H_2O	
$Ca_3(PO_4)_2 \cdot 3.45H_2O$	45.15** / 45.44	– / –	38.16 / 37.90	16.69 / 16.66	1.50 / 1.52
$CaHPO_4 \cdot 2H_2O$	32.56 / 32.03	– / –	41.28 / 40.61	26.16 / 27.36	1.00 / 1.00
$Mg_3(PO_4)_2 \cdot 22H_2O$	– / –	18.24 / 18.24	21.58 / 21.51	60.18 / 60.25	1.50 / 1.50
$MgHPO_4 \cdot 3H_2O$	– / –	22.99 / 23.00	40.80 / 40.50	36.21 / 36.50	1.00 / 1.00
$CaHPO_4 \cdot 2H_2O + MgHPO_4 \cdot 3H_2O$***	15.93 / 14.95	11.38 / 9.20	40.38 / 36.15	30.71 / 38.10	1.00 / 0.98

* M = Ca or Mg.

** Numerator, calculated; denominator, found.

*** Also contains acid-insoluble admixture of SiO_2 (1.6%).

The structure of the initial phosphates and products of their thermal treatment was determined by X-ray phase analysis (XPA) (DRON-2 diffractometer, Cu_{K_α} radiation) and IR spectroscopy (UR-20 spectrometer, frequency range 4000–400 cm^{-1}, in pellets with KBr, 2-mg weighed portions).

The sorption activity of the obtained materials was evaluated on the basis of absorption by these substances of Pb^{2+} ions from 0.2 N solutions of $Pb(NO_3)_2$ [4]. For this purpose, a weighed portion of a ground sorbent (0.09–0.25 mm fraction, 0.2 g) was placed in 25 ml of 0.2 N lead nitrate solution at room temperature and kept for 24 h with periodic stirring. The solution was separated from the solid phase and the residual content of lead ions in the filtrate was determined by complexometric titration. The error in determining the concentration of lead ions in solution was ±5%.

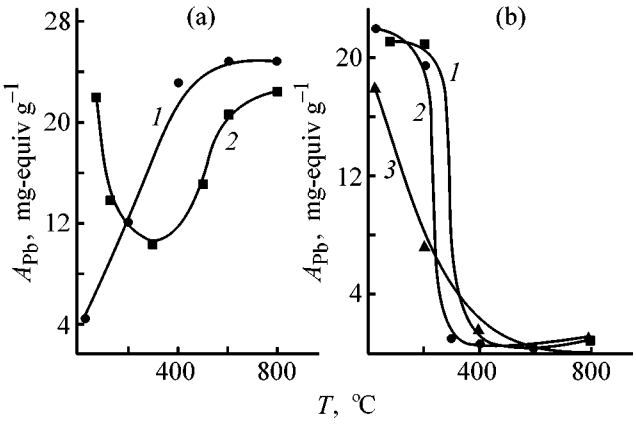

Fig. 1 Changes in sorption capacity of calcium and magnesium phosphates toward lead ions, A_{Pb}, upon thermal treatment. (*T*) Temperature. (a) (*1*) $Mg_3(PO_4)_2 \cdot 22H_2O$ and (*2*) $Ca_3(PO_4)_2 \cdot xH_2O$; (b) (*1*) $CaHPO_4 \cdot 2H_2O$, (*2*) $MgHPO_4 \cdot 3H_2O$, and (*3*) $CaHPO_4 \cdot 2H_2O$–$MgHPO_4 \cdot 3H_2O$.

The results of chemical analysis of the synthesized calcium and magnesium phosphates (Table 1) indicate that their composition corresponds to stoichiometry of hydrophosphates (M/P = 1) and phosphates (M/P = 1.5). Their X-ray and spectral characteristics are in agreement with those reported in the literature [10].

The manner in which the sorption capacity of the phosphates toward lead ions changes upon thermal treatment is shown in Figs 1a and 1b in the form of a plot of the amount A_{Pb} of lead absorbed from a 0.2 N $Pb(NO_3)_2$ solution against the sample heating temperature.

As seen from Fig. 1, the sorption activity of the phosphates changes upon thermal treatment in different ways. For calcium phosphate $Ca_3(PO_4)_2 \cdot 3.45H_2O$, the A_{Pb}–T dependence shows a minimum at 300°C (Fig. 1a). Upon thermal treatment at 20–300°C, the capacity for lead(II) decreases from 20.6 mg-equiv g^{-1} for the initial sample to 10.6 mg-equiv g^{-1} for a sample calcined at 300°C. With temperature raised further, to 800°C, the A_{Pb} value increases to 22.6 mg-equiv g^{-1}.

The sorption capacity of calcium and magnesium hydrophosphates, and a mixture of these, falls upon

thermal treatment irreversibly. The A_{Pb} value for the initial samples is 21.3, 22.1, and 18.1 mg-equiv g^{-1}, respectively. After thermal treatment at 600–800°C, the corresponding values lie in the range from 0.2 to 1.2 mg-equiv g^{-1}.

The sorption capacity of magnesium phosphate $Mg_3(PO_4)_2 \cdot 22H_2O$ grows upon thermal treatment at 20 – 400°C (Fig. 1a) as a result of a considerable loss of mass through dehydration, reaching the maximum value at 400°C, and remains virtually unchanged with temperature elevated further. The sorption capacity of magnesium phosphate in terms of anhydrous salt is virtually unchanged upon thermal treatment.

To explain the observed behavior of the sorption activity of the phosphates, the nature of physicochemical processes occurring in their thermal treatment was studied (Table 2).

The processes of dehydration of calcium and magnesium hydrophosphates and the phase and chemical composition of products formed in all stages of dehydration were described in detail in [10, 12, 13]. According to the available data, calcium and magnesium hydrophosphates polymerize in dehydration to give diphosphates, with calcium diphosphate formed directly from calcium hydrophosphate at 290°C by the scheme

$$CaHPO_4 \cdot 2H_2O \xrightarrow{120^\circ C} CaHPO_4 \xrightarrow{290-400^\circ C} Ca_2P_2O_7. \quad (1)$$

Dehydration of the magnesium salt is a more complex process. In the range 20–600°C, dehydration of magnesium hydrophosphate is accompanied by formation of a multicomponent mixture of amorphous phosphate polymers with 1 to 5 phosphorus atoms in the chain and magnesium oxide. At temperatures higher than 650°C the composition of the system becomes simpler because of the interaction of these components to give a diphosphate. The process can be represented as

$$MgHPO_4 \cdot 3H_2O \xrightarrow{T \le 600^\circ C} \left[\begin{array}{l}\text{Mixture of amorphous } P_1\text{–}P_5 \\ \text{phosphates of Mg and MgO}\end{array}\right] \xrightarrow{T > 600^\circ C} Mg_2P_2O_7 \quad (2)$$

The composition of the products formed in thermal treatment of a mixture of hydrophosphates $CaHPO_4 \cdot 2H_2O + MgHPO_4 \cdot 3H_2O$ in the temperature range 20–800°C has not been described in the literature.

Table 2 Phase and chemical composition and sorption activity of calcium and magnesium phosphates before and after thermal treatment

T, °C	A_{Pb}, mg-equiv g^{-1}	Composition
		$Mg_3(PO_4)_2 \cdot 22H_2O$
20	4.56	$Mg_3(PO_4)_2 \cdot 22H_2O$
200	12.13	Amorphous $Mg_3(PO_4)_2 \cdot xH_2O$
400	23.25	〃
600	24.98	Crystalline $Mg_3(PO_4)_2$ + amorphous phase
800	24.89	Crystalline $Mg_3(PO_4)_2$
		$MgHPO_4 \cdot 3H_2O$
20	22.10	$MgHPO_4 \cdot 3H_2O$
200	19.75	Amorphous phase
300	1.13	Amorphous P_1–P_5 phosphates
600	0.50	Crystalline α-$Mg_2P_2O_7$ + amorphous phase
800	1.20	Crystalline α-$Mg_2P_2O_7$
		$Ca_3(PO_4)_2 \cdot 3.45H_2O$
20	20.60	Amorphous $Ca_3(PO_4)_2 \cdot 3.45H_2O$
120	13.83	Poorly crystalline $Ca_3(PO_4)_2 \cdot xH_2O$
300	10.60	Amorphous phase
500	15.06	〃
600	20.80	Crystalline β-$Ca_3(PO_4)_2$ + amorphous phase
800	22.60	Crystalline β-$Ca_3(PO_4)_2$
		$CaHPO_4 \cdot 2H_2O$
20	21.30	Crystalline $CaHPO_4 \cdot 2H_2O$
200	21.20	Crystalline $CaHPO_4$
400	0.75	Crystalline β-$Ca_2P_2O_7$
600	0.60	〃
800	1.13	〃
		$CaHPO_4 \cdot 2H_2O + MgHPO_4 \cdot 3H_2O$
20	18.10	$CaHPO_4 \cdot 2H_2O + MgHPO_4 \cdot 3H_2O$
200	7.25	$CaHPO_4 \cdot 2H_2O + MgHPO_4 \cdot 3H_2O$ + amorphous phase
400	1.63	Amorphous P_1–P_5 phosphates Ca and Mg
600	0.39	〃
800	0.20	Crystalline β-$Ca_2P_2O_7$ + α-$Mg_2P_2O_7$

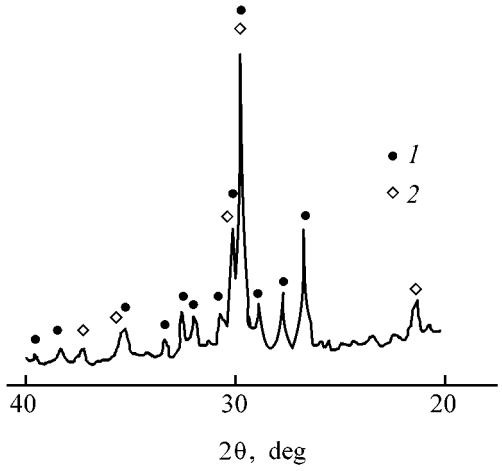

Fig. 2. X-ray diffraction pattern of the product of thermal treatment at 800°C of a mixture of calcium and magnesium hydrophosphates $CaHPO_4 \cdot 2H_2O$ + $MgHPO_4 \cdot 3H_2O$. (2θ) Bragg angle. (*1*) β-$Ca_2P_2O_7$ and (*2*) α-$Mg_2P_2O_7$.

Figure 2 shows an X-ray diffraction pattern of the compound obtained upon calcination of the mixture of hydrophosphates at 800°C. As seen, it contains reflections of calcium and magnesium diphosphates. Double calcium–magnesium diphosphate isolated in [14] from the system $CaO–MgO–P_2O_5$ at a higher temperature of 1050°C was not found in the present study.

Processes of mass loss have been studied in sufficient detail for orthophosphates; however, the information concerning the anionic composition of the forming compounds is rather scarce and contradictory. The final product of dehydration at 800°C is composed of anhydrous orthophosphates, but the issue of whether or not polymerization processes occur in intermediate stages of thermal treatment remains open. It has been noted that amorphous products of $Mg_3(PO_4)_2 \cdot xH_2O$ dehydration contain, in addition to orthophosphate, diphosphate (for a hydrate with x = 22) or di- and tripolyphosphate (for a hydrate with x = 8) [10, 15–17], but no quantitative assessment of these processes has been done. The corresponding information for calcium phosphate is available for a compound of composition $Ca_3(PO_4)_2 \cdot 0.5H_2O$. Up to 1.5–3.0% diphosphate is formed in a certain stage of dehydration of this compound [10].

If the hydrogen bond energy between water of crystallization and the phosphate anion does not exceed 40 kJ mol^{-1}, dehydration proceeds by the molecular mechanism leaving intact the structure of the phosphate anion [10]. Phosphates in which the hydrogen bond energy exceeds the above value are dehydrated by the dissociative mechanism characterized by polymerization of the orthophosphate anion in a certain temperature interval.

To determine the possibility of occurrence of polymerization processes in dehydration of the synthesized hydrated calcium and magnesium phosphates, the energy of their strongest hydrogen bond was evaluated on the basis of IR spectra (Table 3).

The hydrogen bond energy in the synthesized phosphates was calculated using the approximate formula [13]:

$$E = \frac{\Delta\nu}{\nu_0 \times 0.016} \times 4.184,$$

where $\Delta\nu$ is the long-wavelength shift of the frequency of stretching vibrations of the hydroxy group (cm^{-1}), and ν_0 is the frequency of stretching vibrations of the hydroxy group in an isolated water molecule.

In accordance with [16], the ν_0 value is taken to be 3700 cm^{-1}.

The calculated values were 20.0 and 19.8 kJ mol^{-1} for, respectively, $Ca_3(PO_4)_2 \cdot 3.45H_2O$ and $Mg_3(PO_4)_2 \cdot 22H_2O$. According to the existing concepts, dehydration of the calcium and magnesium orthophosphates synthesized must not be accompanied by polymerization. XPA and IR spectral data for the initial phosphates and products of their thermal treatment, presented in Tables 2 and 3, confirm this assumption.

As conclusive evidence in favor of polymerization of the orthophosphate anion in dehydration of calcium and magnesium phosphates would serve appearance of absorption bands associated with vibrations of bridge P–O–P groups in IR spectra of these compounds upon thermal treatment.

As seen from Table 3, products of thermal treatment of calcium and magnesium phosphates show no absorption bands characteristic of vibrations of bridge P–O–P groups and, in particular, symmetric stretching vibrations ν_s(P–O–P) at 650–800 cm^{-1} at any temperature [18–20]. The spectra of calcium and magnesium phosphates contain, in all stages of thermal treatment, only strong absorption bands at 1060–965 and 620–570 cm^{-1}, associated with stretching $\nu(PO_4)$ and deformation $\delta(PO_4)$ vibrations of the orthophosphate anion PO_4 [19]. Thus, calcium and magnesium orthophosphates are dehydrated by the molecular mechanism. The process can be represented schematically as

$$M_3(PO_4)_2 \cdot xH_2O \xrightarrow{20-800^\circ C} M_3(PO_4)_2, \qquad (3)$$

where x = 2.22, and M = Ca or Mg.

Table 3. Peak frequencies ν in IR spectra of $Ca_3(PO_4)_2 \cdot 3.45H_2O$ and $Mg_3(PO_4)_2 \cdot 22H_2O$ and products of their dehydration

Wave number ν (cm^{-1}) of phosphates heated at T°C						Assignment
–	300	800	–	400	800	
$Ca_3(PO_4)_2 \cdot 3.45H_2O$			$Mg_3(PO_4)_2 \cdot 22H_2O$			
415 w	400 br.m	415 w			407 s	$\delta_s(PO_4)$
		430 w	435 m		437 s	
		445 w			488 s	
					509 sh	$\delta_{as}(PO_4)$
		530 w				
569 v.s		565 v.s			578 s	
	580 s		583 s	595 s	592 s	
607 v.s	615 s	610 sh				
		622 v.s			625 v.s	
					640 sh	
967 sh	950 sh	960 m			982 s	$\nu_s(PO_4)$
		990 s			995 s	
		1010 sh				$\nu_{as}(PO_4)$
1035 v.s					1041 v.s	
	1045–1085 br.s	1060 v.s	1075 br.s	1080 s	1078 v.s	
		1090 v.s				
1120 sh	1110 sh	1110 v.s			1108 sh	
		1130 v.s				
1348 w						δ(OH)
1381 m	1385 w					
1410 m	1425 w					
1476 m	1455 w					
1590 m		1600	1620 m			
1617 m	1608 w		1660 m			
1635 m	1635 w					
2345 w						
2367 w						
				2855 w		
				2930 m		
3410 m	3430 br.m	3450 br.w	3420 br.s	3450 m		ν(OH)

Comparison of the presented information on phase and chemical transformations of various phosphates in thermal treatment (Table 2) with changes in their sorption activity (Fig. 1) makes evident that the decrease in the sorption capacity of hydrophosphates and their mixture with the heating temperature increasing in the range 20–600°C is due to the occurrence of polymerization. Polymeric calcium and magnesium phosphates are characterized by lower solubility, compared with monomers, and do not enter into chemical interaction with lead ions; the obtained capacity value (0.2–1.2 mg-equiv g^{-1}) may be due to ion-exchange substitution of lead ions for calcium ions in the structure of these phosphates.

The sorption activity of those phosphates which are not polymerized in thermal treatment is high in all stages of dehydration. Anhydrous calcium and magnesium orthophosphates retain the ability of their hydrated analogues to enter into chemical interaction with lead ions. According to the data obtained, the minimum at 300°C in the A_{Pb}–T curve for $Ca_3(PO_4)_2$ has kinetic origin. In the range 20–300°C, the process of calcium orthophosphate dehydration is the most intensive, which leads to sintering of its particles and to a change in the kinetic parameters of the interaction between the phosphate and lead nitrate solution. With the time of contact between $Ca_3(PO_4)_2 \cdot 3.45H_2O$ calcined at 300°C and lead nitrate solution raised to

4 days and additional grinding performed, a sample sorbed 21.2 mg-equiv g^{-1} of lead(II).

CONCLUSION

Thermal treatment affects differently the properties of hydrated phosphates of alkaline-earth metals. Calcium and magnesium hydrophosphates polymerize upon thermal treatment, and the reaction products—anhydrous diphosphates, do not interact with ions of lead. Hydrated calcium and magnesium orthophosphates are dehydrated by the molecular mechanism and the forming anhydrous orthophosphates retain ability to enter into chemical interaction with lead ions in all stages of thermal treatment.

REFERENCES

1. Suzuki, T., Hatsushika, T., and Hayakawa, Y., *J. Chem. Soc.*, Faraday Trans. 1, 1981, vol. 77, pp. 1059–1065.
2. Suzuki, T., Hatsushika, T., and Miyake, M., *J. Chem. Soc.*, Faraday Trans. 1, 1982, vol. 78, pp. 3605–3611.
3. Suzuki, T., Ishigaki, K., and Miyake, M., *J. Chem. Soc.*, Faraday Trans. 1, 1984, vol. 80, pp. 3157–3165.
4. Shashkova, I.L., Shul'ga, N.V., and Samuskevich, V.V., *Zh. Neorg. Khim.*, 1998, vol. 43, no. 1, pp. 52–57.
5. Shul'ga, N.V., Shashkova, I.L., and Samuskevich, V.V., *Zh. Prikl. Khim.*, 1999, vol. 72, no. 11, pp. 1852–1858.
6. Shcheglova, I.A., Leont'eva, G.V., and Vol'khin, V.V., *Izv. Vyssh. Uchebn. Zaved., Khim. Khim. Tekhnol.*, 1977, vol. 20, pp. 462–467.
7. Shashkova, I.L., Rat'ko, A.I., and Kitikova, N.V., *Zh. Prikl. Khim.*, 1997, vol. 70, no. 11, pp. 1787–1793.
8. Shashkova, I.L., Rat'ko, A.I., and Kitikova, N.V., *Zh. Neorg. Khim.*, 1998, vol. 43, no. 9, pp. 1431–1436.
9. Shashkova, I.L., Rat'ko, A.I., and Kitikova, N.V., *Colloids Surfaces, A, Physicochem. Eng. Aspects*, 1999, vol. 160, pp. 207–215.
10. Shchegrov, L.N., *Fosfaty dvukhvalentnykh metallov* (Phosphates of Divalent Metals), Kiev: Naukova Dumka, 1987.
11. Shashkova, I.L., Kitikova, N.V., Rat'ko, A.I., and D'yachenko, A.G., *Neorg. Mater.*, 2000, vol. 36, no. 8, pp. 990–994.
12. Shchegrov, L.N., Dzyuba, E.D., and Pechkovskii, V.V., *Izv. Akad. Nauk SSSR, Neorg. Mater.*, 1973, vol. 9, no. 10, pp. 1783–1786.
13. Shchegrov, L.N., *Ukr. Khim. Zh.*, 1983, vol. 49, no. 5, pp. 469–472.
14. McCauley, R.A., Hummel, F.A., and Hoffman, M.V., *J. Electrochem. Soc.*, 1971, vol. 118, no. 5, pp. 755–759.
15. Kotlova, A.G., Kobtsev, B.M., and Shchepochkina, N.I., Abstracts of Papers, *IV Vsesoyuznaya konferentsiya "Fizikokhimicheskoe issledovanie fosfatov"* (All-Union Conf. "Physicochemical Investigation of Phosphates"), Minsk, 1976, pp. 148–149.
16. Pechkovskii, V.V., Mel'nikova, R.Ya., Barannikova, T.N., and Dzyuba, E.D., *Zh. Neorg. Khim.*, 1979, vol. 24, no. 3, pp. 651–656.
17. Makatun, V.N. and Shchegrov, L.N., *Usp. Khim.*, 1972, vol. 41, no. 11, pp. 1937–1959.
18. Lazarev, A.N. and Tenisheva, T.F., *Izv. Akad. Nauk SSSR, Neorg. Mater.*, 1969, vol. 5, no. 1, pp. 82–87.
19. Pechkovskii, V.V., Mel'nikova, R.Ya., Dzyuba, E.D., *et al.*, *Atlas infrakrasnykh spektrov fosfatov: Ortofosfaty* (IR Spectra of Phosphates: Orthophosphates), Moscow: Nauka, 1981.
20. Mel'nikova, R.Ya., Pechkovskii, V.V., Dzyuba, E.D., and Malashonok, I.E., *Atlas infrakrasnykh spektrov fosfatov: Kondensirovannye fosfaty* (IR Spectra of Phosphates: Condensed Phosphates), Moscow: Nauka, 1985.

Russian Journal of Applied Chemistry, Vol. 75, No. 2, 2002, pp. 209–212. Translated from Zhurnal Prikladnoi Khimii, Vol. 75, No. 2, 2002, pp. 217–220.
Original Russian Text Copyright © 2002 by Martirosyan, Manukyan, Kostanyan.

SORPTION AND ION-EXCHANGE PROCESSES

Study of Filtration and Adsorption Properties of Calcium Hydrometasilicate

G. G. Martirosyan, A. G. Manukyan, and K. A. Kostanyan

Institute of General and Inorganic Chemistry, Armenian National Academy of Sciences, Erevan, Armenia

Received June 23, 2000; in final form, June 2001

Abstract—The constants and rate of filtration, optimal filtering layer thickness ensuring the maximum rate of filtration, and specific resistance of the filtering layer were determined for calcium hydrometasilicate powders of the C–S–H (I) type, obtained by processing natural diatomites and by reacting alkali-siliceous solution with $Ca(OH)_2$. The effects of heat treatment and carbonization of C–S–H (I) on its filtration and adsorption properties were studied. The filtration and adsorption properties of calcium hydrometasilicates and conventional commercial filtering powders are compared.

Recently, such cheap raw materials as natural diatomites have been increasingly studied and used to synthesize filtering powders and adsorbents [1–8]. It has been established [3, 9] that, under certain conditions, lime treatment of diatomites leads to destruction of their primary structure and formation of calcium hydrosilicates $xCaO \cdot ySiO_2 \cdot zH_2O$ of the C–S–H (I) type (by Taylor's classification [10]) with molar ratio $CaO : SiO_2 < 1.5$.

This study is a continuation of recent investigations [3, 5, 9, 11] devoted to synthesis of calcium hydrometasilicates of the C–S–H (I) type by reaction between $Ca(OH)_2$ solution (lime milk), diatomite, and alkaline-siliceous solution. The aim of the study was to analyze filtration and bleaching properties of the above-mentioned hydrometasilicates in purification of spent organic solvents.

EXPERIMENTAL

The experiments were carried out on a laboratory vacuum filtration installation, in which vacuum was maintained constant during an experiment. This installation was used to measure at ΔP = const across a filter the duration of passage of each 100 ml of a pure organic solvent and a spent solution containing soluble and insoluble admixtures through a layer of the hydrometasilicates under study. For comparison, we carried out experiments under similar conditions with the conventional commercial Special-2 and ZP-200 filtering powders [12] and carbonated calcium metasilicate obtained from alkali-siliceous solution (CCM) [11].

On the basis of the obtained data (Tables 1 and 2; Figs. 1 and 2), we calculated the filtration constants K

Table 1. Selected physicochemical characteristics of filtering powders

Powder	S_{sp}, $m^2\ g^{-1}$	ρ, $kg\ m^{-3}$	G, $kg\ m^{-3}$	pH of water extract
C–S–H (I) obtained from diatomite [3]	200	2200	160	9.5
SCM	92	2300	466	9.0
Special-2	22	2020	350	8.2
ZP-200	100	2170	532	6.95

Table 2. Filtration constants and specific resistance of the filtering layer of powders in filtration of pure white spirit

Powder	m	tan β	$K \times 10^4$, $m^2\ s^{-1}$	$C \times 10^3$, $m^3\ m^{-2}$	$r \times 10^{-10}$, $m\ kg^{-1}$
C–S–H (I) obtained from diatomite [3]	65.0	187.5	107	347.8	0.870
SCM	52.5	82.5	242	635	0.384
Special-2	101.0	347.0	57.7	291.4	1.60
ZP-200	222.0	815.0	24.5	272.0	3.77

1070-4272/02/7502-0209 $27.00 © 2002 MAIK "Nauka/Interperiodica"

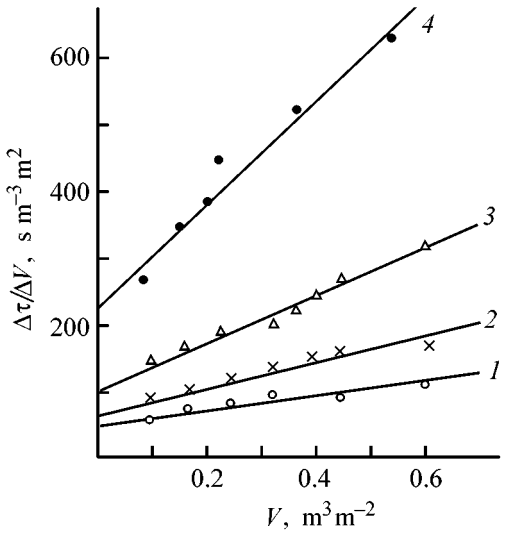

Fig. 1. $\Delta\tau/\Delta V$ vs. filtrate volume V for pure white spirit. (*1*) CCM, (*2*) calcium hydrometasilicate obtained from diatomite, (*3*) Special-2, and (*4*) ZP-200; the same for Fig. 2.

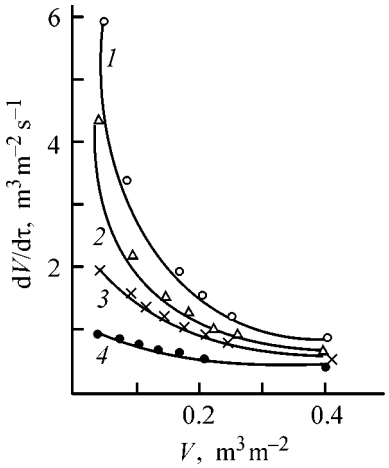

Fig. 2. Filtration rate of spent white spirit $dV/d\tau$ vs. filtrate volume V.

and C related to 1 m^2 of the filtering surface area, the rate of filtration $dV/d\tau$ (m^3 m^{-2} s^{-1}) through a layer of a filtering powder, and the specific resistance r (m kg^{-1}) of the filtering layer (per 1 kg of dry solid substance contained in it) [13]:

$$\frac{dV}{d\tau} = \frac{K}{2(V + C)}, \quad r = \frac{2\Delta P}{\mu G K}.$$

Here V is the volume (m^3) of filtrate passed through 1 m^2 of the filtering surface during a time τ (s); K the filtration constant taking into account the filtration regime and the physicomechanical properties of the precipitate and the solution (m^2 s^{-1}); C the filtration constant characterizing the hydraulic resistance of the filtering cloth (m^3 m^{-2}); ΔP the pressure drop across the filter (kg m^{-2}); μ the viscosity of the filtrate (kg s m^{-2}); and G the mass of dry solid substance precipitated on the filter upon passing 1 m^3 of a filtrate (kg m^{-3}).

Differential thermal analysis curves (DTA) were recorded on an MOM derivatograph (Hungary) with temperature raised at a rate of 5 deg min^{-1}. We determined the specific surface area of samples by the method of low-temperature adsorption of nitrogen by BET [14]; and the density, bulk density, and pH of water extract, by the standard procedures [15].

Table 1 shows that calcium hydrometasilicate obtained from diatomite has a substantially greater adsorption capability than commercial filtering powders, since its specific surface area exceeds by factors of 2 and 9 the specific surface of, respectively, ZP-200 and Special-2 powders. The specific resistance of the filtering layer of calcium hydrometasilicate to pure white spirit is less by factors of 1.8 and 4.3 than that of Special-2 and ZP-200 powders (Tables 2 and 3; Figs. 1 and 2.)

We studied the effect of the heat treatment temperature on the filtering and adsorption properties of calcium hydrometasilicates. It is shown that the specific surface area of C–S–H (I) is almost unchanged as the temperature raised to 550–560°C, irrespective of the $CaO : SiO_2$ molar ratio, and, with the temperature elevated further, to 750°C and more, it decreases abruptly owing to the transformation of porous calcium hydrometasilicate into wollastonite $Ca_3(Si_3O_9)$, which has a substantially more developed crystal structure. The adsorption (decolorizing) properties of calcium

Table 3. Changes in the rate of filtration of pure and spent white spirit through a layer of powders under study at various volumes of the forming filtrate

White spirit	V, m^3 m^{-2}	τ, s	$(dV/d\tau)\times 10^3$, m^3 m^{-2} s^{-1}	τ, s	$(dV/d\tau)\times 10^3$, m^3 m^{-2} s^{-1}	τ, s	$(dV/d\tau)\times 10^3$, m^3 m^{-2} s^{-1}	τ, s	$(dV/d\tau)\times 10^3$, m^3 m^{-2} s^{-1}
		C–S–H (I) [3]		CCM		Special-2		ZP-200	
Pure	0.08–0.4	6.7–67.8	11.8–6.5	4.2–34.2	16.9–11.7	10.2–79.1	7.7–4.13	4.2–217.7	3.51–1.83
Spent	0.04–0.4	9.0–615	4.35–0.65	7.0–540	5.94–0.81	20–746	2.0–0.57	41.8–980	0.96–0.44

hydrometasilicates are improved when the temperature of their heat treatment is raised to 350°C, and, with the temperature elevated further, to 650–800°C, they first slowly and then abruptly deteriorate. The volume of micro- and mesopores in C–S–H (I) samples heated to 350°C seems to change in such a manner that it does not affect the specific surface area of the samples, but improves their adsorption properties with respect to admixtures with appropriate molecule sizes, dissolved in organic solvents. The rate of filtering of organic solvents through a calcium hydrometasilicate layer grows steadily with the temperature of its heat treatment increasing to 750°C.

The data obtained in chemical and thermogravimetric studies suggest that calcium hydrometasilicates are readily carbonized. In this case, their CO_2 content increases 7–12-fold reaching a value of 15% CO 2, and the pH of the water extract decreases from 10 to 8.8. In the DTA curves of carbonated C–S–H (I) samples there appears and steadily grows an endothermic peak at 750–800°C (Fig. 3), associated with decomposition of calcium carbonate [16, 17]. The adsorption and filtering properties of calcium hydrometasilicates are improved 1.2–1.5-fold upon their carbonization.

A distinctive feature of high-quality filtering powders is the incompressibility of the filtering layer, which allows through pores to be preserved in it. These pores can let through the liquid but retain solid particles. It has been shown in our previous studies [5] that particles of calcium hydrometasilicate of the C–S–H (I) type have a shape preventing their packing with formation of a dense filtering layer.

A granulometric study of calcium hydrometasilicate of the C–S–H (I) type by the technique described in [18] showed that particles 20–100 μm in size prevail in the samples. Such a granulometric composition of samples ensures high degree of purification of organic solvents at a sufficiently high filtration rate.

With the aim of making conclusive recommendations concerning a filtering powder for purification of spent organic solvents, calcium hydrometasilicate obtained from diatomites was compared with other powders[1] on various machines with various filter designs. As criteria of complete purification served the intensity of filtration, degree of solvent transparency, and pressure on a filter, which was not to exceed 0.202 MPa.

The experiments showed that the intensity of filtration of spent solvents depends to a considerable extent on the thickness of the filtering powder layer. As seen from the data of Table 4, the optimal amount of calcium hydrometasilicate per 1 m^2 of the filter surface is 320–350 g.

Table 4. Rate of filtration of spent white spirit through a layer of C–S–H (I) [3] of varied thickness (content of insoluble admixtures in the starting solution 0.335 g l^{-1})

m, g	m, g per 1 m^2	l, mm	τ, s	$(dV/d\tau) \times 10^3$, $m^3\ m^{-2}\ s^{-1}$
0.0	0.0	0.15	188.1	2.12
0.2	80	0.25	76.0	5.26
0.4	160	0.40	63.0	6.35
0.6	320	0.75	51.0	7.84
1.0	400	0.95	53.0	7.55
1.5	600	1.25	60.0	6.67
2.0	800	1.60	63.0	6.35
3.0	1200	2.25	66.0	6.1

Note: m is the weight of C–S–H (I) powder, and l is the thickness of the precipitate layer after filtration.

Industrial experiments with batches of clothes showed that spent white spirit becomes transparent on being passed through a layer of calcium hydrometasilicate, and the light transmission of the solvent does not change till the 5th batch of clothes, and becomes 88.5 and 57% after 6 and 14th batches, respectively. The pressure on the filter changed from 0.030 to 0.101 MPa at the beginning of filtration of spent white spirit through a layer of calcium hydrometa-

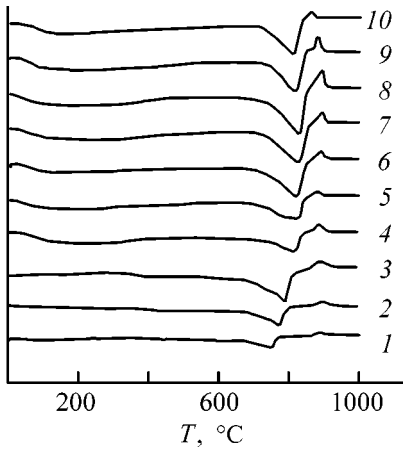

Fig. 3. DTA curves of diatomites treated with $Ca(OH)_2$ solution and carbonated for 15 min. Treatment temperature 95°C, duration 6 h. (T) Temperature. $CaO : SiO_2$ molar ratio in a starting reaction mixture: (*1*) 0.1, (*2*) 0.2, (*3*) 0.3, (*4*) 0.4, (*5*) 0.5, (*6*) 0.6, (*7*) 0.7, (*8*) 0.8, (*9*) 0.9, and (*10*) 1.15.

[1] The tests were carried out at Arabkir dry-cleaning factory in Erevan.

silicate, and from 0.051 to 0.136 MPa at the end of filtration, in treating 1 to 14 batches of clothes, respectively. The color of white spirit passed through a layer of calcium hydrometasilicate appeared to be essentially lighter than that obtained with commercial Special-2 and ZP-200 powders. Moreover, use of calcium hydrometasilicate allowed treatment of 14 batches of clothes, whereas use of Special-2 powder, only 6. The use of calcium hydrometasilicate instead of Special-2 powder made it possible to cut down the solvent losses by 35–45%, shorten the total duration of drycleaning, raise more than twice the average productivity of degreasing machines, and reduce the frequency of filter cleaning 2–3-fold. Similar results were obtained with perchloroethylene used as a solvent.

CONCLUSIONS

(1) The specific resistance of a filtering layer and the main constants and rate of filtration of calcium hydrometasilicate powders obtained upon treatment of natural diatomite and alkali-siliceous solutions were calculated. Compared with the case of conventional commercial filtering powders, the specific resistance of the filtering layer of calcium hydrometasilicate is much lower, and the filtering and adsorption capacity, much better.

(2) The thermal treatment of calcium hydrometasilicate powders at temperatures of up to 350°C and carbonation (to CO_2 content of 15%) improve their filtering and adsorption properties.

(3) Industrial use of calcium hydrometasilicate in purification of spent organic solvents, instead of the conventional commercial filtering powders, improves the quality-related and economic characteristics of the processes and makes higher the productivity of the equipment.

ACKNOWLEDGMENTS

The authors are grateful to staff members of Arbakir factory for the possibility to test the obtained filtering powder (calcium hydrometasilicate).

REFERENCES

1. Dawis, L., *Am. Ceram. Soc. Bull. Columbus Ohio*, 1992, vol. 71, no. 5, p. 795.
2. Mdivishvili, O.M., *Kristallokhimicheskie osnovy regulirovaniya svoistv prirodnykh sorbentov* (Crystal-Chemical Principles of Control over Properties of Natural Sorbents), Tbilisi, 1983.
3. USSR Inventor's Certificate, no. 1 060 567.
4. Diatomite: Filtering out the Competition, *World Ceram. Refract.*, 1990, vol. 1, no. 5, pp. 20–21.
5. Manukyan, A.G., Study of Physicochemical Features of Lime Activation of Local Diatomites and Manufacture of Adsorbing and Filtering Powders on Their Base, *Cand. Sci. Dissertation*, Erevan, 1997.
6. *Syr'evaya baza kremnistykh porod SSSR i ikh ispol'zovanie v narodnom khozyaistve* (Resource Base of Siliceous Rocks in USSR and Their Use in National Economy), Petrov, V.P., Ed., Moscow: Nedra, 1976.
7. USSR Inventor's Certificate, no. 1 599 055.
8. Fedyaev, F.F., Matveeva, L.G., Eremeev, D.N., *et al.*, *Doklady regional'noi konferentsii "Aluminii Urala-96"* (Proc. Reg. Conf. "Ural Aluminum-96"), Krasnoturinsk, 1996, pp. 108–115.
9. Manukyan, A.G., Martirosyan, G.G., Anakchyan, E.Kh., and Kostanyan, K.A., *Zh. Prikl. Khim.*, 1999, vol. 72, no. 11, pp. 1795–1800.
10. Taylor, F.W., *The Calcium Silicate Hydrates—the Chemistry of Cements*, London, New York, 1964, vol. 1.
11. Martirosyan, G.G., Ovsesyan, E.B., and Gukasyan, D.M., Abstracts of Papers, *Vsesoyuznyi seminar "Gidrosilikaty kaltsiya i ikh primenenie"* (All-Union Seminar "Calcium Hydrosilicates and Their Use"), Kaunas, 1980, p. 87.
12. Fedorova, A.F. and Troshchenko, M.A., *Tekhnologiya khimicheskoi chistki i krasheniya odezhdy* (Technology of Dry Cleaning and Dyeing of Clothes), Moscow: Legkaya Industriya, 1970.
13. Pavlov, K.F., Romanov, P.G., and Noskov, A.A., *Primery i zadachi po kursu protsessov i apparatov khimicheskoi tekhnologii* (Examples and Excersizes on the Course of the Processes and Apparatus of Chemical Technology), Leningrad: Goskhimizdat, 1959.
14. Gregg, S.J. and Sing, K.S.W., *Adsorption, Surface Area and Porosity*, London: Academic, 1982.
15. Butt, Yu.M. and Timashev, V.V., *Praktikum po khimicheskoi tekhnologii vyazhushchikh materialov* (Practical Course on Chemical Technology of Binders), Moscow: Vysshaya Shkola, 1973.
16. Pashkevich, A.A., Bronevoi, V.A., and Kraus, I.P., *Termografiya produktov glinozemnogo proizvodstva* (Thermography of Products of Alumina Industry), Moscow: Metallurgiya, 1983.
17. Manukyan, A.G., Martirosyan, G.G., and Kostanyan, K.A., *Khim. Zh. Armenii*, 1999, vol. 52, no. 4, pp. 3–9.
18. *Spravochnik po proizvodstvu stroitelnoi keramiki* (Reference Book on Production of Construction Ceramics), Yushkevich, O.M., Ed., Moscow: Gosstroiizdat, 1961, vol. 1.

Russian Journal of Applied Chemistry, Vol. 75, No. 2, 2002, pp. 213–218. Translated from Zhurnal Prikladnoi Khimii, Vol. 75, No. 2, 2002, pp. 221–226.
Original Russian Text Copyright © 2002 by Nagirnyi, Apostolova, Baskevich, Litvin, Shembel'.

APPLIED ELECTROCHEMISTRY AND CORROSION PROTECTION OF METALS

Electrolytic Synthesis of Binary Oxide Systems Based on Manganese(II) Oxide

V. M. Nagirnyi, R. D. Apostolova, A. S. Baskevich, P. M. Litvin, and E. M. Shembel'

Ukrainian State University of Chemical Engineering, Dnepropetrovsk, Ukraine

Received January 15, 2001

Abstract—Joint anodic deposition of manganese, cobalt, nickel, and chromium oxides, which form binary oxide systems, from two-component sulfate solutions of the constituent metals was studied under different electrolysis conditions.

Multicomponent oxide systems of the type $LiCo_x \cdot Mn_{2-x}O_4$, $LiCo_yMn_{2-y}O_4$, and MnV_2O_5, prepared by "doping" of traditional electrochemically active oxides of manganese, vanadium, etc., are of interest for developing efficient cathode materials for lithium batteries [1–4]. Such materials are mainly prepared by chemical-thermal synthesis of stoichiometric mechanical mixtures of thermally unstable salts of the corresponding metals (with simultaneous modification of the forming oxide compounds in the presence of lithium carbonate or hydroxide, if necessary). The essential drawback of this method is the difficultly controllable synthesis and the contamination of the final product with impurities formed in side reactions. This makes preferable the electrochemical synthesis of complex oxide systems by anodic deposition from aqueous solutions containing salts of co-deposited metals [5, 6]. The electrolytic synthesis is advantageous because of the possibility of preparing homogeneous materials, whose components, unlike the case of mechanical mixtures, have related structures and can interact at the molecular level. Along with this, the electrochemical method allows fabrication ballast-free cathodes by direct deposition of complex oxide systems onto a smooth or gauze stainless-steel substrate. Vanadium(V) oxide, synthesized simultaneously with manganese oxide, shows better electrochemical performance than the individually synthesized material [7].

Therefore, it was appropriate to study the possibility of preparing complex binary systems by joint electrolytic deposition of oxide compounds of manganese, cobalt, nickel, and chromium from mixed aqueous solutions of salts of metals co-deposited under varied electrolysis conditions. Data of this kind are unavailable in the literature.

The electrolysis was performed in a 0.2-dm^3 temperature-controlled glass cell. Smooth plates of technical grade VT-1 titanium served as a cathode. The oxides under study were deposited as compact coatings on two sides of gauze and plate-like 12X18H9T steel anodes of size $10 \times 10 \times 0.15$ and $10 \times 10 \times 0.3$ mm, respectively, at $S_a : S_c = 1 : 5$. An X-ray diffraction analysis was used to study on disperse deposits of weight 0.1–0.15 g, obtained on a smooth VT-1 titanium plate. The solutions were prepared from pure and analytically pure reagents and distilled water. Two-component solutions based on manganese, cobalt, nickel, and chromium sulfates were used in the study. The total concentration of the solutions studied was within the range 0.3–0.4 M at a ratio of the main to doping components from 5 : 1 to 1 : 5. All runs were performed at 85 ± 3°C and pH 2.0–2.5. The electrolysis parameters were chosen on the basis of preliminary experimental tests. The deposition rate V_{dep} (mg cm^{-2} h^{-1}) was determined from the weight gain upon electrolysis per unit surface per unit time. Polarization curves were taken in a special three-chamber cell on a plate-like 12X18H9T steel anode (S_a = 1 cm^2) with surface roughness corresponding to ∇ 7–8 at $S_a : C_c = 1 : 4$ and current densities in the range 0.5–50 mA cm^{-2}. The potentials were measured relative to a silver chloride reference electrode (E = +0.225 V) with a ShCh-4315 digital voltmeter. The X-ray diffraction analysis was done on a DRON-2 diffractometer. The microstructure of the surface of deposits (1–3.5 μm thick films) was studied with a nanoscope. The quantitative composition

1070-4272/02/7502-0213 $27.00 © 2002 MAIK "Nauka/Interperiodica"

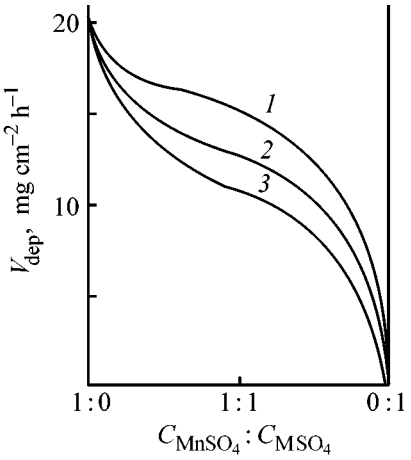

Fig. 1. Deposition rate V_{dep} of binary oxides vs. the concentration ratio of sulfates of co-deposited metals C (M). Total concentration 0.3–0.4 M, T = 85°C, pH 2.0–2.2, i_a = 15 mA cm^{-2}; the same for Fig. 4. System: (*1*) Mn–Co, (*2*) Mn–Ni, and (*3*) Mn–Cr.

of the deposits was estimated approximately by the oxalate technique chemical analysis [8].

Figure 1 shows how the deposition rate of the systems studied varies with the ratio of the main components in mixed solutions under the indicated conditions of electrolysis. With increasing "dopant" concentration in a solution, the deposition rate gradually decreases in all cases. Comparison of the deposition rates of individual manganese and cobalt oxides from their solutions under comparable conditions of electrolysis (20–25 and 2.5–3.0 mg cm^{-2} h^{-1}, respectively) shows that the efficiency of the anodic process decreases steadily with increasing dominating role of delayed formation of the "doping phase" in the anodic deposit (Fig. 1, curve *1*). Similar dependences were obtained for the systems Mn–Ni and Mn–Cr. However, the deposition rate for these systems decreases more sharply with increasing dopant concentration (Fig. 1, curves *2*, *3*). This is accounted for by the fact that, under the given conditions, nickel and chromium oxides cannot be deposited directly from their solutions, and are co-deposited with manganese oxide onto the anode. Apparently, the forming manganese oxide acts as a catalyst, energetically facilitating the transition of the conjugate metal ions into the oxide phase and the formation of stable oxide compounds in the joint anodic process.

The feasible anodic reactions corresponding to the systems studied can be represented by equations (1)–(6) [9, 10] and concurrent redox reactions (7), (8):

$$2Mn^{2+} + 3H_2O \rightarrow Mn_2O_3 + 6H^+ + 2e, \quad E^0 = 1.0\ V, \qquad (1)$$

$$Mn^{2+} + 2H_2O \rightarrow MnO_2 + 4H^+ + 2e, \quad E^0 = 1.23\ V, \qquad (2)$$

$$2Co^{2+} + 3H_2O \rightarrow Co_2O_3 + 6H^+ + 2e, \quad E^0 = 1.8\ V, \qquad (3)$$

$$2Ni^{2+} + 3H_2O \rightarrow Ni_2O_3 + 6H^+ + 2e, \quad E^0 = 1.75\ V, \qquad (4)$$

$$Ni^{2+} + 2H_2O \rightarrow NiO_2 + 4H^+ + 2e, \quad E^0 = 1.68\ V, \qquad (5)$$

$$2Cr^{3+} + 3H_2O \rightarrow 2CrO_3 + 6H^+ + 6e, \quad E^0 = 1.36\ V, \qquad (6)$$

$$Ni_2O_3 + Mn_2O_3 \rightarrow 2NiO + 2MnO_2, \qquad (7)$$

$$2CrO_3 + 3Mn_2O_3 \rightarrow Cr_2O_3 + 6MnO_2. \qquad (8)$$

Reactions (1)–(6) are related to standard redox systems. The standard electrode potentials for these reactions are given according to the data of [9, 10]. However, only reactions (1)–(3) can actually occur under the conditions considered. In the given case, reactions (4)–(6) are concurrent and can proceed to give oxide compounds only simultaneously with manganese oxidation. Reactions (7) and (8) are quite permissible, with account taken of the probable ionic and interphase interaction of conjugate components in anodic deposition under certain conditions. This is confirmed by X-ray diffraction analysis of the corresponding binary systems, in which the presence of all of the oxide phases described by equations (1)–(4) and (6)–(8) was revealed [reaction (5) is intermediate].

Probably, processes of joint deposition of the oxide systems studied may occur stage by stage or following other, more complex schemes. This is indirectly confirmed by comparative analysis of the i_a–E dependences characterizing the process of joint deposition (Fig. 2). A characteristic feature of these dependences is the presence of an intermediate plateau at potentials preceding the ascending branch. The relative position and the character of the corresponding curves depend on the manganese to metal salt concentration ratio Mn : M (where M is Co, Ni, and Cr) in solution. It can be seen in Fig. 2 that raising the "dopant" concentration makes the anodic polarization stronger and the current density lower. In this case, the relative shift of the upper portions of polarization curvers for the same binary system at the concentration ratio in solution varied from 3 : 1 to 1 : 3 is 0.23–0.25 V,

and that of the lower portions at the level of the inflection points, no more than 0.1 V. At current densities lower than 5 mA cm^{-2} the curves virtually merge together, irrespective of the above ratio.

The influence exerted by the nature of a doping component is manifested as enhancement of the anodic polarization in order Co < Ni < Cr, in agreement with the dependences of the deposition rate on the Mn : M ratio in solution (Fig. 1). Comparison of the lower portions of the i_a–E curves for binary systems with a similar dependence of the anodic deposition of manganese oxide from its solutions shows that oxidation of manganese to give oxide is the potential-determining process, irrespective of the Mn : M ratio. This process is accompanied by simultaneous reactions of binary oxide formation and hydrogen evolution, which are more intensive in the range of the upper ascending branches of the curves.

Probably, the less positive anode potentials in the lower portions of the curves result from the occurrence of reactions of the first stage of magnesium oxidation $Mn^{2+} \rightarrow Mn^{3+}$ and oxygen discharge on the initial weakly oxidized stainless-steel surface, proceeding with lower energy expenditure. After a solid oxide film is formed on the anode and the limiting diffusion current of the co-deposited metal ions is reached, the process passes into a new stage (upper portions of the curves), with the corresponding change in the relative rates of the concurrent anodic reactions: O_2 > oxide(Mn–M). The energy balance of the anodic process as a whole is determined by the polarization of electrode reactions invilving oxygen evolution on the anode surface shielded by a solid oxide film and of co-deposition of oxide compounds of the conjugate oxide system. In this case, raising the concentration of the "doping" phase causes a corresponding increase in the anodic polarization. This follows from a comparison of the upper portions of the curves for the systems with Mn : M ratio higher and lower than unity (Fig. 2, curves *3*, *3*'; *4*, *4*'; *5*, *5*'). As seen, the upper portions of curves *3*'–*5*' lie at more positive potentials than the corresponding portion for deposition of cobalt oxide from its solution.

The current density on the surface preliminarily coated with a solid film of the corresponding binary oxide steadily grows with increasing potential and reaches the limiting values for the given binary system without intermediate plateaus (Fig. 2, curve *5*, dashed line). This confirms the considered kinetic origin of the electrode processes studied at different current densities. The last assumption is in accord with the dependences of the deposition rate on the current density, observed for the binary systems studied at various Mn : M ratios (for the example of the Mn–Cr system; Fig. 3). The dependences are similar for all Mn : M ratios: the deposition rate sharply increases in a narrow range of current densities and reaches certain limiting values at i_a = 15–20 mA cm^{-2}. In this case, the limiting values of V_{dep} totally coincide with the corresponding values in the dependence of the deposition rate on the Mn : M ratio at constant current density (Fig. 1, curve *3*) and decrease at higher "dopant" concentrations.

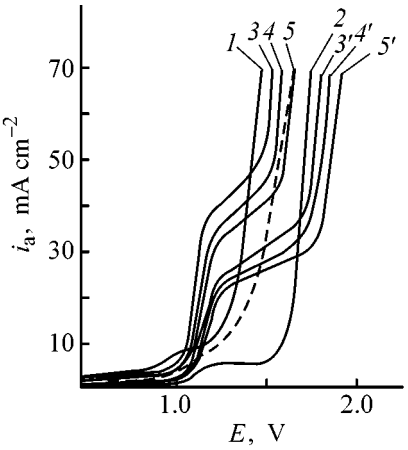

Fig. 2. Current–voltage characteristics of anodic formation of (*1*) manganese and (*2*) cobalt oxides from their solutions and binary oxides from mixed sulfate solutions of co-deposited metals at concentration ratios (*3*–*5*) 3 : 1 and (*3*'–*5*') 1 : 3. Total concentration 0.3–0.4 M, T = 85°C, pH 2.0. (i_a) Current density and (E) potential. System: (*3*, *3*') Mn–Co, (*4*, *4*') Mn–Ni, and (*5*, *5*') Mn–Cr.

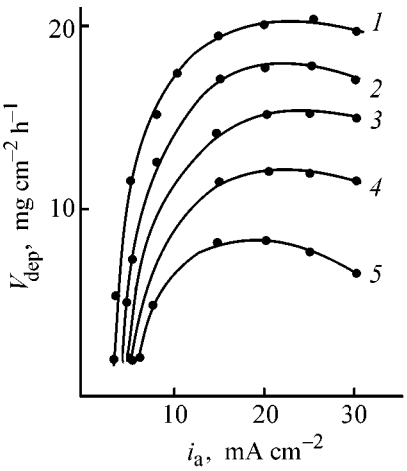

Fig. 3. Deposition rate V_{dep} of the double oxide Mn–Cr vs. anodic current density i_a at various C_{MnSO_4} : $C_{Cr_2(SO_4)_3}$ ratios. Total concentration 0.3–0.4 M, T = 85°C, pH 2.0–2.5. C_{MnSO_4} : $C_{Cr_2(SO_4)_3}$: (*1*) 5 : 1, (*2*) 3 : 1, (*3*) 1 : 1, (*4*) 1 : 3, and (*5*) 1 : 5.

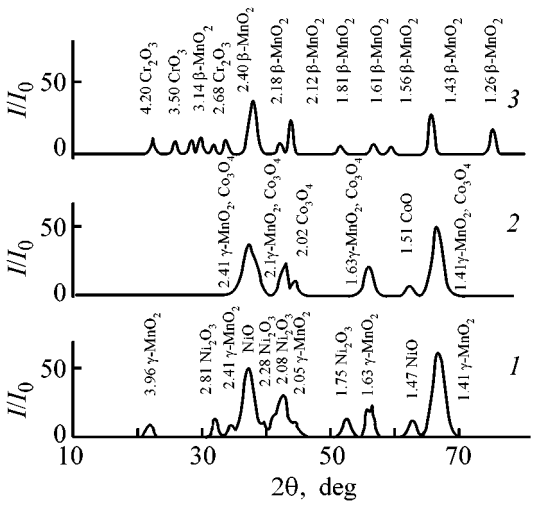

Fig. 4. Diffraction patterns of binary oxides (*1*) Mn–Ni, (*2*) Mn–Co, and (*3*) Mn–Cr, deposited from solutions with concentration ratios $C_{MnSO_4} : C_{MSO_4} = 1 : 3$ and heated in air to 420°C for 7 h. (I/I_0) Relative intensity and (2θ) Bragg angle.

After the limiting values are reached, the deposition rate gradually decreases with increasing current density, which is due to the growing contribution to the energy balance of the anodic process from the hindered reaction of doping phase formation and to the increasing fraction of joint oxygen evolution. This circumstance is in agreement with the current–voltage characteristics of the anodic formation of the corresponding binary systems (Fig. 2). Apparently, the fraction of the doping phase in the binary deposit must grow in the given case.

Such an increase also takes place when the Mn : M ratio in solution is changed toward increased concentrations of the concurrent component. For example, approximate quantitative estimate of the composition of the binary Mn–Co oxide shows that, with the Mn : Co ratio in solution changed from 1 : 2 to 1 : 3, the content of cobalt oxide in the deposit may increase from 12–15 to 20 wt %. For the Mn–Ni and Mn–Cr systems, these values are lower: 10–12 and 5–8 wt %, respectively. Similar relationships are retained for all of the systems studied When the total concentrations of the corresponding components in solution are raised, with other electrolysis conditions being the same. However, at Mn : M < 1 (1 : 2, 1 : 3, etc.) and total concentration above 100 g l^{-1}, the deposition rate decreases considerably owing to the increased contribution of the hindered formation of the doping phase.

According to the results of X-ray diffraction analysis, the materials studied are two-phase systems consisting of oxide compounds formed by joint deposition on the anode. These compound correspond to the most thermodynamically stable forms: MnO_2, CoO, Co_3O_4, NiO, Ni_2O_3, and Cr_2O_3 (Fig. 4). These systems are the most reliably identified by diffractometry at Mn : M = 3 : 1 and after high-temperature treatment at 400, 650, and 720–750°C. Simultaneous modification of the obtained complex oxides in the presence of lithium hydroxide or carbonate is a prerequisite to synthesis of electrochemically active oxide systems in the form of double spinels of the type $LiCo_xMnO_{2-x}O_4$, $LiCr_yMnO_{2-y}O_4$, etc.

Presently, the origin of the structural and molecular correlation in the bulk between the systems studied is unclear. A certain information can be obtained from a comparative analysis of the microstructure and microrelief of the surface of thin-film coatings of the corresponding oxides, deposited onto a smooth stainlesssteel substrate at Mn : M = 1 : 2 (Fig. 5).

Analysis of the presented data shows that the structures of individual oxides and mixed oxides differ significantly. For example, photomicrographs of the surface of the deposits, taken under the same magnification, show that the structure of manganese oxide is coarsely grained crystalline with typical layer-by-layer growth of separate grains (Fig. 5a). At the same time, the cobalt oxide structure is more finely grained, with random orientation of crystals (Fig. 5b).

The structure of co-deposited manganese and cobalt oxides in a mixed anodic deposit essentially differs from the structure of the individual oxides in that a peculiar pattern of finely grained randomly distributed "combs" is formed, which makes the specific surface area of the deposits considerably larger (Fig. 5c).

Deposits with a similar structure are also obtained in joint deposition of manganese and nickel oxides. This is possibly due to the similar mechanisms of formation of the double systems under consideration (Fig. 5d), governed by the interaction of conjugate phases in the stage of their formation and crystallization into grains.

Unlike these systems, Mn–Cr oxide is obtained on the anode in the form of finely grained columnar deposit with rather developed surface (Fig. 5e). These deposits are characterized by ordered structure with virtually symmetric alternation of nearly identical valleys and ridges. Apparently, the mechanism of nucleation and interaction of molecules of the conjugate phases is more intensive in this system, compared with deposition of the binary oxides considered in the present study. This impedes growth of manganese

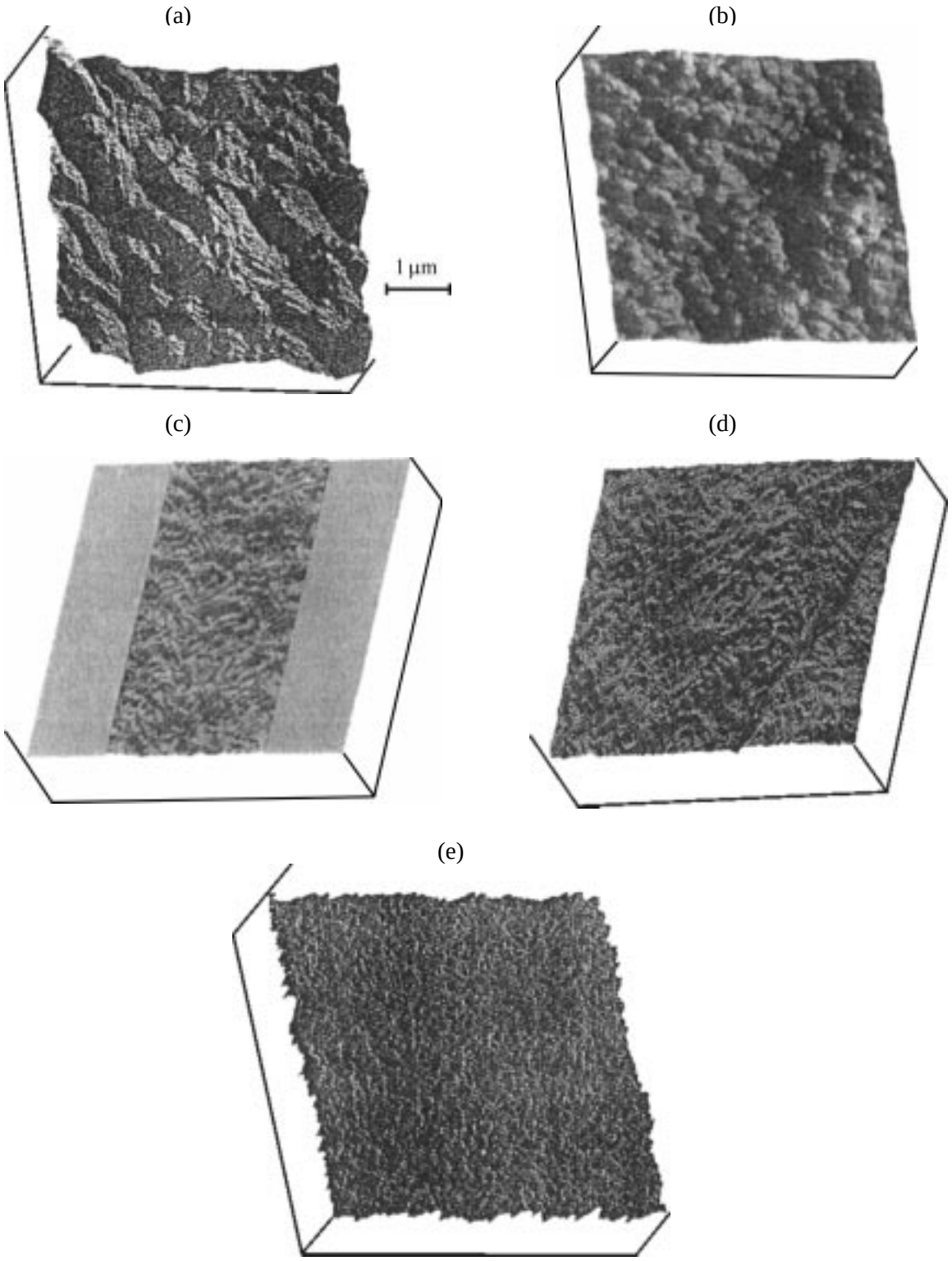

Fig. 5. Photomicrographs of the surface of the electrolytic deposits of (a) MnO_2, (b) Co_2O_3, and binary oxides (c) Mn–Co, (d) Mn–Ni, and (e) Mn–Cr obtained from solutions with 1 : 2 concentration ratio of sulfates of co-deposited metals.

oxide crystals and facilitates their degeneration in the early stage of development.

These data suggest that, from the standpoint of energetics, the binary oxides studied are a certain in-

termediate system between a homogeneous mechanical mixture and the single-phase chemical compound.

CONCLUSIONS

(1) It was demonstrated that complex oxide systems, showing promise as active supports for efficient cathodes of lithium batteries, can be obtained in various combinations (Mn–Co, Mn–Ni, Mn–Cr, etc.) by electrolysis of two-component solutions of Mn(II), Co(II), Ni(II), and Cr(III) sulfates at certain ratios of their concentrations and certain electrolysis parameters.

(2) The necessary condition for electrolytic synthesis of such materials is the presence of a base oxide material, which can be deposited individually on the anode in reasonably high yield, e.g., manganese and cobalt oxides.

(3) Of particular interest are binary oxides of the series studied, synthesized from solutions at 2 : 1–1 : 3 concentration ratios of the main to "doping" metal salts at average total concentration of 0.3–0.4 M. The electrolysis parameters are as follows: temperature 80–85°C, pH 2.0–2.5, and anodic current density 7.5–25 mA cm^{-2}.

REFERENCES

1. Ol'shanskaya, L.N. and Popova, S.S., Abstracts of Papers, *IV Mezhdunarodnaya konferentsiya "Fundamental'nye problemy electrockhimicheskoi energetiki"* (IV Int. Conf. "Fundamental Problems of Electrochemical Energetics"), Saratov (Russia), June 21–23, 1999, pp. 75–77.
2. Kachibaya, E.I, Imnadze, R.A., Pankidze, T.V., *et al.*, Abstracts of Papers, *IV Mezhdunarodnaya konferentsiya "Fundamental'nye problemy electrockhimicheskoi energetiki"* (IV Int. Conf. "Fundamental Problems of Electrochemical Energetics"), Saratov (Russia), June 21–23, 1999, pp. 55–56.
3. Zhang, F., Zavalij, P., and Wittingham, M.S., *Electrochem. Commun.*, 1999, no. 1, pp. 564–567.
4. Baudrin, E., Laruelle, S., Denis, S., *et al.*, *Solid Ionics*, 1999, vol. 123, pp. 139–153.
5. Shembel', E.M., Apostolova, R.D., and Nagirnyi, V.M., *Elektrokhimiya*, 2000, vol. 36, no. 1, pp. 41–48.
6. Shembel, E.M., Apostolova, R.D., Nagirny, V.M., *et al.*, Abstracts of Papers, *The 197th Meet. of the Electrochem. Society*, Toronto (Canada), 2000, p. 105.
7. Le Gal La Salle, A., Guyomard, D., Verbaerre, A., and Piffard, Y., Abstracts of Papers, *9th Int. Meet. on Lithium Batteries*, Edinburg (Scotland), 1998, poster II, Thursday, no. 91.
8. Kolthoff, I.M., Belcher, R., Stenger, V.A., and Matsuyama, G., *Volumetric Analysis*, New York: Wiley, 1957.
9. *Spravochnik po elektrokhimii* (Handbook of Electrochemistry), Sukhotin, A.M., Ed., Leningrad: Khimiya, 1981.
10. Lur'e, Yu.Yu., *Spravochnik po analiticheskoi khimii* (Handbook of Analytical Chemistry) Moscow: Khimiya, 1979.

Russian Journal of Applied Chemistry, Vol. 75, No. 2, 2002, pp. 219–222. Translated from Zhurnal Prikladnoi Khimii, Vol. 75, No. 2, 2002, pp. 227–230.
Original Russian Text Copyright © 2002 by Medvedev, Makrushin, Dubenkov.

APPLIED ELECTROCHEMISTRY AND CORROSION PROTECTION OF METALS

Electrodeposition of Tin from Sulfate Electrolyte in the Presence of Synthanol, Formalin, and Propargyl Alcohol

G. I. Medvedev, N. A. Makrushin, and A. N. Dubenkov

Novomoskovsk Institute of Mendeleev Russian University of Chemical Technology, Novomoskovsk, Russia

Received July 26, 2001

Abstract—The process of electrodeposition of tin from a sulfate electrolyte containing $SnSO_4$, H_2SO_4, synthanol, formalin, and propargyl alcohol was studied.

Previously, electrodeposition of tin from a sulfate electrolyte in the presence of organic additives has been studied [1, 2]. It was shown that electrodeposition in an electrolyte containing synthanol and formalin, together with 1,4-butanediol and 2-butene- and 2-butyne-1,4-diols, yields lustrous coatings. The present communication reports the results obtained in studying electrodeposition of tin from a sulfate acid electrolyte in the presence of synthanol, formalin, and propargyl alcohol.

The investigation was carried out in an electrolyte containing (g l^{-1}): $SnSO_4$ 10–50, and H_2SO_4 90–100. The organic substances were introduced into the electrolyte in the following amounts: synthanol (DS-10) 1–4 g l^{-1}, formalin (37% solution) 1–10 ml l^{-1}, and propargyl alcohol 1–15 ml l^{-1}.

Tin was deposited onto copper substrates to a thickness of 6–15 μm. Polarization curves were measured with a P-5828 potentiostat. The luster was measured with an FB-2 photoelectric luster meter. The degree θ of surface coverage with organic additives was evaluated by the results of polarization measurements, using the formula [3]

$$\theta = 1 - \exp(\Delta E/b),$$

where ΔE is polarization, and b is the constant appearing in the Tafel equation, determined from polarization curves plotted in the ΔE–log i_c coordinates.

The leveling power P of the electrolytes was determined directly by profilometric measurements of the surface of samples with sinusoidal microprofile. The P value was calculated using the formula [4]:

$$P = 2.3a/2\pi h_{av}\log(H_0/H_i),$$

where a is the wave amplitude of the sinusoidal microprofile; h_{av} the average coating thickness (10 μm); and H_0 and H_i the initial and final amplitudes of the sinusoidal microprofile, respectively.

The capacitance of the electric double layer was measured in the course of electrolysis with a P-5021 ac bridge at a frequency of 30 kHz, using the series equivalent scheme.

The electrodeposition was done at 18–25°C with and without electrolyte agitation by means of a magnetic rabble.

The effect of organic additives on the outward appearance of coatings was studied in an electrolyte containing 50 g l^{-1} $SnSO_4$ and 100 g l^{-1} H_2SO_4. It was found that, with synthanol (1–4 g l^{-1}) added to the electrolyte, dull coatings are obtained. With formalin (1–10 ml l^{-1}), or propargyl alcohol (1–15 g l^{-1}), or a mixture of these, poor-quality coatings are deposited. The outward appearance of coatings is much improved if propargyl alcohol is added to an electrolyte containing synthanol (2–3 g l^{-1}) and formalin (6–8 ml l^{-1}). Data on the influence exerted by propargyl alcohol on the outward appearance of the coatings are presented in the table.

It can be seen that lustrous coatings are obtained in the presence of propargyl alcohol. The widest range of current densities at which lustrous coatings are obtained (i_c = 7–12 A dm^{-2}) is observed at propargyl alcohol concentrations of 7–10 ml l^{-1}.

With the formalin concentration outside the above limits, silvery coatings are obtained. At synthanol

1070-4272/02/7502-0219 $27.00 © 2002 MAIK "Nauka/Interperiodica"

Effect of propargyl alcohol on the outward appearance of tin coatings*

c_{pa},** ml l^{-1}	i, A dm^{-2}	Outward appearance of coatings
1–3	1–5	Dull
	6–11	Dull with luster along edges
	12–13	Dull with burn-on
5–6	1–5	Dull
	6–8	Dull with luster along edges
	9–10	Lustrous
	11–13	Lustrous with burn-on
7–10	1–5	Dull
	6	Semilustrous
	7–12	Lustrous
	13	Lustrous with burn-on
11–15	1–5	Dull
	6–7	Semilustrous
	8–10	Lustrous
	11–13	Lustrous with burn-on

* Electrolyte composition (g l^{-1}): $SnSO_4$ 50, H_2SO_4 100, synthanol 2; formalin 6 ml l^{-1}; mechanical agitation.

** c_{pa} is the concentration of propargyl alcohol.

concentrations of less than 2 g l^{-1} (1 g l^{-1}), the working interval of current densities for obtaining lustrous coatings becomes much narrower. At synthanol concentrations exceeding 3 g l^{-1} (4 g l^{-1}), the range of current densities yielding lustrous coatings remains unchanged, but electrolyte frothing is much enhanced, which hinders electrodeposition in an agitated electrolyte.

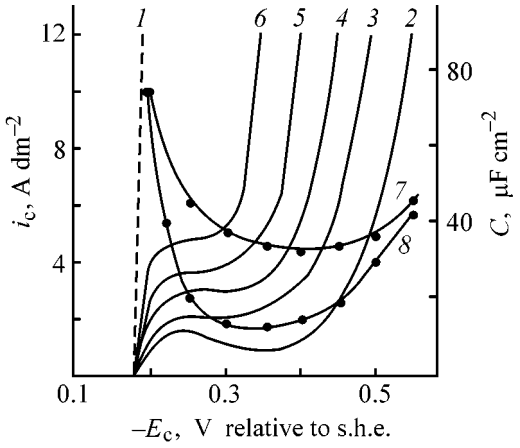

Fig. 1. (*1–6*) Cathodic polarization curves of tin, measured on a rotating disk electrode, and (*7*, *8*) capacitance C of electric double layer vs. electrode potential E_c in tin-plating electrolytes. (i_c) Current density. Electrolyte composition (g l^{-1}): $SnSO_4$ 50, H_2SO_4 100. (*1*, *7*) electrolyte; (*2*, *8*) 1 + 2 g l^{-1} synthanol, 6 ml l^{-1} formalin, and 7 ml l^{-1} propargyl alcohol; (*3*, *4*, *5*, *6*) 2 at disk electrode rotation rates of, respectively, 200, 500, 1000, and 2000 rpm.

In addition to the influence of organic substances, the study was concerned with effect of the $SnSO_4$ concentration on the working range of current densities for obtaining lustrous coatings. The investigation was carried out in an electrolyte containing 2 g l^{-1} synthanol, 6 ml l^{-1} formalin, and 7 ml l^{-1} propargyl alcohol. It was found that lowering the $SnSO_4$ concentration makes narrower the i_c range in which lustrous coatings are obtained. For example, lustrous coatings are obtained in the ranges i_c = 2–5 and 6–10 A dm^{-2} at $SnSO_4$ concentrations of, respectively, 10–20 and 30 g l^{-1}. The H_2SO_4 concentration in the electrolyte should be within 90–100 g l^{-1}. At concentrations lower than 90 g l^{-1} the electrolyte is unstable in operation and the i_c range in which lustrous coatings are obtained becomes narrower. At H_2SO_4 content exceeding 100 g l^{-1} the range of current densities at which lustrous coatings are obtained remains unchanged.

It should be noted that high-quality lustrous coatings are only obtained in an agitated electrolyte, with dull deposits formed otherwise.

The current efficiency (CE) by tin in electrolytes yielding lustrous coatings decreases with increasing i_c and grows as the $SnSO_4$ concentration becomes higher. CE = 95–75% at $SnSO_4$ content of 10–20 g l^{-1} and i_c = 2–5 A dm^{-2}, and CE = 95–90% at $SnSO_4$ content of 30–50 g l^{-1} and i_c = 6–12 A dm^{-2}.

To reveal the influence of organic substances on electrodeposition of tin, cathodic polarization curves were measured on a rotating disk electrode. As seen in Fig. 1, the cathodic polarization is enhanced in the presence of organic substances, with a plateau of limiting current observed in the cathodic polarization curve (curves *1* and *2*). With the disk electrode rotated, the i_{lim} value grows and the cathodic polarization decreases (curves *2–6*). The limiting current in the polarization curves is associated with adsorption of organic substances and formation of an adsorption layer on the cathode surface. This assumption is confirmed by measurements of the capacitance of the electric double layer. As seen in Fig. 1 (curves *7* and *8*), introduction of organic substances into the electrolyte makes the capacitance of the electric double layer lower. At potentials E_c = –0.3…–0.4 V, it decreases from 32 to 10 μF cm^{-2}. At higher cathode potentials, organic substances are desorbed from the electrode surface and the continuity of the adsorption layer is broken, which leads to an increase in the electric double layer capacitance.

Figure 2 presents the degree of coating luster and surface coverage θ as functions of the current density. It can be seen that the degree of coating luster passes through a maximum, and the coverage decreases steadily, with increasing current density (curves *1* and *2*). The θ value at i_c yielding lustrous coatings (i_c = 7–12 A dm^{-2}) varies between 35.0 and 27.7%. It should be noted that lustrous coatings can be obtained in an electrolyte with organic additives only in a certain range of i_c and θ. Presumably, the optimal values of these parameters correspond to the conditions in which the growing deposit has the minimum roughness.

The leveling power *P* was measured in a tin plating electrolyte as a function of the cathode current density (Fig. 2, curve *3*). It can be seen that the tin plating electrolyte with organic additives produces leveling effect. With increasing i_c, the *P* value grows and, at i_c = 10–11 A dm^{-2}, passes through a maximum (*P* = 0.98). At present, the mechanism of surface leveling is commonly explained in terms of the adsorption-diffusion theory [4] whose main concepts are as follows. All leveling additives inhibit electrodeposition of metals, with the degree of inhibition controlled by diffusion as a result of the diffusion-controlled expenditure of the additives in the course of electrolysis. According to [4], polarization curves measured at different rates of disk rotation on a rotating disk electrode model qualitatively the cathodic process of microprojections (fast rotation) or microdepressions (slow rotation). The uneven accessibility of the microprofile is the reason for nonuniform distribution of the supply rate of organic substances to different parts of the microprofile. Since the inhibiting influence exerted by leveling additives on the process of metal electrodeposition grows with increasing rate of additive's diffusion toward the cathode (fast rotation), this effect is manifested to a greater extent on microprojections, and to a lesser extent in microdepressions, which leads to a nonuniform distribution of the electrodeposition rate.

It was proposed on the basis of this circumstance to assess the action of various additives by measuring the cathode potential in an electrolyte with additive(s) in two agitation modes [4]. If the polarization grows with increasing speed of electrode rotation, then it would be expected that additive(s) will exert leveling influence under the given conditions.

Analysis of the cathodic polarization curves in a tin plating electrolyte, measured on a rotating disk electrode (Fig. 1, curves *3*–*6*), shows that they do not model the distribution of the electrodeposition rate

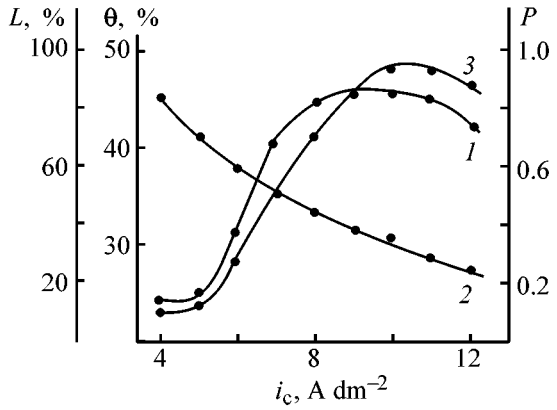

Fig. 2. (*1*) Degree of coating luster, *L*, (*2*) surface coverage θ, and (*3*) degree of leveling, *P*, vs. cathode current density i_c. Electrolyte composition (g l^{-1}): $SnSO_4$ 50, H_2SO_4 100, synthanol 2; formalin 6 ml l^{-1}; propargyl alcohol 7 ml l^{-1}. Mechanical agitation.

over the microprofile. The probable reason is that an adsorption layer of organic substances is formed on the electrode surface. Intensification of the hydrodynamic mode affects the process of formation and disintegration of such a layer. In this case, the rate of tin deposition grows on all parts of the microprofile, i.e., changes in such a way that this appears outwardly just like a manifestation of the antileveling effect.

It should be noted that the same phenomenon is observed in electrodeposition of a Sn–Sb alloy from a sulfate electrolyte in the presence of synthanol, formalin, and 2-butyne-1,4-diol, or synthanol, formalin, and coumarin [5].

The leveling in an electrolyte, in which an adsorption layer of organic substances is present on the electrode surface, can be accounted for on the assumption that this layer disintegrates with increasing speed of disk electrode rotation. This "strips" microprojections to a greater extent as compared with microdepressions. At the same time, a higher rate of supply of organic substances to microprojections is observed with increasing rate of electrode rotation, and the microprojections are more strongly inhibited than microdepressions, which leads to nonuniform distribution of the metal electrodeposition rate over the microprofile surface. The phenomenon of leveling is related to the luster of electroplated coatings, since luster formation is also a process of surface leveling. The leveling eliminates large microirregularities 0.2 to 100 μm and more in size; in luster formation, very fine submicroirregularities (of size about 0.15 μm and less) are smoothed out [6].

Thus, submicro- and microirregularities of the cathode surface are smoothed out in a tin plating elec-

trolyte containing synthanol, formalin, and propargyl alcohol.

Finally, it should be noted that the investigation performed made it possible to develop a sulfate acid tin-plating electrolyte of simple composition, which yields lustrous leveled coatings. The electrolyte composition is as follows (g l^{-1}): $SnSO_4$ 10–50, H_2SO_4 90–100, synthanol (DS-10) 2–3; formalin (37% solution) 6–8 ml l^{-1}; propargyl alcohol 7–10 ml l^{-1}. The process is performed with mechanical agitation of the electrolyte, i_c = 2–12 A dm^{-2}. The current efficiency is 75–95%.

Agitation with air impairs the stability of the electrolyte operation because of the fast oxidation of the electrolyte. The electrolyte temperature is 18–25°C. Above 25°C, the working i_c range in which lustrous coatings are obtained becomes narrower, electrolyte rapidly turns turbid, and a precipitate is formed on the bath bottom, which impairs the quality of the coatings obtained. The anodes should be made of pure tin. To prevent electrolyte contamination with sludge, the anodes are to be placed in sheaths of khlorin or propylene fabric.

The electrolyte is adjusted with respect to $SnSO_4$, H_2SO_4, and formalin, according to chemical analysis data [7]. The electrolyte adjustment with respect to synthanol should be done after 100 A h l^{-1} is passed through the bath by adding 1 g l^{-1} of synthanol. The expenditure of propargyl alcohol is 0.01 ml A^{-1} h^{-1}.

CONCLUSIONS

(1) A study of tin electrodeposition from sulfate acid electrolyte with organic additives demonstrated that, in the case of simultaneous presence of synthanol, formalin, and propargyl alcohol, lustrous coatings are formed at i_c = 2–12 A dm^{-2}, depending on the $SnSO_4$ concentration in the electrolyte.

(2) Cathodic polarization curves were measured on a rotating disk electrode. It was found that organic substances inhibit electrodeposition of tin. In this case, a plateau of limiting current is formed in the polarization curve. With increasing speed of disk electrode rotation, the limiting current grows and the cathodic polarization decreases.

(3) The degree of coating luster and the electrode surface coverage were measured in relation to the current density. It is shown that, with increasing i_c, the degree of luster grows and passes through a maximum, and the surface coverage decreases. The coverage varies between 35.0 and 27.7% in the range of current densities yielding lustrous coatings.

(4) The leveling power of a sulfate acid electrolyte with organic additives was studied. It is established that, in simultaneous presence of synthanol, formalin, and propargyl alcohol, the tin plating electrolyte shows positive leveling whose amount depends on i_c.

(5) The polarization curves obtained at different rates of disk electrode rotation cannot model the distribution of the rate of tin electrodeposition over the microprofile because of the sensitivity of the adsorption layer inhibiting the electrodeposition process to the hydrodynamic mode.

REFERENCES

1. Medvedev, G.I. and Gorbunova, I.M., *Zh. Prikl. Khim.*, 1990, vol. 63, no. 4, pp. 807–812.
2. Medvedev, G.I. and Mashutina, G.G., *Zh. Prikl. Khim.*, 1992, vol. 65, no. 4, pp. 789–795.
3. Valentelis, L.Yu., Kamuntavichene, I.Yu., and Matulis, Yu.Yu., *Tr. Akad. Nauk LitSSR, Ser. B*, 1970, vol. 63, no. 4, pp. 129–136.
4. Kruglikov, S.S., *Itogi nauki i tekhniki: Khimiya. Elektrokhimiya* (Advances of Science and Technology: Chemistry. Electrochemistry), Moscow: VINITI, 1965, pp. 117–151.
5. Medvedev, G.I., Kruglikov, S.S., and Fursova, N.Yu., *Gal'vanotekhn. Obrab. Poverkhn.*, 2000, vol. 7, no. 2, pp. 25–29.
6. Gnusin, N.P. and Kovarskii, N.Ya., *Sherokhovatost' elektroosazhdeniya poverkhnostei* (Irregularity of Electrodeposition on Surfaces), Novosibirsk: Nauka, 1970.
7. Vyacheslavov, P.M. and Shmeleva, N.M., *Kontrol' elektrolitov i pokrytii* (Monitoring and Control of Electrolytes and Coatings), Leningrad: Mashinostroenie, 1965.

Russian Journal of Applied Chemistry, Vol. 75, No. 2, 2002, pp. 223–228. Translated from Zhurnal Prikladnoi Khimii, Vol. 75, No. 2, 2002, pp. 231–236.
Original Russian Text Copyright © 2002 by Krasnov, Kolbasov.

APPLIED ELECTROCHEMISTRY AND CORROSION PROTECTION OF METALS

Optical Characteristics and Structure of Electrochromic Amorphous Tungsten Trioxide Films Electrodeposited from Aqueous Electrolytes

Yu. S. Krasnov and G. Ya. Kolbasov

Institute of General and Inorganic Chemistry, National Academy of Sciences of Ukraine, Kiev, Ukraine

Received September 25, 2001

Abstract—The structure of electrochromic amorphous tungsten trioxide films electrodeposited from an aqueous tungsten-containing electrolyte and specific features of the optical and electrochemical characteristics of these films in different stages of their reversible coloration in a 1 N H_2SO_4 solution were studied.

Electrochromic characteristics of films of amorphous tungsten trioxide α-WO_3, obtained by electrochemical deposition onto cathode from aqueous solutions of tungsten-containing compounds, are comparable with characteristics of similar films obtained by vacuum evaporation and reactive sputtering [1], and, as regards response time and optical contrast in a proton containing electrolyte, are as good as anodic films on tungsten [2, 3]. Electrochromic films have response time of ~0.1 s at a contrast of about 80% in transmission and 95% in reflection [4], whereas electrodes based on anodic films operate only in reflection and need preliminary development of their characteristics by multiple cycling. The electrochromic effect in WO_3 is based on injection into the oxide bulk of electrons from the ohmic contact and the same number of protons from the electrolyte to a concentration of 10^{21}–10^{22} cm^{-3} [1]. The injected electrons are captured to free *d* levels of tungsten, wherefrom they can transit, on absorbing a quantum of light, to neighboring W centers by the charge transfer mechanism [5]. At the same time, films deposited onto cathode from aqueous electrolytes exhibit certain, inherent only in these films, features of structure and of the electrochemical process.

This communication presents the results obtained in a study of reversible changes in the optical absorption spectrum of such films, aimed to reveal the possibility of interpreting such changes with account of the structural features of a deposited layer.

EXPERIMENTAL

α-WO_3 films were obtained by cathodic electrodeposition from an aqueous electrolyte based on sodium tungstate [6], with a transparent conducting SnO_2 layer deposited onto glass used as a cathode. Oxide layers deposited at a cathode current density of about 1 mA cm^{-2} had smooth lustrous surface and exhibited good adhesion to the substrate and clearly pronounced electrochromic properties. The thickness *d* and refractive index *n* of an α-WO_3 layer at a wavelength of 0.6328 μm were determined directly in the course of deposition by means of double-beam laser interferometry [7]. The *d* and *n* values of dried films were measured with a Biolar-PI interference-polarization microscope. The structure of freshly prepared films was studied with optical and scanning electron microscopes, by thermogravimetry, and by IR spectroscopy. The electrochemical and optical characteristics of the fabricated α-WO_3 electrodes were measured in subsequent coloration–decoloration cycles in a 1 N H_2SO_4 solution on a setup described in [4]. For these measurements, the electrodes were placed in a transparent electrochemical cell with a platinum counter-electrode and silver chloride reference electrode, relative to which all electrode potentials *E* of the α-WO_3 layer are given.

The structure of the obtained α-WO_3 films demonstrates that they are X-ray-amorphous and contain a large number of fine pores, which are filled with

1070-4272/02/7502-0223 $27.00 © 2002 MAIK "Nauka/Interperiodica"

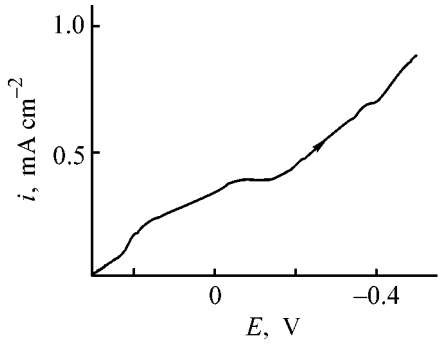

Fig. 1. Current i of coloration of an α-WO_3 film with d = 1 μm vs. cathodic polarization E at sweep rate of 10 mV s^{-1}.

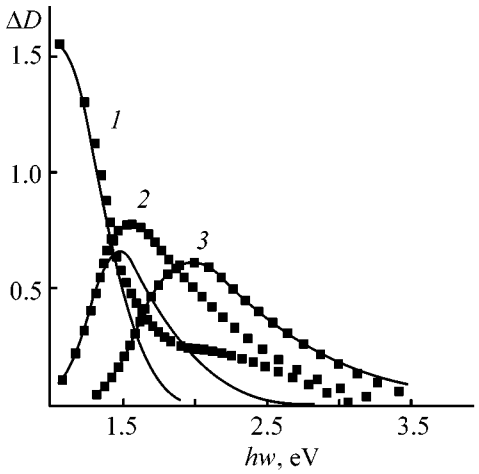

Fig. 2. Spectral distribution of the change ΔD in the optical density of an α-WO_3 layer with d = 1 μm at cathodic polarization E in three successive ranges on the potential scale. (hw) Quantum energy. E (V): (*1*) 0.3–0, (*2*) 0…–0.2, and (*3*) –0.2…–0.4 (*points*). *Solid lines*: three α-WO_3 absorption bands resolved in these spectra.

water molecules in the course of deposition. Most part of free water can be removed from the pores by drying the films in air at room temperature. A certain decrease in the oxide layer thickness, occurring in the process, indicates its densification, which is confirmed by an increase in the refractive index of decolorized α-WO_3 at wavelengths in the range 0.5–0.9 μm, from 1.6–1.7 to 1.9–2.0. In addition to free water in pores, cathodically deposited α-WO_3 layers contain water in capillary-bound and chemically bound (hydrate H_2O) states. The presence of such H_2O molecules is observed in all WO_3 films, irrespective of the preparation technique [1], but the content of the molecules in cathodic deposits (15% according to thermogravimetric analysis) is comparable with the amount of structural water in tungstic acid [8], which is confirmed by IR spectral data. In the region of W–O vibrations, IR spectra of such deposits are similar to the spectrum of yellow tungstic acid, with a broad asymmetric band at 450–1100 cm^{-1}. This band characterizes stretching vibrations of polymer chains of the type …–O–W–O–W–O–… [9] with terminal W=O bonds, whose presence is indicated by the narrow band peaked at 950 cm^{-1} [10, 11]. This gives reason to regard cathodically deposited films as high-polymer oxide compounds of tungsten with varied coordination of oxygen atoms, and the deposit can be represented by the formula $WO_{3-y} \cdot xH_2O$, where $x \approx 2$.

Figure 1 presents the dependence of the cathode current on potential, obtained in coloration of an α-WO_3 layer in a 1 N H_2SO_4 solution. Together with two portions ("waves") of rise in current, between E 0.3 and 0.15 and between –0.15 and –0.35 V, clearly manifested in such electrodes with a cathodically deposited oxide layer [12, 13] and, after cycling, also in anodic α-WO_3 films [3], one more wave is well discernible, having a maximum at $E \approx -0.05$ V. In coloration and decoloration of the electrochromic layer, the electrode current is proportional to the potential sweep rate, but, on passing to a fixed potential, it falls to zero in a time of about 0.1 s. At $E > -0.4$ V, the quasi-equilibrium potential established at the electrode after its disconnection from the power source is virtually equal to the potential which is set at the instant of disconnection (with the difference between these two not exceeding several millivolts). This makes it possible to regard the electrochromic material as a kind of electrolytic capacitor in which the charge of excess electrons captured to free d orbitals of W^{6+} centers, reducing them to W^{5+} [1], is neutralized by the charge of mobile protons in the form of OH_3^+ in channels and pores of the oxide layer. The concentration of injected electrons, N_e, at E = –0.4 V, found by integrating the dependence presented in Fig. 1, is $1.43 \times 10^{21} cm^{-3}$, which corresponds to an oxide in which 30–35% of tungsten atoms are reduced to W^{5+}. It should be noted that, with some α-WO_3 electrodes, a doublet structure of the wave is observed in the range E = –0.15…–0.35 V in the form of two bends in the current–potential dependence, spaced by about 0.15 V.

The optical characteristics of an electrode with a cathodically deposited α-WO_3 layer are presented in Fig. 2. The points represent experimental dependences of the change in optical density on the quantum energy, ΔD–hw. Measurements were done in the course of α-WO_3 layer coloration in three successive ranges of potential, corresponding to the position on the scale of potentials of three waves of the i–E dependence for this electrode in Fig. 1: 0.3–0, 0…–0.2, and –0.2…–0.4 V. In the initial stage of coloration, at a cathodic polarization E of 0.3 to 0 V, a broad

Parameters of three absorption bands in differential optical spectra in Fig. 2 and three types of W centers in the structure of cathodically deposited α-WO_3, corresponding to these bands

Spectrum	hw, eV	$\alpha \times 10^{-4}$, cm^{-1}	$W_{1/2}$, eV	$N_e \times 10^{-20}$, cm^{-3}	f	m_e^*
1	~1	3.57	~0.65	1.0	~1	~1.5
2	1.5	1.5	0.65	1.1	0.43	1.8
3	2.0	1.43	1.12	6.54	0.12	2.0

absorption band peaked at around hw = 1 eV appears in a preliminarily decolorized film (Fig. 2, spectrum *1*). However, its short-wavelength wing is distorted by superposition of one more absorption band with hw_{max} = 2.0 eV, which is identical to that in the range E –0.2…–0.4 V (Fig. 2, spectrum *3*), except that its intensity is 2.7 times lower. The undistorted short-wavelength wing of the band with $hw_{max} \approx 1$ eV, shown in Fig. 2 by a solid line, was obtained by subtraction from the overall spectrum *1* of the contribution from absorption in the band with hw_{max} = 2.0 eV. An analysis of the additional absorption appearing in the film in the next range of E variation, 0…–0.2 V, (Fig. 2, spectrum *2*) demonstrated that in this case, too, there occurs superposition of two bands; one, more intensive, peaked at 1.5 eV, and a band with hw_{max} = 2.0 eV, but having D_{max} 2 times smaller than that in spectrum *3*. The undistorted run of the dependence ΔD–hw, shown by solid line in Fig. 2, was also obtained by subtraction of absorption in the shorter-wavelength band of these two.

The values of hw_{max}, absorption coefficient α_{max}, and half-width $W_{1/2}$, found for the three bands in the presented optical absorption spectra of cathodically deposited α-WO_3, are listed in the table. The table also gives the concentration N_e of excess electrons, on W^{5+} centers, whose optical excitation corresponds to the appearance of each of these bands. The N_e value for the band with hw_{max} = 2.0 eV is found by integration of the i–E dependence (Fig. 1) over the E range –0.2…–0.4 V. The N_e values for this band in two other ranges of E were found by assuming proportionality between N_e and α_{max}. This made it possible to find out that in the initial stage of coloration, before E = 0 V, W centers giving rise to the band with hw_{max} = 2 eV account for 70% of electrons injected into the film, and only 30% is captured by centers responsible for the absorption in the band with $hw_{max} \approx 1$ eV. In the next interval, E 0…–0.2 eV, the fraction of electrons on such W centers is even higher, 75%. It follows from the presented data that, in coloration of αWO_3, more than 90% of the injected electrons is consumed for formation of W centers giving rise to absorption in the band with hw_{max} = 2.0 eV in all the three ranges of potential, although α_{max} for this band is lower than the values for the two other bands.

With hw increasing in the range of fundamental absorption of α-WO_3, the ΔD value in differential spectra *1*–*3* gradually decreases and then becomes negative, which corresponds to the effect of oxide "bleaching" because of the shift of the fundamental absorption edge to higher hw with film coloration in the visible spectral range. To eliminate the contribution from the wing of the absorption band with hw_{max} = 2.0 eV and obtain undistorted ΔD–hw dependences, the extrapolation of the wing of this band to higher hw was taken as zero ΔD.

The spectra of α-WO_3 layer bleaching, obtained for each of the successive ranges on the E scale (as in Fig. 2), are presented in Fig. 3. Each differential spectrum of this kind is in fact the contribution to the fundamental absorption from optical transitions involving only those electrons which were injected into the film in a given range of E. Spectrum *1*, corresponding to the initial interval E 0.3–0 V has an inflection at $hw \approx 3$ eV and an additional shoulder at lower hw, which are absent in spectra *2* and *3*.

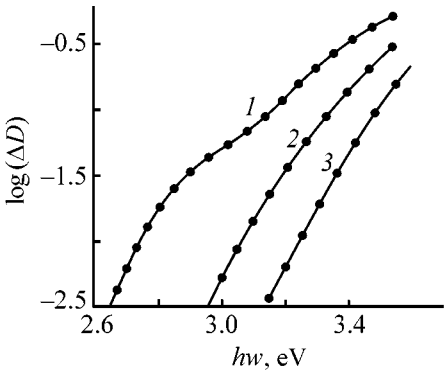

Fig. 3. ΔD–hw dependence in the fundamental absorption range of α-WO_3 layer with d = 1 μm. Polarization potential E (V): (*1*) 0.3–0, (*2*) 0…–0.2, and (*3*) –0.2…–0.4.

In the course of coloration, the quasi-equilibrium potential of the α-WO_3 electrode changes by ΔE = 0.7 V, which much exceeds that expected in accordance with the Nernst equation on the basis of the change in the proton activity ($\Delta E \approx 400$ mV for N_e changing by an order of magnitude). This change in the quasi-equilibrium potential is mainly due to a change in the electrochemical potential of electrons, i.e., is determined by the current position of the Fermi level E_F in the continuous energy spectrum of electronic states of the oxide [14, 15]. A shift of E_F to higher values on the energy scale upon coloration is also indicated by the shift of the fundamental absorption edge of α-WO_3 to higher hw, manifested in the differential spectra in Fig. 3. At a constant rate of E sweep, the coloration current in Fig. 1 can be regarded as a quantity proportional to the density of electronic states. Hence follows that the presented current–potential dependence reflects the distribution of the electronic states over the energy scale in a wide (~0.7 eV) range covered by the interval of E_F variation. The occurrence of three successive waves of rising injection current suggests that the energy spectrum of α-WO_3 includes three broad overlapping bands formed by d orbitals of three types of W centers differently bonded in the film to oxygen atoms and water molecules. Depending on the nature of such bonds, the ionization energies of the corresponding discrete electronic levels forming these bands are different (as also are the positions of these bands on the energy scale): at a difference ΔE between the peaks of separate waves in the current–potential dependence—by approximately $-e\Delta E$ on the average.

Three absorption bands with different positions of hw_{max} appear successively in the optical spectrum of α-WO_3 in the same E ranges which correspond to three waves of the cathodic current in Fig. 1. This confirms the presence appear successively in the structure of a colored cathodically deposited layer of W^{5+} centers of three types with different ionization energies, differing in the quantum energy necessary for initiating a transition of an excess electron to a neighboring W^{6+} center. They are also characterized by unequal probabilities of optical excitation of transitions between charge states of W centers, which is indicated by the oscillator strengths f of the absorption bands, evaluated using the relation [1]

$$f = 0.87 \times 10^{17} \frac{n}{(n^2 + 2)^2} W_{1/2} \frac{\alpha_{max}}{N_e}$$

with $n = 2$ for decolorized α-WO_3. According to these estimates, the higher the hw_{max} of an absorption band, the lower the f value, and the f value calculated for the band with hw_{max} = 2.0 eV for the first two ranges of E (Fig. 2, spectra *1* and *2*) is also equal to 0.12. The table lists effective masses m_e^* of excess electrons on levels of different W^{5+} centers, calculated using the equation [16]

$$m_e^* = 1 + 1.25\, hw_{max}/(6\pi hw_0),$$

where hw_0 is the phonon energy (~0.13 eV [16]).

The obtained m_e^* values are not the same for different W^{5+} centers, being close to the estimates of this parameter for tungsten bronzes Li_xWO_3 and Na_xWO_3 (m_e^* = 1.5 [17] and m_e^* = 2 [18]).

A shift of the absorption band peak to higher hw with decreasing f is observed in colored WO_3 films prepared by reactive sputtering, vacuum evaporation, and ion deposition in the case of broken long-range order and a transition to a more disordered, X-ray-amorphous structure, with double terminal bonds W=O formed instead of the ruptured bridge bonds W–O–W [19, 20]. Lowering the substrate temperature from 200 to 23°C in the course of reactive sputtering leads to an increase in the W=O/W–O–W ratio in the deposited layer from 0.08 to 0.36 and shifts hw_{max} of absorption in coloration from 1.05 to approximately 1.5 eV [19]. Similar changes in the position of hw_{max} of an absorption band, occurring directly in the course of coloration (in an electrolyte with Li^+ cations), were observed for samples of anodized tungsten in analyzing their reflection spectra [2]. The coloration of anodic films is accompanied by an increase in the intensity of the peak at 950 cm^{-1} in Raman spectra, associated with terminal W=O groups [21]. Therefore, the different positions of the absorption peaks hw_{max} in the initial and final stages of coloration are due [2] to the additional disordering of such films upon incorporation of Li^+ cations and to the appearance of W centers with different numbers of terminal W=O groups in the oxide. In a cathodically deposited α-WO_3, the degree of disordering and the number of terminal W=O group are even higher than those in anodic films, and the layer structure includes polymer chains of the type …–O–W–O–W–O–…, with W centers having two groups of this kind each. Therefore, it may be assumed that the main electronic band and the corresponding absorption band with hw_{max} = 2.0 eV are associated with optical excitation of electrons in W centers whose ligand environment includes two terminal oxygen atoms. The doublet structure and the extension of this band to lower energies can be related to different spatial arrangements of two terminal groups in the environment of the tungsten atom and to wide variety of hydrogen bonds of terminal oxygen atoms with water molecules.

The absorption band peaked at around 1 eV is also characteristic of single-crystal WO_3 and films deposited in a vacuum, after their crystallization by annealing at 500°C [1]. For this reason, the corresponding electronic band in a cathodically deposited α-WO_3 can be related to W centers in a regular octahedral ligand environment formed by oxygen atoms. The extension of the wave function of an electron captured by such a W center to neighboring W centers (according to ESR data for a single crystal, the residence time of an electron on neighboring W centers is nearly 2 times longer [22]) leads to an increase in its ionization energy, in agreement with the lower position of E_F on the energy scale upon filling of free levels of this band. As regards centers responsible for the absorption in the band with hw_{max} = 1.5 eV, it may be assumed that they are bonded to a single terminal atom of oxygen.

The probability of an optically induced transition of an excess electron between charge states of the W center and the energy necessary for its activation by absorbed quantum are determined by the overlapping of the electron wave functions in the initial and final states, i.e., depend on the extent of its localization on a W^{5+} center and distance to the nearest unoccupied W^{6+} center. In this connection, the absorption in the band with the lowest energy $hw_{max} \approx 1$ eV and the highest $f \approx 1$ in cathodically deposited α-WO_3 corresponds to excitation of excess electrons with the lowest degree of localization on a W^{5+} center, where the wave function of an electron partially extends, as in the case of a single crystal, to neighboring tungsten atoms. Such W centers are surrounded by bridge atoms of oxygen and their lowest unoccupied *d* orbitals form the lowest-energy electron band and are filled with injected electrons already in the initial stage of film coloration. The absorption in the other two bands, having higher hw_{max}, corresponds to optical excitation of electrons with higher degree of localization, which, according to the table, is confirmed by lower *f* values for these bands and heavier m_e^* of such electrons on discrete *d* levels in the other two, higher-energy electron bands formed by W centers with distorted ligand environment.

The optical gap E_g of α-WO_3 is found from the position of the fundamental absorption edge, for which is taken the point of intersection of extrapolated linear portion of the $D(hw)$ spectrum plotted in the $(Dhw)^{1/2}$–hw coordinates with the abscissa axis [11, 23]. The weak absorption at $hw < E_g$ is attributed to optical transitions involving the "tail" of the density of discrete electronic states with lower energy in disordered amorphous oxide. However, if it is assumed, on the basis of the data obtained, that disordering of WO_3 with disintegration of W–O–W bridge bonds and formation of a large amount of W=O terminal bonds is accompanied by formation of higher-energy electron bands, then it is necessary to regard as the fundamental absorption edge its beginning, lying in spectra *1–3* (Fig. 3) at $hw \approx 2.65$, 2.95, and 3.15 eV. The intervals between these values, equal to approximately 0.3 and 0.2 eV, correspond to $\Delta E_g \approx \Delta E_F \approx -e\Delta E$ between the initial *E* values of 0.3, 0, and –0.2 V, whereas the conventional technique for determining the edge position gives ΔE_g lower than 0.2 eV. With this approach to interpretation of the fundamental absorption spectra of α-WO_3, the region of spectra in Fig. 3, characterized by the highest $\log(\Delta D)$ values, can be attributed to transitions of valence electrons to free levels in the main electron band with the highest density of unoccupied electron states. When discrete levels in the other two bands are filled with injected electrons, they cannot be involved in optical transitions of electrons from the valence band, and, therefore, the additional shoulder associated with such transitions, present at low *hw* in the differential spectrum *1* in Fig. 3, is not observed in spectra *2* and *3*.

CONCLUSIONS

(1) The structure of amorphous oxide layer deposited onto the cathode, which is close to $WO_{3-y} \cdot 2H_2O$, is characterized by the presence of a great number of fine pores filled with water molecules. This leads to low refractive index (decolorized film in contact with electrolyte has n = 1.6–1.7) and makes shorter the time of coloration and decoloration of a layer of electrochromic material because of the high mobility of protons in the form OH_3^+.

(2) The reversible change in optical and electrochemical properties of such films in the course of coloration is associated with successive filling with injected electrons of three overlapping electron bands formed by discrete *d* levels of W centers having in their ligand environment different numbers of terminal oxygen atoms (W=O double bonds). In this case, the electronic Fermi level is shifted upwards on the energy scale, and the fundamental absorption edge of the oxide, to higher *hw* by a value determined by a change in the quasi-equilibrium potential ($\Delta hw \approx \Delta E_F \approx -e\Delta E$).

(3) The differences in hw_{max} position and oscillator strength between the three absorption bands, successively appearing in the optical spectrum in the course of coloration, are determined by the different degrees of localization of excess electrons on

the *d* levels of tungsten in the electron bands formed by these levels.

REFERENCES

1. Channin, D.J., Crandall, R.S., Criscimagna, *et al.*, Electrochromic Displays Based on α-WO_3, in: *Display Devices*, Pankove, J.I., Ed., Berlin: Springer, 1980.
2. Delichere, P., Falaras, P., and Hugot-Le Goff, A., *Thin Solid Films*, 1988, vol. 161, pp. 47–58.
3. Reichman, B. and Bard, A.J., *J. Electrochem. Soc.*, 1979, vol. 126, no. 4, pp. 583–591.
4. Krasnov, Yu.S., Vas'ko, A.T., Patsyuk, F.N., and Sych, O.A., *Ukr. Khim. Zh.*, 1987, vol. 53, no. 9, pp. 951–956.
5. Faughnan, B.W., Crandall, R.S., and Heyman, P.M., *RCA Rev.*, 1975, vol. 36, no. 1, pp. 177–197.
6. Yamase, T., Sasaki, Y., and Motovaki, T., *Inorg. chem. Acta*, 1986, vol. 121, no. 1, pp. 19–22.
7. Krasnov, Yu.S., Patsyuk, F.N., and Sych, O.A., *Ukr. Khim. Zh.*, 1989, vol. 65, no. 12, pp. 1287–1292.
8. Ramans, G.M., Gabrusenoks, J.V., and Veispals, A.A., *Phys. Stat. Sol. (a)*, 1982, vol. 74, pp. K41–K44.
9. Kharitonov, Yu.Ya. and Buslaev, Yu.A., *Izv. Akad. Nauk SSSR, Ser. Khim.*, 1964, no. 5, pp. 808–814.
10. Guery, C., Choquet, C., Dujeancourt, F., *et al.*, *J. Solid State Electrochem.*, 1997, vol. 1, no. 3, pp. 199–207.
11. Shiyanovskaya, I. and Hepel, M., *J. Electrochem. Soc.*, 1998, vol. 145, no. 3, pp. 1023–1028.
12. Krasnov, Yu.S., Patsyuk, F.N., Sandrovskii, A.K., and Vas'ko, A.T., *Elektrokhimiya*, 1984, vol. 20, no. 11, pp. 1470–1475.
13. Sych, O.A., Krasnov, Yu.S., Vas'ko, A.T., *et al.*, *Ukr. Khim. Zh.*, 1991, vol. 57, no. 6, pp. 628–632.
14. Krasnov, Yu.S., Sych, O.A., Patsyuk, F.N., and Vas'ko, A.T., *Elektrokhimiya*, 1988, vol. 24, no. 11, pp. 1523–1526.
15. Voinov, M., *Progr. Batteries Sol. Cells*, 1982, vol. 4, pp. 108–110.
16. Salje, E. and Hoppmann, G., *Phil. Mag. B*, 1981, vol. 43, no. 1, pp. 105–114.
17. Hjelm, A., Granqvist, C.G., and Wills, J.M., *Phys. Rev. B*, 1996, vol. 54, no. 4, pp. 2436–2445.
18. Green, M. and Travlos, A., *Phil. Mag. B*, 1985, vol. 51, no. 5, pp. 501–529.
19. Kubo, T. and Nishkitani, Y., *J. Electrochem. Soc.*, 1998, vol. 145, no. 5, pp. 1729–1734.
20. Yoshimura, T., *J. Appl. Phys.*, 1985, vol. 57, no. 3, pp. 911–919.
21. Delichere, P., Falaras, P., Froment, M., and Hugot-Le Goff, A., *Thin Solid Films*, 1988, vol. 161, pp. 35–46.
22. Schirmer, O.F. and Salje, E., *Solid State Commun.*, 1980, vol. 33, no. 3, pp. 333–336.
23. Nakamura, A. and Yamada, S., *Appl. Phys.*, 1981, vol. 24, no. 1, pp. 55–59.

Russian Journal of Applied Chemistry, Vol. 75, No. 2, 2002, pp. 229–234. Translated from Zhurnal Prikladnoi Khimii, Vol. 75, No. 2, 2002, pp. 237–242.
Original Russian Text Copyright © 2002 by Vorobets, Kovach, Kolbasov.

APPLIED ELECTROCHEMISTRY AND CORROSION PROTECTION OF METALS

Distribution of Ion Species and Formation of Ion Pairs in Concentrated Polysulfide Solutions in Photoelectrochemical Transducers

V. S. Vorobets, S. K. Kovach, and G. Ya. Kolbasov

Vernadskii Institute of General and Inorganic Chemistry, National Academy of Sciences of Ukraine, Kiev, Ukraine

Uzhgorod National University, Uzhgorod, Ukraine

Received August 8, 2001

Abstract—Results of spectrophotometric measurements in concentrated polysulfide solutions used as electrolytes in regenerative photoelectrochemical transducers are presented. The equilibrium constants are determined and the distribution of ions species in the solutions is calculated. The effect of electrolyte solution on the output characteristics of a photoelectrochemical cell based on cadmium selenide and cobalt sulfide was studied.

Concentrated sulfide-polysulfide solutions are commonly used as electrolytes that can stabilize the operation of photoelectrochemical transducers (PECT) based on cadmium chalcogenides. It is believed that sulfide ions are oxidized by holes from the valence band

$$(x + 1)S_x^{2-} + 2h^+ \rightarrow xS_{x+1}^{2-} \quad (1)$$

at the semiconductor photoelectrode [1, 2], and polysulfide ions are reduced

$$xS_{x+1}^{2-} + 2e \rightarrow (x + 1)S_x^{2-}. \quad (2)$$

at the counter electrode. For simplicity, the electrically active species are designated as S_x^{2-}, although their true nature is unknown, since the electrolyte contains simultaneously a number of ions that can enter into electrode reactions (S^{2-}, HS^-, OH^-, S_x^{2-}, where x = 2–5). A comprehensive study of sulfide-polysulfide systems requires reliable methods for analysis of all the species present in these systems, and polysulfide species, in particular.

The distribution of polysulfide forms in an electrolyte is determined by the equilibrium

$$(x - 1)S_{x+1}^{2-} + HS^- + OH^- = xS_x^{2-} + H_2O, \quad (3)$$

where x = 2–4.

The equilibrium constants of the processes described by Eq. (3) were found in [3] from spectral data and refined in [4]. However, these data cannot be used and generalized to concentrated systems since (1) the superposition of absorption bands of HS^- and S^{2-} ions on the absorption bands of polysulfide ions in the UV range at high concentration of these ions in solution was disregarded, and (2) there is no dependence of the equilibrium constants on the ionic strength of the solution. The latter casts doubt on the appropriateness of using the values of the $K_{1/2}$ and $K_{2/3}$ constants, found for solutions with high ionic strength, in the case of solutions with low ionic strength, for which the constant $K_{3/4}$ was determined ($K_{1/2}$, $K_{2/3}$, $K_{3/4}$ are the equilibrium constants for the equilibrium between the polysulfide ions S_2^{2-} and S_3^{2-}, S_3^{2-} and S_4^{2-}, S_4^{2-} and S_5^{2-}, respectively).

In [4], some shortcomings of the calculations made in [3] were taken into account. For example, in determining the optical constants from absorption spectra, a correction was made for the strong absorption by HS^- and S^{2-} ions in the UV range, which leads to a significant change in the results obtained. However, no attempts were undertaken to make corrections to the equilibrium constants for different ionic strengths. Moreover, the second constant of dissociation of H_2S solutions, $K_{a_2} = 10^{-17}$ [5], was used in calculations, whereas rather widely varying pK_{a_2} values (12–17) can be found in the literature [6, 7]. Previously, the K_{a_2} values have been determined for H_2S in solutions with ionic strength I = 4–5 with the use

1070-4272/02/7502-0229 $27.00 © 2002 MAIK "Nauka/Interperiodica"

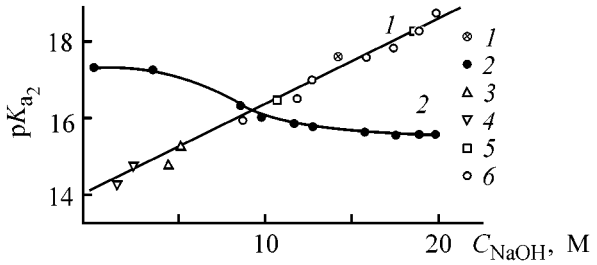

Fig. 1. pK_{a_2} vs. alkali concentration C_{NaOH} according to data obtained in different studies. Data of: (*1*) [4], (*2*) [5], (*3*) [8], (*4*) [6], and (*5*) [7]; (*6*) data of [5] recalculated with account of ion pair formation.

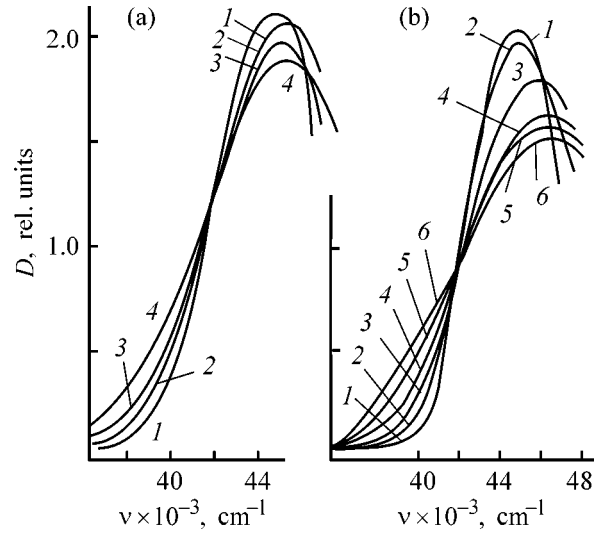

Fig. 2. Absorption spectra of 0.5 M solutions of (a) Na_2S and (b) K_2S in the presence of alkali. (*D*) Optical density and (ν) wave umber; the same for Fig. 3. (a) NaOH concentration (M): (*1*) 0.1, (*2*) 6, (*3*) 8.3, and (*4*) 10.2. (b) KOH concentration (M): (*1*) 0, (*2*) 8, (*3*) 10, (*4*) 13, (*5*) 15, and (*6*) 16.8.

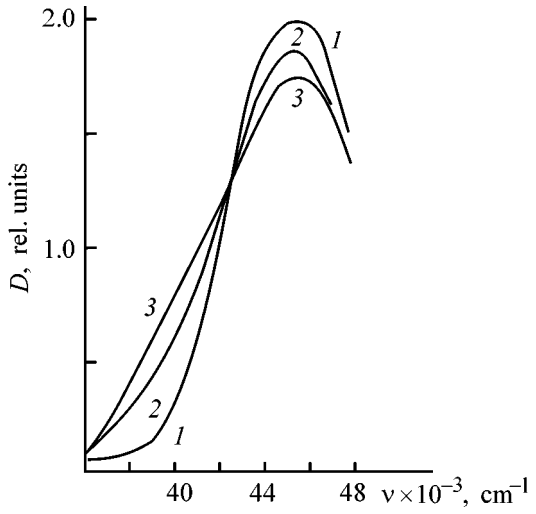

Fig. 3. Absorption spectra of a 15 M KOH–0.5 M K_2S solution in (*1*) formamide, (*2*) water, and (*3*) ethanol.

of a sulfide-selective electrode [8]. Figure 1 presents the pK_{a_2} values obtained in different studies in solutions containing an alkali. It can be seen that pK_{a_2} grows steadily with increasing concentration of OH^- ions. Also presented are the data obtained in [5] from spectra of sulfide solutions, according to which pK_{a_2} decreases with increasing alkali concentration.

Since the scatter of pK_{a_2} values in dilute solutions is known to be strong and data on the distribution of ion species in concentrated polysulfide solutions are virtually lacking, the aim of this study was to analyze the distribution of ion species in such solutions and reveal the reasons for the scatter of pK_{a_2} values, and also to determine the optimal electrolyte composition for PECT.

EXPERIMENTAL

Absorption spectra of concentrated alkaline sulfide and polysulfide solutions of potassium and sodium were studied. The solutions were prepared by dissolving the starting components MOH, M_2S, and S (M = Na, K) in deaerated twice-distilled water. The absorption spectra were measured with a Specord M40 spectrophotometer in cells of thickness $d = (5–35) \times 10^{-4}$ cm in the wave-number range 20 000–50 000 cm^{-1}. The redox potential E_{redox} was measured on a platinum electrode relative to silver chloride reference electrode.

In sodium and potassium sulfide solutions with high alkali content (>5 M) a new absorption band is observed at $\nu = 40 \times 10^3$ cm^{-1} (Fig. 2), which can be attributed to formation of an ion pair of K^+ (Na^+) with S^{2-} ions, rather than with a sulfide ion, as believed in [5] where the formation of an ion pair was ruled out because of the high dielectric constant of water ($\varepsilon = 80$). However, the activity of water falls dramatically at high concentrations of alkali [9] and the dielectric constant of the medium decreases [10], with the result that the probability of ion pair formation increases. In addition, the band at $\nu = 40 \times 10^3$ cm^{-1} depends on the solvent nature. Figure 3 shows absorption spectra of 0.5 M K_2S–15 M KOH solutions in water ($\varepsilon = 80$), formamide ($\varepsilon = 110$), and ethanol ($\varepsilon = 25$). It can be seen that the intensity of the band at $\nu = 40 \times 10^3$ cm^{-1} decreases with increasing dielectric constant of the medium.

One more argument in favor of the formation of ion pairs in concentrated polysulfide solutions is furnished by spectra of the crystal hydrates $Na_2S \cdot 5H_2O$ and $Na_2S \cdot 9H_2O$ [3]. The spectrum of $Na_2S \cdot 9H_2O$

Shows only a single strong band at $\nu = 44 \times 10^3$ cm^{-1}. The spectrum of $Na_2S \cdot 5H_2O$ contains a broad band in the range $\nu = 40 \times 10^3$–45×10^3 cm^{-1}. The structures of the crystal hydrates $Na_2S \cdot 9H_2O$ and $Na_2S \cdot 5H_2O$ are known. In $Na_2S \cdot 9H_2O$, a sulfur atom is surrounded by 12 oxygen atoms so that Na^+ and S^{2-} ions are spatially separated by water molecules. In $Na_2S \cdot 5H_2O$, a sulfur atom is surrounded by five oxygen atoms and one sodium atom, which is in direct contact with the sulfur atom, which virtually corresponds to formation of a contact ion pair. Consequently, the spectral data of [5] can be interpreted as follows: alkali sulfide solutions with alkali content of up to 5 M contain the same ion associates, including Na^+, S^{2-} ions and H_2O, as the crystal hydrate $Na_2S \cdot 9H_2O$.

With increasing alkali concentration, the spectra of aqueous sulfide solutions become similar to the absorption spectra of $Na_2S \cdot 5H_2O$ crystal hydrate, which can be related to the formation of a contact ion pair. In [5], such an explanation was considered, too, but was discarded because the absorption band at $\nu = 40 \times 10^3$ cm^{-1} could not be observed in absorption spectra of alkali metal halide solutions to the point of saturation. However, this fact cannot be regarded as ruling out the formation of ion pairs in alkali solutions, since the solubility of halides is much lower than that of hydroxide, and it is impossible to obtain in halide solutions the same cation concentrations as in alkaline solutions; the behavior of halide solutions markedly differs from that of hydroxide, sulfide, and polysulfide solutions. The average activity of a solution decreases in the series of alkali metal halides from Li to Cs, whereas the average activity of solutions of alkali metal hydroxides, sulfides, and polysulfides grows [11]. Such a difference in behavior can be accounted for in terms of the "local hydrolysis" model. According to this model, an anion interacts with a proton in the hydration shell of a cation

$$M^+...H_2O + A^- = M^+...OH^-...H^+...A^-.$$

As a result, an ion associate is formed, which can be regarded as a noncontact ion pair. The degree of such an association is directly related to the strength of an anion as proton acceptor and the polarizability of protons in the hydration shell. Chlorides, which are weak proton acceptors, will undergo pairing, as a result of local hydrolysis, to a lesser extent than sulfides and hydroxides, which are strong proton acceptors, and also polysulfides, which are bases intermediate in strength. Cations with large and strongly polarized hydration shells, e.g., Li^+, will undergo strong pairing because of the local hydrolysis with anions acting as strong proton acceptors, in contrast to cations having a small primary hydration shell or none at all, as, e.g., Cs^+. Consequently, the absence of the band corresponding to an ion pair in the spectra of chlorides cannot establish that ion pairs cannot be formed in alkaline sulfide (polysulfide) solutions.

The experimentally observed dependence pK_{a_2} on the alkali concentration may be due to a change in the ion distribution in favor of ion pair formation. For example, in strongly concentrated solutions, where ion pairing is manifested, the $[S^{2-}]$ value is low and the constant of sulfide ion hydrolysis, K_h, grows. Consequently, $K_{a_2} = K_w/K_h$, (K_w is the ion product of water) decreases, and $pK_{a_2} = -\log K_{a_2}$ grows, which is observed experimentally (Fig. 1, curve *1*).

The experimental data suggest that the S^{2-} ion forms in aqueous alkaline solutions a noncontact ion pair with water molecules and sodium (potassium) ions:

$$S^{2-} + H_2O + Na^+ = [S^{2-}–H_2O–Na^+].$$

The spectral band associated with such a pair may coincide with the band at 44×10^3 cm^{-1}, known in the literature as the band associated with HS^-. Experimentally, the band at $\nu = 44 \times 10^3$ cm^{-1} furnishes information about the sum of species in the form HS^-, S^{2-}, and $[S^{2-}–H_2O–Na^+]$. The band at $\nu = 40 \times 10^3$ cm^{-1} corresponds to the contact ion pair Na_2S, which is indicated, as already mentioned, by the spectra of the crystal hydrates $Na_2S \cdot 9H_2O$ and $Na_2S \cdot 5H_2O$.

It follows from the aforesaid that, in concentrated sulfide and polysulfide solutions, it is necessary to take into account, in addition to equilibria (3), also the following processes: hydrolysis of the sulfide ion

$$S^{2-} + H_2O = HS^- + OH^- \quad (4)$$

and formation of contact and noncontact ion pairs

$$Kt^+ + A^{z-} = [KtA]^{(z-1)-}, \quad (5)$$

$$Kt(H_2O)_n^+ + A^{z-} = [Kt(H_2O)_mA]^{(z-1)-}, \quad (6)$$

$$Kt(H_2O)_n^+ + A(H_2O)_l^{z-} = [Kt(H_2O)_mA]^{(z-1)-} + (l + n - m)H_2O. \quad (7)$$

In view of the complexity of the system, we perform calculations in terms of a simplified model taking into account Eqs. (4) and (5). The hydrolysis constant of the sulfide ion and the formation constant

of the ion pair, K_1, are related to the activities of the corresponding species by

$$K_h = a_{HS^-} a_{OH^-}/a_{S^{2-}} a_w, \quad (8)$$

$$K_l = a_{NaS^-}/a_{Na^+} a_{S^{2-}}, \quad (9)$$

where a_{NaS^-}, a_w, a_{Na^+}, a_{HS^-}, a_{OH^-}, and $a_{S^{2-}}$ are the activities of the ion pair, water, sodium ions, and hydrosulfide, hydroxide, and sulfide ions, respectively.

If the total concentration of sodium sulfide introduced into solution is denoted by C_{Na_2S}, then

$$C_{Na_2S} = [HS^-] + [S^{2-}] + [NaS^-], \quad (10)$$

where $[HS^-]$, $[S^{2-}]$, and $[NaS^-]$ are the equilibrium concentrations of hydrosulfide ions, sulfide ions, and the contact ion pair, respectively.

Assuming that the band at $\nu = 40 \times 10^3$ cm^{-1} corresponds to the contact ion pair NaS^-, rather than to the sulfide ion, and the band at $\nu = 44 \times 10^3$ cm^{-1}, to a sum of the HS^- and S^{2-} species, rather than to solely HS^-, we can write the expression for the equilibrium constant of the process (4), with account of ion pair formation, as

$$K_l^i = \frac{[S^{2-}]a_w}{[HS^-][OH^-]} = \frac{[NaS^-]a_w}{(C_{Na_2S} - [NaS^-])[OH^-]}, \quad (11)$$

whence follows

$$\frac{K_l^i[OH^-]}{a_w} = \frac{[NaS^-]}{C_{Na_2S} - [NaS^-]}. \quad (12)$$

Introducing the designation $[NaS^-]/(C_{Na_2S} - [NaS^-]) = x$, we obtain $[NaS^-] = xC_{Na_2S}/(1 + x)$.

It follows from spectral data that

$$[NaS^-] = D_l/\varepsilon_l d,$$

where D_l and ε_l are, respectively, the optical density and molar absorption coefficient for the band at $\nu = 40 \times 10^3$ cm^{-1}, and d is the layer thickness.

Solving simultaneously Eqs. (8)–(11), we obtain

$$x^{-1}a_{OH^-} = K_h\gamma_{NaS^-} a_w/K_l\gamma_{HS^-} a_{Na^+} + \gamma_{NaS^-}/K_l\gamma_{S^{2-}}, \quad (13)$$

where γ_{NaS^-}, γ_{HS^-}, and $\gamma_{S^{2-}}$ are the activity coefficients of the respective species.

Plotting $x^{-1}a_{OH^-}$ as a function of a_w/a_{Na^+}, we obtain a straight line whose equation is as follows:

$$x^{-1}a_{OH^-} = 162 + 4933a_w/a_{OH^-}.$$

The corresponding expressions for the constant of sulfide hydrolysis (in a sodium solution) and the constant of ion pair formation have the form

$$K_h = 30.5(\gamma_{HS^-}/\gamma_{S^{2-}}),$$

$$K_l = 6 \times 10^{-3}(\gamma_{NaS^-}/\gamma_{S^{2-}}).$$

Consequently, $pK_{a_2} = 15.48$. Using the presented constants, we recalculated the pK_{a_2} data of [5] (Fig. 1, points *6*). As follows from Fig. 1, the results of [5] recalculated with account of the ion pair formation are in agreement with the data obtained elsewhere [6–8].

A knowledge of the constants K_h and K_l makes it possible to calculate the distribution of ion species in polysulfide electrolytes with known introduced concentrations of alkali metal sulfide, alkali, and sulfur.

Let us write the material balance equations for the introduced sulfide, sulfur, and the hydroxide ion

$$C_{K_2S} = [S^{2-}] + [HS^-] + S_n, \quad (14)$$

$$C_{S^0} = \sum_{n=1}^{4} n[S_{n+1}^{2-}], \quad (15)$$

$$[OH^-] = C_{OH^-} + [HS^-], \quad (16)$$

where C_{K_2S} is the concentration of potassium sulfide introduced into solution, S_n a sum of equilibrium concentrations of polysulfide ions $S_n = \sum_{n=2}^{4}[S_n^{2-}]$, and C_{OH^-} the concentration of potassium hydroxide introduced into solution.

Solving the system of equations (8), (14)–(16), we obtain

$$[OH^-] = \frac{1}{2}\left\{C_{OH^-} - K_h + \sqrt{(K_h + C_{OH^-})^2 + 4K_h(C_{K_2S} - S_n)}\right\}, \quad (17)$$

$$[S^{2-}] = (C_{K_2S} - S_n) \times \left\{\frac{2K_h}{C_{OH^-} - K_h + \sqrt{(K_h + C_{OH^-}) + 4K_h(C_{K_2S} - S_n)}} + 1\right\}. \quad (18)$$

We find he concentrations of separate polysulfide ions and S_n from absorption spectra of polysulfide solutions. Despite the complexity of such spectra, arising from the superposition of individual absorption bands of polysulfide ions, modern software makes it possible to resolve in these spectra separate absorption

bands and to determine their parameters, namely, the position ν_c of a band, its width w, and peak height h. The concentrations of separate polysulfide ions can be determined from the equation

$$D(\nu) = d\sum_{i=2}^{5}[S_i^{2-}]h_i \exp\left\{\left(-\frac{\nu_i - \nu_c}{w_i}\right)^2\right\}, \qquad (19)$$

where $D(\nu)$ is the optical density at i-th point after subtraction of the absorption due to HS^- and S^{2-} ions; ν_c the position of the absorption band; w_i, h_i its width and height, respectively; and d the cuvette thickness.

The results of calculation for a 1 M KOH–1 M K_2S–1 M S solution are presented in the table. The absorption bands were identified in [3, 4]. Our data largely coincide with the results of [4].

Formation of ion pairs in an electrolyte leads to a decrease in the amount of electrically active species involved in the electrode processes occurring at the photo- and counter electrode, which affects adversely the operation of PECT. Consequently, an improvement of the PECT efficiency would be expected on passing to electrolytes less subject to ion pair formation.

With account of the aforesaid, the effect exerted by the electrolyte composition on the output characteristics of a photoelectrochemical cell (PECC) was studied. By the electrolyte composition are understood the concentrations of introduced alkali, and sulfide, and also the sulfur to sulfide ratio X_S. The alkali metal cation markedly affects, not being directly involved in the electrode processes, the PECC operation, improving it in the order Li < Na < K < Cs [11].

Figure 4 presents the characteristics of PECC in polysulfide electrolytes with varied X_S. It can be seen that the short-circuit current I_{sc} grows with X_S increasing up to $X_S = 2$, and starts to fall only in solutions strongly saturated with sulfur ($X_S > 2$). Such a behavior of I_{sc} can be accounted for by the interaction of several factors.

(1) Photooxidized products dissolve more rapidly in solutions with lower sulfur concentration. As believed by the authors of [12], the dissolution of products oxidized at the photoelectrode is the rate-determining stage of the anodic reaction.

(2) Processes of ion pair formation become faster with increasing ionic strength of solution and, consequently, with growing X_S. As already mentioned, ion pairing makes lower the concentration of electrically active species in solution, which impairs charge transfer and diminishes the current.

Species distribution in 1 M KOH–1 M K_2S–1 M S solution

Species	Concentration, M	Mole fraction, U_i^*
HS^-	0.3236	0.324
S^{2-}	0.03745	0.037
S_2^{2-}	0.03522	0.352
S_3^{2-}	0.1713	0.171
S_4^{2-}	0.1156	0.116

* $U_i = [S_i]/\Sigma S_i$.

The dependence of the open-circuit voltage U_{oc} on X_S is different from that of I_{sc} on X_S. It is known that U_{oc} is determined by the difference between the redox potential of a solution, E_{redox} and the flat-band potential of a semiconductor, E_{fb}:

$$U_{oc} = f(E_{redox} - E_{fb}).$$

E_{fb} is independent of the concentration of sulfur introduced into solution up to concentrations of 1 M [13]. As shown by our investigations, E_{redox} shifts to positive values with increasing X_S, changing from –660 mV at $X_S = 0.5$ to –630 mV at $X_S = 2$.

Hence follows that U_{oc} must grow with X_S increasing up to $X_S = 1$, which is the case in the experiment. A slight decrease in U_{oc} in solutions with high concentration of sulfur can be attributed to the influence of other factors (e.g., a shift of E_{fb} of *C*dSe to more positive values with increasing X_S). In this case, the dependence of cell efficiency on X_S (Fig. 4) has an extremum at $X_S = 1.5$.

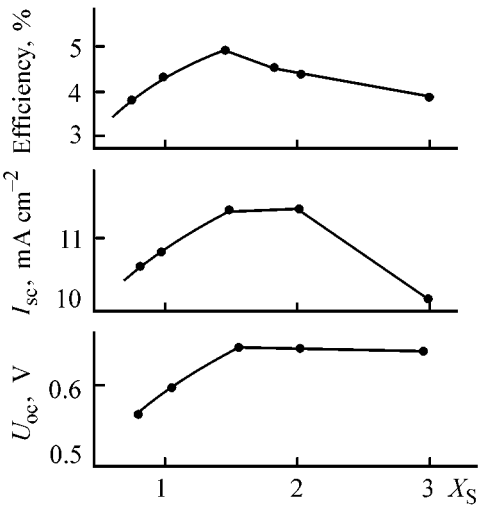

Fig. 4. Efficiency, short-circuit current I_{sc}, and open-circuit voltage U_{oc} vs. sulfur to sulfide ratio X_S. Illumination intensity 75 mW cm^{-2}.

Alkali is introduced into an electrolyte in order to shift the equilibrium of reaction (4) toward formation of the sulfide ion, which, in turn, affects the equilibrium of reaction (1) and, correspondingly, the output parameters of PECC. For example, U_{oc} is 0.6 V for a PECC with electrolyte containing 1 M NaOH, and only 0.54 V for an electrolyte containing no alkali, which is apparently due to a shift of the flat-band potential of the semiconductor to the negative side in view of the increasing concentration of sulfide ions.

With account of the presented calculations and experimental data, the optimal electrolyte is that containing alkali metal hydroxide and sulfide in amounts of 1–2 M each and characterized by $X_S = 1.5$.

CONCLUSIONS

(1) An analysis of published data on the second constant of dissociation of an H_2S solution demonstrated that the scatter of pK_{a_2} values obtained in different studies ($pK_{a_2} = 12–17$) depends on the alkali concentration in the solutions used for measurements.

(2) The observed rise in pK_{a_2} values with increasing alkali concentration can be accounted for by the formation of ion pairs. With account of this circumstance, the equilibrium constants were determined and the distribution of ion species in concentrated solutions of polysulfides used in regenerative photoelectrochemical transducers was calculated.

(3) It is shown that the electrolyte composition strongly affects the output characteristics of photoelectrochemical transducers. An optimization of the composition of the polysulfide electrolyte, carried out with account of the aforesaid, made it possible to raise by 20–25% the conversion efficiency of a photoelectrochemical cell with cadmium selenide photoelectrode and cobalt sulfide counter electrode and to achieve efficiencies of 10–12%.

REFERENCES

1. Hodes, G., Manassen, J., and Cahen, D., *Nature* (London), 1976, vol. 261, no. 559, pp. 403–404.
2. Kuzminskii, Ye.V. and Kolbasov, G.Ya., *Solar Energy Materials, Solar Cells*, 1999, vol. 5, no. 1, pp. 93–115.
3. Giggenbach, W., *Inorg. Chem.*, 1972, vol. 11, no. 6, pp. 1201–1207.
4. Licht, S., Hodes, G., and Manassen, J., *Inorg. Chem.*, 1986, vol. 25, no. 15, pp. 2486–2489.
5. Giggenbach, W., *Inorg. Chem.*, 1971, vol. 10, no. 7, pp. 1333–1338.
6. Ellis, A.J. and Golding, R.M., *J. Chem. Soc.*, 1959, no. 1, pp. 127–130.
7. Meyer, B., Ward, K., Koshlap, K., and Peter, L., *Inorg. Chem.*, 1983, vol. 22, no. 16, pp. 2345–2346.
8. Kovach, S.K., Vorobets, V.S., and Vas'ko, A.T., *Ukr. Khim. Zh.*, 1988, vol. 54, no. 2, pp. 150–154.
9. *Voprosy fizicheskoi khimii rastvorov elektrolitov* (Problems of Physical Chemistry of Electrolyte Solutions), Mikulin, G.I., Ed., Leningrad: Khimiya, 1968.
10. Dobosh, G., *Elektrokhimicheskie konstanty: Spravochnik dlya elektrokhimikov* (Electrochemical Constants: Reference Book for Electrochemists), Moscow: Mir, 1980.
11. Licht, S., Tenne, R., Flaisher, H., and Manassen, J., *J. Electrochem. Soc.*, 1986, vol. 133, no. 1, pp. 52–59.
12. Lando, D., Manassen, J., Hodes, G., and Cahen, D., *J. Am. Chem. Soc.*, 1979, vol. 101, no. 14, pp. 3969–3971.
13. Kolbasov, G.Ya., Karpov, I.I., Pavelets, A.M., and Khanat, L.N., *Elektrokhimiya*, 1985, vol. 21, no. 9, pp. 1236–1238.

Russian Journal of Applied Chemistry, Vol. 75, No. 2, 2002, pp. 235–240. Translated from Zhurnal Prikladnoi Khimii, Vol. 75, No. 2, 2002, pp. 243–248.
Original Russian Text Copyright © 2002 by Protod'yakonova, Aniskin, Sleptsov.

PROCESSES AND EQUIPMENT OF CHEMICAL INDUSTRY

Experimental Study of Gas-Fluid Jet Formed by Single-Flare Atomizer

O. I. Protod'yakonova, S. V. Aniskin, and I. E. Sleptsov

St. Petersburg State Technical University, St. Petersburg, Russia

Received November 15, 2001

Abstract—A gas-fluid jet outflowing from a single-flare atomizer and the possibility of a pronounced change in the nature of the spraying density distribution in a free polydisperse gas-fluid jet with increasing distance from the atomizer nozzle were studied experimentally.

Apparatus with gas-fluid jets formed with single-flare atomizers are widely used in wet cleaning of industrial gas discharges.

In [1, 2], a model of motion of such a jet was developed, possessing certain advantages over the previously proposed models [3]. For example, the gas velocity distribution had been assumed [3] to be uniform across the jet in constructing a model of a gas-fluid jet outflowing from a single-flare atomizer.

The model constructed in [1, 2] was based on the assumption of a nonuniform distribution of gas velocity across the jet, with a maximum on the jet axis. This kind of distribution of the parameter is characteristic of gas jets in general and those developing in a flow of fluid drops, in particular [4].

The hydrodynamic model proposed in [3] takes into account the type of spraying density distribution across the flare. However, this model replaces the real polydisperse flow of drops in a gas-fluid jet with a monodisperse flow with drops whose diameter is equal to the average volume-surface drop size of the polydisperse flow. The model of a gas-fluid jet, developed in [1, 2], takes into account not only the type of the spraying density distribution function, but also the type of the drop size distribution function, i.e., the dispersion composition of the gas-fluid jet. These functions should be set in the boundary conditions for the model equations.

The aim of this study was to confirm experimentally the validity of the model of the flow of a gas-fluid jet, developed in [1, 2]. The calculations performed in terms of this model demonstrated that finely dispersed fractions of drop starting their motion on the flare periphery are shifted toward its axis much faster than fractions with larger drops do [2]. An experimental verification of this result would give reason to consider the model discussed here adequate to the object of study.

To assess the adequacy of the given model, it is necessary to obtain experimentally the spraying density distribution function at different distances from the atomizer nozzle and compare it with a similar function found by solving the model equations.

However, to obtain this solution, it is necessary to specify the boundary conditions of these equations. To accomplish this task, it is necessary to have, first, the analytical form of the spraying density distribution function in the region close to the atomizer nozzle and, second, the drop size distribution function, i.e., a description of the dispersion composition of the drop flow. Obtaining such an information is also a part of the experimental verification of the model of a polydisperse jet, considered here.

Thus, the general task of the given study can be accomplished by solving successively the following two concrete problems.

One of these involves an experimental determination of the analytical form of the spraying density and drop size distribution functions. These functions appear in the boundary conditions of the equations constituting the gas-fluid jet model [2].

The other consists in solving the equations of the model of a gas-fluid jet with the specified boundary conditions and in verifying the adequacy of the gas-fluid jet model by comparing the obtained solution

1070-4272/02/7502-0235 $27.00 © 2002 MAIK "Nauka/Interperiodica"

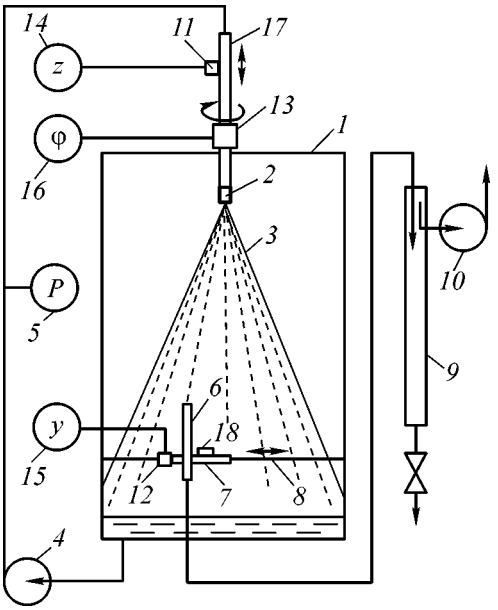

Fig. 1. Schematic of experimental setup: (*1*) chamber; (*2*) atomizer; (*3*) flare; (*4*) pump; (*5*) pressure gage; (*6*) drop trap; (*7*) slide; (*8*) rail; (*9*) separator; (*10*) suction pump; (*11*) vertical coordinate transducer; (*12*) horizontal coordinate transducer; (*13*) flare rotation angle transducer; (*14–16*) voltmeters showing, respectively, the vertical and horizontal coordinates and the angle of flare rotation with respect to a given point; (*17*) tube; and (*18*) cuvette.

to the model equations with experimental data on the spraying density at different distances from the atomizer nozzle.

The experimental setup for studying the hydrodynamics of gas-fluid jets includes chamber *1* with transparent Plexiglas walls, 1.7 m high and 1.2×1.2 m in cross-section. (Fig. 1). A centrifugal-jet atomizer *2* with nozzle diameter of 3 mm and cross-shaped insert serving to create a rather broad flare *3* filled with water drops is mounted in the upper part of the chamber.

As is known, the centrifugal-jet atomizer is a characteristic type of single-flare atomizers. Water flows down to the chamber bottom and then is again fed into the atomizer *2* by a pump *4*. The water pressure before the atomizer is measured with a pressure gage *5*. This pressure was 6 atm in the experiments. The study was performed with an atomizer with nozzle diameter of 3 mm.

The system for measuring the spraying density includes the following elements: drop trap *6*, slide *7*, rail *8*, separator *9* in the upper part, and suction pump *10*. The experimental setup makes it possible to determine the coordinates of a point at which the spraying density is measured, namely, the radial coordinate y and the rotation angle φ of a flare of atomized fluid relative to the given point. The systems for measuring the values of z, y, and φ include resistance transducers *11–13* and digital voltmeters *14–16*, respectively.

The specific feature of the experimental setup consists in that the flare position relative to the trap can be varied by moving the tube *17* in vertical direction and rotating it together with the rigidly fixed atomizer. This allows the trap to be placed at a certain radial angle φ with respect to the flare at a prescribed distance z from the atomizer nozzle. The radial displacement y of the trap is effected by slider *7* moved along rail *8* by an actuating motor with remote control.

The spraying density is measured at any prescribed point of the flare as follows. Drops arriving at the trap pass through its frontal opening having a sharp edge. The sharp edge of the entrance opening of the trap ensures better correspondence between the cross-sectional area of the fluid flow coming into the trap from the flare and the area of the entrance opening of the trap.

A minor amount of air finds its way into the trap together with the fluid. The gas-fluid mixture formed in the trap is transported into separator *9* by suction pump *10*.

As separator serves a burette with a glass tube in contact with the burette wall in its upper part. The fluid passes through the glass tube and flows down along the burette walls. Air is evacuated from the upper part of the separator by the suction pump *10*.

The time τ (s) in which the fluid volume in the burette increases by a prescribed amount V (m^3) is measured. The spraying density J ($m\ s^{-1}$) at a prescribed point of the flare is found using the formula

$$J = V/(F\tau), \qquad (1)$$

where F is the area of the frontal opening of the drop trap (m^2).

Strictly speaking, the flow rate of air evacuated by the suction pump from the separator is to be such that the isokineticity condition, according to which the velocity of the air flow approaching the trap must be equal to the velocity of air in its the entrance cross-section, should be satisfied in fluid uptake by the trap from the polydisperse flow. Satisfying this conditions makes it possible to assert that the gas flow velocity in the drop trapping zone and, consequently, the trajectories of entrapped drops (especially fine

drops) remain invariable in the course of spraying density measurements. Correspondingly, also invariable is the fluid flow in the trap and, consequently, no error occurs in determining the spraying density, all other measurement conditions being the same.

It was established in the experiments performed that varying within certain limits the flow rate of air evacuated by the suction pump from the separator does not lead to any noticeable changes in the results of spraying density measurements, all other experimental conditions being the same. This means that, in the given range of variation of the rate of the air flow passing through the suction pump, minor violations of the isokineticity condition have no essential effect on the accuracy with which the spraying density is determined. In this connection, the spraying densities measured at rates of air flow through the suction pump, falling within the mentioned interval, were used in further calculations.

The experimentally determined spraying densities, obtained at a distance of 0.2 m from the atomizer nozzle, are given in Fig. 2. Each of these values is a result of averaging of eight measurements done with the flare rotation angle successively changed by 45°. It is assumed that the type of spraying density distributions in flare cross-sections lying higher than the 0.2-m level are similar to the given one. On the basis of this assumption, the type of function, illustrated by Fig. 2, was used to formulate boundary conditions for the equations of the model at $z = 0$. To make, if necessary, convenient recalculation of spraying densities for different vertical coordinates z, the spraying densities and flare radius R are presented in Fig. 2 as, respectively, dimensionless quantities I and x. In this case,

$$I = J/\bar{J}, \tag{2}$$

where the average spraying density J is determined in a section circumscribed by a circle of radius R.

Within this section is contained 95% of the flow of atomized fluid.

The radius R was determined experimentally using the formula

$$0.95G_0 = 2\pi\rho_f\int_0^R Jy\,dy, \tag{3}$$

where G_0 is the rate of fluid flow through the atomizer (kg s^{-1}).

The flow coefficient of the fluid passing through the nozzle was determined by the formula

$$\mu = \frac{4G_0}{\pi d_n\sqrt{2P\rho_f}}, \tag{4}$$

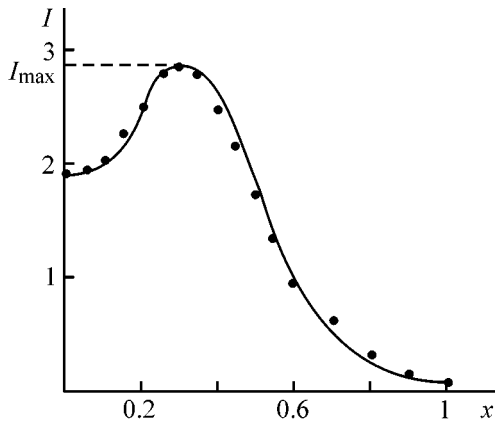

Fig. 2. Plot of the function approximating the experimentally obtained values of the spraying density distribution function. Distance from atomizer nozzle 0.2 m. (I) Relative spraying density and (x) relative radial coordinate.

where P is the fluid pressure before the nozzle (Pa), d_n the nozzle diameter (m), and ρ_f the fluid density (kg m^{-3}).

The aperture angle of the flare of the gas-fluid jet was calculated by the formula

$$\alpha = 2\arctan(R/z). \tag{5}$$

The dimentionless radial coordinate x was calculated by the formula

$$x = y/R. \tag{6}$$

The formula used to approximate the experimental dependence $I = f(x)$ was derived in this study:

$$I = \frac{a}{1 + bx^n} - \frac{c}{1 + dx^n}, \tag{7}$$

where a, b, c, and d are distribution constants.

The curve in Fig. 2 was obtained at the following values of the constants appearing in formula (7)

$$a = 3.0,\ b = 49.0,\ c = 1.06,\ d = 32\,544,\ n = 6.4. \tag{8}$$

The mean error of approximation was 3%.

The dispersion composition of drops of the atomized fluid was determined using the known procedure [5] which consists in drop catching with cuvette *18* containing an immersion medium and subsequent photographing and analysis of the obtained images. As immersion medium served transformer oil.

Drop sampling into the cuvette was done by cutting off a part of the drop flow with a shutter. The proce-

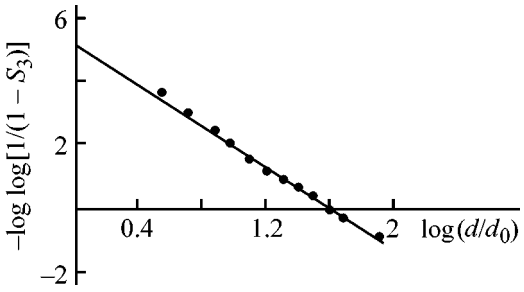

Fig. 3. Experimental distribution function S_3 of the total volume of fluid drops with respect to their size d. Fluid pressure before atomizer, P = 6 atm; atomizer nozzle diameter $d_n = 3 \times 10^{-3}$ m; constant $d_0 = 10^{-5}$ m.

dure ensured capture of a sufficiently large number of drops, which, however, was not large enough to lead to drop merging and overlapping of drop images on a photograph. Drops were photographed in the immersion medium on the background of a coordinate scale, using a Zenit camera with attachment rings. The obtained negatives were projected onto a screen and the size distribution of caught drops was determined.

As is known, the actual drop size distribution in fluid atomization with an atomizer is best described by the integral Rosin–Rammler distribution [5]

$$S = 1 - \exp[-(d/a)^l], \quad (9)$$

where d is drop diameter, and a and l are the distribution constants.

To determine the constants a and l from experimental data, it is necessary to reduce Eq. (2) to linear form

$$-\log\log[1/(1-S)] = 0.3622 + l[\log(a/d_0)] - l[\log(d/d_0)], \quad (10)$$

where d_0 is the constant preset to define the argument scale.

The integral drop size distribution function S for the total volume of drops captured by the cuvette was determined from its values S_j calculated by the formula

$$S_j = \frac{\sum_{i=1}^{j} K_i d_i^3}{\sum_{i=1}^{m} K_i d_i^3}, \quad (11)$$

where d is the average drop size of i-th fraction; K_i the number of drops in i-th fraction; and j the running number of i-th fraction, i = 1, 2, ..., j, ..., m, where m is the total number of fractions used in the measurements.

To calculate S_j by means of formula (4), the number of drops, K_i, was calculated in each of the 14 fractions, into which was divided the whole ensemble of the drops being analyzed, and their average diameter d_i was determined.

For an atomizer with nozzle diameter of 3 mm and water pressure of 6 atm, the diameter of drops constituting the main part of the sample varied within 20–500 μm. The results of measurements processed using formulas (3) and (4) are presented in Fig. 3 which makes it possible to find graphically the constants a and n of the Rosin–Rammler distribution. Constant n is numerically equal to the slope of the straight line in Fig. 3, and constant a, to the intercept on the abscissa axis.

Experimental data processing gave the following values of constants a and n

$$a = 0.34 \times 10^{-3}\,\text{m}, \quad n = 3.1. \quad (12)$$

In this case, the mean error of approximation, i.e., the mean deviation of the S value calculated by formula (9) with account of the obtained constants from the values S_j found experimentally with the use of formula (11) was 6%.

The obtained distribution functions (7) and (9) were used in calculating the spraying density at different distances from the atomizer by means of equations of the hydrodynamic model of free flare [1, 2]. These functions made it possible to specify the boundary conditions for the first and second zones of the jet. The first zone, characterized by fluid jet breakup into drops, is defined in the range from z = 0 to $z = L$ [1], where z is the axis of a cylindrical system of coordinates, coinciding with the atomizer axis and L is the distance from the atomizer nozzle exit section, which is the boundary of that region of gas-fluid jet flow at which the process of fluid flow breakup into drops is considered complete.

In [1], the L value is found from the condition that the volume content β of fluid at any point of the second zone of the jet should be less than 0.02. In calculating the flow of a gas-fluid jet, its cross-section was divided by concentric circles into 16 parts, each belonging to some i-th jet. The partitioning of the gas-fluid jet in question into separate jets, used in the calculation, is presented in Table 1.

It was found that dividing the jet cross-section into more than 16 parts does change significantly the results of calculation of the gas-fluid jet parameters.

As the maximum value of the dimensionless flare radius x_{16} was chosen the value 1.23, which accounted for 99% of the fluid outflow from the atomizer. The x_{16} value was determined from the equality

$$1.9\int_0^{x_{16}} I x \mathrm{d}x = 0.99. \quad (13)$$

The quantity y_i, necessary for specifying the conditions at the boundary of the first flow zone of the gas-fluid jet, was determined using formula (6)

$$y_i = R_\mathrm{n} x_i. \quad (14)$$

The distribution of the fluid flow rate among jets in the first flow zone of the gas-fluid jet, presented in Table 1, was found using the relation

$$G_i = 1.9 G_0 \int_{x_{i-1}}^{x_i} I x \mathrm{d}x. \quad (15)$$

In determining the type of boundary conditions for the second flow zone, characteristic geometric parameters—boundaries between the first and second zones, R and L, were calculated using the formulas

$$R = R_\mathrm{n}\sqrt{I_\mathrm{max}/\beta},\ \beta = 0.02; \quad (16)$$

$$L = \frac{R - R_\mathrm{n}}{\tan(d/2)}. \quad (17)$$

From formulas (16) and (17) follows that R and L depend on I_max, which is determined by the spraying density distribution function. It follows from Fig. 2 that I_max = 2.86, with R = 18 mm and L = 75 mm. In writing down the boundary conditions for the second flow zone of the gas-fluid jet, the polydispersity of the drop flow was accounted for by a distribution function defined by expressions (9) and (12). The drop flow passing through section $z = L$ was divided into six fractions. This decomposition is presented in Table 2.

The quantity h is defined by

$$h = d/a. \quad (18)$$

Its introduction is to some extent convenient in view of the use of the Rosin–Rammler distribution function (9).

The quantity d_j in Table 2 is average volume-surface Sauter diameter for each of the distinguished fractions of the drop flow

$$d_j = a(S_j - S_{j-1}) \Big/ \left(\int_{h_{j-1}}^{h_j} \frac{1}{h}\frac{\partial S}{\partial h}\mathrm{d}h \right). \quad (19)$$

Table 1. Partitioning of the gas-fluid flow into separate jets

i	x_i	$G_i \times 10^3$, kg s^{-1}	i	x_i	$G_i \times 10^3$, kg s^{-1}
1	0.1	4.57	9	0.55	20.6
2	0.2	15.3	10	0.6	16.7
3	0.25	14.1	11	0.65	12.9
4	0.3	18.4	12	0.7	9.62
5	0.35	21.7	13	0.8	12.2
6	0.4	24.0	14	0.9	6.65
7	0.45	24.7	15	1.0	3.74
8	0.5	23.5	16	1.23	3.86

Table 2. Decomposition of the drop flow passing through section $z = L$ into fractions*

j	h_j	d_j, μm	$S_j - S_{j-1}$
1	0.5	117	0.110
2	0.7	202	0.172
3	0.9	268	0.232
4	1.1	333	0.225
5	1.3	398	0.156
6	∞	453	0.105

* j is the fraction index, and h_j is the relative drop diameter setting the upper limit of a fraction.

The difference of the distribution function values S_j and S_{j-1} for j-th fraction has a meaning of the volume fraction of the fluid flow which is accounted for by j-th fraction. From expression (9) follows that this fraction is given by

$$S_j - S_{j-1} = \exp(-h_{j-1}^l) - \exp(-h_j^l). \quad (20)$$

The flow rates G_{kj} of fluid in jets with certain fraction composition, necessary for setting the boundary conditions [2], was calculated with account of the volume fractions of the fluid in the drop flow in each fraction by the formula

$$G_{kj} = G_i(S_j - S_{j-1}) \text{ at } k = i. \quad (21)$$

Thus, the boundary conditions obtained for the first flow zone of the gas-fluid jet at $z = 0$ are defined by relations (14) and (15) and parameter values in Table 1. The boundary conditions for the second flow zone at $z = L$ are defined by relations (17) and (19)–(21) and parameter values in Table 2. The obtained kind of boundary conditions reflects all specific

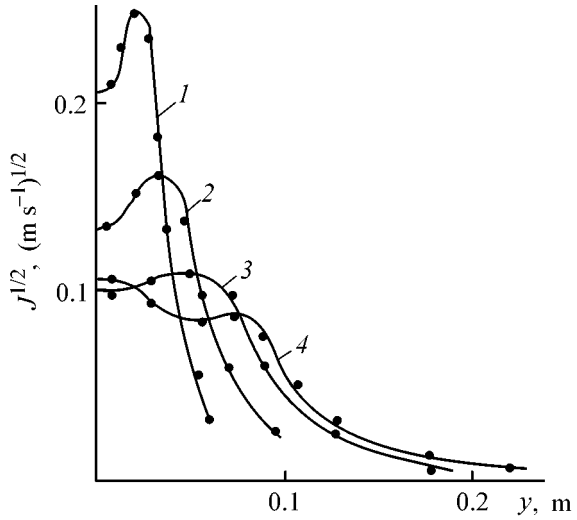

Fig. 4. Distribution of spraying density J along the radius of the flare of the gas-fluid jet. Fluid pressure before atomizer 6 atm, atomizer nozzle diameter $d_n = 3 \times 10^{-3}$ m, flare aperture 25°. Distance from the atomizer nozzle (m): (*1*) 0.3, (*2*) 0.7, (*3*) 0.9, and (*4*) 1.1.

features of the jet flow in the experimental setup under consideration. Therefore, the spraying density distribution at different distances from the atomizer nozzle, found theoretically by solving the equations of the model of the gas-fluid jet just with these boundary conditions, makes it possible to confirm the adequacy of the model correctly, by comparing this distribution with the results of its study on the experimental setup under consideration.

This comparison is illustrated by Fig. 4. The average discrepancy of the theoretical and experimental results does not exceed 7%. The results obtained in the performed experimental study of the flow of a free polydisperse gas-fluid jet confirm the possibility that the type of the spraying density distribution may change with distance from the atomizer nozzle. For example, if this distance is 0.30 m, the spraying density distribution virtually coincides with the initial distribution of this quantity, which has a minimum on the Z axis (Fig. 4), in full agreement with the theoretical results obtained in [2].

It is important to note that calculation of the jet under consideration without taking into account its polydispersity gives no way of revealing theoretically changes in the nature of the spraying density distribution with distance from the atomizer nozzle. The results of an experimental study concerned with this issue confirmed that the spraying density increases in the near-axis region of jet flow through displacement of finely dispersed drop fractions from the periphery of the gas-fluid jet toward its central part. This displacement occurs because of the radial gas motion inside the jet.

The general form of the spraying density distribution with a minimum and maximum at the Z axis, obtained in this study experimentally at different distances from the atomizer nozzle, is, as is known [3], rather characteristic of centrifugal-jet atomizers. It has been believed until now that the type of these distributions is only determined by design features of the atomizer itself and its operation mode and does not change in the development of a gas-fluid jet. However, a study of the hydrodynamics of a polydisperse gas-fluid jet, carried out in the present work, established experimentally that the spraying density distribution also changes in the process of development of this jet, and the dispersion composition of the drop flow affects the nature of this change. Hence follows that hydrodynamic calculation of a free polydisperse gasfluid jet is to be carried out with account of the dispersion composition of the drop flow.

CONCLUSIONS

(1) An experimental study of a gas-fluid jet outflowing from a single-flare atomizer confirms the adequacy of the hydrodynamic model developed in previous investigations of the authors.

(2) The possibility of a significant change in the nature of spraying density distribution in a free polydisperse gas-fluid jet with distance from the atomizer nozzle was confirmed experimentally.

(3) A strong influence exerted by the polydispersity of a drop flow on how the spraying density distribution function changes with distance from the atomizer nozzle was revealed.

REFERENCES

1. Aniskin, S.V. and Protod'yakonova, O.I., *Zh. Prikl. Khim.*, 2001, vol. 74, no. 3, pp. 445–450.
2. Protod'yakonova, O.I., Aniskin, S.V., and Kadashevich, Yu.I., *Zh. Prikl. Khim.*, 2001, vol. 74, no. 11, pp. 1994–2000.
3. Galustov, V.S., *Pryamotochnye raspylitel'nye apparaty v teploenergetike* (Direct-Flow Spraying Apparatus in Heat- and Power Engineering), Moscow: Energoatomizdat, 1989.
4. Katalov, V.I., Gushchin, Yu.I., and Basargin, B.N., *Massoobmennye i teploobmennye protsessy khimicheskoi tekhnologii* (Mass- and Heat-Exchange Processes of Chemical Technology), Yaroslavl: Yarosl. Politekhn. Inst., 1975, issue 2, pp. 13–16.
5. Pazhi, D.G. and Galustov, V.S., *Raspyliteli zhidkostei* (Fluid Sprayers), Moscow: Khimiya, 1979.

Russian Journal of Applied Chemistry, Vol. 75, No. 2, 2002, pp. 241–244. Translated from Zhurnal Prikladnoi Khimii, Vol. 75, No. 2, 2002, pp. 249–252.
Original Russian Text Copyright © 2002 by Vorotyntsev, Drozdov, Kirillov.

PROCESSES AND EQUIPMENT OF CHEMICAL INDUSTRY

Thorough Cleaning of Argon and Germanium Tetrahydride To Remove Admixture of Water by Membrane Gas Separation

V. M. Vorotyntsev, P. N. Drozdov, and Yu. P. Kirillov

Nizhni Novgorod State Technical University, Nizhni Novgorod, Russia

OOO Firma Horst, Moscow, Russia

Received March 19, 2001

Abstract—Thorough cleaning of argon and germanium tetrahydride to remove admixture of water with gas-separating membranes of the Lestosil type was studied. Schemes of the installation and the membrane unit necessary for performing thorough cleaning are presented. The selectivity of radial counterflow membrane units was studied and a mathematical model is presented making it possible to calculate their separating power and evaluate the effect of longitudinal agitation on the cleaning process.

The method of membrane gas separation is beginning to be used for gas cleaning to remove admixture of water. For example, raw natural gas can be cleaned to remove water to a level of $(1.4–1.5) \times 10^{-2}$ vol %, using cellulose acetate membranes [1]. Cleaning of nitrogen to remove water was studied in [2], and that of argon and helium, in [3, 4]. Of interest is to study the process of thorough cleaning of gases to remove admixture of water with highly permeable commercial membranes based on polydimethylsiloxane (of the Lestosil type).

The aim of this work was to study theoretically and experimentally the process of thorough cleaning of gases to remove admixture of water with a membrane of the Lestosil type for the example of germanium tetrahydride and argon.

The cleaning installation is shown schematically in Fig. 1. It comprises a unit for preparing a model mixture and sections for cleaning and analysis. The model mixture is prepared by bubbling a gas under study, contained in cylinder *1*, through water in vessel *2*. The gas pressure in vessel *2*, determining the concentration of water impurity at the temperature of experiment (293 K) is set with reducer *3* and monitored with pressure gage *4*. Reducer *5* is used to set the gas pressure in the high-pressure zone of the membrane unit *6*, monitored with pressure gage *7*. A membrane having higher permeability to water, than to gas being cleaned is employed. In the unit, part of a gas mixture with increased content of water impurity passes through the membrane into the low-pressure zone and may condense in cylinder *8* or be evacuated through cock *9*. Vacuum gages *10* and *11* serve for determining the pressure in the low-pressure zone. The flow rate of a cleaned gas mixture at the exit from the high-pressure zone is monitored with rotameter *12* and controlled with fine adjustment valve *13*. The rotameter *12* shows the total flow rate of the gas mixture at the unit inlet. At closed valve *13*, it shows the rate of the gas flow through the membrane into the low-pressure zone of unit *6*.

As membrane unit was used a counterflow radial element in which the gas mixture moves radially, from periphery to center, in the high-pressure zone and from center to periphery in the low-pressure zone. A schematic of the membrane unit is given in Fig. 2.

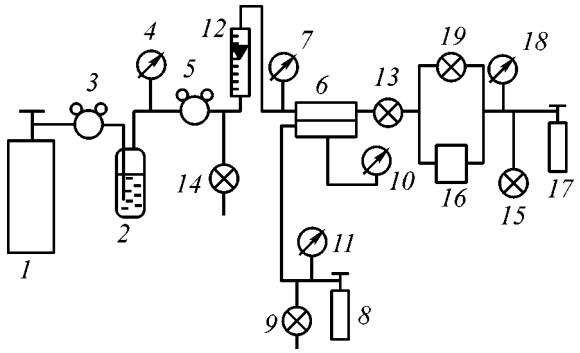

Fig. 1. Membrane installation: (*1, 8, 17*) cylinders, (*2*) bubbler, (*3, 5*) reducers, (*4, 7, 18*) pressure gages, (*6*) membrane unit, (*9, 13–15, 19*) valves, (*10, 11*) vacuum gages, (*12*) rotameter, and (*16*) dew point sensor.

1070-4272/02/7502-0241 $27.00 © 2002 MAIK "Nauka/Interperiodica"

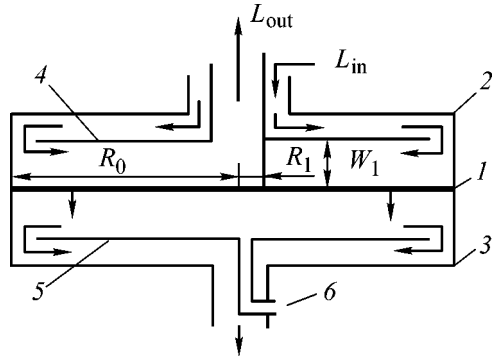

Fig. 2. Schematic of radial countercurrent membrane element: (*1*) membrane; (*2, 3*) high- and low-pressure zones, respectively; (*4, 5*) distributor disks; and (*6*) pipe for connecting a vacuum gage.

The arrows show the motion direction of the gas mixture. On the low-pressure side the membrane is supported by a plate of porous stainless steel or stainless steel mesh lying on a flange with a system of channels for gas mixture removal. The pressure difference between the central and peripheral regions in the chambers of the membrane element was not higher than 5 and 30% in the high- and low-pressure zones, respectively. The clearance in the high-pressure zone of the membrane element, W_1 = 0.1 cm, and the radius of the outlet channel from the high-pressure cavity, R_1 = 0.1 cm.

To perform a thorough cleaning of gases to remove admixture of water, it is necessary to eliminate the effect of the apparatus material, associated with diffusion of water vapor from air through polymeric lining and its desorption from apparatus walls. Therefore, the shut-off valves and fine adjustment stopcocks used in the line for discharge of cleaned gas from the membrane element have no polymeric sealing materials. To eliminate the possibility of water desorption from the apparatus walls, the installation was purged (through valves 9, 14, and 15) with dried gas to make the concentration of water level lower than the minimum experimentally observed value in cleaned gas. Further, a unit for model mixture preparation was connected to the installation, and experiments with a minimum rate of product removal and maximum cleaning efficiency were performed. Then the rate of removal of a cleaned gas mixture was raised using the fine adjustment cock, and, after the installation attained the steady-state mode, the impurity concentration under given process conditions was determined.

In membrane units, the membrane between flanges is sealed with polymeric linings. In the element employed, the sealing lining is situated on the periphery, and, therefore, a gas with water content close to the initial value, rather than cleaned gas, is in contact with polymer linings in both chambers of the unit. This is due to the fact that the gas mixture being cleaned moves from periphery to center in the high-pressure zone of the element, and as a counterflow, from center to periphery, in the low-pressure zone.

In the experiments, a membrane of the Lestosil type with working part diameter of 25.8 cm was used. Membranes of this type show rather high selectivity in separation of water vapor and a number of volatile inorganic hydrides and inert gases. For example, the ratio of permeabilities (separation factor) is 30 for water vapor and argon and 9.5 for water vapor and germanium tetrahydride. The membrane permeabilities to argon and GeH_4 are, respectively, 0.37×10^{-7} and 1.2×10^{-7} mol s^{-1} m^{-2} Pa^{-1}. It was also found that membranes of the given type retain their properties (selectivity and permeability) in inert gases and high-purity GeH_4 for more than three years.

The gases were analyzed for water content with a dew point sensor *16* preliminarily calibrated with a Baikal 3M coulometric hygrometer for low H_2O concentrations. As dew point was taken arithmetic mean temperature of appearance and disappearance of dew. The analysis error determined by the difference of temperatures of dew appearance and disappearance did not exceed 5 and 25% for the experimentally determined maximum and minimum concentration of water, respectively. The rate of gas flow through the sensor was maintained constant, the excess amount of the gas mixture was discharged through an additional line. The pressure in the line of analysis was determined with pressure gage *18*.

In experiments, the separating power of a membrane element (separation factor F) was found as a ratio of concentrations of water in the initial and cleaned mixture, discharged from the high-pressure zone of the element. The initial concentration of water was determined on the installation in the absence of pressure drop across the membrane, i.e., without evacuation of the gas mixture from the low-pressure zone of the element. The initial concentration coincides with the equilibrium content of water, corresponding to water temperature and gas pressure in the vessel for model mixture preparation.

Figure 3 presents experimental values of the separation factor of the membrane element in relation to the reciprocal of the degree of product discharge, $l_{out}^{-1} = L_{in}/L_{out}$. It can be seen that the efficiency of cleaning grows with decreasing rate of product discharge. At equal rates of product discharge, a greater

separation factor is observed for a mixture of argon with water impurity, for which the separation coefficient is higher.

A theoretical study of thorough cleaning of argon and germanium tetrahydride was carried out using equations taking into account the longitudinal mixing of the impurity in the element zones [4]:

$$\frac{1}{\mathrm{Pe}_1}\frac{\mathrm{d}^2c_1}{\mathrm{d}r^2} + \frac{1}{r}\left[\frac{1}{\mathrm{Pe}_1} + 1 - \frac{h}{2}(1 - P)(1 - r^2)\right]\frac{\mathrm{d}c_1}{\mathrm{d}r} + h(1 - \alpha - P)c_1 + Phc_2\alpha = 0, \quad (1)$$

$$\frac{1}{\mathrm{Pe}_2}\frac{\mathrm{d}^2c_2}{\mathrm{d}r^2} + \frac{1}{r}\left[\frac{1}{\mathrm{Pe}_2} - \frac{h}{2}(1 - P)(r^2 - r_1^2)\right]\frac{\mathrm{d}c_2}{\mathrm{d}r} + h[1 + (\alpha - 1)P]c_2 + hc_1\alpha = 0 \quad (2)$$

with boundary conditions

$$\frac{1}{\mathrm{Pe}_1}\frac{\mathrm{d}c_1}{\mathrm{d}r} + c_1 = 1, \ \frac{\mathrm{d}c_2}{\mathrm{d}r} = 0 \text{ at } r = 1, \quad (3)$$

$$\frac{\mathrm{d}c_1}{\mathrm{d}r} = 0, \ \frac{\mathrm{d}c_2}{\mathrm{d}r} = 0 \text{ at } r = r_1, \quad (4)$$

where $c_1 = C_1/C_{1\,\mathrm{in}}$, $c_2 = C_2/C_{1\,\mathrm{in}}$, $r = R/R_0$, $r_1 = R_1/R_0$, $\alpha = Q_\mathrm{A}/Q_\mathrm{B}$, $P = P_2/P_1$, $\mathrm{Pe}_1 = V_\mathrm{in}R_0/D_1$, $\mathrm{Pe}_2 = V_\mathrm{in}W_1R_0/(W_2D_2)$, $h = 2\pi R_0^2Q_\mathrm{B}P_1/L_\mathrm{in}$, $L_\mathrm{in} = 2\pi R_0W_1V_\mathrm{in}\rho$; C is the impurity concentration (mole fraction); D the coefficient of longitudinal mixing ($\mathrm{m^2\ s^{-1}}$); L the flow rate of the gas mixture ($\mathrm{mol\ s^{-1}}$); P the pressure of the gas mixture; Q the membrane permeability ($\mathrm{mol\ m^{-2}\ s^{-1}\ Pa^{-1}}$), R_0 the radius of the working part of the membrane (m); R_1 the radius of a channel for gas mixture discharge from the high-pressure zone (m); R the coordinate along the membrane radius (m); V the gas flow velocity ($\mathrm{m\ s^{-1}}$); W the clearance in a zone (m); ρ the gas density ($\mathrm{mol\ m^{-3}}$); indices: (*1*) high-pressure zone, (*2*) low-pressure zone, (A) impurity component, (B) main component, and (in) inlet of the high-pressure zone.

Equations (1)–(4) describe separation in a membrane element in the case of low impurity concentration in the initial mixture as compared with the concentration of the main component. These equations account for the influence exerted by longitudinal mixing of the impurity in the element cavities on the separation process.

From Eqs. (1)–(4) can be derived two limiting expressions for the separation factor

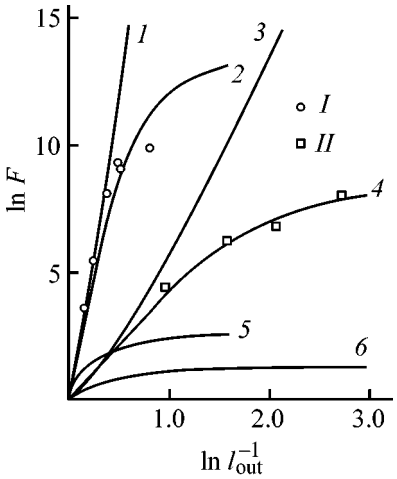

Fig. 3. Separation factor F vs. degree of product discharge l_out. Gas mixture composition: (*1, 2, 5*) argon–water impurity and (*3, 4, 6*) germanium tetrahydride–water impurity. Calculation by equation: (*1, 3*) (5), (*2, 4*) (1)–(4), and (*5, 6*) (6). Experimental data for mixture of water impurity with (*I*) argon and (*II*) germanium terahydride.

$$F = l_\mathrm{out}[1 + h_1(1 - l_\mathrm{out})^{-h_2}\psi(1), \quad (5)$$

$$F = \alpha^* - (\alpha^* - 1)l_\mathrm{out}, \quad (6)$$

where $h_1 = \alpha/(1 - P)$, $h_2 = P\alpha/(1 - P)$, $l_\mathrm{out} = L_\mathrm{out}/L_\mathrm{in}$, $\psi(1) = \int_{l_\mathrm{out}}^{1} l^{-(1+h_1)}(l - l_\mathrm{out})^{h_2}\mathrm{d}l$, $l = L(R)/l_\mathrm{in}$ the running relative flow rate of the gas mixture in the high-pressure zone, $L(R) = 2\pi R_0W_1V(R)\rho$, $\alpha^* = \alpha/[1 + (\alpha - 1)P]$ the effective separation coefficient, $V(R)$ the gas flow velocity in the high-pressure zone at a point with coordinate R ($\mathrm{m\ s^{-1}}$), the index "out" refers to the outlet of the high-pressure zone.

Expressions (5) and (6) correspond, respectively, to the ideal displacement mode in both zones ($\mathrm{Pe}_1 >> 1$, $\mathrm{Pe}_2 >> 1$) and complete mixing mode in the element cavities ($\mathrm{Pe}_1 << 1$, $\mathrm{Pe}_2 << 1$). At $P = 0$, relation (5) gives a simple expression

$$F = l_\mathrm{out}^{(1-\alpha)}. \quad (7)$$

Equation (7) characterizes the maximum possible separating power of the membrane unit. Under real conditions, the limiting values of F, according to Eqs. (5) and (7), are not reached because of the influence of longitudinal mixing, always occurring to some extent in the element zones.

Figure 3 presents theoretical and experimental dependences of the separation factor on the reciprocal of the degree of product discharge, l_out^{-1}, and also theoretical formulas for the limiting formulas (5) and (6)

for the systems argon–water impurity (curves *1* and *5*) and germanium tetrahydride–water impurity (curves *3* and *6*). Experimental points lie between the limiting curves corresponding to formulas (5) and (6). This means that in the membrane element zones there exists longitudinal mixing affecting the separation process and depending on the diffusion coefficients, concentration gradients, and gas flow nonuniformity.

The dependences of the separation factor on the product discharge rate, calculated numerically using the initial equations (1)–(4), were compared with experimental data. It was assumed in theoretical calculations that molecular diffusion occurs in the high-pressure zone, for which the diffusion coefficient can be calculated in terms of the kinetic theory of gases, using the Chapman–Enskog equation [5]. The parameters of the intermolecular potential of GeH_4 were taken from [6].

From the condition of minimum rms discrepancy of the theoretical and experimental dependences were found the values $W_2D_2 = 0.055$ cm^3 s^{-1} (argon–water impurity) and $W_2D_2 = 0.164$ cm^3 s^{-1} (germanium tetrahydride–water impurity) characterizing the longitudinal mixing in the low-pressure zone of the employed membrane units. The extent to which longitudinal mixing affects the cleaning efficiency can also be evaluated on the basis of Fig. 3 by the discrepancy between the experimental points and the limiting curves *5* and *6*. It can be seen that the separation conditions are closer to the ideal displacement conditions for argon, compared with GeH_4. This may be associated with the difference in W_2 values, associated with the low-pressure zone design.

CONCLUSION

The results of the investigation performed indicate that the method of membrane gas separation can be successfully used to clean argon and germanium tetrahydride to remove admixture of water. The employed mathematical model makes it possible to calculate the separating power of a membrane unit, evaluate the longitudinal mixing and choose the optimal technological parameters of the process.

REFERENCES

1. Dytnerskii, Yu.I., Brykov, V.P., and Kagramanov, G.G., *Membrannoe razdelenie gazov* (Membrane Separation of Gases), Moscow: Khimiya, 1991.
2. Pukh, N.N., Saprykin, V.L., Rozhanchuk, V.N., *et al.*, *Khim. Tekhnol.*, 1990, no. 1, pp. 65–68.
3. Drozdov, P.N. and Nosyrev, S.A., *Vysokochist. Veshchestva*, 1993, no. 3, pp. 111–114.
4. Vorotyntsev, V.M., Drozdov, P.N., Kirillov, Yu.P., and Skryagin, V.N., *Teor. Osn. Khim. Tekhnol.*, 1999, vol. 33, no. 2, pp. 184–189.
5. Reid, R.G., Prausnitz, J.M., and Sherwood, T.K., *The Properties of Gases and Liquids*, New York: McGraw-Hill Book Company, 1977.
6. Devyatykh, G.G. and Zorin, A.D., *Letuchie neorganicheskie gidridy osoboi chistoty* (Volatile Inorganic Hydrides of Special Purity), Moscow: Nauka, 1974.

Russian Journal of Applied Chemistry, Vol. 75, No. 2, 2002, pp. 245–247. Translated from Zhurnal Prikladnoi Khimii, Vol. 75, No. 2, 2002, pp. 253–255.
Original Russian Text Copyright © 2002 by Grinberg, Saradzhev, Levin, Ryabenko.

ORGANIC SYNTHESIS AND INDUSTRIAL ORGANIC CHEMISTRY

Preparation of Fine Alumina Powders by Hydrolysis of Aluminum Isopropylate

E. E. Grinberg, V. V. Saradzhev, Yu. I. Levin, and E. A. Ryabenko

Federal State Unitary Enterprise, State Research Institute of Chemicals and Ultra Pure Compounds, Moscow, Russia

Received June 3, 2001

Abstract—Preparation of fine alumina powder by hydrolysis of aluminum isopropylate was studied.

Because of the stringent requirements to purity of materials used in modern industry, a necessity arises for using new raw materials, such as organic compounds of many classes. Prominent among them are metal alcoholates [1]. Hydrolysis, thermolysis, oxidation, and plasma degradation of these compounds are widely used to prepare high-purity metal oxides or hydroxides (sols and gels) [2, 3]. The higher stability of these colloids as compared with those prepared, e.g., by hydrolysis of metal halides is due to the complete absence of ions promoting sol coagulation [4]. Colloid solutions of metal hydroxides obtained from the corresponding alcoholates are widely used as film-forming agents for preparing coatings (e.g. Al_2O_3) by the "solution technology" [5–9].

Topical tasks in development of a procedure for preparing metal oxides by hydrolysis of the corresponding alcoholates are study of the mechanism and determination of the best conditions of formation of metal hydroxide gels. This stage involves determination of particle size, conditions for metal hydroxide dehydration (i.e., temperature of formation of metal oxides), surface area of the powders, their tendency to cake, etc. [4]. The demand for fine powders of high-purity aluminum oxides and hydroxides steadily grows. A promising procedure for preparing 5–30-μm alumina powders is hydrolysis of aluminum isopropylate [10].

As regards to physicochemical properties, aluminum isopropylate is the best suited for industrial production among aluminum alcoholates. The aluminum content in aluminum isopropylate is relatively high and the liquid phase of this compound exists in a wide temperature range which allows its purification by distillation. However, the requirements of high dispersity and purity of the product become mutually conflicting under conditions of liquid-phase hydrolysis. Preparation of fine alumina powder by liquid-phase hydrolysis is complicated by aggregation of the product and incorporation of isorpopanol and water in it. Introduction of various compounds maintaining the dispersity of the system decreases the purity of the product. Hydrolysis under conventional conditions yields highly hydrated aluminum oxides or their mixtures with variable composition. In addition, great volumes of dilute isopropanol solutions formed in this process are difficult to utilize.

A study of hydrolysis of aluminum isopropylate under various conditions showed [11] that the best procedure for preparing fine alumina powder is hydrolysis of aluminum isopropylate by steam, which can be performed as a single-step process:

$$2Al(OPr\text{-}i)_{3(l)} + 4H_2O = Al_2O_3 \cdot H_2O_{(s)} + 6i\text{-}PrOH_{(s)}.$$

In addition, easy control of the water-to-alcoholate ratio makes lower the water consumption and the yield of waste hydrolyzate.

EXPERIMENTAL

Aluminum isopropylate was hydrolyzed in a flow reactor. An aluminum isopropylate melt was sprayed into a reactor with a carrier gas through an injection nozzle. The reactor was heated to 120–160°C and purged simultaneously with steam fed from a steam generator, until the required temperature was reached at the outlet and water drops on the lid and walls of the reactor completely disappeared. Then a melt of aluminum isopropylate was charged into a preheated

1070-4272/02/7502-0245 $27.00 © 2002 MAIK "Nauka/Interperiodica"

Table 1. Conversion K of aluminum isopropylate into boehmite and the particle size d of alumina powder formed by spraying of $Al(OPr\text{-}i)_3$ melt with various carrier gases (temperature inside the reactor 130°C)

Carrier gas	P_n, mm Hg	Feed rate, g min^{-1}		Q_s, mol mol^{-1}	K, wt %	d, μm
		$Al(OPr\text{-}i)_3$	steam			
Technical-grade nitrogen	62	57	20	16.2	81	2–20
Argon	68	34	20	10.0	83	2–20
Air	61	47	20	13.2	82	2–20

Notes: P_n is the residual pressure in the nozzle; Q_s is the overstoichiometric excess of steam.

Table 2. Conversion K of aluminum isopropylate into boehmite and particle size d of alumina at different temperatures of steam–gas mixture inside the reactor

T, °C	P_n, mm Hg	Feed rate, g min^{-1}		K, wt %	d, μm
		$Al(OPr\text{-}i)_3$	steam		
120	63	34	20	85	2–20
140	65	35	20	83	2–20
160	62	34	20	84	2–20

melter and sprayed through the nozzle with a carrier gas fed from a cylinder. Solid hydrolysis products were deposited on the lid and walls of the reactor, and the steam–gas mixture was passed through a condenser where steam and isopropanol vapor were condensed and drained to an attached vessel. The carrier gas and uncondensed vapors were discharged into the atmosphere. After emptying the melter, the steam feed was stopped and the hydrolysis was terminated. The steam generator was detached and reactor was purged with the carrier gas for 5–10 min to remove residual water vapor. Then the reactor was cooled, and the solid hydrolysis products were unloaded. The samples of the powder and condensate were weighed and analyzed.

To optimize the process parameters, we studied the hydrolysis as influenced by the nature of the carrier gas. For example, air can oxidize aluminum isorpopylate and affect the particle size distribution of the hydrolysis products.

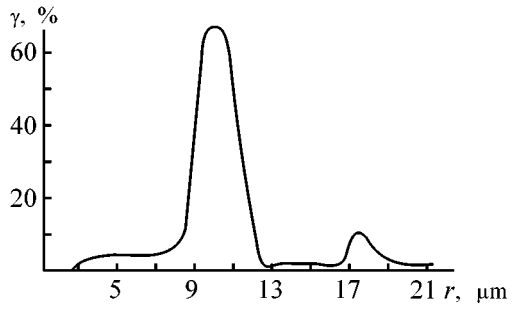

Particle size distribution of alumina: (γ) fraction of particles of size r.

The results of experiments with argon, nitrogen, and air as carrier gases are presented in Table 1. The quality of hydrolysis products and the hydrolysis rate are independent of the nature of the carrier gas. Feeding steam in a tenfold excess over the stoichiometry has no effect on the hydrolysis.

As seen from Table 2, varying the temperature of the steam-gas mixture inside the reactor in the range 120–160°C has no effect on the particle size distribution and degree of hydrolysis of aluminum isopropylate.

The hydrolysis products were studied by DTA and powder X-ray diffraction. The particle size distribution was also determined. All the samples studied were found to be boehmite AlOOH, rather than $Al(OH)_3$ as would be expected from the moderate temperatures in the reaction zone.

The samples were calcined at 550–700°C. After this treatment γ-alumina powders were formed without agglomeration and caking. The particle size ranged from 2 to 20 μm (see figure). The BET surface area of γ-alumina was in the range 235–295 m^2 g^{-1}. This allows considerable simplification of the process flowsheet.

Table 3. Content of impurities in initial aluminum isopropylate and γ-alumina

Compound	Content, wt %									
	Fe	Mn	Ni	V	Cu	Ga	Mg	Na	Si	Cr
$Al(OPr\text{-}i)_3$	10^{-5}	$<10^{-6}$	$<10^{-6}$	$<10^{-6}$	2×10^{-5}	3×10^{-3}	10^{-5}	$<10^{-5}$	3×10^{-4}	$<10^{-6}$
Al_2O_3	2×10^{-4}	3×10^{-6}	3×10^{-6}	$<10^{-6}$	8×10^{-5}	10^{-2}	2×10^{-4}	3×10^{-5}	8×10^{-4}	5×10^{-6}

The slight increase in the impurity content in γ-alumina as compared with the initial aluminum isopropylate (Table 3) is due to a decrease in the weight of the target product. Thus, no additional impurities are introduced in the stages of hydrolysis and calcination, which confirms our initial assumptions.

CONCLUSIONS

(1) Aluminum isopropylate is hydrolyzed with a steam flow by spraying of its melt.

(2) The product of hydrolysis at 120–160°C is a boehmite powder. The chemicals and materials used in this process require no additional purification.

(3) Alumina powders prepared by this procedure do not agglutinate and agglomerate. The deviation of the particle size from the average value is negligible.

REFERENCES

1. Novoselova, A.V., Turova, N.Ya., Turevskaya, E.P. *et al.*, *Izv. Akad. Nauk SSSR, Neorg. Mater.*, 1979, vol. 15, no. 6, pp. 1055–1067.
2. Razuvaev, G.A., Gribov, B.G., Domrachev, G.A., *et al.*, *Metalloorganicheskie soedineniya v elektronike* (Organometallic Compound in Electronics), Moscow: Nauka, 1972.
3. Suikovskaya, N.V., *Khimicheskie metody polucheniya tonkikh prozrachnykh plenok* (Chemical Methods for Preparing Thin Transparent Films), Leningrad: Khimiya, 1971.
4. Zakutinskii, V.L., Study and Development of a Vapor-Phase Procedure for Preparing Finely Divided Aluminum Oxides, *Cand. Sci. Dissertation*, Sverlovsk, 1969.
5. Kozunov, V.A., Synthesis and Physicochemical Study of Aluminum Isopropylate, Aluminum Isopropoxide Chlorides, and Solvate of Aluminum Chloride with Isopropanol, *Cand. Sci. Dissertation*, Moscow, 1979.
6. Zhao, Y.Z. and Zhang, Q., *Trans. NF Soc.*, 1994, vol. 4, no. 2, pp. 21–27.
7. Ogihara, T., *J. Am. Ceram. Soc.*, 1991, vol. 74, no. 9, pp. 2263–2269.
8. Tarar, S.S. and Gunay, V., *Powders Interceram.*, 1996, vol. 45, no. 4, pp. 254–260.
9. Tsai, D.-S., *J. Am. Ceram. Soc.*, 1991, vol. 44, no. 4, pp. 830–831.
10. Dudkin, B.K., Kaneva, S.I., Mastikhin, V.M., *et al.*, *Zh. Obshch. Khim.*, 2000, vol. 70, no. 12, pp. 1949–1955.
11. Zakharchenya, R.I. and Vasilevskaya, T.N., *Zh. Prikl. Khim.*, 1992, vol. 65, no. 12, pp. 2707–2715.

Russian Journal of Applied Chemistry, Vol. 75, No. 2, 2002, pp. 248–253. Translated from Zhurnal Prikladnoi Khimii, Vol. 75, No. 2, 2002, pp. 256–262.
Original Russian Text Copyright © 2002 by Puchkov, Buneeva, Perkel'.

ORGANIC SYNTHESIS AND INDUSTRIAL ORGANIC CHEMISTRY

Pathways of Liquid-Phase Oxidation of Cyclohexanol

S. V. Puchkov, E. I. Buneeva, and A. L. Perkel'

Kuznetsk Coal Basin State Technical University, Kemerovo, Russia

Received September 11, 2001

Abstract—The kinetics of product accumulation in uncatalyzed oxidation of cyclohexanol at 403 K was studied. Along with the compounds originating from oxidation of cyclohexanol at position 1 (cyclohexanone, hydrogen peroxide, 1-hydroxycyclohexyl hydroperoxide), products formed by oxidation of C–H bonds at positions 2–4 were detected: 2-, 3-, and 4-hydroxycyclohexyl hydroperoxides (*cis* and *trans* isomers), 1,2-, 1,3-, and 1,4-dihydroxycyclohexanes (*cis* and *trans* isomers), 2- and 4-hydroxycyclohexanones, and 2-cyclohexenone.

Liquid-phase oxidation of aliphatic and alicyclic hydrocarbons and their oxygen-containing derivatives to carboxylic acids is low-selective because of the multistage oxidation mechanism and possible occurrence of several transformation pathways of the substrate and intermediates [1–3].

In such processes, secondary alcohols are formed along with ketones in the stage of decomposition of secondary hydroperoxides [1–3]. It is commonly believed that their subsequent transformations mainly involve radical-chain oxidation of the activated (by a factor of 16–50 [4–6]) C–H bond at the α-position relative to the functional group, yielding 1-hydroxy hydroperoxide or ketone and hydrogen peroxide [2, 3, 7]. The possibility of oxidation of secondary alcohols at more remote C–H bonds is usually disregarded, and the reactivity of these bonds is assumed to be equal to that of the similar C–H bonds in hydrocarbons. At the same time, the contribution of alternative oxidation pathways must become more significant with increasing chain length and/or ring size in the substrates. Also, the hydroxy group exhibits electron-withdrawing properties and can deactivate the β- and γ-C–H bonds, as observed previously for the acetoxy group in reaction of cyclohexyl acetate with *tert*-butylperoxy radical [8].

The goal of this study was to evaluate, with cyclohexanol as example, the selectivity of liquid-phase oxidation of secondary alcohols. The choice of cyclohexanol was governed by the fact that, with this substrate, the reaction pattern is not disturbed by intramolecular isomerization of the peroxy radical, characteristic of long-chain aliphatic alcohols [9]. We also wished to gain insight into the mechanism of formation of degradation products in liquid-phase oxidation of cyclohexanol and cyclohexane.

EXPERIMENTAL

Cyclohexanol (analytically pure grade) was purified to remove ethers and cyclohexanone by azeotropic distillation of impurities with water, followed by treatment with a saturated solution of sodium hydrosulfite and fractional distillation in an argon flow under reduced pressure. The composition of the resulting sample was as follows (%): main substance (determined by GLC) 99.5 ± 0.1, cyclohexanol ethers (GLC) ≤ 0.01, and cyclohexanone (determined spectrophotometrically as 2,4-dinitrophenylhydrazone [10]) <0.005.

Oxidation of cyclohexanol with molecular oxygen was performed at 403 K in a glass bubbling reactor.

Separate determination of hydrogen peroxide and organic peroxides (1-hydroxycyclohexyl hydroperoxide) was performed by iodometric titration using the catalase enzyme [11]. The total content of cyclohexanone and 1-hydroxycyclohexyl hydroperoxide was determined by GLC (10% Carbowax-6000 on Chromaton N-AW-DHCS, 393 K, internal reference chlorobenzene) after reduction of the samples with triphenylphosphine, and the content of 2- and 4-hydroxycyclohexanones (in the form of acetates), on the same column at 448 K (internal reference decyl acetate). 2-Cyclohexenone was determined on a column

1070-4272/02/7502-0248 $27.00 © 2002 MAIK "Nauka/Interperiodica"

packed with Chromaton N-AW-super + XE-60 silicone at 358 K (internal reference chlorobenzene).

To determine isomeric 2-, 3-, and 4-hydroxycyclohexyl hydroperoxides (*cis*- and *trans*-) and 1,2-, 1,3-, and 1,4-dihydroxycyclohexanes (*cis*- and *trans*-), samples of oxidized alcohol were concentrated under reduced pressure, the peroxides were reduced with a 50% solution of KI in 0.1 M HCl, and the products were extracted with 1,2-dichloroethane. The extract was dried over $MgSO_4$, the solvent was distilled off, and the diols were converted to diacetates by treatment with a 1 : 1 acetic anhydride–pyridine mixture for 2 h at 373 K [12]. A procedure for identification and quantitative determination of isomeric cyclohexanediol diacetates by GLC (20% diethylene glycol succinate on Chromaton N-AW-HMDS and 5% 1,2,3,4,5,6-hexakis-β-cyanoethoxyhexane on Chromaton N-AW-HMDS) is described elsewhere [8].

To accomplish our goals, we studied the kinetics of accumulation of products characteristic of various pathways of cyclohexanol oxidation with molecular oxygen at 403 K: hydrogen peroxide, 1-hydroxycyclohexyl hydroperoxide, cyclohexanone, 2- and 4-hydroxycyclohexanones, 2-cyclohexenone, 2-, 3-, and 4-hydroxycyclohexyl hydroperoxides (*cis*- and *trans*-), and 1,2-, 1,3-, and 1,4-dihydroxycyclohexanes (*cis*- and *trans*-) (Fig. 1). The accumulation curves of hydrogen peroxide, organic hydroperoxides (of which the major product is 1-hydroxycyclohexyl hydroperoxide), and cyclohexanone shows that H_2O_2 and cyclohexanone are accumulated earlier than 1-hydroxycyclohexyl hydroperoxide, with the relative content of the latter increasing with conversion. This fact cannot be attributed to higher rate of hydrogen peroxide decomposition, because it is known [2] that adducts of H_2O_2 or organic hydroperoxides with cyclohexanone decompose faster than free hydroperoxides.

To refine the sequence of formation of products originating from cyclohexanol oxidation at the α-CH bond, we compared [1] the accumulation rates of the reaction products, determined by graphic differentiation of the kinetic curves (Fig. 1). Indeed, the ratios of the accumulation rates of organic hydroperoxides and H_2O_2, and also of organic hydroperoxides and cyclohexanone (Fig. 2) confirm the assumption that, under the experimental conditions, 1-hydroxycyclohexyl hydroperoxide is mainly formed by reversible nucleophilic addition of hydrogen peroxide to cyclohexanone [reaction (1a)], rather than from 1-hydroxycyclohexylperoxy radical [reaction (1b)]:

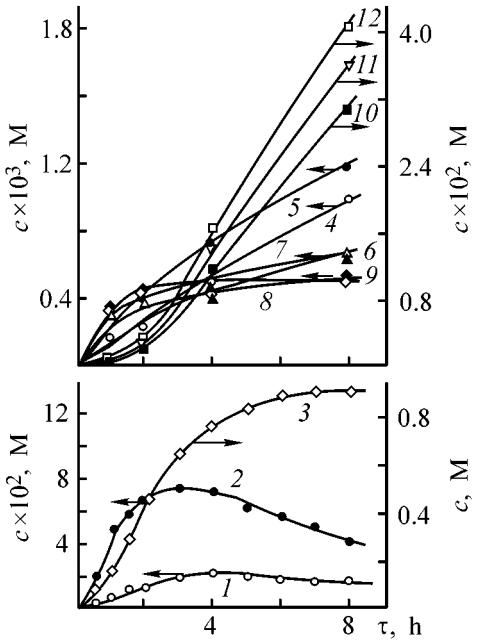

Fig. 1. Kinetic curves of product accumulation in oxidation of cyclohexanol at 403 K: (*c*) product concentration and (τ) time; the same for Fig. 4. (*1*) 1-Hydroxycyclohexyl hydroperoxide, (*2*) hydrogen peroxide, (*3*) cyclohexanone, (*4*) *cis*-2-hydroxycyclohexyl hydroperoxide and *cis*-1,2-dihydroxycyclohexane, (*5*) *trans*-2-hydroxycyclohexyl hydroperoxide and *trans*-1,2-dihydroxycyclohexane, (*6*) *cis*-3-hydroxycyclohexyl hydroperoxide and *cis*-1,3-dihydroxycyclohexane, (*7*) *trans*-3-hydroxycyclohexyl hydroperoxide and *trans*-1,3-dihydroxycyclohexane, (*8*) *cis*-4-hydroxycyclohexyl hydroperoxide and *cis*-1,4-dihydroxycyclohexane, (*9*) *trans*-4-hydroxycyclohexyl hydroperoxide and *trans*-1,4-dihydroxycyclohexane, (*10*) 2-hydroxycyclohexanone, (*11*) 2-cyclohexenone, and (*12*) 4-hydroxycyclohexanone.

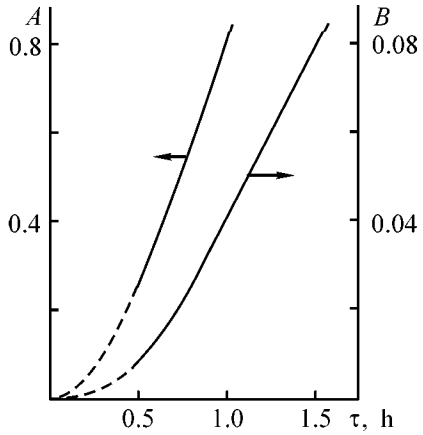

Fig. 2. Ratio of the rates of product accumulation in oxidation of cyclohexanol at 403 K: (*A*) cyclohexanone : 1-hydroxycyclohexyl hydroperoxide and (*B*) hydrogen peroxide : 1-hydroxycyclohexyl hydroperoxide. (τ) Time.

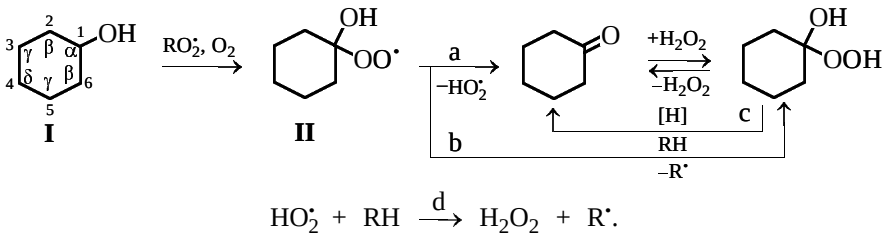

(1)

$$HO_2^{\bullet} + RH \xrightarrow{d} H_2O_2 + R^{\bullet}.$$

These results also show that the oxidation chain in oxidation of cyclohexanol at 403 K is led by the $HO_2^{\bullet}$ radical [reaction (1d)].

In parallel with the products of cyclohexanol oxidation at position 1, *cis* and *trans* isomers of 2-, 3-, and 4-hydroxycyclohexyl hydroperoxides are also accumulated. These compounds, apparently, decompose to give the corresponding dihydroxycyclohexanes and also 2-cyclohexenone and 2- and 4-hydroxycyclohexanones.

Table 1. Variation of the *trans*-to-*cis* isomer ratio C_{trans}/C_{cis} of 2-, 3-, and 4-hydroxycyclohexyl hydroperoxides with time τ of cyclohexanol oxidation at 403 K

Positional isomer	C_{trans}/C_{cis} at indicated τ, h			
	1	2	4	8
2-	1.87	1.90	1.46	1.20
3-	2.0	1.60	1.20	1.00
4-	1.60	1.45	1.30	1.00

Formation of 2-, 3-, and 4-hydroxycyclohexyl hydroperoxides and of 1,2- 1,3-, and 1,4-dihydroxycyclohexanes in the form of *cis* and *trans* isomers is quite natural, because the carbon-centered radical formed in the stage of chain propagation has a planar structure. Figure 1 and Table 1 show that the *trans* isomers somewhat prevail. For 2- and 4-hydroxycyclohexyl hydroperoxides, this may be due to the higher stability of the *trans* isomers. Indeed, the heats of formation of *trans*-1,2- and *trans*-1,4-dimethylcyclohexanes are lower by approximately 8 kJ mol^{-1} than those of the corresponding *cis* isomers [13]. At the same time, the reason for predominant formation of *trans*-3-hydroxycyclohexyl hydroperoxide are unclear, as the *cis* isomer of 1,3-dimethylcyclohexane is more stable than the *trans* isomer [13].

Furthermore, the higher relative content of *trans*-3-hydroxycyclohexyl hydroperoxide can hardly be attributed to the specific features of cyclohexanol oxidation with the $HO_2^{\bullet}$ radical, as the increased yield of this *trans*-1,3 isomer is also observed in reaction of cyclohexyl acetate with *tert*-butylperoxy radical [8].

Possible pathways of cyclohexanol oxidation at positions 2 and 6 (2a), 3 and 5 (2b), and 4 (2c) are shown below:

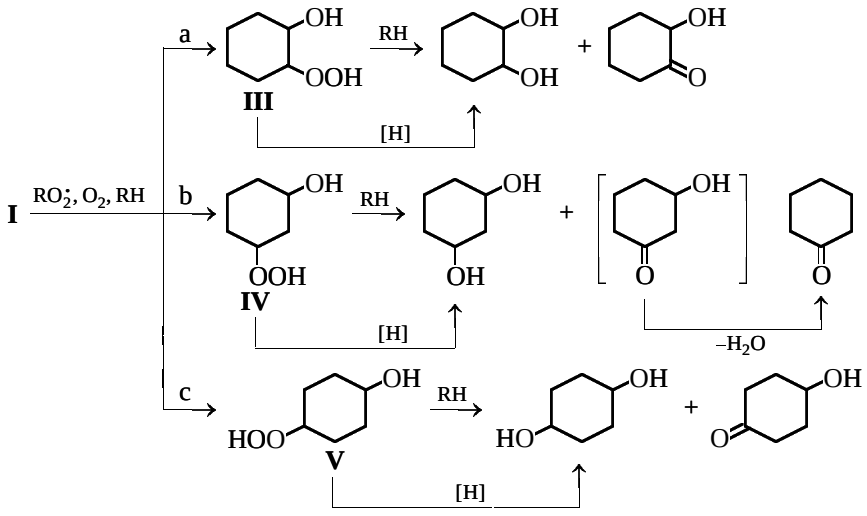

(2)

Assuming that hydroxycyclohexyl hydroperoxides make a major contribution to the total content of hydroperoxides and diols (Fig. 1, curves *4*–*9*), we can evaluate the variation with the oxidation time of the relative mole fraction of each hydroxycyclohexyl hydroperoxide isomer (Fig. 3).

Figure 3 shows that, with conversion, the fractions of *cis*- and *trans*-2- and of *cis*-3-hydroxycyclohexyl hydroperoxides increase, and those of *cis*- and *trans*-4- and of *trans*-3-hydroxycyclohexyl hydroperoxides decrease. Because the decrease in the content of the last two products is accompanied by accumulation of their decomposition products (Fig. 1), the above trend is attributable to different stabilities of the isomers, so that the *trans*-to-*cis* isomer ratio decreases (Table 1). Indeed (Fig. 3), hydroxycyclohexyl hydroperoxides can be ranked in the following order with respect to their stability: *cis*-**III** ≥ *trans*-**III** > *cis*-**IV** > *trans*-**IV** ≥ *cis*-**V** > *trans*-**V**. Such a sequence well correlates with the capacities of hydroxycyclohexyl hydroperoxides for intramolecular hydrogen bonding:

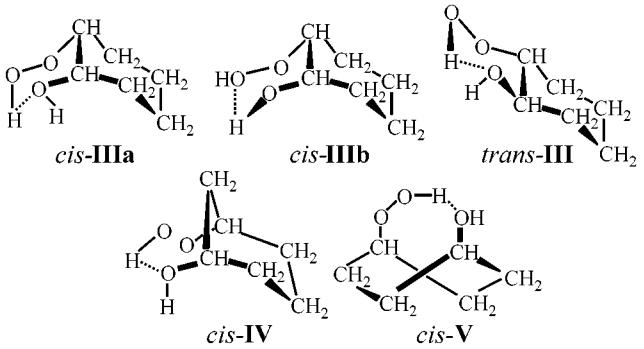

It is known that 1-hydroxycyclohexyl hydroperoxide forms a strong intramolecular hydrogen bond [14]. Since formation of intramolecular hydrogen bonds with six- and seven-membered rings is preferable energetically [15], we should expect formation of a strong hydrogen bond in *cis*-**IIIa**, *cis*-**IIIb**, *trans*-**III**, and *cis*-**IV**.

In principle, hydroxy hydroperoxides can form two types of intramolecular hydrogen bonds via hydrogen atoms of hydroperoxy and hydroxy groups [2, 14]. Because the hydrogen atom of the OO–H bond is more acidic than that of the O–H bond, structure **IIIa** is preferable to **IIIb**. At the same time, although structure *trans*-**III** must be more stable than *cis*-**IIIa** (cf. *cis*- and *trans*-decalins [13]) owing to the steric factor, the difference in their stability can be decreased by the mutual effect of the polar groups of hydroxycyclohexyl hydroperoxides and by solvation effects.

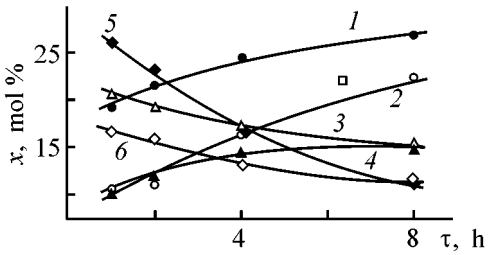

Fig. 3. Variaiton of the relative content of hydroxycyclohexyl hydroperoxide isomers with time of cyclohexanol oxidation at 403 K: (*x*) relative content and (τ) time. (*1*) *cis*-2-Hydroxycyclohexyl hydroperoxide, (*2*) *trans*-2-hydroxycyclohexyl hydroperoxide, (*3*) *trans*-3-hydroxycyclohexyl hydroperoxide, (*4*) *cis*-3-hydroxycyclohexyl hydroperoxide, (*5*) *trans*-4-hydroxycyclohexyl hydroperoxide, and (6) *cis*-4-hydroxycyclohexyl hydroperoxide.

Formation of an intramolecular hydrogen bond in *cis*-4-hydroxycyclohexyl hydroperoxide (*cis*-**V**) is less probable than in 2- and 3-hydroxycyclohexyl hydroperoxides, as such a bond can be only occur in a more strained conformation [16]. In *trans*-3- and *trans*-4-hydroxycyclohexyl hydroperoxides, formation of an intramolecular hydrogen bond with a six-membered ring is impossible, and such bonds with larger rings would hardly be stable.

A strong intramolecular hydrogen bond in hydroxy hydroperoxides must prevent formation of linear intermolecular associates of the hydroperoxides with the substrate

$$\mathrm{ROOH + R'OH \rightleftarrows \underset{\displaystyle H}{\overset{|}{ROO}}\cdots H\text{–}OR' \rightarrow RO^{\bullet} + H_2O + R'O^{\bullet}}, \quad (3)$$

which are known [2] to decompose at higher rates than free hydroperoxides.

2-, 3-, and 4-Hydroxycyclohexanones can form not only by decomposition of the corresponding hydroxycyclohexyl hydroperoxides by reactions (2a), (2b), and (2c), but also by recombination of peroxy radicals:

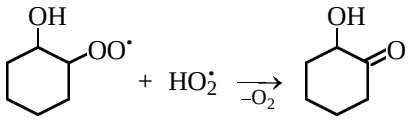

(4)

Since the length of the kinetic chain of cyclohexanol oxidation is more than 100 under the experimental conditions {as calculated from the overall oxidation rate and the parameter $k_p(2k_t)^{-0.5}$ (403 K) = 1.03×10^{-2} $l^{1/2}$ $mol^{-1/2}$ $s^{-1/2}$ [2]}, the contribution of reaction (4) to the product formation is insignificant.

2-Cyclohexenone is probably formed from 3-hydroxycyclohexanone, because is it well known that

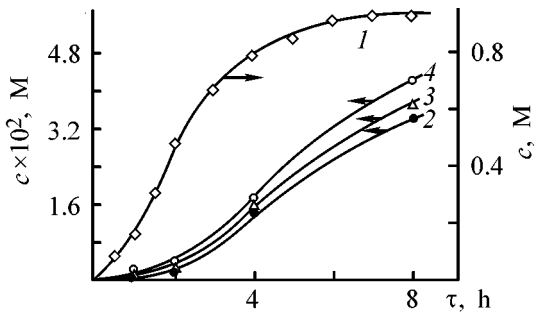

Fig. 4. Kinetic curves of product accumulation in oxidation of cyclohexanol at 403 K. Position of C–H bond: (*1*) 1, (*2*) 2 and 6, (*3*) 3 and 5, and (*4*) 4.

β-keto alcohols are unstable against dehydration [17]. Formation of 2-cyclohexenone from 2-hydroxycyclohexanone is considerably less probable. It is known that α-keto alcohols are dehydrated only under severe conditions [17]. We found that heating of a 0.1 M solution of 2-hydroxycyclohexanone in chlorobenzene at 403 K for 10 h under argon yielded no 2-cyclohexenone.

The kinetic curves of accumulation of cyclohexanone, 2- and 4-hydroxycyclohexanones, and 2-cyclohexenone (Fig. 1) show that hydroxycyclohexanones and 2-cyclohexenone can form in later oxidation stages by oxidative transformations of cyclohexanone.

The accumulation curves of the products characteristic of specific pathways of cyclohexanol oxidation [involving four different types of C–H bonds, schemes (1) and (2)] are shown in Fig. 4, and the initial rates of the product accumulation are listed in Table 2. Assuming that the reactivity of the C–H bond at position 4 is equal to that of the C–H bonds in cyclohexane, we can evaluate the relative reactivities of the C–H bonds in the cyclohexanol molecule (Table 2).

Table 2 shows that the hydroxy group enhances by a factor of more than 200 the reactivity of the C–H bond at position 1 and appreciably decreases the reactivity of the C–H bonds at positions 2 and 3. Similar trends were observed in the reaction of cyclohexyl acetate with *tert*-butylperoxy radical [8].

Table 2. Initial accumulation rates $v_{0,i}$ of products characteristic of specific pathways of cyclohexanol oxidation at 403 K and relative reactivities of the C–H bonds in cyclohexanol

Position of C–H bonds	Number of C–H bonds	$v_{0,i} \times 10^7$, mol l^{-1} s^{-1}	Relative reactivity
1	1	440	215
2, 6	4	1.85	0.22
3, 5	4	2.50	0.30
4	2	4.10	1.00

Oxidation of cyclohexanol, similar to that of cyclohexyl acetate, is a typical example of homolytic substitution in a hydrocarbon chain linked to an electron-withdrawing substituent. The polar (inductive + field) effect of such a substituent decreases the electron density on the hydrogen atom of the C–H bond subject to attack and thus hinders its interaction with electrophilic peroxy radicals [8, 18]. Furthermore, the electron-withdrawing substituent destabilizes the transition state and carbon-centered radicals formed by attack of the C–H bonds at positions 1–3 of cyclohexanol.

However, when a peroxy radical reacts with the C–H bond at position 1, the resulting hydroxyalkyl radical **VIa**, destabilized by the mechanism of the polar effect, is stabilized by conjugation of the unpaired electron with the lone electron pairs of the hydroxy group (structure **VIb**):

$$\underset{\textbf{VIa}}{H{-}\ddot{O}{\leftarrow}\dot{C}H{\leftarrow}R} \leftrightarrow \underset{\textbf{VIb}}{H{-}\dot{O}{=}CH{\leftarrow}R}. \qquad (5)$$

This effect must enhance the reactivity of the α-C–H bond in alcohols as compared with C–H bonds in hydrocarbons.

At the same time, so large (by more than a factor of 200) difference in the reactivities of the C–H bonds at positions 1 and 4 was unexpected. According to [5], at 353 K the reactivity of the α-C–H bond in cyclohexanol toward *tert*-butylperoxy radical exceeds that of the C–H bond in cyclohexane by a factor of 50. With increasing temperature and in going from the less active *tert*-butylperoxy radical to the more active $HO_2^{\bullet}$ radical [6], the difference between the reactivities of the C–H bonds must decrease, rather than increase.

The abnormally high reactivity of the C–H bond at position 1 in cyclohexanol toward the $HO_2^{\bullet}$ radical can be accounted for by assuming formation of a six-membered hydrogen-bonded transition state **VII**:

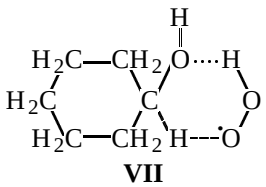

VII

The reaction via state **VII** is more favorable energetically and hence it must occur at a higher rate

than usual hydrogen abstraction from a substrate by a peroxy radical.

It is known [2] that alcohols form with peroxy radicals hydrogen-bonded associates **VIII**. In contrast to peroxy radicals, $HO_2^{\bullet}$ radicals can form associates **IX** of different kind:

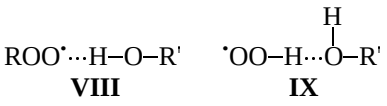

VIII **IX**

Because the hydrogen atom in the $HO_2^{\bullet}$ radical is more acidic and shows stronger electron-withdrawing power than the hydrogen atom of the hydroxy group, and the hydroxyl oxygen, in turn, is a stronger electron donor than the electrophilic oxygen of the peroxy radical, associate **IX** is preferable to **VIII**.

Table 2 shows that oxidation of cyclohexanol by the α pathway initially occurs with fairly high selectivity (~98%), which is due to activation of the C–H bond at position 1 and its deactivation at positions 2 and 3.

The second most reactive C–H bonds in cyclohexanol are the C–H bonds at position 4. As already noted, oxidation of cyclohexanol at these bonds yields 4-hydroxycyclohexyl hydroperoxide, 1,4-dihydroxycyclohexane, and 4-hydroxycyclohexanone. Their further oxidative transformations may result in "burn-out" of two carbon atoms and formation of succinic acid, which, indeed, was detected in products of deep oxidation of cyclohexanol [19].

CONCLUSIONS

(1) In autooxidation of cyclohexanol at 403 K, the reaction chain is led by the $HO_2^{\bullet}$ radical. Along with oxidation products formed by cleavage of the 1-CH bond (cyclohexanone, hydrogen peroxide, 1-hydroxycyclohexyl hydroperoxide), products originating from the attack at the C–H bonds at positions 2–4 are formed: 2-, 3-, and 4-hydroxycyclohexyl hydroperoxides (*cis*- and *trans*-), 1,2-, 1,3-, and 1,4-dihydroxycyclohexanes (*cis*- and *trans*-), 2-cyclohexanone, and 2- and 4-hydroxycyclohexanones.

(2) The different siabilities of isomeric 2-, 3-, and 4-hydroxycyclohexyl hydroperoxides (*cis*- and *trans*-) in the course of cyclohexanol oxidation are due to different extents of their stabilization by an intramolecular hydrogen bond: *cis*- and *trans*-2- and *cis*-3-hydroxycyclohexyl hydroperoxides are the most stable, and *trans*- and *cis*-4- and *trans*-3-hydroxycyclohexyl hydroperoxides, the least stable.

(3) In autooxidation of cyclohexanol effected by $HO_2^{\bullet}$ radical, the C–H bond at position 1 is strongly activated, and the C–H bonds at positions 2 and 3 are appreciably deactivated.

REFERENCES

1. Emanuel', N.M., Denisov, E.T., and Maizus, Z.K., *Tsepnye reaktsii okisleniya uglevodorodov v zhidkoi faze* (Chain Reactions of Liquid-Phase Oxidation of Hydrocarbons), Moscow: Nauka, 1965.
2. Denisov, E.T., Mitskevich, N.I., and Agabekov, V.E., *Mekhanizm zhidkofaznogo okisleniya kislorodsoderzhashchikh soedinenii* (Mechanism of Liquid-Phase Oxidation of Oxygen-Containing Compounds), Minsk: Nauka i Tekhnika, 1975.
3. Perkel', A.L., Voronina, S.G., and Freidin, B.G., *Usp. Khim.*, 1994, vol. 63, no. 9, pp. 793–809.
4. Korcek, S., Chenier, J.H.B., Howard, J.A., *et al.*, *Can. J. Chem.*, 1972, vol. 50, no. 14, pp. 2285–2297.
5. Hendri, D.G., Gould, C.M., Schuetzle, D., *et al.*, *J. Org. Chem.*, 1976, vol. 41, no. 1, p. 1–10.
6. Landolt-Bornstein Zahlwerte, *Funktionen aus Naturwissenschaften und Technik*, Neue Serie, Gruppe II, Berlin: Springer, 1984, vol. 13.
7. Neginskaya, R.V., Freidin, B.G., Dolgikh, V.V., *et al.*, *Zh. Prikl. Khim.*, 1985, vol. 55, no. 11, pp. 2512–2516.
8. Puchkov, S.V., Perkel', A.L., and Buneeva, E.I., *Kinet. Katal.*, 2001, vol. 42, no. 5, pp. 1–8.
9. Freidin, B.G. and Ermolaeva, L.I., *Zh. Prikl. Khim.*, 1970, vol. 43, no. 5, pp. 2512–2516.
10. Perkel', A.L., Freidin, B.G., Voronina, S.G., and Perkel', R.L., *Zh. Anal. Khim.*, 1993, vol. 48, no. 8, pp. 1399–1406.
11. Buneeva, E.I, Puchkov, S.V., Yarysh, O.N., and Perkel', A.L., *Zh. Anal. Khim.*, 1998, vol. 53, no. 8, pp. 882–885.
12. Siggia, S. and Hanna, J.G., *Quantitative Organic Analysis via Functional Groups*, New York: Wiley–Interscience, 1979.
13. *Comprehensive Organic Chemistry. The Synthesis and Reactions of Organic Compounds*, Barton, D. and Ollis, W.D., Eds., vol. 1: *Oxygen Compounds*, Stoddart,, J.F., Ed., Oxford: Pergamon, 1979.
14. Terent'ev, V.A. and Antonovskii, V.L., in *Uspekhi khimii organicheskikh perekisnykh soedinenii i avtookisleniya* (Advances in Chemistry of Organic Peroxides and Autooxidation), Moscow: Khimiya, 1969, pp. 435–442.
15. Dneprovskii, A.S. and Temnikova, T.I., *Teoreticheskie osnovy organicheskoi khimii* (Theoretical Foundations of Organic Chemistry), Leningrad: Khimiya, 1979.
16. March, J., *Advanced Organic Chemistry. Reactions, Mechanisms, and Structure*, New York: Wiley–Interscience, 1985.
17. Fieser, L.F. and Fieser, M., *Advanced Organic Chemistry*, New York: Reinhold, 1962.
18. Perkel', A.L. and Voronina, S.G., *Zh. Prikl. Khim.*, 1999, vol. 72, no. 9, pp. 1409–1419.
19. Zhavnerko, K.A. and Erofeev, B.V., *Vestsi Akad. Navuk Bel. SSR, Ser. Khim. Navuk*, 1968, no. 3, pp. 67–71.

Russian Journal of Applied Chemistry, Vol. 75, No. 2, 2002, pp. 254–256. Translated from Zhurnal Prikladnoi Khimii, Vol. 75, No. 2, 2002, pp. 263–265.
Original Russian Text Copyright © 2002 by Sokolova, Kovzhina, Dmitrieva, Blinova.

ORGANIC SYNTHESIS AND INDUSTRIAL ORGANIC CHEMISTRY

Photodegradation of Azo Dyes with Heterocyclic and Benzene Groups in Polymeric Matrix

N. B. Sokolova, L. P. Kovzhina, N. M. Dmitrieva, and N. V. Blinova

St. Petersburg State Technological Institute, St. Petersburg, Russia

Received May 24, 2001

Abstract—Lightfastness of individual azo dyes with benzene, thiophene, and furan groups and their binary mixtures in cellulose acetobutyrate was studied on an installation for accelerated photochemical aging. The dye pairs in which the components enhance the lightfastness of each other were determined.

Most of fat-soluble orange, red, and claret-colored dyes are azo dyes containing benzene groups with no sulfo groups. These dyes are widely used for coloring polymeric light filter films based on cellulose esters, which are mainly filters of the cutting type (see figure) [1]. However, the majority of azo dyes with benzene groups are characterized by parasitic transmission in the blue region. This drawback can be eliminated by adding yellow dyes having maximal absorption in this spectral range. The main component of the filter dyes are 1-phenyl-3-methyl-5-pyrazolone derivatives and recently developed derivatives of 2-phenyl-5-furanone and 2-phenyl-5-thienone [2, 3].

One of the main requirements to filtering dyes is high lightfastness in a polymeric matrix. Azo dyes have medium lightfastness. It can be increased by adding various photostabilizers, but the better choice is the use of dyes enhancing the lightfastness of one another [4].

In this work we studied the lightfastness of binary mixtures of two types of filter azo dyes: (1) benzene derivatives (red-violet component) and (2) derivatives of five-membered heterocycles, thiophene and furan (yellow component).

We prepared eight film light filters colored with pure dyes **I**–**VIII** (Table 1) and 16 light filters colored with binary mixtures of these dyes.

Dye photodegradation in the films was studied on a Standard Xenon Long-Life Fade Meter XFL-1 providing accelerated photochemical aging. The films were irradiated for 10 h simultaneously with a colorless film of cellulose acetobutyrate polymer. To determine the degree of photodegradation, the absorption at λ_{max} (analytical wavelength) of the dye was recorded 15, 30, 60, 120, 180 min, etc. after the start of the irradiation. To exclude contribution of photodegradation of the polymeric matrix, an irradiated colorless film was used as reference.

The optical density of yellow dyes at the analytical wave length was calculated as the difference between the measured density and the optical density of the red dye. The degree of photodegradation Φ_D for a certain irradiation time was calculated by the equation

$$\Phi_D = \frac{D_0 - D_i}{D_0} \times 100\%,$$

where D_0 and D_i are the optical densities at the analytical wavelength before and after irradiation.

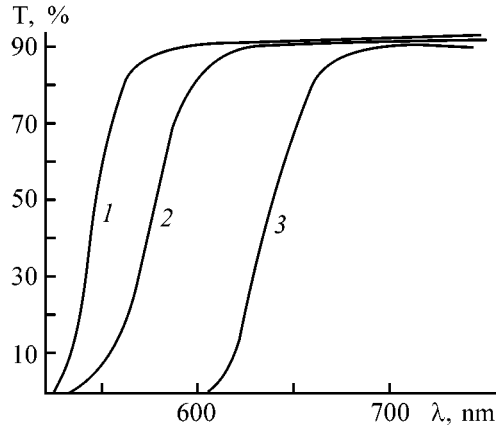

Electronic spectra of red cutting light filters containing (*1*) Fat-Soluble Orange (C.1.12055), (*2*) Disperse Reddish Zh (C.I.11110), and (*3*) Sudan Red 7V (C.I. 26050) azo dyes. (T) Transmission and (λ) wavelength.

1070-4272/02/7502-0254 $27.00 © 2002 MAIK "Nauka/Interperiodica"

Table 1. Polymeric film light filters containing azo dyes

Dye*	Film thickness, nm	λ_{max}	Dye	Film thickness, nm	λ_{max}	Dye	Film thickness, nm	λ_{max}	Dye	Film thickness, nm	λ_{max}
I	0.16	440	**III**	0.16	470	**V**	0.15	520	**VII**	0.15	520
II	0.11	440	**IV**	0.17	480	**VI**	0.15	540	**VIII**	0.17	540

* Dye:

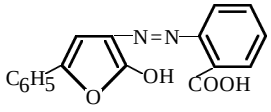

I

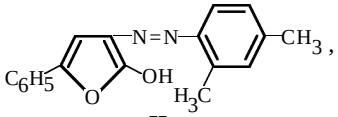

II

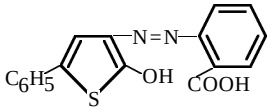

III

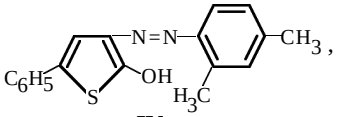

IV

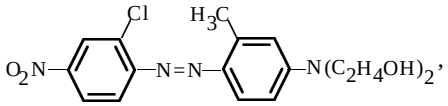

Disperse Bordeaux 2C (C.I.11215)

V

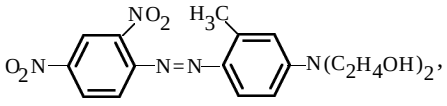

Disperse Violet 4K

VI

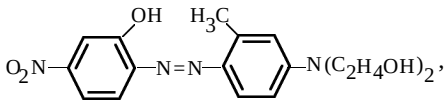

Disperse Ruby C (C.I.11225)

VII

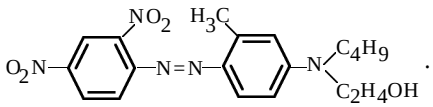

Celliton Violet R (C.I.11195)

VIII

Table 2. Degree of photodegradation of pure monoazo dyes with furan and thiophene groups **I**–**IV** and azo dyes with benzene groups **V**–**VIII** and their binary mixtures in a polymeric matrix after irradiation for 1 h

Dye	Φ_D	$\Delta\Phi_D$	Dye	Φ_D	$\Delta\Phi_D$	Dye	Φ_D	$\Delta\Phi_D$	Dye	Φ_D	$\Delta\Phi_D$
	%			%			%			%	
I	11.72		**I**	13.96	–2.24	**V**	5.26		**V**	2.57	+2.69
II	66.12		**II** + **VII**	64.93	+1.19	**VI**	3.82		**VI** + **III**	1.83	+1.99
III	10.02		**III**	14.40	–4.37	**VII**	3.60		**VII**	–5.91	+9.50
IV	42.21		**IV**	100.00	–57.79	**VIII**	3.29		**VIII**	1.02	+2.27
I	8.89	+2.83	**I**	10.84	+0.88	**V**	2.89	+2.37	**V**	13.18	–7.92
II + **V**	51.86	+14.26	**II** + **VIII**	23.93	+42.19	**VI** + **I**	2.02	+1.74	**VI** + **IV**	5.61	–1.79
III	7.31	+2.71	**III**	5.28	+4.74	**VII**	3.11	+0.50	**VII**	16.17	–12.57
IV	31.39	+10.82	**IV**	47.42	–5.21	**VIII**	1.76	+1.53	**VIII**	5.19	–1.90
I	8.40	+3.31				**V**	7.45	–2.19			
II + **VI**	60.40	+5.72				**VI** + **II**	3.76	+0.06			
III	6.26	+3.76				**VII**	6.25	–2.65			
IV	46.15	–3.94				**VIII**	2.44	+0.85			

The difference between the degrees of photodegradation of each dye in the film in the absence and in the presence of the second dye was calculated as

$$\Delta\Phi_D = \Phi_{D\,pur} - \Phi_{D\,mixt}.$$

The results are presented in Table 2. We compared the degrees of photodegradation after 1-h irradiation, since by this time the accumulation of the photodegradation products affecting the process is negligible. However, the data obtained after 10-h irradiation are also analyzed to give insight into the final steps of dye fade.

As seen from the results presented in Table 2 for the films colored with a single dye, the lightfastness of the azo dyes with benzene groups is higher than

that of the heterocyclic dyes; the azo dyes with thiophene groups are more stable under irradiation than the dyes with furan groups; derivatives of anthranilic acid are more stable to irradiation than derivatives of *m*-xylidine.

The data on the lightfastness of the films containing binary dye mixtures show that the azo dyes with benzene groups containing electron-acceptor substituents, NO_2 and Cl (**V**, **VI**, and **VIII**) decrease the photodegradation of all the heterocyclic dyes, excluding the azo dyes with thiophene groups **IV**. The Azo dye with the electron-donor group at the benzene ring (**VII**) increases photodegradation of heterocyclic azo dyes, and various substituents at the nitrogen atom of the amino group of the benzene ring have no effect on the lightfastness of the dyes. The lightfastness of the azo dyes with benzene groups increases in the presence of heterocyclic azo dyes, irrespective of the heterocycle nature (**I**–**III**). Derivatives of *m*-xylidine decrease the lightfastness of azo dyes with benzene groups, with this effect being the most pronounced for the dye with thiophene groups (**IV**).

These results agree well with the mechanism of photodegradation of heterocyclic azo dyes [5] and with the data on the fade of azo dyes with benzene groups [6]. Photodegradation of azo dyes with benzene groups containing acceptor and donor substituents occurs by the reduction and oxidation mechanism, respectively. Photodegradation of monoazo dyes proceeds by the reduction mechanism. Thus, the synergistic increase in photodegradation of binary dye formulations is observed when these dyes, e.g, **II** and **VIII**, degrade by different mechanisms. In the formulations containing the dyes degrading by the same mechanism, e.g, by the reduction mechanisms for dyes **I**–**IV** and **V**, each component partially "shields" the other component from irradiation, thus increasing its lightfastness. These formulations are preferable for preparing polymeric film light filters.

EXPERIMENTAL

Photodegradation of the films was performed on an installation providing accelerated photochemical aging. The sun irradiation was simulated with a 1.5-kW xenon lamp. Film samples of size 10×40 mm were automatically irradiated according to a certain program at 30°C and 65% humidity in the chamber. A colorless cellulose acetobutyrate film was irradiated simultaneously. Irradiated samples were kept in the dark for 24 h. The absorption spectra were recorded on an SF-16 spectrophotometer using a colorless film irradiated under the same conditions as the reference.

Polymeric film light filters were prepared by casting 10% solution of cellulose acetobutyrate containing a certain amount of the dye onto a polished glass plate restricted by a frame. A chloroform-ethanol mixture (85 : 15 weight ratio) was used as the solvent, and dibutylphthalate, as plasticizer. The system was allowed to stand at 25–28°C for 72 h. 10×10-cm films 0.15 ± 0.02 mm thick were prepared.

CONCLUSION

A mixture of hydrophobic heterocyclic azo dyes prepared from thiophene or furan and anthranilic acid and azo dyes with benzene groups containing electron-acceptor substituents shows promise for preparing polymeric light filtering films.

ACKNOWLEDGMENTS

This work was financially supported by the program "High-School Research in Priority Fields of Science and Technology," section 203.02 (P-06.015).

REFERENCES

1. Sokolova, N.B., Bogdanova, L.A., and Shul'gina, E.S., *Khimiya i tekhnologiya poluprovodnikov i krasitelei* (Chemistry and Technology of Semiconductors and Dyes), Leningrad: Leningr. Tekhnol. Inst. im. Lensoveta, 1990, pp. 4–15.
2. Kovzhina, L.P., Sokolova, N.B., Dmitrieva, N.M., and Pesenko, E.V., *Zh. Prikl. Khim.*, 1996, vol. 69, no. 3, pp. 477–482.
3. Kovzhina, L.P., Sokolova, N.B., and Dmitrieva, N.M., *Zh. Prikl. Khim.*, 1998, vol. 69, no. 3, pp. 453–458.
4. Kovzhina, L.P., Sokolova, N.B., Dmitrieva, N.M., and Vins, T.Yu., *Zh. Prikl. Khim.*, 1999, vol. 72, no. 9, pp. 1507–1509.
5. Kovzhina, L.P., Sokolova, N.B., Dmitrieva, N.M., and Popova, T.N., *Zh. Prikl. Khim.*, 1998, vol. 71, no. 12, pp. 2024–2028.
6. Krichevskii, G.E., *Fotokhimicheskie prevrashcheniya krasitelei i svetostabilizatsiya okrashennykh materialov* (Photochemical Transformations of Dyes and Light Stabilization of Colored Materials), Moscow: Khimiya, 1986.

Russian Journal of Applied Chemistry, Vol. 75, No. 2, 2002, pp. 257–260. Translated from Zhurnal Prikladnoi Khimii, Vol. 75, No. 2, 2002, pp. 266–269.
Original Russian Text Copyright © 2002 by Antonik, Lopyrev, Korchevin, Tomin.

ORGANIC SYNTHESIS AND INDUSTRIAL ORGANIC CHEMISTRY

Phosphorus-Containing Salts of Polyhexamethyleneguanidinium for Protection of Metals from Corrosion, Biological Overgrowing, and Salt Deposition

L. M. Antonik, V. A. Lopyrev, N. A. Korchevin, and V. P. Tomin

Favorskii Institute of Chemistry, Siberian Division, Russian Academy of Sciences, Irkutsk, Russia

Received April 26, 2001

Abstract—The procedure for preparing polyhexamethyleneguanidinium phosphate and polyhexamethyleneguanidinium hydroxyethylidenediphosphonate, protecting metals from corrosion and biological overgrowing, was optimized.

Polyhexamethyleneguanidinium (PHMG) salts exhibiting strong bactericidal activity can be used in medicine for disinfection of toolkits, operating and injection fields, in agriculture in storage of vegetables, in lumber industry as fungicides and preservatives, in wastewater treatment, etc [1–3]. Hence, synthesis of new PHMG salts and study of their properties is of special interest.

We prepared polyhexamethyleneguanidinium phosphate (PHMGP) and previously unknown polyhexamethyleneguanidinium hydroxyethylidenediphosphate (HPPG). Since these salts are potential inhibitors of metal corrosion, they were tested for multipurpose metal protection. Heat-exchange equipment of large-scale productions and pipe lines of circulating systems made from carbon and low-alloy steels can corrode and undergo salt deposition and biological overgrowing from the side of cooling water. However, the inhibitors produced in Russia are low effective, and those produced in other countries are rather expensive and cannot be used for multipurpose metal protection. For example, the well-known preparation of Kurita company, containing mainly polyphosphates, inhibits corrosion and salt deposition. To suppress microorganism growth, Polikrin is added to this preparation.

EXPERIMENTAL

We studied oligomeric PHMGP and HPPG [molecular weight M = 1100–1600 (n = 4–5)] prepared by neutralization of PHMG with phosphoric and 1-hydroxyethylidenediphosphonic (Xydiphone) acids, respectively, in an alcoholic solution [1–4]. The initial base (PHMG) was prepared from metacide hydrochloride [M = 800 (n = 4–5)] [5]. PHMGP and HPPG with M = 7000–8000 were synthesized by polycondensation of guanidinium carbonate and hexamethylenediamine (HMDA) [6]. The results of elemental analysis of the polymers are presented in Tables 1, 2. The IR spectra of the polymers, recorded on a Specord spectrophotometer, contain the following bands (ν_{max}, cm^{-1}): $-CH_2-$ (2920, 2860, and 1470), –NH– (3220–3240), and =NH (1650).

The structure of phosphorus-containing PHMG salts can be described by the general formula

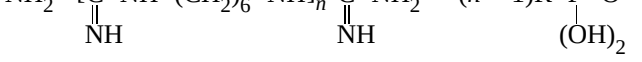

where R = OH, 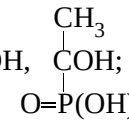 ; n = 4–30.

The inhibition of corrosion, salt deposition and biological overgrowing by solutions of PHMG salts with concentration from 0.01 to 0.1 g l^{-1} was studied under conditions simulating the operation conditions of water circulating systems [7]. The pH of aqueous solutions containing 0.02 g l^{-1} of the polymer and 1 g l^{-1} of NaCl was measured with an ION-1 conductometer (Table 1). The inhibition of metal corrosion was evaluated by electrochemical procedure [8] with the use of a PI-50-1M potentiostat, PR-8 programmer, YaKD-004 automatic recorder, and YaES-1 cell. A silver chloride electrode and a pol-

1070-4272/02/7502-0257 $27.00 © 2002 MAIK "Nauka/Interperiodica"

Table 1. Oligomers prepared from commercial polyhexamethyleneguanidinium hydrochloride (metacide)

Comp. no.	PHMG : acid, mol : mol	Content, %				Yield, %	pH of aqueous solution of the polymers	Comp. no.	PHMG : acid, mol : mol	Content, %				Yield, %	pH of aqueous solution of the polymers
		C	H	N	P					C	H	N	P		
Neutralization with phosphoric acid (PHMGP)								Neutralization with Xydiphone (HPPG)							
1	1 : 2.5	38.83* 42.49	8.82 8.73	22.82 25.61	9.93 7.56	70	7.90	1	1 : 1.3	35.68 44.87	7.98 8.87	16.58 25.30	14.70 7.46	47	7.72
2	1 : 4.0	32.55 34.29	7.77 7.64	19.80 20.67	13.08 12.20	86	7.65	2	1 : 4.0	29.05 30.69	6.83 6.75	13.92 14.50	18.02 17.11	89	6.79
3	1 : 5.0	30.81 31.27	7.01 7.24	18.73 18.85	13.37 13.90	90	5.88	3	1 : 5.0	28.55 28.33	6.80 6.38	12.26 12.69	18.26 18.73	92	5.95

* (Numerator) found and (denominator) calculated.

Table 2. Polycondensation of guanidinium carbonate with hexamethylenediamine in various solvents (τ = 8 h)

Comp. no.	Solvent	*T*, °C	PHMGP					HPPG				
			content, %			yield, %	*n*	content, %			yield, %	*n*
			C	N	P			C	N	P		
4	Toluene	110	31.87	18.35	13.58	77	4	29.17	12.61	18.17	76	5
5	Amyl alcohol	130	32.12	18.11	13.23	83	10	30.65	12.01	18.53	85	10
5'*	"	130	34.56	17.85	12.97	86	25	–	–	–	–	
6	Mesitylene	165	33.47	17.90	12.92	85	15	30.88	12.40	17.98	88	20

* τ = 15 h.

ished and degreased 1-cm^2 steel (St. 20) electrode (test sample) were used as the reference and working electrodes, respectively. An aqueous solution with total salt content of 0.15 g l^{-1} and content of Ca^{2+} cations of 0.03 g l^{-1} was used as the corrosion medium. The measurements were performed at potential sweep rate of 0.2 mV s^{-1} and polarization of +300 mV. In each experiment, the polarization resistance was measured within 24 h. The corrosion current was calculated from the polarization resistance by the Stern–Geary procedure. The corrosion current density (A m^{-2}) is proportional to the corrosion rate. In the absence of inhibitor, the corrosion current density in the being solution tested was 0.48 A m^{-2}. For each salt, three measurements were performed at a certain concentration of the salt in the corrosion solution. The corrosion current and protecting effect of PHMGP-3, PHMGP-5', HPPG-2, and HPPG-6, averaged over three experiments, are presented in Table 3. The results of corrosion experiments with PHMGP-1 and HPPG-1 were poorly reproducible. In Table 3, we present the best data for these salts for a more reliable comparison with other polymeric salts prepared by neutralization of PHMG with equivalent amount of the acid.

Salt deposition in the course of 4-h electrolysis of hard water (2 mg-equiv g^{-1} of Ca^{2+}) at a current density of 1 A m^{-2} and cathodic polarization was estimated gravimetrically. The inhibition of salt deposition was estimated by a fast test [9].

The biocidal properties were estimated from the number of bacteria in 1 ml of water, which, in turn, was determined by the TTC test proposed by Kurita company. The antibacterial action of PHMGP and HPPG on various bacterial stains and the toxicity of these polymers were studied in detail in [1–3].

The preparation conditions and the results of elemental analysis of PHMGP oligomers and HPPG prepared by addition of various amounts of phosphoric and 1-hydroxyethylidenediphosphonic (Xydiphone) acids to an alcoholic solution of metacide with *M* = 800 and *n* = 4–5 are presented in Table 1. It can be seen that the oligomer yield depends on the amount of the acid added. At PHMG : acid molar ratios of 1 : 1.3 and 1 : 2.5, the yield of the reaction products

Table 3. Protective properties of PHMG salts

Inhibitor, g l^{-1} ($[PO_4^{3-}]$, g l^{-1})	Corrosion*		Salt deposition, g m^{-2}	Number of bacteria in 1 ml	Inhibitor, g l^{-1} ($[PO_4^{3-}]$, g l^{-1})	Corrosion*		Salt deposition, g m^{-2}	Number of bacteria in 1 ml
	v, A m^{-2}	α, %				v, A m^{-2}	α, %		
0	0.480	0	300	10^8	PHMGP-3:				
HPPG-1, 0.05	0.300	38	61	10^4	0.02 (0.008)	0.100	76	210	–
HPPG-2:					0.05	0.020	96	1195	–
0.01	0.170	64	21	10^2	"Kurita" 1030** (0.01)	0.300	27	62	10^3
0.05	0.028	94	28	–	PHMGP-5', 0.02	0.0120	97	682	–
0.10	0.018	96	55	–	HPPG-6, 0.02	0.013	97	20	–
PHMGP-1, 0.05	0.317	34	346	10^2					

* (v) Corrosion rate, (α) degree of protection from corrosion. ** Water treated with Polikrin A-511.

does not exceed 47–70% and the results of elemental analysis of these products are inconsistent with the composition of the monomeric unit of the phosphorus-containing PHMG salts, presented in the experimental.

With the PHMG : acid molar ratio raised to 1 : 4 and 1 : 5, the oligomer yield increases to 92%. The results of elemental analysis show that there is single acid molecule per monomeric unit of the macromolecule. The resulting PHMG becomes stable.

Table 2 presents the results of elemental analysis and conditions of synthesis of PHMG salts, performed by polycondensation of guanidinium carbonate with equimolar amount of HMDA at 110–165°C in an organic solvent in which the guanidinium salts are sparingly soluble [6]. Unlike the procedure performed in a melt [4, 5], the synthesis occurs in this case under a solvent layer with stirring of a rather low-viscous white resin, which allows preparation of polymers with M from 7000 to 8000 (n = 4–30) (Table 2). The carbonate anion in the resulting PHMG carbonate can be readily substituted with another anion by treatment with the corresponding acid. Unlike the procedure described in [4–6], the stage of PHMG base formation is absent. A pilot plant for production of PHMGP with an output of 5 t/year, based on this procedure for preparing PHMG salts, has been put in operation [10].

The protective properties of PHMGP, HPPG, and commercial inhibitors (Kurita company) of corrosion, salt deposition, and biological overgrowing are summarized in Table 3. The samples of PHMGP and HPPG have different molecular weights and were prepared by addition of different amounts of the acids.

A preliminary electrochemical study of PHMGP and HPPG showed that these salts are film-forming inhibitors of the mixed anodic-cathodic type. The films formed on the steel surface after 20 h of electrolysis have thickness within 0.1 mm and can be observed visually. These films are formed by reaction of the corrosion products of iron with the phosphorus-containing groups; they prevent access of corroding agents to the metal surface, thus decelerating the corrosion. In 0.01 g l^{-1} solutions of the examined PHMG salts, the steel corrosion is decelerated by a factor of 2.8 (Table 3) as compared with that in water. Raising the concentration of pure PHMGP-3 and HPPG-2 to 0.05 g l^{-1} and using 0.02 g l^{-1} solutions of PHMGP-5' and HPPG-6 with higher molecular weight lead to a sharp (to 97%) increase in the degree of protection. In the presence of these additives, the corrosion is appreciably slower than that in the presence of HPPG-1 and PHMGP-1 prepared with a smaller amount of the acid. In contrast to the last two salts, the growth of bacteria and microorganisms is aqueous solutions of the first four salts is completely suppressed. Further increase in the concentration of PHMG salts to 0.1 g l^{-1} or use of salts with higher molecular weights is unnecessary since the corrosion rate in solutions of these salts remains virtually the same.

The inhibiting powers of the Kurita preparations and PHMG solutions were compared at almost the same concentrations. The corrosion rate in the presence of PHMG salts is lower. At the inhibitor concentration of 0.02 g l^{-1} the protective effect of PHMGP-3 is 3 times higher than that of the Kurita preparations. As the PHMGP concentration is increased to 0.05 g l^{-1}, the protective effect increases by a factor of 26.

Although PHMGP inhibits corrosion and biological overgrowing of metal, it does not protect the metal surface from salt deposition and in some cases even promotes this process (Table 3). At the same time, HPPG suppresses salt deposition already at the concentration of 0.01 g l^{-1}. Thus, HPPG salts can be used to protect

the metal surface from corrosion, salt deposition, and biological overgrowing in water-circulating systems.

CONCLUSIONS

(1) Polyhexamethyleneguanidinium salts with strong protective power were prepared in high yield by neutralization of guanidine with equivalent amount of appropriate acid. Polyhexamethyleneguanidinium salts with molecular weight from 7000 to 8000 were synthesized by polycondensation of guanidinium carbonate with hexamethylenediamine in solvents in which guanidinium salts are sparingly soluble.

(2) Corrosion and biological overgrowing of metal surface are effectively suppressed in presence of polyhexamethyleneguanidinium phosphate in the concentration from 0.01 to 0.05 g l^{-1}. The polymers with higher molecular weight exhibit the same protective effect at their lower concentration in the solution.

(3) Polyhexamethyleneguanidinium hydroxyethylibenebiphosphonate is a better inhibitor of corrosion, salt deposition and biological overgrowing than the commercial Kurita inhibitor.

REFERENCES

1. RF Patent no. 2122865.
2. RF Patent no. 2143905.
3. RF Patent no. 2147299.
4. USSR Inventor's Certificate, no. 944290.
5. Gembitskii, P.A., Boksha, L.F., Boldenkov, G.F, *et al.*, *Khim. Prom–st.*, 1984, no. 2, pp. 82–83.
6. RF Patent no. 2144024.
7. RF Patent no. 2109847.
8. Kharlamov, Yu.A., *Zashch. Met.*, 1977, vol. 15. no. 6, pp. 678–680.
9. Chaplakov, P.E., Polkovnichenko, I.T., Toporkova, N.A., and Penzeva, T.A., *Ingibitory otlozheniya solei: Tematicheskii obzor TsNIIEneftekhim* (Inhibitors of Salt Deposition: Review of TsNIIEneftekhim), Moscow, 1989.
10. Tolstikov, G.A. and Trofimov, B.A., *Byull. Sib. Otd. Ross. Akad. Med. Nauk*, 2000, vol. 96, no. 2, pp. 125–133.
11. *Corrosion*, Shtier, L.L., Ed., London: Butterworths, 1976, 2nd ed.

Russian Journal of Applied Chemistry, Vol. 75, No. 2, 2002, pp. 261–264. Translated from Zhurnal Prikladnoi Khimii, Vol. 75, No. 2, 2002, pp. 270–273.
Original Russian Text Copyright © 2002 by Russavskaya, Silinskaya, Yakimova, Korchevin, Tomin, Deryagina.

ORGANIC SYNTHESIS AND INDUSTRIAL ORGANIC CHEMISTRY

Thiokols Based on Wastes from Epichlorohydrin Production as Components of Rail Lubricants

N. V. Russavskaya, Ya. N. Silinskaya, G. A. Yakimova, N. A. Korchevin, V. P. Tomin, and E. N. Deryagina

Favorskii Institute of Chemistry, Irkutsk, Russia

Received September 27, 2001

Abstract—Preparation of solid polymers with varied content of sulfur by condensation of 1,2,3-trichloropropane-rich wastes from epichlorohydrin production with sodium polysulfide Na_2S_x (x = 1–4) generated by reductive dissolution of sulfur in the hydrazine hydrate–alkali system was studied.

Various organosulfur compounds are used as antiwear and extreme-pressure additives to lubricants [1, 2]. In contrast to other lubricants, formulations for rail lubrication at curved sections of railway lines operate in rather specific conditions, because nonstationary friction appearing at contact of the wheel flange and the lateral surface of the rail head is characterized by large specific loading and periodicity. At this contact, the pressure and temperature increase for short time [3], which can activate the molecules of lubrication formulations and improve their sorption on the rubbing elements. Therefore, sulfur and alkali are added to some rail lubricants [4], because in the presence of surfactants they sulfidize and strengthen the wheel and rail surfaces. However, addition of alkali and surfactants impairs other operation properties of lubricants and increases their corrosion activity and environmental hazard.

Sulfur-containing polymers (thiokols) based on wastes from epichlorohydrin production are often used as additives to rail lubricants.

In industry, thiokols are prepared from dihalo derivatives [1,2-dichloroethane, di(β-chloroethyl) formal, and dichlorodiethyl ether] and sodium polysulfide. To obtain branched macromolecules, minor amounts of 1,2,3-trichloropropane (TCP) are often added [5–7]. As a rule, polymerization of the above components yields rubbery or liquid polymers. Solid polymers, prepared only in the presence of sodium monosulfide Na_2S, contain low-reactive C–S groups, and their use in lubrication formulations is rather difficult. Rubbery polymers are immiscible with other lubricant components, and liquid thiokols are mixed with them only upon prolonged vigorous stirring.

At the same time, the source of raw materials for thiokol production can be significantly expanded owing to chlorine-containing wastes from industrial organic synthesis. At present, utilization of these wastes is a complex environmental problem [8, 9]. In this study, we prepared sulfur-containing polymers from the wastes of epichlorohydrin production, which is the main component of epoxy resins. In industry, it is prepared from propylene in three stages [10], and each stage is accompanied by various side reactions. As a result, more than 500 kg of chlorine-containing wastes are formed per 1000 kg of commercial epichlorohydrin [11]. These wastes are enriched in 1,2-dichloropropane, TCP, dichloropropanols, or epichlorohydrin, depending on the sampling point. Thus, specific compositions of the wastes, which varies within a wide range, is determined by the process conditions and operation stability of industrial units.

EXPERIMENTAL

The polysulfide polymers were prepared using a TCP fraction containing (wt %): 76.6 TCP, 17.4 dichloropropanols, 2.0 1,2-dichloropropane, 2.1 dichloropropenes, and 1.9 other products.

The polymers can be prepared using two different procedures for sodium polysulfide Na_2S_n generation. In the first case (procedure 1), it was prepared by a common procedure used in industrial production of

1070-4272/02/7502-0261 $27.00 © 2002 MAIK "Nauka/Interperiodica"

Table 1. Preparation conditions and properties of polymers*

Polymer no.**	S : NaOH, mol : mol	*n* in Na_2S_n	PY, %	Content in polymer, wt %		S_{theor}, wt %	Polymer appearance
				S	Cl		
1	3 : 1	4	87	60.5	11.4	82.4	Dark brown rubbery material
2	1 : 2	1	82	42.5	15.8	53.6	Light gray powder
3	1 : 1	2	87	66.4	8.3	70.1	Yellowish granules
4	3 : 2	3	91	74.4	3.2	77.8	Yellow granules
5	2 : 1	4	94	82.1	0.5	82.4	Dark yellow granules

* (PY) Polymer yield based on TCP, (S_{theor}) theoretical content of sulfur at complete chlorine substitution.

** Sodium polysulfide synthesized by procedure 1 (polymer no. 1) and procedure 2 using a tenfold molar excess of hydrazine hydrate with respect to sulfur (polymer nos. 2–5).

thiokols, namely, by dissolution of sulfur in 40% aqueous solution of sodium hydroxide [6]:

$$6NaOH + (2n + 1)S \rightarrow 2Na_2S_n + 3H_2O + Na_2SO_3. \quad (1)$$

The resulting sodium sulfite reacts with sulfur, yielding thiosulfate:

$$Na_2SO_3 + S \rightarrow Na_2S_2O_3. \quad (2)$$

In this case thiokols were prepared in the presence of magnesium hydroxide (dispersing agent).

Using this procedure, we obtained from the TCP fraction at hand a dark brown elastomeric product. As seen from Table 1, the residual content of chlorine in the product is rather high, despite that we used the stoichiometric NaOH : S ratio, corresponding to the synthesis of Na_2S_4 by reaction (1).

In the second case (procedure 2), sodium polysulfide was generated by reaction of sulfur with the reductive system hydrazine hydrate–alkali [12]:

$$2nS + N_2H_4 \cdot H_2O + 4NaOH \rightarrow 2Na_2S_n + N_2 + 5H_2O. \quad (3)$$

The last reaction yields no sulfur-containing byproducts (Na_2SO_3 and $Na_2S_2O_3$) and thus *n* is determined by the average sulfur:alkali ratio, so that *n* can be varied from 1 to 4 (Table 1). In this procedure, thiokols are prepared without dispersing agents.

At any *n*, we obtained solid polymeric products, which can be easily ground to a fine powder. The polymer preparation is represented by the following scheme:

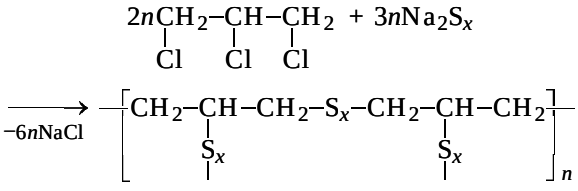

The required polymers were obtained by the two above procedures in a reactor equipped with a stirrer. First, a solution of sodium polysulfide was prepared by reactions (1) or (3), and then TCP was added with stirring. The resulting polymer was filtered off, washed with dilute hydrochloric acid and organic solvent, and dried.

The difference in the composition and properties of the polymers prepared is probably due to the structure of the macromolecules formed and the surface layer of the drops of the monomer or oligomers in the system. Longer polysulfide chains S_3 and S_4 promote the reaction of chlorine atoms at the central carbon in TCP with S_n^{2-} anions, and thus the residual content of chlorine in the polymers prepared by procedure 2 decreases with increasing *n*. The high content of residual chlorine in the polymer prepared by procedure 1 is probably due to the presence of a dispersing agent and high salinity of the reaction mixture. The dispersing agent occurring at the surface of the organic phase drops hinders diffusion of S_n^{2-} anions and thus decreases the degree of TCP sulfuration. In the presence of SO_3^{2-} and $S_2O_3^{2-}$ in the reaction mixture, side reactions of chlorine substitution by these anions may proceed [7]:

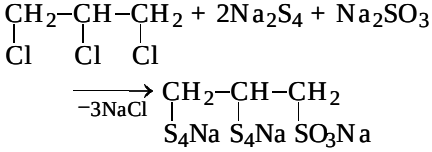

(4)

As a result, we obtain a rubbery polymer with a smaller molecular weight and less developed macromolecular network. In contrast to the polymers prepared by procedure 2, the IR spectrum of the polymer prepared by procedure 1 contains additional bands at 1027 and 1200 cm^{-1}, which suggests the presence of SO_3H and S_2O_3H groups [8].

Table 2. Results of testing of lubricants containing thiokols on a friction machine

Polymer no. (Table 1)	Roller wear (g) in the course of tests					
	after 6 h (with lubricant)		additional 3 h (no lubricant)		additional 6 h (no lubricant)	
	FR	RR	FR	RR	FR	RR
1	0.071	0.051	0.123	0.118	0.561	0.535
2	0.067	0.042	0.183	0.189	0.437	0.394
3	0.062	0.045	0.187	0.194	0.386	0.417
4	0.065	0.039	0.171	0.183	0.287	0.293
5*	0.084	0.076	0.623	0.587	1.325	1.216

* Lubricant without thiokol (15 petroleum coke, 20 diesel oil, and 65% LMWP).

Using procedure 2, we prepared four polymers differing in the content of sulfur and chlorine. These polymers are easily ground and their hardness increases with increasing x.

In the dispersed state, these polymers are easily mixed with a formulation for rail lubrication, which is based on low-molecular-weight polyethylene (LMWP), finely dispersed petroleum coke, and spent locomotive diesel oil [13]. After mixing these four components, a stable lubricant grease is obtained. We used the following formulation, wt %: 60 LMWP, 10 petroleum coke, 20 spent diesel oil, and 10 sulfur-containing polymer.

As seen, the lubrication formulations studied are prepared from available and cheap components. Their antiwear properties were tested on an MI-1M friction machine [14] using the running (RR) and fixed (FR) rollers, whose friction and wearing conditions simulate the wheel-rail friction couple at curved sections of a railway line. The magnitude of the sample wear was determined by weighing the rollers on an analytical balance with an accuracy of 0.0001 g; the results are listed in Table 2.

In the absence of lubricant, the wear after 6 h was as large as 1.464 g for FR and 1.421 g for RR.

To evaluate the enhancing effect of the thiokol additive on the wear resistance of the roller surface, their wear was determined three times in the course of a single test. First the rollers operated for 6 h in the presence of lubricant, whose additional amounts were placed in the contact zone every 10 min. Then the lubricant was removed with acetone and rags, the wear was registered, and the test was continued for 3 h. The wear was registered, and additional treatment for 3 h was performed. The results are listed in Table 2.

As seen, upon polymer addition lubricant not only preserves high antiwear power, but enhances the wear resistance of the surface in the contact zone, because the protective effect is retained after removing the lubricant. This is probably due to the formation of surface iron sulfides or chlorides (at high residual content of chlorine in the polymer). In some cases, sulfuridizing is performed to enhance the surface strength [15]; this accounted for the function of sulfur in the rail lubricants [4] and the effect of sulfur- and chlorine-containing extreme-pressure additives [1].

CONCLUSIONS

(1) Procedures were developed for preparing solid thiokols with varied content of sulfur by reaction of wastes from epichlorohydrin production (enriched in 1,2,3-trichloropropane) and sodium polysuldfide Na_2S_x (x = 1–4) generated by reductive dissolution of sulfur in the hydrazine hydrate–alkali system.

(2) Rail lubricants containing thiokols were studied. These lubricants decrease the wear of the wheel flange and lateral surface of the rail head on passing the curved sections of railway lines not only in the presence of lubricant in the contact zone, but also after its complete removal.

ACKNOWLEDGMENTS

This work was financially supported by the Commission of the Russian Academy of Sciences for Working with Young Scientists (project no. 159).

REFERENCES

1. Kuliev, A.M., *Khimiya i tekhnologiya prisadok k maslam i toplivam* (Chemistry and Technology of

Additives to Oils and Fuels), Leningrad: Khimiya, 1985.

2. Obel'nitskii, A.M., Egorushkin, E.A., and Chernyavskii, Yu.N., *Toplivo, smazochnye materialy i okhlazhdayushchie zhidkosti* (Fuel, Lubricants, and Cutting Fluids), Moscow: Poligraf, 1997.
3. *Iznos rel'sov i koles podvizhnogo sostava* (Wear of Rails and Wheels of the Rolling-Stock), Komarov, K.L. and Karpushchenko, N.I., Eds., Novosibirsk: Sib. Gos. Univ. Putei Soobshch., 1997.
4. *Poverkhnostnye yavleniya i poverkhnostno-aktivnye veshchestva* (Surface Phenomena and Suractants), Abramzon, A.A. and Shchukin, E.D., Eds., Leningrad: Khimiya, 1984.
5. Kirpichnikov, P.A., Averko-Antonovich, L.A., and Averko-Antonovich, Yu.O., *Khimiya i tekhnologiya sinteticheskogo kaychuka* (Chemistry and Technology of Synthetic Rubber), Leningrad: Khimiya, 1970.
6. *Sinteticheskii kauchuk* (Synthetic Rubber), Garmonov, I.V., Ed., Leningrad: Khimiya, 1983.
7. Minkin, V.S., Averko-Antonovich, L.A., and Sukhanov, P.P., *Kauchuk Rezina*, 1994, no. 2, pp. 2–5.
8. Muganlinskii, F.F., Treger, Yu.A., and Lyushin, M.M., *Khimiya i tekhnologiya galogenorganicheskikh soedinenii* (Chemistry and Technology of Organohalogen Compounds), Moscow: Khimiya, 1991.
9. Zanaveskin, L.N., Aver'yanov, V.A., and Treger, Yu.A., *Usp. Khim.*, 1996, vol. 65, no. 7, pp. 667–675.
10. *Promyshlennye khlororganicheskie produkty* (Industrial Organochlorine Products), Oshin, L.A., Ed., Moscow: Khimiya, 1978.
11. Silinskaya, Ya.N., Tomin, V.P., Katul'skii, Yu.N., and Korchevin, N.A., in *Nauka, Tekhnologii, obrazovanie: Sbornik trudov Angarskogo Gos. tekhnol. inst.* (Science, Technology, Education: Coll. of Works of Angarsk State Technological Inst.), Angarsk, 2000, part 2, p. 89.
12. Korchevin, N.A., Turchaninova, L.P., Deryagina, E.N., and Voronkov, M.G., *Zh. Obshch. Khim.*, 1989, vol. 59, no. 8, pp. 1785–1787.
13. Yakimova, G.A., Mel'nichenko, O.V., Maryutin, K.A., *et al.*, in *Transportnye problemy sibirskogo regiona: Sbornik nauchnykh trudov Irkutskogo Inst. inzhenerov transporta* (Transport Problems of Siberian Region: Coll. of Scientific Works of Irkutsk Inst. of Transportation Engineers), Irkutsk, 2000, part 2, p. 122.
14. Zozulya, V.D., *Slovar'-spravochnik po treniyu, iznosu i smazke detalei mashin* (Dictionary-Handbook on Friction, Wear, and Lubrication of Machine Parts), Kiev: Naukova Dumka, 1990.
15. Minkevich, A.N., *Khimiko-termicheskaya obrabotka metallov i splavov* (Chemical and Thermal Treatment of Metals and Alloys), Moscow: Mashinostroenie, 1965.

Russian Journal of Applied Chemistry, Vol. 75, No. 2, 2002, pp. 265–275. Translated from Zhurnal Prikladnoi Khimii, Vol. 75, No. 2, 2002, pp. 274–285.
Original Russian Text Copyright © 2002 by Smirnov, Komarov, Kushch, Ponomareva, Lantsov.

MACROMOLECULAR CHEMISTRY AND POLYMERIC MATERIALS

Structural and Kinetic Features of Formation of High-Strength Epoxy-Amine Cross-Linked Polymers by Combined Polycondensation–Polymerization Process

Yu. N. Smirnov, B. A. Komarov, P. P. Kushch, T. I. Ponomareva, and V. M. Lantsov

Institute for Problems of Chemical Physics, Russian Academy of Sciences, Chernogolovka, Moscow oblast, Russia

Kazan Institute of Construction Engineering, Kazan, Tatarstan, Russia

Received September 13, 2001

Abstract—To control the structural contributions of the polycondensation and polymerization curing of epoxy resins, the curing kinetics of the composites diepoxide–tertiary amine and diepoxide–(primary + tertiary) amines is studied by the isothermal calorimetry.

A specific feature of products formed in curing of epoxy resins with primary amines by the polycondensation mechanism is the presence of tertiary amino groups fixed at the network junctions and of secondary alcohol groups in the hydroxy ether fragments of the interjunction chain [1, 2]. This affects not only the kinetics and mechanism of formation of the cross-linked structure in the course of curing [2, 3–6], but also characteristics of the resulting epoxy-amine cross-linked polymers (EACLPs) [1, 2, 7].

The latter is associated with the fact that these groups can serve as active sites in the physical network [6, 8], causing high cohesion strength of polycondensation (PC) EACLPs. At the same time, polymerization (PM) EACLPs prepared by the mechanism catalyzed by tertiary amines (TAs) demonstrate, unlike PC EACLPs, lower cohesion strength, but higher adhesion to the surface of glass fibers [9, 10].

These differences in the properties of PC and PM cross-linked polymer matrices (CLPMs) are probably due to the features of their structural organization at the chemical, topological, and supramolecular levels [11]. A particularly pronounced difference is observed in the structures of a network junction and an interjunction chain responsible to a significant extent for the mechanical characteristics of EACLPs [12]. In the case of PM EACLPs a more defective, less rigid crosslinked structure is realized, demonstrating higher flexibility [11, 13], which, evidently, facilitates relaxation of internal (thermal) strains, generally concentrated at the CLPM–fiber interface [14], thus increasing the adhesion resistance [9].

Therefore, it was of interest to obtain CLPMs with varied content of PC and PM fragments or the corresponding microvolumes with varied degree of cross-linking. The final purpose of the study is to obtain high-strength epoxy matrices with controlled structural microheterogeneity. As known [15–17], high-strength CLPMs can be designed by forming synthetically a faulted structure with microvolumes having lower degree of cross-linking, i.e., demonstrating lower local modulus of elasticity and higher molecular flexibility.

In this work, we studied the structural and kinetic features of curing of epoxy resins with primary aromatic amines in the presence of tertiary amines with varied reactivity by the combined polycondensation–polymerization mechanism, and also analyzed the structure and relaxation and mechanical characteristics of the resulting PM/PC polymer matrices.

EXPERIMENTAL

As starting materials we used resorcinol diglycidyl ether (RDE) purified by high-vacuum distillation and diaminopyridine (DAP) recrystallized from a methanol–heptane mixture.

As additives we used two types of tertiary amines: reactive TAs [dimethylbenzylamine (DMBA), dimeth-

1070-4272/02/7502-0265 $27.00 © 2002 MAIK "Nauka/Interperiodica"

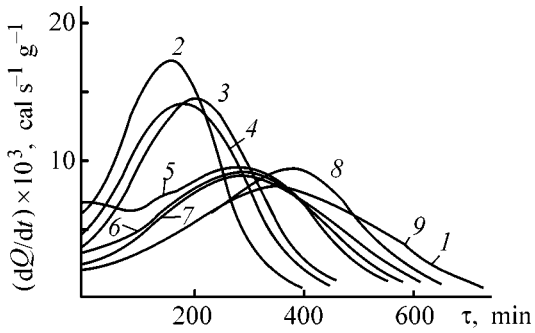

Fig. 1. Rate of heat release, d*Q*/d*t*, vs. the curing time τ at 80°C for RDE–DAP–TA composites. TA: (*1*) no, (*2*) LD, (*3*) DMA, (*4*) α-P, (*5*) DMBA, (*6*) β-P, (*7*) TEA, (*8*) CD, and (*9*) DEA.

ylaniline (DMA), α- and β-picolines (α- and β-P), triethanolamine (TEA), 2,4-lutidine (LD), 2,4,6-collidine (CD)] and inactive diethylaniline (DEA). All the tertiary amines were purified by vacuum distillation from KOH.

The curing kinetics was studied with an EK-2 isothermal fast microcalorimeter and a DAK-1-A microcalorimeter.

Relaxation characteristics of epoxy-amine composites cured according to the following schedule: 70°C, 18 h; 140°C, 6 h; and 160°C, 2 h, were studied in the range of α-relaxation by method of the bending resonance vibrations on a setup described in [18] and in the range of β-relaxation, with a torsion pendulum (free oscillations) [19].

The nuclear magnetic spin-lattice (T_1) and spin–spin (T_2) relaxation times were determined on a pulse coherent relaxometer [11] at a frequency of 17 MHz. The T_2 was measured by the free induction decay and Hahn's methods, and T_1, using 180°–90° pair pulses. Mechanical characteristics (tensile strength σ_t, Young's modulus E_t, and the rupturing deformation ε_t were determined on a 1231U tensile-testing machine at a clamp motion velocity of 1 mm min^{-1}. The total fracture energy A_f was estimated by integration of the area under the fracture curve. The surface fracture energy γ was determined by the procedure described in [20]. Electron micrographs were obtained as in [21].

Effect of TA additives on the kinetics and mechanism of curing. In this section we report on a kinetic study performed in attempt to control the relative contributions of the PC and PM mechanisms by varying the ratio of the corresponding rates of conversion of epoxy groups. This was realized by using TAs with different reactivities and by varying the TA amount and curing temperature.

The differential curves of heat release for the initial system RDE + DAP and the systems RDE + DAP + TA are presented in Fig. 1 (each point in the curves corresponds to a current rate of heat release). As seen, in all the systems curing develops as an autocatalytic process (the initial rate of curing is noticeably lower that the maximal value). The presence of 0.8–1.4 mol % reactive TAs (LD, DMA, α-P, DMBA, β-P, and TEA) noticeably accelerates curing: the initial and maximal rate of heat release increase, and the time in which the maximal rate τ_{max} is reached decreases. Addition of CD has virtually no effect on the initial stage of curing, only shifting the peak rate position to longer time. It should be pointed out that all the indicated TAs can themselves initiate PM conversion of the epoxy groups at the initial rate W_0^{PM} given in Table 1. At the same

Table 1. Kinetic parameters of curing of the investigated composites*

TA	pK_b TA	[TA], mol %	$W_0^{PM}\times10^3$	$W_0^{PC+PM}\times10^3$	$W_{max}^{PC+PM}\times10^3$	k_0	k_{max}	τ_{max}, min
			cal s^{-1} g^{-1}					
–	–	0	–	2.0	7.8	–	–	350
2,4-LD	8.0	1.35	0.5	6.0	17.2	2.4	2.2	165
DMA	8.9	1.33	0.04	3.1	14.6	1.5	1.87	190
α-P	8.0	1.21	0.2	4.3	14.0	1.95	1.80	180
DMBA	8.93	0.87	5.85	7.2	9.5	0.12	1.22	290
β-P	8.3	1.46	0.95	4.1	8.8	1.39	1.13	290
TEA	7.96	1.02	0.04	4.2	8.6	1.27	1.10	290
2,4,6-CD	6.7	1.17	0.04	2.0	9.1	1.0	1.17	380
DEA	7.6	1.20	0	2.0	7.8	1.0	1.0	350

* (W_0^{PM}, W_0^{PC+PM}) Initial rates for the systems RDE + TA and RDE + DAP + TA, respectively; $k_0 = W_0^{PC+PM}/(W_0^{PC} + W_0^{PM})$, where ($W_0^{PC} + W_0^{PM}$), is the estimated total rate for the systems RDE + DAP and RDE + TA; $k_{max} = W_{max}^{PC+PM}/W_{max}^{PC} \times \tau_{max}$ is the time in which the maximal rate is reached at 80°C.

time, addition of DEA, which does not promote polymerization of the epoxy groups, does not influence the curing kinetics at [DEA] < 2 mol %, and at higher concentrations the initial and maximal rates of heat release decrease and the peak rate position shifts toward longer time. Note that the inhibiting effect of DEA on polycondensation has been observed previously with primary aromatic and aliphatic amines [22]. Since addition of DEA does not change significantly the curing mechanism and, correspondingly, the topological structure of EACLPs, it acts as a typical plasticizer which, like DBP, decelerates chemical cross-linking and accelerates physical (relaxation) structurization of EACLPs [23].

A kinetic study to predict the particular contributions of PC and PM mechanisms of conversion of epoxy groups to the final chemical structure appeared to be difficult. The results obtained (Table 1) show that, firstly, there is no correlation between the basicity of TAs (pK_b) and the PM conversion rate, which is caused by the steric accessibility of the nucleophilic center at the nitrogen atom (in the case of DEA this is a crucial factor) [24]. Secondly, there is no correlation between the PM activity of TAs and the gain in the rate of the combined PC–PM curing. This is probably due to the dual behavior of TAs in the polycondensation system. On the one hand, TAs can act as electron donor capable of binding active protons of primary amino groups, thereby making lower the effective concentration of proton donors [22] and decelerating the PC process. On the other hand, primary amino groups, can in their turn, being proton donors, accelerate the PM process under the action of TAs [22]. The cross effect of the PC and PM processes must be strongly dependent on the reactivity and complexing power of the corresponding primary and tertiary amines. The relative rates of these processes are also influenced by the presence of other proton donors, especially of secondary alcohol hydroxy groups formed in opening of epoxy groups by various mechanisms (one OH group per epoxy group in the case of the PC mechanism and per 5–6 epoxy groups in the case of the PM mechanism [25]). Therefore, the PC to PM rate ratio may vary widely in the course of curing. It should be pointed out that combined action of different types of hardeners is not additive, but provides a synergistic effect. It follows from Table 1 that, for most of TAs, the initial rate W_0^{PC+PM} in the combined system RDE + DAP + TA exceeds the sum of the rates $W_0^{PC} + W_0^{PM}$ in separate systems RDE + DAP and RDE + TA. The synergistic effect makes it impossible to estimate from the kinetic data the structural contributions from

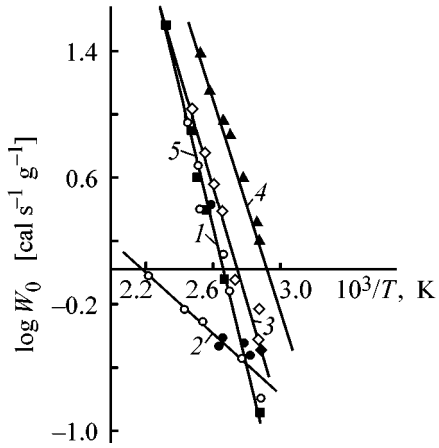

Fig. 2. Arrhenius plots of the initial curing rates in the systems (*1*) RDE + DAP, (*2*) RDE + β-P, (*3*) RDE + DAP + β-P, (*4*) RDE + DAP + DMBA, and (*5*) RDE + DAP + DEA. (W_0) Initial curing rate and (T) temperature.

the PC and PM processes. Evidently, the only way to estimate these contributions adequately estimation is by IR spectroscopic study of the accumulation of OH groups (essentially by the PC mechanism) and C–O–C linear ether groups (PM process) [2, 26–28]. Note that, when using a combination of primary and tertiary amines, changing the curing temperature makes the situation even more complicated. It follows from the Arrhenius plots of the initial curing rates in the systems RDE + DAP, RDE + β-P, RDE + DAP + β-P, RDE + DAP + DMBA, and RDE + DAP + DEA (Fig. 2) that the activation energy of the purely PM process (curve *2*) is considerably lower than that for the PC process (curve *1*) (4.6 and 19.6 kcal mol^{-1}, respectively). Therefore, the activation energy of the combined process decreases too, being 16 kcal mol^{-1} for β-P and 15 kcal mol^{-1} for the more reactive DMBA. In the case of small additions of inactive DEA (curve *5*), the activation energy remains unchanged. The results show that, with increasing curing temperature, the contribution of the PM process must decrease, since W_0^{PC+PM} approaches W_0^{PC}. This should be taken into account in the case when curing proceeds step-by-step, since the PC to PM rate ratio will additionally change in the course of curing, depending on the temperature and treatment time in the corresponding step.

The PM contribution can be controlled by varying the TA concentration only to a limited extent, since the polycondensation kinetics is second-order with respect to a primary amine (T = 70°C), and the order of polymerization varies between 0.6 and 1.0. Therefore, the most effective factor controlling the PM contribution is the TA reactivity which can be varied within two orders of magnitude.

Analysis of the structural organization of EACLPs. (1) Chemically, addition of TA results in increased amount of unreacted secondary amino groups, decreased content of secondary alcohol groups, and formation of double vinylidene bonds via isomerization of the epoxy ring [2, 25, 26, 28]. Lowering the amount of secondary OH groups, serving as network junctions [1, 5, 6], must decrease to certain extent the cohesion resistance of EACLPs. It should be outlined that some of the amines studied, e.g., β-P, can enter the network, as demonstrated by data on its consumption in the course of curing (data were obtained using chromatographic analysis). Although the mechanism of this reaction is not understood exactly, one may suggest that such a behavior of β-P is caused by the possibility of pyridine ring opening with cleavage of the C–N bond [29]. In this case linear products having a system of conjugated bonds can be formed, as evidenced by the intense coloration of the system RDE + DAP + β-P. Therefore, this TA can additionally modify the network chemical structure.

(2) Topologically, addition of TA changes the nature and functionality of the junctions and interjunction chain. Note that, as considered below, the junction functionality can take an important part in formation of mechanical characteristics of cross-linked polymers. A network junction is a major kinetic unit of large-scale segmental motion in EACLPs (α relaxation) [30]. Therefore, the junction functionality must control the effective size of the kinetic unit, i.e., the degree of cooperativity of segmental motion and, correspondingly, the energy dissipated in the course of α relaxation. In the case of PC process (if it proceeds without a side reaction of epoxy groups with secondary alcohol groups and without cyclization), the nitrogen atom is the only branchpoint or junction. In this case, the functionality of EACLP network junction is controlled essentially by the structure of an amine hardener [1]. If the structure of the fragment connecting two primary amino groups has certain flexibility (e.g., in the case of the aliphatic fragment ~CH_2–CH_2~), the junction with a branchpoint at the nitrogen atom can be considered trifunctional. When the connecting fragment is an aromatic ring (pyridine ring in our case), we have a tetrafunctional junction. A typical fragment of a PC cross-linked structure is shown below:

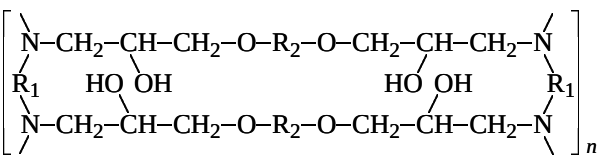

where R_1 and R_2 are aromatic residues of the corresponding diamines and diglycidyl ethers.

In the PM process with a bifunctional epoxy resin, a cross-linked structure with a trifunctional junction and a branchpoint at the nitrogen atom is formed. A typical fragment of PM crosslinked structure formed without side isomerization reactions can be represented as follows:

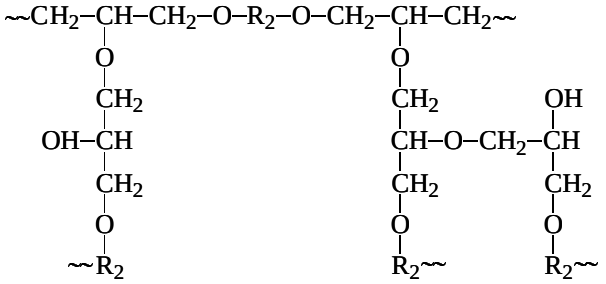

It follows from a comparison of the typical defect-free PC and PM structural fragments that, in the case of the PM network, the interjunction distance must be noticeably shorter than that in the PC network. It would be expected that such a PM cross-linked structure must have higher rigidity (degree of correlated motion of the network junctions) and more hindered segmental motion, resulting in a higher glass transition point T_g. However, our experiments showed that T_g of PM EACLPs (as a parameter characterizing the segmental mobility [31]) appeared to be lower as compared with PC, which is due to higher fault density in PM EACLPs [11]. Therefore, it may be suggested that, with addition of TA, the degree of topological faultiness of the combined EACLP structure must increase too. Indeed, the decrease in T_g with increasing TA content, which becomes more pronounced with increasing TA reactivity (W_0^{PM} in Table 1), supports this hypothesis.

Furthermore, comparison of the regular structural units of the PC and PM networks shows that the difference between them consists in that the interjunction chain contains two hydroxy ether groups (**I**) in the former case, and one or two ether groups (**II**) in the latter:

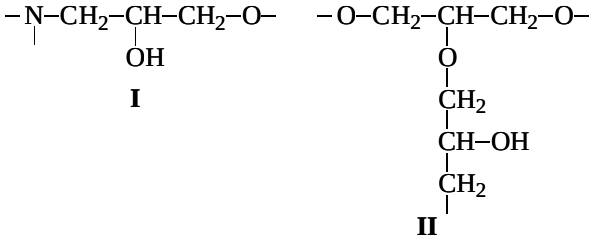

With increasing TA concentration in the system, the content of fragment **I** must decrease, and that of

fragment **II**, decrease. This trend can be revealed by studying the temperature dependence of the mechanical loss tangent tan δ, as a decreasing intensity of the β transition. Indeed, such a confirmation was obtained in [13]. A thorough analysis of β relaxation spectra can be found below. Therefore, addition of TA modifies significantly the topology of EACLPs, the effect being more pronounced with increasing TA reactivity and concentration. These parameters can be optimized on the basis of data on the structural and strain behavior of combined PC–PM EACLPs.

(3) At the supramolecular level of the EACLP structure one may expect increasing degree of microheterogeneity as a result of higher degree of the topological faultiness in the presence of TA. In fact, we observed increased microroughness of the chip surface in the electron micrographs of TA-modified samples. It should be pointed out that the effect of small addition of TAs on the supramolecular structure of epoxy-amine polymer matrices differs significantly from that in epoxy-phenol cross-linked polymer matrices [32]. In the latter case, a small amount of TA suppressed the side reaction producing ether fragments **II**. As a result, the degree of ordering at the topological and, correspondingly, supramolecular levels of the CLPM structure increased. Also, TA considerably affects the supramolecular packing of EACLPs. Figure 3 presents theoretical concentration dependence of the specific volume V_{theor}, obtained on the assumption of additivity of the polymer matrix and TA volumes:

$$V_{theor} = \varphi_{PM} V_{PM} + \varphi_{TA} V_{TA},$$

where V_{PM} and V_{TA} are the specific volumes of the polymer matrix and TA, respectively; φ_{PM} and φ_{TA} are their weight fractions. The same figure shows the experimental concentration dependence of the specific volume V_{exp} of the system RDE + DAP + TA for tertiary amines with different polymerization activities. The results show that the specific volume of the system with more active DMBA increases more rapidly as compared with the theoretical dependence, and with less active β-P and inactive DEA, more slowly, suggesting that DMBA loosens the network structure through its chemical modification, while β-P and DEA act essentially as typical plasticizers [33], filling voids of the free space or promoting relaxation of the excess free volume of the polymer matrix.

Relaxation properties of EACLPs. The TA effect on the EACLP structure is distinctly reflected in evolution of the relaxation properties of these polymers at the local (β process) and segmental levels of molecular mobility (α process). (1) Analysis of β-relaxation spectra of TA-modified EACLPs shows that local motion in PC–PM EACLPs significantly depends on both the TA activity and concentration. The temperature dependences of the dynamic shear modulus G' and mechanical loss tangent tan δ of EACLPs modified with various TAs (4 wt %) or without TA are presented in Fig. 4. In all cases, we

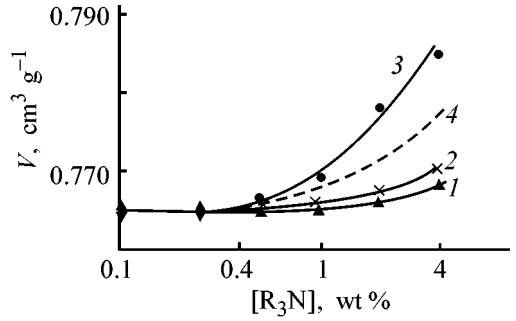

Fig. 3. Specific volume V of the system RDE + DAP + TA vs. the TA concentration [R_3N] (wt %): (*1*) β-P, (*2*) DEA, (*3*) DMBA, and (*4*) theoretical curve.

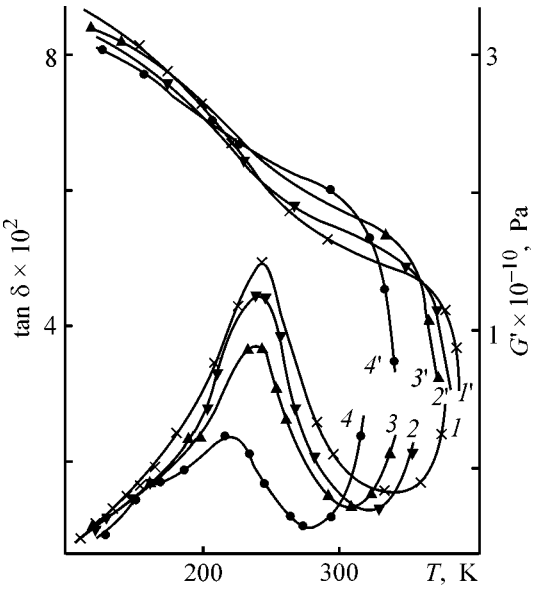

Fig. 4. (*1*–*4*) Mechanical loss tangent tan δ and (*1'*–*4'*) dynamic shear modulus G' of the system RDE + DAP + 4 wt % TA vs. the temperature T (K). TA: (*1*, *1'*) no, (*2*, *2'*) DEA, (*3*, *3'*) β-P, and (*4*, *4'*) DMBA.

Table. 2. Parameters of β transition in hardened composites RDE + DAP + 4 wt % TA

TA	tan $\delta_{max} \times 10^2$	$\Delta G/G$	K	ΔH, eV
–	5.0	0.450	0.111	0.83
DEA	4.4	0.403	0.109	0.55
β-P	3.7	0.357	0.104	0.40
DMBA	2.4	0.309	0.078	0.32

Notes: (tan δ_{max}) β Peak intensity of the mechanical loss, ($\Delta G/G$) degree of relaxation, K = tan $\delta_{max}/(\Delta G/G)$, and ($\Delta H$) effective activation energy of β transition.

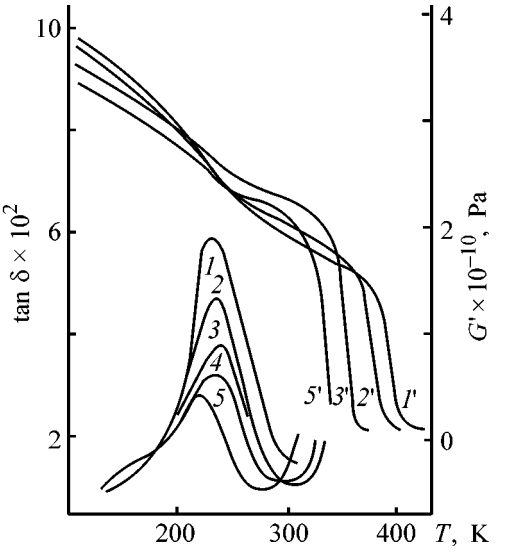

Fig. 5. (*1*–*5*) Mechanical loss tangent tan δ and (*1*′–*5*′) dynamic shear modulus G' in the system RDE + DAP + β-P vs. the temperature T. β-P content (wt %): (*1*, *1*′) 0, (*2*, *2*′) 2, (*3*, *3*′) 4, (*4*, *4*′) 6, and (*5*, *5*′) 10.

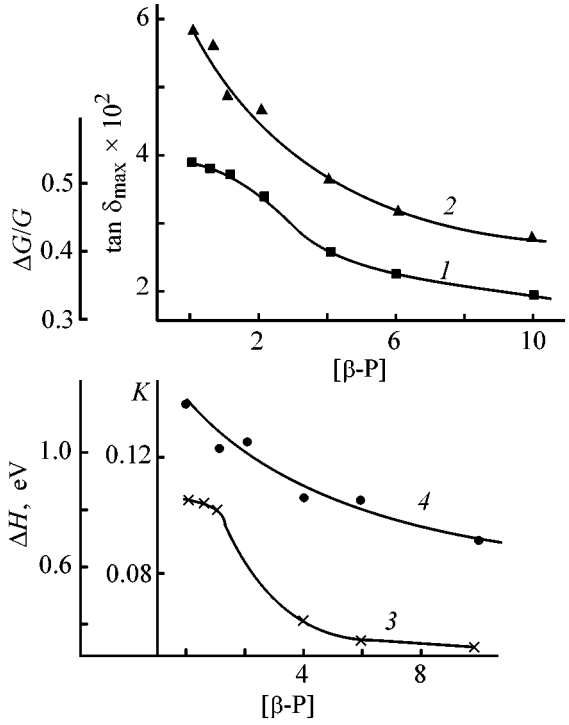

Fig. 6. Parameters of β transition in hardened composites RDE + DAP + β-P vs. the TA concentration [β-P] (wt %): (*1*) degree of relaxation $\Delta G/G$, (*2*) β-peak intensity $\tan\delta_{max}$, (*3*) effective activation energy of β transition ΔH, and (*4*) $K = \tan\delta_{max}/(\Delta G/G)$.

observed spectra typical of epoxy-based polymers [34]. The effect of TA, as expected, increases in the order of the TA activity: DEA < β-P < DMBA. This effect is reflected in the shift of the low-temperature β peak ($\tan\delta_{max}$) toward lower temperature, and, as seen from Table 2, in the decreasing intensity of this peak, decreasing total degree of relaxation $\Delta G/G$ in the vicinity of the β transition ($\Delta G/G = 1 - G_{280}/G_{140}$, where G_{140} and G_{280} are the shear modulus values at 140 and 280 K, respectively), and, finally, in decreasing activation energy of the β process (ΔH). Since β transition is caused by local mobility of the shaft crown type of the hydroxyether fragments **I** [35–37], the observed decrease in the transition parameters can be attributed to decreasing concentration of these structural units. This conclusion is also supported by measured relaxation characteristics of the system RDE + DAP + β-P, as influenced by the TA concentration. It is seen from Figs. 5, 6 that the increasing TA concentration has an effect similar to increasing TA activity. However, the concentration dependences of $\tan\delta_{max}$, $\Delta G/G$, and ΔH tend to level off (Fig. 6), which can be interpreted as follows. In the course of polymerization, the chain-terminating reactions produce polymer network fragments **A** [25]:

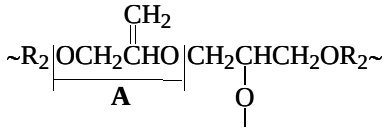

Such fragments are similar in structure to the hydroxy ether fragments responsible for β transition in the PC network. However, they contain no strongly polar OH group. Furthermore, they must demonstrate high flexibility, as containing no nitrogen atom forming a PC network junction. Therefore, it whould be expected that the relaxation of ether fragments **A** proceeds in the vicinity of β transition, but at lower temperature. Indeed, according to [11], the β peak is quite distinctly pronounced and shifted toward low-temperature region in the PM network formed in the system RDE + 5% TA. Similar results were obtained in the systems RDE + DAP + 4% DMBA (Fig. 4, curve *4*) and RDE + DAP + 10% β-P (Fig. 5, curve *5*). The formation of new, more flexible fragments in the PC–PM network is demonstrated by the decrease not only in the activation energy ΔH, but also in $K = \tan\delta_{max}/(\Delta G/G)$, observed with increasing TA activity (Table 2) or concentration (Fig. 6, curve *4*). Since for a purely Debye relaxation peak with a single relaxation time $K = 0.5$ [18], the deviation of the experimental K from the standard value can be regarded as evidence in favor of the occurrence of a spectrum of relaxation times. The decrease in K with increasing TA activity and concentration is an indication of the broadening of this spectrum, specifically, by virtue of the increasing fraction of flexible fragments **A**. Therefore, introduction of flexible PM fragments by

adding TA makes lower the rigidity of the network structure, thus reducing the intrachain cooperativity of local motion [38] and the mechanical energy dissipated at the local level in EACLPs.

At the same time, addition of inactive DEA, not changing the topological structure and not reducing the network rigidity, also decreases the β-peak intensity (peak area) and ΔH of the β process [39]. Such an effect of the inactive TA is due to its plasticizing action, resulting in a decrease in interchain cooperativity of local motion or in the effective size of the kinetic unit of motion [39]. In other words, molecules of low-molecular-weight fluids reduce the effective microviscosity of the medium, thus decreasing the specific mechanical loss.

To conclude, TAs act as chemical or (and) physical plasticizing agents for EACLMs, and, depending on their PM activity and concentration, they can reduce the degree of interchain cooperativity of local motion, thus decreasing the specific mechanical loss.

Note that, in certain cases [40, 41], the mechanical energy dissipated in β process (β-peak area) correlates with the specific impact resilience.

(2) Analysis of α relaxation in PC–PM EACLPs allows understanding of the effect of TAs on the long-range molecular mobility of the segmental type which, as known [42, 43], can play a significant part in static fracture of linear and network polymers. The main contribution of α relaxation consists in dissipation of mechanical load through afterflows at the mouth of a growing crack and relaxation of residual internal strains in the course of curing or of overstrains at the apex of crack in the initial stage of fracture of a cross-linked polymer matrix.

We analyzed the temperature dependences of the nuclear magnetic spin-lattice (T_1) and spin–spin (T_2) relaxation times, using pulse NMR in the vicinity of α transition [11]. A minimum in the temperature dependence of T_1 was found only for the system RDE + 5% TA (Fig. 7, curve *2*), but not for the initial system RDE + DAP (curve *1*). In the case of β-P, the minimum becomes pronounced at a TA concentration above 5 wt %, suggesting that the rigidity of the PC–PM network structure decreases in the presence of TA (in other words, the relaxation capacity of the system increases). An analysis of the decay of cross magnetization (Fig. 7) showed that the decay is described by a single time T_2 (curve *1*') in the case of PC network (initial system RDE + DAP), by two times: short T_{2a} (curve 2') and long T_{2b} (curve *2*") and in the case of PM network (RDE + 5 wt % DMBA) at a temperature above the glass transition point (T_g = 80°C).

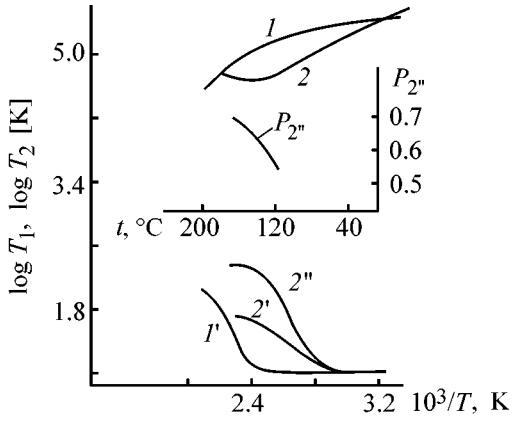

Fig. 7. (*1*, *2*) Nuclear magnetic spin-lattice relaxation time T_1 and (*1*', *2*', *2*") nuclear magnetic spin–spin relaxation time T_2 vs. the temperature T; and population of protons of the more mobile phase $P_{2"}$ vs. the temperature t. (*1*, *1*') PC EACLP and (*2*, *2*') PM EACLP.

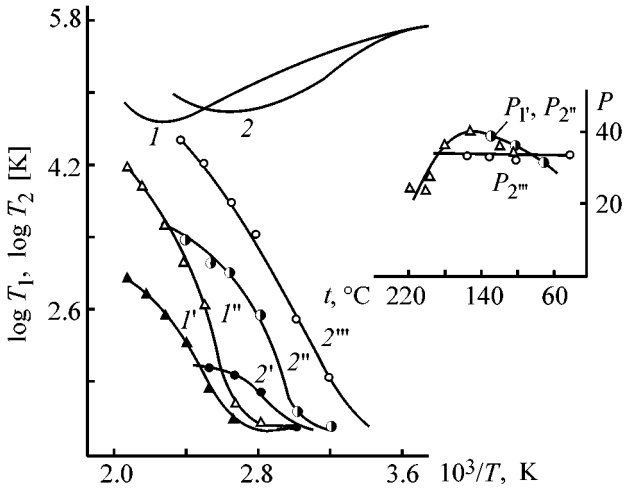

Fig. 8. (*1*, *2*) Nuclear magnetic spin-lattice relaxation time T_1 and (*1*', *1*", *2*', *2*", *2*"') nuclear magnetic spin–spin relaxation time T_2 of the temperature T for the hardened composite RDE + DAP + β-P; and population P of protons of mobile phases vs. the network $P_{1'}$ and $P_{2"}$, and of β-P itself $P_{2'''}$ vs. the temperature t. β-P concentration (wt %): (*1*, *1*', *1*") 10 and (*2*, *2*', *2*", *2*"') 30.

It has been demonstrated previously [11] that this is due to the presence of two kinetic phases formed by protons the PM network and the corresponding fragments (microvolumes) of different topological levels. The short (T_{2a}) and long times (T_{2b}) characterize the behavior of protons in rigid and labile faulty fragments of the PM network, respectively, whose occurrence is caused by the known specific features of the PM process. On varying the β-P concentration in the system RDE + DAP + TA over the range 0–10 wt %, we also found two time parameters T_2 (Fig. 8, curves *1*', *1*"). In this case the short time

Table 3. Effect of β-P concentration on parameters of β transition

[TA], mol %	T_g, K	$E'_{300} \times 10^9$, Pa	$E'_{he} \times 10^7$, Pa	$\tau_\alpha \times 10^2$, s	$\Delta_{1/2}$, K	$\nu \times 10^3$, mol cm^{-3}
0	427	3.53	3.92	5.3	27	3.92
0.25	426	3.43	3.82	4.8	28	3.80
0.5	422	3.72	3.53	4.1	30	3.53
1.0	420	3.72	3.23	3.6	33	3.23
2.0	413	4.12	2.84	2.8	35	2.74
3.0	410	3.72	2.74	2.5	38	2.45

Notes: (E'_{300}, E'_{he}) Dynamic modulus of elasticity at 300 K and in the hyperelastic state, respectively; (τ_α) effective relaxation time of α transition, (ν) cross-linking density, and ($\Delta_{1/2}$) half-width of α peak.

T_{2a} characterizes the behavior of protons in fragments of more rigid PM network, and the long time T_{2b}, the behavior of labile faulty fragments. At a β-P concentration above 30 wt % the cross magnetization decay is described by three time parameters: T_{2a} and T_{2b} (curves *2*' and *2*''), characterizing the relaxation of protons in rigid and flexible faulty fragments of the PC–PM network, and also the longest T_{2c} (curve *2*''') characterizing the behavior of protons of β-P itself, separated out in its own phase, as demonstrated by the coincidence of the estimated fraction of protons in β-P and the measured fraction (population P_c) of protons in the phase characterized by the time T_{2c}. Furthermore, the population of protons in the kinetic phases characterized by the parameters T_{2a} and T_{2b} (whose protons belong just to the network) changes with temperature; the temperature dependence having a maximum (Fig. 8, curves $P_{1'}$ and $P_{2''}$). This suggests that T_{2a} and T_{2b} are close, opening the door for temperature-induced transition of protons from one kinetic phase to another. At the same time, the population of protons in the kinetic phase, characterized by T_{2c}, does not change with temperature (curve $P_{2'''}$), suggesting that their behavior is independent of the polymer matrix (phase separation). To conclude, pulse NMR study of α relaxation shows that the use of TAs provides wide potentialities to control the molecular flexibility within the three modes, which is important in designing materials operating at various load frequencies.

The effects of β-P concentration on the temperature dependences of the dynamic modulus of elasticity E' and mechanical loss tangent tan δ were studied by the method of bending resonance vibrations. The effective number of cross-links decreases with increasing TA concentration, as demonstrated by the decrease in dynamic modulus of elasticity in the hyperelastic state E'_{he} and, correspondingly, in the cross-link density ν (Table 3). The effective ν was determined on assumption of the approximate equality of E'_{he} and the limiting modulus of elasticity E_∞ [18] which, according to the hyperelasticity theory [44], is related to the cross-link density

$$E_\infty = 3\nu RT,$$

where R is the gas constant and T is the absolute temperature.

Addition of TA also decreases other parameters of α relaxation, such as the peak temperature (mechanical glass transition point) T_α and effective time of relaxation of α transition τ_α.

All these trends suggest the decreasing degree of intra- and interchain cooperativity of segmental motion (decreasing effective size of the kinetic unit of this motion) and, as a result, decreasing mechanical loss at α peak ($\tan \delta_{max}$). At the same time, the observed increase in the α-peak half-width $\Delta_{1/2}$ is an indication of the increasing structural and, correspondingly, α-relaxation inhomogeneity in TA-modified EACLPs, which is well consistent with the NMR data. This causes an increase in the total energy dissipated in the course of the α process, determined as $\tan \delta_{max} \Delta_{1/2}$. The results demonstrate that the increasing molecular flexibility of the segmental type in TA-modified EACLPs makes larger the contribution of α relaxation under static load [43] and the energy dissipated in afterflows at the mouth of growing crack [45, 46].

Dilatometric analysis data showed that, in the case of addition of low concentration of inactive DEA or medium-active α-P and β-P, the glass transition point T_g of EACLPs decreases linearly with increasing TA concentration (Fig. 9, curve *1*). This result can be attributed to the essentially plasticizing effect of TAs, changing the interchain cooperativity of segmental motion. At the same time, the observed abrupt decrease in T_g upon addition of minor amounts of DMBA evidences in favor of the fact that TAs also affect on the intrachain cooperativity of long-range motion. It should be pointed out that, in the case of

DMBA, two breaks were detected in the dilatometric curves: the first at a temperature corresponding to T_g of the initial compound RDE + DAP and the second at a temperature decreasing with increasing TA concentration. This is probably due to formation of microheterogeneous PC–PM network structure consisting of microvolumes, rather than large fragments of the PM structure. This finding is consistent with the two different types of the kinetic behavior of protons in the network structure, demonstrated by NMR.

The structural analysis given above allows more adequate interpretation of the trends in the mechanical behavior of EACLPs having a combined PC–PM network structure.

Mechanical properties. Analysis of the experimental data on the effect of TAs on mechanical characteristics of EACLPs (tensile strength σ_t, rupturing deformation ε_t, and Young's modulus E_t) (Fig. 10) revealed the following major trends.

(1) In the case of addition of small amount of inactive DEA (or CD), the tensile strength σ_t remains virtually unchanged (curve *2*). With DMBA (active TA), σ_t decreases (curve *3*), and with β-P or α-P (medium active TAs), the curve passes through a maximum at a TA concentration of 0.5 wt % (curve *1*). In the latter case, the maximal σ_t exceeds the value characteristic of the TA-free compound by 10%.

(2) In the systems with β-P and DEA E_t is virtually constant (curves *1*', *2*') and in those with DMBA, E_t noticeably decreases (curve *3*'). The constancy of E_t in the former case is, evidently, due to the dominant plasticizing effect of small additions [33], when the intrinsic loosening effect of the low-molecular-weight additive is compensated for by the relaxation compaction of the polymer matrix. This is demonstrated by the trend in variation of the EACLP specific volume in the presence of these additives. The decrease in E_t in the presence of DMBA is caused by decreasing rigidity of the PC–PM network structure, as demonstrated by the relaxation data.

(3) At low TA concentrations, ε_t is virtually constant in the case of DEA and DMBA (curves *2*'', *3*'') and passes through a maximum with β-P (note that the peak positions of σ_t and ε_t coincide). It is worth noting that in the latter case a distinctly pronounced plateau of the yield point or hyperelasticity is seen in the deformation failure curves. In this case, the predominance of rough areas is observed in EACLPs on the surface of failure, which is typical of plastic fracture in glassy polymers [47], indicating that the nature of fracture in the combined EACLPs is

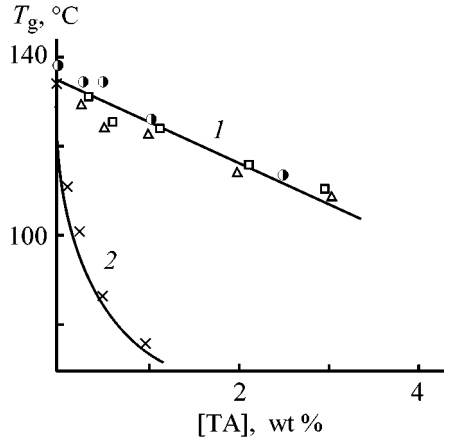

Fig. 9. Glass transition point T_g of the compound RDE + DAP + TA vs. the TA concentration [TA] (wt %): (*1*) DEA, β-P, or α-P; (*2*) DMBA.

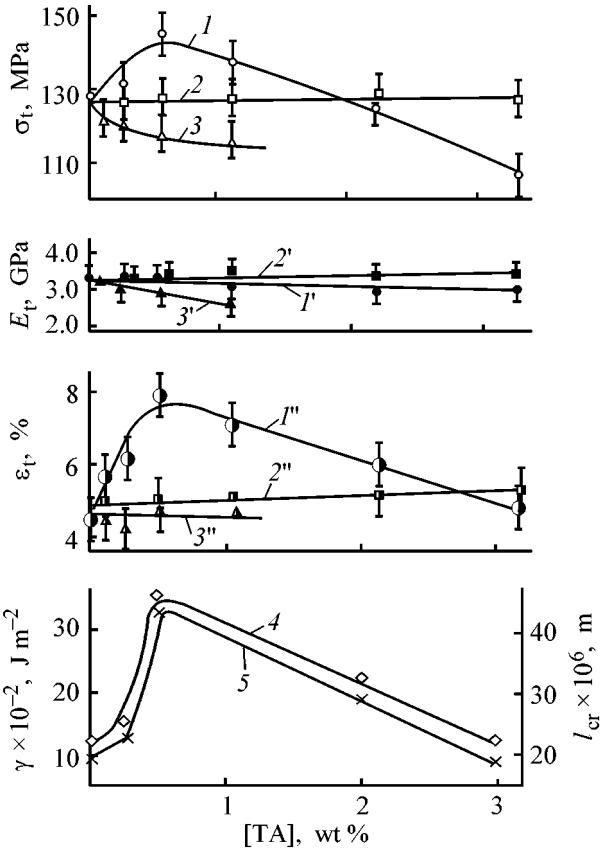

Fig. 10. Mechanical properties of the system RDE + DAP + TA vs. the TA concentration [TA] (wt %): (*1*–*3*) σ_t, (*1*'–*3*') E_t, (*1*''–*3*'') ε_t, (*4*) γ, and (*5*) l_{cr}.

changed. Note also that addition of β-P produces about 200% increase in the deformation characteristics. This is an important result of modification, since the gain in ε_t at constant E_t provides considerable increase in the work of deformation A_d (area under the deformation curve) reflecting the total energy

consumption for deformation and fracture of a material. The A_d value is an important criterion in selecting optimal binders [48] providing high performance of a composite [49].

Let us try to make a simplified analysis of the results obtained using the Griffits equation for the critical strength, relating the major structural parameters of hard materials to each other:

$$\sigma_{cr} = \sqrt{\frac{2E\gamma}{\pi l_{cr}}}.$$

Among these parameters are the modulus of elasticity E (elasticity parameter), surface fracture energy γ (dissipation parameter), and critical size of defect, l_{cr} (structural parameter).

It is seen from Fig. 10 that, with changing β-P concentration, γ also passes through a maximum at about 0.5 wt % TA.

Substituting the E_t, σ_t, and γ values in the equation, we estimated l_{cr} which, like γ, passes through a maximum.

The observed parallelism in the dissipation and structural parameters, which is similar to that reported in [20], suggests that l_{cr} reflects not the size of the critical structural defect in the initial material, but its size in the prerupture state. Therefore, addition of TA has an effect on the rupture initiation stage. Evidently, faulty microvolumes formed in the EACLP structure in the presence of TA favor local (in the mouth of incipient crack) microafterflows, possibly as shear zones observed in faulty EACLPs [51]. As a result of plastic deformation with participation of α relaxation, dissipation of mechanical energy takes place, which grows with increasing α-relaxation cooperativity. This mechanism of action of TA additives can be assigned to the effect of the structural factor. Furthermore, small concentrations of TAs, increasing the local and long-range (segmental) molecular flexibility, favor relaxation of stresses in the mouth of growing crack and delocalization of fracture. The local fracture process involves a large volume of material subjected to deformation [32]. This implies higher deformability of PC–PM EACLPs and, correspondingly, larger size of the prerupture critical defect.

To conclude, taking into account the observed improvement in the mechanical properties (tensile strength and, especially, rupturing deformation) through modification of EACLPs with TAs, and also in the adhesion to glass, TA additives can be recommended as modifiers for EACLPs of various purposes.

CONCLUSIONS

(1) Simultaneous operation of the polycondensation and polymerization curing mechanisms gives a synergistic effect whose intensity is controlled by the structure of a tertiary amine.

(2) The effect of tertiary amines of various reactivities on the local (α-process) and segmental (β-process) molecular flexibility in epoxy-amine cross-linked polymers is studied by the method of bending resonance vibrations, torsion pendulum method (free oscillations), pulse NMR spectroscopy, and dilatometry. The relaxation spectra of various modes of flexibility show that the structural microheterogeneity grows with increasing TA content and reactivity.

(3) The effect of TA additives on mechanical characteristics, such as the tensile strength, Young's modulus, rupturing deformation, and total and surface rupture energies, and also on the rupture mechanism is studied.

ACKNOWLEDGMENTS

The work was financially supported by the Russian Foundation for Basic Research and the Moscow oblast foundation (project no. 01-03-97001).

REFERENCES

1. Salamatina, O.B., Akopyan, E.L., Rudnev, S.N., *et al.*, *Vysokomol. Soedin., Ser. A*, 1983, vol. 25, no. 1, pp. 179–195.
2. Morgan, R.J. and Mones, E.T., *J. Appl. Polym. Sci.*, 1987, vol. 33, no. 4, pp. 999–1006.
3. Arutyunyan, Kh.A., Kinetics and Mechanism of Curing of Epoxy Oligomers with Aromatic Amines, *Cand. Sci. Dissertation*, Chernogolovka, 1974.
4. Blyakhman, E.M., Nikitina, N.N., Zelenina, N.L., and Shevchenko, Z.A., *Vysokomol. Soedin., Ser. A*, 1974, vol. 16, no. 5, pp. 1031–1036.
5. Vladimirov, L.V., Artemenko, S.A., Ivanov, V.V., *et al., Vysokomol. Soedin., Ser. A*, 1980, vol. 22, no. 1, pp. 225–230.
6. Zhorina, L.A., Knunyants, M.I., and Vladimirov, L.V., *Vysokomol. Soedin., Ser. A*, 1986, vol. 28, no. 6, pp. 1310–1315.
7. Morgan, R.L., O'Neal, J.E., and Miller, D.B., *J. Mater. Sci.*, 1974, vol. 14, no. 1, pp. 109–115.
8. Vladimirov, L.V., Zelenetskii, A.N., and Oleinik, E.F., *Vysokomol. Soedin., Ser. A*, 1977, vol. 19, no. 9, pp. 2104–2111.
9. Lee, H. and Nevill, K., *Handbook of Epoxy Resins*, New York: McGraw-Hill, 1967.

10. Partansky, A.M., *Epoxy Resins*, Washington, DC, 1970.
11. Smirnov, Yu.N., Komarov, B.A., Zakirov, I.N., *et al.*, *Vysokomol. Soedin., Ser. B*, 1983, vol. 25, no. 9, pp. 671–674.
12. Irzhak, V.I., Rozenberg, B.A., and Enikolopyan, N.S., *Setchatye polimery: Sintez, struktura, svoistva* (Network Polymers: Synthesis, Structure, and Properties), Moscow: Nauka, 1979.
13. Aniskina, T.A., Smirnov, Yu.N., Shteinberg, V.G., and Rozenberg, B.A., *Vysokomol. Soedin., Ser. A*, 1980, vol. 22, no. 11, pp. 2528–2533.
14. Korotkov, V.N., Chekanov, Yu.A., and Rozenberg, B.A., *Vysokomol. Soedin., Ser. A*, 1994, vol. 36, no. 4, pp. 684–689.
15. Natrusov, V.I., Shatskaya, T.E., Lapitskii, V.A., *et al.*, *Mekh. Kompozit. Mater.*, 1987, no. 2, pp. 315–319.
16. Tarasov, V.P., Smirnov, Yu.N., Shatskaya, T.E., *et al.*, *Vysokomol. Soedin., Ser. B*, 1990, vol. 32, no. 6, pp. 428–431.
17. Smirnov, Yu.N., Magomedov, G.M., Shatskaya, T.E., and Natrusov, V.I., *Vysokomol. Soedin., Ser. A*, 1996, vol. 38, no. 10, pp. 1717–1721.
18. Perepechko, I.I., *Akusticheskie metody issledovaniya polimerov* (Acoustic Methods in Polymer Research), Moscow: Khimiya, 1973.
19. Shteinberg, V.G., Efremova, A.I., and Rozenberg, B.A., *Vysokomol. Soedin., Ser. A*, 1979, vol. 21, no. 6, pp. 1259–1263.
20. Volkov, V.P., Evdokimenko, N.M., Kartsovnik, V.I., *et al.*, *Mekh. Polym.*, 1978, no. 2, pp. 248–251.
21. Shteinberg, V.G., Volkov, V.P., Zaspinok, G.S., *et al.*, *Vysokomol. Soedin., Ser. A*, 1978, vol. 20, no. 12, pp. 2298–2301.
22. Mutin, I.I., Kushch, P.P., Komarov, B.A., *et al.*, *Vysokomol. Soedin., Ser. A*, 1980, vol. 22, no. 8, pp. 1828–1833.
23. Smirnov, Yu.N., Dzhavadyan, E.A., and Golodkova, F.M., *Vysokomol. Soedin., Ser. B*, 1998, vol. 40, no. 6, pp. 1031–1034.
24. Rozenberg, B.A., in *Kompozitsionnye polimernye materialy* (Composite Polymer Materials), Kiev: Naukova Dumka, 1975, pp. 39–59.
25. Kushch, P.P., Lagodzinskaya, G.V., Komarov, B.A., and Rozenberg, B.A., *Vysokomol. Soedin., Ser. B*, 1979, vol. 21, no. 9, pp. 708–711.
26. Pirozhnaya, L.N., *Vysokomol. Soedin., Ser. A*, 1970, vol. 12, no. 11, pp. 2446–2448.
27. Sidyakin, P.V., *Vysokomol. Soedin., Ser. A*, 1972, vol. 14, no. 5, pp. 979–983.
28. Sorokin, M.F., Shode, L.G., and Shteinpress, A.B., *Vysokomol. Soedin., Ser. A*, 1972, vol. 14, no. 2, pp. 309–313.
29. Karrer, P., *Lehrbuch der Organischen Chemie*, Stuttgart: Thieme, 1959.
30. Tarasov, V.P., Smirnov, Yu.N., Erofeev, L.N., *et al.*, *Vysokomol. Soedin., Ser. A*, 1982, vol. 24, no. 11, pp. 2379–2382.
31. Bartenev, G.M. and Frenkel', S.Ya., *Fizika polimerov* (Polymer Physics), Leningrad: Khimiya, 1990.
32. Smirnov, Yu.N. and D'yankova, S.L., *Zh. Prikl. Khim.*, 2000, vol. 73, no. 5, pp. 819–825.
33. Mironova, T.A., Smirnov, Yu.N., Irzhak, V.I., and Rozenberg, B.A., *Vysokomol. Soedin., Ser. B*, 1983, vol. 25, no. 7, pp. 531–534.
34. Pogany, G., *Polymer*, 1970, vol. 11, no. 1, pp. 66–71.
35. Delatycki, O., Shaw, J., and Williams, J., *J. Polym. Sci., Ser. A-2*, 1969, vol. 7, pp. 753–757.
36. Arridge, R.G.C. and Speake, J.H., *Polymer*, 1972, vol. 13, no. 9, pp. 450–458.
37. Oleinik, E.F. and Rudnev, S.N., *Vysokomol. Soedin., Ser. A*, 1980, vol. 22, no. 11, pp. 2482–2490.
38. Shteinberg, V.G., Smirnov, Yu.N., Irzhak, V.I., and Rozenberg, B.A., *Vysokomol. Soedin., Ser. A*, 1981, vol. 23, no. 9, pp. 665–668.
39. Smirnov, Yu.N., Shteinberg, V.G., Mironova, T.A., *et al.*, *Vysokomol. Soedin., Ser. B*, 1983, vol. 25, no. 10, pp. 762–764.
40. Wada, J. and Kazahara, T., *J. Appl. Polym. Sci.*, 1967, vol. 11, no. 9, pp. 1661–1669.
41. Saher, E.A., *J. Appl. Polym. Sci.*, 1975, vol. 19, no. 9, pp. 1421–1428.
42. Aharoni, S.M., *J. Appl. Polym. Sci.*, 1972, vol. 16, no. 12, pp. 3275–3284.
43. Smirnov, Yu.N., Irzhak, V.I., and Rozenberg, B.A., *Vysokomol. Soedin., Ser. B*, 1983, vol. 25, no. 12, pp. 914–916.
44. Treloar, L.R.G., *The Physics of Rubber Elasticity*, Oxford: Clarendon, 1949.
45. Gent, A.N., *J. Mater. Sci.*, 1973, vol. 5, no. 4, pp. 729–736.
46. Morgan, B.J. and O'Neal, J., *J. Polym. Eng. Sci.*, 1978, vol. 18, no. 14, pp. 1081–1086.
47. Gul', V.E., *Struktura i prochnost' polimerov* (Structure and Durability of Polymers), Moscow: Khimiya, 1971.
48. Rozenberg, B.A., Oleinik, E.F., and Irzhak, V.I., *Zh. Vses. Khim. O–va*, 1978, vol. 23, no. 3, pp. 273–284.
49. Corten, H.T., *Razrushenie armirovannykh plastikov* (Fracture of Reinforced Plastics), Moscow: Khimiya, 1967.
50. *Fracture. An Advanced Treatise*, Liebowitz, H., Ed., vol. 7: *Fracture of Nonmetals and Composites*, New York: Academic, 1972.
51. Morgan, R.J. and Mones, E.T., *Am. Chem. Soc. Polym. Prepr.*, 1980, vol. 21, no. 2, pp. 231–232.

Russian Journal of Applied Chemistry, Vol. 75, No. 2, 2002, pp. 276–280. Translated from Zhurnal Prikladnoi Khimii, Vol. 75, No. 2, 2002, pp. 286–290.
Original Russian Text Copyright © 2002 by Solovskii, Pavlov, Korneeva, Harding, Denisov, Nikol'skaya.

MACROMOLECULAR CHEMISTRY AND POLYMERIC MATERIALS

Synthesis of *N*-Vinylpyrrolidone–Crotonic Acid–2-Hydroxyethyl Methacrylate Terpolymers as Carriers of Biologically Active Substances

M. V. Solovskii, G. M. Pavlov, E. V. Korneeva, S. E. Harding, V. M. Denisov, and N. V. Nikol'skaya

Institute of Macromolecular Compounds, Russian Academy of Sciences, St. Petersburg, Russia

Research Institute of Physics, St. Petersburg State University, St. Petersburg, Russia

National Centre of Macromolecular Hydrodynamics, Nottingham University, Nottingham, UK

Received November 2, 2001

Abstract—Water-soluble *N*-vinylpyrrolidone–crotonic acid–2-hydroxyethyl methacrylate terpolymers, potential polymeric carriers for biologically active substances, were prepared. The composition of the terpolymers was determined, their chemical structure was confirmed, and their hydrodynamic characteristics and structural features in aqueous solutions were studied.

N-Vinyl-2-pyrrolidone (VP) terpolymers containing two types of monomeric units with reactive functional groups are of indubitable interest for development of polymeric carriers for biologically active substances (BASs) [1]. Such terpolymers can serve as a basis for preparing hydrophilic polymers with polyfunctional activity by covalent (or ionic and covalent) binding of two BASs with different mechanisms of the biological effect. It is interesting to consider in this respect VP terpolymers **I** containing carboxy and primary hydroxy groups.

In this work, we prepared and studied such terpolymers. These substances were synthesized by ternary radical copolymerization of VP with crotonic acid (CA) and 2-hydroxyethyl methacrylate (2-HEMA). The interest in 2-HEMA is due to the fact that polymers based on it (hydrogels) are biologically compatible with a living body and are used for immobilization of various BASs and fabrication of contact lenses [2–6]. At the same time, VP–CA copolymers are also used for modification of various BASs [7, 8]. Furthermore, CA acts as a chain-terminating agent in the polymerizing monomer mixture.

The kinetics of terpolymerization of VP (M_1) with CA (M_2) and 2-HEMA (M_3) was studied in ethanol at 343 K; the monomer molar ratio was $[M_1] : [M_2] : [M_3] = 65.5 : 14.5 : 20.0$, and the concentration of the initiator, azobis(isobutyronitrile) (AIBN), 1.5 wt %. The total initial concentration of the monomers was 20 wt %. For comparison, we studied under the same conditions the binary copolymerization of VP with 2-HEMA at the molar ratio $[M_1] : [M_2] = 80 : 20$. Copolymerization of VP with 2-HEMA under these

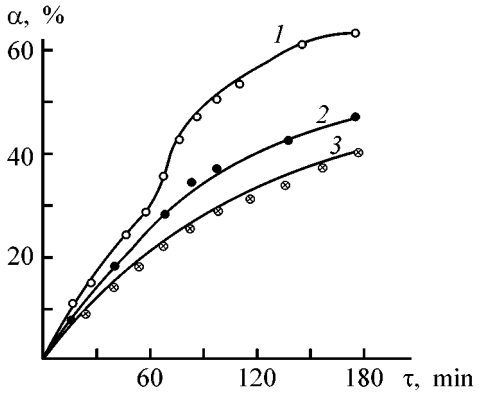

Fig. 1. Conversion α vs. time τ in copolymerization of monomers in ethanol at 343 K in the presence of 1.5 wt % AIBN. Initial concentration of the monomers 20 wt %. Copolymer and molar ratio of monomers: (*1*) VP–2-HEMA, $[M_1] : [M_2] = 75 : 25$; (*2*, *3*) VP–CA–2-HEMA, $[M_1] : [M_2] : [M_3] = 65.5 : 14.5 : 20.0$ and $77.0 : 14.5 : 8.5$, respectively.

1070-4272/02/7502-0276 $27.00 © 2002 MAIK "Nauka/Interperiodica"

Table 1. Terpolymerization of VP (M_1), CA (M_2), and 2-HEMA (M_3) in ethanol at 343 K

Run no.	Initial monomer mixture					Yield in 48 h, %	Terpolymer **I**				
	$[M_1]$	$[M_2]$	$[M_3]$	$[M_1+M_2+M_3]$	[AIBN]		designation	m_1	m_2	m_3	$[\eta]$, dl g^{-1}
	mol %			wt %				mol %			
1	79.5	14.5	6.0	20	1.5	71.0	**I**-1	71.2	11.0	17.8	0.19
2	77.1	14.5	8.4	20	1.5	86.4	**I**-2	66.7	12.9	20.4	0.14
3	70.2	14.5	15.3	20	1.5	90.4	**I**-3	62.0	11.2	26.8	0.15
4	65.6	14.5	19.9	20	1.5	90.6	**I**-4	56.0	10.0	34.0	0.10
5	65.2	19.5	15.3	20	1.5	66.4	**I**-5	58.1	13.9	28.0	0.16
6	55.2	29.5	15.3	20	1.5	48.8	**I**-6	49.8	16.6	33.6	0.09
7	65.2	19.5	15.3	30	1.5	86.5	**I**-7	63.3	17.1	19.6	0.22
8	55.2	29.5	15.3	40	1.5	74.6	**I**-8	52.0	22.3	25.7	0.21
9	82.5	14.5	3.0	20	1.5	70.1	**I**-9	74.3	15.6	10.1	0.13
10	77.5	19.5	3.0	20	3.0	72.9	**I**-10	72.4	15.8	11.8	0.10
11	67.5	29.5	3.0	20	3.0	54.0	**I**-11	62.7	20.7	16.6	0.085
12	65.5	29.5	5.0	15	4.5	42.0	**I**-12	65.9	20.8	13.3	0.04
13	57.5	39.5	3.0	20	3.0	23.2	**I**-13	54.9	30.6	14.5	0.03

conditions is fast (Fig. 1, curve *1*). The copolymer yield is 63% in 3 h. A sharp self-acceleration of the copolymerization (gel effect) is observed in the conversion range 28–47%. The rate of ternary copolymerization of VP with CA and 2-HEMA is lower than the rate of binary copolymerization of VP with 2-HEMA (Fig. 1, curves *1*, *2*), which is due to the presence of CA, which is low-active and prone to degradation chain transfer. The results of preparative synthesis of VP–CA–2-HEMA terpolymers **I** are listed in Table 1. It is seen that at the molar ratio $[M_1] : [M_2] : [M_3] = 65.5 : 14.5 : 20.0$ the terpolymer yield is 45% in 3 h and reaches 90% in 48 h. The terpolymers are enriched, as compared with the initial monomer mixture, in 2-HEMA, which is the most active monomer in the system (Table 1, run nos. 1–13). With increasing content of CA, the yield of the terpolymer and its intrinsic viscosity decrease. An increase in the concentration of the monomer mixture at the same monomer ratio results in increased content of CA in the terpolymer (Table 1, run nos. 5 and 7, 6 and 8), which may be due to diffusion hindrance of the degradation chain termination. As seen from Table 1, it is possible to prepare, by varying the terpolymerization conditions, terpolymers **I** with the intrinsic viscosity ranging from 0.03 to 0.22 dl g^{-1}; CA unit content, from 10.0 to 30.6 mol %; and HEMA unit content, from 10.1 to 34.0 mol %.

Terpolymers **I** are typical anionic polyelectrolytes. They are titrated with alkalis, and their reduced viscosity in aqueous solutions increases with dilution:

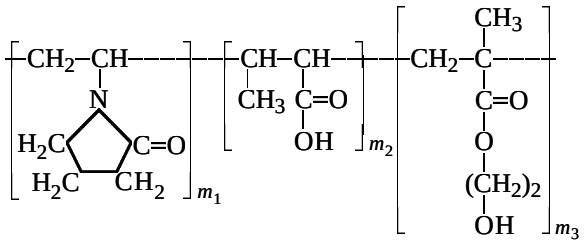

The structure of terpolymers **I** ($m_1 + m_2 + m_3 = 100$ mol %) was confirmed by titration of carboxy groups, elemental analysis for nitrogen, and ^{1}H NMR spectra taken in DMF-d_7. The ^{1}H NMR spectrum of sample **I-2** contains, along with the proton signals of the VP unit, signals originating from the $–OCH_2–CH_2O–$ protons of the 2-HEMA unit (4.15 and 3.85 ppm) and from the methyl protons of the CA (1.15–1.20 ppm) and 2-HEMA (0.75–0.96 ppm) units (Fig. 2).

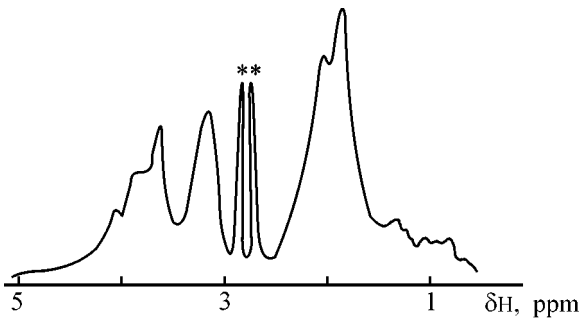

Fig. 2. ^{1}H NMR spectrum of terpolymer **I-2** in DMF-d_7. (δH) Chemical shift. The signals originating from impurities in the solvent are marked with asterisks.

Table 2. Hydrodynamic and molecular characteristics of terpolymers **I***

Terpolymer	0.1 M KCl		0.03 M phosphate buffer solution			
	$D \times 10^7$, $cm^2\ s^{-1}$	d*n*/d*c*, $cm^3\ g^{-1}$	$\overline{M}_w \times 10^{-3}$	$\overline{M}_w/\overline{M}_n$	[h], dl g^{-1}	d*n*/d*c*, $cm^3\ g^{-1}$
I-2	6.25	–	31**	–	0.14	–
I-1	3.5	0.134	50	2.00	0.19	–
I-5	7.1	0.132	50	1.69	0.16	0.160
I-7	5.8	0.172	74	1.99	0.22	0.157

* (*D*) Diffusion coefficient; (d*n*/d*c*) increment of the refractive index.

** M_{SD} was determined from sedimentation diffusion analysis.

As seen from Table 2, terpolymers **I** have low molecular weight with moderate polydispersity. Their forward diffusion coefficients, intrinsic viscosities, and molecular weights allow them to be classed with flexible-chain polymers [9]; the mean length of the Kuhn segment in them is 20×10^{-8} cm.

The viscometric data for VP–CA–2-HEMA terpolymers suggest occurrence of structural transformations in their aqueous solutions. Table 3 shows that, in going from sample **I-1** to **I-2** and **I-6**, the reduced viscosity of their aqueous solutions $\eta_{r,2}$ decreases, which suggests that, the macromolecular globules become more compact as the content of carboxy and hydroxy groups is increased. Because the hydrophobic interactions are enhanced with increasing temperature [10], $\eta_{r,2}$ at 310 K is lower than that at 298 K (macromolecules become more compact). In an aqueous urea solution, the intramolecular hydrogen bonds are broken, and the macromolecular globules unroll; therefore, $\eta_{r,1}$ is higher than $\eta_{r,2}$ for each terpolymer. In contrast to aqueous solutions, in aqueous urea solutions, $\eta_{r,1}$ grows with increasing content of carboxy groups, because mutual electrostatic repulsion of these charged groups causes the macromolecules to unroll to a greater extent. At 310 K, this trend is less pronounced because of the increased role of hydrophobic interactions in structure formation of the terpolymers.

Table 3. Viscometric study of VP–CA–2-HEMA terpolymers in aqueous solutions in the presence and in the absence of urea*

Terpolymer	$\eta_{r,1}$	$\eta_{r,2}$	$\eta_{r,1}$	$\eta_{r,2}$
	dl g^{-1}, 298 K		dl g^{-1}, 310 K	
I-1	0.256	0.169	0.232	0.143
I-2	0.270	0.160	0.252	0.120
I-6	0.423	0.146	0.377	0.107

* ($\eta_{r,1}$, $\eta_{r,2}$) Reduced viscosities of terpolymers in 1 M aqueous urea solution and in water, respectively (c_{terp} = 1.0 g dl^{-1}).

It is important that aqueous solutions of all the VP–CA–2-HEMA copolymers prepared in this work are transparent at "physiological" pH values and temperatures even at a concentration as high as 5 wt %. This fact predetermines the possibility of incorporation into terpolymers **I** of two BASs with different mechanisms of the biological effect. We confirmed this possibility by the example of two-stage fixation on terpolymer **I-2** of Acemin (agent stimulating reparative regeneration of tissues) by the ester bond and of Katamin AB (antiseptic) by the ionic bond stabilized by hydrophobic interactions of long alkyl chains of Katamin AB with macromolecules of the carrier [11]. As a result, we obtained a water-soluble VP copolymer exhibiting reparative and antimicrobial activity and showing promise for treatment of wounds and burns.

EXPERIMENTAL

VP and 2-HEMA were purified by vacuum distillation, and CA, by recrystallization from water with preliminary treatment of the solution with activated charcoal. The physicochemical constants of the monomers agreed with published data. Azobis(isobutyronitrile) was recrystallized three times from ethanol–chloroform (3 : 1); mp 376 K.

The kinetics of ternary copolymerization of VP, CA, and 2-HEMA, initiated with AIBN, in ethanol at 343 K was studied dilatometrically in ampules (4 mm in diameter, 250 mm high) sealed under argon. Variation of the reaction volume in the course of copolymerization was monitored with a KM-6 cathetometer. To determine the conversion, the VP–CA–2-HEMA terpolymer **I** formed was isolated by precipitation

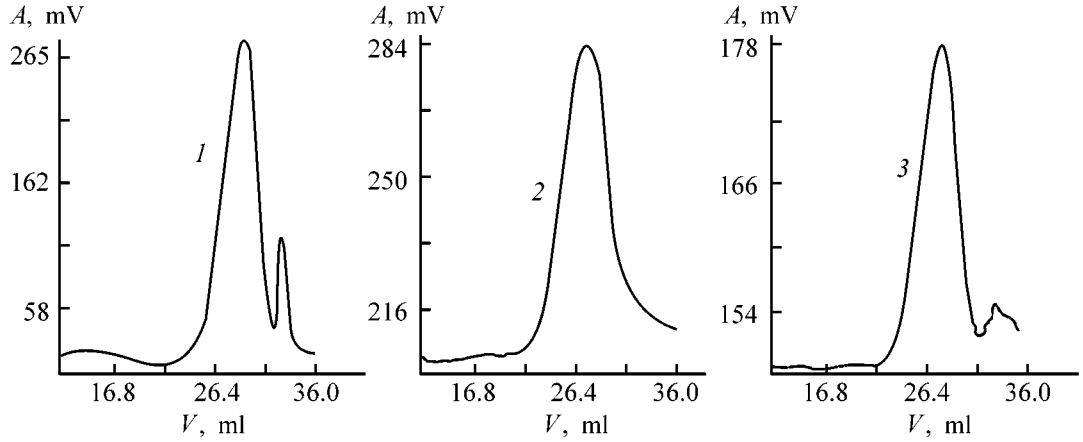

Fig. 3. Chromatograms of terpolymer **I-3**: (*A*) device readings and (*V*) retention volume. Detector: (*1*) refractometric, (*2*) of light scattered at an angle of 90°, and (*3*) viscometric.

into acetone. Preparative synthesis of **I** was performed in large ampules under the conditions indicated in Table 1. The compositions of terpolymers **I** were calculated from the results of analysis for nitrogen and from the content of carboxy groups, determined by titration with 0.1 N aqueous NaOH on a pH 340 titrator.

Terpolymer I-2. A glass ampule was successively charged with 0.1062 g of AIBN (1.5 wt % relative to the sum of monomers) and a solution of a monomer mixture consisting of 5 g (55 mol %) of VP, 0.80 g (15 mol %) of CA, and 1.2 ml (30 mol %) of 2-HEMA in 36 ml of ethanol. The ampule was purged with argon, sealed, and placed in a thermostat kept at 343 K. After heating for 48 h, the ampule was withdrawn, cooled, and opened. Terpolymer **I-2** was isolated by precipitation into diethyl ether, collected on a glass frit, and vacuum-dried. Yield 6.05 g (86.4%). Found, %: N 8.25, 8.47; COOH groups 5.2; m_1 = 6.67, m_2 = 12.9, m_3 = 20.4 mol %; intrinsic viscosity in 0.1 M sodium acetate solution at 25°C [η] = 0.14 dl g^{-1}; M_{SD} = 31000. The ^{1}H NMR spectrum of **I-2** was recorded on a Bruker AC 200 spectrometer in DMF-d_7.

Terpolymers **I** were studied by GPC using simultaneously three detectors [12] (Fig. 3): (1) a refractometric detector (Optilab 901/Wyatt Technology interference refractometer, the United States), (2) a detector recording scattered light of an He–Ne laser (5 mW, λ = 632.28 nm; Wyatt Technology, the United States); and (3) a viscometric detector of the hydrodynamic bridge type (similar to the Winston electric bridge) [13, 14]. The viscometric detector allows detection of the difference between the solution and solvent viscosities at very low concentrations, when the ratio $(\eta - \eta_0)/\eta_0 c$ can be fegarded as intrinsic viscosity. In the course of analysis, the injected volume (100 ml) passes through three series-connected analytical columns TSK G6000PW, G5000PW, and G4000PW (Anachem, UK), allowing separation of macromolecules of reference polyethylene oxide in the range of molecular weights 1×10^3–2×10^6. The eluent was fed at a rate of 0.8 ml min^{-1} at room temperature. The increments of the refractive index d*n*/d*c* were measured in independent experiments on an Optilab 901 interference refractometer. In GPC experiments, 0.05 M phosphate buffer solution was used as solvent.

Figure 4 shows the differential molecular-weight distribution of sample **I-5**, derived from chromatograms *1* and *2* (Fig. 3). The forward diffusion of terpolymer molecules was studied on a device equipped

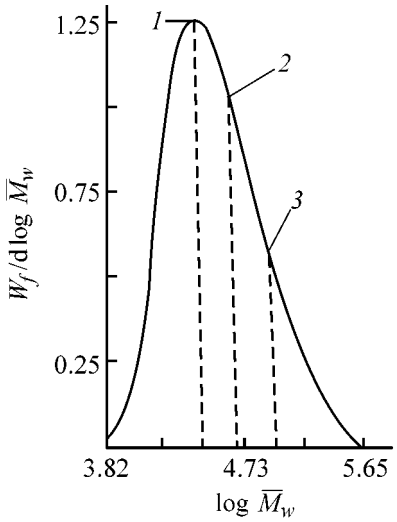

Fig. 4. Differential molecular-weight distribution of terpolymer **I-5**, derived from chromatograms *1* and *2* (Fig. 3). (*1*) $\overline{M}_n$ = 29800, (*2*) $\overline{M}_w$ = 50300, and (*3*) $\overline{M}_z$ = 93700.

with a Lebedev polarization interferometer as the detecting optical system. The Tsvetkov diffusometer and the procedure for calculaing the forward diffusion coefficients are described elsewhere [9, 15]. The solution–solvent boundary was formed in glass cells with optical path length of 3 cm. The diffusion boundary variance σ^2 was calculated from the maximal ordinate and the peak area. From the dependences

$$\sigma^2 = \sigma_0^2 + 2Dt,$$

we calculated the forward diffusion coefficient D (σ_0^2 is the initial variance characterizing the quality of formation of the diffusion boundary). Diffusion experiments were performed in 0.1 M KCl at 299 K. The intrinsic and reduced viscosities of copolymers **I** were determined in 0.1 M aqueous KCl solution at 298 K with an Ubbelohde viscometer.

CONCLUSIONS

(1) New water-soluble terpolymers *N*-vinylpyrrolidone–crotonic acid–2-hydroxyethyl methacrylate were prepared in 48.8–90.6% yield by radical ternary copolymerization in solution, initiated by azobis(isobutyronitrile). The ternary copolymerization kinetics was studied.

(2) The compositions and molecular-weight parameters of the resulting functional terpolymers were determined.

ACKNOWLEDGMENTS

The authors are sincerely grateful to E.F. Panarin for participation in the discussion of the results.

The study was financially supported by the Russian Foundation for Basic Research (project no. 00-15-97318).

REFERENCES

1. Panarin, E.F. and Ushakova, V.N., in *Polimery meditsinskogo naznacheniya* (Polymers for Medicine), Moscow: Inst. Neftekhim. Sinteza, 1988, pp. 66–94.
2. Lavrov, N.A., in *Khimicheskaya tekhnologiya, svoistva i primenenie plastmass* (Chemical Technology, Properties, and Use of Plastics), Leningrad: Leningr. Tekhnol. Inst. im. Lensoveta, 1989, pp. 77–84.
3. Zaks, I.N. and Pernikis, A.B., *Izv. Akad. Nauk Latv. SSR, Ser. Khim.*, 1988, no. 4, pp. 436–440.
4. Rego, I.M. and Huglin, M.B., *Polym. J.*, 1991, vol. 23, no. 12, pp. 1425–1434.
5. Roman, I.C. and Levenfeld, B., *Macromolecules*, 1991, vol. 24, no. 23, pp. 6083–6088.
6. Lavrov, N.A. and Nikolaev, A.F., *Zh. Prikl. Khim.*, 1987, vol. 60, no. 1, pp. 167–170.
7. Solovskij, M.V., Denisov, V.M., Panarin, E.F., *et al.*, *Macromol. Chem. Phys.*, 1996, vol. 197, pp. 2035–2046.
8. Anufrieva, E.V., Panarin, E.F., Pautov, V.D., *et al.*, *Macromol. Chem. Phys.*, 1997, vol. 198, pp. 3871–3881.
9. Tsvetkov, V.N., *Zhestkotsepnye polimernye molekuly* (Rigid-Chain Polymer Molecules), Leningrad: Nauka, 1986.
10. Pchelin, V.A., *Dokl. Akad. Nauk SSSR*, 1970, vol. 194, no. 3, pp. 621–624.
11. Solovskii, M.V., Panarin, E.F., Kochetkova, I.S., *et al.*, Abstracts of Papers, *Aktual'nye problemy sozdaniya lekarstvennykh sredstv: Vserossiiskaya nauchnaya konferentsiya* (Urgent Problems of Drug Development: Russian Scientific Conf.), St. Petersburg: Sankt-Peterb. Khimiko-Farm. Akad., 1996, p. 63.
12. Wyatt, P.J., *Anal. Chim. Acta*, 1993, vol. 272, no. 1, pp. 1–16.
13. Haney, M.A., *Am. Lab.*, 1985, vol. 17, no. 1, pp. 41–46.
14. Harding, S.E., *Prog. Biophys. Molec. Biol.*, 1997, vol. 68, nos. 2/3, pp. 207–232.
15. Tsvetkov, V.N., Eskin, V.E., and Frenkel', S.Ya., *Struktura makromolekul v rastvorakh* (Structure of Macromolecules in Solutions), Moscow: Nauka, 1964.

Russian Journal of Applied Chemistry, Vol. 75, No. 2, 2002, pp. 281–285. Translated from Zhurnal Prikladnoi Khimii, Vol. 75, No. 2, 2002, pp. 291–295.
Original Russian Text Copyright © 2002 by Solovskii, Pek.

MACROMOLECULAR CHEMISTRY AND POLYMERIC MATERIALS

Reasons for Structure–Acid Resistance Correlation in Series of Substituted Phenylpenicillins

M. V. Solovskii and G. Yu. Pek

Institute of Macromolecular Compounds, Russian Academy of Sciences, St. Petersburg, Russia

Shemyakin and Ovchinnikov Institute of Bioorganic Chemistry, Russian Academy of Sciences, Moscow, Russia

Received July 2, 2001

Abstract—The kinetics of acid hydrolysis of phenylpenicillins substituted in the benzene ring were studied at pH 3.0 and temperatures of 20, 25, and 30°C. A Hammett correlation analysis of the reaction was performed.

Antibiotics of the penicillin series significantly differ in stability in acid solutions. Among acid-resistant penicillins, which can be administered perorally, are phenoxymethylpenicillin, Oxacillin, Cloxacillin, etc. Benzylpenicillin, *p*-hydroxybenzylpenicillin, and Methicillin show poor acid resistance.

Penicillins contain a common bicyclic system consisting of fused β-lactam and thiazolidine rings and differ only in the structure of the side acyl group. All the differences between penicillins are largely due to structural features of this substituent, and, from this standpoint, it is appropriate to discuss the difference in acid resistance between penicillins.

Strukov *et al.* [1, 2] believe that the differences in acid resistance of penicillins are associated with the amide–imidol tautomerism of their side chain; however, no explanations for this hypothesis are given. Doyle *et al.* [3] showed that electron-withdrawing substituents in the side aliphatic acyl group enhance the acid resistance of penicillin, but they gave no explanations for this fact either. Therefore, it seemed appropriate to study the acid resistance of specially chosen penicillin derivatives differing in the nature of substituent in the aromatic ring of the side acyl group, with the aim to reveal a correlation between the structure of the side acyl droup, on the one hand, and the rate of penicillin acid cleavage, on the other, and also to find the reason for this correlation.

As objects for our study we chose phenylpenicillins substituted in the side chain. Their side acyl groups are structurally related to benzoic acids, for which the the dissociation constants strongly depend on the electronic effects of substituents. Hence, significant differences in acid resistance must be expected for substituted phenylpenicillins too.

The substituted phenylpenicillins were prepared by acylation of the core compound, 6-aminopenicillanoic acid, with various substituted benzoyl chlorides in aqueous acetone in the presence of sodium hydrogen carbonate [4]. The properties of the resulting sodium salts of substituted penicillins, which show high biological activity, are listed in Table 1. The purity

Table 1. Sodium salts of phenylpenicillins

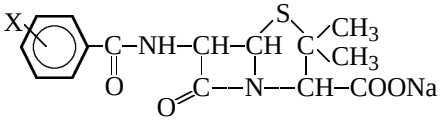

Comp. no.	X	Yield, %	Activity		
			iodometric, μg mg^{-1}	optical α_D^{17}, C = 0.5% in H_2O	biological, MSC,* units ml^{-1}
1	*p*-OCH_3	49	740	+216	0.35
2	*p*-CH_3	56	820	+232	0.40
3	H	61	970	+250	0.50
4	*p*-Cl	45	850	+282	0.78
5	*p*-Br	52	860	+228	0.48
6	*m*-NO_2	61	820	+222	0.50
7	*p*-NO_2	73	850	+252	0.55

* MSC is the minimum suppressing concentration for *Staphylococcus aureus* 60.

1070-4272/02/7502-0281 $27.00 © 2002 MAIK "Nauka/Interperiodica"

Table 2. Methyl esters of phenylpenicillins

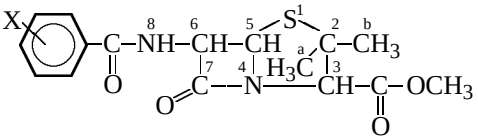

Ester no.*	N calculated (%)	N found** (%)	S calculated (%)	S found** (%)	mp, °C	Iodometric activity, μg mg^{-1}	Optical activity α_D^{17}, C = 0.5%	Optical activity solvent	R_f
1	7.68	7.30	8.79	8.57	174–175	950	+287	Cloroform : ethanol = 2 : 1	0.75
2	8.04	8.02	9.19	9.02	162–163	1000	+252	Cloroform : ethanol = 1 : 1	0.76
3	8.38	8.34	9.59	9.60	116–117	960	+280	Ethanol	0.73
4	7.60	7.73	8.67	8.60	178–179	980	+256	Cloroform : ethanol = 1 : 1	0.79
5	6.78	6.78	7.75	7.43	100–101	990	+280	Ethanol	0.81
6	11.09	11.20	8.44	8.37	88–89	980	+204	Cloroform	0.74
7	11.09	11.16	8.44	8.34	58–59	1000	+290	Cloroform : ethanol = 1 : 1	0.77

* Prepared from the respective compounds in Table 1. ** Average of two determinations.

Table 3. Kinetic characteristics of acid inactivation of phenylpenicillins

Comp. no.*	$K \times 10^3$, min^{-1}, at indicated temperature, °C: 20	25	30	E, kcal mol^{-1}	log(PZ)
1	70.0 ± 0.6	81.0 ± 0.9	117.0 ± 2.0	5.1 ± 0.1	0.83
2	40.0 ± 0.9	47.9 ± 0.5	65.0 ± 0.3	7.8 ± 0.5	2.63
3	18.0 ± 0.6	28.0 ± 0.6	42.2 ± 0.3	14.2 ± 0.2	7.10
4	7.0 ± 0.1	11.3 ± 0.3	17.5 ± 0.2	16.2 ± 0.3	7.23
5	6.7 ± 0.07	10.5 ± 0.1	16.7 ± 0.2	16.0 ± 0.5	7.03
6	–	1.48 ± 0.05	2.60 ± 0.06	20.3 ± 0.6	10.38
7	–	1.19 ± 0.02	2.18 ± 0.04	21.5 ± 0.4	11.09

* Corresponds to Table 1.

of phenylpenicillins, according to iodometric analysis, was 74–97%, which may be due to inactivation of these compounds in the course of isolation and purification. Purification of phenylpenicillins is very difficult because of their instability; therefore, substituted phenylpenicillins were additionally identified in the form of methyl esters. Furthermore, these derivatives appeared to be more convenient for a ^{1}H NMR study of phenylpenicillins than the salts. The properties of methyl esters of the phenylpenicillins substituted in the benzene ring are listed in Table 2. It is seen that these compounds were isolated pure.

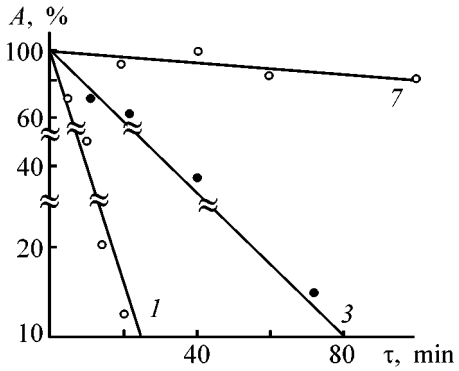

Fig. 1. Acid inactivation of phenylpenicillins. 25°C, pH 3.0; the same for Fig. 2. (*A*) Concentration of non-inactivated substituted phenylpenicillin and (τ) time elapsed from the start of the reaction. *Figures at curves* denote compound nos. in Table 1.

The kinetics of acid inactivation of the chosen penicillins were studied in a glycine buffer solution (pH 3.0) at 20, 25, and 30°C. The initial concentration of the antibiotic in solution was about 1000 units ml^{-1}. Under these conditions, hydrolysis of the amide bond in the β-lactam ring of substituted phenylpenicillins, resulting in their inactivation, is a pseudomonomolecular reaction and is described by a first-order equation, as in the case of other penicillins [5–7].

The parameter $\log[C_0/(C_0 - C_\tau)]$ is a linear function of τ (Fig. 1). The rate constants of acid inactivation of substituted phenylpenicillins and the activation energies of the reactions are listed in Table 3. It is seen that the rate constants of acid hydrolysis of phenylpenicillins differ considerably.

The large difference between the activation energies of hydrolysis of *p*-methoxyphenylpenicillin (5.06 kcal mol^{-1}) and *p*-nitrophenylpenicillin (21.5 kcal mol^{-1}) shows that at the instant of cleavage of the amide bond in the β-lactam ring the penicillin molecule is strongly polarized. The probability factors *PZ* also differ considerably. On the whole, the rate constants of acid inactivation of substituted phenylpenicillins vary in accordance with the polar effect of the substituent.

Examination of the applicability of the Hammett equation to the acid inactivation of phenylpenicillins (Fig. 2) shows that the logarithms of the rate constants of this reaction show a satisfactory linear correlation with the Hammett σ constants in the temperature range studied (in all cases we used common Hammett σ constants [8]). Thus, despite complex structure of penicillins, the description of their inactivation by the Hammett equation is quite adequate. The coefficients ρ at 20, 25, and 30°C, calculated from the slopes of the log *K*–σ straight lines, are –2.00 (r = 0.956), –1.76 (r = 0.996), and –1.65 (r = 0.994), respectively. The negative sign of ρ shows that the inactivation is promoted by donation of the electron density to the reaction center. The coefficients ρ are large in absolute value, which means that acid inactivation of substituted benzylpenicillins is highly sensitive to effects of substituents in the benzene ring of the side acyl group, despite their relatively large distance from the reaction center (amide bond in the β-lactam ring).

To understand why the effect of substituents on the cleavage of the relatively remote bond is so strong, it seemed important to study how the substituents affect the polarization of the amide bond in the β-lactam ring. Such information can be derived from the ^{1}H NMR spectra of the methyl esters of phenylpenicillins. Indeed, if the electronic effect of substituents in the benzene ring on the strength of the amide bond in the β-lactam ring were significant, it would alter the hybridization of the nitrogen atom and hence cause

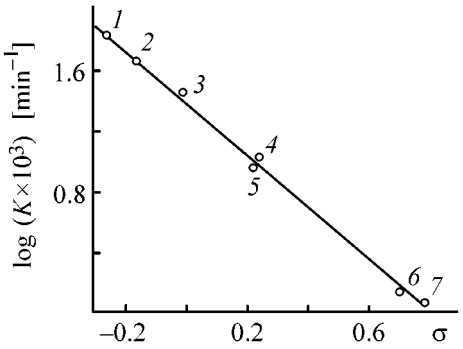

Fig. 2. Correlation between the logarithms of the rate constants *K* of acid activation of substituted phenylpenicillins and the Hammett σ constants of substituents in the benzoyl group. *Figures at curves* are compound nos. in Table 1.

appreciable changes in the coupling constant of the β-lactam protons and in the chemical shift of C^5H.

^{1}H NMR data for methyl esters of phenylpenicillins are given in Table 4. It is seen that for all the compounds the coupling constants $J(H^5–H^6)$ and the chemical shifts δ of the β-lactam protons are very similar. That is, there is no pronounced correlation between the ^{1}H NMR parameters of the lactam ring and the structure of the side chain. The lack of such a correlation suggests that either there is no specific interaction in an inert medium between the amide moiety of the β-lactam ring and the side chain, or this interaction is too weak to be detected by NMR. An increase in the chemical shifts of the C^5H protons with increasing electronegativity of the side chain (Table 4) suggests occurrence of a certain interaction, but this trend is very weakly pronounced. The effect of substituents in the benzene ring is apparently leveled out by the amide group of the side chain, which has a very low transmission factor π = 0.12 [8].

The high absolute values of ρ for the acid inactivation of substituted phenylpenicillins, taking into account the very weak transmission of the inductive ef-

Table 4. ^{1}H NMR data for methyl esters of phenylpenicillins (1 mol % in $CDCl_3$)

Ester no. (Table 2)	a	b	OCH_3	C^3H	C^5H	C^6H	NH	$J(H^5–H^6)$	$J(H^6–NH)$
	$C^2(CH_3)_2$		δ, downfield from TMS, ppm					Hz	
1	1.53	1.70	3.80	4.48	5.64	5.87	6.73	4.0	9.1
2	1.54	1.69	3.81	4.51	5.69	5.88	6.86	4.1	9.1
3	1.53	1.71	3.80	4.50	5.66	5.91	7.03	4.0	8.5
4	1.53	1.69	3.81	4.50	5.67	5.93	6.86	Not determined	Not determined
5	1.52	1.68	3.80	4.50	5.67	5.92	6.73	4.0	8.5
6	1.53	1.73	3.82	4.50	5.71	5.77	7.74	4.0	8.0
7	1.52	1.68	3.78	4.48	5.68	5.82	7.24	Not determined	Not determined

fects to the β-lactam ring by the mechanism of successive polarization of σ bonds, suggest direct participation of the side chain in the limiting stage of the acid inactivation:

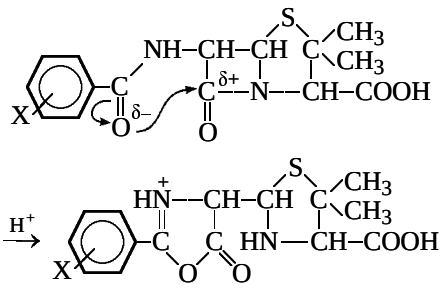

In this case, the electronic effects of substituents are probably transmitted by the field effect mechanism via electrostatic interaction through space between the oxygen atom of the carbonyl group of the side chain and the carbonyl carbon atom of the β-lactam ring. In the process, the rate of formation of a new –O–C– bond with simultaneous cleavage of the amide bond in the β-lactam ring is determined by the electron density (δ– charge) on the oxygen atom of the side chain, which, in turn, strongly depends on the substituent in the benzene ring. Just this factor is responsible for the pronounced dependence of the rate of acid inactivation of phenylpenicillins on the polar effect of substituents in the benzene ring. The effect is similar to that observed in the series of benzoic acids, which is reflected in the linear correlation of $\log K$ with the Hammett σ constants.

The increased δ– charge on the amide oxygen atom of the side chain facilitates closure of the oxazolone ring with cleavage of the β-lactam ring; therefore, electron-donor substituents in the benzene ring noticeably accelerate the reaction. The negative sign of δ–, suggesting the promoting effect of electron donors, is consistent with this mechanism.

EXPERIMENTAL

The ^{1}H NMR spectra were recorded at room temperature, relative to internal TMS, on a JEOL INM-C-60 spectrometer operating at 60 MHz. Samples were taken as 1–2 mol % solutions in $CDCl_3$. The IR spectra were recorded on a UR-10 spectrometer (KBr pellets). The specific optical rotation α_D^T of substituted phenylpenicillins and their methyl esters in solutions was determined with an EPL-1 polarimeter. The iodometric activity of phenylpenicillins and their methyl esters was studied as described in [9]. The TLC study of methyl esters of phenylpenicillins was performed as follows: solutions of the compounds in chloroform (1–1.5 mg ml^{-1}) were applied to plates coated with KSK silica gel (5 μg per spot). Ascending chromatography was performed in a closed chamber, with ethanol as eluent. After separation, the chromatograms were dried for 10 min at 20°C and for 15 min at 100°C, and then developed with iodine vapor. The target compounds gave rust-colored spots.

Phenylpenicillin sodium salt 3. A 0.2 g (0.00093 M) portion of 6-aminopenicillanoic acid was dissolved in a mixture of 20 ml of 0.1 M phosphate buffer solution (pH 6.6) and 4 ml of 10% $NaHCO_3$ solution. To the resulting mixture was added dropwise, with stirring and cooling on an ice bath, a solution of 0.197 g (0.0014 mol; 1.5-fold excess) of benzoyl chloride in 10 ml of acetone. Acylation was performed for 20 min, with addition of $NaHCO_3$ solution to maintain the neutral medium. After reaction completion, the unchanged benzoyl chloride was extracted with diethyl ether and discarded. The cooled aqueous solution was acidified with 1 N HCl to pH 2.0, and the phenylpenicillic acid formed in the process was extracted with 15 ml of diethyl ether. The extract was treated with 12 ml of 0.05 N $NaHCO_3$ to wash the acid back to the aqueous phase in the form of the sodium salt. The product was isolated by lyophilic drying and purified by reprecipitation from aqueous acetone into dry acetone. Yield of phenylpenicillin sodium salt 0.204 g (61%), iodometric activity 970 μg mg^{-1}. IR spectrum, ν, cm^{-1}: 1770 (C=O in β-lactam ring); 1400 (–O–C– in –C(=O)O$^-$ group); 1655, 1490 (C=O in –C(=O)–NH– group).

The sodium salts of phenylpenicillins substituted in the benzene ring were prepared similarly.

Phenylpenicillin methyl ester. A solution of 1.3 ml of diazomethane in 10 ml of diethyl ether was added with stirring to a solution of 0.5 g of phenylpenicillic acid in 50 ml of diethyl ether. The reaction was performed until the gas evolution ceased. Phenylpenicillin methyl ester was isolated by vacuum evaporation of the ether and purified by repeated reprecipitation from ethyl acetate into petroleum ether. Yield 0.208 g (40%); mp 116–117°C. IR spectrum, ν, cm^{-1}: 1770 (C=O in β-lactam ring); 1655, 1520 (C=O in –C(=O)–NH– group); 1720 (C=O in –C(=O)–O– group); 1170 (–O–C–).

Found, %: N 8.34, S 9.60.

$C_{16}H_{18}O_4N_2$.

Calculated, %: N 8.38, S 9.59.

Iodometric activity 960 μg mg^{-1}. Methyl esters of the other phenylpenicillins were prepared similarly.

Dioazomethane was prepared by Arndt's procedure [10].

CONCLUSIONS

(1) Phenylpenicillins substituted in the benzene ring were prepared and identified in the form of methyl esters.

(2) The rate constants of acid hydrolysis of substituted phenylpenicillins correlate with the Hammett σ constants of substituents in the benzene ring, with high (in absolute value) sensitivity coefficients ρ: –2.05, –1.76, and –1.65 for 20, 25, and 30°C, respectively. Contrasingly, the ^{1}H NMR spectra of the lactam moiety are weakly sensitive to the substituents in the benzene ring.

(3) The reaction mechanism, consistent with these facts, was suggested, in which the side acyl group takes an active part in the limiting stage.

ACKNOWLEDGMENTS

The authors are sincerely grateful to E.F. Panarin for initiation of this work and active participation in the discussion of its results and to L.N. Samoilova for determining the antimicrobial activity of phenylpenicillin sodium salts.

REFERENCES

1. Strukov, I.T., *Antibiotiki*, 1963, no. 11, pp. 963–976.
2. Maslova, G.A. and Strukov, I.T., *Antibiotiki*, 1965, no. 11, pp. 1005–1010.
3. Doyle, F.P., Nayler, I.H.C., Smith, H., and Stove, E.R., *Nature*, 1961, vol. 191, pp. 1091–1092.
4. Perron, Y.G., Minor, W.F., Holdrege, C.T., *et al.*, *J. Am. Chem. Soc.*, 1960, vol. 82, pp. 3934–3938.
5. Brandl, E. and Margreiter, H., *Öster. Chem. Ztg.*, 1954, vol. 55, pp. 11–21.
6. Kondrat'eva, A.P. and Bruns, B.P., *Med. Prom–st. SSSR*, 1957, no. 12, pp. 30–34.
7. Inozemtseva, I.I., Kleiner, G.I., Panina, M.A., *et al.*, *Antibiotiki*, 1966, no. 6, pp. 497–500.
8. Zhdanov, Yu.A. and Minkin, V.I., *Korrelyatsionnyi analiz v organicheskoi khimii* (Correlation Analysis in Organic Chemistry), Rostov: Rostov. Univ., 1966.
9. Alicino, I.F., *Anal. Chem.*, 1961, vol. 33, pp. 648–649.
10. Arndt, F., *Organic Synthesis*, Gilman, H., Adams, R., Clark, H.T., *et al.*, Eds., New York: Wiley, 1946, coll. vol. 2. Translated under the title *Sintezy organicheskikh preparatov*, 1949, coll. 2, pp. 174–176.

Russian Journal of Applied Chemistry, Vol. 75, No. 2, 2002, pp. 286–291. Translated from Zhurnal Prikladnoi Khimii, Vol. 75, No. 2, 2002, pp. 296–300.
Original Russian Text Copyright © 2002 by Valueva, Silinskaya, Kipper.

MACROMOLECULAR CHEMISTRY AND POLYMERIC MATERIALS

Optical Properties of Semidilute Solutions of Poly-2-acrylamido-2-methylpropanesulfonic Acid at Varied Ionic Strength of the Medium

S. V. Valueva, I. G. Silinskaya, and A. I. Kipper

Institute of Macromolecular Compounds, Russian Academy of Sciences, St. Petersburg, Russia

Received June 28, 2001

Abstract—Aqueous-salt semidilute solutions of a high-molecular-weight polyelectrolyte, poly-2-acrylamido-2-methylpropanesulfonic acid, were studied by flow birefringence and light scattering methods at varied ionic strength of the medium.

In [1], we studied the optical properties of solutions of a copolymer formed by 2-acrylamido-2-methylpropanesulfonic acid and acrylamide, P(AMPS–AA), with the degree of ionization of 20 %, as influenced by the ionic strength of the medium I and the polymer concentration c at $c > c^*$ (c^* is the solution concentration comparable with the average concentration of the units in the polymer coil and correlating with the parameter inverse to the intrinsic viscosity $[\eta]$ of this polymer in an appropriate solvent [2]). For P(AMPS–AA) in 1 M $NaNO_3$ solution we revealed an fluctuation network of engagements, and in 0.1 M $NaNO_3$ solution, disoriented anisotropic structural macroelements of the fluctuation nature. The macroelements have size comparable with the wavelength of light and are capable of mutual orientation in a gradient field.

The aim of this work was (1) to apply the flow birefringence (BR) and light scattering methods to study the structurization in semidilute solutions of high-molecular-weight flexible-chain polyelectrolyte poly-2-acrylamido-2-methylpropanesulfonic acid (PAMPS; 100% ionic groups) at ionic strength of solution I = 1 M (the case of suppressed electrostatic interactions) and I = 0.1 M {the case of long-range electrostatic interactions; the percolation effect is negligible; $A \sim$ const (A is the equilibrium rigidity of macromolecules) [3–5]} and (2) to compare the results with those for semidilute P(AMPS–AA) solutions reported by us in [1].

EXPERIMENTAL

Our study was concerned with high-molecular-weight ($M_w = 4.6 \times 10^6$) flexible-chain (A = 2 nm [6]) polyelectrolyte PAMPS. We described in detail the molecular and conformational parameters of this sample for the $c < c^*$ region in [7]. The PAMPS solutions were studied ionic strengths I of 1 and 0.1 M ($NaNO_3$).

The solutions and solvents were purified by centrifugation at 15000 rpm for 1.5 h.

We measured the flow BR Δn as dependent on the rotor rotation rate gradient g, polymer concentration c, and ionic strength I by the procedure described in [8]. We used a titanium dinamooptometer with a 4-cm-high internal rotor and a 3×10^{-2}-cm clearance between the rotor and stator. The measurements were conducted at $g < g_c$, where g_c is the rate gradient at which the flow becomes turbulent. Throughout the c and I ranges investigated, the PAMPS solutions exhibit positive BR. The $\Delta n = f(g)$ plots are linear and pass through the origin at all the c and I values studied, which suggests the lack of intermolecular association in the $c > c^*$ region.

Viscometric measurements were conducted on an Ostwald's capillary viscometer, the water outflow time being 120 ± 0.2 at 21°C.

Static light scattering for PAMPS solutions was studied on a Fica photogoniodiffusometer at the vertically incident polarized light with wavelength of 546.1 nm in the range $c \cong 0.01$–0.7% (herefrom, wt %) and angles (with respect to the incident light direction) $\theta = 30°$–$150°$. The results were interpreted in terms of the Debye-Simm theory [9]. The refractive index increment $\partial n/\partial c$ was derived from the results of refractometric studies on an IRF-23 instrument.

1070-4272/02/7502-0286 $27.00 © 2002 MAIK "Nauka/Interperiodica"

The static light scattering was studied for PAMPS solutions on an FPS-3M instrument comprising a photoelectric system for recording the intensity of light scattered at an angle $\theta = 40°–140°$ (incident light wavelength 546.1 nm). The results obtained were interpreted in terms of the Bueche–Stein statistical theory [10].

The angular dependences of the vertically polarized component of the scattered light V_v were measured by a standard technique [9]. Based on the angular dependence of V_v in terms of the Bueche–Stein statistical theory, we determined the isotropic parameters of the structure: average squared fluctuation of the average polarizability of the scattering microvolume $\langle\langle\eta\rangle^2\rangle$ and the correlation radius of the polarizability fluctuations α_v. The isotropic structure parameters are related to the sizes of the macromolecules or associates α_v and to microheterogeneity, which is a function of the density fluctuation $\langle\langle\eta\rangle^2\rangle$.[1]

Based on the concentration dependence of the reduced viscosity η_{sp}/c ($\eta_{sp} \equiv \eta_r - 1$, where η_r is the relative viscosity) in dilute solutions, we determined the intrinsic viscosity $[\eta] \equiv (\eta_{sp}/c)_{c\to 0}$ ($[\eta]_1 = 5.0$ at $I = 1$ M and $[\eta]_2 = 9.0$ at $I = 0.1$ M [7]) and estimated Debye's concentration $c^* \sim [\eta]^{-1}$ above which the solution is semidilute: $c^* \sim 0.20$ % ($I = 1$ M) and $c^* \sim 0.11$ % ($I = 0.1$ M). The viscometric data suggest (1) fairly strong polyelectrolyte swelling of the poly ions with decreasing I ($[\eta]_2/[\eta]_1 = 1.8$) and (2) the existence in 0.1 M $NaNO_3$ solution, along with c^*, of additional critical points ($c \sim 0.2$ and $c \sim 0.5$%) at which the slope of the $\eta_{sp}/c = f(c)$ plot changes (Fig. 1).

The light scattering data for the PAMPS–1 M $NaNO_3$ solution system suggest that the angular dependences $(V_v - 4/3H_v)^{-1/2}$ are linear throughout the concentration range investigated, except at $c = c^* \cong 0.20$%. In this case, the experimental curve exhibits an inflection indicative of the existence in solution of additional, larger scattering elements typical of systems with suppressed polyelectrolyte effect, which are in a state of transition from dilute to semidilute solution and form a fluctuation network of engagements. For the PAMPS–0.1 M $NaNO_3$ solution system we

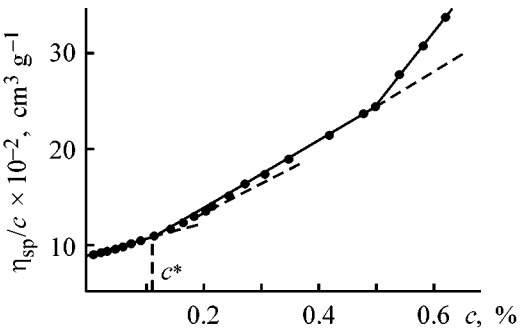

Fig. 1. Reduced viscosity η_{sp} vs. the polymer concentration c for PAMPS solutions at $I = 0.1$ M.

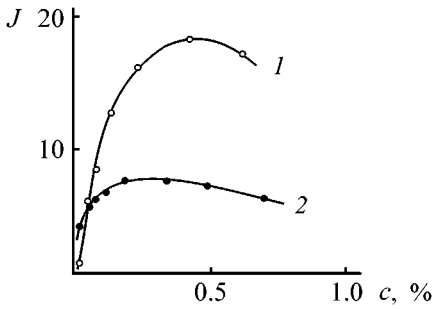

Fig. 2. Reduced intensity of the scattered light J vs. the polymer concentration c for PAMPS solutions at (*1*) $I = 1$ M and (*2*) $I = 0.1$ M.

observed at all the concentrations studied abnormally high light-scattering intensities at $\theta = 40–80°$. By extrapolation to zero scattering angle, we found that the size of the scattering formations is comparable with the wavelength of light. This is, evidently, accounted for by restriction of free fluctuations of the polymer coils in solution owing to incompletely suppressed polyelectrolyte interactions and, correspondingly, by an increase in the correlation radius of these fluctuations. It should be emphasized that the light scattering effects observed for PAMPS at $I = 1$ and $I = 0.1$ M are similar to those for P(APMS–AA) in 1 M and 0.1 M $NaNO_3$ solutions [1].

The concentration dependences of the reduced intensity of scattered light for PAMPS solutions at $I = 1$ and $I = 0.1$ M exhibit maxima in Debye's concentration range at $c^* \sim 0.20$ and $c^* \sim 0.11$%, respectively (Fig. 2). These maxima suggest a decrease in the fluctuation mobility at $c \geq c^*$ due to strong intermolecular interaction, namely, nonelectrostatic interaction at $I = 1$ M (owing to the formation of the fluctuation network of engagements) and polyelectrolyte interaction in 0.1 M $NaNO_3$ solution. It should be emphasized that the extremum in the $I = f(c)$ dependence also suggests the lack of aggregation in the solutions [9].

[1] Because of the lack of the angular dependence for the reduced intensity of anisotropic scattering (horizontal polarized component of the scattered light, H_v) for the systems PAMPS–1 M $NaNO_3$ solution and PAMPS–0.1 M $NaNO_3$ solution, the anisotropic structure parameters (squared average optical anisotropy $\langle\delta\rangle^2$ and the correlation radius of orientation of the optical axes of the scattering volume elements α_H) were not determined for these systems.

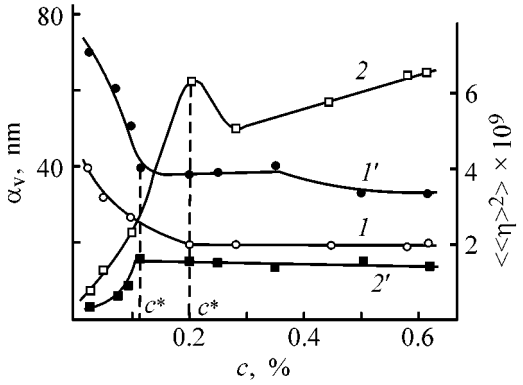

Fig. 3. Concentration dependences of (*1*, *1*′) the correlation radius of the polarizability fluctuations $\alpha\delta_v$, and (*2*, *2*′) the average squared fluctuation of the average polarizability of the scattering microvolume $\langle\langle\eta\rangle^2\rangle$ for PAMPS solutions at (*1*, *2*) I = 1 M and (*1*′, *2*′) I = 0.1 M.

As known, the average correlation radius of the polarizability fluctuations, α_v, for solutions of nonionic flexible-chain polymers initially tends to decrease with growing concentration up to Debye's concentration, to take a value $\alpha_{v,0}$ corresponding to the size of macromolecules $\langle R_g^2\rangle^{1/2}$, and then (at $c > c^*$) tends to increase owing to aggregation of the macromolecules [11].[2] For nonionic polymers with functional groups capable of strong specific interactions (this is, evidently, the case for PAMPS at I = 1 M) a significant increase in the parameter α_v for $c > c^*$ also reflects the intermolecular association in solution [12].

In contrast to nonionic polymer systems, the parameter α_v for PAMPS in 1 M and 0.1 M $NaNO_3$ solutions at $c > c^*$ (it should be mentioned that the c^* values estimated by light scattering studies coincide with Debye's concentrations obtained by viscometry) are significantly lower than the theoretically calculated values [$\alpha_{v,0}$ = 41 at I = 1 M ($[\alpha^2_{v,0} = 1/6\langle R_g^2\rangle$, $\langle R_g^2\rangle^{1/2}$ = 100 nm); $\alpha_{v,0}$ = 57 at I = 0.1 M ($\langle R_g^2\rangle^{1/2}$ = 140 nm)] and remain virtually unchanged at $c > c^*$ (Fig. 3, curves *1*, *1*′). This suggests the lack of intermolecular association in the region of semidilute solution. This is in agreement with the $\Delta n = f(g)$ dependence for PAMPS in 1 and 0.1 M $NaNO_3$ solution. The $\alpha_v = f(c)$ dependence for PAMPS at I = 1 and I = 0.1 M reproduces, on the whole, the analogous dependence for P(AMPS–AA) [1].

The parameter α_v for PAMPS in 0.1 M $NaNO_3$ solution, calculated for the linear section of the angular dependence $(V_v - 4/3H_v)^{-1/2}$, is 35–40 nm at $c > c^*$, which exceeds the analogous value for PAMPS in 1 M $NaNO_3$ solution (α_v = 20 nm). This is consistent with the viscometric data.

In view of the fact that a network of engagemenists probably formed in the system PAMPS–1 M $NaNO_3$ solution in the concentration range studied at $c > c^*$ [1, 13, 14], the parameter α_v evidently characterizes the correlation size of its interstice, and the parameter $\langle\langle\eta\rangle^2\rangle$ increasing at c > 0.3 % (Fig. 3, curve *2*), an increase in the number of engagements. In the case of 1 M solutions of $NaNO_3$ the $\langle\langle\eta\rangle^2\rangle = f(c)$ plot for PAMPS is analogous to that for P(AMPS–AA) [1]. This, probably, suggests a similar behavior of semidilute solutions of polyelectrolytes under depressed electrostatic interactions.

Of special interest is analysis of the concentration dependence of the reduced BR $[\Delta n/(g\eta_0 c)]_{g\to 0}$ (Figs. 4a, 4b; η_0 is the solvent viscosity).[3] High-molecular-weight flexible-chain polymers in dilute solutions with refractive index increment $\partial n/\partial c$ other than zero (in our case, $\partial n/\partial c$ = 0.133 $cm^3\ g^{-1}$) typically exhibit a steadily decreasing concentration dependence of reduced BR, which is due to a decrease in the macroform effect [8]. In our case, the dependence is nonmonotonic: For I = 1 M (Fig. 4, curve *1*) it has a critical point at $c = c^* \cong 0.20$ %; in 0.1 M $NaNO_3$ solution (Fig. 4b, curve *1*) critical points are observed at $c = c^* \cong 0.11$, $c \sim 2$, and $c \sim 0.5$ %. This correlates with the viscometric (Fig. 1) and light scattering (Fig. 3, curves *1*, *1*′) data.

Increase in the reduced BR for PAMPS in 1 M $NaNO_3$ solution at $c > c^*$, suggests similarly, to the light scattering data, formation of a fluctuation network of engagements. It should be noted that $[\Delta n/(g\eta_0 c)]_{g\to 0} = f(c)$ dependences for PAMPS and P(AMPS–AA) in 1 M $NaNO_3$ solution at $c > c^*$ are, on the whole, virtually identical.

The lack, in the case of PAMPS, of an angular dependence of the reduced intensity of anisotropic light scattering in 1 M $NaNO_3$ solution suggests the following. There is no mutual orientation of the segments of macromolecules, while for P(AMPS–AA) with suppressed electrostatic interactions at $c > c^*$ the formation of the fluctuation network of engagements was accompanied by the appearance of microdomain structures, which are mutually oriented macromolecular segments

[2] The size of macromolecules, $\langle R_g^2\rangle^{1/2}$, in 1 M and 0.1 M $NaNO_3$ solutions was estimated using the data on the asymmetry of scattered light in the $c < c^*$ region [7].

[3] In view of the significant curvature of the $\eta_{sp}/c = f(c)$ plot (Fig. 1), we present in Figs. 4a and 4b, the $[\Delta n[g\eta_0 c)]_{g\to 0} = f(c)$ dependence, instead of the widely used $\{\Delta n[g\eta_0(\eta_r - 1)]\}_{g\to 0} = f(c)$ dependence.

[1]. The difference in network morphology of the between the homo- and copolymer is, evidently, due to the fact that in the former, the dipole–dipole interactions dominate, and in the latter case the structure of the solution is significantly affected by hydrogen bonds (e.g., of the $-NH_2...O=C<$ type [1]).

The fluctuation network of engagements is also formed in semidilute solutions with suppressed electrostatic interactions in the case of moderately rigid-chain (A = 6–7 nm) high-molecular-weight [M_w = (6.6–10) × 10^6] polyelectrolytes of various structures [15, 16] (Fig. 4, curves *2*, *3*).

For rigid-chain high-molecular-weight polyelectrolyte (A ~ 17 nm, $M_w = 6 \times 10^6$) [15] we did not record formation of fluctuation network of engagements by the flow BR method (Fig. 4a, curve *4*). Formation of the network in polyelectrolyte solutions is, probably, affected not only by the ionic strength of the medium [13, 14], but also by the equilibrium rigidity of poly ions.

It was shown in [1, 13] that, in semidilute solutions of polyelectrolytes with incompletely suppressed polyelectrolyte effect, the electrostatic repulsion forces between the similarly charged poly ion groups hinder not only formation of associates but also interpenetration of the coils and formation of the fluctuation network of engagements at Debye's point.

Thus, the "abnormal" behavior of the optical anisotropy at I = 0.1 M [increase at c ~ 0.11–0.35 % (Fig. 4b, curve *1*)] cannot be understood from the standpoint of the network structure of solution. As shown by the light scattering studies, the lack of mutual orientation of the segments of PAMPS macromolecules seems to be sufficient for eliminating from consideration also the "microdomain" structure of solution, as in the case of PAMPS in 1 M $NaNO_3$ solution. We can presume (similarly to [1]) the hydrodynamic field-induced orientation of separate polymer chains with respect to each other (formation of "macrodomains"). This once again brings about the macroform effect owing to an increase in the degree of the form asymmetry p of the macromolecule ($p >> p_G$, where p_G is the parameter p for the Gaussian coil [8]). It should be noted that, even at $c < c^*$, the parameter p for the PAMPS macromolecule in 0.1 M $NaNO_3$ solution exceeds that under suppressed electrostatic interactions [7]. The homopolymer studied is a weakly charged species (fairly high ionic strength); hence, macrodomains are evidently formed for the most part via ion pair formation [13, 17, 18]. It should be emphasized, however, that the lack of correlation in orientation of anisotropic elements (according to light scattering data) in the PAPMS–0.1 $NaNO_3$ solution (unlike the data on flow BR) may be due to methodological factors: In studying of polyelectrolyte solutions by the flow BR method, the solution is strongly affected by the gradient field, in contrast to the light scattering method. Also, the polyelectrolyte effect does not allow in the case of interest any unambiguous interpretation of the light scattering data. Thus, the orientation effects in this system can be revealed only by the flow BR studies. In view of the fundamental difference between the methods, flow BR and light scattering, we cannot completely rule out the microdomain structure of the PAMPS–0.1 M $NaNO_3$ solution.

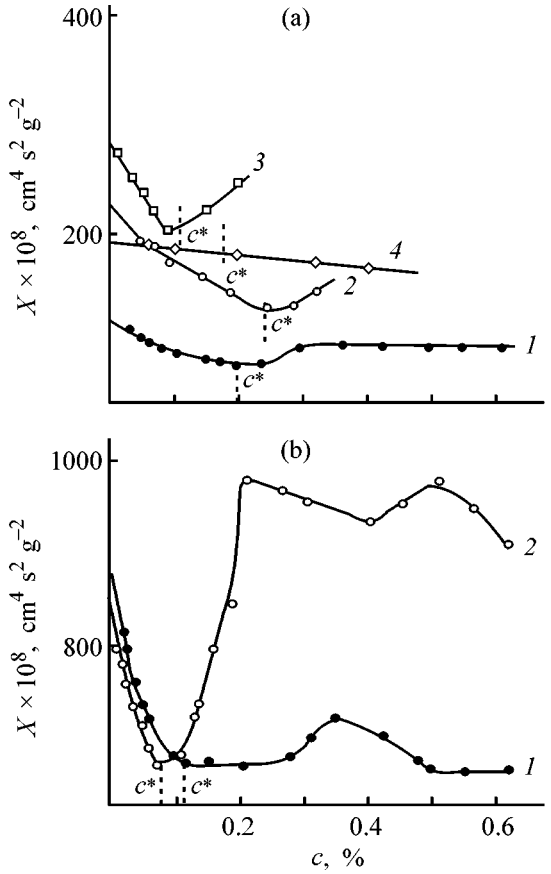

Fig. 4. Concentration dependence of reduced birefringence $[\Delta n/(g\eta_0 c)]_{g\to 0} = X$, for different solutions at (a) I = 1 M and (b) I = 0.1 M. Solution: (a) (*1*) PAMPS, (*2*) P(DMAEMA–AMPS) (DMAEMA is 2-dimethylaminoethyl methacrylate) [15], (*3*) P(DMAEMA–AAc) (AAc is acrylic acid) [16], and (*4*) P(DMAEMA · AMPS) [15]; (b) (*1*) PAMPS and (*2*) P(AMPS–AA).

Comparison of the $[\Delta n/(g\eta_0 c)]_{g\to 0} = f(c)$ dependences for systems PAMPS–0.1 $NaNO_3$ solution and P(AMPS–AA)–0.1 M $NaNO_3$ solution (Fig. 4b, curves *1*, *2*) shows that the effects are significantly stronger in the case of the copolymer, although the

amount of the ionic groups in PAMPS exceeds twofold that in the copolymer. The parameter *p* for PAMPS in 0.1 M $NaNO_3$ solution exceeds that for P(AMPS–AA) [7]. This contradicts the presumed macrodomain structure of the solution in the case of the system PAMPS–0.1 M $NaNO_3$ solution [7]. Evidently, this system is characterized by a microdomain structure of solution.

The morphological difference between the systems PAMPS–0.1 M $NaNO_3$ solution and P(AMPS–AA)–0.1 M $NaNO_3$ solution is clearly illustrated by the concentration dependence of the parameter $\langle\langle\eta\rangle^2\rangle$: In the case of the homopolymer, the $\langle\langle\eta\rangle^2\rangle = f(c)$ plot levels off at $c > c^*$ (Fig. 3, curve *2*'), and the $\langle\langle\eta\rangle^2\rangle = f(c)$ plot shows a clearly pronounced extremum in the case of the copolymer at $c \sim 0.2–0.4$ % [1].

The decrease in the optical anisotropy, suggested by the flow BR studies for PAMPS in 0.1 $NaNO_3$ solution at $c \sim 0.35–0.50$ % and the subsequent attainment of saturation (Fig. 4b, curve *1*) may be due to a greater hindrance to the mutual orientation of the segments at increased polymer concentration.

Our data on the flow BR for the systems PAMPS–0.1 M $NaNO_3$ solution and P(AMPS–AA)–0.1 M $NaNO_3$ solution suggest that the second extremum in the $[\Delta n/(g\eta_0 c)]_{g\to 0} = f(c)$ plot for P(AMPS–AA) (Fig. 4b, curve *2*) is due to the copolymeric nature of the polyelectrolyte.

CONCLUSIONS

(1) The flow birefringence, light scattering, and viscometric studies revealed the structural features of semidilute solutions of high-molecular-weight rigid-chain polyelectrolyte, poly-2-acrylamido-2-methylpropanesulfonic acid, at varied ionic strength of the medium and polymer concentration.

(2) In the case of suppressed electrostatic interactions (I = 1 M) in PAMPS solutions at $c > c^*$, a fluctuation network of engagements is formed. Its morphology differs from that of the fluctuation network forming in solutions of copolymer of 2-acrylamido-2-methylpropanesulfonic acid with acrylamide. In the latter case, the network formation is accompanied by formation of microdomain structures that are, essentially, mutually oriented macromolecular segments.

(3) Comparison of the results of the flow birefringence studies for semidilute solutions of high-molecular-weight polyelectrolytes of different structures in 1 M $NaNO_3$ solution showed that the network formation in polyelectrolyte solutions is affected by the equilibrium rigidity of poly ions.

(4) An assumption is made that, at I = 0.1 M and $c > c^*$, disordered fluctuation microstructures (microdomains) are formed in solutions of poly-2-acrylamido-2-methylpropanesulfonic acid which are capable of hydrodynamic field-induced orientation.

(5) The flow birefringence studies revealed the morphological differences for the systems poly-2-acrylamido-2-methylpropanesulfonic acid–0.1 M $NaNO_3$ solution and copolymer of 2-acrylamido-2-methylpropanesulfonic acid with acrylamide–0.1 M $NaNO_3$ solution. These differences are due to the structural features of the polymers.

REFERENCES

1. Valueva, S.V., Kipper, A.I., Silinskaya, I.G., *et al.*, *Vysokomol. Soedin., Ser. A.*, 2002, vol. 44, no. 2, pp. 305–313.
2. Debye, P., J. *Chem. Phys.*, 1946, vol. 14, no. 10, pp. 636–639.
3. Alexandrovicz, Z., *J. Chem. Phys.*, 1967, vol. 47, no. 11, pp. 4377–4384.
4. Noda, J., Truge, T., and Nagasawa, M., *J. Chem. Phys.*, 1970, vol. 74, no. 4, pp. 710–719.
5. Veselkov, A.N., Moroshkin, V.A., Polyakova, P.D., *et al.*, *Molek. Biol.*, 1976, vol. 10, no. 5, pp. 1050–1060.
6. Valueva, S.V., Kipper A.I., Lyublina, S.Ya., *et al.*, *Vysokomol. Soedin., Ser. A*, 1992, vol. 34, no. 12, pp. 35–44.
7. Valueva, S.V. and Kipper, A.I., *Zh. Prikl. Khim.*, 2001, vol. 74, no. 9, p. 1513–1517.
8. Tsvetkov, V.N., Eskin, V.E., and Frenkel', S.Ya., *Struktura makromolekul v rasrvorakh* (Structure of Macromolecules in Solutions), Moscow: Nauka, 1964.
9. Eskin, V.E., *Rasseyanie sveta rastvorami polimerov i svoistva makromolekul* (Light Scattering by Polymer Solutions and Properties of Macromolecules), Leningrad: Nauka, 1986.
10. *Polymer Blends*, D.P.Paul and Newman, S., Eds., New York, Academic.
11. Kalinina, N.A., Kallistov, O.V., Kuznetsov, N.P., *et al.*, *Vysokomol. Soedin., Ser. A*, 1990, vol. 32, no. 4, pp. 665–670.
12. Kallistov, O.V., Krivobokov, V.V., Kalinina, N.A., *et al.*, *Vysokomol. Soedin., Ser. A*, 1985, vol. 27, no. 5, pp. 968–974.
13. Litmanovich, E.A., Orleneva, A.P., Korolev, B.A.,

et al., *Vysokomol. Soedin., Ser. A*, 2000, vol. 42, no. 6, pp. 1035–1040.

14. Orleneva, A.P., Korolev, B.A., Litmanovich, E.A., *et al.*, *Vysokomol. Soedin., Ser. A*, 1998, vol. 40, no. 7, pp. 1179–1184.
15. Valueva, S.V., Kipper, A.I., Rumyantseva, N.V., *et al.*, *Zh. Prikl. Khim.*, 2000, vol. 73, no. 11, pp. 1183–1185.
16. Valueva, S.V., Kipper, A.I., Rumyantseva, N.V., *et al.*, *Zh. Prikl. Khim.*, 2000, vol. 73, no. 6, pp. 1000–1003.
17. Orleneva, A.P., Dynamic Properties of Concentrated and Semidilute Solutions of Poly(dimethylallylammonium Chloride) and Its Complexes with Sodium Dodecyl Sulfate, *Cand. Sci. Dissertation*, Moscow, 1998.
18. Litmanovich, E.A., Influence of the Concentration Characteristics of Polyelectrolyte Solution on the Composition and Phase State of the Products of Reaction between Poly(dimethylallylammonium Chloride) and Sodium Dodecyl Sulfate, *Cand. Sci. Dissertation*, Moscow, 1999.

Russian Journal of Applied Chemistry, Vol. 75, No. 2, 2002, pp. 292–295. Translated from Zhurnal Prikladnoi Khimii, Vol. 75, No. 2, 2002, pp. 301–304.
Original Russian Text Copyright © 2002 by Sazanov, Ugolkov, Mokeev, Novoselova, Zgonnik.

MACROMOLECULAR CHEMISTRY AND POLYMERIC MATERIALS

Effect of Fullerene on Cyclization of Polyamido Acids

Yu. N. Sazanov, V. L. Ugolkov, M. V. Mokeev, A. V. Novoselova, and V. N. Zgonnik

Institute of Macromolecular Compounds, Russian Academy of Sciences, St. Peterburg, Russia
Institute of Machine Science, Russian Academy of Science, St. Petersburg, Russia

Received October 17, 2001

Abstract—The reaction of fullerene C_{60} with polyamido acid in the stage of its conversion into polyimide was studied by complex thermal analysis. The thermal and kinetic characteristics of this reaction and its probable mechanisms are discussed.

Fullerenes attract the researchers' attention from not only theoretical, but also applied standpoints. Addition of fullerenes C_{60} and C_{70} or their mixtures to finished polymer or in the stage of its formation significantly affect the product characteristics and the polymerization mechanism [1–7]. The effects revealed suggest a polyfunctional role of fullerenes in polyolefin formation.

To proceed with these studies, we examined the effect of fullerenes on the formation of polymers of the polycondensation type, for the example of well-studied polyimides. It is well known that polyimides are formed in two stages. In the first stage, the starting compounds, tetracarboxylic acid dianhydrides and diamines, react in an aprotic polar solvent to form polyamido acid (PAA). In the second stage, dehydration and polycondensation occur under the action of various reagents or upon heating. These reactions are usually monitored by spectral or thermal analysis [8, 9]. These methods are fairly sensitive to quantitative or qualitative changes in the reaction system under the action of any external factors.

In this study, we mainly used calorimetry (differential scanning calorimetry, DSC) and thermal gravimetric analysis (TGA), with account of the kinetic and diffusion factors of polyimide formation.

EXPERIMENTAL

Pyromellitic dianhydride and diaminodiphenyl ether were used as the starting compounds. These reagents were purified by the standard procedure [8].

Since the aim of this work was to determine the time parameters of stabilization of PAA solutions [10], samples were withdrawn for analysis in the first 6–8 days of keeping the initial PAA solution of PAA under the identical conditions at room temperature.

As modifying additives to PAA solution we used fullerene C_{60} purified to 99% and partially cyclized polyacrylonitrile (*m*-PAN) [10], in which 40% of nitrile groups were converted to imine groups to form short ladder structures along the macromolecule. To prepare mixtures, a calculated amount (by weight) of C_{60} powder or jointly ground dry mixture of *m*-PAN and C_{60} in a required ratio was added to a DMF solution of PAA as polyimide (20%) precursor. After stirring for 10 min, the homogeneous mixtures were kept for a certain time (3 h, 1 day, etc. up to 8 days) at room temperature for stabilization and from subjected to thermal analysis. Each experimental series was completed by analysis of films produced from the solution of the mixture with finite aging time. For the system PAA + *m*-PAN + C_{60} (79 : 20 : 1, %) a thermogram of the film produced from the freshly prepared mixture was obtained. In parallel, the thermal behavior of *m*-PAN in solution was studied.

Thermal analysis was carried out on a Noetsch complex thermal analyzer (Germany) at a heating rate of 10 deg min^{-1} and weighed portion of 5 mg; and thermovolumetric analysis, on a TVA installation, heating rate 10 deg min^{-1}, pressure 5×10^{-3} mm Hg, and weighed portion 20 mg.

As shown previously [11, 12], thermal analytical study of a series of thermal and thermochemical processes of PAA formation and its conversion to poly-

1070-4272/02/7502-0292 $27.00 © 2002 MAIK "Nauka/Interperiodica"

imide gives the greatest body of data when quantitative and qualitative measurements are performed directly in the cell of the corresponding device. The DSC curves of PAA solution in DMF, measured in during PAA stabilization in the temperature range 20–400°C, are shown in Fig. 1. The general shape of these curves reflects the main features of thermal effects accompanying the transformation of PAA solutions, up to the temperature of thermal degradation of the resulting polyimide. At the beginning of solution heating, the heat capacity of the sample decreases owing to evaporation of the "free" solvent (unbound to PAA). The inflection in the curve at 60–70°C corresponds to the onset of solvent removal from the solvate shell of PAA, whose formation mechanism has been discussed previously [13, 14]. Subsequent thermal degradation of the solvate complex and imidization of PAA, accompanying this process, are manifested in the DSC curve as an asymmetrical endothermic peak in the range 105–111°C. The pattern observed in this range depends on the time of solution stabilization. Sample no. 1 differs from the other samples in the lack of an inflection in the DSC curve at 60–70°C and presence of a noticeable endothermic peak of water evolution at 133°C. These distinctions suggest that the formation of the stable solvate shell of PAA is complete within 2 days. An interesting feature of the thermal processes in the temperature range studied is the presence of significant endothermic effects for all PAA samples (curves *1*–*5*) with peaks in the range 287–292°C. Since, after heating to 160°C no weight loss is observed, according to the TGA data, up to 500°C, the above endothermic effects can be assigned to the melting of ordered domains of the resulting polyimide. It is most likely that there are mesomorphic structures extremely sensitive to the conditions of sample heating, which is confirmed by the absence of this effect in the case of a film of the same PAA, prepared under some other conditions (curve *0*), and also by noticeably different height and temperature of the peak in the DSC curves for a similar sample kept for 8 days (curve *6*).

The above distinctions show that the structure of PAA and its complexes with solvent is fairly labile and depends on the conditions of PAA synthesis and storage. These factors also have a pronounced effect on the characteristics of the resulting polyimides and their conversion at elevated temperatures [15]. In this connection, PAA solutions have been repeatedly used in practice as reactive components for synthesis of new heat-resistant composite materials. Their reactions with various monomers and polymers were confirmed by complex methods of thermal and spectral

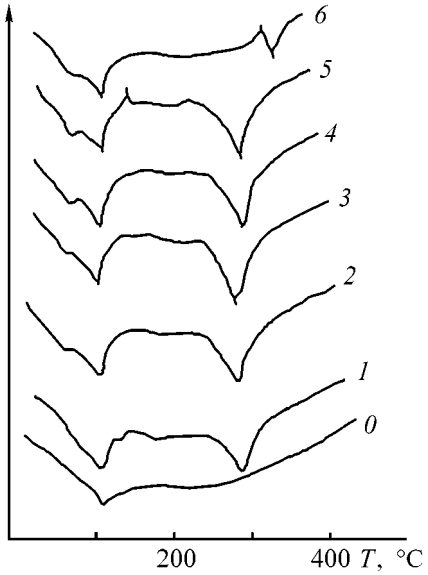

Fig. 1. DSC curves of PAA solution in DMF. (*T*) Temperature; the same for Fig. 3. Keeping time at room temperature, days: (*1*) 3 h, (*2*) 2, (*3*) 3, (*4*) 4, (*5*) 5, and (*6*) 8; (*0*) PAA film.

analysis [16]. In this study, we used as additional components fullerene C_{60} and modified PAN with partial cyclization along the chain.

We first studied the effect of fullerene C_{60} added to PAA solution in amounts of 0.3 and 5.0 wt %. Comparison of the DSC curves obtained under conditions similar to those for analysis of straight PAA did not reveal any significant changes. Irrespective of the C_{60} amount, the same endothermic effects in the temperature ranges 60–70°C and 105–110°C are observed, characterizing the evaporation of the solvent, decomposition of the solvate complex, and release of water with conversion of PAA to polyimide. Small variations of the peak temperatures and areas are independent of fullerene addition. The same is true for the parameters of peaks at approximately 300°C, which are less pronounced than those for straight PAA and do not allow any conclusions about the effect of C_{60} on the structural rearrangements of the polyimide.

When considering the kinetics of evolution of volatile products formed in heat treatment of PAA solution with and without fullerene (Fig. 2), monitored by thermal volumetric analysis (TVA), we can follow a regular trend in the removal of the solvent, bound and unbound to PAA macromolecules. With C_{60}-containing PAA solutions kept for more than 2 days, a splitting of the solvent evolution peak is clearly pronounced. According to calculation of the matter balance, the first peak in curves *2*′ and *3*′ at 60–70°C

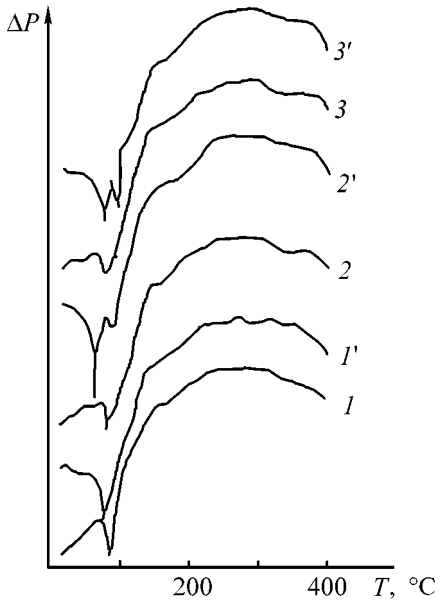

Fig. 2. TVA curves of the solution of PAA in DMF. (ΔP) Rarefaction and (T) temperature. Time of keeping at room temperature (days): (*1*, *1*') 3 h, (*2*, *2*') 2, and (*3*') 3. (*1*'–*3*') In the presence of 5% C_{60}.

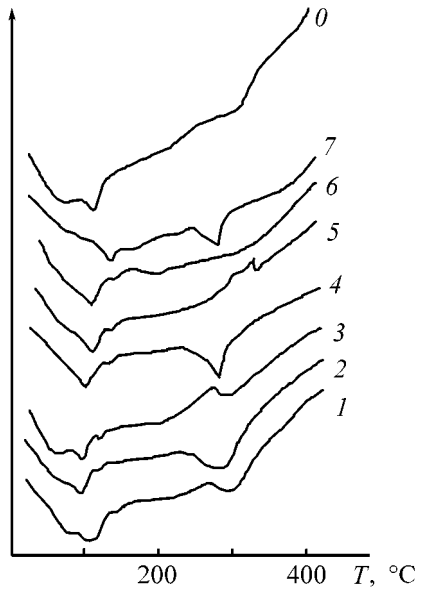

Fig. 3. DCS curves of solution of PAA in DMF + 1.0% C_{60} + 20% *m*-PAN. Time of keeping at room temperature (days): (*1*) 3 h, (*2*) 2, (*3*) 3, (*4*) 4, (*5*) 5, (*6*) 6, and (*7*) 10; (*0*) solution of *m*-PAN.

is assigned to evolution of the solvent unbound to PAA, and the second peak at 85–90°C, to evolution of DMF from its complex with PAA. It is evident that, under conditions of thermal decomposition in a vacuum, fullerene exerts a certain effect on the structural rearrangement of the PAA–solvent complex. A splitting of the peak is observed for curves *1*'–*3*' and not observed for curves *1*–*3*. It should be noted that solvent removal begins immediately after the start of heating. Without special crystallographic studies we cannot explain the mechanism of the effect of fullerene in this stage, but the occurence of this effect is an indisputable fact. As regards the cyclodehydration of PAA, in which water is evolved, the maximum effect is observed as evidenced by calorimetric data (Fig. 1) and the matter balance (Fig. 2),, at approximately 150°C. However, there are certain distinctions in this case, too, especially in the TVA curves. For example, according to DSC analysis, the endothermic effect of cyclodehydration after 2 days of stabilization of PAA solution almost coincides with the endothermic effect of decomposition of the solvate complex PAA-DMF, whereas TVA shows that these processes noticeably differ in temperature. In addition, it is seen that the presence of C_{60} shifts the cyclodehydration peak to higher temperatures by approximately 20–30°C. Under these conditions, fullerene is able not only to form complexes with CO and NH_2 groups of PAA but also to react with carboxy groups. The complexation promotes evolution of the solvent in thermal treatment of PAA in the presence of C_{60}, and chemical reaction of fullerene with carboxy groups hampers imidization.

The parameters of thermal conversion of PAA to polyimide change to a greater extent when *m*-PAN is added, along with C_{60}, to PAA solution. Typical DSC curves of the PAA + *m*-PAN + C_{60} mixture are shown in Fig. 3. When comparing DSC curves in Figs. 1 and 3, we can conclude that addition of partially cyclized PAN to PAA solution affects the activity of the system in both the first and second stages. It is likely that the differences observed are caused by the formation of PAA–*m*-PAN compositions whose activity in complexation has been demonstrated previously [17]; they react with C_{60} to form additional bonds.

CONCLUSION

The effect of fullerene C_{60} added to the polyamido acid derived from pyromellitic anhydride and diaminodiphenyl ether on its thermal conversion to polyimide was studied by complex thermal analysis. It was found that C_{60} affects some kinetic parameters of this reaction, especially when it is activated with modified polyacrylnitrile.

ACKNOWLEDGMENTS

This work was financially supported by the Russian Scientific and Technical Program “Topical Re-

search Lines in Physics of Condensed Media," "Fullerenes and Atomic Clusters" (project no. 98076).

REFERENCES

1. Pozdnyakov, A.O., Pozdnyakov, O.F., Redkov, B.P., *et al., Tech. Phys. Lett.*, 1996, vol. 22, no. 9, pp. 86–87.
2. Pozdnyakov, A.O., Ginzburg, B.M., Pozdnyakov, O.F., and Redkov, B.P., *Zh. Prikl. Khim.*, 2000, vol. 73, no. 1, pp. 135–136.
3. Pozdnykov, O.F., Redkov, B.P., and Pozdnykov, A.O., Abstracts of Papers, *Int. Workshop on New Approaches of Hi-Tech Materials NDTCS*, St. Petersburg, Russia, June 3–7, 1996, D3, pp. 33–34.
4. Shibaev, L.A., Antonova, T.A., Vinogradova, L.V., *et al., Pis'ma Zh. Tekh. Fiz.*, 1997, vol. 23, no. 18, pp. 19–21.
5. Shibaev, L.A., Antonova, T.A., Vinogradova, L.V., *et al., Pis'ma Zh. Tekh. Fiz.*, 1997, vol. 23, no. 18, pp. 81–82.
6. Shibaev, L.A., Antonova, T.A., Vinogradova, L.V., *et al., Pis'ma Zh. Tekh. Fiz.*, 1997, vol. 23, no. 18, pp. 87–89.
7. Mokeev, M.V., Vinogradova, L.V., Zgonnik, V.N., and Gribanov, A.V., Abstracts of Papers, *New Approaches in Polymer Synthesis and Macromolecular Formation, Int. Symp.*, St. Petersburg, June 16–20, 1997, pp. 0–002.
8. Bessonov, M.I., Koton, M.M., Kudryavtsev, V.V., and Laius, L.A., *Poliimidy – klass termostoikikh polimerov* (Polyimides: A Class of Heat-Resistant Polymers), Leningrad: Nauka, 1983.
9. Sazanov, Yu.N., *Termicheskii analiz organicheskikh soedinenii* (Thermal Analysis of Organic Compounds), Leningrad: Nauka, 1991.
10. Novoselova, A.V., Zgonnik, V.N., Spirina, T.N., *et al., Vysokomol. Soedin., Ser. A*, 1993, vol. 35, no. 5, p. 510.
11. Sazanov, Yu.N., Krasilnikova, G.N., and Shcherbakova, L.M., *Eur. Polym. J.*, 1975, vol. 11, no. 3, pp. 801–804.
12. Sazanov, Yu.N., Fedorova, G.N., and Shcherbakova, L.M., *J. Appl. Polym. Sci.*, 1975, vol. 19, no. 12, pp. 2335–2341.
13. Sazanov, Yu.N., Shibaev, L.A., and Dauengauer, S.A., *J. Therm. Anal.*, 1982, vol. 24, no. 1, pp. 75–82.
14. Sazanov, Yu.N., Dauengauer, S.A., Shibaev, L.A., *et al., J. Therm. Anal.*, 1982, vol. 25, no. 5, pp. 441–447.
15. Gribanov, A.V., Sazanov, Yu.N., Beloborodova, E.V., and Fedorova, G.N., *Zh. Prikl. Khim.*, 1999, vol. 72, no. 3, pp. 467–473.
16. Sazanov, Yu.N., *J. Therm. Anal.*, 1990, vol. 36, no. 4, pp. 361–376.
17. Spirina, T.N., Novoselova, A.V., Sazanov, Yu.N., *et al.*, Abstracts of Papers, *X Vsesoyuznoe soveshchanie po termicheskomu analizu* (X All-Union Conf. on Thermal Analysis), Leningrad, August 26–28, 1989, Leningrad: Izd. Akad. Nauk SSSR, 1989, p. 197.

Russian Journal of Applied Chemistry, Vol. 75, No. 2, 2002, pp. 296–301. Translated from Zhurnal Prikladnoi Khimii, Vol. 75, No. 2, 2002, pp. 305–310.
Original Russian Text Copyright © 2002 by Grigor'eva, Stepanenko, Sergeeva .

MACROMOLECULAR CHEMISTRY AND POLYMERIC MATERIALS

Plasticization of Polyvinyl Chloride with Reclaimed Polyvinyl Chloride–Polyurethane Mixture

O. P. Grigor'eva, L. V. Stepanenko, and L. M. Sergeeva

Institute of Chemistry of Macromolecular Compounds, National Academy of Sciences of Ukraine, Kiev, Ukraine

Received July 13, 2001

Abstract—The feasibility was studied of plasticization of rigid polyvinyl chloride with a reclaimed polyvinyl chloride–polyurethane mixture yielded by thermomechanochemical degradation of wastes of polyurethane foam coated with a polyvinyl chloride film. The molecular-weight distribution of the polyurethane component, temperatures of phase transitions, and physicomechanical properties of the polymer systems were studied as influenced by the preparation temperature of the reclaim.

It is well known that polyvinyl chloride (PVC) is for the most part used in the plasticized form. The most widely used plasticizers are low-molecular-weight polar substances of the ester nature, such as, e.g., dioctyl phthalate (DOP), dioctyl sebacate, (DOS), etc. However, low-molecular-weight plasticizers make the properties of the resulting PVC unstable owing to migration of the plasticizer in the bulk of the material and its gradual exudation. In this context, much attention has been recently given to plasticization of PVC with high-molecular-weight compounds and polyurethanes (PUs), in particular, [1–6]. Even in the case of fast segmental diffusion, the polymer plasticizer molecule cannot leave the material surface, which ensures more stable properties of the material. The structural features and the properties of a number of compositions based on PVC/PU mixtures were studied in [2–6]. Also, plasticization of PVC with reclaimed PU was attempted with the aim of preparing materials suitable for sound proofing, pipeline facing, shoemaking, medicine, house-building, etc. [1].

The previous studies of the degradation of secondary PUs in an extruder showed that the products of inexhaustive degradation can be used for preparing polymer materials suitable for diversified applications [7–10]. These studies were concerned with individual polyurethane foams (PUFs) differing in degree of cross-linking (wastes from PUF production, automobile parts, furniture, shoes, etc.).

In this study, we analyzed the possibility of reclaiming a secondary PUF coated with a PVC film (wastes of sound-proofing materials) by thermomechanochemical degradation in an extruder, and also the suitability of the polymer mixture yielded by degradation (PVC/PU reclaim) for plasticizing rigid PVC. We also studied the properties and the phase structure of the plasticized PVC as influenced by the preparation conditions and the concentration of the PVC/PU reclaim introduced.

EXPERIMENTAL

We studied crushed wastes of elastic PUFs coated with a PVC film (10 × 10 × 10 mm crumb). Polyurethane foam was essentially polyesterurethane prepared from an ester (molecular weight M = 2200) and toluylene diisocyanate (TDI, a 65/35 isomer mixture). The trifunctional nature of the initial ester (based on adipic acid, diethylene glycol, and trimethylolpropane) and proper reactant ratio afforded sufficient degree of PUF cross-linking. The PVC film for PUF coating was prepared from rigid PVC (resin) plasticized with commercial plasticizers DOP and DOS. The degrading agent was a mixture of monoethanolamine (MEA) and potassium acetate (PA). The composition and the component ratio for the polymer systems are presented in Table 1.

For thermomechanochemical degradation of PVC–PUF wastes we utilized a mixture of degrading agents in a single-worm laboratory extruder. Prior to being fed into the charging bin of the extruder, the crushed wastes were treated with a mixture of degrading agents. The specially chosen parameters, namely, the geometry of the worm, the temperature gradient

1070-4272/02/7502-0296 $27.00 © 2002 MAIK "Nauka/Interperiodica"

along the worm, and the type and concentration of the above mixture allowed simultaneously partial thermomechanochemical degradation, homogenization, and plasticization of the material being processed. The temperature gradient $T_{in} - T_{end}$ along the worm was varied from 130–170 to 180–200°C. The worm rotation rate was set constant at 35 rpm. The time of material processing in the extruder was 2–4 min. The resulting PVC/PU reclaim was a homogeneous thermoplastic mixture of PVC and PU suitable for subsequent use without further purification or fractionation.

Plasticization of PVC was effected by mixing rigid PVC with commercial plasticizers (DOP : DOS = 2 : 1) and/or PVC/PU reclaim in certain proportions in dimethylformamide solution (10% solution). Films were prepared by casting the polymer solutions onto Teflon supports, followed by solvent evaporation and vacuum treatment of the films to constant weight.

The molecular weights and molecular-weight distributions for PU in the reclaim obtained under various temperature gradients in the extruder were determined by exclusive chromatography on a Du Pont (USA) installation for liquid chromatography in the UV region, with tetrahydrofuran as the solvent. A reference PU sample was synthesized from the same initial polyester P-2200 and excess TDI; the terminal isocyanate groups of the resulting PU were converted to urethane groups by reaction with methanol.

We studied the viscoelastic properties of the films of polymers and polymer blends by DMTA. The measurements were carried out for samples stretched at a frequency of induced sinusoidal vibrations equal to 100 Hz in the temperature range from –130 to +100°C at sample heating rate of 1 deg min^{-1}. The sample size was $5 \times 50 \times 1.0$ mm.

The thermal properties of the samples were studied by DSC on a Mettler TA 4000 calorimeter in the range from –100 to +250°C under nitrogen at sample heating rate of 20 deg min^{-1}.

The tensile strength and relative elongation of the films were measured on an FU-1000 tensile-testing machine at 25°C and sample stretching rate of 50 mm min^{-1}. The sample size was $5 \times 40 \times 1.0$ mm.

The intrinsic viscosity of PVC in cyclohexanone [η] was determined at 25°C.

It is known that, in thermal degradation of densely cross-linked PUF (e.g., semirigid PUF) in the absence of degrading agents, the secondary and main chemical bonds of the polymer chains in PUF are ruptured at high temperatures, 230–250°C [7]. Thermal oxidative degradation of PVC begins upon heating to 120–140°C and is accompanied by partial dehydrochlorination and formation of a conjugated double bond system in the main chain. This substantially improves the thermal stability of PVC, but deteriorates the physicomechanical properties of the polymers [6]. Bowden *et al*. [6] found that, in the case of thermal degradation of PUF coated with a PVC film, dehydrochlorination to give polyenes in PVC at the PUF–PVC interface proceeds at a rate exceeding 6–8-fold that at the air–PVC interface, and this process is accelerated by the residual amine catalyst utilized in synthesis of PUF.

Table 1. Initial materials

Composition	Component content, wt fraction
PVC/PUF composite (sound-proofing material wastes)	46/54
PVC film [0–55 brand, GOST (State Standard) 5960–72–PVC resin	100
Plasticizer:	
DOP	27
DOS	14
Special additives (carbon black, antioxidants, thermostabilizers, etc.)	9
PUF (EShZ brand, TU (Technical Specifications) 6-55-50–90:	
polyester P-2200	100
TDI	38
special additives (catalyst, foam stabilizer, etc.)	7
Formulation for extrusion, PVC/PUF composite	100
Mixture of degrading agents:	
MEA	6
PA	1

Of great importance in this regard is the proper selection of conditions for extrusion of the PVC : PUF composite, so as to ensure cleavage of cross-links in PUF with minimal degradation of the main polymer chains of both polymers (worm design, temperature condition, extrusion rate, chemical nature and concentration of the degrading agents).

Being thermoplastic, the PVC film contained in the PVC/PUF composite studied is easily processed in extruders, and thermostabilizers and antioxidants from the initial formulation favor preservation of the service properties of PVC subjected to energy

Table 2. Influence of extrusion conditions on the intrinsic viscosity of PVC film

PVC : DAM ratio, wt fraction : wt fraction	T_{in}–T_{end}, °C	[η], dl g^{-1}
100 : 0	–	0.56
100 : 0	160–175	0.61
100 : 7	160–175	0.58
100 : 7	170–190	0.57

Table 3. Molecular-weight distribution for PU in the reclaim under different temperature conditions of PVC/PUF composite extrusion

T_{in}–T_{end}	M_n	M_w	M_z	M_w/M_n
130–175	89 100	94 200	108 000	1.06
160–175	81 500	92 600	96 100	1.13
170–180	35 300	46 700	64 100	1.32
180–200	34 000	35 800	37 800	1.05

impact in the extruder for relatively short time. The presence of PUF and degrading agents can accelerate PVC degradation. Table 2 presents the intrinsic viscosities of PVC measured after extrusion under different conditions; it is seen that the intrinsic viscosity of PVC and, hence, its molecular weight, are virtually unaffected by the process temperature and the presence of degrading agents. Certain increase in the intrinsic viscosity of PVC after extrusion may be due to loose cross-linking of its chains, in agreement with the DMTA results.

Let us consider how the extrusion conditions for the PVC/PUF composite affect the properties of its second component, elastic PUF. The composition and the reactant ratio of the composite are such that it has a looser network of cross-links compared with semirigid and rigid PUFs [11]. This allows partial thermal degradation of the composite under the actual conditions at moderate temperature, which yields a soluble polymeric product suitable for processing.

Table 3 presents the molecular-weight distribution for PU in the reclaim as dependent on the extrusion temperature for the PVC/PUF composite. It is seen that the products obtained are linear polymers with fairly high molecular weights. With increasing processing temperature, the absolute values of M_n, M_w, and M_z tend to decrease. Table 3 shows that all the PU samples obtained are polydisperse ($M_w/M_n > 1$). It is seen that the polydispersity of PU tends to grow with increasing the processing temperature initially, but at the maximal processing temperature (180–200°C) it takes the minimum value. This involves, however, a decrease in the molecular weight by a factor of 2.6–2.8, and the parameters M_n, M_w, and M_z become virtually identical. The high molecular weights of PU (M_n, M_w, and M_z) and its narrow molecular-weight distribution ($M_w/M_n \approx 1$) must impart good mechanical properties of the materials on their base.

Thus, data in Tables 2 and 3 suggest that, under the actual extrusion conditions, the main chemical transformations in the PVC/PUF composite involve elastic PUF. Thermal degradation of semirigid PUF occurs primarily at 230–250°C (in extruder). When degrading agents are used, the temperature for degrading the PUF polymer chains is decreased to 200–220°C, which yields oligomeric reactive products (viscous liquids or pastes). These are essentially mixtures of oligocarbamateureas with the initial oligoester, from which PUF was obtained [10].

Extrusion of elastic PUF under the actual conditions yields, even at 130–175°C, linear polyurethaneureas with fairly high molecular weights which are compatible with other polymers and suitable for conventional processing. Table 3 shows that, with the extrusion temperature increasing from 180 to 200°C, the degradation of elastic PUF gets somewhat more profound. The inexaustive degradation products are, most probably, of polyesterurethane nature and contain carbamateurea moieties in the chain [12].

We also analyzed the suitability of the PVC/PU reclaim as plasticizer for rigid PVC. As known, the main effect exerted by plasticizers, both low-molecular-weight and polymeric, consists in their interaction with segments of macromolecules of the main polymer, which ensures a prompter viscoelastic response of the polymer to mechanical impact [13]. Thus, plasticizers increase the molecular mobility of polymer chains and decrease the glass transition point T_g. Therefore, it was of interest to study how the conditions of preparation of the PVC/PU reclaim affect the segmental mobility and the phase transition temperatures of the reclaim constituents, PVC and PU. The DMTA and DSC methods provide exhaustive information about specifically these changes in polymer blends.

Figure 1 presents the temperature dependences of the tangent of the mechanical loss angle tan δ and the elasticity modulus E' of the samples of the initial and extruded PVC, and those of the PVC/PU reclaim obtained at various temperature gradients in the extruder. Table 4 presents the phase transition temperatures for these samples.

The initial PVC has a single T_g (53°C), as judged from the single broad maximum of the mechanical loss angle in the temperature dependence of tan δ (Fig. 1, curve *1*) and the single transition observed in the $E' = f(T)$ plot. The significant width of the tan δ maximum and the decrease in the T_g, compared with nonplasticized PVC ($T_g \cong 80$°C [13]), is known to be due to the presence of the plasticizer in PVC. Also, a secondary relaxation transition is observed in the range from –80 to –30°C, whose mechanism remains to be fully elucidated. It is believed, e.g., that it is due to degradation of the interchain hydrogen bonds [14]. The temperature dependence of tan δ for PVC processed in the extruder (Fig. 1, curve *2*) is virtually identical to that for the initial PVC with only T_g somewhat increased (Table 4), which is probably due to loose cross-linking of PVC during processing.

The temperature dependences of tan δ for the PVC/PU reclaim exhibit three partially overlapping maxima (Fig. 1, curves *3*, *4*). The temperature dependences of the elasticity modulus are indicative of the corresponding transitions. The first low-temperature maximum of tan δ corresponds to T_g of PU, and the second and third maxima, to temperatures intermediate between the glass transition points for PU and PVC. The last fact suggests formation of mixed microphases enriched in PU and PVC, respectively (Table 4). It was impossible to determine T_g for the PVC component by DMTA, as the PVC/PU reclaim samples investigated soften upon stretching and rupture at $T \geq 40$°C. Therefore, we conducted DSC studies and found that T_g of the PVC component tends to decrease (unlike individual PVC, Table 4). Thus, the glass transition points for PU and PVC components tend to approach each other. This suggests a better compatibility of PVC and PU in the PVC/PU reclaim.

Figure 1 (curves *3* and *4*) also suggests that the temperature corresponding to the tan δ maximum remains virtually unchanged with increasing temperature of PVC/PU reclaim preparation. However, the kinetic mobility of the macromolecular segments, especially in the microphase enriched in PU, grows, as evidenced by a significant increase in the tan δ peak height (Fig. 1, curve *4*). This is due to a decrease in the molecular weights and widening of the molecular-weight distribution for the polyurethane component of the reclaim owing to a higher degree of PUF degradation (Table 3).

Figure 2 presents thermograms (DSC data) for the initial PVC film and for PVC/PU reclaim obtained under varied temperature conditions. Table 4 presents the phase transition temperatures for these samples. The thermogram of the initial PVC film (curve *1*) is indicative of two main transitions, one corresponding to T_g of PVC (63°C) and the other, to the melting point of PVC (236°C).

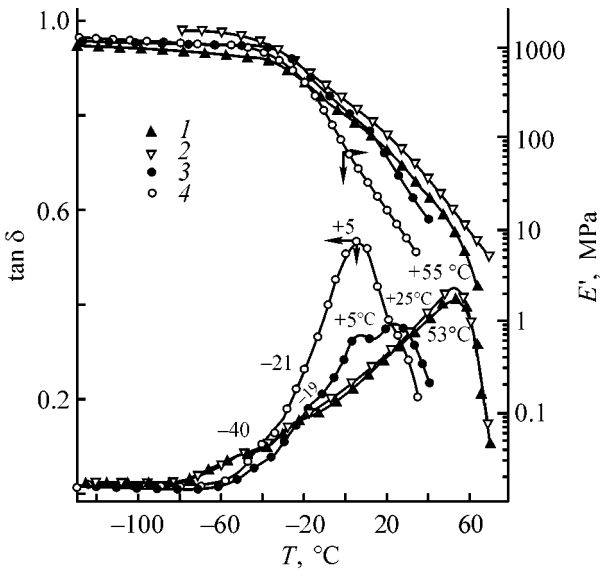

Fig. 1. Temperature dependences of the tangent of the mechanical loss angle tan δ and the elasticity modulus E', of (*1*) initial PVC, (*2*) PVC after extrusion at 130–175°C, and (*3*, *4*) PVC/PU reclaim. Temperature gradient in the extruder, °C: (*3*) 130–175 and (*4*) 160–175.

Let us analyze the thermograms of the PVC/PU reclaim obtained under varied temperature condi-

Table 4. Phase transition temperatures for the initial PVC film and PVC/PU reclaim.

$T_{in}-T_{end}$, °C	Method	Glass transition point T_g, °C				mp, °C
		PU	mixed microphase		PVC	
			PU–EP*	PVC–EP		
PVC						
–	DMTA	–	–	–	53	–
–	DSC	–	–	–	63	236
130–175	DMTA	–	–	–	55	–
130–175	DSC	–	–	–	64	233
PVC/PU regenerate						
130–175	DMTA	–19	5	25	–	–
130–175	DSC	–38	–1	11	59	–
160–175	DMTA	–21	5	24	–	–
160–175	DSC	–40	–2	15	53	–

* EP is enriched phase.

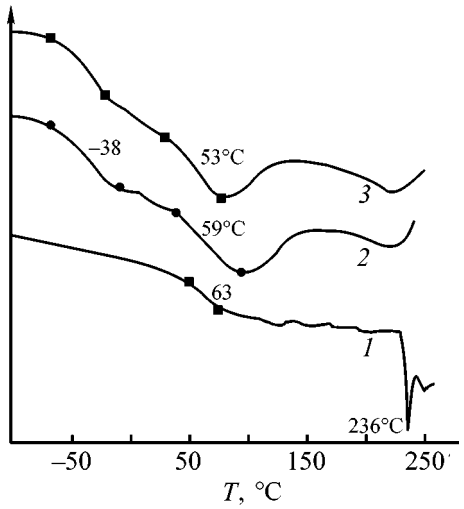

Fig. 2. Thermograms of (*1*) initial PVC and (*2*, *3*) PVC/PU reclaim. (*T*) Temperature, the same for Fig. 3. Temperature gradient in extruder, °C: (*2*) 130–150 and (*3*) 160–175.

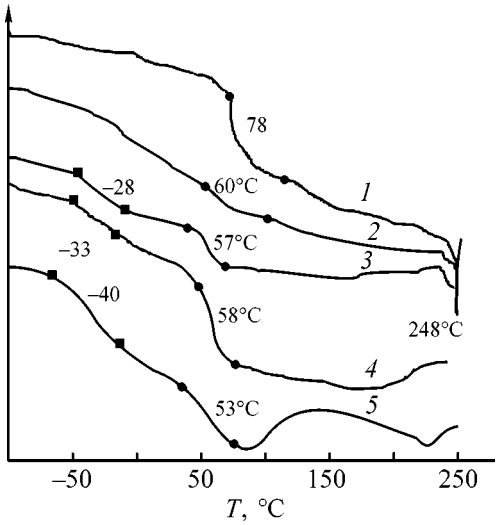

Fig. 3. Thermograms of plasticized PVC. Rigid PVC : polymer reclaim : DOP/DOS ratio: (*1*) 100 : 0 : 0, (*2*) 100 : 0 : 40, (*3*) 100 : 20 : 20, (*4*) 100 : 40 : 0, and (*5*) 0 : 100 : 0.

tions (Fig. 2, curves *2*, *3*). Both curves are indicative of two main transitions corresponding to the glass transition points of the PU and PVC components (Table 4). Also, graphical differentionation of the curves allows identification of less pronounced transitions corresponding to the glass transition points of mixed microphases enriched in the PU and PVC components (Table 4). These results reasonably agree with the DMTA data, and the difference in the absolute values of the glass transition points may be due to different heating rates of the samples (1 and 20 deg min^{-1} for DMTA and DSC, respectively).

Raising the temperature of the PVC/PU reclaim preparation virtually does not affect the T_g of PU, but lowers that of PVC from 59 to 53°C. Thus, the DSC data confirm the conclusion, made on the basis of the DMTA data, about partial mixing of the PVC/PU reclaim components during its preparation and improved compatibility of PU and PVC in the reclaim after rising temperature of its preparation.

Table 5. Glass transition point for the polymer components (DSC data) and physicomechanical properties of plasticized PVC

Rigid PVC : PVC/PU reclaim : DOP/DOS ratio	T_g, °C		Tensile strength, MPa	Relative elongation, %
	PU	PVC		
100 : 0 : 0	–	78	83.1	50
100 : 0 : 40	–	60	65.0	480
100 : 20 : 20	–28	57	68.6	490
100 : 40 : 0	–33	58	80.1	380
0 : 100 : 0	–40	53	16.2	350

Also, the thermograms of the PVC/PU reclaim suggest the following. First, the lack of a peak corresponding to the melting point of the crystalline phase of PVC in both the thermograms may be due to retardation of crystallization by the microphase structure formed in the PVC/PU reclaim because of a limited compatibility of its components and by formation of mixed microphases enriched in PVC or PU. Second, at $T \geq 100$°C the system undergoes afterpolymerization, as evidenced by ascending exothermic curves. Probably, this is due to polymerization of reactive oligomers yielded by thermomechanochemical degradation of the PVC/PU composite.

As known [13], to be suitable as polymer plasticizer for rigid PVC, the PVC/PU reclaim must (i) have $T_g << T_g$ of PVC, (ii) have a sufficiently high molecular weight so as to be classed as "polymer" ($M_n >$ 5000), and (iii) mix well with PVC (at the molecular or segmental level). Our experimental data suggest that the PVC/PU reclaim prepared by us satisfies all these requirements. Also, it contains impurity low-molecular-weight plasticizers DOP/DOS (entering into composition of the initial composite), which improves the miscibility of the components and the material processed.

Figure 3 presents the thermograms, and Table 5, the characteristics of the plasticized PVC (sample of

the PVC/PU reclaim prepared at 160–175°C). The concentrations of the plasticizers DOP and DOS do not include their content in the reclaim. It is seen that the PVC/PU reclaim lowers the T_g of PVC similarly to low-molecular-weight plasticizers DOP/DOS. The fact that the glass transition points for PU and PVC approach each other in the plasticized PVC suggests a decreased degree of segregation in the system. Table 5 shows that addition of reclaimed polymer plasticizers to rigid PVC improves the physicomechanical properties of the resulting material.

CONCLUSIONS

(1) The feasibility is demonstrated of reclaiming secondary polyurethane foam coated with polyvinyl chloride film by thermomechanochemical degradation in extruder. This yields a homogeneous reclaimed polymer mixture polyvinyl chloride–polyurethane, suitable as thermoplastic.

(2) The resulting mixture is both an efficient plasticizer and a modifier of the properties of rigid polyvinyl chloride. By varying the extrusion conditions for the initial material it is possible to modify the microphase structure and to achieve the desired mechanical properties of the reclaimed polyvinyl chloride–polyurethane mixture and, hence, those of plasticized polyvinyl chloride.

(3) Our results can be used not only for utilizing the wastes of polyurethane foam coated with polyvinyl chloride film, but also for saving the initial materials and improving the properties of polymer materials.

REREFENCES

1. Gribanova, N.A., *Plast. Massy*, 1995, no. 4, pp. 8–10.
2. Kim, A.J., Kim, B.K., and Jeong, B.K., *J. Appl. Polym. Sci.*, 1994, vol. 51, no. 13, pp. 2187–2190.
3. Al-Salax, H.A., *Polym. Bull.*, 1998, vol. 40, pp. 477–484.
4. Vilenskii, V.A., Kercha, Yu.Yu., Shtompel', V.I., *et al.*, *Ukr. Khim. Zh.*, 1991, vol. 57, no. 11, pp. 1202–1208.
5. Zhu, Y.O., Huang, Y.J., and Chi, Z.G., *J. Appl. Polym. Sci.*, 1995, vol. 56, no. 9, pp. 1371–1379.
6. Bowden, M. Bradley, J.W., Dix, L.R., *et al.*, *Polymer*, 1994, vol. 34, no. 8, pp. 1654–1657.
7. Stepanenko, L.V., Nedashkovskaya, N.S., Matyushov, V.F., *et al.*, *Plast. Massy*, 1983, no. 8, pp. 31–32.
8. USSR Inventor's Certificate, no. 1168571.
9. USSR Patent, 1836391
10. Stepanenko, L.V., Matyushov, V.F., Lebedev, E.V., and Sergeeva, L.M., *Vestn. Akad. Nauk Ukrain. SSR*, 1987, no. 9, pp. 66–70.
11. Saunders, J.H. and Frish, K.C., *Polyuretanes. Chemistry and Technology. Part 1. Chemistry*, New York: Interscience, 1962.
12. Frisch, K.S., *Polimery*, 1988, vol. 43, no. 10, pp. 579–660.
13. Hammer, C.F. *Polymer Blends*, Paul, D.R. and Newman, S., Eds., vol. 2, New York: Academic, 1978.
14. Nielsen, L.E., *Mechanical Properties of Polymers and Composites*, New York: Marcel Dekker, 1974.

Russian Journal of Applied Chemistry, Vol. 75, No. 2, 2002, pp. 302–304. Translated from Zhurnal Prikladnoi Khimii, Vol. 75, No. 2, 2002, pp. 311–313.
Original Russian Text Copyright © 2002 by Lavnikova, Zheltobryukhov, Rakhimov, Storozhakova.

MACROMOLECULAR CHEMISTRY AND POLYMERIC MATERIALS

Polymerization of Methyl Methacrylate in the Presence of *N*-Acetyl-ε-aminocaproic Acid Acetylamide

I. V. Lavnikova, V. F. Zheltobryukhov, A. I. Rakhimov, and N. A. Storozhakova

Volgograd State Technical University, Volgograd, Russia

Received January 10, 2000; in final form, May 2000

Abstract—The effect of *N*-acetyl-ε-aminocaproic acid acetylamide on radical polymerization of methyl methacrylate initiated with lauroyl peroxide was studied.

To impart new service properties, vinyl polymers are often modified with polymeric fragments containing heteroatoms. One of such modifying agents is polycaproamide (PCA), which is widely used in the fiber production. Upon prolonged storage in air, especially at elevated temperatures and on treatment with ozone, PCA is oxidized to form peroxy groups. Through these groups various vinyl monomers can be grafted to PCA, giving polymers with new service properties [1, 2].

To evaluate the mechanism of graft polymerization, we studied the effect of compounds with amide-containing fragments, namely *N*-acetyl-ε-aminocaproic acid acetylamide (DAPAC), on the polymerization kinetics and properties of vinyl monomers for the example of methyl methacrylate (MMA). DAPAC was prepared according to [3] by successive transformation of *N*-acetyl-ε-aminocaproic acid into acid chloride, amide, and then DAPAC. It is known that addition of some polar fragments to polymethyl methacrylate allows preparation of polymers with high thermal stability and light fastness [4].

The kinetic features of MMA radical polymerization in the presence of DAPAC with lauroyl peroxide initiator were studied by dilatometry [5]. Polymerization did not occur on heating of the reaction mixture at 333–353 K for 2–6 h at DAPAC concentration of $(1.75–43.3) \times 10^{-4}$ mol dm^{-3}, but occurred at DAPAC content decreased to $(0.5–1.7) \times 10^{-4}$ mol dm^{-3}.

The presumed role of DAPAC in polymerization can be illustrated by the following scheme:

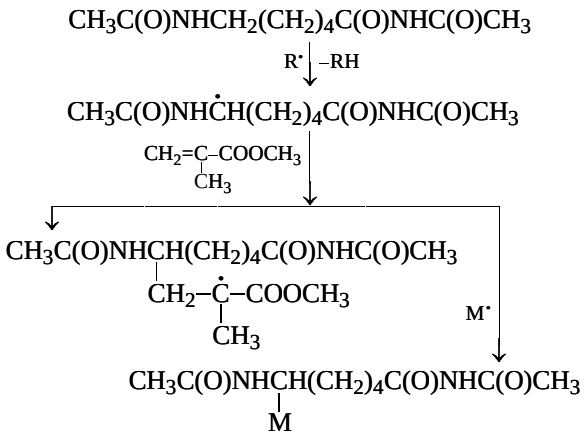

In the presence of oxygen, formation of peroxy radicals and their participation in chain polymerization reactions are possible [6].

The kinetic parameters of MMA polymerization in the presence of lauroyl peroxide and DAPAC are listed in Table 1. Our data show that the initial rates of formation of modified PMMA are higher than those in the absence of DAPAC. The apparent rate constants of MMA polymerization in the presence of DAPAC at low (7.6%) and high (51.9%) conversions can be described by the following equations:

$$K_1 = 6.1 \times 10^{-3}\exp(-75\,000/RT), \quad (1)$$

$$K_2 = 2.0 \times 10^{-3}\exp(-122\,000/RT), \quad (2)$$

where R is the universal gas constant, 8.314 J mol^{-1} K^{-1}.

The apparent rate constants and activation energies at low conversions are similar to those determined

1070-4272/02/7502-0302 $27.00 © 2002 MAIK "Nauka/Interperiodica"

previously. At higher MMA conversion the process decelerates and its activation energy increases. Polymerization of MMA in the presence of DAPAC proceeds more uniformly, and the gel effect V_{max}/V_0 decreases nearly tenfold.

As seen from Table 1, polymerization of MMA in the presence of DAPAC proceeds in the initial stage at higher rates, and the induction period of this process (τ = 720 s) is significantly smaller as compared with that in MMA polymerization without additive (τ = 1020 s) (Table 2). It should be noted that, with increasing DAPAC concentration, the induction period decreases to 60 s. This is probably due to an increase in the concentration of free radicals initiating polymerization. Free radicals can arise in oxidation of DAPAC by oxygen to form peroxy groups. This reaction readily occurs at elevated temperatures due to the presence of labile hydrogen atom in ε-aminocaproic acid. These peroxy groups readily decompose, yielding active radicals [6].

As seen from Table 2, the molecular weight of polymers decreases from 7×10^5 to 0.9×10^5 with the content of DAPAC increasing from 0 to 1.7×10^{-4} mol dm^{-3}. This decrease in the molecular weight of polymers with increasing DAPAC concentration is probably due to the fact that at higher conversions there occurs chain transfer to the DAPAC molecule with the formation of a less-reactive radical (as compared with primary radicals), which decelerates polymerization. In this case, the ratio of the rate constants of chain termination K_t and chain propagation K_p decreases nearly twofold (K_t/K_p = 0.025 [6–8]).

The presence of DAPAC fragments in the polymer macromolecule is confirmed by the presence of the absorption bands typical of amide groups in the IR spectra [9], whereas in the IR spectrum of unmodified PMMA such bands are absent.

The parameters characterizing the thermal stability of PMMA prepared are listed in Table 3.

As seen from Table 3, addition of DAPAC to the polymerization mixture increases the temperature of the polymer degradation by 5–29°C at concentrations of $(0.5–1.7) \times 10^{-4}$ mol dm^{-3}, respectively.

EXPERIMENTAL

The effect of DAPAC on the polymerization of vinyl radicals was studied by dilatometry. Methyl methacrylate was washed with 2–3% sodium chloride solution to remove hydroquinone and with distilled water to neutral reaction for at least 2 h, and dried

Table 1. Kinetic parameters* of MMA polymerization

T, K	$V_0 \times 10^4$	$V_{in} \times 10^3$	$V_{max} : V_0$	$K_{ap} \times 10^4$, s^{-1} at indicated conversion		E_a, kJ mol^{-1} at indicated conversion	
	mol dm^{-3} s^{-1}			7.6	51.9	7.6	51.9
DAPAC concentration 0.6×10^{-4} mol dm^{-3}							
353	44.0	3.4	2	50	15		
343	11.5	1.7	3	15	6	75	122
333	1.6	0.65	8	10	5		
No additive							
353	6.0	–	17	–	54		
343	0.15	–	73	–	32	–	85
333	0.035	–	57	–	12		

* (V_0) Initial rate at MMA concentration of 9.7 mol dm^{-3}, (V_{in}) initiation rate, (K_{ap}) apparent rate constant, and (E_a) activation energy.

Table 2. Viscosity-average molecular weight of modified PMMA

[DAPAC] $\times 10^4$, mol dm^{-3}	MMA concentration, mol dm^{-3}	τ, s	$\frac{[DAC]}{[MMA]} \times 10^4$	$M \times 10^{-6}$	$1/P^* \times 10^4$
0	8.1	1020	0	0.7	1.7
0.5	8.0	720	0.063	0.07	14.3
0.6	7.3	780	0.081	0.38	2.3
0.8	9.4	720	0.085	0.06	16.7
1.1	8.4	120	0.13	0.4	2.5
1.7	8.4	60	0.2	0.09	11.1

* (P) Degree of polymerization.

Table 3. Thermal properties of modified PMMA polymer*

[DAPAC] $\times 10^4$, mol dm^{-3}	T_{dec}, °C	Weight loss (%) at indicated temperature, °C				
		10	20	30	40	50
0	229	242	252	269	273	295
0.5	234	249	254	273	281	302
0.6	241	252	260	278	284	306
0.8	249	258	262	279	287	308
1.1	252	264	273	288	296	310
1.7	258	264	278	283	298	321

* (T_{dec}) Temperature of decomposition onset.

over zeolites calcined at 623 K. Immediately before polymerization, methyl methacrylate was distilled in an argon atmosphere. Then lauroyl peroxide (0.4 wt %) and DAPAC [$(0.5–1.7) \times 10^{-4}$ mol dm^{-3}] were added to the freshly distilled monomer. Nitrogen was bubbled through the resulting solution and the ampules were sealed and placed in a thermostat heated to a required temperature. The kinetics of MMA polymerization was studied by dilatometry in 5-cm^3 glass ampules in the 333–353 K range; the temperature was maintained with an accuracy of 0.1 K. The measurements were performed using a KM-6 cathetometer.

The intrinsic viscosity of polymers η was determined in chloroform at 293 K using a viscometer. The viscosity-average molecular weight was calculated using the following equation [10]:

$$\eta = 0.60 \times 10^4 M^{0.79}.$$

The thermal oxidative degradation of the resulting copolymers was studied by thermal analysis using an MOM derivatograph (100 mg sample, Al_2O_3 reference, 10 deg min^{-1} heating rate, 1/5 DTA sensitivity).

The IR spectra in chloroform were recorded on a Specord M-82 spectrometer.

CONCLUSION

In the initiation stage of methyl methacrylate polymerization, addition of *N*-acetyl-ε-aminocaproic acid acetylamide sharply raises the process rate owing to generation of a large amount of free radicals, which is accompanied by a decrease in the induction period. The ratio of the rate constants of chain termination and chain propagation in the presence of *N*-acetyl-ε-aminocaproic acid acetylamide decreases by half as compared with the reaction without the additive. The resulting polymethyl methacrylate is characterized by smaller molecular weight and higher thermal stability.

REFERENCES

1. Khardin, A.P., Zheltobryukhov, V.F., and Tatarnikov, M.K., *Khim. Volokna*, 1984, no. 4, pp. 9–14.
2. USSR Inventor's Certificate, no. 914 677.
3. Lipatkov, V.A., *Khim.-Farm. Zh.*, 1984, vol. 18, pp. 19–23.
4. Voigt, J., *Die Stabilisierung der Kunststoffe gegen Licht und Warme*, Berlin: Springer, 1966.
5. Toroptseva, A.M., Belgorodskaya, K.V., and Bondarenko, V.M., *Laboratornyi praktikum po khimii i tekhnologii vysokomolekulyarnykh soedinenii* (Laboratory Course on Chemistry and Technology of Macromolecular Compounds), Leningrad: Khimiya, 1972.
6. Rakhimov, A.I., Ozerov, A.A., Zheltobryukhov, V.F., *et al.*, *Khim. Volokna*, 1986, no. 6, pp. 1647–1650.
7. Bagdasar'yan, Kh.S., *Teoriya radikal'noi polimerizatsii* (Theory of Radical Polymerization), Moscow: Nauka, 1966.
8. Odian, G., *Principles of Polymerization*, New York: McGraw-Hill, 1970.
9. Dechant, J., Danz, R., Kimmer, W., *et al.*, *Ultrarotspektroskopieshe Untersuchungen and Polymeren*, Berlin: Akademie, 1972.
10. Rafikov, S.R., Pavlova, S.A., and Tverdokhlebova, I.I., *Metody opredeleniya molekulyarnykh vesov i polidispersnosti vysokomolekulyarnykh soedinenii* (Determination of Molecular Weights and Polydispersity of Macromolecular Compounds), Moscow: Akad. Nauk SSSR, 1963.

Russian Journal of Applied Chemistry, Vol. 75, No. 2, 2002, pp. 305–309. Translated from Zhurnal Prikladnoi Khimii, Vol. 75, No. 2, 2002, pp. 314–318.
Original Russian Text Copyright © 2002 by Kutsenko, Ivanova, Karetnikova, Bobasheva, Bochek, Panarin.

MACROMOLECULAR CHEMISTRY AND POLYMERIC MATERIALS

Characteristics of Aqueous Solutions of Methyl Cellulose–Polymethacrylamidoglucose Mixtures

L. I. Kutsenko, N. P. Ivanova, E. B. Karetnikova, A. S. Bobasheva, A. M. Bochek, and E. F. Panarin

Institute of Macromolecular Compounds, Russian Academy of Sciences, St. Petersburg, Russia

Received June 1, 2001

Abstract—The characteristics of dilute (0.1%) and moderately concentrated (2%) aqueous solutions of methyl cellulose, polymethacrylamidoglucose, and their blends, and also the composition of films based on them were studied by viscosimetry, rheology, and IR spectroscopy. The effect of the mixture composition on the conditions of gel formation in methyl cellulose solutions was studied.

Structural modification of polymers by combining two polymers with different structures in the same solvent is used for production of polymer blends with controllable characteristics. Depending on the chemical composition, rigidity of macromolecular chain, degree of polymerization, and solvent type, the polymers to be blended can form in solution stuctures of various organizations and stabilities. Data are available on the formation of intermolecular structures in polymer systems with components differing in the thermodynamic rigidity of chain: polyacryl acid + methyl cellulose (MC) and polyacrylamide + hydroxyethyl cellulose in aqueous solutions [1, 2]. These data suggest the possibility of purposeful modification of characteristics of cellulose ethers.

In this work, we studied the intermolecular interactions of semirigid-chain MC with flexible-chain polymethacrylamidoglucose (PMAG) in dilute and moderately concentrated aqueous solutions of their blends. The interactions of polymers in solutions were studied by viscosimetry and rheology, and in films, by IR spectroscopy. The structural formulas of monomeric units of MC and PMAG are shown below:

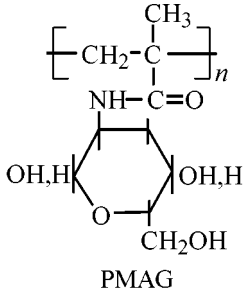

PMAG

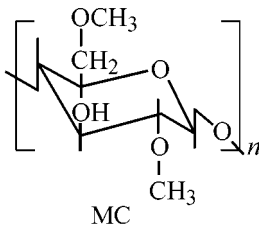

MC

MC is used as a thickening agent or filler in textile, paper, food, and pharmaceutical industry and in agriculture [3]. Polymethacrylamidoglucose belongs to relatively new class of hydrophilic polymers, polyvinylsaccharides, and contains residues of glucosamide structure in the side chain. Such polymers exhibit immunostimulating properties [4] and can be used for modification of polymeric carriers [5]. This study is stimulated by the demand for new modifying agents for MC.

EXPERIMENTAL

The objects of study were commercial sample of MC with degree of substitution DS = 1.7 and degree of polymerization DP_η = 740, and also $PMAG_I$ and $PMAG_{II}$ with DP_η 3600 and 2300, respectively. The MC sample was dissolved in water, and the solution was filtered under a pressure and then subjected to lyophilic drying. The molecular weight and DP_η were determined viscometrically using the Mark–Kuhn–Houwink equation for MC in water [6]:

$$[\eta] = 2.8 \times 10^{-3} M^{0.63}.$$

The PMAG samples were synthesized by radical polymerization of methacrylamidoglucose in water in the presence of 2,2-azobis(2-methylpropanediamine) dihydrochloride as initiator [5].

The molecular weights and DP_η were evaluated using the constants in the Mark–Kuhn–Houwink equation for PMAG in water [5]:

$$[\eta] = 2.3 \times 10^{-3} M^{0.772}.$$

1070-4272/02/7502-0305 $27.00 © 2002 MAIK "Nauka/Interperiodica"

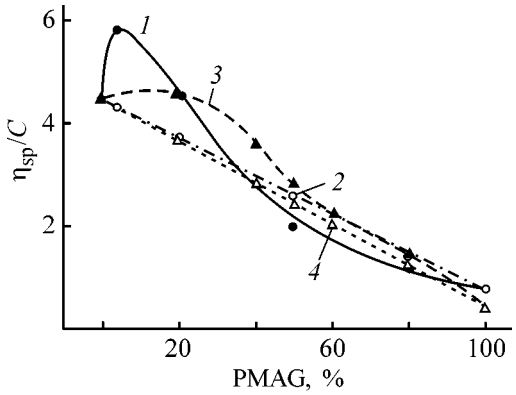

Fig. 1. Reduced viscosity η_{sp}/C of mixtures of dilute (0.1%) solutions of (*1*, *2*) MC–$PMAG_I$ and (*3*, *4*) MC–$PMAG_{II}$ vs. the amount of PMAG. (*1*, *3*) Experimental and (*2*, *4*) calculated.

In aqueous solutions of PMAG, no polyelectrolytic effects were observed [5]. Comparison of the constants α in the Mark–Kuhn–Houwink equations for MC (0.63) and PMAG (0.772) suggests that the shape of MC macrochains in water approaches the statistical Gaussian globule to a greater extent than that of macromolecules of flexible-chain PMAG. This fact can be accounted for by possible formation of intramolecular hydrogen bonds in PMAG macrochains in aqueous solutions [5].

Distilled water was used as solvent. The solutions of polymer mixtures were prepared by mixing equiconcentrated solutions of the initial components in various ratios.

The viscosity characteristics of dilute solutions were measured on a Ubbelohde capillary viscometer at 20°C. The rheological characteristics of the solutions were studied with a Rheotest 2.1 rotation viscometer with the cylinder-cylinder working unit in the range of shear streses 3–600 Pa at 20–50°C. The conditions of gel formation in the solutions were studied, depending on temperature, with a Hoeppler viscometer.

The IR spectra of the samples were recorded on a Bruker IFS-88 Fourier spectrometer. For this purpose, the films were formed from aqueous solutions of the initial MC and $PMAG_I$ and a mixture containing 20% $PMAG_I$. The films were also formed from the upper and lower phases after phase separation of the blend solution. The films were produced by applying the solutions to glass plates with subsequent evaporation of the solvent at room temperature. From the resulting films, KBr pellets were prepared.

Interactions of two different polymers in a common solvent are often studied by viscometry [7–9]. Namely, deviations are recorded of the experimental viscosity of the solutions of polymer blends from the ideal value, evaluated as weight-average viscosity of two components taken separately in the same concentrations. These deviations can be considered a measure of intermolecular interactions of polymers.

In this work, to study interaction of MC and PMAG molecules in aqueous solutions, we determined the reduced viscosity η_{sp}/C of separate components and their blends of various compositions by the formula

$$\frac{\eta_{sp}}{C} = \left(\frac{\eta_{sp}}{C}\right)_1 \frac{C_1}{C} + \left(\frac{\eta_{sp}}{C}\right)_2 \frac{C_2}{C}, \qquad (1)$$

where subscript 1 denotes MC, and subscript 2, PMAG; C is the total concentration of the polymer blend, C_1 and C_2 are concentrations of components 1 and 2, respectively, $C = C_1 + C_2$; $(\eta_{sp}/C)_1$ and $(\eta_{sp}/C)_2$ are the reduced viscosities of components 1 and 2, respectively, at concentration $C = C_1 + C_2$.

The experimental and calculated dependences of the reduced viscosity on the composition of MC–$PMAG_I$ and MC–$PMAG_{II}$ blends are presented in Fig. 1. For the MC–$PMAG_I$ blend, the deviations of the experimental curve from the calculated curve are positive at $PMAG_I$ content of 4 and 20% and negative at $PMAG_I$ content of 50 and 80%. For the MC–$PMAG_{II}$ blend, in which the second component has lower molecular weight, the deviations of the experimental curve from the calculated curve are positive for all the compositions studied. Both positive and negative deviations suggest the occurrence of intermolecular interactions in the systems in hand. The positive deviations can be caused by formation of intermolecular structures whose hydrodynamic volume is greater than that of the separate components. These structures can be formed via interaction of the functional groups of solvated MC and PMAG macromolecules through hydrogen bonds. With increasing fraction of $PMAG_I$ in a mixture, the deviations of the reduced viscosity from the calculated values became negative, which can be caused by formation of more compact structures than those in the case of separate components. Formation of these structures can be caused by weakening of interaction of polymers with the solvent (deterioration of solubility) and by incompatibility or partial compatibility of polymers, i.e., by phase separation in mixtures. This suggestion is confirmed by the increased turbidity of the mixtures of 2% solutions in comparison with the solutions of straight components. Upon storage of these

solutions for 10 days and more, the systems separate into two phases.

The phase composition was analyzed by IR spectroscopy. The IR spectra of the initial components, a mixture of MC with 20% $PMAG_I$, and components of the upper and lower phases of this mixture are shown in Fig. 2. In the IR spectrum of straight MC, there are absorption bands at 2897, 2839, and 942 cm^{-1} characteristic of stretching and bending modes of the CH groups of MC. The spectrum of straight $PMAG_I$ contains absorption bands in the region of 1643 and 1533 cm^{-1} characteristic of C=O groups of PMAG. In the IR spectrum of the film produced from the blend containing 20% $PMAG_I$, there are absorption bands characteristic of MC and PMAG. The spectrum of the film produced from the upper phase suggests that the dominant component of the blend is MC. The upper phase also contains PMAG as suggested by the absorption band at about 1535 cm^{-1} and by the altered shape of absorption band at 1643 cm^{-1}. The lower phase contains PMAG with a certain amount of MC, which is confirmed by the absorption band in the region of 2838 cm^{-1}. It is seen that, in phase separation of the mixed solution, one of the components is dominant in each phase. It is believed that MC and PMAG may be partially compatibile in moderately concentrated solutions of the MC–$PMAG_I$ blend, despite phase separation. This is suggested by significant changes in the systems of intra- and intermolecular hydrogen bonds, as judged from the absorption of hydroxy groups at 3200–3600 cm^{-1}. For example, the peak in the range of absorption of hydroxy groups in the IR spectrum of the film produced from the upper phase is shifted to higher frequences, and the band becomes more asymmetric and narrower. This may be due to the fact that PMAG macrochains appearing in the MC film matrix hinder formation of hydrogen bonds characteristic of MC. The high-frequency shift of the OH band reflects the tendency toward an increase in the fraction of free OH groups or OH groups bonded by weaker hydrogen bonds. In the IR spectrum of the film prepared from the lower phase, the absorption band of the OH groups is broadened, which reflects the significant rearrangement of the system of hydrogen bonds characteristic of straight PMAG. This band is broadened and shifted to lower frequencies, which suggests the formation of stronger hydrogen bonds in comparison with straight MC and $PMAG_I$.

It seems appropriate to study the effect of intermolecular reactions of two polymers in moderately concentrated solutions. For this purpose, we studied rheological characteristics of 2% solutions of MC–$PMAG_I$ and MC–$PMAG_{II}$. The flow curves of solutions of MC, $PMAG_I$, and blends of MC with $PMAG_I$ and $PMAG_{II}$ at 20°C are presented in Fig. 3. The flow curve of MC solution is an incomplete flow curve of a non-Newtonian liquid: the branch of structural viscosity becomes noticeable at a shear stress higher than $\log\tau = 2.4$. The flow curve of $PMAG_I$ solutions in the shear stress range studied suggests non-Newtonian flow of the solutions. This abrupt variation of viscosity with the shear stress is characteristic of structured systems [10]. The viscosity of $PMAG_I$ solution is considerably lower than that of MC solution, which may be due to differences in the behavior of macromolecules of flexible-chain and semirigid-chain polymers in solutions [11]. It can be assumed that in solution of $PMAG_I$ there is a system of hydrogen bonds between solvated macromolecules, which is more sensitive to external effect as compared with MC

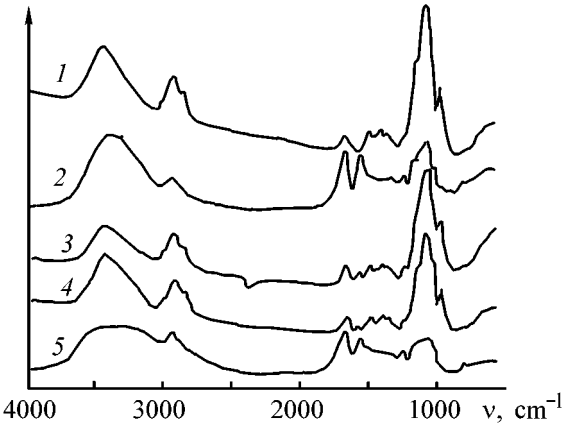

Fig. 2. IR spectra of films produced from solutions of (*1*) MC, (*2*) $PMAG_I$, (*3*) blend of MC with 20% $PMAG_I$, and (*4*) upper and (*5*) lower pahses of the solution of MC with addition of 20% $PMAG_I$. (ν) Wave number.

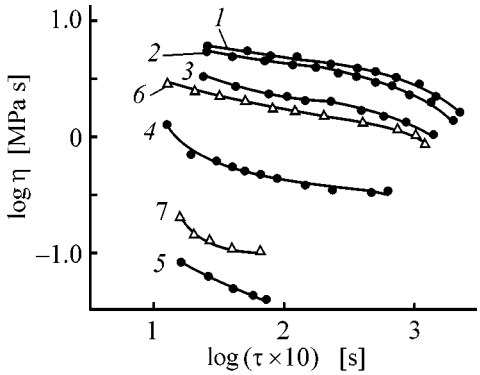

Fig. 3. Flow curves of 2% solutions of (*1*) MC, (*2*) MC with 4% $PMAG_I$, (*3*) MC with 20% $PMAG_I$, (*4*) MC with 50% $PMAG_I$, (*5*) straight $PMAG_I$, (*6*) MC with 20% $PMAG_{II}$, and (*7*) MC with 50% $PMAG_{II}$ at 20°C. (η) Viscosity, and (τ) time; the same for Fig. 5.

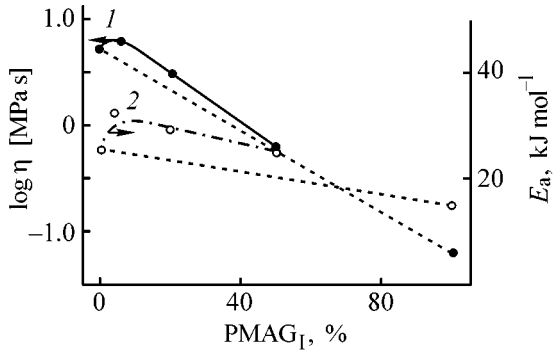

Fig. 4. Dependences of (*1*) viscosity η (log τ = 1.4) and (*2*) E_a of the solutions of the MC–PMAG$_I$ blends on the amount of PMAG$_I$.

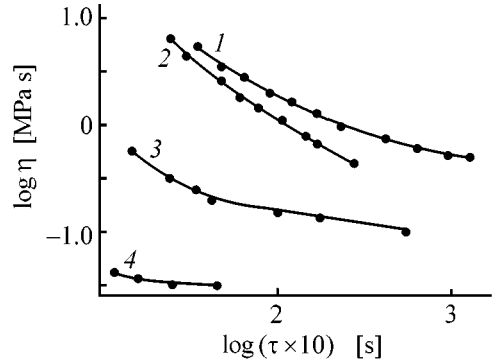

Fig. 5. Flow curves of (*1*) 2% solutions of MC, (*2*) MC with 20% PMAG$_I$, (*3*) MC with 50% PMAG$_I$, and (*4*) PMAG$_I$ at 50°C.

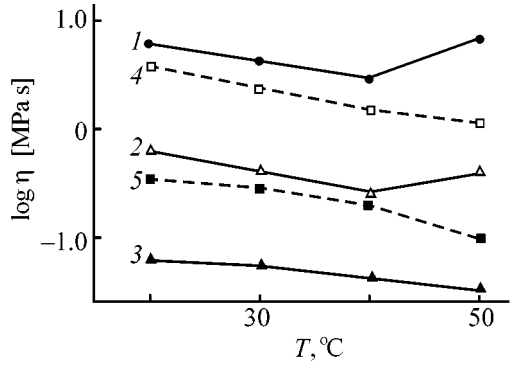

Fig. 6. Temperature dependences of viscosity η of (*1, 4*) MC solutions, (*2, 5*) MC with 50% PMAG$_I$, and (*3*) PMAG$_I$. log τ: (*1–3*) 1.4 and (*4, 5*) 2.7.

solution. With increasing molecular weight of PMAG (Fig. 3, curves *6* and *7*), the external effect on solution viscosity becomes more pronounced.

The rheological behavior of solutions of the initial components and their blends was studied in the temperature range 20–50°C. Based on the temperature dependences of the solution viscosity, we evaluated the activation energies of viscous flow E_a, which reflect the strength of the solution structure [12]. The dependences of the solution viscosity and E_a on the composition of the MC–PMAG$_I$ blend are shown in Fig. 4. It is evident that the viscosity and E_a of the blends are higher than those of the initial MC and PMAG. The positive deviation of viscosity from the additive values may occur for several reasons. On the one hand, as noted in the discussion of the IR spectra, new systems of stronger hydrogen bonds, compared with straight MC, can be formed in the mixtures, which should affect E_a and viscosity. On the other hand, at phase separation the flow mechanism differs from that in a homogeneous solution. The viscosity and E_a can be affected by the shape, number, and stability (strength) of microparticles of the disperse phase, occurring in the solution of the other phase, serving as matrix. Deviations from the additive values may be both negative and positive. Finally, it should be noted that addition of the other polymer, PMAG, to the solution of MC can affect the thermodynamic quality of water as a solvent with respect to MC. Deterioration of the solvent quality will be accompanied by an increase in the viscosity of concentrated solutions and their structurization. This variation of the rheologic characteristics of concentrated solutions with deterioration of the solvent quality is characteristic of cellulose and its derivatives [11].

It is well known that physical thermally reversible gels can be formed upon heating of aqueous solutions of MC. The gelation conditions are affected by many factors, including molecular weight of MC, degree of substitution, and uniformity of distribution of substituents along the macrochain and within glucopyranose units [13–15]. Heating of aqueous solutions of MC is accompanied by gelation, and the shape of the flow curves is changed substantially (Fig. 5). The shapes of the flow curves for MC and MC–PMAG$_I$ blends, except straight PMAG$_I$, are characteristic of physical gels [16, 17]. The viscosity depends critically on the shear stress. The shape of the viscosity–temperature curves depends critically on the chosen shear stress (Fig. 6). At low shear stresses and temperatures above 40°C the viscosity of solutions of MC and MC–PMAG blends increases, which is caused by gelation in the systems. At higher shear stresses this effect is not manifested, since at high shear stresses the structure of thermoreversible gels can be destroyed. It is appropriate to study the gelation conditions on a Hoeppler viscosimeter.

Previously, it has been shown that addition of small amounts of hydrophobic and strongly polar substituents decreases the gel point of aqueous solutions T_{gel} [16, 17]. Decrease in T_{gel} is due to deterioration of interaction of the solvent with polymer owing to an increase in the amount of hydrophobic groups in macro-

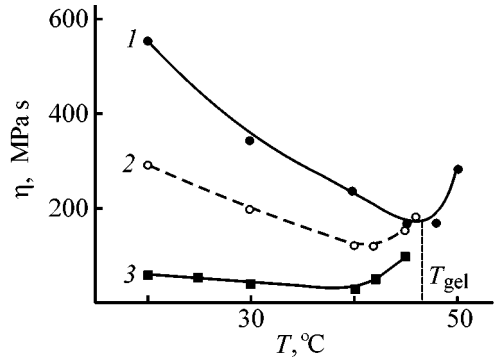

Fig. 7. Vuscosity of solutions of (*1*) MC, (*2*) MC with 20% $PMAG_I$ and (*3*) MC with 50% $PMAG_I$ vs. temperature *T*. (η) Viscosity.

chains. Low-molecular-weight salts added to MC solutions destroy the solvate shell of MC macromolecules, which also leads to a decrease in T_{gel} [18]. It can be expected that addition of another polymer, PMAG, to MC solution can affect the thermodynamics of interaction of MC with water and the gelation conditions. The results of determination of T_{gel} of solutions of MC and MC–PMAG blends are presented in Fig. 7. It is evident that, with increasing weight fraction of PMAG in the mixture, T_{gel} decreases. This trend can be accounted for by the fact that, in the case of incompatibility of polymers in the common solvent, PMAG macromolecules can destroy the hydrate shells of MC macrochains and accelerate their association, with subsequent aggregation. In the case of partial compatibility of the polymers, different macromolecules interact through hydrogen bonds, and mixed associates are formed. The mechanism of aggregation of mixed associates and their physicochemical characteristics may differ from the mechanism of gelation in solutions of straight MC. Thus, addition of PMAG macromolecules to MC solution promotes gelation in solutions at lower temperatures, which suggests the possibility of using PMAG as modifying polymer for control of the structure formation in MC solutions.

CONCLUSIONS

(1) In dilute solutions of methyl cellulose and polymethacrylamidocellulose blends, the experimental values of viscosity differ from the calculated values, which is caused by intermolecular reactions of different polymers.

(2) In moderately concentrated solutions of the above blends, the deviations of viscosity and activation energy from the additive values are positive, which is due to variations in the strength of the solution structure, intermolecular interactions, and phase separation in the systems.

(3) The IR spectra show that after phase separation in the solutions of polymer blends one of the initial polymers prevails in each of the phases, which is characteristic of partial compatibility of polymers.

(4) Addition of polymethacrylamidoglucose to methyl cellulose solutions decreases the gelation point of the systems.

REFERENCES

1. Nikolaeva, O.V., Budtova, T.V., Kalyuzhnaya, L.M., *et al.*, *Vysokomol. Soedin., Ser. A*, 1999, vol. 41, no. 7, pp. 1176–1182.
2. Matveeva, N.A., Ostrovskaya, L.D., Klenkova, N.I., *et al.*, *Cellulose Chem. Technol.*, 1984, vol. 18, no. 2, pp. 155–168.
3. Bytenskii, V.Ya. and Kuznetsova, E.P., *Proizvodstvo efirov tsellyulozy* (Production of Cellulose Ethersand Esters), Moscow: Khimiya, 1974.
4. Panarin, E.F., Ivanova, N.P., Belokhvostova, A.G., *et al.*, *Immunologiya*, 1999, no. 2, pp. 26–28.
5. Pavlov, G.M., Korneeva, E.V., Mikhailova, N.A., *et al.*, *Vysokomol. Soedin., Ser. A*, 1993, vol. 35, no. 10, pp. 1647–1650.
6. Kato, T., Yokoyama, M., and Takabashi, A., *Colloid Polym. Sci.*, 1978, vol. 256, no. 1, pp. 15–21.
7. Williamson, G.R. and Wright, B., *J. Polym. Sci., Part A3*, 1965, vol. 3, no. 11, pp. 3885–3891.
8. Staikos, G. and Bokias, G., *Makromol. Chem.*, 1991, vol. 192, no. 11, pp. 2649–2657.
9. Budtova, T.V., Bel'nikevich, N.G., Belyaev, V.M., *et al.*, *Vysokomol. Soedin., Ser. B*, 1991, vol. 35, no. 7, pp. 520–524.
10. Bochek, A.M. and Petropavlovsky, G.A., *Cellulose Chem. Technol.*, 1995, vol. 29, no. 5, pp. 567–574.
11. Tager, A.A., *Fizikokhimiya polimerov* (Physical Chemistry of Polymers), Moscow: Khimiya, 1978.
12. Tager, A.A., Botvinnik, G.O., and Dreval', V.E., *Uspekhi reologii polimerov* (Advances in Polymer Rheology), G.V. Vinogradov, Ed., Moscow: Khimiya, pp. 229–240.
13. Petropavlovskii, G.A., *Gidrofil'nye chastichno zameshchennye efiry tsellyulozy i ikh modifikatsiya putem khimicheskogo sshivaniya* (Hydrophilic Partially Substituted Cellulose Esters and Ethers and Their Modification by Cross-Linking), Leningrad: Nauka, 1988.
14. Takahachi, Sh.-I., Fujimoto, T., and Miyamoto, T., *et al.*, *J. Polym. Sci., Part A: Polym. Chem.*, 1987, vol. 25, no. 4, pp. 987–994.
15. Hirrien, M., Chevillard, C., Desbrieres, J., *et al.*, *Polymer*, 1998, vol. 39, no. 25, pp. 6251–6259.
16. Bochek, A.M., Nud'ga, L.A., Petrova, V.A., *et al.*, *Zh. Prikl. Khim.*, 2000, vol. 73, no. 2, pp. 304–308.
17. Bochek, A.M., Petropavlovskii, G.A., Kutsenko, L.I., *et al.*, *Zh. Prikl. Khim.*, 2000, vol. 73, no. 1, pp. 152–155.
18. *Cellulose and Cellulose Derivatives*, Bikales, N. and Segal, L., Eds., New York: Wiley, 1971, vol. 1.

Russian Journal of Applied Chemistry, Vol. 75, No. 2, 2002, pp. 310–314. Translated from Zhurnal Prikladnoi Khimii, Vol. 75, No. 2, 2002, pp. 319–324.
Original Russian Text Copyright © 2002 by A. Radbil', Zolin, Shkapova, B. Radbil'.

MACROMOLECULAR CHEMISTRY AND POLYMERIC MATERIALS

Reaction of α-Pinene with Haloacetic Acids

A. B. Radbil', B. A. Zolin, Yu. A. Shkapova, and B. A. Radbil'

Lesma Research and Promotion Limited Liability Company, Nizhni Novgorod, Russia
Lesosibirsk Rosin Extraction Plant, Open Joint-Stock Company, Lesosibirsk, Krasnoyarsk krai, Russia

Received September 25, 2001

Abstract—The reactions of α-pinene with chloro-, bromo-, and trichloroacetic acids, accompanied by isomerization of α-pinene, were studied.

α-Pinene **I**, one of the major components of turpentine, is an important representative of unsaturated monoterpene hydrocarbons. Esters derived from α-pinene show a wide spectrum of scents [1] and are used as components of diverse perfume formulations. Also, these compounds are components of plastics, rubbers, drugs, cosmetics, and disinfectants [2]. Monoterpene esters show particular promise in production of detergents to impart to them pleasant odor and to mask the odor originating from petroleum raw materials used for detergent manufacture [3].

Esters derived from α-pinene are widely used as intermediates in synthesis of biologically and physiologically active substances [2, 4, 5]. Of most interest in this respect is the report [5] on synthesis of borneol with high yield and selectivity by reaction of α-pinene with chloroacetic acid, followed by saponification of the reaction mixture with NaOH. According to other papers [6–8], the yield of borneol esters in reactions of α-pinene with some haloacetic acids does not exceed 20%, with low reaction selectivity.

In this work, we studied the reaction of α-pinene with chloro-, bromo-, and trichloroacetic acids. The results are given in the table and in Figs. 1 and 2.

We found that addition of haloacetic acids to α-pinene is accompanied by its isomerization and yields both mono- and bicyclic terpenoids. As seen from the table, the qualitative composition of the isomerization products is similar in all cases: camphene **II**, dipentene **III**, α-terpinene **IV**, β-terpinene **V**, terpinolene **VI**, and fenchene **VII** are detected. With chloro- and bromoacetic acids, the corresponding fenchol, borneol, and α-terpineol esters are formed, and with trichloroacetic acid, a minor amount of the isoborneol ester is also detected. Furthermore, with

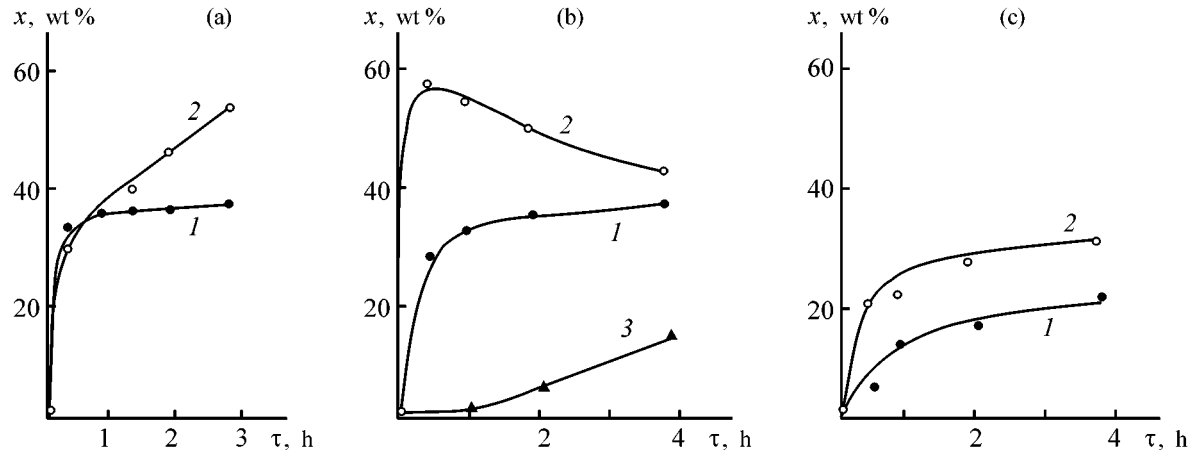

Fig. 1. Curves of product accumulation in reactions of α-pinene with (a) chloro-, (b) trichloro-, and (c) bromoacetic acids (70°C, molar ratio α-pinene : acid = 1 : 1). (*x*) Product content and (τ) time. (*1*) Terpene esters, (*2*) terpene hydrocarbons, and (*3*) polyterpenes; the same for Fig. 2.

1070-4272/02/7502-0310 $27.00 © 2002 MAIK "Nauka/Interperiodica"

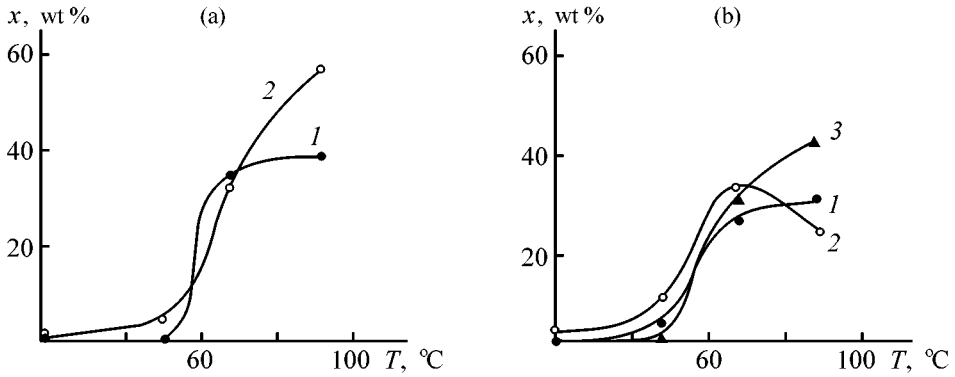

Fig. 2. Influence of temperature *T* on the composition of products formed in reactions of α-pinene with (a) chloroacetic and (b) trichloroacetic acids (1 h, molar ratio α-pinene : acid = 1 : 1).

trichloroacetic acid, oligoterpenes are formed along with the addition and isomerization products.

The yield of products in reactions of α-pinene with haloacetic acids largely depends on the reaction conditions and on particular acid.

Figure 1 illustrates the difference in the rates of accumulation of terpene esters and terpene hydrocarbons in reactions with different acids. In reaction of α-pinene with chloroacetic acid at 70°C, the yields of esters and isomeric terpene hydrocarbons in 0.5 h are 35 and 30%, respectively, with 35% of α-pinene remaining unchanged. After 3 h, the content of terpene hydrocarbons is almost doubled (55%), whereas the content of esters changes insignificantly (Fig. 1a).

Isomerzation of α-pinene into other terpene hydrocarbons is the major transformation pathway in its reaction with bromoacetic acid at the same temperature (Fig. 1c). However, in contrast to chloroacetic acids, the accumulation curves of terpene hydrocarbons and terpene esters are smoother, and even in 4 h the content of these products does not exceed 31 and 20 wt %, respectively, with approximately 50% conversion of α-pinene.

In the reaction of α-pinene with trichloroacetic acid (Fig. 1b), changes in the composition of the reaction products with time are the sharpest. The content of terpene hydrocarbons passes through a maximum. It is seen that the highest (57%) content of isomeric terpene hydrocarbons is attained in 0.5 h, after which it gradually decreases, reaching 43% in 4 h, with simultaneous increase in the content of oligoterpenes. The accumulation pattern of terpene esters is similar to that observed with monohaloacetic acids.

The influence of temperature on the composition of reaction products, examined with chloro- and trichloroacetic acids, is also significant. As seen from Fig. 2, the patterns for terpene esters are similar with both acids. Below 50°C, formation of terpene esters is negligible, and at 65–70°C their content sharply increases. With the temperature rising further, the curve of the ester content flattens out. For α-pinene isomerization products, the patterns observed with chloroacetic and trichloroacetic acids are different. In the first case, the content of terpene hydrocarbons increases steadily with temperature, whereas in the second case their content passes through a pronounced maximum (33–35%) at 70°C. Also, oligoterpenes are formed with trichloroacetic acid, and their content considerably increases with temperature.

It should be noted that oligoterpenes are formed from α-pinene only in the presence of trichloroacetic acid. Furthermore, a distinctive feature of this reaction, as compared witho the reaction with monohaloacetic acids, is its sensitivity to the temperature of reactant mixing (see table). When the starting compounds, α-pinene and CCl_3COOH, are cooled to –5°C, carefully mixed with warming up avoided, and then kept in a thermostat at the required temperature for 1 h, the resulting mixture contains 33% terpene esters, 54% terpene hydrocarbons, and 2% oligoterpenes. When α-pinene is slowly added with stirring to trichloroacetic acid preheated to 70°C and then the mixture is kept at this temperature for 1 h, the content of oligoterpenes sharply increases (to 35%), and the content of terpene hydrocarbons decreases to 36%. The content of terpene esters changes only slightly. Presumably, when α-pinene is mixed with trichloroacetic acid without controlling the temperature, local overheatings due to the heat of reaction cause secondary transformations of terpene hydrocarbons with accumulation of oligoterpenes. A similar assumption was made in [6, 9]. In reactions of α-pinene with chloro- and bromoacetic acids, the temperature of reactant mixing has no effect on the product composition.

Compositions of reaction mixtures from reactions of α-pinene with haloacetic acids

Pinene : acid molar ratio	*T*, °C	τ, h	Reaction mixture composition, wt %							
			α-pinene	α-pinene isomerization produts (monoterpene hydrocarbons)						
				camphene	dipentene	α-terpinene	γ-terpinene	terpinolene	fenchene	total
Chloroacetic acid										
1 : 1	70	0.5	34.8	8.5	12.5	0.4	1.3	3.6	2.5	30.3
1 : 1	70	1	29.5	8.8	15.7	1.5	1.9	4.5	2.7	35.1
1 : 1	70	1.5	24.8	9.0	17.8	1.8	1.9	5.7	2.9	39.1
1 : 1	70	2	18.6	9.0	21.1	2.2	1.9	7.5	3.0	44.7
1 : 1	70	3	9.2	9.0	27.5	2.8	1.8	10.5	3.2	54.8
1 : 1	50	1	95.0	2.0	2.0	0.3	0.2	0.5	–	5.0
1 : 1	90	1	7.0	10.6	24.7	4.0	3.0	9.4	4.0	55.7
2 : 1	70	1	38.2	9.0	16.0	1.5	1.9	5.1	2.8	36.3
Bromoacetic acid										
1 : 1	70	0.5	71.0	9.4	6.7	0.4	1.3	2.0	2.5	22.3
1 : 1	70	1	65.0	9.0	8.5	0.6	1.5	2.5	2.7	24.8
1 : 1	70	2	56.0	10.5	10.1	0.6	1.7	2.7	2.9	28.5
1 : 1	70	4	48.8	10.3	12.1	0.6	1.7	3.1	3.0	30.8
Trichloroacetic acid										
1 : 1	70	0.5	12.7	14.1	27.5	0.4	3.1	9.8	2.5	57.4
1 : 1	70	1	10.5	14.4	25.2	0.4	2.5	9.2	2.4	54.1
1 : 1	70	2	8.0	14.0	23.0	0.2	2.0	9.6	2.7	51.5
1 : 1	70	4	6.6	14.4	16.6	–	1.0	8.0	3.0	43.0
2 : 1	70	1	25.2	14.0	12.5	0.4	1.3	8.4	2.4	47.0
1 : 1*	70	1	1.5	14.0	12.1	–	–	6.5	2.9	35.5
1 : 1*	90	1	–	13.5	6.0	–	–	3.0	3.0	25.5

Pinene : acid molar ratio	*T*, °C	τ, h	Reaction mixture composition, wt %					
			addition products (esters of indicated monoterpene alcohols)					Polyterpenes
			fenchol	borneol	isoborneol	α-terpineol	total	
Chloroacetic acid								
1 : 1	70	0.5	3.6	8.3	–	23.0	34.9	–
1 : 1	70	1	3.8	8.9	–	22.7	35.4	–
1 : 1	70	1.5	3.9	9.4	–	22.9	36.1	–
1 : 1	70	2	3.8	9.6	–	23.3	36.7	–
1 : 1	70	3	4.0	9.0	–	23.0	36.0	–
1 : 1	50	1	–	–	–	–	–	–
1 : 1	90	1	5.8	14.0	–	17.5	37.3	–
2 : 1	70	1	4.0	7.5	–	14.0	25.5	–
Bromoacetic acid								
1 : 1	70	0.5	–	2.1	–	4.6	6.7	–
1 : 1	70	1	–	3.8	–	6.4	10.2	
1 : 1	70	2	–	5.7	–	9.8	15.5	–
1 : 1	70	4	2.4	6.0	–	12.0	20.4	–
Trichloroacetic acid								
1 : 1	70	0.5	1.4	7.6	0.2	20.7	29.9	–
1 : 1	70	1	2.1	8.6	0.9	21.3	32.9	2.5
1 : 1	70	2	2.2	8.9	1.1	22.3	34.5	6.0
1 : 1	70	4	3.3	10.2	1.9	23.0	38.4	12.0
2 : 1	70	1	1.2	7.0	0.2	19.4	27.8	–
1 : 1*	70	1	1.8	6.8	0.4	19.0	28.0	35.0
1 : 1*	90	1	1.7	9.0	0.5	21.3	32.5	42.0

* The reaction was performed without preliminary cooling of the reactants.

As already mentioned, the reaction products formed from α-pinene contain both mono- and bicyclic terpenoids. Terpenoids with various structures of the carbon skeleton are present both in isomerization products and in the esters. Our results are well consistent with the well-known and generally accepted carbocation mechanism of α-pinene isomerization in the presence of acid catalysts [4] (see scheme).

Scheme of α-pinene transformations in the presence of α-haloacetic acids.

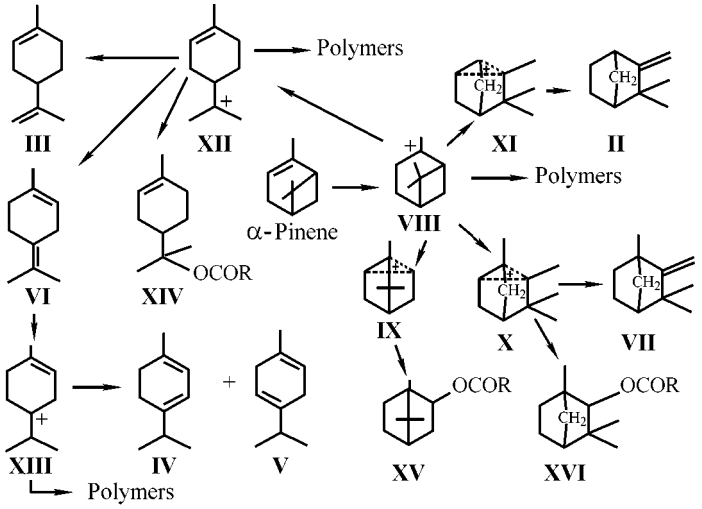

(**II**) Camphene, (**III**) dipentene, (**IV**) α-terpinene, (**V**) γ-terpinene, (**VI**) terpinolene, (**VII**) fenchene, (**VIII**) pinyl cation, (**IX**) bornyl cation, (**X**) fenchyl cation, (**XI**) isocamphyl cation, (**XII**) terpenyl cation, (**XIII**) isomeric terpenyl cation, (**XIV**) terpineol ester, (**XV**) borneol ester, and (**XVI**) fenchol ester.

Protonation of α-pinene gives pinyl cation **VIII**, which undergoes Wagner–Meerwein rearrangement to give carbocations **IX**–**XI**, subsequently transforming into bicyclic terpenoids of the bornane, fenchane, and camphane series. Namely, deprotonation yields hydrocarbons (camphene, **II**; fenchene, **VII**), and addition of the acid anion to carbocations **IX** and **X** gives the corresponding bornyl and fenchyl haloacetates.

Monocyclic terpenoids, such as dipentene **III** and terpinolene **VI**, are formed via terpenyl cation **XII**, which is, in turn, formed by ring opening in pinyl cation **VIII**; α- and γ-terpinenes are formed via carbocation **XIII**.

Transformations occurring in the presence of trichloroacetic acid yield, along with isomeric terpene hydrocarbons and terpene esters (via carbocations **VIII**, **XII**, and **XIII**), also oligoterpenes.

The ratio between the products of α-pinene isomerization and addition of haloacetic acids, and also the ratio between the mono- and bicyclic terpenoids, governed by the rates of the competing isomerization and addition reactions, depend on the reaction conditions and particular haloacetic acid.

It should be noted that, when studying the reactions of α-pinene with chloro- and trichloroacetic acids under similar conditions Markevich *et al*. [6], have not detected the corresponding α-terpineol esters. This could be due to inefficient GLC procedure used in [6] for identification of terpenoids. A packed GLC column with tricresyl phosphate as liquid phase does not provide separation of borneol and α-terpineol esters of haloacetic acids, as shown by our experiments with the corresponding reference compounds under the similar conditions. Therefore, we chose conditions for more efficient GLC analysis.

To confirm the formation of α-terpineol esters of haloacetic acids, the products of the reactions of α-pinene with chloro- and trichloroacetic acids were treated with a 10% solution of NaOH in ethanol. In the resulting mixture, we detected, along with fenchol and borneol formed by saponification of the corresponding haloacetates, also α-terpineol, and the ratio of the alcohols fully coincided with the ratio of the corresponding esters in the initial mixture. All the alcohols were also identified by GLC using the reference compounds. Thus, we can conclude with certainty that α-terpineol haloacetates are major products of the reactions of α-pinene with haloacetic acids.

EXPERIMENTAL

α-Pinene and haloacetic acid were cooled to –5°C and then carefully mixed, with warming up avoided, and transferred to a temperature-controlled reactor equipped with a heated jacket, a stirrer, and a reflux condenser. The temperature in the reactor was maintained constant to within ±0.5°C. The stirrer rotation rate was controlled with a tachometer. After a certain time, the mixture was rapidly cooled, the reaction products were washed with water, excess acid was neutralized with 10% aqueous Na_2CO_3, and the mixture was again washed with water to pH 7 and dried over $MgSO_4$, after which the products were analyzed by GLC. In experiments without preliminary cooling of the reactants, the acid was charged into the reactor and heated with stirring to a certain temperature, after which α-pinene was added, which was regarded as the start of the reaction.

Sodium hydroxide treatment of the product mixtures from reactions of α-pinene with chloro- and trichloroacetic acids was performed as follows. After washing with water to pH 7 and drying over $MgSO_4$, the mixture was charged into a reactor. A twofold excess amount (by volume) of a 10% solution of NaOH in ethanol was added. The mixture was refluxed for 2 h and cooled; the reaction products were extracted with two portions of hexane. The combined extract was washed with water to pH 7 and dried over $MgSO_4$. The solvent was removed, and the products were analyzed by GLC.

The chromatographic analysis was performed on a Chrom-5 chromatograph (flame ionization detector; 3-m stainless steel column; stationary phase 15% PFMS-4 silicone oil on Chromaton N-AW-DMSC, 0.20–0.25 mm; column temperature 110–180°C; vaporizer temperature 250°C; carrier gas nitrogen, flow rate 60 ml min^{-1}). Also, we performed analysis under the same conditions as in [6]: column length 3 m; stationary phase tricresyl phosphate; column temperature 110–180°C; vaporizer temperature 250°C; carrier gas nitrogen, flow rate 60 ml min^{-1}. Tridecane was added as internal reference. The products were identified by comparison with the corresponding reference compounds or by using data on relative retention of terpenoids [4]. The relative error of single analysis at a confidence level of 0.95 was within ±2%. With each sample, five chromatograms were recorded, and the results were averaged.

CONCLUSION

Reactions of α-pinene with chloro-, bromo-, and trichloroacetic acids yield terpene alcohols and esters, which can be used as components or intermediates in syntheses of active substances.

REFERENCES

1. Voitkevich, S.A., *865 dushistykh veshchestv dlya parfyumerii i bytovoi khimii* (865 Aromatic Principles for Perfumery and Domestic Chemistry), Moscow: Pishchevaya Prom–st., 1994.
2. Sandermann, W., *Naturharze Terpentinöl–Tallöl. Chemie und Technologie*, Berlin: Springer, 1960.
3. Osadchii, S.A. and Tolstikov, G.A., *Khim. Inter. Ustoich. Razv.*, 1997, vol. 5, no. 1, pp. 79–93.
4. Rudakov, G.A., *Khimiya i tekhnologiya kamfary* (Camphor Chemistry and Technology), Moscow: Lesnaya Prom–st., 1976.
5. Li Shixin, Gu Shunchun, and Chen Chuanhe, *Linchan Huaxue Yu Gongye*, 1984, vol. 4, no. 4, pp. 10–19.
6. Markevich, R.M., Lamotkin, A.I., and Reznikov, V.M., *Khim. Drev.*, 1985, no. 2, pp. 103–105.
7. Markevich, R.M., Lamotkin, A.I., and Reznikov, V.M., *Khim. Drev.*, 1985, no. 3, pp. 106–108.
8. Markevich, R.M., Lamotkin, A.I., and Reznikov, V.M., *Khim. Drev.*, 1985, no. 5, pp. 96–101.
9. Popov, A.A. and Vyrodov, V.A., *Gidrolizn. Lesokhim. Prom–st.*, 1979, no. 6, pp. 18–20.

Russian Journal of Applied Chemistry, Vol. 75, No. 2, 2002, pp. 315–318. Translated from Zhurnal Prikladnoi Khimii, Vol. 75, No. 2, 2002, pp. 325–328.
Original Russian Text Copyright © 2002 by Nazarova, Anan'eva, Grebennikov.

MACROMOLECULAR CHEMISTRY AND POLYMERIC MATERIALS

Pore Structure of Film Materials Based on Ultra-High-Molecular-Weight Polyethylene

E. V. Nazarova, T. A. Anan'eva, and S. F. Grebennikov

St. Petersburg State University of Technology and Design, St. Petersburg, Russia

Received October 31, 2001

Abstract—The pore structure of xerogel films of ultra-high-molecular-weight polyethylene, prepared by the gel process, was studied by mercury porosimetry and water vapor sorption. Data on the pore size distribution and on the volume and surface area of sorbing pores were obtained.

The majority of commercially produced film materials are solid (monolithic) uniform films. By now, new promising products have been developed, among which a particular place is occupied by porous film materials. Such materials find growing use for filtration and separation of liquid media, and also as separators for chemical power sources, as diaphragms for electric capacitors and electrolytic membranes, and in devices for environmental protection [1, 2].

A versatile procedure for preparing porous polymeric materials is treatment of crystallizing polymers with organic solvents at elevated temperatures [3–5]. These materials can also be prepared by conventional extrusion of gas-filled materials with the formation of a film fabric in the die head [6] or by extrusion of a polymer melt at high flow velocity, followed by annealing of samples crystallized at room temperature, uniaxial drawing of the annealed films, and their thermofixation. This procedure allows preparation of films with various ratios of open and closed pores [2, 7]. One of procedures for preparing porous film materials involves condensation cross-linking and is based on physicochemical processes spontaneously occurring in polymer melts [8]. A promising line in polymer processing is the gel technology, which has recently led to a considerable success in forming highly porous film materials based on ultra-high-molecular-weight polyethylene (UHMWPE) [9–12]. The first stage of the gel process is transfer of a polymer into solution. Suitable solvents are aliphatic, cycloaliphatic, and aromatic hydrocarbons boiling above 100°C, such as octane, nonane, decane, their isomers, higher linear and branched hydrocarbons, petroleum fractions boiling above 100°C, and halogenated hydrocarbons. The main requirement to a solvent is that its evaporation under the process conditions must not be significant. This is necessary to maintain the constant solution concentration and prevent nonuniform distribution of the liquid in the gel. The next stage after polymer dissolution is solidification of the initially liquid solution. In the gel process, as applied to UHMWPE, this is provided by decreasing temperature, rather than by varying the solution composition. The gel formed in the process is a macroscopically connected, three-dimensionally cross-linked system containing significant amounts of a low-molecular-weight liquid and exhibiting elastic properties. In contrast to systems with chemical cross-links, UHMWPE gels are loosely packed systems linked by crystalline junctions [13].

Removal of the solvent from a UHMWPE gel yields a xerogel exhibiting a high total porosity and a uniform structure throughout the volume. Owing to this feature, it is feasible to prepare from UHMWPE xerogels highly porous materials with properties largely depending on the pore structure features [14]. However, data on the pore-size distribution, the presence of pores of a definite size, and the volume and surface area of sorbing pores are virtually lacking.

In this work, we studied experimentally using mercury porosimetry and water vapor sorption, the porosity of UHMWPE xerogel films.

EXPERIMENTAL

Xerogel films were prepared from UHMWPE (average molecular weight 1.5×10^6, UHMWPE-1; or 4.0×10^6, UHMWPE-2) solutions in paraffin. The

1070-4272/02/7502-0315 $27.00 © 2002 MAIK "Nauka/Interperiodica"

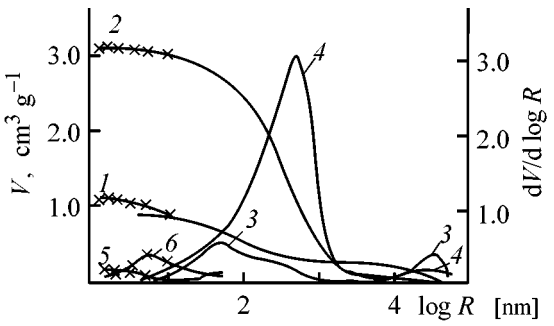

Fig. 1. (*1*, *2*) Integral and (*3*–*6*) differential curves of (*2*, *4*, *5*) UHMWPE-1 and (*1*, *3*, *6*) UHMWPE-2 samples. (*V*) Volume of pressed-in mercury and (*R*) pore radius. Curves *5* and *6* were plotted on the basis of data on water vapor sorption.

UHMWPE solutions were prepared as described in [15]. The choice of the solvent is explained in detail in [11, 12].

Films were cast onto a smooth polished metallic table heated to 60°C, with a heated metallic cover. The table was cooled to room temperature at a rate of 1.6 deg min^{-1}. Solid paraffin was extracted from the gel films in the fixed state with heptane at 70–75°C. After extraction, the films were dried at room temperature to constant weight to obtain porous UHMWPE xerogel films.

To measure the water vapor sorption isotherms, film samples were dried to constant weight at 50°C, cooled in a desiccator over silica gel, and transferred into desiccators with saturated salt solutions.

The drying temperature was chosen taking into account the possible α-relaxation transition at 50–60°C, which consists of several independent relaxation processes. It is believed that at these temperatures the macromolecular chains become mobile, and folds on the plate surfaces in crystals and macromolecules in defective regions can undergo reorientation [16].

The pore structure of xerogel films was studied on Macropores Unit 120 (low pressure) and Porosimeter 2000 Carlo Erba Strumentazions (high pressure) devices. A sample of UHMWPE xerogel film, preliminarily dried at 50°C, was placed in a dilatometer, which was then transferred into a low-pressure porosimeter. After evacuation, the dilatometer was charged with mercury, and air was admitted to atmospheric pressure to fill the coarsest pores with mercury. After that, the dilatometer with the sample was transferred into a high-pressure porosimeter. The pressure in the dilatometer was set by means of in the range from 0.1 to 200 MPa oil in a capillary. As the pressure is increased, pores with the size decreasing from 43000 to 5 nm are filled.

Figure 1 shows the integral structural curves of xerogel film samples prepared from UHMWPE-1 and UHMWPE-2. As seen, for the UHMWPE-1 sample the integral curve ascends more steeply. The maximal volume of pressed-in mercury was 3.04 $cm^3 g^{-1}$ for UHMWPE-1 and 0.92 $cm^3 g^{-1}$ for UHMWPE-2. This is due to the fact that the polymers significantly differing in molecular weight form xerogel films with different pore structures.

The differential curves of pore volume distribution with respect to the pore radius for UHMWPE-1 and UHMWPE-2 samples (Fig. 1) show that the major volume of macropores in the UHMWPE-1 sample corresponds to the pore radius range 70–1250 nm. The UHMWPE-2 xerogel film has a bidisperse pore structure, with maxima at about 47 and 29000 nm. The specific features of the pore structure of these film samples are probably due to different courses of gelation and crystallization of polymer solutions, depending on the UHMWPE molecular weight.

In crystallization from semidilute solutions ($c \geq$ 1%), the morphology of the forming crystals largely depends on the rheological history of the solution. If a solution was subject to shear stresses, knotted fibrillar chains of a shish-kebab structure may form along with lamellar crystals. The shish-kebab structures arise on peculiar precursor structures which are developed in a polymer solution in the course of its flow through a die channel or onto a metallic support. These "flow units" can be represented as alternating "bundles" of stretched macromolecules and clusters of strongly knotted chains. The bundles can crystallize at high temperatures even in the flow field, because of the considerably decreased, owing to stretching, conformational entropy of the molecules composing them [13]. On this basis, it can be assumed that in a solution of the higher-molecular-weight polymer sample, UHMWPE-2, more bundles are formed than in a UHMWPE-1 solution, which ultimately affects the pore structure of the UHMWPE gel and xerogel.

From the porosimetric data, we calculated the specific surface areas of the xerogel samples, assuming the cylindrical shape of the pores, by the formula

$$S = \Sigma \Delta S_i = \Sigma 2 \frac{\Delta V_i}{R_{\text{av}\,i}}, \qquad (1)$$

where S is the specific surface area of the solid ($m^2 g^{-1}$), ΔV_i is the width of an interval of pore radii ($m^3 g^{-1}$), and $R_{\text{av}\,i}$ is the average pore radius in the interval ΔV_i (m).

The specific surface area of the pores with radii larger than 5 nm in UHMWPE-1 and UHMWPE-2 xerogel samples was 50 and 13 $m^2 g^{-1}$, respectively.

The isotherms of water vapor sorption by the UHMWPE-1 and UHMWPE-2 xerogel films are shown in Fig. 2. It is seen that the sorption value is strongly influenced by the molecular weight of a polymer. The sorption by the UHMWPE-2 xerogel film is higher than by the UHMWPE-1 xerogel film. From the sorption isotherms we calculated, using the Kelvin equation, the pore radii:

$$R_{\text{pore}} = \frac{2V_{\text{m}}}{RT\ln(p_s/p)}, \quad (2)$$

where R_{pore} is the pore radius (m), σ is the surface tension of water (71.96×10^{-3} N m^{-1}), V_{m} is the molar volume of water (m^3 mol^{-1}), R is the universal gas constant, T is temperature (K), and p/p_s is the relative water vapor pressure.

Using these data, we supplemented the integral and differential porosimetric curves (Fig. 1) toward smaller pore radii; the curve continuations are marked with *crosses*.

As seen from Fig. 1, the UHMWPE-2 xerogel film has a more developed mesoporous structure (V_{me} = 0.32 cm^3 g^{-1}) as compared with the UHMWPE-1 xerogel film (V_{me} = 0.17 cm^3 g^{-1}). The major fraction of the mesopore volume in the UHMWPE-2 sample corresponds to the pore radius range 3–10 nm. At the same time, macropores prevail in the UHMWPE-1 sample (2.9 cm^3 g^{-1}, against 0.8 cm^3 g^{-1} for UHMWPE-2). This is due to the fact that a solution of UHMWPE with molecular weight of 4.0×10^6 is more viscous, and hence the polymer molecules in it are less mobile. In this case, gelation is accompanied by build-up of considerable internal stresses in the polymer network, which results in shrinkage of the xerogel after solvent removal. The shrinkage of UHMWPE gels is largely associated with crystallization processes in the enriched polymer phase, occurring differently depending on the molecular weight of the polymer.

By the BET procedure, we calculated from the sorption data the specific surface area of the porous xerogel films:

$$A = \frac{a_{\text{m}}}{18} N_{\text{A}} \sigma, \quad (3)$$

where A is the specific surface area (m^3 g^{-1}), α is the landing surface area for water molecule (0.105 nm^2) [17], a_{m} is the adsorption value (g g^{-1}), and N_{A} is the Avogadro number.

The specific surface area of the UHMWPE-1 and UHMWPE-2 xerogel samples was 157 and 98 m^2 g^{-1}, respectively, i.e., for UHMWPE with M 4.0×10^6 it is lower than for UHMWPE with M 1.5×10^6. This fact is due to differences in the course of crystallization of the polymer phase and in the shrinkage of the polymeric skeleton, affecting the features of the forming macro- and mesoporous structure of the xerogel samples.

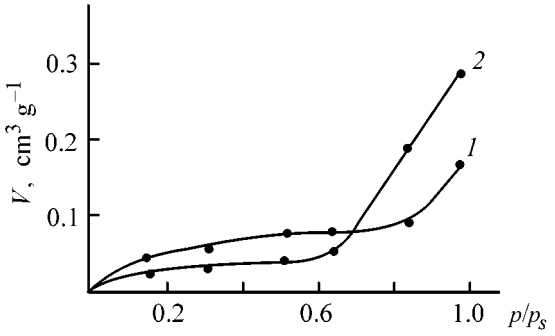

Fig. 2. Isotherms of water vapor sorption by (*1*) UHMWPE-1 and (*2*) UHMWPE-2 xerogel films. (V_s) Sorption value and (p/p_s) relative water vapor pressure.

CONCLUSIONS

(1) As shown by mercury porosimetry, the molecular weight of ultra-high-molecular-weight polyethylene affects the formation of the macroporous structure of the films.

(2) The differential curves of the pore volume distribution with respect to the pore radius were plotted. The specific surface areas of the xerogel films were calculated. This parameter decreases with increasing molecular weight of ultra-high-molecular-weight polyethylene.

(3) As shown by the isotherms of water vapor sorption and by the corresponding BET calculations, the molecular weight of ultra-high-molecular-weight polyethylene appreciably affects the sorption value, the mesopore volume, and the specific surface area of the xerogel films.

REFERENCES

1. Volkov, F.V., *Abstracts of Papers, 4-ya Sankt-Peterburgskaya Assambleya molodykh uchenykh i spetsialistov* (4th St. Petersburg Assmebly of Young Scientists and Specialists), St. Petersburg, December 2–10, 1999, p. 25.
2. Kozlov, A.G., Kuryndin, I.S., Rozova, E.Yu., *et al.*, *Vysokomol. Soedin., Ser. A*, 2000, vol. 42, no. 3, pp. 425–429.
3. Andrianova, G.P., Shilov, V.V., Pakhomov, S.I., *et al.*, *Vysokomol. Soedin., Ser. B*, 1988, vol. 30, no. 5, pp. 360–364.

4. Andrianova, G.P., Pakhomov, S.I., and Zhiryakov, A.V., *Vysokomol. Soedin., Ser. B*, 1990, vol. 32, no. 11, pp. 820–823.
5. Shilov, V.V., Andrianova, G.P., Pakhomov, S.I., *et al.*, *Vysokomol. Soedin., Ser. A*, 1990, vol. 32, no. 6, pp. 1238–1243.
6. Andrianova, G.P., Kalashnikov, V.G., Polyakova, K.A., *et al.*, *Khimiya i tekhnologiya polimernykh plenochnykh materialov i iskusstvennoi kozhi* (Chemistry and Technology of Polymeric Film Materials and Man-made Leather), Moscow: Legkaya i Pishchevaya Prom–st., 1981.
7. Kudasheva, O.V., Rozova, E.Yu., and Karpov, E.A., *Vysokomol. Soedin., Ser. A*, 1997, vol. 39, no. 10, pp. 1635–1640.
8. Vovchuk, A.I., Relationships in Formations and Properties of Film Materials with a Fibrous or Porous Structure, Prepared from Polymer Solutions, *Cand. Sci. Dissertation*, Moscow, 1973.
9. Volkov, F.V., Anan'eva, T.A., and Nachinkin, O.I., Abstracts of Papers, *Mezhdunarodnaya nauchno-tekhnicheskaya konferentsiya "Khimiya-97"* (Int. Scientific and Technical Conf. "Chemistry-97"), Ivanovo, 1997, pp. 14–15.
10. Volkov, F.V., Anan'eva, T.A., and Nachinkin, O.I., *Vestn. Sankt-Peterb. Gos. Univ. Tekhnol. Dizaina*, 1998, no. 2, pp. 46–51.
11. Nazarova, E.V., Anan'eva, T.A., and Grebennikov, S.F., *Fizikokhim. Polim.* (Tver), 2001, no. 7, pp. 33–37.
12. Nazarova, E.V., Anan'eva, T.A., and Mikhailova, Yu.N., *Fizikokhim. Polim.* (Tver), 2001, no. 7, pp. 192–197.
13. Mitchenko, Yu.I., Kuzub, V.I., D'yachkov, A.N., *et al.*, *Poluchenie sverkhprochnykh sverkhvysokomodul'nykh polietilenovykh volokon metodom gel'-tekhnologii: Obzornaya informatsiya. Ser.: Sinteticheskie volokna* (Preparation of Ultrastrong Ultra-High-Modulus Polyethylene Fibers by the Gel Process: Review, Ser.: Synthetic Fibers), Moscow: NIITEKhIM, 1988.
14. Volkov, F.V., Anan'eva, T.A., and Nachinkin, O.I., *Vestn. Sankt-Peterb. Gos. Univ. Tekhnol. Dizaina*, 1998, no. 2, pp. 166–175.
15. Volkov, F.V., Anan'eva, T.A., and Nachinkin, O.I., *Fizikokhim. Polim.* (Tver), 1996, no. 2, pp. 26–31.
16. Andrianova, G.P., *Fizikokhimiya poliolefinov* (Physical Chemistry of Polyolefins), Moscow: Khimiya, 1974.
17. Gregg, S.J. and Sing, K.S.W., *Adsorption, Surface Area and Porosity*, London: Academic, 1982.

Russian Journal of Applied Chemistry, Vol. 75, No. 2, 2002, pp. 319–322. Translated from Zhurnal Prikladnoi Khimii, Vol. 75, No. 2, 2002, pp. 329–332.
Original Russian Text Copyright © 2002 by Oranskaya, Kurbatova, Gornikov, Shklovskaya.

MACROMOLECULAR CHEMISTRY AND POLYMERIC MATERIALS

X-Ray Diffraction Study of Fine Iron Powder Modified with Cross-Linked Dextran

E. I. Oranskaya, G. T. Kurbatova, Yu. I. Gornikov, and N. I. Shklovskaya

Institute of Surface Chemistry, Ukrainian National Academy of Sciences, Kiev, Ukraine

Received April 12, 2001

Abstract—The structure of fine iron powders modified with cross-linked dextran was studied by X-ray diffraction analysis. The parameters of short-range ordering of dextran in the modifying coating were determined as influenced by dextran content. The parameters for quantitative phase analysis was proposed.

Preparation of high-performance magnetically targetable drugs of directional and prolonged action on the basis of fine iron powders (FIPs) with immobilized drugs [1–5] is impossible without creating a magnetic carrier having required capacity for the corresponding drug, controlled, in particular, by thickness or volume of a biocompatible polymeric coating. The polymeric coating formed on the surface of magnetic particles should be tested with respect to its phase state, structure, and composition [6–9]. Such compositions are untypical of quantitative X-ray diffraction (XRD) analysis, because they involve crystalline (iron) and amorphous (dextran) components of different chemical nature; moreover, the scattering power of iron powder is extremely higher [10–12].

The aim of this work was to perform the quantitative phase analysis of FIPs modified with cross-linked dextran and to elucidate the structural features of polymeric modifying coatings.

EXPERIMENTAL

We studied the FIP samples prepared by electrolytic procedure [13] and modified with cross-linked dextran by emulsion polymerization of dextran (molecular weight 70 000) on the powder particle surface in the presence of initiating and cross-linking agents [14] with varied content of the polymer. The concentration of dextran in the modified FIP samples was determined by chemical analysis; the results are listed in the table. We also studied the initial FIP, dextran cross-linked under the conditions similar to those used in modification, and mechanical mixtures of FIP with cross-linked dextran, having the same composition as the modified samples.

The diffraction patterns of the samples we recorded on a DRON-UM1 diffractometer using $Co_{K\alpha}$ radiation (iron filter) in the reflected beam focused according to Bragg–Brentano.

It should be noted that we studied in this work modified FIP samples in which the content of dextran was determined preliminarily by chemical analysis. The mechanical mixtures were prepared using the data of chemical analysis. Thus, comparison and analysis of the diffraction patterns of the modified FIP samples and mechanical mixtures of the same composition can be considered a model diffraction experiment.

The diffraction patterns of the initial FIP, cross-linked dextran, FIP samples modified with dextran at its varied content (solid lines), and mechanical mixtures of the same composition (dotted lines) are shown in Fig. 1. Despite the difference in scattering power between dextran and iron (curves *1*, *2*) and insignificant increase in the scattering of the polymer over the background in the diffraction patterns of the modified FIP samples, identification of the phases and evaluation of the short-range parameter of polymer ordering [10] are possible owing to different locations of the diffraction peak of dextran and diffraction lines of iron (curves *3*–*6*). As seen from these data, cross-linked dextran and dextran in modified FIPs are in the amorphous state. The parameters of the short-range ordering of dextran, calculated from the diffraction patterns, are listed in the table. With the dextran content in the modified samples increasing from 9.9 to 33.8% the short-range ordering parameter grows from 0.412 to 0.420 nm, which suggests a decrease in the packing density of the polymer chains.

1070-4272/02/7502-0319 $27.00 © 2002 MAIK "Nauka/Interperiodica"

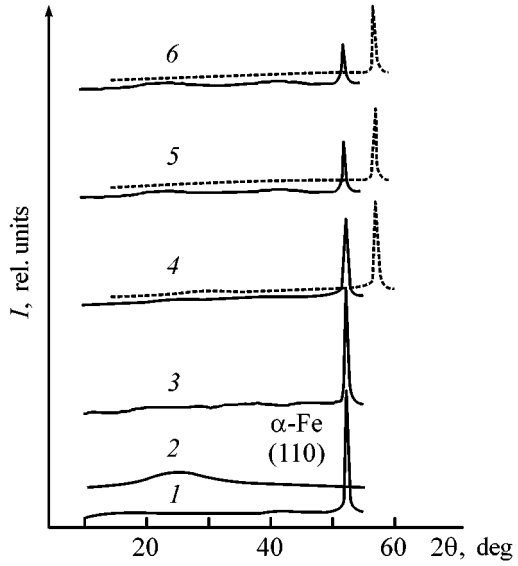

Fig. 1. Diffraction patterns of (*1*) initial FIP, (*2*) cross-linked dextran, and (*3*–*6*) FIP modified with dextran. (*I*) Intensity and (2θ) Bragg angle; the same for Fig. 3. Dextran content, wt %: (*3*) 9.9, (*4*) 15.4, (*5*) 25.2, and (*6*) 33.8. *Dotted lines* are the diffraction patterns of mechanical mixtures of the same composition as modified samples, shifted along both axes for clarity.

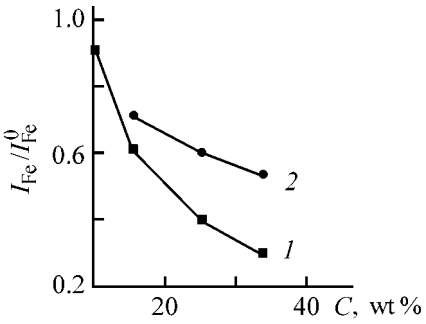

Fig. 2. Ratio of the intensity of the diffraction peak (110) of iron in (*1*) FIP modified with dextran and (*2*) mechanical mixture of FIP and dextran to the intensity of the diffraction peak (110) of iron in the initial FIP I_{Fe}/I_{Fe}^0 vs. the dextran content *C*.

The presence of cross-linked dextran on the FIP particle surface was judged from comparison with the diffraction data for mechanical mixtures of cross-linked dextran and FIP, having the same composition as modified FIP samples. It is known that the intensity of the diffraction lines of one component may decrease when its particles are coated with another component [15, 16]. As seen from our data, the intensity of the diffraction line in the patterns of modified FIPs is lower than that in the case of mechanical mixtures (Fig. 1, *dotted lines*). Thus, cross-linked dextran is present on the surface of the FIP particle.

As known, quantitative analysis is based on the dependence of the intensity of the diffraction peaks of a crystalline compound on its content in the mixture; it is carried out using calibration dependences (as a rule, linear) plotted by various procedures [16]. However, quantitative determination of the dextran content in modified FIPs and mechanical mixtures, using these calibration dependences, is rather difficult because of the small scattering power of dextran as compared with iron.

The content of dextran in the formulations in question can be evaluated from the calibration dependences of the intensity of the diffraction peak (110) on the dextran content in modified FIP samples and mechanical mixtures, using the external standard (unmodified initial FIP). Although these dependences are nonlinear (Fig. 2), they can be used in analysis of the dextran content in the samples studied. However, for more precise evaluation of the concentration dependence, the number of experimental points should be greater.

As seen from the diffraction patterns of modified FIPs and mechanical mixtures, the deviation of the background level from the additive value (determined by summation of the diffraction patterns of cross-linked dextran and unmodified FIP) grows with increasing diffraction angles. In these patterns, the background is about the same in the entire scanning range studied, which is illustrated in Fig. 3 for samples with dextran content of 25.2 wt %.

With increasing dextran content the intensity of the diffraction peak (110) and the background level decreased simultaneously with changes in the angular distribution of the background. This distribution can be quantitatively described with parameters *A*, *B*, and *C*, which characterize variations in the background scattering at the beginning and the end of the diffraction pattern with respect to the background scattering at the end of the diffraction pattern of the initial FIP:

Concentration *C* and short-range ordering parameter of cross-linked dextran *r* in modified FIP

Sample	*C*, wt %	*r*, nm	Sample	*C*, wt %	*r*, nm	Sample	*C*, wt %	*r*, nm
1	–	–	3	9.9	0.412	5	25.2	0.418
2	10.0	0.412	4	15.4	0.416	6	33.8	0.42

$$A = (I^0_{bb} - I_{bb})/I^0_{be}, \quad (1)$$

$$B = (I^0_{be} - I_{be})/I^0_{be}, \quad (2)$$

$$C = (I_{be} - I_{bb})/I^0_{be}, \quad (3)$$

where I_{bb} is the intensity of the background scattering of FIP modified with dextran and mechanical mixture at the beginning of the diffraction pattern, I_{be} is the is the intensity of the background scattering of FIP modified with dextran and mechanical mixture at the end of the diffraction pattern, and I^0_{bb} and I^0_{be} are the intensities of the background scattering of the initial FIP at the beginning and the end of the diffraction pattern.

The dependences of these parameters on the dextran content are shown in Fig. 4. As seen, parameters *A* and *B*, which have different initial values, grow with increasing dextran content, and the rate of this increase is greater for parameter *A*; parameter *C* simultaneously decreases. The dependences of parameters *A*, *B*, and *C* on the dextran content are nearly linear, which simplifies plotting of the calibration dependences, because smaller number of the model compositions is required for this procedure. The concentration dependences for mechanical mixtures with dextran content of up to 15 wt % are similar to those obtained for modified FIPs. With the dextran content increasing further, the dependences for mechanical mixtures deviate from the dependences for modified FIPs, so that the content of dextran in modified samples, determined from the calibration curves for mechanical mixtures, is overestimated. For example, at a dextran content in modified sample, determined by chemical analysis, of 25.2 wt % the value estimated from the calibration dependences for mechanical mixtures is greater by 28%, and at dextran content of 33.8 wt %, by 33%. The calibration curves given in Fig. 2 also give overestimated dextran concentrations. Thus, when using variations in the intensity of the diffraction peak (110) of iron and parameters *A*, *B*, and *C* for quantitative determination of the dextran content in the modified FIP samples, we should introduce appropriate corrections in the calibration dependences for mechanical mixtures.

The features of the diffraction patterns can be explained by assuming that at low content of dextran the polymer layer on the FIP particles is not solid because of the dendritic shape of the FIP particles, determined by the preparation conditions, and, hence, of their large specific surface area. In this case the diffraction patterns of modified FIPs are similar to those recorded for mechanical mixtures. With increasing

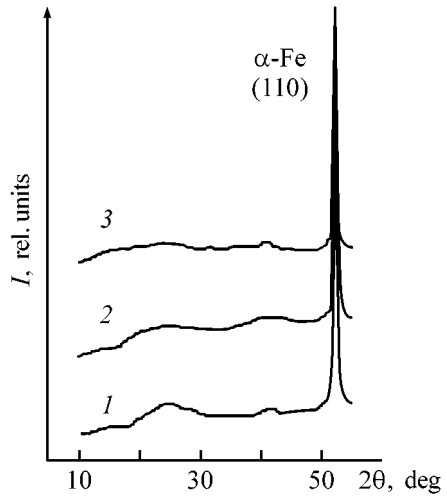

Fig. 3. Diffraction patterns of (*1*) FIP modified with dextran, (*2*) mechanical mixture of FIP with dextran, and (*3*) their additive curve; dextran content 25.2 wt %.

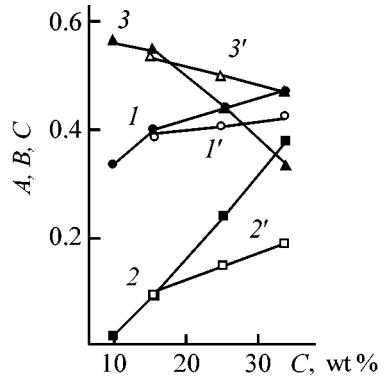

Fig. 4. Parameters (*1*, *1*′) *A*, (*2*, *2*′) *B*, and (*3*, *3*′) *C* for (*1*–*3*) FIPs modified with dextran and (*1*′–*3*′) mechanical mixtures of FIPs and dextran vs. dextran concentration *C*.

content of polymer, its layer on the particle surface becomes solid. Variation in the parameter of short-range ordering of cross-linked dextran in modified FIP does not contradict this assumption. Formation of a solid polymeric coating on the FIP particles with the dextran concentration increasing in the 15–33 wt % range affects the intensity of the diffraction peaks of iron in the modified samples more strongly as compared with mechanical mixtures.

Thus, quantitative phase analysis of modified FIP samples on the basis of the calibration dependences found for mechanical mixtures can be used at polymer concentrations of up to 15 wt %. At higher polymer content the dextran concentrations determined using the calibration curves for mechanical mixtures are overestimated by 20–30%. However, despite the above limitations, our analysis of the intensity of

the diffraction peak (110) and the angular dependence of the background scattering allow us to supplement conclusions concerning the qualitative detection of the dextran coating on the FIP particle surface. The dextran phase in the modified FIPs decreases the intensity of the diffraction peak of iron and affects the angular dependence of the background scattering as compared with those in the initial FIP, and this effect is the most pronounced at the beginning of the diffraction pattern.

CONCLUSIONS

(1) An X-ray diffraction study of a fine iron powder modified with cross-linked dextran showed the possibility of determining the spatial distribution of the polymer modifying the fine iron powder particles. The parameters are proposed, quantitatively describing how the background level in the diffraction patterns of fine iron powder modified with dextran and of the corresponding mechanical mixtures of these components change relative to those in the initial powder as influenced by the dextran concentration.

(2) Cross-linked dextran occurs on the surface of iron particles, and the coating state depends on the polymer content. At low dextran concentrations (up to 15 wt %) its layer is not solid; with the polymer content increasing to 33.8 wt % the coating becomes solid and less compact, which is confirmed by the increase in the short-range ordering parameter of cross-linked dextran in the modifying coating as compared with free cross-linked dextran.

(3) In determining the content of cross-linked dextran in modified fine iron powder from the calibration dependences plotted for mechanical mixtures of dextran and iron powder, appropriate correction parameters should be used.

REFERENCES

1. Morimoto, Y.A., Sugibayashi, K, and Kato, Y.O., *Chem. Pharm. Bull.*, 1981, vol. 29, no. 5, pp. 1433–1438.
2. Akimoto, M. and Morimoto, Y., *Biomaterials*, 1983, vol. 4, no. 1, pp. 49–51.
3. Daviss, S.S., *Manufact. Chem.*, 1986, vol. 57, no. 1, pp. 42–45.
4. Torchilin, V.P., Papisov, M. I., and Smirnov, V.N., *J. Biomed. Mater. Res.*, 1985, vol. 19, pp. 461–466.
5. Alekseev, k.V., Gogotova, M.V., Dobrotvorskii, A.E., *et al.*, in *Meditsina i zdravookhranenie. Farmakologiya i farmatsiya: Obzornaya inaformatsiya* (Medicine and Public Health. Pharmacology and Pharmacy: Review), 1987, issue 1, pp. 1–66.
6. Mikhailik, O.M., Povstugar, V.I., Mikhailova, S.S., et al., *Colloids Surfaces*, 1991, vol. 52, nos. 3/4, pp. 315–324.
7. Mikhailik, O.M., Povstugar, V.I., Mikhailova, S.S., *et al.*, *Colloids Surfaces*, 1991, vol. 52, nos. 3/4, pp. 325–330.
8. Mikhailik, O.M., Fedorenko, O.M., Mikhailova, S.S., *et al.*, *Colloids Surfaces*, 1991, vol. 52, nos. 3/4, pp. 331–338.
9. Fedorenko, O.M., Oranskaya, E.I., and Shklovskaya, N.I., *Zh. Prikl. Spektrosk.*, 1994, vol. 61, nos. 5–6, pp. 447–454.
10. Lipatov, Yu.S., Shilov, V.V., Gomza, Yu.P., and Kruglyak, N.E., *Rentgenograficheskie metody izucheniya polimernykh sistem* (X-ray Diffraction Methods for Analysis of Polymeric Systems), Kiev: Naukova Dumka, 1982.
11. Rusakov, A.A., *Rentgenografiya metallov* (X-ray Diffraction Analysis of Metals), Moscow: Atomizdat, 1977.
12. Gorelik, S.S., Rastorguev, L.R., and Skakov, Yu.A., *Rentgenograficheskii i elektronno-opticheskii analiz* (X-ray Diffraction and Electron-Optical Analysis), Moscow: Metallurgiya, 1970.
13. USSR Inventor's Certificate, no. 1471597.
14. Kurbatova, G.T., Mikhailik, O.M., Oranskaya, E.I., and Shklovskaya, N.I., *Ukr. Khim. Zh.*, 1994, vol. 60, no. 2, pp. 141–145.
15. Kovba, L.M. and Trunov, V.K., *Rentgenofazovyi analiz* (X-ray Phase Analysis), Moscow: Mosk. Gos. Univ., 1976.
16. Zevin, L.S. and Zav'yalova, L.L., *Kolichestvennyi rentgenograficheskii fazovyi analiz* (Quantitative X-ray Phase Analysis), Moscow: Nedra, 1974.

Russian Journal of Applied Chemistry, Vol. 75, No. 2, 2002, pp. 323–325. Translated from Zhurnal Prikladnoi Khimii, Vol. 75, No. 2, 2002, pp. 333–335.
Original Russian Text Copyright © 2002 by Korenman, Podolina, Kharitonova.

BRIEF COMMUNICATIONS

Extraction-Conductometric Determination of Phenol and Cresol in Nonaqueous Concentrates

Ya. I. Korenman, E. A. Podolina, and L. A. Kharitonova

Voronezh State Technological Academy, Voronezh, Russia

Received June 21, 2001

Abstract—Extraction of phenol and cresols with hydrophilic solvents (acetone, acetoacetic ester, and diacetone alcohol) from aqueous-salt solutions [$MgSO_4$, $(NH_4)_2SO_4$, NaCl] was studied. Extraction-conductometric technique for determination of phenol and cresols was developed.

Hydrophilic solvents are widely used for extraction of phenol derivatives from aqueous solutions [1–3]. These solvents are chosen to ensure phenol determination by electrochemical methods directly in the organic extract (without preliminary backwashing).

In this work, we studied extraction of phenol and cresols with hydrophilic solvents from aqueous solutions to develop the technique for their selective determination directly in the nonaqueous concentrates.

EXPERIMENTAL

Phenol and *o*-, *m*-, and *p*-cresols used in our experiments were of pure grade. The extractants (acetone, acetoacetic ester, and diacetone alcohol) were purified prior to use [4]. These hydrophilic solvents form a separate phase upon contact with aqueous solutions of salts [5], e.g., $MgSO_4$, $(NH_4)_2SO_4$, and NaCl. The extraction procedure was similar to that described in [6]. The equilibrium phenol concentration was determined spectrophotometrically on an SF-46 spectrophotometer. The conductometric titration was carried out on a Tesla Semiautomatic Universal Bridge-BM-509 setup equipped with two platinum electrodes (S = 1 cm^2, l = 1 cm) at 20 ± 1°C. A 0.01 M NaOH solution in isopropyl alcohol was used as titrant. Intermolecular interactions between the infinitely water-soluble polar extractant and compounds being extracted involve van der Waals interactions, depending on the polarization of the O–H, C=O, and O–C=O bonds, and hydrogen bonding [7].

The distribution coefficients determined in the systems containing hydrophilic solvent and aqueous salt solution under identical conditions are given in Table 1.

It has been reported [8] that in the aqueous–acetone system solvates are formed in which the phenolic OH group is bound to the acetone carbonyl group through a water molecule. The highest distribution coefficients were observed in extraction of unsubstituted phenol, which is the most hydrophilic among the compounds tested. The hydrophobic CH_3 group in the cresol molecule decreases its affinity for hydrophilic solvents, which makes lower the extractability of cresols as

Table 1. Distribution coefficients of phenol and cresols in a system consisting of hydrophilic solvent and aqueous salt solution (n = 5, P = 0.95, V_w/V_o = 10)

Compound	Distribution coefficient D		
	acetone	acetoacetic ester	diacetone alcohol
$MgSO_4$ salting-out agent			
Phenol	121 ± 8	62 ± 8	218 ± 14
o-Cresol	91 ± 8	42 ± 4	158 ± 7
m-Cresol	98 ± 9	45 ± 4	176 ± 13
p-Cresol	112 ± 7	51 ± 5	205 ± 12
$(NH_4)_2SO_4$ salting-out agent			
Phenol	397 ± 38	204 ± 18	507 ± 34
o-Cresol	252 ± 14	123 ± 11	318 ± 12
m-Cresol	263 ± 18	151 ± 16	346 ± 17
p-Cresol	352 ± 29	168 ± 14	403 ± 24
NaCl salting-out agent			
Phenol	152 ± 13	82 ± 8	255 ± 21
o-Cresol	109 ± 9	51 ± 5	168 ± 12
m-Cresol	117 ± 9	62 ± 6	182 ± 14
p-Cresol	122 ± 13	64 ± 6	206 ± 17

1070-4272/02/7502-0323 $27.00 © 2002 MAIK "Nauka/Interperiodica"

Table 2. Determination of phenol and cresols in an extract based on diacetone alcohol in the presence of ammonium sulfate (n = 5, P = 0.95)

Introduced, mg l^{-3}				Determined, mg l^{-3}		S_R	W, %
phenol	cresols			phenol	cresols (sum)		
	o-	*m*-	*p*-				
1.00	1.00	1.00	1.00	1.00 ± 0.05	3.00 ± 0.15	0.07	5.0
5.00	5.00	5.00	5.00	5.00 ± 0.21	15.00 ± 0.51	0.29	4.3
10.00	10.00	10.00	10.00	10.00 ± 0.36	30.00 ± 0.76	0.50	3.7

compared with phenol. The CH_3 group in the *ortho* position shields the phenolic OH group in cresol molecule and, therefore, hinders its hydration.

The extractive power of an organic solvent depends on the number of functional groups in its molecule [9]. For example, acetoacetic ester and diacetone alcohol molecules contain, along with the C=O polar group, also ester and alcohol groups. Acetoacetic ester in nonaqueous solvents exists as keto and enol tautomers [10].

Owing to intermolecular hydrogen bonding of the enol hydrogen atom and oxygen atom of the β-carbonyl group, a stable six-membered ring is formed. In this ring the proton is deshielded by the oxygen atoms of OH and anisotropic C=O groups. The ester group exhibiting the *I* effect decreases the electron density on the oxygen atom of the carbonyl group and thereby decreases the proton-acceptor power of acetoacetic ester. Therefore, the distribution coefficients of phenol and cresols in the systems consisting of acetoacetic ester and aqueous salt solution are considerably lower than those in a similar system with acetone and diacetone alcohol.

The C=O and OH functional groups of diacetone alcohol increase the efficiency of extraction of phenols from aqueous salt solutions. The highest distribution coefficient (~500) is reached in extraction with diacetone alcohol in the presence of ammonium sulfate.

The extraction involves combined recovery of phenol and cresols. Since the organic solvents suitable for extraction have high permittivity and differentiating power [11], phenols can be determined electrochemically directly in the extract. The best titration curves of phenol and cresols (isomer mixture) were obtained on addition of dimethyl sulfoxide.

The electrochemical determination of phenol and cresols is carried out as follows. Water (500 ml) containing phenol and cresols is placed in a separatory funnel and acidified with H_2SO_4 approximately to pH ~2. Next, ammonium sulfate is added till formation of a virtually saturated solution, diacetone alcohol (50 ml) is added, and the resulting mixture is shaken on a vibro mixer for 15 min. After phase separation, 10 ml of the extract is placed in a conductorymetric cell and titrated with NaOH solution in isopropyl alcohol. Phenol and cresol are determined in the extract using titration curve obtained. Their concentrations are calculated by the equation

$$C_w = \frac{V_a C_a \times 100}{V_{ex} R r},$$

where V_a is the volume of the NaOH solution in isopropyl alcohol, spent for titraration (cm^3); C_a the NaOH concentration in isopropyl alcohol (M); V_{ex} the extract volume (cm^3); R the degree of phenol recovery (%) in extraction with diacetone alcohol from aqueous salt solution; and r the ratio of the equilibrium volumes of the aqueous and organic phases.

The statistically processed data on separate determination of phenol and cresols in aqueous solutions are given in Table 2.

The technique developed by us allows fast extraction-conductometric determination of phenol and cresols.

CONCLUSION

The distribution coefficients of phenol and cresols in systems consisting of a hydrophilic organic solvent and an aqueous salt solution were determined. The highest distribution coefficients were attained in extraction with diacetone alcohol in the presence of ammonium sulfate. The conditions for acid-base conductometric titration of phenol and cresols in nonaqueous concentrates were found. The technique for extraction-conductometric determination of phenol and cresols in the extracts was developed.

REFERENCES

1. Korenman, Ya.I., Kuchmenko, T.A., and Ermolaeva, T.N., *Zh. Prikl. Khim.*, 1991, vol. 64, no. 6, pp. 1231–1232.
2. Kuchmenko, T.A., Extraction with Hydrophilic Solvents, *Cand. Sci. Dissertation*, Leningrad, 1992.
3. Podolina, E.A., Extraction of Phenol and Alkylphenols with Hydrophobic and Hydrophilic Ketones: Relationships and Electrochemical Analysis of Nonaqueous Concentrates, *Cand. Sci. Dissertation*, Moscow, 1995.
4. Korostylev, P.P., *Reaktivy i rastvory v metallurgicheskom analize* (Chemicals and Solutions in Metallurgical Analysis), Moscow: Metallurgiya, 1977.
5. Korenman, Ya.I. and Bortnikova, R.N., *Zh. Anal. Khim.*, 1977, vol. 32, no. 3, pp. 443–445.
6. Korenman, Ya.I., Bobrinskaya, E.V., Ermolaeva, T.N., and Kharitonova, L.A., *Zh. Prikl. Khim.*, 1994, vol. 67, no. 9, pp. 1569–1571.
7. Reid, K.F., *Properties and Reactions of Bonds in Organic Molecules*, London: Longmans, 1968.
8. Smol'skaya, E.L. and Egutkin, N.L., *Zh. Phys. Khim.*, 1994, vol. 68, no. 9, pp. 1591–1595.
9. Korenman, Ya.I., *Koeffitsienty raspredeleniya organicheskikh soedinenii: Spravocnik* (Distribution Coefficients of Organic Compounds: Handbook), Voronezh: Voronezh. Gos. Univ., 1992.
10. Reichardt, Ch., *Solvents and Solvent Effects in Organic Chemistry*, Weinheim: VCH, 1988.
11. Gordon, A.J., and Ford, K.A., *The Chemist's Companion. A Handbook of Practical Data, Techniques, and References*, New York: Wiley, 1972.

Russian Journal of Applied Chemistry, Vol. 75, No. 2, 2002, pp. 326–328. Translated from Zhurnal Prikladnoi Khimii, Vol. 75, No. 2, 2002, pp. 336–338.
Original Russian Text Copyright © 2002 by Radushev, Prokhorenko, Bel'chenko, Podlepyan.

BRIEF COMMUNICATIONS

Synthesis of Copper-Chromium-Barium Catalyst from Tetraamminecopper(II) Nitrate Solutions

A. V. Radushev, E. N. Prokhorenko, M. G. Bel'chenko, and O. V. Podlepyan

Institute of Technical Chemistry, Ural Division, Russian Academy of Sciences, Perm, Russia
Priazov Technical University, Mariupol, Russia

Received December 1, 2000; in final form, July 2001

Abstract—A method is proposed for obtaining copper-chromium-barium catalyst with the use of a nitrate ammonia solution of copper(II), obtained as a result of leaching of a spent copper-chromium-barium catalyst.

Copper-chromium-barium catalyst (CCBC) of general formula $x\mathrm{CuO} \cdot y\mathrm{Cr_2O_3} \cdot \mathrm{BaO}$, where x = 12–14, y = 6–7.5, is commonly used in hydrogenation of organic compounds. The catalyst is obtained by various techniques, with the highest-activity catalyst produced by thermal decomposition of a basic salt $\mathrm{NH_4(CuOH)CrO_4}$. With CCBC used as a suspension in a liquid raw material, e.g., in manufacture of higher alcohols, a waste is produced in the form of a paste consisting of an organic part (35–50%) and a mineral fraction including oxides CuO, $\mathrm{Cr_2O_3}$, BaO, and $\mathrm{SiO_2}$ [1]. A method has been proposed for utilization of spent CCBC by ammonia leaching [2]. It is advisable to use the forming $\mathrm{[Cu(NH_3)_4](NO_3)_2}$ solutions for obtaining fresh CCBC. A study of this possibility is the subject of the present work.

EXPERIMENTAL

Chromium(VI) oxide [GOST (State Standard) 2548–77], barium nitrate of chemically pure grade (GOST 3777–76), aqueous ammonia (GOST 9–77), and nitric acid (GOST 5.1187–72) were used in the study. $\mathrm{[Cu(NH_3)_4](NO_3)_2}$ solution containing (g $\mathrm{l^{-1}}$): Cu(II) 53, $\mathrm{NH_3}$ 29, and $\mathrm{NH_4NO_3}$ 139 was prepared by leaching of degreased spent CCBC. The content of the components and the catalyst activity (nominally 30–36% as regards the degree of acetone hydrogenation) were determined in conformity with TU (Technical Specification) 38-1325–74.

To obtain CCBC, to 200 ml of a nitrate-ammonia solution of copper(II) in a 500-ml vessel containing 10.6 g (0.165 mol) of Cu(II) was added 3.4 g (0.013 mol) of $\mathrm{Ba(NO_3)_2}$ and the mixture stirred at 70°C (solution 1). Into a 100-ml vessel was poured 15 ml of water, 16.5 g (0.165 mol) of $\mathrm{CrO_3}$ was introduced, and the mixture was stirred to complete dissolution (solution 2). A vessel with solution 1 was placed in a UT-15 thermostat at 74 ± 2°C and solution 2 was added. The excess of the sum of Cu(II) and Ba(II) with respect to Cr(VI) was 8.3%. Then, a 55% solution of $\mathrm{HNO_2}$ was added dropwise in the course of 0.5 h to pH 5.5 (about 22 ml). The suspension was stirred for 1 h, filtered under a vacuum, and washed with water (30 ml), with the filtrate and washing water collected separately. Found in the filtrate (g $\mathrm{l^{-1}}$): $\mathrm{NH_4NO_3}$ 365, Cu(II) 2.66, and Cr(VI) 0.027. At pH 6.4, no Cr(VI) and 2.6 g $\mathrm{l^{-1}}$ was found. The precipitate was dried for 30 min at 170°C and then calcined in a muffle furnace at 400°C for 1 h.

The main reaction of CCBC preparation [1] can be represented as

$$\mathrm{Ba(NO_3)_2 + (NH_4)_2CrO_4 \rightleftarrows BaCrO_4\downarrow + 2NH_4NO_3}, \quad (1)$$

$$\mathrm{Cu(NO_3)_2 + (NH_4)_2CrO_4 + NH_4OH} \xrightleftharpoons[65\text{–}80^\circ\mathrm{C}]{\mathrm{pH\ 5.5\text{–}6.2}} \mathrm{NH_4(CuOH)CrO_4\downarrow + 2NH_4NO_3}, \quad (2)$$

$$\mathrm{2NH_4(CuOH)CrO_4} \xrightleftharpoons{380\text{–}420^\circ\mathrm{C}} \mathrm{2CuO \cdot Cr_2O_3 + N_2 + 5H_2O}. \quad (3)$$

The precipitation was done at a 4–5 mol % excess of chromate ions with respect to the sum of Ba(II) and Cu(II) ions; the wastewater was purified to remove the major part of chromium(VI) by sorption of $\mathrm{Cr_2O_7^{2-}}$ on an AB-17 × 8 anion-exchange resin. Additional purification of wastewater to remove Cr(III)

1070-4272/02/7502-0326 $27.00 © 2002 MAIK "Nauka/Interperiodica"

and Cu(II) ions was done by addition of $Ca(OH)_2$; chromium(VI) was preliminarily reduced with iron(II) sulfate. A disadvantage of this method is the large volume of liquid waste (up to 20 m^3 per 1 ton of CCBC).

Let us compare five ways to obtain a fresh catalyst with the use of $[Cu(NH_3)_4](NO_3)_2$ solutions.

(1) Solution of a complex $[Cu(NH_3)_4](NO_3)_2$ was converted by acidification with HNO_3 into copper(II) and ammonium nitrate:

$$[Cu(NH_3)_4](NO_3)_2 + 4HNO_3 \rightleftarrows Cu(NO_3)_2 + 4NH_4NO_3. \quad (4)$$

This solution was used to obtain the catalyst by the method described in [1]. The CCBC activity was 30.1%. The disadvantages of the technique consist in that ammonium nitrate appears in wastewater in amount exceeding 3–3.2-fold that in wastes produced by the known technology and in increased loss of copper(II) into the filtrate (up to 6 g l^{-1}).

(2) To a nitrate-ammonia solution of copper(II) was added HNO_3 till basic salts were formed

$$[Cu(NH_3)_4](NO_3)_2 + 3HNO_3 + H_2O \rightleftarrows (CuOH)NO_3\downarrow + 4NH_4NO_3. \quad (5)$$

The precipitate was filtered off, dissolved in nitric acid, and $Cu(NO_3)_2$ was used to prepare the catalyst by the method described in [1]. The CCBC activity was 30.4%. The loss of copper(II) into the filtrate was diminished, with, however, a large amount of unused ammonium nitrate solution still formed.

(3) Basic salts obtained by variant 2 were added to a solution containing ammonium chromate and barium nitrate at $m_s : m_l \sim 1 : 3.3$. The precipitate was obtained in accordance with the equations

$$Ba(NO_3)_2 + (NH_4)_2CrO_4 \rightleftarrows BaCrO_4\downarrow + 2NH_4NO_3, \quad (6)$$

$$(CuOH)NO_3\downarrow + (NH_4)_2CrO_4 \rightleftarrows NH_4(CuOH)CrO_4\downarrow + NH_4NO_3. \quad (7)$$

Further, the precipitate was processed using the technique described in [1]. The activity of the obtained catalyst was 34.7%. Smaller amounts of wastewater were obtained, the amount of NH_4NO_3 exceeded that produced in the case of the technology reported in [1] only 2–2.2-fold.

(4) Variant 3 at $m_s : m_l \sim 1 : (1.3–1.5)$ was used. The obtained paste with 60% humidity was dried and calcined [1]. The CCBC activity was 30.0%. No wastewater was formed; however, ammonium nitrate remained in the precipitate, forming nitrogen(I) oxide in calcination

$$NH_4NO_3 \xrightarrow{>190°C} NO_2 + 2H_2O. \quad (8)$$

The method is promising if an effective system is available for waste gas purification to remove N_2O and other forming nitrogen oxides.

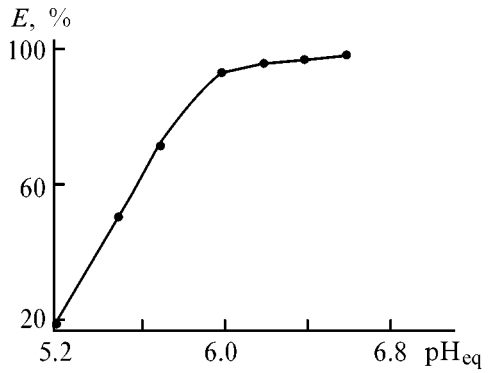

Degree E of copper(II) recovery with carboxylic acids of the C_7–C_9 fraction vs. pH_{eq} of solution obtained after separation of the precipitated catalyst. Concentration (g l^{-1}): Cu(II) 2.6 and NH_4NO_3 365 g l^{-1}; V_w = 25 ml, V_o = 5 ml; τ = 3 min.

(5) Into a nitrate-ammonia solution of copper(II) was introduced under heating a calculated amount of $Ba(NO_3)_2$. Then, an aqueous solution of CrO_3 was added. The pH value was adjusted to 5.8–6.2 by introduction of HNO_3; $m_s : m_l \sim 1 : (5–6)$. The occurring processes can be represented as

$$2Ba(NO_3)_2 + H_2Cr_2O_7 + 4NH_4OH \rightleftarrows 2BaCrO_4\downarrow + 4NH_4NO_3 + 3H_2O, \quad (9)$$

$$2[Cu(NH_3)_2](NO_3)_2 + H_2Cr_2O_7 + 5H_2O \rightleftarrows 2[Cu(NH_3)_2(H_2O)_2]CrO_4 + 4HNO_3, \quad (10)$$

$$[Cu(NH_3)_2](H_2O)_2]CrO_4 + HNO_3 \underset{70–80°C}{\overset{pH\ 5.8–6.2}{\rightleftarrows}} NH_4(CuOH)CrO_4\downarrow + NH_4NO_3 + H_2O, \quad (11)$$

$$[Cu(NH_3)_4](NO_3)_2 + 2HNO_3 + 2H_2O \underset{70–80°C}{\overset{pH\ 5.8–6.2}{\rightleftarrows}} Cu(OH)_2\downarrow + 4NH_4NO_3, \quad (12)$$

$$Cu(OH)_2 \overset{380–420°C}{\rightleftarrows} CuO + H_2O\uparrow. \quad (13)$$

The catalyst activity was 33.0%. The given way to use nitrate-ammonia solutions of copper(II) is the

most appropriate: 3 mol of NH_4NO_3 is produced per 1 mol of $NH_4(CuOH)CrO_4$, which is only 1.5 times that in the technique reported in [1]. At a small (4–8 mol %) excess of copper(II) with respect to Cr(VI) and pH 6.0–6.2, 20–30 mg l^{-1} of chromium(VI) passed into wastewater, and the content of copper(II) did not exceed 2–3 g l^{-1}. This makes unnecessary the ion-exchange purification of the filtrate to remove chromate ions and allows a 3–4-fold decrease in the volume of wastewater, with the NH_4NO_3 concentration simultaneously increased.

The filtrate obtained in variant 5 is a concentrated ammonium nitrate solution (300–370 g l^{-1}) containing 20–30 mg l^{-1} of Cr(VI) and 2–3 g l^{-1} of Cu(II). The solution can be used as recycle solution in ammonia leaching of copper(II) from spent CCBC or as a liquid nitrogen-containing fertilizer. To remove a major part of copper(II), liquid extraction with 100% carboxylic acids of the C_7–C_9 fraction was studied [3]. It can be seen from the figure that 98–99% of copper(II) was recovered at high NH_4NO_3 concentration in a single extraction stage at $V_w : V_o = 5 : 1$ and pH_{eq} 6.4–6.7; the residual content of copper(II) did not exceed 30–50 mg l^{-1}. The capacity of the organic phase with respect to Cu(II) was 15–20 g l^{-1}. Copper(II) was transferred from the organic into the aqueous phase under the action of mineral acids [4] and used to obtain CCBC. The amounts (milligrams) of Cu(II) and Cr(III) upon reduction of Cr(VI) remaining in the $(NH)_4NO_3$ solution are of interest as microelements. Also possible is additional purification of the obtained solution to remove Cu(II) and Cr(III), e.g., by ion floatation [5].

CONCLUSION

Nitrate-ammonia solutions of copper(II), obtained by ammonia leaching of a spent copper-chromium-barium catalyst, are suitable for obtaining a fresh catalyst. The most promising is the method of precipitation of $Cu(OH)_2$ and $NH_4(CuOH)CrO_4$ by treating a tetraammine(II) nitrate solution with HNO_3 at a 4–8 mol % excess of copper(II) with respect to chromate ions, which makes it possible to diminish 3–4-fold the volume of wastewater. The filtrate was purified to remove Cu(II) by extraction with carboxylic acids of the C_7–C_9 fraction. Wastewater containing 300–370 g l^{-1} of ammonium nitrate is proposed as a liquid nitrogen-containing fertilizer.

REFERENCES

1. *Vysshie spirty* (Higher Alcohols), Loktev, S.M., Ed., Moscow: Khimiya, 1970.
2. USSR Inventor's Certificate, no. 1023824.
3. *Ekstraktsiya organicheskimi kislotami i ikh solyami: Spravochnik po ekstraktsii* (Extraction with Organic Acids and Their Salts: Handbook of Extraction), Rozen, A.M., Ed., Moscow: Atomizdat, 1978, vol. 3.
4. Zelikman, A.N., Vol'dman, G.M., and Belyaevskaya, L.V., *Teoriya gidrometallurgicheskikh protsessov* (Theory of Hydrometallurgical Processes), Moscow: Metallurgiya, 1975.
5. Radushev, A.V., Zubareva, G.I., Chekanova, L.G., and Nasrtdinova, T.Yu., *Izv. Vyssh. Uchebn. Zaved., Tsvet. Metall.*, 1999, no. 2, pp. 3–6.

Russian Journal of Applied Chemistry, Vol. 75, No. 2, 2002, pp. 329–331. Translated from Zhurnal Prikladnoi Khimii, Vol. 75, No. 2, 2002, pp. 339–341.
Original Russian Text Copyright © 2002 by Podkopaev, Shibalenkov, Tyumentsev, Semenov, Luchko, Bogoslovskii.

BRIEF COMMUNICATIONS

Manifestation of the Effect of Self-Activation in Formation of Carbon Fiber Structure in High-Temperature Treatment

S. A. Podkopaev, D. N. Shibalenkov, V. A. Tyumentsev, P. V. Semenov, D. V. Luchko, and S. A. Bogoslovskii

Chelyabinsk Electrode Plant, Chelyabinsk, Russia
Ural Electrochemical Combine, Novoural'sk, Russia
Chelyabinsk State University, Chelyabinsk, Russia

Received August 13, 2001

Abstract—X-ray structural analysis was applied to study recrystallization of the material of carbon fiber in high-speed high-temperature (up to ~3200°C) thermomechanical treatment. The time of heating of a fiber bundle is evaluated.

The unique physicomechanical properties of carbon fiber are due to its specific microstructure, including the size of coherent domains and the high degree of texturing of carbon ribbons (layers) with respect to the axis of fibers formed in high-temperature thermomechanical treatment [1–3]. In the course of treatment of a thermally stabilized polyacrylonitrile fiber at temperatures of up to 2300°C, heteroatoms are intensively removed and carbon layers (ribbons) mainly oriented along the filament axis are formed to give an ultradisperse, thermodynamically unstable structure. Subsequent thermomechanical treatment of such carbon fibers at 3000–3200°C leads to further recrystallization, with the result that the mean sizes of coherent domains, L_a and L_c, grow substantially, and the elasticity modulus of the material becomes as high as 500 GPa. It is believed that the structural transformation of carbon fibers in high-temperature thermal treatment is rather slow [3]. The present study is concerned with the effect of heating rate and duration of high-speed thermal treatment of a carbon bundle in the temperature range 3000–3200°C on microstructure formation and carbon fiber properties.

Carbon fiber samples were produced by high-speed high-temperature thermomechanical treatment in argon of 99.999% purity (temperature 3000–3200°C, elongation 5.5–7.6%) of a carbon fiber bundle preliminarily thermally treated at 2300°C in the atmosphere of nitrogen of 99.999% purity. To a fiber bundle comprising 7200 filaments about 8 μm in diameter was applied, in the course of thermal treatment at 3000–3200°C, a constant stretching force of 1.5 kg. The furnace temperature in each thermal treatment mode was controlled to maintain constant the relative elongation ΔL.

At a chosen mode of thermal treatment (see table), a fiber bundle was moved, from the input zone of the furnace, with a temperature of about 600°C, into the isothermal zone with temperature of 3000–3200°C in a time of 0.6 to 0.3 s, with the duration of residence, $\Delta\tau$, in the isothermal field of the furnace decreasing in this case from 2 to 1 s. With decreasing time of residence of the fiber bundle in the isothermal field of the furnace, the temperature was raised somewhat to values at which the relative elongation ΔL reached a prescribed value (the interval ΔT of temperature variation did not exceed 200°C).

X-ray structural studies of carbon fibers were carried out on rectangular black-reinforced plastic arms of 4 × 4-mm cross-section. To fabricate the arms, portions of fiber bundle were impregnated with epoxy resin, placed in parallel rows in a mold, with excess amounts of resin removed, and monolithized. The structural investigations were performed with filtered Cu_{K_α} radiation. The interplanar spacing in coherent domains of the carbon fiber was determined from the centers of gravity of the 002 and 110 diffraction peaks. The mean sizes L_c and L_a were calculated by the Selyakov–Scherrer formula.

According to X-ray structural data, the mean sizes L_c and L_a for initial fiber samples subjected to thermal

1070-4272/02/7502-0329 $27.00 © 2002 MAIK "Nauka/Interperiodica"

Structural parameters and properties of carbon fiber obtained in various thermomechanical treatment modes*

Treatment mode no.	Time of transfer into furnace, s	Δτ, s	Δ*l*, %	L_c	d_{002}	L_a	d_{110}	γ, g cm^{-3}	*E*, GPa
				nm					
1	0.7	2.2	5.6	6.6	0.3448	22	0.1227	1.86	452
2			7.2	7.2	0.3443	21	0.1229	1.86	458
3	0.6	1.8	5.8	8.2	0.3431	27	0.1230	1.90	500
4			7.1	9.4	0.3432	29	0.1230	1.92	510
5	0.5	1.55	6.0	7.8	0.3438	20	0.1229	1.89	470
6			7.6	8.4	0.3433	28	0.1230	1.87	488
7	0.45	1.35	5.96	7.1	0.3443	24	0.1228	1.87	457
8			6.3	7.2	0.3432	27	0.1229	1.98	467
9	0.4	1.2	5.5	6.9	0.3449	22	0.1227	1.83	435
10			6.5	7.3	0.3443	24	0.1228	1.86	480
11	0.3	1.0	6.0	9.6	0.3418	28	0.1230	1.90	490

* γ fiber density, *E* elasticity modulus.

treatment at 2300°C are about 2.2 and 5.5 nm, respectively, with the interplanar spacings $d_{002} \cong 0.354$ and $d_{110} \cong 0.121$ nm. High-speed thermal treatment of such a fiber at 3000–3200°C initiates recrystallization of the ultradisperse carbon material (see table). Let us consider in more detail the influence exerted by modes of thermal treatment of a bundle in a high-temperature furnace on the structure and properties of high-modulus carbon fiber. It is noteworthy that effort was made to maintain constant the relative elongation Δ*L* of a bundle in the course of thermal treatment in each mode (~5.8–5.9%). However, fibers with somewhat shorter or longer Δ*L* were obtained in some modes because of technical difficulties.

The mean sizes L_c and L_a for bundle samples treated in modes 1 and 2 (temperature ~3000°C, residence time of the material in the high-temperature zone 2.2 s) are 6.6 and 22 nm, respectively. On decreasing the treatment duration to 1.8 s, the furnace temperature was raised somewhat to ensure a relative elongation Δ*L* = 5.8–5.9%. As a result of such a thermal treatment, the L_c and L_a of carbon fiber increased substantially to 8.4 and 26,5 nm, respectively. The elasticity modulus *E* also increased to become 500 GPa. During thermal treatment of the fiber bundle at the same Δτ, but somewhat higher temperature (Δ*L* increased to 7.1%), the mass transfer is markedly intensified. The mean sizes of coherent domains along the *c* and *a* axes become as large as nearly 10 and 30 nm, with the elasticity modulus equal to 510 GPa. The density γ of fiber obtained in modes 3 and 4 was the highest (≥1.9 g cm^{-3}).

The mean sizes L_c and L_a for bundle samples obtained upon thermomechanical treatment in modes 5–10 was 4–18% lower (see table, Fig. 1). In this case, the density γ and elasticity modulus *E* decrease. However, after treatment in mode 11 (time of bundle transfer into the isothermal field of the furnace, with temperature of about 3200°C, is approximately 0.3 s, and the duration of isothermal treatment, ~1 s), a certain increase in mean sizes of coherent domains and improvement of physicomechanical properties of fibers were again observed (Fig. 1). Thus, modes of carbon bundle treatment, in which the largest coherent do-

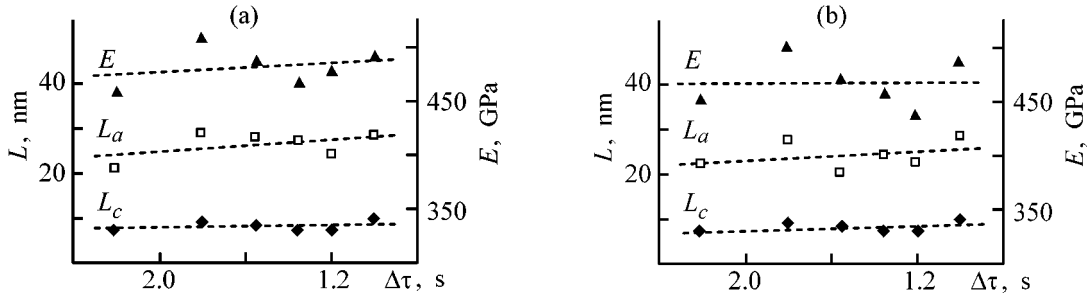

Fig. 1. Mean sizes L_c and L_a of coherent domains and Young's modulus *E* of carbon fiber samples vs. thermal treatment duration Δτ. Furnace temperature corresponds to (a) greatest and (b) smallest relative elongation.

mains are formed, can be distinguished in the temperature-time interval of thermal treatment, considered in this study.

It should also be mentioned that a certain increase in the bundle material treatment temperature in even modes of thermomechanical treatment always initiates a more pronounced mass transfer, compared with modes 1, 3, 5, 7, and 9, respectively. However, cutting down substantially the time of thermal treatment of fiber bundle, $\Delta\tau$, by more than a factor of 2 (to ~1 s) has no significant effect on mean sizes of coherent domains and physicomechanical properties.

The carbon bundle consists of a great number of filaments, its heat conductivity in radial direction is low (0.282 W m^{-1} deg^{-1}) [4]. An estimate of the time of bundle heating (Fig. 2) shows that the residence time of the carbon material in the central part of the bundle at temperatures of about 3200°C is actually shorter by nearly 0.5 s. Thus, depending on a treatment mode, structural transformations in carbon bundle fibers are complete in 1.7 to 0.5 s. It may be assumed that, as in other ultradisperse systems [5, 6], recrystallization centers are formed in microscopic volumes of carbon fiber upon an abrupt rise in material temperature (upon fast transfer of the bundle into a heated furnace). Apparently, further structural transformations develop rather intensively in such local microscopic volumes in a time significantly shorter than the treatment duration. In particular, the time of structural transformations in microscopic volumes of an amorphous carbon film is only 100–200 μs [5]. Therefore, structural transformations of the material of carbon fiber are the most strongly affected in high-speed thermomechanical treatment by the treatment temperature and heating rate, rather than by the duration of heating.

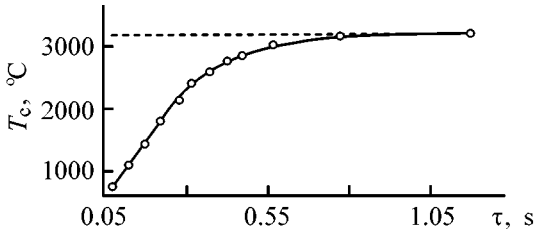

Fig. 2. Time of heating, τ, of a carbon bundle to a temperature T_c.

ACKNOWLEDGMENTS

The study was supported by the Russian Foundation for Basic Research (project no. 99-03-32696).

REFERENCES

1. Tyumentsev, V.A, Podkopaev, S.A., Belenkov, E.A., and Fotiev, A.A., *Zh. Prikl. Khim.*, 1995, vol. 68, no. 8, pp. 1398–1400.
2. Belenkov, E.A., Tyumentsev, V.A., Podkopaev, S.A., *et al.*, *Zh. Prikl. Khim.*, 1998, vol. 71, no. 8, pp. 1379–1381.
3. Fitzer, E., Frohs, W., and Heine, M., *Carbon*, 1986, vol. 24, no. 4, pp. 387–395.
4. Konkin, A.A., *Termo-, zharostoikie i negoryuchie volokna* (Heat-Resistant and Inflammable Fibers), Moscow, 1978.
5. Zakharov, V.P. and Zaliva, V.I., *Neorg. Mater.*, 1973, vol. 9, no. 8, pp. 1325–1329.
6. Shklovskii, V.A. and Kuz'menko, V.M., *Usp. Fiz. Nauk*, 1989, vol. 157, no. 2, pp. 311–338.

Russian Journal of Applied Chemistry, Vol. 75, No. 2, 2002, p. 332. Translated from Zhurnal Prikladnoi Khimii, Vol. 75, No. 2, 2002, p. 342.
Original Russian Text Copyright © 2002 by Wamhoff, Zlotskii, Saprygina.

BRIEF COMMUNICATIONS

Oxidative Dehydrogenation of 4-Arylurazoles

H. Wamhoff, S. S. Zlotskii, and V. A. Saprygina

Kekulé Institut für Organische Chemie und Biochemie der Universität Bonn, Bonn, Germany
Ufa State of University of Petroleum Engineering, Ufa, Bashkortostan, Russia
Reaktiv Research Institute, Ufa, Bashkortostan, Russia

Received July 9, 2001

Abstract—4-Arylurazoles are selectively oxidized with $Fe_2(NO_3)_3 \cdot 9H_2O$ to the corresponding Δ^1-1,2,4-triazoline-3,5-diones.

Recently there has been growing interest in Δ^1-1,2,4-triazoline-3,5-diones, which are extremely active dienophiles and are successfully used in syntheses of fused and polysubstituted heterocycles [1–3]. Also, these compounds react with olefins to form the corresponding secondary amines [4, 5]. The most versatile and widely used route to Δ^1-1,2,4-triazoline-3,5-diones is oxidation of the corresponding urazoles (1,2,4-triazolidine-3,5-diones).

Along with the use of powerful oxidants, such as *tert*-butyl hypochlorite [6], trichloroacetyl isocyanate [7], or nitrogen dioxide [8], procedures have been developed for oxidation with *N*-bromosuccinimide [9, 10] and halogens [11]:

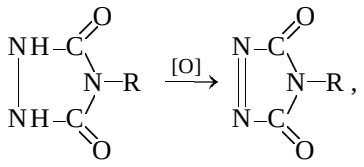

Ia–**Ic** **IIa**–**IIc**

where R = Ph (**a**), 4-ClC_6H_4 (**b**), 3,4-$Cl_2C_6H_3$ (**c**).

In addition to the known procedures, we found that 4-arylurazoles **Ia**–**Ic** can be oxidized to 4-aryl-Δ^1-1,2,4-triazoline-3,5-diones **IIa**–**IIc** with iron(III) nitrate under mild conditions in high yields (65–75%). The reaction occurs in the solid phase, which considerably simplifies the isolation and purification of the target diones **IIa**–**IIc**. A similar procedure has been used previously to prepare substituted semicarbazides [12].

EXPERIMENTAL

4-Aryl-Δ^1-1,2,4-triazoline-3,5-diones IIa–IIc. A mixture of triazolidinedione **Ia**–**Ic** with $Fe_2(NO_3)_3 \cdot 9H_2O$ (molar ratio 1 : 2) was ground in an agate mortar for 5–8 min. The mixture was transferred into dry acetone (15 ml per millimole of **Ia**–**Ic**), concentrated HCl was added to pH ≤ 2, and the resulting bright red liquid was diluted with an equal volume of ice-cold water. The precipitate was filtered off, washed with water, and vacuum-dried. Target compounds **IIa**–**IIc** were obtained in 65–75% yields; their constants agreed with published data [9, 10].

ACKNOWLEDGMENTS

The study was performed within the framework of the Academic Exchange Program of the German Academy (DAAD), grant A/99/09940.

REFERENCES

1. *The Chemistry of Heterocyclic Compounds*, Montgomery, J.A., Ed., New York: Wiley, 1981, vol. 37.
2. Adam, W. and Lucchi, O. de, *Angew. Chem.*, 1980, vol. 92, no. 10, pp. 815–832.
3. Wagner, Th.J., *Synthesis*, 1980, no. 7, pp. 165–214, 769–798.
4. Adam, W., Pastor, A., and Wirth, T., *Org. Lett.*, 2000, vol. 5, pp. 1295–1297.
5. Vassilikogiannakis, G., Stratakis, V., Orfanopoulus, M., and Foote, C.S.D., *J. Org. Chem.*, 1999, vol. 64?, no. 11, pp. 4130–4139.
6. Cookson, R.C., Gupte, S.S., Stevens, J.D.R., and Watts, C.T., *Org. Synth.*, 1971, vol. 51, pp. 121–127.
7. Moore, J.A., Muth, R., and Sorace, R., *J. Org. Chem.*, 1974?, vol. 39, no. 25, pp. 3799–3800.
8. Stickler, J.C. and Pirkle, W.H., *J. Org. Chem.*, 1966, vol. 31, no. 10, pp. 3444–3445.
9. Wamhoff, H. and Wald, K., *Org. Prep. Proced. Int.*, 1975, vol. 7, pp. 251–253.
10. Fieser M. and Fieser, L.F., *Reagents of Organic Synthesis*, New York: Wiley, 1977, vol. 6.
11. Wamhoff, H. and Kunz, G., Angew. Chem., 1981, vol. 93, no. 9, pp. 832–833.
12. Wang, C., Wang, J., and Li, J., *Synth. Commun.*, 1999, vol. 29, no. 15, pp. 2597–2599.

1070-4272/02/7502-0332 $27.00 © 2002 MAIK "Nauka/Interperiodica"

Russian Journal of Applied Chemistry, Vol. 75, No. 2, 2002, pp. 333–334. Translated from Zhurnal Prikladnoi Khimii, Vol. 75, No. 2, 2002, pp. 343–344.
Original Russian Text Copyright © 2002 by Zaikov, Gumargalieva, Artsis.

INFORMATION

XXII Danube Region Colloquium on Natural and Artificial Degradation of Polymers

The XXII Danube Region Colloquium on Natural and Artificial Degradation of Polymers was held from September 17 to 18, 2001, at the Federal Institute for Materials Research and Testing in Berlin (Germany). The Organizing Committee Chairman was Dr. P. Trubiroha. The Colloquium was sponsored by several German research centers. The Colloquium title is of purely historical origin: in the early 1960s, scientists from Austria, Germany, and Hungary organized the first colloquium and named it for the Danube River running across these countries. Now this is an all-Europe conference; however, the original title remained.

Among the conference participants were more than 500 scientists from nine European Countries (Austria, Czech Republic, Germany, Hungary, the Netherlands, Russia, Slovak Republic, Sweden, and Switzerland), representing 30 research centers. In all, there were given 25 lectures devoted to thermal, thermooxidative, photooxidative, biological, hydrolytic, and mechanically induced polymer degradation.

The subject of the report delivered by D. Kockott (Germany) was comparison of natural and artificial aging from the standpoint of using accelerated aging methods for prediction of useful life and shelf-life of polymer articles. J. Boxhammer (Germany) examined in his report accelerated photodegradation of polymers as a way to develop new methods for express evaluation of the photostability of polymer articles in use. The problem of fast test calibration for express evaluation of polymer stability was examined in the report presented by a group of authors [G. Pausch (Germany), R. Raymond, and P. Brennan (the United States)]. Much attention was given by the participants to a report by P. Trubiroha on the kinetic features and mechanism of polymer photodegradation and a search for methods for photostabilization of polymer articles. J. Boxhammer's second contribution concerned the use of various simulated-climate chambers for acceleration of polymer degradation and correlation of the data obtained with natural polymer degradation. The same problems were examined in the report by T. Raabe (Germany).

The effects of temperature and humidity on polymer photodegradation were considered by U. Schultz (Germany) who demonstrated that these factors considerably accelerate photodegradation. In the report presented by I. Jakubowicz (Sweden), special emphasis was placed on degradation and stabilization of polyvinyl chloride (PVC).

The problems of accelerated degradation of polymers used in the automobile industry were considered by T. Franz (Switzerland).

A series of the conference contributions were devoted to polymer biodegradation. Specifically, K.Z. Gumargalieva, G.E. Zaikov, and S.A. Semenov considered the interaction of fungi with polymer, particularly PVC, surface; and the report by I. Stephan (Germany) focused on preparation of biofilms through adhesion of microorganisms to the surface of various polymers.

The participants showed considerable interest in the results reported by a group of authors [J. Pospisil, S. Nespurek, Z. Horak, Z. Krulis (Czech Republic), and W.D. Habicher (Germany)] on the effects of polymer matrix and testing conditions on the behavior and useful life of stabilizers for polymers.

A series of contributions were devoted to the problems of environmental protection and interaction of polymers with polluted atmosphere. T.F. Reichert and U. Pohsner (Germany) reported the effect of the type of air pollution on selection of polymers sufficiently resistant against a given type of pollution. U. Schultz considered the part played by acid rains in polymer photodegradation, and V. Wachtendorf reported the development of new polymeric coatings stable in polluted environment (tests were performed in the US). P. Truberoha, U. Schultz, and V. Wachtendorf reported the effect of acid rains on degradation of polymer films for agricultural use. The effects of various additives on accelerated degradation of polymers were analyzed by M. Zah (Germany).

W. Bachleitner and L. Kranner (Austria) focused in their report on natural and accelerated degradation of polycarbonate, and G. Kalinka, on the study of de-

1070-4272/02/7502-0333 $27.00 © 2002 MAIK "Nauka/Interperiodica"

gradation of the surface of polymer articles. The condition of the surface of polymer articles upon their aging and development of quality control methods were considered by C. Van Teylingen (the Netherlands).

The topics of the latter five reports concerned the analysis and control of natural and accelerated polymer degradation. In particular, B. Ivan and T. Szakacs (Hungary) reported on a study of thermooxidative degradation of PVC by gel chromatography. The report by P. Meinlschmidt (Germany) and G.B. Pausch was devoted to determination of latent defects in polymeric coatings by high-resolution thermography. Three reports were devoted to the use of chemiluminescence for studying thermooxidative degradation of various polymers [L. Matisova-Rychla and J. Rychly (Slovak Republic); K. Germann (Germany); and D. Kockott and V. Wachtendorf].

The next, XXIII Colloquium is planned to be held in 2003. However, the place of the meeting has not been specified yet, since none of the organizers of the XXII Colloquium took an initiative to hold the next conference. So the place and date of the XXIII Colloquium will be decided in 2002. The Abstracts of Papers of the XXII Colloquium are available from the library of the Institute of Chemical Physics, Russian Academy of Sciences (Moscow, Russia).

G.E. Zaikov, K.Z. Gumargalieva, and M.I. Artsis

Russian Journal of Applied Chemistry, Vol. 75, No. 2, 2002, pp. 335–336. Translated from Zhurnal Prikladnoi Khimii, Vol. 75, No. 2, 2002, pp. 345–346.
Original Russian Text Copyright © 2002 by Morachevskii.

Kontseptsiya razvitiya goreniya i vzryva kak oblasti nauchno-tekhnicheskogo progressa (The Concept of Development of Research into Combustion and Explosion as an Avenue of Scientific and Technical Progress), Chernogolovka: Territoriya, 2001, 176 pp.

The book is a collection of papers prepared by a group of leading specialists on the instructions of the Scientific Council on combustion and explosion of the Russian Academy of Sciences. The purpose of this collection is to reflect the present state of R&D in the field of combustion and explosion and to assess the prospects for their development.

In a brief introduction (pp. 6–12), the executive editor of the collection, Academician of the Russian Academy of Sciences A.G. Merzhanov emphasizes that combustion and explosion presently constitute an independent field of knowledge which has its own experimental and theoretical means of investigation. These are based on analysis of nonlinear direct and back couplings between the rates of chemical, phase, and structural transformations, on the one hand, and rates of energy (heat) and mass transfer, on the other. This approach gives insight into the nature of quite a number of specific phenomena that are typical of combustion and explosion. Despite the difference in outward manifestations, the combustion and explosion are processes which are close in their scientific essence and are characteristic of systems possessing a common feature—high energy capacity. The introduction notes the vast possibilities of the science of combustion and explosion and its real advances in practical applications.

The material of the collection is divided into five chapters, some of which contain actually independent sections written by different authors. The first chapter "Some Aspects of Fundamental Investigations into Combustion and Explosion" (pp. 13–77) contains evidence about the main directions of research, to which, in particular, belong initiation and propagation of combustion waves, effect of external physical fields on combustion and explosion, thermodynamics and kinetics of combustion and explosion, and their mathematical modeling.

The second chapter "Shock Waves and Detonation" (pp. 78–93) is concerned with the state and prospects of studies of shock wave and detonation phenomena. Computer simulation of explosion and high-speed impact, studies of states of substance at high pressure and temperature, technological applications of shock and detonation waves, and some other issues are considered.

The third chapter "Scientific Foundations of the Use of Combustion and Explosion in Technology" (pp. 94–131) discusses a variety of topical problems important for the national economy and energy safety of the country. To these belongs, in particular, the use of hydrogen, which is not only a high-energy ecologically safe fuel, but also a convenient energy carrier. It is noted that effective, corrosion-inactive, and ecologically safe inhibitors, capable of controlling the combustion, explosion, and detonation of hydrogen and its mixtures with carbon dioxide, have been developed at the Institute of Structural Macrokinetics and Problems of Materials Science, Russian Academy of Sciences. Another global problem is related to the necessity for eliminating, processing, or utilizating industrial and domestic wastes. According to the authors' data, use of filtration combustion in modes with superadiabatic heating is among the most efficient ways to solve the problem. The essence of the method and results of tests with reactors intended for various purposes are discussed. Of particular interest is the part of the chapter which is devoted to the analysis of heat-and-power facilities of Russia. The part played by Russia in the world's power engineering in the 21st century is very important—more than 13% of the world's oil reserves, 33% of proven natural gas resources, 16% of coal reserves, and 14% of uranium reserved are concentrated in its territory covering approximately 10% of the Earth's land surface, together with a vast economical potential of unconventional power sources and local reserves of organic fuel. In 1999, Russia occupied the third place in the world, after Saudi Arabia and the US, in oil production (304.2 million ton). Production of gas (591 billion m^3)

1070-4272/02/7502-0335 $27.00 © 2002 MAIK "Nauka/Interperiodica"

was approximately 25%, and that of coal (250 million ton), 5.3% of the respective world's figures.

At the same time, the authors mentioned some negative tendencies in the heat-and-power complex of Russia—decline in gas production at the existing deposits, and decrease in production and, especially, refining of oil at domestic refineries, and the resulting reduction of fuel oil resources, and ecological problems. The authors are of the opinion that, in Russia, it is advisable to use coal whose resources will last for 300–500 years. Directions of investigations that could favor a wider and more efficient use of solid fuel and improve the ecological characteristics of its burning are outlined.

The same chapter considers prospects for development of scientific investigations of combustion processes in internal-combustion engines and points to the necessity for increasing the number of energy carriers that can be used in these engines.

The fourth chapter "Technological Processes of Combustion and Explosion" (pp. 132–156) pays much attention to self-propagating high-temperature synthesis (SHS)—a process in which practically valuable solid substances are formed. The technological advantages of SHS lie in its operation principle—use of heat released in chemical reactions instead of heating a substance by means of an external source. SHS processes have found a wide variety of applications (the problem of SHS is being studied in 47 countries all over the world), but there exist even wider prospects. Use of SHS processes in metallurgy is considered.

Among other promising combustion-related technologies discussed in the chapter are oxypyrolysis and production of synthesis gas (mixture of carbon oxide and hydrogen), and preparation of technical-grade carbon (carbon black) and sulfur in incomplete combustion of aromatic hydrocarbons and hydrogen sulfide, respectively. In the industry of Russia, the annual manufacture of synthesis gas constitutes tens of millions of cubic meters, and, therefore, laying scientific foundations of an energy-saving technology of its production is of primary economical importance. A separate section of the chapter is devoted to explosive technologies. They are based of physicochemical and physicomechanical processes occurring in a substance under the action of shock waves. Irrespective of the method used to generate the waves, a pressure surge ($\sim 10^{10}$ Pa) appears in a material, propagating in it at high speed ($\sim 10^3$ m s^{-1}). The response of materials to an extremal action of this kind may vary. This section of the chapter analyzes the history, present state, and prospects for the development of explosive technologies. Of particular interest is the shock-wave impact upon substances and their mixtures that are apt to undergo chemical and phase transformations.

The fifth chapter "Safety and Ecology" (pp. 157–171) gives general consideration to problems associated with safety and reduction of the technological risk for quite a number of branches of national economy. Analysis of the known emergencies shows that more than 60% of these have been accompanied by inflammation and explosion. Special attention is given to such widely occurring natural ecological catastrophes as forest fires, leading to burning-out of vast forest tracts and contamination of the atmosphere, up to its upper layers, with carbon black particles. The authors of the chapter formulate the main lines of studies of safety and ecology in terms of the presently considered concept of development of research into combustion and explosion as an avenue of scientific and technical progress.

Despite the large number of authors and some differences in the presentation styles, the book is rather well written and is of much interest for a wide variety of specialists in various fields.

The concept in question is based on fundamental investigations requiring considerable funds and commitment of the state and major financial and industrial companies. As noted by one of the authors (p. 156), a decline in basic and applied research in all fields of science has been observed since the early 1990s. Insufficient financing, low pay, lack of inflow of young scientists, and difficulties with scientific exchange—all these factors tell on the rate of development and level of scientific investigations. It only remains to hope that the negative tendencies in science and science-intensive industries, associated with the economic recession in Russia, will be overcome and works in the field of combustion and explosion will receive appropriate support.

A. G. Morachevskii

Russian Journal of Applied Chemistry, Vol. 75, No. 2, 2002, p. 337. Translated from Zhurnal Prikladnoi Khimii, Vol. 75, No. 2, 2002, p. 347.
Original Russian Text Copyright © 2002 by Morachevskii.

BOOK REVIEWS

Petrov, G.V., Greiver, T.N., and Lazarenkov, V.G., *Sovremennoe sostoyanie i tekhnologicheskie perspektivy proizvodstva platinovykh metallov iz khromitovykh rud* (Present State and Technological Prospects of Manufacture of Platinum Metals from Chromite Ores), St. Petersburg: Nedra, 2001, 200 pp.

In the 19th century, Russia was the major manufacturer of platinum extracted from gravel deposits of Urals, which had been exhausted long ago and were replaced in the middle of the 20th century by sulfide copper-nickel ores of the Noril'sk–Talnakh region, containing no less than 40% of the world's reserves of platinum metals. This allows Russia to remain a major manufacturer of platinum metals in the 21st century. Even though chromite ores (chromites are spinel minerals with Cr_2O_3 content ranging from 18 to 62%) are unconventional source of platinum metals, they are of interest in view of the growing demand for platinum and its accessories.

Among the authors of this monograph are specialists with many years of experience both in the geology of platinum metals (V.G. Lazarev) and in the development of methods for their dressing in integrated use of the raw material (T.N. Greiver, G.V. Petrov). This allowed discussion of a wide variety of problems.

The book comprises eight small chapters and a reference list including 193 references to publications by mainly Russian authors. The first chapter (pp. 7–28) characterizes the world's mineral resources of platinum metals and the state of their manufacture and consumption. The most prominent exporters of home-manufactured platinum metals are Republic of South Africa, Russia, Canada, and Australia. The first place in manufacture of platinum is occupied by the Republic of South Africa, the largest manufacturer of palladium is Russia.

The second chapter (pp. 29–46) is concerned with chromite ores, their deposits, resources, mining, and dressing, structure of chromite ore consumption, and state of the world's market of ferrochromium. The third chapter (pp. 47–64) considers the processes of concentration of platinum metals in dressing of ores from deposits in the territory of the Republic of South Africa (Bushweld massif). The fourth chapter (pp. 65–106) discusses problems associated with the recovery of platinum metals in dressing of chromite ores from another kind of deposits—zonal massifs characteristic of the platinum-bearing belt of Urals. Specific features of the behavior of chromium and platinum metals in dressing of ores from the Nizhni Tagil deposit and also from deposits of the southeastern part of the Siberian platform are described. The fifth chapter (pp. 107–126) considers the prospects for dressing of platinum-containing chromite ores from other deposits in the territory of the CIS.

The following chapters—sixth (pp. 126–147), seventh (pp. 148–169), and eighth (pp. 170–187), are concerned with various kinds of technological schemes for processing of the platinum-containing concentrates obtained. Combination of various dressing methods under industrial conditions may yield concentrates with content of the sum of platinum metals in the range from 100 to 1000 g per 1 ton. In choosing a technology, the central issue is the method for stripping the concentrate in order to transfer platinum metals into solution, wherefrom they can be extracted by various techniques (sorption on anion-exchange resin, cementation).

In a brief conclusion (pp. 188–189), the authors emphasize that improving the sensitivity and accuracy of analytical determination of platinum metals made it possible to reveal their presence in many kinds of raw materials that are unconventional for the extraction of platinum metals. Particularly topical for Russia is the processing of the chromite ore which is already an important source of platinum metals in foreign countries.

The monograph is marked by high scientific level and is of interest for engineers and researchers in the field of integrated processing of various kinds of complex mineral raw materials.

A.G. Morachevskii

1070-4272/02/7502-0337 $27.00 © 2002 MAIK "Nauka/Interperiodica"

Russian Journal of Applied Chemistry, Vol. 75, No. 2, 2002, p. 338. Translated from Zhurnal Prikladnoi Khimii, Vol. 75, No. 2, 2002, p. 348.
Original Russian Text Copyright © 2002 by Morachevskii, Beloglazov.

BOOK REVIEWS

Ni, L.P., *Fizicheskaya khimiya gidroshchelochnykh protsessov polucheniya oksida alyuminiya* (Physical Chemistry of Hydroalkaline Processes for Production of Aluminum Oxide), Almaty: KazgosINTI, 2001, 148 pp.

This monograph is concerned with an issue that is rather topical for Russia and Kasakhstan. It was written by a known specialist in alumina production and is largely based on results of his many years' investigations. The author made a major contribution to the development of technological schemes for processing of high-silica and high-iron alumina-containing substances and other low-grade aluminum raw materials.

The book comprises five chapters and a list of references to 82 titles. The first chapter (pp. 6–19) gives a general characteristic of the main kinds of aluminum raw materials—bauxites and alkaline and alkali-free aluminosilicates. It briefly describes hydroalkaline methods for alumina production. The second chapter (pp. 20–70) is devoted to the analysis of physicochemical properties of systems, underlying hydroalkaline processes. Much attention is given to the systems containing silicon dioxide and iron(III) oxide. The third chapter (pp. 71–111) occupies the central place in the monograph. The author briefly considers the classical scheme of alumina production by the Baeyer method; various modifications of this method, depending on the type of raw materials being processed; and ways to improve the technology of autoclave leaching of bauxites. The primary aim of improving the autoclave processing in the Baeyer method is to reduce the expenditure of the high-priced caustic alkali. This can be achieved by either raising the temperature of autoclave leaching or replacing sodium hydroxide with soda ash. The monograph analyzes both possible ways. Specific features of processing of high-silica and high-iron bauxites are discussed in detail.

The fourth chapter (pp. 112–133) is concerned with the theory and technology of chemical dressing of high-silica aluminum raw materials. The process is based on the decomposition of high-silica raw materials under the action of acids to give a silicate solution and aluminum-enriched concentrate. Chemical dressing of alkali-free aluminosilicates (kyanite, kaolins and clays, mineral fraction of coals), nepheline ores, and high-silica bauxites is considered. Special attention is given to the processing of silicate solutions. The cost-effectiveness of the technology of chemical dressing is determined largely by the cost and sales volume of products obtained in utilization of silicate solutions. The final fifth chapter (pp. 134–140) contains brief information about autoclave desiliconization of aluminate solutions.

According to the available data, Russia manufactured 3.24 million tons of aluminum in 2000, and the country holds the second place in the world being surpassed only by the United States (3.67 million tons). However, it is known that a considerable part of raw materials is imported. The topicality of using various kinds of low-grade aluminum-containing raw materials in Russia was noted as far back as the 1930s by A.A. Yakovkin (1860–1936), an outstanding physical chemist and technologist.

The book written by L.P. Ni is of indubitable interest for a wide audience of specialists in manufacture of alumina. It can be used as a textbook in chemical-engineering and metallurgical higher-school institutions. The monograph has a clear-cut technological purpose, is well written, and gives a clear picture of the important technological problem.

A.G. Morachevskii, I.N. Beloglazov

1070-4272/02/7502-0338 $27.00 © 2002 MAIK "Nauka/Interperiodica"

Russian Journal of Applied Chemistry, Vol. 75, No. 3, 2002, pp. 339–344. Translated from Zhurnal Prikladnoi Khimii, Vol. 75, No. 3, 2002, pp. 353–358.
Original Russian Text Copyright © 2002 by Shashkova, Rat'ko, Koshevar, Kitikova, D'yachenko.

INORGANIC SYNTHESIS AND INDUSTRIAL INORGANIC CHEMISTRY

Synthesis and Properties of Modified Fillers Based on Calcium and Magnesium Carbonates

I. L. Shashkova, A. I. Rat'ko, V. D. Koshevar, N. V. Kitikova, and A. G. D'yachenko

Institute of General and Inorganic Chemistry, State Scientific Institution, National Academy of Sciences of Belarus, Minsk, Belarus

Received April 24, 2000; in final form, December 2001

Abstract—A possibility of modifying natural carbonate fillers for paint and varnish industry by solutions of salts of some nonferrous metals was studied. Reactions of carbonates with metal ions and physicotechnical properties of the resulting materials were considered.

Paints and paint coatings to approximately 70% consist of fillers: natural or synthetic inorganic powders used in combination with chromatic or achromatic pigments to reduce the cost of paint-and-varnish compositions [1]. Colorless substances are used as fillers, but these components of paints and enamels are not inert. A proper choice of fillers makes it possible to improve physicochemical and physicomechanical properties of the painting systems. Fillers based on alkaline-earth metal carbonates gained the widest acceptance owing to their availability and relatively low price. In recent years, a cycle of studies on using natural carbonates as sorbents of such heavy and nonferrous ions as Cu(II), Fe(III), Cr(III), Pb(II), Ni(II), Co(II), etc., has been carried out and summarized in [2]. It was found that solid carbonates, when in contact with solutions of salts of the above metals, react with them to give difficultly soluble colored compounds with solubility products lower than those of the starting compounds [2–4]. These compounds are M(II) and M(III) carbonates, subcarbonates, or hydroxides.

The carbonates can be partially transformed by a two-stage treatment into other colored chemical compounds of M(II) and M(III), which are also high-quality pigments, for example, hexacyanoferrates(II) or phosphates [5, 7]. Moreover, the phosphates are thermostable up to 1000°C and higher.

According to the obtained data, 30–40% transformation of the starting carbonates into reaction products ensures an intense color of the materials.

The capability of alkaline-earth metal carbonates to selectively sorb ions of nonferrous metals from various solutions offers possibilities of utilizing various metal-containing wastes, including wastes of electroplating productions and of metal working, to produce colored materials.

Here we report on the modification of natural chalk and dolomite[1] with solutions of M(II) and M(III) salts and of $K_4[Fe(CN)_6]$, including modification in the presence of phosphate anion, and on the physicochemical properties of the resulting compounds.

EXPERIMENTAL

We used natural dolomite and chalk as the base of pigments and fillers. According to the differential thermal analysis (DTA) data, dolomite contains 84% calcium–magnesium carbonate, and chalk, 96% calcite $CaCO_3$. To prepare modifying solutions, we used the following salts: $CuCl_2 \cdot 2H_2O$ (pure grade), $CuSO_4 \cdot 5H_2O$ (pure grade), $Cu(NO_3)_2 \cdot 3H_2O$ (chemically pure grade), $Co(NO_3)_2 \cdot 6H_2O$ (pure grade), $Cr(NO_3)_3 \cdot 9H_2O$ (pure grade), $Fe(NO_3)_2 \cdot 9H_2O$ (analytically pure grade), $FeSO_4 \cdot 7H_2O$ (analytically pure grade), $K_4[Fe(CN)_6] \cdot 3H_2O$ (chemically pure grade), and also copper-containing wastes $3Cu(OH)_2 \cdot CuCl_2 \cdot xH_2O$ (x = 1–3) and copper shavings, which were dissolved in nitric acid.

We modified natural carbonates with solutions of M(II) and M(III) salts under static conditions at room temperature. A 100-g portion of natural chalk or dolomite was added to 350 ml of 0.9–1.8 N solution of an M salt [M = Cu(II), Fe(III), Cr(III), Co(II)] and allowed to stand for a day at room temperature with intermittent stirring. Then the solid phase was separated, washed with distilled water, dried in air, and ground

[1] Both are industrially mined in the Vitebsk oblast, Belarus'.

1070-4272/02/7503-0339$27.00 © 2002 MAIK "Nauka/Interperiodica"

in a mortar. To study physicochemical properties, we used the fraction of less than 0.05 μm.

To obtain hexacyanoferrate modifications, we first treated natural carbonates with 0.9 N solutions of $CuCl_2$ and $FeSO_4$ [the solid-to-liquid ratio (g : ml) was $M_s : V_l = 100 : 350$] and then, after washing with distilled water, with a 0.1 N solution of $K_4[Fe(CN)_6]$ ($M_s : V_l = 100 : 750$). The resulting intermediate compounds were treated with potassium dichromate to oxidize Fe(II) by the procedure given in [1].

When obtaining the phosphate modification, we used the product of treating dolomite with a solution of phosphoric acid, which consisted of a mixture of calcium and magnesium hydrophosphates [5]. We colored this mixture with solutions of M(II) and M(III) salts.

We treated carbonates with metal salt solutions for 1 day, though kinetic studies showed that the chemical processes are 80% complete within several hours [3–7].

The concentrations of the modifying salt solutions (0.9–1.8 N) and the ratio between the solid and liquid phases were chosen on the basis of the data on the adsorption of M(II) and M(III) ions by carbonates and phosphates [3–7] in such a way as to ensure partial transformation of the starting phases into the reaction products. The amount of metal ions absorbed from the solution was determined by photometry or by complexometric titration [3, 4, 6, 7] as the difference between their concentrations in the starting solution and in the solution after a contact with a carbonate.

The samples of modified carbonates were heat-treated at 200–800°C.

We determined the specific surface area of the samples S_{sp} ($m^2\ g^{-1}$) by the air adsorption at the liquid nitrogen temperature [8].

The differential thermal analysis (DTA) was carried out with an MOM (Hungary) derivatograph by heating in air at a rate of 10 deg min^{-1} in an open conical crucible. The sample weight was 600 mg.

We determined the phase compositions of the starting carbonates and products of their chemical treatment by the X-ray phase analysis on a DRON-2 diffractometer with the CuK_α radiation.

We determined pH of the aqueous extract, the bulk density, and the oil absorption of modified colored carbonates by the procedures designed for inorganic pigments [9, 10]. The covering power was determined by the visual procedure designed for pigmented paint and varnish materials (relative error ±5%) [9].

The color properties of the materials obtained by the chemical and thermal treatment of natural carbonates are given in Table 1. The combination of chemical and thermal methods for modifying carbonates allowed a wide variety of colored materials to be obtained on their basis. The color intensity of the obtained materials is a function of the modifying solution concentration and is determined by the nature of the modifying agent. A copper chloride solution gave a brighter color than copper nitrate and sulfate solutions.

With the aim to study in detail the physicochemical properties of the colored materials obtained on the basis of chalk $CaCO_3$, dolomite $CaMg(CO_3)_2$, and phosphated dolomite $CaMg(CO_3)_2 \cdot H_3PO_4$, we selected several samples modified in the systems $CaCO_3$–$CuCl_2$, $CaCO_3$–$CuCl_2$–$K_4[Fe(CN)_6]$, $CaCO_3$–$FeSO_4$–$K_4[Fe(CN)_6]$, $CaMg(CO_3)_2$–$Fe(NO_3)_3$, $CaMg(CO_3)_2$–H_3PO_4–$Co(NO_3)_2$, $CaMg(CO_3)_2$–H_3PO_4–$CuCl_2$, and $CaMg(CO_3)_2$–H_3PO_4–$Cu(NO_3)_2$. In the latter case we prepared a solution of copper nitrate from both the reagent-grade salt, $3Cu(OH)_2 \cdot CuCl_2 \cdot xH_2O$ wastes, and copper shavings.

The phase composition, covering power, pH of aqueous extract, density, specific surface area, and oil absorption of the compounds obtained in the listed systems are given in Table 2. Similar properties of the starting nonmodified carbonates are also given there for comparison.

The X-ray phase analysis showed that the products of the reaction of $CaCO_3$ with Cu^{2+} ions and of $CaMg(CO_3)_2$ with Fe^{3+} ions are amorphous: the X-ray patterns contain no reflections of new phases, but involve only the diffraction peaks of the starting $CaCO_3$ or $CaMg(CO_3)_2$ phases. The examination of published data points to the fact that the product of the reaction of the carbonates with iron ions is $Fe(OH)_3$, as Fe(III) does not give carbonates [11]. The reaction is described by the equation

$$3CaMg(CO_3)_2 + 4Fe^{3+} + 6HOH \rightarrow 4Fe(OH)_3 + 3Ca^{2+} + 3Mg^{2+} + 6CO_2. \quad (1)$$

Reactions of chalk with solutions of copper salts can yield various compounds: carbonate, basic carbonates and chlorides, or copper hydroxide. The published information on this problem is rather ambiguous. We used for modification a 1.8 N solution of copper chloride with pH 2.7. After the reaction with calcium carbonate pH of the mother liquor increased to 5.7. It is most probable that under the conditions in

Table 1. Color properties of modified natural carbonates depending on the conditions of the material preparation

Solution, g-equiv l^{-1}	pH	Color before and after heat treatment at indicated temperature, °C				
		starting	200	400	600	800
			Chalk			
$CuSO_4$, 1.8	3.35	Light green	Green	Dark grey	Dark grey	Black
$CuCl_2$, 1.8	2.70	″	″	Dark brown	″	Dark grey
$Fe(NO_3)_3$, 1.8	0.90	Light brown	Light brown	Light brown	Light brown	Brown
$Cr(NO_3)_3$, 1.8	1.00	Blue	″	″	Green (khaki)	Green
$CuCl_2$, 0.9	3.65	Light brown	–	–	–	–
$K_4[Fe(CN)_6]$, 0.1	6.25	″				
$FeSO_4$, 0.9	0.97	Dark blue	–	–	–	–
$K_4[Fe(CN)_6]$, 0.1	6.25	″	–	–	–	–
			Dolomite			
$CuSO_4$, 1.8	3.35	Light green	Green	Gray	Dark gray	Black
$CuCl_2$, 1.8	2.70	″	″	Brown	″	Dark gray
$Fe(NO_3)_3$, 1.8	0.90	Golden brown	Golden brown	Reddish brown	Reddish brown	Brown
$Cr(NO_3)_3$, 1.8	1.00	Gray	Brown	Brown	Green (khaki)	Green
$FeSO_4$, 0.9	0.97	Dark blue	–	–	–	–
$K_4[Fe(CN)_6]$, 0.1	6.25	″	–	–	–	–
			Phosphated dolomite			
$CuSO_4$, 1.8	3.35	Turquoise	Turquoise	Turquoise	Turquoise	Turquoise
$Fe(NO_3)_3$, 1.8	0.90	Light yellow	Light yellow	Light yellow	Light yellow	Light yellow
$Cr(NO_3)_3$, 1.8	1.00	Gray	Brown	Brown	Brown	Gray
$Co(NO_3)_2$, 1.8	4.05	Pink	Violet	Violet	Violet	Violet
$CuCl_2$, 0.9	3.65	Plum violet	–	–	–	–
$K_4[Fe(CN)_6]$, 0.1	6.25	″	–	–	–	–

hand the amorphous product is copper hydroxocarbonate.

When phosphated dolomite was treated with salt solutions, the reflections of new phases resulting from the reaction with Cu^{2+} and Co^{2+} ions were identified in the X-ray pattern of the end products, whereas the peaks of the starting phases (calcium and magnesium hydrophosphates $CaHPO_4 \cdot 2H_2O$ and $MgHPO_4 \cdot 3H_2O$) were, as a rule, absent from the patterns of the modified samples.

According to the X-ray data, the products of the reaction of phosphated dolomite with solutions of cobalt(II) and copper(II) salts are $Co_3(PO_4)_2 \cdot 8H_2O$ and $Cu_3(PO_4)_2 \cdot 3H_2O$. Their formation can be expressed by the equations

$$CaMg(CO_3)_2 + 2H_3PO_4 + 3Co^{2+} + 6H_2O \rightarrow Co_3(PO_4)_2 \cdot 8H_2O + Ca^{2+} + Mg^{2+} + 2CO_2 + 2H^+, \quad (2)$$

$$CaMg(CO_3)_2 + 2H_3PO_4 + 3Cu^{2+} + H_2O \rightarrow Cu_3(PO_4)_2 \cdot 3H_2O + Ca^{2+} + Mg^{2+} + 2CO_2 + 2H^+. \quad (3)$$

The products of chalk modification with potassium hexacyanoferrate(II) exhibit reflections of calcium carbonate and of copper and iron hexacyanoferrates(II).

The content of the starting phase, i.e., of an unreacted carbonate, in colored samples is 54–69%, as calculated from the amount of metal ions absorbed from solutions according to the equations of the corresponding chemical reactions (Table 2). Despite this fact, the synthesized materials are fairly uniformly colored without markedly contrasting disseminations of unchanged carbonates. This fact suggests that particles of unchanged phases are colored at the expense of surface processes: either owing to chemical reactions occurring on their surface or owing to the adsorbed metal ions.

Partial transformation of the carbonate phase into new chemical substances results in a characteristic change in the thermogravimetric parameters of the material. The data of differential thermal analysis of carbonates before and after their modification with M(II) and M(III) solutions are given in the Figs. 1a–1c, which show, in particular, that the starting car-

Table 2. Physicochemical properties of modified and nonmodified natural carbonates

Property	Chalk	Chalk + salt			Dolomite	Dolomite + $Fe(NO_3)_3$
		$CuCl_2$	$CuCl_2$–$K_4[Fe(CN)_6]$	$FeSO_4$–$K_4[Fe(CN)_6]$		
Color	White	Light green	Light brown	Dark blue	Light yellow	Brown
Bulk volume after shaking up, $cm^3\ g^{-1}$	0.83	0.93	0.86	1.16	0.56	0.61
Covering power, $g\ m^{-2}$	515	234	25	12	470	117
Phase composition	$CaCO_3$	$CaCO_3$ + amorphous product	$CaCO_3$ + X***	$CaCO_3$ + Y****	$CaMg(CO_3)_2$	$CaMg(CO_3)_2$ + amorphous product
Content of starting phase, %	100	69	60	57	100	54
pH of aqueous extract	8.0	7.1	8.2	7.1	8.9	6.7
Moisture content, %	0.32	2.43	0.89	3.70	0.17	6.05
Specific surface area S_{sp}, $m^2\ g^{-1}$	1	2	2	–	0	53
Oil absorption, g/100 g	15	18	20	34	13	22

Property	Phosphated dolomite	Phosphated dolomite + chalk			
		$CuCl_2$	$Co(NO_3)_2$	$Cu(NO_3)_2$*	$Cu(NO_3)_2$**
Color	Light yellow	Blue	Pink	Light green	Light green
Bulk volume after shaking up, $cm^3\ g^{-1}$	1.13	1.47	1.03	1.32	1.45
Covering power, $g\ m^{-2}$	674	342	206	252	210
Phase composition	$CaHPO_4 \cdot 2H_2O$ + $MgHPO_4 \cdot 3H_2O$	$Cu_3(PO_4)_2 \cdot 3H_2O$	$Co_3(PO_4)_2 \cdot 8H_2O$	$Cu_3(PO_4)_2 \cdot 3H_2O$ $CaHPO_4 \cdot 2H_2O$	$Cu_3(PO_4)_2 \cdot 3H_2O$
Content of starting phase, %	100	64	64	64	64
pH of aqueous extract	7.3	6.0	6.0	5.8	5.0
Moisture content, %	13.48	5.29	16.40	6.68	17.05
Specific surface area S_{sp}, $m^2\ g^{-1}$	1	24	12	20	83
Oil absorption, g/100 g	28	36	23	37	49

* The solution was obtained by dissolving copper shavings in nitric acid.
** The solution was obtained by dissolving $3Cu(OH)_2 \cdot CuCl_2 \cdot xH_2O$.
*** $X = K_2Cu_3^{II}[Fe^{II}(CN)_6]_2 + K_2Cu^{II}[Fe^{II}(CN)_6]_2$.
**** $Y = Fe_4^{III}[Fe^{II}(CN)_6]_2$.

bonates do not undergo thermal decomposition up to 800–900°C. The materials prepared by modifying dolomite and chalk with $Fe(NO_3)_3$ and $CuCl_2$ solutions, respectively, have quite different thermogravimetric characteristics. As seen from Fig. 1, two ranges of thermal transformations can be distinguished. The first range is 117–550 (Fig. 1a) and 106–567°C (Fig. 1b), and the second range covers higher temperatures. The major process in the second range is carbonate decomposition, whereas the first stage, with endothermic effects at 150–300°C, corresponds to the release of water contained in the chemical compounds, in particular, in iron(III) hydroxide (Fig. 1a) and in unidentified amorphous copper(II) compound (Fig. 1b).

When phosphated dolomite is treated with solutions of copper and cobalt salts, hydrated phosphates of alkaline-earth metals partially transform into hydrated copper and cobalt phosphates, the weight loss substantially decreases, but the temperature range of the substance decomposition does not change appreciably (Fig. 1c).

The modification of natural carbonates with acid solutions of metal salts changes not only their color, but also the other physicochemical characteristics (Table 2). The bulk volume of the materials obtained is 0.61–1.47 $cm^3 g^{-1}$. For the initial chalk and dolomite these values are 0.83 and 0.56 $cm^3 g^{-1}$, respectively. The modified fillers are characterized by pH of aqueous extract of 5–8, whereas the initial carbonates have basic properties, pH of their aqueous extract is 8.0–8.9.

The transformation of natural carbonates in solutions of salts with double- and triple-charged metal ions substantially increases the material surface area owing to two factors. First, compounds with a smaller particle size than in the initial carbonate are formed in the reaction with metal ions and, second, unchanged particles of natural carbonates decrease in size on treating with acid solutions of metal salts owing to their partial dissolution. Thus, the specific surface area of the initial materials, which does not exceed 1 $m^2 g^{-1}$, increases after the modification by more than an order of magnitude: to 12–83 $m^2 g^{-1}$.

The oil absorption of the colored fillers obtained is 12–49 g/100 g, which allows them to be classed with readily dispersible substances. One of the most important characteristics of pigments is their covering power. It is seen from Table 2 that cyanoferrate modifications of carbonates have the best covering power: 12 and 25 g m^{-2}. The material obtained from dolomite modified with $Fe(NO_3)_3$ has the covering power of 117 g m^{-2}, which is fairly close to the value given in [1] for natural iron oxide pigments. For blue, light green, and pink fillers obtained from phosphated dolomite and various copper and cobalt solutions, the covering power is 206–342 g m^{-2}. Therefore, many of the obtained modified samples based on natural carbonates have a satisfactory covering power close to that of commercial pigments.

CONCLUSION

(1) Chemical treatment of alkaline-earth metal carbonates in solutions of copper(II), iron(III), chromium(III), and cobalt(II) salts and of potassium hexacyanoferrate(II) results in their transformation into the corresponding transition metal carbonates, basic carbonates, and hexacyanoferrates(III), and in the presence of phosphate anions, into transition metal phosphates. The process is accompanied by substantial changes not only in color, but also in physicochemical characteristics of the materials.

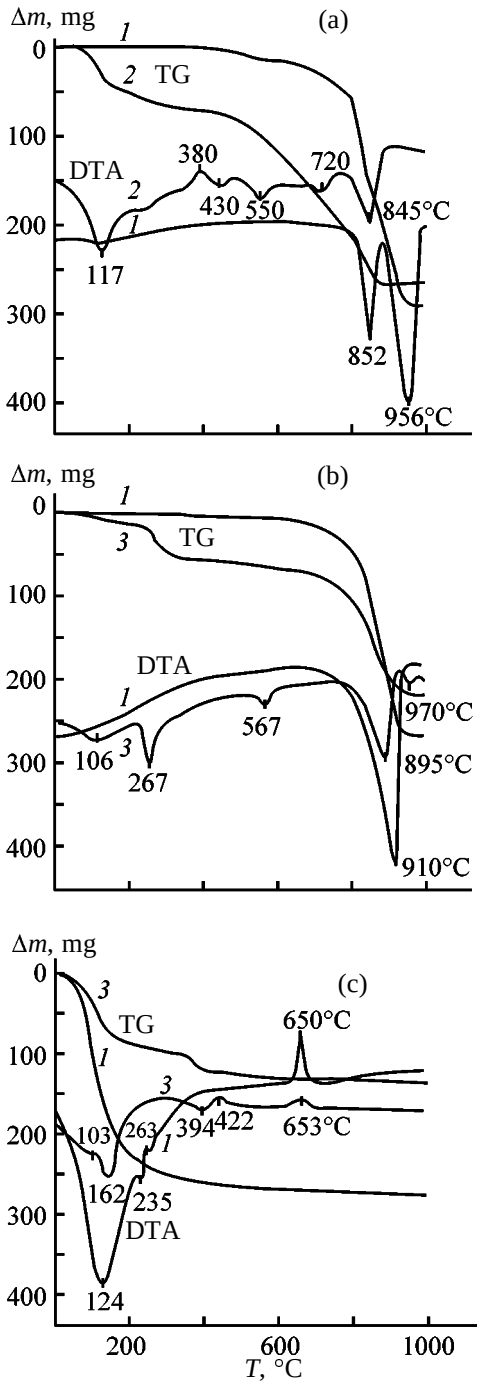

Fig. 1. TG and DTA curves of starting and modified carbonates: (Δ*m*) weight loss and (*T*) temperature. (a) Solomite, (b) chalk, and (c) phosphated dolomite. Material: (*1*) initial, (*2*) modified with $Fe(NO_3)_3$ solution, and (*3*) modified with $CuCl_2$ solution.

(2) The synthesized materials are characterized by satisfactory covering power and oil absorption, allowing them to be considered not only as promising colored fillers of paint and varnish materials, but also as pigments proper.

REFERENCES

1. Belen'kii, E.F. and Riskin, I.V., *Khimiya i tekhnologiya pigmentov* (Chemistry and Technology of Pigments), Leningrad: Khimiya, 1974.
2. Gudz', N.Ya. and Maksin, V.I., *Khim. Tekhnol. Vody*, 1991, vol. 13, no. 5, pp. 428–436.
3. Shashkova, I.L., Rat'ko, A.I., Mil'vit, N.V., *et al*., *Zh. Prikl. Khim*., 2000, vol. 73, no. 6, pp. 914–919.
4. Shashkova, I.L., Rat'ko, A.I., Panasyugin A.S., *et al*., *Zh. Prikl. Khim*., 2001, vol. 74, no. 2, pp. 249–254.
5. Shashkova, I.L., Kitikova, N.V., Rat'ko, A.I., and D'yachenko, A.G., *Izv. Ross. Akad. Nauk, Neorg. Mater*., 2000, vol. 36, no. 8, pp. 990–994.
6. Shashkova, I.L., Rat'ko, A.I., and Kitikova, N.V., *Zh. Prikl. Khim*., 1997, vol. 70, no. 11, pp. 1787–1793.
7. Shashkova, I.L., Rat'ko, A.I., and Kitikova, N.V., *Zh. Prikl. Khim*., 1998, vol. 71, no. 9, pp. 1431–1436.
8. Klyachko-Gurvich, A.L., *Izv. Akad. Nauk SSSR, Ser. Khim*., 1961, no. 10, pp. 1884–1886.
9. Gordovskii, I.A., Indeikin, E.A., and Tolmachev, I.A., *Laboratornyi praktikum po pigmentam i pigmentnym lakokrasochnym materialam* (Laboratory Course of Pigments and Pigment Paint and Varnish Materials), Leningrad: Khimiya, 1990.
10. Ermilov, P.I., Indeikin, E.A., and Tolmachev, I.A., *Pigmenty i pigmentirovannye lakokrasochnye materialy* (Pigments and Pigmented Paint and Varnish Materials), Leningrad: Khimiya, 1987.
11. *Obshchaya khimiya v formulakh, opredeleniyakh, skhemakh: Spravochnoe rukovodstvo* (General Chemistry in Formulas, Definitions, and Schemes: Reference Manual), Tikavyi, V.F., Ed., Minsk: Universitetskoe, 1987.

Russian Journal of Applied Chemistry, Vol. 75, No. 3, 2002, pp. 345–350. Translated from Zhurnal Prikladnoi Khimii, Vol. 75, No. 3, 2002, pp. 359–364.
Original Russian Text Copyright © 2002 by Fedushchak, Il'in.

INORGANIC SYNTHESIS AND INDUSTRIAL INORGANIC CHEMISTRY

Study by Methods of Electron Spin Resonance and Model Oxidation Reaction of Nanosize Metal Powders Obtained in Electric Explosion of Conductors

T. A. Fedushchak and A. P. Il'in

Institute of Petrochemistry, Siberian Division, Russian Academy of Sciences, Tomsk, Russia

Received October 17, 2000

Abstract—Paramagnetic properties of nanopowders obtained by electric explosion of copper, aluminum, cobalt, and platinum conductors have been studied. The possibility of using ESR and model reaction of isopropylbenzene for testing the electric-explosion powders as chemical reagents is discussed.

Nanosize metal powders obtained by electric explosion of a conductor are comparatively new and poorly studied objects. They possess a number of specific properties [1–7]. The electric explosion is a phenomenon consisting in explosive disintegration of a metallic conductor through which a current pulse of high density is passed. The most important characteristics of the electric explosion, determining the grain size and nature of the forming metallic dispersions, are the density of energy introduced into a substance (ratio of energy introduced into a conductor to the sublimation energy of this conductor, ω/ω_s), rate of its introduction, its distribution along and across a wire, chemical composition of the medium in which explosion occurs, etc. [8, 9]. The properties of nanopowders produced by electric explosion (NPEE) are strongly affected by the explosion chamber design, which influences the dynamics of particle dispersion in explosion, and by the mode of nanopowder passivation [10]. Use of NPEEs as chemical reagents or catalysts may be efficient if reproducibility of their properties is ensured in the course of preparation and their reactivity in the corresponding chemical transformations can be prognosticated. The conventional approach relying upon "exit" test of NPEEs by means of low-temperature adsorption of inert gases and differential-thermal (DTA), X-ray phase, elemental, and calorimetric analyses proved to be insufficient. Additional diagnostic studies aimed at adaptation of NPEEs as novel chemical objects are necessary. It seems appropriate in this connection to study the paramagnetic properties of NPEEs. The paramagnetic properties of finely dispersed metallic media have been mentioned in the literature. For example, superparamagnetism is exhibited by nanosize ensembles of ferromagnetic nickel in ultradisperse powders obtained by the method of pulsed plasma channel [11, 12]. The authors attributed this phenomenon to distortion of the domain structure of compact nickel. A conclusion that the observed ferromagnetism has impurity nature was made in [13] on the basis of magnetochemical studies of highly dispersed spherical particles of powdered copper and aluminum. Ushakov *et al*. [14] reported the possibility of concentrating various kinds of impurities, including those of paramagnetic nature, either on the surface of particles of nanopowders produced by electric explosion or in the bulk, depending on preparation conditions. In this case, as shown in [15], NPEEs frequently do not absorb the microwave radiation of the ESR spectrometer.

The aim of this study was to analyze the properties of copper, aluminum, platinum, and cobalt powders obtained under varied electric-explosion conditions by the methods of electron spin resonance (ESR) and model reaction of isopropylbenzene (IPB) oxidation.

As objects of study served numerous samples of metals obtained under varied conditions of electric explosion in various gas media: NPEEs of copper, platinum, cobalt, and aluminum (set 1) and NPEEs of copper (sets 2 and 3). The table lists characteristics and preparation conditions of nanopowders belonging to set 1. For comparison, aerosol and plasmochemical nanopowders of copper and PMS-1 powder were studied under similar experimental conditions.

Here we discuss the basic problem of manifestation of paramagnetic properties in the series of the objects under study. The ESR spectra of copper NPEEs of

1070-4272/02/7503-0345$27.00 © 2002 MAIK "Nauka/Interperiodica"

Conditions of electric explosion for metal nanopowders of set 1, their paramagnetic characteristics, and activity in cumene oxidation*

Sample no.	Sample, 100 mg	Medium	ω/ω_c	D_S, nm	$C_{PMC} \times 10^{20}$, spin g^{-1}	T_{on}^{ox}, °C	Cumene model		
							initial composition of reaction mixture	$(V_{in} - V_{fin}) \times 10^{-3}$, ml min^{-1}	$Q \times 10^{-3}$, mol
1	Cu8	Argon	0.76	78	14.90	188	Cu8 + IPB + AIBN	400, 390	0.141
2	Cu8	"	0.76	78	14.90	188	Cu8 + IPB	760, 750	0.178
3	Cu10	"	0.76	109	3.23	111	Cu10 + IPB + AIBN	1470, 1120	0.503
4	Cu10	"	0.76	109	3.23	111	Cu10 + IPB	1690, 1370	0.589
5	Cu11	Xenon	0.91	112	36.94	138	Cu11 + IPB	810, 560	0.259
6	Al60	Nitrogen	0.73	101	5.11	289	Al60 + IPB	128, 119	0.054
7	Al61	Argon	0.78	123	9.08	355	Al61 + IPB	136, 140	0.052
8	Al62	Xenon	0.74	239	10.10	400	Al61 + IPB	100, 95	0.052
9	Al63	"	1.00	138	2.96	293	Al63 + IPB	105, 101	0.050
10	Al64	Argon	0.86	145	18.51	341	Al64 + IPB	70, 78	0.027
11	Al65	Nitrogen	1.00	93	3.85	350	Al65 + IPB	88, 78	0.032
12	Al66	Argon	0.96	–	0	293	Al66 + IPB	0, 6	0.004
13	Pt3	Xenon	0.82	111	40.10	–	Pt3 + IPB	568, 568	0.279
14	Pt5	"	1.12	30	316.21	–	Pt5 + IPB	630, 625	0.320
15	Cu7	Nitrogen	0.89	86	5.22	125	Cu7 + IPB	1220, 5	0.212
16	Cu9	Argon	0.92	107	29.71	148	Cu9 + IPB	376, 141	0.134
17	Cu12	"	0.78	116	7.68	159	Cu12 + IPB	730, 5	0.123
18	Co2	Nitrogen	–	–	57.1×10^4	155	Co2 + IPB	1740, 0	0.110
19	Co3	"	–	–	65.8×10^4	–	Co3 + IPB	2340, 3	0.149
20	Co4	"	–	–	68.8×10^4	140	Co4 + IPB	2340,3	0.192

* D_S is the surface-average particle diameter; $D_S = 6/\rho S$, where ρ is particle density (g cm^{-3}), S is the specific surface area (m^2 g^{-1}) determined by BET; C_{PMC} is the concentration of paramagnetic centers; T_{on}^{ox} is the temperature of oxidation onset, as indicated by DTA; V_{in}, V_{fin} are the gas absorption rates at the initial and final instants of observation; Q is the amount of O_2 taken up in 10 min; and AIBN is azobis(isobutyronitrile).

sets 2 and 3, plasmochemical and aerosol nanopowders of Cu, and PMS-1 powder show no signals. At the same time, nearly all samples of set 1 (nanopowders of copper, aluminum, cobalt, and platinum) are characterized by high intensity of absorption of microwave radiation. Spectra recorded in the form of a first derivative of the absorption intensity function have the form of irregular, broad, asymmetric lines. Typical ESR spectra are shown in Fig. 1. Their line shape corresponds to the Dyson line, which reflects the presence of conduction electrons [16, 17]. The spacing between the absorption peaks H_{max} is 36–37 mT, and the g factor values vary within the range 1.9–2.2. At liquid nitrogen temperature the spectra are even more broadened and, with temperature increasing from 20 to 100°C, the signal becomes narrower without change in the total area under the spectral curve. Placing solid samples in a high vacuum (with residual pressure of 10^{-4} torr) has no effect on this characteristic, either. The concentration range of paramagnetic centers in nanopowders is (spin g^{-1}) $(3–37) \times 10^{20}$ for copper powders, $(3–18) \times 10^{20}$ for aluminum, $(40–316) \times 10^{20}$ for platinum, and $(57–68) \times 10^{24}$ for cobalt. In aluminum powders Al60–Al65, the concentration of paramagnetic centers decreases by a factor of 2 and more already after 3 months, whereas the paramagnetism of copper nanopowders Cu7–Cu12 remains unchanged. In this case, nanopowders obtained in argon medium degrade at much lower rate, compared with powders obtained in nitrogen.

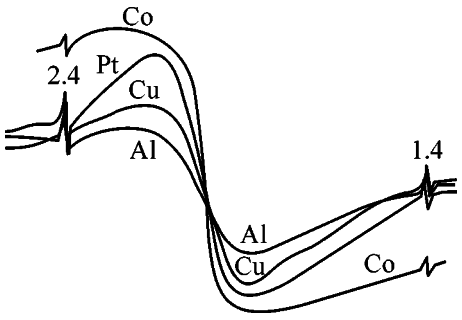

Fig. 1. ESR spectra of Cu, Al, Pt, and Co nanopowders. 2.4 and 1.4 are the g factors of ruby reference.

Previously, the relationship between the energy introduced and dispersity of explosion products has been repeatedly demonstrated. All other conditions being the same, raising the amount of introduced energy leads to higher dispersity of the obtained powders [1]. Comparison of the data presented in the table for Cu8 and Cu10; Cu 11, Cu7, and Cu9; Al60 and Al61; and Al63 and Al66, not only confirms the aforesaid, but also reveals a difference between the initial temperatures of nanopowder oxidation, as indicated by DTA, and between the paramagnetic center concentrations.

ESR analysis characterizes the overall concentration of paramagnetic centers in a sample. Meanwhile, the fundamental questions are those concerning the nature of the powder surface and distribution of paramagnetic centers over this surface and throughout the bulk.

It is known that heterogeneous chemical reactions are highly sensitive to the state of the surface at which they occur. In recent 15 years, an efficient method has been successfully used for studying the surface of solid substances. This method is based on comparison of a thoroughly studied kinetics of the model reaction of IPB oxidation in the case of its homogeneous initiation, on the one hand, and in the presence of heterogeneous surfaces, on the other [18, 19]. It has been established previously in numerous experimental studies that the rate of liquid-phase oxidation of hydrocarbons changes upon introduction into solution of various kinds of solid surfaces (oxides, metals, metal salts, minerals). This effect has been attributed to catalytic and initiating action of the additives. It has been shown that cobalt and manganese oxides affect the stages of not only chain initiation, but also chain termination, whereas metallic copper (micrometer size powders, shavings) affects only the reaction initiation, followed by transfer of radicals into the liquid bulk [18]. As applied to NPEEs, the method of model reactions of liquid-phase oxidation has not been tested as yet.

In this work, we used as a model the low-temperature (60°C) liquid-phase oxidation of IPB initiated by free radicals formed in AIBN decomposition [19]. Nanopowders of Al, Cu, Pt, and Co were used in this reaction together with, and instead of the conventional initiating agent (AIBN).

A 1.5–4.0-fold decrease in paramagnetic center concentration was observed for all of the paramagnetic powders after their being placed in IPB for 10 min and then isolated. For example, the concentration of paramagnetic centers in the system Cu10 + IPB is

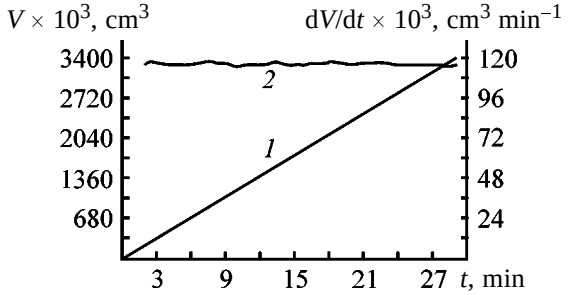

Fig. 2. Kinetics of oxygen uptake in the model reaction of IPB oxidation with oxygen in the presence of AIBN homogeneous initiator. (V) Oxygen uptake, (dV/dt) rate of gas absorption, and (t) time; the same for Figs. 3–5. (*1*) Kinetic curve of oxygen uptake and (*2*) variation of the rate of gas absorption with time; the same for Figs. 3–5.

64×10^{20} spin g^{-1} (see table), being by a factor of 20 higher than that in the initial Cu10 nanopowder, which indicates the development of free-radical processes in this system. For Cu10 isolated from the reaction mixture after being brought in contact with IPB, the corresponding concentration decreases to 1.5×10^{20} spin g^{-1}, i.e., falls by a factor of 2 relative to the initial value. The results obtained confirm the assumption that active centers on the surface of NPEE of set 1, which can initiate the radical reaction of IPB oxidation, have paramagnetic nature. The nature of the surface was studied in more detail by carrying out appropriate kinetic measurements.

The rate of free radical formation in the model reaction of IPB oxidation is commonly found in two ways: from the rate of oxygen uptake and from the rate of inhibitor consumption [19]. In this study, the first method was used on a gasometric installation described in [20].

Figure 2 presents the kinetic curve of oxygen uptake and its derivative, corresponding to the rate of IPB oxidation in the presence of a standard initiating agent (AIBN, 117×10^{-3} cm^3 min^{-1}). The process of gas uptake by all the samples in the initial stage of the reaction was characterized by different observed rate functions and amounts of oxygen taken up. It follows from the table that powders Al61–Al65 of set 1, taken together with IPB but without initiating agent, ensure oxygen uptake on a level not exceeding the standard values. Powder Al66 is nonparamagnetic and remained inert under the conditions of the model reaction. For other nanopowders of copper, platinum, and cobalt, the rate of oxygen uptake by IPB much exceeds the standard value, both with and without initiating agent, which is reflected in Figs. 3 and 4 for the example of Cu10. No definite relationship between the concentration of paramagnetic centers, process

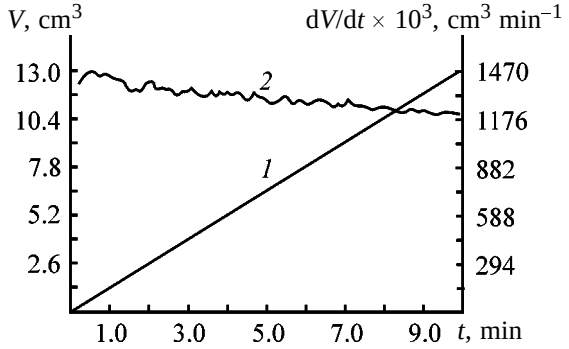

Fig. 3. Kinetics of oxygen uptake by dispersion of Cu10 in IPB in the presence of AIBN initiating agent.

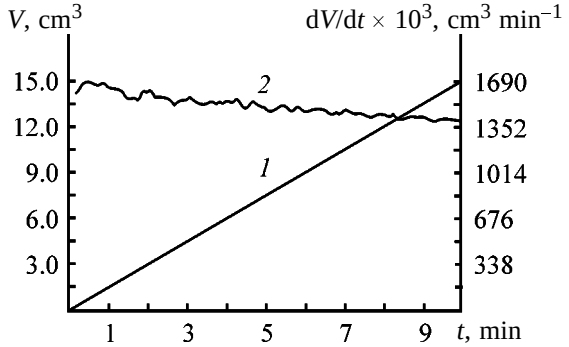

Fig. 4. Kinetics of oxygen uptake by dispersion of Cu10 in IPB. The curve shape is typical of nanopowder nos. 1–14.

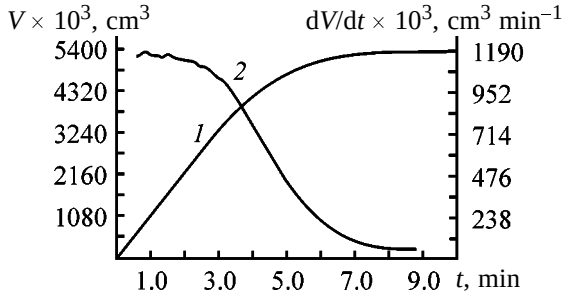

Fig. 5. Typical shape of curves characterizing oxygen uptake by IPB in the presence of nanopowder nos. 15–20.

rate, and amount of absorbed oxygen is observed. For example, nanopowder of platinum (see table, sample no. 13) with a high concentration of paramagnetic centers (40×10^{20} spin g^{-1}) is characterized by a medium, and constant in time, rate of 568×10^{-3} cm^3 min^{-1}. The oxygen uptake is the most intensive on a cobalt powder. These results suggest different concentrations of reactive centers on the particle surface.

According to shapes of the kinetic curves of oxygen uptake by the systems IPB + AIBN + nanopowder and IPB + nanopowder, nanopowders can be classed into two groups. For the first group, a hyperbolic dependence is observed (Fig. 5, curve *1*), adequately reflecting the fast saturation of the system with oxygen (see table, sample nos. 15–20). The second is characterized by gas absorption linearly growing at a constant, comparatively high rate (see table, sample nos. 1–14; typical kinetic curve is shown in Fig. 4, curve *1*). For powders of the first group, the active surface centers are saturated, on the average, in the course of 10 min. Therefore, for all samples the rates and amounts of absorbed oxygen in the table refer just to this time interval. Cu10 and Cu12 samples obtained under similar conditions have different temperatures of oxidation onset (111 and 159°C, respectively). In accordance with the shapes of the kinetic curve, they also belong to different groups. For Cu8, Cu10, and Cu11 powders, the rate of oxygen uptake by the nanopowder dispersion in IPB is the higher, the lower the onset temperature of sample oxidation in air, according to DTA. An analysis of the reaction medium of nanopowders with hyperbolic kinetics of oxygen uptake revealed no products of IPB oxidation. In parallel, oxygen uptake by a suspension of cobalt nanopowder was recorded, even if at low rate [$(28–32) \times 10^{-3}$ cm^3 min^{-1}], in heptane and isooctane, i.e., in a liquid medium stable against oxidation. This possibly means that there is no initiation of IPB oxidation with radicals passing into the bulk of the liquid, during the time interval monitored, and threshold sorption processes occur. Switching the reaction mixture for several minutes into the mode of oxygen bubbling through nanopowder dispersions in IPB results in that the system under study again gains the capacity for short-time gas absorption. Such a cyclic recurrence was verified for all powders of the second group in five cycles. It may be assumed that, under the given particular conditions, activity is exhibited by oxygen-containing surface paramagnetic centers. For nanopowders belonging to the group with hyperbolic kinetics of oxygen uptake, there appears a possibility of separately determining paramagnetic centers on the surface and in the bulk of powder nanoparticles from the difference between the paramagnetic center concentrations in a nanopowder before and after its being brought in contact with IPB and oxygen. In addition, it was found that, upon preliminary evacuation of air, the kinetic behavior of the given powders in the system nanopowder + IPB under conditions of high vacuum (residual pressure 10^{-4} torr) becomes similar to that of powders of the first group, and similar oxidation products are formed.

According to liquid chromatography, the products of IPB oxidation with oxygen in the presence of NPEEs of copper, cobalt, and platinum are composed of a (1–2) : 20 mixture of IPB hydroperoxide and dimethylphenylcarbinol in amount corresponding to 3% IPB conversion. Contrary to published data [18]

concerning IPB oxidation in the presence of micrometer-size copper powders, nanopowders of sets 1 and 3, and aerosol and plasmochemical powders, including coarsely dispersed PMS-1 powder, were inert in the model reaction. This may indicate a different state of their surface.

EXPERIMENTAL

Nanosize powders of copper, platinum, cobalt, and aluminum, produced by electric explosion, were supplied by the Institute of High-Current Electronics, Siberian Division, Russian Academy of Sciences (Tomsk). For the example of set 1, Valevich and Sedoi [8] developed the conditions for uniform volume heating at current densities in the range 5×10^6–5×10^8 A cm^{-2}. This ensured production of powders with increased dispersity, narrow size distribution of particles, and small mass of the coarse fraction (2–3%). Copper nanopowders produced by electric explosion (set 2, explosion in argon, ω/ω_s = 1.2–1.4) were obtained at the Research Institute of High Voltages and at the Russian Center of Science and Engineering, Siberian Division, Russian Academy of Sciences (Tomsk; set 3, argon, ω/ω_s = 1.1–1.5) [9, 10]. The aerosol powder of copper (surface-average diameter of particles of a freshly produced nanopowder from 4 to 6 nm) was supplied by the Krasnaya Zvezda State Enterprise (Moscow), and the plasmochemical nanopowder of copper (200 nm), by the Siberian Chemical Combine (Seversk). An industrial copper powder with micrometer grain size, PMS-1, was obtained by atomization of a melt with subsequent fractionation of particles (40 μm). All powders produced by electric explosion were obtained on installations with electric circuit based on capacitor discharge. A wire 0.3 mm in diameter was fed into the working chamber under lowered pressure of the gas medium (xenon, argon, helium, nitrogen). After a certain amount of powder was produced, the settled powder was collected and studied.

Differential-thermal analysis was made on a Q-1500D derivatograph (Hungary) by the standard procedure (heating rate 10 deg min^{-1}, weighed portion 1×10^{-4} kg). ESR spectra were recorded on a Radiopan SE/X 2544 spectrometer (Poland, Q range) at liquid nitrogen temperature and in the range 20–100°C. The recording was done at a frequency of 9.3 GHz with scanning in the range 0–700 mT in a cylindrical quartz ampule 2 mm in diameter at modulation amplitude of 0.25 mT, scanning time of 16 min, and time constant of 0.3 s. The device was equipped with an attachment for varying the ampule and sample temperature directly in the resonator. The concentration of paramagnetic centers was found by comparing the intensities of ESR signals from the powders under study (area under the curves of microwave absorption derivatives) with that from a reference sample of ruby [17, 21]. The table lists average values of the paramagnetic center concentrations for each sample, calculated from no less than five measurements. The reproducibility was no worse than 5%.

The model reaction of oxidation was studied on a gasometric setup [20] at 60°C in a duck-shaped reactor under standard conditions: 10 cm^3 IPB + 11.2 mg initiating agent [azobis(isobutyronitrile), AIBN] + nanopowder. The initiating agent AIBN was preliminarily purified by recrystallization from ethanol, benzene, and acetone. The kinetic features of gas absorption processes were recorded for various samples and compared for the initial 10-min period of the reaction. The reaction mixture was analyzed on an ELWRO liquid chromatograph (PEG-25M column) and MK-40 IR spectrometer.

CONCLUSIONS

(1) Under certain conditions of electric explosion of such conductors as copper, aluminum, platinum, and cobalt, the forming nanopowders may acquire paramagnetic properties. Paramagnetic centers are distributed over the surface and throughout the volume of nanoparticles, with the concentration of these centers on the surface of copper, cobalt, and platinum nanopowders being higher than in the case of aluminum. The ability of nanopowders to retain paramagnetism in the course of time depends on the chemical composition of the gas medium in which the explosion occurs, with nanopowders obtained in argon being more stable.

(2) The method of a model reaction of isopropylbenzene oxidation reveals surface paramagnetic centers in nanopowders produced by electric explosion and distinguishes even powders of the same type, obtained under similar conditions. The lower the temperature of oxidation onset, the higher the rate of oxygen uptake. In accordance with the nature of gas uptake, powders are divided into two groups. The oxidation reaction occurs only in powders with linear time dependence of the intensity of oxygen uptake. The surfaces of copper and cobalt nanopowders, originally not initiating the model reaction, can be activated by vacuum treatment.

ACKNOWLEDGMENTS

The study was supported by the Integration project no. 20 of the Siberian Division of the Russian Academy of Sciences.

REFERENCES

1. Gusev, A.I., *Nanokristallicheskie materialy: metody polucheniya i svoistva* (Nanocrystalline Materials: Preparation Techniques and Properties), Yekaterinburg: Ural. Otd. Ross. Akad. Nauk, 1998.
2. Il'in, A.P. and Proskurovskaya, L.T., F*iz. Goren. Vzryva*, 1990, vol. 26, no. 2, pp. 71–72.
3. Il'in, A.P., Trushina, L.F., and Rodkevich, N.G., *Fiz. Khim. Obrab. Mater.*, 1995, no. 3, pp. 122–125.
4. RF Patent 2 103 995.
5. Proskurovskaya, L.T., Physicochemical Properties of Ultradisperse Aluminum Powders Produced by Electric Explosion, *Cand. Sci. Dissertation*, Tomsk, 1992.
6. Burtsev, V.A., Kalinin, N.V., and Luchinskii, A.V., *Elektricheskii vzryv provodnikov i ego primenenie v elektrofizicheskikh ustanovkakh* (Electric Explosion of Conductors and Its Use in Electrical Installations), Moscow: Energoizdat, 1990.
7. Lyashko, A.P., Specific Features of Interaction with Water and Structure of Submicrometer Al Powders, *Cand. Sci. Dissertation*, Tomsk, 1988.
8. Valevich, V.V. and Sedoi, V.S., *Izv. Vyssh. Uchebn. Zaved., Fiz.*, 1998, no. 6, pp. 70–74.
9. Ushakov, V.Ya., Ilyin, A.P., Nazarenko, O.P., *et al.*, *Proc. First Korea–Russia Int. Symp. on Science and Technology (CORUS'1997)*, Ulsan, Sept. 1997, pp. 167–171.
10. Lerner, M.I., Control over Formation of Highly Dispersed Particles under Conditions of Electric Explosion of Conductors, *Cand. Sci. Dissertation*, Tomsk, 1988.
11. Morozov, Yu.G. and Petinov, V.I., *Ul'tradispersnye chastitsy i ikh ansambli* (Ultradisperse Particles and Ensembles of These), Kiev: Naukova Dumka, 1982, pp. 122–128.
12. Chuistov, K.V. and Perekos, A.E., *Metallofiz. Noveish. Tekhnol.*, 1997, vol. 19, no. 1, pp. 36–53.
13. Vasil'ev, A.A., Lisetskii, V.N., and Kovalev, D.V., *Materialy nauchno-prakticheskoi konferentsii "Metody issledovaniya v khimii i khimicheskoi tekhnologii"* (Proc. Scientific and Practical Conf. "Methods of Investigation in Chemistry and Chemical Technology"), Tomsk, May 20–22, 1986, pp. 55–61.
14. Ushakov, V.Ya., Ilyin, A.P., Tihonov, D.V., and Yablunovscky, T.V., *Proc. CORUS 2000*, Ulsan, June 2000, part 3, pp. 277–279.
15. Kul'kov, S.N., Sedoi, V.S., Sirotkina, E.E., *et al.*, *Integratsionnye programmy fundamental'nykh issledovanii* (Integration Programs of Basic Research), Novosibirsk: Sib. Otd. Ross. Akad. Nauk, 1998, pp. 239–254.
16. Poole, Ch.P., *Electron Spin Resonance. A Comprehensive Treatise on Experimental Techniques*, New York: Interscience, 1967.
17. Blyumenfel'd, L.A., Voevodskii, V.V., and Semenov, A.G., *Primenenie elektronnogo paramagnitnogo rezonansa v khimii* (Use of Electron Spin Resonance in Chemistry), Novosibirsk: Sib. Otd. Akad. Nauk SSSR, 1962.
18. Gorokhovatskii, Ya.B. and Evmenenko, N.P., *Teoriya i praktika zhidkofaznogo okisleniya* (Theory and Practice of Liquid-Phase Oxidation), Moscow: Nauka, 1974, pp. 209–213.
19. Emanuel', N.M. and Gal, D., *Okislenie etilbenzola (model'naya reaktsiya)* [Oxidation of Ethylbenzene (Model Reaction)], Moscow: Nauka, 1984.
20. USSR Inventor's Certificate no. 723 445.
21. Unger, F.G. and Andreeva, L.N., *Fundamental'nye aspekty khimii nefti. Priroda smol i asfal'tenov* (Fundamental Aspects of Petrochemistry, Nature of Resins and Asphaltenes), Novosibirsk: Nauka, 1995.

Russian Journal of Applied Chemistry, Vol. 75, No. 3, 2002, pp. 351–356. Translated from Zhurnal Prikladnoi Khimii, Vol. 75, No. 3, 2002, pp. 365–370.
Original Russian Text Copyright © 2002 by Vlasov, Murzina, Legin, Ermolenko, Schubert, Schöning, Lut.

INORGANIC SYNTHESIS AND INDUSTRIAL INORGANIC CHEMISTRY

Solid-State Thin-Film Sensors Based on Chalcogenide Materials Obtained by Planar Technology and Pulsed Laser Deposition

Yu. G. Vlasov, Yu. G. Murzina, A. V. Legin, Yu. E. Ermolenko, J. Schubert, M. J. Schöning, and H. Lut

St. Petersburg State University, St. Petersburg, Russia
Research Center, Jülich, Germany
University of Applied Sciences of Aachen, Jülich, Germany

Received July 13, 2001

Abstract—Methods of silicon planar technology and pulsed laser deposition were applied to fabricate fully solid-state chemical sensors for determining ions of copper, lead, cadmium, thallium, and also sulfide and chloride ions on the basis of thin chalcogenide films as ion-sensitive membranes.

Development and study of new types of chemical sensors is presently associated with the achievements of new technologies and, in particular, with advances in the technology of integrated microcircuits. In developing microsensors and single-chip sensor systems, a problem arises of obtaining thin-film membranes by techniques compatible with the technology of microelectronics. It is rather difficult to obtain films of required composition by using the previously known methods of CVD, vacuum evaporation, or irradiation-induced deposition. At the same time, physical and electrochemical characteristics of films, affecting the chemical sensitivity of these films as membranes in chemical sensors, are composition-dependent.

Recently, a new method has appeared, pulsed laser deposition (PLD) [1, 2]. This method has been employed to deposit films of superconducting and magnetic materials. The main distinction of the technique is that the sample stoichiometry is preserved even in the case of multicomponent materials. Previously, the PLD method has been specially developed for obtaining thin films of materials that can be used to fabricate membranes of chemical sensors based on silicon structures [3–5].

The aim of this study was to prepare by PLD onto silicon new thin-film sensors for determining ions of copper, lead, cadmium, and thallium, and also sulfide and chloride ions. With positive results obtained, these sensors could be used in developing multisensor systems of the "electronic tongue" type on a single chip [6, 7].

EXPERIMENTAL

The PLD installation shown schematically in Fig. 1 included a Lambda LPX305 KrF excimer laser with pulse width and energy of, respectively, 20 ns and 1 J pulse^{-1} and wavelength λ = 248 nm. Deposition cycles were performed at room temperature and partial pressure of N_2 of about 0.2 mbar to prevent oxidation of the forming thin films. The process duration was varied between 300 and 600 s. At energy density of 5 J cm^{-2} and pulse repetition frequency of 10 Hz, the thickness of the obtained films varied within 380–1500 nm.

In the installation in question, a focused beam of a KrF excimer laser is used as external energy source to evaporate the material from the target surface and deposit it in the form of a thin film onto a substrate, The interaction between the laser beam and the target,

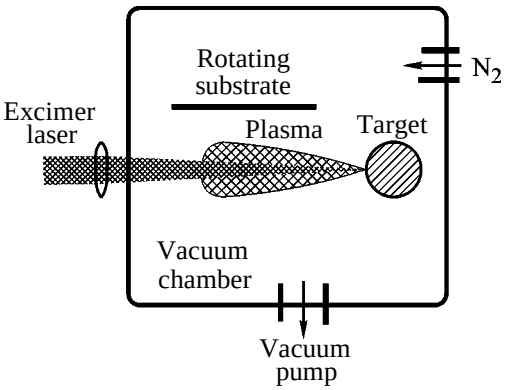

Fig. 1. Schematic of PLD installation for preparing thin-film membranes for chemical sensors.

1070-4272/02/7503-0351$27.00 © 2002 MAIK "Nauka/Interperiodica"

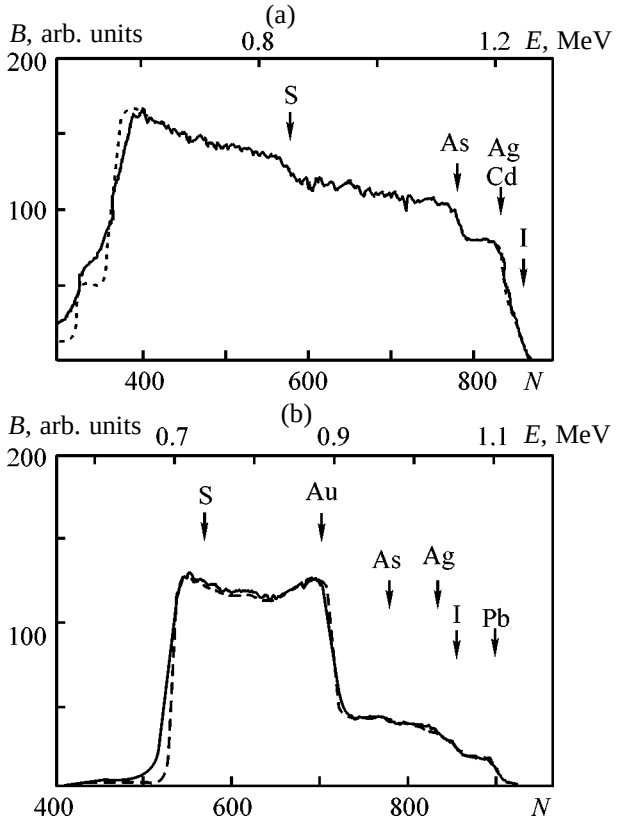

Fig. 2. RBS data for (a) Cd–Ag–I–As–S and (b) Pb–Ag–As–I–S films deposited by PLD onto a gold layer 300 nm thick. (*B*) Normalized output signal, (*N*) channel number, and (*E*) energy. Film thickness (nm): (a) 870 and (b) 300. Solid line: measured data; dashed line: result of their processing by RUMP software [11]; arrows show the corresponding elements.

with duration estimated at several tenths of a second, is divided schematically into four stages [1]: (I) optical irradiation of the target with a short pulse leads to heating of the target surface; (II) the heating is accompanied by melting of the target surface; (III) then substance evaporates from the target surface and multiphoton ionization leads to plasma formation; and (IV) the plasma absorbs laser radiation and controls its further interaction with the surface.

The composition, structure, and thickness of the thin films obtained was studied by Rutherford backscattering spectroscopy (RBS) with the use of He^+ ions with initial energy E_0 = 1.4 MeV and by electron microscopy (JEOL FX4000).

Chalcogenide glasses and polycrystals were used as targets in PLD for fabrication of thin-film membranes of chemical sensors. The targets were 10–12 mm in diameter and 10–12 mm long.

Chalcogenide glasses in the systems Cu–Ag–As–Se–Te, Cd–Ag–As–I–S, Tl–Ag–As–I–S, Pb–Ag–As–I–S, Ag–I–As–S, Ag–I–As–Se, and Ag–As–Te–Se were synthesized from element substances of semiconductor purity in quartz ampules evacuated to residual pressure of 0.1–0.01 Pa in a furnace heated to 1000–1200 K for 5–10 h. Ampules with melt were quenched in air in the temperature range 400–600 K at average cooling rate of 4–6 deg s^{-1}. Ag_2S and AgCl–Ag_2S polycrystals were synthesized by, respectively, precipitation and coprecipitation. The obtained crystalline deposits were compacted under a pressure of 8–10 t cm^{-2}.

Wafers of single-crystal phosphorus-doped *n*-Si with ⟨100⟩ surface orientation, resistivity of 1000–5000 Ω cm, and thickness of 350 ± 40 μm were used as substrates for fabricating chemical sensors. The functional layers of the sensors were structured on the substrates and produced by means of thin-film technology [8]. Ti/Pt, Ti/Pt/Au, and Cr/Au metal contact layers were structured by means of photolithography [4, 5].

The substrates with contact layers were divided into separate elements, and thin-film chalcogenide membranes were prepared by PLD [3–5], using chalcogenide glasses and polycrystals as targets, as described above. The obtained sensors were assembled on printed-circuit boards with appropriate waterproofing.

The electrochemical behavior of the sensors was studied potentiometrically in an electrochemical cell with double liquid junction

Ag	AgCl	KCl (0.1 M)	KNO_3 (0.1 M)	Solution under study	Sensor

The electrode potential of the cell was measured with a V7-23 general-purpose digital voltmeter with accuracy of 0.1 mV. The solution pH was monitored using Ionomer I-130 device with ESL-43-07 glass indicator electrode, calibrated against standard buffer solutions, and silver chloride reference. All measurements were done at room temperature. The ionic strength of the solutions used was maintained constant with 0.1 M KNO_3. The sensor response was studied in solutions containing metal cations (Cd^{2+}, Cu^{2+}, Tl^+, Pb^{2+}, Fe^{3+}, Ni^{2+}, Zn^{2+}, Ca^{2+}, and Mg^{2+}) in the concentration range 10^{-7}–10^{-2} M. The selectivity coefficients were determined using the method of mixed solutions [9, 10].

The effect of the solution pH on the sensor response was studied in solutions with constant concentration of the potential-determining ion, with the pH

Table 1. Comparison of the component composition of PLD-deposited thin films, found by RBS spectroscopy, and that of the material of the corresponding bulk chalcogenide glass target

System	Content, at. %									Thickness, nm
	Ag	Pb	Cd	Tl	As	I	S	Se	Te	
1	20* 19.6	11.6 14	–	–	13.6 13	13.6 19.6	41 33.7	–	–	380
2	16.3 17.2	–	7.5 2.1	–	21.3 25.5	10 12.4	45 42.8	–	–	870
3	20.4 19.7	–	–	9.4 10.6	23 19.7	8.9 10.6	38.3 39.4	–	–	770
4	16.9 10.5	–	–	–	31.3 31.6	8.4 10.5	43.4 47.4	–	–	1020
5	10.5 13.6	–	–	–	31.6 31.8	10.5 9.1	–	47.4 45.5	–	1500
6	15 8.5	–	–	–	42.5 63.8	–	–	34 15	8.5 12.8	1500

* Numerator: RBS (thin film); demoninator: target.

varied by adding solutions of nitric acid and potassium hydroxide and the ionic strength of the working solutions maintained constant with a 2 M KNO_3 buffer solution. To monitor the solution pH in the process, the pH was simultaneously measured with a glass pH electrode preliminarily calibrated against standard buffer solutions. All the solutions were prepared using distilled water. The starting solutions of Cd^{2+}, Cu^{2+}, Tl^{+}, Pb^{2+}, Fe^{3+}, Ni^{2+}, Zn^{2+}, Ca^{2+}, and Mg^{2+} nitrates were prepared by dissolving weighed portions of the corresponding nitrates in distilled water acidified with nitric acid. The concentrations of the thus obtained solutions were found by complexometric titration with potentiometric indication of the end point [9]. Individual solutions of Cd^{2+}, Cu^{2+}, Tl^{+}, Pb^{2+}, Fe^{3+}, Ni^{2+}, Zn^{2+}, Ca^{2+}, and Mg^{2+} nitrates with concentrations in the range 10^{-5}–10^{-1} M were produced by tenfold dilution of the starting solutions. Solutions with lower concentrations (10^{-8}–10^{-5} M) were prepared immediately before the measurements in a Teflon cell by the addition method. Reagents of analytically pure grade were used in the study.

The correspondence between the chemical composition of multicomponent thin films deposited by PLD and that of the corresponding targets was checked by RBS spectroscopy. The results obtained are presented in Fig. 2 for films of Cd–Ag–I–As–S (Fig. 2a, 870 nm) and Pb–Ag–As–I–S (Fig. 2b, 300 nm) deposited onto a 300-nm-thick layer of gold by the PLD technique. The comparative data are given in Table 1. It can be seen that a strong deviation of the thin film composition from the composition of the corresponding bulk target was observed only for the Ag–As–Se–Te system. Thus, there is good correspondence between the component composition of multicomponent thin layers deposited by the PLD method and that of the targets used.

The structure and thickness of the obtained films were analyzed by electron microscopy. The study revealed the presence of crystalline nanophases (with size of about several micrometers), compared with the amorphous nature of chalcogenide glass targets. The film thickness was in the range from 380 to 1500 nm (Table 1).

In order to achieve a transition from the ionic (Ag^{+}) conductivity of the sensitive membrane to the electronic conductivity of a metallic contact and to obtain better adhesion of the thin chalcogenide film to the metallic contact layer, which improves the reproducibility and stability of the sensor response and prolongs its service life, various compositions of metallic contact layers were studied. The composition and thickness of the contact layers were as follows: Ti/Pt (25/175 nm), Ti/Pt/Au (30/50/200 and 30/50/300 nm),

Table 2. Electrochemical characteristics of thin-film sensors

Membrane	Detection limit, M	S, mV/pC	pH	$K_{sel} = K_{ij}$, $E = E_0 + (RT/zF)\ln(a_i + K_{ij}a_j)$
Cu–Ag–As–Se	1×10^{-7} Cu^{2+}	27–29	2–6	Ag^+, Hg^{2+} must be absent; Pb(II) 3×10^{-5}–8×10^{-5}; Cd(II) 2×10^{-5}; Zn(II) 2×10^{-6}; Ni(II) 8×10^{-6}; Co(II) 3×10^{-6}; Ca(II) 7×10^{-6}
Pb–Ag–As–I–S	1×10^{-7} Pb^{2+}	27–29	2–6	Ag^+, Hg^{2+} must be absent; Cd(II) 0.05; Zn(II) 2×10^{-5}; Ni(II) $<10^{-5}$; Co(II) 2×10^{-5}; Fe(II) 8×10^{-4}; Ca(II) 5×10^{-5}
Cd–Ag–As–I–S	4×10^{-7} Cd^{2+}	26–28	2–7	Ag^+, Hg^{2+}, Cu^{2+} must be absent; Pb(II) 32; Zn(II) 2×10^{-4}; Ni(II) 1×10^{-3}; Co(II) 1×10^{-3}; Fe(II) 2×10^{-3}; Ca(II) 3×10^{-5}
Tl–Ag–As–I–S	3×10^{-5} Tl^+	55–58	2–7	Ag^+, Hg^{2+} must be absent; Cu^{2+} 0.5–3; Zn(II) 1×10^{-4}; Pb(II), Cd(II), H^+ 1×10^{-2}; Ca(II), Mg(II) 2×10^{-3}
Ag_2S	4×10^{-7} S^{2-}	28–29	~13	–
Ag_2S–AgCl	1×10^{-5} Cl^-	56–57		I^- must be absent; Br^- ~300

and Cr/Au (25/175 nm). Measurements carried out in the course of 3 months demonstrated that sensors with Cr/Au contact layers are characterized by poorer stability and reproducibility.

(1) Cu sensor. A typical curve describing the dependence of the potential difference across the electrochemical cell, E, on the logarithm of the concentration of the potential-determining ion is presented in Fig. 3, curve *3*. It can be seen that the developed fully solid-state sensors sensitive to copper(II) ions (Cu–Ag–As–I–S system) are characterized by Nernst response in the concentration range 3×10^{-5}–1×10^{-1} M, with the slope of the electrode function equal to 27–29 mV/pCu, and a hyper-Nernst response of the sensor is observed in the range of more dilute solutions. This fact may be due to the influence of redox processes occurring at the membrane|solution interface in the case of a low concentration of the potential-determining ion, which was studied, in particular, for Cu ion-selective electrode with a bulk membrane based on a Te-containing chalcogenide glass [12, 13]. Owing to the strong influence of redox processes at low concentrations of the potential-determining ion, a mixed potential is formed at the membrane|solution interface. However, this behavior of the sensor is reproducible, which allows its use in dilute solutions, too. The detection limit of the sensor was 1×10^{-7} M. The main characteristics of the sensors developed, such as the composition of the thin-film membrane, detection limit, slope S of the electrode function, working pH range, and selectivity coefficients, are presented in Table 2.

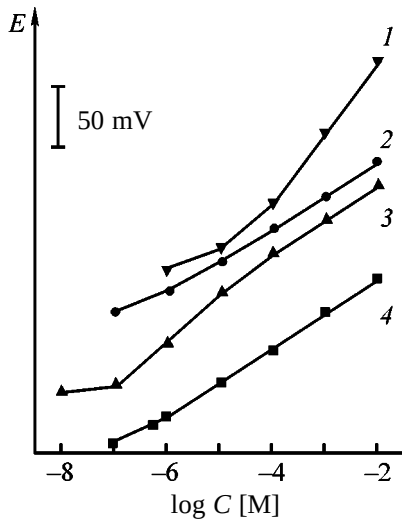

Fig. 3. Calibration curves of (*1*) Tl sensor (Tl–Ag–As–I–S) in $TlNO_3$ solution, (*2*) Cd sensor (Cd–Ag–As–I–S) in cadmium nitrate solution, (*3*) Cu sensor (Cu–Ag–As–Se–Te) in copper nitrate solution, and (*4*) Pb sensor (Pb–Ag–As–I–S) in lead nitrate solution. (*E*) Potential and (*C*) concentration of the potential-determining ion; the same for Fig. 5. (*1*) Solution pH 1.5 adjusted with nitric acid.

The response time of the sensors in stirred solutions does not exceed 30 s in the Cu(II) ion concentration range 1×10^{-4}–1×10^{-1} M, and is about 1–2 min in more dilute solutions.

The effect of the solution pH on the potential of Cu sensors is illustrated in Fig. 4a for two copper(II) ion concentrations, 10^{-4} and 10^{-3} M.

The characteristic rise in the electrode potential, observed with increasing acidity of solutions (pH ≤ 2),

is due to slow membrane dissolution. With the solution acidity lowered, the activity of copper(II) ions decreases because of the formation of hydroxo complexes by metal ions, which accounts for the decrease in the electrode potential and limited applicability of the sensor to direct potentiometric determinations in the alkaline range.

The extent of the hindering influence of foreign ions, i.e., ions different from that determining the potential for a given sensor, in multicomponent solutions on the sensor response was quantitatively evaluated by means of the selectivity coefficients $K_{ij/j}$. Table 2 lists the potentiometric selectivity coefficients found by the method of mixed solutions. As seen from the presented data, a 10^4–10^5 M excess of Pb^{2+} and Cd^{2+} ions and a 10^6–10^5 M excess of Zn^{2+}, Ni^{2+}, Co^{2+}, Ca^{2+}, or Mg^{2+} ions over the Cu^{2+} ion do not hinder analysis for the potential-determining ion.

Experiments concerned with the stability and reproducibility of the behavior exhibited by a Cu-selective sensor were carried out in the course of 8 months. During this period of time, the electrode function, selectivity coefficients, and linearity range remained unchanged, but a drift of the standard potential E_0 was observed, constituting ±5 mV for 10^{-6} M solutions and ±3 mV for 10^{-4} solutions of Cu^{2+} ions. This drift may be due to surface oxidation of the film membrane and gradual change in the surface composition.

(2) Tl, Cd, Pb, Cl, and S sensors. The calibration curves of Tl, Cd, Pb, Cl, and S sensors are presented in Fig. 3 (curves *1*, *2*, and *4*) and Fig. 5 (curves *1* and *2*), respectively. The slopes of the electrode functions and the detection limits were, e.g., 55–59 mV/pTl in the concentration range 5×10^{-5}–10^{-1} M, with detection limit of 3×10^{-5} M, for the Tl sensor (Tl–Ag–I–As–S); 26–28 mV/pCd in the concentration range 10^{-6}–10^{-1} M, with detection limit of 4×10^{-7} M, for the Cd sensor (Cd–Ag–I–As–S); and 56–57 mV/pCl in the concentration range 3×10^{-5}–10^{-1} M, with detection limit of 1×10^{-5} M, for the Cl sensor (Ag_2S–AgCl). All the data are summarized in Table 2.

Unfortunately, it was impossible to fabricate, with the use of chalcogenide glass targets, Ag-selective sensor with stable and reproducible potentiometric response. Possibly, this fact can be accounted for by the high rate of silver ion diffusion in the film, leading to a change in its properties.

The response time of the sensors in agitated solutions of a potential-determining ion does not exceed 30 s at high concentrations and is about 1–2 min in more dilute solutions. The potentiometric selectivity coefficients, and also the working pH ranges, were determined as in the case of the copper-selective electrode and are listed in Table 2. The developed sensors

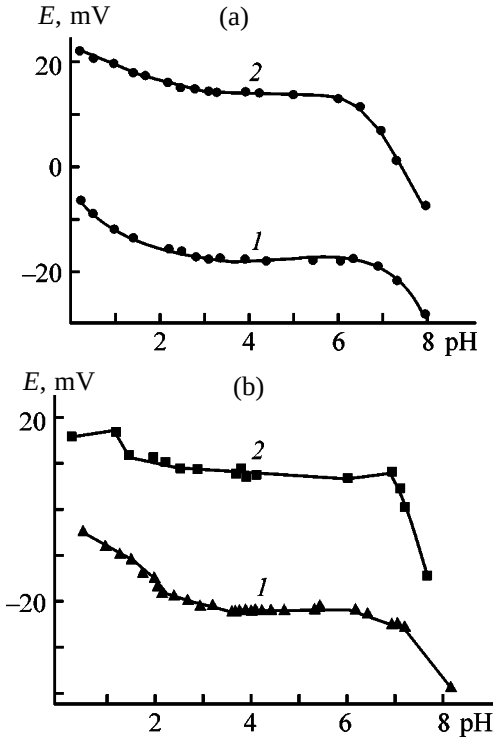

Fig. 4. Effect of solution pH on the response of (a) Cu sensor in solutions with constant concentration of copper(II) ions and (b) Pb sensor in solutions with constant concentration of lead(II) ions. (*E*) Potential. Ion concentration (M): (*1*) 1×10^{-4} and (*2*) 1×10^{-3}. The ionic strength of solution was supported with 2 M buffer solution of potassium nitrate.

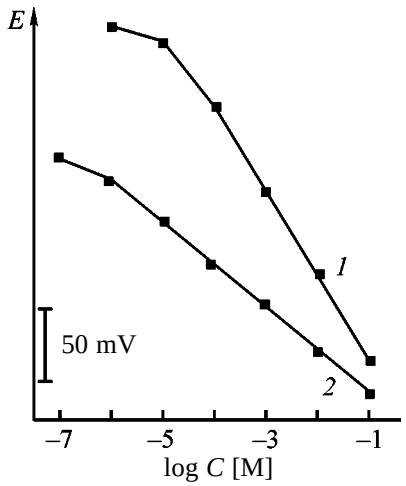

Fig. 5. Calibration curves of (*1*) Cl sensor (AgCl–Ag_2S) in potassium chloride solution and (*2*) S sensor (Ag_2S) in sodium sulfide solution. (*2*) Solution pH 13, adjusted with potassium hydroxide.

exhibit high selectivity with respect to the potential-determining ion in the presence of alkali and alkaline-earth metal ions, and also Ni(II) and Co(II).

The stability and reproducibility of the behavior exhibited by the sensors was inspected during 6 months, with no changes in sensor response parameters observed.

The advantage of the developed thin-film sensors over those with bulk membranes is that their technology is compatible with the technology of integrated microcircuits, which enables mass production of lower-cost and reliable sensors and analytical microsystems based on them. In addition, thin-film sensors can be used in small-size flow-through systems with small volume of solutions to be studied.

The results obtained indicate that the employed method may favor further miniaturization, and multisensor systems can be fabricated with sensor membranes having prescribed composition and, consequently, definite sensor characteristics, which is particularly important in creating such analyzers as "electronic tongue."

CONCLUSIONS

(1) Fully solid-phase chemical sensors were developed in the form of ion-sensitive membranes for determining ions of copper, lead, cadmium, and thallium, and also sulfide and chloride ions on the basis of chalcogenide thin films (300 to 1500 nm).

(2) The membranes were fabricated by the methods of silicon planar technology and pulsed laser deposition. The use of the latter allowed fabrication of membranes with prescribed composition and electrochemical characteristics.

ACKNOWLEDGMENTS

The study was supported by the Russian Foundation for Basic Research (project no. 99-03-32 483).

REFERENCES

1. Chrisey, D.B. and Hubler, G.H., *Pulsed Laser Deposition of Thin Films*, New York: Wiley, 1994.
2. Saenger, K.L., *Proc. Adv. Mater*., 1993, vol. 3, no. 1, pp. 1–24.
3. Schubert, J., Schöning, M.J., Schmidt, C., *et al.*, *Appl. Phys. A*, 1999, vol. 63, no. 4, pp. 803–806.
4. Mourzina, Yu.G., Schöning, M.J., Schubert, J., *et al.*, *Anal. Chim. Acta*, 2001, vol. 433, no. 1, pp. 103–110.
5. Mourzina, Yu.G., Schöning, M.J., Schubert, J., *et al.*, *Sensors Actuators*, 2000, vol. 71, no. 1–2, pp. 13–18.
6. Vlasov, Yu.G. and Legin, A.K., *Fresenius J. Anal. Chem*., 1998, vol. 361, no. 2, pp. 255–260.
7. Vlasov, Yu.G., Legin, A.V., Rudnitskaya, A.M., *et al.*, *Zh. Prikl. Khim*., 1996, vol. 69, no. 6, pp. 958–964.
8. Fatikow, S. and Rembold, U., *Microsystem Technology and Microrobotics*, Berlin: Springer, 1997.
9. Camman, K. and Galster, H., *Das Arbeit mit ionenselektiven Elektroden*, Berlin: Springer, 1996.
10. Guilbault, G.G., *IUPAC Inform. Bull.*, 1978, vol. 1, no. 1, p. 69.
11. Doolittle, L.R., *Nucl. Instr. Meth. B*, 1985, vol. 9, no. 2, pp. 344–348.
12. Vlasov, Yu.G., Bychkov, E.A., and Medvedev, A.M., *Anal. Chim. Acta*, 1986, vol. 185, no. 2, pp. 137–158.
13. Vlasov, Yu.G., Bychkov, E.A., and Seleznev, B., *Sensors Actuators B*, 1990, vol. 2, no. 1, pp. 23–31.

Russian Journal of Applied Chemistry, Vol. 75, No. 3, 2002, pp. 357–361. Translated from Zhurnal Prikladnoi Khimii, Vol. 75, No. 3, 2002, pp. 371–374.
Original Russian Text Copyright © 2002 by Gordeeva, Moroz, Rudina, Aristov.

INORGANIC SYNTHESIS AND INDUSTRIAL INORGANIC CHEMISTRY

Formation of Porous Vermiculite Structure in the Course of Swelling

L. G. Gordeeva, E. N. Moroz, N. A. Rudina, and Yu. I. Aristov

Boreskov Institute of Catalysis, Siberian Division, Russian Academy of Sciences, Novosibirsk, Russia

Received December 19, 2000; in final form, December 2001

Abstract—The effect of swelling conditions on the vermiculite pore structure was studied by X-ray diffraction analysis, mercury porosimetry, and scanning electron microscopy. The closed porosity of the samples was estimated. A possibility for purposeful modification of vermiculite pore structure by varying the swelling temperature and heating rate was evaluated.

Vermiculites belong to minerals of hydromica group, which are formed in the course of hydration and other secondary changes in some micas, particularly in phlogopite and biotite. Two elementary layers of silicon–oxygen tetrahedra, in which silicon is partially replaced by aluminum, and a layer of OH^- groups and magnesium ions form a strongly bound mica stack. A hydrate layer is located between the stacks. This layer consisits of hydrated ions of double-charged metals (mainly Mg^{2+} and Ca^{2+}) [1, 2]. On fast heating (calcination) vermiculites swell, with their volume increasing by a factor of 10–20 owing to vaporization of water from hydrate interstack layers. Swollen vermiculite is used as a construction material because it is a porous material with a low bulk density, high heat-insulating and sound-proof properties, and a high flame resistance. In this regard, a low bulk density of vermiculite is the most important feature; therefore, the influence of the calcination conditions on the bulk density was studied in detail [1, 3].

Recently vermiculite became more attractive for using also in other fields. In particular, it was shown [4] that a composite sorbent based on swollen vermiculite with calcium chloride contained in its pores is capable to absorb a large amount of water (more than 1 g g^{-1}) under static conditions. This property can be important for systems destined for air dehydration and heat accumulation. In view of the fact that the sorption properties of "salt in porous host matrix" composites substantially depend on the pore structure of a matrix [5], we studied in this work in detail the vermiculite pore structure and regular trends in its formation upon calcination.

EXPERIMENTAL

Vermiculites of Kovdor field (KVK-2, fraction 2 ± 0.71 mm) and of Kramer Progetha Basalt-Feuerfest GmbH (Rohvermikulite no. 1, KR-1) were used in the work. The chemical composition of the starting samples is shown in Table 1 [2].

Samples were swollen as follows. A preliminarily dried 0.5-g sample of the initial vermiculite was placed in a furnace heated to 200°C. The furnace temperature was monitored with a thermocouple placed directly over the sample. Then the temperature was linearly increased to 700–1200°C; the sample was kept at a required temperature for 30–60 s and

Table 1. Composition of KVK-2 and KR-1 vermiculites

Component	Composition, %	
	KVK-2	KR-1
SiO_2	34–36	35–41
Al_2O_3	9.1–9.9	6.0–9.5
Fe_2O_3	5.6–6.5	6.0–9.5
MgO	24.7–26.0	21.5–25.5
Tio_2	0.50–0.47	0.6–1.4
FeO	0.20–0.27	–
CaO	1.02–1.22	2.0–6.0
Mn	0.05–0.07	–
K_2O	0.70–0.87	3.0–6.0
Cr_2O_3	–	0.01–0.15
CO_2	–	0.6–2.5
F	–	0.2–0.8
Cl	–	0–0.5
P_2O_5	–	0.2–2.0

1070-4272/02/7503-0357$27.00 © 2002 MAIK "Nauka/Interperiodica"

Table 2. Phase composition of the initial and heated KVK-2 and KR-1 samples

Calcination conditions		Mg-vermiculite		Hydrophlogopite		Biotite *D*, nm
R, deg min^{-1}	*T*, °C	*c*, %	*D*, nm	*c*, %	*D*, nm	
KVK-2 sample						
Initial sample		100	120	100	70	–
60	700	27	40	60	70	–
85	700	31	45	75	70	–
165	700	42	69	93	70	–
1000	1000	14	28	55	70	–
KR-1 sample						
Initial sample		100	55	100	40	–
42	760	25	16	45	20	16
64	760	–	–	45	20	14
117	770	60	10	53	25	11
264	790	35	23	35	33	10
950	960	–	–	25	15	15
169	1220	–	–	–	–	45

* (*R*) Heating rate, (*c*) content relative to the initial sample, and (*D*) size of coherent scattering areas.

taken out of the furnace. The heating rate was 40–200 deg min^{-1}. The maximal heating rate was reached by placing a sample in a furnace preheated to 1000°C. In this case the heating was not linear, and the average heating rate reached 1000 deg min^{-1}.

The phase composition of the initial and swollen samples was studied by X-ray diffraction analysis (XRD) on an HZG-4C diffractometer with a graphite monochromator using CuK_α irradiation. The phase composition was determined using the JCPDS data base [6] and the data [7–9] for reference samples of separate minerals. The relative contents of phases were calculated from the integral intensities of their diffraction peaks, and the crystallite sizes, from the diffraction peak broadening. The pore size distribution was determined on a Micromeritics ASAP 1400 automatic volumetric installation from the nitrogen adsorption isotherms at 77 K and by mercury porosimetry on a Micromeritics Pore Size 9300 apparatus. Electron photomicrographs of samples were taken on an REM-100U scanning electron microscope with a digital image output at accelerating voltage of 30 kV. To create a surface conductive layer, a thin layer of gold was preliminarily deposited on the sample surfaces by thermal vacuum dispersion.

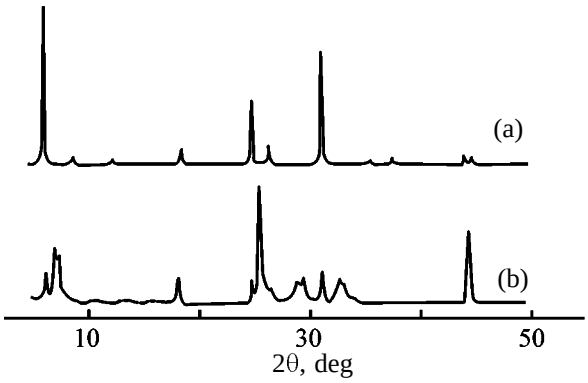

Fig. 1. Diffraction patterns of the initial (a) KVK-2 and (b) KR-1 vermiculites. (2θ) Bragg angle.

According to the XRD data, KVK-2 and KR-1 vermiculites significantly differ in the phase composition (Fig. 1). The former consists mainly of the Mg-vermiculite mineral with pronounced basal reflections (002, 004, 006, 008, 0010, 0012, and 0014). It contains hydrophlogopite as an impurity, which alternates with vermiculite layers with a probability $w \approx 0.06$. Hydrated mica (biotite or phlogopite) is the main phase of the KR-1 sample ($w \approx 0.46$), and Mg-vermiculite is its impurity phase. Thus, both samples contain both vermiculite and hydrated mica layers. However, these layers alternate more uniformly in the KR-1 sample. The difference in the phase composition of the initial samples determines their distinctions in the swelling process. The calcination of the KVK-2 sample at 700°C results in disintegration of Mg-vermiculite (Table 2). The sizes of hydrophlogopite crystallites remain unchanged in the course of the heat treatment, because low-hydrated hydro-

phlogopite undergoes only insignificant changes, which do not lead to its disintegration. Heating of the KR-1 sample to 700°C results in the disintegration of both the Mg-vermiculite (Table 2) and hydrobiotite (hydrophlogopite) phases. The biotite phase appears in the course of the heat treatment. The amounts of the crystallite phases decrease in both samples. The interplanar spacings remain unchanged, because the dehydration at 700°C is reversible [10]. Aluminosilicate layers are destroyed on heating above 1200°C, and the samples become X-ray amorphous [10].

The electron-microscopic patterns of the initial samples are similar (Fig. 2). The samples have a pronounced layered structure. They consist of parallel plates 5–20 μm thick, which are, as it will be clear later, secondary formations. These plates are separated by 0.5–10 μm thick cracks.

On heating, the samples are delaminated under the action of vapor formed in vermiculite hydrate layers (Figs. 3, 4). In this case, two parallel processes occur: (*1*) broadening of the cracks separating secondary plates (Figs. 3a, 3b) and (2) delamination of secondary plates into thinner (primary) layers with a thickness of 0.1–3 μm (Fig. 3b). On heating with a rate less than 200 deg min^{-1} the resulting vapor seems to escape mainly through cracks already available in the initial samples, which leads to the separation of secondary plates. Broadening of the plates at the expense of their delamination into primary layers occurs to a small extent (to 10–50 μm) (Fig. 3c). The structures of swollen vermiculites KVK-2 and KR-1 somewhat differ: secondary plates in KR-1 are delaminated less intensively (especially on edges), and consequently they are of more compact structure (Figs. 3b, 3c).

An increase in the vermiculite heating rate results in more intense delamination of secondary plates into primary layers, and their structure becomes looser (Fig. 4a). Samples obtained by fast heating consist of thin layers with sizes of 0.1–3 μm, which are separated by pores. Some plates take the form of pillows inflated from the inside and linked along the sample perimeter to form closed porosity (Fig. 4b). Samples of both vermiculites, owing to heterogeneity of their structures, have both "cleaved" and "inflated" parts. However, the formation of pillows is more typical for KVK-2 vermiculite. Data on the specific volume of pores and bulk weight of the samples allow us to estimate the volume of closed pores. The bulk weight (ρ_b) of a sample is expressed as the quotient:

$$\rho_b = m/(V_{op} + V_{cl} + V_s + V_t),$$

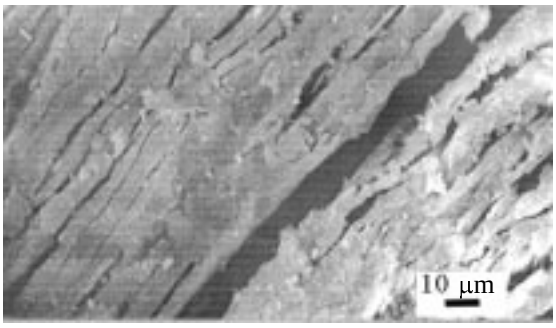

Fig. 2. Electron photomicrographs of the KVK-2 initial sample.

(a)

(b)

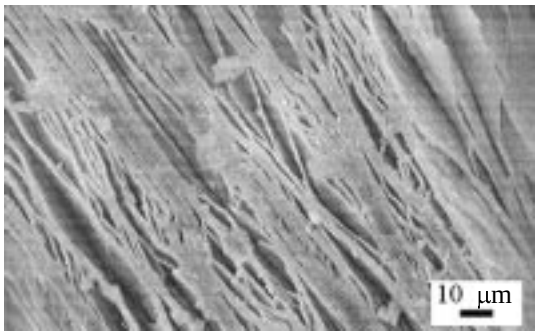

(c)

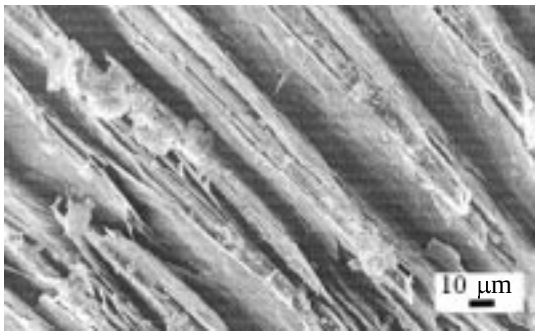

Fig. 3. Samples of (a, b) KVK-2 and (c) KR-1 swollen by heating to 700°C at a rate of 60 deg min^{-1}.

(a)

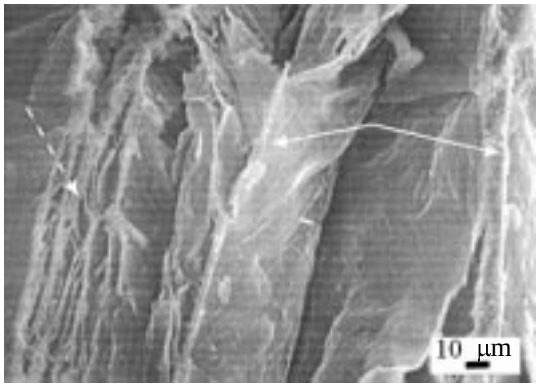

(b)

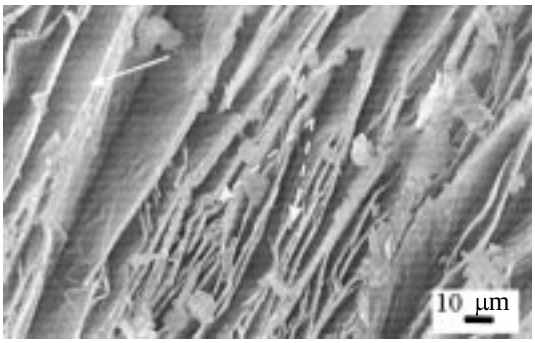

Fig. 4. Samples of (a) KVK-2 and (b) KR-1 swollen by heating to 1000°C at a rate of 1000 deg min^{-1}. Solid arrows indicate areas of closed pores or pillows, and dashed arrows show areas with open pores.

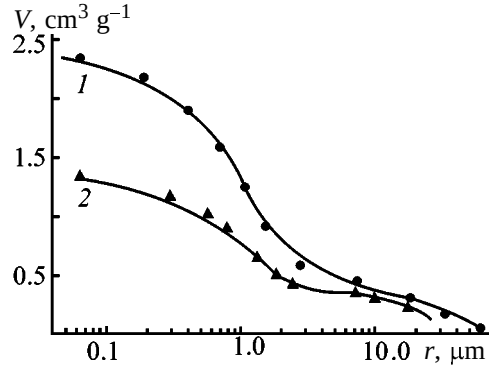

Fig. 5. Influence of the rate of heating to 1000°C on the pore structure of KR-1 vermiculite. (*V*) Pore volume and (*r*) pore radius. Heating rate (deg min^{-1}): (*1*) 1000 and (*2*) 38.

where m is the sample weight (g), V_{op} is the volume of open pores, V_{cl} is the volume of closed pores, V_s is the volume of intergranular space in a sample, $V_t = 1/\rho_t$ is the volume of the solid phase, and ρ_t is the true sample density.

The porosity ε of a layer of granules of different shapes and of the size varying in a wide range is known to be 0.35–0.45 [11]. Taking into account the fact that KVK-2 and KR1 vermiculites swollen by industrial technique have ρ_b of 0.12 and 0.11 g cm^{-3}, V_{op} of 2.6 and 3.5 cm^3 g^{-1}, respectively, and ρ_t of 2.6 g cm^{-3}, we find that the closed pore volume is in the range of 1.5–2.5 for KVK-2 and 0.8–1.8 cm^3 g^{-1} for KR-1. Thus, vermiculite swelling in fact results in formation of a large number of closed pores in addition to open pores, this process occurring to a greater extent in KVK-2 vermiculite.

The volumes of mesopores in both the initial and swollen samples are very small (0.036 and 0.066 cm^3 g^{-1}, respectively). In the course of swelling, numerous macropores with a broad size distribution are formed (Fig. 5). There are macropores of two predominant sizes: pores formed between primary layers, which seem to lie in the range 0.1–1 μm, and pores separating secondary plates from each other, of size in the range 5–50 μm. The specific pore volume increases with increasing heating rate. The volume of large pores (between plates) changes only slightly. The total pore volume increases mainly at the expense of relatively small pores separating layers inside the plates, which is in good agreement with the electron microscopy data. The increase in the calcination temperature from 700 to 1200°C results in a certain decrease in the pore volume (Fig. 5), which seems to be attributable to partial sample sintering. The maximal specific pore volume (2.5 cm^3 g^{-1}) is attained upon heating to 1000°C at a rate of 1000 deg min^{-1}.

CONCLUSION

Swollen KVK-2 and KR-1 vermiculites are characterized by the existence of closed and open pores. Open pores are characterized by a broad size distribution with two predominating pore sizes in the ranges 0.1–1 and 5–50 μm. The structure of open pores depends on the swelling conditions. An increase in the heating rate leads to more uniform swelling and favors the growth of relatively small pores, with the volume of large pores being preserved. The increase in the calcination temperature from 700 to 1200°C results in a decrease in the pore volume. Thus, the pore structure of the resulting samples can be purposefully modified by variation of the vermiculite calcination conditions.

ACKNOWLEDGMENTS

The authors are grateful to the Russian Foundation for Basic Research for partial financial support of the work (project no. 99-03-32312a).

REFERENCES

1. Popov, N., *Proizvodstvo i primenenie vermikulita* (Production and Application of Vermiculite), Moscow: Stroiizdat, 1964.
2. Khvostenkov, S.I., Turkin, A.F., Timoshenko, O.M., and Shandrik, L.L., *Issledovanie nekotorykh fiziko-khimicheskikh svoistv ryada flogopit-vermikulit Kovdorskogo mestorozhdeniya: Kovdorskii vermikulit* (Study of Some Physicochemical Properties of Phlogopite–Vermiculite Family from Kovdor Deposit: Kovdor Vermiculite), Moscow: Nauka, 1966.
3. Gannibal, L.F. and Afanas'ev, V.P., *Issledovanie i primenenie vermikulita* (Study and Applications of Vermiculite), Leningrad: Nauka, 1969.
4. Aristov, Yu.I., Restuccia, D., Tokarev, M.M., *et al*., *React. Kinet. Catal. Lett.*, 2000, vol. 71, no. 2, p. 377.
5. Gordeeva, L.G., Restuccia, D., Tokarev, M.M., *et al*., *Zh. Fiz. Khim.*, 2000, vol. 74, no. 11, pp. 2065–2069.
6. *PCPDF Win. Ver. 1. 30 JCPDS ICDD*, Swarthmore, PA (the United States), 1997, pp. 4–829.
7. *Rentgenografiya osnovnykh tipov porodoobrazuyushchikh mineralov (sloistye i karkasnye silikaty)* (X-ray Diffraction Analysis of the Main Types of Rock-Forming Minerals (Layered Silicates and Tectosilicates)), Frank-Kamenetskii, V.A., Ed., Leningrad, Nedra, 1983.
8. Driz, V.A. and Sakharov, B.A., *Rentgenostrukturnyi analiz smeshanno-sloinykh mineralov* (X-ray Diffraction Analysis of Mixed-Layer Minerals), Moscow: Nauka, 1976.
9. D'yakonov, Yu.S., *Dokl. Akad. Nauk SSSR*, 1964, vol. 154, no. 6, pp. 1347–1350.
10. Keay, J. and Wild, A., *Clay Miner. Bull*, 1961, vol. 4, no. 25, pp. 221–228.
11. Aerov, M.A., Todes, O.M., and Narinskii, D.A., *Apparaty so statsionarnym zernistym sloem* (Apparatus with Fixed Granular Bed), Leningrad: Khimiya, 1979.

Russian Journal of Applied Chemistry, Vol. 75, No. 3, 2002, pp. 362–366. Translated from Zhurnal Prikladnoi Khimii, Vol. 75, No. 3, 2002, pp. 375–379.
Original Russian Text Copyright © 2002 by Morachevskii, Bochagina.

PHYSICOCHEMICAL STUDIES OF SYSTEMS AND PROCESSES

Thermodynamic Analysis of Alloys in the Calcium–Antimony System

A. G. Morachevskii and E. V. Bochagina

St. Petersburg State Technical University, St. Petersburg, Russia

Received January 15, 2002

Abstract—Data on the phase equilibria and thermodynamic properties of alloys in the calcium–antimony system are analyzed.

The component interaction in the calcium–antimony system plays an important role in refining of crude lead with calcium [1, 2]. In this work, we consider and compare data on the phase diagram and thermodynamic properties of the Ca–Sb system and, with due regard to these data, discuss the phase equilibrium in the system Ca–Pb–Sb. The phase diagram and thermodynamic properties of alloys of the Ca–Pb system in the solid and liquid states were considered in detail previously [3].

Data on the compositions of compounds forming in the Ca–Sb system are controversial. In handbooks [4, 5], the phase diagram of this system is taken from [6]. That work reports the congruently melting compound CaSb (mp 985 ± 5°C) and the compounds Ca_3Sb_2 and $CaSb_3$ melting with decomposition, with the respective peritectic horizontals lying at 825 ± 5 and 730 ± 5°C. However, in [7–9] compounds of a different composition were reported. According to a summary of published data made by Okamoto [10], in the system Ca–Sb there are the congruently melting compound $Ca_{11}Sb_{10}$ (mp 1123°C) and three compounds melting with decomposition: Ca_2Sb, Ca_5Sb_3, and $CaSb_2$. The peritectic horizontals corresponding to these compounds lie at 827, 996, and 597°C (Fig. 1).

The thermodynamic characteristics of compounds formed in the Ca–Sb system were studied repeatedly by various methods. However, the results are not always consistent. Certain difficulties arising when comparing data of various researchers are associated with different estimated compositions of the forming compounds. Kubaschewski and Villa [11, 12] give for Ca_3Sb_2 the standard enthalpy of formation ΔH^0_{298} = –728 ± 37.7 kJ mol^{-1} and the standard entropy, S^0_{298} = 157.3 J mol^{-1} K^{-1}. Shchukarev *et al.* [13], using solution calorimetry, obtained for Ca_3Sb_2 ΔH^0_{298} = –477 ± 4 kJ mol^{-1}. From the authors' viewpoint, the exothermic effects studied by the method used in [11] are overestimated.

Min and Sano [14], based on the chemical equilibrium data, estimated the Gibbs energy ΔG^0_T for the reaction

$$3Ca(l) + 2Sb(l) = Ca_3Sb_2(s). \quad (1)$$

In the range 1273–1573 K, the temperature dependence of ΔG^0_T (J mol^{-1}) is expressed by the equation

$$\Delta G^0_T = -726\,300 + 159.3T \pm 24\,600. \quad (2)$$

According to a handbook [15], the dependence $\Delta G^0_T = f(t)$ for reaction (1) in the same temperature range has the following form (J mol^{-1}):

$$\Delta G^0_T = -840\,000 + 176.4T. \quad (3)$$

At 1273 K, the ΔG^0_{1273} values for reaction (1),

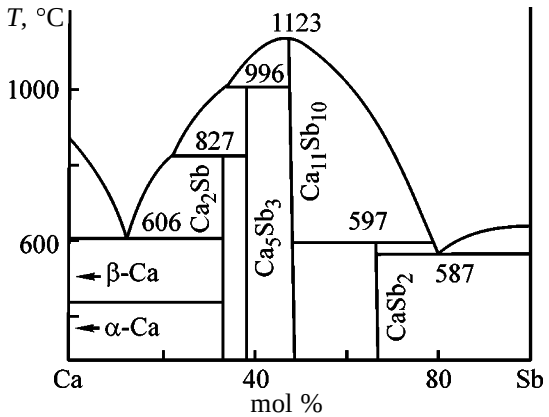

Fig. 1. Phase diagram of the system calcium–antimony [10]. (*T*) Temperature.

1070-4272/02/7503-0362$27.00 © 2002 MAIK "Nauka/Interperiodica"

calculated using Eqs. (2) and (3), are different (–523.5 and –615.4 kJ mol^{-1}). It should be noted, however, that data from [15] are largely based on the results of [11]. It seems appropriate to use Eq. (2).

Ustimov *et al.* [16] measured the solubilities of intermetallic compounds in liquid lead in large-scale experiments (tanks with 400 and 4000 kg of lead) and calculated the Gibbs energy of formation of the compound Ca_3Sb_2 in the solid state at temperatures of up to 714 K. In [16], the following dependence (J mol^{-1}) is presented without reference to calculation details:

$$\Delta G_T^0 = -421\,977 - 210T. \quad (4)$$

Equation (4) differs from Eqs. (2) and (3) primarily in the sign of the temperature coefficient, i.e., in the sign of the reaction entropy.

The cathodic polarization of solid antimony in nitrate (443 K) and chloride (800 K) melts containing calcium was studied in [17]. As will be shown below, interpretation of the results obtained depends on identification of the compounds forming in the system.

The thermodynamic properties of the Ca–Sb system in the middle region of compositions in a wide temperature range (933–1699 K) were studied in detail by Knudsen effusion mass spectrometry [18, 19]. Owing to the limitations of the method, the partial vapor pressure of both components was measured solely in the range of a two-phase equilibrium of $Ca_{11}Sb_{10}$ with Ca–Sb melts at the overstoichiometric content of calcium. This made it possible to calculate the Gibbs energy of formation of $Ca_{11}Sb_{10}$ from the solid components (kJ mol^{-1}):

$$\Delta G_T^0 = -(2184 \pm 15) - (43.5 \pm 12.3) \times 10^{-3} T. \quad (5)$$

In [18, 19], the activity of calcium and antimony in the liquid phase was also determined ($0.502 \le x_{Ca} \le 0.604$, x_{Ca} is mole fraction of calcium in the alloy), with the pure liquid components chosen for standard state. The whole set of the data on the component activity was treated by the authors in terms of the ideal associated solution model with consideration of the CaSb, Ca_2Sb, Ca_3Sb, and Ca_3Sb_2 groups. None of the associates can be considered dominating in a liquid phase, and their enthalpies of formation are comparable (–193.6, –280.8, –316.4, and –562.9 kJ mol^{-1}).

Data on the calcium activity in melts ($0.604 \le x_{Ca} \le 0.635$) in equilibrium with the compound Ca_5Sb_3 allowed estimation of the free energy of formation ΔG_T^0 of this compound from solid antimony and calcium (kJ mol^{-1}):

$$\Delta G_T^0 = -(919 \pm 5) + (34.2 \pm 4.7) \times 10^{-3} T. \quad (6)$$

The results of recent reviews and experimental studies [9, 10, 18, 19] show that, at 443 K, the existence of three phase regions, Sb + $CaSb_2$, $CaSb_2$ + $Ca_{11}Sb_{10}$, and $Ca_{11}Sb_{10}$ + Ca_5Sb_3, is the most probable. In this case, ΔG_{443}^0 of formation of $CaSb_2$, $Ca_{11}Sb_{10}$, and Ca_5Sb_3 from the solid components is –191.1, –1858.6, and –642.2 kJ mol^{-1}, respectively [17]. These values, recalculated to kJ (mol at.)$^{-1}$, are as follows: –63.7 for $1/3\,CaSb_2$, –88.5 for $1/21\,Ca_{11}Sb_{10}$, and –80.8 for $1/8\,Ca_5Sb_3$. Extrapolation of data of [18] to 443 K yields the following ΔG_{443}^0 values (kJ mol^{-1}): –104.9 for $1/21\,Ca_{11}Sb_{10}$ and –113.0 for $1/8\,Ca_5Sb_3$. Unfortunately, the temperature dependences of the Gibbs energy in [18] are given without discussion and comparison with the data of the other researchers [14, 16]. The experimental temperature dependence of ΔG_T^0 is described by the equation [14, 16, 18, 19]

$$\Delta G_T^0 = \Delta H_T^0 - T\Delta S_T^0, \quad (7)$$

where ΔS_T^0 is the entropy of formation of a compound from the pure components in the corresponding aggregation state.

Data on this quantity are controversial. As a rule, for the intermetallic compounds formed with a large exothermic effect, ΔS_T^0 is negative. All the calcium and antimony compounds being discussed, existing or hypothetical, are listed below:

Type	$x_{Ca} : x_{Sb}$	x_{Ca}
$CaSb_3$	1 : 3	0.250
$CaSb_2$	1 : 2	0.33
CaSb	1 : 1	0.500
$Ca_{11}Sb_{10}$	11 : 10	0.524
Ca_3Sb_2	3 : 2	0.600
Ca_5Sb_3	5 : 3	0.625
Ca_2Sb	2 : 1	0.667

As noted above, the main object of the initial thermodynamic studies of the Ca–Sb system was the hypothetical compound Ca_3Sb_2, in which the calcium content is intermediate between the compounds $Ca_{11}Sb_{10}$ and Ca_5Sb_3. The entropy of Ca_3Sb_2 formation from the pure components in a wide temperature range can be estimated using the data of a handbook [15] (Fig. 2). The quantity ΔS_T^0 strongly dependens on the aggregation state of the initial components, taking,

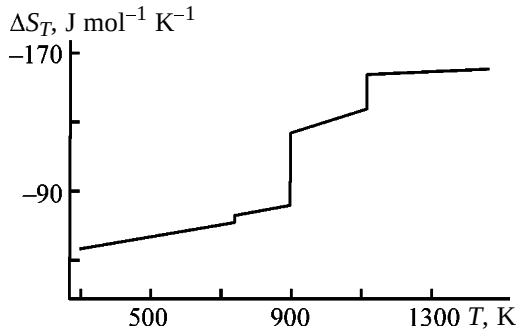

Fig. 2. Entropy of formation ΔS_T^0 of the compound Ca_3Sb_2 vs. temperature T.

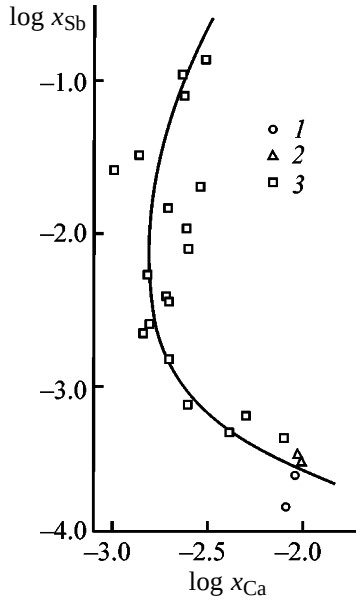

Fig. 3. Composition of the liquid phase in equilibrium with the solid phase in the lead-rich part of the Pb–Ca–Sb system at 400°C [22]. Solid phase: (*1*) $CaPb_3$, (*2*) $CaPb_3$ + Ca_3Sb_2, and (*3*) Ca_3Sb_2.

however, fairly large negative values at all temperatures. Its is reasonable to suggest that at comparable temperatures the ΔS_T^0 values per mole of atoms of the compounds close in the composition ($Ca_{11}Sb_{10}$ and Ca_5Sb_3) should not differ appreciably from the values given in Fig. 2. At the same time, Zaitsev *et al.* [18, 19] give for $1/21\,Ca_{11}Sb_{10}$ $\Delta S_T^0 > 0$ [2.07 J mol^{-1} K^{-1} (1110–1255 K)]. According to the same papers, for the compound $1/8\,Ca_5Sb_3$ $\Delta S_T^0 < 0$ [though it is as small as –4.28 J mol^{-1} K^{-1} (933–1187 K)]. Such discrepancies between the ΔS_T^0 values prevent comparison of experimental data and their recalculation from one temperature to another.

The thermodynamic properties of liquid alloys of the Ca–Sb system ($0.10 \le x_{Ca} \le 0.50$, 800°C) were studied for the first time by the emf method with single-crystalline CaF_2 solid electrolyte. The composition of the alloys was varied coulometrically [20]. The authors showed that, as the mole fraction of calcium is increased from 0.10 to 0.50 at 800°C, its activity changes from 3.16×10^{-10} to 3.50×10^{-9}. In [18, 19], a value of 3.43×10^{-8} was reported for the calcium activity in a liquid alloy with antimony at $x_{Ca} = 0.502$ and 986°C. Taking into account the temperature difference, these data on the calcium activity are in reasonable agreement.

Data on the enthalpy of mixing for liquid alloys in the Ca–Sb system at 1078 K are given in [21]. The extremum in the $\Delta H^0 = f(x_{Ca})$ curve is –67.2 kJ mol^{-1} at $x_{Ca} = 0.52$. The concentration dependence of the thermodynamic functions was described and the short order was estimated using the regular associated solution model. Bouhajib *et al.* [21] postulated formation of only one associate, CaSb, and took into account its interaction with excess pure components (CaSb–Ca and CaSb–Sb) and interaction between the free components. The association is characterized by ΔH_{as} = –158 kJ mol^{-1} and ΔS_{as} = –71 J mol^{-1} K^{-1}. The maximal number of associates was formed close to the composition corresponding to $Ca_{11}Sb_{10}$. The calculated entropy of formation of the CaSb associate in liquid alloys indirectly confirms that the ΔS_T^0 data from [18, 19] for the compounds $Ca_{11}Sb_{10}$ and Ca_5Sb_3 are hardly correct.

From the viewpoint of industrial practice, interaction of calcium with antimony dissolved in liquid lead is of particular interest. No data are available on the thermodynamic properties of Ca–Pb–Sb alloys. In the system Ca–Sb the component interaction is strong [3, 9]. The system Pb–Sb is eutectic, and its properties were repeatedly studied by emf, saturated vapor pressure, and calorimetric methods [2]. The system is characterized by insignificant deviations from the ideal behavior and by a nearly zero enthalpy of mixing.

Fedorov and Shachnev [22] experimentally studied the mutual solubility of calcium and antimony in liquid lead at 400°C. At a very low content of antimony (less than 0.015 wt %) in the solid phase, in equilibrium with the liquid alloy is the compound $CaPb_3$. At higher antimony concentrations (0.020 wt %), two solid compounds are detected: $CaPb_3$ and Ca_3Sb_2. With the antimony concentration increased further, only one compound, Ca_3Sb_2, exists in the solid phase (Fig. 3). No thermodynamic support is given for these results.

As shown previously [3], a value of –118.4 kJ can

be accepted for the Gibbs energy, $\Delta G^0_{673,}$ of the reaction

$$Ca(liq) + 3Pb(liq) = CaPb_3(sol) \quad (8)$$

at 400°C. Correspondingly, the equilibrium constant K_{673} for reaction (8) is 1.55×10^9. Taking into account that

$$K_{673} = a_{CaPb_3}/(a_{Ca} a^3_{Pb}), \quad (9)$$

that $CaPb_3$ is a separate phase, and that the lead activity is nearly unity ($x_{Pb} \sim 0.99$), we obtain a value of 6.45×10^{-8} for the calcium activity in the lead–calcium alloy in equilibrium with $CaPb_3$. In this case, the calcium content in the liquid phase lies within 0.16–0.18 wt % ($x_{Ca} = 0.008$–0.009).

The equilibrium constant for reaction (1) can be written as follows:

$$K_{673} = a_{Ca_3Sb_2}/(a^3_{Ca} a^2_{Sb}). \quad (10)$$

Since Ca_3Sb_2 is a separate solid phase, $a_{Ca_3Sb_2} = 1$, and Eq. (10) takes the form

$$K_{673} = [a^3_{Ca} a^2_{Sb}]^{-1} = K_x K_\gamma, \quad (11)$$

In its turn, $K_x = \prod_x^{-1}$, where K_x is the equilibrium constant expressed via mole fractions, and $\prod_x^{-1}$ is the solubility product, also expressed in mole fractions. In [22], the ratio $x_{Ca} : x_{Sb}$ in the liquid alloys in equilibrium with the solid phase was varied within the wide range: from 33.8 to 0.02. In the process, $\prod_x$ value varied from 1.0×10^{-14} to 1.1×10^{-10} (Fig. 4). To stoichiometry of the forming solid compound corresponds the ratio $x_{Ca} : x_{Sb} = 1.5$.

As noted previously, extrapolation of the ΔG^0_T values, necessary for calculating the equilibrium constant, to relatively low temperatures is difficult. The ΔG^0_{673} value obtained by extrapolation of Eq. (2) to 673 K is –619.1 kJ mol^{-1}. Then, the equilibrium constant of reaction (1) is 1.13×10^{48}. If, according to the equilibrium data, we accept $K_x = 10^{14}$, then K_γ will be $1.13 \times 10^{34.}$ When calcium is present in liquid lead in excess compared to antimony, the activity coefficient of calcium (γ_{Ca}) is mainly determined by the interaction of calcium with lead. As shown in [3], a value of 6.45×10^{-8} for γ_{Ca} can be accepted under these conditions at 400°C. Taking into account K_γ, we obtain the activity coefficient of antimony of 5.7×10^{-7}. However, estimation of ΔG^0_{673} based on the data of [9] gives a different result. For reaction (1) ΔG^0_{673} is

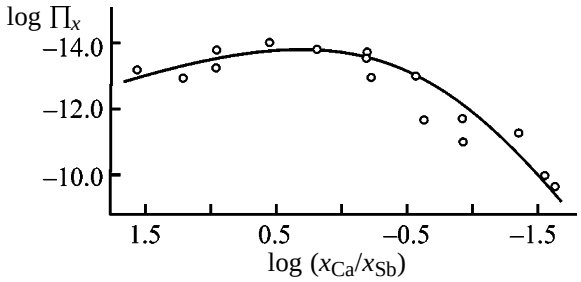

Fig. 4. Solubility product $\prod_x$ (expressed via mole fractions) of the compound Ca_3Sb_2 in the liquid lead at 400°C vs. the ratio of calcium to antimony mole fractions.

–705.9 kJ mol^{-1}. In this case, $K_{673} = 6.17 \times 10^{54}$, $K_\gamma = 6.17 \times 10^{40}$, and the activity coefficient of antimony is 2.46×10^{-10}.

To conclude, the experimental data on the thermodynamic properties of compounds in the system calcium–antimony differ appreciably, which makes any reliable optimization infeasible. This is, to a certain extent, due to the fact that in previous works the central place was given to the compound Ca_3Sb_2, whose existence seems doubtful. The most inconsistent are data on the temperature dependence of the standard Gibbs energy of formation, i.e., on the entropy of alloying.

REFERENCES

1. Smirnov, M.P., *Rafinirovanie svintsa i pererabotka poluproduktov* (Refining of Lead and Reprocessing of Intermediates), Moscow: Metallurgiya, 1997.
2. Kozin, L.F., and Morachevskii, A.G., *Fizikokhimiya i metallurgiya vysokochistogo svintsa* (Physical Chemistry and Metallurgy of High-Purity Lead), Moscow: Metallurgiya, 1991.
3. Morachevskii, A.G., Vaisgant, Z.I., and Bochagina, E.V., *Zh. Prikl. Khim.*, 2000, vol. 73, no. 3, pp. 372–377.
4. Drits, M.E. and Zusman, L.L., *Splavy shchelochnykh i shchelochno-zemel'nykh metallov* (Alloys of Alkali and Alkaline-Earth Metals), Moscow: Metallurgiya, 1986.
5. *Diagrammy sostoyaniya dvoinykh metallicheskikh sistem* (Phase Diagrams of Binary Metallic System), Lyakishev, N.P., Ed., Moscow: Mashinostroenie, 1996, vol. 1.
6. Niyazova, Z.U., Vakhobov, A.V., and Dzhuraev, T.D., *Izv. Akad. Nauk SSSR, Neorg. Mater.*, 1976, vol. 12, no. 7, pp. 1293–1294.
7. Brauer, C., and Müller, O., *Angew. Chem.*, 1961, vol. 73, no. 5, p. 169.

8. Bruzzone, G., and Merlo, F., *J. Less-Common Met*., 1982, vol. 85, no. 2, pp. 285–306.
9. Notin, M., Mejbar, J., Bouhajib, A., *et al.*, *J. Alloys Comp*., 1995, vol. 220, no. 1, pp. 62–75.
10. Okamoto, H., *J. Phase Equil.*, 1997, vol. 18, no. 3, p. 313.
11. Kubaschewski, O., and Villa, W., *Z. Elektrochem*., 1949, vol. 53, no. 1, pp. 32–40.
12. Kubaschewski, O., and Alcock, C.B., *Metallurgical Thermochemistry*, Oxford: Pergamon, 1979.
13. Shchukarev, S.A., Morozova, M.P., and Li, M.-S., *Zh. Obshch. Khim*., 1959, vol. 29, no. 9, pp. 3142–3144.
14. Min, D.J., and Sano, N., *Met. Trans. B*, 1989, vol. 20, December, pp. 863–870.
15. Barin, I., Knacke, O., and Kubaschewski, O., *Thermochemical Properties of Inorganic Substances. Supplement*, Berlin: Springer, 1977.
16. Ustimov, A.M., Kopach, V.G., and Smirnov, M.P., *Tsvetn. Met*., 1992, no. 2, pp. 15–18.
17. Klebanov, E.B., Shibalovskaya, I.I., Morachevskii, A.G., and Stepanova, T.I., *Izv. Vyssh. Uchebn. Zaved., Tsvetn. Metall*., 1988, no. 4, pp. 20–23.
18. Zaitsev, A.I., Shelkova, N.E., Dobrokhotova, Zh.V., *et al.*, *Izv. Ross. Akad. Nauk, Neorg. Mater*., 1997, vol. 33, no. 6, pp. 655–664.
19. Zaitsev, A.I., Shelkova, N.E., and Mogutnov, V.M., *Z. Metallkunde*, 1997, vol. 88, no. 3, pp. 250–255.
20. Delset, J., Delgado-Brune, A., and Egan, J.J., *Calculation of Phase Diagrams and Thermochemistry of Alloy Phases*, Chang, Y.A., and Smith, J.F., Eds., Met. Soc. AIME, 1979, pp. 275–286.
21. Bouhajib, A., Nadiri, A., Yacoubi, A., and Castanet, R., *J. Alloys Comp*., 1999, vol. 287, nos. 1–2, pp. 167–169.
22. Fedorov, P.I. and Shachnev, V.I., *Izv. Vyssh. Uchebn. Zaved., Tsvetn. Metall*., 1962, no. 5, pp. 86–88.

Russian Journal of Applied Chemistry, Vol. 75, No. 3, 2002, pp. 367–369. Translated from Zhurnal Prikladnoi Khimii, Vol. 75, No. 3, 2002, pp. 380–382.
Original Russian Text Copyright © 2002 by Morachevskii.

PHYSICOCHEMICAL STUDIES OF SYSTEMS AND PROCESSES

Thermodynamic Analysis of Alloys of the Lithium–Antimony System

A. G. Morachevskii

St. Petersburg State Technical University, St. Petersburg, Russia

Received December 13, 2001

Abstract—Data on the thermodynamic properties of alloys in the lithium–antimony system are compared and analyzed.

The phase diagram of the lithium–antimony system, according to handbooks [1, 2], has not been established. Only data on the crystal lattice parameters of Li_2Sb and Li_3Sb are reported [1]. The melting point of Li_3Sb lies between 1150 and 1300°C [1] or slightly above 950°C [2].

According to [3], the compound Li_3Sb melts congruently at temperature of about 1150°C; at about 650°C α-Li_3Sb transforms into β-Li_3Sb. Li_2Sb melts with decomposition, and the peritectic horizontal lies at about 825°C. On the lithium side, the eutectic is degenerated, and on the antimony side, the eutectic point lies at 89 mol % Sb and about 590°C. The phase diagram, according to [3], is shown in Fig. 1.

An essentially different phase diagram of the Li–Sb system was obtained in [4]. The author pointed out that the diagram could not be considered completely equilibrium, because preliminary annealing was not performed. The alloys were obtained by electrolysis of a molten eutectic mixture LiCl–KCl with liquid antimony as cathode. The probability of potassium incorporation into the alloy was not discussed in that work. In the Li–Sb system, two congruently melting compounds are formed, Li_3Sb_2 and Li_3Sb (mp 700°C and above 1000°C, respectively) [4]. To lithium antimonide Li_3Sb corresponds a very narrow and intense peak similar to that of the intermetallic compound Mg_3Bi_2 [4]. In addition, incongruently melting compound, $LiSb_2$, with the peritectic horizontal at 610°C, is also formed in the Li–Sb system [4]. The compound Li_3Sb_2 is not revealed on the liquidus curve. Thus, the comparison of the phase diagrams reported in [3, 4] calls for a further study of the system.

Some additional information on the compound compositions and other features of the lithium interaction with antimony can be obtained by comparing and analyzing the results of the thermodynamic studies of the system. In [5], a value of –325.5 and –335.0 kJ mol^{-1} was obtained by solution calorimetry for the enthalpy of formation ΔH^0_{298} of Li_3Sb from the solid elements and from liquid lithium and solid antimony, respectively.

The first data on the Gibbs energy of alloy formation in the Li–Sb system were obtained by Weppner and Huggins [6]. The authors varied the alloy composition coulometrically and measured the potential of the Li–Sb solid alloy in a liquid eutectic mixture LiCl–KCl. The study was performed in a wide temperature range (355–600°C). The reference electrode was the Li–Sb alloy in the two-phase region. Two compounds, Li_2Sb and Li_3Sb, were clearly detected in the potential vs. composition curves in [6]. The solubility of lithium in solid antimony is negligible. Passage from the two-phase region Sb + Li_2Sb to the region Li_2Sb + Li_3Sb at 360°C is accompanied by a very small potential drop. The homogeneity region of Li_3Sb at this temperature is small. Nonetheless, in going from x_{Li} = 0.74990 to x_{Li} = 0.75030 [x_{Li} is lithium mole fraction in the alloy] the lithium activity at 360°C changes from 1.04×10^{-7} to 0.438, and the

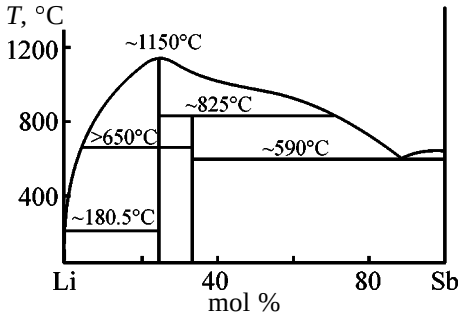

Fig. 1. Phase diagram of the lithium–antimony system [3]. (*T*) Temperature.

1070-4272/02/7503-0367$27.00 © 2002 MAIK "Nauka/Interperiodica"

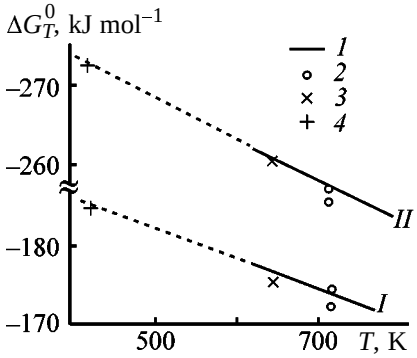

Fig. 2. Gibbs energy ΔG_T^0 of formation of compounds (*I*) Li_3Sb and (*II*) Li_3Sb from pure components, according to the data of various studies. (*T*) Temperature. References: (*1*) [6], (*2*) [7], (*3*) [8], and (*4*) [9].

antimony activity, from 0.297 to 2.78×10^{-22}. Weppner and Huggins [6] obtained the following results: for the reaction 2Li + Sb = Li_2Sb (355–500°C), ΔG_T^0 = = –197.3 + 0.0319*T*, kJ mol^{-1}. Correspondingly, in the given temperature range ΔH_T^0 = –197.3 kJ mol^{-1} and ΔS_T^0 = –31.9 J mol^{-1} K^{-1}. Similarly, for the reaction 3Li + Sb = Li_3Sb (355–500°C), ΔG_T^0 = –293.3 + 0.0492*T* kJ mol^{-1}, ΔH_T^0 = –293.3 kJ mol^{-1}, and ΔS_T^0 = –49.2 J mol^{-1} K^{-1}.

In [7], the polarization curves in the pulsed galvanostatic mode were taken, and switch-off curves were subsequently recorded to study the lithium deposition on liquid and solid antimony electrodes from the liquid electrolytes LiCl (650°C), LiCl–LiF (527°C), and LiCl–KCl (450, 527, and 650°C). The most appropriate temperature for estimating the thermodynamic properties of lithium–antimony compounds is 450°C. A special thermal analysis of the antimony-rich part of the Li–Sb system revealed an eutectic at 472 ± 3°C, which is close to the value of 466°C from [4]. Thus, at 527°C solid antimony is in equilibrium with a liquid alloy. At 450°C, the alloys are in the solid state in the phase regions studied.

The potential of the two-phase region, clearly defined in the polarization curves, is equal to 0.904 ± 0.002 V for the Sb + Li_2Sb system and 0.858 ± 0.002 V for the Li_2Sb + Li_3Sb system. The delays of the potential decrease in the switch-off curves at 450°C for the LiCl–KCl melt are 0.857 ± 0.002 and 0.895 ± 0.002 V. The Gibbs energy of formation of Li_2Sb from liquid lithium and solid antimony is ΔG_{723}^0 = –174.5 kJ mol^{-1}, as calculated from the polarization curve, and –172.7 kJ mol^{-1}, as calculated from the switch-off curve. In [6], the value of –174.2 kJ mol^{-1} is reported.

The Gibbs energy of formation of Li_3Sb from the pure components is ΔG_{723}^0 = –257.3 and –255.4 kJ mol^{-1}, as calculated from the polarization and switch-off curves, respectively. According to [6], ΔG_{723}^0 = –257.7 kJ mol^{-1}.

In a later work [8], the polarization curves in the course of lithium deposition on a solid antimony cathode were taken similarly at 650 K in heterocationic (LiCl–KCl) and homocationic (LiF–LiCl–LiI) electrolytes. At this temperature, the cathode potential relative to the lithium reference electrode in the phase region Sb + $LiSb_2$ was similar in both electrolytes (0.915 ± 0.002 V). This corresponds to the Gibbs energy ΔG_{650}^0 = –176.6 kJ mol^{-1}. With the two-phase system Li_2Sb + Li_3Sb system present at the surface, the electrode potential is 0.879 ± 0.003 V in the LiF–KCl electrolyte and 0.882 ± 0.001 V in the LiF–LiCl–LiI electrolyte. Correspondingly, ΔG_{650}^0 is –261.4 kJ mol^{-1} in the first case and –261.7 kJ mol^{-1} in the second case. The obtained ΔG_{650}^0 values are in good agreement with the data of [6].

At lower temperatures, the alloy formation in the course of lithium deposition on antimony cathode was studied using low-melting electrolytes $LiNO_3$–$LiNO_2$–LiOH and $LiNO_3$–KNO_3 [9].

In this case, the effect of potassium ions on the discharge potential of lithium ions was not revealed. At 150°C, the discharge potential relative to a solid lithium electrode is equal to 0.961 ± 0.003 V for the first phase region (Sb + Li_2Sb) and 0.901 ± 0.002 V for the second phase region (Li_2Sb + Li_3Sb). Correspondingly, the Gibbs energy ΔG_{423}^0 is –185.4 and –272.3 kJ mol^{-1} for Li_2Sb and Li_3Sb, respectively. In going to liquid lithium reference electrode at this temperature, these values change insignificantly (–185.8 and –272.9 kJ mol^{-1}). As seen from Fig. 2, the results of [6–9] are mutually consistent for both compounds of lithium with antimony. The dependence of the Gibbs energy of the Li–Sb solid alloys on the composition at 700°C is shown in Fig. 3.

Data are available on the potentials of lithium deposition from liquid electrolytes on a liquid antimony cathode, indirectly characterizing the component interaction in the liquid state. The polarization curves, reflecting the dependence of the potential of lithium deposition from LiCl and LiCl–KCl liquid electrolytes at 650°C on the logarithm of the current density, are linear in the current density range 2.5×10^{-3}–1.0 A cm^{-2}. In this case, the lithium deposition potential relative to a lithium reference electrode is shifted from 1.6 to 1.0 V [7, 10].

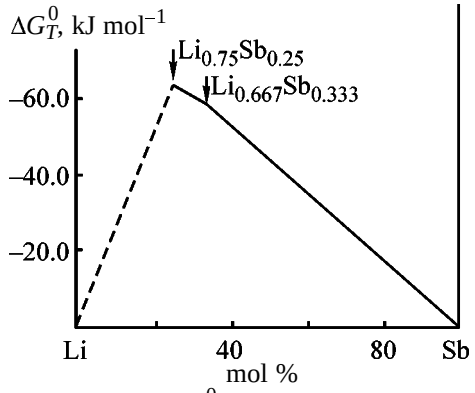

Fig. 3. Gibbs energy ΔG_T^0 vs. composition of the Li–Sb system at 700 K.

In [10], we summarized data on the potentials of lithium deposition from a liquid eutectic mixture LiCl–KCl on various liquid cathodes at a polarizing current density of 0.1 A cm^{-2}. A potential of 0.94 V vs. lithium reference electrode is reported for lithium deposition on a liquid bismuth cathode at 400°C. In [7, 10] we reported a potential of 1.14 and 1.23 V for lithium deposition on liquid bismuth and liquid antimony electrodes, respectively, under similar conditions at higher temperature (650°C). As expected, these values are considerably higher than the potentials of lithium deposition at a similar current density on tin (0.78 V, 400°C) or lead (0.68 V, 400°C).

CONCLUSIONS

(1) Analysis of the whole set of electrochemical data on solid alloys in the lithium–antimony system confirms formation of only two intermetallic compounds: Li_2Sb and Li_3Sb.

(2) The results of electrochemical studies with various liquid electrolytes in a wide temperature range are mutually consistent and allow estimation of the Gibbs energy of formation of Li_2Sb and Li_3Sb from the pure components.

REFERENCES

1. Drits, M.E. and Zusman, L.L., *Splavy shchelochnykh i shchelochno-zemel'nykh metallov* (Alloys of Alkali and Alkaline-Earth Metals), Moscow: Metallurgiya, 1986.
2. *Diagrammy sostoyaniya dvoinykh metallicheskikh sistem* (Phase Diagrams of Binary Metallic System), Lyakishev, N.P., Ed., Moscow: Mashinostroenie, 1999, vol. 3, book 1.
3. Sangster, J., and Pelton, A.D., *J. Phase Equil.*, 1993, vol. 14, no. 4, pp. 514–517.
4. Fedorov, P.I., *Zh. Neorg. Khim.*, 1995, vol. 40, no. 5, pp. 844–846.
5. Shchukarev, S.A., Vol'f, E., and Morozova, M.P., *Zh. Obshch. Khim.*, 1954, vol. 24, no. 11, pp. 1925–1926.
6. Weppner, W. and Huggins, R.A., *J. Electrochem. Soc.*, 1978, vol. 125, no. 1, pp. 7–14.
7. Nikitin, A.V., Demidov, A.I., and Morachevskii, A.G., *Zh. Prikl. Khim.*, 1980, vol. 53, no. 7, pp. 1641–1644.
8. Nikitin, A.V., Demidov, A.I., Morachevskii, A.G., *et al.*, *Zh. Prikl. Khim.*, 1982, vol. 55, no. 4, pp. 915–916.
9. Demidov, A.I., Dukhanin, G.P., and Morachevskii, A.G., *Elektrokhimiya*, 1983, vol. 19, no. 12, pp. 1695–1699.
10. Demidov, A.I., Dukhanin, G.P., Morachevskii, A.G., and Nikitin, A.V., *Izv. Vyssh. Uchebn. Zaved., Tsvetn. Metall.*, 1982, no. 6, pp. 63–65.
11. Temnogorova, N.V., Demidov, A.I., and Morachevskii, A.G., *Izv. Vyssh. Uchebn. Zaved., Tsvetn. Metall.*, 1979, no. 3, pp. 89–96.

Russian Journal of Applied Chemistry, Vol. 75, No. 3, 2002, pp. 370–374. Translated from Zhurnal Prikladnoi Khimii, Vol. 75, No. 3, 2002, pp. 383–387.
Original Russian Text Copyright © 2002 by Sladkov.

PHYSICOCHEMICAL STUDIES OF SYSTEMS AND PROCESSES

Density of Liquid Halogermanes

I. B. Sladkov

St. Petersburg State Technical University, St. Petersburg, Russia

Received June 26, 2001

Abstract—The density of liquid bromo- and iodogermanes was calculated by four independent methods at temperatures between the melting and boiling points. The coefficients of a temperature series of density were established and the accuracy of the results obtained was analyzed. The reliability of the obtained data was confirmed by variation of the molar volume of a liquid substance in the series of halogermanes and halosilanes.

Germanium compounds containing hydrogen and chlorine atoms (chlorogermanes) are widely used for preparing single-crystalline germanium and for manufacturing semiconductor devices. The procedures commonly involve reduction of chlorogermanes with hydrogen. The germanium compounds with hydrogen and bromine (bromogermanes) and those with hydrogen and iodine (iodogermanes) are reduced with hydrogen more readily than chlorogermanes. Therefore, it may be appropriate to use them when the lower process temperature is the decisive factor.

At the same time, bromo- and iodogermanes are studied considerably less than chlorogermanes; presently, many of their physicochemical properties remain unknown. For example, data are lacking on the temperature dependence of the density in the liquid state.

In this work we obtained, using approximate procedures of the thermodynamic similarity principle, the lacking data on the density of these compounds. The reliability of the methods used was tested on related compounds for which experimental data on the density were available.

To calculate the density of liquid bromo- and iodogermanes, we used four independent procedures. Procedure 1 is based on the law of respective states. According to this law, thermodynamically similar substances must have similar reduced volumes in the liquid state at the same reduced temperature. Calculation of the density by procedure 1 involves a choice of a few compounds that are thermodynamically similar to the compounds under consideration, for which the density in the liquid phase, critical temperature T_{cr}, and critical volume V_{cr} are known from the literature. The reduced volumes, $V_{red} = V/V_{cr}$, of these substances in the liquid state, as calculated for a given reduced temperature $T_{red} = T/T_{cr}$, should be close. Their average value can be accepted as the reduced volume of the substances under consideration at a given reduced temperature.

The thermodynamically similar substances should be chosen so as to ensure close values of the complexity factor of intermolecular interaction (ψ-factor) [1], which is the determining criterion of thermodynamic similarity of inorganic molecular compounds. Therefore, we chose chloro- and bromogermanes GeH_2Br_2, $GeBr_4$, GeH_3Cl, GeH_2Cl_2, $GeHCl_3$, and $GeCl_4$, for which data on the density in the liquid state are available from the literature [1]. Tables 1 and 2 present, according to [1], the physicochemical properties necessary for the calculation. In Table 1 the properties of the substances studied (nos. 7–11) are given along with those of the thermodynamically similar compounds (nos. 1–6).

Evidently, the chosen reduced temperatures for calculating the reduced volumes of the substances should correspond to their liquid state. It is infeasible to estimate the lower temperature boundary of the liquid state without data on the melting point. However, the melting point of iodogermanes is unknown. To determine it, we used a correlation between the melting and boiling points for this class of substances (Fig. 1).

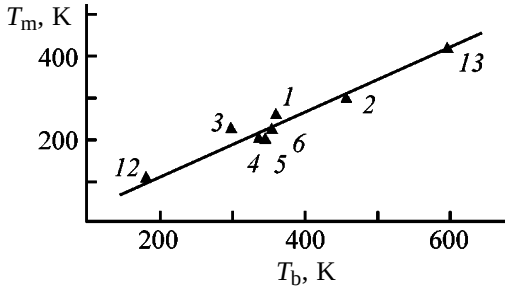

Fig. 1. Correlation between the melting T_m and boiling T_b points of halogermanes. Figures at curves are substance nos. in Table 1; (*12*) SiH_4 and (*13*) SiJ_4.

1070-4272/02/7503-0370$27.00 © 2002 MAIK "Nauka/Interperiodica"

Table 1. Physicochemical properties of halogermanes

Substance no.	Substance	ψ	Parachor Π, $J^{1/4}$ $cm^{5/2}$ mol^{-1}	T_m, K	T_b, K	V_b, cm^3 mol^{-1}	T_{cr}, K	V_{cr}, cm^3 mol^{-1}
1	GeH_2Br_2	0.038	3.64	258	362	97	575	262
2	$GeBr_4$	0.010	5.50	299	460.1	146.3	718	392
3	GeH_3Cl	0.056	2.60	221	302	71.2	486	193
4	GeH_2Cl_2	0.041	3.23	205	343	90.8	545	254
5	$GeHCl_3$	0.021	3.86	202	348.3	107	448	288
6	$GeCl_4$	0.005	4.49	224	356.2	124.1	552	330
7	GeH_3Br	0.059	2.85	241	325	74.0	524	201
8	$GeHBr_3$	0.021	4.61	279	420	125.0	656	337
9	GeH_3I	0.051	3.26	228*	350	84.0	560	228
10	GeH_2I_2	0.027	4.55	279*	420	119.0	660	321
11	$GeHI_3$	0.014	5.84	338*	500	153.0	775	419

* Calculated by Eq. (1).

As seen, this is a clear linear correlation (correlation coefficient 0.9789, root-mean-square error ±8%) described by the equation

$$T_m = 0.735T_b - 29.6. \quad (1)$$

Using Eq. (1), we estimated the melting points of iodogermanes (Table 1).

Then, we found that the liquid state range for halogermanes corresponds to the condition $T_{red} > 0.42$. On the other hand, for halogermanes the reduced temperature corresponding to the boiling point lies within 0.62–0.65. Therefore, we chose three reduced temperatures (0.50, 0.55, and 0.60) at which any of the indicated compounds would be in the liquid state.

The temperature $T = T_{red}T_{cr}$ can be calculated for each reduced temperature and, using the data of Table 2, the density of a liquid substance, its molar volume $V = M/\rho$, and then the reduced volume $V_{red} = V/V_{cr}$ can be determined for this temperature. The results of the calculations for one of the reduced temperatures are listed in Table 3.

As seen from Table 3, the reduced volumes of different substances differ insignificantly. Thus, they can be averaged. As a result, the following averaged values of the reduced volume were obtained at indicated reduced temperatures (in parentheses): 0.332 (0.50), 0.345 (0.55), and 0.359 (0.60). Then for each reduced temperature we determined the temperature $T = T_{red}T_{cr}$, the molar volume of the liquid substance $V = V_{red}V_{cr}$, and its density $\rho = M/V$ (Table 4).

Calculation procedure 2 is based on the linear correlation between the volume of a liquid substance and the parachor Π, existing for related compounds. It is known that the parachor is a complex physicochemical property of a liquid substance relating its molar weight, surface tension, and density. One of the main properties of the parachor is additivity. Thus, it can be calculated for each substance as the sum of the atomic fractions of the constituent elements, taking into account the molecular stoichiometry [1]. Another im-

Table 2. Coefficients for calculating the density ρ, g cm^{-3}, of liquid bromo- and chlorogermanes in the temperature range between the melting and boiling points [1], $\rho = a - 10^{-3}bT + 10^{-6}cT^2$

Substance	*a*	*b*	*c*
GeH_2Br_2	3.975	4.30	0
$GeBr_4$	3.928	2.607	–0.223
GeH_3Cl	2.281	2.40	0
GeH_2Cl_2	2.358	2.20	0
$GeHCl_3$	2.831	3.30	0
$GeCl_4$	2.389	1.266	–1.67

Table 3. Volumes and reduced volumes of liquid substances at $T_{red} = 0.60$

Substance	*T*, K	*V*, cm^3 mol^{-1}	V_{red}
GeH_2Br_2	345.0	94.1	0.327
$GeBr_4$	430.8	141.9	0.338
GeH_3Cl	291.6	70.3	0.339
GeH_2Cl_2	327.0	88.8	0.326
$GeHCl_3$	328.8	103.1	0.324
$GeCl_4$	331.2	120.0	0.340

Table 4. Densities of liquid bromo- and iodogermanes, calculated by various procedures*

Substance	*T*, K	Density, ρ, g cm^{-3}, determined by indicated method				ρ$_{av}$, g cm^{-3}
		1	2	3	4	
GeH_3Br	262.0	2.330	2.187	2.293	2.280	2.272
	288.2	2.242	2.098	2.216	2.208	2.191
	314.4	2.155	2.010	2.135	2.133	2.108
GeH_2Br_2	328.0	2.800	2.794	2.781	2.764	2.785
	360.8	2.695	2.693	2.686	2.676	2.687
	393.6	2.590	2.591	2.588	2.584	2.588
GeH_3I	280.0	2.675	2.511	2.642	2.626	2.613
	308.0	2.574	2.410	2.552	2.543	2.520
	336.0	2.474	2.315	2.459	2.456	2.426
GeH_2I_2	330.0	3.081	2.966	3.053	3.033	3.032
	363.0	2.965	2.856	2.949	2.937	2.927
	396.0	2.850	2.750	2.841	2.836	2.819
$GeHI_3$	387.5	3.266	3.227	3.308	3.294	3.274
	426.3	3.143	3.112	3.195	3.187	3.159
	465.0	3.020	3.002	3.079	3.075	3.044

* Method of: (1) law of respective states, (2) volume–parachor correlation, (3) Mathias–Goldhammer equation, and (4) Rackett equation.

portant property of the parachor is its correlation with many physicochemical properties.

For example, for related substances the parachor correlates well with the molar volume of a liquid. Taking into account the thermodynamic similarity principle, the volumes as functions of parachor must be compared at the same reduced temperatures. The related substances for bromo- and iodogermanes are chlorogermanes.

Using the parachor values calculated by the procedure described in [1], the data of Table 1, and the volumes of the substances at the three above-indicated reduced temperatures, we constructed the V–∏ plots

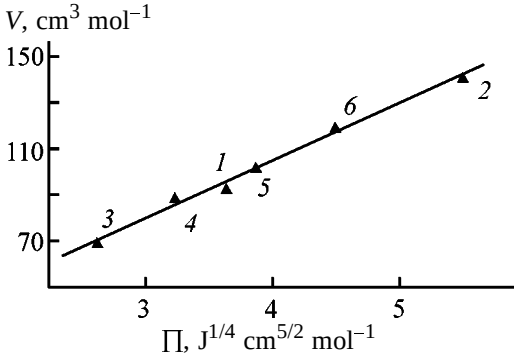

Fig. 2. Correlation between the molar volume of liquid substance *V* and parachor ∏ for T_{red} = 0.6. Figures at curves are substance nos. in Table 1.

for the related substances. Indeed, there is a clear linear correlation between the volume of a liquid substance and parachor (Fig. 2).

Thus, the volume can be calculated from the relation

$$V = A\prod + B. \quad (2)$$

The parameters of relation (2), along with the correlation coefficient *R* and the root-mean-square error *S*, which were determined by the least-squares method, are listed in Table 5. By substituting the parachor values of the substances under consideration into relation (2), we calculated the volumes of these substances and then their density in the liquid state ρ = *M*/*V*. The calculated densities of liquid bromo- and iodogermanes are presented in Table 4.

Procedure 3 uses the Mathias–Goldhammer equation [1]:

$$\rho = \alpha + \alpha(1 - T/T_{cr}) + \beta(1 - T/T_{cr})^{1/3},$$

where

$$\alpha = \rho_b/[2(2 - T_b/T_{cr})],$$

$$\beta = \rho_b/[2(1 - T_b/T_{cr})^{1/3}].$$

The densities calculated by this method are listed in Table 4.

Procedure 4 is based on the Racket equation [1]:

$$\rho = \rho_{cr}B^{y},$$

where

$$y = -(1 - T/T_{cr})^{2/7}.$$

The individual constant B was found using the boiling point parameters:

$$B = (\rho_{cr}/\rho_{b})^{z},$$

where

$$z = 1/(1 - T_{b}/T_{cr})^{2/7}.$$

The densities of liquid bromo- and iodosilanes as calculated by four independent procedures are given in Table 4. As seen, the values obtained by different procedures are in good agreement. Therefore, these values can be averaged to calculate the parameters of a temperature series of density.

To broaden the temperature range, we used the published data for the boiling point (Table 1). As seen from Fig. 3, all points are fitted well by straight lines

$$\rho = a - 10^{-3}bT.$$

The parameters of this dependence for bromo- and iodogermanes, found by the least-squares treatment, are listed in Table 6.

Let us now estimate the accuracy of our results. The root-mean-square error is ±2.5% for method 1 and ±2.4% for method 2 (Table 5). To estimate the accuracy for methods 3 and 4, we calculate the accuracy of the Mathias–Goldhammer and Racket equations for the related substances for which experimental densities are available (Table 2).

To do this, the temperature range between the melting and boiling points was divided in five sections, and the density was calculated for six temperatures, starting from the melting point and completing with the boiling point. The root-mean-square error of the Mathias–Goldhammer and Racket methods calculated for six substances using these data is, respectively, as follows (%): 2.7 and 3.3 for GeH_2Br_2, 0.4 and 0.4 for $GeBr_4$, 0.5 and 0.4 for GeH_3Cl, 0.2 and 0.4 for GeH_2Cl_2, 4.5 and 5.3 for $GeHCl_3$, and 0.8 and 0.2 for $GeCl_4$.

Thus, the overall root-mean-square error of methods 3 and 4 is ±1.7 and ±1.6%, respectively. If the parameter is calculated by several independent methods, and for each method the root-mean-square error is known (as in the case of estimating the densities of the compounds under consideration at each temperature), then the error of the arithmetic mean can be calculated by the method described in [1]. The calculation performed shows that in this work the accuracy in determining the density of liquid bromo- and iodogermanes is ±1.5%.

Table 5. Parameters of the $V = A\prod + B$ dependence

T/T_{cr}	A	B	R	$\pm S$, %
0.50	23.30	4.71	0.9942	2.8
0.55	23.98	5.78	0.9959	2.4
0.60	24.75	6.83	0.9971	2.0

Table 6. Coefficients for calculating the density ρ, g cm^{-3}, of liquid bromo- and iodogermanes at various temperatures, $\rho = a - 10^{-3}bT$

Substance	a	b	R	$\pm S$, %
GeH_3Br	3.01	2.83	0.9925	0.5
GeH_2Br_2	3.78	3.03	0.9999	0.1
GeH_3I	3.446	2.995	0.9923	0.5
GeH_2I_2	4.039	3.06	0.9986	0.2
$GeHI_3$	4.330	2.74	0.9974	0.3

Another way to test the reliability of our data is the method of comparative calculation. To do this, it is necessary to compare the volume variation in a series of related compounds of germanium and silicon. Bromo- and iodosilanes are studied better than the corresponding germanium compounds: for them the parameters for the boiling and critical points and data on the density in the liquid state in the temperature range between the melting and boiling points are available from the literature [1]. Based on these

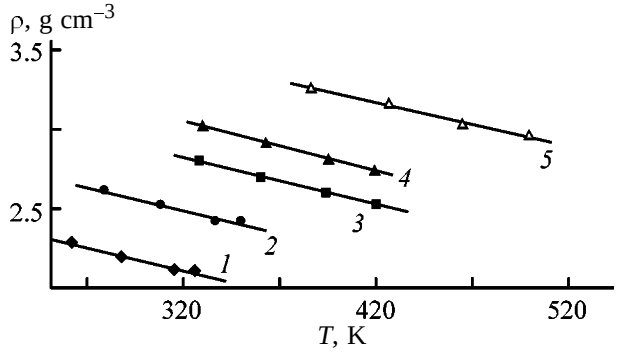

Fig. 3. Density ρ vs. temperature T for liquid bromo- and iodogermanes: (*1*) GeH_3Br, (*2*) $GeHBr_3$, (*3*) GeH_3I, (*4*) GeH_2I_2, and (*5*) $GeHI_3$.

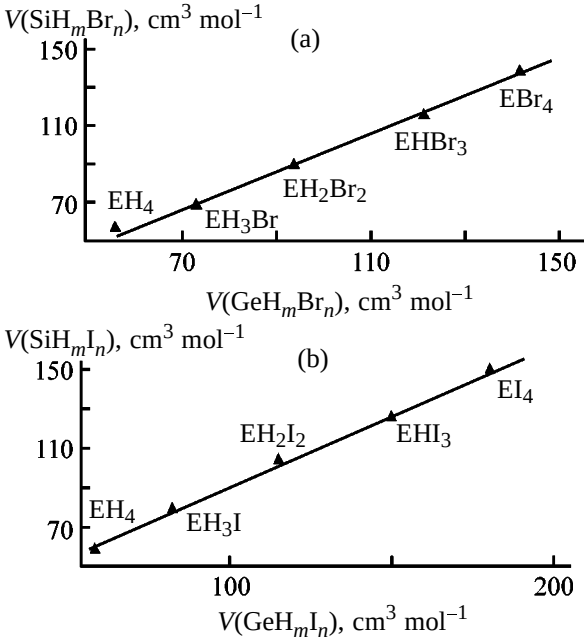

Fig. 4. Variation of the molar volume V of liquid substance for T_{red} = 0.6 in the series of (a) bromogermanes and bromosilanes and (b) iodogermanes and iodosilanes.

data, let us calculate the volumes of liquid bromo- and iodogermanes at a particular reduced temperature, for example, at T_{red} = 0.6. The variation of the volume is shown in Fig. 4a for a series of bromogermanes and in Fig. 4b for a series of iodosilanes and iodogermanes. As seen from these plots, a clear linear correlation exists in both cases. The correlation coefficients are as high as 0.9957 and 0.9989, respectively, and the root-mean-square errors, as low as ±0.7 and ±1.2%, respectively. This fact additionally confirms the high reliability of our results.

CONCLUSIONS

(1) The data on the density of liquid bromo- and iodogermanes, which are lacking from the literature, are obtained by four independent calculation procedures for the temperature range between the melting and boiling points.

(2) The reliability of the data obtained is confirmed by variation of the molar volumes of liquid substances in the series of halogermanes and halosilanes.

REFERENCE

1. Morachevskii, A.G., and Sladkov, I.B., *Fiziko-khimicheskie svoistva molekulyarnykh neorganicheskikh soedinenii* (Physicochemical Properties of Molecular Inorganic Compounds), St. Petersburg: Khimiya, 1996.

Russian Journal of Applied Chemistry, Vol. 75, No. 3, 2002, pp. 375–377. Translated from Zhurnal Prikladnoi Khimii, Vol. 75, No. 3, 2002, pp. 388–390.
Original Russian Text Copyright © 2002 by Prusova, Baranov.

PHYSICOCHEMICAL STUDIES OF SYSTEMS AND PROCESSES

Solubility of 1-Amino-4-Hydroxyanthraquinone in Water–Amide Mixtures

S. M. Prusova and A. V. Baranov

Institute of Solution Chemistry, Russian Academy of Sciences, Ivanovo, Russia

Received June 23, 1999; in final form, May 2000

Abstract—The solubility of a C.I. Disperse Red 15 dye in water and concentrated aqueous solutions of urea and acetamide was studied by isothermal saturation within the 313–353 K temperature range The thermodynamic characteristics of the dye solution were calculated, and the results were analyzed.

The state of a dye in intensifier, which is used in high-speed, high-temperature fixation of disperse dyes on a textile, is poorly studied. This is caused by partial decomposition of intensifiers at high temperatures and low solubility of disperse dyes. At the same time, the state of disperse dyes in water–amide solutions is of interest in terms of fixation of dyes on textile and development of high-speed high-temperature dyeing technology.

The goal of this work was to study the solubility of purified C.I. Disperse Red 15 dye (1-amino-4-hydroxyanthraquinone) in water and mixtures of water with urea and acetamide (water content 30–50%) within the 313–353 K temperature range by isothermal saturation method in order to obtain the thermodynamic parameters of dye solution.

EXPERIMENTAL

To determine the solubility of 1-amino-4-hydroxyanthraquinone, we used a special temperature-controlled device, which is a hermetically sealed tube equipped with a filtering attachment for sampling solid-phase-free solution. The concentration of the dissolved dye in the saturated aqueous solution was determined spectrophotometrically after its extraction with carbon tetrachloride. The relative error of determination of the dye solubility was 1.44%.

1-Amino-4-hydroxyanthraquinone used was prepared from commercial-grade Disperse Red 2C dye as follows. The dye was extracted with acetone and then precipitated with a large excess of distilled water, filtered, washed with water, and dried. The procedure was repeated several times to attain the constant molar absorption coefficient of the dye in the solution. The further purification was performed by the chromatography [1] on a column packed with 100/40 silica gel with toluene as an eluent. Four fractions were isolated, and only the fraction whose electronic spectrum contained the long-wave band with two maxima at 530 and 560 nm was used in the study. These maxima are characteristic of the charge-transfer band of 1-amino-4-hydroxyanthraquinone in toluene [2]. The dye was crystallized from toluene and dried under vacuum. Analytically pure grade amides were used.

The thermodynamic characteristics of solution of the nonionic dye were calculated using phase equilibrium equations. For poorly soluble nonelectrolytes, the activity coefficients are close to unity. Therefore, the concentration can be used instead of activity. The dye solubility was varied within the 0.4×10^{-5}–7×10^{-5} M range depending on the temperature and solvent composition. From data on solubility, the Gibbs energy was calculated:

$$\Delta G^0 = -RT \ln C, \quad (1)$$

where C is the dye concentration in the saturated solution.

As a rule, within a small range of temperature variation the heat of solution ΔH^0 varies weakly, and hence it can be taken as constant. With this assumption, the integration of the isobar equation $d\ln C/dT = \Delta H^0/RT^2$ gives

$$\ln C_2/C_1 = \Delta H^0(T_2 - T_1)/RT_2T_1, \quad (2)$$

where C_2 and C_1 are the dye solubilities at temperatures T_2 and T_1, respectively. Using Eq. (2), we calculated ΔH^0.

1070-4272/02/7503-0375$27.00 © 2002 MAIK "Nauka/Interperiodica"

Effect of solvent on thermodynamics of 1-amino-4-hydroxyanthraquinone solution at 353 K

Solvent	ΔG^0	ΔH^0	$-T\Delta S^0$	ΔG^0	ΔH^0	$-T\Delta S^0$	ΔG^0	ΔH^0	$-T\Delta S^0$
	kJ mol^{-1} at indicated water content, wt %								
	30			40			50		
Urea–water	–	–	–	30.1	17.8	12.3	30.0	17.8	12.2
Acetamide–water	29.3	15.7	14.1	28.5	8.8	19.7	28.3	7.0	21.3
Water	31.9	56.0	–20.2	–	–	–	–	–	–

The entropy of solution can be determined from the relation

$$\Delta G^0 = \Delta H^0 - T\Delta S^0. \quad (3)$$

As the standard state of the substance dissolved in the real solution, we take its state in a hypothetical ideal solution with unit concentration, in which the partial molar volumes, enthalpy, and heat capacity are the same as in infinitely dilute solution. For the solvent in the real solution, the state of pure solvent under standard conditions is taken as the standard state.

The relative errors of the thermodynamic parameters calculated by differentiation of the corresponding equations are ±0.1% for ΔG^0 and ±3% for ΔH^0 and ΔS^0.

Data on the solubility of the dye in various solvents at various temperatures are shown in the figure. As seen, the temperature dependences are linear; the correlation coefficient is 0.999 from the least-squares treatment. Water–amide mixtures dissolve the dye better (curves *2*–*6*) than water (curve *1*).

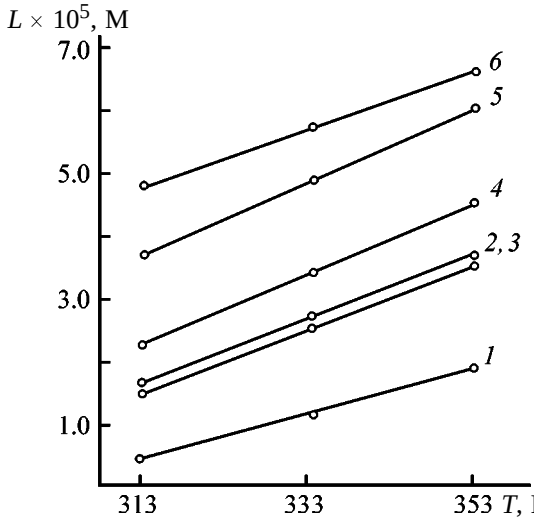

Solubility L of 1-amino-4-hydroxyanthraquinone in (*1*) water, (*2*, *3*) water–urea, and (*3*, *4*) water–acetamide mixtures as a function of the temperature T. Water content (wt %): (*2*, *5*) 40, (*3*, *6*) 50, and (*4*) 30.

Dissolution of 1-amino-4-hydroxyanthraquinone in each water–amide mixture is specific. The solubility of the dye in the mixture with acetamide is higher than in the mixture with urea and noticeable depends on the amide : water ratio.

The calculated thermodynamic characteristics of solution of the dye in water and water–amide mixtures are listed in the table. As seen, the entropy factor largely governs the dissolution of the dye in water. The enthalpy of solution in water is highly positive, which prevents dissolution. In water–amide mixtures, the role of the enthalpy factor in dissolution increases. The enthalpy of solution is independent of water content within the 40–50 wt % range for water–urea mixtures and decreases for water–acetamide mixtures with increasing water content. We believe that it is due to lower structurization of water–acetamide solution as compared to water–urea solution, owing to the structure-breaking effect of the alkyl substituent. This increases the dye dissolvation (see table). The enthalpy contribution to dye solution increases with increasing water content in the water–acetamide mixture. The role of entropy in dye dissolution decreases from water to water–amide mixtures: the entropy becomes negative.

On the whole, dissolution of the dye in water–amide mixtures is less endothermic than in water, and this is due not only to specific interaction of amide molecules with water, but also to the effect of hydrophobic hydration, i.e., liberation of the additional energy as a result of increasing number and strength of H bonds between water and amide molecules surrounding the dye molecules. Hydrophobic hydration, in turn, favors strengthening of associates of organic substances in the solution [3, 5].

CONCLUSIONS

(1) The solubility of 1-amino-4-hydroxyanthraquinone in water and aqueous amides was studied by isothermal saturation within the 313–353 K range. The dissolving power of water–amide mixtures with the 30–50 wt % water content with respect to the dye is higher than that of water. The solubility of 1-amino-4-hydroxyanthraquinone in water–acetamide mixture depends of the mixture composition and is higher than the solubility in water–urea mixture.

(2) The main factor of dissolution of the dye in water is the entropy change. Dissolution of the dye in water–amide mixtures is characterized by increasing enthalpy contribution to the free energy of solution.

REFERENCES

1. *Chromatography: Fundamentals and Applications of Chromatographic and Electrophoretic Methods*, Heftmann, E., Ed., Amsterdham: Elsevier, 1983.
2. Fain, V.Ya., *Tablitsy elektronnykh spektrov antrakhinona i ego proizvodnykh* (Tables of Electronic Spectra of Anthraquinone and Its Derivatives), Moscow: Khimiya, 1970.
3. Petropavlovskii, G.A. and Zimina, T.R., *Zh. Prikl. Khim.*, 1994, vol. 67, no. 5, pp. 705–721.
4. Belousov, V.P. and Panov, M.Yu., *Termodinamika vodnykh rastvorov neelektrolitov* (Thermodynamics of Aqueous Solutions of Nonelectrolytes), Leningrad: Khimiya, 1983.
5. Gordon, J., *The Organic Chemistry of Electrolyte Solutions*, New York: Wiley, 1975.

Russian Journal of Applied Chemistry, Vol. 75, No. 3, 2002, pp. 378–384. Translated from Zhurnal Prikladnoi Khimii, Vol. 75, No. 3, 2002, pp. 391–397.
Original Russian Text Copyright © 2002 by Shul'ga, Samusevich.

SORPTION AND ION-EXCHANGE PROCESSES

Lead(II) Sorption by Magnesium Phosphates

N. B. Shul'ga and V. V. Samusevich

Institute of General and Inorganic Chemistry, National Academy of Sciences of Belarus, Minsk, Belarus

Received May 4, 2000; in final form, July 2001

Abstract—Lead(II) sorption from aqueous solutions by various magnesium phosphates was studied. The sorption kinetics was studied. Magnesium phosphates show high performance in treatment of lead-containing solutions under static and dynamic conditions.

Recently the interest in phosphate sorbents increased again. The sorption of heavy metal ions, including lead, from solutions by zirconium [1, 2] and calcium [2–4] phosphates was studied. It is presumed in these papers that the sorption occurs by the ion-exchange mechanism; however, in certain cases the release of exchanging ions into the solution was out of equivalent stoichiometry [5], which suggests that the process can be complicated by side chemical reactions. Previous data [6] showed that the lead(II) sorption by hydroxyapatite $Ca_{10}(PO_4)_6(OH)_2$ is accompanied by complicated topochemical transformations affecting the sorption parameters.

The ion-exchange properties of magnesium phosphates are poorly understood. Vol'khin *et al.* [7, 8] studied the ion exchange of alkali metals on $MgHPO_4 \cdot 3H_2O$, $Mg_3(PO_4)_2 \cdot 22H_2O$, and $MgNH_4PO_4 \cdot H_2O$. In [9, 10], it was shown that acid magnesium hydrophosphates can be used to sorb copper(II) and also other heavy metal (cadmium, nickel, cobalt, and mercury) ions from solutions. These facts suggest that magnesium phosphates can exhibit a sorption activity toward lead(II).

In this work we studied sorption of lead(II) by various magnesium phosphates. To optimize the sorption process, we have studied the kinetics of lead(II) sorption from dilute (0.1–0.0005 M) solutions of nitrates at 20°C under static conditions. The sorption isotherms were obtained, and the characteristics of magnesium phosphates under study were determined. Based on these data, the optimal sorption conditions were found and solutions contaminated with lead(II) were purified under dynamic conditions.

EXPERIMENTAL

Samples were synthesized by known procedures. Magnesium ammonium phosphate monohydrate $MgNH_4PO_4 \cdot H_2O$ was prepared by combining 1 M solutions of magnesium chloride (chemically pure grade) and ammonium hydrophosphate (analytically pure grade) in a 1 : 3 ratio at 90°C [11]. Crystalline magnesium hydrophosphate trihydrate $MgHPO_4 \cdot 3H_2O$ was prepared by the reaction of a 35% solution of magnesium sulfate (chemically pure grade) and 50% orthophosphoric acid (chemically pure grade), taken in an equimolar ratio, at 40°C [12]. The resulting crystalline samples were analyzed for the contents of lead(II) and magnesium(II) (by complexometric titration with xylenol orange and eriochrome black, respectively, as indicators), phosphorus (photocolorimetrically after formation of molybdenum blue), and nitrogen (by the Kjeldahl method) [13]. The water content was determined by the weight loss of samples on calcination (minus gaseous ammonia in the case of $MgNH_4PO_4 \cdot H_2O$).

Samples prepared for the analysis were dissolved in hydrochloric acid, as the use of, e.g., nitric acid can noticeably distort the results of phosphorus determination. The anlytical data were consistent with the above-given formulas. The X-ray patterns of the crystalline products coincide with published data [14] for the corresponding salts.

Magnesium orthophosphate was prepared by the reaction of solutions of magnesium sulfate (chemically pure grade) and sodium hydrophosphate (analytically pure grade) at pH 9 [15], maintained by adding sodium hydrocarbonate. At 40°C, an X-ray amorphous product is formed, identified by chemical analysis as $Mg_3(PO_4)_2 \cdot 6H_2O$.

When studying lead(II) sorption under static conditions, 0.2 g of a sample under study (from the sieved 100–200-μm fraction) was brought in contact at room temperature with 5×10^{-4}–0.1 M solutions of $Pb(NO_3)_2$ at a certain ratio R between the liquid (ml)

1070-4272/02/7503-0378$27.00 © 2002 MAIK "Nauka/Interperiodica"

Table 1. Chemical compositions of $Pb(NO_3)_2$ solutions and results of X-ray phase analysis of magnesium phosphates before and after lead(II) sorption.* τ = 24 h, T = 20°C, R = 150

c_{eq}, mM	c_0, mM			$\overline{Pb}^{2+}$, mg-equiv g^{-1}	$\overline{Pb}^{2+}$: Mg^{2+}, mol : mol	pH		Phase composition of solid product
	Pb^{2+}	Mg^{2+}	$H_nPO_4^{3-n}$			before sorption	after sorption	
				$Mg_3(PO_4)_2 \cdot 6H_2O$				
2.5	0**	–	0	0.76	–	5.23	–	$Mg_3(PO_4)_2 \cdot 6H_2O$
5.0	0	4.5	0	1.5	1.11 : 1	4.95	–	$Mg_3(PO_4)_2 \cdot 6H_2O$, $Pb_5(PO_4)_3OH$
25.0	0	22.9	–	7.6	1.09 : 1	4.60	3.00	〃
50.0	0.8	45.5	0	14.8	1.12 : 1	4.30	2.55	$Pb_5(PO_4)_3OH$, $Mg_3(PO_4)_2 \cdot 6H_2O$
100.0	39.0	53.1	0	18.3	1.15 : 1	4.05	2.80	$Pb_5(PO_4)_3OH$
				$MgHPO_4 \cdot 3H_2O$				
5.0	0	–	–	1.5	–	4.95	–	$MgHPO_4 \cdot 3H_2O$
10.0	0	–	–	3.0	–	–	–	〃
25.0	0	15.0	3.0	7.6	1.67 : 1	4.60	2.50	$MgHPO_4 \cdot 3H_2O$, $Pb_5(PO_4)_3OH$
50.0	2.5	29.7	0	14.1	1.6 : 1	4.30	2.48	$Pb_5(PO_4)_3OH$, $MgHPO_4 \cdot 3H_2O$
100.0	25.2	39.4	0	22.0	1.9 : 1	4.05	2.39	$Pb_2PO_4NO_3 \cdot H_2O$, $Pb_5(PO_4)_3OH$
				$MgNH_4PO_4 \cdot H_2O$				
5.0	0	0.9	–	1.5	–	4.95	–	$MgNH_4PO_4 \cdot H_2O$
25.0	0	–	–	7.6	1.67 : 1	4.60	3.14	$MgNH_4PO_4 \cdot H_2O$, $Pb_5(PO_4)_3OH$
50.0	0.9	29.8	–	14.9	1.65 : 1	4.30	3.00	$Pb_5(PO_4)_3OH$, $MgNH_4PO_4 \cdot H_2O$
100.0	86.5	9.0	–	3.3	1.50 : 1	4.05	4.74	$MgNH_4PO_4 \cdot H_2O$

* (c_0) Initial concentration of lead(II) in solution, (c_{eq}) equilibrium concentration of ions in solution, and ($\overline{Pb}^{2+}$) amount of sorbed lead.

** The concentration of this component was below the detection limit (less than 5×10^{-5} M for Mg^{2+} and Pb^{2+} and less than 1×10^{-6} for phosphate anions).

and solid (g) phases. To determine the sorption capacity, R was varied from 150 to 28000 (from 30 to 5600 ml of solution per 0.2 g of sorbent), and in kinetic experiments it was chosen in each particular case so as to ensure a constant (1.5-fold) excess of lead(II) at complete transformation of the initial sorbent into the product, irrespective of solution concentration. The resulting water–salt systems were kept at 20°C for various periods (0–48 h) with intermittent stirring. Then the precipitates were separated from the solution, washed with water, and dried in air to constant weight, after which the contents of lead, magnesium, and phosphorus were determined by the above-described techniques. The equilibrium liquid phases were analyzed similarly. The solution pH during sorption was monitored with an EV-74 ionometer in a parallel series of experiments.

When studying sorption under dynamic conditions, we stirred 0.1 g of a sorbent in aqueous suspension with silica in a 1 : 20 ratio and filled with this mixture a column 0.5 cm in diameter and 5 cm high. A dilute 5×10^{-4} M solution of lead nitrate was passed through the column at a constant rate (~1 ml min^{-1}). Eluate samples were taken at regular intervals, and the lead(II) and magnesium(II) contents were determined therein. On this basis, the output curves were plotted and the performance of the column was evaluated with respect to both the degree of solution concentrating and the degree of the sorbent exchange. The phase composition of the sorption product was also

Table 2. Chemical analysis of $Pb(NO_3)_2$ solutions before and after lead(II) sorption by magnesium phosphates. τ = 24 h, T = 20°C

a_0, mmol g^{-1}	R	c_0, mM	$c_{eq}(Pb^{2+})$, mM	$\overline{Pb}^{2+}$, mmol g^{-1}
		$Mg_3(PO_4)_2 \cdot 6H_2O$		
0.375	150	2.5	0	0.38
0.75	150	5.0	0	0.75
3.75	150	25.0	0	3.8
5.0	2500	2.0	0	5.0
7.5	150	50.0	0.8	7.4
7.75	2500	3.1	0	7.8
10.0	2500	4.0	0.35	9.3
14.0	28 000	0.5	0.17	9.3
14.0	2800	5.0	1.6	9.4
14.0	280	50.0	16.8	9.3
15.0	150	100.0	39.0	9.2
20.0	200	100.0	53.0	9.4
		$MgHPO_4 \cdot 3H_2O$		
0.75	150	5.0	0	0.75
1.5	150	10.0	0	1.5
3.75	150	25.0	0	3.8
7.5	150	50.0	2.5	7.1
15.0	15 000	1.0	0.4	9.0
15.0	3000	5.0	2.2	8.4
15.0	600	25.0	6.5	11.1
15.0	300	50.0	12.3	11.3
15.0	150	100.0	25.2	11.2
25.0	500	50.0	27.0	11.5
25.0	250	100.0	56.0	11.0
		$MgNH_4PO_4 \cdot H_2O$		
0.75	150	5.0	0	0.75
3.75	150	25.0	0	3.8
7.5	150	50.0	0.9	7.5
15.0	600	25.0	8.5	9.8
15.0	300	50.0	14.9	10.5
30.0	600	50.0	32.3	10.6

determined. The dilution of the phosphate sorbent with silica (which is almost inert in the process under study) allows the experiment to be carried out much faster. With neat $Mg_3(PO_4)_2 \cdot 6H_2O$, at the same concentration of the initial solution and the same elution rate, the lead(II) breakthrough would occur only after several months.

The X-ray phase analysis of the initial samples and solid products formed in various stages of the sorption was carried out on a DRF-2.0 diffractometer (CuK_α radiation).

The data on the lead(II) sorption under static conditions [24-h contact of $MgHPO_4 \cdot 3H_2O$, $Mg_3(PO_4)_2 \cdot 6H_2O$, and $MgNH_4PO_4 \cdot H_2O$ with solutions of lead(II) nitrate at 20°C] are given in Tables 1 and 2. These data show that, as the lead(II) content in the initial solution per gram of the sorbent (a_0) increases, the amount of the sorbed lead(II) regularly increases irrespective of whether this increase is reached at the expense of increasing solution concentration at a constant volume (Table 1) or at the expense of changing R (Table 2). If the a_0 value is fixed, variation of the concentration of the initial solution (and, correspondingly, of R) only slightly affects the value of sorption. Only with $MgNH_4PO_4 \cdot H_2O$ an anomaly is observed, namely, at R = 150 the increase in the solution concentration from 0.05 to 0.1 M results in a sharp reduction in the amount of the sorbed lead(II) (Table 1). As will be shown below, this unexpected effect is due to the arising diffusion hindrances in delivery of lead(II) ions to the sorbent surface through a layer of the forming sorption product.

The sorption capacities of $Mg_3(PO_4)_2 \cdot 6H_2O$, $MgHPO_4 \cdot 3H_2O$, and $MgNH_4PO_4 \cdot H_2O$, determined from the corresponding isotherms, are as high as 18.8, 22.6, and 21.8 mg-equiv g^{-1}, respectively, whereas one of the best known inorganic sorbents (zirconium phosphate [1]) sorbs no more than 5 mg-equiv (2.5 mmol) of Pb^{2+} per gram. The isotherms in Fig. 1 almost coincide with the ordinate up to high sorption values, which means that high exchange capacity of magnesium phosphates can be reached even at low equilibrium concentrations of lead(II) in solution. This fact makes magnesium phosphates suitable for the purification of both concentrated and very dilute solutions. The data on lead(II) sorption from 0.001–0.1 M $Pb(NO_3)_2$ solutions by various phosphate sorbents at R = 150 (30 ml of solution per 0.2 g of sorbent) are shown in Fig. 2a. Under these conditions, $Mg_3(PO_4)_2 \cdot 6H_2O$ and $MgNH_4PO_4 \cdot H_2O$ completely remove lead(II) from its solutions with an initial concentration of up to 0.05 M, and magnesium hydrophosphate sorbs 95% of lead(II) from 0.05 M solutions. At the same time, zirconium hydrophosphate under these conditions sorbs less than a half of the initial lead(II). With this sorbent, the 100% purification is reached only with 0.005 M and less concentrated solutions.[1]

The initial solution concentration at which lead is completely removed depends on the liquid : solid

[1] The A values for zirconium phosphate were calculated from the sorption isotherms given in [1] for the liquid phase : sorbent ratio of 100 used in that work.

ratio; however, the experimental data obtained at different R values are well fitted by the curves in the coordinates degree of purification–total amount of lead(II) in the initial solution per gram of sorbent (Fig. 2b). This fact allows us to calculate easily in each particular case the amount of the sorbent required for exhaustive purification of the solution. Later, when discussing the kinetic data, we shall consider several cases of deviations of the above-mentioned trend (Fig. 2b, outlying points of curves *1* and *3*), which result from a change in the sorption mechanism.

The sorption rate is of considerable practical importance for the use of sorbents for treatment of solutions to remove heavy metal ions. In the case of inorganic sorbents it can depend in a complicated way on the sorption conditions, sorbent structure, and the concomitant chemical and phase transformations. Let us consider the kinetic features and mechanism of lead(II) sorption by various magnesium phosphates.

If the sorption occurs by the ion-exchange mechanism

$$MgNH_4PO_4 \cdot H_2O + Pb^{2+} \rightarrow PbNH_4PO_4 \cdot H_2O + Mg^{2+}, \quad (1)$$

1 mol of magnesium ammonium phosphate can sorb 1 mol of lead(II). The maximum amount of lead(II) that can be sorbed in the system obtained by mixing 200 mg of the monohydrate and 60 ml of a 0.05 M solution of lead nitrate is 1.29 mmol. At the same time, it was found that the lead(II) concentration in such solution decreases within a day to 0.015 M, which corresponds to the sorption of 2.1 mmol of Pb^{2+}. The excess sorption can result from chemical transformation of magnesium ammonium phosphate either to lead orthophosphate [reaction (2)] or to pyromorphite [reaction (3)]:

$$3MgNH_4PO_4 \cdot H_2O + 3Pb^{2+} \rightarrow Pb_3(PO_4)_2 + 2Mg^{2+} + 2NH_4^+ + H_2O, \quad (2)$$

$$3MgNH_4PO_4 \cdot H_2O + 5Pb^{2+} \rightarrow Pb_5(PO_4)_3OH + 3Mg^{2+} + 3NH_4^+ + H^+. \quad (3)$$

The X-ray phase analysis of the sorption product shows that the process develops according to (3). This equation is also consistent with the experimental molar ratio of the sorbed lead(II) and released magnesium(II), $Pb^{2+} : Mg^{2+}$, which is close to 5 : 3 (Table 1).

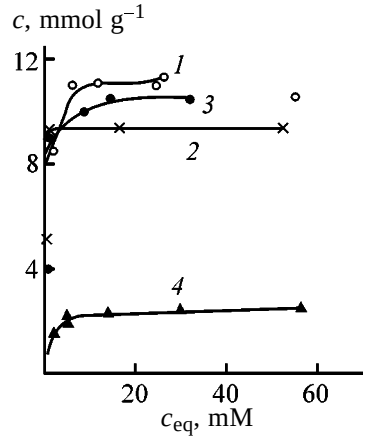

Fig. 1. Isotherms of lead(II) sorption by samples of magnesium phosphates: (c) $\overline{Pb}^{2+}$ concentration in the sorbent and (c_{eq}) Pb^{2+} concentration in the equilibrium solution. Sorbent: (*1*) $MgHPO_4 \cdot 3H_2O$, (*2*) $Mg_3(PO_4)_2 \cdot 6H_2O$, (*3*) $MgNH_4PO_4 \cdot H_2O$, and (*4*) $ZrHPO_4$ [1]; the same for Fig. 2.

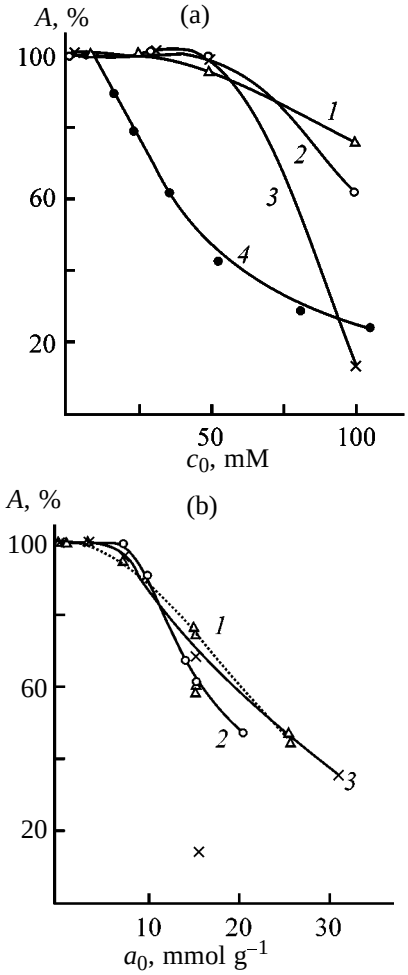

Fig. 2. Plots of the degree of lead removal A from $Pb(NO_3)_2$ solutions by magnesium phosphate samples vs. (a) the initial solution concentration c_0 and (b) total lead(II) content a in the initial solution.

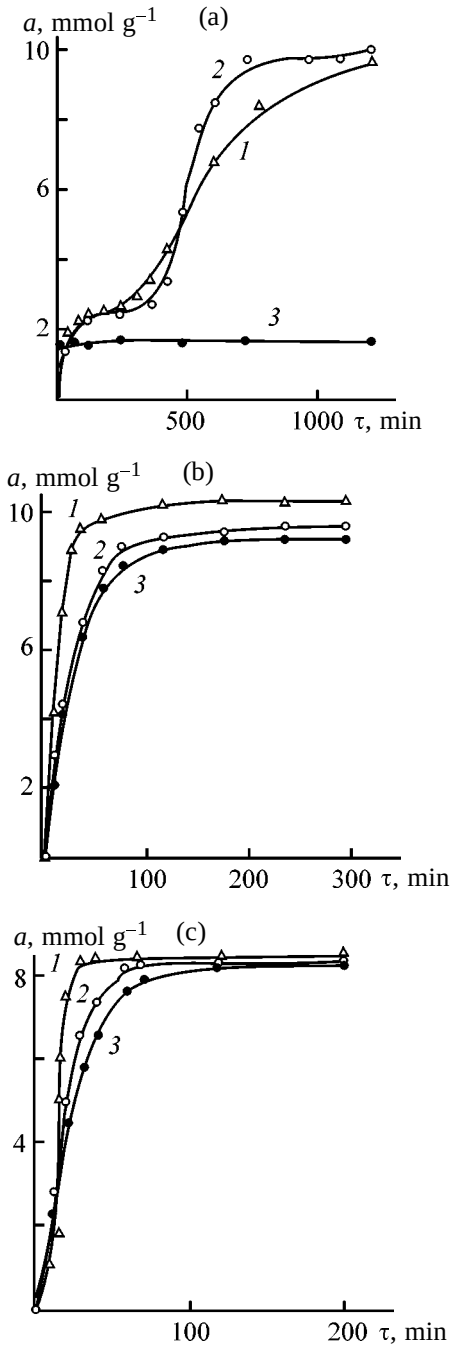

Fig. 3. Kinetic curves of lead(II) sorption by samples of (a) $MgNH_4PO_4 \cdot H_2O$, (b) $Mg_3(PO_4)_2 \cdot 6H_2O$, and (c) $MgHPO_4 \cdot 3H_2O$ from $Pb(NO_3)_2$ solutions. (*a*) Amount of sorbed Pb^{2+} (mmol per gram of sorbent) and (τ) time. Initial solution concentration (mM): (a) (*1*) 25.0, (*2*) 50.0, and (*3*) 100.0; (b) (*1*) 50.0, (*2*) 5.0, and (*3*) 0.5; (c) (*1*) 50.0, (*2*) 5.0, and (*3*) 2.5.

The kinetic curves of lead(II) sorption by magnesium ammonium phosphate from solutions of various concentrations are shown in Fig. 3 [complete transformation of $MgNH_4PO_4 \cdot H_2O$ into pyromorphite $Pb_5(PO_4)_3OH$ corresponds to the sorption of 10.7 mmol of lead(II) per gram of the sorbent]. The process starts at a maximal rate for all concentrations, but then it sharply decelerates at relatively low conversions. The X-ray phase analysis of the products formed in this stage suggests that the plateau in the kinetic curves is due to the formation of an amorphous product preventing the delivery of lead ions to the unchanged sorbent surface. When the system is kept at a constant temperature, the product crystallizes, the hindering layer is destroyed, and the sorption rate increases again. The time required to activate the sorption process is 3.5 and 5 h for 0.025 and 0.05 M solutions of $Pb(NO_3)_2$, respectively. When lead(II) is sorbed from 0.1 M solution of $Pb(NO_3)_2$, after the initial fast sorption (a = 1.8 mmol g^{-1}) the process practically stops, resuming only after 4–5 days. As a result, when $MgNH_4PO_4 \cdot H_2O$ is kept at R = 150 for a day in contact with solutions to be purified, in the plot of the degree of purification A vs. the initial concentration c_0 (Fig. 2a, curve *3*) the point corresponding to c_0 = 0.1 M lies much lower as compared to not only other magnesium phosphates, but also zirconium hydrophosphate. The sorption features are even more pronounced at c_0 = 0.1 M in the plot of A vs. total lead(II) amount in the initial solution a_0, in which the data obtained at different R values are summarized (Fig. 2b). As the contact time τ is varied, the shapes of the concentration dependences of the sorption capacity and degree of purification noticeably change, and, taking into account the kinetic features revealed, we can always choose such a value of τ at which the sorption capacity of the sorbent would be realized to a full extent (in case of the 0.1 M solution it takes more than 10 days).

Thus, when using $MgNH_4PO_4 \cdot H_2O$, the course of sorption is determined by the conditions of diffusion of exchanging ions, which, in their turn, depend on the rate of crystallization of the forming product.

The lead(II) sorption by magnesium phosphate $Mg_3(PO_4)_2 \cdot 6H_2O$ also involves the pyromorphite formation:

$$3Mg_3(PO_4)_2 \cdot 6H_2O + 10\,Pb^{2+} \rightarrow 2Pb_5(PO_4)_3OH + 9Mg^{2+} + 2H^+ + 4H_2O. \quad (4)$$

In this case, the maximal sorption capacity (18.0 mg-equiv per gram of the sorbent) calculated taking into account Eq. (4) is reached in the experiment. Such a reaction pattern is also proved by X-ray phase analysis, $Pb^{2+} : Mg^{2+}$ ratio, and also by a pronounced decrease in the solution pH (Table 1).

Lead(II) sorption from solution by magnesium orthophosphate proceeds with a high rate, which only slightly depends on the concentration of the solution to be purified (Fig. 3b). It should be noted that, in spite of high rates of orthophosphate conversion to pyromorphite, the latter is well crystallized. This seems to be due to the orientating effect of the support; therefore, a dense hindering layer is not formed in this case as it takes place when lead(II) is sorbed on magnesium ammonium phosphate. Only at a 0.05 M lead(II) concentration in the initial solution a small bend appears in curve *1*, indicating diffusion hindrance in the initial process stages.

The lead(II) sorption by crystalline magnesium hydrophosphate $MgHPO_4 \cdot 3H_2O$ is accompanied, as is the case with the other sorbents studied in this work, by the pyromorphite formation

$$3\,MgHPO_4 \cdot 3H_2O + 5Pb^{2+} \rightarrow Pb_5(PO_4)_3OH + 3Mg^{2+} + 4H^+ + 2H_2O, \quad (5)$$

with the theoretical sorption capacity of 19.1 mg-equiv g^{-1} being reached.

The kinetic curves of lead sorption at 20°C and various concentrations of $Pb(NO_3)_2$ solution are shown in Fig. 3c. At concentrations of ≤0.005 M the theoretical capacity is reached within 2 h; however, as the concentration increases, it becomes higher than the value corresponding to scheme (5). The X-ray phase analysis shows that final products formed at low and high concentrations of $Pb(NO_3)_2$ solution are different. When lead is sorbed from 0.05 M $Pb(NO_3)_2$ solution, pyromorphite formed in the initial stages transforms further into crystalline lead nitrate phosphate:

$$Pb_5(PO_4)_3OH + H^+ + 3NO_3^- + Pb^{2+} + 2H_2O \rightarrow 3Pb_2PO_4NO_3 \cdot H_2O. \quad (6)$$

Observation of the crystals in this stage of sorption shows that, as opposed to reactions (1)–(5), the transformation of pyromorphite to nitrate phosphate [Eq. (6)] occurs as spontaneous recrystallization rather than by a topochemical mechanism. As this case can be hardly described as sorption, it is necessary to clearly distinguish the areas of solid-phase (5) and liquid-phase (6) processes.

As found in [16], pyromorphite recrystallizes to nitrate phosphate when the solution pH becomes less than 2.5 as a result of reaction (5). We have calculated that, for the solid-phase sorption mechanism to become operative, the amount of the lead nitrate solution

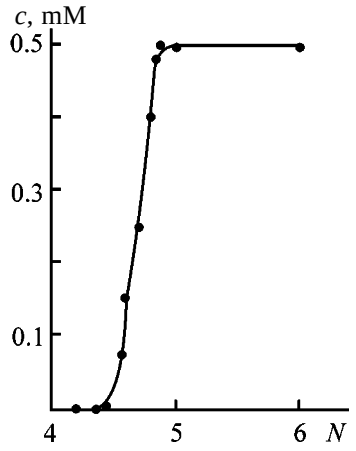

Fig. 4. Output curve of Pb^{2+} sorption on $Mg_3(PO_4)_2 \cdot 6H_2O$ from 5×10^{-4} M solution of $Pb(NO_3)_2$: (c) Pb^{2+} concentration in the purified solution and (*N*) amount of the solution passed through the column (thousand column volumes).

should be more than 300 ml per 0.2 g of magnesium hydrophosphate ($R > 1500$). In this case, the solution concentration is not of crucial importance, it should only be sufficient for the complete transformation by scheme (5). A similar calculation for partial sorption shows that the solid-phase sorption mechanism can become operative also at $R < 1500$. These data give insight into the above-mentioned anomaly, when the use of magnesium hydrophosphate as a sorbent results in the fact that the degree of solution purification *A* takes different values at the equal initial lead(II) content $a_0 = 15$ mmol g^{-1} (Table 2; Fig. 2b, curve *1*). The point is that two of four points were obtained at *R* 300 and 600, and the other two points, at *R* 3000 and 15 000. These latter points lie out of the A–a_0 curve, as, unlike the other points in this curve corresponding to the recrystallization by scheme (6), they reflect the solid-phase transformation by scheme (5).

Thus, it is desirable to carry out lead(II) sorption by $MgHPO_4 \cdot 3H_2O$ at high *R*, which in actual practice corresponds to the treatment of very dilute solutions. However, in this case it is necessary to take into account the possibility of partial dissolution of the sorbent, which prevents its use under dynamic conditions. The solubility of magnesium ammonium phosphate $MgNH_4PO_4 \cdot H_2O$ in dilute solutions is minimal, but the induction period characteristic of this sorbent (the possibility of diffusion hindrance of the process, at least in sorption from concentrated solutions) can also lead to complications in the implementation of the column version of the lead(II) sorption.

Thus, magnesium orthophosphate $Mg_3(PO_4)_2 \cdot 6H_2O$ is the best lead(II) sorbent under dynamic conditions. Figure 4 shows the output curve obtained on

passing a 5×10^{-4} M solution of lead nitrate through a column packed with magnesium orthophosphate deposited on silica of the same particle size as the sorbent. Breakthrough of lead (II) was observed only on passing more than 4000 column volumes of the solution. It should be noted that more than 50% of the theoretical column sorption capacity calculated by Eq. (4) is utilized in this case.

CONCLUSIONS

(1) Magnesium phosphates $MgHPO_4 \cdot 3H_2O$, $Mg_3(PO_4)_2 \cdot 6H_2O$, and $MgNH_4PO_4 \cdot H_2O$ show high performance in the purification of lead-contaminated solutions under static conditions (sorption capacity 22.6, 18.8, and 21.8 mg-equiv g^{-1}, respectively).

(2) Lead(II) sorption by magnesium phosphates from solution is accompanied by complicated topochemical transformations of the sorbents. Proper account of these transformations allows optimization of the sorption process.

(3) The best sorbent for lead(II) under dynamic conditions is magnesium orthophosphate, which allows 4000 column volumes of a 5×10^{-4} M solution to be completely purified; in this case, more than 50% of the theoretical sorption capacity is utilized.

REFERENCES

1. Perekhozheva, T.N. and Shaprygin, L.M., *Zh. Neorg. Khim.*, 1992, vol. 37, no. 2, pp. 280–286.
2. Bortun, A.I. and Kvashchenko, A.P., *Zh. Fiz. Khim.*, 1990, vol. 64, no. 7, pp. 1963–1967.
3. Lazic, S. and Vucovic, Z., *J. Radioanal. Nucl. Chem., Articles*, 1991, vol. 149, no. 1, pp. 161–165.
4. Suzuki, T., Hatsushika, T., and Hayskawa, Y., *J. Chem. Soc., Faraday Trans. 1*, 1981, vol. 77, pp. 1059–1062.
5. Suzuki, T., Hatsushika, T., and Miyake, M., *J. Chem. Soc., Faraday. Trans. 1*, 1982, vol. 78, pp. 3605–3611.
6. Shashkova, I.L., Shul'ga, N.A., and Samusevich, V.V., *Zh. Prikl. Khim.*, 1998, vol. 43, no. 1, pp. 52–57.
7. Vol'khin, V.V., Tatlieva, T.N., and Zil'berman, M.Yu., *Izv. Akad. Nauk SSSR, Neorg. Mater.*, 1976, vol. 12, no. 9, pp. 1634–1638.
8. Vol'khin, V.V., Leont'eva, G.V., and Onorin, S.A., *Izv. Akad. Nauk SSSR, Neorg. Mater.*, 1973, vol. 9, no. 6, pp. 1041–1046.
9. Maki, T. and Okhubo, M., *Nippon Kagaku Kaishi*, 1976, no. 1, pp. 50–58.
10. JPN Patent 75–51090.
11. Mazaeva, M.N., Remen, R.E., and Petrov, E.I., *Khim. Prom–st.*, 1969, no. 4, pp. 275–277.
12. Shchegrov, L. N., *Fosfaty dvukhvalentnykh metallov* (Phosphates of Bivalent Metals), Kiev: Naukova Dumka, 1987.
13. *Sbornik tekhnicheskikh uslovii na khimicheskie reaktivy* (Collection of Technical Specifications for Chemicals), Moscow: Khimiya, 1965, issue 1.
14. *ASTM Standard X-ray Diffraction Powder Patterns, Inorganic*, Philadelphia, 1976.
15. Pechkovskii, V.V., Mel'nikova, R.Ya., Baranchikova, T.I., and Dzyuba, E.D., *Zh. Neorg. Khim.*, 1979, vol. 24, no. 3, pp. 651–656.
16. Shul'ga, N.A., Galkova, T.N., and Samusevich, V.V., *Zh. Neorg. Khim.*, 1999, vol. 44, no. 7, pp. 1064–1070.

Russian Journal of Applied Chemistry, Vol. 75, No. 3, 2002, pp. 385–388. Translated from Zhurnal Prikladnoi Khimii, Vol. 75, No. 3, 2002, pp. 398–400.
Original Russian Text Copyright © 2002 by Ergozhin, Bektenov, Akimbaeva.

SORPTION AND ION-EXCHANGE PROCESSES

Polyfunctional Anion Exchanger as Sorbent of Copper(II) and Vanadium(V) Ions

E. E. Ergozhin, N. A. Bektenov, and A. M. Akimbaeva

Bekturov Institute of Chemical Sciences, Almaty, Kasakhstan

Received February 12, 2001

Abstract—Sorption of copper and vanadium ions from aqueous solutions by cross-linked anion exchanger based on a copolymer of glycidyl methacrylate with styrene and polyethylenimine was studied. The effect of the solution pH on the completeness of sorption is considered.

The continuous and impetuous expansion of the application fields of synthetic polyelectrolytes is stimulating the growing interest in synthesis of ion-exchange polymers. Particular attention is attracted by sorption recovery of metals from aqueous solutions and metal separation, widely used in hydrometallurgy, chemical technology, environmental protection, and analytical chemistry [1, 2]. To enable these applications, a wide variety of ion-exchange resins, membranes, and fibers based on polymer ion exchangers of cation- and anion-exchange type are being manufactured at present. Of much interest for obtaining various ion-exchange polymers are copolymers of glycidyl methacrylate, exhibiting a high reactivity and a number of valuable physicochemical properties. The known methods for preparing ion exchangers of the styrene type are multistage and involve the use of toxic and sometimes difficultly available monomers. Therefore, a promising direction in the field of synthesis of ion exchangers is the use of a copolymer of glycidyl methacrylate and styrene, which allows synthesis of polyelectrolytes with high chemical and thermal stability and mechanical strength and makes it possible to perform reactions under mild conditions with the possibility of controlling the composition and properties of the obtained products [3, 4]. In radical homo- and copolymerization of glycidyl esters, the double bond is cleaved and the epoxy group, whose presence in a macromolecule allows synthesis of infusible and insoluble cross-linked products, is preserved.

In this work, we tested for sorption of metal ions an anion exchanger prepared by modifying with polyethylenimine a copolymer of glycidyl methacrylate and styrene (GMA–ST–PEI) [3].

EXPERIMENTAL

The polyfunctional anion exchanger GMA–ST–PEI was synthesized by the procedure reported in [3]. The IR spectra of the initial and metal-containing anion exchangers were measured in KBr pellets on a UR-20 spectrophotometer. Polymer samples were dried in a vacuum drying box to constant weight prior to each set of experiments. The static exchange capacity (SEC) was determined using the technique described in [5]. A weighed portion (1 g in terms of dried substance) of anion-exchange resin in the OH form was placed in 200 ml of 0.1 N HCl solution. The mixture was kept for 24 h with intermittent stirring. After that the ion exchanger was filtered off, and 25 ml of the filtrate was taken with a pipette and titrated with 0.1 N NaOH solution in the presence of phenolphthalein. The SEC of the anion exchanger (mg-equiv g^{-1}) was calculated by the formula

$$\mathrm{SEC} = \frac{[200F - (200/25)VF_1] \times 0.00365 \times 1000}{36.5g} = \frac{200F - 8VF_1}{10g},$$

where F is the correction factor for 0.1 N HCl solution, V is the volume of 0.1 N NaOH solution (ml), F_1 is the correction factor for 0.1 N NaOH solution, 0.00365 is the titer of 0.1 N HCl solution, 36.5 is the molecular weight of HCl, and g is the weighed portion of anion exchanger (g).

The sorption of copper and vanadium ions was done under static conditions from copper sulfate solution (initial concentration of $CuSO_4 \cdot 5H_2O$ 6.24 g l^{-1})

1070-4272/02/7503-0385$27.00 © 2002 MAIK "Nauka/Interperiodica"

and sodium vanadate (initial concentration of $Na_3VO_4 \cdot 2H_2O$ 6 g l^{-1} in terms of V_2O_5) [6]. To determine the sorption capacity (SC) of the anion exchanger for ions in relation to the solution pH, weighed portions of the polymer (SEC 8.09 mg-equiv g^{-1}, grain size 0.25–0.50 mm, weight 0.10–0.12 g) were placed in six vessels and brought in contact for 6–7 days [6] with a solution containing 20 ml of a solution of a salt of the corresponding metal, sulfuric acid (for maintaining constant the solution pH) in amount of 0 to 12 ml, and water to make the total volume of solution in each vessel equal to 40 ml. The solution pH was measured with an EV-74 pH-meter with the accuracy $\Delta = 0.02$. The content of vanadium ions was found by titration with Mohr's salt in the presence of phenylanthranilic acid. The concentration of copper cations was determined by atomic-absorption spectroscopy.

Chemical modification of the starting polymer GMA–ST, containing active epoxy groups, with aliphatic polyamine PEI was carried out in toluene by the scheme

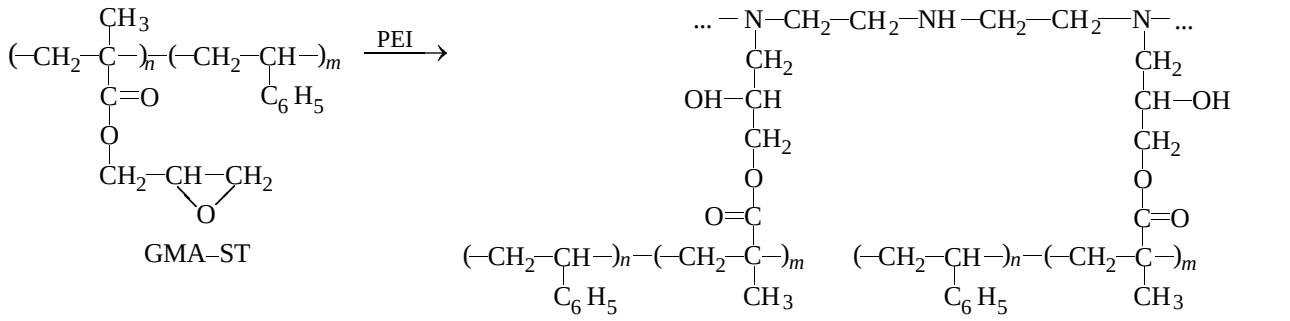

The practical use of ion exchangers involves their prolonged contact with water and aqueous solutions, occurring at elevated temperatures. In the process, physicochemical and technical properties of ion exchangers undergo irreversible changes associated with degradation of the polymer matrix or functional groups. Therefore, the thermal stability is an important factor for these materials. The recent success in studies of the mechanism and kinetics of thermal degradation of ion exchangers allows, in some cases, proper choice of ion exchanger and prediction of the service life and direction of changes in physicochemical properties of ion exchangers [7]. It has been established that two mechanisms of thermal degradation of anion exchangers are possible:

deamination

$$R\text{–}CH_2\text{–}N^+(CH_3)_3OH^- \xrightarrow[\Delta]{H_2O} RCH_2OH + N^+H(CH_3)_3OH^- \quad (1)$$

and dealkylation

$$R\text{–}CH_2\text{–}N^+(CH_3)_3OH^- \xrightarrow[\Delta]{H_2O} RCH_2\text{–}N^+H(CH_3)_2OH^- + CH_3OH. \quad (2)$$

Degradation by the first scheme is accompanied by complete loss of capacity with the formation of nonionic alcohol groups. The second way assumes conversion of functional groups with higher basicity into low-basic groups, with possible insignificant change in the ion exchanger capacity.

The thermal stability of anion exchangers depends not only to the structure of amino groups, but also on the structure of the ion exchanger skeleton. Of three constituents of a swollen ion exchanger (polymer matrix, functional groups, and water), the functional groups are the least stable [7]. Therefore, decomposition of ion exchangers commonly starts with functional groups and primarily affects the exchange capacity (after tests of ion exchangers), which is the quantitative criterion of thermal stability. According to some studies [7, 8], the ion exchanger is more stable in the salt form, compared with the basic form. The anion exchanger in the salt form is characterized by reactions described for an anion exchanger in the hydroxide form, with the exception of dealkylation to give methanol [Eq. (2)]. Therefore, experiments were carried out with samples in the OH form, boiled in water for 48 h. On heating the synthesized anion exchanger in water, its exchange capacity changes somewhat (6.02% loss of capacity). A different behavior is observed for EDE-10P and AV-18 commercial anion exchangers. Their loss of capacity on heating in water

to 100°C for 48 h is 23%, which is nearly 4 times that for the anion exchanger under study. Presumably, the matrix degrades, with decrease in the cross-linking density and elimination of the functional groups of the ion exchanger.

Polyfunctional cross-linked and linear ion exchangers with primary, secondary, and tertiary amino groups exhibit donor properties and, when brought in contact with substances whose molecules have acceptor groups or ions, form coordination compounds via unshared electron pairs at ionogenic groups [9]. It is known that the higher the content of protonated amino groups in the polymer phase, the smaller the number of active centers coordinated with metal. Protonated ligands of coordinated compounds form no coordination compounds with metal ions. In weakly acidic, neutral, or alkaline medium, the unprotonated form of the ion exchanger is in the undissociated state; under these conditions, the interaction of the polymer with metals occurs via coordination bonding. On the whole, it was noted [8] that the sorption capacity of ion exchangers for transition metal ions grows with decreasing acidity of the medium. However, in alkaline solutions metal hydroxides can precipitate, and, therefore, copper ions were recovered with a polyelectrolyte based on GMA–ST–PEI at pH 2–5 (see table).

At pH 4.94, the capacity of the polymer for copper ions is 380 mg g^{-1}. It can be seen from the table that the sorption capacity of the polymer grows with increasing solution pH. The change in the solution color suggests occurrence of complexation.

It is known [6, 8, 10] that many polyfunctional anion exchangers well recover vanadium(V) ions from solutions of its salts. The figure shows the sorption capacity of the anion exchanger under study as a function of the solution pH. For comparison, the figure presents the curve describing the sorption of vanadium ions by a commercial polyfunctional anion exchanger of the EDE-10P brand.

The strong influence of the solution pH on the sorbent capacity is due to the influence of the ionic state of vanadium in solution [11]:

Ionic state of V	pH
VO_4^{3-}	>13
HVO_4^{2-}	8–3
$V_3O_9^{3-}$	8.0–6.6
$V_{10}O_{28}^{6-}$	6.5–6.0
$HV_{10}O_{28}^{5-}$	6.0–3.5
$H_2V_{10}O_{28}^{4-}$	3.2–2.0
VO_2^+	<2

Change in sorption capacity of anion exchanger based on GMA–ST–PEI for copper(II) ions in relation to solution pH

pH_{in}	pH_{eq}	SC, mg g^{-1}	Color of solution after sorption
4.94	5.93	380	Dark blue
2.49	4.42	118	Blue
2.04	3.12	82	″

As a result, the sorption capacity of the anion exchanger grows dramatically in the acid range and decreases with the solution pH growing further. The sorption capacity is as high as 1674 mg g^{-1} (pH 3.30) for the GMA–ST–PEI sorbent and 520 mg g^{-1} for EDE-10P.

The formation of metal ion complexes with anion exchangers was studied by IR spectroscopy. An analysis of the IR spectra of a polymer containing bound copper revealed broadening of bands associated with stretching vibrations of the N–H bond (3000–3400 cm^{-1}) and appearance of absorption in the range 200–360 cm^{-1}, attributable to a coordination bond between metal ions and amino groups. In the spectrum of the anion exchanger saturated with vanadium ions, an absorption band related to decavanadate ion appears at about 960 cm^{-1}.

CONCLUSION

An anion exchanger based on a copolymer of glycidyl methacrylate with styrene and on polyethylenimine can be effectively used for sorption of copper(II) and vanadium(V) ions from weakly acidic solutions.

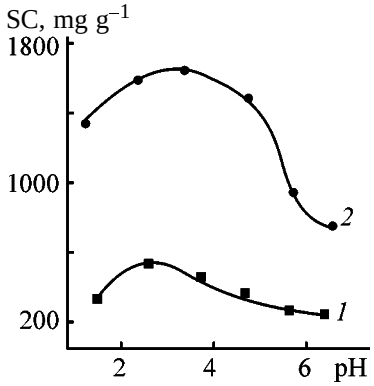

Sorption capacity SC of GMA–ST-based anion exchanger for V_2O_5 vs. solution pH. Sorbent: (*1*) EDE–10P and (*2*) GMA–ST–PEI.

REFERENCES

1. Senyavin, M.M., *Ionnyi obmen v tekhnologii i analize neorganicheskikh veshchestv* (Ion Exchange in Technology and Analysis of Inorganic Substances), Moscow: Khimiya, 1980.
2. Juo, A., Matsufune, S., Ono, H., and Egawa, H., *J. Appl. Polym. Sci*., 1997, vol. 63, no. 10, pp. 1327–1333.
3. Akimbaeva, A.M., Bektenov, N.A., and Ergozhin, E.E., *Izv. Minist. Nauki Vyssh. Obraz. Nats. Akad. Nauk Resp. Kazakhstan, Ser. Khim*., 1999, no. 3, pp. 68–73.
4. Akimbaeva, A.M., Bektenov, N.A., and Ergozhin, E.E., *Izv. Minist. Obraz. Nauki, Ser. Khim*., 2000, no. 1, pp. 67–71.
5. Toroptseva, A.M., Belogorodskaya, K.V., and Bondarenko, V.M., *Laboratornyi praktikum po khimii i tekhnologii vysokomolekulyarnykh soedinenii* (Laboratory Manual of Chemistry and Technology of Macromolecular Compounds), Leningrad: Khimiya, 1972.
6. Bektenov, N.A., Ergozhin, E.E., and Menligaziev, E.Zh., *Izuchenie sorbtsionnoi sposobnosti glitsidilmetakrilatnykh ionoobmennikov po otnosheniyu k ionam nekotorykh metallov* (Investigation of Sorption Capacity of Glycidyl Methacrylate Ion Exchangers for Ions of Some Metals), pp. 45–60.
7. Tulupov, P.E., *Stoikost' ionoobmennykh materialov* (Stability of Ion-Exchange Materials), Moscow: Khimiya, 1984.
8. Ergozhin, E.E. and Menligaziev, E.Zh., *Polifunktsional'nye ionoobmenniki* (Polyfunctional Ion Exchangers), Alma-Ata, 1989.
9. Saldadze, K.M. and Kopylova-Valova, V.D., *Kompleksoobrazuyushchie ionity* (Complexing Ion Exchangers), Moscow: Khimiya, 1980.
10. Ptitsyn, A.N., Zolotavin, V.L., and Maletina, L.E., in *Khimiya i tekhnologiya vanadievykh soedinenii* (Chemistry and Technology of Vanadium Compounds), Perm, 1974, pp. 167–171.
11. Ivakin, A.A., *Tr. Inst. Khim. Akad. Nauk SSSR, Ural. Fil*., 1968, issue 18, pp. 3–11.

Russian Journal of Applied Chemistry, Vol. 75, No. 3, 2002, pp. 389–392. Translated from Zhurnal Prikladnoi Khimii, Vol. 75, No. 3, 2002, pp. 401–403.
Original Russian Text Copyright © 2002 by Pimneva, Pakholkov.

SORPTION AND ION-EXCHANGE PROCESSES

Sorption of M(III) with KFP-12 Phosphonic Cation Exchanger from Chloride Solutions

L. A. Pimneva and V. S. Pakholkov

Tyumen State Architectural Academy, Tyumen, Russia

Received May 10, 2001

Abstract—Sorption by KFP-12 phosphonic anion exchanger of ions of triply charged metals, such as indium, gallium, yttrium, and iron, from chloride solutions was studied. The nature of bonding between sorbed cations and functional groups of the cation exchanger and the mechanism of the ion exchange reaction were elucidated.

This study is a continuation of previous investigations of the phosphonic cation exchanger KFP-12 [1–5]. It is known that phosphate cation exchangers can sorb metal ions via not only ion exchange, but also complexation. It has been established [6] that, owing to the increased electron density on the phosphoryl oxygen atom, the phosphonic cation exchanger KFP-12 via its P=O groups forms strong coordination bonds with metals having unoccupied orbitals.

EXPERIMENTAL

This study is concerned with sorption of gallium, indium, yttrium, and iron ions from 0.3 M MCl_3 solutions containing 0 to 2.0 M HCl by a macroporous phosphonic cation exchanger with exchange capacity of 7.5 mg-equiv g^{-1}. In the ammonium form, the cation exchanger has exchange capacity of 9.9, 7.6, 7.4, and 7.2 mg-equiv g^{-1} (29.6, 22.8, 22.2, and 21.5 mmol g^{-1}) for indium, iron, gallium, and yttrium ions, respectively. The cation exchanger dissociates in two stages, with the apparent dissociation constants pK_1 3.5 and pK_2 8.9, respectively (calculated for α = 0.5). The sorption capacity of the KFP-12 cation exchanger depends on the state of ionic groups, form of the cation exchanger (H^+ , NH_4^+), and pH of the equilibrium solution. The maximum sorption capacity is characteristic of the KFP-12 cation exchanger in the completely ionized state (pH > 3). Under such conditions, metal sorption occurs via not only ionic, but also coordination bonding.

The initial solutions, their preparation, analytical techniques, and experimental procedure were the same as those described in [1–4]. All experiments were carried out at room temperature under static conditions.

The mechanism of sorption of triply charged indium, gallium, yttrium, and iron ions was studied by IR spectroscopy. The IR spectra were recorded on a UR-20 spectrometer in the frequency range 700–1600 cm^{-1}, using the KBr technique. The IR spectra of KFP-12 cation exchanger with sorbed indium, gallium, yttrium, and iron ions were analyzed in comparison with the spectra of the cation exchanger in the H^+ form.

A study of the behavior of triply charged ions of indium, gallium, yttrium, and iron in chloride solutions demonstrated that the ions exist in the form of positively and negatively charged chloride and hydroxo complexes, and also as neutral molecules. It is this factor that governs cation sorption on the phosphate cation exchanger. The sorption strongly depends on the solution acidity and on the ionic form of the cation exchanger. Figure 1 shows how the HCl concentration affects the sorption of Ga, In, Fe, and Y ions by the KFP-12 cation exchanger. The dramatic decrease in the sorption capacity is due to the fact that the fraction of neutral MCl_3 molecules and negatively charged chloride complexes $[MCl_4]^-$, $[MCl_5]^{2-}$, and $[MCl_6]^{3-}$ increases in acid solutions.

The amount of sorbed ions largely depends on the ionic form of the cation exchanger. The sorption capacity of the NH_4^+ form exceeds that of the H^+ form. This is due to the fact that in the course of sorption by the cation exchanger in the NH_4^+ form ammonium ions are displaced by cations of metal and hydrogen. The ion exchange is described by the following reactions:

$$R\text{–}PO(ONH_4)_2 + MCl_2^+ = R\text{–}PO(ONH_4^+)(OMCl_2) + NH_4^+,$$

$$R\text{–}PO(ONH_4)_2 + MCl^{2+} = R\text{–}PO(O_2MCl) + 2NH_4^+,$$

1070-4272/02/7503-0389$27.00 © 2002 MAIK "Nauka/Interperiodica"

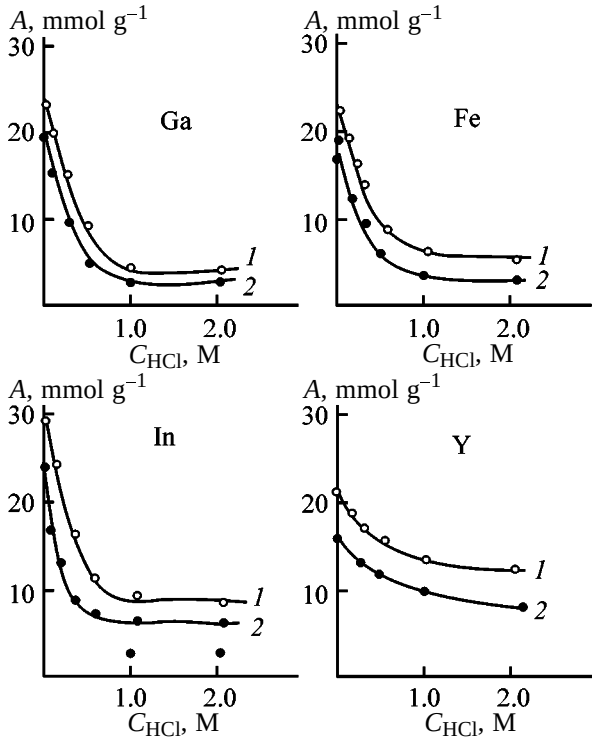

Fig. 1. Effect of HCl concentration C_{HCl} on sorption A of indium, gallium, yttrium, and iron ions from 0.3 M MCl_3 solution. Form of KFP-12 cation exchanger: (*1*) NH_4^+ and (*2*) H^+.

$$2R\text{–}PO(ONH_4^+)_2 + MCl_3 = 2R\text{–}PO(ONH_4^+)(OMCl) + 2NH_4Cl,$$

$$R\text{–}PO(ONH_4)_2 + HCl = R\text{–}PO(OH)_2 + 2NH_4Cl.$$

In sorption of triply charged metal ions from stoichiometric solutions and solutions with a low HCl concentration (up to 0.3 M), the sorption exceeds the total exchange capacity of the KFP-12 cation exchanger for ions of the corresponding metals. Such a behavior of the elements indicates that they are sorbed not only as simple triply charged cations, but also as chloride (MCl^{2+}, MCl_2^+) and hydroxo complexes. The very high sorbability of the triply charged metal ions and hence the high selectivity of the resins with respect to these ions are due to the interaction of metal ions with the ionic groups to form polymeric complexes.

Figures 2 and 3 present the IR spectra of the phosphonic cation exchanger KFP-12 with indium, gallium, yttrium, and iron(III) ions sorbed from chloride solutions. Analysis of the spectra allows conclusions about the nature of bonding between the sorbed ions and ionic groups of the cation exchanger. The spectra of the cation exchanger with sorbed metal ions differ from the spectrum of the initial cation exchanger in

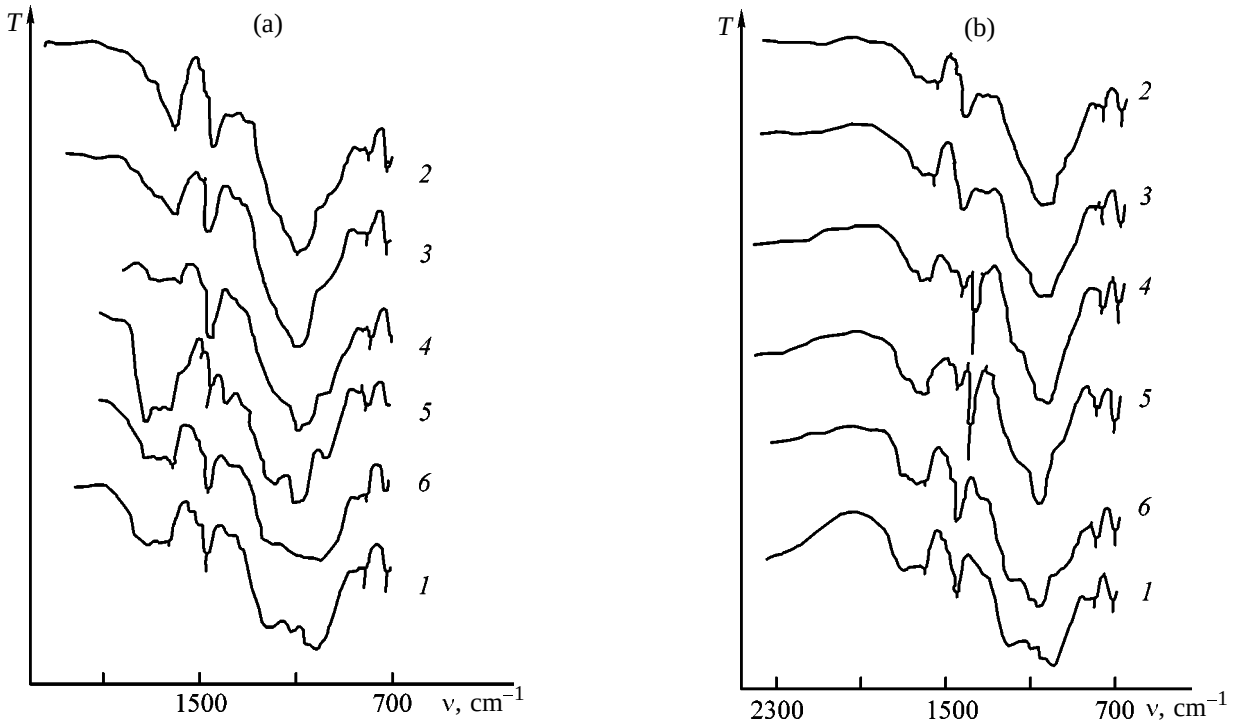

Fig. 2. IR spectra of KFP-12 cation exchanger (*1*) in the H^+ form and (*2*–*6*) after sorption of (a) indium and (b) iron ions. (*T*) Transmission and (ν) wave number; the same for Fig. 3. M^{3+} concentrations (M): (*2*) 0, (*3*) 0.1, (*4*) 0.3, (*5*) 0.5, and (*6*) 1.0.

the H^+ form in that they contain absorption bands at 980 and 1060 cm^{-1}, associated with symmetric and antisymmetric vibrations of the R–PO_3^{2-} group [6–8]. Characteristically, absorption bands at 980 and 1060 cm^{-1} are observed even at minor loading of the cation exchanger (to 15–30%) with metal ions (Fig. 2, curves *5* and *6*). This indicates that hydrogen is replaced by metal in both the hydroxo groups of the phosphonic cation exchanger simultaneously.

The presence of phosphoryl oxygen with increased electron density in the P=O group is responsible for the ability of phosphonic cation exchangers to form strong coordination bonds with metals having unoccupied orbitals. In the spectra of the cation exchanger, the intensity of the absorption band at 1210 cm^{-1} (vibrations of the P=O group) decreases with filling of the cation exchanger and nearly disappears when all ionic groups are replaced (Fig. 2, curves *2* and *3*). The decrease in the intensity of this band points to rupture of hydrogen bonds [7] and to involvement of phosphoryl oxygen in the coordination with the metal ion. It should also be noted that the P=O stretching vibration band at 1210 cm^{-1} in the spectra of the cation exchanger with sorbed metal ions is shifted by 20–30 cm^{-1} to lower frequencies, and just this is observed in complexation [8].

In sorption of gallium and yttrium ions (Fig. 3), protons are replaced in both hydroxy groups of the cation exchanger. This is confirmed by the appearance of a broad absorption band at 1070 cm^{-1}, associated with stretching vibrations of the R–PO_3^{2-} ion, and disappearance of bands at 950, 1100, and 1175 cm^{-1}. The spectra of the cation exchanger saturated with yttrium and gallium ions show the same characteristic absorption bands as the spectra of the indium- and iron-saturated resin.

Thus, the following structural forms are possible in sorption of triply charged metal ions:

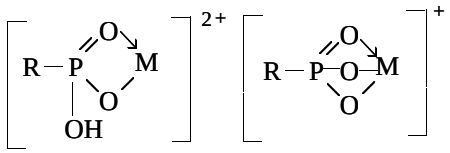

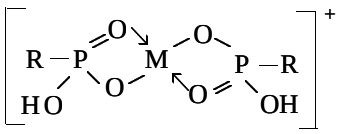

The formation of polymeric complexes is preceded by disintegration of chloride anionic complexes. This is evidenced by the observed sequence of decreasing sorbability, corresponding to the stability series of

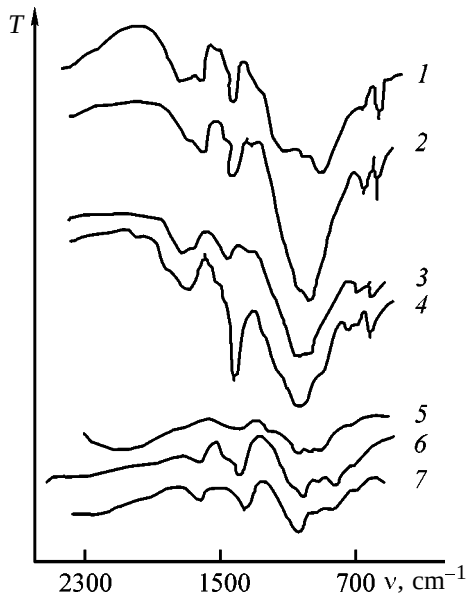

Fig. 3. IR spectra of KFP-12 cation exchanger (*1*) in the H^+ form and after sorption of (*2–4*) gallium and (*5–7*) yttrium ions. M^{3+} concentration (M): (*2*, *5*) 0, (*3*, *6*) 0.1, and (*4*, *7*) 1.0.

chloride complexes of elements (with the exception of indium): In > Fe ≫ Ga > Y. The main reason for the exceptional selectivity of KFP-12 is the interaction of indium with ionic groups to give stronger polymeric complexes.

To conclude, it should be noted that the difference in behavior between In^{3+}, Fe^{3+}, Ga^{3+}, and Y^{3+} in their sorption by the KFP-12 cation exchanger from chloride solutions can be widely used for solving various problems of analytical, preparative, and applied chemistry and technology. The cation exchange can be successfully applied in fine purification of elements forming stable anionic chloride complexes to remove impurities of other elements present in starting solutions as positively charged species.

CONCLUSIONS

(1) The sorption of triply charged gallium, indium, yttrium, and iron ions from chloride-containing solutions with the KFP-12 cation exchanger was studied. The sorption is influenced by the ionic form of the cation exchanger (H^+ and NH_4^+) and the concentration of hydrochloric acid. Metal ions are sorbed from solutions by the cation exchanger in the form of simple and complex positively charged ions.

(2) On the basis of data on sorption and the results of chemical analysis and IR spectroscopy, conclusions

are made concerning the mechanism of ion exchange and nature of bonding between the sorbed cations and functional groups. The complexation between triply charged metal ions and the cation exchanger was revealed.

REFERENCES

1. Topalova, O.V., Pimneva, L.A., Pakholkov, V.S., and Ganyaev, V.P., *Zh. Prikl. Khim.*, 1981, vol. 54, no. 6, pp. 1421–1424.
2. Pimneva, L.A., Ganyaev, V.P., and Pakholkov, V.S., *Zh. Prikl. Khim.*, 1982, vol. 55, no. 5, pp. 1009–1013.
3. Pimneva, L.A., Ganyaev, V.P., and Pakholkov, V.S., in *Ionnyi obmen i khromatografiya* (Ion Exchange and Chromatography), Leningrad: Nauka, 1984, pp. 52–57.
4. Topalova, O.V. and Pimneva, L.A., in *Ionnyi obmen i khromatografiya*, Leningrad: Nauka, 1984, pp. 57–62.
5. Topalova, O.V., Pimneva, L.A., and Goncharova, G.V., *Zh. Prikl. Khim.*, 1984, vol. 57, no. 8, pp. 1859–1861.
6. Kopylova, V.D., Saldadze, K.M., and Mekvibishvili, T.V., *Zh. Fiz. Khim.*, 1972, vol. 46, no. 4, pp. 990 – 992.
7. Bellamy, L.J., *The Infra-Red Spectra of Complex Molecules*, New York: Wiley, 1957.
8. Semushkin, A.M., Yakovlev, V.A., and Ivanova, E.V., *Infrakrasnye spektry pogloshcheniya ionoobmennykh materialov* (IR Absorption Spectra of Ion-Exchange Materials), Leningrad: Khimiya, 1980.

Russian Journal of Applied Chemistry, Vol. 75, No. 3, 2002, pp. 393–395. Translated from Zhurnal Prikladnoi Khimii, Vol. 75, No. 3, 2002, pp. 404–406.
Original Russian Text Copyright © 2002 by Maiboroda, Petrov, Troshkina.

SORPTION AND ION-EXCHANGE PROCESSES

Regeneration of VA-212 Cationic Polyelectrolyte Exhausted in Rhenium(VII) Recovery from Aqueous Solutions by Complexation–Ultrafiltration Technique

A. B. Maiboroda, D. G. Petrov, and I. D. Troshkina

Mendeleev Russian Chemical Engineering University, Moscow, Russia

Received January 20, 2001; in final form, September 2001

Abstract—A procedure was developed for regeneration of VA-212 cationic polyelectrolyte exhausted in recovery of rhenium(VII) from aqueous solutions by complexation–ultrafiltration technique. The regeneration includes polyelectrolyte coagulation by displacement of perrhenate by nitrate anions, ultrafiltration, and dissolution of the filtered sediment with reducing agent.

Water-soluble macromolecular compounds containing ionogenic groups are used for metal ion recovery from aqueous solutions [1]. This technique is preferable as compared to ion-exchange sorption on granulated ion exchangers, mainly because of high rates of sorption of the target ions and their subsequent displacement in the desorption stage.

The complexation–ultrafiltration technique (COUF) is suitable for metal recovery from dilute aqueous solutions. This technique includes binding of the target metal to water-soluble polyelectrolyte, displacement of this metal from the metal–polyelectrolyte complex, and separation of the precipitated polyelectrolyte by ultrafiltration. The term complexation takes into account all types of interactions capable of binding metal to polyelectrolyte, including anion–cation and donor–acceptor contacts. The polyelectrolyte is regenerated by displacement of target metal from metal–polyelectrolyte complex, followed by separation of the coagulated polyelectrolyte by ultrafiltration and, if required, transrformation of the polyelectrolyte to the form suitable for reuse.

The aim of this work was to determine the conditions ensuring the regeneration of VA-212 cationic polyelectrolyte used for anion-exchange recovery of perrhenate anions by the COUF technique.

EXPERIMENTAL

Our experiments were carried out on a laboratory ultrafiltration setup equipped with a membrane flow unit manufactured from hollow polysulfonic fibers [2]. These membranes retain species with the molecular weight exceeding 40 000. VA-212 cationic flocculant containing quarternary ammonium base groups was introduced into aqueous solution to bind perrhenate anions [3]. Prior to further procedures, this solution was concentrated threefold by ultrafiltration.

The IR spectra of the polyelectrolyte (KBr pellets) were recorded on a UR-20 IR spectrometer. The rhenium(VII) content in aqueous solutions was determined by kinetic analysis [4]; variations in the rhenium content in the course of COUF were monitored with short-lived ^{188}Re tracer prepared with an isotope generator [5].

The relationships of rhenium(VII) recovery from process solutions of copper production by the COUF technique were reported in [2, 6]. Data on the aggregative stability of a series of polyelectrolyte solutions, including those of VA-212, in the presence of salts were published in [6]. Displacement of rhenium(VII) from the rhenium–polyelectrolyte complex was studied in [2]. In that work it was found that addition of a nitrate-containing solution causes coagulation of the polyelectrolyte. The coagulation of a polyelectrolyte in the presence of lower electrolytes (salting-out agents) is characterized by a certain coagulation threshold depending on the salting-out agent. As a rule, sodium nitrate is used as the salting-out agent. In this case, the coagulation threshold is equal to 4.84×10^{-2} M at VA-212 polyelectrolyte concentration of 1 g l^{-1} [6].

Displacement of ReO_4^- from its complex with the polyelectrolyte was studied at different sodium nitrate

1070-4272/02/7503-0393$27.00 © 2002 MAIK "Nauka/Interperiodica"

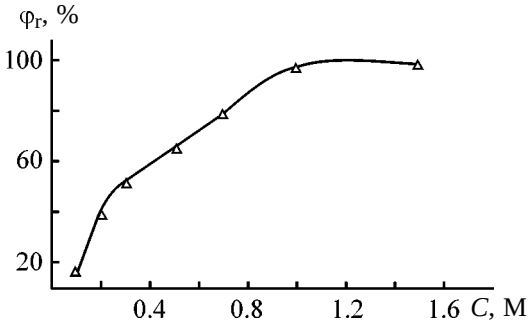

Fig. 1. Degree of VA-212 polyelectrolyte regeneration φ_r as a function of $NaNO_3$ concentration *C*.

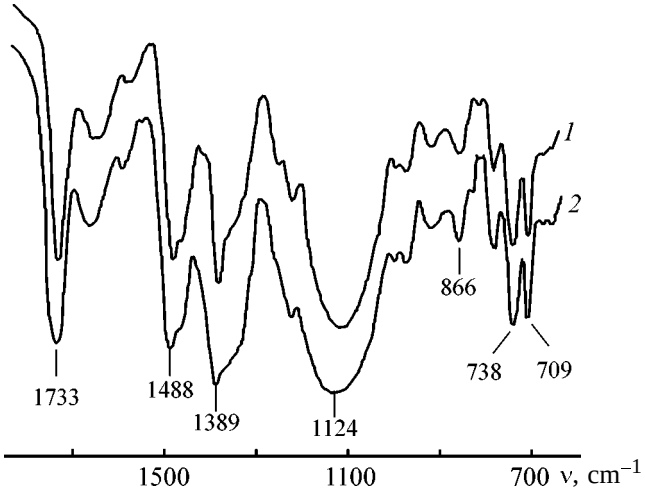

Fig. 2. IR spectra of VA-212 polyelectrolyte. (ν) Wavenumber. (*1*) Polyelectrolyte precipitated with $NaNO_3$; (*2*) polyelectrolyte first precipitated with $NaNO_3$ and then dissolved with Na_2SO_3.

concentrations which were attained by adding the required amount of 4 M sodium nitrate. In the experiments we used rhenium(VII) concentrate containing 0.3 wt % of VA-212 and 4 mg l^{-1} of rhenium(VII) bound to the polyelectrolyte. The resulting suspension of the polyelectrolyte was subjected to ultrafiltration, and the rhenium content in the permeate (filtrate) was determined. The degree of polyelectrolyte regeneration φ_r was calculated by the equation

$$\varphi_r = \frac{C_p}{C_c} \times 100,$$

where C_p is the rhenium concentration in permeate (mg l^{-1}) after addition of $NaNO_3$ into the rhenium concentrate; C_c is the rhenium(VII) concentration in the concentrate (mg l^{-1}), corrected for the volume of the $NaNO_3$ solution added.

The degree of polyelectrolyte regeneration as a function of the sodium nitrate concentration is plotted in Fig. 1. These results show that 1 M is the optimal $NaNO_3$ concentration for regeneration of VA-212 polyelectrolyte. Under these conditions, the high degree of polyelectrolyte regeneration (98%) is reached. Furthermore, the resulting permeate can be processed by hydrometallurgical technique (e.g., by solvent extraction).

The regenerating solution (1 M $NaNO_3$) was continuously added to the concentrate circulating in the ultrafiltration unit. We found that, at the 3 : 1 volume ratio of the regenerating solution and initial concentrate, more than 90% of rhenium passes into the permeate.

To reuse the polyelectrolyte for further rhenium(VII) recovery, its filtered precipitate should be converted to the water-soluble state. We found that washing of this precipitate with distilled water did not lead to dissolution even at the NO_3^- concentration lower than the coagulation threshold. The fast and complete dissolution of VA-212 precipitate is reached on addition of hydrazine (0.005 M) or a mixture containing 0.05 M sodium sulfite and 0.10 M ammonia. The resulting solution was washed with distilled water in the ultrafiltration unit and reused for rhenium recovery.

The possibility of repeated rhenium(VII) recovery using the regenerated polyelectrolyte was studied with return solutions from a concentrating mill processing copper-containing sandstown. It was found [2] that, after five successive recovery–regeneration cycles using sodium nitrate for rhenium(VII) displacement and sodium sulfite for dissolution of the polyelectrolyte precipitate, the change in the degree of rhenium recovery was minor.

The regenerated sample of VA-212 polyelectrolyte was washed with water, separated from the aqueous phase, and characterized IR-spectroscopically. In the IR spectrum, a strong absorption band at 1389 cm^{-1} is due to $\nu_a(NO_3^-)$ vibrations. This band shows that the polyelectrolyte contains NO_3^- anions as the counterions. Comparison of spectra *1* and *2* (Fig. 2) shows also that IR spectrum of the precipitated polyelectrolyte (spectrum *1*) does not change noticeably after its dissolution in the presence of sodium sulfite (spectrum *2*). The precipitation–dissolution processes used by us for regeneration of water-soluble VA-212 polyelectrolyte are governed by interactions between the polyelectrolyte and inorganic electrolyte species. In aqueous solutions, polyelectrolytes form macromolecular globules with the size depending on the supporting electrolyte and its concentration. The internal and external surfaces of these globules are surrounded by

counterions which form an electrical double layer consisting of the dense and diffuse parts. With increasing counterion concentration, the polyelectrolyte ionogenic groups are neutralized. Under these conditions, the macromolucular globules agglomerate under the action of van der Waals forces into large aggregates, and polyelectrolyte coagulates [3]. In our system, polyelectrolyte coagulates owing to displacement of ReO_4^- by NO_3^- anions, with the NO_3^- anions being incorporated in the coagulate.

We found that the precipitated polyelectrolyte is dissolved on adding reducing agents. We believe that dissolution of the precipitated polyelectrolyte is caused by redox reactions occurring on the surface between the macromolecular globules. As seen from the standard electrode potentials of the reactions given below, nitrate anions can be reduced by sulfite anions in alkali solution [7]:

$$NO_3^- + H_2O + 2e \rightarrow NO_2^- + 2OH^-, \quad E^0 = +0.01 \text{ V};$$

$$SO_4^{2-} + H_2O + 2e \rightarrow SO_3^{2-} + 2OH^-, \quad E^0 = -0.93 \text{ V}.$$

Combination of these reactions shows that reduction of nitrate by sulfite anions is characterized by increase in the standard electrode potential: $\Delta E_0 > 0$. Since $\Delta G = -zF\Delta E^0$ (z is the number of electrons participating the redox reaction, F is the Faraday constant), the change of the Gibbs energy in nitrate reduction with sulfite is negative. This fact suggests that nitrate ion can be efficiently reduced with sulfite anions. Taking into account that the reducing power of sulfite anion increases in alkali media, the polyelectrolyte solutions in our experiments were alkalized with ammonia. Ammonia is a convenient agent since it can be removed into the gas phase in hydrometallurgical processing of the permeate.

Our preliminary experiments [6] showed that, at the polyelectrolyte concentration of 1 g l^{-1}, the coagulation threshold of VA-212 is reached at the sulfite concentration equal to 3 M, which by more than two orders of magnitude exceeds that for nitrate anions. Introduction of SO_3^{2-} anions into an aqueous suspension of the coagulated polyelectrolyte results in reduction of NO_3^- to NO_2^-. This reaction apparently occurs in the diffuse part of the electrical double layer of the macromolecules. The decrease in the NO_3^- concentration in the diffuse part of the electrical double layer due to its partial displacement by nitrite anions, characterized by a higher coagulation threshold, causes disaggregation of macromolecular globules and, as a result, their dissolution. Our IR data show that nitrate anions localized in the internal part of globules are not reduced.

Polyelectrolyte can be dissolved also with hydrazine which is capable of reducing nitrate anions. However, taking into account toxicity of hydrazine and its gradual decomposition in aqueous solution, the use of sodium sulfite as the reducing agent is preferable.

CONCLUSIONS

Rhenium(VII) is efficiently recovered from aqueous solution by multistage technique including rhenium binding with VA-212 polyelectrolyte, its coagulation with nitrate anions, and ultrafiltration. The precipitated polyelectrolyte can be reused after dissolution in the presence of a reducing agent.

REFERENCES

1. Tokareva, G.I., Tokarev, N,I., Dytnerskii, Yu.I., *et al*., *Izbiratel'noe kontsentrirovanie metallov v rastvorakh s pomoshch'yu polimernogo svyazyvaniya i ul'trafil'tratsii* (Selective Concentration of Metals in Solutions by Polymeric Binding and Ultrafiltration), Moscow: VNII Ekonomiki Mineral'nogo Syr'ya i Geologorazvedochnykh Rabot, 1988.
2. Troshkina, I.D., Petrov, D.G., Maiboroda, A.B., and Chekmarev, A.M., *Tsvetn. Met*., 2001, no. 4, pp. 71–73.
3. Veitser, Yu.I. and Mints, D.M., *Vysolkomolekulyarnye flokulyanty v protsessakh ochistki prirodnykh i stochnykh vod* (Macromolecular Flocculants in Treatment Processes of Natural and Wastewater), Moscow: Stroizdat, 1984.
4. Demin, Yu.V., Borisova, L.V., and Gatinskaya, N.G., *Zh. Anal. Khim*., 1996, vol. 51, no. 6, pp. 638–641.
5. Kodina, G.E., Tulskaya, T.A., and Gureev, E.V., in *Technetium and Rhenium in Chemistry and Nuclear Medicine*, New York: Raven, 1989, pp. 645–651.
6. Troshkina, I.D., Chekmarev, A.M., Maiboroda, A.B., *et al*., *Proc. Global Conf. on Environment Control in Mining and Metallurgy (GME'99) (May 24–27, 1999, Beijing, China)*, Beijing: International Academic, 1999, pp. 548–553.
7. *Kratkii spravochnik fiziko-khimicheskikh velichin* (Concise Handbook of Physicochemical Quantities), Mishchenko, K.P. and Ravdel', A.A., Eds., Leningrad: Khimiya, 1974.

Russian Journal of Applied Chemistry, Vol. 75, No. 3, 2002, pp. 396–401. Translated from Zhurnal Prikladnoi Khimii, Vol. 75, No. 3, 2002, pp. 407–412.
Original Russian Text Copyright © 2002 by Lamberov, Romanova, Shmelev, Sopin.

SORPTION AND ION-EXCHANGE PROCESSES

Effect of Acid Modification on the Structure and Catalytic Activity of Aluminum Oxide

A. A. Lamberov, R. G. Romanova, I. G. Shmelev, and V. F. Sopin

Kazan State Technological University, Kazan, Tatarstan, Russia

Received July 6, 2001

Abstract—The effect of acetic acid introduced as modifying additive into active aluminum oxide on its structural characteristics is considered. A relationship is established between the structural characteristics, content and features of aprotic acid centers, and catalytic activity of the obtained catalysts in dehydration of methylphenylcarbinol.

One of industrial methods for styrene production is based on dehydration of methylphenylcarbinol (MPC). The main disadvantage of the process is its high energy consumption, resulting from the fact that the reaction is endothermic and proceeds in the gas phase. In this connection, development of effective catalysts making it possible to reduce the energy consumption by lowering the process temperature is a topical problem. It is known that active aluminum oxide (γ-Al_2O_3, AAO) is used as catalyst for dehydration of aromatic alcohols, and the process occurs by the acid–base mechanism [1]. Consequently, the catalyst activity will depend on structural characteristics and distribution of acid–base centers over the surface. It has been shown previously that dehydration proceeds the most efficiently on an AAO surface with the pore diameter distribution peaked at about 150 Å [2]. One of promising ways to change the structure and surface distribution of active centers is to introduce modifying agents into the catalyst composition.

In this paper we analyze the effect of modification with acetic acid on the structure and activity of the catalyst in MPC dehydration to give styrene.

EXPERIMENTAL

Commercial AAO manufactured by the aluminate–nitrate method was modified by impregnation [3]. The thus treated aluminum oxide was dried to constant weight at 110°C and then calcined at 550°C for 2 h.

MPC dehydration was performed in an isothermal reactor at 220°C in the presence of water vapor (MPC : H_2O = 1 : 1) under conditions of incomplete conversion, since only in this case the catalyst activities can be compared. The temperature was maintained constant to within ±5°C, the space velocity of the raw material and water was 5.4 h^{-1}, and the catalyst volume, 50 cm^3.

Liquid catalyzate was analyzed on a Tsvet chromatograph with a thermal conductivity detector and a steel column 2 m long and 3 mm in diameter, stationary phase 12% PEG-20 000 on Porokhrom support (0.25–0.315 fraction), carrier gas helium. The columns and the detector were thermostated at, respectively, 150 and 180°C; the vaporizer was heated to 250°C.

Adsorption measurements aimed at determining the specific surface area, pore volume, and pore diameter distribution were performed by the method of nitrogen desorption on a Micromeritics ASAP-2400 installation. Adsorption isotherms were measured at 200°C, and degassing was done at 500°C to a residual pressure of 10^{-4} mm Hg. The model of slit-like pores open on all sides was used in calculations.

The crystal structure was studied on a DRON-3M diffractometer with FeK_α radiation and secondary beam passed through a graphite monochromator. Diffraction patterns were processed using RIETQUAN 2.3 software [4, 5] applicable to both crystalline and amorphous structures. As reference were used structures represented in the Inorganic Crystal Structure Database (ICSD for WWW).

The acid-base properties of the aluminum oxide surface were studied by IR spectroscopy.[1] The IR

[1] Investigations were carried out under supervision of E.A. Paukshtis (Boreskov Institute of Catalysis, Siberian Division, Russian Academy of Sciences, Novosibirsk).

1070-4272/02/7503-0396$27.00 © 2002 MAIK "Nauka/Interperiodica"

Table 1. Performance of catalysts obtained by AAO treatment with acetic acid in MPC dehydration* (T = 220°C, V_{cat} = 50 cm^3, V_{raw} = V_{water} = 5.4 h^{-1})

Acid concentration C, M	MPC conversion, %, after indicated time, h			S, %	Y, $g_{st}\ g_{cat}^{-1}\ h^{-1}$	ω, %	$V \times 10^4$, $g_{coke}\ g_{st}^{-1}\ h^{-1}$
	2	4	6				
–	28.83	25.30	22.66	89.6	1.66	2.52	19.0
0.83	40.00	28.00	25.0	96.0	1.68	2.68	20.0
1.67	46.48	41.04	44.06	91.4	2.54	2.73	13.4
8.33	57.54	48.71	43.76	89.0	3.09	3.51	14.1
13.3	62.00	51.65	46.99	98.9	3.92	2.75	11.7
17.4	64.46	54.04	48.43	98.1	3.98	1.21	5.0
1.67**	43.07	49.69	8.73	87.4	1.54	–0.65	–3.7

* (S) Selectivity with respect to styrene; (Y) specific yield of styrene; (ω) deactivation rate, $\omega = [(m - m_0)/m_0] \times 100$, where m_0 and m are the catalyst masses before and after test, g; (V) reduced deactivation rate.
** Without calcination.

spectra were recorded at the adsorption temperature, using a Shimadzu 8300 Fourier spectrometer with a resolution of 4 cm^{-1} and a spectrum accumulation factor of 50. The spectra were recorded at –170°C. The detection limit of the concentration of Lewis acid centers was 0.2 μmol g^{-1}. As probes in determining the acid and base centers were used carbon monoxide and deuterochloroform. The concentration of Lewis acid centers was found from the integral intensity of the corresponding bands in the spectrum of adsorbed CO with the use of integral absorption coefficients [6] which depend on the position of the absorption band of CO complexes in the range 2180–2240 cm^{-1}, in accordance with the formula $A_0 = (\nu_{CO} - 2130)$.

The strength of Lewis acid centers was characterized by the heat of CO adsorption, Q_{CO}, found using the correlation equation [6]

$$Q_{CO} = 10.5 + 0.5(\nu_{CO_i} - 2143),$$

where ν_{CO_i} is the vibration frequency of CO adsorbed on ith Lewis center.

The surface OH groups were characterized by the vibration frequency ν_{OH} (cm^{-1}) and the strength on the proton affinity (PA) scale (kJ mol^{-1}). In determining base centers, spectra of a pretreated sample were measured in the ranges 2000–2300 and 3000–3900 cm^{-1} at room temperature, and then adsorption of $CDCl_3$ was performed at the same temperature under saturated vapor pressure of deuterochloroform to completely saturate the base centers.

The catalytic activity of commercial aluminum oxide modified with solutions of acetic acid of various concentrations was studied in MPC dehydration. The catalyst activity was evaluated on the basis of the MPC conversion, specific rate of styrene formation, selectivity of the reaction with respect to styrene, and reduced deactivation rate. As shown in Table 1, the catalyst activity grows with increasing concentration of acetic acid taken for modification. The dependence of the specific rate of styrene formation on the acid concentration (see figure) indicates that the catalyst activity increases dramatically, compared with unmodified AAO, on treating AAO with acetic acid solutions with concentrations of up to 1.67 M. With the concentration of the modifying agent increasing to more than 13.3 M, the catalyst activity grows to a lesser extent. The selectivity of modified samples with respect to styrene is commonly higher.

The dependence of the reduced rate of catalyst deactivation on the concentration of acid taken for modification (see figure) is complex. At low acetic acid concentrations the modified catalyst is deactivated even faster than the initial sample. The rate of catalyst deactivation falls markedly (by 30%) with the

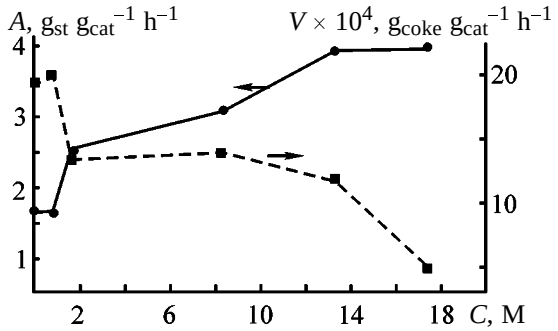

Specific rate A of styrene formation and specific rate V of catalyst deactivation vs. the acetic acid concentration C.

Table 2. Texture characteristics of modified AAO samples

S_{sp}, $m^2\ g^{-1}$ (BET)	Pore volume, $cm^3\ g^{-1}$		Intensity I and position d of peak in pore size distribution				Distribution of volumes $V_i \times 10^2$, $cm^3\ g^{-1}$, in indicated pore size range, Å		
	BET	from desorption branch	d, Å	$I \times 10^3$, $cm^3\ g^{-1}$	d, Å	$I \times 10^3$, $cm^3\ g^{-1}$	37.7–43.8	43.8–108	133.5–175
228	0.70	0.69	42	7.6	153	4.0	3.2	18.1	15.9
214	0.70	0.71	41	4.9	145	4.4	2.3	20.1	17.4
210	0.72	0.73	42	4.8	152	4.4	2.1	19.6	17.5
216	0.66	0.64	43	6.3	145	3.4	1.4	20.7	13.7

acid concentration, increasing from 0.83 to 1.67 M, the decrease in the range from 1.67 to 13.3 M is insignificant, and for a sample modified with glacial acetic acid the rate of deactivation again decreases dramatically. For example, in a sample impregnated with glacial acetic acid the rate of deactivation is approximately 4 times smaller than that in the initial AAO. Thus, the maximum catalytic activity and minimum rate of deactivation under the reaction conditions are observed for a sample obtained by impregnation with glacial acetic acid.

The catalyst performance is strongly affected by conditions of its thermal treatment after modification. For example, a catalyst prepared by treatment with a 1.67 M solution of acetic acid and subsequent drying to constant weight at 100°C failed to show high activity in MPC dehydration, despite the fact that the MPC conversion into styrene was rather high during the first hours of operation. Probably, in the case of this treatment procedure, dehydration involves, during the first hours, acid centers formed on the AAO surface as a result of adsorption of acetic acid, which is not removed completely at 100°C. Subsequently, acid molecules are gradually removed from the surface, which is also indicated by the fact that the catalyst mass gain after 8 h of operation is negative, despite the observable indications of coking. The change in the nature of active centers is also evidenced by the decreasing selectivity with respect to styrene.

To reveal the fundamental aspects of processes occurring in acid modification of AAO, the structural and acid–base characteristics of the catalysts obtained were studied. The isotherms of adsorption belong, for all the samples, to type IV by BDDT classification [8], and, consequently, mesopores prevail in the pore structure of the systems under study. The type of the hysteresis loop (H2 according to IUPAC classification) indicates that the mesoporous system consists of parallel-sided particles with slit-like pores open on all sides [9]. The pore structure of AAO is characterized by mesopores with the size distribution peaked at around 40 and 165 Å. These samples of commercial aluminum oxide were prepared by mixing hydroxides (AH) produced by cold and hot precipitation. The former, as a rule, have finely porous structure and virtually totally determine the left-hand side of the pore-size distribution pattern. The structure of the latter is characterized by larger pores, responsible for the right-hand part of the pattern. In AH mixing, the finely porous hydroxides (cold precipitation) are arranged in larger pores of hot-precipitated AH, making lower their true porosimetric volume.

As shown in [9], contacts between primary particles of finely porous AH, resulting from weak van der Waals interaction, are rather labile and are broken under the action of acids. The contacts between hot-precipitated particles are similar to those in crystals and are broken under the action of acids to a much lesser extent. Probably, similar behavior must be observed for AAO, too.

As seen from Table 2, the action of acetic acid on the AAO structure makes the intensity of the peak at 42 Å in the pore size distribution lower, from 0.0076 to 0.0048 $cm^3\ g^{-1}$, whereas the intensity of the broad peak at 140–150 Å grows from 0.0040 to 0.0044 $cm^3\ g^{-1}$. The observed behavior can be accounted for by deaggregation of finely porous oxides responsible for the peak at 42 Å. As a result, the height of the peak at 42 Å decreases, and the porosimetric volume of larger pores increases owing to the breakdown of finely porous oxides present within these pores. This leads to a decrease in the specific surface area and an increase in the total pore volume. Raising the concentration of the acid to 8.33 M makes this tendency more pronounced.

Since changes in the nature of pore distribution are related to the AAO structure, we studied how the

Table 3. Phase analysis data for AAO samples modified with acetic acid

Phase content, wt %		Crystallite size, Å		Lattice constants, Å		
				β-Al_2O_3		η-Al_2O_3, *a*
β-Al_2O_3	η-Al_2O_3	β-Al_2O_3	η-Al_2O_3	*a*	*c*	
30.6	69.4	8.32	30.05	6.05	25.82	7.91
33.0	67.0	6.09	29.59	6.09	25.22	7.90
35.7	64.3	6.08	31.68	6.08	25.46	7.90

crystal structure of catalyst samples changes upon their modification with acetic acid. According to [10], AAO is composed of aggregates (more than 1000 Å in size) constituted, in their turn, by finely dispersed (~20 Å) oxide particles. The large number of layer displacement defects leads to anisotropic broadening of diffraction peaks. Therefore, the diffraction pattern of X-ray scattering by commercial γ-Al_2O_3 significantly differs from that observed for well-crystallized γ-oxide whose crystal structure is in agreement with reference data (*Fd*3*m* space group, lattice constant 7.9 Å, crystallite size 27 Å). Attempts to use diffraction patterns of the standard γ-Al_2O_3 structure for identification purposes failed to produce satisfactory results even in the case of arbitrary filling with Al^{3+} ions of octahedral and tetrahedral voids formed in the γ-Al_2O_3 structure by O^{2-} ions. That is why the η-Al_2O_3 structure was chosen, making it possible to formally consider the spinel structure with large number of cationic vacancies [11]. The use of the η-Al_2O_3 structure allowed a sufficiently good description of clearly pronounced crystalline diffraction peaks, but failed to do so for broad diffuse peaks. The trial-and-error method revealed that the diffuse component of the diffraction pattern is best described with the use of the β-Al_2O_3 structure. Only this phase, combined with η-Al_2O_3, enables a satisfactory description of the peak of complex shape in the angle range 32°–54°. The proposed two structures were optimized by the least-squares technique, with primary attention given to fitting of parameters characterizing filling with Al^{3+} ions of vacancies between O^{2-} ions and to crystallite sizes. The results obtained in determining the crystallographic parameters are listed in Table 3, whence follows that acetic acid treatment increases the relative content of the finely crystalline phase β-Al_2O_3, and its content grows with increasing acid concentration. Correspondingly decreases the content of the coarsely crystalline phase.

Thus, modification with acetic acid leads to a decrease in the prevalent pore diameter through breakdown of secondary aggregates. As shown previously [2], the optimal pore diameter for dehydration is 150 Å. Modification with acetic acid solutions with concentrations of up to 8.33 M increases the volume of pores with the diameter close to this value, which enhances the catalyst activity.

However, the substantial increase in the reaction rate for the catalyst obtained by modification with glacial acetic acid cannot be accounted for by changes in structural characteristics. Acid modification of AAO leads, in addition to structural changes, to changes in its hydroxyl cover and, consequently, in the distribution of acid and base centers on the surface. Data on the acid–base properties of the catalysts are presented in Table 4. The AAO Lewis centers in the form of complexes with carbon monoxide are characterized by intense bands in the range 2158–2240 cm^{-1}, characteristic of γ-Al_2O_3 [6]. There are four main types of Lewis acid centers on the surface of the aluminum oxides under study: strong (type 1, Q_{CO} = 58–59 kJ mol^{-1} and ν = 2238–2240 cm^{-1}), two types of medium strength (type 2, Q_{CO} = 41–42 kJ mol^{-1} and ν = 2203–2207 cm^{-1}; type 3, Q_{CO} = 33–33.5 kJ mol^{-1} and ν = 2189–2191 cm^{-1}), and weak (type 4, Q_{CO} = 27–27.5 kJ mol^{-1} and ν = 2177–2180 cm^{-1}). In addition, OH groups exhibiting weakly acid properties are identified on the surface (Q_{CO} = 18–18.5 kJ mol^{-1}, ν = 2157–2162 cm^{-1}); upon modification they remain virtually unchanged. It should also be noted that the number of strong centers and medium-strength Lewis acid centers (type 2) is insignificant and constitutes 4.3–4.5% of the total number of aprotic centers. These centers also change only slightly upon modification with acetic acid. The most pronounced changes are observed for centers with medium (type 3) and weak (type 4) strength. For example, upon treatment with 1.67 M acetic acid, the content of type 4 centers decreases from 0.700 to

Table 4. Acidity of the initial catalyst samples and samples modified with acetic acid

$[CH_3COOH]$, M	Lewis centers (L)		OH groups		Base centers			Σ_L/Σ_{base} ratio
	ν_{CO}, cm^{-1}	*n*,* μmol m^{-2}	ν_{CO}, cm^{-1}	*n*, μmol m^{-2}	ν_{CD}, cm^{-1}	*n*, μmol m^{-2}	strong/weak centers	
0 (initial AAO)	2240 2203 2189 2177	0.002 0.140 1.930 0.700 Σ 2.773	2159	0.886	2253 2234	1.228 2.270 Σ 3.498	1.85	0.794
1.67	2239 2203 2190 2177	0.002 0.112 2.080 0.467 Σ 2.661	2158	0.916	2250 2229	0.154 3.019 Σ 3.173	19.6	0.838
17.4	2239 2204 2190 2177	0.002 0.171 2.830 0.870 Σ 3.873	2158	0.960	2254 2242	1.046 2.294 Σ 3.340	2.19	1.16

* (*n*) Number of centers.

0.467 μmol m^{-2}, and that of type 3 centers increases from 1.93 to 2.08 μmol m^{-2} (i.e., by approximately 8%). By contrast, modification with glacial acetic acid increases the content of Lewis acid centers of types 4 and 3, from 1.93 and 0.700 to 2.83 and 0.870 μmol m^{-2}, respectively, which constitutes 46.6 and 24.3%. The total content of Lewis acid centers decreases by 4.3% upon treatment with 1.67 M acetic acid and markedly increases, by 39.6%, upon impregnation with glacial acetic acid.

The spectra of catalysts with deuterochloroform reveal two types of base centers: weak and strong at around 2253 and 2230 cm^{-1}, respectively. The total content of base centers varies within the range 679–797 μmol g^{-1} (3.50–3.17 μmol m^{-2}). Treatment with 1.67 M acetic acid decreases the total number of base centers by approximately 9%. In the process, the ratio of the contents of the strong and weak centers changes from 1.85 to 19.6, i.e., by a factor of more than 10. Upon modification with glacial acetic acid, the total content of base centers decreases by 5%, with the strong/weak center ratio increasing from 1.85 to 2.19. It should also be noted that the vibration frequency ν(C=O) is shifted from 2234 to 2242 cm^{-1}. The ratio between the total contents of Lewis acid and base centers, Σ_L/Σ_{base}, increases upon treatment with 1.67 and 17.4 M solutions of acetic acid from 0.794 for the initial sample to 0.838 and 1.16 (by 5.5 and 46%), respectively.

The change in the distribution of acid–base centers on the aluminum oxide surface is probably due to chemical reaction of the acid with aluminum oxide, resulting in the formation of insoluble base salts of aluminum in the stage of thermal treatment. The presence of the acetate ion is confirmed by the IR spectra containing, for the catalysts modified with acetic acid, two weak absorption bands at 1380 and 1580 cm^{-1}, assigned to symmetric and asymmetric stretching vibrations of the carboxylate ion [12]. It is noteworthy that raising the concentration of the modifying acid results in higher intensity of these absorption bands.

Comparison of the activities of the catalyst and surface acid centers shows that the rate of styrene formation grows in parallel with the increasing content of medium-strength Lewis acid centers (type 3) and increasing ratio between the total contents of Lewis acid and base centers. The revealed pattern suggests that MPC dehydration occurs on medium-strength Lewis acid centers.

CONCLUSIONS

(1) Modification of active aluminum oxide with acetic acid leads to changes in the pore structure and

acid–base properties of the surface, with the type of changes depending on the acid concentration and modification method.

(2) A relationship was established between the structural characteristics, amount and strength of aprotic acid centers, and the catalytic activity of the catalysts obtained.

(3) The maximum activity in dehydration of methylphenylcarbinol is exhibited by catalysts in which modification leads to an increase in the amount of medium-strength Lewis acid centers and in the volume of pores with a size of 130–150 Å.

ACKNOWLEDGMENTS

The study was supported financially by the Russian Foundation for Basic Research (project no. 01-03-32857) and the Universities of Russia foundation of the Ministry of Education of the Russian Federation (project nos. 990078 and 015.05.01.002).

REFERENCES

1. Serebryakov, B.R., Salamov, R.G., Dalin, M.A., *et al.*, *Khim. Prom–st.*, 1977, no. 6, pp. 32–33.
2. Lamberov, A.A., Romanova, R.G., Gibadullin, I.Kh., and Shmelev, I.G., *Zh. Prikl. Khim.*, 2000, vol. 73, no. 11, pp. 1850–1855.
3. Stiles, A.B., *Catalyst Supports and Supported Catalysts. Theoretical and Applied Concepts*, Boston: Butterworths, 1987.
4. Lutterotti, L. and Scardi, P., *J. Appl. Crystallogr.*, 1990, vol. 23, pp. 246–252.
5. Lutterotti, L., Scardi, P., and Maistrelli, P., *J. Appl. Crystallogr.*, 1992, vol. 25, pp. 459–460.
6. Paukshtis, E.A., *Infrakrasnaya spektroskopiya v geterogennom kislotno-osnovnom katalize* (IR Spectroscopy in Heterogeneous Acid–Base Catalysis), Novosibirsk: Nauka, 1992.
7. US Patent 4602119.
8. Gregg, S.J. and Sing, K.S.W., *Adsorption, Surface Area and Porosity*, London: Academic, 1982.
9. Shepeleva, M.N., Fenelonov, V.B., Shkrabina, R.A., and Moroz, E.M., *Kinet. Katal.*, 1986, vol. 27, no. 5, pp. 1202–1207.
10. Ivanova, A.S., Litvak, G.S., Kryukova, G.N., *et al.*, *Kinet. Katal.*, 2000, vol. 41, no. 1, pp. 137–141.
11. Ushakov, V.A. and Moroz, E.M., *Kinet. Katal.*, 1985, vol. 26, no. 4, pp. 968–972.
12. Antipina, T.V., Uvarov, A.V., and Tikhomirova, S.P., *Zh. Fiz. Khim.*, 1967, vol. 41, no. 12, pp. 3059–3065.

Russian Journal of Applied Chemistry, Vol. 75, No. 3, 2002, pp. 402–407. Translated from Zhurnal Prikladnoi Khimii, Vol. 75, No. 3, 2002, pp. 413–418.
Original Russian Text Copyright © 2002 by Zakharchenko.

SORPTION AND ION-EXCHANGE PROCESSES

Recovery of Platinum with Calcium Oxide Sorbent in Ammonia Oxidation

N. I. Zakharchenko

Zhukovsky Aerospace University, Kharkov, Ukraine

Received June 26, 2001

Abstract—The reaction of granulated CaO sorbent with platinum lost in high-temperature oxidation of ammonia was studied. Physicochemical properties of the product and conditions and mechanism of its formation are considered.

Catalytic oxidation of ammonia to nitrogen(II) oxide is the key stage in industrial synthesis of nitric acid [1]. Commercial catalysts (Pt, Rh, and Pd alloys) undergo physicochemical transformations in the process, with their surface structure and chemical composition changed [1–6]. A set of transformations of this kind results in loss of deficient and expensive platinum-group metals. An effective way to reduce the loss of platinum metals is their partial recovery by sorbents mainly based on calcium oxide [1, 7–15].

The mechanism of platinum recovery by calcium-containing sorbents and the chemical aspect of the process are debated in the scientific literature. Atroshchenko *et al*. [9] came to a conclusion that platinum is bound on the surface of the oxide sorbent to form an $x\mathrm{CaO}\cdot y\mathrm{Pt}$ compound. In other studies [10, 11], platinum was found in the sorbent bulk as $4\mathrm{CaO}\cdot\mathrm{PtO_2}$ and $\mathrm{CaO}\cdot\mathrm{Pt_2}$ compounds. In [12, 16], platinum compounds in the sorbent bulk were identified as $\mathrm{Ca_4PtO_6}$ and PtO.

This study is concerned with recovery by calcium oxide of platinum lost in high-temperature oxidation of ammonia and with identification of products formed in the reaction of the lost platinum with calcium oxide.

The calcium oxide sorbent was prepared as follows. As starting compound served calcium oxide of chemically pure grade, which was treated with 80% ethanol (2–3% relative to sorbent weight) and compacted into pellets under a pressure of 150 MPa. Step-like thermal treatment of the sorbent was done in a muffle furnace in air at 473, 673, 873, and 1073 K (for 2 h in each stage). The sorbent was crushed into grains, and fraction with a grain size of $(2–3)\times 10^{-3}$ m was selected.

Since the lost platinum is mainly caught by the surface layer of sorbents [1, 7–14, 17], sorbent grains were ground and subjected to additional forming and thermal treatment in inert medium (argon) following the above scheme in order to intensify the process and raise the yield of the chemical compounds obtained.

The processes of platinum recovery were studied on a flow-through installation with a quartz reactor 5×10^{-1} m in diameter. As catalyst was used platinum in the form of a package of five meshes with a wire diameter of 7.5×10^{-5} m (industrial platinoid alloy nos. 1 and 5 were not used, because Rh and Pd contained in these alloys in addition to Pt would complicate the interpretation of the experimental results). A bed of sorbent grains, of height 1.7×10^{-1} m, was placed directly after the catalyst meshes at a distance of 8.0×10^{-3} m from them.

The temperature of catalytic oxidation of ammonia was maintained at 1073 K, and the pressure in the system, at 0.101 MPa. The content of ammonia in the air–ammonia mixture (AAM) was about 11.5 vol %. The linear flow velocity of AAM was 0.40 m s^{-1} (normal conditions).

X-ray phase analysis of the compounds obtained was carried out on a Siemens D-500 diffractometer with $\mathrm{Cu}K_\alpha$ radiation and graphite monochromator used to analyze the diffracted beam. The phases observed in the diffraction patterns were identified using the JCPDS file contained in the mathematical software package of the diffractometer; some X-ray diffraction pattern were compared with the data of the ASTM file [18].

IR absorption spectra were measured on a Perkin–Elmer 577 spectrometer in the range 200–2000 cm^{-1} with CsI pellets used as matrices.

Differential thermal analysis was made on an

1070-4272/02/7503-0402$27.00 © 2002 MAIK "Nauka/Interperiodica"

MOM Q-derivatograph (Hungary). The temperature was raised at a rate of 300 deg h^{-1} in the interval 293–1273 K, the sample weight was 1×10^{-4} kg, and the duration of catalyst operation and of tests with absorption mass constituted 500 h.

During reactor shutdowns (especially in the final stage of a prolonged experiment), measures were taken for preventing to the maximum possible extent the moisture absorption by the sorbent, leading to its conversion into $Ca(OH)_2$, by purging the reactor at high temperature with dried argon and isolating the argon-filled reactor from humid air by means of moisture absorbents. After being discharged from the reactor, the sorbent was stored in a hermetically sealed vessel filled with dried argon.

X-ray phase analysis of used up sorbent demonstrated that it contained calcium oxide, platinum, and a compound of unknown composition with low line intensities (Fig. 1); no platinum dioxide PtO_2 was found. To confirm the results of X-ray phase analysis, sorbent samples were treated with a 48% solution of HBr at 293 K (PtO_2 dissolves in this reagent, whereas Pt and other its compounds do not [5]). The presence of platinum in solution was determined by the atomic absorption method. Experiments demonstrated that, indeed, there was no platinum dioxide in the sorbent.

Identification of X-ray patterns of a multicomponent mixture is difficult (especially in the cases when lines are closely spaced or insufficiently intense at low concentrations of substances). For this reason, the system was separated into components, with their subsequent identification.

To eliminate the influence of unchanged sorbent on the X-ray patterns of a complex system, the formulation was dissolved in HNO_3 (25 wt %, chemically pure grade) at 308 K. In doing so, account was taken of the fact that neither Pt nor its compounds dissolve at moderate temperatures [5, 19, 20]. The liquid phase was separated from solids and discharged. The solid phase was thoroughly and repeatedly washed with hot double-distilled water (to absence of Ca^{2+} and NO_3^- ions in washing water) and subjected to thermal treatment in inert medium (Ar) at 473–523 K to constant weight.

The X-ray patterns of the solid residue (after dissolution and removal of the unchanged part of the sorbent) contained only line sets with interplanar spacings characteristic of platinum, and less intense lines of a compound of unknown composition (Fig. 1). Based on characteristics of the lines, an assumption was made that the unknown compound belongs to the structural type $M_xPt_3O_4$, where M is Ca, i.e.,

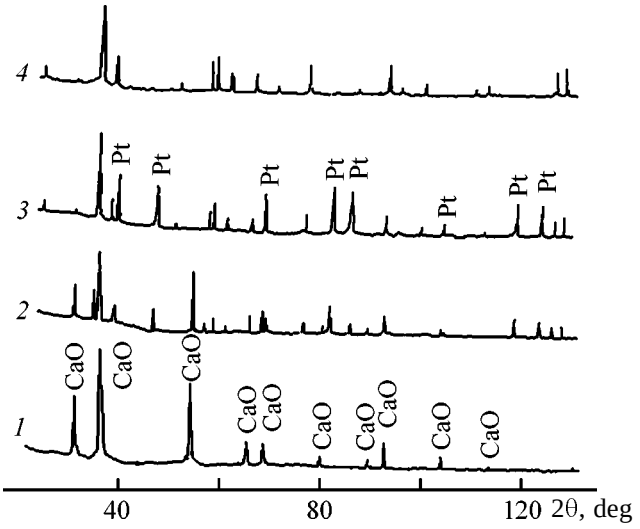

Fig. 1. X-ray patterns of the sorbent and products of platinum recovery. (2θ) Bragg angle. Sorbent: (*1*) starting, (*2*) after 500 h of catalyst operation, and (*3*) after treatment with HNO_3; (*4*) product of sorbent reaction with Pt compounds.

$Ca_xPt_3O_4$. Since this compound does not dissolve even in boiling aqua regia [19], the following analytical procedure was used to isolate it as individual phase. The residue after dissolving CaO was treated with aqua regia at 318 K to recover platinum dissolving under these conditions [5, 19, 20]. The liquid phase was separated, and the solid phase was thoroughly washed in hot double-distilled water (to absence of Ca^{2+} and NO_3^- ions in washing water) and subjected to thermal treatment by the scheme described above. Characteristics of X-ray patterns of the given compound are presented in Table 1.

Table 1. Characteristics of X-ray patterns of the compound $Ca_xPt_3O_4$ (x = 1) found in the sorbent

hkl	*d*, nm	*I*, %	*hkl*	*d*, nm	*I*, %
110	0.4052	18.7	332	0.1222	3.2
200	0.2879	5.5	422	0.1170	3.1
210	0.2564	100.0	510/431	0.1124	6.1
211	0.2340	28.8	520/432	0.1065	26.1
220	0.2028	3.7	521	0.1047	6.7
310	0.1813	7.0	440	0.1013	11.2
222	0.1655	28.5	530/433	0.0983	2.0
320	0.1590	31.0	600/442	0.0955	0.5
321	0.1531	18.1	610	0.0942	6.3
400	0.1433	16.8	611/532	0.0930	7.1
411/330	0.1351	3.9	541	0.0885	2.6
420	0.1283	2.8	622	0.0864	19.8
421	0.1251	26.3	630/542	0.0855	25.0

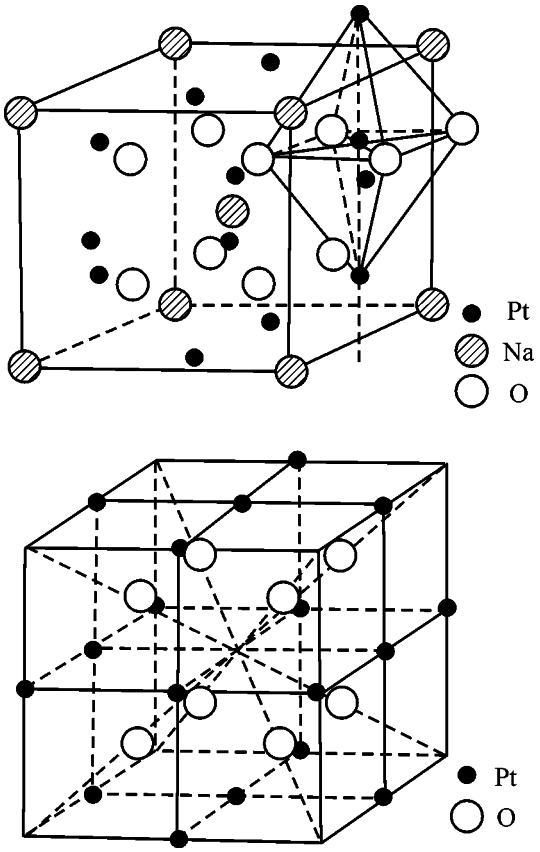

Fig. 2. $Na_xPt_3O_4$ structure by Muller and Roy [21].

The set of lines in X-ray patterns (interplanar spacings, intensities), which is in good agreement with the data of [19] and JCPDS and ASTM files [18], indicates the formation in the sorbent of a chemical compound, $Ca_xPt_3O_4$, having a simple cubic lattice (a = 0.5739 nm) with space group $Pm3n$–O_h^3. The compound $Ca_xPt_3O_4$ belongs to the structural type $Na_xPt_3O_4$ (with x varying between 0 and 1) and is a nonstoichiometric intercalation compound of platinum oxide (Pt_3O_4) [19, 21]. The cubic structure of Pt_3O_4 is constituted by square oxygen prisms occupied by Pt atoms and arranged perpendicularly to one another (Fig. 2). Oxygen atoms occupy cube vertices. Pt atoms center each oxygen face in these prisms. Cubic voids formed by prism intersection are empty. This structure corresponds to the ideal composition $PtO_{1.33}$ [21]. Deviations from the ideal composition Pt_3O_4 can be attributed to formation of interstitial solid solutions. Excess, with respect to the $PtO_{1.33}$, platinum atoms, and also impurity ions Na^+, K^+, Ca^{2+}, and Mg^+, may be introduced into cubic voids of the structure, forming stable nonstoichiometric intercalation compounds of the structural type $Na_xPt_3O_4$ [19, 22, 23]. Compounds with this structure are stable even at a very small number of atoms introduced [19, 22, 23]. In the given case, the compound $Ca_xPt_3O_4$ of the same structural type was formed when Ca^{2+} ions were present in excess.

Table 2. Analytical data for the composition of $Ca_xPt_3O_4$ (x = 1) found in the sorbent

Sample weight, g	Content,* wt %				
	O			Pt (4)	Ca (5)
	1	2	3		
0.3010	–	9.31	–	84.91	–
0.2543	–	9.25	–	84.89	–
0.2855	–	9.28	–	84.90	–
0.1015	9.29	–	–	84.89	5.82
0.0876	9.27	–	–	84.91	5.82
0.1000	–	–	9.30	–	5.79
0.1000	–	–	9.26	–	5.85
Average	9.28	9.28	9.28	84.90	5.82

* Determination method: (*1*) gravimetric, (*2*) volumetric, (*3*) thermogravimetric, (*4*) atomic-absorption, and (*5*) chemical.

The IR spectrum of the compound contains absorption bands at 707, 683, 599, 479, 367, and 230 cm^{-1}, characteristic of the compound of this structural type [24]. The absorption bands at 707 and 599 cm^{-1} can be assigned to Pt–O stretching vibrations, and those at 683 and 479 cm^{-1}, to Ca–O stretching vibrations. The absorption bands at 367 and 230 cm^{-1} characterize O–Pt–O bending vibrations.

To confirm the quantitative composition of nonstoichiometric $Ca_xPt_3O_4$, this compound was analyzed for the content of all the constituent elements by various techniques. The results obtained are presented in Table 2.

The stoichiometric compound $Ca_xPt_3O_4$ (x = 1) must contain (wt %): Pt 84.90, Ca 5.82, and oxygen 9.28. The content of oxygen was determined as an average of the values yielded by three analytical methods: gas-volumetric, thermogravimetric (decomposition of the compound), and from the difference when determining the content of platinum and calcium.

A thermogravigram of the compound $Ca_xPt_3O_4$ is shown in Fig. 3. Heating of the substance (in argon, to prevent high-temperature oxidation of platinum and its sublimation as platinum dioxide vapor [1–5, 20]) in the interval 1183–1223 K leads to the weight loss (6.96%), associated with endothermic decomposition

of the compound in accordance with the equation

$$2Ca_xPt_3O_4 = 2xCaO + 6Pt + (4 - x)O_2. \quad (1)$$

The products of dissociation of the compound are calcium oxide, metallic platinum, and oxygen, which is characteristic of double oxides including a noble metal [25]. The endothermic peak in the DTA curve lies at 1203 ± 5 K.

The X-ray patterns of products of $Ca_xPt_3O_4$ decomposition, cooled in inert medium (Ar), contain, in addition to reflections associated with calcium oxide (0.276, 0.239, 0.169, 0.1447, 0.1383, 0.1203, 0.1072, and 0.0980 nm), also those associated with metallic platinum (0.227, 0.1957, 0.1386, 0.1179, 0.1132, 0.0979, 0.0898, 0.0875, 0.0799, and 0.0754 nm).

For the compound $Ca_xPt_3O_4$, the weight loss in decomposition virtually did not exceed the expected value calculated by Eq. (1) at $x = 1$, which indicates that the influence of platinum sublimation in the form of dioxide

$$Pt(c) + O_2(g) = PtO_2(g) \quad (2)$$

is eliminated in the inert medium. A chemical analysis of the solid residue after $Ca_xPt_3O_4$ decomposition was made by dissolving the mixture in boiling aqua regia and then determining the platinum content in solution by the atomic-absorption method [26]. The content of calcium(II) was found gravimetrically by a standard procedure in the form of calcium carbonate after solution neutralization.

The oxygen content in $Ca_xPt_3O_4$ was determined volumetrically by thermal decomposition of a sample in a sealed ampule placed in a muffle furnace (1273 K, 1.5 h). After fast cooling of the ampule to room temperature, the volume of evolved oxygen was measured with a gas burette. The gas-volumetric analysis confirmed the data of thermogravimetric and chemical methods as regards the content of oxygen in a $Ca_xPt_3O_4$ sample at $x = 1$ (Table 2). Thus, chemical analysis of condensed products of $Ca_xPt_3O_4$ decomposition, and also analysis for the content of oxygen by various techniques, made it possible to determine unambiguously the composition of the compound obtained: $CaPt_3O_4$, i.e., $x = 1$.

The formation of $Ca_xPt_3O_4$ in the sorbent can be accounted for on the basis of a comparative analysis of the conditions of platinum recovery and synthesis of this compound. In [19], $Ca_xPt_3O_4$ ($x = 1$) was synthesized upon prolonged heating in air (823–973 K, $P = 0.101$ MPa) of a mixture of platinum dioxide and

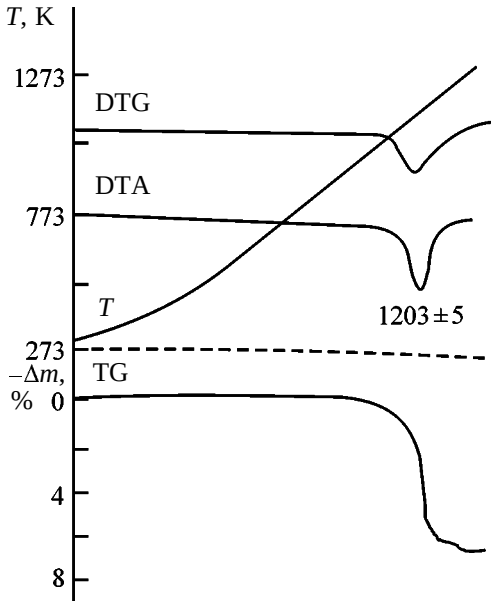

Fig. 3. Thermogravigram of $CaPt_3O_4$. Substance weight 1×10^{-4} kg, heating rate 300 deg h^{-1}. (T) Temperature and (Δm) weight change.

calcium nitrate. In [27], the same compound was obtained by heating a mixture of platinum dioxide, platinum black, and calcium oxide (673–773 K, $P = 0.202$–0.808 MPa) for 300–340 h. $Ca_xPt_3O_4$ was synthesized by introducing calcium ions into voids of the cubic lattice of Pt_3O_4 of the structural type $Na_xPt_3O_4$ [19, 21–23], which is stable at $T \leq 1073$ K. Consequently, formation of $Ca_xPt_3O_4$ assumes the presence of platinum oxide Pt_3O_4 in the starting reaction mixture or formation of this substance in some stage of a complex process.

Introduction of platinum atoms or calcium ions (and also, according to [19, 21–23], of microscopic amounts of Na^+, K^+, Mg^{2+}, Zn^{2+}, and Li^+) leads to formation of a thermally stable nonstoichiometric compound $Ca_xPt_3O_4$ of the structural type $Na_xPt_3O_4$. The composition of $Ca_xPt_3O_4$ varies depending on the concentration of ions introduced into the substance structure (this concentration grows, at constant temperature and pressure, with increasing process time).

Platinum oxide Pt_3O_4 can be obtained by various methods [24, 28]; in particular, by thermal decomposition of platinum dioxide in accordance with the equation

$$3PtO_2 = Pt_3O_4 + O_2. \quad (3)$$

The optimal decomposition temperature is 923–953 K; at higher temperature, platinum dioxide inten-

sively dissociates into platinum and oxygen (at 1173 PtO_2 dissociates completely [28]).

Platinum oxide Pt_3O_4 can also be obtained by oxidation of highly dispersed platinum (platinum black) in oxygen [24, 27] (especially under elevated pressure):

$$3Pt + 2O_2 = Pt_3O_4. \quad (4)$$

In the course of high-temperature oxidation of ammonia, the platinum catalyst undergoes a number of physicochemical transformations [1–6, 20]; in particular, platinum and platinum dioxide appear in the gas phase:

$$Pt(c) = Pt(g), \quad (5)$$

$$Pt(g) + O_2(g) = PtO_2(g). \quad (6)$$

To this should be added sublimation of platinum as platinum dioxide in accordance with Eq. (2).

The products of reactions (2), (5), and (6), Pt and PtO_2, are starting substances in processes used to obtain Pt_3O_4 (in gas phase or on the sorbent surface). Introduction of atoms (ions) of platinum and calcium (or microscopic amounts of K^+, Na^+, Mg^{2+}, and Zn^{2+}, present in the sorbent as impurities and, in part, coming from AAM as contaminants, despite the reagent purification to remove them) into voids in platinum oxide Pt_3O_4 stabilizes a compound of the structural type $Na_xPt_3O_4$ and improves its thermal resistance. The temperature of PtO_2 dissociation should not be exceeded only in the initial stage of synthesis. In later stages, this limitation is lifted since a higher-temperature process of Ca^{2+} ion introduction into the crystal lattice of a compound of the structural type $Na_xPt_3O_4$ occurs, i.e., $Ca_xPt_3O_4$ is formed in accordance with the equation

$$Pt_3O_4 + xCa^{2+} = Ca_xPt_3O_4, \quad (7)$$

where $0 \le x \le 1$.

Analysis of the conditions for absorption by the CaO sorbent of products formed in conversion of the platinum catalyst leads to the following important practical recommendations.

(1) It is necessary to satisfy certain temperature conditions of sorbent operation. The sorbent should be placed at a distance from the catalyst meshes at which its temperature does not exceed the temperature of complete PtO_2 dissociation ($T \le 1173$ K) or the temperature of Pt_3O_4 dissociation. Beginning with the instant of time when a nonstoichiometric compound $Ca_xPt_3O_4$ is synthesized in the sorbent, the sorbent temperature should not exceed the dissociation temperature of this compound (1183–1203 K).

(2) Since the nonstoichiometric compound $Ca_xPt_3O_4$ is formed in the sorbent at the phase boundary CaO–Pt_3O_4, it is necessary to have well-developed interface for accelerating the process. Low rate of the topochemical process leads to accumulation on the sorbent surface of products formed in transformations of the platinum catalyst [Eqs. (2), (4)–(6)]. Dissociation of these compounds enriches the sorbent surface with platinum, and the rate of $Ca_xPt_3O_4$ formation falls. Consequently, the sorbent taken in the form of pellets, coarse grains, or cylinders is inefficient in chemical recovery of products of platinum conversion, since only a small part of its outer surface is used in reaction (7), with deep layers of the sorbent virtually not involved in sorption at all.

(3) To make faster the chemical absorption of platinum-containing components by the sorbent, it is necessary to stabilize platinum oxide Pt_3O_4, i.e., to obtain a nonstoichiometric intercalation compound of the type $Na_xPt_3O_4$. Consequently, the presence in the calcium-containing sorbent of even minor concentrations of ions with small radius and high mobility (e.g., Li^+, Na^+, Mg^{2+}, Zn^{2+}, etc.), which readily penetrate into voids of the cubic lattice of Pt_3O_4 and stabilize it, must exert positive influence on the efficiency of platinum recovery in the form of the chemical compound $Ca_xPt_3O_4$ ($0 \le x \le 1$). When present in the sorbent, ions with larger radius (e.g., Ba^{2+}, Sr^{2+}, Cs^+, Rb^+, etc.) will adversely affect the efficiency of platinum recovery.

(4) In recovery of platinum from a calcium-containing sorbent, account should be taken of the high thermal and chemical stability of the compound $Ca_xPt_3O_4$, and appropriate temperature ($T \ge 1223$ K) and reagents should be used.

CONCLUSIONS

(1) It is established that conversion products of platinum lost in high-temperature oxidation of ammonia are bound chemically by a calcium-containing sorbent to give a nonstoichiometric compound $Ca_xPt_3O_4$ ($0 \le x \le 1$). The extent to which the compound is nonstoichiometric depends on the time of sorbent operation and process parameters.

(2) Data on chemical mechanisms of recovery of platinum lost in high-temperature oxidation of am-

monia by a calcium-containing sorbent can be used to develop theoretical prerequisites for synthesis of effective sorbents.

REFERENCES

1. Karavaev, M.M., Zasorin, A.P., and Kleshchev, N.F., *Kataliticheskoe okislenie ammiaka* (Catalytic Oxidation of Ammonia), Moscow: Khimiya, 1983.
2. Phillips, W.Z., *Trans. ASM*, 1964, vol. 57, no. 1, pp. 33–37.
3. Schafer, V.H. and Tebben, A.Z., *Z. Anorg. Allg. Chem.*, 1960, vol. 304, no. 3–4, pp. 317–321.
4. Karavaev, M.M., Mumchyan, E.G., Arutyunyan, V.A., *et al.*, *Azot. Prom–st.*, 1974, no. 5, pp. 26–29.
5. Holzmann, H., *Platinum Met. Rev.*, 1969, vol. 13, no. 1, pp. 2–8.
6. Kozub, P., Gryn, G., and Goncharov, I., *Platinum Met. Rev.*, 2000, vol. 44, no. 2, pp. 74–84.
7. Darling, A., Selman, G., and Rushforth, R., *Platinum Met. Rev.*, 1970, vol. 14, no. 2, pp. 54–60.
8. Karavaev, M.M., Mumchyan, E.G., Solei, E.M., *et al.*, *Khim. Prom–st.*, 1975, no. 2, pp. 116–117.
9. Atroshchenko, V.I., Loboiko, A.Ya., Sedashova, E.G., *et al.*, *Izv. Vyssh. Uchebn. Zaved., Khim. Khim. Tekhnol.*, 1974, vol. 17, no. 10, pp. 1587–1590.
10. Blasiak, E., Lugowska, M., and Swerczak, R., *Chem. Stosow.*, 1971, vol. 15, no. 2, pp. 225–230.
11. Sikora, H. and Blasiak, E., *J. Am. Ceram. Soc.*, 1972, vol. 55, no. 8, pp. 426–427.
12. *Kataliticheskie i massoobmennye protsessy pod davleniem v tekhnologii neorganicheskikh veshchestv* (Catalytic and Mass-Exchange Processes Performed under Pressure in Technology of Inorganic Substances), Loboiko, A.Ya., Ed., Kharkov: Osnova, 1993.
13. Atroshchenko, V.I., Loboiko, A.Ya., Sedashova, E.G., *et al.*, *Khim. Prom–st.*, 1976, no. 1, pp. 73–75.
14. Karavaev, M.M., Pal'mova, N.A., Telyatnikova, T.V., *et al.*, *Khim. Prom–st.*, 1978, no. 3, pp. 198–200.
15. Kozub, P., Trusov, N., Gryn, G., and Prezhdo, V., *J. Chem. Technol. Biotechnol.*, 2001, vol. 76, no. 2, pp. 147–152.
16. Shushura, O.S., Goncharov, I.I., Loboiko, A.Ya., *et al.*, *Vestn. Kharkov. Gos. Politekh. Univ.*, 1999, issue 39, pp. 44–47.
17. Lavrenko, A.A., Kozub, P.A., Grin' G.I., *et al.*, *Vestn. Nats. Tekh. Univ. Khar'k. Politekh. Inst.: Sb. Nauch. Tr.*, 2001, issue 3, pp. 108–110.
18. *Powder Diffraction Data File*, Philadelphia: ASTM, Joint Committee in Powder Diffraction Standards, 1967.
19. Bergner, D. and Kohlhaas, R., *Z. Anorg. Allg. Chem.*, 1973, vol. 401, no. 1, pp. 15–20.
20. *Blagorodnye metally: Spravochnik* (Noble Metals: Reference Book), Savitskii, E.M., Ed., Moscow: Metallurgiya, 1984.
21. Muller, O. and Roy, R., *J. Less-Common Met.*, 1968, vol. 16, no. 2, pp. 129–133.
22. Collongues, R., *La Non-Stoechiometrie*, Paris: Masson, 1971.
23. Waser, J. and McClanahan, E.D., *J. Chem. Phys.*, 1951, vol. 19, no. 7, pp. 413–417.
24. Goncharenko, G.I., Lazarev, V.B., and Shaplygin, I.S., *Zh. Neorg. Khim.*, 1985, vol. 30, no. 12, pp. 3032–3037.
25. Shaplygin, I.S. and Lazarev, V.B., *Zh. Neorg. Khim.*, 1980, vol. 25, no. 4, pp. 906–909.
26. Yudelevich, I.G. and Startseva, E.A., *Atomno-absorbtsionnoe opredelenie blagorodnykh metallov* (Atomic-Absorption Analysis for Noble Metals), Novosibirsk: Nauka, 1981.
27. USSR Inventor's Certificate no. 1 452 793.
28. Sukhotin, A.M., Gankin, E.A., Kondrashov, Yu.D., *et al.*, *Zh. Neorg. Khim.*, 1971, vol. 16, no. 12, pp. 3190–3194.

Russian Journal of Applied Chemistry, Vol. 75, No. 3, 2002, pp. 408–410. Translated from Zhurnal Prikladnoi Khimii, Vol. 75, No. 3, 2002, pp. 419–421.
Original Russian Text Copyright © 2002 by Bairamov, Ermakov, Vedernikova.

APPLIED ELECTROCHEMISTRY AND CORROSION PROTECTION OF METALS

Behavior of Aluminum in Its Electric-Spark Dispersion in Aqueous Solutions of Some Acids

R. K. Bairamov, A. I. Ermakov, and N. R. Vedernikova

Olimpiya Limited Liability Company, Novomoskovsk, Tula oblast, Russia
Novomoskovsk Institute, Mendeleev Russian University of Chemical Engineering, Novomoskovsk, Tula oblast, Russia

Received May 16, 2001

Abstract—The influence exerted by the nature and concentration of a number of organic and mineral acids on the composition of products formed in electric-spark dispersion of aluminum was studied.

Being a continuation of [1–3], this study is concerned with the effect of organic and mineral studies on the composition of products formed in electric-spark dispersion of aluminum. The experiments were carried out on a setup, and using a procedure, described in [1].

The results obtained in studying the influence exerted by the concentration of working solutions of nitric, hydrochloric, and acetic acids on the composition and amount of spark-erosion products are presented in Fig. 1. Among the products are identified aluminum powder and boehmite and bayerite forms of aluminum hydroxide (AH). As seen, the ω–*C* dependences show different behavior in two ranges. With the concentration of acid solutions increasing in the first range, the content of aluminum powder in spark-erosion products grows steeply (ω_1–*C* dependence). Correspondingly, the fraction of AH decreases (ω_2–*C* dependence). The stronger the acid, the steeper the increase in the content of metal powder in the product. Further increase in the acid concentration affects the amount of metal powder in the product only slightly (portion II of the ω_1–*C* dependence). The observed run of the ω–*C* curves is apparently due to the fact that, as the acid concentration in solution is increased, the mechanism of oxide film formation on the surface of dispersed aluminum particles changes. It has been suggested previously [2, 3] that the energy released in the spark discharge zone is sufficient for atomization of oxygen from oxygen-containing acid residues. The released oxygen may be involved in aluminum oxidation to give a protective oxide film. However, a steep rise in the content of powdered aluminum in the product formed in spark erosion is observed in the first range in a narrow interval of concentrations also in that case when one of acids (hydrochloric) has no oxygen-containing acid residue. Hence, oxygen that oxidizes aluminum originates from sources other than the acid residue of an acid. It is known that hydrogen ions in dilute aqueous solutions of acids are in the hydrated state in the form of hydroxonium H_3O^+.

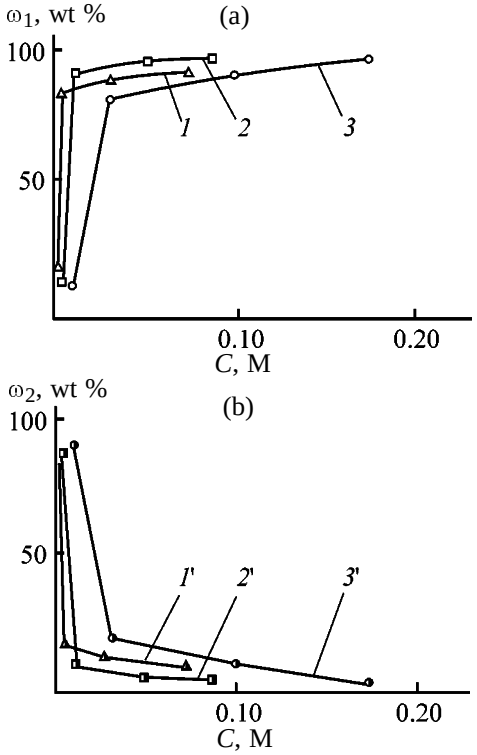

Fig. 1. Content of (a) powdered aluminum, ω_1, and (b) aluminum hydroxide, ω_2, in spark-erosion products vs. acid concentration *C* in the working solution. Temperature of sludge treatment 25°C, treatment time 4 h. Acid: (*1*, *1*′) hydrochloric, (*2*, *2*′) nitric, and (*3*, *3*′) acetic.

1070-4272/02/7503-0408$27.00 © 2002 MAIK "Nauka/Interperiodica"

Effect of additives introduced into working solution on the composition of products formed in electric-spark dispersion of aluminum in sludge processing* and their characteristics**

Additive no.	Component added	C, M	T, °C	τ, h	Product composition, wt %		K	ΔE, kJ mol^{-1}
					AH***	metal		
1	Distilled water	–	90	15	65/35	0	1.8×10^{-16}	910
	Acid:							
2	hydrogen peroxide	0.18	90	12	0/100	0	2.63×10^{-12}	650
3	orthoboric	0.064	90	10	0/100	0	5.8×10^{-10}	1030
	metaboric	–	–	–			7.5×10^{-10}	680
	Boron oxide	–	–	–			–	650
	Acid:				(AH)Σ			
4	acetic	0.15	25	4	5	95	1.75×10^{-5}	680
5	oxalic	0.055	25	4	8	92	5.4×10^{-2}	650
6	nitric	0.045	25	4	4	96	43.6	350
7	hydrochloric	0.035	25	4	10	90	1×10^{7}	–

* (T, τ) Treatment temperature and duration, respectively.
** (K, ΔE) Protolysis constant and energy of atomic oxygen formation.
*** (AH) Content of aluminum hydroxides: (numerator) bayerite and (denominator) boehmite; (Σ) total content of all AH forms.

Presumably, either water or H_3O^+ may serve as a source of oxygen. The mass fraction of aluminum in products of thermal-electric decomposition strongly depends on the nature and concentration of acid in a working solution. In the first range, the stronger the acid, the greater the amount of atomic oxygen formed via thermal-electric decomposition of H_3O^+ ions and, correspondingly, the higher the fraction of aluminum powder in the products. In the second portion of the ω_1–C dependence, the content of metal powder varies slowly with increasing acid concentration. The possible reason is that oxygen produced in thermal decomposition of the oxygen-containing acid residue is involved, together with oxygen formed in decomposition of the hydroxonium ion, in aluminum oxidation in the second range of the dependence. Consequently, the oxidation of aluminum in the given range of concentrations is the slowest and the most incomplete in the case of hydrochloric acid solutions.

Experimental and calculated data for a number of the acids studied are presented in the table. Addition of acid nos. 4–7 to the working solution leads to preferential formation of an oxide film on the aluminum surface. The observed phenomenon is virtually independent of the type of anion. However, this contradicts the conventional concepts of how acids act upon aluminum under nearly standard conditions. The protective oxide film is formed on aluminum in sufficiently concentrated nitric acid solutions. No protective film is formed in hydrochloric acid solutions [4]. At the same time, under conditions of electric-spark dispersion of aluminum in hydrochloric acid solutions, there occurs, at the initial instant of time, even more intensive formation of a protective film than that with nitric and weaker acids. In this case, the experimentally obtained series of influence exerted by the nature and concentration of acids on the intensity of oxide film formation is in good agreement with data on acid protolysis constants [5] (see table).

The composition of products formed in spark dispersion of aluminum is in qualitative agreement with the energy ΔE of atomic oxygen formation from molecules of solution components, calculated by quantum-chemical methods AM1 [6] and PM3 [7]. The table lists the energies necessary for removing an oxygen atom from a molecule to give independent fragments (or a fragment) of the molecule. In calculations, the geometry of fragments was optimized.

On the whole, the observed experimental data are in satisfactory agreement with the individual properties of the components introduced into the working solution, if their acid properties and the energy of atomic oxygen formation are considered simultaneously. In all probability, the acid properties of a component affect the total concentration of the atomic oxygen being formed to even greater extent. Such a conclusion follows not only from the fact that water is the dominant component of the working solution. Free electrons with rather high kinetic energy appear in the spark discharge zone; and these electrons can be involved in reactions. Calculations show that the reac-

tion of formation of atomic oxygen from a hydroxonium ion, proceeding with electron of capture, requires much less energy than formation of atomic oxygen from water:

$$H_3O^+ + e \rightarrow 3H + O, \quad \Delta E = 210 \text{ kJ mol}^{-1}. \quad (1)$$

A calculation in terms of scheme (1) assumed that the electron energy is zero. The energy consumption in formation of atomic oxygen by reaction (1) is much lower than that in reactions of its formation from water or acid residues. Thermodynamic calculations employing data of [8] show that the entropy-related contribution to the total energy in decomposition of a hydroxonium ion is approximately 1.55 times that in decomposition of a water molecule. At a temperature of about 1000 K this quantity is approximately 310 and 200 kJ mol^{-1} for the hydroxonium ion and water molecule, respectively. Consequently, the entropy factor dominates over the enthalpy factor in decomposition of a hydroxonium ion. In decomposition of a water molecule, such a condition is not satisfied at the given temperature. Therefore, one would expect that atomic oxygen is formed in thermal-electric dissociation of just the hydroxonium ion.

Atomic oxygen may also appear in decomposition of acid molecules. However, the decomposition energy proved to exceed by, on the average, a factor of 2 and more that required for atomization of oxygen from water (see table). The concentration of acid molecules in aqueous solutions of weak acids is much higher than that of hydroxonium ions. However, the influence exerted by thermal decomposition of oxygen-containing acid residues to give atomic oxygen on the composition of products of spark erosion of aluminum should also be taken into account for weak acids.

As seen from the table, virtually 100% boehmite is formed when solutions of boric acid and hydrogen peroxide are used. In view of the fact that the protolysis constants of these acids have values intermediate between the constant of water and those of the acids under study, such a composition of the products is as it would be expected. Indeed, the boehmite phase of AH is, formally, also intermediate between the bayerite AH phase (obtained in water) and the oxide phase of aluminum (formed in solutions of stronger acids). Judging from the decomposition energy ΔE of orthoboric acid, it would be expected that decomposition to give atomic oxygen is hindered. However, boric acids are easily dehydrated on heating to form metaboric and other acids. In the end, boric acids completely pass into the gas phase at a temperature of about 2250°C (reached in the spark discharge zone) in the form of monomeric boron oxide B_2O_3. The ΔE value is close to the decomposition energies of the acids, listed in the table. The energy of oxygen atomization for the monomeric form of metaboric acid is close to the atomization energy of oxygen from B_2O_3. Moreover, boric acid markedly differs in nature from the other acids represented in the table: its acid function is associated with protolysis of water bound to boron to form a complex, rather than with protolysis of the acid itself. This circumstance may affect processes occurring in the solution bulk. The case of hydrogen peroxide is characterized by disproportionation with evolution of oxygen. This oxygen may favor formation of AH containing increased fraction of oxygen, namely, boehmite AH (see table).

CONCLUSION

Mineral and organic acids introduced into the working solution markedly affect oxidation of aluminum in the course of its electric-spark dispersion. The possible mechanism of formation of a protective oxide film on the surface of dispersed aluminum is associated with the occurrence of thermal-electric decomposition of the hydroxonium ion and acid molecules to give atomic oxygen under spark discharge conditions.

REFERENCES

1. Bairamov, R.K., Vedernikova, N.R., and Ermakov, A.I., *Zh. Prikl. Khim*., 2001, vol. 74, no. 10, pp. 1703–1705.
2. Bairamov, R.K., Ermakov, A.I., and Vedernikova, N.R., *Zh. Prikl. Khim*., 2001, vol. 74, no. 10, pp. 1706–1708.
3. Bairamov, R.K., Ermakov, A.I., and Vedernikova, N.R., *Zh. Prikl. Khim*., 2001, vol. 74, no. 10, pp. 1708–1710.
4. Glinka, N.L., *Obshchaya khimiya* (General Chemistry), Ermakov, A.I., Ed., Moscow: Integral, 2000.
5. *Spravochnik khimika* (Chemist's Handbook), Nikol'skii, B.P., Ed., Moscow: Khimiya, 1964.
6. Dewar, M.J.S., Zoebisch, E.G., Hearly, E.F., and Stewart, J.J.P., *J. Am. Chem. Soc*. 1985, vol. 107, no. 13, pp. 3902.
7. Stewart, J.J.P., *J. Comp. Chem*., 1989, vol. 10, pp. 209, pp. 221.
8. Karapet'yants, M.Kh. and Karapet'yants, M.L., *Osnovnye termodinamicheskie konstanty organicheskikh i neorganicheskikh veshchestv* (Basic Thermodynamic Constants of Organic and Inorganic Substances), Moscow: Khimiya, 1968.

Russian Journal of Applied Chemistry, Vol. 75, No. 3, 2002, pp. 411–416. Translated from Zhurnal Prikladnoi Khimii, Vol. 75, No. 3, 2002, pp. 422–427.
Original Russian Text Copyright © 2002 by Tumanova.

APPLIED ELECTROCHEMISTRY AND CORROSION PROTECTION OF METALS

Anodic Dissolution, Passivation, and Methods for Electrochemical Polishing of Nb, Ta, and Ti in Low-Temperature Urea–Halide Melts[1]

N. Kh. Tumanova

Vernadsky Institute of General and Inorganic Chemistry, National Academy of Sciences of Ukraine, Kiev, Ukraine

Received April 11, 2001

Abstract—Processes of anodic dissolution of Nb, Ta, and Ti in low-temperature urea–NH_4Cl and urea–NH_4F melts were studied. Methods for electrochemical polishing of metals were developed.

The electrochemical behavior of niobium, tantalum, and titanium, oxidation levels of metal ions formed in melt as a result of anodic dissolution, and equilibrium of metals with their ions in chloride, fluoride, and mixed chloride–fluoride melts have been extensively studied [1–10]. Despite the considerable number of publications, the relevant scientific concepts and results are subject of discussion. The ambiguity of mechanisms of processes at electrodes, described in the literature, is associated with the complexity of multielectron processes occurring in anodic dissolution and deposition of metals and with the formation and stability of poorly soluble intermediate oxyhalides and oxides.

Passing to low-melting ion–organic electrolytes (consisting of an organic compound and an ionic compound) is of interest for solving a number of scientific and applied problems. The scientific interest is primarily associated with the need to reveal the fundamental aspects of the electrochemical behavior of Nb, Ta, and Ti in low-temperature melts containing organic compounds and its general (common to all molten media) and specific features. Another important thing is to determine the stable oxidation states of metals and the structure of complexes formed by niobium, tantalum, and titanium with melt components.

The expediency of practical use of low-temperature melts for electropolishing of Nb, Ta, and Ti is governed by the problem of environment protection. The electrolytes presently used for electropolishing of these metals are based on corrosive acids: hydrofluoric and sulfuric [11]. Use of urea-based melts will improve the environmental and labor conditions and make simpler and less expensive the equipment to be used. No published data on use of low-temperature ion–organic melts for studying the electrochemical behavior of high-melting metals could be found in the literature, except for [12–15].

EXPERIMENTAL

The electrochemical behavior of Nb, Ta, and Ti in urea–halide melts was studied by cyclic voltammetry with the use of a PI-50-1 potentiostat. The surface area of the indicator electrode (Nb, Ta, Ti) was $(5–8)\times10^{-3}$ cm^2. As auxiliary electrode served platinum plate. The electrode potential was measured relative to a silver reference electrode $Ag/AgNO_3$ (0.07 mol kg^{-1})–urea–NH_4NO_3 (16 mol %). Experimental data were obtained in the temperature range 120–140°C in an argon atmosphere. The oxidation states of metal ions passing into melt in electrochemical dissolution were determined by gravimetry and spectroscopically: by electronic (Specord UV/VIS and IKS-14), Raman (DFS-24), and IR (Specord M-80) spectroscopies. The electronic spectra were measured in the course of anodic dissolution of metals, quenched melts were studied by Raman and IR methods. The electrode surface was analyzed with a 09 IOS-1 Auger spectrometer. A layer-by-layer analysis of samples was made in a vacuum, with a beam of Ar^+ ions with an energy of about 3000 eV. The melts were prepared from salts of chemically pure grade, recrystallized and dried in a vacuum.

Two sets of melts were studied: urea–MCl (M =

[1] Reported at the Kola Symposium "Electrochemistry of Less-Common Metals," Apatity, December 4–7, 2000.

1070-4272/02/7503-0411$27.00 © 2002 MAIK "Nauka/Interperiodica"

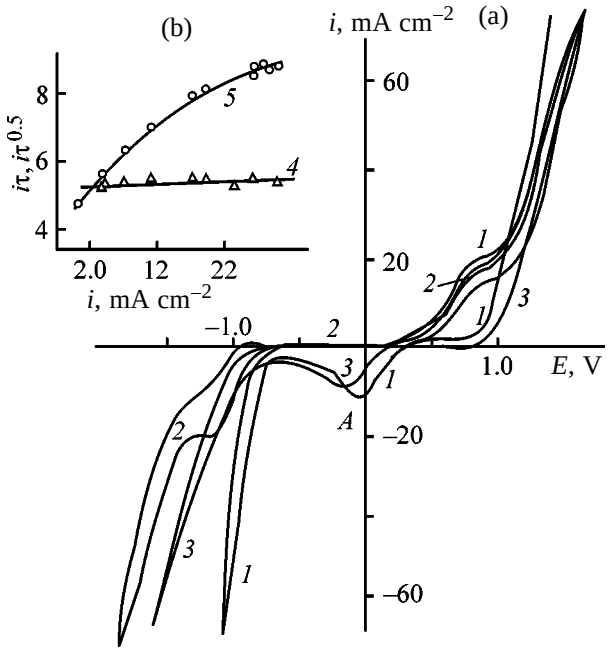

Fig. 1. (a) (*1*–*3*) Voltammograms measured on a Pt electrode in the urea–chloride melt and (b) dependences of (*4*) $i\tau$ and (*5*) $i\tau^{0.5}$ on the current density i for chronopotentiograms of reduction of the anodic reaction product corresponding to waves in curves *1* and *3*. T = 130°C, potential sweep rate 0.1 V s^{-1}. (τ) Transient period (s) and (E) potential. Melt: (*1*) urea–NH_4Cl, (*2*) urea–KCl, and (*3*) the same after preliminary electrolysis.

NH_4^+, K^+, Na^+, Cs^+) and urea–NH_4Cl (Br^-, I^-, F^-). The results of electrochemical studies of the given melts with the use of inert (platinum, glassy carbon) electrodes were reported in [12, 13].

A study of urea–chloride melts of varied composition revealed distinctive features of melts containing ammonium ions. Formation of a compound present both in the gas phase and, in lesser amount, in the melt was revealed in a urea–NH_4Cl melt in anodic polarization of a Pt (glassy carbon) electrode to potentials exceeding that at which the electrolyte decomposes (0.9 V), i.e., under conditions of joint oxidation of Cl^- ions and urea. This compound is reduced at 0.1 V (Fig. 1a, curve *1*); according to chronopotentiometric data (Fig. 1b), the reduction proceeds from an adsorbed layer [13]. The results obtained in an IR study of the anolyte and anode gases, and their comparison with published data [16], made it possible to identify this compound as NCl_3. In the urea–K(Na, Cs)Cl melts, there is no cathodic peak of current, corresponding to NCl_3 reduction, in the reverse portion of the voltammetric curve measured in the first cycle (Fig. 1, curve *2*), and free chlorine is present in the gas phase. Preliminary electrolysis in melts containing alkali metal chlorides, during which urea is isomerized, leads to accumulation of NH_4^+ ions [12]. Simultaneously, a cathodic current peak appears in voltammograms, similar to that observed in urea–NH_4Cl melts (Fig. 1a, curve *3*). In the process, the peak corresponding to Cl_2 gradually disappears from the spectra of the gas phase, and signal indicating formation and accumulation of NCl_3 appears. The fact that the occurring processes and voltammograms obtained on Pt electrodes in urea–NH_4Cl and urea–(alkali metal chloride) melts are identical after 30–40 min of electrolysis indicates that the use of the urea–NH_4Cl melt as solvent is preferable.

A study of systems comprising urea and ammonium salts of varied anionic composition revealed that electrolysis of bromide and iodide melts is accompanied by liberation of free bromine and iodine, imparting, respectively, yellow and brown-yellow color to the melts, which hinders interpretation of the results of electrochemical and, especially, spectroscopic studies. Therefore, the urea–NH_4Cl (16.8 mol %) and urea–NH_4F (10 mol %) melts were chosen for studying the mechanism of anodic dissolution of metals and solving applied problems.

A study of Nb, Ta, and Ti dissolution in the urea–NH_4Cl melt demonstrated that all the metals are passive, but to varied extent.

Niobium is passive in a rather wide range of potentials. Its surface is activated only in the transpassive region at potentials more positive than 1.0 V (Fig. 2a, curve *1*). After activation, the wave of niobium dissolution current can be observed in the reverse portion of the voltammetric curve. Recycling leads to appearance in the forward portion of an anodic current peak (curve *2*), with the current increasing in cycling (curves *3* and *4*) if the electrode polarization reaches the transpassive region. That is, the increase in niobium dissolution current is proportional to the rise in the concentration of NCl_3, which is formed in the transpassive region and activates the surface of the Nb electrode. If the polarization is switched off and the electrode is kept in the melt for a certain time, the voltammetric curve retraces the curve obtained in the first cycle, reflecting the complete passivation of the electrode. Auger spectroscopy was applied to study the surface of the Nb electrode in the steady state and in the case of anodic polarization. In the steady state, the electrode is covered with a passive film mainly composed of urea; with increasing positive potential, the content of Cl^- in the film markedly increases.

According to gravimetric data, niobium passes into

the melt in anodic dissolution as pentavalent ions. The calculated oxidation state n is 5–5.2 for all portions of the anodic curve. The metal is dissolved by the solid-phase mechanism of dissolution of high-melting metals [17]. According to this mechanism, compounds with varied metal oxidation state are formed in the passive film, and the oxidation state increases in going from metal to the film–melt interface. The fact that ions with the highest oxidation state [Nb(V)] are formed in dissolution of Nb is an indirect evidence in favor of the formation of a sufficiently stable passive film on the metal surface. The formation and accumulation of Nb(V) ions in the urea–NH_4Cl melt was indicated by the shift of charge-transfer bands in the UV part of the electronic spectra in the course of anodic dissolution of the metal (at current densities i = 5–50 mA cm^{-2}). The position (36 000, 32 500, and 28 500 cm^{-1}) and the nature of the absorption bands indicate formation of octahedral chloride complexes of niobium, $[NbCl_6]^-$ [18]. A study of quenched melts by other spectroscopic methods confirmed this conclusion. The peaks in Raman spectra at 370, 290, and 180 cm^{-1} are characteristic of $[NbCl_6]^-$ [16]. The IR spectra of melts solidified before and after metal dissolution demonstrated that the frequencies of stretching vibrations of the C–O and N–H bonds remain unchanged. This means that urea is not involved in complexation.

The mechanism of tantalum dissolution in the urea–chloride melt also corresponds to the solid-phase mechanism of dissolution of high-melting metals. The passivation of Ta in the melt is even more pronounced, compared with that of niobium. In the case of Ta, electrode polarization into the transpassive range does not depassivate the surface of the metal surface and lead to its dissolution (Fig. 2b). The dissolution of tantalum requires accumulation of a much greater amount of the depassivating agent than that formed while the electrode is in the transpassive region during a single cycle at potential sweep rate of 10^{-1} V s^{-1}. For a sufficient amount of depassivating agent to be accumulated, the time of electrode polarization in the transpassive region is to be extended. For this purpose, it is necessary to either perform multiple cycling (3–5 cycles, Fig. 2b) or reduce the potential sweep rate to 10^{-2} V s^{-1}. The peak of tantalum dissolution current can also be observed in the voltammetric curve after preliminary electrolysis of the melt for 20–30 min at voltages exceeding 1 V. In reverse portions of the voltammetric curve, the dissolution wave occasionally appears even in those cases when it is absent in the forward portion of the curve. When

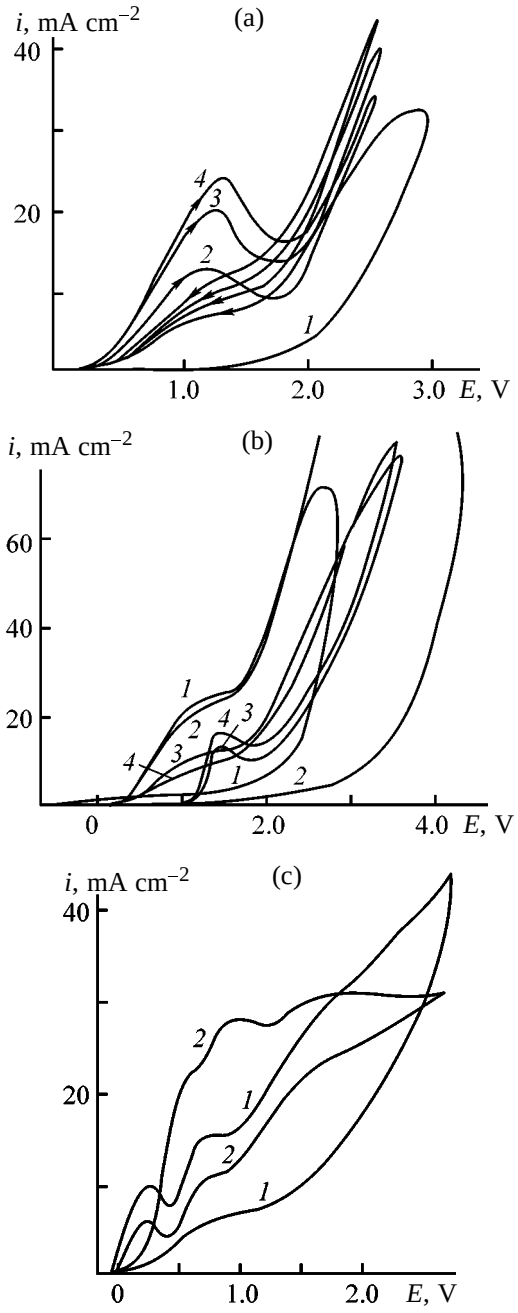

Fig. 2. (*1–4*) Anodic portions of voltammograms obtained successively on (a) Nb, (b) Ta, and (c) Ti electrodes in a eutectic urea–NH_4Cl melt. Potential sweep rate 0.1 V s^{-1}; the same for Fig. 3. (*i*) Current density and (*E*) potential; the same for Fig. 3.

the electrode is placed in the melt, the dissolution peak current decreases in the course of time, to the point of its complete disappearance. This indicates the gradual passivation of the electrode. The stable passivation of the Ta electrode is due to the fact that the urea film formed on the electrode in the melt in

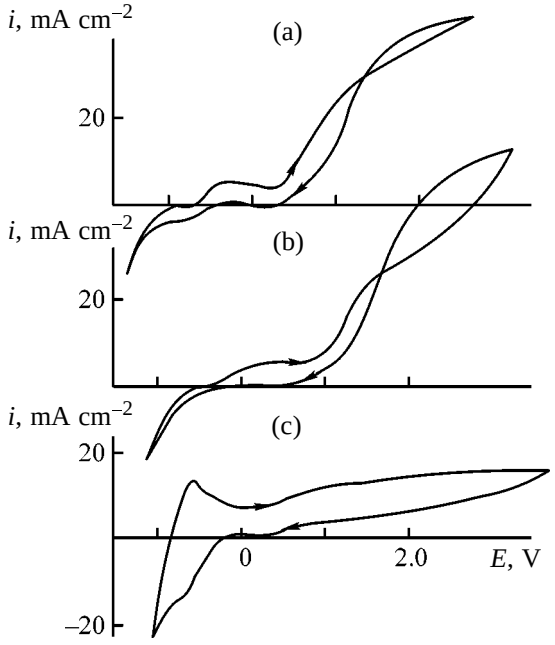

Fig. 3. Voltammograms obtained on (a) Nb, (b) Ta, and (c) Ti electrodes in eutectic urea–NH_4F melt.

the steady state is saturated with oxygen as the electrode is polarized. This leads to formation on the tantalum surface of an oxide film (according to Auger spectroscopy) whose disintegration requires a substantial activity of the depassivating agent.

The formation of tantalum ions with the highest oxidation state, Ta(V), was established gravimetrically and spectroscopically. Electronic spectra were measured during electrolysis in the course of 15–60 min in a wide range of current densities, 5–150 mA cm^{-2}. The peaks in the spectrum (27000, 31000, and 38000 cm^{-1}) correspond to formation of octahedral chloride complexes $[TaCl_6]^-$ [18, 19]. Raman spectra of quenched melts also confirm this conclusion (frequencies 380, 300, and 183 cm^{-1}) [16]. No tantalum ions with lower oxidation states were formed.

Depassivation of the urea film on titanium proceeds rather easily. A region of Ti dissolution is observed in the forward portion of the voltammetric curve in the first cycle (Fig. 2c). This means that the depassivating action of the Cl^- ion is sufficient for disruption of the passive film and dissolution of titanium to give Ti(II) ions in the melt. The electronic spectra obtained after 30 min of electrolysis at current densities in the range 5–20 A cm^{-2} confirm the formation of urea complexes with Ti(II) $Ti[CO(NH_2)_6]^{2+}$, with coordination via oxygen. The IR spectra of quenched melts before and after dissolution of titanium show a decrease in the frequency of vibrations of the C–O bond from 1683 to 1615 cm^{-1}, with the frequencies corresponding to the N–H bond remaining unchanged.

However, with increasing anodic polarization Ti(II) ions are not oxidized further to higher oxidation state (Fig. 2c, curve *1*). According to Auger spectroscopy, the urea film is gradually saturated with oxygen and chlorine. Apparently, an oxychloride film shielding the electrode surface is formed on the titanium surface. If the electrode is polarized into the transpassivation region, two new waves appear in the reverse portion of the voltammetric curve, retained in the forward portion of the curve. These waves reflect the formation of Ti(III) and Ti(IV) ions (as indicated by gravimetry). The formation of Ti(III) ions was also revealed in measuring electronic spectra at current densities of 30–50 A cm^{-2}. The peaks in the spectrum (23000 and 19000 cm^{-1}) correspond to formation of four-coordinate complexes of Ti(III) with urea, $[Ti(CO(NH_2)_2)_4]^{3+}$, coordinated via nitrogen. The IR spectra measured before and after dissolution of titanium at the current densities specified show an increase in vibration frequencies from 1683 to 1720 cm^{-1} for the C–O bond, and a decrease from 1471 to 1400 and from 3400 to 3200 cm^{-1} for, respectively, the C–N and N–H bonds. For Ti(IV) the spectra could not be obtained because of the possible overlapping of the charge-transfer spectrum for Ti(IV) and the spectra of *d–d* transitions in Ti(II) and Ti(III). The formation of Ti(IV) in the third wave of the cyclovoltammograms was confirmed qualitatively, by introducing $TiCl_4$ into the melt.

It follows from the results obtained in studying the electrochemical dissolution of metals in the urea–chloride melt that the electrochemical activity of the metals decreases in the order Ti > Nb > Ta, which is due to the formation of a passive film and is determined by its composition, stability, and solubility in the melt. The electrochemical activities of the metals being different, the methods for electropolishing of Nb, Ta, and Ti in the urea–chloride melt differ in the electrolyte composition and electrolysis conditions: the quality of a treated surface decreases in the order Ti > Nb > Ta.

For obtaining a lustrous metal surface, the electrode polarization is to be performed with the use of reversing current, $i_a/i_c = 3:1$, at total time of a cycle equal to 1 s. For the same purpose, organic surfactants of various kinds (neutral, cationic, and anionic, which are thermally, chemically, and electrochemically stable under the electrolysis conditions) are to be introduced into the urea–NH_4Cl melt.

The treatment can be done in the easiest way, and with the best results obtained, in polishing of titanium. After electrochemical treatment for 5 min in a urea–NH_4Cl melt, the degree of surface finish increases by three points, and the luster reaches a value of 84% [20]. In treatment of niobium, the degree of surface finish can be increased by two points, and the luster becomes 74% upon electrolysis for 10 min [21]. The most difficult is polishing of tantalum. The time of treatment is, in this case, 15 min, the degree of finish increases by one point, and the luster does not exceed 70% [22].

The quality of the metal surface after treatment can be much improved if electrochemical polishing is carried out in urea–fluoride melts.

The mechanism of metal dissolution in a fluoride-containing $CO(NH_2)_2$–NH_4F melt differs from that in a chloride-containing melt. The depassivating agent in the chloride melt is NCl_3 formed in electrolysis of the $CO(NH_2)_2$–NH_4Cl melt, whereas in the fluoride melt this part is played by the F^- ion.

The dissolution of Nb and Ta occurs immediately after the beginning of polarization (Fig. 3). The first wave corresponds to formation of ions with the lower oxidation state (IV), and the second, to their oxidation to Nb(V) and Ta(V) (gravimetry). Polarization of the electrode into the transpassive region does not lead to any significant changes in the shape of the curves. This may indicate that no compound with depassivation action stronger than that of the F^- ion is formed in the given range of potentials.

The formation of pentavalent ions of Nb and Ta in electrochemical dissolution of metals at current densities in the range 5–10 A cm^{-2} was confirmed by electronic and Raman spectroscopies. The shift of the charge-transfer bands in the electronic absorption spectra (from 42 000 to 32 000 cm^{-1} for Nb and from 39 000 to 34 000 cm^{-1} for Ta) is in agreement with the data of Raman spectroscopy for quenched melts (280, 560, and 682 cm^{-1} for niobium and 290, 590, and 694 cm^{-1} for Ta) and corresponds to formation of octahedral complexes of Nb(V) and Ta(V), $[MF_6]^-$.

The wave of Ti dissolution in the urea–fluoride melt (Fig. 3) also appears in the forward portion of the voltammetric curve in the first cycle. However, measurements of the reverse portion of the curve show that poorly soluble compounds of titanium are formed on the metal surface. Auger spectroscopy revealed the formation of titanium oxyfluoride on the anode surface during polarization. The formation of a deposit on the electrode surface can be observed visually in electrolysis for 1 h. After the current is switched off, the deposit gradually dissolves in the urea–NH_4F melt to give octahedral complexes of Ti(III) of the type $[TiF_6]^{3-}$. This indicates that the rate of Ti oxyfluoride formation in polarization exceeds the rate of its dissolution.

The urea–fluoride melt was used as electrolyte for Ta electropolishing as the metal most difficultly treated in the chloride melt. Introduction of even minor amounts of NH_4F (5 mol %) into the eutectic melt urea–NH_4F markedly changes the results of electrochemical treatment. The degree of finish increases by unity, with the luster reaching a value of 80% (in chloride melts the luster does not exceed 70%).

With account of the toxicity of fluoride melts, their practical use is possible, but inexpedient, since the main parameters characterizing the quality of the Nb, Ta, or Ti surface conform to the requirements to a polished surface after electrochemical treatment in the urea–chloride melt.

CONCLUSIONS

(1) A study of the anodic dissolution of Nb, Ta, and Ti in urea–NH_4Cl and urea–NH_4F melts demonstrated that all these metals are passive in urea-based melts and the dissolution mechanism corresponds to the solid-phase mechanism of dissolution of high-melting metals.

(2) The electrochemical dissolution of metals occurs under the action of the depassivating agent, NCl_3, formed in electrolysis of the urea–NH_4Cl melt at potentials exceeding 1.0 V, and of the F^- ion in urea–NH_4F melts. The electrochemical activity of the metals decreases in the order Ti > Nb > Ta in the urea–chloride melt and is about the same in the urea–NH_4F melt. Titanium virtually does not dissolve in the urea–fluoride melt because of the formation of poorly soluble titanium oxyfluoride on the metal surface.

(3) The study of the electrochemical dissolution of Nb, Ta, and Ti in urea-based melts made it possible to develop methods for electrochemical polishing of the metals. The basic parameters characterizing the metal surface quality (degree of finish, luster) conform to the requirements to a polished surface for all the metals studied.

REFERENCES

1. Baraboshkin, A.N., *Elektrokristallizatsiya metallov iz rasplavlennykh solei* (Electrocrystallization of Metals from Molten Salts), Moscow: Nauka, 1976.

2. Ivanovskii, L.I., Lebedev, V.A., and Nekrasov, V.N., *Anodnye protsessy v rasplavlennykh galogenidakh* (Anodic Processes in Molten Halides), Moscow: Nauka, 1983.
3. Konstantinov, V.I., *Elektroliticheskoe poluchenie tantala, niobiya i ikh splavov* (Electrolytic Production of Tantalum, Niobium, and Their Alloys), Moscow: Metallurgiya, 1977.
4. Fairbrother, F., *The Chemistry of Niobium and Tantalum*, Amsterdam: Elsevier, 1967.
5. Gitman, E.B., *Elektrometallurgiya i rafinirovanie titana iz rasplavlennykh solei* (Electrometallurgy and Refining of Titanium from Molten Salts), Kiev: Naukova Dumka, 1970.
6. Tumanova, N.Kh. and Barchuk, L.P., *Gal'vanopokrytiya iz ionnykh rasplavov* (Electroplating from Ionic Melts), Kiev: Tekhnika, 1983.
7. Girginov, A., Tzvetkoff, T.Z., and Bojinov, M., *J. Appl. Electrochem.*, 1995, vol. 25, no. 10, pp. 993–1003.
8. Polyakov, E.G., *Zh. Prikl. Khim.*, 1998, vol. 71, no. 2, pp. 181–193.
9. Inman, D. and White, S.N., *J. Appl. Electrochem.*, 1978, vol. 8, no. 5, pp. 375–390.
10. Senderoff, S., Mellors, G.W., and Reinhart, W.J., *J. Electrochem. Soc.*, 1965, vol. 112, no. 8, pp. 840–845.
11. Ustimenko, V.N., Fundamental Aspects of Nonstationary Passivation of Niobium under Convective Diffusion Conditions, *Cand. Sci. Dissertation*, Simferopol, 1998.
12. Tumanova, N.Kh., Babenkov, E.A., Chernukhin, S.I., *et al.*, *Ukr. Khim. Zh.*, 2000, vol. 66, no. 5, pp. 35–39.
13. Tumanova, N., Babenkov, E., Bojko, O., and Burjak, N., *195th Meet. of the Electrochem. Soc.*, Seattle (the United States), May 2–6, 1999, p. A-913.
14. Mamantov, G., Gilbert, B., Fung, K.W., *et al.*, *Proc. 1st Int. Symp. on Molten Salts*, New York: Electrochem. Soc., 1976.
15. Sun, I.-W. and Hussey, C.L., *Inorg. Chem.*, 1989, vol. 28, pp. 2731.
16. Nakamoto, K., *Infrared and Raman Spectra of Inorganic and Coordination Compounds*, New York: John Wiley & Sons, 1986.
17. Vas'ko, A.T. and Kovach, S.K., *Elektrokhimiya tugoplavkikh metallov* (Electrochemistry of High-Melting Metals), Kiev: Tekhnika, 1983.
18. Lever, A.B.P., *Inorganic Electronic Spectroscopy*, Amsterdam: Elsevier, 1984.
19. Volkov, S.V. and Yatsimirskii, K.B., *Spektroskopiya rasplavlennykh solei* (Spectroscopy of Molten Salts), Kiev: Naukova Dumka, 1977.
20. Ukrainian Patent 99084755.
21. Ukrainian Patent 99042246.
22. Ukrainian Patent 99095374.

Russian Journal of Applied Chemistry, Vol. 75, No. 3, 2002, pp. 417–421. Translated from Zhurnal Prikladnoi Khimii, Vol. 75, No. 3, 2002, pp. 428–432.
Original Russian Text Copyright © 2002 by Apostolova, Shapa, Shempel', Mel'nikov.

APPLIED ELECTROCHEMISTRY AND CORROSION PROTECTION OF METALS

Titanium Dioxide Synthesized by Emulsion Method as a Material for Lithium Current Sources

R. D. Apostolova, N. N. Shapa, E. M. Shempel', and B. I. Mel'nikov

Ukrainian State University of Chemical Engineering, Dnepropetrovsk, Ukraine

Received April 11, 2001

Abstract—Nanostructural titanium dioxide, TiO_2(E), synthesized by the emulsion method, was studied as cathode and anode of a lithium current source.

Titanium dioxide, TiO_2, is used in lithium current sources [1, 2], electrochromic systems [3], and in photocatalysis [4].

Among structural modifications of titanium dioxide, anatase is the most extensively studied as electrode of lithium sources. Nanostructural anatase is a promising cathode [2]; also, it was tested as anode of a lithium-ion battery [1].

The discharge–charging cycle of a TiO_2 electrode in aprotic Li-containing medium is accompanied by a topotactic reaction of lithium ion intercalation into the titanium dioxide lattice:

$$TiO_2 + xLi^+ + xe \rightarrow Li_xTiO_2. \quad (1)$$

The service life of a lithium battery based on TiO_2 is determined by the reversibility of reaction (1), which depends, to a considerable extent, on the procedure for titanium dioxide synthesis. In cathodes based on the anatase [TiO_2(A)], the intercalation of lithium ions is reversible at $x \leq 0.5$. The discharge capacity of the lithium-ion system with TiO_2(A) anode and $TiCoO_2$ cathode in 1 M solutions of $LiN(CF_3SO_2)_2$, EC (ethylene carbonate), and DME (dimethoxyethane) is 50 mA h g^{-1} [1].

To improve the relative discharge characteristics of the TiO_2(A) electrode, various methods were developed for anatase preparation. It was synthesized in the mesophase form and also by applying a thin layer to a conducting substrate for use in thin-film chemical current sources (CCSs) and electrochromic systems. For example, the electrochemical intercalation of lithium ions was studied in TiO_2(A) synthesized by the following methods: cathodic electrodeposition from aqueous solution containing TiO^{2+} ions [5], electrophoresis in organic electrolyte, electron-beam evaporation [6], reaction of titanium carbide with hydrogen peroxide [4], anodic dissolution of titanium in acetonitrile [7], sol–gel formation from titanium alcoholates [8], nanocomposite formation [2], and by other methods.

However, the electrochemical potentialities of TiO_2(A) in the synthesized materials during cycling of lithium batteries are not exhausted to a full measure. This fact stimulates a search for new ways to improve the electrochemical performance of TiO_2(A), including development of new synthesis procedures.

In this work, we studied the electrochemical intercalation of lithium ions into nanostructural TiO_2(A) synthesized by the emulsion method [TiO_2(E)].

The emulsion method for synthesizing TiO_2(E) was proposed and described in detail in [9]. Finely dispersed titanium dioxide was prepared in reverse emulsion from titanium tetrachloride. For this purpose, a 1% solution of oxyethylated lard (surfactant) in benzene, placed in a glass cap, was added to aqueous ammonia without mixing the layers. Then, a conical head of an ultrasonic disperser was plunged into the aqueous phase, and the generator adjusted to a frequency of 22 kHz was switched on. After the emulsification was complete, a titanium tetrachloride solution in benzene was added to the emulsion, with the ultrasonic treatment continued. In the process, titanium tetrachloride diffused into the dispersed phase and was hydrolyzed in the emulsion droplets. The hydrolysis product was centrifuged, dried, and calcined at 350–400°C to remove ammonium chloride and organic substances.

The synthesized products were studied by IR spectroscopic, X-ray diffraction, thermal, and electrochemical analyses. X-ray diffraction patterns were taken on a DRON-2 diffractometer. The IR absorption

1070-4272/02/7503-0417$27.00 © 2002 MAIK "Nauka/Interperiodica"

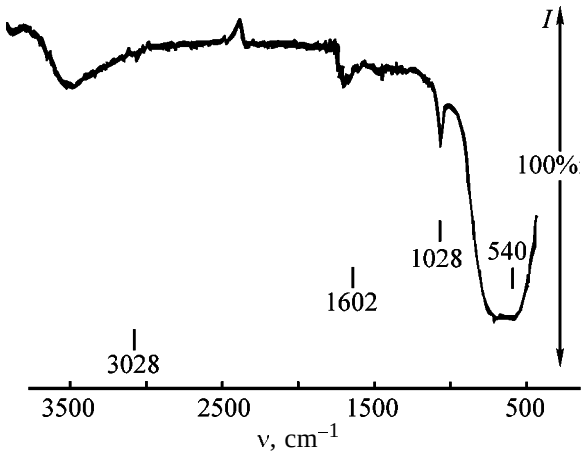

Fig. 1. IR absorption spectrum of TiO_2(E). (*I*) Transmission and (ν) wave number.

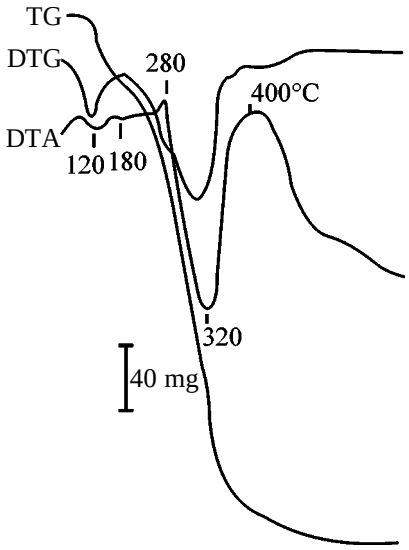

Fig. 2. Thermogravimetric curve of the hydrolysis product of the composition $Ti(OH)_4$ + NH_4Cl.

spectra were recorded on a Specord IR-75 spectrophotometer in the range 400–4000 cm^{-1} using KBr technique. The thermogravimetric curves of 200–300-g TiO_2 samples were obtained on a Q1500-D derivatograph (heating rate 10 deg min^{-1}).

The electrochemical characteristics of TiO_2 were determined in composite electrodes prepared from a grid of 18Cr12Ni10Ti stainless steel, to which the active component containing additives of carbon black and fluoroplastic binder (10 wt % each) was applied as paste, with subsequent drying at 250°C for 2.5–5 h.

The TiO_2 electrode and counterelectrode were assembled as sandwich in commercial KhIT 2325 cells, in which 1 M $LiClO_4$ solution in PC (propylene carbonate) and DME was the electrolyte and a two-layer 110-μm-thick fiber glass was the separator.

The cyclic voltammograms were taken in a sealed three-electrode cell with Li auxiliary electrode and Li/Li^+ reference electrode. The cell was assembled in a glove box under argon.

In study of lithium battery TiO_2 was the cathode and lithium foil, the anode, and in study of lithium-ion current source TiO_2 was the anode and $LiCoO_2$, the cathode. The layered $LiCoO_2$ was synthesized by the thermal method, i.e., by sintering a mixture of dry Li_2CO_3 and Co_3O_4 (Li : Co = 1.05 : 1) at 750°C for 20 h.

The galvanostatic charging–discharge curves of the CCSs and the volt–ampere characteristics of the TiO_2(E) electrode were obtained on a computer-controlled electronic testing bench, at I_{dis} = 0.2 mA and I_{ch} = 0.1 mA. The TiO_2(E) electrode was cycled in the potential range 4.0–0.9 V and then in the narrower range 2.8–0.9 V, with the results changed inappreciably. The cycling range of the $LiCoO_2$ electrode was 3.0–1.1 V.

The X-ray diffraction patterns of TiO_2(E) contain weak diffuse reflections, indicative of finely dispersed powder. The crystallite size estimated from the diffraction patterns is 60 nm. According to the data [9] of transmission electron microscopy, the grain size of TiO_2(E) is 40–60 nm. The emulsification product is a mixture of the TiO_2 structural modifications with anatase as predominant phase [88–90%; *d* (Å): 3.50, 2.47, 2.37, 1.88, 1.68, 1.61, 1.48, 1.36, 1.34, 1.26, and 1.24]. The remainder is rutile [*d* (Å) 3.25 and 1.88] and insignificant amount of orthorhombic titanium oxide [*d* (Å) 2.92 and 2.47].

The physicochemical and electrochemical properties of titanium dioxide depend on the moisture content. The IR spectrum of the synthesized TiO_2(E) confirmed its hygroscopicity (Fig. 1). The absorption spectrum of titanium dioxide, kept in air and then over P_2O_5, has absorption bands attributable to the OH stretching (3440 cm^{-1}) and H–O–H bending vibrations of coordinated water molecules (1640 cm^{-1}). In a humid atmosphere, the titanium–oxygen bonds are not clearly resolved. Only one broad absorption band between 900 and 400 cm^{-1} is present, resembling that in the TiO_2 IR spectrum from [10].

The thermal analysis curves of the heated hydrolysis product of the composition $Ti(OH)_4$ + NH_4Cl have several peaks (Fig. 2). The weight loss (TG and DTG curves) occurs in three stages (at 40–200°C, 200–350°C, and 350–500°C). The DTA curve has three endothermic peaks. The first peak at 110–120°C is due to the water evaporation, the second at 160–

180°C is of uncertain origin, and the third at 320°C is due to NH_4Cl decomposition. The fourth peak at 400–550°C, evidently caused by the decomposition of organic substances, overlaps with the exothermic peak of TiO_2 crystallization at 400–430°C. Above 500°C the weight loss ceases, which confirms the removal of volatile impurities and stabilization of TiO_2.

Thus, the product synthesized by sintering at 400°C is contaminated with organic impurities.

The discharge capacity of the TiO_2(E)/Li system in the first cycle is 600–670 mA h g^{-1}. The discharge curve has two inclined potential plateau: at 1.80–1.60 (*I*) and 1.20–0.9 V (*II*) (Fig. 3a, curve *1*). To them correspond two plateau of the open-circuit potential (OCP): 1.90–1.60 and 1.45–1.35 V (Fig. 3a, curve *2*). The OCP was determined after switching off current, when the change of potential with time did not exceed 1 mV h^{-1}. In charging a TiO_2(E) electrode charged to 0.9 V, the process corresponding to potential plateau *I* is reversible and that corresponding to potential plateau *II*, irreversible (Fig. 3a, curve *3*).

In the second cycle, the discharge capacity of the TiO_2(E) electrode sharply decreases (to 250–270 mA h g^{-1}) (Fig. 3a, curve *4*). The discharge plateau *II* (1.2–0.9 V) in the galvanostatic curve disappears since the second cycle.

In the third cycle, the charging–discharge curve of the TiO_2(E) electrode has the charging (1.80 V) and discharge (1.65 V) potential plateaus (Fig. 3b). The change in the discharge capacity upon TiO_2(E) cycling is reflected in Fig. 3c. Upon subsequent cycling, the discharge capacity decreases, reaching 90 mA h g^{-1} on the 100th cycle.

The cycling voltammetry also shows that the electrochemical intercalation of lithium ions into TiO_2(E) is irreversible. This is seen from Fig. 4: (1) the maximum of the cathode current is smaller than of the anode current, although the total amount of electricity in intercalction is similar to that in Li^+ extraction (Q_{dis}/Q_{ch} = 1.04); (2) the potential difference between the cathode and anode current maxima at the potential scan rate $V = 5 \times 10^{-4}$ V s^{-1} is 0.45–0.55 V. With decreasing scan rate, the potential difference of these maxima decreases (to 0.40–0.50 V at $V = 2 \times 10^{-4}$ V s^{-1} and to 0.32–0.40 V at $V = 1 \times 10^{-4}$ V s^{-1}).

It was determined that the discharge characteristics of TiO_2(E) differ insignificantly from those of TiO_2(BH)-anatase synthesized by traditional base hydrolysis. The discharge curves of TiO_2(BH) are similar to those of TiO_2(E). In the first cycle, the discharge capacity of TiO_2(BH), 550–580 mA h g^{-1}, is

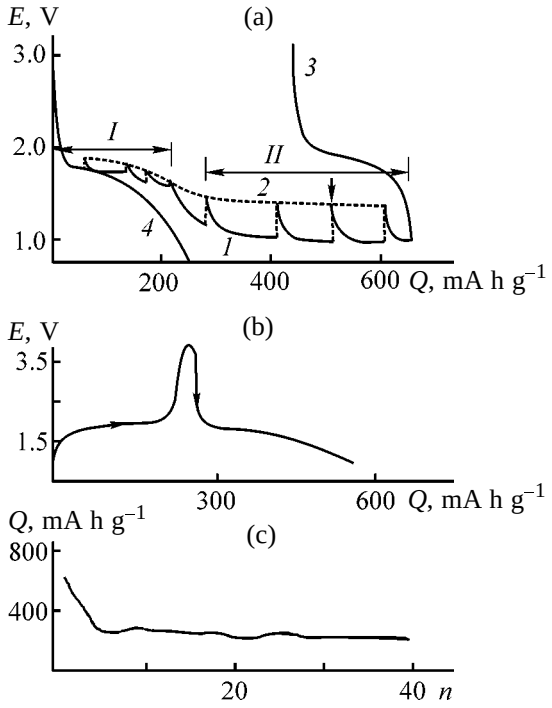

Fig. 3. KhIT 2325 TiO_2(E)/Li current source. I_{dis} = 0.2 mA cm^{-1}, I_{ch} = 0.1 mA cm^{-1}. (*E*) Potential, (*Q*) capacity, and (*n*) cycle number. Curve: (a) (*1*) initial discharge, (*2*) change in OCP upon discharge, (*3*) charging, and (*4*) discharge in the second cycle; (b) charging–discharge in the third cycle; and (c) change in the discharge capacity upon cycling. (a) Vertical arrow indicates the moment of switching on the current.

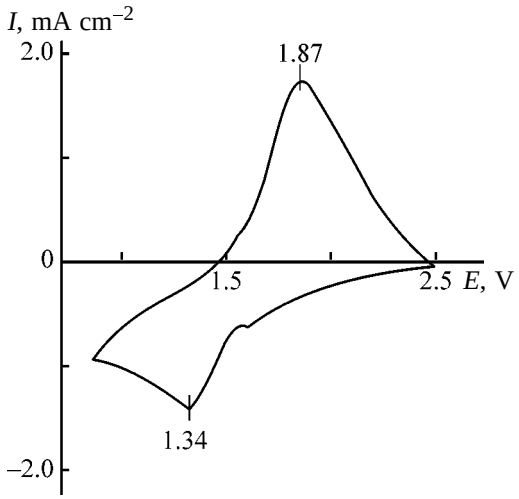

Fig. 4. Cyclic voltammogram of TiO_2(E) for the second cycle. Weight of the cathode active paste 3 mg cm^{-2}, potential scan rate $V = 5 \times 10^{-4}$ V s^{-1}. (*I*) Current and (*E*) potential.

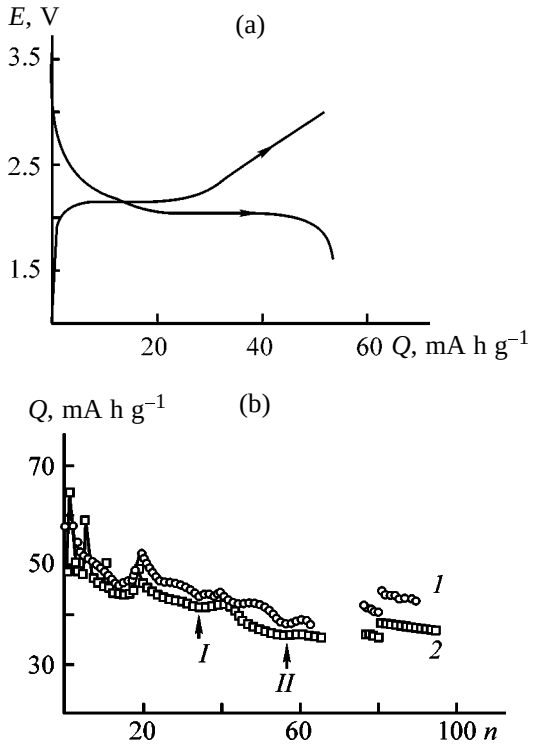

Fig. 5. KhIT 2325 $LiCoO_2/TiO_2$(E) current source. (*E*) Potential, (*Q*) capacity, and (*n*) cycle number. (a) Charging–discharge curve (fifth cycle); (b) change in (*1*) charging and (*2*) discharge capacity upon cycling. Discharge current (mA): (*I*) 0.2 and (*II*) 0.4.

lower than that of TiO_2(E). However, the reversible discharge capacity of titanium dioxide obtained by base hydrolysis is similar to that determined for TiO_2(E).

Our data on the electrochemical intercalation of lithium ions into TiO_2(E) are compared with the published data for TiO_2(A). The open-circuit potentials corresponding to process *I* on the discharge galvanostatic curve of TiO_2(E) lie within the range of the published data: 1.75 [11–13] and 1.80 V [14, 15]. The discharge plateau *II*, which, according to the published data, also disappears at cycling TiO_2(A), is assigned to the film forming at the interface owing to the reaction of titanium dioxide with the electrolyte. In the course of the intercalation of lithium ions, tetragonal TiO_2(A) transforms into orthorhombic Li_xTiO_2, with a maximal value of x differing from the published data: $x = 0.7$ [13] and $x = 1$ [3, 12, 16]. The value $x = 1$ obtained from the X-ray diffraction data is questionable. It is more reasonable for the electrochemical intercalation of lithium ions into TiO_2(A) at room temperature to accept $x = 0.5$ [15, 17, 18]. Our data give $x = 0.60–0.62$ for the maximal degree of lithium ion intercalation on the 30th–40th cycle.

For practical use of electrode materials, the high reversibility of electrochemical conversion and the high rate of lithium intercalation are the necessary conditions. Attempts are made to solve these problems using nanostructural or thin-film materials. However, even for TiO_2(A) thin films, the potential difference between the maxima of the cathode and anode currents exceeds 0.2 V, according to the cyclic voltammogram taken at a scan rate of 2.5×10^{-5} V s^{-1}, i.e., process is irreversible [15]. In thicker porous films, being the objects of our study, the degree of irreversibility is still higher.

It should be taken into account that our results concern anatase containing impurities of other titanium dioxide modifications, including rutile. It was found that the intercalation potential of Li^+ ions into rutile is lower by 0.4 V than into anatase [19]. According to our data, TiO_2-rutile synthesized by thermal hydrolysis showed a 480–500 mA h g^{-1} capacity during the first cycle, when discharged to 0.90 V. Its maximal reversible capacity was 95–100 mA h g^{-1}. Therefore, the specific discharge characteristics of TiO_2(E) with a pure anatase structure can be better.

TiO_2(A) is used as anode of rechargeable lithium-ion batteries [1, 20]. Its theoretical charging capacity is 168 mA h g^{-1}. We tested the TiO_2(E) anode in the lithium-ion system $LiCoO_2/TiO_2$(E). The tests were performed with the applied composite electrodes (active paste weight 10–20 mg cm^{-2}).

The structure of the cathode material $LiCoO_2$ synthesized for the lithium-ion system was confirmed by X-ray diffraction analysis (*d*, Å: 4.67, 2.40, 2.34, 2.20, 2.00, 1.84, 1.55, 1.42, 1.40, 1.34, and 1.22).

The open-circuit potential of the uncharged current source $LiCoO_2/TiO_2$(E) is 0.033–0.040 V. It was charged by intercalating lithium ions into TiO_2(E) and by extracting them from $LiCoO_2$ in the potential range 3.0–1.1 V. The charging-discharge curves are plotted in Fig. 5a. The reversible discharge capacity, as calculated per unit weight of the anode active paste, reached 70–60 mA h g^{-1}, which exceeds the results of [1]. The change in the discharge capacity upon cycling, as calculated per unit weight of the anode active paste, is shown in Fig. 5b. The lithium-ion system studied was not optimized. Its discharge capacity can be enhanced taking into account the material balance of the system.

CONCLUSIONS

(1) Titanium dioxide prepared by emulsion hydrolysis, which is a mixture of TiO_2 structural modi-

fications with anatase prevailing (90%), when used as cathode of a lithium current source, exhibits the initial discharge capacity of 600–650 mA h g^{-1} and the reversible capacity of about 200 mA h g^{-1} on the 30th–40th cycles. The initial discharge capacity of TiO_2(E) anode in the lithium-ion system $LiCoO_2/TiO_2$ is 67–70 mA h g^{-1}, and its reversible capacity after 10 cycles, about 50 mA h g^{-1}. The specific discharge characteristics of TiO_2(E) are similar to those of TiO_2(A) prepared by various procedures.

(2) Compared to titanium dioxide prepared by base hydrolysis, the TiO_2(E) cathode exhibits the higher discharge capacity on the first cycle. The relative discharge characteristics of the TiO_2(E) electrode in a lithium current source can be improved after preparing 100% anatase. In this case, TiO_2(E) will compete with titanium dioxide of anatase structure synthesized by traditional procedures.

REFERENCES

1. Huang, S.J., Kavan, L., Exnar, I., and Gratzer, M., *J. Electrochem. Soc*., 1995, vol. 142, no. 9, pp. L142–L144.
2. Kavan, L., Attia, A., Lenzmann, S.H., *et al*., *J. Electrochem. Soc*., 2000, vol. 147, no. 8, pp. 2897–2902.
3. Ohzuku, T., and Hirai, T., *Electrochim. Acta*, 1982, vol. 27, no. 9, pp. 1263–1266.
4. Lin, W.-J., Tacconi, N.R. de, Smith, R.L., and Rajeshwar, K., *J. Electrochem. Soc*., 1997, vol. 144, no. 2, pp. 497–502.
5. Natarajan, C., and Nogami, G., *J. Electrochem. Soc*., 1996, vol. 143, no. 5, pp. 1547–1550.
6. Krol, R. van de, Goossens, A., and Schoonman, J., *J. Electrochem. Soc*., 1997, vol. 144, no. 5, pp. 1723–1727.
7. Zatti, G., Schiavon, G., and Zecchin, S., *J. Electrochem. Soc*., 1999, vol. 146, no. 2, pp. 637–641.
8. Yuan, J., and Tsujikawa, Sh., *J. Electrochem. Soc*., 1995, vol. 142, no. 10, pp. 3444–3450.
9. Mel'nikov, B.I., Solonukha, A.V., and Shapa, N.N., *Vopr. Khim. Khim. Tekhnol*., 2000, no. 3, pp. 19–21.
10. Nyquist, R.A., and Kagel, R.O., *Infrared Spectra of Inorganic Compounds (3800–45 cm^{-1})*, New York: Academic, 1971.
11. Macklin, W.J. and Neat, R.J., *Solid State Ionics*, 1992, vols. 53–56, pp. 694–703.
12. Ohzuku, T., Kodama, Z., and Hirai, T., *J. Power Sources*, 1985, vol. 14, pp. 153–157.
13. Cava, R.J., Murphy, D.W., Zahurak, S., *et al*., *J. Solid State Chem*., 1984, vol. 53, pp. 64–70.
14. Schlichthorl, G., Park, N.G., and Frank, A.J., *J. Phys. Chem*., 1999, vol. B101, no. 5, pp. 782–787.
15. Krol, R. van de, Goossens, A., and Meulnkamp, E.A., *J. Electrochem. Soc*., 1999, vol. 146, no. 9, pp. 3150–3154.
16. Ohzuku, T., Takehara, Z., and Yoshizawa, S., *Electrochim. Acta*, 1979, vol. 24, no. 2, pp. 219–222.
17. Zachau-Christiansen, B., West, K., Jacobsen, T., and Atlung, S., *Solid State Ionics*, 1988, vol. 30, pp. 1176–1182.
18. Kavan, L., Gratzel, M., Rathousky, J., and Zukal, A., *J. Electrochem. Soc*., 1996, vol. 143, no. 2, pp. 394–400.
19. Kavan, L., Fattakhova, D., and Krtil, P., *J. Electrochem. Soc*., 1999, vol. 146, no. 4, pp. 1375–1378.
20. Exnar, I., Kavan, L., Huang, S.Y., and Gratzel, M., *J. Power Sources*, 1997, vol. 68, pp. 720–731.

Russian Journal of Applied Chemistry, Vol. 75, No. 3, 2002, pp. 422–426. Translated from Zhurnal Prikladnoi Khimii, Vol. 75, No. 3, 2002, pp. 433–437.
Original Russian Text Copyright © 2002 by Malai, Shchukin, Yalamov.

PROCESSES AND EQUIPMENT OF CHEMICAL INDUSTRY

Effect of Particle Surface Heating on the Sedimentation Rate

N. V. Malai, E. R. Shchukin, and Yu. I. Yalamov

Belgorod State University, Belgorod, Russia
Moscow Pedagogical University, Moscow, Russia

Received November 23, 2000; in final form, May 2001

Abstract—The Stokes and Hadamard–Rybchinsky formulas are generalized, making it possible to take into account the temperature dependence of viscosity in a wide range of temperatures and to calculate the force of resistance to motion and velocity of gravitational fall at arbitrary temperature differences between the particle surface and a remote region.

Determining the granulometric composition of disperse systems via their sedimentation is one of the most practicable and widely used methods of dispersion analysis [1]. In cleaning of liquids to remove contaminating particles and dressing of minerals, it is important to accelerate sedimentation. This is commonly achieved in various ways, depending on the kind of particles and their environment. Sedimentometry is based on the relationship between the velocity of particle motion in a viscous medium and the particle size. The velocity of particle motion can be markedly raised by heating the particle surface, since the viscosity of a fluid decreases exponentially with increasing temperature. Of practical and theoretical interest in this regard is description of the gravitational motion of a heated particle in a viscous fluid.

Let us consider the gravitational motion of a uniformly heated hydrosol particle in another, viscous incompressible fluid, which is immiscible with the former and fills the entire space. At infinity, the fluid is at rest. By heated (cooled) particle is understood a particle whose surface temperature differs from that at a distance from the particle. The temperature difference between the particle and the viscous fluid can be maintained steadily via, e.g., heat release in chemical reactions at the particle surface, radioactive decay of the drop substance, external irradiation, etc. In particular, if a flux of electromagnetic radiation (wavelength λ_0, intensity I_0) is incident on the drop, then the energy absorbed by the drop is $\pi R^2 I_0 K_a$, where R is the drop radius and K_a is the absorption factor [2]. If the heat conductivity of the drop much exceeds that of the external medium and $\lambda_0 \gg R$, then the absorbed energy is evenly distributed over the drop surface and, consequently, the drop can be considered uniformly heated.

The heated particle surface affects the heat-transfer properties of the ambient fluid and, in the end, the distribution of the velocity and pressure fields in the vicinity of the particle.

In contrast to previous investigations [3–7], the present study generalizes the Stokes and Hadamard–Rybchinsky formulas to the case of uniformly heated spherical drop in a viscous incompressible fluid at arbitrary temperature difference between the particle surface and remote region with account of the temperature dependence of viscosity.

Of all fluid transfer parameters, the viscosity coefficient depends on temperature most strongly [8]. To take into account the temperature dependence of the dynamic viscosity, we use a formula that describes changes in the viscosity of a fluid in wide range of temperatures with any required accuracy (at $F_n = 0$ this formula can be reduced to the known Reynolds relation [8]):

$$\mu_e = \mu_\infty [1 + \sum_{n=1}^{\infty} F_n (T_e/T_\infty - 1)^n] \exp [-A(T_e/T_\infty - 1)], \quad (1)$$

where A and F_n are constants, $\mu_\infty = \mu_e(T_\infty)$, and T_∞ is the fluid temperature far away from the particle.

Hereinafter the indices e and i refer, respectively, to viscous fluid and heated particle; index ∞ denotes fluid parameters at infinity in an unperturbed flow; and index s refers to values of physical quantities at average surface temperature T_s.

It is known that the fluid viscosity decreases exponentially with increasing temperature [8]. An analysis of the available semiempirical formulas demonstrated that expression (1) describes the variation of

1070-4272/02/7503-0422$27.00 © 2002 MAIK "Nauka/Interperiodica"

viscosity in a wide temperature range in the best way, with any required accuracy. For example, we have $A = 5.779$, $F_1 = -2.318$, $F_2 = 9.118$ for water in the temperature range 0–90°C, with relative error not exceeding 2% ($T_\infty = 273$ K).

It is assumed that the densities, heat conductivities, and specific heats of the fluid and particle are constant, the heat conductivity coefficient of the particle much exceeds that of the medium, and particle motion is rather slow (small particles by Reynolds and Peclet).

It is convenient to introduce a reference system associated with the center of a moving particle (the problem is reduced to analysis of how an infinite plane-parallel flow, whose velocity U_∞ is to be determined, moves past a particle). The distributions of velocity and temperature is axially symmetric with respect to the 0Z axis passing through the drop center in the direction of the velocity vector of the incident flow. Therefore, the analysis uses a spherical system of coordinates in which radius is reckoned from the drop center, and angle θ, from the velocity direction of the incident flow.

In terms of the assumptions made, the equations and boundary conditions for the velocity, pressure, and temperature inside and outside a drop can be written in Stokes approximation in the spherical system of coordinates r, θ, η in the form [9]

$$\nabla P_e = \mu_e \nabla^2 U_e + 2(\nabla \mu_e)\nabla U_e + (\nabla \mu_e) \times (\nabla U_e), \quad \mathrm{div} U_e = 0, \tag{2}$$

$$\mu_i \Delta \mathbf{U}_i = \nabla P_i, \qquad \mathrm{div}\, U_i = 0, \tag{3}$$

$$\Delta T_e = 0, \tag{4}$$

$$r = R, \quad U_r^e = U_r^i = 0, \quad U_\theta^e = U_\theta^i, \quad T_e = T_s, \tag{5}$$

$$r \to \infty, \ \mathbf{U}_e \to U_\infty \cos\theta \mathbf{e}_r - U_\infty \sin\theta \mathbf{e}_\theta, \ T_e \to T_\infty, \ P_e \to P_\infty, \tag{6}$$

$$r \to 0, \quad |\mathbf{U}_i| \neq \infty, \quad P_i \neq \infty, \tag{7}$$

where μ and λ are, respectively, the dynamic viscosity and heat conductivity; P is the pressure; U_r and U_θ are the radial and tangential components of the mass velocity of the fluid, $\mathbf{U}$, in the spherical system of coordinates; $U_\infty = |\mathbf{U}_\infty|$, U_∞ is the velocity of the incident flow, which is to be determined from the condition of vanishing total force acting on the particle ($U_\infty > 0$ if this velocity is directed along the z axis, and $U_\infty < 0$ otherwise); $\mathbf{e}_r$ and $\mathbf{e}_\theta$ are the unit vectors in the spherical system of coordinates; and T_s is the mean temperature of the drop surface.

Conditions (5), assuming impermeability and continuity of the normal and tangential components of the mass velocity and constant particle surface temperature, are taken for the particle surface. As boundary conditions at infinity, i.e., far away from the particle, are taken conditions (6), and the finiteness of the physical quantities characterizing the drop at $r \to 0$ is accounted for by conditions (7).

To obtain a closed problem, the boundary conditions on the surface of a uniformly heated drop are supplemented with the condition of continuity of the stress tensor components (normal and tangential) on the drop surface [9]:

$$-P_e + 2\mu_e \frac{\partial U_r^e}{\partial r} = -P_i + 2\mu_i \frac{\partial U_r^i}{\partial r}, \tag{8}$$

$$\mu_e\left(\frac{1}{r}\frac{\partial U_r^e}{\partial \theta} + \frac{\partial U_\theta^e}{\partial r} - \frac{U_\theta^e}{r}\right) = \mu_i\left(\frac{1}{r}\frac{\partial U_r^i}{\partial \theta} + \frac{\partial U_\theta^i}{\partial r} - \frac{U_\theta^i}{r}\right). \tag{9}$$

The boundary conditions (5)–(9) make it possible to separate variables and reduce the system for perturbed quantities to a system of ordinary differential equations. Solving Eqs. (2)–(4) with boundary conditions (5)–(9) gives the distribution of velocities, pressures, and temperature in the fluid and the drop. After these distributions are found, we can calculate the force acting on a uniformly heated drop and the velocity of its drift.

At $\mathrm{Re}_\infty = \pi_e R U_\infty / \mu_\infty \ll 1$, the incident flow exerts only perturbing influence, and, therefore, the solution to the equations of hydrodynamics and heat transfer is to be sought for as an expansion in the Reynolds number Re_∞. In determining the force acting on a uniformly heated drop and its drift velocity, we restrict the consideration to corrections of the first order of smallness. To find these corrections, it is necessary to know the fields of velocity, pressure, and temperature in the vicinity of the particle. The general solution to the heat conduction equation (4), satisfying the relevant boundary conditions, has the form

$$t_e = 1 + \gamma / y, \qquad \gamma = (T_s - T_\infty)/T_\infty, \tag{10}$$

where γ is a dimensionless parameter characterizing the temperature difference between the particle surface and remote region; $t_e = T_e/T_\infty$, $y = r/R$.

Substituting (10) in (1), we obtain

$$\mu_e = \mu_\infty[1 + \sum_{n=1}^{\infty} F_n(\gamma^n/y^n)]\exp(-A\gamma/y). \quad (11)$$

Formula (11) is further used for determining the velocity and pressure fields in the vicinity of a uniformly heated drop.

Since the viscosity depends only on the coordinate y, the equations of hydrodynamics are solved by separation of variables, with the velocity and pressure fields expanded in Legendre and Gegenbauer polynomials [10]. In particular, the following expressions were derived for the components of the mass velocity U:

$$U_r^e(y,\theta) = U_\infty\cos\theta[1 + A_1G_1(y) + A_2G_2(y)], \quad (12)$$

$$U_\theta^e(y,\theta) = -U_\infty\sin\theta[1 + A_1G_3(y) + A_2G_4(y)], \quad (13)$$

$$U_r^i(y,\theta) = U_\infty\cos\theta(A_3 + A_4y^2), \quad U_\theta^i(y,\theta) = -U_\infty\sin\theta(A_3 + 2A_4y^2), \quad (14)$$

where

$$G_1(y) = -y^{-3}\sum_{n=0}^{\infty}\Delta_n^{(1)}[(n+3)y^n]^{-1},$$

$$G_1^I = dG_1/dy, \quad G_2^I = dG_2/dy,$$

$$G_2(y) = -y^{-1}\sum_{n=0}^{\infty}\Delta_n^{(2)}[(n+1)y^n]^{-1} - \alpha y^{-3}\sum_{n=0}^{\infty}[(n+3)\ln y^{-1} - 1]\Delta_n^{(1)}[(n+3)^2y^n]^{-1},$$

$$\Delta_n^{(1)} = [n(n+5)]^{-1}\sum_{k=1}^{n}\{(n+4-k)[\alpha_k^{(1)}(n+5-k) - \alpha_k^{(2)}] + \alpha_k^{(3)}\}\gamma^k\Delta_{n-k}^{(1)} \quad (n \geq 1). \quad (15)$$

$$G_3(y) = G_1(y) + 0.5yG_1^I, \quad G_4(y) = G_2(y) + 0.5yG_2^I,$$

$$\Delta_n^{(2)} = [(n+3)(n-2)]^{-1}[-6\alpha_n^{(4)}\gamma^n + \sum_{k=1}^{n}\{(n+2-k) \times [\alpha_k^{(1)}(n+3-k) - \alpha_k^{(2)}] + \alpha_k^{(3)}\}\gamma^k\Delta_{n-k}^{(2)} + \alpha\sum_{k=0}^{n}[(2n+5 - 2k)\alpha_k^{(1)} - \alpha_k^{(2)}]\gamma^k\Delta_{n-k-2}^{(1)} \quad (n \geq 3). \quad (16)$$

In calculating the coefficients $\Delta_n^{(1)}$, $\Delta_n^{(2)}$ by means of recurrence formulas (15) and (16), account should be taken that

$$\Delta_0^{(1)} = -3, \ \Delta_0^{(2)} = -1, \ \Delta_2^{(2)} = -1, \ \alpha_0^{(1)} = \alpha_0^{(4)} = -1,$$

$$\alpha_0^{(2)} = 4, \ \alpha_0^{(3)} = -4, \ \alpha_n^{(1)} = F_n, \ \alpha_n^{(2)} = (4-n)F_n + AF_{n-1},$$

$$\alpha_n^{(3)} = 2AF_{n-1} - 2(2+n)AF_n, \ \alpha_n^{(4)} = A^n/n!,$$

$$\alpha = -\gamma\{6\gamma^2\alpha_2^{(4)} - [3(4\alpha_1^{(1)} - \alpha_1^{(2)}) + \alpha_1^{(3)}]\Delta_1^{(2)} + [2(3\alpha_2^{(1)} - \alpha_2^{(2)}) + \alpha_2^{(3)}]\gamma\}/15,$$

$$\Delta_1^{(2)} = -\gamma[6\alpha_1^{(4)} + 2(3\alpha_1^{(1)} - \alpha_1^{(2)}) + \alpha_1^{(3)}]/4.$$

The integration constants A_1–A_4, appearing in Eqs. (12)–(14), are found upon their substitution in the corresponding boundary conditions on the drop surface. With this done, the force acting upon the particle is found by integration of the stress tensor over its surface [9] and has the following form:

$$\mathbf{F} = -4\pi R\,\mu_\infty U_\infty A_2\exp\{-A\gamma\}\mathbf{n}_z, \quad (17)$$

where

$$A_2 = -(N_3 + N_4\,\mu_e^s/3\mu_i^s)/\Delta, \quad \Delta\Big|_{y=1} = N_1 + N_2\,\mu_e^s/\mu_i^s,$$

$$N_4\Big|_{y=1} = 2G_1^I + G_1^{II},$$

$$N_2\Big|_{y=1} = G_2(2G_1^I + G_1^{II}) - G_1(2G_2^I + G_2^{II}),$$

$$N_1\Big|_{y=1} = G_1G_2^I - G_2G_1^I, \quad N_3\Big|_{y=1} = G_1^I,$$

The index s denotes the values of the physical quantities for the mean surface temperature of a uniformly heated drop, T_s; $\mathbf{n}_z$ is the unit vector in the direction of the z axis.

It is noteworthy that the force **F** is calculated on the assumption of a uniform drop motion, which is only possible if the total force acting upon the particle is zero. Since the force (17) is proportional to the velocity and vanishes together with the latter, then, for uniform motion of a heated drop to occur, it is necessary to assume the presence of a certain extraneous force counterbalancing the force (17).

Substituting the explicit form of coefficient A_2 in (17), we obtain the expression

$$\mathbf{F} = 6\pi R\,\mu_\infty U_\infty f_\mu\mathbf{n}_z, \quad (18)$$

$$f_\mu = 2\exp\{-A\gamma[N_3 + N_4\mu_e^s/(3\mu_i^s)]\}/[3(N_1 + N_2\mu_e^s/\mu_i^s)].$$

Let us consider as an example the gravitational fall of a uniformly heated drop. A spherical drop falling under the action of gravitational force in a viscous medium ultimately starts to move at a constant velocity at which the action of the gravitational force is counterbalanced by hydrodynamic forces. The gravitational force acting upon a particle is given, with account of the buoyancy force, by

$$\mathbf{F} = (\rho_i - \rho_e)g\pi R^3\mathbf{n}_z \times 4/3, \quad (19)$$

where g is the gravitational acceleration.

Equating expressions (18) and (19), we obtain the fall velocity of a uniformly heated spherical particle (analog of the Hadamard–Rybchinsky formula):

$$\mathbf{U} = h_\mu \mathbf{n}_z, \quad (20)$$

where

$$h_\mu = \frac{2}{9}R^2\frac{\rho_i - \rho_e}{\mu_\infty f_\mu}g.$$

If $\mu_e^s/\mu_i^s \to 0$ in expressions (18) and (20), then we obtain a formula for the resistance force and the velocity of gravitational fall of a solid uniformly heated particle (analog of the Stokes formula).

Thus, formulas (18) and (20) allow evaluation of the force acting upon a uniformly heated drop and the velocity of its gravitational fall with account of the temperature dependence of viscosity, represented as an exponential-power series at arbitrary temperature differences between the particle surface and a remote region.

In the case when the drop surface is heated to a relatively low extent, i.e., the mean surface temperature differs only slightly from the temperature of the ambient at infinity [$\gamma = (T_s - T_\infty)/T_\infty \to 0$], the temperature dependence of the dynamic viscosity coefficient can be neglected and $G_1 = 1$, $G_1^I = -3$, $G_1^{II} = 12$, $G_2 = 1$, $G_2^I = -1$, $G_2^{II} = 2$, $N_1 = 2$, $N_2 = 6$, $N_3 = 3$, and $N_4 = 6$. In this case, formulas (18) and (20) are transformed into the known expression for a sphere [9, 10].

Mention should be made of some problems concerning the motion of a uniformly heated spherical drop, whose solutions can be found directly from the results obtained here. Let us consider motion of a particle containing uniformly distributed heat sources (drains) with constant power and density q_1, i.e., the motion of a particle with uniform internal heat release. In this case, it is necessary to supplement Eqs. (2)–(4) with an equation describing the distribution of temperature within the drop ($\Delta T_i = q_i/\lambda_i$) and to take into account the equality of temperatures and heat fluxes in the boundary conditions. Then the mean surface temperature of a uniformly heated drop is given by the relation

$$T_s/T_\infty = 1 + q_i R^2/(\lambda_e T_\infty). \quad (21)$$

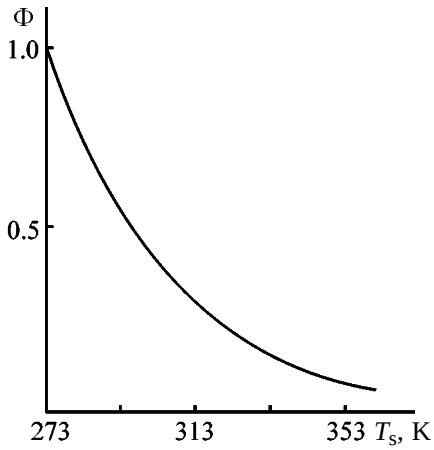

Fig. 1. Contribution to the resistance force, $\Phi = f_\mu/f_\mu\big|_{T_s = 273\ K}$, vs. the mean temperature T_s of the mercury drop surface.

It is noteworthy that, in formulating the problem, the boundary condition (8) for normal stresses, unnecessary in analyzing the flow around a uniformly heated drop, was left out. It can be shown that, upon substitution of the obtained solution for velocity and pressure components, the given boundary condition reduces to identity. This means that, in the approximation employed, the drop remains strictly spherical and its shape should be analyzed in terms of higher-order approximations.

To illustrate the contribution of particle surface heating to the resistance force and the fall velocity of a drop, i.e., to take into account the temperature dependence of viscosity, represented by formula (1), Figs. 1 and 2 show curves relating the values $\Phi = f_\mu/f_\mu\big|_{T_s = 273\ K}$ and $\Phi_1 = h_\mu/h_\mu\big|_{T_s = 273\ K}$ to T_s values for large mercury drops with radius $R = 2 \times 10^{-5}$ m, moving in water at $T_\infty = 273$ K. The curve Φ_1^* is plotted using the formula for small relative temperature differences ($\gamma \to 0$) [9, 10], but with the molecular transfer coefficients taken for $T_e = T_s$. As seen from the presented curves, the drop surface heating

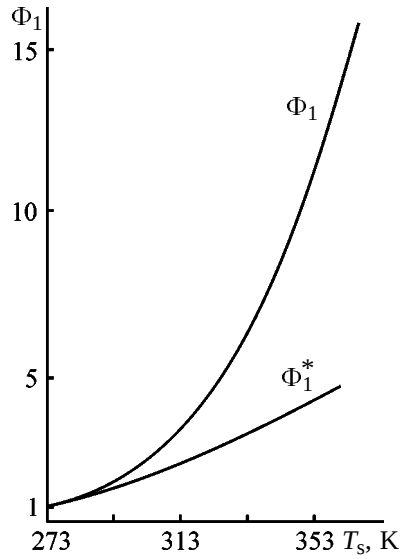

Fig. 2. Fall velocity of mercury drop, $\Phi_1 = h_\mu/h_\mu\big|_{T_S = 273\,\mathrm{K}}$, vs. the mean temperature T_S of the mercury drop surface.

strongly affects the resistance force and the velocity of gravitational fall of the drop. This result can be used in practice for accelerating the sedimentation process [11]. Let us consider selective sedimentation of coal particles in a water flow with temperature of 20°C in a rectangular chamber with length L = 100 cm, width d = 80 cm, and height h = 5 cm. In the absence of heating, the particle velocity in this chamber is 1.109×10^{-2} cm s^{-1}. To this velocity corresponds the volumetric flow rate of cleaned water Q = 0.319 m^3 h^{-1} [11]. The formulas derived in the present study yield Q = 0.356 m^3 s^{-1}, which corresponds to sedimentation accelerated by a factor of 1.12, and, with the particle surface heated to 50°C, we obtain Q = 0.588 m^3 s^{-1}, which already gives an acceleration by a factor of 1.84. Consequently, the use of the derived formulas enables acceleration of particle sedimentation.

CONCLUSIONS

(1) An analytical solution of the problem of a fluid flow around a uniformly heated particle at small Reynolds numbers is described. In solving the hydrodynamics equations, account is taken of the temperature dependence of dynamic viscosity, represented as an exponential–power-law series. The Stokes and Hadamard–Rybchinsky formulas are generalized, which makes it possible to calculate the resistance force and the velocity of gravitational fall at arbitrary temperature differences between the particle surface and a remote region. It is shown that particle surface heating markedly affects the resistance force.

(2) The results obtained can be used in evaluating the settling velocity of spherical hydrosol particles in channels, in designing experimental installations in which a directed motion of hydrosol particles is to be ensured, in developing methods for fine cleaning of fluids to remove hydrosol particles, etc.

REFERENCES

1. Khodakov, G.S. an Yudkin, Yu.P., *Sedimentatsionnyi analiz vysokodispersnykh sistem* (Sedimentation Analysis of Highly Dispersed Systems), Moscow: Khimiya, 1981.
2. Bohren, C.F. and Huffman, D.R., *Absorption and Scattering of Light by Small Particles*, New York: Wiley, 1983.
3. Kuzikovskii, A.V., *Izv. Vyssh. Uchebn. Zaved., Fiz*., 1970, no. 5, pp. 89–94.
4. Acrivos, A. and Taylor, T.D., *J. Phys. Fluids*, 1962, vol. 5, no. 4, pp. 387–394.
5. Naidenov, V.I., *Prikl. Mat. Mekh.*, 1971, vol. 38, no. 1, pp. 162–166.
6. Leonov, A.I., *Prikl. Mat. Mekh*., 1962, vol. 26, no. 3, pp. 33–40.
7. Shchukin, E.R., Malai, N.V., and Yalamov, Yu.I., *Teplofiz. Vys. Temp*., 1988, vol. 25, no. 5, pp. 1020–1024.
8. Bretsznajder, S., *Wlasnosci gazow i cieczy*, Warsaw: Naukowo-Techniczne, 1962.
9. Landau, L.D. and Lifshits, E.M., *Gidrodinamika* (Hydrodynamics), Moscow: Nauka, 1986.
10. Happel, J. and Brenner, H., *Low Reynolds Number Hydrodynamics*, Leiden: Nordhoff, 1973, 2nd ed.
11. Fajita, H., *Mathematical Theory of Sedimentation Analysis*, New York: Academic, 1969.

Russian Journal of Applied Chemistry, Vol. 75, No. 3, 2002, pp. 427–431. Translated from Zhurnal Prikladnoi Khimii, Vol. 75, No. 3, 2002, pp. 438–442.
Original Russian Text Copyright © 2002 by Klenin, Ivanova.

ENVIRONMENTAL PROBLEMS OF CHEMISTRY AND TECHNOLOGY

Spectroturbidimetric Determination of the Size and Concentration of Terrestrial Particles in Potable Water

V. I. Klenin and N. A. Ivanova

Chernyshevsky Saratov State University, Saratov, Russia

Received October 12, 2001

Abstract—A method was proposed for determining the average size and mass-space concentration of terrestrial particles in potable water from the turbidity spectrum. This method was applied to a systematic study of a formazine suspension and potable water samples.

Turbidity of water is due to the presence of terrestrial particles having a colloidal degree of dispersion.

At the present time, GOST (State Standard) 3351–74 [1] is acting in Russia, which prescribes photometric determination of terrestrial particles, with a formazine suspension (prepared from hexamethylenetetramine and hydrazine sulfate) as the reference. The reaction goes to completion, which gives us information about the formazine content in a unit volume of the reaction medium. Several reference suspensions of different concentrations are prepared and their optical densities D are measured on an FEK-56 photocolorimeter with a light filter (λ = 540 nm) in 5-cm cells. The reference cell contains double-distilled water. The calibration plot of D vs. the formazine suspension concentration C, mg dm^{-3}, is constructed. From this plot, the concentration of terrestrial particles in potable water samples is determined. A similar method for determining the terrestrial particle concentration is practiced abroad [2]. This method cannot be treated *a priori* as a correct one, as the turbiidity of colloidal systems is not only a linear function of the concentration but also a complex function of the relative size (size-distribution pattern) and of the relative refractive index of the particles.

Light scattering theories describe the turbidity of a colloidal monodisperse system by the equation [3]

$$\tau = N_2 \pi r^2 K(\alpha, m). \quad (1)$$

Here, τ is the turbidity, cm^{-1}, N_2 is the number of particles in cm^3, r is the particle radius, $K(\alpha, m)$ is the light scattering efficiency factor as a function of the relative size α and the relative refractive index m:

$$\alpha = 2\pi\mu_1 r/\lambda, \quad (2)$$

$$m = \mu_2/\mu_1, \quad (3)$$

μ is the refractive index of the dispersed phase, μ_1 is the refractive index of the dispersion medium, and λ is the wavelength in vacuum.

The procedure prescribed by GOST [1] does not allow for the particle size and the difference between the μ_2 parameters for formazine and terrestrial particles.

The aim of this work was to elucidate the potentialities of the spectroturbidimetric method as applied to determining the mass-space concentration and the size of terrestrial particles in potable water.[1]

The spectroturbidimetric method showed a good performance in characterizing dispersed systems of different nature [3], in particular, in analyzing mineral suspensions in natural water basins [4]. For the latest data concerning disperse systems of different origin, see monograph [5].

EXPERIMENTAL

We found no explanations in published papers and patents why specifically formazine suspension was chosen as the reference for analysis of terrestrial particles in potable water. Thus, we began with studying the properties of the formazine suspension prepared according to the GOST mentioned [1].

Next, we systematically studied potable water samples by the spectroturbidimetric method and by the method prescribed by the GOST. Water samples were taken in various stages of purification, namely,

[1] Our study was concerned with potable water from the water supply systems in Saratov and Saratov oblast.

1070-4272/02/7503-0427$27.00 © 2002 MAIK "Nauka/Interperiodica"

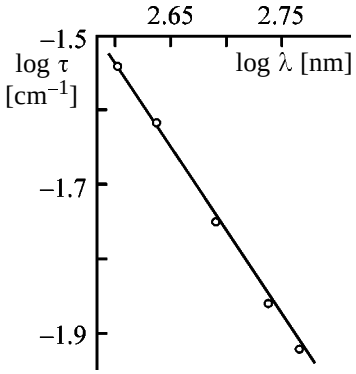

Fig. 1. Variation of the turbidity τ with the wavelength λ for water from the water manifold of the Smorodinka settlement, Perelyub raion.

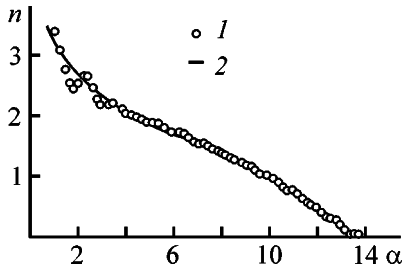

Fig. 2. Variation of $n(\alpha, m)$ with α for $m = 1.15$. System: (*1*) monodispersion and (*2*) polydispersion; the same for Fig. 3.

from the initial water (river, artesian well, water storage basin), from the potable water supply system, and from the water manifold (tap water cock). The optical density spectrum $D(\tau)$ was measured on an FEK-56 instrument at four wavelengths within 400–540 nm in a 5-cm cell. The reference cell contained double-distilled water.

Within a limited wavelength range $\Delta\lambda$, the spectral dependence of the turbidity is described by the Ångström equation [3]

$$\tau = A\lambda^{-n}. \quad (4)$$

Here, n is the wave exponent, or a wavelength index which is a complex function of the relative size α and relative refractive index m.

In log–log coordinates, Eq. (4) describes a straight line (Fig. 1):

$$\log\tau = \log A - n\log\lambda. \quad (5)$$

Thus, n is determined as the slope of the plot of (5). The turbidity, cm^{-1}, was determined by the formula

$$\tau = 2.3D/l, \quad (6)$$

where l is the cell length, cm.

In [3], the exponent $n(\alpha, m)$ was tabulated according to the Mie theory over a wide range of α and m values. For monodispersion particles, the characteristic light scattering functions have the oscillating character, and for polydispersion particles, smoothened approximation formulas are applied [6].

In [7], a routine was devised for processing the data derived by the spectroturbidimetric method on a mini-micro computer (calculators with minimal programming options) using the approximation formulas [6]. Processing of a large body of experimental data for water samples taken from oceans and rivers yielded $m = 1.15$ for terrestrial particles in water [8].

The parameter α for the experimentally determined n is derived from the calibration plot $n(\alpha, m) = f(\alpha)$. Figure 2 shows this dependence for $m = 1.15$.

The average particle size can be calculated by the formula

$$\bar{r} = \frac{\alpha\lambda_{av}}{2\pi\mu}, \quad (7)$$

where λ_{av} corresponds to the middle of the wavelength range where the turbidity was measured, in logarithmic coordinates, or $\lambda_{av} = (\lambda_1\lambda_2)^{1/2} = 469$ nm, where λ_1 and λ_2 are the smallest and the greatest light wavelengths in the working range for λ, respectively.

The mass-space concentration C, g dm^{-3}, of terrestrial particles in the formazine suspension was calculated by the formula [3]

$$C = Sv\tau, \quad (8)$$

$$s = \frac{10.61\rho_2\lambda_{av}}{\mu_1(m-1)}, \quad (9)$$

$$v(\alpha, m) = \frac{2\alpha(m-1)}{K(\alpha, m)} = \frac{2n(m-1)}{\partial K(\alpha, m)/\partial\alpha}, \quad (10)$$

where s is a parameter, g/100 cm^2, and ρ_2 is the particle density.

The wavelength exponent n and the structure factor v are functions of the same arguments, α and m, which allows plotting $v(\alpha, m)$ vs. $n(\alpha, m)$ (Fig. 3).

The above formulas suggest that measuring the disperse system parameters by the spectroturbidimetric method requires the knowledge of the density and refractive index of the substance in the dispersed phase.

The refractive index of the dispersed phase can be determined either directly with a refractometer or from

the refractive index increment for a solution of the substance, or by the spectroturbidimetric method [3, 5], provided that the concentration of the dispersed phase particles is known.

Attempts to prepare a solution of formazine failed, as this polymer is insoluble in most of organic solvents [9]. Therefore, the relative refractive index of the formazine particles was estimated spectroturbidimetrically.

When the mass-space concentration of the suspension is known, the measured turbidity τ can be used for determining by Eq. (8) the *vs* product, which in the $2 < n < 4$ range is strongly dependent on *m*. Using the tables from [5], it is possible to construct a tentative plot of *vs* vs. *m* for a given *n* value (Fig. 4). Then, using the $C/\tau = sv$ ratio and the plot from Fig. 4, it is possible to determine *m*.

The experiments with the formazine suspension showed that the experimental points are concentrated around $m = 1.07$ corresponding to the refractive index of the formazine particles $\mu_2 = 1.426$. Repeated preparations and spectroturbidimetric examinations of formazine suspensions showed good reproducibility of the size of formazine particles formed in independent preparations, namely, the average particle radius was 800 ± 50 nm. The particle size remained unchanged upon diluting the suspension within 230–0.6 mg dm^{-3}.

The formazine particles are fairly large, which allows determination of the formazine particle concentration by two independent methods, spectroturbidimetric and gravimetric.

The formazine dispersion was filtered through a Schott's filter whose pore diameter was *a fortiori* smaller than the formazine particle size. The mass of all the formazine particles in a given volume (0.05–0.5 dm^3) was determined from the Schott's filter mass before and after filtration, with the filter being dried to constant weight.

Below, we compare the particle concentration calculated from the turbidity spectrum C_1 with that determined gravimetrically, C_2, for a formazine suspension with the concentration *C* calculated from the concentrations of the initial substances, which were estimated according to GOST 3351–74.

C, mg dm^{-3}	232	23.2
V, ml	50	500
τ_{483}, cm^{-1}	3.2 ± 0.1	0.31 ± 0.01
n	1.68 ± 0.02	1.68 ± 0.02
$\bar{r}$, nm	800 ± 50	800 ± 50
C_1, mg dm^{-3}	220 ± 10	20.7 ± 0.4
C_2, mg dm^{-3}	215 ± 5	20.6 ± 0.1

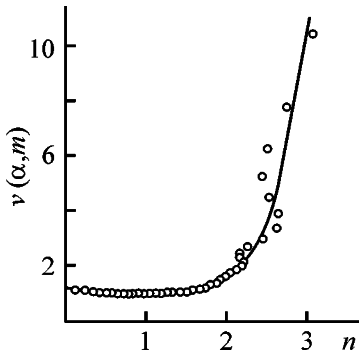

Fig. 3. Variation of the structure factor $v(\alpha, m)$ with the wavelength index *n* for $m = 1.15$.

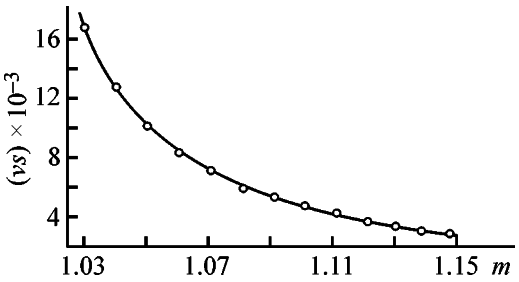

Fig. 4. Variation of the *vs* product with the relative refractive index *m* at *n* = const.

The data obtained by the two independent and absolute methods of determining the formazine concentration reasonable agree. Comparison of these experimental values with those calculated according to the chemical reaction shows that the reaction yield is actually 95%. The parameters were estimated by the methods of interest accurately to within 5% for formazine concentrations of 232 and 23.2 mg dm^{-3}.

The average particle radius for different samples of potable water, as determined spectroturbidimetrically, lies within 70–700 nm. As Eq. (8) incorporates the structure factor [described by Eq. (10)], which is a function of α and *m*, the difference in the mass-space concentrations of the particles determined spectroturbidimetrically and by the method prescribed by the GOST [1] must be the greater, the stronger the sample particle size differs from 800 nm.

The table presents the results of analysis for a number of potable water samples by both methods discussed. It is seen that the content of terrestrial particles in potable water widely varies. As expected, the concentrations determined spectroturbidimetrically and according to GOST [1] differ the stronger, the stronger the size of terrestrial particles differs from that of formazine particles.

Concentration of terrestrial particles as determined from the turbidity spectrum C_1, by the procedure prescribed by GOST [1] C_2, and calculated from the turbidity spectrum without taking into account the terrestrial particle size C_3

Sampling site	n	τ_{483}, cm^{-1}	$\bar{r}$, nm	C_1	C_2	C_3
				mg dm^{-3}		
Perelyub raion, Smorodinka settlement:						
Sestra river	2.20	0.021	180	1.88	0.7	0.6
water supplied to the network	1.9	0.020	260	1.08	0.7	0.77
water manifold	2.4	0.045	130	3.0	0.7	0.8
Saratov raion, Krasnyi Tekstil'shchik settlement:						
artesian well	1.72	0.060	410	2.4	2.3	2.4
water supply line	2.64	0.026	100	5.06	1.4	1.02
Krasnoarmeisk:						
Volga river	1.9	0.070	260	3.63	1.4	2.5
water supplied to the network	2.75	0.037	90	8.6	1.4	1.39
water supply line	2.21	0.048	130	4.15	1.7	1.8

The procedure specified by the GOST neglects the size of terrestrial partciles. To clearly indicate one of the sources of the systematic error in this procedure, we intentionally introduced an error into the calculations involved in the spectroturbidimetric method: We eliminated from formula (8) the structure factor (10) which shows how the turbidity varies with the particle size. This calculation yielded the concentrations C_3 (see table). It is seen that these *a fortiori* erroneous concentrations are close to those estimated according to the GOST.

The plot in Fig. 4 indicates the systematic error in the method prescribed by GOST due to neglecting the difference in the relative refractive indices for formazine (m = 1.07) and terrestrial particles (m = 1.15). The parameters $C/\tau = sv$ for m = 1.07 and m = 1.15 differ by a factor of 2.5. Thus, neglecting the difference in the relative refractive indices is responsible for a 2.5-fold error in the data estimated by the GOST procedure, and, thereby, for overestimation of the concentration of terrestrial particles by a factor of about 2.5 (Fig. 4).

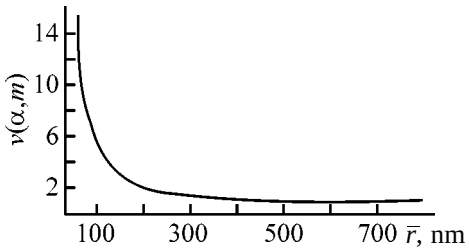

Fig. 5. Structure factor $\nu(\alpha, m)$ as a function of the average particle size $\bar{r}$ for m = 1.15.

Neglecting the difference in the sizes of terrestrial particles and formazine is responsible for underestimation of the concentration of terrestrial particles, the extent of overestimation being the greater, the larger the difference in size between the formazine and terrestrial particles (the latter are always smaller) (Fig. 5). Hence, in certain cases these two errors can compensate each other and, as a result, certain values of the parameters C_2 and C_3 become close to each other (see table).

Standard calibration plots of D vs. C for formazine make sense only for particles ca. 800 nm in size at m = 1.07. The real size of terrestrial particles for different water samples varies, however, within 70–700 nm, and real m is equal to 1.15. The concentration of terrestrial particles varies within 0.5–28.5 mg dm^{-3}. Therefore, the formazine suspension is not an adequate reference for determining the degree of potable water contamination.

The spectroturbidimetric method proposed by us compares advantageously with that prescribed by GOST 3351–74 [1] in that it is an absolute method based on rigorous theories of light scattering by colloidal systems and thus requires no preliminary, especially inadequate, calibrations.

CONCLUSIONS

(1) A spectroturbidimetric method was proposed which, as compared to the empirical method prescribed by GOST, is more rigorous and easier (no

preliminary calibration using absolutely different system is needed).

(2) The spectroturbidimetric method is suitable for determining the average size and concentration of terrestrial particles in potable water from urban water supply system.

REFERENCES

1. *GOST* (State Standard) *3351–74: Potable Water. Methods of Determining the Taste, Odor, Color, and Turbidity*, Moscow: Izd. Standartov, 1986.
2. Berné, F. and Cordonnier, J., *Traitment des eaux*, Paris: Technip, 1991.
3. Klenin, V.I., Shchegolev, S.Yu., and Lavrushin, V.I., *Kharakteristicheskie funktsii svetorasseyaniya dispersnykh sistem* (Characteristic Functions of Light Scattering by Disperse Systems), Saratov: Saratov. Univ., 1976.
4. Vlasova, O.L., Bezrukova, A.G., Mchedlishvili, B.V., *et al.*, *Khim. Tekhnol. Vody*, 1989, vol. 11, no. 3, pp. 237–240.
5. Klenin, V.I., *Termodinamika sistem s gibkotsepnymi polimerami* (Thermodynamics of Systems Comprising Flexible-Chain Polymers), Saratov: Saratov. Univ., 1995.
6. Ramazanov, K.R., Khlebtsov, N.G., Shchegolev, S.Yu., and Klenin, V.I., *Kolloidn. Zh.*, 1983, vol. 45, no. 3, pp. 473–479.
7. Shchegolev, S.Yu. and Khlebtsov, N.G., *Primenenie mini- i mikro-EVM pri opredelenii parametrov dispersnykh sistem spektroturbidimetricheskim metodom* (Application of Mini- and Microcomputers to Determining the Parameters of Disperse Systems by Spectroturbidimetric Method), Saratov: Saratov. Univ., 1984.
8. Shifrin, K.S., *Vvedenie v optiku okeana* (Introduction to Optics of the Ocean), Leningrad: Gidrometeoizdat, 1983.
9. Pulvermacher, G., *Ber.*, 1893, vol. 26, pp. 2360–2363.

Russian Journal of Applied Chemistry, Vol. 75, No. 3, 2002, pp. 432–435. Translated from Zhurnal Prikladnoi Khimii, Vol. 75, No. 3, 2002, pp. 443–446.
Original Russian Text Copyright © 2002 by Porozova, Bekker, Ivshina, Karmanov, Rychkova.

ENVIRONMENTAL PROBLEMS OF CHEMISTRY AND TECHNOLOGY

Structural Changes of Aluminosilicate Materials in the Presence of *Rhodococcus sensu stricto*

S. E. Porozova, V. Ya. Bekker, I. B. Ivshina, V. I. Karmanov, and M. I. Rychkova

Research Center of Powder Materials Science, Perm, Russia
Institute of Ecology and Genetics of Microorganisms, Ural Division, Russian Academy of Sciences, Perm, Russia
Institute of Applied Chemistry, Ural Division, Russian Academy of Sciences, Perm, Russia

Received November 5, 2001

Abstract—The influence of rhodococci on highly porous ceramics based on celsian and cordierite porcelain was studied by X-ray diffraction and IR spectroscopy.

The study of microorganisms involved in restoration of ecosystems affected by human activity is an urgent problem. One of these ecologically trophic bacteria oxidizing natural and man-made hydrocarbons is *Rhodococcus sensu stricto* [1]. Highly porous honeycomb ceramics (HPHC) combining developed macroporosity with the presence of channel micropores [4, 5] are promising supports for biogenic agents. However, even ceramics are affected by rhodococci [4, 5]. Previously we found that rhodococci catalyze not only degradation of aluminosilicate HPHC but also epitaxial processes increasing the weight and strength of the samples. The phase composition of the reprecipitation products formed in thin ceramic films of complex shape is difficult to determine.

In this work we studied structural transformation of aluminosilicate HPHC under the action of *Rhodococcus sensu stricto*.

EXPERIMENTAL

We used pure *R. ruber* IEGM 231 rhodococcus culture[1]. To determine the resistance of the ceramics to the bacterial action, HPHC samples were placed in mineral media containing 0.003% acrylamide as the carbon source and 4.0×10^9 rhodococcus cells per ml. The blank experiment was performed without bacteria. We studied highly porous honeycomb ceramics based on celsian and cordierite porcelain [2]. X-ray diffraction analysis was performed on a DRON-3M diffractometer using β-filtered cobalt radiation.

The IR spectra of ceramic samples kept in the bacterial media for 10 months were recorded on an IFS-66 Fourier spectrometer (Bruker, Germany) under the following conditions: Nujol mulls prepared in an agate mortar, KBr windows, resolution of 1 cm^{-1}, 100 scans. The spectra were brought to the zero baseline. The complex bands were resolved into the components whose location (ν), half-width, and peak (D_p) and integral (D_i) optical densities were determined. Since powders of multiphase ceramics are structurally nonuniform, the shape of separate bands was approximated by the Gaussian functions. Resolution of the complex bands of the initial cordierite porcelain into the components is shown in Fig. 1 as an example. The parameters of these bands are presented in Table 1.

Since the intensity of the absorption bands depends on the thickness of the absorption layer and the content of Nujol in the mull, which were not controlled,

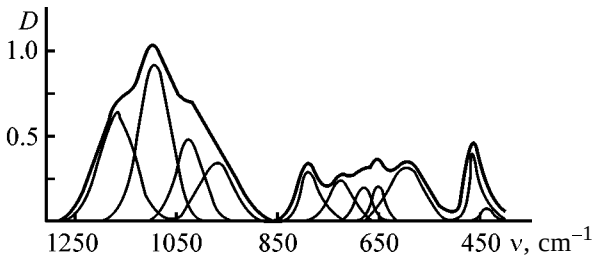

Fig. 1. Resolution of absorption bands of the initial cordierite porcelain into the components: (*D*) optical density and (ν) wave number.

[1] Obtained from the Local Profiled Collection of Alkanotrophic Microorganisms (Institute of Genetics and Ecology of Microorganisms, Ural Division, Russian Academy of Sciences, Perm, Russia).

1070-4272/02/7503-0432$27.00 © 2002 MAIK "Nauka/Interperiodica"

Table 1. Parameters of IR bands of cordierite porcelain

ν, cm^{-1}	D_p	Half-width, cm^{-1}	D_i
431	0.15	25	4.0
468	0.43	30	13.7
594	0.32	82	27.6
650	0.22	31	7.2
680	0.20	35	7.5
724	0.24	58	14.8
789	0.31	44	14.5
965	0.35	88	32.9
1023	0.49	67	34.8
1089	0.93	75	74.8
1165	0.64	82	56.0
1376	0.23	16	3.9

we compared the relative band intensities calculated by the equation

$$A_{rel,j} = D_{i,j}/\Sigma D_i,$$

where $A_{rel,j}$ is the relative intensity, $D_{i,j}$ is the integral optical density of jth band, and ΣD_i is the total optical density.

As seen from Table 2, the absorption bands of celsian porcelain at 1173, 985, 787 cm^{-1} are shifted to lower frequencies after keeping in the aggressive media. The first band is shifted under the action of both the mineral solution (control) and the bacterial suspension (experiment); the second, only under the action of the mineral solution; and the third, only under the action of the bacterial suspension. The action of aggressive media on the bands of cordierite porcelain (1165, 1023, 965, and 680 cm^{-1}) is similar. However, the bands at 1165 and 680 cm^{-1} are shifted to the low frequencies, and the bands at 1023 and 965 cm^{-1}, to higher frequencies. Thus, rhodococci catalyze the processes occurring in cordierite porcelain also in their absence and have a complex effect on celsian porcelain.

The changes in the relative intensity of the absorption bands of the control and experimental samples of HPHC as compared to the initial porcelain are shown in Fig. 2.

The bands at 1160 and 1090–1095 cm^{-1} are in the range of the Si–O stretching vibrations typical for aluminosilicates (850–1250 cm^{-1}) [7, 8]. It should be noted that the bands of isolated SiO_4 tetrahedra appear in the range 800–1050 cm^{-1}, and the bands of silicate polymers, in the range 1000–1200 cm^{-1} [7].

The relative intensity of the characteristic absorption bands of isolated SiO_4 groups decreases and that of polymeric silicates increases after keeping celsian porcelain in the mineral solution. Rhodococci exert the opposite effect: the intensity of the bands of monomeric silicates slightly increases and that of the bands of polymeric silicates decreases appreciably. Thus, inorganic compounds favor glass crystallization, whereas rhodococci initiate structural transformations in the crystalline phases. The shift of the IR bands to the lower frequencies suggests isomorphous substitution of ions.

Fragments of the X-ray pattern of celsian porcelain kept for 10 months in the (*1*) mineral solution and (*2*) bacterial suspension are shown in Fig. 3. The first X-ray pattern is similar to that of the initial material:

Table 2. Wave numbers ν and relative intensities A_{rel} of the bands in the IR spectra of celsian and cordierite porcelain

Celsian porcelain						Cordierite porcelain					
initial		control		experiment		initial		control		experiment	
ν, cm^{-1}	A_{rel}	ν, cm^{-1}	A_{rel}	ν, cm^{-1}	A_{rel}	ν, cm^{-1}	A_{rel}	ν, cm^{-1}	A_{rel}	ν, cm^{-1}	A_{rel}
1173	0.25	1167	0.34	1156	0.17	1165	0.20	1163	0.23	1152	0.28
1090	0.28	1086	0.27	1089	0.20	1089	0.27	1089	0.22	1090	0.16
1036	0.06	1029	0.13	1039	0.11	1023	0.13	1024	0.11	1035	0.12
985	0.26	979	0.07	980	0.29	965	0.12	973	0.11	987	0.17
787	0.03	785	0.04	776	0.07	789	0.05	787	0.06	789	0.05
–	–	–	–	–	–	680	0.03	676	0.04	672	0.03
–	–	–	–	–	–	650	0.03	648	0.01	647	0.01
566	0.02	565	0.04	562	0.05	594	0.10	597	0.14	598	0.09
464	0.08	465	0.08	464	0.10	467	0.05	462	0.06	463	0.06
429	0.02	429	0.02	429	0.02	431	0.01	431	0.02	430	0.02

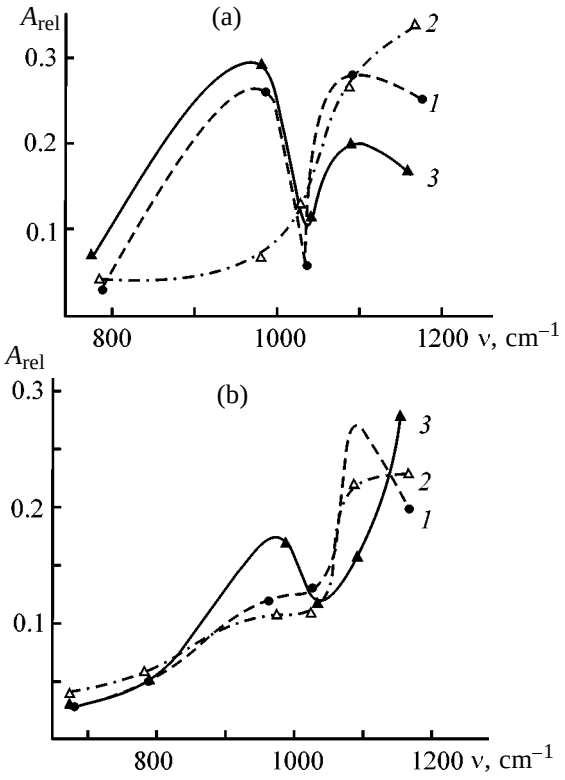

Fig. 2. Relative intensity of absorption bands of (a) celsian and (b) cordierite porcelain. (ν) Wave number. (*1*) Initial sample, (*2*) sample kept in the mineral solution (control), and (*3*) sample kept in a suspension of *R. ruber* IEGM 231 (experiment).

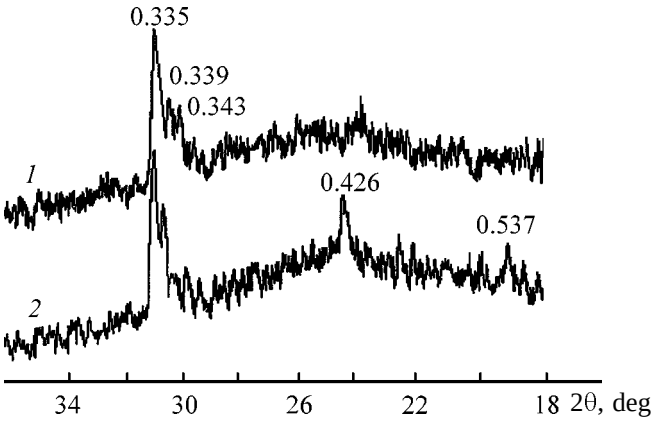

Fig. 3. Fragments of X-ray diffraction patterns of celsian porcelain kept in (*1*) mineral solution and (*2*) bacterial suspension. (2θ) Bragg angle. Interplanar spacings (nm) are given for the most intense reflections.

almost all reflections are assigned to orthorhombic mullite. The ratio of the most intense and closely located reflections of mullite (021), d_α = 0.399 nm and (120), d_α = 0.343 nm, is 1.1, which agrees with the ASTM data. A strong reflection with d_α = 0.335 nm is probably a superposition of the strongest quartz reflection (110), d_α = 0.335 nm, and celsian reflection (220), d_α = 0.335 nm. Probably sillimanite Al_2SiO_5 and hyalophane $0.57KAlSi_3O_8 \cdot 0.43BaAl_2Si_2O_8$ are also present.

After keeping celsian poreclain in the culture media, new reflections appear. In particular, relatively strong reflections with d_α = 0.537 and 0.426 nm are observed in the fragment shown in Fig. 3. The ratio of the most intense and closely located reflections of mullite (021), d_α = 0.399 nm, and (120), d_α = 0.343 nm, increases to 2, which can be due to formation of calcined mullite usually prepared by kaolinite calcination. The (120) reflection with d_α = 0.343 nm is absent in the X-ray pattern of calcined mullite, and the reflection with d_α = 0.537 nm is stronger than that of orthorhombic mullite. The reflection with d_α = 0.426 nm can be assigned to quartz. However, the ratio of the intensities of this reflection and the reflection with d_α = 0.426 nm is 2, differing from the tabulated value (*4*). This is probably due to superposition of the reflections of quartz and potassium barium feldspars of different compositions.

In the case of cordierite porcelain, strong reflections of crystalline α-Al_2O_3 contained in the sample mask weak reflections, which complicates the similar structural study.

CONCLUSIONS

(1) Structural transformations in celsian porcelain in the presence of rhodococci were studied by IR spectroscopy and X-ray diffraction. It was found that rhodococci strongly affect ceramics.

(2) Rhodococci intensify mainly isomorphous substitution in the SiO_4 and AlO_4 groups, thus affecting metamorphism of aluminosilicates.

(3) The kinetics of degradation and epitaxial processes occurring in ceramics in the presence of *rhodococci* can be studied by IR spectroscopy.

ACKNOWLEDGMENTS

We are grateful to V.N. Antsiferov for participation in discussion of the experimental results.

REFERENCES

1. Ivshina, I.B., Pshenichnov, R.A., and Oborin, A.A., *Propanokislyayushchie rodokokki* (Propane Oxidizing Rhodococci), Sverdlovsk: Ural Nauch. Tsentr Akad. Nauk SSSR, 1987.

2. Antsiferov, V.N. and Porozova, S.E., *Vysokoporistye pronitsaemye materialy na osnove alyumosilikatov* (Highly Porous Permeable Materials Based on Aluminosilicates), Perm: Perm Gos. Tekhn. Univ., 1996.
3. Kovalenko, G.A., Semikolenov, V.A., Kuznetsova, E.V., *et al.*, *Kolloidn. Zh.*, 1999, vol. 61, no. 6, pp. 787–795.
4. Alikin, V.N., Kuz'mitskii, G.E., Zabelin, L.V., *et al.*, *Konversiya spetsial'noi tekhnicheskoi khimii: Porokha, topliva, zaryady* (Conversion of Special Applied Chemistry: Gunpowders, Fuels, Charges), Perm: Perm. Nauch. Tsentr, Ural Otd., Ross. Akad. Nauk, 1999.
5. Porozova, S.E., Makarov, A.M., Ivshina, I.B., and Rychkova, M.I., *Zh. Prikl. Khim.*, 1997, vol. 70, no. 12, pp. 1076–1079.
6. Porozova, S.E., Ivshina, I.B., and Rychkova, M.I., Abstracts of Papers, *Materialy i pokrytiya v eksperimental'nykh usloviyakh: issledovaniya, primenenie, ekologicheski chistye tekhnologii proizvodstva i utilizatsii izdelii: Mezdunarodnaya konferentsiya* (Materials and Coatings under Extreme Conditions: Study, Application, Enviromnemtally Clean Production and Utilization: Int. Conf.), Katsiveli, Crimea (Ukraine), September 18–22, 2000, p. 76.
7. Plyusnina, I.I., *Infrakrasnye spektry mineralov* (Infrared Spectra of Minerals), Moscow: Mosk. Gos. Univ., 1976.
8. Eitel, W., *The Physical Chemistry of Silicates*, Chicago: Univ. of Chicago, 1954.

Russian Journal of Applied Chemistry, Vol. 75, No. 3, 2002, pp. 436–440. Translated from Zhurnal Prikladnoi Khimii, Vol. 75, No. 3, 2002, pp. 447–451.
Original Russian Text Copyright © 2002 by Bazanova, Kholodkova, Gostikin.

ORGANIC SYNTHESIS AND INDUSTRIAL ORGANIC CHEMISTRY

Reduction of 4,4'-Dinitrostilbene-2,2'-disulfonic Acid with Hydrogen on Raney Nickel

I. N. Bazanova, N. V. Kholodkova, and V. P. Gostikin

Ivanovo State University of Chemical Engineering, Ivanovo, Russia

Received July 23, 2001

Abstract—Reduction of 4,4'-dinitrostilbene-2,2'-disulfonic acid with hydrogen in aqueous solution on Raney nickel yields a trisazo compound identical to Direct Yellow K dye.

In syntheses of some dyes and optical whitening agents, 4,4'-diaminostilbene-2,2'-disulfonic acid (DAS) is widely used as the diazo component. At present, this acid is prepared from 4,4'-dinitrostilbene-2,2'-disulfonic acid (DNS) by Bechaump reduction [1]. The drawbacks of this process are large amounts of wastewater, the necessity of utilizing the iron slime, and labor-consuming isolation of the target product; they make the process environmentally and economically unacceptable. Heterogeneous-catalytic reduction of DNS with hydrogen in the liquid phase (see scheme) is more efficient and economically feasible. However, this process is accompanied by formation of by-products and intermediates decreasing the yield and quality of DAS. The scheme of catalytic reduction of DNS suggested by Bizhanov and Zhubanov [2] does not reflect all the transformations that DNS undergoes under conditions of catalytic reduction. Bizhanov and Zhubanov proved the possibility of hydrogenation of the C=C double bond in the stilbene moiety with the formation of 4,4'-diaminodibenzyl-2,2'-disulfonic acid (DADB) and *p*-aminotoluenesulfonic acid; they also noted formation in solution of diazo compounds and unidentified unstable colored products. Formation of an unidentified red product in reduction of DNS was noted in [3, 4]. It was suggested that the compound imparting the red color to the reaction mixture in the course of DNS reduction contains an azoxy group [4]. At the same time, DAS can be prepared by hydrogenation of a mixture of azo dyes containing as major component the trisazoxy dye Direct Yellow K (DYK) of the following structure [7]:

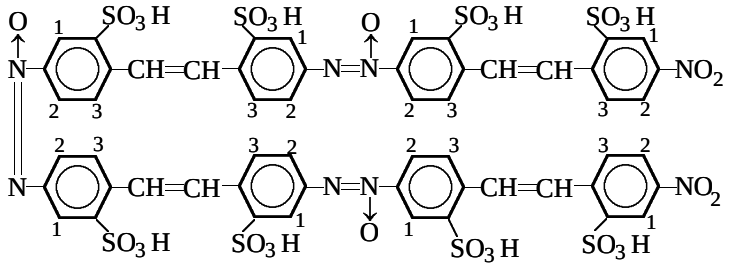

According to the Haber–Lukashevich–Shmonina scheme, nitro compounds are reduced in steps, with the products of incomplete hydrogenation of the NO_2 group being capable to react with each other to form azoxy compounds [6, 7]. Therefore, presumably, heterogeneous-catalytic reduction of DNS can yield a product identical to DYK, imparting the red color to the catalyzate and the cream color to the isolated target product.

Papers concerning the DAS production process discuss the influence of various process conditions on the product quality. This influence cannot be understood without data on intermediates and by-products. Therefore, the goal of this work was to prepare and study intermediates and by-products arising in catalytic reduction of DNS. The results would allow us to suggest a more detailed scheme of DNS reduction with hydrogen on Raney nickel and to find conditions for preparing the purest target product.

1070-4272/02/7503-0436$27.00 © 2002 MAIK "Nauka/Interperiodica"

Scheme of heterogeneous-catalytic reduction of DNS

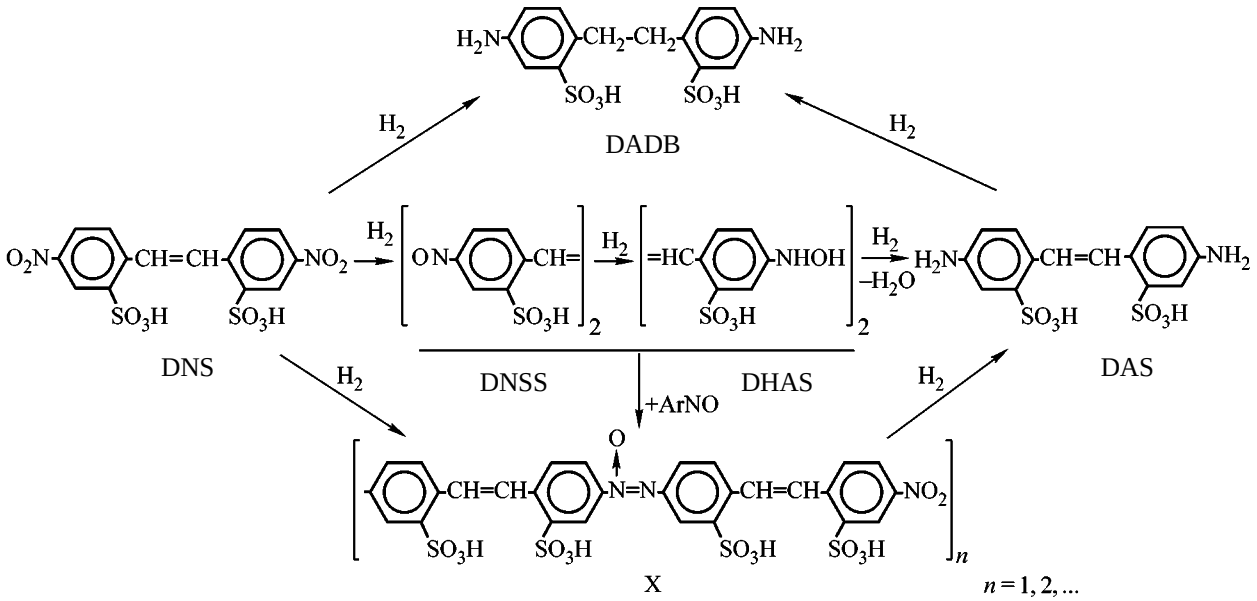

where DNSS is 4,4'-dinitrosostilbene-2,2'-disulfonic acid and DHAS is 4,4'-di(hydroxylamino)stilbene-2,2'-disulfonic acid.

EXPERIMENTAL

Catalytic reduction of DNS with hydrogen was performed at atmospheric pressure in a Vishnevskii apparatus with vigorous stirring of the liquid phase. Raney nickel was prepared by leaching nickel–aluminum alloy (1 : 1 by weight) with a 25% NaOH solution. Crude DNS was purified by double recrystallization, which yielded fine yellow needle-like crystals soluble in water and dimethyl sulfoxide. The intermediate, hereinafter denoted as X, was prepared by reduction of DNS. A reaction vessel was charged with 2 g of the catalyst washed to remove NaOH and with 100 ml of water. The vessel was purged with hydrogen, after which the catalyst was saturated with hydrogen at stirring (1000 rpm) for an additional 10 min. Then 7 g of DNS was added, and reduction was performed at 303 K for 5 min with stirring (4000 rpm). Under these conditions, the reduction yielded a red solution, which was filtered to remove the catalyst and evaporated. The residue was recrystallized from DMF. A red powder was obtained, soluble in water and DMF. Separate experiments showed that intermediate X can be reduced to DAS in the presence of Raney nickel.

The target product, DAS, was prepared by reduction of DNS (1 g) in citrate–phosphate buffer solution (pH 9.5) at 303 K on Raney nickel (1 g). The crude product was recrystallized from water. The resulting flesh-colored needle-shaped crystals were soluble in aqueous alkali. DADB was prepared by hydrogenation of DAS (1 g) in aqueous solution on Raney nickel and isolated by acidification with HCl to pH 2.35. The product was a white amorphous powder. DYK was prepared according to [5] from nitrotoluenesulfonic acid and purified by recrystallization from DMF. The product was a red powder soluble in water and DMF. All the products were sulfo derivatives; they decomposed without melting above 300°C.

To determine the structure of intermediate X, all the above substances were studied by IR and UV spectroscopy. For DYK and product X, we also recorded the ^{1}H NMR spectra and performed elemental analysis. The UV spectra were taken on an SF-46 spectrophotometer in the wavelength range 250–500 nm in aqueous solution (cell thickness 1 cm). The IR spectra were taken on a Specord M80/M85 spectrophotometer in the frequency range 4000–200 cm^{-1} using the KBr technique (0.002–0.0024 g of substance per 0.3 g of KBr, pressing at 6000–1000 atm with continuous evacuation to 10^{-3} mm Hg). The ^{1}H NMR spectra were taken on a Bruker AMX spectrometer (400.13 MHz, DMSO-d_6) relatve to internal TMS.

The C=C double bond was detected by iodination, and the amino group, by diazotization. Elemental analysis was performed by the standard procedure [8].

The UV spectra of DNS, DAS, DADB, product X, and DYK are shown in Fig. 1. The spectra of DNS

Table 1. IR spectra of DNS and its reduction products

Compound	ν, cm^{-1}						
	–CH=CH–	C=C (arom.)	C–H (arom.)	CH_2– (aliph.)	$–NO_2$	$–NH_2$	$–SO_3H$
DNS	1664 vs	1472, 1484, 1576	968, 976	–	752, 848, 876 1348, 1520–1568	–	628, 1080, 1296
DAS	1664	1496, 1568, 1576, 1584, 1608	912, 976	–	–	640, 660, 1256 1496, 3312–3400 3512	628, 1080, 1280
DADB	–	1436, 1508, 1584, 1620	968, 976	2624, 2712, 2960	–	672, 704, 796 908, 1272, 1508 1508, 3280, 3448	624, 1088, 1272
DYK	1664 vs	1472, 1568	976	–	–	–	624, 1128, 1288
X	1664 vs	1456, 1568	968, 976	–	–	–	624, 1128, 1288

and DAS differ insignificantly. The only absorption maximum in the spectrum of DNS (350 nm) corresponds to the π–π^* transition with the electron transfer to the NO_2 group [6]. In the UV spectrum of DAS, there is a maximum at λ = 340 nm, characteristic of aromatic amines [9]. Absorption in the visible range is insignificant. DADB has no absorption maxima in the examined range. The spectra of product X and DYK appeared to be virtually identical. The maximum at about 440 nm is assigned to the n–π^* transition.

The IR spectra of all the compounds listed in Table 1 contain bands assignable to vibrations of the sulfo group and aromatic CH group, skeleton vibrations of benzene rings, and out-of-plane bending vibrations of the C–H bonds in benzene rings. The spectrum of DNS also contains the NO_2 vibration bands, and the spectra of DAS and DADB, the vibration bands of the NH_2 group. Because DADB contains no –CH=CH– bond, in the spectrum of this compound the band at 1664 cm^{-1} is lacking, but bands assignable to stretching vibrations of the aliphatic CH_2 group are observed, which are absent in the spectra of the other substances.

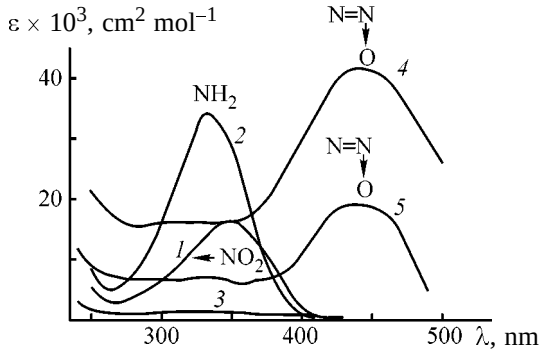

Fig. 1. UV absorption spectra of (*1*) DNS, (*2*) DAS, (*3*) DADB, (*4*) product X, and (*5*) DYK. (ε) Extinction coefficient and (λ) wavelength.

The spectra of product X and DYK contain a whole set of bands confirming the presence of the stilbene double bond, benzene rings, and sulfo group. A distinctive feature of the spectra of X and DYK, as compared to those of the other compounds, is the presence of a strong band at 1300–1304 cm^{-1} belonging to the azoxy group. The fine structure of the spectra of X and DYK in the range 1300–900 cm^{-1} is slightly different, which may be due to partial hydrogenation of double bonds between the benzene rings in the course of catalytic reduction. In other respects, the spectra of DYK and product X virtually coincide.

Comparison of the chemical shifts in the ^1H NMR spectra of product X and DYK (Table 2) shows that all the major fragments in these substances coincide. Insignificant differences are due to the presence of the aliphatic CH_2–CH_2 bond in product X.

Both X and DYK are neither iodinated nor diazotized. Elemental composition of X, found, %: C 42.3; N 7.2; H 2.8. Calculated for DYK, %: C 42.2; N 7.0; H 2.5. The difference between the spectra of DYK and product X may be due to simultaneous transformations of intermediates with different extents of reduction under the conditions of the heterogeneous-catalytic reaction. As a result of the reactions suggested in

Table 2. ^{1}H NMR spectra of DYK and product X

Compound	^{1}H NMR spectrum, δ, ppm					
	H^1 (arom.)	H^2 (arom.)	H^3 (arom.)	–CH=CH–	SO_3H	$–CH_2–CH_2–$
DYK	8.669 (8H)	8.165 d (8H)	6.832 d (8H)	5.390 (8H)	2.611 d (8H)	–
X	8.681 d (8H)	8.166 d (8H)	6.796 d (8H)	5.375 (8H)	2.611 d (8H)	2.337 s

[7], product X contains impurities of azo coupling products with similar properties. Apparently, reduction of DNS occurs via azo coupling of product X with other reaction participants. Thus, heterogeneous-catalytic reduction of DNS in aqueous solution follows a complex pattern involving much more species than it was suggested earlier [2].

We plotted a calibration chart to determine the concentration of X from the optical density of its solutions at 440 nm and, using these data, examined how the concentration of X in hydrogenation products varies with time in the course of DNS reduction (Figs. 2a, 2b). The concentration of X passed through a maximum in the initial period of the reaction. The maximal concentration of X depended on the weight ratio of DNS to the catalyst (the lower this ratio, the lower the maximal concentration of X) and on pH. The highest concentration of X was attained at pH 9.5–9.7. At this pH the reaction was also the most selective with respect to hydrogenation of the NO_2 group to form DAS (the stilbene double bond was not involved). Therefore, formation of X can be considered as a condition for selective formation of the target product.

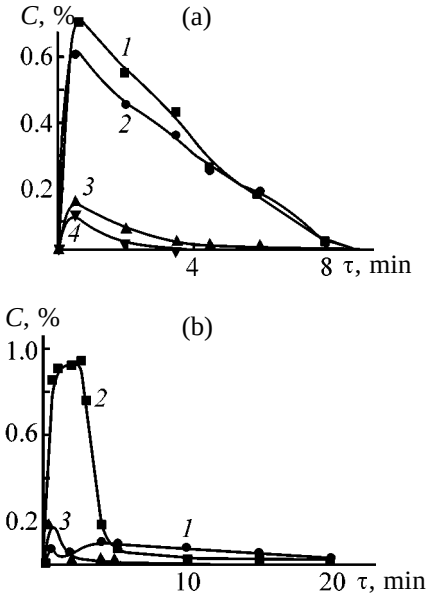

Fig. 2. Concentration of product X *C* as a function of time τ in (a) aqueous and (b) phosphate buffer solutions. 303 K; 0.5 g of DNS. (a) Catalyst weight, g: (*1*) 0.4, (*2*) 0.5, (*3*) 1.0, and (*4*) 2.0. (b) Catalyst weight 1 g; pH: (*1*) 5.64, (*2*) 9.68, and (*3*) 11.00.

We have shown previously [10] that at low weight ratios of DNS to the catalyst the DNS reduction occurs with an induction period. Comparison of the induction period to the time in which the concentration of X reaches a maximum shows that a low rate of hydrogen uptake is associated with formation of this intermediate. Apparently, rapidly forming product X blocks the catalyst surface and prevents further reduction. This is accompanied by partial reduction of X with the metal of the catalyst, primarily with residual aluminum.

The homogeneous stages of coupling of X with reactants play a major role under conditions when the amount of hydrogen on the catalyst surface is insufficient (Figs. 2a, 2b, curves *1*), i.e., at large DNS loads and deficiency of the catalyst. To improve the quality of DAS, such unfavorable conditions should be avoided.

CONCLUSIONS

(1) An intermediate of reduction of 4,4'-dinitrostilbene-2,2'-disulfonic acid in aqueous solution on Raney nickel was detected and studied; it is identical to Direct Yellow K trisazo dye.

(2) Formation of this intermediate explains the kinetic features of reduction of 4,4'-dinitrostilbene-2,2'-disulfonic acid and is the cause of the reaction deceleration. Incomplete reduction of this product results in decreased process selectivity.

REFERENCES

1. Vorozhtsov, N.N., *Osnovy sinteza poluproduktov i krasitelei* (Principles of Synthesis of Intermediates and Dyes), Moscow: Goskhimizdat, 1955.
2. Bizhanov, F.B. and Zhubanov, L.K., *Zh. Prikl. Khim.*, 1990, vol. 63, no. 5, pp. 276–278.

3. FRG Patent 2455394.
4. JPN Patent 59–118780.
5. Stepanov, B.I., *Vvedenie v khimiyu i tekhnologiyu organicheskikh krasitelei* (Introduction to Chemistry and Technology of Organic Dyes), Moscow: Khimiya, 1984.
6. *The Chemistry of the Nitro and Nitroso Groups*, Feuer, H., Ed., New York: Interscience, 1969.
7. Abdrakhmanova, R.M., Shmonina, V.P., and Sokol'skii, D.V., *Kataliticheskoe vosstanovlenie i gidrirovanie v zhidkoi faze* (Catalytic Reduction and Hydrogenation in the Liquid Phase), Ivanovo, 1970.
8. Siggia, S. and Hanna, J.G., *Quantitative Organic Analysis via Functional Groups*, New York: Wiley–Interscience, 1979.
9. Kazitsyna, L.A. and Kupletskaya, N.B., *Primenenie UF, IK i YaMR spektroskopii v organicheskoi khimii* (Use of UV, IR, and NMR Spectroscopy in Organic Chemistry), Moscow: Mosk. Gos. Univ., 1979.
10. Bazanova, I.N. and Shteinbakh, S.V., *Izv. Vyssh. Uchebn. Zaved., Khim. Khim. Tekhnol.*, 1998, vol. 41, no. 1, pp. 50–53.

Russian Journal of Applied Chemistry, Vol. 75, No. 3, 2002, pp. 441–443. Translated from Zhurnal Prikladnoi Khimii, Vol. 75, No. 3, 2002, pp. 452–454.
Original Russian Text Copyright © 2002 by Gaifutdinova, Beresnev.

ORGANIC SYNTHESIS AND INDUSTRIAL ORGANIC CHEMISTRY

Synthesis of Ethyl Benzoate by Ozonolysis of Styrene in the Presence of Ethanol

E. K. Gaifutdinova and V. V. Beresnev

Kazan State Technological University, Kazan, Tatarstan, Russia

Received July 11, 2001

Abstract—Ozonolysis of styrene in the presence of ethanol was studied as a route to ethyl benzoate.

Thanks to the high reactivity of ozone and its selective action on C=C bonds, ozonolysis of unsaturated organic compounds shows promise for industrial synthesis of various compounds with oxygen-containing functional groups [1].

Recently the demand for benzoic acid and its derivatives increased. These compounds are widely used in various branches of the national economy. Benzoic acid esters are used in production of dyes [2], heat-resistant lubricants [3], herbicides [4], alkali-resistant polyester coatings [5], and also as plasticizers for synthetic resins, cellulose ethers and esters, rubbers, and paper, as additives for dyeing fabrics made from manmade fibers [5], as polymerization catalysts [3], drugs [6–8], active ingredients of plant growth regulators [9], and cosmetic means [10].

High selectivity of ozonolysis of unsaturated hydrocarbons gives reasons to hope that synthesis of benzoic acid esters by ozonolysis starting from styrene and alcohols would be commercially feasible.

EXPERIMENTAL

Ozonolysis was performed in a glass bubbler with a porous bottom; it was charged with a styrene (**I**) solution. Ozone was generated by passing oxygen through a glow discharge at 10 kV. The ozone concentration was determined spectrophotometrically at 254 nm. Oxidation was performed to ozone breakthrough, which was detected by coloration of a 15% aqueous KI solution in a wash bottle placed at the reactor outlet (with starch as indicator). In the course of ozonolysis, we withdrew samples to determine the content of available oxygen [11] and of carboxy, carbonyl, and ester groups [12].

The thermal decomposition of ozonides was performed by heating the reaction solutions at 90–100°C for 2–4 h. In the resulting products, we determined the content of carboxy, ester, and carbonyl groups.

The IR spectra were recorded on an IFS-113V Fourier spectrometer in the range 400–4000 cm^{-1} with a resolution of 2 cm^{-1}; samples were prepared as films cast from solution on KBr plates, or as KBr pellets. The GC–MS study of ozonolysis products was performed with a Finnigan-MAT 212 device (INCOS 50 mass spectrometer, Varian 3400 gas–liquid chromatograph, capillary column with grafted SE-30, carrier gas helium, heating from 40 to 300°C at a rate of 15 deg min^{-1}, injector temperature 250°C). The ^{13}C NMR spectra of ozonolysis products were taken on a Bruker MSL 400 spectometer at 100.62 MHz; the chemical shifts were measured relative to TMS [13].

According to the experimental results, ozonolysis of styrene in the presence of ethanol can be described by the following scheme:

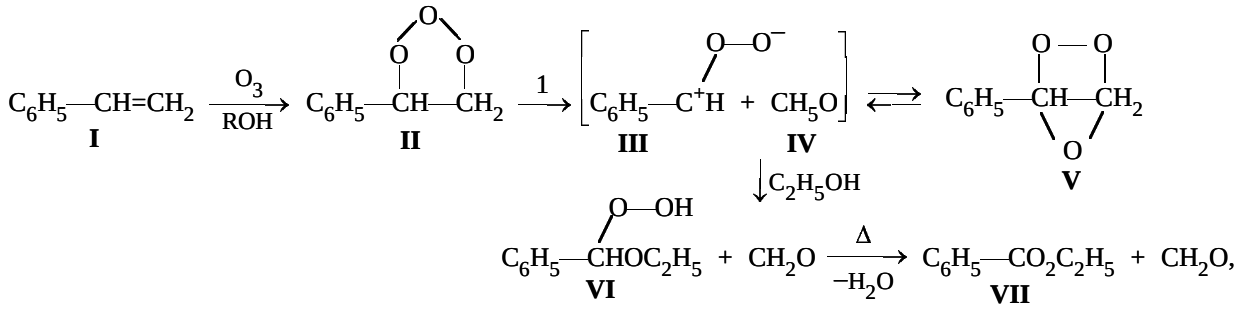

1070-4272/02/7503-0441$27.00 © 2002 MAIK "Nauka/Interperiodica"

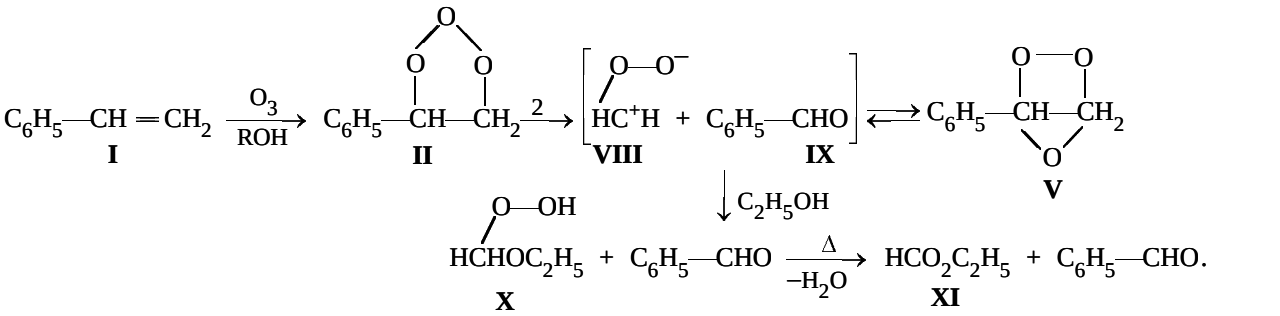

According to this scheme, addition of ozone to the double bond in styrene **I** yields unstable molozonide **II**; in the presence of a terminal double bond the aromatic system remains intact [14]. Molozonide readily decomposes into two fragments: bipolar ion **III** or **VIII** and carbonyl compound **IV** or **IX**. Presumably, owing to the positive inductive effect of the phenyl ring in styrene **I**, formation of the bipolar ion at the phenyl-substituted carbon atom [reaction (1)] is preferable [15]. The pair bipolar ion–carbonyl compound arising in decomposition of molozonide rapidly recombines in the solvent cage to form ozonide **V**. Formation of this compound is preceded by a change in the mutual orientation of fragments **III** and **IV** [reaction (1)], or **VIII** and **IX** [reaction (2)] (turn by 180°). Decomposition of ozonide **V** also yields bipolar ion **III** or **VIII** and carbonyl compound **IV** or **IX**.

Bipolar ion **III** or **VIII** is stabilized by reaction with an added active compound (ethanol) to form ethoxy hydroperoxides **VI** and **X**. In pathway (1), which is apparently preferable (see above), the second reaction product is formaldehyde **IV**. However, its content in the reaction mixture was low, probably because of easy volatilization.

We found that the content of available oxygen increases with the progress of styrene oxidation. We found that at the molar ratio styrene : ethanol = 1 : 1.5 the yield of available oxygen reaches a maximum (8.14 wt %); at the ethanol content increased further, the content of available oxygen decreases.

The IR spectra of alkoxy hydroperoxides contain the following absorption bands (cm^{-1}): 2980 [$\nu(CH_3)$]; 2950 [$\nu(CH_2)$]; 2890 [$\nu(CH_3)$]; 1310 [δ(C–O)]; 1110 [ν(CO)]; 990, 910, and 840 [ν(O–O)] [15].

Alkoxy hydroperoxides are unstable and readily decompose even at room temperature [16]. After storage of a mixture of ethoxy hydroperoxides **VI** and **X** for 2 months at 20°C, the content of available oxygen decreased from 8.1 to 1.9%.

Thermal decomposition of alkoxy hydroperoxides **VI** and **X** was performed at 90–100°C. It is advisable to perform the reaction at elevated temperatures, because at low temperatures formation of esters is too slow. The reaction is accompanied by release of low-molecular-weight inorganic products (e.g., water, which is formed by hydrogen abstraction by the hydroxy radical).

The IR spectra of reaction products contain absorption bands at 1260 [ν(C–O)] and 1715 cm^{-1} [ν(C=O)], confirming the presence of ethyl benzoate. The bands at 1680 and 1690 cm^{-1} belong to benzoic acid, and the band at 1700 cm^{-1} is characteristic of aromatic aldehydes (in particular, benzaldehyde **IX**). The ^{13}C NMR spectrum of the reaction product (after vacuum distillation) confirms its identification as ethyl benzoate [δ_C, ppm: 166 (C=O), 125–135 (Ph), 61.4 (CH_2), 14.6 (CH_3)].

The major reaction products are ethyl benzoate **VII** [63.4 wt %, isolated by vacuum distillation (68°C at 15 mm Hg)] and ethyl formate **XI** (20.4 wt %); the by-products are formaldehyde (6.0 wt %), benzaldehyde (6.3 wt %), formic acid (1.8 wt %), and benzoic acid (2.1 wt %).

CONCLUSION

A procedure was suggested for preparing ethyl benzoate by ozonolysis of styrene in the presence of ethanol, followed by thermal decomposition of the intermediate ozonolysis products.

REFERENCES

1. Razumovskii, S.D. and Zaikov, G.E., *Ozon i ego reaktsii s organicheskimi soedineniyami* (Ozone and Its Reactions with Organic Compounds), Moscow: Nauka, 1974.
2. Orlova, O.V. and Fomicheva, T.N., *Tekhnologiya*

lakov i krasok (Paint and Varnish Technology), Moscow: Khimiya, 1990.

3. *Polymer Blends*, Paul, D.R. and Newman, S., Eds., New York: Academic, 1978, vol. 1.
4. Mel'nikov, N.N. and Baskakov, Yu.A., *Khimiya gerbitsidov i regulyatorov rosta rastenii* (Chemistry of Herbicides and Plant Growth Regulators), Moscow: Goskhimizdat, 1962.
5. Perazich, D.I., Sokolova, A.I., Khailov, V.S., *et al.*, *Benzoinaya kislota: Svoistva, primenenie, proizvodstvo* (Benzoic Acid: Properties, Use, Production), Moscow: NIITEKhIM, 1973.
6. US Patent 53 787 228.
7. JPN Patent Appl. 421 665.
8. FRG Patent Appl. 4 032 037.
9. Baskakov, Yu.A. and Polyakov, A.I., *Karbonovye kisloty i ikh proizvodnye v kachestve regulyatorov rosta rastenii* (Carboxylic Acids and Their Derivatives as Plant Growth Regulators), Moscow: Mir, 1981.
10. Villamo, H., *Kosmeticheskaya khimiya* (Chemistry of Cosmetics), Moscow: Mir, 1990.
11. Alekseev, V.N., *Kolichestvennyi analiz* (Quantitative Analysis), Moscow: Khimiya, 1972.
12. Toroptseva, A.M., Belogorodskaya, K.V., and Bondarenko, V.M., *Laboratornyi praktikum po khimii i tekhnologii vysokomolekulyarnykh soedinenii* (Laboratory Manual on Chemistry and Technology of Macromolecular Compounds), Leningrad: Khimiya, 1972.
13. Kazitsyna, L.A. and Kupletskaya, N.B., *Primenenie UF, IK i YaMR spektroskopii v organicheskoi khimii* (Use of UV, IR, and NMR spectroscopy in Organic Chemistry), Moscow: Mosk. Gos. Univ., 1979.
14. Gaifutdinova, E.K., Synthesis of Carboxylic Acids and Their Derivatives by Ozonolysis of Hydrocarbons with a Terminal Double Bond, *Cand. Sci. Dissertation*, Kazan, 1999.
15. Gaifutdinova, E.K. and Beresnev, V.V., *Zh. Prikl. Khim.*, 1999, vol. 72, no. 5, pp. 865–867.
16. Antonovskii, V.L. and Buzlanova, Sh.M., *Analiticheskaya khimiya organicheskikh peroksidnykh soedinenii* (Analytical Chemistry of Organic Peroxides), Moscow: Khimiya, 1978.

Russian Journal of Applied Chemistry, Vol. 75, No. 3, 2002, pp. 444–448. Translated from Zhurnal Prikladnoi Khimii, Vol. 75, No. 3, 2002, pp. 455–459.
Original Russian Text Copyright © 2002 by Silaev.

ORGANIC SYNTHESIS AND INDUSTRIAL ORGANIC CHEMISTRY

Radiation-Chemical Behavior of C_1–C_4 Alcohols and Their Binary Mixtures

M. M. Silaev

Moscow State University, Moscow, Russia

Received June 19, 2001

Abstract—Data on γ-radiolysis of C_1–C_4 alcohols, practically significant for related fields of chemistry, were summarized.

Studies of γ-radiolysis of C_1–C_4 alcohols and their binary systems gave numerous data significant for related fields of chemistry [1–4]. The kinetics of competing addition of free radicals to double bonds of molecules with formation of 1 : 1 adducts and inhibition with unsaturated substrate [5] was developed, and the applicability of this kinetics to radical-chain oxidation was demonstrated [6]. In this work, we summarize the results that can be used in related fields of research.

The dissociation energies of chemical bonds in alcohol molecules, as data required for preliminary estimation of the probability of radiolytic reactions in alcohol-containing systems, are listed in Table 1.

In [1] we compared γ-radiolysis of aliphatic monohydric C_1–C_3 alcohols and 2-methyl-2-propanol in a wide temperature range (195–503 K) to determine their relative radiation-thermal stability. Such data can be useful in forecasting radiolytic transformations at various temperatures of both individual alcohols whose radiolysis has not been studied experimentally and various mixtures of alcohols with other components. The logarithms of the total yields of the decomposition of C_1–C_3 alcohols at γ-radiolysis as functions of reciprocal temperature are shown in Fig. 1. The effective activation energies E_α of various radiolytic reactions in alcohols: alcohol decomposition, reactions involving rupture of C_α–C and C–O bonds, and α-diol formation (as a result of recombination of α-hydroxyalkyl radicals arizing from the rupture of C_α–H bonds in alcohols) at low temperatures (≤ 293 K), when the thermal decomposition is negligible, are also presented in [1]. The E_α(α-diol) values (equal to 1.3, 5.7, 2.7, and 4.4 kJ mol^{-1} for methanol, ethanol, 1- and 2-propanol, respectively) can be used to extrapolate to higher temperatures, using the Arrhenius equation [10], the initial radiation-chemical yields of α-hydroxyalkyl radicals in alcohols, known for room temperature from ESR data [11].

Addition of α-hydroxyalkyl radicals to olefins and their derivatives in the course of γ-radiolysis leads to formation of molecular products (mainly 1 : 1 adducts) by the chain mechanism [3–5]. It was found that the reactivity of saturated alcohols with respect to γ-diol formation in γ-radiolysis of 2-propen-1-ol in saturated C_1–C_3 alcohols [3] (Fig. 2) and formation of recombination α-diols in γ-radiolysis of individual saturated C_1–C_3 alcohols at low temperatures (before transition to the radiation-thermal mode [1]) increase in the series methanol < 1-propanol < ethanol <

Table 1. Dissociation energies *E* of bonds in the gas phase at 298 K [7]

Alcohol	*E*, kJ mol^{-1}			
	C_α–C	C_α–H	C–O	O–H
Methanol	–	383.7	383.3	428.4
Ethanol	356.1	377.4	381.2	424.7
2-Propen-1-ol	363.6	330.1*	334.7* [8]	
1-Propanol	342.7	381.2*	382.8	427.2
2-Propanol	339.3	379.1	389.1	437.6
2-Methyl-2-propanol	310.0 [9]	–	387.9	434.3

* Calculated using the ratio of the dissociation energies of single-type chemical bonds in the series of ROH/RX pairs (R is saturated or unsaturated hydrocarbon radical C_1–C_3, X is CH_3 or OCH_3 for C_α–H or C–O bonds, respectively); for each bond type these ratios are constant within the limit of relative deviations: no more than 2 and 8% for C_α–H and C–O bonds, respectively.

1070-4272/02/7503-0444$27.00 © 2002 MAIK "Nauka/Interperiodica"

2-propanol.[1] It was shown in [4] that this series correlates with the entropy of formation of H bonds in alcohols, ΔS^0_{298} (it is quantitative characteristic of alcohol association), and the energy $E_{\lambda max}$ corresponding to the wavelength of the absorption band maximum in the spectrum of solvated electrons in alcohols (i.e., energy of electron solvation in alcohols) and inversely correlates with the effective activation energy of the alcohol self-diffusion E_D (Table 2).

The dependences of the radiation-chemical yields of formation of γ-diols, molecular products of addition of α-hydroxyalkyl radicals to 2-propen-1-ol [3], and 1 : 1 adducts of any free saturated radicals with olefins [16] on the concentration of the unsaturated compound have maxima. Using the scheme with competing reactions (parallel reactions in which molecules of the saturated and unsaturated components compete for radical adduct) and the method of steady-state concentrations, we described such nonmonotonic dependences by a kinetic equation with a single parameter α to be determined [6, 17, 18]. This equation describes both the dependences (with a maximum) of the radiation-chemical yield (or formation rate) of the 1 : 1 adduct on the concentration of the unsaturated component in binary systems consisting of saturated and unsaturated components at their comparable concentrations and of the yield (formation rate) of peroxide and alcohol (with the same number of the carbon atoms as in the initial hydrocarbon) on the concentration of molecular oxygen in noncatalytic oxidation by unbranched radical-chain mechanism (when the yields of these products substantially exceed the yields of carbonyl compounds). The above equation also allows determination of the rate constant k_{ad} of addition of a free radical to a double bond:

$$G(1:1\ \text{adduct}) = \frac{\varepsilon G(R_{sat})\alpha l x}{x^2 + (\alpha l + x)x^2_{max}/\alpha l_{max}}, \qquad (1)$$

$$k_{ad} = \alpha l_{max}[2k\varepsilon G(R_{sat})P]^{0.5}/x^2_{max},$$

where ε is the electronic fraction of the saturated component, $G(R_{sat})$ is the initial radiation-chemical yield of α-hydroxyalkyl or any other free saturated radicals (initiation yield), P is the dose rate, l and x are the initial molar concentrations of the saturated and unsaturated initial components ($l > x$), l_{max} and x_{max} are l and x at the curve maximum, respectively, α is the ratio of the rate constants of competing reactions, and $2k$ is the rate constant of the decay of the identical chain-leading free saturated radicals by their collisions with each another.

The constants $2k$ of diffusion-controlled reactions of the mutual decay of the identical hydroxyalkyl

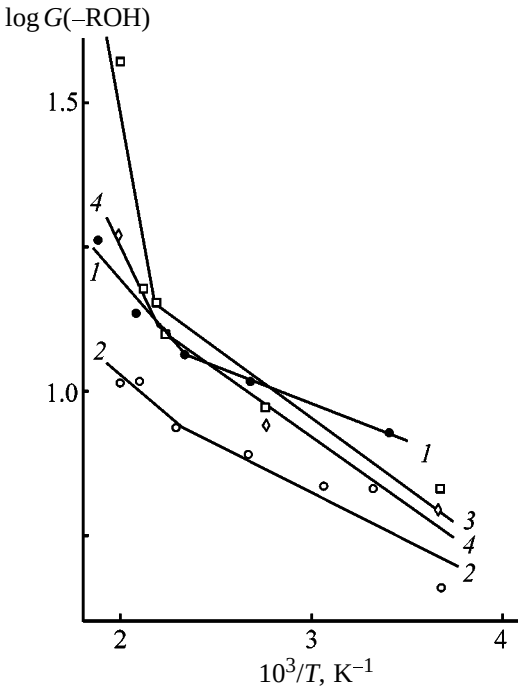

Fig. 1. Yields of alcohol decomposition G(–ROH) (molecules per 100 eV) as a function of temperature T in γ-radiolysis of (*1*) methanol, (*2*) ethanol, (*3*) 1-propanol, and (*4*) 2-propanol.

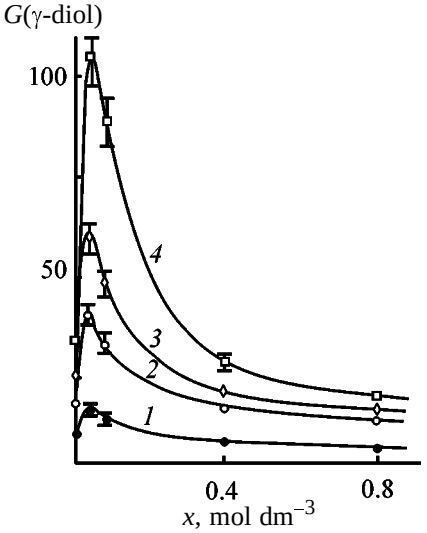

Fig. 2. Yields G(γ-diol) (molecules per 100 eV) of (*1*) 1,4-butanediol, (*2*) 1,4-hexanediol, (*3*) 1,4-pentanediol, and (*4*) 2-methyl-2,5-pentanediol as functions of the initial 2-propen-1-ol concentration x in methanol, 1-propanol, ethanol, and 2-propanol, respectively, at 433 K.

[1] Similar sequence was obtained in [12] for telomerization of 3,3,3-trifluoro-1-propene with saturated alcohols under the action of γ-radiation at 303 K.

Table 2. Effective activation energies E_a of formation of γ-diols in γ-radiolysis of saturated C_1–C_3 alcohol–2-propen-1-ol systems and parameters reflecting structural properties of the medium

Alcohol	E_a [4], kJ mol^{-1}	ΔS^0_{298} [13], J mol^{-1} K^{-1}	$E_{\lambda max}$ [14], kJ mol^{-1}	E_D [15], kJ mol^{-1}
Methanol	27.5	–35.8	191	11.6
1-Propanol	22.6	–61.1	188	17.8
Ethanol	19.5	–63.6	176	19.3
2-Propanol	14.4	–79.9	147	22.2

radicals enter into many kinetic equations combining the rates of formation of any alcohol-derived products with the concentrations of the reacting substances. Figure 3 shows how the experimental 2*k* values for hydroxyalkyl radicals C_2–C_3 in individual alcohols (neutral medium, room temperature), 2*k* values obtained from the self-diffusion coefficients of C_1–C_4 alcohols, and *k* values [10] for hydroxyalkyl radicals in 0.1 M aqueous solutions of C_2–C_4 alcohols with pH 6 (in this case, the use of *k* instead of 2*k* is associated with the lower viscosity of aqueous solutions of alcohols and higher alcohol diffusion coefficients [19, 20], which are practically the same as the diffusion coefficients of the corresponding hydroxyalkyl radicals [10]) correlate with the reciprocal viscosity (fluidity) of the corresponding alcohols. The correlation (a total of 12 points) is linear (correlation coefficient 0.995) and is described by the equation

$$2k = aD = b_{exp}/\eta, \quad (2)$$

where $a = (1.0 \pm 0.13) \times 10^{15}$ m mol^{-1} is the coefficient of Smoluchowski equation for identical species (C_1–C_4 saturated alcohols) at 298 K [20], *D* is the self-diffusion coefficient (m^2 s^{-1}), $b_{exp} = (1.27 \pm 0.05) \times 10^3$ N m mol^{-1}, and η is the viscosity (MPa s) [10].

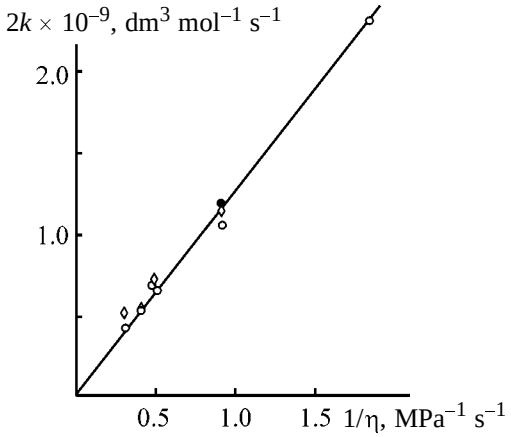

Fig. 3. Rate constant 2*k* of decay of hydroxyalkyl radicals in individual C_1–C_4 alcohols at room temperature as a function of the viscosity η of these alcohols. (*1*) $2k_{exp}$, (*2*) $2k = aD$, and (*3*) $2k = k_{0.1\ M}$.

This equation allows obtaining numeral estimation of unknown 2*k*. Due to the use of the empirical coefficient b_{exp}, the differences between the estimated and experimental (taken as 100%) values of the average alcohol self-diffusion coefficients $D = b_{exp}/a\eta$ and of 2*k* are small as compared to the experimental relative error (< 20%). Only for the self-diffusion coefficient of ethanol and 2*k* of hydroxymethyl radicals such differences are 12.5 and 18%, respectively.

The decay constants 2*k* of the identical hydroxyalkyl radicals at any taken temperature can be found from their room-temperature values by the Arrhenius equation using the known activation energies E_a of these reactions. For the majority of alcohols, within the experimental error, these quantities are approximately equal to the activation energies of self-diffusion E_D or viscous flow E_η [10]. The E_η values were calculated in [10] from the slope of the linear dependences of the logarithms of the viscosity on reciprocal temperature for the majority of C_1–C_8 aliphatic alcohols within the 273–373 K range.

Addition (under the action of γ-radiation) of α-hydroxyalkyl radicals to the carbon atom at the double bond of free (desolvated, monomeric) formaldehyde leads to the chain formation of α-diols [5, 21]. In these processes, the main role in the reactivity of alcohols belongs to desolvation of formaldehyde in alcohol–formaldehyde solutions. Neutral solutions of formaldehyde in alcohols at room temperature are mainly equilibrium mixtures of formaldehyde–alcohol oligomers of various molecular weights, described by the general formula $RO(CH_2O)_nH$, where $n = 1$–4 [22]. The concentration of free (unbound to solvent) formaldehyde (active species capable to accept free radicals) is as low as a fraction of percent of the total formaldehyde concentration [22]. The concentration of free formaldehyde was determined by high-temperature spectrophotometry at 335–438 K for solutions in water, ethandiol, methanol, ethanol, 1- and 2-propa-

nol, and 2-methyl-2-propanol with the analytical formaldehyde concentrations from 1.0 to 8.4 mol dm^{-3} [23]. The free formaldehyde concentration exponentially increases with increasing temperature and can reach several percents of the formaldehyde total concentration, i.e., 19.3% for 2-methyl-2-propanol (alcohol concentration 1.0 mol dm^{-3}, 398 K) (Fig. 4).

The treatment of 101 measurements gave empirical formula combining the free formaldehyde concentration x (mol dm^{-3}) with the temperature T (K) and total formaldehyde concentration in the solution c_0 (measured at room temperature):

$$\log x = -\alpha(10^3/T) + \beta + \gamma \log c_0, \quad (3)$$

where α and β, as parameters of the straight line equation, were calculated by the least-squares method from the dependences of $\log x$ on $1/T$ at c_0 = 1.0 mol dm^{-3} for various solvents; the coefficient γ was obtained as the average slope of the linear dependences of $\log x$ on $\log c_0$ at various fixed temperatures. The coefficients α, β, and γ for each solvent are listed in Table 3.

The deviation of x calculated by Eq. (3) from the experiment does not exceed 25%.

The alcohol concentrations l_T (mol dm^{-3}) in alcohol–formaldehyde solutions at any temperature can be estimated assuming linear dependence of the solution density on the formaldehyde concentration, similar to that for formaldehyde aqueous solutions (0–14 mol dm^{-3}, 291 K), by the formula

$$l_t = \frac{(10^3 d - 21.6 c_0) d_T}{(d + 8.4 \times 10^{-3} c_0) M}, \quad (4)$$

where c_0 is the total formaldehyde concentration (mol dm^{-3}); M is the solvent molecular weight (g mol^{-1}); d and d_T are the densities of the solvent at room temperature and given temperature T (g cm^{-3}), respectively; the dimension of the coefficient 8.4×10^{-3} is 10^3 g mol^{-1}, and that of coefficient 21.6 is g mol^{-1} [25].

We showed [23] that at constant temperature the concentration of free formaldehyde decreases with increasing the solvent dielectric constant (Fig. 4). Water, in which, in spite of its higher polarity, the concentration of free formaldehyde is abnormally high and close to its concentration in 2-propanol (Fig. 4), is an exception. This may be caused by the specific instability of hydrated formaldehyde species and their ready conversion into free formaldehyde at elevated temperatures. Hence, we can assume that the addition of a less polar solvent to more polar alcohol (and of water to methanol or ethanol) will increase the free formaldehyde concentration, similarly to heating of the solution.

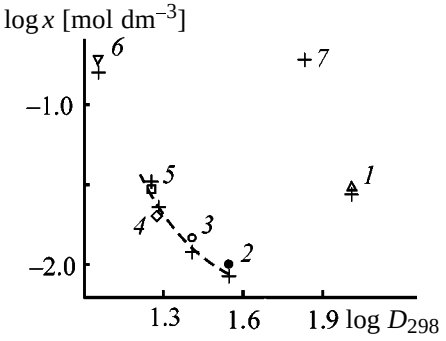

Fig. 4. Experimentally determined concentration x of free formaldehyde in (*1*) water, (*2*) methanol, (*3*) ethanol, (*4*) 1-propanol, (*5*) 2-propanol, and (*6*) 2-methyl-2-propanol as a function of dielectric constant D_{298} of these solvents. Total formaldehyde concentration C_0 1.0 mol dm^{-3}, temperature 395 ± 3 K. (*7*) Values of x in the above solvents calculated by Eq. (3).

CONCLUSIONS

(1) The relative radiation-thermal stability of C_1–C_3 alcohols within the 195–503 K range was determined.

(2) The general kinetic equation for unbranched radical-chain reactions of addition and oxidation, describing the experimental curves with a maximum, was obtained.

(3) An equation for quantitative estimation of the rate constants of reactions describing the decay of identical free hydroxyalkyl radicals at collision with each other from reciprocal viscosity (fluidity) of the corresponding alcohols was derived.

Table 3. Coefficients of empirical Eq. (3) for estimation of free formaldehyde concentration x in polar solvent–formaldehyde mixtures [23]

Solvent	α	β	γ
Water	2.36	4.45	0.80
Ethanediol	1.83	2.60	1.28
Methanol	3.11	5.58	$0.22c_0/\log c_0$
Ethanol	3.10	5.92	$1.10\ (10^3/T)$–1.44
1-Propanol	2.42	4.47	1.30
2-Propanol	2.42	4.64	1.05
2-Methyl-2-propanol	3.19	7.31	0.96

(4) Empirical equations for calculating concentrations of free (desolvated) formaldehyde and the alcohol in alcohol–formaldehyde systems at various temperatures and formaldehyde concentrations were found.

REFERENCES

1. Silaev, M.M., *Vestn. Mosk. Gos. Univ., Ser. 2: Khim.*, 1989, vol. 30, no. 3, pp. 263–268.
2. Silaev, M.M., Afanas'ev, A.M., and Kovalev, G.V., *Khim. Vys. Energ.*, 1993, vol. 27, no. 4, pp. 61–67.
3. Silaev, M.M., *Khim. Vys. Energ.*, 1990, vol. 24, no. 3, pp. 282–283.
4. Silaev, M.M., Kalyazin, E.P., and Bugaenko, L.T., *Khim. Vys. Energ.*, 1990, vol. 24, no. 4, pp. 323–325.
5. Silaev, M.M. and Bugaenko, L.T., *Radiat. Phys. Chem.*, 1992, vol. 40, no. 1, pp. 1–10.
6. Silaev, M.M., *Zh. Fiz. Khim.*, 1999, vol. 73, no. 7, pp. 1180–1184.
7. Gurvich, L.V., Karachevtsev, G.V., Kondrat'ev, V.N., *et al.*, *Energii razryva khimicheskikh svyazei. Potentsialy ionizatsii i srodstva k elektronu* (Dissociation Energies of Chemical Bonds. Ionization Potentials and Electron Affinities), Kondrat'ev, V.N., Ed., Moscow: Nauka, 1974.
8. Benson, S.W., *Thermochemical Kinetics. Methods for the Estimation of Thermochemical Data and Rate Parameters*, New York: Wiley, 1968.
9. Johnson, W.D., *Aust. J. Chem.*, 1975, vol. 28, no. 8, pp. 1725–1731.
10. Silaev, M.M., Bugaenko, L.T., and Kalyazin, E.P., *Vestn. Mosk. Gos. Univ., Ser. 2: Khim.*, 1986, vol. 27, no. 4, pp. 386–389.
11. Fel'dman, V.I., Belevskii, V.N., Milinchuk, A.V., and Bugaenko, L.T., *Vestn. Mosk. Gos. Univ., Ser. 2: Khim.*, 1984, vol. 25, no. 3, pp. 258–264.
12. Zamyslov, R.A., Radiation Synthesis of Fluorine-Containing Alcohols by Radical Polymerization, *Cand. Sci. Dissertation*, Moscow, 1984.
13. Dannhauser, W. and Bahe, L.W., *J. Chem. Phys.*, 1964, vol. 40, no. 10, pp. 3058–3066.
14. Okazaki, K., Idriss-Ali, K.M., and Freeman, G.R., *Can. J. Chem.*, 1984, vol. 62, no. 11, pp. 2223–2230.
15. Partington, J.R., Hudson, R.F., and Bagnall, K.W., *Nature*, 1952, vol. 169, no. 4301, pp. 583–584.
16. Silaev, M.M., *Kinet. Katal.*, 1999, vol. 40, no. 2, pp. 281–284.
17. Silaev, M.M., *Oxid. Commun.*, 1999, vol. 22, no. 2, pp. 159–170.
18. Silaev, M.M., *Neftekhimiya*, 2000, vol. 40, no. 1, pp. 33–40.
19. Valiev, K.A. and Emel'yanov, M.I., *Zh. Stukt. Khim.*, 1964, vol. 5, no. 1, pp. 7–12.
20. Porai-Koshits, A.B., Yakorev, O.P., Sazonov, A.M., and Shmuilovich, G.A., *Izv. Vyssh. Uchebn. Zaved., Khim. Khim. Tekhnol.*, 1981, vol. 24, no. 10, pp. 1230–1235.
21. Silaev, M.M. and Bugaenko, L.T., *Kinet. Katal.*, 1994, vol. 35, no. 4, pp. 509–513.
22. Ogorodnikov, S.K., *Formal'degid* (Formaldehyde), Leningrad: Khimiya, 1984.
23. Silaev, M.M., Rudnev, A.V., and Kalyazin, E.P., *Zh. Fiz. Khim.*, 1979, vol. 53, no. 7, pp. 1647–1651.
24. Walker, J.F., *Formaldehyde*, 2-nd ed., New York: American Chem. Soc., 1953.
25. Silaev, M.M., *Zh. Fiz. Khim.*, 1993, vol. 67, no. 9, p. 1944.

Russian Journal of Applied Chemistry, Vol. 75, No. 3, 2002, pp. 449–451. Translated from Zhurnal Prikladnoi Khimii, Vol. 75, No. 3, 2002, pp. 460–462.
Original Russian Text Copyright © 2002 by Gorbunova, Zapevalov, Saloutin, Chupakhin.

MACROMOLECULAR CHEMISTRY AND POLYMERIC MATERIALS

Reaction of Dinitropolychlorobiphenyls with *O*- and *N*-Nucleophiles as a New Route of Reprocessing Polychlorobiphenyls

T. I. Gorbunova, A. Ya. Zapevalov, V. I. Saloutin, and O. N. Chupakhin

Institute of Organic Synthesis, Ural Division, Russian Academy of Sciences, Yekaterinburg, Russia

Received October 29, 2001

Abstract—The reactivity of a mixture of dinitropolychlorobiphenyls in nucleophilic substitution of aromatic chlorine by polyethyleneoxy and amino groups was studied. New polychlorobiphenyl derivatives were obtained.

Rendering harmless polychlorobiphenyls (PCBs) used as dielectrics, plasticizers, materials for hydraulic devices, etc., remains an urgent problem. According to various sources [1–3], from 100 to 500 thousand tons of PCBs was produced in the former Soviet Union. Although production and use of PCBs was prohibited by WHO in 1990, in some industrial enterprises they are still in use, which increases environmental pollution with PCBs and their derivatives, dibenzodioxins and dibenzofurans [3], which are very stable organic pollutants.

This work continues a search for methods of PCB reprocessing alternative to incineration. As noted previously, an efficient procedure for cleaning transformers to remove residual PCBs (and possibly dioxins) is treatment of the inner surface of a transformer with polyethylene glycols (PEGs) in the presence of alkali metal hydroxides [4, 5] to substitute aromatic chlorine in PCBs by polyethyleneoxy groups. A necessary condition of this process is the use of higher solid PEGs.

We also studied the reaction of a crude mixture of pentachlorobiphenyls (PCB-5) with PEGs of various molecular weights (PEG-3, 13, 35, 65) in the presence of alkali metal hydroxides [6] and found that, under the reaction conditions, two chlorine atoms were substituted by the corresponding alkoxy groups. Alkoxylation occurred under relatively mild conditions (120–130°C, 3–6 h) with a high yield of the target products (95–99%).

However, attempts to perform similar reactions with lower polyethylene glycols, ethylene glycol (EG) and diethylene glycol (DEG), failed: no conversion of PCB-5 was observed. This fact is attributable to structural features of the alkali metal alcoholates formed in the reaction mixture.

It is known that, under common conditions, EG reacts with alkali metal hydroxides or alkali metals to form monoethylene glycolates containing a tightly bound EG molecule [7]:

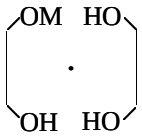

A

M = Na, K

According to [7], structure **A** is stable up to 150°C (at higher temperatures, the substance undergoes carbonization). Formation of such a structure is responsible for deactivation of monoethylene glycolate in nucleophilic substitution of aromatic chlorine. Apparently, with DEG a structure similar to **A** is formed also.

Alcoholates derived from PEG-3 (and from higher PEGs) probably form a similar adduct:

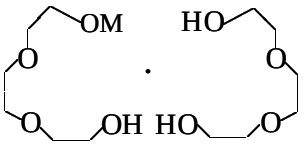

B

However, formation of structure **B** promotes rather than inhibits nucleophilic substitution of chlorine in PCB-5. Presumably, the PEG-3 molecule in **B** behaves as a podand [8]. Although PEG-3 contains no

1070-4272/02/7503-0449$27.00 © 2002 MAIK "Nauka/Interperiodica"

hard terminal donor groups enhancing complexation with metal ions, this molecule can form complexes via terminal hydroxy groups. These groups fulfil two functions simultaneously: coordination with metal ion and stabilization of the alkoxide ion by hydrogen bonding. As a result, interaction of the alkoxide oxygen with the metal cation is weakened, and the reactivity of this species is enhanced as compared to EG and DEG anions.

These data and our previous experimental results [6] suggest that alcoholate anions derived from EG and DEG are unsuitable for nucleophilic substitution of aromatic chlorine in PCB-5. At the same time, it is known that two acceptor substituents (e.g., nitro groups) introduced into *o*- and *p*-positions relative to halogen considerably facilitate substitution of halogen in aromatic compounds by alkoxy groups [9]. Furthermore, alcoholate anion appears to be more reactive when generated from alcohol and alkali metal fluoride [10] as compared to generation from alcohol and alkali metal or its hydroxide:

$$ROH + 2F^- \rightleftarrows RO^- + HF_2^-.$$

In the presence of weak hydrofluoric acid coexisting in solution with alkali metal alcoholates, the alkoxy groups are solvated relatively weakly.

We believe that for exchange of halogen by alkoxy groups derived from EG and DEG the most promising initial substance among the known PCB derivatives is a mixture of dinitropentachlorobiphenyls **I** described in detail in [11]. In this work, alkoxylation of **I** with alcoholates derived from EG and DEG in the presence of KF was performed at 110–130°C for 8–10 h. Analysis of the resulting mixtures **II** and **III** showed substitution of a single chlorine atom in **I** (see scheme). Incorporation of two alkoxy groups is apparently hindered sterically. The presence of such substituents as $O(CH_2CH_2O)_nH$ (n = 1, 2) makes mixtures **II** and **III** suitable initial substances for polycondensations.

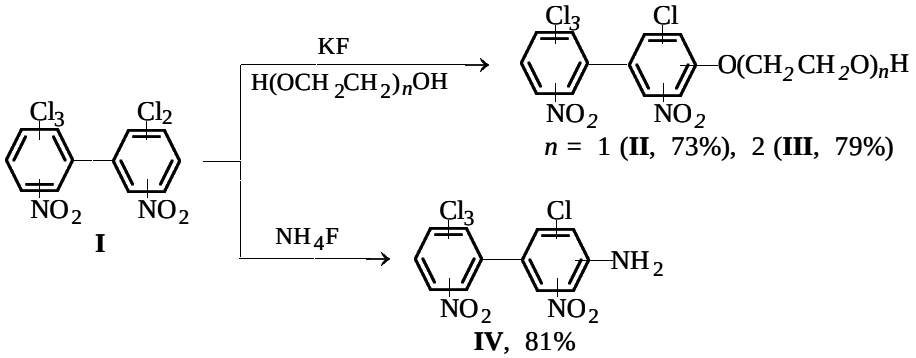

A similar pattern is observed in reaction of PCB derivatives with amino groups. Synthesis of diaminopentachlorobiphenyls by reduction of mixture **I** was reported in [11]. Similar to [10], we performed nucleophilic substitution of aromatic chlorine by amino group. The reaction occurred on heating of **I** with excess ammonium fluoride at 110°C for 8 h and yielded a mixture of aminodinitrotetrachlorobiphenyls **IV** (see scheme). However, both kinds of amino derivatives derived from PCBs are of little promise for preparation of polymers, because the aromatic amino group is a weak ("masked") polymerization center. Apparently, further functional substitution of PCB amino derivatives is required.

EXPERIMENTAL

The IR spectra of **II**–**IV** were recorded on a Specord 75-IR spectrophotometer; samples were cast as films from toluene solution. The IR and analytical data are listed in the table.

(Oxyethylen-ω-ol)dinitrotetrachlorobiphenyls II. A three-necked flask equipped with a power-driven stirrer and a reflux water condenser was charged with 3.2 g (0.055 mol) of KF, 10 ml (11.2 g, 0.18 mol) of EG, and 10.4 g (0.025 mol) of **I**. The mixture was heated on a glycerol bath at 110–130°C for 8 h with vigorous stirring. Then the mixture was cooled, 25 ml of toluene was added, and the mixture was refluxed for 5–10 min. The toluene layer was separated and washed with water, the solvent was evaporated, and the transparent brown residue was dried in a vacuum (5–6 mm Hg) at 60–80°C for 10 min. A mixture of compounds **II** was obtained; yield 8.1 g (73%), mp 53–58°C.

Similarly, from 3.2 g (0.055 mol) of KF, 15 ml (16.5 g, 0.16 mol) of DEG, and 10.4 g (0.025 mol) of

IR and analytical data for **II**–**IV**

Substance	Found, %/Calculated, %				Empirical formula	IR spectrum, ν, cm^{-1}
	C	H	Cl	N		
II	37.97/38.04	1.49/1.82	32.56/32.08	6.49/6.34	$C_{14}H_8Cl_4N_2O_6$	3435 (OH); 1555, 1340 (NO_2); 1100 (C–O–C)
III	39.82/39.53	2.72/2.49	29.68/29.17	5.82/5.76	$C_{16}H_{12}Cl_4N_2O_7$	3380 (OH); 1540, 1320 (NO_2); 1110 (C–O–C)
IV	36.08/36.31	1.07/1.27	36.18/35.72	10.32/10.58	$C_{12}H_5Cl_4N_3O_4$	3490, 1620 (NH); 1550, 1345 (NO_2)

I, 9.6 g (79%) of a mixture of (dioxyethylen-ω-ol)dinitrotetrachlorobiphenyls **III** was obtained as a light brown viscous liquid.

Aminodinitrotetrachlorobiphenyls IV. A round-bottomed flask equipped with a reflux condenser with a $CaCl_2$ tube was charged with 4.1 g (0.01 mol) of **I** and 3.7 g (0.1 mol) of NH_4F. The mixture was heated on a glycerol bath at 110°C for 8 h, after which it was worked up similarly to synthesis of **II**. A mixture of products **IV** was obtained as a transparent brown solid; yield 3.2 g (81%), mp 46–56°C.

CONCLUSION

(1) Reactions of dinitropentachlorobiphenyls with alcoholates derived from ethylene glycol and diethylene glycol, performed in the presence of KF, gave the monoalkoxylation products in yields of 73 and 79%, respectively.

(2) New polychlorobiphenyl derivatives, aminodinitrotetrachlorobiphenyls, were prepared.

ACKNOWLEDGMENTS

The study was financially supported by the Russian Foundation for Basic Research (project no. 01-03-96447).

REFERENCES

1. Tarasov, V.V., *Sb. Nauchn. Tr. Ross. Khim.-Tekhnol. Univ. im. D.I. Mendeleeva*, 1995, no. 173, pp. 24–42.
2. Fedorov, L.A., *Prakt. Sertif.*, 1992, nos. 4–5, p. 28.
3. Petrosyan, V.S., *Priroda*, 2000, no. 2, pp. 13–19.
4. McGraw, M.G., *Electr. World*, 1983, vol. 197, no. 2, pp. 49–72.
5. Tundo, P., Facchetti, S., Tumiatti, W., and Fortunati, U.G., *Chemosphere*, 1985, vol. 14, no. 5, pp. 403–410.
6. Gorbunova, T.I., Zapevalov, A.Ya., Kirichenko, V.E., *et al.*, *Zh. Prikl. Khim.*, 2000, vol. 73, no. 4, pp. 610–614.
7. Mamedov, Sh., *Prostye efiry glikolei* (Glycol Ethers), Baku: Akad. Nauk Azerb. SSR, 1961.
8. *Host Guest Complex Chemistry. Macrocycles. Synthesis, Structure, Applications*, Vögtle, A. and Weber, E., Eds., Berlin: Springer, 1985.
9. Vorozhtsov, N.N., Jr. and Yakobson, G.G., *Zh. Obshch. Khim.*, 1961, vol. 31, no. 11, pp. 3705–3708.
10. Vorozhtsov, N.N., Jr. and Yakobson, G.G., *Zh. Obshch. Khim.*, 1957, vol. 27, no. 6, pp. 1672–1676.
11. Gorbunova, T.I., Zapevalov, A.Ya., Kirichenko, V.E., *et al.*, *Zh. Prikl. Khim.*, 2001, vol. 74, no. 1, pp. 114–117.

Russian Journal of Applied Chemistry, Vol. 75, No. 3, 2002, pp. 452–456. Translated from Zhurnal Prikladnoi Khimii, Vol. 75, No. 3, 2002, pp. 463–467.
Original Russian Text Copyright © 2002 by Shapovalov, Svishcheva.

MACROMOLECULAR CHEMISTRY AND POLYMERIC MATERIALS

Effect of Cationic Surfactants on Association of Pinacyanol with Organic Counterions

S. A. Shapovalov and Ya. A. Svishcheva

Research Institute of Chemistry, Karazin National University, Kharkov, Ukraine

Received November 23, 2001

Abstract—The absorption spectra of aqueous solutions containing associates of pinacyanol and organic counterions (tetraphenylborate, sulfophthalein, and oxyxanthene) were studied as influenced by cationic surfactants. The possibility of developing sensitive procedures for quantitative evaluation (test control) of the content of cationic surfactants in aqueous solutions using pinacyanol associates was analyzed.

At present, interaction of cyanine (polymethine) chromophores with organic ions is widely studied using various media such as aqueous and nonaqueous solutions [1, 2], polyelectrolyte systems [3], thin films [4], and photosensitive materials [5]. The spectral study of such association will furnish information on specific interactions (hydrophobic, van der Waals, and π-electron) of bulk chromophores [6]; it is also urgent for practical use of ionic associates for quantitative determination of the content of cationic surfactants (CSAs) in solutions [6, 7].

Among the cyanine dyes, pinacyanol (1,1'-diethylquino-2-carbocyanine chloride, PNC)

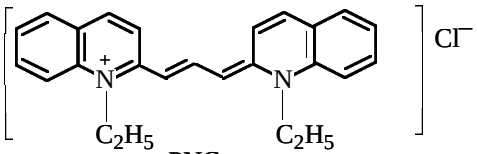

PNC

is of practical interest owing to its pronounced ability to form monomeric, dimeric, and more aggregated structures in aqueous solutions [8]. It was found that PNC forms ionic associates with bulky organic anions such as colorless single-charged tetraphenylborate anion (TPB) [9] and other organic anions including sulfophthalein and oxyxanthene chromophores [7, 10]. Thus, study of interaction of these PNC heteroassociates with ionic surfactants is of particular importance. In this work, we studied the interaction of PNC heteroassociates with CSAs.

EXPERIMENTAL

In this work, we used PNC chloride (Aldrich) and sodium TPB (Apolda, chloride content less than 0.01%); the other reagents (at least analytically pure grade) were used without additional purification. The CSAs [cetylpyridinium bromide (CPB), cetylpyridinium chloride (CPC), and cetyltrimethylammonium chloride (CTMA)] contained 98±1% of the main compound. The dye purity was monitored spectrophotometrically using the extinction coefficients and wavelengths of the absorption peak of the double-charged anions, and by the equilibrium dissociation constants in the case of oxyxanthenes. The required acidity of the solutions was adjusted using acetate buffers (for pH-metry) and hydrochloric acid and sodium hydroxide solutions. The solution pH was monitored with a glass electrode. The absorption spectra of the solutions were registered directly after their preparation at room temperature on Hitachi-U3210 and SF-46 spectrophotometers.

We used phenol red (PR), cresol red (CR), thymol blue (TB), bromothymol blue (BTB), bromocresol purple (BCP), bromocresol green (BCG), and bromophenol blue (BPB) sulfophthalein counterions and fluorescein (FL), eosin (EO), ethyleosin (EE), tetrabromophenylfluorone (TBPF), erythrosine (ER), and Rose Bengal B (RBB) oxyxanthene counterions.

At pH 4.5–9.5 and concentrations smaller than 7×10^{-7} M, PNC occurs in solutions as strongly absorbing single-charged cation (monomer, pK_a 3.5 [12]), which strongly decolorizes at pH ≥10 owing to hydrolysis. It is known [8] that PNC tends to self-associate. The absorption spectra of the PNC monomer exhibit the strongest band at 600 nm (Fig. 1, curve *1*), whereas the strongest band of the dimer ($c \approx 5 \times 10^{-5}$ M) is observed at 545 nm (Fig. 2, curve *1*). Moreover, at $c \geq 5 \times 10^{-4}$ M PNC forms H-aggregates with the absorption maximum at 510 nm.

1070-4272/02/7503-0452$27.00 © 2002 MAIK "Nauka/Interperiodica"

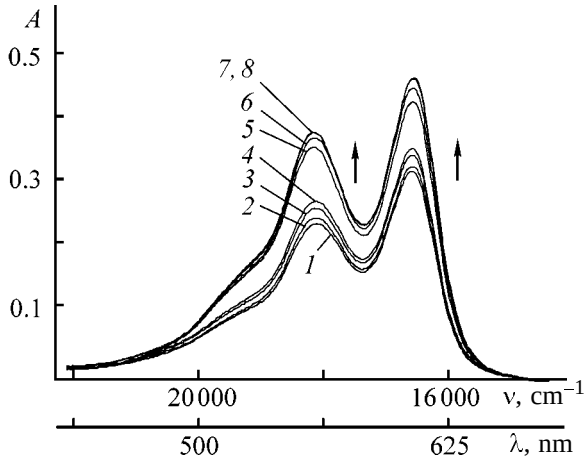

Fig. 1. Absorption spectra of PNC (4.9×10^{-6} M) at various content of CPB in aqueous solutions. Water reference, layer thickness 1.00 cm, pH 6.9; the same for Fig. 3. (*A*) Absorption, (λ) wavelength, and (ν) wave number; the same for Figs. 2–6. c_{CPB}, M: (*1*) 0, (*2*) 10^{-6}, (*3*) 5×10^{-6}, (*4*) 10^{-5}, (*5*) 10^{-4}, (*6*) 3×10^{-4}, (*7*) 6×10^{-4}, and (*8*) 9×10^{-4}.

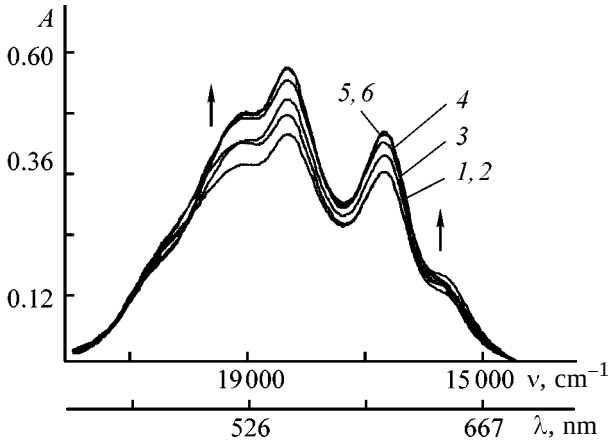

Fig. 2. Absorption spectra of dimeric PNC species (4.9×10^{-6} M) at various content of CPB in aqueous solutions. Water reference, layer thickness 0.20 cm, pH 6.9. c_{CPB}, M: (*1*) 0, (*2*) 5×10^{-6}, (*3*) 10^{-5}, (*4*) 5×10^{-5}, (*5*) 10^{-4}, and (*6*) 10^{-3}.

The premicellar and micellar contents of CSAs do not affect the shape of the absorption bands of both PNC monomer (Fig. 1) and dimer (Fig. 2), which suggests the absence of a strong interaction of the similarly charged chromophore and CSA ions. In contrast, the cationic PNC species readily interact with TPB anion and anionic chromophores listed above. As a result, the absorption of PNC (and in some cases of the chromophore) in solutions decreases by 40–65%, and new absorption bands appear in the spectra [2, 7, 9, 10]. These spectral changes observed at relatively low concentrations of the counterion ($c \geq 10^{-6}$) are similar to those occurring in aqueous solutions upon formation of ionic associates with cations of indopolycarbocyanines [13–15] and rhodamines [16–18].

It should be noted that the heteroassociates decompose in the presence of all the CSAs studied in this work, and the degree of decomposition is determined by the CSA concentration and is almost independent of its anionic component. For example, the ionic associate of PNC and TPB (Fig. 3, curve *1*) starts to decompose at a CTMA concentration of 3×10^{-6} M (Fig. 3, curve *2*). At further CSA addition, the solution absorption increases (Fig. 3, curves *3*–*7*), and at concentrations close to the micellar level $\{(1.0-1.8) \times 10^{-3}$ M [19]$\}$ the initial associate completely breaks down (Fig. 3, curve *8*). In the latter case, the solution spectra are similar to those of PNC in micelles of CTMA, CPC, and CPB (Fig. 1, curve *8*).

The breakdown of associates containing two chromophores (associates of PNC with sulfophthalein or oxyxanthene) is also accompanied by restoration of the absorption bands of their initial species. In these cases (Figs. 4–6), the absorption bands of each counterion are similar to those of the individual chromophores in CSA micelles. The band of the single-charged sulfophthalein anion undergoes a hypsochromic shift (≈ 8–12 nm) with respect to the CSA-free solution (absorption bands at 435 nm, e.g., PR^-, Fig. 4, curve *8*; BTB^-, Fig. 5, curve *6*), whereas in the case of the double-charged anions of sulfophthalein and oxyxanthene the bathochromic shift (≈ 15 nm,

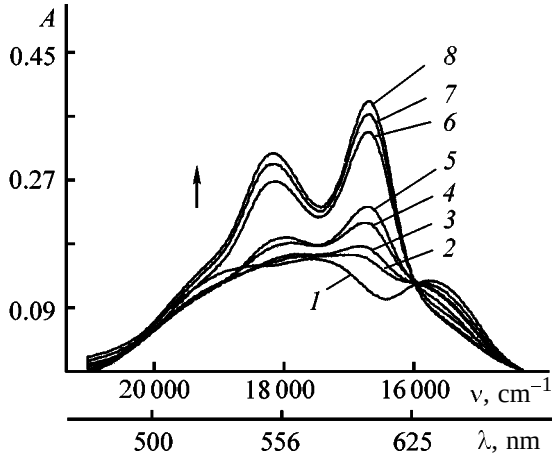

Fig. 3. Absorption spectra of the PNC (4.9×10^{-6} M) + TPB (5×10^{-6} M) system at various content of CTMA in aqueous solutions. c_{CTMA}, M: (*1*) 0, (*2*) 3×10^{-6}, (*3*) 5×10^{-6}, (*4*) 7×10^{-6}, (*5*) 10^{-5}, (*6*) 5×10^{-5}, (*7*) 10^{-4}, and (*8*) 6×10^{-4}.

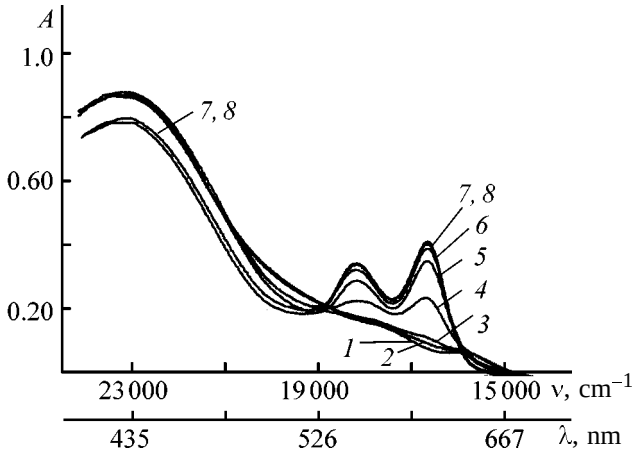

Fig. 4. Absorption spectra of the PNC (4.9×10^{-6} M) + PR (7.1×10^{-5} M) system at various content of CPB in aqueous solutions. Water reference, layer thickness 1.00 cm, pH 4.6. c_{CPB}, M: (*1*) 0, (*2*) 3×10^{-6}, (*3*) 10^{-5}, (*4*) 3×10^{-5}, (*5*) 6×10^{-5}, (*6*) 8×10^{-5}, (*7*) 6×10^{-4}, and (*8*) 9×10^{-4}.

absorption band at 530 nm, e.g. ER^{2-}, Fig. 6, curve *8*) is observed. It should be noted that similar spectral shifts, related to solubilization, were observed for the absorption bands of individual anions of a series of sulfophthalein and oxyxanthene dyes in the CSA micelles [20, 21]. As seen from the comparison of curves *1* and *8* (Fig. 1) and curves *1* and *6* (Fig. 2), in the case of PCN cation such shifts are absent.

Spectral changes observed in the PNC + TPB and PNC + chromophore systems suggest the equilibrium association. Using published analytical procedures [9, 13, 15, 16]; we found that the interaction of the ions can be presented by the following equations:

$$2Ct^+ + An^- \rightleftarrows (Ct^+)_2 \cdot An^- \text{ (for TPB anion);}$$

$$Ct^+ + An^- \rightleftarrows Ct^+ \cdot An^-,$$

$$2Ct^+ + An^{2-} \rightleftarrows (Ct^+)_2 \cdot An^{2-} \text{ (for chromophore anions),}$$

where Ct^+ is a monomeric PNC cation and An^- and An^{2-} are the single- and double-charged anions.

Taking into account the stoichiometric ratios observed, we calculated the thermodynamic equilibrium constants K_{as}. In the case of the PNC–TPB associate, K_{as} was 2.5×10^{13}. With increasing number of the halogen atoms and decreasing number of the alkyl substituents in the sulfophthalein molecule, K_{as} increases (its logarithm is given in parentheses) for both single-charged anions in the series CR^- (4.6) < TB^- (5.3) < PR^- (5.8) ≈ BTB^- (5.9) < BCP^- (6.7), and double-charged anions, CR^{2-} (11.0) ≈ BTB^{2-} (10.9) ≈ BCP^- (11.1) < PR^{2-} (11.8) < BCG^{2-} (12.1) < BPB^{2-} (13.7). Similar phenomenon is observed for oxyxanthenes: FL^- (4.6) < EE^- (5.5) < $TBPF^-$ (6.4), and especially for their double-charged anions: FL^{2-} (9.8) < EO^{2-} (11.3) < ER^{2-} (11.8) < RBB^{2-} (13.5).

Statistically significant differences in K_{as} suggest that the associate formation along with electrostatic factor strongly depends on the structural factor, which, in turn, is determined by specific interaction and thus affects the particle hydrophobicity [6, 11, 22]. As

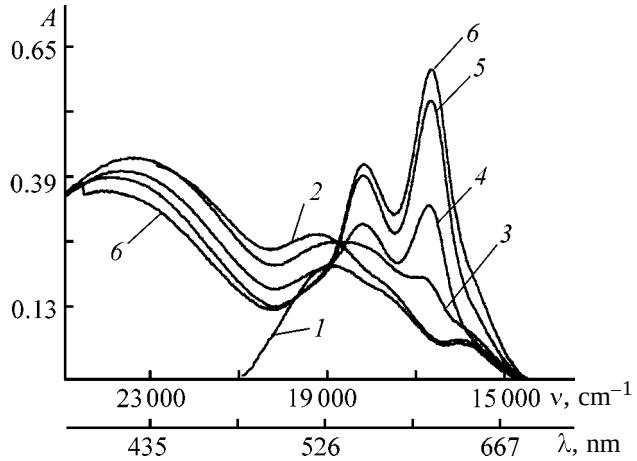

Fig. 5. Absorption spectra of the PNC (5.1×10^{-6} M) + BTB (2.5×10^{-5} M) system at various content of CPB in aqueous solutions. Layer thickness 1.00 cm, pH 4.6. c_{CPB}, M: (*1*) 0, (*2*) 3.1×10^{-6}, (*3*) 10^{-5}, (*4*) 4.8×10^{-5}, (*5*) 4×10^{-4}, and (*6*) 8.1×10^{-4}. Reference solution: (*1*) BTB, 2.5×10^{-5} M and (*2–6*) water.

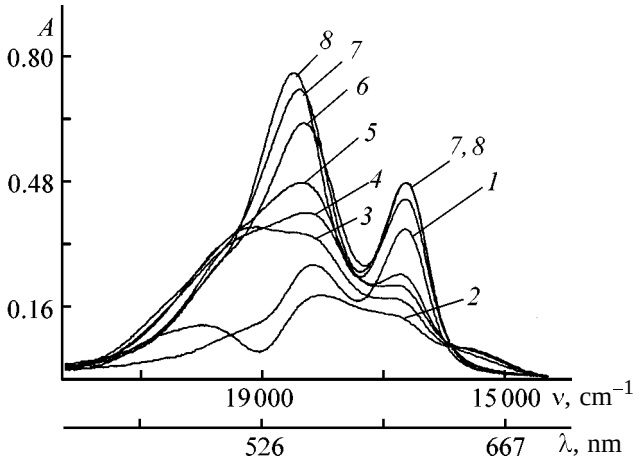

Fig. 6. Absorption spectra of (*1*) PNC (4.9×10^{-6} M), (*2*) PNC associate with double-charged ER, and (*3–8*) solution containing associate with addition of CPB. Layer thickness 1.00 cm, pH 9.2. c_{CPB}, M: (*1, 2*) 0, (*3*) 3×10^{-6}, (*4*) 6×10^{-6}, (*5*) 8×10^{-6}, (*6*) 6×10^{-5}, (*7*) 6×10^{-4}, and (*8*) 9×10^{-4}. Reference solution: (*1, 3–8*) water and (*2*) ER, 4×10^{-6} M.

seen, in the above series the strongest are the associates of BPB and RBB, which contain no alkyl substituents and have the greatest number of the hydrophobic halogen atoms.

The CSAs studied more easily break weaker associates: the breakdown of a stronger associate requires a higher concentrations of CSA, other conditions being equal (in particular, initial concentrations of counterions, relative excess of CSA with respect to counterions, etc.). Such a trend suggests that the surfactant cations (CSA^+) in the premicellar concentration range compete with PNC cations in the associate formation, replacing the latter from the associate with increasing CSA concentration:

$$Ct^+ \ An^- + CSA^+ \rightleftarrows Ct^+ + An^- \cdot CSA^+$$

or

$$(Ct^+)_2 \ An_2^- + CSA^+ \rightleftarrows 2Ct^+ + An^{2-} \cdot CSA^+.$$

In the micellar concentration range, the counterions are essentially separated from each other, but they are surrounded by CSA micelles:

$$Ct^+ \cdot An^- + (x+y)CSA^+ \rightleftarrows (Ct^+)_{xCSA^+} + (An^-)_{yCSA^+}$$

or

$$(Ct^+)_2 \cdot An^{2-} + (2x + y)CSA^+ \rightleftarrows 2[(Ct^+)_{xCSA^+}] + (An^{2-})_{yCSA^+},$$

Thus, in micellar solutions CSA acts both as competitor and medium for the associate component [23].

As seen from the calculated K_{as} values, the PNC associates are fairly strong and dominate in an aqueous solution at a 1.5–3.0-fold excess of an organic anion with respect to a cation. Nevertheless, even insignificant amounts of CSA can affect absorption of the aqueous solution containing associate. It should be noted that these changes occur in a wide range of CSA concentrations up to the micellar level. The optical density of the solution containing fixed amounts of PNC and counterions increases proportionally to the CSA concentration. Thus, the optical density at a given wavelength is a function of the CSA concentration in solution. For example, for PNC–TPB associate in the PCB concentration range 10^{-6}–10^{-4} M and at PNC and TPB concentrations of 4.9×10^{-6} and 10^{-5} M, respectively, the dependence of the optical density on the CSA concentration can be described as follows:

$$A_{600} = (0.098 \pm 0.009) + (2.22 \pm 0.18) \times 10^5 c_{CPB},$$

where A_{600} is the optical density at 600 nm and c_{CPB} is the concentration of CPB in the aqueous solution (M).

These relationships only slightly depend on the solution acidity; neither PNC nor TPB enter into protolytic reactions at pH 4.5–9.5. Therefore, quantitative determination of the CSA concentration using such dependences can exhibit high sensitivity to CSA (nearly 10^{-6} M) with the reliably determined concentrations ranging from 10^{-5} M to the micellar level in the solution pH range 4.5–9.5.

Moreover, some associates can be used for semiquantitative evaluation (test control) of the CSA concentration. In this case, we prepared a series of solutions containing fixed amounts of PNC and counterion (e.g., PNC and EE, both 5×10^{-6} M) and various amounts of CSA (10^{-6}, 5×10^{-6}, 10^{-5}, 5×10^{-5}, and 10^{-4} M). Each solution is characterized by its own color index, because the breakdown of the associate in each solution would be different. To evaluate the CSA concentration in a solution, its aliquot is added to a solution containing PNC and EE, and the color index of the resulting solution is compared with those of the reference solutions, after which the concentration is determined by interpolation.

CONCLUSIONS

(1) In aqueous solution, pinacyanol cation forms ionic associates with colorless (tetraphenylborate) and colored (sulfophthalein, oxyxanthene) anions. Irrespective of the composition, associates decompose in the presence of surfactants.

(2) The associate breakdown in the presence of various surfactants was studied. At the premicellar concentrations, the cationic surfactant competes with a pinacyanol cation, whereas at the micellar concentrations a specific medium is formed, which breaks associates.

(3) The properties of some associates can be used to develop new highly sensitive (up to 10^{-6} M) procedures for semiquantitative (test) and quantitative analysis of the content of cationic surfactants in aqueous solutions. These procedures are based on the proportional dependence of the optical density (coloring) of the solution on the concentration of cationic surfactants.

REFERENCES

1. Ishchenko, A.A., *Stroenie i spektral'no-lyuminestsentnye svoistva polimetinovykh krasitelei* (Structure and

Spectral Luminescence Properties of Polymethine Dyes), Kiev: Nukova Dumka, 1994.

2. Shapovalov, S.A., Mchedlov-Petrosyan, N.O., Koval', V.L., *et al*., Abstracts of Papers, *VII Simpozium "Fizika i khimiya polimetinovykh krasitelei"* (VII Symp. on Physics and Chemistry of Polymethine Dyes), Moscow, 1999, pp. 104–106.
3. Mitra, A. and Chakraborty, A.K., *Indian J. Chem., Ser. A*., 1992, vol. 31, nos. 1–2, pp. 77–82.
4. Kabayashi, M., Yuan, X., Sakai, H., *et al*., *Bull. Chem. Soc. Jpn*., 1992, vol. 66, no. 2, pp. 463–470.
5. Ishchenko, A.A., *Teor. Exp. Khim*., 1998, vol. 34, no. 4, pp. 214–232.
6. Shapovalov, S.A., Koval', V.L., Mchedlov-Petrosyan, N.O., *et al*., *Dopov. Nats. Akad. Nauk Ukr*., 1999, no. 2, pp. 156–161.
7. Shapovalov, S.A., Svishchova, Y.A., and L'vovskaya, M.I., Abstracts of Papers, *VIII Int. Scientific Conf. "The Problems of Solvation and Complex Formation in Solutions,"* Ivanovo, October 8–11, 2001, p. 245.
8. Sheppard, S.E., *Rev. Modern Phys*., 1942, vol. 14, pp. 304–340.
9. Shapovalov, S.A. and Svishcheva, Ya.A., *Vestn. Khar'kov. Nats. Univ., Khim*., 2000, no. 5, pp. 112–116.
10. Svishcheva, Ya.A., L'vovskaya, M.I., Dudnik, O.P., and Shapovalov, S.A., Abstracts of Papers, *Vtoraya vseukrainskaya nauchnaya konferentsiya studentov i aspirantov "Sovremennye porblemy khimii"* (2nd Ukrainian Scientific Conf. of Students and Post-Graduate Students on Modern Problems of Chemistry), Kiev, May 18–21, 2001, p. 111.
11. Shapovalov, S.A. and Svishcheva, Ya.A., Abstracts of Papers, *III Vserossiiskaya konferentsiya molodykh uchenykh "Sovremennye porblemy teoreticheskoi i eksperimental'noi khimii"* (III Russian Conf. of Young Scientists on Modern Problems of Theoretical and Experimental Chemistry), Saratov, September 3–5, 2001, p. 68.
12. Herz, A.H., *Photogr. Sci. Eng*., 1974, vol. 18, no. 2, pp. 207–215.
13. Ishchenko, A.A., Derevyanko, N.A., Popov, S.V., *et al*., *Izv. Ross. Akad. Nauk, Ser. Khim*., 1997, no. 5, pp. 950–955.
14. Shapovalov, S.A., Koval', V.L., Ishchenko, A.A., *et al*., Abstracts of Papers, *VII Int. Conf. "The Problems of Solvation and Complex Formation in Solutions,"* Ivanovo, June 29–July 2, 1998, p. 186.
15. Shapovalov, S.A., Chernaya, T.A., Koval', V.L., *et al*., Vestn. Khar'kov. Nats. Univ., Khim., 1999, no. 3, pp. 138–140.
16. Shapovalov, S.A., Chernaya, T.A., Belyaev, V.G., *et al*., *Vestn. Khar'kov. Nats. Univ., Khim*., 1998, no. 2, pp. 256–258.
17. Shapovalov, S.A., Chernaya, T.A., and Larin, V.I., Abstracts of Papers, *VIII Int. Scientific Conf. "The Problems of Solvation and Complex Formation in Solutions,"* Ivanovo, October 8–11, 2001, pp. 92–93.
18. Shapovalov, S.A., Chernaya, T.A., and Samoilov, E.A., *Vestn. Khar'kov. Nats. Univ., Khim*., 2000, no. 6, pp. 110–112.
19. Abramzon, A.A., Bocharov, V.V., and Gaevoi, G.M., *Poverkhnostno-aktivnye veshchestva: Spravochnik* (Surfactants: Handbook), Leningrad: Khimiya, 1979.
20. Mchedlov-Petrosyan, N.O. and Kleshchevnikova, V.N., *Zh. Obshch. Khim*., 1990, vol. 60, no. 4, pp. 900–911.
21. Mchedlov-Petrosyan, N.O. and Kleshchevnikova, V.N., *Vestn. Khar'kov. Nats. Univ., Khim*., 1993, no. 378, pp. 65–71.
22. Kessler, Yu.M. and Zaitsev, A.L., *Sol'vofobnye effekty. Teoriya, eksperiment, praktika* (Solvophobic Effects. Theory, Experiment, Practice), Leningrad: Khimiya, 1989.
23. Savvin, S.B., Chernova, R.K., and Shtykov, S.N., *Poverkhnostno-aktivnye veshchestva* (Surfactants), Moscow: Nauka, 1991.

Russian Journal of Applied Chemistry, Vol. 75, No. 3, 2002, pp. 457–460. Translated from Zhurnal Prikladnoi Khimii, Vol. 75, No. 3, 2002, pp. 468–471.
Original Russian Text Copyright © 2002 by Raskulova, Volkova, Moskaleva, Khaliullin.

MACROMOLECULAR CHEMISTRY AND POLYMERIC MATERIALS

Properties and Application Prospects of 1-(Vinyloxyalkoxy)propylene 2,3-Oxide Copolymers

T. V. Raskulova, L. I. Volkova, O. N. Moskaleva, and A. K. Khaliullin

Favorskii Irkutsk Institute of Chemistry, Siberian Division, Russian Academy of Sciences, Irkutsk, Russia

Received April 12, 2001

Abstract—Thermal stability, impact strength, folding resistance, and adhesion were studied for copolymers of vinyl chloride and 1-(vinyloxyalkoxy)propylene 2,3-oxides prepared in acetone and dimethyl sulfoxide.

Polyvinyl chloride (PVC) ranks among basic commercial polymers owing to its versatility and low cost. To almost 57% polyvinyl chloride consists of chlorine which is a cheap raw material whose world reserves are virtually unlimited. This specific polymer composition is responsible for both its advantages (strength and resistance to acids and solvents) and disadvantages (high viscosity of melt and low resistance to heat and light). One of the main disadvantages of PVC is that the temperature range of its conversion to the fluid state exceeds the degradation temperature. Therefore, the processing of PVC into articles requires, above all, introduction of stabilizing agents enhancing the thermal stability and plasticizing agents lowering the flow point [1].

However, many additives (especially the most efficient stabilizing agents based on lead, cadmium, and barium compounds) belong to hazard class 1 and 2 compounds [2]. Modern strict safety requirements to PVC composition components imply changing to new types of stabilizing agents free from the above-mentioned toxic metals.

The most widely used phthalate plasticizing agents are regarded as harmless [3, 4]. However, international environmental organizations regularly claim on unsafe application of these agents [5]. A possible reason is that the PVC–plasticizing agent system is metastable, and plasticizing agents can migrate from the composition during exploitation of articles, thereby taking away toxic stabilizing agents. Also, the introduced plasticizing agents inevitably decrease the softening point of the material; as a result, the deformation temperature of even rigid plastics based on PVC does not exceed 80°C.

The desired properties of the materials can be achieved by combining various chemical structures not only physically (by mixing appropriate composition components) but also chemically (copolymerization of the basic monomer with small amounts of a modifying comonomer). Therefore, an alternative line of improving the processability of PVC is copolymerization of vinyl chloride (VC) with a small amount of comonomers containing fairly bulky substituents ("internal" plasticization) and/or groups able of efficiently trapping the evolving hydrogen chloride (self-catalyst of the degradation process) and preventing oxidation processes (internal stabilization).

Vinyl ethers are often used as such comonomers [6–8]. In this case, stabilization is ensured by the specific structure of the copolymer macromolecules: Short blocks of VC units are separated by single vinyl ether units. The rate of elimination of hydrogen chloride is proportional to the length of VC blocks, which makes the copolymer containing no stabilizing groups more stable to thermal degradation than PVC [8]. The plasticizing efficiency of the polymer material is increased in the presence of fairly bulky side substituents in the vinyl ether molecule [9].

One of the main drawbacks of materials based on these copolymers is a lower (compared to PVC) softening point. Therefore, it is necessary to introduce into the monomer composition functional (e.g., epoxy) groups able of forming three-dimensional macromolecular networks and thereby increasing the softening point of the material.

In this connection, copolymers of VC and vinyl ethers containing an oxirane ring seem promising. These copolymers can efficiently trap hydrogen chloride, thereby significantly improving the resistance of copolymers to thermal degradation [10].

The aim of this work is to study the properties of

1070-4272/02/7503-0457$27.00 © 2002 MAIK "Nauka/Interperiodica"

Table 1. Thermal stability of VC–VEP copolymers

Comonomer	Preparation procedure	VEP_n content in copolymer, mol %	$[\eta]$, dl g^{-1}	T_{deg}, °C
– (PVC)	In suspension	–	–	162
VEP_1	In suspension	3.6	0.60	175
		5.3	0.35	180
		20.7	0.27	195
VEP_1, BVE	In suspension	5.3	0.26	252
VEP_2	In acetone	0.8	0.25	248
		8.6	0.23	247
	In DMSO	7.8	0.22	248
VEP_3	In acetone	0.8	0.24	253
		4.1	0.215	243
	In DMSO	2.4	0.23	250
		4.1	0.21	247

copolymers based on VC and 1-(vinyloxyalkoxy)propylene 2,3-oxides (VEP): 1-(vinyloxyethoxy)propylene 2,3-oxide (VEP_1), 1-(vinyloxydiethoxy)propylene 2,3-oxide (VEP_2), and 1-(vinyloxytriethoxy)propylene 2,3-oxide (VEP_3):

$$CH_2CHORCH_2\underset{\backslash\,O\,/}{CH}CH_2,$$

where R = $(CH_2–CH_2–O)$ in VEP_1, R = $(CH_2–CH_2–O)_2$ in VEP_2, and R = $(CH_2–CH_2–O)_3$ in VEP_3.

As shown earlier [10], the thermal stability of copolymers based on VC and VEP_1 increases owing to not only "internal" but also "structural" stabilization. The effect of the latter is manifested in the difference in the thermal stabilities of binary VC–VEP_1 and ternary VC–VEP_1–butyl vinyl ether (BVE) copolymers. The thermal stability of ternary copolymers significantly exceeds that of binary VC–VEP_1 copolymers (Table 1), despite lower content of VEP_1 and hence lower content of epoxy groups.

The thermal stability of VC–VEP_2 and VC–VEP_3 copolymers significantly exceeds that of binary VC–VEP_1 copolymers and is comparable with that of ternary VC–VEP_1–BVE copolymers (Table 1).

By contrast to the VC–VEP_1 system, in the VC–VEP_2 and VC–VEP_3 systems the thermal stability slightly decreases with increasing VEP fraction in the copolymers. Probably, lengthening of the side substituent intensifies degradation processes involving VEP and typical for poly(alkyl vinyl) ethers at temperatures around 250°C.

At the same time, lengthening of the side substituent should enhance the internal plasticization, which naturally increases the impact strength, folding resistance, and adhesion of coatings based on VC–VEP_2 and VC–VEP_3 copolymers. These coatings are formed from concentrated (40–50 wt %) solutions in available organic solvents, individual or mixed. Ordinary PVC is unable of forming lacquer coatings.

Coatings based on VC–VEP copolymers exhibit high impact strength (45–50 kg cm), the maximal folding resistance (1 mm), and high adhesion to metals, depending on the VEP content in copolymer (Table 2). High strength is characteristic for coatings based on copolymers containing over 4 mol % of VEP units. The coating strength is virtually unaffected by the length of the side VEP (VEP_2 or VEP_3) chain.

The adhesion of coatings based on these copolymers is also unaffected by the VEP content. When the VEP content in the copolymers is under 3 mol %, the adhesion of the coatings is moderate (2–3 points according to the lattice notch method), and it increases to a maximum (1 point according to the parallel notch method) with increasing VEP content in the copolymers.

These results can be explained by insufficient plasticizing effect exerted by VEP when in small amounts (up to 3 mol %) in copolymers, which is responsible for moderate strength and low adhesion of the coatings. With over 4 mol % of VEP units in the copolymer, internal plasticization is responsible for enhanced strength and adhesion.

The strength and adhesion characteristics of the coatings based on VC–VEP_2 and VC–VEP_3 copolymers significantly exceed those of coatings based on VC–VEP_1 copolymers (Table 2).

High strength and strong adhesion to various materials of uncured coatings are characteristic only for suspension or emulsion VC–VEP_1 copolymers, because such polymers contain hydroxy groups arising from partial hydrolysis of epoxy groups of VEP units in aqueous medium [10]. Also, the limiting impact strengths for coatings based on suspensions of VC–VEP_1 copolymers were achieved only after curing (Table 2).

The copolymers can be cured by virtually any curing agent suitable for epoxy resins. The thermal stability limit of the cured materials increases to 150–200°C. Moreover, by selecting appropriate curing agents it is possible to additionally increase the thermal stability of copolymers [11, 12]. For example, their modification with nitrogen-containing com-

Table 2. Characteristics of lacquer coatings prepared from VC–VEP copolymers. Method of parallel notches

VEP content in copolymer, mol %	$[\eta]$, dl g^{-1}	Folding resistance, mm	Impact strength, kg cm	Adhesion, points
VC–VEP_1 copolymers (in toluene)				
3.08	0.29	20	15	3*
6.80	0.26	20	15	3*
VC–VEP_2 copolymers (in suspension)				
3.10	0.60	1	45	1
3.10**	0.60	1	50	1
6.75	0.35	1	45	1
6.75**	0.35	1	50	1
VC–VEP_2 copolymers				
0.78	0.25	10	15	3*
8.65	0.24	1	45	1
11.61	0.22	1	50	1
13.06	0.22	1	50	1
26.92	0.20	1	50	1
VC–VEP_3 copolymers				
0.82	0.24	10	15	3*
2.41	0.23	10	15	2*
4.08	0.215	5	20	2
10.37	0.21	1	50	1
16.46	0.21	1	50	1
22.22	0.19	1	50	1
25.76	0.18	1	50	1

* Method of lattice notches.
** After curing with polyethylenepolyamine, 1 wt fraction.

pounds, e.g., quinoxaline-2,3-dithiol or silicon-containing derivatives of ureas, *N*,*N*'-bis(trimethoxysilylmethyl)trimethylurea and *N*,*N*'-bis(dimethylchlorosilylmethyl)trimethylurea, increases the thermal stability of cured copolymers. Nitrogen in these compounds is the basic center, and it is able of accepting the hydrogen chloride evolving in degradation, thus transforming into ammonium cation. For example, the thermal stability limit of the VC–VEP_1 copolymer, which is initially stable up to 180°C, can be increased to 240–280°C by modifying with quinoxaline-2,3-dithiol [11]. Modification of the same copolymer with *N*,*N*'-bis(trimethoxysilylmethyl)trimethylurea makes it more resistant to thermal oxidative degradation, extending its stability range to 310°C [12].

High thermal stability of the copolymers make them suitable as stabilizing and costabilizing agents preventing degradation of PVC and exhibiting synergistic effect with the conventional barium stearates. The bulky side moieties in the VEP units significantly improve the processability of copolymers: The amount of the plasticizing agent consumed in extrusion of the compositions based on VC–VEP_1 copolymers decreases fivefold compared to PVC [10]. Of undoubted interest is the use of the copolymers as polymeric modifying agents for PVC-based plastics.

Thus, VC–VEP copolymers have a set of valuable operation and process characteristics which significantly improve the corresponding characteristics of PVC and make them versatile. These results can be achieved without adding any toxic compounds, which ensures high hygienic safety of the materials based on the copolymers studied.

Technologically, copolymerization is undoubtedly a more sophisticated process than polymerization, and introduction of a comonomer such as VEP will certainly increase the prime cost of the product. However, an easier and cheaper process of synthesizing PVC will inevitably complicate its processing and require expensive equipment for efficient mixing of various components.

EXPERIMENTAL

Both synthesis of the copolymers and their thermogravimetric studies followed the procedure described in [8].

The composition of the copolymers was calculated from the elemental analysis data. The content of chlorine was estimated by the Schoeniger's procedure [13].

The relative viscosity of the copolymers was determined in cyclohexanone at 25°C; it was recalculated to intrinsic viscosity as described in [14].

The characteristics of the coatings based on the copolymers were determined by conventional procedures [15].

CONCLUSIONS

(1) A study was made of the properties of copolymers based on vinyl chloride and 1-(vinyloxyalkoxy)-propylene 2,3-oxides. The thermal stability of all the copolymers significantly exceeds that of straight polyvinyl chloride; it increases with lengthening of the side moiety in 1-(vinyloxyalkoxy)propylene 2,3-oxides.

(2) The characteristics of coatings based on the copolymers (adhesion, folding resistance, and impact strength) are improved with lengthening of the side moiety in 1-(vinyloxyalkoxy)propylene 2,3-oxides.

REFERENCES

1. Ul'yanov, V.M., Rybkin, E.P., Gutkovich, A.P., and Pishin, G.A., *Polivinilkhlorid* (Polyvinyl Chloride), Moscow: Khimiya, 1992.
2. Mukhin, Yu.F., Efimov, A.A., Shestakova, L.M., *et al*., *Sovremennoe sostoyanie problemy stabilizatsii polivinilkhlorida* (Polyvinyl Chloride Stabilization: Current State of the Problem), Moscow: NIITEKhIM, 1988.
3. *Chem. Eng*., 1998, no. 22, pp. 906–908.
4. *Mod. Plast. Int.*, 1997, vol. 27, no. 11, pp. 26–31.
5. Defosse, M.T., *Mod. Plast. Int*., 1999, vol. 29, no. 1, pp. 50–54.
6. Sun, Yi-Jun, Hu, Guo-Hua, and Lambla, M., *Angew. Makromol. Chem*., 1995, vol. 229, no. 1, pp. 1–6.
7. Carter, E., *J. Oil Colour Chem*., 1986, vol. 26, no. 4, pp. 100–103.
8. Khaliullin, A.K., Salaurov, V.N., Shibanova, E.F., *et al*., *Zh. Prikl. Khim*., 1996, vol. 69, no. 4, pp. 653–656.
9. *Paint and Surface Coatings: Theory and Practice*, Lambourne, R., Ed., Chichester: Horwood, 1987. Translated under the title *Lakokrasochnye materialy i ikh primenenie*, St. Petersburg: Khimiya, 1991, pp. 512–521.
10. Raskulova, T.V., Volkova, L.I., Salaurov, V.N., *et al*., *Zh. Prikl. Khim*., 1998, vol. 71, no. 7, pp. 1184–1187.
11. Raskulova, T.V., Volkova, L.I., Elokhina, V.N., and Khaliullin, A.K., Abstracts of Papers, *Vserossiiskaya konferentsiya po khimii i tekhnologii organicheskikh soedinenii sery* (Russian Conf. on Chemistry and Technology of Organic Sulfur Compounds), Kazan, 1995, part 1, p. 191.
12. Raskulova, T.V., Volkova, L.I., Lazareva, N.F., *et al*., Abstracts of Papers, *V Vserossiiskii simpozium "Stroenie i reaktsionnaya sposobnost' kremniiorganicheskikh soedinenii* (V Russian Symp. "Structure and Reactivity of Organosilicon Compounds"), Irkutsk, 1996, p. 116.
13. Klimova, V.A., *Osnovnye mikrometody analiza organicheskikh soedinenii* (Basic Methods of Organic Microanalysis), Moscow: Khimiya, 1975.
14. Berlin, A.A., *Vysokomol. Soedin*., 1966, vol. 8, no. 8, p. 1336.
15. Karyakina, M.I., *Laboratornyi praktikum po ispytaniyu lakokrasochnykh materialov i pokrytii* (Laboratory Course of Testing Paint and Varnish Materials and Coatings), Moscow: Khimiya, 1977, pp. 116, 129, 133.

Russian Journal of Applied Chemistry, Vol. 75, No. 3, 2002, pp. 461–464. Translated from Zhurnal Prikladnoi Khimii, Vol. 75, No. 3, 2002, pp. 472–475.
Original Russian Text Copyright © 2002 by Verezhnikov, Nikulin, Poyarkova, Vostrikova.

MACROMOLECULAR CHEMISTRY AND POLYMERIC MATERIALS

Flocculating Power of Poly-*N*,*N*-dimethyl-*N*,*N*-diallylammonium Chloride of Various Molecular Weights

V. N. Verezhnikov, S. S. Nikulin, T. N. Poyarkova, and Yu. G. Vostrikova

Voronezh State University, Voronezh, Russia

Received October 30, 2001

Abstract—The amount of precipitated rubber in flocculation of SKS-30 ARK butadiene–styrene latex was studied as influenced by the concentration of poly-*N*,*N*-dimethyl-*N*,*N*-diallylammonium chloride cationic polyelectrolyte at various temperatures and concentrations of the latex dispersed phase.

Recently, considerable attention has been given to the use of quaternary ammonium polymeric salts as coagulating agents for recovery of rubbers after emulsion copolymerization [1–5]. This is due to the fact that the amount of these salts required for recovery of rubbers from latexes is 50–100 times smaller as compared with the common coagulating agents (sodium chloride) [6]. As a result, environmental pollution with aqueous salt wastes, which is the main disadvantage in production of emulsion rubbers, can be significantly decreased, and thus utilization of quaternary ammonium salts in production of synthetic rubber is rather promising. At the same time, published data are insufficient for industrial use of these salts. For example, significant scattering in molecular weights and pH of their aqueous solutions can strongly affect the consumption of the reagent required for complete coagulation of the latex. Since under the real industrial conditions the recovery of rubber from a latex depends on such factors as concentration of the dispersed phase and temperature, study of the effect of these parameters is of particular importance.

In [5], we used ungraded commercial cationic polyelectrolyte poly-*N*,*N*-dimethyl-*N*,*N*-diallylammonium chloride (PDMDAAC) as flocculating agent. It was found that the dependence of the fraction of the precipitated polymer on the concentration of the cationic polyelectrolyte passes through a maximum only at relatively small concentrations of the dispersed phase ($\approx$50 g l^{-1}). At higher rubber concentrations in the latex, the flocculation optimum is lost.

In this work, we studied the flocculating power of PDMDAAC of various molecular weights as influenced by the temperature and concentration of the dispersed phase.

We used SKS-30 ARK brand commercial butadiene–styrene latex containing soap emulsifiers based on disproportionated rosin and fatty and resin acids of tall oil.

In the first stage, PDMDAAC was subjected to fractional precipitation in the water–acetone system. The initial commercial PDMAAC sample ($\approx$ 40 wt % concentration) was diluted with water to nearly 10% concentration. Fractionation was performed by addition of acetone into the resulting PDMAAC aqueous solution with subsequent separation of the corresponding fractions. Then each fraction was dried in an oven at 90°C for 4–6 h to remove acetone. We studied three PDMAAC fractions with $\overline{M}_v$ of 172 000, 62 000, and 16 000. The molecular weights were calculated from the Mark–Kuhn–Houwink equation with the following constants: $K = 1.12 \times 10^{-4}$ and $\alpha = 0.82$ [7].

The coagulating power of PDMAAC samples with various $\overline{M}_v$ was evaluated gravimetrically (from the weight of the resulting coagulum) and visually (from the serum transparency).

Coagulation tests were performed as follows. A sample of the SKS-30 ARK latex with a given concentration of the dispersed phase (1.0, 1.5, 2.0, 3.0, 5.0, and 10 wt %) was charged into a vessel equipped with a stirrer and a thermometer and then placed in a thermostat heated to a required temperature. After heating for 10 min, the required amounts of a PDMAAC aqueous solution and 2% sulfuric acid were added with stirring. The content of the acidifying agent was constant (15 kg per ton of rubber). The resulting coagulum was separated from the serum and dried at 75–80°C.

The dependence of the degree of coagulum re-

1070-4272/02/7503-0461$27.00 © 2002 MAIK "Nauka/Interperiodica"

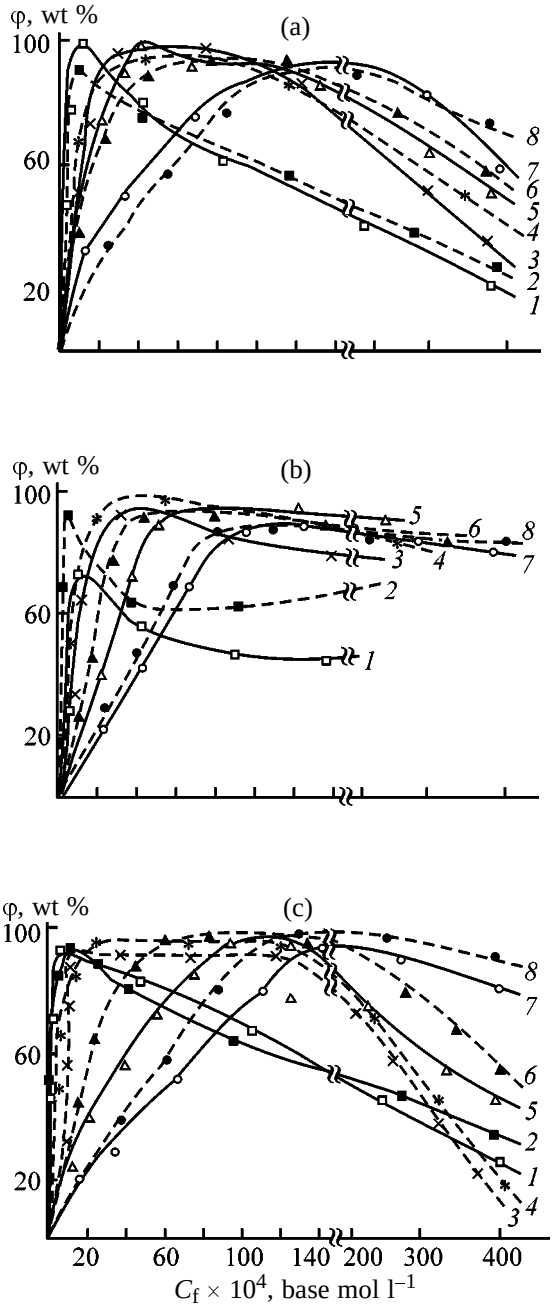

Fig. 1. Degree of coagulum recovery φ from the SKS-30 ARK latex as a function of PDMAAC concentration C_f. Dispersed phase concentration (wt %): (*1, 2*) 1, (*3, 4*) 3, (*5, 6*) 5, and (*7, 8*) 10. Temperature, °C: (*1, 3, 5, 7*) 20 and (*2, 4, 6, 8*) 80. Average molecular weight of PDMAAC, $\overline{M}_v \times 10^{-3}$: (a) 172, (b) 62, and (c) 16.

covery φ on the concentration of the PDMAAC fraction C_f at 20 and 80°C at various concentrations of the dispersed phase C_d are shown in Figs. 1a–1c. With increasing concentration of the dispersed phase, the curves of coagulum recovery $\varphi = f(C_f)$ shift monotonically toward higher concentrations of the flocculating agent. Moreover, with increasing C_d the shape of the recovery curves also changes, and the dependences with a maximum observed at small C_d transform into curves with a plateau or with a very broad maximum.

For dilute dispersions of the polystyrene latex [8], the precipitation curves $\varphi = f(C_f)$ showed a flocculation optimum typical for the flocculation with both charged and uncharged polymers. In all the cases, in the initial stage the flocculation efficiency strongly increased with increasing concentration of a cationic polyelectrolyte, passing through a well-defined maximum at low concentrations of the dispersed phase and flattening out or only slightly decreasing, without pronounced maximum, at high concentrations of the dispersed phase.

These different concentration dependences of the flocculation efficiency at low and high concentrations of the dispersed phase are presumably due to the features of the flocculating effect of the polymeric reagents [8]. The flocculation optimum in the sol flocculation with oppositely charged polymers can be considered as a resultant of two effects: destabilization due to neutralization of the particle surface charge and bridge binding mechanism, with subsequent restabilization due to the surface recharging and formation of a compact adsorption layer of a hydrophilic polymer on the particle surface [9]. These effects initiate the adsorption of the charged polymeric macromolecules on the particle surface, which provides neutralization of the surfactant anions with PDMAAC cationic groups to form an insoluble ionic complex. The flocculant excess promotes formation of a charged protective adsorption layer of the cationic polyelectrolyte macromolecules on the particle surface, which restabilizes the sol and decreases the amount of the recovered coagulum.

As seen from Fig. 1, irrespective of temperature and molecular weight of the polyelectrolyte, this effect is most pronounced for the dilute latex (C_d 1.0 wt %). At higher C_d, the maximum in the φ–C_f dependences becomes more diffuse or flattens out, i.e., the restabilization effect decreases or almost disappears, which is due to relaxation processes occurring in the adsorption layers of macromolecules at the particle surface [10]. With aging, the number of segments bound with the surface increases, whereas the length of the tails and loops of the polymer chain, which occur in the aqueous phase and provide bridging of the neighboring particles, decreases. At smoothening of the polymer macromolecules, the power to form

bridges decreases and a compact protective layer is formed, which decreases flocculation and hence the amount of the coagulum formed. These processes develop in time, and thus the operation period (aging of the adsorption layer) is a decisive factor.

With increasing content of the dispersed phase, the number of collisions between the particles increases and the relaxation time decreases, becoming insufficient for smoothening of the adsorbed molecules, so that they retain the bridging power. As a result, despite recharging, the cationic polyelectrolyte retains a high flocculating power due to the bridging mechanism of the particle binding. The recharging of the latex particles was observed experimentally in the study of the dependence of the electrokinetic potential of the particles on the concentration of the cationic polyelectrolyte added to the latex [5, 8, 9].

As seen from Fig. 1, with increasing temperature from 20 to 80°C the flocculation efficiency increases. This is also confirmed by the dependence of the optimal flocculation concentration (OFC) C_m on the dispersed phase concentration (Fig. 2). Due to the different shape of the precipitation curves at low and high C_d, as C_m we took the flocculant concentration either in a maximum or in a point corresponding to the beginning of the plateau. As seen, for both flocculation temperatures the $C_m = f(C_d)$ dependences are approximately linear, and the results for PDMAAC samples of different molecular weights are fitted by common curves. The slope of these dependence (calculated by the least-squares method) slightly decreases from 13.8×10^{-4} base mol g^{-1} at 20°C to 11.9×10^{-4} base mol g^{-1} at 80°C, which suggests certain decrease in the specific consumption of the flocculant in the flocculation optimum with increasing temperature. This is probably due to increased contribution of effective collisions at higher kinetic energy of the particles.

The above data suggest that temperature can affect the flocculation in the course of restabilization. Owing to the increase in the collision number and decrease in the free path of the particles with increasing temperature, their deactivation due to the smoothening of the adsorption layer should be suppressed, and both the flocculating power of the reagent and the trend toward flattening out of the flocculation curves should increase. However, as seen from Fig. 1, this is not the case. This trend is probably suppressed by the opposite factor: increase with increasing temperature in the mobility of macromolecular chains and in the rate of relaxation processes causing deactivation of the particles.

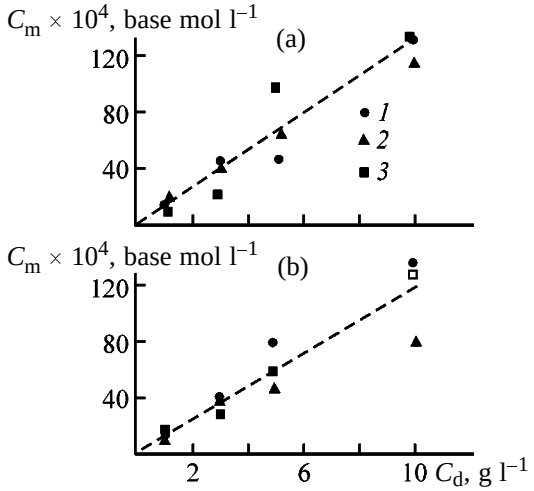

Fig. 2. Optimal flocculation concentration C_m as a function of the dispersed phase concentration in latex C_d. Temperature, °C: (a) 20 and (b) 80. Average molecular weight of PDMAAC fraction, $\overline{M}_v \times 10^{-3}$: (*1*) 172, (*2*) 62, and (*3*) 16.

In practice, the results obtained suggest that, in the course of SKS-30 ARK rubber recovery, the effect of the average molecular weight of PDMAAC flocculant and flocculation temperature is insignificant. This weakens the requirements to the control of the molecular weight of the flocculants and decreases power consumption in the rubber recovery.

Our study of the properties of rubbers, rubber stocks, and vulcanized rubbers showed that the properties of SKS-30 ARK rubber and vulcanized rubber based on it (see table) are almost independent of the molecular weight of PDMAAC and flocculation temperature.

The chemical composition of the rubbers recovered from the latex with PDMAAC aqueous solutions was close to that of the control samples of the rubber recovered with sodium chloride. However, in all the coagulum samples recovered from the latex with PDMAAC, the content of the organic acid soaps was minimal (absent or traces). At the same time, in the coagulum samples recovered from the latex with sodium chloride the soap content varied from 0.0 to 0.2%.

The properties of the vulcanized rubbers based on the rubbers recovered from the latex with cationic polyelectrolytes are similar to the properties of the reference sample. At the same time, the vulcanization rate of the rubber stocks based on SKS-30 ARK rubber recovered from the latex with PDMAAC is higher. As shown in [11, 12], vulcanization is probably accelerated with polymeric quaternary ammonium salt retained in the rubber after coagulation and(or)

Properties of SKS-30 ARK rubber and vulcanized rubbers based on it

Parameter	$\overline{M}_{v(\text{PDMAAC})}$			Reference sample*
	172 000	62 000	16 000	
Mooney viscosity	54	53	54	52
Content, wt %:				
free organic acids	6.6	6.5	6.4	5.7
bound organic acids	–	–	–	0.12
VTS-150 antioxidant	1.3	1.3	1.3	1.3
bound styrene	22.3	22.3	22.3	22.3
ash	0.11	0.13	0.13	0.21
Weight loss at 105°C in 2 h, %	0.10	0.13	0.13	0.19
Vulcanization time, min	60	60	60	80
Elastic recovery, mm	3.0	3.0	3.0	3.0
Stress at 300% elongation, MPa	9.7	9.6	9.4	8.3
Tensile strength, MPa	26.4	25.2	27.0	27.6
Relative elongation at break, %	560	565	580	630
Relative residual deformation after break, %	8	10	10	14
Rebound elasticity, %	39	40	40	42

* Recovered from latex with NaCl.

products of its reactions with the emulsion system components.

CONCLUSIONS

(1) Flocculation of SKS-30 ARK butadiene–styrene latex at various concentrations of the dispersed phase is almost independent of temperature (20–80°C) and average molecular weight of poly-*N*,*N*-dimethyl-*N*,*N*-diallylammonium chloride cationic polyelectrolyte. The flocculating power of the reagent (rubber yield) slightly increases with temperature.

(2) Utilization of poly-*N*,*N*-dimethyl-*N*,*N*-diallylammonium chloride cationic polyelectrolytes of various molecular weights does not require significant changes in the industrial flowsheet of rubber recovery and does not noticeably affect the properties of rubbers and vulcanized rubbers based on them.

REFERENCES

1. Verezhnikov, V.N., Nikulin, S.S., Poyarkova, T.N., and Garshin, A.P., *Vestn. Tambov. Univ.*, 1997, vol. 2, no. 1, pp. 47–52.
2. Garshin, A.P., Nikulin, S.S., Shapovalova, N.N., *et al.*, *Proizv. Ispol'z. Elastom.*, 1994, no. 11, pp. 2–6.
3. Garshin, A.P., Nikulin, S.S., Shapovalova, N.N., *et al.*, *Proizv. Ispol'z. Elastom.*, 1994, no. 12, pp. 9–14.
4. Verezhnikov, V.N., Nikulin, S.S., Krutikov, M.Yu., and Poyarkova, T.N., *Kolloidn. Zh.*, 1999, vol. 61, no. 1, pp. 37–41.
5. Verezhnikov, V.N., Nikulin, S.S., Poyarkova, T.N., and Vostrikova, G.Yu., *Zh. Prikl. Khim.*, 2000, vol. 73, no. 10, pp. 1720–1724.
6. Kirpichnikov, P.A., Averko-Antonovich, L.A., and Averko-Antanovich, Yu.O., *Khimiya i tekhnologiya sinteticheskogo kauchuka* (Chemistry and Technology of Synthetic Rubber), Leningrad: Khimiya, 1987.
7. Wandrey, C., Jaeger, W., and Reinish, G., *Acta Polym.*, 1982, vol. 33, no. 2, pp. 156–159.
8. Verezhnikov, V.N., Poyarkova, T.N., Nikulin, S.S., and Kurbatova, N.A., *Kolloidn. Zh.*, 2000, vol. 62, no. 11, pp. 26–30.
9. Baran, A.A. and Solomentseva, I.M., *Khim. Tekhnol. Vody*, 1983, vol. 5, no. 2, p. 120.
10. Pelssers, E., Cohen, S., and Fleer, G., *J. Chem. Soc., Faraday Trans.*, 1990, vol. 86, no. 9, pp. 1355–1361.
11. Garshin, A.P., Nikulin, S.S., Ryl'kov, A.A., *et al.*, *Proizv. Ispol'z. Elastom.*, 1996, no. 5, pp. 8–10.
12. Garshin, A.P., Nikulin, S.S., Slukina, Z.D., *et al.*, *Proizv. Ispol'z. Elastom.*, 1996, no. 9, pp. 14–19.

Russian Journal of Applied Chemistry, Vol. 75, No. 3, 2002, pp. 465–469. Translated from Zhurnal Prikladnoi Khimii, Vol. 75, No. 3, 2002, pp. 476–480.
Original Russian Text Copyright © 2002 by Kazantsev, Igolkin, Shirshin, Kuznetsova, Spirina, Malyshev.

MACROMOLECULAR CHEMISTRY AND POLYMERIC MATERIALS

Spontaneous Polymerization of 2-Acrylamido-2-methylpropanesulfonic Acid in Acidic Aqueous Solutions

O. A. Kazantsev, A. V. Igolkin, K. V. Shirshin, N. A. Kuznetsova, A. N. Spirina, and A. P. Malyshev

Dzerzhinsk Branch, Nizhni Novgorod State Technical University, Dzerzhinsk, Nizhni Novgorod oblast, Russia

Received October 10, 2001

Abstract—Spontaneous polymerization of 2-acrylamido-2-methylpropanesulfonic acid in the presence of inorganic and organic neutralizing agents in concentrated aqueous solutions is studied. The hypothesis of redox mechanism of the process initiation is discussed.

Water-soluble copolymers based on 2-acrylamido-2-methylpropanesulfonic acid (AMPSA) and its sodium salt are used in oil production and as effective flocculants and additives in paper production [1]. These products are prepared by free radical polymerization of the corresponding monomers using the traditional methods. For methacrylic monomers capable of association (containing ionogenic groups, e.g., *N*,*N*-dialkylaminoethyl methacrylates, or mobile hydrogen atoms, e.g., acrylamide), the methods for spontaneous polymerization in concentrated aqueous solutions are being extensively developed [2, 3]. The AMPSA molecule contains an acid group and a monosubstituted amide group and therefore should also be capable of spontaneous polymerization. Indeed, spontaneous polymerization of AMPSA in water was reported in [4]. At the same time, in the system *N*,*N*-dialkylaminoethyl methacrylate–AMPSA–water (no initiator) a homopolymer of amino methacrylate was obtained, i.e., AMPSA molecules were not involved in spontaneous polymerization [5].

It was demonstrated in preliminary experiments that spontaneous polymerization leading to consumption of C=C bonds and considerable increase in the viscosity of the system goes at a noticeable rate at a temperature above 20°C and pH <7 in concentrated aqueous AMPSA solutions. As the reaction proceeds by the free radical mechanism, it does not occur in the presence of sufficiently large amounts of inhibitors. Furthermore, the monomer solutions remain stable after total neutralization of AMPSA with NaOH and also in the case of excess NaOH.

In this work we studied the features of autoinitiated radical polymerization of AMPSA in acidic aqueous solutions. Figure 1 shows the kinetics of C=C bond consumption in spontaneous polymerization of AMPSA at various degrees of neutralization of the sulfonic acid groups with NaOH. In the absence of the neutralizing agent, the reaction proceeds slowly (curve *7*). The dependence of the initial polymerization rate on the degree of neutralization *K* passes through a maximum at *K* of about 50% (Fig. 2). At larger conversions, the effect of this factor becomes weaker: at the degree of neutralization of AMPSA varied within 10–95%, the conversion of the monomer after 4 h varies within a narrow range from 75 to 88% (Fig. 1). Considerably lower value was obtained only in the absence of NaOH.

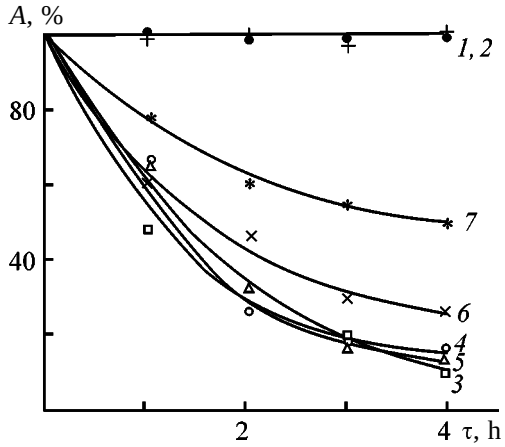

Fig. 1. C=C bond concentration *A* in the system AMPSA–NaOH–H_2O as a function of time τ. $[AMPSA]_0$ = 37 wt %, *T* = 50°C; the same for Fig. 2. Molar ratio AMPSA : NaOH: (*1*) 1 : 1.5, (*2*) 1 : 1, (*3*) 1.1 : 1, (*4*) 4 : 3, (*5*) 4 : 1, (*6*) 10 : 1, and (*7*) 1 : 0.

1070-4272/02/7503-0465$27.00 © 2002 MAIK "Nauka/Interperiodica"

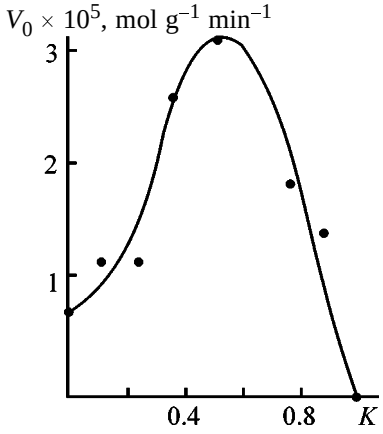

Fig. 2. Initial polymerization rate V_0 as a function of the degree of AMPSA neutralization *K*. Neutralizing agent NaOH.

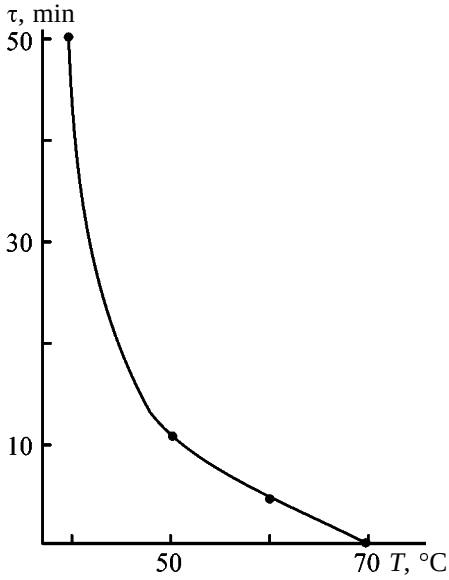

Fig. 3. Induction time of polymerization τ as a function of the temperature *T*. Molar ratio AMPSA : NaOH = 2 : 1, $[AMPSA]_0$ = 31 wt %; the same for Figs. 4 and 6.

Polymerization parameters are strongly influenced not only by the content of free acid groups, but also by the initial monomer concentration M_0. The effect of M_0 on the initial rate V_0 of spontaneous polymerization is illustrated below.

M_0, wt %	$V_0 \times 10^5$, mol g^{-1} min^{-1}
20.0	0
25.0	0.35
37.5	3.10
45.0	3.95
51.5	5.95

The experiments were carried out at the optimal AMPSA : NaOH molar ratio of 2 : 1, temperature of 50°C, and a monomer concentration of 10–50 wt % (the upper limit corresponds to the monomer solubility). The process rate abruptly increases with increasing concentration, which is typical of radical polymerization (either spontaneous and initiated) of associated monomers in water [6]. This is due to the fact that in concentrated solutions monomer associates are formed, facilitating generation of initiators and chain propagation. A significant role of association in autoinitiated polymerization is supported by large orders of the reaction with respect to the monomer. For example, in this work this parameter was determined to be 2.3 at $[AMPSA]_0$ = 50 wt %, AMPSA : NaOH = 1.2 : 1, and T = 70°C. In dilute solutions association of the monomers is hardly probable. Therefore, decreasing initial concentration abruptly decelerates polymerization of associating monomers [6]. In the presence of initiators, dilution considerably decelerates polymerization, and in the absence of initiators at $[AMPSA]_0$ < 20 wt %, spontaneous polymerization was not observed at all in 8 h (50°C), suggesting that the indicated conditions do not favor chain propagation as well as generation of a sufficient amount of radicals initiating polymerization. Therefore, it may be concluded that active species are formed in AMPSA monomer associates.

Additional information important for understanding the process mechanism can be obtained from the temperature dependences of τ (Fig. 3) and also from data on the effect of inhibiting admixtures. The induction time of polymerization at 40–70°C is given in Fig. 3. At 30°C τ ~ 16 h, and with increasing temperature to 50°C τ decreases to 10 min. At 70°C the induction time was too short to be detected. The induction time increases not only with decreasing temperature, but also with introduction of small amounts of inhibitors. For example, with introduction of 0.02 and 0.1 mol % *p*-methoxyphenol (against the monomer concentration) into the system, the induction time at 50°C is 40 and 120 min, respectively (for the experimental conditions, see the caption to Fig. 3). At higher inhibitor concentration (1.0 mol %), no polymerization occurred in the observation period (4 h). The occurrence of the induction time at low temperature in the absence of inhibiting additives can be attributed to the low rate of initiation and also to the presence of trace amounts of inhibiting admixtures in the tested samples of the monomers. However, these admixtures, even if occur, have no significant effect on the initial rate of polymerization after the end of the induction period, since the initial rates at 40–70°C (within this temperature range the induction time decreases from 50 to 0 min)

demonstrate a satisfactory linear correlation in the coordinates $\ln V_0 - 1/T$. This allowed determination of the overall activation energy of polymerization (21.7 ± 4.8 kJ mol^{-1} at $[AMPSA]_0$ = 31% and AMPSA : NaOH = 2 : 1). The activation energy of initiation is hence even lower, which is consistent with data on spontaneous polymerization in water of acrylamide [3] and *N*,*N*-dimethylaminoethyl methacrylate tertiary salts [2].

In many cases the fact that polymerization of methacrylic monomers proceeds without addition of initiators is attributed to formation of peroxy compounds from the initial monomers and oxygen [7, 8]. For the systems studied in this work, this is hardly probable. Thus, we observed no acceleration of polymerization after AMPSA was allowed to stand in air. Furthermore, the process does not occur in neutral and alkaline solutions, and, what is more, polymerization even accelerates after preliminary purging of the reaction mixture with nitrogen, i.e., oxygen has some inhibiting rather than initiating effect. All these findings are inconsistent with the concept of peroxide initiation.

It should be pointed out that the activation energy below 40 kJ mol^{-1} is typical of redox systems (with substance initiation), being considerably lower that those found in thermal homolytic breakdown of weak bonds of initiators (>60 kJ mol^{-1}) [7]. To check for consistency the hypothesis of redox initiation in spontaneous polymerization of AMPSA, we conducted experiments with addition in the system of such a strong reducing agent as sodium metabisulfite. This resulted in elimination of the induction period and acceleration of polymerization (Fig. 4), suggesting the presence in concentrated aqueous AMPSA solutions of some reactive centers acting as weak reducing agents. Evidently, as such reducing agents can serve heteroatoms having a lone pair (nitrogen or oxygen), and as oxidizing agents, electrophilic C=C bonds of the monomer. Initiation of polymerization of methacrylic monomers through electron transfer from a heteroatom to the C=C bond is known from the literature [9]. Possibly, association of monomers in concentrated aqueous solutions is the factor favoring such an initiation.

It is known that the rate of radical polymerization of AMPSA salts in water in the presence of initiators increases with increasing solution ionic strength (for example, with addition of NaCl [10]) and atomic radius of a neutralizing agent cation ($Li^+ < Na^+ < K^+$) [11]. Increasing radius of the cation facilitates its binding to the sulfonate anion, thus decreasing electrostatic repulsion between the growing macroradicals and the monomer molecules. Increasing ionic strength of the solution by adding a low-molecular-weight electrolyte also results in weakened electrostatic repulsion.

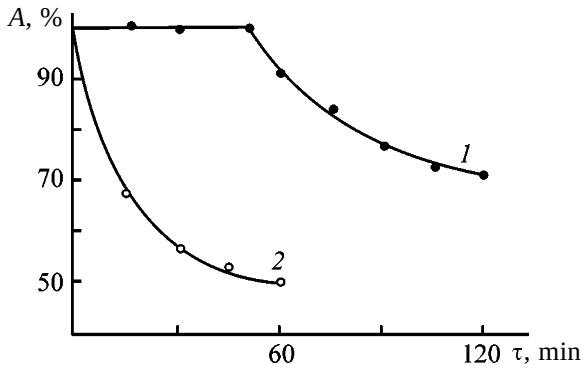

Fig. 4. Concentration of C=C bonds in AMPSA *A* as a function of the polymerization time τ (*1*) in the absence and (*2*) in the presence of $Na_2S_2O_5$. Temperature 40°C, $[Na_2S_2O_5]$ = 0.3 mol % against AMPSA.

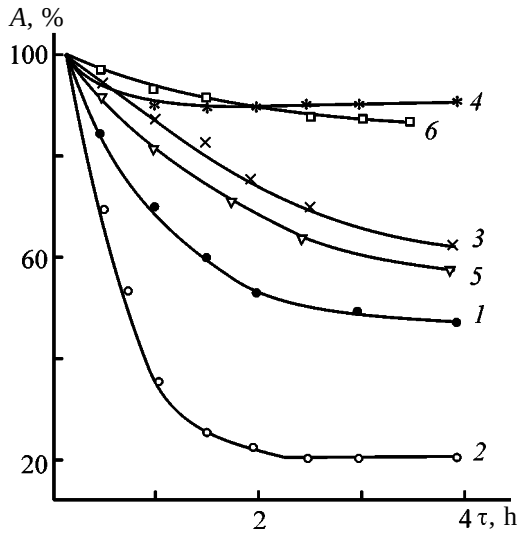

Fig. 5. Effect of neutralizing agent on spontaneous polymerization of AMPSA at 50°C: (*1*) NaOH, (*2*) KOH, (*3*) NH_4OH, (*4*) $N(CH_3)_3$, (*5*) $N(C_2H_5)_3$, and (*6*) $N(C_4H_9)_3$. AMPSA to neutralizing agent molar ratio 2 : 1, [AMPSA] = 31 mol %. (*A*) C=C bond concentration and (τ) time; the same for Fig. 6.

Figure 5 demonstrate data on spontaneous polymerization of AMPSA in the presence of various neutralizing agents. With alkalis, the polymerization rate increases with increasing radius of the cation ($Na^+ < K^+$). More complicated pattern is observed when the sulfonic acid is partly neutralized with ammonia or trialkylamines. Triethylamine, taking the intermediate position in the size of substituents between trimethylamine and tributylamine, is the most

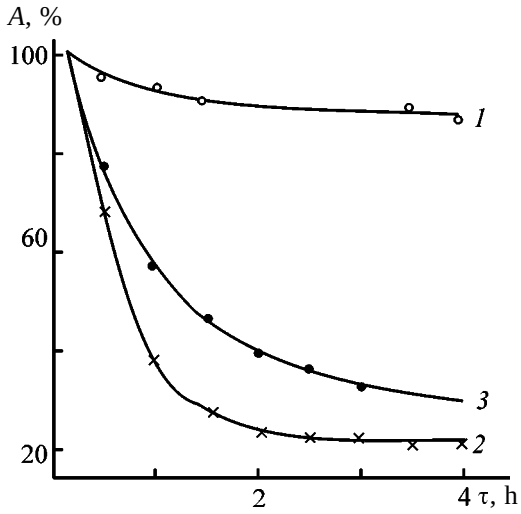

Fig. 6. Effect of electrolytes on spontaneous polymerization of AMPSA at 50°C: (*1*) NaCl, (*2*) Na_2SO_4, and (*3*) $NaNO_3$. [NaA] = 30 mol %.

active among the indicated amines, close in basicity (Fig. 5, curves *4*–*6*). In contrast to polymerization of AMPSA salts, increasing ionic strength of solutions by adding inorganic electrolytes does not necessarily accelerate the process. For example, addition of sodium sulfate or nitrate considerably accelerates polymerization, whereas addition of sodium chloride has the opposite effect (Fig. 6). Note that a noticeable effect of the anion was also observed in studying spontaneous polymerization in water of *N*,*N*-dimethylaminoethyl methacrylate salts with mineral acids, with the hydrochloride being considerably less active that the nitrate or sulfate [2]. The results obtained show that ions occurring in the system considerably affect spontaneous polymerization of AMPSA in aqueous solutions, which is probably due to the fact that different ions differently contribute to packing of the monomeric molecules in the associates.

Analysis of the rate of spontaneous polymerization of AMPSA as a function of the degree of neutralization of the monomer shows that increasing acidity, on the one hand, should facilitate electrophilic activation of the C=C bonds and increase their activity as oxidizing sites, and, on the other hand, should hamper association of the monomers. Furthermore, increasing degree of neutralization by adding a base increases the solution ionic strength, accelerating the process. The observed dependence of the polymerization rate on the monomeric acid to neutralizing agent molar ratio, having a maximum (Fig. 2), is a resultant of these oppositely directed trends. In the case of totally neutralized sulfonic acid groups, the key factor responsible for suppressing spontaneous polymerization is most likely the lack of protonated carbonyl groups. To gain a better insight into the process mechanism, further investigations are needed.

The results obtained in this work provide tools for control of spontaneous polymerization in aqueous AMPSA solutions. If needed (for example, in industrial synthesis of AMPSA copolymers), polymerization can be suppressed. Additionally, autoinitiated polymerization can be used for preparing AMPSA-based homopolymers. In this case, the molecular weight of the products can be controlled by varying the reaction temperature. Thus, the viscosity-average molecular weight of the polymers, determined by the Mark–Houwink equation [12], decreases from 3×10^6 to 1×10^6 with increasing temperature from 40 to 70°C.

EXPERIMENTAL

In the work, we used AMPSA recrystallized from acetic acid (mp 186°C). The polymerization kinetics of AMPSA in the presence of neutralizing agents was studied in water at 20–70°C and an initial AMPSA concentration of 10–50 wt %. Polymerization was monitored by two methods: by the concentration of C=C bonds and with separation of the reaction products by adding acetone. The resulting polymers were additionally washed with acetone and dried in a vacuum (20°C, 2 mm Hg) to constant weight.

The C=C bond concentration was determined by the bromide–bromate titration method. The ^{1}H NMR spectra were registered on a Varian Gemini-300 Fourier-transform spectrometer at a frequency of 75 MHz in D_2O with DMSO as a reference. Infrared spectra were registered on a Specord M-80 spectrometer using the KBr technique.

Poly(2-acrylamido-2-methylpropanesulfonic acid) sodium salt. To 2.25 g of AMPSA in 3.8 ml of water, 1.07 g of 20% NaOH was added, and the solution was allowed to stand at 50°C for 5 h. Then the same portion of 20% NaOH was added for total neutralization of the acid. The polymer was separated from the reaction system by adding 50 ml of acetone. The product was additionally washed with acetone and dried in a vacuum (20°C, 2 mm Hg). Yield 5.8 g (85%). No C=C bonds were detected in the product. ^{1}H NMR spectrum (δ, ppm): 2.9–3.6 ($-CH_2SO_3$), 1.7–2.3 (–CHC=O), and 0.9–2.3 (CH_3– and $-CH_2CH-$). IR spectrum (ν, cm^{-1}): 1668 (C=O), 1548 (amide II), 1220 (amide III), and 1046 and 632 (SO_3^-).

CONCLUSIONS

(1) In concentrated aqueous solutions, 2-acrylamido-2-methylpropanesulfonic acid spontaneously polymerizes at pH <7.

(2) The maximal initial rate of the process is observed at 50% neutralization of 2-acrylamido-2-methylpropanesulfonic acid and depends on the cations and anions occurring in the system.

(3) Experimental data on the effects of the initial concentration, temperature, electrolytes, inhibitors, and reducing agents can be interpreted assuming generation of radical initiators in the monomeric associates through redox reactions involving the C=C bonds and heteroatoms of 2-acrylamido-2-methylpropanesulfonic acid.

REFERENCES

1. Lisovtsev, V.V., Rostokin, G.A., and Kulikova, A.E., in *Khimicheskaya promyshlennost': Akrilaty i polivinilkhlorid* (Chemical Industry: Acrylates and Polyvinyl Chloride), Moscow: NIITEKhIM, 1984, pp. 1–22.
2. Efimova, D.Yu., Shibalovich, V.G., and Nikolaev, A.F., *Zh. Prikl. Khim.*, 2000, vol. 73, no. 5, pp. 815–819.
3. Kurlyankina, V.I., Ushakova, I.L., Molotkov, V.A., *et al.*, *Zh. Obshch. Khim.*, 1999, vol. 69, no. 1, pp. 97–100.
4. Kurlyankina, V.I., Molotkov, V.A., Dobrodumov, A.V., *et al.*, *Dokl. Ross. Akad. Nauk*, 1995, vol. 341, no. 3, pp. 358–363.
5. Valueva, S.V., Kipper, A.I., Rumyantseva, N.V., *et al.*, *Zh. Prikl. Khim.*, 2000, vol. 73, no. 11, pp. 1883–1885.
6. Egorov, V.V., Zaitsev, S.Yu., and Zubov, V.P., *Vysokomol. Soedin., Ser. A*, 1991, vol. 33, no. 8, pp. 1587–1608.
7. *Poliakrilamid* (Polyacrylamide), Kurenkov, V.F., Ed., Moscow: Khimiya, 1992.
8. Pistoia, G. and Voso, M., *J. Polym. Sci., Polym. Chem. Ed.*, 1976, vol. 14, pp. 1811–1813.
9. Strepikheev, A.A. and Derevitskaya, V.A., *Osnovy khimii vysokomolekulyarnykh soedinenii* (Principles of Macromolecular Chemistry), Moscow: Khimiya, 1976.
10. Kurenkov, V.F. and Safin, A.G., *Zh. Prikl. Khim.*, 1997, vol. 70, no. 12, pp. 2030–2034.
11. Kurenkov, V.F. and Safin, A.G., *Zh. Prikl. Khim.*, 1998, vol. 71, no. 1, pp. 136–140.
12. Fisher, L.W., Sochor, A.R., and Tan, J.S., *Macromolecules*, 1977, vol. 10, no. 5, pp. 949–954.

Russian Journal of Applied Chemistry, Vol. 75, No. 3, 2002, pp. 470–473. Translated from Zhurnal Prikladnoi Khimii, Vol. 75, No. 3, 2002, pp. 481–484.
Original Russian Text Copyright © 2002 by Mognonov, Mazurevskaya, Volodarskii.

MACROMOLECULAR CHEMISTRY AND POLYMERIC MATERIALS

Polyamidobenzimidazoles as Polymeric Materials for Cold Climate

D. M. Mognonov, Zh. P. Mazurevskaya, and L. B. Volodarskii

Baikal Institute for Nature Management, Siberian Division, Russian Academy of Sciences, Ulan-Ude, Buryatia, Russia
Institute of Organic Chemistry, Siberian Division, Russian Academy of Sciences, Novosibirsk, Russia

Received July 24, 2001

Abstract—A frost-resistant polyamidobenzimidazole-based polymer composite is synthesized from 3,3',4,4'-tetraaminodiphenyl oxide, diphenyl adipate or diphenyl sebacate, and hexamethylenediamine or ε-caprolactam. As stabilizers for the polymers were used 4-phenyl-2,2,5,5-tetramethyl-3-imidazoline-3-oxide-1-oxyl and carbon black.

It is known that, under conditions of distinctly continental climate with negative annual average temperature, polymeric materials and composites degrade considerably more rapidly than in temperate climatic zones [1]. Through simultaneous effects of solar radiation, moisture, and atmospheric oxygen and ozone, polymers are subject of photooxidative and hydrolytic degradation, resulting in significant decrease in their molecular weight, brittle failure, and rapid deterioration of performance characteristics.

It is obvious that the frost resistance of polymeric materials can be enhanced by modification of the polymer composition and structure [1]. Of particular interest in this context are resonance-stabilized rigid-chain heterocyclic polymers containing aromatic and heterocyclic fragments in their macrochains.

It was demonstrated in [2, 3] that polybenzimidazoles (PBIs) based on aromatic tetramines and diphenyl esters of aromatic or aliphatic dicarboxylic acids can be used as starting materials for preparation of glues and binders for glass fiber reinforced plastics which are capable to maintain high performance at cryogenic temperatures, despite high rigidity of their chain and high glass transition temperature. However, in most cases PBIs are infusible compounds poorly soluble in organic solvents, making it more difficult to process them into goods by modern industrial methods.

Polyamidobenzimidazoles (PABIs) reported in [4–6] are copolymers of PBI and a polyamide whose molecule contains benzimidazole rings and amide bonds. They were synthesized by solid-phase polycondensation from 3,3',4,4'-tetraaminodiphenyl oxide, diphenyl adipate or diphenyl sebacate, and hexamethylenediamine or ε-caprolactam.

Chemical modification of BPIs through introduction of aliphatic fragments in the macrochain increases the chain flexibility and free space of the macromolecule, which has a favorable effect on such properties as the solubility and plasticity. Commercial polyamides, which are low-resistant to the action of climatic factors [7], can be stabilized by introduction of benzimidazole rings [7].

It was demonstrated in preliminary tests of PABI-based films[1] that this class of copolymers show promise for exploitation under conditions of cold climate and strong UV radiation [8]. Good results obtained with the films in environmental tests stimulated study of degradation of pressed samples of such polymers. Shovel-shaped samples obtained by direct pressing of PABI molding powders were exposed for three years at the site of the Institute of Nonmetallic Materials, Yakut Scientific Center, Siberian Division, Russian Academy of Sciences (Yakutsk).

The initial polymer composite was as in [10] and contained (wt %): PABI 97.5–98.1, 4-phenyl-2,2,5,5-tetramethyl-3-imidazoline-3-oxide-1-oxyl 1.0–1.5, and carbon black 0.9–1.0.

The reduced viscosity at 25°C of 0.5% PABI in concentrated formic acid was found to be 2.53–

[1] Tests were conducted in cooperation with the Institute for Physical and Engineering Problems of the Russian North, Yakut Scientific Center, Siberian Division, Russian Academy of Sciences (Yakutsk).

1070-4272/02/7503-0470$27.00 © 2002 MAIK "Nauka/Interperiodica"

Table 1. Mechanical characteristics of polymer films before and after exposure*

R	Solvent	η_r, dl g^{-1}	Initial films		Films after 3-month exposure	
			σ_t, kgf cm^{-2}	ε_b, %	σ_t, kgf cm^{-2}	ε_b, %
–$(CH_2)_8$–	HCOOH	5.2	544	78	821	6
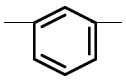	HCOOH	1.5	984	7	795	3
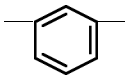	DMF	1.5	812	5	621	3
–$(CH_2)_4$–	DMF	1.2	772	5	Fail in 1 month	
Polyamide**	–	–	630–950	240–450	–	–

* (η_r) Reduced viscosity of 0.5% aqueous polymer solution in formic acid, (σ_t) breaking tensile stress, and (ε_b) elongation at break.
** $NH(CH_2)_6NHCO(CH_2)_4CO$ [9].

4.76 dl g^{-1}. This copolymer is soluble in concentrated sulfuric and formic acids, amide solvents, and tricresol, being also sufficiently heat-resistant [11]. According to TGA data (air; heating rate 5 deg min^{-1}), for polymers **I** and **II** τ_0, τ_5, and τ_{10} are 210–300, 280–360, and 360–400°C, respectively, depending on the elementary unit composition. The latter, in its turn, depends on the starting monomer. The structure of elementary units is as follows:

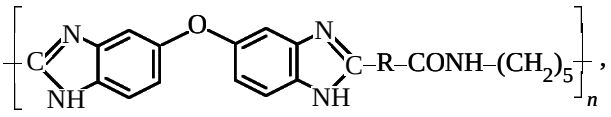

I

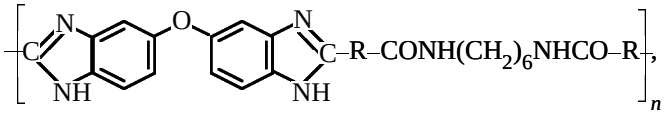

II

where R = –$(CH_2)_4$ (**I**); –$(CH_2)_8$–, 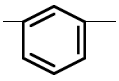 (**II**).

The environmental testing results for the investigated polymer films are summarized in Table 1.

The structure of the radical-type stabilizer 4-phenyl-2,2,5,5-tetramethyl-3-imidazoline-3-oxide-1-oxyl (ST) is as follows:

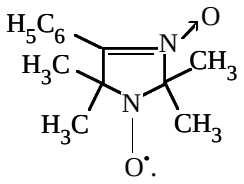

The well-known stabilizer, carbon black, absorbs solar radiation and, being an antioxidant by itself, enhances the inhibiting action of other antioxidants. Furthermore, oxygen-containing functional groups and free radicals present on the carbon black surface are capable to recombine with radicals formed in polymer degradation [12].

The results of 3-year environmental tests under conditions of cold climatic zone of the polymer composites studied in this work are summarized in Table 2. The polymeric materials obtained demonstrate a sufficiently high resistance to the factors of cold climate. Even after a 3-year exposure their elasticity remains at a 69–81% level, whereas for the samples of polyamide-6, ε_b decreased by about 90% after exposure to moderately cold climatic conditions [7]. The first cracks were found on the surface of the polyamide samples after 6–8 months, whereas the polymer composites proposed in this work maintain their surface appearance throughout the entire period of testing. Note that unstabilized PABIs are less stable.

If considering the PABIs studied as a modified polyamide, one may suggest that their increased aging stability is due to the positive effect of benzimidazole fragments in the macrochain. Furthermore, the presence of a radical stabilizer and carbon black also contribute to maintenance of mechanical properties in the course of long exposure.

The initial and exposed samples were characterized by infrared spectroscopy. The spectra show the absorption bands at 1680–1630 cm^{-1} due to vibrations of the >C=O groups of secondary amides (amide

Table 2. Elongation at break of PABI-based polymeric composites after various exposures

Composite no.	ST	Carbon black	ε_b, %, after indicated exposure, months				
	%		initial composite	6	12	24	36
1	–	–	5.0	3.3	1.9	0.9	–
2	1.0	1.0	4.0	4.2	4.0	4.0	3.2
3	1.5	1.0	4.5	4.0	3.7	3.7	2.8
4	1.0	0.9	3.5	3.0	2.7	2.7	2.5
5	1.6	1.0	4.5	4.5	4.0	3.5	3.1
6	1.0	1.0	4.0	4.2	3.7	3.6	3.1
7	1.5	1.0	3.5	3.3	3.2	3.2	2.9

Note: Polyamidobenzimidazoles in composite nos. 1–5 were prepared from 3,3',4,4'–tetraaminodiphenyl oxide, diphenyl adipate, and ε-caprolactam; and in nos. 6–7, from the same tetramine, diphenyl sebacate, and hexamethylenediamine.

I band) and at 1570–1515 cm^{-1} due to bending vibrations of >NH (amide II band). The bands at 800 and 1445 cm^{-1} are indicative of the presence of benzimidazole rings [13]. The intensity of the indicated bands in the stabilized samples only slightly changes with exposure as compared to the unstabilized samples.

For the stabilized pressed samples, TGA data showed that τ_{10} is 340–360°C, only slightly changing in the course of a 3-year exposure. The viscous characteristics, reflecting the molecular weight, decreased by 8–10% in two years, whereas for the unstabilized samples the decrease is 25–30% of the initial.

Finally, the stabilized PABI-based polymer composite demonstrate high resistance to factors of cold climate, moisture, oxygen, and solar radiation, showing promise for manufacture of goods designed for exploitation under inclement climatic conditions of the North and Siberia.

EXPERIMENTAL

Polyamidobenzimidazole was obtained by solid-phase polycondensation of equimolar quantities of 3,3',4,4'-tetraaminodiphenyl oxide, diphenyl adipate or diphenyl sebacate, and hexamethylenediamine or ε-caprolactam. A mixture of the indicated monomers in a reaction vessel was multiply purged with argon by multiple evacuation–admission cycles and then placed into a furnace heated to 200°C. After the reaction mixture fused, the temperature was raised to 260°C over a period of 1–1.5 h, and the mixture was allowed to stand at this temperature for 3.5–4.0 h. After 20–30 min of heating, the melt hardens, and the reaction goes in the solid phase with liberation of water and phenol. Then the reaction vessel was evacuated to 1–2 mm Hg, and polycondensation was continued for 1 h at the same temperature. Finally, the product was cooled to room temperature.

The resulting copolymer was dissolved in concentrated formic acid and separated by adding aqueous ammonia. The products with aliphatic fragments in the macrochain were intimately mixed with the radical stabilizer (1.0–1.6 wt %) and carbon black (0.9–1.0 wt %) and then pressed at 180–190°C and a pressure load of 80–100 MPa to obtain shovel-shaped samples according to GOST (State Standard) 11262–68. In the case of PABIs with aromatic fragments in the macrochain, the pressing temperature was 260°C, and no radical stabilizer was introduced in the composite, since it is unstable at this temperature.

The radical stabilizer was prepared at the Institute of Organic Chemistry, Siberian Division, Russian Academy of Sciences (Novosibirsk) by the procedure described in [14]; mp 103–105°C, decomposition temperature 170–190°C.

Infrared spectra were recorded on a Specord 75-IR spectrometer. Mechanical tests of the pressed samples for the breaking tensile stress and elongation at break were performed on an Instron 1195 general-purpose high-precision tensile-testing machine. Thermogravimetric analysis was carried out on a Q-1000 derivatograph at a heating rate of 5 deg min^{-1}.

CONCLUSION

Composites prepared from a polyamidobenzamidazole, a radical stabilizer, and carbon black by direct hot pressing demonstrate good stress–strain behavior, which is preserved during long-time exposure under conditions of cold climate. These composites outperform any commercial polyamides.

REFERENCES

1. Filatov, I.S., *Klimaticheskaya ustoichivost' polimernykh materialov* (Environmental Stability of Polymeric Materials), Moscow: Nauka, 1983.
2. Izyneev, A.A., Mazurevskii, V.P., Novak, I.S., and Markov, A.D., *Sbornik dokladov Vsesoyuznoi nauchno-tekhnicheskoi konferentsii "Rabotosposobnost' mashin i konstruktsii v usloviyakh nizkikh temperatur: Khladostoikost' materialov"* (Proc. All-Union Sci.-Tech. Conf. "Performance of Machines and Constructions at Low Temperatures: Cold Resistance of Materials"), part 2: *Khladostoikost' polimernykh materialov i izdelii* (Cold Resistance of Polymeric Materials and Goods), Yakutsk: Yakutsk Filial Sib. Otd. Akad. Nauk SSSR, 1974, pp. 143–152.
3. Mazurevskaya, Zh.P., Mognonov, D.M., Etonova, E.M., *et al*., *Sbornik dokladov Vsesoyuznoi nauchno-tekhnicheskoi konferentsii "Rabotosposobnost' mashin i konstruktsii v usloviyakh nizkikh temperatur: Khladostoikost' materialov"* (Proc. All-Union Sci.-Tech. Conf. "Performance of Machines and Constructions at Low Temperatures: Cold Resistance of Materials"), part 2: *Khladostoikost' polimernykh materialov i izdelii* (Cold Resistance of Polymeric Materials and Goods), Yakutsk: Yakutsk Filial Sib. Otd. Akad. Nauk SSSR, 1974, pp. 153–163.
4. USSR Inventor's Certificate no. 390 119.
5. USSR Inventor's Certificate no. 366 727.
6. Mognonov, D.M., Mazurevskaya, Zh.P., Ul'zetueva, I.D., and Izyneev, A.A., *Zh. Prikl. Khim*., 2000, vol. 73, no. 3, pp. 1003–1007.
7. Pavlov, N.N., *Starenie plastmass v estestvennykh i iskusstvennykh usloviyakh* (Natural and Artificial Aging of Plastics), Moscow: Khimiya, 1982.
8. Izyneev, A.A., Filatova, V.Ya., Mazurevskaya, Zh.P., *et al*., *Materialy Vsesoyuznoi konferentsii "Svoistva i primenenie polimernykh materialov pri nizkikh temperaturakh"* (Proc. All-Union Conf. "Properties and Applications of Polymeric Materials at Low Temperatures"), Yakutsk: Yakutsk. Filial Sib. Otd. Akad. Nauk SSSR, 1977, pp. 150–158.
9. *Entsiklopedia polimerov* (Encyclopedia of Polymers), Moscow: Sov. Entsiklopedia, 1974, vol. 2.
10. RF Patent no. 2 022 984.
11. Khakhinov, V.V., Mazurevskaya, Zh.P., Mognonov, D.M., and Il'ina, O.V., *Zh. Prikl. Khim*., 2001, vol. 74, no. 4, pp. 649–652.
12. Voigt, J., *Die Stabilisierung der Kunststoffe gegen Licht und Wärme*, Berlin: Springer, 1966.
13. Bellamy, L.J., *The Infra-Red Spectra of Complex Molecules*, New York: Wiley, 1957.
14. Volodarskii, L.B., Grigor'ev, I.A., Dikanov, S.A., *et al*., *Imidazolinovye nitroksil'nye radikaly* (Imidazoline Nitroxyl Radicals), Novosibirsk: Nauka, 1988, ch. 1.

Russian Journal of Applied Chemistry, Vol. 75, No. 3, 2002, pp. 474–476. Translated from Zhurnal Prikladnoi Khimii, Vol. 75, No. 3, 2002, pp. 485–487.
Original Russian Text Copyright © 2002 by Kozlov, Shustov, Zaikov.

MACROMOLECULAR CHEMISTRY AND POLYMERIC MATERIALS

Role of the Structure of Polymer Melt in Thermal Oxidative Degradation of Heterochain Polyesters

G. V. Kozlov, G. B. Shustov, and G. E. Zaikov

Kabardino-Balkar State University, Nalchik, Kabardino-Balkaria, Russia

Received November 22, 2001

Abstract—A study was made of the fractal dimension of the macromolecular coil as a parameter characterizing the polymer melt structure.

It is generally recognized now that the thermal oxidative degradation of polymers is influenced by their structure [1–3]. However, this influence was quantitatively characterized only for solid-phase crystalline-amorphous polymers, namely, by the degree of crystallinity [3, 4]. Other models utilize semiempirical approaches such as the "cage" model [2], zone model [3], etc. This is due to the lack of a quantitative structural model for amorphous state of both amorphous glassy and polymer melts. This gap can be filled, however, by the recently developed fractal analysis methods [5, 6]. In particular, fractal analysis provides now essentially the only mathematical means for describing the structure of polymer melts [7].

The aim of this work was to elucidate the structure-related factor governing the thermal oxidative degradation of polymer melts.

We studied polyarylates (PArs) based on 1,1-dichloro-2,2-di(*p*-chlorocarbonylphenyl)ethylene and 4,4-isopropylidenediphenol, as well as block copolymers of poly(arylene sulfone oxide arylates) (PASOAs) synthesized from 4,4'-isopropylidenediphenol, a 1 : 1 mixture of tere- and isophthaloyl dichlorides, and dihydroxyl-containing oligo(arylene sulfone) oxide based on 4,4-isopropylidenediphenol and 4,4'-dichlorodiphenyl sulfone with the molecular weight of 4600. The polycondensation procedures utilized for preparing these polymers are presented in the table.

The glass transition point T_g of the polymers was determined by the dielectric method on a Tesla BM-560 coulometer at a frequency of 1 MHz at 293–573 K [8].

Thermal oxidation processes in air were studied by the ampule technique. The working volume of the ampules was 3×10^{-5} l. The initial oxygen content was, on the average, 2.5–3.0 mol O_2 per base mole of the polymer. The studies were carried out at 573–723 K [8]. The main characteristics of PArs and PASOAs are listed in the table.

Let us consider the parameters characterizing the polymer melt structure. Thermal oxidative degradation of PArs and PASOAs was studied at 573–723 K, and the glass transition points of these polymers lie within 463–491 K (see table). As known [9], the temperature of the so-called fluid 1–fluid 2 transition T_{II} can be estimated as

$$T_{II} = (1.20 \pm 0.05)T_g. \quad (1)$$

It follows from Eq. (1) and the table that $T > T_{II}$. At T_{II} the polymer melt transforms from "a fluid with a fixed structure" (exhibiting a residual structural ordering [9]) to a truly liquid state, or a "structureless fluid" [10]. However, the latter term means that the melt at $T > T_{II}$ exhibits no supramolecular structure, whereas the structure of the macromolecular coil in the melt is still an important structure factor (essentially, the only factor operating at $T > T_{II}$).

Polycondensation methods and main characteristics of the polymers

Polymer	Polycondensation method	T_g, K	$\overline{M}_w \times 10^{-3}$
PAr-1	Low-temperature	471	76
PAr-2	High-temperature	476	72
PAr-3	Phase-transfer	462	69
PASOA-1	Low-temperature	472	76
PASOA-2	High-temperature	474	64
PASOA-3	Phase-transfer	491	66
PASOA-4	Emulsion	489	58

1070-4272/02/7503-0474$27.00 © 2002 MAIK "Nauka/Interperiodica"

The structure of supramolecular coil which is a fractal object [11] is most adequately described by its fractal ("Hausdorf") dimension Δ_f characterizing the spatial distribution of the coil elements [7]. The parameter Δ_f can be estimated as follows [12]. The formal kinetics of chemical reactions is described by the equation

$$dQ/dt = k_d(1 - Q). \quad (2)$$

Here, Q is the degree of conversion, t is the reaction time, and k_d is the reaction rate constant.

The general fractal relation which is also used for describing the kinetics of chemical reactions has the form [6]

$$Q \sim t^{(3 - \Delta_f)/2}. \quad (3)$$

By differentiating relation (3) with respect to the time t and equating the derivative dQ/dt to the analogous derivative in Eq. (2), we obtain [12]

$$t^{(\Delta_f - 1)/2} = \frac{C_1}{k_d(1 - Q)}. \quad (4)$$

Here, C_1 is the constant to be estimated from the boundary conditions [12]; the k_d values are taken from [8].

It was shown earlier [3] that the plots of $[N_{O_2}/(1 - K)]^{1/2}$ (N_{O_2} is the amount of the oxygen absorbed, and K is the degree of crystallinity) vs. the time t for polypropylene are straight lines. The parameter $(1 - K)$ determines the portion of the structure of crystalline-amorphous polypropylene which is the site of thermal oxidative degradation (amorphous phase). The structure of PAr and PASOA melts is characterized by the parameter Δ_f. As shown in [13], the processes occurring in fractal spaces (in fractal time) are described by the fractional differentiation and integration methods. In this case, the fractional exponent ν coincides with the fractal dimension of the Cantor set and characterizes the fraction of the states of the system retained within the evolution time t. It should be reminded that the Cantor set is considered in one-dimensional Euclidean space ($d = 1$), and for its fractal dimension holds $d_f < 1$ by definition of the fractal. For fractal objects in Euclidean spaces with higher dimensionalities ($d > 1$), one has to take as ν the fractional part of d_f (in our case, Δ_f):

$$\nu = \Delta_f - (d - 1). \quad (5)$$

Then the parameter ν will characterize the fraction of the fractal (macromolecular coil) preserved after

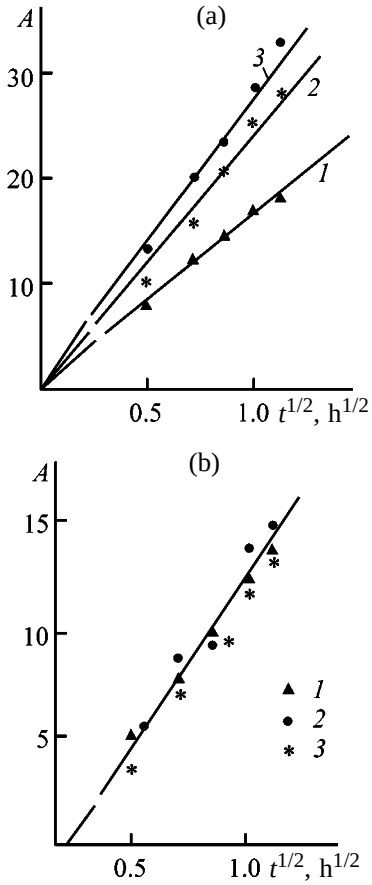

Fig. 1. Normalized amount of absorbed oxygen $N_{O_2}/(3 - \Delta_f)$ A, mole per base mole of polymer, as a function of the time $t^{1/2}$ for (a) PArs and (b) PASOA. Temperature, K: (a) (*1*) 623 (PAr-1), (*2*) 673 (PAr-3), and (*3*) 723 (PAr-3); (b) (*1*) 623 (PASOA-1), (*2*) 673 (PASOA-2), and (*3*) 723 (PASOA-3).

degradation. Evidently, the fraction of the macromolecular coil β breaking down in degradation is determined as

$$\beta = 1 - \nu = 1 - [\Delta_f - (d - 1)] = d - \Delta_f \quad (6)$$

or, taking into account that in this case $d = 3$, as

$$\beta = 3 - \Delta_f. \quad (7)$$

Thus, it should be presumed that specifically parameter β must be used for normalization of N_{O_2}, by analogy with the parameter $(1 - K)$ in the case of solid-phase crystalline-amorphous polymers. Figure 1 shows the plots of $N_{O_2}/(3 - \Delta_f)$ vs. t for PArs and PASOA. These plots can be linearized only with the parameter $t^{1/2}$ as abscissa. This means that the order of the chain termination reaction for PAr and PASOA melts is equal to 0.5. The slopes of the straight lines

in Fig. 1a differ because of different rate constants of the reaction [3].

The most important fact is that the plots shown in Figs. 1a and 1b were linearized using the fractal parameter $(3 - \Delta_f)$. This means that the fractal dimension Δ_f of the macromolecular coil is as unambiguous characteristic for a polymer melt structure as the degree of crystallinity for solid crystalline polymer [3].

The plots shown in Figs. 1a and 1b differ significantly in that the straight lines for PArs pass through the origin, while that for PASOA is shifted along the abscissa. Similar situation was observed in the case of atactic and isotactic polypropylene in [3]. The straight line for the latter is shifted by a certain time period t_0. This shift was explained by linear termination of the chain at the crystalline phase elements playing an important role in the very beginning of the reaction, when free radicals participating in the oxidation reaction are captured by crystalline formations containing no or insignificant amounts of oxygen. Too small, badly shaped crystallites cannot retain free radicals, but as their size and the degree of ordering increase they grow in importance as traps for free radicals. As a result, the oxygen absorption rate decreases and the induction period in the polymer oxidation increases [3]. For the polymers studied by us, this can be explained as follows. As shown in [14], PASOA exceeds PArs in the activation energy of thermal oxidative degradation for identical Δ_f's because of steric hindrances in the PASOA chain. These hindrances can be produced by various types of substituents, side branches, substituents in different positions (*para, ortho, meta*), etc. In this case, the degree of influence of this factor can be estimated using the Hammett's constant [15]. The sterically hindered moieties can serve as free radical traps, as in the case of polypropylene. This decreases the oxygen absorption rate and increases the induction period for oxidation of PAr and PASOA melts.

CONCLUSION

The parameter characterizing the structure of polymer melt is the fractal dimension of macromolecular coil. Sterically hindered moieties in the polymer chain can act as free radical traps, thereby exerting an effect similar to that of inhibitor.

REFERENCES

1. Kovarskaya, B.M., Blyumenfel'd, A.B., and Levantovskaya, I.I., *Termicheskaya stabil'nost' geterotsepnykh polimerov* (Thermal Stability of Heterochain Polymers), Moscow: Khimiya, 1977.
2. Gladyshev, G.L., Ershov, Yu.A., and Shustova, O.A., *Stabilizatsiya termostoikikh polimerov* (Stabilization of Thermally Stable Polymers), Moscow: Khimiya, 1979.
3. Shlyapnikov, Yu.A., Kiryushkin, S.G., and Mar'-in, A.P., *Antiokislitel'naya stabilizatsiya polimerov* (Antioxidative Stabilization of Polymers), Moscow: Khimiya, 1986.
4. Emanuel', N.M., *Vysokomol. Soedin., Ser. A*, 1985, vol. 27, no. 7, pp. 1347–1363.
5. Novikov, V.U. and Kozlov, G.V., *Usp. Khim.*, 2000, vol. 69, no. 4, pp. 378–399.
6. Novikov, V.U. and Kozlov, G.V., *Usp. Khim.*, 2000, vol. 69, no. 6, pp. 572–599.
7. Vilgis, T.A., *Physica A*, 1988, vol. 153, no. 2, pp. 341–354.
8. Batyrova, Kh.M., *Cand. Sci. Dissertation*, Moscow, 1985.
9. Bershtein, V.A. and Egorov, V.M., *Differentsial'naya skaniruyushchaya kalorimetriya v fizikokhimii polimerov* (Differential Scanning Calorimetry in Physical Chemistry of Polymers), Leningrad: Khimiya, 1990.
10. Lobanov, A.M., and Frenkel', S.Ya., *Vysokomol. Soedin., Ser. A*, 1980, vol. 22, no. 5, pp. 1045–1057.
11. Baranov, V.G., Frenkel', S.Ya., and Brestkin, Yu.V., *Dokl. Akad. Nauk SSSR*, 1986, vol. 290, no. 2, pp. 369–372.
12. Dolbin, I.V., Ligidov, M.Kh., Beev, A.A., and Kozlov, G.V., Abstracts of Papers, *Mezhdunarodnaya konferentsiya "Aktual'nye problemy sovremennoi nauki"* (Int. Conf. "Urgent Problems of Modern Science"), Samara: Samar. Gos. Univ., 2000, p. 26.
13. Nigmatullin, R.R., *Teor. Mat. Fiz.*, 1992, vol. 90, no. 3, pp. 354–367.
14. Kozlov, G.V., Dolbin, I.V., and Shustov, G.N., Abstracts of Papers, *Mezhdunarodnaya konferentsiya "Sovremennye problemy organicheskoii khimii, ekologii i bikotekhnologii"* (Int. Conf. "Modern Problems of Organic Chemistry, Ecology, and Biotechnology"), Kaluga: Kaluzh. Gos. Univ., 2001, vol. 1, pp. 15–16.
15. Hammett, L.R., *Physical Organic Chemistry. Reactions, Rates, Equilibria and Mechanisms*, New York: McGraw-Hill, 1970, 2nd ed.

Russian Journal of Applied Chemistry, Vol. 75, No. 3, 2002, pp. 477–479. Translated from Zhurnal Prikladnoi Khimii, Vol. 75, No. 3, 2002, pp. 488–490.
Original Russian Text Copyright © 2002 by Kotel'nikov, Sukhinin, Ermilov.

MACROMOLECULAR CHEMISTRY AND POLYMERIC MATERIALS

Kinetics of Formation and Curing of Oligoether Urethane Allyl Ester

S. A. Kotel'nikov, V. S. Sukhinin, and A. S. Ermilov

Perm State Technical University, Perm, Russia

Received November 5, 2001

Abstract—Kinetic parameters of formation of P-9AD oligoether urethane allyl ester with terminal double bonds and of its curing with dinitrile oxide were determined. The dependence of the rate constant on the allyl alcohol concentration and temperature was studied. The mechanism of reaction of P-9A prepolymer with allyl alcohol was proposed. The kinetic and thermodynamic parameters of curing of oligoether urethane allyl ester with dinitrile oxide were determined. The mechanism of reaction of P-9AD oligoether urethane allyl ester with dinitrile oxide was proposed.

One of procedures for processing filled systems is cross-linking of oligomers via reactive terminal groups in the presence of active curing agents. To simplify the production process and to improve its efficiency and the quality of the product, low-temperature curing agents are developed. Among promising agents of low-temperature rubber curing are nitrile oxides. These agents accelerate polymer curing by a factor of 3–4 and decrease the curing temperature to 0–80°C [1]. Oligoether urethane esters derived from unsaturated alcohols can be cured at low temperatures with nitrile oxides. Although some properties of various unsaturated oligoether urethane esters are reported [2], the kinetics of their formation and curing was poorly studied. In this work we studied the kinetics of formation of P-9AD oligoether urethane ester (prepared from P-9A prepolymer and allyl alcohol) and its curing with dinitrile oxide.

EXPERIMENTAL

P-9AD oligoether urethane ester with terminal double bonds was prepared by reaction of P-9A prepolymer with allyl alcohol. The content of double bonds in the polymer is 3.3 wt %; the density at 25°C is 1.22 g cm^{-1}; the refractive index at 20°C is 1.5080. The kinetics of formation of P-9AD oligoether urethane ester (18–100°C) and of its curing (16–30°C) was monitored by variation with time of the optical density of the characteristic IR bands of the isocyanate groups –N=C=O at 2270 cm^{-1} and of the nitrile oxide groups –C≡N→O at 2290 cm^{-1}. The kinetic parameters of addition of allyl alcohol to P-9A prepolymer are presented in Table 1.

The activation energy (E = 59.1 kJ mol^{-1}) and preexponential factor of the Arrhenius equation (A = 6.09×10^5 l mol^{-1} s^{-1}) were calculated by the least-squares treatment of the data presented in Table 1. The activation enthalpy $\Delta H_0^{\neq}$ was calculated by the equation

$$\Delta H_0^{\neq} = E - RT, \quad (1)$$

where R is the universal gas constant, and T is the temperature, K; $\Delta H_0^{\neq}$ = 56.59 kJ mol^{-1}.

The activation entropy ΔS_0 calculated by the equation

$$\Delta S_0^{\neq} = R[\ln A - \ln(kT)/h - n] \quad (2)$$

(where k is Boltzmann's constant, h is Planck's constant, n is the reaction order) is –126.52 J mol^{-1} deg^{-1}.

Table 1. Kinetic parameters of addition of allyl alcohol to P-9A prepolymer

T, °C	K, l mol^{-1} s^{-1}	ln K
18	1.43×10^{-5}	–11.45
25	3.8×10^{-5}	–10.18
40	8.25×10^{-5}	–9.4
60	3.28×10^{-4}	–8.02
70	6.02×10^{-4}	–7.41
80	1.41×10^{-3}	–6.59
100	3.61×10^{-3}	–5.63

1070-4272/02/7503-0477$27.00 © 2002 MAIK "Nauka/Interperiodica"

Table 2. Dependence of the rate constant on the allyl alcohol concentration

[NCO]	[ROH]	K, l mol^{-1} s^{-1}	[ROH]/[NCO]
M			
1.5	0.94	6.97×10^{-6}	0.63
1.39	1.868	7.89×10^{-5}	1.34
1.35	2.23	1.59×10^{-4}	1.7
1.032	5.53	1.32×10^{-3}	5.16

The rate constant of the reaction of allyl alcohol with the prepolymer at 47°C increases with increasing allyl alcohol concentration, which is due to the catalytic influence of the alcohol (Table 2).

The reaction of allyl alcohol with the urethane prepolymer can be described by the equation [3]

$$RNCO + R'OH \xrightarrow{R'OH} [R-N=C(H-O-R')-O]$$

$$\rightarrow R-N(H-O-R')-C(H-O-R')-O \rightarrow RNHCOR' + R'OH,$$

where R' = $-CH_2-CH=CH_2$.

We suggest that one isocyanate group reacts with two alcohol molecules, one of which is a catalyst. Up to the 75% conversion the dependence is linear, and then the reaction is accelerated, probably owing to catalysis by the urethane groups. The catalytic effect up to 75% conversion is weak, and the reaction is described by the second-order equation

$$-d[NCO]/d\tau = K[NCO]^2. \quad (3)$$

The activation energy E = 59.1 kJ mol^{-1} is slightly higher than that reported in [3] for the reaction of phenyl isocyanate with aliphatic alcohols, which may be due to the higher reactivity of these compounds. The high calculated activation entropy $\Delta S_0^{\neq}$ = –126.52 J mol^{-1} deg^{-1} suggests high ordering of the transition state, which confirms the proposed mechanism of reaction of allyl alcohol with the prepolymer.

P-9AD rubber was cured 3,4,6-triethylisophthalodinitrile di-*N*-oxide

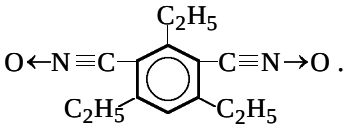

The kinetics of curing in solvents with different dielectric constants was studied at the rubber : solvent volume ratio of 3 : 7. The activation energy and preexponential factor A were calculated by Arrhenius equation from data for two temperatures. The activation enthalpy and entropy (Table 3) were calculated by Eqs. (1) and (2), respectively.

As seen from Table 3, the rate of addition of nitrile oxide groups to the double bonds of the rubber is weakly dependent on the dielectric constant (polarity) of the solvent. This is typical for reactions of 1,3-dipolar cycloaddition [4] where the dipolarphile is the

Table 3. Solvent effect on the kinetic and thermodynamic parameters of addition of dinitrile oxide to P-9AD rubber

Solvent	ε	T, °C	$K \times 10^4$, l mol^{-1} s^{-1}	E, kJ mol^{-1}	A, l mol^{-1} s^{-1}	$\Delta H_0^{\neq}$, kJ mol^{-1}	$\Delta S_0^{\neq}$, J mol^{-1} deg^{-1}
Cyclohexanone	18.3	17	3.47	55.98	4.25×10^6	53.5	–134.5
		30	9.34				
Dimethyl sufoxide	48.9	18	2.41	23.81	4.55	21.33	–248.8
		30	3.56				
Dimethylformamide	36.7	18	1.4	16.02	0.1	13.54	–280
		30	1.82				
Methyl ethyl ketone	18.5	18	1.57	68.34	2.9×10^8	65.86	–99.3
		30	4.78				
2-Ethoxyethanol	15.9	16	2.89	51.04	4.9×10^5	48.56	–152.4
		30	7.71				
Nitromethane	38.6	20	3.4	67.87	8.6×10^7	65.4	–78.04
		30	10.4				
Triacetin	7.19	17	7.3	15.73	0.1	13.2	–280.2
		30	9.4				

double bond of the rubber and the dipolar agents are the nitrile oxide groups of the curing agent. The negative entropy indicates high ordering of the transition state and concerted addition of nitrile oxide groups to the double bonds. The mechanism of this reaction can be described by the following scheme:

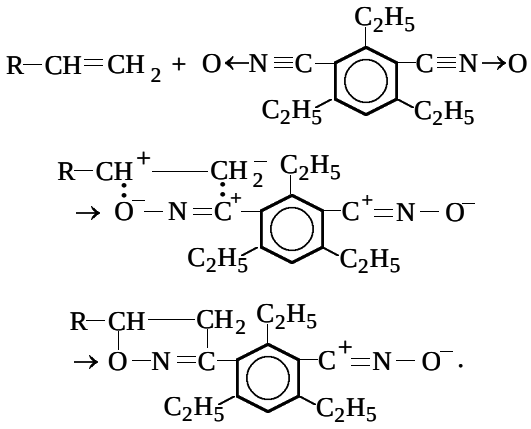

Reaction of P-9AD rubber with 3,4,6-triethylisophthalodinitrile di-*N*-oxide yields a five-membered isoxazoline ring.

CONCLUSIONS

(1) The rate of reaction of P-9A rubber with allyl alcohol at 18–100°C is described by the second-order equation. The acceleration of the reaction with increasing alcohol concentration is due to the catalytic effect of the alcohol.

(2) Reaction of P-9AD unsaturated rubber with 3,4,6-triethylisophthalodinitrile di-*N*-oxide is described by the second-order kinetic equation, with the rate constant being weakly dependent on the dielectric constant of the solvent.

(3) Reaction of P-9AD oligoether urethane ester with 3,4,6-triethylisophthalodinitrile di-*N*-oxide proceeds by the mechanism of concerted 1,3-dipolar cycloaddition.

REFERENCES

1. Antipova, V.F., Petrov, G.N., and Salins, K.Yu., *Primenenie nitriloksidov v kachestve otverditelei kauchukov obshchego naznacheniya* (The Use of Nitrile Oxides as Curing Agents for Rubbers of General Purpose), Zhukov, B.P., Ed., Ser.: *Porokha i tverdye spetsial'nye topliva v narodnom khozyaistve* (Gunpowder and Solid Special Fuels in National Economy), Moscow: TsNIINTKPK, 1990.
2. Berlin, A.A., Korolev, G.V., and Kefeli, T.Ya., *Akrilovye oligomery i materialy na ikh osnove* (Acrylic Oligomers and Materials Based on Them), Moscow: Khimiya, 1983.
3. Saunders, J.H. and Frish, K.C., *Polyurethanes. Chemistry and Technology*, part 1: *Chemistry*, New York: Interscience, 1962.
4. Carey, F.A. and Sundberg, R.J., *Advanced Organic Chemistry*, part A: *Structure and Mechanisms*, New York: Plenum, 1977.

Russian Journal of Applied Chemistry, Vol. 75, No. 3, 2002, pp. 480–482. Translated from Zhurnal Prikladnoi Khimii, Vol. 75, No. 3, 2002, pp. 491–493.
Original Russian Text Copyright © 2002 by Nurmanov, Gevorgyan, Matmuratov, Kasimova, Sirlibaev, Kalyadin.

MACROMOLECULAR CHEMISTRY AND POLYMERIC MATERIALS

Synthesis of Vinyl Phenyl Ether and Its Use for Ammetric Titration of Silver(I)

S. E. Nurmanov, A. M. Gevorgyan, Sh. A. Matmuratov, O. Kasimova, T. S. Sirlibaev, and V. G. Kalyadin

National University of Uzbekistan, Tashkent, Uzbekistan

Received August 16, 2001

Abstract—Catalytic vinylation of phenol with acetylene at atmospheric pressure was studied. The yield of vinyl phenyl ether was determined as influenced by the solvent, reaction temperature, and catalyst amount. The mechanism of formation of vinyl phenyl ether was proposed. Ammetric titration of silver(I) with a solution of vinyl phenyl ether in nonaqueous acetic acid solutions was performed.

It is known [1, 2] that vinyl derivatives are widely used as monomers, cross-linking agents, pharmaceuticals, etc.. Among them vinyl ethers are the most used, since are synthesized from readily available reagents by simple procedures. Preparation of vinyl ethers by vinylation at atmospheric pressure was studied insufficiently.

In this work we studied vinylation of phenol with acetylene at atmospheric pressure and different temperatures in different solvents in the presence of KOH as catalyst. This reaction was performed in benzene, water, and dimethyl sulfoxide (DMSO) (Table 1). In benzene, no vinyl phenyl ether (VPE) was formed, since this solvent is low-polar, has low boiling point, and does not dissolve the catalyst. In water, the VPE yield is low.

In DMSO, KOH–DMSO separated ion pairs are formed, which increases the basicity of the solvent. Phenol transforms into readily dissociating potassium phenolate, which promotes vinylation.

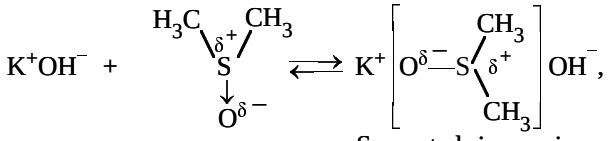

Separated ion pair

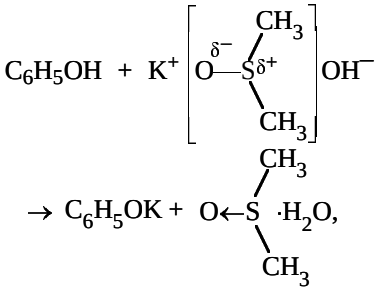

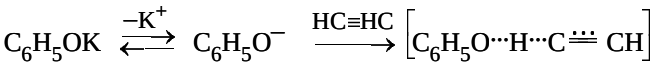

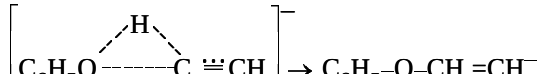

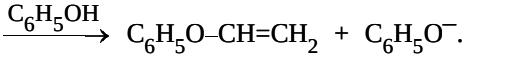

Thus, the VPE yield increases with increase in the dielectric constant and basicity of the solvent.

Since the solubility of gases in liquids decreases with increasing temperature, we studied the temperature dependence of the VPE yield in the presence of various amounts of KOH (3–15 wt % relative to phenol) (Table 2).

As seen from Table 2, no VPE is formed at temperatures below 75°C. At 95–100°C the yield is 17–19%, and at 145–150°C it reaches a maximum of 25–32%.

The structure of VPE was confirmed by IR spectroscopy and by its physicochemical parameters which coincided with the published values.

Thus, synthesis of PVE at atmospheric pressure

Table 1. Yield of VPE as influenced by the solvent (KOH catalyst : phenol weight ratio 0.1)

Solvent	*T*, °C	VPE yield, %
Benzene	76–79	–
H_2O	95–100	Traces
DMSO	95–100	17–19

1070-4272/02/7503-0480$27.00 © 2002 MAIK "Nauka/Interperiodica"

should be performed in DMSO at 145–150°C and the catalyst (KOH) : phenol weight ratio of 0.15.

Vinyl ethers are widely used as biologically active compounds in various branches of science, medicine, and agriculture [3]. However, no data are reported on analytical application of VPE. Its analogs are used as analytical reagents [4]; in this connection, we tested VPE as a titrating agent for determining various metal ions in nonaqueous and mixed solvents. For this purpose, we determined electrochemical properties of VPE.

Previously we found [5] that metal cations can be selectively titrated with VPE solutions in glacial acetic acid and its mixtures with various inert nonaqueous solvents (chloroform, tetrachloromethane, hexane, benzene, dioxane, methyl ethyl ketone, heptane, etc.). The equivalence point (EP) was determined ammetrically with a platinum working electrode.

This procedures can be used for determining metal ions in extracts formed in analysis of multicomponent inorganic materials and in organic materials readily soluble in nonaqueous and mixed solvents.

Preliminary experiments on titration of silver(I), mercury(II), palladium(II), platinum(IV), and other metals with VPE solutions in glacial acetic acid and its mixtures with inert solvents [6, 7] confirmed our assumptions about the shape of the titration curves and the accuracy of the analysis. Complexes of these metals with VPE are sufficiently soluble in nonaqueous and mixed solvents. In all cases the EP determined by extrapolation of the straight line sections of the titration curves to their intersection corresponds to formation of 1 : 1 and 2 : 1 complexes of the titrating agent with monovalent and bivalent metal cations, respectively. This was also confirmed by electrochemical and optical methods and by NMR spectroscopy [8].

To determine Ag^+ in the presence of large amounts of elements interfering with its determination and usually present in tested minerals, jewelries, alloys, and other objects, we proposed a procedure based on extractive separation of Ag^+ ions with subsequent ammetric titration of these anions in the extract with VPE.

An aliquot of a test solution containing no more than 200 mmol of Ag(I) was placed in a separatory funnel and acidified with $HClO_4$ and HCl to the concentration of about 0.2 M. A 0.1 M solution of ethylenediaminetetraacetic acid disodium salt (5 ml) and 1% solution of Thionalide (thioglycolic acid β-naphthylamide) were added. The resulting solution was stirred for 10 min and then silver(I) was extracted for 1–2 min with two 5-ml portions of chloroform [9]. To the combined extract placed in a titration vessel, glacial acetic acid (5 ml) was added. The solution was heated to boil and Thionalidate silver complex was decomposed by adding a saturated solution (30–40 drops) of potassium permanganate or chromium trioxide in glacial acetic acid until the solution became yellow–brown. Then 0.2 M solution (5 ml) of lithium chloride or lithium perchlorate in glacial acetic acid was added. The mixture was heated for several minutes to reduce completely colloidal manganese dioxide to Mn(II) [or Cr(IV) to Cr(III)] and Ag(I) to Ag(0), which was judged by decolorization of the solution. The solution was cooled to room temperature and was ammetrically titrated by the procedure in [6] with a standard (c = 0.0001–0.002 M) VPE solution using two platinum working electrodes.

Table 2. Yield of vinyl phenyl ether in DMSO as influenced by temperature and catalyst amount

c_{KOH}, wt % relative to phenol	T, °C	VPE yield, %
10	75–80	Traces
10	95–100	17–19
10	120–125	23
10	145–150	31
10	155–160	26
3	145–150	9
5	145–150	25
15	145–150	32

The results of silver(I) determination in five different artificial mixtures simulating natural and industrial objects are presented in Table 3. Statistical treatment of these data [10] shows that the procedure proposed allows reliable and selective determination of silver with a high accuracy.

CONCLUSIONS

(1) The best conditions (15% KOH, DMSO, 145–150°C) for preparing vinyl phenyl ether by reaction of phenol with acetylene at atmospheric pressure were determined.

(2) A procedure was developed for determining Ag^+ in systems simulating real objects by ammetric titration with a solution of vinyl phenyl ether in nonaqueous and mixed solvents.

Table 3. Results of ammetic titration of silver(I) extracted from model systems

Mixture composition, mg	Found Ag^+, mg (P = 0.95, $\bar{x} \pm \Delta X$)	n	S	$S_r \times 10^2$
Ag, 0.15 + Au, 0.56 + Co, 20.3 + Pt, 1.39	0.16 ± 0.01	3	0.008	5.1
Ag, 0.15 + Rh, 1.04 + Pd, 5.42 + Os, 3.47	0.15 ± 0.02	4	0.101	6.7
Ag, 0.15 + Ru, 2.56 + Ni, 40.5 + Bi, 30.6	0.15 ± 0.02	4	0.009	5.9
Ag, 0.15 + Fe, 50.7 + Ir, 0.78 + Ni, 20.9	0.16 ± 0.001	4	0.012	8.0
Ag, 0.15 + Co, 40.6 + Fe, 25.3 + Pt, 2.78	0.15 ± 0.02	5	0.007	4.5

* P is the confidence probability, $\bar{x}$ is the average value, ΔX is the confidence interval, n is the number of parallel measurements, S is the standard deviation, and S_r is the relative standard deviation.

REFERENCES

1. Lebedev, N.N., *Khimiya i tekhnologiya osnovnogo organicheskogo i neftekhimicheskogo syr'ya* (Chemistry and Technology of Basic Organic and Petrochemical Raw Materials), Moscow: Khimiya, 1971.
2. Trofimov, B.A., *Usp. Khim.*, 1981, vol. 50, no. 2, pp. 248–272.
3. Trofimov, B.A., *Zh. Org. Khim.*, 1986, vol. 22, no. 9, pp. 1991–2006.
4. Songina, O.A. and Zakharov, V.A., *Amperometricheskoe titrovanie* (Ammetric Titration), Moscow: Khimiya, 1979.
5. Gevorgyan, A.M., Matmuratov, Sh.A., Mukhamedgalieva, U.A., *et al.*, *Khim. Prirodn. Soedin.* (Tashkent), 2001, special issue, pp. 90–91.
6. Gevorgyan, A.M., Matmuratov, Sh.A., Mukhamedgalieva, U.A., *et al.*, Abstracts of Papers, *Konferentsiya "Analiticheskaya khimiya i problemy ekologii"* (Conf. "Analytical Chemistry and Environmental Problems"), Samarkand, 2000, pp. 64–66.
7. Gevorgyan, A.M., Matmuratov, Sh.A., and Kalyadin, V.G., Abstracts of Papers, *Mezhdunarodnaya konferentsiya, posvyashchennaya 100-letiyu so dnya rozhdeniya O.A. Songinoi* (Int. Conf. Devoted to Centennial of O.A. Songina's Birthday), Almaty, 2001, p. 44.
8. Kukushkin, Yu.N., *Khimiya koordinatyionnykh soedinenii* (Chemsitry of Coordination Compounds), Moscow: Vyshsaya Shkola, 1985.
9. Moskvin, L.N. and Tsaritsyna, L.G., *Metody razdeleniya i kontsntrirovaniya v analiticheskoi khimii* (Separation and Concentrating Procedures in Analytical Chemistry), Leningrad: Khimiya, 1991.
10. Doerfel, K., *Statistik in der analytischen Chemie*, Leipzig: Leuna-Merseburg, 1966.

Russian Journal of Applied Chemistry, Vol. 75, No. 3, 2002, pp. 483–485. Translated from Zhurnal Prikladnoi Khimii, Vol. 75, No. 3, 2002, pp. 494–496.
Original Russian Text Copyright © 2002 by Suvorova, Novikova, Passet, Iozep.

MACROMOLECULAR CHEMISTRY AND POLYMERIC MATERIALS

Reactions of Dextran Polyaldehyde with Carboxylic and Sulfonic Acid Amides

O. B. Suvorova, E. V. Novikova, B. V. Passet, and A. A. Iozep

St. Petersburg State Academy of Pharmaceutical Chemistry, St. Petersburg, Russia

Received September 27, 2001

Abstract—Reactions of dextran polyaldehyde with carboxylic and sulfonic acid amides were suggested for modification of polysaccharides with low-molecular-weight compounds. The influence of reaction conditions on the content of fragments incorporated into the polymer was examined.

The majority of aliphatic and all aromatic aldehydes react with amides to form alkylidene- or arylidenebisamides. With diamides of oxalic, malonic, and alkylmalonic acids, cyclic bisamide derivatives are formed. With sulfamides, aldehydes react difficultly to give bisamides [1].

Reactions of polysaccharide polyaldehydes with carboxylic and sulfonic acid amides were not studied previously. Such reactions are of interest as routes to physiologically active polymers, in view of the fact that many biologically active substances are amides, and their conversion to polymeric derivatives would prolong their effect and decrease the toxicity. Therefore, it was interesting to study the reactions of polysaccharide polyaldehydes (with dextran polyaldehyde, DPA, as example) and carboxylic and sulfonic acid amides.

DPA was prepared by a common procedure of polysaccharide oxidation [2], so as to minimize formation of by-products. The oxidant consumption was monitored spectrophotometrically at 222.5 nm [2], and the amount of the released formic acid was determined by volumetric titration. After reaction completion, the mixture was concentrated in a water-jet-pump vacuum at 60°C, dialyzed against water to remove low-molecular-weight reaction products, and again concentrated in a vacuum; the product was precipitated with ethanol. The resulting DPA was a white amorphous powder soluble in water and insoluble in alcohol, acetone, ether, and other organic solvents.

The content of aldehyde groups in DPA was determined by photocolorimetric [3] and oxime [4] methods. The degree of substitution C_{sa} (the number of aldehyde groups in polysaccharide aldehyde per monosaccharide unit) of the DPA samples used in this work varied from 0.73 to 1.1.

Chemical modification of DPA was performed as follows:

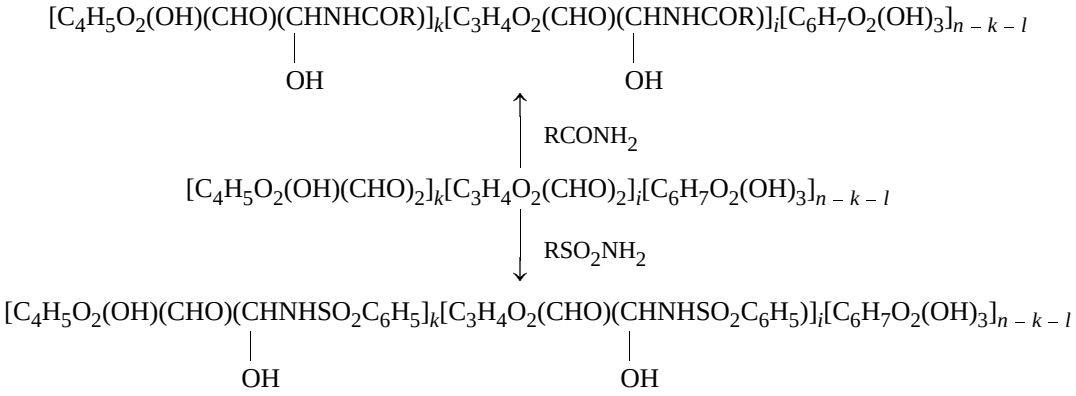

where R = CH_3–, $C_6H_5CH_2$–, and C_5H_4N–.

1070-4272/02/7503-0483$27.00 © 2002 MAIK "Nauka/Interperiodica"

Table 1. Degree of conversion of aldehyde groups C_{ca} in DPA in the reaction with benzenesulfamide (90°C, 6 h)

Molar ratio of amide to aldehyde groups	C_{ca}, %	
	method 1	method 2
4	21	21
5	25	26
6	27	27

* Method: (*1*) elemental analysis and (*2*) conductometric back-titration.

Table 2. Degree of conversion of aldehyde groups C_{ca} in reaction of DPA with acetamide in aqueous solution, as influenced by temperature, time, and reactant ratio

Run no.	T, °C	τ, h	Molar ratio of amide to aldehyde groups	C_{ca}, %
1	90	2	5	6
2	90	3	5	9
3	90	4	5	13
4	90	6	5	20
5	90	10	5	24
6	40	4	5	1
7	60	4	5	2
8	80	4	5	9
9	90	4	5	13
10	100	4	5	24
11	90	6	2	11
12	90	6	3	13
13	90	6	5	19
14	90	6	7	30
15	90	6	10	38

The reactions of DPA with amides were performed in aqueous solution at 40 to 90°C for 1 to 10 h; the molar ratio of amide to aldehyde groups was varied from 2 to 10. After reaction completion, the products were precipitated with ethanol, filtered off, washed with ethanol and ether, and dried in a water-jet-pump vacuum at 60°C for 2 h. The resulting compounds are beige amorphous powders soluble in water and insoluble in alcohol, acetone, and ether.

The absence of the initial amide in the target product was confirmed by TLC.

The reaction products were studied by elemental analysis, conductometric titration, and IR and UV spectroscopy.

The IR spectra of the products contained absorption bands at 1660 cm^{-1}, lacking in the spectra of the initial amides and assignable to the C=O stretching vibrations in the amide group, and at 1570 cm^{-1}, characteristic of the NH bending vibrations in the amide group.

The products of reaction of DPA with benzenesulfamide were examined by elemental analysis and conductometric back-titration of amide NH groups. As seen from Table 1, the results obtained by both methods are quite consistent.

The reaction products were characterized by the degree of substitution C_s (number of low-molecular-weight fragments per monosaccharide unit). The reaction of DPA with amide was characterized by the degree of conversion of aldehyde groups C_{ca} (%), calculated as

$$C_{ca} = (C_s/C_{sa}) \times 100.$$

To determine the best conditions for the reactions of polysaccharides with carboxylic acid amides, we studied how C_{ca} depends on the reaction temperature, time, reactant ratio, and solvent, with acetamide as example. The results are listed in Table 2.

We found that the content of acetamide fragments in the polysaccharide aldehyde sharply increased as the reaction temperature was increased (run nos. 6–10). Therefore, the subsequent experiments were performed at 90°C. The reaction was virtually complete in 6 h (run nos. 1–5). As expected, C_{ca} increased with increasing amide-to-aldehyde molar ratio (run nos. 11–15) and reactant concentrations. However, too large excess of the amide is not appropriate, because its solubility in water is limited. Therefore, in the subsequent experiments we took the amide in a five-fold excess, and the concentration of aldehyde groups was approximately 1 M. When the reaction was performed in ethanol, the conversion decreased from 13 to 5%, because DPA is insoluble in ethanol and therefore the reaction was heterogeneous.

Thus, we chose the following conditions for the reactions of DPA with carboxylic and sulfonic acid amides: aqueous solution, 90°C, 6 h, and molar ratio of amide to aldehyde groups 5 : 1. Under these conditions, we performed the reactions of DPA with amides of acetic, phenylacetic, nicotinic, and thioacetic acids, acetanilide, phthalimide, and benzenesulfamide. This set of compounds includes primary and secondary amides of aliphatic and heterocyclic carboxylic acids, an imide, and a sulfonic acid amide. The degrees of conversion of aldehyde groups C_{ca} in the reactions of DPA with amides are listed below (90°C, 6 h, molar

ratio of amide to aldehyde groups 5 : 1):

Compound	C_{ca}, %
Acetamide (CH_3CONH_2)	19 ± 1
Phenylacetamide ($C_6H_5CH_2CONH_2$)	22 ± 0.5
Thioacetamide (CH_3CSNH_2)	25 ± 1
Nicotinamide ($C_5H_4NCONH_2$)	14 ± 0.5
Benzenesulfamide ($C_6H_5SO_2NH_2$)	25 ± 2
Phthalimide [$C_6H_4(CO)_2NH$]	7 ± 0.5
Acetanilide ($CH_3CONHC_6H_5$)	0

These results show that all the unsubstituted amides of monobasic acids, tested in this work, react with DPA to a similar extent, whereas the secondary amide (acetanilide) does not react with DPA. The low C_{ca} in the reaction of DPA with phthalimide is probably due to the low solubility of the imide in water.

To evaluate the lability of the bond between DPA and the amide fragment, we studied the hydrolytic stability of the acetamide and benzenesulfamide derivatives of DPA in strongly alkaline (pH 13.6) solutions at 18–20°C. We found that about 40% of amide fragments are eliminated in 4 days, and about 90%, in 7 days.

To obtain information on the product structure, we determined by the oxime procedure the content of aldehyde groups that remained unchanged in the reactions with acetamide and benzenesulfamide. We found that, on the average, two aldehyde groups are converted per mole of incorporated amide. These results, in combination with the IR and conductometric titration (for benzenesulfamide) data, suggest formation of a stable six-membered ring (structure **II**):

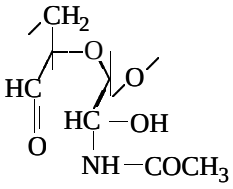

I

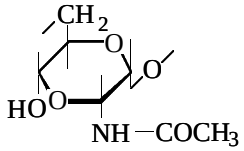

II

CONCLUSION

Polysaccharide aldehydes react with amides of aliphatic and heterocyclic carboxylic, thiocarboxylic, and sulfonic acids. The highest conversion of aldehyde groups in reactions of dextran polyaldehyde with unsubstituted carboxylic acid amides is attained in aqueous solution at 90°C, reaction time of 6 h, and molar ratio of amide to aldehyde groups of 5 : 1.

REFERENCES

1. *Organic Reactions*, Cope, A.C., Ed., New York: Wiley, vol. 14.
2. *Methods in Carbohydrate Chemistry*, Whistler, R.L. and Wolfrom, M.L., Eds., New York: Academic, 1962–1965, vols. 1, 2, 4, 5.
3. Iozep, A.A., Suvorova, O.B., Iozep, L.I., and Passet, B.V., *Zh. Prikl. Khim.*, 1998, vol. 71, no. 7, pp. 1202–1205.
4. Houben–Weyl, *Methoden der organischen Chemie*, vol. 2: *Analytische Methoden*, Stuttgart: Thieme, 1953.

Russian Journal of Applied Chemistry, Vol. 75, No. 3, 2002, pp. 486–490. Translated from Zhurnal Prikladnoi Khimii, Vol. 75, No. 3, 2002, pp. 497–501.
Original Russian Text Copyright © 2002 by Prokshin, Korobova, Vishnyakova, Afanas'ev.

MACROMOLECULAR CHEMISTRY AND POLYMERIC MATERIALS

Estimation of the Effect of Diffusion and Transformation of Lignosulfonates on the Mechanism of Delignification in Sulfite Cooking of Spruce Wood

G. F. Prokshin, E. N. Korobova, A. P. Vishnyakova, and N. I. Afanas'ev

Institute of Environmental Problems of the North, Ural Division, Russian Academy of Sciences, Arkhangelsk, Russia

Received May 28, 2001

Abstract—The contribution of diffusion and transformation of macromolecules to the mechanism of delignification of cell wall in sulfite cooking of spruce wood was quantitatively estimated from variation of the parameters of the Kolmogorov–Erofeev–Avrami equation and hydrodynamic radii of lignosulfonate macromolecules found in the cooking liquor.

In topochemistry of sulfite cooking, it is assumed that an increase in the molecular size and the size of network fragments of lignin in the form of lignosulfonates diffusing into cooking liquor is caused by their sifting through capillaries with increasing sizes in the cellular structure of wood substance. However, actually the pore size was measured after delignification was stopped and wood residue was removed from the autoclave. In this case, the capillary size could be altered as a result of probable relaxation processes occurring after cooking, and also during experimental determination of the capillary volumes by standard procedures.

Spruce wood consists to 95% of long tubular cells (tracheids). The wall thickness in these cells is in the range of $(0.5–4.0) \times 10^{-6}$ m; therefore, the wall and wood as a whole can be considered as a membrane. In terms of its structure, the cell wall presents a layered porous membrane consisting of cellulose fibrils immersed in a lignocarbohydrate matrix subjected to various phase transitions with possible formation and destruction of interpenetrating physicochemical networks (bonds) in solid solutions (gels) in various stages of sulfite cooking [2–4]. Here, the main topochemical processes occurring initially in cooking and completed by formation of soluble lignosulfonates are followed by diffusion transfer of lignosulfonates predominantly in the transverse direction from the central plate into the cell body. For simplicity sake it can be assumed that the driving force of this process is the gradient of lignin concentration in various layers of the cell wall membrane and at its surface facing to the cooking liquor and in the cell capillaries. Therefore, the process kinetics can be described by the Fick diffusion model [5, 6].

Here we report the principle and procedure and analyze the results of quantitative estimation of the contribution of diffusion and relaxation processes in a cell wall in the topochemical stage, made directly in cooking without removal of wood residue from the autoclave. Our procedure involves comparing the variation of the topokinetic equation parameters of delignification and determining the hydrodynamic radii and transformations of lignosulfonate molecules in solutions during sulfite cooking of spruce wood.

EXPERIMENTAL

Delignification was studied by a conventional procedure of wood residue sampling at successive stages of the process. Spruce chips 2–3 mm thick were cooked using three process modes with the acid containing in total 7 wt % SO_2 and 1.1 wt % base (recalculated to Na_2O). In modes I and II, the temperature–time schedule was standard. Mode II differed from mode I in that samples of alkali liquors were taken at each stage with addition of the equal volume of fresh cooking acid to continue the process in subsequent stages. The temperature schedule was as follows: heating to 105°C for 60 min, keeping at 105°C for 90 min (stage 1); heating to 140°C for 90 min (stage 2); keeping at 140°C for 60 min (stage 3), 120 min (stage 4), and 180 min (stage 5). Mode III was based on mode II and differed from the latter in

1070-4272/02/7503-0486$27.00 © 2002 MAIK "Nauka/Interperiodica"

that after sampling of liquors the wood residue (without washing) was poured over with fresh acid and the successive stage of cooking was carried out until the process completion. The prescribed time and temperature were followed with an accuracy of ±1 min and ±1°C, respectively. The yield and content of lignin were determined by the standard procedures [7].

The kinetic curves of delignification in the coordinates α–τ are shown in the figure.

The kinetic constants were evaluated by the Kolmogorov–Erofeev–Avrami equation reflecting the topochemical nature and nonstationary course of the processes:

$$1 - \alpha = \exp(-kt^n), \quad (1)$$

where α is the fraction of lignosulfonates diffusing from the cell wall into cooking liquor; k is the rate constant of multistage topochemical delignification; t is the process time expressed in minutes as conventionally accepted in the delignification kinetics; and n is a parameter indicating variation of the rate constant of a nonstationary process.

By taking the logarithm, the equation is brought to a linear form:

$$\ln(1 - \alpha) = -kt^n, \quad \ln[-\ln(1 - \alpha)] = \ln k + n\ln t,$$

$$\ln\ln[1/(1 - \alpha)] = \ln k + n\ln t.$$

For practical calculations and plotting, it is preferable to use the logarithms to the base 10 rather than e:

$$\log\log[1/(1 - \alpha)] = \log[-(1 - \alpha)]$$

$$= \log K + n\log t + \log\log e. \quad (2)$$

The latter term in Eq. (2), being small (–0.3623), is usually neglected.

At $\log t \to 0$ $\log K = \log K_0$ (this value is graphically determined by the portion intercepted on the ordinate at $\log t = 0$). The parameter K evaluated by this equation is the effective constant expressed in logarithms to the base 0 and in logarithmic coordinates of the Kolmogorov–Erofeev equation.

The advantage of this topokinetic equation is the possibility of describing the nonstationary delignification in the portion before and after the maximum rate by experimental determination of only one quantity, the residual content of lignin in the wood residue or of lignosulfonates in the cooking liquor. The linear feature of the equation in the logarithmic form allows us

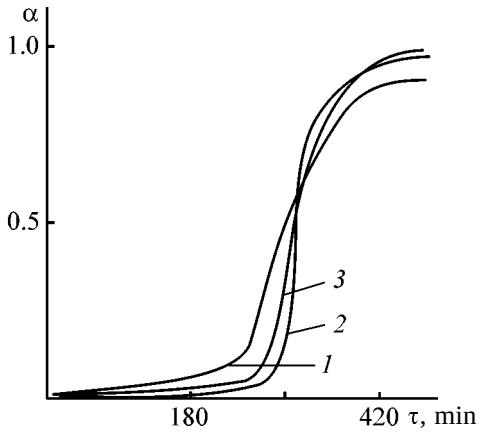

Kinetic curves of delignification: (α) fraction of dissolved lignosulfonates and (τ) time. Cooking mode: (*1*) I, (*2*) II, and (*3*) III.

to find and select graphically the isokinetic linear portions with constant n and $\log K_0$ by the least-squares technique. In this case, it should be noted that K_0 can also be considered as a constant characterizing the relaxation state of the cell wall. The relation of the parameters of the topokinetic equation to the delignification mechanism was estimated from the well-known selection rules for information in topokinetic studies by the Kolmogorov–Erofeev–Avrami equation [8, 9], considering the mechanism of sulfite cooking of cellulose from spruce chips.

A remakable feature of the Kolmogorov–Erofeev–Avrami equation is the possibility of using it for description of the relaxation states of a polymer system [10] at varied process temperature and time. Any such variation of the system characteristics involves certain structural rearrangements depending not only on the temperature and time, but also on the rate of temperature variation in each specific temperature–time schedule.

The parameters n and $\log K_0$ of the logarithmic equation reflect the lifetime of a certain structure of the relaxing polymer system of a wood cell wall. Under the assumption that polymers of cellulose fibers are frozen in delignification processes at commonly used temperatures of cooking, the parameters n and $\log K_0$ characterize the state of the lignocarbohydrate matrix of cell wall. The delignification process is characterized quantitatively by the same constants. Variations of the molecular-weight characteristics of lignin in the process furnish quantitative information on variation of the pore structure of a relaxing cell wall without recovery of wood residue from the cooking liquor.

Table 1. Topokinetic parameters of the main stages of delignification

Curve	60–260 min		270–360 min		370–420 min	
	$-\log K_{01}$	n_1	$-\log K_{02}$	n_2	$-\log K_{03}$	n_3
1	4.25	1.20	6.80	2.40	3.14	1.27
2	3.72	0.75	15.57	5.76	2.06	1.38
3	3.74	0.76	12.61	5.35	3.16	1.84

Table 2. Retention coefficients φ_i of fractions of macromolecules for various intervals of hydrodynamic radii R_{hi} in cooking liquors from successive stages

Stage of cooking	φ_i for indicated R_{hi}, nm				
	<1.5	1.5–3	3–5	5–7	>8
1	1.0	1.0	1.0–1.0	1.0–1.0	1.0
2	0.45	0.45–0.55	0.55–0.72	0.72–1.0	1.0
3	0.70	0.70–0.75	0.75–0.70	0.70–1.0	1.0
4	0.0	0.05	0.05–0.40	0.40–0.55	0.55–1.0

The results of calculations from the experimental data are presented in Table 1.

The hydrodymanic radii of lignosulfonate macromolecules R_h were determined by the laser correlation spectroscopy directly in cooking liquor. The procedure is based on the measurement of the halfwidth of the light scattering spectrum of laser beam from lignin macromolecules in dilute solutions and calculation from these data of the translation diffusion coefficient D and R_h by the well-known Einstein–Stokes formula [11, 12].

The molecular radii of lignosulfonates were measured in samples of the first liquor withdrawn 150 min, the second liquor, 240 min, the third liquor, 360 min, and the fifth liquor, 420 min after the beginning of cooking.

To evaluate the retention coefficient $\varphi(R_{hi})$, the liquor withdrawn in the final, fifth stage of cooking, containing the total set of sizes R_{hi}, was selected as a calibrating mixture. The calculation was carried out by the formula

$$\varphi(R_{hi}) = 1 - [\psi(R_{hi})/f(R_{hi5})] \quad (i = 1, 2, 3\ldots),$$

where $\varphi(R_{hi})$ is the retention coefficient of lignosulfonates with the radius R_{hi}; $\psi(R_{hi})$ is the fraction of the ith interval of radii of lignosulfonate molecules in first–fourth liquors; $f(R_{hi5})$ is the fraction of ith interval of radii of lignosulfonate molecules in the fifth liquor; and i is the number of intervals used for calculation of the retention coefficients.

The calculation results are presented in Table 2.

Variations of the average molecular weights M_w, hydrodynamic radii R_{hi}, the ratio R_{hi}/M_w reflecting branching of molecues in relation to the degree of delignification α, and the fraction of capillaries with the known interval of radii in the wood residue (from published data [1]) are listed in Table 3. The molecular weights M_w were determined on a centrifuge by the nonestablished equilibrium technique [13].

The kinetic curves of delignification in the coordinates α–τ (see figure), evaluated from the results of cooking in mode I (curve *1*) commonly used in industry, are compared with those for mode II, differing in addition of a new portion of fresh acid in each stage (curve *2*), and for mode III differing from cooking in mode II in that in each subsequent stage cooking is performed with the wood residue after cooking in mode II (curve *3*). In view of essential differences in the times and conditions of pretreatment, curves *2* and *3* are brought into coincidence for comparison in the inflection point $\alpha = 0.55$ corresponding to 315 min on the time axis of curve *1*. This procedure allowed us to determine already from the shapes of the primary kinetic curves that in cooking with sampling of liquors and addition of acid (modes II and III) delignification is significantly accelerated and occurs to a greater extent, and the highest rate of the process

Table 3. Characteristics of wood residue and macromolecules in cooking liquor

Stage of cooking	Wood residue				Lignosulfonates		
	yield, %	α	capillaries		$M_w \times 10^{-3}$	R_h, nm	$R_h/M_w \times 10^{-6}$
			radius, nm	% of the total amount			
1	87.7	0.02	1.8–2.4	40	10	2.2	2.2
2	64.2	0.105	1.8–6.0	45	15	2.4	1.6
3	58.9	0.54	2.2–8.0	53	26	3.4	1.3
4	52.6	0.85	2.2–8.0	67	35	4.2	1.2
5	42.5	0.98	2.2–8.0	70	55	4.4	0.8

is observed at $\alpha = 0.55$. This is characteristic of the rate of topochemical processes in solids and hence can be evidence of the topochemical nature of sulfite delignification of the polymeric lignocarbohydrate matrix of cell walls relaxing under conditions predetermined by the temperature–time schedule.

A quantitative distinction in the delignification mechanisms, caused by different sequence and duration of stages 1–3 of cooking in modes II and III, is governed by the numerical values of n and $\log K_0$ (Table 1). It is evident that the process can be divided in three stages: initial (n_1 = 0.75–1.20), active (n_2 = 2.40–5.76), and final (n_3 = 1.27–1.84). In the case of cooking in mode I (without stopping the process and adding fresh acid) all the stages are characterized by smaller numerical differences in the constants $-\log K_0$ and n. According to interpretation of parameters in topokinetic equations [7, 8] and well-known concepts of the delignification mechanism in sulfite cooking, low numerical values of n and $-\log K_0$ in the beginning (60–260 min) and in the end of dlignification (370–420 min) can be assigned to the diffusion mode of the process. The active stage of delignification in mode I at n = 2.40 and $-\log K_0$ = 6.80 substantially differs from those in modes II and III, characterized by n = 5.76–5.35 and $-\log K_0$ = 15.57 and 12.61. These significant differences suggest stronger effect of chemical processes in successive stages of delignification in modes II and III. As seen from comparison of the constants for successive stages of cooking in modes I–III, the relaxation states of the cell system in the active stage of delignification vary significantly. This is caused by differences in the stage-by-stage treatment of the wood residue removed from autoclaves, and hence in the relaxation states of lignocarbohydrate matrix of cell walls. As a result, the process should be considered in terms of molecular relaxation constants and chemical kinetics of delignification.

The effect of changes in pore structure of cell walls as a result of hydrolytic and delignification processes in the lignocarbohydrate matrix on the delignification mechanism in successive sulfite cooking of spruce chips can be estimated by comparing the retention coefficients (Table 2), charactersistics of lignosulfonate macromolecules in solutions, and sizes of capillary pores in wood residue in relation to the degree of delignification (Table 3).

Table 2 shows that at complete retention of macromolecules with the radius greater than 1.5 nm in the first stage of cooking, with increasing extent of delignification (stages 2–4) the retention coefficients of lignosulfonates φ_i gradually decrease for macromolecules with large hydrodynamic radii R_{hi}, up to 7 nm. Macromolecules with the radius greater than 8 nm are completely retained by cell walls in all the stages of cooking. Therefore, it can be concluded that, in the course of structural transformations in the matrix, pores with the size larger than 8 nm were absent or were not formed. In the first stage, retention of macromolecules is apparently caused by plugging or absence of pores in the nondegraded lignocarbohydrate gel in the wood residue. As a result, only low-molecular-weight lignosulfonates can pass into the cooking liquor by the mechanism of molecular diffusion [5, 6]. In stages 2–4, φ_i of molecules with the larger size significantly decreases, and only macromolecules with the radius greater than 8 nm are completely retained. This trend in variation of the sizes of coarse capillaries of the wood residue in particular stages of cooking [1], corresponding to variation of the retention coefficients of lignosulfonates depending on the average hydrodynamic radii R_h, is also followed in variation of the average molecular weight M_w and branching index R_h/M_w of lignosulfonate macromolecules detected in solutions (Table 3).

It was shown previously [5] that macromolecules

of lignosulfonates are separated by ultrafiltration with a synthetic membrane owing to their interaction with the membrane and formation of a gel layer at its surface and in capillaries, and the process itself proceeds in the mode of pre-gel polarization and is characterized by plugging of pores and operation of the molecular-diffusion mechanism of lignosulfonate transfer.

Comparison of data listed in Tables 2 and 3 and topokinetic parameters of delignification (Table 1) gives ground to the statement that, in the first stage of delignification, the process is diffusion-controlled owing to formation of a soft lignosulfonate gel and intramembrane deceleration of lignosulfonate molecules with $M_w < 10^3$, even the least branched (2.2×10^{-6}), and in the final stage it is also diffusion-controlled owing to thin cross-linking and formation of a macromolecular fraction of lignosulfonates with $M_w > 55 \times 10^3$ with the greatest branching (0.8×10^{-6}). It is possible that in the final stage a more rigid lignocarbohydrate gel is formed as a result of thin chemical cross-linking.

The relaxation state of the cellulose component of the cell wall membrane in all the stages does not govern the delignification mechanism in sulfite cooking of cellulose in the ranges of temperature–time schedules with heating and impregnation at 105°C. The delignification rate in this process is governed by modification of characteristics and degradation of the bond network of the lignocarbohydrate matrix relaxing in the process.

CONCLUSION

Variation of the parameters of the Kolmogorov–Erofeev–Avrami topokintic equation, hydrodynamic radii, and coefficients of retention and transformation of macromolecules can be used for quantitative estimation of the contribution of diffusion and mass-transfer to the mechanism of delignification and variation of the porosity of the relaxing matrix of cell walls in sulfite cooking of cellulose produced from spruce chips.

REFERENCES

1. *Kletochnaya stenka drevesiny i ee izmeneniya pri khimicheskikh vzaimodeistviyakh* (Cell Wall of Wood and Its Variations under Effect of Chemical Agents), Riga: Zinatne, 1972.
2. Fengel, D. and Wegener, G., *Wood (Chemistry, Ultrastructure, Reactions)*, Berlin: Walter de Gruyter, 1984.
3. Erin'sh, P.P., *Khim. Drev.*, 1977, no. 1, pp. 8–25.
4. Bogolitsyn, K.G. and Reznikov, V.M., *Khimiya sul'fitnykh metodov delignifikatsii* (Chemistry of Sulfite Delignification Procedures), Moscow: Ekologiya, 1994.
5. Afanas'ev, N.I., Korobova, E.N., and Dyatlova, O.V., *Lesn. Zh.*, 1996, nos. 1–2, pp. 130–135.
6. Afanas'ev, N.I., Structure of Macromolecules in Solutions at Interfaces and Surface-Active Characteristics of Lignosulfonates, *Doctoral Dissertation*, St. Petersburg, 1995.
7. Obolenskaya, A.V., El'nitskaya, Z.P., and Leonovich, A.L., *Laboratornye raboty po khimii drevisiny i tsellyulozy* (Laboratory Works on Chemistry of Wood and Cellulose), Moscow: Ekologiya, 1991.
8. Protashchik, V.A., *Novye zakonomernosti v topokhimii* (New Relationships in Topochemistry), Moscow: Znanie, 1974.
9. Eremin, E.N., *Osnovy khimicheskoi kinetiki* (Principles of Chemical Kinetics), Moscow: Vysshaya Shkola, 1976.
10. Bartenev, G.M. and Frenkel', S.L., *Fizika polimerov* (Polymer Physics), Leningrad: Khimiya, 1990.
11. Afanas'ev, N.I., Noskin, V.A., and Forofontova, S.D., *Khim. Drev.*, 1991, no. 6, pp. 71–73.
12. Afanas'ev, N.I., Ivanova, M.A., and Forofontova, S.D., *Khim. Drev.*, 1993, nos. 4–5, pp. 42–51.
13. Sokolov, O.M., *Opredelenie molekulyarnykh mass ligninov na ul'tratsentrifuge i metodom gel'fil'tratsii* (Determination of Molecular Weights of Lignins on Ultracentrifuge and by Gel Filtration), Leningrad: Leningr. Lesotekh. Akad., 1978.

Russian Journal of Applied Chemistry, Vol. 75, No. 3, 2002, pp. 491–494. Translated from Zhurnal Prikladnoi Khimii, Vol. 75, No. 3, 2002, pp. 502–505.
Original Russian Text Copyright © 2002 by I. P. Deineko, I. V. Deineko, Kornilova.

MACROMOLECULAR CHEMISTRY AND POLYMERIC MATERIALS

Oxidative Ammonolysis of Wood Bark

I. P. Deineko, I. V. Deineko, and L. I. Kornilova

St. Petersburg State Forestry Academy, St. Petersburg, Russia
St. Petersburg State Agricultural University, St. Petersburg, Russia

Received July 20, 2001

Abstract—The influence of temperature (75–100°C), ammonia concentration in solution (1–5%), and oxygen pressure (1–8 MPa) on the yield of the target product (insoluble residue) and nitrogen content in this product in treatment of pine bark with oxygen in aqueous ammonia (oxidative ammonolysis) was studied. The resulting samples were tested in agriculture as nitrogen-containing fertilizers.

In wood felling and processing, large amounts of bark wastes are formed, which are not yet properly utilized. The promising line of utilization of these wastes is their use as fertilizers. The process of production of fertilizers from bark, consisting of composting of the substrate with preliminary addition of nutrients, was considered in detail [1, 2]. The grave drawback of composting is that it is time- (1–4 months) and labor-consuming [2]. The process including treatment of raw materials with oxygen in aqueous ammonia (oxidative ammonolysis) was also proposed for production of nitrogen-containing fertilizers from bark [3]. However, oxidative ammonolysis of bark practically was not studied. In addition, data on the effect of the resulting fertilizer on plants are lacking.

The goal of this work was to study the influence of the process conditions on the yield and characteristics of a nitrogen-containing fertilizer produced from bark by oxidative ammonolysis (oxyammonolysis).

EXPERIMENTAL

The surface part of pine bark (*Pinus Sylvestris*) milled to a fraction of less than 5 mm was used as raw material. The target product of oxidative ammonolysis was the residue insoluble in the reaction medium and presenting a complex of partially oxidized macromolecular components of bark incorporating nitrogen-containing functional groups. The nitrogen content in the product was determined by the Kjeldahl method. The nitrogen content in the initial bark was 0.33%. Two series of the experiments were carried out. In series A, 50 g of bark and 500 ml of aqueous ammonia were placed in a flat-bottomed flask equipped with a reflux condenser, a bubbler, and thermometer. Air was bubbled through the reaction mixture at a flow rate of approximately 20 l h^{-1}. The flask was heated over a period of 1 h to 90 ± 1°C, and this temperature was maintained for 2 h. After completion of the process, the flask was cooled and the reaction mixture was filtered. The residue on the filter was washed with water to neutral reaction, dried at 100°C, and the product yield was determined.

In series B, the experiments were carried out in a rocking (53 s^{-1}) 1-l autoclave equipped with a pressure gage and a thermometer. A 50-g portion of bark and 500 ml of aqueous ammonia were placed into the autoclave, and, after its sealing, oxygen was fed. The autoclave was placed in a heater, stirring was started, and the autoclave was heated to a given temperature. In all runs the process duration was 3 h including the time of reaching the required temperature (1 h). After the process completion, the autoclave was cooled with water and the product was recovered by the same manner as in series A.

The plants were grown in 500 cm^3 vessels. Three tests were performed for each set of conditions. Soddy weakly podzolic medium-loamy soil with a humus content of 2.1–2.5% and pH 5.6–5.9 was used. The content of mobile compounds of phosphorus and potassium was 0.10 g P_2O_5 and 0.10 g K_2O per 1 kg of soil. The efficiency of the samples was determined from the amount of the resulting ground biomass. For monitoring we used (a) fertilizer-free soil and (b) soil with mineral fertilizers (ammonium nitrate, double superphosphate, and potassium sulfate): 0.15 g N, 0.10 g P_2O_5, and 0.10 g K_2O per 1 kg of soil. The samples of series A were tested in growing of corn (three plants per vessel). The samples were taken in the amount corresponding to 0.15 g N per 1 kg of

1070-4272/02/7503-0491$27.00 © 2002 MAIK "Nauka/Interperiodica"

Table 1. Influence of ammonia concentration in solution on characteristics of the product at 90°C

Run no.	C_{NH_3}, wt %	Product yield, %	N, %
1A	1.0	87.3	1.10
2A	2.4	85.1	1.42
3A	3.3	85.9	1.86
4A	5.1	80.7	2.02
5A*	2.8	83.0	1.61

* In run 5A, $CuCl_2$ was added into solution (0.2% of bark weight).

Table 2. Influence of temperature on the product yield and nitrogen content in the product. P_{O_2} = 0.1 MPa and C_{NH_3} = 5.2 wt %

Run no.	*T*, °C	Yield, %	N, %
1ß	75	77.7	1.60
2ß	81	67.7	1.90
3ß	89	68.4	1.92

Table 3. Influence of oxygen pressure on the product yield and nitrogen content in the product at C_{NH_3} = 5.1 wt %

Run no.	*T*, °C	P_{O_2}, MPa	Consumption of O_2, %	Yield, %	N, %
3ß	89	0.1	1.5	68.4	1.92
4ß	87	0.3	4.2	75.3	2.10
5ß	89	0.5	7.0	77.9	2.71
6ß	98	0.5	7.0	78.3	2.83
7ß	91	0.8	11.2	76.8	3.50

Table 4. Effect of nitrogen-containing fertilizers on the productivity of corn

Fertilizer	Weight of dry substance, g	Growth, %
None	2.4 ± 0.2	
$N_{0.1}P_{0.2}K_{0.2}$	3.5 ± 0.2	46.1
Product of run:		
4A	3.8 ± 0.4	58.1
5A	5.5 ± 0.3	126.5

soil. The samples of series B were tested in growing of multimowing rye grass (*Lolium multiflorum*). The following amounts of the samples were used: B_1, 0.15 g N per 1 kg of soil; B_2, 0.30 g N per 1 kg of soil. The productivity was considered from three mowings.

In the first series of the experiments (series A), we examined the influence of the ammonia concentration on the characteristics of the resulting product. Table 1 shows that with increasing concentration of ammonia in solution the yield of the product (insoluble residue) decreases; in parallel, the nitrogen content in the product increases. One run was performed with addition of copper chloride $CuCl_2$. We used copper salt because of the fact that, as found in [4], addition of copper ions to the reaction mixture in oxyammonolysis of lignin results in increased nitrogen content in the product. It was assumed that in oxyammonolysis of pine bark, having fairly high content of lignin and other phenolic compounds [5], addition of copper chloride will result in increased nitrogen content in the product as well. However, Table 1 shows that copper(II) ions did not noticeably affect the yield of insoluble residue and the nitrogen content in this residue. Apparently, nitrogen-containing substances formed in this case have relatively low molecular weight and therefore are readily soluble in the reaction mixture.

In series B, we examined the influence of the process temperature and oxygen pressure on the product characteristics. Oxidative ammonolysis was carried out in a rocking autoclave, in which oxygen was fed to a certain pressure before the run. To prevent fast development of deep oxidation of the substrate, oxygen was taken in relatively low amounts. Table 2 shows that with increasing temperature from 75 to 81°C the product yield significantly decreases. This may be due to the presence of large amounts of alkali-soluble substances in the bark [5], which pass into aqueous-ammonia solutions under conditions of oxidative ammonolysis. With increase in temperature, the nitrogen content in the insoluble residue increases. With further increase in temperature, the yield of the product and the nitrogen content in the product do not vary noticeably, which is apparently caused by small amount of oxygen (1.5 wt % relative to the initial raw material) fed into the system and hence by a low extent of oxidation. Attention is drawn to the fact that in the runs of series B the yield of the insoluble residue is noticeably lower than the yield of the products obtained in series A. This distinction may be due to lower concentration of ammonia in the reaction mixture in series A, as a result of ammonia removal with the air flow in the runs of series A, which decreases the ammonia concentration in the solution by more than 30%.

An increase in the oxygen pressure from 0.1 to 0.5 MPa increases the product yield and the nitrogen content in the product (Table 3).

Table 5. Effect of nitrogen-containing fertilizers on the productivity of multimowing rye grass

Fertilizer	Weight of dry substance, g				Increase, %
	1st mowing	2nd mowing	3rd mowing	total	
None	1.09	0.56	0.10	1.75	
$N_{0.15}P_{0.10}K_{0.10}$	1.63	0.89	0.26	2.78	58.9
Initial bark	–	0.36	1.02	1.38	–21.2
$1B_1$	1.17	0.61	0.26	2.04	16.6
$3B_1$	1.11	0.77	0.25	2.13	21.7
$4B_1$	1.22	0.65	0.22	2.09	19.4
$5B_1$	1.32	0.77	0.26	2.35	34.3
$N_{0.30}P_{0.10}K_{0.10}$	2.43	1.32	0.32	4.07	132.6
$1B_2$	1.38	0.85	0.24	2.47	41.2
$4B_2$	1.51	0.76	0.27	2.54	45.2
$5B_2$	1.76	1.05	0.18	2.99	70.9

The results obtained can be explained by an increase in the amount of quinone structures formed from phenols, whose reactions with ammonia cause accumulation of nitrogen-containing functional groups apparently participating in condensation reactions and forming macromolecular products insoluble in the reaction medium. However, with increasing oxygen pressure to 0.8 MPa the yield of the insoluble residue decreases. This is apparently due to the fact that further increase in the oxygen amount in the system results in acceleration of oxidative degradation reactions yielding water-soluble substances. Since the whole of oxygen added to the system is consumed during the process, an increase in temperature does not affect substantially the product yield (Table 3, run nos. 5B and 6B).

The use of nitrogen-containing samples of series A as fertilizers in growing of corn showed their high performance (Table 4). The greatest positive effect was observed with fertilizers of run 5A, which may be due to the presence of copper ions, playing an important role in photosynthesis.

The experiments with rye grass showed that the initial bark exerts depressing effect on the plant growth. This is caused by the presence in the fresh bark of organic compounds toxic for plants. In oxyammonolysis these compounds are oxidized, react with ammonia, and lose the ability to inhibit the plant growth. Nitrogen-containing samples of series B exert a positive effect on the growth and development of plants (Table 5).

The performance of nitrogen-containing bark products increases with increasing nitrogen content. Since the specific consumption of nitrogen in fertilizers added to soils was the same, the above trend can be explained by an increase in the degree of oxidation of the samples in hand. Indeed, Table 3 shows that the oxygen consumption in preparation of nitrogen-containing fertilizers increases in the series 3B–7B.

Table 5 shows that the performance of organic fertilizers of series B, in contrast to those of series A, was lower than that of mineral fertilizers. The difference between samples of series A and B may be due to higher degree of condensation of organic compounds produced by oxidative ammonolysis under oxygen pressure. As a result, degradation of fertilizers with soil microflora is hindered, and liberation of chemically bonded nitrogen is decelerated. The indirect evidence of this assumption is an increase in the effect of organic fertilizers with increase in their expenditure.

CONCLUSIONS

(1) In treatment of pine bark with oxygen in aqueous ammonia, the bark components react with ammonia to form nitrogen-containing products. The yield of the product and its nitrogen content depend on the process conditions and vary in the ranges 68–87 and 1.10–3.50%, respectively.

(2) The amount of chemically bonded nitrogen in the samples produced by oxidative ammonolysis increases with increasing concentration of ammonia in solution, process temperature, and oxygen pressure in the system.

(3) The resulting nitrogen-containing samples

exhibit high performance as fertilizers in growing of corn and multimowing ray grass.

REFERENCES

1. Varfolomeev, L.A., *Prigotovlenie promyshlennykh kompostov na osnove tverdykh otkhodov derevoobrabotki* (Preparation of Industrial Composts Based on Solid Wastes of Wood Processing), Moscow: VNIITEIagroprom, 1992.
2. Zhidkov, A.V., *Utilizatsiya drevesnoi kory* (Utilization of Wood Bark), Moscow: Lesn. Prom–st, 1985.
3. USSR Inventor's Certificate no. 545 627.
4. Deineko, I.P. and Balin, N.B., *Khim. Drev*., 1981, no. 5, pp. 53–59.
5. Deineko, I. and Deineko, I., *Proc. 5th Eur. Workshop on Lignocellulosics and Pulp. Advances in Lignocellulosics Chemistry for Ecologically Friendly Pulping and Bleaching Technologies*, Aveiro (Portugal), August 30–September 2, 1998, pp. 233–236.

Russian Journal of Applied Chemistry, Vol. 75, No. 3, 2002, pp. 495–498. Translated from Zhurnal Prikladnoi Khimii, Vol. 75, No. 3, 2002, pp. 506–509.
Original Russian Text Copyright © 2002 by Platonov, Proskuryakov, Glybina.

CHEMISTRY OF FOSSIL FUEL

Chemical Composition of the Organic Matter of Oil Shale (Kerogen-70) from Leningrad Oblast (Benzene–Ethanol Extract)

V. V. Platonov, V. A. Proskuryakov, and A. V. Glybina

Tolstoi State Pedagogical University, Tula, Russia
St. Petersburg State Technological Institute, St. Petersburg, Russia

Received August 13, 2001

Abstract—Detailed data are reported on the chemical composition of the benzene–ethanol extract of oil shale (kerogen-70).

Among fossil fuels, oil shales occupy a particular position with respect to both origin and composition, on the one hand, and role as a chemical raw material and power source, on the other hand. The increased hydrogen content in the organic matter of shales (OMS) and, as a result, higher yield of liquid products make oil shales promising as a source of liquid fuel and raw materials for chemical industry.

Integrated processing of oil shales to obtain hydrocarbon raw materials can be set up only after detailed elucidation of the composition of OMS. Such studies will give insight into the composition of the initial biomaterial, its genetic relationship with various OMS compounds, and pathways of biogeochemical transformation of OMS in the course of shale formation and will facilitate development of a process for shale treatment to obtain a wide range of valuable products [1–12].

In this work we studied the chemical composition of the benzene–ethanol extract of shale oil (kerogen-70) from Leningrad oblast.

EXPERIMENTAL

Shale was extracted in a Soxhlet apparatus with a boiling benzene–ethanol (3 : 1 by volume) mixture. The yield of the extract was 6.4% relative to OMS. The molecular structures of the extract components were determined by a combination of methods including elemental, quantitative functional, emission spectrum, and structural-group analyses, cryoscopy, IR and UV/VIS spectroscopy, and capillary gas–liquid chromatography (CGLC).

The average molecular weight of the extract $\overline{M}$ was 298; elemental composition, %: C 73.6, H 10.5, N 0.7, and O + S 15.2; atomic ratio H/C 1.71; degrees of aromaticity 0.19, naphthenicity 0.53, and alkyl substitution 0.28; functional composition (groups, mg-equiv g^{-1}): phenolic (PG) 1.01, keto (KG) 1.33, quinoid (QG) 0.79, carboxy (CG) 0.22; ester groups (EG) and lactone rings (LR) 0.35; iodine number 0.14.

In the IR spectrum of the extract, we identified the absorption bands of the following fragments (ν, cm^{-1}). Fairly strong bands of aromatic rings (3010–3080, doublet 1500/1595, 1450, 675–900, 800–1200). The higher intensity of the low-frequency component of the doublet suggests that monocyclic aromatic structures prevail. Substitution in aromatic rings: monosubstituted compounds (735, 710) prevail, the content of disubstituted compounds (740–760, 820) is lower, and more highly substituted compounds are not detected. The spectra also contain bands of the CH_3 and CH_2 groups in alkanes and cycloalkane structures (2850, 2926–2980, 1370–1380, 1470, 1450), a broad strong band (3380) of alcoholic and phenolic hydroxyls, and some other bands characteristic of alcohols and phenols (1360, 1220, 1330–1420, 635–660). We also observed medium-intensity carbonyl bands characteristic of various compounds: ketones, mainly aliphatic (1690, 1700, 1710, 1720, 1100); α- and γ-pyrones (1720, 1735, 1600–1650, 1540); six- (1735, 750, present in larger amounts) and five-membered (1775, 1720) lactones; and cyclic anhydrides (1750, 1800). Also the spectra contain weak bands of esters with cycloalkane and alkane fragments (3450, 1735–1750, 1160–1210), furan (1570–1605, 1475–1510, 1380–1400, 820–885, 740–800) and pyrrole heterocycles (3490, 1565, 1500), and alkoxy groups (1200–1225, 812, 2990), including methoxy groups (2835).

1070-4272/02/7503-0495$27.00 © 2002 MAIK "Nauka/Interperiodica"

Table 1. Yields and characterisrtics of eluates of the benzene–ethanol extract*

Eluate no.	Yield	Characteristics
1	74.0	*M* 295; C 75.3; H 10.9; N 0.2; O, S 13.6; H/C 1.74; D_a 0.12; D_n 0.55; D_{alk} 0.33; PG 0.06; KG 0.68; QG 0.05; CG 0.02; EG, LR 0.02; IN 0.03
2	10.0	*M* 268; C 74.3; H 9.9; N 0.8; O, S 15.0; H/C 1.60; D_a 0.15; D_n 0.51; D_{alk} 0.34; PG 0.75; KG 1.13; QG 0.56; CG 0.07; EG, LR 0.42; IN 0.09
3	4.5	*M* 235; C 73.3; H 9.7; N 1.5; O, S 15.5; H/C 1.59; D_a 0.36; D_n 0.40; D_{alk} 0.24; PG 1.80; KG 2.40; QG 1.45; CG 0.27; EG, LR 0.85; IN 0.15
4	8.1	*M* 309; C 69.7; H 10.5; N 3.8; O, S 16.0; H/C 1.81; D_a 0.45; D_n 0.45; D_{alk} 0.10; PG 5.79; KG 3.82; QG 4.37; CG 1.15; EG, LR 2.43; IN 0.45
5	0.5	*M* 414; C 54.1; H 6.6; N 2.5; O, S 36.8; H/C 1.46; D_a 0.54; D_n 0.30; D_{alk} 0.16; PG 8.25; KG 7.07; QG 6.95; CG 1.68; EG, LR 2.95; IN 0.95
6	2.9	*M* 465; C 42.4; H 4.0; N 2.5; O, S 51.1; H/C 1.13; D_a 0.60; D_n 0.28; D_{alk} 0.12; PG 10.25; KG 10.05; QG 8.32; CG 2.85; EG, LR 1.22; IN 2.03

* The yields of eluates are given in wt % relative to the OMS extract. (*M*) Molecular weight; (C, H, N, O, S) content of the respective elements, wt %; (H/C) H/C atomic ratio; (D_a, D_n, D_{alk}) degrees of aromaticity, naphthenicity, and alkyl substitution, respectively; groups: (PG) phenolic, (KG) keto, (QG) quinoid, (CG) carboxy, (EG) ester, and (LR) lactone rings; (IN) iodine number.

The conclusions made from the IR spectra are confirmed by the UV/VIS data. The main absorption maxima (λ_{max}, nm) in the UV/VIS spectra belong to unsaturated carboxylic acids and their derivatives (200), flavonols (250, 370), enols (220, 320), benzene rings (200, 260), steroid λ-diketones and their derivatives (280, 340), porphines (450, 480–494, 500–550), possibly nickel porphyrins; and chlorophylls b (456, 598, 646) and a (430, 617, 667).

By emission spectrum analysis, we detected in the extract Fe, Ni, V, Cu, Zn, Co, Mo, Si, Ge, Ga, Ti, Ca, Mg, and Al.

Thus, compounds from the benzene–ethanol extract have a relatively high molecular weight and polyfunctional composition; they contain unsaturated fragments.

To obtain more detailed data on the composition of the initial shale (kerogen-70) and benzene–ethanol extract, it was appropriate to separate the extract into a number of close-cut fractions by adsorption liquid chromatography on ASKM silica gel. This procedure in most cases does not alter the structures of the compounds being separated.

The following eluates were obtained (the eluents are given in parentheses): nos. 1 (C_6H_{14}), 2 (C_6H_{14}–C_6H_6, 1 : 1 by volume), 3 (C_6H_6), 4 ($CHCl_3$), 5 [$(CH_3)_2CO$], and 6 (C_2H_5OH). These eluates were studied by the same physicochemical methods as the initial benzene–ethanol extract (Table 1).

In the IR spectrum of eluate no. 1, we identified strong absorption bands (ν, cm^{-1}) of long alkyl chains and saturated rings (2930, 2970, 2860, 1450, 1460, 1470, 1380, 970, 725) and weak bands of aromatic rings (3060, doublet 1500–1600, a series of bands at 900–1200), unsaturated compounds (3060, 1675, 680, 880), possibly carotenoids, and aliphatic ketones (1695, 1710, 1650, 1720).

By UV/VIS spectroscopy (λ_{max}, nm), we detected unsaturated carboxylic acids and their derivatives (220), carotenoid pigments (440.5, 450, 480–494, 500–550), diketones of the diterpene series (318), flavonols (251, 370), and chlorophylls a (380, 418, 428, 510, 580, 700) and b (428, 465, 675).

By CGLC, we identified in eluate no. 1 *n*-alkanes, isoalkanes, and cycloalkanes (Table 2). The odd/even ratio is 0.99 for alkanes and 0.80 for isoalkanes, indicating that the major role in formation of OMS was played by algal material, although the contribution of terrestrial material is also significant. It should be noted that in diagenesis the reductive conditions prevailed. The distribution of *n*-alkanes has a maximum at C_{21}–C_{27}, on the whole typical of bacterial bioproduction.

The major bands in the IR spectrum of eluate no. 2 (ν, cm^{-1}) are those of long alkyl chains and, to a lesser extent, of saturated rings (2960, 2920, 2856, 2840, 1470, 1460, 1450, 1375, 970, 720) and aromatic (possibly naphthalene) rings (3000–3050, doublet 1500–1600, 750); bands are detected assignable to C=C bonds (3000–3050, 1675, 965, 730–885), keto groups (1695, 1705, 1715), ester groups (1730, 1755,

3470), primary and secondary amines, alcohols (sharp peak at 3400, 3250–3450, shoulder at 3200, 750–850, 1590–1650), and oxygen-containing heterocycles (1570–1605, 1475–1510, 1380–1400, 820–885, 740–800).

According to the UV/VIS spectrum (λ_{max}, nm), eluate no. 2 contains unsaturated carboxylic acids and their derivatives (220), λ-diketones (280, 350), carotenoids (440.5, 450, 480–494, 500–550), diketones of the diterpene series (318), porphyrin rings (520, 560), flavonols (251, 370), and chlorophylls a and b (380, 418, 428, 510, 580, 700, 428, 465, 675).

The IR spectrum of eluate no. 3 contains the bands (ν, cm^{-1}) of aromatic rings (3030–3070, doublet 1500–1600, series of bands at 900–1200), alkyl chains (2920, 2960, 2880, 1470, 1460, 1385 broad split, 730), keto groups (1700, 1715, 1725), ester groups (1750, 1730), and lactone rings (1770, 1785).

By UV/VIS spectroscopy (λ_{max}, nm), we detected in eluate no. 3 carotenoids (440.5, 450, 480–494), saturated and unsaturated ketones (280, 365–368, 380–390), unsaturated lactones, and unsaturated esters (200, 240).

The IR spectrum of eluate no. 4 contains the bands (ν, cm^{-1}) of aromatic rings (3050–3070, doublet 1605/1595, series of bands at 900–1200; impurity of hydroaromatic rings is possible), unsaturated rings (1470, 1270, 970), short aliphatic chains, substituted pyridines and quinolines (3030–3070, 1585–1620, 1570–1575, 1475, 1428), pyrrole rings (3490, 1565, 1500), keto groups (1705, 1715, 1725), ester groups and lactone rings (1730, 1745, 1765, 1785, 1795, 1805), aromatic ethers (990–1090 broad), and primary alcohols (3140–3600 broad).

The UV/VIS spectra (λ_{max}, nm) suggest the presence of unsaturated lactones and esters (222), saturated and unsaturated ketones (280, 365–368, 380–390), flavonol (246, 368) and coumarin (266, 282, 318) derivatives, chlorophyll c (444, 580, 630), bacteriochlorophyll (475), and nickel porphyrin (575, 550); the presence of nickel was confirmed by emission spectrum analysis.

Eluate no. 5 is characterized by a high content of sulfur and oxygen and a low H/C ratio.

Its IR spectrum (ν, cm^{-1}) contains the bands of aromatic rings (3050, doublet 1500/1600, 727), alkyl chains and unsaturated rings (2860, 2940, 2970, 1465, 1470, 1300, 1380 narrow, 1022, 970, 750–920), carboxy groups and ketones, mainly aliphatic (1690, 1715, 1725, 1050), esters and lactones (1735, 1745, 1250–1300, 1100–1150, 1765, 1780, 1790), with a possible impurity of chromone structures; alcoholic and phenolic hydroxyls (3100–3600, 1050 strong broad, 1200, 1310–1410), cyclic ethers (broad band of complex structure at 1180–1290), terpenes (1680, 1648, 890, 810, 680), unsaturated double bonds, and steroid structures (series of bands at 3390, 3200 shoulder, 1612, 1585, 1500, 1435, 1415, 1054, 870, 815).

Table 2. Content* of *n*-alkanes and isoalkanes in eluate no. 2

n-Alkane	Content, wt %	Isoalkane	Content, wt %
$C_{12}H_{26}$	0.05	$C_{12}H_{26}$	0.08
$C_{13}H_{28}$	0.38	$C_{13}H_{28}$	0.13
$C_{14}H_{30}$	0.92	$C_{14}H_{30}$	0.42
$C_{15}H_{32}$	2.20	$C_{15}H_{32}$	0.49
$C_{16}H_{34}$	2.22	$C_{16}H_{34}$	0.82
$C_{17}H_{36}$	2.71	$C_{17}H_{36}$	0.36
$C_{18}H_{38}$	2.18	$C_{18}H_{38}$	0.33
$C_{19}H_{40}$	2.56	$C_{19}H_{40}$	0.20
$C_{20}H_{42}$	2.98	$C_{20}H_{42}$	0.16
$C_{21}H_{44}$	3.73	$C_{21}H_{44}$	0.13
$C_{22}H_{46}$	4.61	$C_{22}H_{46}$	0.26
$C_{23}H_{48}$	4.93	$C_{23}H_{48}$	0.39
$C_{24}H_{50}$	4.73	$C_{24}H_{50}$	0.33
$C_{25}H_{52}$	4.14	$C_{25}H_{52}$	0.33
$C_{26}H_{54}$	3.42	$C_{26}H_{54}$	0.35
$C_{27}H_{56}$	2.69	$C_{27}H_{56}$	0.39
$C_{28}H_{58}$	2.99	$C_{28}H_{58}$	0.29
$C_{29}H_{60}$	3.20	$C_{29}H_{60}$	0.41
$C_{30}H_{62}$	2.95	$C_{30}H_{62}$	0.33
$C_{31}H_{64}$	1.98	$C_{31}H_{64}$	0.37
$C_{32}H_{66}$	1.72	$C_{32}H_{66}$	0.64
$C_{33}H_{68}$	1.18	$C_{33}H_{68}$	0.41
$C_{34}H_{70}$	1.14	$C_{34}H_{70}$	0.49

* Relative to the total weight of hydrocarbons in the eluate.

By UV/VIS spectroscopy (λ_{max}, nm), we detected in eluate no. 5 aliphatic ketones (300), diketones of the diterpene series (319), carotenoids (440, 450, 480–494, 500–550), chlorophyll a (380, 418, 428, 510, 580, 700), nickel and vanadium porphyrins (620, 565, 535, 500, 400), and chlorins (695).

Eluate no. 6 is characterized by a low content of nitrogen and hydrogen and a low H/C ratio.

In its spectrum, we identified the bands (ν, cm^{-1}) of alkyl chains and saturated rings (2980, 2930, 2815, 2826, 1475, 1455, 1380 split, 1260, 970, 720), traces of aromatic rings (3050, doublet 1500–1600, 725), alcohols and phenols (3620, 3400, 3170, 1200, 1155, 1310–1410), carboxy groups (2730, 1300, 1310, 1295), traces of sulfur compounds (1930, 1950), thio-

phenes (1050–1200, 1225–1260, 847, 549), sulfides (630, 680–700), and also skeleton vibration bands of heterocycles or metal complexes of oxygen-containing compounds (465–475).

According to the UV/VIS spectrum (λ_{max}, nm), eluate no. 6 contains chlorophylls a (380, 418, 428, 510, 580, 700) and b (456, 598, 646), saturated ketones (275–290), and polycyclic and aromatic compounds, mainly of the naphthalene series (220, 276, 311).

To conclude, the developed adsorption-chromatographic procedure allowed separation of the benzene–ethanol extract of oil shale (kerogen-70) into close-cut groups appreciably differing in the molecular weight, elemental composition, quantitative content of functional groups, degree of aromaticity, and H/C ratio. The benzene–ethanol extract consists mainly of cycloalkanes and alkanes. The OMS was formed not only from algal material, but also from terrestrial material of higher plants, bacterial bioproducts, animal material, and fungi. Detection of long-chain *n*-alkanes (C_{12}–C_{34}) proves participation of terrestrial higher plants in formation of OMS.

CONCLUSIONS

(1) An adsorption liquid chromatographic procedure was developed for separation of the benzene–ethanol extract of oil shale into a number of close-cut fractions appreciably differing in the molecular weight, elemental composition, and functional groups.

(2) Organic matter of shales was formed with the participation of algal and terrestrial material of higher plants, bacterial bioproducts, animal material, and fungi.

REFERENCES

1. Gordenko, V.M. and Pogrebnova, N.V., *Goryuch. Slantsy*, 1987, vol. 4, no. 2, pp. 120–129.
2. Zhukova, A.V. and Lopatin, V.V., *Goryuch. Slantsy*, 1988, vol. 5, no. 4, pp. 356–364.
3. Lapo, A.V. and Mikhailova, N.S., *Goryuch. Slantsy*, 1988, vol. 5, no. 4, pp. 349–355.
4. Zhmur, S.I., Serova, N.B., and Melamedova, V.S., *Goryuch. Slantsy*, 1986, vol. 3, no. 4, pp. 365–375.
5. Sumberg, A.I., Urov, K.E., and Grinchak, M.B., *Goryuch. Slantsy*, 1987, vol. 4, no. 4, pp. 394–403.
6. Bondar', E.B. and Kuzik, M.G., *Goryuch. Slantsy*, 1986, vol. 3, no. 1, pp. 13–22.
7. Urov, K.E. and Klesment, I.R., *Khim. Tverd. Topl.*, 1981, no. 3, pp. 16–21.
8. Gulyaeva, N.D., Arefeeva, O.A., and Petrov, A.A., *Khim. Tverd. Topl.*, 1977, no. 6, pp. 25–30.
9. Klesment, I.R., *Khim. Tverd. Topl.*, 1987, no. 4, pp. 36–41.
10. Grinberg, I.V. and Strel'kovskaya, A.G., *Khim. Tverd. Topl.*, 1981, no. 3, pp. 13–15.
11. Krypina, S.M. and Kovalev, K.E., *Khim. Tverd. Topl.*, 1989, no. 4, pp. 16–21.
12. Vol'-Epshtein, A.B., Platonov, V.V., and Shpil'berg, M.B., *Khim. Tverd. Topl.*, 1987, no. 3, pp. 69–75.

Russian Journal of Applied Chemistry, Vol. 75, No. 3, 2002, pp. 499–503. Translated from Zhurnal Prikladnoi Khimii, Vol. 75, No. 3, 2002, pp. 510–514.
Original Russian Text Copyright © 2002 by Platonov, Proskuryakov, Shavyrina, Shvykin, Podshibyakin, Sychev.

CHEMISTRY OF FOSSIL FUEL

Chemical Concept of Geodynamic Shocks in Coal Strata

V. V. Platonov, V. A. Proskuryakov, O. A. Shavyrina, A. Yu. Shvykin, S. I. Podshibyakin, and A. I. Sychev

Tolstoi State Pedagogical University, Tula, Russia
St. Petersburg State Technological Institute, St. Petersburg, Russia

Received October 9, 2001

Abstract—A chemical concept of geodynamic shocks in coal strata, accompanied by ejection of coal dust and gas, is suggested.

A dangerous phenomenon in coal mining is geodynamic shock in a coal stratum, accompanied by ejection of enormous amount of coal dust and gas enriched in H_2, CH_4, CO, CO_2, C_2H_6, C_3H_8, and other low-boiling hydrocarbons. This phenomenon causes severe damages and miners' death. Various theories explaining the origin of geodynamic shock mainly take into account the physical characteristics of coal and do not consider at all the features of chemical composition of the organic and mineral components of coal.

Studies of sudden ejections of coal and gas in mines revealed a correlation between ejection danger in coal strata and degree of disturbance of their structure [1–3]. Coals with different degrees of structure disturbance are characterized by different rates of release of adsorbed gaseous products. This fact can be used to reveal zones with ejection danger in coal strata [1, 2]. The capability of coals for fast gas release is associated with formation of a highly developed microporous structure in the course of their dispersion.

Published data concerning mechanical actions on various caustobioliths (lignites, coals, oil shales, peat) and also on graphite, quartz, and various metal oxides show that mechanical actions induce significant changes in the physical structure, enhance the reactivity, and cause release of a large amount of a gas enriched in hydrogen [4–17]. Dispersion of fossil fuels significantly affects the composition of both organic and mineral matter. The organic matter of fuels is hydrogenated, a "mobile molecular phase" appears, the yield of extracts, humic and fulvic acids, and neutral oils grows, the H/C atomic ratio in the residual coal decreases, but the degree of its aromaticity increases; various atomic groups are broken down or altered; the layer size, cluster height, number of layers *n* associated in the cluster, and the distance between aromatic layers decreases. Mechanical action on coals causes, along with increased yield of bitumens, also generation of gaseous products containing, along with O_2, CO_2, and CO, also significant amounts of H_2, CH_4, C_2H_6, C_3H_8, and C_4H_{10}. The composition of gaseous products depends on the origin of coal, grinding procedure (planetary mills, disintegrators, acoustic or ultrasonic treatment, etc.), and medium and time of mechanical activation.

The goal of this work was to study the chemical composition of the initial coals of various technological groups and of their geodynamic shock products, and also to develop a chemical concept of geodynamic shocks in coal strata in relation to the chemical composition of the organic and mineral matter of coals.

The investigation objects were coals of groups E, D, and G, and also the product of sudden ejections of coal and dust in Vostochnaya mine (Donetsk coal basin), the so-called "mad dust."

The results of technical analysis, elemental composition and yield of the benzene–ethanol extract, structural parameters, and elemental and quantitative functional composition of the initial coals and "mad dust" are listed in the table.

The table shows that the initial coals significantly differ in the yield of volatiles (24.8–41.2%), carbon (79.8–88.6%) and hydrogen (5.5–5.9%) content (wt%, daf), yield of the benzene–ethanol extract [2.10–3.52 wt % relative to organic matter of coal (OMC)], average molecular weight, elemental and functional composition, and structural parameters of the extract.

In the IR spectrum of the extracts, we identified the absorption bands (ν, cm^{-1}) of the following fragments: aromatic rings (3030–3100, CH stretching

1070-4272/02/7503-0499$27.00 © 2002 MAIK "Nauka/Interperiodica"

Results of technical and elemental analysis of the initial coals and "mad dust"; yield, elemental and functional composition, and structural parameters of the benzene–ethanol extract*

Parameter	Initial coal			Coal from "mad dust"		
	E	D	G	E	D	G
Technical analysis, wt %:						
W^a	1.2	3.1	1.5	1.8	3.9	1.8
A	9.2	7.5	10.2	11.5	9.2	13.2
V^{daf}	41.2	36.2	24.8	40.1	32.2	23.5
Elemental composition, wt % daf:						
C	79.8	82.4	88.6	76.2	80.2	85.6
H	5.7	5.9	5.5	5.9	6.5	5.8
N	0.8	1.5	2.0	1.0	1.7	2.2
O, S	13.7	10.2	3.9	16.9	11.6	6.4
Benzene–ethanol extract:						
yield, wt % of OMC	2.1	3.1	3.52	9.5	12.4	16.4
molecular weight, amu	382	332	345	425	365	384
elemental composition, wt % daf:						
C	78.2	80.2	86.2	74.2	77.8	82.5
H	5.8	6.1	5.6	6.2	7.2	6.0
N	1.0	1.6	2.1	1.5	2.1	2.6
O, S	15.0	12.1	6.2	18.1	12.9	8.9
structural parameters:						
D_a	0.59	0.52	0.48	0.64	0.58	0.54
D_n	0.25	0.30	0.35	0.30	0.36	0.40
D_{alk}	0.16	0.18	0.17	0.06	0.04	0.06
functional composition, mg-equiv g^{-1}:	0.16	0.18	0.17			
PG	0.12	0.15	0.25	0.25	0.40	0.53
CG	0.13	0.16	0.32	0.31	0.40	0.71
QG	0.45	0.53	0.93	1.25	1.63	2.05
KG	0.05	0.05	0.08	0.15	0.20	0.22
EG, LR	0.10	0.13	0.20	0.35	0.45	0.65
IN	0.10	0.13	0.35	0.35	0.40	0.60

* (W^a, A, V^{daf}) Moisture content, ash residue, and yield of volatiles, respectively, wt % relative to dry sample; (C, H, N, O, S) content of the respective elements, wt % daf; (D_a, D_n, D_{alk}) degrees of aromaticity, naphthenicity, and alkyl substitution, respectively; groups: (PG) phenolic, (CG) carboxy, (QG) quinoid, (KG) keto, (EG) ester, and (LR) lactone rings; (IN) iodine number, mg-equiv g^{-1}.

vibrations; 1575–1605 and 1480–1510, C=C in-plane vibrations; the components of the doublet at 1575–1605 have comparable intensity, which suggests low degree of fusion of aromatic rings; strong bands of the CH_3 and i-C_3H_7 groups (2975–2950, 2885–2860, 1380, 1410–1435); stretching and bending vibration bands of CH and CH_2 groups in aliphatic and cycloalkane fragments (2975–2950, 2850, 2875, 1460, 1260, 1470, 970); stretching vibration bands of O–H (2500–3500, 3500–3550, 955–890) and C–O (1230–1140, 1310–1410, 1395–1440) groups in carboxylic acids and phenols; bands of keto (1700–1725) and ester groups, six- (1795–1750, 1660–1210) and five-membered lactone rings (1760–1795); medium-intensity bands of quinoids groups (1645, 1675); and weak bands of ethers (2835–2878, 1125, 1210–1310) and oxygen-containing furan heterocycles (1570–1605, 820–880, 740–800).

The IR spectra of extracts from "mad dust" are characterized by increased concentration of absorption bands of epoxy groups (2990–3050, 1230–1280, 815), ester groups and lactone rings, especially of aliphatic esters, quinoid rings, and furan heterocycles; the content of carboxy and phenolic groups is also somewhat increased.

The yield of the benzene–ethanol extract from "mad dust" varies from 9.5 (E) to 16.4 (G); the average molecular weight, from 365 to 425; and the degree of aromaticity, from 0.30 (E) to 0.40 (G). The prevailing functional groups are quinoid, carboxy, phenolic, and ester (including lactone rings; see table).

The table shows that mechanochemical breakdown of OMC significantly increases the yield of the benzene–ethanol extract and the quantitative content of functional groups. The solid residue of the coal is enriched in the mineral component, the hydrogen content increases, but the carbon content and the yield of volatiles decrease. For example, for D6 coal the yield of volatiles decreased from 36 to 32.2, and the carbon content, from 82.4 to 80.2; the yield of hydrogen increased from 5.9 to 6.5 wt% daf; the yield of the benzene–ethanol extract increased from 3.1 to 12.4 wt % of OMC; the content of phenolic groups increased from 0.15 to 0.40, carboxy groups, from 0.16 to 0.40, quinoid groups, from 0.53 to 1.63, keto groups, from 0.05 to 0.20, and ester groups and lactone rings, from 0.13 to 0.45 mg-equiv g^{-1}. Similar trends were also observed with coals E and G (see table).

The organic matter of "mad dust" has increased content of hydrogen and oxygen and decreased content of carbon. Hence, mechanochemical breakdown of OMC is accompanied by significant enrichment in hydrogen, but after geodynamic shock the hydrogen content decreases as a result of oxidative processes in "mad dust" and of hydrodealkylation, dehydroxylation of phenols and alcohols, and hydrogenation of quinones and aromatic rings, catalyzed with the finely dispersed material. Thus, we can suggest that tectonic heaves of coal rocks containing organic and mineral matter are accompanied by significant mechanical processes causing primarily crushing of rocks and formation of a large amount of a finely dispersed mass. Cleavage of various chemical bonds is accompanied by release of hydrogen, which promotes hydrogenation of aromatic rings and their transformation into naphthenic rings, degrading more readily, and also hydrodealkylation, dehydroxylation, decarboxylation reactions, etc. Large amounts of hydrogen are adsorbed by finely dispersed coal. Accumulation of hydrogen and pathways of mechanical breakdown of the organic and mineral components of coal undoubtedly depend on their chemical composition.

Detailed studies of various coal products (extracts, semicoking tars, products of destructive thermal hydrogenation in hydrogen-donor solvents and oxidative degradation) show that a significant part of metals in fossil fuels are bound in metal porphyrins, phthalocyanines, phenolates, and carboxylates. Particular attention should be given to Fe, V, Ni, Zn, Cu, Co, and Mo porphyrins, which effectively catalyze release of hydrogen from water and its transfer to aromatic fragments of a coal macromolecule. The structure of metal porphyrins correlates with the degree of metamorphism of fossil fuels. Differences are observed in both the carbon skeleton of the tetrapyrrole macroring and in the central metal ion [18, 19].

Because metal porphyrins show a high catalytic activity in hydrogen release, they should be assumed to be the main hydrogen generators. This process is induced by profound mechanochemical transformations in OMC caused by tectonic forces. Fairly high degree of amorphization of the coal mass, formation of large amounts of reactive radical fragments, high performance of metal porphyrins, especially in the presence of acidic groundwater (typical for zones with a high ejection danger)—all these factors favor release of large amounts of hydrogen. The released hydrogen is accumulated by sorption in the amorphous coal mass. A significant part of hydrogen is involved in hydrogenation, hydrodealkylation, and saturation of low-molecular-weight radicals, yielding large amounts of CH_4, C_2H_6, and C_3H_8, which are also sorbed by the coal mass. Various reactions with hydrogen are also catalyzed with organometallic complexes, especially with complexes of metals with variable oxidation state. To understand processes occurring in OMC at tectonic heaves of coal rocks, it is appropriate to consider a correlation between the tendency of coals to destructive hydrogenation and the chemical composition of their organic mineral material.

It was found experimentally that hydrogenation of OMC is primarily determined by the features of structural organization of separate fragments of the coal macromolecule, their ratio, and structure and quantitative content of functional groups (phenolic, keto, carboxy, ether, ester, alcoholic; lactone and quinoid rings). Coals that are readily hydrogenated are characterized by a definite ratio of hydroaromatic and aromatic fragments, low content of humic acids, phenols, and carboxylic acids, and high content of quinoid, furan, and thiophene rings. Hydroaromatic structures like tetralin, hydroanthracene, dihydrophenanthrene, di- and tetrahydropyrene, dihydrofluoranthene, and dihydroquinoline are effective hydrogen donors. In turn, polycyclic aromatic hydrocarbons and thiophene, furan, and quinoid rings effectively transfer hydrogen to various radical products of OMC degradation [20–23].

Lignites are characterized by a high content of

hydrogen donors (hydroaromatic hydrocarbons, terpenes, azulenes, adamantanes, cycloalkanes), but the content of hydrogen-transfer agents in them is low. The high degree of substitution of structural fragments of the lignite macromolecule with phenolic, keto, ether, ester, carboxy, and alcoholic groups is a negative factor, because hydrogen is consumed for reduction of these groups. This fact suggests that in lignite strata mechanical breakdown of their structure under the action of tectonic forces will not be accompanied by accumulation of large amounts of free hydrogen, and hence the geodynamic shock will be impossible.

In coals containing 80–86% C, the content of hydrogen donors, and also of polycyclic aromatic fragments and of Fe, V, Ni, Cu, Co, and Ti porphyrins, which are effective hydrogen-transfer agents, is high. Furthermore, metal porphyrins are additional hydrogen generators and highly active catalytic systems easily effecting hydrogenation, dehydrogenation, hydrodealkylation, cyclization, and isomerization.

In the presence of hydrogen, polycyclic aromatic structures are hydrogenated to naphthenic structures, which readily degrade with release of large amounts of low-boiling hydrocarbons accumulating in the highly amorphized coal mass, producing a high pressure. It should be noted that accumulation in coal strata of large amounts of hydrogen, lower alkanes, CO, and CO_2 is also favored by low degree of substitution of OMC structural fragments by functional groups (carboxy, phenolic, ether, ester) reducible by hydrogen.

Thus, tectonic heaves of coal strata are accompanied by significant chemical transformations of OMC, with release of large amounts of hydrogen and its subsequent accumulation in the amorphous mass of coal. These processes occur especially actively at the sites of contact of OMC with mineral streaks, which, in turn, should be rich in Al, Fe, V, Co, Ni, Ti, and Si, i.e., in elements catalyzing hydrogenation, dehydrogenation, hydrodealkylation, etc. The main hydrogen generators are metal porphyrins and water.

Apparently, mining of coal strata is accompanied by admission of atmospheric oxygen to areas rich in hydrogen and lower alkanes. As a result, a detonating gas mixture is formed, which causes avalanche-like ejection of enormous amounts of coal dust that was formed in the course of tectonic heaves of coal mineral rocks.

It should be expected that the strength of a geodynamic shock and the amount of the ejected "mad dust" are largely determined by the mine working rate. At a low rate, the intrastratal gas pressure is relieved gradually, and avalance-like ejection of coal dust and gas can be avoided. It was noted that geodynamic shocks are characteristic of moderately amorphized coals and are virtually untypical of highly metamorphized coals (86% C). Highly metamorphized coals are characterized by a high content in their organic matter of polycyclic aromatic fragments, which are hydrogen-transfer agents, and a low content of hydrogen donos. These coals are very strong, so that the highly amorphous mass capable of accumulating hydrogen and alkanes is formed in a low amount. Owing to these factors, the probability of sudden ejections of "mad dust" and gas, associated with disturbance of the structural organization of coals under the action of tectonic forces, is low. It should be expected that the major gases sorbed in the bulk of these coals will be CH_4 and C_2H_6, which, when mixed with oxygen, are less reactive than hydrogen. Furthermore, CH_4 and C_2H_6 are bound with the coal matter more tightly; therefore, they are desorbed more slowly, and the drop of the intrastratal pressure is not so sharp.

When considering the tendency of coal strata to hydrodynamic shock caused by tectonic forces, we should also take into account the stratum porosity, making possible the access of water as a source of hydrogen to the mineral and organic components of coal. Dense rocks are impermeable for water, and virtually no hydrogen is formed.

Significant structural changes in both the organic and mineral components of coal cause generation of large amounts of radical products. They are localized in definite zones. This factor plays also a signifacnt role in subsequent processes occurring in the finely dispersed porous coal mass and capable of causing suddent ejection of coal dust and gaseous products. Probably, preliminarily boring of a coal block is necessary, with pumping of an electrolyte solution, e.g., of mine water enriched in metal ions (Fe^{2+}, Al^{3+}, Ca^{2+}, Mg^{2+}, Ni^{2+}, etc.); this procedure will be more efficient when using acidic ground water. It can be appropriate to use solutions of phenols (especially di- and trihydric). The content of trihydric phenols is fairly high in waters from peat, shale, lignite, and immature coal deposites, in which virtually no sudden ejections of dust and gas under the action of tectonic forces were observed.

It follows from the above consideration that the probability of geodynamic shock in a coal stratum with sudden ejection of finely dispersed coal and gas ("mad dust") under the action of tectonic forces is in-

fluenced by numerous factors. However, it is beyond doubt that the major factor is structural organization and chemical composition of both organic and mineral components of the coal macromolecule, the quantitative ratio of its structural fragments, e.g., hydroaromatic (hydrogen donors) and polycyclic aromatic (hydrogen-transfer agents). An important role is played by the structure of oxygen-containing functional groups substituting various hydrocarbon fragments of OMC, their ratio, structure of metal porphyrin complexes, chemical forms of inorganic and organic sulfur and nitrogen, composition of groundwater and surrounding mineral rocks, coal stratum porosity, and its sorption activity toward hydrogen and lower alkanes.

CONCLUSIONS

(1) Geodynamic shocks in coal strata under the action of tectonic forces have undoubtedly chemical origin and correlate with the composition of the organic and mineral matter of coals.

(2) Tectonic shifts in the bulk of a coal block induce profound mechanochemical transformations causing hydrogenation, dehydrogenation, hydrodealkylation, and thermal cleavage of various chemical bonds. These reactions are promoted by hydrogen, a number of metals, organomineral complexes like metal porphyrins and phthalocyanines, and acidic groundwater.

(3) One of the hydrogen sources is water reacting chemically with various compounds of the mineral matter of coal.

REFERENCES

1. Bubnoff, S., *Z. Berg. Hütten, Salinenwesen*, 1927, no. 75, pp. 15–20.
2. Ettinger, I.L., Zhupakhina, E.S., Shterenberg, L.E., and Yablokov, V.S., in *Razrabotka ugol'nykh mestorozhdenii na bol'shikh glubinakh: Trudy Soveshchaniya (Stalino, oktyabr' 1953 g.)* (Working of Coal Deposites at Large Depths: Proc. Meet. [Stalino (now Donetsk), October 1953]), Moscow: Ugletekhizdat, 1955, pp. 215–229.
3. Ettinger, I.L., Zhupakhina, E.S., and Shterenberg, L.E., *Metody vydeleniya v ugol'nykh plastakh zon, opasnykh po vnezapnym vybrosam* (Methods for Revealing Zones with a Danger of Sudden Ejections in Coal Strata), Moscow: Akad. Nauk SSSR, 1956.
4. Molchanov, V.I., *Dokl. Akad. Nauk SSSR*, 1968, vol. 182, no. 2, pp. 445–448.
5. Polubentsev, A.V., Proidakov, A.G., and Kanitskaya, L.V., *Khim. Tverd. Topl.*, 1988, no. 6, pp. 49–54.
6. Polubentsev, A.V., Proidakov, A.G., Kuznetsova, L.A., *et al.*, *Khim. Tverd. Topl.*, 1992, no. 2, pp. 24–27.
7. Khrenkova, T.M., Goldenko, N.L., and Zimina, E.S., *Khim. Tverd. Topl.*, 1986, no. 1, pp. 82–84.
8. Kirda, V.S. and Khrenkova, T.M., *Khim. Tverd. Topl.*, 1990, no. 2, pp. 15–18.
9. Khrenkova, T.M., Kirda, V.S., and Antonova, V.M., *Khim. Tverd. Topl.*, 1991, no. 5, pp. 17–20.
10. Gontsov, A.A., Gontsova, S.A., and Pakhomova, O.V., *Khim. Tverd. Topl.*, 1992, no. 4, pp. 11–17.
11. Fialkov, A.S., Chuparova, L.D., Varlakov, V.P., *et al.*, *Khim. Tverd. Topl.*, 1992, no. 6, pp. 114–119.
12. Kirda, V.S. and Khrenkova, T.M., *Khim. Tverd. Topl.*, 1992, no. 6, pp. 77–81.
13. Neavel, R.C., *Fuel*, 1976, vol. 35, no. 7, pp. 236–242.
14. Girina, L.V., Luk'yanenko, L.V., Ammosova, Ya.M., *et al.*, *Khim. Tverd. Topl.*, 1991, no. 5, pp. 37–42.
15. Avakumov, E.G., *Khim. Tverd. Topl.*, 1986, no. 1, pp. 82–83.
16. Vol'-Epshtein, A.B., Platonov, V.V., Khrenkova, T.M., *et al.*, *Khim. Tverd. Topl.*, 1987, no. 5, pp. 37–40.
17. Galkina, A.A., Chernyi, Yu.F., Baranov, S.N., *et al.*, in *Vliyanie davleniya na veshchestvo* (Effect of Pressure on Substances), Kiev: Naukova Dumka, 1980, pp. 42–47.
18. Platonov, V.V. and Klyavina, O.A., *Khim. Tverd. Topl.*, 1989, no. 6, pp. 3–12.
19. Platonov, V.V., Klyavina, O.A., Okushko, V.D., and Vol'-Epshtein, A.B., *Khim. Tverd. Topl.*, 1992, no. 4, pp. 27–36.
20. Novikova, I.L., Chemical Composition of the Organic Matter of Lignites from the Near-Moscow Basin and Their Reactivity in Destructive Thermal Hydrogenation in a Hydrogen-Donor Solvent, *Cand. Sci. Dissertation*, St. Petersburg, 1998.
21. Martynov, V.Yu., Chemical Composition of the Organic Matter of Coals from the Yakutia–Sakha Republic and New Fields of Their Application, *Cand. Sci. Dissertation*, St. Petersburg, 1999.
22. Chilachava, K.B., Thermolysis of Tkibuli Coals (Georgia Republic) in Various Organic Solvents, *Cand. Sci. Dissertation*, St. Petersburg, 2000.
23. Sivtsova, E.Yu., New Pathways of Destructive Thermal Hydrogenation of the Organic Matter of Coals from the Kuznetsk Basin, *Cand. Sci. Dissertation*, St. Petersburg, 2000.

Russian Journal of Applied Chemistry, Vol. 75, No. 3, 2002, pp. 504–506. Translated from Zhurnal Prikladnoi Khimii, Vol. 75, No. 3, 2002, pp. 515–517.
Original Russian Text Copyright © 2002 by Mognonov, Dorzhieva, Lbova, Zvontsov, Buraev, Khakhinov.

BRIEF COMMUNICATIONS

Dating of Osteological Material from Archeological Sources Using Thermal Analysis

D. M. Mognonov, T. N. Dorzhieva, L. V. Lbova, I. V. Zvontsov, A. I. Buraev, and V. V. Khakhinov

Baikal Institute for Nature Management, Siberian Division, Russian Academy of Sciences, Ulan-Ude, Buryatia, Russia

Institute of Mongolian, Buddhism, and Tibet Studies, Siberian Division, Russian Academy of Sciences, Ulan-Ude, Buryatia, Russia

Received October 5, 2001

Abstract—It is demonstrated that the absolute age of osteological material from archeological sources can be determined using dynamic thermogravimetric analysis and pyrolysis gas chromatography.

Today, when each branch of science is highly specialized, the fundamental problems are commonly solved using interdisciplinary approaches. Among the humanities, this is especially true in regard to the archeology. As distinct from the history in its narrow sense, the archeology has at its disposal diverse materials which can be analyzed by methods typical of many disciplines, primarily the chemistry and physics [1].

Of vital importance for archeology is maximally exact determination of the period of being of one or another culture and archeological finds, and archeologists are making considerable efforts to determine the absolute and relative age of archeological sources in hand.

One of the basic chronological analysis methods is radiocarbon dating [2–4]. However, it requires development of such a method for synthesis of organic compounds that corresponds to a given radiocarbon registration procedure. In its turn, this requires a considerable amount of the material and increases the analysis time and cost. Furthermore, very sensitive radiometric systems are needed to register the radioactivity at a level of 10^{-11}–10^{-15} Ci [5].

In this work we examined the potentialities of absolute dating of osteological material from archeological sources by dynamic thermogravimetric analysis (DTGA) and pyrolysis gas chromatography. These methods are thought as tentative screening tests of field materials prior to exact dating by the standard methods.

EXPERIMENTAL

Characteristics of the initial osteological material are given in the table. Bone material was preliminarily mechanically cleaned to remove surface soiling. Humic acids were removed by treatment with 0.1–0.5 NaOH at room temperature for 20–24 h. Then the material was treated with ethanol in a Soxhlet apparatus for 4–6 h and dried in a vacuum drier at 60°C and a residual pressure of 1–2 mm Hg. The dry material was ground with a side milling cutter and on a vibrating grinder (agate mortar and ball) to a milling grade of 200 mesh. Dynamic TGA analysis was performed on an OD-103 derivatograph in a platinum crucible (sample 200 mg, air, heating rate 5 deg min^{-1}). Pyrolysis of osteological material was studied at 500°C in a flow pyrolysis cell. The procedure allowed controlled pyrolysis of the material (1–2-mg samples), followed by GC analysis of volatile products (CO_2) with a Chrom-4 chromatograph [1-m column, silica gel L 80–120 mesh, carrier gas (Ar) flow rate 60 mil min^{-1}]. A standard gas mixture (CO_2 + N_2) with a CO_2 concentration of 19.33 vol % was used for calibration.

Osteological material is an element of the skeleton of the vertebrates, characterized by a mineral to organic fraction ratio of 65 : 35. The mineral fraction represents calcium phosphate (85%) and carbonate (10%) containing small amounts of magnesium phosphate (1.5%) and calcium fluoride (0.5%). The organic fraction consists of collagen, protein, fats, etc. [6]. Long-term being of osteological material in buried condition is accompanied by fossilization and, as

1070-4272/02/7503-0504$27.00 © 2002 MAIK "Nauka/Interperiodica"

Characteristics of samples

Sample no.	Sampling year	Horizon, m	Matrix lithology	Available age
1	1998	1.7	Sand, ochre	6225 ± 150
2	1998	1.7	″ ″	6179 ± 65
3	1993	8–9	Brown sand	30 220 ± 270
4	1998	0.58	Bottom-sod loamy sand chestnut soil	3000*
5	1993	708	Subaerial sediments	24 625 ± 190**

* From geoarcheological data. ** Data of the Siberian Division, Russian Academy of Sciences.

a result, decrease in the organic fraction content. Despite numerous attempts made to correlate variations in different characteristics of collagen (nitrogen content, physical and optical properties, and amino acid content) in the course of fossilization, diagenesis of collagen is poorly understood yet. Nevertheless, a fairly simple conceptual model was proposed for collagen degradation, setting up a link between its content and the problem of dating of low-collagen bones [7, 8].

According to the primary classification, collagen is related to insoluble proteins (scleroproteins). It contains abnormally high amounts of glycine, proline, and hydroxyproline. One of every four units in the protein skeleton of collagen is proline or hydroxyproline bound to glycine. The elongated shape of the collagen spiral prevents intramolecular hydrogen bonding. However, the interchain hydrogen bonding is an important factor in collagen diagenesis, including kinetic and transport processes. Therefore, the time of osteological material being buried may be estimated from the amount of polypeptide fragments in the matrix. Knowing the trends of thermal and thermooxidative degradation of collagen in osteological material opens the door for dating this material using thermal analysis.

Since the major structural elements of the polypeptide chain of collagen are aliphatic fragments, its thermal decomposition should be similar to that of synthetic aliphatic polyamides (their thermal stability was studied in detail). It was demonstrated that they decompose even at 300°C, which is accompanied by considerable weight loss, liberation of volatile products, and formation of an insoluble coke-like residue [9]. The thermal decomposition of polyamides accelerates with temperature, especially in air [10].

The thermal analysis data obtained in this work with osteological material are consistent with the above-mentioned trends. For example, the maximal weight loss rate due to exothermic thermooxidative decomposition is observed at about 300°C. With increasing temperature to 400°C, the decomposition rate considerably decreases. Therefore, the weight loss over the temperature range 300–350°C can be used as a parameter characterizing the collagen content in osteological material. It is important that the mineral fraction of osteological material decomposes at much higher temperature (thermal decomposition of calcium carbonate with liberation of CO_2 occurs at 740°C [11]).

The DTGA results obtained for osteological material of various ages (see table) are presented in Fig. 1.

The results obtained demonstrate a clear correlation between the age of osteological material and the organic fraction content in it. The weight loss at 350°C was found to be 16–17, 11–12, and 8–9% for sample nos. 4, 2, and 3, respectively.

Even more illustrative are the results of pyrolysis gas chromatography. The volume of liberated CO_2 decreases linearly with increasing age of osteological material (Fig. 2).

The dependence plotted in Fig. 2 can serve as a calibration curve for determination of the absolute age of bone material from archeological sources.

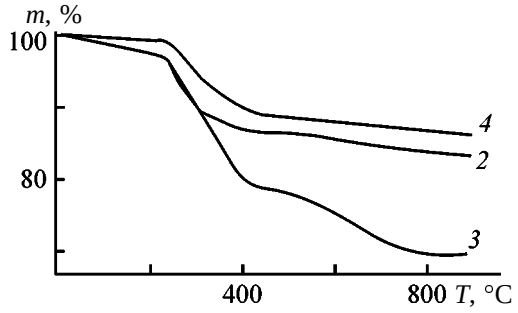

Fig. 1. Dynamic thermogravimetric analysis of osteological material of various ages: (*m*) residual weight and (*T*) temperature. Figures at the curves correspond to the sample numbers in the table.

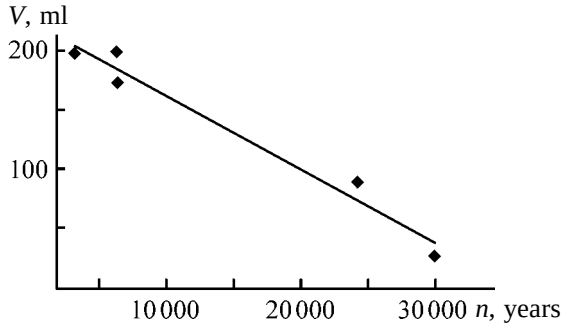

Fig. 2. Volume of CO_2 V liberated in pyrolysis of osteological material of various ages n.

CONCLUSION

Absolute dating of osteological material from archeological sources can be made by the dynamic TGA and pyrolysis gas chromatography methods. Collagen, the organic component of bones of the vertebrates, being buried for a long time, is subject to fossilization, resulting in its decreasing amount. At high temperatures, collagen undergoes thermal and thermooxidative degradation with the amount of the released products depending on the material age.

ACKNOWLEDGMENTS

The work is financially supported by the Russian Foundation for Basic Research (project no. 01-06-8392) and Integrated Projects Foundation, Siberian Division, Russian Academy of Sciences (project no. 85).

REFERENCES

1. Vaganov, P.A., *Fiziki dopisyvayut istoriyu* (Physicists Finish Writing the History), Leningrad: Leningr. Gos. Univ., 1984.
2. Sulerzhitskii, L.D., *Chelovek zaselyaet planetu Zemlya* (Human Beings Are Populating the Earth), Velichko, A.A. and Soffer, O.A., Eds., Moscow: Inst. Geographii, Sib. Otd. Ross. Akad. Nauk, 1997, pp. 184–200.
3. Orlova, L.A., Kuz'min, Ya.V., Plicht, J. van der, and Jull, A.J.T., in *Sovremennye problemy Evraziiskogo paleolitovedeniya* (Modern Problems of Eurasian Paleolithic Research), Novosibirsk: Nauka, 2001, pp. 289–290.
4. *Radiouglerodnaya khronologiya paleolita Vostochnoi Evropy and Severnoi Azii: problemy i perspektivy* (Radiocarbon Chronology of Paleolith in the Western Europe and Northern Asia: Problems and Prospects), Sinitsyn, A.A. and Praslov, N.D., Eds., St. Petersburg: Inst. Istor. Material. Kul'tury, Ross. Akad. Nauk, 1997.
5. Artem'ev, V.V., *Novye metody v arkheologicheskikh issledovaniyakh* (New Methods in Archeological Research), Moscow: Akad. Nauk SSSR, 1963.
6. Orlova, L.A., in *Fiziko-khimicheskie metody issledovanii v geologii* (Physicochemical Methods in Geological Research), Novosibirsk: Nauka, 1981, pp. 153–160.
7. Collins, M.J., Riley, M.S., Child, A.M., and Turner-Walker, A., *J. Archeol. Sci*., 1995, vol. 22, pp. 175–183.
8. Ambrose, S.H. and De Niro, M.J., *Quater. Res*., 1989, vol. 31, pp. 407–422.
9. Korshak, V.V., Slonimskii, G.L., and Krongauz, E.S., *Izv. Akad. Nauk SSSR, Otd. Khim. Nauk*, 1958, no. 2, pp. 221–226.
10. Valco, E.I., and Chiklis, S.K., *J. Appl. Polym. Sci*., 1965, vol. 9, pp. 2855–2877.
11. Erdey, L., Paulik, F., and Paulik, J., *Acta Chim. Hung*., 1956, vol. 10, p. 6.

Russian Journal of Applied Chemistry, Vol. 75, No. 3, 2002, pp. 507–508. Translated from Zhurnal Prikladnoi Khimii, Vol. 75, No. 3, 2002, pp. 518–519.
Original Russian Text Copyright © 2002 by Bykov, Karabanov.

BRIEF COMMUNICATIONS

Correction for Fluctuations of Local Molecular Field in the Debye Method of Dilute Solutions

A. N. Bykov and S. M. Karabanov

Ryazan Plant of Metal–Ceramic Devices, Joint-Stock Company, Ryazan, Russia

Received June 28, 2001

Abstract—A simple method for evaluating the correction for the effect of solvent on the dipole moments of molecules, determined using the Debye method of dilute solutions, is proposed.

As shown by analysis of a vast body of experimental data [1], the properties of strongly polar molecules are poorly described by correlation dependences that well fit nonpolar molecules. The most important characteristic of a polar molecule is its dipole moment μ, which is frequently used in correlating the properties of polar substances [1].

However, this poses the problem of how to choose the dipole moment μ represented in the reference literature by rather widely varying values [2, 3], which is due not only to experimental errors. All correlation dependences for polar substances include the dipole moment μ_0 determined in the gas phase, in which case the influence of other molecules is negligible. At the same time, the main technique used for determining the dipole moments of molecules is the Debye method of dilute solutions. It is this method that has been used to find the majority of presently known dipole moments [3]. As shown by numerous experimental studies [2, 3], the dipole moments μ_s determined by the method of dilute solutions differ from μ_0.

To evaluate the influence exerted by solvent, we performed [4] a full statistical analysis of experimental data for all the 226 substances for which both μ_0 and μ_s are known (the latter was measured in solutions of benzene C_6H_6). Benzene was chosen as the solvent for which the most extensive data on dipole moments of dissolved molecules are available.

As seen from the figure, the μ_s/μ_0 ratio averaged over large groups of substances decreases monotonically with increasing μ_0. The thus obtained statistical dependence of μ_s on μ_0 can already be used to evaluate μ_0 on the basis of data on μ_s. This is all the more important since only data on μ_s are available for many chemical substances.

To evaluate the correction for the solvent effect more precisely, let us consider this issue in more detail. In the method of dilute solutions, the orientational polarizability a_{or} of molecules of a polar component x_2 in an external effective field $\mathbf{F}_{eff}$ is extrapolated to zero concentration of this component. In doing so, it is assumed that at $x_2 \to 0$ polar molecules are oriented in the external field as freely as this occurs in a gas, i.e.,

$$\lim_{x_2 \to 0} a_{or} = \mu_0^2/(3kT). \quad (1)$$

However, an important part may be played in nonpolar liquids by fields of molecular multipoles [5], with $\langle \mathbf{F}^2 \rangle \neq 0$, where $\mathbf{F}$ is the local molecular field at the center of an arbitrarily chosen particle.

In [4], analytical expressions for the μ_s/μ_0 ratio were derived in terms of a statistically substantiated discrete model of a nonpolar solvent. These expressions account for the influence exerted by fluctuations of local molecular fields on μ_s and describe satisfactorily the dependence of the μ_s/μ_0 ratio on μ_0, molecule size, and temperature T.

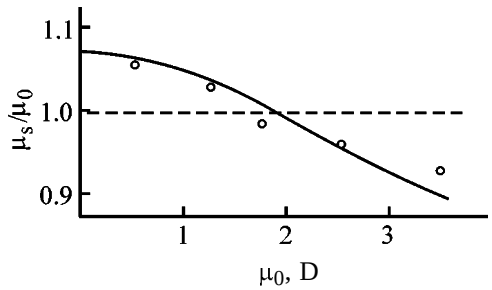

Effect of μ_0 on the μ_s/μ_0 ratio. Curve: theoretical dependence at quadrupole moment of benzene molecules $Q = 5.6 \times 10^{-26}$ CGS units cm^2; points: data obtained in statistical processing of experimental data.

1070-4272/02/7503-0507$27.00 © 2002 MAIK "Nauka/Interperiodica"

Here we propose a simpler method for evaluating the correction for the effect of fluctuations of the local molecular field in nonpolar solvents. Taking, in accordance with the theory of corrections for the effect of solvent [2], that

$$\lim_{x_2 \to 0} a_{or} = \mu_s^2/(3kT) \quad (2)$$

and assuming that

$$\lim_{x_2 \to 0} a_{or} = \lim_{x_2 \to 0} \langle a_{or} \rangle = \langle a_{or} \rangle_0 \quad (3)$$

(where $\langle a_{or} \rangle$ is the average orientational polarizability of polar molecules in an infinitely dilute solution in the presence of fluctuations of local molecular fields in the nonpolar solvent), we obtain for μ_s/μ_0

$$(\mu_s/\mu_0)^2 = [3kT\langle a_{or} \rangle_0]/\mu_0^2, \quad (4)$$

Calculating $\langle a_{or} \rangle$ in terms of the discrete model [4], we have

$$(\mu_s/\mu_0)^2 = \mu/(8.66\mu_0) \times \int_0^\infty (1 - \mathrm{cth}^2 a + a^{-1}\mathrm{cth}\, a - a^{-2})s^3 \exp(-s/1.1)ds, \quad (5)$$

$$a = \mu F/(kT) = \mu s Q\langle r^{-4} \rangle/(kT),$$

where F is the local molecular field strength, $F = sQ\langle r^{-4} \rangle$; r is the intermolecular distance; Q is the quadrupole moment of molecules of the nonpolar solvent; and s is the proportionality factor; $\langle r^{-4} \rangle$ can be readily found in terms of Kirkwood's model of rigid spheres [4].

The μ value can be obtained in the conventional approximation [6]

$$\mu = \mu_0 \frac{\varepsilon_\infty + 2}{3} \frac{2\varepsilon_\infty + 1}{2\varepsilon_\infty + \varepsilon_\infty}, \quad (6)$$

where $\varepsilon_\infty \approx 1.05 n_D$ and n_D is the refractive index of the nonpolar solvent.

The μ_s/μ_0 value can be easily found from (5) by graphical integration since the integrand has a relatively narrow maximum.

The figure presents the dependence of the μ_s/μ_0 ratio on μ_0, plotted theoretically for benzene solutions with the use of (5) and found experimentally by averaging data for all the 226 chemical substances for which data on μ_0 and μ_s in benzene are available [3].

As follows from the figure, the proposed relation (5) describes satisfactorily the dependence of μ_s/μ_0 on μ_0, which allows its use for evaluating the influence exerted by fluctuations of local molecular fields on the μ_s values found using the Debye method of dilute solutions.

REFERENCES

1. Reid, R.G., Prausnitz, J.M., and Sherwood, T.K., *The Properties of Gases and Liquids*, New York: McGraw-Hill, 1977.
2. Smyth, C.P., *Dielectric Behavior and Structure*, New York: McGraw-Hill, 1955.
3. Osipov, O.A., Minkin, V.I., and Garnovskii, A.D., *Spravochnik po dipol'nym momentam* (Reference Book of Dipole Moments), Moscow: Vysshaya Shkola, 1971.
4. Bykov, A.N., *Khim. Fiz.*, 1993, vol. 12, no. 10, pp. 1366–1381.
5. Kielich, S., *Molekulyarna optyka nieliniowa*, Warsaw: UAM, 1977.
6. Fröhlich, H., *Theory of Dielectrics, Dielectric Constants and Dielectric Loss*, Oxford: Clarendon, 1958.

Russian Journal of Applied Chemistry, Vol. 75, No. 3, 2002, pp. 509–510. Translated from Zhurnal Prikladnoi Khimii, Vol. 75, No. 3, 2002, pp. 520–521.
Original Russian Text Copyright © 2002 by Komarova, Sul'man.

BRIEF COMMUNICATIONS

Relationships of Sorption of Heavy Metals (Lead, Nickel, Cobalt) on Biomass Isolated from Production Waste of Megaterin Enzyme Preparation

N. N. Komarova and E. M. Sul'man

Tver State Technical University, Tver, Russia

Received April 18, 2001

Abstract—The biomass of *Bacillus megaterium* cells, containing polypeptides, polysaccharides, and lipids, isolated from production waste of Megaterin enzyme preparation, was tested for sorption recovery of heavy metals (lead, nickel, cobalt) from aqueous solutions. The sorption capacity of this biosorbent and the main relationships of the metal sorption were studied.

Modern processes for water decontamination from various impurities tend to wider use of sorbents prepared from bacterial waste of biotechnological productions [1]. The microbial biomass used as a raw material for preparation of biosorbents is formed in the course of microbial synthesis. This material consists of partly destroyed cells of microorganisms containing biopolymers rich in ionogenic groups [1]. It is known that heavy metal ions are toxic agents. At the same time, heavy metals incorporated in complexes lose toxicity. The biomass of microbial cells can be effective natural sorbent accumulating heavy metals on the cell surface. The aim of this work was to study the sorption capability of microbial biomass for heavy metals.

EXPERIMENTAL

The microbial biomass used in our experiments (*Bacillus megaterium*) was isolated from production waste of Megaterin enzyme preparation.[1] The sorption power of bacterial cells with respect to heavy metals and the optimal conditions for metal sorption were studied using aqueous solutions of cobalt chloride $CoCl_2$, nickel acetate $Ni(CH_3COO)_2$, and lead acetate $Pb(CH_3COO)_2$. The sample of dry biomass taken from the enzyme-producing plant was treated with acetone. Excess acetone was removed by vacuum filtration. Prior to use, the biomass was washed with distilled water to neutral reaction of wash water and dried [1, 2]. A portion of the resulting biomass was introduced into a model solution containing heavy metal ions. The sorption was carried out in a temperature-controlled reactor at stirring. After completion of a sorption experiment, the biomass was separated by centrifuging. The residual content of Co(II), Ni(II), and Pb(II) in the cenrifuged solution was determined spectrophotometrically and fluorometrically [3].

We found that at a constant metal concentration (0.1 g l^{-1}) in solution and a constant solution volume (250 ml) the residual metal content in solution continuously decreased with increasing sorbent weight. The results obtained in the sorption experiments showed that the sorption was maximal at the sorbent concentration of 80–90 g l^{-1}.

The sorption isotherm has a convex shape and is fairly well fitted by Langmuir's equation (Fig. 1). The metal ion concentration in the solution was varied from 0.01 to 0.2 g l^{-1}. Sorption was performed to

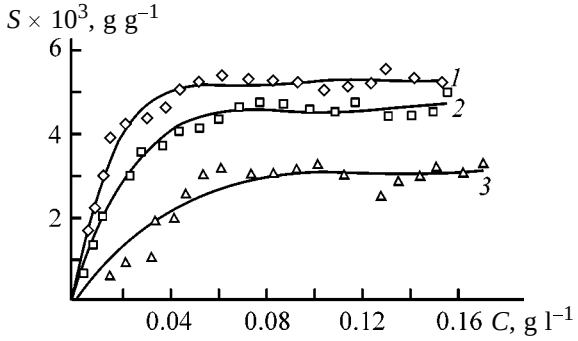

Fig. 1. Sorption isotherms of metals on microbial biomass: (*S*) sorption capacity and (*C*) equilibrium metal concentration in solution. Cation sorbed: (*1*) Pb^{2+}, (*2*) Ni^{2+}, and (*3*) Co^{2+}: the same for Fig. 2.

[1] The material was produced and submitted by the Vyshni Volochek plant of Enzymatic Preparations.

1070-4272/02/7503-0509$27.00 © 2002 MAIK "Nauka/Interperiodica"

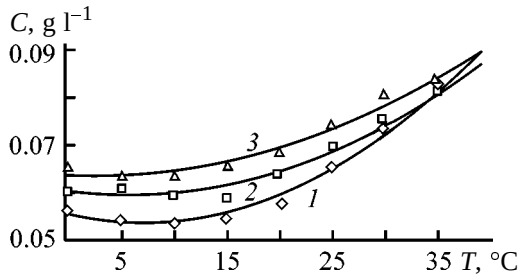

Fig. 2. Residual metal content in solution as influenced by temperature.

complete saturation of the sorbent. In obtaining the sorption isotherms, both the solution volume (250 ml) and the sample weight (80 g l^{-1}) were constant. Figure 1 shows that lead ions exhibit higher affinity for the biomass than nickel and cobalt ions. The sorption capacity of the biomass is 0.0042, 0.0029, and 0.0049 g g^{-1} for nickel, cobalt, and lead, respectively.

The sorption kinetics was studied at different contact times of the biosorbent and solution. A portion of solution was sampled at regular intervals and analyzed for metal. We found that the major fraction of the metals was sorbed within the first 15–20 min. The sorption equilibrium sorption was attained in 30 min. Under these conditions, the following degree of metal recovery was reached (%): Pb 42, Ni 34, and Co 27.

Figure 2 shows that with increasing temperature from 0 to 50°C the sorption of metals slightly decreases. The sorption of metals on the biomass is maximal in the temperature range 0–20°C.

CONCLUSIONS

(1) The biomass of bacterial cells prepared from production waste of Megaterin enzyme preparation is capable of recovering heavy metals (lead, nickel, and cobalt) from aqueous solutions.

(2) The residual metal content in solution decreases with increasing amount of the sorbent. The sorption is maximal at a biomass content of 80–90 g l^{-1}.

(3) The dependences of lead, nickel, and cobalt sorption on their concentration in solution are described by Langmuir's isotherm.

(4) The sorption equilibrium is attained within 30 min. The degree of metal recovery is 42, 34, and 27% for Pb, Ni, and Co, respectively.

(5) The degree of heavy metal recovery is maximal in the temperature range 0–20°C.

Our results show that the biomass of microbial cells prepared from Megaterin production waste is effective and inexpensive sorbent for purification of aqueous solutions to remove heavy metals.

REFERENCES

1. Kirillova L.N., Smirnov, A.V., and Murav'eva, M.B., *Biotechnology*, 1996, no. 4, pp. 35–41.
2. *GOST* (State Standard) *10896–78: Ion Exchangers, Preparation for Testing*.
3. Burger, K., *Organic Reagents in Metal Analysis*, Budapest: Akad. Kiado, 1973.

Russian Journal of Applied Chemistry, Vol. 75, No. 3, 2002, pp. 511–512. Translated from Zhurnal Prikladnoi Khimii, Vol. 75, No. 3, 2002, pp. 522–523.
Original Russian Text Copyright © 2002 by Osadchenko, Tomilov.

BRIEF COMMUNICATIONS

Phase-Transfer Catalysis in Synthesis of Oximes

I. M. Osadchenko and A. P. Tomilov

State Research Institute of Organic Chemistry and Technology, Moscow, Russia

Received September 25, 2001

Abstract—Perfluorinated higher carboxylic acids were tested as phase-transfer catalysts in synthesis of oximes.

The known synthetic routes to oximes are based on reaction of a carbonyl compound with an aqueous solution of a hydroxylamine salt [1–3] in the presence of inorganic compounds, e.g., of NaOH:

$$\underset{\underset{\|}{\mathrm{O}}}{\mathrm{RCR'}} + \mathrm{NH_2OH \cdot HX} + \mathrm{NaOH} \rightarrow \underset{\underset{\|}{\mathrm{NOH}}}{\mathrm{RCR'}} + \mathrm{H_2O} + \mathrm{NaX},$$

where R = Alk; R' = Alk, H, Ar, Ht; X is an inorganic anion.

Because carbonyl compounds, as a rule, are poorly soluble in water, the reaction is usually performed in aqueous alcohol. However, the reaction is slow (5–8 h) and does not go to completion even in the presence of excess hydroxylamine salt. The yield of the oxime based on the taken carbonyl compound usually does not exceed 80%.

To promote the reaction, various phase-transfer catalysts were tested without using an organic solvent. We found that the most effective phase-transfer catalysts for oximation are higher perfluorinated carboxylic acids exhibiting a high surface activity. Addition of these compounds (0.07–0.10 wt %) appreciably shortens the reaction time and allows preparation of oximes in high, sometimes almost quantitative yields. This can be illustrated by several examples.

Acetophenone oxime. (a) A 1-l reaction vessel equipped with a thermometer, a reflux condenser, a stirrer, and a dropping funnel was charged with a solution of 76.5 g (1.1 mol) of hydroxylamine hydrochloride in 200 ml of water and 120 g (1.0 mol) of acetophenone, and a 20% solution of 44 g (1.1 mol) of NaOH was added dropwise with stirring at 36°C until pH 7–8 was attained. The mixture was heated at 60–70°C for 5 h and then cooled to 0–3°C. The resulting crystalline precipitate was filtered off, washed with several portions of ice-cold water, and dried in a desiccator over $CaCl_2$ to constant weight; 100 g of acetophenone oxime was obtained, mp 57°C (published data [2, 3]: 57–58°C); yield 70%.

(b) The reaction was performed similarly to procedure (a) but in the presence of 0.61 g (1.7 mmol) of perfluoroenanthic acid with addition of a 20% NaOH solution at 60–70°C; the mixture was heated at this temperature for 3.5 h. Yield of acetophenone oxime 131.6 g (98%).

(c) The reaction was performed similarly to procedure (a) but in the presence of 0.61 g (2.3 mmol) of perfluorovaleric acid; time of heating at 60–70°C 3 h. Yield of acetophenone oxime 132.3 g (99%).

5-Methyl-3-hexanone oxime. A reaction vessel [the same as in procedure (a)] was charged with 57 g (0.8 mol) of 5-methyl-3-hexanone, 39 g (0.56 mol) of hydroxylamine hydrochloride, 100 ml of water, and 0.6 g (1.65 mmol) of perfluoroenanthic acid; 100 ml of 25% aqueous NaOH was added, keeping the temperature below 35°C, after which the mixture was heated to 67–68°C and kept at this temperature for 3 h. After cooling, the upper layer was separated, washed with three 20-ml portions of cold water, and distilled in a vacuum (10–12 mm Hg). A fraction boiling at 85–95°C was collected. Yield of 5-methyl-3-hexanone oxime 49.7 g (71%); n_D^{20} 1.4424 (published data [4]: n_D^{20} 1.4436).

Salicylaldoxime. Similarly to procedure (a), a 500-ml reactor was charged with 26 g (0.21 mol) of salicylaldehyde, 16 g (0.21 mol) of hydroxylamine hydrochloride, 40 ml of water, and 0.2 g (0.55 mol) of perfluoroenanthic acid; a solution of 9 g (0.225 mol) of NaOH in 30 ml of water was slowly added, after which the mixture was heated to 65–70°C and kept at this temperature for 3 h. After cooling to 5–10°C, the mixture was worked up similarly to procedure (a).

1070-4272/02/7503-0511$27.00 © 2002 MAIK "Nauka/Interperiodica"

Yield of salicylaldoxime 26 g (98%), mp 58°C (published data [5]: 57–59°C).

3-Thioxo-2-butanone oxime. Similarly to synthesis of salicylaldoxime, a reactor was charged with 25.2 g (0.247 mol) of 3-thioxo-2-butanone, a solution of 16 g (0.23 mol) of hydroxylamine hydrochloride in 210 ml of water, and 0.2 g (0.55 mol) of perfluoroenanthic acid, after which a solution of 9 g (0.225 mol) of NaOH in 30 ml of water was added dropwise at 30–35°C. The mixture was heated to 70°C and kept at this temperature for 3 h. After cooling, the mixture was worked up as described above. Yield of 3-thioxo-2-butanone oxime 20.8 g (74%); mp 105–106°C. The structure was confirmed by IR spectroscopy.

Thus, addition of perfluorinated carboxylic acids increases the yield of oximes, shortens the reaction time, and eliminates the necessity of using an organic solvent, which considerably simplifies the oximation process.

REFERENCES

1. Khudenko, A.V., Osadchenko, I.A., and Kaabak, L.V., *Khim. Prom–st.*, 1998, no. 12, pp. 1731–1738.
2. USSR Inventor's Certificate no. 692 832.
3. Pfeifer, P., *J. Prakt. Chem.*, 1924, vol. 108, no. 3, pp. 341–343.
4. Trapesonsjaus, Ch., *Ber.*, 1893, vol. 26, no. 5, pp. 1426–1432.
5. *Dictionary of Organic Compounds*, Heilborn, I. and Banbury, H.M., Eds., London: Eyre and Spottiswoode, 1946, vol. 3. Translated under the title *Slovar' organicheskikh soedinenii*, Moscow: Inostrannaya Literatura, 1949, vol. 3, p. 611.

Russian Journal of Applied Chemistry, Vol. 75, No. 3, 2002, p. 513. Translated from Zhurnal Prikladnoi Khimii, Vol. 75, No. 3, 2002, p. 524.
Original Russian Text Copyright © 2002 by Ginak, Aronova.

BRIEF COMMUNICATIONS

A Procedure for Synthesis of 3-Halomethyl-4-oxothiazolidine-2-thiones

A. I. Ginak and E. B. Aronova

St. Petersburg State Technological Institute, St. Petersburg, Russia

Received October 23, 2001

Abstract—Solid-phase synthesis of 3-halomethyl-4-oxothiazolidine-2-thiones was perforomed.

Halomethyl-4-oxothiazolidine-2-thiones, which are starting compounds for preparing biologically active substances [1], vulcanizing agents [2], and plant growth stimulants [3], are synthesized by a multistage procedure via intermediate hydroxymethyl-4-oxothiazolidine-2-thiones, with subsequent replacement of the hydroxy group in the methyl substituent under the action of $SOCl_2$, PBr_3, or HBr [4]. The procedure involves the use of corrosive media and expensive chemicals; the loss in each stage reaches 25%.

We have developed a single-stage solid-phase procedure for preparing 3-halomethyl-4-oxothiazolidine-2-thiones **IIa**–**IIf** by reaction of the vapors of the corresponding methylene dihalides with crystalline alkali metal salts of 4-oxothiazolidine-2-thiones **I**. It is known [5] that crystals of ambifunctional compounds exhibit anisotropic reactivity on various crystal faces. This property was used to develop a synthetic process. Lithium, sodium, potassium, and cesium salts of 4-oxothiazolidine-2-thiones were crystallized from organic solvents (methanol, acetone, acetonitrile, dimethylformamide), and the crystals that exhibited the strongest anisotropy in alkylation were selected. The reaction progress was monitored by TLC. We found that the most anisotropic were the lithium salts of 4-oxothiazolidine-2-thiones crystallized from methanol: the yield of the target products (see table) exceeded 95%.

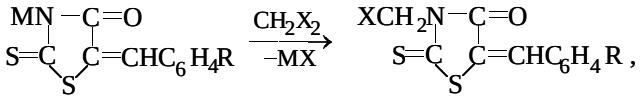

I **IIa**–**IIf**

where M = Li, Na, R, Cs; X = Cl, R = H (**IIa**); X = Br, R = H (**IIb**); X = I, R = H (**IIc**); X = Cl, R = *p*-CH_3 (**IId**); X = Br, R = *p*-CH_3 (**IIe**); X = Cl, R = *m*-NO_2 (**IIf**).

Elemental compositions and melting points of **IIa**–**IIf**

Compound	mp, °C	Found, % / Calculated, %		Formula
		N	S	
IIa	192–193	4.95 / 5.19	23.60 / 23.77	$C_{11}H_8ClNOS_2$
IIb	194–195	4.35 / 4.46	20.23 / 20.41	$C_{11}H_8BrNOS_2$
IIc	187–188	3.65 / 3.88	17.20 / 17.75	$C_{11}H_8INOS_2$
IId	187–188	4.62 / 4.91	22.15 / 22.59	$C_{12}H_{10}ClNOS_2$
IIe	189–190	3.94 / 4.21	4.21 / 19.59	$C_{12}H_{10}BrNOS_2$
IIf	151–152	9.34 / 8.97	8.97 / 20.37	$C_{11}H_7ClN_2O_3S_2$

The reaction was performed in an electrically heated temperature-controlled (70–250°C) tubular reactor (1 cm in diameter, 10 cm high). Alkylating agent vapor was passed through a bed of the substrate.

REFERENCES

1. Brown, F.C., *Chem. Rev.*, 1961, vol. 61, no. 5, pp. 463–521.
2. Sheshina, G.M., Ratnikova, T.V., and Ginak, A.I., *Kauch. Rezina*, 1978, no. 5, pp. 16–18.
3. Mel'nikov, N.N., Volkov, A.I., and Korotkova, O.A., *Pestitsidy i okruzhayushchaya sreda* (Pesticides and Environment), Leningrad: Khimiya, 1977.
4. Borisova, M.A., Ginak, A.I., and Sochilin, E.G., *Zh. Org. Khim.*, 1972, vol. 8, no. 7, pp. 1536–1538.
5. Dymshits, V.A., *Khimiya organicheskikh kristallov* (Chemistry of Organic Crystals), St. Petersburg: Khimiya, 1994.

1070-4272/02/7503-0513$27.00 © 2002 MAIK "Nauka/Interperiodica"

Russian Journal of Applied Chemistry, Vol. 75, No. 3, 2002, p. 514. Translated from Zhurnal Prikladnoi Khimii, Vol. 75, No. 3, 2002, pp. 525.
Original Russian Text Copyright © 2002 by Morachevskii.

BOOK REVIEWS

Buler, Peter, *Fiziko-khimicheskaya termodinamika veshchestva* (Physicochemical Thermodynamics of Substance),

St. Petersburg: Yanus, 2001, 192 pp.

The book is an author's translation of *Physicochemical Thermodynamics of Substance*, previously published in English (St. Petersburg: Yanus, 2000). The author, professor P. Buler, a metallurgist engineer by education, held the chair of chemical technology of glass and glass ceramics of the Ural State Technical University in Yekaterinburg, prior to moving to Germany in 1990. From 1991 till 2000, he had been a professor of the chair of glass and ceramics of Universität Erlangen (Nürnberg). At present, he is a consultant of the same chair. During the whole period of his activities, P. Buler's scientific interests have been associated with investigations into interaction of oxide melts with metals and gases.

The brief introduction and the first chapter, *Substance and Its Internal Energy*, point out the specific features of the author's approach to presentation of the fundamentals of chemical thermodynamics. In particular, doubt is cast on the correctness of using such a function as enthalpy ($H = U + PV$). The main reason is that, although the product PV has the dimensionality of energy, "this product does not come to be energy in the Nature" (p. 24). As seen from the summary (*Symbols and Definitions*) and the subsequent presentation, such notions as Gibbs energy and chemical potential are not used, either. Individual substances and mixing processes are mainly characterized by internal energy (U), free energy ($G = U - TS$), and peculiarly understood entropy. The author writes: "The entropy of a substance is the temperature coefficient of the free energy and cannot be interpreted in any other way" (p. 32).

The second, third, fourth, and fifth chapters consider relations describing changes in the internal energy, free energy, and entropy under various conditions. The author comes to conclusions that are difficult to comment. It is noted, in particular, that, changes in entropy being only associated with changes in energy, the entropy of mixing in the formation of an ideal gas mixture or ideal solution proves to be zero. Correspondingly, changes in free energy are also zero for these systems. The sixth chapter is concerned with phase equilibria in single-component systems, with no mention made of the phase rule.

The seventh chapter considers thermodynamic functions characterizing the formation of binary solutions from pure components. The concepts developed by the author rule out the notion of excess functions and thereby cause a certain confusion of terminology in describing processes of mixing. The eighth chapter discusses the equilibrium between condensed phases in two-component system, without, however, using the term "chemical potential." The ninth chapter is devoted to the liquid–vapor equilibrium, and the tenth considers the equilibrium in chemical transformations. The eleventh chapter presents results of some experimental studies carried out by the author.

One hundred and twenty-five years ago, J.W. Gibbs (1839–1903) published his major work *On the Equilibrium of Heterogeneous Substances*, which was of paramount importance for the development of chemical thermodynamics. The analytical method rigorously and consistently described in this paper was later named by P. Duhem (1907) the method of thermodynamic potentials. The possibilities of the method are manifested to full extent in calculation of phase and chemical equilibria. Any "revision" of this method or abandonment of other fundamental concepts of the classical chemical thermodynamics seems to be unproductive.

The freedom of press is generally accepted all over the world, but it should not be unconditionally extended to scientific publications. A book of such a controversial nature should have been prefaced with an explicit introduction written by a specialist of authority in chemical thermodynamics, with a detailed analysis of merits and demerits and specific features of a publication brought to reader's notice.

A. G. Morachevskii

1070-4272/02/7503-0514$27.00 © 2002 MAIK "Nauka/Interperiodica"

Russian Journal of Applied Chemistry, Vol. 75, No. 4, 2002, pp. 515–520. Translated from Zhurnal Prikladnoi Khimii, Vol. 75, No. 4, 2002, pp. 529–534.
Original Russian Text Copyright © 2002 by C. Radchenko, Bykadorov, Novakov, Zhokhova, Utkina, Otchenashev, F. Radchenko.

INORGANIC SYNTHESIS AND INDUSTRIAL INORGANIC CHEMISTRY

Structuring in Concentrated Solutions of High-Basicity Aluminum Hydroxychloride and in New Coagulant Formulations on Its Base

S. S. Radchenko, N. U. Bykadorov, I. A. Novakov, O. K. Zhokhova, E. E. Utkina, O. P. Otchenashev, and F. S. Radchenko

Volgograd State Technical University, Volgograd, Russia

Volzhskii Polytechnic Institute, Volgograd State Technical University, Volgograd, Russia

Received February 22, 2001; in final form, November 2001

Abstract—Gelation in concentrated solutions of high-basicity aluminum hydroxychloride in the presence of inorganic salts was studied. Comparative evaluation of the coagulation activities of aluminum hydroxychloride and solid formulations on its base in water purification was made.

The scale on which aluminum hydroxychlorides are used in purification of natural and wastewater to remove suspended and colloid impurities [1] motivates the increasing interest in the problem of their performance and availability [2–4]. They can also be used for preparing new coagulants with improved properties [5].

Most of the known methods for production of aluminum hydroxychloride are based on hydrolysis of aluminum chloride formed in the preliminary stage of treatment of an aluminum-containing starting material. All stages of this process have been extensively studied (see reviews [6–8]), and a conclusion was made that various kinds of Al(III) hydroxo complexes can coexist in concentrated aqueous solutions. The composition of these complexes varies from monomeric to polymeric, depending on Al(III) concentration, solution pH, and other factors. As applied to studies aimed at developing new coagulants, it was found important that a new phase of polynuclear hydroxo complexes of aluminum appears in aluminum hydroxychloride solutions at high Al(III) concentration and $[Al^{3+}]/[Cl^{-}]$ ratio exceeding 2 and the solution becomes colloidal [9, 10]. This made it possible to determine conditions for aluminum hydroxychloride structuring with inorganic salts and to obtain on this basis new solid coagulant formulations showing higher performance than the initial aluminum hydroxychloride.

EXPERIMENTAL

The initial aluminum hydroxychloride solution was prepared by reacting granulated aluminum of AG brand [intermediate in manufacture of electrolytic aluminum, TU (Technical Specifications) 48-0107-95–90] with hydrochloric acid [11] and had the following characteristics: Al(III) content 13.2 wt %, dry residue 54.3 wt %, atomic ratio Al^{3+}/Cl^{-} = 2.18, pH 4.6, ρ = 1340 kg m^{-3}.

The electrical conductivity of dilute aluminum hydroxychloride solutions was measured in a conductometric cell with platinum electrodes (S = 1 cm^2, L = 1 cm) with an F-480 ac bridge. Double-distilled water was used.

The structuring was studied with an RV-8M rotation viscometer in the constant shear stress mode. The dynamic viscosity of aluminum hydroxychloride solutions was measured with a VPZh-2 viscometer with a capillary diameter of 0.88 mm.

Solid coagulant formulations were obtained by adding to an aluminum hydroxychloride solution a weighed portion of NaCl or $MgCl_2$ of analytically pure grade (or its solutions) with subsequent stirring with a spatula.

To study the performance of the coagulants, dispersions of kaolin (of "pharmaceutical" brand) were prepared by roiling 1 g of kaolin in 2 l of tap water

1070-4272/02/7504-0515 $27.00 © 2002 MAIK "Nauka/Interperiodica"

Table 1. Characteristics of low-turbid kaolin dispersions in water

Dispersion	Content of dispersed phase, mg l^{-1}	Particle size, nm	pH of medium
1	88	78	7.7
2	16	77	7.6
3	7	47	7.6

(pH 7.6–7.7) and subsequent settling for 12, 24, or 48 h. The thus prepared dispersion was decanted, its upper part was sampled, and the sample was analyzed for the content of the dispersed phase by filtering through a membrane filter. The particle size of the dispersed phase (the most probable value) was found turbidimetrically (Table 1).

The coagulant performance was studied as follows: a freshly prepared kaolin dispersion of prescribed concentration was poured in 12 250-ml cylinders.

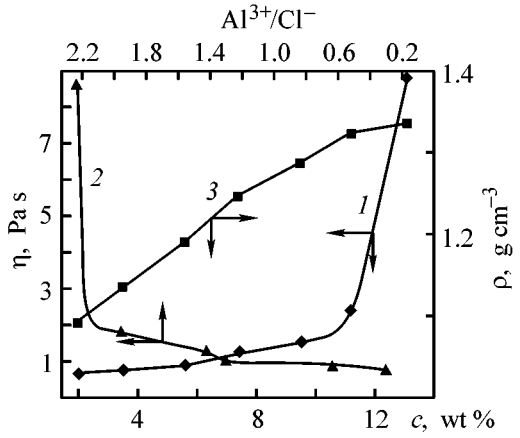

Fig. 1. Dynamic viscosity of the reaction mass, η, vs. (*1*) aluminum concentration *c* and (*2*) Al^{3+}/Cl^{-} ratio, and density ρ vs. aluminum concentration. Reaction temperature 85°C.

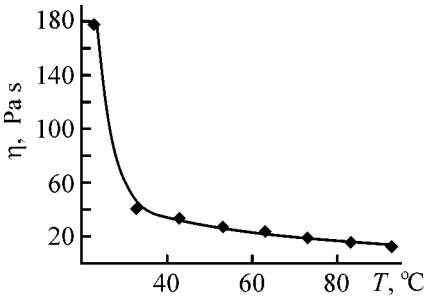

Fig. 2. Dynamic viscosity of aluminum hydroxychloride solution, η, vs. temperature *T*. Dispersed phase concentration 730 g l^{-1}.

A certain volume of a coagulant with a known concentration was introduced into each cylinder. After 12-fold tilting, the dispersion was allowed to settle for 1 h and the upper, over-sediment layer of the dispersion was sampled and its optical density was determined on a Spekol spectrophotometer in a cell with a layer thickness from 1 to 5 cm at incident light wavelength of 640 nm.

The kinetics of sedimentation of coagulant-treated dispersions was studied with an FET turbidimeter. Low-turbid kaolin dispersion was placed in a temperature controlled glass cell (V = 100 cm^3), and a coagulant dose was introduced at working magnetic stirrer (n = 120 rpm). In 5 s the stirrer was switched off, and the optical density of the dispersion was measured in transmitted light (λ = 540 nm) in the course of 1 h. Using the preliminarily constructed calibration plots [12], the optical densities of the dispersion were recalculated into turbidity (mg l^{-1}).

As already noted, the composition and properties of aqueous aluminum hydroxychloride solutions are governed by a number of factors: Al(III) concentration, pH value, etc. These factors largely depend on the conditions of aluminum hydroxychloride preparation. It was found that, when aluminum hydroxychloride is obtained by reacting aluminum with a 10% solution of hydrochloric acid, the properties of the reaction system change dramatically in the course of reaction. For example, on raising the Al(III) content in the reaction mass to more than 10 wt %, the viscosity of the reaction mass grows steeply (Fig. 1, curve *1*). At this Al(III) content the Al^{3+}/Cl^{-} atomic ratio reaches a value of 1.91 (curve *2*). The solution density grows virtually linearly in the course of the reaction (curve *3*). The occurring changes are presumably due to variation of the phase composition of the reaction mass. It is known that aluminum pentahydroxychloride is the final, and the most stable product of hydrolysis of aluminum salts in concentrated solutions [7]. The elemental composition of the product under study in its final state corresponds to this compound.

As shown by viscosity measurements with a concentrated aluminum hydroxychloride solution, the temperature dependence of the dynamic viscosity is nonlinear (Fig. 2). With the temperature increasing to above 23°C, the viscosity falls dramatically. At 80°C, the viscosity is only 10% of its initial value, and it remains virtually unchanged with temperature elevated further. Such a behavior of the system suggests structural interactions in the initial aluminum hydroxychloride solution. With increasing temperature, this structure disintegrates and the system becomes a sol.

The heterogeneous nature of aluminum hydroxychloride solutions is also evidenced by the dependence of the equivalent electrolytic conductivity of the solutions on the Al(III) concentration in these solutions (Fig. 3, curve *1*). The curve for the $\lambda = f(\sqrt{c})$ dependence shows an apparent break at $c = 1.25 \times 10^{-3}$ M. For colloidal solutions such a point characterizes the critical micelle concentration (CMC). Micelle formation in a hydrolytic interaction of aqua hydroxo complexes of Al(III) in aqueous dispersed systems is regarded as an intermediate stage in heterocoagulation with basic salts of aluminum [1]. Measurements of the optical density of an aluminum hydroxychloride solution diluted in the presence of a dye (solubilization technique) gives a CMC of 1.15×10^{-3} M (Fig. 3, curve *2*), i.e., a value close to that found from electrolytic conductivity measurements. Thus, the results of the investigations performed, combined with published data, suggest that a concentrated aluminum hydroxychloride solution is a dispersed system partly structured under standard conditions.

In water treatment technology, the customer's requirements to coagulants frequently refer not only to the performance of coagulants, but also to their aggregative state, storage conditions at low temperature, transportation problems, etc. The liquid form of reagents fails to always satisfy these requirements. The revealed specific features of concentrated aluminum hydroxychloride solutions, and also the known patterns of gelation of silica dispersions [13] close to aluminum hydroxychloride dispersions in particle size in water sols {$(0.12–0.6) \times 10^{-6}$ m for silica [14] and $(0.1–1.5) \times 10^{-6}$ m for particles of sols of aluminum complexes [3, 15]}, suggest that a concentrated aluminum hydroxychloride solution, which is actually a sol, may transform under certain conditions into a gel.

It is known that structuring in dispersed systems is largely influenced by electrolytes [16]. The gelation in aqueous dispersions of aluminum hydroxychlorides was studied upon introduction into these dispersions of a number of inorganic salts in solid state or as solutions. On adding an electrolyte, the dispersion was stirred with a spatula and its viscosity was measured on a rotation viscometer. The gelation time was found as the time elapsed from the instant of electrolyte introduction till the onset of viscosity rise [17]. Table 2 presents the time of gelation, τ_{gel}, in structuring of aluminum hydroxychloride dispersions with various salts.

The mass ratios aluminum hydroxychloride : salt, listed in Table 2, correspond to the minimum gelation time for a respective salt. It should be noted that no gel is formed with aluminum and iron chlorides even after 24 h. It is shown for the example of sodium chloride solution that the gelation time strongly depends on the concentration of the aqueous electrolyte solution (Table 3) introduced into the aluminum hydroxychloride dispersion (volume ratio aluminum hydroxychloride : solution = 10 : 1):

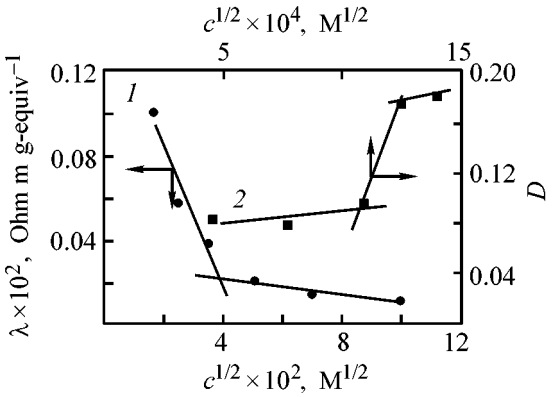

Fig. 3. (*1*) Equivalent electrolytic conductivity λ and (*2*) optical density *D* vs. aluminum hydroxychloride concentration *c*.

c_{NaCl}, %	6.6	10.0	12.0	13.2	16.0	20.0
τ_{gel}, min	60	10	1.5	1.2	0.8	0.5

These data were obtained for an aluminum hydroxychloride dispersion containing 54.3% main substance or 730 g l^{-1} in terms of aluminum pentahydroxychloride.

Table 2. Time of structuring of aluminum hydroxychloride dispersion with inorganic salts at 180°C

Solid salt	Mass ratio aluminum hydroxychloride : salt	τ_{gel}, min
NaCl	1 : 0.10	2
$Al_2(SO)_3$	1 : 0.35	2.5
Na_2SO_4	1 : 0.99	2
NaCl	1 : 0.20	2
$MgCl_2 \cdot 6H_2O$	1 : 0.18	1.5
$MgSO_4$	1 : 0.14	1
$AlCl_3 \cdot 6H_2O$	Varying	No gel formed*
$FeCl_3 \cdot 6H_2O$	1 : 0.25	〃
$MnSO_4 \cdot 6H_2O$	1 : 0.22	1
Natural bischofite	1 : 0.25	1
Natural bischofite (l)	1 : 0.25	1

* No gel formed in 24 h.

Table 3. Effect of dispersed phase concentration in an aluminum hydroxychloride solution on the gelation time

Content of dispersed phase, g l^{-1}	τ_{gel} (min) upon introduction of indicated salt, M		
	NaCl, 3.38	$MgCl_2 \cdot 6H_2O$, 2.27	$Al_2(SO_4)_3$, 0.69
730	0.5	0.5	0.5
710	2.5	3.0	3.5
680	3.5	9.5	35
644	14	90	250
606	90	306	1460
568	1440	1680	4140

Table 4. Content of components in working solutions of coagulants

Coagulant	Content, g l^{-1}		
	Al(III)	NaCl	$MgCl_2$
Aluminum hydroxychloride	1.32	–	–
Formulation 1	1.12	0.91	–
Formulation 2	0.92	–	1.24

As is known, the concentration of the dispersed phase markedly affects the process of sol structuring [17]. Table 3 presents data on the dependence of the time of structuring of an aluminum hydroxychloride dispersion on the content of the dispersed phase in the dispersion. To make the nature and structure of the solutions identical, the following procedure was used. Instead of diluting an aluminum hydroxychloride solution with the maximum content of the main substance, dispersions were prepared by synthesis of aluminum hydroxychloride at varied process duration under conditions ensuring the required Al^{3+}/Cl^- ratio, i.e., leading to formation of aluminum pentahydroxychloride. The concentration of salts (per the whole dispersion volume) was chosen in such a way that the gelation time was minimal and equal for the most concentrated dispersion with different salt added.

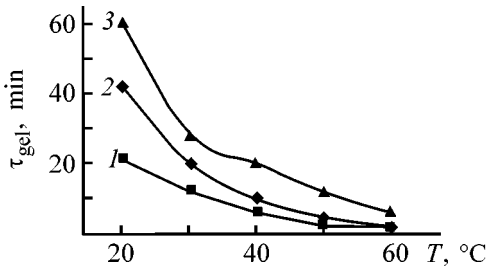

Fig. 4. Gelation time τ_{gel} vs. temperature T of aluminum hydroxychloride mixing with salts. Concentrations: dispersed phase 680 g l^{-1} and salt 1.6 M. Salt: (*1*) NaCl, (*2*) $MgCl_2 \cdot 6H_2O$, and (*3*) $Al_2(SO_4)_3 \cdot 18H_2O$.

As seen from Table 3, the gelation time increases steeply when the concentration of the dispersed phase is made lower than 680 gl^{-1}.

The transition from sol to gel and back is strongly affected by the pH of the medium. To obtain an aluminum hydroxychloride dispersion with the lowest possible pH, gaseous HCl was bubbled through the dispersion. Structuring of such dispersions with various electrolytes demonstrated that, irrespective of the type of salt, the gelation time is virtually the same and does not exceed 1 min at pH 3.7 and higher. Beginning with pH 3.6, the gelation time grows steeply, and no gel at all is formed at pH below 3.0.

As would be expected, the gelation time depends on temperature at which a salt is introduced into the aluminum hydroxychloride dispersion (Fig. 4). With the temperature increasing from 20 to 60°C, the gelation time decreases 10–20-fold.

The gels obtained in aluminum hydroxychloride structuring with electrolytes are X-ray amorphous and possess no thixotropic properties. When dried in air, they crack and are easily powdered mechanically. In gels obtained in the presence of sodium chloride, the strengthening of the coagulation structure results in their spontaneous transformation into a powder. A similar phenomenon was observed in formation of gels of silicic acid [18].

To evaluate the coagulant performance, aqueous dispersions of kaolin with varied content of the dispersed phase (Table 1), close to that in natural water, were subjected to coagulation. The efficiencies of the coagulating action of aluminum hydroxychlorides and gels obtained in the presence of NaCl (formulation 1) and $MgCl_2 \cdot 6H_2O$ (formulation 2) were compared. The working solutions were prepared by dissolving a weighed portion of a reagent (~1 wt %) in 100 ml of distilled water (Table 4).

Preliminarily, a comparative analysis of coagulant hydrolysis was made on the basis of changes in the turbidity of the medium, in which flakes of aluminum hydroxide were formed. For this purpose, the working solution of a coagulant (6 ml) was introduced into a cell with distilled water (V = 100 cm^3) with pre-

Table 5. Rates of hydrolysis of coagulants and sedimentation of hydrolysis products in water with alkalinity of 7.5 mg-equiv l^{-1}*

Coagulant	Rate, mg l^{-1} min^{-1}		Coagulant	Rate, mg l^{-1} min^{-1}	
	hydrolysis	sedimentation		hydrolysis	sedimentation
Aluminum hydroxychloride	0.13	1.54	Formulation 1 Formulation 2	0.72 0.84	2.68 4.70

* According to turbidity measurements.

Table 6. Results of river water purification with coagulants [coagulant dose in terms of Al(III) 5 mg l^{-1}]

Parameter	Permissible level according to GOST 2874–82	Initial water	Treated water		
			aluminum hydroxochloride	1*	2*
pH	6–9	8.2	7.4	7.6	7.5
Turbidity, mg dm^{-3}	≤1.5	2.3	0.4	0.12	0.08
Color, deg	≤20	52	10	5.5	7.5
Number of microbe colonies	≤100	78	3	2	1
Time of attainment of turbidity equal to 0.1 mg dm^{-3}, min	–	100	30	20	15

* 1 and 2 are formulation numbers.

scribed (hydrocarbonate) alkalinity of 7.5 mg-equiv l^{-1}. After short mixing (5 s), the optical density of the cell content was measured at certain intervals of time. The values obtained were recalculated (using a preliminarily plotted calibration graph) to dispersion turbidities (mg l^{-1}). The rate of hydrolysis was expressed as the slope of a tangent to the ascending portion of the turbidity curve. Similarly, the rate of sedimentation was found from the descending portion of the turbidity curve. The thus obtained rates of hydrolysis and sedimentation of hydrolysis products, presented in Table 5, suggest a higher coagulation activity of binary coagulants. Characteristically, the sedimentation rate of products formed in hydrolysis of formulation 2 (aluminum hydroxychloride + $MgCl_2$) much exceeds that of aluminum hydroxychlorides.

Figure 5 presents typical curves describing changes in dispersion turbidity upon introduction of certain doses of aluminum hydroxychloride and formulation 1 (aluminum hydroxychloride + NaCl). Similar curves were obtained for formulation 2 (aluminum hydroxychloride + $MgCl_2$). The same behavior is observed for all the three types of dispersions: equal degrees of clarification of the dispersions are obtained with a dose of binary coagulant that is much lower than that of aluminum hydroxychloride. Table 6 presents the results obtained in tests of the coagulants under study in purification of river water (Volzhskoe reservoir). The tests were done in conformity with GOST (State Standard) 3351–74.

The results of the tests confirm the enhanced, compared with aluminum hydroxychloride, coagulation activity of binary coagulants.

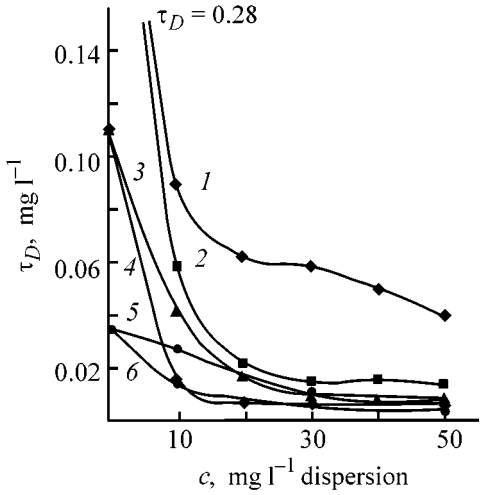

Fig. 5. Turbidity τ_D of kaolin dispersions vs. coagulant dose c in terms of Al(III). (*1, 3, 5*) Aluminum hydroxychloride and (*2, 4, 6*) formulation 1. Dispersion: (*1, 2*) 1, (*3, 4*) 2, and (*5, 6*) 3 (see Table 1).

CONCLUSIONS

(1) The results of the rheological and conductometric studies of concentrated solutions of aluminum hydroxychloride indicate the structuring of these solutions. Introduction of inorganic salts leads to gelation whose rate depends on the concentration of aluminum hydroxychloride, type of salt and its concentration, pH value, and temperature.

(2) The obtained solid formulations of aluminum hydroxychloride with NaCl and $MgCl_2$ exhibit higher coagulating activity in water purification as compared with the starting aluminum hydroxychloride.

REFERENCES

1. Zapol'skii, A.P. and Baran, A.A., *Koagulyanty i flokulyanty v protsessakh ochistki vody* (Coagulants and Flocculants in Water Treatment), Leningrad: Khimiya, 1987.
2. Butchenko, L.I., Shut'ko, A.P., and Mulik, I.Ya., *Khim. Tekhnol. Vody*, 1989, vol. 11, no. 2, pp. 182–185.
3. Kulyasova, A.S. and Fomicheva, T.N., *Zh. Prikl. Khim.*, 1997, vol. 70, no. 3, pp. 371–374.
4. Feofanov, Yu.A. and Litmanova, N.L., *Zh. Prikl. Khim.*, 2000, vol. 73, no. 8, pp. 1390–1391.
5. Bykadorov, N.U., Radchenko, S.S., Zhokhova, O.K., and Utkina, E.E., Abstracts of Papers, *VI Mezhdunarodnaya konferentsiya "Naukoemkie khimicheskie tekhnologii," Moskva, 1999 g.* (VI Int. Conf. "High-End Chemical Technologies," Moscow, 1999), Moscow: MITKhT, 1999, pp. 251–253.
6. Basov, V.P. and Shut'ko, A.I., *Dokl. Akad. Nauk SSSR*, 1976, vol. 230, no. 3, pp. 599–601.
7. Pilipenko, A.T., Falendysh, N.F., and Parkhomenko, E.P., *Khim. Tekhnol. Vody*, 1982, vol. 4, no. 2, pp. 136–150.
8. Gerasimenko, N.G., Solomentseva, I.M., and Surova, L.M., *Khim. Tekhnol. Vody*, 1991, vol. 13, no. 8, pp. 755–760.
9. Fedotov, M.A., Krivoruchko, O.P., and Buyanov, R.A., *Izv. Akad. Nauk SSSR, Ser. Khim.*, 1977, no. 10, pp. 2183–2186.
10. Fedotov, M.A., Krivoruchko, O.P., and Buyanov, R.A., *Izv. Akad. Nauk SSSR, Ser. Khim.*, 1977, no. 12, pp. 2647–2651.
11. RF Patent 2 083 495.
12. *GOST* (State Standard) *2874–82. Potable Water: Photometric Method for Turbidity Determination*, Moscow: Izd. Standartov, 1982.
13. Iler, R.K., *The Chemistry of Silica*, New York: Wiley–Interscience, 1979.
14. Gamera, V.A., Kruglitskii, N.N., Makarov, A.S., and Sperkach, V.S., *Akust. Zh.*, 1986, vol. 32, no. 5, pp. 610–615.
15. Krivoruchko, O.P., Kolomiichuk, V.N., and Buyanov, R.A., *Zh. Neorg. Khim.*, 1985, vol. 30, no. 2, pp. 306–310.
16. *Fiziko-khimicheskaya mekhanika dispersnykh struktur: Sbornik nauchnykh trudov* (Physicochemical Mechanics of Dispersed Structures: Coll. Sci. Works), Kruglitskii, N.N., Ed., Kiev: Naukova Dumka, 1986.
17. Mart'yanova, T.F., Golova, N.L., Kuznetsov, L.L., and Zavlin, P.M., *Zh. Prikl. Khim.*, 1996, vol. 69, no. 6, pp. 1028–1030.
18. Frolov, Yu.G., Shabanova, N.A., and Savochkina, T.V., *Kolloid. Zh.*, 1980, vol. 42, no. 5, pp. 1015–1018.

Russian Journal of Applied Chemistry, Vol. 75, No. 4, 2002, pp. 521–525. Translated from Zhurnal Prikladnoi Khimii, Vol. 75, No. 4, 2002, pp. 535–539.
Original Russian Text Copyright © 2002 by Fedorova, Tsymbulov, Tsemekhman.

PHYSICOCHEMICAL STUDIES OF SYSTEMS AND PROCESSES

Determining the Activity Coefficients of Copper and Nickel Oxides in Melts of the System Cu_2O–NiO

N. A. Fedorova, L. B. Tsymbulov, and L. Sh. Tsemekhman

Gipronikel' Institute, Joint-Stock Company, St. Petersburg, Russia

Received December 14, 2001

Abstract—Equilibria between a copper–nickel alloy and oxide melt of the binary system Cu_2O–NiO were studied and the activity coefficients of copper and nickel oxides at 1573 K in the homogeneity region of the oxide melt (up to 11.6 mol % NiO) were determined. Similar values were also found by calculation from the phase diagram of Cu_2O–NiO.

Autogenous smelting of high-grade nickel containing copper sulfide concentrates obtained by floatation separation of converter matte gives metallic (0.5 to 6 wt % Ni, 0.01 to 1.5 wt % S) and oxide (slag) phases [1, 2]. The distribution of nickel between these phases is largely determined by the exchange reaction

$$(Cu_2O) + [Ni] = (NiO) + 2[Cu], \qquad (1)$$

where parentheses and square brackets designate components of, respectively, the oxide and metallic phases.

Since the interaction of components of the metallic and oxide phases in pyrometallurgical units can be considered from the standpoint of thermodynamic equilibrium, a knowledge is necessary of the activities of these components in melts.

However, detailed data are scarce, especially for oxide melts. With account of difficulties encountered in determining the activities of metal oxides in real multicomponent slag systems (to which may be referred slag formed in smelting of copper concentrates), it is appropriate first to find the activities of copper and nickel oxides in the binary system Cu_2O–NiO. A temperature of 1300°C, characteristic of the industrial processes considered, was chosen for the study.

The required activity coefficients can be determined experimentally by establishing an equilibrium between a copper–nickel alloy and an oxide melt of the system Cu_2O–NiO. Knowing the equilibrium constant of reaction (1), component concentrations in the oxide melt and metal, and the activities of copper and nickel in the metal alloy, we can find the ratio of the activity coefficients of the oxides

$$K_a = \frac{a_{Cu}^2 a_{NiO}}{a_{Ni} a_{Cu_2O}} = \frac{x_{Cu}^2 x_{NiO}}{x_{Ni} x_{Cu_2O}} \frac{\gamma_{Cu}^2}{\gamma_{Ni}} \frac{\gamma_{NiO}}{\gamma_{Cu_2O}}, \qquad (2)$$

where a_i, x_i, and γ_i are the activity, mole fraction, and activity coefficient of component i (i = Ni, Cu, NiO, Cu_2O) in the equilibrium phases, respectively.

From Eq. (2) follows that

$$\gamma_{NiO}/\gamma_{Cu_2O} = K_a(\gamma_{Ni}/\gamma_{Cu}^2)(x_{Ni} x_{Cu_2O}/x_{Cu}^2 x_{NiO}). \qquad (3)$$

Further, it will be shown that, according to the Gibbs–Duhem equation, this ratio can be used to find the activity coefficients of NiO and Cu_2O.

As starting materials served electrolytic copper, powdered metallic nickel produced by the carbonyl technique, and copper(I) oxide of analytically pure grade. A magnesium oxide crucible with a 15-g portion of the charge, comprising 5 g of metallic copper and nickel (with Cu : Ni ratio varied from 99.7 : 0.3 to 88 : 12) and 10 g of copper oxide, was placed in a hermetically sealed alundum reactor in a cold furnace with graphite heater. The charge was heated to the working temperature; the melt was kept at this temperature for 120 min and cooled under argon. After cooling, the alloy and slag were separated, weighed, and analyzed chemically for the content of copper and nickel. Additionally, the alloy was analyzed for the content of oxygen (on LECO analyzer), and the oxide phase, for magnesium (chemically). The content

1070-4272/02/7504-0521 $27.00 © 2002 MAIK "Nauka/Interperiodica"

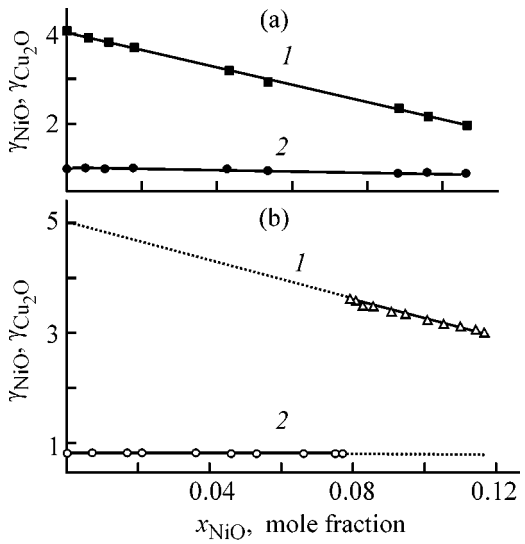

Fig. 1. Activity coefficients (*1*) γ_{NiO} and (*2*) γ_{Cu_2O} vs. nickel oxide content x_{NiO}. (a) Experimental data for 1573 K and (b) calculation on the basis of the phase diagram of the system Cu_2O–NiO.

of magnesium in the oxide melt was in the range 0.2–0.4 wt % in all the experiments, which well allows the influence of magnesium oxide on the equilibrium in the system under study to be neglected.

The time of keeping was chosen on the basis of a set of preliminary experiments carried out at 1300°C for 5 to 240 min, with metallic components taken in the ratio Cu : Ni = 90 : 10. It was found that equilibrium is attained in the system in about 50 min.

The compositions of alloys and oxide melts were varied by gradually increasing the Ni content relative to Cu. The Cu : Ni ratio in the initial charge was decreased until the oxide melt became saturated with respect to NiO. The nickel contents in the alloy and oxide melt, as influenced by the Cu : Ni ratio in the charge, are given below.

Initial Cu : Ni ratio	99.7 : 0.3	98.9 : 1.1	98.3 : 1.7
Ni content in alloy, wt %	0.085	0.16	0.259
Ni content in oxide phase, wt %	0.19	0.42	0.72
Initial Cu : Ni ratio	95.6 : 4.4	92.0 : 8.0	90.0 : 10.0
Ni content in alloy, wt %	0.59	1.29	0.9
Ni content in oxide phase, wt %	1.79	4.12	3.77
Initial Cu : Ni ratio	89.3 : 10.7	88.0 : 12.0	
Ni content in alloy, wt %	1.09	0.88	
Ni content in oxide phase, wt %	4.6	5.3	

On the basis of the thus determined contents of components in the alloy and the oxide melt, the equilibrium constant of reaction (1) [calculated with account of NiO overcooling (K_a = 8.16)], and the activity coefficients of copper and nickel, the ratio $\gamma_{NiO}/\gamma_{Cu_2O}$ was obtained in the NiO content range 0.5–10.6 at. % by means of Eq. (3):

x_{NiO}	0.005	0.010	0.017	0.043
$\gamma_{NiO}/\gamma_{Cu_2O}$	3.86	3.74	3.57	3.05
x_{NiO}	0.05	0.09	0.10	0.106
$\gamma_{NiO}/\gamma_{Cu_2O}$	2.81	2.18	2.04	1.87

Since the alloy was in equilibrium with the oxide melt, it contained, in addition to copper and nickel, also considerable amounts of oxygen (2.7–3.1 wt %), which is close to the solubility limit. Therefore, we calculated the activity coefficients of copper and nickel in the alloy, using the data of [3], where the activities of copper and nickel in oxygen-saturated alloys are presented. It should be noted, however, that the activities of copper and nickel in such alloys virtually coincide with those in oxygen-free alloys [4].

On the basis of the calculated ratios of the activity coefficients, let us find the activity coefficients, using the Gibbs–Duhem equation. For this purpose, let us define the function $\gamma_{NiO}/\gamma_{Cu_2O} = f(x_{NiO})$.

The activity coefficient of NiO is given by

$$\gamma_{NiO} = \gamma_{Cu_2O} f(x_{NiO}). \quad (4)$$

According to the Gibbs–Duhem equation,

$$x_{NiO}\, d\ln\gamma_{NiO} + x_{Cu_2O}\, d\ln\gamma_{Cu_2O} = 0. \quad (5)$$

Substituting (4) in Eq. (5), we obtain

$$x_{NiO}\, d[\ln f(x_{NiO}) + \ln\gamma_{Cu_2O}] + x_{Cu_2O}\, d\ln\gamma_{Cu_2O} = 0,$$

$$x_{NiO}\, d\ln[f(x_{NiO})] + x_{NiO}\, d\ln\gamma_{Cu_2O} + x_{Cu_2O}\, d\ln\gamma_{Cu_2O} = 0,$$

$$(x_{Cu_2O} + x_{NiO})\, d\ln\gamma_{Cu_2O} = -x_{NiO}\, d\ln[f(x_{NiO})],$$

$$d\ln\gamma_{Cu_2O} = -x_{NiO}\, d\ln[\gamma_{NiO}/\gamma_{Cu_2O}].$$

Integrating this equation over the interval 0–x_{NiO}, we obtain the following values of the activities

x_{NiO}	0.005	0.010	0.017	0.043
γ_{NiO}	3.89	3.79	3.65	3.22
γ_{Cu_2O}	1.007	1.014	1.024	1.056
x_{NiO}	0.05	0.09	0.10	0.106
γ_{NiO}	3.00	2.41	2.26	2.09
γ_{Cu_2O}	1.068	1.104	1.111	1.119

The composition dependence of γ_{NiO} and γ_{Cu_2O}, found from experimental data, is presented in Fig. 1a.

Let us compare the activity coefficients obtained from experimental data with the calculated values found on the basis of the phase diagram of Cu_2O–NiO. The procedure for calculating the activities on the basis of the phase diagram has been described in numerous manuals [5, 6] and is widely used in practice. The activity of a component is calculated along the line of its primary crystallization in the phase diagram. Among disadvantages of this method are its not always sufficient accuracy and necessity for making certain assumptions in recalculation of data to a single temperature. Despite these disadvantages, such a calculation can be rather useful for comparison purposes.

The phase diagram of the system Cu_2O–NiO was taken from [7] (Fig. 2). It can be seen from the diagram that the system is simple eutectic. Since the phase diagram of the system Cu_2O–NiO has not been found over the entire range of concentrations, it cannot be stated with full confidence that there is no range of solid solution formation for NiO. However, we assume in calculations that pure NiO crystallizes.

The melting points of Cu_2O and NiO are, respectively, 1502 and 2228 K, and the heats of melting, 65.6 and 42 kJ mol^{-1}. In all calculations, the heat of melting was taken to be temperature-independent.

For any point of the curve of primary crystallization of NiO ($T < T_m$), we can write the equilibrium equation

$$\mu_l = \mu_s,$$

$$\mu_{0,l} + RT\ln a_{NiO} = \mu_{0,s}, \quad \mu_{0,l} = \mu_{0,s} + \Delta\mu_m,$$

$$\Delta\mu_m = \Delta G_m = \Delta H_m - T\Delta S_m = T_m\Delta S_m - T\Delta S_m$$
$$= \Delta S_m(T_m - T) = (42\,000/2228)(2228 - T).$$

At T = 1573 K and x_{NiO} = 0.116, ΔG_m = 12 437.4 J mol^{-1}.

Let us consider the following scheme:

$$\begin{array}{ccc} \mathrm{NiO\,(s,}\ x_{NiO}=1) & \xrightarrow{\ \mathrm{I}\ } & \mathrm{NiO\,(l,}\ x_{NiO}=0.116) \\ & \searrow^{\mathrm{II}} \quad \nearrow_{\mathrm{III}} & \\ & \mathrm{NiO\,(l,}\ x_{NiO}=1) & \end{array}$$

The change in the Gibbs energy is zero for process I. Process II corresponds to melting of pure nickel oxide at $T < T_m$ and $\Delta G \neq 0$. Process III corresponds to transfer of nickel oxide from pure liquid phase to an alloy of the corresponding composition. In this case, the change in the Gibbs energy corresponds to

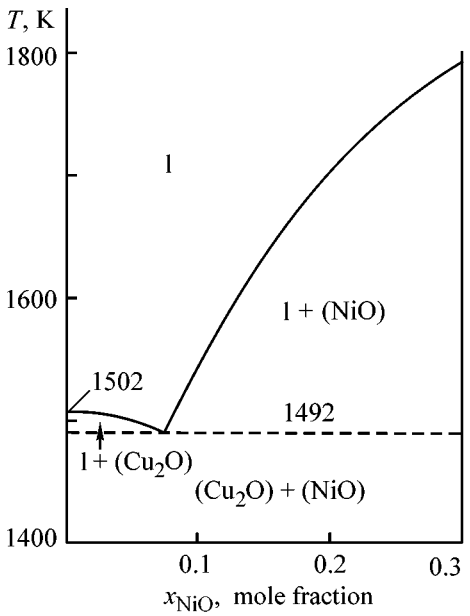

Fig. 2. Fusion diagram of the system Cu_2O–NiO. (T) Temperature.

partial molar energy of NiO in the liquid alloy, $\Delta\bar{G}_{NiO}$, with $\Delta G^{I} = \Delta G^{II} + \Delta G^{III}$. Thus,

$$\Delta\bar{G}_{NiO} = RT\ln a_{NiO} = -\Delta G_{m\,NiO}$$
$$= -(42\,000/2228)(2228 - T). \quad (6)$$

The activities of nickel oxide, calculated along the liquidus line from 1573 to 1492 K (eutectic point), and activity coefficient recalculated to 1573 K over the entire homogeneity region as far as the eutectic point on the assumption of regular solutions are presented in Table 1. To obtain the activity coefficients of NiO for compositions beyond the eutectic point, it is necessary to extrapolate the curve for the activity coefficient of nickel oxide from the initial to zero content (Fig. 1b).

The portion of the liquidus curve along which Cu_2O crystallizes is short (Fig. 2); however, in this case too, the thermodynamic characteristics of Cu_2O in liquid alloys can be calculated along the curve portion in a similar way:

$$\Delta\bar{G}_{Cu_2O} = RT\ln a_{Cu_2O} = -\Delta G_{m\,Cu_2O}$$
$$= -(65\,600/1502)(1502 - T). \quad (7)$$

It should be noted that the region in which solid solutions are formed is negligibly narrow for Cu_2O, with virtually pure component crystallizing. To obtain the activity coefficients of Cu_2O for compositions beyond the eutectic point, it is necessary to extrapolate the curve describing the dependence of the activity

Table 1. Activity coefficients of nickel and copper(I) oxides at 1573 K, calculated for compositions with 7.5–11.6 mol % NiO and 88.4–100 at.% Cu_2O with the use of the phase diagram of Cu_2O–NiO

x	T, K	$\Delta\bar{G}$, J mol^{-1}	a	γ (along liquidus line)	$\Delta\bar{H}$,* J mol^{-1}	γ
			Nickel oxide			
0.116	1573	–13 874.3	0.387	3.335	15 744.66	3.335
0.114	1572	–13 836.6	0.386	3.387	15 935.14	3.384
0.109	1562	–13 761.2	0.378	3.470	16 148.77	3.440
0.105	1552	–13 723.5	0.370	3.528	16 258.69	3.469
0.100	1542	–13 704.7	0.363	3.627	16 508.51	3.536
0.094	1532	–13 497.3	0.355	3.776	16 916.80	3.648
0.090	1522	–13 308.8	0.347	3.860	17 082.22	3.694
0.085	1512	–13 120.3	0.340	3.998	17 412.21	3.789
0.082	1501	–12 931.8	0.332	4.044	17 428.17	3.793
0.080	1500	–12 743.3	0.331	4.136	17 696.37	3.872
0.079	1498	–12 554.8	0.329	4.169	17 773.36	3.895
0.077	1494	–12 366.2	0.326	4.239	17 932.11	3.943
0.075	1492	–12 347.4	0.325	4.333	18 178.18	4.017
			Copper(I) oxide			
0.925	1492	–432.4	0.973	1.044	534.18	1.042
0.932	1494	–345.9	0.977	1.043	528.36	1.041
0.947	1498	–173	0.984	1.041	504.92	1.039
0.964	1500	–86.49	0.992	1.03	370.53	1.029
0.979	1501	–43.24	0.996	1.018	221.49	1.017
1	1502	0	1	1	0	1

* $\Delta\bar{H} = RT\ln\gamma$.

Table 2. Activity coefficients of components of the system Cu_2O–NiO and their ratio at 1573 K in the homogeneity region

x_{NiO}	γ_{NiO}	γ_{Cu_2O}	$\gamma_{NiO}/\gamma_{Cu_2O}$	x_{NiO}	γ_{NiO}	γ_{Cu_2O}	$\gamma_{NiO}/\gamma_{Cu_2O}$
0.116	3.34	1.04	3.20	0.077	3.94	1.04	3.79
0.114	3.38	1.04	3.25	0.075	4.02	1.04	3.86
0.109	3.44	1.04	3.30	0.066	4.09	1.04	3.93
0.105	3.47	1.04	3.33	0.056	4.25	1.04	4.09
0.100	3.54	1.04	3.40	0.046	4.40	1.03	4.26
0.094	3.65	1.04	3.50	0.036	4.56	1.03	4.44
0.09	3.69	1.04	3.55	0.026	4.71	1.02	4.64
0.085	3.79	1.04	3.64	0.017	4.85	1.01	4.79
0.082	3.79	1.04	3.64	0.007	5.00	1.01	4.98
0.080	3.87	1.04	3.72	0	5.11	1.00	5.11
0.079	3.89	1.04	3.74				

coefficient of copper(I) oxide from pure Cu_2O to the line of NiO crystallization (Fig. 1b). The activities of copper oxide, calculated along the liquidus line from 1492 (eutectic point) to 1502 K and activity coefficients recalculated to 1573 K over the entire homogeneity region as far as the NiO crystallization line are presented in Table 1.

Because of the very gradual slope of the liquidus line, the activity coefficient of Cu_2O determined from the fusion diagram may be less accurate than the activity coefficient of NiO. For comparison, we calculated γ_{Cu_2O} from the Gibbs–Duhem equation. Contrary to expectations, the activity coefficients of copper oxide, calculated from the fusion diagram, and

those found by integration of the Gibbs–Duhem equation virtually ideally coincide.

Table 2 presents the activity coefficients of both components of the system Cu_2O–NiO and their ratio at 1573 K for the entire homogeneity region to the line of primary crystallization of NiO (0–11.6 at.% NiO).

Thus, we obtained calculated and experimental activity coefficients of the oxide melt components. Comparison of the values obtained shows that both the results are in good agreement. Figure 3 presents the composition dependence of the ratio of the activity coefficients, $\gamma_{NiO}/\gamma_{Cu_2O}$, obtained on the basis of experimental and calculated data. It can be seen that the experimental values are lower than those calculated. This minor discrepancy can be accounted for by the fact that, in contrast to the calculation based on the phase diagram, the estimate using experimental data is made without any assumptions.

It should also be noted that the experimentally obtained limiting activity coefficient γ_{NiO} = 3.96 is in good agreement with the limiting activity coefficient of nickel oxide found to be 3.2 in [8].

CONCLUSIONS

(1) The activity coefficients of copper and nickel oxides at 1573 K in the homogeneity region of the oxide melt (0 to 11.6 mol % NiO) were found on the basis of a study of the equilibrium between a copper–nickel alloy and an oxide melt of the system Cu_2O–NiO. γ_{Cu_2O} varies between 1.0 and 1.11, and γ_{NiO}, between 2.09 and 3.96.

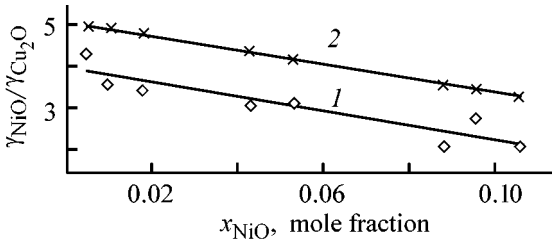

Fig. 3. Ratio of activity coefficients, $\gamma_{NiO}/\gamma_{Cu_2O}$, vs. nickel oxide content x_{NiO} at 1573 K. (*1*) Experimental data and (*2*) calculation.

(2) A conclusion that melts of the system Cu_2O–NiO belong to regular solutions was made on the basis of the data obtained.

REFERENCES

1. RF Patent 2 169 202.
2. Miroevskii, G.P., Golov, A.N., Koklyanov, E.B., and Tsemekhman, L.Sh., *Tsvetn. Met.*, 2001, no. 2, pp. 41–47.
3. Kulkarni, A.D. and Johnson, R.E., *Met. Trans.*, 1973, vol. 4, pp. 1723–1727.
4. Berezutskii, V.V. and Lukashenko, G.M., *Ukr. Khim. Zh.*, 1987, vol. 53, no. 10, pp. 1029–1032.
5. Morachevskii, A.G., *Termodinamika rasplavlennykh metallicheskikh i solevykh sistem* (Thermodynamics of Molten Metallic and Salt Systems), Moscow: Metallurgiya, 1987.
6. Kubaschewski, O. and Alcock, C.B., *Metallurgical Thermochemistry*, Oxford: Pergamon, 1979.
7. Neumann, J.P. and Hsieh, K.C., *Metallurgical Review of MMIJ*, 1987, vol. 4, no. 2, pp. 106–120.
8. Burylev, B.P., Romanov, V.D., and Tsemekhman, L.Sh., *Metally*, 1976, no. 5, pp. 75–77.

Russian Journal of Applied Chemistry, Vol. 75, No. 4, 2002, pp. 526–530. Translated from Zhurnal Prikladnoi Khimii, Vol. 75, No. 4, 2002, pp. 540–544.
Original Russian Text Copyright © 2002 by Lipatova, Losev, Yusova.

PHYSICOCHEMICAL STUDIES OF SYSTEMS AND PROCESSES

Effect of Ultrasonic Field on the State of Starch Hydrogels

I. M. Lipatova, N. V. Losev, and A. A. Yusova

Institute of Chemistry of Solutions, Russian Academy of Sciences, Ivanovo, Russia

Received December 10, 2001

Abstract—Some fundamental aspects of how the primary structure of starch hydrogels with concentration of 1 to 8 wt % disintegrates in an ultrasonic field are discussed. The effect of ultrasonic vibrations on the basic characteristics of starch hydrogels: degree of grain cleavage, viscosity, transparence, and phase composition, is analyzed.

Water–starch gel-like materials are widely used in various industries (textile, food, paper, building, etc.). To ensure the technological usability, starch hydrogels are subjected to thermal, thermochemical, or intensive mechanical treatment [1] in order to destroy their primary structure. The conventional way to prepare gel-like materials from unmodified starches, still employed at domestic plants, is either prolonged cooking (glues, thickeners) or boiling under pressure (size). Both these techniques require much time and thermal energy.

The power intensity and duration of the process can be reduced dramatically by employing mechanical methods [1–3] of preparation of highly dispersed gel-like starch materials, including those with the use of ultrasound. Ultrasonic fields have not found wide application in industry for starch cleavage because of the complexity and poor reliability of the necessary equipment. More promising, in our opinion, is use for these purposes of continuous high-speed rotary-pulsed apparatus (RPA) in which the material treated is subjected to simultaneous action of high-rate shear deformations and ultrasonic field. The influence exerted by conditions of mechanical treatment of starch hydrogels in RPA on disintegration of their primary structure was studied previously [4, 5]. Particular attention was given to dynamic structuring in starch hydrogels under simultaneous action of shear stresses and ultrasonic vibrations in RPA.

The aim of this study was to evaluate the contribution of ultrasonic vibrations to mechanochemical cleavage of starch hydrogels in their treatment in RPA. To solve the problem in hand, disintegration of the primary structure of starch hydrogels under the action of only ultrasound, without shear deformations present in RPA, was studied.

EXPERIMENTAL

As object of study served corn starch [GOST (State Standard) 7697–82]. Starch hydrogels for subsequent ultrasonic treatment were prepared by cooking of a starch suspension on a water bath at 90°C for 15 min.

Starch hydrogels with starch concentration in the range 1–8 wt % were subjected to ultrasonic treatment in a UZDN-2T disintegrator at a frequency F = 22 kHz. The exposure time was 5 to 60 s; the volume density of acoustic energy, found calorimetrically, was 1.34 W cm^{-3}.

The degree of starch grain cleavage (DC, %) was found by centrifugation [6]; the content of the water-soluble fraction of starch, A (%), by the method of hot extraction; and the composition of extracts, spectrophotometrically, using complexation with iodine [7].

The optical densities of solutions were measured on a Spekol-221 spectrophotometer at a wavelength λ = 400 nm.

The starting starch hydrogels are in the form of a dispersion in which swollen starch grains are distributed in a solution of the water-soluble fraction. In starch cleavage by any of the known methods, starch grains disintegrate to a necessary level of dispersity,

1070-4272/02/7504-0526 $27.00 © 2002 MAIK "Nauka/Interperiodica"

determining the technological properties of the gel-like starch material.

The disintegration of the primary structure of starch hydrogels under the action of ultrasonic vibrations is, in fact, the process of dispersion. The term "dispersion" is referred to two different processes: dispersion proper, i.e., disintegration of monolithic particles, and deagglomeration, i.e., rupture of bonds between particles in the agglomerate [8]. Cleavage of starch hydrogels cannot be related with confidence to any of these processes. The specificity of starch hydrogels as microheterogeneous systems consists in that the colloid-disperse phase in these systems is composed on starch grains, which are, in their turn, natural formations with complex morphology. Swollen starch grains can be referred neither to monolithic particles nor to agglomerates, since, on the one hand, they contain finer structural units (fibrils, crystallites), and, on the other, each grain is a unified system with a nucleus and a lipid–polysaccharide shell. One more specific feature of starch dispersions is that the composition and, correspondingly, the viscosity of the dispersed medium change in the course of grain cleavage as a result of partial diffusion of starch macromolecules into solution. For the above reasons, the known procedures for calculating parameters of the dispersion process, developed for common dispersions and, as a rule, based on quite a number of assumptions and limiting conditions including, in particular, the invariable viscosity of the medium, are inapplicable to the case of starch hydrogels [9].

The disintegration of the initial structure of starch hydrogels is accompanied by a decrease in their viscosity, increase in the transparency, and rise in the content of the water-soluble fraction. Analysis of how these parameters vary with increasing time of ultrasonic treatment allows some conclusions on the mechanism of ultrasonic cleavage of starch hydrogels. As seen from Fig. 1, the viscosity reaches a certain maximum value in the very beginning of treatment (τ = 5 s) and then decreases abruptly, with the decrease in viscosity becoming slower after 15 s of ultrasonic treatment. Such a run of the curve describing the decrease in viscosity is in agreement with the run of the curves describing the increase in the degree of cleavage and in the content of the water-soluble fraction. The peak in the viscosity curve is accounted for by the stage of additional swelling which occurs before disintegration of grains because of the removal of their lipid shell limiting the swelling.

It was of interest to compare the rates and mechanisms of grain disintegration in ultrasonic and thermal treatment. For this purpose, one part of the same initial starch hydrogel was subjected to ultrasonic treatment, and another part, to thermal treatment in a closed vessel at a temperature of 105°C and pressure of 1.1 atm without stirring. It was found that the rate of cleavage of starch grains under the action of ultrasound at the volume density of acoustic energy used in the study exceeds by two orders of magnitude and more that in cooking without chemical cleaving agents. For example, an 80% cleavage of grains of a 5% starch hydrogel in cooking without stirring is achieved in 2 h, whereas in the case of ultrasonic treatment the same degree of cleavage is achieved in only 40 s.

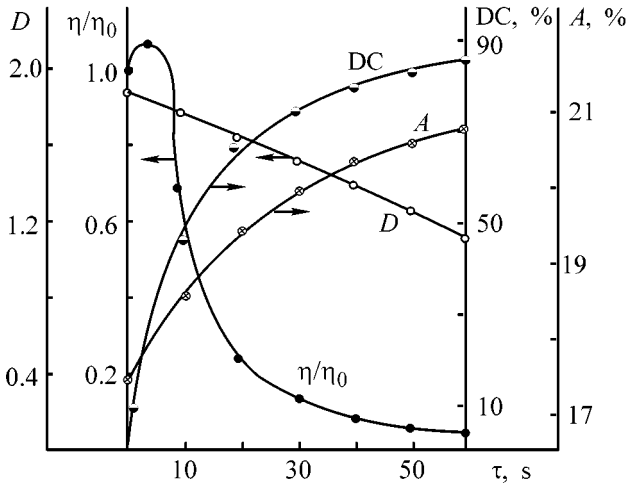

Fig. 1. Optical density D (λ = 400 nm), relative viscosity η/η_0, degree of cleavage DC, and content of water-soluble fraction, A, of starch hydrogels vs. time τ of ultrasonic treatment.

In both cases, the viscosity of hydrogel samples was measured at 80°C to reduce the contribution from the structural component of the viscosity. The viscosity of the hydrogels at this temperature is determined by the content of the water-soluble fraction and the particle size of the colloid-dispersed phase. The same refers to the optical density. As seen from Fig. 2, to the same content of the water-soluble fraction correspond, in the case of ultrasonic cleavage, much lower viscosities and optical densities as compared with those in thermal cleavage, which points to much smaller particle size in ultrasonically treated hydrogels. In thermal cleavage without stirring, the process dominating after the stage of swelling, which also occurs in this case, is diffusion of amylose macromolecules into solution, caused by thermal motion and concentration gradient. Grains weakened by the diffusion start to gradually disintegrate in cooking.

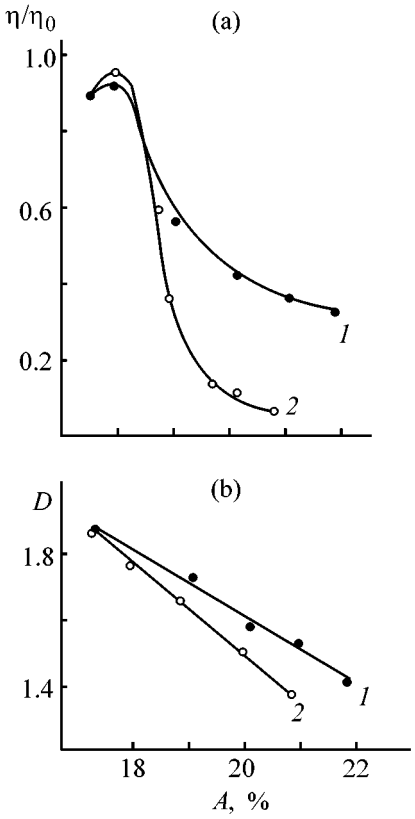

Fig. 2. (a) Relative viscosity η/η_0 and (b) optical density D vs. content A of the water-soluble fraction in cleavage of starch hydrogel (C = 5 wt %). Cleavage: (*1*) thermal (T = 105°C, P = 1.1 atm) and (*2*) ultrasonic (F = 22 Hz, T = 40°C).

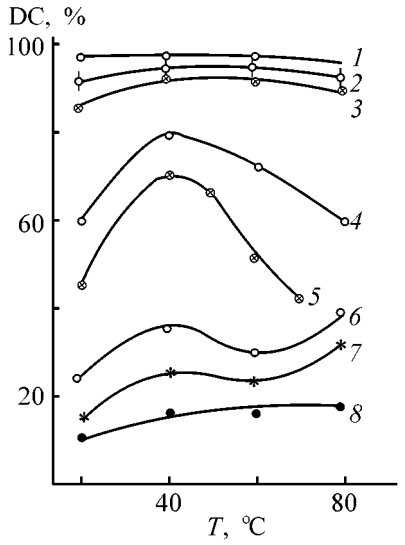

Fig. 3. Degree of cleavage, DC, of starch hydrogels vs. temperature T of ultrasonic treatment. F = 22 kHz, τ = 20 s. Starch concentration C (wt %): (*1*) 1, (*2*) 2, (*3*) 3, (*4*) 3.5, (*5*) 4, (*6*) 5, (*7*) 5.5, and (*8*) 6.

In this connection, a gradual and steady decrease in viscosity is observed.

As is known, the main reason for the high viscosity of uncleaved starch hydrogels is the hydrodynamic effect of swollen grains. Thus, the abrupt decrease in viscosity under ultrasonic treatment indicates disintegration of the majority of swollen starch grains already in the first seconds of ultrasonic treatment.

The key factor in the action of ultrasound on particles of the dispersed phase in a dispersion process is cavitation. In the case of cavitation, dispersion particles mainly disintegrate under the action of impact waves and microjets of liquid, generated by imploding cavitation bubbles. The domination of one or another mechanism in acoustic dispersion is determined by the relative size of cavitation bubbles and particles of the phase [8]. In the case when the particle is much smaller in size than the bubble, no particle fragmentation occurs, but the external layers of the particle as if peel under the action of impact waves. If the particle much exceeds in size the bubble, the initial spherical shape of the latter is distorted and the imploding process is accompanied by formation of high-velocity microjets of the liquid. In this case, the particle disintegration is dominated by the mechanism of wedging at weakened bonds between the structural units.

According to microscopic studies, the size of swollen grains of corn starch is 40–80 μm. The size of cavitation bubbles in water under atmospheric pressure for frequencies of several tens of kilohertz does not exceed tens of micrometers [9], i.e., is of the same order of magnitude as the grain size. There is no reason to expect a noticeable change in this value on passing from pure water to starch hydrogels, since the bubble size is mainly determined by the internal and external pressure, and also by surface tension, which is about the same for water and starch hydrogels [5]. Thus, it would be expected, on the basis of the relative sizes of grains being disintegrated and cavitation bubbles, that both the disintegration mechanisms are operative. Presumably, larger grains are the first to disintegrate. This is due not only to their lower strength [10], but also to the fact that, near the surface of large grains, the spherical shape of cavitation bubbles may be distorted and microjets may form on their implosion, which enhances the wedging effect. In the stage when fragments of large grains and more stable fine grains remain in the volume being treated, the part played by microjets becomes less important because of a change in the relative size of bubbles and particles and the process of cleavage as a whole is slowed down.

We also examined, the influence of the ultrasonic treatment temperature and concentration of starch hydrogels on the efficiency of their ultrasonic cleavage (Fig. 3). For starch concentration of 1 wt % complete cleavage is achieved at any treatment temperature. At other starch concentrations, the efficiency of ultrasonic cleavage increases at 40°C. Because of the multifactor nature of the process of cavitation dispersion, it is difficult to account for this result. In processes of this kind, the optimal temperature is to be found experimentally for each system. The degree of cleavage of starch grains decreases steadily with increasing hydrogel concentration (Fig. 3). This is presumably due, in the first place, to the fact that, at the same density of acoustic energy, its amount per particle being disintegrated decreases with increasing content of these particles in unit volume, i.e., with increasing hydrogel concentration in the case in question. Moreover, account should be taken of the fact that, at the same amount of ultrasonic energy imparted to a given volume of the liquid material, the effectiveness of disintegration of dispersed particles is determined by the erosion activity.

The erosion activity was determined by measuring the mass loss of standard samples of thin (50 μm) aluminum foil submerged in starch hydrogels and placed in parallel to the emitter surface at a distance of 5 mm. The time of exposure was 20 s. Figure 4 shows the erosion activity and degree of starch grain cleavage as a function of the starch concentration. It can be seen that the erosion activity changes only slightly with the concentration varying between 1 and 7%. For gels with concentration of 8%, a much lower damage to the foil was obtained. Thus, in the concentration range 1–7 wt %, both the energy per particle and the erosion activity decrease monotonically with increasing hydrogel concentration. Therefore, it would be, seemingly, expected that the degree of grain cleavage in an ultrasonic field should also decrease monotonically. However, the efficiency of cleavage falls stepwise at starch concentration of 4–4.5%. This behavior is confirmed by concentration dependences of the optical density and content of the water-soluble fraction (Figs. 5a and 5b). It can be seen that, for ultrasonically treated hydrogels, the characteristics mentioned do not vary monotonically with increasing starch concentration, but exhibit a bend at about 4–4.5%. These experimental data can presumably be accounted for as follows. As established previously [5], the curve describing the dependence $\log\log \nu = f(\log C)$ for starch has a clearly pronounced bend at a concentration of 4.5%, indicating a change of the mechanism of viscous flow

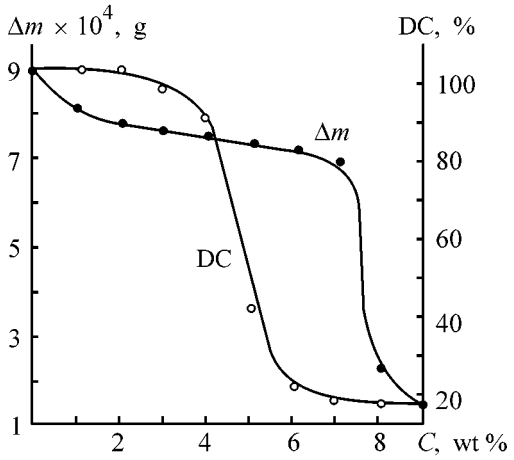

Fig. 4. Erosion activity Δm (F = 22 kHz, τ = 20 s) and degree of cleavage DC of starch hydrogels vs. starch concentration C.

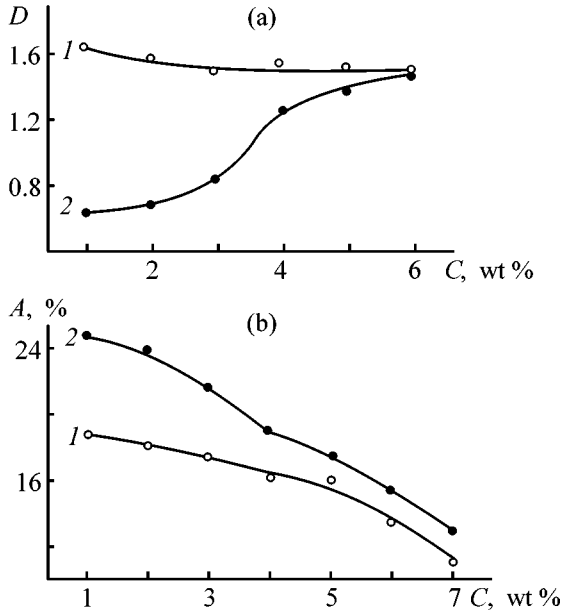

Fig. 5. (a) Optical density D and (b) content A of the water-soluble fraction of starch hydrogels vs. starch concentration C. Sample: (*1*) initial and (*2*) ultrasonically treated (F = 22 kHz, τ = 20 s).

on passing from one concentration range (C < 4.5%) to another (C > 4.5%). Presumably, the presence of a physical network stabilizing the initial structure in hydrogels with C > 4.5% is an additional factor reducing the cleavability of grains.

The most complicated problem encountered in studying the mechanical and, in particular, ultrasonic cleavage of starch is that concerning the degradation of its macromolecules. Determining the molecular weight to monitor the degradation is complicated by

Influence exerted by the time of ultrasonic treatment of starch hydrogels on the peak position in absorption spectra of I_2-amylose complex

C,* %	λ_{max} (nm) of water-soluble fraction at indicated insonification time, s			
	0	20	30	60
1	620.0	611.0	609.0	607.0
2	618.0	612.0	609.0	608.0
3	617.0	612.0	610.0	609.0
4	614.4	613.0	610.0	608.0
5	614.0	612.0	611.0	610.0
6	612.9	610.5	610.0	609.0
7	611.9	609.0	609.0	607.0

* C is the starch concentration

the fraction and phase inhomogeneity of starch hydrogels. To study the extent of degradation of starch hydrogels, we used the method described in more detail in [4]. With this method, changes in the degree of polymerization of starch macrochains can be judged without determining the molecular weight. The method is based on the dependence of the position λ_{max} of the peak in the absorption spectrum of the I_2–amylose complex on the degree of amylose polymerization. In agreement with published data [11], a decrease in the degree of amylose polymerization causes a hypsochromic shift of the absorption peak in the spectrum of the I_2–amylose complex. The watersoluble fraction of starch, mainly composed of amylose judging from λ_{max}, ws used for analysis. The table lists λ_{max} values for the water-soluble fraction, corresponding to the initial and ultrasonically treated samples of hydrogels with various concentrations.

It can be seen from the table that ultrasonic treatment causes a hypsochromic shift of the absorption band of the I_2–amylose complex. Such a shift indicates a decrease in the average degree of amylose polymerization. As shown by analysis, ultrasonic treatment of starch hydrogels for 20 s does not change the concentration of reducing groups. This means that there occurs no degradation of linear macromolecules of amylose with rupture of α-1,4-glucoside bonds. In the case under study, the shift of the absorption band of the I_2–amylose complex is presumably due to accumulation of short amylose fragments formed as a result of amylopectin debranching with rupture of mechanically strained α-1,6 bonds. A similar result was obtained in studying the mechanochemical degradation of starch in treatment of starch hydrogels in RPA [4].

CONCLUSIONS

(1) A fundamental difference between the mechanisms of ultrasonic and thermal cleavage of starch grains in hydrogels was established. This difference consists in that in the former case cavitation cleavage of these grains into fine fragments occurs, and in the latter case grain disintegration is preceded by prolonged period of grain weakening by diffusion.

(2) The highest efficiency of ultrasonic cleavage of starch grains in hydrogels is achieved at a treatment temperature of 40°C.

(3) It was found that, with the content of starch in ultrasonically treated hydrogels becoming higher than a certain critical concentration corresponding to appearance of a physical fluctuation network, the cleavability of starch decreases dramatically.

REFERENCES

1. Lipatova, I.M., Padokhin, V.A., Moryganov, A.P., *et al.*, *Tekstil'naya Prom–st.*, 1998, no. 5, pp. 32–33.
2. Larin, O.V., Lipatova, I.M., Makarova, L.I., and Moryganov, A.P., *Izv. Vyssh. Uchebn. Zaved., Tekhnol. Tekstil. Prom–sti.*, 1999, no. 4, pp. 69–75.
3. FRG Patent DE 3530770.
4. Lipatova, I.M., Yusova, A.A., and Moryganov, A.P., *Zh. Prikl. Khim.*, 2000, vol. 73, no. 8, pp. 1372–1376.
5. Lipatova, I.M., Yusova, A.A., Blokhina, S.V., and Moryganov, A.P., *Zh. Prikl. Khim.*, 2001, vol. 74, no. 9, pp. 1517–1521.
6. Potyagalov, A.F., *Shlikhtovanie osnov* (Warp Dressing), Moscow: Legkaya Industriya, 1965.
7. Shanthy, A.P., *Stärke*, 1980, no. 12, pp. 409–411.
8. Novitskii, B.G., *Primenenie akusticheskikh kolebanii v khimiko-tekhnologicheskikh protsessakh* (Use of Acoustic Vibrations in Chemical Technology), Moscow: Khimiya, 1983.
9. *Ul'trazvukovaya tekhnologiya* (Ultrasound Technology), Agranat, B.A., Ed., Moscow: Metallurgiya, 1974.
10. Andreev, N.R., *Osnovy proizvodstva nativnykh krakhmalov* (Fundamentals of Manufacture of Native Starch), Moscow: Pishchevaya Prom–st., 2001, p. 289.
11. Richter, M., Augustat, S., and Schierbaum, F., *Ausgewählte Methoden der Stärkechemie*, Leipzig: Fachbuchverlag, 1968.

Russian Journal of Applied Chemistry, Vol. 75, No. 4, 2002, pp. 531–534. Translated from Zhurnal Prikladnoi Khimii, Vol. 75, No. 4, 2002, pp. 545–548.
Original Russian Text Copyright © 2002 by Aleksandrov, Lukuttsov, Drabovskaya, Didenkulova, Tsyganova.

SORPTION AND ION-EXCHANGE PROCESSES

Ceramic Cation Exchangers in Ion-Exchange Chromatography

Yu. A. Aleksandrov, A. A. Lukuttsov, A. E. Drabovskaya, I. I. Didenkulova, and E. I. Tsyganova

Lobachevskii State University, Nizhni Novgorod, Russia

Received March 11, 2001

Abstract—The kinetics of attainment equilibrium in sorption and desorption of sodium and potassium ions with foam ceramic cation exchangers with chemically bound phosphate and vanadate groups was studied.

Ionic chromatography is an effective method for analysis of ions. Researchers' efforts are aimed at extending the possibility of the analysis, especially in determining cations. The problem of synthesis of new sorbents for ion-exchange chromatography remains urgent [1].

Small exchange capacity (10^{-3}–5×10^{-2} mmol g^{-1}), resistance to aqueous acids and alkali, and mechanical strength are characteristic of such sorbents.

Transformation of anion exchangers into cation exchangers by modification with phosphoric acid salts was described in [2]. A drawback of a thus obtained cation exchanger is that functional phosphate groups are fixed on the anion exchanger surface by Coulombic forces only, and they are gradually washed away during the process, which decreases the sorbent exchange capacity. Therefore, sorbents with strongly bound functional phosphate groups would be more promising.

In this study, a hydrothermally stable foam ceramic KhIPek [TU (Technical Specifications) 5759-010-10657190–97] [3] was used as a cation exchanger. It was synthesized from alumina with addition of metal oxides. Polymeric aluminosilicate chains were chemically cross-linked with salts of phosphoric acid (sorbent 1) and those of a mixture of phosphoric and vanadic acids (sorbent 2). This exothermic process is accompanied by foaming. The structure of the resulting ceramic is a cellular three-dimensional skeleton similar to that of natural zeolites [4].

The strength of binding of functional groups to the foam ceramics was monitored by the reaction with ammonium molybdate in nitric acid solutions, which is a sensitive and specific test for phosphate ions.

In this study, we examined the possibility of using cation exchangers based on a hydrothermostable foam ceramics with phosphate and vanadate functional groups in ion-exchange chromatography.

EXPERIMENTAL

The sorbents studied were compared with cation exchangers KU × 2-8 (exchange capacity 3–5 mmol g^{-1}) and KANK-KST (0.022 mmol g^{-1}) taken as references.

Foam ceramic sorbents were crushed in a porcelain mortar, and the required fraction was separated by sedimentation.

The sorbent dried in an oven was charged into a 6 × 50 mm standard column of a Tsvet-3006 chromatograph connected to a sample inlet unit and a conductometric detector. Through the column with the sorbent in the H^+ form, washed with water to neutral reaction, we passed aqueous solutions of potassium or sodium nitrate (10^{-4} M) at a flow rate of 6 ml min^{-1}. During the ion exchange, hydrogen ions were liberated, and the conductometric detector recorded the signal as the output sorption curve.

After the attainment of the equilibrium, deionized water was passed through the column at a rate of 6 ml min^{-1} until the stable minimal signal was obtained (the curve of elution of salts from the sorbent intergrain area). After replacing water with 10^{-4} M nitric acid solution, the sodium or potassium ions were eluted from the sorbent at the same flow rate (desorption curve).

The curves of sodium ion sorption are shown in Fig. 1. As seen, they differ in both the equilibrium

1070-4272/02/7504-0531 $27.00 © 2002 MAIK "Nauka/Interperiodica"

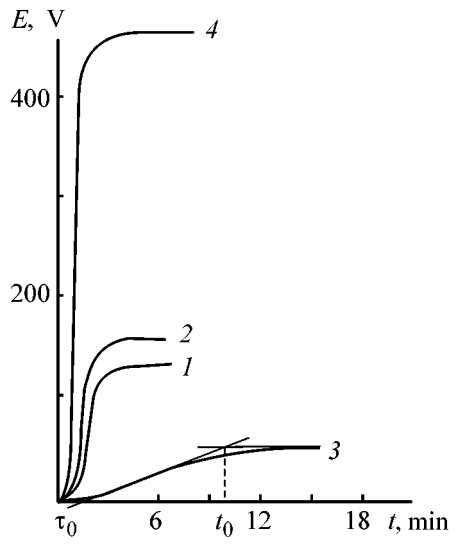

Fig. 1. Time dependence of the signal E of the conductometric detector in sodium ion sorption from the sodium nitrate aqueous solution. 20°C, sodium nitrate concentration 10^{-4} M, flow rate of solution through the column 6 ml min^{-1}; the same for Figs. 2–4. (t) Time, (τ_0) time retardation and (t_0) time in which the equilibrium is attained. (*1*) Sorbent 1, (*2*) sorbent 2, (*3*) KANK-KST, and (*4*) KU × 2-8; the same for Fig. 3.

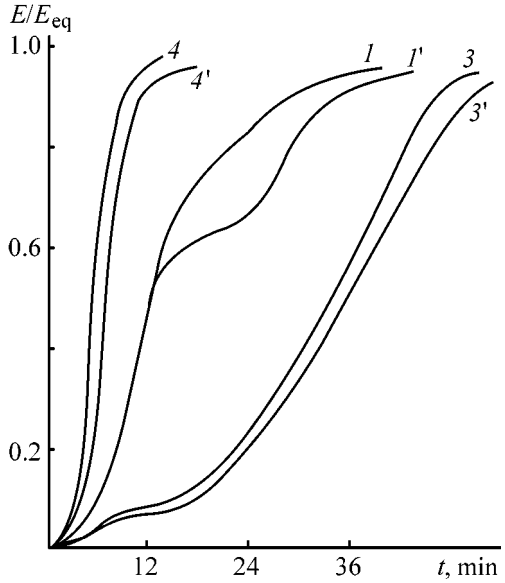

Fig. 2. Ratio of the running signal of the conductometric detector to the equilibrium signal E/E_{eq} vs. time t of (*1, 3, 4*) sodium and (*1'*, *3'*, *4'*) potassium ion desorption with a nitric acid solution passed through the column with the sorbent. (*1, 1'*) Sorbent 1, (*3, 3'*) KANK-KST, and (*4, 4'*) KU × 2-8.

signal value and the retardation time τ_0 and time of attainment of the equilibrium t_0. It is more convenient to monitor the differences in the behavior of the sorbents studied by elution curves normalized to the same value of the equilibrium signal. The normalized curves of desorption of sodium or potassium ions from the sorbents studied are shown in Fig. 2. We found that, with the sodium ion, the equilibrium in sorption, washing with water, and elution with nitric acid solution is attained faster then that with the potassium ion. For sorbent 1 containing only phosphate functional groups, the desorption curve of the potassium ion exhibits a step (Fig. 2). The above differences in behavior between sodium and potassium can be accounted for by the fact that hydrated potassium ions, which are smaller by a factor of 1.46 [5], penetrate into the sorbent cells and are retained on phosphate groups, while sodium ions are mainly fixed by the functional groups of the sorbent surface. Therefore, in sorption of potassium ions with sorbent 1, the exclusion mechanism is along with the ion exchange mechanism operative. The possibility of exclusion on cellular sorbents or on cross-linked polymers is mainly determined by matching between the sizes of cells and hydrated ions or molecules. At low concentrations of the substance (10^{-4} M), the exclusion mechanism can be revealed by conductometry based on equivalent exchange of ions with low specific electrolytic conductivity for hydroxonium ions whose conductivity is an order of magnitude higher.

The output curves allow evaluation of the compactness of sorbent packing in the column from both the retardation time τ_0 and the rate of equilibrium attainment. It was found that the denser the packing, at a lower rate the equilibrium is attained.

Since the packing compactness is related to the size of sorbent grains and to the rate of the equilibrium attainment, we plotted the nomogram

$$\Delta E/\Delta t = 3.12 \times 10^{-2} d - 0.144, \quad (1)$$

where $\Delta E/\Delta t$ is the rate of equilibrium attainment for the output curves (Fig. 1), i.e., the variation of the recorder signal in unit time, and d is the sorbent grain diameter within the 20 (KANK-KST)–1500 μm (KU × 2-8) range.

Using the experimental rates of equilibrium attainment (Fig. 1) and Eq. (1), we calculated the grain sizes of sorbent 1 and sorbent 2 to be 290 and 420 μm, respectively.

The compactness of the sorbent packing can also be quickly estimated from the correlation between the pressure in the column and the retardation time of the sorption curve (Fig. 3). The denser the packing, the slower the flow of the mobile phase through the

column, and hence the longer the retardation time. On the other hand, the packing compactness increases with decreasing sorbent grain size. Correspondingly, a higher pressure is required to press the mobile phase through the column at a definite rate. For sorbents 1 and 2, this pressure does not exceed the level of 6–9 MPa, which is acceptable for liquid chromatography.

One of the main characteristics of any ion exchanger is its exchange capacity. The sorption and desorption output curves allow estimation of this parameter. The height of the step of the output curve, corresponding to the equilibrium signal, is proportional to the sorbent exchange capacity. The nomogram of the logarithm of the exchange capacity as a function of the equilibrium signal (Fig. 1) within the range from 0.022 mmol g^{-1} for KANK-KST sorbent to 4 mmol g^{-1} for KU × 2-8 sorbent is described by the equation

$$\log S = 5.6 \times 10^{-3} h - 1.99, \qquad (2)$$

where S is the sorbent exchange capacity (mmol g^{-1} sorbent), and h is the equilibrium signal of the sorption (desorption) output curves.

For sorbents 1 and 2, the exchange capacities estimated by Eq. (2) amount to 0.06 and 0.09 mmol g^{-1} sorbent, respectively.

To confirm these results, we used potentiometric titration. From the dependence of pH on the volume of alkali solution spent for titration of a sorbent sample in the H^+ form, we calculated the sorbent exchange capacity. The foam ceramic sorbents studied differ in exchange capacity only slightly (by t-test); its average value was 0.040 ± 0.004 mmol g^{-1} sorbent.

Thus, we showed by both potentiomentric titration and calculation by Eq. (2) that the exchange capacities of sorbents 1 and 2 are close to that of KANK-KST and amount to several hundredths of mmol g^{-1}. This level is acceptable for using foam ceramic sorbents to separate cations by ion-exchange chromatography.

The above method allows chromatographic separation of ion mixtures, using a single column without modifying the installation design.

It follows from Fig. 4 that both sorbents allow separation of sodium and potassium ions. In the chromatogram of sorbent 1 (Fig. 4a), two peaks correspond to potassium ions. This fact confirms specific features of the ion exchanger, revealed in dynamic studies of potassium sorption.

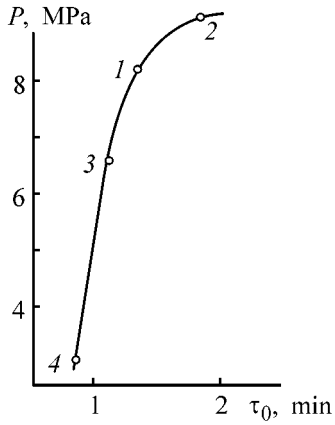

Fig. 3. Correlation between the pressure P in the column and the retardation time τ_0 (see Fig. 1), for the case of a sodium nitrate aqueous solution passed through the column.

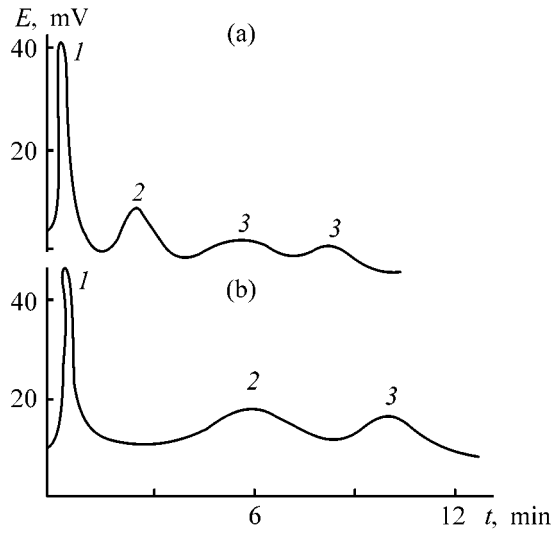

Fig. 4. Chromatogram of NaCl and KCl separation on sorbents (a) 1 and (b) 2. Eluent: aqueous solution of nitric acid. Conductometric detector (Tsvet-3006 chromatograph). (*E*) Detector signal and (*t*) time. (*1*) Cl^-, (*2*) Na^+, and (*3*) K^+.

Comparison of chromatograms in Figs. 4a and 4b shows that sorbent 1 separates ions better than sorbent 2. Since the separation efficiency depends on packing compactness in the column, which, in turn, depends on the grain size, we can conclude that the experimental chromatogram is in good agreement with the grain size of the sorbents calculated on the basis of dynamic studies.

CONCLUSIONS

(1) In sorption with foam ceramic sorbents, sodium ions are sorbed, washed with water from intergrain

space, and desorbed faster than potassium ions. In sorption of potassium ions on sorbent 1, both exchange and exclusion mechanisms are imported.

(2) Foam ceramic sorbents 1 and 2 with low exchange capacity, 0.06–0.09 mmol g^{-1} sorbent, are similar in sorption properties to cation exchangers for ion-exchange chromatography.

(3) Single-column chromatographic separation of potassium and sodium ions was performed, and a possibility was demonstrated of using foam ceramic cation exchangers with chemically fixed phosphate and vanadate groups in the ion-exchange chromatography.

REFERENCES

1. Shpigun, O.A. and Zolotov, Yu.A., Abstracts of Papers *Pervaya Vsesoyuznaya konferentsiya po ionnoi khromatografii* (First Al-Union Conf. on Ion-Exchange Chromatography), Moscow: Inst. Geokhim Anal. Khim. im. V.I. Vernadskogo USSR Acad Sci., June 19–21, 1989, p. 3.
2. Gur'ev, I.A. *et al.*, *Vestn. Nizhegor. Gos. Univ. im. N.I. Lobachevskogo, Khim.*, 1998, issue 1, pp. 59–63.
3. RF Patent 2 091 348.
4. Breck, D.W., *Zeolite Molecular Sieves*, New York: John Wiley & Sons, 1974.
5. Entelis, S.G. and Tiger, R.P., *Kinetika reaktsii v zhidkoi faze* (Kinetics of Reactions in the Liquid Phase), Moscow: Khimiya, 1973.

Russian Journal of Applied Chemistry, Vol. 75, No. 4, 2002, pp. 535–539. Translated from Zhurnal Prikladnoi Khimii, Vol. 75, No. 4, 2002, pp. 549–553.
Original Russian Text Copyright © 2002 by Polyakova, Kolikov, Pisarev.

SORPTION AND ION-EXCHANGE PROCESSES

Sorption of Eremomycin on Carboxylic Cation Exchangers

I. V. Polyakova, V. M. Kolikov, and O. A. Pisarev

St. Petersburg State Technological University, St. Petersburg, Russia

Institute of Macromolecular Compounds, Russian Academy of Sciences, St. Petersburg, Russia

Received November 15, 2001

Abstract—The relationships of sorption of antibacterial antibiotic eremomycin on carboxylic cation exchangers were studied. The difference between gel-like and structurally segregated carboxylic cation exchangers were analyzed by potentiometric titration. The optimal conditions for sorption and desorption of eremomycin were found.

Eremomycin, a modern antibiotic belonging to the group of polycyclic glycopeptides (dalbaheptides), was recovered from a culture broth of INA-238 actinomycetes. This antibiotic produces strong bactericidal effect on Gram-positive microorganisms. At the same time, it does not influence the growth and development of animals and does not change the morphology of internal organs [1].

Eremomycin is a *zwitter*-ion containing three primary amino groups (pK^1_{a1} 6.9, pK^2_{a1} 7.9, and pK^3_{a1} 9.0), phenyl groups (pK^1_{a2} 9.7, pK^2_{a2} 10.4, and pK^3_{a2} 11.35), and a terminal carboxy group (pK_a 3.1). The molecular weight of eremomycin $C_{73}H_{89}N_{10}O_{20}Cl$ is 1540 [2]. Owing to its amphoteric nature, eremomycin can be sorbed on both cation and anion exchangers.

At present, eremomycin is obtained biosynthetically. The initial preparation is purified by multistage extraction and then subjected to chemical modification. Production of eremomycin involves problems associated with the low yield of the target product, toxicity of the by-products, and detrimental environmental effect of the organic solvents [2].

Comparison of sorption characteristics of eremomycin *zwitter*-ion on sorbents of different types and structures is of interest from both scientific and practical viewpoints. Such a comparative study, on the one hand, extends the set of experimental data on sorption of such complicated substances as zwitterions, and, on the other, allows the development of a technique for recovery of this antibiotic from the native solutions containing products of the microbial metabolism.

EXPERIMENTAL

In our experiments, we used crystalline samples of eremomycin sulfate.[1] The content of the main substance, as determined by HPLC analysis, was 98.5%.

The following sorbents were tested: Polysorb [nonionic macroporous sorbent with poly(styrene–divinylbenzene) matrix], polydextran T70, AV-17 × 8 [highly basic anion exchanger based on poly(styrene–divinylbenzene) copolymer], sorbents of BDM type (carboxylic cation exchangers produced by radical copolymerization of methacrylic acid MAA and ethylene glycol dimethacrylate DMEG [3]), and MN-500 {isoporous sulfonated poly(styrene–divinylbenzene) copolymer prepared in the presence of cyclohexane as porophore [4]}.

Potentiometric titration of the sorbents was carried out by the technique of separate weighed samples [5]. A 0.1–0.2-ml portion of distilled water was added to 50 mg of sorbent and stirred for 20 min to completion of swelling. To provide different degrees of ionization of the sorbent α, a calculated volume of a titrated NaOH solution was added. The degree of ionization α was calculated by the equation:

$$\alpha = c_{NaOH} V_{NaOH} \times 1000 / E m_{sorb}, \quad (1)$$

where c_{NaOH} and V_{NaOH} are the concentration (mg-equiv ml^{-1}) and the volume (ml) of the titrant,

[1] The material was prepared in the Scientific Research Institute for New Antibiotics, Russian Academy of Medical Sciences, Moscow, Russia.

1070-4272/02/7504-0535 $27.00 © 2002 MAIK "Nauka/Interperiodica"

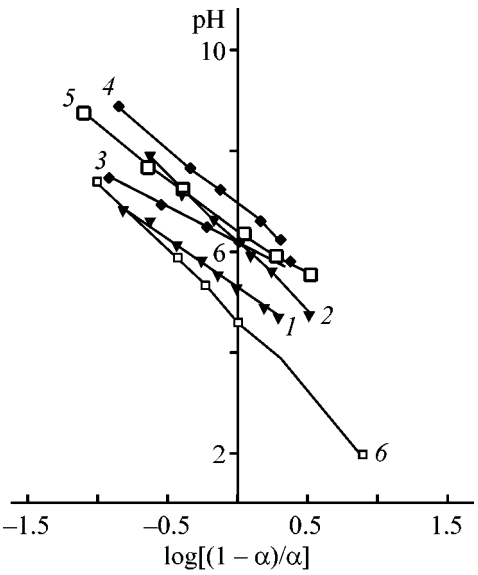

Fig. 1. Potentiometric titration of carboxylic ion exchangers. (α) Degree of ion exchanger ionization. (*1*) BDM-1, (*2*) BDM-3, (*3*) BDM-5, (*4*) BDM-9, (*5*) BDM-1, and (*6*) MN-500.

respectively; E, the total exchange capacity of the sorbent (mg-equiv g^{-1}); and m_{sorb}, the sorbent weight (mg).

After the attainment of equilibriium, the pH of the solution was measured and the curve of potentiometric titration in the Henderson–Hasselbach coordinates

$$pH = f\{\log[(1 - \alpha)/\alpha]\}. \quad (2)$$

was constructed.

The experiments on sorption of eremomycin were carried out in 0.2 M ammonium acetate [6]. The pH was adjusted with HCl (1 M) and NH_4OH (25%). The eremomycin concentration ranged from 0.2 to 1.5 mg ml^{-1}. Such levels are attained in the culture broth due to metabolism of INA-238 actinomycetes.

Table 1. The parameters of the Henderson–Hasselbach equation* for different cation exchangers

Sorbent**	K_{exp}	E, mg-equiv g^{-1}	pK_a	n
BDM-1	7.1	9.9	5.1	1.3
BDM-3	7.0	9.5	5.9	1.7
BDM-5	4.8	8.9	6.3	1.9
BDM-9	4.8	8.5	6.5	1.3
BDM-10.5	5.2	8.4	6.4	1.3
BDM-12	5.5	8.2	6.2	1.3
MN-500	1.4	2.0	4.6	1.4

* pK determined by extrapolation of the linear plot of pH vs. log[(1 – α)/α] to interseption with the abscissa; n the slope of this plot.

** The figure in the sorbent brand refers to the content of the cross-linking agent (mol %).

The sorption kinetics of eremomycin was studied as follows. Distilled water (0.1–0.2 ml) was added to a dry sample of the ion exchanger (50 mg), and the mixture was stirred for 20 min to sorbent swelling. Then, 20 ml of the eremomycin solution in 0.2 M ammonium acetate with eremomycin concentration of 1 mg ml^{-1} was added to the swollen ion exchanger at the prescribed pH. In the course of the kinetic experiment performed at continuous stirring, 0.2-ml samples were taken at regular intervals. The eremomycin concentration in the solution was determined spectrophotometrically at λ = 280 nm, using a calibration curve. In preliminary experiments, we found that the rate of eremomycin sorption is independent of the antibiotic concentration and stirring rate. These experiments also showed that the limiting stage of eremomycin sorption on the cation exchanger is its diffusion into the sorbent granule. The pore-diffusion mechanism of kinetics of eremomycin sorption on the carboxylic cation exchanger was also confirmed in sorption experiments with intermittent separation of the cation exchanger and aqueous phases. In these experiments, sorbent granules were separated from the solution, kept for 20 h, and then returned into the same solution. We found that, on repeated contact of the cation exchanger and solution, the sorption rate increases as compared to that before phase separation. This fact shows that the cation pore-diffusion is the limiting stage of sorption. The internal diffusion coefficient was calculated by the Boyd equation [5]

$$\overline{D} = 0.087 \tan^2 \beta R^2, \quad (3)$$

where $\overline{D}$ is the effective diffusion coefficient ($cm^2 s^{-1}$); R, the radius of the swollen cation exchanger granule (μm); β, the slope the linear part of the plot F vs. $t^{1/2}$; $F = m_t/m_\infty$, the fraction of the total sorption capacity of the sorbent consumed by the sorbate; m_t, the sorption capacity in a time t; and m_∞, is the equilibrium sorption capacity.

The half-saturation time of the sorbent with the antibiotic (F = 1/2) was calculated from the plot of F vs. t.

Figure 1 shows the curves of potentiometric titration of the cation exchangers of BDM type and sulfonic cation exchanger MN-500 in the Henderson–Hasselbach coordinates. The parameters the Henderson–Hasselbach equation for different sorbent types are listed in Table 1.

With increasing degree of cross-linking, the total exchange capacity E of ion exchanger of the BDM type falls because of a decrease in the carboxy group content. The mobility of protons of the carboxy groups of cation exchanger depends on the content of the hydrophobic ethylene glycol dimethacrylate cross-linking units (DMEG) in the cation exchanger matrix. By the character of the influence exerted by the cross-linking agent on pK_a, the carboxylic cation exchangers can be subdivided into two groups: gel-like with DMEG content less than 5 mol % and structurally segregated cation exchangers with DMEG content exceeding 5 mol % [3]. For gel-like cation exchangers, the acidity of the cation exchanger decreases with increasing the DMEG content. As seen from Table 1, this decrease in acidity correlates with the decrease in the swelling coefficient. As the DMEG content is decreased, the sorbent swelling increases owing to the enhancement of the intrapolymeric hydration and increase in the entropy of the expanded matrix. Although these factors facilitate ionization of the carboxy groups, the irreversible sorption of biologically active compounds on these sorbents hinders their effective recovery by preparative-chromatographic technique [6].

The structurally segregated cation exchangers in the H form are characterized by an abnormally strong rise in swellability with increasing content of the cross-linking agent. The enhanced swelling may be due to the loose network structure formed because of the isolation of the double bonds of the cross-linking agent [7, 8]. One of the possible factors hampering cross-linking are hydrophobic interactions between methacrylic acid molecules, resulting in additional structurization of microgel sites in the polymeric network. This is the reason for the rise in acidity of BDM-9 and BDM-12 cation exchangers with increasing DMEG content.

The n term in the Henderson–Hasselbach equation characterizes the influence exerted by the degree of carboxy group ionization on the apparent ionization constant of the cation exchanger. The larger the difference between n and unity, the stronger the effects of ionized carboxy groups on the ionization of non-ionized carboxy groups in the sorbent. This means that, with increasing degree of ionization, the density of distribution of the ion-exchange sites in the polymeric matrix grows. In the absence of mutual effects of the ionized and unionized carboxy groups, the ideal ionization occurs (n = 1). In passing from BDM-1 to BDM-5 gel-like cation exchangers, n increases. This effect is due to the lower concentration of carboxy groups in the loosest BDM-1 cation exchanger, compared to that in BDM-5 gel-like sorbent with strongly cross-linked structure. The segregated sorbents with similar structure have close n. It is of interest that n of BDM-12 cation exchanger, belonging to the structurally segregated sorbent type, is virtually equal to that of BDM-1 gel-like sorbent. This fact shows that these sorbents have approximately the same densities of distribution of ionizable carboxy groups. MN-500 sulfonic cation exchanger exhibits a higher acidity. The n parameter of this sorbent is close to those of structurally segregated cation exchangers, which reflects the similarity in cooperative interaction between the carboxy groups in ionization of these sorbents.

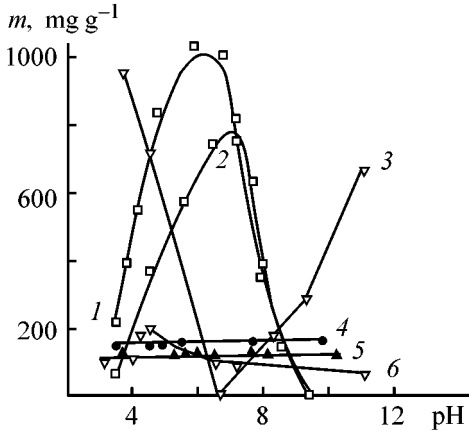

Fig. 2. Specific sorption of eremomycin m vs. pH: (*1*) BDM-3, (*2*) BDM-12, (*3*) MN-500, (*4*) Polysorb, (*5*) dextran T-70, and (*6*) AV-17 × 8.

The potentiometric titration gives insight into the correlation between the sorption capacity of the cation exchanger for eremomycin and the equilibrium pH of the sorbate solution (Fig. 2). The plots of the sorption capacity of carboxylic cation exchangers for eremomycin vs. pH show a sharp maximum at pH ~7 (curves *1* and *2*). We believe that this maximum is due to competition between the electrostatic attraction of the sorbent and antibiotic molecules and the repulsion between their likely charged functional groups. The ionization of carboxy groups of the cation exchanger strongly depends on pH of the sorbate solution. The ascending portion of sorption curves *1* and *2* (Fig. 2) corresponds to gradual dissociation of the carboxy groups and their association with the positively charged amino and phenyl groups of eremomycin (at pH < 7). At pH 3.5, the carboxylic cation exchanger is completely converted to the H form exhibiting some sorption capacity for eremomycin (~100–200 mg g^{-1}). Under these conditions, sorption occurs by the mechanism of hydrophobic interactions between the sorbent and antibiotic [8]. After the maximal sorption is reached at pH close to neutral re-

Table 2. Effect of cross-linking agent content on the sorption characteristics of eremomycin on carboxylic cation exchangers at pH 6.95

Sorbent	$t_{0.5}$, min	$\overline{D} \times 10^4$, $cm^2\ s^{-1}$
BDM-3	1.84	3.82
BDM-5	14.4	0.2
BDM-9	9.4	1.74
BDM-12	1.7	5.62

action, the sorbability of eremomycin gradually decreases with increasing pH, and at pH 9.5–10 the carboxylic cation exchangers lose their sorption power with respect to eremomycin. These data suggest that interaction between eremomycin and carboxylic cation exchanger in the pH range corresponding to the descending portion of sorption curves *1* and *2* is controlled by both transformation of the amino and phenyl groups to the nonionized state and ionization of the eremomycin carboxy groups. In contrast to the acidic pH range corresponding to partial ionization of the carboxy groups of the antibiotic molecule, the carboxy groups of both cation exchanger and antibiotic are completely ionized in the alkaline pH range. Under these conditions, the repulsion between the ionized sorbing sites and antibiotic molecules prevails over the hydrophobic interactions, and, therefore, the cation exchanger loses its sorption power with respect to eremomycin. Thus, eremomycin exhibits in the alkaline pH range a sorption behavior similar to that in the acidic region.

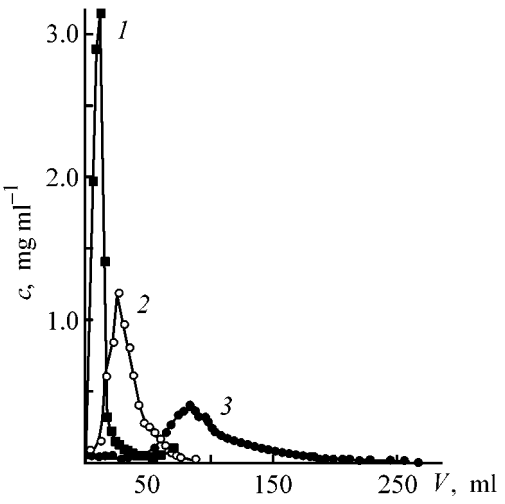

Fig. 3. Elution of eremomycin from structurally segregated BDM-12 cation exchanger. Eluent 0.2 M ammonium acetate. (*c*) Eremomycin concentration in eluate and (*V*) eluent volume. pH: (*1*) 8.6, (*2*) 9.5, and (*3*) 10.5.

The sorption of eremomycin on molecular sorbents and anion exchanger as influenced by pH is shown in Fig. 2 (curves *4*–*6*). These sorption curves are similar: the sorption of eremomycin is virtually independent of pH in the range 3.5–11.5, and its value is lower than that on cation exchangers. The insensitivity of sorption of amphoteric eremomycin molecules to pH and its sharp decrease in the presence of organic solvents [9] suggest that eremomycin is sorbed on the molecular sorbents and anion exchangers mainly by the mechanism of hydrophobic interactions.

A different pattern occurs in sorption of eremomycin on MN-500 sulfonic cation exchanger (Fig. 2, curve *3*). The degree of ionization of sulfonic cation exchanger considerably exceeds that of the carboxylic cation exchanger. Therefore, even at pH 3.5 the ionized sulfo groups of the sulfonic cation exchanger can bind the amino and phenyl groups of the antibiotic, and this sorbent exhibits the maximal sorption capacity for eremomycin zwitterion. With pH increasing to 6–7, the amino and phenyl groups of eremomycin are partially converted to the nonionized state, whereas the carboxy groups become completely ionized. Thus, the sorption of eremomycin on the cation exchanger ceases even in the neutral pH region. The ascending portion of curve *3* (Fig. 2) shows further increase in the eremomycin sorption due to enhancement of hydrophobic interactions between eremomycin and MN-500 cation exchanger at pH ~11.0–11.5.

Since the natural aqueous medium populated with INA-238 actinomicetes has pH ~7, the sorption kinetics of eremomycin on carboxylic cation exchanger was studied at pH 6.95 corresponding to the maximal sorption.

Table 2 shows that for gel-like cation exchangers the half-saturation period becomes longer with increasing content of the cross-linking agent. According to these data, the eremomycin diffusion coefficient and the rate of its sorption decrease with increasing cross-linking of the sorbent. The eremomycin diffusion in BDM-9 and BDM-12 structurally segregated sorbents occurs by a different mechanism. At the DMEG content in the cation exchanger higher than 5 mol %, the antibiotic can diffuse within cation exchanger granules not only through transport channels located in the structural sites with loose network but also through more strongly cross-linked sites surrounding the transport channels [3]. In the cation exchangers with denser polymeric network and rigid channels, eremomycin diffuses only through sites with loose structure and is anchored at the channel walls.

Therefore, the sorption rate of eremomycin on such sorbents grows with increasing content of the cross-linking agent.

Our studies of eremomycin desorption from carboxylic cation exchangers under dynamic conditions were aimed at finding the conditions providing effective desorption of eremomycin at its high concentration in the eluate. We found that eremomycin can be quantitatively desorbed with aqueous acid solution, commonly used for antibiotic elution, only upon addition of an organic solvent. In this procedure the cation exchanger is converted to the H form, whereas eremomycin occurs as the zwitterion.

In elution of eremomycin from BDM-12 cation exchanger with more alkaline aqueous solutions, the elution curve becomes sharper, and desorption of eremomycin becomes more complete (up to 95%) (Fig. 3). Under these conditions, eremomycin is converted from zwitterionic to carboxylate anionic form.

CONCLUSIONS

(1) Combined analysis of data on potentiometric titration and swelling of carboxylic cation exchangers shows that the structural organization of the polymeric matrix considerably affects the ionization constant of the carboxy groups pK_a and the parameter n. The strongest mutual effect of the ionized and nonionized carboxy groups is observed in gel-like cation exchangers.

(2) The opposite effects of ionization of the carboxy groups of cation exchanger, on the one hand, and dissociation of amino, phenyl, and carboxy groups of eremomycin, on the other, on the eremomycin sorption result in a peak in the plot of the eremomycin sorption vs. equiblibrium pH of the sorbate solution.

(3) The equilibrium sorption of eremomycin on cation exchangers is reached sufficiently fast.

(4) Complete elution of eremomycin from BDM-12 carboxylic cation exchanger at high antibiotic concentration in the eluate can be reached by conversion of eremomycin from the zwitterion to the carboxylate anion.

REFERENCES

1. Berdnikova, T.F., Lomakina, N.N., Olsuf'eva, E.N., *et al., Antibiot. Khimioterap.*, 1991, vol. 36, no. 6, pp. 28–32.
2. Gause, G.F. and Braznikova, M.G., *Antibiotics Med. Biotech.*, 1987, vol. 32, no. 3, pp. 571–576.
3. Pisarev, O.A., *Isol. Purif.*, 1996, vol. 2, no. 1, pp. 93–102.
4. Davankov, V.A. and Tsyrupa, M.P., *Pure Appl. Chem.*, 1989, vol. 61, no. 10, pp. 1881–1888.
5. Libinson, G.S., *Sorbtsiya organicheskikh soedinenii ionitami* (Sorption of Organic Compounds on Ion Exchangers), Moscow: Meditsina, 1979.
6. Pisarev, O.A. and Samsonov, G.B., *Prikl. Biokhim. Mikrobiol.*, 1996, vol. 32, no. 3, pp. 281–287.
7. Pisarev, O.A., Dobrodumov, A.V., Denisov, V.M., *et al., Vysokomol. Soedin., Ser. B.*, 1987, vol. 29, no. 1, pp. 4–8.
8. Pisarev, O.A., Samsonov, G.V., and Bogdanova, L.P., *Zh. Prikl. Khim.*, 1993, vol. 66, no. 11, pp. 2825–2828.
9. Polyakova, I.V., Kolikov, V.M., and Pisarev, O.A., *Sorbts. Khromatogr. Prots.*, 2001, vol. 1, no. 5, pp. 833–838.

Russian Journal of Applied Chemistry, Vol. 75, No. 4, 2002, pp. 540–542. Translated from Zhurnal Prikladnoi Khimii, Vol. 75, No. 4, 2002, pp. 554–556.
Original Russian Text Copyright © 2002 by Kravchenko, Shvets, Strelko, Mironyuk.

SORPTION AND ION-EXCHANGE PROCESSES

ESR Characterization of Vegetable Carbon Materials

O. V. Kravchenko, D. I. Shvets, V. V. Strelko, and T. I. Mironyuk

Institute of Sorption and Endoecological Problems, National Academy of Sciences of Ukraine, Kiev, Ukraine

Received December 4, 2001

Abstract—Paramagnetic centers arising in carbonization of vegetable raw materials at 290–450°C were studied.

Preparation of selective carbon-containing sorbents of new generation for solving ecological, medicinal, and other problems requires use of new methods for stage-by-stage monitoring of their production. One of such methods is electron spin resonance (ESR), which is highly sensitive and allows monitoring of variation of paramagnetic characteristics in process optimization and commercial production of the required materials.

For example, the mechanism of formation and the nature of paramagnetic centers (PMCs) in carbon materials have been studied previously [1–6]. The main attention in [3–6] was given to analysis of ESR signals of carbons produced by high-temperature heat treatment.

Here we report on an ESR study of paramagnetic characteristics of intermediate carbon materials produced by power-saving low-temperature carbonization of various vegetable raw materials (wood sawdust, leaves, straw, husk, grape sprat, etc.). Some features of these low-temperature processes were discussed in [5, 6] for the case of carbonization of coke and pitches in oxygen-free medium. In so doing, it was found that the ESR spectra of carbons are complicated and depend on many factors, among them sensitivity to oxygen in thermal treatment. Contrary to these studies, we studied here the nature of active PMCs of carbon materials in carbonization of raw materials in oxygen. The emphasis was placed on a study of this process in the intermediate stages of removal of water and organic substances from the matrix structure.

Finely divided vegetable raw materials were heat treated in air in the range 290–450°C. The ESR spectra were recorded on a computerized upgraded RE-1306M spectrometer. α,α'-Diphenyl-β-picrylhydrazyl and also Mn^{2+} ions in a MgO matrix were used as reference. The spectra were processed as described in [7].

The ESR spectra and variation of the width and intensity of PMC signals with carbonization temperature are shown in Figs. 1 and 2. The results obtained allow the following conclusions.

(1) Contrary to the generally accepted views that the intensity of ESR signal depends linearly on the temperature of heat treatment, we found that, in low-temperature carbonization in the intermediate single-stage mode, there is a clearly pronounced increase in the intensity of the ESR signal in the range 300–350°C.

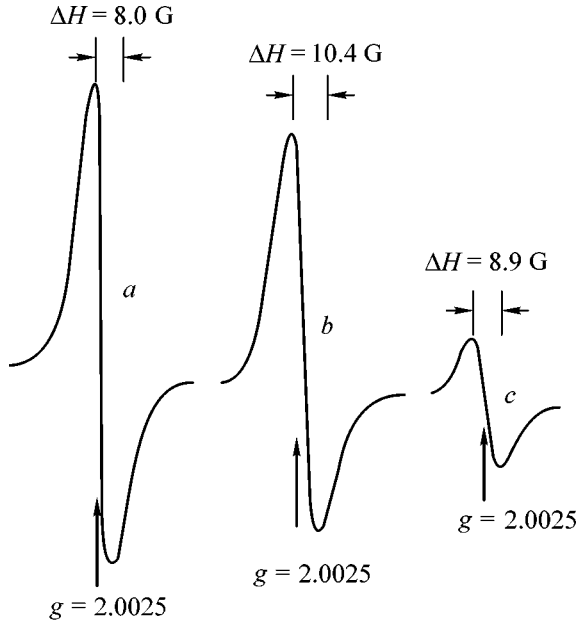

Fig. 1. Influence of the type of raw materials to be carbonized on the ESR signal. (*a*) Pine sawdust, (*b*) straw, and (*c*) leaves.

1070-4272/02/7504-0540 $27.00 © 2002 MAIK "Nauka/Interperiodica"

(2) In the initial (ascending) portion of the curve, a clearly pronounced change in the width of the ESR signals occurs (drop to ΔH = 4 G), which correlates with the weight loss in this temperature range.

(3) With further heating, in the descending portion of the curve (after passing of the maximum), changes are observed both in the line widths of ESR signals (further narrowing to ΔH = 3 G) and in the line shapes (the symmetric line becomes asymmetric, and the degree of asymmetry reaches 1.5–1.6). In this case, the signal asymmetry is retained in a wide temperature range (290–450°C).

The characteristics of PMCs of carbon materials obtained under the optimum conditions of single-stage heat treatment of raw materials substantially differ from the characteristics of samples prepared by two-stage carbonization: the ESR signal is narrowed still further to ΔH = 1.5–2.0 G. In addition, the shape of the ESR signal also depends on the type of a raw material being carbonized.

Hence, the characteristics of the ESR signals of materials produced in the low-temperature intermediate regime of carbonization substantially differ from the characteristics of signal from PMCs typical of high-temperature samples of carbon materials.

In turn, the results obtained suggest that complicated and diverse transformations take place in this temperature range, including those accompanied by formation of structural-sorption parameters of carbon materials, i.e., by transformations of the phase transition type. This is confirmed by the fact that, when the intensities of ESR signals reach a maximum, both the widths (narrowing) and the shapes (appearance of asymmetry) of the ESR signals change simultaneously, which is apparently caused by structural rearrangements and by ordering of interphase structures. It should be noted that the degree and rate of structural-chemical transformations attain a maximum in this temperature range, which can be accounted for by the presence of an extremum corresponding to a phase transition. At the same time, subsequent deceleration of the rise in intensity of the narrowing ESR signal suggests completion of the stage of structural rearrangement, which is confirmed by the appearance of a narrower ESR signal (ΔH = 3.5 G). The appearance of this signal may be due to further ordering of the structures formed in the course of phase transition. However, this phase transition is not completed, as suggested by the fact that the ESR signals become more asymmetric.

If this is the case, we can suggest that qualitative and quantitative changes in the structure of ESR signals reflect both physicochemical and phase transformations in total. Therefore, it can be expected that unusual paramagnetic characteristics should be manifested in atypical behavior of these carbon materials in sorption, desorption, etc. Indeed, studies of carbon materials produced under optimal conditions of carbonization (Fig. 3) revealed their abnormally high sorption capacity [(in particular, for petroleum, up to 12 g g^{-1}; maximum SEC (static exchange capacity) 3.5–4.0 mg-equiv g^{-1}] and nearly absolute hydrophobicity, preserved for a long time (5–6 months). At the same time, samples of carbon materials produced in regimes different from the optimum have nearly opposite characteristcs (low sorption capacity, extremely high moisture capacity, irreproducible SEC, etc.)

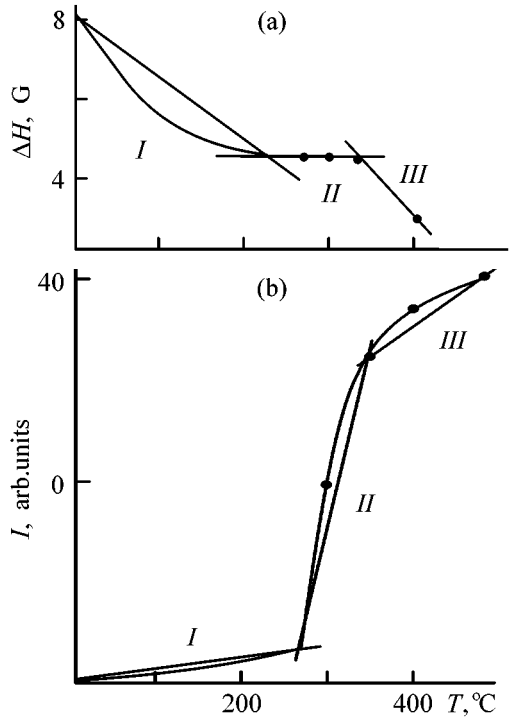

Fig. 2. (a) Width ΔH and (b) intensity I of the ESR signal from carbon materials (sawdust) vs. carbonization temperature T. (*I*) Temperature range in which water is removed; (*II*) intermediate range in which water removal is complete and removal of organic compounds begins; and (*III*) the range in which organic fractions are removed; the same for Fig. 3.

Thus, we can suggest that the abnormal paramagnetic characteristics of carbon materials in the range of transition stage (phase transition) must also be accompanied by abnormal physical and biochemical characteristics. This is confirmed, e.g., by high affinity in immobilization of microorganism strains on these matrices and abrupt variation of the Z-potential in the optimal mode.

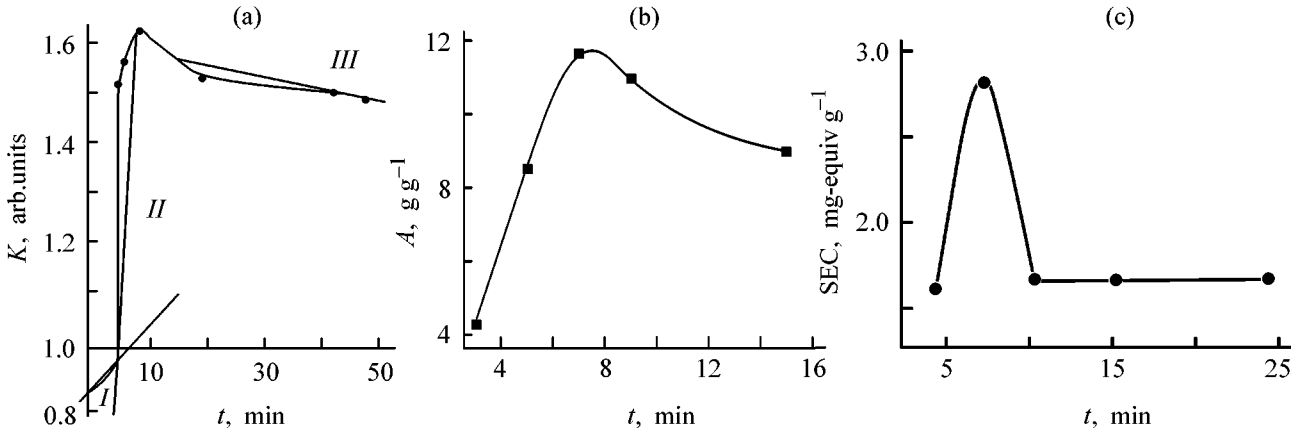

Fig. 3. (a) Degree of asymmetry of ESR signals, *K*, (b) oil capacity, *A*, and SEC of carbon materials (sawdust) vs. carbonization duration *t*.

Data on breaking of the symmetry of ESR signals in a relatively narrow temperature range (290–320°C) deserved special attention. This can be accounted for by a structural rearrangement of the matrix. Hence, the assumption that a phase transition occurs in the course of low-temperature carbonization of the material is confirmed. In addition, analysis of the whole set of varying characteristics of the ESR spectra furnishes valuable data on the specific nature of phase transitions. This opens up new avenues for understanding of processes occurring in phase transitions and also allows the use of new methods for monitoring and control of production of carbon materials with prescribed characteristics and well-defined structural-sorption parameters (pore type and size).

Thus, the study of paramagnetic characteristics of carbons produced by low-temperature carbonization furnishes valuable data on the specific nature of energy-controlled transformations in carbon-containing composites (phase transitions, formation of structural and sorption parameters, energy state of the surface, etc.) and, hence, allows prediction of the characteristics of the newly developed materials.

REFERENCES

1. Lin Chan-Ching, Waters, A.B., and Varnice, M.A., *Carbon*, 1995, vol. 33, pp. 1699–1702.
2. Gutzse, A. and Wieczorek, J., *Carbon*, 1980, vol. 18, pp. 8–10.
3. Hanvin, R., Chicke, P., Qumtoner, M.F., and Uebersfeld, J.C.R., *Acad. Sci. Paris*, 1968, vol. 265, pp. 27–30.
4. Farber, M.S., *Khim. Tverd. Topl.*, 1982, no. 2, pp. 33–39.
5. Makarov, G.P., Bronshtein, A.P., Sanitskii, B.V., *et al.*, *Koks Khim.*, 1971, no. 9, pp. 23–27.
6. Fialkov, A.S., Galeev, G.S., and Tyan, L.S., *Khim. Tverd. Topl.*, 1967, no. 2, pp. 78–84.
7. Ayscough, P.R., *Electron Spin Resonance in Chemistry*, London: Methuen, 1967.

Russian Journal of Applied Chemistry, Vol. 75, No. 4, 2002, pp. 543–547. Translated from Zhurnal Prikladnoi Khimii, Vol. 75, No. 4, 2002, pp. 557–561.
Original Russian Text Copyright © 2002 by Mirzoev, Maiorov, Stepanova, Styrov.

APPLIED ELECTROCHEMISTRY AND CORROSION PROTECTION OF METALS

Ways To Improve the Specific Power of Alkaline Batteries

R. A. Mirzoev, A. I. Maiorov, N. I. Stepanova, and M. I. Styrov

St. Petersburg State Technical University, St. Petersburg, Russia

Received June 26, 2001

Abstract—Principles of designing of ultrahigh-power batteries and their electrodes are formulated on the basis of a theoretical analysis of phenomena limiting the rate of battery discharge. Experimental evidence in favor of the possible practical implementation of the principles proposed is presented.

Modern alkaline batteries have the maximum discharge current of 10 C [A (A h)$^{-1}$] [1]. This means that they can be effectively used at discharge duration more than 100 s. At shorter pulses of discharge current, batteries put out only a minor fraction of the energy stored and, therefore, lose their main advantage, high specific energy, and become inferior to their competitors, electrochemical capacitors. The most widely occurring type of the latter are capacitors with electrodes made of high-porosity carbon materials and electrolyte based on organic solvents. These capacitors operate on the principle of charging–discharge of the double layer. Recently, the demand for energy storage devices for 0.2–100-s pulses has been increasing continuously, which stimulates the rise in manufacture of electrochemical capacitors (in both quantity and quality) [2]. However, this type of energy storage devices has its own disadvantages: low energy storage capacity (only up to 5 W h kg^{-1}), high cost, fire risk, and explosion hazard.

It can be expected that, on changing fundamentally the technology of electrode fabrication and design of batteries, their specific power can be made tens and hundreds of times higher, so that they would compete successfully with electrochemical capacitors in numerous important applications.

(1) Conditions for achieving a high specific power of batteries. The discharge current of battery is limited by four interrelated quantities: internal resistance of electrolyte and current leads, rate of electrochemical processes on electrodes, rate of equalization of charges and potentials across the electrode thickness, and rate of equalization of electrolyte concentration in electrodes and separator.

Each of the quantities mentioned may become rate-determining under certain conditions and limit the discharge current and, consequently, the power of a battery.

The internal resistance of the electrolyte depends on the electrolyte resistance and on the thickness and porosity of the separator:

$$R_e = \rho_e \delta_s \varepsilon^{-\nu}, \quad (1)$$

where R_e is the internal resistance of the electrolyte in separator pores per unit geometric surface area (Ω cm^2), ρ_e the electrolyte resistivity (Ω cm), δ_s the separator thickness (cm), ε the separator porosity, and ν a constant dependent on the shape of separator pores.

At $\nu = 1.5$, the R_e value calculated using formula (1) has an intermediate value obtained using the known formulas of Fricke [3] and Mashovets [4]. Formula (1) shows that the separator must be thin and highly porous.

The internal resistance of a current lead (collector) depends on the collector thickness, resistivity of the material used, and electrode length in the direction of current supply:

$$R_c = \rho_c L^2 / 2\delta_c, \quad (2)$$

where R_c is the collector resistance per unit geometric surface area (Ω cm^2), ρ_c the resistivity of the material (Ω cm), δ_c the thickness (cm), and L the length in the direction of current supply (cm).

From formula (2) follows a quadratic dependence of the resistance of collector on its length. Thus, the electrode length in high-power batteries is limited by the admissible value of the internal resistance.

The rate of electrochemical processes is determined by temperature and specific surface area of particles

1070-4272/02/7504-0543 $27.00 © 2002 MAIK "Nauka/Interperiodica"

of the active paste, which are in contact with the electrolyte and in electronic contact with the collector. The large the total surface area of particles in contact with the collector, the lower the polarization resistance. Consequently, all particles of the active paste in high-power batteries must have reliable electrical contact with the collector, and their total surface area must be as large as possible.

The rate of charge and potential equalization across the electrode thickness is determined by the thickness and effective capacity of the active paste and effective electrolyte resistivity in pores. To a first approximation, the process of potential equalization across the active paste thickness can be regarded as discharge of a volume-porous capacitor through the resistance of electrolyte in pores. The discharge of such a capacitor can be described by an equation similar to the heat conduction or diffusion equation [5]:

$$\frac{\partial E}{\partial t} = a\frac{\partial^2 E}{\partial x^2}, \quad (3)$$

$$a = (C_V \rho_{\text{eff}})^{-1}, \quad (4)$$

$$C_V = \frac{1}{V}\frac{\mathrm{d}Q}{\mathrm{d}E}, \quad (5)$$

where a is a constant similar to the thermal diffusivity coefficient in the heat conduction equation ($\text{cm}^2\ \text{s}^{-1}$), ρ_{eff} the effective electrolyte resistance in the pores of the active paste (Ω cm), and C_V the effective capacity of the active paste per unit volume V (F cm^{-3}).

For example, at a typical specific charge of the active paste equal to 1000 C cm^{-3}, potential ?shift in the course of discharge by 0.2 V, $C_V \approx 5000$ F cm^{-3}, and $\rho_{\text{eff}} \approx 5\ \Omega$ cm the a value is about 4×10^{-5} $\text{cm}^2\,\text{s}^{-1}$.

The time constant τ of discharge of the volume-porous electrode depends on thickness δ_e and a:

$$\tau = \delta_e^2/a. \quad (6)$$

The thinner the electrode, the lower the time constant of discharge, and the faster the equalization of charge and potential within the electrode. In the above example, $\tau \approx 250$ s for an electrode of thickness 1 mm and $\tau \approx 2.5$ s for a 0.1-mm-thick electrode. Consequently, high-power batteries with discharge time constant of less than 100 s must have electrodes with thickness not exceeding several tenths of millimeter.

The rate of equalization of the electrolyte concentration in electrode and separator pores is determined by migration and diffusion of ions and, therefore, is described by an equation of the type (3). The diffusion coefficients of ions in aqueous solutions are on the order of 10^{-5} $\text{cm}^2\ \text{s}^{-1}$, which is comparable with the value of coefficient a in Eq. (3). Hence follows that the time constant of concentration equalization is close to the time constant of potential equalization, found from formula (6), with the principal requirement, small thickness of the electrode, remaining in force.

(2) Possible, in principle, ways to satisfy requirements to design of ultrahigh-power batteries. The design of modern alkaline batteries satisfies none of the four requirements considered above. The contact of active paste particles is ensured by pressure. The collector is, as a rule, a volume-porous body (sintered body, metallic felt, etc.) whose pores are filled with the active paste: particles of oxides, hydroxides, and hydrides mixed with electrolyte, and particles of electronic conductors (metals, carbon). In any case, the electronic contact is far from being ensured for all particles of the active paste. The electrode thickness, as a rule, exceeds 0.5 mm, and, occasionally, even 1 mm. As a result, even the best of modern alkaline batteries for fast discharge (e.g., SANYO no. 1000SCR [1]) have admissible discharge current of 8–10 C.

A radical way to raise the discharge rate is to abandon the active paste in its classical understanding. It was proposed in [6] to use as active paste thin passivating oxide (hydroxide) films formed on the surface of metals, such as, in particular, cadmium, nickel, or their alloys. At film thickness of several nanometers to tens of nanometers, the diffusion path of redox reactions decreases by orders of magnitude. This leads to an increase in the rate of discharge by orders of magnitude. At such a thickness of the active paste, metal particles on which passivating films are formed must have size comparable with the film thickness, i.e., several to tens of nanometers, and large specific surface area, at least several square meters per 1 gram.

With this principle of electrode formation, each particle of the active paste is involved in the redox process, and contact with the collector is conditioned by chemical bonding between the metal and the passivating film, ensuring full use of the "active paste."

One of universal and effective methods for fabricating such electrodes is porous oxidation of metal foils with subsequent electrochemical or chemical reduction of the porous oxide film to metal [7]. This method can be used to obtain cadmium or iron negative electrodes or silver positive electrode. Unfortunately, no satisfactory technology for porous oxidation of nickel could be developed.

Table 1. Specific capacity of electrodes of various batteries

Electrode no.	Electrode	Preparation method	Specific capacity, A h g^{-1}		
			theoretical	battery	
				modern	ultrahigh-power
1	$Fe/Fe(OH)_2$	Porous oxidation	0.596	0.2–0.25	0.05
2	$Cd/Cd(OH)_2$	"	0.417	0.2–0.25	0.07
3	MH*	Electrolytic	–	0.3–0.4	0.08
4	$Ni(OH)_2/NiOOH$	"	0.292	0.2–0.25	0.17
5	$Ni(OH)_2/NiOOH$	Raney nickel technology	0.292	0.2–0.25	0.11
6	Ag/Ag_2O	Porous oxidation	0.231	0.1–0.15	0.08

* MH fabricated by the technology described in [9]; collector, nickel foil.

Table 2. Characteristics of electrodes of various prototypes

Electrode no.	Electrode	Characteristics of electrodes				
		thickness, mm		mass, g		Capacity, C
		collector	active layer	active layer	electrode	
1	Negative cadmium	0.050	0.07	0.112	0.285	28
	Positive nickel oxide (Raney)	0.025	0.067	0.067	0.149	23.7
2	Negative metal hydride	0.030	0.220	0.2	0.307	57
	Positive nickel oxide (electrolytic)	0.030	0.082	0.082	0.189	49

A nickel electrode with highly developed surface, coated with a passivating film and able to work as nickel oxide positive electrode of a battery, was fabricated in two ways. The first method is formation of a nickel–aluminum alloy on the surface of nickel foil by diffusion with subsequent electrochemical or chemical leaching of aluminum from the alloy. This yields a layer of Raney nickel, firmly adhering to a layer of smooth nickel (collector) [6].

The second method, electrolytic, was described in a patent [8]. Both these techniques yield nickel positive electrodes with nickel foil or nickel grid as collector, in which nickel hydroxide ("active paste") has the form of a thin (several to tens of nanometers) layer on the surface of fine nickel particles bound to the collector by strong metallic bonds.

Both the positive (silver oxide, nickel) and the negative electrodes (iron, cadmium, metal hydride) fabricated by the above methods markedly differ from the electrodes of conventional batteries: the mechanical and electrical contact of highly porous metal layers covered with oxide (hydroxide) films (active layers) with the collector is ensured by strong chemical bonds, rather than by mechanical pressing. The contact resistance between the active layers and the collector is so small that it could not be measured.

The specific capacities of the active material of various electrodes are presented in Table 1. The capacity was found from curves of galvanostatic discharge at current density of 0.1 A cm^{-2} (30–60°C). As reference served mercury oxide electrode. For comparison, Table 1 also lists theoretical specific capacities of the same electrodes and the specific electrode capacity of modern batteries.

As follows from Table 1, the specific capacity of electrodes of ultrahigh-power batteries is 2–5 times lower than that of the electrodes of modern batteries. This is due to a much larger fraction of metal in the active material of the electrodes used. Possibly, further improvement of the technology will make the electrode capacity of ultrahigh-power batteries closer to the level of modern batteries. As an example may serve the nickel oxide electrode (Table 1, no. 4).

(3) Characteristics of prototype ultrahigh-power batteries. To assess the feasibility of new ways of battery design, simplest prototype batteries, nickel–metal hydride and nickel–cadmium, were fabricated.

The prototypes had electrodes 20 × 20 mm in size and Lavsan (Russin equivalent of Dacron) fabric with thickness of about 0.1 mm as separator. The characteristics of the electrodes used are presented in Table 2.

Table 3. Characteristics of prototypes of ultrahigh-power batteries

Prototype no.	Mass of prototype without case, g	Discharge current		Voltage, V		Discharge time, s	Specific capacity, A h kg^{-1}	Specific energy, W h kg^{-1}	Average specific power, kW kg^{-1}
		A	A (A h)$^{-1}$, C	initial	final				
1	0.50	0.4	53	1.3	0.8	67.5	15	15.7	0.84
		1.0	133	1.2	0.7	20	11	10.4	1.90
		2.0	266	1.0	0.6	4	4.4	3.5	3
2	0.58	0.4	31	1.3	0.8	115	22	23	0.72
		1.0	78	1.2	0.7	35.5	17	16	1.6
		2.0	157	1.0	0.6	8.5	8.2	6.5	2.7

The electrode capacity was measured at a current density of 0.1 A cm^{-2}.

The characteristics of two prototypes with pairs of electrodes no. 1–no. 3 and no. 2–no. 4 (Table 1) are presented in Table 3. The specific energy and power were calculated per total mass of the electrodes, separator, and electrolyte. The mass of the case and contact units was ignored. Figure 1 presents discharge characteristics of prototype no. 2.

As follows from Table 3 and Fig. 1, prototypes of ultrahigh-power batteries designed on the basis of the principles described above are characterized by sufficiently high power characteristics, exceeding those of modern batteries by an order of magnitude. True, this is achieved with a 3–4-fold loss of specific energy. For example, the best Cd batteries have a specific energy of up to 40 W h kg^{-1}, and the best NiOOH–MH batteries, a specific energy of up to 75 W h kg^{-1}.

A systematic study of the stability of ultrahigh-power batteries in cycling is incomplete as yet. Data are only available for the conditions of "fast" charging–discharge, when 10–30% of the total charge is taken from a prototype, and charging continues for no more than 100 s. Under these conditions, prototype no. 1 endures 1500–2000 cycles, and prototype no. 2, 8000–15 000 cycles.

(4) Technical application and ways to improve ultrahigh-power batteries. To determine the possible fields of application of ultrahigh-power batteries, Fig. 2 presents, in the specific power–specific energy diagram, the areas occupied by the already known energy storage devices. It can be seen that "gaps" corresponding to an order of magnitude in energy and power exist between the electrolytic and electrochemical capacitors and between electrochemical capacitors and batteries. The region corresponding to characteristics of ultrahigh-power batteries fills nearly entirely one of the gaps: that between electrochemical capacitors and batteries. The region between the electrolytic and electrochemical capacitors remains free for the time being. Probably, this gap will be filled in the course of improvement of the technology and design of both of these types of devices [2].

The principal conclusion following from an analysis of Fig. 2 is that ultrahigh-power batteries are energy storage devices with their own field of application. Their nearest competitors are "classical" batteries (having higher specific energy) and electrochemical capacitors (higher specific power). In the application

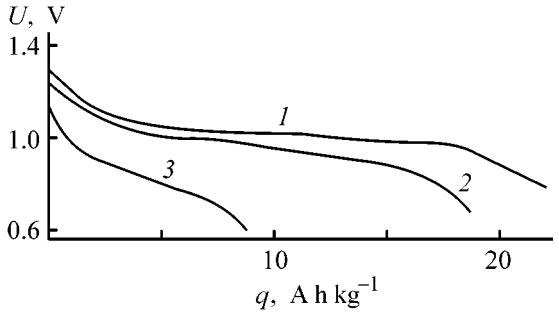

Fig. 1. Discharge characteristics of a prototype ultrahigh-power MH–NiOOH battery. (*U*) Voltage and (*q*) specific capacity. Discharge current (C): (*1*) 31, (*2*) 78, and (*3*) 157.

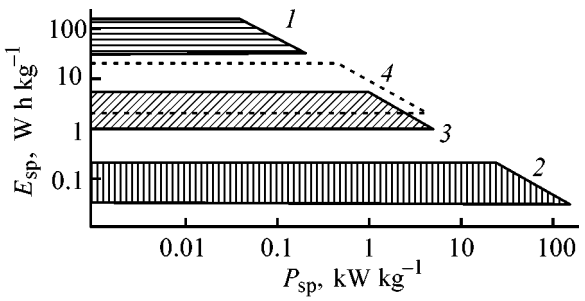

Fig. 2. Relationship between specific energy E_{sp} and specific power P_{sp} of various energy storage devices. Battery: (*1*) modern and (*4*) ultrahigh-power. Capacitor: (*2*) electrolytic and (*3*) electrochemical.

fields requiring specific power higher than 1 kW kg^{-1}, specific energy exceeding 10 W h kg^{-1}, and discharge time of up to 100 s, the ultrahigh-power batteries are the most efficient.

An important field of application of ultrahigh-power electrochemical batteries is the hybrid automobile equipped with both an electric motor and an internal combustion engine. The hybrid automobile allows a 20–25% decrease in fuel consumption and an order-of-magnitude decrease in the amount of hazardous substances in the exhaust gases, which is due to "electric" speeding and energy recuperation in braking. As is known [9], the hybrid automobile requires energy storage devices producing a power of up to 50 kW during an acceleration time of about 10 s, i.e., an energy of more than 500 kJ (more than 150 W h). With account of the fact that repeated starts are possible in real practice, there must be a 2–3-fold energy reserve. The required characteristics can be ensured by using electrochemical capacitors with mass exceeding 100 kg or classical batteries (>200 kg). Both these variants are of little use for economic and technological reasons. Use of ultrahigh-power batteries will allow a substantial decrease in the mass and cost of storage devices, thus creating prerequisites for transition from prototypes of hybrid automobiles to their full-scale production.

REFERENCES

1. Taganova, A.A. and Bubnov, Yu.I., *Germetichnye khimicheskie istochniki toka: Spravochnik* (Hermetically Sealed Chemical Power Cells: Reference Book), Moscow: Khimizdat, 2000.
2. Conway, B.E., *Electrochemical Supercapacitors*, New York: Kluwer, 1999.
3. Fricke, H., *Phys. Rev.*, 1924, vol. 24, no. 1, pp. 275–276.
4. Mashovets, V.P., *Zh. Prikl. Khim.*, 1951, vol. 24, no. 2, pp. 353–355.
5. Mirzoev, R.A. and Umnov, A.B., *Zh. Prikl. Khim.*, 1989, vol. 62, no. 3, pp. 521–526.
6. RF Patent 2 121 728.
7. RF Patent 2 150 533.
8. RF Patent 2 170 468.
9. Corrigan, D., Gow, P., Menjak, I., *et al., 31th Int. Symp. on Automotive Technology and Automation*, Dusseldorf (Germany), June 1998.

Russian Journal of Applied Chemistry, Vol. 75, No. 4, 2002, pp. 548–551. Translated from Zhurnal Prikladnoi Khimii, Vol. 75, No. 4, 2002, pp. 562–565.
Original Russian Text Copyright © 2002 by Kamenev, Kiselevich, Ostapenko, Skachkov.

APPLIED ELECTROCHEMISTRY AND CORROSION PROTECTION OF METALS

Antimony-free Alloys for Unattended (Sealed) Lead Batteries

Yu. B. Kamenev, A. V. Kiselevich, E. I. Ostapenko, and Yu. V. Skachkov

Scientific and Technical Center Elektrotyaga Private Joint-Stock Company, St. Petersburg, Russia

Received October 4, 2001

Abstract—The effect of tin concentration on major characteristics of the Pb–0.08% Ca alloy was studied.

The creation of unattended sealed batteries requires alloys for manufacturing antimony-free positive electrodes. Antimony is known to be able to pass onto a negative electrode through corrosion of current leads, which results in a considerable increase in gassing because of the low overvoltage of hydrogen evolution. In the case of sealed batteries, the gas evolution leads to irreversible loss of water, dehydration of separators, increase in the internal resistance, and, in the end, to a decrease in the battery service life.

The number of publications in the technical literature, concerned with one or another alloy, can be considered a criterion of whether or not the alloy is promising. An analysis covering the period 1960–1995, carried out by the ALABC association (project Pb-001) [1], demonstrated that the Pb–Ca–Sn alloy was most frequently considered among antimony-free alloys (55% of the total number of publications concerned with antimony-free alloys).

We made a similar analysis covering the period 1995–2000, which demonstrated that the Pb–Ca–Sn alloy was the subject of 64.8% of publications in the field in question. There is virtually a consensus on the optimal calcium content (0.07–0.08%). As for the content of tin, opinions of researchers differ widely (0.3–1.8%). In this study, we analyzed the effect of tin concentration in the Pb–0.08% Ca alloy on its main characteristics: ultimate strength σ_S, creep limit σ_C, maximum hardness H_{Smax}, and hardness variation during aging of alloys after casting, afterflow (susceptibility to plastic deformation under static loads less than the ultimate strength), fluidity L, cracking susceptibility in casting CS, corrosion resistance CR, and conductivity of a contact corrosion layer (CCL) at the interface between the current lead and the active paste.

Pb–0.08% Ca alloys containing 0.5, 1.0, and 1.5% Sn served as objects of study. To prevent calcium oxidation during preparation and casting of the alloys, we added 0.010–0.015% aluminum to the alloys [2].

The ultimate strengths and creep limits of the alloys under study, measured 1, 8, and 41 days after sample casting are given in Table 1.

It follows from these data that addition of tin raises the strength of the alloys, especially at tin concentration of 1.5%. It is necessary to note that the increase in the alloy strength takes a long time. This is indicative of the prolonged character of the stabilization process after casting. It was shown in [3] that the strength of the Pb–Ca–Sn alloy continues to increase even after 90 days. The stabilization process can be accelerated either by optimization of the alloy cooling process or by additional heat treatment of samples after casting.

Table 1. Ultimate strengths and creep limits of Pb–Ca–Sn alloys (Ca content in alloy 0.08%)

Sn, %	Aging, day	σ_S	σ_C
		kg mm^{-2}	
0.5	1	3.20	2.10
0.5	8	3.50	2.30
0.5	41	3.91	2.47
1.0	1	3.20	2.12
1.0	8	3.62	–
1.0	41	4.52	2.77
1.5	1	3.22	2.40
1.5	8	3.86	3.16
1.5	41	5.50	3.24

1070-4272/02/7504-0548 $27.00 © 2002 MAIK "Nauka/Interperiodica"

The hardness of the alloys under study, measured 1, 2, 8, 15, 37, and 90 days after casting, is given in Table 2. It can be seen that both the hardness and the strength grow steadily with increasing tin content in an alloy or shelf life of samples after casting.

The aging dynamics can be represented more visually by differential curves $dH_B/d\tau = f(\tau)$ showing how the hardness growth rate varies with time (Fig. 1). Three ranges of growth rate variation can be distinguished in the $dH_B/d\tau = f(\tau)$ curve. The highest rate is observed during the first two days. Then, between the 2nd and 37th day it changes insignificantly, and, finally, during the 37th–90th day it is virtually constant and extremely low. Addition of tin makes the hardness growth rate higher in the second portion of the $dH_S/d\tau = f(\tau)$ curves.

This behavior is in agreement with the modern theory of Pb–Ca alloy hardening [4]. According to this theory, the aging of these alloys after casting occurs in four successive stages of structural transformation, with the corresponding changes in hardness. The first stage, which is about 30 min long, is characterized by an almost twofold increase in hardness. In this stage, the macrocrystalline structure of an alloy becomes finer as a result of formation of new linear grain boundaries. It may be assumed that the reason for the development of new boundaries is that the alloy (supersaturated solid solution α-Pb) tends to make lower its internal energy. In the second stage of structural transformations, grains also become finer, but the boundaries have in this case a sinuous shape owing to minor Pb_3Ca precipitation. The duration of the second stage is 40–50 h. The third stage, beginning approximately 50 h later, is associated with precipitation of thin layers of such compounds as Pb_3Ca at grain boundaries. In this stage, the hardness growth slows down. In the fourth stage, which begins after 25–30 days, Pb_3Ca particles become coarser, with changes in hardness either ceasing or decreasing somewhat (superaging).

An analysis with the $dH_S/d\tau = f(\tau)$ curves in Fig. 1 in terms of this briefly described theory led us to conclude that the first portion of these curves is associated with the first and second stages of structural transformation of the alloy, the second portion, with the precipitation of Pb_3Ca compounds, and the third, with their coagulation. Addition of tin has virtually no effect on the mechanism of hardness growth, but influences the kinetics of its separate stages. The addition of tin is known to decelerate the first and the second transformations, which results in alloy grain coarsening. In addition, Fig. 1 shows that tin accelerates the third transformation stage owing to precipitation, along with Pb_3Ca, of new compounds Pb_3Sn and $(Pb,Sn)_3Ca$. These compounds increase the alloy hardness which depends on the total number of secondary phases.

Table 2. Hardness of Pb–Ca–Sn alloys (Ca content in alloy 0.08%)

Sn, %	H_{Smax}, kg mm^{-2}					
	1 day	2 days	8 days	15 days	37 days	90 days
0.5	15.32	15.75	16.08	16.34	16.88	16.50
1.0	15.45	15.88	16.31	16.78	17.42	17.61
1.5	15.49	15.92	16.52	17.17	17.98	18.45

The effect of tin addition on the alloy creep is shown in Fig. 2. To estimate the creep, we loaded statically cylindrical samples 2.5 mm in diameter at 27.5 MPa and measured the time elapsed till their rupture, which served as a creep parameter. It is seen from Fig. 2 that the alloy resistance to dead loads grows steadily with increasing tin content.

The effect of tin on the fluidity of an alloy and its cracking susceptibility in casting are presented in Fig. 2, which shows that tin makes the fluidity higher and reduces the tendency toward hot cracking. The alloy was cast into a mold with 15 channels 2.5 mm in diameter, hindering its shrinkage in hardening.

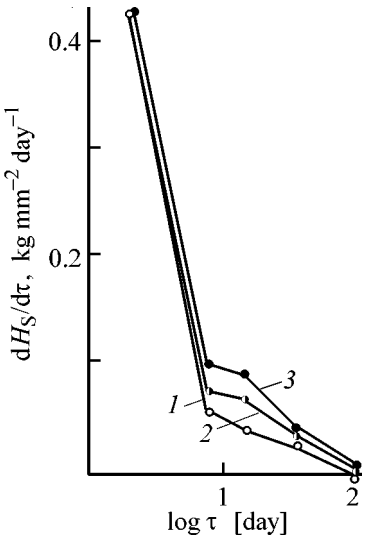

Fig. 1. Hardness growth rate $dH_S/d\tau$ for Pb–0.08% Ca–Sn alloys vs. the duration of alloy aging after casting τ. Sn content in alloy (%): (*1*) 0.5, (*2*) 1.0, and (*3*) 1.5.

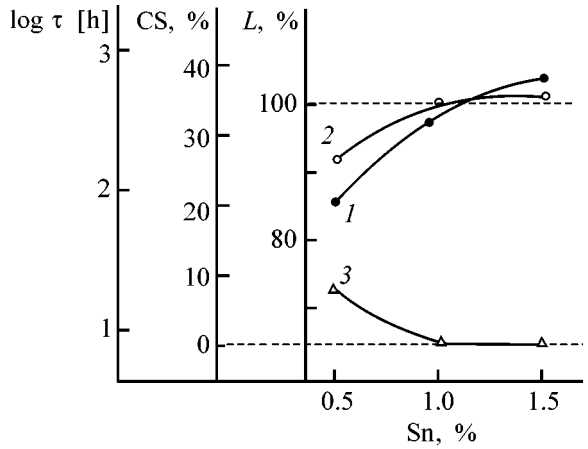

Fig. 2. (*1***)** Creep log τ, (*2*) fluidity *L*, and (*3*) cracking susceptibility in casting CS of the Pb–0.08% Ca alloy vs. the tin content in the alloy.

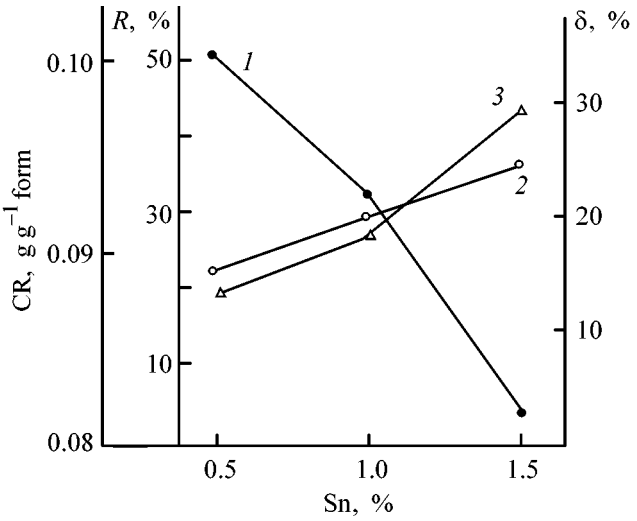

Fig. 3. (*1***)** Corrosion resistance CR, (*2*) fraction of the dense part of the oxide corrosion layer *R*, and (*3*) CCL conductivity δ of the Pb–0.08% Ca alloy vs. the tin content in the alloy.

As a criterion of cracking susceptibility was accepted the ratio of the number of broken veins to their total number in the mold.

We estimated the corrosion rate of the alloys from sample weight losses upon prolonged (300 h) anodic polarization in a sulfuric acid solution of density 1.28 g cm^{-3}. During oxidation, the alloy is covered by an oxide film consisting of two layers: one tightly adjacent to the surface and the other friable, falling off under the action of the evolving oxygen. It is evident that the dense film plays the part of a protective layer ensuring stable existence of passivating clusters [5]. We estimated the fraction of the dense oxide layer, along with the general corrosion losses. For this purpose, we determined the total amount of the oxide formed, P_Σ, and the weight of the dense noncrumbling part of the oxide layer, P_d, using the following formulas:

$$P_\Sigma = (M_{PbO_2}/A_{Pb})\Delta Pb = 1.15\Delta Pb,$$

$$P_d = P_1 - P_2.$$

Here, M_{PbO_2} is the molecular weight of PbO_2, A_{Pb} the atomic weight of Pb, ΔPb the sample weight loss, P_1 the weight of a sample directly after tests (with an oxide layer on the surface), and P_2 the weight of a sample after dissolution of the oxide layer in a hot alkaline solution of sugar.

After that, we calculated the fraction of the dense part of the corrosion layer, *R* (%), from the ratio

$$R = (P_d/P_\Sigma) \times 100.$$

The results of corrosion tests are presented in Fig. 3, which shows that addition of tin decelerates the alloy corrosion and increases the fraction of the dense part of the oxide layer.

A metallurgical study of the samples after corrosion tests demonstrated that the corrosion of the Pb–Ca–Sn alloy has local intercrystallite nature, which determines the dependence of the corrosion rate on the alloy structure. Alloys with low tin content have a finely crystalline structure with large grain boundary area, which predetermines rather high weight losses upon corrosion. As mentioned above, addition of tin noticeably increases the size of alloy grains by hindering the first and the second stages of its structural transformation. In the process, the total surface area of the boundaries decreases, which decelerates the corrosion. Furthermore, as seen from Fig. 3, tin favors an increase in the fraction of the dense part of the passivation film, which must also result in lower corrosion of the alloys.

One of the most important characteristics of alloys is the conductivity of CCL at the interface between the current lead and active paste, since it is across this interface that the overall current generated in electrochemical processes flows. The area of this surface is 10^{-6} of the surface area of the active paste, and any changes in its characteristics will strongly affect the efficiency of the positive electrode and the battery as a whole. If CCL is reduced faster than the active mass in battery discharge, then, when it reaches the oxidation state of $PbO_{1.5}$, it will create a nonconducting barrier in the path of the electron transfer from the active paste into an external circuit and thus

will stop the discharge. It is known [6] that Pb–Ca alloys have CCL that severely constrains the battery capacity, and that addition of tin can raise its conductivity significantly. In this study, we determined the conductivity of CCL formed on alloys from changes in the rate of Fe^{2+} oxidation on a preliminarily oxidized sample surface. Apparently, the rate of this reaction is determined by the rate of electron transfer across the CCL. We polarized the samples of the alloys under study (shaped as disks with smooth surface) at a potential of 700 mV (relative to an Hg/Hg_2SO_4 reference electrode) for 5 min in a vigorously stirred solution of sulfuric acid with density of 1.28 g cm^{-3}. In this case, a film similar to that formed in discharge of the positive active mass appeared on the surface. Then we introduced a $FeSO_4$ solution into the cell and recorded a current step in the current–time curves, resulting from iron(II) oxidation. This step served as a criterion for estimating the conductivity of CCL formed on the alloy under study. The dependence of this parameter on the tin content in the alloy is presented in Fig. 3, which shows that addition of tin leads to an increase in the CCL conductivity in the entire range of concentrations under study. This results from the formation of corrosion films composed of spinel-type double oxides $Pb_{1-x}Sn_xO_2$ with increased *n*-type conductivity [7] and with the known inhibiting effect of tin on the reduction process $PbO_2 \rightarrow PbO_x$ [6].

CONCLUSION

A study of the influence exerted by tin on the major characteristics of the Pb–0.08% Ca alloy, in many respects determining the performance of the positive current leads of batteries, has shown that the alloy containing 1.5% of tin has the best characteristics and can be recommended for use in unattended (sealed) batteries.

REFERENCES

1. Bagshaw, N. and Mayer, M., *ALABC Program Pb-001, Final Rep. Int. Lead–Zinc Research Organization, Inc.*, Research Triangle, NC (USA), Feb., 1995.
2. Dasoyan, M.A. and Kravchenko, G.V., *Sbornik rabot po khimicheskim istochnikam toka Vsesoyuznogo nauchno-issledovatel'skogo akkumulyatornogo instituta* (Coll. of Sci. Works of All-Union Research Inst. of Batteries), Leningrad: Energiya, 1974, pp. 11–17.
3. Miraglio, B.I., *J. Power Sources*, 1995, vol. 53, pp. 53–61.
4. Bourder, L. and Hilder, I., *J. Power Sources*, 1991, vol. 33, pp. 27–51.
5. Popov, Yu.A. and Alekseev, Yu.V., *Elektrokhimiya*, 1985, vol. 21, no. 4, pp. 499–503.
6. Pavlov, D., *J. Power Sources*, 1995, vol. 53, pp. 9–21.
7. Bui, N. and Mattesco, P., *J. Power Sources*, 1998, vol. 73, pp. 30–35.

Russian Journal of Applied Chemistry, Vol. 75, No. 4, 2002, pp. 552–557. Translated from Zhurnal Prikladnoi Khimii, Vol. 75, No. 4, 2002, pp. 566–571.
Original Russian Text Copyright © 2002 by Nagirnyi, Apostolova, Baskevich, Litvin, Shembel'.

APPLIED ELECTROCHEMISTRY AND CORROSION PROTECTION OF METALS

Joint Electrolytic Deposition of Vanadium and Manganese Oxides

V. M. Nagirnyi, R. D. Apostolova, A. S. Baskevich, P. M. Litvin, and E. M. Shembel'

Ukrainian State University of Chemical Engineering, Dnepropetrovsk, Ukraine

Received September 19, 2000; in final form, October 2001

Abstract—The electrolysis conditions and the character of the anodic processes were studied at the joint anodic deposition of vanadium and manganese oxides from mixed sulfate solutions in the form of double oxide systems, which are promising cathode materials of lithium batteries.

Complex multicomponent oxide systems of the type $LiCo_xMn_{2-x}O_4$, $LiCr_yMn_{2-4y}O_4$, and $Co_2V_2O_7 \cdot xH_2O$, prepared by doping of traditional electrochemically active oxides of manganese, vanadium, etc., are interesting cathode materials of lithium batteries, as they have considerably higher electrolytic characteristics compared to basic materials [1–4]. Basically, such systems are mainly prepared by thermal synthesis from stoichiometric mixtures of metal salts. At the same time, there is a great interest in electrochemical synthesis of complex oxide materials by the anodic deposition from mixed aqueous solutions of salts of codeposited metals [5, 6]. The advantage of the electrolytic synthesis is the possibility of preparing uniform structured systems, whose components, unlike simple mechanical mixtures, can interact at the molecular level. This allows ballast-less cathodes to be prepared by the direct deposition of compact oxide coatings onto a smooth or gauze stainless-steel support. Complex vanadium–manganese oxides prepared by the electrolytic deposition from aqueous solutions have the higher electrochemical activity compared to individual components [7]. It was appropriate to study the conditions of joint electrodeposition of the vanadium and manganese oxide compounds from mixed solutions of their salts to obtain on anode in a quantitative yield the complex oxide systems with a controllable phase composition, depending on solution concentrations and electrolysis parameters.

In study, we used mixed solutions of oxovanadium and manganese(II) sulfates of the overall average concentration of 0.3–0.35 M at a concentration ratio (hereinafter, V : Mn) of 5 : 1–1 : 5. Here, the first figures stand for the main component, i.e., for oxovanadium sulfate, and the second, for the doping component. Solutions were prepared from pure and analytically pure grade reagents and distilled water. The electrolysis was performed in a temperature-controlled glass cell 250-ml capacity. The compact coatings were deposited onto gauze and smooth platelike two-side anodes made of 12Cr18Ni9Ti steel of $10 \times 10 \times 0.15$ and $10 \times 10 \times 0.3$ mm size, respectively. Smooth plates of VT-1 commercial titanium with a ratio $S_a : S_c = 1 : 5$ of the anode and cathode surfaces served as cathodes. The tests were performed at 85°C and pH 1.8–2.2. These values were chosen based on the preliminary experimental test and the published data [5, 8] on the electrolytic deposition of vanadium and manganese oxides.

The electrolysis efficiency was estimated from the deposition rate V_{dep} (mg cm^{-2} h^{-1}) and the conventional current efficiency CE_{con} (wt %) by the anodic product, assuming that the whole efficient current is spent for formation of vanadium oxide V_2O_5 [electrochemical equivalent 3.4 g $(A\ h)^{-1}$]. The calculation of the electrochemical equivalent of the anodic product for each value of I_a and V : Mn, and, consequently, the true value of current efficiency is difficult. Despite the arbitrary assumption, the variations of electrolysis efficiency with electrolysis conditions can be, however, judged from correlation of the conventional current efficiency with the deposition rate.

The current efficiency was measured with a copper coulometer. The deposition rate was determined from the mass gain of the anode after electrolysis, which was recalculated per unit surface and unit time.

1070-4272/02/7504-0552 $27.00 © 2002 MAIK "Nauka/Interperiodica"

The polarization curves were taken in a three-chamber cell on a 12Cr18Ni9Ti steel anode polished to a class V 7–8 finish with S_a = 1 cm^2 at I_a = 0.5–50 mA cm^{-2} and the above-indicated temperature and pH values. The potentials were measured relative to a silver chloride reference electrode (E = +0.225 V) with a ShCh-4315 digital voltmeter and then were recalculated to hydrogen scale.

A qualitative phase composition of deposits, along with its approximate quantitative composition (for a few samples), was estimated from comparison of the X-ray diffraction patterns (DRON-2 diffractometer, Cu_{K_α}-radiation) with the calibration graph obtained under the standard conditions [9]. Preliminarily, the "doping" phase (in wt %) in deposits was estimated qualitatively by simple chemical analysis involving dissolution in a hydrogen peroxide solution, which was adjusted to pH 9 with sodium hydroxide, sedimentation (for 24 h), separation, washing, drying at 125°C, weighing of the forming $MnO(OH)_2$, and recalculation to MnO_2. The microstructure and morphology of the surface of deposits (1.5–2.5 μm thick films) was studied with a digital nanoscope (Nona Scope IIIa, Digital Instruments).

Figure 1 shows the deposition rate V_{dep} of the double oxide V–Mn vs. a concentration ratio of the codeposited metal salts in solution. At a low concentration of manganese(II) ions in solution, the deposition rate of the anodic product is somewhat higher than upon deposition from the "straight" oxovanadium sulfate solution and reaches the maximal value at V : Mn = 7 : 1. At further increase in the manganese(II) concentration, the deposition rate decreases sharply, and then the gradual decrease is observed after the ratio V : Mn = 4 : 1 is attained. At V : Mn = 1 : 5, the deposition rate attains the minimal value and virtually passes to the region of zero effect. The specific feature of this process is that the rate of the manganese oxide deposition from the individual solution is higher several-fold than that of the vanadium oxide formation under the comparable electrolysis conditions (20–25 and 5.0–5.5 mg cm^{-2} h^{-1}). This shows that the joint deposition of vanadium and manganese oxides under the conditions studied is a set of complex anodic processes. The kinetics of these processes is to a considerable degree determined by the concurrent redox reactions of ions participating in the electrode process and by the products forming in the different stages of anodic oxidation. The standard electrode potentials of the anodic reactions [10]

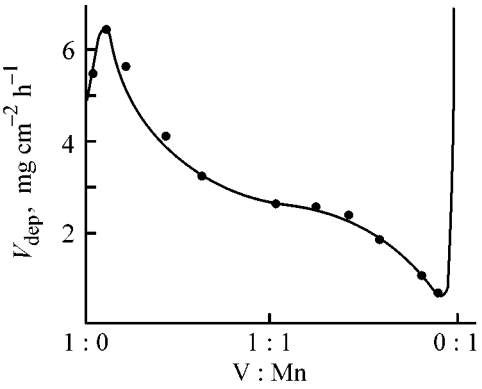

Fig. 1. Rate of deposition V_{dep} of the V–Mn double oxide on anode during the electrolysis of mixed solutions of oxovanadium and manganese(II) sulfates vs. concentration ratio V : Mn. c_Σ = 0.3–0.4 M, I_a = 10 mA cm^{-2}, 85°C, pH 1.9–2.2; the same for Fig. 2.

$$2VO^{2+} + 3H_2O - 2e \rightarrow V_2O_5 + 6H^+,\ E^0 = 1.10\ V; \quad (1)$$

$$Mn^{2+} + 2H_2O - 2e \rightarrow MnO_2 + 4H^+,\ E^0 = 1.23\ V; \quad (2)$$

$$2H_2O - 4e \rightarrow O_2 + 4H^+,\quad E^0 = 1.23\ V \quad (3)$$

are close. Therefore, the given redox reactions can occur in the intermediate and final stages of the electrolysis, when the equilibria are shifted to one side or another owing to the change in the concentration ratio of the initial components. For example, at the low concentrations of manganese(II) ions in a solution, reaction (2) in one of the intermediate oxidation stages is probably complete, yielding an active manganese oxide complex, which can catalyze formation of vanadium(V) oxide:

$$2VO_2^+ + H_2O \rightarrow V_2O_5 + 2H^+.$$

On the contrary, an increase in the manganese ion concentration in solution impedes formation of vanadium(V) oxide and decreases the yield of the total anodic product. This can be ascribed to the increased contribution of the redox reactions, which are responsible for the enhancement of nonproductive energy consumption and the decrease in the efficiency of the electrode reactions. This is supported, in particular, by the fact that, with manganese(II) concentration increased considerably (V : Mn < 1), the deposit color changes to brown owing to the presence of manganese dioxide. The degree of deposition from the solutions at indicated ratio of the component concentrations decreases as the electrolysis time increases (c_Σ = 0.35 M, V : Mn = 1 : 3, 85°C, I_a = 10 mA cm^{-2}, and pH 2.0):

τ, min	15	30	45	60	75	90	100
V_{dep}, mg cm^{-2} h^{-1}	0.04	0.03	0.025	0.02	0.015	0.015	0.013

Deposition rate of anodic product at T = 85°C, I_a = 10 mA cm^{-2}, and pH 2.0

Total concentration of $VOSO_4$ and $MnSO_4$, M	V_{dep} (mg cm^{-2} h^{-1}) at indicated V : Mn ratio		
	3 : 1	1 : 1	1 : 3
2.0	3.0	2.5	2.0
0.35	3.3	2.8	2.4
0.5	3.2	2.3	1.8

For example, after 1 h of electrolysis the anodization rate decreases twofold compared to the initial rate (after the first 15 min). After the solution is stored for 1 day, the initial rate slightly increases (to 0.05 mg cm^{-2} min^{-1}) and then decreases again to the given lower value.

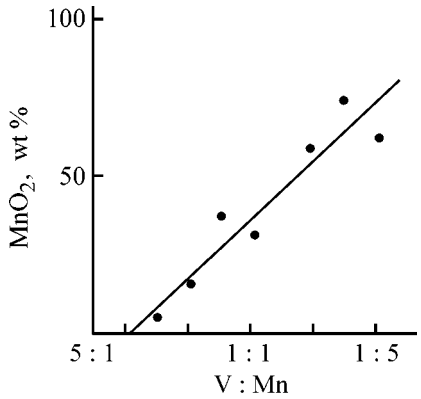

Fig. 2. The concentration of the MnO_2 doping phase in the anodic deposits vs. a ratio V : Mn of the oxovanadium and manganese(II) sulfate concentrations during the electrolysis from solutions.

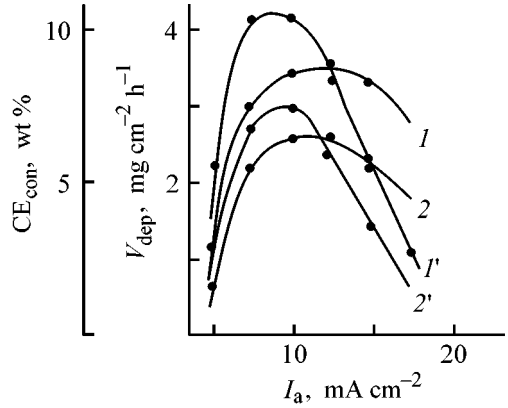

Fig. 3. Dependences of (*1*, *2*) deposition rate V_{dep} and (*1*', *2*') conventional current efficiency by the anodic product CE_{con} on current density I_a during the electrolysis from solutions of oxovanadium and manganese(II) sulfates. c_Σ = 0.3–0.4 M, 85°C, pH 1.9–2.2. V : Mn concentration ratio: (*1*, *1*') 3 : 1 and (*2*, *2*') 1 : 3.

The V_{dep} value and the appearance of deposits are also affected by the total concentration of components in a solution at their different ratios (see table). The decrease in the total concentration decreases the deposition rate and does not affect the character of its dependence on the V : Mn ratio at the optimal total concentration. At higher total concentrations, the electrolysis becomes unstable (the measured V_{dep} values are not reproduced, and the separated deposits have inhomogeneous structure and color). These deviations, along with the intensification of the above side reactions, are also caused by the increased contribution of the cathodic reactions, manifested in formation of loose dark brown films on the cathode.

A decrease in the anodization rate with increasing manganese(II) concentration can be explained by high adsorption activity of vanadium oxide compounds. As a result, adsorption layers rather strongly attached to a substrate can appear on the initial surface of electrode and on the surface of anodic deposit, which would increase the energy barrier of discharge of the manganese(II) ions. In this case, increasing the manganese(II) concentration simultaneously increases the concentration of manganese oxide in the deposit. At V : Mn = 1 : 3, the "doping" phase concentration of more than 50 wt % is attained (Fig. 2). However, its limiting value does not exceed 60 wt %, even at V : Mn = 1 : 5.

The analysis of the dependences of the deposition rate V_{dep} and conventional current efficiency CE_{con} on the current density at various V : M ratios in a solution leads to the similar conclusions (Fig. 3). Evidently, at low and medium current densities (5–10 mA cm^{-2}) the rate of the oxovanadium(IV) ion oxidation by reaction (1) is higher than that of manganese(II) oxidation, irrespective of the V : M ratio. This may be ascribed to the less electropositive standard electrode potential of reaction (1). For this reason, the latter reaction becomes rate-determining in the total anodic process. As a result, with the current density increasing to the optimal value, the deposition rate and the current efficiency by anodic product will increase. The corresponding extremal points on the V_{dep}–I_a curves (Fig. 3, curves *1*, *2*) coincide with the analogous points on the dependence of the deposition rate on the V : Mn ratio (Fig. 1). At current densities above 10 mA cm^{-2}, the manganese(II) oxidation by reaction (2) is predominant: the efficiency of the total process drastically decreases, and the sharp drop of the deposition rate and current efficiency is observed on the V_{dep}–I_a and CE_{con} curves (Fig. 3). It should be noted that the probable contribution of the man-

ganese oxide formation by reaction (2) [electrochemical equivalent 1.62 g $(A\ h)^{-1}$] to the total current efficiency by anodic product (Fig. 3, curves *1*', *2*') does not affect the main character of the dependences considered.

The data presented are confirmed by comparison of the volt–ampere characteristics for individual and joint deposition of vanadium and manganese oxides (Fig. 4). The curves of individual deposition (Fig. 4, curves *1, 2*) form two ascending branches separated with a transition plateau, being more pronounced for vanadium oxide. According to the data of [5], this plateau is of diffusion origin and arises from transition of the anodic process to the region where oxide deposition and oxygen evolution occur jointly. The I_a–E curve of the anodic deposition of manganese oxide has the traditional character (Fig. 4, curve *1*): after the limiting current of the oxidation reaction $Mn^{2+} \rightarrow Mn^{3+}$ is attained, the transition plateau (lower segment of curve) and then the second stage (upper segment) corresponding to the $Mn^{3+} \rightarrow Mn^{4+}$ reaction are observed [8]. The volt–ampere characteristics of the joint separation of vanadium and manganese oxides (Fig. 4, curves *3*–*6*) have another transition plateau owing to the change in the rate ratio of the simultaneous anodic reactions. The corresponding dependences at V : Mn < 1 lie at more positive potentials with respect to those at V : Mn > 1 (Fig. 4, curves *3*, *4*). This shows that the anode overvoltage significantly increases at higher concentrations of the manganese(II) ions in a solution. Correspondingly, the limiting current of the transition plateaus decreases, which agrees with the considered dependence of the rate of the double oxide deposition on the V : Mn ratio (Fig. 1).

The comparison of the I_a–E dependences for individual and joint anodic deposition of vanadium and manganese oxides shows that the lower ascending segments corresponding to them are mainly due to the discharge of oxovanadium ions and formation of the corresponding anodic oxide, which are accompanied by manganese(II) oxidation and oxygen evolution. Probably, the second ascending segment is ascribed to the change in a rate ratio of the concurrent reactions at the increasing rate of manganese(II) oxidation. In the regions of the upper ascending segments, the oxygen evolution, accompanied by intense oxidation of oxovanadium and manganese(II) ions, becomes the potential-determining process.

The nature of the structural and molecular correlation in the bulk of the deposits studied remains controversial. A certain information can be obtained from

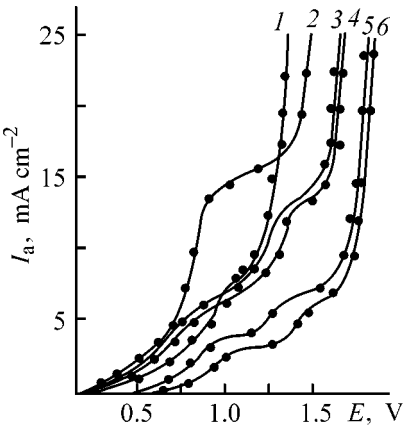

Fig. 4. Volt–ampere curves I_a–E of the anodic deposition of the binary V–Mn oxide from the solutions of oxovanadium and manganese(II) sulfates. c_Σ = 0.3–0.4 M, 85°C, pH 1.9. V : Mn ratio: (*1*) 0 : 1, (*2*) 1 : 0, (*3*) 5 : 1, (*4*) 3 : 1, (*5*) 1 : 5, and (*6*) 1 : 3.

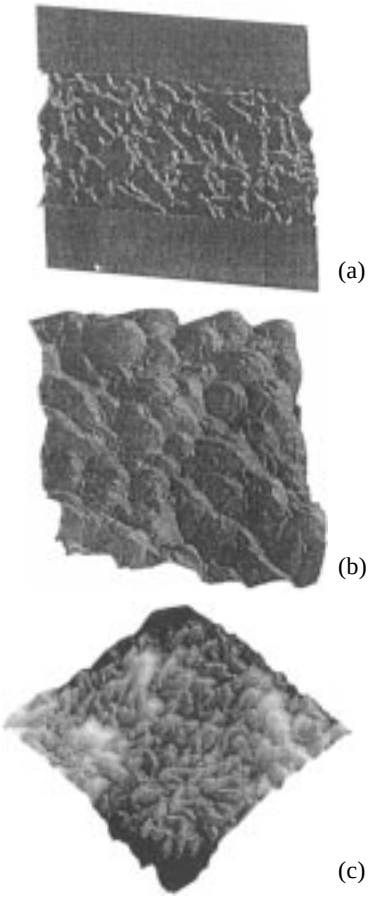

Fig. 5. The microstructure of the surface of thin-film anodic deposits of vanadium(V) and manganese(IV) oxides from sulfate solutions of (a) oxovanadium, (b) manganese(II), and (c) of double oxide obtained from mixed solution with a V : M concentration ratio of 1 : 2. I_a = 10 mA cm^{-2}, 85°C, pH 1.9. Deposits were dried in air at 0°C.

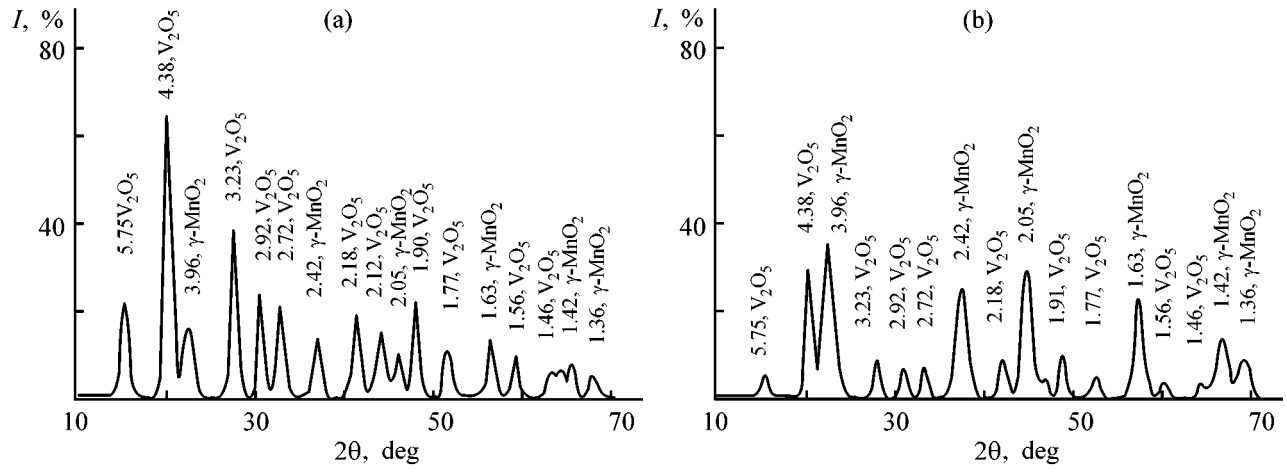

Fig. 6. X-ray diffraction patterns of the double V–Mn oxides, obtained by anodic deposition from solutions. c_Σ = 0.3–0.4 M, I_a = 10 mA cm^{-2}, 85°C, pH 1.9–2.2. Deposits were dried in air at 0°C. (*I*) Intensity and (2θ) Bragg angle. V : Mn ratio: (a) 3 : 1 and (b) 1 : 3. Interplanar spacing are given in Å.

comparison of the microstructure and microrelief of a surface of thin-film deposits of individual vanadium and manganese oxides with the binary oxide V–Mn (Fig. 5). The analysis of the data obtained shows that their nature, determined by electrolysis conditions and solution composition, differs qualitatively. The vanadium oxide deposits are amorphous with a rather developed specific surface area (Fig. 5a). The deposits formed at its joint anodic deposition with manganese oxide have evident crystalline structure (Fig. 5c) nearly similar to block crystalline structure of manganese dioxide deposits (Fig. 5b). Apparently, the structure of deposits of the double oxide system is determined by the fact that manganese dioxide (molecules) tend to form crystalline structures, as it is the energy profitable process (heat of formation of MnO_2 and V_2O_5 is –518 and –1560 kJ mol^{-1}, respectively [11]). The closeness of the crystal systems of rhombic V_2O_5 and γ-MnO_2 can also facilitate this process. Evidently, the mutual influence of originating and growing nuclei of a new phase, which are separated jointly with the oxides, disturbs a regular growth of a part of forming crystalline grains and facilitates formation of deposits with a rather developed surface.

The X-ray diffraction patterns of the double oxides studied, obtained from the solutions differing in the V : Mn ratios, showed that they clearly correspond to the double oxide systems containing both the codeposited oxides as individual phase and the oxide compounds of the type $MnO_2 \cdot V_2O_5$ and $MnO_x \cdot V_2O_{5-x}$. The number of the reflections due to the MnO_2 phase increases proportionally to the manganese(II) ion concentration in a solution (Fig. 6). These data show that, from the energy standpoint, the studied deposits of the double V–Mn oxide system are a certain intermediate system between homogeneous mechanical mixture and single-phase chemical compound.

CONCLUSION

Upon the electrolysis of mixed solutions of oxovanadium and manganese(II) sulfates, vanadium and manganese oxides are jointly deposited on the anode in the form of the double V–Mn oxide system. Such deposits with approximately controllable composition of the codeposited phases can be obtained from the above solutions at the oxovanadium to manganese(II) concentration ratio of 5 : 1–1 : 5, the total concentration of 0.3–0.4 M, 80–85°C, pH 1.9–2.2, and the anodic current density of 7–15 mA cm^{-2}.

REFERENCES

1. Kachibaya, E.I., Kyurkchibasheva, N.R., Dzhaparidze, A.N, and Dam'e, V.N., Abstracts of Papers, *III Vsesoyuznaya konferentsiya "Elektrokhimicheskaya energetika"* (III All-Union Conf. on Electrochemical Energetics), Moscow, 1989, p. 15.
2. Wang, G.X., Bradhurst, D.H., Liu, H.R., and Dou, S.H., *Solid State Ionics*, 1999, vol. 120, pp. 95–101.
3. Amarila, J.M., Martin de Vidales, J.L., and Rojas, R.M., *Solid State Ionics*, 2000, vol. 127, pp. 564–567.
4. Baudrin, E., Laruelle, S., Denis, S., *et al.*, *Solid State Ionics*, 1999, vol. 123, pp. 139–153.

5. Shembel', E.M., Nagirnyi, V.M., Apostolova, R.D., and Chaikovskaya, I.M., *Zh. Prikl. Khim.*, 2000, vol. 73, no. 3, pp. 409–412.
6. Shembel, E., Nagirny, V., Apostolova, R., *et al.*, Abstracts of Papers, *The 197th Meet. of the Electrochemical Society*, Toronto (Canada), May 14–18, 2000, p. 105.
7. Le Gal La Salle, A., Guyomard, D., Verbaere, A., and Piffard, Y., Abstract of Papers, *9th Int. Meet. on Lithium Batteries*, Edinburg (Scotland), July 12–17, 1998.
8. Agladze, R.I., *Elektrokhimiya margantsa* (Electrochemistry of Manganese), Tbilisi: Akad. Nauk Gruz. SSR, 1967.
9. Mirkin, A.I., *Spravochnik po rentgenostrukturnomu analizu polikristallov* (Handbook on X-ray Diffraction Analysis of Polycrystals), Moscow: Fizmatgiz, 1961.
10. *Spravochnik po elektrokhimii* (Handbook on Electrochemistry), Sukhotin, A.M., Ed., Leningrad: Khimiya, 1986.
11. *Kratkii spravochnik po khimii* (A Concise Reference Book on Chemistry), Pilipenko, A.T., Ed., Kiev: Naukova Dumka, 1987.

Russian Journal of Applied Chemistry, Vol. 75, No. 4, 2002, pp. 558–561. Translated from Zhurnal Prikladnoi Khimii, Vol. 75, No. 4, 2002, pp. 572–575.
Original Russian Text Copyright © 2002 by Zarubitskii, Budnik, Omel'chuk, Melekhin, Opanasyuk, Zakharchenko.

APPLIED ELECTROCHEMISTRY AND CORROSION PROTECTION OF METALS

Electrochemical Recovery of Silver from Lead Alloys in Chloride Melts

O. G. Zarubitskii, V. G. Budnik, A. A. Omel'chuk, V. T. Melekhin, V. P. Opanasyuk, and N. F. Zakharchenko

Vernadsky Institute of General and Inorganic Chemistry, National Academy of Sciences of Ukraine, Kiev, Ukraine

Received November 13, 2001

Abstract—Electrochemical separation of lead–silver alloys into the constituents by thin-layer electrolysis in molten electrolytes, with bismuth as metal separator, is studied. It is proposed to determine the extent of component recovery by potentiometry.

Presently, up to 70–80% of silver manufactured in the world is recovered in integrated processing of raw materials containing nonferrous metals. About half of the total output of silver is recovered from lead–zinc ores [1].

At present, the only industrial method used to recover silver and gold from lead and its alloys, obtained from these raw materials, is the so-called Parkes process [2]. This method is based on the ability of silver to react with zinc to form intermetallic compounds characterized by limited solubility in lead. The technique is rather labor-consuming and involves a large amount of recycle products. In this connection, attempts have been repeatedly made to improve the method of silver recovery from intermediates of lead-and-zinc production [3–9]. It has been shown [3–5] that significant progress in improving the given process can be achieved by using electrolysis of molten salts and, in particular, by means of cathode–anode refining [3]. Electrolysis of molten salt mixtures containing zinc compounds makes it possible to combine in the same reactor the silver recovery from lead alloys in the form of its intermetallic compounds with zinc (at the cathode) and decomposition of these compounds to give silver-rich alloys (at the anode). This technique enables a significant decrease in the number of operations and in the amount of recycle products and, consequently, an increase in the extent of silver recovery.

In molten electrolytes, silver has more positive oxidation potential than lead [3], which allows concentration of silver at the anode in the course of electrolysis [3, 6–9]. The accumulation of silver in the anode alloy is 92–95% [9]. However, it should be noted that direct separation of lead–silver alloys into the components in molten salts is complicated by the fact that, when the anode alloy is enriched with silver in the course of electrolysis, the melting point of the alloy grows. This circumstance impairs the efficiency of alloy separation into components and requires that the electrolysis temperature should be raised. The high extent of enrichment with silver under the given conditions of electrolysis of the anodic alloy is achieved when the alloy is in the liquid state [9]. Consequently, there is good reason to believe that alloying of the initial silver-containing lead with a metal that forms sufficiently low-melting and homogeneous alloys with silver and has much more positive oxidation potential, compared with those of lead and silver, can create conditions for successive electrochemical recovery of these metals from the anode to the cathode. A metal possessing the whole set of the above properties is bismuth. In addition, it has been shown [10] that, owing to its ability to form compounds in different oxidation states, bismuth under appropriate conditions is virtually not involved in mass exchange between the electrodes in thin-layer electrolysis.

The present communication reports the results obtained in studying the electrochemical separation of a bismuth-containing Pb–Ag alloy.

EXPERIMENTAL

A Pb–Ag alloy containing 6.2% silver was subjected to electrochemical separation into components. Silver-containing lead was alloyed with bismuth in amount ensuring an Ag : Bi ratio in the ternary alloy

1070-4272/02/7504-0558 $27.00 © 2002 MAIK "Nauka/Interperiodica"

of 1 : (3.7–4.0). At this ratio of the components, the crystallization point of the anode alloy does not exceed (410 ± 10)°C. This allows electrolysis to be performed at a constant temperature, in contrast to electrolysis without adding Bi, when the temperature should be gradually increased because of the growth of the melting point of the alloy.

The ternary alloy obtained was separated in two stages by thin-layer electrolysis [11]. The method consists in that mass exchange between the electrodes occurs through a thin layer of a porous dielectric material containing molten electrolyte in its pores, with the anode–cathode spacing equal to the thickness of this layer [$(0.5–1.0) \times 10^{-3}$ m]. As molten electrolyte served a mixture of the following composition (mol %): NaCl 20, KCl 20, and $ZnCl_2$ 60, with the melting point of 203°C.

In the first stage of electrolysis, lead was extracted from the anode alloy.

A schematic of the electrochemical cell is presented in the figure. A graphite crucible *1*, simultaneously serving as anode current lead, was charged with a ternary alloy to be separated. On the surface of the ternary alloy was placed cathode vessel *2* whose bottom was made of a porous dielectric material *3*. Prior to being placed in the cell, the porous material was impregnated with a molten salt mixture of the composition specified above. The cathode vessel was made of quartz or corundum. As the material of the cathode current lead *5* served graphite or molybdenum. The prescribed temperature mode was provided by heaters *9*. In recovery of lead from cathode to anode, the cathode vessel was additionally charged with lead and electrolysis was carried out with a liquid lead cathode. The electrolyte mixture contained no compounds responsible for the mass transfer between the electrodes. In the first stage of electrolysis, such a compound is lead chloride. It was established experimentally that the concentration of this salt in thin-film electrolysis is as high as 20 wt % even after passing no more than 0.2–0.3 A h of electricity. This concentration is sufficient for ensuring a stable mass exchange between the electrodes. In the process, no zinc is deposited at the cathode from the electrolyte mixture.

The electrolysis was carried out in the temperature range 410–420°C until an anode potential of 0.35–0.40 V relative to a lead reference electrode was reached by the instant when the current was switched off. Composition of electrolyte in the reference electrode (wt %): $PbCl_2$ 20.0, NaCl 8.6, KCl 11.0, $ZnCl_2$ 60.4. It was established that the best characteristics of lead and silver separation are achieved under these

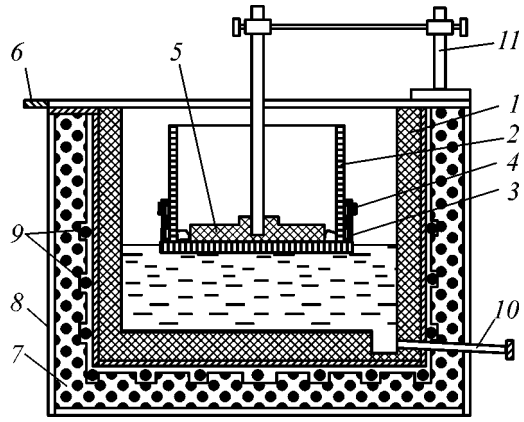

Electrolyzer for silver recovery from its alloys with lead in chloride melts: (*1*) electrolyzer bath (graphite), (*2*) cathode vessel made of a dielectric material, (*3*) membrane made of a porous dielectric material, (*4*) clip for membrane fixation, (*5*) disc-shaped cathode, (*6*) current lead, (*7*) refractory material, (*8*) casing, (*9*) heaters, (*10*) discharge, and (*11*) holder of the cathode current lead.

conditions. This is, to a certain extent, also favored by the fact that the ionization potential of silver is shifted to more positive values upon alloying of silver-containing lead with bismuth, and this shift diminishes silver transfer from anode to cathode. The characteristics of lead recovery from the ternary alloy are listed in Table 1. It can be seen that the conditions of lead recovery from the anode alloy are the most favorable at current densities i $(2–3) \times 10^3$ A m^{-2}. At higher current densities (5×10^3 A m^{-2}) there occurs joint ionization of silver and bismuth, with the content of these components in the cathode metal becoming as high as, respectively, 0.48 and 0.35%. Electrolysis at the optimal current densities (e.g., 3×10^3 A m^{-2}), but during a time in which the potential of the anode alloy reaches values exceeding 0.40 V relative to the above reference electrode potentials, also leads to dissolution of silver and bismuth at the anode and their joint deposition at the cathode. If lead recovery is terminated before the anode potential reaches the values specified above, lead cannot be recovered completely from the anode alloy (Table 1).

Thus, the potential of the anode alloy at the instant of current switching-off is a criterion of lead recovery.

In the second stage of electrolysis, the cathode vessel *2* was extracted from the cell, lead was poured out, the bottom part of the vessel was replaced with a new porous insulator, the insulator was impregnated with molten electrolyte, and the vessel was again placed on the surface of the alloy remaining after lead recovery. As a cathode was used, in the given case, a material not interacting with molten electrolyte and

Table 1. Recovery of lead from the Pb–Ag–Bi alloy

Run no.	Mass of anode alloy, kg	Initial Ag : Bi ratio in the alloy	Electrolysis mode		Content in cathodic lead, wt %		Recovery, %		Residual content of Pb in the anode alloy, wt %
			$i \times 10^{-3}$, A m^{-2}	E_f,* V	Ag	Bi	Pb	Ag	
1	0.1	1 : 4.0	2.0	0.30	0.004	0.001	93.5	99.6	3.50
2	0.2	1 : 3.7	2.0	0.35	0.003	0.001	98.3	99.4	0.03
3	0.1	1 : 3.9	3.0	0.38	0.004	0.003	98.6	99.3	0.02
4	0.2	1 : 4.0	2.5	0.40	0.004	0.001	99.0	99.2	0.03
5	0.1	1 : 4.0	3.0	0.44	0.61	0.15	99.0	90.1	0.002
6	0.1	1 : 3.0	5.0	0.40	0.48	0.35	98.0	92.2	0.02
7	0.1	1 : 4.0	1.0	0.40	0.004	0.001	98.2	99.3	0.02

* (E_f) final polarization potential of the anode alloy.

Table 2. Recovery of silver from Bi–Ag alloy

Run no.	Initial Ag : Bi ratio in the alloy	Electrolysis mode		Content in cathodic silver, wt %		Recovery of silver, %
		$i \times 10^{-3}$, A m^{-2}	E_f, V	Pb	Bi	
1	0.5	1 : 4.0	0.60	10.3*	0.005	98.2
2	0.5	1 : 3.7	0.57	0.01	0.003	89.2
3	0.7	1 : 3.7	0.60	0.01	0.002	98.9
4	1.0	1 : 4.0	0.62	0.02	0.003	98.7
5	0.5	1 : 4.0	0.62	0.01	0.009	98.9
6	0.2	1 : 3.0	0.60	0.03	0.005	91.5
7	2.0	1 : 4.0	0.60	0.04	0.007	92.1

* Silver from the anode residue of Bi–Ag–Pb (3.5%) alloy (Table 1, run no. 1).

forming no alloys with silver. For this purpose, graphite, nickel, molybdenum, and silver were tested. The best (as regards recovery, specific electric energy expenditure, current efficiency) results were obtained with a silver cathode.

As also in the first stage, the initial electrolyte contained no electromotive substance ensuring mass exchange between the electrodes. A stable electrolysis mode was attained immediately after switching on the current. The concentration of silver chloride in the electrolyte layer was no less than 15 wt % after passing 0.2–0.3 A h of electricity. It was established experimentally (Table 2) that the optimal range of current densities in the given stage of electrolysis is $(0.5–1.0) \times 10^3$ A m^{-2}, and temperature, 410–420°C. The electrolysis was carried out till the potential of the anode alloy reached a value of 0.60–0.62 V relative to the lead reference electrode. Under these electrolysis conditions, a finely crystalline silver deposit is obtained at the cathode. At higher current densities, a coarsely crystalline deposit is formed, the current efficiency decreases, and silver purity is impaired. To prevent penetration of silver through the layer of porous dielectric material separating the electrodes, the metal was removed from the cathode at regular intervals. If silver recovery is terminated in the second stage before the necessary anode potential is reached, high silver recovery characteristics cannot be ensured (Table 2, run no. 2). After the potential of the anode residue reaches a value of 0.62 V, the potential becomes virtually independent of the electrolysis duration since only a single potential-determining component, bismuth, remains on the anode. If the electrolysis is continued, the specific electric energy consumption grows (Table 2, run no. 5).

Thus, in the second stage of electrolysis, too, the potential of metal at the anode is the criterion of whether the process should be terminated.

After silver is recovered, bismuth obtained at the anode is used in subsequent operations of alloying with silver-containing lead and in repeated electrolysis.

Since the electrolysis in both the first and the second stages is carried out at exceedingly short interelectrode spacings [$(0.5–1.0) \times 10^{-3}$ m], the proposed

method is characterized by low specific consumption of electric energy and components. The average specific consumption of electric energy is estimated to be 0.12–0.15 and 0.3–0.4 kW h kg^{-1} in the stages of recovery of, respectively, silver and lead.

CONCLUSIONS

(1) An electrochemical method for separation of lead–silver alloys into components in molten electrolytes was proposed. The process is based on thin-film electrolysis with the use of bismuth as a metal separator. The method ensures high degree of alloy separation into components at low specific consumption of electric power and electrolyte.

(2) The extent of recovery of the components from the alloy can be monitored by the potential of the anode residue at the instant of current switching-off.

REFERENCES

1. Malyshev, V.M. and Rumyantsev, D.V., *Serebro* (Silver), Moscow: Metallurgiya, 1987.
2. *Osnovy metallurgii* (Fundamentals of Metallurgy), Greiver, N.S., Ed., Moscow: Metallurgizdat, 1962, vol. 2.
3. Delimarskii, Yu.K. and Zarubitskii, O.G., *Elektroliticheskoe rafinirovanie tyazhelykh metallov v ionnykh rasplavakh* (Electrolytic Refining of Heavy Metals in Ionic Melts), Moscow: Metallurgiya, 1975.
4. USSR Inventor's Certificate no. 510857.
5. Delimarskii, Yu.K., Budnik, V.G., Zarubitskii, O.G., and Melekhin, V.T., *Khim. Tekhnol.*, 1977, no. 1, pp. 3–5.
6. Kleespies, E.K., Bennetts, J.P., and Henrie, T.A., *J. Metals*, 1970, vol. 22, no. 1, pp. 42–44.
7. Zarubitskii, O.G., Dugel'nyi, A.P., Omel'chuk, A.A., *et al.*, *Tsvetn. Met.*, 1991, no. 3, pp. 30–32.
8. Omelchuk, A.A. and Zarubitskii, O.G., *Electrochim. Acta*, 1999, vol. 44, no. 11, pp. 1779–1787.
9. Zarubitskii, O.G., Opanasyuk, V.P., Omel'chuk, A.A., and Zakharchenko, N.F., *Zh. Prikl. Khim.*, 2001, vol. 74, no. 2, pp. 206–210.
10. Omel'chuk, A.A., Budnik, V.G., and Zarubitskii, O.G., *Ukr. Khim. Zh.*, 1995, vol. 61, no. 12, pp. 111–114.
11. Omel'chuk, A.A., *Ukr. Khim. Zh.*, 2001, vol. 67, no. 7, pp. 37–44.

Russian Journal of Applied Chemistry, Vol. 75, No. 4, 2002, pp. 562–564. Translated from Zhurnal Prikladnoi Khimii, Vol. 75, No. 4, 2002, pp. 576–578.
Original Russian Text Copyright © 2002 by Devyatkin, Pisanenko, Shapoval.

APPLIED ELECTROCHEMISTRY AND CORROSION PROTECTION OF METALS

Chemical and Electrochemical Behavior of Carbonate Melts Containing Silicon Oxide

S. V. Devyatkin, A. D. Pisanenko, and V. I. Shapoval

Vernadsky Institute of General and Inorganic Chemistry, National Academy of Sciences of Ukraine, Kiev, Ukraine

Received January 30, 2001; in final form, July 2001

Abstract—The optimal conditions of electrochemical synthesis of silicon carbide in carbonate melts containing silicon oxide were determined on the basis of thermodynamic calculations and data of cyclic voltammetry.

Carbonate melts have found wide use as electrolytes for fuel cells [1] and for treatment of castings. The behavior of molten carbonates has been studied extensively. At the same time, use of carbonates as supporting molten electrolytes in electrolysis aimed to obtain solid deposits is poorly studied. In [2, 3], the possibility of carbon deposition at the cathode in these media was examined.

Alkali metal carbonates react rather well with a number of metals [4] and dissolve oxides of refractory metals and *p* elements (B, Al, Si, Ge, etc.) [5]. The range of potentials in which carbonate melts do not decompose is 1.6-V-wide, but cathodic depolarization of electrochemical synthesis is possible because of the low energy of formation of silicon and titanium carbides [6] (ΔG_f^0 = –65 kJ mol^{-1} for SiC and ΔG_f^0 = –173 kJ mol^{-1} for TiC at 1000 K). Synthesis of carbides in molten carbonates may occur in the given range of potentials. Therefore, it may be considered promising to use carbonate melts to synthesize carbides. Commonly, a binary K_2CO_3–Li_2CO_3 (mp 492°C) or ternary eutectic K_2CO_3–Na_2CO_3–Li_2CO_3 (mp 397°C) are used [7]. However, lithium carbonate is poorly soluble in water [8], and, therefore, a binary eutectic K_2CO_3–Na_2CO_3 (mp 720°C) was chosen as object of study [7].

Potassium and sodium carbonates are well soluble in water, which makes unnecessary use of acid for washing of the cathode product. In [9], silicon carbide was obtained from an SiO_2 (20%)–Li_2CO_3 melt at 1050°C. However, the synthesis mechanism was not studied. Electrolysis was performed at elevated temperature because of the high concentration of the higher-melting component, silicon oxide. Silicon carbide is widely used in the industry, since its exhibits high hardness, refractoriness, oxidation resistance, and semiconducting properties.

The aim of this study was to analyze the ?interaction of molten alkali metal carbonates with silicon oxide and the electrochemical behavior of this system, and to choose the optimal conditions of electrochemical synthesis of silicon carbide.

To prognosticate processes occurring in the systems, the Gibbs energy, ΔG^0, were calculated for a number of chemical reactions possible in molten carbonates at 750°C. The results obtained are presented in the table. It can be seen that silicon oxide is infinitely soluble in molten carbonates because of exchange reactions (4)–(6). The solubility of carbon dioxide in molten carbonates at 750°C is 10^{-4} mol cm^{-3} (~0.22 wt %) [10]. Carbon dioxide dissolves in molten carbonates without chemical reaction, and, consequently, its solubility is directly proportional to pressure, i.e., is described by the Raoult law. Having positive Gibbs energies, molten carbonates of potassium, sodium, and lithium are not susceptible to decomposition [reactions (2) and (3)]. Introduction of silicon oxide into a melt leads in all cases to formation of free carbon dioxide. Consequently, to stabilize carbonate melts containing silicon oxide, it is necessary to create an excess pressure of carbon dioxide. Redox reactions (7)–(22) have positive Gibbs energies and do not occur under the given conditions. Thus, it may be suggested on the basis of thermodynamic calculations that electrochemical synthesis of silicon carbide from carbonate melts containing silicon oxide is possible.

EXPERIMENTAL

Voltammetric measurements were carried out in two hermetically sealed quartz cells under elevated

1070-4272/02/7504-0562 $27.00 © 2002 MAIK "Nauka/Interperiodica"

Gibbs energies, ΔG^0, of reactions (1)–(22) at 750°C

Reaction		ΔG^0, kJ	Reaction		ΔG^0, kJ
$Li_2CO_3 = Li_2O + CO_2$	(1)	88.892	$K_2CO_3 = K_2O + C + O_2$	(12)	629.839 (–1.632)
$Na_2CO_3 = Na_2O + CO_2$	(2)	187.731	$CO_2 = CO + 1/2O_2$	(13)	193.326 (–1.002)
$K_2CO_3 = K_2O + CO_2$	(3)	233.970	$CO = C + 1/2O_2$	(14)	202.542 (–1.050)
$Li_2CO_3 + SiO_2 = Li_2SiO_3 + CO_2$	(4)	–88.478	$CO_2 = C + O_2$	(15)	395.868 (–1.026)
$Na_2CO_3 + SiO_2 = Na_2SiO_3 + CO_2$	(5)	–46.478	$SiO_2 = Si + O_2$	(16)	723.953 (–1.878)
$K_2CO_3 + SiO_2 = K_2SiO_3 + CO_2$	(6)	–39.428	$SiO_2 + CO_2 = SiC + 2O_2$	(17)	1055.266 (–1.367)
$Li_2CO_3 = 2Li + C + 3/2O_2$	(7)	919.656 (–1.588)*	$Li_2CO_3 + SiO_2 = Li_2O + SiC + 2O_2$	(18)	1144.158 (–1.482)
$Na_2CO_3 = 2Na + C + 3/2O_2$	(8)	844.991 (–1.459)	$Na_2CO_3 + SiO_2 = Na_2O + SiC + 2O_2$	(19)	1242.996 (–1.482)
$K_2CO_3 = 2K + C + 3/2O_2$	(9)	850.496 (–1.469)	$K_2CO_3 + SiO_2 = K_2O + SiC + 2O_2$	(20)	1289.236 (–1.670)
$Li_2CO_3 = Li_2O + C + O_2$	(10)	484.761 (–1.256)	$CO_2 + Na_2SiO_3 = Na_2O + SiC + 2O_2$	(21)	896.616 (–1.162)
$Na_2CO_3 = Na_2O + C + O_2$	(11)	583.599 (–1.512)	$CO_2 + K_2SiO_3 = K_2O + SiC + 2O_2$	(22)	942.856 (–1.222)

* The electromotive force V in a circuit in which a given current-forming reaction proceeds is given in parentheses.

pressure of carbon dioxide at 750°C. In one case, a platinum crucible served as a container for the melt and an auxiliary electrode, with platinum wire (S = 0.2 cm^2) as working electrode and oxygen–platinum reference electrode in air. In the other, glassy carbon crucible with working electrode (S = 0.8 cm^2) and reference electrode made of glassy carbon rods were used. Prior to experiments, reagents of chemically pure grade were recrystallized and silicon oxide was dried at 300°C. As cathode materials in electrolysis were used platinum and stainless steel. After electrolysis, cathode deposits were analyzed by X-ray diffraction analysis, Auger spectroscopy, and electron microscopy.

The rise in current observed in the anodic range of potentials in voltammetric curves obtained on a glassy carbon electrode in carbonate melts containing no SiO_2 is due to oxygen evolution, and the rise in the cathodic region, to deposition of carbon and alkali metal (Fig. 1a). The range of potentials in which there are no redox reactions is 0.5 V narrower in the case of glassy carbon electrodes, compared with that for platinum electrodes. This is due to the formation of carbon oxides on glassy carbon subjected to anodic polarization. In titration of the melt with silicon oxide to a concentration of 5×10^{-4} mol cm^{-3}, which corresponds to the limiting solubility of carbon dioxide, the rise in current observed in the cathodic range of potentials in the voltammetric curves obtained on a platinum electrode is due to discharge of carbon dioxide dissolved in the melt to elemental carbon (Fig. 1b). A peak of anodic current, associated with oxidation of carbon, is observed in the reverse run. No anodic current peak is observed on the glassy carbon electrode.

Stable platinum monocarbide exists only in the gas phase [11]. Thermodynamic characteristics of platinum carbide cannot be found in the literature, and, therefore, it is impossible to assess the possibility of formation of a compound of platinum and carbon at 1023 K. With increasing silicon oxide concentration in the melt, a new peak of anodic current appears in voltammetric curves (Fig. 1c) on both platinum and glassy carbon electrodes. The potential at which this current peak is observed is independent of silicon ox-

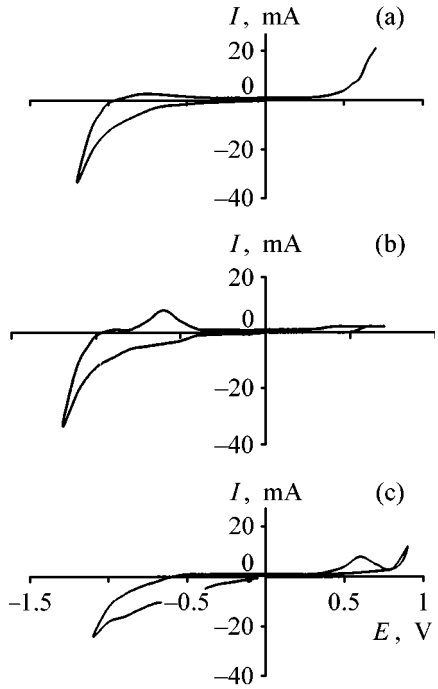

Fig. 1. Cyclic voltammetric curves obtained in (a) carbonate melt and (b, c) in carbonate melt containing SiO_2. Temperature 750°C, potential sweep rate 0.1 V s^{-1}. (I) Current and (E) potential. Electrode: (a, c) glassy carbon and (b) platinum. SiO_2 concentration (mol cm^{-3}): (b) 1×10^{-5} and (c) 9×10^{-5}.

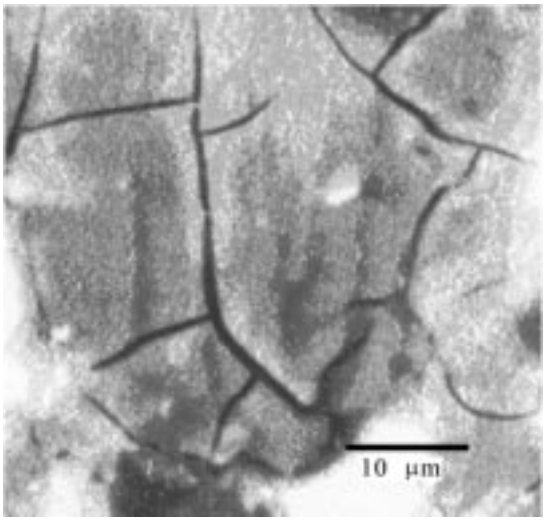

Fig. 2. Electron micrograph of the surface of a silicon carbide film obtained by electrolysis. Magnification 1500.

ide concentration and potential sweep rate at silicon oxide concentrations exceeding 5×10^{-4} mol cm^{-3}. The cathodic process corresponding to the appearance of a new peak of anodic current in the reverse run proceeds at potentials corresponding to residual currents and merges with the background. To shift the potential corresponding to the cathodic process by 24 mV, the carbon dioxide pressure is to be raised to 10 atm.

The results of voltammetric studies suggest that electrochemical synthesis of silicon carbide occurs on glassy carbon and platinum electrodes in molten carbonates containing silicon oxide under elevated carbon dioxide pressure and cathodic polarization.

To confirm the results obtained, electrolytic experiments were performed. By electrolysis of an Na_2CO_3–K_2CO_3–SiO_2 (5%) melt at 750°C, CO_2 pressure of 1 atm, and current density not exceeding 0.2 A cm^{-2}, carbon coatings were produced on steel and platinum, with a glassy layer of 20% carbon and 80% platinum formed on the latter. Under certain electrolysis conditions, coatings of black α-SiC (with increased carbon content) were obtained on steel. Figure 2 illustrates the surface morphology of an SiC coating obtained on steel by means of electrolysis. The coating had block structure with a grain size of 10–20 μm. The carbide coating was dense, had high hardness, easily scratched glass, and possessed semiconducting properties.

CONCLUSIONS

(1) Carbonate melts containing silicon oxide are unstable because of the occurrence of an exchange reaction to give carbon dioxide. This process can be stabilized by creating a carbon dioxide atmosphere with elevated pressure over the melt.

(2) The optimal conditions of electrochemical synthesis of silicon carbide in carbonate melts containing silicon oxide are found.

REFERENCES

1. Cassir, M. and Belhomme, C., *Plasmas Ions*, 1999, vol. 2, no. 1, pp. 3–15.
2. Delimarskii, Yu.K., Grishchenko, V.F., Tumanova, N.Kh., and Shapoval, V.I., *Ukr. Khim. Zh.*, 1970, vol. 36, no. 2, pp. 136–140.
3. Ingram, M.D., Baron, B., and Janz, G.J., *Electrochim. Acta*, 1966, vol. 11, no. 11, pp. 1629–1639.
4. Manukhina, T.I., Sannikov, V.I., and Penyagina, O.P., *Vzaimodeistvie metallov i splavov s rasplavlennymi karbonatami shchelochnykh metallov* (Interaction of Metals and Alloys with Molten Alkali Metal Carbonates), Yekaterinburg: Ural. Otd. Ross. Akad. Nauk, 1999.
5. Orel, V.P. and Dmitruk, B.F., *Issledovaniya v oblasti khimii rasplavov i tverdykh elektrolitov* (Investigations in Chemistry of Melts and Solid Electrolytes), Kiev: Naukova Dumka, 1985, pp. 71–88.
6. Barin, Ih., *Thermodynamic Data of Pure Substances*, Weinheim: VCH, 1993.
7. *Diagramma plavkosti solevykh sistem* (Fusion Diagram of Salt Systems), Posypaiko, V.P., Ed., Moscow: Metallurgiya, 1977, part 2.
8. Nekrasov, B.V., *Osnovy obshchei khimii* (Fundamentals of General Chemistry), Moscow: Khimiya, 1969, vol. 2.
9. Elwell, O., *Mater. Res. Bull.*, 1982, vol. 17, no. 6, pp. 697–706.
10. *Solubility Data Series: Gases in Molten Salts*, Tomkins, R. and Bansal, P., Eds., Oxford: Pergamon, 1991, vol. 45/46.
11. Fromm, E. and Gebhardt, E., *Gase und Kohlenstoff in Metallen*, Berlin: Springer, 1976.

Russian Journal of Applied Chemistry, Vol. 75, No. 4, 2002, pp. 565–568. Translated from Zhurnal Prikladnoi Khimii, Vol. 75, No. 4, 2002, pp. 579–582.
Original Russian Text Copyright © 2002 by Devyatkin, Kaptay.

APPLIED ELECTROCHEMISTRY AND CORROSION PROTECTION OF METALS

Physical, Chemical, and Electrochemical Behavior of Boron Oxide in Cryolite–Alumina Melts

S. V. Devyatkin and G. Kaptay

Vernadsky Institute of General and Inorganic Chemistry, National Academy of Sciences of Ukraine, Kiev, Ukraine
University of Miscolc, Miscolc, Hungary

Received January 26, 2001; in final form, July 2001

Abstract—Preparation of aluminum alloys in an aluminum electrolyzer considerably reduces the cost price of the resulting ligatures. Introduction of new oxides into molten cryolite frequently disturbs the electrolyzer operation. The behavior of boron oxide in molten cryolite and the possibility of stabilizing the electrolyzer operation were studied.

Introduction of boron-containing compounds in the course of aluminum electrolysis is used to remove impurities of heavy metals, inhibit carbon anode combustion, and obtain boron-containing aluminum ligatures [1–3]. Introduction of boron-containing compounds into a cryolite–alumina bath leads, in some cases, to a rise in the process temperature and to deviation from the optimal process parameters of the electrolyzer. It has been shown [4–6] that boron(III) is irreversibly reduced in chloride and fluoride melts to elemental boron in a single stage. The data of [7] are indicative of a single-stage reduction of boron oxide in cryolite. However, the problem of increasing vapor pressure upon introduction of boron oxide into molten cryolite and possible ways to overcome this difficulty were not considered in [7]. Therefore, the aim of this study was to analyze the physical, chemical, and electrochemical behavior of boron oxide and its compounds in an aluminum electrolyzer.

EXPERIMENTAL

Voltammetric studies were carried out in two cells: a platinum crucible with platinum wire as working electrode (S = 0.2 cm^2) and oxygen–platinum reference electrode in air and also a glassy carbon crucible (auxiliary electrode) with glassy carbon working and reference electrodes in argon at 1000–1020°C. We used in our experiments the Greenland cryolite Na_3AlF_6, boric acid, and α- and γ-Al_2O_3 (alumina).

Among the components of a cryolite–alumina–boron oxide melt at 1000°C [8] boron oxide has the lowest density ρ and surface tension γ:

Melt	ρ, g cm^{-3}	γ, mN cm^{-1}
B_2O_3(l)	1.518	830
Al_2O_3(l)	3.03	10 000
Na_3AlF_6(l)	2.095	1360

The density and the surface tension of the higher-melting compound Al_2O_3 in liquid state were extrapolated to 1000°C. These data suggest that, when boron oxide is introduced into a cryolite–alumina bath, a boron oxide film will cover the melt surface with the subsequent formation of gaseous boron trifluoride:

$$2AlF_3(l) + B_2O_3(l) = Al_2O_3(l) + 2BF_3(g). \quad (1)$$

This can account for the unlimited solubility of boron oxide in molten cryolite [1]. The Gibbs energy of the exchange reaction (1) is –77 kJ, as calculated using reference data [9]. The voltammetric curves of cryolite–alumina melt, measured upon introduction of boron oxide, show peaks characteristic of a cryolite–alumina melt. Therefore, boron passes in a gas phase instead of being accumulated in the melt.

This problem can be solved by creating conditions for dissolution of boron oxide in the bulk of the melt, by decreasing the boron oxide activity, and by shifting the equilibrium of reaction (1) to the left. For this purpose, it is necessary to add a complex compound of boron and aluminum to the melt. We studied the formation of a compound from boric acid and γ-Al_2O_3 by thermogravimetry (Fig. 1). Water-containing components were specially selected so that the particle

1070-4272/02/7504-0565 $27.00 © 2002 MAIK "Nauka/Interperiodica"

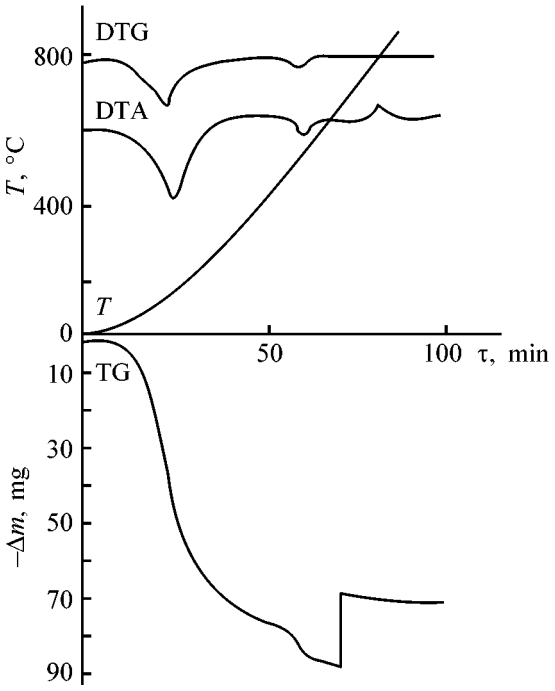

Fig. 1. Thermogravigram of an H_3BO_3–γ-Al_2O_3 sample (500 mg). (*T*) Temperature, (μ) weight change, and (τ) time.

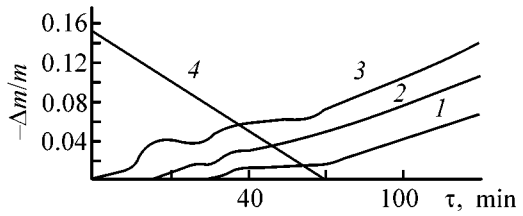

Fig. 2. (*1*)–(*3*) Sample weight $\Delta m/m$ and (*4*) temperature *T* vs. time τ. Sample: (*1*) cryolite, (*2*) cryolite + 10 wt % (B_2O_3 : 2γ-Al_2O_3) mixture, (*3*) cryolite + 10 wt % B_2O_3 : *n*Al_2O_3 compound.

surface was activated by water evaporation upon heating. The DTA curve in Fig. 1 exhibits two endothermic peaks related to water vaporization from boric acid and γ-Al_2O_3 [10] and an endothermic peak at 770°C corresponding to the formation of a compound by the reaction

$$n\mathrm{Al_2O_3} + m\mathrm{B_2O_3} = n\mathrm{Al_2O_3} \cdot m\mathrm{B_2O_3}. \quad (2)$$

This was confirmed by X-ray analysis and IR spectroscopy. A favorable property of this compound is its nonhygroscopicity, in contrast to boron oxide transforming into boric acid in air.

In the phase diagram of the Al_2O_3–B_2O_3 system, there are two incongruently melting compounds: $Al_4B_2O_9$ (mp 1308 K) and $Al_{18}B_4O_{33}$ (mp 2223 K) [11]. Formation of boron oxyfluoride compounds in a cryolite–alumina melt is also possible:

$$\mathrm{NaF} + n\mathrm{B_2O_3} = \mathrm{NaF} \cdot n\mathrm{B_2O_3}. \quad (3)$$

The phase diagram of the NaF–B_2O_3 system was presented in [12]. In this system, there are two compounds: $NaF \cdot B_2O_3$ (mp 913 K) and $NaF \cdot 2B_2O_3$ (mp 933 K). Th thermodynamic characteristics of boron oxyfluoride compounds are unknown, and, therefore, it is impossible to assess the probability of their existence in the melt.

In a number of works [13, 14], it was proposed to introduce sodium tetraborate $Na_2B_4O_7$ into cryolite, but the increasing activity of the alkali metal in the melt makes higher the probability of cathode bottom failure through incorporation of sodium.

Below are presented the results of thermodynamic calculations [9] of possible electrochemical reactions in a cryolite–alumina melt containing boron oxide and its compounds with aluminum and sodium oxides at 1273 K:

Reaction	Δ*G*, kJ	Δ*E*, V
$Al_2O_3 = 2Al + 3/2O_2$	1219.082	–2.106
$B_2O_3 = 2B + 3/2O_2$	960.740	–1.660
$Al_4B_2O_9 = 2Al_2O_3 + 2B + 3/2O_2$	1002.114	–1.731
$Al_4B_2O_9 = 4Al + 2B + 9/2O_2$	3546.438	–2.042
$Na_2B_4O_7 = Na_2O + 4B + 3O_2$	2208.673	–1.908
$Na_2B_4O_7 = 2Na + 4B + 7/2O_2$	2444.506	–1.809
$Na_2B_4O_7 = 2NaBO_2 + 2B + 3/2O_2$	978.817	–1.690
$2NaBO_2 = Na_2O + 2B + 3/2O_2$	1229.856	–2.124
$NaBO_2 = Na + B + O_2$	732.844	–1.899

Comparison of the decomposition potentials of boron, aluminum, and sodium oxides and their compounds shows that the potential of sodium tetraborate decomposition into boron and sodium is more electropositive than the potential of alumina decomposition, which may lead to an increase in the concentration of the alkali metal in aluminum. Correspondingly, the probability of graphite failure upon incorporation of sodium increases. Therefore, it is preferable to introduce a compound of boron and aluminum oxides into the melt.

The weight loss of pure molten cryolite and molten cryolite containing a mixture of boron and aluminum oxides and also their compounds was monitored by thermogravimetry (Fig. 2). It is seen from the figure that introduction of boron oxide as a compound with aluminum oxide diminishes the weight loss resulting from boron trifluoride formation. Therefore,

voltammetric studies were carried out by titration of the cryolite–alumina melt with a preliminarily prepared compound $2Al_2O_3 \cdot B_2O_3$.

Glassy carbon cell. When the compound $2Al_2O_3 \cdot B_2O_3$ is introduced into a cryolite melt, a new more electropositive peak, compared with the background curve characteristic of the cryolite–alumina melt, appears in the cathodic part of the cyclic voltammetric curve (Fig. 3). In the concentration range under study, the peak height linearly depends on the boron oxide content in the melt. A sharp fall of the cathode current after the peak and also the linear dependence of the peak current and potential on the polarization rate indicate the cathode passivation through formation on its surface of a layer having electrical conductivity different from that of the electrode. In this case, a semiconductor material, boron, is formed, which has electrical conductivity lower than that of glassy carbon, but higher than that of the melt [15]. Since the cathodic peak is not of diffusion nature, it is impossible to calculate the kinetic parameters of this electrochemical process. No anodic peak was observed in the entire range of polarization rates, which is also due to passivation of the working electrode.

Platinum cell. In the case of a cryolite–alumina melt, we observed three cathodic and anodic peaks, which are more electropositive than the background rise. These peaks correspond to reduction of aluminum on platinum with the formation of Pt–Al intermetallic compounds. The calculated potentials of depolarization of aluminum reduction through formation of intermetallic compounds [16] are close to the potentials obtained from the voltammetric curves (Fig. 4a):

Peak *I*:	$3Pt + Al = Pt_3Al$,	$\Delta E = +0.98$ V;
Peak *II*:	$Pt_3Al + Al = Pt_3Al_2$,	$\Delta E = +0.66$ V;
Peak *III*:	$Pt_3Al_2 + Al = 3PtAl$,	$\Delta E = +0.43$ V.

A new cathodic peak *B* appear on the top of peak *I* in the cyclic voltammetric curves (Figs. 4b and 4c) recorded in an Na_3AlF_6–Al_2O_3–B_2O_3 melt. The limiting current of this peak linearly depends on the concentration of boron oxide in the melt. The peak potential is shifted to the electronegative side with increasing boron oxide concentration and potential sweep rate. A forewave of boron reduction yielding a Pt–B compound was observed in voltammetric curves measured in an LiF–KF–B_2O_3 melt at 700°C on a Pt electrode [17]. In our case, we did not observe the forewave corresponding to the formation of a Pt–B compound. The aforesaid suggests that the new peak is attributable to irreversible three-electron reduction of boron.

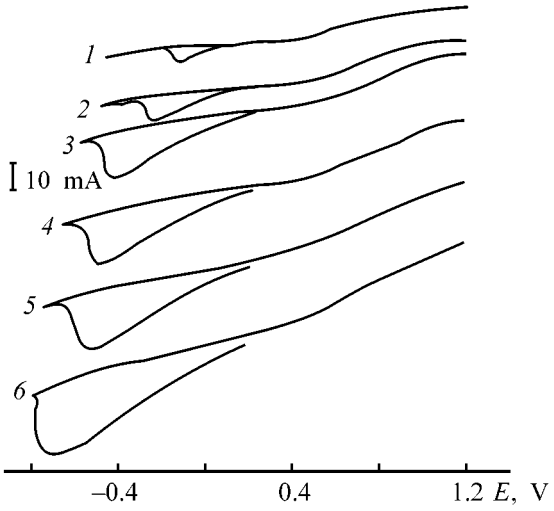

Fig. 3. Cyclic voltammetric curves for molten cryolite containing 1.54×10^{-4} mol cm^{-3} of Al_2O_3 and 7.4×10^{-5} mol cm^{-3} of B_2O_3 at 1273 K. Glassy carbon working and reference electrodes. (*E*) Potential. Polarization rate *V* (V s^{-1}): (*1*) 0.01, (*2*) 0.02, (*3*) 0.05, (*4*) 0.1, (*5*) 0.2, and (*6*) 0.5.

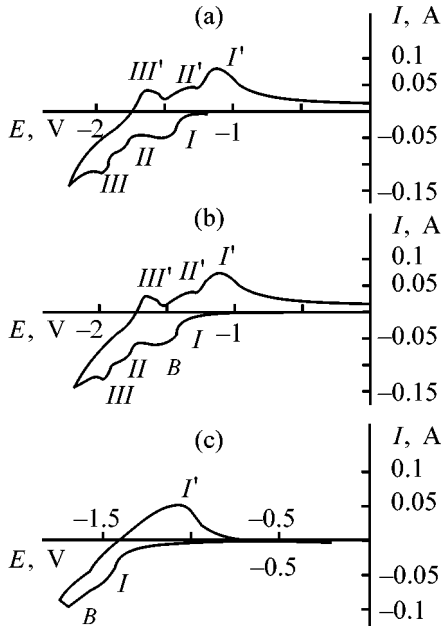

Fig. 4. Cyclic voltammetric curves for the systems: (a) Na_3AlF_6–Al_2O_3 (2×10^{-4} mol cm^{-3}), (b) Na_3AlF_6–Al_2O_3 (1.12×10^{-3} mol cm^{-3})–B_2O_3 (3.8×10^{-5} mol cm^{-3}), and (c) Na_3AlF_6–Al_2O_3 (1.12×10^{-3} mol cm^{-3})–B_2O_3 (1.9×10^{-4} mol cm^{-3}). Temperature 1020°C, $V = 0.5$ V s^{-1}, Pt working electrode ($S = 0.2$ cm^2), reference electrode O^{2+}/O_2 (Pt). (*I*) Current strength; (*E*) potential.

Introduction of boron oxide as a compound with aluminum oxide into molten cryolite does not result in its considerable losses, since the electrochemical reduction of boron is the most electropositive process.

CONCLUSION

A study of the physical, chemical, and electrochemical behavior of boron oxide and its compound with aluminum oxide in molten cryolite enabled stabilization of the melt. Boron oxide, when added to molten cryolite in the form of a compound with aluminum oxide, is reduced in a single stage to elemental boron. This process occurs at less negative potentials than aluminum reduction.

REFERENCES

1. Belyaev, A.I., *Fiziko-khimicheskie protsessy pri elektrolize alyuminiya (rol' okislov v alyuminievoi vanne)* (Physicochemical Processes in Aluminum Electrolysis (Role of Oxides in Aluminum Bath)), Moscow: Metallurgizdat, 1947.
2. Karnaukhov, E.N., Kulesh, M.K., Ryzhev, V.A., *et al.*, *Izv. Vyssh. Uchebn. Zaved., Tsvetn. Metall.*, 1978, vol. 1, pp. 55–58.
3. Krymov, A.P., Bugaenko, V.V., Nerubashchenko, V.V., and Chernov, R.V., in *Elektrokhimicheskie i termodinamicheskie svoistva ionnykh rasplavov* (Electrochemical and Thermodynamic Properties of Ionic Melts), Kiev: Naukova Dumka, 1977, pp. 69–71.
4. Polyakova, L.P., Bukatova, G.A., Polyakov, E.G., *et al.*, *Elektrokhimiya*, 1995, vol. 31, no. 12, pp. 1348–1353.
5. Kuznetsov, S.A., *Elektrokhimiya*, 1996, vol. 32, no. 7, pp. 829–835.
6. Devyatkin, S.V., Kaptay, G., Shapoval, V.I., *et al.*, in *Refractory Metals in Molten Salts*, Kluwer, 1998, 1998, pp. 73–80.
7. Ray, S.C. and Skyllas-Kazacos, M., *Electrochim. Acta*, 1992, vol. 37, no. 10, pp. 1787–1796.
8. Janz, G.J., *NISI Properties of Molten Salts: Single Salts and Salts Mixtures Data*, New York, 1991, Electronic Version 2.0.
9. Barin, Ih., *Thermodynamic Data of Pure Substances*, Weinheim: VCH, 1993.
10. Kaptay, G., *Kohaszat. BVK*, 1968, no. 101, pp. 429–436.
11. Gliesse, P.J.M. and Foster, W.R., *Nature*, 1962, vol. 195, no. 4836, pp. 69–70.
12. Pavlikov, V.N., Yurchenko, V.A., Lugovskaya, E.S., *et al.*, *Zh. Neorg. Khim.*, 1974, vol. 19, no. 7, pp. 1597–1600.
13. Makyta, M., Danek, V., Haarberg, G.M., and Thonstad, J., *J. Appl. Electrochem.*, 1996, vol. 26, no. 4, pp. 319–324.
14. Anghel, E.M., Pavlatou, E., Balasoiu, M., and Zuca, S., *Advance in Molten Salts: From Structural Aspects to Waste Processing*, Gaune-Escard, M., Ed., New York: Begell House, 1999, pp. 23–31.
15. MacDonald, D.D., *Transient Techniques in Electrochemistry*, New York: Plenum, 1977.
16. Boer, F.R. de, Boom, R., Mattens, W.C.M., *et al.*, *Cohesion in Metals*, Amsterdam: North-Holland, 1988, vol. 1.
17. Makyta, M., Matiasovsky, K., and Fellner, P. *Electrochim. Acta*, 1984, vol. 29, no. 12, pp. 1653–1657.

Russian Journal of Applied Chemistry, Vol. 75, No. 4, 2002, pp. 569–572. Translated from Zhurnal Prikladnoi Khimii, Vol. 75, No. 4, 2002, pp. 583–586.
Original Russian Text Copyright © 2002 by Vasil'eva, Rudnev, Tyrina, Lukiyanchuk, Kondrikov, Gordienko.

APPLIED ELECTROCHEMISTRY AND CORROSION PROTECTION OF METALS

Phase Composition of Coatings Formed on Titanium in Borate Electrolyte by Microarch Oxidation

M. S. Vasil'eva, V. S. Rudnev, L. M. Tyrina, I. V. Lukiyanchuk, N. B. Kondrikov, and P. S. Gordienko

Far-Eastern State University, Vladivostok, Russia

Institute of Chemistry, Far-Eastern Division, Russian Academy of Sciences, Vladivostok, Russia

Received May 7, 2001

Abstract—The effect of oxidation conditions, temperature and concentration of the electrolyte, and its transformation from the true to colloidal solution on the phase composition and electrical resistance of coatings was studied.

Titanium and other rectifying metals are commonly anodized to prepare various coatings, for example, catalytic, catalyst supporting, and anticorrosion coatings. Controllable synthesis of films of a prescribed composition and crystalline structure is necessary for development of efficient protective coatings and new materials. One of promising methods of their synthesis is microarch oxidation (MAO), i.e., the formation of oxide coatings on metals and alloys in the regime of electrical breakdowns in aqueous and nonaqueous electrolytes. The method allows the chemical and phase composition, and, consequently, physicochemical properties of the anodic coatings on rectifying metals to be varied within wide range [1–3].

The conditions appearing in breakdowns (high temperature and considerable pressure drop) should result in the formation of anodic titanium oxide of rutile modification, which is a more thermodynamically stable phase highly resistant to chemical aggressive media. At the same time, previous experimental data showed that anatase, rutile, and amorphous inclusions in various combinations are formed in various electrolytes [2–7].

All the mentioned titanium dioxide modifications possess different physicochemical and corrosion–mechanical properties. For this reason, controllable synthesis of prescribed oxide structures is an urgent problem.

A few assumptions exist concerning the formation of anatase and rutile modifications of titanium oxide upon anodization: Koche *et al.* [8] believe that the transition anatase→rutile is temperature-induced; according to [2, 3, 5, 7], formation of one or another modification of TiO_2 is influenced by the anionic composition of the electrolyte.

The electrolyte anions can affect the phase composition of MAO films via generation of nuclei of the corresponding titanium oxide modification, similarly to a way in which the anionic composition of aqueous titanium salts used for titanium oxide deposition predetermines the polymerization type [2, 3]. Moreover, the ratio of these phases can be varied within a rather wide range owing to variations of the amount of the certain electrolyte components selectively dissolving anatase or rutile [7]. The phase composition of MAO coatings is largerly dependent on the formation conditions [1–3].

The elemental composition of MAO coatings sharply varies on passing from the colloidal to true solution [9, 10]. Under these conditions, the phase composition should vary.

In this work, we study the phase composition and electrical resistance of the coatings obtained by oxidation under different conditions of electrical breakdowns in an electrolyte containing sodium tetraborate. Also, we determined the change in the phase composition on passing from the colloidal to true electrolyte.

EXPERIMENTAL

Prior to anodizing, VT1-0 titanium samples ($2.5 \times 0.5 \times 1$ cm) were polished mechanically. Then, chemical polishing in a mixture of concentrated acids (HF : HNO_3 = 3 : 1) was done at 60–80°C for 2–3 s to remove the surface metal layer and obtain a standard state of the surface [11]. After that, samples were washed with distilled water and dried in air.

1070-4272/02/7504-0569 $27.00 © 2002 MAIK "Nauka/Interperiodica"

Influence of conditions of titanium anodization and sodium tetraborate concentration c on the rutile amount I_r in MAO films

i, A cm^{-2}	c, M	T, °C	I_r	Electrolyte state
0.05	0.1	13	1	True
	0.2	14	0.85	Colloidal
	0.2	33	1.22	True
	0.3	21	0.96	Colloidal
0.1	0.1	18	1.15	True
	0.2	19	0.97	Colloidal
	0.2	48	1.38	True
	0.3	26	1.65	Colloidal
	0.3	42	1.73	True
0.2	0.1	25	1.32	〃
	0.2	29	1.29	〃
	0.2	48	2.05	〃
	0.3	31	2.16	Colloidal
	0.3	41	2.39	True

Oxide films on titanium were obtained by microarch oxidation in an electrolyte containing sodium tetraborate. Solutions were prepared from chemically pure grade reagents. True solution was prepared by dissolving sodium tetraborate in a solution heated to 60°C and then gradually cooling to a required temperature.

The coatings were formed in the galvanostatic mode (i = 0.05–0.2 A cm^{-2}, oxidation time 10 min). As power supply served a TER4-100:46ON thyristor transducer delivering a pulsed current of positive polarity. The MAO was performed in a 250-ml heat-resistant glass vessel with a spiral hollow cathode of Cr18Ni9Ti stainless steel cooled with tap water. The electrolyte temperature was varied within 10–50°C. The electrolyte was continuously stirred with a magnetic stirrer. After oxidizing, samples were washed with distilled water and dried in air.

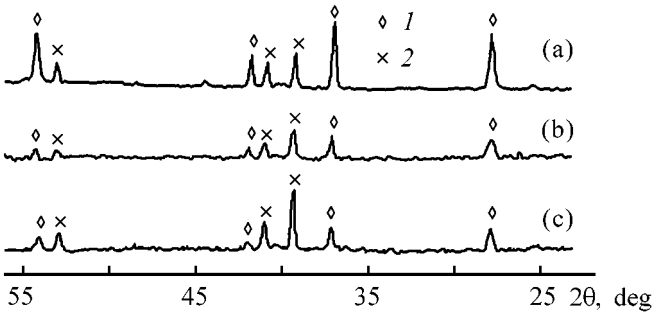

Fig. 1. Diffraction patterns of the MAO coatings formed in a tetraborate electrolyte under the different oxidation conditions. $Na_2B_4O_7$ concentration (M): (a, b) 0.3 and (c) 0.1; Current density (A cm^{-2}): (a, b) 0.1 and (c) 0.05. Temperature (°C): (a) 34, (b) 19, and (c) 12. (*1*) TiO_2 (rutile) and (*2*) Ti.

The phase composition of coatings was determined on a DRON-2.0 diffractometer (Cu_{K_α} radiation). The elemental composition of the surface was determined on a JXA-5A X-ray spectral microprobe analyzer. The electrical resistance of the films was measured with an R5021 alternating current bridge in a 3% NaCl solution. The counter electrode was platinum gauze. The measurements were made within a 1 cm^2 surface; the remaining surface and the edges of coating were insulated with lacquer.

The state of the solutions prepared is dependent on the electrolyte concentration and temperature. Transparent solutions, true over the entire temperature range studied, contain 0.1 M sodium tetraborate. In solutions containing 0.2 and 0.3 M sodium tetraborate, colloidal and suspended particles are formed at low temperature. With increasing temperature, the particle size decreases, and the colloidal solution transforms into true solution (a 0.2 M solution at 28–30°C and a 0.3 M solution at 32–38°C).

The table and Figs. 1 and 2a show how the concentration of tetraborate electrolyte and its state, dependent on temperature and MAO conditions, affect the phase composition of the coatings. As seen, the films obtained in borate electrolyte contain only the rutile modification of TiO_2, irrespective of the oxidation conditions. The relative amount of rutile, I_r, was estimated from the ratio of the reflection intensity of the studied sample (for three intense reflections) to the intensity of the sample anodized at i = 0.05 A cm^{-2}, c = 0.1 M, and T = 12°C (Fig. 1c). The amount of the rutile modification depends on the electrolyte state and oxidation conditions. In the electrolyte containing 0.1 M sodium tetraborate, the rutile amount increases with increasing current density. Anodization in a more concentrated electrolyte is influenced to a greater extent by the electrolyte state.

The content of the rutile modification in a coating and the electrical resistance of coatings formed in 0.3 M $Na_2B_4O_7$ solutions at i = 0.1 A cm^{-2} are presented in Fig. 2 as functions of electrolyte temperature. With increasing temperature, the rutile content increases, attaining the maximal value in the transition region with respect to the state of tetraborate solution of the given concentration (32–38°C). The amount of the crystalline phase in the coating formed at higher temperatures in the unsaturated solution sharply decreases. The rutile content is maximal on passing from the colloidal to true solution (Fig. 2a). In

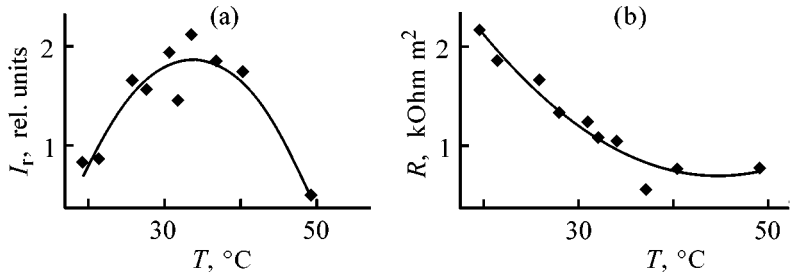

Fig. 2. Influence of temperature T on (a) rutile amount I_r and (b) electrical resistance R of the coatings formed in the electrical breakdown mode in a 0.3 M $Na_2B_4O_7$ electrolyte at current density of 0.1 A cm^{-2}.

the process, the elemental composition of the films varies insignificantly. For example, the titanium content changes from 60.6 to 60 wt %, and the sodium content, from 0.06 to 0.11 wt %. It should be noted that the method used for elemental analysis of coatings does not allow determination of light elements, boron in particular.

In a transition range from the colloidal to true solution, the content of the rutile modification in the coating and the electrical resistance of coatings show a certain correlation (Fig. 2). The increase in the rutile amount decreases the electrical resistance. However, in unsaturated electrolyte, no correlation was observed.

As known, titanium and other rectifying metals are anodized in an electrolyte containing borate and fluoride ions [12]. In this connection, we studied how addition of 0.5 M NaF to an electrolyte containing 0.1 M sodium borate affects the phase composition of coatings:

i, A cm^{-2}	0.05	0.1	0.2	0.2
I_r/I_a	1.02	0.85	1.32	2.43
T, °C	12	13	18	65

With NaF additive, the phase composition of the forming coatings is changed: titanium dioxide of the anatase modification is formed, with the rutile to anatase ratio dependent on oxidation conditions. A ratio I_r/I_a of the rutile to anatase amounts in the analyzed sample was calculated from the corresponding reflection intensities (for the three most intense reflections) and compared to the sample obtained at i = 0.05 A cm^{-2} and T = 12°C. The anatase amount is larger in coatings oxidized at i = 0.1 A cm^{-2} than in those oxidized at i = 0.05 A cm^{-2}. However, at i = 0.2 A cm^{-2} this ratio is changed, i.e., the rutile modification of titanium dioxide becomes predominant. This can be ascribed to the increased temperature, and, consequently, enhanced chemical interaction between the coating and electrolyte, which occur at higher current densities in the region adjacent to the electrical breakdown channels. As a result, anatase, as a less stable titanium dioxide modification, dissolves. This result is confirmed by the fact that, as the electrolyte temperature at i = 0.2 A cm^{-2} increases, the content of the rutile modification of TiO_2 grows.

Only rutile modification of titanium oxide is present in the MAO coatings obtained in the tetraborate electrolyte. This result can be explained using Gordienko's assumptions [2, 3]. It is evident that in the tetraborate electrolyte the borate ions enter the coordination sphere of titanium(IV) in a solution or on the anode surface with distortion of its octahedral surrounding. As a result, the nuclei of the rutile modification of titanium oxide are preferentially formed. The influence of the current density on the phase composition of a coating can be explained by the fact that, with increasing current density, the sparking power and, consequently, both the local temperature and the electrolyte temperature increase, thus facilitating formation of the rutile phase, a high-temperature titanium oxide modification.

Apart from the current density, the electrical resistance and the phase composition of coatings are also affected by the electrolyte concentration, which can be explained by a specific action of boron oxide. Boron oxide, B_2O_3, melts at 450°C [13] and in molten state can dissolve many oxides, with the oxide crystal lattice passing to the active state owing to deformation. Moreover, the energy of the B–O bond (18 254.45 kJ mol^{-1}) is higher than that of the Ti–O bond (12 158.47 kJ mol^{-1}). For this reason, boron oxide can loosen the crystal lattice of titanium oxides and facilitate defect formation, intensifying of the solid-state reaction at lower temperatures [14]. Thus, the higher the sodium tetraborate concentration, the stronger the influence exerted by it on the coating characteristics. The change in the rutile amount in the range 18–38°C can be largely associated with the electrolyte state.

A 0.3 M concentration of $Na_2B_4O_7 \cdot 10H_2O$ is attained at 38°C [15]. It is found experimentally that

the colloidal solution cooled with a stainless steel spiral starts transforming into true solution within 32–38°C, i.e., in the region where the maximal amount of the rutile modification is formed. In the transition region, the colloid size decreases gradually with increasing temperature. The increase in the number of colloids participating in microplasma-assisted anodic reactions results in the fact that colloids, while entering reaction zone, form the B_2O_3 phase, which affects the phase composition of the coatings. Probably, a drastic decrease in the amount of the crystalline phase in coatings formed at an electrolyte temperature above 38°C is due to transformation of the colloidal solution into true solution and to disappearance of colloids of a certain size.

As noted above, in the temperature range corresponding to transformation of the colloidal solution into true solution the rutile content in the coatings correlates with their electrical resistance. For films formed at higher temperature, the electrical resistance is constant. Probably, the growth of the crystalline phase in this temperature range produces a more defective structure, thus decreasing the electrical resistance.

CONCLUSIONS

(1) Coatings on titanium obtained in borate electrolyte by microarch oxidation contain solely the rutile modification.

(2) The rutile amount depends on the electrolyte state and is maximal in the range of transformation of the colloidal solution into true solution.

(3) The electrical resistance and the phase composition of the coating correlate.

(4) Titanium oxide of anatase modification is present in borate electrolyte containing NaF.

REFERENCES

1. Chernenko, V.I., Snezhko, L.A., and Papanova, I.I., *Poluchenie pokrytii anodno-iskrovym elektrolizom* (Preparing Coatings by Anodic Spark Electrolysis), Leningrad: Khimiya, 1991.
2. Gordienko, P.S., *Obrazovanie pokrytii na anodnopolyarizovannykh elektrodakh v vodnykh elektrolitakh pri potentsialakh iskreniya i proboya* (Formation of Coatings on Anodically Polarized Electrodes in Aqueous Electrolytes at Sparking and Breakdown Potentials), Vladivostok: Dal'nauka, 1996.
3. Gordienko, P.S., and Gnedenkov, S.V., *Mikrodugovoe oksidirovanie titana i ego splavov* (Microarch Oxidation of Titanium and Titanium Alloys), Vladivostok: Dal'nauka, 1997.
4. McAller, J.F., and Peter, L.M., *J. Electrochem. Soc.*, 1982, vol. 129, no. 6, pp. 1252–1260.
5. Malygin, V.V., and Kvasova, N.A., Abstracts of Papers, *VI Vsesoyuznaya konferentsiya po elektrokhimii* (VI All-Union Conf. on Electrochemistry), Moscow, June 21–25, 1982, vol. 3, p. 92.
6. Jahalov, F., and Zahavi, J., *Electrochim. Acta*, 1970, vol. 15, no. 9, pp. 1429–1435.
7. Gordienko, P.S., and Khrisanfova, O.A., *Vliyanie ionnogo sostava elektrolita i rezhima oksidirovaniya na fazovyi i elementnyi sostav pokrytii, poluchennykh na metallakh* (The Influence of Ionic Composition and Oxidation Mode on the Phase and Elemental Composition of Coatings on Metal Substrates), Vladivostok, 1989. Available from VINITI, May 6, 1989, no. 2986V–83.
8. Koche, A., Bador, R., Banyssonx, G., and Romand, M., *Analusis*, 1978, vol. 6, no. 9, pp. 383–388.
9. Rudnev, V.S., Yarovaya, T.P., Boguta, D.L., *et al.*, *Elektrokhimiya*, 2000, vol. 36, no. 12, pp. 1457–1462.
10. Rudnev V.S., Yarovaya, T.P., and Boguta, D.L., *J. Electroanal. Chem.*, 2001, vol. 497, no. 1–2, pp. 150–158.
11. Grilikhes, S.Ya., *Obezzhirivanie, travlenie i polirovanie metallov* (Degreasing, Etching, and Polishing of Metals), Leningrad: Mashinostroenie, 1977.
12. GDR Patent 156003.
13. *Fiziko-khimicheskie svoistva okislov. Spravochnik* (Physicochemical Properties of Oxides. Reference Book), Samsonov, G.V., Ed., Moscow: Metallurgiya, 1978.
14. Pishch, I.V., in *Khimiya kislorodnykh soedinenii bora* (Chemistry of Oxygen Compounds of Boron), Riga: Latv. Gos. Univ., 1981, pp. 108–110.
15. Kirgintsev, A.N., Trushnikova, L.N., and Lavrent'eva, V.G., *Rastvorimost' neorganicheskikh soedinenii v vode: Spravochnik* (The Solubility of Inorganic Compounds in Water. Reference Book), Leningrad: Khimiya, 1972, pp. 208–209.

Russian Journal of Applied Chemistry, Vol. 75, No. 4, 2002, pp. 573–578. Translated from Zhurnal Prikladnoi Khimii, Vol. 75, No. 4, 2002, pp. 587–592.
Original Russian Text Copyright © 2002 by Lukiyanchuk, Rudnev, Andenko, Kaidalova, Panin, Gordienko.

APPLIED ELECTROCHEMISTRY AND CORROSION PROTECTION OF METALS

Anodic-Spark Oxidation of Aluminum Alloy in Tungstate Electrolytes

I. V. Lukiyanchuk, V. S. Rudnev, N. A. Andenko, T. A. Kaidalova, E. S. Panin, and P. S. Gordienko

Institute of Chemistry, Far-Eastern Division, Russian Academy of Sciences, Vladivostok, Russia

Received September 3, 2001; in final form, February 2002

Abstract—The effect of Na_2WO_4 concentration, electrolyte depletion, and replacement of sodium tungstate by ammonium paratungstate on the specific features of formation and on the phase and elemental composition of coatings formed on AMtsM aluminum alloy in anodic-spark oxidation was studied.

Tungsten-containing oxide layers deposited on metallic surfaces are of interest because of their semiconducting, corrosion-resistant, catalytic, and decorative properties. As shown previously [1], even prespark oxidation of aluminum in tungstate electrolytes leads to incorporation of tungsten into anodic oxide films. In the process, tungsten is concentrated in the outer layer of the coatings, with its content being about 0.72 ± 0.05 at.%. The WO_3 phase was revealed in coatings upon anodic-spark oxidation of rectifying metals in 0.05 M Na_2WO_4 [2]. When 0.1 M Na_2WO_4 is used as electrolyte [3], coatings containing aluminum tungstates appear on AD-1 aluminum alloy in the initial stage, and then, as the electrolyte is being depleted and the quantity of electricity expended for coating formation grows, tungsten oxides and tungsten bronzes are formed. Thus, analysis of published data shows that the coating composition in the first place depends on the electrolyte concentration. The present study is aimed to reveal the effect of concentration and the depletion of the tungstate electrolyte on the composition and parameters of coatings on aluminum alloy.

EXPERIMENTAL

Electrolytes were prepared using distilled water and analytically pure grade $(NH_4)_{10}[H_2W_{12}O_{42}] \cdot 10H_2O$ and $Na_2WO_4 \cdot 2H_2O$. Ammonium paratungstate was dissolved with heating to 70°C. The electrochemical cell and the method of pretreatment of aluminum samples have been described previously [4]. Oxide layers on AMtsM alloy samples $40 \times 10 \times 1$ mm in size were formed in the galvanostatic mode at current densities i 3 and 5 A dm^{-2} in the course of t 10, 30, and 60 min. The process temperature did not exceed 20°C. After treatment, samples with coatings were thoroughly washed first with tap and then with distilled water and dried in air at room temperature.

The sparking voltage was evaluated by the appearance of the first visually observed sparks on the anode surface or by analyzing the forming curves $U = f(t)$ (from the beginning of deviation of the time dependence of the voltage across electrodes from linear behavior). As the electrolyte depletion Q^* (C l^{-1}) was taken the quantity of electricity, normalized to solution volume, passed through the electrochemical cell before the beginning of oxide layer formation on the electrode.

The phase composition of the coatings was studied by X-ray phase analysis (XPA) on a DRON-2.0 diffractometer (Cu_{K_α} radiation). The elemental composition of the coatings was determined on a JEDE JXA-5A X-ray spectral analyzer. The film thickness was measured with an MBI microscope in reflected light on coating cross sections as an average of 10–15 measurements with accuracy of ±2 μm.

Table 1 presents the concentrations of Na_2WO_4 solutions, pH values, electrical resistivities α of initial solutions and those after anodic-spark oxidation, and phase composition of coatings formed on aluminum alloy at i = 3 A dm^{-2} and varied duration of anodic-spark treatment, and also at different extents of electrolyte depletion Q^*. All the electrolytes exhibit weakly alkaline reaction due to hydrolysis of tungstate ions. Raising the Na_2WO_4 concentration leads to a change in the pH of the initial solutions, increase in electrical conductivity, and lowering of the sparking

1070-4272/02/7504-0573 $27.00 © 2002 MAIK "Nauka/Interperiodica"

Table 1. Characterization of anodizing electrolytes with various concentrations *c* of sodium tungstate and phase composition of coatings formed at current density of 3 A dm^{-2}

c, M	Characteristics of electrolyte				Phase composition		
	initial		after anodizing				
	pH	$\alpha \times 10^3$, $(\Omega\ \mathrm{cm})^{-1}$	pH	$\alpha \times 10^3$, $(\Omega\ \mathrm{cm})^{-1}$	1	2	3
0.01	7.08	1.5	9.48	1.5	$Al_2O_3 + Al(OH)_3$	$Al_2O_3 + Al(OH)_3$	$Al_2O_3 + WO_3$
0.02	7.42	2.9	11.05	2.93	Al_2O_3	Al_2O_3	$Al_2(WO_4)_3 + ?(Al_xWO_3 + Na_2W_2O_7 + Na_2W_4O_{13})$
0.04	7.98	5.4	10.47	5.5	$Al_2O_3 + Al(OH)_3$	$Al_2O_3 + Al(OH)_3$	〃
0.05	7.95	6.7	11.64	6.7	WO_3	$Al_2(WO_4)_3 + ?(Al_xWO_3 + Na_2W_2O_7 + Na_2W_4O_{13})$	〃
0.06	7.93	7.9	12.07	7.9	$H_{0.33}WO_3 + WO_{2.9}$	〃	〃
0.07	8.0	8.9	12.23	9.2	$Al_2(WO_4)_3 + ?(Al_xWO_3 + Na_2W_2O_7 + Na_2W_4O_{13})$	〃	〃
0.08	8.06	9.9	12.18	10.2	〃	〃	〃
0.1	8.11	12.4	12.80	13.4	〃	〃	$Al_xWO_3 + H_{0.33}WO_3 + Na_2W_4O_{13}$

Note: Oxidation mode: (1) t = 10 min, undeveloped electrolyte; (2) t = 10 min, Q^* = 1440–1800 C l^{-1}; and (3) t = 30–60 min, Q^* = 1800–5040 C l^{-1}; "?" denotes possible presence of the indicated phases.

voltage U_s and final voltage U_f of forming (Fig. 1a). For an undepleted electrolyte, the dependence $U_s = f(c)$ is linear, and $U_f = f(c)$, nonlinear. Moreover, the concentration affects the thickness h of the coatings formed and their elemental and phase composition (Figs. 1b and 1c, Table 1), and also their outward appearance (Fig. 2).

Figure 1c presents only the content of W, Al, and O in the coatings, with the content of other elements (Na, Mn, Fe) not exceeding 0.5 wt %. From data in Fig. 1 and Table 1, three ranges of the Na_2WO_4 concentration (M) influencing on the composition of the coatings can be distinguished: (I) 0.01–0.04, (II) 0.05–0.06, and (III) 0.07–0.1. In electrolytes with low sodium tungstate concentrations (region I), thin (3–4 μm) moire coatings (with light and dark areas) containing aluminum oxides and hydroxides are formed (Table 1). The content of tungsten in such coatings is 12–19 wt %.

The composition of coatings formed at intermediate concentrations (region II) is affected by the extent of electrolyte depletion. At $Q^* < 720$ C l^{-1}, green

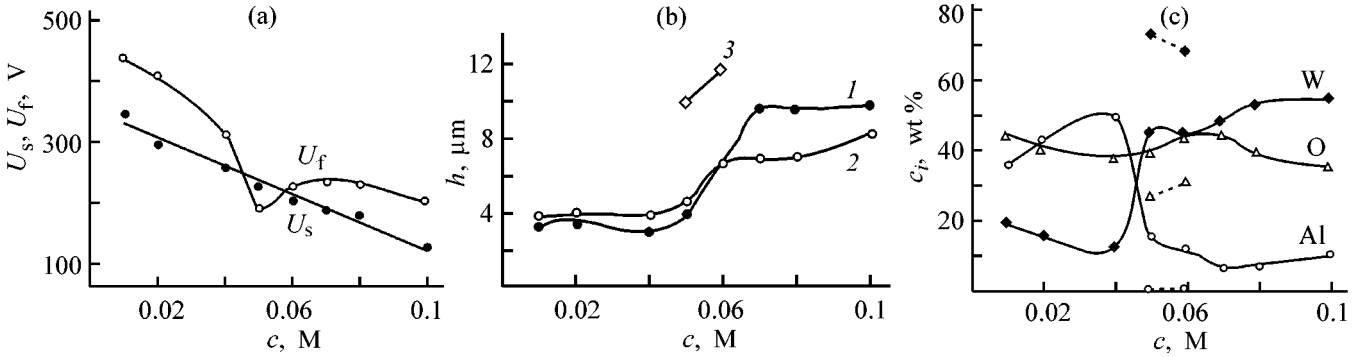

Fig. 1. (a) Sparking voltage U_s and final voltage U_f across electrodes, (b) coating thickness h, and (c) content c_i of main elements in coatings vs. concentration c of sodium tungstate. Current density i = 3 A dm^{-2}, t = 10 min. (b) (*1*, *2*) Dark parts of coatings, formed in, respectively, undepleted and depleted electrolyte; (*3*) green coatings. (c) Oxygen content in the coatings was determined from the difference; *dashed lines*: content of elements in green coatings.

10–12-μm-thick coatings are formed. WO_3 and $WO_{2.9}$ phases are present in their composition (Table 1). Formation of tungsten oxides on rectifying metals has been observed previously [2] in a 0.05 M Na_2WO_4 solution, but at higher current density (i = 16 A dm^{-2}). In the case under study, tungsten oxide layers are formed on the anode surface at Na_2WO_4 concentrations of 0.05–0.06 M by the linear discharge mechanism [5]. At Q^* > 720 C l^{-1}, green areas disappear, aluminum tungstate is formed, and the concentration of tungsten in the coatings decreases from 70 to 45 wt %.

At high Na_2WO_4 concentrations (region III), black coatings with thickness of up to 10 μm were obtained. The $Al_2(WO_4)_3$ phase was detected in them, although presence of sodium polytungstates is not impossible since the content of sodium is as high as 0.35 wt %. The concentrations of tungsten and aluminum in such coatings are 44–55 and 6–15 wt %.

Over nearly the entire range of Na_2WO_4 concentrations studied (0.02–0.08 M), making longer the duration of anodic-spark oxidation of an aluminum alloy (or raising the quantity of passed electricity $Q = it$) in depleted electrolytes gives coatings with identical composition, which contain the $Al_2(WO_4)_3$ phase (Table 1). In region III, raising the Q value favors formation of three-layered coatings. A black film with greenish tint is formed on a gray film and is overgrown by a green film of tungsten trioxide (Fig. 2).

Electrolyte development affects not only the outward appearance and composition of coatings (especially noticeable for coatings obtained in region II), but also the parameters of their formation (Fig. 3). In the first place, the ionic composition of the electrolytes is changed. With increasing Q^*, first colloids and then WO_3 precipitates are formed, the concentration of WO_4^{2-} ions decreases, and pH grows. The depletion of an electrolyte containing 0.1 M Na_2WO_4 leads, already at Q^* = 360 C l^{-1}, to a change in pH value by more than 3 units (Fig. 3b).

To account for the rise in pH on the basis of the results of [3, 6], the following scheme of chemical and electrochemical processes in anodic-spark oxidation of aluminum and its alloys in tungstate electrolytes may be suggested.

Hydroxide ions are formed at the cathode through electrochemical discharge of water molecules:

$$2H_2O + 2e \rightarrow 2OH^- + H_2\uparrow. \quad (1)$$

A film of aluminum hydroxide grows on the anode, and hydroxonium ions are generated:

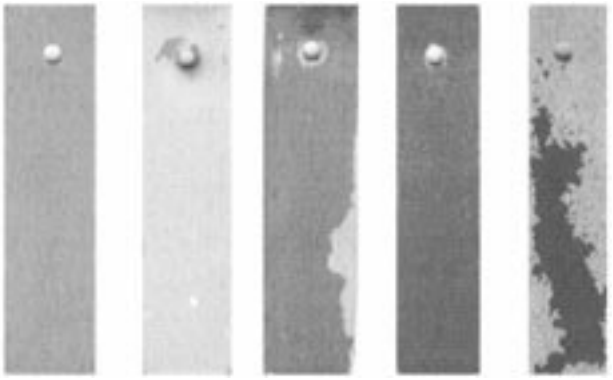

Fig. 2. Effect of Na_2WO_4 concentration on the outward appearance of coatings obtained in the course of anodic-spark treatment in (*1–4*) undepleted and (*5*) depleted electrolytes. Current density i = 3 A dm^{-2}. Time t (min): (*1–4*) 10 and (*5*) 30. Na_2WO_4 concentration (M): (*1*) 0.02, (*2*) 0.05, (*3*) 0.06, (4) 0.07, and (*5*) 0.1.

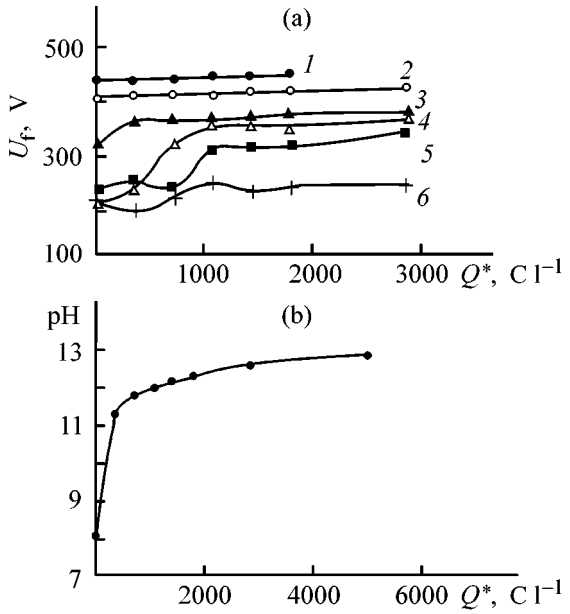

Fig. 3. Effect of electrolyte depletion Q^* on (a) final voltage of coating formation U_f and (b) pH value of 0.1 M Na_2WO_4. (a) Na_2WO_4 concentration (M): (*1*) 0.01, (*2*) 0.02, (*3*) 0.04, (*4*) 0.05, (*5*) 0.06, and (*6*) 0.1.

$$2Al + 9H_2O \rightarrow Al_2O_3 + 6H_3O^+ + 6e. \quad (2)$$

A decrease in pH in the near-anode layer promotes formation of isopolyanions (IPA) [7]:

$$nWO_4^{2-} + pH^+ \rightleftarrows H_xW_nO_{[4n-(1/2)(p-x)]}^{(2n-p)-} + 1/2(p-x)H_2O. \quad (3)$$

It is noteworthy that decomposition of tungsten IPA in the solution bulk would be expected at pH > 8 [8].

Table 2. Characterization of anodizing electrolytes containing 0.1 M tungsten(VI) and phase composition of precipitates

Electrolyte no.	Composition	Characteristics of electrolyte				Phase composition of precipitates	
		initial		after anodizing			
		pH	$\alpha \times 10^3$, $(\Omega\ \mathrm{cm})^{-1}$	pH	$\alpha \times 10^3$, $(\Omega\ \mathrm{cm})^{-1}$	from initial electrolyte	from electrolyte after anodizing
1	Na_2WO_4	8.11	12.4	12.80	13.4	–	$Na_{10}[H_2W_{12}O_{42}] \cdot 12H_2O + WO_3$
2	$Na_2WO_4 + (NH_4)_{10}[H_2W_{12}O_{42}]$	6.71	7.5	7.65	8.2	$Na_2(NH_4)_8[H_2W_{12}O_{42}] \cdot 12H_2O$	$Na_2(NH_4)_8[H_2W_{12}O_{42}] \cdot 12H_2O + WO_3$
3	$(NH_4)_{10}[H_2W_{12}O_{42}]$	6.45	3.2	6.91	3.2	$(NH_4)_{10}[H_2W_{12}O_{42}] \cdot 10H_2O$	$(NH_4)_{10}[H_2W_{12}O_{42}] \cdot 10H_2O + WO_3$

Reaction (3) may give sodium polytungstates which are retained on the surface of anodic films by capillary forces or by adsorption. The final product of polycondensation is tungstic acid. Formation of gel layers of hydrated tungsten oxide already in prespark anodizing of aluminum in tungstate electrolytes was observed in [6]. Dehydration of $WO_3 \cdot nH_2O$, initiated by microdischarges in the near-anode space, leads to appearance of tungsten oxides in the composition of coatings (region II).

Formation of aluminum tungstate in the coatings was attributed in [3] to solid-phase interaction of the anodic aluminum oxide with negatively charged hydrosol of tungsten(VI) oxide. Also possible is another mechanism of its formation. When sparks appear at the anode surface, metal ions pass into solution more intensively [9]. Interaction of aluminum ions with tungstate ions may lead to deposition of a difficultly soluble compound $Al_2(WO_4)_3$ [10] at the anode–electrolyte interface. Aluminum ions may be present in solution at the given pH values in the form of hydroxoaluminate anionic complexes. With aluminum ions accumulated in the electrolyte, formation of aluminum tungstate can also be observed on the anode surface. The formation of this compound in anodic-spark oxidation of titanium in aluminate–tungstate electrolytes has also been reported [11].

Irrespective of what tungsten-containing compound, WO_3 or $Al_2(WO_4)_3$, is formed, consumption of WO_4^{2-} anions at the anode and generation of OH^- at the cathode make higher the pH of electrolyte possessing no buffer properties.

Replacement of tungstate ions by hydroxide ions would have resulted in higher electrolytic conductivity of a solution, since the mobility of OH^- is higher [at 20°C the limiting electrical conductivity at infinite dilution $\lambda_{20}^{\infty}(OH^-) = 217.73$, $\lambda_{20}^{\infty}(1/2WO_4^{2-}) = 76.34\ \Omega^{-1}\ \mathrm{g\text{-}equiv^{-1}\ cm^2}$] [12]. The constant (within experimental error) electrolytic conductivity can be accounted for by changes in the number and mobility of carriers, including those caused by formation of IPA and colloid particles.

Changes in the coating composition may be due to the influence of concentration and depletion of electrolyte on the pH value. At pH > 11.2, gel layers of hydrated tungsten(VI) oxide cease to form on the surface of the aluminum anode, and transfer of aluminum ions to solution is enhanced [6]. After the depletion of the electrolyte, pH is lower than 11.2 at $c \le 0.04$ M and exceeds this value at c 0.05 M (Table 1). Consequently, it would be expected that the concentration of aluminum ions in the electrolyte decreases and aluminum tungstate is formed in the coatings beginning with $c \ge 0.05$ M. Indeed, formation of $Al_2(WO_4)_3$ in coatings deposited in the course of 10 min from depleted electrolytes onsets just at this concentration; however, in undepleted electrolytes $Al_2(WO_4)_3$ is only formed at $c \ge 0.07$ M. It is known [11] that the near-anode layer is acidified in anodic spark electrolysis. Possibly, changes in the composition of coatings are associated with changes in the electrolyte pH, concentrations of tungstate ions, and forms in which these ions are present in the near-anode space. Presumably, the amount of tungsten IPA appearing in the near-anode layer is insufficient for tungsten oxide coatings to be formed in region I, and sufficient in region II. In region III, dissolution of Al_2O_3 is enhanced because of the increasing pH of the depleted electrolyte, and coatings of different composition are formed.

To verify the assumption that the forms of occurrence of tungstate ions affect the composition of forming coatings, sodium tungstate was completely or partly replaced by ammonium paratungstate in such a way

Table 3. Phase composition of coatings formed in electrolytes nos. 1–3 containing 0.1 M tungsten(VI)

Electrolyte no. (Table 2)	Phase composition of coatings at indicated formation time, min			
	10		30	
	1	2	3	4
1	$Al_2(WO_4)_3$	$Al_2(WO_4)_3$	$Al_x(WO_4)_3 + H_{0.33}WO_3 + Na_2W_4O_{13}$	æ-Al_2O_3 + Al_xWO_3
2	$WO_3 + WO_{2.9}$	〃	$WO_3 + WO_{2.9}$	$Al_2(WO_4)_3$
3	WO_3	WO_3	WO_3	WO_3

Note: Oxidation mode: (1) i = 3 A dm^{-2}, Q = 18 C cm^{-2}; (2) i = 5 A dm^{-2}, Q = 30 C cm^{-2}; (3) i = 3 A dm^{-2}, Q = 54 C cm^{-2}; and (4) i = 5 A dm^{-2}, Q = 90 C cm^{-2}.

that the total concentration of tungsten in the electrolyte remained constant. The composition, pH value, and electrolytic conductivity of the initial electrolytes and those after anodizing are presented in Table 2.

Replacement of sodium tungstate with ammonium paratungstate changes the outward appearance and phase composition of coatings (Table 3). Coatings obtained in 0.1 M Na_2WO_4 contain aluminum tungstate, and aluminum–tungsten and (or) hydrogen bronzes are formed with increasing current density and time of anodic-spark treatment. The composition of coatings obtained in electrolyte no. 2 depends on the current density. The coatings contain tungsten oxides at i = 3 A dm^{-2}, and aluminum tungstate is formed at i = 5 A dm^{-2}. Coatings formed from the paratungstate electrolyte are identical in composition to those formed in a 0.05–0.06 M solution of Na_2WO_4 and contain tungsten trioxide.

Table 2 presents the compositions of precipitates formed in electrolytes obtained upon storage of both depleted and undepleted solutions for 1 month in sealed glass vessels. Tungsten(VI) oxide is formed after anodic-spark electrolysis in all the three electrolytes. Precipitates of double ammonium sodium paratungstate are formed in both undepleted and depleted electrolytes nos. 2 and 3, respectively. Precipitation of sodium paratungstate from electrolyte no. 1 at pH > 12 contradicts published data [7, 8, 10]. At such pH values, tungsten IPA can be only formed in the course of electrolysis, the more so as no precipitate was formed in undepleted electrolyte no. 1.

The formation of tungsten trioxide in the coatings upon replacing the tungstate electrolyte with a paratungstate one and precipitation of sodium paratungstate from a 0.1 M solution of Na_2WO_4 subjected to electrolysis confirm the assumption that tungsten IPA are formed in the near-anode layer and their concentration affects the coating composition.

Formation of bronzes and nonstoichiometric tungsten oxides (Tables 1, 3) at the anode has been attributed previously [3] to the action of hydrogen which is a product of water thermolysis under the action of microbreakdowns [13, 14]. A decrease in the oxidation level of elements contained in oxide coatings that are formed on aluminum in anodic spark treatment, compared with their oxidation level in the electrolyte, was also reported in [5] for vanadate–phosphate electrolytes. Bronze-containing coatings may be of interest for further study of their electrical and catalytic properties.

CONCLUSIONS

(1) Three ranges of the Na_2WO_4 concentration affecting formation and composition of oxide layers formed on aluminum alloy in its anodic-spark treatment are distinguished.

(2) It is shown that raising the Na_2WO_4 concentration and making longer the time of anodic-spark oxidation in depleted electrolyte lead to formation of coatings with identical compositions, containing the $Al_2(WO_4)_3$ phase.

(3) Anodic-spark oxidation of aluminum at sodium tungstate concentrations of 0.07–0.1 M in solution and $Q \geq 54$ C cm^{-2} leads to formation of tungsten oxide bronzes $H_{0.33}WO_3$ and Al_xWO_3 in the coatings.

(4) Tungsten trioxide is formed in coatings in an undepleted electrolyte only in a narrow range of Na_2WO_4 concentrations. An assumption is made that WO_3 formation is associated with the presence of isopolytungstate anions in the near-anode region. This is confirmed by the formation of similar layers on replacing sodium tungstate in the electrolyte with ammonium tungstate and by the results of studies of the precipitates formed in the electrolytes.

REFERENCES

1. Skeldon, P., Shimizu, K., Thompson, G.E., and Wood, G.C., *Thin Solid Films*, 1985, vol. 123, no. 2, pp. 127–133.
2. Gruss, L.L. and McNeil, W., *Electrochem. Technol.*, 1963, vol. 1, no. 9–10, pp. 283–287.
3. Rudnev, V.S., Morozova, V.P., Yarovaya, T.P., *et al.*, *Zashch. Met.*, 1999, vol. 35, no. 5, pp. 524–526.
4. Lukiyanchuk, I.V., Rudnev, V.S., Kaidalova, T.A., *et al.*, *Zh. Prikl. Khim.*, 2000, vol. 73, no. 6, pp. 926–929.
5. Gordienko, P.S. and Rudnev, V.S., *Elektrokhimicheskoe formirovanie pokrytii na alyuminii i ego splavakh pri potentsialakh iskreniya i proboya* (Electrochemical Formation of Coatings on Aluminum and Its Alloys at Sparking and Breakdown Potentials), Vladivostok: Dal'nauka, 1999.
6. Morlige, J.R., Skeldon, P., Thompson, G.E., *et al.*, *Electrochim. Acta*, 1999, vol. 44, pp. 2423–2435.
7. Launay, J.P., Boyer, M., and Chauveau, F., *J. Inorg. Nucl. Chem.*, 1976, vol. 38, no. 2, pp. 243–247.
8. Sazonova, O.I., Rozantsev, G.M., and Kholin, Yu.V., *Zh. Neorg. Khim.*, 1998, vol. 43, no. 11, pp. 1894–1899.
9. Li, Y., Shimada, H., Masatoshi, S., Shigyo, K., *et al.*, *J. Electrochem. Soc.*, 1994, vol. 144, no. 3, pp. 866–876.
10. Mokhosoev, M.V. and Shevtsova, N.A., *Sostoyanie ionov molibdena i vol'frama v vodnykh rastvorakh* (State of Molybdenum and Tungsten Ions in Aqueous Solutions), Ulan-Ude: Buryatskoe Knizhnoe, 1977.
11. Khrisanfova, O.A., Volkova, L.M., Gnedenkov, S.V., *et al.*, *Zh. Neorg. Khim.*, 1995, vol. 40, no. 4, pp. 558–562.
12. *Kratkii spravochnik fiziko-khimicheskikh velichin* (Concise Reference Book of Physicochemical Quantities), Mishchenko, K.P. and Ravdel', A.A., Eds., Leningrad: Khimiya, 1967.
13. Ragalyavichus, R. and Yusis, Z., *Chemija* (Lithuania), 1992, no. 2, pp. 45–50.
14. Gordienko, P.S. and Yarovaya, T.P., Processes of Gas Evolution on Titanium Alloys, *Preprint of Inst. of Chemistry, Far-Eastern Div., USSR Acad. Sci.*, Vladivostok, 1989.

Russian Journal of Applied Chemistry, Vol. 75, No. 4, 2002, pp. 579–581. Translated from Zhurnal Prikladnoi Khimii, Vol. 75, No. 4, 2002, pp. 593–595.
Original Russian Text Copyright © 2002 by Tereshchenko, Likhachev, Izotov.

APPLIED ELECTROCHEMISTRY AND CORROSION PROTECTION OF METALS

Influence of the Composition of Chloride-containing Solutions on the Corrosion of 12Cr18Ni10Ti Steel

O. L. Tereshchenko, V. A. Likhachev, and M. V. Izotov

Kirovo-Chepetsk Chemical Plant, Joint-Stock Company, Kirovo-Chepetsk, Kirov oblast, Russia
Vyatka State Technical University, Kirov, Russia

Received April 17, 2001

Abstract—The corrosion activity of chloride-containing solutions formed in production of ternary nitrogen–phosphorus–potassium fertilizers was studied. The inhibiting effect of hydroxide ions on the corrosion of 12Cr18Ni10Ti steel during the evaporation of solutions of nitrogen–phosphorus–potassium fertilizers was evaluated.

Production of complex ternary fertilizers (NPK) involves the use of potassium chloride, which significantly enhances the corrosion activity of the working medium. Therefore, introduction of potassium chloride into NP-containing solutions before evaporation is unacceptable. The structural material of evaporators is 12Cr18Ni10Ti steel. In the presence of chloride ions, the steel is subject to local forms of corrosion, i.e., point corrosion (pitting) and corrosion cracking under the action of stress. To avoid these and other undesirable phenomena, potassium chloride is introduced into evaporated NP-containing pulp before granulation.

In the course of drying, grinding, sorting, and packing of ternary fertilizers, a considerable amount of dust is formed, which should be returned to the process cycle to make the process economically and environmentally acceptable.

A portion of dust is catched by scrubbers sprayed with condensed process steam. The resulting dilute solutions of fertilizers should be evaporated prior to returning to the process cycle.

Therefore, it is necessary to examine whether 12Cr18Ni10Ti steel evaporators used for preparing binary nitrogen–phosphorus (NP) fertilizers can be used for the evaporation of dilute solutions containing NPK and chloride ions.

In this work, we studied the corrosion of 12Cr18Ni10Ti steel in multicomponent media of various compositions containing chloride ions.

As known, chloride ions inevitably enhance the corrosion activity of solution. This is especially true for pitting corrosion of stainless steels [1–3], which can also undergo a fast corrosion cracking under a stress [4, 5]. For example, solutions containing 0.01, 0.1, and 3.0 wt % sodium chloride at 245–250°C and a 32 kgs mm^{-2} load cause Cr18Ni10B steel samples to degrade in 49.4, 0.6, and 0.8 h, respectively [6]. Other types of anions (phosphate, nitrate, and hydroxide ions) makes solutions less corrosive. For example, 12Cr18Ni10Ti steel evaporators can operate for 8–10 years without repair under the following conditions: reaction mixture containing (g l^{-1}) 120–180 NaOH, 180–200 NaCl, and 0.15–0.25 $NaClO_3$, T = 140–150°C, and P = 4.0–5.0 atm; reaction mixture containing (g l^{-1}) 180–260 NaOH, 140–210 NaCl and 0.35–0.40 $NaClO_3$, T = 120–130°C, and P = 2.5–3.0 atm; reaction mixture containing (g l^{-1}) 230–340 NaOH, 210–75 NaCl, and 0.40–0.80 $NaClO_3$, T = 90–95°C, and P = 620–650 mm Hg [7].

Gorodnichii *et al.* [8] established the boundaries of stability of high-alloy steels (12 compositions) in boiling chloride–nitrate, chloride–sulfate, and chloride–phosphate solutions. These boundaries are mainly determined by the ratio of anion concentrations in a solution and by solution pH. The studied anions were arranged in the following order with respect to the inhibiting effect: PO_4^{3-}, NO_3^-, and SO_4^{2-}.

Uhlig and Revie [1] reported the similar data on the inhibiting effect of different anions. According to the authors' data, the inhibiting effect of the anions decreases in the following order: OH^-, NO_3^-, SO_4^{2-},

1070-4272/04/7504-0579 $27.00 © 2002 MAIK "Nauka/Interperiodica"

Solution compositions and potentials (relative to standard hydrogen electrode) of 12Cr18Ni10Ti steel at 90°C

Component, parameter	Content (wt %) and potential (V) in solution						
	no. 1	no. 2	no. 3	no. 4	no. 5	no. 6	no. 7
NH_4NO_3	8.4	33.4	–	–	8.7	–	–
$NH_4H_2PO_4$	5.9	23.6	–	–	–	–	–
KNO_3	–	–	9.7	30.3	–	–	–
K_3PO_4	–	–	10.0	31.2	–	–	–
KCl	5.8	23.0	5.3	16.5	6.9	6.6	25.4
KOH	–	–	1.0	1.9	–	–	–
pH at 20°C	5.1	3.1	10.5	11.0	5.8	6.2	6.0
E_{cor}	–0.15	0.01	–0.10	–0.54	0.03	–0.03	–0.08
E_{pp}	1.58	1.50	0.70	0.57	1.29	0.31	0.08
E_{rp}	1.22	1.32	0.70	0.55	1.32	0.04	–0.10
ΔE_{pp}	1.73	1.49	0.80	1.09	1.26	0.34	0.16
ΔE_{rp}	1.37	1.31	0.80	1.11	1.29	0.07	–0.02

and ClO_4^-. However, the combined effect of the three anions, PO_4^{3-}, NO_3^-, and Cl^-, has not been studied yet.

EXPERIMENTAL

Initially, corrosion of 12Cr18Ni10Ti steel was studied electrochemically by the method of polarization curves [GOST (State Standard) 9.912–89]. The test samples were polarized in the potentiodynamic mode from the steady-state corrosion potential in the solutions under consideration to determine the bases of pitting resistance.

The 2-mm wires of 12Cr18Ni10Ti steel were glued to a polyvinyl chloride mounting with epoxy resin. The samples were finished with abrasive papers at the grain size decreased gradually to 7–10 μm in final finishing. After finishing, samples were washed with water, degreased with ethyl alcohol, and dried on a filter paper.

The test were performed in a glassy three-electrode cell thermostated at 90°C. Platinum was auxiliary electrode, and a saturated silver chloride electrode was reference (E = 0.201 V relative to standard hydrogen electrode). The polarization curves were taken with a P-5827M potentiostat and a PDP-4-002 two-coordinate plotting potentiometer.

A steel sample was kept in a test solution for 1 h to establish the steady-state corrosion potential E_{cor} and then was anodically polarized at a potential scanning rate of 1 mV s^{-1}. The potential was scanned in the opposite direction after the anode current density reached 0.1 A cm^{-2}.

The pitting potential E_{pp} and the repassivation potential E_{rp} were determined from the direct and inverse polarization curves plotted in the E–log i coordinates [GOST 9.912–89]. The E_{cor}, E_{pp}, and E_{rp} values obtained in three parallel measurements were averaged.

The pitting resistance bases, ΔE_{pp} and ΔE_{rp}, were calculated by the formulas $\Delta E_{pp} = E_{pp} - E_{cor}$, and $\Delta E_{rp} = \Delta E_{rp} - E_{cor}$. The values of the pitting resistance bases allowed determination of the susceptibility of steel to pitting corrosion.

In this work, we used solutions that are formed upon washing of evaporators and treatment of gases to remove dust. The resulting dulite solutions contain all components of complex NPK fertilizers. Evaporation of such solutions yields a valuable ternary fertilizer.

We tested four multicomponent solutions modeling a working medium of production of ternary fertilizers (solution nos. 1 and 3 before evaporation and solution nos. 2 and 4 after evaporation). Three one- and two-component solutions were also studied for comparison. The experimental bases of pitting resistance in the solutions studied are given in the table.

The polarization curves for each solution are shown in Figs. 1a–1g. The following conclusions can be made:

(1) Solutions containing only chloride ions (solution nos. 6 and 7) are rather corrosive. The bases of pitting resistance of 12Cr18Ni10Ti steel in these solutions are very low (Figs. 1a, 1b).

(2) Introduction of nitrate ions into solutions containing chloride ions yields a positive effect. In solution no. 5 the pitting and repassivation potentials

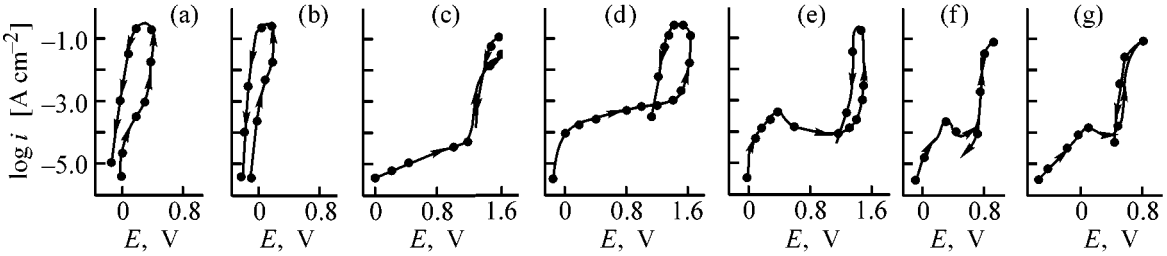

Fig. 1. Direct and inverse polarization curves E–log i of 12Cr18Ni10Ti steel in solution at 90°C. Solution composition (wt %): (a) KCl, 6.6; (b) KCl, 25.4; (c) NH_4NO_3, 8.7; KCl, 6.9; (d) NH_4NO_3, 8.4; $NH_4H_2PO_4$, 5.9; KCl, 5.8; (e) NH_4NO_3, 33.4; $NH_4H_2PO_4$, 23.6; KCl 23.0; (f) KNO_3, 9.7; K_3PO_4, 10.0; KCl, 5.3; KOH, 1.0; (g) KNO_3, 30.3; K_3PO_4, 31.2; KCl, 16.5; KOH, 1.9.

are shifted toward positive values by nearly 1 V (Fig. 1c).

(3) When phosphate and nitrate ions are simultaneously present in chloride solutions, the pitting potentials of 12Cr18Ni10Ti steel are shifted even more toward positive values (soluton nos. 1 and 2), i.e., pitting formation is impeded. At the same time, the extended hysteresis loops on the direct and inverse polarization curves confirm impeded repassivation of the forming pittings (Figs. 1d, 1e), which is undesirable.

(4) Introduction of potassium hydroxide into Cl^--, PO_4^{3-}-, and NO_3^--containing solutions in an amount ensuring conversion of the ammonium to potassium salts, ammonia removal, and maintenance of pH > 9 (solution nos. 3 and 4) results in disappearance of the hysteresis loop (Figs. 1f, 1g). This shows favorable conditions of pitting repassivation and should decrease the local corrosion of 12Cr18Ni10Ti steel in the given solutions.

To confirm results obtained by electrochemical method, ringlike samples with a welded seam made of 12Cr18Ni10Ti steel were placed in flasks with a reflux condenser and subjected to corrosion in solution nos. 1–4 at bp 140–160°C for 400 h. After completing tests, the overall corrosion rate was determined gravimetrically.

Solution no.	1	2	3	4
v, mm year^{-1}	0.001	4.0	0.001	0.001

The corrosion tests showed that, upon evaporation of dilute chloride-containing solutions of ternary fertilizers containing NH_4^+ and Cl^- ions at pH from 3 to 5, the corrosion activity of solutions increased by three orders of magnitude (solution no. 2). Thus, evaporation of dilute chloride-containing solutions of ternary fertilizers can cause considerable corrosion damage of evaporators made of 12Cr18Ni10Ti steel.

CONCLUSION

With potassium hydroxide added to dilute chloride-containing solutions of the NPK ternary fertilizers in amounts ensuring removal of ammonia and at pH above 9, the corrosion effect of these solutions is decreased considerably, which allows their evaporation to be performed in 12Cr18Ni10Ti steel apparatus.

REFERENCES

1. Uhlig, H.H. and Revie, R.W., *Corrosion and Corrosion Control. An Introduction to Corrosion Science and Engineering*, New York: Wiley, 1963.
2. Klinov, I.Ya., *Korroziya khimicheskoi apparatury i korrozionnostoikie materialy* (Corrosion of Chemical Equipment and Corrosion-Resistant Materials), Moscow: Mashgiz, 1960.
3. Man, H.C. and Gabe, D.K., *Metal Corrosion, Proc. 8th Int. Congr., 7th Congr. of Eur. Federation of Corrosion (111th Event)*, Mainz, 6–11 Sept. 1981. Frankfurt-on-Main, 1981, vol. 1, pp. 163–167.
4. Kolesnikov, V.A., Miroshnikov, N.A., and Benzhakov, L.M., *Tekh. Nauki* (Alma-Ata), 1975, no. 18, pp. 167–170.
5. Desjardins, D., Duiggali, M., and Petit, M.C., *Mem. Etud. Sci., Rev. Met.*, 1981, vol. 78, no. 5, pp. 233–241.
6. Sukhotin, A.M. and Zotikov, V.S., *Soprotivlenie materialov* (Materials Resistance), Leningrad: Khimiya, 1975.
7. Sukhotin, A.M. and Labutin, A.L., *Korroziya i zashchita khimicheskoi apparatury* (Corrosion and Protection of Chemical Equipment), Leningrad: Khimiya, 1972, vol. 6.
8. Gorodnichii, A.P., Rozenblyum, R.G., Khabarova, E.V., *et al., Khim. Prom–st.*, 1990, no. 2, pp. 34–37.

Russian Journal of Applied Chemistry, Vol. 75, No. 4, 2002, pp. 582–584. Translated from Zhurnal Prikladnoi Khimii, Vol. 75, No. 4, 2002, pp. 596–598.
Original Russian Text Copyright © 2002 by Subbotin, Vorob'eva, Gudkov, Yakerson, Kustov.

CATALYSIS

Temperature Hysteresis in CO Oxidation on Copper Oxide Catalyst Applied to a Steel Gauze

A. N. Subbotin, M. P. Vorob'eva, B. S. Gudkov, V. I. Yakerson, and L. M. Kustov

Zelinsky Institute of Organic Chemistry, Russian Academy of Sciences, Moscow, Russia

Received November 21, 2001

Abstract—The temperature hysteresis during the heterogeneous catalysis was studied by an example of model reaction of CO oxidation on copper oxide catalyst applied to a stainless steel gauze.

Over several years, we have been developing a concept that the local overheating of active centers is the main process responsible for the temperature hysteresis in heterogeneous catalysis [1–3]. Such overheating is due to impeded removal of heat from the active centers in the course of exothermic reactions.

Recently, the methods of preparation were proposed and the properties were studied of new heterogeneous catalysts based on a metal gauze [4, 5]. These catalysts, containing supporting and (or) catalytically active metals immobilized on the surface of stainless steel gauze, have a number of advantages, of which the most important is the high heat-exchange coefficient. This makes such catalysts especially promising for reactions with a large positive heat effect.

Here we attempted to use such gauze catalysts to confirm the hypotheses explaining the temerature hysteresis in terms of the local overheating of active centers. The test was performed by an example of the model reaction of carbon monoxide oxidation on copper-containing catalysts.

EXPERIMENTAL

A stainless steel gauze made of a 50-μm-thick wire was used as metallic support of a catalyst. Prior to depositing oxide layer, the gauze surface was treated electrochemically and then by chemical etching.

Two types of catalyst samples were prepared: (1) a steel gauze to which copper oxide was applied directly (CuO/gauze) and (2) a stainless steel gauze to which aluminum oxide and then copper oxide were applied (CuO/Al_2O_3/gauze).

The CuO/gauze catalyst was prepared by electrochemical deposition of copper from a $CuSO_4$ solution with subsequent oxidation. The deposition current was 500 mA. Two parallel copper plates were cathode. The metallic copper was oxidized by calcination in air (flow rate 3 l h^{-1}) at 550°C for 4 h. After calcination, the CuO/gauze sample contained 140 mg CuO.

The CuO/Al_2O_3/gauze catalyst was supported with a steel gauze preliminarily coated with Al_2O_3. Aluminum oxide was deposited electrophoretically [4]. For this purpose, a gauze cathode was plunged into aluminum hydroxide sol containing 5.5 g l^{-1} AlO(OH). The deposition was performed at direct current and a 30 V voltage for 2 min. After that, the sample was dried at room temperature for 24 h and calcined at 550°C for 2 h. Copper oxide was introduced by impregnation of the support with a $Cu(NO_3)_2$ solution followed by calcination in air flow at 550°C for 2 h. The resulting sample contained 25 mg CuO and 100 mg Al_2O_3.

The copper–aluminum–calcium catalyst containing 20% CuO and 80% Talum, a mixture of calcium mono- and dialuminates [3, 6], and platinum foil were used for comparison.

Carbon monoxide was oxidized with atmospheric oxygen in an automated catalytic installation with forced circulation of the reaction mixture at various CO : O_2 ratios and a total flow rate of 8 l h^{-1}. The reactor temperature was raised and lowered in small steps, and time at which the system was kept at each new temperature was sufficient to attain a constant composition of the reaction mixture (commonly, up to 10 min).

The CO content in the reaction mixture was determined by gas chromatography (column 1.5 m long and 2 mm in diameter, packed with a Porapak Q).

1070-4272/02/7504-0582 $27.00 © 2002 MAIK "Nauka/Interperiodica"

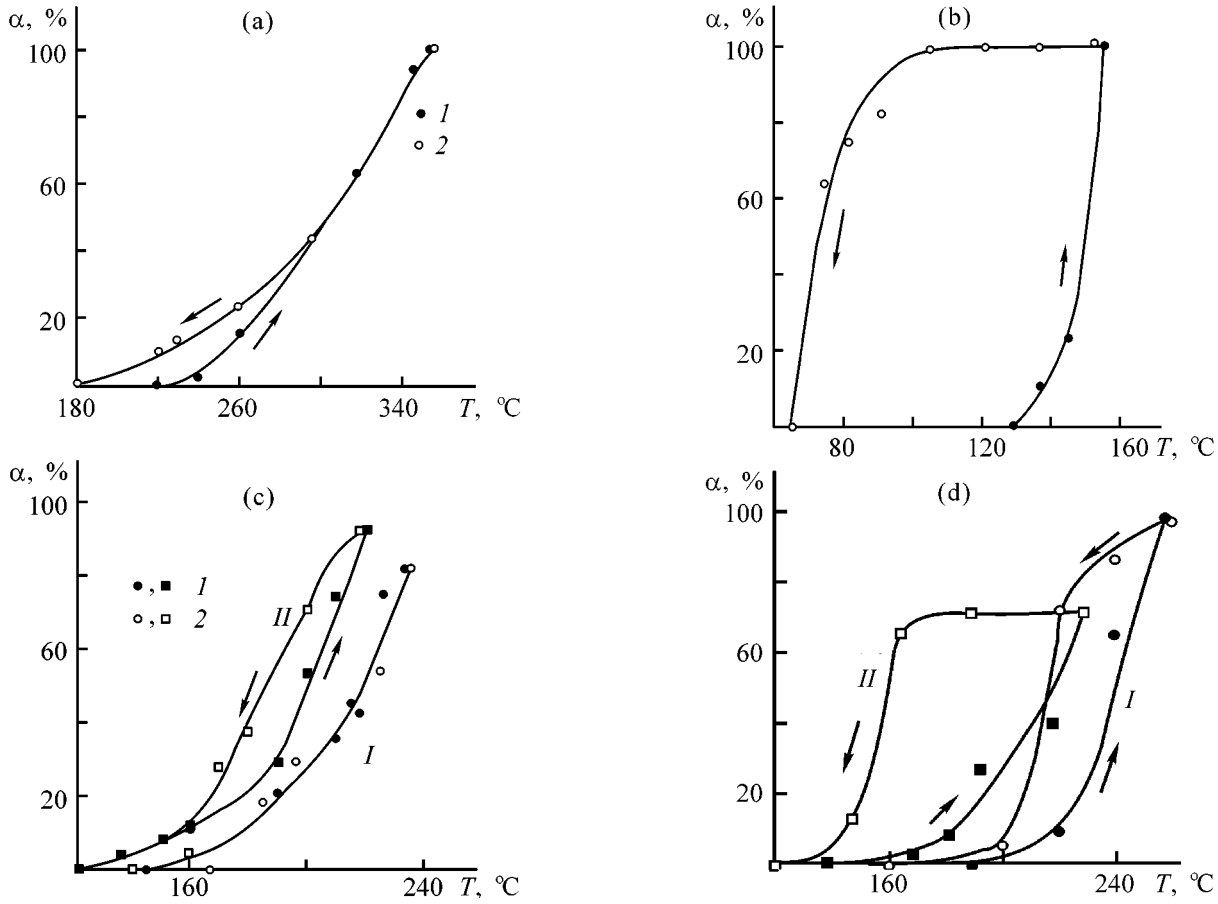

Fig. 1. Degree of CO oxidation α vs. temperature *T* on (a) Pt foil, (b) CuO/Talum, (c, d) CuO/gauze (*I*) and CuO/Al_2O_3/gauze (*II*) catalysts. (*1*) Heating and (*2*) cooling. CO content (%): (a) 7, (b) 14, (c) 11 (*I*) and 10 (*II*), (d) 32 (*I*) and 38 (*II*).

According to the temperature hysteresis concepts, the heat released from the active center of a catalyst in the course of exothermic reaction commonly has no time to dissipate completely. The major dissipation channel is heat transfer through the catalytic mass in the reactor. However, in dispersed solids, to which belongs the majority of catalysts, the conduction of heat via contact is impeded not only by the support but also by the low-active mass of the catalyst itself, which contains rather rarely "interspersed" active centers. As a result, the local temperature of an active center becomes higher than the average temperature measured by a thermocouple in the catalyst bed. Thus, the true reaction temperature under these conditions is higher than its measured value considered as reaction temperature. When the supply of heat from the outside is stopped or limited, i.e., reactor starts cooling, the true temperature of an active center remains higher than the measured temperature. As a result, the descending branch (cooling) on the temperature dependence is shifted to the left with respect to the ascending branch, i.e., an anticlockwise hysteresis loop appears. In light of this concept, the lower the heat conductivity of the catalytic mass under other equal conditions, the more marked the hysteresis. Bulk metals are known to have the highest heat conductivity, and, consequently, they should have the lowest hysteresis effect.[1]

Indeed, during the oxidation of CO on platinum foil, the ascending and descending branches of the temperature dependence diverge only slightly (Fig. 1a). At the same time, for the copper–aluminum–calcium catalyst the hysteresis loop is quite considerable (Fig. 1b).

Evidently, applying catalytically active component to a steel gauze should facilitate removal of heat from the active centers and, consequently, decrease the hysteresis effect. With a heat-insulating layer of aluminum oxide applied between copper oxide and steel gauze, the hysteresis effect should be more considerable.

Figure 1c shows the temperature dependences of the degree of CO conversion on the CuO/gauze and

[1] This concept is developed in more detail in [1, 2].

CuO/Al_2O_3/gauze samples at the close compositions of the reaction mixture. As seen, on the first of them the hysteresis is completely absent, whereas on the second one, a hysteresis (through insignificant) is observed.

Markedly different dependences were also obtained on the same samples at other composition of the reaction mixture, namely, at CO excess (Fig. 1d). It was shown previously [7] that the growth of the CO content extends the hysteresis loop. In line with this, the hysteresis loops are, as a whole, broader in Fig. 1d than in Fig. 1c. At the same time, even in the latter case, a heat-isolating film of aluminum oxide between copper oxide and steel gauze increases the hysteresis effect.

Thus, the results obtained confirm once again that the local overheating of active centers by excess heat released in an exothermic reaction is the main cause of temperature hysteresis in heterogeneous catalysis. These results also show that steel gauze catalytic systems ensure efficient heat release from the reaction zone, and, consequently, create the more favorable conditions of the process.

CONCLUSIONS

(1) The temperature hysteresis in CO oxidation with atmospheric oxygen on copper oxide applied to a steel gauze is more pronounced in the case when a heat-insulating layer of aluminum oxide is present between copper oxide and the gauze. This confirms the concept that the local overheating of active centers is the main cause of the temperature hysteresis.

(2) The catalyst applied to a gauze made of steel wire ensures efficient heat removal in an exothermic reaction and creates more favorable process conditions.

ACKNOWLEDGMENTS

The work was financial by supported by the Russian Foundation for Basic Research (project no. 00-03-032 169).

REFERENCES

1. Subbotin, A.N., Gudkov, B.S., and Yakerson, V.I., *Izv. Ross. Akad. Nauk, Ser. Khim.*, 2000, no. 8, pp. 1379–1385.
2. Yakerson V.I., Gudkov B.S., and Subbotin A.N., *Russ. J. Phys. Chem.*, 2000, vol. 74, suppl. 3, pp. S498–S505.
3. Subbotin, A.N., Gudkov, B.S., Yakerson, V.I., *et al.*, *Zh. Prikl. Khim.*, 2001, vol. 74, no. 9, pp. 1463–1465.
4. Vorob'eva, M.P., Greish, A.A., Ivanov, A.V., and Kustov, L.M., *Appl. Catal. A: General*, 2000, vol. 199, pp. 257–261.
5. Vorob'eva, M.P., Greish A.A., Stakheev, A.Yu., *et al.*, *Stud. Surf. Sci. Catal.*, 2000, vol. 130B, pp. 1127–1132.
6. Yakerson, V.I., and Golosman, E.Z., *Usp. Khim.*, 1990, vol. 59, pp. 778–806.
7. Gudkov, B.S., Subbotin, A.N., Dykh, Zh.L., and Yakerson, V.I., *Dokl. Ross. Akad. Nauk*, 1997, vol. 353, no. 3, pp. 347–349.

Russian Journal of Applied Chemistry, Vol. 75, No. 4, 2002, pp. 585–588. Translated from Zhurnal Prikladnoi Khimii, Vol. 75, No. 4, 2002, pp. 599–602.
Original Russian Text Copyright © 2002 by Mamedov, Gagarin, Kharlampidi.

ORGANIC SYNTHESIS AND INDUSTRIAL ORGANIC CHEMISTRY

Effect of Acetophenone on Liquid-Phase Dehydration of Dimethylphenylmethanol

E. M. Mamedov, M. A. Gagarin, and Kh. E. Kharlampidi

Kazan State Technological University, Kazan, Tatarstan, Russia

Received September 25, 2001

Abstract—The acid-catalyzed liquid-phase dehydration of dimethylphenylmethanol to α-methylstyrene was considered. The scheme and mathematical model of liquid-phase dehydration of dimethylphenylmethanol were proposed, and the effect of acetophenone on the reaction kinetic parameters was studied.

Combined production of phenol and acetone by the cumene method is a widely used process of chemical technology [1]. It yields, along with the target products, many by-products, including dimethylphenylmethanol (DMPM). DMPM is formed through nonselective consumption of cumene hydroperoxide in the stages of cumene oxidation and acid decomposition of hydroperoxide into phenol and acetone. The presence of DMPM in the reaction mixture leads to formation of products impairing the quality of commercial phenol.

As noted in [2–7], DMPM can be dehydrated to obtain α-methylstyrene (α-MS), which is the initial monomer for production of various polymeric materials.

At present, α-MS is prepared in Russia mainly by high-temperature catalytic dehydrogenation of cumene [8]. This process is very power-consuming. Therefore, development and promotion of a process for α-MS production from DMPM, which finds no commercial application yet, is of practical interest.

Dehydration of DMPM to α-MS can be performed in both gas and liquid phases. We consider here the liquid-phase process as the most cost-efficient.

EXPERIMENTAL

DMPM obtained by base decomposition of cumene hydroperoxide was used as a raw material [1]. The sample contained (wt %) DMPM 91.7, acetophenone (ACP) 7.6, α-MS 0.53, cumene 0.28, and cumene hydroperoxide 0.50. A 0.5 M solution of sulfuric acid in acetic acid was taken as catalyst. Kinetic studies were performed in a temperature-controlled glass cell equipped with a magnetic stirrer. During the reaction, an inert gas (nitrogen) was bubbled through the reaction mixture. The reaction course was monitored chromatographically by the concentrations of the initial substances and reaction products [9].

Initially cumene was taken as a reaction medium, since it was the initial substance in DMPM synthesis, which eliminates the stage of additional purification of alcohol.

It is commonly believed [10, 11] that the acid-catalyzed dehydration of alcohols in the liquid phase proceeds via formation of carbocation by the scheme

$$\mathrm{ROH} + \mathrm{H^+} \rightleftarrows \mathrm{ROH_2} \rightleftarrows \mathrm{R^+} + \mathrm{H_2O} \rightleftarrows \text{Olefin} + \mathrm{H_2O} + \mathrm{H^+}, \quad (1)$$

where R is a hydrocarbon radical.

It was found experimentally that DMPM dehydration in cumene decelerates in the course of time (Fig. 1), which is probably due to inhibition of the catalyst by water formed, rather than to attainment of a chemical equilibrium. Special experiments showed that α-MS is not hydrated under these conditions. Since water exhibits higher proton affinity than the other reaction components, its accumulation in the system can cause resolvation of protons with water and, as a result, a decrease in the catalyst activity.

In experiments with various initial DMPM concentrations (Fig. 1), we found that the DMPM dehydration is first-order with respect to the substrate and that the reaction selectivity with respect to α-MS is 100%. The use of special procedures [12] and analysis of the

1070-4272/02/7504-0585 $27.00 © 2002 MAIK "Nauka/Interperiodica"

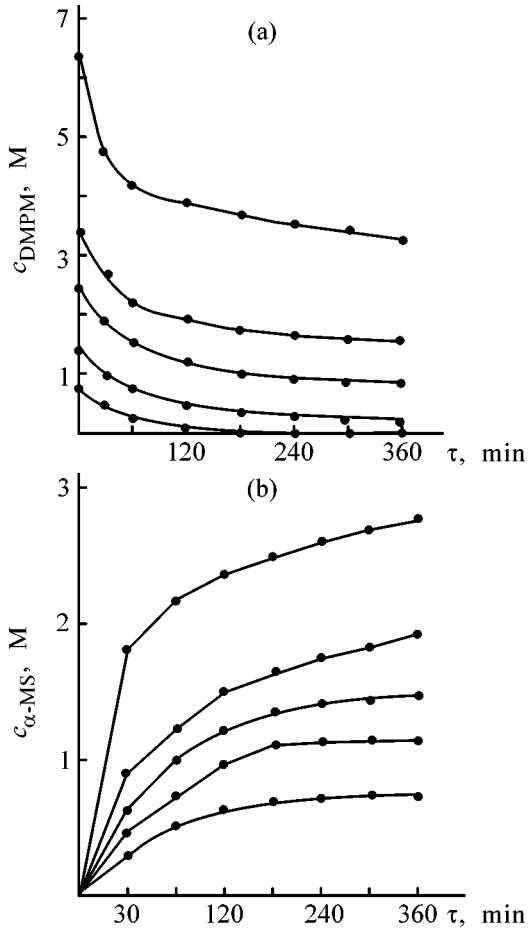

Fig. 1. Kinetic curves of (a) DMPM dehydration and (b) α-MS accumulation in cumene at various initial DMPM concentrations. $c_{H_2SO_4} = 5 \times 10^{-3}$ M, 80°C. (c_{DMPM}) DMPM concentration, ($c_{\alpha\text{-MS}}$) α-MS concentration, and (τ) time.

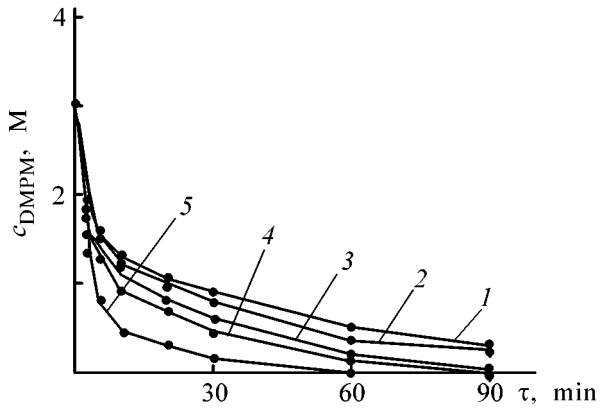

Fig. 2. Effect of the ACP concentration on the kinetics of DMPM dehydration in cumene. $c^0_{DMPM} = 3$, $c_{H_2SO_4} = 5 \times 10^{-3}$ M, 110°C; the same for Figs. 3, 4. (c_{DMPM}) DMPM concentration and (τ) time; the same for Fig. 5. ACP concentration (M): (*1*) 0.28, (*2*) 0.57, (*3*) 1.50, (*4*) 2.10, and (*5*) 5.0.

kinetic data allowed us to suggest a scheme of DMPM conversion, which takes into consideration the stage of catalyst inhibition:

$$\text{DMPM} + \text{cat}_a \underset{k_{-1}}{\overset{k_1}{\rightleftarrows}} [X] \xrightarrow{k_2} \alpha\text{-MC} + H_2O + \text{cat}_a,$$
$$\text{cat}_a \xrightarrow{k_i} \text{cat}_i, \qquad (2)$$

where cat_a and cat_i are the active and inactive forms of the catalyst; [X] is the intermediate; k_1 and k_{-1} are constants of [X] formation and decomposition, respectively; k_2 is the rate constant of decomposition of [X] with the formation of reaction products; and k_i is the rate constant of catalyst inhibition.

When conversion of [X] into the reaction products is the limiting stage, the concentration of the active form of the catalyst is described by the equation

$$c^a_{cat} = c^0_{cat} \exp(-k_1\tau), \qquad (3)$$

where c^a_{cat} is the concentration of the active form of the catalyst, c^0_{cat} is the initial concentration of the catalyst, and τ is the reaction time.

Thus, the DMPM concentration c_{DMPM} changes in time by the equation

$$-\frac{dc_{DMPM}}{d\tau} = k_{app} c_{DMPM} \exp(-k_i\tau), \qquad (4)$$

where k_{app} is the apparent rate constant defined by

$$k_{app} = k_2 \frac{k_1}{k_{-1}} c^0_{kat}. \qquad (5)$$

Integration of Eq. (4) gives a kinetic equation for DMPM in the integral form, which adequately describes all the experimental data:

$$c_{DMPM} = c^0_{DMPM} \exp\left\{\frac{k_{app}}{k_i}[\exp(-k_i\tau) - 1]\right\}, \qquad (6)$$

where c^0_{DMPM} is the initial DMPM concentration.

Since ACP always accompanies DMPM in phenol and acetone production, it was interesting to study the effect of ACP on DMPM dehydration. ACP, as a more polar solvent than cumene, must undoubtedly affect the process.

To reveal this effect, we performed experiments at 110°C, varied initial ACP concentration, and equal other conditions. It was found that ACP is not consumed; its concentration determined chromatographically remained unchanged. The kinetics of the DMPM dehydration in cumene with various ACP additives is shown in Fig. 2, and the constants calculated by

Eq. (6) and the initial reaction rates v_0 are listed in the table. The initial reaction rates were determined by differentiation of the kinetic curves. The selectivity of DMPM dehydration under these conditions was also 100%.

As seen, the initial reaction rate and the degree of DMPM conversion grow with increasing ACP concentration in the system, which is probably due to a change in the solvent properties, namely, in its dielectric constant.

The dielectric constant of a mixture of substances can be determined from the equation [13]

$$\log \varepsilon = n_1 \log \varepsilon_1 + n_2 \log \varepsilon_2 + \ldots + n_i \log \varepsilon_i, \quad (7)$$

where ε_i is the dielectric constant of ith component and n_i is the mole fraction of ith component of the mixture.

Using Eq. (7), we calculated ε of a mixture of cumene and ACP and correlated the results with the reaction rate. Figure 3 shows the dependence of the apparent dehydration rate constant on ACP concentration, and Fig. 4, the dependence of $\log k_{app}$ on the Kirkwood parameter (KP), which characterizes the solvent polarity [13] and is defined by

$$KP = (\varepsilon - 1)/(2\varepsilon + 1). \quad (8)$$

As seen (Fig. 3), the reaction rate grows with increasing solvent polarity.

In accordance with the classic Arrhenius theory of reaction kinetics, a certain energy barrier must be overcome before conversion of the initial substances into the reaction products. The solvent can change the activation Gibbs energy due to different degrees of solvation of the initial reactants and the activated complex [13]. The degree of solvation is determined by the electric charge of the reacting species: it grows with increasing charge. Reactions in which the activated complex has higher charge density (is more polar) than the initial molecule are accelerated in more polar solvents.

A similar trend is observed in dehydration of DMPM at its various initial concentrations in ACP (Fig. 5): the reaction is accelerated with increasing solvent polarity (Fig. 6). However, the dependence of the apparent rate constant on KP is nonlinear, which suggests the effects of the specific and nonspecific solvation. The rate constants of DMPM dehydration in ACP calculated by Eq. (6) and the initial reaction rates are listed in the table.

Kinetic parameters of DMPM dehydration $c_{H_2SO_4} = 5 \times 10^{-3}$ M, 110°C

c^0_{DMPM}	c_{ACF}	$v_0 \times 10^3$, mol l^{-1} s^{-1}	$k_{app} \times 10^3$	$k_i \times 10^3$	DMPM conversion, %
M			s^{-1}		
Dehydration in cumene					
3	0.28	5.656	3.525	3.225	87
3	0.57	5.698	3.525	2.933	90
3	1.50	6.241	4.176	2.979	98
3	2.10	6.659	4.650	2.901	95
3	5.00	8.446	6.067	2.231	99
Dehydration in acetophenone					
0.71	a*	15.000	34.00	7.537	100
1.47	a	13.000	13.000	2.917	100
2.96	a	9.453	5.755	1.933	99
4.32	a	11.000	4.311	1.674	98
5.14	a	4.194	4.153	3.581	80
6.38	a	4.119	3.384	4.334	65

* Acetophenone as solvent.

Thus, we can assume that, under conditions of DMPM dehydration, the activated complex is more polar than the initial DMPM molecule. This is confirmed by quantum-chemical calculations of the DMPM molecule and transition complex (protonated DMPM), which were performed using the MORAC program. Calculations showed that dipole moments of

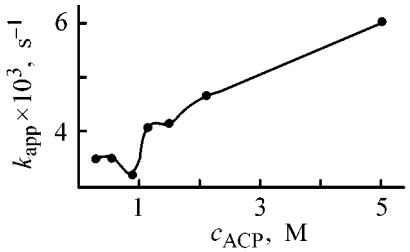

Fig. 3. Apparent rate constant of DMPM dehydration k_{app} in cumene vs. ACP concentration.

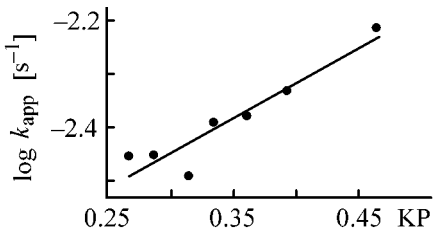

Fig. 4. Effective rate constant of DMPM dehydration k_{app} in cumene with various ACP content vs. Kirkwood parameter KP.

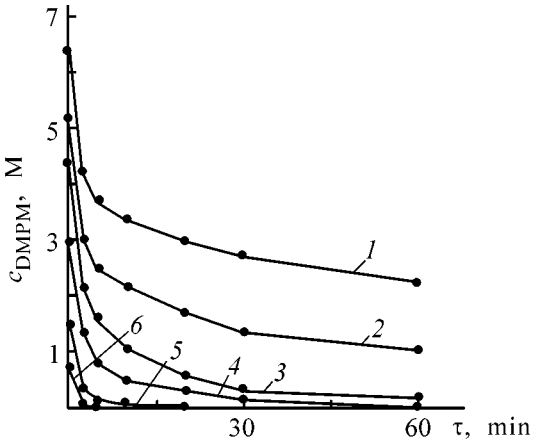

Fig. 5. Kinetic curves of DMPM dehydration in ACP. $c_{H_2SO_4} = 5 \times 10^{-3}$ M, 110°C; the same for Fig 6. Initial concentration of DMPM (M): (*1*) 6.38, (*2*) 5.14, (*3*) 4.32, (*4*) 2.96, (*5*) 1.47, and (*6*) 0.71.

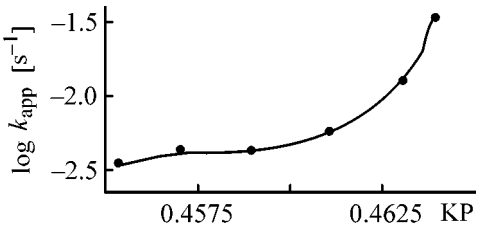

Fig. 6. Apparent rate constant of DMPM dehydration k_{app} in ACP vs. Kirkwood parameter KP.

DMPM and protonated DMPM are 1.549 and 1.915 D, respectively. This fact, combined with the above results, accounts for the acceleration of DMPM dehydration in the presence of acetophenone as a more polar compound.

CONCLUSIONS

(1) The kinetics of dimethylphenylmethanol dehydration in cumene and in acetophenone was studied; it was shown that acetophenone accelerates dehydration.

(2) The rate of dimethylphenylmethanol dehydration in acetophenone is higher than that in cumene under the same conditions.

(3) Dehydration of dimethylphenylmethanol in both cumene and acetophenone is characterized by 100% selectivity; its conversion reaches 87% in cumene and 99% in acetophenone at substrate concentration of 3 M and 110°C.

REFERENCES

1. Kruzhalov, B.D. and Golovanenko, B.I., *Sovmestnoe proizvodstvo fenola i atsetona* (Combined Production of Phenol and Acetone), Moscow: Goskhimizdat, 1963.
2. CSSR Patent 248562B1.
3. JPN Patent 61293936A2.
4. Polyanskii, N.G. and Polyanskaya, N.L., *Tr. Tambovsk. Inst. Khim. Mashinostr.*, 1969, no. 3, pp. 84–91.
5. GDR Patent 161239.
6. Zuolin, Z. and James, H.E., *J. Org. Chem.*, 1996, vol. 61, no. 1, pp. 324–328.
7. US Patent 5245090.
8. Safronov, V.S., Bogomolova, G.Ya., Smirnov, B.Yu., *et al.*, *Khim. Prom–st.*, 1991, vol. 31, no. 8, pp. 461–468.
9. McNair, H.M. and Bonelli, E.J., *Basic Gas Chromatography*, Walnut Creek, CA: Varian Aerograph, 1967.
10. Fiezer, L.F. and Fiezer, M., *Advanced Organic Chemistry*, New York: Reinhold, 1962; Fiezer, L.F. and Fiezer, M., *Current Topic in Organic Chemistry*, New York: Reinhold, 1964.
11. Lebedev, N.N., Manakov, M.N., and Shvets, V.F., *Teoriya khimicheskikh protsessov osnovnogo organicheskogo i neftekhimicheskogo sinteza* (Theory of Chemical Processes of Basic Organic and Petrochemical Synthesis), Moscow: Khimiya, 1984.
12. Shmidt, R. and Sapunov, V.N., *Non-Formal Kinetics*, Weinheim: Chemie, 1982.
13. Reichardt, Ch., *Solvents and Solvent Effects in Organic Chemistry*, Weinheim: VCH, 1988.

Russian Journal of Applied Chemistry, Vol. 75, No. 4, 2002, pp. 589–597. Translated from Zhurnal Prikladnoi Khimii, Vol. 75, No. 4, 2002, pp. 603–611.
Original Russian Text Copyright © 2002 by Kalnin'sh.

MACROMOLECULAR CHEMISTRY AND POLYMERIC MATERIALS

Thermal Electronic Excitation of Perfluoroolefins

K. K. Kalnin'sh

Institute of Macromolecular Compounds, Russian Academy of Sciences, St. Petersburg, Russia

Received December 24, 2001

Abstract—The electronic structure of the known intermediates of perfluoroolefins was analyzed from the standpoint of thermal electronic excitations. The calculated (*ab initio* DZ) energies of the perpendicular triplet state T_1 of the perfluorolefins are compared with the experimental enthalpies of formation of the intermediates. A new mechanism of cyclodimerization of tetrafluoroethylene is proposed, including its thermal excitation into the lowest triplet state as the limiting stage.

Tetrafluoroethylene (TFE) and its fluorinated analogs are used as initial monomers in preparing fluorinated polymers and resins which find extensive industrial and agricultural application. Of great importance for understanding of the mechanism of polymerization and various chemical transformations of monomers is elucidation of the nature of elementary chemical processes and the structure of intermediates species. Buravtsev *et al.* [1–3] studied systematically TFE C_2F_4, hexafluoropropylene C_3F_6, perfluoro-1-butene 1-C_4F_8, perfluoro-2-butene 2-C_4F_8, and a number of other fluorinated derivatives. They revealed extremely interesting properties of these compounds, exceeding ethylene and its derivatives in thermal stability (at 700–1500 K). Buravtsev and Kolbanovskii heat-treated perfluoroethylenes to "prepyrolysis" temperatures in the gas phase in a free-plunger adiabatic compression setup and reported existence of previously unknown intermediates. It was found that, kinetically, the forward and backward reactions of formation of the intermediates are first-order reactions, which suggests the monomolecular character of the reactions [6]. Therefore, the chemical formulas of the intermediates are identical to those of the initial compounds; they were designated as $C_2F_4^*$, $C_3F_6^*$, 1-$C_4F_8^*$, 2-$C_4F_8^*$, and *iso*-$C_4F_8^*$.

A kinetic spectroscopic study revealed two absorption bands of the intermediates in the UV and visible regions, whose positions (nm) are as follows: 236.5 and 500 for $C_2F_4^*$, 240 and 477.5 for $C_3F_6^*$, and 242.5 and 460 for 1-$C_4F_8^*$. These positions differ from those for the initial compounds C_2F_4 (188 nm) and C_3F_6 (185 nm). Studies at different temperatures showed that the new bands are actually those of true intermediates, rather than "hot bands" in the spectra of perfluoroolefins. Special experiments on generating the same intermediates from different compounds showed that the intermediates directly participate in formation of new chemical compounds. For example, the TFE intermediate $C_2F_4^*$ degrades into two difluorocarbenes (DFCs) $:CF_2$ which add to $C_2F_4^*$ to give hexafluoropropylene:

$$C_2F_4 \rightleftarrows C_2F_4^* \rightleftarrows :CF_2 + :CF_2, \quad (1)$$

$$C_2F_4^* + :CF_2 \rightleftarrows C_3F_6^* \rightleftarrows C_3F_6. \quad (2)$$

Elucidation of the nature of these remarkable species, prefluoroolefin intermediates, is of much scientific interest. Now, there is no doubt that they reflect certain common properties of reactive species and, in the case of fluoroolefins, directly participate in chemical transformations of molecules.

Buravtsev and Kolbanovskii characterize the nature of these species as follows [13]: "The $C_2F_4^*$, $C_3F_6^*$, 1-$C_4F_8^*$, and 2-$C_4F_8^*$ intermediates formed in the gas phase upon heating the corresponding perfluoroolefins are the previously unknown, lowest excited singlet states of these perfluoroolefins, since formation of the triplet states of perfluoroolefins in the gas-phase thermal monomolecular reactions is spin-forbidden." In the same work, Buravtsev and Kolbanovskii state further that "the structures of 1,2-biradicaloids $C_2F_4^*$, $C_3F_6^*$, 1-$C_4F_8^*$, 2-$C_4F_8^*$, and *iso*-$C_4F_8^*$, revealed in light absorption studies, remain to be proved both experimentally and theoretically." Clearly, the scheme proposed by these authors (see above) does not fully disclose the properties of the intermediates.

1070-4272/02/7504-0589 $27.00 © 2002 MAIK "Nauka/Interperiodica"

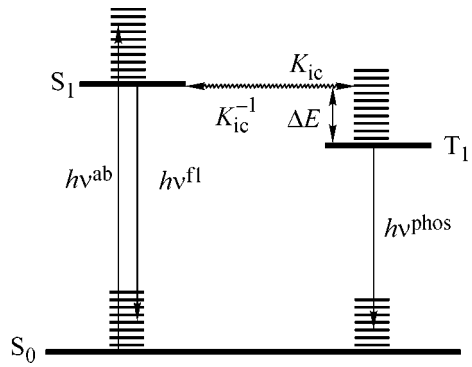

Fig. 1. Energy scheme of thermally activated delayed fluorescence.

In this work, we explain the unique experimental data reported by Buravtsev and Kolbanovskii from another standpoint based on the concept of thermal electronic excitation in chemical reactions as a unique physicochemical process [14]. The assumed triplet nature of the intermediates is supported by the results of nonempirical quantum-chemical calculations. In [15–17], we demonstrated that the triplet excited molecules and complexes are involved in polymerization/depolymerization reactions.

The *ab initio* quantum-chemical calculations were carried out with PC GAMESS routine, version 5.4, in the 6-31G* basis. Also, *ab initio* calculations in the DZ basis were carried out by the HyperChem routine, issue 6.0. The same routine was utilized for optimization of the molecular geometry by the AM1 method, whose results served as the initial approximation for the *ab initio* calculations. The singlet excited states were optimized by AM1 semiempirical methods, using WinMOPAC-2.0 routine. The triplet state energies were calculated in the spin-unrestricted Hartree–Fock approximation, as the differences of the total energies (*ab initio*) or heats of formation (semiempirical methods) of the molecules in the triplet and singlet configurations.

The species with unpaired electrons were additionally characterized by the spin population S_p, which is essentially the difference of the charge densities of alpha and beta electrons. The electronic absorption spectra of the initial olefin molecules and their electronically excited species were calculated by the ZINDO/S semiempirical method (HyperChem-6.0 routine).

Thermal population of the triplet states. In [14], we developed a concept stating that the elementary processes involved in cleavage and formation of a chemical bond are underlain by electronic (thermal-, electric-, or mechanical-) excitation as a fundamental physicochemical process. Therefore, elucidation of the nature of thermally activated intermediates of TFE and its derivatives is clearly related to the problem of thermal electronic excitation of molecules and molecular complexes, which is essentially the population of electronic states.

By contrast to the population of electronic states (forward process), the degradation of electronic energy (reverse process) can be studied in detail. For example, Hunter *et al.* [18] studied degradation of the electronic energy of the triplet state of benzene, 40 000 cm^{-1}, by examining the optoacoustic effect. They showed that, after the excitation event takes place, the electronic energy is transferred to more than ten neighboring molecules, thereby exciting stretching vibrations of the C–H bonds with a frequency of about 3000 cm^{-1}. This is followed by vibrational relaxation (V–V) at a rate of 5×10^{-9} s atm. The vibrational and translational energy exchange (V–T process) proceeds for the lowest-frequency vibrations of benzene, 404 cm^{-1}, at a tenfold lower rate.

Importantly, the exchange efficiency depends on the energy separating the vibrational states [19]. For nonradiative transitions from excited S and T levels, the transition rate is inversely proportional to the energy difference between the $v = 0$ levels of the states involved [20, 21]. This is accounted for by the fact that the rate of a nonradiative electronic transition is determined by the vibrational overlap integral, which is the smaller, the greater the separation between the initial and final states. The same law must be valid for the rates of transitions to higher energy levels.

The restriciton following from the spin exclusion of transitions between the states with different multiplicities (S and T), which is almost strictly obeyed in the case of photoexcitation, is lifted to a significant extent in the case of thermally activated transitions. This follows from high degradation rates of triplet energy [20]. The fact that thermal S–T transitions are not forbidden is clearly demonstrated by the so-called thermally activated delayed fluorescence (Fig. 1). No fluorescence is observed at low temperatures, since under these conditions only the level of the triplet with $v = 0$ is populated. Thermal activation by ΔE, followed by reverse intercombination $S_1 \leftarrow\sim\sim T_1$, yields excited singlets deactivated by fluorescence quantum emission. The fluorescence-to-phosphorescence intensity ratio is described by the exponential dependence

$$\frac{I_{fl}}{I_{phos}} = \exp\left(\frac{E_S - E_T}{kT}\right), \quad (3)$$

which is suitable for estimating the singlet–triplet splitting. At the same time, the E_S–E_T separation is equal to the difference between the fluorescence and phosphorescence frequencies. A comparison of these parameters for a number of dyes with small singlet–triplet splitting revealed close agreement between the activation energy and the single–triplet splitting derived from spectroscopic data. For example, for Acridine Orange $E_S - E_T$ = 31.4 kJ mol^{-1} and E_a = 29.7 kJ mol^{-1} [22].

Turning back to TFE and its analogs, the above data suggest the following. Contrary to the conclusion made by Buravtsev and Kolbanovskii in [13], the spin exclusion does not act in reality in the case of the $T_1 \leftarrow\!\sim\!\sim S_0$ transition, and the rate of transition between the S_0 and T_1 states is the higher, the smaller the energy separation $E(T_1)$–$E(S_0)$. Upon heating to 700–900 K, TFE molecules in the gas phase undergo electronic transition to the excited triplet state, which is deactivated nonradiatively, $S_0 \leftarrow\!\sim\!\sim T_1$. The fact that the lifetime of the experimentally detected TFE* intermediates and analogs makes milliseconds proves once again their triplet nature. The lifetime of singlet excited states S_1 is significantly shorter, namely, under 10^{-9} s.

The energy of triplet states $E(T_1)$ is always lower than that of singlet states $E(S_1)$ [20], and this is a general conclusion. The $E(S_1)$–$E(T_1)$ energy difference, which is termed the singlet–triplet splitting, is large for π–π^* states (up to 292.6 kJ mol^{-1}) but small for n–π^* and charge-transfer states (20.9–41.8 kJ mol^{-1}). For ethylene C_2H_4, the triplet state energy $E(T_1)$ was estimated at 341.2 kJ mol^{-1} [20] (341.9 kJ mol^{-1} according to *ab initio* 6-31G** calculations for the $T_1 \leftarrow S_0$ vertical transition), and the singlet–triplet splitting, at 289.2 kJ mol^{-1} [20] (242.0 kJ mol^{-1} as calculated by the AM1 semiempirical method).

Triplet nature of the TFE intermediates. In the case of TFE, the T_1 triplet energy is also much lower than the S_1 singlet energy (see the calculated data below). Therefore, the singlet nature of the intermediates of TFE $C_2F_4^*$ and its analogs, suggested in [13], is inconsistent with the known relations between the energies of singlet and triplet levels. Noteworthy, Buravtsev *et al.* [8–11] established the biradical nature of the intermediates from the experimental chemical equilibria. This important conclusion disclosing the high chemical activity of the intermediates is consistent with the triplet hypothesis, but contradicts the concept of the singlet nature of the intermediates. Indeed, excited singlets S_1, having two outer electrons with antiparallel spins, do not exhibit properties of biradicals, unlike triplets having essentially biradical nature responsible for their paramagnetism and high reactivity.

Let us turn to the quantum-chemical calculations for the intermediates, which were inexplicitly criticized by Buravstev and Kolbanovskii in [13]. In the opinion of these authors, their own data presented in that work (in particular, the calculated results for the transition state TS) do not account for the structural features of the intermediates. Buravstev and Kolbanovskii [13] take a traditional approach to the chemical reaction mechanism, describing the reactive states of the molecules by the so-called transition states TS. The point is, however, that the TS calculations in the traditional version do not describe the chemical process adequately. A fundamentally different approach developed in [14] is underlain by the concept stating that the reaction states of the molecules have the meaning of electronic states of molecular systems, which can be studied experimentally. These states are determined as electronically excited relaxed (equilibrium) states of the molecules or their complexes, which have low energies (<1 eV) and, therefore, can be thermally populated.

This makes of special interest the absorption spectra of intermediates of perfluoroolefins, recorded by Buravtsev and Kolbanovskii, as this is a rare, maybe even unprecedented, case of directly observed thermally activated reaction states of molecules at high temperatures (700–1000 K) in the gas phase. It should be noted that most of organic molecules cannot be thermally excited into electronic states because of degradation, which typically begins long before the required temperature is attained. For example, according to [13], the lowest electronic state of TFE has an energy of 75.2 ± 8.4 kJ mol^{-1} (vs. 86.8 kJ mol^{-1} from *ab initio* calculations) and this level can be thermally populated. At the same time, for ethylene C_2H_4 the T_1 energy is almost twice that for TFE, namely, 169.5 kJ mol^{-1} (*ab initio* calculation). In the latter case, the Boltzmann factor $\exp(-\Delta E/RT)$ at 700 K is negligible (10^{-13}), which is responsible for the extremely low population of the level and hence for the very low process rate.

The views concerning the electronic excitation as a necessary stage of a chemical process [14] suggest that the reactive species (intermediate, in terms of [13]) preceding formation/rupture of a chemical bond is a biradical. As applied to the [2 + 2] cyclodimerization reaction of TFE

$$C_2F_4 + C_2F_4 \overset{kT}{\rightleftarrows} C_2F_4^* + C_2F_4 \rightleftarrows C^{\bullet}F_2 + C^{\bullet}F_2\cdots CF_2{=}CF_4 \overset{kT}{\rightleftarrows} C^{\bullet}F_2{-}(C^{\bullet}F_2\cdots C^{\bullet}F_2){-}C^{\bullet}F_2 \rightleftarrows C^{\bullet}F_2{-}CF_2{-}CF_2{-}C^{\bullet}F_2 \overset{kT}{\rightleftarrows} \boxed{F}, \quad (4)$$

this means that the formation of stable cyclobutane $\boxed{F}$ is preceded by a number of radical stages, each involving thermal electronic excitation, and CF_2CF_2 does not directly add to CF_2CF_2:

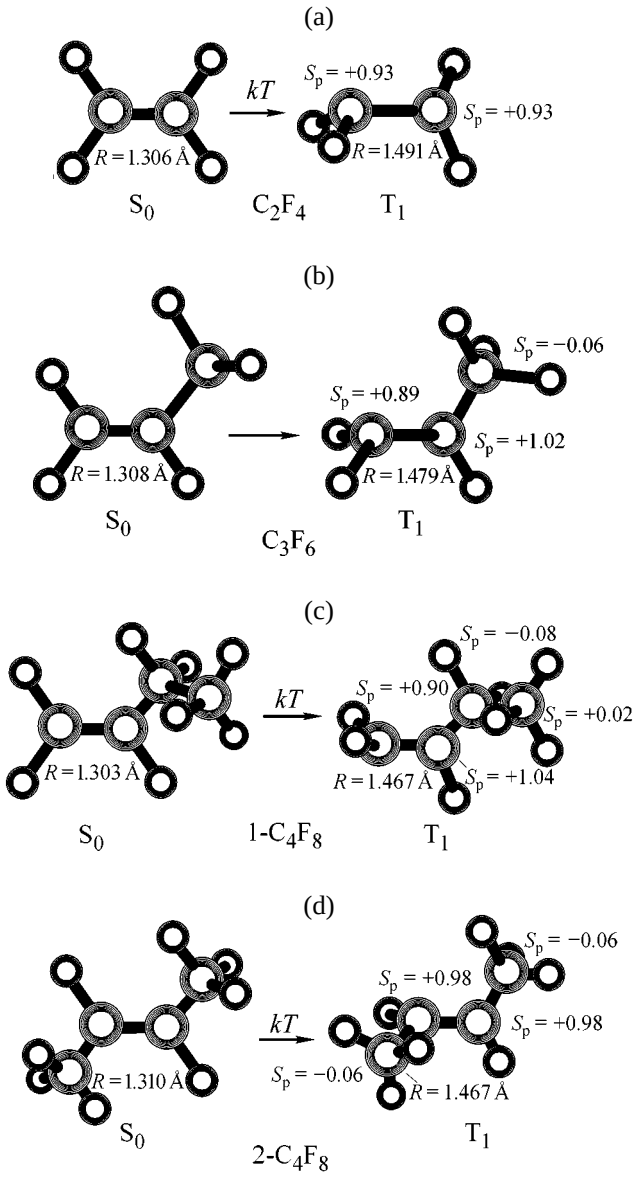

Fig. 2. Optimized (*ab initio* DZ) steric structure of (a) C_2F_4, (b) C_3F_6, (c) 1-C_4F_8, and (d) 2-C_4F_8 in the ground singlet S_0 and excited T_1 states. Indicated are the C=C bond lengths and spin populations at carbon atoms of the double bond.

$$C_2F_4 + C_2F_4 \rightleftarrows \boxed{F}. \quad (5)$$

This excludes, as incomplete, one-step reaction of the type (5), where radical stages are hidden and are not manifested experimentally, e.g, because of their high rate and small lifetime of radical species. In this connection, it should be noted that the radical mechanism of [2 + 2] cyclodimerization of C_2F_4 was confirmed experimentally in [8, 12].

Structure of the olefin molecules in electronically excited state. The triplet, so-called "phantom" states of olefins, e.g., stilbene [23, 24], are known to have a perpendicular configuration. *Cis–trans* isomerization (rotation by 180° about the C=C bond) proceeds specifically via this state. The triplet states of ethylene and other olefins have biradical character, be the configuration perpendicular (equilibrium state) or planar (vertical transition). The radical centers are located at the carbon atoms involved in the double $C^{\bullet}$–$C^{\bullet}$ bond. The decrease in the C=C bond order (degradation of the double bond) under triplet excitation has electronic origin and is not directly related to transition of the molecule into perpendicular configuration. For example, the C–C bond order in ethylene decreases from p = 2.0 to p = 1.0 as a result of vertical transition $T_1 \leftarrow S_0$ which leaves unchanged the initial planar structure.

The molecules of perfluoroolefins C_2F_4 and C_3F_6 (Figs. 2a, 2b) and 1-C_4F_8 and 2-C_4F_8 (Figs. 2c, 2d) in the ground singlet state have planar structures, except in the case of the 1-C_4F_8 molecule in which the CF_3 group lies outside the plane of the central C–C moiety (Figs. 2c, 2d). In the triplet state T_1, these molecules undergo rotation about the C=C bond and take a close-to-perpendicular configuration (Figs. 2a–2d). For fluoroolefins, and especially for TFE, the F–C–C angle at the $C^{\bullet}$ radical centers markedly decreases from 123°–125° for S_0 to 113°–114° for T_1. At the same time, the H–C–C angle for olefins decreases only slightly as a result of transition to the triplet state, namely, from 121.8° for S_0 to 121.2° for T_1. In the optimized singlet excited state, the molecules of olefins and their fluorinated analogs also have nonplanar configuration, but, unlike the case of triplets, the singlet state S_1 is characterized by strictly perpendicular location of the bonds [dihedral angles H–C–C–H (F–C–C–F) are equal to 90°].

Despite the similar steric structures of the olefin molecules in the triplet and singlet excited states, the electronic structures of these molecules differ substantially. Figures 2a–2d show that in the triplet state

the maximal positive spin population S_p is close to unity and is concentrated at the carbon atoms of the double C=C bond, which in the T_1 state degrades to ordinary bond. Also, the spin density distribution S_p is weakly dependent on the type of substituent at the double bond (H, F, or C). This means that olefin molecules in the triplet state are biradicals with all the ensuing consequences, both spectral and chemical. The triplets of the olefins must have characteristic ESR spectra, and they must behave chemically as radical (biradical) species, e.g., participate in dimerization or addition reactions [Eq. (4)] yielding biradical species.

Absorption spectra of olefins. The singlet state S_1 cannot be a biradical by definition and, therefore, must not exhibit paramegnetism typical of triplets. Also, the absorption spectra of the singlets S_1 and triplets T_1 would be expected to differ, though this is not confirmed by the available published data. For the initial olefins, the calculated $S_1 \leftarrow S_0$ spectra reasonably agree with the experimental data (Table 1). In the visible and UV regions of the spectrum, we observe two triplet–triplet transitions allowed by the selection rules, each region containing one transition. The lowest in energy $T_2 \leftarrow T_1$ transition, corresponding to excitation of an unpaired electron, is observed in the visible region, and the $T_3 \leftarrow T_1$ transition observed in the UV region is due to electron excitation from the second double-occupied molecular orbital.

Calculation of the absorption spectra of excited molecules, such as intermediates of perfluoroolefins, is a sophisticated task. Nonempirical calculation yields extremely unsatisfactory results, and semiempirical calculations also present certain difficulties. Table 1 lists the energies calculated by the ZINDO/S method tested previously in solving such problems. It is seen that, for the two experimentally observed transitions, namely, $T_2 \leftarrow T_1$ in the visible and $T_3 \leftarrow T_1$ in the UV region, the experimental and calculated (in our case, evaluated) data agree reasonably.

Energies of triplet and singlet excited states. The triplet hypothesis was most adequately substantiated by calculations of the energies of triplet equilibrium (optimized) states of perfluoorolefins. Specifically these electronic states, which are the lowest in energy, are populated in thermal excitation. The *ab initio* calculation yields the difference of the total energies of the molecules in the triplet T_1 and singlet S_0 configurations, which is defined as the triplet state energy and should be compared with the experimental enthalpies of the intermediates. Buravtsev and Kolbanovskii reported in [13] the same experimental

Table 1. Calculated (ZINDO/S) singlet–singlet $S_1 \leftarrow S_0$ and triplet–triplet $T_{2,3}$–T_1 absorption spectra of olefins

Molecule	$S_1 \leftarrow S_0$	$T_2 \leftarrow T_1$	$T_3 \leftarrow T_1$
	nm		
C_2F_4	186.7 (188)* / 0.55***	544 (500)**	243 (236.5)**
C_3F_6	184.1 (185)* / 0.57***	543 (477.5)**	213 (240)**
C_4F_8-1	178.7 / 0.57***	490 (460)**	231 (242.5)**
C_4F_8-2	159.7 / 0.51***	310	202 (240)**

* Experimental data from [25].

** Experimental data from [13].

*** Oscillator strength.

value of the enthalpy of the formation reaction, ΔH, for all the four intermediates considered, $C_2F_4^*$, $C_3F_6^*$, 1-$C_4F_8^*$ and 2-$C_4F_8^*$, namely, 75.2 ± 8.4 kJ mol^{-1} (18.0 kcal mol^{-1}).

The energy of the triplet states of TFE calculated *ab initio* in the DZ basis agrees reasonably with the experimental enthalpy of formation of $C_2F_4^*$ (Table 2). At the same time, the extensively used 6-31G* basis somewhat overestimates, and the semiempirical AM1 method underestimates, the triplet energy $E(T_1)$–$E(S_0)$. As to the DZ basis, it also satisfactorily describes other molecules with unfilled shells. For example, the inconsistency between the experimental value of the enthaply of C_2F_4 decomposition into two carbenes $:CF_2$, 290.8 ± 5 kJ mol^{-1} [26] and the calculated value of 235 kJ mol^{-1} [27] mentioned in [13], is eliminated in the case of the *ab initio* DZ calculation yielding $\Delta H = 283.5$ kJ mol^{-1} .

The remaining three perfluorolefins from Table 2 are characterized by higher triplet energies exceeding that for TFE by 20.9–33.4 kJ mol^{-1}, this difference being preserved for all the calculation methods. Common reasoning suggests a certain difference $E(T_1)$–$E(S_0)$ for the fluoroolefins considered, though the experiment yields identical enthalpies of formation for the intermediates, namely, 75.2 kJ mol^{-1} [13]. This conclusion is supported by the regular shift of the band maxima in the pulse absorption spectra of the intermediates [13] upon introducing substituents into the ethylene molecule, namely, a red shift of the short-wavelength band and a blue shift of the long-wave band in the vis-

Table 2. Calculated energies of the triplet T_1 and singlet S_0 states of olefins

Molecule	$E(T_1)$–$E(S_0)$, kJ mol^{-1}			ΔH_{exp}, kJ mol^{-1} [13]	$E(S_1)$–$E(S_0)$, AM1 method	$E(T_1)$–$E(S_1)$
	ab initio, basis		AM1 method			
	6-31G*	DZ			kJ mol^{-1}	
C_2F_4	103.1	86.8	54.1	75.2	294.0	239.9
C_3F_6	133.9	112.2	74.0	75.2	285.5	211.2
C_4F_8-1	126.9	116.2	76.6	75.2	282.1	205.5
C_4F_8-2	138.1	115.9	81.6	75.2	365.0	283.4
C_2H_4	176.2 (344.2)*	169.5	137.1		379.0	241.9 (290)*
C_3H_6	181.0	174.3	130.4		366.1	235.7
C_4H_8-1	181.7	174.3	129.8		361.4	231.6
C_4H_8-2	179.5	175.9	124.4		381.7	257.3

* The data in parentheses are the experimental data taken from [20].

ible region. It should be noted that Buravtsev and Kolbanovskii also report other enthalpies of formation of the intermediates, e.g., $\Delta H = 71 \pm 4$ kJ mol^{-1} (17 kcal mol^{-1}) for 1-$C_4F_8^*$, and 2-$C_4F_8^*$ in [4] and 92 ± 3 kJ mol^{-1} (22 kcal mol^{-1}) for $C_2F_4^*$ in [8]. In this study, we used the data from the latest work [13], which are, evidently, the most reliable.

The triplet energies for perfluoroolefins exceed those for olefins by approximately a factor of 1.5 (Table 2), which suggests the stabilizing role of the unshared electron pair of the fluorine atoms. Specifically this important fact is responsible for the lowering of the triplet levels toward thermally achievable energies (<1 eV), and favors observation of thermally activated transitional spectra. As far as we know, such experiments are very troublesome in the case of H forms of the olefins . The incorporated fluorine atoms also stabilize other species, e.g., 1,4-biradical participating in [2 + 2] cyclodimerization [Eq. (4)]. In the opinion of Buravtsov and Kolbanovskii [13], this stabilization (by 104.5 kJ mol^{-1}) [28] (our *ab initio* DZ calculations yield 148.8 kJ mol^{-1}) accounts for the more intensive [2 + 2] cyclodimerization of C_2F_4, compared to C_2H_4. In reality, the 1,4-biradical is only an intermediate species with low energy (Figs. 3a, 3b), and the potential barrier of the reaction, which governs the reaction rate, is determined by the triplet state of the olefins.

As already mentioned, the singlet configuration of the fluoroolefin intermediates, discussed in [13], is inconsistent with the experimental evidence of the biradical character of the intermediates. A more serious objection to the singlet hypothesis is that the energies of the singlet excited states are high and exceed severalfold the experimental enthalpies of formation of the intermediates (Table 2). These results were obtained by AM1 semiempirical calculations which describe satisfactorily the singlet ground S_0 and excited S_1 states. Table 2 lists the optimized, equilibrium energies $E(S_1)$–$E(S_0)$. As to vertical, optical transitions, their energies are significantly greater, and the corresponding absorption bands lie, as already mentioned, in the vacuum UV region (<200 nm).

Table 2 also lists the calculated singlet–triplet splittings $E(T_1)$–$E(S_1)$ which take for small molecules, such as ethylene, the maximal values of up to 300 kJ mol^{-1} [20]. These splittings are, on the average, identical (ca. 240 kJ mol^{-1}) for olefins and their fluorinated derivatives, though the latter are characterized by a somewhat lower energy of the singlet S_1 state. The above-cited data suggest that the singlet S_1 excited levels of fluoroolefins and, moreover, of their hydrogencontaining analogs are located much higher (by ≥3 eV) than their corresponding triplet levels and are inaccessible for thermal population under the actual conditions.

Mechanism of [2 + 2] cyclodimerization of ethylene and perfluoroethylene. Let us consider the mechanism of TFE cyclodimerization in the light of our concepts reported in [14] and the new data from [1, 8, 13]. The radical pathway of this reaction naturally stems from the general statement that mono- or bimolecular thermal reactions proceed via relaxed electronically excited states of the molecules and their complexes, which typically have triplet and, hence, radical (biradical) character [14]. Direct experimental verification of this mechanism, with the [2 + 2] cyclo-

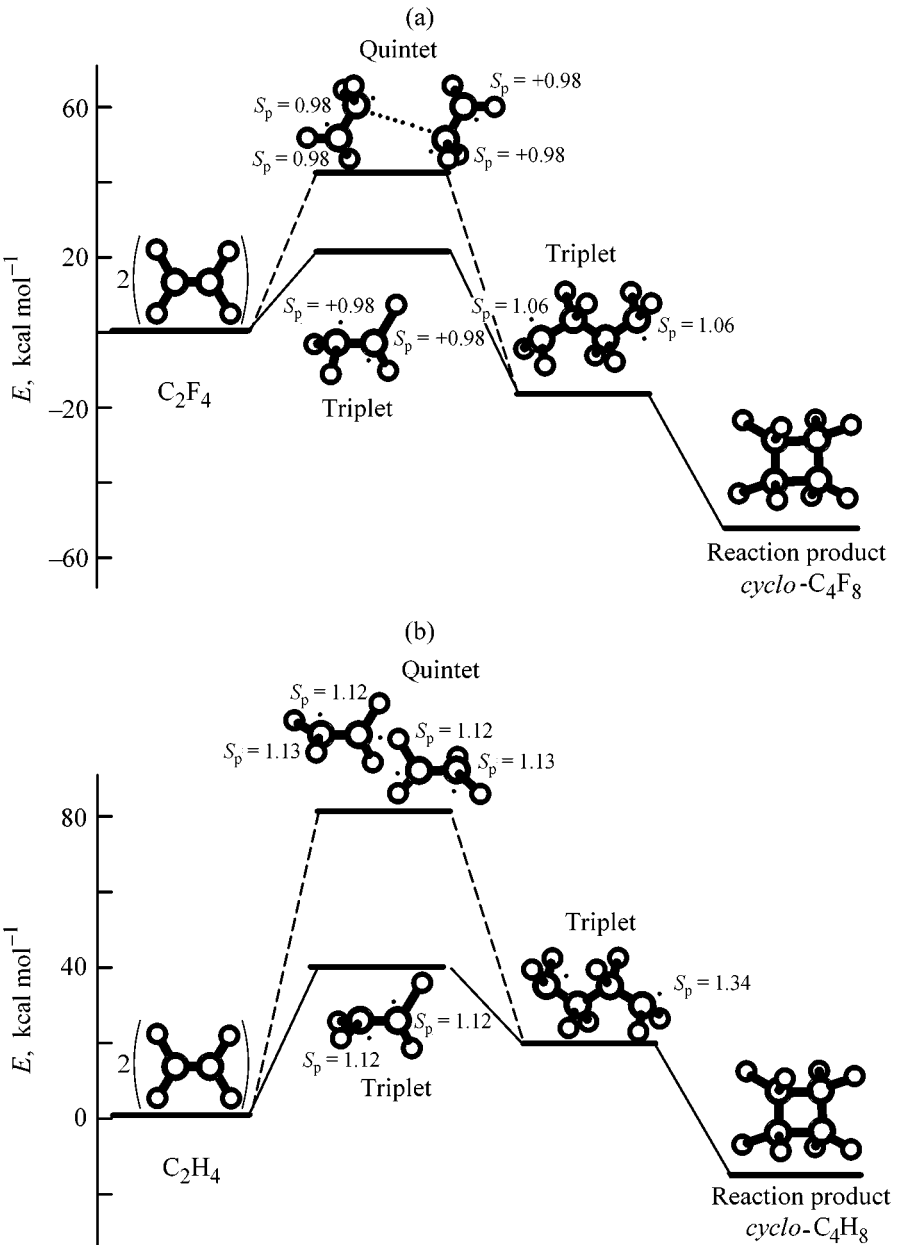

Fig. 3. Energy diagrams of the cyclodimerization reaction for (a) C_2F_4 and (b) C_2H_4. (E) Energy.

dimerization reaction of TFE as an example [8, 13], is of much importance for understanding of the nature of this and many other reactions. The hypothetical ionic mechanism [8] also has an essentially radical nature, as such reactions necessarily involve electronic transfer generating radical (radical ion) species.

Figures 3a and 3b present the energy diagrams for the dimerization reactions of TFE and ethylene, based on the results of *ab initio* DZ calculations. It is assumed that the potential barrier of the reaction is determined either by a quintet (a complex of two molecules in the triplet state) or a triplet state of the olefins. In the latter case, it should be presumed that reaction (4) proceeds via collision of two excited TFE molecules. This collision yields the intermediate 1,4-biradical [Eq. (4)], and this process, evidently, does not require additional thermal activation. Then, taking the activation energy of the forward aggregate reaction (5) $E_a(5)$ [stages from Eq. (4) and Fig. 3a] equal to the triplet energy of TFE, 86.8. kJ mol^{-1} (Table 2) and the heat of forward reaction (5) ΔH = 221.0 kJ mole^{-1} (from *ab initio* DZ calculations; cf. experimental value of 222 kJ mol^{-1} [29]), the activation energy for reverse reaction (5) will be $E_a(-5)$ =

86.8 + 221.0 = 307.8 kJ mol^{-1}. The experimental activation energy for decomposition of octafluorocyclobutane

$$2C_2F_4 \leftarrow \textit{cyclo}\text{-}C_4F_8 \quad (6)$$

is 331 ± 5 kJ mol^{-1} [1], which somewhat exceeds the calculated value of 307.8 kJ mol^{-1}. However, the same work [1] contains data reported by other authors, which suggest that E_a^{exp} (6) varies within 311–316 kJ mol^{-1}.

The alternative reaction pathway via the quintet state yields a less satisfactory agreement between the calculated, $E_a(6)$ = 394.6 kJ mol^{-1}, and the experimental [1], $E_a^{exp}(6)$ = 331 kJ mol^{-1}, values. Also, this pathway assumes generation of the triplet ^{3}TFE from the TFE molecule in the ground state:

$$\underset{\text{Triplet}}{C^{\bullet}F_2\text{–}C^{\bullet}F_2} + CF_2\text{–}CF_2 \rightleftarrows \underset{\text{Quintet}}{C^{\bullet}F_2\text{–}C^{\bullet}F_2\cdots C^{\bullet}F_2\text{–}C^{\bullet}F_2}. \quad (7)$$

However, in the arising quintet state (E = 397.5 kJ mol^{-1}), at least in the framework of the *ab initio* basis sets we used, interaction between its two constituent triplet molecules is weak (e.g., only 0.04 kJ mol^{-1} in the case of C_2H_4). This makes more probable the pathway of reaction between the two triplet TFE molecules to give a 1,4-biradical

$$\underset{\text{Triplet}}{C^{\bullet}F_2\text{–}C^{\bullet}F_2} + \underset{\text{Triplet}}{C^{\bullet}F_2\text{–}C^{\bullet}F_2} \rightleftarrows \underset{\text{Triplet}}{(C^{\bullet}F_2\text{–}CF_2\cdots CF_2\text{–}C^{\bullet}F)}$$

$$\rightleftarrows \underset{\text{1,4-Biradical (triplet)}}{C^{\bullet}F_2\text{–}CF_2\text{–}CF_2\text{–}C^{\bullet}F_2} \quad (8)$$

and *cyclo*-C_4F_8 as the end product.

It is assumed that the reaction follows pathway (8) (Figs. 3a, 3b): two triplet molecules come within a distance of approximately 3 Å from each other, which is followed by intercombination $S_0 \leftarrow\!\sim\!\sim T_1$ and disappearance of one of the triplets, and the resulting $^3(C^{\bullet}F_2\text{–}CF_2\cdots CF_2\text{–}C^{\bullet}F)$ complex is converted into a radical species $^3(C^{\bullet}F_2\text{–}CF_2\text{–}CF_2\text{–}C^{\bullet}F)$ in the triplet configuration, which was termed 1,4-biradicaloid in [8, 13]. *trans*-1,4-Biradical has a symmetric structure with terminal radical centers accommodating the spin population S_p = 1.34, and the $C^{\bullet}F_2\text{–}CF_2$ and $CF_2\text{–}CF_2$ bond lengths are 1.52 and 1.53 Å, respectively. This 1,4-biradical is easily isomerized into *cis* structure which is stabilized, via the second intercombination stage $S_0 \leftarrow\!\sim\!\sim T_1$ toward the ground singlet state S_0, as the reaction product, cyclobutane. The C–C bond length in the symmetric (D_{4h}) molecule of cyclo-$C_4F(H)_8$ is 1.55 Å.

The absorption spectrum of 1,4-biradical C_4F_8 (230 nm) was for the first time recorded directly in the millisecond range in [12]. The lifetime of the hydrogen analog C_4H_8 is significantly shorter and, depending on the pumping energy, amounts to 300–800 fs [29]. In the case of interest, the 1,4-biradical C_4H_8 has, however, the *cis* configuration favoring cyclization and, thus, decreasing the lifetime of the species. It can be assumed that the 1,4-biradical C_4F_8 (230 nm) [12] in the triplet electronic state takes the *trans* configuration.

CONCLUSIONS

(1) The thermally activated intermediates of perfluoroolefins described in the literature are essentially the initial olefins in the triplet electronically excited state. The calculated (*ab initio* DZ) triplet energies of perfluotoolefins reasonably agree with the experimental enthalpies of formation of intermediates. The calculated triplet–triplet absorption spectra reasonably agree with the transitional absorption spectra of the intermediates.

(2) A mechanism of cyclodimerization of tetrafluoroethylene is proposed, which involves thermal excitation into the triplet state, collision of two triplet molecules, their transformation (after $S_0 \leftarrow\!\sim\!\sim T_1$ intercombination) into the triplet 1,4-biradical, and formation of *cyclo*-C_4F_8 from *cis*-1,4-biradical after the second intercombination along the pathway toward the ground state S_0.

REFERENCES

1. Buravstev, N.N., Grigor'ev, A.S., and Kolbanovskii, Yu.A., *Kinet. Katal.*, 1985, vol. 26, no. 1, pp. 7–14.
2. Buravstev, N.N., Grigor'ev, A.S., and Kolbanovskii, Yu.A., *Kinet. Katal.*, 1989, vol. 30, no. 1, pp. 21–30.
3. German, L.S., Grigor'ev, A.S., Kolbanovskii, Yu.A., and Chepik, S.D., *Kinet. Katal.*, 1989, vol. 30, no. 1, pp. 221–223.
4. Buravstev, N.N., Kolbanovskii, Yu.A., and Ovsyannikov, A.A., *Zh. Org. Khim.*, 1994, vol. 30, no. 12, pp. 1802–1809.
5. Buravstev, N.N., German, L.S., Grigor'ev, A.S., *et al.*, *Mendeleev Commun.*, 1993, pp. 133–134.
6. Buravstev, N.N., Kolbanovskii, Yu.A., and Ovsyannikov, A.A., *Izv. Ross. Akad. Nauk, Ser. Khim.*, 1995, no. 10, pp. 2048–2050.

7. Buravstev, N.N., Kolbanovskii, Yu.A., and Ovsyannikov, A.A., *Izv. Ross. Akad. Nauk, Ser. Khim.*, 1996, no. 1, pp. 64–67.
8. Buravstev, N.N., Kolbanovskii, Yu.A., and Ovsyannikov, A.A., *Mendeleev Commun.*, 1994, pp. 48–50.
9. Buravstev, N.N., Kolbanovskii, Yu.A., and Ovsyannikov, A.A., *Mendeleev Commun.*, 1994, pp. 190–191.
10. Buravstev, N.N., Kolbanovskii, Yu.A., and Ovsyannikov, A.A., *Dokl. Ross. Akad. Nauk*, 1997, vol. 357, no. 6, pp. 775–778.
11. Buravstev, N.N., Kolbanovskii, Yu.A., and Ovsyannikov, A.A., *Dokl. Ross. Akad. Nauk*, 1998, vol. 358, no. 1, pp. 57–61.
12. Buravstev, N.N. and Kolbanovskii, Yu.A., *J. Fluorine Chem.*, 1999, vol. 96, pp. 35–42.
13. Buravstev, N.N. and Kolbanovskii, Yu.A., *Zh. Prikl. Khim.*, 2002, vol. 75, no. 4, pp. 612–619.
14. Kalnin'sh, K.K., *Elektronnoe vozbuzhdenie v khimii* (Electronic Excitation in Chemistry), St. Petersburg: Sankt-Peterb. Gos. Univ. Tekhnol. Dizaina, 1998.
15. Kalnin'sh, K.K., *Zh. Fiz. Khim.*, 2000, vol. 74, no. 1, pp. 117–124.
16. Kalnin'sh, K.K. and Podol'skii, A.F., *Zh. Strukt. Khim.*, 2001, vol. 42, no. 6, pp. 1071–1084.
17. Kalninsh, K.K., *Phys. Chem. Chem. Phys.*, 2001, vol. 3, no. 20, pp. 4542–4546.
18. Hunter, T.F., Stock, M.G., and Webb, N., *J. Chem. Soc., Faraday Trans. 2*, 1979, vol. 75, no. 5, pp. 738–751.
19. Birks, J.B., *Photophysics of Aromatic Molecules*, London: Wiley, 1970.
20. Barltrop, J.A. and Coyle, J.D., *Excited States in Organic Chemistry*, London: Wiley, 1975.
21. Jamshidi, G. and Kummler, R.R., *J. Chem. Soc., Faraday Trans. 2*, 1979, vol. 75, no. 8, pp. 1205–1207.
22. Motoda, Y. and Kubota, Y., *Bull. Chem. Soc. Jpn.*, 1979, vol. 52, no. 3, pp. 693–696.
23. Gorner, H. and Schulte-Frohlinde, D., *J. Phys. Chem.*, 1978, vol. 85, no. 25, pp. 2653–2659.
24. Caldwell, R.A. and Schwerzel, R.E., *J. Am. Chem. Soc.*, 1972, vol. 94, no. 3, pp. 1035–1037.
25. Sharpe, S., Hartnett, B., Sethi, H.S., and Sethi, D.S., *J. Photochem.*, 1987, vol., 38, pp. 1–3.
26. Schug, K.P. and Wagner, H.G., *Ber. Bunsenges. Phys. Chem.*, 1978, vol. 82, pp. 719–725.
27. Trinquier, G. and Barthelat, J.C., *J. Am. Chem. Soc.*, 1990, vol. 112, no. 25, pp. 9121–9130.
28. Getty, S.F. and Border, W.T., *J. Am. Chem. Soc.*, 1991, vol. 113, no. 11, pp. 4334–4335.
29. Atkinson, B. and Trenwith, A.B., *J. Chem. Soc.*, 1953, pp. 2082–2087.
30. Pedersen, S., Herek, J.L., and Zewail, A.H., *Science*, 1994, vol. 266, pp. 1359–1364.

Russian Journal of Applied Chemistry, Vol. 75, No. 4, 2002, pp. 598–605. Translated from Zhurnal Prikladnoi Khimii, Vol. 75, No. 4, 2002, pp. 612–619.
Original Russian Text Copyright © 2002 by Buravtsev, Kolbanovskii.

MACROMOLECULAR CHEMISTRY AND POLYMERIC MATERIALS

Mechanism of Hexafluoropropylene Formation in Gas-Phase Pyrolysis of Tetrafluoroethylene

N. N. Buravtsev and Yu. A. Kolbanovskii

Topchiev Institute of Petrochemical Synthesis, Russian Academy of Sciences, Moscow, Russia

Received September 6, 2001

Abstract—The consecutive formation of short-lived intermediates during tetrafluoroethylene conversion into hexafluoropropylene by gas-phase pyrolysis under conditions of pulsed adiabatic compression was studied by kinetic spectroscopy. The process mechanism was determined in detail. The ways for improving the pyrolysis procedure were considered.

Development of processes for preparing hexafluoropropylene C_3F_6 is and urgent problem since this compound is starting reagent in production of fluorinated rubbers. The only process for C_3F_6 production is pyrolysis of tetrafluoroethylene C_2F_4. Since C_2F_4 is relatively expensive, special attention is focused on its consumption coefficients and on improvement of the process selectivity. The main problems are to decrease the yield of fluorocoke and perfluorobutenes C_4F_8, one of which, perfluoroisobutylene *i*-C_4F_8, is highly toxic [1].

In this work, the mechanism of formation of C_3F_6 and the by-products in C_2F_4 pyrolysis was studied in detail with the aim to improve the technology of C_3F_6 production.

Previous concepts of the mechanism of pyrolytic synthesis of C_3F_6 were only based on studies of the stable reaction products [2–23]. Also, formation of difluorocarbene $:CF_2$ in thermolysis was detected by UV spectroscopy [24–31]. The absorption of other intermediates was not studied. Based on the results of these works, the mechanism of C_3F_6 formation can be represented as two processes:

Process 1 [6, 11, 23]

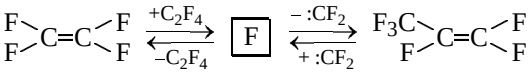

Process 2 [9, 12–14, 21–24, 26]

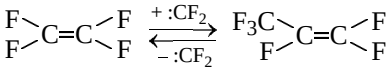

Scheme 1.

Our previous kinetic data on pyrolysis of octafluorocyclobutane cyclo-C_4F_8 [18] did not confirm the occurrence of the first process. The second process, reaction of $:CF_2$ with C_2F_4, can proceed by three possible mechanisms (a)–(c) [32]:

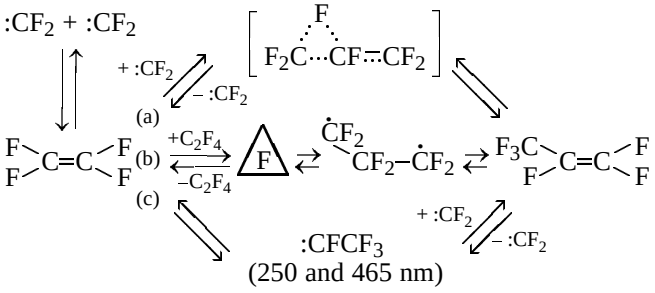

Scheme 2.

Pathway (b) was rejected on the basis of a kinetic study of pyrolysis of perfluoromethylcyclopropane CF_3-cyclo-C_3F_5, which selectively decomposed into C_2F_4 and C_3F_6 in 1 : 2 ratio [33]. This ratio and the absence of C_4F_8 in the reaction products indicate that the 1,3-biradical formed via opening of the three-membered CF_3-cyclo-C_3F_5 ring does not isomerize and is converted into C_3F_6 and $:CF_2$. Our previous study of thermolysis of CF_3-cyclo-C_3F_5 by kinetic spectroscopy [34, 35] showed that the formation of the 1,3-biradical precedes formation of $:CF_2$. In accordance with the principle of macroscopic reversibility, the reverse process, cycloaddition of $:CF_2$ to C_3F_6, is also a biradical reaction (see Scheme 3).

This indicates that cycloaddition of $:CF_2$ to C_2F_4 can also occur in two steps. However, according to Skell's hypothesis [36], reactions of singlet carbenes

1070-4272/02/7504-0598 $27.00 © 2002 MAIK "Nauka/Interperiodica"

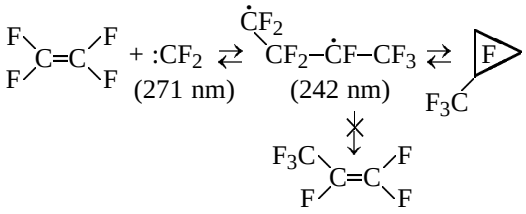

Scheme 3.

with olefins are one-step, as follows from stereoselective *syn* addition of the carbens [37]. The stereoselectivity of this reaction, whose two-step mechanism was confirmed experimentally, is due to the fact that the cyclization of singlet 1,3-biradical is faster than its isomerization by rotation around the C–C bond.

As follows from Scheme 2, the only way to determine the mechanism of C_3F_6 formation [(a) or (b)] is to study spectroscopically the kinetics of transformations of the short-lived intermediates of reaction 2. This study was the aim of the present work.

Homogeneous heating of the gaseous reaction mixture was performed by adiabatic compression [38]. The stable pyrolysis products were analyzed and identified by GLC, GC–MS, and IR spectroscopy. The reaction kinetics of short-lived intermediates was studied by millisecond kinetic spectroscopy in the UV–Vis region [39]. Similar intermediates were generated from different compounds. The kinetics of the examined reactions, including elementary steps involving the detected intermediates, was simulated mathematically [40]. The enthalpies of reversible reactions initial reagent ⇄ primary intermediate were determined from the kinetic spectroscopy data obtained after attainment of the equilibria [41, 42].

First of all, we found whether pathway (c), involving formation of $:CFCF_3$, is actually followed. The electronic spectrum of this radical contains the characteristic band at 465 nm [43]. This band was not observed in the absorption spectra of intermediates of C_2F_4 pyrolysis (Fig. 1). This is possible in two cases: (1) if $:CFCF_3$ is not formed indeed or (2) its concentration is lower than the sensitivity limit of the spectroscopic equipment.

To check the second possibility, we used the results of a study of $C_2F_5SiF_3$ pyrolysis [39]. The formation of $:CFCF_3$ in the course of pyrolysis under adiabatic compression was reliably indicated by the absorption at 465 nm. Up to the complete conversion of $C_2F_5SiF_3$, the final reaction products are SiF_4 and *cis*-2-C_4F_8, the product of steroselective recombination of $:CFCF_3$ radical (hear and hereinafter, the location of the double bond is indicated by the locant).

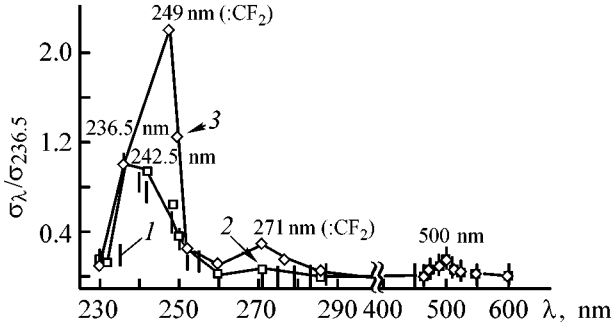

Fig. 1. Absorption spectra of the intermediates of flash pyrolysis of (*1*) 5 vol % C_2F_4 in Xe (890 K), (*2*) 10 vol % C_2F_4 in Ar (1000 K), and (*3*) 5 vol % C_2F_4 in Ar (1170 K). ($\sigma_\lambda/\sigma_{236.5}$) Ratio of molar extinction coefficients; (λ) wavelength.

At higher temperature in a pulse, *cis-trans* isomerization of 2-C_4F_8 was observed after complete conversion of $C_2F_5SiF_3$.

Thus, the direct experiments at temperatures of industrial pyrolysis allowed us to rule out pathway (c) of C_3F_6 synthesis via formation of $:CFCF_3$. Hence, the only possible pathway of C_3F_6 formation is insertion of $:CF_2$ into the C–F bond. However, the detailed mechanism of the synthesis remains unknown.

Previously [34] we detected for the first time the absorption of unknown primary intermediates formed on heating perfluoroolefins to "prepyrolysis" temperatures. Experiments with different initial concentrations of perfluoroolefins showed the first order of the direct and reverse reactions of formation of these intermediates, i.e., these reactions are monomolecular [44]. Thus, the composition of the primary intermediates is identical to that of perfluoroolefins. Hereinafter, these intermediates are denoted by $C_2F_4^*$, $C_3F_6^*$, 1-$C_4F_8^*$, 2-$C_4F_8^*$, and *iso*-$C_4F_8^*$ (here and hereinafter, the asterisk indicates an excited state).

The UV absorption spectra of these intermediates contain the bands with $\lambda_{max}^{(1)}$ 236.5 ($C_2F_4^*$), 240 ($C_3F_6^*$ and 2-$C_4F_8^*$), and 242.5 nm (1-$C_4F_8^*$) [44]. These bands differ from the characteristic UV bands of C_2F_4 (λ_{max} = 188 nm) and C_3F_6 (λ_{max} = 185 nm) [29]. The $:CF_2$ spectrum contains bands in the range 236.5–242.5 nm [45]. However, the absorption of $C_2F_4^*$, $C_3F_6^*$, and 1-$C_4F_8^*$ was observed at temperatures lower than that of $:CF_2$ generation.

In this work, we studied the spectral properties of $C_2F_4^*$, $C_3F_6^*$, and 1-$C_4F_8^*$ having absorption bands in the visible region at $\lambda_{max}^{(2)}$ of 500, 477.5, and 460 nm, respectively (Fig. 2). A specific feature of the electronic absorption spectra of these intermediates is

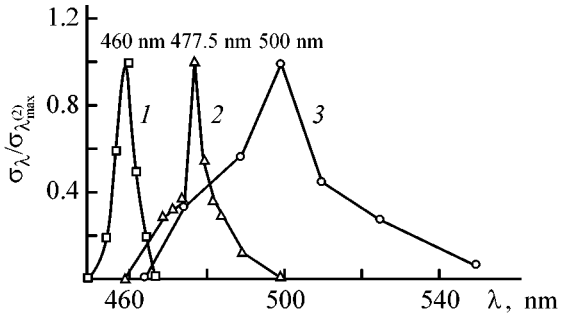

Fig. 2. Visible absorption bands of primary intermediates of pyrolysis of (*1*) 1.2 vol % 1-C_4F_8 (1010 K), (*2*) 1 vol % C_3F_8 (1160 K), and (*3*) 5 vol % C_2F_4 (890 K) in argon (stable pyrolysis products are not detected chromatographically). ($\sigma_\lambda/\sigma_{\lambda^{(2)}_{max}}$) Ratio of molar extinction coefficients and (λ) wavelength.

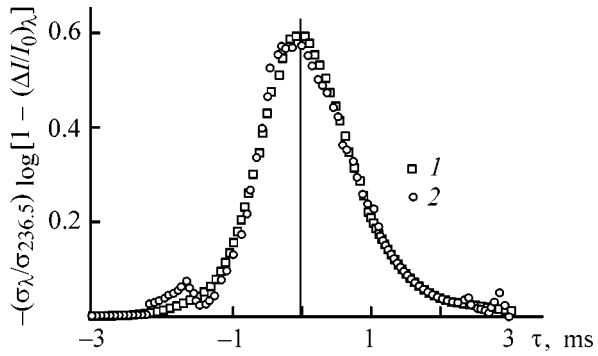

Fig. 3. Absorption of $C_2F_4^*$ intermediate formed in flash heating of 5 vol % C_2F_4 + Xe mixture to T_{max} = 890 K [temperature at the maximal compression (τ = 0 ms)], normalized to the maximal value, vs. time τ. $\sigma_\lambda/\sigma_{236.5}$ is the ratio of molar extinction coefficients, $(\Delta I)_\lambda = (I_0 - I)_\lambda$ the difference in absorption at λ (nm) before and after passage through the reaction mixture, and $(\Delta I/I_0)_\lambda$ the relative absorption (%). λ (nm): (*1*) 236.5 and (*2*) 500.

the presence of two bands, one in the UV and the other in the visible region. The fact that the absorption at $\lambda^{(1)}_{max}$ = 236.5 and $\lambda^{(2)}_{max}$ = 500 nm, normalized to the maximal absorption, varies with time during C_2F_4 heating similarly (Fig. 3) allows these bands to be assigned to the same singlet intermediate $C_2F_4^*$. The absence of long-wave shifts of these bands at higher temperatures (Fig. 1) indicates that they are due to true intermediates and are not "hot bands" [46] in the perfluoroolefin spectra.

The low-energy singlet intermediates $C_2F_4^*$, $C_3F_6^*$, and 1-$C_4F_8^*$, and 2-$C_4F_8^*$ formed by monomolecular reactions of the respective perfluoroolefins at elevated temperatures have been unknown previously.

The enthalpies of formation of $C_2F_4^*$, $C_3F_6^*$, 1-$C_4F_8^*$, and 2-$C_4F_8^*$ are similar and equal to ΔH_r^0 = 75.2 ± 8.4 kJ mol^{-1} [36, 41, 42, 47, 48]. All these intermediates contain the C=C double bond with no less than two fluoride subsituents. The absorption of $C_2F_4^*$, $C_3F_6^*$, 1-$C_4F_8^*$, and 2-$C_4F_8^*$ in the UV–Vis region is due to electronic rearrangement of these fragments.

We failed to determine the structure of these intermediates by millisecond IR spectroscopy. Matrix isolation is complicated by their fast isomerization into the initial perfluoroolefins. The only way to gain insight into the structure of these intermediates was quantum-chemical calculation. The results of these calculations are shown in Fig. 4. The structure of $C_2F_4^*$ is not described by any of the structures calculated in [49–54], with the activation energy of formation of :$CFCF_3$ being higher than that of :CF_2, However, it should be noted that the *ab initio* calculations of the energy of molecules with unpaired electrons do not always agree with experimental data. For example, the calculated enthalpy of decomposition of C_2F_4 into two :CF_2 species is 235 kJ mol^{-1}, whereas the experimental value is 290.8 ± 5 kJ mol^{-1} [27].

Clearly, the π bond in $C_2F_4^*$, $C_3F_6^*$, 1-$C_4F_8^*$, 2-$C_4F_8^*$ and *iso*-$C_4F_8^*$ has a decreased order but is not fully ruptured since the enthapy of equilibrium perfluoroolefin $\rightleftarrows$ intermediate (75.2 + 8.4 kJ mol^{-1}) is appreciably lower than the energy of rupture of the π bond (197.3–211.5 kJ mol^{-1} [48]). Thus, $C_2F_4^*$, $C_3F_6^*$, 1-$C_4F_8^*$, 2-$C_4F_8^*$, and *iso*-$C_4F_8^*$ must, to a certain extent, resemble biradicals. In accordance with the IUPAC classification [55], they can be termed 1,2-biradicaloids. Previously, we showed [47, 56–58] that these species do exhibit biradical properties.

Formation of 1,2-biradicaloid $C_2F_4^*$ does not contradict the two-step reversible decomposition of C_2F_4 into two carbenes :CF_2 [56, 57].

$$C_2F_4 \underset{-1}{\overset{1}{\rightleftarrows}} C_2F_4^* \underset{-2}{\overset{2}{\rightleftarrows}} :CF_2 + :CF_2$$

Scheme 4.

Ab initio calculations of [2 + 2]-cyclodimerization processes [59] showed that the biradical mechanism, not forbidden by the Woodward–Hoffmann theory [60], is more energetically favorable than the concerted mechanism. The energy of the 1,4-biradical calculated by various *ab initio* procedures [61] is lower by 104.5 kJ mol^{-1} than that of its hydrocarbon analog. That is why, in tetrafluoroethylene pyrolysis, the energy contribution of biradical [2 + 2] cyclodimerization is appreciable, unlike its contribution to thermal conversion of C_2H_4 [62].

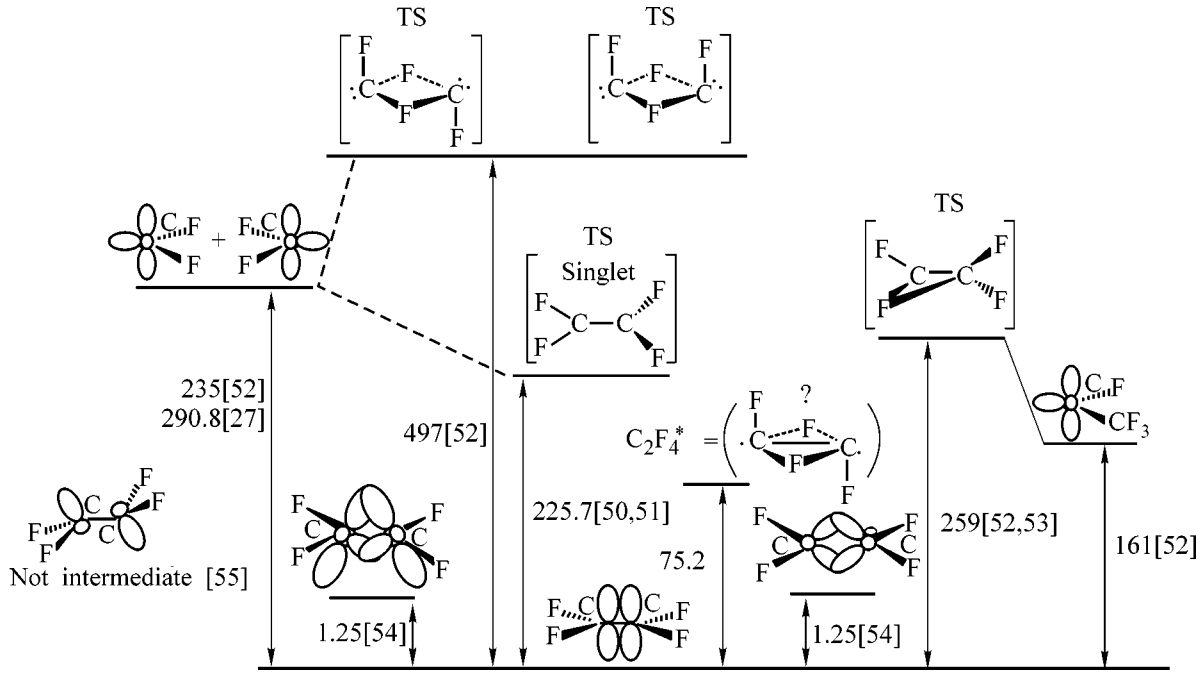

Fig. 4. *Ab initio* relative energies (kJ mol^{-1}) of $C_2F_4^*$ and species formed in the C_2F_4–TS (transition state) system.

The suggested mechnasim of [2 + 2] cyclodimerization of tetrafluoroethylene is presented in Scheme 5. Reaction (3) is addition of 1,2-biradicaloid to the double bond of $C_2F_4^*$:

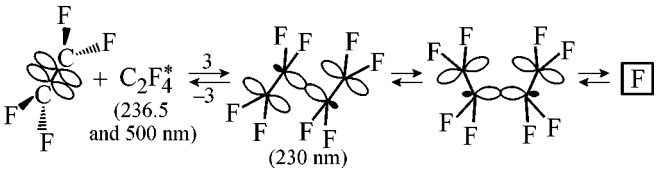

Scheme 5.

Thus, involvement of $C_2F_4^*$ in biradical [2 + 2] cyclodimerization of C_2F_4, which was proved by direct experiments, confirms biradical properties of this intermediate and indicates that a 1,4-biradical is formed by reaction of C_2F_4 with previously unknown singlet 1,2-biradicaloid $C_2F_4^*$.

The biradical nature of $C_2F_4^*$ was also confirmed by the results of a study of C_3F_6 pyrolysis [37] proceeding via reversible (4,4)-extrusion of $:CF_2$ from the CF_3 group of the C_3F_6 molecule:

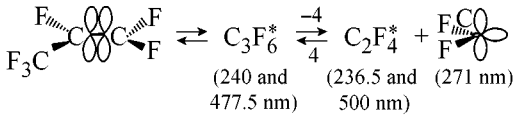

Scheme 6.

It should be noted that, at temperatures of industrial pyrolysis, C_3F_6 is formed by reaction (4), whereas the equilibrium addition of $:CF_2$ to the double bond of C_2F_4 (Scheme 3) at these temperatures is shifted to the initial compounds. Hence, the perfluorocyclopropane formation makes no contribution to the C_3F_6 synthesis. The formation of $C_3F_6^*$ and $C_2F_4^*$ 1,2-biradicaloids and the $:CF_2$ extrusion from the CF_3 groups of the biradicals were indirectly confirmed by a study of the thermolysis of compounds containing no CF_2 groups: strained epoxy compound 2-C_4F_8O [52] and 2-C_4F_8 [58]. Generally, $:CF_2$ is extruded from the CF_3 groups at radical centers of primary intermediates. Only after the appearance of a 1,3-biradical or 1,2-biradicaloid 2-$C_4F_8^*$, $:CF_2$ is extruded from the CF_3 group at the radical center:

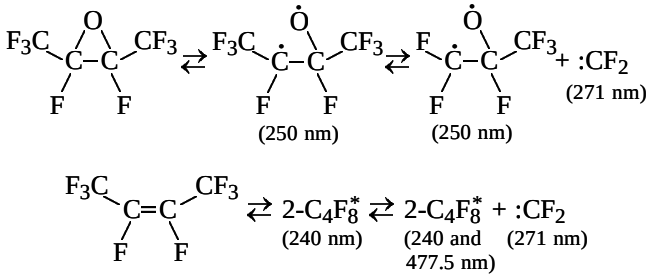

Scheme 7.

The reverse reaction is insertion of $:CF_2$ into the C–F bond at the radical center of 1,3-biradicals or

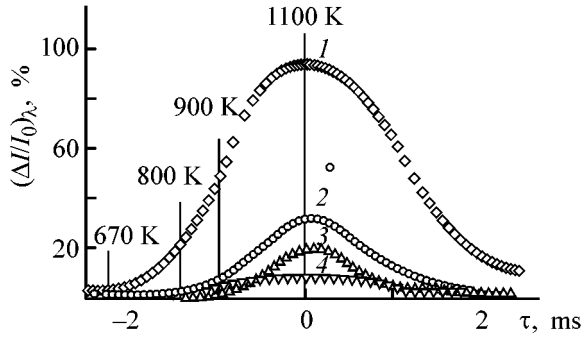

Fig. 5. Absorption of intermediates of flash pyrolysis of C_2F_4 (5 vol % in Ar) vs. time τ. $(\Delta I/I_0)_\lambda$ Relative absorption (%); the same for Fig. 6. λ (nm): (*1*) 236.5 ($C_2F_4^*$), (*2*) 230 (1,4-perfluorotetramethylene), (*3*) 271 ($:CF_2$), and (*4*) 477 ($C_3F_6^*$).

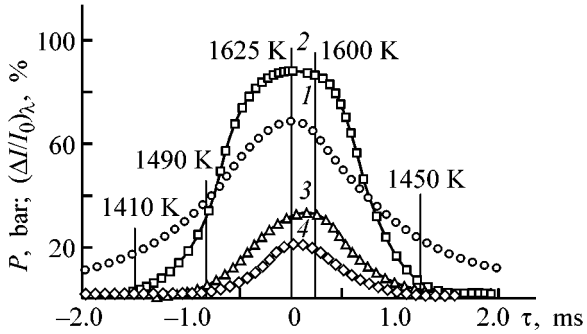

Fig. 6. (*1*) Vapor pressure *P* and (*2*–*4*) light absorption of intermediates of flash pyrolysis of C_3F_6 (1 vol % in Ar) vs. time τ. λ (nm): (*2*) 240 ($C_3F_8^* + C_2F_4^*$), (*3*) 500 ($C_2F_4^*$), and (*4*) 271 ($:CF_2$).

1,2-biradicaloids. In accordance with the above scheme and the principle of microscopic reversibility, the formation mechanism of 2-C_4F_8 is similar to that of C_3F_6 and involves insertion of $:CF_2$ into the C–F bond at the radical center of the primary carbon atom of 1,2-biradicaloid $C_3F_6^*$. Clearly, $:CF_2$ insertion into the C–F bond at the radical center of the secondary carbon atom of 1,2-biradicaloid $C_3F_6^*$ must yield *iso*-C_4F_8. The exception is synthesis of 1-C_4F_8, probably occurring via $:CF_2$ insertion into either a C–F bond of the CF_3 group or a weakened C–C bond at the radical center on the secondary carbon atom of 1,2-biradicaloid $C_3F_6^*$. However, these mechanisms were not confirmed experimentally. It should be noted that $:CF_2$ insertion into the C–C bond has not been reported yet.

Thus, detailed mechanism of formation of C_3F_6 and perfluoroolefins C_4F_8 in the course of gas-phase pyrolysis of C_2F_4 can be described by Scheme 8. This scheme is fully consistent with the sequence of formation of stable products in pyrolysis of C_2F_4 [18, 21], cyclo-C_4F_8 [18], C_3F_6 [21], and C_4F_8 [21]. The migration of double bond in normal perfluorobutenes described in [21], is also included in this scheme [33]:

$$C_2F_4 \underset{-1}{\overset{1}{\rightleftarrows}} C_2F_4^* \underset{-2}{\overset{2}{\rightleftarrows}} :CF_2 + :CF_2$$

(236.5 and 500 nm) (271 nm)

$$C_2F_4^* + C_2F_4 \underset{-3}{\overset{3}{\rightleftarrows}} F_2\dot{C}-CF_2-CF_2-\dot{C}F_2 \rightleftarrows \boxed{F}$$

(230 nm)

$$C_2F_4^* + :CF_2 \underset{-4}{\overset{4}{\rightleftarrows}} C_3F_6^* \rightleftarrows C_3F_6$$

(240 and 477.5 nm)

$$C_3F_6^* + :CF_2 \underset{-5}{\overset{5}{\rightleftarrows}} 1\text{-}C_4F_8^* \rightleftarrows 1\text{-}C_4F_8$$

$$C_3F_6^* + :CF_2 \underset{-6}{\overset{6}{\rightleftarrows}} 2\text{-}C_4F_8^* \rightleftarrows 2\text{-}C_4F_8$$

$$C_3F_6^* + :CF_2 \underset{-7}{\overset{7}{\rightleftarrows}} \textit{iso}\text{-}C_4F_8^* \rightleftarrows \textit{iso}\text{-}C_4F_8$$

$$\textit{cis}\text{-}2\text{-}C_4F_8 \underset{-8}{\overset{8}{\rightleftarrows}} \textit{trans}\text{-}2\text{-}C_4F_8$$

Scheme 8.

Experimental detection of the intermediates included in Scheme 8 does not prove their actual participation in the C_3F_6 formation. To prove the involvement of these intermediate in C_3F_6 synthesis, we generated similar intermediates from different compounds, i.e., used the method similar to independent organic synthesis.

The use of this method is based on the principle of microscopic reversibility, valid for completely homogeneous reversible thermal processes in the gas phase. In accordance with this principle, the same intermediates and stable compounds formed in the forward and reverse reactions must appear in the course of time in forward and reverse sequences.

The first intermediate of C_2F_4 pyrolysis (Fig. 5), $C_2F_4^*$ (236.5 and 500 nm), is formed at 670 K. Then 1.4-perfluorotetramethylene (230 nm) appears at 800 K. On further heating to 90 K, $:CF_2$ (271 nm) and $C_3F_6^*$ (240 and 477.5 nm) are formed virtually simultaneously. The sequence of formation of these intermediates in C_3F_6 pyrolysis (the reverse reaction) is reverse (Fig. 6). As seen from Fig. 6, the first intermediate, $C_3F_6^*$ (240 and 477.5 nm), is formed at 1410 K, and only at 1490 K simultaneous formation of $C_2F_4^*$ (236.5 and 500 nm) and $:CF_2$ (271 nm) is observed.

This indicates decomposition of $C_3F_6^*$ into these two intermediates. 1,4-Perfluorotetramethylene is not formed under conditions of C_3F_6 pyrolysis owing to the high temperature of the process (>1490 K). Since monomolecular degradation of 1,4-perfluorotetramethylene is appreciably faster than the bimolecular reaction of its formation, the concentration of this intermediate is lower than the detection limit. The fact that the maximal absorption at 271 ($:CF_2$) and 500 nm ($C_2F_4^*$) is observed at different times suggests the occurrence of an additional (along with $C_3F_6^*$ decomposition) pathway of $C_2F_4^*$ formation by recombination of $:CF_2$ [reaction (2)].

Thus, the results of direct experiments confirm the proposed Scheme 8. The structure of intermediates (1,2-biradicaloids $C_2F_4^*$, $C_3F_6^*$, 1-$C_4F_8^*$, 2-$C_4F_8^*$, and *iso*-$C_4F_8^*$) detected by light absorption was, however, confirmed neither experimentally nor theoretically.

Based on the results of this work, we propose three ways to improve the procedure of C_3F_6 production by C_2F_4 pyrolysis.

(1) High-temperature pyrolysis of perfluoroolefins by flash bulk heating at cold reactor walls raises the yield of the target product, since C_2F_4 is not consumed under these conditions in side reaction of fluorocoke formation. A reactor constructed on the basis of a standard diesel will not only produce such heating but also convert the reaction heat into mechanical work or electricity [63].

(2) The second direction is based on the fact that perfluorobutenes are formed only after the appearance of C_3F_6 in the reaction mixture. Mathematical modeling of the kinetics of reactions included in Scheme 8 shows that the yields of cyclo-C_4F_8 and C_4F_8 olefins, including highly toxic *iso*-C_4F_8, can be decreased by quenching the products at a rate of 105 deg s^{-1}. The quenching can be performed, e.g., by injection of cyclo-C_4F_8 or cold bottoms formed after C_3F_8 recovery from the pyrolysis products.

(3) Previously [18, 21], we showed that pyrolysis of C_2F_4 at 1100–1280 K and to less than 20% conversion yields only two products, cyclo-C_4F_8 and C_3F_6. Under these conditions, unreacted C_2F_4 can be recycled after separation of the pyrolysis products, thus preventing *iso*-C_4F_8 formation. The accumulated cyclo-C_4F_8 can be selectively converted into C_2F_4 by pyrolysis at 1050–1250 K, which should be performed to no more than 35% conversion [37].

The advisability of using these approaches in thermal production of C_3F_6 can be determined by feasibility studies.

CONCLUSIONS

(1) Synthesis of C_3F_6 by gas-phase pyrolysis of C_2F_4 involves insertion of $:CF_2$ into the C–F bond at the radical center of the 1,2-biradicaloid $C_2F_4^*$.

(2) Formation of C_4F_8 olefins in the course of gas-phase pyrolysis of C_2F_4 involves insertion of $:CF_2$ into the C–F (and probably C–C) bonds at the radical centers of the 1,2-biradicalod $C_3F_6^*$.

(3) The enthalpy of formation of 1,2-biradicaloids $C_2F_4^*$ and $C_3F_6^*$ from the respective perfluoroolefins is 75.2 ± 8.4 kJ mol^{-1}. The absorption spectra of these intermediates contain two bands at 236.5 and 500, and 240 and 477 nm, respectively.

(4) The theoretically predicted stabilizing effect of the F atoms was experimentally confirmed by the millisecond absorption spectra of 1,3- and 1,4-perfluoro biradicals. Indeed, the lifetime of biradical hydrocarbon analogs is shorter by several orders of magnitude.

(5) Three pathways to improve the procedure of C_3F_6 production were proposed.

ACKNOWLEDGMENTS

This work was financially supported by the Presidium of the Russian Academy of Sciences within the framework of the subprogram “Basic Research into Chemical Bond and Chemical Structure.”

REFERENCES

1. Maksimov, B.N., Barabanov, V.G., Serushkin, I.L., *et al.*, *Promyshlennye ftororganicheskie produkty* (Industrial Fluorine-Containing Organic Products), Leningrad: Khimiya, 1990.
2. Atkinson, B. and Trenwith, A.B., *J. Chem. Phys.*, 1952, vol. 20, no. 3, pp. 754–755.
3. Lacher, J.R., Tompkin, G.W., and Park, J.D., *J. Am. Chem. Soc.*, 1952, vol. 74, no. 7, pp. 1693–1696.
4. Atkinson, B. and Trenwith, A.B., *J. Chem. Soc.*, 1953, no. 7, pp. 2082–2089.
5. Atkinson, B. and Atkinson, V.A., *J. Chem. Soc.*, 1957, no. 5, pp. 2086–2091.
6. Butler, J.N., *J. Am. Chem. Soc.*, 1962, vol. 84, pp. 1393–1398.
7. Lifshitz, A., Carroll, H.F., and Bauer, S.H., *J. Chem. Phys.*, 1963, vol. 39, no. 7, pp. 1661–1665.
8. Dasey, J.R. and Litter, J., *Can. J. Chem.*, 1969, vol. 47, no. 9, p. 3871.

9. Cohen, N. and Heicklen, J., *J. Chem. Phys.*, 1965, vol. 43, no. 3, pp. 871–873.
10. Atkinson, B. and Stocwell, P.B., *J. Chem. Soc. B*, 1966, no. 9, pp. 984–989.
11. Atkinson, B. and McKeagan, D., *Chem. Commun.*, 1966, no. 7, pp. 189–190.
12. Matula, R.A., *J. Phys. Chem.*, 1968, vol. 72, no. 8, pp. 3054–3056.
13. Politanskii, S.F., *Kinet. Katal.*, 1969, vol. 10, no. 3, p. 500.
14. Simmie, J.M., Quiring, W.J., and Tschuikow-Roux, E., *J. Phys. Chem.*, 1969, vol. 73, no. 11, pp. 3830–3833.
15. Bauer, S.H., Hou, K.C., and Resler, E.L., *Phys. Fluids Suppl. I*, 1969, vol. 12, part 2, no. 5, p. 125.
16. Atkinson, B. and Tsiamis, C., Int. *J. Chem. Kinet.*, 1979, vol. 11, no. 10, p. 1029.
17. Martinez, R.I., Huie, R.E., Herron, J.T., and Braun, W.J., *J. Phys. Chem.*, 1980, vol. 84, no. 6, p. 2344.
18. Buravtsev, N.N., Grigor'ev, A.S., and Kolbanovskii, Yu.A., *Kinet. Katal.*, 1985, vol. 26, no. 1, pp. 7–14.
19. Chowdhury, P.K., Rao, K.V.S.R., and Mittal, J.P., *J. Phys. Chem.*, 1988, vol. 92, no. 1, p. 102.
20. Mel'nikovich, S.V. and Moin, F.B., *Kinet. Katal.*, 1988, vol. 29, no. 2, p. 257.
21. Buravtsev, N.N., Grigor'ev, A.S., and Kolbanovskii, Yu.A., *Kinet. Katal.*, 1989, vol. 30, no. 1, pp. 21–30.
22. Ainagos, A.F., *Kinet. Catal.*, 1991, vol. 32, no. 3, pp. 720–725.
23. Bauer, S.H. and Javanovic, S., Int. *J. Chem. Kinet.*, 1998, vol. 30, no. 1, pp. 171–177.
24. Dalby, F.W., *J. Chem. Phys.*, 1964, vol. 41, no. 8, pp. 2297–2303.
25. Modica, A.P. and LaGraff, J.E., *J. Chem. Phys.*, 1965, vol. 43, no. 9, pp. 3383–3392.
26. Tyerman, W.J.R., *J. Chem. Soc.*, Faraday Trans., 1969, vol. 65, no. 557, pp. 1188–1198.
27. Schug, K.P. and Wagner, H.Gg., *Ber. Bunsenges. Phys. Chem.*, 1978, vol. 82, no. 7, pp. 719–725.
28. Sarkar, S.K., Palit, D.K., Rao, K.V.S.R., and Mittal, J.P., *Chem. Phys. Lett*, 1986, vol. 131, no. 4, p. 303.
29. Sharpe, S., Hartnett, B., Sethi, H.S., and Sethi, D.S., *J. Photochem.*, 1987, vol. 38, no. 1, pp. 1–13.
30. Chowdhury, P.K., Pola, J., Rao, K.V.S.R., and Mittal, J.P., *Chem. Phys. Lett.*, 1987, vol. 142, no. 2, pp. 252.
31. Zhitnev, Yu.N., Timofeev, V.V., and Ignat'eva, N.Yu., *Khim. Vys. Energ.*, 1994, vol. 28, no. 6, pp. 553–560.
32. Longfellow, C.A., Smoliar, L.A., Lee, Y.T., Yeh, C.Y., and Lin, S.M., *J. Phys. Chem.*, 1997, vol. 101, no.4, p. 338.
33. German, L.S., Grigor'ev, A.S., Kolbanovskii, Yu.A., and Chepik, S.D., *Kinet. Katal.*, 1989, vol. 30, no. 1, pp. 221–223.
34. Buravtsev, N.N., Kolbanovskii, Yu.A., and Ovsyannikov, A.A., *Zh. Org. Khim.*, 1994, vol. 30, no. 12, pp. 1802–1809.
35. Buravtsev, N.N. and Kolbanovskii, Yu.A., *J. Fluorine Chem.*, 1999, vol. 96, no. 1, pp. 35–42.
36. Skell, P.S. and Woodworth, R.C., *J. Am. Chem. Soc.*, 1956, vol. 78, no. 17, pp. 4496–4497.
37. Jones, M., Ando, W., Hendrick, M.E., et al., *J. Am. Chem. Soc.*, 1972, vol. 94, no. 21, pp. 7469–7479.
38. Kolbanovskii, Yu.A., Shchipachev, V.S., Chernyak, N.Ya., *et al.*, *Impul'snoe szhatie v khimii i tekhnologii* (Pulse Compression in Chemistry and Technology), Moscow: Nauka, 1982.
39. Buravtsev, N.N., German, L.S, Grigor'ev, A.S., *et al.*, *Mendeleev Commun.*, 1993, no. 4, pp. 133–134.
40. Buravtsev, N.N., *Cand. Sci. Dissertation*, Moscow, 1989.
41. Buravtsev, N.N., Kolbanovskii, Yu.A., and Ovsyannikov, A.A., *Izv. Ross. Akad. Nauk, Ser. Khim.*, 1996, no. 1, pp. 64–67.
42. Bilera, I.V., Buravtsev, N.N., and Kolbanovskii, Yu.A., *Izv. Ross. Akad. Nauk, Ser. Khim.*, 1998, no. 1, pp. 28–34.
43. O'Gara, J.E. and Dailey, W.P., *J. Am. Chem. Soc.*, 1992, vol. 114, no. 10, pp. 3581–3590.
44. Buravtsev, N.N., Kolbanovskii, Yu.A., and Ovsyannikov, A.A., *Izv. Ross. Akad. Nauk, Ser. Khim.*, 1995, no. 10, pp. 2048–2050.
45. King, D.S., Schenck, P.K., and Stepherson, J.C., *Mol. Spectr.*, 1978, vol. 78, no. 1, p. 1.
46. Barltrop, J.A. and Coyle, J.D., *Excited States in Organic Chemistry*, London: J. Wiley and Sons, 1975.
47. Buravtsev, N.N., Kolbanovskii, Yu.A., and Ovsyannikov, A.A., *Mendeleev Commun.*, 1994, no. 2, 48–50.
48. Borisov, Yu.A., *Izv. Ross. Akad. Nauk, Ser. Khim.*, 1998, no. 4, pp. 605–607.
49. Schmidt, M.W., Trong, P.N., and Gordon, M.S., *J. Am. Chem. Soc.*, 1987, vol. 109, no. 17, pp. 5217–5227.
50. Jeffers, P.M., *J. Phys. Chem.*, 1972, vol. 76, no. 20, pp. 2829–2832.
51. Trinquier, G. and Barthela, J.C., *J. Am. Chem. Soc.*, 1990, vol. 112, no. 25, pp. 9121–9130.
52. So, S.P., *J. Phys. Chem.*, 1993, vol. 97, no. 46, pp. 11908–11911.

53. Carter, E.A. and Godard, W.A., *J. Am. Chem. Soc.*, 1988, Vol. 110, no. 12, pp. 4077–4079.

54. Tringuier, G. J. *Am. Chem. Soc.*, 1990, vol. 112, no. 6, pp. 2130–2137.

55. *IUPAC: Organic Chemistry Division: Commission on Physical Organic Chemistry. Glossary of Terms Used in Physical Organic Chemistry*, Muller, P., Ed., 1994, p. 63.

56. Buravtsev, N.N., Kolbanovskii, Yu.A., and Ovsyannikov, A.A., *Mendeleev Commun.*, 1994, no. 5, pp. 190–191.

57. Buravtsev, N.N. and Kolbanovskii, Yu.A., *Dokl. Ross. Akad. Nauk*, 1997, vol. 357, no. 6, pp. 755–778.

58. Buravtsev, N.N. and Kolbanovskii, Yu.A., *Dokl. Ross. Akad. Nauk*, 1998, vol. 358, no. 1, pp. 57–61.

59. Bernardi, F., Bottoni, A., and Olivucci, M., *J. Chem. Soc., Faraday Trans.*, 1994, vol. 90, no. 12, pp. 1617–1630.

60. Woodward, R.B. and Hoffmann, R., *Angew. Chem.*, Int. Ed., 1969, vol. 8, p. 693.

61. Getty, S.F. and Border, W.T., *J. Am. Chem. Soc.*, 1991, vol. 111, no. 11, pp. 4334–4335.

62. Quick, L.M., Knecht, D.A., and Back, M.H., *Int. J. Chem. Kinet.*, 1972, vol. 4, no. 1, pp. 61–68.

63. Buravtsev, N.N., Kolbanovskii, Yu.A., Ovsyannikov, A.A., and Plate, N.A., *Khim. Prom–st.*, 1995, no. 1, pp. 4–7.

Russian Journal of Applied Chemistry, Vol. 75, No. 4, 2002, pp. 606–610. Translated from Zhurnal Prikladnoi Khimii, Vol. 75, No. 4, 2002, pp. 620–624.
Original Russian Text Copyright © 2002 by Gribanov, Sazanov, Mokeev.

MACROMOLECULAR CHEMISTRY AND POLYMERIC MATERIALS

Role of Structural Characteristics of Aromatic Polyimides in Carbonization

A. V. Gribanov, Yu. N. Sazanov, and M. V. Mokeev

Institute of Macromolecular Compounds, Russian Academy of Sciences, St. Petersburg, Russia

Received January 9, 2002

Abstract—The influence of the structural characteristics of polyimides belonging to four standard classification groups was analyzed. The main factors responsible for formation of ordered and/or turbostratic carbon structures in the course of carbonization were studied for the example of film and fibrous materials.

The majority of published data on heat resistance of polyimide materials are related to poly(pyromellitimide diphenyl oxide) (PPM), the first and the most widely used aromatic polyimide [1, 2]. This polyimide is still the most demanded; however, some service characteristics of articles made from it do not meet the modern requirements. In this connection, one of the ways to modify polyimide materials was to vary the chemical structure of the initial components, tetracaboxylic acid dianhydrides and aromatic diamines. By now, active synthetic efforts have resulted in laboratory preparation of several hundreds of polyimides of various structures. For a number of reasons, only a few of these have found real practical use. Published data [3–6] on the heat resistance and mechanical strength of film and fibrous materials based on some polyimides differing in structure from PPM are insufficient to understand the proceses occurring in these compounds at temperatures above 300–400°C. Much less is known about the carbonization process, i.e., conversion to the carbon state, although production of carbon materials by carbonization of polyimide polymers is of prime interest.

Previously [7, 8], we have established some features of high-temperature conversion, i.e., carbonization of PPM polyimide. Here, using the previously developed approach, we make an attempt to elucidate the influence of the chemical structure of aromatic polyimides on their conversion to a carbonized product under similar conditions.

EXPERIMENTAL

Films and fibers produced according to [9] were used as samples of polyimide materials. With respect to their chemical structure, the polyimides studied belong to all the four groups of the standard classification [9]:

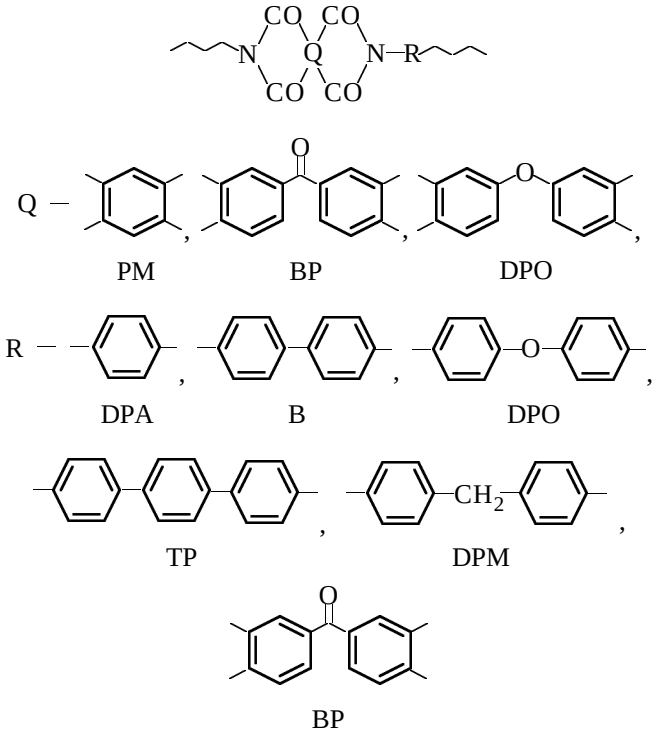

where PM is the pyromellitic core, BP is benzophenone, DPO is diphenyl oxide, PPA is *p*-phenylenediamine, B is benzidine, TP is terphenyl, and DPM is diphenylmethane.

In what follows, the first abbreviation will refer to the dianhydride moiety, and the second, to the diamine moiety.

1070-4272/02/7504-0606 $27.00 © 2002 MAIK "Nauka/Interperiodica"

To study the carbonization and the structure of the reaction products, we used thermal gravimetric analysis (TGA) in a vacuum and an inert gas medium in combination with mass spectrometry, thermal volumetric analysis (TVA) of the kinetics of gas release, and complex spectral analysis of the final products and intermediates with the use of high-resolution ^{13}C NMR in solids and X-ray photoelectron spectroscopy (XPES). Some reactions were monitored by DTA. Thermal analysis was carried out using a Du Pont-951 thermal analyzer (TGA), a Mettler thermal balance connected to a Balzer quadrupole mass spectrometer, a Vacuum-Generator X-ray emission spectrometer, a Bruker CXP-100 NMR spectrometer, and a thermal volumetric installation [10].

Up to now, the universally accepted criterion for estimation of the carbonization ability of polymers has been the amount of the coke residue formed in a certain regime of heat treatment. Therefore, when comparing quantitative data on carbonization of polyimides, it is reasonable to consider this characteristic first.

As shown for PPM as an example, carbonization of polyimides begins and proceeds most intensively in the temperature range 500–650°C. In this range, it is of most interest to compare the weight loss and the kinetics of gas release, depending on the structure of the elementary unit of polyimide. The TGA curves of the initial stage of carbonization of polyimides are shown in Fig. 1. It is evident that the most heat-resistant in the temperature range 500–550°C are polyimides of classes A and B, whose structure is rigid because the diamine component contains no "hinged" atoms and groups. For these polyimides (PM–PPA and PM–B) the coke number in the given temperature range is 2 times that of flexible-chain polyimides such as, e.g., BP–PPA and BP–B. This behavior of rigid-chain polyimides corresponds to thermal characteristics of aromatic model compounds of the phenylene series [11]. In the cases when such hinged groups or atoms as –O–, $–CH_2–$, –C(O)–, etc. are incorporated in the polyimide structure, thermal degradation, most likely, starts at these bonds.

Homolytic degradation of benzimide rings with release of carbon oxides begins in the same temperature range.

The curves of simultaneous thermal gravimetric and mass spectrometric analyses of PM–B polyimide (Fig. 2) show a typical pattern of thermal degradation of polyimides. A noticeable weight loss accompanied by release of a number of gaseous products of degradation of benzimide ring (CO, CO_2, H_2O, HCN, H_2, etc.) occurs specifically in the range 500–550°C. The set of these products suggests that the initial phase of carbonization is similar to that considered previously for the example of PPM [8]. However, detailed comparison of these data for various structures of polyimides other than PPM reveals certain qualitative and quantitative distinctions between them in the composition of gaseous carbonization products. For example, for polypyromellitimides in which the diamine fragment consists of phenylene rings (PM–PPA, PM–B, and PM–TP), according to mass-spectrometric data, the products of the initial stage of carbonization consist mainly of carbon oxides, i.e., products of decomposition of benzimide rings. The distinction in the amount and ratio of these products

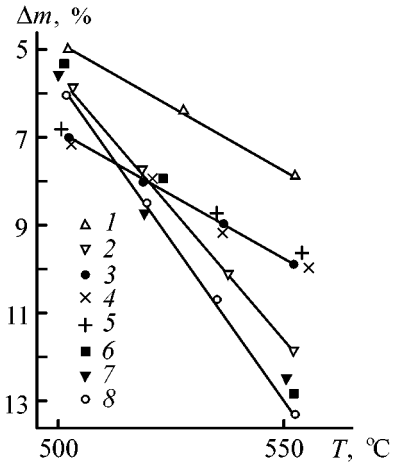

Fig. 1. TGA curves of the initial stage of carbonization of polyimides. (Δ*m*) Weight loss and (*T*) temperature, the same for Fig. 2. (*1*) PM–PPA, (*2*) DPO–DPO, (*3*) DPO–PPA, (*4*) PM–B, (*5*) DPO–P, (*6*) BP–PPA, (*7*) BP–B, and (*8*) PPM.

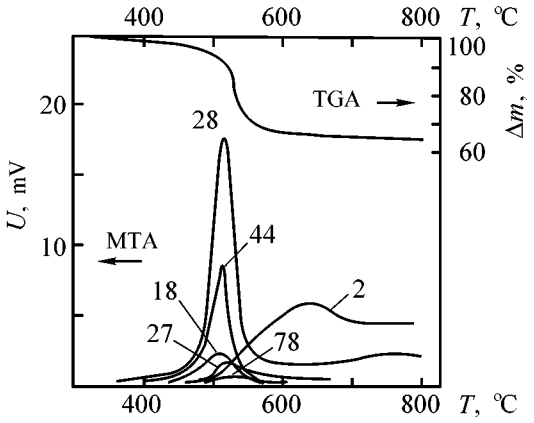

Fig. 2. Curves of simultaneous TGA–MTA of PM–B fiber: (*U*) voltage of ionic current. Figures at MTA curves are weight numbers of pyrolysis products, *m*/*e*.

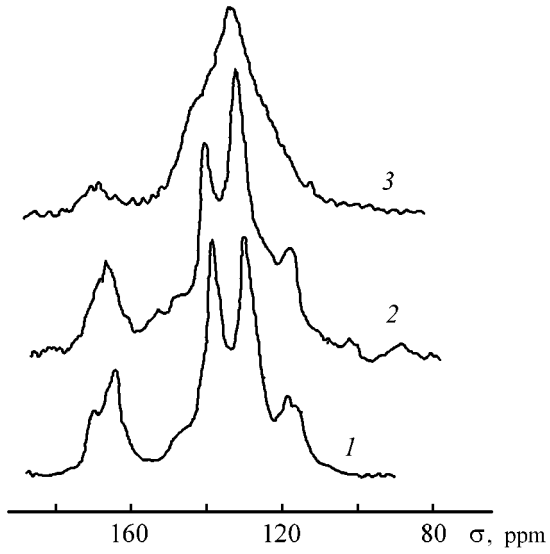

Fig. 3. High-resolution ^{13}C NMR spectra of PM–PPA and its carbonization products: (δ) Chemical shift, the same for Figs. 4 and 6. Temperature, °C: (*1*) 25, (*2*) 575, and (*3*) 600.

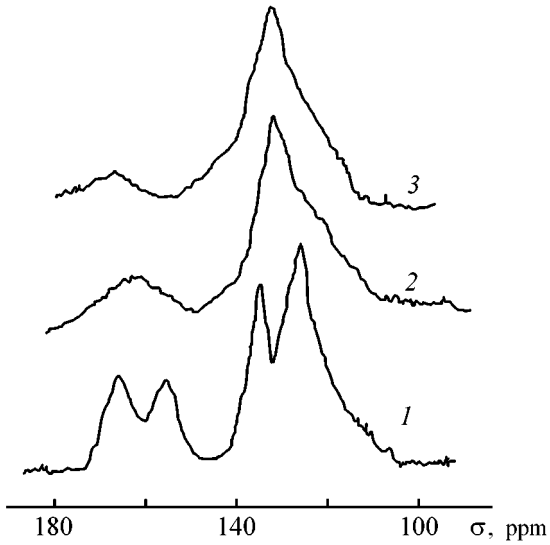

Fig. 4. High-resolution ^{13}C NMR spectra of DPO–DPO and carbonization products. Temperature, °C: (*1*) 25, (*2*) 500, and (*3*) 550.

is caused by different types of structural packing of macromolecules in these polyimides [12]. As regards polyimides with "hinged" bonds in the diamine and dianhydride components, the presence of noticeable amounts of HCN, ammonia, benzonitrile, dicyanobenzene, phenol, and biphenyl in the mass spectra suggests diversity of the initial events in thermal degradation of these polyimides. It should be noted that thermal degradation in a vacuum of polyimides containing methylene, diphenyl oxide, and benzophenone fragments favors secondary cross-linking of solid carbonization residues. This follows from comparison of the amounts of carbonized polyimides formed by heating to 800°C. It is seen from the TGA data that this amount is 80–75% for the DPO–B and DPO–PPA film samples, less by 10% for PM–DPO, PM–B, and PM–PPA, and, on the average, 60–65% for fibrous samples.

As a rule, the main weight loss due to removal of volatile carbonization products is complete by 650°C. Upon further heating, the primary carbonized structure becomes thickened owing to dehydrogenation and removal of residual heteroatoms.

As in the case of PPM, the most interesting data on the influence of chemical structure on the mechanism of conversion of polyimides into carbonizate with ordered and/or disordered structure were obtained using ^{13}C NMR in solids.

A comparison of the high-resolution ^{13}C NMR spectra of rigid-chain PM–PPA and PM–B polymers produced at various temperatures of heat treatment (Fig. 3) showed primarily the high stability of polymer units in this group of polyimides. Up to 600°C, the main signals vary insignificantly. The behavior of the signal at 164 ppm, corresponding to the carbonyl carbon of the imide ring, exhibits a specific feature: even at temperatures higher than 600°C there is a weak signal in this range of spectrum, which suggests the presence of a small amount of carbonyl groups even at these temperatures. On heating at 550°C, a shoulder at 150–155 ppm appears in the spectra. It is well known that this range corresponds to a carbon atom of a benzene ring directly bonded to an oxygen atom. Hence, we can assume a slight increase in the amount of Ph–O–Ph bonds (this is more pronounced in the spectra of PM–PPA than those of PM–B). The appearance of this shoulder is most probably due to formation of new bonds in the polymer through exogenic oxidation. On heating PPM polyimide, the intensity of the signal at 155 ppm decreases out of proportion to the intensity of the carbonyl signal at 164 ppm [13]. However, formation of new Ph–O–Ph bonds could not be detected against the background of the Ph–O–Ph bonds already present in the diamine fragment of PPM. Here, the appearence of oxyphenyl groups in PM–PPA and PM–B was detected for the first time.

Polyimides containing the DPO fragment show different trends in evolution of the NMR spectra upon heating. Even at 500°C the signals become strongly broadened (Fig. 4). The signals corresponding to carbonyl carbons (164 ppm) and quaternary carbons of the imide ring (137 ppm) abruptly decrease in intensity and become significantly broadened. Simultane-

ously, the width of the signal at 130 ppm increases significantly, which suggests rapid growth of a heteroaromatic carbon structure. Since the weight loss at these temperatures is insignificant, these changes in the spectra can be accounted for by interchain cross-linking and rapid formation of a heteroaromatic structure at relatively low temperature. This is also suggested by the coalescence of the signals at 164 and 155 ppm.

These observations are well supplemented by the spectral characteristics of the C, O, and N atomic states of the polymers in carbonization, obtained using XPES. The spectra of intermediates obtained in carbonization of polyimides (heating in a vacuum to 600°C) are shown in Fig. 5. Comparison of the O1*s* spectra shows that, contrary to PPM polyimide, for which the intensity of the signal of the C=O group does not exceed 40–45% of the total intensity of the oxygen signal (in the initial sample, 4 : 1), the similar ratio for the DPO–DPO polyimide is higher, although the initial proportions are lower (2 : 1). This fact suggests that the cleavage of the imide ring in DPO–DPO with increasing temperature is somewhat slower than that in PPM polyimide, and cross-linking through oxygen bridges is less active. Analysis of the oxygen spectra of rigid-chain polymers PM–PPA and PM–B containing no diphenyl oxide oxygen in the chain shows that, with increasing temperature, the C–O–C interchain bonds are formed (the spectral line at 533.6 eV). These conclusisons are confirmed by analysis of the C1*s* lines. It is seen that carbonization is the fastest in this stage for PPM, in good agreement with the curves of weight loss at 600°C. For all the polymers studied in this work, the initial singlet of nitrogen transforms on heating into a multiplet with different binding energies. In PM–B and PM–PPA, the contribution of this spectral line (E = 400.4 eV) in the multiplet is significantly higher than that in PPM and DPO–DPO polyimides. This fact suggests that the content of the residual imide rings in rigid-chain polyimides is significantly higher than that in semicrystalline PPM and flexible-chain DPO–DPO.

Carbonization proper, as a transition from linear to three-dimensional carbon structure, is completed on heating to 800–900°C and is characterized by the formation of a polyaromatic quasi-graphite carbon structure. The ^{13}C NMR spectra of carbon residues of various polyimides were compared with the spectrum of graphite (Fig. 6). A downfield shift of the signal of carbonizates by 5 ppm for PPM and PM–PPA and by 10 ppm for DPO–DPO is attributable to the difference between the resulting carbon structure and the ideal polyaromatic structure of graphite. Comparison of the half-widths of the signals is of greater interest. We believe that the more broadened signal of the DPO–DPO carbonizate suggests the preferable formation of turbostratic irregular structures, while the half-width of the signal of rigid-chain PPA is

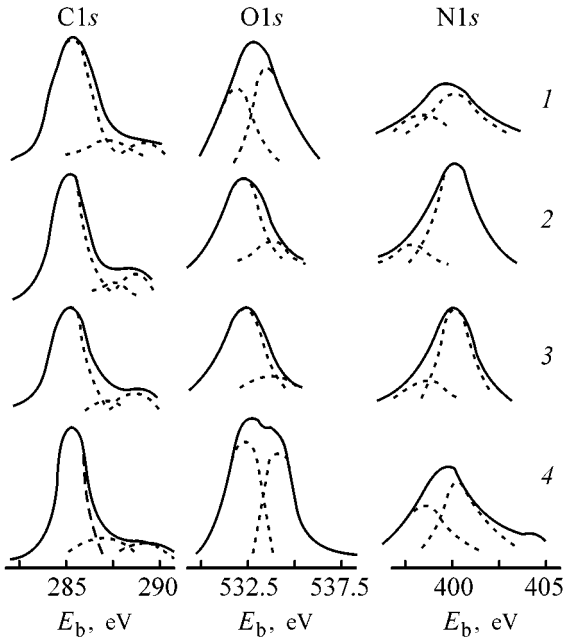

Fig. 5. XPE spectra of polyimides heated to 600°C (C1*s*, O1*s*, and N1*s* lines): (*1*) PPM, (*2*) PM–B, (*3*) PM–PPA, and (*4*) DPO–DPO. (E_b) Binding energy.

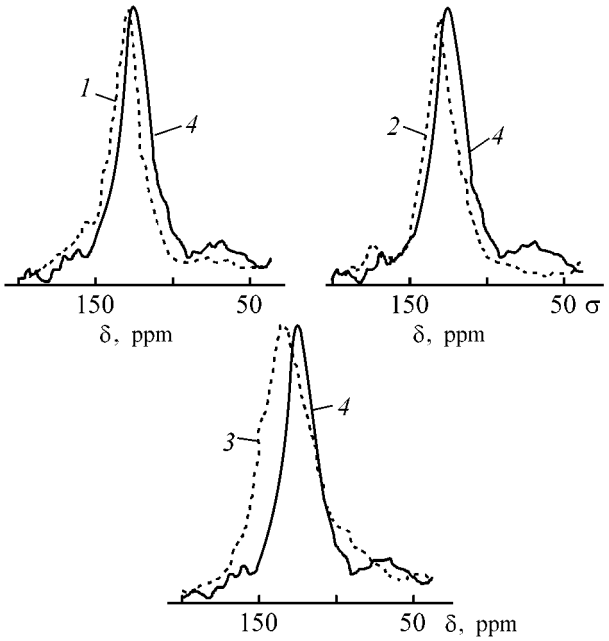

Fig. 6. High-resolution ^{13}C NMR spectra of carbonizates of polyimides (*1*) PPM, (*2*) PM–PPA, and (*3*) DPO–DPO; (*4*) spectrum of graphite, as reference.

close to that of the signal of graphite, which apparently reflects its structural similarity to graphite.

CONCLUSIONS

(1) The model of interchain cross-linking of PPM polyimide is applicable to polyimides of various chemical structures.

(2) Carbonization of rigid-chain polyimides of class A is governed by layered packing of macromolecules, which results in the formation of ordered centers of subsequent graphitization.

(3) Carbonization of flexible-chain polymers of class D is developed through formation of turbostratic structures owing to the significant segmental mobility of macromolecules in these polyimides.

(4) The mechanism of carbonization of polyimides of classes B and C is mainly governed by the parameters of heat treatment.

REFERENCES

1. Gribanov, A.V. and Sazanov, Yu.N., *Zh. Prikl. Khim.*, 1997, vol. 70, no. 6, pp. 881–902.
2. Sazanov, Yu.N., *Zh. Prikl. Khim.*, 2001, vol. 74, no. 8, pp. 1217–1234.
3. Sekei, T., Koton, M.M., Sazanov, Yu.N., *et al.*, *Khim. Volokna*, 1977, no. 1, pp. 25–27.
4. Koton, M.M., Bessonov, M.I., and Sazanov, Yu.N., *Plast. Massy*, 1981, no. 5, pp. 22–26.
5. Kabilov, Z.A., Miunov, T.M., Shibaev, L.A., *et al.*, *Thermochim. Acta*, 1979, vol. 28, pp. 333–347.
6. Yasunori, Y., *Kogyo Zaizyo*, 1997, vol. 45, no. 4, pp. 99–102.
7. Gribanov, A.V., Sazanov, Yu.N., Beloborodova, E.V., and Fedorova, G.N., *Zh. Prikl. Khim.*, 1999, vol. 72, no. 3, pp. 467–473.
8. Gribanov, A.V. and Sazanov, Yu.N., *Zh. Prikl. Khim.*, 2000, vol. 73, no. 10, pp. 1705–1709.
9. Bessonov, M.I., Koton, M.M., Kudryavtsev, V.V., and Laius, L.A., *Poliimidy – klass termostoikikh polimerov* (Polyimides: A Class of Heat-Resistant Polymers), Leningrad: Nauka, 1983.
10. Sazanov, Yu.N. and Sysoev, V.A., *Eur. Polym. J.*, 1974, vol. 10, pp. 867–869.
11. Sazanov, Yu.N. and Shibaev, L.A., *Acta Polym.*, 1980, vol. 31, no. 1, pp. 1–10.
12. Sazanov, Yu.N., Antonova, T.A., Stepanov, N.G., *et al.*, *Acta Polym.*, 1991, vol. 42, nos. 2/3, pp. 119–125.
13. Gribanov, A.V., Shibaev, L.A., Koltsov, A.I., *et al.*, *J. Thermal Anal.*, 1987, vol. 32, no. 3, pp. 815–823.
14. Gribanov, A.V., Milevskaya, I.S., Lukasheva, N.V., *et al.*, *Vysokomol. Soedin., Ser. A*, 1989, vol. 31, no. 8, pp. 1572–1576.

Russian Journal of Applied Chemistry, Vol. 75, No. 4, 2002, pp. 611–618. Translated from Zhurnal Prikladnoi Khimii, Vol. 75, No. 4, 2002, pp. 625–632.
Original Russian Text Copyright © 2002 by Smirnov, Volkov.

MACROMOLECULAR CHEMISTRY AND POLYMERIC MATERIALS

Effect of Functionality of Oligophenolic Hardener on Structural and Kinetic Features of Formation and on Properties of Epoxy–Phenolic Cross-Linked Polymers

Yu. N. Smirnov and V. P. Volkov

Institute for Problems of Chemical Physics, Russian Academy of Sciences, Chernogolovka, Moscow oblast, Russia

Institute of Synthetic Polymeric Materials, Russian Academy of Sciences, Moscow, Russia

Received October 2, 2001

Abstract—Kinetics of the reaction of resorcinol diglycidyl ether with novolac phenol–formaldehyde resins of various functionalities were studied over a wide temperature range by isothermal calorimetry. The effects of the functionality of oligophenols on curing of epoxy-phenolic composites, structure of the resulting polymer at the chemical, topological, and supramolecular levels, its mechanical and relaxation properties, and the mechanism of its fracture were analyzed.

Success in synthesis of high-performance cross-linked polymers at low production cost depends to a considerable extent on understanding of relationships between the structure of the starting reagents, synthesis conditions, product structure, and product properties. Goal-seeking analysis of these interlinks is known as structural-kinetic approach [1–5]. In these works, the effects of various low-molecular-weight fluids, chemically active tertiary amines [1, 2, 5], and physically active plasticizers [1, 3] on the kinetics and mechanism of curing, relaxation and mechanical characteristics, and fracture of polymers were examined for the examples of epoxy–amine [1–3, 5] and epoxy–phenolic cross-linked polymers [4].

It is known [6–10] that oligophenols obtained by condensation of phenol and formaldehyde, among them novolac phenol–formaldehyde resins (NPFRs) [6], are widely used as cheap hardeners for epoxy resins of various purposes. However, only very limited published data are available concerning the effect of the molecular weight or functionality of NPFRs on the kinetics of their reaction with epoxides and also on the mechanical characteristics of novolac epoxy composites [11]. Therefore, the goal of this work was to analyze the effect of the molecular weight or functionality of NPFRs on the kinetics and mechanism of curing, structural organization at various levels, and properties of epoxy–phenolic cross-linked polymers (EPCLPs) using the structural-kinetic approach.

EXPERIMENTAL

As an epoxy resin we used resorcinol diglycidyl ether purified by high-vacuum distillation. A novolac phenol–formaldehyde resin was synthesized by the procedure described in [12] and used without further purification. The average functionality of the novolac resin was controlled by varying the phenol-to-formaldehyde ratio.

As reference compounds we used the monofunctional phenol studied previously [13, 14] and also SF-010 commercial high-molecular-weight novolac resin [GOST (State Standard) 18694–73]. Phenol and sulfolane (used as a strongly solvating agent) were purified by high-vacuum distillation. The reactivity of the epoxy and phenol groups was characterized by the initial rates, which were determined from differential calorimetric curves obtained on an EK-2 fast-response calorimeter over a wide temperature range [15].

Phenolic rings of oligophenols can be bound to each other via *ortho,ortho*, *ortho,para*, and *para,para*

1070-4272/02/7504-0611 $27.00 © 2002 MAIK "Nauka/Interperiodica"

Characteristics of novolac phenol–formaldehyde resins

Resin	P_1 : FA, mol : mol	$\overline{M}_n$		$\overline{M}_w$, GPC	$\overline{M}_n / \overline{M}_w$	$\overline{f}_n$	P_1	P_2	P_3	HMWF	[OH]
		IE*	GPC				%				
N_{10}	10 : 1	205	232	362	1.66	2.3	0.73	59.8	37.1	3.1	16.8
N_{11}	10 : 2	246	288	378	1.25	2.81	2.0	41.0	19.2	38.0	16.6
SF-0121**	–	–	308	390	1.27	3.0	1.65	42.3	26.4	31.3	16.9
N_9	10 : 3	338	328	431	1.31	3.19	–	34.2	18.3	47.5	16.6
N_6	10 : 4	346	360	475	1.27	3.52	0.88	31.1	15.3	53.6	16.6
N_7	10 : 5	363	392	672	1.62	3.82	1.35	22.6	13.8	63.6	16.6
N_4	10 : 6	424	426	927	2.02	4.1	1.65	20.1	11.8	68.1	16.4
SF-010**	–	590	450	1630	2.71	4.45	5.34	12.4	9.7	77.9	16.8
N_1	10 : 7	645	556	1274	2.29	5.32	–	14.7	10.6	74.7	16.3

* Determined from the heat of condensation (indirect ebullioscopy). ** Commercial brand.

methylene bridges [16]. Below is given typical oligophenol structure

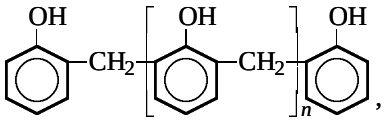

where n = 0–10.

A gel-permeation chromatographic study of NPFRs showed that the oligophenols obtained are characterized by a broad distribution over molecular weights and, therefore, with respect to functionalities (Fig. 1). As seen from the table, with variation of the phenol-to-formaldehyde molar ratio (P_1 : FA) from 10 : 1 to 10 : 7, the mean molecular weight of NPFR $\overline{M}_n$ increases from 232 to 556, and the mean functionality $\overline{f}_n$, determined from $\overline{M}_n$ and the hydroxy group content (see table), from 2.3 to 5.32. In this case, the contents of fractions with n = 0 (P_2) and n = 1 (P_3) and of high-molecular-weight fractions (HMWF) noticeably change, as also does the excess phenol content P_1^e. At the same time, the phenol group content (wt %) in NPFRs remains practically unchanged, regardless of their functionality. From the kinetic standpoint, this must cause the equality of the rates of curing with these resins. However, the calorimetric data obtained over a wide temperature range appeared to be unexpected.

With increasing functionality of NPFRs, the activation energy E_a of the reaction of the diepoxide with oligophenols considerably decreases (Fig. 2a); the

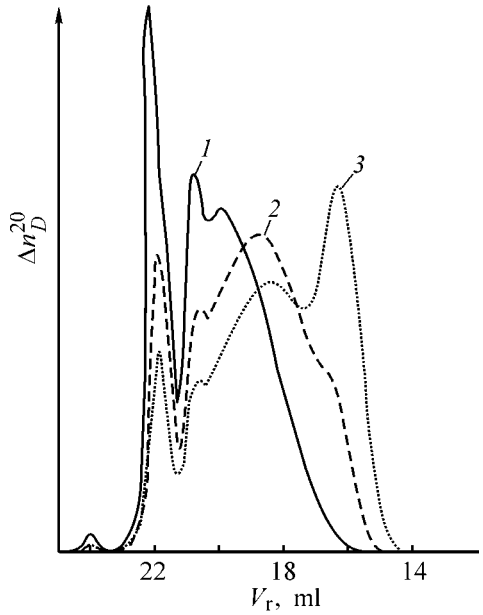

Fig. 1. Gel chromatograms of NPFRs. (Δn_D^{20}) Refractive index difference and (V_r) retention volume. Average functionality $\overline{f}_n$ of NPFRs: (*1*) 2.3, (*2*) 3.5, and (*3*) 5.3.

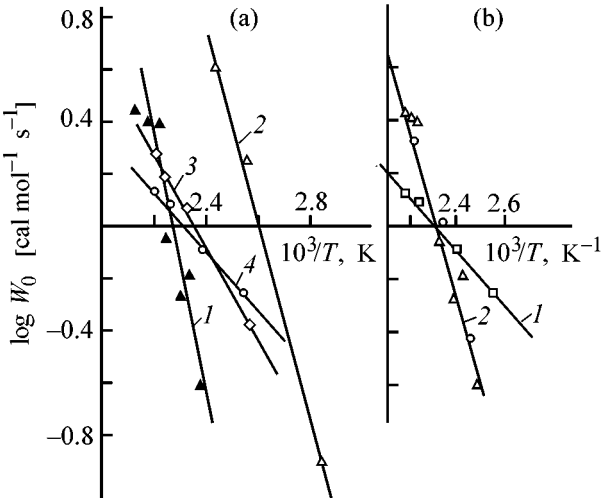

Fig. 2. Arrhenius plots of the initial rates W_0 of curing in the bulk of epoxy–phenolic polymers obtained with (a) NPFRs of various mean functionalities $\overline{f}_n$ and (b) at $\overline{f}_n$ = 5.3 in the presence or absence of monophenol. (T) Temperature; the same for Fig. 3. (a) $\overline{f}_n$: (*1*) 1, (*2*) 2.3, (*3*) 3.5, and (*4*) 5.3. (b) Monophenol concentration (wt %): (*1*) 0 and (*2*) 6.

monofunctional phenol demonstrates the highest E_a. Addition of a small amount of phenol (6 wt %, which is a typical concentration of phenol as an impurity in commercial NPFRs) to a mixture containing oligophenol with $\overline{f_n}$ 5.3 also considerably increases E_a (Fig. 2b).

Note that the increasing activation energy of curing is an important factor in molding goods from prepreg-based composite materials [17]. The higher E_a, the lower the reactivity of a binder (the longer the prepreg shelf life) at a given temperature of storage and the higher the reactivity at the temperature of molding. Therefore, optimization of the NPFR functionality allows control of the prepreg performance.

It was demonstrated in studying the kinetics of curing of the same composites in sulfolane that the functionality of NPFRs has practically no effect on E_a. In this case, E_a of all the NPFRs studied becomes equal to that of phenol (Fig. 3), which can be attributed to the clearly pronounced tendency of phenols toward self-association. It is typical of monophenols to form linear (**I**) or cyclic (**II**) associates:

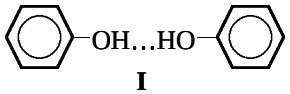

I

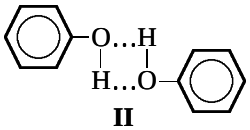

II

It is known [13, 18] that, the higher the degree of saturation of hydrogen bonds and the degree of delocalization of the electron density in autocomplexes, the more stable and the less reactive they are. More stable cyclic associates of monophenols, having higher enthalpy of complexation (6–8 kcal mol^{-1}), must increase the activation energy of the reaction of oligophenols with epoxides. That is why the reaction of the diepoxide with monophenol is characterized by the highest E_a.

In oligophenols, formation of cyclic intermolecular associates is hindered by steric factors, and intramolecular association, evidently, dominates in this case. The resulting chains of oligophenols roll up into globules [19]. This trend must become more pronounced with increasing molecular weight of oligophenols. Therefore, the reactivity of phenol groups in oligophenols can increase as a result of formation of less stable associates, but the steric accessibility of these groups to reagents may be lower as compared to monophenols

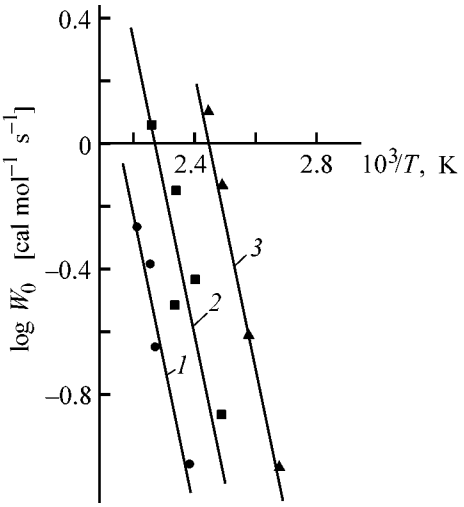

Fig. 3. Arrhenius plots of the initial rates of curing W_0 of epoxy–phenolic composites in sulfolane for NPFRs of various mean functionalities $\overline{f_n}$: (*1*) 1, (*2*) 2.3, and (*3*) 5.3.

because of the globular structure. As an illustration, with the functionality of NPFR increasing from 2.3 to 5.3, the degree of epoxidation of the oligophenols with epichlorohydrin decreases from 81 to 63%, while in the case of monophenol it is 90–95%.

Note that, with the use of polyphenols as curing agents, the topological limit of curing of the final cross-linked polymer (α_∞ = 0.85 [20]) is lower than that of epoxy–amine polymers (α_∞ = 0.95 [21]). This result was attributed in [20] to stronger steric hindrance in epoxy–phenolic systems with respect to interaction of functional groups, with the possible globular structure of the phenolic hardener disregarded. Introduction of sulfolane (highly solvating agent) results in breakdown of the associates of phenol groups and formation of complexes with the solvent, thus saturating all the hydrogen bonds in the reaction system (in this case, open conformations of oligophenols can be formed). All this explains the observed rise in the activation energy. Introduction of a small amount of monophenol to high-functionality oligophenols must also favor formation of more stable H complexes, causing increase in E_a.

It follows from the results obtained that association plays an important part in curing of epoxides with oligophenols. The practical aspects of this effect have been considered elsewhere [22]. At the same time, high degree of association in oligophenols (especially in high-molecular-weight fractions) can reduce α_∞ and create prerequisites for formation of a microheterogeneous cross-linked structure. It was demonstrated in [4] that formation of a cross-linked structure involves two reactions: main reaction (1), in which the epoxy

groups are consumed in the polycondensation (PC) process with participation of the phenol groups of EPCLP, and side reaction (2), in which the epoxy groups react with secondary alcohol groups [products of reaction (1)] by the polymerization (PM) mechanism:

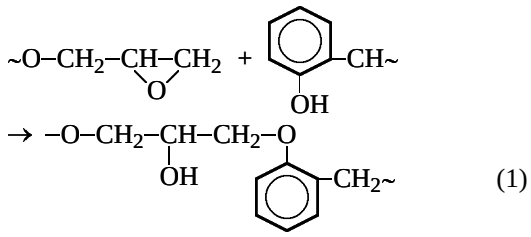

(1)

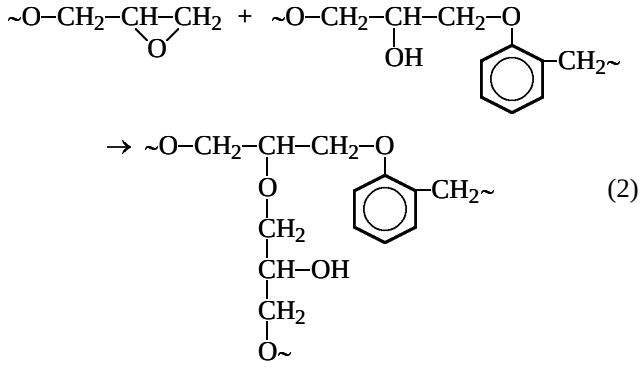

(2)

The typical unit of a cross-linked structure formed in the purely PC process is hydroxy ether fragment **III** of the interjunction chain:

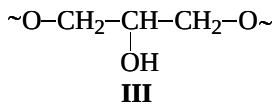

III

whereas ether fragment **IV** is the characteristic unit of a cross-linked structure formed in a side PM reaction:

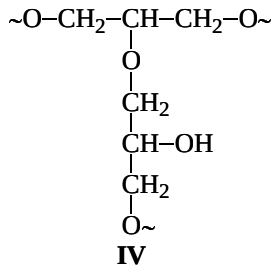

IV

Note that hydroxy ether fragments **III** of the interjunction chain formed by the PC mechanism may serve as a flexible link decreasing the degree of cooperativity of motion of network junctions as the major kinetic unit of large-scale segmental motion [23]. Furthermore, the secondary alcohol group of fragment **III**, which is the major unit of the H-bonded network structure in EPCLPs [24], controls to a considerable extent the properties of these polymers in the glassy state. In its turn, the ether fragment **IV** is an additional junction in the chemical network formed by the PM mechanism. The appearance of this junction changes the length and nature of the interjunction chain, deteriorating the relaxation and mechanical characteristics of EPCLPs.

It follows from the kinetic results that the functionality of NPFRs has a strong effect on the structure of the resulting cross-linked polymers. The structure and properties of cured EPCLPs were mainly studied at an epoxy to phenol group ratio of 1 : 0.5. This was caused by the fact that the oligophenol content in the epoxy-phenolic composite is a key factor controlling its viscosity as a binder for wet winding. Taking into account that the strength of EPCLPs decreases with increasing epoxy to phenol group ratio [24], the selected ratio was accepted as the optimal from the standpoint of the product performance. Such a selection of this ratio suggests *a priori* a high contribution of the PM process to the formation of the crosslinked structure of EPCLPs. However, this contribution must also depend on the degree of conversion of the phenol groups, i.e., on their steric accessibility, depending, in its turn, on the functionality of the oligophenols.

It should be pointed out that epoxyphenolic composites were cured in the presence of 1% triethanolamine (TEA) as a catalyst, with stepwise rise in the temperature, which allows separation of reactions (1) and (2) in time and provides completeness of PM reaction (2) in the final stages of curing [4]. Chemical analysis for the epoxy groups in cured EPCLPs showed that, regardless of the NPFR functionality, the conversion with respect to the epoxy groups is 94–96%, i.e., it is constant to within the determination error. This result shows that the observed evolution in the structure and properties of EPCLPs is directly governed by the functionality of NPFRs.

The effect of the functionality of oligophenols on the structure of cross-linked epoxy–phenolic polymers is manifested differently at the molecular, topological, and supramolecular levels [25].

This effect is not pronounced at the molecular level at the given initial ratio of the reactive groups and practically constant conversion of the epoxy groups.

Topologically, the structure can be characterized, to a first approximation, by the number of cross-links and also by the sol fraction content. The effective cross-link density was determined (with the front fac-

tor disregarded) from the modulus of elasticity in the hyperelastic state [26]:

$$G_\infty = 3\rho RT/\overline{M} = 3\nu RT,$$

where ν is the effective cross-link density; ρ, the density; $\overline{M}$, the mean molecular weight of the interjunction chain; R, the gas constant; and T, the measurement temperature.

The dependence of the effective cross-link density ν on the mean functionality of NPFR (Fig. 4) passes through a maximum at $\overline{f_n}$ = 3.5–4.0. For the same polymers, we determined the sol fraction content which is commonly used as an integral parameter characterizing the degree of topological faultiness of the cross-linked structure, associated with formation of rings, linear chains, or with the presence of unreacted components [25]. Figure 4 demonstrates that the sol fraction content Z (wt %) as a function of the hardener functionality passes through a minimum at $\overline{f_n}$ approximately corresponding to the maximal ν.

Thus, the dependences of both the parameters characterizing the topology of the cross-linked structure on the hardener functionality show extrema. The variation trends of these parameters are evidently caused by the increasing functionality of network junctions and, as a result, by changing relative contributions of the PC and PM mechanisms to formation of the cross-linked structure in the course of curing. It may be suggested that, at low hardener functionality, the PC process dominant in the initial stages of curing must produce essentially linear chains. Further cross-linking of these chains in the course of gelation proceeds by reaction (2). At medium functionality of the hardener (about 3.5), cross-linking must proceed by the PM mechanism [reaction (1)], at least at the microscopic level (formation of microgels). In this case, the PM mechanism promotes further monolithization, i.e., linking of separate microblocks or cross-linked microaggregates to form a macroscopic block or network.

The expected course of cross-linking at various hardener functionalities is confirmed by experimental data on the evolution of mechanical properties of the composites in curing (Fig. 5). For NPFR of low functionality, the rise in the relative shear modulus G_{rel} in the course of curing is strongly extended in time, although the initial heat liberation rate for this resin is considerably higher.

The decrease in the cross-link density and increase in the sol fraction with NPFR functionality increasing further are probably due to lower steric accessibility of their phenolic hydroxyls as a result of intramolecular self-association to give globular species. It is clear that the increase in steric hindrances must be accompanied by a decrease in the epoxy to phenol group ratio, i.e., the contribution of the secondary reaction (2) involving the alcohol hydroxy groups must increase. Furthermore, partly or totally unreacted high-molecular-weight fractions of polyphenols must accumulate in the resulting polymer composite. They can serve as a polymeric binder making the sol fraction content higher and the cross-link density lower, which is supported by the results of dynamic mechanical tests using the bending resonance vibration method. The relaxation spectra of EPCLPs in the initial stages of curing demonstrate the presence of a high-temperature φ peak, whose intensity decreases with increasing reaction temperature or time, in addition to the basic relaxation peak (α peak). This is particularly typical of commercial high-melting NPFRs, e.g., SF-010, containing high-molecular-weight fractions. In the relaxation spectra of low-melting NPFRs of low functionality these peaks are not found.

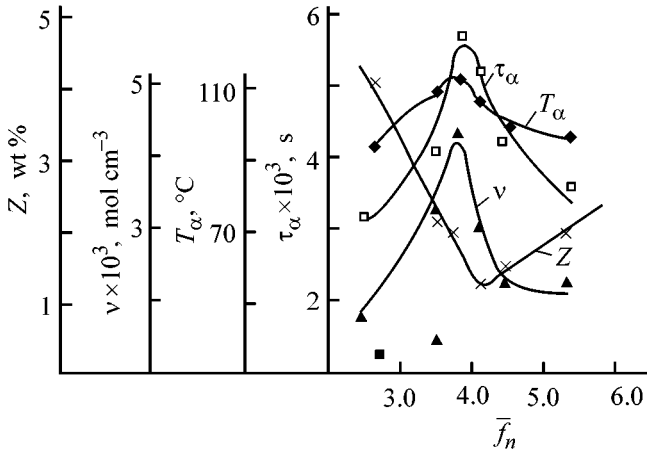

Fig. 4. Sol fraction content Z, cross-link density ν, peak temperature T_α, and relaxation time τ_α of α transition vs. the mean functionality $\overline{f_n}$ of NPFRs.

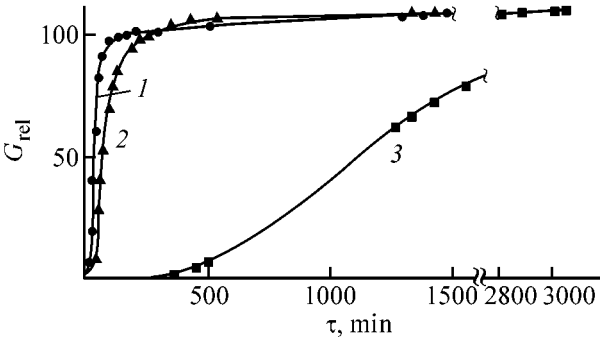

Fig. 5. Relative shear modulus G_{rel} vs. the curing time τ for NPFRs with various mean functionalities $\overline{f_n}$: (*1*) 5.32, (*2*) 3.52, and (*3*) 2.3.

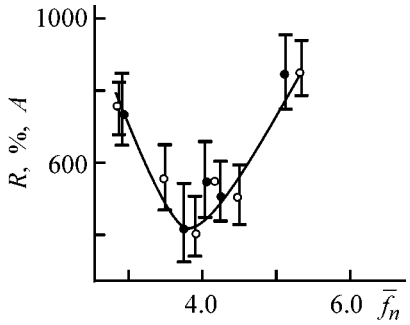

Fig. 6. Average grain size R in electron micrographs and the degree of inhomogeneity A (from low angle electron scattering data) vs. the mean functionality of NPFR.

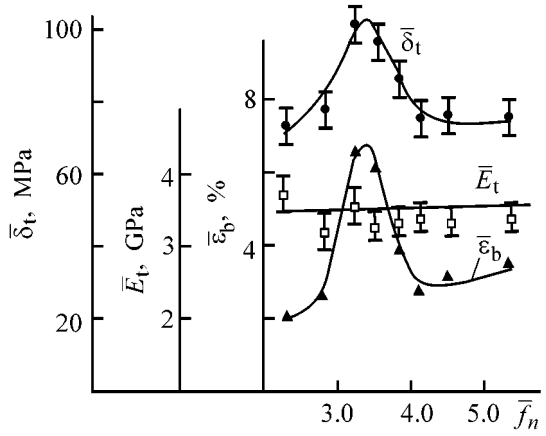

Fig. 7. Tensile strength $\overline{\delta}_t$, Young modulus $\overline{E}_t$, and elongation at break $\overline{\varepsilon}_b$ vs. the mean functionality of NPFR.

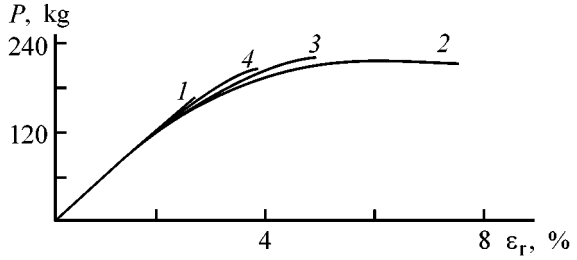

Fig. 8. Stress–strain curves for the strongest EPCLP samples obtained with NPRF of various functionalities. (P) Stress and ($\overline{\varepsilon}_r$) rupturing deformation. $\overline{f_n}$: (*1*) 2.3, (*2*) 3.52, (*3*) 3.82, and (*4*) 5.3.

To conclude, the functionality (or the molecular weight) of NPFRs can influence the mechanism of curing by changing the relative contributions of reactions (1) and (2). As a result, the proportion of the hydroxy ether and ether fragments of the cross-linked structure may change, thus modifying the structure at the topological level.

The supramolecular organization of these polymers was studied by electron microscopy and low-angle X-ray scattering. With increasing hardener functionality, the microroughness of the chip surface of the polymers in the electron micrographs of EPCLPs initially decreases and then starts to increase. In this case, the size of supramolecular species (globules) passes through a minimum near $\overline{f_n} \approx 3.5$ (Fig. 6). The degree of inhomogeneity, estimated from the low-angle X-ray scattering data, also passes through a minimum at approximately the same $\overline{f_n}$. It should be pointed out that the peak values of the parameters characterizing the supramolecular structure fall into the same range of $\overline{f_n}$, suggesting some genetic relation between the two levels of the structural organization of EPCLPs, similarly to the case described in [4].

To examine the structure–properity interrelations, we studied the structural, deformation, and elastic characteristics of EPCLPs obtained with NPFR of various functionalities. With increasing $\overline{f_n}$, the tensile strength $\overline{\delta}_t$ and elongation at break $\overline{\varepsilon}_b$ change in parallel (Fig. 7), and their dependences on $\overline{f_n}$ demonstrate maxima at $\overline{f_n}$ close to 3.5. At the same time, the Young modulus $\overline{E}_t$ is virtually independent of $\overline{f_n}$. The linear section in the stress–strain curves of EPCLP samples obtained with NPRF of low and high functionality (Fig. 8) corresponds to brittle fracture. For the samples with $\overline{f_n}$ ranging from 3.0 to 4.0, the contribution of forced elastic deformation increases noticeably. In the limiting case, at $\overline{f_n} = 3.5$, we can find a distinctly pronounced plateau corresponding to forced rubberlike elasticity.

Changes in the structural and deformation properties with varying NPFR functionality are accompanied by alteration of the fracture mode in the cross-linked polymers. It should be pointed out that, depending on $\overline{f_n}$, the areas of the smooth and rough fracture zones change, which is typical of a transition from brittle to forced elastic fracture [27]. The observed change of the mode of fracture can be attributed to the action of two major factors: (1) variation in the relaxation characteristics of EPCLPs as a result of modification of the cross-linked structure at the topological level and (2) variation in the degree of structural heterogeneity or changing size of supramolecular forms, as directly follows from the well-known Griffits equation for the critical strength, relating the major structural parameters to each other [28]:

$$\sigma_{cr} = \sqrt{\frac{2E\gamma}{\pi l_{cr}}}.$$

Among these parameters are the modulus of elasticity E (elasticity parameter), surface fracture energy γ (dissipation parameter), and defect critical size l_{cr} (structural parameter characterizing local stress).

Since the modulus of elasticity remains virtually unchanged, the strength variation may be due to a change in γ or (and) l_{cr}. It is worth noting that the strength and the major characteristics of the α relaxation process, caused by long-range segmental mobility, pass through a maximum at approximately the same $\overline{f_n}$ of NPFR (Fig. 4). Among the dissipation parameters are the peak (or glass transition) temperature T_α, effective cross-link density ν, and relaxation time τ_α determined from the resonance condition $\omega\tau_\alpha = 1$ in dynamic mechanical tests of EPCLPs by the resonance bending vibration method with dead-ended samples. The results obtained are indicative of extremal increase in the effective size of the kinetic unit of segmental motion. This may suggest [29] that, in the polymeric system studied, the parameters of the α process control the energy dissipated in EPCLP under static stress. The larger the effective size of the kinetic unit of segmental motion, the greater, evidently, the volume of the yielded region at the mouth of a growing crack and the higher the dissipated energy.

At the same time, we can speak about the correlation between the structural characteristics and the dimensions of supramolecular structures. Evidently, in this case, the size of supramolecular structures may be equated, to a first approximation, to the critical defect size in the Griffits equation. Therefore, the larger the supramolecular form, the more pronounced will be the local overstrains at the boundary surface, and the sooner the catastrophic failure of the polymeric material will start.

CONCLUSIONS

(1) The functionality of novolac phenol–formaldehyde resins controls the degree of structural heterogeneity at the topological and, particularly, supramolecular levels, thus causing differences in the structural and deformation characteristics of epoxy–phenolic cross-linked polymers and also in their fracture mode.

(2) Decision on the optimal commercial hardeners should be made taking into account the effect of their functionality on both the processing and performance characteristics of epoxy–phenolic composites.

ACKNOWLEDGMENTS

The authors are grateful to A.I. Kuzaev, A.I. Efremova, and G.S. Zaspinok for their help in conducting the experiments.

REFERENCES

1. Smirnov, Yu.N., Golodkova, F.M., and Dzhavadyan, E.A., *Vysokomol. Soedin., Ser. B*, 1998, vol. 40, no. 6, pp. 1031–1034.
2. Smirnov, Yu.N. and Lapitskii, V.A., *Zh. Prikl. Khim.*, 1998, vol. 71, no. 11, pp. 1863–1867.
3. Smirnov, Yu.N., Golodkova, F.M., and Ponomareva, T.I., *Zh. Prikl. Khim.*, 2000, vol. 73, no. 4, pp. 634–638.
4. Smirnov, Yu.N. and D'yankova, S.L., *Zh. Prikl. Khim.*, 2000, vol. 73, no. 5, pp. 819–825.
5. Smirnov, Yu.N., Komarov, B.A., Kushch, P.P., *et. al.*, *Zh. Prikl. Khim.*, 2002, vol. 75, no. 2, pp. 274–285.
6. Nikolaev, A.F., *Sinteticheskie polimery i plasticheskie massy na ikh osnove* (Synthetic Polymers and Plastics Based on Them), Moscow: Khimiya, 1964.
7. Lee, H. and Nevill, K., *Handbook of Epoxy Resins*, New York: McGraw-Hill, 1967.
8. Andrievskaya, G.D., *Vysokoprochnye orientirovannye stekloplastiki* (High-Strength Oriented Glass-Reinforced Plastics), Moscow: Nauka, 1966.
9. Trizno, M.S. and Nikolaev, A.F., *Epoksidno-novolachnye bloksopolimery i oblasti ikh primeneniya* (Epoxy–Novolac Block Copolymers and Areas of Their Application), Leningrad: Dom Nauchno-Tekh. Propagandy, 1970.
10. Kryzhanovskii, V.K., *Iznosostoikie reaktoplasty* (Wear-Resistant Thermosetting Plastics), Leningrad: Khimiya, 1984.
11. Smirnov, Yu.N., Naidovskii, E.S., Volkov, V.P., *et al.*, Abstracts of Papers, *Vtoraya Vsesoyuznaya konferentsiya po khimii i fizikokhimii polimerizatsionnosposobnykh oligomerov* (The 2nd All-Union Conf. on Chemistry and Physical Chemistry of Polymerizable Oligomers), Alma-Ata, 1979, p. 52.
12. Serenson, W.R. and Campbell, T.W., *Preparative Methods of Polymer Chemistry*, New York: Interscience, 1961.
13. Volkov, V.P., Naidovskii, E.S., Komarov, B.A., *et al.*, *Vysokomol. Soedin., Ser. A*, 1982, vol. 24, no. 12, pp. 2520–2526.
14. Komarov, B.A., Volkov, V.P., Boiko, G.N., *et al.*, *Vysokomol. Soedin., Ser. A*, 1983, vol. 25, no. 7, pp. 1431–1435.
15. Dzhavadyan, E.A., Galyuk, O.S., and Rozenberg, B.A., *Zavod. Lab.*, 1979, no. 3, pp. 228–230.
16. Siling, M.I., Matyukhina, O.S., Mochalova, O.A., *et al.*, *Vysokomol. Soedin., Ser. A*, 1969, vol. 11, no. 9, pp. 1943–1951.

17. Smirnov, Yu.N., Shatskaya, T.E., Natrusov, V.I., and Lapitskii, V.A., *Plast. Massy*, 1986, no. 7, pp. 24–26.
18. Geiseler, G. and Seidel, H., *Die Wasserstoffbruckenbindung*, Berlin: Akademie, 1977.
19. Pshenitsina, V.P., Shabadash, A.N., and Fremel', T.V., *Dokl. Akad. Nauk SSSR*, 1963, vol. 153, no. 3, pp. 650–652.
20. Hale, L., Macosko, Ch.W., and Bair, E., *Macromolecules*, 1991, vol. 24, pp. 2610–2619.
21. Oleinic, E.F., *Adv. Polym. Sci.*, 1986, vol. 80, pp. 49–95.
22. Smirnov, Yu.N. and Volkov, V.P., *Plast. Massy*, 2001, no. 12, pp. 26–29.
23. Tarasov, V.P., Smirnov, Yu.N., Erofeev, L.N., *et al.*, *Vysokomol. Soedin., Ser. A*, 1982, vol. 24, no. 11, pp. 2379–2382.
24. Smirnov, Yu.N., Rozenberg, B.A., Mileiko, S.T., *et al.*, *Plast. Massy*, 1984, no. 4, pp. 17–20.
25. Irzhak, V.I., Rozenberg, B.A., and Enikolopyan, N.S., *Setchatye polimery: Sintez, struktura, svoistva* (Cross-Linked Polymers: Synthesis, Structure, and Properties), Moscow: Nauka, 1979.
26. Perepechko, I.I., *Akusticheskie metody issledovaniya polimerov* (Acoustic Methods in Polymer Research), Moscow: Khimiya, 1973.
27. Gul', V.E., *Struktura i prochnost' polimerov* (Structure and Durability of Polymers), Moscow: Khimiya, 1971.
28. Berry, J.P., *Fracture. An Advances Treatise*, Liebowitz, H., Ed., vol. 7, part 2: *Fracture of Nonmetals and Composites*, New York: Academic, 1972.
29. Smirnov, Yu.N., Irzhak, V.I., and Rozenberg, B.A., *Vysokomol. Soedin., Ser. B*, 1983, vol. 25, no. 12, pp. 914–916.

Russian Journal of Applied Chemistry, Vol. 75, No. 4, 2002, pp. 619–628. Translated from Zhurnal Prikladnoi Khimii, Vol. 75, No. 4, 2002, pp. 633–642.
Original Russian Text Copyright © 2002 by Shibryaeva, Popov, Zaikov.

MACROMOLECULAR CHEMISTRY AND POLYMERIC MATERIALS

Structural Effects in Oxidation of Polypropylene

L. S. Shibryaeva, A. A. Popov, and G. E. Zaikov

Emanuel' Institute of Biochemical Physics, Russian Academy of Sciences, Moscow, Russia

Received August 2, 2001; in final form, February 2002

Abstract—Structural rearrangements occurring in the course of oxidation of isotropic and oriented samples of isotactic polypropylene were studied. The mechanisms of structural rearrangement in intercrystallite regions of isotropic and oriented samples were examined. The character of relaxation transitions in oriented polypropylene was studied in relation to the structures of the initial fibrils and of interfibrillar and intrafibrillar regions.

The heat resistance of a polymeric material is determined by its capability to preserve structural parameters in the course of thermal oxidative degradation. Elucidation of the features of structural rearrangements that accompany thermal oxidation allows more adequate evaluation of the performance limit of a polymeric material under particular conditions. At the same time, oxidation modifies a polymer, affecting its structural parameters and properties. Modification of a polymer by oxidation can improve its compatibility with other polymers. Therefore, elucidation of regular trends in the effect of oxygen on the polymer structure is of practical importance.

The influence of the polymer structure on its oxidation has been studied extensively, whereas data on the effect of oxidation and thermal degradation on the polymer structure are scarce [1–10]. Changes in the molecular structure of a polymer in the course of oxidation are poorly understood.

The goal of this study was to reveal regular trends in structural changes occurring in isotactic polypropylene (PP) in the course of its thermal oxidation and to examine the influence of the initial structure [isotropic (iPP) or oriented (oPP) sample] on these trends.

EXPERIMENTAL

We used isotactic PP of the Moplen brand with the following characteristics: M_w = (3.3–3.6) × 10^5, M_n = (3.6 – 4.1) × 10^4, intrinsic viscosity η = 1.53 dl g^{-1} (tetralin, 135°C), density d = 0.92 g cm^{-3}, degree of isotacticity 96%. The polymer was studied in the form of films prepared by pressing under nitrogen at 180°C and a pressure of 10 MPa in the quenching mode. Uniaxial orientational extension of films was performed by local heating at 130°C. The relative elongation reached 600–950% (λ = 6.0–9.5). The thickness of isotropic films varied within 40–100 μm, and that of oriented films, within 10–20 μm.

The structure and volume of crystalline regions of the initial and oxidized PP samples was determined by X-ray diffraction (XRD) using Ni-filtered Cu_{K_α} radiation. The degree of crystallinity was evaluated by differential scanning calorimetry (DSC; DSM-2M device) and was also monitored by IR spectroscopy (M-80 spectrometer), using the intensity ratio of the bands at 1220 and 1256 cm^{-1} [11].

The thermal parameters were determined by DSC at a scanning rate of 16 deg min^{-1}; the polymer sample weight was varied from 2 to 20 mg. The calorimeter was calibrated against indium (mp 156.6°C).

The microstructure, or conformational composition, of polymeric chains was determined by IR spectroscopy from the structure-sensitive bending vibration bands of CH_2 and CH_3 groups, and also from the intensity of the bands originating from coupling of the rocking vibrations of these groups with the stretching vibrations of the carbon skeleton (500–1500 cm^{-1}) [11–17].

The structure of oriented samples (degree of crystallinity æ, conformational composition of macromolecules, orientation of macrochains in the crystalline and amorphous regions) was determined by polarization IR spectroscopy. The polarization spectra were recorded with Hitachi polarizers. The optical densities were calculated by the formula $D^0 = (D_{||} + 2D_\perp)/3$, where $D_{||}$ and $D_\perp$ are the optical densities of bands in the spectra measured with the incident bean polarization parallel and perpendicular to the orientation axis, respectively.

1070-4272/02/7504-0619 $27.00 © 2002 MAIK "Nauka/Interperiodica"

Table 1. Structural parameters of unoxidized and oxidized samples of isotropic and oriented PP films

Sample	Degree of extension λ	State	Major period $d \pm 5\%$	Crystallinity index $X \pm 5\%$	Large-angle reflections
iPP	0	Unoxidized	180	64	Rings
	0	Oxidized	185	62	"
oPP	6	Unoxidized	178	60	Strokes
	6	Oxidized	178	60	Points
	9	Unoxidized	187	60	Strokes
	9	Oxidized	187	60	Points

The orientation of macrochains in crystalline and amorphous regions was characterized by the Freser orientation factor f [17], which is related to the IR dichroism value $R = D_{||}/D_{\perp}$ by

$$f = (R - 1)(R_0 + 2)/(R + 2)(R_0 - 1), \qquad (1)$$

where $R_0 = 2\text{cotan}^2\,\alpha$, and α is the transition moment angle (angle between the direction of the transition moment vector of the vibration, **M**, and the electrical vector of the beam, **E**).

This angle ranges from 0° to 55° for *A* bands (manifested in IR spectra with parallel polarization) and from 55° to 90° for *E* bands (manifested in IR spectra with perpendicular polarization). Correspondingly, $0 < R_0 \le \infty$ for *A* bands and $1/\infty \le R_0 < 1$ for *E* bands.

From the polarized spectra, we obtained the IR dichroism values R for each band. To calculate the orientation factors by formula (1), we took the angles α from [17].

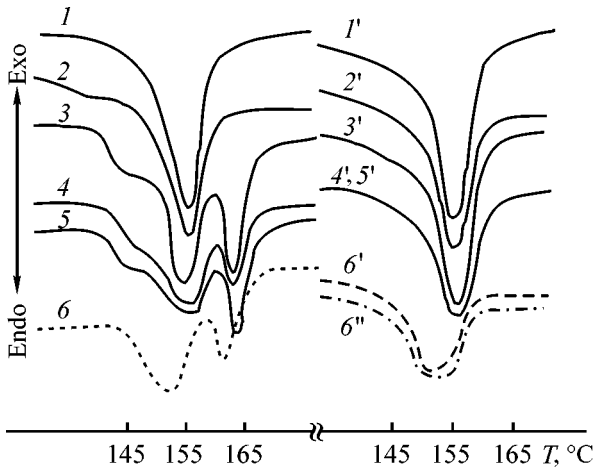

Fig. 1. Endotherms of melting of the initial and oxidized (130°C, P_{O_2} = 20 MPa) PP samples. (*T*) Temperature; the same for Fig. 5. Endotherm of (*1*–*6*) first melting, (*1*'–*6*') second melting after recrystallization, and (*6*") third melting. Oxidation time (min): (*1*, *1*') unoxidized sample, (*2*, *2*') 5, (*3*, *3*') 30, (*4*, *4*') 60, (*5*, *5*') 85, and (*6*, *6*', *6*") 120.

The kinetics of oxygen uptake by PP was studied with a manometric unit [18]. The nonvolatile oxidation products were studied by IR spectroscopy. The content of carbonyl (>C=O) and hydroxy groups was determined from the intensities of bands in the ranges 1700–1800 and 3320–3600 cm^{-1}, respectively; the OH groups in blocks absorbed at 3420, and isolated OH groups, at 3560 cm^{-1}. For the molar extinction coefficients used to calculate the concentrations of the carbonyl and hydroxy groups, we took the values of 220 and 70 kg mol^{-1} cm^{-1} [5].

The accuracy of determination of the structural and kinetic parameters was 10–15%. The conformational composition and composition of the oxidation products were determined simultaneously in the same experiment.

Isotropic PP samples. The endotherms of melting of iPP crystallites (initial and oxidized) are shown in Fig. 1. As seen from Fig. 1, thermal oxidation of the polymer significantly affects the shape of the melting peak of its crystallites; the extent of the observed changes depends on the time and extent of oxidation. In the initial stage, a low-temperature shoulder appears. With increasing oxidation time, it grows in intensity, and one more, high-temperature, peak appears. Thus, the thermogram of oxidized PP contains three peaks, one of which lies more than 10°C lower, and the other, higher than the melting point of crystallites in unoxidized PP. At large extents of oxidation, when carbonyl and hydroxyl-containing products are accumulated in significant amounts, the intensity of the low-temperature peak considerably increases, and the intensity of the high-temperature peak and the temperature of its maximum decrease (Fig. 1). Appearance of new peaks in the endotherms of melting of oxidized PP suggests changes in the modification or size of the crystallites. However, XRD data show that the modification of the PP crystallites remains unchanged (Table 1).

Recrystallization of oxidized PP after melting results in disappearance of both high- and low-temperature peaks (Fig. 1). In the endotherms of second melting of PP a single peak with the melting point close to that of the initial PP is observed, except in the case of the most deeply oxidized samples, instead of three peaks. The single melting peak is preserved after repeated recrystallizations. In the more deeply oxidized samples, recrystallization also results in that the endotherm of melting becomes more similar to that of the initial sample, but there are still two peaks, and the melting point after one and two recrystallizations remains lower than that of the initial polymer. It should be noted that the enthalpies of melting and hence the degrees of crystallinity, æ, increase slightly in the initial stage of PP oxidation. However, with increasing oxidation time, the difference between ΔH of the first and repeated meltings grows. After remelting, ΔH and æ decrease. It is also significant that the endotherms of the first and second meltings give noticeably different dependences of æ on the oxidation time. Namely, in the first case, α first increases and then decreases with increasing oxidation time, whereas in the second case it decreases monotonically (Fig. 2).

The presence of a low-temperature peak and its growth in intensity with simultaneous decrease in the degree of PP crystallinity suggest breakdown of crystalline regions and amorphization of crystallites, induced by thermal oxidative degradation. The appearance of fine PP crystallites in further oxidation stages is confirmed by the preservation of the low-temperature peak in the DSC curve recorded after recrystallization.

Nevertheless, the presence of several peaks in the endotherm of first melting of PP and their disappearance after remelting indicate that changes in the melting point of the crystallites in the oxidized samples are not necessarily associated with changes in the structure and size of the crystallites and may be due to changes in the thermodynamic parameters or to relaxation processes in interlamellar tie chains [19]. The fact that oxidation of PP does not change significantly the crystallization temperature T_{cr} (Fig. 2) suggests, most likely, the occurrence of relaxation processes in interlamellar tie chains, which precede melting of the crystallites or accompany their intrachain cooperative melting. This is also indicated by the appearance of a high-temperature endothermic peak.

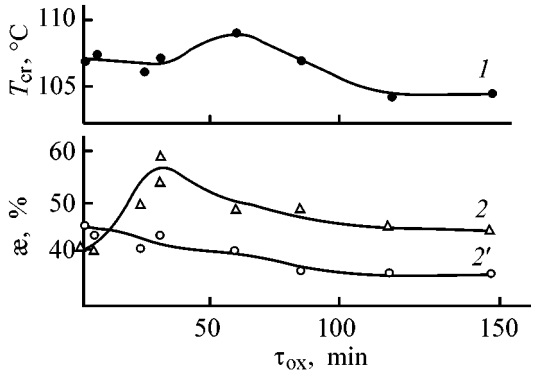

Fig. 2. Variation of the (*1*) crystallization temperature T_{cr} and (*2*, *2*′) degree of crystallinity æ, determined from DSC data, in the course of iPP oxidation. T = 130°C, P_{O_2} = 150 mm Hg; the same for Fig. 4. (τ_{ox}) Oxidation time. Curve *2* was obtained using data on the heat of first melting, and curve *2*′, using data obtained after recrystallization.

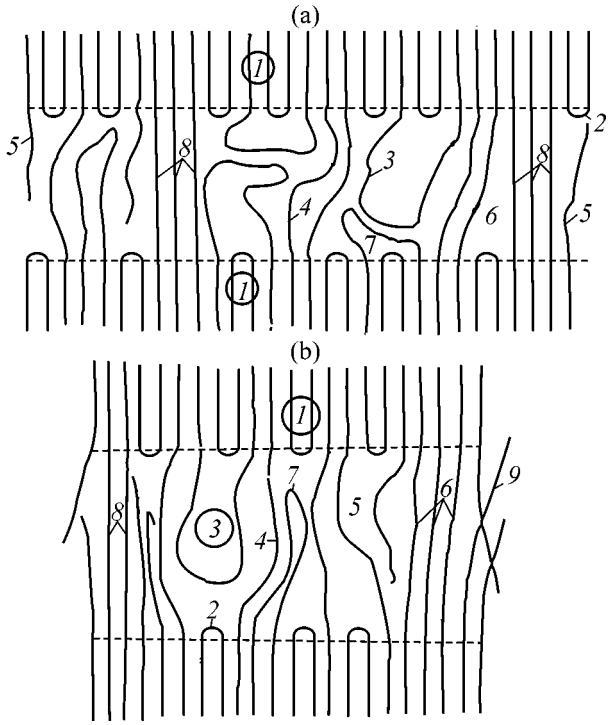

Fig. 3. Interlamellar layer in (a) iPP and (b) oPP: (*1*) crystalline cores of lamellas, (*2*) regular folds with suppressed mobility, (*3*) long irregular loops, (*4*) folded tie chains, (*5*) long terminal chains, (*6*) weakly folded tie chains, (*7*) folds in which the motion is restricted by the crystals, (*8*) fully straightened tie chains with the ends fixed in lamellas, and (*9*) interfibrillar tie chains.

In accordance with the generally accepted scheme [20], interlamellar layers in IPP have a conformational structure (Fig. 3a). Between the crystalline cores of lamellas *1* and regular folds with suppressed mobility *2*, there are macromolecular elements with different conformational mobilities below the melting point T_m: long irregular loops *3*, folded tie chains *4*, and long ends of molecules *5* emerging from the crystals; weakly folded tie chains *6* and folds *7* in which the motions are restricted by the crystals to the greater

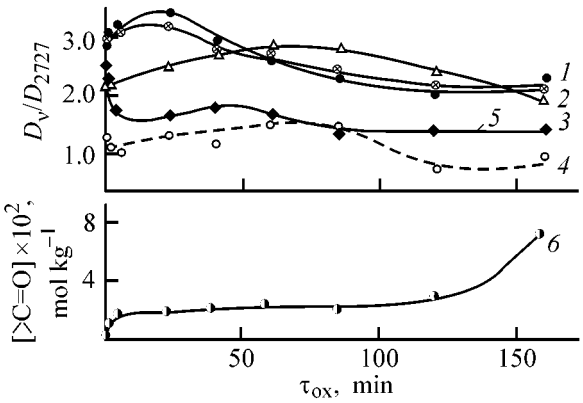

Fig. 4. Variation with oxidation time τ_{ox} of the (*1*–*5*) relative intensities D_ν/D_{2727} of the IR bands and (*6*) the content of carbonyl groups [>C=O], as determined from D_{1720}/D_{2727}. ν, cm^{-1}: (*1*) 840, (*2*) 998, (*3*) 975, (*4*) 810, and (*5*) 1155.

extent, the lower the extent of chain folding ($y = l/h$, where h is the distance between the molecule ends, and l is the length of the molecular contour); and straightened tie chains *8* with ends fixed in lamellas. Apparently, the relaxation processes in these irregular loops and folded tie chains occur at temperatures considerably lower than T_m of the crystallites and cannot affect their melting. The motions in straightened tie chains fixed by the crystals are defrosted as the rotational-isomeric composition of these chains changes by the mechanism of $T \rightarrow G$ transitions [21]. Defrosting will occur with the onset of melting of the smallest lamellas and will determine relaxation at temperatures 10–15°C lower than T_m. The most probable reason for the appearance of the lowtemperature shoulder in the DSC curve of oxidized PP is folding of the least folded interlamellar tie chains formed by thermal oxidation as a result of high-temperature annealing. The rise in intensity of the low-temperature shoulder with increasing time of PP oxidation is probably indicative of an increase in the content of straightened tie chains in the helical *TG* conformation in the intercrystallite regions of oxidized samples.

On the one hand, the high-temperature peak may be due to relaxation processes in maximally straightened chains in interlamellar regions, which can form "strands" similar to those appearing in oriented PP samples [20, 22]. On the other hand, this peak may belong to the high-melting fraction of crystallites, formed owing to the fact that crystallization of straightened tie chains, which prevent crystallite formation, is accelerated in the course of oxidative degradation.

Changes in the structure of macromolecules in the course of oxidation were monitored by IR spectroscopy. The results are shown in Fig. 4. The initial period of the polymer oxidation is characterized by enrichment in straightened, and depletion of folded conformations, i.e., by occurrence of relaxation $G \rightarrow T$ transitions. Upon longer oxidation, the content of straightened chains reaches a maximum and then starts to decrease monotonically. This is indicated by the variation of the band intensities at 975 and 998, and at 840 and 810 cm^{-1}. The content of folded conformers in amorphous regions of PP (a band at 1155 cm^{-1}) in the course of oxidation first decreases sharply, then increases, and, finally, decreases slowly again (Fig. 4). The changes in the relative content of the folded and straightened conformers correspond to $G \rightarrow T$ transitions in the initial stage of oxidation. With the progress of oxidation, in the stage of accumulation of carbonyl-containing oxidation products, the content of straightened conformers decreases, and that of folded conformers grows. As carbonyl compounds are accumulated further, the content of both conformers decreases (Fig. 4).

It should be noted that the bands at 998 and 975 cm^{-1} start to grow in intensity earlier than the bands at 810 and 840 cm^{-1}. The peaks in the curves of the intensities of the latter bands vs. oxidation time are shifted toward longer times. Apparently, all the four bands describe the features of the chain structure in different PP regions. This is confirmed by the IR spectra of the iPP samples treated with boiling concentrated HNO_3. It is known [3] that such a treatment breaks down the chains in the amorphours regions, with the crystallites remaining intact. We found that, after the acid treatment, the intensity of the bands at 998 and 975 cm^{-1}, belonging to regular structures, decreases slightly, and the intensity of the band at 840 cm^{-1} either remains unchanged or increases somewhat, depending on the chosen reference band. Thus, the bands at 975 and 998 cm^{-1} characterize the presence of long helical sections in tie chains, mainly in amorphous intercrystallite regions, whereas the band at 840 cm^{-1} is more sensitive to changes in the chain structure in PP crystallites. Apparently, the different trends in variation of the intensities of these bands (Fig. 4) should not be attributed to different rates of structural rearrangements of chains in lamellas and of interlamellar tie chains, considered separately; more likely, they reflect correlations between these rearrangements.

Apparently, the factors affecting the polymer structure in the course of thermal oxidation are high temperature and oxygen, i.e., annealing and thermal oxidative degradation. Comparison of changes observed in the structure of PP macrochains in the course of

Table 2. Structure of polymeric chains in the initial PP samples and in PP samples heat-treated in oxygen and in an inert atmosphere (T = 130°C, P_{O_2} = 150 mm Hg)

τ, min	[>C=O]	[OH]	[>C=O]/[OH]	$\frac{D_{975}}{D_{1300}}$ ($\frac{D_{975}}{D_{1300}}$)	$\frac{D_{998}}{D_{1300}}$ ($\frac{D_{998}}{D_{1300}}$)	$\frac{D_{840}}{D_{1300}}$ ($\frac{D_{840}}{D_{1300}}$)	$\frac{D_{1155}}{D_{1300}}$ ($\frac{D_{1155}}{D_{1300}}$)	$\frac{D_{1220}}{D_{1256}}$
	mol kg^{-1}							
0 (oxygen)	0	0	–	2.13 (43.8)	2.1 (42.5)	1.7 (32.5)	1.65 (33.8)	0.38
5 (oxygen)	1.5×10^{-2}	5.0×10^{-2}	0.3	3.0 (52.5)	2.8 (37.5)	1.9 (35.0)	1.58 (32.5)	0.39
23 (oxygen)	1.6×10^{-2}	5.0×10^{-2}	0.3	3.04 (49.7)	3.15 (58.3)	2.7 (41.7)	1.58 (24.2)	0.32
40 (oxygen)	1.9×10^{-2}	5.0×10^{-2}	0.4	3.1 (56.4)	3.16 (57.5)	2.3 (40.8)	2.0 (36.4)	0.60
85 (oxygen)	1.9×10^{-2}	4.7×10^{-2}	0.4	2.8 (48)	2.7 (46.7)	3.15 (54.7)	1.46 (25.3)	0.56
120 (oxygen)	3.0×10^{-2}	5.0×10^{-2}	0.6	2.2 (32)	2.3 (35)	1.0 (20)	0.9 (16.7)	0.35
5 (ultrapure nitrogen)	0	0	–	2.7 –	2.3 –	2.1 –	2.2 –	0.35 –
15 (ultrapure nitrogen)	0	0	–	3.0 –	2.8 –	2.9 –	1.9 –	0.39 –
25 (ultrapure nitrogen)	0	0	–	3.7 –	2.9–3.2 –	3.2 –	1.7 –	0.42 –

heat treatment in air and in a vacuum at the same temperature shows that, initially, the changes are mainly due to the effect of high temperature (Table 2). At large extents of oxidation, a low-melting crystallite fraction appears as a result of degradation of both interlamellar tie chains and crystallites (probably, of their plane surfaces) in the course of high-temperature oxidation.

A sharp decrease in the extent of folding of tie chains in the iPP samples under consideration, observed after short oxidation, is associated with specific features of the molecular structure of intercrystallite regions of the unoxidized polymer, namely, with the distribution with respect to contour length of chains fixed between lamellas. Such a decrease may be due to the conformational state of macromolecules in which single $G \rightarrow T$ transitions decrease the extent of folding, or to the high content of tie chains in which these transitions occur [22, 24]. Apparently, the same factors determine the rate of variation of the crystallite structure.

Oriented PP samples. An X-ray diffraction study of oPP samples showed that the morphology of PP crystallites does not change after orientational extension. The crystallites in oPP become more oriented (Table 1), which agrees with previous data [5, 20, 22]. The thermograms of melting of the isotropic and oriented samples differ appreciably (Fig. 5). The endotherms of oPP melting consist of two overlapping peaks. As a result of melting and subsequent recrystallization of oPP, the low-temperature shoulder disappears, and T_m of the remaining peak decreases (Fig. 5). A low-temperature shoulder appearing in the

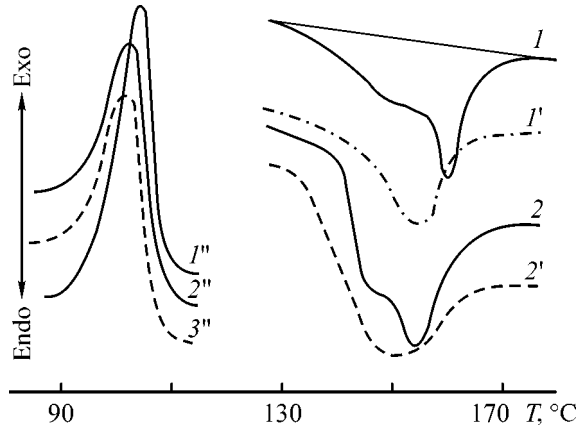

Fig. 5. (*1*, *1'*, *2*, *2'*) Endotherms of melting and (*1"*–*3"*) exotherms of crystallization of (*1*, *1'*, *1"*) initial and (*2*, *2'*, *2"*, *3"*) oxidized (130°C, P_{O_2} = 150 mm Hg) oPP samples (λ = 9). (*1*, *2*) First melting; (*1'*, *2'*) melting after recrystallization; and (*3"*) peak of oPP crystallization after second melting.

Table 3. Changes in the conformational pattern and orientation of oPP macrochains (λ = 9) in the course of its oxidation in the isometric mode and under free shrinkage conditions (T = 130°C, P_{O_2} = 150 mm Hg)

τ_{ox}, min	$\frac{D^0_{840}}{D^0_{900}}$	$\frac{D^0_{998}}{D^0_{900}}$	$\frac{D^0_{945}}{D^0_{900}}$	$\frac{D^0_{955}}{D^0_{900}}$	R_{840}	R_{998}	$\frac{D^0_{1715}}{D^0_{900}}$	$\frac{D^0_{3410}}{D^0_{900}}$
Isometric mode								
0	2.5	3.1	0.6	0.5	34	18	0.1	0.1
30	2.5	3.1	0.5	0.5	34	18	0.1	0.1
58	2.9	3.4	0.5	0.5	34	19	0.1	0.1
118	2.9	3.3	0.3	0.2	30	17	0.4	0.3
188	2.7	3.0	0.3	0.3	26	18	0.4	0.3
268	2.6	3.9	0.4	0.3	43	22	0.4	0.3
Free shrinkage conditions								
0	3.7	4.4	0.6	0.8	37	15	0.1	0.1
15	2.7	3.3	0.3	0.2	20	12	0.5	0.2
42	3.0	3.9	0.3	0.1	19	12	0.8	0.4
177	2.8	3.1	0.7	0.5	22	14	3.3	1.5

endotherm of the first melting of oPP may be due to melting of linear systems in amorphous regions consisting of intrafibrillar and interfibrillar tie chains (Fig. 3b) in the maximally straightened 3_1 helical conformation characteristic of PP crystallites. In contrast to crystallites, the linear systems show no three-dimensional ordering [19, 20, 22]. The change in the shape of the oPP endothermic peak after recrystallization is probably due to the breakdown of the linear systems. This is also indicated by the shape of the oPP crystallization peak and by its T_{cr}, which is close to T_{cr} of iPP (Fig. 5).

Structural rearreangements in the course of thermal oxidation of oPP samples with different degrees of extension were monitored by XRD, DSC, and IR spectroscopy. The structural parameters of unoxidized and oxidized oPP, determined by XRD, are listed in Table 1. It is seen that, in the course of low-temperature oxidation (below the melting point of the crystallites), the major period and the degree of oPP crystallinity change insignificantly. The orientation of crystallites changes noticeably. According to the IR spectra, oxidation of oPP results in structural changes of polymeric macrochains. The following specific features of the IR spectra of oPP samples should be noted. A decrease in the intensity of bands after treatment of oPP with boiling concentrated HNO_3 shows that both bands of regular structures at 840 and 998 cm^{-1} belong to macrochains in amorphous regions. By the intensities of these bands, it is possible to monitor the variation of the content of straightened conformers in intercrystallite regions of oPP. In some experiments, to determine the content of folded conformers, we used, along with the band at 1155 cm^{-1}, also the bands at 528 and 460 cm^{-1}. We also used the bands at 945, 955, and 962 cm^{-1}, which are the low-frequency shoulders of the band at 975 cm^{-1}. These bands are sensitive to stresses and stress relaxation in intrafibrillar tie chains [25]. Wool [25] showed that the intensities of these bands are a measure of accumulation of local strains in tie chains.

An analysis of the kinetic curves characterizing variation of the intensities of these bands in the IR spectra of oPP samples with different λ in the course of oxidation showed that the physical processes accompanying the oxidation depend on the initial oPP structure and on the oxidation conditions.

Changes in the conformational compositions of chains, occurring in the course of thermal oxidation of oPP with λ = 9 under isometric conditions (l = const) and in the free shrinkage mode, are given in Table 3. As seen from these data, the observed changes depend on the oxidation mode. Oxidation of oPP in the isometric mode initially affects the rotameric composition of the chains: the content of straightened chains increases, that of folded conformers decreases, and local stresses in tie chains increase. The first trend is indicated by the rise in the intensity of the bands at 998 and 840 cm^{-1} and the decrease in the intensity of the band at 1155 cm^{-1}, and the latter trend, by growth of the bands at 945, 955, and 962 cm^{-1}. With the progress of oxidation, relaxation of stresses occurs, and the intensities of the bands at 945, 955, and 962 cm^{-1}

Table 4. Changes in the structure of oPP (λ = 9) macrochains (conformational pattern and orientation) in the course of annealing in an inert atmosphere in the isometric mode and under free shrinkage conditions (T = 130°C)

τ_{ann}, min	$\frac{D^0_{840}}{D^0_{900}}$	$\frac{D^0_{998}}{D^0_{900}}$	$\frac{D^0_{975}}{D^0_{900}}$	$\frac{D^0_{945}}{D^0_{900}}$	R_{840}	f_{840}	R_{998}	f_{998}	R_{975}	f_{975}	R_{945}
Isometric mode											
0	2.2	2.8	3.2	0.3	53.0	0.95	25.5	1.0	6.6	0.76	0.3
18	2.9	3.4	3.9	0.4	55.0	0.95	24	1.0	6.5	0.76	0.2
43	2.8	3.5	3.8	0.2	69.0	0.96	20	1.0	6.4	0.76	0.1
73	3.1	3.5	3.7	0.4	50.0	0.95	20	1.0	7.5	0.80	0.04
178	3.0	3.7	3.9	0.4	60.0	0.95	15	0.96	7.2	0.79	0.02
Free shrinkage conditions											
0	3.3	4.1	4.6	0.4	32.0	0.9	19.0	1.0	6.0	0.7	0.1
18	3.8	5.9	4.2	0.6	34.0	0.9	4.0	0.6	6.6	0.8	0.3
43	3.3	5.2	4.2	0.6	33.0	0.9	5.0	0.7	5.0	0.7	0.2
73	3.1	5.5	3.8	0.5	32.0	0.9	3.6	0.5	6.0	0.8	0.3
178	3.2	5.1	3.9	0.5	30.0	0.9	5.0	0.7	5.0	0.7	0.2

decrease. It should be noted that the decrease in the intensity of these bands coincides in time with the appearance of terminal >C=O groups. This process is not accompanied by noticeable changes in the isomeric composition of the chains. Only upon prolonged oxidation the chains tend to become more regular. However, this is not accompanied by accumulation of large amounts of carbonyl groups.

Oxidation under free shrinkage conditions proceeds differently. Even in the first 20 min of oxidation, the content of the regular conformers decreases drastically, and the content of folded conformers grows, with a simultaneous decrease in the stresses in tie chains (the intensity of the bands at 945, 955, and 962 cm^{-1} decreases). This is accompanied by accumulation of carbonyl-containing oxidation products. After these products are accumulated in oPP in large amounts, the local stresses in tie chains start to build up again, in proportion with [>C=O], both in the isometric oxidation mode and under free shrinkage conditions (Table 3).

Changes in the structure of the chains in the course of thermal oxidation are accompanied by changes in their orientation (Table 3). Oxidation in the isometric mode causes a certain increase in the orientation of tie chains. Oxidation under free shrinkage conditions is initially accompanied by disorientation of macromolecules (the dichroism of the bands at 840 and 998 cm^{-1} decreases), and then, by an increase in the orientation of regular chains. The XRD data indicate that the orientation of crystallites in oxidized oPP samples increases (Table 2).

Changes in the chain structure in the course of oPP oxidation depend on the initial structure of a sample. In the sample with λ = 9.5, characterized by the larger degree of extension and lower degree of folding (or by higher content of tie chains), oxidation under the same conditions in the free shrinkage mode also causes a change in the conformational composition of chains due to $T \rightarrow G$ relaxation transitions (a decrease in the content of straightened chains is accompanied by an increase in the content of folded chains). However, this transition is appreciably delayed. Instead of relaxation of stresses existing in tie chains of an unoxidized sample, stresses build up, and relaxation occurs only after oxidation for more than 50 min. This sample is also characterized by decelerated accumulation of oxidized products as compared with the sample with λ = 9. However, in this sample, too, the onset of accumulation of carbonyl groups corresponds to a decrease in stresses in tie chains and to an increase in the content of folded conformers (the intensity of the bands at 945, 955, and 965 cm^{-1} decreases, and that of the bands at 528 and 1155 cm^{-1} increases).

Experiments on heat treatment of an oPP sample with λ = 9 in an inert atmosphere, with the other conditions being the same as those in oxidation (Table 4), shows that changes in the structural features of the chains (conformational pattern and local stresses) in the initial stage are independent of the annealing conditions. In the isometric mode and under free shrinkage conditions, the orientation of chains in the crystallites (R_{840}) and the content of straightened conformers increase, whereas the content of folded

Table 5. Correlation between the structural characteristics and parameters of oxidation of oPP samples (T = 130°C, P_{O_2} = 600 mm Hg)

Sample	Oxidation parameters						Structural parameters					
	N_{O_2}, mol kg^{-1}	τ, min	$\frac{D^0_{1710}}{D^0_{900}}$	$\frac{D^0_{3410}}{D^0_{900}}$	$\frac{D^0_{1710}}{D^0_{3410}}$	$\frac{D^0_{3410}}{D^0_{3560}}$	$\frac{D^0_{840}}{D^0_{900}}$	$\frac{D^0_{998}}{D^0_{900}}$	$\frac{D^0_{975}}{D^0_{900}}$	f_{840}	f_{998}	f_{975}
I, λ = 6	0	0	–	–	–	–	2.3	2.9	3.8	0.96	0.99	0.70
	1.0	130	0.85	0.80	1.1	4.5	3.2	4.0	4.1	0.94	0.80	0.80
II, λ = 6	0	0	–	–	–	–	2.1	2.7	3.4	0.96	0.99	0.70
	1.0	137	1.4	0.90	1.6	3.0	2.8	3.0	3.5	0.95	1.0	0.80
Free shrinkage conditions												
III, λ = 9	0	0	–	–	–	–	3.0	3.9	4.4	0.96	1.0	
	1.0	140	1.06	0.60	1.8	2.5	1.3	1.9	2.9	0.85	1.0	
Isometric mode												
IV, λ = 9	0	0	–	–	–	–	3.2	3.6	4.2	0.96	1.0	
	1.0	112	1.0	0.7	1.4	3.0	2.5	2.8	3.2	0.95	1.0	

conformers decreases. Local stresses in tie chains are preserved for a long time even under free shrinkage conditions. The oxidation mode affects the orientation factor of the band at 998 cm^{-1}. In oPP annealed under free shrinkage conditions, the dichroism of this band and, correspondingly, the orientation factor drastically decrease. The orientation factor of the band at 945 cm^{-1} decreases too.

Comparison of changes occurring in the oPP structure upon oxidation and annealing under identical conditions shows that, in oxidation, the initial portion of the curves characterizing structural changes of polymeric chains reflects relaxation conformational transitions and build up of stresses in tie chains due to the effect of high temperature. The relaxation of local stresses in tie chains and the decrease in the content of straightened conformers (increase in the content of folded conformers), occurring with further progress of oxidation, are due to oxidative degradation of tie chains.

The role of oxidation in structural rearrangements is related to the dependence of the relaxation rate on the oxygen concentration. At increased oxygen pressure, the content of regular conformers in the initial stage decreases faster, and the maximally straightened chains become less oriented (the dichroism of the bands at 998 and 840 cm^{-1} decreases). Simultaneously increases the rate of accumulation of nonvolatile oxidation products.

The experimental data listed in Tables 3 and 4 illustrate the correlation between the relaxation and oxidation processes. The acceleration of structural rearrangements promotes oxidation of oPP. As shown previously, the initial rate of accumulation of >C=O groups varies in parallel with the rate of stress relaxation in tie chains. However, the concentration of products in the oriented polymer depends on the rate of chain folding ($T \rightarrow G$ transitions) and increases with decreasing content of straightened conformers; the folded conformers are consumed in oxidation. It should be noted that this dependence is determined by the initial structure of PP and, being pronounced in oriented samples, is not manifested noticeably in iPP. In further oxidation stages, as carbonyl groups are accumulated in appreciable amounts, these groups start to affect the conformational composition of the chains, their orientation, and stresses in tie chains. With increasing [>C=O], the chains become more oriented, and the stresses in tie chains grow. The IR dichroism and the orientation factors of the bands at 998, 975, and 840 cm^{-1}, as well as the intensities of the bands at 945, 955, and 962 cm^{-1}, increase.

A clearly defined correlation between the structure of the chains in various oPP samples, their relaxation characteristics, and kinetic parameters of oxidation follows from Table 5. It is seen that the relaxation processes determine not only the oxidation rate but also the composition of oxidation products. The rates of oxidation and accumulation of volatile products, and also their composition differ significantly for oPP samples that have the same degree of extension but differ in the structure of the chains or in the oxidation modes. In samples differing in the initial chain struc-

ture and oxidation conditions, the relaxation processes are different and occur at different rates. This is manifested in the kinetics of particular oxidation stages, in the contributions of the intermolecular and intramolecular chain transfers, and, as a result, in the ratios of the carbonyl and hydroxy groups and of the block and isolated hydroperoxy groups (Table 5). With respect to these ratios, the oPP samples under consideration can be ranked in the following order: **I** < **II** < **III** < **IV**.

In this order, the contribution of the intermolecular transfer of the oxidation kinetic chain grows, as indicated by an increase in the ratio of the carbonyl and hydroxy groups and in the content of isolated hydroxy groups relative to the total OH content. The first in this order is oPP sample **I** with $\lambda = 6$; in this sample, relaxation of interfibrillar chains is manifested in that the orientation factor of the band at 998 cm^{-1} decreases appreciably, and that of the band at 975 cm^{-1} increases. In sample **II** with $\lambda = 6$, these chains do not relax; sample **III** with $\lambda = 9$ is oxidized in the isometric mode when relaxation of all the chains is hindered; and sample **IV** with $\lambda = 9$ is oxidized under free shrinkage conditions.

In this connection, an important question arises: Relaxation of what chains (interfibrillar or intrafibrillar) exerts a stronger effect on the rate of the polymer oxidation? To answer this question, we annealed an oPP sample with $\lambda = 9$ at 130°C in an inert atmosphere under free shrinkage conditions. In the process, the dichroism (orientation factor) of the band at 998 cm^{-1} decreased. After annealing, the sample was divided in two portions, one of which was subjected to oxidation under free shrinkage conditions, and the other, in the isometric mode. If accumulation of solid oxidation products were mainly determined by the relaxation rate of interfibrillar tie chains, then the oxidation mode would have no effect on the rate of product accumulation. However, the oxidation in the isometric mode was actually considerably slower than that under free shrinkage conditions. In the isometric mode, high concentrations of oxidation products were not attained, in contrast to oxidation under free shrinkage conditions, which yielded significant amounts of oxidation products in a considerably shorter time.

Comparison of changes in the conformational composition of chains, which occur in these samples in the course of their oxidation, demonstrated, above all, the different changes in the local stresses in tie chains. In the IR spectrum of PP oxidized under free shrinkage conditions, in contrast to the spectrum of a similar sample oxidized in the isometric mode, the intensities of the bands at 945, 955, and 962 cm^{-1}, and also at 998 and 840 cm^{-1} rapidly decrease, as also does the dichroism of the band at 840 cm^{-1}. Taking into account the fact that the relaxation of tie chains in interfibrillar amorphous regions of both samples occurred before the onset of oxidation, we can state that the changes in the conformational pattern and in the local stresses, occurring in the course of oxidation, are associated with the relaxation processes in tie chains of intrafibrillar amorphous interlayers.

Oxidation of a similar sample after shrinkage of not only interfibrillar but also intrafibrillar chains (at 155°C, when the mobility of interlamellar chains is defrosted owing to partial fusion of crystallites) is considerably faster than oxidation after shrinkage of interfibrillar chains only.

CONCLUSIONS

(1) Structural rearrangements in the course of oxidation of an isotropic sample involve changes in the structure of both crystallites (annealing of crystallites) and intercrystallite regions (conformational transitions). The main mechanisms of structural rearrangements occurring in oriented polypropylene in the course of its oxidation are relaxation conformational transitions and relaxation of stresses in tie chains.

(2) The relaxation properties and the oxidation rate are interrelated. The oxidation rate of an oriented polymer is determined by its molecular structure and hence by the character and rate of relaxation processes that accompany oxidation. The relaxation processes, in turn, affect the oxidation kinetics.

REFERENCES

1. Regel', V.R., Slutsker, A.I., and Tomashevskii, E.E., *Kineticheskaya priroda prochnosti tverdykh tel* (Kinetic Nature of the Strength of Solids), Moscow: Nauka, 1974.
2. Krisyuk, B.E., Popov, A.A., and Zaikov, G.E., *Vysokomol. Soedin., Ser. A*, 1980, vol. 22, no. 2, pp. 329–334.
3. Emanuel', N.M. and Buchachenko, A.L., *Khimicheskaya fizika molekulyarnogo razrusheniya i stabilizatsii polimerov* (Chemical Physics of Molecular Degradation and Stabilization of Polymers), Moscow: Nauka, 1988.
4. Popov, A.A., Rapoport, N.Ya., and Zaikov, G.E., *Okislenie orientirovannykh i napryazhennykh polimerov* (Oxidation of Oriented and Stressed Polymers), Moscow: Khimiya, 1987.

5. Shibryaeva, L.S., Kiryushkin, S.G., and Zaikov, G.E., *Polym. Degrad. Stab.*, 1992, vol. 36, no. 1, pp. 17–30.
6. Zuev, Yu.S., *Razrushenie polimerov pod deistviem agressivnykh sred* (Degradation of Polymers in Aggresive Media), Moscow: Khimiya, 1972.
7. Minsker, K.S., Kolesov, S.V., and Zaikov, G.E., *Starenie i stabilizatsiya polimerov na osnove vinilkhlorida* (Aging and Stabilization of Polymers Based on Vinyl Chloride), Moscow: Nauka, 1982.
8. Odinokova, I.L., Zherdev, Yu.V., and Zelenev, Yu.V., *Vysokomol. Soedin., Ser. B*, 1991, vol. 33, no. 4, pp. 297–299.
9. Amerik, Yu.B., Shirokova, L.A., Sleptsov, S.A., and Filatova, M.P., *Vysokomol. Soedin., Ser. B*, 1992, vol. 34, no. 1, pp. 61–65.
10. Blinov, N.N., Popov, A.A., Rakovski, S.K., *et al., Vysokomol. Soedin., Ser. A*, 1989, vol. 31, no. 10, pp. 2212–2217.
11. Kissin, Yu.V., *J. Polym. Sci., Part A-2*, 1983, vol. 21, no. 10, pp. 2085–2096.
12. Kissin, Yu.V., *Eur. Polym. J.*, 1972, vol. 8, pp. 487–499.
13. Dechant, J., Danz, R., Kimmer, W., *et al., Ultrarotspektroskopische Untersuchungen an Polymeren*, Berlin: Akademie, 1972.
14. Miyamoto, T. and Inagaki, H., *J. Polym. Sci., Part A-2*, 1969, vol. 7, no. 6, pp. 963–981.
15. Miyazawa, T., Ideguchi, Y., and Fukushima, K., *J. Chem. Phys.*, 1963, vol. 38, no. 11, pp. 2709–2720.
16. Kissin, Yu.V., *Isospecific Polymerization of Olefins*, New York: Springer, 1985.
17. Samuels, R.J., *Makromol. Chem., Part 1*, 1981, vol. 4, pp. 241–270.
18. Shlyapnikov, Yu.A., Kiryushkin, S.G., and Mar'-in, A.P., *Antiokislitel'naya stabilizatsiya polimerov* (Antioxidative Stabilization of Polymers), Moscow: Khimiya, 1986.
19. Bershtein, V.A. and Egorov, V.M., *Differentsial'naya skaniruyushchaya kalorimetriya v fizikokhimii polimerov* (Differential Scanning Calorimetry in Physical Chemistry of Polymers), Leningrad: Khimiya, 1990.
20. Marikhin, V.A. and Myasnikova, L.P., *Nadmolekulyarnaya struktura polimerov* (Supramolecular Structure of Polymers), Leningrad: Khimiya, 1977.
21. Birshtein, T.M. and Ptitsyn, O.B., *Konformatsiya makromolekul* (Conformation of Macromolecules), Moscow: Nauka, 1964.
22. Egorov, E.A., Zhizhenkov, V.V., Marikhin, V.A., *et al., Vysokomol. Soedin., Ser. A*, 1985, vol. 27, no. 8, pp. 1637–1642.
23. Wunderlich, B., *Macromolecular Physics*, New York: Academic, 1973.
24. Gabaraeva, A.D. and Shishkin, N.I., *Vysokomol. Soedin., Ser. A*, 1973, vol. 15, no. 3, pp. 406–411.
25. Wool, R.P., *Polym. Eng. Sci.*, 1980, vol. 20, no. 12, pp. 805–815.

Russian Journal of Applied Chemistry, Vol. 75, No. 4, 2002, pp. 629–635. Translated from Zhurnal Prikladnoi Khimii, Vol. 75, No. 4, 2002, pp. 643–649.
Original Russian Text Copyright © 2002 by Pesetskii, Makarenko.

MACROMOLECULAR CHEMISTRY AND POLYMERIC MATERIALS

Grafting of Glycidyl Methacrylate to Polypropylene in an Extruder, Initiated with Organic Peroxides

S. S. Pesetskii and O. A. Makarenko

Belyi Institute of Mechanics of Metal–Polymer Systems, State Scientific Institution, National Academy of Sciences of Belarus, Gomel, Belarus

Received January 8, 2002

Abstract—The efficiency of grafting of glycidyl methacrylate to polypropylene and the degree of degradation of macromolecules, evaluated from the melt flow index, were studied in relation to the structure of the peroxide initiator.

Reactive extrusion is widely used for production of a wide set of polymeric products [1]. In this process, the starting polymers are usually polyolefins, which is largely due to their availability, low cost, and wide use in engineering, and also to the possibility of controlling the physicochemical properties of the resulting materials by chemical modification. In particular, reactive extrusion is used for chemical modification of olefin polymers and copolymers and their blends by grafting polar monomers to their macromolecules with the aim to enhance adhesion or to prepare polymer–polymer systems [1, 2].

Chemical reactions in a polymer melt in an extruder occur, as a rule, by the radical mechanism [1–3]. Most often, these reactions are initiated with organic peroxides. Examples of such reactions are graftings to polypropylene (PP) of acrylic acid and its derivatives [4, 5], maleic anhydride [6–9], glycidyl methacrylate (GMA) [10–14], and oxazoline [15–20].

Under conditions of fast processes characteristic of reactive extrusion, the course of grafting and concomitant transformations are largely influenced not only by the chemical activity of a peroxide initiator, but also by its solubility in the main components of the reaction mixture: a polymer and a monomer [21, 22]. The influence of the mutual solubility of the components is particularly strong at poor mixing efficiency, which is characteristic of, e.g., single-screw mixer–extruders [21].

The influence of the peroxide structure on the kinetics of monomer grafting to PP was considered in [23]. All the peroxides used in [23] had asymmetric structure and simultaneously were monomers containing a carboxy group. Therefore, decomposition of the peroxides was accompanied by their grafting to the macromolecules. It was found that peroxides generating methyl radicals in decomposition afford higher efficiency of grafting than peroxy acids generating ethyl radicals.

In this work, we considered the specific features of GMA grafting to PP in the presence of peroxide initiators that exhibit increased affinity for the polymer. Previously [21], we showed for the example of grafting of methylenebutanedioic acid to polyethylene that such peroxides ensure the highest yield of the grafted products. With peroxides exhibiting increased affinity for the monomer, the grafting efficiency was lower.

EXPERIMENTAL

In our study, we used PP of Kaplen brand [Moscow Oil Refinery, 01030 grade, TU (Technical Specifications) 2211-015-00203521–95, density 0.905 g cm^{-3}, melting point (determined by differential scanning calorimetry) 169°C] and organic monoperoxides (*tert*-butyl peroxide, TBP; dicumyl peroxide, DCP, Orgsintez Joint-Stock Company, Russia) and diperoxides {2,5-dimethyl-2,5-di(*tert*-butylperoxy)hexane (L-101), 2,5-dimethyl-2,5-di(*tert*-butylperoxy)-3-hexene (L-130), both ELF Atochem, France; di(*tert*-butylperoxyisopropyl)benzene (Perk-14, P-14), Aldrich; 2,2-di(*tert*-butylperoxy)-5,5,6-trimethylbicyclo[2.2.1]heptane (D-1); and 2,2-di(3-methyl-1-butyn-3-ylperoxy)-3,5,6-trimethylbicyclo[2.2.1]heptane (D-2) [24]}.

The structures and properties of these peroxides are given in Table 1. The solubility parameters δ of the

1070-4272/02/7504-0629 $27.00 © 2002 MAIK "Nauka/Interperiodica"

Table 1. Characteristics of peroxide initiators

Peroxide	Structural formula	Solubility parameter δ, $(J\ cm^{-3})^{0.5}$	Available oxygen content, %
DCP	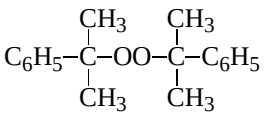	17.4	5.92
L-101	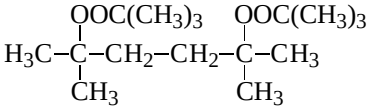	15.5	11.03
TBP	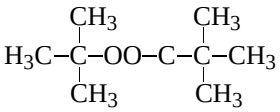	15.3	10.95
D-1	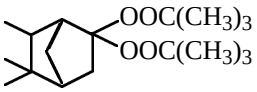	16.1	10.17
D-2	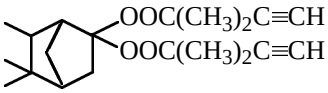	16.3	9.57
L-130	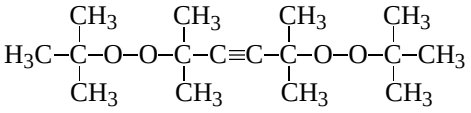	15.0	10.2
P-14	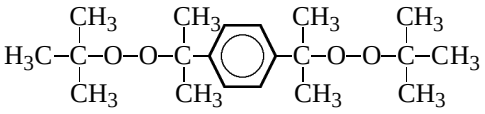	16.4	9.0

peroxides were calculated, as in [21], by the method of group contributions [25, 26].

The parameters δ were calculated for 25°C (298 K). Naturally, these parameters are temperature-dependent. However, the paramaters δ of polymers and low-molecular-weight compounds vary with temperature similarly [27]:

$$\ln \delta_T = \ln \delta_{298} - \beta k(T - 298),$$

where δ_T and δ_{298} are the δ values at a temperature T and at 298 K, respectively; k the coefficient approximately equal to unity for polyolefins and 1.25 for peroxides and GMA; and β the linear coefficient of thermal expansion.

Therefore, characterization of the solubility of peroxides and GMA in PP by the solubility parameters determined for 25°C is fairly adequate. The calculated solubility parameters of PP and GMA at 25°C are 16.1 and 29.8 $(J\ cm^{-3})^{0.5}$, respectively.

As in [21], graftings were performed in a single-screw extruder (screw diameter 36 mm, L/D = 20) under the following conditions: screw rotation rate 27 rpm (shear rate about 30 s^{-1}); temperatures in zones I and II–IV 175 and 190°C, respectively.

The grafting was characterized by the grafting efficiency defined as the ratio of the grafted monomer to its total introduced amount. As in [21], the grafting efficiency α (wt %) was determined with film samples (40–60 μm thick) by IR absorption spectroscopy, using the formula

$$\alpha = \frac{D_\tau}{D_0} \times 100,$$

where D_0 and D_τ are, respectively, the optical density of the GMA carbonyl absorption band (1735 cm^{-1})

Table 2. Characteristics of thermal stability of peroxides (thermal analysis data) and their half-lives in benzene*

Peroxide	$T_{o.d}$	$T_{e.d}$	$T_{m.d}$	Δm, % (TG)	T_m, °C (DTA)	Exothermic peak, °C (DTA)		Parameters of decomposition of peroxides in benzene (0.2 M)	
	°C (DTG)					onset	maximum	T, °C	$\tau_{0.5}$, min
DCP	131	202	162	74.5	43	131	162	177	1
L-101	118	176	155	94.0	–	123	162	177	1
L-130	133	195	177	93	–	145	183	193	1
P-14	148	192	182	82	58	150	185	180	1
TBP	15**	125**	103**	96.0**	–	30**	98**	160	1
D-1	95	125	117	84.0	52	96	118	185	0.6
D-2	85	110	104	86.0	40	86	104	192	2–2.5

* ($T_{o.d}$, $T_{e.d}$, $T_{m.d}$) Temperatures of the onset, end, and maximal rate of decomposition, respectively; (Δm) weight loss; and (T_m) melting point.

** Characteristics of vaporization and partial decomposition of TBP.

in the initial PP sample and that in the PP sample after grafting and extraction of the residual unchanged monomer with acetone at 40°C [28]. In calculations, we used as internal reference the band at 465 cm^{-1} characterizing the skeleton vibrations of PP macromolecules. The viscosity of the polymer melt was evaluated by the melt flow index (MFI), which was determined at 210°C and a load of 2.16 kg with an IIRT-AM device (Ekodatchik Private Company, Tula, Russia). Thermal decomposition of peroxides was studied with a Q-1500 derivatograph (MOM, Hungary) at a heating rate of 5 deg min^{-1} and sample weight of 100 mg. The results are given in Table 2.

The structure of functionalized PP was examined by differential scanning calorimetry with a DSM-3A microcalorimeter (Institute of Biological Instrument Making, Russian Academy of Sciences) at a sample weight of 4 mg and heating rate of 16 deg min^{-1}. The changes in the sample crystallinity were characterized by the crystallinity index, which was defined as the ratio of the crystallization peak area of the functionalized PP to that of the initial polymer. Measurements were performed with samples heated in a calorimetric cell to 190°C and kept at this temperature for 1 min.

Table 1 shows that all the chosen peroxides exhibit increased thermodynamic affinity for the polymer. Peroxides D-1, D-2, and P-14, whose solubility parameters are the closest to that of PP, must be the most soluble in PP. The solubility parameter of L-101 is also close to that of PP, which suggests good solubility of this peroxide in the polymer melt {according to [29], in the absence of strong specific interactions between solvent and solute molecules, the solvent and solute are thermodynamically compatible when their solubility parameters differ by no more than 2 $(J\ cm^{-3})^{0.5}$}. Thus, none of the peroxides is compatible with GMA.

The results of thermal analysis (Table 2) show that the chosen peroxides significantly differ in thermal stability. It should be noted that the data obtained for the solid peroxides (CDP, D-1, D-2, P-14) are more reliable: For these compounds, the temperatures of the onset and maximal rate of decomposition, determined from the DTG and DTA curves, are in good agreement. For liquid peroxides L-101 and L-130, the DTA peaks are slightly shifted to higher temperatures relative to the DTG peaks, which may be due to evaporation of the compounds. With TBP, which is highly volatile, thermal analysis does not give reliable information on decomposition. Dicumyl peroxide is the most thermally stable, and *gem*-diperoxides D-1 and especially D-2, as expected, are the least thermally stable. D-1 actively decomposes in the range 95–125°C with a maximum at 117°C (DTG data), and D-2, at 85 to 110°C with a maximum at 104°C.

Evaluation of the half-lives of peroxides in a moving PP melt subjected to shear stresses (calculated shear rate 30 s^{-1}) appeared to be impossible. However, since the temperature in the reaction zone of the extruder was as high as 190°C, and the residence time of the melt in this zone was 1.25 min, the decomposition of peroxides must be complete (cf. half-lives of the peroxides in benzene, Table 2; the half-lives must not change significantly in going from benzene to the polyolefin melt).

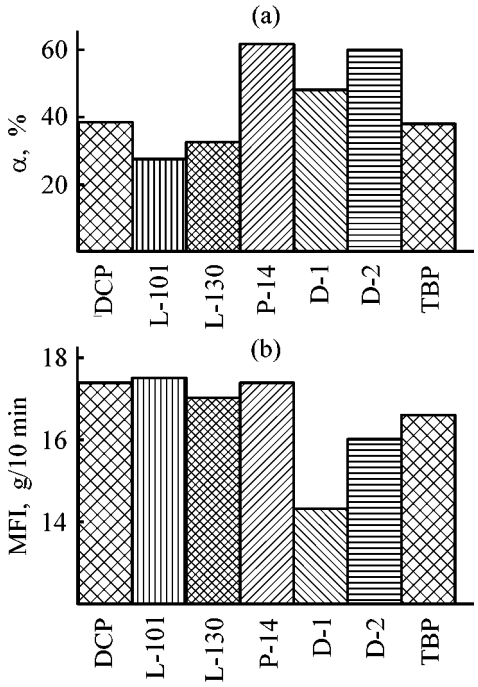

Fig. 1. Influence of peroxides on (a) efficiency of GMA grafting α and (b) melt flow index MFI of the PP-*graft*-GMA melt. Concentration, wt %: peroxides 0.2 and GMA 1.0.

Figure 1 shows how the grafting efficiency and MFI are influenced by the structure of a peroxide. It should be noted that, here and hereinafter, experiments were performed under the same temperature conditions in the extruder. According to [22], peroxide-initiated GMA grafting is not significantly affected by temperature variation in the range 170–200°C. It is known that grafting of monomers to PP is usually accompanied by competing degradation of macromolecules. Therefore, the main problem in preparation of a functionalized polymer is to ensure the highest yield of the grafted product with the molecular weight preserved. The melt flow index directly characterizes the molecular weights of the initial and grafted (PP-*graft*-GMA) polypropylene and is very sensitive to β-cleavage of the PP chain [30].

It is known that the structure of the peroxide affects significantly the characteristics of the resulting graft copolymer. It should be noted that the highest grafting efficiencies α were obtained with P-14, D-1, and D-2, which are the most soluble in PP. With D-1 and D-2, the degree of degradation of PP-*graft*-GMA was the lowest, as judged from the lowest MFI. A somewhat lower α (and, correspondingly, higher MFI) was obtained with TBP.

The peroxides D-1, D-2, and TBP are the least thermally stable among the peroxides tested in this work; their active decomposition (onset of the exothermic peak in the DTA curve, Table 2) starts at 96, 86, and 30°C. In our procedure, the temperature in the reactant loading zone of the extruder is 175°C. In this zone, the peroxides and GMA dissolve in the PP melt, and the peroxides decompose to radicals. Because the affinity of D-1, D-2, and TBP for the polymer is higher than that for GMA, and GMA is less soluble in PP than the peroxides, the radicals, apparently, mostly attack PP macromolecules. The resulting macroradicals then react with GMA to give PP-*graft*-GMA and are involved in β-cleavage resulting in degradation of the polymer. Since the grafting efficiency is relatively low even with the least thermally stable peroxide initiator, TBP, we can assume that the arising macroradicals have a fairly long half-life (the total residence time of the reaction mixture in the extruder was 1.5 min). This result confirms the previously found possibility [21] of using peroxides with low thermal stability to initiate grafting of unsaturated monomers to polyolefin macromolecules by reactive extrusion.

tert-Butyl peroxide, being highly volatile, is partially evaporated in the extruder loading zone. Therefore, its actual concentration in the reaction zone at the beginning of grafting will be lower than that of the other peroxides. However, in decomposition of TBP, the yield of active radicals $^{\bullet}CH_3$ and $^{\bullet}OC(CH_3)_3$ is higher, compared to the other peroxides [31]. Therefore, the concentration of macroradicals will be high even in the extruder loading zone. Because GMA is relatively poorly soluble in PP, effective molecular contact of the active macroradicals with the monomer is not attained in this zone, and a significant part of macroradicals are deactivated by the β-cleavage pathway. Therefore, PP-*graft*-GMA prepared in the presence of TBP initiator apparently, has lower α and higher MFI as compared to D-1 and D-2 initiators (Fig. 1).

The different initiating activities of the *gem*-diperoxide D-2 and its saturated analog D-1 may be due to the following. Decomposition of D-1 generates a weakly active biradical

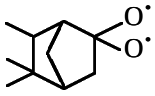

A

and two $^{\bullet}OC(CH_3)_3$ radicals whose fragmentation gives active methyl radicals $^{\bullet}CH_3$ [21, 31]. Decomposition of D-2 generates biradical **A** and two $^{\bullet}OC(CH_3)_2C{\equiv}CH$ radicals, which are less active than $^{\bullet}CH_3$ [31]. Despite the higher content of available oxygen in D-1 as compared to D-2 and formation of

more active radicals in its decomposition, the α values are higher with D-2 and the extent of macromolecule degradation is greater (Figs. 1a, 1b). This means that the chemical activity of the peroxide is not the decisive factor affecting the yield of the graft copolymer and grafted products. D-2 is better soluble in PP melt than D-1. Therefore, D-2 initiates the grafting and macromolecule degradation more efficiently than D-1. On the whole, the molecular weight of PP-*graft*-GMA decreases with D-1 and D-2 to a lesser extent than with the other peroxide initiators. This fact may be due to a reaction of tertiary PP macroradicals with biradical A, yielding inactive products.

The most active initiator of both grafting and degradation is P-14 (Figs. 1a, 1b). As compared to the other peroxides, it is better soluble in PP and more thermally stable (Table 2). The temperature interval of P-14 decomposition is the optimal for GMA grafting. The maximal amount of free radicals will be generated at the moment when PP is melted completely and the monomer is well dispersed in the melt. Hence, the solubility in the polymer and the thermal stability of a peroxide initiator are the major factors governing the GMA grafting and macromolecule degradation.

The decreased α in initiation with peroxides L-101 and L-130, which are structurally similar to P-14 (Fig. 1a), is apparently due to their lower solubility in PP. Therefore, the concentrations of the forming macroradicals are insufficient to initiate grafting, and these macroradicals are mainly consumed in β-cleavage reactions (Fig. 1b).

The yield of PP-*graft*-GMA with DCP initiator is approximately the same as that with L-101, although the content of available oxygen in DCP and the affinity of DCP for PP are lower (Table 1). Probably, these factors are compensated for by favorable features of thermal behavior of DCP. The temperature range of its decomposition, as in the case of P-14, is the optimal for grafting under our experimental conditions.

As the concentration of the peroxide initiator is increased, both α and MFI grow, with the degree of PP degradation increasing to a greater extent [30]. Under our experimental conditions (Fig. 2), the increase in the DCP concentration from 0.1 to 0.3 wt % did not cause significant changes in MFI, and α even decreased somewhat. As compared to [30], the concentration of GMA was considerably lower under our experimental conditions (1 wt % against 6–10), and the concentration of the initiator was also lower and varied within narrower limits. Figure 2 shows that initiation of grafting is the most efficient at a

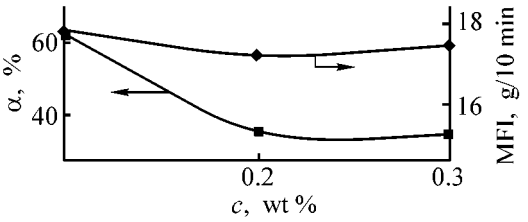

Fig. 2. Influence of DCP concentration *c* on the efficiency of GMA grafting to PP α and on the melt flow index of PP-*graft*-GMA. GMA concentration 1.0 wt %.

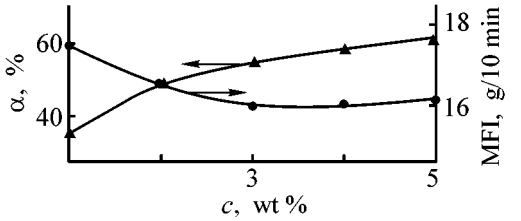

Fig. 3. Influence of GMA concentration *c* on the efficiency of its grafting to PP α and on the melt flow index of PP-*graft*-GMA. DCP concentration 0.3 wt %.

DCP concentration of 0.1 wt %. Hence, increased concentrations of the initiator are not appropriate in grafting of relatively small amounts of GMA to PP. Excess free radicals generated by decomposition of the peroxide are, probably, spent for oligomerization of ungrafted GMA occurring concurrently with GMA grafting and PP degradation [30].

With increasing GMA concentration in the reaction mixture, the grafting efficiency increased, as expected [30], and the degree of macromolecule degradation decreased (Fig. 3). However, the extent to which the monomer suppressed the degradation of macromolecules was appreciably lower than, e.g., with D-1 initiator (Figs. 1b, 3). Therefore, to obtain an optimal

Table 3. Structural characteristics of PP functionalized with GMA in the presence of DCP, according to DSC data

Content, wt %		T_m	T_{cr}	$\Delta T = T_m - T_{cr}$	I_{cr}
GMA	DCP	°C			
0	0	169.0	110.0	59.0	1.0
1.0	0.1	168.5	118.5	50.0	1.32
1.0	0.2	164.5	117.5	47.0	1.37
1.0	0.3	164.0	115.5	48.5	1.27
2.0	0.3	165.0	117.0	48.0	1.23
3.0	0.3	163.5	117.0	46.0	1.4
5.0	0.3	165.8	117.5	48.3	0.93

ratio between grafting and chain cleavage, it is preferable to choose appropriate peroxide and take it in appropriate concentration, rather than to vary the concentration of the monomer.

Grafting of methylenebutanedioic acid to LDPE does not affect significantly the crystallinity of the polymer [32, 33]. Only at relatively high concentrations of the peroxide initiator, when functionalized polyethylene transforms into a highly viscous, partially cross-linked product, crystallization decelerates somewhat, and, according to DSC, the crystallinity decreases by 8–12%.

In contrast to polyethylene, PP undergoes degradation in the course of peroxide-initiated grafting of monomers. Taking into account the higher rate of PP crystallization and its dependence on the viscosity of the polymer melt [34], we expect that the structural changes in this polymer after grafting will be more significant. Indeed, as seen from Table 3, functionalized PP prepared by grafting of GMA exhibits higher crystallinity than the initial polymer. Only PP-*graft*-GMA prepared in the presence of 5 wt % GMA and 0.3 wt % DCP has lower crystallinity (I_{cr} = 0.93). In all the cases, grafting leads to a decrease in the melting point and an increase in the crystallization point of the polymer. The extent of variation of both parameters depends on the composition insignificantly: The difference $\Delta T = T_m - T_{cr}$, equal to 59°C for PP, varies within 46–50°C for PP-*graft*-GMA. Hence, even at the lowest peroxide concentration (0.1 wt %), the viscosity of the melt and the molecular weight of the polymer change to such an extent that the crystallization is appreciably accelerated.

The dependences of I_{cr} on the peroxide concentration pass through a maximum, or through a maximum and a minimum (Table 3). These changes are due to variations of the melt viscosity, grafting efficiency, and, probably, degree of the monomer oligomerization [10–14, 30]. The lower I_{cr} of PP-*graft*-GMA prepared in the presence of 5 wt % GMA and 0.3 wt % DCP is probably due to oligomerization of the monomer. Like other high-molecular-weight additives, oligo(glycidyl methacrylate) can prevent crystallization, affecting the mobility of macromolecules.

CONCLUSIONS

(1) To ensure high yield of the grafted product, it is appropriate to use peroxides that exhibit high thermodynamic affinity for polypropylene and decompose in the temperature range matching the temperature of reactive extrusion. These conditions are met to the greatest extent by di(*tert*-butylperoxyisopropyl)benzene.

(2) To attain the desired balance between the grafting efficiency and the degree of degradation of macromolecules, it is preferable to properly choose the peroxide and its concentration, rather than to vary the monomer concentration.

(3) Grafting of glycidyl methacrylate can be initiated with peroxides that decompose at temperatures considerably lower than the temperature in the main reaction zone of the extruder.

(4) Irrespective of the type of the peroxide, grafting of glycidyl methacrylate is accompanied by β-cleavage of macromolecules, which raises the melt flow index; this increase is significant even at a minimal peroxide concentration (0.1 wt %).

(5) Degradation of polypropylene macromolecules in the course of functionalization accelerates its crystallization from the melt (crystallization occurs at temperatures 5–8.5°C higher than the crystallization point of the initial polypropylene; the crystallinity increases by 20–60%). At high concentration of glycidyl methacrylate (5 wt %), the crystallinity of functionalized polypropylene is lower than the initial value, which is probably due to oligomerization of the monomer.

ACKNOWLEDGMENTS

The authors are grateful to A.P. Yuvchenko for placing samples of D-1 and D-2 peroxides at their disposal.

REFERENCES

1. Xantnos, M., *Reactive Extrusion: Principles and Practice*, Munich: Hanser, 1992.
2. Moad, G., *Prog. Polym. Sci.*, 1999, vol. 24, pp. 81–142.
3. Moad, G. and Solomon, D.H., *The Chemistry of Free Radical Polymerization*, Oxford: Pergamon, 1995.
4. Oromehie, A.R., Hashemi, S.A., Meldrum, I.G., and Waters, D.N., *Polym. Int.*, 1997, vol. 42, pp. 117–120.
5. Lin, N.C., Xie, H.Q., and Baker, W.E., *Polymer*, 1993, vol. 34, pp. 4680–4687.
6. De Roover, B., Devaux, J., and Zegras, R., *J. Polym. Sci., Part A: Polym. Chem.*, 1996, vol. 34, pp. 1195–1202.
7. De Roover, B., Sclavons, M., Carlier, V., *et al.*, *J. Polym. Sci., Part A: Polym. Chem.*, 1995, vol. 33, pp. 829–842.

8. Mulhaupt, R., Duschek, T., and Rieger, B., *Macromol. Chem. Macromol. Symp.*, 1991, vols. 48/49, pp. 317–332.
9. Mulhaupt, R., Duschek, T., and Rosch, J., *Polym. Adv. Technol.*, 1993, vol. 4, pp. 465–474.
10. Sun, Y.-J., Hu, G.-H., and Lambla, M., *Angew. Makromol. Chem.*, 1995, vol. 229, pp. 1–13.
11. Sun, Y.-J., Hu, G.-H., and Lambla, M., *J. Appl. Polym. Sci.*, 1995, vol. 57, pp. 1043–1054.
12. Lin, N.C., Xie, H.Q., and Baker, W.E., *Polymer*, 1993, vol. 34, pp. 4680–4687.
13. Chen, L.-F., Wong, B., and Baker, W.E., *Polym. Eng. Sci.*, 1996, vol. 36, pp. 1594–1607.
14. Huang, H. and Liu, N.C., *J. Appl. Polym. Sci.*, 1998, vol. 67, pp. 1957–1963.
15. Rosch, J., Holger, W., Muller, P., *et al., Macromol. Symp.*, 1996, vol. 102, pp. 241–254.
16. Tang, F. and Huyser, E.S., *J. Org. Chem.*, 1997, vol. 42, pp. 2160–2163.
17. Vaino, T., Hu, G.-H., Lambla, M., and Seppala, J.V., *J. Appl. Polym. Sci.*, 1996, vol. 61, pp. 843–852.
18. Vaino, T., Hu, G.-H., Lambla, M., and Seppala, J.V., *J. Appl. Polym. Sci.*, 1997, vol. 63, pp. 883–894.
19. Liu, N.C. and Baker, W.E., *Polymer*, 1994, vol. 35, pp. 988–994.
20. Worner, C., Rosch, J., Hohn, A., and Mulhaupt, R., *Polym. Bull.*, 1996, vol. 36, pp. 303–309.
21. Pesetskii, S.S., Jurkowski, B., Krivoguz, Y.M., and Kelar, K., *Polymer*, 2001, vol. 42, pp. 469–473.
22. Hogt, A.H., Jelemic, J., and Meijer, J., *Polymer Processing Eur. Meet.*, Stuttgart, September 26–28, 1995, p. 3.2.
23. Assoun, L., Manning, S.C., and Moore, R.B., *Polymer*, 1998, vol. 39, pp. 2571–2578.
24. Yuvchenko, A.P., Beresnevich, A.B., Zhukovskaya, N.A., *et al., Zh. Obshch. Khim.*, 1988, vol. 24, no. 9, pp. 1889–1893.
25. Askadskii, A.A. and Matveev, Yu.M., *Khimicheskaya struktura i svoistva polimerov* (Chemical Structure and Properties of Polymers), Moscow: Khimiya. 1983.
26. Van Krevelen, D.W., in *Properties of Polymers. Their Correlation with Chemical Structure; Their Numerical Estimation and Prediction from Group Additive Contributions*, Amsterdam: Elsevier, 1990, pp. 184–225.
27. Hildebrand, J.H. and Scott, R.L., in *The Solubility of Nonelectrolytes*, New York: Dover, 1964, 3rd ed., pp. 432–438.
28. Makarenko, O.A., in *Polikom-2000: Trudy nauchno-tekhnicheskoi konferentsii* (Polikom-2000: Proc. Scientific and Technical Conf.), Gomel, 2000, pp. 155–157.
29. Coleman, M.M., Serman, C.J., Bhagwagar, D.E., and Painter, P.C., *Polymer*, 1990, vol. 31, pp. 1187–1197.
30. Chen, L.-F., Wong, B., and Baker, W.E., *Polym. Eng. Sci.*, 1996, vol. 36, no. 12, pp. 1594–1599.
31. Antonovskii, V.L., *Organicheskie peroksidnye initsiatory* (Organic Peroxide Initiators), Moscow: Khimiya, 1972.
32. Pesetskii, S.S., Jurkowski, B., Krivoguz, Y.M., and Urbanowicz, R., *J. Appl. Polym. Sci.*, 1997, vol. 65, pp. 1493–1501.
33. Jurkowski, B., Pesetskii, S.S., Olkhov, Y.A., *et al., J. Appl. Polym. Sci.*, 1999, vol. 71, pp. 1771–1785.
34. *Polypropylene: Structure, Blends and Composites*, Kocsis, K.Y., Ed., London: Chapman and Hall, 1995.

Russian Journal of Applied Chemistry, Vol. 75, No. 4, 2002, pp. 636–640. Translated from Zhurnal Prikladnoi Khimii, Vol. 75, No. 4, 2002, pp. 650–654.
Original Russian Text Copyright © 2002 by Perminov, Modyanova, Ryabkov, Sevbo, Gailyunas, Kuchin.

MACROMOLECULAR CHEMISTRY AND POLYMERIC MATERIALS

Epoxy Composites Modified with Finely Dispersed Fillers

V. P. Perminov, A. G. Modyanova, Yu. I. Ryabkov, O. A. Sevbo, I. A. Gailyunas, and A. V. Kuchin

Institute of Chemistry, Komi Scientific Center, Ural Division, Russian Academy of Sciences, Syktyvkar, Komi Republic, Russia

Institute of Organic Chemistry, Ufa Scientific Center, Russian Academy of Sciences, Ufa, Bashkortostan, Russia

Received August 8, 2001

Abstract—The thermal stability and mechanical strength of composites based on ED-20 epoxy oligomer cured with isomethyltetrahydrophthalic and methylendic anhydrides was studied as influenced by the nature and properties of finely dispersed inorganic fillers, such as carbon black, aluminum oxide, and silica nanoparticles.

Modern industry requires development of new polymeric materials with specific properties, especially with enhanced strength, hardness, and heat resistance. Owing to high mechanical and adhesion characteristics and strong resistance to various solvents and aggressive solutions, composite polymeric materials based on epoxy resins are widely used in industry. These epoxy resins are cured in a wide temperature range without liberation of volatile compounds. The main disadvantage of epoxy binders is their low softening point; the strength of polymers drastically decreases on heating to temperatures close their glass-transition point.

The properties of epoxy polymers can be easily controlled both by selection of the epoxy oligomer–curing agent system and by addition of fillers [1–3]. Almost all natural and artificial materials with suitable properties, including polymers, can be used as fillers for polymeric composites. A combination of a polymer with filler allows preparation of materials with desired processability and performance. Usually, primary attention is given to the effect of fillers on the mechanical strength of polymers, but fillers also decrease the fluidity and thermal and chemical volume shrinkage, increase moldability and dimensional stability, decrease inflammability, and improve friction or antifriction, electrical, thermal, and other properties.

To find an optimal combination of the polymer and filler, it is necessary to take into account not only their nature, shape, size, and distribution of nanoparticles, but also their interaction at the interface. The chemical composition is the main characteristic of fillers, and in most cases it determines the possibility of their use. The reactivity of fillers, being the surface property directly related to the chemical composition, is of particular importance [4].

By now, various properties of filled epoxy polymer have been studied (Table 1), but primary attention was focused on coarse fillers with particle size larger than 1 μm, and at relatively high degree of polymer filling (>10 wt %).

The effect of "small addition" [10], namely, improvement of physical and mechanical properties of polymer at small and very small degrees of filling is rather promising. It was found that, upon addition of a filler, the glass-transition point of a polymer T_g may increase, and a greater increase is observed at small degrees of filling (Table 1). Very often, with increasing degree of filling the rise in T_g terminates even at very low concentrations, and it remains almost constant up to fairly high concentrations of the solid additive. The effect of "small addition" is pronounced only in the case of filling of a polymer with solid particles smaller than 1 μm in diameter (d), which follows from the data on the length of tie chains binding various supramolecular structures. The nanoparticles are accumulated in boundary sections, and thus even insignificant amounts of a solid additive can affect the flexibility of tie chains and hence the physical

1070-4272/02/7504-0636 $27.00 © 2002 MAIK "Nauka/Interperiodica"

Table 1. Properties of filled epoxy materials [5–9]

Parameter	Filler,* wt %	d, μm	Parameter	Filler,* wt %	d, μm
Glass-transition temperature T_g, K:	TiO_2:		Coefficient of cubic thermal expansion $\alpha \times 10^6$, deg^{-1}	Quartz:	
413 (408)**	1	0.15	175 (160)*	10	20–40
416	5	0.15	175	20	20–40
420	100	0.15	150	40	20–40
	Quartz:			ABS:	
328.5	5	0.4	150	10	20–40
335	17.2	0.4	143	20	20–40
338	32.8	0.4	130	40	20–40
			Compression strength, σ_{com}, MPa:	CNP:	
Young's modulus of elasticity $E \times 10^{-4}$, kg cm^{-2}:			103 (102)	20	10
			118	70	10
1.35 (1.35)	5	0.4	110	80	10
1.55	17.2	0.4			
2.50	32.8	0.4	Thermal stability (reduced decomposition temperature T_{dec}), K:	Graphite:	
3.7 (1.5)	10	20–40	571 (576)	10	5–10
6.3	20	20–40	590	20	5–10
9.2	30	20–40	584	30	5–10
11.7	40	20–40		TiO_2:	
	ABS:		571	10	2
5.0	10	20–40	571	20	2
8.0	20	20–40	567	30	2
10.8	30	20–40		V_2O_5:	
			547	10	5–10
			525	20	5–10
			515	30	5–10

* (ABS) Aluminoborosilicate glass; (CNP) carbonyl nickel powder.

** Data for unfilled polymer are given in parentheses.

and mechanical properties of the polymer. The stability of the polymer properties upon further increase in the filler content is due to the fact that additional amounts of the filler cannot penetrate into boundary regions (owing to their complete filling), and thus their effect on the already ordered structures is insignificant.

The aim of this work was to improve the thermal and mechanical properties of epoxy materials, with the low viscosity of the resin and curing agent in the uncured state preserved, because this composite is used as binder in production of glass-fiber-reinforced plastics by the winding procedure. Special attention was focused on nanosize fillers that enhance the heat resistance and strength of polymer at low degrees of filling [2, 3].

EXPERIMENTAL

In our work, we used formulations based on ED-20 epoxy–4,4'-isopropylidenediphenol oligomer, cured with isomethyltetrahydrophthalic (MTHPA) and methylendic (MEA) anhydrides and filled with K-354 carbon black (specific surface area S_{sp} = 137 $m^2 g^{-1}$, effective particle size 10–30 nm), alumina (S_{sp} = 50–70 $m^2 g^{-1}$, effective particle size 20–30 nm), and silica (S_{sp} = 40–60 $m^2 g^{-1}$, effective particle size 20–30 nm). The nanopowders of alumina and silica were prepared by an original procedure [11].

Various fillers (1–10 wt % degree of filling) were added to an epoxy binder containing (wt. parts): 100 ED-20, 80 MTHPA or MEA, 5 EDOS plasticizer, and 1.5 activator 2,4,6-tris(dimethylaminomethyl)phenol. The components were mixed at 70–90°C; filler particles were first homogenized in a low-viscosity hardener and then mixed with a resin and other components. The formulation was cured at 160°C for 3 h.

The thermal stability of the resulting composites was studied by differential thermogravimetry in the 293–1050 K range at a heating rate of 10 deg min^{-1}; the temperature was measured with an accuracy of

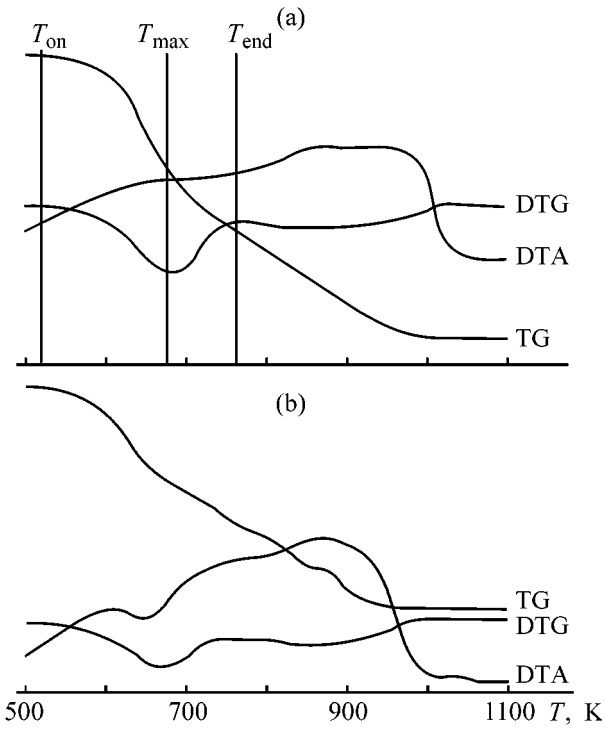

Fig. 1. Thermogravimetric curves of cured epoxy binder containing (a) no filler and (b) Al_2O_3 nanoparticles (2.5 wt %).

±0.5 deg. The samples were prepared by mechanical grinding of the cured formulations. The experimental data on the weight loss $m = f(T)$ (TG), rate of weight loss $dm/dT = f(T)$ (DTG), and thermal effects (DTA) are shown in Figs. 1a and 1b. Using these results, we calculated the reduced decomposition temperatures and evaluated the thermal stability of various materials (Table 2).

Table 2. Temperature and weight parameters of decomposition of MTHPA-cured polymers

Filler, wt %	T_{on}	T_{max}	T_{end}	α_{end}	T_{dec}, K
	K				
–	520	678	753	0.609	611
C:					
0.5	515	663	766	0.642	605
1.0	583	673	788	0.691	646
2.0	571	648	783	0.696	635
5.0	538	688	798	0.655	628
Al_2O_3, 2.5	555	670	737	0.568	634
–	618*	698*	750*	0.663*	662*
C, 1.0	638*	688*	763*	0.681*	678*

* MEA-cured polymer.

The reduced decomposition temperature T_{dec}, as a criterion of thermal stability, was calculated by the following equation:

$$T_{dec} = (1 - \alpha_{end})(T_{end} - T_{on}) + T_{on},$$

where T_{on} and T_{end} are the temperatures of the onset and end of the rapid decomposition interval corresponding to the peak in the DTG curve, and α_{end} is the weight loss at T_{end}.

More adequately, the thermal stability of a material can be evaluated by considering the TG and DTG curves in combination.

As seen from Table 2, composites cured with MEA are more thermally stable than those cured with MTHPA (the onset temperature of rapid decomposition and the reduced temperature of decomposition increase by 98 and 51°C, respectively). Fillers significantly enhance the thermal stability of the epoxy compositions. Addition of carbon (1 wt %) raises T_{dec} by 16–35°C, whereas with carbon content increasing to 5 wt %, the thermal stability of the composite slightly decreases. This is probably due to the ability of the active surface of carbon to adsorb the functional groups of the curing agent, which must participate in the oligomer hardening. As a result, defective regions appear in the cured polymer, and, thus, the thermal stability of the material decreases with increasing carbon filler content.

The tensile strength was measured on an FPZ-10 tensile-testing machine (velocity of the mobile clamp 10 mm min^{-1}) using 200 × 10 × 3 mm plate samples. The results of tests performed at various temperatures are listed in Table 3.

As seen from Table 3, the formulations cured with MTHPA have higher strength than those cured with MEA. The formulations containing 2 wt % carbon have the highest strength (at 23°C). With increasing degree of filling, the mechanical strength of this polymer becomes lower than the strength of the unfilled material by 23–32%, which is probably due to the increase in the content of defective regions as a result of adsorption of the functional groups of the hardener on the carbon surface. At 115°C, the highest strength (10 times the strength of the unfilled polymer) is typical of composites containing mixed fillers (SiO_2 + Al_2O_3 or C + Al_2O_3) or pure alumina. The observed strengthening of the structure upon addition of alumina or silica is attributable to the active surface of these oxides. The surface of alumina and silica contains hydroxy groups, which can form hydrogen bonds with the polymer molecules. As

Table 3. Mechanical properties of MTHPA-cured polymers containing fillers

Filler, wt %	Tensile strength (MPa) at indicated temperature, °C			Young's modulus of elasticity, MPa	Relative elongation (%) at indicated temperature, °C		
	23	115	130		23	115	130
–	54.0	1.45	1.14	3758	1.77	15.7	10.6
–	42.6*	–	3.25*	3696*	1.15*	–	19.9*
C:							
0.5	50,2	–	1.76	3341	1.62	–	10.0
1.0	33.5	4.79	2.57	3315	1.19	30.1	14.3
1.5	54.1	–	1.94	3305	1.82	–	13.8
2.0	67.2	–	2.08	3449	2.33	–	11.7
5.0	36.6	–	1.96	3263	1.2	–	9.7
10.0	41.4	–	1.8	3393	1.44	–	8.7
Al_2O_3, 1.0	32.0	14.5	3.68	3580	0.95	36.4	19.3
SiO_2:							
1.0	58.8	6.66	2.26	3553	1.95	27.9	15.6
5.0	33.9	–	2.43	3336	1.07	–	14.6
(SiO_2+Al_2O_3), 1.0	52.3	15.0	2.84	3325	1.79	38.7	15.7
(C+Al_2O_3), 1.0	28.7	12.4	2.79	3302	0.93	29.4	15.7

* MEA-cured polymer.

compared with silica, the alumina surface is more active in chemical reactions with electron-donor molecules of the polymer. Along with hydroxy groups, the alumina surface can also contain other active centers, e.g., Lewis acid centers formed by coordination-unsaturated aluminum atoms. Hence, in the case of alumina, the coordination interaction between the Lewis centers and polymer molecules occurs simultaneously with the formation of hydrogen bonds. As a result, the epoxy composites filled with oxides exhibit enhanced strength at elevated temperature.

CONCLUSIONS

(1) Composites based on ED-20 epoxy resin cured with isomethyltetrahydrophthalic (MTHPA) and methylendic (MEA) anhydrides and filled with nanoparticles of carbon black, alumina, and silica were prepared. The thermal stability and mechanical strength of these materials was studied.

(2) Addition of fillers to epoxy polymer enhances its thermal stability and mechanical strength at elevated temperature.

(3) The composites containing filler (2 wt % carbon or 1 wt % silica) exhibit the highest strength at 23°C. At elevated temperatures all the fillers enhance the strength properties of the polymers, and the highest strength is observed for the materials filled with alumina, silica, and mixed fillers. Strengthening of the polymer structure upon addition of oxide fillers is due to the presence on their surface of hydroxy groups, which can form hydrogen bonds with the polymer molecules, and in the case of alumina, additional coordination bonds can arise from the interaction of the surface Lewis acid centers (coordination-unsaturated aluminum atoms) and polymer.

REFERENCES

1. Lapitskii, V.A. and Kritsuk, A.A. , *Fiziko-mekhanicheskie svoistva epoksidnykh polimerov i stekloplastikov* (Physical and Mechanical Properties of Epoxy Polymers and Glass-Reinforced Plastics), Kiev: Naukova Dumka, 1986.
2. Lee, H. and Nevill, K., *Handbook of Epoxy Resins*, New York: McGraw-Hill, 1967.
3. *Napolniteli dlya polimernykh kompozitsionnykh materialov (spravochnoe posobie)* (Fillers for Polymeric Composite Materials. Handbook), Kats, G.S. and Milevski, D.V., Eds., Moscow: Khimiya, 1981.
4. Bryk, M.T., *Polimerizatsiya na tverdoi poverkhnisti neorganicheskikh veshchestv* (Polymerization on the Solid Surface of Inorganic Compounds), Kiev: Naukova Dumka, 1986.
5. Anisimov, Yu.N., Dobrova, L.P., and Anisi-

mov, A.Yu., *Zh. Prikl. Khim.*, 1998, vol. 71, no. 5, pp. 790–795.

6. Zakordonskii, V.P., Gnatyshin, S.Ya., and Soltys, M.N., *Zh. Prikl. Khim.*, 1998, vol. 71, no. 9, pp. 1524–1528.
7. Trostyanskaya, E.B., Poimanov, A.M., Nosov, E.F., and Bel'nik, A.R., *Mekh. Polim.*, 1969, no. 6, pp. 1018–1022.
8. Trostyanskaya, E.B., Poimanov, A.M., and Nosov, E.F., *Vysokomol. Soedin.*, 1973, vol. 15, no. 3, pp. 612–620.
9. Shut, N.I., Sichkar', T.G., and Voznyi, P.A., *Kompoz. Polim. Mater.*, 1985, issue 24, pp. 18–21.
10. Solomko, V.P., *Mekhan. Polim.*, 1976, no. 1, pp. 162–166.
11. Sevbo, O.A., in *Fiziko-khimicheskie problemy sozdaniya keramiki spetsial'nogo i obshchego naznacheniya na osnove sinteticheskikh i prirodnykh materialov* (Physicochemical Problems of Preparation of Ceramics for Special and General Purposes, Based on Synthetic and Natural Materials), Syktyvkar, 1998, pp. 141–147.

Russian Journal of Applied Chemistry, Vol. 75, No. 4, 2002, pp. 641–644. Translated from Zhurnal Prikladnoi Khimii, Vol. 75, No. 4, 2002, pp. 655–658.
Original Russian Text Copyright © 2002 by Kurenkov, Zaitseva, Kirdyashova.

MACROMOLECULAR CHEMISTRY AND POLYMERIC MATERIALS

Effect of Alkali Metal Cation on Copolymerization of Acrylamide with Salts of 2-Acrylamido-2-methylpropanesulfonic Acid in Aqueous Solutions

V. F. Kurenkov, O. A. Zaitseva, and G. N. Kirdyashova

Kazan State Technological University, Kazan, Tatarstan, Russia

Received December 17, 2001

Abstract—The kinetics of radical copolymerization of acrylamide with lithium, sodium, and potassium 2-acrylamido-2-methylpropanesulfonates in concentrated aqueous solutions in the presence of potassium persulfate as initiating agent at pH 9 and 50°C was studied by dilatometry.

Owing to high hydrophilicity and high resistance to salts, hydrolysis, and heat, and also high thickening, flocculating, and structuring power, copolymers of acrylamide (AA) with salts of 2-acrylamido-2-methylpropanesulfonic acid (H-AMS)

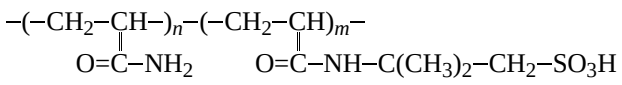

are widely used in drilling, petroleum production, and water treatment [1, 2]. This fact, and also the observed features of radical copolymerization of the ionic monomers [3–5], which are unusual from the viewpoint of classical theory, call for development of new procedures for direct synthesis of AA copolymers with H-AMS salts with various service properties. One of the factors strongly affecting the radical copolymerization of salts of unsaturated acids in ionizing media is the kind of cation. Previously, we have studied the effect of cations on polymerization of H-AMS salts with single- [6] and double-charged [7] cations in aqueous solutions, and also on the flocculation [8] and thermal properties of the resulting polymers [9]. In this work, we studied the kinetics of radical copolymerization of acrylamide with lithium, sodium, and potassium 2-acrylamido-2-methylpropanesulfonates in aqueous solutions and the molecular properties of the resulting copolymers, as influenced by the kind of cation.

EXPERIMENTAL

In our work, we used acrylamide purchased from Mitsubishi Chem. Ind. Ltd. (Japan) (mp 84.5°C), H-AMS purchased from Lubrizol Corp. (United Kingdom) (mp 185°C), distilled water, and other chemically pure grade reagents. Lithium, sodium, and potassium 2-acrylamido-2-methylpropanesulfonates were prepared by potentiometric titration of aqueous H-AMS solutions with aqueous solution of LiOH, NaOH, and KOH to pH 9; the resulting salts were used as aqueous solutions.

The procedures of copolymerization, dilatometric measurements, copolymer isolation, and tests were presented previously in [10]. The shift of the meniscus of the reaction mixture in a dilatometer capillary in the course of kinetic measurements was monitored with a KM-8 cathetometer; the dilatometers were temperature-controlled with an E3E thermostat (Germany) with an accuracy of ±0.05°C.

The solution acidity was measured with a pH-121 pH-millivoltmeter with an ESL-63-07 working glass electrode and an EVL 1M-3 silver chloride reference electrode.

The molecular weight of copolymers M was determined from the intrinsic viscosity [η], because [η] ~ M according to the Mark–Kuhn–Houwink equation. The intrinsic viscosity [η] of copolymer solutions was measured in a 0.5 M NaCl solution at 25°C, using a VPZh-3 viscometer (d_c = 0.43 mm). The content of ionic groups in the copolymer was determined from the content of sulfur [11].

Copolymerization of AA (M_1) with Li-, Na-, and K-AMS salts (M_2) was carried out in concentrated aqueous solutions ([M_1] + [M_2] = 10–30 wt %) at

1070-4272/02/7504-0641 $27.00 © 2002 MAIK "Nauka/Interperiodica"

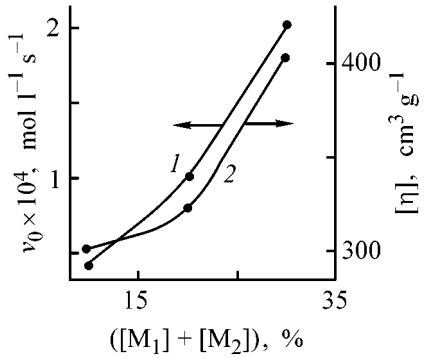

Fig. 1. (*1*) Initial rate of copolymerization of AA with Na-AMS v_0 and (*2*) intrinsic viscosity of copolymers [η] vs. concentration of the initial monomer mixture ([M$_1$] + [M$_2$]). Initial molar ratio [M$_1$] : [M$_2$] = 1 : 1.

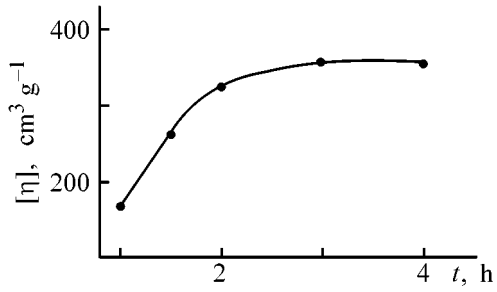

Fig. 2. Intrinsic viscosity of AA and Na-AMS copolymers [η] vs. copolymerization time. ([M$_1$] + [M$_2$]) = 15%, initial molar ratio [M$_1$] : [M$_2$] = 7 : 3, [PP] = 5.86×10^{-3} M.

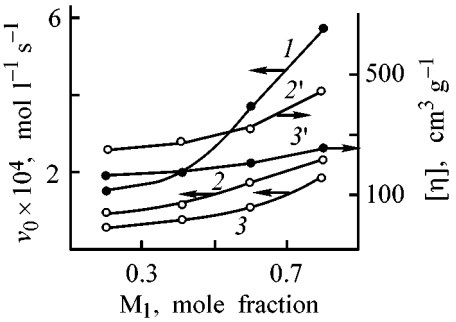

Fig. 3. (*1–3*) Initial rate of copolymerization v_0 of AA with H-AMS salts and (*2*', *3*') intrinsic viscosity of copolymers [η] vs. AA content in the initial monomer mixture M$_1$. ([M$_1$] + [M$_2$]) = 15 wt%. (*1*) Li-AMS, (*2*, *2*') Na-AMS, and (*3*, *3*') K-AMS.

pH 9 and 50°C in the presence of potassium persulfate (PP) as initiating agent. Constant pH 9 was maintained in the reaction mixture (1) to provide constant rate of initiation at solution ionic strength varying [12] as a result of changes in the concentration of the ionic monomers and of increasing conversion in the course of copolymerization, (2) to hinder hydrolysis of H-AMS salts [13], and (3) to prevent imidization of amide groups in concentrated aqueous solutions [14]. Variation of the ionic strength of solutions at changing concentration of the ionic monomer does not affect the reactivity of AA and of the corresponding propagating radical, because the rate of AA polymerization in aqueous solutions is independent of salt additions [15]. Copolymerization was carried out under homogeneous conditions, and no spontaneous polymerization was observed in the absence of the initiating agent.

First, we studied copolymerization of AA and Na-AMS as influenced by the concentration of the initial monomer mixture, which was varied within the range ([M$_1$] + [M$_2$]) = 10–30%; the initial molar ratio [M$_1$] : [M$_2$] was 1 : 1, other experimental conditions being equal. In all cases, the initial portions of the kinetic curves were linear, and, using them, we determined the initial copolymerization rates v_0 at low conversions (<3%). The kinetic curves of copolymerization, obtained by the dilatometric procedure (in a time τ = 2 h), are shown in Fig. 1. As seen, v_0 and [η] of copolymers grow with increasing ([M$_1$] + [M$_2$]) concentration in the reaction mixture, which agrees with the general pattern of radical copolymerization.

The variation of [η] in the course of copolymerization of AA and Na-AMS is illustrated in Fig. 2. The intrinsic viscosities of copolymers grow with increasing reaction time and become nearly constant at τ = 2 h; thus, in our further tests [η] was determined after a 2-h reaction.

The effect of the alkali metal cation in the H-AMS salts on their copolymerization with AA was studied at various initial molar ratios [M$_1$] : [M$_2$], ([M$_1$] + [M$_2$]) = 15%, other experimental conditions being the same. The dependences of v_0 and [η] of copolymers on the content of AA in the initial reaction mixture M$_1$ are shown in Fig. 3. In all the AA-Me-AMS systems, v_0 and [η] grow with increasing M$_1$, which suggests higher reactivity of AA in copolymerization as compared with H-AMS salts. A comparison of the experimental data at fixed [M$_1$] : [M$_2$] > 4 : 6 (Fig. 2) showed that both v_0 and [η] increase in the following order: $K^+ < Na^+ < Li^+$.

The dependences of the current composition of copolymers (conversion <3%) on the content of AA in the course of AA copolymerization with Li-, Na-, and K-AMS are shown in Fig. 4. These dependences correspond in all the systems studied to the following relative activities of the monomers: $r_1 = k_{11}/k_{12} > 1$ (for AA) and $r_2 = k_{22}/k_{21} < 1$ (for H-AMS salts),

which confirms the higher reactivity of AA in copolymerization, compared with H-AMS alkali metal salts. As seen from Fig. 4, enrichment of copolymers in AA units is observed in a wide concentration range in all the systems studied. Moreover, at fixed M_1, the content of the ionic units in copolymers increases in the order $K^+ < Na^+ < Li^+$ (Fig. 4, passing from curve *1* to curve *3*).

To explain the observed trends, let us consider the ionization equilibrium of the ionic groups of the H-AMS salts and their units in growing macroradicals in aqueous salt solutions:

$$\underset{\text{I}}{A^-X^+} \rightleftarrows \underset{\text{II}}{A^- \| X^+} \rightleftarrows \underset{\text{III}}{A^- + X^+}, \qquad (1)$$

where A^- is the anion of the monomer or macroradical; X^+ is the cation; and I, II, and III are contact ion pairs, ion pairs separated with a solvent, and free ions, respectively.

As known, the sulfonate groups in the H-AMS salts and in the units of these salts in copolymers are completely ionized in aqueous solutions. With increasing ionic strength and degree of binding of alkali metal cations with polysulfonate anions, the ionization equilibrium (1) is shifted to the left; as a result, the relative content of various ionic species with different reactivities change, and the intra- and intermolecular electrostatic interactions in the reaction system decrease. This, in turn, affects the polymerization constants and relative activities of the monomers in copolymerization, r_1 and r_2, which are actually the apparent characteristics of the process; therefore, we did not determine them.

It is known [16] that the degree of alkali metal cation binding in solutions of AA copolymers with H-AMS salts increases in the order $K^+ < Na^+ < Li^+$. In this order, the electrostatic repulsion of similarly charged monomers (H-AMS salts) and macroradicals with the terminal ionic groups decreases, which makes k_{22} and v_0 larger (Fig. 3) and causes the observed enrichment of the copolymer with ionic groups (Fig. 4) in the order $K^+ < Na^+ < Li^+$.

Contrary to the above data on copolymerization of AA and H-AMS alkali metal salts, in homopolymerization of H-AMS salts in aqueous solutions [6], v_0 varied with the cation nature in the opposite direction, namely, v_0 decreased in the order $K^+ > Na^+ > Li^+$. This can be accounted for by similar order of changes in binding of the alkali metal cations with H-AMS salt homopolymers [16]. A similar difference in the

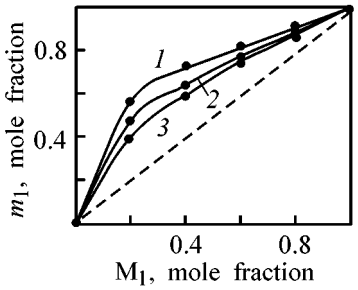

Fig. 4. Content of AA units m_1 in AA copolymer with (*1*) K-AMS, (*2*) Na-AMS, and (*3*) Li-AMS as influenced by the mole fraction of AA in the initial monomer mixture M_1. ($[M_1] + [M_2]$) = 15%; conversion <3%.

trends observed in copolymerization of H-AMS salts with *N*-vinylpyrrolidone and in homopolymerization of H-AMS salts in aqueous solutions was found in [17, 18]; for copolymerization of methyl methacrylate with lithium, sodium, and potassium methacrylates and homopolymerization of alkali metal methacrylates in methanol solutions, such a difference was observed in [19].

Thus, the kinetic parameters of copolymerization of AA with H-AMS salts of single-charged cations and the properties of the resulting copolymers can be controlled by varying the type of cation in the ionic monomer.

CONCLUSIONS

(1) The v_0 and [η] values grow with increasing concentration of the monomer mixture (acrylamide + alkali metal 2-acrylamido-2-methylpropanesulfonate) and content of acrylamide in the reaction system; v_0 increases in the order $K^+ < Na^+ < Li^+$, and [η], on passing from K^+ to Na^+ and with increasing conversion.

(2) The content of the ionic groups in the copolymers increases in the order $K^+ < Na^{2+} < Li^+$; as a result, copolymers enriched in nonionic acrylamide units are formed in all the systems studied.

ACKNOWLEDGMENTS

The work was financially supported by the Foundation of Basic Natural Science of the Ministry of Education of the Russian Federation (project no. 97-0-9.4-59) and the Foundation of Research and Development of the Republic of Tatarstan [project no. 19-03/2000 (F)].

The authors are grateful to T.A. Romanova (Central Research Institute of Geology of Nonmetalliferous Mineral Resources) for elemental analysis of copolymers.

REFERENCES

1. McCormick, C.L., J. Macromol. *Sci. Chem., Ser. A*, 1985, vol. 22, nos. 5–7, pp. 955–982.
2. Lisovtsev, V.V., Rostokin, G.A., and Kulikova, A.E., in *Khimicheskaya promyshlennost': Akrilaty i polivinilkhlorid* (Chemical Industry: Acrylates and Polyvinyl Chloride), Moscow: NIITEKhIM, 1984, pp. 1–20.
3. Kabanov, V.A. and Topchiev, D.A., *Polimerizatsiya ionizuyushchikhsya monomerov* (Polymerization of Ionizable Monomers), Moscow: Nauka, 1975.
4. Bekturov, E.A., Myagchenkov, V.A., and Kurenkov, V.F., *Polimery i sopolimery stirolsul'fokisloty* (Polymers and Copolymers of Stryrenesulfonic Acid), Alma-Ata: Nauka, 1989.
5. Kurenkov, V.F. and Myagchenkov, V.A., *Zh. Prikl. Khim.*, 1999, vol. 72, no. 6, pp. 881–890.
6. Kurenkov, V.F. and Safin, A.G., *Zh. Prikl. Khim.*, 1998, vol. 71, no. 1, pp. 136–140.
7. Kurenkov, V.F., Safin, A.G., and Almazova, E.I., *Zh. Prikl. Khim.*, 1998, vol. 71, no. 10, pp. 1704–1708.
8. Kurenkov, V.F., Safin, A.G., and Merkanina, O.N., *Zh. Prikl. Khim.*, 1998, vol. 71, no. 9, pp. 1015–1018.
9. Kurenkov, V.F. and Safin, A.G., *Zh. Prikl. Khim.*, 1998, vol. 71, no. 11, pp. 1927–1929.
10. Kurenkov, V.F., Khairulin, M. R., and Utikeeva, A.R., *Zh. Prikl. Khim.*, 1999, vol. 72, no. 7, pp. 1177–1181.
11. Charlot, G., *Les methods de la chimie analytique. analyse quantitative minerale*, Paris: Masson, 1961.
12. Kolthoff, I.M. and Miller, I.K., *J. Am. Chem. Soc.*, 1951, vol. 73, no. 7, pp. 3055–3059.
13. *2-Acrylamido-2-Methylpropane Sulfonic Acid Monomer*, Wickliffe, Ohio (USA): Lubrizol, 1994.
14. USSR Inventor's Certificate, no. 235997.
15. Topchiev, D.A., Shakirov, R.Z., Kalinina, L.P., *et al.*, *Vysokomol. Soedin., Ser. A*, 1972, vol. 14, no. 3, pp. 581–586.
16. Kurenkov, V.F., Kolesnikova, I.Yu., and Solov'ev, D.A., *Zh. Prikl. Khim.*, 2001, vol. 74, no. 3, pp. 490–493.
17. Kurenkov, V.F., Zaitseva, O.A., and Karyagina, S.V., *Vestn. Kazan. Tekhnol. Univ.*, 2000, nos. 1–2, pp. 121–126.
18. Kurenkov, V.F., Zaitseva, O.A., Khartan, Kh.-G., and Lobanov, F.I., *Vestn. Kazan. Tekhnol. Univ. (Suppl.)*, 2001, nos. 1–2, pp. 199–214.
19. Hamoudi, A. and McNeill, I.C., *Eur. Polym. J.*, 1978, vol. 14, pp. 177–180.

Russian Journal of Applied Chemistry, Vol. 75, No. 4, 2002, pp. 645–648. Translated from Zhurnal Prikladnoi Khimii, Vol. 75, No. 4, 2002, pp. 659–663.
Original Russian Text Copyright © 2002 by Bochek, Yusupova, Zabivalova, Petropavlovskii.

MACROMOLECULAR CHEMISTRY AND POLYMERIC MATERIALS

Rheological Properties of Aqueous *H*-Carboxymethyl Cellulose Solutions with Various Additives

A. M. Bochek, L. D. Yusupova, N. M. Zabivalova, and G. A. Petropavlovskii

Institute of Macromolecular Compounds, Russian Academy of Sciences, St. Petersburg, Russia

Received June 1, 2001

Abstract—Rheological properties of moderately concentrated aqueous solutions of carboxymethyl cellulose in the H form with various additives were studied.

It is known that carboxymethyl cellulose sodium salt (NaCMC) is readily soluble in water at a degree of substitution (DS) above 0.4. Aqueous solutions of NaCMC are used in food, cosmetic, fragrance, and textile industries, in petroleum production, and also in manufacture of detergents [1]. Heavy metal (Ag, Pb, Zr, Cu) salts precipitate NaCMC from solutions [2]. Introduction of Cr(III) into an NaCMC solution may result in the formation of a gel, in which syneresis proceeds in the couse of time [3]. With increasing Cr(III) concentration, the solution viscosity grows and cross-linking occurs.

The viscosity and structural organization of CMC solutions depend on the degree of its neutralization [1, 4, 5]. On passing from the Na to H form (HCMC), the solution viscosity increases and cross-linking occurs. Dry HCMC is insoluble in water, and its aqueous solutions can be prepared by passing NaCMC solutions through strongly acidic cation-exchange resins [1]. When an HCMS solution free from granules of a cation-exchange resin is allowed to stand at 5–10°C, gelation starts, caused by accumulation of weakly dissociated carboxy groups in the polymer macromolecules [1, 4]. The resulting HCMS gel is stable in time. We observed no syneresis or polymer degradation even after keeping an HCMC solution for a year at 5–10°C in an oxygen-free atmosphere [4]. Thus, a gel obtained from aqueous HCMC is a three-dimensional (3D) cross-linked system formed through intra- and intermolecular hydrogen bonding between the carboxy and hydroxy groups of HCMC and water molecules.

Addition of heavy metal salts to HCMC solutions initiates chemical cross-linking through carboxy groups of the polymer. It was of considerable scientific and practical interest to study the effect of various additives (heavy metal salts and weak bases and acids) on the rheological properties of aqueous HCMC solutions and also to elucidate the mechanisms of action of these additives on gelation.

Therefore, we studied in this work the features of gelation in aqueous HCMC solutions with various additives.

EXPERIMENTAL

As a starting material we used commercial NaCMC (degree of substitution DS 0.46; degree of polymerization DP_η 460). The degree of polymerization was determined viscometrically using an NaCMC solution in 6% NaOH. We used in calculations the relationship $[\eta] = 7.3 \times 10^{-3} M^{0.93}$ [1]. The degree of substitution in NaCMC was estimated from the sodium content by Eq. (1).

$$DS_{Na} = \frac{162n}{2300 - 80n}, \quad (1)$$

where n is the Na content in the polymer (wt %).

The sodium content in CMC was determined by conductometric titration with 0.1 N HCl. The degree of substitution of HCMC by carboxy groups DS_{COOH} was estimated by Eq. (2).

$$DS_{COOH} = \frac{162m}{4500 - 58m}, \quad (2)$$

where m is the carboxy group content (wt %).

The carboxy group content was determined by conductometric titration with 0.1 N NaOH. The DS_{Na} and DS_{COOH} were coincident in the CMC samples studied.

1070-4272/02/7504-0645 $27.00 © 2002 MAIK "Nauka/Interperiodica"

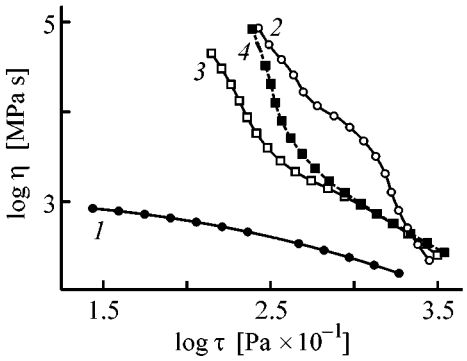

Fig. 1. Flow curves of 3% aqueous solutions of (*1*) HCMC and (*2–4*) HCMC with various additives: (*2*) $CuCl_2$, (*3*) urea, and (*4*) boric acid. Additive concentration 0.5 mol/mol COOH. (η) Viscosity and (τ) shear stress. Flow curves were obtained 1 h after solution preparation.

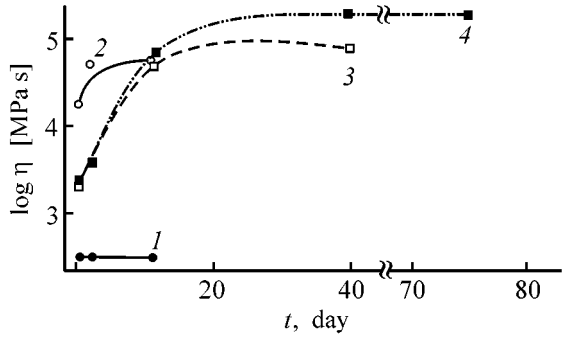

Fig. 2. Viscosity η of 3% aqueous solutions of (*1*) HCMC and (*2–4*) HCMC with various additives: (*2*) $CuCl_2$, (*3*) urea, and (*4*) boric acid vs. time *t*. Additive concentration 0.5 mol/mol COOH; log τ = 2.7.

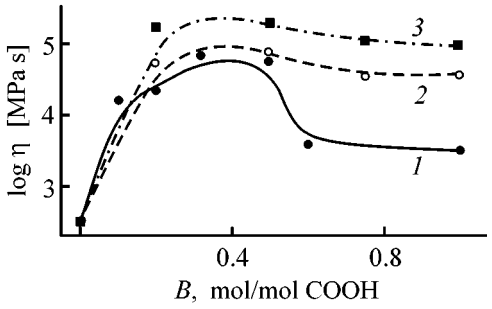

Fig. 3. Viscosity η of 3% aqueous HCMC solutions (log τ = 2.7) vs. additive concentration *B* (mol/mol COOH): (*1*) $CuCl_2$, (*2*) urea, and (*3*) boric acid. Time elapsed after solution preparation (days): (*1*) 3, (*2*) 11, and (*3*) 40.

Commercial NaCMC may contain low-molecular-weight impurities, particularly, chlorides used in cellulose carboxymethylation [1]. To remove foreign compounds, the sample was pretreated in a Soxhlet apparatus with hot 70% aqueous isopropanol for 4 h to negative reaction for chloride ($AgNO_3$) and then vacuum-dried at 50°C for 12 h. The DS_{Na}, DS_{COOH}, and DP_η were determined for thus treated samples.

The initial 3% aqueous NaCMC solution was prepared by dissolution in distilled water at room temperature with stirring for 5 h. Then the solution was filtered under pressure through a three-layer fabric (coarse calico) filter and then centrifuged for 1 h at 5000 rpm.

To convert NaCMC into the H form, we used commercial KU-2 sulfonic cation-exchange resin. A fixed amount of the resin was added to an NaCMC solution, and a mixture was stirred vigorously. In a 3% NaCMC solution the total conversion into the H form took 5 h. The resulting solution showed pH 3.0 (degree of neutralization α = 0). It preserved its fluidity for 24 h at 5–10°C, and then gelation started.

As additives to HCMC we used 20% aqueous solutions of $CuCl_2$ and urea and 2% boric acid.

The rheological properties of HCMC with various additives were studied with a Rheotest 2.1 rotation vis- cometer (cylinder–cylinder working unit) under a shear stress of 3–600 Pa. Solutions of HCMC appeared to be more cross-linked as compared to the initial NaCMC solution [4].

Figure 1 shows the flow curves of HCMC solutions containing various additives in amount of 0.5 mol/mol COOH. The curves were measured 1 h after the solution preparation. Introduction of any of the additives used induces cross-linking of the HCMC solution, considerably increasing its viscosity. The observed strong dependence of the viscosity on the shear stress is typical of thermoreversible physical gels [6] and chemically cross-linked systems [7]. After introduction of an additive with stirring, the solution viscosity increases, approaching saturation (Fig. 2). The time required for reaching the limiting viscosity is different for systems with different additives. This parameter is the highest in the case of boric acid and the lowest in the system with $CuCl_2$. Therefore, the effect of the additive content on the rheological properties of the solutions was studied after reaching the limiting viscosity, i.e., the systems with $CuCl_2$, urea, and boric acid were allowed to stand for 3, 11, and 40 days, respectively, prior to measurement.

It follows from Fig. 3 that the trend of viscosity variation with the additive concentration depends on particular additive, i.e., the additives differently interact with the polymer macromolecules.

Upon addition of $CuCl_2$ the viscosity increases up to a salt concentration of 0.5 mol/mol COOH, then decreases, and, finally, becomes constant. It is known that salts of copper, lead, and other heavy metals precipitate NaCMC from aqueous solutions [2]. At

a $CuCl_2$ concentration of up to 0.5 mol/mol COOH we did not observe noticeable turbidity. It may be suggested that the initial increase in the viscosity is due to cross-linking of the polyelectrolyte macromolecules by reaction (3):

$$\begin{aligned} &2\text{Cell}-\text{O}-\text{CH}_2-\overset{\overset{\text{O}}{\|}}{\text{C}}-\text{O}-\text{H} + \text{CuCl}_2 \\ &\rightarrow \text{Cell}-\text{O}-\text{CH}_2-\overset{\overset{\text{O}}{\|}}{\text{C}}-\text{O}-\text{Cu}-\text{O}-\overset{\overset{\text{O}}{\|}}{\text{C}}-\text{CH}_2-\text{O}-\text{Cell} \\ &+ 2\text{HCl}. \end{aligned} \quad (3)$$

To confirm the possibility of reaction (3), we determined the copper concentration in the systems just after addition of $CuCl_2$ in amount of 0.5 and 1.0 mol/mol COOH and 3 days after. Copper was determined [8] in the solution after removal of the precipitated polymer. The copper concentration in the solution decreased by 16.0 and 12.0%, respectively, against the initial value. Therefore, only partial chemical cross-linking by reaction (3) occurs, which is due to the fact that $CuCl_2$ is added to an acid solution, and the equilibrium is shifted to the left. Nevertheless, even partial cross-linking noticeably increases the solution viscosity.

The decrease in the solution viscosity at an additive concentration above 0.5 mol/mol COOH is accompanied by the appearance of a noticeable turbidity, which is an indication of phase separation occurring in the system as a result of either polymer precipitation in the presence of copper or syneresis of the chemically cross-linked network.

In the systems HCMC–urea and HCMC–boric acid, the viscosity reaches a maximum at an additive concentration of 0.5 mol/mol COOH and then slightly decreases.

Urea is a weak base [9]. In an acidic HCMC solution (pH 3.0) it occurs in the undissociated form, and the following reactions can take place:

$$\begin{aligned} &\text{Cell}-\text{O}-\text{CH}_2-\overset{\overset{\text{O}}{\|}}{\text{C}}-\text{O}-\text{H} + \text{NH}_2-\overset{\overset{\text{O}}{\|}}{\text{C}}-\text{NH}_2 \\ &\rightarrow \text{Cell}-\text{O}-\text{CH}_2-\overset{\overset{\text{O}}{\|}}{\text{C}}-\overset{-}{\text{O}}\text{H}_3\overset{+}{\text{N}}-\overset{\overset{\text{O}}{\|}}{\text{C}}-\text{NH}_2, \end{aligned} \quad (4)$$

$$\begin{aligned} &2\text{Cell}-\text{O}-\text{CH}_2-\overset{\overset{\text{O}}{\|}}{\text{C}}-\text{O}-\text{H} + \text{NH}_2-\overset{\overset{\text{O}}{\|}}{\text{C}}-\text{NH}_2 \\ &\rightarrow \text{Cell}-\text{O}-\text{CH}_2-\overset{\overset{\text{O}}{\|}}{\text{C}}-\overset{-}{\text{O}}\text{H}_3\overset{+}{\text{N}}-\overset{\overset{\text{O}}{\|}}{\text{C}}-\overset{+}{\text{N}}\text{H}_3\overset{-}{\text{O}}-\overset{\overset{\text{O}}{\|}}{\text{C}}-\text{CH}_2-\text{O}-\text{Cell}, \end{aligned} \quad (5)$$

$$\text{---NH}_2-\overset{\overset{\text{O}}{\|}}{\text{C}}-\text{NH}_2\text{---}. \quad (6)$$

The formation of an amine salt of CMC in the reaction of HCMC with ethylenediamine (EDA) was reported in [10]. Similar reaction (4) can also proceed with urea. After formation of a film from a solution of HCMC with urea, cross-linking of the macrochains by reaction (5) may occur, as in the case of EDA [10]. Formation of H bonds between urea molecules and carboxy and hydroxy groups of the polymer (6) may also occur. It should be suggested for the system under consideration that the formation of a salt (4) and hydrogen bonding (6) are dominating processes. The formation of an H-bonded network is a slower process as compared to the chemical reaction occurring in the system with $CuCl_2$. As a result, the limiting viscosity is reached in a longer time in the systems with urea and boric acid. Reaction (5) could not be realized in this work, since it requires heating of the films formed in the system at a temperature above 100°C [10].

With the urea concentration increasing above 0.5 mol/mol COOH the viscosity decreases slightly, which can be due to the presence of free urea capable of forming additional H bonding, thus stabilizing the system and decelerating the syneresis. Among other factors is dilution of the solution, i.e., decrease in the polymer concentration. Generally, formation of additional H bonds makes the solution more viscous, and a decrease in the polymer concentration, less viscous. We observed no syneresis in the system with urea even after its being kept for more than 40 days, which suggests that this system is a mixture of the amine salt of CMC, stabilized through H bonds, with water molecules also involved in H bonding.

Introduction of boric acid into HCMC solutions increases the solution viscosity up to the additive concentration of 0.4–0.5 mol/mol COOH. With the additive concentration increasing further the viscosity decreases slightly. In this case, the polyacid (HCMC having $K \approx 5.0 \times 10^{-5}$ [1] is close to acetic acid in strength) reacts with even weaker boric acid ($K_1 = 6.0 \times 10^{-10}$, $K_2 = 5 \times 10^{-13}$, and $K_3 = 4 \times 10^{-14}$ [11]). In aqueous solutions, boric acid occurs as a weakly dissociated hydroxide, $B(OH)_3$. It was suggested also that boric acid can form a donor–acceptor bond with one water molecule, giving rise to one more boron hydroxide species [11]:

$$H_2OB(OH)_3 \rightleftarrows H^+ + [B(OH)_4]^-.$$

The occurrence of weakly dissociated boron hydroxide species $B(OH)_3$ and $[B(OH)_4]^-$ in HCMC solutions suggests that the increase in the HCMC solution viscosity and its cross-linking are caused by formation of a 3D H-bonded network, in which the indicated boron hydroxide species serve as network points, i.e., H bonds are formed between the OH groups of boron hydroxide and COOH and OH groups of the polymer. One of the possible models for H bonding is presented below.

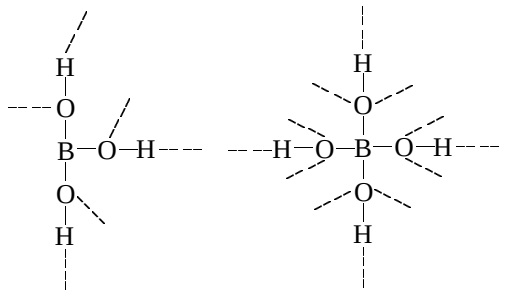

It should be pointed out that introduction of aqueous boric acid in a solution of the stronger acid, HCMC, shifts the equilibrium of $[B(OH)_4]^-$ formation to the left. Therefore, involvement of this form of boron hydroxide in H bonding is hardly probable. Hydrogen bonding can involve both protons and oxygen atoms of ionic boron species. The process is kinetically controlled, and the limiting viscosity is reached in 40 days. The resulting gel is quite stable, and no syneresis is observed. As in the case with urea, no considerable decrease in the viscosity was observed with the boric acid concentration increasing above 0.5 mol/mol COOH. This can be interpreted as follows. Occurrence of free boric acid in the system increases the density of H bonds, which must increase the solution viscosity. The observed insignificant decrease in the viscosity is probably due to dilution of the polymer solution as a result of addition of a dilute boric acid solution (2 wt %).

Finally, introduction of $CuCl_2$ in HCMC solutions initiates gelation by the mechanism of chemical cross-linking at the carboxy groups with Cu^{2+} ions. In the course of time, the gel undergoes syneresis. In the system with urea, the gelation mechanism includes formation of CMC amine salt and a 3D H-bonded network. In the case of boric acid, gelation proceeds through H bonding. Gels formed in the systems with urea (weak base) and boric acid (weak acid) are stable in time (no syneresis). Therefore, an increased viscosity of HCMC solutions and cross-linking of HCMC-based systems can be achieved by various methods, which expands the potentialities of their practical use as thickeners. Weak bases and acids can be used to obtain stable HCMC-based gels, depending on a field of application.

CONCLUSIONS

(1) Rheological characteristics of moderately concentrated solutions of H-carboxymethyl cellulose can be modified with additives of various natures.

(2) Introduction of $CuCl_2$ into HCMC solutions initiates formation of a chemically cross-linked gel, which undergoes syneresis.

(3) Introduction of weak base or acid into HCMC solutions increases the viscosity as a result of formation of a 3D H-bonded network with participation of water molecules.

(4) Aqueous HCMC solutions modified with various additives can be used to prepare stable gels.

REFERENCES

1. Petropavlovskii, G.A., *Gidrofil'nye chastichno zameshchennye efiry tsellyulozy i ikh modifikatsiya putem khimicheskogo sshivaniya* (Hydrophilic Partially Substituted Cellulose Ethers and Their Modification by Chemical Cross-Linking), Leningrad: Nauka, 1988.
2. *Cellulose and Cellulose Derivatives, part IV*, Bikales, N.M. and Segal, L., Eds., New York: Wiley, 1971.
3. Medvedeva, V.V., Myasnikova, L.I., Semchikov, Yu.D., *et al., Vysokomol. Soedin., Ser. B*, 1998, vol. 40, no. 3, pp. 492–497.
4. Yusupova, L.D., Bochek, A.M., and Petropavlovskii, G.A., *Zh. Prikl. Khim.*, 1994, vol. 67, no. 7, pp. 1187–1191.
5. Bochek, A.M., Petropavlovskii, G.A., Yusupova, L.D., *et al., Zh. Prikl. Khim.*, 1997, vol. 70, no. 12, pp. 2048–2052.
6. Bochek, A.M. and Petropavlovskii, G.A., *Cell. Chem. Technol.*, 1995, vol. 29, no. 5, pp. 567–574.
7. Buyanov, A.L., Revel'skaya, L.G., Petropavlovskii, G.A., *et al., Zh. Prikl. Khim.*, 1992, vol. 65, no. 2, pp. 679–685.
8. Přibil, R., *Komplexony v chemické analyse*, Prague: Československé Akad., 1957.
9. Petropavlovskii, G.A. and Zimina, T.R., *Zh. Prikl. Khim.*, 1994, vol. 67, no. 5, pp. 705–721.
10. Petropavlovskii, G.A., Larina, E.I., and Borisova, T.I., *Cell. Chem. Technol.*, 1984, vol. 187, no. 3, pp. 283–292.
11. Nekrasov, B.V., *Osnovy obshchei khimii* (Fundamentals of General Chemistry), Moscow: Khimiya, 1973, vol. 2.

Russian Journal of Applied Chemistry, Vol. 75, No. 4, 2002, pp. 649–655. Translated from Zhurnal Prikladnoi Khimii, Vol. 75, No. 4, 2002, pp. 664–672.
Original Russian Text Copyright © 2002 by Platonov, Proskuryakov, Podshibyakin, Domogatskii, Shvykin, Shavyrina, Chilachava.

CHEMISTRY OF FOSSIL FUEL

Genetic Relationship of Organic Bases of the Quinoline and Isoquinoline Series from Lignite Semicoking Tars with the Initial Biological Material

V. V. Platonov, V. A. Proskuryakov, S. I. Podshibyakin, V. V. Domogatskii, A. Yu. Shvykin, O. A. Shavyrina, and K. B. Chilachava

Leo Tolstoy State Pedagogical University, Tula, Russia

St. Petersburg State Technological Institute, St. Petersburg, Russia

Received May 10, 2001; in final form, November 2001

Abstract—The genetic relationship of quinoline and isoquinoline compounds present in semicoking tars of Kimovsk lignites (near-Moscow fields) with the initial vegetable material is discussed. Transformation pathways of the native compounds in the course of lignite formation are suggested.

Recently there has been a considerable progress in detailed studies of biological markers bearing information about the initial biomaterial, primary sedimentation, and hence about further diagenesis and catagenesis. Such studies formed a new direction in geoorganic chemistry. Alkaloids form one of the most important groups of lignite biomarkers. Structural studies of individual nitrogen-containing heterocycles isolated from lignites give insight into their genesis. Extensive data have been obtained [1] on the composition of various extracts and tars formed in low-temperature semicoking of lignite from the Kimovsk open pit, near-Moscow fields.

It was found that the major organic bases of semicoking tars (SCTs) are nitrogen-containing heterocycles boiling below 300°C (wt % of fraction): pyridine (1.2), C_1-alkylpyridines (2.1), C_2-alkylpyridines (5.8), C_3-alkylpyridines (6.5) >C_4-alkylpyridines (8.9), alkylquinolines (5.0), alkylisoquinolines (10.4), hydrogenated quinolines (10.2), polycyclic aromatic compounds (5.5), indoles (5.6), alkylindoles (5.4), C_3-alkylindoles (5.0), >C_4-alkylindoles (1.2), carbazoles (3.9), and hydrogenated benzopyrroles (12.3).

The share of quinoline and isoquinoline derivatives in nitrogen-containing compounds is fairly high; therefore, it seemed of interest to study the genesis of these structures in the organic matter of lignites (OML). A detailed study of organic bases from lignite SCT by IR, UV, ^{1}H NMR, and ^{13}C NMR spectroscopy, cryoscopy, preparative thin-layer chromatography, GC–MS, and elemental and quantitative functional analyses allowed identification of compounds **I**–**XXVII** characterizing structural fragments of OML and elucidation of the features of nitrogen distribution (see scheme 1).

Scheme 1.

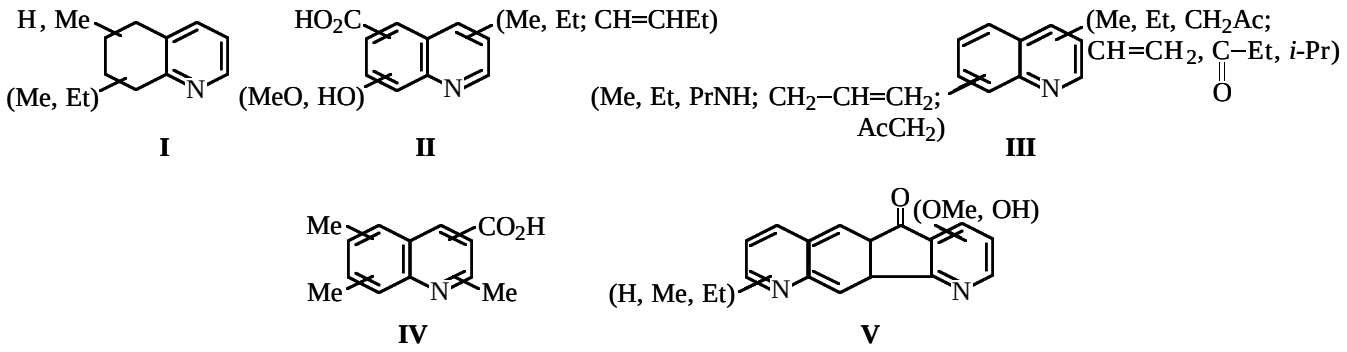

1070-4272/02/7504-0649 $27.00 © 2002 MAIK "Nauka/Interperiodica"

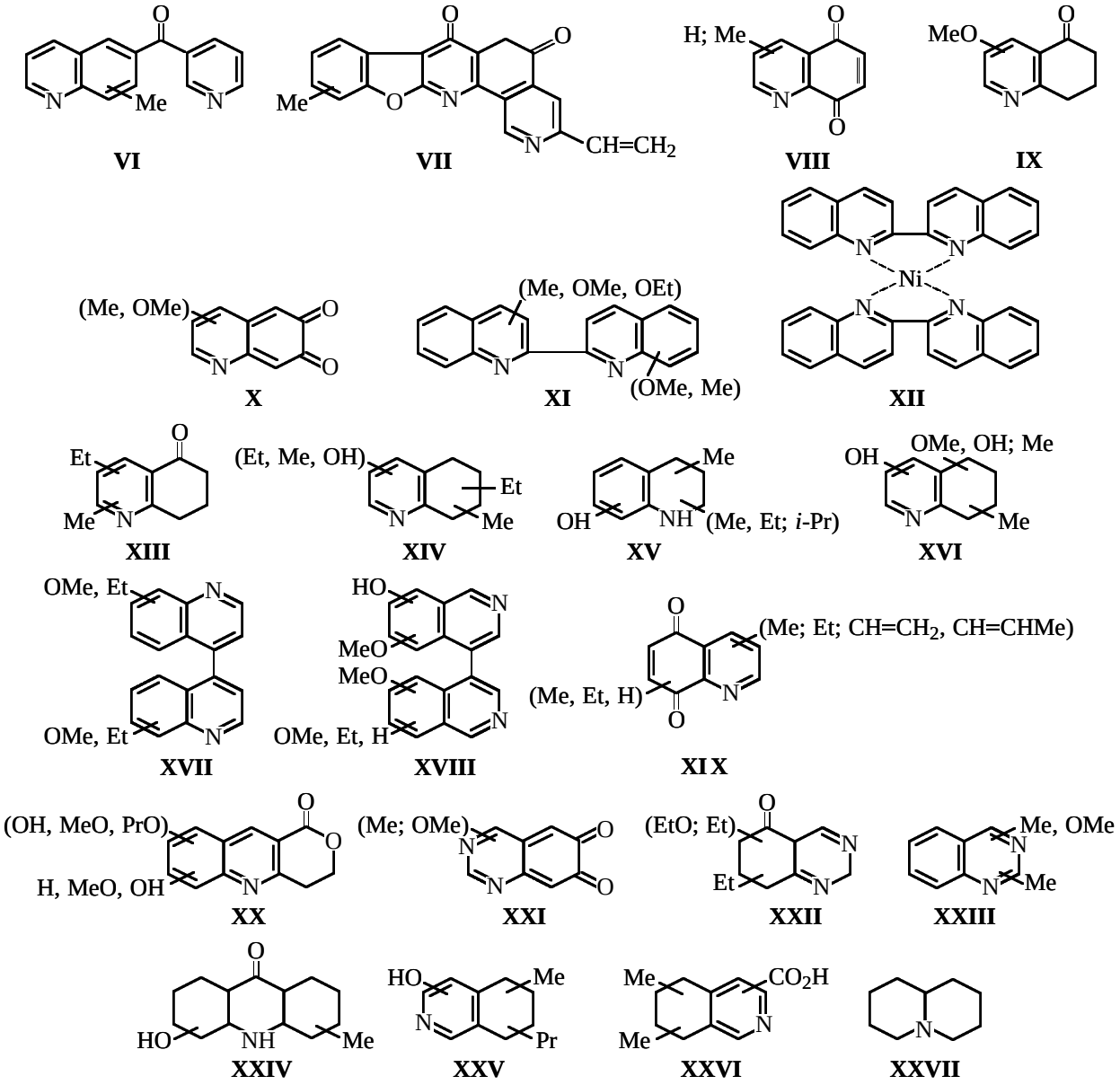

In this connection, it was necessary to pay attention to biomarkers that give insight into the relationship between the nitrogen-containing lignite fragments and the biological material. Structures **I**–**XXVII** in OML should be associated with vegetable alkaloids, because so strong enrichment of the initial organic matter with oxygen-containing and alkyl groups by other pathways of biogeochemical degradation seems improbable. Alkaloids occur most widely in Angiospermae, especially in *Papaveraceae*, *Ranunculaceae*, *Leguminosae*, *Rubiaceae*, *Solanaceae*, and some other families. In algae, fungi, mosses, ferns, and Gymnospermae, alkaloids occur relatively seldom; therefore, as noted in numerous papers [2], the content of heterocyclic nitrogen in sapropelic caustobioliths is relatively low. The fact that alkaloids are distributed among botanic families nonuniformly gives reason to consider them as fairly selective biological markers. It should be noted that the group of quinoline and especially isoquinoline alkaloids is characterized by the largest number of representatives and diversity of their structures. This is confirmed by a large content of quinolines and isoquinolines in SCT [1].

To reveal a genetic relationship between this group of nitrogen-containing compounds and natural alkaloids, we performed their structural classification based on the structure of the heterocycle. Structures **I**–**XVII**, **XIX**, and **XX** were classed with the quinoline series; structures **XVIII**, **XXV**, and **XXVI**, with the isoquinoline series; **XXI**–**XXIII**, with the quinazoline series; and structure **XXVII** belongs to belong to the group of natural alkaloids of the quinolizidine series.

Distribution of various groups of alkaloids in the biological material

Plant family	Quinolines	Isoquinolines	Quinazolines	Quinolizines
Rutaceae	+	+	++	
Rubiaceae	++	+		+
Papaveraceae		++		
Ranunculaceae		+		+
Acantaceae		+	+	
Leguminosae		+		++
Chenopodiaceae		+		+
Berberidaceae		+		+
Solanaceae		+		+
Menispermaceae		+		+
Fungi producing alkaloid precursors in OML		+	+	+

A comparison of the molecules isolated from OML with various natural compounds allowed the former compounds to be classed with biomarkers of the second kind, in which the thermodynamically stable molecular core is preserved, but substituents have underwent changes in the course of biogeochemical transformation of the organic matter of the initial vegetable material, or in the course of semicoking (SC). The structures of the organic bases allow fairly accurate identification of families, genera, and even species of plants from which lignite was formed (see table).

A large number of quinolines and isoquinolines are produced by the *Rutaceae*, *Rubiaceae*, *Leguminosae*, and *Solanaceae* families. Alkaloids of the quinoline series occur in almost all the families, but in *Papaveraceae* their content is the highest. The theory of the biological conservatism of plants gives grounds to state that evolutionary precursors of these plant families were involved in the primary sedimentations. Also, a very important part in the stage of peat genesis was played by fungi which produced various aliphatic amines and polypeptides. Under the action of microbial enzymes, these compounds transformed into various nitrogen-containing heterocycles, including those of the classes under consideration.

The preservation of the quinoline and isoquinoline cores in OML is due to their fairly high thermodynamic stability. It has been noted that these structures are linked to the peripheral part of the coal macromolecular network; however, owing to increased stability, they are also involved in formation of the polymeric core of a caustobiolith macromolecule. That is why data on recovery of nitrogen-containing heterocycles by nondestructive methods (e.g., extraction) are scarce [1]. A large number of such structures, detected in SCT, were released in the course of thermal degradation of the polymeric matrix. For example, the following mechanism can be suggested for formation of quinoline in pyrolysis of coal:

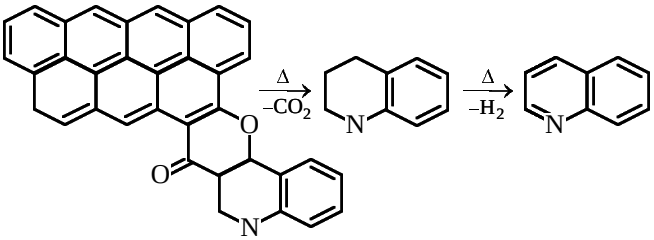

Quinolines formed in thermal degradation of caustobioliths and occurring in the nature contain, as a rule, a reduced (di- or tetrahydro) heteroring. This fact gives grounds to state that, in chemical transformations occurring in the course of semicoking or of biosynthesis in the initial vegetable material, isoquinolines are formed by decarboxylation of aromatic amino acids, many of which have been identified in aqueous extracts of coals. One of the major producers of isoquinolines in the modern flora is the *Papaveraceae* family. Representatives of this family contain such alkaloids as, e.g., morphine, codeine, papaverine, etc. One of possible pathways of biochemical transformations of native compounds is as follows:

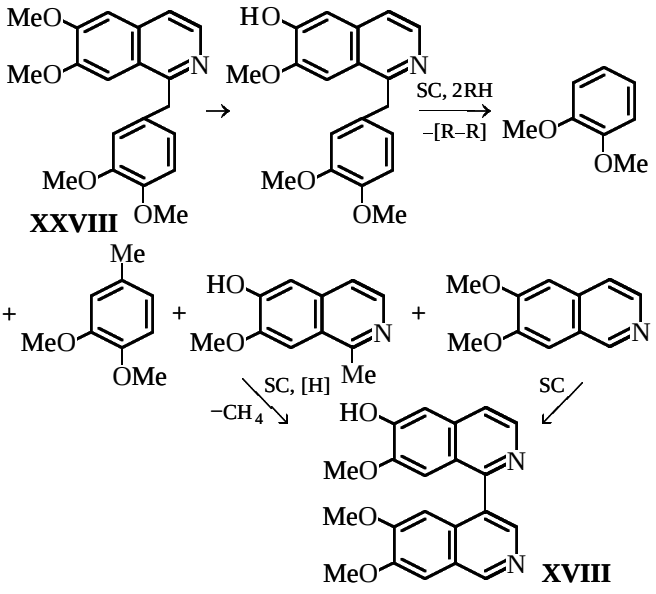

Papaverine **XXVIII** undergoes enzymatic demethoxylation. In the course of semicoking, one phenyl radical undergoes radical elimination, and two isoquinoline fragments are coupled to form product **XVIII** identified in SCT. In the course of biogeochemical and subsequent thermochemical transformations, such a structure can be yielded by degradation of polymethylene bridges in such compounds as salsoline (*Solanaceae*) and laudanine (*Papaveraceae*). It has been found previously [3] that the organic matter of some lignites contains isoquinoline lactams (isoquinolones), which are presumably formed by amination in aqueous solutions of the corresponding isocoumarins. Substituted isoquinolones were also isolated from SCTs of lignites from the near-Moscow fields. The involvement of plants producing alkaloids in the primary sedimentation suggests that isocoumarin lactams could also be formed by oxidative degradation of the corresponding substituted isoquinolines. For example, skulerine **XXIX**, which belongs to the subclass of diisoquinolines occurring mainly in the *Papaveraceae*, *Menispermaceae*, and *Berberidaceae* families in both hydrogenated and dehydrogenated forms, gives hydrogenated isoquinolone **XXX**:

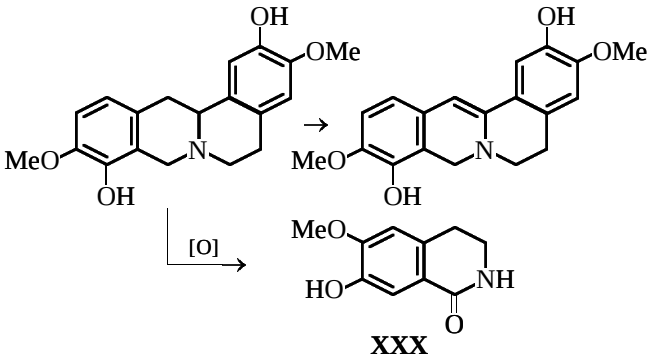

XXX

Hydrogenated rings in nitrogen-containing alkaloids can act as hydrogen donors in various coal treatment processes. Correspondingly, the higher the content of hydrogenated isoquinolines in OML, the more facile is the destructive thermal hydrogenation of this caustobiolith.

A more detailed comparative analysis of the chemical structures identified in SCT showed that the nitrogen-containing organic bases in OML do not always correspond to the natural isoquinoline and quinoline alkaloids; hence, biogeochemical transformation does not always account for the formation of particular structures in the organic matter of a caustobiolith.

It is widely believed that alkaloids are formed from amino acids under the action of microbial enzymes in the stage of peat genesis. Changes in the composition of the organic matter initially buried in sediments and the degree of decomposition of the organic matter supplied to the sediments will depend on the extent and nature of microbial activity [2]. Microbial oxidation can cease in any stage, and the selective effect of microorganisms can result in concentration of biologically more stable organic residues and of nitrogen-containing heterocyclic systems. Enzymes are either accumulated in the organic matter, increasing its weight, or favor transformation of organic substances into water-soluble or colloidal forms. Thus, isoquinolines of OML can be formed *in vitro* from the corresponding amino acids containing a phenylethylamine residue under the action of various microbial enzymes. It is believed that an important part is played in the process by formaldehyde (the primary product of CO_2 assimilation), which acts as a methylating and ring-closing agent, as shown for isoquinolines. Furthermore, in the course of lignite formation, isoquinolines can also be formed from acyclic alkaloids. This group of alkaloids consists of aliphatic amines formed in the course of life activity of fungi (degradation of polypeptide fungal toxins) in the peat genesis stage.

Gymnospermae can also be involved in OML formation. Below we show as example the scheme of formation of isoquinoline **XXXII** from ephedrine **XXXI**, suggesting participation of coniferous plants in primary sedimentation. As far as modern coniferous plants are concerned, ephedrine was isolated from plants of the *Ephedra* (*Gnetaceae* family) genus and from *Taxus laceata* (*Taxaceae*). The reaction occurs *in vitro* and is effected by enzymes:

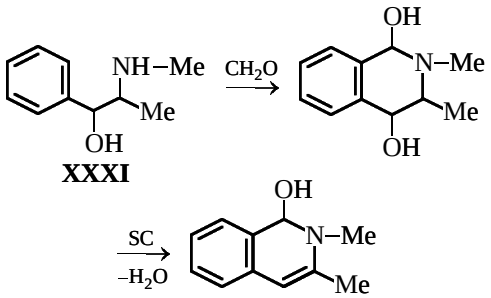

XXXI

XXXII

It is important that, as compared to isoquinolines, quinoline alkaloids are considerably less abundant in the flora and occur in a very narrow group of families. For example, two structurally related alkaloids, skimmianine and dictamnine, have been isolated from two closely related *Rutaceae* plants, namely, *Skimmia japonica* and *Dictamnus albus* [4]. Below is given the scheme of biogeochemical transformations of skimmianine **XXXIII** under conditions of lignite formation:

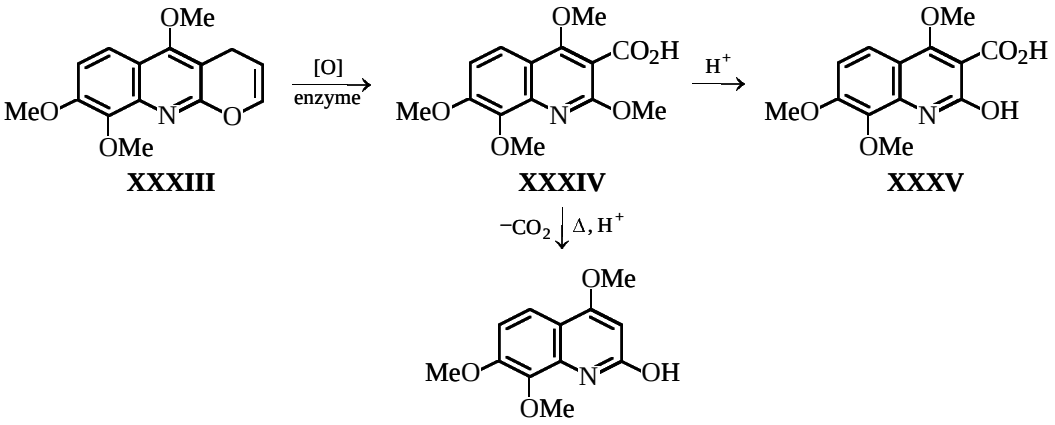

XXXIII **XXXIV** **XXXV** **XXXVI**

The reaction occurs via skimmianic acid **XXXIV** and yields two substituted isoquinoline structures **XXXV** and **XXXVI**, identified in lignite SCT.

It is interesting that more than half of natural compounds containing a quinoline core belong to the group of quinine alkaloids, which is inherent in certain species, namely, *Cinchona* and *Remija* (*Rubiaceae* family). Presumably, the evolutionary precursors of these species, producing a large number of quinine alkaloids (quinoline group), such as cinchonine, quinine, quinidine, hydrocinchonine, hydroquinine, hydroquinidine, homoquinine, quinallene, aricine, cusconine, paricine, etc., could be the suppliers of aromatic and hydroaromatic substituted isoquinolines to OML. Below is given the scheme of possible biogeochemical transformations of quinine **XXXVII**:

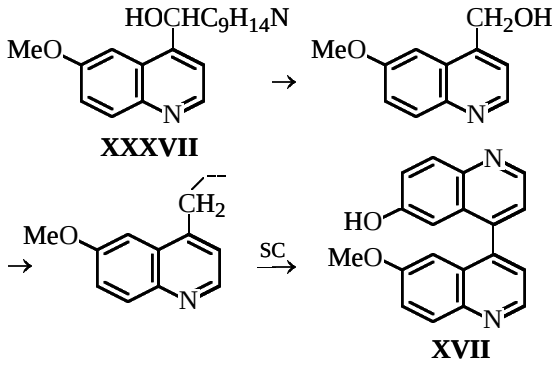

XXXVII **XVII**

The first stage of microbiological degradation of quinine is accompanied by elimination of the quinuclidine core. After that, the structure becomes incorporated via the methylol substituent in the periphery of the lignite macromolecular network. In the course of SC, the quinoline fragments may undergo radical coupling to give structure **XVII** identified in SCT of near-Moscow lignites.

Of particular interest is formation of substituted 2,2'-biquinoline **XL**. Firstly, this structure was presumably formed from the natural quinolines cusparine **XXXVIII** and galipine **XXXIX**, which are produced in the modern flora by *Calipea cusparia*:

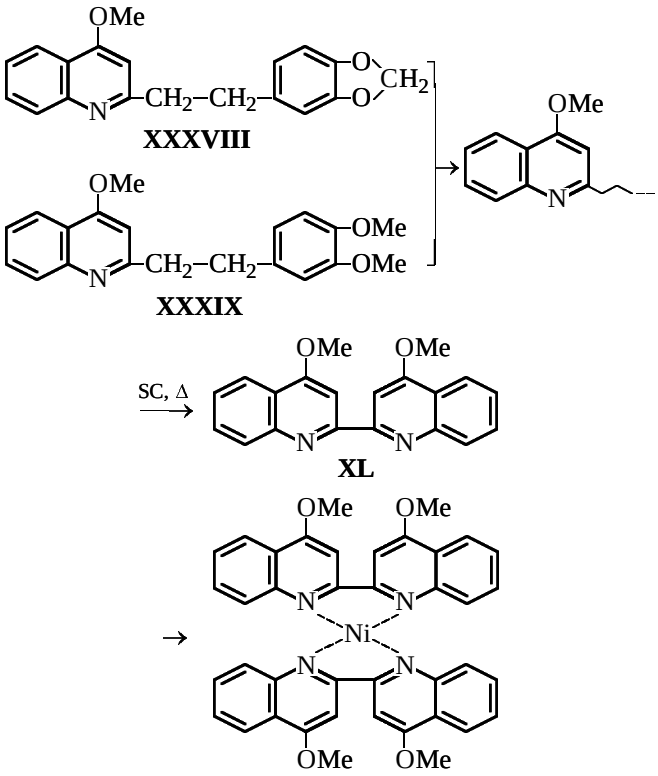

XXXVIII **XXXIX** **XL**

After structures **XXXVIII** and **XXXIX** become incorporated in the lignite matrix via alkyl radicals in 2-position, the 2,2'-biquinoline structure is formed by free-radical thermochemical degradation. Under the conditions of degradation of the polymeric molecule, two molecules of such a dimer react with the mineral matter of coal to form chelates with various metals.

For example, a similar nickel complex **XII** was identified in SCT. Presumably, nickel and other elements pass into such chelates from metal porphyrins, which results in metal migration in the course of thermochemical reactions.

Secondly, some authors note that 2,2'-biquinoline is formed in 15% yield by heating of quinoline with nickel on alumina at 325°C. Thus, the quinoline dimer is synthesized either from molecules that have been already eliminated from the matrix or from biogeochemically transformed quinoline alkaloids conserved in lignite pores.

Detailed analysis also reveals inconsistency between the relatively small number of natural quinoline alkaloids and fairly large number and diversity of nitrogen-containing organic bases incorporating the quinoline core. This fact is attributable to the formation of quinolines, similarly to isoquinolines, from amino acid residues in the biochemical stage *in vitro* of lignite formation under the action of enzymes. Also, as noted in [5], pyrolysis of lignite SCT is accompanied by ring extension: The content of nitrogen atoms incorporated in six-membered aromatic heterocycles increases, whereas the content of five-membered rings decreases. Hence, one of the pathways of thermochemical transformations of nitrogen is the formation of six-membered heterocycles in general, and of quinoline cores in particular. For five-membered heterocyclic systems, ring extension under conditions of thermal degradation of lignites is quite possible. The scheme of thermochemical transformation of indoles **XLI** into quinolines **XLII** is shown below:

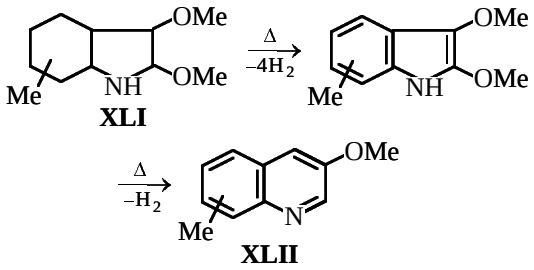

Compounds structurally similar to **XLII** were identified in lignite SCT in a fairly large amount. Thus, a significant part of quinolines could be formed from indole compounds in the course of semicoking. Furthermore, these reactions are promoted by carbonyl compounds whose content in primary tars is fairly high, because the caustobiolith under consideration has a low degree of metamorphism and high degree of oxidation (with oxygen mainly occurring in keto and quinoid groups). Taking into account the degree of metamorphism of caustobiolith, we find that the

Scheme 2.

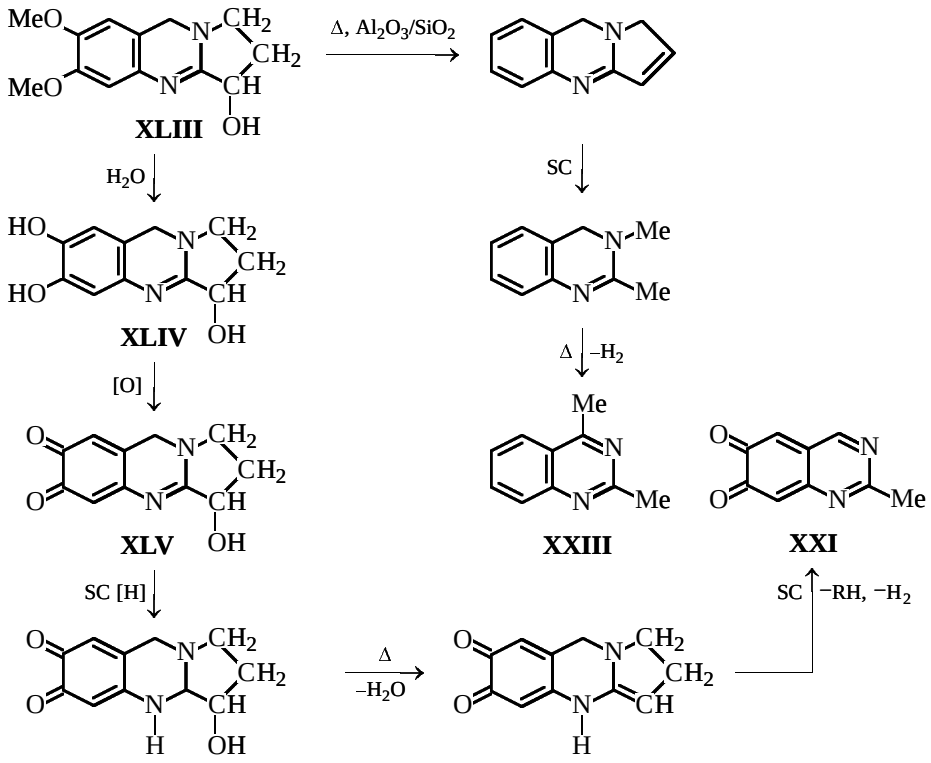

yield of indoles from coals is considerably higher than that from lignites, i.e., indoles exhibit increased thermodynamic stability. Comparison of the compositions of SCTs from coals and lignites shows that the content of quinolines in coals is higher than that in lignites, which confirms the assumption that quinolines are formed from substituted indoles. This assumption is also supported by the fact that indole alkaloids prevail in modern flora, and isoquinolines are present in a considerably smaller amount, being produced by a fairly narrow group of plants. It is significant that indoles are produced in large amounts by fungi; therefore, we can make an important conclusion that substituted quinolines originate from the activity of fungi that produce indole compounds undergoing subsequent thermochemical transformations.

Structures **XXI**–**XXIII** in OML are attributable to participation of plants producing a relatively small group of quinazoline alkaloids in the primary sedimentation. These compounds are produced by *Acanthaceae* and *Rutaceae* plants; also, they are microbial metabolites. For example, peganine (vasicine) **XLIII** was isolated from two species, *Peganum harmala* and *Adhatoda vasica*. The process can occur by two different pathways yielding structures **XXI** and **XXIII**. The pathway of formation of *o*-quinoid compound **XXI** is of particular interest. Vasinine, most probably, undergoes enzymatic hydroxylation in the *o*-position in the stage of peat genesis to form structure **XLIV**, which is oxidized by atmospheric oxygen under aerobic conditions with the participation of bacteria, yielding quinone **XLV**. It was noted previously that the introduction of hydroxy groups into an aromatic substrate is effected by bacteria of the genera *Pseudomonas* and *Nocardia*, and also by *Aspergillus niger* fungus (see scheme 2).

Quinolizine compounds **IV**, **VII**, and **VIII** are still more specific alkaloids than quinazolines. The involvement of the biological material producing compounds of this class is responsible for the presence in the organic matter of near-Moscow lignites of substances with structure similar to **XXVII**. The quinolizine core usually occurs in alkaloids in the fully reduced quinolizidine form, e.g., in *Leguminosae* family and in lupines, in particular. When heated in aromatic hydrocarbons, lupinine **XLVI** isomerizes in the course of enzymatic processes into epilupinine **XLVII**:

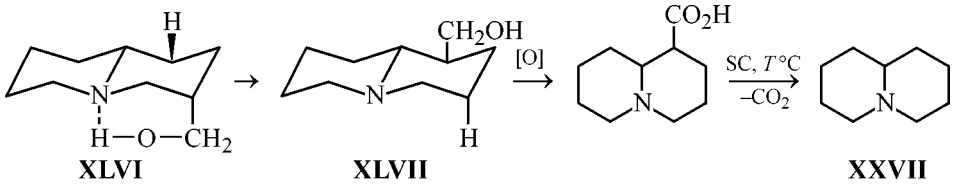

XLVI **XLVII** **XXVII**

This fact suggests that the primary alcoholic group in lupinine occurs in the less sterically favorable axial position owing to hydrogen bonding. The hydrogenated quinolizidine rings are hydrogen donors in thermal transformations of OML; therefore, the presence of structures similar to **XXVII** in the organic matter positively affects various processes of coal treatment.

CONCLUSIONS

(1) A genetic relationship was revealed between quinolines and isoquinolines detected among organic bases of semicoking tars of near-Moscow lignites, on the one hand, and vegetable alkaloids and fungal metabolites, on the other.

(2) Pathways of possible biogeochemical transformations of the initial nitrogen-containing compounds in the course of lignite formation and semicoking were suggested.

REFERENCES

1. Polovetskaya, O.S., Chemical Composition of Organic Bases from Semicoking Tar of Near-Moscow Lignites and Thermochemical Transformations of These Bases, *Cand. Sci. Dissertation*, St. Petersburg, 1999.
2. *Organic Geochemistry. Methods and Results*, Eglinton, G. and Murphy, M.T.J., Eds., Berlin: Springer, 1969.
3. Podshibyakin, S.I., Genetic Relationship between the Pyrone Group Compounds in the Organic Matter of Kansk–Achinsk Lignite and the Initial Biological Material, *Cand. Sci. Dissertation*, St. Petersburg, 2000.
4. Orekhov, A.P., *Khimiya alkaloidov* (Alkaloid Chemistry), Moscow: Akad. Nauk SSSR, 1955.
5. Bronshtein, A.P., Makarov, T.N., Akulov, P.V., and Grigor'ev, N.P., *Khim. Tverd. Topl.*, 1979, no. 6, pp. 65–74.

Russian Journal of Applied Chemistry, Vol. 75, No. 4, 2002, pp. 656–658. Translated from Zhurnal Prikladnoi Khimii, Vol. 75, No. 4, 2002, pp. 673–675.
Original Russian Text Copyright © 2002 by Tolstoi.

BRIEF COMMUNICATIONS

Synthesis of $Ce_4MnO_x \cdot nH_2O$ Layers on Silica Gel Surface by Ionic Layer Deposition

V. P. Tolstoi

St. Petersburg State University, St. Petersburg, Russia

Received November 29, 1999, in final form, July 2000

Abstract—The possibility of synthesizing $Ce_4MnO_x \cdot nH_2O$ nanolayers on silica gel surface by ionic layer deposition was examined. The layers synthesized were studied by X-ray photoelectron spectroscopy, UV-Vis diffuse reflection spectroscopy, and powder X-ray diffraction.

According to [1–3], nanolayers of metal oxides and hydroxides can be synthesized on solid surfaces by ionic layer deposition in two ways. In the first case, a layer of adsorbed cations is oxidized to higher oxidation states to form compounds significantly less soluble at pH values in use (scheme I). In the second, cations are converted to more difficulty soluble peroxide compounds (scheme II). For example, nanolayers of hydrated CeO_{2+x} have been synthesized previously [1] by oxidation of an adsorbed layer of Ce^{3+} ions to Ce^{4+}.

The aim of this study was to synthesize nanolayers of hydrated double cerium manganese oxide by ionic layer deposition according to scheme I. These oxides are widely used as solid electrolytes with oxygen conductivity, adsorbents, catalysts, etc.

EXPERIMENTAL

As reagents in the synthesis, we used $CeCl_3$ and $KMnO_4$ aqueous solutions with KOH added to pH 9–10. The Ce(III) → Ce(IV) oxidation in a layer of an adsorbed hydroxide was assumed to be effected by MnO_4^- ions, which also form upon reduction a poorly soluble compound incorporated in the layer. The working concentration of the reagents was selected on the basis of the data [3] on MnO_2 nanolayer synthesis by ionic layer deposition. Merck 60 silica gel with specific surface area of 360 $m^2\ g^{-1}$, average pore size of 12 nm, and granulometric composition of 0.2–0.63 mm was used as a support. To carry out the synthesis, a 0.5-g weighed sample of silica gel was placed in a beaker containing 200 ml of a $CeCl_3$ solution. The solution with silica gel was kept for 30 min with intermittent stirring and, after the sedimentation of silica gel particles, the excess amount of the solution was decanted. Then silica gel was washed four times by decanting with distilled water, the contact time being in each case 5 min. Then 200 ml of $KMnO_4$ (KOH) solution was poured in the beaker and the mixture was kept for 30 min with intermittent stirring. After sedimentation of silica gel particles, the excess amount of the solution was removed. Then the silica gel sample was decanted with distilled water four times.

One treatment sequence of this kind constituted a single cycle of ionic layer deposition resulting in the formation of a nanolayer of synthesized compound on the silica gel surface. Subsequent layers were synthesized by multiple repetition of elementary ionic layer deposition cycles.

The layers synthesized were studied by diffuse reflection (DR) spectroscopy in the UV and visible spectral regions, X-ray photoelectron spectroscopy (XPS), and powder X-ray diffraction. Diffuse reflection spectra were recorded on a Perkin–Elmer Lambda-9 spectrophotometer (scan rate 50 nm min^{-1}, slit program 2 nm). X-ray photoelectron (XP) spectra were obtained on a Perkin–Elmer 5400 spectrometer, using Mg_{K_α} line as exciting radiation. The quantitative content of each element of the layer was determined with an accuracy no worse than 10%. The X-ray diffraction patterns of silica gel samples with layers synthesized were obtained on a DRON-3.0 diffractometer (Cu_{K_α} radiation).

As follows from the diffuse reflection spectrum (Fig. 1), a strong absorption band in the range of 300–

1070-4272/02/7504-0656 $27.00 © 2002 MAIK "Nauka/Interperiodica"

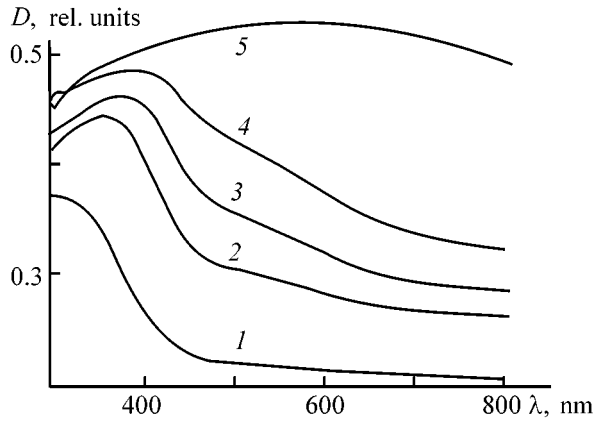

Fig. 1. Diffuse reflection spectra of silica gel samples with nanolayers of (*1–4*) $Ce_4MnO_x \cdot nH_2O$ synthesized by ionic layer deposition and (*5*) $MnO_2 \cdot nH_2O$ synthesized by six cycles of ionic layer deposition. (*D*) Optical density; (λ) wavelength. Number of ionic layer deposition cycles: (*1*) 1, (*2*) 3, (*3*) 6, and (*4*) 10.

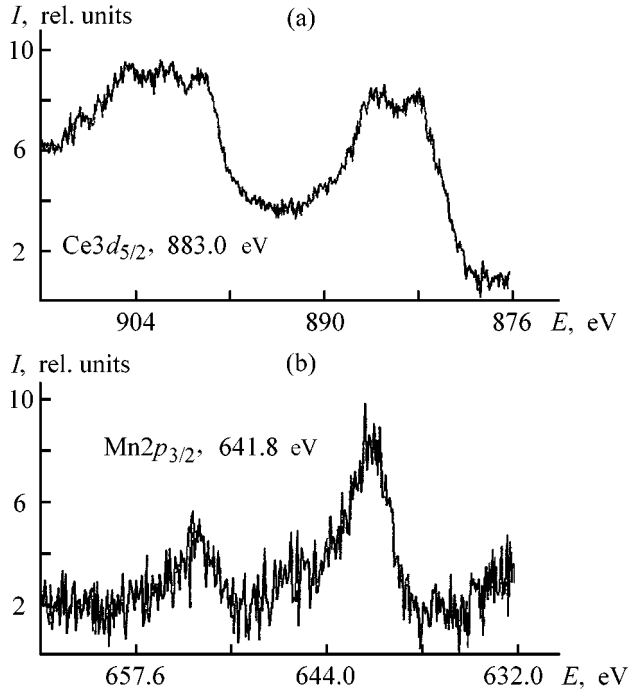

Fig. 2. XPS spectrum of a $Ce_4MnO_x \cdot nH_2O$ layer synthesized by 10 ionic layer deposition cycles on silica gel surface. (*I*) Intensity and (*E*) bond energy. Range: (a) Ce and (b) Mn.

400 nm appears after the first ionic layer deposition cycle. Subsequent cycles result in an increase in its intensity approximately in proportion to the number of ionic layer deposition cycles, and a weaker band appears in the range 450–600 nm. Unfortunately, it was impossible to construct quantitative dependences of the optical density (absorption) on the number of ionic layer deposition cycles, because adequate quantitative models for diffuse reflection spectra are presently available only for the concentrations of substances under study that are much less than those corresponding to one monolayer thickness. However, the spectra obtained, taken together with ellipsometric data for Mn-containing layers [3], suggest that the thickness of the layers synthesized grows stepwise with increasing number of ionic layer deposition cycles.

As for the composition of the layer synthesized, comparison of its spectrum with that of an MnO_2 layer (Fig. 1, spectrum *5*) synthesized by ionic layer deposition [3] shows that it contains no manganese(IV) ions which are characterized by a broad absorption band in the range 400–800 nm.

A more detailed information on the composition of the layer synthesized was obtained from an XP spectrum (Fig. 2). Indeed, manganese is characterized by a peak at 641.8 eV, corresponding to $2p_{3/2}$ electrons of Mn(III) [4]. Cerium has a peak at 883.0 eV, which is difficult to assign owing to the lack of reference data on Ce(IV) compounds. However, the data of [4] allow us to state that this peak does not refer to Ce(III). At the same time, the ratio of the intensities of Ce and Mn bands is, with regard to the experimental error, 4 : 1, which indirectly confirms the presence of cerium in oxidation state +4, because the transition $Mn(VII) \rightarrow Mn(III)$ requiring four electrons is clearly identified in the layer of adsorbed ions on the surface upon synthesis. If the Ce/Mn ratio is four, these four electrons can be provided by a one-electron reaction $Ce(III) \rightarrow Ce(IV)$ and the above-mentioned peak corresponds to Ce in oxidation state +4.

Thus, the surface reactions can be described by the following schemes. Treatment of silica gel with a $CeCl_3$ solution and removal of the excess amount of the solution with water lead to replacement of chlorine ions by hydroxide in the layer of adsorbed cerium ions to form a hydrate–hydroxide cerium complex $\equiv Si–OH \cdot Ce(OH)_3$ or a $\equiv Si–OCe(OH)_2$ complex. This scheme is confirmed by the absence of chlorine bands in the XP spectrum. Further, cerium(III) reacts with a $KMnO_4$ solution to give cerium(IV) and manganese(III), and a new poorly soluble compound is formed. Cerium(IV) and manganese(III) hydroxides and oxides are known to be difficulty soluble at pH corresponding to this synthesis, and, thus, an equilibrium in solutions is shifted toward their formation on the surface in the form of a layer. The only problem in this scheme is the mechanism of transition of four electrons from cerium(III) to the permanganate ion, because the probability of simultaneous transition of four electrons is extremely low. However, a step-by-step transition can be assumed: an intermediate

adsorbed complex of MnO_4^- is first formed with one adsorbed cerium(III) ion, then with two cerium(III) ions, etc. A hydrate–hydroxide complex of Mn(III) bound with four hydrate–hydroxide complexes of Ce(IV) located at vertices of a tetrahedron or a square is likely to be formed in the last stage of such a reaction. The formation of such a complex is quite probable from the steric viewpoint. If ionic layer deposition is repeated many times, a layer of proportionally greater thickness is formed on the surface. According to the XRD data, a layer of this kind, synthesized by ten ionic layer deposition cycles, is X-ray amorphous. Apparently, such a layer contains water molecules and hydroxide ions in addition to Ce and Mn ions. Consequently its formula can be written as $Ce_4MnO_x \cdot nH_2O$. Unfortunately, we are presently unable to determine the amounts of oxygen atoms and water molecules in a layer, owing to its small thickness.

CONCLUSION

Successive and multiple treatments of silica gel surface with $CeCl_3$ and $KMnO_4$ (KOH) solutions, carried out by ionic layer deposition, results in the formation of a $Ce_4MnO_x \cdot nH_2O$ surface layer. The thickness of this layer is determined by the number of ionic layer deposition cycles.

ACKNOWLEDGMENTS

The author is grateful to A.V. Shchukarev and E.I. Puzidarova for recording the XP spectrum and to I.V. Murin and A. Reller for fruitful discussion of the results obtained.

This work was financially supported by the "Universities of Russia" program.

REFERENCES

1. Tolstoi, V.P. and Ehrlich, A.G., *Thin Solid Films*, 1997, vol. 307, pp. 60–64.
2. Tolstoi, V.P., *Zh. Prikl. Khim.*, 1999, vol. 72, no. 8, pp. 1259–1261.
3. Tolstoi, V.P., Murin, I.V. and Reller, A., *Appl. Surf. Sci.*, 1997, vol. 112, pp. 255–257.
4. Moulder, Y.E., Stickle, W.F., Sobol, P.E., and Bomben, K.D., *Handbook of X-ray Photoelectron Spectroscopy*, Minnesota (USA): Perkin–Elmer Corp., Phys. Electron. Division, 1992.

Russian Journal of Applied Chemistry, Vol. 75, No. 4, 2002, pp. 659–661. Translated from Zhurnal Prikladnoi Khimii, Vol. 75, No. 4, 2002, pp. 676–677.
Original Russian Text Copyright © 2002 by Nikulicheva, Tikhova, Fadeeva.

BRIEF COMMUNICATIONS

Separation of Multicomponent Mixture of Naphthalene Derivatives by Reversed-Phase High-Performance Liquid Chromatography

O. N. Nikulicheva, V. D. Tikhova, and V. P. Fadeeva

Vorozhtsov Institute of Organic Chemistry, Siberian Division, Russian Academy of Sciences, Novosibirsk, Russia

Received July 17, 2001; in final form, December 2001

Abstract—Separation of a mixture of naphthalene derivatives by reversed-phase high-performance liquid chromatography with UV detection was studied. Chromatographic characteristics were calculated for nine compounds, including naphthalene.

Naphthalene and its derivatives are intermediates in the synthesis of organic dyes, medicines, and surfactants; they also serve as auxiliary agents in the industry of polymeric materials. Many of these compounds are toxic, and some of them are carcinogenic [1]. This necessitates permanent monitoring of these compounds in production zones and the environment.

Certain naphthalenes can be determined by spectrophotometric, chemiluminescent, and chromatographic methods [2–9]. Among these methods, high-performance liquid chromatography (HPLC) seems the most promising, as it affords analysis of multicomponent mixtures of various naphthalene derivatives.

This work is aimed at studying the conditions of separation of a mixture of nine derivatives of naphthalene, having different functional groups, in methanol and water by reversed-phase HPLC with UV detection.

EXPERIMENTAL

We carried out chromatographic studies at room temperature on a Milikhrom-1 chromatograph with UV detector and a steel column (64 × 2 mm) packed with Separon C18 sorbent. The column efficiency was 2100 TP for naphthalene. The measurements were made on the optical density scale 1.6 – 0.4 at λ = 280 nm. This wavelength allowed detection of all the components under study. We injected methanolic (1 μl) and aqueous (10 μl) solutions of the components. As mobile phase served methanol and a water–methanol mixture in a micropump chamber; the methanol concentration in water was 50, 60, 80, and 100 vol %. The eluent flow rate was 100 μl min^{-1}, and each run took 15–25 min.

The optimal conditions of separation were elucidated with an artificial mixture of straight substances prepared by mixing 1 mg ml^{-1} methanolic solutions of the components. To this end, we used nine compounds of naphthalene series: naphthalene, α-naphthol, β-naphthol, α-naphthylamine, 1,5-dihydroxynaphthalene, 1,7-dihydroxynaphthalene, 1,5-dinitronaphthalene, 2-nitroso-1-naphthol, and disodium 1,5-naphthalenedisulfonate.

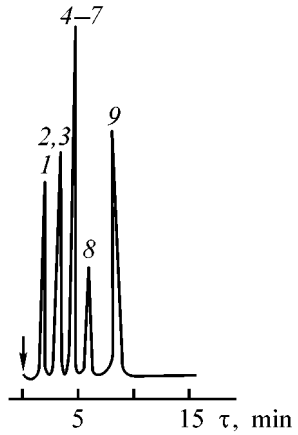

Fig. 1. Chromatogram of a mixture of naphthalene derivatives. Eluent methanol, wavelength 280 nm, flow rate 200 μl min^{-1}. (τ) Time. The *figures at peaks* correspond to the compound nos. in the table; the same for Fig. 2.

1070-4272/02/7504-0659 $27.00 © 2002 MAIK "Nauka/Interperiodica"

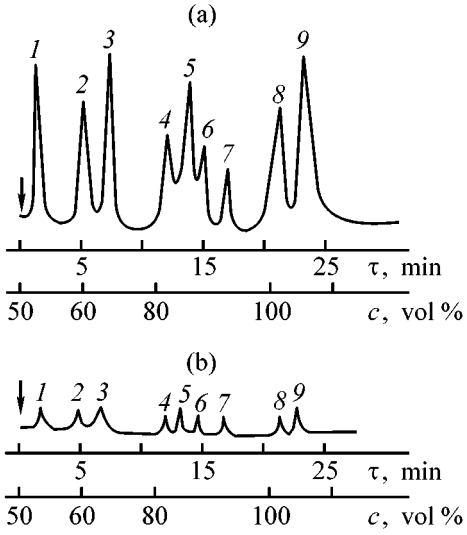

Fig. 2. Chromatograms of (a) naphthalene derivatives in methanolic solution and (b) water with added naphthalene derivatives. Eluent aqueous solution of methanol, wavelength 280 nm, eluent flow rate 100 μg min^{-1}. (τ) Time, and (*c*) methanol concentration in water, vol %.

Our study showed that exhaustive separation of the mixture components cannot be achieved with methanol (100%) as eluent (Fig. 1). Hence, we used as mobile phase for mixture separation methanol–water mixtures containing 50, 60, 80, and 100 vol % methanol (Fig. 2a). The peaks were identified by the retention time of individual compounds; for compounds with close retention times we used the method of additives. Based on our data on separation of methanolic solutions, we calculated the following chromatographic characteristics of the compounds under study: reduced capacity coefficients k', selectivity with respect to adjacent component pairs α, and their resolution R_s [11] (see table).

Parameters of chromatographic separation of naphthalene derivatives*

Compound no.	Compound	τ, min	$k' \pm 0.11$	$\alpha \pm 0.07$	$R_s \pm 0.21$
1	Disodium 1,5-naphthalene-disulfonate	1.33	0.25	16.33	1.96
2	1,5-Dihydroxy-naphthalene	5.47	4.16	1.46	1.02
3	1,7-Dihydroxy-naphthalene	7.50	6.07	1.87	2.08
4	2-Nitroso-1-naphthol	13.12	11.38	1.08	0.75
5	α-Naphthylamine	14.06	12.26	1.12	0.67
6	β-Naphthol	15.62	13.74	1.14	0.84
7	α-Naphthol	17.66	15.66	1.34	2.39
8	1,5-Dinitro-naphthalene	23.34	21.02	1.07	1.63
9	Naphthalene	24.91	22.50	–	–

* τ_m = 1.06 min is the dead time of the column.

To elucidate the chromatographic behavior of a mixture of the compounds studied in water, we also prepared an artificial mixture. The concentration of each component in the mixture was 0.4 μg ml^{-1}; for disodium 1,5-naphthalenedisulfonate and naphthalene it was 0.1 μg ml^{-1}. The sensitivity of the instrument was increased to a maximum, so that the noise level did not prevent detection of the signal to be measured. The chromatogram of this mixture is shown in Fig. 2b. As seen, it is feasible to determine certain naphthalene derivatives in water in concentrations of 0.1–0.4 μg ml$^{-1.}$ The root-mean-square deviation is no greater than 12%.

CONCLUSIONS

(1) The chromatographic characteristics, namely, reduced capacity coefficients, selectivity with respect to adjacent component pairs, and their resolution, were determined by reversed-phase high-performance chromatography for nine compounds of the naphthalene series, including unsubstituteed naphthalene.

(2) Conditions of chromatographic separation of these compounds in aqueous medium were chosen, and the detection limit of individual components was estimated at 0.4 μg ml^{-1}; for disodium 1,5-naphthalenesulfonate and naphthalene this concentration is 0.1 μg ml^{-1}.

REFERENCES

1. Donaldson, N., *The Chemistry and Technology of Naphthalene Compounds*, London: Edward Arnold, 1958.
2. Hill, P., Newbery, J.E., Parry-Jones, K., and High J., *Resolut. Chromatogr. Chromatogr. Commun.*, 1983, vol. 6, no. 11, pp. 625–629.
3. Rosini, C., Altemura, P., Pini, D., *et al.*, *J. Chromatogr.*, 1985, vol. 348, no. 1, pp. 79–87.
4. Pietrogrande, M.C., Bio, Y., and Bighi, C., *J. Chromatogr.*, 1985, vol. 349, no. 1, pp. 63–68.

5. Ayangar, N.R. and Bhide, S.R., *J. Chromatogr.*, 1989, vol. 464, no. 1, pp. 201–207.
6. Zheltukhin, I.A. and Kalisterova, N.A., *Metody analiza i kontrolya kachestva produktsii: Nauchno-tekhnicheskii referativnyi sbornik* (Product Quality Control and Analysis Methods: Scientific and Technical Coll. of Abstracts), Moscow: NIITEKhIM, 1989, issue 2, pp. 12–14.
7. Yaleano Diaz, T., Acedo, M.J., Munoz de la Pena, A., *et al.*, *Analyst*, 1994, vol. 119, no. 6, p. 1151–1155.
8. Al-Tamzah, S.A. and Towhshend, A., *Anal. Chim. Acta*, 1987, vol. 202, no. 1, pp. 247–250.
9. Matveeva, E. Ya., Kalinichenko, I.B., and Pilipenko, A.T., *Zh. Anal. Khim.*, 1987, vol. 42, no. 10, pp. 1905–1908.
10. Yashin, Ya.I. and Yashin, A.Ya., *Zh. Anal. Khim.*, 1999, vol. 54, no. 9, pp. 949–956.
11. Schoenmakers, P.J., *Optimization of Chromatographic Selectivity. A Guide to Method Development*, Amsterdam: Elsevier, 1986.

Russian Journal of Applied Chemistry, Vol. 75, No. 4, 2002, pp. 662–664. Translated from Zhurnal Prikladnoi Khimii, Vol. 75, No. 4, 2002, pp. 678–679.
Original Russian Text Copyright © 2002 by Yapryntseva, Kolosnitsyn, Yatsyk, Krasnogorskaya.

BRIEF COMMUNICATIONS

Anodic Dissolution of Molybdenum and Tungsten in a Solution of Sodium Sulfate

O. A. Yapryntseva, V. S. Kolosnitsyn, N. A. Yatsyk, and N. N. Krasnogorskaya

Institute of Organic Chemistry, Ufa Research Center, Russian Academy of Sciences, Ufa, Bashkortostan, Russia
Ufa State Aviation Technical University, Ufa, Bashkortostan, Russia

Received July 11, 2001

Abstract—The electrochemical dissolution of molybdenum and tungsten in a 0.5 M solution of sodium sulfate at various temperatures was studied. The conditions of the efficient recovery of molybdenum from the binary metal system Mo–W were determined.

In modern lamp manufacturing, molybdenum core is removed from incandescent bodies by chemical dissolution of molybdenum from the binary metal system Mo–W. The tungsten loss during molybdenum dissolution should not exceed 5% [1]. The etching solution contains 56% nitric acid and 78% sulfuric acid at a volume ratio of 1 : 3 [1]. The chemical dissolution is environmentally hazardous process yielding strongly acidic solutions containing approximately (wt %) 1.6–3 Mo(VI), 18 H_2SO_4, 8 HNO_3, SO_2, and nitrogen oxides. The Mo(VI) concentration in washing solutions attains 8 mg l^{-1} against maximum permissible concentration of 0.0012 mg l^{-1}. This level cannot be ensured by purification of wastewater.

In [2], we proposed to use the anodic dissolution of molybdenum instead of chemical dissolution. The dissolution of molybdenum in salt solutions is intense [3, 4]. At the same time, the rate of the anodic dissolution of tungsten is considerably lower.

In this work, we studied the conditions of the preferable dissolution of molybdenum from the binary metal system Mo–W in sulfate solutions. For this purpose, the anodic dissolution of molybdenum and tungsten in a 0.5 M solution of sodium sulfate was studied at various temperatures.

EXPERIMENTAL

The specific features of the anodic dissolution of molybdenum and tungsten were studied by voltammetric method using a YASE–2 temperature-controlled glassy three-electrode cell with separated electrode spaces. The working electrodes were prepared from molybdenum wire. Platinum auxiliary electrode and silver chloride reference electrode were used (all potentials are given relative to this electrode).

The electrochemical study was performed in the potentiodynamic mode with a PI-50-1 potentiostat and a PR-8 programmer. The curves were recorded with ENDIM, Kh-306, and Kh-307/1 two-coordinate recorders.

The temperature in the electrochemical cells and electrolyzers was maintained at a prescribed value with liquid and air laboratory thermostats.

Measurements were performed in a 0.5 M solution of Na_2SO_4. Chemically pure reagents and distilled were used. Prior to the experiment, the electrodes were trimmed with a no. 0 abrasive paper and washed in the electrolyte to be tested.

The steady-state potential of molybdenum in a 0.5 M Na_2SO_4 solution was 0.121 V. When the potential was changed from the steady-state potential to +1.5 V with a scanning rate from 10 to 100 mV s^{-1}, the maximum of the anodic current was observed on the corresponding voltammograms, depending on potential scan rate V_{sc} (Fig. 1a). With growing V_{sc}, the current peak potential shifts to the anodic region, and the peak current increases. At the polarization varied in the opposite direction, no current maximum

1070-4272/02/7504-0662 $27.00 © 2002 MAIK "Nauka/Interperiodica"

was observed. The shape of the obtained voltammograms suggests occurrence of processes limiting molybdenum dissolution [3, 5]. Among possible processes are formation of sparingly soluble compounds on the electrode surface (passivation) or impeded removal of the reaction products (diffusion) into the solution [5].

With the temperature increased to 60°C at a constant scan rate V_{sc}, the peak current increases and the peak potential is shifted (by 0.15–0.2 V) toward negative potentials. The currents corresponding to the inverse branches of the voltammograms also increase with temperature.

The voltammograms on tungsten have two current peaks at all scanning rates V_{sc} (Fig. 1b). This shows that at least two stages control the process. The current peaks were also observed on the inverse branches of the voltammograms. With the temperature raised to 60°C at a constant scanning rate, the peak currents grow by an order of magnitude and the peak potentials are shifted toward negative potentials.

The comparison of the peak currents for anodic dissolution of Mo and W showed that the rate of the anodic dissolution of molybdenum considerably exceeds that of tungsten. In the case of molybdenum, the dissolution is limited by liquid diffusion, and in the case of tungsten, by formation of passivating oxide film on the electrode (solid diffusion). The results of the study are in agreement with the data of [6, 7].

Using the data obtained, we calculated the efficiency coefficients of the anodic dissolution of molybdenum at various potentials and temperatures by the formula

$$K_{ef} = i_{Mo}/i_W,$$

where i_{Mo} and i_W are the densities of the anodic dissolution currents of Mo and W, respectively, at the same potential.

The results obtained are plotted in Fig. 2. As seen, with increasing temperature the efficiency coefficient of the anodic dissolution of Mo decreases. It is the most promising to recover molybdenum from the binary metal system Mo–W at 20°C and at potentials within 0.7–0.9 V.

The results of the study were tested on incandescent bodies anodically polarized under the steady-state conditions. It was shown that the surface of the tungsten helices obtained meets the regulations.

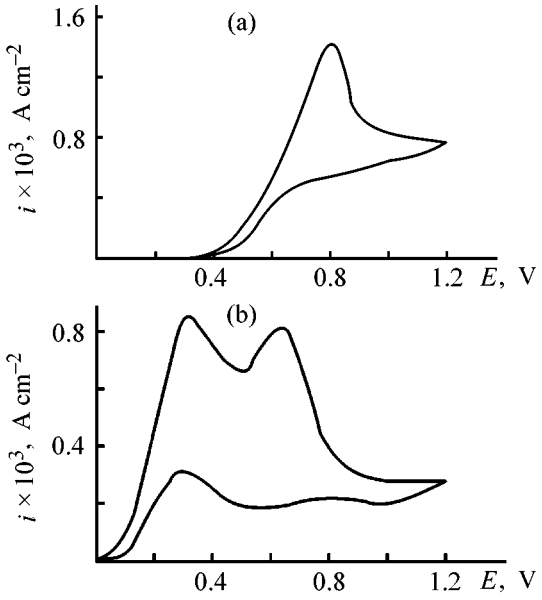

Fig. 1. Volt–ampere curves on (a) molybdenum and (b) tungsten in a 0.5 M Na_2SO_4 solution. Potential scanning rate 10 mV s^{-1}, temperature 20°C. (i) Anodic current density and (E) potential.

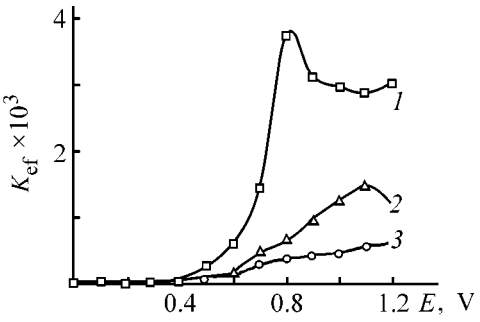

Fig. 2. The efficiency coefficient K_{ef} of the anodic dissolution of molybdenum vs. potential E. Temperature (°C): (*1*) 20, (*2*) 40, and (*3*) 60.

CONCLUSIONS

(1) The study of the effect of temperature on the rate of the anodic dissolution of molybdenum and tungsten in a 0.5 M Na_2SO_4 solution showed that for tungsten the dissolution rate depends on temperature to a considerably greater extent than for molybdenum.

(2) The efficiency coefficient of the anodic dissolution of molybdenum as a function of potential was determined at various temperatures. The efficiency of molybdenum dissolution is the highest (K_{ef} = 4000) at 20°C and a potential of 0.8 V.

REFERENCES

1. Ul'mishek, L.G., *Proizvodstvo elektricheskikh lamp nakalivaniya* (Manufacturing Electrical Incandescent Lamps), Leningrad: Gosenergoizdat, 1958.
2. Kolosnitsyn, V.S., Yatsyk, N.A., Yapryntseva, O.A., *et al.*, *Materialy Mezhregional'noi konferentsii "Otkhody-2000"* (Proc. Inter-Regional Conf. "Wastes-2000"), Ufa, 2000, pp. 63–65.
3. Davydov, A.D., and Kozak, E., *Vysokoskorostnoe elektrokhimicheskoe formoobrazovanie* (High-Speed Electrochemical Shaping) Moscow: Nauka, 1990.
4. Atanasyants, A.G., *Anodnoe povedenie metallov* (Anodic Behavior of Metals), Moscow: Vysshaya Shkola, 1989.
5. Galus, Zb., *Teoretyczne Podstawy Elektroanalisy Chemiczne*j, Warsaw: Naukowe, 1977.
6. Kozlova, N.B., Noskov, A.V., Lilin, S.A., and Zuev, A.V., *Zh. Prikl. Khim.*, 1999, vol. 72, no. 1, pp. 101–104.
7. Kolosnitsyn, V.S., Yatsyk, N.V., Ponomarev, V.K., *et al.*, *Bashkir. Khim. Zh.*, 1999, vol. 6, no. 1, pp. 50–53.

Russian Journal of Applied Chemistry, Vol. 75, No. 4, 2002, pp. 665–666. Translated from Zhurnal Prikladnoi Khimii, Vol. 75, No. 4, 2002, pp. 680–681.
Original Russian Text Copyright © 2002 by Kukharev, Stankevich, Klimenko, Kovalyuk, Bayandin.

BRIEF COMMUNICATIONS

Substituted *N*-(2-Hydroxyethyl)-1,3-thiazolidin-4-ones: Synthesis and Anticorrosive Properties

B. F. Kukharev, V. K. Stankevich, G. R. Klimenko, E. N. Kovalyuk, and V. V. Bayandin

Favorskii Institute of Chemistry, Siberian Division, Russian Academy of Sciences, Irkutsk, Russia
Angarsk State Technological Institute, Angarsk, Irkutsk oblast, Russia

Received December 28, 2001

Abstract—A one-pot procedure was developed for synthesis of *N*-(2-hydroxyethyl)-1,3-thiazolidin-4-ones in 64–68% yield by reactions of monoethanolamine with carbonyl compounds and mercaptoacetic acid. The synthesized compounds were characterized by IR and ^{1}H NMR spectra, and their anticorrosive properties were studied.

Nitrogen-containing alcohols and some sulfur-containing organic compounds are known to exhibit anticorrosive properties [1–3]. In this work, we prepared, with the aim to reveal anticorrosive properties of other amino alcohol derivatives, a series of substituted *N*-(2-hydroxyethyl)-1,3-thiazolidin-4-ones and studied them as inhibitors of carbon dioxide and hydrogen sulfide corrosion of steel. One of routes to *N*-(2-hyroxyethyl)-1,3-thiazolidin-4-ones is reaction of oxazolidinies with mercaptoacetic acid [4]. Oxazolidines are, in turn, prepared by condensation of carbonyl compounds with 1,2-amino alcohols [5–7]:

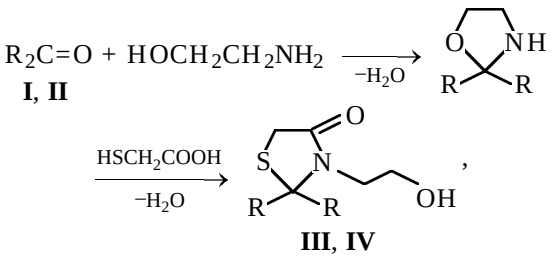

I, **II** **III**, **IV**

where R = H (**I**, **III**): R + R = $(CH_2)_5$ (**II**, **IV**).

With this synthesis scheme, the yield of *N*-(2-hydroxyethyl)-1,3-thiazolidin-4-ones **III** and **IV** is 62–63% [4]. The initial oxazolidines were prepared from monoethanolamine and the corresponding carbonyl compounds in 90–94% yield [6, 7].

In this study, we examined the possibility of combining in one-pot synthesis the stages of preparation of oxazolidines and their subsequent transformation into *N*-(2-hydroxyethyl)-1,3-thiazolidin-4-ones.

When developing the synthesis procedure, we took into account the conditions under which the separate stages were performed in [4, 6, 7]. We used benzene as solvent. Condensation of monoethanolamine with carbonyl compounds **I** and **II** was performed by refluxing an equimolar mixture of the reactants, with azeotropic distillation of water. After the release of water was complete, a stoichiometric amount of mercaptoacetic acid was added, and the mixture was refluxed until the release of the next portion of water was complete.

The yield of *N*-(2-hydroxyethyl)-1,3-thiazolidin-4-ones **III** and **IV** under these conditions was 70 and 68%, respectively. The yield of thiazolidinones is the highest at the equimolar ratio of monoethanolamine and carbonyl compounds. With 10% molar excess of the carbonyl compound, the yield decreased by 6–10%, and with 10% molar excess of monoethanolamine, it decreased by 20–25%.

To evaluate the inhibiting power of **III** and **IV**, we studied their effect on steel corrosion under conditions simulating steel corrosion in petroleum production [8].

The anticorrosive activity was evaluated gravimetrically with St. 3 steel samples of size 2 × 20 × 6 mm, according to GOST (State Standard) 9.505–86, in a 1% NaCl solution saturated with CO_2 in the presence of hydrogen sulfide. Tests were performed at 20, 40, and 60°C for 3 h. At a 10^{-3} M concentration of **III** or **IV** and varied temperature, we obtained the following protective effect *Z* (%): **III**, 95.9 (20°C), 80.5 (40°C), and 45.5 (60°C); **IV**, 96.3 (20°C), 83.3 (40°C), and

1070-4272/02/7504-0665 $27.00 © 2002 MAIK "Nauka/Interperiodica"

62.7 (60°C). Thus, search for new corrosion inhibitors among thiazolidinone alcohols shows much promise.

EXPERIMENTAL

In syntheses, we used commercial paraform (99.3% purity), cyclohexanone, monoethanolamine, and mercaptoacetic acid, which were purified by distillation to the main substance content of no less than 99.8%.

N-(2-Hydroxyethyl)-1,3-thiazolidin-4-one III. A mixture of 30.5 g (0.5 mol) of monoethanolamine, 15.1 g (0.5 mol) of paraform, and 100 ml of benzene was refluxed with a Dean–Stark trap until the release of water was complete. Then, 46.1 g (0.5 mol) of mercaptoacetic acid was added, and the mixture was refluxed until the release of water was complete. The mixture was cooled and distilled to give 47.9 g (65%) of **II**; bp 176–178°C at 3 mm Hg; mp 63–64°C. IR spectrum (thin film, ν, cm^{-1}): 1630 (C=O), 3300 (OH). ^{1}H NMR spectrum ($CDCl_3$, 90 MHz), δ, ppm: 3.49 t (2H, NCH_2), 3.56 d (2H, SCH_2CO, ^4J 1.4 Hz), 3.76 t (2H, OCH_2), 4.0 s (1H, OH), 4.54 d (2H, SCH_2N, ^4J 1.4 Hz).

Found, (%): C 40.97, H 6.03, N 9.28, S 21.63.

$C_5H_9NO_2S$.

Calculated, (%): C 40.80, H 6.16, N 9.52, S 21.78.

N-(2-Hydroxyethyl)-1-thia-4-azaspiro[4.5]decan-3-one IV was prepared similarly from 30.5 g (0.5 mol) of monoethanolamine, 49.1 g (0.5 mol) of cyclohexanone, and 46.1 g (0.5 mol) of mercaptoacetic acid. Yield 73.5 g (68%); bp 200–203°C at 2 mm Hg; mp 86–87°C. IR spectrum (thin film, ν, cm^{-1}): 1630 (C=O), 3420 (OH). ^{1}H NMR spectrum ($CDCl_3$, 90 MHz), δ, ppm: 1.08–1.79 m [10H, $(CH_2)_5$], 3.44 t (2H, NCH_2), 3.50 s (2H, SCH_2CO), 3.74 t (2H, OCH_2), 4.08 s (1H, OH).

Found, (%): C 55.63, H 7.88, N 6.55, S 14.99.

$C_{10}H_{17}NO_2S$.

Calculated, (%): C 55.78, H 7.96, N 6.51, S 14.89.

CONCLUSIONS

(1) Conditions were found for one-pot synthesis of *N*-(2-hydroxyethyl)-1,3-thiazolidin-4-ones from monoethanolamine, carbonyl compounds, and mercaptoacetic acid. The product yield is higher than that in the two-stage synthesis with intermediate isolation of oxazolidines.

(2) The protective effect of *N*-(2-hydroxyethyl)-1,3-thiazolidin-4-ones against carbon dioxide and hydrogen sulfide corrosion of steel reaches 96%.

REFERENCES

1. Grigor'ev, V.P. and Ekilik, V.V., *Khimicheskaya struktura i zashchitnoe deistvie ingibitorov korrozii* (Chemical Structure and Protective Effect of Corrosion Inhibitors), Rostov-on-Don: Rostov. Gos. Univ., 1978.
2. Kukharev, B.F., Stankevich, V.K., Klimenko, G.R., *et al.*, *Zh. Prikl. Khim.*, 2000, vol. 73, no. 1, pp. 161–163.
3. Eidemiller, Yu.N., Rakhmankulov, D.L., and Golubeva, I.V., Abstracts of Papers, *Vserossiiskii simpozium "Khimiya organicheskikh soedinenii sery i kremniya"* (Russian Symp. "Chemistry of Organic Compounds of Sulfur and Silicon"), Irkutsk, 2001, p. 184.
4. Kukharev, B.F., Stankevich, V.K., and Klimenko, G.R., *Izv. Ross. Akad. Nauk, Ser. Khim.*, 1997, no. 12, pp. 2221–2223.
5. Bergman, E.D., *Chem. Rev.*, 1953, vol. 53, no. 2, pp. 309–352.
6. Laurent, P.A., *Bull. Soc. Chim. Fr.*, 1967, no. 2, pp. 571–575.
7. Cope, A.C. and Hancock, E.M., *J. Am. Chem. Soc.*, 1942, vol. 64, pp. 1503–1506.
8. Saakiyan, A.S. and Efremov, A.P., *Zashchita neftepromyslovogo oborudovaniya ot korrozii* (Corrosion Protection of Petroleum Extraction Equipment), Moscow: Nedra, 1982.

Russian Journal of Applied Chemistry, Vol. 75, No. 4, 2002, pp. 667–668. Translated from Zhurnal Prikladnoi Khimii, Vol. 75, No. 4, 2002, pp. 682–683.
Original Russian Text Copyright © 2002 by Kashparova, Kagan, Kashparov, Zhukova.

BRIEF COMMUNICATIONS

Synthesis of 2,2,6,6-Tetramethylpiperidine Derivatives

V. P. Kashparova, E. Sh. Kagan, I. S. Kashparov, and I. Yu. Zhukova

South-Russian State Technical University (Novocherkassk Polytechnic Institute), Novocherkassk, Rostov oblast, Russia

Received October 29, 2001; in final form, January 2002

Abstract—Diazotization of 4-amino-2,2,6,6-tetramethylpiperidine in acetic or sulfuric acid affords 2,2,6,6-tetramethyl-1,2,3,6-tetrahydropyridine in high yield. Under the same conditions, the corresponding nitroxyl radical transforms into 4-hydroxy-2,2,6,6-tetramethylpiperidine-1-oxyl.

Recently, there has been much interest in synthesis of 2,2,6,6-tetramethylpiperidine derivatives, which are widely used for stabilization of polymers and monomers against light and heat [1, 2]. In this work, we studied the synthesis of nitroxyl radicals and sterically hindered amines by diazotization of 4-amino-2,2,6,6-tetramethylpiperidine **I** and 4-amino-2,2,6,6-tetramethylpiperidine-1-oxyl **II**. Compound **I** is commercially available and is used for production of polymer photostabilizers.

Diazotization of **I** in the presence of HCl or HBr gave 1,2,5,6-tetrahydro-2,2,6,6-tetramethylpyridine **III** in 80% yield. Under these conditions, 4-chloro-2,2,6,6-tetramethylpiperidine **IV** or 4-bromo-2,2,6,6-tetramethylpiperidine **V** is formed in 10–15% yield, along with **III**.

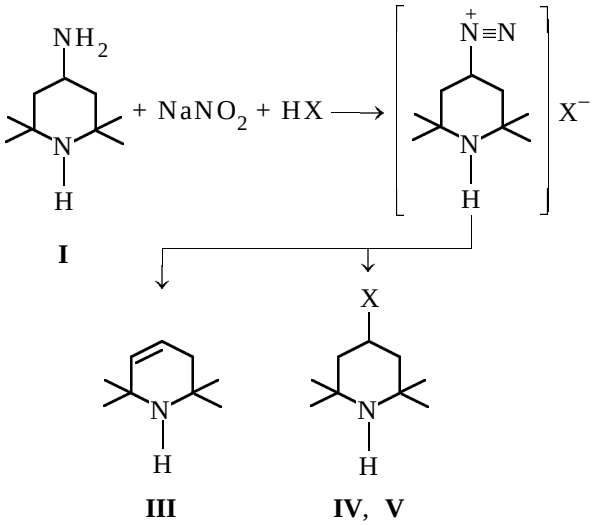

where X = Cl (**IV**), Br (**V**).

The best result was obtained when diazotization was performed in the presence of acetic or sulfuric acid (yield of **III** 90%). This is due to the fact that the acetate and sulfate ions are less nucleophilic than the chloride and bromide ions. Thus, the proposed reaction can be used for preparing **III**. Oxidation of **III**–**V** with hydrogen peroxide in the presence of Na_2WO_4 yields the corresponding nitroxyl radicals [3].

Of particular interest is diazotization of 4-amino-2,2,6,6-tetramethylpiperidine-1-oxyl **II**:

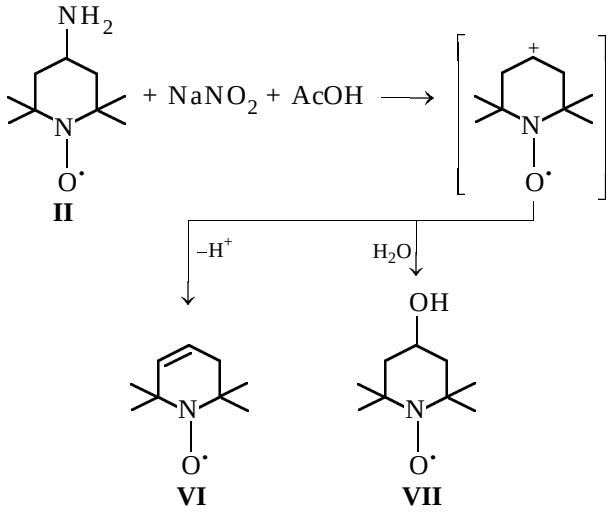

This reaction cannot be performed in the presence of mineral acids, as the radical center decays under these conditions [4]. However, the reaction can be performed in the presence of 30% acetic acid, which leaves the radical center intact. The nitroxyl group strongly affects the reaction course. The yield of **VI** is as low as 10% (cf. **III**), and the major product (80% yield) is 4-hydroxy-2,2,6,6-tetramethylpiperi-

1070-4272/02/7504-0667 $27.00 © 2002 MAIK "Nauka/Interperiodica"

dine-2-oxyl **VII** (cf. **IV** and **V**). Probably, the reaction pathway depends on the basicity of the initial substances. With **I**, elimination of N_2 and HX is the prevailing process.

When diazotization of **I** is performed in glacial acetic acid, the only reaction product is 4-acetylamino-2,2,6,6-tetramethylpiperidine **VIII**. Compound **II** is also acylated with glacial acetic acid at room temperature; the yield of 4-acetylamino-2,2,6,6-tetramethylpiperidine-1-oxyl **IX** is 95%. According to [5], 2,2,6,6-tetramethylpiperidine derivatives are only acylated with acetic anhydride.

EXPERIMENTAL

2,2,6,6-Tetramethyl-1,2,5,6-tetrahydropyridine III and 4-chloro-2,2,6,6-tetramethylpiperidine IV. To a solution of 7.8 g (0.05 mol) of amine **I** in 10 ml of water, 9 ml of HCl (ρ = 1.19 g ml^{-1}) was added. Then, a solution of 5.2 g (0.075 mol) of $NaNO_2$ in 10 ml of water was added dropwise with stirring. In the course of the reaction, the pH was maintained within 3–5 by adding aqueous HCl (1 : 1). After the reaction was complete, the mixture was alkalized first with K_2CO_3 and then with KOH to pH 10–12, after which it was extracted with benzene (3 × 10 ml). The benzene extracts were combined, the solvent was evaporated, and the residue was distilled under atmospheric pressure. Yield of **III** 5.5 g (80%), bp 143–145°C (cf. bp 145–146°C [3]). The residue was recrystallized from methanol. Yield of colorless crystalline compound **IV** 0.9 g (10%), mp 37–38°C; the compound was identified using a mixing test with an authentic sample [6].

When the reaction was performed in HBr, the yield of **III** was 80%, and that of 4-bromo derivative **V**, 10%; mp 43–45°C (from methanol; cf. mp 44–45°C [6]).

2,2,6,6-Tetramethyl-1,2,5,6-tetrahydropyridine-1-oxyl VI and 4-hydroxy-2,2,6,6-tetramethylpiperidine-1-oxyl VII. To a solution of 8.5 g (0.05 mol) of **II** in 40 ml of distilled water, 20 ml of glacial acetic acid was added, the mixture was cooled to 5°C, and a solution of 6.4 g (0.075 mol) of $NaNO_2$ in 20 ml of water was gradually added. The resulting mixture was stirred for 2 h, alkalized with a KOH solution to pH 10–11, and extracted with benzene (3 × 50 ml). The benzene extracts were combined, the solvent was removed, and the residue was treated with hexane (50 ml). Compound **VI** passed into hexane, and compound **VII** remained in the residue. After removal of the solvent, 0.9 g (12%) of **VI** was obtained; mp 34–35°C (cf. mp 33°C [3]). The insoluble product **VII** was purified by column chromatography (l = 50 cm, r = 1.5 cm, sorbent Al_2O_3, Brockmann grade II, eluent CH_2Cl_2). Yield of **VII** 6.8 g (80%). The mixing test with an authentic sample gives no depression of the melting point [3].

4-Acetylamino-2,2,6,6-tetramethylpiperidine-1-oxyl IX. To 30 ml of glacial acetic acid, we added with stirring 2.6 g (0.015 mol) of radical **II**. The stirring was continued for 1 h, after which the mixture was alkalized with a KOH solution to pH 10–11 and extracted with methylene chloride (3 × 30 ml). The organic extracts were combined and dried over Na_2SO_4; the solvent was removed. The remaining red-orange crystalline compound **IX** (3.3 g, 95%) was recrystallized from water; mp 145–146°C. The compound was identified by a mixing test with an authentic sample and by comparison of the IR spectra [3].

CONCLUSIONS

(1) Diazotization of 4-amino-2,2,6,6-tetramethylpiperidine in HCl, HBr, H_2SO_4, and dilute AcOH affords 2,2,6,6-tetramethyl-1,2,5,6-tetrahydropyridine in 80–90% yield.

(2) Diazotization of 4-amino-2,2,6,6-tetramethylpiperidine-1-oxyl in 30% AcOH gives 4-hydroxy-2,2,6,6-tetramethylpiperidine-1-oxyl in 80% yield.

(3) In glacial AcOH, 4-amino-2,2,6,6-tetramethylpiperidine and the corresponding radical are converted virtually completely to the corresponding *N*-acetyl derivatives.

REFERENCES

1. Dagonneau, M., Ivanov, V.B., Rozantsev, E.G., *et al.*, *J. Macromol. Sci.*, 1982–1983, no. 2, pp. 169–202.
2. Rozantsev, E.G., Sholle, V.D., Ivanov, V.B., *et al.*, in *Polymer Stabilization and Degradation*, Washington DC: Am. Chem. Soc., 1985, pp. 11–37.
3. Rozantsev, E.G., *Svobodnye iminoksil'nye radikaly* (Free Iminoxyl Radicals), Moscow: Khimiya, 1970.
4. Avrutskaya, I.A., Kagan, E.Sh., Smirnov, V.A., and Fioshin, M.Ya., *Nitroksil'nye radikaly: sintez, khimiya i prilozheniya* (Nitroxyl radicals: Synthesis, Chemistry, and Applications), Moscow: Nauka, 1987.
5. Dagonneau, M., Sholle, V.D., Rozantsev, E.G., *et al.*, *Synthesis*, 1984, no. 11, pp. 895–916.
6. Rozantsev, E.G., Golubev, V.A., and Neiman, M.B., *Izv. Akad. Nauk SSSR, Ser. Khim.*, 1965, no. 2, pp. 391–393.

Russian Journal of Applied Chemistry, Vol. 75, No. 4, 2002, pp. 669–671. Translated from Zhurnal Prikladnoi Khimii, Vol. 75, No. 4, 2002, pp. 684–685.
Original Russian Text Copyright © 2002 by Svetlakov, Nikitin, Orekhova.

BRIEF COMMUNICATIONS

Oxidation of Tetrahydrofuran and 1,4-Butanediol with Nitric Acid

N. V. Svetlakov, V. G. Nikitin, and A. O. Orekhova

Kazan State Technological University, Kazan, Tatarstan, Russia

Received August 13, 2001; in final form, January 2002

Abstract—Preparation of succinic acid by oxidation of tetrahydrofuran and 1,4-butanediol with nitric acid was studied.

One of practically important aliphatic dicarboxylic acids is succinic acid (SA). Owing to its unique biological properties, this acid is widely used in medicine and agriculture [1, 2].

Succinic acid is prepared in industry [3] by reduction of maleic and fumaric acids. The production process is being constantly improved [4, 5]. A promising procedure for preparing SA is oxidation of butadiene rubber with ozone [6]. Oxidation of tetrahydrofuran (THF) with nitric acid [7] is also of practical interest. However, this procedure is poorly studied.

Tetrahydrofuran was oxidized with nitric acid of various concentrations (97–30%) at a temperature lower than 25°C. THF vigorously reacts with concentrated HNO_3 (80–97%) with liberation of nitrogen oxides and heat. Already 30–40 min after mixing of the reactants, crystalline SA starts to precipitate. The oxidation is complete in 3–4 h after mixing the reactants. The SA yield is 80–85%. An additional amount of SA is precipitated after prolonged storage of the filtrate. The total yield exceeds 90%.

Oxidation of THF with 40–60% nitric acid is less exothermic. The liberation of nitrogen oxides, whose composition was not studied, is less vigorous. Oxidation of THF with 30% HNO_3 continues for several days. The SA yield was 40–45%, which is due to losses with spent nitric acid.

Nitric acid with a concentration higher than 70% contains nitronium cation, which is a strong electrophile [8]. We suggested that, in concentrated HNO_3, nitronium cation must cleave the C–O bond of THF to form 1,4-butanediol dinitrate (BDN). To confirm this assumption, we performed the reaction of THF with fuming nitric acid at temperatures lower than 0°C. After reaction completion, the reaction mixture was diluted with water and extracted with chloroform. As determined by elemental and spectral analysis, the isolated liquid product was BND.

1,4-Butanediol dinitrate thus obtained is converted into SA by treatment with nitric acid at 25–30°C.

These results suggest that SA can also be prepared by oxidation of 1,4-butanediol (BD) with nitric acid. 1,4-Butanediol was oxidized with 30–97% HNO_3 at 25–30°C. At nitric acid concentration higher than 80%, vigorous liberation of heat and nitrogen oxides was observed. In 3–4 h, precipitation of crystalline SA from the reaction mixture and liberation of nitrogen oxides were complete.

The yield of SA prepared by oxidation with 80% HNO_3 is as high as 90%. When 60–40% nitric acid is used, the SA yield decreases to 40–60%. This is due to dissolution of SA in spent HNO_3. The SA loss can be decreased if the spent nitric acid is recycled by mixing with concentrated HNO_3.

Since alcohols are *O*-nitrated readily and fast [9], BDN is apparently the intermediate of BD oxidation with concentrated nitric acid.

It is known than BDN can be prepared by esterification of BD with a mixture of sulfuric and nitric acid at temperatures below 0°C. At higher temperatures BDN is unstable [10]. BDN was oxidized to SA by the above procedure. The SA yield was 85%. Nitrogen oxides evolved in BD oxidation probably affect the oxidation. For example, N_2O_4, NO, and

1070-4272/02/7504-0669 $27.00 © 2002 MAIK "Nauka/Interperiodica"

N_2O_3 readily react with alcohols to form nitrous acid esters [11], which are subsequently converted into the carboxylic acid.

Preparation of SA by oxidation of BD has the following advantages over THF oxidation: reaction occurs under milder conditions, the reaction temperature can be easily controlled, the SA yield is sufficiently high, and BD is appreciably cheaper than THF.

EXPERIMENTAL

The IR spectra of SA (Nujol mull) and BDN (thin film between KBr discs) were recorded on a UR-20 spectrometer. The 1H NMR spectra of the reaction products were recorded at room temperature in acetone-d_6 on a Tesla-497 spectrometer operating at 100 MHz. HMDS was used as internal reference. THF and BD were of pure grade. Nitric acid solutions were prepared by dilution of 97% nitric acid (technical grade) with distilled water to the required concentration.

THF oxidation. To 80% nitric acid (56.7 g of 100% HNO_3, 0.9 mol), THF (10.18 g, 0.15 mol) was added with stirring at a temperature below 25°C. Crystalline SA started to precipitate 30–40 min after mixing the reactants. When heat evolution and liberation of nitrogen oxides terminated, the reaction was considered complete. Then the mixture was allowed to stand for 3–4 h and after that cooled to 0°C. SA was filtered off on a glass frit under reduced pressure produced by a water-jet pump and dried. Yield 14.8 g (89%). Melting point of the product recrystallized from water was 185°C [2]. ^{1}H NMR (δ, ppm): 2.5 s (4H, CH_2), 7.0 br. s (2H, 2OH). IR (ν, cm^{-1}): 1700 (C=O), 2500–3000 (COOH).

Preparation and oxidation of BDN. To 97% HNO_3 (57.7 g, 0.9 mol) THF (10.18 g, 0.15 mol), was added with stirring at a temperature from –10 to 0°C. Then the reaction mixture was allowed to stand for 15 mim and poured into a water–ice mixture. The resulting solution was extracted with three 50-ml portions of chloroform, and the extract was dried over Na_2SO_4. The solvent was removed, and BDN was purified by distillation. Yield 9.7 (38%); bp 103–104°C (4 mm Hg); n_D^{20} = 1.4450 {bp 104–105°C (4 mm Hg); n_D^{20} = 1.4470 [9]}. IR (ν, cm^{-1}): 870, 1280, 1650 (ONO_2). ^{1}HNMR (δ, ppm): 2.4 s (4H, CH_2), 4.2 s (4H, OCH_2).

Found, %: C 26.16, H 4.14, N 15.16.
$C_4H_8O_6N_2$.
Calculated, %: C 26.66, H 4.44, N 15.15.

BDN was oxidized as described. The reaction mixture was allowed to stand at 20°C for 14 h after mixing the reactants. Yield of SA 84%.

BD oxidation. To 80% nitric acid (56.7 g of 100% HNO_3, 0.9 mol) stirred at 25–30°C, BD (13.5 g, 0.15 mol) was added at the rate at which liberation of nitrogen oxides was not vigorous. When 35–40 min passed after the beginning of BD addition, SA started to precipitate. The reaction completion was judged from cessation of heat evolution and change of the color of the reaction mixture from brown to yellow. The reaction mixture was allowed to stand at 20°C for additional 2–3 h. SA was filtered off and dried. Yield 16 g (90%), mp 185°C (from water).

The NMR and IR spectra of SA prepared by this procedure were identical to those of SA prepared from THF.

BD oxidation with nitric acid solutions of other concentrations was performed similarly. The reaction completion was judged from cessation of heat evolution and end of liberation of nitrogen oxides, and from SA precipitation.

Preparation of BDN from BD and BDN oxidation. To a mixture of 94% H_2SO_4 (36.8 g, 0.38 mol) with 97% HNO_3 (30.2 g, 0.47 mol), BD (8 g, 0.08 mol) was added at a temperature below 10°C. The reaction mixture was allowed to stand at this temperature for 30 min and then poured into cold water. The resulting solution was extracted with two 50-ml portions of chloroform. The extract was washed with water and dried over Na_2SO_4. The solvent was removed, and BDN was purified by distillation. The properties of the product were in agreement with published data [10].

Oxidation of BDN to SA with 80% HNO_3 was performed similarly. Yield 85–90%.

REFERENCES

1. Kondrasheva, M.N., *Terapevtichesko e deistvie yan–tarnoi kisloty* (Therapeutic Effect of Succinic Acid), Pushchino: ONTI Nauchn. Tsentra Biol. Issled., Akad. Nauk SSSR, 1976.
2. Ivanitskii, Yu.Yu., Golovko, A.I., and Sofronov, G.A., *Yantarnaya kislota v sisteme sredstv metabolizma i korrektsiya funktsional'nogo sostoyaniya i rezistent–nosti organizma: Uchebnoe posobie* (Succinic Acid in Metabolism and Correction of Functional State and Resistance of a Body: Textbook), St. Petersburg: Ozdorovitel'nye Tekhnologii, 1998.
3. Freidlin, G.N., *Alifaticheskie dikarbonovye kisloty*

(Aliphatic Dicarboxylic Acids), Moscow: Khimiya, 1978.

4. RF Patent no. 2135458.
5. RF Patent no. 2129540.
6. RF Patent no. 2036895.
7. Ponomarev, A.A., *Sintezy i reaktsii furanovykh veshchestv* (Syntheses and Reactions of Furan Derivatives), Saratov: Saratov. Gos. Univ., 1960.
8. Veretennikov, E.A., Lebedev, B.A., and Tselinskii, I.V., *Zh. Org. Khim.*, 2001, vol. 37, no. 7, pp. 1016–1020.
9. Orlova, E.Yu., *Khimiya i tekhnologiya brizantnykh vzryvchatykh veshchestv* (Chemistry and Technology of Brisant Explosives), Moscow: Oborongiz, 1960, pp. 301–355.
10. Ficher, F., Siegrist, W., and Buess, H., *Helv. Chim. Acta*, 1935, vol. 18, pp. 18–25.
11. *Comprehensive Organic Chemistry. The Synthesis and Reactions of Organic Compounds*, vol. 2: *Nitrogen Compounds*, Sutherland, I.O., Ed., Oxford: Pergamon, 1979.

Russian Journal of Applied Chemistry, Vol. 75, No. 4, 2002, p. 672. Translated from Zhurnal Prikladnoi Khimii, Vol. 75, No. 4, 2002, p. 685.
Original Russian Text Copyright © 2002 by Aronova, Ginak.

BRIEF COMMUNICATIONS

Solid-Phase Synthesis of Triethylammonium Salt of 4-Oxothiazolidine-2-thione

E. B. Aronova and A. I. Ginak

St. Petersburg State Technological Institute, St. Petersburg, Russia

Received December 23, 2001; in final form, January 2002

Abstract—A procedure was developed for solid-phase synthesis of triethylammonium salt of 4-oxothiazolidine-2-thione.

3-R-Substituted 4-oxothiazolidinethiones are natural biologically active substances. They are plant growth stimulants [1] and metabolites of amino acid synthesis in cells [2]; their synthetic analogs exhibit a wide spectrum of biological activity, from herbicides [3] to antitumor agents [4]; also, these compounds are used as complexones for noble metals. The main synthetic route to these compounds involves nucleophilic substitution in polar solvents in the presence of bases. In the process, the main reaction of electrophile addition to the sulfur or nitrogen atom of the heterocycle is accompanied by base hydrolysis of the initial and final products with ring cleavage. This side reaction significantly decreases the yield of the target products and complicates their purification. It is known [5] that the nucleophilic substitution is preceded by the formation of salts of the substrate with a base, and in some cases, these intermediate salts are isolated to prevent hydrolysis. However, synthesis of these salts is also labor-consuming and requires proper choice of solvents for neutralization and crystallization.

To eliminate these drawbacks, we attempted to prepare alkylammonium salt of 4-oxothiazolidine-2-thione by solid-phase synthesis. Crystalline 4-oxothiazolidine-2-thione **I** was treated with triethylamine vapor at 50–120°C in a tubular reactor with false bottom. The reaction gives no by-products, and the desired 4-oxothiazolidine-2-thione triethylammonium salt **II** is formed in 98% yield.

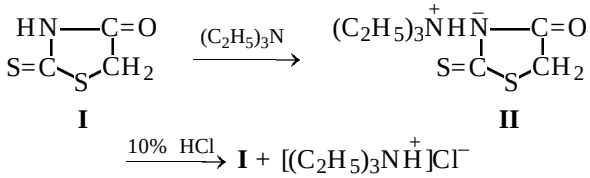

The resulting product contains no impurities and does not require additional purification. Its composition was confirmed by elemental analysis, and the structure, by a mixing test with an authentic sample.

Found, (%): N 11.8, S 27.3.

$C_9H_{18}N_2OS_2$.

Calculated (%): N 12.0, S 27.4.

REFERENCES

1. Brown, F.C., *Chem. Rev.*, 1961, vol. 61, no. 5, pp. 463–521.
2. Zvonkova, E.N., Zotchik, N.V., Fillipovich, E.N., *et al.*, *Khimiya biologicheski aktivnykh prirodnykh soedinenii* (Chemistry of Biologically Active Natural Compounds), Moscow: Khimiya, 1970.
3. Mel'nikov, N.N., Volkov, A.I., and Korotkova, O.A., *Pestitsidy i okruzhayushchaya sreda* (Pesticides and the Environment), Leningrad: Khimiya, 1977.
4. Pluijgers, C.N., Berg, J., and Thorn, D.D., *Recl. Trav. Chim. Pays-Bas*, 1969, vol. 88, no. 1, pp. 241–253.
5. Ginak, A.I., Volkova, A.A., Ramsh, S.M., and Sochilin, E.G., *Zh. Org. Khim.*, 1980, vol. 16, no. 1, pp. 122–125.

1070-4272/02/7504-0672 $27.00 © 2002 MAIK "Nauka/Interperiodica"

Russian Journal of Applied Chemistry, Vol. 75, No. 4, 2002, pp. 673–674. Translated from Zhurnal Prikladnoi Khimii, Vol. 75, No. 4, 2002, pp. 687–688.
Original Russian Text Copyright © 2002 by Shaglaeva, Lebedeva, Pirogova, Sultangareev, Es'kova, Petrova, Khaliullin.

BRIEF COMMUNICATIONS

Copolymerization of 1-Vinylpyrazole with Vinyl Chloride

N. S. Shaglaeva, O. V. Lebedeva, G. A. Pirogova, R. G. Sultangareev, L. A. Es'kova, E. P. Petrova, and A. K. Khaliullin

Favorskii Institute of Chemistry, Siberian Division, Russian Academy of Sciences, Irkutsk, Russia

Received December 19, 2001

Abstract—Copolymerization of vinyl chloride with 1-vinylpyrazole was studied. The copolymerization constants were determined. The chemical structure of the copolymers was studied by NMR and IR spectroscopy.

In [1–3], we studied copolymerization of *N*-vinyl-4,5,6,7-tetrahydroindole, 2-methyl-5-vinylpyridine, and 1-vinyl-1,2,4-triazole with vinyl chloride (VC) and showed that copolymers are formed at any initial ratio of the monomers and that copolymerization is accompanied by dehydrochlorination of the resulting macromolecules. Therefore, revealing the effect of the structure of the azole ring on the degree of dehydrochlorination in the course of copolymerization and on the composition and properties of the resulting copolymers remains a topical problem.

In this work, we studied radical copolymerization of 1-vinylpyrazole (1-VPR) with VC.

The reaction yielded powders soluble in DMF, DMSO, *N*-methyl-2-pyrrolidone, and benzene. The IR spectra of the VPR–VC copolymers contain absorption bands at 1400–1525 cm^{-1}, corresponding to vibrations of the pyrazole ring; the bands at 1650 and 960 cm^{-1}, characteristic of the residual double bond, are lacking.

As seen from Table 1, copolymers are formed at any ratio of the monomers within the examined range and are always enriched in VPR units.

As the VPR content in the initial mixture is increased, the copolymer yield and intrinsic viscosity grow. In contrast to copolymerization of VC with *N*-vinyl-4,5,6,7-tetrahydroindole, 1-vinyl-1,2,4-triazole, and 2-methyl-5-vinylpyridine, copolymerization of VC with VPR is not accompanied by elimination of HCl, which is confirmed by the absence of signals from –CH=CH– groups in the ^{13}C NMR spectrum. For the system VPR–VC, we determined at low conversions the copolymerization constants: $r_{VPR} = 0.79$, $r_{VC} = 0.015$. From these quantities, we calculated the parameters of the molecular structure of the copolymers (Table 2).

An increase in the VPR content in the initial mixture makes formation of the alternating copolymers less probable. In contrast to polyvinyl chloride, the VPR–VC copolymers prepared in this work are soluble in a wide range of organic solvents; they can be processed under milder conditions as compared to VC and vinylidene chloride homopolymers.

It is known [4] that polyvinyl chloride and polyvinylidene chloride can form only dilute (≤5%) solutions in mixtures of acetone, butyl acetate, and cyclo-

Table 1. Copolymerization of VPR with VC (solvent DMF; [AIBN] = 1.5 wt %, 60°C, τ = 6 h)

Initial mixture composition, mol %		Polymer composition, mol %, as calculated from content of				Yield, wt %	[η], dl g^{-1}
		N		Cl			
VPR	VC	VPR	VC	VPR	VC		
0.16	0.84	0.28	0.72	0.23	0.77	3.25	0.08
0.23	0.77	0.54	0.46	0.55	0.45	4.52	0.10
0.42	0.58	0.61	0.39	0.62	0.38	6.00	0.87
0.68	0.32	0.73	0.27	0.74	0.26	7.25	0.93
0.85	0.15	0.84	0.16	0.84	0.16	8.43	1.60

1070-4272/02/7504-0673 $27.00 © 2002 MAIK "Nauka/Interperiodica"

Table 2. Activity factors and microstructural parameters of copolymers of VPR (M_1) with VC (M_2)

M_1, mole fraction		Probability of diad formation			Mean length of sequences	
initial mixture	copolymer	m_1–m_2	m_1–m_1	m_2–m_2	l_1	l_2
0.1	0.24	0.0377	0.2734	0.6889	1	14
0.3	0.48	0.2452	0.5677	0.2990	2	2
0.5	0.59	0.4055	0.4335	0.1609	2	1
0.7	0.74	0.6668	0.2896	0.0437	3	1
0.9	0.92	0.9154	0.0820	0.0026	12	1

hexanol. The limited solubility of the copolymers precludes use of their solutions for varnishing. We found that VPR–VC copolymers can form solutions with concentration as high as 50%, which meets the modern requirements to varnishes.

Thus, VPR–VC copolymers exhibit a number of interesting properties, different from those of the VC homopolymer, and can find new applications.

EXPERIMENTAL

Copolymerization of monomers was performed in sealed ampules at 60°C in the presence of azobis(isobutyronitrile) under argon. The reaction mixture was dissolved in DMF, and the copolymer was precipitated with acetone. After reprecipitation into acetone, the copolymers were vacuum-dried to constant weight. The intrinsic viscosity was determined in DMF at 20°C by the dilution procedure. The relative activity constants were calculated by the Fineman–Ross and Kelen–Tudos methods, using a program developed by G.I. Deryagina and the Mortimer–Tidwell experimental design method. In the calculations, we used experimental data for low (≤10%) conversions. The IR spectra were measured on a Specord 75-IR spectrometer (KBr pellets, mulls in mineral oil). The ^{13}C NMR spectra of copolymer samples were recorded with proton noise decoupling on a Varian VXR-500 spectrometer (working frequency 125.5 MHz) in DMSO-d_6 at a relaxation delay of 2.5 s and 90° pulse. Chromium tris(acetylacetonate) (0.02 M) was used as relaxant.

CONCLUSIONS

(1) Radical copolymerization of 1-vinylpyrazole with vinyl chloride is not accompanied by dehydrochlorination; 1-vinylpyrazole is more reactive.

(2) Incorporation of 1-vinylpyrazole units in the copolymer increases its solubiity in organic solvents.

REFERENCES

1. Shaglaeva, N.S., Mikhaleva, A.I., Sarapulova, G.I., *et al.*, *Izv. Ross. Akad. Nauk, Ser. Khim.*, 1997, no. 12, pp. 2267–2268.
2. Lebedeva, O.V., Shaglaeva, N.S., Pirogova, G.A., *et al.*, *Zh. Prikl. Khim.*, 2000, vol. 73, no. 8, pp. 1399–1400.
3. Lebedeva, O.V., Shaglaeva, N.S., Pirogova, G.A., and Fedorov, S.V., *Zh. Prikl. Khim.*, 2001, vol. 74, no. 8, pp. 1374–1375.
4. *Poluchenie i svoistva polivinilkhlorida* (Synthesis and Properties of Polyvinyl Chloride), Zil'berman, E.N., Ed., Moscow: Khimiya, 1968.

Russian Journal of Applied Chemistry, Vol. 75, No. 4, 2002, pp. 675–676. Translated from Zhurnal Prikladnoi Khimii, Vol. 75, No. 4, 2002, pp. 689–690.
Original Russian Text Copyright © 2002 by Polezhaeva, Polezhaev, Levdanskii, Kuznetsov.

BRIEF COMMUNICATIONS

Synthesis and Properties of Low-Temperature Solder Creams Based on Polyester Resin and Diethyldibenzylammonium Bromide

N. I. Polezhaeva, I. V. Polezhaev, V. A. Levdanskii, and B. N. Kuznetsov

Institute of Chemistry and Chemical Technology, Siberian Division, Russian Academy of Sciences, Krasnoyarsk, Russia

Received September 10, 2001

Abstract—Synthesis and properties of solder creams based on polyester resin modified with rosin and diethyldibenzylammonium bromide were studied. The feasibility of using diethyldibenzylammonium bromide as soldering flux in low-temperature solder creams was analyzed.

The modern trend in the development of electronics is the increase in the number of components per unit volume, which is achieved by wide use of microassemblies and functional microelectronic devices. Electronic devices are produced to a significant extent by hybrid integrated methods. In this case, the passive section of the hybrid microchips (HMCs) can be produced by both thick- and thin-film procedures. The working hours of the manual hybrid-circuit packaging comprised nearly 50% of the total working hours of the HMC production, and a decrease in the manual operation is a topical problem.

At present, the component leads are connected to thick-film pads of the chips by various methods: adhesion connection, welding, and soldering. Soldering with low-temperature creams is the most widely used and effective method [1].

The organic fraction of the solder cream contains three main components: flux, binder, and solvent [2]. These components provide the required consistence of the solder cream, low melting temperature, and high adhesion to the surface being soldered.

The flux in the solder cream is analogous to the common fluxes; it removes oxide films from the surface of metals being soldered and solder, protects the contact surfaces from oxidation during soldering, and decreases the surface tension of molten solder at the metal–solder flux interface. Thus, the flux must meet the following requirements: necessary activity in the given temperature range, low corrosion activity and toxicity, stability upon prolonged storage, and easy elimination after soldering.

This paper continues our study aimed at the development of low-temperature noncorrosive solder creams [3, 4].

EXPERIMENTAL

We used diethyldibenzylammonium bromide (DEDBAB) flux. The solder cream was prepared as follows: DEDBAB (2 g) was added to the polyester resin (15 g) modified with rosin synthesized as described in [3]. The components were thoroughly mixed.

The parameters of the thermal-oxidative decomposition of the resulting mechanical mixture of polyester resin, DEDBAB, and flux were studied by dynamic thermogravimetry [5]. For more correct determination of the temperature of the onset of sample decomposition, we recorded TG, DTG, and DTA curves. The thermogravimetric curves were registered on an MOM Q-1000 device (Hungary) in the programmed-heating mode. The sample (0.03 g) was heated in a platinum crucible in air at a heating rate of 10 deg min^{-1}. The scales of the balance, DTA galvanometer, and DTG galvanometer were 50 mg, 1/3 and 1/10, respectively.

The thermal stability of the polyester resin with added DEDBAB was determined from the temperature of the onset of sample decomposition [T_{dec}^{DTA} is the temperature at which the exothermic effect (related to oxidation) appears in the DTA curve, and T_{dec}^{DTG} is the temperature at which the DTG curve starts to deviate from the horizontal] [6]. The results are listed in the table.

1070-4272/02/7504-0675 $27.00 © 2002 MAIK "Nauka/Interperiodica"

Thermal stability of the samples, calculated from dynamic thermogravimetry data

Sample	T_{dec}^{DTG}	T_{dec}^{DTA}	T_{dec}^{av*}
	°C		
Polyester resin	540	460	500
Polyester resin + DEDBAB	500	460	480

* $T_{dec}^{av} = (T_{dec}^{DTG} + T_{dec}^{DTA})/2$.

As seen from the table, for the polyester resin mixed with DEDBAB, the average decomposition temperature (T_{dec}^{av}) is lower as compared to straight polyester resin, which is probably due to an increase in the chemical activity and specific surface area of the mixture [5].

Our analysis of the TG and DTA curves recorded for DEDBAB flux shows that the sample decomposes in the 160–220°C range, which suggests that DEDBAB can be used in solder creams with melting point lower than 230°C.

To study the properties of the solder cream based on the polyester resin containing DEDDBAB, the mixture was placed on chip pads (obtained by the thick-film procedure using silver-containing and silver–palladium conducting formulations) and thin-film copper guides coated with tin or gold. The solder creams were prepared using the POSK 50-18 and POIn 52 solders; the tinning temperature was 180 ± 10 and 150 ± 10°C, respectively. The fusing mode of the solder cream must provide aggregation of the solder particles and wetting of the contact surfaces. Usually, the fusing temperature is 30–50°C higher than the melting point of the straight solder, and in this case fusing and wetting proceed in 10–30 s [7].

The quality of tinning was studied using an MBS-9 microscope (8–16× magnification). The surface area of untinned sections of the contact pads was determined using a measuring microscope. The wetting coefficient K_w (%) was calculated from the following equation:

$$K_w = \frac{S_1 + S_2 + \ldots + S_n}{S_0},$$

where S_1, S_2, …, S_n are the areas of the untinned sections of the contact pad (mm^2), and S_0 is the total area of the contact pad (mm^2).

In the case of the solder cream based on polyester resin and DEDBAB flux, the quality of tinning was fairly high [according to GOST (State Standard) V 20.39.304–76], because the untinned area was less than 20% of the total surface area being tinned.

The adhesion of the solder cream layer to a contact pad after fusion was determined by the anchor-film method on an MP-05 tensile-testing machine.

The tests were performed as follows. Four brass rods with heads about 2 mm in diameter were soldered to four (2×2 mm) contact pads of a test-chip, using the solder cream. Then the soldered junctions were tested on a tensile-testing machine. The post-fusion adhesion of the solder cream to a contact pad was determined from the breakout force.

The post-fusion adhesion of the solder cream to contact pads prepared by the thick- and thin-film procedures was no less than 50 and 25 kg cm^{-2}, respectively. In most cases, the strength of the soldered junction was higher than the adhesion of the contact pad to the support.

CONCLUSIONS

(1) The composition and preparation procedure of low-temperature solder creams based on polyester resin binder and diethyldibenzylammonium bromide flux were developed.

(2) By thermal stability, tinning quality, and adhesion strength, the mixtures obtained meet the requirements to solder creams.

REFERENCES

1. Krasov, V.G., Petrauskas, G.B., and Chernozubov, Yu.S., *Tolstoplenochnaya tekhnologiya v SVCh mikroelektronike* (Thick-Film Methods in Ultrahigh Frequency Microelectronics), Moscow: Radio i Svyaz', 1985.
2. Guth, L.A., *Circuits Manuf.*, 1989, vol. 29, no. 2, pp. 56–69.
3. Polezhaeva, N.I., Polezhaeva, I.V., Levdanskii, V.A., and Kuznetsov, B.N., *Zh. Prikl. Khim.*, 2001, vol. 74, no. 4, pp. 684–685.
4. Polezhaeva, N.I., Polezhaev, I.V., Levdanskii, V.A., and Kuznetsov, B.N., Abstracts of Papers, *IX Konferentsiya "Destruktsiya i stabilizatsiya polimerov"* (IX Conf. on Degradation and Stabilization of Polymers), Moscow, 2001, pp. 150–151.
5. Wendlandt, W.Wm., *Thermal Methods of Analysis*, New York; Wiley, 1974.
6. Prokopchuk, N.R., *Vestsi Akad. Navuk. Bel. SSR, Ser. Khim. Navuk*, 1984, no. 4, pp. 119–121.
7. Trizna, Yu.P., Panov, L.I., Koretskii, V.N., and Rogovskii, V.F., *Tekhn. Sredstv Svyazi*, 1979, issue 2, pp. 61–64.

Russian Journal of Applied Chemistry, Vol. 75, No. 4, 2002, pp. 677–679. Translated from Zhurnal Prikladnoi Khimii, Vol. 75, No. 4, 2002, pp. 689–690.
Original Russian Text Copyright © 2002 by Raskulova, Moskaleva, Volkova, Kanitskaya, Khaliullin.

BRIEF COMMUNICATIONS

Copolymerization of 1-(Vinyloxyalkoxy)-2,3-epoxypropanes with Vinyl Chloride

T. V. Raskulova, O. N. Moskaleva, L. I. Volkova, L. V. Kanitskaya, and A. K. Khaliullin

Favorskii Institute of Chemistry, Siberian Division, Russian Academy of Sciences, Irkutsk, Russia

Received January 30, 2001; in final form, November 2001

Abstract—Binary radical polymerization of vinyl chloride with 1-(vinyloxyalkoxy)-2,3-epoxypropanes in acetone and dimethyl sulfoxide was studied. The copolymerization constants and the microstructural parameters of the resulting copolymers were calculated.

Vinyl ethers are widely used in syntheses of organic chemicals, polymers, and copolymers exhibiting valuable properties [1–4], and also in production of modified polyvinyl chloride materials [5, 6]. We have shown [7] that copolymers of vinyl chloride (VC) with *n*-butyl vinyl ether surpass polyvinyl chloride in heat resistance and solubility in organic solvents. One of the major drawbacks of copolymers of VC with vinyl ethers is their lower, compared to the homopolymers, softening point. Therefore, it is appropriate to introduce into vinyl ethers functional groups (e.g., epoxy groups) capable of forming three-dimensional macromolecular networks and thus increasing the softening point of the material [8].

In this work, we studied radical copolymerization of VC with 1-(vinyloxyalkoxy)-2,3-epoxypropanes (VEPs)

$$CH_2{=}CH{-}O{-}R{-}CH_2{-}\underset{\diagdown\,O\,\diagup}{CH}{-}CH_2,$$

where R = CH_2–CH_2–O [1-(2-vinyloxyethoxy)-2,3-epoxypropane, VEP_1], (CH_2–CH_2–O)$_2$ {1-[2-(2-vinyloxyethoxy)ethoxy]-2,3-epoxypropane, VEP_2}, and (CH_2–CH_2–O)$_3$ (1-{2-[2-(2-vinyloxyethoxy)ethoxy]-ethoxy}-2,3-epoxypropane, VEP_3).

Copolymerization in the VC–VEP systems yielded copolymers in the form of yellow or light gray powders (at the VEP content in the initial monomer mixture ≤30%) or yellow oily substances (at the VEP content in the initial monomer mixture >30%).

The IR spectra of the copolymers show no absorption in the range 1620–1650 cm^{-1}, characteristic of the vinyl group. The presence of oxirane rings is confirmed by the bands at 765, 820, 915, 960, 1230, and 3060 cm^{-1}. The ^{13}C NMR spectra of the copolymers contain broadened signals suggesting the presence of units of both monomers, δ, ppm: 43.9 (–CH_2O–), 44.9–47.4 (>CH_2), 51.04 (–CHO–), 58.59–56.6 (>CHCl), and 68.2–72.7 (–CH_2–CH_2–O–). The signals assignable to the =CH_2 (86.7 ppm) and =CH–O– (152.7 ppm) groups are absent.

Experimental data on copolymerization in the systems VC–VEP are listed in the table. The content of VEP in the copolymers increases in parallel with its content in the initial monomer mixture. In the entire range of the initial mixture compositions, the copolymers are enriched in the VC units relative to the monomer mixture, which indicates that VEPs are less reactive than VC. This is also indicated by the copolymerization constants *r* (see table). With increasing solvent polarity [in going from acetone to dimethyl sulfoxide (DMSO)], the reactivity of the monomers relative to the like radical decreases, as indicated by decreased copolymerization constants. Such a solvent effect on the monomer reactivity may be due to the volume effects [9].

The microstructural parameters of the copolymers, calculated from the copolymerization constants (see table), show that the macromolecules are built of long blocks of VC units (L_1) separated by single VEP units (L_2). When the VEP content in the initial mixture is increased, or when the copolymerization is performed in DMSO, the length of VC blocks in the copolymers decreases.

The viscosity of the copolymers decreases with an increasing content of VEP units (Fig. 1). The relative viscosities in the VC–VEP_1 system are lower than those in the VC–VEP_2 and VC–VEP_3 systems.

1070-4272/02/7504-0677 $27.00 © 2002 MAIK "Nauka/Interperiodica"

General relationships of copolymerization in the VC–VEP (M_2) systems

Initial mixture composition, mol %		Copolymer composition, mol %		Yield, %	Solvent, *r*	L_1^*	Initial mixture composition, mol %		Copolymer composition, mol %		Yield, %	Solvent, *r*	L_1^*
VC	VEP	VC	VEP				VC	VEP	VC	VEP			
VC–VEP_2 system							VC–VEP_3 system						
95	5	99.22	0.78	40.8	Acetone;	71	95	5	99.18	0.82	24.7	Acetone;	58
85	15	91.35	8.65	73.0	$r_1 = 3.69$,	22	85	15	95.92	4.08	81.8	$r_1 = 3.00$,	18
75	25	86.94	13.06	75.5	$r_2 = 0.17$	12	75	25	89.63	10.37	86.1	$r_2 = 0.20$	10
50	50	73.08	26.92	84.0		5	50	50	77.78	22.22	88.6		4
95	5	97.11	2.89	50.8	DMSO;	36	95	5	97.59	2.41	41.3	DMSO;	48
85	15	92.16	7.84	81.3	$r_1 = 1.84$,	11	85	15	95.91	4.09	80.3	$r_1 = 2.29$,	14
75	25	88.39	11.61	83.9	$r_2 = 0.10$	7	75	25	83.54	16.46	84.3	$r_2 = 0.12$	8
50	50	70.38	29.62	86.1		3	50	50	74.24	25.76	88.9		3

* (*L*) Mean block length; $L_2 = 1$.

In all the systems studied, the copolymer yield grows with increasing VEP content in the initial monomer mixture (see table). This effect becomes more pronounced in going from VEP_1 to VEP_2 and then to VEP_3 and is manifested irrespective of the solvent polarity. The product yield increases because of the involvement of larger amounts of VC (Fig. 2).

EXPERIMENTAL

Copolymerization was performed at 70°C in glass ampules under argon, in the presence of 1.0 wt % AIBN initiator. Copolymers were purified by double reprecipitation with methanol from acetone, after which they were dried in a vacuum oven to constant weight.

The composition of the copolymers was determined by elemental analysis (chlorine content) and ^{13}C NMR spectroscopy. The ^{13}C NMR spectra of copolymer samples were recorded with proton noise decoupling on a Varian VXR-500 spectrometer (working frequency 125.5 MHz) in DMSO-d_6 and acetone-d_6 at a relaxation delay of 2.5 s and 90° pulse. Chromium tris(acetylacetonate) (0.02 M) was used as relaxant.

The IR spectra were recorded on a Specord IR-75 spectrometer from thin films and KBr pellets.

The relative viscosity of copolymers was determined with an Ubbelohde viscometer at 25°C. Copolymers were taken as 1 wt % solutions in cyclohexanone. The relative viscosity was recalculated to the intrinsic viscosity according to [10].

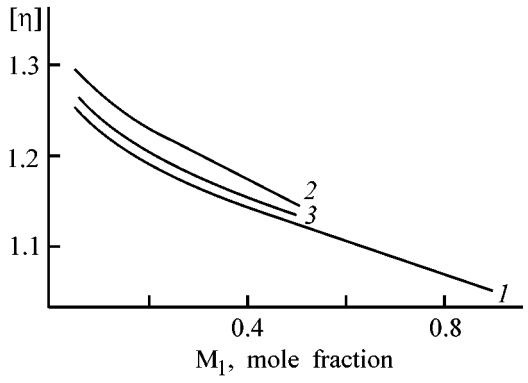

Fig. 1. Intrinsic viscosity [η] of VC–VEP copolymers prepared in acetone vs. mole fraction M_1 of VEP in the initial monomer mixture: (*1*) VEP_1, (*2*) VEP_2, and (*3*) VEP_3.

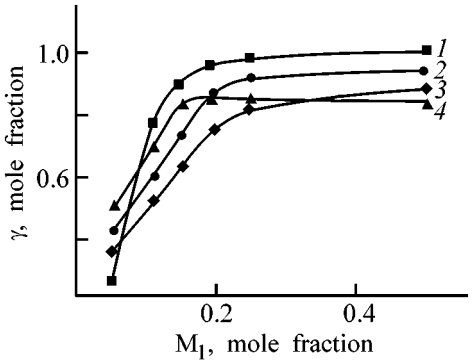

Fig. 2. VC conversion γ vs. mole fraction M_1 of VEP in the initial monomer mixture. Systems: (*1, 2*) VC–VEP_2 and (*3, 4*) VC–VEP_3; solvent: (*1, 3*) acetone and (*2, 4*) DMSO.

The copolymerization constants were determined by the least-squares method, using the Mortimer–Tidwell method of experimental design. In calculations, we used data obtained at monomer conversions ≤10%. The error of determining the constants was 3%.

CONCLUSIONS

(1) In radical copolymerization of vinyl chloride with 1-(vinyloxyalkoxy)-2,3-epoxypropanes, the latter compounds are less reactive than vinyl chloride.

(2) With increasing content of 1-(vinyloxyalkoxy)-2,3-epoxypropanes in the reaction mixture, the intrinsic viscosity of the product decreases, but the copolymer yield grows.

REFERENCES

1. Shostakovskii, M.F., *Prostye vinilovye efiry* (Vinyl Ethers), Moscow: Khimiya, 1952.
2. Nikolaev, A.F., *Sinteticheskie smoly i plastmassy na ikh osnove* (Synthetic Resins and Plastics Based on Them), Moscow: Nauka, 1966.
3. Mikhant'ev, B.I., *Monomery i vysokomolekulyarnye soedineniya* (Monomers and Macromolecular Compounds), Voronezh: Voronezh. Univ., 1969.
4. Zhubanov, B.A., Shaikhutdinov, E.M., and Osadchaya, E.F., *Prostye vinilovye efiry v reaktsiyakh radikal'noi polimerizatsii* (Vinyl Ethers in Radical Polymerizations), Alma-Ata: Nauka, 1985.
5. Sun, Yi-Jun, Hu, Guo-Hua, and Lambla, M., *Angew. Makromol. Chem.*, 1995, vol. 229, pp. 1–7.
6. Carter, E., J. *Oil Colour Chem.*, 1986, vol. 26, no. 4, pp. 100–105.
7. Khaliullin, A.K., Sallaurov, V.N., Shibanova, E.F., *et al.*, *Zh. Prikl. Khim.*, 1996, vol. 69, no. 4, pp. 653–656.
8. Raskulova, T.V., Volkova, L.I., Salaurov, V.N., *et al.*, *Zh. Prikl. Khim.*, 1998, vol. 71, no. 7, pp. 1184–1189.
9. Raskulova, T.V., Moskaleva, O.N., Volkova, L.I., *et al.*, *Vysokomol. Soedin., Ser. B*, 2001, vol. 43, no. 3, pp. 557–561.
10. Berlin, A.A., *Vysokomol. Soedin.*, 1966, vol. 8, no. 8, pp. 1336–1341.

Russian Journal of Applied Chemistry, Vol. 75, No. 4, 2002, pp. 680–682. Translated from Zhurnal Prikladnoi Khimii, Vol. 75, No. 4, 2002, pp. 694–696.
Original Russian Text Copyright © 2002 by Tishchenko, Iozep, Ivin.

BRIEF COMMUNICATIONS

Reaction of Dextran Polyaldehyde with Aminohydroxypyrimidines

E. V. Tishchenko, A. A. Iozep, and B. A. Ivin

St. Petersburg State Academy of Pharmaceutical Chemistry, St. Petersburg, Russia

Received December 6, 2001

Abstract—Reaction of dextran polyaldehyde with aminohydroxypyrimidines is proposed as a procedure for modifying polysaccharides with low-molecular-weight compounds. The influence exerted by the reaction temperature and time and by solution pH on the number of incorporated heterocyclic fragments was examined.

Many heterocyclic structures are fragments of molecules that are responsible for functioning of living bodies. Heterocyclic compounds are widely used in syntheses of biologically active substances and, in particular, such drugs as fluorouracil, methotrexate, and idoxurin. Unfortunately, all these drugs exhibit side effects and toxicity; they are rapidly eliminated from the body. At the same time, it is known that modification of drugs with polysaccharides is a way to decrease their toxicity, prolong their effect, and provide the required lipophilic–hydrophilic balance. Therefore, the goal of this study was to develop a procedure for binding 5- and 6-aminouracils and 2-amino-4,6-dihydroxypyrimidine with dextran polyaldehyde (DPA).

Chemical modification of DPA was performed by the scheme

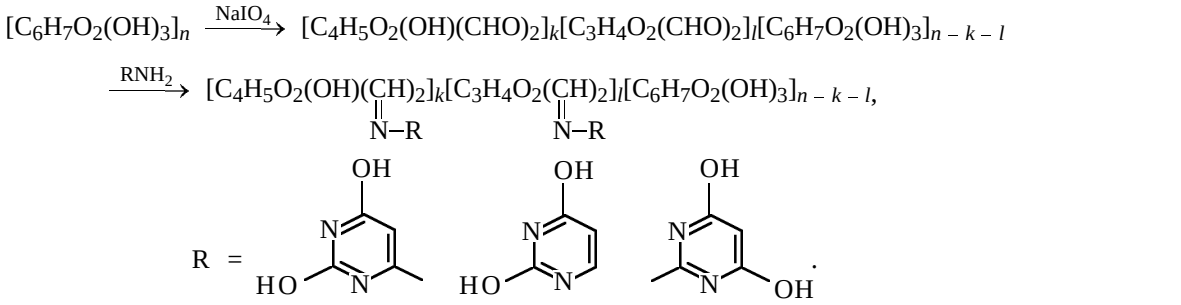

Dextran was oxidized with sodium metaperiodate in 0.1 N formate buffer solution (pH 4) in the course of 48 h at 6–8°C [1]. The oxidant consumption was monitored spectrophotometrically (λ 222.5 nm), and the amount of the released formic acid was determined by titration. To isolate the target product, the reaction mixture was dialyzed to remove low-molecular-weight substances and concentrated in a vacuum (20–25 mm Hg) at 50°C; DPA was precipitated with ethanol, filtered off, washed with alcohol and ether, and dried for 2–3 h in a vacuum (20–25 mm Hg) at 60°C.

The compounds synthesized were characterized by the degree of substitution C_{sa} (number of aldehyde groups per monosaccharide unit of the polymer); the content of aldehyde groups was determined by the oxime and hydroxamic methods [2, 3]. In this work, we used DPA with C_{sa} = 0.86.

Reactions of DPA with heterocyclic amines were performed at 20–80°C for 0.5–48 h at a molar ratio of the heterocyclic compound and DPA aldehyde groups of 3 : 1 and pH 4–10.2. The reaction was heterogeneous, since the major fraction of the amine occurred in the solid phase and dissolved with the progress of the reaction with DPA. After reaction completion, excess undissolved substances were filtered off, and the reaction product was precipitated with ethanol, filtered off, washed with ethanol and ether, and dried for 2–3 h in a vacuum (20–25 mm Hg) at 60°C. The absence of low-molecular-weight compounds in the products was checked by thin-layer chromatography.

1070-4272/02/7504-0680 $27.00 © 2002 MAIK "Nauka/Interperiodica"

The products are white, light yellow, or light brown amorphous powders insoluble in water, alcohol, ether, and most of other organic solvents, but soluble in aqueous alkalis.

The IR spectra of the products contain strong absorption bands at 1630 and 1720 cm^{-1}, which can be assigned to C=N and C=O stretching vibrations of the heterocyclic fragment incorporated in the polysaccharide aldehyde molecule.

The UV spectra of solutions of the reaction products in 0.02 N NaOH contain absorption bands that are absent in the spectrum of the polyaldehyde but are similar to the bands observed in the spectra of the initial heterocycles (see table).

Heterocyclic polyaldehyde compounds were characterized by the degree of substitution C_s (number of heterocyclic fragments per monosaccharide unit), which was calculated from the results of elemental analysis; the reactivity of DPA and aminopyrimidines was judged from the degree of conversion of aldehyde groups C_{ca} (%), which was calculated by the formula

$$C_{ca} = (C_s / C_{sa}) \times 100.$$

The conditions for incorporation of aminohydroxypyrimidines in the polyaldehyde molecule were determined from data on the influence exerted by the reaction temperature and time and by solution pH on the degree of substitution in reaction products of DPA and 6-aminouracil (Figs. 1a, 1b).

As expected, the number of heterocyclic fragments in the reaction products of DPA and 6-aminouracil grows from 0.01 to 0.58 mol mol^{-1} as the temperature is raised from 20 to 80°C. However, the temperature dependence of the degree of substitution reflects not only the increase in the reactivity, but also, probably, the fact that the solubility of 6-aminouracil in water and, hence, its concentration in solution grow with temperature (Fig. 1a).

With the solution pH increasing from 4 to 10.2, the degree of conversion of DPA aldehyde groups in the reaction with 6-aminouracil grows virtually linearly from 1.4 to 63.6%. This trend is apparently related to ionization of 6-aminouracil, formation of soluble anionic species, and increase in its concentration in the solution.

At 20°C, the conversion is low even at long reaction times (Fig. 1b); the curve of conversion vs. time flattens out, with the limit of 21.1% reached in 45 h. At 50°C, the content of heterocyclic fragments in the polysaccharide aldehyde increases considerably more rapidly: the conversion reaches 65% in 24 h.

Positions of bands in the electronic absorption spectra of aminohydroxypyrimidines and heterocyclic polyaldehyde derivatives (HC–DPA) (2×10^{-4} M solutions of substances in 0.02 N NaOH)

Amine	λ_{max}, nm	
	free amine	HC–DPA
5-Aminouracil	216, 288	216, 290
6-Aminouracil	216, 264	216, 268
2-Amino-4,6-dihydroxypyrimidine	208, 258	210, 262

As shown previously [4], with amine taken in the reaction with DPA in an amount exceeding 3 mol per mole of aldehyde groups, the degree of substitution does not increase further. Furthermore, large excess of 6-aminouracil is not appropriate because of its low solubility in water.

The results obtained allowed us to choose the best conditions for the reaction of DPA with 6-aminouracil: 80°C, 2 h, pH 10, and molar ratio of the amine to aldehyde groups 3 : 1. However, even under these conditions, the degree of conversion of the aldehyde groups does not exceed 87%, which may be due to side reactions of the polyaldehyde in alkaline solutions, which make smaller the amount of aldehyde groups capable of reacting with the heterocyclic compound. When DPA was kept under these conditions in the absence of 6-aminouracil, the content of aldehyde groups in DPA decreased approximately by half.

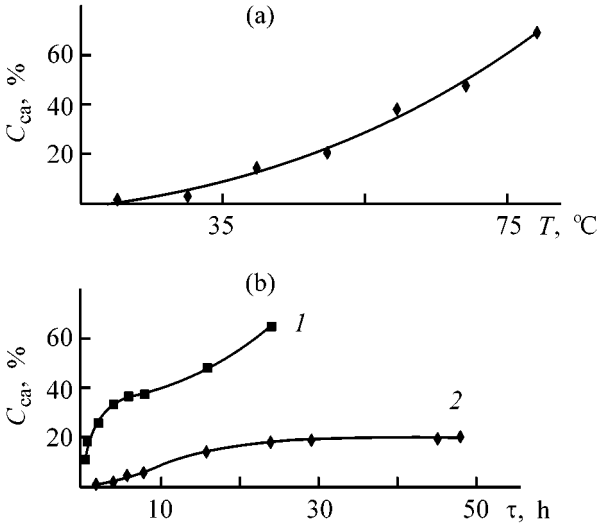

Fig. 1. Degree of conversion C_{ca} in reaction of 6-aminouracil with DPA vs. (a) temperature T and (b) time τ at (*1*) 50 and (*2*) 18–20°C.

Experiments on modification of DPA under these conditions with 5-aminouracil, 2-amino-4,6-dihydroxypyrimidine, 6-methyluracil, and uracil showed that 5-aminouracil is appreciably more reactive than 6-aminouracil (C_{ca} = 92%), 2-amino-4,6-dihydroxypyrimidine is less reactive (C_{ca} = 23%), and 6-methyluracil and uracil do not react with DPA at all under these conditions. This fact suggests that, under these conditions, aminouracils react with DPA via the amino group.

CONCLUSION

Dextran polyaldehyde can be modifed with aminohydroxypyrimidines. Its reactions with 5- and 6-aminouracils (80°C, 2 h, molar ratio of amine to aldehyde groups 3 : 1, pH 10) allow binding of up to 0.79 mol of the heterocyclic compound per monosaccharide fragment.

REFERENCES

1. *Methods in Carbohydrate Chemistry,* Whistler, R.L. and Wolfrom, M.L., Eds., New York: Academic, 1962–1965.
2. Houben–Weyl, *Methoden der organischen Chemie,* vol. 2: *Analytische Methoden,* Stuttgart: Thieme, 1953.
3. Iozep, A.A., Suvorova, O.B., Iozep, L.I., and Passet, B.V., *Zh. Prikl. Khim.*, 1998, vol. 71, no. 11, pp. 1859–1863.
4. Suvorova, O.B., Study of Reactions of Polysaccharides with *S*- and *N*-Nucleophiles, Aimed at Development of New Biologically Active Substances, *Cand. Sci. Dissertation,* St. Petersburg, 1999.

Russian Journal of Applied Chemistry, Vol. 75, No. 4, 2002, pp. 683–684. Translated from Zhurnal Prikladnoi Khimii, Vol. 75, No. 4, 2002, pp. 697–698.
Original Russian Text Copyright © 2002 by Morachevskii.

Vladimir Vladimirovich Skorchelletti (To the Centenary of His Birthday)

Vladimir Vladimirovich Skorchelletti, a scientist and lecturer, made a major contribution to investigations of corrosion and corrosion protection of metals and to improvement of teaching of theoretical electrochemistry and fundamentals of metal corrosion. For many years he was a member of the Editorial Board of *Zhurnal Prikladnoi Khimii* (Russian Journal of Applied Chemistry).

V.V. Skorchelletti was born on May 17, 1902, in Odessa but lived in St. Petersburg from childhood. His father was a shipbuilding engineer and technical director of Baltiiskii plant, and his mother, an opera soloist at Mariinsky Theater. Having completed his secondary education in 1920, Vladimir Vladimirovich entered the mining faculty of the Mining Institute. At those years, such known scientists as N.S. Kurnakov, N.I. Stepanov, N.P. Aseev, and K.F. Beloglazov were among professors of this oldest institution of higher education. Skorchelletti's labor activities started after he graduated from the institute in 1925 and were originally associated (untill 1929) with Nevsky machine-building plant and department of shipbuilding in Leningrad. From February to December 1927, he was on a business trip to Germany where he familiarized himself with the technology of shaped steel casting at quite a number of plants.

In June 1929, Skorchelletti was invited to work at the Central Institute of Metals, established in Leningrad by that time, where he studied corrosion and chemical resistance of alloys. In 1932, he organized and headed a laboratory of metal corrosion, one of the first of this kind in the country. Skorchelletti's close scientific cooperation with A.I. Shultin (1898–1978), also a graduate of the Mining Institute (1926), proved to be rather fruitful.

Skorchelletti and Shultin's papers on chemical stability of cast iron alloyed with tin and copper, and also with antimony and copper, were published in a special collection *Voprosy khimicheskoi stoikosti splavov* (Problems of Chemical Stability of Alloys, Moscow, Leningrad: Gosmashmetizdat, 1933). The same papers discussed the stability of various kinds of alloyed cast iron used for fabrication of sulfuric acid pumps and the chemical stability of steel alloyed

with tin and copper and of steel with high content of aluminum. Already these first studies combined the high scientific level with the solution of specific applied problems.

Further development of Skorchelletti and Shultin's investigations in the field of corrosion and metal protection was reflected in their joint monograph *Khimicheskoe razrushenie metallov* (Chemical Degradation of Metals, Moscow–Leningrad: Metallurgizdat, 1934). The authors subjected to thorough critical analysis the theory of local elements, widely accepted at that time, and formulated a modern approach to corrosion as a redox reaction, whose possibility of occurrence is determined by thermodynamic properties of the system. The electrochemical mechanism of corrosion assumes that oxidation and reduction are described by characteristic relationships between potential and current, with the current expressing the rate of corrosion. The corrosion kinetics is governed by the kinetics of metal oxidation and oxidant reduction.

1070-4272/02/7504-0683 $27.00 © 2002 MAIK "Nauka/Interperiodica"

These concepts were further developed in Shultin's works and were entirely shared and supported by Skorchelletti.

The same monograph paid, for the first time, much attention to theoretical analysis and experimental verification of the law established in 1919 by G. Tammann (1861–1938), according to which the corrosion resistance of metallic solid solutions changes stepwise at compositions which are multiples of 1/8 of the least active component. Critically assessing all objections to Tammann's theory, Skorchelletti points to conditions under which the "*n*/8 law" is obeyed and mentions that Tammann's theory explains in a simple and logical way all the phenomena observed in corrosion of binary solid solutions. Also, the chemical stability of two-phase alloys is discussed.

Skorchelletti and Shultin were the first to systematize the material on chemical stability of iron alloys on the basis of the available published data and numerous investigations of their own [*Khimicheskaya stoikost' splavov na zheleznoi osnove: Spravochnaya kniga* (Chemical Stability of Iron-based Alloys: Reference Book, Moscow–Leningrad: GONTI, 1938)]. This publication had no analogues in the world literature and required vast authors' work on assessment of the chemical stability of alloys in wide variety of media, including acids, their mixtures, and alkali and salt solutions.

A large paper concerned with measurements of capacitance, transient resistance, and potentials, carried out to study the passive state of metals, was published by Skorchelletti in *Proceedings of the Second Conference on Metal Corrosion* (Moscow, 1940). Rather fine investigation techniques were employed to obtain interesting new data on properties of passivating layers.

As early as 1932, Skorchelletti began teaching at the Polytechnic Institute, and, since 1936, when the Institute of Metals was reorganized, all his scientific activities were associated with Leningrad Polytechnic Institute, where he delivered courses of general chemistry and metal corrosion, and, later, physical chemistry and theoretical chemistry. From 1941 to 1943, he was with the front-line forces.

In 1959, Skorchelletti published his fundamental work *Teoreticheskaya elektrokhimiya* (Theoretical Electrochemistry), highly appreciated by specialists and widely used as a textbook on electrochemistry. The book was twice republished in the subsequent years. Of particular interest were its chapters concerned with electrochemical kinetics and occurrence of spontaneous processes. One more book, *Teoreticheskie osnovy korrozii metallov* (Theory of Metal Corrosion, Leningrad: Khimiya, 1973), was published by Vladimir Vladimirovich in 1973.

His postwar scientific activities were associated with the most important problems of corrosion and metal protection. By means of original experiments, he studied the conditions necessary for the appearance on the metal surface of a layer of adsorbed water, which can serve as electrolyte, and demonstrated the electrochemical nature of atmospheric corrosion. Together with A.M. Borshchevskii and L.P. Baturova he continued to pay much attention to investigation of passivity of metals and alloys and conditions under which an oxidized state of the surface is formed in various media. Skorchelletti' s works put forward a new approach to corrosion cracking. He established the important role played in this process by electrocapillary phenomena changing the surface strength of a metal. The influence of various factors on the corrosion cracking of brass in ammonia solution was studied in detail (together with V.A. Zaitsev). A large number of corrosion studies was performed under Vladimir Vladimirovich's supervision by industrial request.

Skorchelletti was among those who organized publication of the first country's journal devoted to metal protection *Korroziya i bor'ba s nei* (Corrosion and Corrosion Protection) (1935–1941) and repeatedly published his works in this journal.

Before 1918, Vladimir Vladimirovich studied at May Gymnasium, one of the best men's gymnasiums in St. Petersburg, which gave to Russia dozens of outstanding persons of science, culture, and art during the period of its existence (1857–1918). Skorchelletti was a broadly educated person, fluently spoke foreign languages, and was an excellent draftsman.

For his pedagogical and scientific activities he was decorated with a number of State awards.

Vladimir Vladimirovich died of a serious disease on November 7, 1984, at the age of 82. All those who knew him, his colleagues and pupils, will preserve thankful memory of this true scientist, excellent lecturer, and exclusively modest man of principle. He devoted fifty years of his life to corrosion protection of metals—experimented, dug up parts of truth, generalized new facts, and taught the youth.

A. G. Morachevskii

Russian Journal of Applied Chemistry, Vol. 75, No. 4, 2002, pp. 685–686. Translated from Zhurnal Prikladnoi Khimii, Vol. 75, No. 4, 2002, p. 699.
Original Russian Text Copyright © 2002 by Morachevskii.

========== BOOK REVIEWS ==========

Naboichenko, S.S., *Metallurg Nikolai Baraboshkin* (Metallurgist Nikolai Baraboshkin), Yekaterinburg: Ural'sk. Univ., 2001, 584 pp.

The book is devoted to 120th anniversary of Prof. N.N. Baraboshkin's birthday, a prominent specialist in chemistry of platinum-group metals, pedagogue, and one of organizers of higher metallurgical education in the Urals.

Nikolai Nikolaevich Baraboshkin was born on October 24 (November 6, new style), 1884, in St. Petersburg; his parents originated from peasants of Moscow guberniya. After graduating from a nonclassical secondary school ("real'noe uchilishche") in 1899, he entered one of the oldest higher education institution of Russia, Empress Catherine II Mining Institute in St. Petersburg (founded in 1773). The time of his education was prolonged substantially, since Nikolai Nikolaevich participated in numerous expeditions of various purposes and also carried out scientific investigations on his own. Among N.N. Baraboshkin's teachers were such known professors as N.A. Iossa, D.P. Konovalov, I.F. Shreder, N.S. Kurnakov, and N.P. Aseev. Having graduated from the institute in the beginning of 1915, N.N. Baraboshkin went to Yekaterinburg and commenced organization of the first Russia's plant for platinum refining. By that time he had already shown himself as one of the most talented representatives of the chemical school founded by Academician Kurnakov. N.N. Baraboshkin and N.I. Podkopaev's works on analysis of platinum ore and products of its processing were widely known. N.N. Baraboshkin was the first to analyze, with exhaustive completeness, Ural placer platinum and, in particular, determined the content of ruthenium in the soluble part of platinum black sands.

The book reconstructs, on the basis of a great number of archival documents, the history of construction of the refining plant in Yekaterinburg. The plant brought, into service in 1916, produced nearly 267 tons of platinum till the beginning of 1921, despite some interruptions of operation in 1917–1918. Later, methods for obtaining other platinum-group metals: palladium (1922), iridium (1923), rhodium (1925), osmium (1927), and ruthenium (1930), were developed under N.N. Baraboshkin's supervision.

Naboichenko pays much attention to Baraboshkin's involvement in organiztion of higher education in Yekaterinburg. In October 1914, a decision was made to found the Mining Institute, and it was opened in October 1917. Already beginning in 1915, Nikolai Nikolaevich took active part in composing the curricula of the institute and providing equipment for its laboratories; he became a lecturer, and taught the assay techniques, in 1917; professor in 1919, and the dean of the Metallurgical Faculty in 1920. After opening of the Ural State University in 1921, Baraboshkin became professor of the Chair of Metallurgy of Nonferrous Metals. Later, he established the Chair of the Metallurgy of gold, platinum and less common metals and chair of the theory of metallurgical processes at the Ural Polytechnic Institute. Baraboshkin's merits in organization of training, in the Urals, of metallurgy engineers of every description are quite remarkable.

N.N. Baraboshkin actively promoted the foundation of the specialized Research Institute of Nonferrous Metals in Yekaterinburg in 1930 and was its scientific supervisor. A large number of academic and applied studies were carried out with his direct participation. Of importance for the industry of the Ural region were investigations in the field of metallurgy of nickel, copper, selenium, and arsenic.

Nikolai Nikolaevich Baraboshkin died on June 15, 1935.

The appendix to the book includes a list of Baraboshkin's works, a list of publications about the scientist, and notes his followers. Baraboshkin's son, Aleksei Nikolaevich Baraboshkin (1925–1995), academician of the Russian Academy of Sciences, had headed, over several years, the Institute of

1070-4272/02/7504-0685 $27.00 © 2002 MAIK "Nauka/Interperiodica"

High-Temperature Electrochemistry, Ural Scientific Center, Russian Academy of Sciences, in Yekaterinburg.

The author of this, undoubtedly useful book is a corresponding member of the Russian Academy of Sciences, rector of the Ural State Technical University (Ural Polytechnic Institute). He pays much attention to the history of metallurgy in the Urals. The book contains a large number of previously unpublished documents, materials from archives, recollections of persons who knew Baraboshkin, an outstanding scientist and citizen, at different times. All those who are interested in the history of science and technology, in general, and history of the modern industry of nonferrous and noble metals in Russia, in particular, will read this book with keen interest and gratitude to its author.

A. G. Morachevskii

Russian Journal of Applied Chemistry, Vol. 75, No. 5, 2002, p. 687. Translated from Zhurnal Prikladnoi Khimii, Vol. 75, No. 5, 2002, p. 705.
Original Russian Text Copyright © 2002 by the Editorial Board.

Valentin Borisovich Aleskovskii (on the 90th Anniversary of His Birthday)

On June 3, 2002, Valentin Borisovich Aleskovskii, doctor of chemical sciences, corresponding member of the Russian Academy of Sciences, honored scientist and technologist of the Russian Federation, and professor of the Chemical Faculty of St. Petersburg State University, was 90.

Valentin Borisovich graduated from the Leningrad Technological Institute (LTI) in 1937 and then worked at the same institute. In 1941–1945, he served at the fronts of World War II, and then again returned to LTI. He defended his doctoral dissertation in 1952, was rector of the Leningrad Technological Institute in 1965–1975, and headed the Leningrad State University (LGU) in 1975–1985.

Aleskovskii is an outstanding scientist in the field of solid state chemistry and technology of inorganic materials and the author of more than 450 publications, including 12 monographs and textbooks, and more than 150 inventions. Aleskovskii's investigations are mainly concerned with the nature and chemical transformations of solids, including those of highly organized substances. He created a new direction in the solid state chemistry: chemistry of highly organized substances.

The part played by Aleskovskii in the foundation and development of solid state chemistry in our country is tremendous. He organized the first chairs of chemistry of solids (LTI, 1967) and solid state chemistry (LGU, 1978). Aleskovskii is a talented teacher who has trained a group of specialists in physical chemistry of solids, who are working in our country and abroad, and created a productive scientific school "Chemistry of Highly Organized Substances." More than 25 doctors and 100 candidates of sciences are among his disciples.

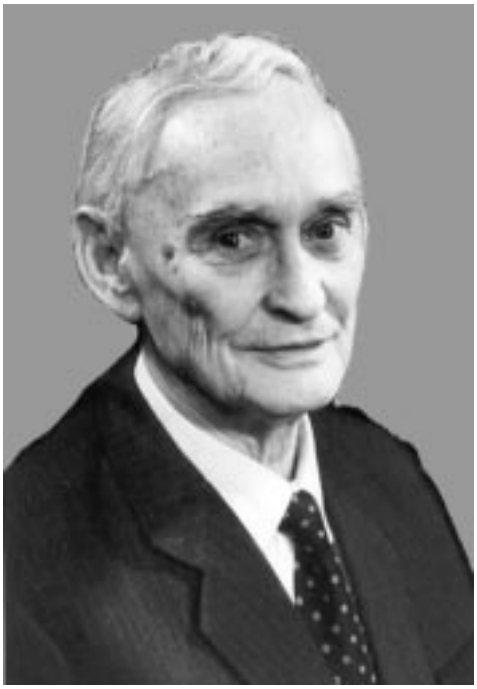

For his scientific and pedagogic activities and participation in the defense of the Motherland, Aleskovskii has been decorated with a large number of State awards and honorary titles.

We heartily congratulate Valentin Borisovich on his glorious jubilee and wish him sound health and creative longevity.

1070-4272/02/7505-0687$27.00 © 2002 MAIK "Nauka/Interperiodica"

Russian Journal of Applied Chemistry, Vol. 75, No. 5, 2002, pp. 688–695. Translated from Zhurnal Prikladnoi Khimii, Vol. 75, No. 5, 2002, pp. 706–713.
Original Russian Text Copyright © 2002 by Aleskovskii.

A Way To Develop an Environmentally Safe Technology

V. B. Aleskovskii

Abstract—It is known that the fastest way to develop environmentally safe technologies is to model natural processes. This can be done using processes of chemical assembling and self-assembling, which are, similarly to biosynthesis, processes of production and materialization of information. The previously unknown chemical-informational laws controlling these processes are considered. The notion of information is represented as a property of substance to adapt to the existence conditions via structuring under external actions.

The world community, concerned with the progressing deterioration of the environment, adopted in 1992 the "Strategy of Stable Development." However, its implementation and, in particular, taking nature-protecting measures, which require enormous expenditure, fail, nevertheless, to produce noticeable results: the technological impact on the nature builds up. An adequate survival strategy of coevolution of humans and the environment was proposed by N. Moiseev [1]. From this strategy follows that it is high time to create a technology whose processes would be harmoniously incorporated in the ecosystem of the planet. Fortunately, this is possible.

In the middle of the XX century, the influx of new knowledge virtually washed away the classical scientific picture of the world. According to Prigogine [2, p. 13], the world cannot already be regarded as a kind of museum where every bit of information is preserved. The world consists of processes destroying and generating the information and structure. These processes occur in open physical systems under joint action on the substance of flows of energy and information under conditions of strong departure from thermodynamic equilibrium. Our planet is an oasis in which "the interplay of nonlinear dynamic processes in systems of this kind very frequently leads to self-organization..." [3, p. 450]. In the course of evolution, an ideal process of substance organization, biosynthesis, was formed. The substance is structured in this process at minimum energy consumption. A major part of the substance is incorporated into the most complicated supramolecular structures, living bodies, and a minor part, into such structures as H_2O and CO_2. As is known, this is a complex process in which matrix synthesis (transcription of the genetic information) is conjugated with molecular self-assembling (translation of this information) [4].

However, some outdated scientific concepts are still alive. One of these is the concept of "nonstoichiometry," adopted in the early XX century. According to this concept, a solid substance cannot have constant stoichiometric composition because of its not being defect-free [4]. This concept could be shaken neither by the known existence of biopolymers, nor by the discovery among biosynthesis products of solid substances with constant composition (oxalates, carbonates, and phosphates, e.g., hydroxyapatites), nor even by the fact that synthesis of individual polyatomic chemical substances has been carried out and numerous researchers have successfully mastered its techniques, e.g., the method of molecular layer deposition (for a review of early works, see [5, 6]).[1]

Technologists disoriented by this concept are unaware of the fact that they have at their disposal pure, individual solid substances, together with the widely occurring substances of variable composition, which are to be freed from "impurities," i.e., unnecessary components of the corresponding solid solutions. This circumstance hinders the development of technology, and especially that of "high technology."

Individual polyatomic chemical substances (those same substances which are assumed to be nonexistent according to the above-mentioned outdated concepts) were synthesized in the early 1960s. Polymers were obtained abroad [7], and solid compounds of constant composition, in the former Soviet Union [5, 6]. About 20 years later, it was found [8] that the absence of individual polyatomic chemical substances among the surrounding substances is due to the fact that they cannot adapt to existence conditions and should be synthesized by special methods based on the same principles as biosynthesis.

(1) Molecular layer deposition and chemical assembling. In developing a catalyst for decomposition of hydrogen peroxide with a low water content

[1] Among these researchers was T. Suntola, responsible for the fact that the method of molecular layer deposition is not quite correctly termed atomic layering epitaxy (ALE).

1070-4272/02/7505-0688$27.00 © 2002 MAIK "Nauka/Interperiodica"

(1952), various functional groups (FG) were grafted to the silica skeleton of a silica gel by means of irreversible chemisorption. In this process, with the chemisorption occurring via chemical condensation, the skeleton of a sorbent (silica gel, in particular) is overbuilt with new structural units, e.g., the following:

$$\equiv Si–OH + ClSi(CH_3)_3 \rightarrow \equiv Si–O–Si\equiv(CH_3)_3 + HCl. \quad (1)$$

For process (1) to be complete, chemisorption was carried out far from equilibrium during a time sufficient for the entire surface of the sorbent to be covered with a monolayer of structural units.

A study of this process allowed understanding of the fact that "destruction in one or another way of organic groups of methylsilylated silica gel and hydration of silicon liberated in the process may presumably lead to hydrated silica with completed skeleton... And, repeating chemisorption and hydrolysis procedures, one can build up monolayer by monolayer the mass of silica" [9, p. 28].[2] Experience suggests (for a review of early works, see [10]) that deposition of monolayers of appropriate structural units on the surface of a solid in this way can produce not only silica, but also various other solids of constant composition. The deposition onto a surface of a number of identical monolayers, or a single monolayer, was termed molecular layer deposition, and synthesis of monolayers with varied composition, alternating in a prescribed sequence, was named chemical assembling [10, 11].

Molecular layer deposition (MLD) is a process of synthesis of simple substances and not-too-complex compounds and, in particular, binary compounds. This method is used, e.g., for obtaining silicon dioxide by synthesizing one its monolayer after another on the surface of pores in silica gel. For this purpose, air-dry silica gel is treated at 180°C for approximately 1 h in a flow of thoroughly purified nitrogen saturated with water vapor. As a result, the silica gel surface is completely covered with a monolayer of silanol functional groups, which gives polysilicic acid (PSA) $[SiO_2]_aOH_2$, a solid compound of constant composition, where a is the number of moles. The PSA surface is treated at the same temperature in a flow of nitrogen, bringing $SiCl_4$ vapor and carrying away hydrogen chloride, by-product of $SiCl_4$ condensation with hydrated silica gel. When this reaction is complete, which is indicated by ceased liberation of HCl, the PSA surface is completely covered with a monolayer of (≡SiCl), which gives polysilicic acid chloride, $[SiO_2]_aO_2SiCl_2$. Hydrolysis of this chloride by the same method as that used for hydration of silica gel yields a monolayer of (≡Si–OH) whose addition to the PSA skeleton transforms this solid acid into its homologue, $[SiO_2]_{a+1}OH_2$. Performing molecular layer deposition of, alternately, (≡SiCl) and (≡Si–OH) monolayers again and again, one can synthesize a silicon dioxide layer of desired thickness with hydrated surface, which is one of higher homologues of polysilicic acid, $[SiO_2]_{a+n}OH_2$, where n is the number of moles equal to the number of MLD cycles. An MLD cycle consists of a pair of solid-state or, more precisely, supramolecular chemical reactions: condensation of completely hydrated silica gel, $[SiO_2]_aOH_2$, with silicon tetrachloride [reaction (2)] and condensation of the product formed in reaction (2) with water molecules [reaction (3)]:

$$[SiO_2]_aOH_2 + SiCl_4 \rightarrow [SiO_2]_aOSiCl_2 + 2HCl, \quad (2)$$

$$[SiO_2]_aOSiCl_2 + H_2O \rightarrow [SiO_2]_aOSi(OH)_2 + 2HCl. \quad (3)$$

The MLD technique has been used to obtain quite a number of simple solid substances and solid compounds of constant composition, and also their isomers, including polymorphic modifications.

Nanostructures reproducible with atomic precision, including $(SiO_2)_m/Si_n$ nanostructures differing in the number n of silica monolayers, have been synthesized for the first time [10]. Such a structure is a single crystal of silicon on whose faces is deposited, by the MLD method, a silicon–oxygen layer of a precisely known thickness (10 nm). The thickness of the layer synthesized was determined ellipsometrically. Measurements of the thickness of the silicon dioxide layer synthesized in 10, 20, 30, 40, 50, and 60 cycles (2) + (3) demonstrated that synthesis of the given layers proceeds with quite satisfactory reproducibility. For example, it was found by measuring the layer thickness in five sets of samples obtained after 50 MLD cycles that its deviation from the average value (equal to 4.25 nm) is ±0.1 nm. As expected, the thickness of layers in the set of samples linearly depends on the number of MLD cycles.

Chemical assembling (CA) is done by alternating in a prescribed sequence cycles of molecular deposition of monolayers of different compositions. This gives solid compounds with both periodic and nonperiodic regular structure. Synthesis by CA is carried out following a program that sets the number and alternation sequence of different cycles, their duration,

[2] This casual mention in [9] was actually the first published report on chemical assembling.

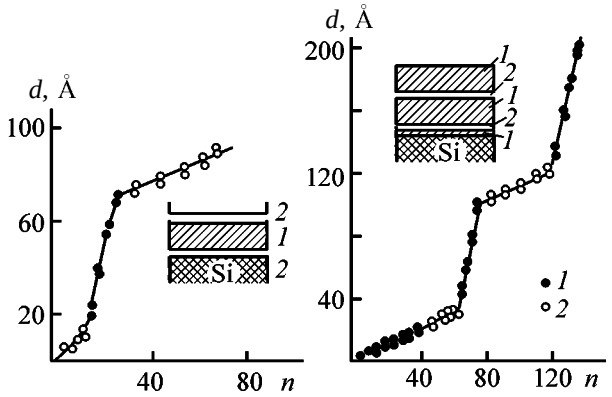

Fig. 1. Thickness d of synthesized layer vs. number n of MLD cycles. Layers: (*1*) TiO_2 and (*2*) SiO_2.

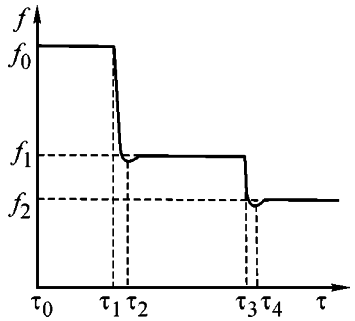

Fig. 2. Variation of the oscillation frequency f of a quartz resonator with time τ during an MLD cycle.

and thermodynamic and physicochemical conditions of synthesis. This technique has been employed to synthesize quite a number of individual solid chemical substances. For example, phosphorus and titanium chlorides and water were used to obtain all the 14 different nanostructures that can be constructed from four phosphorus–oxygen (P) and titanium–oxygen (T) monolayers: TTTP, TPTT, TTPP, etc. Their study demonstrated that the composition and properties, e.g., solubility and catalytic activity, of products composed of the same number of the same structural units T and P, but alternating in different order, are not identical. The products whose outer layer consisted of P structural units exhibited virtually zero catalytic activity in hydrolysis of CCl_4, whereas structures with outer layer composed of T units were exceedingly active. Measurements of the contact potentials of nanostructures of the given type, grown on a silica or titania substrate, revealed that the contact potential decreases as the number of layers constituting this substrate increases to 6–8 monolayers for silica and 4 monolayers for titanium oxide, and then remains constant.

Synthesis of individual complex supramolecular chemical substances is conducted by the program specifying the starting compounds, reactions, procedures, synthesis mode, and, in the first place, the sequence of MLD cycles. The formation in the course of chemical assembling of a multilayer structure of total thickness d is described by the equation

$$d_n = d_1n_1 + d_2n_2 + \ldots + d_in_i, \qquad (4)$$

where d_n is the nanostructure thickness, d_i is the thickness of a monolayer in ith layer, n_i is the number of MLD cycles necessary for ith layer to be formed, and d_in_i is the thickness of ith monolayer belonging to the given nanostructure.

The thicknesses d_1, d_2, …, d_i of monolayers composed of different structural units (silica and titania) are unequal, and, therefore, the slope angles of portions of the $d = f(n)$ curve with the n axis (α_1, α_2, …, α_i), given by the dependence $\tan\alpha = d/n$, are not equal either.

As expected, the plot of the dependence $d = f(n)$ (Fig. 1) is a broken curve with slopes of its separate linear portions and thicknesses of the corresponding layers of different compositions exactly equal to the values predicted theoretically and, at the same time, known from crystal chemistry. The coincidence of slopes for TiO_2 and SiO_2 layers, observed in the initial portion, indicates that the structure of the first monolayers coincides with the structure of the silica matrix.

Chemical assembling is rather slow, for obvious reason, under atmospheric pressure, and much faster under conditions of dynamic vacuum. "Dynamic synthesis" of chalcogenide nanostructures (including superlattices) composed of monolayers of cadmium and zinc sulfides and selenides is performed as follows [11, 12]. Ultrapure dimethyl- or diethylzinc and dimethylcadmium are taken. Substrates are prepared from mica, indium antimonide or arsenide, fused silica, or single-crystal silicon. Silicon wafers are treated first plasmochemically and then with hydrogen fluoride vapor. Arsenide or antimonide wafers are cleaned with 3% solution of bromine in methanol and then washed with ethanol. The synthesis is carried out at 290–300 K, pressure of 500 Pa, exposure of 5–10 s, and cycle duration of chemical assembling equal to 2 min.

The synthesis is commenced with substrate saturation with hydrogen sulfide and continued as follows: evacuation to 10^{-2} Pa, initial instant of time τ_0 (Fig. 2); admission of an organometallic compound of zinc or cadmium at a pressure of 500 Pa, initial instant of time τ_1; evacuation of gaseous reaction prod-

ucts and excess amounts of reactants to 10^{-2} Pa, initial instant of time τ_2; admission of hydrogen sulfide at 500 Pa, 5–10 s, initial instant of time τ_3; and evacuation to a pressure of 10^{-2} Pa, initial instant of time τ_4.

The thickness of the layers being synthesized is determined in the course of synthesis ellipsometrically and, simultaneously, found from the mass gain measured using a quartz resonator. This method is used to construct precision superlattices. Their parameters (thickness D; number of periods k; number of monolayers of different compositions, n and m; and monolayer thicknesses d_1 and d_2) are specified by the program

$$D = k(nd_1 + md_2). \quad (5)$$

St. Petersburg scientific school has synthesized by the method of chemical assembling films of diamond, silicon, silicon dioxide, and complicated supramolecular solid compounds of constant composition, e.g., various polypyrosilicic acid derivatives, of the type of iron(III) oxychloride pyrosilicate $[SiO_2]_{a-1}[OSi\cdot(OFeCl_2)_2]_{1-n}(OSiO)_n$, and many others [11, 12].

Smirnov [13] considered the chemistry of nanostructures. Malygin [14] laid foundations of the technology of chemical assembling of materials, and Alekhin [15] developed chemical and process principles of nanostructure synthesis.

(2) Principles of chemical treatment. The main specific feature of synthesis by chemical assembling is that it is programmed: reactions alternate in a prescribed sequence and occur in an open system during a time necessary for their full completion [11, 16]. As also in the case of catalysis, a solid reactant plays here an exceedingly important part of a stationary phase. A flow of reactants along the surface of a solid makes this solid-state process irreversible, with the surface serving as a matrix for assembling of the target product on it and, simultaneously, as a quantum and electron exchanger, thermostat, and heat exchanger discharging into the environment the energy released in the process. As already mentioned, the synthesis program specifies the starting substances and reactants and sets thermodynamic and other conditions under which reactions and procedures are carried out.

(3) Chemical self-assembling and assembling of polyatomic units. J.M. Lehn and D.J. Cram, followers of Pedersen's scientific school, developed a method for synthesizing highly organized individual chemical substances, which is based on intermolecular

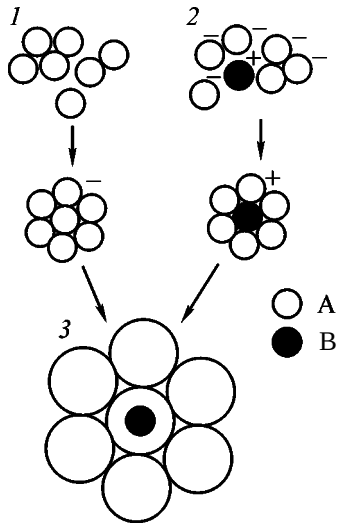

Fig. 3. Scheme of liquid-phase synthesis of quaternary supramolecular structures (*3*) from sols of structured globules (*1*) A and (*2*) B.

interaction of complementary molecules and macromolecules, method of autoensembling, and that of molecular self-assembling, similar to the homonymous biosynthesis process. The mutual complementarity of properties, structures, and forms, ensuring the "recognition" and linkage of complementary structural units in the very first collision in thermal motion, is specified by the information contained in them.

This method was applied in [17] to obtain polymolecular ensembles as models of electronic, photonic, and ionic devices. A number of chemical models of natural prototypes, from ion-conducting channels to artificial cells, have been created.

The method of "unit assembling," which combines chemical assembling and molecular self-assembling, has been proposed for synthesizing particularly complex structures. Nanoglobules of, e.g., Aerosil doped, if necessary, with one or another substance (compound of nickel, iron, etc.) are coated by the method of chemical assembling in a prescribed sequence with doped layers of thickness ranging from one to tens of nanometers, composed of monolayers of different compositions. This gives structured nanoglobules in the form of various nanostructures. These nanounits are used to obtain, e.g., by the sol–structure method, similar to the known sol–gel method, ultracomplex and, in particular, quantum structures (Fig. 3).

Linkage of polyatomic units with one another by the method of "chemical welding" [12] gives various precision nanodevices.

(4) Structural organization of substance. As is known, the substance is an hierarchical multilevel dynamic system of interacting structural units composed of lower-rank structural units, in their turn constituted by even lower-rank structural units consisting of subunits, etc., to particles of incredibly small size (on the order of 10^{-33} cm). All substances consist of atoms and are at one of the following three structural levels: molecular, supramolecular (prebiotic), or biological. In contrast to substances of the first and third kinds, which are chemically individual substances, supramolecular substances occur only as solid solutions.

It was shown in [8] that formation of an individual chemical substance is rather unlikely, and that of individual polyatomic substances (polymers and solids of constant composition), even exceedingly unlikely.

Low-molecular-weight, i.e., low-atomic compound AB is obtained in the individual state when reactants A and B are taken in a certain excess and their residual amounts are removed from the reaction sphere and the equilibrium is thereby shifted to the right, toward AB formation. However, if the reaction product is a polyatomic high- or supramolecular substance, then an inseparable mixture of all innumerable compounds composed of A and B and also their isomers and homologues, rather than a single compound, is formed in the equilibrium process. In this case, the structural units contained in a supramolecule (solid) being synthesized should be dosed and linked in certain order. The point is that a multitude of N compounds, rather than a single compound, can be formed in chemical synthesis from n atoms of m elements. In the process, the probability of formation of one of these compounds, namely, an individual chemical species of interest for us, depends on the number N, given by the rules of combinatorial analysis:

$$N \cong m^n. \tag{6}$$

The number N is small for low-atomic, low-molecular-weight compounds, and exceedingly great for polyatomic (high- and supramolecular) compounds. For example, for hydrocarbon $C_{34}H_{66}$, comprising 100 atoms, $N \approx 2^{100} \approx 10^{30}$. Thus, the number of possible synthesis products depends both on the number of atoms of the elements constituting the target product and on the number of these elements, i.e., on the extent to which this individual substance is polyatomic. As follows from S. Shchukarev's observations [18], each supramolecular compound is a member of a vast family including all innumerable compounds of those same elements which constitute the given individual chemical substance, together with isomers and homologues of all these compounds. With the exception of comparatively scanty low-molecular-weight analogs and homologues, all of them have identical properties, being, therefore, formed simultaneously as mixture of compounds in the form of a solid solution. The probability of formation in the course of chemical synthesis of a mixture of all the possible N products is unity:

$$P = N/N = 1. \tag{7}$$

The probability of formation of one of these in individual state is given by

$$P_i = 1/N. \tag{8}$$

Only simple substances are formed with probability equal to unity, since, in this case too, $N = 1$ and

$$P = 1/N = 1/1 = 1. \tag{9}$$

Thus, the probability P_i of formation of an individual chemical substance is the lower, the larger the number N of chemical compounds that can be formed from the given number of atoms of the given elements. And, since this number is incredibly enormous for individual polyatomic substances, the probability of formation of individual high- and supramolecular substances approaches zero; the probability of formation of a mixture of isomorphic compounds is unity. That is why only low-molecular individual compounds are produced in chemical synthesis, with the corresponding mixtures, imaginary compounds of variable composition, formed instead of individual high- and supramolecular compounds. At the same time, not only polyatomic chemical compounds, but also much more complex biological products, whose appearance is seemingly utterly incredible, are continuously formed in cells of any organism. The secret of biosynthesis is known: information is produced in its course. But what the problem at hand has to do with information?

According to Shannon's theory, the quantity of information contained in a text depends on the probability of its formation from the symbols constituting this text. This theory formed a foundation of informatics, which studies the laws and methods of accumulation, processing, and transmission of information. This information is drawn from the knowledge acquired by studying the nature. However, information can also be obtained directly in structuring processes. It is important that this opens up a possibility of

shifting the focus of acquisition of new knowledge to structuring processes, with any amount of information extracted directly in synthesis processes. This was made clear by an analysis of data obtained in studying the mechanism of biosynthesis, and also by a certain development of the theory.

(5) Complementary theorem. Prigogine established (1947) that, under external conditions hindering the attainment of equilibrium by a system, the steady state of the system corresponds to the minimum production of entropy. Under the action of a sufficiently high-power flux of energy, the substance of the nonequilibrium system acquires a dissipative structure, which is dynamic and disintegrates when these conditions disappear for gases and liquids, and stationary, preserved when an external action is terminated, for solids.

According to Prigogine [2], the dissipative structure appearing when a system attains the steady state is a random structure, one of the innumerable multitude of structures whose formation is possible with the same probability at the bifurcation point. At present, in view of the theory of structural organization, it is seen that this is not the case.

As is known, the quantities of information and entropy are related by

$$I + S = \text{const.} \quad (10)$$

Relation (10) is a universal law according to which the corresponding amount I of information is produced simultaneously with entropy S, with a decrease in entropy necessarily entailing an increase in the quantity of information. Since $S = 0$ and $I = 1$ in full order, const = 1. Thus,

$$I + S = 1. \quad (11)$$

At $S_{\min}$

$$I_{\max} = 1 - S_{\min}. \quad (12)$$

When the entropy produced in the given process falls to a minimum and the quantity of information produced reaches a maximum, a structure is formed. In this case, the entropy is conveyed to the medium and the information is imparted to the substance, forming its structure.

The production of entropy in this process is a result of decoherentization of the energy flux acting upon the substance. Another result is the saturation of substance with information brought from the outside by this flux. Hence follows that the structure appearing in the given process at the bifurcation point is not accidental, as it follows from the theory of self-organization, but is programmed by the information brought by the flux generating the given structure. If this is the case, then the major factor in the formation of dissipative structures is information, and not entropy (indicated as a key parameter by Prigogine's thermodynamic theorem).

(6) What is information? By information is understood the quantity of information contained in any object of interest for us: text, solid (supramolecule), etc. There exists a mathematically exact definition of information, but here "we deal with just the numerical expression of the volume of information, irrespective of its conceptual content" [3, p. 431]. The meaning of the notion of information is revealed by the theorem presented above. It follows from this theorem that information is a property of substance to adapt to the existence conditions.

The information and structure both appear and disintegrate together. Thus, the structure and information are a single whole. A decrease in entropy production to a minimum in the course of structuring indicates that, when the system passes to a steady state, the degradation of energy acting upon the system decreases, i.e., the "energy conductivity" of the system increases as a result of dissipative structuring. This means that, being structured and saturated with information, the substance belonging to the given system accommodates itself to the changing conditions. In other words, the ability to interact with the medium, to condense, to undergo polymorphic transitions, and to evolve in general, is imparted to the inert matter by the information contained in it.

All the existing things, from the universe to each newly discovered "elementary" particle (quantum of radiation), have structure and, consequently, contain information. The structure is the "flesh" of the substance, and information is its "soul," i.e., something programming in a literal sense the existence of the substance. True, information differs, as heaven from earth, from Aristotle's entelechy enveloped in dense mystical fog. It suffices to say that, as also the substance itself, information can well be described scientifically. It is discrete and diverse, similarly to the substance itself.

Phase transformations of a substance result from its saturation with different portions of information. The structure and properties of a substance change stepwise at certain critical amounts of information. For example, a laminar flow becomes turbulent at a certain Reynolds number, acquiring a more complex

vortex structure, which contains an increased amount of information, and new properties, e.g., the property to centrifuge suspensions.

The property of a substance structured under external action and saturated with information to adapt to the existence conditions and give birth to alike is inherent in all kinds of substance, including radiation, but is manifested only in interaction of appropriate carrier and detector of information. Formation of dissipative structures is no exception. Production of entropy in this process is a result of decoherentization of the energy flux acting upon the substance and saturation of the substance with information brought from the outside. Hence follows that the structure appearing in the given process at the bifurcation point is not accidental, as follows from the theory of self-organization, but is programmed by the information brought by the flux generating the given structure. Generally speaking, information generates information, and structure gives birth to structure. For example, it is known that the information produced in the course of biosynthesis is generated by genetic information.

Matter quanta of increasing mass, structural units of substance of increasing rank, are elementary particles, atoms, molecules, supramolecules, cells, and living bodies. The last kind of structural units appeared after structures (cells) gained the capacity to reproduce, and the history of living, biological individuals began. However, in order to exist, individual polyatomic chemical species must possess a much greater amount of information than low-atomic species. The latter, even if these are compounds of the same elements, e.g., H_2O and H_2O_2, do not loose completely their individuality when mixed with one another because of their having distinctly different properties. They can be separated without using chemical methods. Polyatomic chemical species are a different matter. Each of them is a member of an unimaginably vast family of compounds consisting of atoms of the same elements bound in different ratios (having different compositions) and also their innumerable isomers and homologues. By virtue of the law of degeneracy of large quantities, these species have nearly, or exactly the same properties and are, therefore, formed as families, in closest mixture with one another. These are the solid solutions which are recognized as "nonstoichiometric compounds" surrounding us. The probability of formation of any individual polyatomic compound tends to zero. To raise it to unity, it is necessary to produce a sufficiently large quantity of information in the course of synthesis. We could not conjecture this before making closer acquaintance with biosynthesis and becoming aware of the fact that chemical assembling and self-ensembling, artificial processes for synthesis of individual polyatomic chemical substances, are, similarly to the corresponding biological prototypes, processes for production and materialization of information.

(7) Way to create an environmentally acceptable technology. Synthesis of individual polyatomic chemical substances is becoming a matter of routine. Maybe it is high time to go further: start to create processes for synthesis of living substance? And this substance must not necessarily be organic, since the main indications of life are individuality of substance and its ability to reproduce, preserved over generations. Consequently, it is necessary to synthesize individual superpolyatomic chemical substances saturated with a sufficiently large amount of information, equal to [19]

$$I = \log_2 N, \tag{13}$$

where N is very large quantity whose order can be readily found by formula (6).

However, there is one more, no less important, but more topical, vitally important task. Here, we are dealing with the development—instead of the existing, actually destructive technology, using only rich raw materials, deadening the soil, water, and atmosphere with wastes and discharges—of a new chemical-informational technology whose processes would be harmoniously included in the ecosystem of the planet.

As predicted by Frenkel [20], the creation of such a technology will apparently be based on imitation of living systems and be implementation of principles of molecular cybernetics. As far back as the 1970s, he demonstrated that synthesis processes are described by a hyperbolic dependence of the amount T of work expended in them on the quantity I of information produced in these processes, i.e., IT = const. It is owing to this dependence that biosynthesis, a process in which, in principle, unlimited quantities of information are generated, occurs under exceedingly mild conditions with extremely high efficiency.

A limited amount of genetic information introduced by DNA chains in biosynthesis is transcribed, translated, and multiplied, being imparted in the course of self-assembling of protein molecules to the substance of biological tissues at a minimum expenditure of energy. It may be assumed in this connection that the technology based on the biosynthesis principles will be low-temperature liquid-phase programmable technology with completely utilizable wastes.

It is apparent that, even if the entire mankind occupied itself with invention, it would not develop anything more perfect and, at the same time, simpler than that created by nature. Therefore, it would be necessary to make it a rule to create anything new and complex following the natural samples, using processes of production and materialization of information and programming them with appropriate genetic information transferred, when necessary, by the chemical assembling method (replication) from one or another natural carrier to artificial matrices.

The solution of these problems is ensured by the development of the information theory [21–23] and chemistry of highly organized substances [24], and by investigations of the physicochemical aspect of the theory of information and chemical informatics.

Thus, a way to develop processes harmoniously incorporated in the ecosystem of the planet has been outlined.

ACKNOWLEDGMENTS

The author is deeply grateful to his dear colleagues, members of the scientific school of the chemistry of highly organized substances, for fruitful collaboration. The study was supported by the Russian Foundation for Basic Research (project no. 00-15-97356).

REFERENCES

1. Moiseev, N.N., *Vopr. Filosof.*, 1995, no. 1, pp. 1–30.
2. Prigogine, I., *From Being to Becoming: Time and Complexity in the Physical Sciences*, San Francisco: Freeman, 1980.
3. Kadomtsev, B.B., *Usp. Fiz. Nauk*, 1994, vol. 164, no. 5, pp. 449–530.
4. *Khimicheskaya entsiklopediya v 5 tomakh* (Chemical Encyclopedia in 5 vols.), Knunyants, I.L., Moscow: Sov. Entsiklopediya, 1995, vol. 1, p. 253; vol. 4, p. 79.
5. Aleskovskii, V.B., *Zh. Prikl. Khim.*, 1974, vol. 47, no. 10, pp. 2145–2157.
6. Aleskovskii, V.B., *Vestn. Akad. Nauk SSSR*, 1975, vol. 6, pp. 48–52.
7. Merrifield, R.B., *J. Am. Chem. Soc.*, 1963, vol. 85, pp. 2149–2167.
8. Aleskovskii, V.B., *Vestn. Sankt-Peterb. Gos. Univ., Ser. 4*, 1992, issue 4, no. 25, pp. 75–76.
9. Kol'tsov, S.I. and Aleskovskii, V.B., *Silikagel', ego stroenie i svoistva* (Silica Gel, Its Structure and Properties), Leningrad: Goskhimizdat, 1963.
10. Aleskovskii, V.B., *Stekhiometriya i sintez tverdykh soedinenii* (Stoichiometry and Synthesis of Solids), Leningrad: Nauka, 1976.
11. Aleskovskii, V.B., *Khimiya nadmolekulyarnykh soedinenii* (Chemistry of Supramolecular Compounds), St. Petersburg: Sankt-Peterb. Gos. Univ., 1996.
12. Aleskovskii, V., *Macromol. Symp.*, 1998, vol. 136, p. 1.
13. Smirnov, V.M., *Khimiya nanostruktur: Sintez, stroenie, svoistva* (Chemistry of Nanostructures: Synthesis, Structure, and Properties), St. Petersburg: Sankt-Peterb. Gos. Univ., 1996, p. 108.
14. Malygin, A.A., *Napravlennyi sintez tverdykh veshchestv* (Directed Synthesis of Solids), Aleskovskii, V.B., Ed., Leningrad: Leningr. Gos. Univ., 1987, issue 2, pp. 32–59.
15. Alekhin, A.P., Chemical and Process Principles of Low-Temperature Formation of Insulator–Semiconductor Interfaces, *Doctoral Dissertation*, Moscow, 1999.
16. Aleskovskii, V.B., *Khimiko-informatsionnyi sintez: Nachatki teorii. Metody* (Chemical-Informational Synthesis: Fundamentals of the Theory. Methods), St. Petersburg, 1998.
17. Lehn, J.M., *Supramolecular Chemistry*, New York: VCH, 1995.
18. Shchukarev, S.A., *Vestn. Leningr. Gos. Univ.*, 1947, no. 5, pp. 5–25.
19. Kolmogorov, A.N., *Teoriya informatsii i teoriya algoritmov* (Theory of Information and Theory of Algorithms), Moscow: Nauka, 1987.
20. Frenkel, S., *Sov. Sci. Rev.*, 1971, March, pp. 110–118.
21. Zhdanov, Yu.A., *Entropiya informatsii v organicheskoi khimii* (Entropy of Information in Organic Chemistry), Rostov-on-Don: Rostov. Univ., 1979.
22. Klimantovich, Yu.L., *Usp. Fiz. Nauk*, 1999, vol. 169, no. 4, pp. 443–452.
23. Bal'makov, M.D., *Usp. Fiz. Nauk*, 1999, vol. 169, no. 11, pp. 1273–1279.
24. Aleskovskii, V.B., *Zh. Prikl. Khim.*, 1997, vol. 70, no. 6, pp. 994–1001.

Russian Journal of Applied Chemistry, Vol. 75, No. 5, 2002, pp. 696–699. Translated from Zhurnal Prikladnoi Khimii, Vol. 75, No. 5, 2002, pp. 714–717.
Original Russian Text Copyright © 2002 by Tolchev, Pervushin, Kleshchev.

INORGANIC SYNTHESIS AND INDUSTRIAL INORGANIC CHEMISTRY

Thermal Transformations of Hydrated Titanium Dioxide with a Globular Structure of Aggregates

A. V. Tolchev, V. Yu. Pervushin, and D. G. Kleshchev

Chelyabinsk State Pedagogical University, Chelyabinsk, Russia

Received December 13, 2001

Abstract—The phase and chemical transformations in hydrated titanium dioxide with a globular structure of aggregates, prepared by thermal hydrolysis of aqueous solution of oxotitanium(IV) sulfate and calcined in air at 200–1100°C, were studied. The effect of modifying additives (potassium, zinc, magnesium, and phosphorus compounds) and seed crystals of rutile-like structure on the kinetics and temperature of the polymorphous transition of anatase into rutile, morphology of crystals, and particle size of the resulting product was studied.

In a sulfate method of synthesis of titanium dioxide pigment of anatase and rutile modifications, hydrated titanium dioxide (HTD), which was obtained by thermal hydrolysis of titanium(IV) sulfate solutions, is calcined at ~900°C in air [1, 2]. HTD samples prepared in open reactors at atmospheric pressure by standard procedure have the empirical composition $TiO_2 \cdot xSO_3 \cdot nH_2O$, with x and n depend on the hydrolysis conditions, and are finely crystalline powders (crystal size 10–20 nm [2]) tending to the form dense irregular polydispersed aggregates. The thermal treatment of HTD results in the dehydration, desulfation, and the anatase $\rightarrow$ rutile phase transition [2–5]. The latter two processes are accompanied by coalescence and sintering of TiO_2 crystals [6–8]. To control the phase composition and particle size of TiO_2 in HTD, the modifying additives and seed crystals (SCs) of rutile-like structure are added before calcination. Potassium, silicon, and phosphorus compounds increase the temperature of the anatase $\rightarrow$ rutile transition, whereas zinc, magnesium, and iron compounds, as well as seed crystals, act oppositely [2]. Owing to the HTD dispersity, titanium dioxide obtained by the traditional procedure is characterized by a broad size distribution of globules. This results in the deterioration of its pigment properties.

HTD obtained by thermal hydrolysis of titanium(IV) sulfate solutions at 130–170°C is a nearly monodisperse powder with a globular structure of aggregates. Its calcination should result in the formation of anatase and rutile crystals of the same shape and size.

In this work, we studied the effect of seed crystals and modifying additives on the phase transitions and chemical transformations of such HTD and on the particle size of the resulting titanium dioxide.

EXPERIMENTAL

Hydrated titanium dioxide with a globular structure of aggregates (Fig. 1) and an average globule size $D \sim 250$ nm was obtained by thermal hydrolysis of 1.25 mol g^{-1} aqueous solution of chemically pure grade oxotitanium(IV) sulfate at 130°C for 1 h. To separate the mother liquor and remove free sulfuric acid, the deposit was filtered under pressure and washed with distilled water until the absence of sulfate ions in the filtrate.

Water-soluble compounds of potassium, phosphorus, magnesium, and zinc, which are widely used

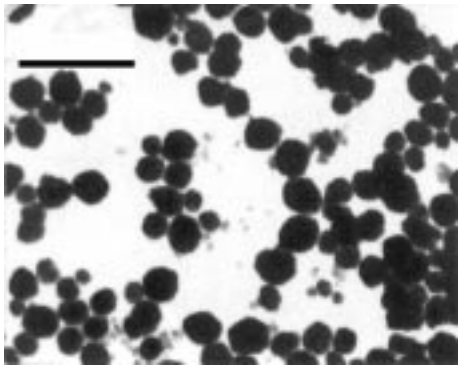

Fig. 1. Photomicrograph of the HTD sample with globular structure of aggregates, obtained by thermal hydrolysis of oxotitanium(IV) sulfate solution at 130°C. Magnification 10000. The bar corresponds to 10 μm.

1070-4272/02/7505-0696$27.00 © 2002 MAIK "Nauka/Interperiodica"

Composition of modifying additives, temperature T_1 of the anatase → rutile transition, and particle size of titanium dioxide*

Sample no.	Modifying additive, wt %**	Aggregate size, μm		T_1, °C
		anatase	rutile	
1	–	0.2–0.6 (m)	0.7–1.5	900
2	KOH, 1.0	0.2–0.4 (m)	0.7–1.5	950
3	H_3PO_4, 0.4	0.4–1.0 (m)	1.0–2.5	1000
4	KOH, 1.0 + H_3PO_4, 0.7	0.4–0.8	0.8–2.0	1000
5	KOH, 1.0 + H_3PO_4, 0.4	0.2–0.4	0.6–1.5	950
6	SCs, 2.0	0.2–0.4 (m)	0.4–0.8	800
7	$ZnCl_2$, 0.8	0.2–0.4 (m)	1.0–2.5	800
8	$MgCl_2$, 0.6	0.2–0.4 (m)	1.0–2.0	825
9	KOH, 0.8 + $ZnCl_2$, 0.8 + SCs, 1.0	0.2–0.3 (m)	0.6–1.0	800
10	KOH, 0.8 + $MgCl_2$, 0.6 + SCs, 1.0	0.2–0.3 (m)	0.4–0.8	825
11	KOH, 0.3 + $ZnCl_2$, 0.6 + H_3PO_4, 0.2 + SCs, 2.0	0.2–0.4	0.4–1.0	950
12	KOH, 0.3 + $MgCl_2$, 0.5 + H_3PO_4, 0.2 + SCs, 2.0	0.2–0.4	0.4–1.0	950

* Anatase and rutile samples were obtained by calcining HTD for 2 and 4 h at temperatures 25°C lower and higher than T_1; (m) stands for the anatase globules of mosaic structure.

** Weight percentage with respect to TiO_2 in HTD, in terms of the corresponding oxide.

for synthesizing titanium dioxide pigment of anatase and rutile modifications, were modifying additives [2]. To attain the uniform distribution throughout the sample bulk, the modifying additives in the form of aqueous solutions of KOH, H_3PO_4, $MgCl_2$, and $ZnCl_2$ (all chemically pure grade) were added to concentrated HTD suspensions with vigorous stirring. In some tests, rutile crystals, obtained by the method described in [2], were introduced into HTD suspension as a seed. The composition of the modifying additives in the HTD samples is given in the table.

The HTD samples obtained were dried at 100°C to constant mass, ground, and subjected to isothermal calcination at 200–1100°C for 0.5–5 h in air.

The phase composition and particle size of the samples were determined by X-ray phase analysis (DRON–3 diffractometer, filtered CuK_α radiation) and transmission electron microscopy (UEMV-100K electron microscope), and their chemical composition, by volumetric chemical analysis and thermogravimetry [MOM derivatograph (Hungary)]. The unit cell parameters a and c of HTD and anatase were determined from the (116) and (220) reflections with polycrystalline MgO reference (chemically pure grade). The average size of the crystals D was estimated by the Selyakov–Scherrer formula [9]. In this case, it was taken into account that, according to the approximation results [(200) and (400) reflections of HTD and (004) and (008) reflections of anatase] and the data of [3], small crystals produce the main contribution to the physical broadening β of the reflections. The degree of the phase transition of anatase into rutile was determined by standard procedure of quantitative X-ray phase analysis [10]. The determination accuracy was ±1.5 wt % at a 0.95 confidence level.

According to chemical analysis, the initial HTD sample has the composition $TiO_2 \cdot 0.035SO_3 \cdot 0.61H_2O$. The DTA curves have two broad endothermic peaks due to HTD dehydration (at 150–500°C) and desulfation (at 600–900°C).

The X-ray phase analysis showed that the initial HTD has an anatase-like structure with increased, however, unit cell parameters a and c (a = 0.31812 ± 0.0007 and c = 0.9530 ± 0.0005 nm). The average size of the HTD crystals is 16 nm. The comparison of the sizes of aggregates and crystals showed that each globule contains about 4000 randomly oriented primary HTD crystals.

In the temperature range of dehydration, the unit cell parameters of the samples monotonically decrease to the values typical of anatase [11], with the reflection half-width remaining virtually constant: a = 0.3785 ± 0.0007 and c = 0.9514 ± 0.0005 nm. The desulfation is accompanied by a sharp narrowing of all the anatase reflections, which shows that the average size of the crystals increases (16 nm at 500°C and 90 nm at 900°C). The diffraction patterns of the samples thermally treated at 900°C and above contain, along with anatase reflections, also rutile reflections.

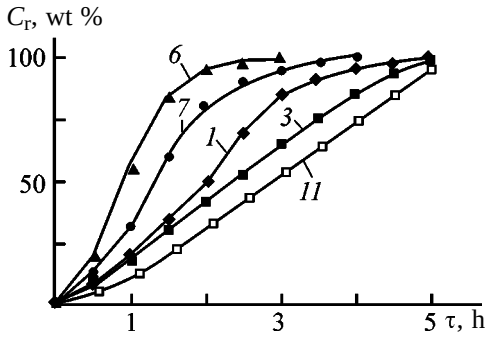

Fig. 2. Rutile content C_r in titanium dioxide vs. time of isothermal calcination τ of the HTD samples. Calcination temperature (°C): (*1*) 925, (*3*) 1025, (*6, 7*) 825 and (*11*) 975. Curve nos. are sample nos. in the table.

The rutile content monotonically increases with calcination time (Fig. 2).

No significant changes in the globule shape and size upon HTD dehydration and desulfation were revealed by electron microscopy. In the anatase sample obtained at 600°C, the globules have a mosaic structure, which confirms formation of 15-nm pores or cavities in the course of dehydration. With calcination temperature increased above 900°C, the number of defects in the globules is decreased and their average size is increased to approximately 75 nm. Upon the phase transition of anatase into rutile, the size of the titanium dioxide globules sharply increases. The photomicrographs of the rutile sample obtained at 975°C revealed the single crystals of about 0.2 μm size with the morphology close to that of the initial HTD globules. The bulk of the sample consists of irregular aggregates of up to 1.5 μm size, formed by sintering of several spherical globules.

The thermal transformations in the modified samples at $T_1 \leq 750$°C are similar to those in the initial HTD. At higher calcination temperatures, the modifiers affected the anatase coalescence and (or) the polymorphous transition of anatase into rutile, as well as the particle size of titanium dioxide (see table).

The effect produced on the HTD transformations by each individual modifier is as follows: (a) magnesium and zinc compounds, as well as seed crystals, decrease by ~100°C the temperature T_1 of the anatase → rutile transition. At the same time, they facilitate sintering of rutile crystals into dense aggregates; (b) phosphoric acid retards anatase coalescence, increases by ~100°C the temperature T_1, and promotes formation of large aggregates of anatase and rutile; (c) potassium hydroxide does not noticeably affect the size of titanium dioxide aggregates and increases by ~50°C the temperature of the rutile formation. When several modifiers producing opposite effects on the anatase → rutile transition are added into HTD simultaneously, the modifier whose individual influence is greater produces the greater effect. Note that potassium hydroxide and phosphoric acid, jointly introduced into HTD, intensify mass exchange in titanium dioxide. This is manifested in "healing" of defects in the surface layer of anatase globules, which maintain initial form and size, and also in the formation of nearly isometric rutile crystals.

Comparison of the experimental results and published data [2, 3] shows that HTD formed by thermal hydrolysis from titanium(IV) sulfate solutions has an approximately 3 times smaller water content and has the 100–150°C higher transition temperature than the samples synthesized at atmospheric pressure.

When discussing the localization of water molecules and sulfate ions in HTD and the processes occurring upon their thermal desorption, it should be noted that variations of the unit cell parameters *a* and *c* upon dehydration agree, on the whole, with the data of [3] and show that the water (or at least its part) can enter the HTD crystal. In the course of dehydration, cavities and channels appearing at the crystal boundaries owing to H_2O diffusion within the HTD globules form their pore structure, which is observed on the photomicrographs of the dehydrated samples.

It may be assumed that, according to Belov's data [12], sulfate ions are located on the surface of the initial HTD crystals and form chemical bonds stabilizing the surface layer of crystals. In the course of breakdown of sulfate ions and removal of SO_3, two types of active centers are formed on the surface of anatase crystals: Ti(III) ions and unsaturated O^{2-} radicals [13]. As a result, the surface layer becomes unstable, which facilitates the mass exchange of crystal-forming complexes between anatase single crystals (coalescence). Since at relatively low temperatures (600–900°C) the mass exchange occurs via surface diffusion [14], the coalescence can be localized within a single globule. This fact can explain why HTD globules and anatase crystals acquire a similar shape.

Unlike topochemical solid-state reactions of dehydration and desulfation [14], the phase transitions in finely dispersed systems can proceed by the dissolution–deposition mechanism [15] involving formation of nuclei of the equilibrium phase (rutile), dissolution of crystals of metastable phase (anatase), and transfer of crystal-forming complexes to rutile nuclei and their incorporation into them. Since the probability of nucleus formation is proportional to the equilibrium concentration of the crystal-forming complexes c_{cfc},

which, in its turn, varies regularly with temperature, the nucleation is the limiting stage at relatively low calcination temperatures. This can explain the decreased temperature of the anatase → rutile phase transition in the HTD samples with added seed crystals of a rutile-like structure and in those with added magnesium and zinc compounds. The latter interact with TiO_2 with formation of titanates, which, having rutile-like crystal structure, act as seed crystals [2].

The anatase → rutile transition is exothermic. The calculations performed in [6] on samples consisting of anatase crystals, which are in contact between each other, showed that the phase transition, while starts, results in an approximately 140°C overheating of the anatase crystals in the boundary layer, which intensifies the polymorphous transition within a single polycrystalline globule. Therefore, under the conditions of hindered diffusion, the configuration of the rutile crystals being formed is largely determined by the initial HTD structure, including contacts between neighboring globules, and the resulting rutile crystals have no regular morphology.

The experimental data on the effect of H_3PO_4 and $KOH + H_3PO_4$ additives on the thermal transformations of HTD and the dispersion composition of titanium dioxide can be unambiguously judged in the framework of the given model. For example, in the samples modified with phosphoric acid, phosphate ions can replace sulfate ions with the formation of stronger chemical bonds with Ti(IV) ions [2]. This decreases c_{cfc}, and, as a consequence, hinders the anatase coalescence and increases the temperature of the anatase → rutile transition. Moreover, compared to SO_4^{2-} ions, PO_4^{3-} ions can form a larger number of bonds, including those with atoms of the surface layer of neighboring globules. As a result, the size of the anatase and rutile aggregates increases. The joint introduction into HTD of potassium hydroxide and phosphoric acid yields potassium phosphates. In this case, the enhanced mass exchange in the titanium dioxide samples may be due to the formation of fusible eutectics, leading to the increase in the surface diffusion coefficient of the crystal-forming titanium(IV) complexes.

CONCLUSIONS

(1) The temperature ranges of dehydration, desulfation, and the anatase → rutile phase transition, occurring in calcination in air of hydrated tianium dioxide with globular structure of aggregates, obtained by thermal hydrolysis of oxotitanium(IV) sulfate solution at 130°C, were refined.

(2) The effect of modifying additives of potassium, magnesium, zinc, and phosphorus compounds, as well as seed crystals of rutile-like structure, on the thermal transformations of hydrated titanium dioxide and its particle size were studied.

ACKNOWLEDGMENTS

This work was supported by the Russian Foundation for Basic Research (proiect no. P 2001 URCHEL 03–03).

REFERENCES

1. Schmid, R., Mronga, N., Radtke, V., and Seeger, O., *Eur. Coat. J.*, 1997, no. 7, pp. 702–705.
2. Dobrovol'skii, I.P., *Khimiya i tekhnologiya oksidnykh soedinenii titana* (Chemistry and Technology of Oxide Compounds of Titanium), Sverdlovsk: Ural. Otd. Akad. Nauk SSSR, 1988.
3. Pervushin, V.Yu., Denisova, T.A., Tolchev, A.V., *et al.*, *Zh. Neorg. Khim.*, 1985, vol. 30, no. 4, pp. 855–859.
4. Sullivan, W.F. and Coleman, J.R., *J. Inorg. Nucl. Chem.*, 1962, vol. 24, no. 3, pp. 645–652.
5. Gannary, F. and Pasquevich, D.M., *J. Am. Ceram. Soc.*, 1999, vol. 82, no. 7, pp. 1915–1921.
6. Sheinkman, A.I., Tyumentsev, V.A., and Fotiev, A.A., *Izv. Akad. Nauk SSSR, Neorg. Mater.*, 1984, vol. 20, no. 10, pp. 1692–1694.
7. Suzuki, A., and Tukuda, R., *Bull. Chem. Soc. Jpn.*, 1969, vol. 42, no. 7, pp. 1853–1859.
8. Cladrow, E.M., and Eller, H.G., *J. Chem. Eng. Data*, 1969, vol. 6, no. 2, pp. 318–326.
9. Umanskii, Ya.S., Skakov, Yu.A., Ivanov, A.N., and Rastorguev, L.N., *Kristallografiya, rentgenografiya i elektronnaya mikroskopiya* (Crystallography, X-ray Diffraction Analysis, and Electron Microscopy), Moscow: Metallurgiya, 1982.
10. *GOST* (State Standard) *9808–84: Titanium Dioxide Pigment: Technical Specifications.*
11. *Powder Diffraction File: Search Manual, Fink Method Inorganic*, Swarthmore, 1977, card no. 21-1272.
12. Belov, N.V., *Dokl. Akad. Nauk SSSR*, 1950, vol. 71, no. 1, pp. 61–64.
13. Gusev, V.B., Kleshchev, D.G., and Kalinichenko, I.I., *Zh. Prikl. Khim.*, 1985, vol. 58, no. 1, pp. 33–36.
14. Brown, M.E., Dollimore, D., and Galway, A.K., *Reactions in the Solid State*, New York: Elsevier, 1980.
15. Kleshchev, D.G., Sheinkman, A.I., and Pletnev R.N., *Vliyanie sredy na fazovye i khimicheskie prevrashcheniya v dispersnykh sredakh* (Solvent Effect on the Phase and Chemical Transformations in Disperse Systems), Sverdlovsk: Ural. Otd. Akad. Nauk SSSR, 1990.

Russian Journal of Applied Chemistry, Vol. 75, No. 5, 2002, pp. 700–705. Translated from Zhurnal Prikladnoi Khimii, Vol. 75, No. 5, 2002, pp. 718–723.
Original Russian Text Copyright © 2002 by Reva, Vorob'eva.

INORGANIC SYNTHESIS AND INDUSTRIAL INORGANIC CHEMISTRY

Oxidation, Hydrolysis, and Colloid Formation in Storage of $SnCl_2$ Aqueous Solutions

O. V. Reva and T. N. Vorob'eva

Research Institute of Physicochemical Problems, Belarussian State University, Minsk, Belarus

Received May 7, 2001; in final form, February 28, 2002

Abstract—Oxidation of Sn(II), hydrolysis, and colloid formation in storage of acidic and alkaline $SnCl_2$ solutions were studied as influenced by various ligands. The correlation between these processes was analyzed, and the composition of the colloids and precipitates was determined.

Tin-containing solutions, among them $SnCl_2$ aqueous solutions, are used for plating with tin and its compounds. In these solutions, Sn(II) can be reduced to metal by various procedures: addition of appropriate water-soluble reductants, use of a reducing metal support, and disproportionation. These procedures allow production of protective-decorative wear-resistant and solderable coatings. The combined reduction of tin and other metals is also widely used [1–9]. Films based on SnO_2 can be prepared by a sol–gel process based on hydrolysis of tin-containing compounds. These films are used in production of selective gas sensors and liquid-crystalline indicators [10–13]. The hydrolysis of $SnCl_2$ is used also for activation of dielectric surface, with the aim of subsequent metal coating, by predeposition of discontinuous films based on tin hydroxo complexes [1–3, 14–21]. The Sn(II) compounds are oxidized with atmospheric oxygen. It was found that UV irradiation of discontinuous films, promoting their oxidation with atmospheric oxygen, results in loss of their reducing power. This effect is used for selective activation of separate sites of the support surface [14–18].

As a rule, films based on pure metallic tin and its alloys, and also tin-containing oxo and hydroxo compounds are deposited from acidic (pH 1–3) or alkaline (pH 9–12) $SnCl_2$ solutions containing tin complex ions. In these solutions, a set of complexes are formed [1–5, 19–24]. These complexes are slowly hydrolyzed to give polycondensed and polymerized species which, even at thorough adjustment of pH, are converted to colloid particles capable of coagulation and sedimentation. Depending on the rate and features of these processes, they can play either positive or negative role in both the coating with metallic tin and its alloys and predeposition of discontinuous films. Colloid particles must have definite composition, size, and concentration to obtain tin-containing films with definite characteristics. For example, if in preparation of tin hydroxide films, along with sorption of colloid particles of nanometer size, coarser particles with a size of a few tens of nanometers are also sorbed, the coating adhesion deteriorates and looser films are formed. In subsequent palladium deposition on such loose films by reduction of Pd(II) in solution, the palladium particles are distributed nonuniformly over the film surface. All these drawbacks are also typical of metallic films deposited from solutions containing nonuniform palladium particles as catalyst [1, 9, 16, 19–21]. It was found [4–6] that, in cathodic electroplating, the sorption of nanometer tin-containing colloid particles favorably changes the overvoltage and improves the film microstructure [4–6]. In sorption of coarse colloid particles formed in hydrolysis of Sn(II) on the cathode surface, loose films are formed. Under these conditions, the tin deposition is suppressed because of passivation of the growing film surface. To eliminate Sn(II) hydrolysis, various procedures were developed including not only pH adjustment, but also introduction into the coating solutions of appropriate ligands (chloride, citrate, tartrate, diphosphate, fluoride, and fluoroborate anions) [14, 22, 23] and colloid stabilizers (gelatin, polyethylenepolyamine, phenol, etc.) [5, 24].

At present, in production of tin-containing films and coatings with prescribed characteristics by their deposition from $SnCl_2$ solutions, the optimal conditions and procedures are chosen empirically. In this connection, it is important to study the effect of colloid formation, coagulation, and sedimentation on the composition of the coating solutions in their storage. These factors are poorly understood. Data on the

1070-4272/02/7505-0700$27.00 © 2002 MAIK "Nauka/Interperiodica"

composition of colloid particles and also on the effect of the storage time on the composition, size, and concentration of the colloid particles are lacking. Data on colloid formation in alkaline tin-containing coating solutions also are extremely scarce. It is known that Sn(II) is fairly rapidly oxidized with atmospheric oxygen [14, 16, 19–21, 25–27]. In the majority part of published works, the kinetics of Sn(II) oxidation was studied in hydrogen chloride solutions, and different kinetic equations were reported [19–21, 26, 27]. These equations do not take into account the fact that, simultaniously with Sn(II) oxidation, the hydrolysis of the oxidized species proceeds, which is followed by colloid formation and sorption of hydrolyzed tin-containing species on the solid surface [1, 2]. Neglect of these factors can be responsible for the discrepancy between the above-noted kinetic equations. To date, only sparse data were reported on the correlation between Sn(II) oxidation and hydrolysis, relationships of colloid formation in storage of $SnCl_2$ solutions, and factors influencing the coagulation and sedimentation of colloid particles.

Therefore, we performed a combined study of Sn(II) oxidation, hydrolysis, colloid formation, coagulation, and sedimentation in storage of both acidic and alkaline $SnCl_2$ aqueous solutions in the presence of various ligands. The correlation between these processes was studied as influenced by the composition of solutions.

EXPERIMENTAL

The compositions of $SnCl_2$ aqueous solutions used in our experiments are listed in Table 1. These solutions were placed in approximately spherical 1-l flasks, to ensure the minimal ratio of the glass surface to solution volume, and stored in the dark at $20 \pm 2°C$. The solutions were kept without stirring under conditions of free diffusion of oxygen. The oxygen concentration in the solutions was constant ($\sim 1.3 \times 10^{-3}$ M) owing to its easy transfer from air. Under these conditions, the equilibrium between the solutions and atmospheric oxygen was reached within 20 min which is considerably less than the time required for formation of detectable amounts of oxidized tin species (several hours or days). The Sn(II) concentration in solutions was determined by titration with iodine under a CO_2 atmosphere at HCl concentration of 1.5 M. This procedure ensures the tin(II) determination in amounts as small as 0.0025 M [28]. In the separate experiments, we found that this analytical procedure allows determination of Sn(II) occurring in the form not only of truly soluble species but also of colloid particles soluble in 1.5 M HCl. In determination of the total amount of Sn(II) and Sn(IV), Sn(IV) was preliminarily reduced with aluminum cuttings in a CO_2 atmosphere [29]. The relative error of Sn(II) determination does no exceed 5%. The reproducibility of the analytical results was no less than 90%. To estimate the sorption loss of tin on a glass surface, the total concentration of Sn(II, IV) was determined before and after the contact of the tin-containing solution with a glass plate for a prescribed time.

Table 1. Composition of tested solutions

Solution no.	$SnCl_2$	Medium
	c, M	
1	0.11	HCl, 0.11
2	0.11	HCl, 0.06
3	0.11	HCl, 0.11 + KCl, 1.60
4	0.11	HCl, 0.66
5	0.11	HCl, 0.66 + KCl, 1.60
6	0.22	NaOH, 1.40 + EDTA, 0.01
7	0.22	NaOH, 1.50 + $NH_3 \cdot H_2O$, 0.4
8	0.22	NaOH, 2.50
9	0.22	NaOH, 1.00 + $KNaC_4H_4O_6$, 0.28

Electron-microscopic and electron diffraction studies were carried out on an EM-125 transmission electron microscope. The specimens for electron-microscopic study of solid particles formed in the $SnCl_2$ solutions were prepared by placing a drop of the colloid solution or suspension on a collodion film. The powder electron diffraction patterns of the same samples were obtained with the electron microscope in the microdiffraction mode. The phase composition of the solid was determined from no less than four diffraction maxima at the accuracy of determination of the interplanar spacings no less than 0.01–0.02 Å. The diffractometer was equipped with a Powder Diffraction File software based on the ICPDC-89 data bank.

We found that, with increasing storage time, the Sn(II) content in $SnCl_2$ aqueous solutions gradually decreases. We believe that the main process causing the depletion of Sn(II) solution are as follows: Sn(II) oxidation, hydrolysis of tin-containing compounds, formation of tin-containing sols, coagulation, and sorption of the coagulated species on the surface of the flask walls. In storage of acidic Sn(II) solutions, the Sn(II) content rapidly decreases in the first 5–10 days, after which the tin loss becomes slower. With increasing HCl concentration, Sn(II) loss from solution decreases. The effect of the HCl concentration on the Sn(II) loss is demonstrated in Table 1. These data

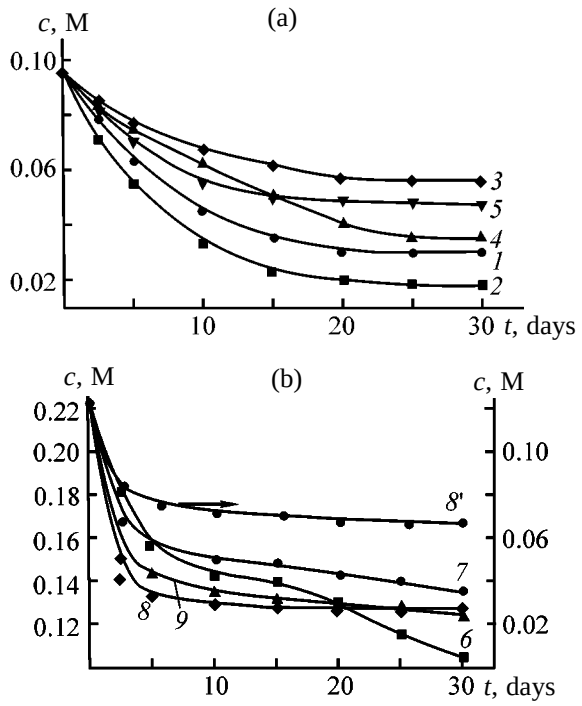

Fig. 1. Sn(II) concentration c in $SnCl_2$ solutions as a function of the storage time t. Solution: (a) acidic and (b) alkaline; the same for Fig. 2. The solution numbers (Table 1) are indicated at the corresponding curves; (*8'*) alkaline solution no. 8 with $SnCl_2$ concentration of 0.11 M.

show that, in solution no. 1, about 50% of Sn(II) was lost in the course of 10-day storage. In passing to solution no. 2 with the lowest HCl concentration, the tin loss increased to 60%. At the same time, at the maximal HCl concentration of 0.66 M (solution no. 4), only about 30% of Sn(II) was lost. We found that addition of excess KCl to $SnCl_2$ solutions decreases the Sn(II) loss to the same extent as the addition of excess HCl (solution nos. 3 and 5, Table 1). In the presence of a 15-fold excess of chloride anions introduced as KCl (solution nos. 3 and 5), the oxidation of Sn(II) in the late stage of storage (after 15–30 days) was noticeably slower than in solutions with a 6-fold excess of chloride anions introduced as HCl only. In storage of acidic $SnCl_2$ solutions containing predominantly Sn(II) aqua and hydroxychloride complexes (solution nos. 1 and 2), the average rate of the Sn(II) loss within the first five days was approximately 8×10^{-3} mol l^{-1} day^{-1}. In storage of solutions with prevalence of tin chloride complexes (solution nos. 3–5), the rate of Sn(II) loss decreased by a factor of 2.

In storage of $SnCl_2$ alkaline (solution nos. 6–9, Fig. 1b) and acidic (solution nos. 1–5, Fig. 1a) solutions, the shape of the kinetic curves and the rate of Sn(II) loss are similar. In the main part of our experiments, we used alkaline $SnCl_2$ solutions with the Sn(II) concentration twice that in the acidic solutions. The similar alkaline solutions are applied, as a rule, in production of tin films by Sn(II) dispropotionation and electroplating. Figure 1b shows that, in passing from acidic to alkaline solutions, the fast stage of Sn(II) loss is shortened by a factor of two and the loss is faster. The increase in Sn(II) loss in alkaline solutions correlates with the higher $SnCl_2$ concentration in them. The minimal Sn(II) loss occurred in storage of $SnCl_2$ solutions containing $NH_3 \cdot H_2O$ as an additive (solution no. 7). The stabilization of $SnCl_2$ alkaline solutions on addition of tartrate and ethylenediaminetetraacetate anions was insignificant. The fastest Sn(II) loss occurred in storage of $SnCl_2$ solutions within the first 10 days. The enhanced stability of Sn(II) to oxidation in acidic $SnCl_2$ solutions is caused by complexation of Sn(II) with chloride anions on addition of a 6–15 fold excess of this ligand. In alkaline solutions oxidation of Sn(II) can be eliminated by addition of a 6–7-fold excess of NaOH along with the two-fold excess of $NH_3 \cdot H_2O$.

As seen from Fig. 1, in storage of acidic $SnCl_2$ solutions for 10–15 days, the Sn(II) loss is decelerated by a factor of 8–10. For alkaline solutions, the same deceleration is observed after 3–5-day storage. Within these periods, the oxygen concentration in $SnCl_2$ solutions does not change noticeably and the Sn(II) content in them remains sufficiently high (no less than 20–70% of the initial $SnCl_2$ concentration). Therefore, most likely, the nearly complete cessation of the Sn(II) loss after 10–15 day storage is caused by the fact that by this time the most reactive complexes have been already oxidized, and only species that are the most stable to oxidation and hydrolysis remain in the solution. The exception are solution nos. 4, 6, and 7 in which transformations of tin-containing compounds continue at a low rate. The total amount of Sn(II) + Sn(IV) sorbed on flask walls is about 0.005–0.008 mol m^{-2}, which is substantially smaller than the tin loss in storage of $SnCl_2$ solutions.

In storage of $SnCl_2$ solutions, a small precipitate is gradually formed. In acidic $SnCl_2$ solutions, this precipitate usually becomes visible within 30–45 days after preparation of fresh solution. In the solution no. 2 with the minimal content of chloride anions, the visible precipitation is observed within a shorter time (12 days). The weight fraction of this initially formed precipitate is no more than 8 wt % of the total $SnCl_2$ amount in the fresh solution. In further storage, the weight of the precipitate slightly increases. In alkaline

Table 2. Sn(II) and Sn(IV) loss in storage (5 and 10 days) of $SnCl_2$ solutions due to oxidation, colloid formation, and adsorption

Sample no.	Sn(II) concentration, M (A)		Difference between the initial Sn(II) concentration and Sn(II) + Sn(IV) determined, M (B)		Sn(II) and Sn(IV) loss, % (B : A)	
	5 days	10 days	5 days	10 days	5 days	10 days
1	0.035	0.052	0.022	0.030	63	58
2	0.042	0.062	0.027	0.032	64	52
3	0.017	0.025	0.010	0.015	58	60
4	0.022	0.035	0.013	0.017	58	51
5	0.025	0.040	0.007	0.012	28	30
6	0.065	0.075	0.062	0.066	95	88
7	0.053	0.070	0.053	0.061	100	87
8	0.068	0.085	0.046	0.051	68	60
9	0.090	0.092	0.044	0.051	49	55

solutions, the precipitate is formed within the first day after preparation of the fresh solution, and its amount varies from 4 to 9 wt % of the initial $SnCl_2$ content. After storage for 10 days, the weight fraction of this precipitate increases to 7–15 wt % . The precipitate formation is the fastest in solution no. 6. In further storage, the precipitation sharply decelerates. The slowest precipitation was observed in solution no. 7.

Our results show that precipitation of tin-containing compounds cannot be responsible for Sn(II) depletion in storage of acidic $SnCl_2$ solutions for 12–30 days. The Sn(II) loss found by us in storage of $SnCl_2$ alkaline solutions exceeds the expected Sn(II) depletion due to precipitation by a factor of 2–5. These facts suggest the existence of additional factors along with the sorption and precipitation, responsible for decrease in the Sn(II) concentration. To elucidate these additional factors, we determined the total concentration of Sn(II) + Sn(IV) in the solutions as influenced by the storage time. The kinetic curves (Fig. 2) show that, in storage of both the acidic and alkaline solutions, the total content of analytically determinable tin-containing compounds decreases. This fact only partly can be attributed to precipitation of tin compounds, which is particularly typical of alkaline solutions. Most likely, the "loss" of tin is caused by the fact that a certain tin fraction occurs as an analytically undeterminable colloid insoluble in 1.5 M HCl.

The data on the Sn(II) and Sn(II) + Sn(IV) loss are listed in Table 2. These data show that, after storage, more than a half of the initial Sn(II) cannot be determined in solutions even after reduction of Sn(IV). In most cases, the total Sn(II) and Sn(IV) loss ranges from 50 to 70%. In solution no. 5 with prevalence of chloride complexes, the fraction of undeterminable tin-containing species is considerably lower. In solution nos. 6 and 7, within the storage time tin almost completely transforms into undeterminable species.

The difference between the initial and current tin amounts shows that, in storage of both acidic and alkaline $SnCl_2$ solutions, colloid species insoluble in 1.5 M HCl are formed. The tin amount contained in these colloids cannot be determined by titration with iodine.

In storage of $SnCl_2$ solutions, Sn(II) oxidation correlates with colloid formation. Oxidation of Sn(II)

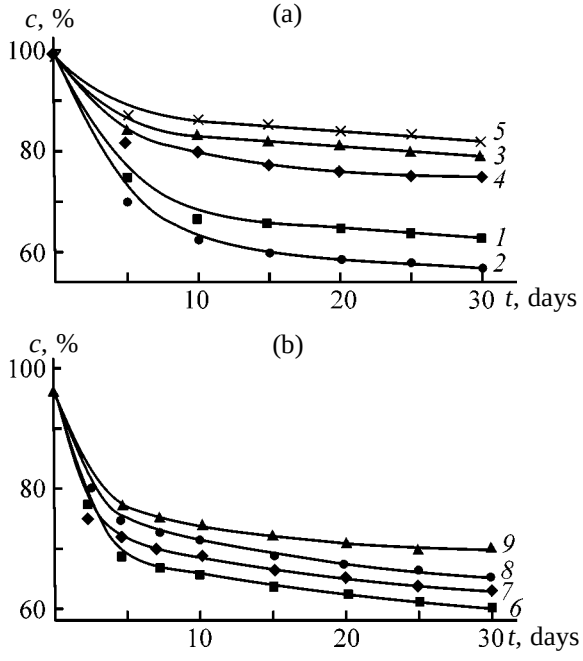

Fig. 2. Total relative Sn(II) + Sn(IV) concentration c in $SnCl_2$ solution as a function of the storage time t. The solution numbers (Table 1) are indicated at the corresponding curves.

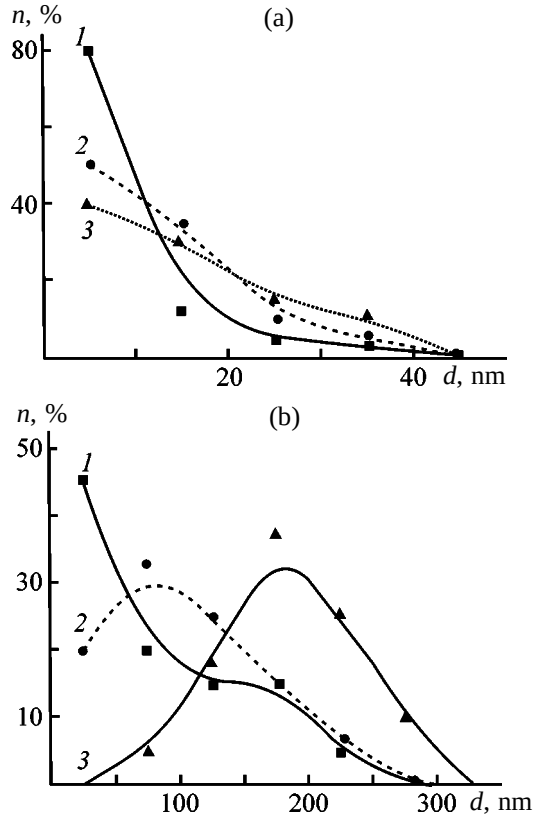

Fig. 3. Size distribution of colloid particles in (a) solution no. 1 and (b) solution no. 2 (Table 1). (*n*) Fraction of particles with a given size, and (*d*) particle size. Storage time (days): (a) (*1*) 0, (*2*) 15, and (*3*) 25; (b) (*1*) 1, (*2*) 7, and (*3*) 15.

promotes the colloid formation, and colloid particles are enriched in Sn(IV). The Sn(II) : Sn(IV) molar ratio is approximately 1 : 3 both in the precipitates formed spontaneously and in those obtained by coagulation of the colloid particles with a strong electrolyte. Such a pattern is observed with both the acidic and alkaline $SnCl_2$ solutions, irrespective of the storage time. The electron-microscopic study showed that about 80% of colloid particles formed in the freshly prepared acidic $SnCl_2$ solutions have a size in the range 5–20 μm (Fig. 3a). The amount of coarser (40–60 nm) particles is no more than 1-2% of the total number of the colloid particles in the freshly prepared acidic solutions and increases to 8–10% during 30-day storage. At the similar storage time, the colloid formation is considerably slower in solutions containing excess H^+ and Cl^- ions than in those containing aqua and hydroxo complexes. Thus, excess H^+ and Cl^- ions suppress the colloid formation and coagulation of colloid particles. In storage of alkaline $SnCl_2$ solutions, the colloid particles also are coarsened and their size exceeds that of colloids formed in acidic solutions by an order of magnitude (Fig. 3b). For example, the main fraction (about 50%) of colloid particles formed in freshly prepared alkaline solutions have a size in the range 20–50 nm. Upon storage of these solutions for 15 days, the size of the particles increases to 15–150 nm. After 30-day storage, aggregates with a size of 150–300 nm are formed, and their fraction is no less than 70%. The coarsening of the colloid particles in storage of solutions is accompanied by a decrease in the content of fine colloids. The electron diffraction phase analysis showed that the precipitates isolated from acidic $SnCl_2$ solutions include the phases of Sn(II, IV) hydroxychlorides and other oxo and hydroxo complexes: SnO_2, $Sn_4(OH)_6Cl_2$, Sn_3O_4, $Sn_{21}Cl_{16}(OH)_{14}O_6$, and $Sn_3O_2(OH)_2$. The precipitates isolated from alkaline solutions include, along with the phases of hydroxo complexes $Sn_3O_2(OH)_2$ and $Na_2[Sn(OH)_6]$, also the phase of metallic tin (β-Sn).

Our results show that Sn(II) is lost by simultaneously occurring Sn(II) oxidation to Sn(IV) and hydrolysis. With increasing Sn(IV) concentration, the hydrolysis rate increases. The hydrolysis products polymerize to form colloid particles including Sn(II) hydroxychloride and hydroxo complexes and also stannic acids capable of converting into SnO_2 and Sn_3O_4. More than a half (with respect to mole fraction) of the tin-containing oxidized and hydrolyzed species are insoluble in 1.5 M HCl and cannot be determined by titration with iodine. Due to gradual coagulation and sedimentation of colloids, the precipitates are formed whose chemical composition is similar to that of the colloid particles. The size of the colloid particles ranges from units to tens of nanometers. The colloid particles formed in acidic solutions are finer than those formed in alkaline solutions. The colloid solutions concerned are sufficiently stable, and therefore their existence should be taken into account in electrodeposition of multicomponent films based on metallic tin and its dioxide.

CONCLUSIONS

(1) In storage of both acidic and alkaline $SnCl_2$ solutions containing different ligands, the Sn(II) concentration decreases by 10–70% within 5–10 days, and then the Sn(II) loss decelerates.

(2) The decrease in Sn(II) concentration is caused by Sn(II) oxidation, hydrolysis, and formation of colloid particles containing Sn(II) and Sn(IV) in the 1 : 3 ratio. In acidic solutions, the colloids are formed including poorly crystalline SnO_2, Sn_3O_4, $Sn_4(OH)_6Cl_2$, $Sn_{21}O_{16}(OH)_{14}O_6$, and $Sn_3O_2(OH)_2$. In

alkaline solutions, the colloids consist of poorly crystalline $Sn_3O_2(OH)_2$, $Na_2[Sn(OH)_6]$, and β-tin.

(3) In storage for 5 days, about 50–70% of the initial Sn(II) is converted to colloid particles. The colloid solutions are fairly stable to coagulation and sedimentation. The tin contained in the colloid particles cannot be determined titrimetrically, which should be taken into account in analysis of tin-plating solutions.

(4) The oxidation of Sn(II) and simultaneous hydrolysis of tin-containing compounds can be controlled by complexation with chloride and hydroxide anions at their 5–10-fold excess.

REFERENCES

1. Shalkauskas, M. and Vashkyalis, A., *Khimicheskaya metallizatsiya plastmass* (Electroless Metal Plating of Plastics), Leningrad: Khimiya, 1985, 3rd ed.
2. *Khimicheskoe osazhdenie metallov iz vodnykh rastvorov* (Electroless Metal Plating from Aqueous Solutions), Sviridov, V.V. Ed., Minsk: Universitetskoe, 1987.
3. *Electroless Plating: Fundamental and Applications*, Mallory, G.O. and Hajdu, J.B. Eds., Orlando: Amer. Electroplaters and Surface Finishers Soc., 1990.
4. Gruev, I.D., Matveev, N.I., and Sergeeva, N.G., *Elektrokhimicheskie pokrytiya izdelii radioelektronnoi apparatury* (Electroplated Coatings in Radioelectronics Parts), Moscow: Radio i Svyaz', 1988.
5. *Spravochnik gal'vanotekhnika* (Handbook of Electroplater), Ginberg, A.M., Ed., Moscow: Metallurgiya., 1987.
6. Tyutina, K.M. and Kosmodamianskaya, L.V., *Zh. Vsesoyuzn. Khim. O–va. im. D.I. Mendeleeva*, 1988, vol. 33, no. 2, pp. 146–152.
7. Afanas'eva, Z.F., Sviridov, V.V., and Shevchenko, G.P., *Zh. Prikl. Khim.*, 1993, vol. 66, no. 6, pp. 1224–1229.
8. Shevchenko, G.P., Afanas'eva, Z.F., and Sviridov, V.V., *Vestsi Akad. Navuk Resp. Bel., Ser. Khim. Navuk*, 1990, no. 2, pp. 115–119.
9. Vorob'eva, T.N. and Reva, O.D., in *Sintez, struktura i svoistva neorganicheskikh veshchestv i kolloidnykh sistem: Tematicheskii Sbornik Inst. Obshchei i Neorganicheskoi Khimii Nats. Akad. Nauk Belarusi, NII Fiziko-Khimicheskikh Problem Belarus. Gos. Univ.* (Synthesis, Structure, and Properties of Inorganic Compounds and Colloid Systems: Topical Collection of the Inst. of General and Inorganic Chemistry, National Acad. Sci. of Belarus, and Research Inst. of Physicochemical Problems, Belarussian State Univ.), Minsk: Belsens, 2000, pp. 196–206.
10. Senguttuvan, T.D. and Malhotra, L.K., *J. Phys. Chem. Solids*, 1997, vol. 58, no. 1, pp. 19–24.
11. Tsyrlina, G.A., Roginskaya, Yu.E., and Postovalova, G.G., *Elektrokhimiya*, 1998, vol. 34, no. 6, pp. 569–574.
12. Nasr, C., Kamat, P.V., and Hotchandani, S., *J. Electroanal. Chem.*, 1997, vol. 420, pp. 201–207.
13. Orlik, D.R., Ivanovskaya, M.I., and Kol', K.D., *Zh. Anal. Khim.*, 1995, vol. 50, no. 11, pp. 1173–1177.
14. Sharp, D.J., *Plating*, 1971, vol. 58, no. 8, pp. 786–790.
15. Mance, A.M., Gaarencefroom, S.W., and Waldo, R.A., *J. Electrochem. Soc.*, 1991, vol. 138, no. 2, pp. 417–421.
16. Vorob'eva, T.N., Reva, O.V., Rukhlya, V.A., *et al.*, *Vestsi Akad. Navuk Bel. SSR, Ser. Khim. Navuk*, 1994, no. 2, pp. 94–100.
17. Reva, O.V. and Vorob'eva, T.N., *Zh. Prikl. Khim.*, 1998, vol. 71, no. 3, pp. 498–502.
18. Reva, O.V., Vorob'eva, T.N., and Sviridov, V.V., *Sci. Appl. Photo*, 1999, vol. 41, no. 4, pp. 331–339.
19. Rozovskii, G.I., Petretite, L.I., Shalkauskas, M.I., and Misyavichus, A.K., *Tr. Akad. Nauk Lit. SSR, Ser. B*, 1976, vol. 1, issue 92, pp. 3–11.
20. Rozovskii, G.I., Petretite, L.I., Shalkauskas, M.I., and Kimtene, D.P., *Tr. Akad. Nauk Lit. SSR, Ser. B*, 1976, vol. 2, issue 93, pp. 23–29.
21. Petretite, L.I., Rozovskii, G.I., Shalkauskas, M.I., and Kimtene, D.P., *Tr. Akad. Nauk Lit. SSR, Ser. B*, 1976, vol. 4, issue 95, pp. 19–24.
22. Fugivara, C.S., Sumojdo, P.T.A., Cardoso, A.A., and Benedetti, A.V., *Analyst*, 1996, vol. 121, no. 4, pp. 541–545.
23. Duncan, G.T. and Banter, J.C., *Plat. Surface Finish.*, 1989, vol. 176, no. 9, pp. 54–57.
24. Medvedev, G.I., Zhuravlev, V.I., and Fursova, N.Yu., *Zh. Prikl. Khim.*, 1998, vol. 71, no. 7, pp. 1113–1120.
25. Spivakovskii, V.B., *Analiticheskaya khimiya olova* (Analytical Chemistry of Tin), Moscow: Nauka, 1975.
26. Kutner, E. and Matseevskii, B., *Kinet. Katal.*, 1969, vol. 10, no. 5, pp. 997–1003.
27. Codina, G., Kostin, I., and Triphonenkova, A., *J. Radioanal. Nucl. Chem. Lett.*, 1990, vol. 146, no. 1, pp. 57–64.
28. Paul, R.C., Sooch, K.S., Vaidya, O.S., and Narula, S.P., *Anal. Chim. Acta*, 1969, vol. 46, no. 1, pp. 131–137.
29. Alekseev, V.N., *Kolichestvennyi analiz* (Quantitative Analysis), Moscow: Khimiya, 1987.

Russian Journal of Applied Chemistry, Vol. 75, No. 5, 2002, pp. 706–711. Translated from Zhurnal Prikladnoi Khimii, Vol. 75, No. 5, 2002, pp. 724–729.
Original Russian Text Copyright © 2002 by Fakeev, Kurmanguzhina, Sukhanovskaya.

INORGANIC SYNTHESIS AND INDUSTRIAL INORGANIC CHEMISTRY

Purification of Calcium Nitrate Solutions by Coprecipitation of Impurities with Hydrated Aluminum Oxide

A. A. Fakeev, L. K. Kurmanguzhina, and A. I. Sukhanovskaya

State Research Institute of Chemicals and Ultrapure Substances, Moscow, Russia

Received June 6, 2001

Abstract—Coprecipitation of 3*d*-element impurities from solutions of calcium nitrate with hydrated aluminum oxide (collector) was studied using radioactive tracers. The structure of the collector was studied by ^{1}H NMR and IR spectroscopy.

In chemical industry, calcium nitrate is a key compound for preparing practically important calcium products (carbonate, fluoride, phosphate, chromate, oxalate, etc.) [1, 2].

Recently, ultrapure calcium compounds (carbonate, phosphate, and fluoride) have found application in manufacturing optical fibers, optical glasses, single crystals, luminophores, etc. Therefore, it is urgent to develop a method for thorough purification of calcium nitrate, which is the most accessible raw material.

The prospects of using the known methods for purification of calcium nitrate were considered in detail [3]. Two purification methods were studied experimentally: crystallization from aqueous solutions and coprecipitation of impurities with inorganic collectors. The efficiency of using calcium hydroxide, calcium carbonate, and hydrated oxides of aluminum and zirconium as inorganic collectors was checked with radioactive tracers, and hydrated oxides of aluminum and zirconium showed much promise in this respect [3].

Despite a great deal of works concerning coprecipitation of impurities with collectors, use of this process in purification of inorganic substances is largely limited by complexity and insufficient understanding of the occurring processes [4–7].

Collectors show promise in technology of ultrapure substances, as they provide highly efficient simultaneous removal of a great number of impurities to virtually zero residual concentration in the solution. The isomorphism and isodimorphism, though complicating crystallization of the majority of salts from aqueous solutions [8], in the given case play the positive role, facilitating coprecipitation of impurities.

In this work, we studied the purification of aqueous solutions of calcium nitrate using an inorganic collector, hydrated aluminum oxide (HAO).

EXPERIMENTAL

Since at present the efficiency of coprecipitation of impurities with inorganic collectors cannot be calculated theoretically, the conditions of purification of calcium nitrate solutions with HAO were studied experimentally.

As collector for purification of aqueous solutions of calcium nitrate, we chose HAO of the composition $Al_2O_3 \cdot nH_2O$, precipitated in a purified solution by addition of calculated amounts of aluminum nitrate $Al(NO_3)_3 \cdot 9H_2O$ [ultrapure 17–3 grade, TU (Technical Specifications) 6-09-3657–74)] and aqueous ammonia [chemically pure grade, GOST (State Standard) 3760–64].

Aluminum(III) is readily hydrolyzed in aqueous solutions: the precipitation starts at pH 4 and is complete at pH 7.5–8.2 [9]. At pH 4–7, the precipitate is amorphous and contains aquahydroxo complexes of various compositions, whereas at pH 8–11 it contains crystalline particles [10].

Solutions of calcium nitrate were prepared from analytically pure grade $Ca(NO_3)_2 \cdot 4H_2O$ (GOST 4142–77). Its concentration was 20 wt %, as at higher concentrations the solution becomes too viscous, which hinders sedimentation and separation of the collector, whereas at lower concentration the process becomes less efficient because of large volumes of water to be evaporated.

The study was performed using ^{59}Fe, ^{60}Co, ^{54}Mn,

1070-4272/02/7505-0706$27.00 © 2002 MAIK "Nauka/Interperiodica"

^{63}Ni, ^{51}Cr, and ^{64}Cu radioactive tracers. The γ-radiation was measured with a BDIS 3-05 device equipped with a thallium-activated NaI detector and a PS-2 scaler. The accuracy of the radioactive measurements was 2–3 rel %.

The β-radiation (^{63}Ni) was measured with scintillating granules [11]. The measurement accuracy was ±10 rel. %. The purification coefficient K_p was calculated as the ratio of the specific activities of the initial and purified calcium nitrate solutions [8].

To a 20% calcium nitrate solution (50 ml), we added calculated volumes of tracer solutions. The mixture was stirred, and the radioactivity was measured. After that, we added the calculated amount of a 20% solution of aluminum nitrate and then, gradually with stirring, 25% aqueous ammonia to pH 7.5–8 (pH-262 pH meter). After that, the mixture was stirred for 0.5 h. The precipitated collector was separated on a TsLN-2 centrifuge, and the purified solution was taken for the radioactivity measurement. The solution pH was maintained at 7.5–8.0 in all the tests, unless otherwise stated. The impurity elements were added in concentrations excluding formation of individual phases of the corresponding metal hydroxides. The collector weight was constant in all the experiments, except those on choosing the precipitation conditions.

In experiments on choosing the collector weight, the content of iron(III) and copper(II) impurities in a solution before and after purification was determined by the extraction-photometric procedure: iron(III), in the form of dibenzoylmethanate and copper, in the form of diethyldithiocarbamate (detection limit 5×10^{-6} and 4×10^{-6} wt %, respectively) [12].

The ^1H NMR spectra were recorded on a W 2112 NMR spectrometer (Varian, the United States) at –193°C and room temperature.

The IR spectra were recorded on a Specord 75-IR spectrophotometer in the 400–4000 cm^{-1} range (KBr pellets). The error in determining the band maximum frequencies did not exceed 3–4 cm^{-1}.

We studied how the collector weight, the time of contact of a solution with a collector, solution pH, the concentration of microimpurities, and the oxidant affect the process efficiency and then chose the conditions of purification of calcium nitrate solutions with HAO.

The kinetics of coprecipitation of impurities from a 20% solution of calcium nitrate with HAO was studied with ^{59}Fe and ^{64}Cu tracers. The iron(III) and copper(II) concentrations were 1×10^{-4} and 5×10^{-5} wt %, respectively, solution pH was 7.5–8.0, and the amount of $Al(NO_3)_3 \cdot 9H_2O$ added was 2 g per 100 g of $Ca(NO_3)_2$. Iron(III) and copper(II) impurities were chosen as typical double- and triple-charged ions differently interacting in the systems $M(NO_3)_n$–$Al(NO_3)_3$–$NH_3 \cdot H_2O$–H_2O (M is Fe or Cu) at 25°C, constant aluminum(III) concentration, and pH 7 and 9 [13, 14].

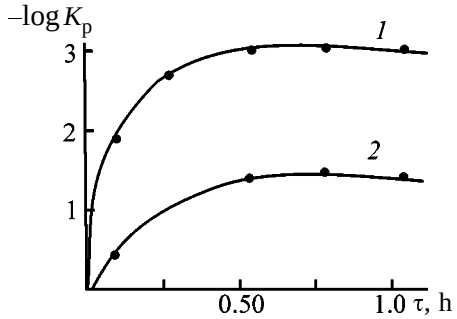

Fig. 1. K_p of a 20% solution of calcium nitrate on HAO vs. τ. (*1*) Fe(III) and (*2*) Cu(II).

Our results (Fig. 1) show that the equilibrium is virtually attained within 30 min. Increasing the process time did not considerably increase the purification coefficient. Therefore, the time of contact of a collector with a solution was 30 min in all subsequent tests.

The study of the $M(NO_3)_n$–$Al(NO_3)_3$–$NH_3 \cdot H_2O$–H_2O systems [M is Cu(II), Mn(II), Ni(II), Fe(III), or Cr(III)] at 25°C in a wide range of component concentrations by the method of isomolar series at a constant concentration of aluminum nitrate and pH 7–10 [13–17] showed that, in the range of low concentrations, the distribution of 3*d*-element impurities is uniform. The minimal collector weight ensuring thorough purification of a calcium nitrate solution was determined from the results on the coprecipitation of iron(III) and copper(II) impurities with HAO. The contact time was 30 min, the iron(III) and copper(II) concentrations were 2×10^{-4} and 7×10^{-5} wt %, respectively, solution pH was 7.5–8.0, and the concentration of the calcium nitrate solution was 20 wt %.

Our results (Table 1) show that the addition of a small amount of the collector-forming compound (0.73–1.11 g) results in virtually complete coprecipitation of iron(III); the copper(II) impurity is captured to a slightly lesser extent. Therefore, 2.0 g of $Al(NO_3)_3 \cdot 9H_2O$ should be added per 100 g of $Ca(NO_3)_2$.

In the course of the aluminum nitrate hydrolysis, a series of its hydroxo complexes, from $Al(OH)_2^+$, $Al_2(OH)_2^{4+}$, $Al_3(OH)_4^{5+}$, $Al_7O_2(OH)_{14}^{3+}$ to the limiting composition $[Al_{13}(OH)_{32 \pm 2}]^{7+}$, are formed in solution

Table 1. Content of impurities in 20 wt % $Ca(NO_3)_2$ solution depending on the weight of the collector-forming compound

$m_{Al(NO_3)_3 \cdot 9H_2O}$, g/100 g $Ca(NO_3)_2$	Fe(III)	Cu(II)
	wt %	
0.73	1×10^{-5}	1×10^{-5}
1.11	5×10^{-6}	7×10^{-6}
2.00	$<5 \times 10^{-6}$	4×10^{-6}
4.40	$\leq 5 \times 10^{-6}$	$\leq 4 \times 10^{-6}$
11.10	$<5 \times 10^{-6}$	$\leq 4 \times 10^{-6}$

[9, 18, 19]. The aluminum aquahydroxo and aquaoxohydroxo complexes, via hydrogen bonds and van der Waals forces, form three-dimensional cluster structures, which act as nuclei of the dispersed phase of the collector. The NMR spectra showed that, in the sol particles being formed, the aluminum ion has tetrahedral and octahedral ligand surrounding, indicating the presence of $[Al_{13}(OH)_{32 \pm 2}]^{7+}$, $Al_2(OH)_2^{4+}$, and $Al(H_2O)_6^{3+}$ complexes [20].

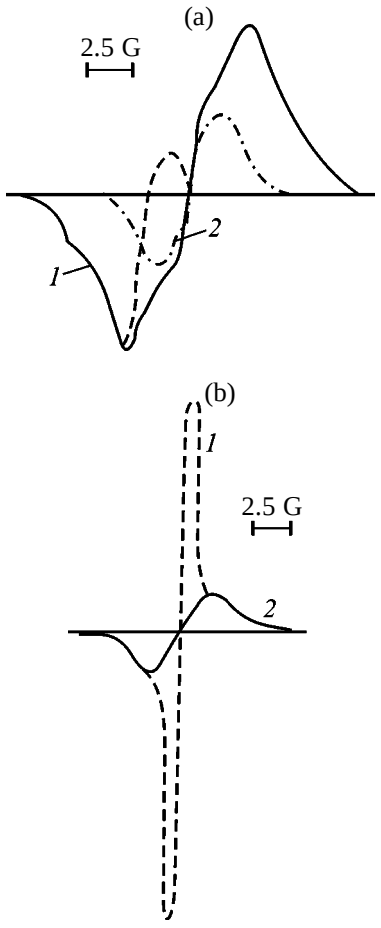

Fig. 2. ^1H NMR spectrum of HAO at (a) –193 and (b) 20°C. (*1*) H_2O and (*2*) OH groups.

We used ^1H NMR and IR spectroscopy to ascertain the role of OH groups and H_2O molecules on the HAO surface in the course of the coprecipitation and the nature of the forming solid phases.

The ^1H NMR spectrum (the first derivative of the absorption line) of the HAO sample that was precipitated at pH 6–8 and has the composition $Al_2O_3 \cdot 6H_2O$ (Fig. 2a), taken at –193°C, is the sum of a doublet from water molecules (δ_H = 12–13 G) and a singlet belonging to OH groups (δ_H = 5–6 G). The share of OH protons in the total amount of the absorbing species (xOH + $2y$$H_2O$) is small and can be determined by graphic integration of the corresponding lines. Water is weakly bound on the HAO surface and at 20°C is mobile on the NMR time scale (rotation, translation) (Fig. 2b). Therefore, at –193°C the doublet due to the rigid lattice of water molecules transforms into a strong narrow singlet (Fig. 2b) superimposing on the OH line, whose parameters are virtually the same at –193 and 20°C. Comparatively high mobility of the water molecules at room temperature is explained by the HAO structure and by hydrogen bonding of H_2O molecules [21]. Our results show that the HAO collector, when precipitated at room temperature, contains OH groups and water molecules coordinated via H bonds.

The IR spectrum of HAO contains structureless absorption bands in the ranges 3000–3600 (H_2O and OH stretching vibrations) and 1400–1600 cm^{-1} (OH^-, H_2O, NH_4^+ bending, and NO_3^- stretching vibrations), and a broad absorption band in the range 400–500 cm^{-1}. In the 3000–3600 cm^{-1} range, the absorption band with a 500 cm^{-1} half-width has no single maxima and is commonly assigned to the stretching vibrations of water molecules hydrogen-bonded with hydroxide ions or each other. The 1400–1600 cm^{-1} range cannot be assigned unambiguously, since it corresponds to bending vibrations of OH groups, water molecules, and NH_4^+ ions and to NO_3^- stretching vibrations [22, 23]. A weak band at 1050 cm^{-1} may be assigned to bending vibrations of Al–O–H bonds. A broad band in the range 400–500 cm^{-1} shows that Al–O oxygen atoms form bonds with other groups, probably with H_2O [22]. The IR spectrum of HAO does not contain narrow bands at 3025, 3290 (boehmite), 3533, 3454 (bayerite), and 3518, 3616 cm^{-1} (hydrargillite), characteristic of OH stretching vibrations. This shows that, in HAO, isolated OH groups are absent and all OH groups form hydrogen bonds with H_2O molecules.

Thus, the ^{1}H NMR and IR study of HAO revealed a large mobility of H_2O molecules and OH groups and showed the possibility of formation of bridging bonds (hydrogen, ol, or oxo bonds) with metal cations.

The speciation of impurities in a solution being purified is largely determined by its pH [8, 9, 24]. The study was performed using radioactive tracers. The concentration of the iron(III), chromium(III), copper(II), manganese(II), and cobalt(II) impurities was 2×10^{-4}–2×10^{-5} wt %, time of contact with a collector, 30 min, and the weight of the collector-forming compound, 2.0 g $Al(NO_3)_3 \cdot 9H_2O$ per 100 g $Ca(NO_3)_2$. The coprecipitation of the iron(III), chromium(III), manganese(II), and cobalt(II) impurities is maximal at pH 8.0–8.5, and that of copper(II), at pH 6.0–6.5 (Fig. 3a). The distribution factor of iron(III) and chromium(III) impurities is virtually pH-independent ($K_p \geq 1000$). Comparison of the data on the Fe(III) behavior (Fig. 3a, Table 1) shows that K_p does not depend on pH and HAO weight. This means that it is uniformly distributed throughout the AHO volume and exists in the nonsorbable forms [6]. The K_p value for copper(II) decreases from 280 to 21 as pH is increased from 6.0 to 9.0. This results from the fact that stable and well soluble complexes $[Cu(NH_3)_4]^{2+}$ are formed in a solution at higher ammonia concentrations [8]. The IR, ^{1}H NMR, and ESR spectra showed that, at low concentrations, virtually all Cu(II) ions coprecipitate with HAO in the form of copper hydroxide. This is due to the replacement of protons of hydroxy groups and to complex formation [13, 25]. The coprecipitation of Mn(II) is a complex process: at pH increased in the range 6.2–8.2, K_p increases, and then it decreases owing to the amphoteric properties of HAO. The ESR spectra show that, at low concentrations and pH 7.0–8.5, Mn(II) is uniformly distributed throughout the HAO precipitate and exists in the form of $[Mn(H_2O)_6]^{2+}$. According to the X-ray phase analysis data, at pH above 9.0, manganese hydroxide is formed and is partially oxidized [15]; the precipitation of $Mn(OH)_2$ is complete at pH ~10.4 [8]. The coprecipitation of cobalt(II) with HAO increases at higher pH values, which is consistent with the data [26, 27] on its state in aqueous solutions.

The effect of H_2O_2 oxidant on the behavior of Cu(II), Mn(II), Co(II), and Cr(III) impurities in coprecipitation from a solution of calcium nitrate was studied using radioactive tracers. After introducing the tracer, the content was treated with an H_2O_2 solution [5 ml of 30% solution per 100 g $Ca(NO_3)_2$] and stirred for 1 h at 60–70°C. Our results show that addition of H_2O_2 facilitates copper(II), manganese(II), and cobalt(II) precipitation (Table 2). Under these conditions, copper forms a peroxide complex [28, 29] detected by ESR (paramagnetic complex with $g_{||}$ = 2.28±0.005, $A_{||}$ = 173.5±5 Oe) [30], whose coprecipitation with HAO increases K_p.

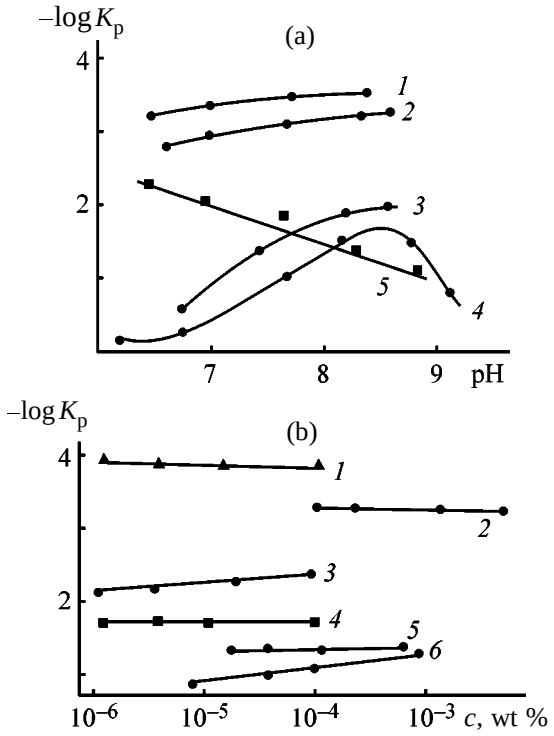

Fig. 3. K_p of a 20% calcium nitrate solution on HAO as a function of (a) pH and (b) impurity concentration c. (*1*) Cr(III), (*2*) Fe(III), (*3*) Co(II), (*4*) Mn(II), (*5*) Cu(II), and (*6*) Ni(II).

The published data on the formation of Mn(II) peroxo complexes are controversial [31, 32]. In HAO precipitates containing manganese(II), obtained at pH 8 in a solution with added H_2O_2, only two known paramagnetic complexes have been revealed by ESR spectroscopy [15]. This means that, under these condi-

Table 2. Effect of H_2O_2 on the purification coefficient of $Ca(NO_3)_2$ solutions with respect to copper(II), manganese(II), cobalt(II), and chromium(III) impurities on HAO

Impurity, wt %	pH	K_p	
		without H_2O_2	with H_2O_2
^{64}Cu, 1×10^{-4}	8.1	34±1	119±3
^{54}Mn, 5×10^{-5}	8.2	35±1	78±2
^{60}Co, 1×10^{-5}	8.2	61±2	187±5
^{51}Cr, 5×10^{-5}	8.1	3000±50	200±6

tions, manganese(II) peroxo complexes are not formed [32] and no marked oxidation of manganese(II) occurs. The observed purification effect (Table 2) may be assigned to some modification of the HAO surface by the formation of peroxide bridging bonds.

The fact that the purification of calcium nitrate solutions by coprecipitation of cobalt(III) impurity with HAO becomes more efficient on adding H_2O_2 can be explained by $Co(OH)_2$ oxidation to $Co(OH)_3$ [33], whose solubility product is considerably lower [$SP_{Co(OH)_2} = 1.6 \times 10^{-18}$, $SP_{Co(OH)_3} = 1 \times 10^{-45}$] [8]).

The purification factor with respect to chromium(III) decreases upon adding H_2O_2 (Table 2). This is due to its partial oxidation to chromium(VI), which does not coprecipitate with HAO [34, 35]. The observed purification effect (Table 2) can be explained by the fact that a part of Cr(III), along with oxidation to Cr(VI), forms chromium(V) peroxo complexes, which coprecipitate with HAO [36].

In a series of experiments, the concentration of microimpurities in the initial calcium nitrate solution was varied from 10^{-3} to 10^{-6} wt %. The study was performed using radioactive tracers by the procedure described above. The results show that the microimpurity concentration does not affect the purification coefficient in this range (Fig. 3b).

Considering the data on coprecipitation of impurities from aqueous calcium nitrate solutions with HAO in combination with the results of studying the processes occurring in the system by modern analytical methods [isomolar series; physicochemical analysis with constant concentration of aluminum(III) and varied concentration of 3*d*-element impurity; X-ray phase analysis; ^{1}H NMR, IR, and ESR spectroscopy] [13–17, 25, 30], we can conclude that the impurities are captured owing to the formation of bridging bonds with a collector. At pH 6–10, the main 3*d*-element species in nitrate solutions are hydrated cations and hydroxo complexes. Owing to complexation and replacement of protons of OH groups in polymeric chains, the distribution of impurities throughout HAO is uniform in the range of the microconcentrations (10^{-4}–10^{-5} wt %), which is in satisfactory agreement with the data of [4, 5].

The appearance of bridging bonds results in the formation of a complex compound whose structural fragment in the case of Cu(II) has the form

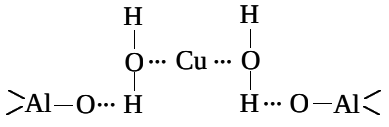

Taking into account the well developed HAO surface, the first stage of coprecipitation is adsorption of hydrated Cu(II) ion. The process mechanism can be presented by the following scheme (fragment) [4, 5, 34]:

$$Al^{3+} \rightleftarrows AlOH^{2+} + Cu(H_2O)_6^{2+} \rightleftarrows AlOCu(H_2O)_5^{+}$$
$$\rightleftarrows AlOCuOH(H_2O)_4^{2+} \rightleftarrows \ldots \rightleftarrows AlOCu(OH)_x^{(5-x)+}$$

As the concentration of 3*d* elements on HAO increases, their distribution becomes nonuniform owing to the formation of large aggregates of the corresponding hydroxides. This results in the ordering of the HAO structure and facilitates formation of chemical compounds (aluminates) for Cu(II), Mn(II), and Ni(II) impurities, and solid solutions for Fe(III) and Cr(III) impurities [37].

CONCLUSIONS

(1) The parameters of the efficient purification of calcium nitrate solutions were found.

(2) The ^{1}H NMR and IR spectra of hydrated aluminum oxide confirmed the large mobility of H_2O molecules and OH groups and showed the possibility of formation of bridging bonds with 3*d*-element ions. The mechanism of coprecipitation was proposed.

REFERENCES

1. Karyakin, Yu.V. and Angelov, I.I., *Chistye khimicheskie veshchestva* (Pure Chemical Substances), Moscow: Khimiya, 1974.
2. Fakeev, A.A., *Vysokochist. Veshch.*, 1987, no. 4, pp. 26–35.
3. Fakeev, A.A. and Sukhanovskaya, A.I., *Zh. Prikl. Khim.*, 2001, vol. 74, no. 12.
4. *Soosazhdenie s gidratirovannymi oksidami: Sbornik trudov Tadzhikskogo gos. univ.* (Coprecipitation with Hydrated Oxides: Coll. of Works of Tadzhik State Univ.), Dushanbe: Tadzhik. Gos. Univ., 1972, issue 1.
5. *Soosazhdenie s gidroksidami: Sbornik trudov Tadzhikskogo gos. univ.* (Coprecipitation with Hydroxides: Coll. of Works of Tadzhik State Univ.), Dushanbe: Tadzhik. Gos. Univ., 1977, issue 2.
6. Egorov, Yu.V., *Statika sorbtsii mikrokomponentov oksigidratami* (Statics of Sorption of Microcomponents with Hydroxides), Moscow: Atomizdat, 1975.
7. Pechenyuk, S.I., *Usp. Khim.*, 1992, vol. 61, no. 4, pp. 711–733.
8. Stepin, B.D., Gorshtein, I.G., and Blyum, G.Z., *Metody polucheniya osobo chistykh neorganicheskikh ve-*

shchestv (Methods of Preparation of Ultrapure Inorganic Substances), Leningrad: Khimiya, 1969.

9. Nazarenko, V.A., Antonovich, V.P, and Nevskaya, E.M., *Gidroliz ionov metallov v razbavlennykh rastvorakh* (Hydrolysis of Metal Ions in Dilute Solutions), Moscow: Atomizdat, 1979.
10. Linsen, B.G., and Heggerda, J.J., *Physical and Chemical Aspects of Adsorbents and Catalysts*, Linsen, B.G., Ed., London: Academic, 1970. Translated under the title *Stroenie i svoistva adsorbentov i katalizatorov*, Moscow: Mir, 1973, pp. 190–232.
11. Ekkerman, V.M., Seredenko, T.N., and Solomonov, V.M., *Radiokhimiya*, 1973, vol. 15, no. 4, pp. 601–604.
12. Chulakin, M.S., Sukhanovskaya, A.I., Krasil'shchik, V.Z., *et al*., *Metody analiza chistykh khimicheskikh reaktivov* (Methods of Analysis of Pure Chemicals), Moscow: Khimiya, 1984.
13. Kurmanguzhina, L.K., Marov, I.N., Evtikova, G.A., *et al*., *Zh. Neorg. Khim*., 1981, vol. 26, no. 9, pp. 2341–2345.
14. Kurmanguzhina, L.K., Marov, I.N., Evtikova, G.A., *et al*., *Zh. Neorg. Khim*., 1982, vol. 27, no. 6, pp. 1490–1493.
15. Kurmanguzhina, L.K., Marov, I.N., Evtikova, G.A., and Fakeev, A.A., *Zh. Neorg. Khim*., 1983, vol. 28, no. 1, pp. 61–64.
16. Kurmanguzhina, L.K. and Fakeev, A.A., *Khim. Reakt. Osobochist. Veshch.: Tr. Inst. Khim. Reakt. Osobochist. Veshch*., 1982, no. 44, pp. 113–118.
17. Kurmanguzhina, L.K., Marov, I.N., Evtikova, G.A., and Fakeev, A.A., *Zh. Neorg. Khim*., 1983, vol. 28, no. 10, pp. 2538–2541.
18. Pilipenko, A.T., Falendysh, N.F., and Parkhomenko, E.P., *Khim. Tekhnol. Vody*, 1982, vol. 4, no. 2. pp. 136–150.
19. Petrosyants, S.P. and Buslaev, Yu.A., *Zh. Neorg. Khim*., 1999, vol. 44, no. 1, pp. 1766–1776.
20. Dudkin, B.N., Kaneva, S.I., Mastikhin, V.M., and Pletnev, R.N., *Zh. Obshch. Khim*., 2000, vol. 70, no. 12, pp. 1949–1956.
21. Kvlividze, V.I., in *Svyazannaya voda v dispersnykh sistemakh* (Bound Water in Disperse Systems), Moscow: Mosk. Gos. Univ., 1970, no. 1, pp. 47–50.
22. Golovanova, G.F., Kvlividze, V.I., and Kiselev, V.F., in *Svyazannaya voda v dispersnykh sistemakh* (Bound Water in Disperse Systems), Moscow: Mosk. Gos. Univ., 1977, no. 4, pp. 178–209.
23. Akhmanova, M.V., Malofeeva, G.I., and Andreeva, N.P., *Zh. Neorg. Khim*., 1976, vol. 31, no. 3, pp. 447–453.
24. Davydov, Yu.P., *Sostoyanie radionuklidov v rastvorakh* (State of Radionuclides in Solutions), Minsk: Nauka i Tekhnika, 1978.
25. Kurmanguzhina, L.K., Akhmanova, M.V., Nirsha, B.M., *et al*., *Zh. Neorg. Khim*., 1984, vol. 29, no. 10, pp. 2576–2581.
26. Vdovina, E.D., Davydov, Yu.P., and Radyuk, R.I., in *Poluchenie i vydelenie radioaktivnykh izotopov* (Preparation and Separation of Radioactive Isotopes), Tashkent: Fan, 1983, pp. 248–250.
27. Belousova, M.Ya., Sorption of Some Elements (Iron, Nickel, and Cobalt) with Magnesium Hydroxide and Its Use for Concentrating, *Cand. Sci. Dissertation*, Moscow, 1970.
28. Frei, V., *Coll. Czech. Chem. Commun*., 1962, vol. 27, no. 2, pp. 430–438.
29. Johnson, G.R., Nazhat, N.B., and Saadalla-Nazhat, R.A., *J. Chem. Soc., Faraday Trans*., 1988, vol. 84, no. 2, pp. 501–510.
30. Kurmanguzhina, L.K., Marov, I.N., Evtikova, G.A., *et al*., *Zh. Neorg. Khim*., 1984, vol. 29, no. 5, pp. 1331–1332.
31. Lunenok–Burmakina, V.A., in *Neorganicheskie perekisnye soedineniya* (Inorganic Peroxide Compounds), Moscow: Nauka, 1975, pp. 27–38.
32. Bielski, B.H., and Chan, P.S., *J. Am. Chem. Soc*., 1978, vol. 100, no. 6, pp. 1920–1921.
33. Ivanov, V.M., Busev, A.I., and Smirnova, L.I., *Zh. Neorg. Khim*., 1970, vol. 25, no. 6, pp. 1149–1153.
34. Novikov, A.I., and Ruzankin, V.I., *Radiokhimiya*, 1974, vol. 16, no. 6, pp. 761–764.
35. Tsunenobu, S., Shiro, G., Jamazaki, H., and Nishikawa, J., *Bull. Inst. Chem. Res. Kyoto Univ*., 1977, vol. 55, pp. 429–440.
36. Zhang, L. and Lay, P.A., *Inorg. Chem*., 1998, vol. 37, no. 8, pp. 1729–1733.
37. Alekseeva, I.P., Dushina, A.P., and Aleskovskii, V.B., *Zh. Obshch. Khim*., 1976, vol. 46, no. 10, pp. 2161–2166.

Russian Journal of Applied Chemistry, Vol. 75, No. 5, 2002, pp. 712–714. Translated from Zhurnal Prikladnoi Khimii, Vol. 75, No. 5, 2002, pp. 730–733.
Original Russian Text Copyright © 2002 by Mitrofanova.

INORGANIC SYNTHESIS AND INDUSTRIAL INORGANIC CHEMISTRY

Complexation of Calcium Ions with Dicarboxylic Acids in Aqueous Solutions

G. V. Mitrofanova

Mining Institute, Kola Scientific Center, Russian Academy of Sciences, Apatity, Murmansk oblast, Russia

Received July 11, 2001; in final form, December 2001

Abstract—Complexation of calcium ion with malonic, succinic, glutaric, and adipic acids at 25°C and ionic strength I = 0.3 (KCl) was studied by pH-potentiometric titration.

Monocarboxylic acids obtained from vegetable raw material are the traditional collecting agents in apatite flotation from apatite–nepheline ores. However, permanent increase in the cost of these reagents and their short supply make urgent the search for new collecting agents obtained from inexpensive raw materials. It is known that introduction of a second functional group into a collecting agent molecule changes its flotation properties. Among the bifunctional compounds capable to be collectors, dicarboxylic acids are of interest as the basis of new synthetic reagents capable to substitute collectors of vegetable origin in apatite flotation [1].

In dressing of apatite-containing ores under conditions of circulating water supply, the liquid phase of the flotation pulp contains substantial amounts of calcium (up to 30 mg l^{-1}), which decreases the activity of reagents and increases their consumption. Therefore, it is important to study complexation of dicarboxylic acids with calcium ions.

The reference data on stability constants of calcium complexes with these acids [2–4] either are inconsistent (i.e., for succinic acid) or refer to formation of only one complex. The known stability constants of calcium complexes with malonic, succinic, glutaric, and adipic acids, recalculated by Davies equation to zero ionic strength, are listed in Table 1.

In this work, complexation of calcium ion with malonic, succinic, glutaric, and adipic acids was studied, and the stability constants of the compounds formed were determined.

EXPERIMENTAL

Complexation was studied by pH-potentiometric titration at 25°C and ionic strength of 0.3 (KCl). Preliminarily we determined under the same conditions the protonation constants of the corresponding acid dianions B_i, required to calculate the complexation constants [5].

The pH of solutions was measured with glass and Ag/AgCl electrodes on an I120.1 ionometer with an error of 0.01 pH unit.

Preliminary studies with 5×10^{-3}–5×10^{-2} solutions at $Ca^{2+} : H_2L = 1 : 1$ [5] showed the absence of calcium complexes in the solution [the formation function $\bar{n} = (c_L - L_f)/c_M$ calculated from the experimental data was negative]. Therefore, we took more concentrated solutions of acids (0.10–0.15 M) and added calcium nitrate (0.1 M, I = 0.3). The concentration ratio $Ca^{2+} : H_2L$ was 1 : 5 and 1 : 3.

The dicarboxylic acids were recrystallized three times from ethanol and dried at reduced pressure. The acid concentration in the solution was set gravimetrically and refined by pH-potentiometric titration. Chemically pure grade calcium nitrate and potassium chloride were used. The calcium concentration was determined by complexometric titration. The KOH

Table 1. Stability constants of calcium complexes with dicarboxylic acids

Acid	$\log \beta^0_{CaL}$	References
Malonic H_2Mal	2.50, 2.16,	[2]
	2.75, (1.25)*	[3]
Succinic H_2Suc	2.00	[4]
	2.40, 1.90	[2]
	2.10 (0.99)	[3]
Glutaric H_2Gl	1.76	[2]
Adipic H_2Ad	2.19	[4]

* In parentheses is $\log \beta^0_{CaHL^+}$.

1070-4272/02/7505-0712$27.00 © 2002 MAIK "Nauka/Interperiodica"

concentration in the solution prepared by dilution of the saturated KOH solution [5] was refined by potentiometric titration. All solutions were prepared with freshly boiled distilled water.

Solutions of the acid H_2L, calcium nitrate, and potassium chloride were placed into a temperature-controlled cell, and pH was measured after addition of 0.1-ml portions of 0.3 M KOH. The equilibrium was considered to be attained when pH of the solution remained constant for 2–3 min. A glass electrode was calibrated by buffer solutions before each series of measurements. The calibration curve was plotted by the least-squares method and then was used for refining the pH values of the solutions studied. After the titration procedure, the ionometer was checked by a buffer with pH 4.01. When the buffer pH measured with the ionometer differed from the above value by more than 0.02 pH unit, the result was discarded.

The protonation constants B_1 and B_2 of malonic, succinic, glutaric, and adipic acid anions were determined by titration at 25°C and ionic strength $I = 0.3$ (KCl). The experimental data were treated by the least-squares method with the approximation confidence no less than 0.99. For each acid, 6–8 independent determinations were obtained. The protonation constants of the anions of the dicarboxylic acids studied are listed in Table 2. The $\log B_1$ error was determined as probable deviation of the arithmetic mean at a confidence probability of 0.95.

The equilibria of acid dissociation (1) and (2) and of Ca^{2+} complexation with products of H_2L acid dissociation (3)–(5) were taken into consideration:

$$H^+ + HL^- \rightleftarrows H_2L, \quad (1)$$

$$H^+ + L^{2-} \rightleftarrows HL^-, \quad (2)$$

$$Ca^{2+} + HL^- \rightleftarrows CaHL^+, \quad (3)$$

$$Ca^{2+} + L^{2-} \rightleftarrows CaL, \quad (4)$$

$$Ca^{2+} + 2L^{2-} \rightleftarrows CaL_2^{2-}. \quad (5)$$

Since alkali and alkaline-earth metals form no hydroxide complexes at pH < 6, the Ca^{2+} hydrolysis was not taken in account.

To calculate the equilibrium concentrations of species, we used the mass action law and equations of the material balance:

$$c_L = [H_2L] + [HL^-] + [L^{2-}] + [CaL] + [CaHL^+] + [CaL_2^{2-}],$$

$$c_H = 2[H_2L] + [HL^-] + [H^+] + [CaHL^+],$$

Table 2. Protonation constants of dicarboxylic acid anions. $I = 0.3$, $T = 25$°C

Acid	$\log B_1$	$\log B_2$
Malonic	5.20 ± 0.01	7.85 ± 0.02
Succinic	5.22 ± 0.02	9.23 ± 0.02
Glutaric	4.99 ± 0.08	9.18 ± 0.04
Adipic	5.03 ± 0.04	9.31 ± 0.04

$$c_M = [Ca^{2+}] + [CaL] + [CaHL^+] + [CaL_2^{2-}],$$

$$B_1 = \frac{[HL]}{[L^{2-}][H^+]}, \qquad B_2 = \frac{[H_2L]}{[L^{2-}][H^+]^2},$$

$$\beta_{CaL} = \frac{[CaL]}{[Ca^{2+}][L^{2-}]}, \qquad \beta_{CaHL^+} = \frac{[CaHL^+]}{[Ca^{2+}][HL^-]},$$

$$\beta_{CaL_2^{2-}} = \frac{[CaL_2^{2-}]}{[Ca^{2+}][L^{2-}]^2},$$

where c_L, c_H, and c_M are the total concentrations of the ligand, H^+, and metal ion, respectively; B_1 and B_2 are the protonation constants of dicarboxylic acid anion; and β_{CaL}, β_{CaHL^+}, and $\beta_{CaL_2^{2-}}$ are the stability constants of the corresponding calcium species.

The formation function $\bar{n}$ is

$$\bar{n} = \frac{[H^+][L^{2-}]\beta_{CaHL^+}B_1 + \beta_{CaL}[L^{2-}] + 2\beta_{CaL_2^{2-}}[L^{2-}]^2}{1 + [H^+][L^{2-}]\beta_{CaHL^+}B_1 + \beta_{CaL}[L^{2-}] + 2\beta_{CaL_2^{2-}}[L^{2-}]^2}.$$

After transform, it becomes

$$\bar{n} + (\bar{n} - 1)[H^+][L^{2-}]\beta_{CaHL^+}B_1 + (\bar{n} - 1)[L^{2-}]\beta_{CaL} + (\bar{n} - 2)[L^{2-}]^2\beta_{CaL_2^{2-}} = 0.$$

The experimental data were treated by the least-squares method assuming (to a first approximation) $\beta_{CaHL^+} = 0$. The complex formation constants obtained under these conditions were used for refining the calculation. The finally obtained constants β_{CaL}, β_{CaHL^+}, and $\beta_{CaL_2^{2-}}$ for calcium complexes with malonic, succinic, glutaric, and adipic acids at $I = 0.3$ (KCl) and 25°C were recalculated to zero ionic strength by Davies equation.

The complexation constants obtained independently by approximation of the experimental data to the $y = a + bx + cz$ form with a confidence probability of 0.95 and a confidence interval not exceeding a factor of 2 are listed in Table 3.

Table 3. Stability constants of calcium complexes with dicarboxylic acids

Acid	$\log\beta^0_{CaL}$	$\log\beta^0_{CaHL^+}$	$\log\beta^0_{CaL_2^{2-}}$
Malonic	2.47 ± 0.05	0.08 ± 0.01	3.73 ± 0.1
	2.48 ± 0.05*	–	3.77 ± 0.08*
Succinic	2.08 ± 0.02	0.86 ± 0.05	3.41 ± 0.06
Glutaric	1.75 ± 0.07	0.92 ± 0.07	2.72 ± 0.09
Adipic	1.78 ± 0.05	0.82 ± 0.08	3.25 ± 0.08

* Without taking into consideration formation of protonated complex.

Calculations showed that, for malonic acid, formation of the $CaHL^+$ complex can be neglected. The stability constants obtained with and without regard to formation of $CaHL^+$ are virtually the same.

For malonic and succinic acids, the logarithms of stability constants $\log\beta^0_{CaMal}$ and $\log\beta^0_{CaSuc}$ are close to those obtained in [2, 3], respectively. For glutaric acid, $\log\beta^0_{CaGl}$ is virtually the same as in [2]. For the 1 : 1 complex with adipic acid, we obtained $\log\beta^0_{CaAd}$ = 1.78, which substantially differs from the value of 2.19 reported in [4] and can be thought to be more reliable because of taking into account formation of the protonated complex.

It follows from Table 3 that the stability of 1 : 1 complexes decreases in the order malonic > succinic > glutaric ~ adipic acid. Two carboxy groups in the acid molecule allow formation of chelates with metal ions. In accordance with the Tschugaeff rule, complexes with five- and six-membered rings are the most stable. Among the acids considered, only malonic acid can form a six-membered ring with calcium ion, which agrees with the maximal value of the stability constant. Bukolov *et al*. [7] proposed probable structures for metal ion complexes with succinic and glutaric acids, in which weakly stable seven- and eight-membered rings are formed. Close stability constants for calcium complexes with glutaric and adipic acids ($\log\beta^0_{CaGl} \sim \log\beta^0_{CaAd}$) obtained by us suggest that glutaric acid forms long-chain complexes similar to complexes with adipic acid [7]. The same trend toward decrease in the stability of the complex with increasing distance between the carboxy groups is also observed for 1 : 2 complexes. The stability constants of protonated complexes are approximately the same for succininc, glutaric, and adipic acids; for malonic acid, $\log\beta^0_{CaHMal^+}$ is very small, i.e., this complex is not present in solution in noticeable amounts.

CONCLUSIONS

(1) The stability constants of 1 : 1 and 1 : 2 calcium complexes with malonic, succinic, glutaric, and adipic acids were determined by potentiometric titration.

(2) The stability constants decrease with the increasing number of carbon atoms between carboxy groups of the dicarboxylic acid molecule.

ACKNOWLEDGMENTS

The author is grateful to S.I. Pechenyuk (Institute of Chemical Technology of Rare Elements and Mineral Raw Materials, Kola Scientific Center, Russian Academy of Sciences) for the assistance.

REFERENCES

1. Ivanova, V.A., Shlykova, G.A., and Mitrofanova, G.V., in *Optimizatsiya protsessov obogashcheniya mineral'nogo syr'ya* (Optimization of Dressing Mineral Raw Materials), Apatity, 2001, pp. 50 – 69.
2. Peacock, M. and James, J.C., *J. Chem. Soc*., 1951, no. 9, pp. 2233–2239.
3. Campi, E., *Ann. Chim.* (Rome), 1963, vol. 53, no. 1, pp. 96 –116.
4. Topp, N.E. and Davies, C.W., *J. Chem. Soc*., 1940, no. 1, pp. 87–93.
5. Kumok, V.N. and Skorik, N.A., *Laboratornye raboty po khimii kompleksnykh soedinenii* (Laboratory Works on Chemistry of Complex Compounds), Tomsk: Tomsk. Univ., 1983.
6. Inczedi, J., *Analytical Application of Complex Equilibria*, Budapest: Akad. Kiado, 1976.
7. Bukolov, I.E., Astakhov, K.V., Zimin, V.I., and Tairov, V.S., *Zh. Neorg. Khim*., 1962, vol. 7, no. 7, pp. 1577–1582.

Russian Journal of Applied Chemistry, Vol. 75, No. 5, 2002, pp. 715–719. Translated from Zhurnal Prikladnoi Khimii, Vol. 75, No. 5, 2002, pp. 734–738.
Original Russian Text Copyright © 2002 by Belyaev, Rubets, Kalinkin, Nuzhdin.

INORGANIC SYNTHESIS AND INDUSTRIAL INORGANIC CHEMISTRY

Analysis of Electrical Properties of Thin Film Samples in the Course of Phase Transformations of Cadmium Sulfide and Telluride Solid Solutions

A. P. Belyaev, V. P. Rubets, I. P. Kalinkin, and M. Yu. Nuzhdin

St. Petersburg State Technological Institute, St. Petersburg, Russia

Received June 3, 2000; in final form, September 2001

Abstract—Phase transformations in layers of cadmium sulfide and telluride solid solutions, synthesized under nonequilibrium conditions, are studied. Thermally activated decomposition of a single-phase CdS_xTe_{1-x} solution containing an α_1 phase (x_1 = 0.4–0.6) into two phases, α_2 (x_2 = 0.1–0.2) and α_3 (x_3 = 0.78–0.99), is chosen as a model process. Electron diffraction patterns and temperature dependences of photoconductivity and conductivity, measured both in the course of phase transformations and after them, are presented. The results of electrical studies are compared with structural data.

Solid solutions based on compounds of Group II and VI elements (II–VI compounds) show promise as materials for microelectronics owing to their widely varying properties. These materials are used in developing photoelectric converters, detectors of ionizing radiation, and sensors of gaseous chemical compounds. Among the factors hindering their wider use are phase transformations occurring in solid solutions in the course of time. In this connection, an attempt is made here to trace the course of transformations in a typical system, CdS–CdTe [1]. There has been virtually no reports on experimental studies of this kind. This is presumably due to the limited sensitivity and complexity of continuous monitoring by means of structural analytical methods widely used to study the phase composition of substance.

It is known that the electrical properties of a substance are the most sensitive to its structural state. The prospects for use of electrical properties to analyze materials were mentioned already by Kurnakov [2]. However, studies concerned with application of electrical measurements to analysis of phase transformations are still virtually lacking. Here we attempt to use current transport measurements as a tool in analysis of thermally activated phase transformations in CdS_xTe_{1-x} solid solutions.

EXPERIMENTAL

Samples obtained in a vacuum (residual pressure 10^{-3} Pa) by the thermal shield method under strongly nonequilibrium conditions were studied [3, 4]. A mechanical mixture of CdS and CdTe powders taken in 40 : 60 (at. %) ratio was subjected to thermal evaporation. Small sheets of mica (muscovite) served as substrates for condensation. The nonequilibrium conditions were chosen because of the necessity to obtain samples prone to phase transformations.

The thus prepared samples were CdS_xTe_{1-x} films with polycrystalline structure, composed of 0.1–0.2-μm crystals of the cubic modification and definite chemical composition. The composition of the solid solution was constant within a sample. Samples with $0.4 < x < 0.6$ were studied. The uniformity of the solid solution throughout the sample volume and its specific composition were found by electron diffraction. All structural and morphological studies were carried out with EMR-100 electron diffractometer and PEM-100 electron microscope. The electron diffraction patterns were identified using the ASTM file.

The sample thickness was varied in the range 0.30–0.50 μm. Within a sample, the layer thickness was constant and invariable in the course of experiments. The thickness was measured on an MII-4 microinterferometer with accuracy of ±0.03 μm.

All the techniques employed to measure electrical and photoelectric characteristics [5] were chosen with account of the fact that solid solution layers are semiconducting film materials [6]. Electrical measurements were carried out in a vacuum (residual pressure 10^{-3} Pa), in which samples were kept for several days.

1070-4272/02/7505-0715$27.00 © 2002 MAIK "Nauka/Interperiodica"

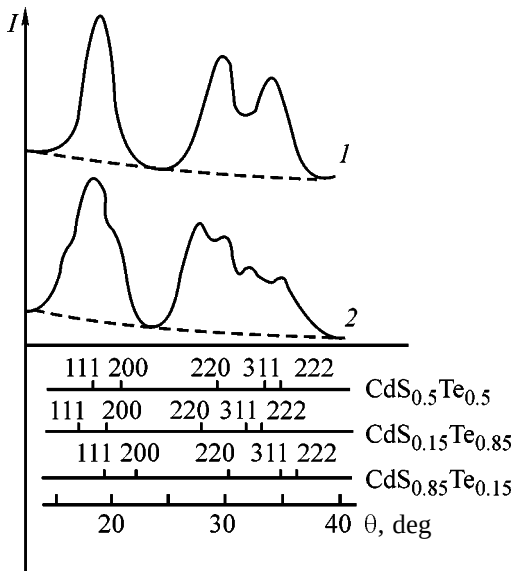

Fig. 1. Electron diffraction patterns of films of the system CdS–CdTe (*1*) before and (*2*) after annealing: (*I*) Intensity and (θ) diffraction angle. Figures above the abscissa axis are crystallographic indices of crystal planes responsible for the peaks in the electron diffraction patterns of a solid solution with the composition indicated on the right.

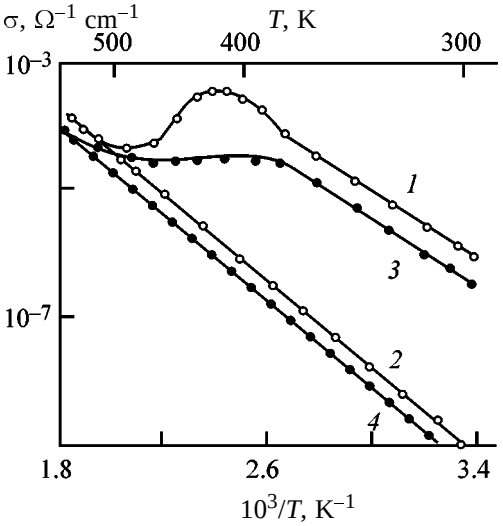

Fig. 2. (*1, 3*) Variation of electrical conductivity σ in the course of phase transformations in cadmium sulfide–telluride layers (x = 0.5) under heating at a rate v_T and (*2, 4*) temperature dependences of the conductivity of these layers after phase transformations. (*T*) Temperature. Heating rate v_T (K s^{-1}): (*1, 2*) 0.05 and (*3, 4*) 0.2.

The measurements were done in the current mode with the use of a V7-30 electrometer and electrostatic shields at electric field strength of 100 V cm^{-1}. The electrical conductivity of the films was measured in the dark and under illumination (photoconductivity). For this purpose, silver contacts were deposited onto $0.4 \times 0.4 \times h$-cm samples, where $2h$ is the layer thickness. The choice of the material of contacts is governed by the necessity for obtaining contacts with properties having no effect on the electrical conductivity to be measured. The contact properties were judged from the initial portions of current–voltage characteristics. No nonlinearities or asymmetry of electrical properties were revealed.

The contacts spaced by 0.4 cm were deposited by thermal evaporation of silver.

The effect of surface charge transport on the electrical properties and the contribution of the ionic charge transport were studied by measuring band and transient characteristics. No asymmetry of electrical properties acquired under the action of electric field was revealed.

Integral photoelectric characteristics of the samples were studied under irradiation with light of a 90-W incandescent lamp with tungsten filament (rated filament temperature 2270 K). Spectral characteristics were measured on a DMR-4 monochromator. In doing so, a signal induced by a single light quantum was taken as analytical signal. The radiation intensity was measured with a nonselective radiation detector, radiation thermocouple.

The sample temperature was maintained constant in measurements with an accuracy of ± 0.1 K or varied at a constant rate of 0.05–0.20 K s^{-1}. Heating at higher rate was done with a beam of electrons having energy of several thousand electronvolts, directed onto a copper substrate holder.

The possible influence of the probing electric field on phase transformations was monitored by comparing the properties of samples that underwent phase transformations under the action of electric field with those of samples not subjected to electric field.

The effect of temperature on the properties of the contacts was monitored by comparing the electrical properties of samples with contacts deposited before annealing with those of samples having contacts deposited after the heat treatment.

The measurement results were processed by methods of mathematical statistics. The relative measurement error did not exceed several percent. The main experimental results are presented in Figs. 1–5.

Figure 1 shows typical electron diffraction patterns of freshly prepared and annealed films of the solid solution. Curve *1* points to the presence in the freshly prepared film of only a single phase, α_1, corresponding to a composition with x_1 = 0.5. Curve *2*, measured

with annealed samples, indicates the appearance in the bulk of the sample of two phases, α_2 and α_3, of the solid solution CdS_xTe_{1-x}, with compositions x_2 = 0.15 and x_3 = 0.85. The phase segregation of annealed samples was also revealed by analysis of an optical transmission spectrum [7].

The method of sample annealing and the rate of heating in annealing had no effect on electron diffraction patterns. Electron microscopic studies revealed no differences, either. The size of crystallites constituting the film remained unchanged: on the order of several tenths of a micrometer.

The difference in annealing methods affected the electrical and photoelectric properties of the objects of study. Figure 2 shows typical differences in the temperature dependences of electrical conductivity, associated with the annealing rate. Curves *1, 2* and *3, 4* were obtained in annealing with heating rates of, respectively, 0.05 and 0.2 K s^{-1}. Curves *1* and *3* characterize the electrical conductivity of freshly prepared samples. These curves differ in the presence, or absence, of a region with increased rate of conductivity change. At a heating rate of 0.05 K s^{-1} the conductivity increases at a temperature of about 360 K and then rapidly decreases; further, the temperature dependence of conductivity is linear in the coordinates $\ln\sigma$–$10^3/T$ (with activation energy of 0.72 eV). At heating rate of 0.2 K s^{-1} there is no region with increased rate of conductivity change (curve *3*). Irrespective of the annealing rate, the linear temperature dependence is preserved further, in subsequent heating and cooling runs (curves *2* and *4*), over the entire temperature range.

The same linear temperature dependence with the same activation energy was reproduced for each particular sample after its being brought in contact with the atmosphere.

Keeping samples in a vacuum at the highest annealing temperature for 5–6 h had no effect on their conductivity at this temperature. As a result of annealing (in any mode), the dark electrical conductivity of the samples decreased manyfold (by three orders of magnitude, Figs. 1 and 2).

Samples with similar properties could be obtained from freshly prepared samples by shock heating with electron beam.

A photoconductivity study revealed the influence of the heating rate on the electrical and optical properties of the samples: the lower the heating rate, the higher the photoconductivity to dark conductivity ratio. For example, for a part of a sample annealed

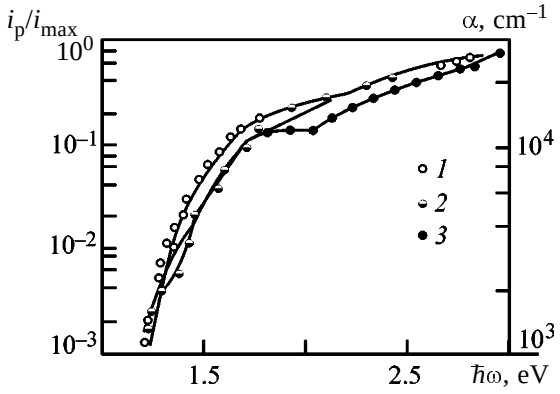

Fig. 3. (*1, 3*) Spectral dependences of the photocurrent and (*2*) absorption edge of cadmium sulfide–telluride layers. (i_p/i_{max}) Relative photocurrent, (α) absorption coefficient, and ($\hbar\omega$) quantum energy. Sample: (*1, 2*) annealed and (*3*) freshly prepared.

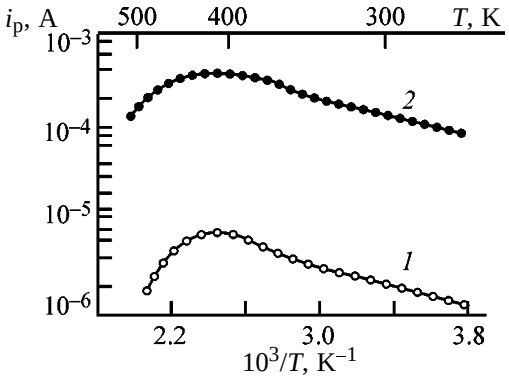

Fig. 4. Photocurrent in cadmium sulfide–telluride samples (x = 0.5) annealed at heating rates of (*1*) 0.2 and (*2*) 0.5 K s^{-1} vs. temperature T. (i_p) Photocurrent.

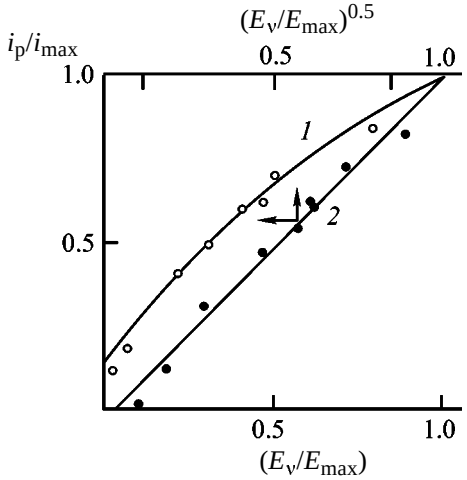

Fig. 5. Current–light characteristics of a cadmium sulfide–telluride sample (x = 0.5) annealed at a rate of 0.05 K s^{-1}. (i_p/i_{max}) Relative photocurrent and (E_v/E_{max}) relative sample illuminance. Characteristic: (*1*) total and (*2*) high-illuminance portion.

at a heating rate of 0.05 K s^{-1} (Fig. 2, curves *1* and *2*) this ratio was ~10^3 at room temperature, whereas the part of the same sample heated by the shock method exhibited virtually zero photosensitivity. Freshly prepared samples increased their photoconductivity 2–3-fold under the action of light.

Comparison of the photoconductivity spectra of the samples (Fig. 3) shows that annealing has virtually no effect on the shape of the spectra.

Figure 4 presents the temperature dependences of photocurrent in samples annealed at different rates. The run of these dependences is nearly independent of the sample heating rate. Figure 5 shows current–light characteristics of cadmium sulfide–telluride.

To conclude, it should be noted that structural studies revealed no differences in the phase composition and microstructure of layers subjected to thermal treatment at different heating rates. Only photoelectric measurements demonstrated their significant distinctions.

Let us now discuss the experimental results obtained. As seen from the electron diffraction patterns (Fig. 1, curve *1*), a freshly prepared sample is formed of a single-phase CdS_xTe_{1-x} solid solution of strictly defined composition with $x_1 = 0.5$. However, according to the equilibrium phase diagram [8], the composition $0.4 < x < 0.6$ corresponds to the region of limited mutual solubility, in which the stability of a single-phase solid solution must be lost entirely. The contradiction between the experiment and theory is eliminated if the elastic stress appearing in samples that have been formed under nonequilibrium conditions is taken into account [4, 9]. Such a stress in a II–VI solid solution favors formation of samples with increased Gibbs energy [7], a single-phase $CdS_{0.5}Te_{0.5}$ solid solution in the given case. Heating of such systems must lead to overcoming of the activation barrier keeping them in a state with increased energy and, consequently, to a phase transformation, and, in the case under study, to decomposition of the single-phase solid solution into several phases.

The results obtained are fully consistent with the aforesaid. Figure 1 shows that the electron diffraction method reveals in the sample only a single phase ($CdS_{0.5}Te_{0.5}$ solid solution) before, and two phases ($CdS_{0.15}Te_{0.85}$ and $CdS_{0.85}Te_{0.15}$ solid solutions), after annealing. In this case, the phase composition falls into the regions of mutual solubility in the equilibrium phase diagram [8].

Thus, it can be stated that we have analyzed a phase transformation of the system from a metastable state (single-phase solid solution) into the equilibrium state (mixture of two solid solutions).

Transition of the system from the metastable into the equilibrium state is only possible via a fluctuation, i.e. through nucleation and growth of new phase nuclei. This process occurs in the course of time. Naturally, the conditions existing during this period of time must affect both the kinetics of phase transformation and the properties of the phases formed. Therefore, samples subjected to annealing at different heating rates acquire different electrical and photoelectric properties. The electrical and photoelectric studies reveal differences undetectable by the electron diffraction technique.

Let us analyze the phase transformation of a solid solution with account of the dynamics of its electrical and photoelectric properties. Condensed layers of a solid solution belong to disordered systems [3]. Charge transport at high temperature in such systems occurs at the so-called mobility edge E_μ, which corresponds to the energy of carriers at which they can be involved in current transport. This process is described by the following expression [6], which qualitatively satisfies the experimental data obtained in the present study (Fig. 2):

$$\sigma = \sigma_0 \exp[-(E_\mu - E_F)/kT], \quad (1)$$

where σ_0 is a pre-exponential factor (Ω^{-1} cm^{-1}), E_μ is the mobility edge (eV), E_F is the Fermi level (eV), k is the Boltzmann constant (eV K^{-1}), and T is temperature (K).

The occurrence of current transport at the mobility edge is also evidenced by results of calculations. A kind of a conduction test is representation of conductivity in the form $\sigma = C\exp(-E/kT)$ with subsequent calculation of the parameter C [6]. For the samples studied, the factor C is on the order of 10^3 Ω^{-1} cm^{-1} both before and after annealing, in good agreement with the data of [6] and the σ_0 value in expression (1). Thus, it may be considered proven that current transport occurs at the mobility edge both in the course of the phase transformation and after it.

A significant change in conductivity in current transport at the mobility edge is only possible via a change in the Fermi level position. This may occur for two reasons: because of a change in the band gap and through a change in the density of states in the gap. No experimental evidence in favor of the first factor has been found. The photoconductivity spectrum remained virtually unchanged after the phase transformation (Fig. 3, curves *1* and *3*). By contrast, the results of photoelectric studies support the second

assumption. In the first place, it should be noted that the photoconductivity spectrum has no falloff at high energies (Fig. 3). Consequently, the recombination rates at the surface and in the bulk are rather close and a high density of states exists in the gap. The high density of states favors monomolecular recombination, which is reflected in the linear run of the current–light characteristic of the systems studied (departure from linearity at high excitation intensities is due to the influence of nonequilibrium carriers on the random field [10]).

The monomolecular photocurrent i_p (A cm^{-1}) can be described by the following expression [6]:

$$i_p = e E_e \mu_D \nu \tau, \quad (2)$$

where e is the elementary charge (C), E_e is the electric field strength (V cm^{-1}), μ_D is the carrier mobility (cm^2 V^{-1} s^{-1}), ν is the generation intensity of nonequilibrium carriers (s^{-1} cm^{-1}), and τ is the lifetime of nonequilibrium carriers (s).

The μ_D value is, as a rule, weakly dependent on states in the band gap. It is considered an intrinsic property of the material. This parameter is commonly responsible for the temperature dependence of the photocurrent. Figure 4 is in agreement with the aforesaid. The run of the temperature dependences of the photocurrent is independent of the annealing mode and, consequently, of the photosensitivity of the samples.

By contrast, the lifetime τ is rather sensitive to the density of states at the Fermi level and weakly depends on temperature [6]. Consequently, the difference in the photoelectric properties of the samples studied is due just to the difference in the density of states at the Fermi level. An additional argument in favor of this conclusion is the absence of IR quenching of photoconductivity, which is known to be characteristic of materials with sensitizing centers.

Thus, it may be stated that the photosensitive properties acquired by samples of a cadmium sulfide–telluride solid solution in the course of their phase transformations are due to a change in the density of states at the Fermi level. The density of states in the band gap, in its turn, determines the Fermi level position, and the Fermi level, as shown above, governs the conductivity of a disordered system. Therefore, it seems natural to relate changes in conductivity in the course of annealing to changes in the density of states. Consequently, curves *1* and *3* in Fig. 2, reflecting changes in the conductivity of a cadmium sulfide–telluride solid solution in the course of phase transformations, simultaneously describe changes in the Fermi level position and in the density of states in the course of thermally activated decomposition of a single-phase solid solution CdS_xTe_{1-x}. However, the relatively long response time of the recording equipment tells upon the results obtained at high heating rates, and, therefore, there is no region with increased rate of change in conductivity in curve *3* (Fig. 2).

CONCLUSIONS

(1) Changes in electrical conductivity, observed in the course of thermally activated decomposition of the solid solution, reflect the occurring changes in the density of states in the system and those in the Fermi level position.

(2) The thermally activated decomposition of the solid solution is accompanied by a steplike change in the position of the Fermi level in the system and its subsequent monotonic relaxation to a new equilibrium value.

(3) The process of thermally activated decomposition of the solid solution is accompanied by a short-term increase in the density of states in the system.

ACKNOWLEDGMENTS

The study was supported by the Russian Foundation for Basic Research (project no. 02-03-32 405).

REFERENCES

1. Murav'eva, K.K., Rubets, V.P., and Kalinkin, I.P., *Zh. Prikl. Khim.*, 1988, vol. 51, no. 5, pp. 962–967.
2. Kurnakov, N.S., *Izbrannye trudy* (Selected Works), Moscow: Akad. Nauk SSSR, 1961, vol. 1.
3. Belyaev, A.P. and Kalinkin, I.P., *Thin Solid Films*, 1988, vol. 158, pp. 25–36.
4. Belyaev, A.P., Rubets, V.P., and Kalinkin, I.P., *Izv. Ross. Akad. Nauk, Neorg. Mater.*, 1998, vol. 34, no. 3, pp. 281–287.
5. Kovtonyuk, N.F. and Kontsevoi, Yu.A., *Izmereniya parametrov poluprovodnikovykh materialov* (Measurements of Parameters of Semiconducting Materials), Moscow: Metallurgiya, 1970.
6. Mott, N. and Davis, E.A., *Electron Processes in Non-Crystalline Materials*, Oxford: Clarendon, 1979.
7. Belyaev, A.P., Rubets, V.P., and Kalinkin, I.P., *Fiz. Tekh. Poluprovodn.*, 1997, vol. 31, no. 5, pp. 635–638.
8. Saraie, J., Kato, H., Yamada, N., *et al.*, *Phys. Status Solidi (a)*, 1997, vol. 39, no. 1, pp. 331–336.
9. Vityuk, V.Ya., Sanitarov, V.A., Kalinkin, I.P., and Zapleshko, N.N., *Izv. Akad. Nauk SSSR, Neorg. Mater.*, 1982, vol. 18, no. 7, pp. 1126–1129.
10. Belyaev, A.P., Rubets, V.P., and Kalinkin, I.P., *Fiz. Tekh. Poluprovodn.*, 1997, vol. 31, no. 2, pp. 222–226.

Russian Journal of Applied Chemistry, Vol. 75, No. 5, 2002, pp. 720–723. Translated from Zhurnal Prikladnoi Khimii, Vol. 75, No. 5, 2002, pp. 739–742.
Original Russian Text Copyright © 2002 by Ibragimova, Vorob'ev-Desyatovskii, Tikhomolova, Ermilova.

SORPTION AND ION-EXCHANGE PROCESSES

Sorption of $[Au(CN)_2]^-$ Ions from Cyanide Solutions with Activated Carbon Fiber

R. I. Ibragimova, N. V. Vorob'ev-Desyatovskii, K. P. Tikhomolova, and O. A. Ermilova

St. Petersburg University of Technology and Design, St. Petersburg, Russia
St. Petersburg State University, St. Petersburg, Russia

Received November 21, 2001

Abstract—Sorption of $[Au(CN)_2]^-$ ions from cyanide aqueous solutions with activated carbon fiber was studied, and the effect of the gas phase composition and additives (phenol, hydroquinone, ethanol, Na_2SO_3, $Na_2S_2O_3$) on sorption was considered. The results are compared with data on interaction of C_{60} with $[Au(CN)_2]^-$.

Sorption of Au(I) from cyanide aqueous solutions with carbon sorbents is believed to be the most promising hydrometallurgical process of gold recovery. In spite of its long history, which began in 1894 [1], the mechanism of $[Au(CN)_2]^-$ adsorption is still the matter of discussion. We can formulate the following viewpoints.

(1) The $[Au(CN)_2]^-$ ion is sorbed by activated carbon owing to donor–acceptor interaction between the delocalized carbon π system and the vacant Au(I) *d* orbital [2].

(2) The main mechanism of sorption is the ion exchange, i.e., substitution of anions, e.g., chloride ions, in the carbon matrix by the $[Au(CN)_2]^-$ ion [3].

(3) During sorption, Au(I) in $[Au(CN)_2]^-$ is completely [to Au(0)] or partially reduced. In the latter case, the degree of Au oxidation in the carbon matrix n varies within the $0 < n < 1$ range [4, 5].

(4) The $[Au(CN)_2]^-$ sorption is accompanied by formation of the polymeric insoluble compound $[Au(CN)]_\infty$ in the sorbent phase [6].

(5) The Au(I) sorption with activated carbon involves sorption of ion pairs $M[Au(CN)_2]_n$ ($M = Na^+$, $n = 1$; Ca^{2+}, $n = 2$, etc.) in the sorbent pores [7–9].

In practice, sorption of $[Au(CN)_2]^-$ with activated carbon proceeds in air, i.e., from the solution saturated with oxygen and nitrogen. It is known [10] that the gas phase composition affects sorption of ions with activated carbon. For instance, sorption of cations increases in a hydrogen atmosphere, and the carbon capacity for anions, in an oxygen atmosphere. Frumkin [11] considered the activated carbon–water–oxygen system as an oxygen electrode. On the carbon surface, the following reactions proceed:

$$O_2 + H_2O + 4e \rightarrow 4OH^-, \quad (1)$$

$$O_2 + H_2O + 2e \rightarrow OH^- + HO_2^-. \quad (2)$$

Reaction (1) corresponds to occurrence of hydroxide anions in the electrical double layer (but not in the solution bulk). Both reactions accompany sorption of $[Au(CN)_2]^-$ ion and can affect it.

Up to now, almost all studies of Au(I) sorption from cyanide solutions were performed with granulated activated carbon. Fibrous structure of the sorbent allows increase in the sorption rate due to decrease in the external and internal diffusion resistance to mass transfer, as compared to granulated sorbents. In addition, fibrous carbon sorbents can exist as various textiles including nonwoven materials, which allows more convenient design of the sorption process.

Thus, fibrous activated carbon is a promising sorbent of gold. It should be noted that the chemical composition of the surface layers of fibrous carbon sorbents is similar to the composition of the surface layers of granulated activated carbon.

This work is the first paper devoted to study of the mechanism of $[Au(CN)_2]^-$ sorption from alkaline cyanide solutions on activated carbon fibers (ACFs) and presents data on effect of the gas phase composition on the $[Au(CN)_2]^-$ sorption and electrochemical transformations of the sorbent surface due to metal sorption. In addition, sorption properties of ACF and complexation of C_{60} with $[Au(CN)_2]^-$ were compared.

1070-4272/02/7505-0720$27.00 © 2002 MAIK "Nauka/Interperiodica"

Table 1. Effect of the gas phase composition over the solution on sorption of $[Au(CN)_2]^-$ anion with ACF

Gas phase	Initial $[Au(CN)_2]^-$ concentration, mM	$[Au(CN)_2]^-$ sorbed, mmol g^{-1} sorbent	V_{O_2}*	
			ml	mmol
Oxygen	0.0	0.0	0.08	~0.004
	4.5	0.43	0.45	0.020
	8.0	0.57	0.25	0.011
	9.0	0.58	0.32	0.014
Air	9.0	0.77	N.d.**	N.d.
Argon	9.0	0.76	0.0	0.0

* (V_{O_2}) Volume of oxygen sorbed.

** (N.d.) Not determined.

EXPERIMENTAL

ACF was prepared by carbonization of hydrated cellulose fiber in a nitrogen atmosphere at 1500°C [12]. The carbon content in the product amounted to 90%. Carbonized fiber was activated with water vapor at 800°C, which ensures its high porosity and increased sorption activity. The ACF specific surface area measured by the low-temperature nitrogen adsorption (SORTY 1750 Carlo Erba Strumentazione, Italy) was 1300 $m^2 g^{-1}$.

The content and halfwidth of meso- and micropores were determined from the benzene vapor sorption isotherm. The elemental analysis of ACF was performed on a CHN-3 analyzer.

The elemental composition of ACF (wt %) was as follows: C 97.5, H 1.7, and N 0; pore structure characteristics ($cm^3 g^{-1}$): mesopores 0.11 and micropores 0.36; micropore halfwidth 0.73 nm.

$Na[Au(CN)_2]$ was prepared by the method described in [13]. In volumetric experiments, the solution volume was 20 ml, and the fiber sample weight, 0.2 g. In experiments on sorption with various additives, the gold concentration was 0.45 mM, solution volume, 250 ml, and fiber sample weight, 0.25 g.

The content of sorbed gold(I) was determined as the difference between its initial and residual concentrations on a SpectrAA 110 Varian device (Australia).

To determine the effect of the gas phase composition on $[Au(CN)_2]^-$ sorption with ACF, we used a volumetric device described in [14]. Experiments were performed in air, oxygen, and argon (Table 1).

To study the sorption in argon, the solution and ACF were separately deoxygenated by passing argon for 1 h. In all the experiments, the time of contact of ACF with the solution in the volumetric device was 40 min.

It follows from Table 1 that the rate of $[Au(CN)_2]^-$ sorption with ACF in the oxygen atmosphere is substantially lower than in air and argon, and the process is accompanied by increased (by a factor of 3–5) sorption of oxygen (as compared to sorption from solution containing no $[Au(CN)_2]^-$).

Such a character of $[Au(CN)_2]^-$ sorption at increased oxygen content suggests that the processes of Au(I) and oxygen sorption with carbon fiber are interrelated.

According to Frumkin's concept [10], sorption of oxygen with ACF is an electrochemical process accompanied by one- or two-electron oxygen reduction. In the case of one-electron reduction, highly reactive species, e.g., O_2^- radical ion or $OH^\bullet$ radical, can be formed as intermediates. These species can react both with the sorbent surface and with $[Au(CN)_2]^-$. As a result, the rate of Au(I) sorption can decrease and the rate of oxygen uptake can increase. Thus, the reactions of $[Au(CN)_2]^-$ sorption may be radical.

To confirm this assumption, we studied $[Au(CN)_2]^-$ sorption with ACF in the presence of various additives: hydroquinone, phenol, ethanol, sodium sulfite, and sodium thiosulfate. The first two compounds are known as effective oxidation inhibitors [15] scavenging $RO^\bullet$ and $RO_2^\bullet$ radicals. Both these compounds are well sorbed with activated carbons and can be used for suppressing Au(I) sorption at cyanidation of gold ores containing impurities of carbonaceous materials [16].

Ethanol is also an effective radical scavenger and can be used for "cold" (nonautoclave) desorption of Au(I) from activated carbon. Sodium sulfite is an effective reagent for deoxygenation of aqueous solu-

Table 2. Kinetics of Au(I) sorption from aqueous solutions in the presence of various additives

Additive, 0.1 M	Au(I) content, mmol g^{-1}, in ACF at indicated τ, min				
	60	120	180	1200	1440
–	0.193	0.197	0.198	0.217	0.217
Hydroquinone	0.000	0.000	0.000	0.000	0.000
Phenol	0.000	0.000	0.000	0.000	0.000
Na_2SO_3	0.204	0.211	0.217	0.224	0.224
$Na_2S_2O_3$	0.223	0.240	0.244	0.253	0.253

* (τ) Time of contact with gold-containing solution.

tions. Its reduction under the action of solvated electron or H• and R• radicals is unlikely, but sulfite is fairly efficient as inhibitor of radical oxidation. Finally, $Na_2S_2O_3$ does not noticeably decrease the oxygen concentration in water and is substantially less efficient as radical scavenger; however the $[Au(S_2O_3)_2]^{3-}$ ion, in contrast to the cyanide complex, is not sorbed with activated carbon. The results are listed in Table 2.

As seen, phenol and hydroquinone completely inhibit the $[Au(CN)_2]^-$ sorption, while sodium sulfite and thiosulfate increase the sorption rate.

With ethanol (20 vol %) introduced into 0.02 mM $[Au(CN)_2]^-$ solution, the Au(I) content in the ACF phase amounts to 0.004 mmol g^{-1} (constant at the contact time varied within 1–24 h), while without ethanol the Au(I) content under the same conditions is about 0.02 mmol g^{-1}.

To determine how Au(I) cyanide complexes interact with the carbon surface, we studied certain electrochemical properties of ACF before and after sorption. The electrophoretic mobility of the finely divided fractions of fiber (after grinding of ACF to the size no more than 1×10^{-4} M) was measured on a microelectrophoretic device [17], and their migration to electrode with the opposite charge sign was observed.

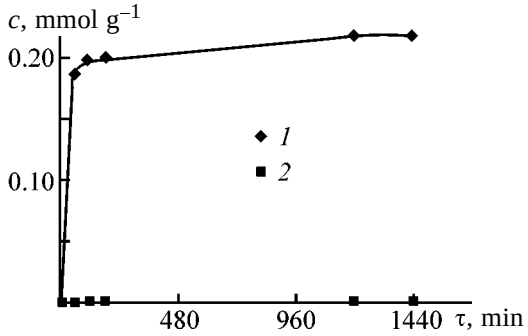

Kinetics of Au(I) sorption from aqueous solutions with various carbon materials. (*c*) Au(I) content in ACF; (τ) time. Sorbent: (*1*) ACF and (*2*) C_{60}.

It was found that the initial ACF has the ξ potential of 7.2 mV and positive sign of the surface charge. After $[Au(CN)_2]^-$ sorption, the ξ potential becomes 22.4 mV, and the sign of the surface charge becomes negative. Previously, Adams *et al*. [8] observed the change of the sorbent surface charge sign after $[Au(CN)_2]^-$ sorption on granulated activated carbon. The change of surface charge shows that the Au(I) species sorbed on the ACF surface are negatively charged.

We believe that $[Au(CN)_2]^-$ chemisorption cannot be explained by formation of donor–acceptor bond between Au(I) and the π system of the carbon surface. Two facts support this assumption.

First, the concentration of the free CN^- ion in the solution during sorption exceeds by an order of magnitude the $[Au(CN)_2]^-$ concentration. The CN^- ion forms strong π bonds with the gold atom and is characterized by a strong *trans* effect. As a result, the π bond between the $[Au(CN)_2]^-$ ion and graphite [in the case of formation of the Au(I) complex, with the gold coordination number greater than 2] should be labile, and hence, the η^n coordination π bond between the ACF surface and Au(I) atom should be unstable and dissociate under the action of excess of CN^- ions. However, desorption of $[Au(CN)_2]^-$ from the ACF surface occurs under rigid conditions [18] and takes long time. Thus, formation of bonds between the $[Au(CN)_2]^-$ ion and π system of graphite is hardly probable.

Second, we found that under the same conditions fullerene C_{60} does not react with $[Au(CN)_2]^-$ ions (see figure). It should be noted that the η^5-ligand properties of fullerene and its derivatives are well known [19].

We assume that the difference in behavior of ACF and C_{60} with respect to the $[Au(CN)_2]^-$ ion may be due to the fact that fullerene C_{60} contains no impuri-

ties, in contrast to ACF whose surface contains atoms of various elements chemically bound with carbon (mainly hydrogen and oxygen atoms). The ACF surface is very defective owing to different orientation of graphenes [20], while the C_{60} surface is practically defect-free. In addition, it was shown that C_{60} derivatives are scavengers of radicals (i.e., O_2^-) [21], while the ACF surface, on the contrary, generates them. This is confirmed by formation of H_2O_2 in the activated carbon–O_2–H_2O system [10].

CONCLUSIONS

(1) The rate of $[Au(CN)_2]^-$ sorption from aqueous cyanide solutions decreases with increasing oxygen content in the solution.

(2) In the presence of effective radical scavengers (hydroquinone, phenol, ethanol), the rate of $[Au(CN)_2]^-$ sorption on activated carbon fiber sharply decreases.

(3) Microelectrophoretic data show that sorption of $[Au(CN)_2]^-$ ion on activated carbon fiber is accompanied by changing sign of the sorbent surface charge. This shows that the chemisorbed Au(I) species are negatively charged.

(4) Under the same conditions, fullerene C_{60} does not interact with $[Au(CN)_2]^-$ in aqueous solutions.

REFERENCES

1. Gross, J. and Scott, W., *Precipitation of Gold and Silver from Cyanide Solution on Charcoal*, Washington: US Goverment, 1927.
2. Ivanova, L.S., Grabchak, S.L., Grabovskii, A.I., *et al*., *Adsorbtsiya Adsorbenty*, 1980, issue 8, pp. 58–61.
3. Tarkovskaya, I.A. and Stavitskaya, S.S., *Ross. Khim. Zh.*, 1995, vol. 39, no. 6, pp. 45–50.
4. Dudarenko, V.V., Strelko, V.V., *et al.*, *Ukr. Khim. Zh.*, 1985, vol. 51, no. 7, pp. 708–712.
5. Grabovskii, A.I., Ivanov, L.S., Korostyshevskii, N.B., *et al*., *Zh. Prikl. Khim.*, 1976, vol. 48, no. 6, pp. 1379–1381.
6. McDougal, G.M., Hancock, R.D., Nikol, M.G., *et al*., *J. South. Afr. Inst. Min. Met*., 1980, no. 9, pp. 344–356.
7. Kuz'minykh, V.M. and Tyurin, N.G., *Izv. Vyssh. Uchebn. Zaved., Tsvetn. Metall*., 1986, no. 4, pp. 65–70.
8. Adams, M.D. and Fleming, S.A., *Met. Trans*., 1989, vol. 20b, no. 6, pp. 315–325.
9. Voiloshnikov, G.I. and Chernov, V.K., Abstracts of Papers, *Mezhdunarodnaya nauchno-prakticheskaya konferentsiya "Sovremennye dostizheniya v ugol'nosorbtsionnykh protsessakh* (Int. Scientific and Practical Conf. "Progress in Coal Sorption Processes"), Irkutsk, September 16–20, 1996, p. 24.
10. Garten, V.A. and Weiss, D.E., *Rev. Pure Appl. Chem*., 1957, vol. 7, no. 7, pp. 69–122.
11. Frumkin, A.N., *Potentsialy nulevogo zaryada* (Zero Charge Potentials), Moscow: Nauka, 1982.
12. Lysenko, A.A., Vorob'ev-Desyatovskii, N.V., Simanova, S.A., *et al*., Abstracts of Papers, *Mezhdunarodnaya konferentsiya po kolloidnoi khimii i fiziko-khimicheskoi mekhanike* (Int. Conf. on Colloid Chemistry and Physicochemical Mechanics), Moscow, October 4–8, 1998, p. 78.
13. *Handbuch der präparativen anorganischen Chemie*, Brauer, G., Huber, F., *et al*., Eds., Stuttgart: Enke, 1978, vol. 2.
14. Emanuel', N.I., Zaikov, G.E., and Maizus, Z.I., *Rol' sredy v radikal'no-tsepnykh reaktsiyakh okisleniya organicheskikh soedinenii* (Role of Medium in Radical-Chain Reactions of Oxidation of Organic Compounds), Moscow: Nauka, 1973.
15. Denisov, E.T., *Kinetika gomogennykh khimicheskikh reaktsii* (Kinetics of Homogeneous Chemical Reactions), Moscow: Vysshaya Shkola, 1988.
16. Maslenitskii, I.N., Chugaev, L.V., Borbat, V.F., *et al*., *Metallurgiya blagorodnykh metallov* (Metallurgy of Precious Metals), Moscow: Metallurgiya, 1987.
17. Grigorov, O.N., Karpova, I.F., Tikhomolova, K.P., *et al*., *Rukovodstvo k prakticheskim rabotam po kolloidnoi khimii* (Handbook on Practical Works in Colloid Chemistry), Leningrad: Khimiya, 1983.
18. Meretukov, M.A. and Orlov, A.M., *Metallurgiya blagorodnykh metallov (zarubezhnyi opyt)* (Metallurgy of Precious Metals (Foreign Experience)), Moscow: Metallurgiya, 1991.
19. Konarev, D.V. and Lyubovskaya, R.N., *Usp. Khim*., 1999, vol. 68, no. 1, pp. 23–44.
20. Fenelonov, V.B., *Poristyi uglerod* (Porous Carbon), Novosibirsk: Ins. Kataliza, Sib. Otd. Ross. Akad. Nauk, 1995.
21. Chiang, L.Y., Lu, F.J., and Lin, J.T., *J. Chem. Soc., Chem. Commun*., 1995, no. 6, pp. 1283–1284.

Russian Journal of Applied Chemistry, Vol. 75, No. 5, 2002, pp. 724–726. Translated from Zhurnal Prikladnoi Khimii, Vol. 75, No. 5, 2002, pp. 743–745.
Original Russian Text Copyright © 2002 by Kirillov, Panezhda, Belousova, Grigor'eva, Pozhidaev, Vlasova, Voronkov.

SORPTION AND ION-EXCHANGE PROCESSES

Uranium(VI) Sorption on Polysilsesquioxanes with Various Organic Functional Groups

A. I. Kirillov, E. V. Panezhda, L. I. Belousova, O. Yu. Grigor'eva, Yu. N. Pozhidaev, N. N. Vlasova, and M. G. Voronkov

Favorskii Institute of Chemistry, Siberian Division, Russian Academy of Sciences, Irkutsk, Russia
Irkustk State University, Irkutsk, Russia

Received June 18, 2001; in final form, December 2001

Abstract—Sorption of UO_2^{2+} on polysilsesquioxanes with thiourea dioxide, acetamide, phthalimide, and malonamide functional groups was studied.

Proceeding with systematic study of ion-exchange and complexing properties of polysilsesquioxanes with organic functional groups [1–3], we studied in this work sorption of uranyl cations on the following sorbents: poly[*N*,*N*'-bis(3-silsesquioxanylpropyl)thiourea dioxide] $\{[O_{1.5}Si(CH_2)_2NH]_2C(SO_2)\}_n$ (**I**) [4], poly[*N*-(3-silsesquioxanylpropyl)acetamide] $[O_{1.5}Si\cdot(CH_2)_3NHC(O)CH_3]_n$ (**II**) [5], poly[*N*,*N*'-bis(3-silsesquioxanylpropyl)phthalamide] $\{[O_{1.5}Si(CH_2)_3\cdot NHCO]_2C_6H_4\}_n$ (**III**) [6], and poly[*N*,*N*-'bis(3-silsesquioxanylpropyl)malonamide] $\{[O_{1.5}Si(CH_2)_3\cdot NHCO]_2CH_2\}_n$ (**IV**).

Extraction [7] and sortion [8–11] recovery and analysis of uranium(VI) have been extensively studied. However, data on the use of organosilicon polymers, in particular, polyorganosiloxanes, are scarce. Since uranyl cations form stable complexes with O,N-containing ligands [7], we examined polymers **I**–**IV** as uranyl sorbents. Kinetic study of UO_2^{2+} sorption on polymers **I**–**IV** showed that in all cases the sorption equilibrium was attained within 30 min, with the major portion being sorbed within the first 5–10 min (Fig. 1a).

The degree of U(VI) recovery increases with increasing pH of the solution (Fig. 1b), which is likely due to stronger sorption of hydrolyzed UO_2^{2+} species. At pH > 2.5, UO_2OH^+ [12] is formed, and at pH 5 $UO_2(OH)_2$ starts to precipitate from 1.1×10^{-4} M UO_2^{2+} solution.

To simulate uranium(VI) sorption from highly saline waters, we studied UO_2^{2+} sorption as influenced by the NaCl concentration in the solution. Appreciable decrease in the UO_2^{2+} recovery at the NaCl concentration higher than 1.0 M may be due to both ionic

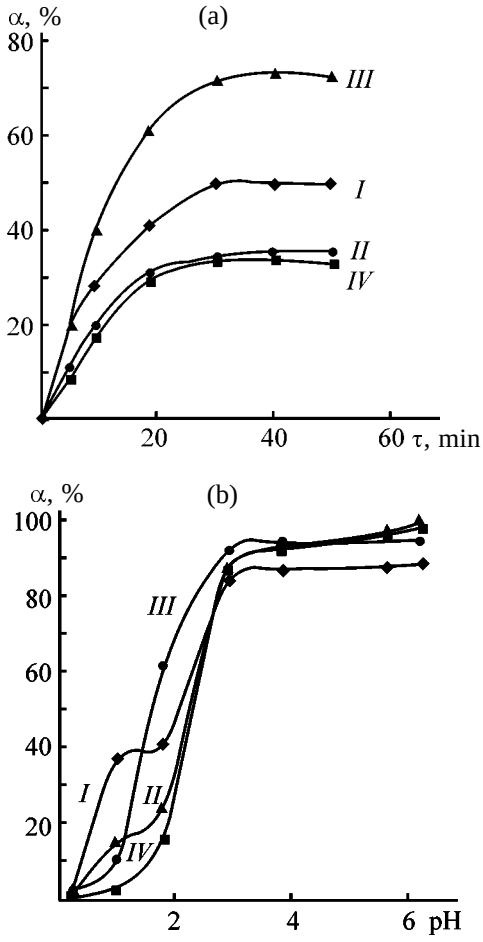

Fig. 1. Degree of uranium(VI) recovery α with polymers **I**–**IV** as a function of (a) phase contact duration τ and (b) pH. Eluent volume 20 ml; U(VI) weight 600 μg; sorbent weight 20 mg; pH 2, T = 20°C. Roman figures *I*–*IV* at the curves are polymer nos. **I**–**IV**.

1070-4272/02/7505-0724$27.00 © 2002 MAIK "Nauka/Interperiodica"

strength effect and competing complexation with Cl^- in the solution.

We studied the degree of uranium recovery as influenced by the UO_2^{2+} concentration in the solution. The static sorption capacities (SSC) of polymers **I**–**IV** and distribution coefficients of uranium *D* between solution and these polymers (Table 1) were determined from the sorption isotherms. High distribution coefficients make polymers **I**–**IV** promising for recovery of uranium(VI) traces from solution. Polymers **I**–**IV** are more effective uranium(VI) sorbents than many of organic chelating sorbents such as Polyarsenazo-*n* (SSC 70 mg g^{-1}) [9], resin with amidoxime functional groups (SSC 36–60 mg g^{-1}) [10], and organosilicon analogs, e.g., PSTM-3 sorbent (SSC 15 mg g^{-1}) [11].

The results of UO_2^{2+} desorption from polymers **I**–**IV** are presented in Table 2. Uranium(VI) is almost completely desorbed from these sorbents with 5% sodium carbonate or 6 M HCl.

To determine the sorption mechanism, we studied the IR spectra of polymer **I** before and after saturation with UO_2^{2+}. Disappearance of the ν(S=O) bands at 1100 cm^{-1} and weakening of the ν(C=N) band at 1695 cm^{-1} in the spectrum of polymer **I** saturated with uranium(VI) suggest that UO_2^{2+} and UO_2OH^+ are coordinated with thiourea dioxide groups in the zwitter-ionic form [4]:

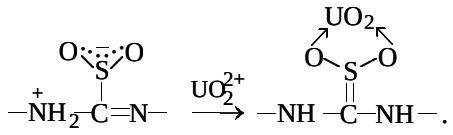

With **II**–**IV**, uranium(VI) is probably sorbed on deprotonated (imidate) acetamide fragments of the polymers by the ion-exchange mechanism:

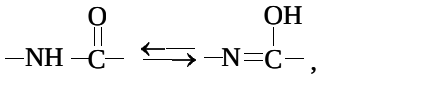

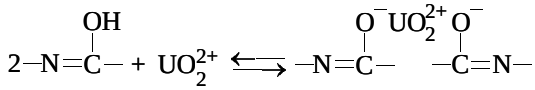

In this case, formation of uranyl chelates is also possible.

To estimate the interfering effect of other cations on the U(VI) recovery from multicomponent solutions, we studied sorption of Cu(II), Zn(II), Cd(II), Co(II), and Ni(II) on polymers **I, II**, and **IV** in a wide pH range. The static exchange capacities of **I, II**, and **IV** for these cations and the distribution coefficients of the cations between the solution and sorbent, determined under the best conditions of U(VI) sorption, are presented in Table 3. As seen from Table 3, polymers **II** and **IV** are more effective sorbents of these metals than polymer **I**. The sorption capacity of polymers **I, II**, and **IV** for Cu(II) is the highest.

Table 1. Static sorption capacity of the polymers and uranium(VI) distribution coefficient *D* at pH 3

Sorbent	SSC, mg g^{-1}	$D \times 10^{-3}$, $cm^3\ g^{-1}$
I	120	7.3
II	80	1.6
III	110	7.0
IV	127	7.8

Table 2. Uranium(VI) desorption under static conditions. Eluent volume 20 ml, U(VI) content in the sorbent 600 μg

Desorbent (5%)	Degree of desorption, %			
	I	**II**	**III**	**IV**
Sodium carbonate	99	100	100	100
Tartaric acid	74	68	46	76
Hydrochloric acid*	100	100	97	100
Citric acid	38	70	30	35

* 6 M

In all cases, Cd(II), Zn(II), and Cu(II) at U(VI) : metal ion = 1 : 1 and Ni(II) and Co(II) at U(VI) : metal ion = 1 : 10 do not interfere with the uranium(VI) recovery. U(VI) can be quantitatively recovered from solutions with prevailing total content of the examined metals. For example, the uranium recovery with polymer **I** [*n* = 4, *p* = 0.95, 0.2 g] from a solution (200 ml) containing Cu(II), Cd(II), Zn(II) (0.5 mg l^{-1}), Co(II), Ni(II) (5 mg l^{-1}), and NaCl (6×10^4 mg l^{-1}) is as follows:

Introduced U(VI), mg l^{-1}	Recovered U(VI), mg l^{-1}
0.05	0.045 ± 0.007
0.10	0.09 ± 0.02
0.50	0.51 ± 0.07
0.90	0.87 ± 0.03
2.00	1.96 ± 0.04

EXPERIMENTAL

Polymers **I**–**IV** are pale yellow powders insoluble in water and organic solvents and stable up to 200°C.

Table 3. Static sorption capacity of polymers **I**, **II**, and **IV** and distribution coefficients of Cd(II), Zn(II), Cu(II), Ni(II), and Co(II) at pH 3

Ion	**I**		**II**		**IV**	
	SSC, mg g^{-1}	D, cm^3 g^{-1}	SSC, mg g^{-1}	D, cm^3 g^{-1}	SSC, mg g^{-1}	D, cm^3 g^{-1}
Cd(II)	15	170	24	780	35	840
Zn(II)	12	170	28	410	36	580
Cu(II)	36	245	80	700	88	860
Ni(II)	6	110	8	120	9	380
Co(II)	10	140	14	250	15	308

Sorption properties of polymers **I**–**IV** were studied at room temperature under static conditions. A weighed portion of the polymer was mixed with a solution with definite pH and metal ion concentration.

A standard 1 mg ml^{-1} U(VI) solution was prepared from $UO_2(NO_3)_2 \cdot 6H_2O$ of chemically pure grade. The uranium(VI) content in solutions was determined spectrophotometrically with arsenazo III [13]. The absorption was measured on a Specol 10 spectrophotometer.

The concentrations of Cu(II), Zn(II), Cd(II), Co(II), and Ni(II) in the solution were determined by atomic absorption spectroscopy [14].

REFERENCES

1. Voronkov, M.G., Vlasova, N.N., and Pozhidaev, Yu.N., *Zh. Prikl. Khim.*, 1996, vol. 69, no. 5, pp. 705–718.
2. Voronkov, M.G., Vlasova, N.N., and Pozhidaev, Yu.N., *Appl. Organomet. Chem.*, 2000, no. 14, pp. 287–303.
3. Voronkov, M.G., Vlasova, N.N., and Pozhidaev, Yu.N., *Khim. Inter. Ustoich. Razv.*, 2000, no. 8, pp. 75–81.
4. Vlasova, N.N., Pozhidaev, Yu.N., Raspopina, O.Yu., and Voronkov, M.G., *Zh. Obshch. Khim.*, 1999, vol. 69, no. 9, pp. 1446–1449.
5. Pozhidaev, Yu.N., Zhila, G.Yu., Belousova, L.I., *et al.*, *Dokl. Ross. Akad. Nauk*, 1993, vol. 330, no. 6, pp. 719–722.
6. Pozhidaev, Yu.N., Belousova, L.I., Vlasova, N.N., and Voronkov, M.G., *Zh. Obshch. Khim.*, 1997, vol. 67, no. 5, pp. 763–764.
7. Vinogradov, A.P., *Analiticheskaya khimiya urana* (Analytical Chemistry of Uranium), Moscow: Izd. Akad. Nauk SSSR, 1962.
8. Burcik, I., *Radioakt. Ziv. Prostr.*, 1984, no. 3, pp. 133–145.
9. Shvoeva, O.P., Kuchava, G.P., Myasoedova, G.V., *et al.*, *Zh. Anal. Khim.*, 1987, vol. 62, no. 8, pp. 1457–1460.
10. Nalan, K. and Hiroaki, E., *Sep. Sci. Technol.*, 1994, vol. 29, no. 1, pp. 135–150.
11. Voronkov, M.G., Vlasova, N.N., Pozhidaev, Yu.N., *et al.*, *Dokl. Akad. Nauk SSSR*, 1991, vol. 320, no. 3, pp. 658–662.
12. Morachevskii, Yu.V. and Tserkovnitskaya, I.A., *Osnovy analiticheskoi khimii redkikh elementov* (Fundamentals of Analytical Chemistry of Rare Elements), Lenindrad: Leningr. Gos. Univ., 1980.
13. Savvin, S.B., *Organicheskie reagenty gruppy arsenazo III* (Organic Reagents of Arsenazo III Group), Moscow: Atomizdat, 1971.
14. Britske, M.E., *Atomno-absorbtsionnyi spektrokhimicheskii analiz* (Atomic Absorption Spectrochemical Analysis), Moscow: Khimiya, 1982.

Russian Journal of Applied Chemistry, Vol. 75, No. 5, 2002, pp. 727–732. Translated from Zhurnal Prikladnoi Khimii, Vol. 75, No. 5, 2002, pp. 746–751.
Original Russian Text Copyright © 2002 by Makarychev-Mikhailov, Goryacheva, Rudnitskaya, Vlasov.

SORPTION AND ION-EXCHANGE PROCESSES

Tetraphenylporphyrin Sensors with High Cross Sensitivity for "Electronic-Tongue" Analyzers

A. V. Legin, S. M. Makarychev-Mikhailov, O. E. Goryacheva, A. M. Rudnitskaya, and Yu. G. Vlasov

St. Petersburg State University, St. Petersburg, Russia

Received February 1, 2002

Abstract—Tertaphenylporphyrin-based film sensors were prepared with anionic and cationic lipophilic ionic additives introduced into polyvinyl chloride membranes plasticized with various solvents. The data obtained with these sensors were used to calculate the parameters of the cross sensitivity of the sensors. A multisensor system of the "electronic tongue" type was developed on the basis of the sensors studied.

Chemical sensors and sensor systems form a rapidly developing class of analytical instruments with a wide variety of fields and objects of application. Porphyrins and their derivatives play increasingly important part in chemical analysis [1], with chemical sensors constituting one of the most important fields of application of porphyrins and metal porphyrins. Highly selective electrodes for determining chloride [2, 3], nitrite [4, 5], thiocyanate [6], salicylate [7], and other anions have been developed on their base. In view of the specific interaction between metal porphyrins and anions, the selectivity of sensors of this kind markedly differs from the selectivity of sensors based on classical anion exchangers, quaternary ammonium salts characterized by the so-called Hofmeister selectivity series [8].

At present, active research is also being conducted in the field of cation-sensitive sensors, in particular, nickel(II)-sensitive devices [9, 10], on the basis of porphyrins and related compounds, but the selectivity of sensors of this kind is poor. Nevertheless, such sensor materials may be of much interest.

Using a multisensor system of the "electronic tongue" type, including sensors that are weakly selective but exhibit high cross sensitivity (CS) to various solution components [11, 12], one can analyze multicomponent media with complex composition. The response of sensors belonging to the system contains information about many components of the complex solution; the multidimensional analytical signal generated in such a system is commonly processed using modern methods of mathematical statistics, e.g., image recognition and multidimensional calibration. The use of multisensor systems enables quantitative determination of many ions and other components whose activity or concentration cannot be determined by the conventional potentiometric techniques. The "electronic tongue" enables multicomponent quantitative analysis, with several substances determined in a complex liquid medium simultaneously. In addition, multisensor systems can be used to perform integrated qualitative analysis (identification, recognition, classification) of various liquid media.

In terms of the "electronic tongue" concept, specific requirements are imposed upon the sensors, the main of which is high cross sensitivity understood as the sensitivity of a sensor material to, simultaneously, several or many solution components, which are not necessarily ionic, and high reproducibility of characteristics of the system in operation in complex media. Previously, parameters for evaluation of the cross sensitivity and possible ways of search for new sensor materials have been proposed [13].

Tetraphenylporphyrin is rather promising membrane-active component (MAC) owing to its ability to form complexes with numerous cations [14]. Although some selective sensors on the basis of tetraphenylporphyrin have already been reported [9], the appearance of a new approach to evaluation of the sensor sensitivity requires a reconsideration of the views about the possibilities of many known MACs. For example, not-too-highly selective sensors exhibiting reproducible cross sensitivity can be successfully used to create multisensor systems. Polymer film cation-sensitive sensors based on MAC of varied nature have been studied previously [15].

1070-4272/02/7505-0727$27.00 © 2002 MAIK "Nauka/Interperiodica"

Table 1. Concentration of components of sensor membranes

Component	Concentration, wt %, in indicated membrane								
	1	2	3	4	5	6	7	8	9
TPP	1.5	1.5	–	1.5	1.5	–	1.5	1.5	–
PTPB	–	0.4	–	–	0.4	–	–	0.4	–
DOS	65.5	65.1	67	–	–	–	–	–	–
o-NPOE	–	–	–	65.5	65.1	67	–	–	–
TOP	–	–	–	–	–	–	65.5	65.1	67
PVC	33	33	33	33	33	33	33	33	33

The aim of this work was to analyze the sensitivity characteristics of film sensors with tetraphenylporphyrin-based polyvinyl chloride membranes plasticized with solvents of varied nature, with anionic and cationic lipophilic ionic additives introduced into these membranes. The selectivity coefficients of the sensors were determined and the effect of the pH value on the sensor response was studied. The CS parameters of the sensors were calculated. The possibility of using sensors in a multisensor system of the "electronic tongue" type was analyzed.

EXPERIMENTAL

The following reagents were used in the study: *meso*-tetraphenylporphyrin (TPP), potassium tetra(*p*-chlorophenyl)borate (PTPB), tetradecylammonium chloride (TDACl), di(2-ethylhexyl) sebacate (DOS), *o*-nitrophenyl octyl ether (*o*-NPOE), tri(2-ethylhexyl) phosphate (TOP), high-molecular-weight polyvinyl chloride (PVC), and tris(hydroxymethyl)aminomethane (TRIS) of Selectophore® or "analytical reagent" grade, purchased from Fluka (Switzerland), and tetrahydrofuran manufactured by Akros Organics (Belgium) and distilled from potassium hydroxide prior to use. All the salts, acids, and bases (Ekros, St. Petersburg) were of chemically pure or analytically pure grade. Double-distilled water was used in all the experiments.

Sensor membranes were prepared using a standard procedure. Weighed portions of membrane components were placed in THF and the mixture was stirred with a magnetic rabble till complete dissolution. The resulting cocktail was poured into a weighing bottle with flat bottom and allowed to stay to complete THF evaporation (~48 h). Discs 6 mm in diameter were cut from the membrane obtained and glued onto the edge of plastic electrode cases. Prior to measurements, the sensors were soaked in a 0.01 M sodium chloride solution. The electrode case was filled with the same solution; Ag/AgCl was the internal reference electrode. Three sensors with membranes of each composition were used in all measurements, with each measurement replicated at least thrice. The compositions of the membranes studied (including blank membranes, i.e., those containing no membrane-active components) are presented in Table 1.

The emf measurements were carried out in the following electrochemical cell:

$$\mathrm{Ag}\left|\begin{matrix}\mathrm{AgCl}\downarrow,\\ \mathrm{KCl_{sat}}\end{matrix}\right|\begin{matrix}\text{Solution}\\ \text{studied}\end{matrix}\Big|\text{Membrane}\Big|\begin{matrix}\text{0.01 M. NaCl,}\\ \mathrm{AgCl}\downarrow\end{matrix}\Big|\mathrm{Ag}. \quad \text{(I)}$$

As reference electrode served EVL1M3 electrode (Gomel). The pH values were measured with a glass hydrogen electrode of the ESL-43-07 type, calibrated against standard buffer solutions. Sensor signals were recorded with a 30-channel electronic voltmeter with high input resistance, connected to a computer. The accuracy of emf measurements was 0.1 mV. All measurements were carried out at room temperature ($20 \pm 2°C$).

The selectivity coefficients were determined by the methods of biionic potentials (BIP) and mixed solutions, recommended by IUPAC [16]. In the BIP method, 0.1 M solutions of metal chlorides or nitrates was used. In the method of mixed solutions, the background concentration of interfering ions was 10^{-4} M. The effect of the pH value on the electrode response was studied in a solution containing 0.01 M TRIS and 0.5 M sodium chloride (pH 10.5), to which sulfuric acid was added dropwise.

When developing an analyzer of the "electronic tongue" type for experiments on recognition of specific objects,[1] a multisensor system comprising sensors

[1] Three samples of 100% apple juice from different manufacturers (samples I–III) were studied, together with a sample of an apple drink containing 12% juice (sample IV).

with each of the compositions studied was developed. The sensor signals were recorded 5 min after sample stirring. Between measurements, the sensors were washed several times with double-distilled water for 2–3 min. Measurements were repeated 3–4 times for each sample, with the order in which the samples were measured changed to reduce systematic errors associated with the action of samples on the sensor materials. The resulting data of high dimensionality were mainly processed by the principal component analysis. The results were processed using license software Unscrambler 6.11 (CAMO ASA, Norway, 1998).

The slopes of the calibration plots of the emf of the electrochemical cell (I) against the activity of a wide variety of cations in pure nitrate or chloride solutions are presented in Table 2. Most of sensors exhibited noticeable sensitivity to nearly all of the cations studied. Previously, it has also been shown that TPP-based sensors show a nearly Nernst function with respect to nickel(II).

Table 2 shows that, on the whole, sensors containing PTPB exhibit higher slopes. Nevertheless, the slopes are frequently smaller than the theoretical values. This can be accounted for by the fact that sensors preliminarily soaked in sodium chloride solution, rather than in a solution of the potential-determining ion, were used in all measurements. The super-Nernst slope of the sensor function in the case of copper(II) and lead(II) ions can be accounted for by variation of the solution pH with the ion concentration due to hydrolysis of salts or by the possible contribution of nonexchange sorption.

In addition to the sensors listed in Table 1, TPP-based sensors, also containing an anion-exchanger (TDACl), were fabricated. Electrodes of this kind exhibited a partial anionic function (with slopes less than 40 mV/pA). The anionic function of the membranes with anion exchanger indicates that TPP in the membrane is rather a neutral carrier [17]. These membranes were of no interest for the present study.

To reveal the effect of pH on the sensor response, the *E*–pH dependence was studied (Fig. 1). Membranes with TOP as plasticizer are insensitive to pH in the range studied. This refers both to modified (Table 1, compositions 7 and 8) and to blank (composition 9) membranes. Membranes plasticized with DOS and containing TPP exhibit weak pH sensitivity at pH < 4, and membranes without cation exchanger, also at pH > 8. The blank membranes based on DOS show virtually zero pH function. Membranes plasticized with *o*-NPOE exhibit a pH function with

Table 2. Slopes of the linear portion of the calibration plot

Cation	Slope, mV/pX, for indicated membranes (Table 1)					
	1	2	4	5	7	8
Na^+	52±4	55±3	45±6	40±4	57±2	58±2
NH_4^+	40±3	52±4	23±4	33±3	55±2	55±2
K^+	42±4	56±4	26±3	43±5	51±2	52±2
Rb^+	36±4	48±3	15±4	41±5	39±2	41±2
Mg^{2+}	26±4	30±5	22±3	23±4	34±3	36±3
Ca^{2+}	20±4	23±3	18±4	15±3	22±3	30±2
Sr^{2+}	23±3	25±2	21±3	19±3	22±2	32±1
Ba^{2+}	14±3	16±3	6±3	8±3	14±2	27±2
Mn^{2+}	15±3	29±2	12±3	14±3	32±3	32±1
Co^{2+}	17±3	25±4	15±3	20±3	26±2	30±1
Ni^{2+}	18±3	22±4	17±3	15±4	20±2	30±2
Cu^{2+}	37±3	44±3	20±3	48±4	44±2	43±2
Zn^{2+}	25±3	26±2	15±3	22±4	32±2	33±3
Cd^{2+}	24±3	27±2	19±4	24±2	41±3	40±2
Pb^{2+}	25±2	31±3	13±5	41±4	38±2	47±3

slopes of 30–35 mV/pH in the neutral and acid regions. The slope is smaller in membranes containing PTPB. The pH sensitivity of DOS-based sensors in the acid region can be accounted for by the tendency toward porphyrin protonation [18], and the pH sensitivity of sensor membranes plasticized with *o*-NPOE is probably largely due to the influence exerted by the solvent-plasticizer itself.

The selectivity coefficients of the sensors, determined using the BIP method, are presented in Fig. 2. The selectivity coefficients with respect to singly charged ions, found for sensor membranes plasticized with DOS and *o*-NPOE, are in agreement with the lipophilic series for these cations, and this agreement is more pronounced for membranes containing a cation exchanger (PTPB). Membranes plasticized with DOS show no noticeable selectivity with respect to

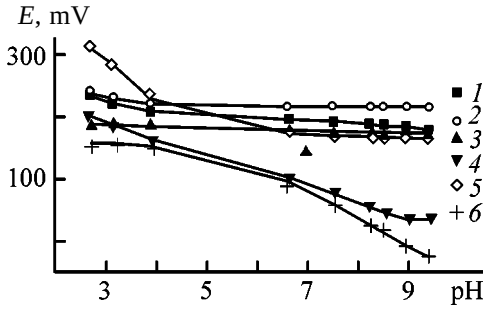

Fig. 1. Sensor response *E* vs. pH. Supporting electrolyte 0.5 M NaCl and 0.01 M TRIS. (*1*–*6*) Membrane compositions (Table 1).

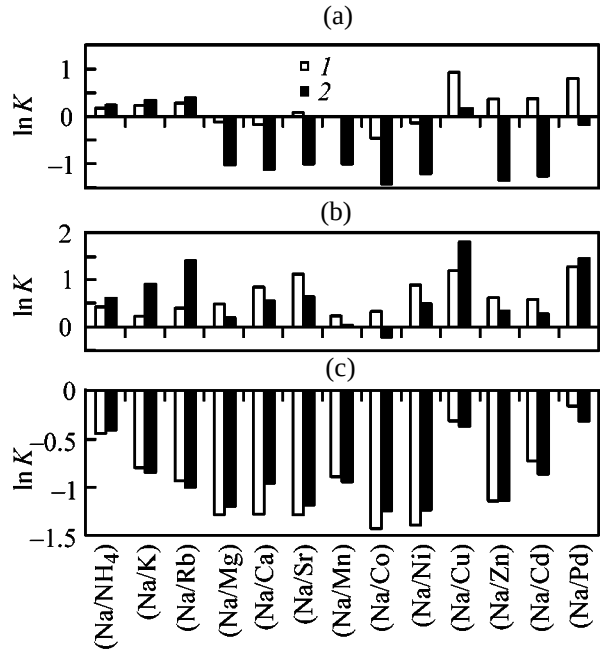

Fig. 2. Selectivity coefficients K(Na/X) measured by the BIP method. Sensor membrane: (*1*) TPP-based and (*2*) TPP- and PTPB-based. Plasticizer: (a) DOS, (b) *o*-NPOE, and (c) TOP.

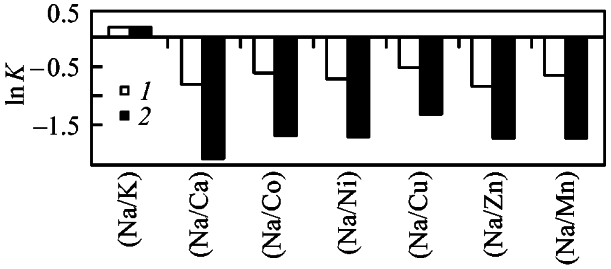

Fig. 3. Selectivity coefficients K(Na/X) measured by the method of mixed solutions. Sensor membrane plasticized with DOS: (*1*) TPP-based and (*2*) TPP- and PTPB-based.

cations of alkaline-earth metals. The logarithms of their selectivity coefficients are close to zero, whereas for membranes with an ion additive they are nearly unity. Sensors based on *o*-NPOE exhibit selectivity that increases with cation lipophilicity, with the selectivity of membranes with cation exchanger being, on the whole, lower. The results obtained are in agreement with the known data on the effect of solvent-plasticizer on the membrane properties: the more polar solvent, *o*-NPOE, shows better ability to solvate double-charged anions. The low selectivity of the sensors with respect to ions of alkali and alkaline-earth metals can be accounted for by the ability of these metals to form only labile, coordination-unsaturated complexes with porphyrin, mainly of the ionic type [19]. Another situation is observed in the case of transition metal ions. The ability of porphyrin to form stable over-plane complexes, in which the pyrrolenine nitrogen atoms are coordinated with a metal ion and pyrrole protons remain in their original positions, has been confirmed experimentally; however, published data on formation constants of such complexes with a wide variety of transition metals in various solvents are unfortunately lacking. Nevertheless, the data of [20] show that the formation constants of copper(II) complexes exceed by two orders of magnitude those for zinc(II). These data are in qualitative agreement with the experimental selectivity coefficients of the sensors with respect to ions of these metals. The selectivity coefficient series for membranes plasticized with DOS and *o*-NPOE are similar, but in sensors based on *o*-NPOE the selectivity with respect to transition metal ions is more pronounced. The highest selectivity is observed for copper(II) and lead(II) ions.

Sensors with membranes plasticized with TOP are characterized by negative logarithms of the selectivity coefficients with respect to all the ions.

The selectivity coefficients measured by the method of mixed solutions are in good agreement with the data obtained by the BIP technique (Fig. 3).

The slopes of the calibration plots, obtained for the sensors in solutions of varied nature, were used to calculate the cross sensitivity parameters (Table 3): average cationic slope

$$S_{av} = n^{-1} \sum_i S_i, \quad (1)$$

nonselectivity factor

$$f = S_{av}/s^2, \quad (2)$$

and reproducibility factor

$$K_{av} = n^{-1} \sum_i (S_i/s_i^2), \quad (3)$$

where S_i is the slope of the electrode function of

Table 3. Parameters of cross sensitivity of sensors

Membrane	S_{av}, mV/pX	F	K
1	28(11)*	0.22	2.7
2	34(13)	0.19	4.1
4	18(10)	0.19	1.4
5	27(13)	0.17	2.2
7	35(13)	0.21	7.6
8	39(10)	0.39	13.4

* rms deviation of S is given in parentheses.

a sensor in a solution of *i*th ion, *n* is the number of ions, *s* is the rms deviation of the average cationic slope, and s_i is the rms deviation of S_i.

The cross sensitivity parameters of TPP-based sensors were calculated using the slopes of the electrode function in solutions of 15 cations and their standard deviations. The data obtained are listed in Table 3.

The average slopes of the electrode function (cationic slope of the sensors) S_{av} is within the range 18–39 mV/pX. This parameter is the most important, and the higher its value, the better the cross sensitivity of a sensor. The rms deviation of the average slope *S* is commonly used to calculate the nonselectivity factor. The nonselectivity factor, characterizing the uniformity of distribution of the sensor sensitivity to various cations, takes values in the range from 0.17 to 0.39, and the higher this factor, the more uniform the selectivity of a membrane material with respect to various ions. Finally, the reproducibility factor characterizes the reproducibility of the electrode function of sensors. This factor is commonly calculated using the rms deviation of the cationic slopes of sensors, found on the basis of three calibrations against solutions of individual ions. The reproducibility factor is within the range 1.4–13.4. Correspondingly, the higher this value, the better the reproducibility of the sensor signal. The calculated cross sensitivity parameters show a rather high cross sensitivity for all of the sensors studied. The best cross sensitivity is observed for sensor nos. 7 and 8 with membranes plasticized with TOP, and also membranes based on DOS and *o*-NPOE, containing an ionic additive.

The results of tests of a multisensor system with TPP-based sensors in recognition of specific objects are presented in Fig. 4.

The system reliably distinguishes apple juices of various manufacturers and differentiates all 100% juices from an apple drink. Thus, the system can be used in practice for monitoring the quality and identifying apple juices.

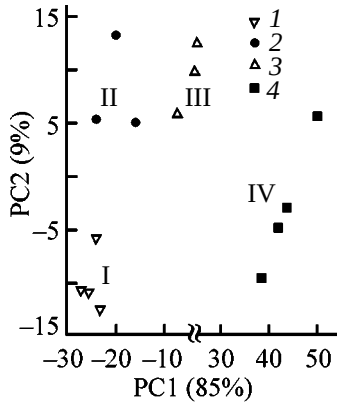

Fig. 4. (*1–4*) Recognition of samples I–IV. The result of principal component analysis is presented in the form of a plot of scores; PC1 and PC2 are the first and second principal components, respectively; percentages in parentheses are the explained variances for a given principal component.

CONCLUSION

Tetraphenylporphyrin-based polyvinyl chloride sensor materials plasticized with solvents of varied nature and containing cationic lipophilic additives were developed and studied. It was established that the properties of sensor materials containing tri-(2-ethylhexyl) phosphate are mainly determined by the solvent-plasticizer itself. A pronounced contribution to the properties of sensors based on di(2-ethylhexyl) sebacate and *o*-nitrophenyl octyl ether comes from the lipophilic additive and *meso*-tetraphenylporphyrin. The selectivity of the sensors was measured by the methods of biionic potentials and mixed solutions and their high cross sensitivity to cations of alkali, alkaline-earth, and transition metals. A multisensor system of the "electronic tongue" type was developed on the basis of sensors with *meso*-tetraphelylporphyrin and was successfully used to recognize various drinks.

REFERENCES

1. Biesaga, M., Pyrzynska, K., and Trojanowicz, M., *Talanta*, 2000, vol. 51, no. 2, pp. 209–224.
2. Huser, M., Morf, W.E., Fluri, K., *et al.*, *Helv. Chim. Acta*, 1990, vol. 73, no. 5, pp. 1481–1496.
3. Park, S.B., Matuszewski, W., Meyerhoff, M.E., *et al.*, *Electroanalysis*, 1991, vol. 3, no. 9, pp. 906–916.
4. Gao, D., Gu, J., Yu, R.Q., *et al.*, *Analyst*, 1995, vol. 120, no. 2, pp. 499–502.
5. Malinowska, E. and Meyerhoff, M.E., *Anal. Chim. Acta*, 1995, vol. 300, no. 1–3, pp. 33–43.
6. Gao, D., Gu, J., Yu, R.Q., *et al.*, *Fresenius J. Anal. Chem.*, 1995, vol. 351, no. 6, pp. 484–488.
7. Kibbey, C.E., Park, S.B., De Adwyler, G., *et al.*, *J. Electroanal. Chem.*, 1992, vol. 335, nos. 1–2, pp. 135–149.
8. Morf, W.E., *The Principles of Ion-Selective Electrodes and Membrane Transport*, Budapest: Akademiai Kiado, 1981.
9. Gupta, V.K., Jain, A.K., Singh, L.P., *et al.*, *Anal.*

Chim. Acta, 1997, vol. 355, no. 1, pp. 33–41.

10. Gupta, V.K., Prasad, R., Kumar, P., *et al.*, *Anal. Chim. Acta*, 2000, vol. 420, no. 1, pp. 19–27.
11. Vlasov, Yu.G., Legin, A.V., Rudnitskaya, A.M., *et al.*, *Zh. Anal. Khim.*, 1997, vol. 52, no. 11, pp. 1199–1205.
12. Vlasov, Yu.G., Ermolenko, Yu.E., Legin, A.V., *et al.*, *Zh. Anal. Khim.*, 1999, vol. 54, no. 5, pp. 542–549.
13. Vlasov, Yu., Legin, A., and Rudnitskaya, A., *Sens. Actuators B*, 1997, vol. 44, no. 1–3, pp. 532–537.
14. Inada, Y., Nakano, Y., Inamo, M., *et al.*, *Inorg. Chem.*, 2000, vol. 39, no. 21, pp. 4793–4801.
15. Legin, A.V., Rudnitskaya, A.M., Smirnova, A.L., *et al.*, *Zh. Prikl. Khim.*, 1999, vol. 72, no. 1, pp. 105–112.
16. Umezawa, Y., Umezawa, K., and Sato, H., *Pure Appl. Chem.*, 1995, vol. 67, no. 3, pp. 508–518.
17. Schaller, U., Bakker, E., Spichiger, U.E., *et al.*, *Anal. Chem.*, 1994, vol. 66, no. 3, pp. 391–398.
18. Valiotti, A.B., Kopylova, E.A., and Abakumova, R.A., *Zh. Fiz. Khim.*, 1995, vol. 69, no. 12, pp. 2176–2178.
19. *Porfiriny: struktura, svoistva, sintez* (Porphyrins: Structure, Properties, and Synthesis), Enikolopyan, N.S., Ed., Moscow: Nauka, 1985.
20. Funahashi, S., Yamaguchi, Y., and Tanaka, M., *Inorg. Chem.*, 1984, vol. 23, no. 15, pp. 2249–2253.

Russian Journal of Applied Chemistry, Vol. 75, No. 5, 2002, pp. 733–739. Translated from Zhurnal Prikladnoi Khimii, Vol. 75, No. 5, 2002, pp. 752–758.
Original Russian Text Copyright © 2002 by Novoselova, Gab.

APPLIED ELECTROCHEMISTRY AND CORROSION PROTECTION OF METALS

Electrode Reactions on Synthetic Diamond and Cubic Boron Nitride in Ionic Melts[1]

I. A. Novoselova and A. I. Gab

Vernadsky Institute of General and Inorganic Chemistry, National Academy of Sciences of Ukraine, Kiev, Ukraine

Received November 13, 2001

Abstract—The behavior and corrosion resistance of synthetic diamond and cubic boron nitride in chloride, chloride–oxide, and oxide salt melts at 750–900°C were studied by potentiometric and voltammetric methods.

Considerable recent attention of electrochemists has been focused on diamond as a new electrode material whose behavior in aggresive media is characterized by unique chemical, physical, and electrochemical features [1, 2]. All the studies were carried out in aqueous and organic electrolytes, mainly with film diamond and diamond-like electrodes doped and modified with various dopants (B, N, Pt). No such researches were made in molten media because of difficulties in designing a diamond electrode suitable for the operation in salt melts at high temperatures. Furthermore, diamond materials were used as inert electrodes for the implementation of processes that are difficult to realize on usual electrodes such as platinum or glassy carbon (for example, electrolytic reduction of nitrate ions to ammonia [3]).

This work is concerned with deposition of high-melting metals on grains of dielectrics. Plating of grains of superhard materials by high-melting metals is one of the most radical ways for improving the performance of abrasive tools [4]. This problem was first solved for diamond [5]. To explain the appearance of the electrode function of dielectric diamonds in salt melts, the concept of surface conductivity arising from redox reactions on the diamond–ionic melt interfaces was offered [6, 7]. Having extended the range of supports, we were able to metal-plate cubic boron nitride, which is the closest structural analog of diamond. In was also shown [8] that these two dielectrics exhibit a similar electrochemical behavior in salt melts. This work summarizes earlier data and new experimental data on the electrochemical behavior of diamond and cubic boron nitride (c-BN).

[1] Reported at the X Kola Seminar "Electrochemistry of Rare Metals," Apatity, December 4–7, 2000.

EXPERIMENTAL

In this work we used dielectric powders of single crystals of AS15 and ASS diamonds (grain size 650/500, 315/250, and 160/125 μm) and of KR cubic boron nitride c-BN (grain size 200/160 and 160/125 μm), and also compact c-BN pelletized in disks of diameter 6.45 mm and thickness 0.66 mm.[2]

Synthetic diamonds were synthesized from the system Ni–Mn–C under static conditions and purified to remove the residual melt-solvent by acid methods (boiling with $K_2Cr_2O_7$–H_2SO_4). Cubic boron nitride of KR grade was obtained from hexagonal boron nitride at high pressures and temperatures in the field of thermodynamic stability of the cubic modification using magnesium as a process stimulant. To isolate the cubic modification of boron nitride from the synthesis products, we treated them with dilute solutions of hydrochloric acid and with a mixture of molten potassium and sodium hydroxides. The content of the cubic modification in thus isolated c-BN crystals was 99% [9].

Pelletized compact c-BN was obtained by solid-phase polymorphic transition of hexagonal graphite-like form of boron nitride at high pressures (about 8.5 GPa) and temperatures (1573–2273 K).

The impurity content of the samples under study is given in Table 1.

We determined the dc resistivity of natural diamond and compact c-BN at 1023 K with an R5083 bridge. The resulting values are given below:

Material	Natural diamond	AS15 (500/400)	c-BN
ρ, Ω m	7.2×10^8	2.7×10^6 [10]	4.7×10^2

[2] The samples were prepared in the Institute of Superhard Materials, National Academy of Science of Ukraine.

1070-4272/02/7505-0733$27.00 © 2002 MAIK "Nauka/Interperiodica"

Table 1. Impurity content of diamond and cubic boron nitride

Sample	Contents of impurities, wt %					
	Si	Fe	Mg	Al	Ca	Ti
AC15 (315/250)	0.05–0.1	0.03–0.08	0.003–0.005	0.002–0.003	0.01–0.02	–
KP (200/160)	0.09	0.02	0.8	0.01	0.05	0.01
Blende c-BN	0.02	0.002	0.004	0.002	0.05	–
Sample	Contents of impurities, wt %					
	C	O	B	Ni	Mn	Co
AC15 (315/250)	–	–	0.033–0.040	0.90–2.20	0.80–1.75	0.001–0.002
KP (200/160)	0.3	0.20	–	–	–	–
Blende c-BN	0.04	0.08	–	–	–	–

The resistivities of diamond and cubic boron nitride at the experimental temperatures allow them to be classed with dielectric materials.

Potentiometric and voltammetric mesurements were carried out in a three-electrode electrochemical cell with a PI-50-1.1 potentiostat and a PR-8 programmer. Voltammograms were recorded on an LKD 4-003 device at scanning rates from 0.02 to 0.2 V s^{-1}. The electrode potentials were recorded on Shch68003 and F4800 high-resistance voltmeters. The experiments were carried out in an electric furnace at 973–1173 K. The working electrode in a three-electrode cell was a platinum-grid container filled with a dielectric powder and immersed in a melt with the aid of a platinum wire. This electrode was called a combined platinum–dielectric electrode (CPDE), as it contains two phases: platinum as a conductive phase and diamond or c-BN powder as a dielectric phase. Further studies have shown that both phases participate in electrochemical processes.

We used a lead electrode Pb | NaCl–KCl–$PbCl_2$ in chloride and chloride–oxide melts as a reference electrode [11]. A platinum or glassy carbon crucible served as a container for a melt and simultaneously as an anode.

The graphite electrode was a rod of diameter 5 mm made from spectrally pure graphite. Its upper part, which extended from a melt, was covered with a porcelain tube. A platinum wire served as a current lead. A pellet of cubic boron nitride was immersed in a melt with the aid of a platinum wire.

The chemicals in use were of chemically pure and analytically pure grades. Before and after each experiment, we controlled the weight and appearance of powders and made their X-ray phase analysis using a DRON 3.0 X-ray diffractometer.

To deposit coatings, we used nickel grids and current leads to a dielectric material powder and tungsten or molybdenum rods of diameter 10 mm, which served as anodes. Metal-plated grains were separated from the remaining electrolyte by decanting after 30-min boiling in distilled water.

The thermogravimetric studies were carried out on a Q-1500D derivatograph, and atomic absorption analysis, on a PYE UNICAM SP 9 atomic absorption spectrophotometer. The X-ray emission spectra were taken on an RSM-500 X-ray ultrawave spectrometer with oil-free evacuation. The ESR spectra were recorded on an SE/X 2547 (Radiopan corporation) radiospectrometer of 3-cm range at room temperature.[3]

To estimate the chemical resistance of the diamond and c-BN, we have carried out thermodynamic analysis of possible reactions of these substances with oxygen-containing compounds of Group IV–VI elements [12]. On this basis, we constructed series of such compounds in the order of increasing oxidizing power toward the dielectrics under study (at 1000 K). For diamond, such a series is as follows: Na_2CO_3, Na_2O, Na_2WO_4, Na_2MoO_4, $Na_2W_2O_7$, CO_2, WO_3, Na_2SO_4, Na_2CrO_4, $Na_2Mo_2O_7$, MoO_3, SO_3, and CrO_3.

[3] The X-ray emission spectra were taken in the Institute of Materials Science Problems, National Academy of Sciences of Ukraine. The ESR spectra were taken in the Institute of Superhard Materials, National Academy of Sciences of Ukraine.

Table 2. Gibbs energies ΔG_T^0 of reactions of cubic boron nitride with oxygen-containing compounds of Group VI elements

Reaction	ΔG_T^0, kJ, at indicated T, K			
	900 K	1000 K	1100 K	1200 K
$8BN + 4Na_2WO_4 = 8NaBO_2 + 3N_2 + 2W_2N$	–333.66	–362.37	–380.43	–401.36
$8BN + 4Na_2MoO_4 = 8NaBO_2 + 3N_2 + 2Mo_2N$	–473.08	–499.82	–518.90	–540.99
$8BN + 4WO_3 = 4B_2O_3 + 2W_2N + 3N_2$	–379.91	–428.94	–477.73	–526.43
$8BN + 4MoO_3 = 4B_2O_3 + 2Mo_2N + 3N_2$	–601.12	–648.10	–694.75	–741.03
$8BN + 2Na_2W_2O_7 = 4NaBO_2 + 2W_2N + 3N_2 + 2B_2O_3$	–293.59	–341.79	–381.23	–414.36
$8BN + 2Na_2Mo_2O_7 = 4NaBO_2 + 2Mo_2N + 3N_2 + 2B_2O_3$	–454.59	–501.58	–549.11	–589.48

Table 3. Results of corrosion tests of AS-15 (315/250) diamonds in Na_2WO_4 melts at 1173 K

Addition to melt, 20 mol %	Δm, %	$V \times 10^{-1}$, g m^{-2} h^{-1}	Δm, %	$V \times 10^{-1}$, g m^{-2} h^{-1}	Δm, %	$V \times 10^{-1}$, g m^{-2} h^{-1}
	at indicated test duration, h					
	1.0		2.0		5.0	
–	1.39	7.24	2.22	5.92	5.23	5.51
WO_3	1.49	7.84	2.33	6.14	4.78	4.13
MoO_3	2.47	13.01	3.62	9.53	9.75	10.27

The series for cubic boron nitride is $Na_2W_2O_7$, Na_2WO_4, CO_2, Na_2CO_3, WO_3, Na_2MoO_4, Na_2SO_4, $Na_2Mo_2O_7$, MoO_3, Na_2CrO_4, SO_3, and CrO_3.

It is evident that the "mildest" oxidizing agents for diamond and c-BN are tungstate, ditungstate, sodium carbonate, and carbon dioxide, i.e., on the one hand, redox processes in melts containing these compounds can occur on the surface of the dielectric materials under study, and, on the other hand, the corrosion of these latter should not be very strong.

It is necessary to note that, according to our thermodynamic analysis, the nitrides Mo_2N and W_2N of high-melting metals can be formed in the reactions of c-BN with Na_2MO_4, $Na_2M_2O_7$, and MO_3 (M = Mo, W) along with the high-melting metals and their dioxides (Table 2). However, our thermogravimeric study of the behavior of cubic boron nitride in the system Na_2WO_4–WO_3 has not revealed changes in the weight and phase composition of c-BN, and by the data of the atomic absorption analysis this melt contains no boron. Therefore, the occurrence of the reactions listed in Table 2, despite their high negative Gibbs energies, was not proved experimentally.

We studied corrosion of diamond and c-BN in halide, halide–oxide, and oxide melts during long-run tests. Changes in the weight and phase composition of the powders under study in the system NaCl–KCl (1 : 1) were detected neither in air nor in argon atmosphere. Addition of sodium tungstate (or molybdate) in amounts of up to 50 mol % into this melt results in minor weight losses Δm (up to 1% in 2 h). The bubbling of CO_2 through the NaCl–KCl melt (1 : 1) does not change the appearance and weight of the dielectric powders either.

Weight losses Δm of both diamond and c-BN were detected in melts of sodium tungstate and oxide mixtures based on it (Table 3). No changes in the phase compositions of the powders under study were found in the corrosion tests.

It follows from Table 3 that the weight loss of diamonds increases with addition of 20% of WO_3 or MoO_3 into an Na_2WO_4 melt. The corrosion rate V decreases as the time of keeping the sample in the melts increases.

Chemical reactions occurring in the melts under study can be described by the following equations:

$$Na_2WO_4 + 3C \rightarrow W + 3CO + Na_2O,$$

$$\Delta G = 176.22 \text{ kJ};$$

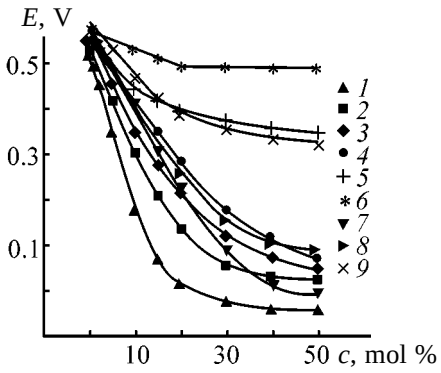

Fig. 1. Potential E as a function of concentration c of (*1, 2, 6–9*) Na_2WO_4 and (*3–5*) Na_2MoO_4, as measured in an NaCl–KCl (1 : 1) melt on various electrodes. Electrode: (*1–3*) combined diamond AS15 (160/125), (*2–4*) combined diamond AS15 (315/250), (*5, 6*) platinum, (*7*) combined c-BN KR (250/200), (*8*) combined c-BN KR (160/125), and (*9*) compact c-BN.

$$2Na_2W_2O_7 + 3C \rightarrow 2W + 3CO_2 + 2Na_2WO_4,$$

$$\Delta G = -84.66 \text{ kJ};$$

$$2Na_2Mo_2O_7 + 3C \rightarrow 2Mo + 3CO_2 + 2Na_2MoO_4,$$

$$\Delta G = -263.73 \text{ kJ}.$$

A high-melting metal formed on the surface of diamonds apparently dissolves in oxide melts.

Using X-ray emission spectroscopy and electron spin resonance (ESR), we have studied how the treatment of diamonds in various melts [equimolar mixture NaCl–KCl, equimolar mixture NaCl–KCl–CO_2 (pressure 10 atm), Na_2WO_4, and Na_2WO_4–xWO_3 (MoO_3)] at 1023 K affects the surface texture of the diamonds. The ESR experiments have not revealed any conductive (metallic) films on the surface of diamonds after their 3-h keeping in the above melts in the absence of current. We have shown by X-ray emission spectroscopy that the treatment with melts results in a rupture of bond between the surface carbon atoms and atoms of other elements adsorbed on the diamond surface during synthesis and subsequent removal of the residual melt-solvents from the diamonds. In this case, recombination of C–C bonds, reconstruction of the diamond surface, and filling of the surface carbon atoms with electrons can take place. Ihm *et al*. [13], using the self-consistent pseudopotential method, calculated the electronic structure of (111) diamonds and drew on this basis a rather interesting conclusion: an ideal surface of diamonds should have a metallic conductivity.

Thus, our thermodynamic analysis and experimental data on the chemical behavior of diamonds in oxide melts qualitatively give the same results and demonstrate that the redox reactions on the interface give rise to an electrochemical equilibrium and to the appearance of an intrinsic electrolytic potential.

The potentiometric study of the behavior of combined diamond and c-BN electrodes in chloride–oxide systems was carried out by measuring emfs of the following circuits:

$$\text{Pt, dielectric} \mid \text{NaCl–KCl (1 : 1)} \parallel \text{NaCl–KCl (1 : 1)–2.5 mol \% } PbCl_2 \mid \text{Pb}, \quad (1)$$

$$\text{Pt, dielectric} \mid \text{NaCl–KCl (1 : 1)–}x\text{Na}_2\text{WO}_4(\text{Na}_2\text{MoO}_4) \parallel \text{NaCl–KCl (1 : 1)–2.5 mol \% } PbCl_2 \mid \text{Pb}, \quad (2)$$

$$\text{Pt, dielectric} \mid \text{NaCl–KCl (1 : 1)–}CO_2\text{ (bubling)} \parallel \text{NaCl–KCl (1 : 1)–2.5 mol \% } PbCl_2 \mid \text{Pb}, \quad (3)$$

where dielectric is diamond or c-BN.

We found that the potential of combined diamond and c-BN electrodes in a pure chloride melt NaCl–KCl (1 : 1) coincides with the potential of platinum. Addition of Na_2WO_4 (or Na_2MoO_4) into the melt results in the displacement of potentials of the combined electrodes to the negative region (Fig. 1). The compact c-BN electrode behaves similarly to the combined c-BN electrode. In this case, the following relation was observed: the finer the grains of a dielectric material, the greater the deviations of its potential from the platinum potential. The potentials of all the combined electrodes under study became more negative than the potentials of platinum, which served as a metal container.

Bubbling CO_2 through an NaCl–KCl (1 : 1) melt also results in displacement of potentials of graphite, platinum, and combined platinum–dielectric electrodes to the negative region, the potential of a combined diamond electrode approaching the potential of the graphite electrode [7]. When the gas feeding is terminated, the initial potentials of all the electrodes are restored.

The potentials of combined platinum–diamond electrodes (CPDE) in oxide melts appreciably differ from the potential of platinum. They are sensitive to the variations of acid–base properties of melts. When acid components (WO_3 and MoO_3) are added, the potential of a combined dielectric electrode is shifted to the positive region, and basic additions (Na_2CO_3)

Table 4. Effect of MoO_3 concentration on steady-state potentials E of electrodes in an Na_2WO_4 melt at 1173 K

Electrode	E, V, at indicated MoO_3 concentration, mol %						
	0	2	4	8	12	16	20
Platinum	–0.60	–0.19	–0.16	–0.06	–0.04	–0.03	–0.02
CPDE ASS (630/500)	–0.97	–0.79	–0.73	–0.62	–0.62	–0.61	–0.56
CPDE AS15 (315/250)	–0.98	–0.74	–.0.71	–0.63	–0.60	–0.61	–0.60
Graphite	–1.24	–0.87	–0.79	–0.65	–	–	–
Molybdenum	–(1.3–1.5)	–1.00	–0.94	–0.85	–0.80	–0.76	–0.73

* Potentials are given relative to the reference electrode Na_2WO_4–0.2 mol % $WO_3 \mid O_2$, Pt.

shift it to the negative region of potentials [6]. The results of our potentiometric study of the behavior of combined platinum–diamond, graphite, and metallic (Pt and Mo) electrodes in an oxide melt at varied concentration of molybdenum oxide are given in Table 4.

Table 4 shows that the CPDE potential in pure melt of sodium tungstate is more negative that the potential of the platinum electrode approximately by 400 mV, and this difference increases to 600 mV when molybdenum oxide is added. At the same time, the CPDE potential is more positive by 200 mV than the potential of the graphite electrode in a tungstate melt, but these potentials become almost equal as molybdenum oxide is added. The potential of the molybdenum electrode in all experiments was more negative than the CPDE potential.

We can assume that the potential-determining processes on graphite and combined platinum–diamond electrodes are similar and can be described by the following electrode reaction:

$$C + O^{2-} \rightleftarrows C \mid O_{ads} + 2e.$$

We can write the following expression for the potential of this electrode:

$$E = E^0 + \frac{RT}{2F}\ln\frac{[C \mid O_{ads}]}{[O^{2-}]} = E^0_* + \frac{2.3RT}{2F}pO^{2-},$$

where $E^0_* = E^0 + \frac{RT}{2F}\ln[C \mid O_{ads}]$.

Correspondingly, the equation of the electrode reaction and the potential of the combined c-BN electrode can be presented as [6]

$$BN + 2O^{2-} \rightleftarrows BO_2^- + 1/2N_2 + 3e,$$

$$E = E^0 + \frac{RT}{3F}\ln\frac{[BO_2^-][N_2]^{1/2}}{[BN][O^{2-}]}.$$

In this work we have studied the CPDE behavior at 750°C by voltammetry in the following systems:

$$NaCl–KCl\,(1:1)–0.5\ M\ Na_2WO_4–0.05–0.15\ M\ NaPO_3, \quad (4)$$

$$NaCl–KCl\,(1:1)–0.5\ M\ Na_2MoO_4–0.05–0.20\ M\ NaPO_3. \quad (5)$$

These systems were developed for the electrolytic deposition of tungsten, molybdenum, and their carbides on metallic electrodes [14].

The cyclic I–E curves obtained on a platinum electrode and CPDE are given in Fig. 2. The presence of current maxima in the curves is characteristic of the processes with a mixed kinetics when the rates of the charge transfer and mass transfer of ions are comparable. This is confirmed by the dependence of the peak potentials on the potential scanning rate. It follows from Table 5 that diamond powder AS15 (315/250) behaves as an electroconductive constituent of an electrode: the cathode current peak $I_{p(c)}$ increases as compared to the platinum electrode, and its

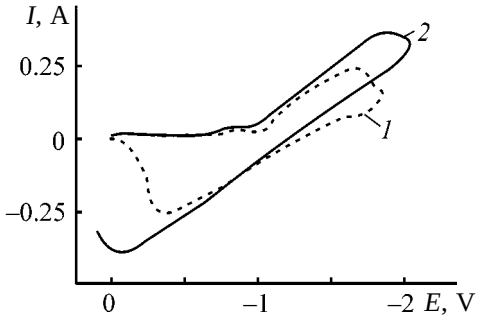

Fig. 2. Voltammograms obtained on (*1*) platinum electrode and (*2*) CPDE in the melt NaCl–KCl–0.5 M Na_2MoO_4–0.15 M $NaPO_3$ at 1023 K. Polarization rate 0.1 V s^{-1}. (*I*) Current and (*E*) potential.

Table 5. Characteristics of cyclic voltammograms obtained on a platinum electrode and on CPDE in the system NaCl–KCl–0.05 M Na_2MoO_4–0.15M $NaPO_3$

Electrode	$I_{p(c)}$, A	$E_{p(c)}$	$E_{p/2(c)}$	$E_{p(a)}$	$E_{p(c)} - E_{p(a)}$	$E_{p/2(c)} - E_{p(c)}$	αn_α
		V					
Platinum	0.215	–1.68	–1.28	–0.36	1.32	0.40	0.408
CPDE	0.320	–1.90	–1.35	0.08	1.82	0.55	0.298

Table 6. Coating thickness h and degree of diamond plating Δm by carbides of high-melting metals at various electrolysis durations τ

τ, min	Δm, wt %	h, μm	Δm, wt %	h, μm
	W_2C		Mo_2C	
30	0.38	0.01	0.63	0.035
60	10.56	0.30	7.62	0.44
90	12.40	0.40	8.00	0.46

potentials are strongly stretched along the potential axis. More positive peak potentials of anode current $E_{p(a)}$ as compared to the platinum electrode, seem to result from a chemical reaction between a generated high-melting metal and diamond. Therefore, the product formed in the cathode cycle on CPDE (a carbide phase) is more difficult to dissolve than a high-melting metal formed on platinum. Apparent charge-transfer coefficients αn_α for the cathode process, calculated by the equation for irreversible charge transfer [15], are given in Table 5.

$$E_{p/2(c)} - E_{p(c)} = 1.857\ RT/\alpha n_\alpha F.$$

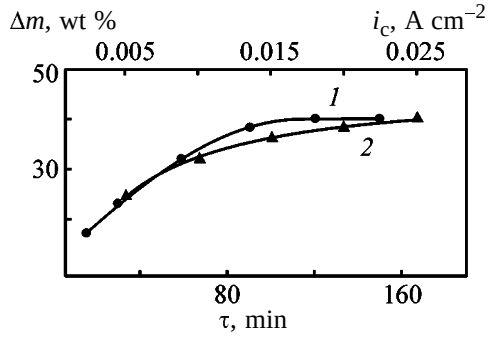

Fig. 3. Degree of c-BN plating Δm with molybdenum carbide as a function of (*1*) electrolysis duration τ and (*2*) cathode current density i_c measured in the melt NaCl–LiF (3 : 1)–1.3 mol % Na_2MoO_4–1 mol % Na_2CO_3 at 1173 K.

The degree of irreversibility of the electrode process on a diamond electrode is much greater.

Knowing the specific surface area of diamond powders in use, we determined the fraction of the surface participating in the electrode process. We found that this fraction increases with increasing $NaPO_3$ concentration from 0 to 18.10% for system (4) and from 3.30 to 13.00% for system (5).

The voltammetric study of the CPDE behavior in systems (4) and (5) allowed us to determine the optimal conditions for the electrodeposition of carbides of high-melting metals (W_2C, Mo_2C) on diamond. Electrolyte composition (mol %): NaCl 45.00–47.30, KCl 45.00–47.30, Na_2MoO_4 (or Na_2WO_4) 5.00–8.00, and $NaPO_3$ 0.40–2.00. Current density i_c = (7–10) × 10^{-3} A cm^{-2}, temperature 750–800°C. The optimal electrolysis duration, as follows from Table 6, is 60 min.

Continuous solid coatings of molybdenum carbide on cubic boron nitride were obtained from the system NaCl–LiF (1 : 1)–1.3 mol % Na_2MoO_4–1 mol % Na_2CO_3.

When this system is used for plating c-BN with molybdenum carbide, the degree of plating depends on the cathode current density and the electrolysis time (Fig. 3). At T = 1173 K, τ = 90 min, and i_c = 0.02 A cm^{-2}, we obtained a solid Mo_2C coating on c-BN with the thickness h 4.80 μm.

Continuous and well adhering to the support coatings of high-melting metals (Mo, W) were obtained on c-BN from the following systems: NaCl–LiF (1 : 1)–2.5 mol % Na_2MoO_4 at T = 1173 K, i_c = 0.02 A cm^{-2}, τ = 45 min, Δm = 14.6 wt %, h = 1.02 μm; Na_2WO_4–1 mol % WO_3 at T = 1173 K, i_c = 0.20–0.30 A cm^{-2}, τ = 90 min, Δm = 220 wt %, h = 7.80 μm.

The optimal systems and conditions for the deposition of coatings of high-melting metals and their carbides on diamond and c-BN are given in Table 7.

Table 7. Optimal conditions for the deposition of coatings of high-melting metals and their carbides with thickness *h* on dielectric materials

Dielectric	Coating	System	*T*, K	i_c, A cm^{-2}	τ, min	*h*, μm
Diamond	Mo_2C	NaCl–KCl (1 : 1)–5 mol % Na_2MoO_4–0.75 mol % $NaPO_3$	1073	0.075	60	0.46
	W_2C	NaCl–KCl (1 : 1)–6 mol % Na_2WO_4–0.4 mol % $NaPO_3$	1073	0.010	60	0.40
c-BN	Mo_2C	NaCl–LiF (3 : 1)–1.3 mol % Na_2MoO_4–1 mol % Na_2CO_3	1173	0.020	90	4.80
	Mo	NaCl–LiF (3 : 1)–2.5 mol % Na_2MoO_4	1173	0.020	45	1.02
	W	Na_2WO_4–1 mol % WO_3	1123	0.220	90	7.80

CONCLUSIONS

(1) Potentials of combined dielectric electrodes (diamond and c-BN) in pure chloride melts coincide with the potential of platinum. In this case, no weight and phase changes take place in the dielectrics.

(2) When weak oxidizing agents (Na_2WO_4, Na_2MoO_4, and CO_2) are added to a chloride melt, minor weight losses (up to 1 wt %) of diamond and c-BN are observed. The potential of a combined platinum-dielectric electrode becomes more negative than the potential of platinum, the deviations of the potentials depending on the grain size. Electroplated coatings of tungsten and molybdenum carbides up to 0.50 μm thick can be obtained from halide–oxide electrolytes.

(3) Both diamond and c-BN have their interinsic potentials in purely oxide melts based on sodium tungstate. These potentials are more negative than the potential of platinum. The potential of a combined platinum–dielectric electrode depends on acid–base properties of a melt. The corrosion of the dielectrics is determined by the concentration of acid additions and corresponds to the series of oxidizing powers constructed on the basis of the thermodynamic analysis.

ACKNOWLEDGMENTS

This work was financially supported by the Scientific and Technical Center of Ukraine (project no. 1622).

REFERENCES

1. Pleskov, Yu.V., *Usp. Khim.*, 1999, vol. 68, no. 5, pp. 416–429.
2. Rao, T.N. and Fujishima, A.F., *Diamond Relat. Mater.*, 2000, no. 9, pp. 384–389.
3. Tenne, R., Patel, K., Hashimoto, K., and Fujishima, A., *J. Electroanal. Chem.*, 1993, vol. 347, nos. 1–2, pp. 409–415.
4. *Paika i metallizatsiya sverkhtverdykh instrumental'nykh materialov* (Soldering and Metal Plating of Superhard Tool Materials), Naidich, Yu.V., Ed., Kiev: Naukova Dumka, 1977.
5. Shapoval, V.I., Kushkhov, Kh.B., and Malyshev, V.V., *Poroshk. Metall.*, 1986, no. 7, pp. 43–45.
6. Kushkhov, Kh.B., Shapoval, V.I., and Baraboshkin, A.N., *Dokl. Akad. Nauk SSSR*, 1990, vol. 312, no. 6, pp. 1405–1408.
7. Kushkhov, Kh.B., Novoselova, I.A., and Shapoval, V.I., *Elektrokhimiya*, 1993, vol. 29, no. 7, pp. 904–906.
8. Malyshev, V.V., Novoselova, I.A., Gab, A.I., and Shapoval, V.I., *Poverkhnost'*, 1997, no. 9, pp. 70–74.
9. Bogatyreva, G.P., Zusmanov, E.R., Kotova, N.V., *et al.*, *Poverkhnost'*, 1997, no. 10, pp. 99–108.
10. Aleshin, V.G., Smekhnov, A.A., Bogatyreva, G.P., and Kruk, V.B., *Khimiya poverkhnosti almaza* (Chemistry of the Diamond Surface), Kiev: Naukova Dumka, 1990.
11. Alabyshev, A.F., Lantratov, M.F., and Morachevskii, A.G., *Reference Electrodes for Fused Salts*, Washington: Sigma, 1965.
12. Malyshev, V.V., Novoselova, I.A., Gab, A.I., *et al.*, *Teor. Osn. Khim. Tekhnol.*, 2000, vol. 34, no. 4, pp. 435–448.
13. Ihm, J., Louie, S.G., and Cohen, M.L., *Phys. Rev. Bull.*, 1978, no. 2, vol. 17, pp. 769–775.
14. Novoselova, I.A., High-Temperature Electrochemical Synthesis of Molybdenum and Tungsten Carbides under Excess Pressure of Carbon Dioxide, *Cand. Sci. Dissertation*, Kiev, 1988.
15. Galus, Zb., *Teoretyczne podstawy elektroanalisy chemicznej*, Warsaw: Naukowe, 1971.
16. Novoselova, I.A., Malyshev, V.V., Gab, A.I., and Shapoval, V.I., *Sverkhtverd. Mater.*, 2001, no. 3, pp. 3–9.

Russian Journal of Applied Chemistry, Vol. 75, No. 5, 2002, pp. 740–744. Translated from Zhurnal Prikladnoi Khimii, Vol. 75, No. 5, 2002, pp. 770–772.
Original Russian Text Copyright © 2002 by Ol'shanskaya, Astaf'eva.

APPLIED ELECTROCHEMISTRY AND CORROSION PROTECTION OF METALS

Thermodynamics of Lithium Intercalates in Carbonized Fabric

L. N. Ol'shanskaya and E. N. Astaf'eva

Technological Institute, Saratov State Technical University, Engels, Saratov oblast, Russia

Received August 31, 2001; in final form, January 2002

Abstract—The method of quasi-equilibrium galvanostatic curves was applied to study the thermodynamics of lithium deintercalation from the system Li_xC_6 (solid phase)/Li^+ (solution) in the interval 293–323 K and the thermodynamic characteristics (ΔG, ΔS, ΔH) of lithium intercalation compounds in a carbonized fabric in relation to the degree of intercalation x.

The basic challenge in fabrication of rechargeable lithium power cells (LPCs) is creating high-energy-capacity reversible negative electrodes on the basis of lithium. The processes of charging–discharge of LPC electrodes, involving conversion of some chemical compounds into others, entail changes in thermodynamic functions: Gibbs energy ΔG, entropy ΔS, and enthalpy ΔH. Knowledge of these parameters may be of key importance not only for predicting electrochemical processes occurring in the system, but also for improving the LPC operation [1–4].

Compounds produced by lithium intercalation into carbon-containing materials (CCMs): coke, carbonized fabrics, fibers, pyrocarbon, etc., are widely used today as the active substance of negative electrodes for lithium-ion batteries [5–22]. The mechanism and kinetics of intercalation/deintercalation of lithium in the CCM structure have been the subject of numerous studies [5–21]. However, insufficient attention has been given to the thermodynamics of lithium intercalates in CCMs.

In this work we analyze the thermodynamic functions of lithium deintercalation from the Li_xC_6 compound formed in the structure of a carbonized fabric (CF) of the ELUR brand in a 1 M solution of $LiClO_4$ in a 1 : 1 (v : v) mixture of propylene carbonate and dimethoxyethane, PC + DME.

EXPERIMENTAL

The carbonized fabric ELUR is a fabric 50 cm wide and ~68 μm thick. Curved bent fibrils predominate in the CF structure. Voids with pore size of 10–50, 50–200 nm and more have nearly cylindrical shape and are oriented along the fibers. In the directions normal to the fiber axis, there are pores whose average diameter is approximately 1.6 nm. The cross-sectional structure of the fabric fibers shows no radial component, being preferably lamellar. It can withstand the disintegrating action of lithium being intercalated into the fabric and an increase in the interlayer spacing. Carbonized fabric has disordered structure.

Working electrodes were prepared from CF as follows: a layer of inert binder (F-42 L fluoroplastic, 10 wt %) dissolved in acetone was deposited onto a separator made of nonwoven polypropylene, and a fabric was manually rolled over it. After that, the electrodes were dried at 80°C in an oven to remove acetone. The thickness of the solid active layer after rolling and drying did not exceed 50–55 μm. Finished electrodes, having the form of spatulas with the working surface area of 1 cm^2, were fixed in a metallic holder. With account taken of the sufficient conductivity of the starting carbon materials and its increase upon formation of intercalation compounds with graphite [20, 22, 23], no additional metallic current leads were used.

Li_xC_6 electrodes were formed in the FC structure by the method of cathodic intercalation [9, 10] in the fifth cycle in a 1 M solution of $LiClO_4$ in 1 : 1 PC + DME [with water content not exceeding $(5–7) \times 10^{-3}$%] at a cathodic polarization potential E_c = –3.1 V relative to a nonaqueous silver chloride reference electrode (NSCRE) in the working solution. The intercalation time was 2 h, and the temperature range studied, 293–323 K (with a step of 5 K). Electrochemical measurements were carried out in a hermetically sealed three-electrode cell with cathode and anode spaces separated by glass frits. As counterelectrodes served 3 cm^2 plates of A 99.99 aluminum; as reference electrode was used NSCRE in the working electrolyte solution. To eliminate the diffusion poten-

1070-4272/02/7505-0740$27.00 © 2002 MAIK "Nauka/Interperiodica"

tial, LiCl crystals were introduced into the working solution of $LiClO_4$ [9, 24]. The silver chloride reference electrode is reversible and stable in the solvents used in the study [24]. The stability of the electrode potential was constantly monitored. If the solution turned yellow (in approximately 6 months), the electrodes were prepared anew. The NSCRE potentials measured relative to the standard aqueous silver chloride and lithium reference electrodes at different temperatures are presented in the table. Temperature measurements were done in a UTU-4 ultrathermostat, with temperature maintained constant to within ±0.1°C. The cell and the reference electrode were thermostated in a hermetically sealed dry vessel equipped with additional thermometers for visual inspection of the temperature of the electrolytes (at the working and reference electrodes). In each set of experiments, 3–5 parallel runs were done, and the results were processed by the least-squares method [25–27].

Figure 1 presents the equilibrium galvanostatic discharge curves E_{eq}–x of lithium deintercalation, measured at discharge current of 0.075 mA cm^{-2} (~5 mA g^{-1}). The difference between the curves obtained in the cathodic and anodic runs did not exceed 3–5 mV, which allowed them to be considered rather close to equilibrium [21, 28]. The process of lithium intercalation/deintercalation in the system studied, Li/Li^+(solution)/Li_xC_6, is described by the equation

$$Li_xC_6 + mLi^+ + me^- + \square_{vacancy} \rightleftarrows Li_{x+m}C_6. \quad (1)$$

No side reactions proceed in the system under study, and the lithium intercalation/deintercalation is accompanied by redistribution of the electron density in the forming phases Li_xC_6 and $Li_{x+m}C_6$. Owing to the small radius of the Li^+ ion (r_{Li^+} = 0.068 nm) [29] as compared to the interlayer spacings and voids in CF (~0.350–1.6 nm), the processes occur reversibly and at high rate.

Three regions of potential variation with x can be distinguished in the E_{eq}–x curves obtained ($x = Q_{eq}/Q^*$, where Q^* = 339 mA h g^{-1} is the theoretical specific capacity of Li_xC_6 at x = 1). In portion *I*, the reaction product is a compound of the composition $Li_{0.3 \le x \le 0.5}C_6$. This region is characterized by a decrease in potential, and a simultaneous decrease in x, with increasing temperature. This points to acceleration of lithium deintercalation from the structure of the active material with increasing temperature. In portion *II*, a steeper decrease in potential is observed until $x \approx 0.23$ is reached. In the vicinity of this x value, the electrode potential is independent of temperature. Further, deintercalation of lithium from the structure of carbonized fabric (portion *III*) is accompanied by a more stable and less steep run of E_{eq} at elevated temperatures, whereas at 293–308 K the potential decreases in the course of discharge. Such a behavior of the E_{eq}–x curves may be due to processes occurring in the solid phase of the active substance and to structural transformations in the lithium–graphite electrode, which are affected, as shown by the experimental data obtained, by temperature. Information about processes occurring in discharge can be obtained by analysis of how thermodynamic characteristics vary with the degree of intercalation x and the equilibrium potential established in the system Li_xC_6 (solid phase)/Li^+ (solution) in different stages of the anodic process

Potentials of NSCRE in 1 M solution of $LiClO_4$ in PC + DME (1 : 1) saturated with LiCl, measured relative to standard aqueous silver chloride and lithium reference electrodes

T, °C	Potential, V		
	NSCRE/SCRE	NSCRE/(Li/Li^+)	Ag/AgCl [29]
10	–0.0732	3.0662	0.23142
15	–0.0709	3.0613	0.22875
20	–0.0663	3.0571	0.22557
25	–0.0608	3.0534	0.22234
30	–0.0560	3.0475	0.21904
35	–0.0544	3.0432	0.21565
40	–0.0506	3.0393	0.21208
45	–0.0461	3.0361	0.20835
50	–0.0443	3.0314	0.20449

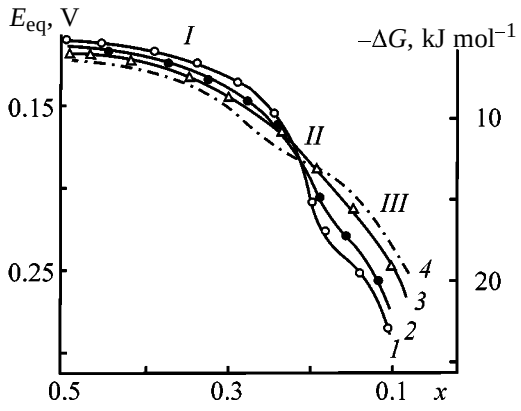

Fig. 1. Equilibrium potential E_{eq} and Gibbs energy ΔG of Li_xC_6 electrode in 1 M solution of $LiClO_4$ in PC + DME (1 : 1) vs. degree of intercalation, x. Temperature (K): (*1*) 293, (*2*) 298, (*3*) 308, and (*4*) 323.

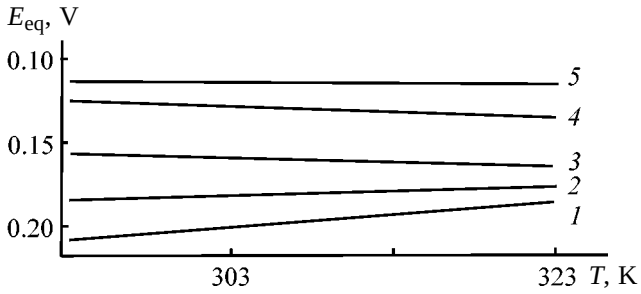

Fig. 2. E_{eq}–T dependence for Li_xC_6 electrode in 1 M solution of $LiClO_4$ in PC + DME (1 : 1). Degree of intercalation x: (*1*) 0.20, (*2*) 0.23, (*3*) 0.25, (*4*) 0.35, and (*5*) 0.50.

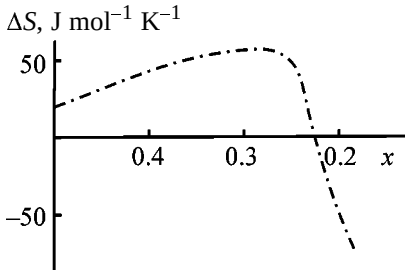

Fig. 3. ΔS–x dependence for Li_xC_6 electrode in 1 M solution of $LiClO_4$ in PC + DME (1 : 1).

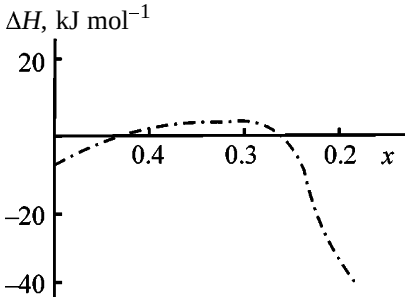

Fig. 4. Effect of the degree of intercalation x on the molar enthalpy, ΔH, of lithium deintercalation from the lithium–graphite electrode in 1 M solution of $LiClO_4$ in PC + DME (1 : 1).

in the temperature range 293–323 K:

$$\Delta G(x,T)_{eq} = -EF, \quad \Delta S(x,T)_{eq} = F(dE/dT)_{eq},$$

$$\Delta H = \Delta G + T\Delta S, \qquad (2)$$

where $F = 964585$ C mol^{-1} is the Faraday number.

To determine the temperature coefficient $(dE/dT)_{eq}$, the dependences E_{eq}–x (Fig. 1) were replotted in the coordinates E_{eq}–T for different x (Fig. 2). The results show that the temperature coefficient $(dE/dT)_{eq}$ is positive in the interval $0.5 > x > 0.23$, approximately equal to zero at $x \approx 0.23$, and negative at $x < 0.23$. The sign of the temperature coefficient determines the relationship between ΔG and ΔH [1, 2]. This allows evaluation of the heat effect and nature of the reaction (Peltier heat, exo- or endothermic process) and calculation of the entropy [1–4].

The dependences E_{eq}–T, ΔG–x, ΔS–x, and ΔH–x, obtained in this study and presented in Figs. 1–4, can be interpreted as follows. At positive temperature coefficient $(dE/dT)_{eq} > 0$ in the interval $0.23 < x \le 0.50$, ΔS is positive (Fig. 3). In this case, $T\Delta S > 0$, i.e., the work done by the electric current exceeds the heat effect of the corresponding process (1). This leads to energy deficiency in the system (endothermic reaction). The lithium deintercalation process is accompanied by energy expenditure and experiences certain hindrance associated, in all probability, with structural transformations in the electrode material [5, 13, 14, 21, 28] (lattice expansion, phase transformations).

A rise in ΔH, giving way to a plateau, is observed in the ΔH–x plot (Fig. 4) in the initial stage of lithium deintercalation at $0.23 \le x \le 0.50$. Analysis of changes in the entropy of the system in the coordinates ΔS–x (Fig. 3) also shows that lithium deintercalation is accompanied in the initial stage by an increase in ΔS, which may be due to structural ordering of the compound Li_xC_6 at these x values. The subsequent lithium deintercalation results in that $(dE/dT)_{eq} \approx 0$ at $x \approx 0.23$ and the potential E_{eq} is temperature-independent. The work is done in the system at the expense of enthalpy, without heat exchange, and lithium deintercalation proceeds without hindrance: the ΔS and ΔH values decrease (Figs. 3, 4).

At $x < 0.23$, $T\Delta S < 0$ $(dE/dT < 0)$ and the process is exothermic. According to the laws of thermodynamics, the work done by electric current in this case is lower than the heat effect of the reaction [1–4]. An excess amount of energy appears in the system: in all probability, the parameters of the compound Li_xC_6 change (recombination of excess energy is possible).

On the basis of the data of [3, 4, 21, 30, 31] and the analogy between processes occurring in intercalate formation from substances with lamellar, channel-like, or tunnel structure, some suggestions can be made about the mechanisms of the processes and the structural changes in the Li_xC_6 electrode. In the initial stage of deintercalation $(0.50 > x \ge 0.23)$, the structure of the compound Li_xC_6 changes significantly. Lithium ions leaving the lattice are, in all probability, surrounded in this case by lithium bound both to intercalated lithium ions and to carbon particles (the so-called short-range-order lithium occupying vacant

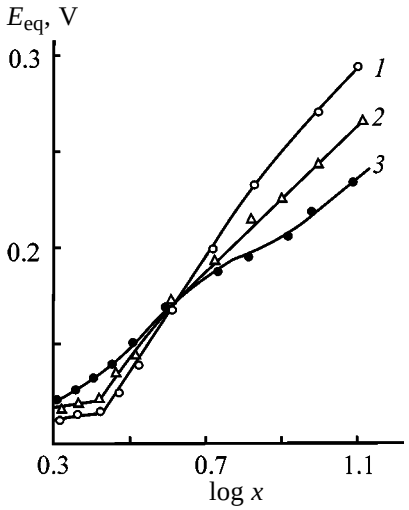

Fig. 5. E_{eq}–log x dependence for Li_xC_6 electrode in 1 M solution of $LiClO_4$ in PC + DME (1 : 1). Temperature (K): (*1*) 298, (*2*) 308, and (*3*) 323.

adjoining sites [12, 13, 17]). This must enhance deformation interactions between lithium species and lead to a change in the lattice parameters of Li_xC_6, which affects the thermodynamic properties of the system: ΔH and ΔS grow with decreasing x. At $x \approx 0.23$, lithium is surrounded in the structure by free vacancies. In this case, the thermodynamic characteristics are stabilized and lithium deintercalation is accompanied by a decrease in ΔH and ΔS. The subsequent decrease in ΔH and ΔS of the system at $x < 0.23$ can be accounted for by lattice recombination in the carbonized fabric.

The occurrence of structural transformations in the Li_xC_6 compound is confirmed by the E_{eq}–log x dependence obtained at different temperatures, in which three (at 293, 298, 303, and 308 K) to four (at 313 and 323 K) straight-line portions characteristic of the case of structural changes in the carbon material in the course of lithium deintercalation (or intercalation) can be distinguished [21, 32].

CONCLUSION

The choice of the interval of degrees of intercalation $0.5 > x > 0.1$ for measuring quasi-equilibrium curves can be accounted for as follows. At very small x values ($x < 0.08$), the intercalation/deintercalation process (1) is already not the only potential-determining process (corrosion and chemical processes may occur in parallel). At the same time, at large x and potentials close to the lithium electrode potential, parasitic processes (impurity reduction in electrolyte etc.) are accelerated. As a result, the current efficiency becomes less than unity, and the experimental curve cannot longer be considered as close to equilibrium.

REFERENCES

1. Vetter, K.J., *Elektrochemische Kinetik*, Berlin: Springer, 1961.
2. Daniels, F. and Alberty, R.A., *Physical Chemistry*, New York: Wiley, 1975, 4th ed.
3. Shutaikina, S.M., Ol'shanskaya, L.N., Evpalov, D.A., and Popova, S.S., Abstracts of Papers, *Sovremennye problemy teoreticheskoi i eksperimental'noi khimii: Vserossiiskaya konferentsiya molodykh uchenykh* (Modern Problems of Theoretical and Experimental Chemistry: Russian Conf. of Young Scientists), Saratov: Saratov. Gos. Univ., June 25–26, 1997, pp. 258–259.
4. Gavrilyuk, V.I. and Plakhotnik, V.N., *Zh. Fiz. Khim.*, 1994, vol. 68, no. 8, pp. 1373–1376.
5. Dai, Y., Wang, Y., Eshkerari, Y., *et al.*, *J. Electrochem. Soc.*, 1998, vol. 145, no. 4, pp. 1179–1183.
6. Atsashi, F., Minori, Y., Zempachi, O., *et al.*, *J. Electrochem. Soc.*, 1998, vol. 145, no. 1, pp. 172–178.
7. Billand, D., Herry, F.X., and Willman, P., *J. Power Sources: 18th. Int. Power Sources Symp.* (Stratford-upon-Avon, April 1993), p. 374.
8. Zhend, T., Xue, J.S., and Dohn, J.R., *Chem. Mater.*, 1996, vol. 8, no. 2, pp. 389–393.
9. Kabanov, B.N., Chekavtsev, A.V., Petukhova, P.I., *et al.*, *Elektrokhimiya*, 1986, vol. 22, no. 3, pp. 415–417.
10. Pominova, T.V., Popova, S.S., and Ol'shanskaya, L.N., *Elektrokhimiya*, 2000, vol. 36, no. 4, pp. 448–454.
11. Volgin, M.A., Churikov, A.V., Konoplyantseva, N.A., *et al.*, *Elektrokhimiya*, 1998, vol. 34, no. 7, pp. 761–768.
12. Danil'chuk, T.N., Petrova, G.N., Efimov, O.N., *et al.*, *Elektrokhimiya*, 1998, vol. 34, no. 7, pp. 770–777.
13. Imanishi, N., Kumai, K., Kokugam, H., *et al.*, *Solid State Ionics*, 1998, vol. 107, nos. 1–2, pp. 135–144.
14. Levi, M.D. and Aurbach, P., *J. Electroanal. Chem.*, 1997, vol. 421, nos. 1–2, pp. 79–88.
15. Skundin, A.M. and Egorkina, O.Yu., *Elektrokhimiya*, 1997, vol. 33, no. 4, pp. 464–468.
16. Volgin, M.A., Churikov, A.V., and L'vov, A.L., *Elektrokhimiya*, 1999, vol. 35, no. 12, pp. 1462–1468.
17. Imanishi, N., Kashiwagi, H., Ishikawa, T., *et al.*, *J. Electrochem. Soc.*, 1993, vol. 140, no. 2, pp. 315–320.
18. Volgin, M.A., Kulikov, L.N., Konoplyantseva, N.A., *et al.*, *Elektrokhim. Energet.*, 2001, vol. 1, nos. 1–2, pp. 50–55.

19. Piao, T., Park, S.M., and Dobital, C.-H., *J. Electrochem. Soc*., 1999, vol. 146, no. 8, pp. 2794–2798.
20. Fialkov, A.S., *Uglerod, mezhsloevye soedineniya i kompozity na ego osnove* (Carbon and Intercalation Compounds and Composites on Its Base), Moscow: Aspekt, 1997.
21. Skundin, A.M. and Egorkina, O.Yu., *Elektrokhimiya*, 1995, vol. 31, no. 4, pp. 373–375.
22. Ubbelohde, A.R. and Lewis, F.A., *Graphite and Its Crystal Compounds*, Oxford: Clarendon, 1960.
23. *Spravochnik po kompozitsionnym materialam* (Reference Book of Composites), Lyubin, D.Zh., Ed., Moscow: Mashinostroenie, 1988, vol. 1.
24. Butler J.N., *Adv. Electrochem. Electrochem. Eng*., 1970, vol. 7, pp. 77–175.
25. Sautin, S.N., *Planirovanie eksperimenta v khimii i khimicheskoi tekhnologii* (Design of Experiments in Chemistry and Chemical Technology), Leningrad: Khimiya, 1975.
26. Zakgeim, A.Yu., *Vvedenie v modelirovanie khimikotekhnologicheskikh protsessov* (Introduction to Simulation of Processes of Chemical Technology), Moscow: Khimiya, 1973.
27. Gordon, A.J. and Ford, R.A., *The Chemist's Companion. A Handbook of Practical Data, Techniques and References*, New York: Wiley–Interscience, 1972.
28. Takami, N., Saton, A., Ohsaki, T., *et al*., *Electrochim. Acta*, 1997, vol. 42, no. 6, pp. 2437–2543.
29. Rabinovich, V.A. and Khavin, Z.Ya., *Kratkii khimicheskii spravochnik* (Concise Chemical Reference Book), Leningrad: Khimiya, 1978.
30. Terina, E.M. and Ol'shanskaya, L.N., *Aktual'nye problemy elektrokhimicheskoi tekhnologii: Sbornik trudov molodykh uchenykh. Engel's, mai 2000 g.* (Topical Problems of Electrochemical Technology: Coll. of Sci. Works of Young Scientists, Engels, May 2000), Saratov: Saratov. Gos, Tekh. Univ., 2000, pp. 19–22.
31. Sanches, L., Farcy, J., and Pereira-Ramos, J.P., *Electrochim. Acta*, 1998, vol. 43, no. 8, pp. 935–941.
32. Imanishi, N., Ohashi, S., Ichikawa, T., *et al*., *J. Power Sources*, 1992, vol. 39, no. 2, pp. 185.

Russian Journal of Applied Chemistry, Vol. 75, No. 5, 2002, pp. 745–751. Translated from Zhurnal Prikladnoi Khimii, Vol. 75, No. 5, 2002, pp. 763–769.
Original Russian Text Copyright © 2002 by Efremov, Tesakova, Mamaeva, Golosman.

CATALYSIS

Synthesis of Cement-Containing Nickel–Copper Catalytic Systems Using Formic Acid Aqueous Solutions

V. N. Efremov, G. M. Tesakova, I. A. Mamaeva, and E. Z. Golosman

Novomoskovsk Institute of Nitrogen Industry, Novomoskovsk, Tula oblast, Russia

Received September 25, 2001; in final form, February 2002

Abstract—Regular trends in the formation of phase composition, structure, and mechanical strength of nickel–copper catalysts used for treatment of process and off-gases were considered in relation to the concentration (5.0–60.0 wt %) of formic acid aqueous solutions used in their preparation. The optimal conditions of the preparation process were determined.

In modern industrial installations, oxygen is removed from process gases with platinum and palladium catalysts, the use of which is limited by high cost and short supply of these metals. A series of NKO-type cement-containing nickel–copper catalysts were developed[1] [1] for a wide range of catalytic processes, in which PK and APK catalysts with platinum and palladium active components are the most active. As opposed to these catalysts, the use of NKO-type catalysts requires their preliminary reduction by a hydrogen-containing gas at 350–450°C. In some cases it is difficult to provide such temperatures in the existing installations.

The goal of this work was to develop a mechanically strong and highly active nickel–copper catalyst, which can be activated in an inert medium at low temperatures (180–280°C).

There are various procedures for the preparation of nickel–copper catalytic systems. These procedures mainly consist in deposition of an active component on a support by impregnation, coprecipitation, or fusion of catalyst components and mixing active components with the support.

Published data on the use of salts of carboxylic acids and of carboxylic acids themselves as liquid reagents in catalyst production suggest the possibility of obtaining supports and also high-performance catalysts that are activated at low temperatures (150–250°C) in a stream of inert gases.

There are three main directions of using carboxylic acids in catalyst production: for preparing high-performance catalyst supports [2–6], for synthesizing catalytic systems [7–14], and for regenerating dead catalysts [15–18].

[1] Developed at the Novomoskovsk Institute of Nitrogen Industry.

EXPERIMENTAL

As the raw material we used substances applied in the synthesis of cement-containing nickel-copper catalytic systems: nickel(II) (NSC) and copper(II) (CSC) subcarbonates, and technical-grade calcium aluminate (talum), which is a mixture of calcium monoaluminate ($CaO \cdot Al_2O_3$, CA) and dialuminate ($CaO \cdot 2Al_2O_3$, CA_2). Samples were synthesized by mixing the initial components in the presence of formic acid aqueous solution, the concentration of which was varied within 5.0–60.0 wt %. The mixing (liquid : solid ratio from 1 : 1 to 1.5 : 1) was carried out at 60–80°C. The catalyst mass with 15–20% moisture content was dried at 100°C, crushed, and pressed at 650 MPa into cylindrical pellets 6.0 mm in diameter and 5.0 mm high.

The X-ray phase analysis (XPA) of the samples was carried out on a DRON-2 diffractometer with CuK_α radiation, and the thermogravimetric analysis, on a Q-1500 D derivatograph. The stages of phase formation in inert media were studied in the linear heating mode on a thermochromatographic installation. The specific surface area was measured on a Tsvet-211 device by thermal desorption of argon. The mechanical strength was determined by crushing granules with application of load on their faces. The catalytic activity in oxygen hydrogenation was studied under atmospheric pressure on a laboratory flow-through installation with a four-channel reactor. The input gas mixture contained 2.0 vol % O_2, 6.0 vol % H_2, and remainder argon. The tests of the catalytic activity were carried out at the space velocity of

1070-4272/02/7505-0745$27.00 © 2002 MAIK "Nauka/Interperiodica"

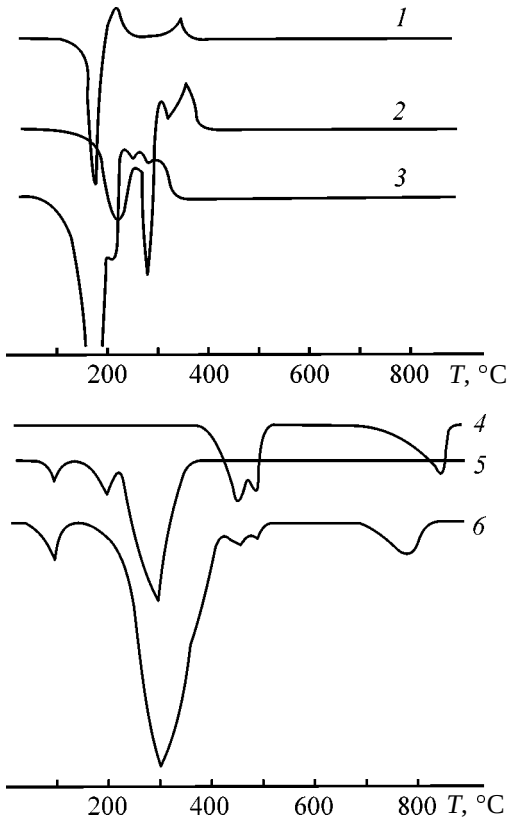

Fig. 1. DTG curves of samples treated with 40% aqueous solution of formic acid: (*1*) CSC, (*2*) NSC, (*3*) 50 wt % CSC + 50 wt % NSC, (*4*) $CaCO_3$, (*5*) γ-Al_2O_3, and (*6*) talum. (*T*) Temperature; the same for Fig. 2.

6000 h^{-1}. The degree of oxygen conversion was taken as a measure of the catalytic activity.

The characteristic decomposition temperature of the initial NSC $NiCO_3 \cdot 2Ni(OH)_2 \cdot 4H_2O$ is 320°C. The specific surface area of NiO obtained by NSC calcination does not exceed 40 $m^2 g^{-1}$. The compound $CuCO_3 \cdot Cu(OH)_2$ (CSC) decomposes at T_{max} = 280°C to CuO, which has disordered crystal lattice and specific surface area of no more than 10–20 $m^2 g^{-1}$.

According to the XPA data, treatment of the initial NSC with formic acid gives nickel formate $Ni(HCOO)_2 \cdot 2H_2O$, and treatment of CSC, anhydrous copper formate $Cu(HCOO)_2$.

Figure 1 shows the rates of the weight loss by samples of NSC, CSC, and their mixture (50 wt % NSC–50 wt % CSC) treated with 40% aqueous solution of formic acid under conditions similar to the conditions of the synthesis. Nickel formate decomposes in two stages (Fig. 1, curve *2*). The first stage (230°C) corresponds to the loss of water of crystallization, and the second (290°C), to exhaustive decomposition of nickel formate, which passes at a high rate, as shown by the intensity of the second peak. The further heating of the sample in the oxidizing atmosphere results in oxidation of the formed nickel (370°C). Copper formate (Fig. 1, curve *1*) decomposes in one stage (180°C). The resulting metallic copper is oxidized first to Cu_2O (220°C) and then to CuO (355°C).

It is known [19] that salts of carboxylic acids and, in particular, nickel and copper formates decompose in oxidant-free media to give metals. The decomposition of these salts is exothermic and occurs with a high rate at relatively low temperatures.

The decomposition temperature of formates can be considerably lowered [20] by adding a formate with a lower decomposition temperature. The decomposition of a mixture of Ni(II) and Cu(II) formates (Fig. 1, curve *3*) is characterized by two intensive exothermic peaks. The exothermic effect at T_{max} = 180°C is due to decomposition of $Cu(HCOO)_2$ and dehydration of $Ni(HCOO)_2 \cdot 2H_2O$, and that at T_{max} = 215°C, to decomposition of $Ni(HCOO)_2$. Thus, the presence of copper formate in a sample decreases the decomposition temperature of nickel formate from 290 to 215°C. At the same time, it cannot be ruled out that a double Cu(II) and Ni(II) salt such as $CuNi(HCOO)_2 \cdot 2H_2O$ can form under the experimental conditions of processing the NSC and CSC mixture [21]. This salt can also decompose in two stages.

To understand phase formation processes occurring in the course of the synthesis of cement-containing nickel–copper catalytic systems, we studied samples obtained by treatment of active aluminum oxide, $CaCO_3$, and calcium aluminate with a 40% aqueous solution of formic acid. The DTG curves of these samples are shown in Fig. 1. The experimental data indicate that treatment of aluminum oxide and $CaCO_3$ with HCOOH yields anhydrous aluminum and calcium formates (Fig. 1, curves *4*, *5*). In the case of treated talum (curve *6*), the peak at 300°C corresponding to the decomposition of aluminum formate prevails. Furthermore, two exothermic peaks were recorded at 350 and 420°C, which are characteristic of the calcium formate decomposition. The endothermic peak at 790°C corresponds to the decomposition of $CaCO_3$ formed by calcium formate thermolysis. The effect of heat treatment on the specific surface area of talum S_{sp} ($m^2 g^{-1}$) treated by aqueous solution of formic acid is given below.

This dependence passes through a maximum (140 $m^2 g^{-1}$) at 280°C. When preparing cement-containing nickel–copper catalytic systems (25 wt % NiO–10 wt % CuO– 65 wt % talum), we found that, at

T, °C	S_{sp}, $m^2\ g^{-1}$
150	5.0
200	10.0
220	25.0
250	70.0
280	140.0
300	135.0
350	80.0
400	45.0

room temperature, the reaction of a mixture of the initial components (NSC + CSC + talum) with an aqueous solution of formic acid occurs at a relatively low rate, which reaches a maximum at 70–75°C. This temperature is optimal for the reaction of the mixture of components and also of each component separately with an aqueous solution of formic acid. For comparison, we prepared a catalyst sample (no. 1) using distilled water. The experimental data obtained by derivatography (Fig. 2) and by X-ray phase analysis allowed us to subdivide the samples under study in three groups depending on the concentration (%) of formic acid aqueous solution used in the stage of mixing: no. 1, H_2O, no. 2, 5.0, and no. 3, 10.0 (first group); no. 4, 15.0, no. 5, 20.0, no. 6, 25.0, and no. 7, 30.0 (second group); and no. 8, 40.0, no. 9, 50.0, and no. 10, 60.0 (third group).

The study of thermal transformations of the samples (Fig. 3) allowed us to establish the sign of thermal effects, determine a mode of heat treatment, and, using also the XPA data, identify phases formed in the course of the preparation. Thermal transformations of all the samples under study involve weight loss, its value increasing as the concentration of HCOOH is increased. The XPA data show that sample no. 2 is almost identical to sample no. 1. The phase composition of these samples includes NSC and CSC, mixed nickel and copper subaluminate, CuO, $CaO \cdot Al_2O_3$, $CaO \cdot 2Al_2O_3$, and a minor amount of nickel, copper, aluminum, and calcium formates (for sample no. 2). The increase in the HCOOH concentration to 10% (sample no. 3) results in increased conversion of the initial components. Sample no. 5 prepared by treatment with 20% HCOOH solution considerably differs in the phase composition from the previous samples. In its phase composition, two types of nickel and copper subaluminates dominate: (1) standard Ni(II) and Cu(II) subaluminates (SA-I) having basic interplanar spacings d = 7.6 and d = 3.8 Å, respectively; (2) Ni(II) and Cu(II) subaluminates differing from standard subaluminates by the fact that their structure contains an additional anion $(HCOO)^-$ (SA-II). They are characterized by the basic interplanar spacings d = 11 and d = 5.5 Å, respectively.

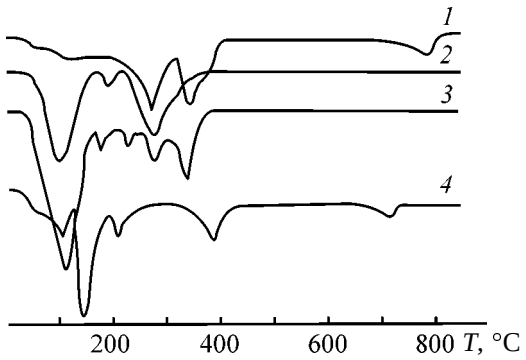

Fig. 2. DTG curves of catalyst samples prepared using aqueous solutions of formic acid. HCOOH concentration (%): (*1*) 0, (*2*) 5, (*3*) 20, and (*4*) 30.

Metal subaluminates can contain various anions replacing their OH^- groups [22], e.g., CO_3^{2-}, NO_3^-, etc. The formula of SA-I in the general form can be written as $MAl_2(OH)_8$ (M = Ni, Cu, Zn, Mg, etc.), and the formula of SA-II, as $MAl_2(OH)_{8-x}(HCOO)_x$, i.e., as a metal subaluminate formate.

A number of well pronounced effects due to the decomposition of SA-II-type compounds and also of Ni(II) and Cu(II) formates were detected in the range 120–280°C for sample no. 5 (Fig. 2, curve *3*).

The further increase in the acid concentration to 30% (Fig. 2, curve *4*) results in preferential formation of compounds such as SA-II, i.e., of Ni(II) and Cu(II) subaluminoformates. Furthermore, in this sample the amount of the formed Ni(II), Cu(II), Al(III), and Ca(II) formates increased, and a certain amount of NSC, CA, CA_2, CuO, and $CaCO_3$ was present.

The phase composition of sample no. 8 contains mainly Ni(II), Cu(II), Al(III), and Ca(II) formates; only small amounts of Ni(II) and Cu(II) subaluminate formates were detected. The use of a 50% aqueous solution of the acid (sample no. 9) promotes the formation of Ni(II), Cu(II), Al(III), and Ca(II) formates. The further increase in the acid concentration to 60% does not affect the phase composition. The phase of $CaCO_3$, which is a product of the exchange reaction of NSC and CSC with talum in the mixing stage, was detected in all the samples. The heat treatment of the samples increases the content of this phase. An additional amount of $CaCO_3$ is formed as a result of the decomposition of Ca(II) formate.

One of the main stages in formation of an active catalytic structure is the catalyst activation, and such characteristics as catalytic activity, mechanical strength, and service life depend on the conditions of this stage.

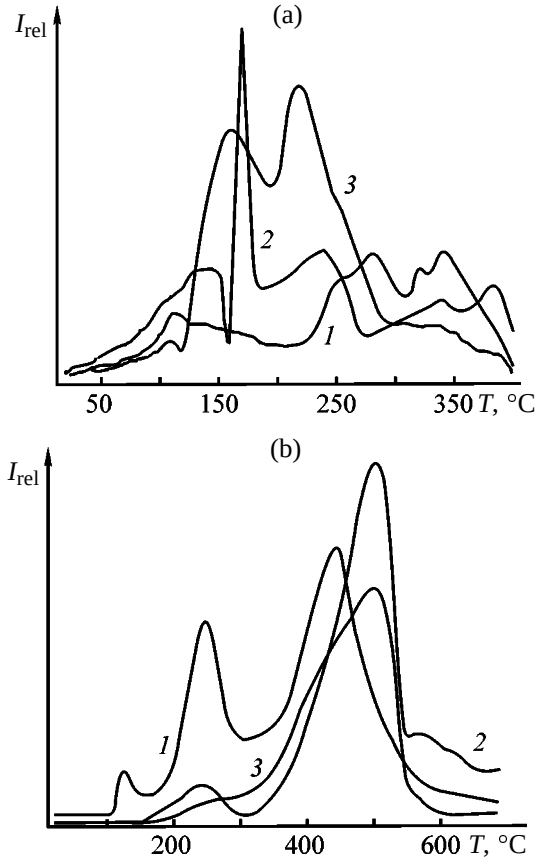

Fig. 3. Thermochromatograms of catalyst samples prepared using aqueous solutions of formic acid and activated in (a) helium and (b) hydrogen. (I_{rel}) Relative intensity and (T) temperature. Concentration of HCOOH (%): (*1*) 5, (*2*) 30, (*3*) 40.

We studied reduction of the samples on a thermochemical installation allowing temperature-programmed reduction in various gas media and temperature modes. The curves of temperature-programmed reduction at linear heating rate of 5 deg min^{-1}, obtained in helium and hydrogen streams, respectively, are shown in Figs. 3a and 3b. These data show that the thermolysis of samples in a helium stream is in fact the stage of their activation. This process, which occurs in the range 125–400°C, is multistage. We can subdivide the samples under study into three groups with respect to the nature of activation. Sample nos. 2 and 3 comprise the first group, for which the main activation process takes place in the range 200–400°C with a rather small intensity. The second group (sample nos. 4 and 5) is characterized by occurrence of the activation in three stages (130–170, 200–300, and 300–400°C). In the third group, the activation is more intense and involves two stages (170–190°C and 215–225°C), corresponding to the decomposition of nickel and copper formates in an inert gas stream. The temperature-programmed reduction data well correlate with the data of the X-ray phase and thermal analyses.

After activation, samples were cooled in a helium stream to room temperature and then heated in a hydrogen stream in a linear heating mode (Fig. 3b). For comparison, we studied simultaneously sample no. 1 prepared with distilled water. At temperatures below 300°C, no effects corresponding to the reduction of active components were detected, which suggests that the catalysts were completely activated in the inert gas stream. For all the sample under study, the curves of temperature-programmed reduction in hydrogen contain a single strong peak in the range 350–550°C, which corresponds to the low-temperature catalytic decomposition of calcium carbonate [23]. The shift of T_{max} of decomposition of this phase, as compared to this effect in sample no. 1, results from the presence of dispersed nickel and copper with a highly developed surface in all the samples except for sample no. 1.

The specific surface area, mechanical strength, and catalytic activity of samples reduced with hydrogen are given in the table. We chose the activation temperatures taking into account the data of the thermogravimetric, X-ray, and thermochromatographic analyses.

Products of the talum hydration and of its reaction with nickel and copper subcarbonates, and partially products of the decomposition of nickel and copper formates make the major contribution to the surface area development in sample no. 2, whereas in sample nos. 4–10 these are products of the decomposition of nickel and copper subaluminoformates (SA-II) and subaluminates formates (SA-I). In these samples the specific surface area, which was measured by argon thermal desorption on a Tsvet-211 instrument, is the total active surface area of nickel and copper. The fact that this surface area mainly corresponds to the active components is confirmed by the data on the surface area of talum treated with a 40% aqueous solution of formic acid and calcined in an inert medium at 240°C. The S_{sp} of this sample does not exceed 10–15 $m^2 g^{-1}$.

When developing new catalysts and improving available catalysts, a special attention is given to their strength properties principally determining their service life. The greatest decrease (30–50%) in the mechanical strength takes place during activation of catalysts. This is due to phase transformations causing changes in their crystalline and porous structures. Our experimental data on the mechanical strength of both starting samples and samples activated in an argon stream at 180°C are given in the table.

Specific surface area S_{sp} of samples, their mechanical strength P, and degree of oxygen conversion α at various activation temperatures T_a in argon stream

Sample no.	c_{HCOOH}, wt %	S_{sp}, $m^2 g^{-1}$, at indicated T_a, °C				P, MPa		α, %, at indicated T_a, °C		
		180	240	280	380	initial	at 180°C	150	160	180
1	0	100	110	120	120	29	32	0	0	0
2	5.0	145	155	120	125	35	15	5	12	50
3	10.0	5	30	65	95	60	55	5	15	80
4	15.0	25	30	70	145	73	90	5	18	100
5	20.0	20	45	95	105	100	93	7	22	100
6	25.0	45	60	105	150	105	50	10	28	100
7	30.0	45	70	100	145	58	23	10	30	100
8	40.0	90	100	155	120	42	8	12	32	100
9	50.0	85	95	95	90	30	3	15	35	100
10	60.0	110	100	100	80	28	2	15	35	100

The catalytic activity in oxygen hydrogenation was determined at a space velocity of 6500 h^{-1}. The working gas mixture contained 2.0 vol % O_2, 6.0 vol % N_2, and the remainder Ar. The catalytic activity of the samples was judged from the degree of oxygen conversion (see table). Prior to the experiments, the samples were activated at 150, 160, and 180°C for 1 h in an argon stream at W = 6500 h^{-1}. It is seen that, as the concentration of formic acid increases, the catalytic activity (after activation at 150 and 160°C) monotonically increases and reaches a maximum for sample nos. 8–10. The increase in the activation temperature to 180°C sharply increases the catalytic activity, and sample no. 4 ensures almost 100% oxygen conversion. Under these activation conditions, however, sample no. 1 still exhibits zero catalytic activity.

We also tested the catalytic properties of sample nos. 4–7, activated under similar conditions, in the course of carbon monoxide hydrogenation. The experiments were carried out at a pressure of 3.0 MPa, space velocity of 30 000 h^{-1}, and carbon monoxide concentration at the reactor inlet of 0.6–0.75 vol %. We evaluated the catalytic activity in this process by the temperature of the 10 ppm CO breakthrough and found that sample nos. 6 and 7 have the maximal activity (220 and 215°C, respectively). These data indicate high catalytic performance of the system under study. Based on the experimental data, we chose for practical applications a catalyst with the composition 10 wt % CuO–25 wt % NiO–65 wt % talum prepared using 20% aqueous solution of formic acid in the stage of mixing.

We have studied in detail variation of the phase composition of this sample on its heating in air and argon flows, using a GPVT-1500 high-temperature X-ray camera. The phase composition of the initial catalyst sample includes Ni(II) subcarbonate, Ni(II) and Cu(II) subaluminates, mixed Ni(II) and Cu(II) subaluminoformate, Ni(II), Cu(II), Al(III), and Ca(II) formates, and also CuO, CA, and CA_2 phases. The heating to 100°C results in the decomposition of mixed Ni(II) and Cu(II) subaluminoformate to mixed Ni(II) and Cu(II) subaluminate. This phase transformation results in a considerable increase in the intensity of reflections of mixed Ni(II) and Cu(II) subaluminate in the X-ray pattern. The heating to 175°C promotes partial decomposition of formates. At the same temperature, Ni(II) and Cu(II) subaluminates start to decompose with the removal of interlayer water, as indicated by the shift of the SA-I lines to larger angles (d = 7.2 Å). The heating to 200°C induces further SA-I decomposition with the shift of the interplanar spacing to d = 6.9 Å. The decomposition of Ni(II), Cu(II), and Al(III) formates is complete at 250°C and yields nickel and copper, which are converted to NiO and CuO in this oxidizing medium. The thermolysis of aluminum formate yields γ-Al_2O_3. The X-ray pattern contains only reflections of Ca(II) formate. The decomposition of SA-I also continues, its interplanar spacing decreases in this case to d = 6.7 Å. At 300°C, calcium(II) formate starts to decompose to give $CaCO_3$, whereas the decomposition of SA-I approaches completion. Its interplanar spacing d becomes equal to 6.2 Å. The intensity of diffraction reflections of this phase in the X-ray pattern considerably decreases. The further temperature increase by 50°C results in complete decomposition of calcium

formate, as indicated by an increase in the intensity of $CaCO_3$ reflections. Mixed Ni(II) and Cu(II) subaluminate also completely decomposes. Nickel subcarbonate starts to decompose intensively to form finely dispersed nickel oxide. At 400°C, its decomposition is complete. The phase composition of the catalyst after thermolysis at this temperature includes the following compounds: NiO, CuO, $CaO \cdot 2Al_2O_3$, $CaO \cdot Al_2O_3$, and $CaCO_3$. The phase composition remains unchanged on cooling to ambient temperature.

The evolution of the phase composition of this sample on heating in an argon stream is almost identical, except for the fact that the dispersed Ni and Cu phases originating from the decomposition of Ni(II) and Cu(II) formates are not oxidized.

The studies of phase composition and phase transformations occurring on heating in both air and inert gas streams, of the activation stage, and also of changes in the specific surface area and mechanical strength allow us to make a substantiated choice of the scheme of the catalyst preparation. According to this scheme, the catalyst should be prepared as follows. The initial components (NSC, CSC, and talum) are mixed in the presence of 15–20% aqueous HCOOH in mixers equipped with heaters. The mixing occurs most intensively at 70–75°C. The catalyst mass with 15–20% moisture content is dried at 100–110°C in rack dryers, then crushed, mixed with graphite, and molded either as cylindrical pellets or as rings with external diameter of 10–15 mm and height not greater than 10 mm. The prepared catalyst is loaded in a reactor and activated in a stream of an inert or working gas at 180–280°C.

The experimental batch of the catalyst[2] in amount of 300 kg was tested in deoxygenation of electrolytic hydrogen.[3] The catalyst was activated in a working gas stream (hydrogen + 0.5 vol % O_2) at 180°C, which is lower by 100–120°C than the activation temperature of NKO-2-3 catalyst used in this process. The time of attaining the working conditions was reduced by 12–15 h. The residual oxygen content in the purified hydrogen did not exceed 0.002–0.005 vol % [24].

CONCLUSIONS

(1) The evolution of the phase composition of cement-containing nickel–copper catalysts synthesized using aqueous formic acid involves the formation of both mixed nickel copper subaluminate and mixed nickel copper subaluminoformate, and also of nickel, copper, aluminum, and calcium formates. The quantitative ratio of these phases depends on the concentration of the aqueous solution of formic acid used.

(2) The mutual influence of metal formates on their decomposition temperature was established.

(3) The optimal concentration of formic acid aqueous solution was chosen, which allowed preparation of mechanically strong and highly active catalysts.

(4) The scheme of catalyst production taking into account basic parameters of the preparation process was offered.

[2] Manufactured in Novomoskovsk Institute of Nitrogen Industry on industrial equipment for production of catalysts.

[3] The tests were carried out in electrolysis shop 2 of the Azot Joint-Stock Company, Novomoskovsk.

REFERENCES

1. Efremov, V.N., Golosman, E.Z., Fainshtein, V.I., and Yakerson, V.I., *Khim. Prom–st.*, 1996, no. 2, p. 95–102.
2. JPN Patent Pending 54-155 191.
3. US Patent 3 846 540.
4. US Patent 4 379 134.
5. Votol, A., Ishido, J., and Osada, K., *J. Nat. Chem. Lab. Ind.*, 1983, vol. 78, no. 8, pp. 384–387.
6. Buman, R.K. and Mironovich, A.A., *Izv. Akad. Nauk Latv. SSR, Ser. Khim.*, 1974, no. 2, pp. 167–170.
7. Vlasov, E.A., Zaevskova, O.L., Selivestrova, N.B., and Deryuzhkina, V.I., Abstracts of Papers, *Vsesoyuznoe soveshchanie "Nauchnye osnovy prigotovleniya katalizatorov"* (All-Union Conf. "Scientific Foundations of Catalyst Preparation"), Novosibirsk, 1983, pp. 22–23.
8. Vlasov, E A., Kozlov, A.I., Redin, V.N., *et al.*, in *Ochistka promvybrosov i utilizatsiya otkhodov* (Treatment of Industrial Rejects and Waste Utilization), Leningrad: Leningr. Tekhnol. Inst. im. Lensoveta, 1985, pp. 104–108.
9. Chusuei, C.C., Brookshier, M.A., and Goodman, D.W., *Langmuir*, 1999, vol. 15, no. 8, pp. 2806–2808.
10. JPN Patent Pending 52-46 559.
11. Kozlov, A.I., Kozlyak, M.I., and Dmitrieva, L.P., *Vestsi Akad. Navuk Bel. SSR, Ser. Khim. Navuk*, 1976, no. 3, pp. 33–36.
12. US Patent 4 400 309.
13. JPN Patent 52-48 559.
14. USSR Inventor's Certificate no. 774 584.
15. FRG Patent 3 151 805.

16. FRG Patent Pending 3151905.
17. Angelidis, T.N. and Papadakis, V.G., *Appl. Catal*., 1997, vol. 12, nos. 2–3, pp. 193–206.
18. RF Patent 2153396.
19. Khimchenko, Yu.I., Vasilenko, V.P., Radkevich, L.S., *et al*., *Poroshk. Metall*., 1977, no. 5, pp. 7–13.
20. Lazerko, G.A., Torkaiko, E.M., and Zaretskii, M.V., *Zh. Neorg. Khim*., 1984, vol. 29, no. 5, pp. 1214–1216.
21. Itkina, L.S., Portnova, S.M., Antsyshkina, A.S., and Krasilov, Yu.I., *Zh. Neorg. Khim*., 1985, vol. 30, no. 7, pp. 1807–1815.
22. Yurieva, T.M., *React. Kinet. Catal. Lett*., 1985, vol. 29, no. 1, pp. 49–54.
23. Golosman, E.Z., Efremov, V.N., Karamanenko, S.V., and Yakerson, V.I., *Kinet. Katal*., 1983, vol. 24, no. 5, pp. 1220–1226.
24. Golosman, E.Z., *Khim. Tekhnol*., 2000, no. 12, pp. 25–35.

Russian Journal of Applied Chemistry, Vol. 75, No. 5, 2002, pp. 752–754. Translated from Zhurnal Prikladnoi Khimii, Vol. 75, No. 5, 2002, pp. 770–772.
Original Russian Text Copyright © 2002 by Erofeev, Shabalina, Koval', Minakova.

CATALYSIS

Influence of Modification of Pentasils with Alkaline-Earth Metals on Their Acid and Catalytic Properties in Conjugate Conversion of Methanol and Propane–Butane Fraction

V. I. Erofeev, L. B. Shabalina, L. M. Koval', and T. S. Minakova

Board of Scientific and Technical Development, Tomsk Petrochemical Plant, Joint-Stock Company, Tomsk, Russia
Tomsk State University, Tomsk, Russia

Received November 5, 2001

Abstract—Acid and catalytic properties of Pentasils in conjugate conversion of methanol and propane–butane fraction, as influenced by their modification with Ca, Sr, Ba, and Mg, were studied.

It is known [1–4] that zeolite-containing catalysts based on high-silica zeolites (HSZ) of the ZSM type are effective catalysts of a number of petrochemical and oil-refining processes. The aim of this work was to study the catalytic activity of Pentasils in conjugate conversion of methanol and propane–butane fraction (PBF) into lower olefins as influenced by modification of Pentasils with alkaline earth metal (AEM) cations and to correlate the catalytic activity with the surface acidity of the samples.

EXPERIMENTAL

High-silica zeolites of Pentasil type with silicate ratio of 30 were prepared by the hydrothermal procedure from alkaline aluminosilica gels in the presence of a structure-forming organic cation [5]. Modification was performed by impregnation of the HSZ in the H form with Mg, Ca, Sr, and Ba salts. The content of these metals recalculated to their oxides was 2 wt %. Identification and determination of the degree of crystallinity of the HSZs were performed by IR spectroscopy and X-ray diffraction analysis (Mo anode, Ni filter). All the samples belong to the ZSM-5 zeolite type with 90–95% degree of crystallinity.

The initial compounds for the conjugate process were commercial methanol produced by Tomsk Petrochemical Plant Joint-Stock Company and PBF (1.7 wt % ethane, 61.4 wt % propane, 32.4 wt % butane, and 4.5 wt % isobutane) produced by Surgut Gas Processing Plant. Conjugate conversion of methanol and PBF was performed on a laboratory flow unit. The initial methanol–PBF mixture (4 : 1 weight ratio) was fed into a quartz reactor with a fixed catalytic bed. The reaction products were analyzed on an LKhM-80 chromatograph with a thermal conductivity detector. The catalytic activity of zeolites was estimated by the yield of C_2–C_4 alkenes based on the feed. The coking of the catalyst was studied by differential thermal analysis (DTA) with an MOM derivatograph (Hungary). The acid properties of the zeolites were studied by temperature-programmed desorption (TPD) of ammonia at a heating rate of 10 deg min^{-1} [6].

As seen from Table 1, the ethylene and propylene yields on H-HSZ increases from 3.6 to 14.8 and from 4.5 to 14.2% with increasing temperature from 500 to 650°C, respectively. The temperature dependences of the ethylene and propylene yield on modified Pentasils pass through extrema. With all the tested catalysts the content of C_2–C_4 alkenes in the gas phase is maximal at 600°C. Modification of the initial H-HSZ with Mg^{2+} and Ca^{2+} increases the yield of C_2–C_4 alkenes and decreases the arene yield. Modification with Sr^{2+} and Ba^{2+} decreases the yield of the target products and increases the yield of C_2–C_4 alkanes and coking of the catalyst surface (Table 2). The fact that the content of C_2–C_4 alkanes in the reaction products formed on Ba-HSZ is higher and the yield of aromatic hydrocarbons is lower than those on H-HSZ indicate deactivation of the catalysts by coking.

The maiximal yield of C_2–C_4 alkenes (56%) was obtained on Mg-HSZ. The yield of ethylene and propylene on Ca-HSZ was lower (51.2%).

The DTA curves of zeolite-containing catalysts clogged with coke under similar conditions of conjugate conversion of methanol and PBF show pro-

1070-4272/02/7505-0752$27.00 © 2002 MAIK "Nauka/Interperiodica"

Table 1. Products of conjugate conversion of methanol and PBF on zeolite-containing catalysts. Methanol space velocity 2 h^{-1}; methanol : PBF ratio = 4 : 1

Catalysts	T, °C	Yield of conversion products, wt %, based on the feed							Content of C_2–C_4 alkenes in the gas phase, rel. %
		total of H_2, CO, and CH_4	C_2–C_4 alkanes	C_2–C_4 alkenes			gaseous products	arenes	
				ethene	propene	butene			
H-HSZ	500	6.2	49.1	3.6	4.5	3.5	66.6	31.8	17.4
	550	7.4	40.7	8.1	9.5	5.7	71.1	26.7	32.8
	600	10.3	25.8	13.7	13.1	6.6	68.6	29.0	48.7
	650	20.7	19.9	14.8	14.2	4.0	70.7	25.8	46.7
Mg-HSZ	500	4.4	44.8	6.3	8.6	5.7	69.5	27.7	29.6
	550	6.5	32.3	12.5	13.9	7.1	72.0	25.3	46.5
	600	10.7	22.7	17.6	17.4	6.3	73.8	23.6	56.0
	650	27.5	9.4	18.4	16.1	3.8	70.7	24.4	54.2
Ca-HSZ	500	3.2	43.9	9.9	6.8	5.2	68.9	28.4	31.8
	550	5.4	37.3	10.6	13.3	7.6	73.9	22.8	42.6
	600	9.1	24.4	15.8	17.3	6.4	77.2	20.2	51.2
	650	17.0	23.5	15.2	15.7	3.8	72.6	24.2	47.8
Sr-HSZ	500	4.8	47.6	6.5	4.2	5.4	68.2	29.5	23.6
	550	6.1	34.7	11.2	12.4	6.5	70.7	26.8	42.6
	600	10.6	29.4	14.4	15.0	5.1	73.5	24.3	46.9
	650	21.2	24.4	11.7	12.8	3.3	69.8	26.0	39.8
Ba-HSZ	500	4.9	52.9	4.6	6.1	4.6	72.8	25.1	20.1
	550	5.9	40.0	9.3	11.3	7.6	73.9	22.9	38.2
	600	9.8	32.1	13.6	14.7	5.7	75.2	22.5	45.3
	650	15.7	30.8	10.8	13.0	4.7	72.3	22.7	39.4

nounced exoeffects with maxima in the range 460–660°C, which are due to coke burning-out. The most friable low-temperature coke is formed on Ca-HSZ. The T_{max} of coke burning-out from this sample is shifted by 30°C to lower temperatures as compared to the other samples (Table 2). The temperatures of the onset and completion of coke burning-out on this catalyst are also lower. The densest high-temperature coke is formed on Sr-HSZ.

This difference in the catalytic properties of the HSZs can be due to a change in their acidity after modification with alkaline-earth metals. The study of the acid properties of the zeolite-containing catalysts by ammonia TPD showed that the acidity of H-HSZ substantially changes after impregnation with AEMs (see figure). With Mg^{2+}, Sr^{2+}, and Ba^{2+}, the number of low-temperature centers increases and that of high-temperature centers decreases (Table 3). The total acidity of these samples decreases after modification.

Introduction of Ca^{2+} into H-HSZ increases the total amount of the acid centers from 1215 to 1294 μmol g^{-1} owing to a sharp increase in the number of low-temperature Lewis centers. The increase in the selectivity of cojugate conversion of methanol and PBF into C_2–C_4 olefins and the decrease in coke formation on the catalysts after modification with calcium ions are probably due to an increase in the number of strong Brønsted acid centers in the sample. The maximal decrease in the concentration of strong Brønsted acid centers was observed after modification with magnesium cations (from 535 μmol g^{-1} in the initial H-HSZ to 336 μmol g^{-1} in Mg-HSZ). This

Table 2. Amount of coke deposits on zeolite-containing catalysts in conjugate conversion of methanol and PBF

Catalysts	Temperature of coke burning-out from the catalyst, °C			Coke formation, mg/100 mg zeolite
	T_{onset}	T_{max} of peak	T_{fin}	
H-HSZ	490	580	640	10.7
Mg-HSZ	500	580	640	11.8
Ca-HSZ	470	550	620	7.0
Sr-HSZ	500	580	660	11.7
Ba-HSZ	460	580	640	13.8

Table 3. Acid properties of zeolite-containing catalysts determined by ammonia TPD

Catalyst	T_{max} of peak, °C		Number of acid centers, μmol g^{-1}		
	form I	form II	form I	form II	total
H-HSZ	208	411	683	532	1215
Mg-HSZ	206	362	753	336	1089
Ca-HSZ	213	425	808	486	1294
Sr-HSZ	208	406	722	466	1188
Ba-HSZ	215	403	703	430	1133

change in the nature of the acid centers is manifested in the shift of the desorption peaks I and II in the DTA curves of modified catalysts as compared to those of the initial H-HSZ (Table 3).

Thus, the acidity of H-HSZ and hence the catalytic activity and selectivity of the catalyst can be controlled by modification of the zeolite with AEMs. The selectivity of conjugate conversion of methanol and propane–butane fraction into C_2–C_4 olefins increases in the following order: Ba < Sr < Ca < Mg.

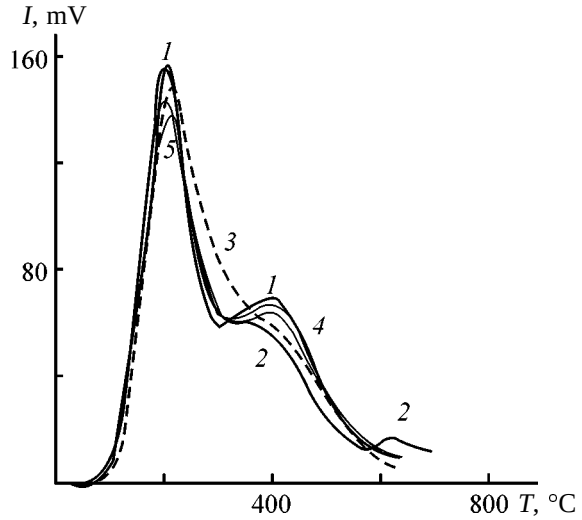

Curves of ammonia desorption from (*1*) H-HSZ, (*2*) Mg-HSZ, (*3*) Ca-HSZ, (*4*) Sr-HSZ, and (*5*) Ba-HSZ at 100°C. (*I*) Intensity and (*T*) temperature.

CONCLUSIONS

(1) Introduction of Mg, Ca, Sr, and Ba into Pentasil increases the strength and concentration of weak Lewis acid centers of the catalyst and substantially decreases the concentration of strong Brønsted acid centers, which increases the yield of C_2–C_4 olefins in conjugate conversion of methanol and propane–butane fraction.

(2) The selectivity of conjugate conversion of methanol and propane–butane fraction into C_2–C_4 olefins increases in the following order: Ba < Sr < Ca < Mg.

REFERENCES

1. Novak, Z., Gunschel, G., Lunch, I., and Anders, K., *Neftekhimiya*, 1987, vol. 27, no. 6, pp. 736–749.
2. Minachev, Kh.M., Kharson, M.S., Dergachev, A.A., *et al.*, *Dokl. Akad. Nauk SSSR*, 1991, vol. 317, no. 2, pp. 378–381.
3. Minachev, Kh.M. and Dergachev, A.A., *Izv. Ross. Akad. Nauk, Ser. Khim.*, 1993, no. 6, pp. 1018–1028.
4. Vosmerikov, A.V. and Erofeev, V.I., *Zh. Prikl. Khim.*, 1994, vol. 67, no. 7, pp. 1152–1156.
5. RF Patent 1527154.
6. Vosmerikov, A.V. and Erofeev, V.I., *Zh. Fiz. Khim.*, 1995, vol. 69, no. 5, pp. 787–790.

Russian Journal of Applied Chemistry, Vol. 75, No. 5, 2002, pp. 755–760. Translated from Zhurnal Prikladnoi Khimii, Vol. 75, No. 5, 2002, pp. 773–778.
Original Russian Text Copyright © 2002 by Post, Dolmatov, Marchukov, Sushchev, Veretennikova, Sal'ko.

PRODUCTION AND USE OF NEW MATERIALS

Industrial Synthesis of Ultradisperse Detonation Diamonds and Some Fields of Their Use

G. Post, V. Yu. Dolmatov, V. A. Marchukov, V. G. Sushchev, M. V. Veretennikova, and A. E. Sal'ko

Tekhnolog Special Engineering and Design Office, St. Petersburg State Technological Institute, St. Petersburg, Russia

Received April 2, 2001

Abstract—The cluster nature of detonation-synthesized ultradisperse diamonds (UDD) is considered. The industrial cycle employed for obtaining ultradisperse diamonds is described, with different variations of this process and the basic principles of design of the necessary equipment noted. Priority product areas and advantages of use of ultradisperse diamonds in metal–diamond electrochemical coatings and polymer–diamond composites are discussed in detail.

Detonation-synthesized ultradisperse diamonds (UDD, or nanodiamonds) are a promising component for development and creation of composite materials and coatings of a new generation [1–4].

Ultradisperse diamonds were discovered in the Soviet Union in the early 1960s in the carbon black formed in detonation of explosive mixtures of a certain composition. It was found that, in view of the ultrasmall particle size (smaller by three orders of magnitude than the size of dynamically synthesized diamond) and specific conditions of formation, UDD exhibit quite a number of unique properties uncharacteristic of diamond and, in particular, the high and peculiarly manifested chemical activity.

The aim of this study was to generalize and systematize data on UDD properties, variations of UDD preparation techniques, optimal technology of chemical purification of nanodiamonds, and advantages of UDD application in the most important fields related to surface treatment: electroplating and polymer chemistry.

Nanodiamonds are characterized by average particle size of 4–6 nm [5, 6], cubic crystal lattice with lattice constant $a = 0.3562 \pm 0.0003$ nm, density of 3.05–3.25 g cm^{-3} [7], and microstresses of about 10 GPa [7]. The specific surface area of UDD is 250–450 m^2 g^{-1}, pore volume 0.3–1.1 cm^3 g^{-1}, and average pore diameter 8–10 nm [8, 9]; the density of proton-donor groups is 0.34–2.52 μg-equiv m^{-2} [10]. The quantitative elemental composition of UDD is as follows (wt %): carbon 80–90, hydrogen 1–2, nitrogen 1–3, and oxygen 8–15 [7, 11]. The onset temperatures of UDD oxidation in air is 430–450°C, and that of graphitization in an inert medium, 1100°C.

A UDD particle is composed, being a cluster formation, of a relatively dense and ordered crystal-like core and loose, chemically labile periphery. The diamond core is the bearer of the basic "diamond" properties of UDD, namely, the thermal and chemical stability, heat and temperature conductivity, low electrical conductivity, X-ray diffraction pattern, quasi-abrasivity, and quasi-hardness. The peripheral structures of the cluster are responsible for such substance characteristics as sign and amount of surface charge on UDD particles; absorption, adsorption, and chemisorption; chemical composition of surface functional groups; and colloid stability of UDD particles in liquid and other media. In UDD clusters, both the core and the stabilizing shell are mainly composed of carbon atoms. In this case, a continuous transition is possible from the diamond lattice to nondiamond periphery via a system of skeleton, polyhedral, and polycyclic structures and networks. The cluster boundary is stabilized by products of interaction of peripheral carbon atoms with the substance of the surrounding medium: gaseous detonation products, air, oxidizing mixtures in chemical purification, and modifying reagents. The peripheral structures play a decisive part in aggregation of diamond clusters and their interaction with the host substances of composite materials and coatings.

The structure of the outer peripheral shell of a

1070-4272/02/7505-0755$27.00 © 2002 MAIK "Nauka/Interperiodica"

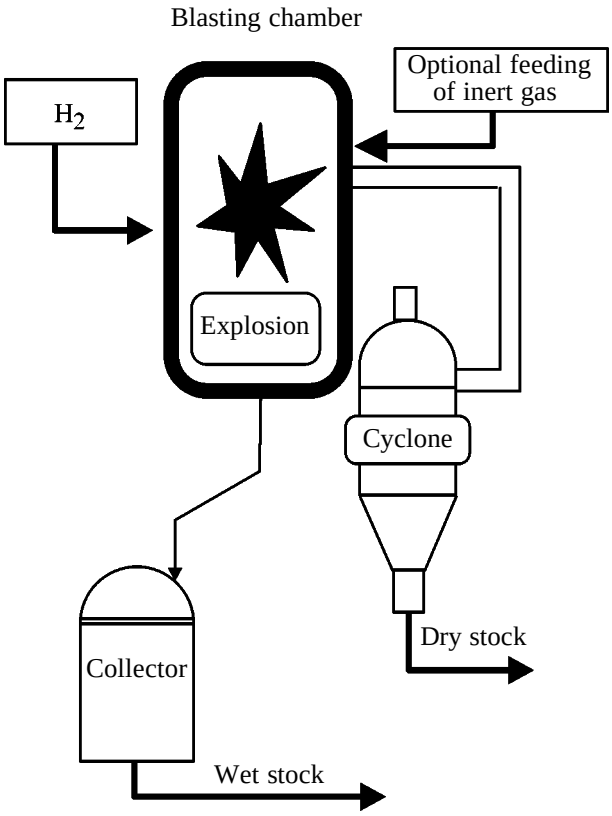

Fig. 1. Scheme of detonation synthesis of UDD.

diamond cluster was analyzed by various methods, including thermal desorption. The composition of desorption products is complex and diverse. In addition to hydrocarbons, they contain oxygen- and nitrogen-containing compounds formed in oxidation of the carbon surface. Benzene and C_7–C_{10} homologues are widely represented, being exceeded in abundance only by alkanes C_{10}, among which *n*-decane predominates.

The major bridged alicyclic compounds are camphene and terpene $C_{10}H_{16}$. Such a composition of the desorption products points to low probability of finding diamond structures proper at the phase boundary. These structures are also stabilized in a UDD cluster by various transition structures.

So dissimilar and diverse fragments are integrated in a single particle and, further, in an ensemble of particles by the rule of fractals via discontinuous filling of a random volume with a mass of substance [12]. In our opinion, the fact that the experimental values of the fractal dimensionality of UDD (2.1–2.3) do not correspond to any particular type of aggregation (cluster–cluster, cluster–particle) [13] can be rationalized just with account of the structural nonuniformity of the primary cluster, ambiguous interaction of clusters with one another and with separate carbon-containing molecules, and also in view of the strongly nonequilibrium conditions of UDD formation.

UDD synthesis based on detonation conversion of high-power blend explosives with subsequent chemical treatment of condensed explosion products has been studied in sufficient detail, both theoretically and in practical regard [5, 6, 14–16]. These studies served as a basis for the development of several pilot installations,[1] which successfully demonstrated the possibility of commercial manufacture of the new product in amounts of tens to hundreds of kilograms of UDD per year.

The production at Tekhnolog Special Engineering Design Office includes detonation synthesis (Fig. 1), chemical purification and washing of UDD to remove acid, conditioning of the product, and modification of diamonds (Fig. 2). The production infrastructure also includes systems for catching and utilization of acid vapor and gases, treatment and recycling of nitric acid, and water treatment.

Detonation synthesis is carried out in special blasting chambers with volume, as a rule, in the range 1–20 m^3. The chambers are made of low- and high-alloy steels. The optimal chambers are those made of low-alloy steel (e.g., boiler steel), clad from the inside with corrosion- and impact-resistant alloys. The chambers are equipped with gas-transport lines and a system for removal and catching of condensed detonation products.

The blasted charge (cast of pressed) is, as a rule, a mixture of TNT and hexogen in approximately 50 : 50 ratio. The charge mass ranges from 0.5 to 2.0 kg. The blasting can be done in three variants: (1) in the medium of detonation products or in inert gases (nitrogen, carbon dioxide) with a yield of condensed explosion products (diamond stock, DS) of 3 to 8 wt % and UDD content in DS of 30–45%, (2) in water with DS yield of 6–12% and UDD content of DS equal to 50–63%, and (3) with charge in an ice shell with DS yield of 8 to 16 wt % and UDD content in DS of 60–75%.

In the case of blasting in a gas medium, the temperature mode of the apparatus ensures separation of water vapor from the carbon condensate. Such a DS is characterized by finely dispersed state, high specific surface area, and its own hydrophilic–hydrophobic balance of surface active centers. The level of noncarbon DS contamination is largely determined, at any

[1] Altai Scientific and Production Association, Biisk; Tekhnolog Special Engineering Design Office, St. Petersburg; etc.

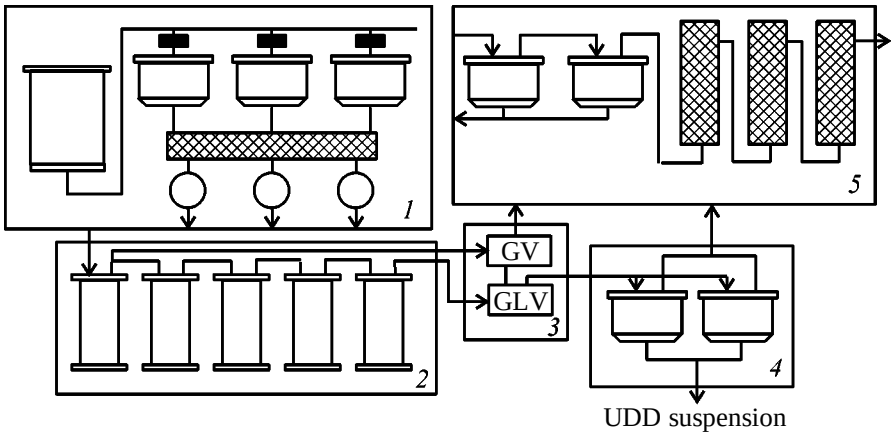

Fig. 2. Chemical purification of UDD. (*1*) Preparation, activation, and batching of suspension; (*2*) barothermal oxidation; (*3*) unit for high pressure relief (GV, gas valve; GLV, gas–liquid valve); (*4*) receiver of UDD suspension; and (*5*) system for environment protection.

kind of blasting, by the material of walls of the blasting chamber and by the chamber volume relative to the charge.

These properties directly affect the applicability of DS as a structuring and modifying agent in synthesis of composites and coatings based on organic matrices (polymers, lubricants, cutting fluids, etc.).

The diamond stock produced in "dry" blasting (in gas medium) has the following composition (wt %): UDD 30–45 and total carbon 88–92; at ash content (mainly metal oxides) of 2–5% and moisture content of 8–14%.

Blasting a charge in water or ice not only makes higher the yield of DS and UDD in terms of the starting explosives, but also markedly changes the hydrophilic–hydrophobic balance of the surface active centers. Nevertheless, a DS of this kind can be used for the same purposes as "dry" DS, naturally, after appropriate treatment. The composition of a "water" blasting DS[2] is as follows (wt %): UDD 50–63 and total carbon 88–95, at ash content of 1.5–3.0%. The "ice" blasting DS[3] contains (wt %) UDD up to 75 and total carbon 88–95, at ash content of 1–2%.

The UDD proper is obtained by barothermal oxidation of DS with aqueous nitric acid (Fig. 2) [17–20]. In this process, DS is thoroughly mixed with the acid and fed into the reaction zone by high-pressure batcher pumps. The acid suspension passes through a cascade of electrically heated titanium reactors and is heated in steps to 280–300°C, thermostated, and then cooled and supplied into the high-pressure relief unit. The relief is done with a complex heterophase mixture: liquid saturated with gases and containing up to 3% diamond particles. Compressed air is fed into the suspension receiver for blowing to remove nitrogen oxides. Clarified UDD suspension in spent nitric acid is directed at regular intervals to the washing unit. The purification is performed continuously in automated mode with UDD output capacity of up to 1 kg (5000 carat) an hour (up to 5 tons a year).

The advantages of using nitric acid as oxidizing agent is that it exerts combined effect on all impurities in DS: nondiamond carbon and particles of metals and oxides, most of carbides [19]. Under high-temperature conditions, the reactivity of nitric acid is much enhanced. As a result, the target reactions occur at high rate, which favors organization of a high-output-capacity process.

Nondiamond carbon in DS is nonuniform in structure and chemical activity [21], and, therefore, the process can be conditionally divided into three stages: preliminary oxidation (10–20% of nondiamond carbon); oxidative breakdown of nondiamond carbon (65–80% of its amount); and additional oxidation of the most stable nondiamond structures, with prescribed oxidation level of diamond particles achieved (5–15% of nondiamond carbon).

The final stage is thermostating of the suspension at a temperature ensuring complete breakdown of nondiamond structures into gases and formation on the diamond particle surface of a stable and uniform coating of oxygen-containing functional groups.

Carrying out this complex multistage process in

[2] Manufactured by Tekhnolog Special Engineering and Design Office.

[3] Manufactured by Russian Research Institute of Technical Physics, Russian Federal Nuclear Center.

a continuous mode required a solution of diverse design and process problems. As experience shows, it is advisable to use controlled heat supply into a rather extended zone. As regards the UDD quality, this means that the degree of decomposition of the nondiamond carbon and the oxidation of the diamond surface will be constant and reproducible.

The second advantage of the purification method employed is that the oxidation products are mainly gaseous compounds. Consequently, the main reaction products are not accumulated in spent acid, which facilitates its recycling.

The technical solutions were based on detailed kinetic studies of the process. The specific design of high-pressure reactors assumes the presence of an air-cooled damping gas volume over flows of the liquid reaction mixture. The volume of the forming gases is estimated at 3.5–5 $m^3 h^{-1}$.

Nitric acid and nitrogen oxides can be regenerated in high yield and used in acid recycling. The extent of acid recycling is 75%, which markedly affects the economic and, what is more, environmental characteristics of the process. A severe problem is presented by UDD washing to remove acid and salt solutions. The small particle size, high sorption capacity, and the colloid stability of suspension, which grows in the course of washing, require a serious approach to the problem. Practice has demonstrated the advantage of intensive separation of finely dispersed suspensions and, in particular, tangential filtration on membrane filters and porous partitions [22].

An even more important problem is the necessity for modification of the surface properties of purified UDD, since it is this factor that affects the applicability of UDD in one or another process or composite. Methods for modifying the surface properties of nanodiamonds are diverse. This may be a purely thermal treatment of a suspension, treatment with various chemical reagents in various media with simultaneous action of high or low temperature, various physical methods. All these treatments markedly change the aggregative state of UDD, relative amounts of hydrophilic and hydrophobic groups on the diamond surface, sorption properties, surface charge, etc. Fine details of the processes of synthesis, chemical purification, and modification of UDD may strongly affect both the physicochemical properties and the performance of diamonds in composite materials and coatings.

We developed various methods for modification of the UDD surface, which allow production of that kind of diamonds, which is best suited for a particular field of their application.

The peculiar composition and complex structure of UDD cause a dualism of their properties, manifested in various physicochemical interactions, and the resulting unique influence on processes involving UDD. On the one hand, UDD inherit such characteristic properties of diamond as resistance to corrosive media, uncommon electrical properties, and high microhardness. On the other hand, the well-developed surface and the presence of a shell composed of dissimilar functional groups lead to a pronounced chemical activity, manifested under certain conditions, and even to the ability to reduce ions to free metals, by decomposing at room temperature aqueous solutions of K_2PdCl_4 and $Fe(C_2H_3O_2)_2$.

At present, 3 or 4 plants in Russia retain indisputable priority of "pathfinders" in the field of UDD synthesis and application. A number of plants in industrially developed countries introduce some processes of UDD application (predominantly metal–diamond electrochemical coatings), but there is no published evidence of any advances of their own in this field, with the exception of a Japanese concern Tokyo Daiyamondo Kogu Seisakusho K.K.

In processes aimed at creating new materials with the use of UDD, these latter act, as a rule, as a strong structure-forming agent. A common factor in these processes is the rather low expenditure of nanodiamonds (frequently, fractions of a percent), i.e., the useful effect is achieved not by changing the properties of a product manufactured, but by modification in the presence of UDD of the course of the corresponding process, be it polymerization, formation of lubricant films, or electrochemical deposition of metals. As a result, the structure of the final product may be altered to such an extent that its service characteristics will change fundamentally.

At present, the priority directions of UDD application are electrochemical and chemical metal–diamond coatings, polymer–diamond composites (film coatings, membranes, rubbers, plastics), lubricant oils, medicine (gastroentherological and antitumor preparations, immobilizers, adsorbents, etc.), polishing systems, and diamond ceramics (electronics, cutting tools).

The first to be developed in the early 1980s were chromium–diamond coatings on blade and pressing tools [1, 23]. As a rule, standard chromium plating electrolytes were used, containing a suspension of colloid UDD particles in amounts of 10–30 $g l^{-1}$. The content of UDD in a coating was in the range from 0.3 to 1.5 wt %. A chromium–diamond coating ex-

tends the service life of tools and articles 2–10-fold. Later, a similar study was carried out in Japan [24].

Nickel–diamond coatings are ideal choice for wear protection of machinery. The service life of articles with a coating of this kind is 5–20 times that for articles with purely nickel or other nickel composite coatings [1, 3, 25]. The UDD content of the electrolyte is 2 to 20 g l^{-1}, and the content of diamonds in a nickel film, from tenths of percent to 7–8% (this parameter is affected by a wide variety of factors, including the state of the surface of an article being treated). In electroless nickel plating, the content of UDD in the electrolyte is 15 to 80 g l^{-1}. At the same time, use of UDD of UDD-SPT brand [TU (Technical Specifications) 05 121 441-275–95] allows a decrease in the nanodiamond concentration in the electrolyte to 2 g l^{-1} at the equally high strengthening of the nickel coating by a factor of 4–12.

Introduction of UDD into an acid copper plating electrolyte gave nonporous copper coatings with 1.5 times higher microhardness, 2 times higher coating elasticity, 9–10 times lower wear, and manyfold higher corrosion resistance; the throwing power of an electrolyte with UDD increased by a factor of 3. The process of copper plating with UDD was described in detail in [4].

Approximately half the electroplated coatings in the world are those of zinc. Their main purpose is to protect articles from corrosion, especially under unfavorable conditions (sea water and atmosphere, tropics, industrially contaminated air, etc.). Previous studies have shown that the corrosion resistance of zinc–diamond coatings increased, without additional treatment, by 60–100%; microhardness, by 30%; and throwing power of the electrolyte, by 20–35% [4, 26–28]. Surface phosphatization raises the corrosion resistance by 200–250%, making it close to that of cadmium coatings.

Use of UDD in tin plating markedly decreases the porosity of a coating (by a factor of 3–9), raises its corrosion resistance, and makes the wear resistance 3 times higher [1, 4, 27]. In this case, the soldering ability and electrical properties of the coating remain virtually unchanged.

The wear resistance of silver coatings increases by a factor of 3–10, and the microhardness becomes as high as 180 kg mm^{-2} [1, 4].

The wear resistance of gold coatings increases by a factor of 1.8–5.5 at average UDD content in a coating of 0.1% [1, 28].

The wear resistance of an anodic film of aluminum and its alloys, filled with UDD in the course of electrolysis, increased by a factor of 10–13, the mass (filling) of the coating became 2–3.5 times higher, and corrosion resistance and dielectric properties grew substantially [1, 4, 29]. The coating is virtually pore-free and has good outward appearance.

Kinetic studies in copper, tin, and zinc plating electrolytes demonstrated that UDD do not change the mechanism of the process, their influence being associated with the surface-adsorption interaction of the most energetically active nanodiamond particles with growing metal crystals.

The common features of metal–diamond films are as follows: (1) markedly enhanced adhesion and cohesion, (2) increased microhardness and wear resistance, (3) improved corrosion resistance and lower porosity, (4) much higher antifriction, and (5) high throwing power of electrolyte.

The use of UDD and DS as active fillers of polymer formulations and, in particular, film coatings proved to be very efficient [1, 30–32]. For example, the process that we developed for cold vulcanization and filling with UDD yields coatings with the following characteristics. Fluoroelastomer-based coatings have approximately 50 times lower permeability to hydrocarbons and polar solvents, 2 times higher elastic and strength parameters, and high resistance to thermal aging. Polysiloxane-based coatings have 3 times higher tensile strength (154 against 53 MPa) at also approximately 3 times greater absolute elongation (1970 against 730%), with the set of elastic and strength characteristics improved by a factor of 3–5.

A film-forming material for creating antifriction coatings on metal surfaces was developed on the basis of fluoropolymers and UDD, with a previously unachievable coefficient of dry friction on metal (<0.01) obtained.

Fluoropolymeric films with UDD are interior coatings of fuel tanks, depositories, and any other surfaces, which are resistant to the action of corrosive media.

Polysiloxane films with UDD are anti-icing heat- and radiation-resistant coatings (aerials, hulls of Arctic ship, cases of radio beacons and radio buoys, plane wings and fuselage, etc.).

The developed process of hot curing of industrial polymers with UDD ensured higher wear resistance and better elastostrain, radiation-resistant, antifriction, and protective properties of composites. The content of UDD in the formulations is 0.1 to 2.0 wt %. The new properties of rubbers make them efficient in fric-

tion units, seals (including those in outer circuits of nuclear reactors), and coatings protecting from the action of corrosive media.

Ultradisperse diamonds constitute one of the most interesting objects of study and application. According to specialists' prognoses, it is UDD that are capable of occupying a key position in manufacture of composite materials and coatings of a new generation, with the result that the demand for UDD will form and soar.

CONCLUSIONS

(1) Ultradisperse diamonds have the form of a cluster–cluster system of the fractal type, possessing an uncommon combination of properties.

(2) Three main methods for synthesis of UDD are described: in the gas medium, in water, and in ice.

(3) The optimal version of the UDD purification process is proposed: oxidation of impurities with dilute nitric acid at high temperature and pressure.

(4) Good service characteristics of metal–diamond electroplated coatings and polymer–diamond films are analyzed in detail.

REFERENCES

1. Dolmatov, V.Yu., *J. Superhard Mater.*, 1998, vol. 20, no. 4, pp. 70–73.
2. Greiner, N.R., Phillips, D.S., Johnson, J.D., *et al.*, *Nature*, 1988, vol. 333, no. 5, pp. 440–442.
3. Chukhaeva, S.I., Detkov, P.Ya., Tkachenko, A.P., *et al.*, *Sverkhtverd. Mater.*, 1998, no. 4, pp. 77–81.
4. Dolmatov, V.Yu. and Burkat, G.K., *Sverkhtverd. Mater.*, 2000, no. 1, pp. 84–95.
5. Savvakin, G.I., Kotko, V.A., Ostrovskaya, N.F., and Kurdyunov, A.V., *Poroshk. Metall.*, 1988, no. 10, pp. 78–82.
6. Xu, T., Xu, K., and Xhao, J., *Mater. Sci. Eng. B*, 1996, vol. 38, no. 1, pp. L1–L4.
7. Vereshchagin, A.L., Komarov, V.F., Mastikhin, V.M., *et al.*, *Doklady V Vsesoyuznogo soveshchaniya po detonatsii. Krasnoyarsk, 5–12 avg. 1991 g.* (Proc. V All-Union Meet. on Detonation, Krasnoyarsk, August 5–12, 1991), Chernogolovka, 1991, vol. 1, pp. 99–103.
8. Baraboshkin, K.S., Gubarevich, T.M., and Komarov, V.F., *Kolloidn. Zh.*, 1992, vol. 54, no. 6, pp. 9–12.
9. RF Patent 2046094.
10. Gubarevich, T.M., Turitsyna, O.F., and Poleva, L.I., *Zh. Prikl. Khim.*, 1992, vol. 65, no. 6, pp. 1269–1273.
11. Gubarevich, T.M., Kulagina, L.S., and Larionova, I.S., *Doklady V Vsesoyuznogo soveshchaniya po detonatsii. Krasnoyarsk, 5–12 avg. 1991 g.* (Proc. V All-Union Meet. on Detonation, Krasnoyarsk, August 5–12, 1991), Chernogolovka, 1991, vol. 1, pp. 130–134.
12. *Fractals in Physics (Proc. Sixth Trieste Int. Symp. on Fractals in Physics, ICTP, Trieste, Italy, July 9–12, 1985)*, Pietronero, L. and Tosatti, E., Eds., Amsterdam: North-Holland, 1986.
13. Petrov, Yu.I., *Klastery i malye chastitsy* (Clusters and Fine Particles), Moscow: Nauka, 1986.
14. Volkov, K.V., Danilenko, V.V., and Elin, V.P., *Fiz. Goren. Vzryva*, 1990, vol. 26, no. 3, pp. 123–125.
15. Savvakin, G.I. and Trefilov, V.I., *Dokl. Akad. Nauk SSSR*, 1991, vol. 321, no. 1, pp. 99–103.
16. Sakovich, G.V., Gubarevich, V.D., Vereshchagin, A.L., *et al.*, *Zh. Vses. Khim. O–va. im. D.I. Mendeleeva*, 1990, vol. 35, no. 5, pp. 600–602.
17. USSR Inventor's Certificate no. 1826067.
18. USSR Inventor's Certificate no. 1658558.
19. Gubarevich, T.M., Sataev, R.R., and Dolmatov, V.Yu., *Doklady V Vsesoyuznogo soveshchaniya po detonatsii. Krasnoyarsk, 5–12 avg. 1991 g.* (Proc. V All-Union Meet. on Detonation, Krasnoyarsk, August 5–12, 1991), Chernogolovka, 1991, vol. 1, pp. 135–139.
20. RF Patent 2109683.
21. Dolmatov, V.Yu., Gubarevich, T.M., Pyaterikov, V.F., *et al.*, *Zh. Prikl. Khim.*, 1993, vol. 66, no. 8, pp. 1882–1885.
22. Solokhina, A.V., Ignatenko, A.V., and Sataev, R.R., *Zh. Prikl. Khim.*, 1991, vol. 64, no. 8, pp. 1751–1753.
23. PCT Patent Appl. (WO 89/07668) 43824 17.
24. JPN Patent Appl. 5-10695 (A).
25. Timoshkov, Yu.V., Orekhovskaya, T.I., Kurmashev, V.I., *et al.*, *Gal'vanotekh. Obrab. Poverkhn.*, 1999, no. 4, pp. 20–25.
26. RF Patent 2169798.
27. Burkat, G.K. and Dolmatov, V.Yu., Abstracts of Papers, *Vserossiiskaya nauchno-prakticheskaya konferentsiya "Gal'vanotekhnika i obrabotka poverkhnosti"* (Russian Scientific and Practical Conf. "Electroplating and Surface Treatment"), Moscow: Ross. Khimiko-Tekhnol. Univ. im. D.I. Mendeleeva, 1999, pp. 15–16.
28. Dolmatov, V.Yu., Burkat, G.K., Saburbaev, V.Yu., and Veretennikova, M.V., *Sverkhtverd. Mater.*, 2000, no. 4, pp. 43–47.
29. RF Patent 2169800.
30. Voznyakovskii, A.P., Levintova, E.A., and Dolmatov, D.Yu., Abstracts of Papers, *4th Eur. East-West Conf. and Exhibition on Material and Process*, St. Petersburg, October 17–21, 1993, p. 80.
31. RF Patent 2100389.
32. Voznyakovskii, A.P., Dolmatov, V.Yu., and Levintova, E.A., *Doklady mezhdunarodnoi konferentsii po kauchuku i rezine* (Proc. Int. Conf. on Rubber), Moscow, September 27–October 1, 1994, vol. 2, pp. 80–87.

Russian Journal of Applied Chemistry, Vol. 75, No. 5, 2002, pp. 761–767. Translated from Zhurnal Prikladnoi Khimii, Vol. 75, No. 5, 2002, pp. 779–785.
Original Russian Text Copyright © 2002 by Protod'yakonova, Aniskin.

PROCESSES AND EQUIPMENT OF CHEMICAL INDUSTRY

Hydrodynamic Model of Restrained Flare of Atomized Fluid

O. I. Protod'yakonova and S. V. Aniskin

St. Petersburg Technological Institute of Plant Polymers, St. Petersburg, Russia

Received January 16, 2002

Abstract—A flow model of a restrained gas–fluid jet with a cocurrent flow is constructed, taking into account the nonuniformity of gas velocity distribution across the jet and the polydisperse composition of drops.

The chemical and related branches of industry, where a problem is encountered of gas discharge cleaning, widely employ mass-exchange apparatus with atomized fluid jets whose development is restrained by apparatus walls. Among the known examples of such apparatus are Venturi ejector scrubbers and straight-flow spraying apparatus with cylindrical and rectangular cross section. In apparatus of this kind, a gas–fluid jet develops in a surrounding gas flow with certain initial velocity. This gas flow is a cocurrent flow with respect to the gas–fluid jet.

Of much practical interest is evaluation of the ejection effect arising in a spraying apparatus for the following reasons.

The fluid flowing out of the atomizer imparts momentum to the surrounding gas. As a result, the gas velocity increases and a gas jet is formed inside the fluid flare. After this jet comes in contact with the apparatus walls, the nonuniformity of the gas velocity across the apparatus diminishes. The kinetic energy of the gas jet also decreases and, correspondingly, its potential energy grows. Consequently, the pressure in the gas flow increases in the course of gas–fluid jet motion. As a result, the pressure difference between the initial and the following (downstream) parts of the apparatus grows. Thus, the ejection effect arises, resulting in that the gas fed into the apparatus inlet is entrained by the gas–fluid jet and moves in the same direction as this jet, forming a cocurrent flow. If a spraying mass-exchange apparatus of this kind is a part of a hydraulic system along which a gas flow moves, then the existence of the ejection effect described above enables the apparatus to perform in the same system also the function of a fan (the so-called flow booster), which can in some cases lower the energy expenditure for gas transport in the system.

The presently known models of flows of this kind have a number of disadvantages [1, 2]. The most significant of these are the lack of a method for determining the gas jet boundaries, the assumption of uniform distribution of the velocity and pressure of gas across the jet, and the failure to take into account the polydispersity of fluid drops, which is particularly important in calculations of heat- and mass-exchange processes in spraying apparatus. Our earlier models are free of these disadvantages [3, 4]. However, these models are only applicable to describing a jet with motion not restrained by apparatus walls, having no cocurrent flow.

A general scheme illustrating the structure of the gas–fluid flow in a straight-flow spraying apparatus is presented in Fig. 1. The apparatus comprises an atomizer *1* in a cylindrical case *2*. The gas flow processed in the apparatus is fed into it from above at a certain constant rate. The fluid fed into the atomizer under pressure is dispersed into drops moving inside the apparatus by inertia and forming a conical flare. The fluid motion velocity in the apparatus exceeds that of the gas. The gas flow from the near-wall region is drawn into this flare to form a gas jet. This process is responsible for the continuous rise in gas flow rate within the fluid flare, which expands as the fluid jet moves along the apparatus. At a certain distance from the atomizer, the gas flow rate inside the flare becomes equal to that at the apparatus inlet. Further increase in the gas flow rate inside the fluid flare may occur, before the flare comes in contact with the apparatus walls, only via gas circulation in the near-wall region. In this case, the circulation also encompasses that region which lies below the point of contact between the fluid flare and the apparatus walls.

It should, however, be noted that, at a certain combination of operating conditions (such as gas and fluid velocities, flare angle, apparatus diameter, drop size,

1070-4272/02/7505-0761$27.00 © 2002 MAIK "Nauka/Interperiodica"

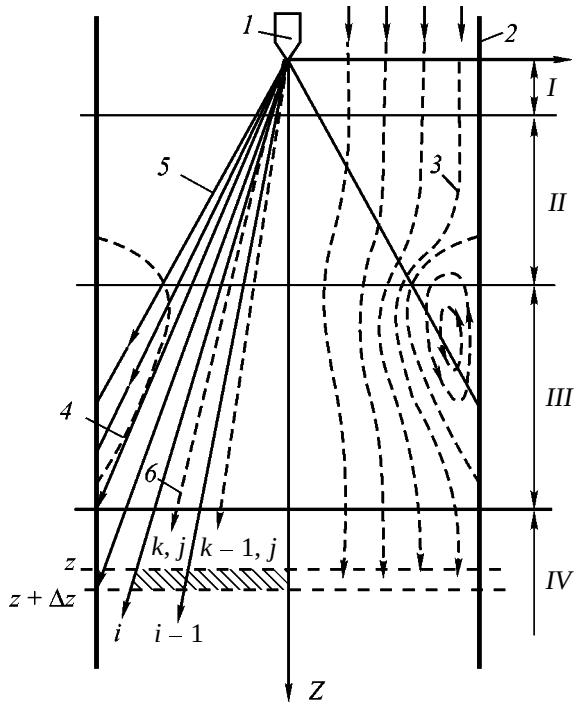

Fig. 1. Schematic of gas–fluid flow in a cylindrical straight-flow spraying apparatus. (*1*) Atomizer, (*2*) apparatus wall, (*3*) lines of gas flow, (*4*) inner boundary of the near-wall gas circulation region, (*5*) line of fluid flow, (*6*) line of flow of a drop jet of *j*th fraction, $j = 1, 2, \ldots, m$ (where m is the number of fraction composed of drops with the maximum size). (*I*) Zone of fluid jet breakdown, (*II*) zone of drop flow of a gas–fluid jet with a cocurrent gas flow, (*III*) zone of gas–fluid jet flow with a near-wall region of gas circulation, and (*IV*) zone of gas–fluid jet flow after the instant of contact between the gas jet and the apparatus wall.

atomizer nozzle diameter, etc.) and also on varying the shape of the spraying apparatus, e.g., with a Venturi tube used instead of a cylinder, there may be no gas circulation in the apparatus. After the fluid flare comes in contact with the apparatus wall, fluid drops settle on the wall to form a downflowing fluid film.

The gas jet inside the fluid flare reaches the apparatus walls after the fluid flare comes in contact with the apparatus walls. Owing to the presence of the above-described gas circulation zone in the near-wall region, the point of contact between the gas jet inside the fluid flare and the apparatus wall may lie below the point of contact between the fluid flare and the apparatus wall. After the gas jet comes in contact with the apparatus wall, the gas velocity profile across the jet is flattened out, with the kinetic energy of the gas jet transformed into its potential energy, characterized by gas pressure.

In accordance with specific features of the gas–fluid jet flow, the jet is conditionally divided, in constructing its mathematical description, into four zones with, to a certain extent, different natures of flow of media. The existence of these zones makes necessary construction of separate mathematical models of flow for each of these zones. The hydrodynamic models of the selected zones of the gas–fluid jet can be used as elements in constructing a general model of a restrained flare of atomized fluid, by combining these elements with the help of appropriate boundary conditions.

Let us consider the first zone of the gas–fluid jet flow (Fig. 1). In this zone, the continuous flow of the fluid outflowing from the atomizer breaks up into drops. Since this flow is swirling because of the atomizer design features, the tangential component of the fluid velocity is transformed into the radial component in the course of flow disintegration into drops. As a consequence, the jet flare angle increases, with the resulting gas–fluid jet having a conical shape.

The distribution of the fluid flow across the flare can be characterized by dimensionless volume density of the liquid phase, β, defined as the fraction of the liquid phase in the space occupied by the gas–fluid mixture. Any cross section of the gas–fluid jet, perpendicular to the Z axis, is characterized by a certain distribution of β over the cross-sectional area. Such a distribution has a certain maximum value $\beta_z^{\max}$.

By analogy with [3], we consider that the first zone of the gas–fluid jet is confined between the lower boundary of the atomizer nozzle, wherefrom the fluid flow runs, and the coordinate $z = L_1$, on reaching which $\beta_z^{\max}$, decreasing in the Z axis direction, takes a value of 0.02. We assume that the relative motion of phases in this zone can be represented as gas filtration through a certain porous medium formed by disintegrating fluid flow and characterized by constant equivalent channel diameter. Then we can use, in describing mathematically the gas–fluid jet flow in this zone, the equations derived in [3].

Let us write an equation describing the momentum change in the flare in a horizontal layer of height dz at a certain arbitrary distance z from the nozzle exit section. The form of this layer, further used to illustrate equations of the mathematical models for the distinguished flare zones, is specified in the bottom part of Fig. 1.

$$\frac{\mathrm{d}}{\mathrm{d}z}\sum_{i=1}^{i}(\rho_g Q_{gi} V_{zi}) - \rho_g V_{z,\,i+1}\sum_{i=1}^{i}\mathrm{d}Q_{gi}/\mathrm{d}z + \sum_{i=1}^{i}(\mathrm{d}w_{zi}/\mathrm{d}z - gG_i/u_{zi}) + \pi\sum_{i=1}^{i}(y_i^2 - y_{i-1}^2)\mathrm{d}P_i/\mathrm{d}z = 0, \qquad (1)$$

where ρ_g is the gas density, kg m^{-3}; Q_g, the volumetric gas flow rate, m^3 s^{-1}; V_z, the gas velocity in the Z axis direction, m s^{-1}; W_z, the flux of the fluid momentum in the direction of the Z axis, N; y and z, the radial and vertical coordinates, respectively, m; P_i, the gas pressure, Pa; i, the fluid jet index; and y_i, the radial coordinate of the intersection of ith line of fluid flow with the cross section (Fig. 1).

It should be noted that, in deriving this equation, the whole volume of the fluid flare is divided in n jets forming a structure of coaxial conical fluid tubes (Fig. 1). In this case, the indices of fluid jets, and also indices of lines of flow delimiting the corresponding fluid jets from the outside, coincide in the adopted indexation system. The equation describes how the flux of momentum changes in an elementary layer of height dz of a gas–fluid jet delimited by ith line of flow (shaded region in Fig. 1).

The equation describing how the momentum varies along the radial coordinate y in an elementary layer of height dz in the gas–fluid jet, which is valid for conditions of a minor variation of the gas flow momentum in this direction, has the form

$$\sum_{i=1}^{i} dW_{yi}/dz + 2\pi \sum_{i=1}^{i} y_i(P_{i+1} - P_i) = 0, \qquad (2)$$

where W_{yi} is the flux of the fluid momentum in the Y axis direction, N.

The equation of gas flow rate conservation in the Z axis direction in a jet layer of height dz, written with account of the fact that part of the gas flow moves into this layer from the outside, has the form

$$\sum_{i=1}^{i} dQ_{yi}/dz + 2\pi y_i v_{y,i+1}, \qquad (3)$$

where v_y is the radial component of the gas flow velocity, m s^{-1}.

Relations closing the set of Eqs. (1), (2), and (3) were considered in detail in [3].

Introducing a function $y_w(z)$ defining the apparatus wall coordinates, we can formulate boundary conditions for these equations with account of the fact that the diameter of the fluid jet outflowing from the jet nozzle is small in comparison of the apparatus diameter. At $z = 0$:

$$G_i = G_{i0};\ u_{zi} = u_{zi0};\ u_{yi} = u_{yi0};$$

$$u_{yi} = u_{yi0};\ y_i = 0;\ v_{z,n+1} = v_0;\ P_i = P_0; \qquad (4)$$

$$\sum_{i=1}^{n} Q_{gi} = 0; \quad Q_{g,n+1} = \pi y_c^2.$$

At $y = 0$:

$$v_{y1} = 0. \qquad (5)$$

At the outer boundary of the jet, i.e., at $y_n < y < y_w$:

$$v_{z,n+1} = Q_{g0} - \pi \sum_{i}^{n} (y_i^2 - y_{i-1}^2) v_{zi}/[\pi(y_w^2 - y_n^2)],$$

$$v_{y,n+1} = (2\pi y)^{-1}(dQ_{g,n+1}/dz), \qquad (6)$$

$$dP_{n+1}/dz = -v_{z,n+1}(dv_{z,n+1}/dz).$$

Let us construct a model of restrained flow of a polydisperse gas–fluid jet for the second zone (Fig. 1). In this zone, the dispersion composition of drops becomes constant, and motion of each drop becomes independent of the motion of other drops. In formulating model equations, we divide the jet flare into m mutually penetrating flares, each composed of drops of the same size. As in constructing the model of a gas–fluid flow for the first zone, we divide the space occupied by each of the above m fluid flares along the radial coordinate by lines of fluid flow into n jets in such a way that the fluid flow rate in each of these jets is constant.

Let us denote the number of a drop fraction by index j, and the number of a fluid jet, by index k. Then the following condition will be satisfied for arbitrary kth fluid jet composed of drops of jth fraction:

$$G_{kj} = \text{const}. \qquad (7)$$

Let us consider a disperse fluid flare composed of drops of one of the fractions $j = 1, 2, \ldots, m$.

We choose a number j corresponding to the fraction composed of maximum-size drops, i.e., $j = m$, and select within the second flow zone an elementary layer of height Δz, delimited along the radial coordinate by lines of fluid flow k and $k - 1$, in the flare in question. This layer will be denoted by a pair of indices k and m, which characterize the number of fluid jet (coinciding with the number of the line of flow) and the number of fraction with drops of maximum size. The layer of the dispersed fluid jet, considered here and denoted by indices k and m, occupies a unit space, denoted by index i to make convenient derivation of further equations of the model. Through this space pass, in motion of a gas–fluid jet, fluid jets

containing drops of all fractions j. As is known, owing to the difference between trajectories of drops of different sizes, the jets composed of drops of one fraction are shifted along the radial coordinate relative to drops of another fraction (Fig. 1). As a result of this shift of jets, they may pass through the selected unit space i entirely, partly, or may not enter this element at all. Thus, k fluid jets and j drop fractions may pass, in principle, through the unit space i. The fraction G of the fluid flow rate of an arbitrary fluid jet kj passing through unit space i can be expressed using the coefficient θ_{ikj}. Then, the expression for the total flow rate of the fluid passing through a unit space i in motion of the gas–fluid jet takes the form

$$G_i = \sum_k^n \sum_j^m \theta_{ikj} G_{kj}. \quad (8)$$

Expressions for W_{zi} and W_{yi} can be obtained similarly, which enables use of Eqs. (1), (2), and (3) for describing the second flow zone. Relations closing these equations were reported in [4].

These relations must be supplemented with boundary conditions taking into account the restrained nature of the gas–fluid flow. At $z = L_1$:

$$G_{kj}^{(2)} = G_{kj0}, \qquad \sum_{j=1}^m \theta_{kj} G_{kj}^{(2)} = G_i,$$

$$u_{zkj}^{(2)} = u_{zi}^{(1)},\ u_{ykj}^{(2)} = u_{yi}^{(1)},\ v_{zi}^{(2)} = v_{yi}^{(1)},\ v_{yi}^{(2)} = v_{yi}^{(1)},$$

$$v_{z,n+1}^{(2)} = v_{z,n+1}^{(1)},\ y_i^{(2)} = y_{kj}^{(2)} = y_i^{(1)},\ P_i^{(2)} = P_i^{(1)}.$$

At $y = 0$ and at $y_n < y < y_w$, the boundary conditions are identical to those for the first zone, (5) and (6).

The next stage of our theoretical study of the flow in a restrained flare of atomized fluid consists in construction of a model for the third flow zone of those selected in Fig. 1.

A distinctive feature of the third flow zone of the gas–fluid jet consists in that the gas flow rate inside this jet becomes higher than the gas flow rate at the apparatus inlet. This is due to an increase in the gas flow velocity in the jet flare, resulting from further rise in the momentum imparted by the fluid phase to the gas flow. This feature, however, does not entail any change in the basic equations used to describe the second flow zone of the gas–fluid jet. Thus, the system of equations for the third flow zone, considered here, must include Eqs. (1), (2), (3), (7), and (8). The distinction of the model for the third zone from that for the second is in the kind of boundary conditions for the equations mentioned. At $z = L_2$:

$$G_{ki}^{(3)} = G_{ki}^{(2)},\ u_{zki}^{(3)} = u_{zkj}^{(3)},\ u_{ykj}^{(3)} = u_{ykj}^{(2)},$$

$$v_{zi}^{(3)} = v_{zi}^{(2)},\ v_{yi}^{(3)} = v_{yi}^{(2)},\ v_{z,n+1}^{(3)} = v_{z,n+1}^{(2)},$$

$$y_{kj}^{(3)} = y_{kj}^{(3)}, \quad P_i^{(3)} = P_i^{(2)}. \quad (10)$$

At $y = 0$, the condition (5) is preserved.

In formulating conditions at the outer boundary of the flare, account should be taken of the following. By virtue of the law of conservation of the flow rate of gas passing through the apparatus, a local excess of gas flow velocity in any jet flow zone over that at the apparatus inlet is only possible when the motion direction of a part of the gas flow changes in the near-wall region to the opposite as a result of formation of the corresponding circulation flows.

It seems natural to assume that this change in flow direction occurs at the outer boundary of the gas–fluid jet flare. Then the boundary condition accounting for this fact can be written in the form

$$v_{z,n+1} = 0. \quad (11)$$

It is known that, in the case of gas flow circulation, the gas pressure in the near-wall region is equalized and it may be considered that at the outer boundary of the flare

$$P = \text{const}. \quad (12)$$

When the fluid flare comes in contact with the apparatus walls, the gas pressure in the gas–fluid jet may increase stepwise by ΔP as a result of abrupt deceleration of the gas flow. In terms of the formalism used, it is believed that, after the gas–fluid jet touches the apparatus walls, its outer boundary successively moves, as the fluid falls onto the wall, inside the flare from line of flow with number $i = n$ (Fig. 1) to that with number $n - 1$, then to line of flow $n - 2$, etc., within the gas circulation zone.

This feature must be taken into account by the boundary conditions for the flow velocity and pressure of gas. For example, depending on the index of the line of flow, i_b, along which the corresponding boundary is established, the conditions (11) and (12) have the following form.

At $i_b = n$:

$$v_{z,n+1} = 0, \qquad P_{n+1} = P_{n+1}^{(2)},$$

At $i_b = n - 1$:

$$v_{z,n} = 0, \quad p_n = P_{n+1}^{(2)} + \Delta P_n, \tag{13}$$

at $i_b = n - 2$:

$$v_{z,n-1} = 0, \quad P_{n-1} = P_{n+1}^{(2)} + \sum_{i=n-1}^{n} \Delta P_n,$$

etc., where $P_{n+1}^{(2)}$ is the gas pressure in the near-wall region at the boundary separating the second and third zones of the gas–fluid jet: ΔP_i is the pressure jump in the near-wall region, which results from deceleration of ith gas jet in its collision with the apparatus wall.

In view of the fact that the gas flow velocity v_z decreases to zero under the conditions (13), the momentum of ith gas jet is completely transformed into gas pressure:

$$\Delta P_i = \frac{\pi_g Q_i v_{zi}}{\pi y_w^2}. \tag{14}$$

and, thus, the flow model of the gas–fluid jet in the third zone is constructed.

Let us now construct a gas–fluid jet flow model for the fourth zone. The specific features of this zone are the following: adhesion of the gas jet to the walls and leveling-out of the gas flow velocity distribution across the apparatus, which is known to be accompanied by an increase in gas pressure. Similarly to the case of the third zone, these features do not entail any need to change the type of the basic equations (1), (2), (3), (7), and (8), used to describe the flow of the gas–fluid jet in the second zone.

Let us formulate the boundary conditions for these equations. For this purpose, we consider a method for determining the coordinate z of a cross section that is the upper boundary of the zone in question. If there is no flow separation from the apparatus walls, i.e., there is no third zone of the gas–fluid jet, then it seems natural to regard as the beginning of the fourth zone the coordinate z at which nth line of fluid flow touches the apparatus wall. In this case, the conditions at this boundary completely coincide with the conditions (10). If, however, there is flow separation from the apparatus walls and there exists the third flow zone in the gas–fluid jet, then the boundary between the third and fourth zones is found from the following considerations. The zone of gas circulation in the near-wall region ends at this boundary and the gas jet adheres to the apparatus walls. This means that the gas flow tube, within which a gas flow moves with flow rate Q_0, again comes in contact with the apparatus walls after flow separation from these walls in the third zone. It is this flow tube that is the boundary of the near-wall circulation zone (Fig. 1).

In terms of the formal concepts used in modeling the flow of the gas–fluid jet under consideration, the boundary between the third and fourth zones is found as follows. A jet cross section passing through the point at which an arbitrary ith line of flow (i_w) touches the wall may be considered, to a first approximation, as the boundary between the third and fourth zones if the line of gas flow, belonging to a flow tube delimiting a gas flow q_{g0}, passes between the lines of fluid flow i_w and $i_{(w-1)}$. Then the following condition is satisfied:

$$\sum_{i=1}^{i_w} Q_{gi} > Q_{g0} > \sum_{i=1}^{i_w - 1} Q_{gi}. \tag{15}$$

The accuracy of finding the position of the sought-for boundary by calculation improves with increasing number n of jets into which the gas–fluid flare is divided in constructing the model.

The conditions at the boundary between the third and fourth zones are as follows.

At $z = L_3$:

$$G_{kj}^{(4)} = G_{kj}^{(3)}, \quad u_{zkj}^{(4)} = u_{zkj}^{(3)}, \quad u_{ykj}^{(4)} = u_{ykj}^{(3)}$$

$$y_i^{(4)} = y_i^{(3)}, \quad y_{kj}^{(4)} = y_{kj}^{(3)}, \quad P_i^{(4)} = P_i^{(3)} + \Delta P_w.$$

where

$$\Delta P_w = \rho[(v_{ziw}^{(3)})^2 - (v_{ziw}^{(4)})^2]. \tag{16}$$

For the boundary region satisfying the condition

$$y \le y_{i-1}: \quad v_{zi}^{(4)} = v_{zi}^{(3)}, \quad v_{yi}^{(4)} = v_{yi}^{(3)}. \tag{17}$$

In the boundary region satisfying the inequality $y_{iw} \le y \le y_{i,w-1}$, the boundary conditions must take into account the stepwise change in gas flow velocity and pressure, resulting from an abrupt change in the nature of the gas flow (in this part of the boundary), consisting in that there occurs a transition from circulation gas motion to motion without circulation at a constant flow rate Q_0, which is established at the instant of gas flow adhesion to the apparatus walls. These boundary conditions have

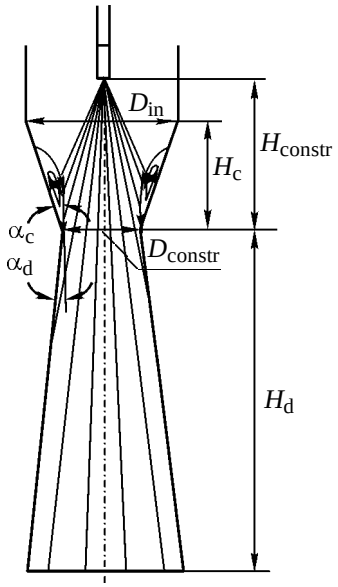

Fig. 2. Basic design parameters of a jet scrubber. (D_{in}) Inlet diameter, (D_{constr}) constriction diameter, (H_{constr}) distance between the atomizer and the constriction section, (H_d) diffuser length, (α_c) confuser angle, (α_d) diffuser angle, and (H_c) confuser length.

the following form:

$$v_{zi\text{w}}^{(4)} = \left[Q_0 - \sum_{i=1}^{i\text{w}-1} Q_i\right]/[\pi(y_{i\text{w}}^2 - y_{i\text{w}-1}^2)]^{-1},$$

$$v_{yi}^{(4)} = -(2\pi y_{i\text{w}-1}^{(3)})^{-1} \sum_{i=1}^{i\text{w}-1} \mathrm{d}Q_i^{(3)}/\mathrm{d}z. \qquad (18)$$

At the apparatus wall, the following condition must be satisfied:

$$v_y = 0. \qquad (19)$$

Thus, the resulting model of the gas–fluid jet for the fourth zones includes Eqs. (1), (2), (3), (7), and (8), and boundary conditions (16)–(19).

The developed hydrodynamic model of the restrained flare of a gas–fluid jet can be verified by comparing the distribution of the statistical pressure $P(z)$ along the flare length, calculated by numerical solution of the model equations by the Runge–Kutta method, with the results of an experimental study of this distribution in a jet scrubber [5]. In [5], a jet scrubber with the case in the form of a Venturi tube was studied.

The design characteristics of a jet scrubber, which appear as constants in the expressions for y_w and are presented in Fig. 2, have the following values: D_{in} = 0.2 m, D_{constr} = 0.126 m, H_c = 0.36 m, H_d = 0.7 m, α_c = 12°, and α_d = 6°. The gas flow velocity at the apparatus inlet was v_{g0} = 3.5 m s^{-1}. The atomizer used in the experiments had the following parameters: nozzle diameter d_n = (3±0.01) mm, flow coefficient μ = (0.9±0.01) mm, flare angle α = 48°, and fluid pressure before the atomizer P_f = 0.6 MPa.

The experimentally obtained [5] values of the spraying density distribution function along the radial coordinate can be approximated by the following formula [6]:

$$I = \frac{a}{1 + bx^n} - \frac{c}{1 + dx^n}, \qquad (20)$$

where I is the relative spraying density, and x is the relative radius.

The I and x values are given by

$$I = J/\bar{J}, \quad x = y/R, \qquad (21)$$

where J, $\bar{J}$ are the spraying density and average spraying density, m s^{-1}, over an area delimited by radius R, through which 95% of the fluid passes.

The constants a, b, c, d, and n, appearing in formula (20), were found by calculation from the condition that this formula ensures the best fit to the experimentally obtained [5] values of the spraying density distribution function: a = 2.93, b = 47.7, c = 2.17, d = 20 158, and n = 15.4. The I value calculated using the above constants makes it possible to determine the fluid flow rate G_i in ith jet, which appears in the boundary conditions (14), using the formula [6]

$$G_i = 1.9\, G_0 \int_{x_{i-1}}^{x_i} I x \mathrm{d}x, \qquad (22)$$

The G_{kj} value, appearing in the boundary conditions (9), (10), and (16), is determined with account of the dispersion composition of the drop flow in the gas–fluid jet.

In the case under study, we can characterize the dispersion composition of the drop flow, using the results obtained in [16], owing to the fact that the impermeability and operation characteristics of the centrifugal-jet atomizer, reported in [5] and [6], are identical, except for the flare angle. However, as is known [1], the effect of this parameter on the dispersion composition of drop flow in the gas–fluid jet is negligible.

Under the hydrodynamic conditions considered here, the dispersion composition of the drop flow can be described by the Rosin–Rammler distribution [6]:

$$S_j = 1 - e^{-(dj/a)^l}, \quad (23)$$

where S_j is the volume fraction of drops with size smaller than d_j, and a and l are distribution constants: $a = 0.34 \times 10^{-3}$ m and $l = 3.1$.

With account of (23), the G_{kj} value is found as follows:

$$G_{kj} = (S_j - S_{j-1})G_i \text{ at } k = i. \quad (24)$$

As additional boundary conditions, necessary for solving numerically the equations of our hydrodynamic model with account of the specific conditions of an experimental study of a restrained flare of atomized fluid in a jet scrubber, we used the following simple relations:

$$P_0 = -38\text{Pa}, \; u_{zi0} = \mu(2\rho_l/\rho)^{1/2}\cos(\alpha_i/2),$$
$$u_{yi0} = u_{zi}\tan(\alpha_i/2), \quad (25)$$

where α_i is the angle of deflection of ith jet from the Z axis.

The distribution function of the statistical pressure $P(z)$ along the gas–fluid jet was plotted in Fig. 3 on the basis of a numerical solution to the equations of our hydrodynamic model of a restrained flare of atomized fluid, with the boundary conditions considered above.

The points in Fig. 3 represent the values of the function $P(z)$, obtained in [5] in an experimental study of a restrained flare of atomized fluid in a jet scrubber. It should be noted that the results obtained in solving numerically the equations of our hydrodynamic model take into account the specific features of all the four flow zones of the gas–fluid jet, which were observed in its experimental study. The rms deviation of the theoretical and experimental $P(z)$ values related to the total pressure drop across the jet scrubber (142 Pa) was 6%.

CONCLUSIONS

(1) A one-dimensional integral hydrodynamic model of a restrained flare of atomized fluid in a jet scrubber is constructed. The model takes into account the real distribution of the spraying density and the dispersion composition of the flow of fluid drops.

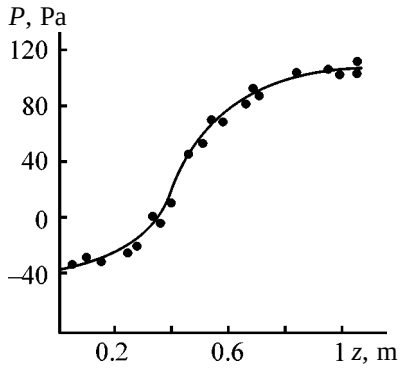

Fig. 2. Distribution of statistical pressure in a jet scrubber. (P) Statistical pressure and (z) distance from the atomizer.

(2) Comparison of the distribution of static pressure in a jet scrubber, obtained by solving numerically the equations of the model of a restrained flare of atomized fluid, with experimental data confirms the validity of the hydrodynamic model constructed in the present study.

REFERENCES

1. Galustov, V.S. and Pazhi, D.G., *Osnovnye tekhniki raspylivaniya zhidkostei* (Basic Methods of Fluid Atomization), Moscow: Khimiya, 1984.
2. Aniskin, S.V., in *Okhrana okruzhayushchei sredy ot zagryazneniya proizvodstvennymi vybrosami* (Environment Protection from Industrial Contaminants), Leningrad, 1977, issue 5, pp. 179–181.
3. Aniskin, S.V. and Protod'yakonova, O.I., *Zh. Prikl. Khim.*, 2001, vol. 74, no. 3, pp. 445–450.
4. Protod'yakonova, O.I. and Aniskin, S.V., *Zh. Prikl. Khim.*, 2001, vol. 74, no. 12, pp. 1994–2000.
5. Aniskin, S.V., Maksimov, V.F., Galustov, V.S., *et al.*, in *Okhrana okruzhayushchei sredy ot zagryazneniya proizvodstvennymi vybrosami* (Environment Protection from Industrial Contaminants), Leningrad, 1981, issue 9, pp. 155–161.
6. Protod'yakonova, O.I., Aniskin, S.V., and Sleptsov, I.E., *Zh. Prikl. Khim.*, 2002, vol. 75, no. 2, pp. 243–248.

Russian Journal of Applied Chemistry, Vol. 75, No. 5, 2002, pp. 768–770. Translated from Zhurnal Prikladnoi Khimii, Vol. 75, No. 5, 2002, pp. 786–788.
Original Russian Text Copyright © 2002 by Illarionova, Abramova, Illarionov.

ORGANIC SYNTHESIS AND INDUSTRIAL ORGANIC CHEMISTRY

Chromatographic Analysis of Isoniconitic Acid Hydrazide Derivatives

E. A. Illarionova, L. V. Abramova, and A. I. Illarionov

Irkutsk State Medical University, Irkutsk, Russia
Irkutsk Institute of Railway Transport Engineers, Irkutsk, Russia

Received November 5, 2001

Abstract—A highly sensitive and selective procedure was developed for determining specific impurities of isonicotinic acid hydrazide and vanillin in Metazid and Ftivazide preparations by thin-layer chromatography.

One of the principal characteristics of drugs is their purity. In this work, we chose for our studies derivatives of isonicotinic acid hydrazide, Metazid and Ftivazide, which are widely used in medicine as antitubercular drugs.

In accordance with the preparation procedure, Metazid can contain as specific impurities isonicotinic acid hydrazide (INAH) and formaldehyde. The initial compounds for preparing Ftivazide are INAH and vanillin whose content in the product should be monitored. According to the existing regulations [1, 2], the content of these specific impurities in Metazid and Ftivazide should be determined chemically. Isonicotinic acid hydrazide is determined with iodine in the presence of starch, and vanillin, by the reaction with phenolphthalein in the presence of alkali. These procedures are low-selective, because their results can be affected by oxidizing and reducing agents.

The drugs under consideration and the possible impurities contain different functional groups and therefore show different physicochemical properties. In this connection, it seems appropriate to detect them by such a quick, selective, and sensitive method as thin-layer chromatography (TLC) [3].

The goal of this study was development of a procedure for detecting and separating impurities in Metazid and Ftivazide by TLC.

EXPERIMENTAL

The test solutions of Metazid and Ftivazide were prepared by dissolving 5 g of the preparation in 10 ml of 95% ethanol (hereinafter, ethanol). The solutions were subsequently filtered. Standard solutions of INAH and vanillin were prepared by dissolving 0.01 g of the substances in 100 ml of ethanol.

Structural features of Metazid, Ftivazide, and the possible impurities suggest that the best sorbent for their separation is silica gel. It is an acidic sorbent allowing separation of substances that differ in acid–base properties. In our studies we tested several brands of silica gel.

The chromatograms were developed by UV irradiation (λ 254 nm). The detection sensitivity was 0.5 μg.

To choose the best mobile phase (MP), we studied the chromatographic behavior of Metazid, Ftivazide, INAH, and vanillin in a series of solvents. The results are listed in the table. It is seen that the mobility of the compounds increases with increasing solvent polarity. Therefore, we chose as the major components of the mobile phase chloroform and ethanol, which significantly differ in the polarity. The compositions of the solvent systems and the results of chromatographic analysis of Ftivazide and Metazid are given in Figs. 1 and 2.

Our results show that, in chloroform, vanillin is the most mobile, and Ftivazide, Metazid, and INAH show low mobility because of their poor solubility (Figs. 1, 2, MP no. 1). Isonicotiic acid hydrazide in chloroform shows the same chromatographic mobility as Ftivazide and Metazid. In ethanol, all the compounds are more mobile (Figs. 1, 2, MP no. 2). The difference between the retention factors of Ftivazide and INAH increases considerably, but the bands of Ftivazide and vanillin become closer. The bands of INAH and Metazid are separated, but ΔR_f is as small as 0.07.

The subsequent experiments were performed with

1070-4272/02/7505-0768$27.00 © 2002 MAIK "Nauka/Interperiodica"

Chromatographic mobility of Ftivazide, Metazid, INAH, and vanillin in various solvents

MP	ε	R_f			
		Ftivazide	vanillin	INAH	Metazid
Water	80.40	0.24	0.64	0.36	0.21
Methanol	31.20	0.81	0.84	0.42	0.38
Ethanol	27.80	0.71	0.80	0.44	0.37
Acetone	21.50	0.67	0.73	0.30	0.32
Ethyl acetate	6.40	0.00	0.44	0.00	0.00
Chloroform	5.20	0.00	0.32	0.00	0.00
Ether	4.30	0.00	0.16	0.01	0.00
Hexane	1.89	0.00	0.00	0.00	0.00
2-Propanol	18.30	0.50	0.48	0.31	0.28
Benzene	2.28	0.00	0.01	0.00	0.00

binary mobile phases consisting of chloroform (major solvent) and ethanol. By varying the content of ethanol in MP, we chose a chromatographic system (Fig. 1, MP no. 4) allowing separation of Ftivazide, vanillin, and INAH. However, the Ftivazide band in this case has an irregular shape. To obtain a Ftivazide band with clear and regular boundaries, we added 25% ammonia and glacial acetic acid. Addition of 25% ammonia to MP results in that the Ftivazide band becomes well-bounded, but the bands of the other substances virtually coalesce (Fig. 1, MP nos. 6, 7). Replacement of 25% ammonia by glacial acetic acid allows separation of Ftivazide, vanillin, and INAH (Fig. 1, MP nos. 8–10). However, the mobility of vanillin increases considerably, and its band approaches the front, which is undesirable. To decrease the mobility of vanillin, we added to MP a fourth component, 25% ammonia (Fig. 1, MP nos. 11–13). By varying the amounts of glacial acetic acid and 25% ammonia, we obtained an optimal MP for monitoring the purity of Ftivazide (Fig. 1, MP no. 11): chloroform–ethanol–glacial acetic acid–25% ammonia, 9 : 1 : 1 : 0.5.

The results of chromatographic study of Metazid and INAH show that the MP with glacial acetic acid ensures good separation of the substances (Fig. 2, MP nos. 8–10). However, higher values of R_f, especially for Metazid, are desirable. This was attained by increasing the content of ethanol in MP (Fig. 2, MP nos. 15–17). Our experiments showed that the best MP for monitoring the Metazid purity is chloro-

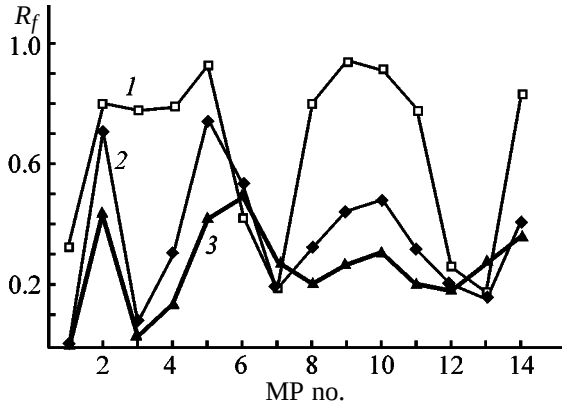

Fig. 1. R_f of (*1*) vanillin, (*2*) Ftivazide, and (*3*) INAH as a function of the mobile phase composition. Mobile phase no.: 1, chloroform (Cl); 2, ethanol (Et); 3–5, Cl–Et (9 : 0.5, 9 : 1, 9 : 2, respectively); 6 and 7, Cl–Et–25% ammonia (Am) (9 :1: 0.25 and 9 : 1 : 0.5, respectively); 8–10, Cl–Et–glacial acetic acid (AA) (9 : 1 : 0.25, 9 : 1 : 0.5, 9 : 1 : 1, respectively); and 11–13, Cl–Et–AA–Am (9 : 1 : 1 : 0.5, 9 : 1 : 0.5 : 1, 9 : 1 : 0.25 : 1, respectively).

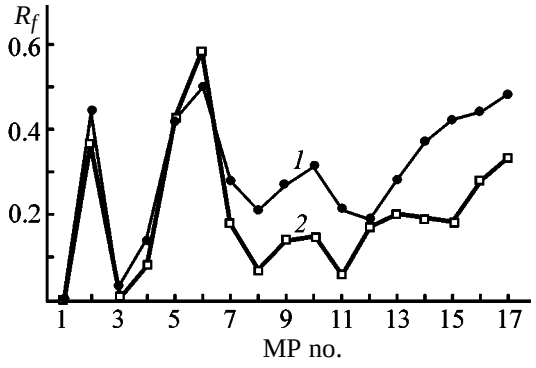

Fig. 2. R_f of (*1*) INAH and (*2*) Metazid as a function of the MP composition. Mobile phase no.: 1, Cl; 2, Et; 3–5, Cl–Et (9 : 0.5, 9 : 1, 9 : 2, respectively); 6 and 7, Cl–Et–Am (9 : 1 : 0.25, 9 : 1 : 0.5, respectively); 8–10, Cl–Et–AA (9 : 1 : 0.25, 9 : 1 : 0.5, 9 : 1 : 1, respectively); 11–13, Cl–Et–AA–Am (9 : 1 : 1 : 0.5, 9 : 1 : 0.5 : 1, 9 : 1 : 0.25 : 1, respectively; and 14–17, Cl–Et–AA (9 : 2 : 0.5, 9 : 2 : 1, 9 : 3 : 1, 9 : 4 : 1.5, respectively).

form–ethanol–glacial acetic acid (9 : 4 : 1.5, Fig. 2, MP no. 17).

The procedure for determining the Ftivazide purity was as follows. A 0.5-g portion of Ftivazide sample was shaken with 10 ml of ethanol for 5 ml and filtered. The resulting solution (0.02 ml; 1 mg) was applied to the start line of a Silufol UV-254, Armsorb UV-254, or other suitable plate (7.5 × 15 cm). In the vicinity, 0.01 ml of 0.01% solution of a reference INAH sample in ethanol and 0.02 ml of a 0.01% solution of a reference vanillin sample in ethanol were applied. The plate with the samples was dried in air for 5 min and then placed in a chamber containing a chloroform–ethanol–glacial acetic acid–25% ammonia solvent mixture (9 : 1 : 1 : 0.5) and chromatographed in the ascending mode. After the solvent front passed 3/4 of the plate length, it was taken out of the chamber, dried in air for 10 min, and examined under UV light (λ 254 nm). The spots of INAH and vanillin in the chromatogram of the test sample should not exceed in size and color intensity the spots of the corresponding reference samples (content no higher than 0.1 and 0.2%, respectively).

By this procedure, we analyzed ten commercial batches of Ftivazide. In all the samples we detected INAH and vanillin impurities, but their content did not exceed the prescribed limits (0.1 and 0.2%, respectively). The retention factors were as follows: Ftivazide, 0.32–0.35; INAH, 0.21–0.23; and vanillin, 0.79–0.81. The sizes and color intensities of the impurity spots did not exceed those of the references.

The purity of Metazid was determined similarly. Along with the test sample, 0.01 mol of a 0.01% solution of INAH reference sample in ethanol was applied to the start line. The plate with the applied samples was dried in air for 5 min and then placed in a chamber containing the chloroform–ethanol–glacial acetic acid solvent mixture (9 : 4 : 1.5) and chromatographed in the ascending mode. The resulting chromatogram was worked up as described above. The spot of the INAH impurity should not exceed in the size and color intensity the spot of the INAH reference (≤0.1%).

By this procedure, we analyzed ten commercial batches of Metazid. In all the samples, INAH impurity was detected, but its content did not exceed 0.1%. The retention factors were as follows: Metazid, 0.33–0.35 and INAH, 0.48–0.50. The sizes and color intensities of the impurity spots did not exceed those of the reference.

The developed procedures for monitoring the purity of Ftivazide and Metazid by thin-layer chromatography were approbated in the Quality Control Department, Usol'e-Sibirskoe Chemical and Pharmaceutical Combine, Joint-Stock Company. These procedures were included into the projects of the pharmacopoeia items of the enterprise for these drugs.

CONCLUSION

(1) Chromatographic behavior of Ftivazide, Metazid, and their possible impurities in various mobile phases was studied; the feasibility was demonstrated for their chromatographic separation at properly chosen composition of the mobile phase.

(2) Quick and selective procedures for checking the purity of Ftivazide and Metazid were developed, using TLC under the experimentally determined optimal conditions.

REFERENCES

1. *Farmakopeinaya Stat'ya* (Pharmacopoeia Item) *42-2468–96: Metazid: Coll. of Items*, Pershin, G.N., Ed., Moscow: Medgiz, 1960.
2. *Farmakopeinaya Stat'ya* (Pharmacopoeia Item) *42-3266–96: Ftivazide: Coll. of Items*, Pershin, G.N., Ed., Moscow: Medgiz, 1954.
3. Bolliger, H.R., Brenner, M., and Günshirt, H., *Dünnschicht Chromatographie. Ein Laboratoriumshandbuch*, Stahl, E., Ed., Berlin: Springer, 1962.

Russian Journal of Applied Chemistry, Vol. 75, No. 5, 2002, pp. 771–776. Translated from Zhurnal Prikladnoi Khimii, Vol. 75, No. 5, 2002, pp. 789–794.
Original Russian Text Copyright © 2002 by Dmitriev, Trukshin, Smykalov.

ORGANIC SYNTHESIS AND INDUSTRIAL ORGANIC CHEMISTRY

A Study of Trichloroethylene Hydrofluorination Using a Kinetic Model[1]

A. V. Dmitriev, I. G. Trukshin, and P. Yu. Smykalov

Prikladnaya Khimiya Russian Scientific Center, St. Petersburg, Russia

Received January 17, 2002

Abstract—The kinetic features of catalytic hydrofluorination of trichloroethylene and 2-chloro-1,1,1-trifluoroethane on chromium fluoride/magnesium fluoride catalyst were studied. The effect of pressure and addition of various components of the reaction mixture at the reactor inlet was studied using the developed model.

The procedure of production of 1,1,1,2-tetrafluoroethane by gas-phase catalytic hydrofluorination of trichloroethylene is well known in the world practice and is commercially used by various companies. There are many patents related to this procedure of tetrafluoroethane production [1–3] and to the catalyst production [4, 5]. In gas-phase fluorination processes, chromium(III) compounds in the form of fluorides and oxofluorides are mainly used.

At the same time, there are no published data on the kinetics and mechanism of hydrofluorination of trichloroethylene, which are necessary to design the reaction unit.

The goal of this work was to study experimentally this process on the chromium fluoride/magnesium fluoride catalyst and, based on the developed kinetic model, to study the effect of pressure and addition of various components of the reaction mixture (hydrogen chloride, 1,1-difluoroethylene, 1,1,1-trifluoroethane, and pentafluoroethane) at the reactor inlet.

EXPERIMENTAL

The study was carried out on a continuous installation consisting of a nickel reactor with electrical heating, units for dosing the initial reagents, and a system for collection and analysis of the synthesis products. The total capacity of the reactor was 1000 cm^3; the inner diameter was 36 mm. The reactor temperature was monitored by a multizone thermocouple. Hydrogen fluoride and 2-chloro-1,1,1-trifluoroethane were fed into the reactor through nickel capillaries. The flow rate of these reagents was set using the calibrating plot of the flow rate vs. the pressure in the service vessels, which, in turn, was produced by their temperature control. Trichloroethylene was fed into the reactor with a dosing pump. The flows of the initial reagents were mixed and fed into a coil-type evaporator equipped with electrical heating, and then into the reactor. After washing with water, neutralization, and drying, the reaction mixture was collected in a glass condenser cooled with a mixture of dry ice and $CCl_4/CHCl_3$.

The reaction mixture was analyzed on a Tsvet-500M chromatograph equipped with a heat conductivity detector. The 2-m chromatographic column was packed with ASK silica gel impregnated with liquid paraffin (10%).

The products were identified by gas chromatography–mass spectrometry on a Hewlett–Packard device equipped with an Al_2O_3/KCl capillary column (l = 50 m).

To determine the kinetic parameters, the experiments were performed in the reactor with a fluidized bed of the chromium fluoride/magnesium fluoride catalyst.[2]

The initial 2-chloro-1,1,1-trifluoroethane and trichloroethylene were purified by fractional distillation.

When developing the kinetic model, the following assumptions were made: the process is kinetically controlled; the catalyst activity is constant in time;

[1] Reported at the Third International Conference "Chemistry, Technology, and Application of Fluorine Compounds," St. Petersburg, June 6–9, 2001.

[2] This catalyst (chromium fluoride applied to magnesium fluoride) is produced by the pilot plant of the Prikladnaya Khimiya Russian Scientific Center and is used in various hydrofluorination processes.

1070-4272/02/7505-0771$27.00 © 2002 MAIK "Nauka/Interperiodica"

the catalyst can operate as a fluorine transfer agent; thermal decomposition of synthesis products is insignificant [6]; in the course of synthesis, products of asymmetric structure are mainly formed; only one fluorine atom in CrF_3 participates in exchange with chlorine atom; and the reaction of CrF_3 with HCl is significantly faster than the reaction of CrF_3 with chlorine-containing organic compounds.

With these assumptions, the process scheme can be presented as a series of successive stages considering the processes related to production of 2-chloro-1,1,1-trifluoroethane from trichloroethylene and subsequent fluorination to 1,1,1,2-tetrafluoroethane:

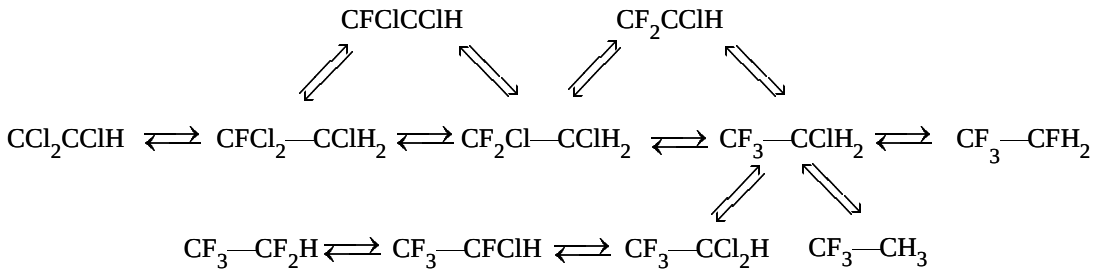

$$CF_3–CClH_2 + =Cr–F \rightleftarrows CF_3–CFH_2 + =Cr–Cl \quad \{k_1/k_{-1}\}, \quad (1)$$

$$=Cr–Cl + HF \rightleftarrows =Cr–F + HCl \quad \{k_2/k_{-2}\}, \quad (2)$$

$$=Cr–F + 2CF_3–CClH_2 \rightleftarrows [=Cr–F \cdot 2CF_3–CClH_2] \quad \{k_3/k_{-3}\}, \quad (3)$$

$$[=Cr–F \cdot 2CF_3–CClH_2] \rightleftarrows CF_3–CH_3 + CF_3–CCl_2H + =Cr–F \quad \{k_4/k_{-4}\}, \quad (4)$$

$$CF_3–CCl_2H + =Cr–F \rightleftarrows CF_3–CFClH + =Cr–Cl \quad \{k_5/k_{-5}\}, \quad (5)$$

$$CF_3–CFClH + =Cr–F \rightleftarrows CF_3–CF_2H + =Cr–Cl \quad \{k_6/k_{-6}\}, \quad (6)$$

$$CF_3–CClH_2 + =Cr–Cl \rightleftarrows CF_2Cl–CClH_2 + =Cr–F \quad \{k_7/k_{-7}\}, \quad (7)$$

$$CF_2Cl–CClH_2 + =Cr–F \rightleftarrows [=Cr–F \cdot CF_2Cl–CClH_2] \quad \{k_8/k_{-8}\}, \quad (8)$$

$$[=Cr–F \cdot CF_2Cl–CClH_2] \rightleftarrows CF_2=CClH + HCl + =Cr–F \quad \{k_9/k_{-9}\}, \quad (9)$$

$$CF_2=CClH + HF + =Cr–F \rightleftarrows [CF_2=CClH \cdot HF \cdot =Cr–F] \quad \{k_{10}/k_{-10}\}, \quad (10)$$

$$[CF_2=CClH \cdot HF \cdot =Cr–F] \rightleftarrows CF_3–CClH_2 + =Cr–F \quad \{k_{11}/k_{-11}\}, \quad (11)$$

$$CF_2Cl–CClH_2 + =Cr–Cl \rightleftarrows CFCl_2–CClH_2 + =Cr–F \quad \{k_{12}/k_{-12}\}, \quad (12)$$

$$CFCl_2–CClH_2 + =Cr–Cl \rightleftarrows CCl_3–CClH_2 + =Cr–F \quad \{k_{13}/k_{-13}\}, \quad (13)$$

$$CCl_3–CClH_2 + =Cr–F \rightleftarrows [CCl_3–CClH_2 \cdot =Cr–F] \quad \{k_{14}/k_{-14}\}, \quad (14)$$

$$[CCl_3–CClH_2 \cdot =Cr–F] \rightleftarrows CCl_2=CClH + HCl + =Cr–F \quad \{k_{15}/k_{-15}\}, \quad (15)$$

$$CCl_2=CClH + HF + =Cr–F \rightleftarrows [CCl_2=CClH \cdot HF \cdot =Cr–F] \quad \{k_{16}/k_{-16}\}, \quad (16)$$

$$[CCl_2=CClH \cdot HF \cdot =Cr–F] \rightleftarrows CFCl_2–CClH_2 + =Cr–F \quad \{k_{17}/k_{-17}\}, \quad (17)$$

$$CFCl_2–CClH_2 + =Cr–F \rightleftarrows [CFCl_2–CClH_2 \cdot =Cr–F] \quad \{k_{18}/k_{-18}\}, \quad (18)$$

$$[CFCl_2–CClH_2 \cdot =Cr–F] \rightleftarrows CFCl=CClH + HCl + =Cr–F \quad \{k_{19}/k_{-19}\}, \quad (19)$$

$$CFCl=CClH + HF + =Cr–F \rightleftarrows [CFCl=CClH \cdot HF \cdot =Cr–F] \quad \{k_{20}/k_{-20}\}, \quad (20)$$

$$[CFCl=CClH \cdot HF \cdot =Cr–F] \rightleftarrows CF_2Cl–CClH_2 + =Cr–F \quad \{k_{21}/k_{-21}\}. \quad (21)$$

Based on the developed scheme of this catalytic process, using the methods of pathways for com-

plicated reactions [7], we derived a kinetic model considering the stages of formation of 2-chloro-1,1,1-trifluoroethane and 1,1,1,2-tetrafluoroethane. In so doing, each reaction was considered as a multistage process [8]. The developed model describes variation of the concentrations of HF, HCl, CF_3–$CClH_2$, CF_3–CFH_2, CF_3–CH_3, CF_3–CCl_2H, CF_3–CFClH, CF_3–CF_2H, CF_2Cl–$CClH_2$, C_2HCl_3, CF_2=CClH, $CFCl_2$–$CClH_2$, and CFCl=CClH:

$$\frac{dc_1}{d\tau} = k'_{-7}c_8 - k_7c_1c_{11} - k'_1c_1 + k_{-1}c_3c_{11} + k'_{10}c_2c_{10} - k_{50}c_1 - 2k_3c_1^2 + 2k_nc_1^2 + 2k_tc_4c_{11},$$

$$\frac{dc_3}{d\tau} = k'_1c_1 - k_{-1}c_3c_{11},$$

$$\frac{dc_4}{d\tau} = k'_3c_1^2 - k_nc_1^2 - k_tc_4c_{11},$$

$$\frac{dc_5}{d\tau} = k'_3c_1^2 - k_nc_1^2 - k_tc_4c_{11} - k'_5c_5 + k_{-5}c_6c_{11},$$

$$\frac{dc_6}{d\tau} = k'_5c_5 - k_{-5}c_6c_{11} - k'_6c_6 + k_{-6}c_7c_{11},$$

$$\frac{dc_7}{d\tau} = k'_6c_6 - k_{-6}c_7c_{11},$$

$$\frac{dc_8}{d\tau} = k_{-12}c_2c_{12} - k_{12}c_8c_{11} - k'_{-7}c_8 + k_7c_1c_{11} - 0.5k'_8c_8 + 0.5k'_{-9}c_{10}c_{11} + k'_{20}c_2c_{13},$$

$$\frac{dc_9}{d\tau} = -k'_{16}c_2c_9 + k_\Sigma c_8c_{11} + k_\sigma c_9c_{11},$$

$$\frac{dc_{10}}{d\tau} = 0.5k'_8c_8 - 0.5k'_{-9}c_{10}c_{11} - k'_{10}c_2c_{10} + k_{50}c_1,$$

$$\frac{dc_{12}}{d\tau} = k'_{16}c_2c_9 - k_{-12}c_2c_{12} + k_{12}c_8c_{11} - 0.5k'_{18}c_{12} + 0.5k'_{-19}c_{11}c_{13},$$

$$\frac{dc_{13}}{d\tau} = 0.5k'_{18}c_{12} - 0.5k'_{-19}c_{11}c_{13} - k'_{20}c_2c_{13},$$

$$c_2 = c_2^0 - 3(c_1 - c_1^0) - 4(c_3 - c_3^0) - 3(c_4 - c_4^0) - 3(c_5 - c_5^0) - 4(c_6 - c_6^0) - 5(c_7 - c_7^0) - 2(c_8 - c_8^0) - 2(c_{10} - c_{10}^0) - (c_{12} - c_{12}^0) - (c_{13} - c_{13}^0),$$

Table 1. Rate constants and activation energies of the process stages

Rate constant	$\ln k_i$	E, kcal mol^{-1}	Rate constant	$\ln k_i$	E, kcal mol^{-1}
k_Σ	43	50	k_σ	$\to 0$	
k'_1	11.7	18.3	k_n	$\to 0$	
k_{-1}	15.6	12.2	k_t	8.5	5
k'_5	30.5	33.7	k'_3	26.2	35
k_{-5}	36.9	32.3	k'_{-9}	23.7	20
k'_6	11	15	k_{50}	29.5	45
k_{-6}	22.7	20	k'_{-12}	82.8	77.6
k_7	43.5	50	k_{12}	0.8	2.1
k'_{-7}	20.5	20	k'_{18}	38.7	34.9
k'_8	17	20	k'_{-19}	58.7	49.6
k'_{10}	12.2	10	k'_{20}	46.7	38.8
k'_{16}	33.8	29.9			

$$c_{11} = c_{11}^0 + (c_1^0 - c_1) + 2(c_5^0 - c_5) + (c_6^0 - c_6) + 2(c_8^0 - c_8) + 3(c_9^0 - c_9) + (c_{10}^0 - c_{10}) + 3(c_{12}^0 - c_{12}) + 2(c_{13}^0 - c_{13}),$$

where c_1 is the concentration of CF_3–$CClH_2$ (Freon 133a), c_2 is that of HF, c_3 is that of CF_3–CFH_2 (Freon 134a), c_4 is that of CF_3–CH_3 (Freon 143a), c_5 is that of CF_3–CCl_2H (Freon 123a), c_6 is that of CF_3–CFClH (Freon 124a), c_7 is that of CF_3–CF_2H (Freon 125), c_8 is that of CF_2Cl–$CClH_2$ (Freon 132a), c_9 is that of C_2HCl_3 (trichloroethylene), c_{10} is that of CF_2=CClH (1,1-difluorochloroethylene), c_{11} is that of HCl, c_{12} is that of $CFCl_2$–$CClH_2$ (Freon 131), c_{13} is that of CFCl=CClH (1-fluoro-1,2-dichloroethylene); and k_i are the kinetic constants:

$$k_\Sigma = 2\frac{k'_{14}k_{13}k_{12}}{k'_{-13}k_{-14}},\ k_\sigma = \frac{k_{-14}k'_{14}k'_{-15}}{k_{-15}k'_{-13}},\ k_n = \frac{k_{-3}k'_3}{k_{-3} + k_4},$$

$$k_t = \frac{k_{-3}k'_{-4}}{k_{-3} + k_4},\ k_{50} = \frac{k_{-1}k'_{10}}{k'_{10} + k_{11}},$$

$$k'_i = k_i[\text{=Cr–F}];\ [\text{=Cr–F}] \approx \text{const}.$$

The constants were determined by regression analysis. The functional to be minimized was the weighted sum of squared deviations of the experimental and calculated concentrations. As a procedure of numerical integration, we used the LSODA method designated for solving rigid systems of differential equations [9]. The functional was minimized by the Gauss–Newton method.

The kinetic constants obtained are listed in Table 1. The developed kinetic model is adequate in the

Table 2. Hydrofluorination of 2-chloro-1,1,1-trifluoroethane and trichloroethylene. Residence time 10 s

Concentration at reactor inlet, M			Concentration at reactor outlet, M
initial reactants	component added		
2-Chloro-1,1,1-trifluoroethane*			
$c_1^0 = 0.003733$, $c_2^0 = 0.01493$			$c_3 = 0.75\times10^{-3}$, $c_4 = 0.3\times10^{-4}$, $c_7 = 0.53\times10^{-5}$, $c_{10} = 0.75\times10^{-5}$
$c_1^0 = 0.003733$, $c_2^0 = 0.01493$	CF_3–CH_3:	$c_4^0 = 0.3\times10^{-4}$	$c_4 = 0.47\times10^{-4}$
		$c_4^0 = 0.6\times10^{-4}$	$c_4 = 0.63\times10^{-4}$
$c_1^0 = 0.003733$, $c_2^0 = 0.01493$	CF_3–CF_2H:	$c_7^0 = 0.53\times10^{-5}$	$c_7 = 0.63\times10^{-5}$
		$c_7^0 = 1.6\times10^{-5}$	$c_7 = 0.82\times10^{-5}$
$c_1^0 = 0.003733$, $c_2^0 = 0.01493$	CF_2 = CClH:	$c_{10}^0 = 0.1\times10^{-4}$	$c_{10} = 0.75\times10^{-5}$
		$c_{10}^0 = 0.8\times10^{-4}$	$c_{10} = 0.1\times10^{-4}$
$c_1^0 = 0.003733$, $c_2^0 = 0.01493$	HCl:	$c_{11}^0 = 0.7\times10^{-5}$	$c_{10} = 0.7\times10^{-5}$
		$c_{11}^0 = 0.7\times10^{-4}$	$c_{10} = 0.7\times10^{-5}$
		$c_{11}^0 = 0.7\times10^{-3}$	$c_{10} = 0.7\times10^{-5}$, $c_3 = 0.5\times10^{-3}$
Trichloroethylene**			
$c_2^0 = 0.01991$, $c_9^0 = 0.005856$			$c_4 = 0.35\times10^{-9}$, $c_7 = 0.45\times10^{-13}$, $c_{10} = 0.3\times10^{-4}$
$c_2^0 = 0.01991$, $c_9^0 = 0.005856$	CF_3–CH_3:	$c_4^0 = 1\times10^{-5}$	$c_4 = 0.45\times10^{-5}$
$c_2^0 = 0.01991$, $c_9^0 = 0.005856$	CF_3–CF_2H:	$c_7^0 = 1\times10^{-5}$	$c_7 = 0.87\times10^{-5}$
$c_2^0 = 0.01991$, $c_9^0 = 0.005856$	CF_2 = CClH:	$c_{10}^0 = 0.3\times10^{-4}$	$c_{10} = 0.42\times10^{-4}$

* Molar ratio HF : CF_3–$CClH_2$ = 4 : 1, 380°C
** Molar ratio HF : C_2HCl_3 = 3.4 : 1, 200°C.

following intervals of the process parameters: temperature 175–420°C; molar ratio of reactants HF : $C_2H_2ClF_3$ = (2–18) : 1 and HF : C_2HCl_3 = (3.4–13.6) : 1.

Using this kinetic model, we studied the influence of the process parameters on the main reaction stages. The influence of pressure was studied under the following conditions: molar ratio of reactants HF : C_2HCl_3 = 3.4 : 1, 200°C (first stage); HF : Freon 133a = 4 : 1, 380°C (second stage); and contact time τ = 10 s. The course of the process was analyzed at a pressure of 1, 3, 6, and 10 atm. The results of evaluation (Figs. 1, 2) show the following.

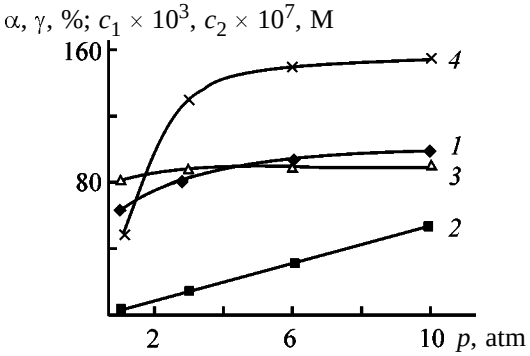

Fig. 1. Hydrofluorination of trichloroethylene: (*1*) conversion of trichloroethylene α, (*2*) concentration of 2-chloro-1,1,1-trifluoroethane $c_1 \times 10^3$, (*3*) selectivity with respect to 2-chloro-1,1,1-trifluoroethane γ, and (*4*) concentration of 1,1,1,2-tetrafluoroethane $c_2 \times 10^7$; (*p*) pressure.

(1) In the stage of trichloroethylene hydrofluorination with hydrogen fluoride to Freon 133a, conversion of trichloroethylene increases (to 95–97%) with increasing pressure to 6 atm, the selectivity with respect to Freon 133a increases up to a pressure of 3 atm and then becomes practically constant (approximately 90%); the concentration of Freon 134a increases up to a pressure of approximately 6 atm and then increases insignificantly, but the yield of by-products increases. Thus, increase of the pressure above 6 atm is not appropriate.

(2) In the stage of hydrofluorination of Freon 133a

Table 3. Hydrofluorination of 2-chloro-1,1,1-trifluoroethane*

Run no.	Component added	Mixture composition, %	
		at reactor inlet (without HF)	at reactor outlet (without HF and HCl)
1	–	CF_3–$CClH_2$ 97.02, others 2.98	CF_3–$CClH_2$ 71.45, CF_3–CFH_2 23.24, CF_3–CF_2H 2.38, CF_3–CH_3 1.86, others 1.08
2	CF_3–CF_2H	CF_3–$CClH_2$ 92.79, CF_3–CFH_2 0.46, CF_3–CF_2H 3.88, others 2.87	CF_3–$CClH_2$ 69.98, CF_3–CFH_2 22.29, CF_3–CF_2H 5.06, CF_3–CH_3 1.82, others 0.85
3	CF_3–CF_2H	CF_3–$CClH_2$ 85.79, CF_3–CFH_2 0.24, CF_3–CF_2H 12.43, CF_3–CH_3 0.04, others 1.5	CF_3–$CClH_2$ 64.89, CF_3–CFH_2 23.99, CF_3–CF_2H 7.82, CF_3–CH_3 2.11, others 1.19
4	–	CF_3–$CClH_2$ 99.69, CF_3–CH_3 0.12, others 0.19	CF_3–$CClH_2$ 62.96, CF_3–CH_3 3.56, CF_3–CFH_2 30.48, CF_3–CF_2H 2.08, others 0.92
5	CF_3–CH_3	CF_3–$CClH_2$ 99.0, CF_3–CH_3 0.68, others 0.32	CF_3–$CClH_2$ 64.23, CF_3–CH_3 3.58, CF_3–CFH_2 28.98, CF_3–CF_2H 2.44, others 0.77
6	CF_3–CH_3	CF_3–$CClH_2$ 92.49, CF_3–CH_3 7.14, others 0.37	CF_3–$CClH_2$ 60.58, CF_3–CH_3 8.48, CF_3–CFH_2 27.08, CF_3–CF_2H 2.73, others 1.13
7	–	CF_3–$CClH_2$ ~ 100	CF_3–$CClH_2$ 82.39, CF_3–CFH_2 16.93, CF_2=CClH 0.15, others 1.13
8	Mixture of CF_3–CFH_2 and CF_2 = CClH	CF_3–$CClH_2$ 71.45, CF_3–CFH_2 25.41, CF_2 = CClH 1.56, others 1.58	CF_3–$CClH_2$ 56.66, CF_3–CFH_2 41.12, CF_2=CClH 0.10, others 2.12

* Reactor with fixed catalyst bed, V = 0.25 l (run nos. 1–3) and with fluidized catalyst bed, V = 0.4 l (run nos. 4–8); molar ratio HF : CF_3–$CClH_2$ = 8.3 : 1 (run nos. 1–3), 10 : 1 (run nos. 4–6), 19.6 : 1 (run nos. 7 and 8); temperature 400 (run nos. 1–3), 420 (run nos. 4–6), and 380°C (run nos. 7 and 8); residence time 4.8 (run nos. 1–3), 6.1 (run nos. 4–6), and 4.3 s (run nos. 7 and 8; with addition of a mixture of CF_3–CFH_2 and CF_2=CClH, 3 s).

with hydrogen fluoride, an increase in the pressure results in decreased conversion of Freon 133a; in this case, the conversion is decreased to the greatest extent in the pressure range from 1 to 3 atm (from 22.3 to 15.8%). At a higher pressure, the conversion becomes practically constant (14.6–14.9%). Thus, elevated pressure has a detrimental effect on this stage.

Calculated data on the effect of adding various components of the reaction mixture at the reactor inlet are listed in Table 2.

Our results show that addition of 2-chloro-1,1-difluoroethylene decreases the degree of its formation in the course of synthesis, i.e., in the process a mixture of Freon 134a and 2-chloro-1,1-difluoroethylene can be supplied to the reactor inlet for subsequent recovery. In a similar manner, addition of Freons 125 and 143a into the initial mixture decreases the degree of their formation in the course of synthesis. However, the presence of hydrogen chloride in the initial mixture in the stage of formation of Freon 134a from Freon 133a decreases the yield of Freon 134a. The results of the experiments confirmed the validity of evaluation of the influence of the process parameters (Table 3).

CONCLUSIONS

(1) Study of the process of 1,1,1,2-tetrafluoroethane production using the developed kinetic model describing the process in the temperature range 175–420°C at a molar ratio of reagents HF : $C_2H_2ClF_3$ = (2–18) : 1, HF : C_2HCl_3 = (3.4–13.6) : 1 showed that an increase in pressure to 6 atm has a positive effect on the conversion and selectivity in hydrofluorination

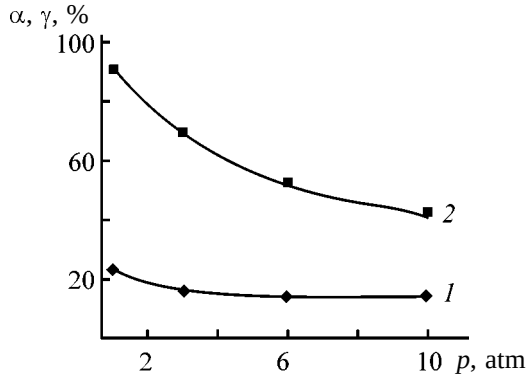

Fig. 2. Hydrofluorination of 2-chloro-1,1,1-trifluoroethane: (*1*) conversion of 2-chloro-1,1,1-trifluoroethane α and (*2*) selectivity with respect to 1,1,1,2-tetrafluoroethane γ; (*p*) pressure.

of trichloroethylene. However, in hydrofluorinaton of 2-chloro-1,1,1-trifluoroethane, an increase in pressure to 3 atm adversely affects the process.

(2) A partial return of by-products (pentafluoroethane, 1,1,1-trifluoroethane, and 2-chloro-1,1-difluoroethylene) to synthesis decreases their formation in the synthesis.

(3) Owing to reversibility of 2-chloro-1,1,1-trifluoroethane hydrofluorination, the presence of hydrogen chloride in the initial reaction mixture adversely affects the process of 1,1,1,2-tetrafluoroethane production. Removal of hydrogen chloride from the reaction area is favorable for increasing the yield of the target product.

REFERENECES

1. EP Patent 408005.
2. JPN Patent 05279276.
3. US Patent 5723700.
4. US Patent 51555082.
5. WO Patent 9810862.
6. Dmitriev, A.V., Trukshin, I.G., and Vishnyakov, V.M., Abstracts of Papers, *3-ya Mezhdunarodnaya konferentsiya "Khimiya, tekhnologiya i primenenie ftorsoedinenii"* (Third Int. Conf. "Chemistry, Technology, and Application of Fluorine Compounds"), St. Petersburg: Teza, 2001.
7. Bezdenezhnykh, A.A., *Inzhenernye metody sostavleniya uravnenii skorostei reaktsii i rascheta kineticheskikh konstant* (Engineering Approach to Setting up of Equations for the Reaction Rates and Evaluating Kinetic Constants), Leningrad: Khimiya, 1973.
8. Trukshin, I.G., Smykalov, P.Yu., Goncharov, E.P., *et al.*, Abstracts of Papers, *1-ya Mezhdunarodnaya konferentsiya "Khimiya, tekhnologiya i primenenie ftorsoedinenii v promyshlennosti"* (First Int. Conf. "Chemistry, Technology, and Application of Fluorine Compounds in Industry"), St. Petersburg: Teza, 1994.
9. Petzold, L.R., *SIAM J. Sci. Stat. Comput.*, 1983, vol. 4, pp. 136–148.

Russian Journal of Applied Chemistry, Vol. 75, No. 5, 2002, pp. 777–780. Translated from Zhurnal Prikladnoi Khimii, Vol. 75, No. 5, 2002, pp. 795–798.
Original Russian Text Copyright © 2002 by Sazanov, Podeshvo, Mikhailov, Fedorova, Goikhman, Lebedeva, Kudryavtsev.

MACROMOLECULAR CHEMISTRY AND POLYMERIC MATERIALS

Polymeric Materials Derived from Vanillic Acid

Yu. N. Sazanov, I. V. Podeshvo, G. M. Mikhailov, G. N. Fedorova, M. Ya. Goikhman, M. F. Lebedeva, and V. V. Kudryavtsev

Institute of Macromolecular Compounds, Russian Academy of Sciences, St. Petersburg, Russia

Received January 23, 2002

Abstract—Film and fibrous materials derived from vanillic acid, one of promising products from processing of industrial lignin, were prepared and characterized. Thermochemical reactions of degradation and carbonization of films and fibers of vanillic acid polyesters and polyamides were considered, and the main relationships of thermal transformations of the materials were revealed.

Industrial lignin is one of major intermediates in chemical processing of wood. Subsequent processing of lignin yields such important products as vanillin, vanillic acid (VA), phenol and its derivatives, pyrocatechol, etc. [1, 2]. From the viewpoint of polymer chemistry, VA (3-methoxy-4-hydroxybenzoic acid) is of the most interest among these products. On the one hand, the presence of a side methoxy group increases the solubility and fusibility of polyamides (PAs) and polyesters (PEs), which simplifies production of materials therefrom. On the other hand, a new possibility is opened up for synthesis of PEs with mesogenic groups in the backbone chain, by analogy with synthesis of PEs from *p*-hydroxybenzoic acid [3, 4]. As for polyamides derived from VA, they show promise as heat-resistant binders exhibiting enhanced adhesion in production of prepregs from technical fabrics.

In our study, we used the following polyesters and polyamides derived from VA:

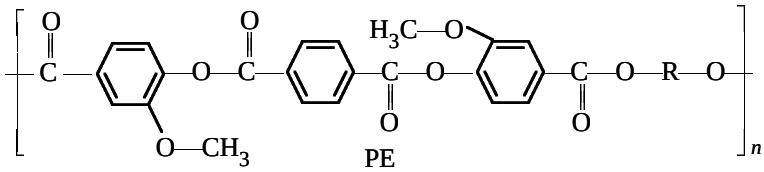

PE

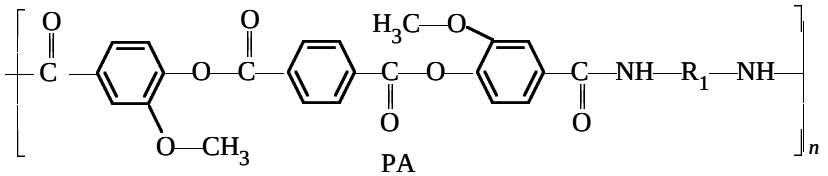

PA

where R = $-(CH_2)_6-$ (PE-1), $-(CH_2)_{10}-$ (PE-2), 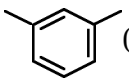 (PE-3), 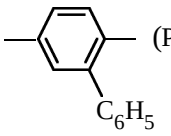 (PE-4),

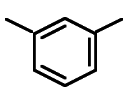 (PA-1), 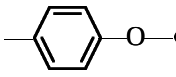 (PA-2), 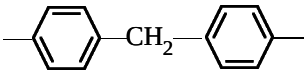 (PA-3),

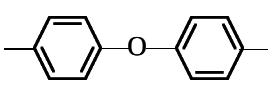 (60%) + 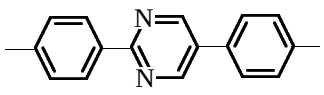 (40%) (PA-4).

1070-4272/02/7505-0777$27.00 © 2002 MAIK "Nauka/Interperiodica"

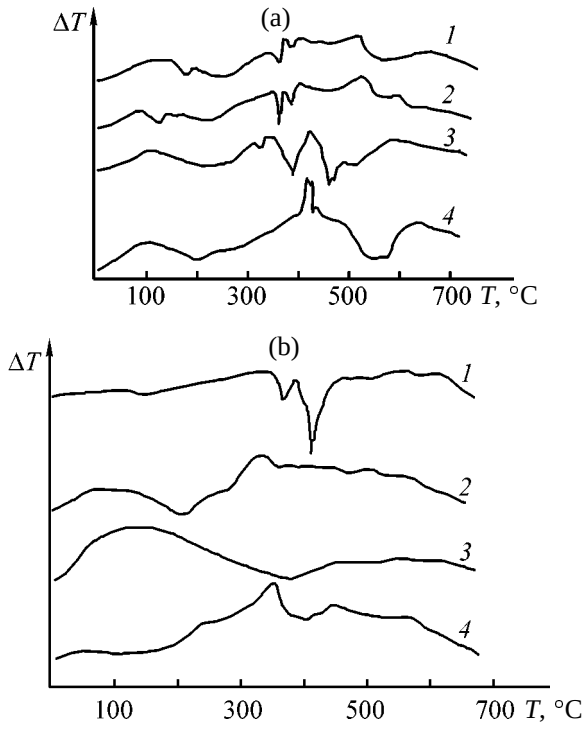

Fig. 1. DTA curves of (a) polyesters and (b) polyamides derived from VA. (*T*) Temperature. (a) (*1*) PE-1, (*2*) PE-2, (*3*) PE-3, ad (*4*) PE-4; (b) (*1*) PA-1, (*2*) PA-2, (*3*) PA-3, and (*4*) PA-4; the same for Fig. 2.

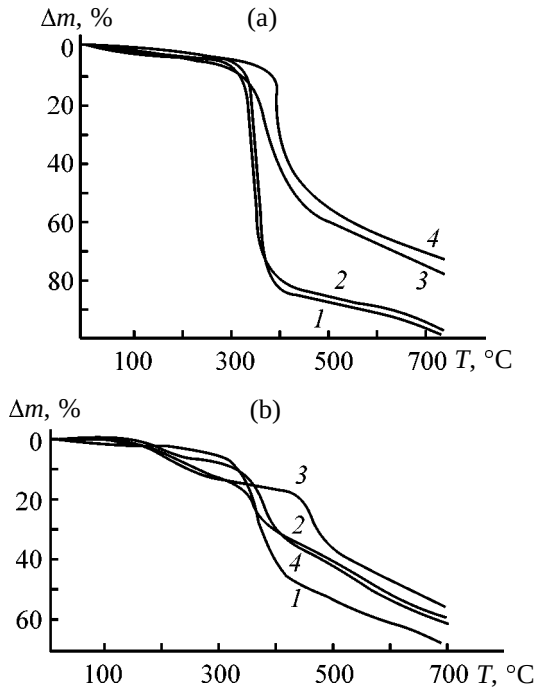

Fig. 2. TG curves for (a) polyesters and (b) polyamides derived from VA. (Δ*m*) Weight loss and (*T*) temperature.

The polymers were prepared as described in [3]. Polymer films were cast from solutions in *N*-methylpyrrolidone on glass supports and dried to constant weight at 115–120°C. The films were 30–50 μm thick. Fibers were formed on a PIFV-01 installation by a wet procedure, using a 1/0.4 die and an ethylene glycol–ethanol (1 : 1 by volume) precipitation bath.

The films and fibers were tested on an Instron-1145 tensile-testing machine. The following parameters were determined: tensile strength σ_t, enlogation at break ε_b, and modulus of elasticity *E*. Thermal analysis (TGA and DTA) was performed with an MOM derivatograph (Hungary), model C, heating rate 10 deg min^{-1}, sample weight 50 mg.

All the polymers prepared are soluble in aprotic polar solvents. Solutions for forming films and fibers were mainly prepared in *N*-methylpyrrolidone; the solubility in dimethylformamide and dimethylacetamide was also estimated qualitatively. The forming solutions had the instrinsic viscosity at 25°C ranging from 3.0 to 3.5 dl g^{-1}.

Data on fusion and softening of samples were obtained by thermal analysis, primarily DTA. Figures 1a ad 1b show the DTA curves of VA polyesters and polyamides; the endothermic effects observed with some samples are due to melting. It can be readily seen that the quantitative characteristics of these effects (peak temperatures and areas) depend on the chemical structure of radicals R and R_1. For example, PE with long aliphatic units in the chain (PE-1, PE-2) show noticeable ordering: Mesomorphic structures are observed, responsible for the endothermic minima at 127 and 190°C. As the aliphatic units are replaced by aromatic groups, especially by those with a pendant phenyl substituent (PE-4), the structural ordering of the macromolecule is broken. The inflections of the DTA curves of PE-3 and PE-4 samples at 235 and 204°C indicate their softening (Fig. 1a, curves *3*, *4*). As for the other thermal characteristics of these samples, asymmetric phenyl substituents in PE-4 render the structure fully amorphous, whereas in the PE-3 sample the *m*-phenylene moiety allows preservation of certain ordering. This is indicated by an endothermic effect (DTA curve with a maximum at 347°C) and by appreciable heat absorption with a maximum at 393°C, accompaied by only insignificant weight loss (Fig. 2a, curve *3*), which allows this effect to be assigned to the polymer melting. As the temperature is increased further, the melt undergoes thermal degradation with release of large amounts of volatiles, mainly carbon oxides according to mass spectrometry.

A different pattern was observed on heating PE-4

in the range 403–445°C corresponding to the onset of the thermal degradation of the polymer. In this case, no endothermic effects of melting are observed, and the DTA curve shows exothermic effects of thermal oxidative degradation with maxima at 431–442°C.

The thermal behavior of VA polyamides appreciably differs from that of VA polyesters. As far as the morphology is concerned, the DTA curves suggest that only PA-1 shows certain ordering, whereas the other PAs have an amorphous structure; this result is consistent with the previous X-ray diffraction and DSC data [5]. Also, as shown by TG curves, in almost all the PA samples the onset of thermal degradation with release of volatiles is observed at approximately 170°C. According to mass spectrometry, initially the polymer–solvent solvation complexes, characterized by relatively high energy in the case of PA [6], are broken down. When the temperature reaches 290–300°C, thermal degradation of the PA backbone starts, with the release of pyrolysis products reaching a maximum at 330–430°C. Calculated data and results of the analysis of the gaseous thermal degradation products, performed for PA-1, show that the thermal degradation of PA is a superposition of cleavage of the ester and amide bonds, with the predominant release of carbon oxides:

Product	O	N	CO	CO_2	H_2O	NH_3	$(CH_3)_2CO$
Content, %	26.0*	5.0	35.3	31.8	22.7	6.1	16.6
of initial structure	–	–	20.2	28.3	6.5	3.0	8.4

* Numerator: content of O, N, and volatiles after complete degradation of PA-1; denominator: actual release of volatiles in the stage of intense degradation (330–430°C).

Thus, examination of the initial stage of thermal transformations of the polymers shows that the fusibility and solubility of PEs are associated with formation of oriented structures, and the solubility and softening of PAs are associated with formation of stable solvation complexes with the solvent.

The TG curves of polyesters (Fig. 2a) show that the PEs containing aliphatic units in the polymer chain are less heat-resistant than PEs containing aromatic grops. This difference is especially noticeable for the degradation rates in the range 335–460°C. By the end of this interval, aliphatic PEs volatilize to approximately 80%, whereas their aromatic analogs at the same temperature lose no more than 25% of their weight. On further heating, PE-3 and PE-4 transform into carbonization products, with the yield of the coke residue of 30–40%. It should be noted that the mesogenic oriented structure allows PEs to withstand dynamic heating to 335°C without noticeable weight loss. For PEs with pendant aromatic substituents in the chain, in which the mobility is restricted by the steric factor, the temperature of the thermal degradation onset increases to 405°C.

Deformation-strength characteristics of films and fibers from PEs and PAs

Polymer bas	σ_t, MPa	ε_b, %	*E*, GPa
Film:			
PE-2*	283	234.0	2.18
PE-3*	68	67.0	1.58
PA-1	125	17.4	3.43
PA-2	159	15.6	4.07
PA-3	136	20.8	2.69
PA-4	225	18.5	5.94
PA-4 fiber	525	14.1	17.8

* Calculated for the initial cross section area of the sample.

For PAs, the pattern of thermal degradation is complicated by decomposition of solvation complexes, stable to 170–180°C. The rate of their degradation, the temperature interval of the solvent release, and the weight of the volatiles evolved in the process depend on the chemical structure of R_1. Active thermal degradation occurs at 310–500°C; the width of this interval for each particular sample is about 70–100°C. The temperature range of degradation depends on the structure of R_1, because its structure governs the intermolecular interaction of PA chains and the mechanism of cross-linking competing with thermal degradation. For example, PA-3 exhibits a plateau of thermal stability in the range 325–440°C, which is due to cross-linking following cleavage of methylene bridges, as noted in [7]. For PA-4, the heat resistance is enhanced by pyrimidine rings introduced into the polymer chain. As for carbonization, all the PAs show a noticeable tendency to cross-linking (coke residue about 40–50%), which makes them promising as heat-resistant binders.

The deformation-strength characteristics of PEs and PAs (see table) show that, with respect to the strength and elasticity, these materials well compete with aromatic compounds of the same class, described in [8].

It should be noted that the mechanical characteristics of PA samples are appreciably improved on introducing rigid 2,5-bis(aminophenyl)pyrimidine fragments into the polymer chain (PA-4); in the course of fiber forming, these fragments exert a cross-linking effect on the system and allow preparation of fibers

with high strength and elasticity without additional thermal and plasticizing stretchings.

CONCLUSIONS

(1) A series of new aliphatic and aromatic polyesters with mesogenic groups in the polymer chain were prepared; from these substances, soluble and fusible materials in the form of films and fibers were prepared by a simple process.

(2) Aromatic polyamides derived from vanillic acid exhibit enhanced heat resistance and are capable of forming fibers and films characterized by a high coke residue in thermal carbonization.

REFERENCES

1. *Khimiya drevesiny: Sbornik statei* (Wood Chemistry: Coll. of Papers), Ivanov, M.D., Ed., Moscow: Lesnaya Prom–st., 1982.
2. Evtuguin, D.V., Deineko, I.P., and Lu Gui Sheng, *Proc. 7th Int. Symp. on Wood and Pulping Chemistry*, Beijing (China), May 25–28, 1993, vol. 3, pp. 577–582.
3. Grigor'ev, A.I., Matveeva, G.A., Bilibin, A.Yu., *et al.*, *Vysokomol. Soedin., Ser. B*, 1984, vol. 26, no. 3, pp. 143–145.
4. Matveeva, G.A. and Grigor'ev, A.I., *Vysokomol. Soedin., Ser. B*, 1992, vol. 34, no. 1, pp. 15–18.
5. Goikhman, M.Ya., Podeshvo, I.V., Mikhailov, G.M., *et al.*, *Zh. Prikl. Khim.*, 1997, vol. 70, no. 11, pp. 1885–1889.
6. Magomedova, N.S., Chetkina, L.A., Bel'skii, V.K., *et al.*, *Zh. Strukt. Khim.*, 1986, vol. 27, no. 5, pp. 118–122.
7. Sazanov, Yu.N., Kabilov, Z.A., Muinov, T.M., *et al.*, *Thermochim. Acta*, 1979, vol. 28, no. 2, pp. 333–344.
8. Korshak, V.V. and Frunze, T.M., *Sinteticheskie geterotsepnye polimery* (Synthetic Heterochain Polymers), Moscow: Akad. Nauk SSSR, 1962.

Russian Journal of Applied Chemistry, Vol. 75, No. 5, 2002, pp. 781–784. Translated from Zhurnal Prikladnoi Khimii, Vol. 75, No. 5, 2002, pp. 799–802.
Original Russian Text Copyright © 2002 by Grishin, Semenycheva, Pavlovskaya.

MACROMOLECULAR CHEMISTRY AND POLYMERIC MATERIALS

Synthesis of Polymethyl Methacrylate in the Presence of 1,3-Diphenyl-1-hydroxytriazene and Nitrobenzene

D. F. Grishin, L. L. Semenycheva, and M. V. Pavlovskaya

Research Institute of Chemistry, Lobachevskii Nizhni Novgorod State University, Nizhni Novgorod, Russia

Received December 17, 2001; in final form, February 2002

Abstract—Radical polymerization of methyl methacrylate in the presence of 1,3-diphenyl-1-hydroxytriazene and nitrosobenzene as sources of stable nitroxyl radicals was studied.

Recently there has been a considerable progress in a new field of radical polymerization, pseudoliving polymerization. Several approaches were suggested to perform such processes, in particular, introduction into a polymerizing system of stable radicals, e.g., nitroxyl [2,2,6,6-tetramethyl-1-piperidinyloxyl (TEMPO) and its analogs] or carbon-centered, or of iniferters combining the functions of initiators and chain-terminating agents. The most widely used iniferters are alkoxyamines, alkylthiocarbamates, phenylazotriphenylmethane, hexaphenylethane, etc. [1–5]. These compounds effectively control the chain propagation only at temperatures above 100°C and are used exclusively in polymerization of styrene or its analogs, or in copolymerization of styrene with other monomers.

In previous studies, to control the chain propagation under conditions of radical initiation, it was suggested to use spin traps: *C*-phenyl-*N*-*tert*-butylnitrone (PBN) [6–9] and 2-methyl-2-nitrosopropane (MNP) [10], and also a binary iniferter, 1-*tert*-butyl-3-phenyl-1-hydroxytriazene (BPT) + oxidant [11, 12]. These chain-terminating agents allow controllable synthesis of polymers based on (meth)acrylates and even vinyl chloride to high conversions in the range 50–70°C, i.e., at temperatures close to those used in commercial syntheses of the polymers; this is a significant advantage over the previously known chain-terminating agents (phenylazotriphenylmethane, TEMPO, etc.).

In this work, to perform low-temperature controllable radical polymerization of methyl methacrylate (MMA), we suggested to use nitrosobenzene (NB) and 1,3-diphenyl-1-hydroxytriazene (DPT). Using the results obtained and published data [5, 10, 11], we analyzed how the structure of the organic radical in the nitroxyl spin adduct affects the kinetic parameters of MMA polymerization and the molecular-weight characteristics of the polymer.

EXPERIMENTAL

DPT [13] and NB [14] were prepared by published procedures. Dicetyl peroxydicarbonate (DPC) used as initiator, and also the monomers and solvents were purified by common procedures. The physicochemical constants of the chemicals used agreed with the reference data. The polymerization kinetics was monitored gravimetrically, dilatometrically [15], and thermographically [16]. The molecular weight M of the polymer was determined viscometrically [17] and by gel permeation chromatography (GPC) with a Waters device (the United States) equipped with five Styrogel columns (pore diameter 10^5, 3×10^4, 10^4, 10^3, and 250 Å) and an R-403 (Waters) differential refractometer as detector. The eluent was tetrahydrofuran (THF). Calibration was performed with close-cut polystyrene references [18].

The kinetic study of MMA polymerization showed that, in the presence of 0.05–0.15 mol % DPT and 0.1 ml % DPC (widely used radical polymerization initiator), the gel effect regularly decreases with increasing DPT concentration and appears at higher conversions (Fig. 1a). These data are in good agreement with the previously published data on synthesis of polymethyl methacrylate (PMMA) in the presence of BPT [11] and are, on the whole, typical of polymerization under conditions of living chains and reversible inhibition.

Additional information on the mechanism of the polymer chain propagation can be derived from the molecular-weight characteristics of the polymers synthesized. As seen from Fig. 2, a pronounced increase of M of the polymer at the instant of the gel effect for PMMA (curve *1*) synthesized in the presence of DPC initiator is not manifested when DPT is added to the

1070-4272/02/7505-0781$27.00 © 2002 MAIK "Nauka/Interperiodica"

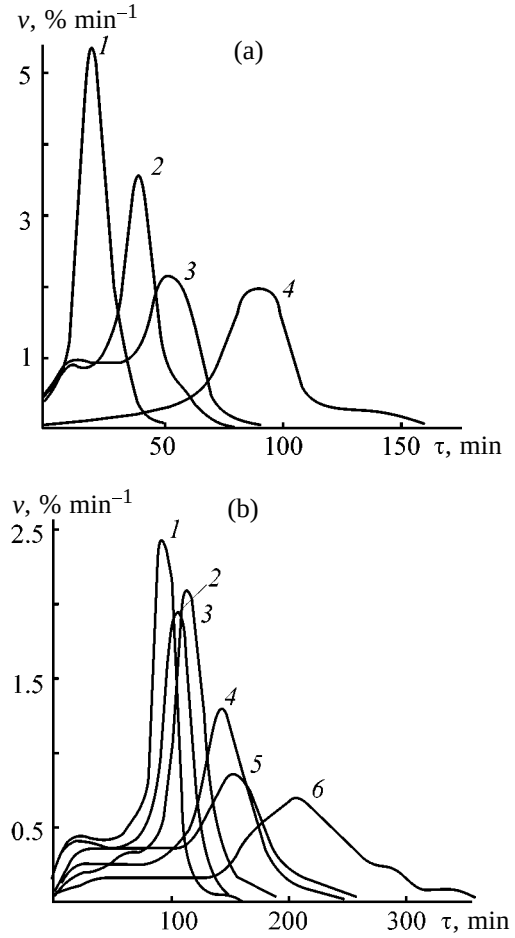

Fig. 1. Differential curves of MMA polymerization initiated by 0.1 mol % DPC in the presence of (a) DPT and (b) NB. (v) Polymerization rate and (τ) time. DPT concentration, mol %: (*1*) 0, (*2*) 0.05, (*3*) 0.1, and (*4*) 0.15. NB concentration, mol %: (*1*) 0, (*2*) 0.015, (*3*) 0.02, (*4*) 0.03, (*5*) 0.04, and (*6*) 0.05. Temperature, K: (a) 343 and (b) 323.

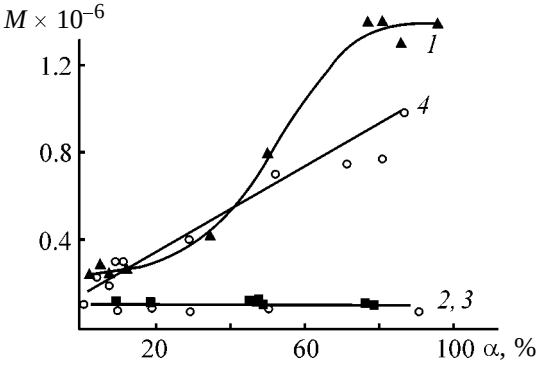

Fig. 2. Effect of DPT and NB on the pattern of variation of the (*1*, *2*, *4*) viscosity-average and (*3*) number-average molecular weight M of PMMA with conversion α. Initiator 0.1 mol % DPC, 323 K; the same for Fig. 3. (*1*) No additives; additive, mol %: (*2*, *3*) DPT, 0.2 and (*4*) NB, 0.06.

reaction mixture (curve *2*). Furthermore, the polydispersity coefficients calculated from the GPC data are 1.4–1.5 at high conversions and are considerably lower than those of the polymer prepared without DPT (see table).

Our results, in total with published data [11, 12, 19], suggest that, in this case, similar to polymerization of acrylic monomers in the presence of BPT, oxidation of DPT with peroxide [reaction (1)] or its reaction with alkoxy radicals [reaction (2)] generates NB, which subsequently reacts with the propagating polymer radical to form stable nitroxyl radical [reaction (3)] terminating the polymer chain [reaction (4)]:

$$\mathrm{Ph{-}N{=}N{-}\underset{\displaystyle OH}{\underset{|}{N}}{-}Ph} \xrightarrow{(O)} \mathrm{Ph^{\bullet} + N_2 + Ph{-}N{=}O}, \qquad (1)$$

$$\mathrm{Ph{-}N{=}N{-}\underset{\displaystyle OH}{\underset{|}{N}}{-}Ph + RO^{\bullet} \rightarrow ROH + Ph{-}N{=}N{-}N{-}Ph}, \qquad (2)$$

$$\mathrm{\downarrow O^{\bullet}}$$

$$\mathrm{Ph^{\bullet} + N_2 + Ph{-}N{=}O}$$

$$\mathrm{\sim Ph^{\bullet} + Ph{-}N{=}O \rightarrow \sim Ph{-}\underset{\displaystyle O^{\bullet}[X^{\bullet}]}{\underset{|}{N}}{-}Ph}, \qquad (3)$$

$$\mathrm{\sim P_n^{\bullet} + {}^{\bullet}X \underset{k_d}{\overset{k_t}{\rightleftarrows}} \sim P_n{-}X}, \qquad (4)$$

(k_p above the propagation arrow)

where $\sim P_n$ is the propagating radical.

To confirm the suggested mechanism, we have studied radical polymerization of MMA in the presence of NB additions. In accordance with the suggested scheme [Eqs. (1)–(3)] and previous data [11], the nitroso compound generated in the course of polymerization should be responsible for formation of stable nitroxyl radicals and subsequent synthesis of the polymer in the controllable mode.

We found that addition of NB in amounts comparable with that of the initiator decreases the gel effect and shifts it to higher conversions (Fig. 1b). Correspondingly, the unimodal curves of molecular-weight distribution (MWD) of PMMA samples are regularly shifted toward higher M (Fig. 3), and the molecular weight of the polymer linearly grows with conversion (Fig. 2), which is one of the most important evidences of the polymerization in the living chain mode.

It should be noted that, in contrast to NB, when the polymerization of MMA is performed in the presence of DPT, M of the polymer does not noticeably increase with conversion (Fig. 2). This may be due to

Molecular-weight characteristics of PMMA (initiator 0.1 mol % DPC, 323 K)

Conversion	$M_n \times 10^{-4}$	$M_w \times 10^{-4}$	$M_\eta \times 10^{-4}$	M_w/M_n
No additive				
14	16	28	26	1.8
53	23	64	55	2.8
72	52	149	134	>2.9
1,3-Diphenyl-1-hydroxytriazene added				
10	7	13	12	1.8
19	8	12	11	1.5
30	7	12	11	1.5
51	9	14	11	1.7
80	8	12	11	1.5

participation of DPT in chain transfer reactions involving both the phenyl moieties and the labile hydrogen atom of the hydroxy group. Furthermore, relatively low values of M of PMMA synthesized in the presence of DPT may also be due to relatively fast exhaustion of the initiator (DPC) at the beginning of the polymerization, since DPC participates simultaneously in thermal initiation of the polymerization and in the reaction with DPT [reaction (1)]. As a result, no "dead" high-molecular-weight polymer, yielded by a common radical polymerization and contributing to the overall molecular weight of the polymer, is formed. This assumption is indirectly confirmed by relatively low polydispersity coefficients, remaining virtually constant throughout the polymerization (see table).

Comparison of our results with published data on polymerization of MMA in the presence of BPT [11, 12] shows that, despite a good correlation between the results obtained with two different hydroxytriazenes (DPT and BPT), the latter compound is more promising as chain-terminating agent. This may be due to the presence in BPT [and hence in the nitroxyl spin adduct formed from BPT, reactions (1)–(3)] of bulky *tert*-butyl radical. Published data show [19, 20] that the structure of the organic radical at the nitroxyl moiety largely affects the rate constants of the forward (K_t) and reverse (k_d) reactions (4) and also the bond energy in the adduct [~P_n–X]. In particular, nitroxyl radicals with a bulky *tert*-butyl group are more effective as chain-terminating agents in radical polymerization than TEMPO and nitroxyl spin adducts containing an aromatic ring.

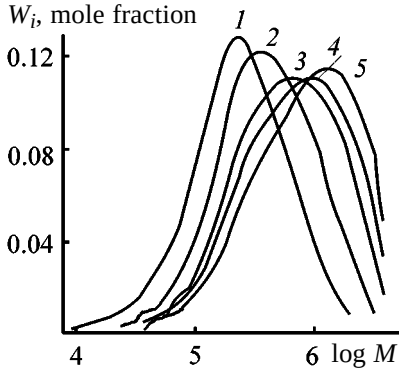

Fig. 3. Molecular-weight distribution of PMMA: (W_1) mole fraction and (M) molecular weight. NB concentration 0.06 mol %. The high-molecular-weight wing of the MWD is not shown because of limited sensitivity of the gel chromatograph in this range of M. Conversion, %: (*1*) 8, (*2*) 30, (*3*) 52, (*4*) 72, and (*5*) 89.

At the same time, an interesting feature of MMA polymerization in the presence of DPT should be noted. DPT actually allows synthesis of PMMA with a constant, independent of conversion molecular weight, which can be important in production of low-molecular-weight castable organic glass.

CONCLUSION

1,3-Diphenyl-1-hydroxytriazene and nitrosobenzene show promise as agents controlling the lifetime of a polymeric chain under energetically favorable conditions. These agents can be used for developing simple and efficient processes for production of low-molecular-weight polymethyl methacrylate in a controlled mode.

ACKNOWLEDGMENTS

The study was financially supported by the Russian Foundation for Basic Reseacrh and the Competitive Center for Basic Natural Science, Ministry of Education of the Russian Federation.

REFERENCES

1. Smirnov, B.R., *Vysokomol. Soedin., Ser. A,* 1990, vol. 32, no. 3, pp. 583–589.
2. Matyjaszewski, K., *Controlled Radical Polymerization*, Oxford: Oxford Univ. Press, 1998.
3. Otsu, T. and Matsumoto, A., *Adv. Polym. Sci.*, 1998, vol. 136, no. 1, pp. 75–127.
4. Korolev, G.V. and Marchenko, A.P., *Usp. Khim.*, 2000, vol. 69, no. 5, pp. 447–475.
5. Grishin, D.F. and Semenycheva, L.L., *Usp. Khim.*, 2001, vol. 70, no. 5, pp. 486–510.

6. Grishin, D.F., Semenycheva, L.L., and Kolyakina, E.V., *Dokl. Ross. Akad. Nauk*, 1998, vol. 362, no. 5, pp. 634–637.
7. Grishin, D.F., Semenycheva, L.L., and Kolyakina, E.V., *Vysokomol. Soedin., Ser. A*, 1999, vol. 41, no. 4, pp. 609–614.
8. Grishin, D.F., Semenycheva, L.L., Sokolov, K.V., and Kolyakina, E.V., *Vysokomol. Soedin., Ser. B*, 2000, vol. 42, no. 7, pp. 1263–1265.
9. Grishin, D.F., Semenycheva, L.L., and Kolyakina, E.V., *Vestn. Nizhegorod. Univ., Khim.*, 2000, no. 2, pp. 156–164.
10. Grishin, D.F., Semyonycheva, L.L., and Kolyakina, E.V., *Mendeleev Commun.*, 1999, no. 6, pp. 250–254.
11. Grishin, D.F., Moykin, A.A., Smirnova, E.P., *et al.*, *Mendeleev Commun.*, 2000, no. 5, pp. 152–154.
12. Grishin, D.F., Semenycheva, L.L., Pavlovskaya, M.V., and Sokolov, K.V., *Zh. Prikl. Khim.*, 2001, vol. 74, no. 9, pp. 1546–1550.
13. Abakumov, G.A., Cherkasov, V.K., and Razuvaev, G.A., *Dokl. Akad. Nauk SSSR*, 1971, vol. 197, no. 4, pp. 823–825.
14. *Organic Syntheses*, Blatt, A.H., Ed., New York: Wiley, 1944. Translated under the title *Sintezy organicheskikh preparatov*, Moscow: Inostrannaya Literatura, 1952, vol. 3.
15. *Praktikum po khimii i fizike polimerov* (Practical Course of Polymer Chemistry and Physics), Kurenkov, V.F., Ed., Moscow: Khimiya, 1990.
16. Arulin, V.I. and Efimov, L.I., *Tr. Khim. Khim. Tekhnol.* (Gor'kii), 1970, issue 2, pp. 74–77.
17. Rafikov, S.R., Pavlov, S.A., and Tverdokhledova, I.I., *Metody opredeleniya molekulyarnykh vesov i polidispersnosti vysokomolekulyarnykh soedinenii* (Methods for Determining the Molecular Weights and Polydispersity of Macromolecular Compounds), Moscow: Khimiya, 1963.
18. Moris, S., *J. Liq. Chromatogr.*, 1990, vol. 13, no. 9, pp. 1719–1721.
19. Mercier, C. le, Lutz, J.-F., Margue, S., *et al.*, in *Controlled/Living Radical Polymerization*, Washington, DC: Am. Chem. Soc., 2000, pp. 109–122.
20. Grishin, D.F., Ignatov, S.K., Razuvaev, A.G., *et al.*, *Vysokomol. Soedin., Ser. A*, 2001, vol. 43, no. 10, pp. 1742–1749.

Russian Journal of Applied Chemistry, Vol. 75, No. 5, 2002, pp. 785–789. Translated from Zhurnal Prikladnoi Khimii, Vol. 75, No. 5, 2002, pp. 803–807.
Original Russian Text Copyright © 2002 by Kuznetsov, Kabanova, Kurskii, Grishin.

MACROMOLECULAR CHEMISTRY AND POLYMERIC MATERIALS

Features of Emulsion Copolymerization of Butyl Methacrylate and Zinc Methacrylate Acetate in the Presence of Nonionic Emulsifiers

N. V. Kuznetsova, L. V. Kabanova, Yu. A. Kurskii, and D. F. Grishin

Research Institute of Chemistry, Lobachevskii State University, Nizhni Novgorod, Russia
Razuvaev Institute of Organometallic Chemistry, Russian Academy of Sciences, Nizhni Novgorod, Russia

Received September 21, 2001; in final form, January 2002

Abstract—The kinetic parameters of radical copolymerization of butyl methacrylate and zinc-containing monomer were studied as influenced by the structure and concentration of various emulsifiers such as oxyalkylated alcohols and alkylphenols. Some physicochemical properties of the resulting copolymers were determined.

It is known [1] that the features of radical polymerization in the presence of nonionic emulsifiers differ from those typical for the process performed in the presence of ionic compounds. Based on the constancy of the polymerization rate up to high conversion, cubic dependence of the particle number on the emulsifier concentration, and independence of the particle size from conversion, it was proposed that in this case polymerization proceeds not through the formation of micelles yielding the latex particles, as in the case of ionic emulsifiers, but in the surface layers of the monomer droplets [2].

Study of how the structure and concentration of various emulsifiers (such as oxyethylated alcohols, alkylphenols, and propylene oxide) affect the kinetics of emulsion polymerization and properties of the resulting polymers revealed the following trends in emulsion polymerization in the presence of nonionic emulsifiers.

(1) The increase in the emulsifier concentration relative to the monomer causes certain decrease in the particle size, which is accompanied by increase in the number of the particles and their total surface area; as a result, the polymerization rate and molecular weight of the product increase [3, 4].

(2) The increase in the degree of oxyethylation in a series of various emulsifiers increases the surface activity of the emulsifier [5, 6] owing to the increase in the surface area occupied by a single surfactant molecule in the adsorption layer on the particle surface (with addition of one $–CH_2–CH_2–O–$ group the surface area S increases by 0.055 nm^2). With increasing surface activity, the stability of the initial monomer emulsion and of the resulting latex increases; simultaneously, the particle size decreases and the process rate correspondingly increases.

The above assumptions are based on the data on the emulsion polymerization of styrene in the presence of oil-soluble initiators such as azobis(isobutyronitrile) (AIBN) and benzoyl peroxide (BP) [3–6]. It was supposed that polymerization proceeds in the particle bulk, although the initiator degradation can proceed in the surface layers of the latex particles [6]. Also, in the case of styrene the coordination and chemical interaction between the monomer and emulsifier molecules is virtually absent.

Previously [7], in our study of copolymerization of zinc-containing monomers with acrylates, we suggested that emulsion copolymerization of zinc methacrylate acetate (MAcZn) with alkyl methacrylates in the presence of a water–soluble redox system and a nonionic emulsifier based on oxyethylated alkylphenols proceeds in the adsorption layer on the particle surface. Due to almost total insolubility of MAcZn in methacrylate monomers, polymerization in the particle bulk is impossible. At the same time, the interaction of the zinc-containing monomer with oxyethylated emulsifiers cannot be ruled out [8].

In this work we studied the effect of the nature and concentration of oxyethylated emulsifiers on the kinetics of emulsion polymerization of butyl methacrylate (BMA) with MAcZn and the properties of the resulting products.

1070-4272/02/7505-0785$27.00 © 2002 MAIK "Nauka/Interperiodica"

EXPERIMENTAL

Zinc methacrylate acetate was prepared by reaction of zinc oxide and a mixture of acetic and methacrylic acids in water at equimolar component ratio [9]. Then zinc dimethacrylate precipitate insoluble in water was filtered off. The content of zinc diacetate was determined from the NMR spectra.

The emulsion copolymerization of MAcZn and BMA was performed in the presence of the ammonium persulfate–sodium dithionite–iron(II) sulfate redox system and nonionic emulsifiers DS-10 [monoalkyl ethers of polyethylene glycol and primary fatty alcohols of the general formula $C_nH_{2n+1}O(C_2H_4O)_mH$, where n = 10–18, m = 8–10] and OP-7 and OP-10 [monoalkylphenyl ethers of polyethylene glycol of the general formula $C_nH_{2n+1}C_6H_4O(C_2H_4O)_mH$, where n = 8–10, m = 6–7 (OP-7) and m = 10–12 (OP-10)]. The monomer : water weight ratio was 1 : 6.

The polymerization rate was monitored by the amount of unchanged monomers in the samples taken from the reaction mixture in the course of polymerization. The polymer was precipitated with isopropanol. The content of BMA was determined on a Tsvet-100 chromatograph equipped with a flame-ionization detector (2 m column length, PEG-6000 sorbent, helium carrier gas, flow rate 35 ml min^{-1}, 120°C). The content of unchanged zinc methacrylate acetate was determined spectrophotometrically [10] after washing out the residual monomer from preliminarily dried samples with subsequent analysis for the content of Zn^{2+} ions in the washing waters.

The effective radius R of the latex particles was determined by turbidimetry [11].

The number of particles in 100 g of latex was calculated from the equation

$$N = m/m_1,$$

where $m = 15A$ is the weight of the polymer (g) per 100 g latex, A is the conversion, $m_1 = 4/3\pi R^3/\rho$ is the weight of a single latex particle (g), R is the effective radius of the latex particles (m), and ρ is the polymer density (g m^{-3}).

The total surface area of the latex particles S (m^2) was calculated from the equation

$$S = NS_1,$$

where $S_1 = 4\pi R^2$ is the surface of a single latex particle (m^2).

The molecular weight of the chain between the cross-links was determined by the Flory–Rehner method [12]. The content of the gel fraction in the polymer was measured by extraction in butyl acetate [13].

The NMR spectra were registered on a Bruker DPX-200 spectrometer with working frequencies of 200 (^{1}H), 12.5 (^{67}Zn), and 44.4 MHz (^{113}Cd) using ampules 10 mm in diameter. A weighed portion of zinc or cadmium methacrylate acetate was dissolved in D_2O (2 ml) or a mixture of D_2O and H_2O (1 : 10). Emulsifiers were added into this solution before the NMR measurements. The molar ratio of the emulsifier and zinc or cadmium salt was determined by ^{1}H NMR spectroscopy.

Study of the radical copolymerization of BMA and MAcZn in the presence of oxyethylated alkylphenols with various degrees of oxyethylation (OP-4, OP-7, and OP-10) showed that the emulsion polymerization occurs only with OP-7 and OP-10 emulsifiers.

The BMA–MAcZn copolymerization in the presence of OP-4 emulsifier is extremely slow, conversion in 24 h does not exceed 3%. The emulsion of the initial monomers is unstable and rapidly segregates, and the size of the initial emulsion and final latex is greater than 170 nm. Realization of the emulsion mechanism starting from certain degree of the emulsifier oxyethylation was observed previously, e.g. in homopolymerization of styrene [5]. This is probably due to the small surface activity of emulsifiers with small degrees of oxyethylation, which is insufficient to provide required stability and dispersion of the emulsion and thus realization of the mechanism of emulsion polymerization.

It was found that the increase in the concentration of OP-7 and OP-10 emulsifiers decreases the particle size and thus makes the system more disperse (see table). As seen by the example of OP-10, with increasing emulsifier content the process rate increases (Fig. 1), which is largely determined by the degree of emulsion dispersion [4]. In this case, the compliance of the dependences derived by Medvedev *et al*. for radical polymerization with participation of nonionic emulsifiers in the surface layer of the latex particles [$V \approx S$ (Fig. 2), $N \approx c_e^3$ (Fig. 3), and $V \approx N^{1/5}$ (Fig. 4), where V is the polymerization rate (% conversion/min), S is the total surface area of the latex particles (m^2), N is the number of particles, c_e is the emulsifier concentration (wt % with respect to monomer)] indicates that copolymerization of BMA and MAcZn proceeds in the adsorption layers on the latex particle surface.

Effect of emulsifiers on the properties of BMA–zinc methacrylate acetate copolymer*; concentration of zinc methacrylate acetate 6.5 mol %

Emulsifier	c_e, wt %	$N_c \times 10^5$, mol cm^{-3}	R, nm	M_c, g mol^{-1}	G, wt %	α, wt %
DS-10	6.7	–	>170	–	–	41.7
	10.0	–	>170	–	–	51.1
	12.0	300	121	3700	–	86.2
	16.7	283	114	3750	–	–
	20.0	300	110	3500	–	98.7
	23.4	297	104	3500	–	96.5
	26.7	264	98	3600	–	94.6
OP-7	6.7	–	>170	–	–	–
	10.0	–	>170	–	–	–
	13.3	5.3	110	17 000	–	–
	16.7	5.1	95	17 800	–	–
	20.0	5.2	85	17 500	–	–
OP-10	3.4	–	>170	–	44.2	31.3
	5.0	–	>170	–	49.6	58.4
	6.7	–	>170	–	–	93.0
	8.4	–	>170	–	–	98.0
	9.0	2.4	156	41 500	52.0	–
	10.0	2.2	132	41 000	63.0	100
	11.7	2.2	78	42 000	86.7	93.5
	13.1	2.3	38	40 000	–	–

* N_c is the effective density of the polymer cross-linking, R is the effective radius of the latex particles, M_c is the molecular weight of the chain between the cross-links, G is the content of the insoluble gel fraction in the polymer, and α is the conversion in 24 h.

At the same time, comparison of the size of the latex particles stabilized with various emulsifiers (see table) showed that, the larger the size of the emulsifier molecule and the higher the degree of its oxyethylation, the smaller the size of the latex particles. The different performance of oxyethylated alcohol DS-10 and OP-10 with the same degree of oxyethylation (n = 10) is probably due to different area of the phase boundary stabilized with a single surfactant molecule [5, 6, 14].

The emulsifier structure, in particular, the degree of its oxyethylation affects the polymer properties, especially the degree of its cross-linking. It was proposed previously [15] that the cross-linking in the zinc-

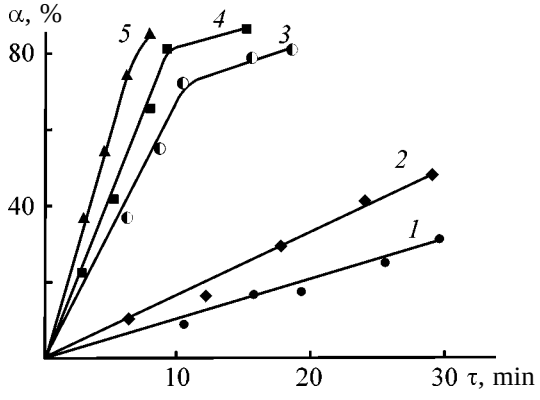

Fig. 1. Kinetic curves of emulsion polymerization of the BMA–6.5 mol % MAcZn system. (α) Conversion and (τ) time. Content of OP-10 emulsifier, wt % with respect to monomer: (*1*) 3.4, (*2*) 5.0, (*3*) 9.0, (*4*) 10.0, and (*5*) 13.1.

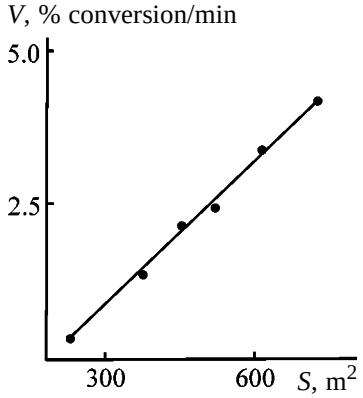

Fig. 2. Rate V of emulsion copolymerization of the BMA–6.5 wt % MAcZn system in the presence of OP-10 emulsifier as a function of the total particle surface area S.

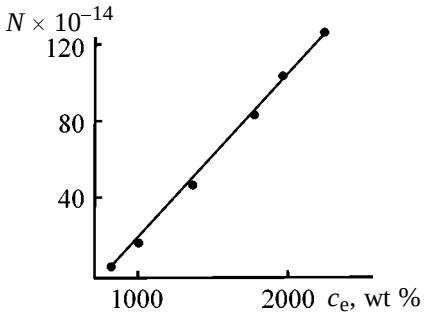

Fig. 3. Number of particles N in emulsion copolymerization of the BMA–6.5 wt % MAcZn system in the presence of OP-10 emulsifier as a function of the emulsifier concentration c_e.

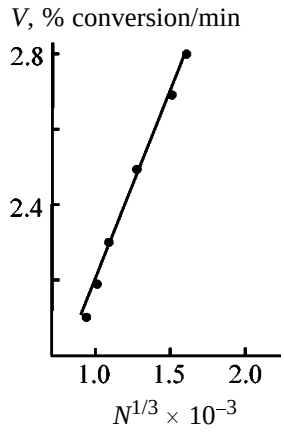

Fig. 4. Rate V of emulsion copolymerization of the BMA–6.8 wt % MAcZn system in the presence of OP-10 emulsifier as a function of the number of particles N.

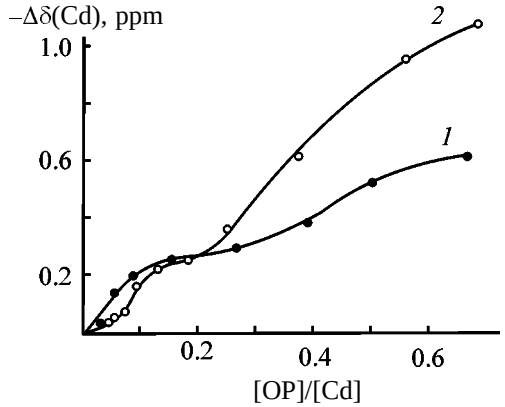

Fig. 5. Chemical shift $-\Delta\delta$(Cd) as a function of the [OP]/[Cd] molar ratio. Emulsifier: (*1*) OP-7 and (*2*) OP-10.

containing polymers is due to complexation of zinc ions with the functional groups of the polymer. Owing to the reaction of the zinc-containing monomer with an emulsifier in the adsorption layer on the particle surface, the polymer cross-linking depends on the emulsifier structure. The larger the size of the emulsifier molecule and the higher the degree of its oxyethylation, the lower the efficiency of the polymer cross-linking N_c, which is probably due to the steric hindrance.

It should be noted that the effective density of the polymer cross-linking depends only on the emulsifier structure, but is independent of its concentration (see table). As shown by the example of OP-10 emulsifier, the increase in the emulsifier concentration increases the content of the cross-linked fraction in the polymer (G). These features of the behavior of the zinc-containing monomer are probably due to the reaction of MAcZn with the emulsifier in the adsorption layer on the particle surface.

The ^{67}Zn NMR signals are broadened owing to the quadrupole moment of the ^{67}Zn nucleus; the width of the zinc methacrylate acetate signal in D_2O exceeds 1200 Hz. With increasing emulsifier concentration, the signal becomes still broader and finally disappears. The quadrupole broadening depends on the symmetry of distribution of the electrical charges around the nucleus. This symmetry is probably decreased owing to the substitution of the water molecules in the zinc environment by the ether fragments of the emulsifier molecule.

Since observation of the chemical shift of ^{67}Zn is rather difficult, in our study we used the monomer containing the closest analog of zinc, cadmium methacrylate acetate. As seen from Fig. 5, with increasing content of emulsifier the chemical shift of the ^{113}Cd signal [$\Delta\delta$(Cd)] increases. The chemical shift observed in presence of OP-10 emulsifier is greater than that with OP-7 emulsifier. This agrees with weaker interaction of OP-7 emulsifier with cadmium methacrylate acetate. In the case of zinc methacrylate acetate, the weaker interaction with OP-7 emulsifier corresponds to higher density of cross-linking of the polymer prepared in the presence of OP-7 emulsifier.

CONCLUSIONS

(1) Realization of the emulsion mechanism of copolymerization of zinc methacrylate acetate with butyl methacrylate depends both on the type of the nonionic emulsifier (oxyethylated alcohol and alkylphenols) and the degree of oxyethylation. Copolymerization of zinc methacrylate acetate with butyl methacrylate proceeds in the adsorption layers on the surface of the latex particles.

(2) The emulsifier structure, in particular, the degree of its oxyethylation affects such physicochemical properties of the polymer as effective density of cross-linking and content of the cross-linked gel fraction. The effective density of cross-linking is independent of the emulsifier concentration.

(3) The interaction of zinc methacrylate acetate with oxyethylated emulsifiers such as oxyethylated alcohols and alkylphenols was confirmed by NMR spectra. The efficiency of this interaction depends on the degree of the emulsifier oxyethylation.

REFERENCES

1. Pavlyuchenko, V.N., *Kinetika polimerizatsii i molekulyarnye kharakteristiki polimerov* (Polymerization Kinetics and Molecular Properties of Polymers), Leningrad: Plastpolimer, 1982.
2. Eliseeva, V.I., Ivanchev, S.S., and Kuchanov, S.I., *Emul'sionnaya polimerizatsiya i ee primenenie v promyshlennosti* (Emulsion Polymerization and Its Industrial Use), Moscow: Khimiya, 1976.
3. Gritskova, V.I., Ustinova, Z.M., and Fodiman, N.M., *Kolloidn. Zh.*, 1965, vol. 27, no. 3, pp. 338–340.
4. Dudukin, V.V., Medvedev, S.S., and Gritskova, I.A., *Dokl. Akad. Nauk SSSR*, 1967, vol. 172, no. 5, pp. 1125–1128.
5. Zuikov, A.V., Gritskova, I.A., Bedina, Zh.A., and Medvedev, S.S., *Vysokomol. Soedin., Ser. A*, 1972, vol. 14, no. 4, pp. 252–254.
6. Medvedev, S.S., Zuikov, A.V., Gritskova, I.A., and Dudukin, V.V., *Vysokomol. Soedin., Ser. A*, 1971, vol. 13, no. 6, pp. 1397–1403.
7. Kabanova, K.V., Kuznetsova, N.V., and Aleksandrov, Yu.A., *Zh. Prikl. Khim.*, 2000, vol. 73, no. 3, pp. 480–484.
8. Baran, A.A., *Polimersoderzhashchie dispersnye sistemy* (Polymer-Containing Disperse Systems), Kiev: Naukova Dumka, 1986.
9. Pomogailo, A.D. and Savost'yanov, V.S., *Metallsoderzhashchie monomery i polimery na ikh osnove* (Metal-Containing Monomers and Polymers Based on Them), Moscow: Khimiya, 1989.
10. Babko, A.K. and Pilipenko, A.T., *Kolorimetricheskii analiz* (Colorimetric Analysis), Leningrad: Khimiya, 1952.
11. *Laboratornye raboty i zadachi po kolloidnoi khimii* (Practical Works on Colloidal Chemistry), Frolov, Yu.G., Ed., Moscow: Khimiya, 1986.
12. Rogers, C.E., Stannett, V., and Szwarc M., *J. Phys. Chem.*, 1959, vol. 63, no. 9, pp. 1406–1418.
13. Rafikov, S.R., Budtov, V.P., and Monakov, D.B., *Vvedenie v fizikokhimiyu rastvorov polimerov* (Introduction to Physical Chemistry of Polymer Solutions), Moscow: Nauka, 1978.
14. Avetisyan, I.S., Bakaeva, T.V., and Pospelova, K.A., *Kolloidn. Zh.*, 1963, vol. 25, no. 2, pp. 143–145.
15. Kabanova, L.V., Kuznetsova, N.V., Aleksandrov, Yu.A., *et al.*, *Kolloidn. Zh.*, 1999, vol. 61, no. 2, pp. 211–214.

Russian Journal of Applied Chemistry, Vol. 75, No. 5, 2002, pp. 790–794. Translated from Zhurnal Prikladnoi Khimii, Vol. 75, No. 5, 2002, pp. 808–812.
Original Russian Text Copyright © 2002 by Voron'ko, Derkach, Izmailova.

MACROMOLECULAR CHEMISTRY AND POLYMERIC MATERIALS

Rheological Properties of Gels of Gelatin with Sodium Alginate

N. G. Voron'ko, S. R. Derkach, and V. N. Izmailova

Murmansk State Technical University, Murmansk, Russia
Moscow State University, Moscow, Russia

Received May 4, 2000; in final form, February 2002

Abstract—Effect of anionic polysaccharide, sodium alginate, on the rheological characteristics of gelatin gels is studied. It follows from the rheological curves that low-temperature gelatin gels with sodium alginate can be classified with elastoviscoplastic systems. Multicomponent gels obtained with the two gel-forming agents demonstrate synergism of the rheological characteristics.

Thanks to their specific gel-forming, emulsifying, and stabilizing characteristics, systems protein–polysaccharide–water are widely used in pharmacy, microbiology, medicine, and other branches. Hydrogels based on gelatin and anionic polysaccharides find wide applications in the food industry, being of interest in view of developing new synthetic food substances [1, 2].

Gels of gelatin are two-phase lyophilic disperse systems. Thermoreversible structurization in gelatin gels occurs on cooling below 35°C through renaturation of collagen-like spirals followed by separation of a new phase (aggregates of gelatin macromolecules) and formation of a three-dimensional gel structure [3, 4]. Contacts between the aggregates can be realized through H bonding and also through hydrophobic and Coulombic interactions. A model for the structural network in gelatin gel can be thought as a combination of elastic (triple collagen-like spirals serving as network junctions) and viscous chain units (disordered polypeptide fragments). These units form an infinite cluster characterized by a set of rheological parameters typical of a solid [5]. Mechanical properties of gelatin gels are thoroughly studied in [3, 6–11] using rheological methods.

Complexation of proteins with anionic polysaccharides, including that of gelatin with sodium alginate (NaAlg), is examined in [1, 12, 13]. The resulting complexes are considered as gelforming agents of a new type, on the basis of which food gels with various properties can be obtained [14–16]. Rheological properties of such gels are insufficiently studied yet.

Therefore, the goal of this work is to study rheological characteristics of multicomponent gels of gelatin with sodium alginate. Particularly, we studied the effect of the anionic polysaccharide concentration on the rheological behavior of gelatin gels. Sodium alginate was added in low concentrations at which the polysaccharide itself does not act as a structuring agent, but has a positive synergistic effect on the gel-forming properties of the mixed systems.

EXPERIMENTAL

In the work we used food-grade gelatin 250. Isoelectric point pI 4.9; moisture content 10.4 wt % (20°C); and ash content (20°C) 0.87. The molecular-weight distribution determined by HPLC is given in Fig. 1a. The weight-average molecular weight M_w was found to be 109 000.

Also we used food-grade sodium alginate (produced by the Arkhangelsk Algal Pilot Plant). This polysaccharide is a sodium salt of alginic acid, whose molecules consist of the residues of β-*D*-mannuronic and α-*L*-guluronic acids:

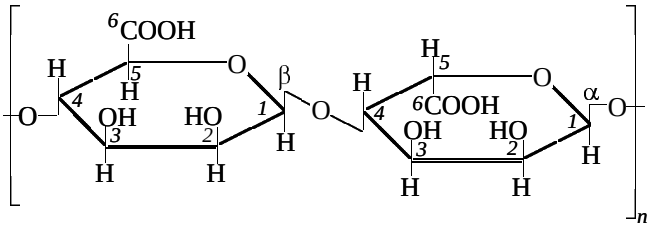

β-*D*-mannuronic acid residue

α-*L*-guluronic acid residue

The molecular-weight distribution of NaAlg, determined by HPLC, is given in Fig. 1b; M_w = 366 000, moisture content 12.6 wt % (20°C), ash content 17.1 wt %, and content of fraction insoluble in boiling water 0.3 wt %.

1070-4272/02/7505-0790$27.00 © 2002 MAIK "Nauka/Interperiodica"

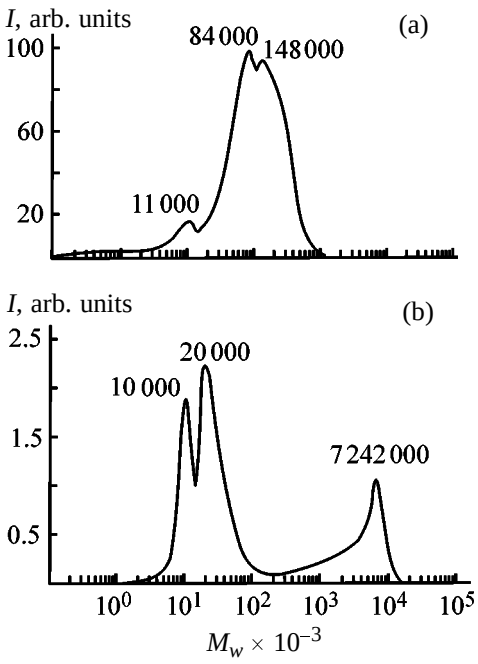

Fig. 1. Molecular-weight distribution determined by HPLC: (a) gelatin and (b) sodium alginate. (*I*) Peak intensity and (M_w) weight-average molecular weight.

In this work we studied low-concentration gels (c_g = 1%, c_{NaAlg} = 0.0001–0.15%) at 16°C and pH 5.3–6.0. It should be pointed out that NaAlg does not form gels under these conditions. It is typical for this polysaccharide to form ionotropic rather than thermotropic gels [17].

Turbidimetric results obtained at pH 5.8–6.0 (pH > p*I*) showed that gelatin interacts with NaAlg with formation of finely dispersed insoluble complexes. The effective size of the resulting particles in the bulk was determined at 40°C by the light scattering variance method (turbidity spectrum) [18]. The effective radius *R* of the particles increases with time from 50–100 to 590–920 nm, depending on the NaAlg concentration in the system (see table). The occurrence of an induction period as well as the observed variation in the particle size in time suggest that complexation proceeds by the nucleation mechanism. The system, representing a suspension of particles of insoluble complexes, remained stable over the observation period (6 days), i.e., no macroscopic phase separation was observed.

Variation of the effective radius of particles *R* with time *t* in aqueous gelatin–sodium alginate systems at c_g = 1.0% and various sodium alginate concentrations (T = 40°C, pH 5.8–6.0)

t, h	*R*, nm, at indicated c_{NaAlg}, %		
	7×10^{-4}	1.3×10^{-3}	1.4×10^{-2}
0	50	60	100
3	50	60	110
6	50	80	110
28	220	310	320
50	390	920	590
77	740	920	590
144	–	920	590

Formation of the complexes from the likely (negatively) charged macromolecules of gelatin and anionic polysaccharide (pH > p*I*) can proceed through hydrophobic interaction, hydrogen bonding, and also salt-like interaction between positively charged amino acid (lysine and arginine) residues of gelatin and negatively charged groups of the polysaccharide. Formation of similar complexes of proteins with polysaccharides was examined in [1]. The observed aggregative stability of the system is probably due to the fact that the resulting complexes are likely charged, which prevents aggregation and macroscopic phase separation. At pH < p*I*, gelatin reacts with NaAlg with formation of neutral complexes, resulting in separation of the system into two phases accompanied by coacervation [19].

Rheological characteristics of low-concentration mixed gelatin–NaAlg gels was measured at 16±0.1°C with shear stress using a Polimer RPE-1M.2 rotary concentric-cylinder viscometer (radius of outer cylinder 20.0 mm, outer to inner cylinder radius ratio R_o/R_i = 1.03). The effective viscosity was determined over the shear rate range $\dot{\gamma}$ = 0.7–708.8 s^{-1}. The shear stress was estimated by Eq. (1):

$$\tau = \eta\dot{\gamma}, \quad (1)$$

where τ is the shear stress (Pa) and η is the effective viscosity (Pa s).

The Reynolds number was found to be no more that 254.6, confirming the laminar type of motion in the investigated systems in measuring the effective viscosity.

It is known that rheological characteristics of gelatin-based gels change with time as a result of structurization processes occurring in the gels below the gelation temperature [3]. Gelation in gelatin-based systems was demonstrated to be a kinetically controlled process, which, once starting, continues prac-

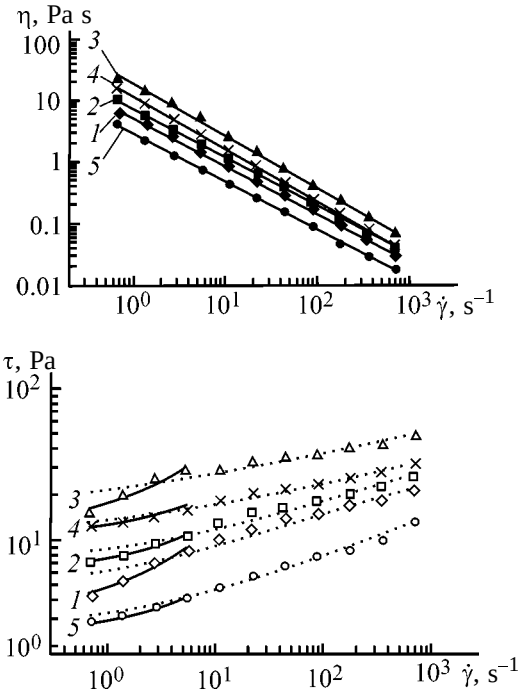

Fig. 2. Flow curves of multicomponent gels of gelatin with sodium alginate. c_g = 1.0%, 16°C, pH 5.2–5.6, and time of gel formation 4 h; the same for Fig. 3. (η) Effective viscosity, (τ) shear stress, and ($\dot{\gamma}$) shear rate. c_{NaAlg} (%): (*1*) 0, (*2*) 7.0×10^{-4}, (*3*) 1.3×10^{-3}, (*4*) 1.8×10^{-3}, and (*5*) 1.4×10^{-2}. Dashed and solid lines in the τ–$\dot{\gamma}$ plot refer to the Herschell–Bulkley and Casson's models, respectively.

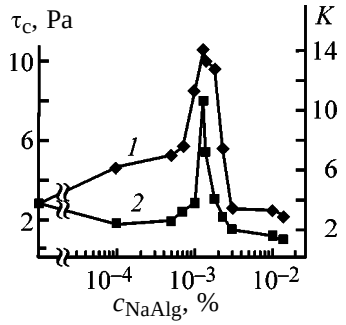

Fig. 3. Rheological characteristics of gelatin gels with sodium alginate: (*1*) yield point τ_c and (*2*) consistency index *K*. (c_{NaAlg}) Sodium alginate concentration.

tically endlessly [20], making rheological study difficult. Nevertheless, it appeared possible to determine the time of gel formation after which the mechanical characteristics increased only slightly. The strength of the gelatin–NaAlg gels studied is practically saturated in 4–5 h at 16°C.

As an example, Fig. 2 shows the flow curves of gelatin–NaAlg gels, measured 4 h after the gelation started. The effective viscosity is a function of the shear rate, the shape of this function being dependent on the component ratio in the system. For the case of simple shear in the nonlinear viscoelastic range, the shear stress fits the Herschell–Bulkley model [21, 22]:

$$\tau = \tau_c + K\dot{\gamma}^n, \quad (2)$$

where τ_c is the yield stress (Pa), *K* is the consistency index, and *n* is the flow index (0.20–0.35 for the systems studied).

There is an initial section of the elastic state in the flow curves, where the shear stress is below the yield stress: $\tau < \tau_c$. In this region, elastic deformations are totally reversible, and the system can be described by the modulus of elasticity. At the same time, it follows from the results obtained in [23] that gelatin gels with a viscosity of 10^8–10^{11} Pa s demonstrate long-time steady afterflow linearly depending on the concentration, suggesting the lack of the equilibrium modulus of elasticity in physical gelatin gels.

The rheological behavior of the gels studied at low shear rates (0.7–5.5 s^{-1}) can be described with a sufficient accuracy by the Casson's model [21, 22]:

$$\tau^{1/2} = \tau_c^{1/2} + (\eta_p\dot{\gamma})^{1/2}, \quad (3)$$

where η_p is the plastic viscosity (Pa s).

For the gels studied, the plastic viscosity varies within the range from 0.06 to 0.95 Pa s.

As seen from Fig. 2, both models reproduce quite adequately the rheological behavior of the gels. The yield stress values, characterizing the strength of the gels, estimated using the Herschell–Bulkley and Casson's models, differ from each other by no more than 6%. Therefore, analysis of the rheological curves (Fig. 2) allows classification of low-concentration gelatin–NaAlg gels with elastoviscoplastic systems.

As an example, Fig. 3 shows the dependences of the yield stress τ_c (curve *1*) and consistency index *K* (curve *2*) on the NaAlg concentration. It is seen that the rheological characteristics of the gels are controlled by the component ratio. The curves show distinctly pronounced maxima, i.e., combination of gelatin and NaAlg provides a synergistic effect. The peak values of the rheological characteristics are observed at $c_{NaAlg} = 1.3 \times 10^{-3}$%, at which complexes with the maximal effective radius of particles are formed (see table). Similar results were obtained also for other rheological parameters such as the flow index *n*

and plastic density η_p. With increasing NaAlg concentration ($c_{NaAlg} > 1.8 \times 10^{-3}$%) the rheological characteristics abruptly decrease, and at $c_{NaAlg} > 3.0 \times 10^{-3}$% they become lower than those of gelatin gels containing no NaAlg.

The rheological methods are sensitive to evolution of the microscopic structure of the gels [4]. The maximal strength of the gelatin–NaAlg gels (Fig. 3) corresponds, evidently, to the maximal number of salt-like bonds formed between the components at pH > p*I*. In this case, the effective particle size is the maximal (see table). It was demonstrated in [24] that the degree of spiralization of the gelatin macromolecules in mixed gels decreases and the thermal stability of triple-stranded collagen-like spirals increases with increasing relative NaAlg concentration, as for association of gelatin with low-molecular-weight surfactants [25]. Stabilization of the three-dimensional structure of gelatin–NaAlg gels, as compared to straight gelatin gels, was attributed in [24] to transformation of the initial salt-like bonds with formation of an electrostatically bonded network. This is most clearly pronounced at pH below the isoelectric point of gelatin and with long aging of the gel (for more than 15 h) [6]. Evidently, high content of NaAlg in the system (in our case $c_{NaAlg} > 3.0 \times 10^{-3}$%) suppresses to a considerable extent the interactions, primarily electrostatic, between the likely charged macromolecules of gelatin and the polysaccharide. As a result, gelatin gels filled with sodium alginate are formed [15].

CONCLUSION

Rheological behavior of gelatin gels with the anionic polysaccharide, sodium alginate, is studied for various gel compositions at pH above the isoelectric point of gelatin. Rheological parameters (yield point, consistency index, and plastic viscosity) of multicomponent gels measured under shear stress conditions are characterized by a distinctly pronounced composition dependence, reaching the maximal values at a fixed component ratio [$(1.3–5.4) \times 10^{-3}$ g NaAlg per gram gelatin). Low-concentration gels (c_g 1%, c_{NaAlg} 0.0001–0.15%) represent elastoviscoplastic systems.

Combination of two gel-forming agents, gelatin and sodium alginate, provides synergism in the rheological properties of the resulting multicomponent gels.

ACKNOWLEDGMENTS

The work was financially supported by the Russian Foundation for Basic Research (project no. 01-03-32129a).

REFERENCES

1. Tolstoguzov, V.B., *Novye formy belkovoi pishchi* (New Forms of Protein Food), Moscow: Agropromizdat, 1987.
2. Morrison, A., Sworn, G., Clark, R.C., *et al*., Physical Chemistry and Industrial Application of Gellan Gum, *Progress in Colloid and Polymer Science*, Nishikari, K., Ed., 1999, vol. 114, no. 2, pp. 127–148.
3. Izmailova, V.N. and Rebinder, P.A., *Strukturoobrazovanie v belkovykh sistemakh* (Structure Formation in Protein Systems), Moscow: Nauka, 1974.
4. Clark, A.H., *Food Polymers, Gels, and Colloids*, Cambridge: Roy. Soc. Chem., 1990.
5. Izmailova, V.N., Yampol'skaya, G.P., Levachev, S.M., *et al*., *Zh. Nauch. Prikl. Fotogr*., 2001, vol. 46, no. 4, pp. 34–43.
6. Tolstogusov, V.B., *Food Hydrocolloids*, 1995, vol. 9, no. 4, pp. 317–332.
7. Djabourov, M., *Contemp. Phys*., 1988, vol. 29, no. 3, pp. 273–288.
8. Ross-Murphy, S.B., *Polymer*, 1992, vol. 33, no. 5, pp. 2622–2634.
9. Te Nijenhuis, K., *Adv. Polym. Sci*., 1997, vol. 130, no. 2, pp. 167–189.
10. Carvalho, W. and Djabourov, M., *Rheol. Acta*, 1997, vol. 36, no. 6, pp. 591–609.
11. Normand, V. and Ravey, J.C., *Rheol. Acta*, 1997, vol. 36, no. 6, pp. 610–617.
12. Tolstoguzov, V.B., Braudo, E.E., Grinberg, V.Ya., and Gurov, A.N., *Usp. Khim*., 1985, vol. 54, no. 10, pp. 1738–1759.
13. Braudo, E.E., Plashchichina, L.G., and Tolstogusov, V.B., *Carbohydr. Polym*., 1984, vol. 4, no. 2, pp. 23–48.
14. Bogdanov, V.D. and Safronova, T.M., *Strukturoobrazovanie i rybnye kompozitsii* (Structure Formation and Fish Composites), Moscow: VNIRO, 1993.
15. Muchin, M.A., Streltsova, Z.A., Wajnerman, E.S., and Tolstogusov, V.B., *Nahrung*, 1978, vol. 22, no. 10, pp. 867–873.
16. Guedj, S. and Capra, J., *Imag. Sci*., 1997, vol. 45, no. 4, pp. 201–204.
17. Lapasin, R. and Pricl, S., *Rheology of Industrial Polysaccharides: Theory and Applications*, Glasgow: Chapman and Hall, 1995.

18. Klenin, V.I., *Termodinamika system s gibkotsepnymi polimerami* (Thermodynamics of Flexible-Chain Polymer Systems), Saratov: Saratov. Univ., 1995.
19. Vainerman, E.S., Grinberg, V,Ya., and Tolstoguzov, V.B., *Vysokomol. Soedin., Ser. A*, 1974, vol. 16, no. 2, pp. 252–256.
20. Ross-Murphy, S.B., *Imag. Sci*., 1997, vol. 45, no. 4, pp. 205–209.
21. Vinogradov, G.V. and Malkin, A.Ya., *Reologiya polimerov* (Rheology of Polymers), Moscow: Khimiya, 1977.
22. Mildman, S., *Techenie polimerov* (Polymer Flow), Moscow: Mir, 1971.
23. Higgs, P.G. and Ross-Murphy, S.B., *Int. J. Biol. Macromol*., 1990, vol. 12, no. 4, pp. 233–240.
24. Mukhin, M.A., Preparation and Physicochemical Characteristics of Composite Gels of Gelatin with Sodium Alginate, *Cand. Sci. Dissertation*, Moscow, 1983.
25. Izmailova, V.N., Derkach, S.R., Zotova, K.V., and Danilova, R.G., *Kolloidn. Zh*., 1993, vol. 55, no. 3, pp. 54–90.

Russian Journal of Applied Chemistry, Vol. 75, No. 5, 2002, pp. 795–799. Translated from Zhurnal Prikladnoi Khimii, Vol. 75, No. 5, 2002, pp. 813–817.
Original Russian Text Copyright © 2002 by Sidorovich, Praslova, Vinogradova, Melenevskaya, Zgonnik.

MACROMOLECULAR CHEMISTRY AND POLYMERIC MATERIALS

Calorimetric Properties of Different Kinds of Polymers Containing C_{60} Fullerene

A. V. Sidorovich, O. E. Praslova, L. V. Vinogradova, E. Yu. Melenevskaya, and V. N. Zgonnik

Institute of Macromolecular Compounds, Russian Academy of Sciences, St. Petersburg, Russia

Received July 9, 2001

Abstract—Transformations of polymers containing C_{60} fullerene: poly-*N*-vinylpyrrolidone with the complex and covalent-graft structure, polyphenylene oxide with the complex structure, and polyethylene glycol and polystyrene with beam structure, were studied by differential scanning microcalorimetry. The observed effects were assigned to the change in nanofragmentary topology on heating.

Fullerenes and fullerene-containing compounds, including polymers, are of scientific and practical interest. Fullerene molecules are characterized by nanometric ordering owing to the presence of developed π-electron system in their molecules. A domain structure ordered at a distance of up to 60 nm is formed in solutions of C_{60}-containing polymers with starlike and complex structures [1, 2]. Okamura *et al.* [3] showed that ordering of the polymer in solutions appreciably depends on the solvent: the domain structure is formed in aromatic solvents and is absent in nonaromatic solvents. Hence, the solid-state properties of fullerene-containing polymers can depend on their structural transformations in solution.

In this work we studied the influence of the type of C_{60}–polymer interaction on calorimetric properties of fullerene-containing polymers [poly-*N*-vinylpyrrolidone (PVP), polyphenylene oxide (PPO), polyethylene glycol (PEG), and polystyrene (PS)] with complex, graft, and starlike structures.

EXPERIMENTAL

Thermograms of the polymers were recorded on a DSM-2M scanning microcalorimeter in the temperature range 30–400°C with the scanning rate of 16 deg min^{-1} (8 deg min^{-1} for graft PVP). Several successive scans were made. To determine the content of volatile products (residual solvents or thermolysis products), the capsules were weighed after the measurements. The threshold sensitivity of the calorimeter was 0.04 mW.

In Table 1, we summarize the main preparation procedures of the polymers, data on the structure and content of C_{60} in the polymer, and the parameters of molecular structure of the polymers with different nature of C_{60} bonding: complex in PVP 1 (C-C_{60}), PVP 2 (C-C_{60}), and PPO (C-C_{60}); covalent graft in PVP 3 (gr-C_{60}); covalent in hexagonal star PS_6-C_{60}; and covalent cross-linked in trigonal star PEG_3-C_{60}.

Table 1. Main properties of the examined polymers

Sample no.*	Polymer	C_{60}, %	Molecular properties**
1	PVP 1 (C-C_{60}) [4]	1	MW = 10^4
2	PVP 2 (C-C_{60}) [4]	1	MW = 10^3, MWD = 1.5
3	PVP 3 (gr-C_{60})	3	Partially cross-linked with irregular network
4	Precursor of PVP 1 (C-C_{60}) PVP 1 (C-C_{60})	0	MW = 70×10^3, broad MWD
5	PPO (C-C_{60})	1	MWD = 1.5
6	Initial PPO	0	MW = $(55–100) \times 10^3$
7	PS_6-C_{60} [5]	2	MWD = 1.03
8	Initial PS	0	MWD = 1.05–1.1
9	PEG_3-C_{60}	0.5	MW = 10^3, partially cross-linked

* Sample nos. 5, 6 are films; the other polymers are powders; sample nos. 3, 9 were prepared by reaction of C=O groups with $C_{60}(R)_n$ molecules containing CMt bonds, R is *t*-BuO; sample nos. 4, 6 are commercial products; sample no. 5 was prepared from toluene solution.

** (MW) Molecular weight and (MWD) molecular-weight distribution.

1070-4272/02/7505-0795$27.00 © 2002 MAIK "Nauka/Interperiodica"

Sample nos. 1 and 2 were prepared by mixing 1% solutions of C_{60} in toluene and PVP in chloroform. The resulting solution was evaporated to dryness. The dry residue containing 1% C_{60} and 99% PVP was dissolved in distilled water, and unchanged C_{60} was filtered off. Powdered C_{60}–PVP complex was obtained by lyophilic drying of the filtrate. Complexes of polymer nos. 1 and 2 with C_{60} were prepared from commercial PVP with MW = 70×10^3 and from the polymer with a lower polydispersity (MW = 1×10^3), respectively.

Graft polymer no. 3 was prepared by activation of C_{60} with *t*-BuOK [4]. The first step involves addition of three *t*-BuOK molecules to C_{60}:

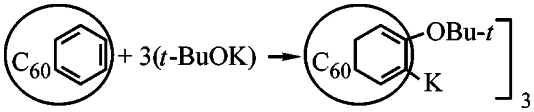

The second step is reaction of the C_{60}-C group with the carbonyl groups of pyrrolidone rings

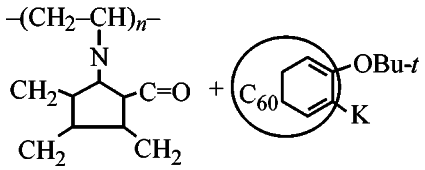

to form both (a) linear and (b) partially cross-linked polymer containing C_{60}.

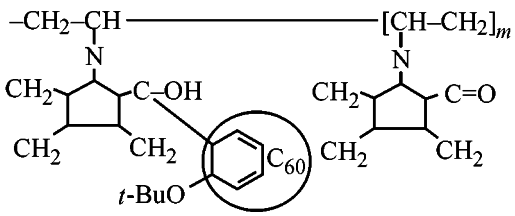

(a)

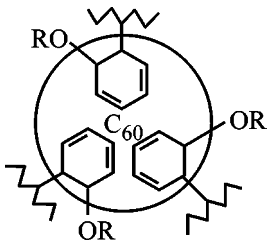

(b)

(R) OBu-*t*, (⩙⩙) PVP chain.

PEG_3–C_{60} was prepared by reaction of C_{60} with polyethylene glycol dialkoxide, which, in turns, was obtained by reaction of polyethylene glycol with metallic potassium in toluene. In this case, two terminal OK groups of polyethylene glycol dialkoxide react with C_{60} to form cross-linked polymer.

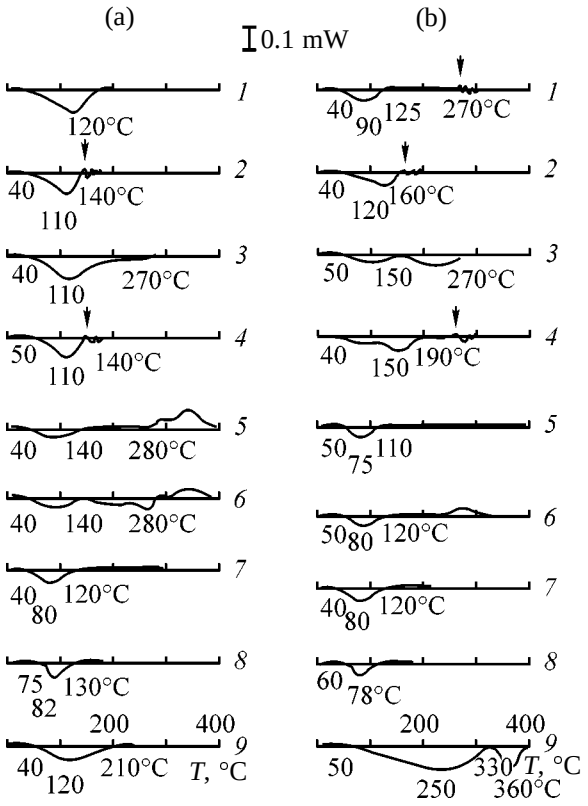

Fig. 1. Thermograms [(a) first scan and (b) second scan] of fullerene-containing and initial polymers. Scanning rate 16 deg min^{-1}, power of the thermal effect 0.1 mW. (*T*) Temperature; the same for Fig. 2. Intense liberation of volatile products is indicated with an arrow. Figures to the right of the curves corresponds to sample nos. in Table 1.

Polymer no. 7 was prepared by reaction of C_{60} with polystyryl lithium chains [5]:

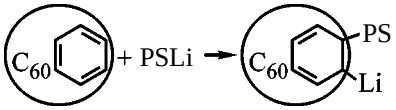

The thermograms of the fullerene-containing and initial polymers are shown in Figs. 1a (first scan) and 1b (second scan). The total thermal effect $\Sigma\Delta H$, the peak temperatures T_{max} of these effects in the first and second scans, and the weight loss of capsules after scanning Δm are summarized in Table 2.

The endothermic peaks have a peculiar shape of a hole but not the shape of step or sharp maxima typical for vitrification or melting, respectively. Such peaks are typical for vitrification with liberation of volatile products. Similar results were obtained when studying soprtion of water by PVP [6].

Figure 1 and Table 2 show that introduction of C_{60} into PVP polymers strongly affects their calorimetric

Table 2. Total thermal effect $\Sigma\Delta H$, peak temperature T_{max}, width ΔT of endothermic and exothermic peaks, and weight loss Δm

Sample no.	First scan							Second scan			
	endoeffect			exoeffect			Δm, %	endoeffect			Δm, %
	$\Sigma\Delta H$, kJ kg^{-1}	T_{max}, °C	ΔT, °C	$\Sigma\Delta H$, kJ kg^{-1}	T_{max}, °C	ΔT, °C		$\Sigma\Delta H$, kJ kg^{-1}	T_{max}, °C	ΔT, °C	
1	220	120	130	–	–	–	–16	17	90	85	0
2	143	110	100	–	–	–	–12	24	125	90	– 2
3	260	110	230	–	–	–	–21	190	125, 240, 365*	220 (100, 120)**	–15.8
4	120	100	90	–	–	–	–7.3	26	110	150	–2.3
5	11	75	100	72	350	120	–5.3	3	75	60	0
6	12	80	180, (100, 80)**	28	330	90	–4	4	70	70	0
7	11	80	1.80	–	–	–	–12	9	80	1.80	–6.3
8	10.7	82	55	–	–	–	–	7.4	78	40	0
9	–	130	170	–	–	–	–4.5	650	250, 360***	350 (280, 70)**	–47

* Peak temperatures of separate effects after the third scan.
** Width ΔT of separate peaks.
*** Peak temperatures T_{max} of separate effects after the second scan.

properties. The peaks of polymer nos. 1 and 3 are broader than that of the initial polymer no. 4.

The thermal effect of graft polymer no. 3, registered in the first and second scans, is broader by 130–140°C than that of the initial polymer. It should be noted that no intense evolution of gaseous products was observed on heating of this sample to 290°C, whereas, on the first heating of the initial polymer no. 4, gaseous products evolved at 140°C.

This cannot be due to the presence of large amounts of impurities in the polymer, since the weight loss Δm of the initial polymer is smaller than that of the fullerene-containing polymers. Hence, PVP polymer with grafted C_{60} undergoes thermolysis at higher temperatures. It should also be noted that the endothermic effect manifested in the first scan as a single peak is resolved into two peaks in the second scan. Thus, introduction of C_{60}, on the one hand, enhances the thermal stability of the polymer and, on the other hand, results in the formation of energetically different fragmentary structures during the first heating.

Formation of energetically different structures during the first heating of graft PVP is confirmed by three scans of the thermogram (Fig. 2). Comparison of the first and third scans (scanning rate 16 deg min^{-1}) with the second scan (scanning rate 8 deg min^{-1}) shows temperature redistribution of the endoeffect. In the second slower scan, a three-step thermal effect appears after the single peak. In the third scan, the three-step peak is also observed; at temperatures below 300°C the peaks are noticeably shifted, but above 300°C the thermogram does not appreciably differ from that obtained in the second scan. Since in this case no intense liberation of volatile thermolysis products is observed up to 400°C, these peaks can be assigned to transformations of the structural topology of the sample.

Introduction of fullerene into PVP [sample PVP 2 (C-C_{60})] does not appreciably improve the thermal properties of the polymer. $\Sigma\Delta H$ and ΔT_{endo} of the

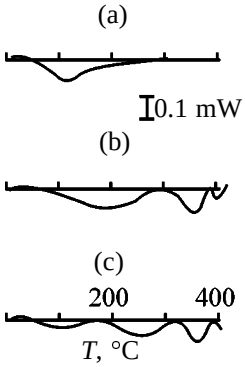

Fig. 2. (a) First, (b) second, and (c) third scans of the PVP 3 (gr-C_{60}) thermograms Thermal effect power 0.1 mW. Scanning rate (deg min^{-1}): (a, c) 16 and (b) 8.

modified polymer, measured in the first scan, are only slightly higher than those of the initial polymer. The onset temperatures of intense evolution of volatile thermolysis products are the same. In the second scan, the total thermal effects are the same, and the temperature of intense evolution of volatile thermolysis products of the modified polymer is lower.

In the first scan, the thermal properties of polymer no. 1 with the complex structure are substantially better than those of the initial polymer: $\Sigma\Delta H$ is higher by 100 kJ kg^{-1} and ΔT_{endo} is higher by 40°C. In addition, no intense thermolysis was observed up to 200°C (thermolysis of the initial polymer starts at 140°C). Hence, formation of a complex structure in PVP 1 (C-C_{60}) increases the thermal stability of the polymer. However, in the second scan the onset temperature of intense liberation of volatile products of PVP 1 (C-C_{60}) and the initial polymer are the same, with $\Sigma\Delta H$ of PVP 1 (C-C_{60}) being slightly lower. This indicates degradation of the complex after the first heating.

Thus, the thermal properties of fullerene-containing polymer nos. 1 and 2 substantially differ. The thermal properties of PVP 2 (C-C_{60}) prepared from the polymer with the lower molecular weight are virtually similar to those of the initial PVP. These results reflect the influence of the structural genesis, in particular, molecular properties of the initial polymer, on the thermal behavior of the modified polymers.

The first scan of the thermogram of PPO (C-C_{60}) complex shows both endo- and exoeffects. $\Sigma\Delta H$ and ΔT of the endoeffect are virtually identical to those of the initial polymer, whereas in the case of the exoeffect these parameters increased by a factor of 2 and by 30°C, respectively. No effects stronger than the determination error were observed in the second scan, which indicates the absence of energetic transformations with thermal effects in both the complex and the initial PPO polymer. Hence, after the first heating PPO is transformed into a thermodynamically stable state. Introduction of C_{60} affects the exothermic but not the endothermic peak and increases the degree of the polymer cross-linking, which is confirmed by $\Sigma\Delta H$ of the first and the second scan and by the fact that the resulting polymer becomes insoluble.

The thermogram of trigonal-star PEG (first scan) contains a broad endothermic peak (ΔT = 170°C). In the second scan, it is broadened to 400°C to form a doublet which, as in the case of PVP 3 (gr-C_{60}), is induced by the first heating.

The endoeffect in the thermograms of fullerene-containing styrene is broader by 100°C than that of the initial PS. The fact that this effect lasts to intense evolution of volatile products indicates higher thermal stability of the modified polymer.

The published data on structural transformations of C_{60}-containing polymers, determined by other methods, agree with our results and their interpretation. The study of free PEG and graft PEG (C-C_{60}) by mass-spectrometric thermal analysis showed an increase in the thermal stability of graft PEG whose pyrolysis temperature increased to 400°C [7]. Quantum chemical calculation of the bonding between C_{60} and PVP and PEG confirmed that formation of grafted and complex structures is thermodynamically favorable [8]. The results of [7, 8] and our calorimetic study show that the thermal stability of graft PVP and graft PEG increases to 400°C. These data agree with the data on the onset temperature of thermolysis of the starlike polymer determined by MTA [9], on the use of C_{60} as inhibitor of thermal oxidative degradation and antioxidant [10, 11], and on the vitrification temperature of PS determined by DSC [12].

The most important result of this work is revealing two- and three-step endoeffects on heating of graft PVP and trigonal-star PEG. These peaks are due to a complex topology of the molecular structure with nanofragmentary separation of these polymers, which changes on heating. The nanodomain structure of the fullerene-containing polymer is formed in solution [1, 2] and is retained in the solid state [13]. Since the size of domains and their bonding energy differ, the nanofragment structure substantially changes on heating, which affects the calorimetric properties.

Thus, DSC performed in a wide temperature range and under different operating conditions gives an insight into high-temperature transformations of fullerene-containing polymers. The mechanism of these transformations can be determined by comparison of DSC and MTA data.

CONCLUSION

The graft structure of C_{60}-containing poly-*N*-vinylpyrrolidone polymers is the most stable. Formation of the complex structure in fullerene-containing polymers strongly depends on the molecular properties of the initial polymer. Multistep enodeffects observed in a wide temperature range in the thermograms of poly-*N*-vinylpyrrolidone with covalent graft structure and in polyphenylene oxide with the complex structure suggest fragmentary structure of these polymers, with its topology changing on heating.

ACKNOWLEDGMENTS

This work was financially supported by the Russian Foundation for Basic Research (project no. 00-03-33083a) and by the program "Urgent Trends in Solid State Physics," subprogram "Fullerenes and Atomic Clusters" (project no. 98076).

REFERENCES

1. Klenin, S.I., Sushko, M.L., Dumpis, M.A., *et al*., *Zh. Tekh. Fiz*., 2000, vol. 70, no. 3, pp. 27–32.
2. Sushko, M.L., Self-Organization and Control of Long-Range Order in Solutions of Fullerene-Containing Polymers, *Cand. Sci. Disseration*, St. Petersburg, 2000.
3. Okamura, H., Tezanchi, T., Minda, M., *et al*., *Macromolecules*, 1997, vol. 30, no. 18, pp. 5279–5289.
4. Jamakoshi, J.N., Jagami, T., and Fukuhava, R., *J. Chem. Soc., Chem. Commun.*, 1994, pp. 517–519.
5. Melenevskaya, E.Yu., Vinogradova, L.V., Litvinova, L.S., *et al*., *Vysokomol. Soedin., Ser. A*, 1998, vol. 40, no. 2, pp. 247–254.
6. Lebedeva, T.L., Fel'dshtein, M.M., Kuptsov, S.A., and Plate, N.A., *Vysokomol. Soedin., Ser. A*, 2000, vol. 42, no. 9, pp. 1504–1523.
7. Shibaev, L.V., Antonova, T.A., Vinogradova, L.V., *et al*., *Zh. Prikl. Khim*., 1998, vol. 71, no. 5, pp. 835–842.
8. Yakimanskii, A.V. and Ginzburg, B.M., *Zh. Prikl. Khim*., 2000, vol. 73, no. 4, pp. 688–690.
9. Ginzburg, B.M., Pozdnyakov, A.O., Pozdnyakov, O.F., and Redkov, B.P., *Zh. Prikl. Khim*., 2000, vol. 73, no. 3, pp. 484–490.
10. Troitskii, B.B., Troitskaya, L.S., Yakhnov, A.S., and Domrachev, G.A., *Dokl. Ross. Akad. Nauk*, 1998, vol. 363, no. 1, pp. 79–81.
11. Troitskii, B.B., Troitskaya, L.S., Domrachev, G.A., *et al*., *Dokl. Ross. Akad. Nauk*, 2000, vol. 375, no. 6, pp. 796–798.
12. Berstein, V.A., Egorov, V.M., Egorova, L.M., *et al*., *J. Non-Cryst. Solids*, 1998, vol. 235–237, pp. 476–484.
13. Karnacheva, G.P., *Vysokomol. Soedin., Ser. A*, 2000, vol. 42, no. 11, pp. 1974–1999.

Russian Journal of Applied Chemistry, Vol. 75, No. 5, 2002, pp. 800–804. Translated from Zhurnal Prikladnoi Khimii, Vol. 75, No. 5, 2002, pp. 818–822.
Original Russian Text Copyright © 2002 by Karabanova, Novikova, Sergeeva, Lutsyk.

MACROMOLECULAR CHEMISTRY AND POLYMERIC MATERIALS

Gradient Semiinterpenetrating Polymer Networks Based on Polyurethane and Polyvinylpyrrolidone

L. V. Karabanova, T. I. Novikova, L. M. Sergeeva, and E. D. Lutsyk

Institute of Chemistry of Macromolecular Compounds, National Academy of Sciences of Ukraine, Kiev, Ukraine

Received March 11, 2001; in final form, April 2002

Abstract—Common and gradient semiinterpenetrating polymer networks based on polyurethane and polyvinylpyrrolidone were prepared. The physicomechanical and IR spectroscopic parameters of these networks were determined and compared.

Among diverse polymeric composites suggested in the recent years, composites with a gradient of properties are of particular interest. Among such materials are gradient interpenetrating polymer networks (IPNs); their preparation and properties are described in [1–8].

With the progress of new technologies (aerospace, computer, biotechnologies), a demand arose for materials with highly specialized functions. To meet these demands, functional gradient materials were developed. Their properties (hardness, conductivity, dielectric constants, etc.) continuously change across the thickness of the material.

Typical functional gradient materials are characterized by continuous changes in the composition, microstructure, and properties from one surface to another, which gives rise to multifunctional characteristics.

Gradient interpenetrating polymer networks as representatives of gradient functional materials can be considered as stack of layers of polymer blends with the composition and properties gradually changing from the surface to the center of the sample.

In this connection, it seemed interesting to study and compare the properties of common and gradient semi-IPNs similar in the chemical nature.

EXPERIMENTAL

Semi-IPNs and gradient semi-IPNs were prepared on the basis of three-dimensional polyurethane (PU) and linear polyvinylpyrrolidone (PVP).

The polyurethane network was prepared in two stages. First, we prepared an adduct of trimethylolpropane with toluene diisocyanate by reaction of 1 g-equiv of trimethylolpropane with 1.5 g-equiv of toluene diisocyanate at 338 K. The reaction was performed until the theoretically calculated content of isocyanate was attained. Then, three-dimensional polyurethane was prepared by reaction of polyethylene glycol adipate (molecular weight M = 2000) with the adduct of trimethylolpropane with toluene diisocyanate (equivalent ratio 1 : 2) at 353 K under nitrogen:

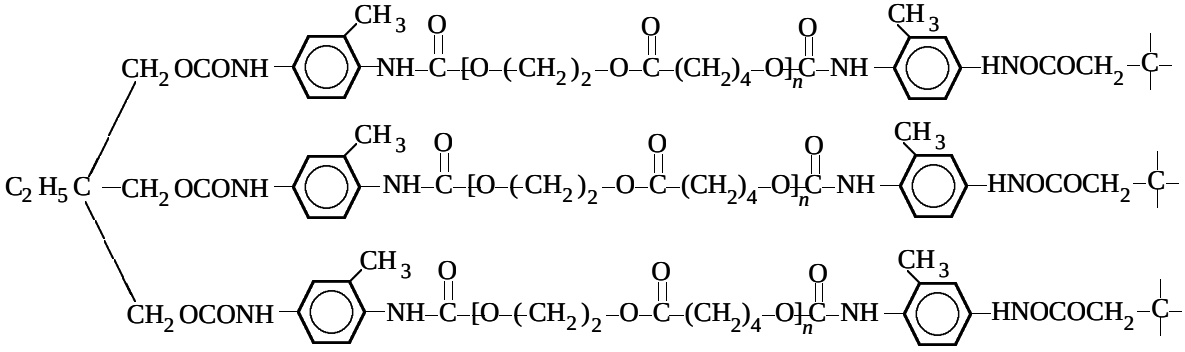

1070-4272/02/7505-0800$27.00 © 2002 MAIK "Nauka/Interperiodica"

The unchanged components were removed from the polyurethane network by extraction with ethyl acetate in a Soxhlet apparatus.

Semi-IPNs and gradient semi-IPNs were prepared by successive polymerization. The polyurethane network was allowed to swell in a monomer (*N*-vinylpyrrolidone) containing a photopolymerization initiator.

To obtain semi-IPN, the polyurethane after swelling in the monomer was kept in a hermetically sealed vessel to attain equilibrium distribution of the components, after which photopolymerization was performed.

Gradient semi-IPNs were formed by swelling of the polyurethane network in the reaction mixture for a definite time estimated from the preliminarily obtained data on the swelling kinetics. Then, without attaining the equilibrium distribution of the components, photopolymerization of *N*-vinylpyrrolidone was performed.

As a result, we obtained a series of semi-IPNs with different content of the components and a block of gradient semi-IPN 6 mm thick with an overall PVP content of 24.1%.

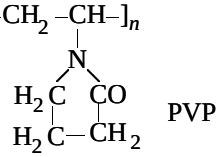

PVP

The systems obtained were studied by IR spectroscopy and by sorption of solvent vapors [10]. The physicomechanical tests were performed on an Instron machine by standard procedures. Thin chips at different distances from the surface of the gradient semi-IPN were obtained with a microtome.

The depth distribution of polymers in gradient systems is usually studied by layer-by-layer elemental analysis [11–13]. However, the qualitative elemental composition of PU and PVP is similar, and layer-by-layer elemental analysis in this case is of little use. Therefore, to study the depth distribution of PVP (overall content 24.1%) in a block of gradient semi-IPN, we choose IR spectroscopy.

The IR spectra of the initial PU, PVP, and semi-IPNs of several concentrations were measured on a Specord M80 spectrophotometer in the range 4000–300 cm^{-1}, using KBr technique (3 mg sample per 600 mg KBr).

Examination of the IR spectra of PU, PVP, and semi-IPNs with definite component ratios showed that the absorption bands of PU at 1740 cm^{-1} and of PVP at 1678 cm^{-1} are the best suited for quantitative determinations.

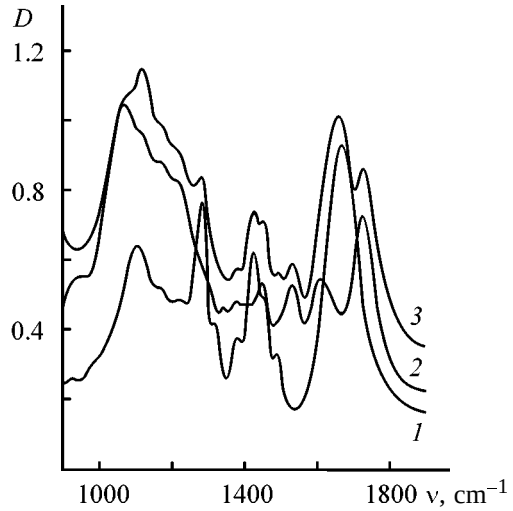

Fig. 1. IR spectra of (*1*) PVP, (*2*) PU, and (*3*) semi-IPN containing 57.3% PVP. (*D*) Optical density and (ν) wave number; the same for Fig. 2.

The IR spectra of PVP, PU, and semi-IPN with a PVP content of 57.3% are shown in Fig. 1. It is seen that, in the spectrum of the semi-IPN, the bands at 1740 (PU) and 1678 cm^{-1} (PVP) partially overlap.

The separation of particular absorption bands, determination of their spectroscopic characteristics, and calculation of the peak areas and intensities were performed using the Band Separation software adapted to the Specord M80 spectrophotometer [14]. The error in calculating the peak areas and intensities was 3–5%.

To perform an IR study of the gradient semi-IPN sample (overal PVP content 24.1%), we made thin chips at different distances from the sample surface. The chips were pulverized and pelletized with KBr.

Figure 2 shows the spectra of gradient semi-IPN specimens taken at different distances from the sample surface. The overall spectrum was mathematically resolved into components in the range 1960–1600 cm^{-1}.

Components a_1–a_5 correspond to vibrations of the C=O bonds in PVP, and components a_6–a_8, to vibrations of the C=O bonds in PU.

In the spectra of the surface layers of the gradient semi-IPN block (Fig. 2a), the major band is that at 1655 cm^{-1}, characterizing vibrations of the C=O bonds in PVP. In the layers located at a depth of about 1.5 mm from the sample surface (Fig. 2b), the carbonyl band of PVP decreases in intensity, and that of PU (1740 cm^{-1}) grows.

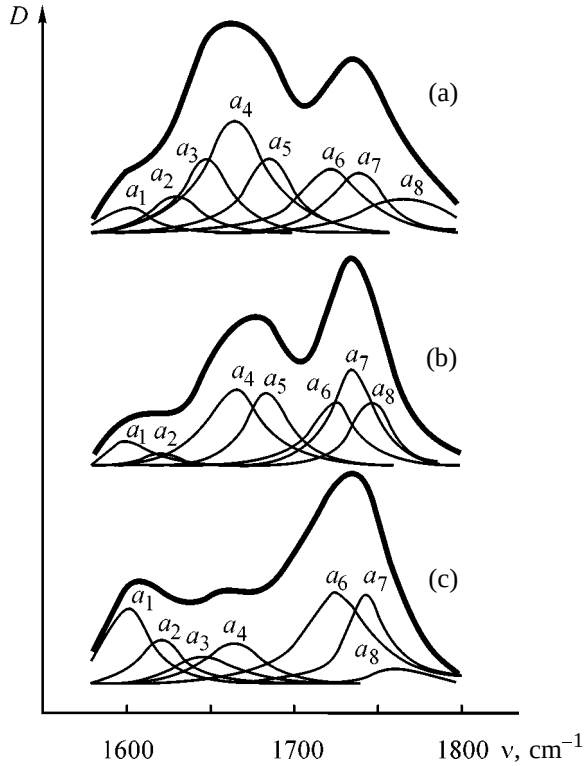

Fig. 2. IR spectra of the (a) first (surface) layer of gradient semi-IPN, (b) second layer of gradient semi-IPN, and (c) core of the gradient semi-IPN block, with mathematical resolution into components in the range 1800–1600 cm^{-1}.

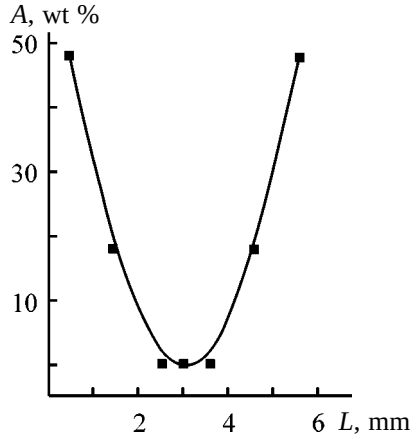

Fig. 3. Concentration depth profile of PVP in the sample of gradient semi-IPN: (*A*) PVP concentration and (*L*) depth.

In the layer located in the center of the gradient block of semi-IPN (Fig. 2c), the PVP vibration band is virtually absent. This fact shows that PVP is concentrated in the surface layers of the gradient block and that its content decreases in going to the sample core.

Based on the results of the IR study of semi-IPN samples, we constructed a calibration plot for the intensity ratio of the C=O vibration bands in PU and PVP. The calibration plot does not pass through the origin, because a number of components a_i in the spectra of PU and PVP overlap. This fact was taken into account when calculating the gradient of the PVP distribution in gradient semi-IPNs.

The quantitative calculation of the PVP content from the IR data for various layers of the gradient semi-IPN allowed construction of the concentration depth profile of PVP in a 6 mm thick sample of gradient semi-IPN (Fig. 3). It is seen that the PVP concentration in the sample varies by a parabolic law. In the surface layers of the sample, the PVP concentration is as high as 48.1%; at a depth of 1.5 mm, it is 17.5%; and at a depth of 2.5 mm it is close to zero. The fourth layer (sample core) contains PU only.

In curing of a gradient system, the conditions of transition from the range of compatibility to the two-phase state are different across the sample, because the ratio of the first network to the monomer, from which the polymer creating the concentration gradient is formed in the course of curing, changes from the surface to the depth of the sample.

In the course of curing, owing to kinetic factors, the components are not completely separated into two phases; instead, nonequilibrium structures with different levels of microphase segregation are "frozen." It was interesting to study how the thermodynamic compatibility of the components changes with the depth. For this purpose, we studied the sorption of vapors of low-molecular-weight compounds with samples of the initial polymers and with layers of the gradient block and performed calculations of the thermodynamic parameters.

Figure 4 shows the isotherms of benzene vapor sorption at 298 K by samples of PU and PVP and by layers of the gradient block of semi-IPN. With PU, the sorption isotherm (curve *1*) has a shape typical of sorption by polymers in the hyperelastic state. With PVP (Fig. 4, curve *2*), at $P/P_0 < 0.45$, the sorption is low, which is due to close packing of macromolecules in the glassy state [15]; in the range of the relative vapor pressures of the solvent $P/P_0 > 0.45$, the polymer undergoes devitrification, which is followed by a sharp increase in the benzene vapor sorption.

Layers of the gradient semi-IPN demonstrated a complex sorption behavior (Fig. 4, curves *3*–*5*). For the surface layer of the gradient block (48.1% PVP), in the range of relative vapor pressures 0–0.4, the isotherm is similar to that of pure PVP, but the sharp increase in the vapor sorption after devitrification is

Physicomechanical properties of semi-IPNs of definite compositions and of layers of gradient semi-IPN based on PU and PVP

Sample	Elongation at break, %	Breaking stress	Young's modulus	Adsorption energy at break, N mm^{-1}
		MPa		
PU	215.3	4.5	4.9	6.4
Semi-IPN, PVP, %:				
7.1	123.4	9.60	17.4	6.3
13.3	82.5	13.5	49.3	5.8
22.5	70.4	15.9	130.6	7.2
30.4	76.9	25.8	411.9	13.7
41.0	68.6	26.4	473.2	14.3
57.3	57.1	28.9	691.4	13.6
Gradient semi-IPN, layer:				
first	65.3	27.1	485.4	13.2
second	80.6	14.8	103.2	7.1
third	176.3	6.2	9.3	6.7
fourth	211.5	4.7	5.1	6.4
Semi-IPN, 24.2% PVP	73.2	19.2	196.4	8.9
Gradient semi-IPN, 24.1% PVP	70.1	25.1	390.2	12.6

not observed. As the PVP content in the layers of the gradient block decreases (curves *4*, *5*), the isotherms acquire the shape characteristic of PU (curve *1*).

The fact that blends formed at different depths differ in the component ratio and structure is also confirmed by physicomechanical tests (see table).

As seen from the table, for semi-IPNs, with increasing PVP content, the elongation at break decreases, and the breaking stress and the adsorption energy at break regularly increase. The Young's modulus increases with increasing PVP content: In going from PU to the semi-IPN with the highest (57.3%) PVP content, the Young's modulus increases by more than two orders of magnitude.

For chips of the gradient block, the trends are as follows (see table). The parameters of the fourth layer (core) are close to those of PU. The physicomechanical characteristics of the surface (first) layer are close to those of the semi-IPN with 41.0% PVP. The parameters of the third and fourth layers are consistent with the low content of PVP in these layers, as determined by IR spectroscopy.

Comparison of the physicomechanical parameters of the semi-IPN and gradient semi-IPN (at equal overall PVP content, see table) shows that the gradient semi-IPN exhibits a higher failure energy. The growth of the Young's modulus is especially pronounced: For the gradient semi-IPN it is higher by a factor of approximately 2. These data show that creation of a gradient structure in a polymeric material allows its mechanical properties to be substantially improved. A number of hypotheses were advanced in [1] to account for this phenomenon. According to one of them, gradient IPNs are considered as a set of an infinite number of layers whose compositions and Young's moduli gradually change. Under strain, all

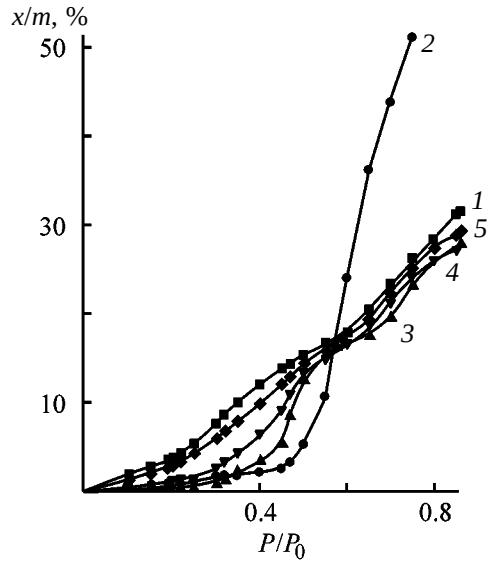

Fig. 4. Isotherms of benzene vapor sorption at 298 K by (*1*) PU, (*2*) PVP, and (*3*–*5*) layers of the gradient semi-IPN with the overall PVP content of 24.1%. (*x*/*m*) Sorption and (P/P_0) relative vapor pressure. The layers are numbered in the direction from the surface (*3*) to the core (*5*).

the layers are stretched to an equal extent, and the stress in each layer corresponds to its modulus. Such a stress distribution favors plastic deformation rather than brittle failure and increases the failure energy.

CONCLUSIONS

(1) Gradient semiinterpenetrating polymer networks can be considered as sets of layers of incompatible polymer blends, differing in the composition and extent of heterogeneity.

(2) An IR study showed that the concentration depth profile of polyvinylpyrrolidone in a gradient semiinterpenetrating polymer network is parabolic. The concentration of polyvinylpyrrolidone changes from 48.1% in the surface layer to 0 in the sample core.

(3) The physicomechanical properties of gradient semiinterpenetrating polymer networks vary along the concentration gradient. At different depths from the surface layers with different morphologies and physicomechanical parameters are formed.

REFERENCES

1. Martin, G.C., Enssani, E., and Shen, M., *J. Appl. Polym. Sci.*, 1981, vol. 26, no. 5, pp. 1465–1473.
2. Akovali, G., Biliyar, K., and Chen, M., *J. Appl. Polym. Sci.*, 1976, vol. 20, no. 9, pp. 2419–2427.
3. Lipatov, Yu.S., Sergeeva, L.M., Karabanova, L.V., *et al.*, *Mekh. Kompoz. Mater.*, 1988, no. 6, pp. 1028–1033.
4. Sergeeva, L.M. and Lipatov, Yu.S., *Fizikokhimiya mnogokomponentnykh polimernykh sistem* (Physical Chemistry of Multicomponent Polymer Systems), Kiev: Naukova Dumka, 1986.
5. Lipatov, Yu.S. and Karabanova, L.V., *Advances in Interpenetrating Polymer Networks*, Lancaster: Technomik, 1994, vol. 4.
6. Karabanova, L.V., Sergeeva, L.M., Lutsyk, E.D., and Kuznetsova, V.P., *Vysokomol. Soedin., Ser. A*, 1996, vol. 38, no. 10, pp. 1700–1705.
7. Karabanova, L., Pissis, P., Kanapitsas, A., and Lutsyk, E., *J. Appl. Polym. Sci.*, 1998, vol. 68, pp. 161–171.
8. Khozin, V.G., Timofeeva, N.V., and Abdrakhmanova, L.A., *Zh. Prikl. Khim.*, 1994, vol. 67, no. 9, pp. 1533–1542.
9. Harrick, H.J., *Internal Reflection Spectroscopy*, New York: Wiley, 1967.
10. Tager, A.A., *Fizikokhimiya polimerov* (Physical Chemistry of Polymers), Moscow: Khimiya, 1978.
11. Wang, J.S. and Matyjaszewski, K.V., *Macromolecules*, 1995, vol. 28, pp. 7527–7536.
12. Akovali, G. and Labban, A., *IUPAC Macro: Int. Symp. on Macromolecules (Florence, 1980): Preprints*, Pisa, 1980, vol. 3, pp. 264–267.
13. Dror, M., Elsabee, M.L., and Berry, G.C., *J. Appl. Polym. Sci.*, 1981, vol. 26, no. 6, pp. 1741–1757.
14. Ishchenko, S.S., Novikova, T.I., Pridatko, A.B., and Lebedev, E.V., *Zh. Prikl. Khim.*, 1995, vol. 68, no. 7, pp. 1198–1201.
15. Tager, A.A. and Tsilipotkina, M.V., *Usp. Khim.*, 1978, vol. 47, no. 1, pp. 152–175.
16. Tager, A.A., *Vysokomol. Soedin., Ser. A*, 1977, vol. 19, no. 8, pp. 1654–1663.
17. Tager, A.A., *Vysokomol. Soedin., Ser. A*, 1988, vol. 30, no. 7, pp. 1347–1359.
18. Razinskaya, I.N., Tager, A.A., Izvozchikova, V.A., *et al.*, *Vysokomol. Soedin., Ser. A*, 1985, vol. 27, no. 8, pp. 1633–1639.
19. Bershtein, V.A., Yakushev, P.N., Karabanova, L., *et al.*, *J. Polym. Sci., Polym. Phys.*, 1999, vol. 37, no. 4, pp. 429–441.
20. Lipatov, Yu.S., *J. Macromol. Sci., Rev. Macromol. Chem. Phys.*, 1990, vol. 30, no. 2, pp. 209–216.

Russian Journal of Applied Chemistry, Vol. 75, No. 5, 2002, pp. 805–810. Translated from Zhurnal Prikladnoi Khimii, Vol. 75, No. 5, 2002, pp. 823–828.
Original Russian Text Copyright © 2002 by Bochek, Gofman, Sukhanova, Vylegzhanina, Kuznetsov.

MACROMOLECULAR CHEMISTRY AND POLYMERIC MATERIALS

Microporous Polyimide Films Based on Blends of Polyamido Acid and Cellulose Derivatives

A. M. Bochek, I. V. Gofman, T. E. Sukhanova, M. E. Vylegzhanina, and Yu. P. Kuznetsov

Institute of Macromolecular Compounds, Russian Academy of Sciences, St. Petersburg, Russia

Received June 1, 2001; in final form, November 2001

Abstract—The effect of a blowing agent, cellulose diacetate, on the structural nonuniformity and physicomechanical properties of polyimide films was studied by thermogravimetric analysis and scanning electron microscopy. Changes in the gas permeability of the films in the course of thermal degradation of the blowing agent were estimated. The feasibility was demonstrated of using these films for fabrication of composite membranes.

Membrane processes are widely used in various branches of industry for separation and purification of liquids and gases. Polymer membranes used as filters are characterized by a wide range of pore size: from 0.001 to 1 μm. Such membranes are produced by various procedures, including addition to the initial forming solutions of polymeric blowing agents, followed by their removal in the course of precipitation or heating. The latter procedure is used, in particular, for production of microporous membranes based on aromatic polyimides (PIs) [1]. In this case, thermal cyclization of PI prepolymer, polyamido acid (PAA), is combined with removal from the film of residual solvent and blowing agent. In this case, blowing agents with a high boiling point are chosen, such as phenanthrene, α-chloronaphthalene, etc. The microporous membranes prepared by this procedure are of interest primarily for filtration of corrosive liquid or gaseous media at high temperatures, thanks to unique properties of aromatic PIs [2–4]. Also, membranes based on PIs can be used as supports in forming diffusion composite membranes. An advantage of such chemically resistant supports is that forming of the diffusion layer from a solution of another (chemically different) polymer can be performed using any solvents.

The goal of this work was to prepare microporous polyimide films from blens of PAA with a polymeric blowing agent, cellulose diacetate (CDA). We have studied the features of thermal degradation of CDA in the course of thermal cyclization of PAA and the influence of this additive on the physicomechanical properties, structural characteristics, and gas permeability of porous polyimide films.

EXPERIMENTAL

As the initial material we used 20% solution of poly-4,4'-oxydiphenylenepyromellitamido acid (PAA–PM) (Plastik Research and Production Association, Moscow), to which a 10% solution of CDA in DMF was added. The degree of polymerization of CDA was 570, and the degree of substitution, 2.37.

The compatibility of PAA-PM and CDA solutions was studied photocolorimetrically with a KFK-2 device at 20°C and λ = 670 nm. On mixing of dilute (2%) solutions of PAA-PM and CDA in any proportions, the optical density of solutions did not increase, whch indicates that the solutions are compatible. However, addition of even small amounts of a more concentrated (10%) CDA solution to a concentrated (20%) PAA-PM solution caused phase separation, detected visually (turbidization) and photocolorimetrically. An emulsion of CDA in PAA-PM solutions was formed.

Unfortunately, the full compatibility of dilute solutions of PAA and CDA is of little practical use, because drying of solutions in the course of film preparation is accompanied by a continuous growth of the concentration and inevitably leads to the phase separation. Therefore, in the subsequent experiments we used a 20% solution of PAA-PM and a 10% solution of DA in DMF. It should be noted that the occurrence of phase segregation requires thorough choice of the

1070-4272/02/7505-0805$27.00 © 2002 MAIK "Nauka/Interperiodica"

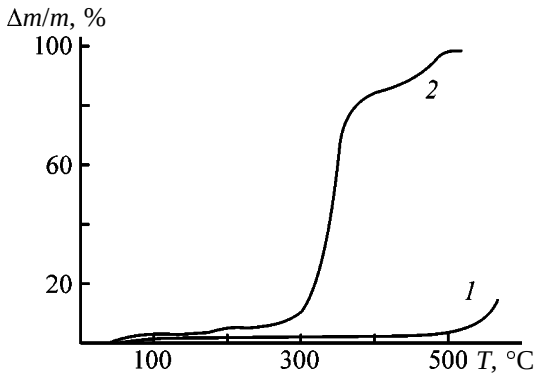

Fig. 1. Weight loss $\Delta m/m$ of (*1*) PM and (*2*) CDA films on heating. Heating rate 5 deg min^{-1}; the same for Fig. 2. (*T*) Temperature; the same for Fig. 2.

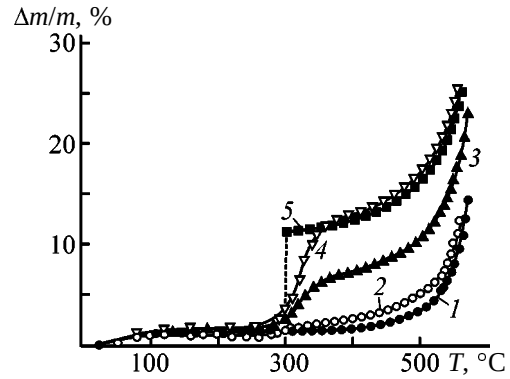

Fig. 2. Weight loss $\Delta m/m$ on heating of polyimide films prepared from PM with addition of CDA. CDA content in the initial polymer blend, %: (*1*) 0, (*2*) 3.25, (*3*) 15, and (*4*, *5*) 30. (*5*) In the course of heating, the sample was kept at 300°C for 3 h.

conditions for preparing the initial solutions of the polymer blends.

Solutions of PAA-PM and CDA were mixed with an ultrasonic disperser and mechanically, with a glass stirrer. In the former case, the solutions strongly warmed up, and even short sonication resulted in a sharp decrease in the viscosity, indicating unacceptable decrease in the molecular weight of PAA-PM. The PI films prepared by this method exhibit poor mechanical characteristics: even at low (<5%) CDA concentrations in a PAA-PM–CDA blend, the resulting PI films were brittle and unsuitable for use. Therefore, in the subsequent experiments we used a stirrer.

PAA-PM–CDA films were prepared by casting of solutions onto glass supports with a laboratory die, followed by drying at 80°C. Thermal cyclization of PAA in films, accompanied by thermal degradation of CDA and removal of the degradation products from the films, was performed under conditions of step heating (50°C steps, keeping at each temperature for 0.5 h). Initially, cyclization was performed in a vacuum. Cyclized films differ from common PI films by considerably enhanced adhesion to glass; therefore, cyclization was performed with a free film of dried PAA after its separation from the support. An additional advantage of cyclization under such conditions is easier removal of CDA thermal degradation products from the film.

To optimize the conditions for film preparation, it was necessary to determine the best conditions for the heat treatment, and primarily the final temperature. To complete the cyclization of PAA, the temperature should not be lower than 300°C. At the same time, on heating the films above 400°C PI starts to degrade [2]. Within this interval, it was necessary to find a temperature ensuring sufficient extent of CDA degradation and complete removal of the degradation products from the film.

To find conditions for CDA degradation, films prepared from PAA-PM–CDA blends and heated for cyclization at 300°C (lower boundary of the temperature range of interest), and also films of pure CDA and PM were studied by thermogravimetric analysis (TGA).

The weight loss curves obtained with PM and CDA are shown in Fig. 1. The CDA film was cast from a solution in DMF with subsequent vacuum drying at 150°C to constant weight (16 h). The PM film was prepared under the same conditions as films from the PM–CDA blend (cyclization at 300°C). Active decomposition of CDA with release of volatiles starts at 250–280°C (Fig. 1, curve *2*). The process sharply accelerates on heating to 300°C, above the glass transition point T_g. By the moment of reaching the temperature of 380°C, more than 80% of CDA passes into the gas phase. After that, the release of volatiles continues with a lower intensity and is accelerated again at 450°C. At 500°C, the sample fully decomposes, and the degradation products pass to the gas phase. The weight loss of the PM film becomes noticeable only above 450°C.

In PI films prepared from PAA-PM–CDA blends, intense weight loss is observed at temperatures from 300 to 360–380°C (Fig. 2). The lower temperature boundary of the weight loss depends on the thermal history of the sample. Since the weight of pure PM films does not change noticeably in this temperature range, this process can be attributed with confidence to removal of volatile products of CDA thermal degradation. It is seen that, after heating at 300°C, a significant amount of CDA remains in the films (Table 1); the degradation products of the residual CDA are actively removed on heating to 360–380°C.

Figures 1 and 2 show that efficient removal of volatile products of CDA degradation is ensured by heating the films to 380°C. However, mechanical tests of the films (Table 2) show that introduction of CDA into PAA-PM results in considerably decreased elongation at break ε_b of the polyimide film. The same effect is observed when the heat treatment of the films is completed at higher temperatures. The practically acceptable value of ε_b of the films should be no less than 5–6%. When the heating is completed at 300°C, ε_b reaches this minimal value at 30% content of CDA in PAA-PM. The TGA data show that the amount of CDA remaining in the films at 300°C is significant. When the heat treatment is completed at higher temperatures, the elongation at break decreases to an unacceptable level.

To optimize the heat treatment conditions, we performed an experiment on isothermal heating in a self-generated atmosphere of films whose cyclization was completed at 300°C (initial CDA content in PAA film 30%). Additional heating was performed in the course of thermogravimetric tests. At 300°C, the heating was stopped, and the film was kept at this temperature to constant weight. The results are shown in Figs. 2 and 3. It is seen that such conditions ensure the maximum possible removal of products of DCA thermal oxidative degradation. However, the total weight loss due to removal of CDA degradation products from the film is somewhat lower than the content of CDA in the initial films. This may be due to several factors: the presence of ash in film pores after CDA carbonization, the presence of residual CDA in closed or blind pores, and partial removal of CDA degradation products from the films already in the stage of thermal cyclization performed by heating to 300°C.

Our results show that, to efficiently remove CDA from PM films, heat treatment in air (i.e., thermal oxidative degradation of CDA), rather than heating in a vacuum, is preferable. Therefore, in the subsequent experiments we chose a procedure involving cyclization of PAA in air followed by isothermal heating of the film in air at the final temperature of cyclization. Under such conditions, we attained efficient removal of CDA from the film without its heating above 300°C. In the process, the elongation at break remained sufficiently high.

The mechanical and thermomechanical tests of the films were performed with a UTS 10 universal installation (UTS Testsysteme, Germany). In the course of tensile tests at room temperature, we determined the modulus of elasticity E, tensile strength σ_t, induced hyperelasticity limit σ_h, and elongation at break ε_b.

Table 1. Characteristics of the heat resistance of polyimide films prepared from PAA with additions of CDA (cyclization completed at 300°C)

CDA content in initial PAA, %	$\Delta m/m$, %	T_1	T_5	T_{10}
		°C		
0	–	467	541	562
3.25	1	451	534	557
15	5.6	421	509	547
30	10.7	410	496	531

* ($\Delta m/m$) Weight loss in the course of TGA of cyclized films (before the onset of polyimide thermal degradation); (T_1, T_5, T_{10}) temperatures corresponding, respectively, to 1, 5, and 10% weight loss of PI films in the course of TGA (Figs. 1, 3).

Table 2. Mechanical and thermomechanical characteristics of polyimide films prepared from PAA with additions of CDA*

Sample no.**	CDA content in initial mixture, %	E, GPa	σ_h, MPa	σ_p, MPa	ε_b, %	T_g, °C
1	0	2.51	101	140	106	356
2	3.25	2.42	96	106	30	350
3	15	2.35	82	87	19	340
4	30	2.01	–	57	6	330
5	30	2.39	–	41	2	–
6	30	2.24	–	63	6	353

* (E) Modulus of elasticity, (σ_h) induced hyperelasticity limit, (σ_t) strength, and (ε_b) elongation at break.

** Sample nos. 1–4: cyclization at 300°C; sample no. 5: cyclization at 400°C; sample no. 6: cyclization at 300°C followed by heating in air at 300°C for 2 h.

In the course of heating at a rate of 5 deg min^{-1}, we determined the glass transition point T_g.

Our results (Table 2) demonstrate high level of the strength characteristics of the films. Although, as

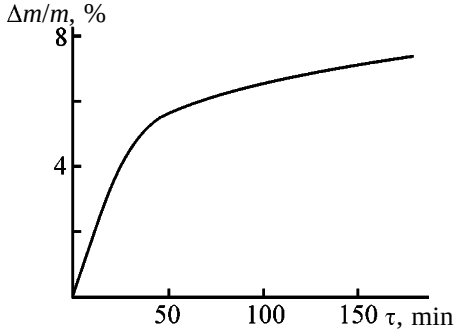

Fig. 3. Weight loss $\Delta m/m$ of a PM film, prepared from PAA with addition of 30% CDA by heating in a vacuum to 300°C, in the course of subsequent isothermal heating in air at 300°C (Fig. 2, curve *5*). (τ) Heating time.

noted above, increased content of CDA in the initial blend results in noticeable decrease in the elongation at break and hence in the strength of the polyimide film, in all cases the σ_t values remain acceptable for practice.

The results of the tests (Table 2) show that addition of CDA to PAA affects the structure of the PI formed by cyclization: plasticization effects are observed. Indeed, as the initial concentration of CDA in PAA is increased, the modulus of elasticity, induced hyperelasticity limit, and glass transition point of the polyimide films monotonically decrease.

To confirm this conclusion, PM films prepared from PAA-PM with addition of 30% CDA and heated in the course of imidization to 300°C in a vacuum were additionally heated in air for 2 h at 300°C. It was shown that such a heating allows more complete removal of CDA degradation products from the film. After the repeated heat treatment, the modulus of elasticity and the glass transition point of the film increase (Tale 2, sample no. 6).

As the concentration of CDA in PAA is increased, the heat resistance of PI films noticeably decreases (Table 1). For example, as the CDA concentration is increased from 0 to 30%, the temperature T_5, corresponding to 5% weight loss of the film in the course of TGA, decreases by 45°C. Since at these temperatures the film contains neither residual CDA nor gaseous products of its degradation, we can suggest that the presence of CDA or initial products of its degradation affects the PI structure at the cyclization stage. At the same time, in all cases the heat resistance of the films remains sufficiently high.

We have estimated the pore concentration in the films from comparison of their density with that of the pure PM film. This was necessary, in particular, for correct calculation of the film strength parameters (E, σ_h, σ_t) from the results of mechanical tests. We found that the volume concentration of pores in the materials was insignificant. For example, the density of PM films prepared from pure PAA was ρ = 1.403 g cm^{-3}, whereas the density of PI films prepared from the blend of PAA with 30% CDA was 1.385 g cm^{-3}.

The morphology of the films prepared from PAA-PM–CDA blends was studied by scanning electron microscopy with an Akashi MSM-V device (Japan). Prior to microscopic examination, the sample surface was coated with a 20-nm gold layer by thermal vacuum sputtering (VEF device, Akashi, Japan). The electron micrographs of both surfaces and transverse chips of the films were obtained, and the pore size and pore distribution across the thickness of the films prepared under different conditions were determined.

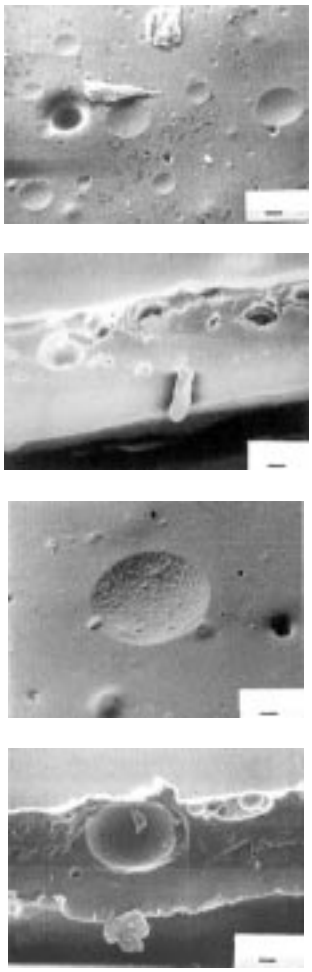

Fig. 4. Electron micrographs of polyimide films prepared from PAA-PM–CDA blends (CDA content 30%) and heated to (a, b) 300 and (c,d) 400°C. (a, c) Free surface and (b, d) transverse chip. The bars correspond to 10 μm.

The electron micrographs of the upper (free) and lower (contacting the support in the course of casting) surfaces of the films heated to 300°C show that the structure of the films is highly nonuniform. The upper surface has a rough relief (Fig. 4a), with open pores 2–10 μm in diameter and spherical pits of 10–40 μm size, probably originating from degradation of coarse CDA particles. A large amount of open pores is also observed on the lower surface of the film; these pores were probably produced by release of volatiles from the film (1–3-μm pores) and degradation of coarse aggregated CDA particles (larger, 10–30-μm, pores).

On the transverse chip (Fig. 4b), we see close pores 2–20 μm in diameter, concentrated mainly in

Table 3. Permeability *P* for oxygen and nitrogen of polyimide films prepared from blends with different CDA content

Sample no.	CDA content, %	Heating to indicated *T*, °C (vacuum)	*P*, barrer*		$\alpha = P(O_2)/P(N_2)$
			$P(O_2)$	$P(N_2)$	
1	0	280	0.22	0.048	4.6
2	15	300	0.1	0.05	2
3	30	300	5.5	4.8	1.14
4	2.4	400	262	250	1.05
5	15	400	660	625	1.05
6	15	300 + 2 h at 300**	721	673	1.07
7	0	285**	0.61	0.1	6.1
8	10, phenanthrene	3 h at 100** + 5 h at 200**	$P(H_2) = 81\,000$		2.1 (H_2CO)

* 1 barrer = 1×10^{-10} cm^3 cm cm^{-2} cm^{-1} Hg.
** In air.

the sample layers adjacent to the free surface, which suggests partial segregation of the PAA-PM–DCA blend. The presence of very large pores of 50–60 μm size is indicative of inefficient dispersion of CDA in the blend.

After heating to 400°C, the general morphology of the film surface does not change (Fig. 4c), but the pores undergo contraction. In the section view (Fig. 4d), we see close pores, which are distributed across the sample thickness more uniformly than in the previous case. On the inner surface of coarse pores, there are residues of carbonized degradation products of coarse CDA particles. Apparently, the differences in the morphology of the chips are due to nonuniform distribution of CDA throughout the bulk of the initial film, rather than to changed conditions of the heat treatment.

To assess the possibility of using these materials as membranes, we determined their gas permeability. For the PI films prepared from blends with different initial content of CDA and heat-treated at different temperatures, we determined the permeability coefficients *P* for oxygen and nitrogen by a chromatographic procedure with a PGD-1 device at a pressure differential of 1 atm. The data obtained (Table 3) are compared with the permeabilities of the nonporous PM film [5] and of the porous film obtained from PAA-PM with phenanthrene as blowing agent [1] (sample nos. 7 and 8, respectively).

Table 3 shows that, for the films prepared from blends containing up to 15% CDA and heated in a vacuum to 300°C, the gas permeability is comparable to that of a pure PM film. As the CDA concentration is increased to 30%, with the same treatment conditions, *P* increases by 1–2 orders of magnitude, and the gas selectivity is lost, which is probably caused by an increase in the free volume due to thermal degradation of CDA. This trend is manifested still more strongly in samples from which CDA was removed to a maximal extent (heating to 400°C, prolonged isothermal heating at 300°C in air, sample nos. 4–6). The permeability of such samples increases by more than three orders of magnitude, the selectivity is also lost, but the films exhibit barrier properties with respect to water and ethanol at pressures of up to 4 atm.

Along with the characteristics of the films prepared by us, we also present in Table 3 the published data on the gas permeabillity of microporous PI films (sample no. 8) prepared as described in [1]. These films show a considerably higher (by two orders of magnitude) gas permeability than the films prepared by us. This fact, in combination with the morphological features of the films considered above and with their barrier properties with respect to liquids, allows certain conclusions about the causes of the observed effects.

Increase in the gas permeability by 3–4 orders of magnitude as a result of CDA removal from the film is mainly due to formation of large amounts of close (blind) pores observed on the transverse chip. At the same time, the lack of gas selectivity suggests formation of through channels; however, their amount per unit surface area is apparently low.

Thus, the films prepared are hardly suitable as filtering materials. At the same time, fairly high gas permeability in combination with high levels of chemical stability, mechanical strength, and heat resistance makes these films promising as supports for compo-

site diffusion (gas separation or pervaporation) membranes. It seems feasible to apply to the surface of such supports diffusion coating layers of various polymers, including those similar to PAA, with subsequent thermal cyclization.

CONCLUSIONS

(1) Mixing of solutions of cellulose diacetate and poly-4,4'-oxydiphenylenepyromellitamido acid, followed by degradation of cellulose diacetate in the course of thermal cyclization of the polyamido acid, allows preparation of porous polyimide films.

(2) Additions of cellulose diacetate to the initial solution of poly-4,4'-oxydiphenylenepyromellitamido acid affect the heat resistance and physicomechanical properties of the cyclized polyimide films.

(3) The procedure for preparing the initial solutions of poly-4,4'-oxydiphenylenepyromellitamido acid and cellulose diacetate and the imidization conditions strongly affect the shape and size of pores and their distribution in the polymer matrix.

(4) The gas permeability for nitrogen and oxygen of the polyimide films prepared from blends of poly-4,4'-oxydiphenylenepyromellitamido acid and cellulose diacetate was studied. These microporous films are suitable as strong, heat-resistant, and chemically stable supports for multilayer composite diffusion membranes.

REFERENCES

1. JPN Patent Appl. 57-170936.
2. Bessonov, M.I., Koton, M.M., Kudryavtsev, V.V., *et al.*, *Poliimidy – klass termostoikikh polimerov* (Polyimides: A Class of Heat-Resistant Polymers), Leningrad: Nauka, 1983.
3. Kochi, M., Isoda, S., Yokota, R., *et al.*, *Polyimides: Synthesis, Characterization, and Applications*, Mittal, K.L., Ed., New York: Plenum, 1984, vol. 2, pp. 671–682.
4. *Polyamic Acids and Polyimides: Synthesis, Transformations, and Structure*, Bessonov, M.I. and Zubkov, V.A., Eds., Boca Raton: CRC, 1993.
5. Kim, T.H., Koros, W.J., Husk, G.R., *et al.*, *J. Membrane Sci.*, 1988, vol. 37, pp. 45–62.

Russian Journal of Applied Chemistry, Vol. 75, No. 5, 2002, pp. 811–813. Translated from Zhurnal Prikladnoi Khimii, Vol. 75, No. 5, 2002, pp. 829–831.
Original Russian Text Copyright © 2002 by Gogotov, Parilova, Khaliullin.

MACROMOLECULAR CHEMISTRY AND POLYMERIC MATERIALS

Inhibition of Styrene Thermal Polymerization by Formulations Based on Quinone Dioxime and Sterically Hindered Phenols

A. F. Gogotov, M. V. Parilova, and A. K. Khaliullin

Angarsk Petrochemical Company, Joint-Stock Company, Angarsk, Irkutsk oblast, Russia
Favorskii Institute of Chemistry, Siberian Division, Russian Academy of Sciences, Irkutsk, Russia

Received December 4, 2001

Abstract—A formulation based on quinone dioxime and a mixture of sterically hindered phenols *tert*-butylpyrocatechol–2,2'-methylenebis(6-*tert*-butyl-4-methylphenol) (Agidol-2) was suggested for inhibiting terpolymerization of styrene.

Styrene, like many other monomers, extremely readily polymerizes on heating; therefore, its industrial distillation should be performed in the presence of inhibitors. At Russian styrene-producing plants, the most widely used and reliable inhibitor of styrene thermal polymerization is *p*-quinone dioxime (QD) [1, 2]. a typical scavenger of alkyl radicals. It is used in combination with various synergistic additives [3]. In other countries, there has been a trend toward using various soluble inhibiting systems based on more effective compounds, in particular, on inhibitors of the latest generation, nitroxyl radicals [4]. Many of the modern inhibiting systems are not commercially produced in Russia, and therefore research groups at the enterprises make efforts to improve commercially used QD-containing formulations, with the aim to enhance their performance and decrease the consumption of the main inhibitor. Such drawbacks of QD as poor solubility in aromatic hydrocarbons and high cost are a common knowledge.

The goal of this study was to extend the range of inhibiting formulations, to decrease the QD consumption, and to enhance the efficiency of inhibiting thermal polymerization of styrene in the course of its distillation from process solutions.

The performance of the inhibiting formulations was evaluated under laboratory conditions using pure freshly distilled styrene; experiments were performed without passing an inert gas. The temperature in all the experiments was maintained at 119 ± 1.5°C. The heating time after adding an inhibitor or inhibiting formulation was 7 h. The polymer yield was determined by taking samples at 1-h intervals and distilling off the unchanged monomer on a boiling water bath at reduced pressure (20 mm Hg). The experimental results are listed in the table.

One of the possible ways to improve the performance of inhibiting formulations is the use of QD in combination with various coinhibitors, most often phenolic compounds, exhibiting a synergistic effect [3]. Some of such formulations were suggested previously, e.g., QD + sterically hindered phenols (SHPs) [5, 6] (run no. 5), QD + methoxylated phenols [7, 8] (run no. 6), and QD + fraction of dihydric phenols from coke-chemical production (pyrocatechol fraction, PCF) [9, 10] (run nos. 7, 8). With these formulations, the efficiency of inhibiting thermal polymerization of styrene was considerably enhanced, but the consumption of QD was not appreciably reduced. The highest inhibiting efficiency was observed at a QD consumption of 0.017–0.011 wt % relative to styrene. Better results, with a decrease in consumption of the main inhibitor, were attained by using as a coinhibitor *N*,*N*-dimethyl-3,5-di-*tert*-butyl-4-hydroxybenzylamine (Mannich base, MB). For example, with the formulation QD + MB + SHP [2], the QD consumption was as low as 0.002–0.003 wt % relative to styrene, although the optimal level in commercial production of styrene is somewhat higher: 0.0046–0.006 wt % (run no. 11). Nevertheless, even such consumptions are lower by a factor of 3–4 than those of the previously used formulations. Run no. 10 shows that straight QD, when taken in such amounts, does not ensure the required inhibiting effect.

One of the possible ways to decrease the QD consumption is increasing the content of coinhibitors in the system. Actually, as the consumption of QD as an individual inhibitor is decreased, the inhibition effi-

1070-4272/02/7505-0811$27.00 © 2002 MAIK "Nauka/Interperiodica"

Choice of optimal conditions of adding components of the inhibiting formulation

Run no.	Components of inhibiting formulation, wt % relative to styrene*	Polymer yield, %, at indicated heating time, h					
		2	3	4	5	6	7
1	QD, 0.03	0.31	0.47	1.22	2.57	5.25	14.6
2	QD, 0.03 + PNP, 0.03	0.52	0.81	1.54	3.87	8.80	12.1
3	QD, 0.017	0.62	0.95	1.82	5.00	11.1	19.9
4	QD, 0.017 + PNP, 0.017	0.52	1.10	4.74	11.1	20.6	23.7
5	QD, 0.017 + (PNP, 0.017), 2 h	0.62	0.99	4.32	8.60	14.3	17.1
6	QD, 0.017 + (TBPC, 0.005 + Ionol, 0.001), 2 h	0.62	1.16	2.39	4.91	8.93	9.72
7	QD, 0.017 + PSBP, 0.017, 2 h	0.23	0.33	0.52	0.73	0.91	1.56
8	QD, 0.011 + PCF, 0.005, 2 h	0.28	0.42	0.54	0.68	0.75	1.58
9	QD, 0.017 + PCF, 0.005, 2 h	0.31	0.35	0.37	0.66	0.87	1.06
10	QD, 0.0046	0.26	0.89	4.72	16.7	29.3	–
11	QD, 0.0046 + 0.2(MB, 0.023 + PNF, 0.012) + 0.8(MB + PCF), 2 h	0.20	0.78	1.52	3.46	9.54	18.0
12	QD, 0.0046 + 0.2(MB, 0.023 + PCF, 0.012) + 0.8(MB + PCF), 2 h	0.19	0.32	0.35	0.45	0.55	0.85
13	QD, 0.004 + 0.2(A-2, 0.015 + TBPC, 0.023) + 0.8(A-2 + TBPC), 2 h	0.25	0.32	0.40	0.60	0.62	0.77
14	QD, 0.004 + 0.2(A-2, 0.01 + TBPC, 0.015) + 0.8(A-2 + TBPC), 2 h	0.29	0.38	0.49	0.63	0.83	1.17
15	QD, 0.004 + 0.2(A-2, 0.023 + TBPC, 0.015) + 0.8(A-2 + TBPC), 2 h	10.3	44.1	–	–	–	–
16	QD, 0.00144 + 0.3(A-2, 0.015 + TBPC, 0.023) + 0.7(A-2 + TBPC), 2 h	0.08	0.26	0.37	0.52	0.63	0.75
17	QD, 0.00099 + 0.4(A-2, 0.015 + TBPC, 0.023) + 0.6(A-2 + TBPC), 2 h	0.14	0.23	0.36	0.40	0.55	0.61

* (PNF) *p*-Nitrophenol, (TBPC) *tert*-butylpyrocatechol, (PSBP) *p-sec*-butylphenol, (PCF) pyrocatechol fraction, (MB) Mannich base, and (A-2) Agidol-2.

ciency increases; when QD is used without coinhibitors, it should be taken in increased amounts to attain the required effect (see table, run nos. 1, 3, 6). The QD consumption can be decreased by using PNP as coinhibitor and by choosing appropriate dosage mode (simultaneously with the main inhibitor or in portions at definite time intervals; run nos. 2, 4, 5).

Experiments showed that the inhibition efficiency can be enhanced by replacing less active coinhibitors by more active agents. An example is replacement of PNP, a relatively low-effective component of the QD + PNP formulation [1], by a synergistic mixture of mono- and dihydric SHPs, namely, TBPC and Ionol (weight percentage of QD, TBPC, and Ionol relative to styrene 0.017, 0.005, and 0.001, respectively [5]).

With another inhibiting system consisting of QD, MB, and PCF ([11] (run no. 12), the polymer yield was considerably reduced as compared to the similar system containing PNP instead of PCF [2] (run no. 11); the percentages of QD, MB, and PNP or PCF were varied within 0.0023–0.0046, 0.012–0.023, and 0.006–0.023, respectively. When the QD consumption is reduced to so great extent, it is very important to ensure stable inhibiting effect. However, the performance of the QD + MB + PNP system drastically decreases even at a slightly reduced content of the main inhibitor, and the inhibiting effect is observed only during a relatively short time.

Therefore, we suggested an inhibiting formulation allowing the consumption of QD to be reduced further. This formulation exhibits stable performance and effectively suppresses styrene polymerization. It includes QD as the main inhibitor and a mixture of 2,2'-methylenebis(6-*tert*-butyl-4-methylphenol) (Agidol-2) with TBPC as a coinhibiting and antioxidant component. With this system, the QD consumption could be decreased to 0.001 wt % and even lower value. As compared to the formulation QD + MB + PNP, the consumption of phenols (0.038 wt %) differed insignificantly from that of MB + PNP (0.035 wt %), and

the QD consumption was somewhat lower (0.004 against 0.0046 wt %).

In the new formulation (run no. 13), as compared to QD + MB + PCF (run no. 12), we replaced MB and PCF by a mixture of Agidol-2 (a monohydric bisphenol) and TBPC (QD + A-2 + TBPC). It is noted in the literature [12] that replacement of mononuclear phenolic compounds in inhibiting systems by binuclear compounds (e.g., diphenylolpropane) enhances the inhibiting power of the formulations. Data obtained in run no. 13 show that such a replacement, indeed, somewhat improves the results (the yield of the polymer in 7 h decreased from 0.85 to 0.77%). When the total concentration of the inhibitors is reduced, with their ratio and the QD concentration remaining the same, the results get worse (run no. 14). Increase in the amount of Agidol-2 (run no. 15), with the amount of QD being the same, drastically weakens the inhibiting power of the formulation.

As seen from the table, replacement of a mixture of MB and PCF (run no. 12) by the above-mentioned SHP mixture (run nos. 16, 17) enhances the inhibiting effect and allows the consumption of QD to be reduced to 0.00144–0.00099 wt % relative to the monomer, whereas with the QD + MB + PCF system the QD consumption can be reduced only to 0.004 wt % at a relatively high consumption of the sum of the inhibitors (0.035 wt %). Experiments showed that decrease in the consumption of the main inhibitor requires certain compensation, i.e., increase in the consumption of the coinhibitors loaded simultaneously with QD. The reduce the consumption of QD, the larger amount of coinhibitors should be added. The best results are obtained when 30–40% of the coinhibitor mixture is added simultaneously with QD, and the remaining amount, after 2 h. Our experiments also showed that the optimal ratio of TBPC to A-2 is 1.5 : 1, i.e., the consumption of the dihydric phenol in such formulations should be higher than that of the monohydric phenol; the total consumption of the phenols is 0.025–0.038 wt %. It is seen that the best result can be attained at a lower consumption of the main inhibitor (run nos. 13, 16, 17).

Thus, our experiments showed that further decrease in the QD consumption in inhibiting formulations preventing thermal polymerization of styrene in the course of its distillation is quite feasible and can be attained both by using more effective coinhibitors and by varying the relative amounts of the inhibitor and coinhibitors at their initial simultaneous loading.

CONCLUSION

In inhibiting thermal polymerization of styrene, the consumption of the main inhibitor (quinone dioxime) can be considerably reduced, without decreasing the inhibition efficiency, by using quinone dioxime in combination with two sterically hindered phenols: *tert*-butylpyrocatechol and 2,2'-methylenebis(6-*tert*-butyl-4-methylphenol) (Agidol-2). The optimal ratio of the phenols in the mixture and the optimal amount of coinhibitors added simultaneously with quinone dioxime were determined.

REFERENCES

1. USSR Inventor's Certificate no. 441263.
2. USSR Inventor's Certificate no. 968041.
3. Denisov, E.T. and Kovalev, G.I., *Okislenie i stabilizatsiya reaktivnykh topliv* (Oxidation and Stabilization of Jet Fuels), Moscow: Khimiya, 1983.
4. Jones, C., *Chem. Week*, 1996, vol. 158, no. 49, p. 32.
5. RF Patent 2129112.
6. Gogotov, A.F., Novichikhin, D.N., Voitik, V.S., *et al.*, *Neftepererab. Neftekhim.*, 1999, no. 12, pp. 34–36.
7. RF Patent 2138473.
8. Gogotov, A.F., Batura, I.I., Voitik, V.S., *et al.*, *Neftepererab. Neftekhim.*, 1999, no. 12, pp. 23–26.
9. RF Patent 2136646.
10. Gogotov, A.F., Novichikhin, D.N., Voitik, V.S., *et al.*, *Neftepererab. Neftekhim.*, 1999, no. 10, pp. 23–27.
11. RF Patent 2152377.
12. Karakuleva, G.I., Vinogradova, I.V., Belyaev, V.A., *et al.*, *Ingibirovanie polimerizatsii diolefinov v protsessakh ikh vydeleniya i khraneniya: Obzor* (Inhibition of Diolefin Polymerization in the Course of Isolation and Storage: Review), Moscow: TsNIITEneftekhim, 1974.

Russian Journal of Applied Chemistry, Vol. 75, No. 5, 2002, pp. 814–817. Translated from Zhurnal Prikladnoi Khimii, Vol. 75, No. 5, 2002, pp. 832–835.
Original Russian Text Copyright © 2002 by Ostanina, Dul'tseva, Suvorov, Chupakhin.

MACROMOLECULAR CHEMISTRY AND POLYMERIC MATERIALS

Polymers Based on Epoxy Resins and Functional Derivatives of Polychlorobiphenyls

N. Yu. Ostanina, L. D. Dul'tseva, A. L. Suvorov, and O. N. Chupakhin

Institute of Organic Synthesis, Ural Division, Russian Academy of Sciences, Yekaterinburg, Russia

Received November 13, 2001; in final form, January 2002

Abstract—A new way to utilize polychlorobiphenyls was suggested: transformation of Sovol base hydrolysis products into glycidyl ethers and titanates. The resulting products were tested as components of epoxy compounds which are subsequently cured to obtain three-dimensional polymer networks.

The problem of rendering harmless polychlorobiphenyls (PCBs), which were widely used in various branches of industry, is extremely urgent, because these compounds are stable ecotoxicants. One of the ways to solve this problem is chemical processing (utilization) of PCBs by their functional substitution followed by transformation into useful nontoxic products [1, 2]. In particular, it seems promising to prepare cross-linked polymers from which the diffusion of the components into the environment will be *a fortiori* low.

In this work, we examined the possibility of using glycidyl ethers and titanates prepared from the products of base hydrolysis of Sovol [3, 4] as components of epoxy compounds. Glycidyl ether resins are prepared by treatment with epichlorohydrin of products of Sovol base hydrolysis in ethylene glycol (SEG) or diethylene glycol (SDEG). Titanates SEG-Ti and SDEG-Ti are prepared by interchange of tetrabutoxytitanium with the ethers produced by Sovol hydrolysis. The compositions of these compounds correspond to the formulas

$$C_{12}H_{4.09}Cl_{4.74}(OH)_{0.46}(OCH_2CH_2OH)_{0.07}(OCH_2\underset{\backslash\ /}{CH}{-}CH_2)_{0.64}\quad \text{SEG}$$
$$O$$

$$C_{12}H_{4.69}Cl_{3.61}(OH)_{0.79}(OCH_2CH_2OCH_2CH_2OH)_{0.64}(OCH_2\underset{\backslash\ /}{CH}{-}CH_2)\quad \text{SDEG}$$
$$O$$

$$Ti[(O)_{0.8}C_{12}H_{5.4}Cl_{3.62}(OCH_2CH_2O)_{0.184}]_{3.24}(OC_4H_9)_{0.76}\quad \text{SEG-Ti}$$

$$Ti[(O)_{1.06}C_{12}H_{4.69}Cl_{3.61}(OCH_2CH_2OCH_2CH_2OH)_{0.64}]_{2.86}(OC_4H_9)_{1.14}\cdot$$
$$4.4(OH)_{1.06}C_{12}H_{4.69}Cl_{3.61}(OCH_2CH_2OCH_2CH_2OH)_{0.64}\quad \text{SDEG-Ti}$$

SEG and SDEG were used as active diluents of epoxy copounds with common curing agents such as hexamethylenediamine (HMDA) or isomethyltetrahydrophthalic anhydride (*i*-MTHPA). These ethers were added in amounts of 15–46 wt % into the compounds with HMDA and 30 or 40 wt % into the compounds with *i*-MTHPA.

The titanates SEG-Ti and SDEG-Ti were used themselves as curing agents for epoxy resins. The molar ratio of the resins and titanates was varied from 2 to 32. SEG-Ti is incompatible with the epoxy resin; therefore, it was preliminarily dissolved in Laprol L-503 (a polyether based on propylene oxide).

As epoxy component we took ED-20 commercial resin. The diluent in the reference compound was dibutyl phthalate (DBP). As catalysts we used the complex of BF_3 with *p*-toluidine (UP-605/5) and oligoethylene glycol phthalate titanate (EGPT) [5].

The compound formulations and the properties of

1070-4272/02/7505-0814$27.00 © 2002 MAIK "Nauka/Interperiodica"

Composition and properties of initial compounds and polymers*

Compound no.	Components			T_{gel}	T_g	τ_{sh}, MPa	c_δ, %	Δm, %	y, kJ m^{-2}
	base	diluent	catalyst	°C					
1	ED-20 + HMDA, 5–7	SEG, 15–48	–	<70	45–62	8.4–9.6	74	–	–
2	ED-20 + HMDA, 7	DBP, 15	–	<70	–	14.1	–	–	–
3	ED-20 + *i*-MTHPA 20–25	SEG, 30–40	UP-605/5, 0.5–1	<70	36–61	3.3–4.9	67–77	1.5–14	9.6
4	〃	〃	EGPT, 5	130–150	64–78	–	79–95	2.7–5	–
5	ED-20 + SEG-Ti, 9–44	L-503, 20	–	80–150	34–52	–	75–97	8–33	7.8–15.9
6	ED-20 + SDEG-Ti, 16–54	–	–	110–150	38–67	–	56–92	7–15	1.4–13.9
7	ED-20 + EGPT, 10–50	–	–	160–190	40–90	–	75–100	8	20–50

* (τ_{sh}) Shear strength of steel adhesive joint, (c_δ) gel fraction content, (Δm) weight loss at 250°C (DTA), and (y) specific impact resilience.

the resulting polymers are listed in the table. It is seen that, for the compounds containing, along with the common curing agents, also SEG and SDEG, the gel point T_{gel} is below 70°C for the compound with HMDA and 130–150°C for the compound with *i*-MTHPA. In the case of the systems with *i*-MTHPA, such samples can be obtained only at the ether content not exceeding 30 wt %. At a higher ether content, addition of catalysts is required.

Figure 1 shows the thermomechanical curves (TMCs) of a series of polymers cured with HMDA (curves *1*) and *i*-MTHPA (curves *4–7*) in the presence of SEG as diluent. Curve *1*, lacking the hyperelasticity plateau, refers to the polymer cured with HMDA containing almost 50% SEG. This polymer is characterized by thin cross-linking and poor mechanical strength; the sample is fully deformed even at 100°C. At the SEG content decreased to 30%, highly cross-linked and mechanicaly strong polymers are formed (curves *2*, *3*). Polymers with better properties are formed when the maximal heating temperature is much higher than T_{gel} (curve *2*).

The physicomechanical and thermal properties of the polymers and the content of the gel fraction in the samples cured with HMDA under various conditions are listed in the table. It is seen that the glass transition point T_g varies within 45–62°C, the gel fraction content reaches 74%, and the shear strength of steel adhesive joint is 8.4–9.6 MPa. Although such adhesion strength is lower than that attained in the steel–steel couple with commercially available epoxy compounds, it is sufficiently high for practical use.

Since the working life of the compounds under consideration is short (up to several hours), they are suitable as adhesives to be prepared immediately before use.

The TMCs of the samples cured with *i*-MTHPA (curves *4–7*) indicate formation of highly cross-linked mechanically strong polymers. With EGPT, the glass

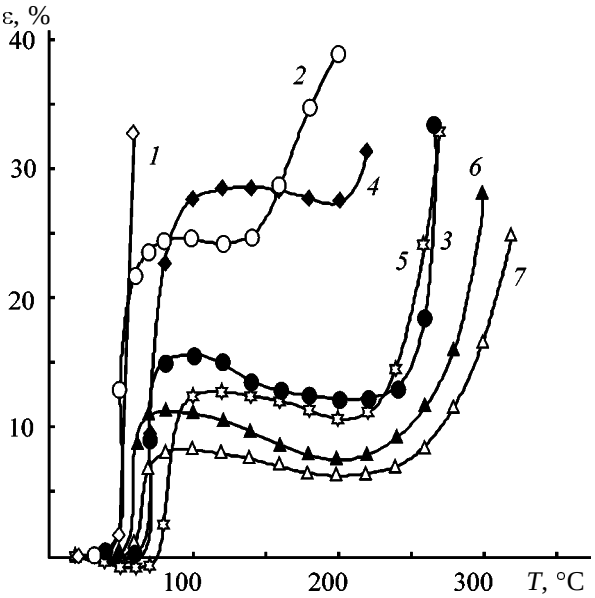

Fig. 1. Thermomechanical curves of the polymers prepared from various compounds. (ε) Deformation and (*T*) temperature. Compound: (*1–3*) ED-20–HMDA–SEG and (*4–7*) ED-20–*i*-MTHPA–SEG. SEG content, %: (*1*) 47.5, (*2*, *3*, *5*, *7*) 30.0, and (*4*, *6*) 40.0. T_{max}, °C: (*1*, *3–7*) 180 and (*2*) 70. Catalyst, %: (*4*, *5*) EGPT, 5.0; (*6*, 77) UP-605/5, 0.5.

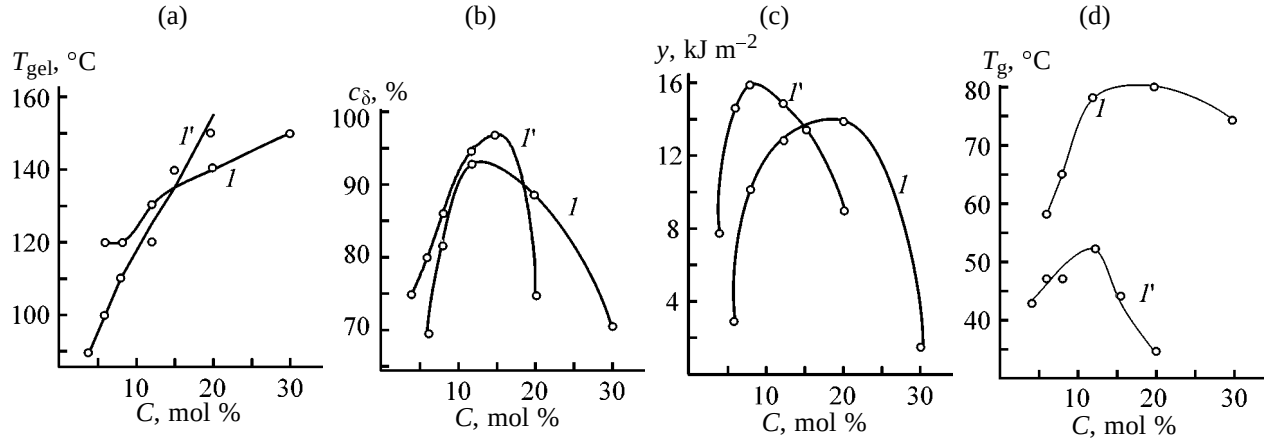

Fig. 2. (a) Gel points of compounds T_{gel} and (b) gel fraction content c_δ, (c) specific impact resilience y, and (d) glass transition point T_g of polymers as functions of the curing agent content c for the compounds containing (*1*) SDEG-Ti and (*1*') SDEG-Ti + L-503.

transition point is higher (curve *4*, *5*), and with UP-605/5, the hyperelasticity plateau is more extended (curves *6*, *7*).

The glass transition points of sample nos. 3 and 4, determined from the TMCs and listed in the table, vary from 36 to 78°C depending on the amount and nature of the catalyst. The τ_{sh} values for these samples are close, irrespective of the composition and curing temperature, and are considerably lower than those for the HMDA-cured systems. The cross-linking in this case is 95% complete. The weight loss in most cases does not exceed 10%. For one of the polymers, we determined the specific impact resilience y, which proved to be sufficiently high: 9.6 kJ m^{-2}.

Thus, the compounds cured with *i*-MTHPA demonstrate a high level of thermal and physicomechanical properties. The polymers prepared in the presence of EGPT are more cross-linked and have higher softening point and higher heat resistance. In contrast to compounds with amines (see table, compound no. 1), the working life of these compounds reaches several days. They can be used as adhesives and are promising as casting compounds.

Figure 2 shows the concentration dependence of the properties of the initial compounds and polymers for the samples in which the titanates themselves are used as curing agents. Figure 2a shows that the gel point of the titanate-containing compounds decreases as the titanate content is increased. The working life of these compounds reaches several months and considerably exceeds the working lives of the above-considered compounds containing SEG or SDEG along with traditional curing agents. The plots of y, T_g, and gel fraction content vs. composition of the initial compound (Figs. 2b–2d) pass through maxima. The highest level of these parameters is attained for the compounds containing 8–25 (for SDEG-Ti) or 8–15 (for SEG-Ti) mol of the resin per mole of the curing agent. Thus, for the polymers cured with SEG-Ti, the optimal properties are attained in a narrower composition range shifted toward higher content of the curing agent. The maximal values of the parameters of the polymers cured with SEG-Ti and SDEG-Ti (see table, compound nos. 5, 6) are fairly high, approximately equal, and close to the parameter values for the previously studied polymers based on epoxy resin and EGPT (compound no. 7), successfully used as adhesives, binders, and casting compounds [6]. The observed differences in the properties of the polymers cured with SEG-Ti and SDEG-Ti, in particular, lower T_g values in the maximum for the polymers based on SEG-Ti (Fig. 2), are due to different chemical nature of the systems.

Thus, we have shown that glycidyl and titanate derivatives of PCBs can be used for preparing epoxy polymers. The resulting products are insoluble, three-dimensionally cross-linked glassy polymers exhibiting hyperelasticity in the range 40–250°C. A wide range of concentrations prividing a high level of physicomechanical and thermal properties of the polymers makes it possible to choose a formulation ensuring the required characteristics of the product. The fairly high level of heat resistance and mechanical properties makes these compounds suitable for practical applications, which opens up a new opportunity to utilize PCBs.

EXPERIMENTAL

Compounds containing HMDA and SDEG-Ti were prepared by mixing the components on heating (50–

70°C), and those containing *i*-MTHPA and SEG-Ti were prepared at room temperature. The ready compounds, except those containing HMDA, were heated in a vacuum (55–80°C) until the foaming ceased. The compounds were cured under conditions with the maximal temperature T_{max} of 70 or 180°C.

The temperature of gelation onset T_{gel} was determined visually as the temperature at which stepwise heating of the compound (10°C steps, 1 h at each temperature) yields an elastic product.

The thermomechanical studies were performed at a constant load of 8 kg cm^{-2}. The thermomechanical curves were plotted as temperature dependences of the deformation ε (%). The glass transition points T_g were determined from TMCs.

The gel fraction content was determined by exhaustive extaction of polymer samples with acetone in a Soxhlet apparatus.

The specific impact resilience was determined with an MK-0.5 pendulum impactor.

The DTA curves were obtained on an OD-102 derivatograph in air in the dynamic mode at a heating rate of 5 deg min^{-1}.

The shear strength of steel–adhesive–steel joints τ_{sh} was determined with a ZDM 5/91 machine.

CONCLUSIONS

(1) Glycidyl ethers and titanates prepared from products of base hydrolysis of Sovol were used for preparing epoxy polymers.

(2) The temperatures of gelation onset, the conditions and extent of curing of the compounds, and the main physicomechanical and thermal characteristics of the polymers were determined in a wide range of the component ratios.

(3) Regular trends were revealed in variation of the polymer properties depending on the qualitative and quantitative compositions of the compounds. The best attained properties are close to those of the known epoxy polymers, which makes the new compounds and polymers suitable for practical use.

ACKNOWLEDMENTS

The study was financially supported by the Russian Foundation for Basic Research (project no. 01-03-96447).

REFERENCES

1. Zanaveskin, L.N. and Aver'yanov, V.A., *Usp. Khim.*, 1998, vol. 67, no. 8, pp. 788–800.
2. Gorbunova, T.I., Zapevalov, A.Ya., Kirichenko, V.E., *et al.*, *Zh. Prikl. Khim.*, 2001, vol. 74, no. 1, pp. 114–117.
3. Kalyuzhnaya, S.A., Yatluk, Yu.G., Suvorov, A.L., and Chupakhin, O.N., Abstracts of Papers, *Ekologicheskie problemy promyshlennykh regionov: Nauchno-tekhnicheskaya konferentsiya v ramkakh mezhdunarodnoi vystavki "Uralekologiya. Tekhnogen. Metallurgiya-2001"* (Environmental Problems of Industrial Regions: Scientific and Technical Conf. in the Framework of Int. Exhibition "Ural Ecology. Technogenic Impact. Metallurgy-2001"), Yekaterinburg, March 28–29, 2001, p. 72.
4. Yatluk, Yu.G., Kalyuzhnaya, S.A., Gorbunova, T.I., *et al.*, Abstracts of Papers, *Ekologicheskie problemy promyshlennykh regionov: Nauchno-tekhnicheskaya konferentsiya v ramkakh mezhdunarodnoi vystavki "Uralekologiya. Tekhnogen. Metallurgiya-2001"* (Environmental Problems of Industrial Regions: Scientific and Technical Conf. in the Framework of Int. Exhibition "Ural Ecology. Technogenic Impact. Metallurgy-2001"), Yekaterinburg, March 28–29, 2001, p. 91.
5. USSR Inventor's Certificate no. 478848.
6. Suvorov, A.L., Dul'tseva, L.D., and Ostanina, N.Yu., in *Tekhnologiya* (Technology), Ser.: *Konstruktsii iz kompozitsionnykh materialov* (Structures from Composite Materials), Interbranch Scientific and Technical Collection of the Russian Research Inst. of Interbranch Information, State Missile Center, and Scientific and Production Association of Applied Mechanics, Moscow, 1996, issue 1, pp. 32–38.

Russian Journal of Applied Chemistry, Vol. 75, No. 5, 2002, pp. 818–821. Translated from Zhurnal Prikladnoi Khimii, Vol. 75, No. 5, 2002, pp. 836–839.
Original Russian Text Copyright © 2002 by Lin, Vorob'eva.

MACROMOLECULAR CHEMISTRY AND POLYMERIC MATERIALS

Transfer of Metal Compounds at Contact Oxidation of Polyethylene on Copper

D. G. Lin and E. V. Vorob'eva

Skorina State University, Gomel, Belarus

Received December 25, 2001

Abstract—Transfer of metal into the polymer bulk during contact oxidation of polyethylene films on a copper support was studied. The metal distribution in the sol and gel fractions of the polymer was determined.

Oxidation of polyethylene at contact with catalytically active metals (including copper) is accompanied by dissolution of the support and transfer of the metal into the polymer bulk [1–3]. This phenomenon, first detected in [4], was confirmed by various methods: visual registration of disappearance of the fine metal layer under the polymer film [4]; measurements of the electrical conductivity of this layer [5]; microscopic study of the disappearance of metal particles in the polymer during its oxidation [6]; IR and ESR spectroscopy of polymer films separated from the metal supports after oxidation [7, 8]; and determination of the metal traces in the ash residue of the polymer sample [9].

The IR spectra of polymeric films containing transferred metal contain absorption bands at 1500–1600 cm^{-1} typical for the ionized carboxy group in metal salts (metal carboxylates). In a polymer, metal carboxylate can occur as both anhydrous salt and hydrate [8]. The experimental results suggest the carboxylate mechanism of transfer of active metals into the oxidizing polymers. Copper carboxylate is detected at fairly large distance, hundreds of micrometers, from the adhesion contact boundary. The mechanism of the metal transfer during contact oxidation of polyethylene is still poorly studied. Two schemes of the metal transfer are assumed [8]: diffusion of low-molecular-weight metal carboxylates or "relay" diffusion of metal ions with participation of the carboxy groups. At present, unambiguous data on what transfer mechanism prevails are lacking. Moreover, data based on the direct measurements of the content of metal transferred into the polymer and its distribution between the gel and sol fractions are lacking; the effect of the oxidative cross-linking of macromolecules on the metal transfer is also poorly understood. In this work, we studied the above problems by the example of polyethylene–copper adhesion composite.

EXPERIMENTAL

We used unstabilized high-density polyethylene prepared at low pressure on complex organometallic catalysts [GOST (State Standard) 16338–85, 20306-005 brand). The 100-μm-thick films were prepared from the polymer powder. The films were then oxidized in the molten state on preliminarily cleaned copper (M1 brand) and aluminum (A99 brand) foils. After oxidation, these films were separated from the supports and used in our tests.

We determined the degrees of oxidation and oxidative cross-linking of the polymer and the content of transferred copper.

The degree of polyethylene oxidation was characterized by the extinction coefficient [the ratio of the optical density to the film thickness (cm)] of the absorption band at 1720 cm^{-1} in the IR spectra of the polymer films.

The degree of oxidative cross-linking of macromolecules was determined as the content of the gel fraction in the sample (%), which was recovered from the polymer after boiling in *o*-xylene for 2 h.

The content of copper in the polymer was determined by polarography [9] using solutions prepared from the ash residue of the polymer. The sample was ashed by a two-stage thermal treatment [10], and the resulting ash residue was dissolved in a supporting electrolyte. The resulting solution was studied on a PU-1 device equipped with a mercury dropping electrode; the copper content was determined using calibration curves. In the quantitative analysis, we

1070-4272/02/7505-0818$27.00 © 2002 MAIK "Nauka/Interperiodica"

used both polymer films separated from the supports and the gel fraction recovered from the samples. The difference between the metal contents in the film and gel fraction allows determination of the copper content in the sol fraction (soluble fraction of the sample).

Data on the accumulation of carbonyl groups and copper in the polyethylene films and on the progress of oxidative cross-linking are given in Fig. 1. Metal becomes detectable in the polymer simultaneously with carbonyl groups (Fig. 1, curves *1* and *3*), whereas traces of the insoluble phase appears 1 h later (Fig. 1, curve *2*). All the dependences are plotted as ascending curves with saturation (stabilization), though the pronounced stabilization section is typical only for the kinetic curve of accumulation of the carbonyl groups (Fig. 1, curve *1*). However, stabilization of the content of the carbonyl groups is probably an apparent process. From our viewpoint, in the course of oxidation the dynamic equilibrium is attained between the carbonyl groups in acidic oxidation products (absorption band at 1720 cm^{-1}) and in low-molecular-weight fatty acids participating in the reactions yielding copper-containing compounds (products of the contact reactions). During oxidation on the support, the polyethylene film accumulates significant amounts of copper: up to several tenths of percent.

As seen, in the initial stage of oxidative cross-linking the kinetic curves of metal accumulation in the gel fraction and in the film as a whole approximately coincide (Fig. 1, middle sections of curves *3* and *4*). Hence, in this oxidation stage the copper content in the soluble polymer fraction is also similar. At prolonged oxidation, copper accumulates more actively in the gel fraction (Fig. 1, curves *3* and *4* diverge from each other). For example, after oxidation for 10.5 h, the content of copper in the cross-linked fraction reaches 0.52%, with the film as a whole containing 0.45% Cu and the minor sol fraction, only 0.18% Cu. The increased copper concentration in the gel fraction is probably due to the fact that, with increasing density and branching of the oxidative cross-links, the greater number of low-molecular-weight copper-containing compounds are encapsulated in the polymer network and cannot be recovered by boiling in *o*-xylene. As a result, only copper compounds with a linear structure and a small molecular weight are recovered from the sample. In this stage of oxidation, the content of metal in the films changes only slightly, because the polymer cross-linking hinders the metal transfer (Fig. 1, curve *3*).

Thus, the metal transfer into the polymer bulk almost ceases on passing of the polyethylene film into

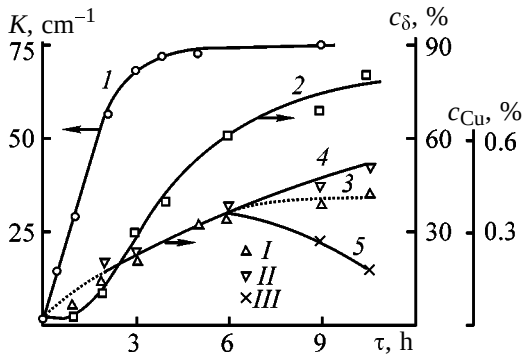

Fig. 1. (*1*) Extinction coefficient K of the absorption band at 1720 cm^{-1}, (*2*) content of the gel fraction c_δ, and (*3*–*5*) content of copper c_{Cu} in polyethylene films as functions of the time τ of their oxidation at 150°C on copper supports. Variation of the metal concentration in the (*I*) film, (*II*) gel fraction, and (*III*) sol fraction.

the inhibited state, and formation of the cross-linked structure causes redistribution of the metal between the sol and gel fractions of the polymer. At denser cross-linking of polyethylene, the copper content in the gel fraction is significantly greater than that in the sol fraction.

To elucidate the mechanism of the copper transfer (diffusion of low-molecular-weight metal carboxylates or "relay" transfer of copper ions with participation of carbonyl groups) at contact oxidation of polyethylene, we performed the following experiment. A series of 100-μm polyethylene films was oxidized on a copper support at 150°C for 10.5 h. Then, they were separated from the support, and the samples for measurements were prepared as follows. Two films of equal thickness of unoxidized (film I) and oxidized (film II) polyethylene were put in contact (as a two-layer stack) and then were melted on an inactive support (aluminum foil). In the sample, film II was in contact with a support, whereas film I was placed on the top, i.e., it formed the outer layer of the stack. The scheme of the sample is shown in Fig. 2. The resulting stack was placed in an oven and heated in air at 150°C; then the sample was cooled and films I and II were separated from each other. The changes in the content of copper, gel fraction, and carbonyl groups in the films during their heat treatment are illustrated by Figs. 2 and 3.

The redistribution of copper between films I and II is shown in Fig. 2; the total content of metal in the sample is 100%. As seen, at contact thermal treatment copper passes from film II into film I, and nearly 30% of copper occurring in film II transfers into film I during 8-h heat treatment.

The kinetics of various processes occurring in

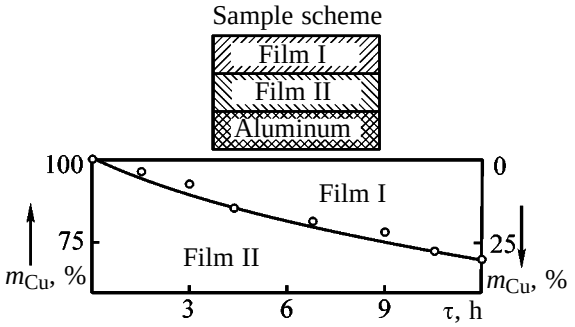

Fig. 2. Redistribution of copper m_{Cu} during heat treatment at 150°C of a stack consisting of a film oxidized on a copper support (film II) and an unoxidized film (film I). (τ) Time.

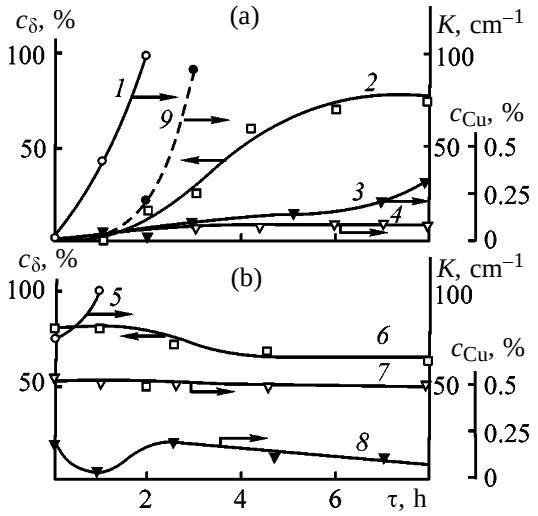

Fig. 3. (*1, 5*) Extinction coefficient K of the absorption band at 1720 cm^{-1}, (*2, 6*) content of the gel fraction c_δ, and content of copper c_{Cu} in the (*4, 7*) gel and (*3, 8*) sol fractions of polyethylene films (a) I and (b) II as influenced by the time τ (h) of oxidation of their stack at 150°C. (*9*) Variation of the extinction coefficient during oxidation of polyethylene film on the aluminum support.

films I and II are shown in Fig. 3. In the initial stage of the thermal treatment ($\tau \leq 1$ h), copper disappears from the soluble fraction of film II almost completely, its content becomes as low as 6% of the total copper content in the sample (Fig. 2; Fig. 3, curve *8*), whereas the content of the gel fraction in film II remains constant (Fig. 3, curve 6). Simultaneously, the same amount of copper appears in film I (Fig. 2). These data suggest that the copper transfer from the bottom film proceeds by the diffusion of low-molecular-weight metal-containing compounds in the sol fraction of film II. As for metal occurring in the gel fraction of film II, it is retained in the film during its thermal treatment.

Copper compounds passing into film I catalyze the oxidative transformations of the polymer, which is confirmed by the higher rate of accumulation of carbonyl groups in film I as compared with the film oxidized on the inert support (Fig. 3, curves *1* and *9*).

In the course of the thermal treatment of film II, intensive accumulation of oxidation products is resumed (Fig. 3, curve *5*). In our opinion, this is probably due to the transfer of the low-molecular-weight oxidation products from intensively oxidized film I and further oxidation of film II, owing to a decrease in the concentration of copper-containing compounds in the film. As known [1], inhibition of polyethylene oxidation at contact with a copper support is due to the accumulation of the critical content of copper, and the residual content of copper in film II (decreased as a result of the metal transfer into film I) does not provide inhibition of the oxidative degradation of the polyethylene film.

At further thermal treatment of the sample ($\tau \geq 1$ h), the oxidative cross-links in film II partially degrade (Fig. 3, curve *6*), which increases the content of the sol fraction; simultaneously occurs further accumulation of copper in film I. It should be noted that the concentration of copper in the gel fraction of film II remains constant (Fig. 3, curve *7*). This suggests that, with decreasing content of the gel fraction in film II, copper still passes into film I by the mechanism of diffusion of low-molecular-weight copper-containing compounds. After a decrease in the initial stage of the process, the copper content in the sol fraction of film II passes a weakly defined maximum (Fig. 3, curve *8*). This maximum is probably due to competition of two processes: increase in the content of the sol fraction in film II (with the corresponding increase in the metal content) and transfer of copper-containing compounds into film I (with the corresponding decrease in the metal content in the sol fraction of film II).

Copper passing into film I is distributed between the sol and gel fractions nonuniformly. In the cross-linked fraction of the polymer, the content of metal in the course of thermal treatment remains almost unchanged, being as low as 0.08% (Fig. 3, curve *4*). This fact suggests that the cross-linked structure is formed in the most rapidly oxidized areas of the polymer (small metal content), i.e., the cross-links appear predominantly in the course of oxidation. In the sol fraction of film I, the content of copper monotonically increases during its heat treatment, and after 8-h heating the metal content reaches 0.3% (Fig. 3, curve *3*). Thus, copper compounds obviously cannot

pass into the gel fraction of the film and are accumulated in its soluble fraction.

CONCLUSION

Our tests showed that the diffusion of low-molecular-weight copper carboxylates, which are the products of contact reactions, is the most probable mechanism of the metal transfer at contact oxidation of polyethylene on a copper support.

REFERENCES

1. Lin, D.G., Scientific Principles of Preparing Layered Metal–Polymer Materials for Mechanical Engineering Based on Thermoplastics and Elastomers, *Doctoral Dissertation*, Gomel', 1993.
2. Lin, D.G., *J. Appl. Polym. Sci*., 1994, vol. 54, no. 13, pp. 1789–1793.
3. Lin, D.G. and Vorob'eva, E.V., *Zh. Prikl. Khim*., 2001, vol. 74, no. 6, pp. 998–1002.
4. Belyi, V.A., Egorenkov, N.I., and Pleskachevskii, Yu.M., *Vysokomol. Soedin., Ser. B*, 1970, vol. 12, no. 9, pp. 643–644.
5. Belyi, V.A., Egorenkov, N.I., and Pleskachevskii, Yu.M., *Dokl. Akad. Nauk Bel. SSR*, 1970, vol. 14, no. 8, pp. 716–718.
6. Egorenkov, N.I. and Tsyganyuk, V.N., *Vysokomol. Soedin., Ser. B*, 1975, vol. 17, no. 5, pp. 393–394.
7. Egorenkov, N.I., Lin, D.G., and Belyi, V.A., *Dokl. Akad. Nauk SSSR*, 1972, vol. 207, no. 2, pp. 397–400.
8. Egorenkov, N.I., Regular Trends in Variation of the Adhesion, Friction, and Physicochemical Properties of Polymeric Films on Metal Supports at Thermal Treatment, *Doctoral Dissertation*, Kiev, 1986.
9. Sviridenko, V.G., Eliseeva, I.M., and Lin, D.G., *Vysokomol. Soedin., Ser. B*, 1989, vol. 31, no. 4, pp. 885–887.
10. USSR Inventor's Certificate no. 1026119.

Russian Journal of Applied Chemistry, Vol. 75, No. 5, 2002, pp. 822–828. Translated from Zhurnal Prikladnoi Khimii, Vol. 75, No. 5, 2002, pp. 840–846.
Original Russian Text Copyright © 2002 by Kuprina, Timofeeva, Vodolazhskaya.

MACROMOLECULAR CHEMISTRY AND POLYMERIC MATERIALS

Electrochemical Preparation of Chitin Materials

E. E. Kuprina, K. G. Timofeeva, and S. V. Vodolazhskaya

State Research and Design Institute for Fishing Fleet (GYPRORYBFLOT), St. Petersburg, Russia

Received September 21, 2001; in final form, January 2002

Abstract—Electrochemical processes for preparation of various chitin materials are examined. Physicochemical and biochemical properties of the products are studied, particularly the effect of deproteinization and degreasing of chitin materials on their sorption and other characteristics.

Materials based on the natural polysaccharide chitin are of steadily growing interest in view of their use as sorbents for environmental remediation (treatment of industrial wastewaters, potable water, and soils) and also for medical purposes. The reason is that natural sorbents are generally nontoxic and biologically active. Along with anion-exchange capacity, among useful properties of chitin is its cation-complexing ability.

However, the existing methods for manufacture of chitin materials, based on deproteinization, demineralization, and decolorization of raw material (shells of crustaceans, fungi, and insects) using alkalis, acids, oxidants, or enzymatic agents are cost-inefficient and not environmentally safe. Furthermore, the use of chemically corrosive reagents often deteriorates the quality of chitin and associated products (proteins, lipids) as a result of chemical or oxidative degradation [1]. The necessity in performing repeated deproteinization and demineralization with intermediate washings to neutral reaction makes the process multistage, also considerably increasing the product cost.

In some application areas (water and soil treatment to remove heavy and transition metals and radionuclides), such intermediate products of chitin manufacture as chitin–glucan, chitin–protein, and chitin–mineral complexes are competitive [2, 3]. In addition to low cost, among the advantages of, for example, chitin–mineral complexes, chisites, is high sorption capacity for heavy and transition metals (up to 2–3 mg-equiv g^{-1}), which is higher by an order of magnitude as compared to straight chitin.

In mid-1990s, an electrochemical process for preparation of chitin materials was developed as an alternative to the traditional methods [4].

It is known that electrochemical methods are fairly efficient in processing biological raw materials, as providing a direct effect of the electromagnetic field on a substrate (without intermediate transformation of the energy) [5]. By virtue of heterogeneity of the electrical properties, a shell-containing raw material is readily polarized, charged, and yielded to the strength of the electromagnetic field. As a result, all the mass-transfer processes accelerate, the cell structure transforms, and the penetrability of membranes and cells increases as well as the extraction rate.

The essence of the electrochemical method for chitin manufacture is that a shell-containing raw material as an aqueous salt emulsion is processed in a specially designed electrolyzer. In this case, deproteinization, demineralization, and decolorization proceed under the effect of the electromagnetic field. The OH^- and H^+ ions, produced as a result of electrolysis of water, and a number of low-molecular-weight products control pH and the redox potential [6]. The process demonstrates such advantages as environmental safety and the possibility of realizing deproteinization, demineralization, and decolorization in one stage at very low alkali and acid concentrations (0.05–0.1%) without intermediate washings to neutral reaction of the medium.

However, while deproteinization proceeds quite rapidly at low solid to liquid phase ratio (1 : 6), completion of demineralization requires 12–24 h at a considerably higher solid to liquid phase ratio, thus reducing the efficiency and profitability of the electrochemical process. Furthermore, owing to low reagent concentrations in the process, the resulting chitin is characterized by increased (by 6–10%) content of lipids, which, as known, shield the reaction centers of chitin, deteriorating its performance [7].

Therefore, the goal of this work was to develop a profitable electrochemical process for production of chitin with improved sorption characteristics.

1070-4272/02/7505-0822$27.00 © 2002 MAIK "Nauka/Interperiodica"

EXPERIMENTAL

As a raw material for preparation of chitin materials, we used the freshwater crustacean *Gammarus pulex* in the dispersed frozen or dry form. Chitin-based materials were prepared by two different methods involving deproteinization only, or deproteinization and demineralization. A raw material in the form of an aqueous salt emulsion (particle size $d \le 5 \times 10^{-3}$ m) at a fixed solid to liquid phase ratio was processed in an electrolyzer at a current density of 300–500 A m^{-2} for 30–40 min. Deproteinization was performed at pH ≥ 12.4. Then the system was heated to 60°C and allowed to stand at this temperature for 45 min. Demineralization was carried out at pH ≤ 2.0. Then the system was allowed to stand for 12–18 h at room temperature. In other experiments, deproteinization was performed off the electrolyzer by treating the raw material with a catholyte representing an electrochemically activated solution at pH > 12.0, prepared in the cathode cell of the electrolyzer. The anode material was platinized titanium, and the cathode material, stainless steel. A membrane was prepared from a sulfonic cation-exchange material. The products prepared by this method were supplied with names ended with el, for example, chitinel and chisitel.

For comparison, we prepared a sample of chisite by deproteinization of the dispersed raw material with 4% NaOH (solid to liquid phase ratio 1 : 10) at 65°C for 2.5 h [8].

Total nitrogen and mineral residue after calcinations were determined according to GOST (State Standard) 7636–85.

To determine the water-retaining capacity (WRC), a sample was held in distilled water for 20 h, filtered through a fabric, and centrifuged at 4000 rpm for 10 min. The WRC was estimated as

$$\mathrm{WRC} = [(m_1 - m_0)/m_0] \times 100\%,$$

where m_0 and m_1 are the sample weights after drying to constant weight at 105°C and after centrifugation, respectively.

Infrared spectra were registered on a Perkin–Elmer 16 PC FTIR spectrometer using KBr technique. Samples (2 mg) were vacuum-dried at 80°C for 12 h and mixed with KBr (100 mg). Then disks (0.5 mm thick) were pressed and vacuum-dried at 110°C for 24 h. The infrared spectra were processed using PeakFit software pack for Windows.

Sorption characteristics of chitin materials were studied in the static mode using an original technique. In one series of experiments we used solutions containing Cu^{2+} in a low concentration (up to 0.7 mM), which is typical of potable water, and in another series, solutions containing up to 30.0 mM, simulating industrial wastewater. The static sorption capacity SC was estimated from the sorption isotherms:

$$\mathrm{SC} = (c_0 - c_{eq})\Gamma,$$

where c_0 and c_{eq} are the initial and equilibrium metal concentrations (mM) and Γ is the liquid to solid phase ratio.

In the experiments with low copper concentration, a weighed portion of a sorbent (0.25 g) was poured over with 50 ml of a 0.5 to 0.7 mM copper solution (solid to liquid phase ratio 1 : 200). One day after, the residual equilibrium copper concentration in the solution was determined. The copper concentration in the initial and equilibrium solutions was determined as follows. A 50-ml sample of the solution was acidified with 2–3 drops of dilute (1 : 1) HCl. The sample was then placed into a separating funnel, and 12.5 ml of 0.3 g l^{-1} lead diethyldithiocarbamate in carbon tetrachloride was added. The funnel was vigorously shaken for 2 min, and the phases were separated. The organic phase was analyzed for copper spectrophotometrically at a wavelength of 440 nm.

In the experiments with high copper concentration, the sorption isotherm was obtained at constant copper concentration (29.3 mM) and variable weight of a sorbent sample (0.2–1.0 g in 50 ml of the solution). In these experiments, the copper concentration was determined on a KFK2 photoelectric colorimeter at a wavelength of 750 nm.

The degree of deacetylation of chitin-based materials was determined by potentiometric titration of a suspension of the sample in 0.1 N NaOH with 0.1 N HCl in the presence of a supporting electrolyte. The amount of NH_2 groups was estimated by the standard method [9].

The lipid concentration was determined by extraction using the Folch method. The fractional composition and percentage of individual lipids were determined by TLC on KSK silica gel using the solvent system hexane–diethyl ether–acetic acid (70 : 30 : 2). The fractional compositions of phospholipids was studied by TLC. The phospholipid content was determined colorimetrically [10]. The fatty acid composition of phospholipids was studied by GLC (with pre-

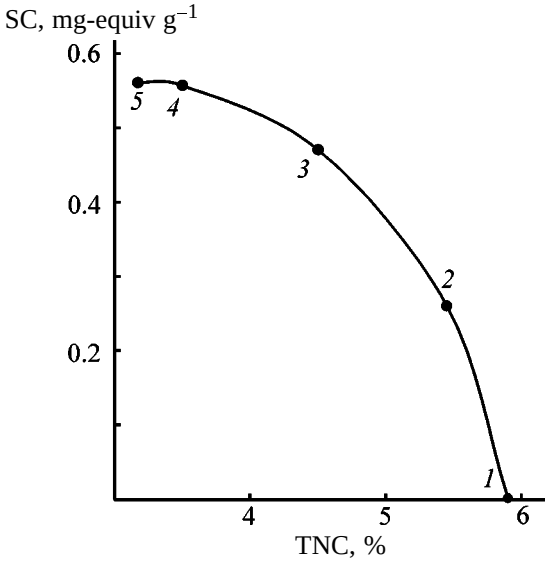

Fig. 1. Static sorption capacity (SC) for copper of chitin-based materials as a function of the degree of deproteinization expressed via the total nitrogen content TNC. The numbers at the points correspond to the sample numbers (see text).

liminary methylation of samples) on a Perkin–Elmer chromatograph [10].

It is known that, in the shell, proteins are in immediate vicinity of chitin fragments. This organic matrix is surrounded by the mineral phase (complex calcide mosaic) [11]. Therefore, removal of the protein component provides access to functional groups of chitin.

We studied the effect of the degree of deproteinization of the shell on its sorption characteristics. For this purpose, samples of chitin materials were prepared using various methods for deproteinization of dispersed *Gammarus*: treatment with water (sample no. 1); treatment for 6 h with the alkaline catholyte solution remaining after deproteinization of the previous portion of the raw material (sample no. 2); double treatment with the alkaline catholyte solution (sample no. 3); as for sample no. 2, but with aftertreatment in the cathode cell of the electrolyzer (sample no. 4); and double treatment in the cathode cell of the electrolyzer with intermediate heat treatment between the stages (sample no. 5).

The sorption capacity for copper of the resulting samples as a function of the degree of deproteinization is shown in Fig. 1.

The results show that the degree of deproteinization has a considerable effect on the sorption capacity (SC of sample nos. 4, 5 is higher by a factor of 1000 than that of the initial raw material). The maximal SC (0.28 mmol g^{-1}) is realized at high degree of deproteinization (TNC = 3.5%).

To provide the desired high degree of deproteinization, we developed a process for preparing highly deproteinized chitin materials, chisitels (see scheme below).

In addition to the basic stage of electrochemical deproteinization II in the cathode cell of the electrolyzer, the process flowsheet includes preliminary deproteinization I (pretreatment of the raw material in the catholyte solution representing a waste from the deproteinization II). This operation allows the required degree of deproteinization to be attained at reduced by half energy and reagent consumption and the pollution of the electrolyzer elements with protein-lipid components to be decreased. The previous electrochemical process included double treatment of the raw material in an electrolyzer [4].

It is known that chitin-containing materials demonstrate high affinity for lipids, causing the need in their degreasing. Lipids shield the reaction centers of polar functional groups in chitin substances, thus deteriorating their reactivity, sorption capacity for metal ions, and also organoleptic characteristics [7].

There is only limited information on the methods for degreasing of chitin-containing materials. This is probably due to the fact that, in preparation of chitosans, which are mostly used in sorption processes, from chitins in concentrated alkaline solutions, lipids are practically totally decomposed and removed. We demonstrated that in the proposed electrochemical process the lipid content in the resulting chisitel is twice that in the product obtained by the alkaline method. The reason is that in our process deproteinization proceeds under mild conditions ([OH$^-$] <0.1%).

Organic solvents commonly used for degreasing (alcohols, ethers, etc.) provided a desired effect only with multiple and long-time extraction at elevated temperature. Furthermore, organic solvents are toxic and fire hazardous.

To understand the fate of chitin–lipid complexes in electrochemical preparation of chitin from crustaceans and to select a method and conditions for degreasing of chisitel, we made a characterization of lipids of raw materials [*Gammarus*, chisitel I (see process flowsheet), and chisite].

It follows from Tables 1 and 2 that lipids of *Gammarus* consist essentially of neutral lipids and free fatty acids (FFAs). Increased FFA content, as known, is a result of high activity of lipolytic enzymes. The major fraction of fatty acids (64.1%) is represented by

Process flowsheet for preparation of chisitel.

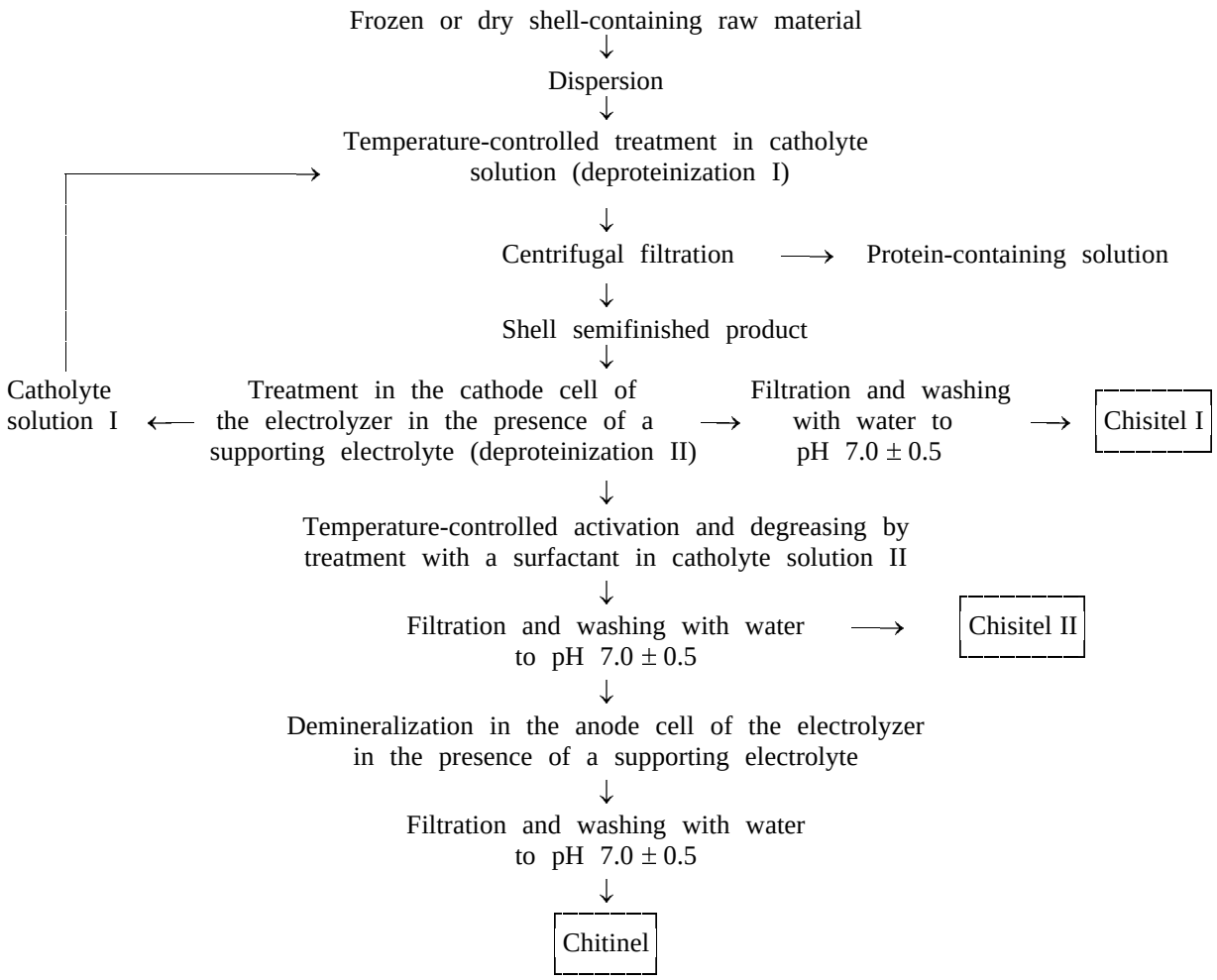

Table 1. Fractional composition of lipids

Fraction	Content, mg %			
	Gammarus	chisite*	chisitel I	chisitel II
Phospholipids, among them:	263.00	343.06	315.40	27.60
phosphatidylserine	11.18	–	–	–
sphingomyelin	53.15	–	–	–
phosphatidylcholine	81.77	–	–	–
phosphatidylethanolamine	72.48	–	–	–
diphosphatidylglycerol	13.89	–	–	–
phosphatidylinositol	30.53	–	–	–
Mono-, diglycerides	323.85	451.96	590.53	61.60
Triglycerides	1020.94	694.30	885.30	130.00
Free fatty acids	1136.21	1230.67	1954.67	180.80
Cholesterol, cholesteryl esters	46	–	–	–

* Obtained by alkaline treatment.

Table 2. Fatty-acid composition of lipids

Fatty acids	Content, % of the total fatty acids		
	Gammarus	chisite	chisitel I
Saturated	35.9	1.1	0.9
Monounsaturated	38.0	8.8	7.7
Polyunsaturated	26.1	90.1	91.4

unsaturated, primarily monounsaturated acids. It was demonstrated that the fractional composition of lipids of *Gammarus* is similar to that of small sea crustaceans [12], i.e., a degreasing process suitable for *Gammarus* can be then expanded to other kinds of raw material.

It is also known that, in the traditional deproteinization with NaOH, the relative contents of neutral lipids and FFAs decrease to a more considerable extent as compared to the electrochemical process. This is due to the fact that hydrolysis of neutral lipids and saponification of free fatty acids in the cathode cell occurs to a considerably lesser extent, as a result of lower OH^- concentration and temperature [13].

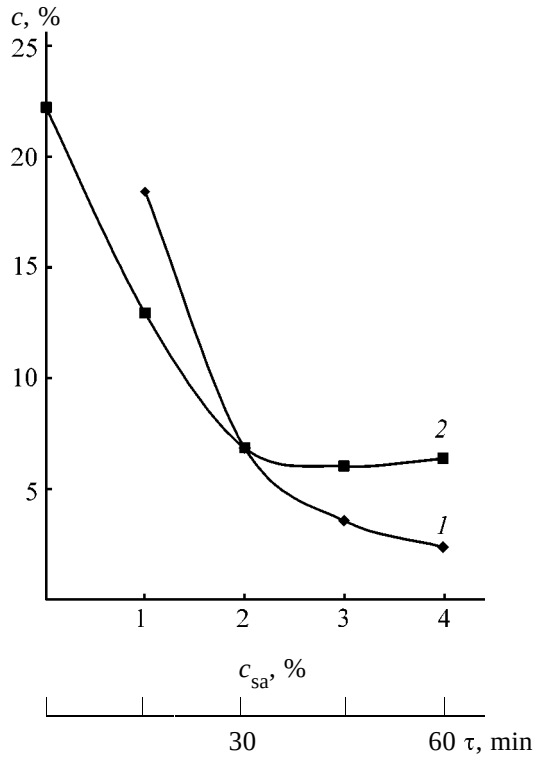

Fig. 2. Lipid content c in chisitel as a function of (*1*) surfactant concentration c_{sa} and (*2*) treatment time τ. Temperature 82°C; τ = 30 min (*1*); and c_{sa} = 2% (*2*).

Analysis of the fatty-acid composition of lipids showed (Table 2) that, in both alkaline and electrochemical deproteinization, the most active process is hydrolysis of saturated and monounsaturated lipids. As a result, their relative content in chitin–mineral complexes significantly decreases.

It is known that base hydrolysis of liquid and solid fats with formation of water-soluble products does not control the efficiency of degreasing action of a reagent. The key factor is the capacity to decrease the surface tension at the water–fat interface [13]. Therefore, we proposed to use anionic surfactants [7] for degreasing chitin materials obtained by the electrochemical method. The function of surfactants is to decrease the surface tension and to increase the wettability of the shell. Also they favor dispersion of solid lipids and emulsification of liquid lipids, preventing their secondary deposition onto the chitin surface.

We optimized the degreasing parameters (surfactant concentration, solid to liquid phase ratio, temperature, and treatment time) (Fig. 2) and demonstrated that it is advisable to perform degreasing simultaneously with the stage deproteinization II (this simplifies the process flowsheet, increasing the profitability).

The use of surfactants instead of conventional organic solvents eliminates fire hazard, decreases the process cost, and provides decrease in the lipid content in chisitel from 17–23 to 1–3%.

Physicochemical and biochemical characteristics of the shell-containing raw material, chisite, chisitels, and chitinel are summarized in Table 3. The results show that all the chisitels differ from chitinel by higher ash content, which is due to the lack of the demineralization stage. The total nitrogen content, characterizing the degree of deproteinization, is higher in chisitel obtained electrochemically than in that obtained by treatment with NaOH by 1.2% on the average.

Degreasing allowed increase in the specific surface area of chisitel from 2.0 to 11.0 $m^2 g^{-1}$.

Sorption isotherms show that, among the chitin materials studied, chisitel II is the most efficient sorbent for copper (Fig. 3).

As compared to chitinel, chisitels demonstrate better sorption of copper even at low copper concentration (<0.5 mM), while conventional ion-exchange resins are practically inoperative at such a low concentration; in this case the degree of recovery approaches 80–90%. This suggests high binding energy and sorp-

Table 3. Physicochemical and biochemical characteristics of chitin-containing materials

Parameter	*Gammarus*	Chisite	Chisitel I	Chisitel II	Chitinel
Total nitrogen, %	8.9	4.8	3.5	3.5	6.1
Ash content, %	17.5	27.0	28.1	27.8	0.8
WRC, %	–	58.9	71.8	44.8	89.2
Lipids, % of dry weight	10–12	12–14	20–23	1–3	30–36

tion by the complexation mechanism, which is typical of chitin materials.

The static sorption capacity of chisitel II (3.2 mmol g^{-1}) is higher by an order of magnitude than that of chitinel (Fig. 3), approaching SC of chitosans [2], which cannot be explained by only the presence of mineral salts of the carbonate–phosphate type.

It is well known [14] that carbonates and phosphates of such metals as Ca, Mg, and others are capable of sorbing metal ions by the mechanism of heterogeneous exchange at the phase boundary. For this to be realized, their specific surface area should be at least 100–200 $m^2 g^{-1}$. In the chitin materials studied in this work, this parameter is only 1.8 and 11.0 $m^2 g^{-1}$ for chitinel and chisitel, respectively. The degree of deacetylation, also influencing the sorption characteristics, is practically the same in these materials, being 0.2–0.3. Therefore, one may suggest that sorption processes in chitin–mineral complexes occur by virtue of metal complexation to acetamide groups, as demonstrated by infrared spectroscopic data. Indeed, a 10-cm^{-1} high-frequency shift of the absorption band due to bending vibrations of amides I (C=O…H–N) at 1656 cm^{-1}, caused by intermolecular interaction, was observed in the IR spectra of chisitel containing adsorbed Cu^{2+} ions, suggesting that the bond energy increases by virtue of metal complexation. An additional evidence in favor of such specific interaction is provided by the fact that the intensity of the amide I band in the spectrum of chisitel containing adsorbed Cu^{2+} ions increases by 40%, while that of amide II (C–O…H–N) at 1565 cm^{-1}, caused by intramolecular interaction, decreases. In the absorption spectra of chisitels, the intensities of these bonds are practically the same.

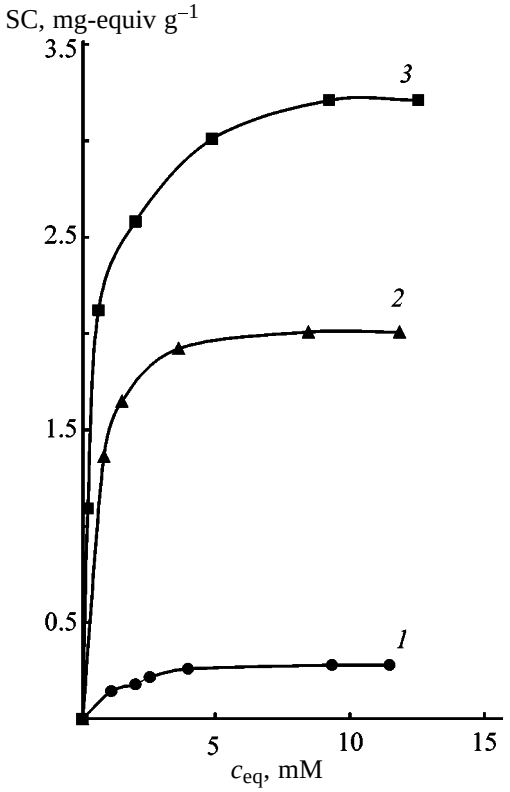

Fig. 3. Copper sorption isotherms: (*1*) chitinel, (*2*) chisitel I, and (*3*) chisitel II. (SC) Static exchange capacity and (c_{eq}) $Cu(NO_3)_2$ concentration in the equilibrium solution.

CONCLUSIONS

(1) An electrochemical process is developed for preparation of the chitin–mineral complex, chisitel, with a high sorption capacity for Cu^{2+}.

(2) A method for degreasing of chitin-containing materials is proposed, based on the use of an anionic surfactant.

(3) The sorption capacity of chisitels increases and the water-retaining capacity decreases with increasing degrees of deproteinization and degreasing.

REFERENCES

1. Kuprina, E.E., Kozlova, I.Yu., and Timofeeva, K.G., *Sovremennye tendentsii v sposobakh polucheniya i primeneniya khitina i khitozana: Obzornaya informatsiya* (Modern Trends in Preparation and Application of Chitin and Chitosan: A Review), *Obrabotka ryby i moreproduktov* (Processing of Fish and Seafood), Moscow: Nauchno-Issled. Inst. Ekon. Razvit. Rybn. Khoz–va., 1999, no. 3(1).

2. Nud'ga, L.A., Ganicheva, S.I., Petrova, V.A., *et al*., *Zh. Prikl. Khim*., 1997, vol. 70, no. 2, pp. 242–246.
3. Seliverstov, A.F., Ershov, B.G., and Trifonova, S.V., *Zh. Prikl. Khim*., 1997, vol. 70, no. 1, pp. 148–152.
4. USSR Inventor's Certificate 175 188.
5. Byval'tsev, A.I., Liakumovich, A.G., and Agadzhanyan, S.I., *Materialy VI Vsesoyuznoi konferentsii po elektrofizicheskim metodam obrabotki pishchevykh produktov i sel'skokhozyaistvennogo syr'ya* (Proc. VI All-Union Conf. on Electrophysical Methods for Treatment of Food Stuff and Farm Raw Materials), Moscow, 1989, p. 203.
6. RF Patent 2 059 390.
7. Kuprina, E.E., Krasavtsev, V.E., Kozlova, I.Yu., *et al*., *Materialy V Vsesoyuznoi konferentsii "Novye perspektivy v issledovanii khitina i khitozana"* (Proc. V All-Union Conf. "New Prospects in Studying Chitin and Chitosan"), Moscow, May 25–29, 1999, Moscow: VNIRO, pp. 37–41.
8. No, H.K., Meyers, S.P., and Lee, K.S., *J. Agr. Food Chem*., 1989, vol. 37, no. 3, pp. 575–579.
9. Polyanskii, N.G., Gorbunov, G.V., and Polyanskaya, N.L., *Metody issledovaniya ionitov* (Methods for Studying Ion Exchangers), Moscow: Khimiya, 1976.
10. *Metody biokhimicheskikh issledovanii (lipidnyi i energeticheskii obmen): Uchebnoe posobie* (Biochemical Research Methods (Lipid and Energy Exchange): A Handbook), Prokhorova, M.I., Ed., Leningrad: Leningr. Gos. Univ., 1982.
11. Giraud-Guille, M., in *Chitin in Life Sciences: 1st Summer School of the European Chitin Soc. "EUCHIS,"* Banyuls-sur-Mer (France): Jacques Andre, 1996, pp. 1–10.
12. *Spravochnik po khimicheskomu sostavu i tekhnologicheskim svoistvam vodoroslei, bespozvonochnykh i morskikh mlekopitayushchikh* (A Handbook of Chemical Composition and Technological Characteristics of Algae, Invertebrates, and Marine Mammalians), Bykov, V.P., Ed., Moscow: VNIRO, 1999.
13. Pavlov, B.A. and Terent'ev, A.P., *Kurs organicheskoi khimii* (A Course of Organic Chemistry), Moscow: Khimiya, 1972.
14. Shul'ga, N.V., Shashkova, I.L., and Samuskevich, V.V., *Zh. Prikl. Khim*., 1999, vol. 72, no. 11, pp. 1852–1854.

Russian Journal of Applied Chemistry, Vol. 75, No. 5, 2002, pp. 829–833. Translated from Zhurnal Prikladnoi Khimii, Vol. 75, No. 5, 2002, pp. 847–851.
Original Russian Text Copyright © 2002 by Tikhova, Shakirov, Fadeeva, Dergacheva, Samutenko, Fedorova.

MACROMOLECULAR CHEMISTRY AND POLYMERIC MATERIALS

NMR Study of Structural Changes in Humic Acids of Meadow Soddy Soils

V. D. Tikhova, M. M. Shakirov, V. P. Fadeeva, M. I. Dergacheva, L. V. Samutenko, and L. V. Fedorova

Institute of Organic Chemistry, Siberian Division, Russian Academy of Sciences, Novosibirsk, Russia
Institute of Soil Science and Agricultural Chemistry, Siberian Division, Russian Academy of Sciences, Novosibirsk, Russia
Sakhalin Agriculture Research Institute, Far Eastern Scientific Center, Russian Agricultural Academy, Yuzhnosakhalinsk, Novoaleksandrovskoe, Russia

Received June 21, 2001; in final form, January 2002

Abstract—Quantitative and qualitative changes in humic acids of meadow soddy soils, occurring under the action of various fertilizer systems, were studied by ^{13}C and ^{31}P NMR.

NMR spectroscopy is an extremely promising method of studying the structure of soil organic substance whose main components are humic acids (HAs). Since the late 1970s, various soils were extensively studied by ^{13}C and ^{1}H NMR [1]. In 1980, ^{31}P NMR was first used for studying alkaline soils extracts [2]. Only this method allowed identification of various forms of phosphorus addition to HA macromolecule and estimation of quantitative relationships between these species. Therefore, this method is widely used for studying various types of soils and soil fractions [3–5]. Data on transformations of soil organic components under the action of cultivation are limited [6].

Here we report on the quantitative and qualitative changes proceeding in HAs of meadow soddy soils under the action of various fertilizer systems, as studied by ^{13}C and ^{31}P NMR.

EXPERIMENTAL

We studied the HAs of soils subjected to the action of fertilizers under the stationary field conditions.[1] Peat–manure compost (C) was used as an organic fertilizer. A mixture of granulated ammonium nitrate NH_4NO_3, granulated double superphosphate $Ca(H_2PO_4)_2$, and potassium chloride KCl were used as mineral fertilizers. The amount and composition of the added fertilizers are listed in Table 1. Humic acids were recovered by the standard procedure [7].

The total phosphorus content was determined spectrophotometrically with the vanadium–molybdenum reagent after combustion of the samples in a flask filled with oxygen.

To obtain NMR spectra, 50 mg of an HA sample was dissolved in 0.5 ml of a 0.5 M NaOH solution in D_2O and placed into an ampule of 5 mm outer

Table 1. Amount and composition of the added fertilizers

Sample no.	Note	Amount of added fertilizers, kg ha^{-1}
1	Control (no fertilizers)	–
2	1NPK	N60P90K90*
3	1C	100×10^3 C
4	2C	200×10^3 C
5	1NPK + 2C	N60P90K90 + 200×10^3 C
6	3NPK + 1C	N180P270K270 + 100×10^3 C
7	3NPK + 2C	N180P270K270 + 200×10^3 C

* (NPK) Active elements of a mineral fertilizer (nitrogen, phosphorus, and potassium); the number to the right of the corresponding element corresponds to the amount of this element in kilograms added per hectare of the soil, evaluated from the formulas of components of the mixed fertilizer.

[1] The experiments were carried out at the Novoaleksandrovskoe pilot station (Sakhalin Island) since 1990. The soil of the pilot parcel was meadow soddy, medium-loamy, and old arable. At the pilot plots, feed crop rotation was maintained for 8 years. The fertilizers were added three times at 1-year intervals and then, after three years (in 1994). In all runs, the soil samples were withdrawn from a depth of 0–20 cm.

1070-4272/02/7505-0829$27.00 © 2002 MAIK "Nauka/Interperiodica"

Table 2. Relative content of various carbon-containing functional groups in HAs from soils with added fertilizers (^{13}C NMR data)

Sample no.	Carbon with indicated chemical shift, ppm					
	aliphatic			polysaccharide, 65–90	aromatic, 90–160	carboxy, 160–200
	CH_3, 0–45	CH_2, 45–65	total, 0–65			
1	38.3	6.1	44.4	6.4	25.6	23.6
2	33.5	10.4	43.9	10.5	32.4	13.2
3	35.4	9.3	44.7	7.9	30.5	16.9
4	37.0	5.8	42.8	4.4	34.3	18.5
5	35.7	9.4	45.1	8.8	32.8	13.2
6	34.5	3.6	38.1	5.9	36.1	19.7
7	33.8	7.1	40.9	5.3	34.8	19.0

diameter. The ^{13}C and ^{31}P NMR spectra were recorded on a Bruker DRX-500 spectrometer at 125.76 and 202.46 MHz, respectively. To exclude the nuclear Overhauser effect, the ^{13}C NMR spectra were recorded with proton decoupling in the INVGATE mode, and the ^{31}P NMR spectra, in the single resonance mode.

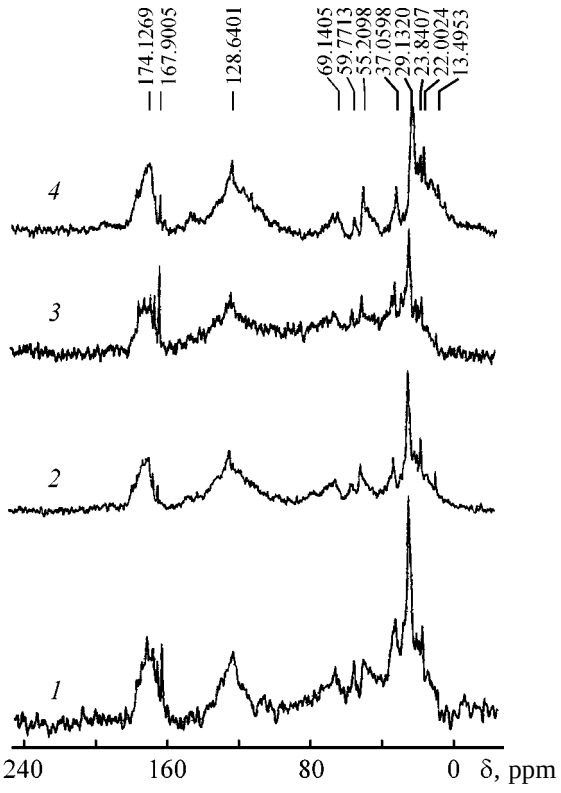

Fig. 1. ^{13}C NMR spectra of the HA samples: (δ) chemical shift; the same for Fig. 4. Figures at curves are sample nos. in Table 1; the same for Fig. 4.

Tetramethylsilane (TMS) and 85% H_3PO_4 were used as external references. The spectra were recorded at pulse delay of 1 s.

Typical ^{13}C NMR spectra of the studied HAs are shown in Fig. 1. They allow distinction and quantitative evaluation of the relative content of the following fragments of HA macromolecule: alkyl (aliphatic) carbon (0–65 ppm); carbon in carbohydrates, alcohols, and acetals, designated as polysaccharide carbon (65–90 ppm); aromatic carbon (90–160 ppm); and carboxylic carbon (160–200 ppm). These are the commonly adopted intervals in which ^{13}C NMR spectra of HAs are integrated, though the limits of these intervals can differ by 5–10 ppm [8]. The relative content of individual carbon-containing functional groups in HAs was estimated by integration of the signals in the above intervals. The results are given in Table 2. The relative standard deviation of the results of tenfold manual integration did not exceed 3%.

Humic acids recovered from control soils are characterized by a low fraction of aromatic carbon (25.6%). The remaining carbon is distributed in macromolecules among aliphatic groups, polysaccharides, and carboxyls in the 44.4 : 6.4 : 23.6 ratio.

All the fertilizers taken in the indicated amounts decrease the amount of carboxy groups in HAs (Fig. 2): organic, by 6.7–5.1% and mineral, by more than 10%. The shapes of the ^{13}C NMR spectra of carboxylic carbon (160–200 ppm), namely, significant decrease in the number of narrow signals at 170 ppm, suggest that addition of mineral fertilizers affects so-called "peripheral" acids weakly bonded to aromatic compounds. These acids, entering into the reaction with additional cations of fertilizers, are hydrolyzed. The remaining carboxy groups are bonded to the

bulky aromatic "core" of HA and are manifested in the spectrum as a broadened structureless peak (Fig. 1). Organic fertilizers do not affect the fraction of weakly bonded acids (narrow lines in the spectrum of sample no. 3, as well as in the spectrum of control sample); however, an increase in the amount of weakly bonded acids results in increased fraction of acids bonded to the core.

All the fertilizers taken in the indicated amounts increase the relative amount of aromatic carbon in HAs (90–160 ppm). This increase is maximal for sample no. 5 (close to 11%) and minimal for sample no. 3 (approximately 5%). The characteristics of sample nos. 2 and 5 are practically the same. This suggests that mineral fertilizers exert a decisive effect on the HA structure, and the effect of compost against this background is insignificant. A minor difference between sample nos. 2 and 5 is observed only for aliphatic and polysaccharide carbon. The maximal amount of the added organomineral fertilizers (sample nos. 6 and 7) gives the maximal increase in the relative content of aromatic carbon.

The use of mineral or organic fertilizers does not appreciably affect the relative content of aliphatic carbon, except the case when triple doses of mineral fertilizers were used. In this case, the amount of aliphatic carbon somewhat decreased. This combination of changes in the relative content of aromatic and aliphatic carbon in HAs suggests the decisive role of high concentrations of salts entering into composition of mineral fertilizers in hydrolysis of aromatic and aliphatic fragments of HA.

The use of mineral fertilizers (sample no. 2) results in the maximal increase in the polysaccharide carbon fraction (by a factor of almost 2 in comparison with the control sample): addition of the organic fertilizer (sample no. 5) somewhat moderates this effect. Addition of organic fertilizers somewhat increases the fraction of polysaccharides (sample no. 3), but an increase in the amount of organic fertilizers (sample no. 4) brings the amount of polysaccharides to the minimum. The use of organomineral fertilizers (sample nos. 6, 7) somewhat decreases, in comparison with the control sample, the fraction of carbon atoms surrounded by oxygen atoms.

Even with the use of large amounts of fertilizers, the ratio of aromatic and aliphatic carbon in the HAs studied differs essentially from that in HAs of chernozem, the richest soil in which the relative fractions of aromatic and aliphatic carbon are 53.4 and 13.3%, respectively [9].

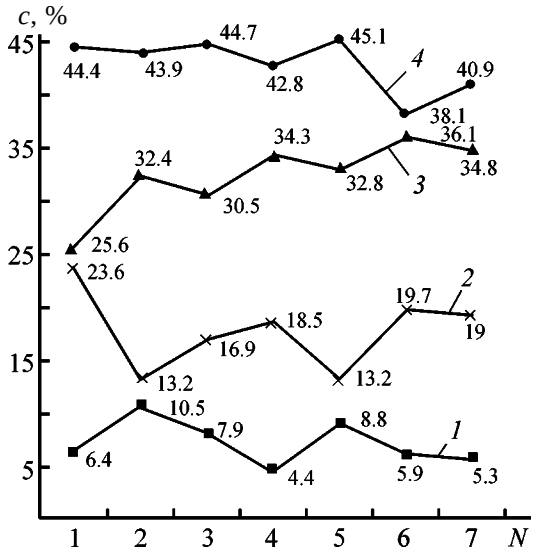

Fig. 2. Relationship between various carbon-containing functional groups in the samples of HAs studied: (*c*) content of functional groups in HA and (*N*) sample no. in Table 1. Carbon: (*1*) polysaccharide, (*2*) carboxy, (*3*) aromatic, and (*4*) aliphatic.

In the course of soil formation, phosphorus entering into the composition of mineral phosphates of soil-forming rocks is incorporated into the soil organic substance and is accumulated in the soil, being the important reserve of phosphorus supply to plants. Incorporation of inorganic phosphorus of fertilizers into soil organic substance proceeds indirectly through involvement of phosphorus in biological processes in the soil. The results of numerous studies suggest that the use of organic and inorganic fertilizers increases the content of organic phosphorus P_{org} in various soils. However, the phosphorus content can decrease during soil cultivation, which is caused either by increased activity of phosphatase and intensity of mineralization of organophosphorus compounds, or by chemical transformations of the initial organophosphorus compounds increasing their solubility and migration activity. On the whole, the resources of organic phosphorus in the soil are more stable in comparison with inorganic phosphates [6].

According to elemental analysis, humic acids recovered from the control soils are characterized by low content of phosphorus, 0.60%. According to ^{31}P NMR, monophosphate esters (77.8%), mineral orthophosphate (9.95%), and diphosphate esters (12.25%) constitute the major fraction of phosphorus compounds (Fig. 3).

Elemental analysis shows (Table 3) that addition of 1NPK, 2C, and 1NPK + 2C significantly (by a factor

Table 3. Ratio between various phosphorus-containing species in HAs of the soils with added fertilizers (^{31}P NMR data)

Sample no.	P,* %	Mineral orthophosphate		Monophosphate esters		Diphosphate esters	
		abs. %	rel. %	abs. %	rel. %	abs. %	rel. %
1	0.60	0.06	9.95	0.47	77.80	0.07	12.25
2	2.05	0.20	9.98	1.60	78.38	0.23	11.64
3	0.86	0.13	14.8	0.63	73.60	0.10	11.60
4	1.68	0.22	13.07	1.18	70.33	0.28	16.61
5	1.75	0.19	10.99	1.24	71.33	0.31	17.68
6	0.66	0.09	13.60	0.51	77.30	0.06	9.1
7	0.60	0.04	6.70	0.47	78.62	0.09	14.67

* Data of elemental analysis.

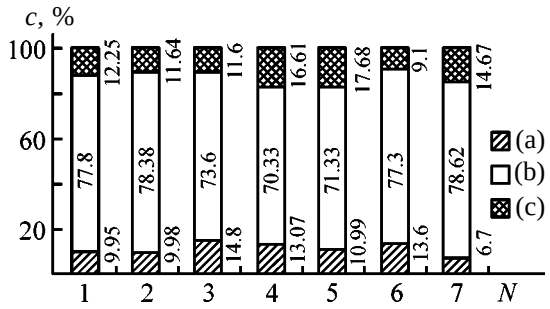

Fig. 3. Ratio between phosphorus-containing species in the HA samples: (*c*) content of various phosphorus-containing species in HA and (*N*) sample no. in Table 1. (a) Mineral orthophosphate, (b) monophosphate esters, and (c) diphosphate esters.

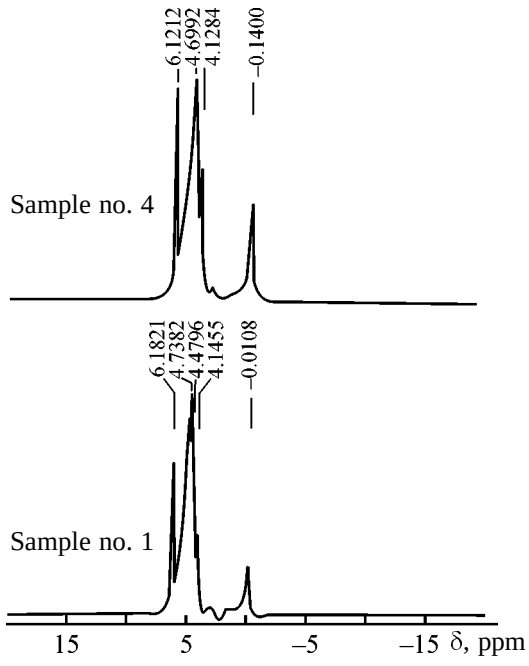

Fig. 4. ^{31}P NMR spectra of HA samples.

of 2–3) increases the phosphorus content in HAs. The use of 1C increases the phosphorus content in HA insignificantly. The maximal amounts of organomineral fertilizers (in sample nos. 6 and 7) do not exert an appreciable effect; the phosphorus content in these samples is comparable with that in the control sample. It can be assumed that large amounts of mineral fertilizers suppress the microbiological activity in the soil and prevent phosphorus incorporation into the HA macromolecule.

Typical ^{31}P NMR spectra of HAs are shown in Fig. 4. The identified signals correspond to the following phosphorus-containing compounds [6]: narrow signal at 6.2–5.8 ppm suggests the presence of mineral orthophosphate ion; in the range of chemical shifts from 5.8 to 3.5 ppm, phosphate monoesters are identified (inositol phosphates, saccharophosphates, and mononucleotides); and a signal in the range from 0.5 to –0.5 ppm corresponds to phosphate diester bond in phospholipids and nucleic acids.

The relative content of individual phosphorus compounds in HAs was estimated by integration of the intensity of the signals in the above intervals. The relative standard deviation of the results of tenfold manual integration did not exceed 1%.

According to data obtained, monophosphate esters (70–80%), mineral orthophosphate (10–15%), and diphosphate esters (10–15%) constitute the major portion of phosphorus compounds in HAs (Fig. 3).

Addition of mineral fertilizers does not change the ratio of phosphorus-containing species in HAs (though its absolute value increases by a factor of 3), and addition of organic fertilizers decreases the fraction of monophosphates owing to increase in the fractions of mineral orthophosphate (sample no. 3) and diphosphates (sample no. 4). Addition of organic fertilizers to 1NPK also decreases the fraction of

monophosphates owing to increase in the amount of diphosphates. The use of maximal amounts of mineral fertilizers in combination with a small amount of compost (sample no. 6) does not alter the amount of monoesters, but decreases the relative content of diesters owing to increase of the amount of mineral orthophosphate. Addition of a larger amount of organic fertilizers (sample no. 7) somewhat increases the fraction of monoesters; in this case, the fraction of monoesters noticeably increases and the amount of mineral orthophosphate reaches the maximum in the series in hand.

CONCLUSIONS

(1) The use of organic fertilizers decreases the amount of carboxy groups in humic acids of the soils by 6.7–5.1%, and the use of mineral fertilizers, by more than 10%; the relative amount of aromatic carbon increases by 5–11%. With addition of mineral fertilizers, the fraction of polysaccharide carbon reaches a maximum. With most of fertilizer systems, the relative content of aliphatic carbon does not noticeably change, though the triple dose of mineral fertilizers decreases its fraction by 3–6%.

(2) Even with addition of large amounts of fertilizers, the ratio of aromatic and aliphatic carbon in the humic acids appreciably differs from that in the chernozem humic acids.

(3) Addition of mineral fertilizers does not affect the ratio of phosphorus-containing species in humic acids, though the absolute value of phosphorus content increases by a factor of 3; addition of organic fertilizers increases the microbiological activity of the soil and decreases the fraction of stable monoesters.

REFERENCES

1. Preston, C.M., *Soil Sci*., 1996, vol. 161, no. 3, pp. 144–166.
2. Newman, R.H. and Tate, K.R., *Commun. Soil Sci. Plant Anal*., 1980, no. 11, pp. 835–842.
3. Tikhova, V.D., Shakirov, M.M., Fadeeva, V.P., and Dergacheva, M.I., *Zh. Prikl. Khim.*, 2000, vol. 73, no. 7, pp. 1206–1209.
4. Makarov, M.I., *Pochvovedenie*, 1997, no. 4, pp. 458–466.
5. Makarov, M.I., *Vestn. Mosk. Gos. Univ., Ser. 17: Pochvovedenie*, 1998, no. 1, pp. 27–32.
6. Makarov, M.I., Nedbaev, N.P., Kurmysheva, N.A., and Efremov, V.F., *Agrokhimiya*, 1997, no. 7, pp. 5–11.
7. Orlov, D.S., Grishina, L.A., and Eroshicheva, N.L., *Praktikum po biokhimii gumusa* (Laboratory Manual on Humus Biochemistry), Moscow: Mosk. Gos. Univ., 1969.
8. Orlov, D.S., *Gumusovye kisloty pochv i obshchaya teoriya gumifikatsii* (Soil Humic Acids and General Theory of Humification), Moscow: Mosk. Gos. Univ., 1990.
9. Tikhova, V.D., Shakirov, M.M., Fadeeva, V.P., and Dergacheva, M.I., *Zh. Prikl. Khim.*, 1998, vol. 71, no. 7, pp. 1173–1176.

Russian Journal of Applied Chemistry, Vol. 75, No. 5, 2002, pp. 834–839. Translated from Zhurnal Prikladnoi Khimii, Vol. 75, No. 5, 2002, pp. 852–857.
Original Russian Text Copyright © 2002 by Platonov, Shvykin, Proskuryakov, Podshibyakin, Chilachava, Khmarin, Solov'ev.

CHEMISTRY OF FOSSIL FUEL

Development and Optimization of the Procedure of Gas-Chromatographic Elemental Analysis of High-Carbon Solid Fossil Fuels

V. V. Platonov, A. Yu. Shvykin, V. A. Proskuryakov, S. I. Podshibyakin, K. B. Chilachava, E. M. Khmarin, and A. S. Solov'ev

Tolstoy Tula State Pedagogic University, Tula, Russia
St. Petersburg State Technological Institute, St. Petersburg, Russia

Received August 13, 2001; in final form, December 2001

Abstract—A procedure was developed for gas-chromatographic elemental analysis of coals. The conditions of exhaustive oxidation of weighed microportions of the coals were optimized. The procedure of calculating the results of analysis was modified with the aim to improve its reproducibility.

The elemental composition of the organic matter (OM) of solid caustobioliths is one of their most important characteristics governing their properties such as, e.g., the capability for destructive hydrogenation, coking, plastic state formation, etc. One of the best and promptest automated methods of elemental analysis (EA) is gas chromatography. It is equal, or sometimes superior, in precision and reproducibility to the classic EA. However, EA of solid fossil fuels has so far followed old classic procedures [1, 2]. The use of modern micromethods, in particular, gas chromatography has been extremely limited.

This is due, above all, to the lack of reliable methods of exhaustive oxidation of weighed microportions of fossil fuel under conditions of pyrolysis. Most of catalyzing oxidants used as additives to ensure exhaustive combustion and obtain a gas mixture to be further analyzed chromatographically prove to be inefficient in the case of fossil fuels. The organic matter of the latter is typically a highly condensed, high-carbon, high-molecular-weight matrix. The presence of a mineral fraction, sometimes very substantial, ever more complicates exhaustive oxidation of the fuel under the conditions of analysis.

With efficient micromethods of EA, the analytical procedure is significantly simplified and accelerated and can be carried out on a commercial scale with the precision remaining equal to that of classic methods. This makes urgent development and optimization of micromethods of gas-chromatographic EA of fossil fuels and, in particular, search for efficient catalyzing oxidants able of exhaustive oxidation of weighed microportions of fuel under EA conditions.

Published data suggest that modern elemental microanalysis utilizes effective oxidants such as silver permanganate $AgMnO_4$ and its thermal degradation product (Körbl catalyst SPTDP), as well as Co_3O_4, MnO_2, WO_3, and Cr_2O_3 [3–5]. Among these, the first-named four reagents act primarily as oxygen donors. It should be noted that SPTDP also acts as a catalyst and a reagent partially absorbing halogens and sulfur. The function of WO_3 is, essentially, that of binding the interfering elements into thermally stable salts [4, 5]. Fadeeva and Moryakina [6] studied such catalysts as NiO, V_2O_5, MnO_2, PbO_2, Cr_2O_3, WO_3, and their mixtures and showed that some of these compounds (NiO, V_2O_5, Cr_2O_3, WO_3) catalyze surface burning, and others (MnO_2, PbO_2) are oxygen donors. The highest performance was exhibited by MnO_2, NiO, and PbO_2; V_2O_5 performs somewhat worse, and WO_3 proved to be the least effective. Individual oxides were found to strongly corrode the combustion tube, while their mixtures proved to be less aggressive. Fadeeva and Moryakina [6] developed a very effective oxidizing catalyst with the following composition, %: MnO_2 64, Cr_2O_3 13, PbO_2 13, and SiO_2 10.

Thus, numerous and diverse inorganic compounds and their mixtures were suggested as oxidative additions to the specimen to be burnt. However, these do not include silver compounds such as, e.g., Ag_2O_2 or $Ag_2Cr_2O_7$, which are promising as active oxidants for

1070-4272/02/7505-0834$27.00 © 2002 MAIK "Nauka/Interperiodica"

gas-chromatographic EA. As to Ag_2O_2, it is an effective oxygen donor superior in the oxygen content to $AgMnO_4$. The silver metal yielded by its degradation is an effective catalyst of surface oxidation. This made reasonable testing the suitability of these oxidants for gas-chromatographic EA.

Conventional calculational methods, such as, e.g., those described in [4] utilizing response factors for the elements to be analyzed, do not accurately account for the errors associated with the oxidant proper. These methods yield an averaged value of the "zero peak" of the oxidant which is to be subtracted in the appropriate formulas from the peak value for the substance to be analyzed or the reference. This necessitates modification of the formulas for calculating the response factors and the weight fractions of the elements analyzed to accurately account for the errors associated with the oxidants utilized.

The aim of this work was to modify the gas-chromatographic EA procedure as applied to analysis of coals so as to improve its precision and reproducibility.

Our study was concerned with coal from the Sangarskaya mine, Yakutsk coal field.

The analyses were carried out on an Carlo Erba-1100 gas-chromatographic analyzer.

The procedure proposed by the manufacturer is intended for EA of individual organic compounds or their mixtures; it exhibited fairly high precision and reproducibility. We attempted application of this procedure to EA of fossil fuels and certain products thereof such as lignites and coals, shales, sapropel, peat, humic acids, and various extracts thereof. The results of analysis proved to be very distorted, namely, the content of all the elements determined, especially carbon, was considerably (by ~40–50%) underestimated, and also the reproducibility of analysis was considerably deteriorated, i.e., the content of C, H, and N elements proved to be appreciably scattered around the average values. We attempted to explain this phenomenon by the presumed unsuitability of the V_2O_5 oxidant, proposed by Carlo Erba, for exhaustive oxidative pyrolysis of the analyzed fossil fuels (and some of their products) under the actual conditions. These fuels are typically highly condensed, high-molecular-weight, and high-carbon compounds (coals) or have a significant mineral constituent which strongly complicates analysis (lignites, sapropels, and extracts thereof).

The unsuitability of V_2O_5, suggested by the manufacturer as oxidant for analyzing fossil fuels and products thereof, necessitates selection of oxidants able of efficiently oxidizing the above-mentioned compounds during the analytical cycle.

Using the procedure from [7], we prepared certain amount of individual $AgMnO_4$. We tested this compound as a substitute to V_2O_5 in EA of fossil fuels and products thereof and found that $AgMnO_4$ is significantly superior to V_2O_5: Unlike the latter, $AgMnO_4$ exhaustively oxidizes the OM even in substances with a very high mineral component, e.g., in sapropels.

Exhaustive oxidation of the OM from fossil fuels with $AgMnO_4$ was confirmed by model experiments on analysis of artificial 9-nitroanthracene–TiO_2 mixtures of the known elemental composition. The results of analysis proved to be highly accurate and reproducible even for TiO_2 content in the mixture of up to 90 wt %.

However, our studies revealed some major drawbacks of $AgMnO_4$. This compound is prepared by the exchange reaction between $AgNO_3$ and $KMnO_4$ and necessarily comprises water incorporated into the crystal lattice. This water cannot be fully eliminated even by heating in a vacuum because of thermal instability of $AgMnO_4$ which begins to decompose above 100°C. Certain amount of NO_3^- anions is also incorporated into the resuting $AgMnO_4$ crystals, which generates unavoidable, though minor, zero peaks of nitrogen associated with the oxidant proper.

Unlike V_2O_5, which withstands heating to 400°C without decomposition, $AgMnO_4$ cannot be freed by calcination from trace amounts of organic substances, contributing to the zero peaks of C, H, and N, either. But the strongest effect is exerted by the coprecipitated water responsible for major zero peaks of hydrogen. In view of the fact that the standard procedure prescribes taking oxidant in approximately the same amount as the substance being analyzed, rather than weighing, the zero peaks of C, H, and N, when in small amounts in the oxidant (which is easily attainable for V_2O_5 by calcining at 400°C), will be low and not strongly dependent on the oxidant mass fluctuations. Therefore, these latter will not significantly contribute to the error and only insignificantly affect the reproducibility of analysis.

With $AgMnO_4$ as oxidant, major amounts of C, H, and N (especially H) in the oxidant will be responsible for major fluctuations of the zero peak values owing to the oxidant mass fluctuations. This necessitated modification of the analytical and calculational procedures to accurately account in analysis of every

sample for the contribution from zero peaks due to the oxidant. Also, it proved to be necessary to change the mode of charging the combustion reactor with the oxidant, as with CuO wire in the high-temperature zone of the reactor the latter is rapidly fused with reduced copper metal, plugging the tube.

The nitrogen content of fossil fuels is typically low and seldom exceeds 2–3%, while the carbon content often proves to be very high (60–80%). This makes desirable selecting among individual organic compounds the appropriate reference with the elemental composition approximately identical to that of fossil fuels. Also, of much interest is testing silver compounds other than $AgMnO_4$, as well as PbO_2, as potential oxidants for EA.

We suggested the following modifications to the analytical procedure:

(1) To replace cyclohexanone 2,4-dinitrophenylhydrazone by 9-nitroanthracene, whose elemental composition is closer to that of coals, namely (%): C 75.34, H 4.04, N 6.28, and O 14.34.

(2) To change the mode of charging the combustion reactor by placing in succession the beds of the CuO wire (10 cm), Cr_2O_3 (9 cm), and quartz crumble (1 cm). Cr_2O_3 efficiently catalyzes exhaustive burning in excess oxygen of the products formed from inexhaustive burning of the samples analyzed such as, e.g., CO. This does not deteriorate the burning conditions and the reactor does not get plugged with fused copper wire.

(3) To modify the sample weighing procedure and the calculational procedure so as to accurately account in each analytical run for the errors introduced by the C, H, and N from the oxidant proper. After weighing the sample in an aluminum container and adding the oxidant, the filled container is weighed once again. This yields the precise mass of the oxidant added to the sample in each run. The resulting value of the oxidant mass m_{ox} is then substituted into the modified calculational formulas. For "blank" analytical runs, the container with the oxidant taken separately is also weighed so as to determine m_{ox}. Next, the specific value of the zero peak of the oxidant is calculated by the formula

$$y^0_{e(sp)} = y^0_e/m_{ox},$$

where y^0_e is the zero signal for a given element in the blank run (area or height of C, H, and N chromatographic peaks for the oxidant sample), m_{ox} is the mass of the oxidant sample, and $y^0_{e(sp)}$ is the specific zero signal in a single run for a given element.

From the results of several blank runs, it is possible to calculate the average value of the specific zero peak

$$\bar{y}^0_{e(sp)} = n^{-1}\sum_{i=1}^{n} y^0_{e(sp)}.$$

The resulting $y^0_{e(sp)}$ value is to be substituted into the modified calculational formulas:

$$K_e = \frac{\omega^e_{ref} m_{ref}}{y^e_{ref} - m_{ox}\bar{y}^0_{e(sp)}},$$

$$\bar{K}_e = n^{-1}\sum_{i=1}^{n} K_{ei},$$

$$\omega^e_{sam} = \frac{\bar{K}_e(y^e_{sam} - m_{ox}\bar{y}^0_{e(sp)})}{m_{sam}},$$

where K_e is the response factor for the corresponding element; ω^e_{ref} is the mass fraction of the element analyzed in the reference; m_{ref} is the mass of the reference with the known elemental composition; m_{sam} is the mass of the sample with unknown elemental composition; m_{ox} is the mass of the oxidant added; y^0_{ref} is the value of the analytical signal (chromatographic peak area or height) of the given element for the given reference; y^e_{sam} is the analytical signal of the element for the given sample of unknown elemental composition; $\bar{K}_e$ is the averaged response factor of the given element as calculated for at least two (better, three–four) values of K_e; $y^0_{e(sp)}$ is the value of the specific zero signal of the given element for a single blank run with individual oxidant; $\bar{y}^0_{e(sp)}$ is the averaged value of the specific zero signal of the given element; and n is the number of analytical runs for the reference or of the blank runs for the oxidant.

These modifications allow precisely accounting for the errors in each run due to the presence of C, H, and N in the oxidant, which significantly improves the reproducibility of analysis.

(4) To wrap with metal wire the containers charged with samples and oxidants before placing them in automated sample dosing unit. This prevents the oxidants from spilling out of the container during the weighed sample discharge, which improves the reproducibility of analysis as well. Also, the specimens do not jam at the combustion reactor inlet.

(5) To replace V_2O_5 by other oxidants, namely, $AgMnO_4$, Ag_2O_2, $Ag_2Cr_2O_7$, and PbO_2, in studies on

optimizing the combustion regime. The three first-named oxidants were prepared by the procedures described in [7, 8], and the latter was taken as-received (analytically pure).

The oxidants prepared, as well as PbO_2 and V_2O_5, were tested with the aim to elucidate their suitability and efficiency in burning coal samples during chromatographic EA. To this end, the samples were placed into the dosing unit in the following order: reference (9-nitroanthracene), oxidant (pure), three coal specimens, reference, oxidant, three coal specimens, reference, oxidant, four coal specimens, reference, oxidant, and reference.

The analyses were carried out in the dynamic mode, in an oxygen-enriched medium, at the rate of helium flow through the C, H, and N channels of 30 ml min^{-1} and that through the reference channel, of 20 ml min^{-1}. The analyzed coal samples with oxidant in the sealed aluminum containers were burnt in a tube of a stainless-steel reactor charged in the above-described manner. The combustion temperature was 1050°C. The combustion products of coal and final oxidation products of gas came then to a U-shaped reactor charged with copper metal heated to 650°C, where excess O_2 and SO_2 were absorbed and nitrogen oxides were reduced. Next, the analyzed gas mixture containing He, N_2, CO_2, and water vapor (at 120°C) came into a 4-m chromatographic column packed with Al_2O_3-supported Chromosorb-102, where the gas mixture was separated. Katharometer served as detector. The content of C, H, and N was calculated from the heights of their chromatographic peaks. The containers, first empty and then filled with a coal sample or reference, were weighed on a Cahn electromagnetic balance. The weights of the coal and reference specimen were about 0.5 mg. After adding the oxidant to the specimen, the container was weighed on a VLA-200M analytical balance to determine the mass of the oxidant added. After weighing, the containers were wrapped before placing them in the corresponding cells of the ring-shaped dosing unit for samples, and the system was hermetically sealed and blown through with a helium stream. The samples were supplied manually. Each analytical run took 12–15 min.

For $AgMnO_4$, we carried out two analytical series. In the first series, we analyzed coal by the old, unmodified, procedure utilizing unwrapped containers and unmodified weighing system and calculational procedure not accounting precisely for errors due to the oxidant. In the second series, we analyzed ten coal specimens by the modified procedure described above. Other oxidants were tested by the modified procedure only. Based on the results of analyses, we calculated the following parameters: the content of the elements analyzed ω_e; the arithmetic means of the content of the elements analyzed $\bar{\omega}_e$; standard deviations in a single run for each element S_e; estimated standard deviations of the content of each element S_e^2; confidence intervals $\bar{\omega}_e \pm t_{p,f}(S_e/10^{1/2})$, where $t_{p,f}$ is the Student's t-distribution coefficient; $t_{0.95;9} = 2.26$ for the confidence probability $p = 0.95$ and the significance level $f = 9$.

$AgMnO_4$, Ag_2O_2, and PbO_2 proved to be the most effective oxidants for coal analysis. Under pyrolysis conditions, they decompose presumably according to the following equations:

$$3AgMnO_4 = 3Ag + Mn_3O_4 + 4O_2,$$

$$Ag_2O_2 = 2Ag + O_2,$$

$$2PbO_2 = 2PbO + O_2.$$

The released oxygen is spent for sample burning and oxidation of aluminum containers. All the three oxidants gave reproducible results, the $\bar{\omega}_e$ values falling within the following confidence intervals as calculated using the Student's coefficients:

$AgMnO_4$:

$$\bar{\omega}_C = 70.73 \pm 3.36 \times 10^{-2} \approx 70.73 \pm 0.03,$$

$$\bar{\omega}_H = 5.15 \pm 1.50 \times 10^{-2} \approx 5.15 \pm 0.02,$$

$$\bar{\omega}_N = 0.99 \pm 8.57 \times 10^{-3} \approx 0.99 \pm 0.01;$$

Ag_2O_2:

$$\bar{\omega}_C = 70.72 \pm 7.86 \times 10^{-2} \approx 70.72 \pm 0.08,$$

$$\bar{\omega}_H = 5.16 \pm 1.20 \times 10^{-2} \approx 5.16 \pm 0.01,$$

$$\bar{\omega}_N = 0.98 \pm 7.86 \times 10^{-3} \approx 0.98 \pm 0.01;$$

PbO_2:

$$\bar{\omega}_C = 70.74 \pm 2.07 \times 10^{-2} \approx 70.74 \pm 0.02,$$

$$\bar{\omega}_H = 5.16 \pm 1.5 \times 10^{-2} \approx 5.16 \pm 0.02,$$

$$\bar{\omega}_N = 0.99 \pm 1.2 \times 10^{-2} \approx 0.99 \pm 0.01.$$

The reproducibility (agreement between the estimated standard deviation of the average and the confidence interval limits for all the elements analyzed)

was the best for $AgMnO_4$ and PbO_2. A somewhat worse reproducibility for carbon (by a factor of ~5.4 lower than that of $AgMnO_4$) was achieved for Ag_2O_2. This is probably due to a greater (by a factor of ~50) value of the zero peak for carbon $\bar{y}^0_{C(sp)}$ in the case of Ag_2O_2 compared to $AgMnO_4$. This is presumably due to the presence of Ag_2CO_3 impurity in the Ag_2O_2 prepared.

Under the actual conditions, silver dichromate decomposes by the scheme

$$Ag_2Cr_2O_7 = 2Ag + Cr_2O_3 + 2O_2.$$

The decomposition of this oxidant yields free oxygen, silver metal, and chromium(III) oxide. The latter, similar to silver metal, efficiently catalyzes surface oxidation. Our experimental data showed, however, that with $Ag_2Cr_2O_7$ the sample combustion is fairly calm and almost flameless, with its rate and intensity being lower compared to the three first-named oxidants for which an instantaneous bright flash is observed. This lower degradation rate is, probably, responsible for incomplete oxidation of carbon in the sample and for underestimated C content as calculated from the analytical data.

Within the confidence interval for $Ag_2Cr_2O_7$ we obtained the following results: $\bar{\omega}_C = 60.61 \pm 2.36$, $\bar{\omega}_H = 5.15 \pm 0.025$, and $\bar{\omega}_N = 0.98 \pm 0.01$.

Thus, for $Ag_2Cr_2O_7$, compared to $AgMnO_4$, Ag_2O_2, and PbO_2, there is a systematic, by ~10%, underestimation of the carbon content. The reproducibility, as estimated from the random deviation of the mean, is also worse by a factor of approximately 5×10^3. At the same time, both the calculated values and the corresponding random deviations and confidence intervals for H and N are fairly consistent with those for $AgMnO_4$, PbO_2, and Ag_2O_2. Thus, $Ag_2Cr_2O_7$ is unsuitable for analyzing carbon in coals, though suitable for analyzing nitrogen and hydrogen.

It should be noted that, with PbO_2 as oxidant, the EA of coals, though providing exhaustive burning and good reproducibility, is accompanied, unfortunately, by prominent oxidative corrosion of combustion tubes. This is due presumably to the high temperature evolving in oxidation of aluminum containers by the aluminothermic reaction

$$3PbO_2 + 4Al = 3Pb + 2Al_2O_3.$$

Major amount of heat evolving in this reaction and the oxygen-enriched atmosphere are responsible for fast burn-out of the tubular combustion reactor. This sets certain limits on application of individual PbO_2. At the same time, with $AgMnO_4$ and Ag_2O_2 aluminum containers do not undergo intensive oxidation, whereas the specimen burns efficiently. This fact justifies the use of individual $AgMnO_4$ and Ag_2O_2.

The worst oxidant among those tested is V_2O_5, which degrades under the actual conditions by the equation

$$2V_2O_5 = 4VO_2 + O_2.$$

Thermal degradation of this oxidant is significantly slower compared to the others. The input of the specimens (even individual organic compounds) is not accompanied by a flash. Slow degradation is evidently responsible for inexhaustive oxidation of the organic constituent of difficultly combustible fossil fuels. The confidence intervals are as follows: $\bar{\omega}_C = 29.03 \pm 5.00$, $\bar{\omega}_H = 4.36 \pm 0.89$, and $\bar{\omega}_N = 0.35 \pm 0.02$.

Thus, with V_2O_5, compared to $AgMnO_4$, there is a systematic underestimation of the content of the elements analyzed, namely, by factors of approximately 2.4, 1.2, and 2.8 for C, H, and N, respectively. Also, for the same elements, the reproducibility of analysis decreased by factors of approximately 2.2×10^4, 3.5×10^3, and 4, respectively. This makes V_2O_5 virtually unsuitable for coal analysis.

The results of a comparative study of the old and new, improved, analytical procedures also gave very interesting results. The old procedure for EA, namely, not accounting precisely for the error due to oxidant but utilizing $AgMnO_4$ as oxidant, exhibits virtually the same precision which is worse, however, compared to the improved procedure, namely, by factors of approximately 3.0, 6.6, and 12.8 for C, H, and N, respectively. The corresponding confidence intervals are as follows: $\bar{\omega}_C = 70.73 \pm 5.79 \times 10^{-2} \approx 70.73 \pm 0.06$, $\bar{\omega}_H = 5.16 \pm 3.86 \times 10^{-2} \approx 5.16 \pm 0.04$, and $\bar{\omega}_N = 0.98 \pm 3.07 \times 10^{-2} \approx 0.98 \pm 0.03$.

Thus, the reproducibility of the improved gas-chromatographic EA procedure is higher by a factor of 7.5 on the average.

CONCLUSIONS

(1) The procedure of gas-chromatographic elemental analysis of solid fossil fuels was improved, which substantially increased the reproducibility of analysis.

(2) The suitability of Ag_2O_2 and $Ag_2Cr_2O_7$ as oxidants in gas-chromatographic elemental analysis was proved for the first time.

(3) The best oxidants for elemental analysis of coals are $AgMnO_4$, Ag_2O_2, and PbO_2. To improve the reproducibility of carbon determination, Ag_2O_2 should be freed from Ag_2CO_3 impurity.

(4) The use of PbO_2 in elemental analysis is limited by its strong oxidative-corrosion action on the combustion tube material.

(5) V_2O_5 proves to be unsuitable for elemental analysis of coals; the use of $Ag_2Cr_2O_7$ for gas-chromatographic elemental analysis of coals is restricted to analysis of nitrogen and hydrogen.

REFERENCES

1. Kamneva, A.I. and Platonov, V.V., *Teoreticheskie osnovy khimicheskoi tekhnologii goryuchikh iskopaemykh* (Theoretical Principles of Chemical Technology of Fossil Fuels), Moscow: Khimiya, 1990.
2. Shpirt, M.Ya., Ignatova, N.N., and Archakova, T.G., *Khim. Tverd. Topl.*, 1991, no. 4, pp. 21–29.
3. Körbl, J., *Microchim. Acta*, 1956, no. 12, pp. 1705–1721.
4. *Metody kolichestvennogo organicheskogo elementnogo mikroanaliza* (Methods of Quantitative Organic Elemental Microanalysis), Gel'man, N.E., Ed., Moscow: Khimiya, 1987.
5. Kissa, E. and Seepere-Yllo, M., *Microchim. Acta*, 1967, no. 3, pp. 287–296.
6. Fadeeva, V.P. and Moryakina, I.M., *Izv. Sib. Otd. Akad. Nauk SSSR, Ser. Khim. Nauk*, 1981, no. 14, issue 6, pp. 113–118.
7. *Handbuch der präparativen anorganischen Chemie*, Brauer, G. *et al.*, Eds., Stuttgart: Enke, 1978, vol. 2; 1981, vol. 3.
8. Karyakin, Yu.V. and Angelov, I.I., *Chistye khimicheskie veshchestva* (Pure Chemical Substances), Moscow: Khimiya, 1974.

Russian Journal of Applied Chemistry, Vol. 75, No. 5, 2002, pp. 840–845. Translated from Zhurnal Prikladnoi Khimii, Vol. 75, No. 5, 2002, pp. 858–863.
Original Russian Text Copyright © 2002 by Begak, Syroezhko, Fedorov.

CHEMISTRY OF FOSSIL FUEL

Trace Contaminants in Tars and Bitumens from West-Siberian and Yarega Crude Oils

O. Yu. Begak, A. M. Syroezhko, and V. V. Fedorov

Mendeleev Research Institute of Metrology, Federal State Unitary Enterprise, St. Petersburg, Russia
St. Petersburg State Technological Institute, St. Petersburg, Russia

Received January 28, 2002

Abstract—The trace contaminant levels were determined for ten tar samples and six bitumen samples available from Kirishi, Yaroslavl, and Ukhta refineries, as well as from Neste (Finland).

High quality of road bitumens[1] is of decisive importance for lengthening the lifetime of asphalt concrete pavement [1]. In recent years the quality of tar[2] used as raw material for bitumen preparation was stabilized. Also, bitumen production (Kirishi refinery) widely utilizes bitumen compounding with tars and vacuum gas oils, which significantly improves the performance characteristics of commercial road bitumens. BDUS 70/100 and BDUS 100/130 (produced by the KINEF Limited Liability Company) bitumens substantially exceed in quality BND 40/60, BND 60/90, and BND 90/130 bitumens that were previously produced by this enterprise. However, the possibilities for improving the bitumen quality at the enterprise are not exhausted.

As known, bitumens with close group and chemical compositions obtained from the same raw material often differ in the thermal stability (penetration P_{25} and ductility $D_{h.t.}$ sharply decrease after heat treatment). The above parameters strongly depend on the amount and composition of the impurity metals and nonmetals both in the initial tars and commercial products. This study was devoted to elucidation of this dependence in the case of raw materials available from the above-listed refineries.

EXPERIMENTAL

Ten samples of BDUS 70/100 and BDUS 60/90 bitumens and tars from bitumen installations at the KINEF Limited Liability Company and bitumen samples from Yaroslavl refinery were taken on May 17–24, 2001. Bitumens from the Ukhta refinery and Neste were prepared in September 1999 and were stored for two years in closed reservoirs under laboratory conditions, at room temperatures.

All the tar and bitumen samples (Tables 1, 2) were studied by a common scheme: (a) determination of the acid numbers, ANs, mg KOH g^{-1}; (b) determination of the content of trace contaminants by mass spectrometry with ionization in inductively coupled plasma (ICP-MS) on a CG Plasma Quad Turbo Plus (England) instrument: Weighed portions (75–100 mg) of tars and bitumens were degraded by a 1 : 2 mixture of concentrated boiling nitric and hydrochloric acids for 3 h on a sand bath, and the trace contaminants were transferred to the aqueous phase, which was followed by multielement analysis of the resulting solutions; (c) deasphalting of tars and bitumens by cold or hot precipitation (in a Soxhlet apparatus); (d) separation of the recovered malthenes into polar and nonpolar components using dimethylformamide (DMF); (e) exhaustive deasphalting of polar and nonpolar components of tars and their corresponding bitumens; (f) chromatographic separation of polar and nonpolar components of tars and bitumens into group components and IR, ^{1}H NMR, and ^{13}C NMR studies; and (g) elemental analysis and X-ray diffraction study of the initial tars and bitumens, malthenes, asphaltenes, and polar and nonpolar components.

The entire complex of investigations was aimed at revealing the most significant differences in quality standard and substandard bitumens and tars.

We found (Table 1) that, on storage for 6 months under laboratory conditions, tars get harder, and their penetration significantly decreases, for example, ap-

[1] The major suppliers of oxidized road bitumens in Northwest Russia are Kirishi, Yaroslavl, and Ukhta refineries. The two first-named enterprises are engaged in processing of the commercial mixture of West-Siberian crude oils, and Ukhta refinery, in processing of high-resin heavy Yarega crude oil. Also, bitumens are supplied by Nafta, Finland.

[2] The KINEF Limited Liability Company has undertaken major reconstruction of the vacuum block of the AVT-6 installation.

1070-4272/02/7505-0840$27.00 © 2002 MAIK "Nauka/Interperiodica"

Table 1. Characterization of tars from KINEF Limited Liability Company

Experiment no.	Initial parameters		Parameters measured after aging*				
	P_{25}, mm × 0.1	conventional viscosity, s	P_{25}, mm × 0.1	ANs, mg KOH g^{-1}			ring-and-ball softening point, °C
				tar	NPCs**	PCs**	
1	387	84	231	11.4			44
2	344	92	185	17.1			35.4
3	329	90	201	7.28			37.4
4	309	94	128	17.86			35.9
5	305	89	155	4.24	–	9.2	45.4
6	313	92	212	9.57			45.2
7	315	93	187	12.84			48.8
8	380	93	160	3.87			42.5
9	390	92	183	4.97	4.3	12.3	44.2
10	320	93	151	6.74			44.3

* Measurements taken in November 2001; the same for Table 2.
** PCs and NPCs refer to polar and nonpolar components, respectively.

Table 2. Characterization of bitumens studied*

Sample no.**	Sample	AN, mg KOH g^{-1}	Ring-and-ball softening point, °C		P_{25}, mm × 0.1		D_{25}, cm	P_{25}, %	$D_{h.t.}$, cm
			initial	after aging	initial	after aging			
1	70/100	9.02	46	49.9	81	53	150	72	113
2	90/130	3.80	47	–	98	–	150	70	98
3	70/100	13.8	45	48.6	81	42.1	>150	69	105
4	70/100	17.8	46	–	84	48.3	140	68	108
5	70/100	18.2	49	–	82	49	150	71	115
6	60/90	12.4	49	53	78	47.9	>150	76	86
7	70/100	9.2	47	50.3	75	43.2	147	75	102
8	60/90	15.5	48	47.3	79	39.7	149	72	96
9	70/100	–	48	–	85	–	141	71	140
10	70/100	–	46	48.6	86	–	>150	66	131
11	70/100	31.2	45	45	90	54.8	147	72	130
12	70/100	8.92	46	–	85	47.5	150	66	116
13	Ukhta refinery	30.9	49		74	34			
14	″	52.0	45		68	30.2			
15	Yaroslavl refinery	15.6	47	47.3	81	74	148	76	121

* The acid numbers of PCs and NPCs of bitumen nos. 4 and 6, measured in November 2001, are 19.6 and 12.4, and 14.7 and 10.7 mg KOH g^{-1}, respectively.
** BDUS sample nos. 1–12 were prepared at Kirishi refinery.

proximately twofold for tar nos. 5 and 9, which were studied in detail by a complex of physicochemical methods.

It should be noted that the acid numbers of bitumen nos. 13 and 14 (Table 2) are fairly large (30.9–52 mg KOH g^{-1}). As carboxy groups intensively interact with the active centers of mineral fillers, the content of these groups governs the durability of the asphalt concrete pavement. Evidently, bitumen nos. 13 and 14 (Ukhta refinery) will ensure a greater durability of the pavement than bitumen nos. 1–12 (KINEF Limited Liability Company).

Interestingly, the acid numbers of bitumen no. 15 (Table 2) are close to those of the similar bitumen

Table 3. Content of trace contaminants in tars from KINEF Limited Liability Company

Element	Content, ppm, in indicated specimen									
	no. 1 (387)*	no. 2 (344)	no. 3 (329)	no. 4 (309)	no. 5 (305)	no. 6 (313)	no. 7 (315)	no. 8 (380)	no. 9 (390)	no. 10 (393)
Na	606	553	253	233	121	100	66	114	121	234
Mg	74	167	22	111	44	8.4	9.7	34	4.4	84
Ca	<0.1	631	0.1	0.1	212	0.1	0.1	0.1	135	18
Sr	3.6	2.3	0.66	0.8	1.7	0.1	1.1	0.1	1.8	3.3
Ba	14	41	14	572	15	9.1	20	5.3	12	12
Al	270	30	23	46	24	0.1	0.1	12	12	47
Bi	20.1	2.6	0.1	0.1	8	0.1	0.1	5.4	41	2.3
Pb	1.4	5.7	1.7	2.8	7	1.9	1.7	2.4	17	10
Cd	0.01	3.4	0.01	0.01	0.01	0.01	0.01	0.01	0.01	0.01
Se	0.01	24	0.01	0.01	0.01	5.5	0.01	5.7	0.01	2.5
P	0.1	42	3.2	0.1	0.1	0.1	0.1	0.1	0.1	0.1
Ti	25	7.5	6.4	2.1	1.0	2.7	0.1	0.6	6.4	2.5
Mo	1.7	1.3	0.5	0.9	2.5	0.1	0.1	0.36	0.3	4.3
Zr	4.1	2.4	17	4.7	1.6	0.7	0.01	0.85	1.9	4.3
W	–	–	–	–	13	–	–	–	1.4	–
Cr	0.01	0.01	0.01	25	6.6	0.01	0.01	0.01	4.1	0.01
Fe	183	777	110	42	280	175	23	76	163	98
Mn	0.01	5.4	0.01	0.01	4.7	0.01	0.01	0.01	4.1	0.01
Cu	11	254	10	5.7	98	5.1	5.5	12	63	106
Co	0.01	0.5	0.1	0.01	1.2	0.1	0.1	0.01	1.7	1.7
V	14	30	38	11	52	15	19	95	53	19
Ni	5.1	20	6.5	3.6	76	4.3	9.2	9.2	60	8.27
I	0.1	0.1	166	0.1	0.01	0.1	0.1	938	148	46
Sn	–	–	–	–	6.2	–	–	–	10.7	–
Br	0.1	3.3	47	0.1	0.01	18	15	3.5	0.06	10
V/Ni	2.74	1.5	5.84	3.05	0.68	3.49	2.06	10.3	0.88	0.19
Σ	1213				1265				1253	

* The figures in parentheses are penetrations P_{25}.

no. 8 from Kirishi refinery. However, in thermal stability (resistance to aging), bitumens from Kirishi refinery are exceeded by those from Yaroslavl refinery.

It is seen that bitumen nos. 1–12 have fairly good initial parameters (ring-and-ball softening point, P_{25}, D_{25}) and fully satisfy the requirements set on BND bitumens. Interestingly, acid numbers of the bitumens of virtually the same brand (BDUS 70/100) differ significantly (range from 3.8 to 31.2). The acid numbers of the analogous bitumens from Neste and from Ukhta and Yarislavl refineries vary more widely. For example, bitumen from Neste has the acid number of 15.1 mg KOH g^{-1}, that from Ukhta refinery, 52 (ring-and-ball softening point 45°C) and 30.9 (ring-and-ball softening point 49°C), and that from Yaroslavl refinery, 15.6 mg KOH g^{-1} (ring-and-ball softening point 47°C) (Table 2). It should be noted that the adhesion properties of the bitumens studied are determined not only by the nature but also by the content of polar groups (including carboxylic).

Tables 3 and 4 present the results of analysis of the tar and bitumen specimens studied.

It should be noted that the total error of the ICP-MS method is no greater than 20%. As seen from Table 3, the tars differ significantly in the content or elements such as Mg, Na, Al, P, Ti, Ca, Fe, Mn, V, Ni, Sr, Zr, I, Ba, Bi, and Pb.

The tars chosen for detailed studies by a complex of physicochemical methods (samples with P_{25} = 305 and 390 mm × 0.1) were characterized by increased iron content and fairly high content of vanadium, nickel, sodium, calcium, and copper. Tar sample with P_{25} = 390 mm × 0.1 had a high iodine content.

Table 4. Content of trace contaminants in bitumens from different refineries*

Element	Content, ppm, in indicated sample					
	no. 1 (46)**	no. 2 (49)	no. 3 (48)	no. 4 (51)	no. 5 (49)	no. 6 (47)
Na	68	140	100	387	293	151
Mg	32	42	21	27	45	121
Ca	100	106	32	57	93	179
Sr	0.7	2.2	0.1	0.1	0.3	3.3
Ba	11	15	5.6	24	4.1	15
Al	9.5	22	5.8	0.1	0.1	69
Bi	8.0	7.0	0.1	0.1	0.5	0.1
Pb	4.17	5.5	1.2	1.4	0.7	6.2
Cd	0.25	0.01	0.01	0.01	0.01	1.5
Se	0.16	0.21	7.3	0.01	5.4	17
P	0.12	0.1	0.1	8.3	3.2	0.1
Ti	1.2	5.2	1.4	0.1	3.0	2.0
Mo	0.6	0.27	3.7	1.2	3.8	1.2
Zr	1.4	1.9	3.9	0.01	0.5	2.2
W	0.23	2.2	–	–	–	–
Cr	3.2	4.4	0.01	1.3	0.01	0.01
Fe	146	252	89	43	259	156
Mn	3.5	4.8	0.01	0.01	0.01	1.9
Cu	37	80	10	3.5	19	175
Co	1.2	1.4	0.01	0.1	0.6	1.0
V	49	51	11	9.3	115	18
Ni	52	66	7.3	6.5	54	17
I	0.01	28	47	0.1	13	0.1
Sn	2.6	2.2	–	–	–	–
Br	0.1	0.05	7.6	0.1	11	27
V/Ni	0.94	0.77	1.5	1.43	2.12	1.05
Σ	532.45	767.43	443.14	570.24	896.83	964.6

* Bitumen sample: nos. 1 and 2 from KINEF Limited Liability Company; nos. 3 and 4, from Ukhta refinery; no. 5, from Neste, and no. 6, from Yaroslavl refinery.

** The figures in parentheses are the ring-and-ball softening points, °C.

The total content of trace contaminants in tar sample no. 5 was 1265, and in tar sample no. 9, 1253 ppm.

The dominating elements for bitumens selected among those prepared from tars with P_{25} = 305 and 390 mm × 0.1 are Mg, Na, Fe, Cu, Ni, and V, and for bitumen no. 2 (Table 4), I. The vanadium and nickel contents in these samples are comparable (0.77–0.94 ppm).

The fact that the content of trace contaminants in bitumens tends to decrease relative to the corresponding tars is, evidently, explained by their dilution with vacuum distillates in the compounding stage.

It should be noted that these impurity elements can exert a catalyzing action on oxidation of tars into bitumens and on their structure at the molecular and supramolecular levels. The reason is that heavy metals (in particular, vanadium and nickel) occur in resin–asphaltene substances as metal–porphyrin complexes and are linked by coordination bonds to nitrogen atoms in these complexes.

Tables 3 and 4 show that there exists certain correlation between the contents of microelements in tars (sample nos. 5 and 9) and in their corresponding bitumens (sample nos. 1 and 2, Table 4). Nevertheless, all the bitumens studied differ in the content of each of the 25 elements analyzed.

Similar to tars, impurity Na, Mg, Ca, Ba, Fe, Cu, V, Ni, and I dominate in the bitumens studied.

It should be noted that the total content of trace

contaminants in tars exceeds that in their corresponding bitumens. Evidently, oxidation with atmospheric oxygen is responsible for dissolution in the resulting distillate products and water (distillate) of a substantial amount of alkali netals, in particular, sodium. A portion of the alkaline-earth elements, evidently, is hydrolyzed. At the Kirishi refinery, the characteristics of commercial bitumens (P_{25}, D_{25}) are adjusted by adding the starting tars and vacuum gas oils. As the content of trace contaminants in tars videly varies with the batch, this fact can explain the experimental data obtained.

The initial tars (sample nos. 5 and 9), which will be further studied in detail, are distinguished (see below) by a fairly high content of trace contaminants Na, Ca, Fe, V, and Ni (Table 3). The studied samples differ in the content of Mg, Ca, Al, Bi, Pb, Mo, and Fe by factors of 10, 1.57, 2, 5.12, 2.43, 8.3, 9.3, and 1.72, respectively. In tars we quantitatively identified (Table 3) 3*d* elements (Ni, V, Co, Cu, Mn, Fe, Cr), which catalyze the homolytic degradation of hydroperoxides forming from oxidation of tars into bitumens, as well as Group VI elements (W, Mo), which catalyze heterolytic degradation of these hydroperoxides. Such *s* elements as Mg, Ca, Sr, and Ba also form complexes with oxygen-containing compounds of the initial tars and bitumens. However, their catalytic effect is substantially weaker compared to 3*d* elements [2].

The dominating trace contaminants in tar no. 5 are Na, Mg, Ca, Ba, Al, W, Fe, Cu, V, and Ni, and in tar no. 9, Na, Ca, Ba, Al, Bi, Pb, Fe, Cu, V, Ni, I, and Sn. Tar nos. 1–10 differ fairly substantially in the content of trace contaminants. Table 3 does not contain data for tars with identical content of trace elements, that is, each initial tar and bitumen has its individual content of trace elements. Each tar is characterized by the maximal content of specific element (one of several). However, the set of the dominating microelements is fairly constant for virtually all tars. The main trace contaminants are the following elements (including organometallic compounds): Na, Mg, Ca, Ba, Al, Fe, Cu, V, and Ni.

Evidently, the total amount of about 1 g kg^{-1} tar is sufficient for trace contaminants to act as a catalyst in the oxidation stage. The effect of this catalyst is manifested in each tar in a specific way, that is, tar oxidation into bitumen and its cross-linking are affected by this factor. Eventually, this affects the consumer properties (above all, thermal stability) of the resulting bitumens.

The above data are insufficient for making a conclusion as to what trace contaminants (when all of them occur in comparable amounts) are desirable in tar and what are not. Undoubtedly, 3*d* elements (Fe, Cu, V, and Ni) exert the strongest influence on oxidation and probably cross-linking of bitumens. This influence is much stronger than that of *s* elements (Na, Mg, Ca, Ba).

Notably, unlike Kirishi refinery, bitumens available from Ukhta and Yaroslavl refineries, as well as from Neste, do not contain tin and tungsten. The total contents of trace contaminants, both metals and nonmetals, in the bitumens studied (Table 4) are comparable. Heavy oil residues (tars and bitumens) are characterized by the occurrence of porphyrin complexes of vanadium and nickel [3]. The content of these elements in the bitumens proved to differ substantially. Moreover, the vanadium-to-nickel ratios differ as well (Table 4).

Thus, each of the tars and bitumens studied (Tables 3, 4) has its specific content of trace contaminants, both metals and nonmetals, which undoubtedly affects the commercial characteristics of bitumens both during their production and under operation as road pavements.

CONCLUSIONS

(1) Tars available from Kirishi refinery, when stored for 6 months under laboratory conditions in closed reservoirs, get harder, as indicated by approximately twofold increase in their conventional viscosity and decrease in penetration.

(2) Tars available from Kirishi refinery differ substantially in the content of active carboxy groups (3.87–17.86 mg KOH g^{-1}). BDUS 70/100 bitumens prepared from the above-mentioned tars are characterized by a fairly widely varying content of active carboxy groups (3.8–31.2 mg KOH g^{-1}). Bitumens available from the Ukhta refinery have the maximal content of carboxy groups.

(3) Tars available from Kirishi refinery differ significantly in the amount of Mg, Na, Al, P, Ti, Ca, Fe, Mn, V, Ni, Sr, Zr, Ba, Bi, and Pb. Similar to tars, the trace contaminants contained in the maximal amounts in the bitumens studied are Na, Mg, Ca, Ba, Al, Fe, Cu, V, Ni, and I.

(4) The tars and bitumens studied contain up to 25 trace contaminants, both metals and nonmetals, whose total content varies within 443–1265 ppm.

(5) The total content of trace contaminants in

bitumens available from Kirishi refinery is lower than in tars owing to dilution of the commercial product by vacuum gas oil.

REFERENCES

1. Kolbanovskaya, A.S. and Mikhailov, V.V., *Dorozhnye bitumy* (Paving Bitumens), Moscow: Transport, 1973.
2. Syroezhko, A.M., *Zhidkofaznoe okislenie alkanov, tsikloalkanov, ikh kislorodsoderzhashchikh proizvodnykh kislorodom i ozonom v prisutstvii soedinenii s- i d-elementov* (Liquid-Phase Oxidation of Alkanes, Cycloalkanes, and Their Oxygen-Containing Derivatives with Oxygen and Ozone in the Presence of Compounds of *s* and 3*d* Elements), Leningrad: Leningr. Tekhnol. Inst. im. Lensoveta, 1984.
3. Khudyakova, T.S., Rozental', D.A., and Malikova, I.A., *Adgezionnye svoistva neftyanykh bitumov i sposoby ikh korrektirovki: Tematicheskii obzor* (Adhesion Properties of Oil Bitumens and Ways To Adjust Them: Topical Review), Moscow: TsNIITEneftekhim, 1991, issue 3.

Russian Journal of Applied Chemistry, Vol. 75, No. 5, 2002, pp. 846–848. Translated from Zhurnal Prikladnoi Khimii, Vol. 75, No. 5, 2002, pp. 864–865.
Original Russian Text Copyright © 2002 by Uritskaya, Kitaev, Belova.

BRIEF COMMUNICATIONS

Kinetics of Cadmium Sulfide Precipitation from Aqueous Thiourea Solutions

A. A. Uritskaya, G. A. Kitaev, and N. S. Belova

Ural State Technical University, Yekaterinburg, Russia

Received December 26, 2000; in final form, August 2001

Abstract—Kinetics of cadmium sulfide precipitation with thiourea from solutions of cadmium(II) ammine complexes under conditions of spontaneous nucleation of the solid phase in the bulk of solution was studied.

Cadmium sulfide is widely used in semiconductor devices [1]. One of the methods for obtaining cadmium sulfide as precipitates and thin films on the surface of dielectrics is its chemical precipitation with thiourea from alkaline solutions of cadmium complexes [2]. The properties of semiconducting materials based on CdS essentially depend on their preparation procedure.

In this work we studied the kinetics of chemical precipitation of cadmium sulfide. When thiourea is added to an alkaline solution of a complex cadmium salt, the transparent solution becomes turbid owing to formation of the CdS solid phase by the reaction

$$[Cd(NH_3)_n]^{2+} + (NH_2)_2CS + 2OH^- = CdS + nNH_3 + H_2NCN + 2H_2O. \quad (1)$$

The surface of the solid phase forming under conditions of homogeneous nucleation continuously changes owing to an increase in the size of CdS particles during the process.

The kinetics of this heterogeneous process was monitored by sampling from a reactor. The cadmium(II) concentration in samples was determined with Dithizone [3]. The experiments were carried out at 298, 308, and 318 K. Working solutions were prepared in volumetric flasks by combining appropriate volumes of the starting solutions in the following sequence: 1 M solution of cadmium sulfate, 25% aqueous ammonia, 0.5 M solution of thiourea, 1 M solution of alkali, and distilled water.

Typical kinetic curves are S-shaped, which is characteristic of heterogeneous autocatalytic processes. Since cadmium sulfide is formed by the reaction of two compounds, a complex cadmium salt and thiourea, we described the reaction rate by the equation

$$\omega = d(c_{0,A} - c_A)/dt = K_{exp}(c_{0,A} - c_A)^{2/3} c_A c_B, \quad (2)$$

where $c_{0,A}$ and c_A are the concentrations of the complex cadmium salt (M) at $t = 0$ and $t > 0$, respectively; $c_{0,B}$ and c_B are the concentrations of thiourea (M) at $t = 0$ and $t > 0$; $(c_{0,A} - c_A) = (c_{0,B} - c_B) = x$ is the amount of cadmium sulfide (M) formed in time t from the beginning of the reaction; $(c_{0,A} - c_A)^{2/3} = x^{2/3}$ is a quantity proportional to the surface area of CdS particles formed in a homogeneous solution.

The number of particles is assumed to remain constant, and their weight and size increase in the course of the process [4].

Equation (2) is integrated by reducing it to the tabular integral [5]. After introducing the dimensionless parameters $a = c_A/c_{0,A}$ and $b = c_{0,B}/c_{0,A}$, the equation takes the form

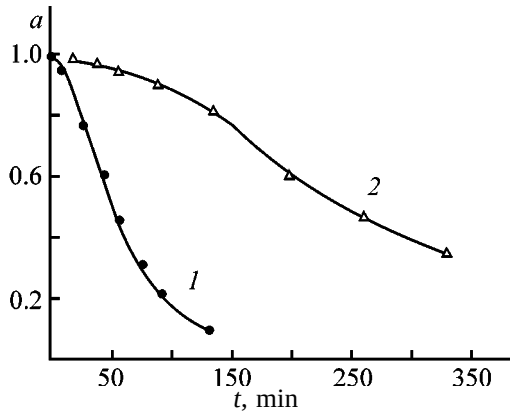

Fig. 1. Kinetic curves at 308 K: (*a*) $c_A/c_{0,A}$ and (*t*) time. pOH and c_{NH_3} (M): (*1*) 1.4 and 1; (*2*) 1.8 and 1.25; the same for Fig. 2.

1070-4272/02/7505-0846$27.00 © 2002 MAIK "Nauka/Interperiodica"

$$Z(a,t) = 0.5\ln\frac{[1-(1-a)^{2/3}]^3}{2} - \frac{1}{2b^{2/3}}\ln\frac{[b^{1/3}-(1-a)^{1/3}]^3}{b-(1-a)}$$
$$- 3^{1/2}\arctan\frac{2(1-a)^{1/3}+1}{3^{1/2}} + \frac{3^{1/2}}{b^{2/3}}\arctan\frac{2(1-a)^{1/3}+b^{1/3}}{b^{1/3}3^{1/2}}$$
$$- \frac{3^{1/2}(1-b^{2/3})}{b^{2/3}}\arctan 3^{-1/2} = c_{0,A}^{5/3}(1-b)K_{exp}t. \quad (3)$$

Equation (3) is linear in the coordinates $-Z(a, t)$–t (Fig. 2) with the slope $K_{op} = c_{0,A}^{5/3}(1 - b)K_{exp}$. From Eq. (3), we calculated the experimental rate constant of the reaction K_{exp}. This constant depends on temperature and carries information on the influence of all the substances involved in the process.

The results of treating the experimental data by Eq. (3) (MathCAD 2000 Professional package) are given in Fig. 2. The obtained data allow us to determine the reaction order n_i with respect to each reagent from the experimental rate constants of the reaction at various initial concentrations of the ligand and thiourea and various pH. We calculated the kinetic orders with respect to the components by the equation

$$\ln K_{exp} = \ln K_i + n_i \ln c_i. \quad (4)$$

The graphic solution of Eq. (4) is given in Fig. 3.

The kinetic studies showed that the rate of cadmium sulfide formation is proportional to the product of the concentrations of the reaction mixture components, raised to the following powers:

Reactant	n_i
$[Cd(NH_3)_n]^{2+}$	1.0
OH^-	1.0
$(NH_2)_2CS$	1.0
NH_3	–3.0

The experimental constants obtained by processing the kinetic curves by Eq. (3) at 289, 308, and 318 K allowed us to determine the activation energy of the process by Arrhenius equation (Fig. 4).

The activation energy of the process is 77 843 J mol^{-1}. The pre-exponential factor of the Arrhenius equation was calculated from the true rate constant K_0 of reaction (1) related to unit concentrations of the reaction mixture components (with regard to the reaction order with respect to the reactants):

$$K_0 = \frac{K_{exp}c_{NH_3}^3}{c_{OH}} = 1.27 \times 10^{17}. \quad (5)$$

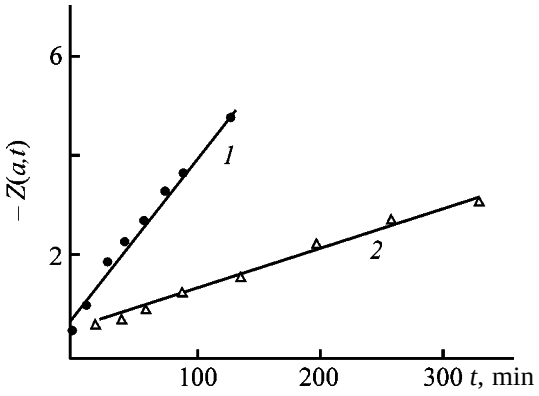

Fig. 2. Plot of $Z(a,t)$ vs. time t at 308 K.

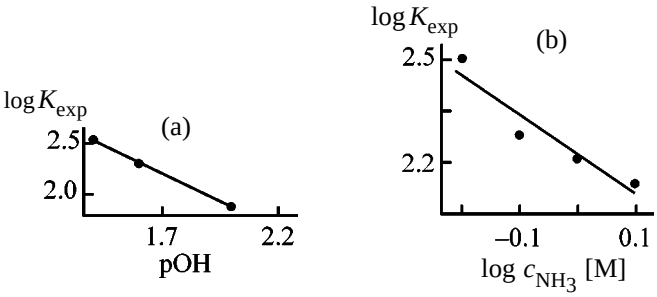

Fig. 3. Graphic determination of the reaction order with respect to the concentrations of (a) OH^- ions and (b) ammonia c_{NH_3}.

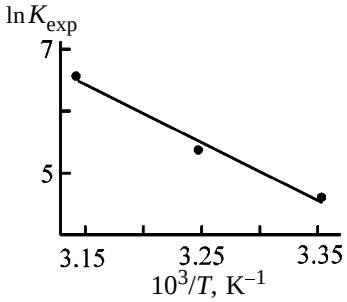

Fig. 4. Determination of the activation energy by Arrhenius equation. (T) Temperature.

From the experimental data on cadmium sulfide precipitation with thiourea from ammonia solutions, we obtained a kinetic equation allowing evaluation of conditions that provide the required reaction rate; the rate, in turn, governs the morphology of the precipitate or film of cadmium sulfide:

$$dx/dt = 1.27 \times 10^{17}\exp(-77\,844/8.134T)x^{2/3}c_{NH_3}^{-3}c_{OH^-}$$
$$\times (c_{0,A} - x)(c_{0,B} - x). \quad (6)$$

ACKNOWLEDGMENTS

The study was financially supported by the Russian Foundation for Basic Research (project no. 01-03-96518).

REFERENCES

1. Chopra, K.L. and Das, S.R., *Thin Film Solar Cells*, New York, 1983.
2. Yatlova, L.E., Uritskaya, A.A., Kitaev, G.A., and Dzyuba, T.A., *Zh. Prikl. Khim.*, 1993, vol. 66, no. 9, pp. 1995–2000.
3. Ivanchev, G., *Ditizon i ego primenenie* (Dithizone and Its Application), Moscow: Inostrannaya Literatura, 1962.
4. Delmon, B., *Introduction a la cinetique heterogene*, Paris: Technip, 1969.
5. Dwight, H.B., *Tables of Integrals and Other Mathematical Data*, New York: MacMillan, 1961.

Russian Journal of Applied Chemistry, Vol. 75, No. 5, 2002, pp. 849–851. Translated from Zhurnal Prikladnoi Khimii, Vol. 75, No. 5, 2002, pp. 866–868.
Original Russian Text Copyright © 2002 by Natorkhin.

BRIEF COMMUNICATIONS

Effect of KBr Additions on NiS Anodic Dissolution in Sulfate Electrolytes

M. I. Natorkhin

St. Petersburg State Technical University, St. Petersburg, Russia

Received October 21, 1999; in final form, July 2001

Abstract—Electrochemical behavior of nickel sulfide (NiS) in 0.5 M solutions of Na_2SO_4 and $CuSO_4$ at pH 2.0–2.2 and T = 90°C was studied. A possibility was shown for depassivation and efficient dissolution of nickel sulfides upon addition of KBr to the electrolyte.

Oxidative dissolution of sulfides of non-ferrous metals is a promising hydrometallurgical process [1–3]. As found previously [4, 5], autoclave leaching by H_2SO_4 solution results in active dissolution of nickel sulfides with H_2S evolution. However, utilization of the forming H_2S is a serious problem, and therefore efforts are made to develop alternative procedures for leaching of nickel concentrates.

In this study we examined the effect of bromide ions on the anodic dissolution of nickel sulfide in acidic sulfate solutions.

According to [6], autoclave leaching of lower nickel sulfides (Ni_3S_2 and Ni_7S_6) results in stepwise formation of sulfides with increasing sulfur content, up to NiS. Therefore, for our study we chose β-NiS with 50% nickel content obtained by a direct synthesis from cathodic nickel (N0 grade) and sulfur (analytically pure grade) [7]. The working electrode was made by soldering a piece of nickel sulfide to a copper holder. The back side of the electrode was insulated with nitrolacquer. The working surface of the electrode (surface area 1 cm^2) was smoothed out with a flint-paper no. 0 and washed with alcohol and distilled water. Electrolytes was prepared using Na_2SO_4 and $CuSO_4 \cdot 5H_2O$ (both analytically pure grade). Solution pH 2.0–2.2 was adjusted with a solution of H_2SO_4 (ultrapure grade). Potassium bromide was of chemically pure grade.

The study was carried out by cyclic voltammetry (CVA) on a PI-50-1.1 potentiostat and a PDP4-002 recorder in a YaES-1 standard electrochemical cell at 90 ± 0.5°C (Fig. 1). The temperature was controlled with a UTU-2/77 thermostat. We used the following three-electrode scheme: nickel sulfide sample as a working electrode, platinum auxiliary electrode, and saturated silver chloride reference electrode (the potentials are referenced to standard hydrogen electrode).

To carry out the experiments, we filled the cell with 50 ml of 0.5 M solutions of $CuSO_4$ or Na_2SO_4 with a KBr addition. The nickel(II) content in the anolyte was determined by the known photometric procedures [8, 9].

The anodic dissolution of nickel sulfide in $CuSO_4$ solution is accompanied by electrode passivation

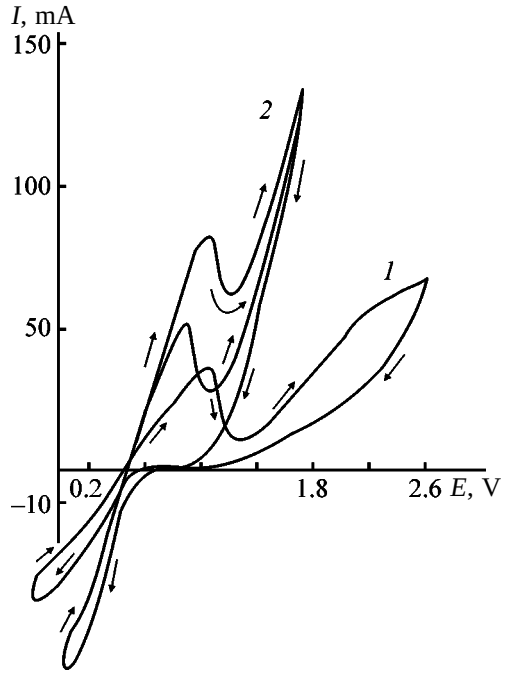

Fig. 1. Cyclic voltammograms of NiS (50%) in solutions of (*1*) 0.5 M $CuSO_4$ and (*2*) 0.5 M $CuSO_4$ + 100 g l^{-1} KBr at pH 2.1. Temperature 90 ± 0.5°C, scanning rate 100 mV s^{-1}; the same for Fig. 3. (*I*) Anode current and (*E*) potential; the same for Fig. 3.

1070-4272/02/7505-0849$27.00 © 2002 MAIK "Nauka/Interperiodica"

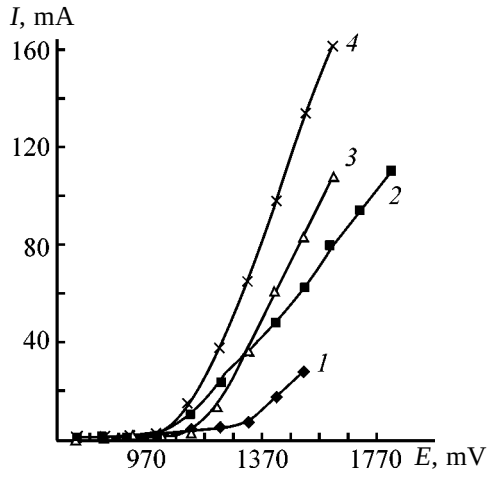

Fig. 2. Stationary currents for NiS electrode in 0.5 M $CuSO_4$ solution. Temperature 90°C, pH 2.1–2.2. (*I*) Current and (*E*) potential; the same for Fig. 4. Addition of KBr (g l^{-1}): (*1*) 20, (*2*) 40, (*3*) 100, and (*4*) 200.

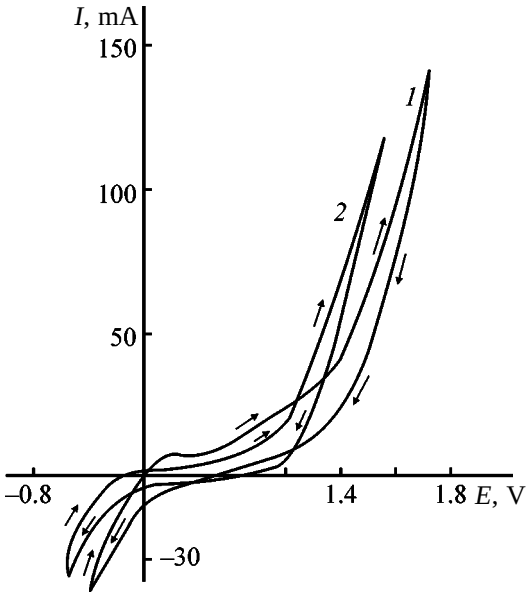

Fig. 3. Cyclic voltammograms of NiS (50%) in solutions of (*1*) 0.5 M Na_2SO_4 and (*2*) 0.5 M Na_2SO_4 + 40 g l^{-1} KBr at pH 2.0.

owing to the formation of a dense black-blue Cu_2S film at the potential of +1170 mV. Sodium chloride is known as a depolarizer of this process [10, 11]. Chlorides are inconvenient for industrial use because, first, chloride depolarization becomes apparent at a relatively high concentration of chloride ions [11], and, second, chloride ions prevent subsequent nickel electroextraction. Bromide ions forms stronger complexes with Cu(I) than chloride ions: $\log\beta_{Cu(I)}$ is 5.92 for Br^{-1} and 5.35 for Cl^{-1} [12]. We performed the experiments with KBr additions (Fig. 2). The effect of these additions becomes appreciable at a KBr concentration of 40 g l^{-1}. In the process, a blue solution of copper sulfate changes its color for green owing to the formation of Cu(I) complex compounds, nickel sulfide is actively dissolved, and a thin yellow deposit of elemental sulfur and foxy drops of bromine are formed on the electrode surface.

The electrochemical behavior of nickel sulfide changes in the absence of copper(II) ions. The CVA curves for nickel sulfide (50%) in 0.5 M Na_2SO_4 solution and in the same electrolyte with addition of 40 g l^{-1} of KBr are shown in Fig. 3. A small anode maximum corresponding to the NiS dissolution and to its conversion to a passive state is observed in the direct branch of the potential scanning curve. Up to potentials of +970 (curve *2*) and 1370 mV (curve *1*), the sulfide dissolves only slightly. Starting from the potential of +970 mV, bromide ions are oxidized to evolve elemental bromine on the electrode surface:

$$2Br^- - 2e = Br_2^0,\ E^0 = +1065\ \text{mV (SHE)}.$$

Elemental bromine is precipitated as fine drops on the surface of the working electrode over the yellow layer of elemental sulfur. We failed to detect free bromine by the reaction of eosin formation [13] in the cell volume, probably owing to the fact that bromine is poorly soluble in water at 90°C [14] and reacts with water:

$$3Br_2 + 3H_2O = 5HBr + HBrO_3.$$

In addition, drops of free bromine do not stay too long on the surface and penetrate into the bulk of the electrode, giving rise to pitting corrosion and promoting additional dissolution of nickel sulfide.

We calculated the partial currents of nickel(III) passing into the solution (Fig. 4) by the Faraday law using the nickel(II) concentration found in the anolyte after dissolution of the working electrode for 15 min at a prescribed potential. The curves of these currents vs. voltage resemble to some extent the CVA curves. The equivalent nickel(II) current (i.e., the current required for the dissolution of the nickel amount found in the cell volume by the photometric technique) appeared to be significantly higher than the integral current measured with a potentiostat. This may be due to secondary dissolution of nickel sulfide in elemental bromine deposited on the electrode surface.

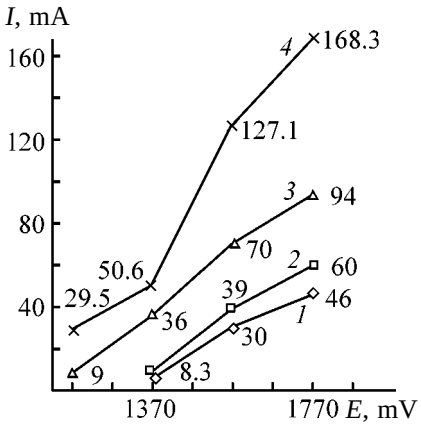

Fig. 4. Partial nickel(II) currents for NiS (50%) dissolution in solutions of (*1*) and (*2*) Na_2SO_4 and (*3*) and (*4*) 0.5 M Na_2SO_4 + 40 g l^{-1} KBr at 90°C. Current: (*1, 3*) NiS and (*2, 4*) partial.

CONCLUSIONS

(1) An addition of KBr to a solution of copper sulfate results in the depolarization of the anodic dissolution of NiS. The addition becomes effective at the KBr concentration of 40 g l^{-1}.

(2) Anodic dissolution of nickel sulfide in the presence of bromide ions results in deposition of elemental bromine on the sulfide surface, which causes pitting corrosion and secondary oxidation of nickel sulfide with elemental bromine. The pitting corrosion leads to rapid breakdown of NiS.

REFERENCES

1. Chizhikov, D.M., Gulyanitskaya, Z.F., and Pliginskaya, L.V., *Elektrometallurgiya medno-nikelevykh sul'fidnykh splavov v vodnykh rastvorakh* (Electrometallurgy of Copper–Nickel Sulfide Alloys in Aqueous Solutions), Moscow: Nauka, 1977.
2. Sinel'nikov, N.V. and Makarov, S.N., *Gidrometallurgiya medi i nikelya* (Hydrometallurgy of Copper and Nickel), Moscow, 1976.
3. Ogorodnikov, Yu.I. and Ponomareva, E.I., *Elektrovyshchelachivanie khal'kogenidnykh materialov* (Electroleaching of Chalcogenide Materials), Alma-Ata: Nauka, 1983.
4. Borbat, V.F. and Leshch, I.Yu., *Novye protsessy v metallurgii nikelya i kobal'ta* (New Processes in Nickel and Cobalt Metallurgy), Moscow: Metallurgiya, 1976.
5. *Gidrometallurgiya: Sbornik perevodov* (Hydrometallurgy: Coll. of Translations), Laskorin, B.N., Ed., Moscow: Metallurgiya, 1978.
6. Muravchik, B.L. and Kipnis, A.Ya., *Zh. Prikl. Khim.*, 1982, vol. 55, no. 12, pp. 2650–2654.
7. Ivanov, I.S., *Zh. Prikl. Khim.*, 1968, vol. 41, no. 4, pp. 1017–1020.
8. Marczenko, Z., *Kolorymetryczne oznaczanie pierwiastkow*, Warsaw: Naukowa-Techniczne, 1968.
9. Sandell, E.B., *Colorimetric Determination of Traces of Metals*, New York: Interscience, 1959.
10. Sladkov, G.A. and Burygina, E.Kh., *Zh. Prikl. Khim.*, 1988, vol. 51, no. 7, pp. 1489–1492.
11. Kheifets, V.L. and Gran', G.V., *Elektroliz nikelya* (Electrolysis of Nickel), Moscow: Metallurgiya, 1975.
12. Podchainova, V.N. and Simonova, L.N., *Med'* (Copper), Moscow: Nauka, 1990.
13. Charlot, G., *Les methods de la chimie analytique. Analyse quantitative minerale*, Paris: Masson, 1961, 4th ed.
14. Ksenzenko, V.I. and Stasinovich, D.S., *Khimiya i tekhnologiya broma, ioda i ikh soedinenii* (Chemistry and Technology of Bromine, Iodine, and Their Compounds) Moscow: Khimiya, 1979.

Russian Journal of Applied Chemistry, Vol. 75, No. 5, 2002, pp. 852–853. Translated from Zhurnal Prikladnoi Khimii, Vol. 75, No. 5, 2002, pp. 869–870.
Original Russian Text Copyright © 2002 by Binkauskene.

BRIEF COMMUNICATIONS

Procedure for Estimating Nickel Plating Rates

E. Binkauskene

Institute of Chemistry, Vilnius, Lithuania

Received March 22, 2000

Abstract—A method was developed for quick determination of nickel plating rates in sulfate and chloride nickel plating solutions using the Hull cell.

One of topical directions of upgrading nickel plating processes is the development of electrolytes ensuring sufficient intensity of the electrodeposition at reduced concentrations of precursor salts. This is important, on the one hand, for decreasing the amount of toxic nickel(II) salts in electroplating sewage and, on the other hand, for reducing the nickel plating cost (saving of anodes and nickel salts). No reequipment is necessary in this case. However, up to now there are no sufficiently simple and reliable methods for reproducible quantitative estimation of the rate of nickel plating from the electrolytes used in electroplating. The method applied for the total assessment of electrolytes using the Hull cell [1] is unsuitable. The method of rotating disk electrode [2] requires a certain hydrodynamic regime to be maintained during the experiments and therefore is too complicated for industrial use and is not commonly accessible.

The aim of this study was to develop a quick procedure for estimating the rate of nickel plating from nickel solutions in a Hull cell using data furnished by the method of rotating disk electrode. This quick method was tested using five model systems of dilute nickel solutions as example.

EXPERIMENTAL

We used $NiSO_4 \cdot 7H_2O$, $NiCl_2 \cdot 6H_2O$, and H_3BO_3 of chemically pure grade and Na_2SO_4 and $MgSO_4 \cdot 7H_2O$ of analytically pure grade. A sulfate nickel plating solution contained (g l^{-1}) $NiSO_4$ 140, $NiCl_2$ 30, and H_3BO_3 30; in certain cases, we added saccharin (1.5, to reduce the inner tension in electroplated coatings [3]) and sodium or magnesium salts (to increase the electrical conductivity and throwing power of the electrolytes). A chloride nickel plating solution with the same nickel content was also used. A rotating titanium disk electrode built in a fluoroplastic case with a visible surface area of 2 cm^2 served as working electrode. We carried out polarization measurements in a temperature-controlled H-shaped cell with the electrode spaces separated by a diaphragm from Schott glass no. 4. The electrolysis was performed in the galvanostatic mode. We measured the potentials vs. saturated silver chloride electrode. The electrolyte temperature was 30°C, the electrode rotation rate, 950 rpm, and pH, 4.0. From the data obtained, we constructed partial polarization curves of the metal deposition. The current efficiency with respect to nickel was determined by weighing the coatings separated from the titanium support.

The method used for the general assessment of electrolytes in a Hull cell [1] was modified. First, a nickel layer was deposited on the cathode in the electrolyte under study for 5 min at a current of 0.5 A, and then the current was increased in 0.05 A steps, with keeping at every step for 30 s. We stopped increasing current when it attained the critical value I_{cr} at which hydrogen bubbles began to evolve on the nearest edge of the cathode to give a narrow strip of blackening (scorching). We did not stir the solution in the Hull cell, since the bubbling with compressed air gives no way for detecting the onset of hydrogen evolution on the cathode edge. A copper plate of 0.5 dm^2 area served as cathode. The experiments were carried out at 50°C.

The cathodic partial polarization curves obtained on a rotating disk electrode in the course of nickel plating are shown in Fig. 1. It is seen that the introduction of sodium sulfate (curve *2*) into the Watts electrolyte (curve *1*) results in an approximately 75 mA decrease in the current at which low-grade coatings start to form. This corresponds to a decrease in the current density j_c and in the rate of electrodeposition by 3.5 A dm^{-2} and 0.75 μm min^{-1}, respectively. Addition of magnesium sulfate and saccharin

1070-4272/02/7505-0852$27.00 © 2002 MAIK "Nauka/Interperiodica"

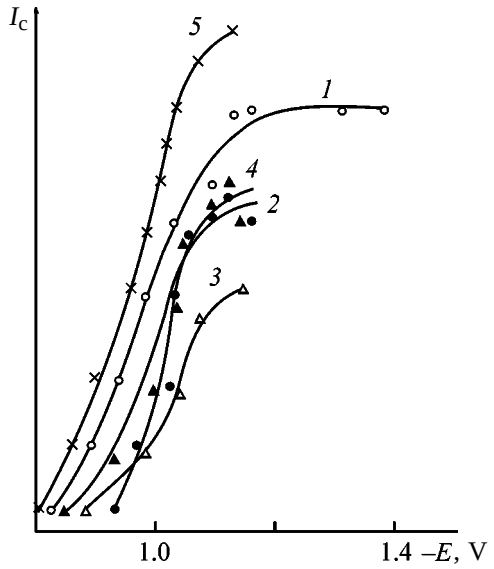

Fig. 1. Partial current I_c of nickel plating as a function of potential E, as measured with a rotating disk electrode in various nickel plating solutions. Temperature 30°C, pH 4.0, n = 950 rpm. Electrolyte composition, g l^{-1}: (*1*) $NiSO_4$, 140; $NiCl_2$, 30; H_3BO_3, 30; (*2*) the same as for *1* + Na_2SO_4, 70; (*3*) the same as for *2* + $MgSO_4$, 20 + saccharin, 1.5; (*4*) the same as for *1* + saccharin, 1.5; and (*5*) $NiCl_2$, 148; Na_2SO_4, 70, H_3BO_3, 30.

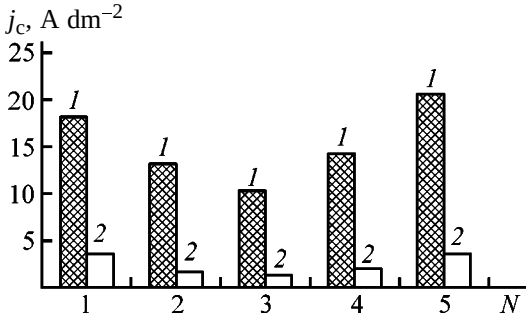

Fig. 2. Limiting current density j_c as a function of the composition of nickel solution for (*1*) rotating disk electrode and (*2*) Hull cell. (*N*) Electrolyte number (as in Fig. 1).

(curve *3*) strengthens the negative effect. In the chloride nickel plating solution (curve *5*), as compared to the sulfate electrolyte (curve *2*), the current at which low-grade coatings start to form is approximately 150 mA higher, which corresponds to an increase in the electrodeposition rate by 1.50 μm min^{-1}.

In spite of the fact that the character of the liquid flow in the vicinity of a rotating disk electrode is rather far from the real nickel plating conditions, the method is flawless from the viewpoint of the stability of the hydrodynamic conditions [2], which eventually allows the mass transfer to be described quantitatively. Hence, the rates of nickel plating determined for five model compositions of electrolytes allow optimization of the deposition rate measurements using the Hull cell.

The cell is connected to an electric circuit with a fixed current of 2 or 1 A, depending on the presence or absence of stirring and heating of the cell, with its size being standard [1] and the size of the cathode being 50 × 100 mm. Usually the nearest edge of the cathode is not scorched under these conditions. Scorching is observed only at a deficiency of nickel salts or at a substantial excess of luster-producing agents or strong foreign inhibitors. To estimate the electrodeposition rate in a solution without stirring, it is necessary to determine experimentally the minimal values of I_{cr} in the cell circuit at which the evolution of hydrogen bubbles on the nearest edge of the cathode, accompanied by scorching, becomes visible. If this condition is met, j_c on the cathode of the Hull cell must correspond to j_c in the polarization curve, which should not exceed the limiting current density j_c observed in the corresponding nickel plating solution.

The limiting values of j_c determined on a rotating disk electrode and in a Hull cell under identical conditions are correlated in Fig. 2. In spite of the fact that the actual values differ from each other by almost an order of magnitude, their dependences on the composition of electrolytes obtained by both methods are in good agreement. Consequently, the advanced procedure using the Hull cell can be used for predicting the nickel plating rates.

REFERENCES

1. Nohse, W., *The Investigation of Electroplating and Related Solutions with the Aid of the Hull Cell*, Teddington: Draper, 1996, pp. 1–25, 33–35, 98–114, 124.
2. Pleskov, Yu.V. and Filinovskii, V.Yu., *Vrashchayushchiisya diskovyi elektrod* (Rotating Disk Electrode), Moscow: Nauka, 1972.
3. *Blestyashchie elektroliticheskie pokrytiya* (Lustrous Electroplated Coatings), Matulis, Yu.Yu., Ed., Vilnius: Mintis, 1969.

Russian Journal of Applied Chemistry, Vol. 75, No. 5, 2002, pp. 854–855. Translated from Zhurnal Prikladnoi Khimii, Vol. 75, No. 5, 2002, pp. 871–872.
Original Russian Text Copyright © 2002 by Sukhanov, Ivashkevich.

BRIEF COMMUNICATIONS

Mutual Transformations of Isomers in *N*-Methyl-5-vinyltetrazole Copolymers

G. T. Sukhanov and O. A. Ivashkevich

Altai Federal Research and Production Center, Biisk, Altai krai, Russia

Received December 18, 2000

Abstract—Mutual transformations of N^1 and N^2 isomeric derivatives of 5-vinyltetrazole polymers in the absence of a solvent were studied.

Polymeric materials based on vinyltetrazoles exhibit a combination of unique properties, in particular, high heat resistance (T = 230–380°C) at a high energy capacity (Q_{comb} up to 2800 kcal kg^{-1}, ρ = 1.32–1.5 g cm^{-3}) and a high nitrogen content (up to 65%) [1], high sorption capacity for environmentally hazardous ions of heavy and transition metals [2], and physiological activity of some derivatives [3, 4].

Mutual transformations of 1,5 and 2,5 isomers of disubstituted low-molecular-weight tetrazole derivatives in solution are described in [5, 6]. Since the physicochemical properties of tetrazoles are largely dependent on the position of substituent at the nitrogen atom of the heteroring, it is important to study possible mutual transformations of isomeric derivatives of *N*-substituted 5-vinyltetrazole polymers.

When studying transformations occurring in a copolymer of 1-methyl-5-vinyltetrazole (1-MVT) and 2-methyl-5-vinyltetrazole (2-MVT) on storage and heating in the absence of a solvent, we detected mutual transformation of the 1-MVT and 2-MVT isomeric units. At 20–25°C, the relative content of the 2-MVT units slowly grows. An equilibrium is attained at the ratio 1-MVT : 2-MVT = 1 : 3. Prolonged heating at 80°C, on the contrary, results in a slow increase in the 1-MVT fraction (by 1% in 25–30 h).

By analogy with the chemistry of tetrazole monomers [5, 6], mutual transformations of N^1 and N^2 isomers are facilitated by alkylating agents or by formation of the corresponding tetrazolium salts. Therefore, it can be suggested that, under polymerization conditions, *N*-methyl-5-vinyltetrazole units undergo partial quaternization.

An ^{1}H NMR study of the products (PVT-M, M-PVT, see below) formed in heterophase methylation of poly-5-vinyltetrazole (PVT) with dimethyl sulfate showed that the spectrum of the M-PVT copolymer, along with the signals of the monomethylated products (methyl groups of 1-MVT, 3.6 ppm, and 2-MVT units, 4.2 ppm) [7], contains a weak signal at 4.6 ppm, which can be assigned [8] to the products of "second" exhaustive methylation with formation of *N*,*N*'-dimethyl-5-vinyltetrazolium methyl sulfate (TS) fragments.

The samples of poly-1-methyl-5-vinyltetrazole (PMVT-1), poly-2-methyl-5-vinyltetrazole (PMVT-2), PVT-M, and M-PVT prepared under conditions excluding formation of TS showed no evidence of mutual transformation of the isomers under similar conditions. Apparently, mutual transformation of 1-MVT and 2-MVT units occurs via TS.

EXPERIMENTAL

Polymers and copolymers of 1-MVT and 2-MVT were prepared by two pathways: a sequence of polymer-analogous transformations [1] polyacrylonitrile → PVT → 1-MVT–2-MVT copolymer (M-PVT) and radical copolymerization of freshly distilled 1-MVT and 2-MVT (PVT-M) in the bulk in the presence of azobis(isobutyronitrile) (0.5 mol %) at 65°C or homopolymerization of 1-MVT (PMVT-1) or 2-MVT (PMVT-2), followed by reprecipitation of the resulting polymers from dimethylformamide solution into methanol. The conditions of PVT synthesis are given in [9].

Changes in the isomeric composition of the polymers were monitored by IR spectroscopy (Perkin–Elmer spectrometer, model 684) using KBr technique (4 mg polymer per 600 mg KBr), namely, by changes in the intensities of the bands at 1100 (characteristic of stretching–bending vibrations of the ring in PMVT-

1070-4272/02/7505-0854$27.00 © 2002 MAIK "Nauka/Interperiodica"

1) and 734 cm^{-1} (characteristic of out-of-plane bending vibrations of the ring in PMVT-2) [8].

The ^1H NMR spectra were recorded on an INM PS-100 spectrometer (~3% solutions of polymers in DMSO-d_6, 353 K).

The degree of methylation of PVT was determined by titration of dimethylformamide solutions of the polymers, from the sum of the residual N–H groups of the acid and alkali metal ions.

To a solution of 0.1 mol of PVT and 0.06 mol (6.34 g) of sodium carbonate in 75 ml of water at 35–40°C, we added 110 ml of methylene chloride and then, dropwise over a period of 60 min, 0.12 mol (15.12 g) of dimethyl sulfate. The mixture was allowed to stand for 30 min, after which methylene chloride was distilled off, the mother liquor was decanted, and the polymer was reprecipitated two times from aqueous acetone into isopropyl alcohol. Yield 9.9 g (90%), degree of alkylation 99.9%. IR spectrum, ν, cm^{-1}: 734 (δ_{ring}), 1041, 1100 (ν, δ_{ring}); 1494, 1525 (C=N). ^1H NMR spectrum, δ, ppm: 3.6 (3H, N^1–CH_3), 4.2 (3H, N^2–CH_3), 4.6 (3H, N^4–CH_3). Content, wt %: 1-MVT 44.4 and 2-MVT 54.6.

CONCLUSION

In copolymers of *N*-methyl-5-vinyltetrazoles containing an impurity of *N*,*N*'-dimethyl-5-vinyltetrazolium salt units, in the absence of a solvent, the 1-methyl-5-vinyltetrazole and 2-methyl-5-vinyltetrazole units undergo mutual transformations. At 20±5°C, the content of the second component grows, and an equilibrium is attained at a component ratio of 1 : 3. Heating of such a copolymer at 80°C causes a reverse process: increase in the fraction of 1-methyl-5-vinyltetrazole units (by 1% in 30 h).

REFERENCES

1. Sukhanov, G.T., Komarov, V.F., Kizhnyaev, V.N., *et al.*, Abstracts of Papers, *II Ural'skaya konferentsiya* (II Ural Conf.), Perm, 1997, pp. 5–6.
2. Kizhnyaev, V.N., Synthesis, Study, and Chemical Modification of Polymers Derived from Vinyltetrazoles, *Cand. Sci. Dissertation*, Irkutsk, 1987.
3. Smirnov, A.I., Kizhnyaev, V.N., Aparin, P.G., ad Vasil'eva, L.S., Abstracts of Papers, *IX Vsesoyuznyi nauchnyi simpozium "Sinteticheskie polimery meditsinskogo naznacheniya"* (IX All-Union Scientific Symp. "Synthetic Polymers for Medical Purposes"), Zvenigorod, 1991, p. 52.
4. Kruglova, V.A., Annenkov, V.V., Moskvina, L.T., *et al.*, *Khim.-Farm. Zh.*, 1989, vol. 23, no. 2, pp. 195–199.
5. Isida, T., Kozima, S., Nabika, N., and Sisido, K., *J. Org. Chem.*, 1971, vol. 36, pp. 3807–3813.
6. Podgurskii, A.I., Zlotin, S.G., Krayushkin, M.M., and Luk'yanov, O.A., *Izv. Akad. Nauk SSSR, Ser. Khim.*, 1985, no. 1, pp. 236–240.
7. Ivashkevich, O.A., Gaponik, P.N., Lesnikovich, A.I., *et al.*, *Vysokomol. Soedin., Ser. B*, 1991, vol. 33, no. 4, pp. 275–279.
8. Zhivich, A.B., Koldobskii, G.N., and Ostrovskii, V.A., *Khim. Geterotsikl. Soedin.*, 1990, no. 12, pp. 1587–1599.
9. Sukhanov, G.T., Gareev, G.A., Kizhnyaev, V.N., and Kirillov, L.G., Abstracts of Papers, *III Vsesoyuznoe soveshchanie po khimii reaktivov* (III All-Union Meet. on Chemistry of Reagents), Moscow, 1989, vol. 3, p. 184.

Russian Journal of Applied Chemistry, Vol. 75, No. 5, 2002, pp. 856–860. Translated from Zhurnal Prikladnoi Khimii, Vol. 75, No. 5, 2002, pp. 873–877.
Original Russian Text Copyright © 2002 by Morachevskii.

HISTORY OF CHEMISTRY AND CHEMICAL TECHNOLOGY

70th Anniversary of the Foundation of Russia's Aluminum Industry

Among nonferrous metals, aluminum holds the first place in the production volume. The prospects for this metal are favorable: the demand for aluminum will grow steadily. The annual rise in aluminum consumption is 2.5–3.0% [1, 2].

In 1998, for the first time in its history, the Russian aluminum industry produced more than 3 million tons and in 1999, 3146.2 thousand tons of aluminum. Russia is second in the world in production of primary aluminum only to the United States and first in export amounting to 90% of the metal produced. The share of aluminum in the total export of nonferrous metals by Russia is 46% [3].

According to the available estimates, the production of primary aluminum in Russia will grow within the next few years owing to intensification of the already existing plants and possible construction of new ones. It is expected that the metal production will be 3.7 and 4.2 million tons in, respectively, 2005 and 2010. In the course of the recovery of the national economy, the annual rise in the aluminum consumption within the country, according to different estimates, will be in the range from 50 to 200 thousand tons. This communication briefly outlines the history of setting up the aluminum production in Russia.

Metallic aluminum was first obtained in 1825 by H.Ch. Oersted (1777–1851), a Danish physicist, by reacting aluminum chloride with potassium amalgam. Later, in 1827, F. Wöhler (1800–1884), a German physicist, replaced potassium amalgam in this process with metallic potassium. The further development of methods for producing aluminum is associated with French scientists L. Le Chatelier (1815–1873) [father of H. Le Chatelier (1850–1936), a famous physical chemist] and H. Sainte-Claire Deville (1818–1881). In 1855, L. Le Chatelier developed a method for producing alumina from bauxites, based on heating of powdered bauxites and soda in a reverberating furnace, subsequent separation of sodium aluminate from iron oxide, and treatment of the resulting solution with carbon dioxide. In 1854, Sainte-Claire Deville proposed to reduce the double salt $AlCl_3 \cdot NaCl$ with metallic sodium. In 1856, this method was applied to obtain 25 kg of aluminum. The double salt was, in turn, obtained by heating a mixture of Al_2O_3, NaCl, and carbon in a flow of chlorine, and metallic sodium, by reduction of Na_2CO_3 with carbon at high temperature.

Nikolai Nikolaevich Beketov.

N.N. Beketov (1827–1911), professor of Kharkov University and Academician of the Russian Academy of Sciences since 1886, continued in Russia the studies on mutual displacement of metals, commenced by him in France, and found that aluminum can be obtained by the reaction of cryolite with magnesium (1865). Aluminum was produced during a certain period (1886–1890) at a plant in Germany.

In 1885–1888, a small plant producing aluminum by Sainte-Claire Deville's method existed near Moscow, but the cost of the metal was too high. Aluminum, its properties and alloys, and production process were the subject of several books published in Russia [4, 5].

1070-4272/02/7505-0856$27.00 © 2002 MAIK "Nauka/Interperiodica"

During the period when the chemical method was used (from 1854 till 1890), i.e., for more than thirty years, only about 200 tons of aluminum was produced by all plants.

On April 23, 1886, Paul Heroult (1863–1914) in France, and independently on July 9 of the same year, Charles Hall (1863–1914) in the United States, claimed patents for a method for obtaining aluminum by electrolysis of alumina dissolved in molten cryolite. These dates signify the birth of the modern aluminum production and, simultaneously, the beginning of wide use of aluminum in engineering.

The commercial production of aluminum by electrolysis was commenced in France in 1889. The presence of large high-quality bauxite deposits (with SiO_2 content <3%) and rich hydroelectric resources favored the successful development of aluminum industry in this country. The development of the industrial technology was much promoted by C. Bayer (1847–1904), an Austrian chemist-technologist, who, when working at Russian chemical plants, proposed a rather perfect way to produce alumina from bauxites. This method was used already in the first French plants. To the centennial anniversary of Bayer's method, Habashi devoted a paper published in 1988 [6].

By 1912, aluminum was commercially produced already in nine Western countries, with about 60 thousand tons of the metal smelted annually; however, the theory of electrolysis of alumina–cryolite melts was not developed, and physicochemical properties of the electrolyte were known poorly.

In Russia, the electrolytic production of aluminum was initially studied in St. Petersburg at two higher school institutions: Institute of Electrical Engineering and Polytechnic Institute. Both the institutes started, already in the beginning of the XX century, training of specialists in applied electrochemistry. Professors A.A. Krakau (1855–1909) and N.A. Pushin (1875–1947) at the Institute of Electrical Engineering and V.A. Kistyakovskii (1865–1952, academician of the Academy of Sciences of the USSR since 1929) and P.P. Fedot'ev (1864–1934, corresponding member of the Academy of Sciences of the USSR since 1933) took active part in this process.

In 1909–1914, Pushin and co-workers actively studied electrolytic production of aluminum [7]. In particular, they studied equilibria in binary fluoride systems, including those in the system $NaF–AlF_3$. The absence at that time of any reliable evidence concerning bauxite deposits in Russia forced Pushin to obtain alumina from a Ural mineral soimonite (corundum) containing in anhydrous form (wt %) Al_2O_3 63, SiO_2 13, Fe_2O_3 18, CaO 3, and MgO 1. Alumina was produced in amount of 7 kg, but the content of SiO_2 could not be made less than 1%.

Pavel Pavlovich Fedot'ev.

Electrolysis of fluoride melts with dissolved alumina at 800–900°C was used to obtain for the first time 0.4 kg of aluminum entirely from domestic raw materials. The researchers aimed to obtain aluminum, even if not very pure, but yet produced "...from exclusively Russian materials, i.e., those of Russian origin" [7].

Thorough investigations were also performed in 1910–1912 by P.P. Fedot'ev and V.P. Il'inskii (1885–1964). They studied the binary system $NaF–AlF_3$, solubility of Al_2O_3 in cryolite, interaction of aluminum with cryolite–alumina melts, decomposition potential of electrolyte in an aluminum bath, formation of aluminum carbide in the bath, and specific features of the anodic process [8, 9]. The authors proposed the optimal composition of the electrolyte and studied all the basic phenomena accompanying electrolysis. Experiments were performed in a laboratory electrolyzer at a current of 200 A. This study laid foundation of in-depth research into the electrolytic production of aluminum and exerted profound influence on the subsequent experimental studies.

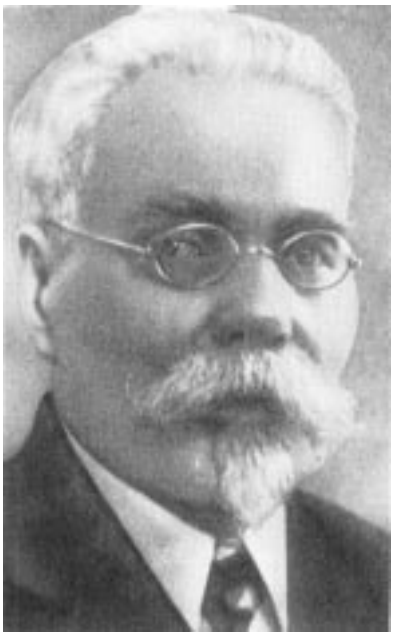

Aleksandr Yakovlevich Yakovkin.

In 1915, Prof. A.N. Kuznetsov (1877–1946) and E.I. Zhukovskii (1892–1965), staff members of the Mining Institute in Petrograd, proposed a method for producing alumina from various kinds of low-grade raw materials, which consisted in smelting in an ore-thermal furnace of aluminosilicates mixed with barium carbonate, carbon, and iron shavings [10]. This smelting yielded a slag containing barium aluminate and ferrosilicon. To isolate pure aluminum hydroxide, the slag was subjected to hydrothermal treatment.

In 1916, a bauxite deposit was discovered near Tikhvin (now in Leningrad oblast). In view of the situation in the country at that time, a geological survey of the deposit was started only in 1920 by a group of geologists headed by professor S.F. Malyavkin (1876–1937). By 1923, it was found that, in the nearest future, the Tikhvin deposit of bauxites can meet the demands of the USSR for aluminum; the low cost of bauxite mining was also noted.

However, these bauxites had a high SiO_2 content (up to 18%) and required development of a new technology for their processing. A search for the most efficient flowsheet for processing of Tikhvin bauxites was commenced at scientific institutions in Leningrad. Such well-known scientists as A.A. Yakovkin (1860–1936), N.P. Aseev (1871–1952), and G.G. Urazov (1884–1957, academician of the Academy of Sciences of the USSR since 1946) took part in these studies. In all stages, much attention was given to the problem of aluminum production from domestic raw materials by such outstanding Russian chemists as academicians V.N. Ipat'ev (1867–1952), V.I. Vernadsky (1863–1945), and N.S. Kurnakov (1860–1941). In the years of World War I, lieutenant-general Ipat'ev headed the Chemical Committee, an institution created to ensure rapid development of the Russian chemical industry and provide the front-line forces with means of chemical protection. In 1915–1916, the scientist did a tremendous work on creating the military-chemical industry in Russia. In 1918–1926, Ipat'ev held high positions in the Soviet State machinery, was a member of the Presidium of the All-Russia Council of National Economy and chairman of the Central Chemical Directorate. In 1919, he headed a special State Committee of Aluminum.

The necessity for obtaining aluminum from domestic ores was stated by Vernadsky and Kurnakov as far back as March 1915 at a meeting of the Department of Physical and Mathematical Sciences of the Academy of Sciences. Vernadsky wrote in 1916 that aluminum has bright future, both in the form of alloys and as pure metal. He mentioned that this is one of most abundant elements of the earth's crust. In 1916, a Directorate for Construction of Aluminum Plants was formed, headed by A.P. Kurdyumov (1857–1926), but no practical results followed under the conditions of that time.

In March 1919, Kurnakov made large efforts to coordinate studies of bauxites, carried out at different institutions. In 1922, Kurnakov and Urazov made a joint report at the III Mendeleev Congress, "Thermal Analysis of Clays and Bauxites," in which they underlined the vital importance of the bauxite rocks found near Tikhvin for creation of the Russian aluminum industry [11]. Urazov, one of Kurnakov's disciples, commenced extensive studies of the chemical and physicochemical properties of domestic bauxites already in 1920. The method of thermal analysis was for the first time applied to determine the mineralogical composition of the rocks.

In 1925 (March 30–April 6), the First All-Union Symposium on nonferrous metals was held. One of the most topical problems discussed at the Symposium was associated with setting up aluminum production in the Soviet Union. This problem was discussed in a report by Kurnakov and co-workers "On Use of Tikhvin Bauxites To Obtain Aluminum" [12]. At the same Symposium, Malyavkin delivered a report on advances in exploration and the expected resources of bauxites in the Tikhvin region [13].

Much attention was given to studies of various

techniques for dressing of Tikhvin bauxites by K.F. Beloglazov (1887–1951), a professor of the Mining Institute.

A key contribution to the development of a technology for processing of high-silica bauxites was made by Prof. Yakovkin, who performed his studies at the Russian Institute of Applied Chemistry. The process was based on sintering of bauxites with soda and lime, which was proposed by G. Muller as far back as 1880 (German Patent 12947 of April 13, 1880). In large-scale laboratory experiments, Yakovkin optimized the composition of the starting stock for the Tikhvin bauxites and developed, together with I.S. Lileev (1882–1966), a method for fractional precipitation of aluminum hydroxide from an aluminate solution (USSR Patent 3985 of November 30, 1927). Later, a desiliconization procedure was introduced to eliminate the fractional precipitation and obtain high-quality alumina. Yakovkin wrote [14]: "The researchers did not aim to develop a certainly original production technique. The task was more moderate: to find the simplest method applicable to our bauxites."

The Second All-Union Symposium on Nonferrous Metals (March 27–April 5, 1927) also paid much attention to processing of domestic bauxites. In an extensive report, Urazov (together with Ya.E. Vil'nyanskii and Yu.V. Morachevskii) considered in detail theoretical foundations of the lime–sodium method for producing alumina from natural aluminosilicates [15]. Lileev reported the results of studies concerned with alumina production from Tikhvin bauxites by sintering.

A pilot production of aluminum from entirely domestic raw materials was organized at Krasnyi Vyborzhets plant in Leningrad under the supervision of P.P. Fedot'ev with participation of his son N.P. Fedot'ev (1897–1969) and Yu.V. Baimakov (1894–1980), chief metallurgist of the plant. Alumina was obtained at the Pilot Plant of the Institute of Applied Chemistry from Tikhvin bauxites by the Muller–Yakovkin–Lileev method. Cryolite and carbon materials used in the process were produced in Russia. The current in the electrolyzers was 2000–2200 A. The first batch of aluminum (8 kg) was produced on March 27, 1929. In the same year, the construction of the Pilot aluminum plant in Leningrad was commenced, which was finished in May 1930. Its aim was to develop a commercial process of aluminum production and to test under industrial conditions various electrolyzer designs for aluminum plants of the country. Baimakov was the chief engineer of the plant; two electrolyzers were designed by N.P. Fedot'ev.

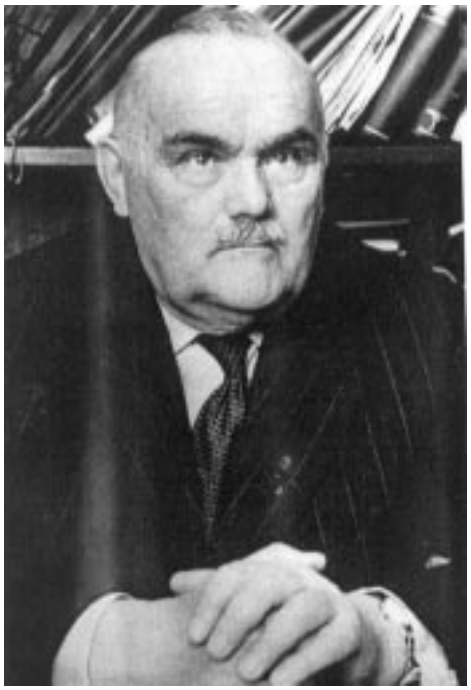

Yurii Vladimirovich Baimakov.

The world production of aluminum grew swiftly in the beginning of the XX century: it increased 30-fold during the period from 1900 to 1927 [16] to become 219.7 thousand tons in 1927, 243.2 thousand tons in 1928, and 264.4 thousand tons in 1929. The actual output capacity of aluminum plants all over the world was as high as 325 thousand tons already in 1925 [17].

On September 14, 1929, the Soviet Government finally defined the scale and schedule of construction of first aluminum plants. A decision was made to construct a plant with annual aluminum output capacity of 5 thousand tons on the basis of Volkhov hydroelectric power station, whose first units were put in operation on December 19, 1926, and a plant producing 15 thousand tons of aluminum annually on the basis of Dnieper hydroelectric power station (Dneproges) whose construction was started in May 1932.

After the Government decision, the production process to be used at these plants was discussed at a special meeting in Moscow. Kurnakov explicitly supported use of the Muller–Yakovkin–Lileev method for the Volkhov aluminum combine and the Kuznetsov–Zhukovskii method for the Dnieper aluminum combine. The latter technique, being more power-consuming, required less expensive electric power that could only be provided by Dneproges. Both the combines were to use Tikhvin bauxites as raw material.

The construction on the Volkhov riverbank was commenced in June 1930. Baimakov, later a professor of the Polytechnic Institute in Leningrad (from 1934 to 1974), was appointed its chief engineer. The construction was fast and the plant was put into operation in the first half of 1932. On May 14, 1932, the first batch of aluminum was obtained (in the initial stage, imported raw materials were used: French alumina and anodes, and cryolite from Greenland). This day is commonly considered the birthday of the domestic aluminum industry. By the end of 1933, the combine reached its designed output capacity [18].

In 1930, the construction of the Dnieper Aluminum Combine was commenced near the hydroelectric power station. Zhukovskii, later a professor of the North-Caucasian Mining and Smelting Institute (from 1938 till 1965), was the chief engineer of the project. The first set of electrolyzers was put in operation in June 1933, and the alumina production, in April 1934. At those years, the Dnieper plant was one of the largest in Europe.

At present, 11 aluminum plants are in operation in Russia, which include such giants as Bratsk and Krasnoyarsk plants having no analogs in the output capacity in the world. The annual output of aluminum by each of these plants exceeded 800 thousand tons (in 1998, 844 and 802 thousand tons at the Bratsk and Krasnoyarsk combines, respectively).

At the same time, the established Russia's resources of the main aluminum raw material, high-quality bauxites processable by the simplest and most economical Bayer method, are scanty. According to the available estimates, after the disintegration of the Soviet Union, about 50% of Russian aluminum is produced from imported raw materials. At the same time, the share of raw materials in the production cost of aluminum is rather high. The complicated economical and environmental problems associated with the operation of aluminum plants in Russia and new kinds of market relationships in the domestic aluminum industry were analyzed in detail in [19].

REFERENCES

1. Zel'berg, I., *Metallosnab. Sbyt*, 2001, January, pp. 26–29.
2. Lankin, V.P. and Sysoev, A.V., *Nauchnye i teoreticheskie issledovaniya v metallurgii legkikh metallov* (Scientific and Theoretical Studies in Metallurgy of Light Metals), St. Petersburg: VAMI, 2000, pp. 5–7.
3. Lavrishchev, V.M., *Metallurg*, 2000, no. 6, pp. 5–7.
4. Korenblit, A.I., *Alyuminii, ego dobyvanie, svoistva, obrabotka, splavy i soedineniya, naibolee vazhnye v tekhnike* (Aluminum, Its Mining, Properties, Processing, Alloys, and Compounds Most Important for Technology), Moscow, 1888.
5. Zhukov, N., *Alyuminii i ego metallurgiya* (Aluminum and Its Metallurgy), Moscow, 1893.
6. Habashi, F., *CIM Bull*., 1988, vol. 81, no. 909, pp. 70–74.
7. Pushin, N.A., Dishler, E.E., and Maksimenko, M.S., *Izv. Elektrotekh. Inst*., 1914, no. 10, pp. 213–224.
8. Fedot'ev, P.P. and Il'inskii, V.P., *Izv. Sankt.-Peterb. Politekh. Inst., Otd. Tekh., Estestvozn. Matem*., 1912, vol. 18, no. 1, pp. 147–196.
9. Fedot'ev, P.P., *Khimiko-tekhnologicheskie ocherki* (Essays on Chemical Technology), Moscow: Izd. Vsekhimproma, 1936.
10. Kaluzhskii, N.A. and Taits, A.Yu., *Otechestvennaya metallurgiya alyuminiya – ot pervykh shagov do promyshlennogo proizvodstva* (Domestic Metallurgy of Aluminum: from First Steps to Industrial Production), Moscow: Metallurgiya, 1991.
11. Kurnakov, N.S. and Urazov, G.G., *Trudy III Mendeleevskogo s"ezda po chistoi i prikladnoi khimii* (Proc. III Mendeleev Congr. on Pure and Applied Chemistry), Petrograd: NKhTI, 1923, pp. 37–38.
12. Kurnakov, N.S., Il'inskii, V.P., Britske, E.V., and Sheinin, S.D., *Trudy Pervogo Vsesoyuznogo soveshchaniya po tsvetnym metallam* (Proc. I All-Union Meet. on Nonferrous Metals), Moscow, 1925, pp. 447–468, 483–484.
13. Malyavkin, S.F., *Trudy Pervogo Vsesoyuznogo soveshchaniya po tsvetnym metallam* (Proc. I All-Union Meet. on Nonferrous Metals), Moscow, 1925, pp. 77–93.
14. Yakovkin, A.A., *Legk. Met*., 1932, nos. 5–6, pp. 25–31.
15. Urazov, G.G., Vil'nyanskii, Ya.E., and Morachevskii, Yu.V., *Trudy Vtorogo Vsesoyuznogo soveshchaniya po tsvetnym metallam* (Proc. II All-Union Meet. on Nonferrous Metals), Moscow, 1927, issue 4, pp. 378–391.
16. Tatariiskii, V.S., *Legk. Met*., 1932, no. 1, pp. 12–17.
17. Mikhel'son, M.I. and Purits, M.F., *Legk. Met*., 1932, nos. 5–6, pp. 38–44.
18. Belyaev, A.I., *Tr. Inst. Istor. Estestvozn. Tekh*., 1959, vol. 20, pp. 3–152.
19. Sokolov, V.M., Yagol'tsiner, M.A., Zel'tser, E.V., *et al*., *Alyuminievaya promyshlennost' Rossii v rynochnykh usloviyakh* (Aluminum Industry of Russia in Market Conditions), Kuleshov, V.V., Ed., Novosibirsk: Inst. Ekon. Organiz. Prom. Proizv., Sib. Otd. Ross. Akad. Nauk, 1997.

A. G. Morachevskii

Russian Journal of Applied Chemistry, Vol. 75, No. 6, 2002, pp. 861–865. Translated from Zhurnal Prikladnoi Khimii, Vol. 75, No. 6, 2002, pp. 881–885.
Original Russian Text Copyright © 2002 by Yaroshenko, Savos'kin, Magazinskii, Shologon, Mysyk.

INORGANIC SYNTHESIS AND INDUSTRIAL INORGANIC CHEMISTRY

Synthesis and Properties of Thermally Expandable Residual Graphite Hydrosulfite Obtained in the System HNO_3–H_2SO_4

A. P. Yaroshenko, M. V. Savos'kin, A. N. Magazinskii, V. I. Shologon, and R. D. Mysyk

Litvinenko Institute of Physicoorganic and Coal Chemistry, National Academy of Sciences of Ukraine, Donetsk, Ukraine

Received January 15, 2002

Abstract—Synthesis of bloating residual graphite hydrosulfide with the use of an oxidizing system, fuming nitric acid–concentrated sulfuric acid, was studied at ultralow expenditure of reagents and their separate introduction into the reaction mass. Important parameters of the process were revealed and their effect on the properties of the target product was determined. Ways to diminish to the maximum possible extent the adverse influence of by-products formed in the stage of graphite oxidation on the properties of the target product were found.

Nitric acid, one of the cheapest and most accessible oxidants, is widely used in synthesis of thermally expandable residual graphite hydrosulfites (RGH) [1–6]. Previously, an approach to RGH synthesis at "ultralow" expenditure of components of the intercalation solution has been developed for the example of graphite oxidation in the system chromic anhydride–sulfuric acid [7, 8]. In the present study, the same approach is applied to graphite oxidation in the system fuming nitric acid–concentrated sulfuric acid.

Formation of intercalation compounds of graphite in the system graphite–HNO_3–H_2SO_4 can be described by the following reactions [7]:

$$C_n + Ox \rightarrow C_n^+ + Red, \quad (1)$$

$$C_n^+ + A^- + HA \rightarrow C_n^+A^- \cdot HA. \quad (2)$$

Nitric acid oxidizes the graphite matrix, and sulfuric acid supplies intercalating species (HSO_4^-) and solvating ligands for them. The final product is graphite hydrosulfite.

To control the process of RGH synthesis with the use of the system HNO_3–H_2SO_4 and to vary purposefully the properties of the products obtained, a knowledge is necessary of the nature of active species directly involved in reactions (1) and (2), by-products and their influence on the process of graphite oxidation and on the structure and properties of the graphite intercalation compounds obtained.

Fuming nitric acid, its mixtures with concentrated sulfuric acid, and also mixtures of sulfuric and aqueous nitric acids have been long, and successfully, used in various industrial chemical processes for oxidation and nitration of alkanes, alkenes, arenes, and many other classes of organic compounds. These systems are used to obtain explosives and serve as a medium for carrying out inorganic reactions [9]. The data accumulated for these reactions can be used to describe processes occurring in RGH synthesis with nitric acid oxidizing the graphite matrix.

It is known that fuming nitric acid self-ionizes

$$2HNO_3 \rightleftarrows NO_2^+ + NO_3^- + H_2O, \quad (3)$$

with the content of ionization products depending on temperature. In most cases, the ability of fuming HNO_3 to oxidize and to nitrate is due to the presence of nitronium cations NO_2^+ in the acid.

Formation of graphite nitrate in the system graphite–fuming nitric acid is described by the following scheme [10]

$$\left.\begin{aligned} 2HNO_3 &\rightleftarrows NO_2^+ + NO_3^- + H_2O, \\ C_n + NO_2^+ &\rightarrow C_n^+ + NO_2\uparrow, \\ NO_3^- + mHNO_3 &\rightarrow NO_3^- \cdot mHNO_3, \\ C_n^+ + NO_3^- \cdot mHNO_3 &\rightarrow C_n^+ \cdot NO_3^- \cdot mHNO_3. \end{aligned}\right\} \quad (4)$$

1070-4272/02/7506-0861 $27.00 © 2002 MAIK "Nauka/Interperiodica"

The forming nitrogen dioxide is partly removed into the gas phase and partly reacts in the liquid phase by the scheme [11]

$$\left.\begin{aligned} 2NO_2 + H_2O &\rightarrow HNO_2 + HNO_3, \\ 3HNO_2 &\rightarrow HNO_3 + 2NO + H_2O. \end{aligned}\right\} \quad (5)$$

Introduction of water into fuming nitric acid suppresses the self-ionization reaction (3): the content of nitronium cations NO_2^+ and, consequently, the oxidizing ability of HNO_3 decrease. At water content of 5–8 wt %, NO_2^+ species are no longer formed in nitric acid. It is noteworthy that treatment of graphite with dilute aqueous solutions of nitric acid does not yield intercalation compounds of graphite, and use of fuming nitric acid gives graphite nitrite only in the second stage.

In H_2SO_4–HNO_3 mixture, nitric acid is ionized to give nitronium cation by the scheme

$$HNO_3 + H_2SO_4 \rightleftarrows NO_2^+ + HSO_4^- + H_2O. \quad (6)$$

A similar reaction proceeds in mixtures of HNO_3 with other strong acids, e.g., $HClO_4$, H_2SeO_4, HF, or HBr. Use of H_2SO_4–HNO_3 mixtures makes it possible to achieve a higher concentration of nitronium cations in the reaction mass, compared with that in fuming HNO_3. In addition, NO_2^+ cations in the system HNO_3–H_2SO_4 completely disappear at much higher content of water, compared with the case of nitric acid.

The equilibrium constant of reaction (6) is 30 – 42 [9]. This means that, at a sufficient excess of nitric acid and low content of water, nitric acid is nearly completely ionized to give a nitronium cation. With increasing content of water and nitric acid, the degree of conversion of the acid into the nitronium cation becomes lower. As a result, the concentration of undissociated nitric acid and nitrate anions in the system decreases. Below are given degrees α of conversion of anhydrous nitric acid into the nitronium cation in HNO_3–H_2SO_4 mixtures of varied composition [9]:

H_2SO_4 : HNO_3, wt % : wt %	α	H_2SO_4 : HNO_3, wt % : wt %	α
95 : 5	1.0	40 : 60	0.167
90 : 10	1.0	20 : 80	0.098
85 : 15	0.8	10 : 90	0.059
80 : 20	0.625	0 : 100	0.01
60 : 40	0.288		

Analysis of the results of oxidation and nitration of various organic compounds in the system H_2SO_4–HNO_3 shows that nitrogen oxides formed in the reaction mass decelerate the main reactions, lower the concentration of sulfuric acid, react with the starting substrates, and, in some cases, complicate the process control [9].

The main primary by-product is nitrogen dioxide. It can react by reactions (5) or disproportionate to form nitrosonium cation and nitrate anion:

$$2NO_2 \rightleftarrows NO^+ + NO_3^-. \quad (7)$$

Nitrosonium cations further react with bisulfate anions to give nitrosylsulfuric acid:

$$NO^+ + HSO_4^- \rightarrow NOHSO_4. \quad (8)$$

Thus, $NOHSO_4$, H_2O, and NO_3^- species are accumulated in the reaction mass in the course of nitration and oxidation in the system HNO_3–H_2SO_4 (as nitric acid is spent), the concentration of sulfuric acid decreases, and, consequently, the main process becomes slower.

It is known that nitrosylsulfuric acid forms stable complexes with aromatic hydrocarbons (Battge complexes), e.g., $(C_6H_6)_n \cdot (NOHSO_4)_{n1} \cdot (H_2SO_4)_{n2}$ and $(C_6H_5CH_3) \cdot 2(NOHSO_4) \cdot 3(H_2SO_4)$ [6]. Complexes of this kind are decomposed by introduction into the reaction mass of an excess amount of nitric acid at 40–50°C. The most stable complexes with $NOHSO_4$ are formed by benzene, whereas homologues of benzene form less stable complexes.

Nitrosylsulfuric acid is stable in solutions of sulfuric acid with concentration exceeding 75 wt %. Lowering the H_2SO_4 concentration to 70 wt % leads to fast decomposition of $NOHSO_4$:

$$2NOHSO_4 + H_2O \rightarrow 2H_2SO_4 + N_2O_3. \quad (9)$$

It has also been proposed to decompose nitrosylsulfuric acid by its oxidation with oxygen, persulfates, and chromic anhydride [9]. For example, in the case of oxidation with oxygen, the reaction is described by the equation

$$2NOHSO_4 + O_2 + 2H_2O \rightarrow 2H_2SO_4 + 2HNO_3. \quad (10)$$

Let us consider in terms of the above concepts data on the influence exerted by the process conditions on the characteristics of RGH synthesized in the system fuming nitric acid–concentrated sulfuric acid.

RGH was synthesized using natural scaly graphite of the GT-1 brand from Zaval'evskoe deposit, concentrated sulfuric acid of chemically pure grade (d =

Bloating coefficient of RGH in relation to the duration of treatment of graphite with sulfuric (τ_1) and nitric (τ_2) acids

Variant*	τ_1, min	τ_2, min	K_v, $cm^3\ g^{-1}$	τ_1, min	τ_2, min	K_v, $cm^3\ g^{-1}$
1	5	10	85	10	5	106
	10	10	82	10	10	83
	20	10	84	10	20	65
	30	10	83	10	30	56
	40	10	85	10	40	49
	60	10	86	10	60	39
2	5	10	127	5	5	100
	10	10	125	5	10	127
	20	10	115	5	20	92
	30	10	107	5	30	93
	40	10	106	5	40	65
	60	10	99	5	60	51

* Acid expenditure, cm^3/100 g: H_2SO_4 24, HNO_3 6 (variant 1); H_2SO_4 40, HNO_3 8 (variant 2).

1.836 g cm^{-3}, 95.8 wt %) and fuming nitric acid (d = 1.518 g cm^{-3}).

RGH samples were obtained using the scheme of successive introduction of components of the intercalation solution into the reaction mass. In what follows, the acid expenditures are given in cubic centimeters per 100 g of starting graphite.

A glass reactor was charged with 25 g of graphite and stirring was switched on. At the instant when the stirring started, the first component of the intercalation solution (fuming nitric acid or concentrated sulfuric acid) was fed into the reactor and the reaction mass was stirred for a time τ_1. Then the second component of the intercalation solution was introduced into the reactor and stirring was continued for a time τ_2. The parameters τ_1 and τ_2, and also expenditures of the components of the intercalation solution and order of their introduction, were varied.

Upon completion of the acid treatment of graphite, the oxidized graphite was washed with water on a filter to washing water pH 5–6 and dried at 100–110°C to constant weight. For all of the RGH samples obtained, the product yield in terms of the starting graphite, mass loss in bloating, and bloating coefficient K_v ($cm^3\ g^{-1}$) at 900°C were determined. The data on the yield of the product were used to calculate the content m_i of intercalate in it.

The bloating coefficient was found in the shock-heating mode as follows. A 150-cm^3 stainless steel cuvette was placed in a muffle furnace heated to 900°C. A weighed portion of the product (m = 0.2–0.3 g) was introduced into the heated cuvette in the furnace and kept there for 60 s. Bloated graphite was carefully transferred into a glass graduate and the volume V (cm^3) occupied by the graphite was measured. The bloating coefficient was found using the relation $K_v = V/m$ as arithmetic mean of three parallel measurements. The admissible discrepancy between the K_v values found in parallel runs is 5%.

Graphite was treated with acids in two variants. In variant 1, graphite was treated with sulfuric acid (40 cm^3/100 g, τ_1 = 10 min) and then with fuming nitric acid (8 cm^3/100 g, τ_2 = 10 min). In variant 2, first fuming nitric acid (8 cm^3/100 g, τ_1 = 10 min) and then sulfuric acid (40 cm^3/100 g, τ_2 = 10 min) were added to graphite. In synthesis by variant 1, the evolution of nitrogen oxide, observed visually after nitric acid was introduced, terminated 3–4 min after the beginning of HNO_3 introduction into the reactor. In variant 2, evolution of nitrogen oxide was observed upon introduction of any of the acids into the reactor. The K_v values for RGH samples obtained in two variants of acid introduction into the reactor are given below:

Variant of synthesis	Order of introduction of acids	K_v, $cm^3\ g^{-1}$
1	H_2SO_4, HNO_3	110
2	HNO_3, H_2SO_4	125

It follows from the data presented that the coefficient of RGH bloating is virtually independent of the order in which the acids are introduced into the reactor.

The influence exerted by the duration of treatment of graphite with sulfuric and nitric acids was studied for both variants of acid introduction into the reactor. The data obtained for varied parameters τ_1 and τ_2 are presented in the table for variants 1 and 2.

The data in the table indicate that, for both variants of acid introduction, the decisive influence on the parameter K_v is exerted by the duration of reaction mass treatment with the second component of the intercalation solution—τ_2. The optimal duration of treatment of graphite with each component of this solution is 5–10 min. Unexpectedly, it was found that raising the parameter τ_2 leads to a dramatic decrease in K_v of the final product. Raising the reaction time in the second stage from 5–10 to 60 min results in a decrease in the bloating coefficient of the final product by a factor of 2.5–3 for both variants of synthesis.

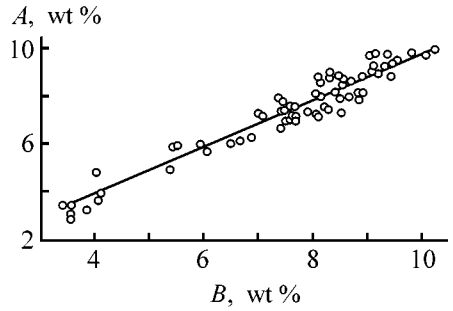

Fig. 1. Mass loss A of RGH in bloating at 900°C vs. intercalant content B in the samples. $y = 0.99x$, $R^2 = 0.93$.

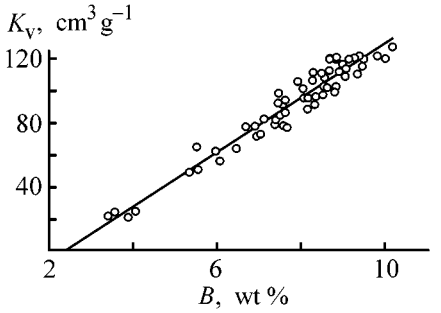

Fig. 2. Bloating coefficient K_v of RGH at 900°C vs. intercalant content B in the samples. $y = 16.91x - 39.46$, $R^2 = 0.96$.

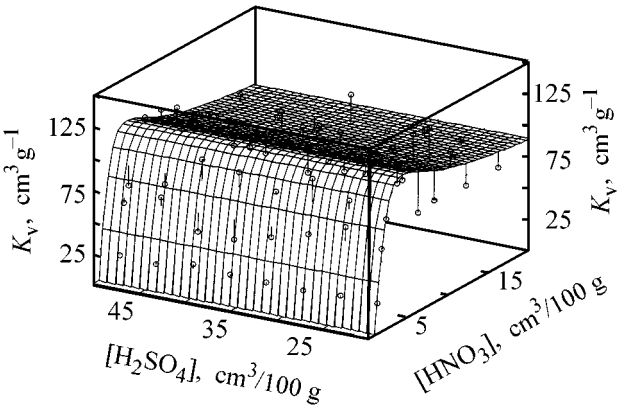

Fig. 3. Bloating coefficient K_v of RGH at 900°C vs. expenditures of sulfuric and nitric acids used in the synthesis stage.

The RGH properties were studied in relation to the expenditure of the components of the intercalating solution under standard conditions for the case of an acid treatment of graphite by variant 1, i.e., first with sulfuric, and then with nitric acids. The expenditure of sulfuric acid was varied within the range 20–48 cm^3/100 g with a step of 4 cm^3/100 g, and that of nitric acid, in the range 1–16 cm^3/100 g with a step of about 2 cm^3/100 g. In this case, the duration of treatment of graphite in each stage was $\tau_1 = \tau_2 = 10$ min.

It was found that the loss of mass in bloating of RGH samples depends linearly on the intercalant content in the samples (Fig. 1). The slope of the straight line obtained is close to unity, which indicates a virtually complete removal of the intercalating agent from the RGH matrix in bloating. Figure 2 presents the dependence of the bloating coefficient of RGH samples at 900°C on the content of intercalant in these samples. The linear run of the dependence may indicate an invariable chemical nature of the intercalant over the entire range of its content in the samples studied.

It also follows from the data in Fig. 2 that, for RGH samples, there exists a threshold content of the intercalating agent, approximately equal to 2.3 wt %, below which no bloating must be observed at 900°C. The dependence of the bloating coefficient of RGH samples at 900°C on the expenditure of acids in synthesizing these samples is represented in Fig. 3 as a three-dimensional diagram. This dependence has the form of a plateau with a precipice at nitric acid expenditures of about 3 cm^3/100 g.

Unexpectedly, it was found that the whole set of experimental data is described, with a correlation coefficient of 0.93, by a single-parameter equation taking into account only the dependence of K_v on the expenditure of fuming nitric acid, [HNO_3]:

$$K_v = 59.55 + 128.67/[HNO_3]^{0.5} - 449.6\exp(-[HNO_3]). \quad (11)$$

In this case, the expenditure of sulfuric acid in the range studied has, to a first approximation, no effect on the bloating coefficient of the final product. These data indicate that even an expenditure of sulfuric acid of 20 cm^3/100 g ensures an acidity of the medium that is sufficient for the intercalation process to occur. This amount of sulfuric acid is also sufficient for ensuring the required amount of hydrosulfate anions to be intercalated into graphite.

At small expenditures of fuming nitric acid, raising the amount of acid introduced from 0 to ~3 cm^3/100 g leads to a steep rise in the bloating coefficient of the product. With the expenditure of nitric acid raised further, this parameter decreases gradually to a certain extent. The dramatic increase in the parameter K_v at small expenditures is presumably due to a rise in the degree of oxidation of the graphite matrix, caused by an increase in the content of the oxidizing agent—nitronium cations, in the reaction mass. Further increase in the expenditure of fuming nitric acid makes the acidity of the reaction mass lower, which leads to a decrease in the concentration of nitronium cat-

ions. This, in turn, lowers the degree of oxidation of the graphite matrix and, as a result, leads to a decrease in the bloating coefficient of the final product.

A dramatic decrease in the bloating coefficient of the final product was observed on making longer the reaction duration in the second stage of synthesis (parameter τ_2). This can be accounted for as follows. In both variants of synthesis, a mixture of fuming nitric acid and concentrated sulfuric acid is formed in the reaction mass in the second stage. Immediately after the introduction of the second reagent there begins intensive oxidation of graphite, which is complete in 5–10 min. Simultaneously with the onset of graphite oxidation, nitrogen oxides appear in the reaction mass and nitrosylsulfuric acid starts to accumulate in the system. This acid forms stable complexes (of the type of Battge complexes [9]) with the matrix of the graphite intercalation compound and, being a reducing agent, presumably promotes the deintercalation process which leads to a decrease in the bloating coefficient of the final product. Theoretical analysis of reactions whose occurrence is possible in the system studied made it possible to account for the experimentally observed dependences of the bloating coefficient of the final product on process parameters.

CONCLUSION

The data obtained in studying the influence exerted by synthesis conditions on the properties of final products in the system graphite–fuming nitric acid–concentrated sulfuric acid indicate that products with practically acceptable characteristics can be synthesized at exceedingly low, compared with those in the conventional methods, expenditures of sulfuric and nitric acids. To obtain a high-quality product, it is necessary to strictly observe the process parameters and especially the duration of treatment of the reaction mass with the second reagent.

REFERENCES

1. Avdeev, V.V., Monyakina, L.A., Nykol'skaya, I.V., *et al.*, *Carbon*, 1992, vol. 30, no. 6, pp. 819–823.
2. Avdeev, V.V., Sorokina, N.E., Nikol'skaya, I.V., *et al.*, *Neorg. Mater.*, 1997, vol. 33, no. 6, pp. 699–702.
3. US Patent 3404061.
4. US Patent 4895713.
5. USSR Inventor's Certificate, no. 1657473.
6. US Patent 6149972.
7. Yaroshenko, A.P., Popov, A.F., and Shapranov, V.V., *Zh. Prikl. Khim.*, 1994, vol. 67, no. 2, pp. 204–211.
8. Yaroshenko, A.P. and Savos'kin, M.V., *Zh. Prikl. Khim.*, 1995, vol. 68, no. 8, pp. 1302–1306.
9. Orlova, E.Yu., *Khimiya i tekhnologiya brizantnykh vzryvchatykh veshchestv* (Chemistry and Technology of High Explosives), Leningrad: Khimiya, 1973.
10. Forsman, W.C., Mertwov, H.E., and Wessbecher, D.E., *Carbon*, 1988, vol. 26, no. 5, pp. 693–699.
11. Cotton, F.A. and Wilkinson, G., *Advanced Inorganic Chemistry*, New York: Interscience, 1966.

Russian Journal of Applied Chemistry, Vol. 75, No. 6, 2002, pp. 866–874. Translated from Zhurnal Prikladnoi Khimii, Vol. 75, No. 6, 2002, pp. 886–894.
Original Russian Text Copyright © 2002 by Voskresenskaya, Skorik.

INORGANIC SYNTHESIS AND INDUSTRIAL INORGANIC CHEMISTRY

Complexation and Intramolecular Redox Decomposition of Cerium(IV) Hydroxo Complexes with Oxycarboxylic Acids

O. O. Voskresenskaya and N. A. Skorik

Joint Institute for Nuclear Research, Dubna, Moscow oblast, Russia
Tomsk State University, Tomsk, Russia

Received January 15, 2001; in final form, March 2003

Abstract—Spectrophotometry, pH-metry, and kinetic method were applied to study the complexation and redox decomposition of cerium hydroxo complexes formed in the systems Ce^{4+}–SO_4^{2-}–H_mL, where H_mL (m = 2, 3, 4) are, respectively lactic, malic, and tartaric acids.

A study of thermodynamic and kinetic characteristics of complexation and redox decomposition of complexes formed in the first stage of oxidation by cerium(IV) of polar organic compounds is of theoretical and practical interest. It is rather important in connection with the problem of stabilization of unstable oxidation states of metals [1–4] and use of these systems as a source of radicals in radical polymerization [5, 6], and also in view of their other applications—analytical [7], in a theoretical study of the electron transfer rates in intermediate complexes [8], and in separation of a mixture of rare-earth elements [1–3].

For example, separation of a mixture of rare-earth elements is based on the ability of cerium to form compounds in which it is in oxidation state +4. This leads to a pronounced difference between the properties of cerium compounds and those with rare-earth elements in oxidation state +3 and improves the efficiency of methods for separation of rare-earth elements. However, the problem of cerium stabilization in this "anomalous" oxidation state, especially in complexation with oxyacids, has been studied insufficiently.

Previously, the influence exerted by the stability constants of complexes, reducing ability of ligands, their denticity, and other factors on the rate of the redox interaction in systems containing cerium(IV) and organic ligands (carboxyl-containing complexons, oxycarboxylic acids, etc.) [3]. It has been established that there is a correlation between the rate of the redox interaction in the systems and the instability constant of cerium(IV) complexes. No simple relationship could be revealed between the stability of the complexes and the rate and apparent activation energy of the redox interaction in cerium(IV) complexation with oxyacids [3]. It has been shown that intramolecular redox interaction cannot be completely eliminated in systems of this kind, with only its partial suppression possible [3, 4].

As characteristics of the redox interaction were employed the conditional rate of the redox process, its apparent activation energy, and reducing power of an organic ligand [3]. Such a direct characteristic of the kinetic activity of the complexes as rate constant of their intracomplex redox decomposition was not determined in the previous studies mentioned here. It is also evident that such a property of an organic ligand as its reducing capacity may play an important part in the case of a bimolecular (free-radical), but not intermediate, mechanism occurring in oxidation of oxy acids by cerium(IV) [9]. A study of the problem of stabilization in the given context is inseparable from a study of the mechanism and kinetics of the redox process occurring in the systems.

The kinetics of oxidation of oxycarboxylic acids by cerium(IV) was studied in [5, 9–13]. In [10–12], a mechanism of the redox process was postulated, in which an intermediate complex is formed and the decomposition of this complex is the rate-determining stage of the process. However, it has been noticed that kinetic data are insufficient for confirming the formation of such an intermediate complex [11]. A synergistic effect of the carboxylic and hydroxy groups of α oxyacids, and also intermediate and free-radical mechanisms of oxidation of organic ligand by ceri-

1070-4272/02/7506-0866 $27.00 © 2002 MAIK "Nauka/Interperiodica"

um(IV) for, respectively, oxy acids and succinic dicarboxylic acids have been noted [9]. A bridge mechanism of electron transfer in such an intermediate has been suggested and necessity for revealing the states in which the metal and ligand are present in this complex has been indicated [13].

It is noteworthy that the complexation pre-equilibrium in the redox process has not been studied specially, being either postulated or studied using methods yielding only effective complexation constants related to a fixed pH value and indeterminate form of the ligand and metal in the complex. At the same time, the kinetic dependences themselves were interpreted on the basis of assumptions about the composition, structure, and reactivity of the complexes and characterized by effective rate constants. Data on the rate constants of intramolecular decomposition of cerium(IV) complexes with organic ligands are unavailable in the literature. Of interest in this regard are generalized methods for investigation of complexation, proposed in this study, and their application to analysis of the kinetics and thermodynamics of the initial stages of the processes mentioned, the mechanism of these processes, and the reactivity of intermediate complexes involved.

A comparative evaluation of the effective formation constants of intermediate cerium(IV) complexes with lactic α oxyacid and other hydroxyl-containing compounds in a perchlorate medium was made in [5]. The composition and stability of complexes have been studied in a nitrate medium for the malate complex $[Ce(NO_3)_zMalt]^{2-z}$ [3, 14] and binuclear tartrate complex of cerium(IV) $[Ce_2(NO_3)_zTart]^{6-z}$ [3, 15]. Other researchers [3, 14, 15] could not study the complexation in a sulfate medium in the systems we investigated.

In the present study, the methods commonly used to investigate complexation and generalized to the case of kinetically active complexes were applied to determine in a sulfate medium the composition, stability constants β_1, rate constants k_2, and activation energy of intramolecular redox decomposition of lactate, malate, and tartrate hydroxo complexes of cerium(IV) $[CeOH\ H_{m-x}L]^{3-x}$ (m = 2, 3, 4) formed in the first stage of oxidation by cerium(IV) of the above-mentioned organic ligands:

$$CeOH^{3+} + H_{m-x}L^{x-} \overset{\beta_1}{\rightleftarrows} [CeOHH_{m-x}L]^{3-x} \xrightarrow{k_2} Ce^{3+} + \cdot LH_{m=1-x}^{x-} + H_2O, \quad (1)$$

$$\beta_1 = k_1/k_{-1}, \quad k_1 >> k_{-1} >> k_2.$$

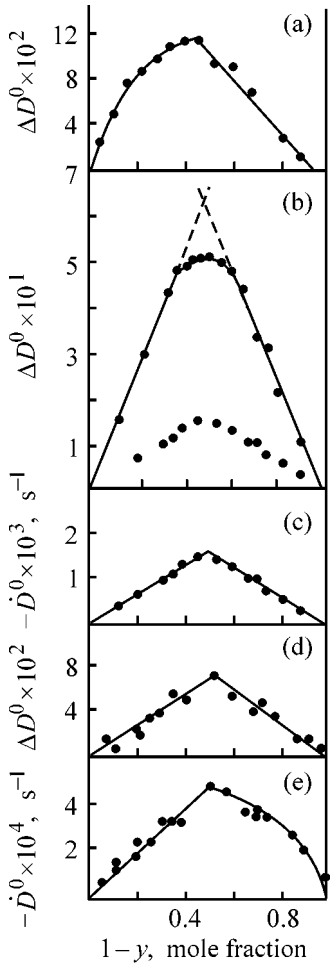

Fig. 1. (a, b, d) ΔD^0–composition and (c, e) $-\dot{D}^0$–composition diagrams for isomolar series of solutions. (y) Content of ligand. System: (a) Ce(IV)–SO_4^{2-}–H_2Lact (c_{tot} = 2.46×10^{-2} M, pH 2.87, I = 2, T = 25.0°C, λ = 400 nm), (b–e) Ce(IV)–SO_4^{2-}–H_4Tart [(b, c) c_{tot} = 1.17×10^{-2} M, pH 2.24, I = 2, T = 24.0°C, λ = 400 nm; (d, e) c_{tot} = 1.03×10^{-3} M, pH 2.3, I = 2, T = 25.0°C, λ = 340 nm].

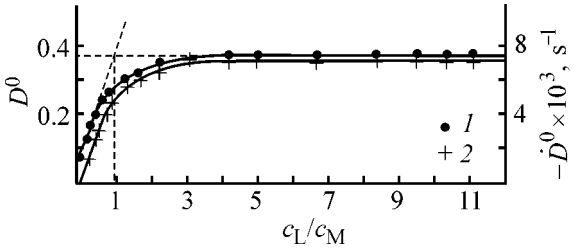

Fig. 2. (*1*) D^0–c_L/c_M and (*2*) $-\dot{D}^0$–c_L/c_M diagrams for the system Ce^{4+}–SO_4^{2-}–H_3Malt. c_M = 1.88×10^{-3}, c_L = 3.00×10^{-4}–2.11×10^{-2} M; pH 2.70; I = 2; T = 18.0°C; λ = 400 nm; D_∞^0 = 0.376; D_M = 0.09.

The number x of protons displaced from the ligand H_mL in complexation was determined. The mechanism of the redox process observed in the systems

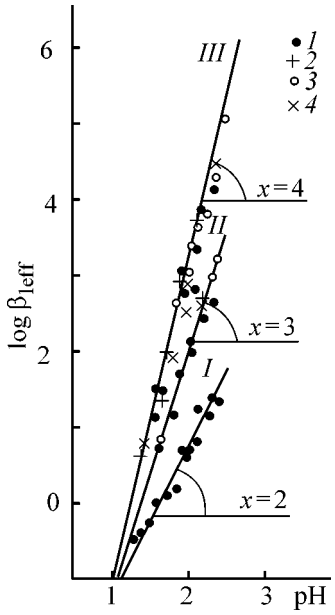

Fig. 3. $\log \beta_{1eff}$–pH diagrams. System: (*I*) Ce^{4+}–SO_4^{2-}–H_2Lact ($c_M = 6.0 \times 10^{-3}$, $c_L = 3.0 \times 10^{-2}$ M; $I = 2$; $T = 18.0$°C; $\lambda = 400$ nm); (*II*) Ce^{4+}–SO_4^{2-}–H_3Malt [(*1*) $c_M = 2.14 \times 10^{-3}$, $c_L = 2.00 \times 10^{-3}$ M; $T = 17.7$°C; (*2*) $c_M = 2.04 \times 10^{-3}$, $c_L = 2.00 \times 10^{-3}$ M; $T = 28.0$°C; and (*3*) $c_M = 3.21 \times 10^{-3}$, $c_L = 3.00 \times 10^{-3}$ M; $T = 27.0$°C; $I = 2$, $\lambda = 400$ nm]; (*III*) Ce^{4+}–SO_4^{2-}–H_4Tart [(*1*) $c_M = 1.22 \times 10^{-3}$, $c_L = 1.20 \times 10^{-3}$ M; $T = 28.0$°C; (*2*) $c_M = c_L = 2.14 \times 10^{-3}$ M; $T = 28.0$°C; (*3*) $c_M = 2.04 \times 10^{-3}$, $c_L = 2.00 \times 10^{-3}$ M; $T = 28.0$°C; and (*4*) $c_M = 3.02 \times 10^{-3}$, $c_L = 1.65 \times 10^{-3}$ M; $T = 24.0$°C; $I = 2$, $\lambda = 400$ nm].

was studied, and the law governing its rate was established.

The composition of intermediate complexes formed in the systems Ce^{4+}–SO_4^{2-}–H_mL at the instant of mixing of the reaction mixture components was studied by the methods of isomolar series (Fig. 1) and molar ratios (Fig. 2). The results obtained indicate that 1 : 1 complexes are predominant in all the systems in the pH range studied. The formation of complexes with 1 : 1 composition in the systems studied was additionally confirmed by using kinetic analogues of the above methods [Figs. 1c and 1e; Fig. 2, curve *2*; Eq. (16)], which are particularly appropriate in the cases of low yield or low light absorption by the complexes.

The data on the composition of the complexes, obtained in the present study, is in agreement with the assumption that an intermediate cerium tartrate complex of composition 1 : 1 is formed in oxidation of tartaric acid by cerium(IV) [10, 12] and also with the conclusions of [5] that the 1 : 1 composition of intermediate organocerium complexes is independent of the denticity of the organic ligand and can be regarded as their proof. The composition of the malate complex of cerium(IV) in a sulfate medium coincides with that in a nitrate medium, established in [3. 14].

The form in which a coordinated ligand is present in the complexes and their stability constants were determined using the *D*–pH method [16]. As the dominant form of cerium(IV) in the pH range studied was taken the monohydroxo form $CeOH^{3+}$ [17].

The number *x* of protons displaced from the ligand molecule H_mL by metal ion in attainment of equilibrium

Table 1. Stability constant and rate constant of redox decomposition of lactate complex with cerium(IV) by the $\dot{D}^0$–pH* method ($c_M = 6 \times 10^{-3}$, $c_L = 3 \times 10^{-2}$ M; $I = 2$; $T = 18.0$°C; $\lambda = 400$ nm; $D_\infty^0 = 0.610$)

D^0	D_M	$-\dot{D}^0$, s^{-1}	pH	$c_K^0 \times 10^3$, M	$\log \beta_{1eff}$	$\log \beta_{1eff} f$	$\log k_{app}$	$\log k_2$
0.307	0.300	1.0×10^{-5}	1.24	0.059	–0.48	15.35	$\bar{1}.23$	$\bar{3}.23$
0.304	0.300	1.5×10^{-5}	1.35	0.077	–0.36	15.25	$\bar{1}.28$	$\bar{3}.28$
0.304	0.299	3.0×10^{-5}	1.50	0.097	–0.26	15.05	$\bar{1}.49$	$\bar{3}.49$
0.309	0.300	4.0×10^{-5}	1.61	0.174	0.00	15.09	$\bar{1}.36$	$\bar{3}.36$
0.311	0.301	4.5×10^{-5}	1.70	0.194	0.05	14.96	$\bar{1}.37$	$\bar{3}.37$
0.311	0.297	8.5×10^{-5}	1.83	0.268	0.20	14.85	$\bar{1}.50$	$\bar{3}.50$
0.322	0.294	1.6×10^{-4}	1.94	0.532	0.52	14.95	$\bar{1}.48$	$\bar{3}.48$
0.332	0.294	1.5×10^{-4}	1.94	0.720	0.68	15.12	$\bar{1}.32$	$\bar{3}.32$
0.328	0.277	1.8×10^{-4}	2.03	0.864	0.74	15.00	$\bar{1}.32$	$\bar{3}.32$
0.327	0.284	2.7×10^{-4}	2.06	0.792	0.72	14.91	$\bar{1}.53$	$\bar{3}.53$
0.331	0.298	3.2×10^{-4}	2.12	0.900	0.81	14.89	$\bar{1}.56$	$\bar{3}.56$
0.339	0.274	4.3×10^{-4}	2.20	1.302	0.98	14.90	$\bar{1}.52$	$\bar{3}.52$
0.347	0.215	4.2×10^{-4}	2.27	1.896	1.22	15.00	$\bar{1}.35$	$\bar{3}.35$
0.357	0.217	4.4×10^{-4}	2.33	1.956	1.38	15.05	$\bar{1}.35$	$\bar{3}.35$
0.342	0.175	4.5×10^{-4}	2.43	2.184	1.33	14.86	$\bar{1}.31$	$\bar{3}.31$

* $\log \beta_1 = 14.97 \pm 0.18$, $\log k_2 = \bar{3}.40 \pm 0.10$ (18°C).

Table 2. Stability constants, rate constant, and activation energy of malate complex with cerium(IV), determined by the D^0, $\dot{D}^0$–pH* method [$c_M = 2.14 \times 10^{-3}$, $c_L = 2.00 \times 10^{-3}$ M; $I = 2$; $T = 17.7$°C; $\lambda = 400$ nm; $D^0_\infty = 0.310$ (run no. 1); $c_M = 3.21 \times 10^{-3}$, $c_L = 3.00 \times 10^{-3}$ M; $I = 2$; $T = 27.0$°C; $\lambda = 400$ nm; $D^0_\infty = 0.246$ (run no. 2)]

D^0	D_M	$-\dot{D}^0 \times 10^4$, s^{-1}	pH	$c^0_K \times 10^3$, M	log k_{app}	log k_2	log β_{1eff}	log β_1
				Run no. 1				
0.228	0.227	0.4	1.67	0.024	$\bar{1}$.23	$\bar{3}$.23	0.76	18.31
0.231	0.228	0.3	1.79	0.073	$\bar{1}$.61	$\bar{3}$.61	1.26	18.45
0.229	0.220	0.9	1.90	0.200	$\bar{1}$.65	$\bar{3}$.65	1.76	18.61
0.230	0.215	1.1	2.05	0.316	$\bar{1}$.54	$\bar{3}$.55	2.01	18.64
0.244	0.210	2.1	2.27	0.680	$\bar{1}$.49	$\bar{3}$.49	2.55	18.34
0.250	0.212	2.7	2.42	0.775	$\bar{1}$.54	$\bar{3}$.55	2.67	18.01
0.262	0.208	3.2	2.38	1.060	$\bar{1}$.48	$\bar{3}$.48	3.02	18.48
0.309	0.128	5.0	2.69	1.988	$\bar{1}$.40	$\bar{3}$.40	–	–
0.310	0.111	4.9	2.75	2.000	$\bar{1}$.39	$\bar{3}$.39	–	–
0.305	0.094	5.0	2.85	1.954	$\bar{1}$.40	$\bar{3}$.40	–	–
0.315	0.085	5.0	2.96	2.000	$\bar{1}$.40	$\bar{3}$.40	–	–
0.306	0.066	5.1	3.07	1.967	$\bar{1}$.41	$\bar{3}$.41	–	–
				Run no. 2				
0.158	0.155	1.0	1.68	0.095	0.02	$\bar{2}$.20	1.02	18.54
0.160	0.155	2.0	1.85	0.158	0.10	$\bar{2}$.28	1.26	18.28
0.162	0.150	3.7	1.96	0.360	0.01	$\bar{2}$.19	1.68	18.38
0.162	0.148	5.0	2.06	0.412	0.08	$\bar{2}$.26	1.75	18.15
0.167	0.148	5.1	2.06	0.559	$\bar{1}$.96	$\bar{2}$.14	1.94	18.34
0.185	0.140	7.8	2.20	1.227	$\bar{1}$.80	$\bar{2}$.00	2.85	18.83

* log $\beta_1 = 18.39 \pm 0.18$, log $k_2 = \bar{3}.43 \pm 0.10$ (17.7°C) (run no. 1); log $\beta_1 = 18.42 \pm 0.24$, log $k_2 = \bar{2}.17 \pm 0.10$ (27°C), $E = 133.0 \pm 1.3$ kJ mol^{-1} (run no. 2).

Table 3. Stability constant and rate constant of redox decomposition of tartrate complex with cerium(IV), determined by the D^0, $\dot{D}^0$–pH* method ($c_M = 1.22 \times 10^{-3}$, $c_L = 1.20 \times 10^{-3}$ M; $I = 2$; $T = 28.0$°C; $\lambda = 400$ nm; $D^0_\infty = 0.317$)

D^0	D_M	$-\dot{D}^0 \times 10^3$, s^{-1}	pH	$c^0_K \times 10^3$, M	log β_{1eff}	log k_{app}	log k_2
0.170	0.155	0.20	1.74	5.18×10^{-5}	28.25	3.86	$\bar{3}$.98
0.163	0.150	0.30	1.79	9.34×10^{-5}	27.97	3.21	$\bar{3}$.90
0.167	0.154	0.35	1.80	9.57×10^{-5}	27.95	3.66	$\bar{3}$.96
0.173	0.156	0.40	1.81	1.27×10^{-4}	28.05	3.12	$\bar{3}$.89
0.171	0.151	0.45	1.90	1.45×10^{-4}	27.76	3.10	$\bar{3}$.88
0.172	0.153	0.45	1.98	1.33×10^{-4}	27.44	3.36	$\bar{3}$.92
0.217	0.155	1.70	2.22	4.59×10^{-4}	27.34	3.70	$\bar{3}$.96
0.238	0.146	1.50	2.35	6.46×10^{-4}	27.24	–	–
0.273	0.152	1.60	2.38	8.78×10^{-4}	27.72	–	–
0.279	0.150	1.25	2.44	9.27×10^{-4}	27.67	–	–
0.292	0.121	1.30	2.50	1.05×10^{-3}	27.98	–	–

* log $\beta_1 = 27.76 \pm 0.32$, log $k_2 = \bar{3}.93 \pm 0.04$ (28°C).

$$CeOH^{3+} + H_mL \overset{R_1}{\rightleftarrows} [CeOHH_{m-x}L]^{3-x} + xH^+, \quad (2)$$

$$R_1 = \frac{[CeOHH_{m-x}L][H]^x}{[CeOH][H_mL]} = \beta_{1eff}[H]^x, \quad (3)$$

was evaluated graphically as the slope of the plot of log β_{1eff} against pH

$$\log \beta_{1eff} = \log R_1 + x\,\mathrm{pH} \quad (4)$$

by comparing the D^0–pH data of series nos. 2–4 (D^0 is light absorption by the reaction mixture at instant of time $\tau = 0$).

As follows from analysis of the dependence of log β_{1eff} on pH (Fig. 3, Tables 1–3), the high-charge

Table 4. Stability constant and rate constant of redox decomposition of malate complex with cerium(IV), determined by the D^0, $\dot{D}^0$–c_L/c_M* method ($c_M = 1.88 \times 10^{-3}$, $c_L = 3.00 \times 10^{-4}$–$2.11 \times 10^{-2}$ M; pH 2.70; $I = 2$; $T = 18.0$°C; $\lambda = 400$ nm; $D^0_\infty = 0.376$; $D_M = 0.090$)

D^0	$-\dot{D}^0 \times 10^3$, s^{-1}	c_L/c_M	$c^0_K \times 10^3$, M	log k_{app}	log k_2	log β_1
0.132	1.5	0.16	0.296	$\bar{1}.70$	$\bar{3}.52$	19.08
0.180	2.5	0.32	0.592	$\bar{1}.63$	$\bar{3}.45$	19.17
0.215	3.1	0.48	0.822	$\bar{1}.58$	$\bar{3}.40$	18.50
0.240	4.0	0.64	0.986	$\bar{1}.61$	$\bar{3}.43$	18.22
0.260	4.5	0.80	1.117	$\bar{1}.60$	$\bar{3}.42$	18.09
0.279	5.0	0.96	1.243	$\bar{1}.60$	$\bar{3}.42$	18.05
0.306	5.5	1.27	1.420	$\bar{1}.59$	$\bar{3}.41$	18.01
0.327	6.0	1.60	1.558	$\bar{1}.59$	$\bar{3}.41$	18.03
0.350	6.5	2.23	1.709	$\bar{1}.58$	$\bar{3}.40$	18.11
0.364	7.0	3.19	1.801	$\bar{1}.59$	$\bar{3}.41$	18.24
0.370	7.0	4.15	1.841	$\bar{1}.58$	$\bar{3}.40$	18.41
0.374	7.4	5.10	1.866	$\bar{1}.60$	$\bar{3}.42$	18.75
0.374	7.3	6.70	1.866	$\bar{1}.59$	$\bar{3}.41$	18.60
0.375	7.5	8.45	1.873	$\bar{1}.60$	$\bar{3}.42$	18.76
0.379	7.6	9.55	1.880	$\bar{1}.61$	$\bar{3}.43$	–
0.375	7.5	10.40	1.873	$\bar{1}.60$	$\bar{3}.42$	18.73
0.377	7.5	11.20	1.880	$\bar{1}.60$	$\bar{3}.42$	–

* $\log \beta_1 = 18.45 \pm 0.34$, $\log k_2 = \bar{3}.42 \pm 0.03$ (18.0°C).

ion $CeOH^{3+}$ displaces 2, 3, or 4 protons from the ligand molecule in complexation with, respectively, lactic, malic, and tartaric acids. In this case, similarly to that of interaction of oxyacids with the cations Sc^{3+}, Ga^{3+}, In^{3+}, and Th^{4+} [18], protons of the oxy groups of oxyacids are displaced because of the high coordination numbers of rare-earth elements and the effective negative charge on electron-donor oxygen atoms.

Consequently, the complexation pre-equilibrium in oxidation of the acids under consideration by cerium(IV) can be represented as

$$CeOH^{3+} + L^{x-} \overset{\beta_1}{\rightleftarrows} [(CeOH)L]^{3-x} \qquad (5)$$

or, which is equivalent in terms of the theory of ionic equilibria,

$$CeOH^{3+} + L^{x-} \overset{\beta_1}{\rightleftarrows} [(CeO)HL]^{3-x}, \qquad (6)$$

where $x = 2$, 3, and 4 for, respectively, H_2Lact, H_3Malt, and H_4Tart.

It is noteworthy that, in a sulfate medium, the formula $[CeOHL]^{3-x}$ should be only regarded as an abbreviated designation of all the possible substances with variable number of ions of the ionic background $\Sigma_y\Sigma_z[(NH_4)_yCeOHL(SO_4)_z]^{3-x+y-z}$, where y and z can be estimated by the inequalities $y \geq 0$, $0 \leq z \leq 3$ [19].

For the complexation equilibrium (5), the equilibrium constant β_1:

$$\beta_1 = \frac{[CeOHL]}{[CeOH][L]} \qquad (7)$$

(charges are omitted) was calculated from the data of the series D^0–pH and the ascending portion of the saturation curve by the formula

$$\beta_1 = \frac{c^0_K}{(c_M - c^0_K)(c_L - c^0_K)} f = \beta_{1eff} f, \qquad (8)$$

$$f = 1 + \sum_{i=1}^{m} B_i [H]^i$$

for each point of the dependence

$$\log \beta_1 = \log \beta_{1eff} + \log f \qquad (9)$$

with the subsequent averaging of the $\log \beta_1$ values obtained (Tables 1–4).

The agreement between the results obtained by different methods (D–pH, molar ratios) in determining the stability constants for, e.g., the malate complex of cerium(IV) ($\log \beta_1 = 18.39$, $\log \beta_1 = 18.45$, Tables 2

and 4) indicates that the basic equilibria in solution are taken into account correctly. The $\log \beta_1$ value for the complex $[CeOHL]^{3-x}$ (x = 2, 3, 4), found in a sulfate medium by averaging data of two to four series for each of the systems, grows in order $H_2Lact < H_3Malt < H_4Tart$ with increasing ligand denticity from $\log \beta_1 = 14.97 \pm 0.18$ for H_2Lact to $\log \beta_1 = 27.83 \pm 0.23$ for H_4Tart.

The kinetics and mechanism of the redox process observed in the system was studied by analyzing the dependence of its initial rate $-\dot{D}^0$ on the equilibrium concentration of hydrogen ions at the initial concentration of the organic ligand in terms of the generalizations of the D^0–pH and D^0–c_L/c_M methods to the case $\dot{D}^0 \neq 0$ (see below), which can be named the D^0, $\dot{D}^0$–pH and D^0, $\dot{D}^0$–c_L/c_M methods, respectively.

The rate constants of the redox decomposition of $[CeOHL]^{3-x}$ complexes were calculated from the data of series D^0–pH, D^0–c_L/c_M (supplemented with the dependences $\dot{D}^0$–pH, $\dot{D}^0$–c_L/c_M) with the use of the equilibrium concentrations of the complex, calculated from the series D^0–pH, D^0–c_L/c_M (Tables 1–4):

$$c_K^0 = \begin{cases} \dfrac{D^0 - D_M}{D_\infty^0 - D_M} c_M, & c_M < c_L; \\ \dfrac{D^0 - D_M}{D_\infty^0 - D_M} c_L, & c_L < c_M, \end{cases} \quad (10)$$

where c_M and c_L are the initial concentrations of the metal ion and ligand, D_M the optical density of the metal ion solution, and D_∞^0 the light absorption by the reaction mixture at the instant of time $\tau = 0$, corresponding to a yield of the complex equal to unity.

The analysis of nonlinear dependences $\dot{D}^0$–pH (Fig. 4) and $\dot{D}^0$–c_L/c_M (Fig. 2) within the series D^0, $\dot{D}^0$–pH, D^0, $\dot{D}^0$–c_L/c_M was supplemented with analysis of linear dependences $\dot{D}^0$–c_K^0 (Fig. 5):

$$-\dot{D}^0 = A + k_{app} c_K^0, \quad (11)$$

allowing, in particular, graphical evaluation of the rate constants of the intramolecular redox decomposition.

An analytical calculation of the logarithm of the apparent rate constant of intramolecular redox decomposition was carried out for each point of the dependence

$$\log k_{app} = \log \dot{D}^0 - \log c_K^0 \quad (12)$$

with the subsequent averaging of the $\log k_{app}$ values obtained.

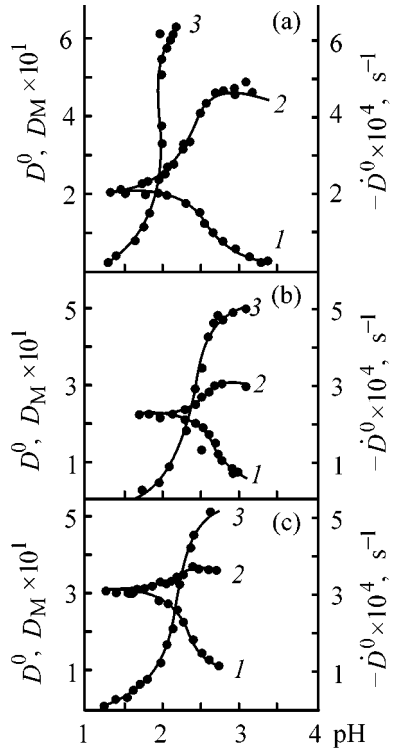

Fig. 4. (*1*) D^0–pH, (*2*) D_M–pH, and (*3*) $-\dot{D}^0$–pH diagrams. System: (a) Ce^{4+}–SO_4^{2-}–H_4Tart ($c_M = c_L = 2.14 \times 10^{-3}$ M, I = 2, T = 28.0°C, λ = 400 nm), (b) Ce^{4+}–SO_4^{2-}–H_3Malt ($c_M = 2.14 \times 10^{-3}$, $c_L = 2.00 \times 10^{-3}$ M; I = 2; T = 17.7°C; λ = 400 nm), (c) Ce^{4+}–SO_4^{2-}–H_2Lact ($c_M = 6.0 \times 10^{-3}$, $c_L = 3.0 \times 10^{-2}$ M; I = 2; T = 18.0°C; λ = 400 nm).

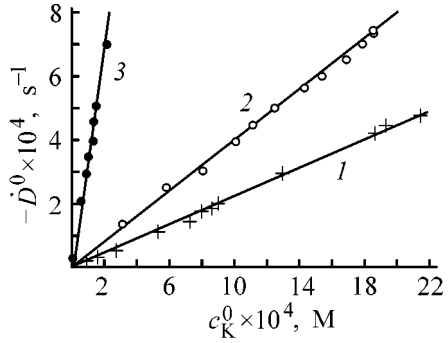

Fig. 5. $-\dot{D}^0$–c_K^0 diagrams. System: (*1*) Ce^{4+}–SO_4^{2-}–H_2Lact ($c_M = 6.0 \times 10^{-3}$, $c_L = 3.0 \times 10^{-2}$ M; I = 2; T = 18.0°C; λ = 400 nm); (*2*) Ce^{4+}–SO_4^{2-}–H_3Malt ($c_M = 1.88 \times 10^{-3}$, $c_L = 3.00 \times 10^{-3}$–$2.11 \times 10^{-2}$ M; pH 2.70; I = 2; T = 18.0°C; λ = 400 nm); (*3*) Ce^{4+}–SO_4^{2-}–H_4Tart ($c_M = c_L = 2.14 \times 10^{-3}$ M; I = 2, T = 28.0°C, λ = 400 nm).

Since the apparent rate constants of redox decomposition of the complexes, k_{app} ($l\ mol^{-1}\ s^{-1}$) depend on their extinction coefficients:

$$k_{app} = \varepsilon_K l / k_2 \quad (13)$$

(l is the thickness of the absorbing layer of the solution), logarithms of the true rate constants k_2 (s^{-1}) of the intramolecular redox decomposition were also calculated (Tables 1–4):

$$\log k_2 = \log k_{app} - \log \varepsilon_K l. \quad (14)$$

The calculated k_2 values were used to evaluate, in accordance with the formula

$$E = 2.303R \frac{\log k_{2\,T_2} - \log k_{2\,T_1}}{\Delta T} T_1 T_2 \quad (15)$$

[R = 8.314 J K^{-1} mol^{-1} is the gas constant, T the absolute temperature (K); $\Delta T = T_2 - T_1$, $T_2 > T_1$], the activation energy of redox decomposition of the complexes (Table 2).

The fact that the dependence $\dot{D}^0 = f(c_K^0)$ remains linear in the concentration ranges under study (Fig. 5) and the constancy of the calculated $\log k_{app}$ value within the series D^0, $\dot{D}^0$–pH, D^0, $\dot{D}^0$–c_L/c_M (Tables 1–4) indicate that a single kinetically active complex is predominant in the systems; and the equality to zero of its free term A (Fig. 5) points to the absence of any contribution from the bimolecular pathway to the process within the concentration ranges studied. Thus, we have an intermediate mechanism of oxidation of the organic ligand by cerium(IV).

In this case the initial rate of the redox process, found using generalized methods of isomolar series and molar ratios, depends on the yield of the complex

$$-\dot{D}^0 = k_{app} c_K^0 = \begin{cases} k_{app}\alpha_K^0 c_M, & c_M < c_L; \\ k_{app}\alpha_K^0 c_L, & c_L < c_M; \end{cases} \quad (16)$$

[$\alpha_K^0 = (D^0 - D_M)/(D_\infty^0 - D_M)$ is the yield of the complex at instant of time $\tau = 0$] and reaches a maximum simultaneously with its maximum yield—at the stoichiometric ratio of the components. In the case in question, this indicates that an intermediate complex of composition 1 : 1 is formed in the system (Figs. 1c and 1e; Fig. 2, curve *2*).

The logarithm of the apparent rate constant of redox decomposition of the complexes, $\log k_{app}$ (12), grows in the order lactic < malic < tartaric acid from $\bar{1}.39 \pm 0.06$ to 0.11 ± 0.04 (18°C). However, the logarithms of true rate constants, $\log k_2$, calculated using expression (14), are constant and equal to $\bar{3}.40 \pm 0.05$ for all the complexes (18°C). The activation energy of intramolecular decomposition also takes a constant, within experimental error, value $E = 132.71 \pm 1.40$ kJ mol^{-1} for H_2Lact, H_3Malt, and H_4Tart.

The rate constants and activation energy of intramolecular redox decomposition, obtained in the present study, are in agreement with the corresponding rate constants and activation energy ($\log k_2 = \bar{3}.36 \pm 0.06$, recalculated to 18°C) and activation energy ($E = 131.8 \pm 1.2$ kJ mol^{-1}) for cerium tartrate $[(CeOH)_2Tart]^{2+}$ [20] and quinate complexes of cerium(IV) $CeOHL]^+$ [21].

The rise in the rate pseudoconstants, observed in going from H_2Lact to H_3Malt [12] and from H_2Malt to H_4Tart [3, 19], is, thus, only apparent and reflects the increase in the extinction coefficients of the complexes in the series in question. Not only the composition of the intermediate complex [5], but also its reactivity are found to be independent, in the given series, of the denticity of the organic ligand. The rise in the stability of the complexes $[CeOHL]^{3-x}$ (x = 2, 3, 4) with increasing ligand denticity is not accompanied by stabilization of cerium(IV) in this series of oxyacids.

The independence of the true rate constants k_2 and the activation energy E of intramolecular redox decomposition from the denticity of oxyacids can be accounted for (as is done in [20]) by the common (single-electron) mechanism of electron transfer via one and the same bridge group in the complexes $[CeOHL]^{3-x}$ (x = 2–4). According to the assumption made in [13], this group is the oxo group of the ceryl ion, which can form a hydrogen bond with the alcohol hydroxyl of tartaric acid. In terms of the theory of ionic equilibria this is equivalent to the formation of a hydrogen bond between a deprotonated alcohol hydroxyl of anions of oxyacids and the hydroxy group of monohydroxo ion of cerium(IV) [Eqs. (5) and (6)].

Thus, the following structure of the intermediate complexes formed in oxidation by cerium(IV) of the ligand series under consideration—H_2Lact (**I**), H_3Malt (**II**), and H_4Tart (**III**), can be suggested:

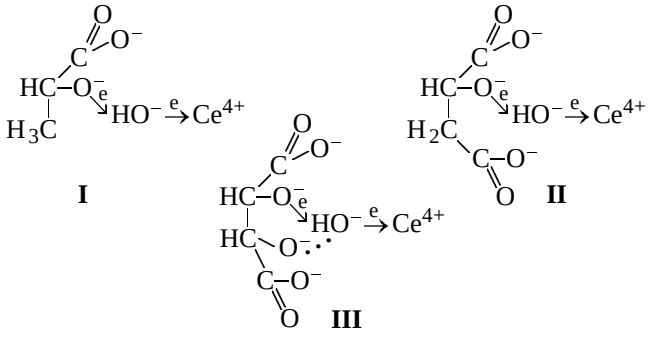

The equation for the initial rate of the redox process occurring in the systems can be represented, with account of expressions (3), (7), and (12), as

$$-\frac{dc_M}{dt} = k_2R_1[CeOH^{3+}][H_mL][H^+]^{-x}$$

$$= k_2\beta_1[CeOH^{3+}][H_{m-x}L^{x-}] \quad (x = m = 2, 3, 4). \quad (17)$$

This equation establishes the type of the functional dependence of the rate on the equilibrium concentration of hydrogen ions in solution and indicates that oxyacids are involved in the redox process not as molecules, contrary to the previous assumption, but as L^{x-} anions, where $x = 2, 3, 4$.

To conclude, it should be mentioned that the redox reactions analyzed in the present study can be, apparently, regarded as indicator reactions [22] for the corresponding complexation pre-equilibria and used not only to solve the inverse problem of determining the rate constants of intramolecular redox decomposition, but also to tackle with the direct problem of finding the equilibrium concentrations of the complexes (and, as a consequence, of their stability constants) by kinetic methods.

EXPERIMENTAL

Twice recrystallized lactic H_2Lact, malic H_3Malt, and tartaric H_4Tart acids, oxycarboxylic acid of chemically pure grade, and cerium(IV) sulfate $Ce(SO_4)_2 \cdot 4H_2O$ of analytically pure grade were used in the study. The required ionic strength of solution, $I = 2$, was created with ammonium sulfate of analytically pure grade. The initial solutions wee prepared from precisely weighed portions. The concentration of organic acid solutions was refined by pH-metric titration with a NaOH solution containing no CO_3^{2-} ions. The content of cerium (IV) in the salt and a freshly prepared solution were determined by back titration with Mohr's salt in the presence of ferroin [23] before and after an experiment.

The optical density of the solutions was recorded with a Specord UV VIS recording spectrophotometer and a KF-5 photoelectrocolorimeter with MEA-4 recording unit, mainly at a wavelength of 400 nm. As the time of reaction onset was taken the instant at which the mixing vessel, in which the starting components were placed, was turned upside-down. The initial optical density of the reaction mixture of the metal and the ligand D^0 was found by linear extrapolation of the kinetic curves plotted in semilogarithmic coordinates to the instant of time $\tau = 0$. The solutions were thermostated using a Wobser thermostat.

The pH value was measured in a mixture of components, after the recording of the optical density ($\tau \approx 1$ min and also $\tau \approx 10$ min), and in cerium(IV) sulfate solutions with a pH-673 precision pH meter.

The step constant of protonation of the carboxy group in the lactic acid anion was also determined at an ionic strength $I = 2$

$$æ_2 = \frac{[H_2L]}{[HL][H]}. \quad (18)$$

The value $\log æ_2 = 3.72 \pm 0.02$, obtained for H_2Lact, is in agreement with $\log æ_2 = 3.69$ ($I = 2$) [7]. The logarithms of step constants of protonation of carboxy groups in the malic acid anion ($\log æ_1 = 3.22$, $\log æ_2 = 4.71$) were taken from [24], and those for the tartaric acid anion ($\log æ_1 = 2.95$, $\log æ_2 = 4.11$), from [25].

Since, according to the dissociation constants of oxy groups, oxyacids are weak acids, the following value of the logarithm of the dissociation constant of the oxy group was used in calculations for all oxyacids: $\log B_1 = 14.6$ (obtained by averaging the data of [16, 25]; in [25], the value of $\log B_1$ was determined by mathematical modeling). The logarithms of the total protonation constants $B_i = [H_iL] / [L][H]^i$, $i > 1$, were taken to be as follows: $\log B_2 = 18.31$ for H_2Lact; $\log B_2 = 19.31$, $\log B_3 = 22.53$ for H_3Malt; and $\log B_2 = 25.90$, $\log B_3 = 30.01$, and $\log B_4 = 32.96$ for H_4Tart.

CONCLUSIONS

(1) A generalization of the methods used to study complexation (D–pH method and methods of molar ratios and isomolar series) to the case on nonzero rate of redox decomposition of complexes was proposed.

(2) The above methods were used to determine the composition, stability constants, true rate constants, and activation energies of intramolecular redox decomposition of hydroxo complexes of cerium(IV) with a number of organic ligands; the law governing the rate of the redox process occurring in the systems and its intermediate mechanism was established.

(3) The absence of stabilization of cerium(IV), with the stability of its complexes increasing in the series of the α oxycarboxylic acids considered, and the independence of the reactivity of these complexes from the denticity of an organic ligand were demonstrated.

(4) The independence of the rate constants and activation energy of redox decomposition of complexes from the denticity of oxyacids was interpreted in

terms of the bridge mechanism of redox decomposition as transfer of an electron via one and the same bridge group in the complexes $[CeOHL]^{3-m}$ (m = 2, 3, 4).

(5) A conclusion was made that the redox reactions considered in the present study can be used as indicator reactions in investigating the corresponding complexation equilibria by kinetic methods.

REFERENCES

1. Kiselev, Yu.M., *Zh. Neorg. Khim.*, 1999, vol. 44, no. 5, pp. 711–717.
2. Kiselev, Yu.M., *Zh. Neorg. Khim.*, 1998, vol. 43, no. 5, pp. 759–767.
3. *Koordinatsionnaya khimiya redkozemel'nykh elementov* (Coordination Chemistry of Rare-Earth Elements), Spitsyn, V.I. and Martynenko, L.I., Eds., Moscow: Mos. Gos. Univ., 1974.
4. Kiselev, Yu.M., *Vestn. Mos. Gos. Univ.*, 1998, vol. 38, no. 1, pp. 3–10.
5. Sarana, N.V., in *Trudy Leningradskogo tekhnologicheskogo instituta tsellyulozno-bumazhnoi promyshlennosti* (Coll. of Sci. Works of Leningrad Technol. Inst. of Pulp and Paper Industry), 1969, no. 24, pp. 56–59.
6. Dolgoplosk, B.A. and Tinyakova, E.I., *Okislitel'no-vosstanovitel'nye sistemy kak istochnik svobodnykh radikalov* (Redox Systems as a Source of Free Radicals), Moscow: Nauka, 1972.
7. Inczedi, J., *Analytical Application of Complex Equilibria*, Translation Editor J.Tyson, Budapest: Academia Kiado, Coll House: Ellis Horwood, 1976.
8. Duka, G.G., Batyr, D.G., Romanchuk, L.S., and Sychev, A.Ya., *Koord. Khim.*, 1990, vol. 16, no. 1, pp. 93–106.
9. Rao, B.M., Sastrys, T.P., and Parekh, T., *Z. phys. Chem.*, 1983, vol. 264, no. 5, pp. 906–920.
10. Krishna, B. and Tewari, K.C., *J. Chem. Soc.*, 1961, no. 25, pp. 3097–3102.
11. Mehrotra, R.N. and Chosh, S., *Z. phys. Chem. (DDR)*, 1965, vol. 230, no. 3/4, pp. 231–239.
12. Lahid, A. and Alexander, A., *J. Chem. Soc. Dalton Trans.*, 1974, no. 23, pp. 2521–2530.
13. Luzan, A.A. and Yatsimirskii, K.B., *Zh. Neorg. Khim.*, 1968, vol. 13, no. 12, pp. 3216–3221.
14. Vakhramova, G.P., Pechurova, N.I., and Spitsyn, V.I., *Izv. Akad. Nauk SSSR, Ser. Khim.*, 1974, no. 10, pp. 2361–2366.
15. Vakhramova, G.P., Pechurova, N.I., and Spitsyn, V.I., *Zh. Neorg. Khim.*, 1974, vol. 19, no. 10, pp. 2722–2725.
16. Kostromina, N.A., Kumok, V.N., and Skorik, N.A., *Khimiya koordinatsionnykh soedinenii* (Chemistry of Coordination Compounds), Moscow: Vysshaya Shkola, 1990.
17. Trubacheva, L.V. and Pechurova, N.I., *Zh. Neorg. Khim.*, 1981, vol. 26, no. 12, pp. 3254–3258.
18. Skorik, N.A. and Artish, A.S., *Zh. Neorg. Khim.*, 1985, vol. 30, no. 8, pp. 1994–1997.
19. Bachmann, K. and Lieser, K.H., *Ber. Bunsgesell. Phys. Chem.*, 1963, vol. 67, no. 8, pp. 810–816.
20. Voskresenskaya, O.O. and Skorik, N.A., *Zh. Neorg. Khim.*, 2000, vol. 45, no. 12, pp. 2090–2098.
21. Voskresenskaya, O.O. and Skorik, N.A., *Zh. Neorg. Khim.*, 2000, vol. 45, no. 4, pp. 719–726.
22. Yatsimirskii, K.B., *Kinetic Methods of Analysis*, Oxford: Pergamon, 1966.
23. Kolthoff, I.M., Belcher, R, Stenger, V. A., and Matsuyama, G., *Volumetric Analysis*, vol. III, *Titration Methods: Oxidation–Reduction Reactions*, New York: Interscience, 1957.
24. Sillen, L.G. and Martell, A.E., Stability Constants of Metal–Ion Complexes: *Special publication no. 17*, London: Chemical Soc., 1964.
25. Dobrynina, N.A. and Martynenko, L.I., *Problemy sovremennoi khimii koordinatsionnykh soedinenii* (Problems of Modern Chemistry of Coordination Compounds), Burkov, K.A., Ed., Leningrad: Len. Gos. Univ., 1989, p. 98.

Russian Journal of Applied Chemistry, Vol. 75, No. 6, 2002, pp. 875–877. Translated from Zhurnal Prikladnoi Khimii, Vol. 75, No. 6, 2002, pp. 895–897.
Original Russian Text Copyright © 2002 by Gerasimova, Okhrimenko, Zhdanova.

INORGANIC SYNTHESIS AND INDUSTRIAL INORGANIC CHEMISTRY

A Study of the Composition of a Solid Phase Isolated on Heating Acid Solutions of Titanium(IV) Sulfate

L. G. Gerasimova, R. F. Okhrimenko, and N. M. Zhdanova

Institute of Chemistry and Technology of Rare Elements and Mineral Resources, Kola Scientific Center, Russian Academy of Sciences, Apatity, Russia

Received: March 11, 2001; in final form, December 2001

Abstract—The mechanism of solid phase formation in hydrolysis of titanium(IV) sulfate solutions was studied at elevated temperature (boiling).

Thermal treatment of acid solutions of titanium(IV) sulfate, with precipitation of hydroxides, is used to manufacture titanium dioxide of pigment and nonpigment brands, each of which must meet the certain requirements to the dispersity, impurity content, solubility of particles in organic and aqueous media, etc. [1, 2]. The conditions of thermal treatment of the solutions affect the composition of the forming solid phase and, consequently, the above properties of the final technological product. In spite of numerous studies in this field, data on the structure of titanium(IV) hydroxide are controversial. Some researchers classed it with acids, namely, metatitanic acid $H_2TiO_3 \cdot nH_2O$ [1], and others, with the hydrated oxides $TiO_2 \cdot nH_2O$ or hydroxides of the type $TiO(OH)_2 \cdot nH_2O$ [3, 4]. Apparently, both standpoints have right to exist, since the structure and composition of titanium hydroxide depend on the preparation conditions. It is known, in particular, that the solid phase separated in the first stage of heating (thermal hydrolysis) of an acid sol ution of titanium(IV) sul- fate contains two OH groups bound to a single titanium(IV) atom. Prolonged heating of such systems results in splitting of hydroxide groups and transformation of metatitanic acid into hydrated titanium dioxide. In addition, the solid phase contains sulfate groups bound to titanium(IV). The relative content of the components and the character of bonding between them depend on the composition of the initial solution (c_{TiO_2}, $c_{H_2SO_4}$, impurity components) and the conditions of its thermal treatment (time and temperature) [1].

In this communication, we present the results obtained in a study of the solid phase separated from acid solutions of titanium(IV) sulfate upon thermal hydrolysis under comparable conditions. Such data, being of theoretical and practical importance, are lacking from the literature.

We used in the study acid solutions of titanium(IV) sulfate, prepared from the salts $TiOSO_4 \cdot H_2O$ [oxotitanium(IV) sulfate monohydrate] and $(NH_4)_2TiO(SO_4)_2 \cdot H_2O$ (ammonium monooxodisulfate titanate mohohydrate). The titanium(IV) concentration in solutions was 1.5 M in terms of TiO_2; the content of free sulfuric acid in $TiOSO_4 \cdot H_2O$ solutions was varied from 0.25 to 0.5 M, and that in $(NH_4)_2TiO(SO_4)_2 \cdot H_2O$ solutions, from 0.1 to 0.5 M at a 0.15–0.75 M content of free ammonium sulfate.

The experimental procedure was as follows. A solution to be studied was placed in a heat-resistant three-necked flask equipped with a stirrer, reflux condenser, and a thermometer, heated to the boiling point (103°C), and boiled for 3 h. The phase composition of the precipitate formed in the solution under heating was analyzed by X-ray phase analysis, and the content of OH groups bound to titanium(IV) in the precipitate was found by the known procedure [5]. For this purpose, a sample of the suspension was filtered in a vacuum on a dense glass filter, the precipitate was washed with water, its weighed portion (0.2 g) was placed in water (15 ml), to which ammonium solution was added to pH 8.25. Then 50–70 ml of a potassium fluoride solution (250 g l^{-1} KF) and several drops of phenolphthalein were added and the mixture was titrated with 0.1N HCl solution, first, every 2 min (during the first 30 min), then, every 30 min (during the first 3 h), and, finally, every 24 h.

1070-4272/02/7506-0875 $27.00 © 2002 MAIK "Nauka/Interperiodica"

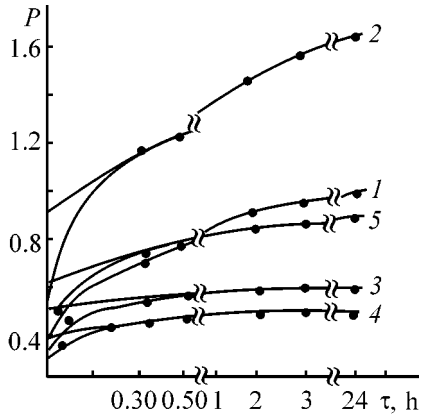

Fig. 1. Variation of the composition of the precipitates obtained from titanium(IV) sulfate solutions heated to the boiling point. c_{Ti} = 1.5 M in terms of TiO_2. (*P*) Amount of OH groups per Ti(IV) and τ time. Solution composition (M): (*1*) 0.25 H_2SO_{4f} and 0.25 $(NH_4)_2SO_{4f}$; (*2*) 0.5 H_2SO_{4f} and 0.15 $(NH_4)_2SO_{4f}$; (*3*) 0.1 H_2SO_{4f} and 0.75$(NH_4)_2SO_{4f}$; (*4*) 0.25 H_2SO_{4f}; and (*5*) 0.5 H_2SO_{4f}; the same for Fig. 2.

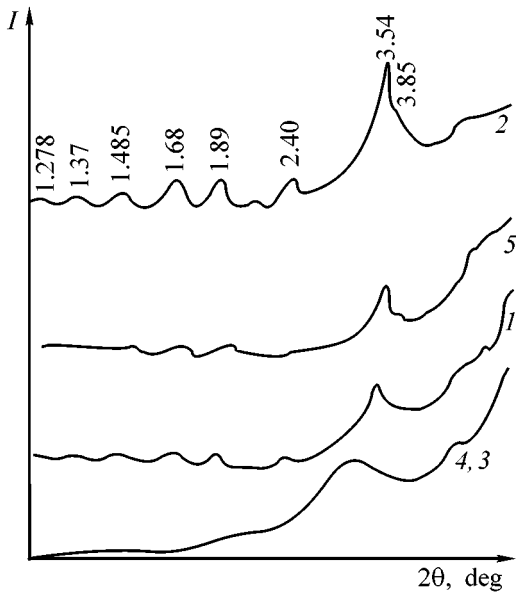

Fig. 2. X-ray diffraction patterns of precipitates obtained from acid solutions of titanium(IV) sulfate. (*I*) Intensity and (2θ) Bragg angle.

In reaction with potassium fluoride, two successive processes occur: fast replacement by fluoride ions of free (terminal) OH groups bound to titanium(IV) and slow rupture of bridging bonds [6, 7]. The replacement of OH groups by fluoride ions is intensive during about 15 min. Then the process decelerates somewhat, and, after 25–30 min, its rate decreases markedly. The amount of active (terminal) OH groups bound to titanium(IV) was found graphically from the intersection with the ordinate axis of the tangent to the flat portion of the curve corresponding to the 0–30 min interval.

The number of the bridging oxo bonds, $Ti^{(IV)}$–O–$Ti^{(IV)}$, was determined from the results of precipitate titration with HCl solution 24 h after the introduction of KF into a suspension. For this purpose, the number of active OH groups was subtracted from the value obtained from the intersection of the ordinate axis with the tangent to the *P*-vs.-τ curve for $\tau \geq 24$ h (Fig. 1).

The correlation between the composition of the acid titanium(IV) sulfate solution, heated to the boiling point (103°C), and the amount of active and inactive OH groups in the precipitates forming under the given conditions is presented in Fig. 1. With increasing acidity, the number of active OH groups in $TiOSO_4 \cdot H_2O$ solutions grow 1.5-fold, with the number of inactive groups increasing by an order of magnitude (curves *4*, *5*). For $(NH_4)_2TiO(SO_4)_2 \cdot H_2O$ solutions with similar basicity, the character of the correlation between the solution composition and the number of active and inactive OH groups in the precipitates is the same, with the quantitative parameters being, however, markedly higher (curves *1*, *2*). In the solid phase precipitated from a $(NH_4)_2TiO(SO_4)_2 \cdot H_2O$ solution with the lowest concentration of H_2SO_{4f} and high concentration of $(NH_4)_2SO_{4f}$, inactive OH groups are virtually absent (curve *3*).

The table presents the compositions of the solid phases precipitated from acid sulfate solutions boiled for 2 and 3 h. Analysis of the data suggests that the effect of solution acidity on the precipitate composition is, in this case, weaker than that in the initial period of heating. The precipitates 3 and 4 contain virtually no inactive OH groups. This points to a different mechanism of solid phase formation in thermal hydrolysis.

The X-ray diffraction patterns of the precipitates obtained from acid titanium(IV) solutions boiled for 3 h (Fig. 2) were taken on a DRON–2 diffractometer (Cu_{K_α} radiation, graphite monochromator, 2 deg min^{-1} counter velocity). The reflection intensities show that sample 2 is decrystallized to a larger extent than the other samples. The crystalline impurity phase is titanium dioxide of anatase modification, formed via particle growth involving Ti–O–Ti– polymeric chains, with their subsequent further incorporation into micelles, i.e., by the crystal-chemical mechanism [8]. The content of the crystalline phase in precipitates 1 and 5 decreases; precipitates 3 and 4 are completely X-ray-amorphous. Such precipitates are formed by

Variation of the c_{OH}/c_{Ti} ratio P in the precipitates

τ, h	OH group	P in a sample*				
		1	2	3	4	5
2	Active	0.38	0.32	0.33	0.34	0.38
	Inactive	0.20	0.24	0.07	0.05	0.11
3	Active	0.32	0.28	0.32	0.27	0.28
	Inactive	0.13	0.13	0.05	0.02	0.10

* Suspension was sampled after indicated boiling time τ; the sample number is the same as the number of the solution composition in Fig. 1.

the colloid-chemical mechanism, with particles growing via cross-linking of hydroxo complexes by OH groups to form colloid particles with loose structure. The colloid-chemical mechanism of precipitate formation is initiated both by the low solution acidity and by the presence of ammonium sulfate in solution [9].

A comparison of the precipitates obtained from $(NH_4)_2TiO(SO_4)_2 \cdot H_2O$ and $TiOSO_4 \cdot H_2O$ solutions heated under similar conditions demonstrated that, in the absence of ammonium sulfate, the solid phase is largely formed by the colloid–chemical mechanism.

CONCLUSION

A study of the thermal hydrolysis of acid solutions of titanium(IV) sulfate with the formation of a hydroxide precipitate demonstrated that, depending on the solution acidity and on the content of ammonium sulfate in solution, two mechanisms, crystal-chemical and colloid-chemical, are responsible for the solid phase formation, and this fast determines the structure of the resulting precipitate.

REFERENCES

1. Belen'kii, E.F. and Riskin, I.V., *Khimiya i tekhnologiya pigmentov* (Chemistry and Technology of Pigments), Moscow: Khimiya, 1976.
2. Weiser, H.W. and Miligen, W.O., *Chem. Rev.*, 1975, vol. 25, no. 1, pp. 1–30.
3. Biryuk, L.I., Goroshchenko, Ya.G., Khandros, E.L., *et al.*, *Ukr. Khim. Zh.*, 1971, vol. 37, no. 112, pp. 1221–1224.
4. Biryuk, L.I., Goroshchenko, Ya.G., Khandros, E.L., *et al.*, *Ukr. Khim. Zh.*, 1973, vol. 39, no. 5, pp. 504–506.
5. Gerasimova, L.G., Okhrimenko, R.F., and Zhdanova, N.M., *Lakokrasochn. Mater. Primen.*, 1998, no. 3, pp. 13–15.
6. Gerasimova, L.G., *Pigmenty i napolniteli iz prirodnogo titansoderzhashchego syr'ya i tekhnogennykh otkhodov* (Pigments and Fillers Obtained from Natural Titanium-containing Raw Materials and Technological Wastes), Apatity: Kol'sk. Nauchn. Tsentr, Ros. Akad. Nauk, 2001.
7. Limar', T.V., Savos'kina, A.I., Andreeva, V.I., *et al.*, *Zh. Neorg. Khim.*, 1968, vol. 14, no. 9, pp. 2307–2312.
8. Motov, D.L., Gerasimova, L.G., and Kharchenko, T.T., *Izuchenie termogidroliza v sisteme* TiO_2–H_2SO_4–$(NH_4)_2SO_4$–H_2O *pri poluchenii dioksida titana* (A Study of Thermal Hydrolysis in the System TiO_2–H_2SO_4–$(NH_4)_2SO_4$–H_2O in Production of Titanium Dioxide), Available from VINITI, 1984, no. 29.
9. Gerasimova, L.G., Gershenkop, A.Sh., and Okhrimenko, R.F., *Neorg. Mater.*, 2001, vol. 37, no. 5, pp. 631–635.

-
Russian Journal of Applied Chemistry, Vol. 75, No. 6, 2002, pp. 878–882. Translated from Zhurnal Prikladnoi Khimii, Vol. 75, No. 6, 2002, pp. 898–902.
Original Russian Text Copyright © 2002 by Vasil'eva, Morozova, Lapshin, Konakov.

INORGANIC SYNTHESIS AND INDUSTRIAL INORGANIC CHEMISTRY

A Porous Ceramic Based on Aluminomagnesium Spinel

E. A. Vasil'eva, L. V. Morozova, A. E. Lapshin, and V. G. Konakov

Grebenshchikov Institute of Silicate Chemistry, Russian Academy of Sciences, St. Petersburg, Russia

Received February 11, 2002

Abstract—Powdered precursors of an aluminomagnesium spinel were synthesized by joint crystallization of magnesium and aluminum salts from solutions. The sequence of stages of the $MgAl_2O_4$ formation was studied in relation to the nature of initial reagents and temperature of heat treatment. Optimal modes of sintering of the aluminomagnesium spinel for obtaining ceramic materials with porosity greater than 50% were determined.

Presently, procedures for manufacturing construction and functional ceramics are being intensively developed in order to create a new generation of materials for modern technology. The topicality of the problem is due to unique properties of ceramic materials consisting of crystallites with size of about 10–100 nm. Much attention is given to preparation and use of porous materials based on various ceramic formulations, including ceramics with aluminomagnesium spinel as a component.

The $MgAl_2O_4$ spinel has thermodynamically stable structure, resistance to corrosive media, low heat-conductivity, and high dielectric characteristics, and, therefore, materials on its base are of great practical interest for electrochemical engineering.

The aim of this study was to obtain a high-permeable porous matrix of an aluminomagnesium spinel for creating galvanic cells with salt bridges made of fluorides of alkali and alkaline-earth metals, which could find wide use in monitoring the activity of oxygen ions in oxide melts in industrial glass manufacture, black and non-ferrous metallurgy, and cement production [1].

Various methods of $MgAl_2O_4$ synthesis have been described in the literature [2–8]. From the technological standpoint, the simplest way to obtain this material is solid-phase synthesis from magnesium and aluminum oxides. However, this procedure involves high temperatures synthesis and sintering of ceramics (1600–1800°C), which makes it impossible to achieve the required open porosity (>50%) and homogeneous distribution of pores in ceramic compacts. It was shown in [9] that a ceramic based on aluminomagnesium spinels with stable porous structure can be obtained by sintering at rather low temperatures (<1400°C) nanosize precursor powders thermally activated at a temperature below 860°C.

To obtain precursor powders with sintering activity, we chose the method of joint crystallization from a mixture of solutions of magnesium nitrate $Mg(NO_3)_2 \cdot 6H_2O$ (analytically pure grade) and various aluminum compounds, with the subsequent decomposition and heat treatment of the crystals obtained. Aluminum nitrate $Al(NO_3)_3 \cdot 9H_2O$ (chemically pure grade), aluminum isopropylate $Al[(CH_3)_2CHO]_3$, and aluminum hydroxide (boehmite) AlO(OH) were used as Al_2O_3 sources.

The starting reagents, taken in the following stoichiometric ratios:

I, $Mg(NO_3)_2 \cdot 6H_2O + 2Al(NO_3)_3 \cdot 9H_2O$,

II, $Mg(NO_3)_2 \cdot 6H_2O + Al(NO_3)_3 \cdot 9H_2O + Al[(CH_3)_2CHO]_3$,

III, $Mg(NO_3)_2 \cdot 6H_2O + 2Al[(CH_3)_2CHO]_3$,

IV, $Mg(NO_3)_2 \cdot 6H_2O + 2AlO(OH)$,

were dissolved in water acidified to pH 4 with nitric acid. The salt solutions were thoroughly stirred and evaporated on a water bath in the course of 3 h, after which the remainder was calcined in a muffle furnace at 250°C (2 h).

The thus synthesized powders I–IV were studied by differential thermal analysis (DTA, Netzsch dif-

1070-4272/02/7506-0878 $27.00 © 2002 MAIK "Nauka/Interperiodica"

fractometer) and X-ray phase analysis (XPA, D-500/HS Siemens diffractometer). Thermal effects corresponding to the instant of $MgAl_2O_4$ formation were not recorded by the DTA method in any of the cases. Comparison of DTA and XPA data for the powders obtained with the relevant published data on dehydration and decomposition of the starting compounds (200–500°C) [10] shows that the temperature ranges of these processes and those of spinel crystallization of amorphous precipitates overlap. According to the XPA data, the initial stage of formation of compounds with spinel structure is already observed at 300°C, and all main spinel peaks are recorded in the X-ray patterns of samples I–IV annealed at 400°C (see, e.g., Fig. 1). The characteristic redistribution of peak intensities and the narrowing of peaks in the X-ray patterns of samples I–IV at above 400°C (Fig. 2) indicate the occurrence of crystallization, ending at about 900°C in the formation of a normal $MgAl_2O_4$ phase (lattice parameter a = 0.806–0.808 nm, ratio of peak intensities I_{400}/I_{311} = 0.57–0.62). Such a two-stage scheme of $MgAl_2O_4$ formation and crystallization from amorphous precipitates has been proposed earlier by Bratton [11]. According to this scheme, a number of solid solutions based on spinel phases $MgAl_2O_4$, γ-Al_2O_3, and MgO* are formed in the amorphous oxide matrix in the intermediate stage (350–400°C). In the second stage (above 400°C), solid-phase reactions between these solid solutions result in the crystallization of the normal $MgAl_2O_4$ phase. The acceleration of the crystallization of aluminomagnesium spinel above 800°C is related, in the first place, to increasing rate of magnesium oxide diffusion at this temperature.

The heat treatment mode, as well as individual properties of the reagents and, in particular, specific features of structural transformations of starting aluminum compounds in thermal decomposition affect the course of the $MgAl_2O_4$ crystallization. According to the XPA data (Fig. 2), α-Al_2O_3 can be formed in amounts of no more than 5%, in addition to the main spinel phase, under conditions of fast heating in calcination of systems I–III in the range 900–1200°C. At the same time, with boehmite used [system IV], the α-Al_2O_3 phase is not detected. It is known that the γ-Al_2O_3 formation in thermal decomposition of boehmite is completed earlier (<500°C) than in the case of nine-water aluminum nitrate (>650°C), and the subsequent transformation of spinel phases to corundum occurs in the case of boehmite at a temperature considerably higher (about 1100°C) than that for the salt (820°C) [12]. It is probable that, in fast heating of amorphous precipitates I–III to 900–

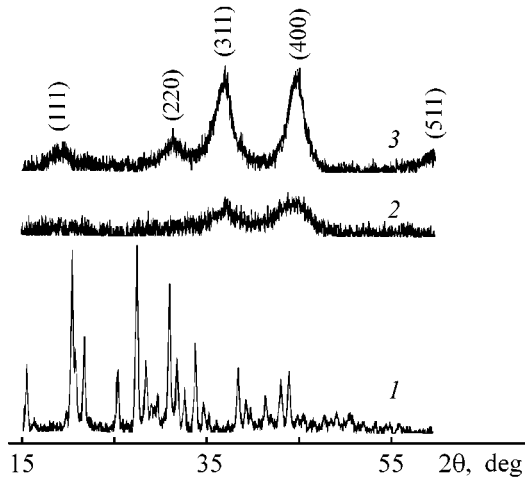

Fig. 1. Sequence of formation of a spinel phase in thermal decomposition of solutions of aluminum and magnesium nitrates (system I). (2θ) Bragg angle; the same for Fig. 2. Temperature (°C), time (h): (*1*) 150, 1; (*2*) 300, 2; (*3*) 400, 2.

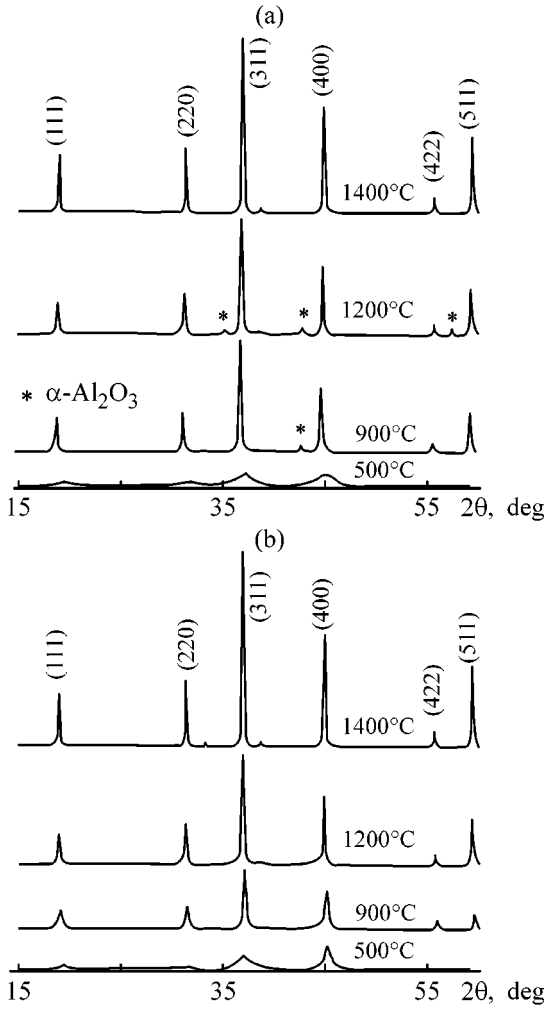

Fig. 2. Effect of the nature of starting aluminum compounds on the $MgAl_2O_4$ formation in the range 500–1400°C. System: (a) I and (b) IV.

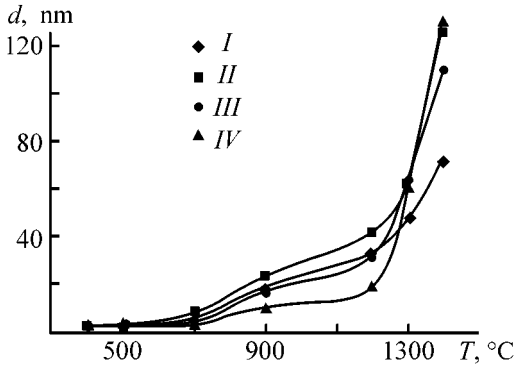

Fig. 3. Change in average size of spinel crystallites, *d*, in the range 400–1400°C. (*T*) Temperature. (*I–IV*) Systems I–IV, respectively.

1200°C, the intermediate γ-Al_2O_3 phase has no time to react completely with MgO and its unreacted part is converted to α-Al_2O_3. The peaks of α-Al_2O_3 are absent from the X-ray patterns of powders I–III calcined above 1200°C, in good agreement with the considerable increase in the solubility of aluminum oxide in $MgAl_2O_4$ at above 1100°C [13].

We determined the average size of primary spinel crystallites formed in precursor powders I–IV heat-treated at 400–1400°C from the Fourier transform of the 311 peak, corrected for the instrumental broadening. In is seen from Fig. 3 that, in the nucleation stage, the size of primary particles of the spinel phase (3–5 nm) is virtually independent of the nature of the starting reagents. In the crystallization stage (400–900°C), the growth rate of crystallites is slow owing to the low diffusion coefficients of the oxides. The crystallite growth becomes essential above 1200°C.

We thermally activated the resulting nanosize precursor powders I–IV of aluminomagnesium spinel at 400°C for 2 h. Compacts pressed from the activated powders I–IV were used to study the effects of sintering temperature and cellulating agents on the formation of porous structure of ceramic materials. The samples were sintered in a silit furnace in air at 1100–1400°C. The total porosity of the samples was calculated from the apparent density of the sintered compacts. The open porosity was determined by hydrostatic weighing. The size distribution of pores was characterized using mercury porosimetry. The main aim of this stage of the study was to obtain sintered ceramic compacts with open porosity greater than 50%.

The initial calcination was carried out at 1400°C (2 h). The porosity of the sintered samples was 30–33%. Calcination at higher temperatures is in expedient, as it leads to gradual "slamming" of a part of pores, formation of closed porosity, and compaction of the sample [4]. The lower temperature boundary of compact sintering was 1100°C. At this temperature, sintered samples were obtained only from powder IV. The above-described formation of α-Al_2O_3 on the surface of spinel crystallites is one of possible reasons for the loosening of samples I–III at 1100°C. A similar effect was noted earlier in [14].

Well-sintered samples of activated powders I–IV were synthesized with the calcination temperature raised to 1150–1300°C. However, the porosity of the material increased by no more than 5% as compared with the samples sintered at 1400°C (see table). A comparison of the total porosity of the samples with their open porosity determined by hydrostatic weighing demonstrated that the closed porosity of the samples did not exceed 3%.

The method proposed did not reveal any advantages of using the expensive aluminum isopropylate as an additive to aluminum nitrate [system II] or as the only source of aluminum [system III]. The main characteristics of porous ceramics (phase and granulometric composition, porosity parameters, shrinkage, and mechanical strength) found for systems I–III coincide within the experimental error. The data in the table show that use of boehmite in synthesis of precursor powders results in a 4–8% decrease in the porosity of the sintered compacts. At the same time, the strength of the ceramics synthesized from powder IV was the highest.

Influence exerted by calcination temperature and by cellulating agent (C) on the shrinkage $\Delta L/L$ and total porosity P_{tot} of ceramic materials prepared from $MgAl_2O_4$

Calcination mode	Parameter	Sample			
		I	II	III	IV
		%			
1150°C, 4 h	$\Delta L/L$	15	15	18	23
	P_{tot}	36	38	36	31
	$\Delta L/L^*$	9	14	16	13
	P^*_{tot}	65	53	53	55
1300°C, 2 h	$\Delta L/L$	16	15	18	23
	P_{tot}	34	38	36	30
	$\Delta L/L^{**}$	17	16	19	21
	P^{**}_{tot}	59	60	60	53

* 20% C added to the blend.

** 30% C and 5% NH_4F added to the blend.

Thus, we failed to obtain sintered ceramics with porosity greater than 50% by simply varying the temperature mode and selecting Al_2O_3 sources.

It is known that one of methods used for creating porous structures is introduction of burning-out additives into a powder to be sintered. In this study, we used highly dispersed activated carbon introduced into the stock before pressing compact samples.

Well-sintered materials with required strength and porosity were obtained by introducing 20% activated carbon (calcination mode 1150°C, 4 h). To sinter samples with higher content of activated carbon (30%), we introduced a sintering component NH_4F (5%) into the stock and raised the calcination temperature to 1300°C (2 h) (see table). The closed porosity of the samples was less than 3%. It is seen from the table that the introduction of carbon into precursor powders allowed us to raise the porosity of samples by more than 25% and to exceed in all cases the required open porosity of 50%. It was also found that the technological procedures applied in the study (use of various initial aluminum compounds in synthesis of precursor powders, variation of the amount of the burning-out additive, variation of the sintering mode, and introduction of a sintering additive) make it possible to control the pore size distribution in a wide range. As an illustration, Fig. 4 presents data obtained by mercury porosimetry for the porous structures of three $MgAl_2O_4$ ceramics. It can be seen that macropores with radius from 0.5 to 3 μm dominate in all the samples. These macropores are formed in the spinel matrix through burning-out of carbon and migration of the combustion products. Raising the sintering temperature to 1300°C and introducing an NH_4F additive makes the pore size distribution narrower and leads to elimination of pores with radius less than 1 μm. Irrespective of the nature of an initial powder-precursor I–IV, the ceramics synthesized under these conditions had similar porous structures (Fig. 4c). At the same time, Figs. 4a and 4b demonstrate a direct dependence of the porous structure of the materials sintered at 1150°C on the nature of a precursor powder used. For example, with powder I (1150°C, 4 h, 20% C), a ceramic with bimodal pore size distribution and a considerable (up to 40%) fraction of pores with radius less than 100 nm was obtained. The average radius of such pores is about 15 nm. This value well agrees with the average size of spinel phase crystallites, which is about 30 nm at 1150°C, as seen from Fig. 3. This coincidence suggests that the porosity is of intercrystallite nature. A possible reason for the additional loosening of the spinel matrix of materials obtained from precursors I–III, compared with the samples obtained from a boehmite-based powder, was discussed above in considering the data on sintering of ceramics at 1100°C without carbon additives.

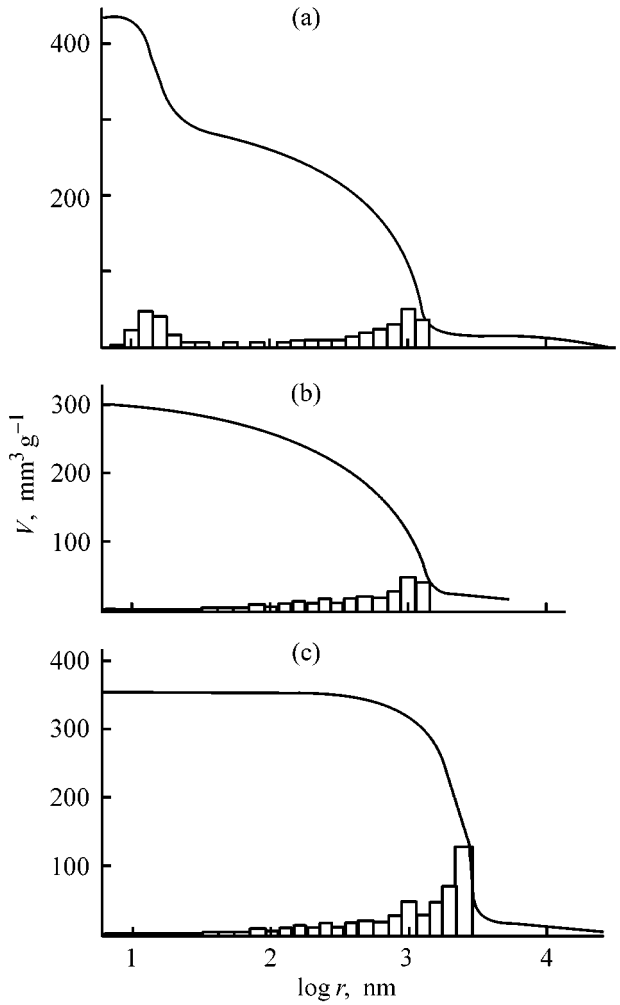

Fig. 4. Pore size distribution in samples of $MgAl_2O_4$ ceramics obtained under various conditions. (V) Volume of pores and (r) pore radius. (a) System I, 1150°C, 4 h, 20% C; (b) system IV, 1150°C, 4 h, 20% C; and (c) system I, 1300°C, 2 h, 30% C, 5% NH_4F.

CONCLUSIONS

(1) Nanosize sintering-active precursor powders of aluminomagnesium spinel were synthesized. Ceramic materials with open porosity exceeding 50% were obtained by introducing a burning-out carbon additive into the stock. The effect of phase transformations and dispersity of spinel powders on the specific features of sintering of the ceramics was determined.

(2) The possibility of controlling the porous structure of spinel materials by varying the source of alu-

minum oxide in synthesis of precursor powders, by changing the sintering modes of ceramics, and by introducing burning-out and sintering additives into the stock was demonstrated.

ACKNOWLEDGMENTS

This study was supported financially by Presidium of the Russian Academy of Sciences according to the results of expertise of the sixth competition between scientific projects presented by young scientists of the Russian Academy of Sciences in the field of fundamental and applied research. Project "Development of a Method for Monitoring P_O Oxide Melts," headed by V.G. Konakov.

REFERENCES

1. Konakov, V.G., Kozhina, E.L., and Shults, M.M., *Fiz. Khim. Stekla*, 2001, vol. 27, no. 2, pp. 279–287.
2. Skomorovskaya, L.A., *Steklo Keram.*, 1993, no. 4, pp. 18–19.
3. Morozova, L.V., Panova, T.I., and Lapshin, A.E., *Zh. Prikl. Khim.*, 1999, vol. 72, no. 4, pp. 547–551.
4. Itatani, K., Sacai, H., and Scott Howell, F., *Br. Cer. Trans. J.*, 1989, vol. 88, no. 1, pp. 13–16.
5. Varnier, O., Hovnanian, N., Larbot, A., *et al.*, *Mat. Res. Bull.*, 1994, vol. 29, no. 5, pp. 479–488.
6. Bailey, J.T. and Russel, R., *Am. Ceram. Soc. Bull.*, 1968, vol. 47, no. 11, pp. 1025–1029.
7. Sarkar, R. and Banerjee, G., *Sci. Sintering*, 2000, vol. 32, no. 2, pp. 61–68.
8. Laobuthee, A., Wongkasemjit, S., Traversa, E., and Laine, R.M., *J. Eur. Ceram. Soc.*, 2000, vol. 20, pp. 91–97.
9. Bratton, R.J., *Am. Ceram. Soc. Bull.*, 1969, vol. 48, no. 11, pp. 1069–1075.
10. *Khimicheskaya entsiklopediya* (Chemical Encyclopedia), Knunyants, I.L., Ed., Moscow: Sovetskaya Entsiklopediya, 1988, vols. 1 and 2.
11. Bratton, R.J., *Am. Ceram. Soc. Bull.*, 1969, vol. 48, no. 8, pp. 759–762.
12. Dzis'ko, V.A., Karnaukhova, P.B., and Tarasova, D.V., *Fiziko-khimicheskie osnovy sinteza okisnykh katalizatorov* (Physicochemical Foundations of the Synthesis of Oxide Catalysts), Novosibirsk: Nauka, 1978.
13. Collongues, R., *La Non-Stoechiometrie*, Paris: Masson et C, 1971.
14. Kashcheev, I.D. and Semyannikov, V.P., *Ogneupory Tekhn. Keram.*, 2000, no. 9, pp. 20–23.

Russian Journal of Applied Chemistry, Vol. 75, No. 6, 2002, pp. 883–887. Translated from Zhurnal Prikladnoi Khimii, Vol. 75, No. 6, 2002, pp. 903–907.
Original Russian Text Copyright © 2002 by Elesin, Pavlov, Berdov, Mashkin, Oglezneva.

INORGANIC SYNTHESIS AND INDUSTRIAL INORGANIC CHEMISTRY

Mechanism of Hydration Conversion of Portland Cement in Calcium Polysulfide Solution

M. A. Elesin, A. V. Pavlov, G. I. Berdov, N. A. Mashkin, and I. M. Oglezneva

Novosibirsk State Architectural University, Novosibirsk, Russia

Institute of Inorganic Chemistry, Siberian Division, Russian Academy of Sciences, Novosibirsk, Russia

Received April 6, 2001; in final form, March 2002

Abstract—The hydraulic activity of portland cement in a solution of polysulfide CaS_n was studied. The characteristics of this activity are determined by the alkalinity of the liquid phase and by chemical transformations of the reagent. Generalizations are made, concerning the choise of parameters of joint conversion of the cement and polysulfide at lowered pH values, which ensure direct hardening.

The parameters of hydration hardening of portland cement largely depend on mineral salt additives differently affecting the hardening process. Water-soluble salts of calcium, whose efficiency is accounted for by the action of the Ca^{2+} cation on hardening, are frequently used in practice. This cation exerts positive influence on hardening when introduced in compounds with a wide variety of anions, which is indicated by the list of known additives: gypsum of various kinds, anhydrite, and calcium chloride, formate, nitrate, nitrite, and thiosulfate.

Among the water-soluble potassium salts, ISO preparation, obtained by dissolution of sulfur in calcium hydroxide, has gained wide recognition [1–3]. The interest in this preparation is due, on the one hand, to the ability of ISO to enhance the activity of portland cement, shown in the patent literature, and, on the other, to its low cost and plentiful availability. However, testing the preparation on portland cements manufactured by domestic plants demonstrated that, depending on experimental conditions (mineralogical and chemical composition of cements, thermomoist treatment mode, and amount of additive in tempered paste), its effect on the hardening characteristics may vary, being not always positive. In particular, in the case of a certain excess of dissolved sulfur in the liquid phase, the final parameters of hardening, determined at the age of 28 days, are impaired by the unrecoverable loss of strength by the samples in the course of hardening, which is to some extent characteristic of portland cements as a whole.

The aim of this study was to analyze the mechanism of activation of minerals in portland cement subjected to hydration in a polysulfide solution and to substantiate the choice of a proper scheme for hydration hardening of a modified mixture in dependence on the mineralogical and chemical composition of portland cement.

EXPERIMENTAL

Comparative evaluation of the action of ISO on the binding properties of the portland cement paste of standard thickness was done by studying its effect on the hardening characteristics of cubic samples under normal temperature and humidity conditions (room temperature, air humidity of no less than 90%). The samples were prepared from clinker paste into which gypsum and ISO were introduced in varied ratio in the tempering stage. Clinker[1] ground to 11% residue on sieve no. 008 was used in the experiments. The chemical composition of the clinker (wt %) was as follows: SiO_2 20.73, Al_2O_3 6.86, Fe_2O_3 4.63, CaO 65.46, MgO 1.38, and SO_3 0.45. The additive was prepared in the form of a liquid preparation, originally containing calcium polysulfide and thiosulfate in equimolar ratio, by dissolution of powdered sulfur in a heated lime suspension. The amount of the additive in the samples was controlled by the mass of dissolved sulfur, varied by changing its concentration in the tempering solution. The pH value and the con-

[1] Clinker manufactured by Chernorechenskii cement plant.

1070-4272/02/7506-0883 $27.00 © 2002 MAIK "Nauka/Interperiodica"

Strength and rate of its build-up in relation to the content of gypsum in portland cement and concentration of dissolved sulfur in the liquid tempering phase

c_S, g l^{-1}	$c_{CaSO_4 \cdot 2H_2O}$, %	Water/cement	Paste cementing, h–min		Ultimate compression strength (MPa) after indicated time, days				Rate of strength build-up (% relative to standard) after indicated time, days			
			start	end	3	7	14	28	3	7	14	28
0	0	0.32	0–55	3–25	11.5	32.8	38.8	39.8	21	49	43	53
0	7.5	0.23	2–35	3–25	55.0	64.5	87.2	73.2	100	100	100	100
0.5	0	0.30	2–10	3–40	25.2	34.5	49.0	58.7	46	53	56	80
1.0	0	0.30	2–05	4–10	26.0	35.6	54.2	66.0	47	54	62	90
1.5	0	0.31	3–10	5–30	24.8	34.8	52.0	53.0	45	54	60	72
5.0	0	0.40	3–55	6–27	17.6	19.2	21.3	23.7	32	30	24	32
0.5	7.5	2.25	2–20	3–20	55.7	66.3	89.6	101	101	102	102	123
1.0	7.5	0.30	2–15	3–10	56.0	66.0	91.7	93.2	102	102	105	127
1.5	7.5	0.31	2–15	2–55	57.8	66.5	88.8	91.8	103	105	102	125
5.0	7.5	0.29	2–10	2–50	57.0	68.0	82.5	71.2	104	105	95	97
20	7.5	0.26	1–40	2–15	69.0	57.0	83.8	71.15	125	98	96	98
100	7.5	0.25	0–18	0–35	74.2	74.8	53.9	67.5	135	116	62	92

centration of hydration products in the liquid phase were found by the known methods [4] by analyzing samples of solutions squeezed out of the cement paste.

The chemical activity of a preparation can be judged from its ability to decelerate the hardening of a clinker paste or, conversely, to accelerate this process through joint action with calcium sulfate contained in portland cement. According to the results of experiments (see table), in which a portland cement containing 7.5% gypsum dihydrate served as standard, even minor amounts of the preparation (in terms of dissolved sulfur) inhibit cementation of the clinker paste. At the same time, joint addition of ISO and gypsum converts the portland cement paste into a fast-cementing mass hardening at increased rate. However, the experimental data presented here are characterized by wide scatter relative to the standard final strength parameters. These parameters may deviate from the standard values both toward improvement, indicating the potentially high strength reserve of the modified system, and toward deterioration of the results obtained.

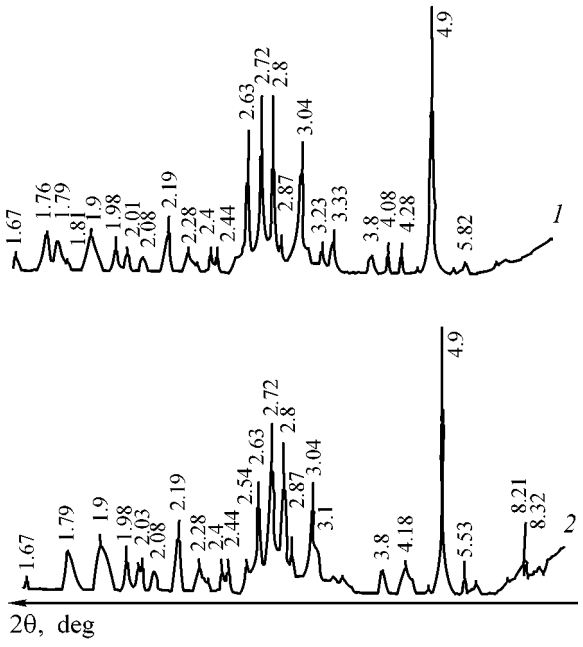

Fig. 1. X-ray diffraction patterns of cement stones. (2θ) Bragg angle. (*1*) Portland cement–water and (*2*) portland cement–ISO (c_S = 180 g l^{-1})

According to experimental data, the improvement of the binding properties of the modified portland cement, which became possible under conditions of a stable hardening rate, is due to changes in the mineralogical and chemical composition of the new formations. For example, the shortening of the paste cementation time correlates with the predominance in the hydroaluminate phase of a new complex salt, $Ca_8Al_4O_{12}SO_4S_2O_3 \cdot 24H_2O$, identified by the presence in the X-ray diffraction pattern (Fig. 1) of diffraction peaks with $d \times 10^8$ = 832 and 418 m. In accordance with the commonly adopted, in cement practice, way of composition presentation, the stoichiometric formula can be represented as $3CaO \cdot Al_2O_3 \cdot CaS_2O_3 \cdot xH_2O \cdot 3CaO \cdot Al_2O_3 \cdot CaSO_4 \cdot (24 - x)H_2O$, composed of, respectively, the thiosulfate and sulfate forms of hydrosulfoaluminate. The absence of mono- and trisulfate forms of hydrosulfoaluminate, typical of portland ce-

ments hydrated in water, as a separate phase in the hydroaluminate structures obtained after different times of hardening indicates that substitution of the sulfate ion by the thiosulfate group is possible in this compound.

Significant changes occur in the hydrosilicate phase. This is demonstrated by X-ray diffraction patterns indicating the presence of tobermorite-like hydrosilicates and more compositionally and structurally complex hydrosilicates $2CaO \cdot Al_2O_3 \cdot SiO_2 \cdot 8H_2O$ with $d \times 10^8$ 821, 553 m and $Ca_2Fe_5^{2+}[Si_8O_{22}][OH]_2$ with $d \times 10^8$ 254, 203 m, which can condense into stronger microconglomerate structures under the action of intergrain cohesion forces.

Additional data on changes in the structure and phase composition of portland cements hydrated in a polysulfide solution are furnished by IR spectra (Fig. 2) obtained on a JFS-66 Fourier spectrometer in the range 400–4000 cm^{-1}. These data mainly refer to the range corresponding to vibrations of the silica fragment. For example, in going from the starting cement to that hydrated in water, the frequency of stretching vibrations is shifted from 924 to 974 cm^{-1}, which indicates the strengthening of the S–O bond because of the disappearance of the originally isolated silica tetrahedra and their polymerization into a silica network. Remarkably, in going from spectrum *2* to spectrum *3*, the stretching vibration frequency shifts further, to 997 cm^{-1}. The increase in the degree of tetrahedron polarization in the modified mixture is probably favored by strong amorphization of hydrosilicate particles, whose exceedingly high dispersity is responsible for their colloid properties.

Changes also occur in the range corresponding to vibrations of the sulfate ion. Instead of the structurally broadened band of stretching vibrations of the S–O bond (1115 and 1151 cm^{-1}) in the starting cement, a broad band appears in the case of cement hydrated in water or CaS_n solution. The bands in the range of deformation vibrations are also broadened as a result of formation of complex salts similar to calcium hydrosulfoaluminate. The sulfate group in the structure of these salts is in a more strongly chemically bound state. At the same time, it should be noted that the intensity of the broadened band of stretching vibrations markedly grows in passing from spectrum *2* to spectrum *3*. This is due, as mentioned above, to the possible partial or total (depending on the concentration of dissolved sulfur) substitution of the sulfo group in the hydrosulfoaluminate.

The observed changes in the structure and composition of new formations, and the resulting improvement of the hardening parameters, are related to the ability of CaS_n polysulfide, as a weakly hydrolyzable salt, to stabilize the solvent pH at a lower level (Fig. 3), compared with the conventional aqueous portland cement suspensions, and also to chemical transformations of the salt. It has been established [4] that the polysulfide contained in the liquid phase of the cement paste is subject to transformation by the scheme

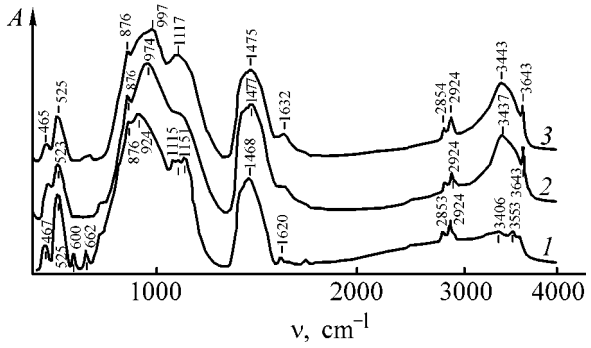

Fig. 2. IR absorption spectra of portland cements. (*A*) Absorption and (ν) wave number. Sample: (*1*) initial, (*2*) hydrated in water, and (*3*) hydrated in CaS_n solution (c_S = 180 g l^{-1}).

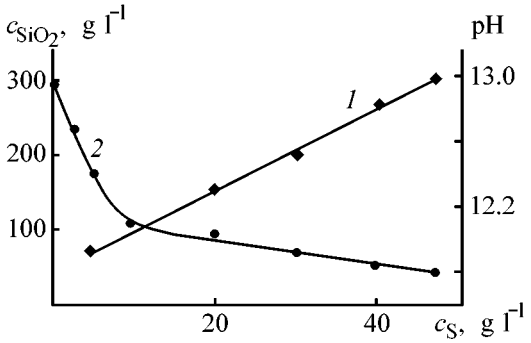

Fig. 3. (*1*) Silica concentration c_{SiO_2} and (*2*) pH vs. concentration c_S of dissolved sulfur.

$$2HS_n^- + 2(n-1)OH^- + (n+1)O_2 \rightarrow nS_2O_3^{2-} + H_2O, \quad (1)$$

$$S_n^{2-} + 6Fe^{3+} + 6OH^- = S_2O_3^{2-} + 6Fe^{2+} + (n-2)S^0 + 3H_2O, \quad (2)$$

$$(n+2)S^0 + 6OH^- = S_n^{2-} + S_2O_3^{2-} + 3H_2O, \quad (3)$$

according to which it serves as a source generating the thio salt, which is an element of the hardening structure. At the same time, the inhibition of hydration, observed experimentally upon excessive lowering of the pH value and weakly catalytic action of hydrosulfoaluminates, is caused by complications in the protolytic reaction involving the basic mineral—

alite, since it is associated with low pH as a reflection of the equilibrium $Ca(OH)_2$ concentration in a solution of the weakly hydrolyzable CaS_n. The high supersaturation of the solution with respect to the equilibrium concentration of calcium hydroxide and the redistribution in the system between $CaOH^+$ and hydroxide proper in favor of the latter make the hydrolytic stage a surface reaction, which is controlled from the very beginning by solvent diffusion through a hydroxide film. Such a concept of the passivation mechanism is consistent with the rather high activity of the protonation event itself. This high activity is due to the increased mobility of the H^+ ion (compared with Ca^{2+}), which, in addition, can be transferred by the so-called go-ahead scheme via hydrogen bonds in the structured film of water. Consequently, the introduction of this ion into the crystal lattice and the very event of protonation weakly depend on the mode of interphase transitions.

The aforesaid suggests as a primary version accounting for the decrease in the hydraulic activity of the mineral $3CaO \cdot SiO_2$ in a CaS_n solution the passivation of the surface first by the crystallizing $Ca(OH)_2$ and then, additionally, by the barrier created by Ca^{2+} ions.

The property of the modified system to combine simultaneously an increased energy of interaction between protolysis products and solvent with enhanced resistance to the solvent flow toward the particle surface can account for the seemingly contradictory phenomena of increased dissolving ability of water and the simultaneously reduced hydraulic activity of silicates. This general property of portland cement binders objectively restricts the possibility of obtaining, under normal conditions at lowered alkalinity of the liquid phase, low-basic hydrosilicate dispersions forming stable structures. The kinetics of such processes strongly depends on the energy parameters of interphase transformations and, as a rule, reaches technologically acceptable values under hydrothermal conditions of autoclave hardening. In the case of a portland cement system modified with polysulfide, this problem, i.e., elimination of the diffusion resistance and activation of silicate minerals, is solved by combining mineral hydration with a chemical transformation of the polysulfide into a thiosulfate structurally bound in the hydrosulfoaluminate. In such a variant of hydration conversion of cement, the disturbance of the dynamic equilibrium in the system $Ca(OH)_{2\,solid} \rightarrow Ca(OH)_{2\,dissolved}$, which initiates hydration, is ensured by the involvement of the dissolved hydroxide in the reaction of ionization of polysulfide sulfur with zero degree of oxidation. The increase in the hydraulic activity of silicates, in its turn, facilitates the attainment of the saturation concentration with respect to silica and mass nucleation of crystal hydrates in the bulk of the liquid phase and makes closer the rates of formation of the basic structures. As a result, the acceleration of the hardening process becomes noticeable, and the process itself, more stable and productive.

Such an interpretation of the mechanism of inhibition of cement hydration in a polysulfide solution can be considered sufficiently substantiated also in the case when there exists an induction period, occurring in common portland cement systems in the initial stage of the process, soon after the spontaneously beginning hydration. The problem of its nature remains to be discussed. Of the known versions, those deserve attention, which give insight into the hydrolytic nature of the hydration conversion of silicate minerals and, in particular, relate the inhibition to incongruent decomposition of $3CaO \cdot SiO_2$ and passivation of the particle surface by crystallizing calcium hydroxide, in one case [5], and to formation by Ca^{2+} ions sorbed from the solution of a barrier limiting the mass exchange, in the other [6]. In the case of ISO, both these phenomena occur as a result of surface reactions in which strong covalent bonds are protonated and the calcium ion is hydrated. However, in both these cases, the hindered stage is represented functionally as induction of the crystallization energy of hydrates, with the limiting supersaturation of the liquid phase reached and critical mass of nuclei of calcium hydroxide formed, after which there occurs its mass crystallization initiating the protolytic reaction.

Noteworthy are two concepts interpreting the driving force of the hydration conversion of portland cement. According to one of these [7, 8], the end of the induction period and continued hydration are enabled by the osmotic pressure formed as a result of the increasing difference between the concentration of calcium hydroxide in solution in the zone of contact under the semipermeable hydrate shell and that in the intergrain space. According to the other [9], the flow of solvent toward the surface is due to a build-up of the difference of electric potentials at the phase boundary with increasing excess of the Ca^{2+} ion sorbed on the surface. It is noteworthy that both these phenomena are physical in nature and, from the standpoint of the mechanism of reaction inhibition described in this communication, are due to accumulation on the surface being hydrated of protolysis products weakly diffusing into solution. Their importance presumably varies between different stages of portland cement hardening. In any case, it is the

accumulation of energy in the system and transformation of this energy into acceleration of hydration that ensure the achievement of a sufficiently high strength of the cement stone in a technologically acceptable interval of time.

CONCLUSIONS

(1) The binding properties of portland cement in a CaS_n solution are determined, on the one hand, by the lowered concentration of $Ca(OH)_2$ in the liquid phase, compared with the conventional suspensions, and, on the other, by ionization of zero-charge polysulfide sulfur and liberation of a thio salt serving as an element of the hardening structure.

(2) The improvement of the hardening parameters of a portland cement mixture in the presence of a polysulfide in the liquid phase is due to a change in the phase composition and structure of both the hydrosulfoaluminate dispersion determining the time of paste cementation and the hydrosilicate suspension responsible for the final parameters of the process.

(3) In the presence of an excess amount of CaS_n in the binder mixture, the inhibition of cement hydration is due to deceleration of the protolytic reaction of the basic mineral ($3CaO \cdot SiO_2$) with the solvent, caused by surface passivation first by the crystallizing $Ca(OH)_2$ and then by the ionic barrier appearing as the diffusion resistance builds-up in the hydration shell.

REFERENCES

1. US Patent 4193811.
2. US Patent 4198245.
3. US Patent 4193809.
4. Kurbatova, I.I., *Sovremennye metody khimicheskogo analiza stroitel'nykh materialov* (Modern Methods for Chemical Analysis of Building Materials), Moscow: Stroiizdat, 1972.
5. Malinin, Yu.S., Lopatnikova, L.Ya., and Guseva, V.I., *K voprosu o gidratatsii i tverdenii portlandtsementa* (To the Problem of Hydration and Hardening of Portland Cement), Moscow: Stroiizdat, 1964.
6. *Dobavki v beton: Spravochnoe posobie* (Additives to Concrete: Reference Book), Ramachandran, V.S., Ed., Moscow: Stroiizdat, 1988.
7. Volzhenskii, A.V., Burov, Yu.S., and Kolokol'nikov, V.S., *Mineral'nye vyazhushchie veshchestva* (Mineral Binders), Moscow: Stroiizdat, 1979.
8. Elesin, M.A., Pavlov, A.V., Sokol'skaya, Yu.B., and Mashkin, N.A., *Izv. Vyssh. Uchebn. Zaved.*, Stroitel'stvo, 2000, no. 4, pp. 37–44.
9. Koshmai, A.S. and Mchedlov-Petrosyan, O.P., *Tsement*, 1980, no. 7, pp. 4–5.

Russian Journal of Applied Chemistry, Vol. 75, No. 6, 2002, pp. 888–890. Translated from Zhurnal Prikladnoi Khimii, Vol. 75, No. 6, 2002, pp. 908–910.
Original Russian Text Copyright © 2002 by Glazov, Dukhanin, Losev.

PHYSICOCHEMICAL STUDIES OF SYSTEMS AND PROCESSES

Saturated Vapor Pressure Over Melts of the Binary System $NaNO_2$–KNO_3

V. I. Glazov, G. P. Dukhanin, and V. A. Losev

Volgograd State Technical University, Volgograd, Russia

Received January 22, 2002

Abstract—The partial pressures of sodium nitrite and potassium nitrate over melts of the binary system $NaNO_2$–KNO_3 were measured at 798, 823, and 848 K. Negative deviations of the vapor pressure from Raoult's law, which decrease with increasing temperature, are established. Coefficients *A* and *B* of the Clausius–Clapeyron equation, partial molar heats of vaporization, activity and activity coefficient are calculated as functions of composition for potassium nitrate.

Molten nitrites and nitrates of alkali metals, and systems based on them, are used as high-temperature heat carriers in vulcanization of extruded rubber articles, in thermal treatment of metals, and in preparing heat-resistant lubricants [1]. For this reason, a study of physicochemical properties of nitrite–nitrate molten salt systems is of both theoretical and practical importance.

In the present study, we measured the saturated vapor pressure *P* over melts of varied composition of the binary system $NaNO_2$–KNO_3 and the partial pressures of the components at 798, 823, and 848 K. The experimental procedure and the method used for determining the saturated vapor pressure of individual molten salts were described in [2]. Mass-spectrometric data [3, 4] for vapors of alkali nitrite and nitrate revealed monomer molecules coexisting with salt melts in the vapor phase. This enabled calculation of the saturated vapor pressure over pure components and their mixtures [5–7].

The results of measurements of the saturated vapor pressure over sodium nitrite and potassium nitrate melts of various compositions at 798 and 848 K are presented in Fig. 1. As seen, the concentration dependence of the saturated vapor pressure in the $NaNO_2$–KNO_3 system shows negative deviations from Raoult's law, which decrease with increasing temperature. Under isothermal conditions, the saturated vapor pressure over the binary melts decreases monotonically with increasing content of potassium nitrate in a mixture. In the regions with component content of less than 5 mol %, the saturated vapor pressure as a function of composition is adequately described by Raoult's law. At equimolar content of the components the extent of negative deviations increases.

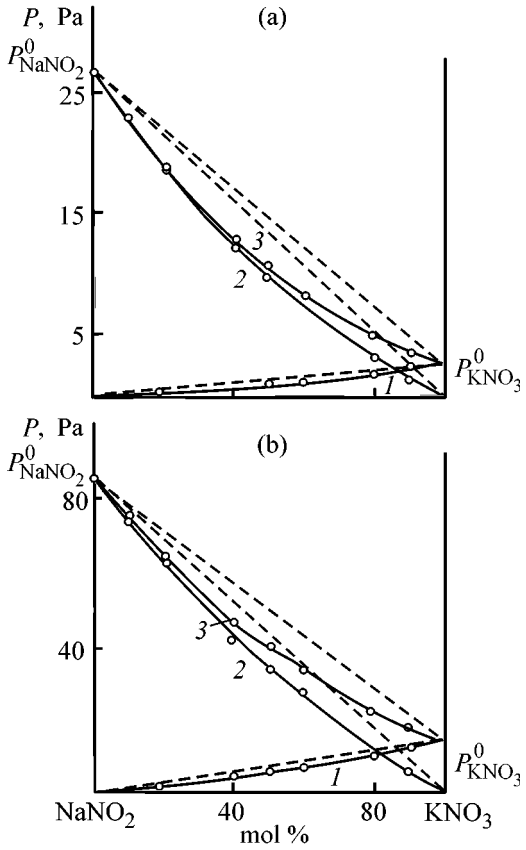

Fig. 1. Vapor pressure *P* over melts of the system $NaNO_2$–KNO_3 (mol %) at (a) 798 and (b) 848 K. $P^0_{NaNO_2}$ and $P^0_{KNO_3}$ are saturated vapor pressures over pure components. (*1*, *2*) Partial pressure of KNO_3 and $NaNO_2$, respectively, and (*3*) total pressure.

1070-4272/02/7506-0888 $27.00 © 2002 MAIK "Nauka/Interperiodica"

Table 1. Saturated vapor pressure P_{KNO_3}, coefficients A and B of the Clausius–Clapeyron equation, and partial molar heat of vaporization $\Delta H_{vap}^{KNO_3}$ of potassium nitrate in the system $NaNO_2$–KNO_3

c_{KNO_3} in melt, mol %	P_{KNO_3} (Pa) at indicated temperature T, K			$A \times 10^{-3}$, K	B, Pa	$\Delta H_{vap}^{KNO_3} \times 10^{-3}$, J mol^{-1}
	798	823	848			
10	0.087	0.272	0.773	12.96	15.18	28.24
20	0.234	0.613	1.786	12.08	14.50	231.26
40	0.598	1.620	4.049	11.43	14.10	218.77
50	0.836	2.180	5.432	11.32	14.09	216.80
60	1.016	2.769	6.744	11.24	14.09	215.19
80	1.617	4.187	10.066	10.79	13.73	206.62
90	2.023	5.093	12.165	10.66	13.66	204.13
100	2.483	6.140	14.38	10.33	13.34	197.69

The system $NaNO_2$–KNO_3 is characterized by a simple fusion diagram of eutectic type [8]. The nature of the concentration dependences of the saturated vapor pressure curves for the $NaNO_2$–KNO_3 system is determined by the predominance of interaction between the unlike species upon replacement of a part of Na(I) cations with K(I) cations in the monomer molecules.

Because the saturated vapor pressures of sodium nitrite and potassium nitrate differ widely, the total saturated vapor pressure over the system is determined by the $NaNO_2$ partial pressure.

The temperature dependence of the potassium nitrate vapor pressure over melts of various compositions is adequately described by the Clausius–Clapeyron equation $\log P_{KNO_3} = B - A/T$. The coefficients of the equation are given in Table 1. Figure 2 shows the $\log P_{KNO_3} = f(1/T)$ plot for potassium nitrate at its varied content in the melt.

The partial molar heats of vaporization of potassium nitrate from the melts of the corresponding compositions were calculated from the slope of the straight lines in Fig. 2:

$$\Delta H_{vap}^{KNO_3} = 2.34RA,$$

where R is the gas constant (8.314 J mol^{-1} K^{-1}).

With decreasing content of potassium nitrate in the system, the heat of vaporization increases, i.e., the strength of interaction between the unlike species grows. The experimental data and results of their processing are presented in Table 1. The coefficient of linear correlation of $\log P$ as a function of $1/T$ varies from 0.81 (at low content of KNO_3) to 1.

The experimentally determined values of the saturated vapor pressure over the pure components, P_i^0 (where i is KNO_3 and $NaNO_2$), and their partial pressures P_i in the system were used to calculate the activities $a_i = P_i/P_i^0$ and the activity coefficients $\gamma_i = a_i/N_i$ for potassium nitrate in the $NaNO_2$–KNO_3 binary system [N_i is the KNO_3 content of the melt (mol %)] [9]. The results of calculation are presented in Table 2.

As seen, the activity of potassium nitrate exhibits negative deviations ideality, and, therefore, the calculated activity coefficients are less than unity.

In the system $NaNO_2$–KNO_3 the extent of departure from ideality is smaller than that in the previously studied system $NaNO_2$–KNO_3 [7]. This may be accounted for by weakening interaction between

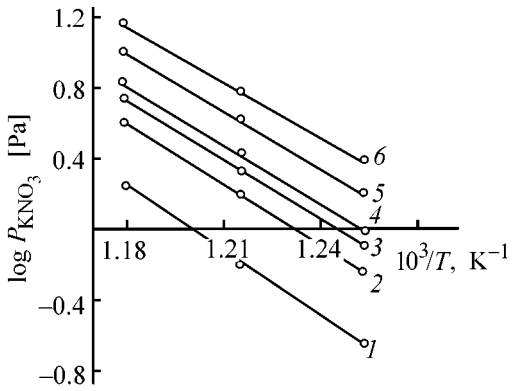

Fig. 2. Vapor pressure of potassium nitrate P_{KNO_3} in the system $NaNO_2$–KNO_3 vs. temperature T. KNO_3 content in the melt (mol %): (*1*) 20, (*2*) 40, (*3*) 50, (*4*) 60, (*5*) 80, and (*6*) 100.

Table 2. Activity a and activity coefficient γ of potassium nitrate in the system $NaNO_2$–KNO_3

Parameter	KNO_3 content in the melt, mol %						
	10	20	40	50	60	80	90
				T = 798 K			
a	0.035	0.094	0.241	0.337	0.410	0.652	0.814
γ	0.350	0.470	0.600	0.673	0.690	0.814	0.904
				T = 823 K			
a	0.044	0.099	0.264	0.355	0.451	0.682	0.829
γ	0.440	0.500	0.660	0.710	0.750	0.850	0.920
				T = 848 K			
a	0.054	0.124	0.282	0.378	0.468	0.700	0.845
γ	0.540	0.620	0.704	0.750	0.780	0.875	0.940

the unlike species [Na(I)–K(I)] upon replacement of the NO_3^- anion with NO_2^-.

REFERENCES

1. Chechetkin, A.V., *Vysokotemperaturnye teplonositeli* (High-Temperature Heat Carriers) Moscow: Energiya, 1971.
2. Glazov, V.I., Golod, V.F., and Golovanov, P.S., *Zh. Prikl. Khim.*, 1984, vol. 57, no. 6, pp. 2351–2352.
3. Bogarat'yan, N.V., and Nikitin, O.T., *Vestn. Mos. Gos. Univ., Khimiya*, 1977, vol. 4, no. 18, p. 388.
4. Verkhoturov, E.N., Makarov, A.V., and Nikitin, O.T., *Vestn. Mos. Gos. Univ., Khimiya*, 1977, vol. 4, no. 18, p. 392.
5. Suvorov, V.A., *Termodinamicheskaya khimiya paro-obraznogo sostoyaniya* (Thermodynamic Chemistry of Vapor State), Leningrad: Khimiya, 1970.
6. Glazov, V.I., Golovanov, P.S., and Dukhanin, G.P., *Zh. Prikl. Khim.*, 1990, vol. 63, no. 1, pp. 193–195
7. Glazov, V.I., and Dukhanin, G.P., *Zh. Prikl. Khim.*, 1992, vol. 65, no. 8, pp. 1907–1911.
8. Voskresenskaya, N.K., Evseeva, N.N., Berul', S.I., and Vereshchetina, I.P., *Spravochnik po plavkosti solevykh sistem* (Reference Book of Fusibility of Salt Systems), Moscow: Akad. Nauk SSSR, 1961, vol. 2.
9. Morachevskii, A.G., *Termodinamika zhidkikh splavov* (Thermodynamics of Liquid Alloys), Leningrad: Len. Politekh. Inst., 1981.

Russian Journal of Applied Chemistry, Vol. 75, No. 6, 2002, pp. 891–893. Translated from Zhurnal Prikladnoi Khimii, Vol. 75, No. 6, 2002, pp. 911–912.
Original Russian Text Copyright © 2002 by Glazov, Dukhanin, Losev.

PHYSICOCHEMICAL STUDIES OF SYSTEMS AND PROCESSES

Partial Saturated Vapor Pressure of Sodium Nitrite Over the System $NaNO_2$–KNO_3

V. I. Glazov, G. P. Dukhanin, and V. A. Losev

Volgograd State Technical University, Volgograd, Russia

Received March 4, 2002

Abstract—The partial pressure of sodium nitrite in the system $NaNO_2$–KNO_3 was measured at 798, 823, and 848 K. The dependence of the logarithm of the $NaNO_2$ pressure on inverse temperature is presented. Coefficients *A* and *B* of the Clausius–Clapeyron equation and the partial molar heats of vaporization are calculated. The activity and activity coefficient of sodium nitrite are determined. The dependences of activity and activity coefficient of sodium nitrite and potassium nitrate are presented as functions of composition of the $NaNO_2$–KNO_3 system. The consistency of the activity coefficients is verified using the Redlich–Kister integral.

Proceeding with investigations of the physicochemical and thermodynamic properties of molten nitrite–nitrate systems [1–3], we studied the partial pressure of saturated vapor of sodium nitrite over the system $NaNO_2$–KNO_3.

The method used to prepare salts and the experimental installation have been described previously [1]. The saturated vapor pressure of sodium nitrite over the melts of the $NaNO_2$–KNO_3 system of varied composition was measured at 798, 823, and 848 K.

Table 1. Vapor pressure P_{NaNO_2}, coefficients *A* and *B* of the Clausius–Clapeyron equation, and partial molar heats of vaporization $\Delta H_{vap}^{NaNO_2}$ of sodium nitrite in the $NaNO_2$–KNO_3 system

c_{NaNO_2} in a melt, mol %	P_{NaNO_2} (Pa) at indicated temperature *T*, K			$A \times 10^{-3}$, K	*B*, Pa	$\Delta H_{vap}^{NaNO_2} \times 10^{-3}$, J mol^{-1}
	798	823	848			
10	1.36	3.02	5.79	8.306	10.558	159.04
20	3.08	6.22	12.11	8.025	10.545	153.66
40	7.39	14.48	27.38	7.702	10.521	147.47
50	9.66	18.61	34.60	7.469	10.345	143.01
60	12.20	23.18	42.30	7.319	10.258	140.14
80	18.66	35.26	63.15	7.158	10.241	137.05
90	22.74	42.18	75.18	6.996	10.126	133.95
100	26.61	48.82	86.50	6.934	10.114	132.77

Table 2. Activity *a* and activity coefficient γ of sodium nitrite in the system $NaNO_2$–KNO_3

Parameter	$NaNO_2$ content in the melt (mol %) at temperature, K																				
	798							823							848						
	10	20	40	50	60	80	90	10	20	40	50	60	80	90	10	20	40	50	60	80	90
a	0.051	0.12	0.27	0.36	0.46	0.70	0.85	0.062	0.13	0.29	0.38	0.47	0.72	0.86	0.067	0.14	0.31	0.40	0.50	0.73	0.87
γ	0.51	0.60	0.67	0.72	0.76	0.87	0.95	0.62	0.64	0.74	0.76	0.79	0.90	0.96	0.67	0.70	0.77	0.80	0.84	0.91	0.97

1070-4272/02/7506-0891 $27.00 © 2002 MAIK "Nauka/Interperiodica"

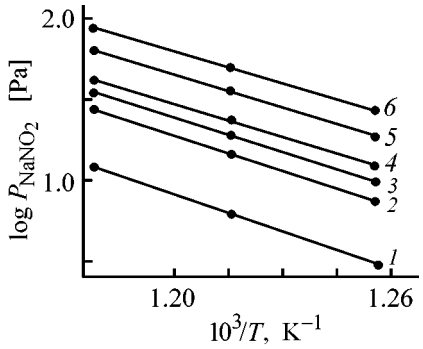

Fig. 1. Saturated vapor pressure P_{NaNO_2} of sodium nitrite in the system $NaNO_2$–KNO_3 vs. temperature T. $NaNO_2$ content in the melt (mol %): (*1*) 20, (*2*) 40, (*3*) 50, (*4*) 60, (*5*) 80, and (*6*) 100.

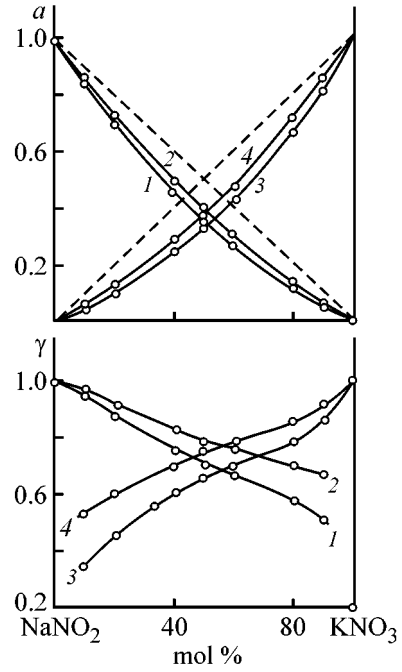

Fig. 2. Activity a and activity coefficient γ of sodium nitrite and potassium nitrate in the system $NaNO_2$–KNO_3. Temperature (K): (*1*, *3*) 798 and (*2*, *4*) 848.

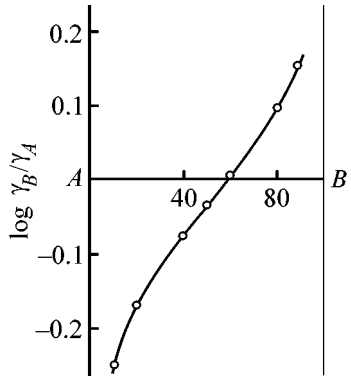

Fig. 3. Verification of the consistency of the activity coefficients for the $NaNO_2$–KNO_3 system, using the Redlich–Kister integral at T = 848 K. (*A*) $NaNO_2$ and (*B*) KNO_3.

The temperature dependence of sodium nitrite vapor pressure is well described by the Clausius–Clapeyron equation $\log P = B - A/T$. The results of measurements of the sodium nitrite vapor pressure over the system, the calculated coefficients of the Clausius–Clapeyron equation, and the partial molar heats of vaporization of $NaNO_2$ are presented in Table 1.

Figure 1 shows the logarithm of the sodium nitrite pressure over the melts of various compositions as a function of inverse temperature. The linear correlation coefficient of $\log P$ as a function of $1/T$ varies from 0.81 (at low sodium nitrite content) to 1.

As shown previously [3], the concentration behavior of the partial pressure curves for sodium nitrite and potassium nitrate exhibits negative deviations from Raoult's law. Under isothermal conditions, the sodium nitrite vapor pressure increases steadily with decreasing content of the second component.

With decreasing content of sodium nitrite in the system, the heat of its vaporization increases, i.e., the interaction between the unlike species becomes stronger.

The experimental values of the saturated vapor pressure P_i^0 over pure components (KNO_3, $NaNO_2$) were used to calculate the activities a_i and activity coefficients γ_i of sodium nitrite in the $NaNO_2$–KNO_3 system. The results of calculations are given in Table 2. The activity and activity coefficient of potassium nitrate in the system studied have been reported previously [3].

Figure 2 shows the activity and activity coefficient of sodium nitrite and potassium nitrate as functions of the composition of the system at 798 and 848 K. As seen, the activities of sodium nitrite and potassium nitrate exhibit negative deviations from ideality. For this reason, the calculated activity coefficients are smaller than unity.

The isotherms of activity of potassium nitrate show large negative deviations. This is due to an increase in the cationic radius. The negative deviations indicate a certain extent of complexation in the system and the predominance of interaction between the unlike cations (Na–K). With increasing temperature, the negative deviations become less pronounced.

The independently obtained activity coefficients of the components of the $NaNO_2$–KNO_3 system must correspond to the Gibbs–Duhem equation. The thermodynamic consistency of the data on the activity

coefficients was verified using the Redlich–Kister integral [4]:

$$\int_{N_B=0}^{N_B=1} \log \gamma_B/\gamma_A \mathrm{d}N_B = 0.$$

The verification results are plotted in Fig. 3. It can be seen that the activity coefficients of the components of the $NaNO_3$–KNO_3 system are in satisfactory agreement with the Gibbs–Duhem equation.

REFERENCES

1. Glazov, V.I., Golod, V.F., and Golovanov, P.S., *Zh. Prikl. Khim.*, 1984, vol. 57, no. 6, pp. 2351–2352.
2. Glazov, V.I., Golovanov, P.S., and Dukhanin, G.P., *Zh. Prikl. Khim.*, 1990, vol. 63, no. 1, pp. 193–195.
3. Glazov, V.I., Dukhanin, G.P., and Losev, V.A., *Zh. Prikl. Khim.*, 2002, vol. 75, no. 6, pp. 908–910.
4. Morachevskii, A.G., *Termodinamika rasplavlennykh metallicheskikh i solevykh sistem* (Thermodynamics of Molten Metal and Salt Systems), Moscow: Metallurgiya, 1987.

Russian Journal of Applied Chemistry, Vol. 75, No. 6, 2002, pp. 894–899. Translated from Zhurnal Prikladnoi Khimii, Vol. 75, No. 6, 2002, pp. 913–919.
Original Russian Text Copyright © 2002 by Tikhomolova, Urakova.

SORPTION AND ION-EXCHANGE PROCESSES

Interaction of Co(II), Ni(II), and Cu(II) with Quartz Surface in Aqueous Solutions at Varied pH

K. P. Tikhomolova and I. N. Urakova

St. Petersburg State University, St. Petersburg, Russia

Received November 30, 2001

Abstract—Sorption/desorption of Co(II), Ni(II), and Cu(II) on quartz was studied in aqueous solutions at pH 3.0, 5.0, and 7.3 [for Co(II) and Ni(II)] and 3.0 and 5.0 [for Cu(II)].

Specific adsorption in disperse systems containing aqueous solutions of various metal salts has been a subject of a great number of experimental and theoretical works. However, some points related to the adsorption mechanism are not understood yet.

The classical theory of electrical double layer (Gouy's theory) formally treats the resultant action of two forces, electrostatic (Coulombic) and diffusion, without taking into account the adsorbate (metal cation in our case) nature. In other words, this theory considers nonspecific adsorption. However, in many cases the classical theory cannot reproduce experimental results adequately. In these cases, the necessity arises to involve specific interactions into consideration, depending on the metal nature and speciation in the solution bulk. Many questions of specific adsorption have been studied insufficiently. To solve these questions, new approaches have been developed [1–19]. A series of works have been based on the concept of the determining role of complexation [7, 9–19], with the term complex is used in different senses. The chemical (coordination) concept of specific adsorption from aqueous solutions on oxides is also related to this research [16].

In this work, we studied adsorption of double-charged cations of 3*d* metals [Co ($3d^7$), Ni ($3d^8$), and Cu ($3d^9$)]. In the experiments we used quartz (SiO_2) from the Kyshtym deposit (99.8% α-quartz). The sample preparation procedure was as follows. Quartz was ground into a powder in a steel ball mill, washed first with dilute sulfuric acid to negative reaction for iron and then with distilled water to neutral reaction, sieved to obtain a desired fraction, dried at about 110°C, and, finally, poured over with distilled water. In the adsorption–desorption experiments, we employed the fraction with equivalent particle diameter d_e of 40–70 μm. The specific surface area S_{sp} of this fraction was determined from adsorption of nitrogen (BET) and Methylene Blue to be 0.20–0.21 $m^2\ g^{-1}$.

Adsorption of the metals on dispersed quartz was monitored by the M(II) concentration in the solution bulk, c_M. Hereinafter quartz after adsorption is called modified. Also, we determined the amount of adsorbed M(II) per unit area of the adsorbent surface Γ (mol m^{-2}). The M(II) concentration in the solution was determined spectrophotometrically on a Specol-10 instrument: Co(II) with Nitroso R salt (λ = 520 nm), Ni(II) with PAN (λ = 540 nm), and Cu(II) with Xylenol Orange (λ = 580 nm). The Γ was estimated from the change in the metal concentration in the aqueous phase. The error of spectrophotometric determinations was within 0.5–3.0%.

The working solutions were prepared from M(II) nitrates. The characteristics of these solutions are as follows: M(II) concentration 10^{-4} M; pH 3.0, 5.0, and 7.3 [only for Co(II) and Ni(II)]; and ionic strength 10^{-3} M. The ionic strength and the desired pH were adjusted by adding KNO_3, KOH, or HNO_3. In addition to the working solutions, we used reference solutions with the same pH values and ionic strengths, but containing no M(II).

The solution pH values were chosen was made in view of the following considerations. Firstly, the initial necessary condition was that the adsorbate solution should be a true solution, i.e., a solution containing only species of molecular dimensions. The systems with Co(II) and Ni(II) meet this requirement at all the three pH values, and in the case of Cu(II), hydroxide particles are formed at pH 7.3. Note that, accord-

1070-4272/02/7506-0894 $27.00 © 2002 MAIK "Nauka/Interperiodica"

ing to the speciation diagrams given in [18] and constructed using potentiometric titration data,[1] Co(II) and Ni(II) occur as aqua ions at the indicated three pH values, and Cu(II), practically totally as aqua ions at pH 3.0 and 5.0. Secondly, in the case of Cu(II), pH 5.0 is only slightly lower than pH 5.8 of dimerization with the formation of $[Cu_2(OH)_2]^{2+}$, and pH 7.3 is lower than the pH of formation of Co(II) and Ni(II) hydroxides (7.8 and 8.5, respectively). Finally, pH strongly affects the amounts of negatively charged $[\equiv SiO]^-$ and neutral active sites $[SiOH]^0$ on the quartz surface. As stated previously [16, 17], these surface groups can serve as ligands, i.e., they can participate in the formation of surface complexes with an adsorbed cation as acceptor; $[\equiv SiO]^-$ being a more reactive ligand than $[SiOH]^0$.

Taking into account the very high sensitivity of the surface properties to even extremely slight variations in the chemical composition of the surface, and to make comparative analysis of results obtained for various metals, all the experiments were carried out with the same quartz sample.

To estimate the degree of dissociation of the quartz surface sites at various pH values, we used the known method of continuous potentiometric titration [20]. Before starting titration of the quartz dispersion, the sample was dried a little on a paper filter, and then a weighed portion was taken and equilibrated with a solution at pH 3. The ionic strength of both the solution and the dispersions was 10^{-3} M (KNO_3). In the course of titration, pH varied from 3 to 10. The amount of OH^- ions consumed in the course of titration is equal to the amount of the $[\equiv SiO]^-$ groups formed on the surface. The potentiometric titration data are presented in Fig. 1.

Before starting the adsorption–desorption experiment, a quartz sample was poured over with the supporting electrolyte solution at a fixed pH. The solution was refreshed at regular intervals over a period of 1–2 days. If no specific interaction occurs in the dispersion at a given pH, this time is enough for the formation of an electrical double layer. Then the solution was decanted, the solid phase was washed with a fresh portion of the supporting electrolyte, and the adsorption experiment started at once.

Adsorption was studied by the static method, and desorption, by the static and electroosmotic displacement methods differing in the effect on the adsorption layer (stronger in the second case [21]). In all cases, we used in the desorption stage M(II)-free solutions (supporting electrolyte solutions). Publications devoted to the potentialities of the electroosmotic technique for this purpose are extremely scarce [19, 21, 22]. The main concern of these works is mostly soil compaction or consolidation grouting [23].

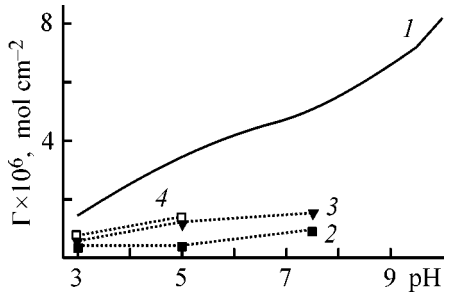

Fig. 1. Specific adsorption Γ vs. pH: (*1*) OH^-, (*2*) Co(II), (*3*) Ni(II), and (*4*) Cu(II).

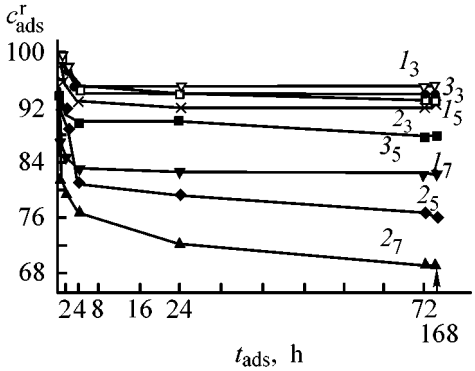

Fig. 2. M(II) concentration in the liquid phase, c^r_{ads} (in percent relative to the metal concentration in the initial working solution c_0) as a function of the adsorption time t_{ads}. Adsorbed ion: (*1*) Co(II), (*2*) Ni(II), and (*3*) Cu(II). The subscripts denote pH of the initial working solution.

In all the adsorption experiments, we used dispersions containing 2 g of a quartz powder and 20 ml of fresh working solution. Weighing bottles were hermetically sealed. After a fixed time t_{ads} varied from 1 to 7 days, the weighing bottle was opened, and the solution was removed by decantation and analyzed for pH and M(II). The solid phase (modified quartz) was then used in the desorption experiment.

In static desorption, modified quartz was placed in a weighing bottle, poured over with 20 ml of supporting electrolyte at the same pH as in the adsorption stage, and sealed. Then we used the same procedure as in the adsorption experiments.

In electroosmotic desorption experiments, the electric field was applied to a diaphragm formed from modified quartz (dc field strength 10 V cm^{-1}).

[1] Since the metal and supporting electrolyte concentrations in [18] differ from those in this study, to refine M(II) speciation, we performed potentiometric titration.

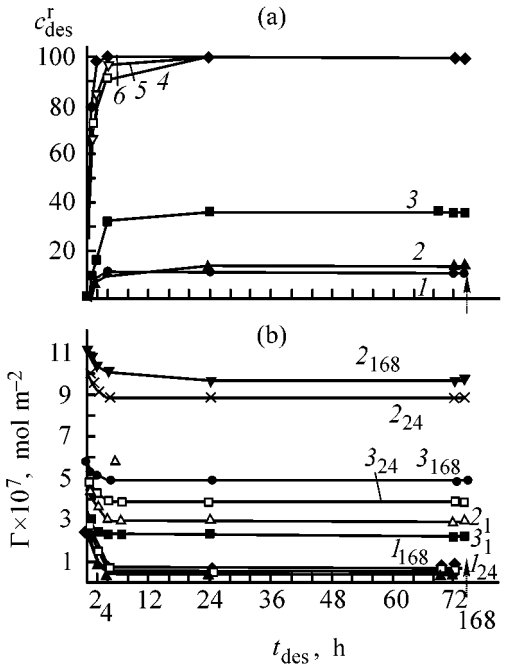

Fig. 3. (a) Ni(II) concentration in the liquid phase at pH 5.0 in the course of the desorption experiment, c^r_{des} (in percent relative to the concentration in the working solution after the adsorption stage) and (b) the specific adsorption of Co(II), Ni(II), and Cu(II) Γ (mol cm^{-2}) at pH 5.0 vs. the desorption time t_{des}. (a) (*1*–*3*) Static desorption and (*4*–*6*) electroosmotic displacement. t_{ads}: (*1*, *4*) 7 days, (*2*, *5*) 1 day, and (*3*, *6*) 1 h. Adsorbed ion: (*1*) Co(II), (*2*) Ni(II), and (*3*) Cu(II); the same for Fig. 4. The subscripts denote the adsorption time in the adsorption stage, expressed in hours.

The amount of desorbed metal was estimated from the M(II) concentration in the filtrate and the filtrate volume.

Variation of the M(II) concentration in the aqueous phase, c^r_{ads} (in percent relative to the metal concentration in the initial working solution c_0) in the course of the adsorption experiment is shown in Fig. 2.

Adsorption of all the three ions grows with increasing solution pH. The c^r_{ads} and adsorption rate are different for different ions. At any pH, the adsorption rate decreases in the order Ni(II) > Cu(II) > Co(II).

For all the three ions, c^r_{ads} approaches saturation at a sufficiently long adsorption time. The time of equilibrium attainment, t^{eq}_{ads}, is found to exceed 1 h and to be much longer than that in ion-exchange processes, when counterions are fixed in the surface layer only by the Coulombic forces.

The time of equilibrium attainment decreases in the order Ni(II) > Cu(II) > Co(II). For Ni(II) t^{eq}_{ads} = 1–3 days, becoming longer with increasing pH; and for Co(II) and Cu(II), t^{eq}_{ads} = 2–4 and 4 h at both pH values.

The relationship between t^{eq}_{ads} and the firmness of metal fixation in the adsorption layer was studied in the static and electroosmotic experiments with varied t_{ads}. As a parameter characterizing the desorption efficiency we used c^r_{des} written as

$$c^r_{des} = (c_{des}V_{des}) \times 100/(c_{ads}V_{ads}),$$

where c_{des} is the current M(II) concentration in the course of desorption; V_{ads} and V_{des} are the volumes of the liquid phase in the course of adsorption and desorption, respectively; and c_{ads} is the M(II) concentration in the working solution after adsorption.

According to the static desorption data, t_{ads} strongly influences the desorption efficiency. With increasing t_{ads}, the firmness of M(II) fixation on the quartz surface grows; the more so with increasing pH. Figure 3a shows the time dependences of c^r_{des}, obtained for Ni(II) in both the static and electroosmotic desorption experiments (t_{ads} 1 h, 1 and 7 days; pH 5.0). It is clearly seen from the electroosmotic desorption data that, with increasing t_{ads}, the same c^r_{des} is attained in a longer time.

Figure 3b shows the desorption curves obtained for Co(II), Ni(II), and Cu(II) by the static method at pH 5.0 (t_{ads} 1 h, 1 and 7 days). The results show that the effect of t_{ads} on $\Gamma_{des} = \Gamma_{ads} - (c_{des}V_{des}/S_{sp})$, where $[\Gamma_{ads} = (c_0 - c_{ads})V_{ads}/mS_{sp}$ and m is the adsorbent weight], is considerably lower for Co(II) than for Ni(II). Note that this effect is quite clearly pronounced in the case of dispersions consisting of a Cu(II) solution at pH 5.0 and modified quartz (t_{ads} 1 h, 1 and 7 days).

It has been demonstrated by several authors that, after an adsorbate enters the surface reaction zone, surface processes can be extended in time relative to the time of the equilibrium attainment, determined using the parameter c_{ads}. In particular, this refers to the phenomenon of specific adsorption [21]. Our data on static desorption provide an additional evidence in favor of this view (Figs. 2, 3b).

Figure 4 shows how the amount of adsorbed M(II) varies with time in sorption and in static and electroosmotic desorption experiments (all the desorption experiments were performed with quartz modified for 7 days).

First, the results show that, at any experimental pH, the limiting amount of adsorbed M(II) increases in the order Co(II) < Cu(II) < Ni(II) (Fig. 4a).

Let us now analyze the most significant features of desorption (Figs. 4b, 4c). Under any experimental conditions studied, the highest desorption efficiency is observed for Co(II). In static desorption, the residual amount of Co(II) adsorbed on the quartz surface was estimated to be about 5, 20, and 45% at pH 3.0, 5.0, and 7.3, respectively. Since the electroosmotic displacement involves a more severe treatment, the fact of rapid total desorption of the metal ions is quite natural [19, 21, 22]. Therefore, our results show that the bonds formed by Co(II) with the surface sites of quartz are the weakest among the metals studied.

As for Ni(II), Fig. 4b shows that static desorption of Ni(II) is rapid, but inefficient process [residual amount of adsorbed Ni(II) is 80, 85, and 87% at pH 3.0, 5.0, and 7.3, respectively]. Only electroosmotic displacement provides total desorption of Ni(II), but it requires longer time than that for Co(II), suggesting firmer fixation of Ni(II). Therefore, Ni(II) forms fairly strong bonds with the active sites of quartz at any pH studied.

The parameters of static desorption of Cu(II) at pH 5.0 virtually coincide with those of Ni(II), and at pH 3.0, they take an intermediate position between Co(II) and Ni(II).

Similarly to the other metals investigated, Cu(II) is totally desorbed by the electroosmotic method, regardless of pH.

In addition to the potentiometric titration data, Fig. 1 also shows the pH dependences of the amounts of all the adsorbed cations. It is clear that the positive charge due to adsorption of M(II) at the quartz–solution interface ($\Sigma|e_M^+|$) is twice the product $\Gamma_M N_A$. Recalculation of Γ (mol m^{-2}) given in Fig. 1 to the corresponding amount of the positive charge in EDL and its comparison with the amount of the negative charges localized on the surface groups $[\equiv SiO]^-$ ($\Sigma|e^-| = \Gamma_{SiO} N_A$) show that $\Sigma|e^-| > \Sigma|e_M^+|$ in all cases.

In this connection, let us estimate the significance of the $[\equiv SiO]^-$ and $[\equiv SiOH]^0$ surface centers as centers determining the electric field of the surface layer and also as ligands of the surface complexes. Taking into account the inequality given above, it may be suggested that the $[\equiv SiO]^-$ sites contribute significantly to the specific adsorption through an essentially Coulombic interaction M(II)–$[\equiv SiO]^-$. The role of the Coulombic forces, as the longest-range forces, is restricted to attraction of the M(II) ions to the zone of action of short-range forces responsible for specific adsorption.

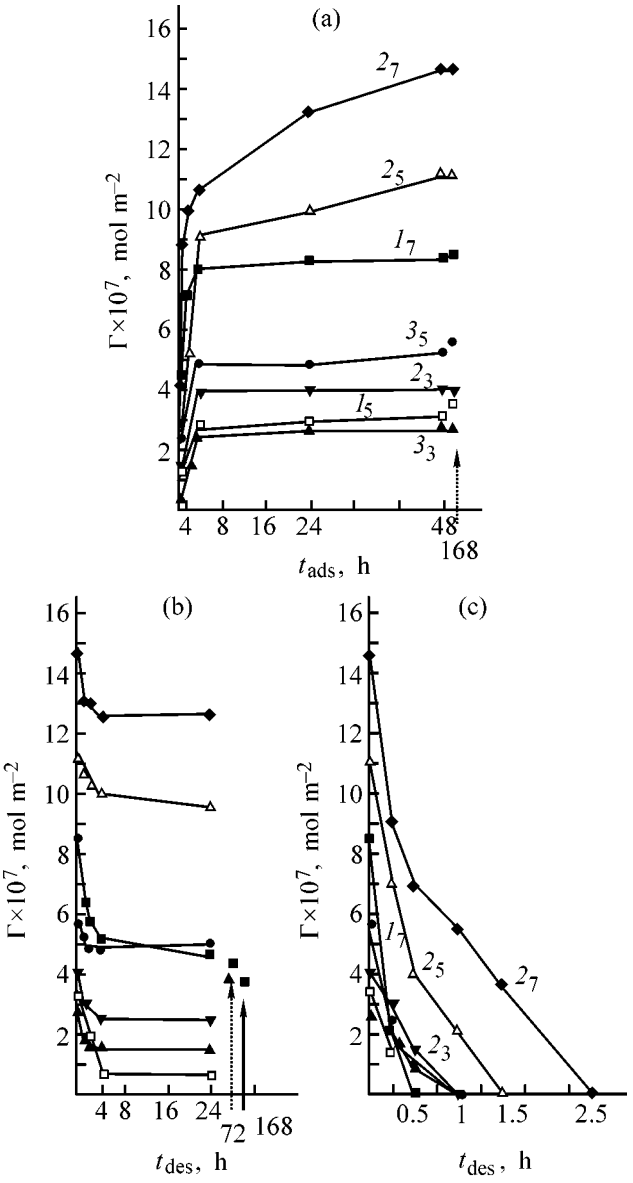

Fig. 4. Amount of M(II) adsorbed on the unit surface area of quartz, Γ, vs. (a) adsorption time t_{ads} and (b, c) desorption time t_{des} at t_{ads} = 168 h. Desorption method: (b) static and (c) electroosmotic. Subscripts denote pH of the initial working solution.

Evidently, the M(II) aqua cations are bound to primarily $[\equiv SiO]^-$ groups on the quartz surface. At the same time, the interaction of M(II) with $[\equiv SiOH]^0$ cannot be ruled out. Also, the forces retaining the adsorbate at the $[\equiv SiO]^-$ active site cannot be restricted to the Coulombic interactions only. The following facts additionally count in favor of the specific adsorption of M(II) on the active site of the quartz surface. In solutions with pH 3.0 and 5.0, in which the initial Ni(II) and Cu(II) concentrations were lower by a factor of 10 than the total concentration of all

other cations, the electrical neutrality of EDL is provided by considerably higher amounts of the Ni(II) and Cu(II) ions, compared to the amounts corresponding to their adsorption as indifferent ions. Indeed, it follows from the recalculated data of Fig. 1 that in the systems containing Ni(II) and, to a lower but also remarkable extent, in Cu(II)-containing systems, the ratio $\Sigma|e_M^+|/\Sigma|e^-|$ is considerably above 0.1–0.2. Moreover, in the case of Ni(II), this ratio only slightly differs from 0.85 at pH 3.0 and 0.8 at pH 5.0; the corresponding values for Cu(II) are 0.5 and 0.6.

At present, the coordination chemistry in aqueous solution is extensively studied. There is a great body of data on the effect of the nature of metals and ligands on the strength and structure of coordination bonds M–L. To our knowledge, such data on surface complexes are lacking in the literature.

At the same time, the force field at the interface is very asymmetrical. Its strength drops from a high value to zero over molecular ranges [19]. Therefore, we analyzed the correlation of the experimental data obtained with coordination model of adsorption, by analogy with consideration of the effect of metal ions and ligands on the formation of the bulk and surface complexes. Of course, this is not the literal meaning. We only point out the known general trends in the effect of the nature of M(II) and L on the properties of the surface complexes formed.

The observed relatively weak fixation of Co(II) on the quartz surface can be attributed to the well-known fact that the coordination numbers 4 and 6, corresponding to the tetrahedral and octahedral surroundings of Co(II), respectively, are the most typical of this cation. Complexes of Co(II) with monodentate ligands, having an oxygen atom as a donor center, are mostly labile [24–26].

The desorption results obtained by the static method suggest that, in the case of Ni(II), donor–acceptor bonds must be relatively strong. For d^8 complexes of Ni(II), both coordination numbers 4 (tetrahedral or square-planar structure) and 6 (octahedron) are typical. According to the crystal field theory, ligand substitution in d^8 complexes by the S_N1 or S_N2 mechanism is slow [27]. Most likely, Ni(II) complexes formed on the α-quartz surface have square-planar or octahedral configuration.

In the systems with Cu(II), like in those with Ni(II), the lack of noticeable desorption in the static mode suggests the formation of relatively strong donor–acceptor bonds between Cu(II) as a central atom and the oxygen atom of the surface ligand $[\equiv SiO]^-$. Note also that, for d^9 complexes of Cu(II), the most typical structures of the inner coordination sphere are square-planar and octahedral.

CONCLUSIONS

(1) The adsorption efficiency of Co(II), Ni(II), and Cu(II) on quartz increases in the order Co(II) < Cu(II) < Ni(II), growing with pH. The time of attainment of the adsorption equilibrium varies in the same order, ranging from 2 h to 3 days.

(2) Desorption of M(II) from quartz depends on a desorption procedure used. In the static desorption, the desorption efficiency of Co(II) is higher than that of Ni(II) at all the experimental pH values and than that of Cu(II) at pH 5.0. At pH 3.0 the static desorption of Cu(II) is lower than that of Co(II), but higher than that of Ni(II). In electroosmotic replacement, all the cations are totally desorbed quite rapidly (in at least 2.5 h).

(3) In both static and electroosmotic desorption modes, the desorption efficiency depends on the adsorption time. In static desorption, the metal cations adsorbed in 1 h are desorbed more efficiently that at an adsorption time of 1 and 7 days. In electroosmotic displacement mode, the same equilibrium c_{des}^r is attained in longer time with increasing t_{ads}.

ACKNOWLEDGMENTS

The study was supported financially by the Russian Foundation for Basic Research (project no. 00-15-97 357).

REFERENCES

1. Bibik, E.E., *Zh. Prikl. Khim.*, 1999, vol. 72, no. 6, pp. 916–920.
2. Yates, D.E., Levin, S., and Healy, T.W., *J. Chem. Soc., Faraday Trans.*, 1974, no. 10, pp. 1807–1812.
3. James, R.O., Stiglich, R.J., and Healy, T.W., *J. Colloid Interface Sci.*, 1972, vol. 40, no. 1, pp. 42–45.
4. Damaskin, B.B., Gorichev, I.G., and Batrakov, V.V., *Elektrokhimiya*, 1990, vol. 26, no. 4, pp. 400–406.
5. Matievich, E., *J. Colloid Interface Sci.*, 1973, vol. 43, no. 2, pp. 217–245.
6. Chernoberezhskii, Yu.M., Bykova, N.I., and Yanklovich, A.I., in *Termodinamika i struktura gidroksokompleksov v rastvorakh* (Thermodynamics and Structure of Hydroxo Complexes in Solutions), Leningrad: Leningr. Gos. Univ., 1983, pp. 152–156.
7. Gorichev, I.G., Batrakov, V.V., and Shaplygin, I.S.,

Izv. Ross. Akad. Nauk, Neorg. Mater., 1994, vol. 30, no. 10, pp. 1219–1234.

8. Lyklema, J., *Adsorption from Solution at the Solid/Liquid Interface*, Parfitt, G.D. and Rochester, C.H., Eds., London: Academic, 1983. Translated under the title *Adsprbtsiya iz rastvorov na poverkhnostyakh tverdykh tel*, Moscow: Mir, 1986, pp. 261–293.
9. Devis, I.A., James, R.D., and Leckie, J.O., *J. Colloid Interface Sci.*, 1978, vol. 63, no. 3, pp. 480–499.
10. Sparnay, M.J., *The Electrical Double Layer*, Oxford: Pergamon, 1972.
11. Lygin, V.I., Farikov, A.Dzh., and Tugushev, R.E., *Zh. Fiz. Khim.*, 1995, vol. 69, no. 2, pp. 315–317.
12. Huang, C.P. and Stumm, W., *J. Colloid Interface Sci.*, 1973, vol. 43, pp. 409–420.
13. Stumm, W., Huang, C.P., and Jenkis, S.R., *Croat. Chem. Acta*, 1970, vol. 43, no. 2, pp. 223–245.
14. Stumm, W., Huang, C.P., and Dalang, F., *Croat. Chem. Acta*, 1976, vol. 48, no. 4, pp. 491–504.
15. Shindler, P.W., Furst, B., Dick, R., and Wolf, P.U., *J. Colloid Interface Sci.*, 1976, vol. 55, no. 3, pp. 469–475.
16. Aleksandrova, L.K. and Tikhomolova, K.P., *Kolloidn. Zh.*, 1988, vol. 50, no. 1, pp. 100–107.
17. Tikhomolova, K.P. and Tsukanova, V.M., *Zh. Prikl. Khim.*, 1997, vol. 70, no. 3, pp. 353–370.
18. Baes, C.F. and Mesmer, R.E., *The Hydrolysis of Cations*, New York: Wiley, 1976.
19. Tikhomolova, K.P., *Elektroosmos* (Electroosmosis), Leningrad: Khimiya, 1989.
20. Ahmed, S.M., in *Oxide and Oxide Films*, New York: Wiley, 1972, pp. 319–517.
21. Tikhomolova, K.P., Kaufman, Yu.V., and Urakova, I.N., *Zh. Prikl. Khim.*, 2001, vol. 74, no. 8, pp. 1258–1264.
22. Tsukanova, V.M., Interaction of Aqua and Hydroxo Species of Pb(II), Cu(II), and Hg(II) with the SiO_2 Surface in Context of the Chemical Concept of Specific Adsorption, *Cand. Sci. (Chem.) Dissertation*, St. Petersburg, 1996.
23. Zhinkin, G.N., *Elektroosmoticheskoe zakreplenie gruntov v stroitel'stve* (Electroosmotic Grouting of Grounds in Construction), Leningrad: Stroiizdat, 1966.
24. Cotton, F.A. and Wilkinson, G., *Basic Inorganic Chemistry*, New York: Wiley, 1976.
25. Kukushkin, Yu.N., *Khimiya koordinatsionnykh soedinenii* (Chemistry of Coordination Compounds), Moscow: Vysshaya Shkola, 1985.
26. Spice, J.E., *Chemical Binding and Structure*, New York: MacMillan, 1964.
27. Cotton, F.A. and Wilkinson, G., *Advanced Inorganic Chemistry*, New York: Interscience, 1966.

Russian Journal of Applied Chemistry, Vol. 75, No. 6, 2002, pp. 900–904. Translated from Zhurnal Prikladnoi Khimii, Vol. 75, No. 6, 2002, pp. 920–923.
Original Russian Text Copyright © 2002 by Afzaletdinova, Murinov, Reznik, Vasil'eva.

SORPTION AND ION-EXCHANGE PROCESSES

Extraction of Iridium(IV) from Hydrochloric Acid Solution with Bis(piperidinoethylthioethyl)-1-phenyl-1-ethanone

N. G. Afzaletdinova, Yu. I. Murinov, L. B. Reznik, and E. V. Vasil'eva

Institute of Organic Chemistry, Ufa Scientific Center, Russian Academy of Sciences, Ufa, Bashkortostan, Russia

Received August 14, 2001; in final form, January 2002

Abstract—A bidentate organic compound containing nitrogen and sulfur donor atoms was tested as a reagent for extraction of iridium(IV) from aqueous solutions. The composition of the extractable Ir(IV) complex was determined by ^{1}H NMR, UV, and IR spectroscopy and elemental analysis.

Because of the kinetic inertness of Ir(IV) halide complexes, iridium is weakly extracted from aqueous hydrochloric acid solutions with organic sulfides. It is known that extraction of kinetically inert complexes of iridium(III) and ruthenium(III) is accelerated when using reagents containing simultaneously sulfur and nitrogen atoms [1].

In this work, we studied the extraction of iridium(IV) from hydrochloric acid solutions with bis(piperidinoethylthioethyl)-1-phenyl-1-ethanone (L) $C_6H_5COCH[CH_2SCH_2CH_2N(C_5H_{10})_2]$ synthesized by the procedure reported in [2].

The purity of L was monitored by elemental analysis, thin-layer chromatography, and ^{13}C and ^{1}H NMR spectroscopy. This reagent is a viscous light yellow liquid with specific odor.

It is known that iridium(IV) is an oxidant. It was reported in [3] that, in extraction of iridium(IV) with octylaniline, iridium(IV) is reduced to iridium(III).

We found that, on keeping iridium(IV) solutions in water or 2–3 M HCl or on their stirring with a pure diluent (*m*-xylene, chloroform) for 90 min, the iridium(IV) concentration does not change.

In our experiments, we used iridium(IV) salt K_2IrCl_6 of pure grade and iridium(III) salt K_3IrCl_6 synthesized by the procedure reported in [4]. The working solutions were prepared by dilution of a stock solution with 3 M HCl.

The total iridium(IV) content in solutions was determined spectrophotometrically [5]. Extraction was carried out in temperature-controlled cells at organic to aqueous phase ratio of 1 : 1 at 20 ± 0.5°C. The phases were stirred with a magnetic stirrer.

The electronic spectra (ES) were recorded in quartz cells on a Specord M-40 spectrophotometer. The ^{1}H NMR spectra of the organic extracts diluted with deuterochloroform were registered on a Bruker AM-300 spectrometer (300 MHz). The electrical conductivity of the organic extracts was measured in acetone solutions on a Radelkis OK-102/1 conductometer (Hungary). The IR spectra of the extractant, extracts, and extracted complexes were recorded on a Specord M-80 spectrophotometer in the range 4000–200 cm^{-1} using KRS-5 disks for the range 4000–400 cm^{-1} and polyethylene disks for 400–200 cm^{-1}.

Our previous testing showed that, in extraction of iridium(IV) from 2–3 M HCl, the equilibrium distribution was attained within a contact time not exceeding 10 min. All the subsequent experiments were performed at this contact time.

It is known that, in hydrochloric acid medium, both aminoketo sulfides and amino sulfides are converted to the corresponding salts due to protonation of the amine nitrogen atom [1]. Therefore, iridium(IV) can be recovered from 2–3 M hydrochloric acid solutions with the reagent L in the form of ionic associates by the mechanism of interphase anion exchange:

$$[IrCl_6]^{2-} + C_6H_5COCH\{CH_2SCH_2CH_2\ddot{N}H(C_5H_{10})_2\}_2 \cdot 2H\ddot{C}l \rightarrow C_6H_5COCH\begin{matrix}\diagup\ CH_2SCH_2CH_2\ddot{N}H^+(C_5H_{10})_2 \\ \\ \diagdown\ CH_2SCH_2CH_2\ddot{N}H^+(C_5H_{10})_2\end{matrix} [IrCl_6]^{2-} + 2Cl^-$$

1070-4272/02/7506-0900 $27.00 © 2002 MAIK "Nauka/Interperiodica"

Table 1. Position of absorption bands in the electronic spectra of iridium(IV) chloride complexes in aqueous HCl and of iridium(IV) extract with solution of L in chloroform

$[IrCl_6]^{2-}$	Assignment and frequency, cm^{-1}		
	$^1A_1 \rightarrow {}^1T_1$	$^1A_1 \rightarrow {}^2T_1$	$^1A_1 \rightarrow {}^3T_1$
Binuclear form	27778 s	23000 m	20408 w [6]
Mononuclear form, 2 M HCl		23840 m, 23041 m	20534 s [5, 6]
Extract from 3 M HCl, I_{cont} (min):			
10		23804 s, 23040 s	20543 s
30*	27500 s	23000 m	19800 s
Extract from 2 M HCl, I_{cont} (min):			
10		23840 s, 23040 s	20480 s
30**	27200 m	23000 w	19750 m

* At saturation of the organic phase with iridium(IV) ions on the contact with iridium(IV) solution in 3 M HCl.

** At saturation of the organic phase with iridium(IV) ions on the contact with iridium(IV) solution in 2 M HCl.

The set of absorption bands in the ESs of both the aqueous solution and organic phases after their 10-min contact shows that iridium is present in the form of the octahedral anion $[IrCl_6]^{2-}$ (Table 1, Fig. 1) [6, 7]. In spite of the fact that iridium(IV) is a strong oxidant, no Ir(III) appeared in the aqueous phase after extraction. Owing to resistance of the extractant to oxidation, the extraction does not affect the electronic spectra of iridium in the aqueous solution.

Measurements of the electrical conductivity of an extract diluted with acetone showed that the extraction complex is an electrolyte of the 2 : 1 type (λ = 190 Ω^{-1} m^2 mol^{-1}).

The IR spectrum of a complex of L with HCl, formed in iridium(IV) extraction from hydrochloric acid solution, contains a band at 2550 cm^{-1}, belonging to NH stretching vibrations in the $\equiv NH^+$ cation. The formation of this cation also shows that Ir(IV) is extracted in the form of a tertiary ammonium salt containing iridium in the form of $[IrCl_6]^{2-}$ anionic complex. The band of $\equiv NH^+$ stretching vibrations in the range 2700–2250 cm^{-1} is typical of tertiary ammonium salts [9].

To choose the optimal conditions for extraction of iridium(IV) with ketoamine sulfide we studied how the extraction of Ir(IV) depends on the HCl concentration in the aqueous phase. Figure 2 shows that, with

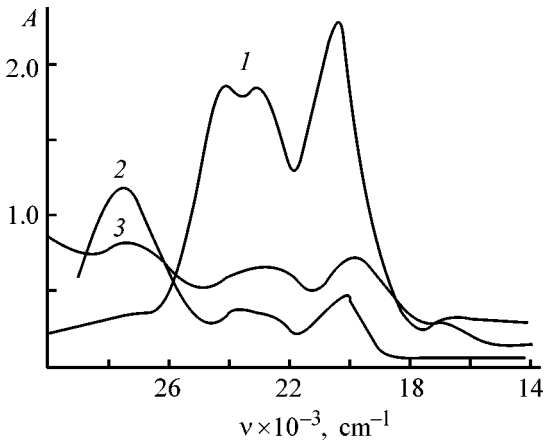

Fig. 1. Electronic spectra of iridium(IV) extracts: (*A*) optical density [8] and (ν) wave number. HCl concentration in the aqueous phase (M): (*1*, *2*) 3 and (*3*) 2. Contact time (min): (*1*) 10 and (*2*) 30.

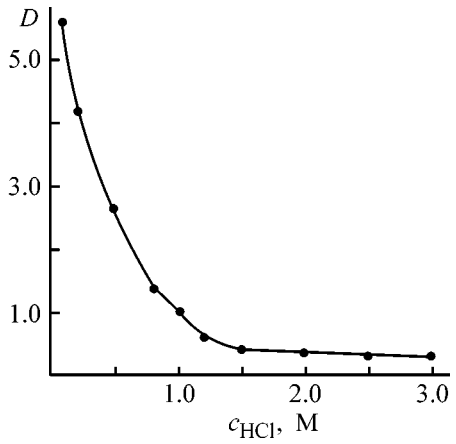

Fig. 2. Distribution factor of iridium(IV) $D = (c_{Ir(IV)})_{org}/(c_{Ir(IV)})_{aq}$ vs. HCl concentration in the aqueous phase. Concentration (M): Ir(IV) 0.0005 and (L) 0.005.

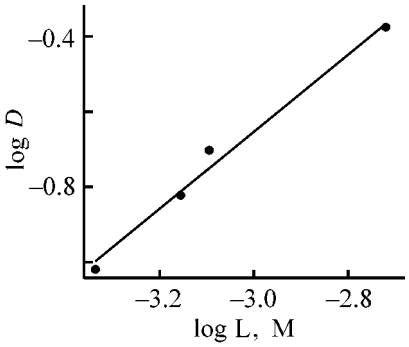

Fig. 3. Distribution factor of iridium(IV) vs. concentration of the free reagent at c_{HCl} 2 M.

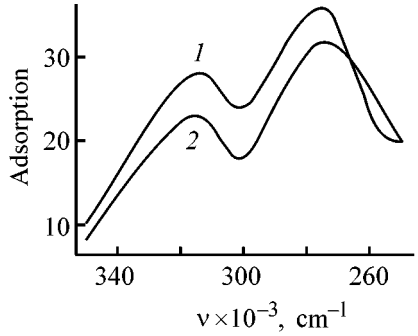

Fig. 4. IR spectra of iridium(IV) complexes with reagent L obtained by extraction from its hydrochloric acid solutions under saturation conditions. (ν) Wave number. HCl concentration in aqueous phase (M): (*1*) 3 and (*2*) 2.

increasing HCl concentration, the distribution coefficient of iridium(IV) D decreases. This suggests that the initial solution contains a large amount of readily extractable iridium(IV) chloride complexes which are converted to poorly extractable species with increasing HCl concentration.

The extraction of iridium(IV) from 2 M HCl was studied in more detail. To determine the composition of the iridium(IV) complex extracted with L from 2 M HCl, we studied how the proton concentration at a constant ionic strength [NaCl + HCl] = 2 M affects the iridium(IV) distribution factor. Our results show that the slope of the dependence $\log D = f(c_{H^+})$ is close to 2, i.e., iridium(IV) is extracted in the form of a negatively charged iridium(IV) anionic complex $[IrCl_6]^{2-}$.

The number of extractant molecules incorporated into the iridium-containing extractable complex was evaluated by the dilution method. Figure 3 shows that the extractable complex contains one molecule of L.

The chemical shifts of proton signals in the ^1H NMR spectra of free reagent L and of the extracts obtained by contacting L with both straight aqueous HCl (2 and 3 M) and iridium(IV) solution in HCl (2 and 3 M) for 10 and 30 min, respectively, are listed in Table 1. Comparison of the ^1H NMR spectra shows that the additional chemical shift on protonation is the strongest for protons of the mehylene groups at the nitrogen atom, while the chemical shifts of protons at the sulfur atom are minor. In extraction of iridium(IV) from 2 and 3 M HCl, the appearing signals at 11.34 and 11.60 ppm are due to protonation of the nitrogen atom of L (Table 2).

Table 2. Chemical shifts of protons in the ^1H NMR spectra of pure reagent L and its complexes with HCl and iridium(IV) in deuterochloroform

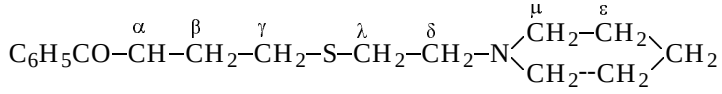

Sample	Proton chemical shift in ^1H NMR spectra δ (ppm) and additional chemical shift Δδ, ppm							
	α	β	γ	λ	δ	μ	ε	NH^+
L(δ)	3.85	3.12	2.57	2.46	2.32	1.52	1.33	–
L · HCl(δ)	3.90	3.08	2.72	3.63	3.50	1.84	1.43	11.34
Δδ*			0.15	1.17	1.18	0.32	0.10	11.34
Extract [T_{cont} = 10 min, 2 M HCl(δ)]	3.92	3.07	2.73	3.49	3.50	1.80	1.42	11.60
Δδ			0.16	1.03	1.17	0.28	0.09	0.32
Extract [T_{cont} = 30 min, 2 M HCl(δ)]	3.90	3.20	2.70	3.40	3.40	1.75	1.40	11.60
Δδ			0.13	0.95	1.08	0.23	0.07	0.34

* The additional chemical shift is defined as the difference between the proton chemical shifts δ in the spectra of pure L and its extraction complex with HCl and iridium(IV).

Table 3. Elemental composition of ionic associates of iridium(IV) chloride anionic complexes with reagent L*

Compound $[Ir_2Cl_{10}L_2]$	Calculated						Found						mp, °C
	wt %												
	C	H	N	S	Cl	Ir	C	H	N	S	Cl	Ir	
I from 3 M HCl	35.8	4.7	3.5	7.9	22.0	23.9	36.0	4.6	3.2	7.3	23.0	23.7	109–110
II from 2 M HCl	35.8	4.7	3.5	7.9	22.0	23.9	35.6	4.6	3.7	8.0	23.0	23.5	108–110

* This compound is a red-brown powder.

Under the conditions of saturation of the organic phase ($c_{Ir(IV)}$ = 0.005 and c_L = 0.05; contact time 30 min) binuclear complexes are obtained (Table 3, Fig. 1).

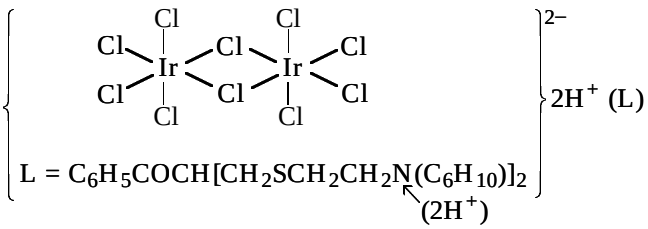

The electronic spectra of extracts saturated with iridium(IV) contain bands at 28000 and 23000 cm^{-1}, which, according to [6], indicate a polynuclear structure of the extractable complexes. Figure 1 shows that, in the UV spectra of complex **I** obtained by extraction of iridium(IV) from 3 M HCl, the absorption band at 28000 cm^{-1} is stronger compared to complex **II** obtained by extraction from 2 M HCl. This result agrees with published data [6, 7], which show that the fraction of extractable polynuclear Ir(IV) complexes increases with increasing acid concentration in aqueous phase.

An elemental analysis of these complexes showed that their composition corresponds to a dimeric structure with Ir : Cl : L = 2 : 10 : 1.

Measurements of the electrical conductivity of the extracts diluted with acetone suggested that the extracted complex is a 2 : 1 type electrolyte (λ = 190 $\Omega\,m^2\,mol^{-1}$).

We found that prolongation of the phase contact to 30 min does not affect the ^1H NMR spectra substantially (Table 2). This fact confirms our assumption that, in extraction of iridium(IV) from concentrated (>2 M) HCl solutions, the sulfur atoms of the reagent molecule do not enter to a significant extent the inner coordination sphere of iridium(IV). Iridium(IV) is extracted as ionic associates.

The long-wave length IR spectra of complexes **I** and **II** are given in Fig. 4. The similarity of these spectra shows that, at HCl concentrations in the aqueous phase higher than 2 M, iridium(IV) is recovered in the form of ionic associates containing bridging cloride ions. In the IR spectra, a broad strong band at 316 cm^{-1} is due to the stretching vibrations ν_μ(Ir–Cl) of terminal bonds [10, 11]; and the strong absorption band at 274 cm^{-1} is due to vibrations of the bridging chloride anions in the extractable complexes.

CONCLUSIONS

(1) A bidentate reagent containing electron-donor sulfur and nitrogen atoms was tested in extraction of iridium(IV) from aqueous (2 and 3 M) HCl.

(2) The composition of iridium(IV) complexes extracted from aqueous HCl was studied by ^1H NMR, UV, and IR spectroscopy and elemental analysis. Depending on the phase contact time, either mononuclear or binuclear iridium(IV) chloro complexes are extracted in the form of ionic associates with the reagent.

REFERENCES

1. Afzaletdinova, N.G., Murinov, Yu.I., Nikitin, Yu.E., and Vasil'eva, E.V., Abstracts of Papers, *V Vsesoyuznaya Konferentsiya "Organicheskie reagenty v analiticheskoi khimii"* (V All-Union Conf. "Organic Reagents in Analytical Chemistry"), Kiev, 1983, part 1, p. 55.
2. Krivonogov, V.P,. Shayakhmetova, R.M., and Dronov, V.I., *Zh. Prikl. Khim.*, 1981, vol. 54, no. 11. pp. 2505–2509.
3. Shul'man, R.S., Mustafaev, R.F., Gindin, L.M., and Chernobrov, A.S., *Izv. Sib. Otd. Akad. Nauk SSSR, Ser. Khim. Nauk*, 1977, no. 9, issue 4, pp. 58–62.

4. *Sintez kompleksnykh soedinenii metallov platinovoi gruppy: Spravocnik* (Synthesis Platinum Metal Complexes: Handbook), Moscow: Nauka, 1964.
5. Ginzburg, S.I., Ezerskaya, N.A., and Prokof'ev, I.V., *Analiticheskaya khimiya platinovykh metallov* (Analytical Chemistry of Platinum Metals), Moscow: Nauka, 1972.
6. Buslaeva, T.M. and Simanova, S.A., *Koord. Khim.*, 1999, vol. 25, no. 3, pp. 165–176.
7. Andreyanov, A.D., Iofa, B.Z., and Nesmeyanov, A.N., *Vestn. Mosk. Gos. Univ.*, 1975, no. 3, pp. 306–309.
8. Babko, A.K. and Pilipenko, A.T., *Fotometricheskii analiz* (Photometric Analysis), Moscow: Khimiya, 1968.
9. Kazitsyna, L.A. and Kupletskaya, N.B., *Primenenie UF, IK i YaMR spektroskopii v organicheskoi khimii* (Application of UV, IR, and NMR Spectroscopy in Organic Chemistry), Moscow: Vysshaya Shkola, 1971.
10. Sinitsyn, N.M., Borisov, V.B., Kozlov, A.S., *et al.*, *Zh. Neorg. Khim.*, 1982, vol. 27, no. 1, pp. 164–169.
11. Allen, E.F. and Wilkinson, W., *J. Chem. Soc. (A)*, 1972, no. 5, p. 613.

Russian Journal of Applied Chemistry, Vol. 75, No. 6, 2002, pp. 905–910. Translated from Zhurnal Prikladnoi Khimii, Vol. 75, No. 6, 2002, pp. 924–928.
Original Russian Text Copyright © 2002 by Nagirnyi, Apostolova, Baskevich, Litvin, Shembel'.

APPLIED ELECTROCHEMISTRY AND CORROSION PROTECTION OF METALS

Electrolytic Deposition of Cobalt(III) Oxide in the Presence of Nickel(II) and Chromium(III) Ions

V. M. Nagirnyi, R. D. Apostolova, A. S. Baskevich, P. M. Litvin, and E. M. Shembel'

Ukrainian State University of Chemical Technology, Dnepropetrovsk, Ukraine

Received August, 23, 2001; in final form, January 2002

Abstract—Preparation conditions and nature of anodic processes in electrolytic deposition of cobalt(III) oxide in the presence of nickel(II) and chromium(III) ions from mixed aqueous solutions of their sulfates were studied. The deposits obtained are of interest for creating effective cathode materials for lithium batteries.

Cobalt(III) oxides in compounds with lithium are effective cathode materials for lithium batteries. Among their advantages mention should be made of high energy capacity and satisfactory stability in cycling [1–3]. According to the results of numerous studies [4–6], these characteristics of cobalt(III) oxide are much improved when complex oxide systems of the types Ni_xCo_{1-x}, $Cr_yCo_{1-y}O_2$, etc., are used. The possibility of obtaining and the preferable parameters of electrolysis in anodic deposition of cobalt(III) oxide from an aqueous solution of its sulfate have been established previously [7]. It has been shown that quantitative amounts of deposits, which are binary oxide systems, are formed on the anode in electrolysis of manganese(II) and cobalt(II) sulfate solutions mixed in a certain ratio [8]. The phase composition of the systems can be controlled to a certain extent by choosing the solution composition and process parameters.

It seemed appropriate to study the nature of anodic processes in electrolytic deposition of cobalt(III) oxide from aqueous sulfate solutions in the presence of nickel(II) and chromium(III) ions in order to determine whether its electrolytic alloying with oxide compounds of these metals is possible. No relevant evidence could be found in the literature.

As objects of study served sulfate solutions of the metals at varied ratio of their concentrations. The concentration of cobalt(II) sulfate in an additive-free solution was 0.09 M, and the total concentration, 0.12–0.13 M for the Co–Ni system and 0.09–0.1 M for the system Co–Cr at salt concentration ratios of 1 : 1–1 : 5 and 1 : 1–5 : 1, respectively, (the figures in the first and second positions refer to, respectively, the base and alloying component). The solutions were prepared from pure and analytically pure reagents and distilled water. The electrolysis was carried out in a 200-ml glass cell. The materials under study were deposited in the form of compact coatings onto smooth $1 \times 1 \times 0.03$-cm smooth plate anodes made of 12Kh18N9T steel (on both sides) at $S_a : S_c$ ratio of 1 : 5. Dispersed deposits with mass of 0.1–0.15 g for X-ray structural analysis were obtained on a smooth plate of VT-1 technical-grade titanium. Smooth plates of the same material served as cathodes. All experiments were done at a temperature of 85°C and pH 2.5–3.0, with these values of the parameters chosen on the basis of preliminary experiments. The deposition rate V_d (mg cm^{-2} h^{-1}) was determined from the anode mass gain after electrolysis per unit area per unit time. A copper coulometer was connected to the circuit to measure the current efficiency by the anodic product. The current efficiency was calculated on the assumption that the entire useful current was expended for formation of cobalt oxide Co_2O_3 [electrochemical equivalent 3.08 g (A h)$^{-1}$]. Polarization curves were measured in a three-chamber cell on an anode made of 12Kh18N9T steel (∇ 7–8, S_a = 1 cm^2, $S_a : S_c$ = 1 : 5) at the above-mentioned electrolysis parameters in the range I_a = 0.5–60 mA cm^{-2}. The potentials were measured relative to silver chloride reference electrode (φ = +0.255 V) with a V7-16A digital instrument. The phase composition of the deposits was determined qualitatively and, approximately, quantitatively using X-ray structural data obtained on a DRON-2 diffractometer, compared with reference data by means of a calibration plot [9]. The microstructure and surface morphology of the deposits were studied on thin-film coatings (2.5–3.5 μm) with a digital nanoscope (Nano Scope IIIa, Digital Instruments).

1070-4272/02/7506-0905 $27.00 © 2002 MAIK "Nauka/Interperiodica"

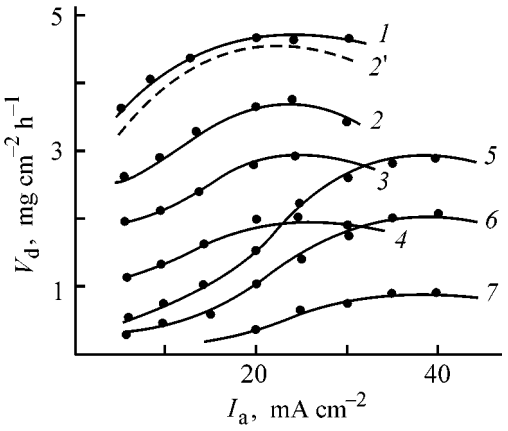

Fig. 1. Deposition rate V_d of electrolytic oxide materials vs. anode current density I_a in electrolysis of (*1*) cobalt(II) sulfate solution, and also in the presence of nickel(II) and chromium(III) sulfate (c_{tot} 0.12–0.13 and 0.09–0.1 M, respectively). Temperature 85°C, pH 2.5–3.0. Co : Ni: (*2*) 1 : 1, (*2'*) 1 : 1 (at double excess of total concentration), (*3*) 1 : 3, and (*4*) 1 : 5; Co : Cr: (*5*) 5 : 1, (*6*) 3 : 1, and (*7*) 1 : 1.

Figure 1 presents the dependences of the deposition rate V_d on the anode current density I_a for deposition of cobalt(III) oxide from a sulfate solution without additives and in the presence of nickel(II) and chromium(III) ions at different ratios of the component concentrations (henceforth Co : M), with all other conditions being the same. A common feature of all the dependences is that V_d gradually increases with I_a to a certain limiting value and then tends to decrease slowly. The extremal points of the dependences are shifted to higher I_a values in the interval 15–25 mA cm^{-2} with increasing relative content of the alloying component in solution. In the same order decrease the V_d values—from 4.7 mg cm^{-2} h^{-1} for cobalt(III) oxide to 1.9 mg cm^{-2} h^{-1} for the system Co–Ni at Co : M = 1 : 5. In the presence of chromium(III), the extrema of the V_d–I_a dependences lie at higher current densities (35–40 mA cm^{-2}), with their numerical values not exceeding 3.0 mg cm^{-2} h^{-1} even upon a fivefold decrease in the relative content of the alloying component in solution (Co : M = 5 : 1). At the same ratio Co : M = 1 : 1, the corresponding value for the system Co–Ni is 5 times that for the system Co–Cr.

Such a significant difference in character between the processes under consideration is due to their specific nature, governed by the kinetic and energy characteristics of the reactions occurring simultaneously at the anode. Only cobalt(III) oxide is deposited quantitatively under real conditions from aqueous solutions of cobalt salts in anodic oxidation of Co(II) in accordance with the reaction equation

$$2Co^{2+} + 3H_2O - 2e \rightarrow Co_2O_3 + 6H^+,\ E^0 = 1.83\ V\ [10]. \quad (1)$$

Under standard conditions, nickel does not form stable oxide compounds with oxidation level exceeding 2; nevertheless, it is thermodynamically possible that a nickel oxide Ni_2O_3 is formed by the reaction

$$2Ni^{2+} + 3H_2O - 2e \rightarrow Ni_2O_3 + 6H^+,\ E^0 = 1.75\ V\ [10]. \quad (2)$$

However, this reaction is impossible in an aqueous solution because of its complete suppression by oxygen being liberated and oxidation of the surface layers of the anode base. In contrast to the case of nickel(II), the transition $Cr^{3+} \rightarrow Cr^{6+}$ occurs under standard conditions via anodic oxidation of the corresponding salt from solution by the reaction

$$2Cr^{3+} + 7H_2O - 6e \rightarrow Cr_2O_7^{2-} + 14H^+,\ E^0 = 1.33\ V\ [10]. \quad (3)$$

Kinetically, formation of molecular oxide compounds of chromium (Cr_2O_3, CrO_3), with the simultaneous deposition of a compact coating on the anode surface, is complicated by the multiple-stage nature of such a process and the suppressing influence of the competing reaction of oxygen liberation. Quantitative deposition of nickel and chromium oxides under the conditions studied is enabled by codeposition on the anode in the form of an alloying phase in the binary oxide system when reactions (2) and (3) are combined with reaction (1). This is presumably favored by a decrease in energy expenditure in the overall anodic process, which may result from the simultaneously occurring reactions of interphase and interion interactions of the forming and reacting substances.

The effect of alloying components in the form of nickel(II) and chromium(III) salts in cobalt(II) sulfate solutions is manifested in a significant decrease in the rate of formation of the anode deposit, nearly independently of the total concentration of salts in solution for the Co–M systems under study. Even in the case of a twofold excess of the total concentration of the salts in a solution with Co : Ni = 1 : 1 with respect to the optimal concentration of cobalt(II) sulfite in an additive-free solution, the dependence V_d–I_a for the binary oxide Co–Ni runs below the corresponding dependence for cobalt(III) oxide (Fig. 1, curves *1* and *2'*). The decrease in the rate of the overall process, observed on raising the relative content of the alloy-

Table 1. Current efficiency at varied Co : M ratio in solution (temperature 85°C, pH 2.5–3.0)

Co : M, mol : mol	CE (wt %) at I_a, mA cm^{-2}					
	5	10	20	25	30	35
Co : Ni:						
1 : 0	19	13	7.3	4.7	–	–
1 : 1	15	8.3	5.6	4.0	–	–
1 : 3	12	7.0	5.2	3.7	–	–
1 : 5	9.6	5.0	3.5	2.4	–	–
Co : Cr:						
1 : 1	–	–	0.5	0.65	0.8	0.8
3 : 1	–	–	1.7	1.8	1.8	1.9
5 : 1	–	–	2.3	2.4	2.5	2.4

Table 2. Content of alloying phase, $c_{a.ph}$, in anodic deposits at varied Co : M ratio in solution (temperature 85°C, pH 2.5–3.0)

Co : M, mol : mol	$c_{a.ph}$ (wt %) at I_a, mA cm^{-2}				
	15	20	25	30	35
Co : Ni:					
1 : 1	–	–	1.5	2.0	–
1 : 3	–	1.0	2.0	3.0	–
1 : 5	1.5	3.0	3.0	5.0	–
Co : Cr:					
1 : 1	–	–	1.5	2.0	2.5
3 : 1	–	–	1.0	1.5	2.0
5 : 1	–	–	–	0.5	1.0

ing component in the system Co–Ni should be presumably attributed to an increase in the unproductive contribution of reaction (2) toward anodic polarization and to deceleration of cobalt(II) oxidation [reaction (3)]. Possibly, this mechanism occurs with higher probability in the presence of chromium(III) ions because of the less positive standard potential of reaction (1), compared with that for reaction (3). This results in that chromium(III) oxidation by reaction (1) at the anode may be faster than reaction (3), which leads to the corresponding deceleration of the process of cobalt(II) oxidation and to the formation of an anodic deposit. In the end, this causes an increase in the share of oxygen, liberated as a by-product, in the overall anodic process. This is clearly seen when analyzing the dependences of the current efficiency by anodic deposits on the current density for different Co : M ratios in solution (Table 1). In the system Co–Ni, the current efficiency (CE) is inversely proportional to the current density and concentration of the alloying component in solution, with the maximum CE in the I_a range studied not exceeding 20 wt % for cobalt(II) sulfate solution. This may indicate a key role of the concomitant reaction of oxygen liberation in the kinetics of the anodic processes under study. These phenomena are even more pronounced in the system Co–Cr, in which the yield of the anodic product is only noticeable at $I_a \geq 20$ mA cm^{-2} and remains nearly unchanged with increasing I_a. A probable reason for the independence of CE from the current density is a rise in the oxygen overvoltage with increasing amount of the oxide phase of chromium in the anodic deposit. With decreasing relative concentration of chromium(III) ions in solution, the CE increases; however, even at Co : Cr = 5 : 1 the CE values fluctuates within 2.3–2.5 wt %, which is apparently due to the increasing rate of oxygen liberation under the given conditions.

The presence of alloying oxide phases of nickel(II) and chromium(III) in the anodic deposits studied is confirmed by the results of X-ray diffraction analysis, which indicate that anodic materials deposited in electrolysis of cobalt(II) sulfate solutions in the presence

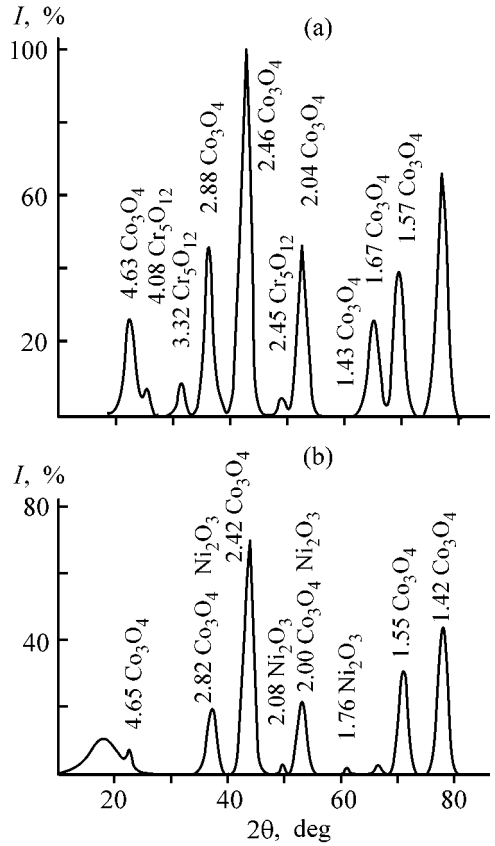

Fig. 2. X-ray patterns of oxide systems (a) Co–Ni and (b) Co–Cr, obtained by anodic deposition from solutions with Co : M of 1 : 3 and 3 : 1, respectively, after thermal treatment at 300°C for 7 h. I_a (mA cm^{-2}): (a) 20 and (b) 30. (*I*) Intensity and (2θ) Bragg angle.

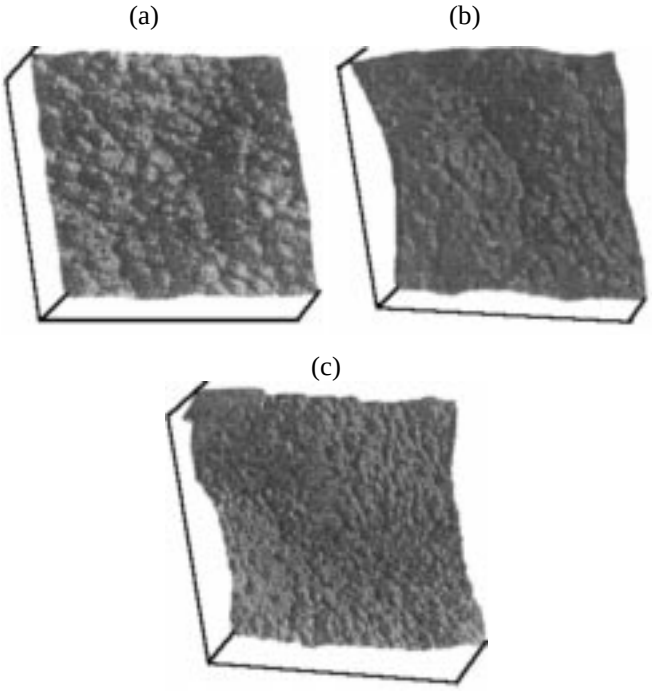

Fig. 3. Surface microstructure of (a) anodic deposit of cobalt(III) oxide and also (b) Co–Ni and (c) Co–Cr deposits obtained from solutions with Co : M concentration ratios of, respectively, 1 : 3 and 3 : 1.

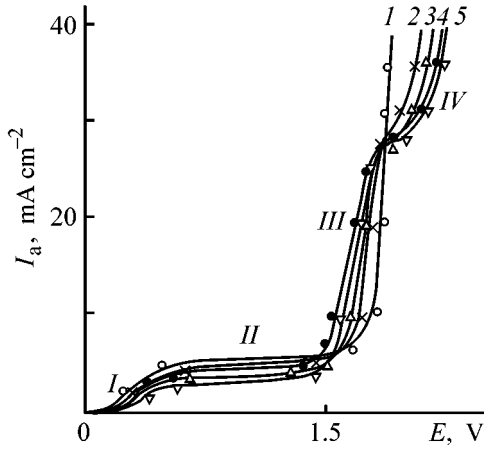

Fig. 4. I_a–E dependences for anodic processes of deposition of (*1*) cobalt(III) oxide from a sulfate solution and (*2*–*5*) oxide systems from solutions with varied Co : M concentration ratio. Temperature 85°C, pH 2.5. Co : Cr: (*2*) 5 : 1 and (*4*) 1 : 1; Co : Ni: (*3*) 1 : 1 and (*5*) 1 : 5.

of nickel(II) and chromium(III) ions are complex multiphase systems composed, under standard conditions, of thermodynamically stable oxide compounds: Co_2O_3, Co_3O_4, NiO, Ni_2O_3, Cr_2O_3, and CrO_3, and also some single-phase compounds of the type $M_xCo_{1-x}O_2$, where M = Ni, Co (Fig. 2). According to approximate estimate, the content of the alloying phase (wt %) in the deposits under study (Table 2) depends on the concentration of the corresponding component in solution and on the current density; however, even in the limiting cases, this content does not exceed 2.5 and 5 wt % for, respectively, the Co–Cr and Co–Ni systems.

The codeposition of the alloying phase markedly affects the kinetics of formation of the anodic deposit and formation of its structure. Comparison of the surface microreliefs and microstructures of the deposits under study (Fig. 3) indicates that their structure changes fundamentally with electrolysis conditions. Cobalt oxide (Fig. 3a) is mainly composed of rather coarse chaotically oriented crystalline grains of globular type. In the presence of nickel(II) and chromium(III) ions, the anodic deposits become finely crystalline, with a certain tendency toward formation of spheroidal blocks preserved in the first case (Fig. 3b) and a more uniform and ordered finely grained structure formed in the second (Fig. 3c). This is more clearly manifested after thermal treatment of deposits at 300°C, after which the binary oxides obtained show a pronounced crystalline structure, more ordered in the case of the Co–Cr binary system with a characteristic layer-by-layer growth of separate crystalline grains. The formation of structures of this kind is possibly due to interaction of the codeposited phases at the molecular level, accompanied by suppression of the growth of "base" cobalt(III) oxide crystals by the molecules of the alloying component.

The above dependences and relations, determined by the nature of the anodic processes under study, are in satisfactory agreement with the voltammetric characteristics measured at different Co : M concentration ratios and constant temperature and pH (Fig. 4). The I_a–E dependences presented can be divided into four regions (*I*–*IV*) defined by the nature of the processes under study at different polarizing currents. The portions of the curves in region *I* apparently reflect the oxygen liberation process, which follows from the coincidence of their position with the potential range of its liberation under the given conditions [10]. The shift of these portions to higher potentials corresponds to the increase in the concentration of the alloying components in solutions in the sequence Co–(Co–Cr)–(Co–Ni), which points to the important part played by the alloying components in the kinetics of the anodic process. In the given case, this is manifested in that the oxygen overvoltage grows in the same order, which is, possibly, a con-

sequence of the influence exerted by the total concentration background in region *I* with predominant effect of cobalt(II) and nickel(II) ions. This is partly indicated by the fact that the portion of the curve (in region *I*) (Fig. 4, curve *4*) for a solution with Co : Cr = 1 : 1 lies at more positive potentials than a similar portion (Fig. 4, curve *2*) for a solution with 5 times lower concentration of the chromium salt (Co : Cr = 5 : 1) and by a more pronounced shift of the potential in the presence of nickel(II) ions at the same Co : M concentration ratio.

The transition plateaus in region *II* are arranged in order of decreasing polarizing current in accordance with the increasing relative concentration of the alloying component in solution, which is in agreement with their above-mentioned influence on the polarization of the electrode process. The appearance and position of the curve portions in region *III* are mainly determined by the relative rates of cobalt(III) oxide deposition and oxygen liberation, with account of the influence exerted by concurrent reaction in which nickel(II) and chromium(III) ions are oxidized. Apparently, the stronger the influence exerted by these latter, the stronger the hindrance to the reaction of cobalt(II) oxidation, the larger the increase in the rate of oxygen liberation, and, consequently, the more pronounced the decrease in the polarization of the overall anodic process. This corresponds to the shift of the ascending portions of the curves in region *III* toward less positive potentials with increasing relative concentration of the second component in solution (Fig. 4). Simultaneously with an increase in the polarizing current, the concentrations of ions of the metals being codeposited and of the products of their oxidation in the near-electrode become higher, with the resulting limitation of the deposition rate of cobalt oxide. This, in the end, gives rise to conditions favorable for formation at the anode of alloying oxide phases simultaneously with that of cobalt(III) oxide. In this case, the anodic polarization is markedly enhanced, which, correspondingly, causes the subsequent inflection of the curves and their transition to the ascending portions of region *IV*. These latter characterize the process of joint formation of cobalt(III) oxide and associated alloying phases, with a simultaneous increase in the oxygen discharge overvoltage on a substrate with changing nature. The shift of the curve portions in region *IV* to positive potentials becomes more pronounced in accordance with the increasing relative concentration of ions of the alloying components in solution. For example, at the same concentration ratio Co : M = 1 : 1 in solution the process of binary oxide formation in the system Co–Ni (Fig. 4, curve *3*) is less polarized than that in the system Co–Cr (Fig. 4, curve *4*). Possibly, this is a consequence of both the more pronounced decrease in the rate of the overall process in the presence of chromium(III) ions and to increased oxygen evolution on the substrate formed in the given system. At the same time, a fivefold increase in the concentration of nickel(II) ions in solution (Co : Ni = 1 : 5) causes a shift of the corresponding portion of the curve (Fig. 4, curve *5*) to potentials with respect to the similar portion for a solution with Co : Cr = 1 : 1 (Fig. 4, curve *4*).

Thus, analysis of the I_a–E dependences for anodic deposition of cobalt(III) oxide in the presence of nickel(II) and chromium(III) ions under different electrolysis conditions supplements to a certain extent the data on the nature of the processes under study and allows refinement of the working parameters of electrolytic deposition of mixed oxide systems Co–Ni and Co–Cr from sulfate solutions.

CONCLUSIONS

(1) A study of the deposition conditions and the nature of the occurring anodic processes revealed that complex binary oxide systems Co–Ni and Co–Cr are formed at the anode in electrolytic deposition of cobalt(III) oxide in the presence of nickel(II) and chromium(III) ions.

(2) The most favorable conditions for quantitative formation at the anode of these oxide materials with prescribed characteristics are achieved at 80–85°C and pH 2.5–3.0 at salt concentration ratios in solution of, respectively, 1 : 1–1 : 5 and 5 : 1–1 : 1 and anode current densities of 10–25 and 25–35 mA cm^{-2} for the systems Co–Ni and Co–Cr.

REFERENCES

1. Levi, M.D., Salitra, G., Markovsky, *et al.*, *J. Electrochem. Soc.*, 1999, vol. 146, no. 4, pp. 1279–1290.
2. Yoshio, M., Noguchi, H., Tominaga, K., and Tonaka, H., *Battery Materials*, vol. 11, pp. 158–165.
3. Potyomkin, G.A., Postnikov, A.Y., Malishev, A.U., and Kozhukar, N.G., *The 197th Meeting of the Electrochem. Soc., May 14–18, 2000*, Toronto, 2000, p. 165.
4. Ol'shanskaya, L.N. and Popova, S.S., *Materialy IV Mezhdunarodnoi konferentsii "Fundamental'nye problemy elektrokhimicheskoi energetiki" Saratov, 21–*

23 iyunya 1999 g. (Proc. IV Int. Conf. "Fundamental Problems of Electrochemical Power Engineering," Saratov, June 21–23, 1999), Saratov, 1999, pp. 75–77.

5. Baudrin, E., Laruelle, S., Denis, S., *et al., Solid State Ionics*, 1999, vol. 123, pp. 139–153.
6. Gover, R.K.B., Yonemura, M., Hirano, A., *et al., J. Power Sources*, 1999, vol. 81–89, no. 9, pp. 558–562.
7. Apostolova, R.D., Nagirnyi, V.M., and Shembel', E.M., *Elektrokhimiya*, 1998, vol. 34, no. 7, pp. 778–784.
8. Shembel, E.M., Apostolova, R.D., Nagirny, V.M., *et al., The 197th Meeting of the Electrochem. Soc., May 14–18, 2000*, Toronto, 2000, p. 105.
9. Mirkin, A.I., *Spravochnik po rentgenostrukturnomu analizu polikristallov* (Handbook of X-ray Diffraction Analysis of Polycrystals), Moscow: Fizmatgiz, 1961.
10. Vetter, K.J., *Electrochemische Kinetik*, Berlin: Springer, 1961.

Russian Journal of Applied Chemistry, Vol. 75, No. 6, 2002, pp. 911–914. Translated from Zhurnal Prikladnoi Khimii, Vol. 75, No. 6, 2002, pp. 929–932.
Original Russian Text Copyright © 2002 by Timinskas, Cheshunene, Kurtinaitene, Skominas.

APPLIED ELECTROCHEMISTRY AND CORROSION PROTECTION OF METALS

Preparation of Anodized Aluminum for Electrodeposition of Metals (Co–Cu System) into Pores of Oxide

A. Timinskas, A. Cheshunene, M. Kurtinaitene, and V. Skominas

Institute of Chemistry, Vilnius, Lithuania

Received June 14, 2001; in final form, November 2001

Abstract—Conditions under which anodized aluminum is treated first in a dilute solution of phosphoric acid and then in a fluoroborate immersion solution in order to deposit a multilayer system of cobalt and copper in the pores in the oxide were studied.

One of promising newest directions in the electrochemistry of metals is deposition of various metals, including multilayer functional systems, from a single solution into pores of specially pretreated membranes [1–3].

The method of deposition of coatings with varied composition from a single solution is commonly used when it is necessary to obtain multilayer coatings with layers having different properties. Use of a single solution in deposition of such coatings markedly simplifies the technology employed. Nevertheless, this technique has a number of limitations and is rather complicated. First of all, it is necessary to use electroplating solutions with two or more kinds of discharging metal ions, and the deposition potentials of metals forming separate layers must differ to a sufficient extent. Electrodeposition of such multilayer functional systems into pores of specially pretreated membranes has been studied insufficiently, and, therefore, some problems concerning the mechanism of deposition processes are incompletely understood. One of such problems is, e.g., diffusion of discharging ions within narrow pores in membranes.

An attempt was made in the present study to use for metal electrodeposition a membrane of anodic aluminum oxide (ADOM brand), obtained in a solution of certain composition. This composition was chosen in such a way that anodizing could be done at voltages sufficiently high for obtaining pores with large diameter. These conditions were satisfied by a 0.045 M (0.4%) solution of oxalic acid at a voltage of 90 V. The anodizing was carried out for 80 min, and then the voltage was lowered stepwise by 10 V every 5 min. The anodizing process was terminated on reaching a voltage of 0.1 V.

Since the membrane thus obtained could not be separated from the aluminum base and the barrier layer formed at pore bottom had high ohmic resistance hindering the electrodeposition of metals, this barrier layer was to be removed. During the process of stepwise voltage lowering, the barrier layer thickness decreases somewhat; however, its complete removal is impossible [4]. It is proposed to use for this purpose a two-stage chemical treatment of anodized aluminum. The first stage involves treatment with a 0.08 M solution of phosphoric acid, and the second, with a fluoroborate immersion solution of composition (M): $Ni(BF_4)_2$ 0.87, $Zn(BF_4)_2$ 0.17, and NH_4BF_4 0.38; pH 4. This solution is commonly used to prepare the surface of aluminum and its alloys for electroplating [5, 6]. The process of barrier layer removal was monitored by changes in the potential of anodized aluminum in relation to duration of treatment in the immersion solution (Fig. 1). The barrier layer was considered removed when the potential of anodized aluminum reached a value of about –0.8 V, corresponding to a steady-state potential in treatment of air-oxidized aluminum with the immersion solution (the potentials are given relative to standard hydrogen electrode).

As it can be seen from Fig. 1, curve *1*, the potential shifts toward negative values on submerging anodized aluminum in the immersion solution. The change in potential is rather fast initially, but slows down in the course of time, with the potential of –0.8 V attained in 16–17 min. It is known that treatment

1070-4272/02/7506-0911 $27.00 © 2002 MAIK "Nauka/Interperiodica"

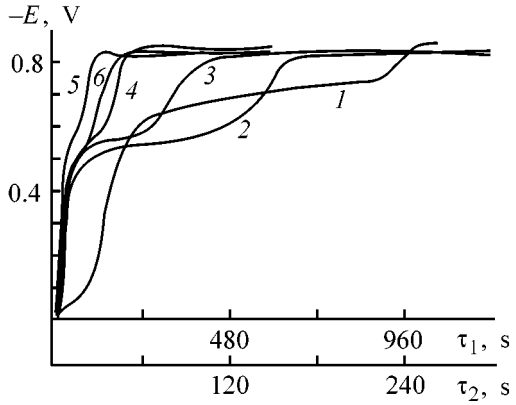

Fig. 1. Potential E of anodized aluminum vs. time of its exposure, (*1*) τ_1 and (*2–6*) τ_2, to immersion solution at different durations of the first stage of treatment. Time of treatment (h): (*1*) 0, (*2*) 0.5, (*3*) 1, (*4*) 2, (*5*) 3, and (*6*) 5.

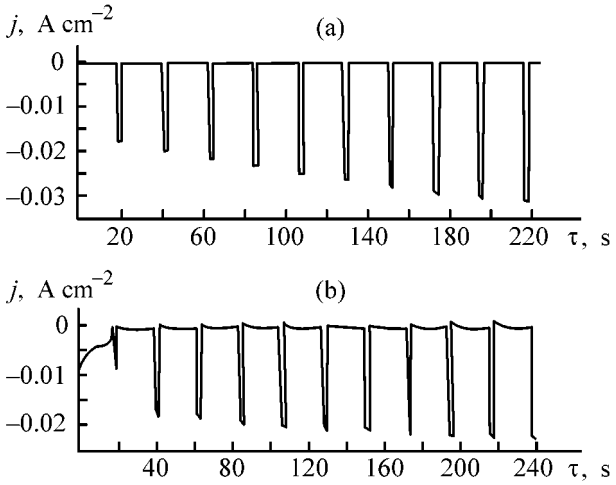

Fig. 2. Current density *j* of pulsed deposition of the Co–Cu system vs. time τ, measured on anodized aluminum in different pretreatment modes. Pulse duration (s): Cu 20, Co 2. Potential amplitude (V): Cu –0.2, Co –0.9. Treatment duration: first stage: (a) 0.5 and (b) 5 h; second stage: (a, b) 10 min.

of anodized aluminum in a phosphoric acid solution leads to widening of pores in aluminum oxide [7]. Therefore, prior to being treated in the immersion solution, anodized aluminum was additionally treated with a phosphoric acid solution. As shown by the experiments (Fig. 1, curves *2–5*), the additional treatment makes the changes in potential faster. For example, after treatment for 0.5 h in a phosphoric acid solution, the shift of potential toward negative values in the immersion solution is accelerated by approximately a factor of 5–6, with the potential reaching the value of –0.8 V in 3 min (Fig. 1, curve *2*). On raising the duration of aluminum treatment in phosphoric acid solution further, the potential of –0.8 V is reached in the immersion solution even faster (Fig. 1, curves *3–6*). However, treatment for more than 2 h does not affect significantly the rate of change in potential (Fig. 1, curves *4* and *5*). Thus, successive two-stage treatment of anodized aluminum in a phosphoric acid solution and immersion solution is a rather efficient way to activate pores in anodic aluminum oxide. This treatment leads to an increase in pore diameter and dissolution of the barrier layer formed at pore bottom.

A multilayer system Co–Cu was deposited into the pores of aluminum prepared by the method described. This was done using a solution of composition (M): $CoSO_4$ 0.5, $CuSO_4$ 0.01, and H_3BO_3 0.65. The electrodeposition was carried out by alternating two potentiostatic pulses. Copper was deposited during the first of these (0 to –0.4 V), and cobalt with minor amount of copper during the second (–0.7 to –0.9 V). The potentials chosen are commonly used in deposition of the given metals onto metal electrodes. The duration of separate pulses was selected depending on the required thickness of metal layer to be deposited. Since copper deposition occurs in the potential range employed at the limiting current, the copper layer thickness was only controlled by varying the deposition duration. The cobalt layer thickness could be controlled by varying the deposition duration or the potential. The results obtained in pulsed deposition demonstrate that the current of cobalt electrodeposition grows with increasing number of cycles on anodized aluminum not subjected to treatment in a phosphoric acid solution or treated in this solution for a relatively short period of time (Fig. 2a). This phenomenon virtually disappears with increasing time of exposure of anodized aluminum (for no less than 2 h) in a phosphoric acid solution. Typical variation of currents in separate pulses with the time of metal deposition is shown in Fig. 2b.

The electrodeposition of the Co–Cu system into pores of aluminum oxide differs from the deposition onto a copper electrode in that the deposition current on anodized aluminum is approximately 20% of the deposition current observed in deposition of these metals on a copper cathode under the identical conditions. Apparently, this is due to the fact that pores into which the metals are deposited occupy only a part of the entire surface area of anodized aluminum.

The area occupied by pores on the surface of anodized aluminum was evaluated. This was done using electron micrographs of the surface of anodized aluminum (Fig. 3a). Calculations show that, after the first stage of treatment of anodized aluminum for 3–5 h, the pore diameter is, on the average, 60 nm and

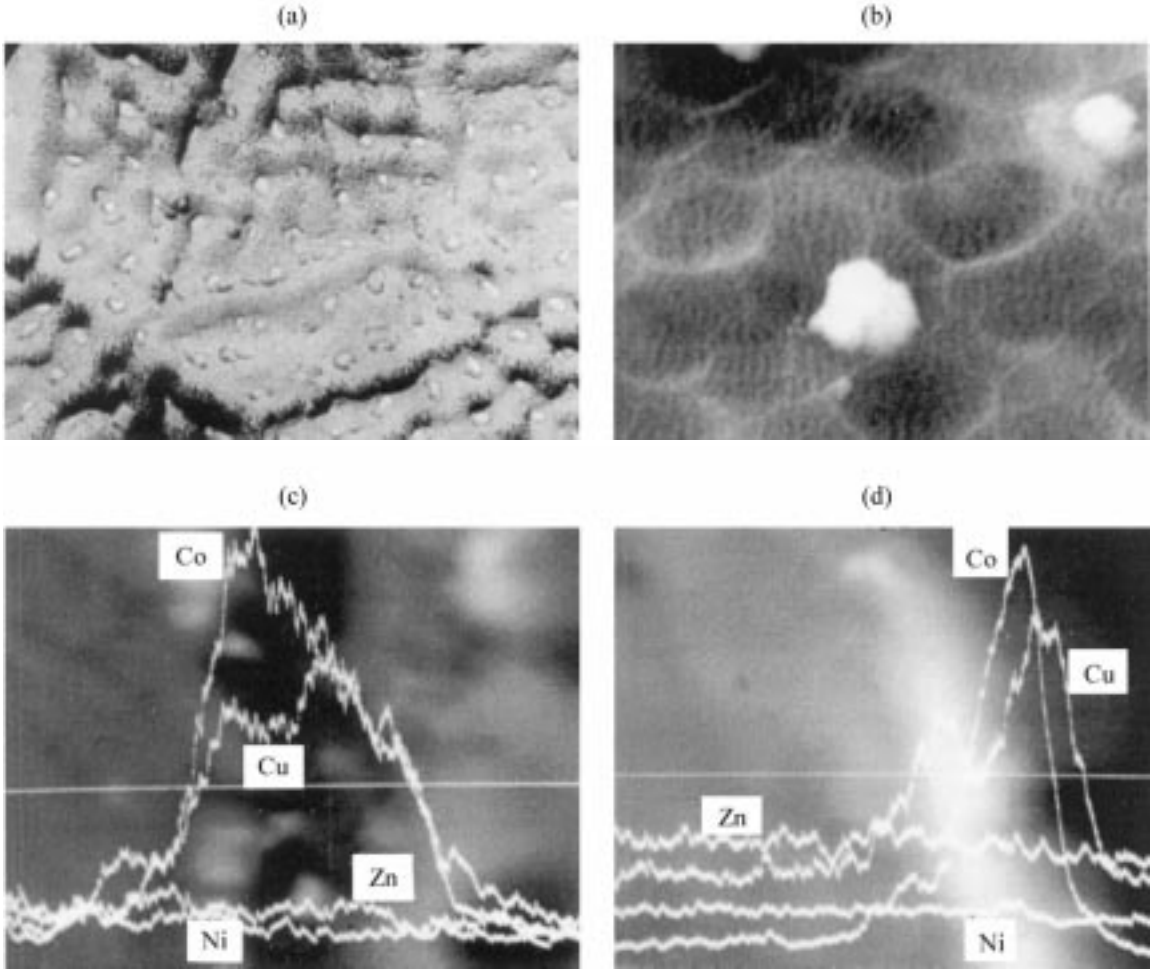

Fig. 3. Electron micrographs of the surface of anodized aluminum (a) before and (b) after deposition of the Co–Cu system and (c, d) shapes of signal from a cross-section of aluminum oxide containing the Co–Cu system, obtained in different pretreatment modes. Magnification: (a) 45000, (b) 10000, and (c, d) 5000. Treatment time: first stage (h): (a) 5, (b, c) 3, and (d) 0.5; second stage (min): (b, c) 10.

pores occupy 10–15% of the entire surface area. Comparison of the pore areas with the relative deposition currents on anodized aluminum and copper cathode shows that the current density in pores is 1.5–2.0 times that on the copper cathode. Possibly, this is associated with specific features of diffusion of the metal ions into a large number of small pores constituting a kind of a microelectrode system [8]. Under these conditions, the contribution of radial diffusion to the total diffusion flux commonly grows, resulting in a higher current density.

SEM studies demonstrated that, after the oxide pores are filled in a more prolonged deposition of the multilayer Co–Cu system, metals being deposited extend over the surface. This process is also accelerated by the higher deposition rate in separate places of the surface of anodized aluminum (Fig. 3b). It may be assumed that this is favored by defects of anodic oxide, formed in anodizing and subsequent treatment of aluminum.

The metals were determined in pores of anodic aluminum oxide by microprobe analysis. For this purpose, sections of anodized aluminum subjected to two-stage treatment with subsequent electrodeposition of the Co–Cu system were fabricated. As shown by the data obtained (Figs. 3c and 3d), Co and Cu are found in the oxide bulk, irrespective of the duration of treatment in a phosphoric acid solution. These metals are present in the bottom layer of the oxide.

The data obtained indicate that the two-stage treatment of anodized aluminum favor metal electrodeposition into the oxide pores at potentials close to those of electrodeposition of the same metals onto metal electrodes. This enables deposition of various metal systems possessing required functional properties into pores of anodized aluminum.

CONCLUSION

A study of the voltammetric characteristics of deposition and determination of the places of copper and cobalt localization in pores of anodic aluminum oxide demonstrated that two-stage treatment of anodized aluminum in a phosphoric acid solution and then in a fluoroborate immersion solution creates conditions favorable for metal deposition at pore bottom at potentials close to those commonly used in electrodeposition of these metals on metallic electrodes.

ACKNOWLEDGMENTS

The authors thank E. Matulenis for help in SEM studies.

REFERENCES

1. Piraux, L., George, J.M., and Despres, J.F., *Appl. Phys. Lett.*, 1994, vol. 65, no. 19, pp. 2484–2486.
2. Martin, R. *Charles*, *Science*, 1994, vol. 266, pp. 1961–1966.
3. Hornyak, G., Kröll, M., and Pugin, R., *Chem. Eur. J.*, 1997, vol. 3, no. 12, pp. 1951–1956.
4. Furneaux, R.C., Rigby, W.R., and Davidson, A.P., *Nature*, 1989, vol. 337, pp. 147–149.
5. USSR Inventor's Certificate, no. 836213.
6. Timinskas, A. and Kaushpedas, Z., *Chemija*, 1993, no. 3, pp. 44–57.
7. AlMawlawi, D., Coombs, N., and Moskovits, M., *J. Appl. Phys.*, 1991, vol. 70, no. 8, pp. 4421–4425.
8. Zagidulin, D., Timinskas, A., and Skominas, V., *Chemija*, 2001, vol. 12, no. 1, pp. 71–75.

Russian Journal of Applied Chemistry, Vol. 75, No. 6, 2002, pp. 915–918. Translated from Zhurnal Prikladnoi Khimii, Vol. 75, No. 6, 2002, pp. 933–936.
Original Russian Text Copyright © 2002 by Natorkhin.

APPLIED ELECTROCHEMISTRY AND CORROSION PROTECTION OF METALS

Effect of $K_2Cr_2O_7$ Addition on Anodic Dissolution of NiS in Acid Sulfate and Ammonia Electrolytes

M. I. Natorkhin

State Technical University, St. Petersburg, Russia

Received October 21, 1999; in final form, July 2001

Abstract—The depassivating effect of $K_2Cr_2O_7$ additions on the electrochemical dissolution of nickel sulfide in 0.5 M solutions of $CuSO_4$ and Na_2SO_4 and in 5.8 M NH_4OH was studied at 90°C.

The interest in studying the autoclave leaching of nonferrous metal sulfides remains rather intense [1, 2]. Electrochemical modeling of autoclave leaching is of considerable importance in these studies [3, 4]. It has been shown earlier [5] that the anodic dissolution of nickel sulfides in acid copper sulfate electrolytes rapidly decelerates in the course of time owing to the formation of a Cu_2S passivating film on the nickel sulfide surface. However, Cu_2S is known to be soluble in $FeCl_3$ and $K_2Cr_2O_7$ solutions, which is often used in analytical practice [6] and in industrial leaching of sulfides [7].

The aim of this study was to make an attempt to eliminate nickel sulfide passivation in $CuSO_4$ solutions by adding $K_2Cr_2O_7$ and to analyze the electrochemical behavior of nickel sulfide in chromium-containing electrolytes.

We choose NiS synthesized by the known procedure [8, 9] as an object of study. A working electrode was fabricated by soldering a nickel sulfide sample to a copper rod 2 mm in diameter in such a way that its working surface area was 1 cm^2. Backsides of NiS and copper rod were insulated with nitro lacquer. The working surface of the electrode was smoothed with no. 0 flint-paper and washed with alcohol and distilled water before experiments. Electrolytes were prepared using Na_2SO_4 (analytically pure), $CuSO_4 \cdot 5H_2O$ (chemically pure), NH_4OH (analytically pure), and H_2SO_4 (special-purity grade). As an additive we used $K_2Cr_2O_7$ (chemically pure).

Electrochemical experiments were carried out by a three-electrode scheme [10] in a YaES-1 electrochemical cell, using a PI-50-1.1 potentiostat and a PDP4-002 recording potentiometer. The cell temperature was maintained at 90 ± 0.5°C with a UTU-2/77 thermostat. Platinum wire was used as a counter electrode and saturated silver chloride electrode as a reference. All potentials are given relative to the standard hydrogen electrode.

Cyclic voltammograms (CVA) of NiS, obtained in a pure 0.5 M $CuSO_4$ (pH 2.1) solution and in a solution with $K_2Cr_2O_7$ additive, are shown in Fig. 1. It is seen that the passivation region corresponding to the forward CVA run (curve *3*) disappears as the

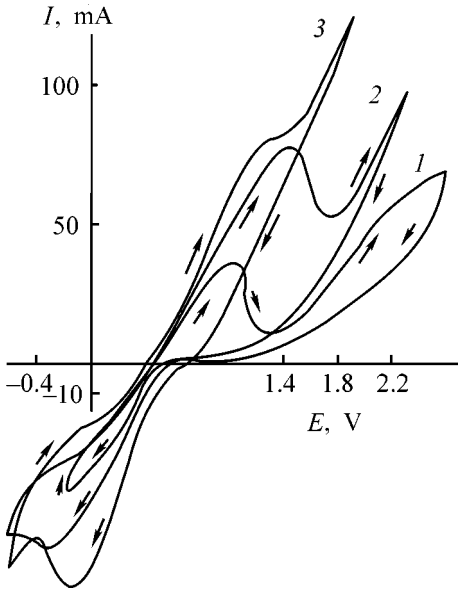

Fig. 1. Cyclic voltammograms obtained on NiS in (*1*) 0.5 M $CuSO_4$ solution (pH 2.1) and (*2*, *3*) the same solution with $K_2Cr_2O_7$ additions. T = 363 K, V_s = 100 mV s^{-1}; the same for Figs. 2 and 4. (*I*) Current and (*E*) potential; the same for Figs. 2 and 4. $K_2Cr_2O_7$ concentration (g dm^{-3}): (*1*) 0, (*2*) 3, and (*3*) 30.

1070-4272/02/7506-0915 $27.00 © 2002 MAIK "Nauka/Interperiodica"

Current I in relation to time τ of exposure to 0.5 M $CuSO_4$ solution with $K_2Cr_2O_7$* additive

τ, s	I (mA) at indicated E, V				
	0.77	0.97	1.17	1.37	1.57
0	17/14	18/32	26/50	26/73	29/94
5	16/13	16/29	13/49	13/71	26/92
10	14/12	12/25	8/48	11/70	19/90
15	12/11	10/24	7/47	10/69	18/90
20	11/10	7/24	6/47	9/69	18/89
25	10/9	6/24	5/47	9/69	18/88
30	9/9	6/24	4/47	9/68	18/87
35	8/8	5/24	3/47	8/69	17/87
40	8/8	5/23	3/46	8/68	17/86
45	7/8	4/23	3/46	7/68	17/86
50	7/8	4/23	3/46	7/68	17/86
55	6/8	4/23	3/46	7/68	17/86
60	6/8	4/23	2/46	7/68	16/86

* I values are given for two different concentrations of $K_2Cr_2O_7$: for 3 g dm^{-3} in the numerator and for 30 g dm^{-3} in the denominator.

dichromate concentration becomes higher. Making longer the exposure of the working electrode to 0.5 M $CuSO_4$ containing 30 g dm^{-3} of $K_2Cr_2O_7$ under potentials of 0.8–1.0 V results in the formation of a thin gray-black film with small bright specks. The dependence of the current on the duration of exposure under various potentials to a 0.5 M $CuSO_4$ solution containing 3.0 and 30 g dm^{-3} of $K_2Cr_2O_7$ is shown in the table.

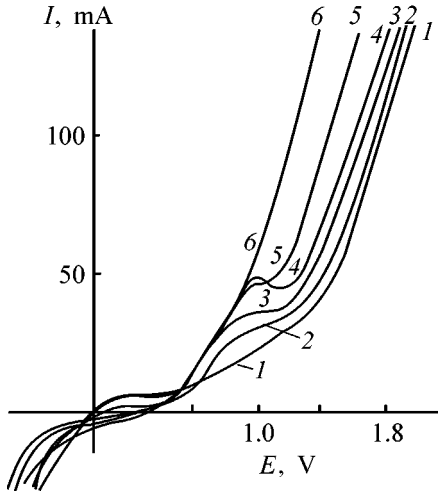

Fig. 2. Voltammetric curves obtained on NiS in (*1*) 0.5 M solution of Na_2SO_4 and (*2*–*6*) in the same solution with $K_2Cr_2O_7$ additive. $K_2Cr_2O_7$ concentration (g dm^{-3}): (*1*) 0, (*2*) 3, (*3*) 6, (*4*) 12, (*5*) 24, and (*6*) 48.

According to the data in the table, addition of $K_2Cr_2O_7$ makes itself evident even at low electrode potentials and $K_2Cr_2O_7$ concentrations. As the $K_2Cr_2O_7$ concentration increases, the dissolution of NiS becomes stable: the current remains almost constant in time.

Forward runs of CVA curves obtained on NiS in a pure 0.5 M Na_2SO_4 solution and in the same solution with $K_2Cr_2O_7$ additive are shown in Fig. 2. No passivation occurs in sulfate solutions containing no copper ions. Addition of $K_2Cr_2O_7$ makes the currents of NiS dissolution higher. However, at a $K_2Cr_2O_7$ concentration of 12 g dm^{-3} (curve *4*), a narrow passivation area appears in the forward CVA run. Its appearance is attributable to a secondary process of sulfur oxidation to sulfate ions, as in the case of anodic dissolution of a Fe–S alloy [11]. At high potassium dichromate concentrations, no sulfur was detected on the electrode surface and within the cell volume, with a slight inflection appearing in the polarization curves.

The stationary currents of NiS dissolution are shown as functions of potential and potassium dichromate concentration in a three-dimensional diagram (Fig. 3). It is necessary to point out that an increase in the $K_2Cr_2O_7$ concentration from 30 to 48 g dm^{-3} results in the appearance of a rather flat "top," and an intermediate "plateau" is observed in the concentration range 18–24 g dm^{-3}. Thus, minor addition of $K_2Cr_2O_7$ results in an increase in the rate of NiS dissolution in the Na_2SO_4 solution, whereas raising the potassium dichromate concentration to more than 30 g dm^{-3} is inexpedient. A slight decrease in the rate of NiS dissolution is observed at potassium dichro-

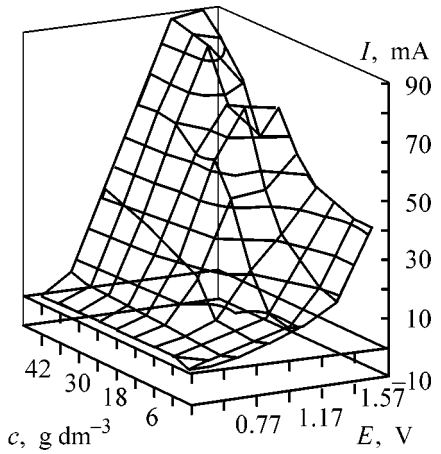

Fig. 3. Stationary NiS dissolution currents I vs. potential E and $K_2Cr_2O_7$ concentration c.

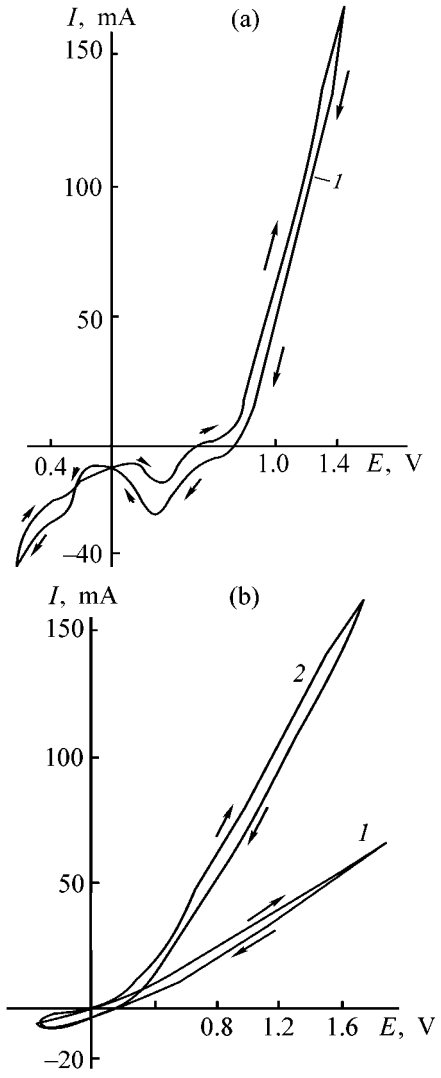

Fig. 4. Cyclic voltammograms obtained on NiS in (a) 0.5 M solution of $K_2Cr_2O_7$ and (b) 5.8 M solution of NH_4OH with $K_2Cr_2O_7$ additions. $K_2Cr_2O_7$ concentration (g dm^{-3}): (*1*) 6 and (*2*) 30.

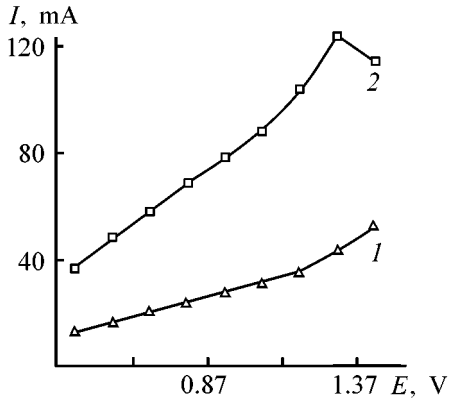

Fig. 5. Stationary currents *I* of NiS dissolution vs. the potential *E* in 5.8 M NH_4OH solution with $K_2Cr_2O_7$ additions. $K_2Cr_2O_7$ concentration (g dm^{-3}): (*1*) 6 and (*2*) 30.

mate concentrations of 42–48 g dm^{-3} at potentials from 1.37 to 1.57 V.

Since a passivation region appears in the sulfate–dichromate systems with increasing $K_2Cr_2O_7$ concentration, it was of interest to study the dissolution of NiS in dichromate solutions containing no sulfate ions. Figure 4 shows, a CVA curve for NiS in pure 0.5 M $K_2Cr_2O_7$. It is seen that no NiS passivation is observed at potentials in the range 1.0–1.4 V, and uniform dissolution occurs. Sulfur is completely oxidized to the sulfate ion in a 0.5 M $K_2Cr_2O_7$ solution.

Nickel sulfide dissolves most completely in ammonia solutions. To prepare the electrolytes, we used 10% (5.8 M) NH_4OH solution because it is sufficiently stable at 90°C [12, 13]. Nickel sulfide is insoluble in pure aqueous ammonia solutions under anodic polarization. Addition of $K_2Cr_2O_7$ makes higher the rate of NiS dissolution (Fig. 4b), no passivation region being observed in the CVA curve within the potential range under study. Raising the $K_2Cr_2O_7$ concentration leads to an increase in the rate of NiS dissolution. The currents of NiS dissolution remain almost unchanged in the course of time. The stationary currents are given for certain potentials in Fig. 5. It can be seen that NiS dissolution is decelerated at high potentials and high $K_2Cr_2O_7$ concentrations. No sulfur is formed, as is the case of 0.5 M $K_2Cr_2O_7$. The electrode surface retains its pure white-yellow color. Raising the ammonia concentration to 13.4 M at 58–60°C leads to solution boiling and cracking of the nickel sulfide surface. This cracking seems to be similar to corrosion cracking of brasses in aqueous ammonia solutions [14].

CONCLUSIONS

(1) Potassium dichromate depassivates the anodic dissolution of NiS in $CuSO_4$, Na_2SO_4, and NH_4OH solutions.

(2) The optimal concentration of potassium dichromate is in the range 6–30 g dm^{-3}. The sulfide sulfur completely oxidizes to SO_4^{2-} in NiS dissolution in solutions containing $K_2Cr_2O_7$.

REFERENCES

1. Chizhikov, D.M., Gulyanitskaya, Z.F., and Pliginskaya, L.V., *Elektrometallurgiya medno-nikelevykh sul'fidnykh splavov v vodnykh rastvorakh* (Electrometallurgy of Copper–Nickel Sulfide Alloys in Aqueous Solutions), Moscow: Nauka, 1977.

2. Ogorodnikov, Yu.I. and Ponomareva, E.I., *Elektrovyshchelachivanie khal'kogenidnykh materialov* (Electroleaching of Chalcogenide Materials), Alma-Ata: Nauka, 1983.
3. Sladkov, G.A. and Burygina, E.Kh., *Zh. Prikl. Khim.*, 1988, vol. 61, no. 7, pp. 1489–1492.
4. Makarov, G.V., Batrakova, Yu.A., and Nasipkalieva, Sh.I., *Zh. Prikl. Khim.*, 1980, vol. 53, no. 7, pp. 1542–1546.
5. Makarov, G.V., Amerkhanova, Sh.K., and Batrakov, V.V., *Zh. Prikl. Khim.*, 1990, vol. 63, no. 5, pp. 999–1003.
6. Podchainova, V.N. and Simonova, L.N., *Med'* (Copper), Moscow: Nauka, 1990.
7. Sinelshchikova, N.V. and Makarov, S.N., *Gidrometallurgiya medi i nikelya* (Hydrometallurgy of Copper and Nickel), Moscow, 1976.
8. Ivanov, I.S., *Zh. Prikl. Khim.*, 1986, vol. 59, no. 4, pp. 1017–1020.
9. *Handbuch der Praparativen Anorganischen Chemie*, von Brauer, G., Fehlhammer, W.P., Glemser, O. *et al.*, Eds., Stuttgart: Ferdinand Enke, 1981, Bd 3.
10. Bakhchisaraits'yan, N.G., Borisoglebskii, Yu.V., and Burkat, G.K., *Praktikum po prikladnoi elektrokhimii* (Practical Training in Applied Electrochemistry), Leningrad: Khimiya, 1990.
11. Simanova, S.A., Bashmakov, V.I., Troshina, O.N., *et al.*, *Zh. Prikl. Khim.*, 1993, vol. 66, no. 1, pp. 27–30.
12. Goronovskii, I.T., Nazarenko, Yu.P., and Nekryach, E.F., *Kratkii spravochnik po khimii* (Brief Handbook of Chemistry), Kiev: Naukova Dumka, 1987.
13. Kuri Khamid, Abaev, G.N., and Kireev, V.A., *Zh. Prikl. Khim.*, 1996, vol. 69, no. 3, pp. 389–392.
14. Zaitsev, V.A., Luk'yanenko, T.N., and Topanov, V.P., *Zh. Prikl. Khim.*, 1996, vol. 69, no. 5, pp. 799–802.

Russian Journal of Applied Chemistry, Vol. 75, No. 6, 2002, pp. 919–925. Translated from Zhurnal Prikladnoi Khimii, Vol. 75, No. 6, 2002, pp. 937–943.
Original Russian Text Copyright © 2002 by Shaidarova, Gedmina, Brus'ko, Zabirov, Ulakhovich, Budnikov.

APPLIED ELECTROCHEMISTRY AND CORROSION PROTECTION OF METALS

Inversion-Voltammetric Determination of Heavy Metal Ions on Electrodes Modified with Mono- and bis-*N*-Thiophosphoryl Thiourea

L. G. Shaidarova, A. V. Gedmina, V. V. Brus'ko, N. G. Zabirov, N. A. Ulakhovich, and G. K. Budnikov

Kazan State University, Kazan, Tatarstan, Russia

Received February 6, 2002

Abstract—A method is proposed for determining Ni^{2+}, Co^{2+}, Cu^{2+}, Cd^{2+}, and Pb^{2+} ions by inversion voltammetry on carbon-paste electrodes modified with *N*-diisopropoxythiophosphoryl-*N*'-phenyl thiourea and its derivatives: *N*,*N*'-bis-(diisopropoxythiophosphorylamidothiocarbonyl)-1,5-diamino-3-oxapentane, *N*,*N*'-bis-(diisopropoxythiophosphorylamidothiocarbonyl)-1,8-diamino-3,6-dioxaoctane and *N*,*N*'-bis-(diisopropoxythiophosphorylaminothiocarbonyl)-1,10-diaza-18-crown-6.

A promising approach to improvement of the efficiency of electrochemical methods for determining heavy metal ions uses chemically modified electrodes (ChME) [1]. The electrode surface can be modified by various methods. Immobilization of a modifier into a carbon-paste electrode (CPE) deserves special attention. Compared with other electrodes, the CPE has more developed working surface and shows enhanced adsorption of various organic and inorganic substances. This property is widely used for adsorption concentration, including that of metal ions, in inversion voltammetry (IVA) [1–3]. Combining ChME with a variety of IVA improves the sensitivity and selectivity of analysis. Carbon-paste electrodes modified with O-, N-, and S-containing compounds are commonly used in IVA for determining various metal ions [4]. The high sensitivity of the IVA method for determining metal ions with the use of ChME is ensured by combination of concentration in the form of a surface-bound complex with a modifier and subsequent quantitative electrochemical determination. Recently, macrocyclic compounds capable of forming complexes of the host–guest type have been used as organic reagents and CPE modifiers [5–7].

The expansion of the ChME range via immobilization of new organic reagents is of indubitable interest from the standpoint of development of IVA techniques. The presence in the molecule of an organic compound of several functional groups enabling different complexation mechanisms (chelate and guest–host) may improve the sensitivity of metal ion determination.

The present study is concerned with the possibility of determining a number of metal ions (Ni^{2+}, Co^{2+}, Cu^{2+}, Cd^{2+}, and Pb^{2+}) by inversion voltammetry with electrodes modified with *N*-diisopropoxythiophosphoryl-*N*'-phenyl thiourea, TPhTU, (**I**) and its crown-containing or open-chain analogs: *N*,*N*'-bis(diisopropoxythiophosphorylamidothiocarbonyl)-1,5-diamino-3-oxapentane (**II**), *N*,*N*'-bis(diisopropoxythiophosphorylamidothiocarbonyl)-1,8-diamino-3,6-dioxaoctane (**III**) and *N*,*N*'-bis(diisopropoxythiophosphorylaminothiocarbonyl)-1,10-diaza-18-crown-6 (**IV**):

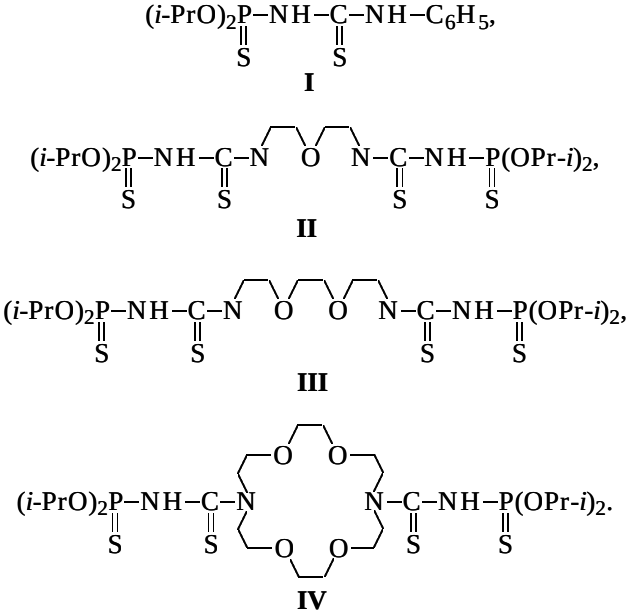

I

II

III

IV

1070-4272/02/7506-0919 $27.00 © 2002 MAIK "Nauka/Interperiodica"

Table 1. Parameters of voltammograms of oxidation and reduction of mono and bis-*N*-thiophosphoryl thioureas on a graphite electrode in acetone ($c = 5 \times 10^{-4}$ M)

Compound	$E_{1/2}$, V	i, μA	tan β, mV	ΔE_{ca}, mV	I_c/I_a	$\Delta\log i/\Delta\log v$*
			Oxidation			
I	0.96	8.5	60	60	0.92	0.51
	1.35	8.0	100	–	–	–
II	1.01	6.4	62	62	0.87	0.49
	1.40	6.0	80	–	–	–
III	1.06	6.2	62	63	0.85	0.52
	1.42	5.9	90	–	–	–
IV	0.89	6.1	59	61	0.82	0.54
	1.26	6.9	110	–	–	–
			Reduction			
I	–1.34	6.5	60	55	0.95	0.50

* (v) Rate of potential sweep.

Purposeful selection of organic reagents as ChME modifiers requires a knowledge of the chemical properties of TPhTM and crown-containing and open-chain *N*-thiophosphoryl thioureas, and also of the electrochemical activity of the ligands themselves and metal complexes on their base.

N-Thiophosphorylated thioureas belong to NH acids since they contain two acceptor groups, thiocarbonyl and thiophosphoryl, at the nitrogen atom. These groups draw the electron density off nitrogen, which markedly raises the mobility of hydrogen atoms. To evaluate the acid–base properties, potentiometric titration was performed in a water–ethanol medium and the dissociation constants were calculated using Gran's method [8]. Crown-containing and open-chain bisthiophosphoryl thioureas are weak dihydric acids with close pK_1 and pK_2 values: pK_1 8.5 and pK_2 9.3 for compound **II** and pK_1 9.2 and pK_2 10.2 for compound **IV**. Comparison of the acid properties of crown-containing and open-chain bisthiophosphoryl thioureas with the acidity of their mono analogue [pK_a 8.1 for compound **I**] shows that the macrocycle and the ethylene oxide fragment exert no significant influence on the acidity of the proton in the NH group.

The compound TPhTM forms with heavy metal ions complexes of composition ML_2 with the formation of a chelate site MS_4 [9]. The bisthiophosphoryl thioureas under consideration contain several functional groups, which leads to formation of complexes with composition M_2L_2. An X-ray structural analysis revealed that two molecules of a bidentate ligand form binuclear complexes with metal atom [10]. Spectral data (IR, ^{31}P and ^{1}H NMR), also indicating the formation of an M_2L_2 complex with two chelate sites MS_4, were presented in [10]. The influence exerted by the structure of ligand molecules on the stability of the corresponding complexes was studied for the example of complexes with cobalt(II). The stability constants of the complexes were determined by redox potentiometric titration in acetone, using a sulfide–disulfide reversible system [11]. The step constants $\log\beta_1$ of cobalt complexation with compounds **I**, **IV**, and **II**, calculated using the Bjerrum method, are, respectively, 5.4, 5.8, and 6.2. The data obtained suggest that the stability of complexes with bisthiophosphoryl thioureas somewhat exceeds that of the mono analogue. Introduction of a macrocyclic fragment into the TPhTM molecule enhances the specificity of the metal–ligand interaction and, correspondingly, raise the stability of the forming complexes. The most stable is the complex with compound **II**. The difference in structure between mono- and bisthiophosphoryl thioureas, and also between their complexes with metals, affects the parameters of their voltammograms.

The compound TPhTM oxidizes on a graphite electrode to form two waves (Table 1). The first wave corresponds to reversible transfer of a single electron. The electrochemical reversibility of the first wave was confirmed using several known diagnostic criteria [wave slope, tan β, (~59 mV) in the classical voltammogram; difference of the potentials of the cathodic and anodic peaks, $\Delta E_{ca} \approx 59$ mV; ratio of cathodic to anodic peak currents in the cyclic voltammograms, I_c/I_a, close to unity]. As done in [12], it may be assumed that the thiocarbonyl group is oxidized in the first stage; at the second wave potentials, products of electron transfer are oxidized further. The voltammograms of crown-containing and open-chain derivatives are identical and largely coincide with that of their mono analogue (Table 1). Apparently, electrooxidation schemes of mono- and bisthiophosphoryl thioureas are the same. The observed insignificant shift of $E_{1/2}$ into the anodic range of potentials can be accounted for by steric factors, and the decrease in current, by an increase in their molecular weight.

Among the *N*-thiophosphoryl thioureas considered here, only TPhTM is reduced on the graphite electrode in acetone at potentials of about –1.4 V (Table 1). As follows from the data of cyclic voltammetry, the electrochemical signal corresponds to reversible single-electron transfer and, in accordance with the results of [12], the electrode process corresponds to reversible reduction of the thiocarbonyl

Table 2. Parameters of voltammograms of oxidation and reduction of Co(II), Ni(II), and Cd(II) complexes with mono and bis-*N*-thiophosphoryl thioureas on a graphite electrode in acetone ($c = 5 \times 10^{-4}$ M)

Metal ion	Compound	$E_{1/2}$, V	i, μA	tan β, mV	ΔE_{ca}, mV	I_c/I_a	$\Delta\log i/\Delta\log v$
			Oxidation				
Co(III)	**I**	0.87	9.0	55	59	0.90	0.50
		1.04	17.0	62	63	0.87	0.55
		1.32	20.0	90	–	–	0.40
	II	0.76	21.5	40	38	0.95	0.55
		1.09	26.0	60	62	0.85	0.50
		1.38	11.0	110	–	–	0.45
	III	0.74	22.0	35	33	0.85	0.50
		0.98	24.0	63	64	0.97	0.54
		1.40	15.0	90	–	–	0.55
	IV	0.79	20.0	30	35	0.88	0.45
		1.13	19.6	65	61	0.81	0.48
		1.24	10.0	85	–	–	0.40
Ni(II)	**I**	0.85	10.0	55	58	0.87	0.45
		1.02	18.0	62	60	0.90	0.49
		1.27	21.0	95	–	–	0.52
	III	0.81	18.0	34	35	0.88	0.45
		1.01	22.0	60	62	0.95	0.55
		1.36	15.0	76	–	–	0.50
Cd(II)	**I**	1.15	24.0	60	65	0.85	0.55
		1.45	17.0	85	–	–	0.60
	III	1.11	19.0	65	66	0.9	0.44
		1.37	10.0	95	–	–	0.55
			Reduction				
Co(II)	**I**	0.55	6.0	–	–	–	0.88
		1.40	7.0	58	60	0.87	0.56
	II	0.56	9.5	–	–	–	0.78
	III	0.58	10.0	–	–	–	0.85
	IV	0.52	11.0	–	–	–	0.80
Ni(II)	**I**	0.74	5.0	–	–	–	0.75
		1.42	7.5	62	64	0.95	0.58
	III	0.78	12.0	–	–	–	0.86
Cd(II)	**I**	0.69	6.2	–	–	–	0.85
		1.45	8.0	65	62	0.87	0.60
	III	0.68	10.0	–	–	–	0.80

group. Bisthiophosphoryl thioureas are not reduced in the potential range in question (down to –1.8 V). Probably, the thiocarbonyl group in these compounds is reduced at more negative potentials. The difference in behavior between mono- and bisthiophosphoryl thioureas is due to the presence in the TPhTM molecule of a benzene nucleus whose π-electron-acceptor properties favor transfer of an electron to the ligand molecule and its delocalization. No effect of this kind is observed in the case of bisthioureas.

In electrooxidation of metal complexes, different numbers of waves can be observed, depending on the ligand nature. Table 2 presents parameters of voltammetric characteristics of metal complexes that could be isolated and whose structure could be studied [9, 10]. The results obtained in studying the electrochemical behavior of copper(II) complexes with mono- and bisthiophosphoryl thioureas were reported in [12]. According to cyclic voltammetry, the first wave is reversible and single-electron for Co(II) and

Ni(II) complexes with TPhTM. As a standard of single-electron transfer was used the oxidation current of a nickel complex with diethyl dithiocarbamate [13]. Commonly, Co(II) and Ni(II) complexes with a coordination site MS_4 are oxidized in the first stage to form particles in which metal is in the oxidation state +3. By analogy with the results of [13], it may be assumed that oxidation of Co(II) and Ni(II) complexes with TPhTM also follows the scheme

$$M(II)L_2 - e \rightleftarrows M(III)L_2.$$

Co(II) and Ni(II) complexes with bisthiophosphoryl thioureas, and also with their analogues, are oxidized in the first stage reversibly, with two electrons involved in the electrochemical reaction ($\tan\beta \approx 30$ mV) as a result of the binuclear structure of the complexes. The subsequent waves probably correspond to oxidation of the ligand bound in the complex, since their half-wave potentials are shifted to a more anodic region than the $E_{1/2}$ of the waves corresponding to oxidation of a free ligand. In electrooxidation of Cd(II) complexes with the compounds under consideration, waves are recorded in the range of potentials exceeding 1.0 V, in which the ligands themselves exhibit electrochemical activity. Therefore, by analogy with the electrochemical behavior of complexes with nontransition metals [13], it may be assumed that a coordinated ligand is involved in the reaction of electrochemical oxidation. All the reactions of electrooxidation of metal complexes are diffusion-controlled ($\Delta\log i/\Delta\log v \approx 0.5$).

In reduction of metal complexes with TPhTM, two waves are recorded in the voltammogram. The absence of waves in the anodic portions of the cyclic voltammograms of the complexes of Co(II), Ni(II), and Cd(II), considered here, in the first stage indicates that the reduction is irreversible. The first stage probably corresponds to a change in the metal oxidation state, M(II) $\rightarrow$ M(0), and the second manifests itself in the range of potentials corresponding to reduction of a free ligand and, therefore, is associated with reduction of the thiocarbonyl group. Since bisthiophosphorylated thioureas are electrochemically inactive in the working range of potentials, the electrochemical signals observed in voltammograms of metal complexes with these ligands can be attributed to a change in the oxidation state of the central atom in a complex. Comparison of wave heights for complexes with TPhTM and bisthiophosphoryl thioureas shows (Table 2) a twofold increase in signal intensity for the latter, which may be due to involvement in electron transport of two active centers (two central atoms in the M_2L_2 molecule), in contrast to a single center in the mono analogue. It should be noted that electroreduction of metal complexes with bisthiophosphoryl thioureas is complicated by adsorption, which manifests itself in that a strong adsorption peak is recorded. The rate constant of the electrode process ($\Delta\log i/\Delta\log v \approx 0.8$) points to an adsorption contribution to the limiting current value. In addition, voltammograms of the Cd(II) complex show an overvoltage of reduction of the supporting electrolyte, proceeding in this case at $E \approx -2.5$ V. For Co(II) and Ni(II) complexes, catalytic currents of hydrogen evolution are observed at $E > -1.4$ V, with the electrochemical signals having the form of narrow peaks exceeding in intensity 50–100-fold the level of the single-electron diffusion current and evolution of gas in the form of bubbles observed on the electrode surface.

The results obtained in studying the electrochemistry of complex compounds of Co(II) and Ni(II) with mono and bis-*N*-thiophosphoryl thioureas suggest that anodic voltammetry should be chosen for determining ions of these metals in view of the reversibility of the electron transfer, M(II) $\rightleftarrows$ M(III). In this case, inversion-voltammetric determination of Co^{2+} and Ni^{2+} ions involves concentration of metal ions on the surface of a modified electrode in the form of a complex with modifier under open-circuit conditions. As a supporting electrolyte for the concentration stage was chosen, to prevent formation of insoluble hydroxides, an ammonia buffer solution with pH 9–10. The electrochemical stage includes preliminary electrolysis at a potential of +0.7 V and potential sweep into the cathodic region. An inversion voltammogram shows peaks corresponding to reduction of Ni(III) and Co(III) complexes (Fig. 1a). The processes occurring at the electrode can be represented as (for ML_2):

$$M^{2+} + 2HL_{(ads)} \rightarrow M(II)L_{2(ads)} + 2H^+,$$

$$M(II)L_{2(ads)} - e \rightarrow M(III)L_{2(ads)},$$

$$M(III)L_{2(ads)} + e \rightarrow M(II)L_{2(ads)}.$$

The choice of the electrolysis potential E_e is based on the fact that the cathodic peak grows in intensity on shifting the potential into the anodic region to 0.7 V, and, upon further shift, oxidation of the ligand itself becomes possible, which enhances the chemical noise. The inversion current grows with increasing accumulation time t_a and reaches a limiting value after accumulation for 1 min.

It is undesirable to determine in a similar way Pb^{2+}, Cd^{2+}, and Cu^{2+} ions since they are oxidized at

more positive potentials and their signal may overlap with the signal associated with the oxidation of the ligand or supporting electrolyte.

Anodic voltammetry was chosen to determine Pb^{2+}, Cd^{2+}, and Cu^{2+} ions. The accumulation of these metal ions on a ChME was performed on the background of an acetate buffer solution with pH 4–5. A voltammogram was recorded after preliminary electrolysis at negative potentials. The analytical signal corresponds to oxidation of a metal to oxidation state (0). The metal is not bound in a complex and is adsorbed on the electrode surface after electrolysis of the surface-bound complex [12]. The processes occurring at the electrode can be represented (for ML_2) as:

$$M^{2+} + 2HL_{(ads)} \rightarrow M(II)L_{2(ads)} + 2H^+,$$
$$M(II)L_{2(ads)} + 2e \rightarrow M(0)_{(ads)} + 2L^-_{(ads)},$$
$$M(0)_{(ads)} - 2e \rightarrow M^{2+}.$$

Figure 1b shows an inversion voltammogram obtained in determining Pb^{2+}, Cd^{2+}, and Cu^{2+} on a CPE modified with compound **II**. The voltammogram was recorded in the ac mode under the following conditions: E_e = –1.0 V, time of electrolysis t_e = 20 s, potential sweep from –1.0 to 0.0 V, rate of potential sweep $v = 10^{-1}$ V s^{-1}.

The inversion currents are mainly determined by the stability of the forming complexes with the CPE modifier. It was found that for all the metal ions the compounds can be arranged in order of increasing inversion currents as **I** ≤ **IV** ≤ **II**, **III**. However, the differences between the currents are only slight. For example, the following currents were obtained in determining Ni^{2+} ions (μA): 96 (**I**), 100 (**IV**), and 105 (**II**), (**III**). Since use of bisthiophosphoryl thioureas as modifier does not lead to any significant increase in the inversion current, compared with the mono analogue, it may be concluded that complexes with approximately the same stability are formed, which is confirmed by the $\log \beta_1$ values presented above.

The choice of a supporting electrolyte in the accumulation stage is governed by the acid-base properties of ligands and metal ions. For example, in determining Pb^{2+}, Cd^{2+}, and Cu^{2+} ions, the maximum inversion currents were recorded in the case of accumulation in an acetate buffer solution in which these metals are in the form of aqua complexes, and in determining Co^{2+} and Ni^{2+} ions, in an ammonia buffer solution, in which the metal ions are in the form of soluble ammonia complexes. Changing the nature of the supporting electrolyte in the electrochemical stage

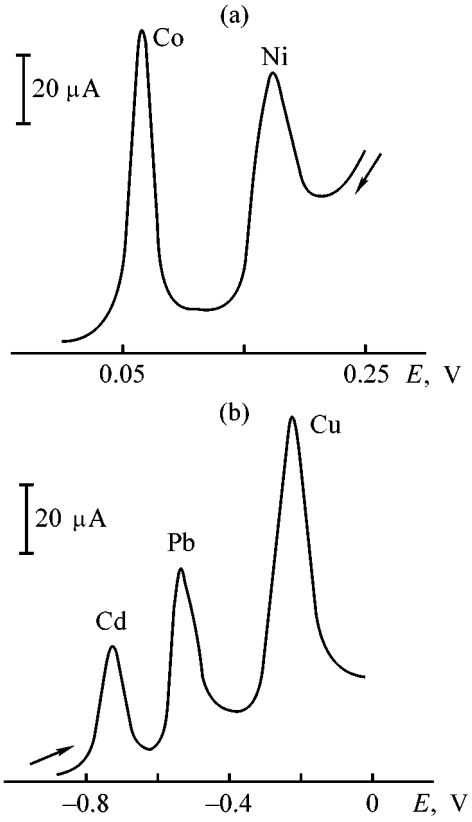

Fig. 1. Inversion voltammograms obtained on ChME with compound **II** on the background of a 0.1 M NaCl solution after stage of accumulation of (a) Co^{2+} and Ni^{2+} and (b) Pb^{2+}, Cd^{2+}, and Cu^{2+} ions. Concentration of metal ions 1×10^{-4} M. (*E*) Potential. Background buffer solution: (a) ammonia, pH 9.0; (b) acetate, pH 4.5.

leads to an increase in the degree of accumulation of any of the metals under consideration in the following order: $CH_3COO^- < ClO_4^- < NO_3^- < Br^- < Cl^-$. This is due to the fact that chloride anions are the best electron carriers among the anions in question.

The ability of compound **IV** to form not only chelate complexes with a coordination site MS_4, but also complexes of the guest–host type with a crown ether fragment manifested itself in inversion-voltammetric determination of Pb^{2+} ions. Changing the nature of a cation in the supporting electrolyte affects the analytical signal recorded. The inversion current obtained on the background of KCl (i = 195 μA) much exceeds that measured with NaCl as supporting electrolyte (i = 112 μA). In view of the competitive complexation, an inverse dependence would be expected, since the stability constants of metal complexes with the crown-compound diaza-18-crown-6 are larger in the case of potassium ions ($\log \beta_{NaL^+}$ = 0.1, $\log \beta_{KL^+}$ = 0.8) [5]. Probably, the effect of the electrolyte on the amplitude of the electrochemical signal

Table 3. Conditions of inversion-voltammetric determination of metal ions on CPE modified with compound **II**

Metal ion	Experimental conditions		E_p, V	c_{min}, M (mg l^{-1})	Maximum permissible concentration, mg l^{-1}
	accumulation stage	electrochemical stage			
Cu(II)	Acetate buffer solution, pH 4.5, t_a=60 s	0.1 M NaCl, E_e = –1.0 V, t_e = 20 s, E = –1.0…0.0 B	–0.15	3×10^{-8} (0.002)	0.1
Pb(II)			–0.56	9×10^{-9} (0.002)	0.1
Cd(II)			–0.75	5×10^{-8} (0.006)	0.01
Ni(II)	Ammonia buffer solution, pH 9.0, t_a = 60 s	0.1 M NaCl, E_e = –1.0 V, t_e = 20 s, E = 0.7–0.0 V	0.15	8×10^{-8} (0.005)	0.1
Co(II)			0.05	9×10^{-8} (0.005)	1.0

is due to the formation of a more stable heteronuclear complex with Pb^{2+} ions and alkali metal cation, by analogy with the data obtained previously for similar complexes with crown ethers [14].

A comparison of the voltammetric characteristics demonstrated that use of bisureas as CPE modifier does not lead to any significant increase in the current, compared with the case of TPhTM; however, bisthiophosphoryl thioureas are more chemically stable than their mono analogue and are electrochemically inert in a wider range of potentials, which depresses the chemical noise level. The best metrological performance ($S_r < 0.07$ in the concentration range studied) was observed with ChME based on compound **II**. A linear dependence of the peak current on the concentration of metal ions was observed in the range 1×10^{-7}–1×10^{-3} M.

Thus, inversion-voltammetric determination of the metal ions considered was done by oxidation or reduction of metal complexes adsorbed on ChME, after preliminary electrolysis. The conditions under which metal ions were determined by IVA are presented in Table 3. The results obtained demonstrate that the techniques proposed extend the range of determinable concentrations and make lower the detection limit c_{min}. The achieved c_{min} values are much lower than the maximum permissible concentrations (MPC).

EXPERIMENTAL

The procedure for determining heavy metal ions by inversion voltammetry includes the stages of concentration of metal ions in the form of a complex compound on the electrode surface and quantitative determination of the surface-bound complex by ac voltammetry. The metal accumulation was done from a solution in the presence of a supporting electrolyte under open-circuit conditions; the time of accumulation was chosen depending on the nature and concentration of a metal. Then the electrode was transferred into an electrochemical cell with another indifferent electrolyte for recording a voltammogram.

Voltammograms were recorded with a PU-1 polarograph, cyclic voltammograms were measured with a PI-50-1.1 potentiostat. A three-electrode cell was used in recording the voltammetric curves. As indicator, reference, and auxiliary electrodes served, respectively, a stationary glassy carbon electrode with apparent surface area of 0.01 cm^2 or modified CPE, saturated calomel electrode, and platinum wire.

The modified CPE was prepared from activated carbon, with Vaseline oil as binder and mono- or bisthiophosphoryl thiourea as modifier, taken in a 60 : 38 : 2 ratio. Chemically modified electrodes were prepared as described in [16]. The electrode surface was refreshed mechanically.

Compounds **I**–**IV** and their complexes with metals were synthesized by procedures described in [9–10]. Working solutions of mono- and bisthiophosphoryl thioureas under study and their complexes were prepared by dissolving their precisely weighed portions in a freshly distilled solvent.

Sets of metal ion solutions were prepared by diluting the initial standard solutions whose precise concentration was determined titrimetrically.

Acetone purified by the known methods [17] was used as solvent in studying the electrochemical properties. As indifferent electrolyte served a 0.1 M solution of $LiClO_4$ of chemically pure grade. Inversion voltammograms were recorded on the background of ammonia and acetate buffer solutions and on the background of NaCl, KCl, KNO_3, and Na_2SO_4 salts with concentration of 0.1–0.5 M.

Potentiometric measurements were carried out with a pH-150 pH meter. The pK values of the ligands were determined in an aqueous-alcoholic solution (80%)

with a glass electrode calibrated in aqueous-alcoholic solutions of HCl with known concentration [18]. The stability constants of metal complexes were found by measuring the potential of a platinum electrode in acetone at varied M : L ratio, using the following galvanic cell:

$$Pt \mid R'_2P(S)NHC(R'')S–SC(R'')HN(S)PR'_2,$$

$$R'_2P(S)NHC(S)R'', \ M^{2+}, \ LiClO_4 \mid KCl, \ AgCl \mid Ag.$$

CONCLUSIONS

(1) An inversion-voltammetric method for determining heavy metal ions (Ni^{2+}, Co^{2+}, Cu^{2+}, Cd^{2+}, and Pb^{2+}) on a carbon-paste electrode modified with mono- or bis-*N*-thiophosphoryl thioureas was developed.

(2) It was shown that conditions under which the electrochemical signal is recorded depend on the nature of metal. In the case of Ni^{2+} and Co^{2+} ions, peaks associated with reduction of complexes of metals in the oxidation state +3, obtained after preliminary electrolysis at E = 0.7 V, were used as analytical signals. In determining Pb^{2+}, Cd^{2+}, and Co^{2+} ions, peaks associated with oxidation of electrodeposited metal (0), obtained after electrolysis at E = –1.0 V of metal complex formed on a chemically modified electrode, were recorded.

(3) A comparison of the voltammetric characteristics demonstrated that use of a bisthiophosphoryl thiourea as modifier of the carbon-paste electrode does not lead to any significant increase in current, compared with the case of *N*- diisopropoxythiophosphoryl-*N*'-phenyl thiourea; however, in contrast to their mono analogue, bisthiophosphoryl thioureas are chemically more stable and electrochemically inert in a wider range of potentials. The best metrological performance was obtained on a chemically modified electrode based on *N*,*N*'-bis-(diisopropoxythiophosphoryl-amidothiocarbonyl)-1,5-diamino-3-oxapentane.

ACKNOWLEDGMENTS

The study was supported by the Russian Foundation for Basic Research (project no. 00-03-32 742).

REFERENCES

1. Budnikov, G.K., Maistrenko, V.N., and Murinov, Yu.I., *Vol'tamperometriya s modifitsirovannymi i ul'tramikroelektrodami* (Voltammetry with Modified and Ultramicroelectrodes), Moscow: Khimiya, 1993.
2. Brainina, Kh.Z., Neiman, E.Ya., and Slepushkin, V.V., *Inversionnye elektroanaliticheskie metody* (Inversion Electroanalytical Methods), Moscow: Khimiya, 1988.
3. Vydra, F., Štulik, K., and Julákova, E., *Rozpouštecí Polarografic a Voltametrie*, Praha: Nakladatelstvi technicke literatury, 1977.
4. Ulakhovich, N.A., Medyantseva, E.P., and Budnikov, G.K., *Zh. Anal. Khim.*, 1993, vol. 48, no. 6, pp. 980–998 .
5. *Host Guest Complex Chemistry Macrocycles. Synthesis, Structures, Applications*, Vogtle, V. and Weber, E., Eds., Berlin: Springer, 1985.
6. Yatsimirskii, K.B. and Lampeka, Ya.D., *Fizikokhimiya kompleksov metallov s makrotsiklicheskimi ligandami* (Physical Chemistry of Metal Complexes with Macrocyclic Ligands), Kiev: Naukova Dumka, 1986.
7. Shaidarova, L.G., Budnikov, G.K., and Ulakhovich, N.A., *Teoriya elektroanaliticheskoi khimii i metod inversionnoi vol'tamperometrii (TEAKh i IV – 2000)* [Theory of Electroanalytical Chemistry and Method of Inversion Voltammetry (TEAKh and IV-2000)], Tomsk, 2000, pp. 207–224.
8. Bykova, L.N., Mar'yanov, B.M., Papkova, E.N., and Chesnokova, O.Ya., *Zh. Anal. Khim.*, 1992, vol. 47, no. 6, pp. 1090–1095.
9. Zabirov, N.G., Galyautdinov, N.I., Shcherbakova, V.A., and Cherkasov, R.A., *Zh. Obshch. Khim.*, 1990, vol. 60, no. 6, pp. 1247–1251.
10. Zabirov, N.G., Brus'ko, V.V., Kashevarov, S.V., *et al., Zh. Obshch. Khim.*, 2000, vol. 70, no. 8, pp. 1294–1302.
11. Ulakhovich, N.A., Shaidarova, L.G., and Budnikov, G.K., *Zh. Neorg. Khim.*, 1987, vol. 32, no. 3, pp. 769–681.
12. Shaidarova, L.G., Gedmina, A.V., Ulakhovich, N.A., *et al., Zh. Obshch. Khim.*, 2002, vol. 72, no. 1, pp. 1–7.
13. Ulakhovich, N.A., Budnikov, G.K., and Fomina, L.G., *Zh. Obshch. Khim.*, 1980, vol. 50, no. 7, pp. 1620–1625.
14. Shaidarova, L.G., Glebov, A.N., Al'-Gakhri, M.A., *et al., Koord. Khim.*, 1993, vol. 19, no. 8, pp. 647–650.
15. Bespamyatnov, G.P., Bogushevskaya, K.K., Bespamyatnova, A.V., *et al., Predel'no-dopustimye kontsentratsii vrednykh veshchestv v vozdukhe i v vode* (Maximum Permissible Concentrations of Hazardous Substances in Air and Water), Leningrad: Khimiya, 1975.
16. Shaidarova, L.G., Zaripova, S.A., Tikhonova, L.N., *et al., Zh. Prikl. Khim.*, 2001, vol. 74, no. 5, pp. 728–732.
17. Weissberger, A. and Proskauer, E.S., *Organic Solvents. Physical Properties and Methods of Purification*, Riddig, J.A. and Toops, E.E., Eds., New York: Intersci., 1955.
18. Bates, R.G., *Determination of pH. Theory and Practice*, New York: Wiley, 1964.

Russian Journal of Applied Chemistry, Vol. 75, No. 6, 2002, pp. 926–930. Translated from Zhurnal Prikladnoi Khimii, Vol. 75, No. 6, 2002, pp. 944–948.
Original Russian Text Copyright © 2002 by Legin, Makarychev-Mikhailov, Kirsanov, Vlasov.

APPLIED ELECTROCHEMISTRY AND CORROSION PROTECTION OF METALS

Solid-Contact Polymer Sensors Based on Composite Materials

A. V. Legin, S. M. Makarychev-Mikhailov, D. O. Kirsanov, and Yu. G. Vlasov

St. Petersburg State University, St. Petersburg, Russia

Received February 5, 2002

Abstract—Ammonium and nitrate polymer sensors with solid contact, based on composites formed by a mixture of a membrane cocktail with metallic silver and silver chloride, were developed and studied for the first time.

Beginning with the appearance of an analytical technique employing chemical sensors (electrodes), the researchers' attention has been attracted to improvement of the design of the existing sensors, especially in their practical use. A topical issue in applied problems and industrial analysis is use of entirely solid sensors without liquid filling typical of many polymer sensors. Using an entirely solid contact gives a number of advantages over the conventional liquid contact, e.g., possibility of simple miniaturization of sensors, extended temperature range of their operation, arbitrary spatial position of the electrode in measurements, prolonged shelf life, etc.

The basic requirements to the solid contact for ion-selective electrodes were formulated in [1]: existence of a fast reversible reaction in which the carrier type is changed at the interface between the membrane and the current lead (as a rule, the membrane exhibits ionic conduction, and the current lead, electronic type) absence of side processes at this interface and buffering of the contact zone with respect to the potential-determining ion.

Meeting these requirements must ensure stable and reproducible signal of a solid-contact sensor (electrode) for a long time. Such a solid contact was created and has been successfully functioning for glass and crystalline membranes [2], but in the case of polymer film membranes, attempts to create a reversible solid contact have encountered severe difficulties. The first proposed were the wire electrode with a coating [3] and selectrode [4]. These sensors, however, show a noticeable drift of the standard electrode potential, which is due to charge transfer blocking at the interface between the membrane and the current lead. Of interest among recent advances are solid contacts based on electrically conducting polymers (polythiophene, polypyrrole, polyaniline) [5–7]. Conducting polymers with electron or hole conduction are to ensure a change of the type of carrier in transfer across the interface between the membrane and the solid contact and, as a result, make the standard potential of the sensor stable. By practical application of this idea showed that electrodes fabricated from conducting polymers possess noticeable redox sensitivity and are characterized by drift of the standard potential.

The approach to fabrication of a solid contact, taken in this study, consists in using composites for creating at the internal interface (membrane|contact) a chemically stable gradient layer with mixed ionic and electronic conduction. This could reduce the drift of the standard potential and ensure stable and reproducible sensor signal during a long period of time.

The aim of this study was to develop solid-contact potentiometric sensors based on membranes of plasticized polyvinyl chloride (PVC), which are reversible with respect to ammonium and nitrate ions. These two kinds of sensors were chosen in view of their wide occurrence and multiple fields of application. However, the method proposed for obtaining a solid contact with the use of gradient layers can be used for other kinds of sensors. The present study is concerned with such working characteristics of sensors as sensitivity, long-term stability of the standard potential, selectivity coefficients, and redox sensitivity. The method of electrochemical impedance spectroscopy was applied to determine, for the example of ammonium sensors, the contribution of the solid contact to the total resistance of a membrane.

The properties of solid-contact sensors are compared with those of ion-selective electrodes with internal liquid filling.

1070-4272/02/7506-0926 $27.00 © 2002 MAIK "Nauka/Interperiodica"

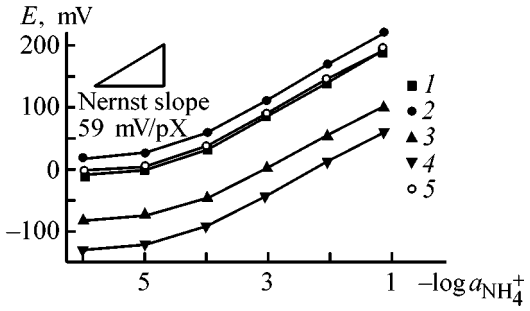

Fig. 1. Calibration plot for ammonium sensors. (*E*) Potential; the same for Fig. 4. (*1*, *2*) TK-1, (*3*, *4*) TK-2, and (*5*) standard electrode with liquid filling.

EXPERIMENTAL

The membranes studied were fabricated from reagents purchased from Fluka (Switzerland). All salts and organic solvents were of chemically pure grade. The solutions were prepared using twice-distilled water.

The composition of PVC-plasticized membranes for the ion-selective electrodes studied is given below:

Membrane	Component, wt %
NO_3^-	Tridodecylmethyl ammonium nitrate, 2 PVC, 33 Diethylhexyl cebacate, 65
NH_4^+	Nonactine, 1 Potassium tetra(*p*-chlorophenyl)borate, 0. PVC, 33 Diethylhexyl cebacate, 65.5

The sensor membranes were prepared by the standard procedure. Weighed portions of membrane components were placed in tetrahydrofuran (THF) and the mixture was stirred with a magnetic stirrer to complete dissolution. The cocktail obtained was poured in a weighing bottle with flat bottom and allowed to stand to complete evaporation of THF (~48 h). Discs 6 mm in diameter were cut out from the membrane obtained. A solid composite contact was deposited onto one side of the disc. The composite was composed either of the membrane material proper, dissolved in cyclohexanone, and metallic silver dispersed in this solution (henceforth TK-1) or of the membrane material with a mixture of Ag and AgCl dispersed in it (henceforth TK-2).

In depositing the composite material onto the membrane surface, a layer with mixed conduction, ionic because of the membrane formulation and electronic as a result of the presence of metallic silver, is formed. A current lead in the form of a copper wire was submerged in the formulation deposited onto the membrane. The assembly was left till complete evaporation of cyclohexanone, and then the membrane was glued into a plastic electrode case. Four sensors were fabricated for each of the two types of solid contacts and two conventional sensors with liquid filling. The numerical values of various electrode characteristics, reported in the present communication, are averaged over sensors of the same kind.

The potentiometric measurements were done with a galvanic cell

$$\mathrm{Cu}\,|\,\mathrm{Ag}\,|\,\underset{\downarrow}{\mathrm{AgCl,\ KCl_{sat}}}\,|\,\text{Solution under study}\,|\,\text{Membrane}\,|\,\text{Composite}\,|\,\mathrm{Cu}$$

The readings were taken with a multichannel electronic digital voltmeter with high input resistance. The stability and reproducibility of the standard potential, and also the sensitivity, were studied by periodically calibrating the sensors in solutions of salts of the potential-determining ion in the concentration range 10^{-6}–10^{-1} M. The selectivity coefficients were determined by the method of biionic potentials in 0.1 M solutions, in conformity with the IUPAC recommendations [8].

The redox sensitivity of the sensors was measured using a series of solutions containing the redox pair $K_3[Fe(CN)_6]/K_4[Fe(CN)_6]$ in ratios of 100/1, 10/1, 1/1, 1/10, and 1/100, The solutions were prepared on the background of 0.01 M of the potential-determining ion in order to model the real conditions of sensor operation. A platinum electrode was also used to compare the redox response.

The electrochemical impedance of the ammonium membranes was measured with computer-controlled Agilent Technologies instruments. The measurements on the membranes under study were carried out in two symmetric cells. In the first of these (liquid contact), both sides of a membrane were in contact with a 0.01 M ammonium chloride solution, and silver electrodes served as working electrodes. In the second cell, the electric contact between a membrane and the external electric circuit was effected by the composite layers under study, deposited onto both sides of the membrane.

A typical calibration curve is shown for the example of ammonium sensors in Fig. 1. A study of the sensor sensitivity demonstrated that the slope of the electrode function is, on the average, 55.4 ± 0.6 mV/pX for NH_4^+ sensors and 53.6 ± 0.5 mV/pX for NO_3^- sensors, irrespective of the contact type. The results obtained in studying the long-term stability of the sensors are presented in Figs. 2a and 2b in the form of the dependence of the slope on the service life of a sensor. Ammonium sensors exhibited stable performance for 7 months, after which the slope decreased by 6–7 mV (Fig. 2a). Probably, this is due to washing-out and onset of decomposition of the main membrane-active substance, nonactine. The slopes of the electrode functions of nitrate sensors increased somewhat during the first 2–3 weeks and then remained constant within experimental error during the entire time of experiment, for about 8 months (Fig. 2b).

The standard sensor potential varied during this time as follows (Fig. 3). During the first 15–20 days after the sensor fabrication, a drift of E^0 toward more negative values by up to 40–50 mV was observed, which is probably due to permeation of electrolytes through the membrane and occurrence of stabilization processes at the interface between the membrane and the solid contact. Then the potentials leveled off and changed only slightly during more than 5 months. In the subsequent 2 months of experiment, a somewhat wider scatter of E^0 values was observed for ammonium electrodes and a certain tendency toward a decrease in the standard potential for nitrate sensors. Interestingly, the E^0 scatter within a series of three identical electrodes was rather wide, being as large as 80 mV. In the course of time, the standard potentials became closer within a series and the E^0 scatter between different sensors of the same composition was no more than 20 mV. Between calibration measurements, two sensors of each type were stored in a 0.01 M solution of the salt of the potential-determining ion, and two sensors of each type, in air. It was found that storage in air is preferable for ammonium sensors, which ensured higher reproducibility of electrode characteristics in a regular calibration measurement. Apparently, this is due to relatively intensive washing-out of nonactine and ionic additive from a membrane stored in the solution. For nitrate solid-contact sensors, no significant difference in behavior between electrodes stored in air and in solution was observed. This may be due to the higher lipophilicity of the tridodecylmethyl ammonium cation and, consequently, to lower extent of its washing-out from the membrane in solution.

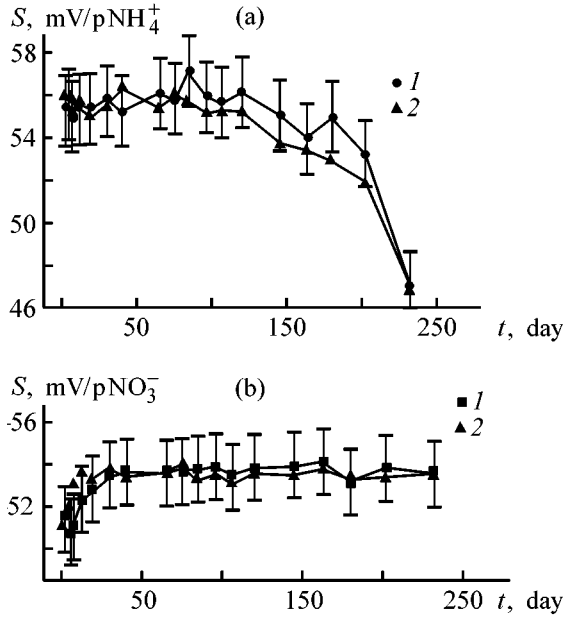

Fig. 2. Long-term stability of the slope S for (a) ammonium and (b) nitrate sensors. (t) Time; the same for Fig. 3. (*1*) TK-1 and (*2*) TK-2.

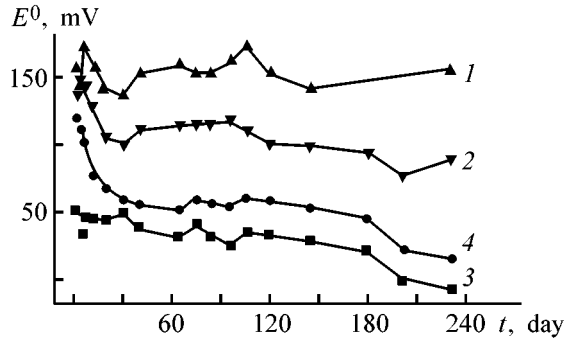

Fig. 3. Long-term stability of the standard potential E^0 of sensors. Sensor: (*1*, *2*) ammonium and (*3*, *4*) nitrate. (*1*, *3*) TK-1 and (*2*, *4*) TK-2.

The selectivity coefficients of sensors, found in this study, are independent of the type of contact, and the characteristics of the solid-contact sensors do not differ from those of the conventional electrodes with liquid filling. For ammonium sensors, $\log K^{pot}_{NO_3X}$ is -2.5 ± 0.1 for sodium ions, -0.83 ± 0.07 for potassium, -3.1 ± 0.2 for calcium, and -2.7 ± 0.2 for magnesium. For nitrate sensors, $\log K^{pot}_{NO_3X}$ is -1.73 ± 0.04 for the chloride ion, -0.55 ± 0.07 for the bromide ion, and -2.3 ± 0.1 for the sulfate ion. The selectivity coefficients of the solid sensors under study toward a number of interfering ions are in good agreement with the available published data, mainly concerning the sensors with liquid filling [9, 10].

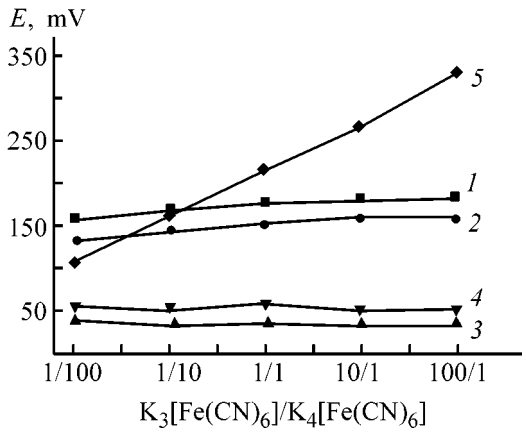

Fig. 4. Redox sensitivity of (*1*, *2*) nitrate sensors with different types of contact and (*3*, *4*) ammonium sensors in $K_3[Fe(CN)_6]/K_4[Fe(CN)_6]$ solution. (*1*, *3*) TK-1, (*2*, *4*) TK-2, and (*5*) response of a platinum electrode—theoretical function with a slope of 59 mV/pX.

It can be seen from Fig. 4 that the sensors developed show no noticeable redox sensitivity. In this regard they compare favorably with electrodes based on conducting polymers, which expands the field of their possible application. The absence of redox sensitivity is due to the fact the change in the type and parameters of conduction and carriers mainly occurs in the composite gradient layer at the internal interface of the membrane and does not affect the bulk properties of the material and the properties of the outer surface of the membrane.

The conductivity of ammonium membranes with liquid contact and composite solid contacts of different compositions is as follows:

Contact	$-\log \sigma_{298}$
TK-1 (metallic silver dispersed in the membrane cocktail)	6.7 ± 0.1
TK-2 (mixture of silver chloride and metallic silver, dispersed in the membrane cocktail.	6.83 ± 0.05
Liquid contact (0.01 M NH_4Cl solution, Ag/AgCl electrode)	6.80 ± 0.08

The total conductivity indicates that the solid contact does not affect noticeably the electrical resistance of the membrane. The lack of a polarization branch in the impedance locus points to an unhindered transport of charge carriers (electrons) at the interface between the membrane and the solid contact. It may be concluded that the value observed is largely the bulk resistance of the membranes.

With technique employed for depositing a composite layer from an organic solvent, the surface of the sensor membrane itself is to some extent dissolved. This leads to the formation of a gradient layer between the membrane and the current lead. It is within this gradient layer that a gradual transition from mainly ionic conduction in the bulk of the membrane to purely electronic conduction in the metallic current lead occurs. The impedance of the gradient layer does not exceed the bulk resistance of the membrane, and the electron (or hole) conduction induced in this layer is sufficient for stable operation of the composite material and the sensor as a whole. Thus, the use of composite layers enables an efficient change of conduction type near the contact and yields polymer sensors with long service life and stable analytical characteristics.

CONCLUSIONS

(1) Polymer (polyvinyl chloride) chemical sensors (ammonium and nitrate) with solid contact based on composites consisting of a membrane cocktail proper and metallic silver or a mixture of silver and silver chloride, dispersed in the membrane cocktail, have been developed.

(2) The slope of the electrode function is 55.4 ± 0.6 mV/pX NH_4^+ sensors and 53.6 ± 0.5 mV/pX for NO_3^- sensors, irrespective of the type of contact.

(3) The slope remains unchanged for 8 months for nitrate sensors and 6 months for ammonium sensors. The standard potentials change during 15–20 days after sensor membrane preparation by 40–50 mV and then remain stable for more than half a year.

(4) The sensors obtained show no redox sensitivity. The solid contact based on the composites proposed does not increase the electrical resistance of the membranes, with the conductivity remaining at the level $-\log \sigma_{298} = 6.8 \pm 0.1$ for the ammonium sensors. The solid contact technology developed in the study enables easy miniaturization of sensors and can be recommended for use in, e.g., flow-injection analysis.

ACKNOWLEDGMENTS

The authors are grateful to P. Viscor and J. Mortensen (Roskilde University, Denmark) for participation in organization and discussion of impedance experiments.

REFERENCES

1. Nikolskii, B.P. and Materova, E.A., *Ion-Selective Electrode Rev.*, 1985, vol. 7, no. 1, pp. 3–39.
2. Shul'ts, M.M., Pisarevskii, A.M., Volkov, S.E., *et al.*, *Fiz. Khim. Stekla*, 1981, vol. 7, no. 4, pp. 426–432.
3. Catrall, R.W. and Freiser, H., *Anal. Chem.*, 1971, vol. 43, no. 13, pp. 1905–1913.
4. Ruzicka, J. and Tjell, J., *Anal. Chim. Acta*, 1970, vol. 51, no. 1, pp. 1.
5. Bobacka, J., Lewenstam, A., and Ivaska, A., *Anal. Chim. Acta*, 1999, vol. 385, nos. 1–3, pp. 195–202.
6. Sun, B. and Fitch, P.G., *Electroanalysis*, 1997, vol. 9, no. 6, pp. 494–497.
7. Lindfors, T. and Ivaska, A., *Anal. Chim. Acta*, 2000, vol. 404, no. 1, pp. 101–110.
8. Umezawa, Y., Umezawa, K., and Sato, H., *Pure Appl. Chem.*, 1995, vol. 67, no. 3, pp. 507–518.
9. Wegmann, D., Weiss, H., Ammann, D., *et al.*, *Microchim. Acta*, 1984, vol. 3, no. 1, pp. 1–16.
10. Ma, S.C., Chaniotakis, N.A., and Meyerhoff, M.A., *Anal. Chem.*, 1988, vol. 60, no. 20, pp. 2293–2299.

Russian Journal of Applied Chemistry, Vol. 75, No. 6, 2002, pp. 931–934. Translated from Zhurnal Prikladnoi Khimii, Vol. 75, No. 6, 2002, pp. 949–952.
Original Russian Text Copyright © 2002 by Kamenev, Ostapenko, Kozerog, Skachkov.

APPLIED ELECTROCHEMISTRY AND CORROSION PROTECTION OF METALS

Conductivity of Contact Corrosion Layer at Interface between Current Lead and Active Paste in Lead Battery

Yu. B. Kamenev, E. I. Ostapenko, K. V. Kozerog, and Yu. V. Skachkov

Research Center, AOZT Elektrotyaga, St. Petersburg, Russia

Received October 4, 2001; in final form, March 2002

Abstract—The conductivity of the contact corrosion layer at the interface between the current lead and the active paste in a lead battery was studied.

The corrosion layer formed on the current lead surface plays an important part in battery operation. For example, it was shown in [1] that corrosive destruction of current leads may limit the service life of batteries to 1500 cycles; sag of the active paste, to 200–300 cycles; and low conductivity of the corrosion layer (CL) at the interface between the current lead and the active paste, to 20–30 cycles. Such a strong influence of the CL characteristics on the working capacity of a battery stems from the fact that, in the end, the entire current generated by the active paste passes through this layer. According to [1], the ratio between the surface area of the active paste and the contact surface area of the electrode is on the order of 10^6. Thus, any, even very small, change in the CL characteristics may produce a substantial effect. The most important characteristic of the CL is its electrical conductivity. It is known [2] that the critical value of the stoichiometric coefficient of the compound PbO_x is approximately 1.5. At lower values, an increase in the oxidation level leads to an insignificant rise in conductivity because of the higher defectiveness of the PbO crystal lattice as a result of its saturation with oxygen. At $x \approx 1.5$, the PbO lattice transforms into the PbO_2 lattice having higher electronic conductivity.

Another important characteristic is the rate of CL reduction ($PbO_2 \rightarrow PbO_x$) in discharge. Apparently, if this rate is high, the CL is rapidly reduced to a low-conducting oxide and the process of active paste discharge is markedly decelerated. If the rate of active paste reduction exceeds that of blocking layer formation, its utilization factor will be higher.

Design of low- or zero-maintenance batteries requires that their positive current leads should be made of alloys with low or zero content of antimony. This is due to the fact that antimony, characterized by relatively low overvoltage of hydrogen evolution, may accumulate at the negative electrode as a result of corrosion of the positive current lead and favor an increase in the gas evolution rate. The latter leads to limited applicability of the batteries in closed compartments not equipped with special ventilation systems and also makes more expensive the maintenance of batteries, involving their frequent filling-up with water.

It was shown in [3] that expenditure for maintenance of stationary batteries over their entire service life (10–15 years) is comparable with their original cost. In the case of sealed batteries, high rate of gas evolution is unacceptable because it leads to irreversible loss of capacity and shorter service life. However, lowering the content of antimony in the alloy impairs their mechanical and casting properties and markedly raises the CL resistance. Consequently, the content of antimony in the alloys can only be lowered in the case of their additional alloying.

The most promising alloying elements are Sn, As, and Ag. Such additives improve the mechanical characteristics of low- and zero-antimony alloys and also favor an increase in the conductivity of CL. The latter occurs for, at least, three reasons. First, these additives affect the structure of oxides in the CL through the formation of compounds of the type $Pb_{1-x}K_xO_2$, where K = Sb, Sn, As, Ag, characterized by increased electronic conductivity [4]. Second, they hinder PbO_2 reduction to poorly conducting PbO_x oxides with

1070-4272/02/7506-0931 $27.00 © 2002 MAIK "Nauka/Interperiodica"

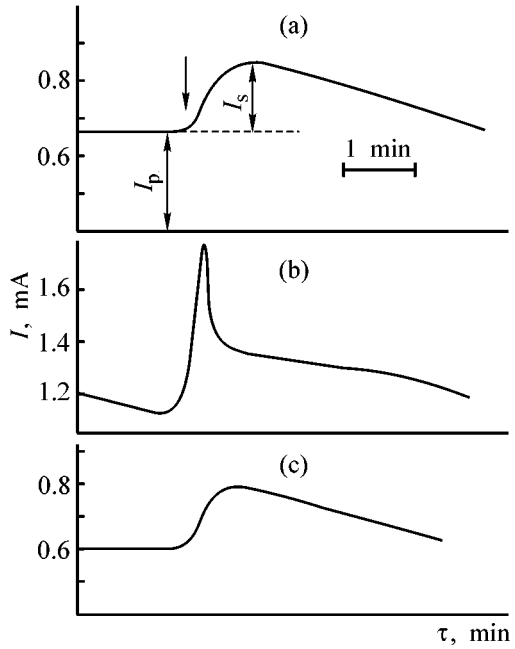

Fig. 1. *I*–τ curves obtained for (a) Pb–Sb–Sn and (b, c) Pb–Sb (5.5%) alloys. Time of keeping at a potential of 700 mV (min): (a, b) 3 and (c) 180.

$x < 1.5$ [4]. Finally, addition of tin or antimony favors formation in the CL of amorphous "gel zones" relieving the internal stresses in the layer, whose appearance is due to bulk changes in the transitions $PbO_2 \leftrightarrow PbO_x \leftrightarrow PbSO_4$. The build-up of stresses may lead to cracking of the CL and to an increase in its resistance because of the decreasing area of the conducting surface [1].

This study is concerned with the effect of tin additives on the conductivity of CLs formed on low- and zero-antimony alloys.

As objects of study served Pb–Sb (1.5–3.0%)–Sn 0.0–3.0% and Pb–Ca (0.07%)–Sn (0.5–1.5)% alloys and, for comparison, the widely used alloy Pb–Sb (5.5%) (named henceforth commercial).

Samples of the alloys under study were cast in the form of discs 20 mm in diameter. To obtain a mirror-smooth surface, ensuring a relatively constant specific surface area, the samples were dressed and compressed between two chromium-plated steel mirrors. After being deformed, the samples were annealed at 180°C. An area in the form of a circle 18 mm in diameter was selected on the mirror-smooth surface of a sample and the rest of the surface was coated with a nitrocellulose lacquer. Thus, all the samples had approximately the same surface area.

The conductivity of the oxide layer formed on the surface of test alloys was evaluated electrochemically. For this purpose, a sample was placed in a three-electrode thermostated cell containing 50 ml of sulfuric acid with density of 1.28 g cm^{-3}. The electrolyte was stirred with an MM2 magnetic stirrer. The electrolyte temperature of 30 ± 0.5°C was maintained with a UT-2 ultrathermostat. A mercury sulfate electrode was used as reference, and lead electrode, as auxiliary electrode. The samples were polarized with a PI-50-1 potentiostat with PR-8 programming unit. The current was recorded with a PDA-1 *X*–*Y* recorder.

An oxide film on the sample surface was formed in the potentiostatic mode in the potential range 1500–700 mV at a sweep rate of 1 mV s^{-1}. Then the electrode was kept for 3 min at the final sweep potential of 700 mV. Such a polarization ensured the formation of oxide films similar to those appearing on alloys of the positive current leads in deep discharge of batteries. After 3 min of potentiostatic polarization, 2 ml of a 0.02 M solution of $FeSO_4$ was introduced into the electrolyte under stirring, with a steplike increase in the anode current observed in the *I*–τ curve.

At a potential of 700 mV, the electrode is in passive state, to which corresponds a constant value of the passivation current I_p. Introduction of iron ions into the solution enables occurrence of the reaction $Fe^{2+} \rightarrow Fe^{3+} + e$ at the electrode. The rate of this reaction depends on the rate of electron transfer through the oxide film, i.e. is governed by the conductivity of this film. Thus, the conductivity of the oxide layer on the current lead surface can be judged from the amplitude of the step in the anode current, I_s, observed upon introduction of $FeSO_4$ into the solution, and the effect of the alloy composition on this conductivity can be studied. To eliminate the influence of the electrode area on the absolute value of the anode current step, the ratio of the currents, I_s/I_p, was used as a measure of the CL conductivity.

Figure 1a shows a typical *I*–τ curve obtained for Pb–Sb (1.5–3.0%)–Sn (1.5–3.0%) alloys. It can be seen that introduction of iron sulfate into the solution under stirring leads to the appearance of an anode current step. For the commercial alloy Pb–Sb (5.5%) the shape of the *I*–τ curve (Fig. 1b) is somewhat different from that for the curves obtained for low-antimony alloys. It can be seen from Fig. 1b that the passivation current does not become constant by the instant of $FeSO_4$ introduction into the solution, and a sharper peak of the anode current is observed after $FeSO_4$ introduction, with its subsequent rapid decrease. The occurrence of the peak in the anode current, which much exceeds the passivation current, indicates that addition of iron sulfate gives rise to an intensive ox-

idation process whose rate decreases abruptly, remaining approximately equal to the Fe(II) → Fe(III) process rate characteristic of ternary alloys.

The shape of the I–τ curve for the commercial alloy can be accounted for by the following mechanism of the occurring processes. It is known that the passivating film formed on lead–antimony alloys with high content of Sb is not so dense as that on lead [5]. Consequently, it would be expected that the passivating film formed upon polarization of the Pb–Sb (5.5%) electrode at the final sweep potential for 3 min has through pores allowing iron(II) ions to reach the alloy surface. In this case, the rate of the Fe(II) → Fe(III) process will be high because the hindrance to electron motion, present when this process occurs on the surface of oxide layers with denser structure, is lacking.

The accumulation of a considerable amount of Fe(III) ions in the CL pores leads to build up of positive charge in the solution, which must be compensated for by a counter flow of HSO_4^- anions. However, it is known that passivating layers formed at a potential of 700 mV have an outer sulfate layer creating a considerable diffusion resistance to motion of sulfate ions. To ensure the electroneutrality of the solution in pores, an electrophoretic flow of electrolyte, directed toward the solution, may appear. Possibly, the most mobile H^+ ions are the first to be removed from the pores. This leads to alkalization of the solution inside the pores and creates conditions for precipitation of a poorly soluble hydroxide $Fe(OH)_3$, which, in its turn, blocks the through pores and displaces the process of oxidation of iron(II) ions to the outer interface between metal oxide and the solution. In view of the limited electronic conductivity of PbO_x, the current decreases abruptly and the I_s value characterizes the conductivity of the given oxide.

The mechanism proposed is supported by the fact that, with the formation time of a passivating film on the Pb–Sb (5.5%) alloy increasing to 180 min, denser oxide layers are formed and no sharp anode current peak is observed in the I–τ curves after introduction of iron sulfate into the solution (Fig. 1c). In this case, the steady-state current is independent of the time of preliminary polarization.

Figure 2 (curve *1*) presents the dependence of the parameter I_s/I_p, characterizing the conductivity of the passivating layer, on the content of antimony in the binary alloy Pb–Sb. It follows from the figure that lowering the content of antimony in the Pb–Sb alloy leads to a pronounced decrease in the conductivity of oxide corrosion layers formed on the surface of these alloys. Such a decrease in the conductivity of

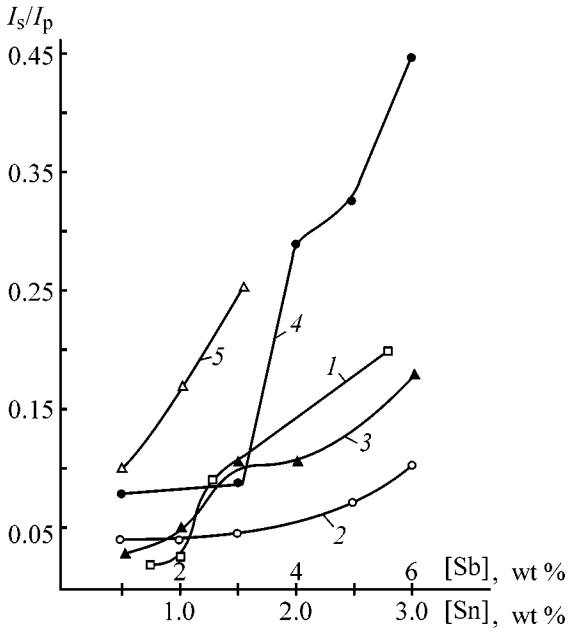

Fig. 2. I_s/I_p parameter vs. the content of (*1*) Sb and (*2–5*) Sn in Pb–Sb alloys. (I_p) Passivation current and (I_s) peak current. Alloy: (*1*) Pb–Sb, (*2*) Pb–Sb (1.5%), (*3*) Pb–Sb (2.0%), (*4*) Pb–Sb (2.5%), and (*5*) Pb–Ca (0.07%).

the contact layer makes necessary additional alloying of low-antimony alloys. Figure 2 (curves *2–4*) shows the dependences of the parameter I_s/I_p on tin content for low-antimony alloys (1.5–2.5% Sb). It can be seen that the dependences are rather complex, which is, in the first place, due to a change in the phase composition of the Pb–Sb alloys upon introduction of tin and to the corresponding change in the composition and structure of passivating films formed in oxidation. However, the principal, and practically important, feature is that addition of tin makes the electronic conductivity of oxide layers higher for all of the low-antimony alloys. For example, for a Pb–Sb (1.5%) alloy, the parameter I_s/I_p grows nearly twofold with the content of tin increasing from 0 to 3%. For the Pb–Sb (2.0%) and Pb–Sb (2.5%), the parameter in question grows approximately 6-fold. It is important to note that the Pb–Sb (2.5%)–Sn (2–3)% alloys have much higher conductivity than the commercial Pb–Sb (5.5%) alloy.

As already mentioned, the effect of tin on the conductivity of the corrosion layer formed on Pb–Sb alloys is due to its influence on the semiconducting properties of oxides. Tin ions are incorporated in the PbO_2 and PbO_x structure to form oxides of the spinel type, $Pb_{1-x}Sn_xO_2$, characterized by higher conductivity.

Moreover, it is known [4] that tin catalyzes the reactions:

$$PbO + (1 - x)O \rightarrow PbO_x,$$

$$PbO_x + (2 - x)O \rightarrow PbO_2,$$

which favors preservation of a high conductivity of oxides on the alloy surface in discharge of the positive active paste.

Figure 2 (curve *5*) shows the dependence of I_s/I_p on the content of tin for antimony-free Pb–Ca (0.07%) alloys. It can be seen that the parameter I_s/I_p grows with the content of tin increasing in the range 0.5–1.5%. At tin content exceeding 1%, the CL conductivity becomes higher than the conductivity of films formed on the commercial Pb–Sb (5.5%) alloy.

CONCLUSION

High CL conductivity can be achieved by introducing tin in amounts less than 2.0–2.5% for alloys containing less than 3% antimony and no less than 1.0% tin for antimony-free Pb–Ca (0.07%) alloys.

REFERENCES

1. Pavlov, D., *J. Power Sources*, 1995, vol. 53, pp. 9–21.
2. Douglas, D.L., Mao, G.M., and Collins, D.H., *J. Power Sources*, Oriel, Newcastle-upon-Tyne, 1973, vol. 4, pp. 561–567.
3. Hattori, S. and Kono, M., *ILZRO Project LE-276*, Rep. no. 5. Research Triangle Park, NC, USA, 1980.
4. Bui, N. and Mattesco, P., *J. Power Sources*, 1998, vol. 73, pp. 30–35.
5. Kamenev, Yu.B. and Rusin, A.I., in *Sbornik rabot po khimicheskim istochnikam toka* (Coll. of Works on Chemical Power Cells), Leningrad: Energiya, 1978, issue 13, pp. 3–6.
6. Pavlov, D. and Iordanov, N., *J. Electrochem. Soc.*, 1970, vol. 117, no. 9, pp. 1103–1109.

Russian Journal of Applied Chemistry, Vol. 75, No. 6, 2002, pp. 935–938. Translated from Zhurnal Prikladnoi Khimii, Vol. 75, No. 6, 2002, pp. 953–955.
Original Russian Text Copyright © 2002 by Ivanova, Boldyrev, Ivanov, Sokol'skii, Makeeva.

APPLIED ELECTROCHEMISTRY AND CORROSION PROTECTION OF METALS

Comparative Characteristics of Chemical Power Cells Based on MnO_2–Zn Systems with Various Manganese Dioxide Samples

N. D. Ivanova, E. I. Boldyrev, S. V. Ivanov, G. V. Sokol'skii, and I. S. Makeeva

Vernadskii Institute of General and Inorganic Chemistry, National Academy of Sciences of Ukraine, Kiev, Ukraine
National University of Aviation, Kiev, Ukraine

Received September 4, 2001; in final form, February 2002

Abstract—The relationship between the catalytic activity of various manganese dioxide samples and the electrical characteristics of chemical power cells with cathode materials on their base was studied.

Chemical power cells (CPC) with cathode mass based on manganese dioxide find widest application. About 70–80% of the total amount of power cells manufactured are CPCs with manganese dioxide. This can be attributed to the fact that CPCs of this kind have an almost horizontal discharge curve, are efficient in a wide temperature range, and their cathode material is less expensive as compared with other oxide materials. In addition, manganese dioxide is stable in aqueous and organic electrolytes, i.e., the 1.5–3.0-V electrochemical systems operate on its basis.

CPCs predominantly employ electrolytic γ-manganese dioxide (EMD-2), since it is more active as compared with other modifications [1].

The wide use of this compound in CPCs brings forth the problem of raising its activity, in particular, via directional disordering of the manganese dioxide structure. All other conditions being the same, the most active compounds are those whose structure is characterized by a larger number of defects [2–4], nonstoichiometric compounds among them, e.g., MnO_x ($1.7 < x < 2$) [1].

The aim of this study was to determine how the electrical characteristics of CPCs depend on the catalytic activity of various samples of manganese dioxide. In this connection, we studied various samples of this compound, differing in the preparation procedures, for the electrochemical system manganese dioxide–zinc.

EXPERIMENTAL

We studied the following manganese dioxide samples: synthesized electrochemically: no. 1, from fluorine-containing electrolytes (EMD_u) [5]; no. 2, from sulfate electrolyte (EMD-2), Georgia, OST (All-Union Standard) 6-22-34–76; and chemically: no. 3 (CMD_p) at Pridneprovskii chemical plant, TU (Technical Specifications) 14312708, 174–94; and no.4 (CMD) of special-purity grade.

Chemical analysis was carried out by the known procedures. The total manganese was determined in the samples by redox titration with $KMnO_4$. The percentage of Mn^{4+} was estimated using oxalic acid. The content of manganese(II) was determined by the procedure given in [6]. The difference between the total manganese and the content of manganese (IV) [after correction for content of manganese(II)] corresponded to the experimental content of manganese(III) ions [7]. The data on the content of manganese ions were given in terms of MnO_2, Mn_2O_3, and MnO; the x value was calculated for all the samples from the content of differently charged manganese ions in a sample under study [8]:

$$x = \frac{2 + 1.5R}{1 + R}, \quad R = \frac{[Mn^{3+}]_s^1}{[Mn^{3+}]_s^1}.$$

We carried out electrochemical studies in 9 N aqueous solutions of analytically pure KOH at 18–20°C. Pellets of diameter 4 mm served as working electrodes.

The weighed portions for preparing cathode samples were chosen in such a way that the sample thickness was almost the same (0.55 ± 0.02 mm). The electric contact with the pellets was effected by pressing

[1] In terms of Mn_2O_{3s}, MnO_{2s}.

1070-4272/02/7506-0935 $27.00 © 2002 MAIK "Nauka/Interperiodica"

Table 1. Composition of manganese dioxide samples and their catalytic activity

Sample no.	$MnO_{2\,total}$	MnO	Mn_2O_3	MnO_2	$k \times 10^{-5}$, s^{-1}
	wt %				
1	90.5	0.9	17.9	81.6	21.0
2	94.0	0.6	7.2	90.0	10.0
3	99.7	0.8	2.5	96.6	18.1
4	99.7	–	2.5	98.3	3.0

Table 2. Electrolytic reduction of manganese dioxide samples (sweep rate 2 mV s^{-1})

Sample no.	I (mA cm^{-2}) at indicated E, mV		
	50	–50	–150
1	0.12	0.20	0.26
2	0.06	0.10	0.14
3	0.12	0.20	0.30
4	0.01	0.02	0.06

a pellet with a constant force to a current lead made of 1Kh18N10T stainless steel. The case of this device was made of fluoroplastic.

Polarization measurements were carried out in a standard cell with a platinum auxiliary electrode of area 4 cm^2. The electrode potential was measured relative to a mercury oxide reference electrode in the same solution. The studies were performed on a PI-50-1 potentiostat with an LKD-4-003 XY self-recorder. Each measurement was done with a new pellet. The reproducibility of the experiments was not worse than 15–20 mV. The content of hydroxide groups was determined by thermogravimetry on an MOM derivatograph (Hungary) with an Al_2O_3 reference and heating in air within the range 20–600°C. To estimate the catalytic activity, we used the model reaction of hydrogen peroxide decomposition [9], readily occurring in aqueous medium at room temperature. We studied the hydrogen peroxide decomposition by gasometry. The volume of released oxygen was recalculated to the normal conditions. A weighed portion of a manganese dioxide sample under study was 10 mg, the concentration of hydrogen peroxide (4.92 M) was determined by titration with 0.1 N solution of potassium permanganate. The catalytic activity of the samples was evaluated by the reaction rate constant determined graphically in accordance with the equation

$$W = kc^n,$$

where W is the reaction rate, k is the rate constant, and n is the reaction order.

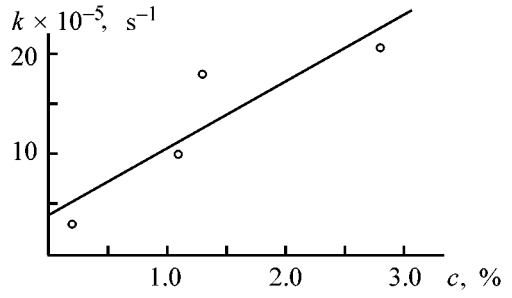

Fig. 1. Catalytic activity k in the model reaction of hydrogen peroxide decomposition vs. concentration c of hydroxy groups on the surface.

We determined the electrical characteristics on model CPCs of 1142 type. The cathode mass consisted of manganese dioxide (85%), an electrically conducting component (10%), and a binder (5%). We prepared the model CPCs by the standard procedure. The discharge characteristics were recorded at external loads of 5.6, 1.0, and 0.3 kΩ.

The data on the composition of the samples and their catalytic activity are given in Table 1. The reaction of hydrogen peroxide decomposition is first-order for all the samples under study. The highest catalytic activity is observed for the manganese dioxide sample obtained electrochemically from a fluorine-containing electrolyte, and the lowest, for the β-modification of manganese dioxide with stoichiometric composition (sample no. 4).

It is known that the catalytic activity is largely determined by the concentration of atomic defects (charge carriers) and their mobility [1]. This accounts for the observed relationship between the catalytic activity and the concentration of surface hydroxy groups, which fix defects of the Mn^{n+}/Mn^{n+1} type. In this case, differently charged Mn^{3+} and Mn^{4+} ions are present in the lattice at the same crystallographic positions [4, 6] (Fig. 1).

It should be noted that the total number of OH groups in the samples of electrochemically synthesized manganese dioxide, especially in sample no. 1 (5–7%), is much greater than that in sample no. 2 (2–3%). The catalytic activity of sample no. 1 is also higher. A correlation is observed between the catalytic

and electrochemical activities. We estimated the electrochemical activity by the current of manganese dioxide electrolytic reduction in the alkali medium at certain potentials (Table 2). The first portion of the *I–E* plot characterizes the electrolytic reduction of manganese dioxide on the electrode surface. Indeed, the rate of the process is in this case proportional to the catalytic activity of manganese dioxide (Fig. 2).

Sample nos. 1 and 3 are the most active. In order of increasing catalytic and electrochemical activity the samples under study can be arranged as follows: nos. 1, 3 > no. 2 > no. 4.

These data are in agreement with the electrochemical characteristics of real chemical power cells. Noteworthy is the possibility of achieving high current densities (5 mA cm^{-2}) in CPCs with cathode material based on manganese dioxide no. 1. The chemical power cell can operate under severe conditions, i.e., at a smoll external ohmic load resistance, which virtually does not occur with other samples and is impossible with sample no. 4.

It follows from these data that an increase in the number of defects in the crystal lattice of manganese dioxide makes higher the catalytic and electrochemical activity, which allows the rate of the electrochemical process to be raised essentially.

Sample no. 3, produced by Pridneprovskii chemical plant, is rather close to sample no. 1 in its characteristics. Since the chemical method of manganese dioxide synthesis is substantially less expensive than the electrochemical method, and the plant can produce manganese dioxide in any quantities (it works on the basis of the largest Nikopol deposit of MnO_2), we should pay attention to this sample. By modifying this product to a certain extent, we obtained a cathode material which is highly competitive with the best samples of manganese dioxide, including foreign analogs. After modification, its capacity exceeds that reported in the advertising brochures of the leading companies, being 105 mA h for the same cell type (for comparison, the capacity of LR 43 cells manufactured by Toshiba is 80 mA h, as also that of Varta cells).

The discharge characteristics of model Zn–MnO_2 cells are presented in Fig. 3. The curves for sample nos. 2 and 3 are measured after modification. Sample no.1 shows the maximal height of the discharge plateau and the longest discharge time because of its defective structure. The chemical modification as a method for disordering the structure further allowed, in accordance with the concept mentioned above, improvement of the characteristics of CPCs with cathodes made of samples nos. 2 and 3 by 15–20%.

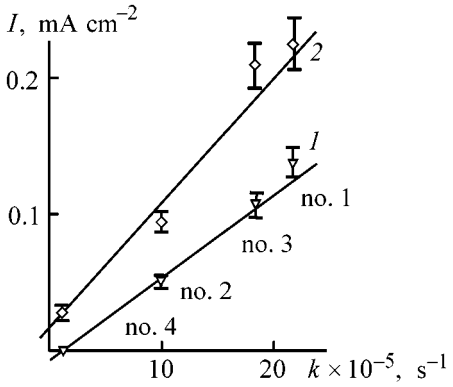

Fig. 2. Current *I* in the initial stage of electrolytic reduction vs. the catalytic activity *k* of manganese dioxide samples under study at $V = 20$ mV s^{-1}. Potential (mV): (*1*) +50 and (*2*) –50.

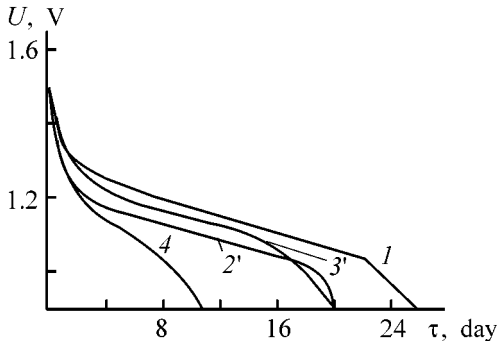

Fig. 3. Discharge characteristics of MnO_2–Zn cells at a load of 5.6 k for the manganese dioxide samples under study. (*U*) Voltage and (τ) time. Curves *1* and *4* correspond to, respectively, sample nos. 1 and 4; and *2'* and *3'*, to modified sample nos. 2 and 3.

CONCLUSIONS

(1) The catalytic activity of manganese dioxide can be used to characterize it as a starting material.

(2) A satisfactory correlation is observed between the catalytic and electrochemical activities of the cathode materials for chemical power cells.

(3) The expediency of using modified chemical manganese dioxide in chemical power cells based on the Zn–MnO_2 system is demonstrated.

REFERENCES

1. Ivanova, N.D., Ivanov, S.V., Boldyrev, E.I., and Mishchenko, A.B., *Zavisimost' electrokataliticheskikh svoistv dioksida margantsa ot ego strukturnykh parametrov* (Electrocatalytic Properties of Manganese Diox-

ide in Relation to Its Structural Parameters), Available from VINITI, 1987, Moscow.

2. Ivanova, N.D., Filatov, K.V., Boldyrev, E.I., *et al.*, *Dokl. Akad. Nauk Ukrainy*, 1992, no. 11, pp. 136–139.
3. Ruetschi, P. and Giovanioli, R., *J. Electrochem. Soc.*, 1988, vol. 135, no. 11, pp. 2663–2669.
4. Brenet, J., *J. Power Sources*, 1979, vol. 4, no. 2, pp. 183–189.
5. Ivanova, N.D., Boldyrev, E.I., Pimenova, K.N., *et al.*, *Zh. Prikl. Khim.*, 1998, vol. 71, no. 7, pp. 1209–1211.
6. *Metody chimicheskogo analiza materialov i polufabrikatov, primenyaemykh v istochnikakh toka* (Methods for Chemical Analysis of Materials and Semi-finished Products Used in Power Cells), Moscow, 1965.
7. Parida, K.M., Kanungo, S.B., and Sant, B.R., *Electrochim. Acta*, 1981, vol. 26, no. 3, pp. 435–443.
8. Kozawa, A. and Yeager, J.F., *J. Electrochem. Soc.*, 1968, vol. 115, no. 10, pp. 1003–1007.
9. Zhabrova, G.M., Roginskii, S.Z., and Oranina, E.A., *Zh. Obshch. Khim.*, 1954, vol. 24, no. 1, pp. 10–18.

Russian Journal of Applied Chemistry, Vol. 75, No. 6, 2002, pp. 939–941. Translated from Zhurnal Prikladnoi Khimii, Vol. 75, No. 6, 2002, pp. 956–958.
Original Russian Text Copyright © 2002 by Nersisyan, Nedezhina, Ten'kovtsev, Khailova.

APPLIED ELECTROCHEMISTRY AND CORROSION PROTECTION OF METALS

Electrolyte Redistribution in Sealed Nickel–Cadmium Batteries with Combined Electrode Design in the Course of Their Prolonged Operation

E. P. Nersisyan, D. S. Nedezhina, V. V. Ten'kovtsev, and I. V. Khailova

OAO Research Design and Technological Battery Institute Istochnik, St. Petersburg, Russia
St. Petersburg State Technical University, St. Petersburg, Russia

Received December 19, 2001

Abstract—Studies of the electrolyte redistribution in a sealed nickel–cadmium battery with combined electrode design, fabricated using the separation fabric recommended for replacing the previously used and presently laid off perchlorovinyl fabric, were carried out.

A specific feature of the design of sealed nickel–cadmium batteries widely used in various fields of technology is the strict limitation on the amount of electrolyte and the use of a fabric woven from alkali-resistant polymer fibers as separator material. These design features ensure relatively free transport of oxygen evolved in charging at the surface of the cadmium electrode, with its subsequent ionization. In this connection, a number of requirements are imposed on the separator material, which ensure, together with good gas permeability, a uniform distribution of the electrolyte throughout the battery. Unfortunately, alkali-resistant polymer fibers that can be used to fabricate the separator are, as a rule, highly hydrophobic. One of the best separator materials is that based on perchlorovinyl fibers, which show good performance in batteries for various purposes. However, the termination, for environment protection reasons, of the industrial manufacture of perchlorovinyl fibers required that a new separator material with characteristics close to those of the perchlorovinyl fabric should be created. As a result of a series of experimental-technological studies [1], a polypropylene-based separator materials has been developed, whose characteristics are the closest to those of the previously manufactured separator based on perchlorovinyl fibers (Table 1), although the material developed is inferior in its hydrophilicity to the perchlorovinyl material.

This communication presents the results obtained in studying the electrolyte redistribution in batteries with separator made of polypropylene separator fabric of the 5254–96 brand [TU (Technical Specification) 8378-476-36545028–99) in the course of their prolonged operation.

EXPERIMENTAL

The investigation was performed on NKGK-90SA sealed nickel–cadmium batteries having, in addition to the working electrodes, also an auxiliary gas-diffusion oxygen electrode made of activated carbon and connected to the cadmium electrode. All the batteries were equipped with pressure sensors limiting the battery charging on an increase of the internal oxygen pressure to 1.5 atm.

The content of electrolyte in the separator was evaluated by measuring the content of alkali at four

Table 1. Comparative characterization of separator fabrics

Parameter	Fabric	
	raised chlorine 86009 brand	polypropylene brand 5254–96
Thickness, mm, under pressure of 1000 g cm^{-2}	0.32–0.45	0.38–0.45
Electrolyte retention, g cm^{-2}	0.033–0.047	0.031–0.033
Relative electrical resistance	2.0–2.6	2.0–2.7

1070-4272/02/7506-0939 $27.00 © 2002 MAIK "Nauka/Interperiodica"

Table 2. Basic parameters of batteries after different times of operation*

N**	C, A h	Open-circuit voltage, V	R, $\Omega \times 10^{-4}$	KOH content, g				Σ KOH, g
				separator	edge	spacer	carbon	
6	112.0	1.21	6.5	12.8	5.7	0.6	4.2	23.3
25	117.0	1.20	6.5	13.3	5.2	1.3	8.3	28.0
100	118.0	1.20	7.5	11.9	4.4	0.6	10.4	28.7
250	111.0	1.25	7.5	5.1	2.7	1.0	15.0	23.8
400	117.0	1.25	6.9	4.3	1.9	1.0	20.5	27.7

* Originally, 380 g of electrolyte containing 102 g of alkali in terms of KOH was poured in the battery; mass of dry carbon 16 g.
** N is the number of cycles.

levels of the separator material along its height. Simultaneously, the content of alkali in the separator edge projecting beyond the electrode plates, in the spacer of separator fabric separating the plate unit from carbon, and in the carbon itself was monitored.

Balance calculations of the content of electrolyte in terms of potassium hydroxide were carried out using data obtained in analyzing the separator material. The analysis was made by the classical titrimetry, which allows simultaneous determination of the total alkali content and degree of carbonization [2].

The content of lithium hydroxide, which is also introduced into the electrolyte, was found by a conductometric method specially developed for this purpose [3].

Table 2 and Fig. 1 present data that allow complete characterization of battery parameters in different stages of operation.

To electrical parameters of the battery belong: discharge capacity C (A h) of the battery to a voltage of 1.0 V after its charging under control of pressure sensor; open-circuit voltage of a battery discharged to 1.0 V; and the ohmic component R of the internal resistance of 50%-charged battery.

As follows from the data obtained, intensive electrolyte redistribution between the separated plate unit and dry carbon occurs in the first cycles. In further operation, the electrolyte gradually flows down into the carbon, with, however, the relative redistribution of alkali over the height of the separator material remaining virtually unchanged, which indicates a constant electrolyte composition as regards the total alkali (in terms of KOH) (Fig. 2).

The process of carbonization is interrupted in those parts of the separator, which are not in contact with the electrodes by 25th cycle (Fig. 3). The content of carbonates in the separator material lying higher than the plate unit is markedly higher. The rise in carbonization of the electrolyte on the spacer terminates in further cycling, and the carbonization even decreases at the separator edge. In the main parts of the separator, which are in contact with the working electrodes, the increase in the degree of carbonization of the carbon and the separator occur in parallel. Simultaneously with the drainage of the electrolyte into carbon, accumulation of lithium compounds is ob-

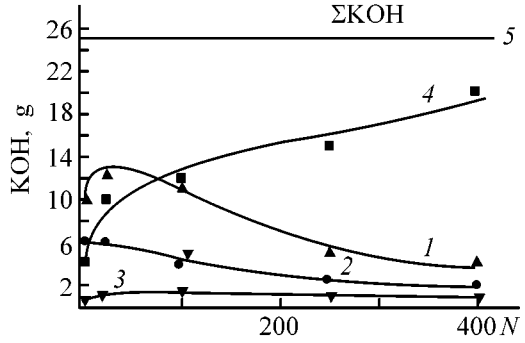

Fig. 1. Balance redistribution of the total alkali ΣKOH (with the exception of the amount of electrolyte contained in working electrodes) in prolonged cycling of the battery. (KOH) Content of KOH in the samples under study and (N) number of cycles. (*1*) Separator, (*2*) edging, (*3*) spacer, (*4*) carbon, and (*5*) sum total.

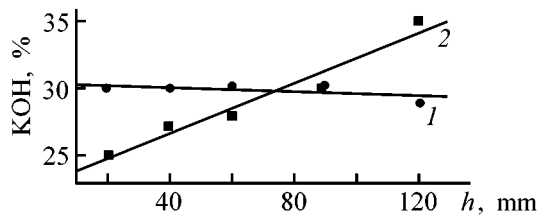

Fig. 2. Electrolyte distribution along the separator height h with respect to the total mass at different times of cycling. (KOH) Content of KOH relative to its total content. Number of cycles: (*1*) 25 and (*2*) 250.

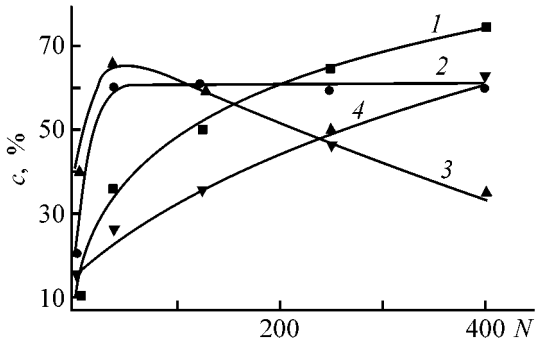

Fig. 3. Degree of electrolyte carbonization in different parts of a battery subjected to prolonged cycling. (*c*) Content of carbonates and (*N*) number of cycles. (*1*) Separator, (*2*) edging, (*3*) spacer, and (*4*) carbon.

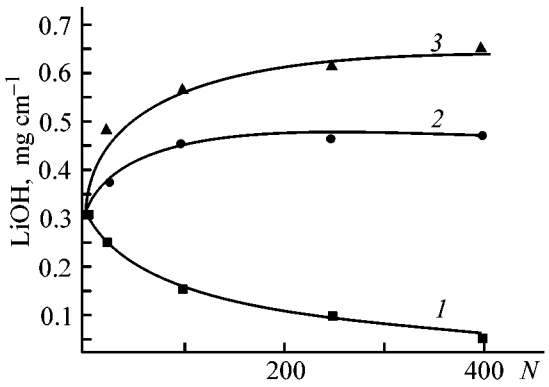

Fig. 4. LiOH content in different layers of the separator in prolonged cycling of a battery. (*N*) Number of cycles. (*1*) Top, (*2*) mid part, and (*3*) bottom.

served in the lower parts of the separator (Fig. 4). The mass and composition of the electrolyte in carbon, determined to within 5%, suggest that lithium compounds accumulate in the auxiliary electrode. Compared with LiOH content in the electrolyte filling the battery in its fabrication (~10% in terms of alkali), the content of LiOH in carbon increases dramatically.

The accumulation of lithium compounds in the bottom part of the separator and in the carbon is due to low solubility of lithium carbonate, which falls with increasing temperature. It is known that warming-up of a battery, associated with the intensive operation of the carbon electrode, is observed just in the bottom part of a battery.

The investigation performed indicates that prolonged operation of a sealed nickel–cadmium battery under terrestrial conditions leads to drainage, under the action of the gravity force, of the electrolyte in the separator and accumulation of the alkali in the carbon. Special additional studies of batteries exhibiting a dramatic decrease in capacity demonstrated that the critical mass of electrolyte in the separator, at which the internal resistance increases, is lower by approximately a factor of 10 than the initial value. For example, a test sample with 2 times smaller amount of electrolyte, which lost half the initial capacity by 130th cycle, had an internal resistance 10 times higher that the common value [73×10^{-4} Ω against $(6.5–7.5) \times 10^{-4}$]. Visual inspection demonstrated that the separator is virtually dry. At its edges, a large amount of salts (carbonates) is accumulated. An analysis revealed that the total content of alkali in the separator is, in terms of KOH, 2.6 g instead of 25 g (standard value for an efficiently operating battery; Table 2).

Under zero-gravity conditions, phenomena of this kind cannot be so pronounced. Presumably, this is the reason why the battery that operated at the Mir space station for five years retained both its initial electrical parameters and its chemical composition [4].

CONCLUSIONS

(1) Balance calculations of the electrolyte distribution in an NKGK sealed battery fabricated using a new separator material—woven polypropylene, were carried out.

(2) It was shown that the electrolyte mass is preserved (to within 5%), being only redistributed among the separator and carbon. Li^+ ions accumulate in carbon and lower parts of the separator in the form of a poorly soluble carbonate. The maximum extent of carbonization is observed at those parts of the separator, which are not in contact with the working plates.

(3) The electrolyte concentration (total alkali in terms of KOH) is not changed noticeably in prolonged operation of a battery.

REFERENCES

1. Ivanova, N.V., Nersisyan, E.P., and Ten'kovtsev, V.V., *Zh. Prikl. Khim.*, 2000, vol. 73, no. 4, pp. 584–587.
2. *Analiticheskaya khimiya: Kolichestvennyi analiz* (Analytical Chemistry: Quantitative Analysis), Moscow: Khimiya, 1972.
3. Morozova, I.V., Ten'kovtsev, V.V., and Nadezhina, L.S., *Zh. Prikl. Khim.*, 1999, vol. 72, no. 2, pp. 220–222.
4. Ten'kovtsev, V.V., Nadezhina, L.S., Nersisyan, E.P., and Morozova, I.V., *Zh. Prikl. Khim.*, 2000, vol. 73, no. 6, pp. 929–934.

Russian Journal of Applied Chemistry, Vol. 75, No. 6, 2002, pp. 942–945. Translated from Zhurnal Prikladnoi Khimii, Vol. 75, No. 6, 2002, pp. 959–962.
Original Russian Text Copyright © 2002 by Zhizhkun, Chernaya, Trusov.

CATALYSIS

Liquid-Phase Heterogeneous Oxidation of Hydroxypivalaldehyde with Oxygen in Alkaline Aqueous Solution in the Presence of Supported Palladium Catalyst

S. V. Zhizhkun, S. S. Chernaya, and S. R. Trusov

Riga Technical University, Riga, Latvia

Received July 10, 2001; in final form, February 2002

Abstract—The kinetics of a model reaction of hydroxypivalaldehyde oxidation with molecular oxygen in alkaline aqueous solution in the presence of 4% Pd/Al_2O_3 was studied with the aim of searching for promising heterogeneous catalysts for *D*-glucose oxidation.

Previously [1–3] we have shown that *D*-glucose can be rapidly and selectively oxidized with molecular oxygen in the presence of sodium nitrite in strongly acidic aqueous solutions. *D*-Gluconic or *D*-glucaric acid is formed, depending on the conditions of catalytic oxidation. Although the oxidation in the presence of sodium nitrite is highly selective, a search for catalysts allowing this process to be performed on the industrial scale is a topical problem. Oxidation of organic compounds on supported heterogeneous catalysts is widely used in practice. The use of these catalysts appreciably increases the oxidation selectivity [4]. It is known [5] that *D*-glucose derivatives can be oxidized to *D*-glucuronic acid in weakly alkaline solutions in the presence of a heterogeneous catalyst, 1.8% Pd/C. However, this process is slow and complex, especially in the stage of isolation of the oxidation products. There are no reports on heterogeneous catalytic oxidation of *D*-glucose to *D*-gluconic and *D*-glucaric acids. Our previous results [1–3, 6] and published data [5, 7] show that the kinetics of catalytic oxidation of *D*-glucose with oxygen is complex. However, the features of chemical transformations of reaction centers in these reactions can be revealed using similar model substrates. To simulate *D*-glucose oxidation, we studied in this work the oxidation of hydroxypivalaldehyde (HPA), which, as *D*-glucose, contains terminal hydroxy and aldehyde groups:

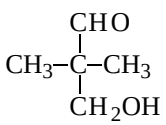

HPA

The presence of hydroxy and aldehyde groups in an HPA molecule suggests that its oxidation is similar to that of *D*-glucose. The absence of "internal" hydroxy groups (which are present in *D*-glucose) in HPA has no effect on the reactivity of the terminal groups being oxidized and does not complicate the kinetic study of the catalytic oxidation. The study of HPA oxidation was also stimulated by the fact that its oxidation products, hydroxypivalic acid (HPAc) and dimethylmalonic acid (DMMA)

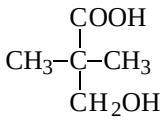

HPAc

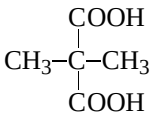

DMMA

are precursors of plasticizers of a new generation. For HPA oxidation we used the conventional industrial heterogeneous supported catalyst, 4% Pd/Al_2O_3. No data on the kinetics of HPA oxidation with oxygen in the presence of heterogeneous palladium catalysts have been reported. However, palladium catalysts are successfully used in oxidation of various alcohols and aldehydes [8–10].

EXPERIMENTAL

Kinetic experiments on liquid-phase catalytic oxidation of HPA were performed in a temperature-controlled gasometric unit in a closed volume under conditions providing kinetic control of the reaction. The oxidation was performed in alkaline aqueous solutions in a glass reactor magnetically stirred at 3000 rpm. The volume of the liquid phase of the system being

1070-4272/02/7506-0942 $27.00 © 2002 MAIK "Nauka/Interperiodica"

oxidized was 3 ml. The process was initiated by adding NaOH. The oxidation rate was monitored by the rates of oxygen uptake and accumulation of the oxidation products. The oxidation products were analyzed by GLC on a Tsvet-500 chromatograph equipped with a 5-m steel column, 2.2 mm i.d., packed with 5% OV-17 on Chromaton N-AW-DMCS. The column was heated to 60–150°C at a rate of 10 deg min^{-1}; the vaporizer temperature was 200°C. Nitrogen was the carrier gas.

Since these are no published data on use of 4% Pd/Al_2O_3 supported catalysts in HPA oxidation with molecular oxygen, we optimized the oxidation conditions by the Box-Wilson procedure [11]. We found that the most important parameters affecting the HPA oxidation were the amount of catalyst, temperature, and NaOH concentration. The experimental results were fitted by the equation

$$Y = 13.590 + 0.848X_1 + 1.768X_2 + 2.025X_3, \quad (1)$$

where Y is the volume (ml) of oxygen taken up within 30 min; X_1 is the catalyst concentration (wt %), $X_1 = \omega_{cat} \times 100\%$, where $\omega_{cat} = m_1/m_2$ is the content of heterogeneous catalyst (wt %), m_1 is the weight of 4% Pd/Al_2O_3 (g), and m_2 is the weight of the system being oxidized (g); X_2 is the NaOH concentration (M); and X_3 is temperature (K).

A kinetic study of the catalytic oxidation of HPA was performed under conditions optimized by experimental design. The concentrations of HPA and NaOH were varied from 0.2 to 1.2 and 0 to 1.2 M, respectively; T = 293–323 K; P_{O_2} = 0.21–1 atm; $\omega_{cat} = (0.1–1.8) \times 10^{-2}$ wt %. The total pressure in the system was maintained constant (1 atm).

As determined by both gas volumetric analysis and GLC, the HPA oxidation occurs in two consecutive steps. The first step is formation of hydroxypivalic acid by the reaction

$$2C(CH_3)_2(CH_2OH)(CHO) + O_2 \xrightarrow[NaOH]{4\%\ Pd/Al_2O_3} 2C(CH_3)_2(CH_2OH)(CHOH). \quad (I)$$

Hydroxypivalic acid is oxidized further to dimethylmalonic acid

$$C(CH_3)_2(COOH)(CH_2OH) + O_2 \xrightarrow[NaOH]{4\%\ Pd/Al_2O_3} C(CH_3)_2(COOH)_2 + H_2O. \quad (II)$$

This step obviously involves formation of dimethylmalonic acid monoaldehyde. However, this reaction is too fast for the aldehyde to be detected in the oxidation products.

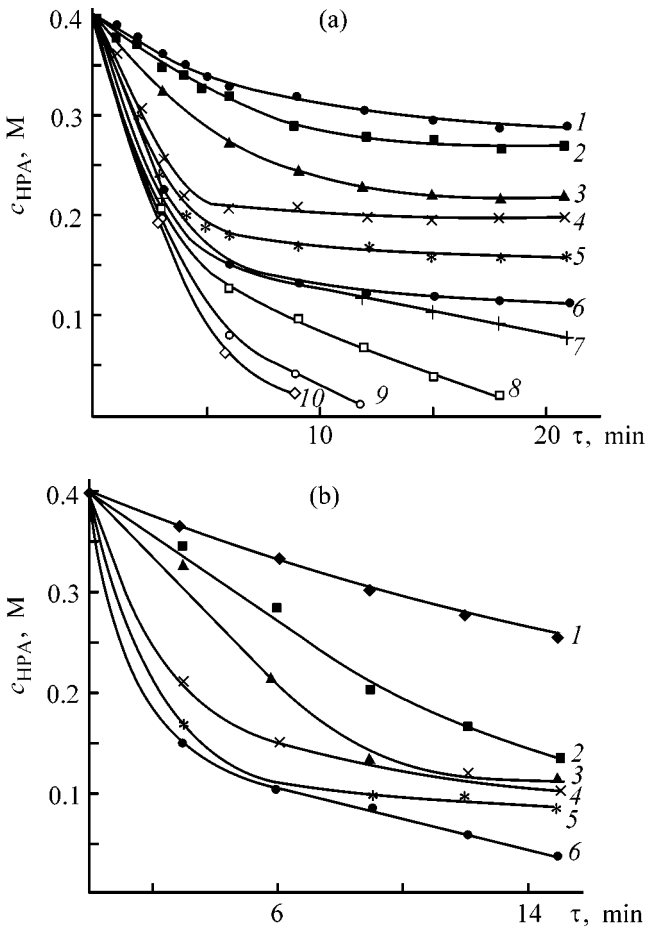

Fig. 1. Kinetic curves of HPA oxidation with oxygen: (a) at weight fraction of the catalyst $\omega_{cat} \times 10^2$: (*1*) 0.1, (*2*) 0.2, (*3*) 0.4, (*4*) 0.6, (*5*) 0.7, (*6*) 0.8, (*7*) 1.0, (*8*) 1.2, (*9*) 1.5, and (*10*) 1.8, T = 313 K; (b) (*1*) at 293, (*2*) 303, (*3*) 308, (*4*) 313, (*5*) 318, and (*6*) 323 K, $\omega_{cat} = 1 \times 10^{-2}$. Initial HPA and NaOH concentration 0.4 and 0.7 M, respectively, p_{O_2} = 1 atm.

In this work, we studied in detail the kinetics of the first step of HPA oxidation [reaction (I)]. All results of gas-volumetric measurements were recalculated in accordance with the stoichiometry of reaction (I) to the current HPA concentration c_{HPA} (M).

A mathematical treatment of the kinetic data showed that the reaction is first-order with respect to HPA in the whole range of HPA concentrations, i.e., at ω_{cat} = const

$$W = k_1 c_{HPA}, \quad (2)$$

$$k_1 = k_2 p_{O_2}, \quad (3)$$

where W is the rate of HPA oxidation (mol l^{-1} s^{-1}), and k_1 and k_2 are the rate constants of oxidation (s^{-1}).

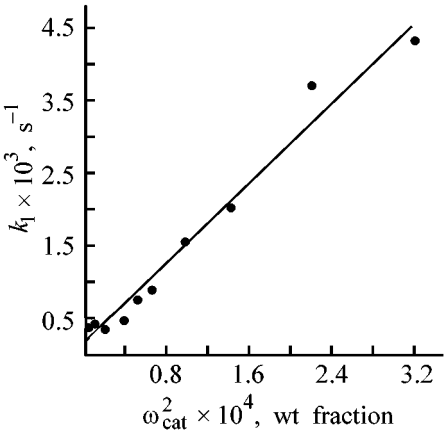

Fig. 2. Rate constant k_1 vs. the initial content of the catalyst, ω_{cat}. T = 313 K and p_{O_2} = 1 atm.

Figures 1a and 1b show how the rate of catalytic oxidation of HPA with oxygen depends on the catalyst content and temperature, respectively. We found that, under the above conditions, HPA oxidation starts at NaOH concentration of 0.3 M and higher. The results of a treatment of the kinetic data on HPA oxidation with oxygen in the presence of 4% Pd/Al_2O_3 are presented in the table.

These data show that at $c_{NaOH} \geq 0.3$ M and p_{O_2} = 1 atm.

Oxidation of HPA with oxygen in the presence of 4% Pd/Al_2O_3 at p_{O_2} = 1 atm

c_{HPA}	c_{NaOH}	$\omega_{cat} \times 10^2$	T, K	$k_1 \times 10^3$, s^{-1}
M				
0.2–0.7	0.7	1	313	1.55
0.4	0.3–1.2	1	313	1.55
0.4	0.7	0.1	313	0.313
0.4	0.7	0.2	313	0.333
0.4	0.7	0.4	313	0.351
0.4	0.7	0.6	313	0.521
0.4	0.7	0.7	313	0.769
0.4	0.7	0.8	313	0.909
0.4	0.7	1.2	313	2.00
0.4	0.7	1.5	313	3.67
0.4	0.7	1.8	313	4.33
0.4	0.7	1	293	0.521
0.4	0.7	1	303	1.39
0.4	0.7	1	308	1.50
0.4	0.7	1	318	1.67
0.4	0.7	1	323	2.22

$$\frac{\partial k_1}{\partial c_{NaOH}} = 0; \quad \frac{\partial k_1}{\partial \omega_{cat}}, \frac{\partial k_1}{\partial T} > 0. \tag{4}$$

The dependence of the oxidation rate on the catalyst content is shown in Fig. 2. The results presented in Fig. 2 and the table can be described by the equation

$$k = a + b\omega_{cat}^2, \tag{5}$$

where a and b are constants equal to 0.17×10^{-3} and 1.35×10^{-3} s^{-1}, respectively.

As seen from Eq. (5), the reaction is second-order with respect to the content of 4% Pd/Al_2O_3 supported heterogeneous catalysts.

A mathematical treatment of the temperature dependence of the rate constant of catalytic oxidation at $\omega_{cat} = 1 \times 10^2$, c_{NaOH} = 0.7 M, and p_{O_2} = 1 atm gave the following Arrhenius equation:

$$k_1 = 1.2 \times 10^8 \exp(-66\,510/RT), \tag{6}$$

with activation energy of the process equal to 66 510 J mol^{-1}.

On the basis of the above relationships, the kinetic equation for W (mol l^{-1} s^{-1}) of HPA oxidation to hydroxypivalic acid in the presence of 4% Pd/Al_2O_3 in alkaline aqueous solution ($c_{NaOH} \geq 0.3$ M) can be described by the equation

$$W = kc_{HPA}p_{O_2}\omega_{cat}^2. \tag{7}$$

It is known [12] that liquid-phase oxidation of hydrocarbons with molecular oxygen in the presence of heterogeneous supported catalysts may involve the step of oxygen activation by the reaction

$$S...S + O_2 \longrightarrow [S–S...O_2^{\delta-}], \tag{III}$$

where S is a catalyst.

Since water is a polar electron-donor solvent, it favors charge transfer to an electron-acceptor oxygen molecule when both are sorbed on the catalyst surface [13]:

$$H_2O \overset{\delta^+}{—} S \overset{\delta^-}{—} O_2.$$

As a result, molecular oxygen is intensively activated, with generation of radicals by a heterogeneous reaction, which do not escape into the liquid phase. As a results, nonchain intraspheric or purely heterogeneous selective catalytic oxidation occurs. Clearly, the mechanism of HPA oxidation with molecular oxygen in the presence of 4% Pd/Al_2O_3 is similar, which

is confirmed by the experimental dependence (7). The features of HPA oxidation with oxygen in the presence of 4% Pd/Al_2O_3 suggest that the kinetics of *D*-glucose oxidation under similar conditions will be similar. The process will also occur in two steps. In the first step, formation of *D*-gluconic acid is possible, which will be further oxidized to *D*-glucaric acid.

CONCLUSIONS

(1) A kinetic study of liquid-phase oxidation of hydroxypivalaldehyde with molecular oxygen in the presence of a heterogeneous catalyst, 4% Pd/Al_2O_3, showed that the oxidation occurs in two steps. Hydroxypivalic acid formed in the first step is oxidized to dimethylmalonic acid in the second step.

(2) A kinetic equation of hydroxypivalaldehyde oxidation to hydroxypivalic acid was derived. The activation energy of this process was determined.

REFERENCES

1. Grigor'eva, I.A., Chernaya, S.S., Trusov, S.R., *et al.*, *Latv. Khim. Zh.*, 1993, no. 6, pp. 707–713.
2. LR Patent LV 10857 B.
3. Grigor'eva, I.A., Chernaya, S.S., Trusov, S.R., *et al.*, *Latv. Khim. Zh.*, 1997, no. 4, pp. 19–23.
4. Blyumberg, E.A. and Norikov, Yu.D., *Itogi Nauki Tekh., Ser: Kient. Katal.*, 1984, vol. 12, pp. 103–109.
5. Fel'dman, D.P., Voitenko, A.D., Shimanskaya, M.V., *et al.*, *Khim.-Farm. Zh.*, 1984, vol. 18, no. 11, pp. 1356–1360.
6. Borovko, N.A., Chernaya, S.S., and Trusov, S.R., *Zh. Prikl. Khim.*, 1999, vol. 72, no. 11, pp. 1842–1846.
7. Fel'dman, D.P., Voitenko, A.D., Shimanskaya, M.V., *et al.*, *Khim.-Farm. Zh.*, 1983, vol. 17, no. 2, pp. 61–68.
8. Hiroshi, K., Akio, K., Isao, K., *et al.*, *Appl. Catal. A: General*, 1993, vol. 95, no. 2, pp. 143–169.
9. Mitsuo, A., Shinji, N., Toshiyuki, S., *et al.*, *Bull. Chem. Soc. Jpn.*, 1993, vol. 66, no. 5, pp. 1511–1515.
10. Shlangen, I.W.A., Neuhaus, G.W., Mandani, M., et al., *Allgem. Praktt. Chem.*, 1992, vol. 334, no. 6, pp. 465–473.
11. Adler, Yu.P., Markova, E.V., and Granovskii, Yu.V., *Planirovanie eksperimenta pri poiske optimal'mykh uslovii* (Experimental Design in Searching for Optimal Conditions), Moscow: Nauka, 1976.
12. Norikov, Yu.D., Blyumberg, E.A., Bochorshvili, Sh.K., *et al.*, *Dokl. Akad. Nauk SSSR*, 1975, vol. 223, no. 5, pp. 1187–1190.
13. Burov, V.A., Norikov, Yu.D., Salukvadze, L.V., *et al.*, *Dokl. Akad. Nauk SSSR*, 1977, vol. 237, no. 6, pp. 1384–1387.

Russian Journal of Applied Chemistry, Vol. 75, No. 6, 2002, pp. 946–949. Translated from Zhurnal Prikladnoi Khimii, Vol. 75, No. 6, 2002, pp. 963–966.
Original Russian Text Copyright © 2002 by Malkov, Davidyan, Filippov, Rotinyan.

ENVIRONMENTAL PROBLEMS OF CHEMISTRY AND TECHNOLOGY

Plasmochemical Neutralization of Ozone-Destroying Chladones and Fluorine- and Chlorine-containing Wastes[1]

Yu. P. Malkov, A. A. Davidyan, Yu. E. Filippov, and M. A. Rotinyan

Prikladnaya Khimiya Russian Scientific Center, St. Petersburg, Russia

Received January 17, 2002

Abstract—A plasmochemical technique for neutralizing ozone-destroying chladones and fluorine- and chlorine-containing wastes is considered. Experimental results obtained on applying this technique to neutralization of some halogen-containing substances are presented, together with the information gained on using the technological scheme of the process in designing and constructing an industrial installation for neutralizing wastes of a plant manufacturing polytetrafluoroethylene.

The intensive development at the end of the XX century of the chemistry and technology of production of fluorine-containing compounds, associated with creation of new materials for various branches of industry, led to their wide introduction into the modern technology. Unfortunately, many of these materials, manufactured on large scale, proved to be ecologically unsafe. No less dangerous are industrial wastes formed in manufacture of virtually all halogen-containing products. Of these halogen-containing compounds, special mention should be made of ozone-destroying chladones. They are highly chemically stable and, when finding way to the environment, can reach the stratosphere to be decomposed there by UV radiation, to liberate atomic chlorine destroying the ozone layer.

The Vienna Convention for the Protection of the Ozone Layer and the Montreal Protocol on Substances that deplete the Ozone Layer envisage not only termination of the manufacture of the above-mentioned fluorine- and chlorine-containing substances, but also their obligatory elimination. Thus, the problem of neutralizing ozone-destroying substances of any kind acquires international importance, and creation of a reliable and efficient technology for performing this elimination becomes a top priority ecological task.

The complexity of solving the problem at hand consists in that incorrect use of thermal techniques for this purpose may give rise to extremely hazardous secondary compounds, such as dioxins, difluoro- and chlorophosgenes, octofluoroisobutylene, benzopyrene, etc. The most dangerous of these are dioxins formed in high temperature processes involving carbon and any chlorine compounds. For example, intensive formation of 2,3,7,8-tetrachlorodibenzo-*p*-dioxin occurs at temperatures in the range from 750 to 900°C, and its effective decomposition onsets only at 1200–1400°C [1–5]. In the same temperature range, the content of phosgene starts to decrease steeply. At a temperature of 1350°C its concentration decreases to the maximum permissible value for the working zone air [6].

The data presented indicate that effective and safe neutralization of organohalogen compounds should be carried out at temperatures of no less than 1400°C. Such conditions are very difficult to create with the use of the conventional thermal techniques with furnace units operating on gas fuel. The most promising is the plasmochemical technique employing plasma generators—plasmatrons, for pyrolysis. Electric arc plasma generators have gained wide acceptance. The choice of these generators is due to the fact that they possess the following important properties: high concentration of energy in a small volume, possibility of achieving very high temperatures of the plasma-forming gas (5000°C and more), convenient control of the temperature mode in a wide range of temperatures, high electrical and thermal efficiency, use as plasma-forming media of any technologically necessary gases (oxidizing, reducing, inert), and simplicity of the process automation because of the fast response of the electric arc.

[1] Report at the 3rd International Conference "Chemistry, Technology, and Use of Fluorine-containing Compounds," St. Petersburg, June 6–9, 2001.

1070-4272/02/7506-0946 $27.00 © 2002 MAIK "Nauka/Interperiodica"

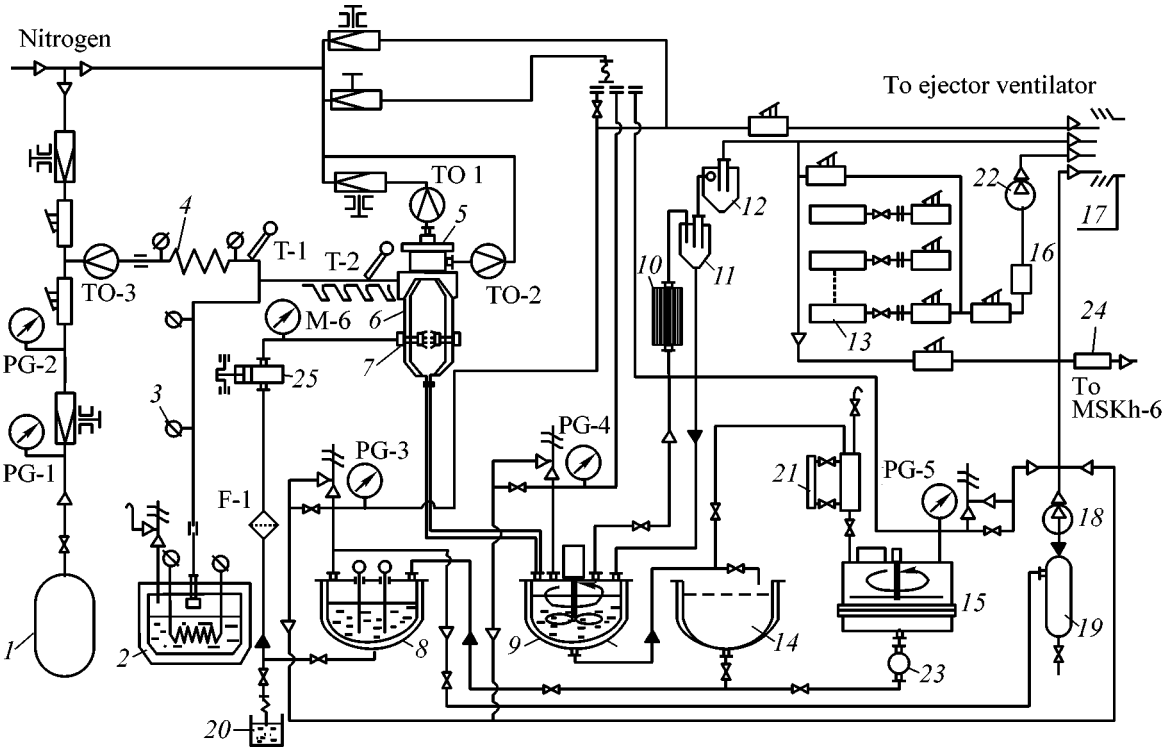

Schematic of a pilot plasmochemical installation: (*1*) cylinder with chladone, (*2*) water evaporator, (*3*) tubular steam heater, (*4*) tubular electric heater, (*5*) plasmatron, (*6*) reactor, (*7*) alkaline solution atomizer, (*8*) vessel with alkaline solution, (*9*) receiver vessel, (*10*) heat exchanger, (*11*) drop separator, (*12*) cyclone, (*13*) sampling devices, (*14*) nutsch filter, (*15*) pressure filter, (*16*) liquid nitrogen trap, (*17*) ejector ventilator, (*18*) vacuum pump, (*19*) trap for liquid phase, (*20*) vessel for water discharge, (*21*) measuring vessel, (*22*) vacuum pump, (*23*) inspection port, (*24*) liquid nitrogen trap, and (*25*) alkaline solution dosing pump. (PG) pressure gages, (T) thermocouples, and (TO) throttling orifices.

Our analysis demonstrated that all the plasmochemical techniques the authors are aware of, created both in Russia and abroad, have some disadvantages hindering their use under industrial conditions. For this reason, a search for a plasmochemical technique for processing of halogen-containing substances, which would be applicable in industrial installations, has been conducted at the Prikladnaya khimiya Russian Scientific Center for several years. As a result of extensive experimental studies, a method has been developed [7], which, in our opinion, best satisfies the requirements to ecologically safe and efficient neutralization.

The essence of this technique is that halogen-containing wastes, both liquid and gaseous, are subjected to pyrolysis in a plasma jet and to oxidation on supplying into the installation of air or steam in amounts required for complete oxidation of carbon contained in the waste to CO_2. In the process, halogens react in the high-temperature zone of the reactor with hydrogen contained in the wastes or in the steam.

The heating of halogen-containing substances and their pyrolysis and oxidation in the plasmochemical technique proposed can be conditionally divided into two stages. The first, preliminary stage proceeds outside the reactor at temperatures close to those of thermal decomposition of the substances being neutralized, but not exceeding these temperatures. In this stage, liquid substances are heated to make lower their viscosity, atomized, evaporated, and the resulting vapors and gaseous components are again heated.

The aim of the first stage is to prepare the wastes being neutralized for the second, main stage of pyrolysis and oxidation in the reactor at the minimum possible residence time of the reaction products in the high-temperature zone. Performing the process in two stages enables a substantial decrease in the dimensions of the reactor, in which corrosion-active components are at very high temperatures, significant reduction of the loss of heat from the hightemperature zone, and pronounced lowering of reactor fabrication costs because of the small reactor dimensions.

To develop this technique, we created a pilot installation with a plasmochemical unit comprising an EDP-109/200 industrial plasmatron, small-size reactor, and a unit for quenching and neutralization of pyrol-

Parameters of plasmochemical neutralization of halogen-containing compounds

Parameter	Substance being neutralized			
	chladone 12	mixture of chladones 13 and 14 with air	wastes from manufacture of chladone 134a	pentachlorobiphenyl
Plasmatron power, W	120	120	91	120
Plasma jet temperature, °C	5231	5241	4732	5247
Flow rate of feed into plasmatron, kg h^{-1}:				
air	–	–	27.4	–
nitrogen	32.4	32.4	13.7	32.4
Flow rate of feed into reactor, kg h^{-1}:				
air	–	22.0	14.5	–
steam	29.1	15.8	–	33.9
Flow rate of substances being neutralized, kg h^{-1}	59	50	73	22
Component temperature at reactor inlet, °C	350	630	20	605
Temperature of pyrolysis products in reactor, °C	2080	2859	2079	2000
Specific energy expenditure, kW h kg^{-1}	2.62	5.43	1.25	5.70
Composition of waste gases, vol %:				
N_2	66.7	72.2	96.1	82.7
CO_2	21.9	14.9	2.1	3.7
CO	7.1	6.1	0.7	10.2
H_2	2.1	0	0	2.8
O_2	1.9	6.4	0.7	0.1
Ar	0.3	0.4	0.4	0.5

ysis products. The output capacity of the unit satisfied the industrial requirements, which enabled, together with a search for optimal conditions of neutralization of halogen-containing compounds, simultaneous improvement of the unit design to increase its reliability and service life.

The figure presents a technological scheme of the pilot plasmochemical installation. Its main units include: (*1*) cylinder with chladone or other substance to be neutralized; (*2*) water evaporator supplying steam into the reactor; (*3*) and (*4*) electric heaters of, respectively, steam and chladone; (*5*) plasmatron; (*6*) reactor with (*7*) quenching and neutralization unit; (*8*) vessel for aqueous solution of alkali; (*9*) vessel receiver for spent alkaline solution; (*10*) heat exchanger; (*11, 12*) cyclones–drop separators for separating residual amounts of the liquid phase from gaseous products discharged into the environment; (*13*) devices for sampling the gas phase for analysis; (*14*) nutsch filter; and (*15*) pressure filter; the last two used to separate salts precipitated in the spent alkaline solution. The installation was used to test neutralization modes of various halogen-containing substances, both gaseous and liquid. As an example, the table presents parameters of neutralization processes for four different compounds.

The specific energy expenditures for neutralization of these compounds, given in the table, are significantly different. This is accounted for by the different thermal stabilities of these compounds, and also by their different contents of halogens and carbon, which make necessary supply into the reactor of sufficient amounts of steam or air to bind halogens into hydrogen halides, and carbon, into gaseous oxides CO_2 and CO.

As seen from the table, the highest energy expenditure is observed for neutralization of a mixture of chladones 13 and 14 with air and for pentachlorobiphenyl. In the first case, a large amount of chladon 14 (tetrafluorometane), the most stable organofluoric compound, was contained in the mixture being neutralized. The high energy expenditure for pentachlorobiphenyl neutralization is due not only to its high thermal stability, but also to the large content of chlorine (~54%) and carbon (~44%) in this compound and its high viscosity (14000 cSt at 20°C) and boiling point (390°C).

The efficiency of the plasmochemical technique for neutralization of halogen-containing compounds was tested not only on the pilot installation. The scheme of this technological process and also the results of experimental studies were used in designing an industrial installation for processing wastes of a plant for polytetrafluoroethylene production.[2] Its construction costs were much lower than those for creation of a similar installation with furnace units operating on gaseous fuel. This industrial installation is used to neutralize gaseous and liquid industrial wastes containing up to 12 different ozone-destroying chladones and other fluorine- and chlorine-containing organic substances.

[2] The installation comprising three plasmochemical units designed at the Prikladnaya khimiya Russian Scientific Center was constructed in China and has been in operation since 1998.

REFERENCES

1. Fedorov, L.A., *Dioksiny kak ekologicheskaya opasnost': retrospektiva i perspektivy* (Dioxins as Ecological Threat: Retrospect and Prospects), Moscow: Nauka, 1993.
2. Ahling, B. and Lindskog, A., *Chemosphere*, 1977, vol. 6, no. 8, pp. 461–468.
3. Junk, J.A. and Richard, J.J., *Chemosphere*, 1981, vol. 10, no. 12, pp. 1237–1241.
4. Redford, D.P., Haile, C.L., and Lucas, R.M., in *Human and Environmental Risks of Chlorinated Dioxins and Related Compounds*, Tucker, R.E., Young, A.L., and Gray, A.P., Eds., New York: Plenum, 1983, pp. 143–152.
5. Shaub, W.M. and Tsang, W., *Human and Environmental Risks of Chlorinated Dioxins and Related Compounds*, Tucker, R.E., Young, A.L., and Gray, A.P., Eds., New York: Plenum, 1983, pp. 731–748.
6. Dmitriev, V.I., Ovchinnikov, V.G., Romashev, A.S., *et al., Khim. Prom–st.*, 1988, no. 3, pp. 145–147.
7. RU Patent 2 105 928.

Russian Journal of Applied Chemistry, Vol. 75, No. 6, 2002, pp. 950–953. Translated from Zhurnal Prikladnoi Khimii, Vol. 75, No. 6, 2002, pp. 967–970.
Original Russian Text Copyright © 2002 by Plokhov, Matasova, Utkin, Vodzinskii.

ENVIRONMENTAL PROBLEMS OF CHEMISTRY AND TECHNOLOGY

Specific Features of Ion-Exchange Zinc(II) Extraction from Washing Water of Zinc Plating

S. V. Plokhov, I. G. Matasova, V. A. Utkin, and V. Yu. Vodzinskii

Nizhni Novgorod State Technical University, Nizhni Novgorod, Russia

Received October 2, 2000; in final form, August 2001

Abstract—Specific features of ion-exchange purification of washing water formed in zinc plating in an alkaline medium are considered. The parameters of extraction of zinc ions and regeneration of ion-exchange resins are optimized.

A two-stage technological scheme based on combination of filtration, sorption, ion exchange, and electrolysis, followed by recovery of metal ions, has been proposed for purification of washing water after acidic or neutral zinc plating [1–4]. Filtration is used to remove mechanical impurities, suspensions, and oil; sorption on activated carbon serves to remove organic surfactants. Zinc ions are extracted from solutions by ion exchange onto a cationite. Eluates obtained in regeneration of ion-exchange resins are subjected to electrolysis to recover metallic zinc. Such a wastewater treatment reduces irreversible zinc loss and water consumption, and thereby improves the economical industrial indexes by decreasing pollution taxes and recycling the metal. The use of this method to purify washing water from alkaline (zincate) zinc plating has a number of specific features.

The goal of this study was to analyze ion-exchange purification of washing water from zinc plating and to optimize the technological parameters of metal ion recovery.

As objects of study served model solutions and real washing water (pH 12–13) from metal plating in an electrolyte of composition [5] (g l^{-1}): zinc oxide 10–17, sodium hydroxide 90–120, brightening compounds NBTz-O 4–6 and NBTz-K 4–6. Model solutions contained (g l^{-1}): Zn(II) as ZnO 0.05–3.0, NaOH 0.5–35.0. In addition, real washing water contained the brightening compounds NBTz-O and NBTz-K (0.1–0.2 g l^{-1} each) and metal impurity ions (g l^{-1}): iron(III) up to 0.01; tin(IV), lead(II), copper(II), and chromium(IV) up to 0.005 each. Removal of these ions from washing water is not considered here. Zinc extraction by ion exchange was studied on a laboratory installation with a glass column (i.d. 0.018 m, ratio between inner diameter and height of swollen ion-exchange resin bed 1 : 9). Weights of ion-exchange resins (KU-1 cationite and AV-17-8 anionite) were 25.49 and 27.30 g, respectively. The concentration of zinc(II) ions in solutions was determined spectrophotometrically [6] and by atomic-absorption method [7, 8] on SF-26 and Saturn SF-115 spectrophotometers, respectively. The analytical error was not greater than ±2%.

Metal ions are present in electrolytes of alkaline zinc plating in the anionic form [9]. Accumulation of Zn(II) in washing water results in that not only soluble anions $[Zn(OH)_n]^{-(n-2)}$ with n = 3, 4 are formed, but also white flocculent precipitate $Zn(OH)_2$ (Table 1), which leads to great loss of zinc on filters

Table 1. Amount of Zn(II) in precipitate in relation to the accumulation time of Zn(II) and its concentration in washing water

$c_{Zn(II)}$, g l^{-1}	Amount of Zn(II) in precipitate (% of Zn(II) in washing water) after indicated time, h			
	3	24	48	72
0.05	–	10	26.7	60
0.1	6.9	60	82	100
0.25	30.6	92	93	100
0.5	50	92	94.6	97.3
1.0	30	88	91.6	93.3
1.5	30	79	84	88.8
2.0	20	60	70	81.3
3.0	–	4.4	35.5	60

1070-4272/02/7506-0950 $27.00 © 2002 MAIK "Nauka/Interperiodica"

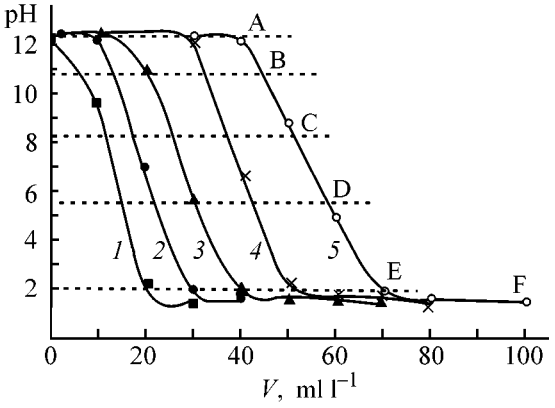

Fig. 1. pH of zincate solutions vs. volume V of 1.8 M solution of sulfuric acid added. Concentration of Zn(II) and NaOH in zincate solutions (g l^{-1}): (*1*) 0.5 and 5.0, (*2*) 0.75 and 7.5, (*3*) 1.0 and 10.0, (*4*) 1.5 and 15.0, and (*5*) 2.0 and 20.0.

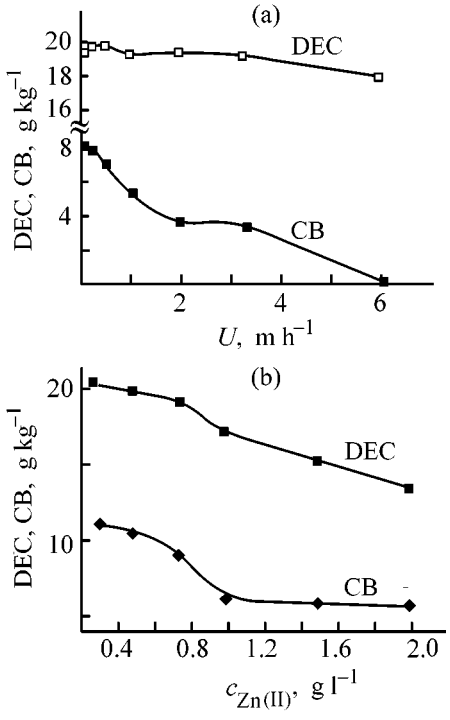

Fig. 2. DEC and CB vs. (a) water flow rate U and (b) zinc ion concentration $c_{Zn(II)}$ in water. Cationite KU-1; (a) Zn(II) concentration 1.0 g l^{-1}, (b) water flow rate 0.5 m h^{-1}.

and in pipe-lines if the above-mentioned technological scheme is used.

Moreover, it was found that ion-exchange extraction of Zn(II) (after filtration of washing water and sorption of surfactants) is insufficiently effective. The efficiency of ion exchange was estimated by the dynamic exchange capacity (DEC) and capacity to breakthrough (CB). By DEC was understood the maximum weight of Zn(II), that can be adsorbed by 1 kg of a swollen ion-exchange resin in a given mode of water treatment till the ion-exchanger inlet and outlet concentrations become equal to each other. The capacity to breakthrough is the maximum weight of Zn(II) that can be adsorbed by 1 kg of a swollen ion-exchange resin in a given mode of water treatment until zinc(II) ions appear at the outlet of the ion-exchange column. The DEC and CB of AB-17-8 anionite for $c_{Zn(II)}$ = 0.35 g l^{-1} at water flow rates (through the inner section of the column) from 0.1 to 6.0 m^3 m^{-2} h^{-1} are 5.0–14.5 and 0.8–8.7 g kg^{-1} of resin, respectively. The values obtained are not sufficiently high owing to the loss of zinc for precipitation.

To reduce the loss of zinc for precipitation and to improve the characteristics of ion exchange, washing water was treated before purification with 1.8 M sulfuric acid (1 : 5), which led to dissolution of the zinc hydroxide precipitate and destroyed complex zinc ions to give transparent solutions containing zinc ions. The amount of acid necessary for such a treatment was found by pH-metric titration of solutions modeling the washing water.

The curves of pH-metric titration of zincate solutions show several characteristic portions (Fig. 1). Portion 0A corresponds to neutralization of free sodium hydroxide. Portion AD characterizes an equilibrium between solution and precipitate, with portions AB (to pH 10.8) and CD (8.3–5.6) corresponding to incomplete formation and dissolution of the precipitate, respectively. Almost complete formation [Zn(II) concentration in solution less than 5×10^{-4} g l^{-1}] is achieved at pH 10.8–8.3. In this case, zinc is present in the precipitate not only as hydroxide, but also as a basic salt of the type $ZnSO_4 \cdot Zn(OH)_2$ [9]. Portion DF is the most interesting for the subsequent zinc recovery from washing water by ion exchange. Complete dissolution of the precipitate can be, in principle, achieved in portion DE (pH 5.6–2.0), but this process is very slow. Portion EF, where precipitate dissolves fast, is more convenient for practical purposes. In this region, the solution has high buffer capacity, and, therefore, it is advisable to treat washing water with acid until pH 1.9–1.8 is reached, with complete dissolution achieved in 0.5 h.

After treatment with sulfuric acid, washing water coming to ion-exchange purification (pH 1.8–1.9) contains Zn(II) in cationic form, so that cationite can be used for its recovery. In this study, we used KU-1 cationite in the H^+ form for technological and economical reasons. A study of various types of cationites de-

monstrated that, although the DEC of many of these cationites is somewhat higher, KU-1 is more than twice less expensive.

According to the present knowledge [10, 11], ion exchange involves a fast chemical stage and slower stages of ion diffusion within phases. Consequently, the DEC and CB values must be affected by the concentration of zinc ions in washing water and by its flow rate. The slower the flow rate (Fig. 2a), the higher the CB value (probably owing to prolonged contact of water with the resin). The greatest increase in the CB value is observed when the rate is changed from 1.0 to 0.5 $m^3 m^{-2} h^{-1}$. Within other flow rate ranges, the change in CB is not so significant. Thus, the water flow rate of no greater than 0.5 $m^3 m^{-2} h^{-1}$ can be assumed optimal.

The DEC and CB values are affected to a greater extent by the Zn(II) concentration in washing water (Fig. 2b). The characteristics of ion exchange are impaired when the Zn concentration becomes higher, which is obviously due to insufficient time of water contact with the resin. The greater $c_{Zn(II)}$, the more pronounced this effect. With the concentration increasing to 0.75 g l^{-1}, the DEC and CB decrease only slightly, so that $c_{Zn(II)}$ should be not greater than 0.75 g l^{-1} to achieve sufficiently high characteristics of ion exchange.

The regeneration of an ion-exchange resin is affected by the concentration of a regenerating solution (sulfuric acid) and its flow rate. The effect of acid concentration on ionite regeneration was studied under static conditions. A cationite saturated with zinc ions was washed with water and dried to constant weight. Ionite samples of the same weight (4 g) were placed in H_2SO_4 solutions of various concentrations. The efficiency of regeneration was estimated by amount of Zn(II) passing into the liquid phase (Table 2).

According to the data presented, the fastest regeneration is observed at H_2SO_4 concentration of 100 g l^{-1}. This concentration can be assumed optimal, and just this concentration was used in studying the influence exerted by the flow rate of the regenerating solution on the efficiency of zinc extraction from the cationite by the dynamic method.

In the range 0.1–0.5 $m^3 m^{-2} h^{-1}$, the flow rate of the regenerating solution passed through a cationite affects the rate of zinc extraction from the cationite only slightly. At higher flow rates the efficiency of regeneration decreases dramatically. For this reason, we recommend an H_2SO_4 solution flow rate of 0.5 $m^3 m^{-2} h^{-1}$, at which the degree of zinc recovery is 90 %.

Table 2. Amount of Zn(II) recovered from cationite in relation to regeneration duration and sulfuric acid concentration

$c_{H_2SO_4}$, g l^{-1}	Amount of Zn(II) (g) recovered in indicated time, h			
	1	3	8	24
200	0.048	0.062	0.071	0.088
150	0.034	0.062	0.087	0.090
100	0.036	0.064	0.090	0.096
50	0.034	0.064	0.072	0.077
25	0.020	0.038	0.051	0.069

Analyzing the dependence of Zn(II) extraction on the volume of regenerating solution passed (Fig. 3), we can determine the reasonable degree of regeneration. We recommend that Zn(II) should be recovered to 80% degree of extraction, because only a quarter of a solution volume required for complete regeneration is consumed in this case. Such regeneration conditions impair somewhat the DEC and CB, which should be taken into account in apparatus design.

One and the same volume of H_2SO_4 solution can be used for regeneration twice, with the Zn(II) concentration in the eluates being 5.0 g l^{-1}. According to the technological scheme, the solutions obtained are subjected to electrolysis, with the result that zinc is deposited onto the cathode as a foil (current density 3–10 A dm^{-2}, 18–25°C, aluminum cathodes, lead

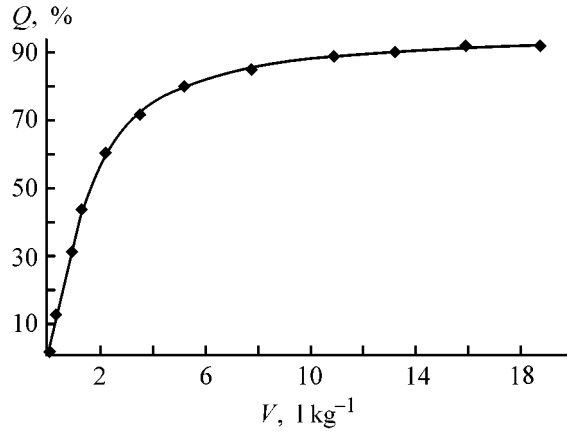

Fig. 3. Degree of extraction of zinc ions, *Q*, in cationite regeneration vs. volume *V* of regenerating solution passed. H_2SO_4 concentration 100 g l^{-1}, solution flow rate 0.5 m h^{-1}.

anodes, no stirring) [12] and can be recycled as anode material in zinc plating, and the H_2SO_4 solution can be used again for regeneration of ion-exchange resins.

CONCLUSIONS

(1) It is established that washing water from zinc plating in alkaline media, treated with 1.8 M solution of sulfuric acid to pH 1.8–1.9, can be purified by cation exchange followed by metal recovery by a technological scheme similar to that proposed for waste water from neutral or acidic zinc plating. The consumption of the H_2SO_4 solution is 20 to 70 ml per liter of washing water.

(2) The optimal parameters of cation-exchange zinc extraction from preliminarily neutralized zincate washing water are as follows: concentration of metal ions in water ≤ 0.75 g l^{-1}, flow rate of water through a cationite ≤ 0.5 m^3 m^{-2} h^{-1}, ionite regeneration with H_2SO_4 solution (100 g l^{-1}) at a flow rate of this solution of 0.5 m^3 m^{-2} h^{-1} to 80 % degree of recovery, Zn(II) concentration in eluates 5 g l^{-1}.

REFERENCES

1. Plokhov, S.V., Vinogradov, S.N., Ershov, D.A. *et al., Zh. Prikl. Khim.*, 1999, vol. 72, no. 7, pp. 1154–1157.
2. Plokhov, S.V. and Matasova, I.G., *Parametry ionoobmennoi otchistki promyvnyjh vod khloristoammoniinogo tzinkovaniya* (Characteristics of Ion-Exchange Purification of Washing Water from Ammonium Chloride Zinc Plating), 2000, Nizhni Novgorod, Available from VINITI, no. 518-VOO, 11 p.
3. Vinogradov, S.N. and Plokhov, S.V., Abstracts of Papers, *Vserossiskaya konferentsiya po galvanotekhnike i obrabotke poverkhnosti* (All-Russian Sci.-Pract. Conf. on Electroplating and Surface Treatment), Moscow: RKhTU, 1999, pp. 23–24.
4. Plokhov, S.V., *Sbornik materialov II Mezhdunarodnoi nauchno-prakticheskoi konferentsii "Ekologiya i zhizn'"* (Proc. II Int. Sci.-Pract. Conf. "Ecology and Life"), Penza, 1999, part 2, pp. 55–56.
5. *GOST* (State Standard) *9.305.-84: Inorganic Metallic and Nonmetallic Coatings: Procedures in Technological Processes for Coating Formation*, 1984.
6. Lur'e, Yu.Yu. and Rybnikov, A.I., *Khimicheskii analiz proizvodstvennykh stochykh vod* (Chemical Analysis of Industrial Waste Waters), Moscow: Khimiya, 1974.
7. L'vov, B.V., *Atomno-adsorbtzionnyi spektral'nyi analiz* (Atomic-Adsorption Spectral Analysis), Moscow: Nauka, 1966.
8. *GOST 22 001–87: Reagents and Ultrapure Substances: Method of Atomic-Adsorption Spectrometry: Determination of Admixtures of Chemical Elements*, 1987.
9. Zubchenko, V.L., Ed., *Gibkie avtomatizirovannye gal'vanicheskie linii: Spravochnik* (Versatile Automated Electroplating Lines: Handbook), Moscow: Mashinostroenie, 1989.
10. Ashirov, A., *Ionoobmennaya ochistka stochnykh vod, rastvorov i gazov* (Ion-Exchange Purification of Waste Waters, Solutions, and Gases), Leningrad: Khimiya, 1983.
11. Kokotov, Yu.A. and Pasechnik, V.A., *Ravnovesie i kinetika ionnogo obmena* (Equilibrium and Kinetics of Ion Exchange), Leningrad: Khimiya, 1970.
12. Plokhov, S.V. and Matasova, I.G., *Ekologiya Prom–st. Rossii*, 2000, Sept., pp. 10–12.

Russian Journal of Applied Chemistry, Vol. 75, No. 6, 2002, pp. 954–958. Translated from Zhurnal Prikladnoi Khimii, Vol. 75, No. 6, 2002, pp. 971–975.
Original Russian Text Copyright © 2002 by Kovaleva, Zemnukhova, Nikitin, Koryakova, Speshneva.

ENVIRONMENTAL PROBLEMS OF CHEMISTRY AND TECHNOLOGY

Biological Properties of Antimony(III) Fluoride Complexes[1]

E. V. Kovaleva, L. A. Zemnukhova, V. M. Nikitin, M. D. Koryakova, and N. V. Speshneva

Institute of Chemistry, Far-East Division, Russian Academy of Sciences, Vladivostok, Russia

Received January 17, 2002

Abstract—Result of a study of how antimony trifluoride and fluoride complexes MSb_2F_7 (M = K, Rb, Cs, Tl, NH_4), $MSbF_4$ (M = Na, K, Rb, Cs, NH_4), and M_2SbF_5 (M = Na, K, Rb, Cs, Tl, NH_4) affect the growth of associations of marine bacteria and vital activity of marine alga *Ulva Fenestrata* are presented. The possible ways of using Sb(III) fluoride compounds are discussed.

Complex antimony(III) fluorides attract interest owing to the revealed high mobility of fluoride ions in the crystal lattice of a number of compounds and their suitability as solid electrolytes, piezoelectrics, and ferroelectrics. The preparation and physicochemical properties of antimony(III) fluoride complexes were reviewed in detail in [1, 2]. The information on the part played by antimony(III) in biochemical processes is scarce; biological properties of fluoride complexes are virtually unknown. There are data on the inhibiting effect of some antimony(III) fluoride complexes, when in concentrations of 10^{-5}–10^{-6} M, on the growth of tumor cells of Ehrlich carcinoma and on *Strongylocentrotus intermedius* urchin embryos [3].

The aim of this work was to study the influence exerted by antimony(III) fluoride complexes of the composition MSb_2F_7, $MSbF_4$, and M_2SbF_5 (M = Na, K, Rb, Cs, NH_4, Tl), as well as by their synthetic precursors, namely, alkali metal and ammonium fluorides and antimony oxide and trifluoride, on two test-objects, marine bacteriocenosis and marine algae *Ulva fenestrata*, belonging to the benthos community of the Sea of Japan.

EXPERIMENTAL

The fluoride complexes of antimony(III) MSb_2F_7, $MSbF_4$, and M_2SbF_5 (M = Na, K, Rb, Cs, NH_4, Tl) were synthesized by the procedures described in [2, 4–6] from aqueous solutions of chemically pure grade antimony(III) fluoride, alkali metal fluorides, and thallium carbonate (all water-soluble).

The bactericidal activity of the compounds synthesized was studied by the method of diffusion of a substance being tested into agar containing the test-object [7]. The experiments were conducted as follows. Petri dishes were filled with agarized medium, ribopeptone agar. The solidified agarized plates were uniformly seeded with a bacterial suspension extracted from seawater. Next, the prepared surface was covered with small hollow glass cylinders (0.8 cm in diameter and 1.0 cm high) into which solid substances to be tested (10^{-3} mol) were introduced. For germination of the marine bacteriocenosis, the Petri dishes were kept at a constant temperature of 28°C for 48 h. After the experiments, we measured the sizes of the bacterial growth suppression areas and bacterial growth areas. The toxicity of the substances was judged from the radius of the no-growth area (NGA, cm).

The effect of the compounds on green alga *U. fenestrata* was monitored by variation of the oxygen concentration in the medium (indicating the effect of the substance on the most important metabolic processes in plants: photosynthesis and respiration [8]). The experiments were carried out in 1-l aquariums filled up to the top with seawater. A 5 g portion of thallomes of freshly collected alga was placed in each aquarium, whereupon 0.01 g of the test substance was introduced (this particular weighed portion was selected in preliminary experiments), except for the reference reservoir. Some of the aquariums were kept for 24 h at room temperature (22–24°C) under natural illumination conditions so as to elucidate how the substances studied

[1] Reported at the Third International Conference "Chemistry, Technology, and Application of Fluorine Compounds," St. Petersburg, July 6–9, 2001.

1070-4272/02/7506-0954 $27.00 © 2002 MAIK "Nauka/Interperiodica"

affect photosynthesis. The remaining aquariums (prepared in a similar way) were kept for 1 day in the dark so as to elucidate how the tested compounds affect the alga respiration. After the experiments, we determined the amount of oxygen dissolved in the water from the aquariums by Winkler's method [9].

The mechanism by which fluoride ions influence the vital activity of various organisms is well understood [10–13]. Fluoride ions rank among microelements with fairly high physiological activity, namely, inhibiting enzymatic processes. The biological effect of these compounds is determined by the stability of the bonds and the possibility of their hydrolysis, rather than by the amount of fluorine contained in the molecule. The inhibiting effect of simple fluorides on the vital activity of microorganisms varies with their composition. For example, the toxic effect of NaF is typically lower than that of other fluorides [11], and NH_4F is a widely spread bactericide [10]. At the same time, fluorine ranks among elements indispensable to normal functioning of organisms, and, when in small concentrations, can stimulate biological processes.

Antimony(III) compounds exceed in toxicity antimony(V) compounds and are classed with the so-called thiol poisons [14, 15]. They react selectively with thiol groups belonging to various macromolecules of biological organisms, above all, enzymatic and other albuminous moieties, as well as to certain amino acids. It was found that SbF_3 forms with glycine four types or complexes, where glycine is either coordinated to antimony atom via the oxygen atom from deprotonated carboxy group or forms strong hydrogen bonds between the fluoride complex ions of antimony(III) [16]. As far as we know, the effect of antimony(III) fluoride complexes on biological objects remains, however, to be elucidated.

Our data on how antimony(III) fluoride complexes, fluorides of alkali metals, ammonium, and thallium, and antimony(III) oxide affect the growth of marine alga associations are presented in Table 1. Tables 2 and 3 present analogous data concerning photosynthesis and respiration of marine alga *U. fenestrata*.

Let us consider how the fluoride compounds affect the marine bacteriocenosis (Table 1). The strength of the bactericidal effect of antimony(III) fluoride and oxide and simple fluorides MF (M = Na, K, Rb, NH_4) on associations of marine bacteria, expressed in the NGA size, varies from 0.4 to 1.5 cm. These substances can be arranged in order of decreasing toxicity as $NH_4F > SbF_3 > NaF > KF \cdot 2H_2O$, $RbF > Sb_2O_3$.

Table 1. Bactericidal effect of substances (10^{-3} mol) on the vital activity of marine bacteriocenosis*

Compound		NGA size, cm
initial	complex	
NH_4F		1.5
SbF_3	KSb_2F_7, $NH_4Sb_2F_7$	1.0
	$NaSbF_4$	0.8
	$RbSbF_4$, $CsSbF_4$	0.7
NaF	NH_4SbF_4	0.6
	$RbSb_2F_7$	0.5
$KF \cdot 2H_2O$, RbF	$CsSb_2F_7$, Tl_2SbF_5	0.4
	K_2SbF_5	0.3
	$TlSb_2F_7$	0.2
Sb_2O_3		0.1

* Stimulating effect is exhibited by $KSbF_4$ and M_2SbF_5 (M = Na, Rb, Cs, NH_4).

Table 2. Effect of alkali metal fluorides, antimony(III) trifluoride and oxide, and antimony(III) fluoride complexes on photosynthesis of marine alga *U. fenestrata*

Compound	c_{O_2}, mg ml^{-1}		Change in c_{O_2}, %
	experiment	reference	
Activation			
$K_2Sb_2F_7$	7.56	6.49	16.5
Rb_2SbF_5	6.94	6.49	6.9
K_2SbF_5	6.90	6.49	6.3
$RbSb_2F_7$	6.52	6.49	0.4
Inhibition			
Na_2SbF_5	0	4.52	100
$NaSbF_4$	0	4.52	100
$RbSbF_4$	0.43	10.25	95.8
Tl_2SbF_5	2.12	10.25	79.3
$TlSb_2F_7$	2.50	10.25	75.6
CsF	2.68	10.25	73.8
$KSbF_4$	1.29	4.52	71.4
$CsSbF_4$	2.16	4.52	52.1
SbF_3	6.87	10.25	33.0
RbF	6.95	10.25	32.2
$KF \cdot HF$	7.80	10.25	23.9
Cs_2SbF_5	5.19	6.49	20.0
Sb_2O_3	9.06	10.25	11.3
$CsSb_2F_7$	6.05	6.49	6.8

The highest toxicity of NH_4F is probably due, above all, to the ability of the cation to easily form hydrogen bonds with other (in this case, organic) compounds or their moieties, so that the fluoride ion is involved into enzymatic processes occurring in bacteria. Antimony trifluoride exceeds antimony(III)

Table 3. Effect of alkali metal fluorides, antimony(III) trifluoride and oxide, and antimony(III) fluoride complexes on respiration of marine alga *U. fenestrata*

Compound	c_{O_2}, mg ml^{-1}		Change in c_{O_2}, %
	experiment	reference	
Activation			
SbF_3	0	1.01	100
RbF	0	1.01	100
CsF	0	1.01	100
$CsSb_2F_7$	0	1.55	100
$TlSb_2F_7$	0	1.01	100
$KSbF_4$	0	1.071*	100
$RbSbF_4$	0	1.01	100
$CsSbF_4$	0	1.071*	100
Rb_2SbF_5	0	1.55	100
Tl_2SbF_5	0	1.01	100
$KF \cdot HF$	0.04	1.01	96.0
KSb_2F_7	0.28	1.55	81.9
Sb_2O_3	0.21	1.01	79.2
K_2SbF_5	0.44	1.55	71.3
$RbSb_2F_7$	0.65	1.55	58.0
Inhibition			
Na_2SbF_5	0.1	0.071*	40.8
Cs_2SbF_5	1.91	1.55	23.2

* Experiments carried out in September–October 2000; the remaining experiments, in July–August 2000.

oxide in the inhibiting effect on the vital activity of marine bacteria and is close in its NGA size to NH_4F. Antimony(III) oxide exhibits the lowest toxicity with respect to marine bacteriocenosis throughout the group of the substances studied by us. The lack of toxic effect of Sb_2O_3 on *Pimephales promelas* embryo and larval growth was revealed in [17]. Thus, all the synthetic precursors of antimony(III) complexes, namely, MF (M = Na, K, Rb, NH_4), SbF_3, and Sb_2O_3, inhibit marine bacteriocenosis; the degree of their toxicity, expressed in the NGA size, varies within 0.1–1.5 cm.

In the group of antimony(III) fluoride complexes, the biocidal activity toward associations of marine bacteria is exhibited by MSb_2F_7 (M = K, Rb, Cs, NH_4, Tl), $MSbF_4$ (M = Na, Rb, Cs, NH_4), and M_2SbF_5 (M = K, Tl) (Table 1). The NGA sizes of these compounds vary within 0.2–1.0 cm. As to $KSbF_4$ and M_2SbF_5 (M = Na, Rb, Cs, NH_4), they, by contrast, stimulate bacteria growth.

Table 1 shows that the toxicity of heptafluorodiantimonate(III) ions toward marine bacteria decreases in order KSb_2F_7, $NH_4Sb_2F_7$ > $RbSb_2F_7$ > $CsSb_2F_7$ > $TlSb_2F_7$ and, evidently, depends on the structure of the complexes [2, 6, 18]. The MSb_2F_7 structures are composed of the M^+ cations and dimeric complex anions $[Sb_2F_7]^-$. Compounds with Rb^+ and NH_4^+ cations are isostructural. The structure of the $[Sb_2F_7]^-$ anion depends on the cation nature. For example, the structure of KSb_2F_7 consists of polymeric chains formed by alternating octahedra $Sb(1)F_5E$ (E is unshared electron pair of Sb^{3+}) and trigonal bipyramids $Sb(2)F_4E$ linked by asymmetric fluoride bridges. In the case of $CsSb_2F_7$, the symmetric bridging fluoride ion links two SbF_3 molecules, thus forming dimeric $Sb_2F_7^{2-}$ groups combined into layers connected by Cs^+. The structural motif for $RbSb_2F_7$ is intermediate between those for analogous compounds with M = K and Cs. The coordination polyhedra for Sb(III) are trigonal bipyramids $Sb(1)F_4E$ and $Sb(2)F_4E$, integrated into layers separated by rubidium cations. The most complex structure is exhibited by $TlSb_2F_7$, whose unit cell contains six nonequivalent positions of Sb(III) forming two polyhedron types: SbF_5E octahedra and SbF_4E trigonal bipyramids integrated into a hexanuclear $[Sb_6F_{21}]^{3-}$ ring.

Complex tetrafluoroantimonates(III) are not isostructural [2, 18], but $MSbF_4$ (M = Na, Rb, Cs, NH_4) compounds have a common, polymeric, structure of the anions, unlike $KSbF_4$, where the anion has a tetrameric structure $[Sb_4F_{16}]^{4-}$. The structural dissimilarity is responsible for the difference in the biocidal properties of these substances (Table 1): $MSbF_4$ (M = Na, Rb, Cs, NH_4) inhiibit the bacterial growth similarly (unlike MSb_2F_7), with the NGA size varying within 0.6–0.8 cm. By contrast, $KSbF_4$ stimulates bacterial growth.

Complexes from the series M_2SbF_5 (M = Na, K, Rb, Cs, NH_4, Tl) are composed of isolated SbF_5^{2-} anions and metal cations, and all of them, except Na_2SbF_5, are isostructural [2, 18]. The antimony polyhedron is a square pyramid completed to an octahedron by the E pair, SbF_5E. A weak inhibiting effect on the growth of marine bacteria is only exhibited by two pentafluoroantimonates(III) with K^+ and Tl^+ cations, for which the respective NGA sizes are 0.3 and 0.4 cm (Table 1). The remaining compounds from the M_2SbF_5 series (M = Na, Rb, Cs, NH_4) intensify the growth of marine bacteria. The different biological activities exerted by isostructural pentafluoroantimonates(III) are, probably, due both to the nature of the cation and to certain, previously revealed, specific features of the electronic and crystal structures of these complexes [2]. For example, pentafluoroantimonates(III) of potassium and thallium differ at room temperature from the other M_2SbF_5 compounds

in anomalous behavior of a number of $^{121, 123}$Sb NQR parameters (signal intensity, asymmetry parameter of the electric field gradient); K_2SbF_5, in addition, exhibits a number of phase transitions involving changes in the structure and heat capacity.

Let us consider how the substances tested affect the photosynthesis in *U. fenestrata* alga (Table 2). This process is stimulated by four antimony(III) fluoride complexes: MSb_2F_7 and M_2SbF_5 (M = K, Rb). The greatest activating effect is exhibited by KSb_2F_7; and the remaining three compounds exert insignificant ($RbSb_2F_7$, the weakest) effect on the bio test.

Compounds MSb_2F_7 (M = Cs, Tl), $MSbF_4$ (M = Na, K, Rb, Cs). M_2SbF_5 (M = Na, Cs, Tl), MF (M = K, Rb, Cs), SbF_3, and Sb_2O_3 exhibit algicidity by inhibiting photosynthesis and decreasing the content of dissolved oxygen in water relative to the reference runs. Our experiment on determining the amount of dissolved oxygen in seawater shows (Table 2) that, among simple substances, the strongest algicidal effect is exerted by cesium fluoride, and the weakest, by Sb_2O_3. The algicidal power of the fluoride complexes of Sb(III) on photosynthesis of *U. fenestrata* alga depends on the composition of a complex and can increase or, by contrast, decrease relative to the initial simple compounds used for their synthesis. For example, the powers of all the three antimony(III) fluorocomplexes with Cs^+ cation are weaker as compared with CsF. In accordance with the toxicity relative to simple compounds, these complexes form the series (Table 1): CsF > $CsSbF_4$ > SbF_3 > Cs_2SbF_5 > $CsSb_2F_7$.

At the same time, photosynthesis of the alga is more strongly suppressed by $RbSbF_4$ than by RbF.

The respiratiom of *U. fenestrata* alga also depends on the composition of a substance present in the aquarium (Table 3). A toxic effect, manifested in suppression of the respiration function of plants, is only exhibited by two Sb(III) fluoride complexes, namely, M_2SbF_5 (M = Na, Cs). These same compounds suppress photosynthesis as well (Table 2). The compound with the Na^+ cation is more toxic in the light, and that with the Cs^+ cation, in the dark. According to Table 3, the remaining substances, both simple and complex, which suppress oxygen release during photosynthesis (Table 2), proved to stimulate alga respiration. The dark sensitivities of the alga to the substances tested are different. In the simple compound group, plant respiration is the least affected by antimony(III) oxide, and in the fluoride complex group, by $RbSb_2F_7$.

CONCLUSIONS

(1) The effect of alkali metal and ammonium fluorides, as well as that of antimony(III) fluoride, oxide, and fluoride complexes, on the vital activity of marine bacteriocenosis and marine green alga *U. fenestrata* was assessed.

(2) SbF_3 and compounds of composition $MSbF_4$ and MSb_2F_7 (except for M = K) and M_2SbF_5 (M = K, Tl) exhibit strong bactericidal effect; $KSbF_4$ and M_2SbF_5 (M = Na, Rb, Cs, NH_4), by contrast, stimulate bacteria growth.

(3) Most of solutions of Sb(III) fluoride compounds, when in concentration of 0.01 g l^{-1}, inhibit photosynthesis in algae and activate their respiration.

(4) Biological properties of the compounds studied are, evidently, due both to the properties of the ions [fluoride ions, antimony(III) ions, and cations] consituting the molecule and to the properties of the compounds themselves (composition, crystal lattice structure, electronic structure features). The compounds acting as inhibitors are promising for development of antifouling pastes and paints.

REFERENCES

1. Buslaev, Yu.N. and Davidovich, R.L., *Koord. Khim.*, 1989, vol. 15, no. 11, pp. 1444–1465.
2. Zemnukhova, L.A., Synthesis, NQR Spectroscopy, and Structure of Coordination Compounds of Antimony(III), Bismuth(III), Indium(III), and Tellurium(IV), *Doctoral Dissertation*, Vladivostok, 1998.
3. Zemnukhova, L.A. and Mamontova, V.A., Abstracts of Papers, *XVI Int. Symp. "Fluorine Chemistry,"* Durham (the United Kingdom), 2000, pp. 1P-2.
4. Davidovich, R.L. and Zemnukhova, L.A., *Koord. Khim.*, 1975, vol. 1, no. 4, pp. 477–481.
5. Ballard, J.G., Birchall, Th., Fuorcade, R., and Mascherpa, G., *J. Chem. Soc., Dalton Trans.*, 1976, no. 23, pp. 2409–2412.
6. Udovenko, A.A., Gorbunova, Yu.E., Davidovich, R.L., *et al.*, *Koord. Khim.*, 2000, vol. 26, no. 9, pp. 662–665.
7. Rodina, A.G., *Metody vodnoi mikrobiologii* (Methods of Aquatic Microbiology), Moscow: Nauka, 1965.
8. Polishchuk, R.A., *Biologicheskie osnovy bor'by s obrastaniem* (Biological Principles of Antifouling Effect), Kiev: Naukova Dumka, 1973, pp. 155–193.
9. *Rukovodstvo po metodam khimicheskogo analiza morskikh vod* (Manual on Chemical Analysis of Seawater), Orodovskii, S.G., Ed., Gidrometeoizdat, 1977.
10. *Vrednye veshchestva v promyshlennosti* (Harmful

Substances in Industry), Lazarev, N.V. and Gadaskina, I.D., Eds., Leningrad: Khimiya, 1977, vol. 3.

11. Taradin, Ya.I., Goremykina, L.F., Sukharenok, B.L., and Pisarenko, G.I., *Samoochishchenie i bioindikatsiya zagryaznennykh vod* (Self-Purification and Bioindication of Contaminated Water), Moscow: Nauka 1980, pp. 179–184.
12. Hughes, M.N., *The Inorganic Chemistry of Biological Processes*, London: Wiley, 1974.
13. *Soedineniya ftora. Sintez i primenenie* (Fluorine Compounds. Synthesis and Application), Ishikawa, I., Ed., Moscow: Mir, 1990.
14. Arzamastsev, E.V., *Gig. Sanit.*, 1964, no. 12, pp. 16–20.
15. Oksengendler, G.I., *Yady i protivoyadiya* (Poisons and Antidotes), Leningrad: Nauka, 1982.
16. Davidovich, R.L., Logvinova, V.B., Zemnukhova, L.A., *et al.*, *Koord. Khim.*, 1991, vol. 17, no. 10, pp. 1342–1348.
17. Le-Blanc, G.A. and Dean, J.W., *Bull. Environ. Contam., Toxicol.*, 1984, vol. 32, no. 5, pp. 565–569.
18. Udovenko, A.A. and Volkova, L.M., *Koord. Khim.*, 1981, vol. 7, no. 12, pp. 1763–1812.

Russian Journal of Applied Chemistry, Vol. 75, No. 6, 2002, pp. 959–961. Translated from Zhurnal Prikladnoi Khimii, Vol. 75, No. 6, 2002, pp. 976–978.
Original Russian Text Copyright © 2002 by Moldavskii, Furin, Shkul'tetskaya, Eifman.

ORGANIC SYNTHESIS AND INDUSTRIAL ORGANIC CHEMISTRY

Fluorination of Organic Compounds with Cobalt Trifluoride and Elemental Fluorine in the Presence of Cobalt Trifluoride[1]

D. D. Moldavskii, G. G. Furin, L. V. Shkul'tetskaya, and B. Ya. Eifman

Prikladnaya Khimiya Russian Scientific Center, St. Petersburg, Russia

Received January 17, 2002

Abstract—Fluorination of organic compounds with cobalt trifluoride and elemental fluorine in the presence of cobalt trifluoride was studied. Fluorination with elemental fluorine proceeds under external-kinetic control at a constant rate. Examples of fluorination with elemental fluorine of certain fluorinated olefins and polyfluorinated paraffins in the presence of CoF_3 are presented.

Cobalt trifluoride is a common fluorinating agent for synthesis (including commercial production) of perfluorinated organic compounds (paraffins, ethers, etc.) form hydrocarbon and unsaturated analogue [1, 2]. In the reaction, cobalt trifluoride is reduced to difluoride:

$$CoF_3 + C_nH_{2n+2} \rightarrow CoF_2 + C_nF_{2n+2} + HF.$$

Fluorination with cobalt trifluoride is characterized by low yield (30–40%) of target products, limited productivity because of the low content of available fluorine (16.30 wt %; the actual consumption is lower by a factor of 1.2–3), and noticeable amount of residual hydrogen-containing and unsaturated compounds (up to 1 wt %), instead of 1×10^{-3}–5×10^{-4} wt % required in medicine, electronics, and other branches of industry. Therefore, other synthesis methods should be searched for. One of them is catalytic fluorination of fluorine-containing organic compounds with elemental fluorine. Higher fluorides of metals with variable oxidation state, including nickel, copper, and cobalt fluorides [3–5], are usually used as such catalysts. In this work, we studied fluorination of monohydroperfluorotripropylamine $C_3F_6HN(C_3F_7)_2$ (**I**) and monohydroperfluorotributylamine $C_4F_8HN(C_4F_9)_2$ (**II**) with cobalt trifluoride and with elemental fluorine in the presence of cobalt trifluoride. Compounds **I** and **II** are the main process impurities in electrochemical synthesis of perfluorotripropylamine $(C_3F_7)_3N$ and perfluorotributylamine $(C_4F_9)_3N$, respectively. Their content in crude products reaches 30 wt %.

Fluorination was performed in a reactor packed with CoF_3. In the first case, a mixture of vapors of a compound to be fluorinated and fluorine was supplied, and in the second case, nitrogen was introduced instead of fluorine at the same flow rate. The figure shows the kinetics of fluorination of monohydroperfluorotributylamime (**II**).

Curve *2* describing the rate of fluorination with CoF_3 is characteristic for reactions whose initial stage proceeds on the surface of a solid reactant (CoF_3 in this case) under external-kinetic control. Since CoF_3 is consumed in the surface layer, the reaction becomes diffusion-controlled, which accounts for the observed decrease in the reaction rate [6]. It should be noted that the initial section of curve *2* is rather difficult for analysis, and the majority of papers on CoF_3 fluorination kinetics contain only data for the diffusion region, in which the decrease in the reaction rate is neglected and the rate is considered to be constant [6, 7]. Studies of fluorination of fluorinated methanes [7] and hexafluoropropane [8] have shown that the fluorination reaction is first-order.

Fluorination with elemental fluorine in the presence of CoF_3 (curve *1*) proceeds under external-kinetic control since the CoF_3 concentration in the surface

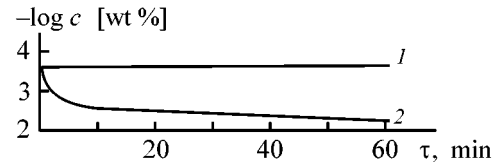

Relative rate of fluorination of **II**: (*c*) concentration of **II** and (τ) time. Fluorination with (*1*) CoF_3–F_2 and (*2*) CoF_3.

[1] Reported at the 3th International Conference "Chemistry, Technology, and Application of Fluorinated Compounds," St. Petesrburg, June 6–9, 2001.

1070-4272/02/7506-0959 $27.00 © 2002 MAIK "Nauka/Interperiodica"

Table 1. Fluorination of CoF_2 and hydrogen-containing impurities of perfluorotributylamine [contact time τ = 5 min, $(C_4F_8H)_3N$ initial concentration 17.5 wt %]

T, °C	Content, wt %		*T*, °C	Content, wt %	
	available fluorine (CoF_3)	hydrogen-containing compounds		available fluorine (CoF_3)	hydrogen-containing compounds
200	13.0 (79.4)	7.5	350	16.0 (97.5)	2.1
250	13.6 (83.0)	4.8	400	16.38 (100)	0
300	15.4 (94.0)	3.2	450	16.38 (100)	0

Table 2. Fluorination of certain hydrogen-containing and unsaturated compounds with elemental fluorine on CoF_3

Compound		*T*, °C	τ, min	$A^* \times 10^{-4}$, wt %	Yield, mol%
fluorinated	fluorinated				
$C_3F_7CFH–CHF_2$	C_5F_{12}	230–280	5	6	94.4
$C_2F_4HN(C_2F_5)_2$	$(C_2F_5)_3N$	270–330	5	5	95.5
$C_3F_6HN(C_3F_7)_2$	$(C_3F_7)_3N$	320–380	10	6	96.0
$C_4F_8HN(C_4F_9)_2$	$(C_4F_9)_3N$	360–410	13	7	93.2
$C_5F_{10}HN(C_5F_{11})_2$	$(C_5F_{11})_3N$	380–430	16	8	90.1
$C_4F_8HOC_4F_8H$	$(C_4F_9)_2O$	300–350	5	5	96.5
$(C_3F_7)_2CF–CF=CF_3$	C_9F_{20}	320–380	6	5	97.0
cyclo $C_6F_9–C_2F_5$	cyclo $C_6F_{11}–C_2F_5$	300–360	7	5	96.4

* (*A*) Residual content of hydrogen-containing and unsaturated compounds.

layer is constant owing to timely or even advance supply of fluorine:

$$RH + CoF_3 \rightarrow RF + HF + CoF_2,$$
$$CoF_2 + F_2 \rightarrow CoF_3.$$

This is illustrated by the data on fluorination of CoF_2 and compound **II** at various temperatures presented in Table 1.

It follows from the kinetics of fluorination of **I** that this reaction is second-order. The activation energy amounts to 37.5 kJ mol^{-1}. The equation of the reaction rate is as follows:

$$\log V = \log \text{const} - 4.56E/RT.$$

It should be noted that the catalytic fluorination is characterized by high yield of the target products and their insignificant degradation.

Data on catalytic fluorination of certain hydrogen-containing and unsaturated compounds are listed in Table 2.

The results make evident the difference between fluorination with CoF_3 and that with fluorine in the presence of CoF_3 as a catalyst.

In the first case, the fluorination rate is low and decreases with time; the process is limited by the content of available fluorine, which prevents its being performed in the continuous mode. The residual content of hydrogen-containing or unsaturated compounds in the resulting products is substantial ($> 1 \times 10^{-3}$ wt %), which requires additional purification. In the second case, the fluorination rate is fairly high and constant; the process has no time limitation, which allows it to be performed in the continuous mode; the residual content of hydrogen-containing compounds is less than 1×10^{-3} wt %.[2]

EXPERIMENTAL

The UV spectra were recorded on a UF-26 spectrophotometer; the fluoride ion was determined with an ET-1 fluoride-selective electrode. In chromatographic analysis, a heat-conductivity detector was used; carrier gas helium, solid phase Silokhrom, liquid phase 20% α,α,α-tri(β-cyanoethyl)acetophenone, 2 m × 3 mm

[2] The catalytic fluorination process was implemented at the pilot plant of the "Prikladnaya Khimiya" Russian Scientific Center.

column. The GC-MS analysis was performed on a Hewlett-Packard device comprising an HP-5890 gas chromatograph, an HP5972 mass-selective detector, and a Vectra 5/100 working station with software for data processing and Wiley138.L and NBS75K.L database.

Chromatographic separation was performed on a 30 m HP-5MS capillary column in the programmed-heating mode. Chromatograms were recorded by the total ion current within the 35–700 mass range. The impurities were identified by comparing the mass spectra of separated mixture components with those from the Wiley138.L and NBS75K.L databases and by calculation.

The kinetics of fluorination of **I** was studied in a vertical reactor made from a nickel tube (inner diameter 36 mm). The reactor was packed with CoF_3 with bed height of 300 mm. A thermocouple pocket was arranged along the reactor axis. The temperature variation throughout the bed did not exceed 3°C. From a batcher, a mixture of **I** (25 wt %) with $(C_3F_7)_3N$ (75 wt %) and fluorine were supplied at definite and constant rates into a mixer-evaporator, which was a 500-mm nickel tube 36 mm in diameter, equipped with a controllable heater. The fluorine excess did not exceed 20% relative to the stoichiometry. From the evaporator, the reaction mixture passed through a catalyst bed (with particle size of 0.035–0.05 mm) and condensed in a trap cooled with liquid nitrogen. After process completion, the trap was warmed to room temperature and weighed, and the reaction products were analyzed by GLC. Low-boiling products containing fluorine and HF were neutralized in a column with lime and analyzed by GLC. The experiments were performed at 150, 180, 220, and 250°C.

The fluorination rate constants and activation energy [9] were calculated from the concentration-vs.-time plots for 150, 180, 220, and 250°C.

ACKNOWLEDGMENTS

The work was financially supported by ISTC.

REFERENCES

1. Kornilov, V.V., Kosteev, R.A., Maksimov, B.N., *et al.*, *Zh. Prikl. Khim.*, 1995, vol. 68, no. 9, pp. 1409–1418.
2. *Advances in Fluorine Chemistry*, vol. I–II, Stacey, M., Tatlow, J.C.,and Sharpe, A.G., Eds., London: Butterworths Scientific Publications, (1960–1961).
3. Zakharov, V.Yu., Denisov, A.K., and Novikova, M.D., *Zh. Org. Khim.*, 1994, vol. 30, no. 12, pp. 1844–1846.
4. Zakharov, V.Yu., Denisov, A.K., and Novikova, M.D., Abstracts of Papers, *Mezhdunarodnaya konferentsiya "Khimiya, tekhnologiya i primenenie ftorsoderzhashchikh soedinenii v promyshlennosti"* (Int. Conf. "Chemistry, Technology, and Application of Fluorine-Containing Compounds in Industry"), St. Petersburg, 1994, p. 11.
5. Moldavsky, D.D., Bisren, T.A., Kaurova, G.I., and Furin, G.G., *J. Fluorine Chem.*, 1999, vol. 94, pp. 157–167.
6. Rozovskii, A.Ya., *Katalizator i reaktsionnaya sreda* (Catalyst and Reaction Medium), Moscow: Nauka, 1988.
7. Asovich, V.S. and Kosteev, R.A., *Zh. Prikl. Khim.*, 1994, vol. 67, no. 8, pp. 1320–1323.
8. Asovich, V.S., Kornilov, V.V., Kosteev, R.A., and Maksimov, B.N., *Zh. Prikl. Khim.*, 1994, vol. 67, no. 1, pp. 103–106.
9. Leidler, K., *Reaction Kinetics*, vol. I: *Homogeneous gas reactions*, vol. II: *Reactions in Solution*, Oxford: Pergamon, 1963.

Russian Journal of Applied Chemistry, Vol. 75, No. 6, 2002, pp. 962–964. Translated from Zhurnal Prikladnoi Khimii, Vol. 75, No. 6, 2002, pp. 979–981.
Original Russian Text Copyright © 2002 by Kalechits, Osinovskii, Matveenko, Ol'khovik.

ORGANIC SYNTHESIS AND INDUSTRIAL ORGANIC CHEMISTRY

Synthesis of 2-Hydroxy-1-Naphthaldehyde under Conditions of Heterogeneous Catalysis

G. V. Kalechits, A. G. Osinovskii, Yu. V. Matveenko, and V. K. Ol'khovik

Institute of Chemistry of New Materials, Belarussian National Academy of Sciences, Minsk, Belarus

Received February 7, 2002

Abstract—A procedure was developed for synthesis of 2-hydroxy-1-naphthaldehyde by Reimer–Tiemann fluorination of 2-naphthol under conditions of heterogeneous catalysis.

Aromatic *o*-hydroxy aldehydes readily enter cyclizations and are therefore important synthetic precursors of carbocyclic and heterocyclic compounds. For example, 2-hydroxy-1-naphthaldehyde **I** is widely used for preparing various luminophores, optical whiteners [1, 2], analytical reagents [3], and drugs.

In synthesis and study of various benzocoumarin derivatives, a need arose for relatively large amounts of **I**. Published procedures for preparing **I** [4–7], despite high yields (up to 80%), are complicated by use of expensive and deficient reagents, which are often toxic.

The most acceptable route to **I**, free of the above drawbacks, is formylation of 2-naphthol **II** by the Reimer–Tiemann reaction; however, in the classical version of this procedure, the yields are as low as 38–48% [8], and isolation of a high-purity product is difficult, which makes this procedure unsuitable for large-scale syntheses.

To raise the yield and obtain high-purity product, we examined the possibility of formylation of **II** with chloroform in alkaline solution under conditions of heterogeneous catalysis [9]. Although the Reimer–Tiemann reaction usually does not require catalysts, it was shown in [10] that the use of tertiary ammonium salts for preparing salicylaldehyde from phenol increases the yield of the target product by more than a factor of 2.

Along with the low cost and availability of the starting compounds (naphthol **II**, chloroform, alkali), an advantage of the heterogeneous-catalytic synthesis in alkaline solution is the formylation at the *o*-position and the minimum extent of condensation of the forming aldehyde **I** with the initial naphthol **II**. The possibility of such a condensation in acid solutions with the formation of dibenzoxanthene derivatives and oligomeric substances contaminating the target product was noted in [11].

Aldehyde **I** was prepared by the scheme

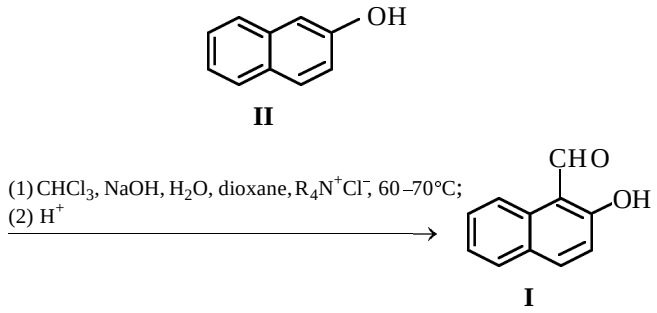

It is well known that the reactive species in the Reimer–Tiemann reaciton is dichlorocarbene :CCl_2. The mechanism of dichlorocarbene generation under conditions of heterogeneous catalysis is also understood in detail [12]. The reaction scheme can be described as follows. At the phase boundary, chloroform is deprotonated to give trichloromethylide anion:

$$HCCl_{3(org.\ phase)} + Na^+_{(aq.\ phase)} + OH^-_{(aq.\ phase)} \rightleftarrows CCl^-_{3(interface)} + Na^+_{(interface)} + H_2O. \quad (1)$$

This is followed by exchange with the quaternary ammonium salt (2) and generation of carbene (3) (the reaction is reversible):

$$CCl^-_{3(interface)} + [R_4N^+X^-]_{(org.\ phase)} \rightleftarrows [R_4N^+CCl^-_3]_{(org.\ phase)} + X^-_{(aq.\ phase)}, \quad (2)$$

$$[R_4N^+CCl^-_3]_{(org.\ phase)} \rightleftarrows [R_4N^+Cl^-]_{(org.\ phase)} + [CCl_2]_{(org.\ phase)}. \quad (3)$$

1070-4272/02/7506-0962 $27.00 © 2002 MAIK "Nauka/Interperiodica"

The carbene formed irreversibly reacts with the substrate:

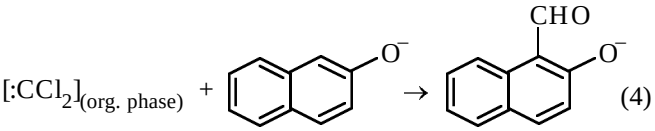

(4)

The reaction was performed in a two-phase aqueous-organic system. The organic phase was 1,4-dioxane or a mixture of 1,4-dioxane with a branched alcohol in a ratio varying from 10 : 1 to 30 : 1. Branched alcohols were added to raise the solubility of sodium naphtholate in the organic phase. As catalysts we tested quaternary ammonium salts: tetrabutylammonium (TBAC), benzyltriethylammonium (TEBAC), and benzyltrimethylammonium (TMBAC) chlorides (0.1–0.4 mol %). Dichlorocarbene was generated from excess chloroform and 40% aqueous NaOH. The reaction was performed at 60–70°C.

The experimental results (see table) show that the Reimer–Tiemann formylation of naphthol **II** under conditions of heterogeneous catalysis gives the target product in a yield 1.5–2 times higher than that in the classical version of this reaction.

The best results were obtained with tetrabutylammonium chloride as phase-transfer catalyst; however, as seen from the table, with the yields the other catalysts are only slightly lower.

It should be noted that this procedure is very easy. Most of the impurities are removed in the stage of isolation of the hydroxy aldehyde sodium salt, so that the target product can be obtained 98% pure without vacuum distillation.

Heterogeneous-catalytic synthesis of hydroxy aldehyde **I** (65–70°C)

Catalyst, mol %	Organic phase,* ml	Yield, %
BuN^+Cl^-:		
0.4	*i*-BuOH, 5	78
0.1**	*i*-AmOH, 5	68**
0.2	*i*-BuOH, 5	73
0.3	*i*-PrOH, 15	76
TEBAC:		
0.1	*i*-BuOH, 5	71
0.2	*i*-PrOH, 15	73
0.4	*i*-AmOH, 10	77
TEMAC:		
0.1	*i*-BuOH, 5	70
0.2	*i*-BuOH, 5	74
0.4	*i*-BuOH, 5	78

* In all runs, the second component is dioxane (150 ml).
** At 68–72°C.

EXPERIMENTAL

The ^1H NMR spectra were recorded on a Tesla BS-587A spectrometer (100 MHz, internal reference TMS). The IR spectra were taken on a Specord M-80 spectrometer in the range 400–4000 cm^{-1}, using KBr pellets. The melting points were determined on a Boetius stage.

2-Hydroxy-1-naphthaldehyde I. A flask equipped with stirrer, thermometer, reflux condenser, and dropping funnel was charged with 144.2 g (1 mol) of naphthol **II** and 400 ml of 40% NaOH. The mixture was stirred for 0.5 h to obtain a homogeneous solution. Then the mixture was cooled to 65–70°C, and 1.15 g (0.004 mol) of a quaternary ammonium salt and 130 ml of a 30 : 1 mixture of 1,4-dioxane with a branched alcohol were added. This was followed by addition of chloroform (155.2 g, 1.3 mol) at a rate ensuring reaction temperature within 70°C. After adding the whole amount of chloroform, the mixture was stirred at 65–70°C for an additional 1 h and cooled to 20°C; 2-hydroxy-1-naphthaldehyde sodium salt was filtered off. The resulting crystalline product was washed successively with 1% NaOH and a 20 : 1 mixture of dioxane with 1% aqueous NaOH. The wet residue was transferred into a flask and stirred for 1 h with 300 ml of 10–15% aqueous HCl. The precipitate of aldehyde **I** was filtered off, washed with water to neutral reaction and negative reaction for chloride ions, and dried in a desiccator over $CaCl_2$. Yield 78%, mp 80–82°C, main substance content 98%.

The physicochemical and spectral characteristics of **I** are in agreement with reference data [8].

CONCLUSIONS

(1) 2-Naphthol is regioselectively formylated under conditions of the heterogeneous-catalytic version of the Reimer–Tiemann reaction to give 2-hydroxy-1-naphthaldehyde.

(2) This procedure allows preparation of a high-purity target product in 75% yield.

REFERENCES

1. Krasovitskii, B.M. and Bolotin, B.M., *Organicheskie lyuminofory* (Organic Luminophores), Moscow: Khimiya, 1984.

2. Dorlars, A., Schellhammer, C.-W., and Schroeder, J., *Angew. Chem.*, 1975, vol. 87, no. 19/21, pp. 683–786.
3. Busev, A.I., *Sintez novykh organicheskikh reagentov dlya neorganicheskogo analiza* (Synthesis of New Organic Reagents for Inorganic Analysis), Moscow: Mosk. Gos. Univ., 1972.
4. Buehler, C.A. and Pearson, D.E., *Survey of Organic Syntheses*, New York: Wiley–Interscience, 1970.
5. Blazevic, N. and Kolbah, D., *Synthesis*, 1979, no. 1, pp. 161–166.
6. Gross, H., Rieche, A., and Matthey, G., *Chem. Ber.*, 1963, vol. 96, no. 1, p. 308.
7. Casiraghe, G., Casnati, C., Poglia, G., and Sortoi, G., *J. Chem. Soc.*, Perkin Trans. 1, 1980, no. 9, pp. 1862–1865.
8. *Organic Syntheses*, Blatt, A.H., Ed., New York: Wiley, 1944. Translated under the title *Sintezy organicheskikh preparatov*, Moscow: Inostrannaya Literatura, 1952, coll. 3.
9. BY Patent 970298.
10. Sasson, Y. and Yanovich, M., *Tetrahedron Lett.*, 1979, no. 39, pp. 3753–3756.
11. Isagawa, K., Kimuro, Y., and Kwan, S., *J. Org. Chem.*, 1974, vol. 38, no. 21, pp. 3171–3172.
12. Dehmlow, E.V. and Dehmlow, S.S., *Phase Transfer Catalysis*, Weinheim: Chemie, 1983, 2nd ed.

Russian Journal of Applied Chemistry, Vol. 75, No. 6, 2002, pp. 965–968. Translated from Zhurnal Prikladnoi Khimii, Vol. 75, No. 6, 2002, pp. 982–985.
Original Russian Text Copyright © 2002 by Lazareva, Yakovleva, Shinkareva.

MACROMOLECULAR CHEMISTRY AND POLYMERIC MATERIALS

Rheological and Electrical Characteristics of Polyvinyl Alcohol Composites with Phosphoric Acid

T. G. Lazareva, O. V. Yakovleva, and E. V. Shinkareva

Institute of General and Inorganic Chemistry, Belarussian National Academy of Sciences, Minsk, Belarus

Received October 17, 2001; in final form, February 2002

Abstract—Rheological and electrical properties of fluid PVA-based composites with phosphoric acid are studied. Formation of ordered liquid-crystal structures in the PVA matrix with addition of phosphoric acid to the system is assumed, with the structural ordering dependent on the polymer to acid ratio and solution temperature.

Composites of polyvinyl alcohol (PVA) with inorganic and poly acids (silicotungstic, phosphoric, polyacrylic, polymethacrylic) can find wide application for preparation of membranes, various coatings, paper sizing formulations, etc. Addition of polyacids or inorganic acids to PVA solutions produces hydrogen-bonded complexes [1]. The rheological and electrical properties of PVA composites with water-soluble cellulose ethers (carboxymethyl cellulose, methyl cellulose) and silicotungstic acid have been studied previously [2–4]. The rheological characteristics of the composites as influenced by the temperature, shear stress and rate, and composition suggested the possibility of formation of anisotropic liquid-crystal (LC) structures. Proceeding with these studies, we examined in this work the rheological and electrical properties of PVA-based composites with phosphoric acid H_3PO_4.

EXPERIMENTAL

The test samples were prepared by adding fixed amounts of 90% phosphoric acid to a 10% aqueous polyvinyl alcohol (PVA 16/1) solution at room temperature to obtain composites containing 15, 25, and 40 wt % H_3PO_4. The mixtures were stirred for 30 min on an LR10 laboratory stirrer. The viscosity η was measured on a Rheotest-2 rotary viscometer over the shear rate range from 3 to 1312 s^{-1} at a temperature of 20–80°C. The electrical conductivity æ and dielectric loss tangent tan δ were determined on an E7-15 instrument at a frequency of 1 kHz.

Figure 1 shows the viscosity η as a function of the shear rate $\dot{\gamma}$ for a series of the composites at various temperatures. Raising the temperature to 70°C and higher results in a more pronounced effect of the shear rate for the composites containing from 15 to 25 wt %

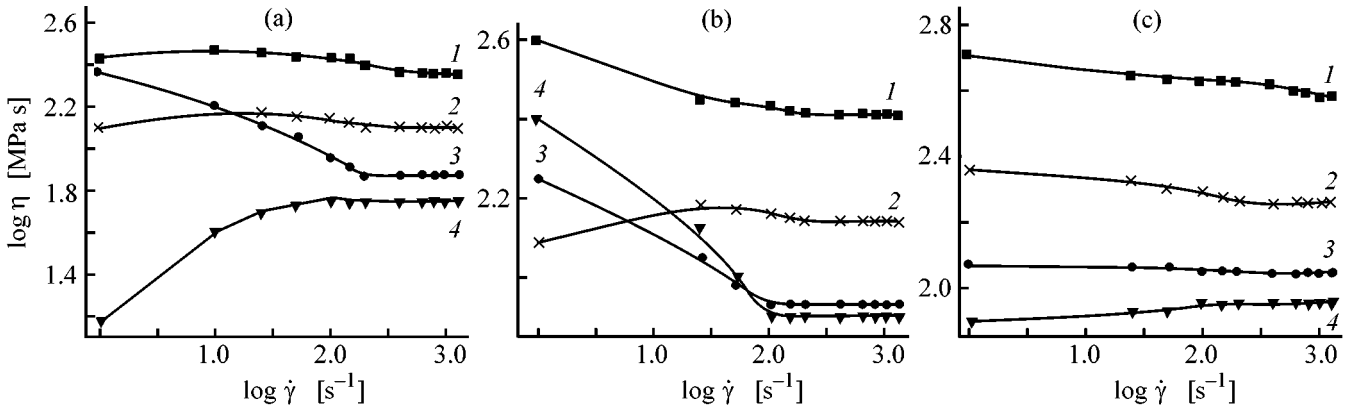

Fig. 1. Dynamic viscosity η vs. the shear rate $\dot{\gamma}$ for PVA-based composites with varied H_3PO_4 content. H_3PO_4 content (wt %): (a) 15, (b) 25, and (c) 40. Temperature (°C): (*1*) 30, (*2*) 50, (*3*) 70, and (*4*) 80.

1070-4272/02/7506-0965 $27.00 © 2002 MAIK "Nauka/Interperiodica"

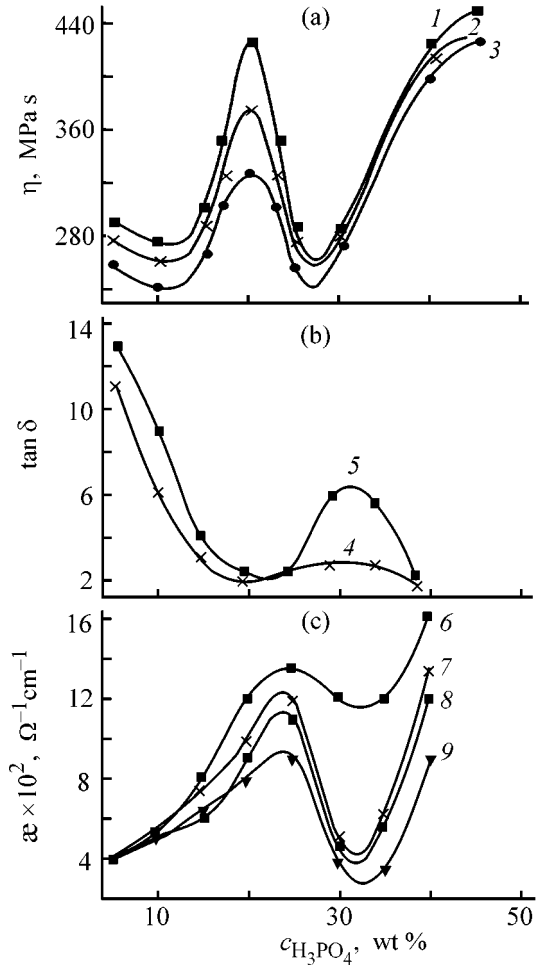

Fig. 2. (a) Dynamic viscosity η at 30°C, (b) dielectric loss tangent tan δ, and (c) conductivity æ vs. the phosphoric acid concentration $c_{H_3PO_4}$. Shear rate $\dot{\gamma}$ (s^{-1}): (*1*) 27, (*2*) 81, and (*3*) 243. Temperature (°C): (*4*, *6*) 30, (*5*, *7*) 60, (*8*) 70, and (*9*) 80.

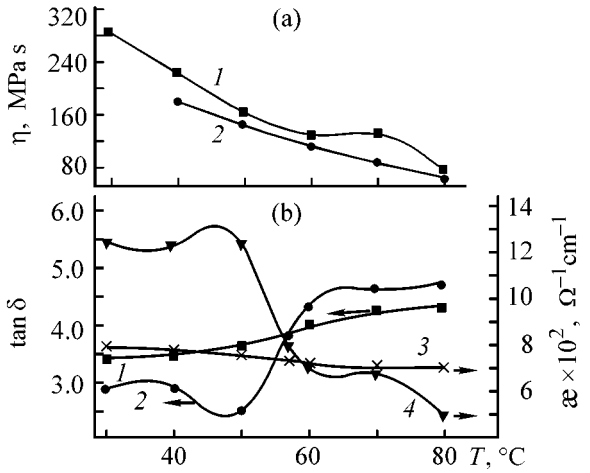

Fig. 3. (a) Dynamic viscosity η at a shear rate of 81 s^{-1} and (b) dielectric loss tangent tan δ and conductivity æ vs. temperature *T*. Phosphoric acid concentration (wt %): (a) (*1*) 30 and (*2*) 15 and (b) (*1*, *3*) 15 and (*2*, *4*) 30.

H_3PO_4. Depending on temperature, the viscosity may increase or decrease with increasing shear rate. This can be attributed to weakening intermolecular interactions and growing molecular flexibility of large aggregates of macromolecules in the polymer matrix with increasing temperature and also to aggregation of macromolecules in the mechanical field [5]. With the phosphoric acid content increasing to 40 wt %, the effect of the shear rate on the viscosity becomes less pronounced (Fig. 1c).

Figure 2 shows the dependences of the viscosity η, dielectric loss tangent tan δ, and conductivity æ on the phosphoric acid concentration in the composites based on 10% aqueous PVA. The composition dependence of the viscosity (Fig. 2a) passes through a maximum at $c_{H_3PO_4}$ = 20 wt % at 30°C. With the shear rate increasing from 27 to 243 s^{-1}, the effect becomes less pronounced. An anomalous behavior of the viscosity is also observed in the composition dependences of tan δ and æ (Figs. 2b, 2c). Comparison of Figs. 2a and 2b shows that the maximum in the concentration dependence of η at $c_{H_3PO_4}$ = 20 wt % corresponds to the minimum in the concentration dependence of tan δ, and vice versa, the maximal tan δ corresponds to the minimal η at an acid content of about 30 wt %. Conversely, the concentration dependences of the viscosity and conductivity are nearly parallel (Figs. 2a, 2c).

The temperature dependences of the viscosity, tan δ, and æ for the composites containing 15 and 30 wt % H_3PO_4 are given in Fig. 3. At low shear rate we observed an anomalous behavior of the viscosity within the temperature range 60–80°C for the composite containing 30 wt % H_3PO_4. With increasing temperature, tan δ grows and æ decreases; the effect being more pronounced for the composite containing 30 wt % H_3PO_4. Taking into account data from [6], demonstrating anomalous viscosity-vs.-temperature curves for the systems with LC structures, one may suggest that the temperature affects the degree of ordering in the PVA–H_3PO_4 system. If so, the effect must be dependent on the molar ratio of the components, at which the LC state occurs and an increase in the flexibility of separate fragments of the polymer chain is observed.

Products differing in structure are formed in the reaction of PVA with phosphoric acid derivatives [4]:

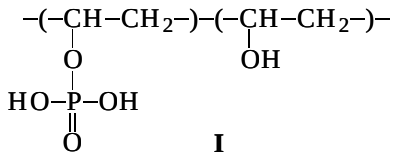

I

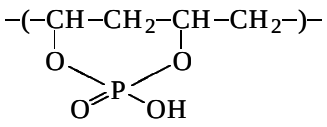

II

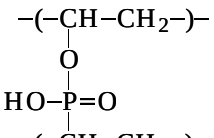

III

Also, it is not improbable that hydrogen-bonded structures **IV**–**VI** can be formed.

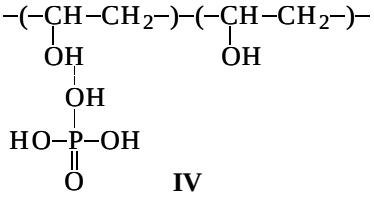

IV

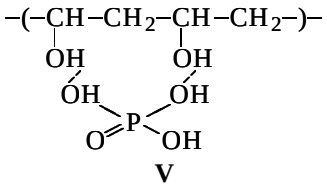

V

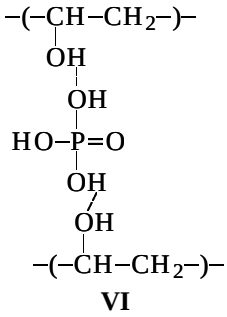

VI

The structure of such complexes resembles to a certain extent that of comb-shaped polymers, in which, as known, LC state can be formed. The occurrence of side chains is responsible for anomalous rheological, electrical, and some other properties.

It is known that transition to the LC state can be studied by rheometry [7]. Viscosity discontinuity in the temperature or concentration curves allows quite reliable determination of phase transition points, particularly for the transition from the isotropic to the anisotropic state. Also, transition points can be determined on applying external fields (mechanical, electrical, or magnetic).

Our experimental data show that, the nature of flow changes in the PVA–H_3PO_4 system in the mechanical field is characteristic of both the plastic (Fig. 1a, curve *3*; Fig. 1b, curves *3*, *4*) and dilatant types of behavior (Fig. 1a, curve *4*), depending on the phosphoric acid concentration, temperature (plastic behavior becomes more pronounced with increasing temperature), and shear rate, which is due to structural reorganization.

It is known that anomalous viscous behavior of LC polymers is manifested in the appearance of a maximum in the concentration dependence of the viscosity [8]. Particularly, it was demonstrated in [9] that, with increasing concentration, the decline in the viscosity is followed by an increase in the anisotropic range. With increasing shear rate, this effect becomes less pronounced. Similar results were observed for the PVA–H_3PO_4 system with variable component ratio. According to the concept proposed in [8], the decrease in the viscosity anisotropy with increasing shear rate is associated with the orientation of the isotropic solution in the mechanical field. The observed anomalous viscosity curves and the decrease in the viscosity discontinuity with increasing shear rate are caused by superposition of two factors: inherent LC state, as dependent on the system composition, and the effect of the mechanical field. Data of Fig. 2 give evidence in favor of the formation of an ordered LC phase having lower segmental flexibility.

In lyotropic or thermotropic LC polymers, reaching a certain concentration or temperature changes the bonding nature, which is reflected in the composition–property relationships [10]. In this case, a step-by-step transition from a semidilute to a concentrated isotropic solution occurs, accompanied by the formation of inclusions of an LC phase, followed by reaching their percolation threshold. Then, at a certain concentration, interpenetrating phases, and, finally, a continuous LC phase are formed with the presence of an emulsion of isotropic droplets in the LC matrix. Firther, gel-like or rigid inclusions are formed in the LC phase, which is followed by gelation. The observed anomalous behavior of the viscosity and electrical characteristics, as dependent on the phosphoric acid concentration and the solution temperature, suggest some complex transitions in both the molecular and supramolecular structures in the system.

To conclude, the observed similarity of the viscous behavior of LC polymers and that of PVC-based composites with phosphoric acid suggests that an isotropic–anisotropic transition may also occur in hydrogen-bonded structures in the polymer–acid systems.

CONCLUSIONS

(1) Polyvinyl alcohol composites with phosphoric acid demonstrate a discontinuity in the viscosity curves and also an anomalous behavior of such electrical characteristics as the electrical loss tangent and conductivity.

(2) Formation of ordered liquid-crystal structures in the PVA–phosphoric acid system is assumed, with the structural order being dependent on the PVA–acid molar ratio and temperature.

REFERENCES

1. Lazareva, T.G., Il'yushchenko, I.A., and Alimov, I.F., *Vysokomol. Soedin., Ser. A*, 1994, vol. 36, no. 9, pp. 1481–1485.
2. Lazareva, T.G. and Vashuk, E. V., *Int. J. Modern Phys. B*, 1994, vol. 10, nos. 23–24, pp. 2983–2989.
3. Lazareva, T.G., Vashuk, E. V., Alimov, I.F., *et al.*, *Proc. Conf. on Smart Structures and Materials: Smart Materials Technologies and Biomimetics*, San Diego, CA (the United States), Febr. 26–March 2, 1996, pp. 267–278.
4. Bayer, E. Grothwohl, P., and Geckeler, K., *Angew. Makromol. Chem.*, 1983, no. 113, pp. 141–142.
5. Papkov, S.P. and Kulichikhin, V.G., *Zhidkokristallicheskoe sostoyanie polimerov* (Liquid-Crystal State of Polymers), Moscow: Khimiya, 1977.
6. *Zhidkokristallicheskie polimery* (Liquid-Crystal Polymers), Plate, N.A., Ed., Moscow: Khimiya, 1988.
7. Schramm, G., *A Practical Approach to Rheology and Rheometry*, Karlsruhe: Gebrueder HAAKE, 1994.
8. Hermans, J., *J. Colloid Sci.*, 1962, vol. 17, no. 4, pp. 638–648.
9. Miller, W.G., *Pure Appl. Chem.*, 1974, vol. 38, pp. 37–62.
10. Yakobsons, E. and Faikel'son, L.A., *Mekh. Kompozit. Mater.*, 1997, vol. 33, no. 6, pp. 821–839.

Russian Journal of Applied Chemistry, Vol. 75, No. 6, 2002, pp. 969–973. Translated from Zhurnal Prikladnoi Khimii, Vol. 75, No. 6, 2002, pp. 986–990.
Original Russian Text Copyright © 2002 by Trifonov, Lapikov, Malygin.

MACROMOLECULAR CHEMISTRY AND POLYMERIC MATERIALS

Reactivity of Phenol-Formaldehyde Microspheres toward PCl_3, $VOCl_3$, and CrO_2Cl_2 Vapors

S. A. Trifonov, V. A. Lapikov, and A. A. Malygin

St. Petersburg State Technological Institute, St. Petersburg, Russia

Received October 30, 2001

Abstract—The products of reactions between $POCl_3$, $VOCl_3$, and CrO_2Cl_2 vapors and phenol-formaldehyde microspheres were studied by chemical analysis and spectroscopy.

Studies of chemical reactions occurring on solid surfaces are of both theoretical and applied interest in, e.g., assessing the reactivity of solid matrices [1, 2]. At the same time, chemical modification, e.g., by molecular layering (ML), which allows selective chemical reactions to be carried out on a solid matrix surface, is utilized for controlling the functional characteristics (adsorption, catalytic, thermal-oxidative, electrophysical, etc.) of substances and materials [3–5]. The foresaid is also true of solid polymer matrices, for which the chemical structure of the surface (elemental chemical composition and occurrence on the surface of various moieties or functional groups) also affects both their performance characteristics and the rate of reactions with other materials [6, 7]. The ML technique shows high performance in controlling the thermal-oxidative properties of phenol-formaldehyde, epoxy, polyamide, and polyvinyl chloride polymers [8, 9]. In this context, studies of the chemical transformations accompanying the gas-phase modification of solid polymer matrix with volatile low-molecular-weight agents will allow not only understanding of the reactions between the element oxide additions introduced and the polymer surface, but also elucidation of their influence on the physicochemical properties of a material.

EXPERIMENTAL

We carried out chemical analysis and spectroscopic [by IR and X-ray photoelectron spectroscopy (XPS)] studies of phenol-formaldehyde microspheres (PFMs) of the BV-01 brand [TU (Technical Specification) 6-05-221-258–77] modified with phosphorus(III) chloride and vanadium(V) and chromium(VI) oxychlorides. The element oxide groups were introduced in a flow-through reactor charged with a weighed portion of PFM (2 g) at room temperature in a dried carrier gas (nitrogen) stream. The extent of the chemical reaction between PCl_3, $VOCl_3$, and CrO_2Cl_2 and the reactive groups of the polymer material was estimated from the concentration of the elements in the modified specimens [10, 11]. Upon completion of the reaction between low-molecular-weight volatile chlorides and PFMs the latter were treated with a flow of dried carrier gas until unchanged initial compounds and formed gaseous products were completely removed from the reaction chamber. The choice of specific modifiers was governed by the fact that phosphorus, vanadium, and chromium compounds in various combinations are used for controlling the thermal-oxidative properties of polymer materials. Also, it was of interest to assess the reactivity of PFMs toward agents exhibiting various redox characteristics (PCl_3 is reductant, and $VOCl_3$ and CrO_2Cl_2 are oxidants).

The XPS[1] studies were carried out on a Perkin–Elmer PH-5000-400 instrument with Mg_{K_α} (1253 eV) exciting radiation. The residual pressure in the chamber of the spectrometer with a semispherical analyzer (energy resolution 0.1 eV) was 10^{-9} torr. The inaccuracy of quantitative analysis was about 10%. The spectrum was calibrated based on the binding energy of C1*s* carbon electrons, 285 eV. The polymer samples were pressed into indium pellets.

The IR spectra[2] of the initial and modified samples were recorded on an FSM-1201 IR Fourier spectrom-

[1] X-ray photoelectron spectra were recorded at the Mekhanobr-Analit Joint-Stock Company (St. Petersburg).

[2] IR spectra were recorded at the Monitoring Scientific and Production Association (St. Petersburg).

1070-4272/02/7506-0969 $27.00 © 2002 MAIK "Nauka/Interperiodica"

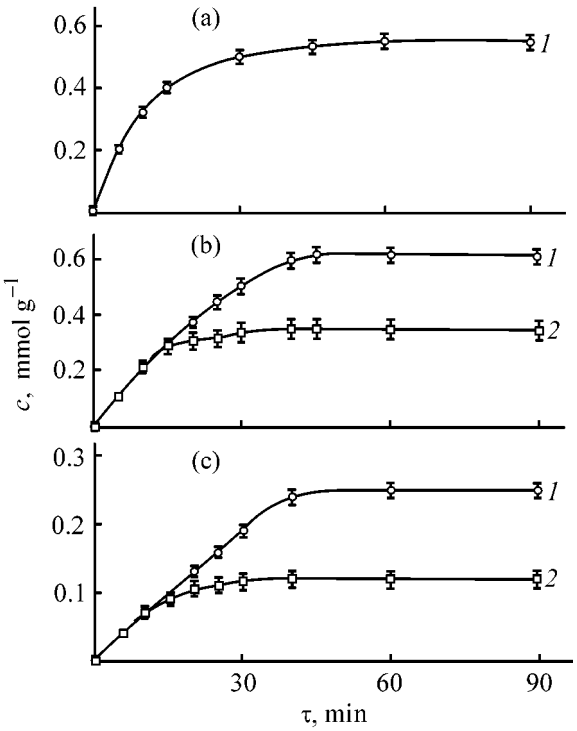

Fig. 1. Variation of the content of elements, *c*, in PFMs with the time of treatment τ with (a) phosphorus trichloride, (b) vanadium(V) oxychloride, and (c) chromium(VI) oxychloride vapors. (*1*) Total concentration of elements in the modified samples and (*2*) V(V) and Cr(VI) concentration.

eter (500–4000 cm^{-1} range, resolution 1 cm^{-1}, self-compensating interferometer). The samples were mixed and pressed with KBr.

To choose the optimal modification modes for the polymer material, we studied how its characteristics vary with the time of treating PFM samples with PCl_3, $VOCl_3$, and CrO_2Cl_2 vapor. Gas-phase treatment of the microspheres was carried out under conditions described in [12], namely, at room temperature, in a flow of air dried to the dew point (–50…–55°C) after the polymer was predried for 60 min.

Figures 1a–1c show how the content of the elements in the microspheres varies with the time of their treatment with the modifier vapor. It is seen that, under the conditions chosen, the total concentration of the elements in the samples attains a constant value within 45–60 min. However, the concentrations of the modifiers in the solid phase after their reaction with the reactive groups of the polymer matrix differ to a certain extent, depending on the chemical nature of the reactant. The maximal amounts of the elements, mmol g^{-1}, in the polymer are as follows: phosphorus(III) 0.56 (Fig. 1a), vanadium (V^{5+}, V^{4+}, and V^{3+}) 0.62 (Fig. 1b, curve *1*), and chromium (Cr^{6+}, Cr^{3+}) 0.25 (Fig. 1c, curve *1*).

We have shown previously [12] that, in reactions with phosphorus(III) chloride, the phosphorus-containing groups are grafted primarily at the phenol hydroxy groups of the microspheres. The appearance of a minor amount of phosphorus in the oxidation state +5 (5–10% of the total amount of the element) in the modified samples may be due to oxidation of PCl_3 in the gas phase to $POCl_3$ and its subsequent chemisorption on the polymer.

Chemical analysis showed that, when PFMs are treated with vanadium(V) oxychloride and chromium(VI) oxychloride vapor, the concentration of the elements in the modified samples in the highest oxidation state [V(+5), Cr(+6)] ceases to change after 15–20 min of synthesis (Figs. 1b and 1c, curves *2*). Since $VOCl_3$ and CrO_2Cl_2 are oxidants, the increase in the content of the modifiers by 50% of the total concentration of the additives may be due to appearance among the reaction products of modifying elements in a lower oxidation state [Cr(+3), V(+3, +4)]. This is probably due to grafting of vanadium- and chromium-containing moieties via redox reactions with the reactive groups of the polymer material.

Thus, in the initial stage of modification of the microspheres with $VOCl_3$ and CrO_2Cl_2 vapors, the element-containing moieties can be grafted by exchange reactions with the phenolic OH groups without changing the oxidation states of the elements, as evidenced by the presence of vanadium(V) and chromium(VI) in the samples (Figs. 1b, 1c, curves *1*). However, it should also be taken into account that phenol-formaldehyde polymers tend to oxidize even during preparation and storage in air [13]. The benzene ring in phenols is easily oxidized. In reactions with oxidants, the orienting action of the hydroxy group is responsible for activation of the carbon atom in the *para* position, which enters into the reaction yielding *p*-benzoquinone and its transformation products [14]. Evidently, treatment of the polymer with a vapor of a modifier with pronounced oxidizing power for a certain time causes structural rearrangement of the polymer surface, thus decreasing the chemical activity and accessibility of the phenol hydroxy groups of the matrix. This, evidently, involves redox reactions between $VOCl_3$ and CrO_2Cl_2, on the one hand, and the reactive centers (e.g., benzene rings, methylene groups), on the other, yielding carbonyl groups. The difference in the concentrations of the modifiers in the vanadium- and chromium-containing microspheres (0.62 vs. 0.25 mmol g^{-1}) may be due to the

difference in oxidizing power between vanadium(V) and chromium(VI). Treatment of PFMs with vapor of CrO_2Cl_2, which is a powerful oxidizing agent for organic compounds [15], causes more substantial changes in the polymer chain, thus decreasing the accessibility of the phenol hydroxy groups to the reactant.

Figure 2 presents an IR Fourier transmission spectrum of the initial microspheres. It contains absorption bands characteristic of phenol-formaldehyde polymers, peaked at [16] 760, 820, and 880 cm^{-1} (bending vibrations of the C–H bonds in substituted benzenes); 1200 cm^{-1} (stretching vibrations of the C–O bond); 1355 cm^{-1} (bending vibrations of phenol hydroxyls); 1475 and 1600 cm^{-1} (stretching vibrations of the C=C bond in the benzene ring); 2850, 2920, and 3010 cm^{-1} (stretching vibrations of the C–H bond in aliphatic and aromatic hydrocarbons); and 3400 cm^{-1} (stretching vibrations of the OH groups.

Chemical modification of the microspheres with PCl_3, $VOCl_3$, and CrO_2Cl_2 vapors changes the spectral characteristics of the polymer. The IR spectra of all the samples are characterized either by disappearance (Fig. 3a) or marked decrease in the intensity (Figs. 3b, 3c) of the absorption band at 1355 cm^{-1}, associated with bending vibrations of the hydroxy group of phenol, and by appearance of new bands at 510–560 cm^{-1}, associated with stretching vibrations of the E–Cl bond (Figs. 3a–3c) [16].

The IR spectra vary to a certain extent with the modifying agent. In the IR spectrum of the phosphorus-containing sample, a new band, associated with stretching vibrations of the P–O–Ar bond appears at 1000 cm^{-1}, and bands at 2360 and 2500 cm^{-1} due to stretching vibrations of the P–H and O–H bonds in phosphorus oxy acids (Fig. 3a). The last two absorption bands are, evidently, due to chemisorption of phosphorus oxychloride on the solid polymer [16].

When chromium-containing groups are introduced into the material, an absorption band at 1650 cm^{-1} appears, originating from stretching vibrations of the C=O bond in carbonyl compounds (Fig. 3c) [16]. The IR spectrum of the vanadium-containing microspheres contains an absorption band near 1010 cm^{-1}, associated with stretching vibrations of the V–O bond [16] (Fig. 3b). A higher reactivity of $VOCl_3$, compared with chromium-containing additives, is manifested in the appearance in the spectrum of two absorption bands at 1650 and 1710 cm^{-1} due to vibrations of the C=O bond. The intensity of the absorption band at 820 cm^{-1} for the samples treated with $VOCl_3$ and CrO_2Cl_2 vapors decreases, which is probably due to

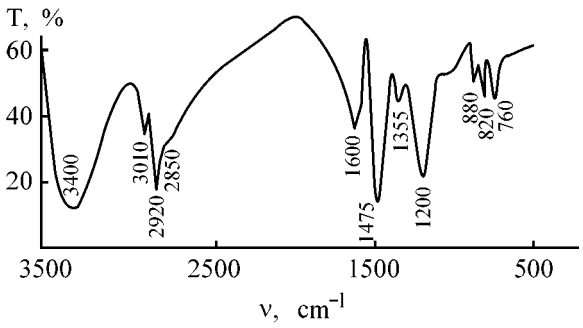

Fig. 2. IR spectrum of the initial PFMs. (T) Transmission and (ν) wave number; the same for Fig. 3.

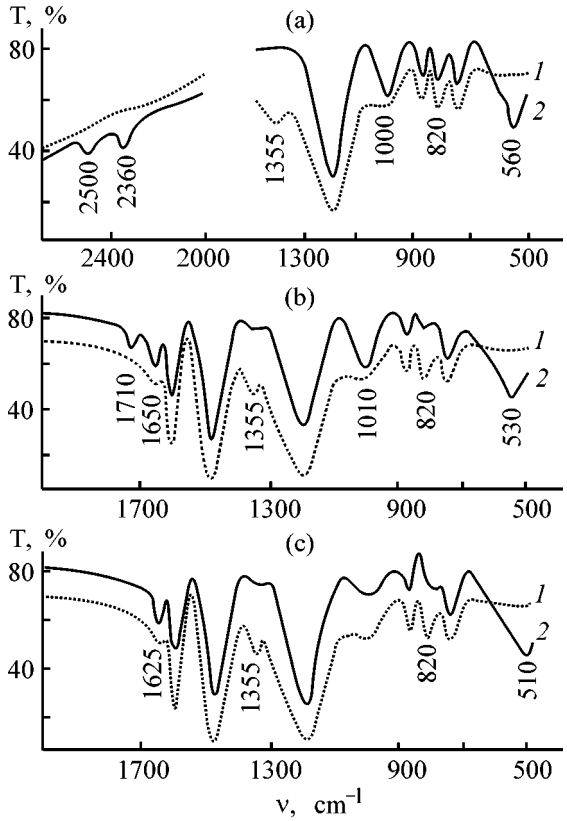

Fig. 3. IR spectra of (a) phosphorus-, (b) vanadium- and (c) chromium-containing PFMs. Sample: (*1*) initial and (*2*) modified.

the change in the substitution pattern in the benzene ring owing to redox reactions between inorganic agents and the polymer matrix [16] (Fig. 3b, 3c).

Figures 4 and 5 show the XPS spectra of the initial and modified PFM samples. The XPS spectrum of the initial microspheres in the C1*s* range contains a band at a binding energy of 285.0 eV, characteristic of the C–H groups, and a band at 286.2 eV. The latter band can be attributed to alcoholic, ester, or ether C–O groups occurring in the chain of the polymeric

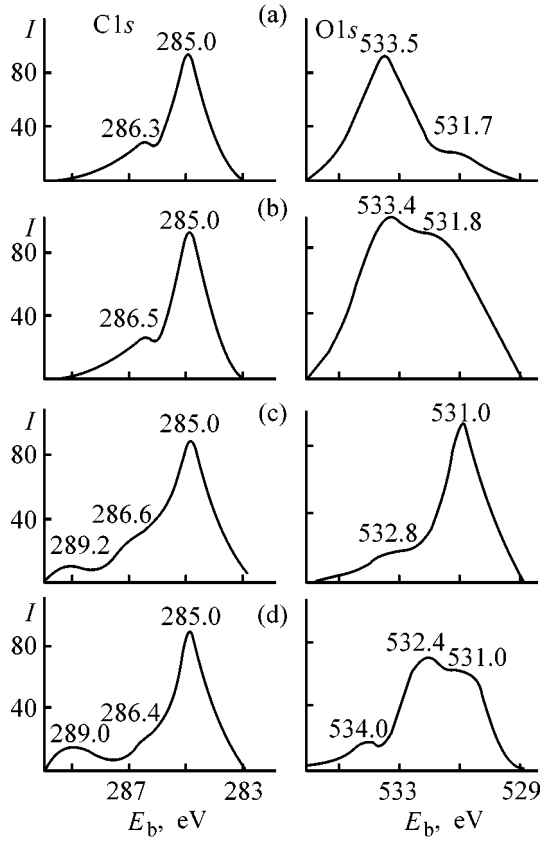

Fig. 4. C1*s* and O1*s* bands in the XPS spectra of (a) initial and (b–d) modified PFMs. (*I*) Relative intensity and (E_b) binding energy; the same for Fig. 5. Modifying agent: (b) PCl_3, (c) $VOCl_3$, and (d) CrO_2Cl_2.

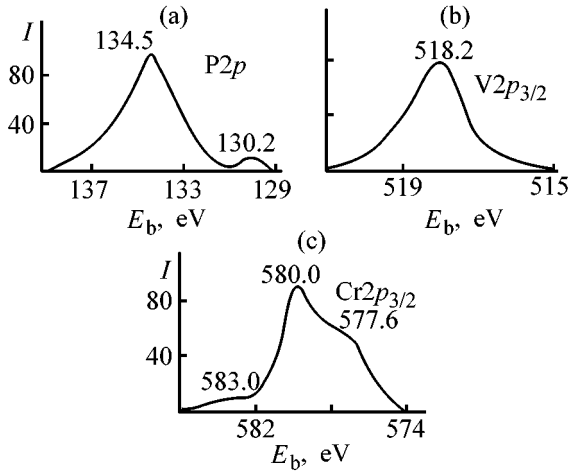

Fig. 5. (a) P2*p*, (b) V2$p_{3/2}$, and (c) Cr2$p_{3/2}$ XPS spectra of the modified PFMs.

material [17]. This is also evidenced by the peaks of the O1*s* electrons with binding energies of 533.5 and 531.7 eV (Fig. 4a).

The phosphorus-containing moieties introduced do not affect the binding energy of the C1*s* electrons, which can, evidently, suggest the lack of chemical reactions between the carbon-containing moieties in the polymer chain and phosphorus(III) chloride (Fig. 4a). However, the XPS spectrum of the modified PFMs is characterized by the appearance of lines in the higher-energy region corresponding to the binding energies of P2*p* electrons of 134.5 and 130.2 eV (Fig. 5a). These peaks are, probably, due to formation of phosphorus-oxygen groups linked to aromatic rings [17]. Our data suggest that this chemical reaction can yield not only phenyl phosphorous moieties with the modifying agent in the same oxidation state (130.2 eV) but also moieties of the $(PhO)_3PO$ type yielded by oxidation of phosphorus(III) chloride in the gas phase during modification. This is also evidenced by an increase in the intensity of the band of O1*s* electrons with binding energy of 531.8 eV (Fig. 4b) [18].

Chemical modification of the microspheres with vapor of vanadium and chromium oxychloride (modifying agents with pronounced oxidizing power) is responsible for the appearance in the XPS spectra of carbon of a shoulder with the binding energy of 1*s* electrons equal to 289.2 eV (Fig. 4c, 4d). This band can be accounted for by formation of carboxy groups (>C=O bond) [17] resulting from redox reactions in the polymer matrix with $VOCl_3$ and CrO_2Cl_2. Also, grafting of vanadium-containing moieties to microspheres is responsible for the appearance in the XPS spectra of the modified samples of lines with the binding energy of $2p_{3/2}$ electrons equal to 518.2 eV (Fig. 5b), and for the increase in the intensity of the band of O1*s* electrons with binding energy of 531.0 eV (Fig. 4c). According to published data [18], these changes may be due to formation of vanadium compounds in different oxidation states (V^{3+}, V^{4+}, V^{5+}).

The XPS spectrum of chromium-containing samples of PFMs contains three bands associated with different oxidation states of the element. The appearance of the bands with the binding energy of Cr 2*p* electrons equal to 583.0 eV is due to the presence in the polymer of the modifying agent containing chromium in the oxidation state +6. This probably suggests an exchange reaction between CrO_2Cl_2 and phenol hydroxy groups. The peak with the binding energy of 580.0 eV, as well as the band of O1*s* electrons with the binding energy of 531.0 eV (Fig. 4), may be due to the presence in the polymer of moieties with binding energies intermediate between those of 2*p* electrons of chromium(VI) and chromium(III) [19].

The redox reaction between the modifying agent and the reactive groups of the microshperes, yielding carbonyl bonds, is probably evidenced by the appearance of a band with binding energy of 577.6 eV (Fig. 5c), characteristic of chromium in the oxidation state (+3), and the above-mentioned shoulder in the XPS spectra of carbon with the binding energy of 289.0 eV (Fig. 4d).

Thus, our spectroscopic studies suggest grafting of modifying additives to the solid polymer both by substitution of the hydrogen atoms in phenol hydroxy groups, which probably proceeds according to the scheme

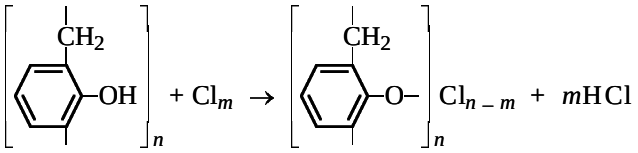

(ECl_m = PCl_3, $VOCl_3$, CrO_2Cl_2), and by redox reactions between the elements introduced [in the case of vanadium(V) and chromium(VI) oxychlorides] and the reactive groups of the material.

CONCLUSION

Chemical analysis and spectroscopic studies point to the occurrence of a chemical reaction between the modifying agents and reactive groups of the polymeric material. For all of the modified samples, the element-containing groups are introduced by exchange reactions with phenol hydroxy groups. When the microspheres are treated with vapor of $VOCl_3$ or CrO_2Cl_2 (modifying agents with pronounced oxidizing powers), the reactive centers of the polymer matrix (e.g., benzene rings and methylene bridges) are partially oxidized, yielding carbonyl moieties.

ACKNOWLEDGMENTS

The authors are grateful to S.D. Dubrovenskii for assistance in interpreting the X-ray photoelectron spectra. This work was financially supported by the Russian Foundation for Basic Research (project no. 01-03-32345).

REFERENCES

1. Petrova, L.I., Malkov, A.A., and Malygin, A.A., *Vzaimodeistvie oksida alyuminiya s khloridom titana i oksokhloridami fosfora i vanadiya* (Reaction of Aluminum Oxide with Titanium Chloride and Phosphorus and Vanadium Oxochlorides), Available from VINITI, May 5, 1995, no. 1264-V95.
2. Malkov, A.A., Malygin, A.A., and Sosnov, E.A., *Zh. Prikl. Khim.*, 1988, vol. 61, no 1, p. 29–35.
3. Malkov, A.A., Malygin, A.A., and Trifonov, S.A., *Metod molekulyarnogo naslaivaniya – osnova noveishei pretsizionnoi tekhnologii* (Molecular Layer Deposition Method as the Basis for the Novel Precision Technology), Available from VINITI, July 8, 1992, no. 2205-B92.
4. Malygin, A.A., *Zh. Prikl. Khim.*, 1996, vol. 69, no. 10, pp. 1585–1593.
5. Zarko, V.I., Kozub, G.M., Malkov, A.A., *et al.*, *Zh. Prikl. Khim.*, 1992, vol. 65, no. 7, pp. 1556–1560.
6. Povstugar, V.I., Kodolov, V.I., and Mikhailova, S.S., *Stroenie i svoistva poverkhnosti polimernykh materialov* (Structure and Properties of Polymer Material Surface), Moscow: Khimiya, 1988.
7. Malygin, A.A. and Tsvetkova, M.N., *Zh. Prikl. Khim.*, 1990, vol. 63, no. 8, pp. 1714–1718.
8. Trifonov, S.A., Malygin, A.A., Nikolaev, V.A., *et al.*, *Plast. Massy*, 1985, no. 6, pp. 21–23.
9. Trifonov, S.A., Semenova, E.Yu., and Malygin, A.A., *Zh. Prikl. Khim.*, 1996, vol. 69, no. 11, pp. 1917–1920.
10. Balandina, V.A., Gurvich, D.B., and Kleshcheeva, M.S., *Analiz polimerizatsionnykh plastmass* (Analysis of Polymerization Plastics), Leningrad: Khimiya, 1967,
11. Charlot, G., *Les methods de la chimie analytique. Analyse quantitative minerale*, Paris: Masson, 1961, 4th ed.
12. Trifonov, S.A. and Malygin, A.A., *Zh. Obshch. Khim.*, 1998, vol. 68, no. 12, pp. 1994–1998.
13. Aseeva, R.M. and Zaikov, G.E., *Gorenie polimernykh materialov* (Combustion of Polymeric Materials), Moscow: Nauka, 1981.
14. Chichibabin, A.E., *Osnovnye nachala organicheskoi khimii* (Basic Principles of Organic Chemistry), Moscow: Goskhimizdat, 1963.
15. Golodets, G.I., *Geterogenno-kataliticheskoe okislenie organicheskikh veshchestv* (Heterogeneous Catalytic Oxidation of Organic Substances), Kiev: Naukova Dumka, 1978.
16. Kazitsyna, L.A. and Kupletskaya, N.V., *Primenenie UF-, IK-, YaMR- i mass-spektroskopii v organicheskoi khimii* (Application of UV, IR, NMR, and Mass Spectrocopy in Organic Chemistry), Moscow: Mosk. Gos. Univ., 1979.
17. Wagner, C., Riggs, W., and Davis, L., *Handbook of X-Ray Photoelectron Spectroscopy*, Minnesota 55344: Perkin Elmer, 1978.
18. Nefedov, V.I. *Rentgenoelektronnaya spektroskopiya khimicheskikh soedinenii: Spravochnik* (X-Ray Photoelectron Spectroscopy of Chemical Compounds: Reference Book), Moscow: Khimiya, 1984.
19. Martsenyuk-Kukharuk, A.P., Beletskii, I.I., Plyuto, I.V., *et al.*, *Dokl. Akad. Nauk SSSR*, 1991, vol. 31, issue 2, pp. 400–403.

Russian Journal of Applied Chemistry, Vol. 75, No. 6, 2002, pp. 974–979. Translated from Zhurnal Prikladnoi Khimii, Vol. 75, No. 6, 2002, pp. 991–997.
Original Russian Text Copyright © 2002 by Kuznetsova, Gudkin, Mishaeva.

MACROMOLECULAR CHEMISTRY AND POLYMERIC MATERIALS

Oligomerization of Bifunctional Aldehyde in Reactions with Bipolar Ions

N. P. Kuznetsova, L. R. Gudkin, and R. N. Mishaeva

Institute of Macromolecular Compounds, Russian Academy of Sciences, St. Petersburg, Russia

Received February 7, 2002

Abstract—Formation of glutaraldehyde oligomers (tri- and pentamers) in reaction of glutaraldehyde with bipolar ions (monoaminoacetic, α-aminoglutaric, and α,ε-diaminocaproic acids and glutatione tripeptide) was studied.

In many methods of protein modification with a bifunctional cross-linking agent, glutaraldehyde (GA), the main attention is paid to carbonyl-amine reactions. These reactions play an important part in various biochemical processes [1]. Therefore, their study in model systems is of interest. In chemical cross-linking of proteins in neutral aqueous solutions, stable Schiff bases are formed by the reaction of protein amino groups with GA functional groups [2, 3]. These bases do not dissociate because of the parallel aldol condensation of GA to give α,β-unsaturated oligomers immobilized on a protein molecule [4].

Previously, we have shown that the GA condensation with glycine involves some parallel reactions [5]. It follows from a comparison of the rate constants that the condensation to give stable aldimine bond (Schiff base) is 20 times faster than the formation of α,β-unsaturated GA oligomers produced by aldol condensation (products were monitored by UV spectroscopy at 267 and 235 nm, respectively) [6]. Hence, we can suggest that a Schiff base is formed initially, being then stabilized by the formation of conjugated double bonds in the course of GA oligomerization (aldol condensation involving the second free aldehyde group of GA).

In this work, the influence exerted by the nature of the bipolar ion on the condensation and, first of all, on the GA oligomerization was studied for the example amino acids and peptides containing, along with carboxy and amino groups (glycine), also sulfhydryl (glutathione), second carboxy (glutathione, glutamic acid), or second amino (lysine) group.

EXPERIMENTAL

Differently charged amino acids: monoaminoacetic (glycine, Glu), α,ε-diaminocaproic (lysine, Lys), α-aminoglutaric (glutamic acid, Glu), and γ- glutamylcysteinylglycine (glutathione, GSH) were studied.

A commercial 25% aqueous solution of GA (Reanal, Hungary) was purified with activated carbon. Its purity was evaluated spectrophotometrically from the ratio of the optical densities of the bands at 235 and 280 nm, D_{235}/D_{280} = 0.4–0.5. Glutaraldehyde exists in aqueous solution at pH 3 as a mixture of the aldehyde proper and its hydrated species. The optical density at λ = 280 nm is due to absorption by the aldehyde group, with molar absorption coefficient ε = 4.2 l mol^{-1} cm^{-1} [7]. The band at λ = 235 nm (ε = 1530 l mol^{-1} cm^{-1}) appears only in the spectra of GA alkaline solutions (pH > 8) and belongs to GA α,β-oligomers with conjugated double bonds (ethylene and carbonyl) formed by aldol condensation [8]

$$\mathrm{CHO{-}(CH_2)_3{-}[CH{=}\overset{\displaystyle HC=O}{\overset{|}{C}}{-}(CH_2)_2]_{\mathit{n}}{-}CHO.}$$

The reactions of GA with bipolar ions were studied in aqueous solutions (pH 6.8–7.2) at 20°C by UV spectroscopy [SF-26 (Russia) and Specord (Germany) spectrophotometers] and pH-metry (Radiometer, Denmark). The reaction products were fractionated by GPC on a 90 × 1.5 cm column packed with Sephadex G-25 (LKB-Pharmacia, Sweden) and eluted with water. The average distribution coefficient K_{av} was deter-

1070-4272/02/7506-0974 $27.00 © 2002 MAIK "Nauka/Interperiodica"

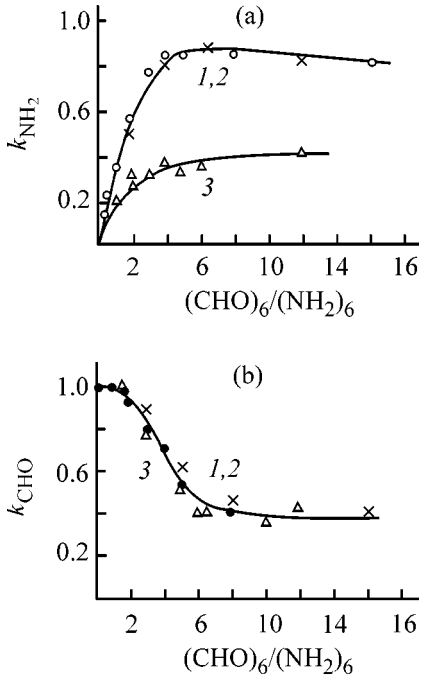

Fig. 1. Degree of conversion k of (a) amino and (b) aldehyde groups in GA condensation with amino acids vs. the initial molar ratio of the functional groups of the components $(CHO)_0/(NH_2)_0$. Reaction time 1 h, 20°C, [GA] = 0.38, [Gly] = [Glu] = 0.4, [Lys] = 0.2 M (or 0.4 with respect to NH_2 groups); pH of amino acid solutions 6.8–7.2; the same for Fig. 2. System: (*1*) GA–glycine, (*2*) GA–lysine, and (*3*) GA–glutamic acid.

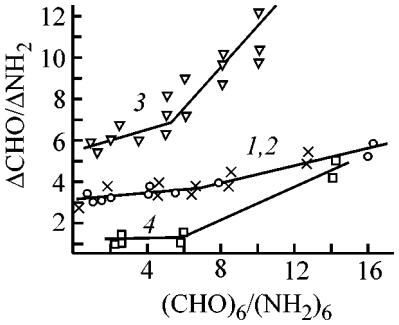

Fig. 2. Overequivalent binding of GA aldehyde groups with respect to amino groups $\Delta CHO/\Delta NH_2$ vs. the initial molar ratio of the functional groups $(CHO)_0/(NH_2)_0$. GA condensation with (*1*) glycine, (*2*) lysine, (*3*) glutamic acid, and (*4*) glutathione.

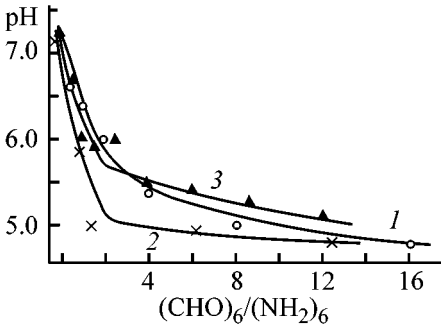

Fig. 3. pH of the reaction mixture vs. the initial molar ratio of functional groups of the components $(CHO)_0/(NH_2)_0$. Reaction time 1 h, 20°C. GA condensation with (*1*) glycine, (*2*) lysine, and (*3*) glutamic acid.

mined by the standard procedure from the corresponding eluate volumes:

$$K_{av} = (V_e - V_0)/(V_0 - V_t),$$

where V_e is the elution volume of the stable GA derivative with bipolar ion, and V_0 and V_t are the elution volumes of dextran-2000 and KI, respectively.

The aldehyde groups were analyzed by reaction with hydroxylamine hydrochloride [9], the amino groups, with 2,4,6-trinitrobenzenesulfonic acid [10], and the sulfhydryl groups, by the Ellman method with 5,5'-dithiobis(2-nitrobenzoic acid) [11]. The degree of conversion of the functional groups (k_{CHO}, k_{NH_2}, k_{SH}) in stable Schiff bases (which do not dissociate under competitive action of hydroxylamine hydrochloride) was estimated as the ratio of the ΔNH_2, ΔCHO, and ΔSH groups that reacted within a definite time interval, to their initial amount $(NH_2)_0$, $(CHO)_0$, and $(SH)_0$, respectively.

The GA condensation with amino acids proceeds in neutral solutions rapidly; with the limiting conversion being attained within 10–15 min [5, 6]. The degree of conversion of amine and aldehyde groups in reaction of GA with glycine, lysine, and glutamic acid (within 1 h) as a function of the initial molar ratio $(CHO)_0/(NH_2)_0$ is shown in Figs. 1a and 1b. The degree of conversion of glycine and lysine functional groups changes with increasing GA concentration similarly and reaches the limiting value of 0.8–0.9 with respect to amino groups. For glutamic acid, k_{NH2} increases only to 0.4 even at excess of GA.

In all cases, the GA aldehyde groups reacted in overequivalent amount as compared with the consumed amino groups of the bipolar ion. (Fig. 2). As the initial molar ratio of GA to glycine or lysine increases, the ratio of the bound aldehyde and amino groups changes similarly, and $\Delta CHO/\Delta NH_2$ varies from 3 to 5. For the GA–glutamic acid system, this ratio varies from 6 to 12, and for the reaction of GA with

Table 1. Degree of conversion of functional groups and ratio of reacted aldehyde and amine groups in GA condensation with glycine or glutamic acid (Reaction time 1 h; 20°C; pH of the initial solution of amino acid 7.0; concentration of components in the GA–glycine system 0.26, and in GA–glutamic acid system, 0.2 M)

$(CHO)_0/(NH_2)_0$, mol/mol	k_{CHO}	k_{NH_2}	ΔCHO	ΔNH_2	ΔCHO/ΔNH_2, mol/mol	$(CHO)_0/(NH_2)_0$, mol/mol	k_{CHO}	k_{NH_2}	ΔCHO	ΔNH_2	ΔCHO/ΔNH_2, mol/mol
			M						M		
GA–glycine						GA–glutamic acid					
0.7	1.00	0.48	0.084	0.031	2.7	0.75	1.00	0.19	0.134	0.023	5.8
2.0	0.94	0.58	0.116	0.037	3.1	2.0	0.59	0.24	0.113	0.021	5.4
4.0	0.70	0.86	0.174	0.054	3.2	5.0	0.38	0.26	0.126	0.015	8.4
8.0	0.40	0.84	0.100	0.026	3.8	8.0	0.21	0.21	0.078	0.007	11.1

the tripeptide, from 1 to 3. It should be noted that at low initial ratios of the components (up to 4–6), $\Delta CHO/\Delta NH_2$ is constant in all cases, but at larger excess of aldehyde groups (up to 16) it increases, and this increase is the greater, the lower the degree of conversion of amino acid amino groups (e.g., for dicarboxylic glutamic acid).

As the acid products are accumulated as a result of formation of stable Schiff bases in the reaction of GA with amino acid, the pH of the reaction mixture decreases (Fig. 3). For all the bipolar ions studied, the dependences of pH on the initial $(CHO)_0/(NH_2)_0$ molar ratio show a bend: sharp initial decrease in pH [to $(CHO)_0/(NH_2)_0 \sim 4$] is followed by a weak variation at high GA concentrations.

Figures 1–3 show two stages of the GA condensation with differently charged amino acids: the first, at low initial molar ratios $(CHO)_0/(NH_2)_0$ [from 0.25 to ~(4–6)], and the second, at larger ratios (>6).

In the first case, the formation of a stable Schiff base is accompanied by oligomerization of GA already linked to amino acid (Fig. 2); in the process, binding of the amino acid reaches a maximum. The observed free aldehyde groups may be the aldehyde groups belonging to the GA oligomer formed. At very small initial ratios (at a large excess of the amino acid), the aldehyde groups are consumed completely (Fig. 1b). At the same time, an overequivalent consumption of the aldehyde groups with respect to amino groups (i.e., GA oligomerization) is observed too. Probably, the reaction products can associate via reaction of free aldehyde groups belonging to the oligomeric fraction of GA.

In the second case, at a large excess of the aldehyde groups, stable Schiff bases are formed by condensation; this process is accompanied by simultaneous GA oligomerization, as in the first case. In all the systems studied, the amount of the overequivalent aldehyde groups consumed increases in comparison with that of the amino groups. For instance, for the GA–glycine and GA–lysine systems (the GA–glutathione system is close to them), the ratio of the consumed groups $\Delta CHO/\Delta NH_2$ increases from 3 (which is characteristic of low initial ratios of the components) to about 5. For the GA–glutamic acid system at low degree of amino group conversion, these changes are substantial: from 6 to 12 and more.

The GA–glycine and GA–glutamic acid systems are compared in Table 1.

As follows from Table 1, with increasing $(CHO)_0/(NH_2)_0$ ratio, the degree of conversion of glycine amino groups in the GA–glycine system (at constant glycine concentration in the solution) increases to 0.84–0.86 due to formation stable Schiff bases, while for the GA–glutamic acid system it reaches only 0.24–0.26 at substantially increased amount of the reacted aldehyde groups.

GA reacts in a specific way with glutathione tripeptide containing, along with amino and two carboxy groups, a sulfhydryl group. Glutaraldehyde can react with both primary amino group and sulfhydryl group. At the initial molar ratio $(CHO)_0/(NH_2 + SH)_0 < 6$ (Fig. 2, curve *4*), a stoichiometric binding of GA and tripeptide functional groups is observed. The positions of CHO groups in the GA molecule and of NH_2 and SH groups in the glutathione molecule are complementary, which suggests that the reaction with GA involves intramolecular cross-linking in the tripeptide molecule, and one molecule of bifunctional GA is consumed per glutathione molecule.The results of GA binding with glutathione at increasing pH of the reaction medium are listed in Table 2.

Table 2. Degree of conversion and ratio of reacted functional groups in the GA–glutathione system [reaction time 20 min; 20°C; $(CHO)_0/(NH_2 + SH)_0$ = 2.5 mol/mol]

pH_{GSH}	pH_{res} of solution	ΔpH	k_{NH_2}	k_{SH}	k_{NH_2}/k_{SH}	$\Delta CHO/\Delta(NH_2 + SH)$, mol/mol
5.3	5.1	0.2	0.71	0.48	1.48	1.4
6.0	5.5	0.5	0.73	0.43	1.69	1.6
7.2	6.4	0.8	0.77	0.75	1.00	1.0
8.0	6.9	1.1	0.85	0.75	1.13	1.0

Table 3. Degree of conversion and ratio of reacted functional groups in GA condensation with glutamic acid [reaction time 30 min; 20°C; $(CHO)_0/(NH_2)_0$ = 8 mol/mol]

pH_{Glu}	pH_{res} of solution	ΔpH	k_{NH_2}	k_{SH}	$\Delta CHO/\Delta NH_2$, mol/mol
6.1	5.5	0.6	0.32	0.35	10.7
7.5	6.0	1.5	0.35	0.42	11.3
9.8	8.3	1.5	–	0.70	–
12.3	10.5	1.8	0.40	0.92	20.0

It follows from Table 2 that, with increasing pH, the GA condensation with glutathione (molar ratio of the functional groups 2.5) proceeds with growing conversion of the functional groups. In all cases, equivalent binding of functional groups of GA and tripeptide is observed.

Reasing the GA content in the reaction mixture at $(CHO)_0/(NH_2 + SH)_0 > 6$ (Fig. 2, curve *4*) leads to overequivalent binding of aldehyde groups, $\Delta CHO/\Delta(NH_2 + SH) \approx 3$, which corresponds, as in the case of other bipolar ions studied, to formation of GA oligomers, probably, separately with each reactive group of glutathione.

A specific feature of the GA condensation with dicarboxylic glutamic acid is the abnormally high degree of binding of GA aldehyde groups at extremely low conversion of amino groups of glutamic acid (Figs. 1a, 1b). The low degree of conversion of these amino groups may result from insufficient amount of the reactive unprotonated amino groups (nucleophiles), which may be due to suppression of their dissociation because of the existence of two carboxy groups in the molecule of glutamic acid. The consumption of aldehyde groups sharply increases at high GA concentrations in the reaction mixture (Fig. 2) and increasing pH of glutamic acid solution (Table 3).

It follows from Table 3 that the degree of conversion of amino groups in glutamic acid slightly increases with pH increasing within the interval 6–12 because of the increase in the amount of unprotonated (reactive) amino groups. With increasing pH, the GA ability to form α,β-unsaturated oligomers also increases. At an excess of GA in the solution, the ratio of the reacted aldehyde groups to amino groups in the GA–glutamic acid system may reach 20.

To account for the observed specific features of GA condensation with glutamic acid, the reaction products were fractionated on a column with Sephadex G-25 at 10°C. Two experimental procedures were used under the same other conditions. In the first

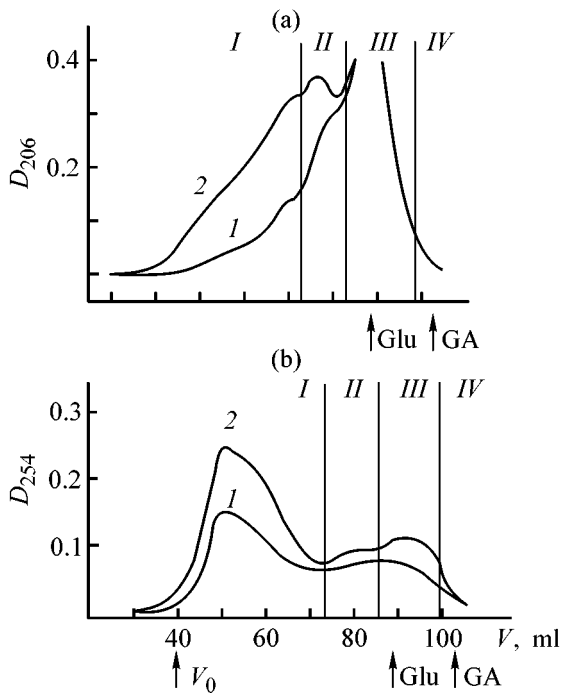

Fig. 4. Gel chromatography on column with Sephadex G-25 of products of GA condensation with glutamic acid (fractions *I–IV*), obtained at 20°C in (*1*) 20 min and (*2*) 2 h. (D_{206}, D_{254}) Optical density and (*V*) volume. (a) Reaction is stopped by addition by sodium borohydride, monitoring of products at 206 nm; (b) reaction products are not reduced, monitoring of products at 254 nm, elution with water at a rate of 30 ml h^{-1}.

Table 4. Fractionation of products of GA condensation with glutamic acid on a column with Sephadex G-25* [reaction time 2 h; 20°C; $(CHO)_0/(NH_2)_0$ = 8 mol/mol]

Reaction product, %	K_{av}	D_{235}/D_{280}	$\Delta CHO/\Delta NH_2$, mol/mol	Fraction mass, %
Fraction:				
I	0.10	2.4 ± 0.1	4.8 ± 0.6	2–4
II	0.48	2.7 ± 0.3	5.0 ± 0.6	18–21
III	0.71	3.0 ± 0.1	5.8 ± 0.2	58–66 (Glu_{free})
IY	0.88	5.0 ± 0.6	–	8–10 (GA_{free})
GA (pH 3.2)	0.88	0.5	–	–
GA (pH 10)	–	2.5	–	–
Glu	0.62	–	–	–

* Results of several experiments.

case, the reaction was stopped by adding sodium borohydride, which reduces both azomethine and carbonyl double bonds. The reaction products were eluted with water and monitored spectrophotometrically at 206 nm (the region of absorption of glutamic acid carboxy groups). Figure 4a shows two chromatograms of products obtained at reaction times of 20 min and 2 h. As seen, the amount of glutamic acid bound in high-molecular-weight products (probably, owing to association of low-molecular-weight components) increases with time.

In the second case, the reaction products were not reduced, and the reaction mixture was introduced into the column directly (Fig. 4b). The fractions obtained were monitored at 254 nm {257–270 nm is the absorption range of aldimine bonds in the stable reaction products [6, 12, 13]; the initial components in the concentrations used do not absorb in this range}. In the four fractions obtained, the amounts of the residual aldehyde and amino groups were determined spectrophotometrically, then the fractions were dried lyophilically, their masses were measured, and the content of nitrogen was found. The amount of strongly bound glutamic acid in the fractions was determined as the difference between the total nitrogen and nitrogen belonging to the free amino groups. The GA amount was determined as the difference between the fraction mass and the amount of amino acid in this fraction, taking into account GA dehydration at the aldol condensation. The yield of products from the column was 90–95%. The results are presented in Table 4.

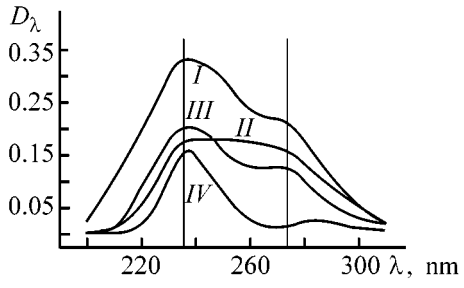

Fig. 5. Differential UV spectra of fractions *I–IV* of products formed in GA condensation with glutamic acid (from Fig. 4b) relative to solution of glutamic acid. (D_λ) Optical density and (λ) wavelength.

Fraction *I*, which amounts to 2–4% of the lyophilically dried reaction mass, is characterized by high optical density at 254 nm. This corresponds to a high content of azomethine bonds in the product. It is known that the separating power of Sephadex G-25 with respect to branched dextrans is limited to the molecular masses of several thousands. In fractions *I* and *II*, no free aldehyde groups were found. These products have molecular mass substantially larger than 1000 and are probably associates of low-molecular-weight products. The active product of the condensation reaction and unchanged glutamic acid are concentrated in fraction *III*. It is interesting that, in fraction *III*, despite a large excess of free glutamic acid, aldehyde groups are detected in substantial amounts and apparently do not react with glutamic acid. We suggest that, in this case, glutamic acid forms with GA common unstable Schiff bases, which are broken down in the reaction with hydroxylamine hydrochloride used to determine free aldehyde groups.

It should be noted that, in the first three fractions of products of the GA condensation with glutamic acid, the ratio of consumed aldehyde groups to amino groups, $\Delta CHO/\Delta NH_2$, is constant, 5–6. This fact suggests that the pentamer with molecular mass of about 600–700 is the main product of GA condensation with glutamic acid.

Fraction *IV* contains free GA and only trace amounts of glutamic acid. The ratio of the optical densities D_{235}/D_{280} in fraction *IV*, which is higher than that in the other fractions, suggests that GA exists in the form of small (probably cyclic) oligomers, since the elution volume of the fraction is close to that of monomeric GA.

The differential UV spectra of four fractions obtained in condensation of GA with glutamic acid are shown in Fig. 5. All the fractions show absorption at 235 nm, characteristic of conjugated double bonds (ethylene and carbonyl) in the products of the GA aldol condensation. Fractions *I–III* show absorption at 260–270 nm, characteristic of aldimine bond in

the stable Schiff bases. Products of fraction *IV* exhibit, along with band 235 nm due to products of aldol condensation of GA, a weak band at 280 nm belonging to the GaA aldehyde group [7].

Thus, in all the GA–bipolar ion systems studied, the composition of reaction products changes with increasing GA concentration. At low ratios of the components $[(CHO)_0/(NH_2)_0 < 4]$, amino acids form with GA products in which GA exists as oligomer (mainly trimer). At $(CHO)_0/(NH_2)_0 > 6$, a higher oligomer (pentamer) is formed. It was noted in [14] that aldol condensation of GA in alkaline media or at its prolonged storage yields GA trimers and pentamers.

The specific feature of the GA reaction with dicarboxylic amino acids is the low degree of conversion of amino groups (up to only 0.4) even in the presence of an excess of GA. Account should be taken of the fact that we monitored only stable Schiff bases containing conjugated double bonds. We can suggest that dicarboxylic glutamic acid prevents intense formation of stable Schiff bases, probably due to sterical factors, but can form usual unstable Schiff bases, which are readily hydrolyzed into the initial components. At the same time, glutamic acid can initiate formation of stable oligomers of GA itself, present in the reaction mixture in excess, while in straight GA solutions no oligomerization proceeds under similar conditions.

The results obtained can be applied to GA polycondensation with proteins: for instance, they confirm that, for intermolecular cross-linking of proteins with excess carboxy groups (with isoelectric points in the acid region), a greater amount of the cross-linking agent and longer condensation time (compared with proteins whose isoelectric points lie in neutral and alkaline regions) are required.

CONCLUSIONS

(1) A study of the condensation of glutaraldehyde with differently charged bipolar ions (glycine, lysine, glutamic acid) at a molar ratio of the functional groups of the initial components varied from 0.25 to 16.0 revealed overequivalent binding of aldehyde groups with amino groups. The reaction products contain amino acid bound with the glutaraldehyde trimer at $(CHO)_0/(NH_2)_0 < 4$ and with the glutaraldehyde pentamer at $(CHO)_0/(NH_2)_0 > 6$. These oligomers are not formed in neutral and weakly acid solutions of glutaraldehyde, containing no bipolar ions.

(2) The highest degree of conversion in the glutaraldehyde-glutamic acid system is 0.4 (cf. 0.8–0.9 for glycine and lysine). Correspondingly, the overequivalent ratio of the reacted aldehyde groups changes from 5–6 to 12 with increasing molar ratio of the initial components. In the presence of glutamic acid, excess glutaraldehyde can form oligomers in weakly acidic solutions, in contrast to straight glutaraldehyde solutions under the same conditions.

(3) Condensation of glutaraldehyde with glutathione may involve intramolecular cross-linking at complementary mutual orientation of the functional groups, when the stoichiometric ratio of the total amount of amino and sulfhydryl groups to the reacted aldehyde groups is attained. At excess of glutaraldehyde $[(CHO)_0/(NH_2)_0 > 6$ mol/mol], the aldehyde groups are consumed in overequivalent amounts to form glutaraldehyde oligomers (trimers) bound with each functional group of the tripeptide separately.

REFERENCES

1. Feeney, R.E., Blankenhorn, G., and Dixon, H.B.F., *Adv. Protein Chem.*, 1975, vol. 29, pp. 135–203.
2. Richard, F.M. and Knowles, J.R., *J. Mol. Biol.*, 1968, vol. 37, no. 1, pp. 231–233.
3. Monsan, P., Puzo, G., and Mazarguil, H., *Biochemie*, 1975, vol. 57, nos. 11–12, pp. 1281–1292.
4. Kuznetsova, N.P., Gudkin, L.R., Kol'tsova, S.V., and Mishaeva, R.N., *Vysokomol. Soedin., Ser. A*, 1996, vol. 38, no. 10, pp. 1668–1673.
5. Kuznetsova, N.P., Mishaeva, R.N., and Gudkin, L.R., *Zh. Prikl. Khim.*, 1999, vol. 72, no. 7, pp. 1171–1177.
6. Kuznetsova, N.P., Mishaeva, R.N., Pisarev, O.A., and Gudkin, L.R., *Zh. Prikl. Khim.*, 2000, vol. 73, no. 5, pp. 796–801.
7. Kawahara, J., Ohnori, T., Ohkubo, T., *et al.*, *Anal. Biochem.*, 1992, vol. 201, no. 1, pp. 94–98.
8. Margel, S., *J. Polym. Sci., part 2*, 1984, vo. 22, no. 1, pp. 3521–3533.
9. Roe, H.R. and Mitchel, G., *Anal. Chem.*, 1951, vol. 23, no. 12, pp. 1758–1760.
10. Fields, R., *Biochem. J.*, 1971, vol. 124, no. 3, pp. 581–590.
11. Ellman, G.L., *Arch. Biochem. Biophys.*, 1959, vol. 82, no. 1, pp. 70–77.
12. Hopwood, D., Allen, C.R., and McCabe, M., *Histochem. J.*, 1970, vol. 2, no. 2, pp. 137–150.
13. Kuznetsova, N.P. and Samsonov, G.V., *Vysokomol. Soedin., Ser. A*, 1986, vol. 28, no. 3, pp. 643–648.
14. Tashima, T., Kawakami, U., Harada, M., *et al.*, *Chem. Pharm. Bull.*, 1987, vol. 35, no. 10, pp. 4169–4180.

Russian Journal of Applied Chemistry, Vol. 75, No. 6, 2002, pp. 980–984. Translated from Zhurnal Prikladnoi Khimii, Vol. 75, No. 6, 2002, pp. 998–1002.
Original Russian Text Copyright © 2002 by Salimgareeva, Sannikova, Kolesov, Leplyanin.

MACROMOLECULAR CHEMISTRY AND POLYMERIC MATERIALS

Influence of Dibenzyl-*o*-carborane on Radiation Aging of Polymethyl Methacrylate

V. N. Salimgareeva, N. S. Sannikova, S. V. Kolesov, and G. V. Leplyanin

Institute of Organic Chemistry, Ufa Scientific Center, Russian Academy of Sciences, Ufa, Bashkortostan, Russia

Received December 10, 2001; in final form, January 2002

Abstract—Radiation aging of polymethyl methacrylate produced in the presence of dibenzyl-*o*-carborane was studied. The influence of dibenzyl-*o*-carborane addition on the thermomechanical properties of the resulting polymer was analyzed.

High-energy radiation significantly affects the physicochemical characteristics of polymer materials. The composition, structure, electrical conductivity, creep rate, and tensile strength of a polymer are changed, which results in deterioration of its performance. To decrease or prevent these consequences, stabilizing additives incorporated into the polymer chain or present as mechanical impurities are added. Various classes of organic compounds show protective properties. For example, polymethyl methacrylate (PMMA) is stabilized with compounds containing bivalent sulfur [1] and aromatic hydrocarbons [2]. Owing to a vacant *d* orbital of sulfur and the π-electron system of the benzene ring, aromatic and organosulfur compounds act as "energy sponges" absorbing and dissipating in the form of heat or fluorenscence the energy absorbed by the polymer. Aromatic compounds effect intermolecular energy transfer without any significant variations. Sulfur-containing compounds undergo cleavage across the S–S (or C–S) bond to form the corresponding stable thiyl radicals which deactivate active polymer radicals initiating degradation (or cross-linking) of macromolecules.

Organosulfur and aromatic compounds also exert inhibiting effect on thermal degradation of irradiated polymer, initiated by "defects" arising in the macromelecule (tertiary carbon atoms and unsaturation) under the action of high-energy radiation [3, 4].

Radiation-induced chemical processes in polymers are also affected by boron-containing compounds, among which carboranes are of particular interest. Carboranes are boron compounds with cage structure necessarily incorporating one or more carbon atoms. Owing to delocalization of valent electrons, boranes exhibit properties typical of aromatic systems, such as high thermal stability and low reactivity toward various agents [5]. Their ability to absorb energy is used in synthesis of radiation-resistant polymers to raise the strength of adjacent bonds in the macrochain [5, 6]. For example, addition of carboranes to polyethylene as a comonomer in copolymer of ethylene and isopropylene carborane supresses cross-linkings of macromolecules under the action of gamma radiation [7].

It was of interest to examine the influence of carboranes on the radiation resistance of polymethyl methacrylate for the example of dibenzyl-*o*-carborane (DBOC).

EXPERIMENTAL

Dibenzyl-*o*-carborane 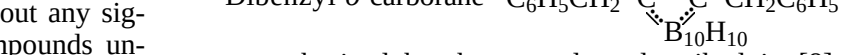
was synthesized by the procedure described in [8]; mp 151–152°C; compound with limited solubility in methyl methacrylate (MMA) and polymethyl methacrylate (PMMA); the solubility of DBOC in MMA is approximately 15%, and the compatibility of DBOC with PMMA is preserved at concentrations not exceeding 10 wt %.

The characteristics of PMMA were studied on block samples produced by polymerization of MMA in the bulk at 40°C until complete conversion of the monomer in the presence of 0.05 wt % initiating agent (dicyclohexyl peroxydicarbonate, CPC) and up to 10 wt % DBOC.

The polymerization kinetics was studied by dilatometry at 40 ± 0.2°C. To remove the stabilizing

1070-4272/02/7506-0980 $27.00 © 2002 MAIK "Nauka/Interperiodica"

agent, MMA was treated with 10% aqueous sodium carbonate, washed with water to neutral reaction, dried over calcined $CaCl_2$, and distilled in a vacuum. The purity of the monomer was checked by chromatography. CPC was recrystallized from methanol and dried in a vacuum at room temperature to constant weight; decomposition temperature 35–40°C.

The thermal oxidative stability of polymers was estimated thermogravimetrically on an MOM derivatograph (Hungary) in air. The weighed portion of polymer chips was 100 mg, and the heating rate, 5 deg min^{-1}.

Thermomechanical tests were carried out on an installation with programmed heating by the method of permanent loading of the samples. The load was 0.13 MPa, and the heating rate, 0.04 deg s^{-1}. The glass transition point T_g and flow point T_f were determined from intersections of tangents to the initial sections of inflections in the thermomechanical curves.

The radiation resistance of PMMA was estimated from variation of T_g, T_f, and decomposition point T_d after gamma irradiation of discs 4 mm high on an Issledovatel' installation equipped with a ^{60}Co source. The irradiation dose was varied from 0 to 8.0 Mrad. The irradiation dose rate was 0.7 Mrad h^{-1}.

The chain transfer constants K_z/K_p in polymerization were determined according to the procedure described in [9].

It is well known that, under the action of ionizing radiation, PMMA degrades with random cleavage of the chain: T_f of the irradiated samples abruptly decreases even at small irradiation doses (Fig. 1, curve *1*), since it varies in direct proportion to the molecular weight of the polymer.

Carborane inhibits the PMMA degradation proceeding under the action of gamma radiation, which is manifested in a less pronounced decrease in T_f of the polymer prepared in the presence of DBOC, compared with the polymer prepared in the absence of carborane (Fig. 1, curves *1* and *2*). It seems likely that the polymer is protected owing to the ability of carboranes to absorb and dissipate the incident radiation energy. It is evident that the polymer is also protected by aromatic fragments of DBOC, dissipating the absorbed radiation energy before chemical transformations proceed in the polymer matrix. In addition, there is a possibility of deactivation of free radicals appearing under the action of high-energy radiation by carborane or products of its radiation-induced transformations.

Polymethyl methacrylate produced in the presence of DBOC is a homopolymer of methyl methacrylate

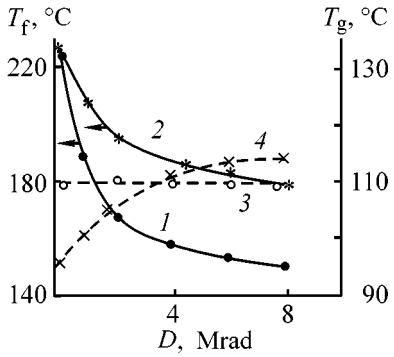

Fig. 1. (*1*, *2*) Flow point T_f and (*3*, *4*) glass transition point T_g of PMMA (*1*, *3*) without additives and (*2*, *4*) with addition of 10 wt % DBOC vs. the irradiation dose *D*.

containing carborane in the form of mechanical impurities. DBOC, having high thermal and chemical stability, does not react with the growing macroradical in polymerization of MMA: the rates of polymerization of monomer both in the presence and in the absence of this compound are the same. Hence, DBOC does not inhibit radical polymerization. In addition, it does not participate in chain transfer: in the presence of DBOC, the molecular weight of the resulting polymer does not change, and the relative inhibition constant K_z/K_p is zero. The macroradical adds neither to aromatic ring owing to abstraction of H atom from the benzene ring nor to the carborane core. It is evident that the reaction conditions are not sufficiently rigorous to form bonds between the carbon atoms of vinyl groups and boron atoms of carboranyl groups. Structures with such bonds were found, along with polyvinyl structures, e.g., in radiation polymerization of 1-vinyl-*o*-carborane [10].

The carborane group is characterized by a large dipole moment (4.5 D for *o*-carborane) and presence of delocalized electrons [11]. These groups can enhance the intermolecular interaction. For example, under isothermal heating in a vacuum and in the presence of oxygen the ester bond in polyarylates containing *o*- and *m*-carborane is cleaved even at 225–325°C. In parallel, the amount of B–H bonds decreases and the B–O–B bonds appear in the carborane fragments, which results in the formation of cross-linked structures [12]. In the presence of oxygen, these structures are formed by the reaction of carborane fragments with oxygen, and in a vacuum, by the reaction with oxygen-containing groups of macromolecules.

Under gamma irradiation of PMMA containing DBOC, carborane or products of its radiation transformations can react with oxygen-containing groups of PMMA (ester groups $-COOCH_3$). In the IR spectra,

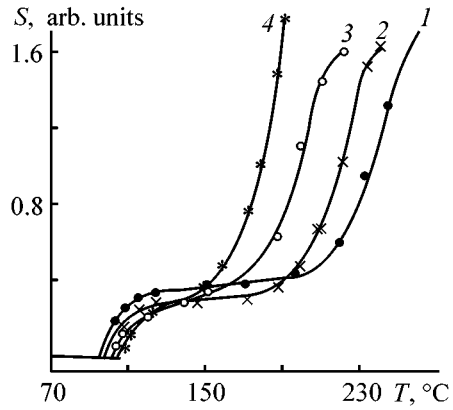

Fig. 2. Thermomechanical curves of (*1*) unirradiated and (*2*–*4*) irradiated samples of PMMA samples with addition of 10 wt % DBOC. (*S*) Strain and (*T*) temperature. Irradiation dose *D* (Mrad): (*2*) 1.0, (*3*) 4.6, and (*4*) 6.0.

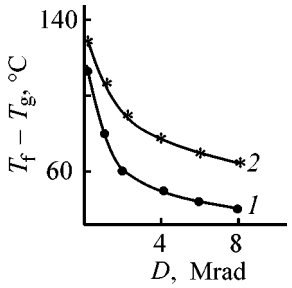

Fig. 3. Dependence of $T_f - T_g$ on irradiation dose *D* for PMMA (*1*) without additive and (*2*) with addition of DBOC.

there are no changes in the intensities of the absorption bands at 2580–2600 and 1740–1720 cm^{-1}, corresponding to the B–H modes of the carborane core [12] and carbonyl group in the ester fragment; in addition, the absorption band at 1420 cm^{-1} characteristic of the B–O–B bond is absent. However, this does not preclude the possibility of cross-linking of macromolecules via these bonds. The concentration of carborane fragments in the polymer does not exceed 4.4 wt %, and only part of these fragments, not detectable by IR spectroscopy, enter into the reaction.

The observed increase in T_g of the samples containing DBOC after irradiation (Fig. 1, curve *4*) can be accounted for by the appearance of cross-linking, resulting in decreased segmental mobility of macromolecules. Another reason for an increase in T_g of the polymer can be formation of di-, tri-, and tetramers from DBOC under gamma irradiation. For example, these oligomers with the C–C bond are formed in gamma radiolysis of *o*-carborane and 1-phenyl-*o*-carborane [13]. An increase in the molecular weight of the plasticizer, resulting in increased viscosity of the system, must also result in a higher T_g of the sample, in contrast to PMMA without an additive, whose T_g does not noticeably change with increasing irradiation dose and is 110°C (Fig. 1, curve *3*).

Dibenzyl-*o*-carborane in irradiated and nonirradiated PMMA affects the flexibility of macromolecules only slightly and acts as a plasticizer. In the unirradiated polymer, T_g decreases from 110 to 95°C with the content of DBOC increasing from 0 to 10 wt %. In PMMA subjected to gamma irradiation, the plasticizing effect of DBOC is retained up to irradiation dose of 3.5 Mrad: curve *3* lies below curve *4* (Fig. 1).

The thermomechanical curves presented in Fig. 2 are characteristic of linear polymers. Irradiated and unirradiated samples of PMMA containing DBOC are characterized by the presence of glassy, hyperelastic, and plastic states. However, when passing from unirradiated to irradiated samples, the level of hyperelastic deformation decreases somewhat, which suggests the formation of cross-links. The decrease in T_f of the polymer at increasing or constant T_g, occurring under the action of gamma irradiation, results in narrowing of the temperature range of hyperelasticity. The decrease in the $T_f - T_g$ difference for the polymer with addition of DBOC (Fig. 3, curve *2*) is less pronounced than that for the straight polymer (Fig. 3, curve *1*).

Dibenzyl-*o*-carborane not only exhibits radiation-protective effect in radiation aging but also inhibits thermal degradaton of this polymer preliminarily subjected to gamma irradiation. It is well known that at high temperature PMMA degrades by the depolymerization mechanism, in which the primary free radicals are generated by cleavage of "weak bonds" of macromolecule (terminal double bonds, bonds between two tertiary carbon atoms). DBOC does not react with the growing macroradical in polymerization of MMA and does not affect the number of weak bonds in the polymer; therefore, it does not affect the thermal stability of PMMA. The temperatures of the degradation onset and intense degradation do not vary with the concentration of carborane increasing from 0 to 10 wt % and are 250–255 and 290–300°C, respectively. The DTA and DTG curves are characterized by the same shape for PMMA with addition of DBOC and straight PMMA. In the DTA and DTG curves, there are no exothermic peaks caused by oxidation processes and there is an endothermic effect suggesting predominance of thermal degradation of irradiated and unirradiated samples.

The irradiated samples of straight PMMA and PMMA containing DBOC degrade in different ways. The T_d values of the polymer with additives exceed

the corresponding characteristics of the straight polymer at irradiation doses of up to 8 Mrad (Fig. 4). Under the action of radiation, the C–C and C–H bonds are cleaved to form, along with low-molecular-weight products, macroradicals able to participate in further reactions, e.g., initiation of thermal degradation of PMMA. Therefore, irradiation decreases its thermal stability, especially at temperatures above 250°C, which is clearly seen when comparing curves *1* and *3* in Fig. 5. The retention of higher decomposition temperatures of polymers with addition of DBOC as compared with the straight polymer is apparently caused by lower concentration of macroradicals owing to the protection of PMMA against radiation aging in the presence of this compound.

The increase in T_d of DBOC-containing PMMA upon gamma irradiation (Fig. 4, curve *2*) can be accounted for by assuming that oxygen-containing groups of macroradicals react with carborane fragments of the additive to form B–O–B bonds, which results in strengthening of the neighboring C–C bonds in the polymer macrochain. The reaction of DBOC with two macromolecules must result in formation of cross (bridging) chemical bonds, yielding a polymer of three-dimensional network structure. Owing to the "cage effect," free radicals arising in the network polymer under the action of gamma radiation recombine, having no time to leave the cage.

The stabilizing effect of DBOC additive on the thermal aging of irradiated PMMA is manifested both in the initial stages of weight loss and in the range of intensive degradation of the polymer. It should be noted that the thermal stability of irradiated samples increases in the same range of irradiation doses in which their softening point increases (up to 3–4 Mrad). Further irradiation does not alter the thermal stability and thermomechanical properties of the irradiated polymer: the dependences of T_d and T_g on irradiation dose flatten out (Fig. 1, curve *4*; Fig. 4, curve *2*).

Thus, PMAA containing DBOC and subjected to gamma irradiation is characterized by higher thermal stability and softening point than the straight polymer.

CONCLUSIONS

(1) Dibenzyl-*o*-carborane exhibits radiation-protective properties in radiation aging of polymethyl methacrylate. It inhibits thermal degradation of irradiated polymer.

(2) Gamma irradiation of polymethyl methacrylate containing dibenzyl-*o*-carborane raises the thermal stability and softening point of the polymer, apparently owing to the reaction of oxygen-containing groups of macromolecules with carborane fragments of the additive occurring in the polymer matrix in the form of mechanical impurity.

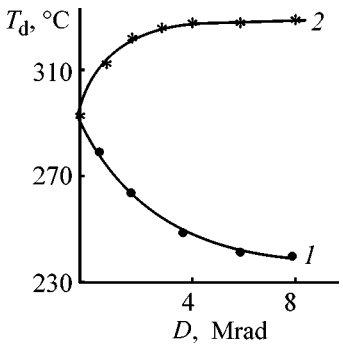

Fig. 4. Temperature of intensive degradation, T_d, of (*1*) PMMA without additive and (*2*) PMMA with addition of 10 wt % DBOC vs. irradiation dose *D*.

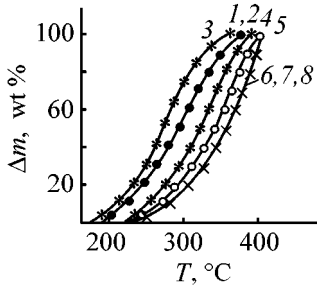

Fig. 5. Weight loss Δ*m* of (*1*, *2*) unirradiated and (*3*–*8*) irradiated samples (*1*, *3*) without addition and (*2*, *4*–*8*) with addition of DBOC vs. temperature *T*. Irradiation dose *D* (Mrad): (*3*) 1.2, (*4*) 1.0, (*5*) 2.0, (*6*) 4.0, (*7*) 6.0, and (*8*) 8.0.

ACKNOWLEDGMENTS

We are sincerely grateful to M.M. Teplyakov for submitting dibenzyl-*o*-carborane.

REFERENCES

1. Salimgareeva, V.N., Leplyanin, G.V., Vorob'eva, A.I., and Rafikov, S.R., *Bashkir. Khim. Zh.*, 1995, vol. 2, nos. 3–4, pp. 27–31.
2. *The Radiation Chemistry of Macromolecules*, Dole, M., Ed., New York: Academic, 1972, vol. 1.
3. Leplyanin, G.V., Salimgareeva, V.N., Malyarchuk, E.S., and Rafikov, S.R., *Vysokomol. Soedin., Ser. B*, 1979, vol. 21, no. 3, pp. 176–178.
4. *Radiation Effects on Organic Materials*, Bolt, R.O. and Carroll, J.G., Eds., New York: Academic, 1963.
5. Grimes, R.N., *Carboranes*, New York: Academic, 1970.

6. *Uspekhi v oblasti sinteza elementoorganicheskikh polimerov* (Advances in Synthesis of Heteroorganic Polymers), Korshak, V.V,, Ed., Moscow: Nauka, 1988.
7. Bogomazova, N.V., Leshchenko, S.S., Soboleva, N.S., and Karpov, V.L., *Vysokomol. Soedin., Ser. B*, 1978, vol. 20, no. 5, pp. 340–344.
8. Zakharkin, L.I. and Kazantsev, A.V., *Izv. Akad. Nauk SSSR, Ser. Khim.*, 1965, no. 12, pp. 2190–2193.
9. Gladyshev, G.P., *Polimerizatsiya vinil'nykh monomerov* (Polymerization of Vinyl Monomers), Alma-Ata: Akad. Nauk Kaz. SSR, 1964.
10. Wright, J.R. and Klingen, T.J., *J. Inorg. Nucl. Chem.*, 1972, vol. 34, no. 10, pp. 3284–3286.
11. Osipov, O.A., Minkin, V.I., and Garnovskii, A.D., *Spravochnik po dipol'nym momentam* (Dipole Momenta: A Handbook), Moscow: Vysshaya Shkola, 1971.
12. Zhuravleva, I.V., Vinogradova, N.K., and Pavlova, S.A., *Vysokomol. Soedin., Ser. A*, 1981, vol. 23, no. 10, pp. 2351–2359.
13. Klingen, T.J. and Mathur, M.A., *J. Inorg. Nucl. Chem.*, 1977, vol. 39, no. 9, pp. 1477–1480.

Russian Journal of Applied Chemistry, Vol. 75, No. 6, 2002, pp. 985–988. Translated from Zhurnal Prikladnoi Khimii, Vol. 75, No. 6, 2002, pp. 1003–1006.
Original Russian Text Copyright © 2002 by Novikova, Tishchenko, Iozep, Passet.

MACROMOLECULAR CHEMISTRY AND POLYMERIC MATERIALS

Influence of Synthesis and Isolation Conditions on Properties of Dextran Polyaldehyde

E. V. Novikova, E. V. Tishchenko, A. A. Iozep, and B. V. Passet

St. Petersburg State Academy of Pharmaceutical Chemistry, St. Petersburg, Russia

Received November 22, 2001; in final form, February 2002

Abstract—The content of aldehyde groups in dextran polyaldehyde was studied in relation to the pH of the reaction mixture in dextran oxidation and isolation of polyaldehyde.

There are indications in the literature that dextran polyaldehyde (DPA) samples prepared by oxidation of dextran with sodium metaperiodate at 18–20°C for 1 day and then isolated at pH in the range from 3.2 to 8.0 differ in spectral characteristics [1–3]. It was suggested that this is due to keto–enol tautomerism of DPA. In acid solutions, approximately half of aldehyde groups are in the free state and hydrated form. The other half is involved in intermolecular hemiacetal bonds. With increasing pH, the intermolecular networks are broken, and hydrated aldehyde groups form mainly hemiacetal rings with aldehyde groups of the oxidized unit.

Since DPA is used for constructing polymeric drugs, it is of prime importance to ensure the reproducibility of its initial properties. Therefore, the goal of this study was to elucidate the influence exerted by conditions of DPA synthesis and isolation and by the pH of the DPA solution on its characteristics.

To find how the pH of the reaction medium in oxidation of α-glycol groups of the polysaccharide affects the properties of the polyaldehyde, the reaction of dextran with sodium periodate (0.75 or 1 mol of $NaIO_4$ per monosaccharide unit) was performed in aqueous solutions with pH from 1.9 to 5.6 at 6–8°C for 4 h until the oxidant consumption ceased (monitored spectrophotometrically at 222.5 nm [4]). The required acidity was adjusted with 0.1 formate buffer solution, or by adding solutions of HCl and NaOH; pH was monitored with an I-160 laboratory pH meter. The products were isolated as described in [5], analyzed by the oxime [6] and hydroxamic [7] methods, and characterized by the degree of substitution, C_{sa} (number of aldehyde groups per monosaccharide unit). The number of 2,4-oxidized monosaccharide fragments in the polyaldehyde (moles per mole of DPA monomeric unit) was determined from the amount of formic acid formed in oxidation of dextran, which, in turn, was determined by titration with 0.1 N NaOH. The number of 2,3- and 2,4-oxidized fragments, x, was calculated by the formula

$$x = a - 2b,$$

where a is the number of moles of consumed $NaIO_4$, and b is the number of moles of released formic acid per mole of dextran monosaccharide units.

Viscometric studies, performed with a VPZh-2 viscometer (glass capillary diameter 0.56 mm) in water at 21°C showed that the intrinsic viscosity of DPA samples prepared by oxidation of dextran at different pH is approximately the same (0.92 ± 0.04 l mol^{-1}) and equal to that of the initial dextran (0.95 l mol^{-1}). This fact suggests that, under the reaction conditions, cross-linking is improbable, or its extent is equal in DPA samples prepared at different pH. As expected, the solubility of DPA samples decreases as compared to the initial polysaccharide. For example, whereas dextran dissolves at room temperature, DPA dissolves only upon heating.

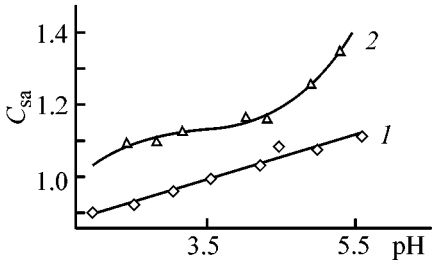

Fig. 1. Degree of substitution, C_{sa}, of DPA, calculated from the results of periodate oxidation, vs. pH of dextran solution (*1*) in formate buffer solution and (*2*) in water (before oxidation).

1070-4272/02/7506-0985 $27.00 © 2002 MAIK "Nauka/Interperiodica"

Table 1. Characteristics of DPA samples prepared by oxidation of dextran in 0.1 N formate buffer solution

Solution pH	$NaIO_4$ consumption, mol mol^{-1}	Number of oxidized fragments		C_{sa}^*	
		2,4-	2,3-	1	2
1.9	0.75	0.30	0.15	–	0.90
2.5	0.75	0.29	0.17	–	0.92
3.0	0.75	0.27	0.21	0.96	0.96
3.5	0.75	0.25	0.25	–	1.00
4.2	0.75	0.23	0.29	1.0	1.04
4.5	0.75	0.21	0.33	0.95	1.08
5.0	0.74	0.20	0.34	1.11	1.08
5.6	0.75	0.19	0.37	0.96	1.12

* (1) Determined by the oxime method and (2) from $NaIO_4$ consumption; the same for Table 2.

Table 2. Characteristics of DPA samples prepared by oxidation of dextran in water

Solution pH		$NaIO_4$ consumption, mol mol^{-1}	Number of oxidized fragments		C_{sa}	
initial	final		2,4-	2,3-	1	2
2.4	1.8	0.90	0.36	0.18	0.87	1.09
2.8	2.1	0.90	0.35	0.20	0.87	1.10
3.2	2.3	0.90	0.34	0.23	0.87	1.13
3.6	2.3	0.90	0.33	0.24	0.91	1.14
4.0	2.4	0.92	0.33	0.25	0.89	1.17
4.3	2.4	0.91	0.33	0.26	0.88	1.17
4.9	2.5	0.93	0.30	0.33	0.93	1.26
5.3	2.8	0.92	0.24	0.43	0.84	1.35

We found (Tables 1, 2) that, in oxidation of dextran in a buffer solution and in water, the amount of the consumed oxidant is approximately constant (~0.75 and 0.92 ± 0.02 mol per mole of monosaccharide units, respectively) irrespective of pH. The total number of aldehyde groups in DPA samples, calculated from the results of periodate oxidation, increases in both cases by 24% as the pH is raised from 1.9–2.4 to 5.6–5.3 (Fig. 1). However, C_{sa} is a virtually linear function of pH in the formate buffer solution, whereas in oxidation of dextran in water the acidity exerts a stronger effect on the total degree of substitution at pH > 5. At lower pH, the mean C_{sa} of DPA samples is 0.89 ± 0.04 (from elemental analysis) and 1.15 ± 0.07 (from results of periodate oxidation).

In periodate oxidation, the yield of formic acid and hence the number of 2,4-oxidized monosaccharide fragments in DPA decrease with increasing pH of the initial dextran solutions. Here, as in the case of the overall degree of substitution, the number of 2,3- and 2,4-oxidized DPA fragments depends linearly on the pH at which dextran was oxidized in buffer solution and in a more complex fashion in aqueous solutions (Figs. 2a, 2b).

With increasing pH of the reaction mixture in periodate oxidation, the ratio of the 2,4- and 2,3-oxidized fragments changes. Correspondingly, the structure of the polymer chain changes, so that, even at close or the same content of aldehyde groups capable of reacting with a nucleophile, the structure of DPA samples may be essentially different. For example, DPA samples prepared in the buffer solution at pH 1.9 and 5.6 contain, respectively, 15 and 37% 2,3-oxidized fragments; the content of glucopyranose fragments in the samples prepared by dextran oxidation in water at the initial pH 2.5 is approximately 1.5 times that in the samples oxidized at pH 5.3, at approximately equal (0.84–0.87) degree of substitution C_{sa} determined by the oxime method.

In oxidation of dextran in water, the pH of the reaction mixture steadily decreases (due to formation of formic acid), and by the end of the reaction it is lower than the initial value by 0.6–2.6. The final pH in oxidation of dextran solution is the same (2.3–2.4) at different pH values (from 3.2 to 4.3) of the initial dextran solutions. Correspondingly, the composition

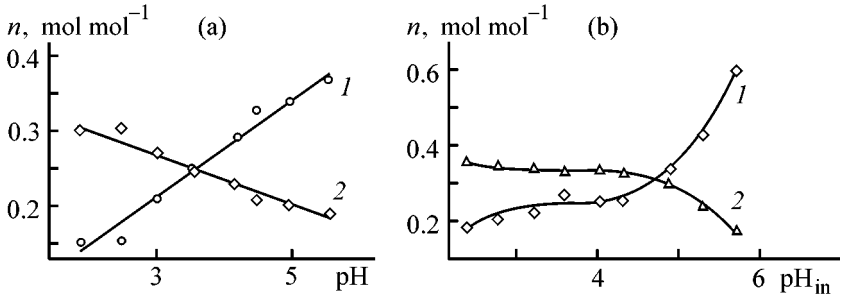

Fig. 2. Number *n* of (*1*) 2,3- and (*2*) 2,4-oxidized monosaccharide units in DPA vs. (a) pH of the buffer solution used in dextran oxidation and (b) initial pH of dextran solution in water in oxidation with sodium periodate.

of the DPA samples obtained under these conditions are also close: 33–34% 2,4-oxidized fragments, 26–23% 2,3-oxidized fragments, and 41–43% monosaccharide fragments.

We also found that, for DPA samples prepared by oxidation in water, C_{sa} determined by the oxime method is always lower than it whould be expected on the assumption that the oxidant is fully consumed for α-glycol oxidation. The difference between the C_{sa} values determined by the oxime method and from the periodate consumption is larger for the samples obtained by dextran oxidation at higher pH. This fact confirms the assumptions made by us and other authors [1–3] that 2,3- and 2,4-oxidized fragments can form stable lactol rings, which are not opened in reactions of polyaldehydes with hydroxylamine:

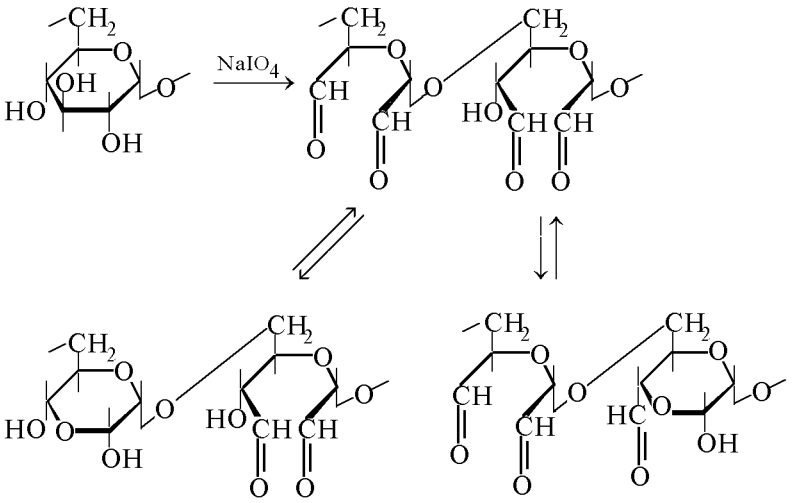

To verify the assumption that not only 2,3-, but also 2,4-oxidized units of the polyaldehyde can form cyclic lactols, we performed oxidation of dextran with excess sodium periodate at pH 2.64 and 5°C until the oxidant uptake ceased. An analysis by the oxime method of the samples containing exclusively 2,4-oxidized fragments showed that the content of aldehyde groups capable of reacting with nucleophiles is only half that expected from the periodate consumption. This may be due to formation of inter- and intramolecular lactols, and also to steric factors.

The influence exerted by conditions of DPA isolation from solution on its characteristics was examined with a sample prepared by oxidation of 10 g of dextran with sodium metaperiodate (0.5 mol of $NaIO_4$ per mole of monosaccharide units) in 1 l of formate buffer solution at pH 4. The mixture obtained by oxidation was dialyzed against water for 2 days, and the resulting solution was concentrated in a vacuum (residual pressure 20–25 mm Hg) at 50°C to 100 ml and divided in five portions; the pH of each portion was adjusted in the range from 2.8 to 5.6, and it was kept for 10 min. To the resulting DPA solutions, ten volumes of ethanol were added, and the products were isolated as described above. The degree of substitution was determined using the hydroxamic reaction.

As expected, the resulting samples had different contents of free aldehyde groups. The highest C_{sa} values were observed in the samples precipitated at pH 3.6–4.0. With pH decreasing to 2.8 or increasing to 5.6, C_{sa} decreased by 8–10% (Fig. 3).

Modification of polysaccharides with amines, phenols, and other compounds is often performed at pH > 7. To determine how C_{sa} of DPA varies in alkaline solutions in the absence of nucleophiles, the

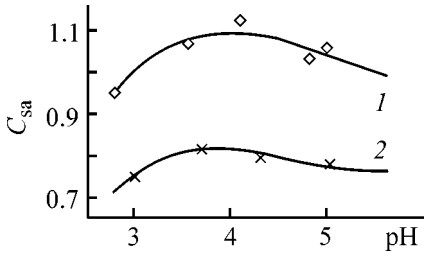

Fig. 3. C_{sa} of DPA samples, determined by the hydroxamic method, vs. pH of their solutions in the stage of precipitation with ethanol. Temperature of oxidation, °C: (*1*) 20, (*2*) 5.

polyaldehyde (C_{sa} = 0.65) was kept for 2 h in 0.02 N NaOH at 15–20°C. At definite intervals, samples were taken, and the amount of aldehyde groups in DPA was determined by the hydroxamic method.

We found that, under these conditions, C_{sa} of this DPA sample decreased to the following level: 15 min, 0.6; 45 min, 0.4; 60 min, 0.35; and 100 min, 0.32. That is, the content of aldehyde groups in DPA decreased approximately by half in 1.5 h, and this process was irreversible. The initial C_{sa} value was not restored after keeping in an acidic solution (pH 3.5) the DPA sample treated with alkali. Such transformations of DPA may involve not only keto–enol tautomerism but also aldol and crotonic condensations and oxidation.

CONCLUSIONS

(1) The ratio of 2,3- and 2,4-oxidized fragments in dextran polyaldehyde formed by oxidation of dextran with sodium metaperiodate is mainly determined by the pH of the reaction solution.

(2) To prepare samples with reproducible characteristics, oxidation of dextran and isolation of dextran polyaldehyde should be performed in the range pH 3.6–4.3.

REFERENCES

1. Drobchenko, S.N., Isaeva-Ivanova, L.S., Grachev, S.A., and Bondarev, G.N., *Vysokomol. Soedin., Ser. B*, 1990, vol. 32, no. 4, pp. 254–258.
2. Drobchenko, S.N., Isaeva-Ivanova, L.S., Kulintseva, I.V., *et al.*, *Vysokomol. Soedin., Ser. B.*, 1991, vol. 33, no. 3, pp. 220–224.
3. Bondarev, G.N., Drobchenko, S.N., and Isaeva-Ivanova, L.S., *Vysokomol. Soedin., Ser. A*, 1994, vol. 36, no. 7, pp. 1109–1112.
4. *Methods in Carbohydrate Chemistry*, Whistler, R.L. and Wolfrom, M.L., Eds., New York: Academic, 1962–1965.
5. Suvorova, O.B., Iozep, A.A., and Passet, B.V., *Zh. Prikl. Khim.*, 2001, vol. 74, no. 6, pp. 988–992.
6. Houben–Weyl, *Methoden der organischen Chemie*, Stuttgart: Thieme, 1953.
7. Iozep,, A.A., Suvorova, O.B., Iozep, L.I., and Passet, B.V., *Zh. Prikl. Khim.*, 1998, vol. 71, no. 7, pp. 1202–1205.

Russian Journal of Applied Chemistry, Vol. 75, No. 6, 2002, pp. 989–993. Translated from Zhurnal Prikladnoi Khimii, Vol. 75, No. 6, 2002, pp. 1007–1011.
Original Russian Text Copyright © 2002 by Bochek, Kalyuzhnaya.

MACROMOLECULAR CHEMISTRY AND POLYMERIC MATERIALS

Interaction of Water with Cellulose and Cellulose Acetates as Influenced by the Hydrogen Bond System and Hydrophilic–Hydrophobic Balance of the Macromolecules

A. M. Bochek and L. M. Kalyuzhnaya

Institute of Macromolecular Compounds, Russian Academy of Sciences, St. Petersburg, Russia

Received January 16, 2002.

Abstract—Interaction of cellulose and cellulose acetates of different degrees of substitution with water, ethanol, and chloroform was studied by the sorption technique. The factors determining the solubility in water of cellulose acetates with degrees of substitution varied in a narrow range were studied.

Interest in water-soluble cellulose acetates (CAs) is due to a number of their peculiar properties. Films and fibers of water-soluble CAs, unlike water-soluble cellulose ethers (methyl cellulose, ethyl cellulose, etc.), can be readily saponified to form hydrated cellulose fibers and films insoluble in water [1–3]. Cross-linked CA films can also be prepared. Water-soluble CAs are also used for preparing drugs with prolonged effect and as a binder for tablets; in textile industry, they are used to improve the crease resistance of fabrics [3–5].

There are several methods for preparing CAs [1–3, 6–8]. Water-soluble CAs are prepared only by homogeneous saponification of cellulose triacetate (CTA) [1, 6]. Cellulose acetates with degree of substitution (DS) from 0.4 to 1.0 are water-soluble [2, 3, 6–9]. Cellulose acetates prepared by direct acetylation to the same DS are only partially soluble in water (20–25 wt %) [7]. The mechanism of dissolution of CAs in water and the factors preventing dissolution in water of CAs prepared by direct acetylation have been extensively studied both in Russia and in other countries. The studies performed in Russia mainly concern preparation and properties of water-soluble CAs [1–3].

The distribution of acetate substituents in glucopyranose rings and along the macromoleculesis of CAs prepared by direct acetylation is nonuniform. The reactivity of the OH groups of cellulose in acetylation decreases in the order $C_6 > C_2 > C_3$. Homogeneous saponification of CTA with acetic acid involves two processes: hydrolysis (saponification) of acetate groups and ester interchange of hydroxyl groups until an equilibrium is attained [1]. Hence, water-soluble CA can be regarded as cellulose derivative with uniform distribution of substituents in the macromolecules of the natural polymer. The CA solubility in water depends on the location of substituents at the anhydroglucoside chains. Experiments on tritylation of water-soluble CAs (introduction of triphenylmethyl substituents at the C_6 position) showed that acetate groups are in the C_2 and C_3 positions [2, 3]. The primary OH groups (C_6 position) remain unsubstituted, and the distribution of acetate groups over positions C_2 and C_3 is random.

A study of the solubility in water of CAs prepared by three homogeneous procedures [7] showed that CAs with uniform distribution of the substituents over the C_6, C_2, and C_3 positions of glucose units are water-soluble. The decisive influence on the solubility of CA in water is exerted by relative substitution degree of the secondary OH groups. Aqueous CA solutions show no gelation on heating, unlike solutions of methyl and ethyl cellulose. Kamide *et al.* studied the solubility in water of CAs prepared by two methods. They also noted that the solubility strongly depends on the substitution at the C_2 and C_3 positions of the polymer units. They suggested that, for CA to be soluble in water, the OH groups at the C_3 position must be substituted. The degree of substitution at this position must be higher than the critical value estimated at 0.2 [8]. Introduction of hydrophobic substituents at the C_3 position ruptures the $OH_{(3)}\cdots O'_5$ intramolecular hydrogen bond and increases the mobility of macromolecules.

1070-4272/02/7506-0989 $27.00 © 2002 MAIK "Nauka/Interperiodica"

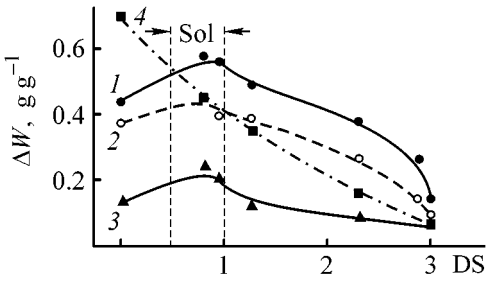

Fig. 1. Water sorption ΔW on cellulose and CA measured at (*1*) 280, (*2*) 293, and (*3*) 310 K and (*4*) calculated by the Van Krevelen procedure, vs. DS. The region of water-soluble CAs is bounded by vertical dashed lines; the same for Figs. 2a and 3.

The influence of the supramolecular structure of CAs on their solubility in water was noted in all the above works. The substituents in water-soluble CAs are uniformly distributed inside the glucopyranose rinds and along the polymeric chains [7–10].

When CA is dissolved in water, H bonds are formed between the solvent molecules and the OH and C=O groups of the acetyl substituents [3]. Introduction of a small number of hydrophobic substituents breaks down the regular structure of cellulose macromolecules and makes the supramolecular structure of the polymer disordered [1]. Hence, the solubility of CA in water depends on both physical (degree of crystallinity and uniformity of substituent distribution) and chemical factors (solvation of hydroxy and acetate groups) [1].

In this work, we studied the solubility of CAs in water as influenced by changes in hydrogen bond network of natural cellulose and in the hydrophilic–hydrophobic balance of its macromolecules. The interaction of cellulose and CA was studied by sorption of solvent vapor at different temperatures.

EXPERIMENTAL

Cellulose acetates with DS of 0.80, 0.95, 1.26, 2.30, 2.88, and 3.00 were prepared by homogeneous saponification of CTA [3]. CA films were prepared by casting CA solutions in water-acetic acid mixture on Teflon plates. To reach complete dissolution of the samples, the solvent composition was varied depending on the DS of the polymer. A film of hydrated cellulose was prepared by saponification of a film of water-soluble CA with DS = 0.80 with a sodium methylate solution [11].

The sorption of saturated solvent vapor on the films at 280–310 K was measured with a McBain spring balance with sensitivity of about 1 mg mm^{-1} (~0.01% error).

To find out how the change in the network of H-bonds of cellulose and in the hydrophilic–hydrophobic balance of the macromoleculs affect the thermodynamic affinity of the polymers for water, we studied the interaction of cellulose and CAs with different DSs with water, ethanol, and chloroform. Ethanol and chloroform can also form hydrogen bonds with the OH groups of the polymer, with ethanol being both donor and acceptor of protons and chloroform being proton donor only [12]. In addition, the hydrophilicity of these compounds varies: ethanol is unlimitedly miscible with water and chloroform is only sparingly soluble in water. The interaction of these solvents with OH groups of cellulose can be estimated from their interaction with water.

Previously, we have found [13] that the energy of H bonds in cellulose is up to 25.0 kJ mol^{-1}. Since the energy of hydrogen bonds in water lies in the range 18.0–21.0 kJ mol^{-1} [14], cellulose is insoluble in water. Cellulose is soluble in tertiary amine *N*-oxides forming H bonds with a polymer with energy higher than 25.0 kJ mol^{-1} [15]. Acetate derivatives of cellulose with DS from 0.4 to 1.0 are water-soluble [3, 7, 8].

Myagkova *et al.* [16, 17] showed that the enthalpy of mixing of CA with water is the factor determining the CA solubility. However, the cellulose structure changes after introduction of a small amount of acetate groups [1, 3], which in turn, affects the network of H bonds in the natural polymer. Introduction of bulky polar substituents into cellulose macromolecules changes fundamentally the polymer properties: network of H bonds, density, molar volume, heat capacity, glass transition point, thermal stability, etc. [18].

Figure 1 shows how the water sorption by cellulose acetate varies with DS at different temperatures. The $\Delta W = f(\mathrm{DS})$ functions pass through a maximum in the DS range corresponding to solubility of CA in water. The presence of the maximum suggests the influence of two processes on the solubility of CA in water. The dependence of water sorption on the DS, calculated by the Van Krevelen procedure [19], is also shown in the figure. It should be noted that the calculated dependence shows no maximum. Only the contribution of various groups to the sorption was taken into account in the calculation, and changes in the degree of crystallinity during swelling and in the system of intermolecular interactions in CA with changing DS were disregarded. As the temperature increases, the water sorption decreases owing

to weakening of CA-water interactions. It should be noted that a maximum in the $\Delta W = f(\mathrm{DS})$ dependence for CA was not always observed [16, 17]. The reason for this phenomenon is considered below.

To evaluate the polymer solubility in a specific solvent, Askadskii *et al*. took into account the surface tension at the solvent–polymer interface and the wettability γ of the polymer surface with the solvent [20, 21]. In this work, we performed similar studies.

The dependence of the solvent sorption at 293 K on the DS and the variation of the surface energy γ of the polymers in going from cellulose to cellulose diacetate (CDA) with DS = 2.40 are shown in Figs. 2a–2c. As seen from Fig. 2a, γ of pure cellulose (curve *2*) is 66.5 mN m^{-1} [22]. The surface energy of commercial CDA is 39–40 mN m^{-1} [23]. The surface tension of water (72.5 mN m^{-1}, curve *3*) is higher than that of cellulose [24]. Introduction of acetate groups into the cellulose macromolecule increases the difference between the surface tension of the polymer and the solvent, i.e., makes the polymer more hydrophobic, decreases the weattability of the polymer with water, and prevents diffusion of solvent molecules in the polymer matrix. As the DS increases further, the difference in γ increases so that CTA virtually does not interact with water. Presumably, the right-hand boundary of the DS range of water-soluble CAs is determined or bounded by the increasing polymer hydrophobicity.

The plots of ethanol and chloroform sorption vs. DS (Fig. 2b and 2c) show that at least two factors affect the solvent–polymer interaction. One of these, the difference in the surface energy of the polymer and the solvent, is manifested to a varied extent.

The $\Delta W = f(\mathrm{DS})$ dependence for ethanol is similar to that for water. However, the ethanol sorption is appreciably lower, which agrees with the data of [16]. The surface energy of CAs with DS > 2.0 approaches that of the solvent; however, cellulose and CA are insoluble in ethanol and swell only slightly. This suggests that the mechanism of interaction of ethanol with CA is similar to that of water, and the energy of ethanol interaction with the functional groups of the polymer is lower.

Cellulose acetate with DS = 3.0 (cellulose triacetate) is soluble in chloroform (Fig. 2c). At DS = 0.8 the sorption passes through a weak minimum. At higher DS the CA-solvent interaction increases. As in the case of ethanol, the surface energies of the polymer and the solvent approach each other, which favors solvent diffusion into the polymer matrix. The fact that CAs with high DS are insoluble in

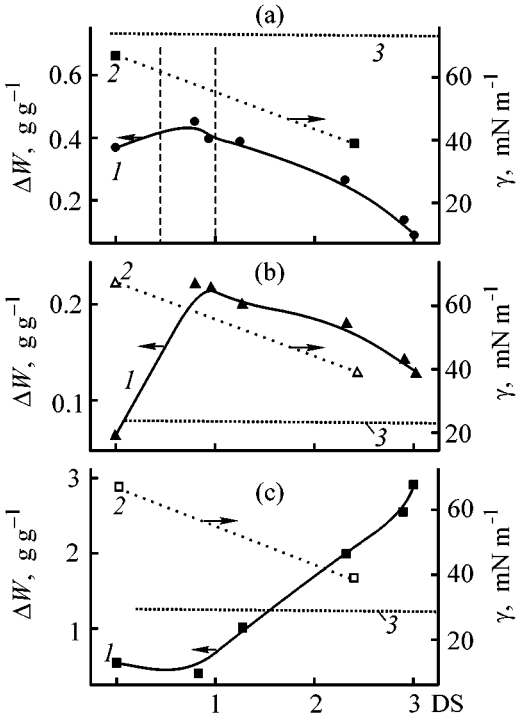

Fig. 2. (*1*) Sorption of (a) water, (b) EtOH, and (c) $CHCl_3$ ΔW at 293 K and (*2*) surface energy of the polymers γ vs. DS; (*3*) the surface energy of liquids.

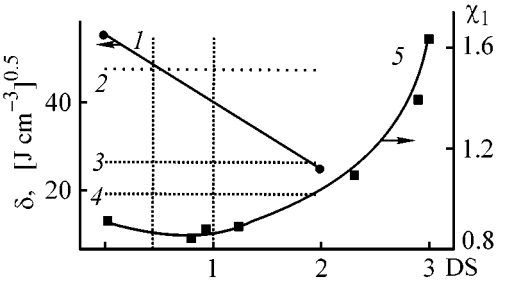

Fig. 3. Solubility parameters δ of (*1*) CA, (*2*) water, (*3*) EtOH, and (*4*) $CHCl_3$, and (*5*) χ_1 interaction parameter vs. DS.

ethanol and chloroform indicates the difference in the specific interaction of these solvents with CA.

Previously, we have shown that the energy contribution of hydrogen bonds and dipole–dipole interactions to the cohesion energy density of CA sharply decreases and the contribution of the dispersion forces grows with increasing DS. The solubility parameter δ and its components for methanol and chloroform are $\delta = 26.5$, $\delta_d = 15.8$, $\delta_p = 8.8$, $\delta_h = 19.4$ and $\delta = 19.0$, $\delta_d = 17.8$, $\delta_p = 3.1$, $\delta_h = 5.7$ $(\mathrm{J\ cm^{-3}})^{0.5}$, respectively [24]. Comparison of the solubility parameters shows that H bond formation makes a major contribution to the cohesion energy density in ethanol, and the contribution of the dispersion interactions is lower.

At the same time, the main contribution in chloroform is due to the dispersion interactions and the energy contribution from H bonding is lower. These different types of interaction cause different mechanisms of interaction of these solvents with CA.

The solubility parameters of water, ethanol, chloroform, and CA and the plot of the parameter of CA–water interaction χ_1 vs. DS are presented in Fig 3. The Flory–Huggins parameter χ_1 was calculated by the equation

$$\ln a_1 = \ln(P_1/P_1^0) = \ln(1 - \varphi_2) + \varphi_2 + \chi_1\varphi_2^2, \quad (1)$$

where a_1 is the solvent activity and P_1/P_1^0 is the relative vapor pressure of the solvent.

The experiments were performed at the saturated pressure of the solvent: $a_1 = P_1/P_1^0 = 1$, $\ln a_1 = 0$. The volume fraction of the swollen polymer was calculated by the equation

$$\varphi_2 = \frac{1}{1 + \frac{d_2}{d_1}(\Delta W)}, \quad (2)$$

where ΔW is the amount of the solvent sorbed (g g^{-1}), and d_2 and d_1 are the polymer and solvent densities, respectively.

The density was determined by the flotation procedure.

The δ-vs.-DS dependence obtained previously [13] is shown in Fig. 3 (curve *1*). Cellulose acetate is soluble in water when the δ values of the polymer and solvent are close and χ_1 values are minimal. Hence, to make CA water-soluble, the energy contribution of H bonding to the cohesion energy density, which prevails in the initial cellulose, should be decreased. Introduction of a small number of acetate groups appreciably decreases the number of H bonds in cellulose and their energy in the case of uniform distribution of these groups in the macromolecules and glucoside units. As a result, CA becomes water-soluble. Upon further increase in the content of acetate groups, the difference between the surface energies of the polymer and solvent strongly grows (hydrophobization of the polymer), and the polymer becomes insoluble. This is confirmed by the fact that cellulose propionates prepared similarly are hydrophobic and insoluble in water [1].

Superposition of the two trends, the decrease in the contribution of the H bonds to the cohesion energy density of the polymer and the hydrophobization of the macromolecules, affects the thermodynamic affinity of CA for water. Strengthening in the polymer–water interaction up to DS = 1.0 (a decrease in the parameter χ_1 of the polymer–solvent interaction) indicates that rupture of the H bonds in the polymer and a decrease in δ of CA exert a prevailing effect. At higher degrees of substitution the interaction weakens owing to polymer hydrophobization. A decrease in the average energy of H bonds of the OH groups of CA with increasing number of acetate substituents was found in [3].

It should be noted that the degree of crystallinity of CAs with DS ≥ 0.5 sharply decreases [1]. In the order cellulose–water-soluble CA–CTA, the polymer crystallinity may change substantially depending on the conditions of CA saponification and isolation of the products from the solution. The porosity and the specific surface area of CAs depend on the conditions of their precipitation from solution [16]. These factors strongly affect the solvent sorption and can result in disappearance of the maximum in the $\Delta W = f(\mathrm{DS})$ curve at DSs corresponding to the water-soluble polymer. Probably this was the case in [17].

Thus, the solubility of CAs in water is due to a decrease in the energy and, probably, number of H bonds of cellulose (supramolecular level). Introduction of acetate groups makes the macromolecules hydrophobic (molecular level) and insoluble in water. Swelling of water-soluble CAs cannot reach a maximum owing to cellulose crystallization.

CONCLUSION

The factors determining the solubility of cellulose acetates were studied at the molecular and supramolecular levels. At the supramolecular level, the solubility of cellulose acetates in water is due to a decrease in the energy (and probably number) of hydrogen bonds of cellulose. Introduction of acetate groups makes the macromolecules hydrophobic (molecular level) and insoluble in water.

REFERENCES

1. Petropavlovskii, G.A., *Gidrofil'nye chastichno zameshchennye efiry cellulozy i ikh modifikatsiya putem khimicheskogo sshivaniya* (Hydrophylic Partially Substituted Cellulose Ethers and Esters and Their Modification By Chemical Cross-Linking), Leningrad: Nauka: 1988.
2. Rakhmanberdyev, G., Water-Soluble Cellulose Acetate, *Cand. Sci.*, Leningrad, 1968.

3. Rakhmanberdyev, G., Petropavlovskii, G.A., and Usmanov, Kh.U., *Cellulose Chem. Technol.*, 1978, vol. 12, no. 2, pp. 153–176.
4. Mukhamedzhanov, M., Zainutdinov, U.N., and Mukhamedkarimova, M.G., Abstracts of Papers, *Vsesoyuznaya nauchnaya konferentsiya "Problemy modifikatsii prirodnykh i sinteticheskikh voloknoobrazuyushchikh polimerov"* (All-Union Scientific Conf. "Problems of Modification of Natural and Synthetic Fiber-Forming Polymers"), Moscow, October 29–30, 1991, p. 81.
5. Rakhmanberdyev, G., alulbekov, S., Mukhamedzhanov, M., *et al.*, Abstracts of Papers, *Vesoyuznaya nauchnaya konferentsiys "Problemy modifikatsii prirodnykh i sinteticheskikh voloknoobrazuyushchikh polimerov"* (All Union Scientific Conf. "Problems of Modification of Natural and Synthetic Fiber-Forming Polymers"), Moscow, October 29–30, 1991, p. 90.
6. Malm, C.J., Barkey, K.T., Salo, M., *et al., Ind. Eng. Chem.*, 1957, vol. 49, no. 1, pp. 79–83.
7. Miyamoto, T., Sato, Y., Shibata, T., *et al., J. Polym. Sci., Poly. Chem. Ed.*, 1985, vol. 23, no. 5, pp. 1373–1381.
8. Kamide, K., Okajima, K., Kowsaka, K., *et al., Polym. J.*, 1987, vol. 19, no. 12, pp. 1404–1412.
9. Kamide, K. Saito, M., and Abe, T., *Polym. J.*, 1981, vol. 13, no. 5, pp. 421–431.
10. Usmanov, T.I., Suleimanova, R.T., Karimova, U.G., *et al., Khim. Drev.*, 1987, no. 5, pp. 81–87.
11. Okamura, K., Fujita, M., and Umezawa, T., *Bull. Kyoto Univ. Forests*, 1981, no. 53, pp. 254–260.
12. Pimentel, J. and McKlenan, O., *Vodorodnaya svyaz'* (Hydrogen Bonds), Moscow: Mir, 1964.
13. Bochek, A.M. and Petropavlovsky, G.A., *Cellulose Chem. Technol.*, 1993, vol. 27, no. 6, pp. 587–596.
14. Karyakin, A.V. and Kriventsova, G.A., *Sostoyanie vody v organicheskikh i neorganicheskikh soedineniyakh* (State of Water in Organic and Inorganic Compounds), Moscow: Nauka, 1973.
15. Bochek, A.M., Petropavlovsky, G.A., and Yakimansky, A.V., *Cellulose and Cellulose Derivatives: Physico-Chemical Aspects and Industrial Applications*, Kennedy, J.F., Phillips, G.O., Williams, P.O., and Piccullel, L., Eds., Cambridge, England: Woodhead, 1995, pp. 131–137.
16. Myagkova, N.V., Hydrodynamic and Thermodynamic Properies of Cellulose Acetate Solutions as Influenced by the Substitution Degree, *Cand. Sci. Dissertation*, Tashkent, 1988.
17. Khamrakulov, G., Myagkova, N.V., and Budtov, V.P., *Vysokomol. Soedin., Ser. B*, 1994, vol. 36, no. 5, pp. 845–849.
18. Askadskii, A.A., Bolobova, A.V., Kondrashchenko, V.I., *et al., Vysokomol. Soedin., Ser. A*, 2000, vol. 42, no. 3, pp. 517–529.
19. Van Krevelen, D.W., *Properties of Polymers. Correlations with Chemical Structure*, Amsterdam: Elsevier, 1972.
20. Askadskii, A.A., MAtveev, Yu.I., and Matevosyan, M.S., *Vysokomol. Soedin., Ser. A*, 1990, vol. 23, no. 10, pp. 3157–3166.
21. Matveev, Yu.I. and Askadskii, A.A., *Vysokomol. Soedin.*, 1994, vol. 36, no. 3, pp. 436–443.
22. Van Hazendonk, J.M., van Putten, C.J., and Keurenjes, J.T.F., *Cellulose and Cellulose Derivatives: Physico-Chemical Aspects and Industrial Applications*, Kennedy, J.F., Phillips, G.O., Williams, P.O., and Piccullel, L., Eds., Cambridge, England: Woodhead, 1995, pp. 107–114.
23. Olsen, D.A. and Osteraas, A.J., *J. Appl. Polym. Sci.*, 1969, vol. 13, no. 7, pp. 1523–1535.
24. Van Krevelen, D.W and Hoftyzer, P.J., *Properties of Polymer: Their Estimation and Correlation with Chemical Structure*, Amsterdam; Elselvier, 1976, 2nd ed.

Russian Journal of Applied Chemistry, Vol. 75, No. 6, 2002, pp. 994–996. Translated from Zhurnal Prikladnoi Khimii, Vol. 75, No. 6, 2002, pp. 1012–1014.
Original Russian Text Copyright © 2002 by Mozyreva, Kireeva, Driker, Kazuto.

MACROMOLECULAR CHEMISTRY AND POLYMERIC MATERIALS

Possibility of Using Organophosphonates in the First Stage of Cellulose Whitening

E. A. Mozyreva, S. A. Kireeva, B. N. Driker, and E. V. Kazuto

Ural State Forestry University, Yekaterinburg, Russia

Received November 5, 2001; in final form, January 2002

Abstract—The influence of organophosphonates on decomposition of equilibrium peracetic acid was studied in the temperature range 50–70°C and pH 4.5–5.0.

One of the promising ways to produce whitened cellulose is to use peroxo compounds, such as peracetic acid and hydrogen peroxide [1]. As a rule, cellulose is whitened in several steps, but the key one is the first stage aimed to complete lignin removal. The efficiency of using formulations based on peroxo compounds is largely governed by the presence of heavy metal ions in the reaction medium and in the material to be treated. Their presence results in catalytic decomposition of these compounds, which deteriorates economical characteristics of delignification and whitening.

It is well known that complexones binding catalyst ions in the reaction mixture into stable complexes enhance the efficiency of peroxo compounds in cellulose whitening [2].

The aim of this work was to study the effect of organophosphonate complexones [3] on the decomposition of equilibrium peracetic acid and on the efficiency of the first stage of whitening of sulfite cellulose.

As object of study served peracetic acid prepared by the procedure described in [4] and containing unreacted acetic acid and hydrogen peroxide. The content of peracetic acid was 15–16%, and that of hydrogen peroxide, 9–10%.

As complexones we used organophosphonates (OPs) with varied number of functional groups and varied length of the hydrocarbon radical: nitrilotrimethylenephosphonic (NTMP), ethylenediaminetetramethylenephosphonic (EDTMP), diethylenetriaminepentamethylenephosphonic (DTPP), methyliminodimethylenephosphonic (MIDP), ethyliminodimethylenephosphonic (EIDMP), butyliminodimethylenephosphonic (BIDMP), and hexyliminodimethylenephosphonic (HIDMP) acids, and also IDMS, inhibitor of deposotition of mineral salts [TU (Technical Specification) 2415-124-166 70872–96], a mixture of organophosphonates in which NTMP and MIDP are the main components:

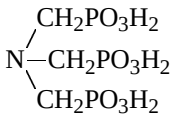
NTMP

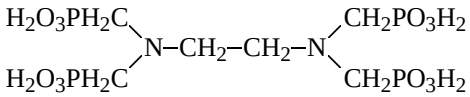
EDTMP

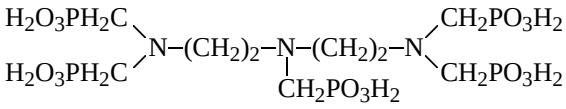
DTPP

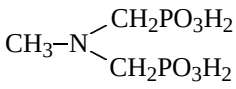
MIDP

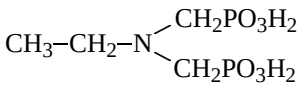
EIDMP

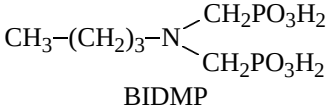
BIDMP

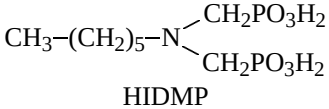
HIDMP

1070-4272/02/7506-0994 $27.00 © 2002 MAIK "Nauka/Interperiodica"

Table 1. Rate of decomposition of equilibrium peracetic acid (pH 4.5–5.0) in the presence of organophosphonates and Fe^{3+} catalyst

OP, catalyst	Decomposition rate $K \times 10^{-6}$ (mol l^{-1} s^{-1}) at indicated temperature, °C					
	50		60		70	
	CH_3COOOH	H_2O_2	CH_3COOOH	H_2O_2	CH_3COOOH	H_2O_2
–	5.00	6.94	16.45	9.80	52.18	9.12
Fe^{3+}	19.52	17.65	47.70	27.08	296.78	64.84
Fe^{3+} + OP:						
NTMP	3.87	4.55	17.18	8.24	49.71 (10.01)*	10.22 (23.41)
EDTMP	1.48	2.21	2.63	5.64	39.47 (0.685)	8.48 (0)
DTPP	0.85	1.37	3.859	7.19	11.81 (0.493)	5.39 (0)
MIDP	1.75	2.45	2.30	4.04	45.78 (5.54)	7.48 (3.80)
EIDMP	1.37	1.35	3.03	3.87	30.32 (3.73)	7.38 (2.70)
BIDMP	1.43	2.205	2.54	3.09	32.11 (4.06)	7.61 (3.43)
HIDMP	1.18	1.59	3.03	3.05	30.32 (3.25)	7.60 (4.11)

* Data for M : OP = 1 : 3 are given in parentheses.

The decomposition kinetics of equilibrium peracetic acid was studied in the temperature range 50–70°C with stirring (Re 12 500) for solutions with initial concentration of 0.039 M and pH 4.5–5.0, which corresponds to the conditions of delignification and whitening. Fe^{3+} ions, catalyzing decomposition of peroxo compounds, were added to the reaction mixture in amount of 1 mg l^{-1}, corresponding to their real content in the reaction medium in cellulose whitening.

The content of CH_3COOOH and H_2O_2 in the reaction mixture was determined by the well-known procedure [5]. The experimental data processed according to the equation of second-order reaction [6] are listed in Table 1.

In the presence of Fe^{3+} ions in the temperature range 50–70°C, the decomposition rate of both CH_3COOOH and H_2O_2 increases by a factor of 3–6 at pH 4.5–5.0. It is evident from Table 1 that all the organophosphonates used noticeably decrease the decomposition rate of peroxo compounds. With increasing amount of functional groups in the reactant molecule, the decomposition rate of both CH_3COOOH and H_2O_2 noticeably decreases. In this case, the effect of organophosphonates is enhanced both with increasing temperature and with variation of the molar ratio M : OP. In our opinion, this suggests the occurence of a chemical reaction between organophosphonates and metal ion and increased stability of the resulting complexes.

For all the organophosphonates differing in the length of hydrocarbon radical, the decomposition rate of CH_3COOOH and H_2O_2 noticeably decreases in the temperature range studied. However, the variation of the length of the hydrocarbon radical does not affect significantly the kinetic parameters of decomposition.

With account of the experimental data on the effect of organophosphonate on the decomposition kinetics of peroxo compounds, we prepared the whitening formulations containing equilibrium peracetic acid (PAA) and organophosphonates. It is well known that the quality of the initial cellulose, namely, lignin content (Kapp number), governs the result of whitening. Therefore, we used, as an initial fibrous product for whitening, crude sulfite cellulose (CSC) with various initial whiteness, 62.6 and 59.2%, and Kapp number 18.0 (CSC I) and 26.0 (CSC II), respectively. In the first stage, cellulose was whitened under standard conditions: temperature 70°C, duration 60 min, cellulose concentration 10 wt %, pH 4.5–5.0, and expenditure of whitening formulation 3% in terms of absolutely dry cellulose. Organophosphonates were added in the amount corresponding to the Fe^{3+} content in a material to be treated (0.007–0.01%) at a molar ratio M : OP = 1 : 3. The results are given in Table 2.

Peracetic acid without addition of organophosphonates only slightly affects delignification and whitening of cellulose, which is suggested by the residual amount of CH_3COOOH and H_2O_2 in the mother liquors, Kapp number, and whiteness of the half-finished product. In delignification of the cellulose sample CSC I with solution of equilibrium peracetic acid in the absence of organophosphonates, the Kapp number decreases from 18 to 13. For sample CSC II, this parameter decreases from 26 to 21. Addition of or-

Table 2. Effect of organophosphonates on the efficiency of the first stage of whitening

OP	Kapp number	Whiteness, %	Iron content, %	Residual content, %	
				CH_3COOOH	H_2O_2
			CSC I		
–	12.85	70.50	0.0070	2.11	57.39
MIDP	10.50	76.40	0.0028	6.95	69.52
EIDMP	11.00	74.70	0.0025	14.78	73.10
BIDMP	10.77	72.00	0.0020	20.00	73.35
HIDMP	11.94	75.30	0.0027	20.00	77.21
			CSC II		
–	21.95	60.08	0.0070	4.20	48.78
NTMP	19.67	68.7	0.0017	21.10	78.90
EDTMP	16.40	74.10	0.0020	19.00	77.16
DTPP	18.05	69.00	0.0019	12.50	72.25
IDMS	17.44	72.90	0.0025	19.00	73.49

ganophosphonates promotes both more complete removal of lignin and increase in the degree of whiteness. The Kapp number decreases to 10–12 for sample CSC I and to 16–19 for sample CSC II. Depending on the length of the hydrocarbon radical of organophosphonate, the degree of whiteness increases from 70.50 to 72.00–76.40%; with organophosphonates differing in the amounts of functional groups, this parameter ranging from 60.08 to 69.00–74.10%.

Most likely, the mechanism of the positive influence exerted by organophosphonates on delignification and whitening consists in the formation of stable coordination compounds with heavy metal ions present in cellulose, which decreases their negative catalytic effect on the decomposition of peroxo compounds. Therefore, peroxo compounds are more completely used in the main process.

The high residual content of H_2O_2 in the equilibrium peracetic acid in mother liquors offers an opportunity for their use in subsequent stages of cellulose whitening.

CONCLUSIONS

(1) Organophosphonates exert stabilizing effect on the components of whitening solutions, CH_3COOOH and H_2O_2. Is is evident that this is caused by the formation of stable coordination compounds of organophosphonates with Fe^{3+} ions.

(2) Composites based on the equilibrium peracetic acid and organophosphonates can be used in the first stage of whitening of sulfite cellulose.

REFERENCES

1. Akim, G.L., *Tsellyuloza. Bumaga. Karton*, 1997, nos. 3–4, pp. 12–14.
2. Kovaleva, N.E., Study of Influence of Complexones and Metal Complexonates on Decomposition of Hydrogen Peroxide, *Cand. Sci. Dissertation*, Moscow, 1997.
3. Dyatlova, N.M., Temkina, V.Ya., and Popov, K.I., *Komleksony i kompleksonaty metallov* (Complexones and Metal Complexonates), Moscow: Khimiya, 1988.
4. Weygand-Hilgetag, *Organisch-chemische Experimentierkunst*, Leipzig: Johann Ambrosius Barth, 1964.
5. Obolenskaya, A.V. and Shchegolev, V.P., *Prakticheskie raboty po khimii drevesiny i tsellyulozy* (A Practical Manual on Chemistry of Wood and Cellulose), Moscow: Lesn. Prom–st., 1965.
6. Driker, B.N., Mozyreva, E.A., Rostova, N.V., and Ageev, A.Ya., *Zh. Prikl. Khim.*, 2000, vol. 73, no. 4, pp. 678–679.

Russian Journal of Applied Chemistry, Vol. 75, No. 6, 2002, pp. 997–1000. Translated from Zhurnal Prikladnoi Khimii, Vol. 75, No. 6, 2002, pp. 1015–1018.
Original Russian Text Copyright © 2002 by Anisimov, Savin.

MACROMOLECULAR CHEMISTRY AND POLYMERIC MATERIALS

Carbon Fabric Reinforced Composites Based on Modified Epoxy Resins and Prediction of Their Strength Characteristics

Yu. N. Anisimov and S. N. Savin

Mechnikov State University, Odessa, Ukraine

Received March 27, 2000; in final form, July 2001

Abstract—The strength characteristics of composites based on four types of modified epoxy resins and reinforced with carbon fabric were studied as influenced by the filler content. The experimental and theoretical strength parameters of the composites were compared. The correlation between the adhesion strength at the polymeric binder-filler boundary and the impact resilience of the composites was evaluated; a procedure was proposed for predicting the impact resilience of the reinforced composites.

Composite materials based on polymeric binders and reinforced with carbon fibers and fabric have high strength properties and find many applications in aerospace industry and ship building [1, 2]. The nature of polymeric binder and the adhesion properties at the interface between the polymeric matrix and the carbon fabric strongly affect the properties of the reinforced composites, especially in the case of various epoxy binders [1, 3]. The electrical conductivity and strength properties of a series of composites based on modified epoxy resins filled with carbon black and graphite were studied in [3]; the possibility of predicting the strength properties of fiber glass fabric reinforced composites with similar binders was analyzed in [4].

The aim of this work was to study the strength properties of carbon fabric–reinforced composites based on modified epoxy resins and to develop a procedure for calculating their strength properties, taking into account the adhesion characteristics at the interface between the polymeric binder and the carbon fabric boundary.

EXPERIMENTAL

In this work, we used the following polymeric binders: T-10 epoxy-silicone resin [TU (Technical Specifications) 6-02-616–85], UP-637 epoxy-resorcinol resin (TU 6-06-271–86), and ED-20 epoxy-4,4'-isopropylidenediphenol resin [GOST (State Standard) 10587–84], whose characteristics are given in [4, 5]. The filled composites were cured at 20°C using B brand polyethylene polyamine (PEPA) [TU 6-02-596–86] at its content of 14–17 wt % relative to the epoxy resin. The EPU-1 epoxy-polyurethane resin contained 16.5 wt % epoxy groups, and its average relative molecular weight was 1600; all other characteristics of the resin are given in [5]. This resin was cured at 20°C using UP-583 product of condensation of formaldehyde and diethylenetriamine (TU 6-05-341–88) at its content of 14 wt % relative to the epoxy resin.

The composites were reinforced with UTM-8-1 brand carbon satin fabric based on heat-treated polyacrylonitrile fiber (92% carbon content, 0.01–0.05 mm in diameter). The composites were prepared as follows. The binder and the curing agent were deposited on carbon fabric sheets with a putty knife, and the resulting stacks were pressed with a roller. These stacks were cured at 20°C for no less than 24 h. The tensile strength (σ_t) and the ultimate strength at static bending (σ_b) of the resulting composites were studied using the procedures described in [4, 6] according to GOSTs 14236–81 and 9650–81, respectively. In our experiments, we determined the average parameters using at least three samples of each composite. The impact resilience of the composites (a_i) was studied using $60 \times 8 \times 6$ mm rectangular samples with no notches on an MK-05 impact tester with a 40-mm distance between the bearings [6] (GOST 9454–88).

The dependence of the tensile strength of the carbon fabric–reinforced composites based on modified epoxy resins on the filler content (in the range of 0.25–0.60 wt fraction) showed that the highest σ_t is observed for the composites based on ED-20 binder at a filler content of 0.35–0.40 wt fraction (see table).

1070-4272/02/7506-0997 $27.00 © 2002 MAIK "Nauka/Interperiodica"

Characteristics of carbon fabric–reinforced composites based on modified epoxy resins* (modulus of elasticity of the carbon fabric E_1 = 250 000 MPa, surface tension of the carbon fabric γ_1 = 55 mJ m^{-2})

Epoxy resin	m_1, wt fraction	E_2	A	B	α	σ_t, MPa		σ_b, MPa		a_i, kJ m^{-2},		γ mJ m^{-2}		A_a, MPa
		MPa				experimental	calculated	experimental	calculated	experimental	calculated	γ_2	γ_{12}	
ED-20,	0.20	2000	367.2	329.2	1.25	170	236	202	251	–	50	–	–	–
	0.35		178.0	70.1	1.81	450	486	460	506	72	101	36	2.0	41
	0.50		120.9	47.2	1.82	472	502	480	535	75	107	–	–	–
	0.60		96.7	36.8	1.83	448	484	461	500	68	100	–	–	–
T-10	0.25	1600	363.3	375.6	1.10	130	182	174	205	–	41	–	–	–
	0.35		175.9	82.6	1.75	342	396	406	452	60	90	32	3.1	36
	0.50		120.2	54.3	1.79	354	412	423	460	–	92	–	–	–
UP-637,	0.25	2340	366.8	294.2	1.32	198	206	225	280	–	56	–	–	–
	0.35		177.2	69.4	1.84	504	552	512	563	86	113	41	1.0	45
	0.50		120.5	47.9	1.85	526	564	514	566	–	110	–	–	–
EPU-1	0.25	2170	363.2	285.6	1.28	186	250	212	263	–	53	–	–	–
	0.35		176.9	77.3	1.78	472	515	482	528	78	106	38	1.6	43
	0.50		119.0	53.8	1.79	483	520	494	532	–	106	–	–	–

* (m_1) Filler content; (E_2) modulus of elasticity of the polymeric matrix; (A, B) coefficients in Eqs. (1)–(5); (α) coefficient; (γ_2, γ_{12}) surface tension of the polymeric binder and interphase surface tension, respectively; (A_a) adhesion strength.

With the filler content increasing to 0.5–0.6 wt fraction, σ_t first slightly increases and then decreases. A similar trend is observed for all the other reinforced composites based on epoxy resins, studied here. In a series of composites with the optimal content of the reinforcing filler (0.35 wt fraction), the tensile strength depends on the binder: it increases in passing from T-10 to EPU-1 resin and reaches the highest values with UP-637 binder. In the last case, σ_t significantly exceeds the results obtained with composites based on ED-20 epoxy resin (see table). It should be noted that the dependences of σ_t and σ_b of the reinforced composites on the type of the epoxy binder are similar to those determined previously for unfilled resins and to that of the modulus of elasticity of the polymeric matrix (see table). As seen from the comparison with the strength properties of fiber glass–reinforced composites based on the same binders [4], σ_t of the corresponding carbon fabric–reinforced com posites is 2–2.5 times higher, which agrees with published data for other carbon–reinforced composites [1, 2]. The optimal content of the filler in the carbon fiber–reinforced composites is significantly lower than that for fiber-glass fabric composites (0.6 wt fraction) [4].

A theoretical analysis of the prestressed-deformed state of reinforced composites is commonly made by solving a model problem by the boundary layer procedure [7, 8]. In this case, the reinforced composite is analyzed as a planar layered material, in which sheets of a carbon or fiber-glass fabric are separated by layers of a binder, with boundary layers between them. These boundary layers are regarded as orthotropic materials with zero modulus of elasticity in the tension direction [7]. Using methods of theoretical mechanics to solve the two-dimensional problem of prestressed-deformed degradation of a reinforced composite [8], the tensile strength σ_t and the ultimate bending strength σ_b can be determined by the equations [7]

$$\sigma_t = -E_1\frac{D_{a2}}{D_{a1}}\left(-\frac{P_l}{D_{a1}+D_{a2}} + \varepsilon_{a1} - \varepsilon_{a2}\right)\left(1 - \frac{\mathrm{ch}\alpha X}{\mathrm{ch}X}\right), \quad (1)$$

$$\sigma_b = -\alpha\frac{D_{a1}D_{a2}}{D_{a1}+D_{a2}}\left(-\frac{P_t}{D_{a2}} + \varepsilon_{a1} - \varepsilon_{a2}\right)\frac{\mathrm{sh}\alpha X}{\mathrm{ch}X}, \quad (2)$$

where E_1 is the modulus of elasticity of the carbon fabric reinforcing the material (250 000MPa) [1]; E_2 is the modulus of elasticity of the polymeric matrix (2000 MPa for ED-20 resin [4], data for the other modified epoxy resins are listed in the table); $D_{a1} = E_1F_1$ and $D_{a2} = E_2F_2$ are, respectively, the rigidities of the reinforcing component and the polymeric matrix at tension; F_1 and F_2 are the respective cross section areas; P_l and P_t are the longitudinal and transverse loads on the polymeric composite; ε_{a1} and ε_{a2} are the tensor components of deformation of the car-

bon fabric and polymeric matrix (MPa m^{-2}); α can be calculated from Eq. (3):

$$\alpha = \sqrt[4]{\frac{6E_1E_2}{G_{1,2}(E_1h_1 + E_2h_2)h_2^2}}, \quad (3)$$

$G_{1,2}$ is the shear modulus of the boundary layer in the composite, taken as 30 000 MPa m^{-1} [7].

The quantities h_1 and h_2, varying with the content of the reinforcing filler in the composites, characterize the layer thickness of the carbon fiber and polymeric matrix.

Equations (1)–(3) can be presented in the general form:

$$\sigma_t = A\left(1 - \frac{\mathrm{ch}\alpha X}{\mathrm{ch}X}\right), \quad (4)$$

$$\sigma_b = \alpha B\left(1 - \frac{\mathrm{ch}\alpha X}{\mathrm{ch}X}\right), \quad (5)$$

where A and B are the corresponding coefficients in Eqs. (1) and (2).

The properties of carbon fabric required for calculations were taken from [1, 9]. The calculations were performed on a PC using special software; the content of the reinforcing filler was varied within 0.25–0.60 wt fraction range with a step of 0.05 wt fraction. The dependences of σ_t and σ_b on the type of modified epoxy resin and the content of the reinforcing carbon fabric are given in the table.

As seen, our calculated and experimental data on σ_{st} and σ_b are reasonably consistent, which confirms the reliability of our model calculations of the strength characteristics of the reinforced composites studied. Our calculations confirmed the experimental fact that that the increase in the filler content over 0.35–0.40 wt fraction does not enhance further the tensile strength of the composites (see table). The calculated σ_t and σ_b exceed the experimental values by 15–20%, and such a deviation is quite acceptable in the theoretical mechanics of composites [7, 8]. The highest strength properties were found for the filled composites based on the UP-637 epoxy-resorcinol resin, which also agrees with our calculations (see table).

The impact resilience a_i, which determines the dynamic strength of the composites [1, 4, 7], is the most important performance characteristic of composites. The experimental a_i values for the reinforced composites are significantly smaller than the corresponding data for fiber glass fabric–reinforced composites based on the same binders [4] (see table), which agrees with the known data on the relatively low impact and shear strength of carbon composites [2, 9, 10]. To a first approximation, the ultimate strength at static bending can be compared with a work for the dynamic break and thus the viscosity of components can be calculated from the ratio similar to those determined for fiber-glass–reinforced composites [4, 7]:

$$a_i = 0.2\sigma_b. \quad (6)$$

The experimental a_i values significantly exceed the experimental data (see table), which is probably due to structural defects in the real composites as compared with an ideal model used in σ_b calculations. The relative changes in the calculated a_i, as influenced by the type of the polymeric binder, agree with the experimental data (see table), which confirms the possibility of predicting this important characteristic of reinforced composites.

The adhesion strength at the interface between the polymeric binder and the carbon fabric, which is characterized by the work of adhesion A_a, specifically affects the main strength properties of the reinforced composites [4, 9, 11]. In [9], a procedure was proposed for experimental evaluation of the adhesion strength, and A_a values were presented for composites reinforced with fiber glass fabric and carbon fabric, with three of four types of polymeric binders used in this work. With increasing A_a of the reinforced composites studied, their main strength properties increase proportionally (see table), and the highest adhesion strength was observed in the case of UP-637 epoxy-resorcinol binder. At the same time, the degree of filler–binder interaction can be quantitatively evaluated from the dispersion fraction of the interfacial surface tension γ_{12}, using the following equation [4, 11]:

$$\gamma_{12} = \gamma_1 + \gamma_2 - 2(\gamma_1\gamma_2)^{0.5}, \quad (7)$$

where γ_1 and γ_2 are the surface tensions of the filler and polymeric binder, respectively.

As shown previously for composites reinforced with fiber glass fabric, based on modified epoxy resins [5], γ_{12} decreases simultaneously with increasing adhesion strength and impact resilience of composites [4]. Using data on the surface tension of carbon fiber [9] and polymeric matrices [4], we calculated by Eq. (7) the interfacial surface tension γ_{12} of the reinforced composites (see table). The work of adhesion of composites A_a and their impact resilience a_i were correlated to the interfacial surface tension (see figure). The lowest γ_{12} for composites based on epoxy-resorcinol resin corresponds to the highest adhesion and dynamic strength (see table, figure), which agrees with trends found for fiber glass fabric–reinforced

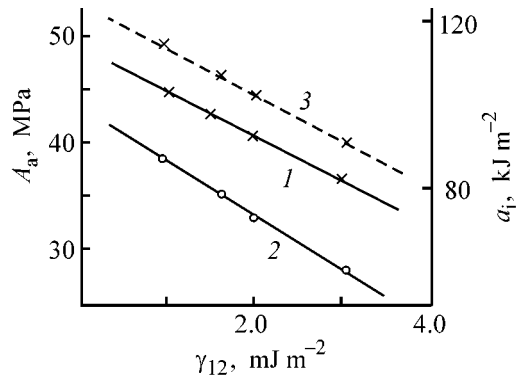

(*1*) Adhesion strength at the polymeric binder–carbon fabric interface between the A_a and (*2*, *3*) impact resilience of composites a_i vs. the interfacial surface tension γ_{12}; 0.35 wt fraction content of the filler in composites. (*1*, *2*) Experimental and (*3*) calculated data.

composites [4]. Using the above dependences (Fig. 2) and the least-squares procedure, we obtained with high reliability the following equations for A_a and a_i:

$$A_a = 49.0 - 4.2\gamma_{12}, \quad (8)$$

$$a_i = 97.2 - 12.1\gamma_{12}. \quad (9)$$

The experimental values of A_a and a_i and those evaluated from Eqs. (8) and (9) are in reasonable agreement (see table, figure). Thus, using a comprehensive approach to the prediction of the strength properties of polymeric composites proposed in [11], which takes into account the strength properties of the polymeric matrix and reinforcing filler [Eqs. (4), (5)] and the adhesion strength and the surface tension at the interface between the polymeric binder and the carbon fiber, we can select the optimal polymeric binders to prepare reinforced composites with improved strength properties.

CONCLUSION

Comparison of experimental and theoretical data on the strength parameters of carbon fabric–reinforced composites based on modified epoxy resins demonstrated the possibility of predicting their properties to prepare reinforced composites with improved strength.

REFERENCES

1. *Carbon Fibres and Their Composites*, Fitzer, E., Ed., Berlin: Springer, 1985.
2. Mikhailin, Yu.A. and Miichenko, I.P., *Plast. Massy*, 1993, no. 3, pp. 5–14.
3. Anisimov, Yu.N., Grekhova, O.B., and Anisimov, A.Yu., *Zh. Prikl. Khim.*, 1999, vol. 72, no. 7, pp. 1181–1185.
4. Anisimov, Yu.N., Kolodyazhnyi, A.V., and Grekhova, O.B., *Zh. Prikl. Khim.*, 1999, vol. 72, no. 8, pp. 1385–1390.
5. Anisimov, Yu.N., Dobrova, L.P., and Anisimov, A. Yu., *Zh. Prikl. Khim.*, 1998, vol. 71, no. 5, pp. 790–795.
6. Tsurpal, I.A., Baraban, N.P., and Shvaiko, V.M., *Soprotivlenie materialov* (Strength of Materials), Kiev: Vishcha Shkola, 1988.
7. Freidin, A.S. and Turusov, R.A., *Svoistva i raschet adgezionnykh soedinenii* (Properties and Calculation of Adhesion Joints), Moscow: Khimiya, 1990.
8. Cherepanov, G.P., *Mekhanika razrusheniya kompozitsionnykh materialov* (Failure of Composite Materials), Moscow: Nauka, 1983.
9. Gorbatkina, Yu.A., *Adgezionnaya prochnost' v sistemakh polimer-volokno* (Adhesion Strength in Polymer-Fiber Systems), Moscow: Khimiya, 1987.
10. Favre, J.P. and Marienne, M.C., *Int. J. Adhesion Adhesives*, 1981, vol. 1, no. 6, pp. 511–515.
11. Lipatov, Yu.S., *Fiziko-khimicheskie osnove napolneniya polimerov* (Physicochemical Principles of the Polymer Filling), Moscow: Khimiya, 1991.

Russian Journal of Applied Chemistry, Vol. 75, No. 6, 2002, pp. 1001–1005. Translated from Zhurnal Prikladnoi Khimii, Vol. 75, No. 6, 2002, pp. 1019–1023.
Original Russian Text Copyright © 2002 by Safiullina, Sergeeva, Sopin, Zenitova.

MACROMOLECULAR CHEMISTRY AND POLYMERIC MATERIALS

Filling of Castable Polyurethanes with Solid Wastes from Petrochemical Production

T. R. Safiullina, E. A. Sergeeva, V. F. Sopin, and L. A. Zenitova

Kazan State Technological University, Kazan, Tatarstan, Russia

Received December 10, 2001; in final form, February 2002

Abstract—Physicochemical properties of castable polyurethanes based on polyethylene glycol adipate and mixture of 2,4- and 2,6-toluylene diisocyanate (NCO : OH molar ratio 1.6) and filled to 10 wt % with silica gel (waste from petrochemical production) were studied.

Solid wastes, including those from chemical production, are the main sources of lithosphere pollution. Their accumulation in various branches of industry is determined by the existing level of processing of raw materials and by their inexhaustive utilization. Removal (transportation) of the wastes and their storage (design and maintenance of slag-heaps and slurry tanks) are rather expensive [1, 2].

Solid wastes from petrochemical production include rejected and spent gas-purifying filters based, in particular, on silica gel and alumina. Hence, treatment to recycle these compounds is an urgent problem.

It is known that materials of similar composition are used as fillers of various polymeric composites and rubbers [3]. However, these fillers are rather expensive and scarce. Hence, use of wastes containing silicon as alternative fillers of polymeric materials and, in particular, castable polyurethanes (PUs) is a promising way of their safe utilization [4, 5].

EXPERIMENTAL

In this work, we studied castable polyurethanes prepared from polyethylene glycol adipate (PEGA, $M \approx 2000$) and a mixture of 2,4- and 2,6-toluylene diisocyanate (TDI, 80/20) at a PEGA : TDI molar ratio of 1.6 [6]. Preliminarily ground to 10–50 μm spent gas-purifying filters based on silica gel [GOST (State Standard) 3956–76] and pearlite [GOST 10832–91] were used as fillers.

The properties of filled PUs at elevated temperatures were studied by differential scanning calorimetry on a DSC-111 device (Setaram) and thermogravimetric analysis on a TGS-2 automated recording unit (Perkin–Elmer) in the 20–500°C temperature range with heating rate of 5 deg min^{-1}. The effective density of the network ν_e/V was determined from the axial compression measured on a relaxometer according to the Cluff-Glading method [7]. The physicochemical parameters were evaluated according to GOSTs.

As seen from Fig. 1c, the shape of the DSC curves after filling of the polyurethanes with silica gel is retained. The effect of the fillers on the sample properties can be analyzed using the TG curves (Fig. 1a).

At temperatures higher than 244°C, the samples intensively lose weight. At lower temperatures, the polymer loses about 1.0–1.5 wt %, which is probably due to liberation of adsorbed moisture and other volatile products. In the 244–446°C range, the sample

Table 1. Thermal degradation of PU and amount of residue in relation to content of silica gel and pearlite fillers

Content, wt %	Temperature of intensive weight loss, °C		Amount of residue, wt%
	onset	end	
Silica gel			
0	330	415	8
1	335	420	10
3	345	425	11
5	350	425	12
10	355	430	14
Pearlite			
0	324	439	8.0
1	328	440	8.6
3	335	447	9.0

1070-4272/02/7506-1001 $27.00 © 2002 MAIK "Nauka/Interperiodica"

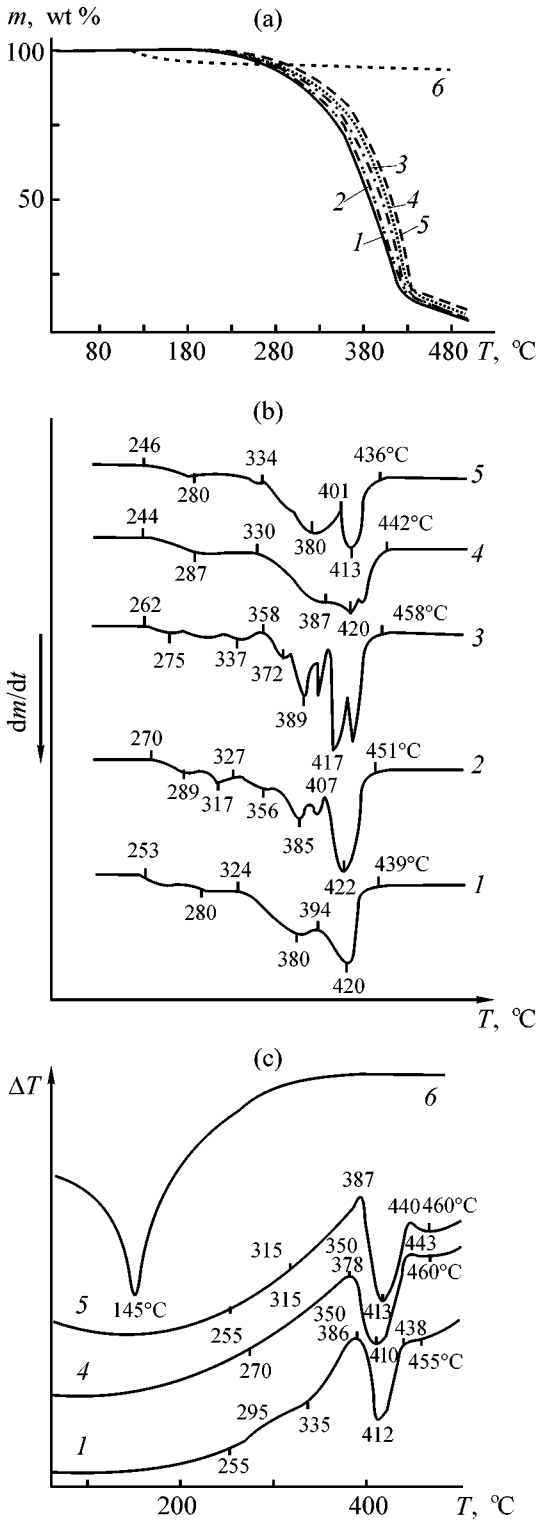

Fig. 1. (a) TG, (b) DTG, and (c) DSC curves of polyurethane filled with silica gel. (*m*) Weight, (d*m*/d*t*) rate of weight loss, and (*T*) temperature; the same for Fig. 2. Silica gel concentration (wt %): (*1*) 0, (*2*) 1, (*3*) 3, (*4*) 5, and (*5*) 10; (*6*) straight silica gel.

degrades, and at temperatures higher than 446°C the TG curve flattens out. As seen, the greater the PU filling degree, the larger the polymer residue (Table 1).

With increasing degree of filling, the temperature of the onset of intensive weight loss increases, i.e., the thermal stability of the composite is enhanced (Table 1). The shape of the TG curves also changes: the weight loss proceeds in two steps, the first step is less pronounced, whereas the second is more intensive.

As for the DTG curve, with increasing degree of filling, its shape becomes more complex and additional peaks appear (Fig. 1b). Such a course of weight loss and the shape of the DTG curves suggest changes in the mechanism of thermal degradation.

The DTG curves of silica gel indicate the presence of adsorbed water, which is liberated in the 80–130°C range. The endothermic peak in the DSC curve of silica gel at 145°C is also due to water liberation (Fig. 1c, curve *6*). Upon further heating of silica gel to 500°C, the weight losses reaches 13 wt %. Such a run of the DSC curves is probably due to the silica gel structure, which is characterized by highly developed surface of micropores, retaining adsorbed water even at temperatures higher than 100°C. The possibility that it contains the crystallization water which is removed only at temperatures higher than 400°C [8] (Fig. 1a) cannot be ruled out, either.

To prepare SKU-OM brand polyurethane, the initial compounds should be dried in a vacuum at elevated temperatures, because moisture deteriorates the quality of the resulting items, reacting with isocyanate to give gaseous products forming gas inclusions:

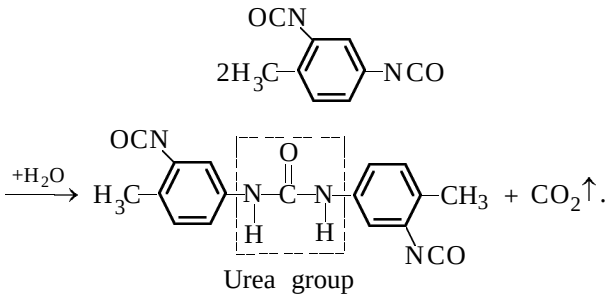

In our tests, we used preliminarily dried silica gel, but, as seen from Fig. 1a, the content of water in the micropores reaches 5 wt %.

In synthesis and thermal treatment of PU under relatively mild conditions (up to 80 ± 5°C), water contained in micropores and partially crystallization water do not affect noticeably the quality of the polyurethane items. However, water is liberated at ele-

vated temperatures during thermal analysis and reacts with the products of PU thermal degradation. This process is accompanied by breakdown of allophanic, urethane, and other fragments forming the urethane network, and liberated water probably reacts with the isocyanate group formed through bond rupture. Since the reaction of isocyanates with water is significantly faster than the other possible reactions with compounds containing the active hydrogen atom, we assume that the reaction through the isocyanate group is the most probable [9]. As a result, more thermally stable urea groups are formed [10]:

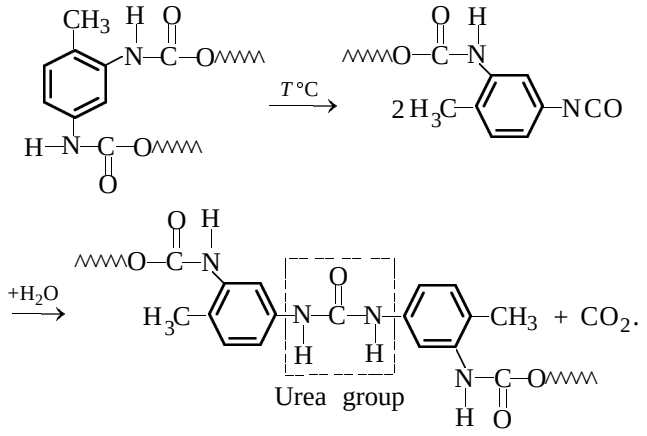

As seen from Fig. 2c, the shape of the DSC curves is almost independent of the degree of polyurethane filling with pearlite.

The effect of the degree of filling on the PU thermal properties can be more clearly seen from the TG and DTG curves (Figs. 2a and 2b).

The shapes of the TG curves of the initial polyurethane and PU filled with pearlite are similar, but in the case of filled composites they lie somewhat higher. With increasing degree of filling, the shape of the DTG curves changes and additional peaks appear (Fig. 2b). The appearance of these peaks suggests that the thermal degradation of the filled PUs becomes more complex and passes several stages as compared with the unfilled polymer. A similar phenomenon was observed in PUs filled with silica gel, and the weaker changes in the case of pearlite filler are probably due to certain differences in the filler structure and smaller degrees of filling as compared with silica gel.

The weight loss of pearlite is illustrated in Fig. 2a (curve *4*). The TG curves show that the content of water in pearlite is significantly lower than that in silica gel.

In the case of pearlite, the dependences of the thermal properties of polyurethanes on the degree of filling (1–3 wt %) are similar to those for silica gel (Figs. 1, 2), because pearlite mainly consists of silica. The only difference is that pearlite has a less developed structure due to the smaller content of micropores. Therefore, the content of adsorbed water in

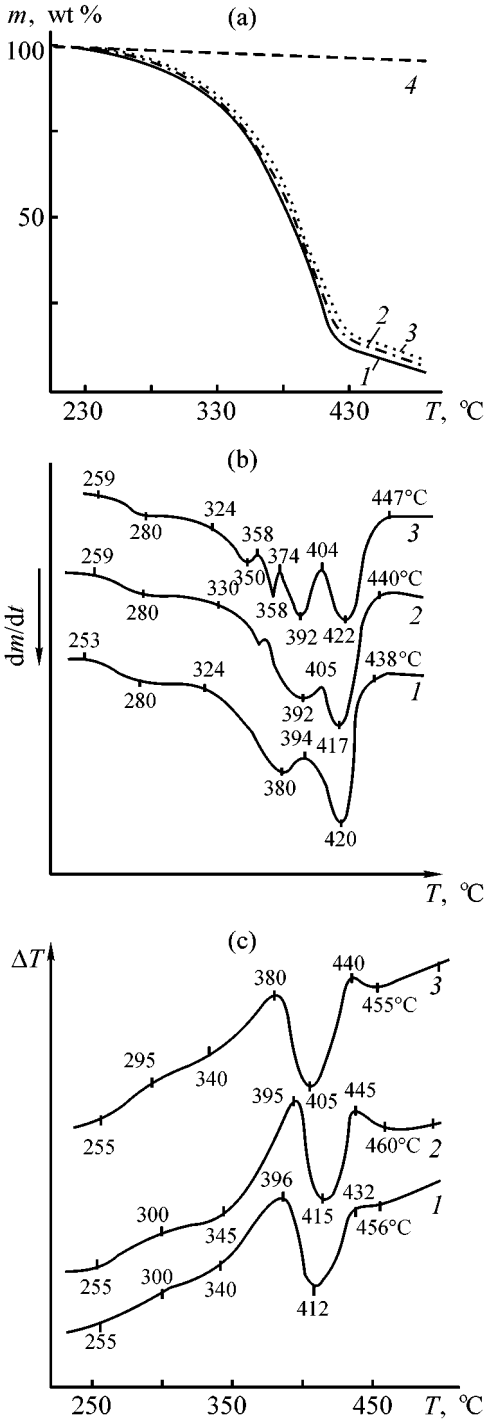

Fig. 2. (a) TG, (b) DTG, and (c) DSC curves of polyurethane filled with pearlite. Pearlite concentration (wt%): (*1*) 0, (*2*) 1, and (*3*) 3; (*4*) pearlite.

Table 2. Effective network density in PU in relation to content of fillers

Filling, wt %	$\nu_e/V \times 10^2$ (mol m^{-3}) at indicated temperature, °C		
	100	120	150
Silica gel			
0	3.828	1.826	0.241
1	5.133	4.508	1.900
3	5.516	5.113	1.706
5	5.603	5.665	1.785
10	6.717	5.627	2.599
Pearlite			
1	5.834	4.643	1.480
3	6.795	4.583	2.039

pearlite is smaller than that in silica gel [8] (Table 1). Moreover, pearlite is a light friable material with high bulk density, and its addition in large amounts to the polymer is rather difficult.

As seen from the above data, filling with silica gel enhances the thermal stability of polyurethanes. However, a study of the effective density of the polymer network can give more comprehensive information on the performance of polyurethane items at elevated temperatures (Table 2).

Above 100°C, the physical bonds are predominantly broken and the ν_e/V value is due to the chemical network in the polymer. This network consists of weak allophanic bonds, which break at 100–120°C. Above 120°C, ν_e/V is a function of more thermally stable chemical bonds, such as urethane and triisocyanurate.

As seen from Table 2, with increasing degree of filling, the effective density of the polymer network increases in the entire temperature range studied. At 150°C, unfilled PU completely degrades to form the linear product, whereas filling with silica gel and pearlite significantly enhances the thermal stability of the composites.

We developed a scheme for preparing SKU-OM type castable polyurethane:

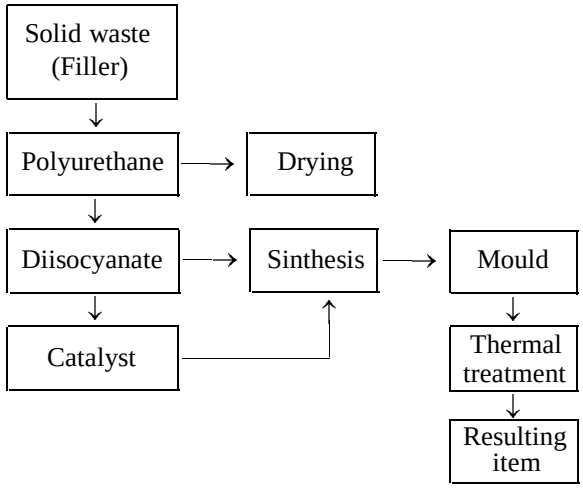

The effect of the content of silica gel filler on the physical and mechanical properties of the resulting PU is illustrated in Table 3. With increasing filler content, the hardness of the composites significantly increases, the elasticity slightly decreases, and the strength remains approximately constant. However, raising the filler content to more than 10 wt % promotes aggregation of the filler and its separation into an individual phase, which impairs the strength properties of the composites. Aggregation of silica-containing fillers in the polyurethane matrix is probably due to the presence of silanol groups at their surface, which existed in the initial filler or were

Table 3. Properties of polyurethane composite as influenced by the type of the filler

Parameter	Silica gel, wt %					Pearlite, wt %	
	0	1	3	5	10	1	3
Nominal stress at 100% elongation, MPa	2.3	2.0	2.9	2.9	3.2	2.6	2.7
Nominal stress at 300% elongation, MPa	5.2	5.9	8.3	8.2	8.5	7.2	7.8
Nominal tensile strength, MPa	20.4	18.7	18.9	20.2	19.7	23.3	22.8
Relative elongation, %	360	350	330	340	340	350	340
Elongation set, %	0	0	0	0	0	0	0
Rebound elasticity, %	50	48	50	46	45	48	47
Hardness according to TIR-1, rel. units	60	61	64	64	65	62	64

formed during preparation. These groups are proton donors, and thus such proton acceptors as isocyanates and amines can form strong bonds with the silicate filler surface [11]. Since the rigid aggregates in PU, formed by diisocyanate, form a separate phase [12], the filler chemically bound with such a rigid block also forms a separate phase, i.e., it agglomerates in the polymer bulk.

Thus, using our experimental data, we developed a new environmentally sound and economically profitable procedure for utilization of silica-containing wastes from petrochemical production for preparing SKU-OM castable polyurethane with enhanced thermal stability.

CONCLUSIONS

(1) Utilization of solid silica-containing industrial wastes from petrochemical production as a way to reduce environmental pollution was studied.

(2) Silica- and pearlite-containing wastes can be used as inert cheap fillers providing thermal stabilization of the polymer.

(3) With increasing content of the filler, the effective density of the network in filled polyurethane increases by nearly a factor of two, simultaneously the temperature of the onset of intensive weight loss increases by 25°C.

(4) A procedure was developed for preparing castable polyurethane filled with silica, which decreases the costs of production and allows solution of environmental problems.

REFERENCES

1. Stepen', R.A., Repyakh, S.M., and Buka, E.S., *Osnovy ekologii: Uchebnoe posobie* (Fundamentals of Ecology: Textbook), Krasnoyarsk: Sib. Gos. Tekhnol. Univ., 2000, 2nd ed.
2. *Ocnovy i menedzhment promyshlennoi ekologii* (Fundamentals and Management of Industrial Ecology), Mukhutdinov, A.A., Ed., Kazan: Magarif, 1998.
3. Koshelev, F.F., Korneev, A.E., and Bukanov, A.M., *Obshchaya tekhnologiya reziny* (General Technology of Rubber), Moscow: Khimiya, 1978.
4. Lyubartovich, S.A., Morozov, Yu.L., and Tret'yakov, O.B., *Reaktsionnone formovanie poliuretanov* (Reactive Molding of Polyurethanes), Moscow: Khimiya, 1990.
5. Lipatov, Yu.S., *Fizikokhimiya napolnennykh polimerov* (Physical Chemistry of Filled Polymers) Kiev: Naukova Dumka, 1980.
6. RF Patent 914574.
7. Kimel'blat, V.I., Zenitova, L.A., and Rozental', N.A., *Izuchenie prostranstvennoi setki lit'evykh polimochevinuretanovykh elastomerov* (Study of the Three-Dimensional Network of Poly(urea-Urethane) Elastomer), Kazan: Kazan Khim.-Technol. Inst., 1979.
8. Samsonov, G.V., Borisova, A.L., Zhidkova, T.G., *et al.*, *Fiziko-khimicheskie svoistva okislov: Spravochnik* (Physicochemical Properties of Oxides: Handbook), Moscow: Metallurgiya, 1978.
9. Saunders, J.H. and Frish, K.C., *Polyuretanes. Chemistry and Technology*, part 1, *Chemistry*, New York: Interscience, 1962.
10. Apukhtina, N.P., *Fizikokhim. Polim.*, 1970, issue 7, pp. 137–145.
11. *Napolniteli dlya kompozitsionnykh materialov* (Fillers for Composite Materials), Kats, G.S and Milevski, D.V., Eds., Moscow: Khimiya, 1981.
12. Vilenskii, V.A., Kostyuk, L.I., Shtompel', V.I., *et al.*, *Vysokomol. Soedin., Ser. A*, 1991, vol. 30, no. 11, pp. 2452–2459.

Russian Journal of Applied Chemistry, Vol. 75, No. 6, 2002, pp. 1006–1008. Translated from Zhurnal Prikladnoi Khimii, Vol. 75, No. 6, 2002, pp. 1024–1026.
Original Russian Text Copyright © 2002 by Kaputskii, Mardykin, Gaponik, Lesnyak, Kostyuk, Mil'chanina.

CHEMISTRY OF FOSSIL FUEL

Synthesis of Petroleum Polymeric Resin by Cationic Polymerization of the C_9 Fraction

F. N. Kaputskii, V. P. Mardykin, L. V. Gaponik, V. P. Lesnyak, S. V. Kostyuk, and T. L. Mil'chanina

Research Institute of Physicochemical Problems, Belarussian State University, Minsk, Belarus

Received January 10, 2002

Abstract—Cationic oligomerization of the C_9 fraction of liquid pyrolysis products of petroleum raw materials, catalyzed by aluminum trichloride diphenyl ether complex, was studied, and a procedure was developed for preparation of a petroleum polymeric resin and petroleum polymerizate to be used as film-forming agents in paint-and-varnish materials.

Petroleum polymeric resins (PPRs) are widely used in production of synthetic drying oils, lacquers, and paints, and also as binders in various adhesive, rubber, and other formulations; the fields of their applications are steadily expanding. These products successfully substitute natural and manmade components of various materials, ensuring the same or even better performance of these materials [1].

PPRs are, as a rule, prepared by cationic (catalytic) or radical (thermal or initiated) polymerization of the C_9 fraction recovered from liquid pyrolysis products of hydrocarbons in production of ethylene and propylene from petroleum raw materials. Catalytic synthesis of PPRs has a number of advantages over thermal or initiated polymerization; primarily, it occurs at a higher rate (within 1–2 h) and with quantitative yield of the product, which creates prerequisites for waste-free production of the resins [2]. Furthermore, the yield of the catalytically prepared resin may even exceed 100% based on the monomer, which is due to incorporation of aromatic solvent molecules into the polymeric chain as a result of chain transfer to the solvent [3]. The C_9 fraction is a mixture of monomers (styrene, dicyclopentadiene, indene derivatives, etc.) and nonpolymerizable hydrocarbons; their ratio affects both the polymerization course and the yield and properties of the resins. The composition and properties of the fraction also depend on the raw material and pyrolysis conditions.

In this work, we studied catalytic polymerization of the C_9 fraction of varied origin with the aim to obtain petroleum polymerizate (PP) and PPRs with required physicochemical properties and to use the resulting products as film-forming agents in paint-and-varnish materials.

We have shown previously [4] that donor–acceptor complexes of $AlCl_3$ with dibutyl and diphenyl ethers, ethyl acetate, and urea exhibit high activity in cationic polymerization of the C_9 fraction. For further studies, we chose the complex with diphenyl ether, which can be fairly readily prepared, is highly stable, and is the most suitable for industrial use. The results of oligomerization of fractions **A** (bp 150–175°C, Stavropol'polimer, Budennovsk, Stavropol krai) and **B** (bp 106–180°C, Neftekhim, Nizhni Novgorod) are listed in the table. Fraction **A** is characterized by higher content of dicyclopentadiene and lower content of nonpolymerizable aromatic hydrocarbons, and fraction **B**, by higher content of styrene and low-boiling hydrocarbonds that cannot be converted into resins (toluene, xylenes, ethylbenzene, etc.). Fractions **A** (run nos. 1–8) and **B** (run nos. 9–12) were used both without pretreatment and after preliminary purification, drying, and distillation. Polymerization of crude fraction **A** yields a PPR with low molecular weight and low softening point (run nos. 1–3), which results in a poor quality of the coatings. In this case, the initial C_9 fraction should be subjected to vacuum distillation, since simple distillation does not improve appreciably the properties of PPRs (run nos. 3, 6). To obtain light heat-resistant resins, the fraction should be additionally treated prior to vacuum distillation (run no. 4). In this case, the resulting resins are less colored and have a high softening point. We found that the optimal con-

1070-4272/02/7506-1006 $27.00 © 2002 MAIK "Nauka/Interperiodica"

Oligomerization of the C_9 fraction of hydrocarbon pyrolysis products with $AlCl_3 \cdot OPh_2$ cationic catalyst (fraction volume 20 ml; modifier maleic anhydride, 2% relative to the fraction; deactivator ethylene oxide, 4% relative to the fraction; oligomerization time 60 min)

Run no.	Fraction	Catalyst, % of fraction	$T_{in} \rightarrow T_{max}$, °C	Characteristics of resins			
				yield, % based on fraction	color by iodometric scale	T_s, °C	M
1	Crude	1.0	4 → 46	50	15–20	57–60	395
2	Dried over $CaCl_2$	1.0	4 → 50	50	15–20	67–73	420
3	Distilled at P_{atm} (150–170°C)	1.0	5 → 48	45	10–15	61–68	410
4	Treated with maleic anhydride and $AlCl_3 \cdot Ph_2O$ and distilled at 43–59°C/4 mm Hg	1.0	5 → 52	56	5–10	87–93	760
5	Distilled at 40–70°C/5 mm Hg	0.5	5 → 37	33	10–15	59–64	540
6	″	1.0	5 → 52	51	10–15	66–70	600
7	″	1.5	5 → 54	54	15–20	63–68	530
8	″	2.0	5 → 53	59	15–20	70–76	660
9	Crude	1.0	3 → 60	59	10–15	60–65	610
10	Distilled at 40–82°C/5–13 mm Hg	1.0	5 → 80	60	5–10	80–85	640
11*	″	1.0	4 → 60	58	5–10	72–78	595
12**	Crude	1.5	10 → 60	60	5–10	65–70	550

* No maleic anhydride added.

** A pilot batch was produced (1800 kg).

centration of the catalytic complex is 1–1.5 wt % relative to the fraction (run nos. 5–8).

With decreasing amount of the catalyst, both the yield of polymer and its softening point decrease (run no. 5). Taking the catalyst in larger amounts does not further improve the properties of the resins and therefore is not appropriate (run no. 8). Under equal other conditions, fraction **B** is more active in polymerization (run nos. 9, 10) than fraction **A** (run nos. 1, 6). When the reaction is performed without adding maleic anhydride (which enhances the adhesion and thus improves the quality of PPR-based films), the yield and the color on the iodometric scale remain unchanged, but the softening point and molecular weight become lower (run no. 11).

Based on these results, we developed a waste-free catalytic process for production of petroleum polymerizate and PPR. It should be noted that the properties of the PPR from the pilot batch (run no. 12) are in good agreement with the properties of the resins prepared in a lab (run nos. 9, 10).[1] Fraction **B** is preferable for commercial use, as it requires no additional treatment (purification, distillation).

For quickly assessing the quality of the fraction under industrial conditions, we proposed the following procedure: A catalyst solution with 1.5 wt % $AlCl_3$ (relative to the fraction) is added to 100 ml of the fraction, cooled to 10°C. If the temperature of the polymerizing mixture rises to approximately 100°C within 3–5 min, the fraction is suitable for oligomerization. The resin content of the polymerizate can be determined from an experimental correlation between the percentage of the dry residue in the resin solution, its density, and conventional viscosity (outflow time) (see figure).

It should be particularly emphasized that the polymerizates obtained by our procedure have properties similar to those of petroleum polymeric drying oil. For preparing a lacquer, it is the most appropriate to use 60% PPR solutions, readily prepared by diluting or concentrating the polymerizates. The lacquer samples thus prepared exhibit high strength and good water resistance; they quickly dry but show poor elasticity and adhesion. To improve these parameters, we chose appropriate modifiers (dibutyl phthalate and KhT polymer) [5] and developed a formula of

[1] A pilot batch of the polymerizate was produced by the Ozocerite Plant, Joint-Stock Company, Svisloch, Belarus, and subsequently used for manufacturing NP-114 lacquer.

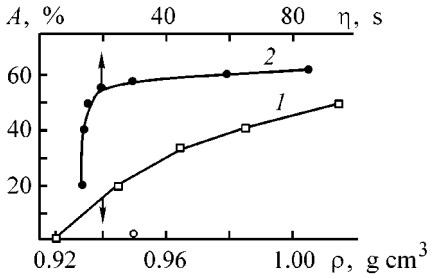

Correlation of the dry residue content *A* at 20°C with (*1*) PPR solution density ρ and (*2*) conventional viscosity η.

an enamel based on oil polymerizates, which is an analog of PF-115 enamel and even surpasses it in hardness and resistance to static action of water.

EXPERIMENTAL

Aluminum chloride diphenyl ether complex was prepared under argon at room temperature in a three-necked flask equipped with a stirrer and a dropping funnel. To a suspension of $AlCl_3$ in toluene, an equimolar amount of a toluene solution of diphenyl ether was added with stirring. For polymerization, we took approximately 1.0 M solutions of the catalyst. The aluminum content was determined by the Wenninen–Ringbom method, and the chlorine content, by the Volhard method.

Oligomerization was performed in a three-necked flask equipped with a stirrer, a dropping funnel, a thermometer, and a cooling water bath. The flask was charged with the C_9 fraction and cooled to 4–8°C, after which the catalyst was added at a rate allowing the reaction temperature to be maintained within 60°C. After the temperature reached a maximum and started to decrease, a definite amount of maleic anhydride was added at 50–55°C. After the temperature decreased to 30°C, the catalyst was deactivated with a solution of ethylene oxide in toluene. The resulting polymerizate was analyzed and directly used for preparing paint-and-varnish formulations. The polymeric oil resin was isolated by distilling off volatile hydrocarbonds at atmospheric pressure and in a vacuum. The composiiton of the fractions was determined by GLC on a Chrom-5 chromatograph equipped with a flame ionization detector; the molecular weight of the resin, cryoscopically in benzene; the softening point, with a Thiele device; and color, using the iodometric scale. The film-forming properties of the polymerizate [TU (Technical Specifications) of Belarus Republic 05568283.017–99] and resins were studied using stationary equipment at the Progress Scientific and Production Enterprise (Minsk).

CONCLUSIONS

(1) The process parameters of oligomerization of C_9 fractions of various compositions were determined, and procedures were developed for synthesis of petroleum polymeric resin or petroleum polymerizate with required physicochemical and technical parameters to be used as film-forming agents in paint-and-varnish materials (drying oils, lacquers, enamels).

(2) The revealed relationships of the oligomerization allowed scaling of the process. Pilot batches of petroleum polymerizate, NP-114 lacquer, and NP-115 enamel (an analog of PF-115 enamel) were produced.

REFERENCES

1. Dumskii, Yu.V., *Neftepolimernye smoly* (Petroleum Polymeric Resins), Moscow: Khimiya, 1988.
2. Kostyuk, S.V., Lesnyak, V.P., Gaponik, L.V., *et al.*, Abstracts of Papers, *Mezhdunarodnaya nauchno-tekhnicheskaya konferentsiya "Novye tekhnologii retsiklinga vtorichnykh resursov"* (Int. Scientific and Technical Conf. "New Technologies of Recycling of Secondary Resources"), Minsk, October 24–26, 2001, pp. 44–47.
3. Kaputskii, F.N., Mardykin, V.P., Kostyuk, S.V., and Gaponik, L.V., *Vestsi Nats. Akad. Navuk Resp. Bel., Ser. Khim. Navuk*, 1999, no. 2, pp. 96–99.
4. Kaputskii, F.N., Mardykin, V.P., Gaponik, L.V., *et al.*, *Vestsi Nats. Akad. Navuk Resp. Bel., Ser. Khim. Navuk*, 2000, no. 3, pp. 48–51.
5. Kaputskii, F.N., Mardykin, V.P., Gaponik, L.V., *et al.*, Abstracts of Papers, *Mezhdunarodnaya nauchno-tekhnicheskaya konferentsiya "Razrabotka importozameshchayushchikh tekhnologii i materialov v khimicheskoi promyshlennosti"* (Int. Scientific and Technical Conf. "Development of Processes and Materials in Chemical Industry To Substitute Imported Products"), Minsk, December 20–22, 1999, pp. 142–146.

Russian Journal of Applied Chemistry, Vol. 75, No. 6, 2002, pp. 1009–1013. Translated from Zhurnal Prikladnoi Khimii, Vol. 75, No. 6, 2002, pp. 1027–1031.
Original Russian Text Copyright © 2002 by Fedorov, Syroezhko, Begak, Proskuryakov, Borovikov .

CHEMISTRY OF FOSSIL FUEL

Modified Paving Bitumens Based on Tar and Petroleum Polymeric Resins

V. V. Fedorov, A. M. Syroezhko, O. Yu. Begak, V. A. Proskuryakov, and G. I. Borovikov

St. Petersburg State Technological Institute, St. Petersburg, Russia

Mendeleev Russian Research Institute of Metrology, State Unitary Enterprise, St. Petersburg, Russia

Slantsy Plant, Joint-Stock Company, Slantsy, Leningrad oblast, Russia

Received October 2, 2001

Abstract—Modification of tar with petroleum polymeric resins yields paving-grade bitumens with enhanced cohesion. With respect to the heat resistance and other parameters, these bitumens meet the requirements of GOST (State Standard) for BND 90/130 paving bitumens.

Rheological and physicochemical characteristics of bitumens are improved by adding various polymers, synthetic rubbers, or rubber crumb [1] in amounts of 1–5%. Blending bitumen with a polymer or a polymer with a solvent requires special equipment ensuring efficient mixing.

Thermopolymeric resins obtained from products of naphtha pyrolysis, having softening points of 80–95°C (Pyroplast, dark resin; Pyroplast-2, light resin), which are produced in compliance with TU (Technical Specifications) 381091–79 and 14689–73, are readily blended with bitumens and petroleum tar on standard apparatus of asphalt-concrete plants. These additives impart to bitumens and tar high heat resistance and plasticity, improve their adhesion to mineral fillers, and enhance the cohesion strength of a pavement [2]. Addition of 1–3% petroleum polymeric resins (PPRs) has been noted to improve such physicomechanical properties of bitumen as ductility, plasticity, elasticity, adhesion strength, and cohesion strength, whereas larger (8–10%) additions of PPRs produced a somewhat weaker effect. At the same time, as noted in [3], such modifiers exert a positive effect mainly on the cohesion of bitumens, decreasing their plasticity (penetration). This study is aimed at refining the effect of these modifiers.

EXPERIMENTAL

The ring-and-ball softening point (°C) was determined according to GOST 9950–83; penetration, according to GOST 11508–78; ductility, according to ASTM D2872–77 standard; and brittle point, according to GOST 11507–78 and by calculation using the Gun formula [4]

$$T_s - T_{br} = 70 - 7PI,$$

where T_s is the softening point (°C), T_{br} is the brittle point (°C), and PI is the penetration index (determined from a nomogram) [4].

The heat resistance of bitumens and modified formulations was determined by a standard procedure. Samples were placed in stainless steel cups (bed height 4 mm, sample weight 60 ± 1 g). The samples were heat-treated at 160°C for 5 h, after which the softening point, penetration P, ductility D, and weight loss Δm (%) were measured.

The adhesion of binder samples to a mineral filler was determined by aqueous cooking with granite and gabbro-diarite (3–5-mm fraction). The filler : bitumen ratio was 15 : 0.6. The cooking was performed for 30 min on a standard grid. The adhesion was evaluated from the weight loss of the material through washout of the binder with boiling water from the filler surface. The specific surface area of the 3–5-mm fraction is close to that of fillers used in Russian plants for production of asphalt concrete.

The water absorption of the binder was determined by the formula

$$W = (W_1/W_2) \times 100\%,$$

1070-4272/02/7506-1009 $27.00 © 2002 MAIK "Nauka/Interperiodica"

Table 1. Component ratios and technical characteristics of binders

Sample no.	Binder, %	Resin	Resin added, %	T, °C	T_{br}^{*}, °C	P_{25}, mm	T_s, °C	Meets requirements to BND paving bitumem
	Tar:							
1	100	–	0	–		265	38.5	–
2	95	P-46	5	110	–23.5	198	43.0	130/200
3	90	P-46	10	110	–25.9	125	45.5	90/130
4	80	P-46	20	110	–25.5	61	50.1	60/90
5	95	Politer	5	110	–33.6	154	41.3	130/200
6	95	P-132	5	110	–31.7	134	43.2	130/200
7	90	P-132	10	110	–21	144	44.8	130/200
8	85	P-132	15	110	–25	107	47.1	90/130
9	99	SIR**	1	120	–26.4	186	42.2	130/200
10	95	SIR	5	120	–26.9	163	42.4	130/200
11	90	SIR	10	120	–43	~130	40.3	130/200
12	85	SIR	15	120	–30.4	~100	45.2	90/130
	BDUS 70/100:							
13	100	–	0	–	–22.9	68	49.9	60/90
14	99	P-46	1	110	–29.1	71	47.9	60/90
15	95	P-46	5	110	–27.1	58	50.6	40/60
16	90	P-46	10	110	–30.7	48	50.5	40/60
17	85	P-46	15	110		45	50.6	40/60

* Calculated.
** Styrene–indene resin.

where W is the water absorption of the material, %; W_1, the weight of a dry spherical sample of the material (g); and W_2, the weight of the same sample after saturation with water (g).

To prepare a modified bitumen, a metallic crucible placed in an electric oven was charged with a definite portion of tar, the temperature was raised to the required level (110–120°C), and a powdered petroleum polymeric resin (<0.25 mm) was added. The mixture was stirred manually with a metallic stirrer for 10 min. The temperature was chosen taking into account the viscosity of the components (Table 1); it was maintained constant to within ±3°C throughout the stirring time.

Mechanical tests of the samples were performed as follows. The binder was applied as a thin layer onto overlapping steel plates. After 4 days, the force required to break the adhesive joint was determined on a tensile-testing machine. The test was performed with 3–4 samples, and the arithmeric mean was calculated.

To prepare samples of asphalt concrete pavements, a <0.25-mm fraction of mineral fillers (granite, gabbro-diarite, marble) was mixed with bitumen or a bitumen-based formulation taken in amount of 10 wt %. The resulting composites were molded in pellets (15.8 mm in diameter, 8 mm high), which were subjected to a compression test on a press until deformation became detectable.

As the raw material for preparing modified bitumens (binders), we used petroleum tar with ring-and-ball softening point of 38.5°C and petroleum polymeric resins produced in compliance with TU 2451-012-00 149 452–99.

The softening points of the resins were as follows: light thermopolymeric resin P-46, 94°C; P-132, 86°C; styrene–indene resin, 96°C; and Politer, 95°C.

Figure 1 shows how the content of P-46 petroleum polymeric resin affects the softening points of the binary formulations based on petroleum tar and BDUS bitumen. It is seen that, for the formulations based on tar, the softening point grows approximately linearly (except in the initial portion of the curve) with increasing content of P-46, whereas for the formulations based on BDUS 70/100 additions of the same resin affect the softening point insignificantly.

Figure 1b shows that, in the formulations based on tar and bitumen, the penetration decreases with increasing content of P-46, with this trend being more pronounced for the former formulations.

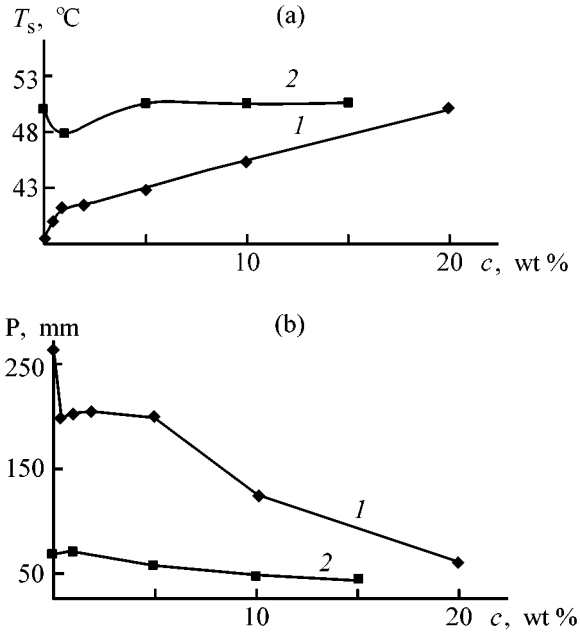

Fig. 1. (a) Softening point T_S and (b) penetration P of formulations vs. the petroleum polymeric (thermopolymeric) resin P-46 *c*: (*1*) tar and (*2*) BDUS 70/100 bitumen.

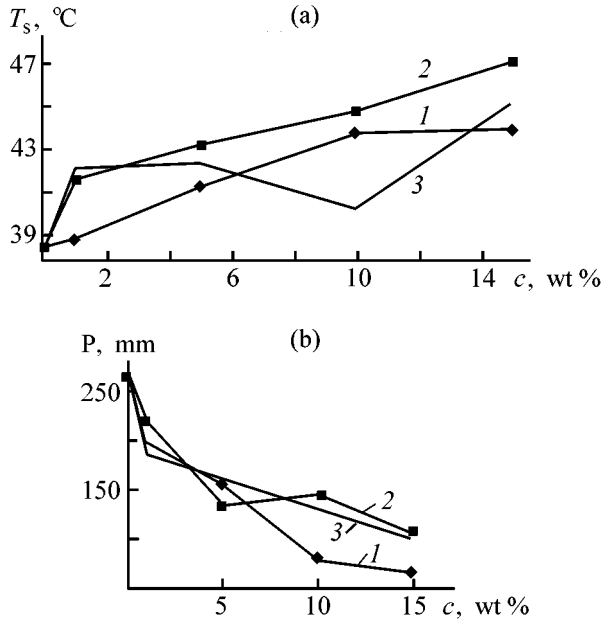

Fig. 2. (a) Softening point T_S and (b) penetration P of formulations based on petroleum tar vs. resin content *c*. Resin: (*1*) Politer, (*2*) P-46, and (*3*) styrene–indene.

Figures 2a and 2b show how the resins added affect, respectively, the softening points and penetrations of the formulations based on tar. The curves in Fig. 2a are similar in shape to those in Fig. 1a, except the curve of the softening point vs. content of the styrene–indene resin. This resin is poorly compatible with tar, and uniform blend cannot be obtained. Figure 2b shows that the penetration of the formulations decreases with increasing content of petroleum polymeric resins.

The requirements to paving bitumens, prescribed by GOST 22245–90, are listed in Table 2.

Among bitumens with satisfactory properties, obtained from tar and thermopolymeric resins, we chose sample nos. 6, 11, 16, 19, 22, and 23 (Table 1), which were tested for compliance with the GOST requirements to paving bitumens. The parameters characterizing the heat resistance of the modified bitumens are listed in Table 3.

Table 3 shows that formulation no. 6 meets all the requirements of GOST to BND paving bitumens. This formulation was subsequently subjected to mechanical tests (strength of a sample with mineral filler) and, together with the other samples, to heat resistance tests.

The parameters of binder-to-filler adhesion are given in Table 2 as mean values of 2–4 measurements. With respect to adhesion to granite, the formulations under consideration (Table 4) are inferior to BDUS 70/100 paving bitumens, but well compete with this bitumen when used with a gabbro-diarite filler. However, the adhesion of these formulations to gabbro-diarite is lower than that of the best samples of Russian bitumens based on high-resin high-viscosity Yarega crude oil. Bitumen sample nos. 6, 9, 14, and 16, meeting the GOST requirements to paving bitumens, were tested for heat resistance, with ductility determined before and after heat treatment (Table 5).

It is seen that the ductility of BDUS 70/100 bitumen (indirectly characterizing the bitumen cohesion) decreases after the heat treatment, whereas that of the formulations based on tar and petroleum polymeric

Table 2. Characteristics of BND bitumens

BND	P_0, mm	T_S,* °C	D_{25},* cm	T_{br}, °C	T_f, °C
40/60	13	51	45	–12	230
40/60	20	47	55	–15	230
90/130	28	43	65	–17	230
130/200	35	40	70	–18	220
200/300	45	35	–	–20	220

* The lower limits are indicated.

Table 3. Heat resistance of modified bitumens*

Sample no.	Δ*m*, %	T_s, °C		P_{25}, mm	
		I	II	I	II
6**	0	44.9	45.5	124	125
9**	0.19	43.3	41.3	117	154
11	0.25	47.7	44.0	43	66
14**	0.18	44.5	44.8	104	144
16**	0.23	43.0	42.2	107	186
22	0.2	53.0	50.6	42	58
23	0.3	52.6	50.5	36	48

* (I) Before and (II) after heat treatment; the same for Table 5.

** Meet requirements to paving bitumen brands; the same for Tables 4 and 5.

Table 5. Ductility of modified bitumens*

Sample no. (Table 1)	Ductility, cm	
	with granite	with gabbro-diarite
BDUS 70/100	75	61
6	61.5	80
9	74	≥100
11	>100	>100
14	76	>100
16	54.5	97
22	>100	
23	93	>>100

* The measurement limit of ductilometer used was 100 cm.

Table 4. Adhesion characteristics of modified bitumens

Sample no. (Table 1)	Adhesion, %	
	before heat treatment	after heat treatment
BDUS 70/100	72.7	49.8
Tar	52.6	48.9
6	56.7	65.9
9	38.6	Not determined
11	63.5	″
14	25.4	″
16	68.8	″
22	54.9	″
23	66.4	″
Bitumen from Ukhta Oil Refinery, T_s = 54°C, P_{25} = 55 mm	89.4	

Table 6. Shear and compression tests of various binder samples

Filler	Sample no. 6	BDUS 70/100	Tar
Compression stress before appearance of detectable deformation, kg cm^{-2}			
Granite	26.9	9.0	1.8
Gabbro-diarite	27	8.4	14.9
Marble	25.4	17.9	4.8
Shear stress, kg cm^{-2}			
–	0.79	1.87	0.42

resins increases, which is important from the practical viewpoint.

The results of mechanical tests of model pavement samples based on formulation no. 6 are listed in Table 6.

Quality bitumens of KINEF Ltd. (mean data for five samples) have the following characteristics: T_s = 43–46°C, P_{25} = 92–97 mm, D_{25} = 147–150 cm, and D_{25} after heat treatment 113–125 cm.

In shear tests, the break of an adhesive joint of metallic plates occurs within the bitumen layer (cohesion break). Since the ductility of sample no. 6 after heating is 80 cm and that of BDUS 70/100 is higher, the trends observed with the shear strength are quite understandable. BND 90/130 bitumen has lower ductility parameters after heating, compared with sample no. 6 (Tables 1, 5). Sample no. 6 in the initial state is characterized by D_{25} = 61.5 cm; for BND 90/130, this value after heat treatment is lower owing to aging (as shown by numerous ductility measurements for laboratory samples and commercial batches of BND bitumens produced from the commercial mixture of West-Siberian crude oils).

From the binders and mineral components, we prepared model pavement samples. The results of compression tests of these samples are listed in Table 6. It is seen that, with all the fillers tested, the model pavement based on formulation no. 6 (90% petroleum tar, softening point 38.5°C, and 10% P-46 petroleum polymeric resin, softening point 94°C) surpasses in compression strength a similar pavement based on BDUS 70/100 commercial bitumen.

CONCLUSION

A paving bitumen formulation, meeting the technical requirements to BND 90/130 paving bitumen, was developed on the basis of tar and light petroleum polymeric resin from thermal polymerization of C_9 naphtha pyrolysis fraction.

REFERENCES

1. Grudnikov, I.B., *Proizvodstvo neftyanykh bitumov* (Production of Oil Bitumens), Moscow: Khimiya, 1983.
2. Kolbanovskaya, A.S. and Mikhailov, V.V., *Dorozhnye bitumy* (Paving Bitumens), Moscow: Transport, 1973.
3. Khudyakova, T.S., Rozental', D.A., and Malikova, I.A., *Adgezionnye svoistva neftyanykh bitumov i sposoby ikh korrektirovki: Tematicheskii obzor* (Adhesion Properties of Oil Bitumens and Methods for Adjusting Them: Topical Review), Moscow: TsNIITEneftekhim, 1991, issue 3.
4. Gun, R.B., *Neftyanye bitumy* (Oil Bitumens), Moscow: Khimiya, 1989.

Russian Journal of Applied Chemistry, Vol. 75, No. 6, 2002, pp. 1014–1019. Translated from Zhurnal Prikladnoi Khimii, Vol. 75, No. 6, 2002, pp. 1032–1037.
Original Russian Text Copyright © 2002 by Begak, Syroezhko, Fedorov.

CHEMISTRY OF FOSSIL FUEL

Relationship between the Performance of Tars and Bitumens from Commercial West-Siberian Crude Oil and Their Structural-Group Composition

O. Yu. Begak, A. M. Syroezhko, and V. V. Fedorov

Mendeleev Russian Research Institute of Metrology, State Unitary Enterprise, St. Petersburg, Russia

St. Petersburg State Technological Institute, St. Petersburg, Russia

Received January 28, 2002

Abstract—The structural-group compositions of polar and nonpolar components of malthenes from tars of West-Siberian crude oil and of quality bitumen BDUS 70/100 and substandard bitumen BDUS 60/90 produced from these tars are compared.

According to Pfiffer [1], bitumens are subdivided in three types with respect to their colloidal state: (a) sol, (b) sol–gel, and (c) gel. This classification reflects the viscosity characteristics of bitumens but disregards their chemical composition. It is based on the assumption that the main components of bitumen (paraffins, naphthenes, arenes, resins, asphaltenes) interact via dispersion forces. It has been shown [2] that the primary elements of the disperse structure of bitumens are colloidal (2–10-nm) micelles having the shape of a sphere or a flattened ellipsoid. These micelles are mainly formed by stacking association of planar polyaromatic plates, mainly beloging to asphaltenes and resins, and, to a lesser extent, to mono-, bi-, and polycycloaromatic compounds, with partial overlap of their electron shells.

Kolbanovskaya [3] subdivided bitumens in three types with respect to their disperse structure. Her classification is based on the ratio of asphaltenes, resins, and oils. However, the colloidal stability of bitumens and their physicochemical properties are determined not only by the ratio of oils, resins, and asphaltenes, but also by their specific chemical features.

The experience of using bitumens shows that, if the oil fraction of a bitumen has high content of naphthenoaromatic rings, such a bitumen shows colloidal stability and exhibits high level of physicochemical parameters (penetration P_{25}, ductility D_{25}). If the amount of the oil fraction is low, or it contains mainly paraffinic and naphthenic components, the colloidal stability of the bitumen is lower, and its ductility and strength parameters are worse. The goal of this study was to reveal specific features of structural-group components of tars and bitumens produced from a commercial mixture of West-Siberian crude oils at the Kirishi Oil Refinery.

EXPERIMENTAL

We studied two samples of tars and bitumens prepared by oxidation of these; their characteristics are listed in Table 1.

Table 1. Content of asphaltenes, malthenes, and polar and nonpolar components in tars and bitumens

Product	Yield, wt %, based on tar or bitumen			
	malthenes	asphaltenes	PCs	NPCs
Residue:				
P_{25} = 305 mm × 0.1, conventional viscosity 89 s	89.55	10.45	16.6	83.4
P_{25} = 390 mm × 0.1, conventional viscosity 92 s	88.62	11.38	15.1	84.9
BDUS:				
70/100, P_{25} = 84 mm × 0.1, ring-and-ball softening point 46°C, D_{25} = 140	80.7	19.3	21.1	78.9
60/90, P_{25} = 78 mm × 0.1, ring-and-ball softening point 49°C, D_{25} > 150	79.0	21.0	21.4	78.6

1070-4272/02/7506-1014 $27.00 © 2002 MAIK "Nauka/Interperiodica"

Deasphalting of tars and bitumens was performed by cold and hot Golde procedures [4, 5] in Soxhlet apparatus.

Polar components were recovered from malthenes of tars and bitumens by extraction with dimethylformamide (DMF) (see scheme). Group separation of polar (PC) and nonpolar (NPC) components was performed on silica gel [4]. The boundaries of fractions were determined by characteristic luminescence on a filter paper under UV irradiation. Paraffinic and naphthenic compounds (PNCs) show no specific luminescence. Monocycloaromatic compounds (MCACs) exhibit a blue emission. The emission of bi- (BCACs) and polycycloaromatic (PCACs) compounds is green. Toluene resins (TRs) are yellow-brown under UV light, and alcohol–toluene resins (ATRs) are black. The partitioning scheme of vacuum residue and bitumen is as follows:

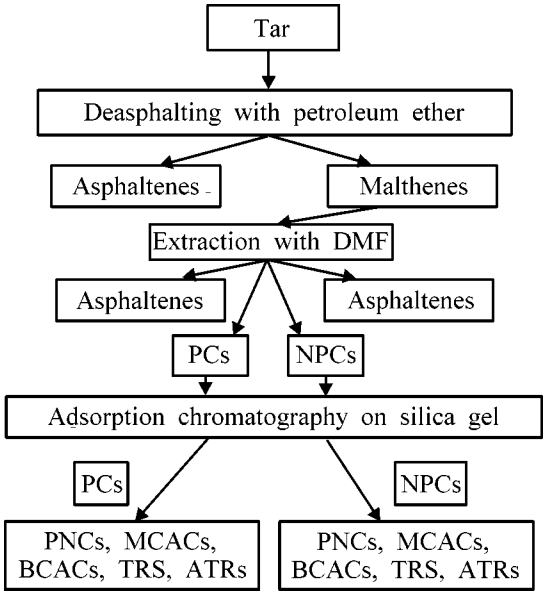

The yields of asphaltenes, malthenes, PCs, and NPCs, and also the group composition of the tar and bitumen samples are listed in Table 1. It is seen that the yields of malthenes from tars are close (88.62–89.55%). The differences in the yields of the polar and nonpolar components are also insignificant (~1.5 wt %).

Upon oxidation of these tars to obtain BDUS 70/100 and BDUS 60/90 paving bitumens, the yield of maltenes decreased to 79–80.7%, and the content of asphaltenes increased.

In the initial tars, the asphaltene content is 10.45–11.38%, whereas in the corresponding bitumens, it varies within 19.3–21%. The yield of polar components from bitumens is 4.3–6.3% higher than that from the corresponding tars. The tar characterized by initial penetration of 390 mm × 0.1 and conventional viscosity of 92 s was oxidized to a greater extent (ring-and-ball softening point 48°C) as compared to a tar with initial penetration of 305 mm × 0.1 and conventional viscosity of 89 s. In a bitumen sample with a higher softening point, the content of polar components increased by 1.8%.

Table 2 shows that the content of oils and resins in both polar and nonpolar components of the tars under consideration and corresponding bitumens is noticeably different. In the tar with P_{25} = 305 mm × 0.1, whereas the oils/resins ratio in NPCs is 2.06, whereas in the corresponding fraction of BDUS 70/100 bitumen, it is appreciably lower: 1.73. In polar components of both tars and the corresponding bitumens, the yield of resins is higher, and the above ratio is 1.37 for the tar and 1.25 for bitumen.

The tar with higher penetration (P_{25} = 390 mm × 0.1) is characterized by higher content of oils in both nonpolar and polar components.

The oils/resins ratio in the NPCs of this tar is 2.46, whereas in the tar with P_{25} = 305 mm × 0.1, it is 2.06, and in the PCs of these tars, it is 1.60 and 1.37, respectively.

It should be noted that both samples of tars differ not only in penetration, but also in conventional viscosity, which suggests their essentially different structural types. These differences were also manifested in the stage of oxidation to paving-grade bitumens. From the tar with P_{25} = 305 mm × 0.1, quality bitumen of BDUS 70/100 grade was obtained, whose softening point, penetration, ductility, and also retained penetration and ductility after heat treatment met the requirements. At the same time, from the tar sample with higher conventional viscosity (92 s), larger penetration, and higher oils/resins ratio, it was possible to obtain only harder bitumen BDUS 60/90, exhibiting not only higher softening point (Table 1), but also lower heat resistance. After standard heat treatment (5 h, 160°C), its ductility decreased from more than 150 to 96 cm, and the penetration decreased to 72% of the initial level. For the more heat-resistant quality bitumen BDUS 70/100, the same heat treatment resulted in a decrease in the ductility to 108 cm and in the penetration to 76% of the initial level.

It is interesting that the bitumen BDUS 60/90 obtained from the tar sample with P_{25} = 390 mm and oxidized to a bitumen with higher softening point is characterized by higher oils/resins ratio for both polar

Table 2. Results of group analysis of tars and corresponding bitumens

Fraction	Tar				Bitumen			
	residue 1*		residue 2**		BDUS 70/100		BDUS 60/90	
	NPCs	PCs	NPCs	PCs	NPCs	PCs	NPCs	PCs
	wt %							
PNCs	22	10.6	20.1	10.0	14.2	7.4	15.8	7.2
MCACs	18.7	23.1	22.4	17.1	30.1	30	22.8	17.4
BCACs and PCACs	26.6	23.8	28.6	34.4	19.1	18.7	27.8	32.7
TRs	13.2	18.8	11.2	14.5	18.4	18.1	14.1	15.4
ATRs	19.5	23.9	17.7	24.0	18.2	26.8	19.5	27.3
Oils	67.3	58.3	71.1	61.5	63.4	56.1	66.4	57.3
Resins	32.7	42.7	28.9	38.5	36.6	44.9	33.6	42.7
Oils/resins	2.06	1.37	2.46	1.60	1.73	1.25	1.98	1.34
Resins/Σ(MCACs + BCACs and PCACs)	0.72	0.91	0.57	0.75	0.74	0.92	0.66	0.85
TRs/ATRs	0.67	0.79	0.63	0.60	1.01	0.68	0.72	0.56
MCACs/BCACs and PCACs	0.70	0.97	0.78	0.60	1.57	1.60	0.82	0.53

* P_{25} = 305 mm × 0.1, conventional viscosity 89.0 s.

** P_{25} = 390 mm × 0.1, conventional viscosity 92 s.

and nonpolar components as compared to BDUS 70/100 quality bitumen.

It is known that the heat resistance of bitumens largely depends on the degree of aromaticity of both the initial tars and the bitumens obtained from them. The heat resistance (possible range of variation of the softening point, penetration, ductility, and brittle point) is affected not only by the extent of oxidation, which is indirectly evaluated by the acid number and oxygen content (elemental analysis), but also by the content of oils, resins, and asphaltenes, and also of aromatic compounds in oils.

It should be noted that not only the total content and ratio of these substances are important, but also their composition (molecular weights; content of polar components, depending on the number of heteroatoms and paramagnetic centers in the system; degree of association of these components; their aromaticity) and the nature of trace impurities (metal complexes). It is noted in the literature that, if polycyclic arenes prevail among aromatic hydrocarbons of oils, the molecules in tars and bitumens are packed into micelles more densely, ensuring higher heat resistance of such bitumens.

Our results show that the ratio of MCACs to BCACs and PCACs is not the only significant factor; the degree of aromaticity of these compounds exerts even stronger influence. It is also clear that, to obtain a heat-resistant bitumen, it is necessary to find the optimal ratio between oils and resins. The excessive amount of oils in the tar with P_{25} = 390 mm × 0.1 results in that their content in the bitumen produced from this tar is also excessive, and the degree of structurization (colloidal stability of the bitumen of type 3, according to Kolbanovskaya's classification) will be lower in this case. As the solvency of malthenes K_s of the oil component increases and the asphaltenes/resins ratio decreases, the colloidal structure of the bitumen becomes less strong:

$$K_s = C_a + 1/3\,C_n,$$

where C_a and C_n are, respectively, the carbon contents in the aromatic and naphthenic structures of malthenes (%).

It seems appropriate to compare quantitatively the group components of the tars and bitumens produced from them. In the quality tar (P_{25} = 305 mm × 0.1), the content of PNCs is 22% in NPC and 10.6% in PC; in the tar with P_{25} = 390 × 0.1 mm, these parameters are similar: 20.1 and 10%, respectively.

For the corresponding bitumens, these parameters are 14.2 and 7.2% for BDUS 70/100 and 15.8 and 7.2% for BDUS 60/90, respectively, i.e., they tend to decrease in going from the tars to bitumens but do not differ significantly between the quality and substandard products.

The content of arenes and resins in the polar components tends to grow in going from the initial tars to bitumens obtained from them. The total content

of MCACs + BCACs and PCACs in NPC and PC of the tar is 45.3–46.9%, and that in the quality bitumen BDUS 70/100, 48.7–49.2%, i.e., oxidation of the tar increases the content of aromatic structures.

In the less heat-resistant bitumen BDUS 60/90, the total content of MCACs + BCACs and PCACs is virtually the same as in the initial tar, ranging from 50.4 to 51.6% for both NPC and PC. It should be noted that the MCACs/BCACs ratio in the heat-resistant bitumen BDUS 70/100 is higher than in BDUS 60/90.

Thus, the most significant differences between the group compositions of the quality (heat-resistant) and substandard bitumens and of the tars are observed in the ratio of resins to sum of arenes in oils. In the quality bitumen BDUS 70/100 and the corresponding tar, this ratio is higher than in the less heat-resistant bitumen BDUS 60/90, in both nonpolar and polar components.

The polar components of tars and the corresponding bitumens are characterized by higher ratio of resins to the sum of arenes than the nonpolar components. Also, in both NPC and PC of the quality bitumen, the ratio of toluene and toluene–alcohol resins and, as already noted, the ratio of MCACs to BCACs and PCACs are higher.

Thus, the heat resistance of bitumen depends not only on the ratio of group components of the tar and bitumen prepared from it, but also on the forming structure (types 1–3). The bitumens under consideration belong to structural type 3 (according to Kolbanovskaya's classification). Probably, the colloidal stability of the forming structures is the highest if the oil fraction contains sufficient amounts of aromatic carbon in MCACs and TRs, with required amount of carbon in cyclic structures. The distribution of heteroatoms is also important.

The optimal structurizing power of asphaltenes and resins should be combined with the optimal ratio of MCACs to BCACs and PCACs to provide formation of the most aggregation-stable (and hence the least temperature-sensitive) structure. Apparently, the penetration and ductility of such a structure would change to the minimal extent in the course of aging, under the action of a mineral filler, or upon heating to simulate the bitumen aging.

Apparently, the major factors determining the aggregative stability of the three-dimensional (3D) coagulation structure of bitumens are the concentration of the dispersed asphaltene phase and its chemical affinity for oils and resins (dispersion medium). Formation of the kinetically stable state of the coagulation structure of bitumens is complete within the first several days after its mechanical or thermal breakdown.

Table 3. Group composition of tars

P_{25}, mm × 0.1	PNCs	Arenes (BCACs + MCACs)	Resins	Asphaltenes
	wt %			
425	10.3	54.2	24.4	11.1
424	9.8	54.6	22.7	12.9
409	11.4	50.9	26.2	11.5
456	11.9	54.9	20.5	12.7
463	11.9	52.4	24.2	11.5
478	7.6	61.7	20.1	10.6
Average: 442.5	10.48	54.78	23.01	11.7

Numerical analysis of small-angle X-ray diffraction patterns shows that the structural state of the disperse system of bitumens is characterized by the presence of microheterogeneities of the first and second order. Interestingly, some authors believe that the size of these microheterogeneities is independent of the component composition and chemical nature of bitumens [6]. This viewpoint seems to be doubtful. In [6], first-order microheterogeneities are interpreted as a primary structural unit with a nucleus of the phase of asphaltene molecules (2–6 nm in diameter), and second-order microheterogeneities, as asphaltene aggregates (about 10 nm in diameter) formed by condensation structurization within a complex structural unit.

The aggregative stability of the 3D coagulation structure of bitumens is determined not only by the concentration of asphaltenes forming the dispersed phase but also by the adsorption factor, namely, the chemical affinity of asphaltenes for the oil and resin components forming the dispersion medium. This affinity is characterized by the lyophobicity index L defined as the difference between the degrees of aromaticity (C_{ar} fraction) of asphaltenes, on the one hand, and oil and resin components, on the other, since specifically the presence of condensed aromatic systems in tars is the necessary condition for their association to form lamellar-block structures. Khryashchev [7] noted that L is independent of the extent of bitumen oxidation but is determined by the chemical composition of the initial tars, amounting to 0.18, 0.28, and 0.31 for bitumens prepared from tars of West-Siberian, Romashkino, and Arlansk crude oils, respectively. Hence, the 3D coagulation structure of

Table 4. Characteristics of bitumens

Parameter	Sample no.					
	1	2	3	4	5	6
Ring-and-ball softening point, °C	45	45	48	43.5	48.5	48
Density, g cm^{-3}	1.0188	1.023	1.0235	1.0196	1.0218	1.019
P_{25}, mm × 0.1	79	76	67	123	84	78
D_{25}, cm	150	146	126	118	131	138
Penetration retained after heat treatment,% of P_{25}	66/52.1	67/50.9	71/47.6	57/70	71/59.6	60/46.8
Ring-and-ball softening point after heat treatment, °C	49	49.5	50	49	52	54
D_{25} after heat treatment, cm	132	118	54	94	56	81
PNCs, %	10.3	10.0	11.1	10.4	9.4	7.8
MCACs + BCACs, %	44.6	43.4	39.1	46.8	46.2	46.4
Resins, %	29.9	28.3	30.6	28.5	27.1	23.8
Resins/Σ(MCACs + BCACs)	0.67	0.65	0.78	0.61	0.59	0.51
Asphaltenes, %	15.2	18.3	19.2	14.3	17.3	22

bitumens from Romashkino and Arlansk crude oils will be more stable, and these bitumens will be more heat-resistant than those produced from West-Siberian crude oils. The enthalpy of formation of the 3D coagulation structure of bitumens per unit weight of asphaltenes is independent of the extent of their oxidation and is determined by the nature of the initial tar, amounting to 27, 21, and 9 kJ kg^{-1} for bitumens produced from tars of West Siberian, Romashkino, and Arlansk crude oils, respectively [6].

The lyophobicity index linearly correlates with the rate constant of condensation structurization of the bitumens in hand:

$$K = K_0(L - 0.13),$$

where $K_0 = 8.5 \times 10^{-3}$ year.

Hence follows that disperse petroleum systems with $L < 0.13$ are thermodynamically stable.

For comparison, we present the group composition of a wider set of tar and bitumen samples from KINEF Ltd. (Tables 3, 4).[1] Table 3 shows that the group composition of tars and bitumens is approximately constant. However, in bitumens, compared to the initial tars, the content of arenes (sum MCACs + BCACs and PCACs) tends to decrease, with the content of resins and asphaltenes increasing. The higher heat resistance, as judged from the increase in the softening point (Table 4) and less significant decrease in the penetration and ductility after heat treatment, is observed at the optimal ratio of the sum of MCACs + BCACs, resins, and asphaltenes (sample nos. 1 and 2 in which the ratio of resins to the sum of MCACs + BCACs is 0.65–0.67). Bitumens with $D_{25} < 100$ cm are considered to be substandard after heat treatment for 5 h at 160°C.

It is seen that all the samples (Table 4), except sample no. 4, correspond only to the BND 40/60 hard bitumen grade after heat treatment, i.e., their properties changed to fall beyond the limits prescribed for the initial grade.

Table 4 shows that bitumens prepared from tars of commercial West-Siberian crude oil exhibit poor heat resistance: Their penetration after heat treatment (5 h, 160°C) decreases by 29–43%, the softening point increases by 2–6%, and the ductility decreases appreciably. According to the requirements to BDUS 70/100 bitumens, the ductility retained after heat treatment should be no less than 100 cm. Only sample nos. 1 and 2 meet this requirement. Nevertheless, all the bitumens (Table 4) are in full compliance with the GOST (State Standard) for BND paving bitumens.

CONCLUSIONS

(1) The structural-group compositions of polar and nonpolar components of malthenes from tars of commercial West-Siberian crude oil and from paving bitumens BDUS 70/100 (heat-resistant) and BDUS 60/90 (with low heat resistance), prepared by oxidation of

[1] Samples of tars and bitumens were obtained in May 2000 from AVT-6 and Bitumnaya-2 installations, respectively.

these tars, were compared. The content of the disperse phase, asphaltenes, is approximately equal for the examined samples of tars (10.45–11.38%) and bitumens (19.3–21%). With increasing solvency of malthenes (at constant content of oils) and with decreasing ratio of asphaltenes to resins, the colloidal structure of the bitumen becomes less stable.

(2) Quality bitumen BDUS 70/100 differs from substandard bitumen BDUS 60/90 in the higher content of aromatic structures.

(3) In the quality bitumen BDUS 70/100 and the corresponding tar, the ratio of resins to sum of arenes is higher than in the less heat-resistant bitumen BDUS 60/90, both in the nonpolar and polar components.

(4) The polar components of tars and of the corresponding bitumens are characterized by higher ratio of resins to the sum of arenes, compared to the nonpolar components.

(5) The nonpolar and polar components of the quality bitumen are characterized by higher ratios of toluene to toluene–alcohol resins and of mono- to bi- and polycyclic aromatic compounds.

(6) The colloidal stability of the forming structures is the highest if the oil fraction contains a sufficient amount of aromatic carbon in monocycloaromatic compounds and toluene resins and also a necessary amount of carbon in cyclic naphthenic structures. The decisive factors affecting the aggregative stability of the 3D coagulation structure of bitumens are the concentration of the disperse phase (asphaltenes) and its chemical affinity for oils and resins forming the dispersion medium.

REFERENCES

1. Pfiffer, J.P., *The Properties of Asphaltic Bitumens*, London: Elsevier, 1950.
2. Bodan, A.N., *Khim. Tekhnol. Topl. Masel*, 1982, no. 12, pp. 22–24.
3. Kolbanovskaya, A.S. and Mikhailov, V.V., *Dorozhnye bitumy* (Paving Bitumens), Moscow: Transport, 1973.
4. Kolbanovskaya, A.S., *Tr. SoyuzdorNII* (Moscow), 1968, issue 27, pp. 120–125.
5. Pechenyi, B.G., *Bitumy i bitumnye kompozitsii* (Bitumens and Bitumen Compounds), Moscow: Khimiya, 1990.
6. Posadov, I.A., Popov, O.G., Proskuryakov, S.V., *et al.*, Neftekhimiya, 1981, vol. 25, no. 3, pp. 412–416.
7. Khryashchev, A.N., Association of Resin and Asphaltene Components of Crude Oil, *Cand. Sci. Dissertation*, Leningrad, 1991.

Russian Journal of Applied Chemistry, Vol. 75, No. 6, 2002, pp. 1020–1023. Translated from Zhurnal Prikladnoi Khimii, Vol. 75, No. 6, 2002, pp. 1038–1041.
Original Russian Text Copyright © 2002 by Shunin, Filippova, Okhotina, Liakumovich, Samuilov.

CHEMISTRY OF FOSSIL FUEL

Possibilities of Production and Use of Rubber–Bitumen Compounds

D. G. Shunin, A. G. Filippova, N. A. Okhotina, A. G. Liakumovich, and Ya. D. Samuilov

Kazan State Technological University, Kazan, Tatarstan, Russia

Received December 19, 2001

Abstract—Procedures are discussed for production of rubber–bitumen compounds based on spent rubber items. A possibility of using these binders for paving is studied experimentally.

The main problem with road building is the poor quality of bitumens used in asphalt-concrete pavements [1]. One of the ways to improve the quality of the binders is their modification with polymers and rubber crumb from reprocessing of tire industry wastes.[1] Simultaneously, utilization of spent rubber would solve a serious environmental problem. The largest amount of worn rubber is collected in the form of tires and inner tubes [2]. They contain valuable kinds of rubber, such as natural, isoprene, butadiene, butadiene–styrene, etc. Under certain conditions of rubber crumb treatment in bitumen formulations, the valuable properties of rubber components become operative [3]. The resulting rubber–bitumen compounds (RBCs) exhibit elasticity, increased softening point, decreased brittle point, and enhanced strength. These properties allow RBCs to be used both as binders for asphalt concretes and as mastics for pavement repair. Asphalt concrete prepared with RBC exhibits high performance, enhanced wear and heat resistance, and resistance to aging. As a result, the pavement quality grows, and its service life becomes a factor of 1.5–2 longer.

EXPERIMENTAL

When developing RBC, it is necessary first to find conditions for introducing rubber crumb into a bitumen or plasticizer, under which the crumb would act not merely as a filler but also as a modifier improving the bitumen properties. For this purpose, the crumb should be preliminarily devulcanized. It is subjected to thermomechanical treatment in the presence of plasticizers: oil tar, commercial oils, various wastes, and low-viscous and paving bitumens [4]. The process is performed at high temperatures (200–260°C) for 15–20 h with vigorous stirring. Under these conditions, the rubber crumb swells in the oil fraction of a plasticizer, with weakening of the intermolecular bonds. Under severe conditions of thermomechanical treatment in the course of devulcanization, these weakened bonds are broken to leave rubber fragments. Then the resulting concentrate is mixed with a bitumen. Devulcanization can be performed faster (within 1–2 h) by adding appropriate agents [5].

In this study, we examined how the physicomechanical characteristics of RBC are affected by various plasticizers, temperature, plasticizer-to-bitumen ratio, and rubber crumb concentration. We also used rubber crumb of varied origin (tire treads, inner tubes, spent rubber items, reclaim) and size (from 0.5 to 3 mm).[2]

Our initial experiments were aimed at choosing a plasticizer and devulcanization conditions. Rubber crumb was devulcanized at 200–220°C with vigorous stirring. As plasticizers were used BND 90/130 paving bitumen, petroleum tar, and PN-6 oil at various crumb-to-plasticizer ratios (from 1 : 1 to 1 : 4). When

[1] Procedure developed at the Center for Elastomers, Kazan State Technological University.

[2] We used reclaim from Chekhov plant (devulcanizate of tire tread rubbers, mixture of SKI, SKD, and SKS rubbers, 0.5 mm fraction; butadiene–styrene rubber crumb produced by Kvart Joint-Stock Company, 0.5–1 mm fraction; and crumb from Leninogorsk plant (crushed inner tube rubber, 0.5–1.3 mm fraction). Experimental data were obtained with the Leninogorsk rubber crumb, bitumen from Sanbit Joint-Stock Company (Nizhnekamsk), and petroleum tar from Nizhnekamskneftekhim Joint-Stock Company.

1070-4272/02/7506-1020 $27.00 © 2002 MAIK "Nauka/Interperiodica"

using bitumen as plasticizer, it should be borne in mind that prolonged heat treatment of bitumens at so high temperatures results in their rapid aging. With oil, the adhesion of the binder to mineral fillers is considerably worse. The best plasticizer is petroleum tar, which is close to bitumen in composition but contains more oils (in which the rubber crumb swells).

Initially, we added rubber crumb in 10 wt % amount. For the resulting compounds, we determined the main physicomechanical parameters of bitumen: depth of needle penetration (penetration P), ring-and-ball softening point T_p, and Fraas brittle point T_{br}. Also, we determined the parameters characterizing the quality of rubber: relative elongation ΔL, ultimate tensile strength H, and elasticity E.

In devulcanization of rubber crumb, we obtained a concentrate of rubber crumb in petroleum tar; the ratio of the crumb to plasticizers was 1 : 4. With a smaller amount of plasticizer, the fluid compound could not be obtained; with its larger amount, the properties were unsatisfactory. Petroleum tar was mixed with bitumen, since the results obtained with straight tar were also unsatisfactory.

The tar to bitumen ratio in concentrate preparation was varied from 1 : 3 to 3 : 1.

Rubber crumb was swollen in plasticizers for 1 h, after which bitumen was added and the process was continued for another 2 h. Initially, the process was performed at 220°C. The compounds were prepared with continuous vigorous stirring. The physicomechanical quality characteristics of the RBC are given in Table 1.

The adhesion of the samples, determined according to GOST (State Standard) 11 508–74, is similar to that of the control sample (BND 60/90 paving bitumen). As seen from Table 1, with decreasing amount of petroleum tar, the softening point of RBC increases, the relative elongation and elasticity decrease, but the strength grows.

Then we varied the concentration of rubber crumb in a compound. We prepared compounds containing 7 and 15 wt % rubber crumb, at the component ratio in the concentrate rubber crumb : tar : bitumen = 1 : 2 : 2 (220°C). The components were vigorously stirred. The results are listed in Table 2.

Apparently, the parameters characterizing the binder (bitumens) vary regularly: As the penetration (indirect characteristic of viscosity) decreases with increasing rubber crumb content, the softening point grows, as also do the strength parameters. The relative elongation and elasticity pass through a maximum. The optimal content of rubber crumb in a compound is 10 wt %. Then we examined the effect of temperature on the physicomechanical parameters of RBC. We performed additional experiments at lower temperatures: 180 and 150°C. The rubber crumb content in RBC was 10 wt %, and the rubber crumb : tar : bitumen ratio, 1 : 2 : 2. The synthesis was performed for 3 h with vigorous stirring. The results are listed in Table 3.

It is seen that the penetration increases with temperature, whereas the softening point does not change. Hence, at low temperatures, the rubber crumb chiefly behaves as a filler. At higher synthesis temperatures, the relative elongation at break, elasticity, and ultimate strength increase. The best temperature for the

Table 1. Physicomechanical parameters of RBC at various component ratios

RBC component ratio*	P, mm × 0.1	T_p, °C	T_{br}, °C	ΔL, %	E, %	H, MPa
BND 60/90	60	47	–17			
1 : 3 : 1 (2)	81	51	–31	450	69	0.93
1 : 2 : 2 (3)	69	56	–31	445	60	1.03
1 : 1.5 : 2 (4)	55	60	–30	350	52	1.7
1 : 1 : 3 (5)	48	64	–30	350	53	2.1

* Rubber crumb : oil tar : bitumen. In parentheses are sample nos.; sample no. 1 is BND 60/90.

Table 2. Physicomechanical parameters of RBC at varied rubber crumb content c

Sample no.	c, wt %	P, mm × 0.1	T_p, °C	ΔL, %	E, %	H, MPa
1	7	70	52	280	57	0.65
2	10	69	56	445	69	1.03
3	15	54	58	400	66	1.25

Table 3. Physicomechanical parameters of RBC prepared at different temperatures

Sample no.	T, °C	P, mm × 0.1	T_p, °C	ΔL, %	E, %	H, MPa
1	150	52	51	260	60	0.71
2	180	55	54	430	62	0.90
3	220	69	56	445	69	1.03

Table 4. Characteristics of asphalt concrete prepared using RBC

Sample	Bulk weight, g cm^{-3}	Water absorption	Swelling	Ultimate compression strength, kg cm^{-2}				Water resistance coefficient	Bitumen content, wt %
		vol %		R_{20}	R_w	R_{50}	R_0		
RBC	2.39	1.21	0.3	31.2	28.1	14.1	10.6	0.9	5.9
GOST 9128–97		1.5–4.0		22.0		10	≤12	0.85	5–6.5

process is 220°C. Higher temperatures are not appropriate, because specifically at this temperature bitumen is produced in oxidation apparatus and is unloaded from it.

The brittle point of RBC is not given in Tables 2 and 3, because it was about –30°C or higher for almost all the compounds. The adhesion of almost all the RBC samples, measured according to GOST 11508–74, was the same as for sample no. 1.

Thus, for RBCs prepared at the optimal temperature of 220°C, varied ratio of petroleum tar and bitumen, and varied content of rubber crumb, the penetration falls within 48–81, and the softening point, 51 to 64°C. These are the main parameters characterizing the quality and application fields of bitumen. Bitumens with penetration higher than 60 are used as binders for mineral fillers in asphalt concretes. The softening point of BND 60/90 paving bitumens is no less than 47°C, and that of BND 90/130 bitumens, no less than 45°C (GOST 9128–97). The softening point of modified bitumens must be higher. Our results show that the RBCs with penetration higher than 60 (Tables 1, 2, RBC nos. 1, 2) are suitable as binders for asphalt concretes. To assess the quality of an asphalt concrete prepared with a rubber–bitumen binder (RBB), a pilot laboratory batch (2 kg) of the RBC was prepared, which was tested in the Paving Laboratory, Tatneftedor Ltd. (Bugulma).

Table 5. Comparison of rubber–bitumen and polymer–bitumen binders

Sample no.	Sample	P, mm × 0.1	T_p, °C	T, °C	E, %
	RBC:				
1	KSTU	69	56	–30	69
2	MOR	63	47	–28	57
3	PBB (OST 218.010–98)	61–90	≥54	≤–20	80

Table 6. Parameters of mastics for pavement repair

Sample	P, mm × 0.1	T_p, °C	T_{br}, °C	ΔL, %	H, MPa	E, %
KSTU	48	64	–30	350	0.48	53
Tatneftedor Ltd.	60	55	–25	–	–	50
Dormast Private Company	90	100	–35	350	0.13	30

The parameters of the asphalt concrete prepared with RBC are listed in Table 4.

The parameters of our RBB are compared in Table 5 with those of RBB produced by the Moscow Oil Refinery (MOR) and of polymer–bitumen binders (PBBs) prepared with butadiene–styrene thermoelastoplastic [OST (Branch Standard) 218.010–98]. The RBB samples contain 10 wt % rubber crumb.

As seen from Table 5, the parameters of the rubber–bitumen binder developed at the Kazan State Technological University (KSTU) exceed those of the binder from MOR, containing rubber crumb, and well compete with those of the polymer–bitumen binders prepared with thermoelastoplastics.

Thus, the parameters of asphalt concrete prepared using RBC exceed those prescribed by GOST 9128–97 for bitumen-containing asphalt concretes.

Rubber–bitumen compounds with penetration less than 60 and softening point higher than 56°C (Table 1, nos. 3, 4; Table 2, no. 3; Table 3, no. 2) can also be used in road building as pavement-repair mastics and for filling cracks and joints. In Table 6 we compare the parameters of our mastic with those of the mastic developed by Tatneftedor Ltd. and containing SKEPT rubber and of the mastic developed by Dormast Private Company (Naberezhnye Chelny) and containing rubber crumb and DST rubber.

As seen, the rubber–bitumen mastics developed by KSTU and containing wastes from tire industry well compete in quality with mastics developed by road-building institutions and containing SKEPT and DST rubbers and surpass them in strength.

To determine the amount of rubber crumb not incorporated into RBC (under the optimal conditions), we washed the flask with CCl_4 after the synthesis and decanting of the products, because CCl_4 dissolves virtually all the components of petroleum tar and bitumen. Then the solution was filtered. Virtually no rubber crumb was detected on the filter. The same result was obtained in 3–5 replications. Thus, the crumb was almost fully incorporated into the compound.

The degree of devulcanization of rubber crumb in the compound and the percentage of its incorporation into bitumen can be determined by treatment with appropriate solvents. To do this, 1 g of RBC was dissolved in CCl_4, and the solution was filtered. The extent of devulcanization was judged from the presence or absence of rubber crumb on the filter. In this experiment, no rubber crumb was detected on the filter either, suggesting its complete devulcanization with hydrocarbons, plasticizers, and bitumen. Three to five experiments were performed with RBC samples prepared under optimal conditions.

CONCLUSOINS

(1) Among various kinds of plasticizers for rubber crumb, the best is petroleum tar, which is similar in composition to bitumen but contains aromatic and saturated oils promoting swelling of any kind of rubber crumb.

(2) The optimal conditions for rubber crumb compounding with bitumen are as follows: 220°C, rubber crumb to plasticizer ratio 1 : 4, and rubber crumb content in rubber–bitumen compounds from 7 to 12%.

(3) Ways to control the physicomechanical parameters of rubber–bitumen compounds were found. The process developed allows preparation of binders for asphalt concretes used in road building and of mastic for pavement repair.

(4) Rubber crumb from reprocessing of tire industry wastes is a relatively cheap and available modifier improving the bitumen properties. The binders prepared surpass in the parameters the binders produced by the Moscow Oil Refinery and well compete with polymer–bitumen binders produced with styrene–butadiene copolymer (OST 218.010–98) and with mastics produced by Dormast Private Company.

(5) Asphalt concrete prepared using the rubber–bitumen binder developed in this study meets the requirements of GOST 9128–97.

(6) Our results combined with published data, suggest that the service life of pavements made using rubber–bitumen binders will be longer by a factor of 1.5–2.

(7) Utilization of rubber crumb in road building will allow the amount of rubber crumb produced by reclaiming facilities to be considerably increased, which will decrease environmental pollution with spent rubber.

REFERENCES

1. Rudenskaya, I.N., *Neftyanye bitumy* (Petroleum Bitumens), Moscow; Rosvuzizdat, 1963, p. 10.
2. Rozental', D.A., Tabolina, L.S., and Fedosova, V.A., *Modifikatsiya svoistv bitumov polimernymi dobavkami* (Modification of Bitumen Properties with Polymeric Additives), Moscow: TsNIITEneftekhim, 1988.
3. Rozental', D.A., Bereznikov, A.V., Kudryavtseva, I.R., *et al., Bitumy: Poluchenie i sposoby modifikatsii* (Bitumens: Production and Modification Procedures), Leningrad: Leningr. Tekhnol. Inst., 1979.
4. Gorshenina, G.I. and Mikhailov, N.V., *Polimer-bitumnye izolyatsionnye materialy* (Polymer–Bitumen Waterproofing Materials), Moscow: Nauka, 1967.
5. Abrosimov, A.A., *Ekologicheskie aspekty proizvodstva i primeneiniya nefteproduktov* (Environmental Aspects of Production and Use of Petroleum Products), Moscow: TsNIITEneftekhim, 1999.

Russian Journal of Applied Chemistry, Vol. 75, No. 6, 2002, pp. 1024–1025. Translated from Zhurnal Prikladnoi Khimii, Vol. 75, No. 6, 2002, pp. 1042–1043.
Original Russian Text Copyright © 2002 by Ostanova, Chubarov, Drozdov, Patrushev, Tatarenko.

BRIEF COMMUNICATIONS

Solubility of Lead Nitrate in Aqueous Solutions of Nitric Acid and Zinc Nitrate

S. V. Ostanova, A. V. Chubarov, S. V. Drozdov, V. V. Patrushev, and A. A. Tatarenko

Institute of Chemistry and Technology, Siberian Division, Russian Academy of Sciences, Krasnoyarsk, Russia

Received November 2, 2001

Abstract—Solubility of lead nitrate in the system H_2O–$Zn(NO_3)_2$–HNO_3 was studied using the simplex-lattice design method. The equations describing the effect of nitric acid and zinc nitrate concentrations on the content of lead nitrate in solution at 25 and 55°C were derived.

In developing hydrometallurgical schemes for reprocessing of lead–zinc ores with the use of nitric acid, data on the mutual solubility of lead and zinc nitrates and on their salting-out with nitric acid are necessary. However, published data on the solubility of $Pb(NO_3)_2$ in nitrate medium are insufficient [1].

In this work, the solubility of lead nitrate in the system HNO_3–$Zn(NO_3)_2$–H_2O was studied.

EXPERIMENTAL

Synthetic lead nitrate obtained by a procedure described in [2], chemically pure zinc nitrate, nitric acid, and distilled water were used as starting reagents.

The equilibration time was established experimentally to be 40–42 h. The experiments runs were performed during 50 h at 25 ± 0.1 and 55 ± 0.1°C. After the experiments were complete, the liquid phase was sampled and the content of lead(II) was determined by atomic absorption spectroscopy and titrimetry [3, 4], and the concentration of nitric acid, by titrimetry [4]. The solid precipitate was filtered off, washed with water and ethanol to remove mother liquor, dried at 80–82°C, and subjected to X-ray phase analysis.

The results obtained were processed by the simplex-lattice method of experiment design [5]. The vertices of the concentration triangle represented the components (in terms of initial concentrations): X_1, distilled water (55.56 M); X_2, $Zn(NO_3)_2$ (1.53 M); and X_3, HNO_3 (3.2 M). As Y functions served the Pb^{2+} concentrations (M) in solution.

The experimental data were used to estimate the coefficients of the polynomials of incomplete third order, having the following form:

$$Y_{25} = 1.500X_1 + 0.338X_2 + 0.275X_3 - 1.068X_1X_2 + 1.014X_2X_3 - 2.006X_1X_3 + 1.500X_1X_2X_3 \quad (25°C),$$

$$Y_{50} = 2.00X_1 + 0.531X_2 + 0.377X_3 - 1.198X_1X_2 + 1.992X_2X_3 - 2.918X_1X_3 + 1.071X_1X_2X_3 \quad (55°C).$$

The root-mean-square error in determining Y was 3%. Verification of the equations with the use of the data obtained in the experiments demonstrated that they adequately describe the experimental data with 97% probability.

The obtained equations were used to plot isoconcentration lines for lead nitrate (see Figs. 1a and 1b).

$Pb(NO_3)_2$–HNO_3–H_2O system. It is known that nitric acid salts-out lead nitrate [2, 6]. The fundamental aspects of this process and the solubility of lead nitrate have been studied previously [6]. The solubility data show that, with increasing nitric acid concentration in the system studied, the solubility of lead nitrate markedly decreases to attain a minimum at the point with the highest concentration of nitric acid.

$Pb(NO_3)_2$–$Zn(NO_3)_2$–H_2O system. To our knowledge, no published data are available on the solubility of lead nitrate in aqueous solutions of zinc nitrate. The data obtained indicate that, in the system studied, the solubility of lead nitrate is considerably higher than that in nitric acid, with the run of the isoconcentration lines following the general pattern. An X-ray phase analysis of the precipitates revealed lead nitrate and no other compounds of lead(II) or zinc.

$Pb(NO_3)_2$–$Zn(NO_3)_2$–HNO_3–H_2O system. A study of the $Pb(NO_3)_2$ solubility in aqueous solutions of zinc nitrate and nitric acid showed that the decrease in

1070-4272/02/7506-1024 $27.00 © 2002 MAIK "Nauka/Interperiodica"

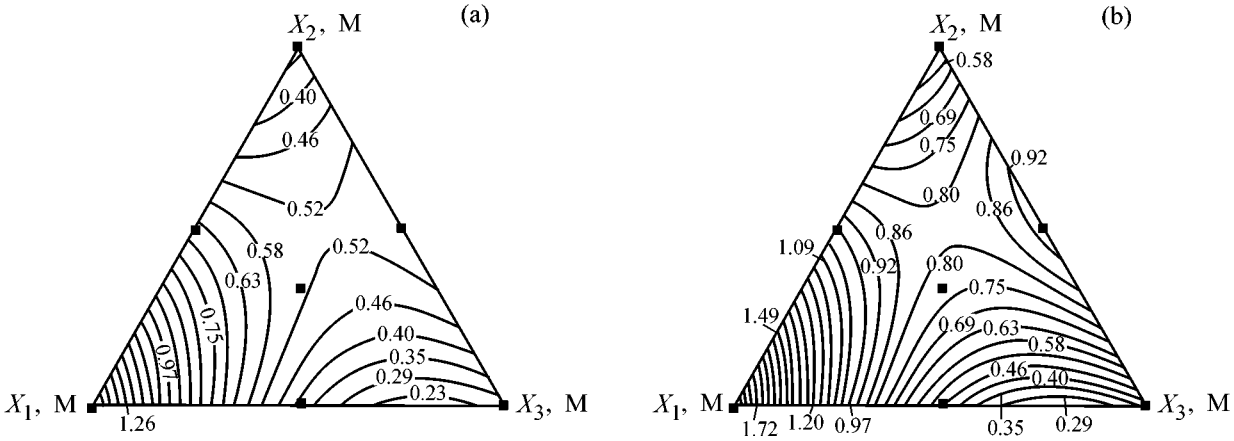

Fig. 1. Isoconcentration lines for $Pb(NO_3)_2$ (M) at (a) 25 and (b) 55°C.

the lead nitrate concentration in solutions becomes more pronounced in solutions with increased nitric acid concentration. The maximum concentration of lead nitrate is observed at the points corresponding to concentrations of 0.81 M $Zn(NO_3)_2$ and 1.50 M HNO_3 at 25°C and at the points with concentrations of 0.83 M $Zn(NO_3)_2$ and 1.47 M HNO_3 at 55°C, with the lead nitrate concentration in solution becoming 0.56 and 0.96 M, respectively. The calculated and experimental solubilities in the given system are presented in the isoconcentration triangles. When zinc nitrate and nitric acid are present in solution simultaneously, the observed behavior is evidently the same as that in the above-presented systems.

A comparison of the lead nitrate solubilities at 25 and 55°C showed that, with increasing temperature, the $Pb(NO_3)_2$ solubility grows and the general tendency is preserved.

It should be noted that an X-ray phase analysis performed for all the points considered revealed only lead nitrate in the precipitate.

CONCLUSIONS

(1) A study of the solubility of lead nitrate in the system H_2O–$Zn(NO_3)_2$–HNO_3 showed that the decrease in the Pb(II) concentration with increasing nitric acid and zinc nitrate concentrations is due to the effect of the NO_3^- ion.

(2) Only a single salt, lead nitrate, precipitates in the system studied.

(3) The regression equations describing the lead nitrate solubility at 25 and 55°C were calculated and used to plot isoconcentration lines.

REFERENCES

1. Lochmann, J. and Pedlik M., *Hydrometallurgy*, 1995, no. 37, pp. 89–96.
2. Karyakin, Yu.V. and Angelov, I.I., *Chistye khimicheskie veshchestva* (Pure Chemicals), Moscow: Khimiya, 1974.
3. Fainberg, S.Yu. and Filippova, R.A., *Analiz rud tsvetnykh metallov* (Analysis of Non-Ferrous Metal Ores), Moscow: Metallurgiya, 1963.
4. Alekseev, V.I., *Kolichestvennyi analiz* (Quantitative Analysis), Moscow: Khimiya, 1972.
5. Akhnazarova, S.L. and Kafarov, V.V., *Optimizatsiya eksperimenta v khimii i khimicheskoi tekhnologii* (Optimization of Experiment in Chemistry and Chemical Technology), Moscow: Vysshaya Shkola, 1978.
6. Ostanova, S.V., Drozdov, S.V., Pashkov, G.L., *et al.*, *Zh. Prikl. Khim.*, 2001, vol 74, no. 10, pp. 1701–1703.

Russian Journal of Applied Chemistry, Vol. 75, No. 6, 2002, pp. 1026–1028. Translated from Zhurnal Prikladnoi Khimii, Vol. 75, No. 6, 2002, pp. 1044–1046.
Original Russian Text Copyright © 2002 by Bazarov, Fedorov, S. Bazarova, Zh. Bazarova.

BRIEF COMMUNICATIONS

Electrical Properties of Molybdates in the Systems M_2MoO_4–$AMoO_4$–$Zr(MoO_4)_2$

B. G. Bazarov, K. N. Fedorov, S. T. Bazarova, and Zh. G. Bazarova

Baikal Institute of Nature Management, Siberian Division, Russian Academy of Sciences, Ulan-Ude, Buryatiya, Russia

Buryat State University, Ulan-Ude, Buryatiya, Russia

Received February 13, 2002

Abstract—The temperature dependence of conductivity of molybdates in the systems M_2MoO_4–$AMoO_4$–$Zr(MoO_4)_2$ was studied. The starting molybdates and molybdates of 5 : 1 : 3 and 1 : 1 : 1 compositions, formed in the systems, exhibit mixed conduction, turning ionic at high temperatures. The sharp bends in linear portions of the temperature dependence of conductivity coincide with the temperatures of polymorphic transitions in the corresponding molybdates.

Previously, the ternary salt systems K_2MoO_4–$AMoO_4$–$Zr(MoO_4)_2$ have been studied [1–3] and formation of molybdates with three dissimilar cations: potassium, doubly charged metal, and zirconium, was established.

The compounds obtained have general formulas $K_5A_{0.5}Zr_{1.5}(MoO_4)_6$ (5 : 1 : 3)[1] and $KA_{0.5}Zr_{0.5}(MoO_4)_2$ (1 : 1 : 1),[1] where A = Mg, Mn, Ni, Co, Cu, Zn, or Cd.

As shown by investigations, the structures of these complex molybdates have the form of skeletons constituted by ZrO_8 and AO_8 octahedra and MoO_4 tetrahedra connected via oxygen atoms. The structures of these compounds contain large voids, which can accommodate cations of alkali metals and, in particular, potassium [4, 5].

At an appropriate geometrical arrangement of channels and their filling with potassium cations, conditions for fast ionic transport may be fulfilled in skeleton structures and the compounds in question may possess properties of solid electrolytes.

The aim of this study was to analyze the electrical properties of starting molybdates forming the systems M_2MoO_4–$AMoO_4$–$Zr(MoO_4)_2$ and ternary molybdates of compositions 5 : 1 : 3 and 1 : 1 : 1.

[1] Molar ratio of starting molybdates.

The temperature dependences of conductivity σ, dielectric constant ε, and dielectric loss tangent $\tan\delta$ were studied on an experimental setup by the method proposed by Vest and Tallan [6]; the values of σ, ε, and $\tan\delta$ were measured under ac conditions on an E8-4 ac bridge with an R-5025 resistance box serving to extend the range of $\tan\delta$ measurements in the samples. The dc current was measured with an E6-13A teraohmmeter at fixed voltages across a sample (30 and 60 mV).

The electronic transport numbers t_e were found as the ratio of the electronic conductivity σ_e, measured under dc conditions, to the total conductivity $\sigma_e + \sigma_i$, measured under ac conditions at a chosen temperature of experiment (σ_i is the ionic conductivity).

Samples for electrical measurements had the form of pellets 1 mm thick with area of 74–75 mm^2. The pellets were obtained by compaction of powdered preparations, with their subsequent annealing at a temperature equal to 2/3 T_m of the corresponding compound.

As electric contacts served platinum paste fired-in at 500°C on the pellet surface.

Figure 1 presents in the form of Arrhenius plots the temperature dependences of conductivity of a part of molybdates studied, which are the conventional straight lines. The activation energies of conductivity,

1070-4272/02/7506-1026 $27.00 © 2002 MAIK "Nauka/Interperiodica"

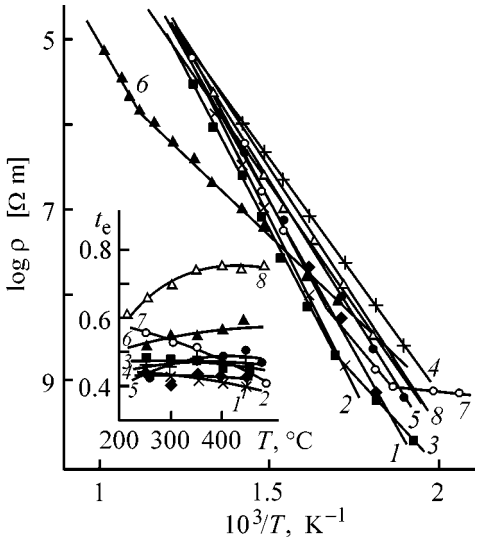

Fig. 1. Electrical resistivity ρ and electronic transport numbers t_e vs. temperature T. Sample: (*1*) $K_5Mn_{0.5}Zr_{1.5}(MoO_4)_6$, (*2*) $K_4MnZr_6(MoO_4)_{15}$, (*3*) $KMn_{0.5}Zr_{0.5}(MoO_4)_2$, (*4*) $K_2Zr(MoO_4)_3$, (*5*) $K_8Zr(MoO_4)_6$, (*6*) $Zr(MoO_4)_2$, (*7*) K_2MoO_4, and (*8*) $MnMoO_4$.

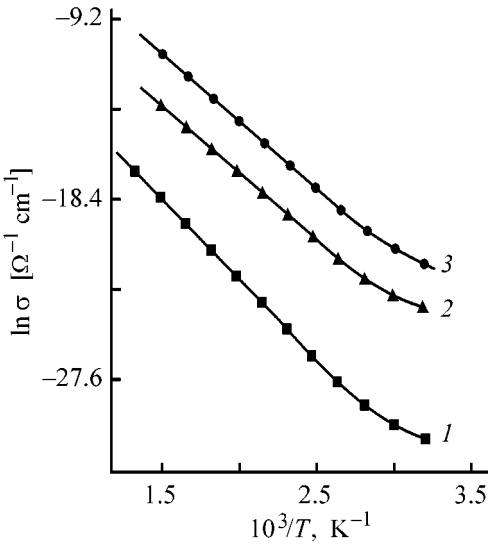

Fig. 2. Electrical conductivity σ of single crystals vs. temperature T. Sample: (*1*) $K_5Mg_{0.5}Zr_{1.5}(MoO_4)_6$, (*2*) $K_5Zn_{0.5}Zr_{1.5}(MoO_4)_6$, and (*3*) $K_5Cd_{0.5}Zr_{1.5}(MoO_4)_6$. E_a (eV): (*1*) 0.806, (*2*) 0.578, and (*3*) 0.591.

E_a, were found from the slopes of these lines for the molybdate samples studied. The experimental values of E_a and σ for the molybdates are presented in the table.

Analysis of the temperature dependences of the electronic transport numbers shows that the ceramic molybdate samples studied exhibit mixed electronic-ionic conduction with predominance of the ionic component at high temperatures of experiment.

Noteworthy are the close values of E_a and comparable values of σ for the ternary molybdates (see table). This circumstance suggests that one and the same ions are charge carriers in these complex oxides of different compositions.

It should be noted that sharp bends are observed in the linear portions of the temperature dependence of conductivity of zirconium and potassium molybdates (Fig. 1, curves *6* and *7*). These bends are not associated with transition from extrinsic to intrinsic conduction. An analysis of the experimental data demonstrated that the positions of the bends on the temperature axis correspond to the temperatures of polymorphic transitions in zirconium and potassium molybdates.

Electrical conductivity σ and activation energy of conductivity, E_a, of the molybdates studied

Sample no.	Compound	$\sigma \times 10^{-3}$, Ω^{-1} m^{-1} (400°C)	E_a, eV	Sample no.	Compound	$\sigma \times 10^{-3}$, Ω^{-1} m^{-1} (400°C)	E_a, eV
1	K_2MoO_4	1.36	0.63	9	$K_5Mn_{0.5}Zr_{1.5}(MoO_4)_6$	1.23	0.62
2	$MnMoO_4$	1.27	0.47	10	$K_5Cd_{0.5}Zr_{1.5}(MoO_4)_6$	2.03	0.54
3	$Zr(MoO_4)_2$	0.76	0.37	11	$Tl_5Mg_{0.5}Zr_{1.5}(MoO_4)_6$	0.74	0.47
4	$K_2Zr(MoO_4)_3$	1.87	0.45	12	$Tl_5Cd_{0.5}Zr_{1.5}(MoO_4)_6$	1.45	0.49
5	$K_8Zr(MoO_4)_6$	2.66	0.52	13*	$K_5Mg_{0.5}Zr_{1.5}(MoO_4)_6$	0.8×10^{-6}	0.806
6	$K_4MnZr_6(MoO_4)_{15}$	0.91	0.63	14*	$K_5Zn_{0.5}Zr_{1.5}(MoO_4)_6$	0.18×10^{-4}	0.578
7	$KMn_{0.5}Zr_{0.5}(MoO_4)_2$	0.79	0.64	15*	$K_5Cd_{0.5}Zr_{1.5}(MoO_4)_6$	0.11×10^{-3}	0.591
8	$K_5Mg_{0.5}Zr_{1.5}(MoO_4)_6$	1.00	0.63				

* Single-crystal samples.

It can be seen from Fig. 1 that at high temperature the electronic transport numbers for manganese molybdate show predominance of the electronic conduction over the ionic one. Presumably, this is due to the fact that manganese atoms in this compound are in variable oxidation state, and electron exchange occurs between differently charged atoms in an electric field.

The rise in ionic conductivity on changing A^{2+} at the same singly and quadruply charged (K and Zr) cations in the order Mg $\rightarrow$ Mn $\rightarrow$ Cd (sample nos. 8–10) can be attributed to an increase in the size of voids through which potassium cations move. This confirms the general tendency characteristic of skeleton structures: with increasing size of multiple-charge cations contained in the rigid skeleton, doubly charged cations in the given case, the activation energy and electrical resistance decrease. The decrease in ionic conductivity on passing from potassium compounds to their thallium analogues (sample nos. 8 and 11, 10 and 12) can be attributed to hindered motion of the thallium ion, which is larger than the potassium ion. Since the sizes of zirconium(IV) and molybdate ions remain constant, the free volume of the structure, accessible to singly charged cations, decreases with their increasing radius at invariable doubly charged metal ion (sample nos. 8, 10 and 11, 12), and purely steric hindrance to migration builds up [7].

The low activation energies of conductivity and the sufficiently high ionic conductivity of the ternary molybdates studied class these compounds with solid electrolytes.

A comparison of the conductivities of ceramic and single-crystal samples of the same composition (Fig. 2) revealed higher σ for the ceramic samples. This is presumably due to facilitated migration of conduction ions in an electric field between grains in the ceramic samples.

ACKNOWLEDGMENTS

The study was supported financially by the Russian Foundation for Basic Research (project no. 01-02-17890a).

REFERENCES

1. Bazarov, Zh.G., Bazarov, B.G., Klevtsova, R.F., *et al.*, *Zh. Neorg. Khim.*, 1994, vol. 39, no. 6, pp. 1007–1009.
2. Bazarova, Zh.G., Arkhincheeva, S.I., Batueva, I.S., *et al.*, *Khim. Interes. Ustoich. Razvitiya*, 2000, vol. 8, pp. 25–29.
3. Bazarova, B.G., Klevtsova, R.F., Bazarova, Zh.G., *et al.*, *Izv. Ross. Akad. Nauk, Ser. Khim.*, 1999, no. 6, pp. 1036–1039.
4. Klevtsova, R.F., Bazarova, Zh.G., Glinskaya, L.A., *et al.*, *Zh. Strukt. Khim.*, 1994, vol. 35, no. 3, pp. 11–15.
5. Klevtsova, R.F., Bazarova, Zh.G., Glinskaya, L.A., *et al.*, *Zh. Strukt. Khim.*, 1995, vol. 36, no. 5, pp. 895–899.
6. Vest, R.W. and Tallan, N.W., *J. Appl. Phys.*, 1965, vol. 35, p. 543.
7. Burmakin, E.I., *Tverdye elektrolity s provodimost'yu po kationam shchelochnykh metallov* (Solid Electrolytes with Conduction by Alkali Metal Cations), Moscow: Nauka, 1992.

Russian Journal of Applied Chemistry, Vol. 75, No. 6, 2002, pp. 1029–1031. Translated from Zhurnal Prikladnoi Khimii, Vol. 75, No. 6, 2002, pp. 1047–1048.
Original Russian Text Copyright © 2002 by Panasyugin, Golikova, Il'inykh, Strukova.

BRIEF COMMUNICATIONS

Sorption Concentration of Radiocesium on NaX Zeolite Modified with $Cu_2[Fe(CN)_6]$

A. S. Panasyugin, N. B. Golikova, N. P. Il'inykh, and O. V. Strukova

Belarussian State Polytechnic Academy, Minsk, Belarus

Institute of Environmental Problems, Belarussian National Academy of Sciences, Minsk-Sosny, Belarus

Research Institute, Belarussian State University, Minsk, Belarus

Received September 18, 2001; in final form, January 2002

Abstract—Sorption of ^{137}Cs on NaX zeolite modified with $Cu_2[Fe(CN)_6]$ was studied under dynamic conditions.

After the Chernobyl accident, about 23% of territory of the Belarus Republic was contaminated with radionuclides. The contaminated territories include river basins. Since the natural aquatic systems are zones of the most active migration of radionuclides, a more thorough monitoring of radionuclides, primarily ^{137}Cs, in water is required.

Before determination, radionuclides should be concentrated using any appropriate procedure: vaporization, coprecipitation, or sorption. The most effective is sorption, especially on sorbents highly selective for cesium. For these purpose, we used a sorbent based on NaX zeolite, which was modified with $Cu_2[Fe(CN)_6]$ by a procedure similar to that described in [1]. The optimal conditions for sorption of ^{137}Cs under dynamic conditions were found by us in column experiments.

All sorption experiments were carried out on standard columns 10 mm in diameter and 50 mm high. The volume of a filtering bed was 5 ml at its height of 43–45 mm; the sorbent grain size was 1.5–2.2 mm.

The optimal conditions for sorption of ^{137}Cs were determined in batch experiments by passing the initial model water containing ^{137}Cs (2×10^5 Bq l^{-1}) through a column at different filtration rates. The chemical composition of the initial model water was as follows (mg l^{-1}): suspended matter 17.1 ± 1.7, dry residue 349.5 ± 8.3, sodium 5.8 ± 0.15, potassium 1.0 ± 0.1, ammonium <0.1, calcium 37.6 ± 3.9, magnesium 6.4 ± 0.44, total iron 0.2 ± 0.02; anions: chloride 8.1 ± 0.79, sulfate 4.1 ± 0.02, nitrate 2.2 ± 0.04, hydrocarbonate 164.7 ± 1.24, bromide 0.1 ± 0.01, fluoride 0.13 ± 0.01; and silica 10.77 ± 1.0. The total hardness was 2.47 ± 0.06; the carbonate hardness, 2.46 ± 0.06 mg-equiv l^{-1}; and pH 8.3 ± 0.06. The chemical composition of this model solution meets GOST (State Standard) for potable water.

The filtration rate of the model water through a sorption column was varied from 50 to 150 column volumes per hour. Once a certain number of column volumes of water was passed, a portion of the filtrate was sampled. After completion of the sorption experiment, the activities of the upper and lower parts of the column were measured.

The ^{137} Cs activity was measured on an RUB-01 P4S radiometer equipped with a BDZhB-06P1 detection unit. The relative error of the activity measurement did not exceed $\pm 7\%$.

From the data on ^{137}Cs activity in the initial and filtered water, the decontamination factor K_{dec} from cesium and the degree of cesium sorption S (%) were calculated by the equation:

$$K_{dec} = A_0/A_f, \quad S = \frac{A_0 - A_f}{A_0} \times 100,$$

where A_0 and A_f are the ^{137}Cs activities in the initial and filtered water, respectively. The sorption parameters were calculated as described in [2–5].

Figure 1a shows that the efficiency of sorption recovery of high-activity water from ^{137}Cs, passed through a column packed with NaX zeolite modified with $Cu_2[Fe(CN)_6]$, is sufficiently high at filtration rates ranging from 50 to 150 column volumes per

1070-4272/02/7506-1029 $27.00 © 2002 MAIK "Nauka/Interperiodica"

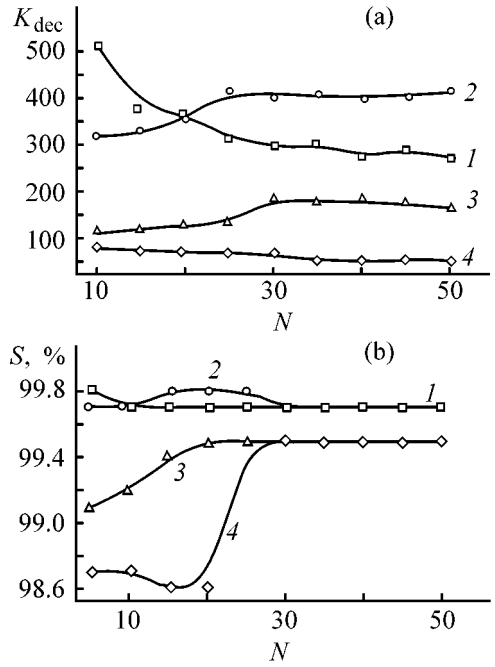

Fig. 1. Cesium decontamination factor K_{dec} and degree of cesium sorption S vs. the number of column volumes of water passed through a column packed with NaX–Cu zeolite at different filtration rates. Filtration rate V (h^{-1}): (*1*) 50, (*2*) 75, (*3*) 100, and (*4*) 150.

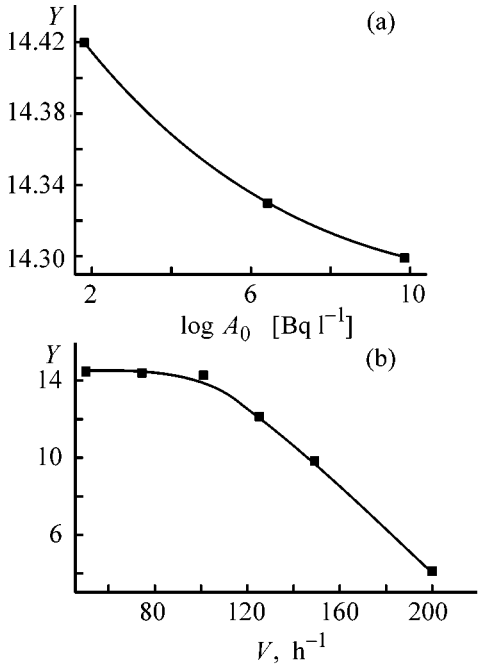

Fig. 2. Ratio of ^{137}Cs activities in the upper and lower parts of the column Y vs. (a) initial water activity A_0, and (b) filtration rate of radioactively contaminated solution V.

hour. Although K_{dec} decreases from 513 to 85, the degree of Cs sorption S remains high: 98.5–99.8% (Fig. 1b). In the first stage of filtration, the decontamination factor either increases or decreases, depending on the filtration rate. In further filtration, the filtering power of the filtering unit is stabilized, and a constant degree of decontamination is attained. Figures 1a and b show that the optimal filtration rate is 75 column volumes per hour. The dependences shown in Figs. 1a and 1b are similar to those reported in [6–13].

Our further experiments on sorption of ^{137}Cs on NaX–Cu zeolite were carried out at the optimal filtration rate of 75 column volumes per hour. In these experiments, the ^{137}Cs content in the initial water ranged from $2\ 10^5$ to 6.2 Bq l^{-1} at the volume of passed water ranging from 50 to 6000 column volumes. Under these conditions, the degree of ^{137}Cs sorption was 96–98%.

We found that, at the optimal filtration rate, the ^{137}Cs level in the initial water does not noticeably affect the ^{137}Cs distribution along a column. Figure 2a shows that, in the range of the ^{137}Cs activity from 2×10^5 to 6.2 Bq, the ratio of the ^{137}Cs activities in the upper and lower parts of the column varies within a very narrow interval, from 14.3 to 14.4.

In filtration of water containing ^{137}Cs in amount of 6.2 Bq l^{-1} at the rate of 200 column volumes per hour, the degree of ^{137}Cs sorption was 95.0–96.0 %.

With the filtration rate increasing from 50 to 200 column volumes per hour, the leading edge of sorption is smeared. As a result, the ratio of ^{137}Cs activities in the upper and lower parts of the column decreases from 14.4 to 4 (Fig. 2b).

CONCLUSION

NaX zeolite modified with $Cu_2[Fe(CN)_6]$ effectively sorbs cesium. The most efficient removal of ^{137}Cs is achieved in filtration of radioactively contaminated drinking water at a rate of 75 column volumes per hour.

REFERENCES

1. USSR Inventor's Certificate, no. 330 195.
2. *Ionity v khimicheskoi tekhnologii* (Ion Exchangers in Chemical Engineering), Nikol'skii, B.P. and Romankov, P.G., Eds., Leningrad: Khimiya, 1982.
3. Saldadze, K.M. and Kopylova-Valova, V.D., *Kompleksoobrazuyushchie ionity* (Complexing Ion Exchangers), Moscow: Khimiya, 1980.

4. Kaganovskii, A.M., *Adsorbtsiya i ionnyi obmen v protsessakh vodopodgotovki i ochistki stochnykh vod* (Adsorption and Ion Exchange in Water Treatment and Decontamination of Wastewater), Kiev: Naukova Dumka, 1983.
5. Berry, J.A. *et al.*, *Radiochim. Acta*, 1988, vols. 44–45, pp. 135–141.
6. Kudryavtsev, G.V., Bernadyuk, S.Z., and Lisichkin, G.V., *Usp. Khim.*, 1989, vol. 58, no. 4, pp. 622–627.
7. Betenkov, N.D., Gubanova, A.I., and Egorov, Yu.V., *Radiokhimiya*, 1976, vol. 18, no. 4, pp. 622–627.
8. Ampflett, S.V., McDonald, Z.A., and Redman, M.I., *J. Inorg. Nucl. Chem.*, 1958, vol. 6, no. 3, pp. 220–235.
9. Helfferich, F., *Ionenaustaucher*, Weinheim: Chemie, 1959, vol. 1.
10. Kuznetsov, Yu.V., Shchebetkovskii, V.N., and Trusov, A.G., *Osnovy ochistki vody ot radioaktivnykh zagryaznenii* (Foundations of Water Decontamination from Radioactive Pollutants), Moscow: Atomizdat, 1974.
11. Egorov, Yu.V., in *Soosazhdenie i adsorbtsiya radioaktivnykh elementov* (Coprecipitation and Adsorption of Radionuclides), Moscow: Nauka, 1965, pp. 113–117.
12. Del Deblio, J.A., *Radiochim. Acta*, 1991, vols. 52–53, part 1, pp. 181–186.
13. Nikashina, V.A., Zaborskaya, E.Yu., Makhalov, E.M., *et al.*, *Radiokhimiya*, 1974, vol. 16, no. 6, pp. 753–756.

Russian Journal of Applied Chemistry, Vol. 75, No. 6, 2002, pp. 1032–1033. Translated from Zhurnal Prikladnoi Khimii, Vol. 75, No. 6, 2002, pp. 1049–1050.
Original Russian Text Copyright © 2002 by Kudyshkin, Abdurakhmanova, Ruban, Voropaeva, Rashidova.

BRIEF COMMUNICATIONS

Synthesis of Polyvinylpyrrolidone under Secondary Inhibition Conditions

V. O. Kudyshkin, T. R. Abdurakhmanova, I. N. Ruban, N. L. Voropaeva, and S. Sh. Rashidova

Institute of Polymer Chemistry and Physics, Academy of Sciences of Uzbekistan Republic, Tashkent, Uzbekistan

Received February 7, 2002

Abstract—A new approach to controlling the molecular weight of polyvinylpyrrolidone in radical polymerization is considered. When the reaction is performed in the presence of a stable nitroxyl radical, 2,2,6,6-tetramethylpiperidyl-1-oxyl, the effect of secondary inhibition is manifested after the end of the induction period. This effect can be used for preparing polymers with prescribed molecular weights.

The molecular weight M of polyvinyllactams, and in particular, polyvinylpyrrolidone (PVP) in radical polymerization can be controlled by weak inhibition and chain-transfer reactions [1]. Previous studies have shown that the post-induction period in polymerization of some vinyl monomers in the presence of stable nitroxyl radicals is characterized by secondary inhibition, which can occur by a catalytic or common mechanism [2, 3]. Here we show that the post-induction inhibiting effect in radical polymerization can be used for preparing PVP of desired molecular weight.

EXPERIMENTAL

The reaction mixture consisting of the monomer, initiator (AIBN), solvent (dioxane), and inhibitor (2,2,6,6-tetramethylpiperidyl-1-oxyl, TEMPO) was placed in glass ampules. The mixture was deaerated by repeated freeze–pump–thaw cycles (residual pressure 0.13 Pa). The synthesis was performed at 60°C. The polymers were reprecipitated into diethyl ether. The polymerization kinetics was studied dilatometrically. The intrinsic viscosity of the polymers was determined in water at 25°C. The experimental data were processed in the Huggins–Kraemer coordinates. For all the samples, the sum of the Huggins and Kraemer constants $K_H + K_K \approx 0.5$. The molecular weights were calculated by the equation $[\eta] = 3.1 \times 10^{-4} M_w^{0.61}$ [1].

The figure shows how the PVP yield varies in the course of synthesis. Immediately after the end of the induction period t_{ind}, a non-steady-state period is observed in which the polymerization rate grows. Then the system reaches a steady state, and VP polymerizes at a constant rate v_p, which is lower than in the absence of TEMPO (see figure, table). The decreased polymerization rate is due, among other things, to partial decomposition of the initiator during the induction period. However, the fact that the product $v_p[I]^{-0.5}$ (where [I] is the AIBN concentration by the end of the induction period) decreases with increasing TEMPO concentration in the initial mixture (see table) shows that the decreased v_p cannot be accounted for solely by the lower initiation rate. Apparently, adducts formed by reaction of active radicals with TEMPO can react with chain propagation radicals, producing weak secondary inhibition after the end of the induction period [5]. This process must affect the molecular weight of PVP. Indeed, despite the fact that the reaction occurs under con-

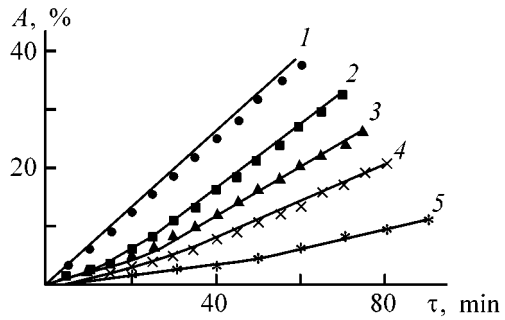

PVP yield, A, vs. synthesis time τ. [TEMPO] × 10^3, M: (*1*) 0, (*2*) 1.17, (*3*) 2.35, (*4*) 3.52, and (*5*) 4.71. Induction period, min: (*1*) 0, (*2*) 80, (*3*) 140, (*4*) 225, and (*5*) 355.

1070-4272/02/7506-1032 $27.00 © 2002 MAIK "Nauka/Interperiodica"

Kinetics of post-induction polymerization of VP and molecular weights of PVP ($[I]_0 = 2.7 \times 10^{-2}$ M)

$[TEMPO] \times 10^3$, M	$v_p \times 10^4$, mol l^{-1} s^{-1}	$(v_p[I]^{-0.5})^* \times 10^3$, s^{-1}	φ**	Yield, %	[η], dl g^{-1}	$M_\eta \times 10^{-3}$
0	3.66	2.23	–	29	0.14	22
				47	0.21	44
				65	0.27	66
				98	0.30	78
1.17	3.10	1.93	0.87	19	0.11	15
				95	0.28	70
2.35	2.34	1.48	0.66	18	0.10	13
				96	0.28	70
3.52	1.75	1.13	0.51	61	0.22	47
				97	0.27	66
4.71	1.22	0.82	0.37	26	0.11	15
				56	0.20	40
				67	0.22	47
				71	0.23	51
				98	0.25	58

* The initiator concentration by the end of the induction period was calculated using the decomposition rate constant $K_{dec} = 0.85 \times 10^{-5}$ s^{-1} for AIBN at 60°C [4].

** (φ) Deceleration factor.

ditions of secondary inhibition more slowly than under common conditions, and the molecular weight of the resulting PVP is lower than that of the polymer prepared in the absence of TEMPO. This is seen for the example of PVP samples obtained at high conversions.

CONCLUSION

Polymerization of vinylpyrrolidone in the presence of a stable nitroxyl radical, 2,2,6,6-tetramethylpiperidinyl-1-oxyl, occurs with secondary inhibition in the post-induction period. This reaction controls the molecular weight of the polymer and can be used for controlling the radical polymerization of vinylpyrrolidone.

REFERENCES

1. Kirsh, Yu.E., *Polivinilpirrolidony i drugie poli-N-vinilamidy* (Polyvinylpyrrolidones and Other Poly-*N*-vinylamides), Moscow: Nauka, 1998.
2. Il'in, A.A., Smirnov, B.R., Golikov, I.V., and Mogilevich, M.M., *Vysokomol. Soedin., Ser. A*, 1993, vol. 35, no. 6, pp. 597–598.
3. Il'in, A.A. and Smirnov, B.R., *Vysokomol. Soedin., Ser. A*, 1992, vol. 34, no. 11, pp. 53–55.
4. Odian, G., *Principles of Polymerization*, New York: McGraw-Hill, 1970.
5. Kudishkin, V.O., Abdurakhmanova, T.R., Ahymbetova, G.D., *et al.*, Abstracts of Papers, *3th IUPAC Sponsored Symp. on Free Radical Polymerization: Kinetics and Mechanism*, Lucca (Italy), 2001, p. 74.

Russian Journal of Applied Chemistry, Vol. 75, No. 6, 2002, pp. 1034–1035. Translated from Zhurnal Prikladnoi Khimii, Vol. 75, No. 6, 2002, pp. 1051–1052.
Original Russian Text Copyright © 2002 by Zaikov.

INFORMATION

X Enikolopov Symposium

X Enikolopov Symposium (March 13, 2002, Moscow) was held at the Enikolopov Institute of Synthetic Polymeric Materials, Russian Academy of Sciences (RAS). Academician Nikolai S. Enikolopov (1924–1993) was one of the most outstanding chemists of the former USSR. The area of his scientific interests covered chemical physics, chemical kinetics, and physics and chemistry of polymers and composite materials. He was a founder and the first director of the Institute of Synthetic Polymeric Materials, RAS. The symposium was organized by RAS (Department of General and Technical Chemistry together with the Scientific Council on Macromolecular Compounds) with active participation of the Enikolopov Institute of Synthetic Polymeric Materials, RAS (Moscow); Semenov Institute of Chemical Physics, RAS (Moscow); Institute for Problems of Chemical Physics, RAS (Chernogolovka, Moscow oblast); and Moscow Physicotechnical Institute (Dolgoprudnyi, Moscow oblast).

The conference participants were 150 scientists from 25 research centers of Russia and other republics of the former Soviet Union.

The symposium program included five plenary lectures delivered by Enikolopov's disciples working in different branches of chemical science.

The first lecture, entitled Quantum-Scale Colloidal Metallic Particles and Structures, was given by V.I. Roldugin (Institute of Physical Chemistry, RAS, Moscow). In this lecture, particular emphasis was placed on methods for preparation of colloid dispersions of nanoparticles, including the methods of chemical and radiation-induced reduction, condensation in a gas flow, methods for preparation of nanoparticles as individual chemical compounds, and also on use of colloid systems for obtaining nanoparticles. Also the lecturer outlined the important contribution of stabilizers physicochemical properties of nanodispersions. Then he considered the features of the electronic structure of metallic nanoparticles, level quantization and statistics, the chemical potential of electrons in small particles, and the effect of the electronic structure on the thermal, magnetic, and optical properties of nanoparticles.

Particular interest was aroused in the audience by data on the contact potential between particles of different sizes, charge transfer in nanostructures, equilibrium distribution of charges in an ensemble of polydisperse particles, and the contribution of this effect to the stability of dispersions. Other aspects of the problem considered in the lecture were the role of colloid processes in the formation of nanostructures, self-organization of nanoparticles into ordered structures, and, finally, physicochemical properties of nanoparticles.

The second lecture, entitled Langmuir's Monolayers in Mesomorphic Polysiloxanes and Their Self-Organizing Collapse, was given by Yu.K. Godovskii (Karpov Physicochemical Institute, Moscow). The lecturer demonstrated that Langmuir's polymeric monolayers may collapse under pressure to form highly ordered polylayers. A self-organized collapse of this type was observed in mesomorphic cyclic-linear polysiloxanes. The lecturer reported the results of the thermodynamic, rheological, and structural studies of monolayers and self-organized polylayers formed at the water–air interface or on a solid surface.

The third lecture, given by S.M. Mezhikovskii (Institute of Chemical Physics, RAS), was devoted to the dynamics of the structure of oligomer blends in the course of establishment of a thermodynamic equilibrium. The lecturer considered the relaxation processes in oligomers and polymer–oligomer blends at various levels of structural hierarchy (molecular, supramolecular, topological, and phase). The author analyzed the experimental results from the standpoint of traditional concepts of anomalous effects. The temperature, concentration, and time dependences of a number of macroscopic characteristics of the systems investigated were interpreted in terms of the aggregate structure of oligomeric fluids. The lecturer also discussed some theoretical models allowing qualitative and, occasionally, quantitative description of the so-called anomalous effects, making it possible to classify them with natural features.

The fourth lecture, given by O.N. Efimov (Institute of Problems of Chemical Physics, RAS), was devoted to conducting polymers and carbon nanostructures.

1070-4272/02/7506-1034 $27.00 © 2002 MAIK "Nauka/Interperiodica"

The author focused on the materials for energy accumulation and transformation, known as synthetic metals. The author overviewed general trends in design of such materials, including composites, and also the prospects for their use in designing energy-converting devices, such as hydrogen and electrochemical energy storage units, electroluminescent diodes, solar cells, sensors, etc.

The last, fifth lecture was devoted to analysis of transition zones in polymer blends (A.E. Chalykh, Institute of Physical Chemistry, RAS). The lecturer formulated a general concept of formation of transition zones and their structure in conjugated phases.

The equilibrium, interdiffusion, and structure of the transition zones were demonstrated to be interrelated. Both in amorphous phase separation and in crystal–crystal and liquid-crystal phase equilibria, gradient structures are formed, corresponding to the phase diagram. The extension of the transition zone depends on the conditions of phase conjugation and the component interaction rate. The phase boundary is one of the elements of the transition zone. In glass transition in solutions, the transition zone is in the nonequilibrium state.

Leading scientists working in the field of polymer physics and chemistry participated in discussions at the symposium. It was demonstrated that Enikolopov's ideas are being successfully developed by his disciples and by the disciples of his disciples.

The next XI Enikolopov Symposium will be held on March 13, 2003 at the Enikolopov Institute of Synthetic Polymeric Materials, RAS.

G. E. Zaikov

Russian Journal of Applied Chemistry, Vol. 75, No. 6, 2002, pp. 1036–1037. Translated from Zhurnal Prikladnoi Khimii, Vol. 75, No. 6, 2002, pp. 1053–1054.
Original Russian Text Copyright © 2002 by Morachevskii.

Shchegolev, V.I. and Lebedev, O.A., *Elecktroliticheskoe poluchenie magniya* (Electrolytic Production of Magnesium), Moscow: Publ. House Ruda i Metally, 2002, 386 pp.

In the 1980s, the magnesium industry of the USSR was one of the most successfully developing segments of nonferrous metallurgy, highly competitive in its scientific and technological level with the similar industries abroad. There were three high-output-capacity titanium-magnesium combines and two magnesium plants in the country. The highest output of magnesium in the USSR in those years was up to 160 thousand tons a year, with 95 thousand tons consumed for titanium production by reduction of titanium tetrachloride with magnesium. The geopolitical changes which occurred in the 1990s resulted in that only two plants out of five remained on the territory of Russia in Perm oblast: titanium-magnesium combine (Berezniki) and magnesium plant (Solikamsk). Their rated output capacities are, respectively, 35 and 20 thousand tons of magnesium a year. The monograph by V.I. Shchegolev and O.A. Lebedev covers a wide range of issues associated with electrolytic manufacture of magnesium from various kinds of raw materials, including information about preprocessing of raw materials, choice of electrolyte, electrolyzer designs, refining of raw magnesium, production of magnesium alloys, and manufacture of high-purity metal. The book comprises an introduction, 15 chapters, a reference list for the entire monograph, and an appendix.

The brief introduction (pp. 3–8) presents evidence of mainly historical nature about magnesium production and creation of the domestic magnesium industry. The Dneprovskii magnesium plant was put into operation on December 23, 1935, and the Solikamsk magnesium plant, on March 10, 1936. The first chapter (pp. 8–17) describes the physicochemical properties of magnesium and its interaction with various reagents. The second chapter (pp. 17–25) summarizes the presently available data on the world production of primary and secondary magnesium and main fields of application of magnesium and its alloys. At present, approximately 80% of magnesium is obtained in the world's technological practice electrolytically, and up to 20% thermally. The largest manufacturer of magnesium in the world is the US. Special attention is given by the authors to the development of magnesium production in China in the recent decade. In 1997, China manufactured 80 thousand tons of magnesium, and the present magnesium production capacity of this country is estimated to be approximately 170 thousand tons. China has, in addition to rather large plants, up to 200 small plants producing magnesium by the thermal method.

The very small third chapter (pp. 27–32) briefly characterizes the main types of magnesium raw materials. The fourth chapter (pp. 32–52) discusses technological schemes for magnesium production by electrolysis, bath feeding with carnallite or magnesium chloride of varied origin, and work by a combined scheme. The fifth chapter (pp. 58–68) is devoted to phisicochemical aspects of the technology of dehydration of chloride-magnesium raw materials. The sixth (pp. 68–98) and seventh (pp. 98–109) chapters describe the apparatus and technology for dehydration of carnallite and crystal hydrates of magnesium chloride. The eighth chapter analyzes in detail various methods for purification of chloride-magnesium raw materials to remove various impurities. The main kind of Russia's raw materials for manufacture of commercial magnesium (Solikamsk magnesium plant) is dehydrated carnallite not subjected to any special treatment. At the same time, preliminary electrolyte purification is necessary for achieving high and stable characteristics on modern diaphragmless electrolyzers.

The ninth chapter (pp. 140–215) discusses the physicochemical properties of salt systems, used in deciding on the electrolyte composition, and formulates main requirements to an industrial electrolyte for ensuring a high current efficiency by magnesium and chlorine, the minimum voltage across the electrolyzer, and lowered sludge formation. The tenth and eleventh chapters (pp. 216–240 and 240–266) describe various designs of electrolyzers with and without diaphragm, analyze their advantages and disadvantages, and advise on how on technological processes are to be carried out, depending on electrolyzer design and type of magnesium-chlorine raw materials (carnallite, magnesium chloride). The twelfth chapter (pp. 267–294) considers possible directions of improvement of the apparatus-technological schemes for electrolytic pro-

1070-4272/02/7506-1036 $27.00 © 2002 MAIK "Nauka/Interperiodica"

duction of magnesium. The authors mention among such directions creation of a flow-line technology of electrolysis and optimization and intensification of operation of a separate electrolyzer. The chapter also considers fundamentally new concepts of the technology and apparatus for electrolytic manufacture of magnesium and the technology for production of granulated magnesium and magnesium powders and discusses some ecological problems and, in particular, those associated with utilization of spent electrolyte.

The thirteenth chapter (pp. 294–316) is devoted to refining and casting of raw magnesium. It analyzes the reasons for the appearance of impurities, requirements imposed by standards on primary magnesium, and methods of its purification. The fourteenth chapter (pp. 316–324) presents evidence on production of magnesium alloys with manganese, zinc, aluminum, zirconium, and other alloying components. The same chapter discusses processing of scrap and waste aluminum alloys. The fifteenth chapter (pp. 324–345) is concerned with manufacture of high-purity magnesium.

The bibliography (pp. 345–357) contains references to 252 publications of mainly domestic authors. The appendix (pp. 358–363) presents evidence concerning the thermodynamic characteristics of various compounds of magnesium and a number of salts used as additives to the electrolyte of the magnesium bath.

The authors of the monograph did an ample amount of work on collecting, systematizing, and analyzing an extensive body of data, furnishing an exhaustive notion of the modern state of magnesium manufacture by electrolysis. The book reflects numerous investigations carried out by staff members of the All-Russia Aluminum-Magnesium Research and Design Institute (St. Petersburg), who made a major contribution to the creation of the domestic magnesium industry.

There is no escape from mentioning that the problem of whether or not it is appropriate to feed baths with dehydrated carnallite, which leads to batch electrolysis, was rather controversial when designing the Solikamsk magnesium plant. A.F. Antipin (1890–1960), one of leading specialists in electrometallurgy of light metals and a corresponding member of the Academy of Sciences of the USSR, believed till the end of his life that this decision was an error. In this connection, an economic assessment of the advisability of this process would be of interest under the present-day market conditions. Unfortunately, the problems of economy and competitiveness of Russian magnesium on the world market are not dealt with in the monograph.

In earlier monographs and textbooks, many important physicochemical laws related to metallurgy of magnesium were illustrated with much more convincing and clear curves than those in the book under discussion. This refers both to processes of carnallite dehydration and to physicochemical properties of the electrolyte and effect of various components on its most important properties. The quality of Figs. 14, 20, 38, 67, and 104 is poor and Fig. 64 is simply erroneous. In our opinion, many apparatus layouts are overladen with unimportant details, which only makes difficult their perception. For unknown reason, names of authors of investigations are mentioned, but no appropriate references are given. The polygraphic design of the book is very well done.

The monograph by V.I. Shchegolev and O.A. Lebedev is of indubitable interest for a wide audience of specialists in manufacture of magnesium and its alloys. The book will be of use for post-graduate students, masters, and undergraduates specialized in metallurgy of light metals or applied electrochemistry.

A. G. Morachevskii

Russian Journal of Applied Chemistry, Vol. 75, No. 7, 2002, pp. 1039–1050. Translated from Zhurnal Prikladnoi Khimii, Vol. 75, No. 7, 2002, pp. 1057–1068.
Original Russian Text Copyright © 2002 by Kurenkov, Hartan, Lobanov.

REVIEWS

Degradation of Polyacrylamide and Its Derivatives in Aqueous Solutions

V. F. Kurenkov, H.-G. Hartan, and F. I. Lobanov

Kazan State Technological University, Kazan, Tatarstan, Russia
Stockhausen GmbH&Co KG, Krefeld, Germany
Stockhausen Eurasia Company, Moscow, Russia

Abstract—General features of degradation of polyacrylamide and its anionic and cationic derivatives under the action of radical degradative agents are considered. The molecular weight of these polymers can be controlled by varying the structure and concentration of the degradative agent and salt additions, the concentration, molecular weight, and composition of the initial (co)polymer, and the process temperature and time.

Polyacrylamide (PAA) and acrylamide (AA) copolymers are widely used in various branches of engineering. Depending on particular purpose, it is appropriate to use PAA and AA copolymers with different characteristics (primarily molecular weight, MW). For example, high-molecular-weight (co)polymers are used as flocculants, thickeners, gel-forming agents, and lubricants, whereas low-molecular-weight (co)polymers are suitable as dispersing agents, coagulants, mud stabilizers, and crude oil thinners [1–4]. However, in the synthesis stage, it is not always feasible to prepare polymers with optimal MW and molecular-weight distribution (MWD); therefore, the MW and MWD of commercially available samples of PAA and AA copolymers are often far from the optimum for a given application. Therefore, it is necessary to develop reliable, simple, and quick procedures for controlling the MW of these polymers. A promising way to solve this problem is controllable degradation [5]. Degradation decreases the MW of polymers and affects their structure and physicochemical characteristics [6], which may deteriorate their performance. However, in some cases degradation can also produce a positive effect. For example, partial degradation of rubbers is used in industry to simplify their processing and application, and degradation of natural polymers allows production of valuable low-molecular weight compounds (e.g., of glucose from starch and of amino acids from proteins; degradation of isoprene rubber yields oligomers suitable as additives to fuels, oils, and paints). Furthermore, controllable degradation can be used to determine the structure and MWD of polymers, to prepare block and graft copolymers, and to study polymer aging and stabilization [5–7]. Some data on degradation of PAA in aqueous solutions are given in a review [8] and a monograph [2].

This review summarizes the data included in [2, 8] and obtained more recently on the degradation kinetics of PAA and its anionic and cationic derivatives in aqueous solutions under the action of radical degradative agents. We also examine the possibility of controlling the MW of the polymers by varying the structure and concentration of the degradative agent and salt additions, the concentration, molecular weight, and composition of the initial (co)polymer, and the process temperature and time.

DEGRADATION AND STABILITY OF POLYACRYLAMIDE AND ITS DERIVATIVES IN AQUEOUS SOLUTIONS

Degradation of PAA and its derivatives in aqueous solutions can occur in the course of synthesis, storage, and use of polymers under the separate or combined action of heat, light, ionizing radiations, mechanical effects, and biological factors.

As noted in [9–16], the viscosity of aqueous solutions of purified technical-grade PAA with $\overline{M}_\eta = 1.5 \times 10^6$ at room temperature in the dark decreased with time; the process occurred without stirring and was intensified by stirring. For example, the viscosity of a 3% aqueous solution of PAA at 25°C decreased by 13.3% in 1 month, and the solution became opalescent; in mixtures of water with 2-propanol, the viscosity did not decrease, and the solution remained transparent [12]. In contrast to high-molecular-weight polymers, the viscosity of solutions of low-molecular-weight PAA did not change in storage [17–19].

The stability of PAA solutions in storage was studied in [20–22]. The observed decrease in the intrinsic viscosity [η] of PAA solutions was attributed

1070-4272/02/7507-1039$27.00 © 2002 MAIK "Nauka/Interperiodica"

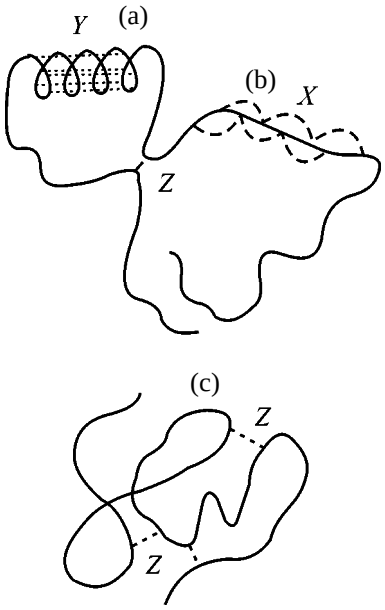

Fig. 1. Conformational transformations of PAA macromolecule in water in storage [22]. State: (a) initial, (b) transition (high viscosity), and (c) final (low viscosity). (*X*, *Y*, *Z*) Various types of H bonds.

to conformational transformations of macromolecules with the redistribution of intramolecular hydrogen bonds (Fig. 1). In the initial PAA solutions, H bonds of different types are formed (*X*, *Y*, *Z*), which accounts for the high viscosity of solutions. In storage, the H bonds of types *X* and *Y* are gradually broken, but the H bonds of type *Z* are preserved, which results in contraction of macromolecular globules and decrease in [η] [22].

The effect of various additions on degradation in storage of a copolymer of AA with sodium acrylate (Na-AA) ($\overline{M}_\eta = 6.5 \times 10^6$, content of Na-AA units 10 mol %) was studied in [23]. It was shown that, after keeping 0.1% solutions of the copolymer at 50°C for 28 days in the presence of Cu^{2+} and Fe^{2+} ions (10^{-3}% relative to the polymer), the reduced viscosity decreased. The intrinsic viscosity [η] of the copolymer also decreases in the presence of some other additives (7×10^{-4} M) in the order thiourea > sodium disulfite > urea > formaldehyde. This is due to degradation of macromolecules under the action of residual amounts of the initiator, potassium peroxosulfate (PP). Addition of reductants induces decomposition of PP and cleavage of backbone chains. Formaldehyde is also a component of redox systems with hydroperoxides [24, 25], and formation of hydroperoxides in storage of copolymer solutions in air is not excluded. An effective agent stabilizing the viscosity in storage of solutions of AA–Na-AA copolymer is KI [23].

After storage in the dark of dry polyacrylglycine cyanamide prepared by radical polymerization in the presence of PP, the viscosity [η] of its solutions decreases [26]. When, in the polymerization stage, PP is taken in smaller amounts, the solutions of high-molecular-weight PAA become more stable in storage, as judged from their viscosity [12].

When exposed to ionizing radiation, high-molecular-weight PAA undergoes degradation in 0.5% solutions and cross-linking in more concentrated solutions; with polymethacrylamide, only degradation was observed [27].

In the presence of bacteria and mold, PAA solutions get turbid with time, and a loose pink precipitate is formed. The microbial activity can result in a 4–5-fold decrease in the MW of PAA [28]. To prevent microbial degradation, bactericides such as Hexachlorophene, Diaphene, pentachlorophenol, etc., are added to polymer solutions [29].

Aqueous solutions of PAA are also unstable to the effect of a hydrodynamic field, deteriorating the polymer properties significant for practice. Stirring of PAA solutions at 4000 and 7000 rpm for 1 h decreases [η], after which it does not change further. According to GPC, the MW decreases from 5×10^6 to $(2.5–3.5) \times 10^6$ [30]. The decrease in [η] under the action of a hydrodynamic field [31] was attributed to a decrease in the size of macromolecular globules and in the flexibility of macromolecules. These factors prevent conformational transformations and orientation of macromolecules in a flow, which decreases the hydrodynamic performance of PAA. As found in [32–34], when solutions of nonhydrolyzed and hydrolyzed PAA are subjected to a shearing hydrodynamic field (at rate gradients of 3×10^3 or 6×10^3 s^{-1} for 30 min), the MW does not change, but the intrinsic viscosity [η], root-mean-square radius of inertia, and second virial coefficient decrease owing to changes in the structural and conformational characteristics of macromolecules [34]. The highest stability was noted for solutions of hydrolyzed PAA at pH 11.5. As shown in [35], at equal shear rate, the flow in dilute solutions of AA–Na-AA copolymers in 1 M NaCl decreases the MW by a factor of 3, and in semidilute solutions this decrease is less pronounced.

Ultrasonic treatment can cause degradation of PAA in aqueous solutions [36, 37]. Mechanical degradation of PAA is enhanced with increasing MW of the polymer and with decreasing solvency of the medium.

Table 1. Variation of molecular characteristics of partially hydrolyzed PAA in the course of thermal degradation in aqueous solutions (pH 7) in the presence of oxygen at 60°C

Characteristic	Time, days							
	0	3	10	34	40	51	75	100
$\overline{M}_w \times 10^{-6}$	3.4	2.2	1.9	1.5	1.2	0.9	0.7	0.5
$\Delta\overline{M}_w/\overline{M}_w$, %	0	35	45	56	64	73	79	83
Content of Na-AA units, mol %	31	31	31	31	34	37	39	41

In a flow through a porous medium, the MW of AA–Na-AA copolymer decreases [38].

The stability of aqueous PAA solutions is largely affected by temperature. A GPC study of the thermal degradation of PAA with $\overline{M}_\eta = 2.9 \times 10^6$ showed that, after keeping the solutions at 50°C for 5 days, the MWD curves change only slightly [39], whereas at 75°C the degradation of PAA with $\overline{M}$ 4.8×10^5 and 2.9×10^6 becomes appreciable.

Oxygen also affects the stability of aqueous PAA solutions. As shown in [40], oxidative degradation of PAA occurs in the presence of dissolved oxygen (~1%), and additions of sodium hydrosulfite and formaldehyde inhibit the polymer oxidation at 120–150°C.

When aqueous solutions of partially hydrolyzed PAA ($\overline{M}_w = 3.4 \times 10^6$, 31 mol % Na-AA units) are kept at 60°C in the presence of atmospheric oxygen, the MW decreases in time (Table 1) [2]. The MW sharply decreases in the first 10 days and more slowly, in the subsequent 10–100 days. The observed decrease in MW cannot be attributed to a change in the degree of hydrolysis of the polymer, since in the first 10 days $\overline{M}_w$ decreased by approximately 65%, whereas the degree of hydrolysis remained unchanged. Apparently, this result is due to the presence in commercial polymer samples of residual initiators, which entered into redox reactions with oxygen and induced degradation of the macromolecules [2]. With purified polymers, oxygen caused no degradation in the temperature range 60–100°C, and $\overline{M}_w$ remained unchanged [42, 42]. The degradation of PAA in aqueous solutions can also be induced by ozone. Ozonolysis of PAA with $\overline{M}_\eta = 3.5 \times 10^5$ in 0.1 and 1% aqueous buffer solutions is slow at pH 2 and faster at pH 10 [43]. With an increase in the oxygen consumption, the number of breaks in macromolecules increases, and $[\eta]$ decreases. The ozonolysis efficiency is determined by the concentrations of dissolved ozone and OH^- ions, temperature, and MW and structure of the polymer [44]. The rate of PAA degradation in aqueous solutions at pH $\leq$ 5.75 is independent of the OH^- concentration and at pH 5.8–8.9 is described by the equation

$$-d\overline{M}_\eta/dt = k_{pAA}[O_3][HO^-]^{0.5}\overline{M}\eta^{1.5},$$

where $k_{pAA} = 1.44 \times 10^{14} \exp(-94 \times 10^4/RT)$.

Thermal degradation of PAA and AA–Na-AA copolymers ($\overline{M}_\eta = 7.6 \times 10^6$) at 150°C is efficiently suppressed by Na_2SO_3 (binding oxygen) and Na_2EDTA (binding metal ions) [45].

The properties of aqueous solutions of PAA and its derivatives can be stabilized by various additives: alkali metal nitrites and iodides, thiocyanates, thiourea, dithionites, benzothiazole, sulfites, pyrosulfites, thiosulfites, mixtures of a guanidine derivative with 50% mercaptobenzothiazole or its salts, glycols, ethers, esters, ketones, etc. [2–8]. As stabilizers in drying of PAA solutions are used cyanamide, guanidine, succinimide, urea, or their mixtures.

The experimental data show that degradation of the polymers can be intensified by active residual impurities, oxygen, and heating. Therefore, to prevent undesirable degradation, the synthesized polymer should be purified to remove residual initiators and impurities by, e.g., reprecipitation or extraction. Residual ionic impurities (initiators, pH-controlling agents, surfactants, modifiers, complexing agents, stabilizers, etc.) can be removed by ion exchange and dialysis. Degradation of macromolecules can also be prevented by excluding access of oxygen to polymer solutions and removing oxygen from them [46]. Also, the polymers should be stored, dissolved, and used at temperatures as low as possible. The effect exerted by the structure of the polymers on the thermal stability of their solutions [47] should also be taken into account.

Despite the above-noted negative effect of degradation on the properties of polymer solutions, in some cases controllable degradation can be used to obtain

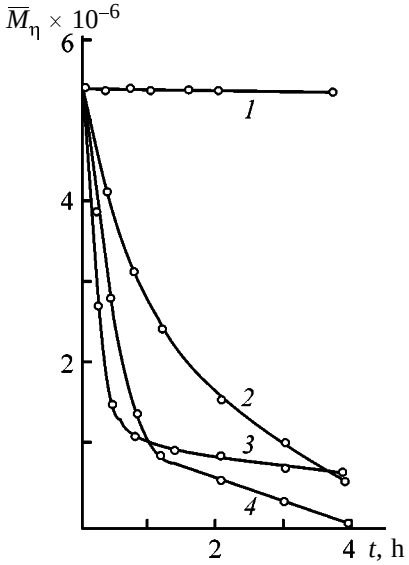

Fig. 2. $\overline{M}_\eta$ as a function of time *t* in degradation of PAA (initial $\overline{M}_\eta = 5.3 \times 10^6$) in the presence of various additives. Additive: (*1*) none, (*2*) ammonium persulfate, (*3*) H_2O_2–$FeSO_4$, and (*4*) PP. [Additive]/[PAA] 5%.

a polymer with the desired molecular weight. Below we discuss the degradation of PAA and its anionic and cationic derivatives in aqueous solutions under the action of radical degradative agents.

DEGRADATION OF POLYACRYLAMIDE AND ITS DERIVATIVES IN AQUEOUS SOLUTIONS IN THE PRESENCE OF RADICAL INITIATORS

Degradation of polyacrylamide. The main features of degradation of commercial PAA ($\overline{M}_\eta$ 0.95×10^6, 5.3×10^6, and 6.3×10^6) in 0.4% aqueous solutions at 50°C under the action of radical degradative agents were studied in [48, 49]. The kinetic studies were performed viscometrically by the procedure described in [50]. In the course of degradation, [η] of PAA in 0.5 M NaCl at 25°C was determined and $\overline{M}_\eta$ was found by the equation [51]

$$[\eta] = 7.19 \times 10^{-3} \overline{M}_\eta^{0.77}.$$

The effect of radical initiators (PP, ammonium peroxosulfate) and the H_2O_2–$FeSO_4$ redox system on variation of $\overline{M}_\eta$ in the course of PAA degradation in aqueous solutions is shown in Fig. 2. It is seen that $\overline{M}_\eta$ does not change in the absence of initiators (curve *1*) and decreases on adding them (curves *2*–*4*). This is due to degradation of the backbone chains under the actions of radicals R$^\bullet$ generated by thermal decomposition of the initiators. The degradation could start from "weak" units of the chain, primarily from the units with abnormal (head-to-head) structure formed by recombination of macroradicals under conditions of PAA preparation. The presence of such abnormal units in PAA macromolecules was confirmed in [52]. The radical R$^\bullet$ abstracts an H atom from the polymer chain, which, at low polymer concentration in solution, results in cleavage of C–C bonds in the backbone [53, 54].

The chain degradation of PAA under the action of radicals R$^\bullet$ can be represented as follows:

Chain initiation:

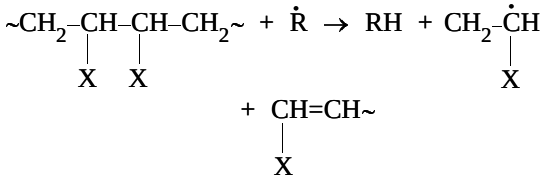

Chain propagation:

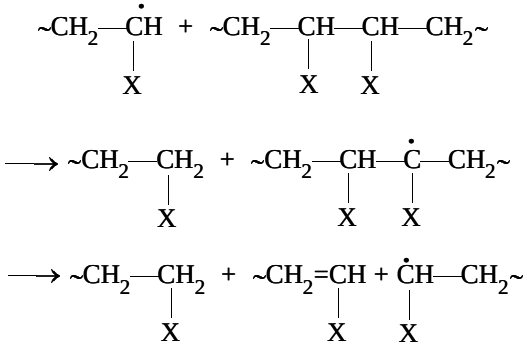

Chain transfer:

intermolecular

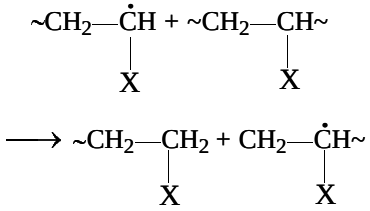

intramolecular

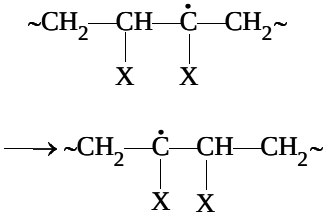

Chain termination:

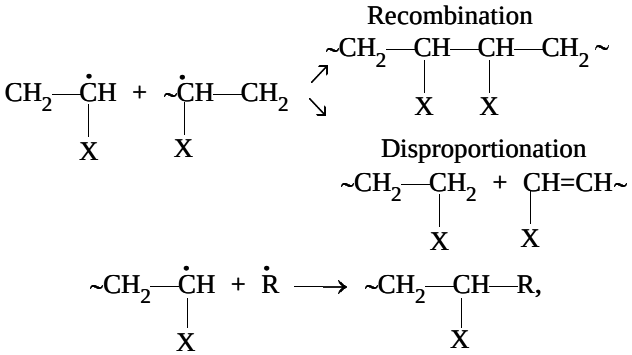

where X = –$CONH_2$.

For simplicity sake, the fact that PAA degradation can be initiated by different radicals (e.g., sulfate radical ions $SO_4^{\bullet}$ or $OH^{\bullet}$ radicals formed by decomposition of PP in water) is not reflected in the scheme. According to the scheme, degradation of PAA under the action of radical initiators is random.

Figure 2 shows that all the initiators used cause active degradation of PAA chains and allow $\overline{M}_\eta$ of the polymer to be decreased to a widely varied level. For example, after degradation for 4 h under the action of PP, the $\overline{M}_\eta$ of PAA decreases by more than an order of magnitude: from 5.3×10^6 to 0.2×10^6 (Fig. 2, curve *4*).

As the initiator concentration is increased in the range [PP] = 1–7% (relative to PAA), $\overline{M}_\eta$ decreases, because degradation becomes more active (Fig. 3). From data in Fig. 3, we can determine the number of breaks α per macromolecule:

$$\alpha = [(\overline{M}_\eta)_0/(\overline{M}_\eta)_t] - 1,$$

where $(\overline{M}_\eta)_0$ is the initial molecular weight of PAA before degradation, and $(\overline{M}_\eta)_t$ is the PAA molecular weight after degradation for time t.

Variation of α in the course of PAA degradation is shown in Fig. 4; α grows with increasing concentration of the degradative agent and degradation time. However, α does not exceed 0.5 in 4 h, which rules out formation of low-molecular-weight products. The absence of noticeable depolymerization was confirmed by gravimetric analysis. As shown in [55, 56], the initial MWD of the polymer can be quickly and reliably estimated from the data on degradation kinetics. Using this approach, we determined the MWD width for the initial PAA sample from data in Fig. 4:

$$D = \overline{M}_w/\overline{M}_n,$$

where $\overline{M}_w$ and $\overline{M}_n$ are, respectively, the weight-average and number-average molecular weights.

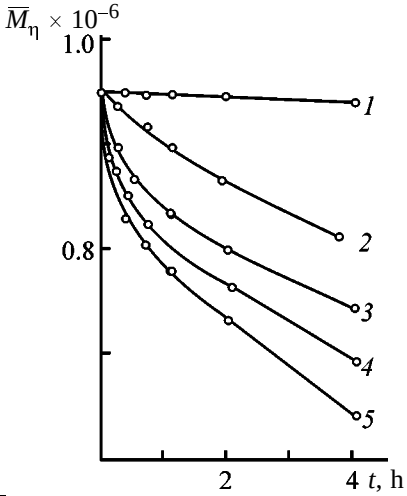

Fig. 3. $\overline{M}_\eta$ as a function of time t in degradation of PAA (initial $\overline{M}_\eta = 0.95 \times 10^6$) in the presence of various concentrations of PP initiator. [PP]/[PAA], %: (*1*) 0, (*2*) 1, (*3*) 3, (*4*) 5, and (*5*) 7.

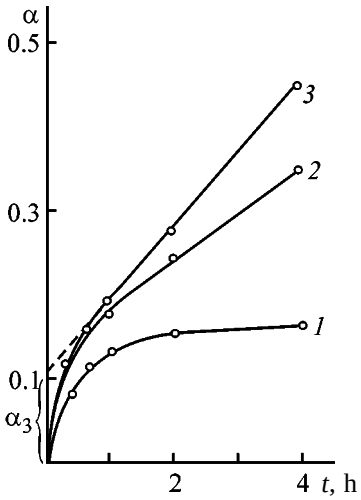

Fig. 4. Number of breaks α per macromolecule as a function of time t in degradation of PAA (initial $\overline{M}_\eta = 0.95 \times 10^6$). [PP]/[PAA], %: (*1*) 1, (*2*) 5, and (*3*) 7.

According to [55, 56], D is determined by

$$D = 2\alpha + 2,$$

where α is the mean length of portions intercepted on the ordinate by the tangents to the curves in Fig. 4. The quantity D found for PAA with $\overline{M}_\eta = 0.95 \times 10^6$ is 2.3, i.e., it somewhat exceeds the most probable value of 2 [5]. In a similar way, we determined D for the PAA sample with $\overline{M}_\eta = 6.3 \times 10^6$; it appeared to be equal to 3.1. Thus, the MWD of the initial PAA sample with $\overline{M}_\eta = 6.3 \times 10^6$ is broader than that of the sample with $\overline{M}_\eta = 0.95 \times 10^6$. The increased polydispersity of PAA with respect to MW was also revealed by light scattering [57, 58] and other methods for estimating MWD [20].

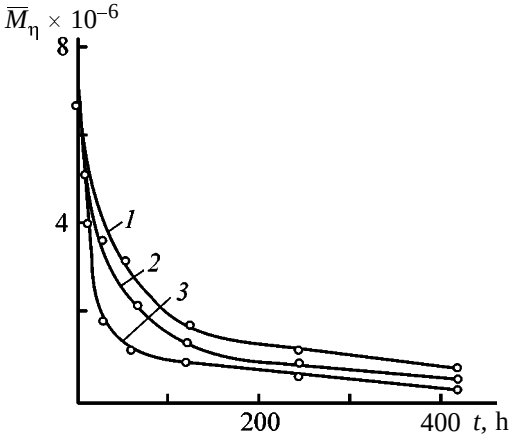

Fig. 5. $\overline{M}_\eta$ of AA–Na-AA copolymers as a function of degradation time *t*. [PP]/[Copolymer] = 1.5%; the same for Fig. 6. Content of Na-AA units, mol %: (*1*) 7, (*2*) 29, and (*3*) 39.

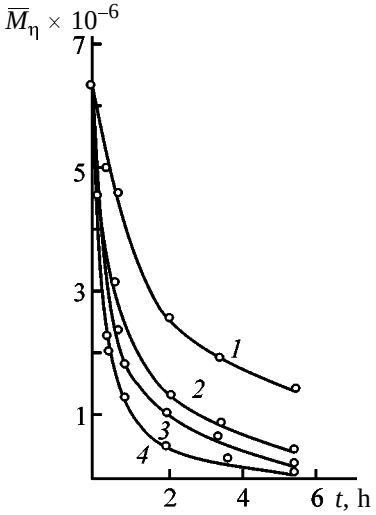

Fig. 6. $\overline{M}_\eta$ of AA–Na-AA copolymers (13 mol % Na-AA units) as a function of degradation time *t* at various NaCl concentrations. [NaCl]/[Copolymer], %: (*1*) 0, (*2*) 1, (*3*) 5, and (*4*) 50.

The difference between the molecular characteristics ($\overline{M}_\eta$ and MWD) of the PAA samples is reflected in their degradation rates. Under equal conditions, PAA with $\overline{M}_\eta = 6.3 \times 10^6$ degrades faster than the sample with $\overline{M}_\eta = 0.95 \times 10^6$ [50]. This is due to the presence in longer macromolecules of the larger number of "weak" units as sites of probable chain break; this result is well consistent with the general trends in chain degradation of polymers [6].

One of the factors promoting degradation of polymers is heating. Increasing temperature in the range 40–70°C accelerates degradation of PAA in aqueous solutions under the action of PP [50] owing to faster decomposition of the initiator. As a result, $\overline{M}_\eta$ of PAA appreciably decreases.

Thus, it is feasible to control $\overline{M}_\eta$ of commercial PAA by partial degradation of the polymer in aqueous solutions under the action of radical degradative agents (e.g., PP, ammonium peroxosulfate, H_2O_2–$FeSO_4$). The extent of degradation grows with increasing initiator concentration, $\overline{M}_\eta$ of the initial polymer, and degradation temperature and time.

Degradation of acrylamide–sodium acrylate copolymers. Specific features of degradation of AA–Na-AA copolymers

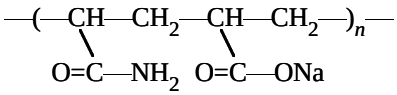

were studied in aqueous [59] and aqueous-salt [60, 61] solutions. Degradation was performed in 0.1 and 0.4% solutions at 40–70°C in the presence of PP (0.5–5 wt % relative to the copolymer). Copolymers of various compositions were prepared by base hydrolysis of PAA]62]; $\overline{M}_\eta$ was determined by the Mark–Kuhn–Houwink equation $[\eta] = K\overline{M}_\eta^\alpha$, and $[\eta]$ was measured in 0.5 M NaCl at 25°C. The constants K and α varied depending on the content of Na-AA units; their values were taken from [63]. The content of Na-AA units was determined by potentiometric titration [64]; analysis of technical-grade polymer in natural water was performed according to [65].

Variation of $\overline{M}_\eta$ of AA–Na-AA copolymers with degradation time is shown in Fig. 5. The chosen conditions allowed $\overline{M}_\eta$ of all the copolymer samples to be varied in a wide range.

To find how the conformational state of the copolymer macromolecules affects their degradation, the reaction was performed in aqueous-salt solutions [60, 61]. Addition of low-molecular-weight salts alters electrostatic interactions of the ionic group of the copolymer and allows the effective size of macromolecular globules to be varied in a wide range. It was found that the degradation accelerates with increasing NaCl concentration (Fig. 6). The $\overline{M}_\eta$ varied in a range covering 1.5–2 orders of magnitude. Similar results were obtained in the presence of KCl, LiCl, and CH_3COONa. The effect of salts on degradation is associated with variation of the solution ionic strength μ. With increasing μ, the acrylate ions in the macromolecular chain become shielded with Na^+ ions to a greater extent. As a result, according to viscometric data, the reduced viscosity η_{sp}/c of solutions of AA–Na-AA copolymers decreases. The intrinsic viscosity $[\eta]$ and the root-mean-square size of macromolecular globules $\langle r^2\rangle^{1/2}$ vary in parallel, as follows from the Flory equation $[\eta] = \Phi\langle r^2\rangle^{3/2}/\overline{M}$.

A decrease in $\langle r^2 \rangle^{3/2}$ and weakening of electrostatic repulsion between the fixed charges in the chain and the $SO_4^{\bullet}$ radical ions generated by decomposition of PP and initiating degradation resulted in acceleration of the copolymer degradation with increasing μ.

At low concentration of the added salts (1 wt % relative to the copolymer), $\overline{M}_\eta$ of degraded AA–Na-AA copolymer (29 mol % Na-AA units) increased in the order $K^+ < Na^+ < Li^+$ [60]. According to published data for polyacrylic acid [66–69] and copolymers of AA with acrylic acid salts [70], the degree of cation binding with the polyanions decreases in the order $K^+ > Na^+ > Li^+$. Therefore, the electrostatic repulsion between the acrylate ion and the $SO_4^{\bullet}$ radical ions grows in going from K^+ to Li^+, which weakens the degradation of the copolymer. The nature of the salt anion also affects the copolymer degradation. Namely, with NaCl $\overline{M}_\eta$ decreases to a considerably greater extent than with CH_3COONa added in the same concentration [61].

Figure 7 shows how $\overline{M}_\eta$ of AA–Na-AA copolymers degraded for various times depends on the content of Na-AA units. The curves pass through a maximum at 13 mol % Na-AA units. Apparently, in this case an optimal combination of the charge density, flexibility, and $\langle r^2 \rangle^{1/2}$ is attained. Figure 7 also shows that, as the degradation time is made longer, the maximum becomes less pronounced (going from curve *1* to curve *4*). Presumably, the above effect is leveled out by more efficient degradation of long macromolecules.

In [71] we studied degradation of partially hydrolyzed PAA in 0.4% aqueous solutions under the action of PP (5 wt % relative to the polymer) at 50°C. The degradation performed for 4 h resulted in 3.5- and 2.3-fold decreases in $\overline{M}_\eta$ of the polymers with the degree of hydrolysis of 16.2 and 42.0 mol %, respectively.

A combination of PAA hydrolysis and degradation also deserves attention as a way to control $\overline{M}_\eta$ of partially hydrolyzed PAA [62, 72]. The reaction was performed in 2.4% aqueous solutions of PAA with $\overline{M}_\eta = 3 \times 10^6$ in the presence of alkali and PP at 30–70°C. An increase in the PP concentration had no effect on hydrolysis but caused a decrease in $\overline{M}_\eta$ due to degradation of the macromolecules. The influence of the NaOH concentration on the process is illustrated by Fig. 8. In the absence of NaOH, no hydrolysis occurs (curve *1*), and an increase in the NaOH concentration accelerates hydrolysis (curves *2*–*4*). Degradation is also intensified owing to acceleration of PP decomposition (curves *1*'–*3*'). Heating affects

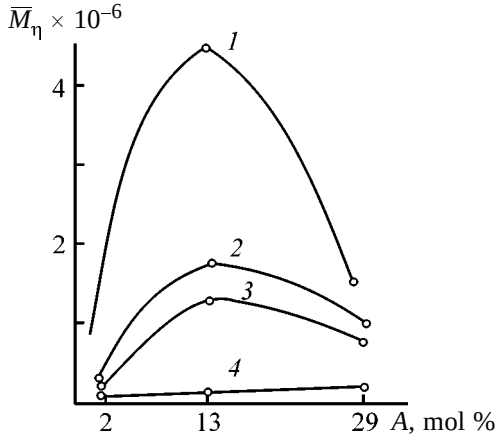

Fig. 7. $\overline{M}_\eta$ of degraded AA–Na-AA copolymers as a function of the content of Na-AA units *A*. [Copolymer] = 0.1%; content of PP and KCl 1.5 wt % relative to copolymer; 50°C. Degradation time, min: (*1*) 20, (*2*) 115, (*3*) 200, and (*4*) 320.

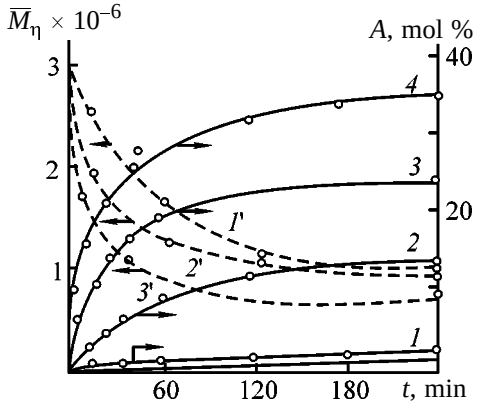

Fig. 8. (*1*–*4*) Content of Na-AA units *A* in AA–Na-AA copolymer and (*1*'–*3*') $\overline{M}_\eta$ as functions of time *t* of hydrolysis of PAA at 60°C in the presence of NaOH. [PAA] = 0.343 base mol l^{-1}; [PP] = 0.033 wt % relative to PAA. [NaOH], M: (*1*, *1*') 0, (*2*) 0.12, (*3*, *2*') 0.44, and (*4*, *3*') 0.73.

the degradation similarly. Thus, it is feasible to prepare partially hydrolyzed PAA with both $\overline{M}_\eta$ and composition being controlled.

A promising and relatively accessible procedure for controlling MW of polymers is ultrasonic degradation (USD) in solution [73, 74]. Myagchenkov and Krikunenko [75] applied ultrasonic treatment to control MW and MWD of partially hydrolyzed PAA in aqueous solutions. They found that USD of partially hydrolyzed PAA ($\overline{M}_\eta = 5.4 \times 10^6$, 18.1 mol % Na-AA units) can decrease MW by more than an order of magnitude, with the average composition and compositional heterogeneity of the samples remaining constant. The molecular characteristics of the degradation products, determined by GPC, are listed in Table 2 [75]. It is seen that $\overline{M}_n$, $\overline{M}_w$, and $\overline{M}_z$ decrease in the course of degradation, both in the absence and in the

Table 2. Molecular characteristics of samples of partially hydrolyzed PAA degraded under ultrasonic treatment in aqueous and aqueous-salt solutions* ($\overline{M}_\eta = 5.4 \times 10^6$, 18.1 mol % Na-AA units)

t, s	[NaCl], M	$\overline{M}_\eta \times 10^{-3}$	$\overline{M}_w \times 10^{-3}$	$\overline{M}_z \times 10^{-3}$	$U = (\overline{M}_w)/(\overline{M}_n) - 1$
60	0	119.6	263.6	449.0	1.21
60	0.5	153.2	298.8	482.5	0.95
100	0	43.7	84.4	139.8	0.93
100	0.002	49.8	100.6	172.4	1.02
100	0.05	100.4	178.5	272.6	0.78
100	0.5	103.6	187.7	288.9	0.79
600	0	20.3	45.0	80.1	1.22
600	0.5	44.6	87.6	137.9	0.97

* (*t*) Degradation time; ($\overline{M}_z$) *z*-average MW.

presence of 0.5 M NaCl. According to Table 2, the Schulz parameter of the samples decreases in the course of degradation, approaching the theoretical value $U = 1$, which suggests random degradation [5, 50], The MWD curves and the values of $\overline{M}_n$, $\overline{M}_w$, and $\overline{M}_z$ (for t = const) show that the USD efficiency decreases with increasing μ (adding NaCl). The quantities [η] and $\overline{M}_\eta$ (viscometric data) vary similarly. The lower degree of degradation is due to smaller $\langle r^2 \rangle^{1/2}$, which is confirmed by viscometric analysis of hydrolyzed PAA in aqueous-salt solutions. In contrast to the hydrolyzed polymer, additions of NaCl exert no noticeable effect on $\langle r^2 \rangle^{1/2}$ in solution of nonhydrolyzed PAA; therefore, with this polymer, USD is not noticeably influenced by μ [75].

Degradation of copolymers of acrylamide with potassium *p*-styrenesulfonate. Degradation of copolymers of AA with potassium *p*-styrenesulfonate (K-SSA)

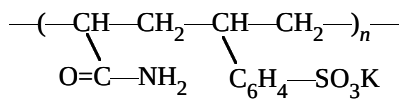

was performed in 0.4% aqueous solutions in the presence of PP in a helium atmosphere at 50°C [76, 77]. The results show that it is feasible to control MW of the copolymers of various compositions within a wide range (covering an order of magnitude), with the chemical composition of the macromolecules being preserved. According to data on degradation of sodium poly-*p*-styrenesulfonate [78], macromolecules of AA–K-SSA copolymer can be randomly cleaved at both acrylamide and styrenesulfonate units. The MW can be decreased by increasing the PP concentration and degradation temperature and time. Figure 9 demonstrates as an example the influence of temperature on degradation of AA–K-SSA copolymers. As the temperature is increased from 30 to 60°C, [η] decreases (with [PP] and *t* being the same), which is apparently due to faster decomposition of the initiator.

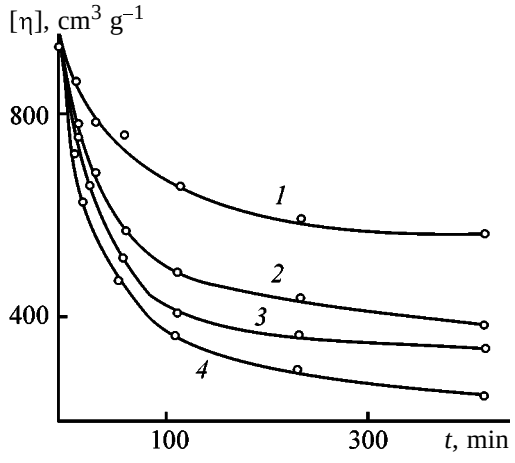

Fig. 9. Plot of [η] vs. time *t* of degradation of AA–K-SSA copolymer (8.4 mol % K-SSA units) at (*1*) 30, (*2*) 40, (*3*) 50, and (*4*) 60°C. [PP] = 1.5 wt % relative to copolymer.

Degradation of copolymers of acrylamide with sodium 2-acrylamido-2-methylpropanesulfonate. The degradation of copolymers of AA with the sodium salt of another strong acid, 2-acrylamido-2-methylpropanesulfonic acid (Na-AMS)

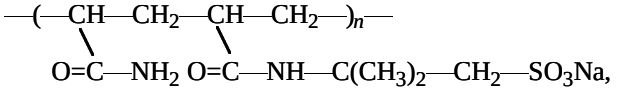

was studied in [79]. As shown by viscometry, PP-initiated degradation in 0.4 and 0.5% solutions at 40 and 50°C yields shorter macromolecules as compared to the initial sample. The intrinsic viscosity [η] of AA–Na-AMS copolymers of various compositions can be controlled by varying the PP concentration and the degradation temperature and time.

Degradation of copolymers of acrylamide with (acrylamidopropyl)trimethylammonium chloride. Copolymers of AA with (acrylamidopropyl)trimethylammonium chloride (APTMAC)

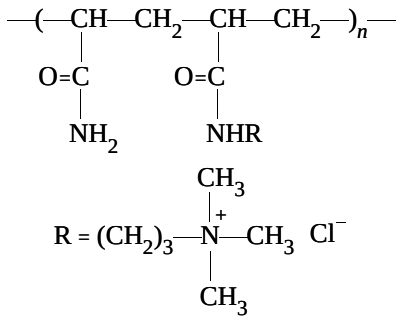

with controlled MW were prepared by degradation in 0.1% solutions initiated by hydrogen peroxide and PP (30–50°C), or by persulfate–bisulfite redox system (25°C) [80]. The characteristics of the initial copolymers are listed in Table 3. The performance of these initiators in copolymer degradation is characterized by a significant decrease in [η]. The degradation is promoted by increasing concentration of degradative agents and in going from H_2O_2 to PP, and also by increasing temperature. Sample B, similar in composition to sample C but having higher initial MW (Table 3), degrades to a greater extent, which is consistent with published data [6].

The influence of the concentration of the AA–APTMAC copolymer (33 mol % ionic units) on its degradation is illustrated in Fig. 10. In the tested concentration range, [η] appreciably decreases with increasing degradation time. In more concentrated copolymer solutions, the degradation is less pronounced. This may be due to increased viscosity, which hinders diffusion of the active species.

Figure 11 shows the plots of [η] vs. degradation time for PAA (sample A, curve *1*), AA–APTMAC copolymer (sample B, curve *2*), and AA–Na-AA copolymer (sample D, curve *3*). Experimental data were obtained under identical degradation conditions for the polymers having approximately equal initial intrinsic viscosities [η]; the content of ionic units in the copolymers was also approximately equal (Table 3). Figure 11 shows that the degradation rate decreases in the order PAA > AA–APTMAC copolymer > AA–Na-AA copolymer. The faster degradation of the AA–APTMAC copolymer, compared to AA–Na-AA copolymer, may be due to electrostatic attraction between the $SO_4^{\bullet-}$ radical ions and the cationic units of the AA–APTMAC macromolecule, whereas in the AA–Na-AA macromolecule the $SO_4^{\bullet-}$ radical ions are repelled from the negatively charged ionic units.

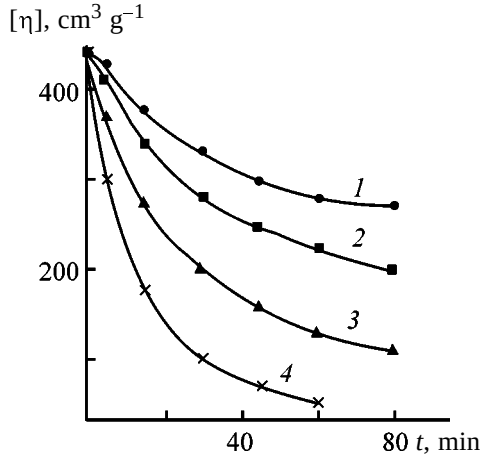

Fig. 10. Plot of [η] vs. degradation time *t* for aqueous solutions of AA–APTMAC copolymer (33 mol % APTMAC units) of various concentrations c_p at 50°C, [PP] = 0.06% (in water). c_p, %: (*1*) 0.5, (*2*) 0.4, (*3*) 0.3, and (*4*) 0.1.

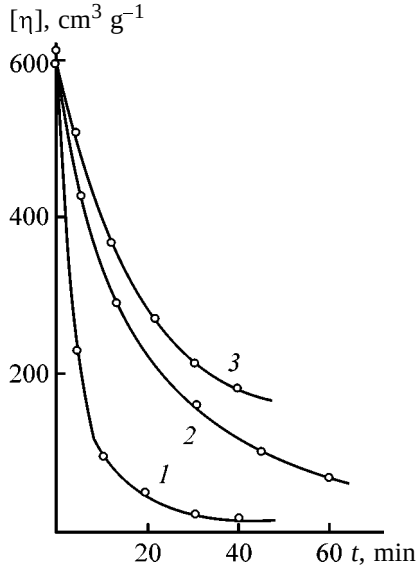

Fig. 11. Plot of [η] vs. degradation time *t* for aqueous solutions of (*1*) PAA, (*2*) AA–APTMAC copolymer, and (*3*) AA–Na-AA copolymer at 50°C. c_p = 0.1 and [PP] = 0.04% (in water).

Table 3. Characteristics of PAA and of AA–APTMAC and AA–Na-AA copolymers

Sample	[η], $cm^3\ g^{-1}$	Content of indicated units, mol %		
		AA	APTMAC	Na-AA
A	600	100	–	–
B	610	73	27	–
C	440	67	33	–
D	600	72	–	28

Thus, by partial degradation in aqueous solutions, it is feasible to control MW of AA–APTMAC copolymers in a wide range covering an order of magnitude.

To conclude, degradation of PAA and its anionic and cationic derivatives in aqueous solutions in the presence of radical degradative agents at 25–60°C is an efficient, reliable, simple, and accessible method for controlling within a wide range (covering two and more orders of magnitude) the MW of commercial (co)polymers. In the process, the chemical composition of the copolymer macromolecules is not altered. The MW of (co)polymers can be adjusted by varying the nature and concentration of the degradative agent and of low-molecular-weight salts added, the concentration, MW, and chemical composition of the initial (co)polymer, and the degradation temperature and time. These data can be used for preparing (co)polymer samples with the required molecular weight under conditions of (co)polymer application in the stage of solution preparation.

The occurrence of degradation should also be taken into account in copolymerization of AA with ionic monomers in water and aqueous-salt solutions in the presence of radical initiators. Degradation is one of the factors complicating copolymerization of ionic monomers [77, 81, 82] and affecting the kinetic and statistical parameters of radical copolymerization.

The degraded polymers and copolymers of various molecular weights show much promise for practice. For example, degraded AA–Na-AA copolymers (MW 7×10^3–5.4×10^4) can be used in medicine as cryoprotectors in conservation of blood components and other biological objects. Samples of AA–Na-AA copolymers with MW $(1.7–6.2) \times 10^4$ positively affect donor erythrocytes: In aqueous solutions of these copolymers, erythrocytes are fully protected from hemolysis and preserve the initial morphological structure.

AA–Na-AA copolymers with MW 0.75×10^3–9×10^4 show high performance as binders and viscosity stabilizers for suspensions of kaolin, calcium carbonate, and other pigments used in paper production [84].

Degraded AA–K-SSA copolymers ($[\eta]$ = 200–700 $cm^3\ g^{-1}$) show high performance as flocculants for kaolin and ocher suspensions [76]. The sedimentation rate of an ocher suspension with these copolymers is by a factor of 2–4.5 higher than with PAA, and for a kaolin suspension it is higher by a factor of 6–7 [77].

Laboratory and commercial tests confirmed the efficiency of using degraded copolymers of AA with dimethylaminoethyl methacrylate hydrochloride [MW $(0.55–6.54) \times 10^5$] as conducting coatings for cellulose triacetate (CTA) and poly(ethylene terephthalate) (PET) films [85]. The electrical conductivity of coatings based on the copolymer exceeds by 7–8 orders of magnitude that of uncoated PET films and by 5–6 orders of magnitude that of uncoated CTA films. The half-time of charge leakage $\tau_{1/2}$ from uncoated PET and CTA films exceeds 120 s, and for the coated films it is less than 1 s. The films not only impart high conductivity to PET and CTA films, but also make their surface lustrous.

Degraded AA–APTMAC copolymers (27 mol % ionic units, $[\eta]$ = 90–200 $cm^3\ g^{-1}$), depending on the copolymer concentration c_p, can act as effective coagulants and stabilizers of kaolin suspensions. For example, with respect to a 0.25% kaolin suspension, the copolymer with $[\eta]$ = 90 $cm^3\ g^{-1}$ behaves as a coagulant at $c_p < 15$ mg l^{-1} and as a stabilizer at $c_p >$ 15 mg l^{-1}. As compared to a mineral coagulant (aluminum sulfate), the organic coagulant (copolymer) ensures a 3.5 times higher coagulating effect at 3–5 times lower concentrations. The efficiency of sedimentation of kaolin suspensions increases when the organic coagulant is used in a combination with a flocculant, AA–Na-AA copolymer ($\overline{M}_\eta = 4.6 \times 10^6$, 11 mol % Na-AA units).

REFERENCES

1. Halverson, F. and Panzer, H.P., in *Kirk–Othmer Encyclopedia of Chemical Technology*, New York: Wiley, 1980, 3rd ed., vol. 10, pp. 489–505.
2. *Poliakrilamid* (Polyacruylamide), Kurenkov, V.F., Ed., Moscow: Khimiya, 1992.
3. Kurenkov, V.F. and Myagchenkov, V.A., in *Polymeric Materials Encyclopedia*, Boca Raton, FL: CRC, 1996, vol. 1, pp. 47–54.
4. Kurenkov, V.F., in *Handbook of Engineering Polymeric Materials*, Morganville, NJ: Dekker, 1997, ch. 3, pp. 61–72.
5. Berlin, A.A., Vol'fson, S.A., and Enikolopyan, N.S., *Kinetika polimerizatsionnykh protsessov* (Polymerization Kinetics), Moscow: Khimiya, 1978.
6. Grassie, N. and Scott, G., *Polymer Degradation and Stabilisation*, Cambridge: Cambridge Univ., 1985.
7. Plate, N.A., Litmanovich, A.D., and Noa, O.V., *Makromolekulyarnye reaktsii* (Macromolecular Reactions), Moscow: Khimiya, 1977.
8. MacWilliams, D.C., *Functional Monomers*, Vacum, R.H. and Nyguist, E.B., Eds., New York: Dekker, 1973, vol. 1, pp. 1–197.

9. Narkis, N. and Rebhuhn, M., *Polymer*, 1966, vol. 10, no. 6, pp. 507–514.
10. Shyluk, W.P. and Stow, F.S., *J. Appl. Polym. Sci.*, 1969, vol. 13, pp. 1023–1034.
11. Gardner, K.L., Murphy, W.R., and Geehan, T.G., *J. Appl. Polym. Sci.*, 1978, vol. 22, pp. 881–893.
12. Haas, H.C. and MacDonald, R.L., *J. Polym. Sci., Polym. Lett. Ed.*, 1972, vol. 10, pp. 461–467.
13. Recasens, F. and Subirana, J.A., in *IUPAC Int. Symp. on Macromolecular Chemistry*, Madrid, 1974, vol. 1, pp. 466–475.
14. Darscus, R.L., Jordan, D.O., Kurucsev, T., *et al.*, *J. Polym. Sci., Part A-3*, 1965, pp. 1941–1954.
15. Alfrey, T., Fuoss, R.M., Morawetz, H., *et al.*, *J. Am. Chem. Soc.*, 1952, vol. 74, pp. 438–442.
16. Chemelir, M., Kunschner, A., and Barthell, E., *Angew. Makromol. Chem.*, 1980, vol. 89, pp. 145–153.
17. McNeill, I.C. and Zulfigar, M., *J. Polym. Sci., Polym. Chem. Ed.*, 1978, vol. 16, pp. 2465–2474.
18. Montgomery, W.H., *Water Soluble Resins*, Davidson, R.L. and Sittig, M., Eds., New York: Reinhold, 1968, pp. 175–184.
19. Korotkina, O.Z., Magdinets, V.V., Savitskaya, M.N., *et al.*, *Zh. Prikl. Khim.*, 1965, vol. 38, no. 11, pp. 2533–2537.
20. Kulicke, W.-M. and Klein, J., *Angew. Makromol. Chem.*, 1978, vol. 69, pp. 189–195.
21. Kulicke, W.-M. and Kniewske, R., *Makromol. Chem.*, 1980, vol. 181, pp. 823–836.
22. Kulicke, W.-M., Kniewske, R., and Klein, J., *Prog. Polym. Sci.*, 1982, vol. 8, no. 4, pp. 373–468.
23. Nakonechnyi, I.I., Baiburdov, T.A., and Kurenkov, V.F., *Zh. Prikl. Khim.*, 1991, vol. 64, no. 5, pp. 1062–1065.
24. Catherin, G. and Marchal, Y., *Rev. Inst. Franc Petrole*, 1979, vol. 34, no. 5, pp. 719–732.
25 Voigt, J., *Die Stabilisierung der Kunststoffe gegen Licht und Wärme*, Berlin: Springer, 1966.
26. Haas, H.C., MacDonald, R.L., and Schuler, A.N., *J. Polym. Sci., Part A-1*, 1970, vol. 8, pp. 3405–3414.
27. Alexander, P. and Charlesby, A., *J. Polym. Sci.*, 1957, vol. 23, pp. 355–362.
28. Gareishina, A.Z., Yayus, L.I., Gazizov, A.Sh., *et al.*, *Neftepromysl. Delo Transport. Nefti*, 1984, no. 8, pp. 17–19.
29. Prazdnikov, Z.F., Veber, V.I., and Kostyuk, T.V., *Neftepromysl. Delo Transport. Nefti*, 1985, no. 6, pp. 61–63.
30. Nagashiro, W. and Tsunoda, T., *J. Appl. Polym. Sci.*, 1977, vol. 21, no. 4, pp. 1149–1153.
31. Povkh, I.L., Makogon, B.P., Stupnikova, T.V., *et al.*, *Dopov. Akad. Nauk Ukr. RSR, Ser. B: Geol., Khim. Biol. Nauki*, 1986, no. 10, pp. 31–33.
32. Makogon, B.P. and Smetankina, V.I., *Vysokomol. Soedin.*, 1988, vol. 30, no. 7, pp. 542–545.
33. Makogon, B.P., Smetankina, V.I., and Bondarenko, T.A., *Izv. Vyssh. Uchebn. Zaved., Khim. Khim. Tekhnol.*, 1989, vol. 32, no. 4, pp. 92–95.
34. Klenin, S.I., Lyubina, S.Ya., Baranovskaya, I.A., *et al.*, *Vysokomol. Soedin., Ser. A*, 1990, vol. 32, no. 2, pp. 439–444.
35. Farinato, R. and Yen Wei, S., *J. Appl. Polym. Sci.*, 1987, vol. 33, no. 7, pp. 2353–2368.
36. Henglein, A., *Makromol. Chem.*, 1954, vol. 14, pp. 15–24.
37. Myagchenkov, V.A., Krikunenko, O.V., and Churikov, F.I., *Ul'trazvukovaya destruktsiya vodorastvorimykh (so)polimerov* (Ultrasonic Degradation of Water-Soluble (Co)polymers), Kazan: Kazan. Gos. Tekhnol. Univ., 1998.
38. Hashemzadeh, A. and Kulicke, W.-M., *Chem. Eng. Technol.*, 1986, vol. 58, no. 4, pp. 325–327.
39. Klein, J. and Westerkamp, A., *J. Polym. Sci., Polym. Chem. Ed.*, 1981, vol. 19, pp. 507–512.
40. Knight, B.L., *Am. Inst. Chem. Eng. Symp. Ser.*, 1973, vol. 69, no. 127, pp. 40–42.
41. Muller, G., *Polym. Bull.*, 1981, vol. 5, pp. 31–38.
42. Muller, G., *Polym. Bull.*, 1981, vol. 5, pp. 39–45.
43. Suzuki, J., Iizuka, S., and Suzuki, S., *J. Polym. Sci.*, 1978, vol. 22, pp. 2109–2117.
44. Morooka, S., Ikemizu, K., and Kato, Y., in *Proc. 3rd Pacific Chemical Engineering Congr.*, Seoul, May 8–11, 1983, vol. 4, pp. 289–294.
45. Martischius, F.-D. and Heide, W., Abstracts of Papers, *Drug Reduction: 3rd Int. Conf.*, Bristol, July 2–5, 1984, part D9, pp. 1–3.
46. Knight, B.L., *J. Pet. Technol.*, 1973, vol. 25, pp. 618–623.
47. Bhuiyan, A.L., *Polymer*, 1984, vol. 25, no. 12, pp. 1699–1710.
48. Myagchenkov, V.A., Kurenkov, V.F., and Akhmed'yanova, R.A., *Vysokomol. Soedin., Ser. B*, 1984, vol. 26, no. 15, pp. 340–344.
49. Kurenkov, V.F. and Tazieva, E.D., *Zh. Prikl. Khim.*, 1994, vol. 67, no. 7, pp. 1162–1166.
50. *Praktikum po khimii i fizike polimerov* (Practical Course of Polymer Physics and Chemistry), Kurenkov, V.F., Ed., Moscow: Khimiya, 1995, pp. 117–121.
51. Klein, J. and Conrad, K.-D., *Macromol. Chem.*, 1980, vol. 181, pp. 227–234.
52. Arcus, C.L., *J. Chem. Soc.*, 1949, no. 3, pp. 2732–2736.
53. Bresler, S.E., Dolgoplosk, B.A., Krol', V.A., *et al.*, *Zh. Obshch. Khim.*, 1956, vol. 26, no. 8, pp. 2201–2209.

54. Dolgoplosk, B.A., Erusalimskii, B.L., Kuren'gina, T.N., and Tinyakova, E.I., *Izv. Akad. Nauk SSSR, Otd. Khim. Nauk*, 1960, no. 2, pp. 311–316.
55. Berlin, A.A. and Enikolopyan, N.S., *Vysokomol. Soedin., Ser. A*, 1968, vol. 10, no. 7, pp. 1475–1478.
56. Berlin, A.A., Khakimdzhanova, M.A., Karmilova, L.V., and Enikolopyan, N.S., *Vysokomol. Soedin., Ser. A*, 1968, vol. 10, no. 7, pp. 1496–1504.
57. Eskin, V.E., *Rasseyanie sveta rastvorami polimerov* (Light Scattering in Polymer Solutions), Moscow: Nauka, 1973.
58. Myagchenkov, V.A., Kuznetsov, E.V., and Kurenkov, V.F., *Tr. Kazan. Khim.-Tekhnol. Inst.*, 1967, no. 36, pp. 336–340.
59. Kurenkov, V.F., Nagel', M.A., Kosterina, E.N., and Myagchenkov, V.A., in *Khimiya i tekhnologiya elementoorganicheskikh soedinenii i polimerov* (Chemistry and Technology of Organoelement Compounds and Polymers), Kazan: Kazan. Khim.-Tekhnol. Inst., 1984, pp. 34–38.
60. Kurenkov, V.F., Trifonova, M.N., Terent'eva, G.I., and Myagchenkov, V.A., in *Fiziko-khimicheskie osnovy sinteza i pererabotki polimerov* (Physicochemical Principles of Polymer Synthesis and Processing), Gor'kii: Gor'k. Gos. Univ., 1987, pp. 74–78.
61. Kurenkov, V.F., Trifonova, M.N., Kropotova, N.A., and Myagchenkov, V.A., in *Khimiya i tekhnologiya elementoorganicheskikh soedinenii i polimerov* (Chemistry and Technology of Organoelement Compounds and Polymers), Kazan: Kazan. Khim.-Tekhnol. Inst., 1987, pp. 106–112.
62. Kurenkov, V.F., Hartan, H.-G., and Lobanov, F.I., *Zh. Prikl. Khim.*, 2001, vol. 74, no. 4, pp. 529–540.
63. Klein, J. and Conrad, K.-D., *Macromol. Chem.*, 1978, vol. 179, no. 6, pp. 1635–1639.
64. Kurenkov, V.F., Baiburdov, T.A., and Stupen'kova, L.L., in *Fiziko-khimicheskie osnovy sinteza i pererabotki polimerov* (Physicochemical Principles of Polymer Synthesis and Processing), Gor'kii: Gor'k. Gos. Univ., 1985, pp. 79–86.
65. Churikov, F.I., Snigirev, S.V., and Kurenkov, V.F., *Zavod. Lab., Diagn. Mater.*, 1998, no. 6, pp. 9–10.
66. Wall, F.T. and Doremus, R.H., *J. Am. Chem. Soc.*, 1954, vol. 76, pp. 1557–1561.
67. Crescenzi, V., De Chirico, A., and Ripamonti, A., *Ricenca Sci.*, 1959, vol. 29, no. 7, pp. 1424–1430.
68. Crescenzi, V., De Rosa, V., and Mandarella, D., *Ricenca Sci.*, 1960, vol. 30, no. 11, pp. 1680–1687.
69. Strauss, U.P. and Schlesinger, M.S., *Z. Phys. Chem.*, 1978, vol. 82, no. 5, pp. 571–574.
70. Akhmed'yanova, R.A., Kurenkov, V.F., Kuznetsov, E.V., and Myagchenkov, V.A., *Vysokomol. Soedin.*, 1981, vol. 23, no. 6, pp. 417–421.
71. Kurenkov, V.F., Gerkin, R.V., Ivanov, V.S., and Luk'yanov, V.S., *Izv. Vyssh. Uchebn. Zaved., Khim. Khim. Tekhnol.*, 1998, vol. 41, no. 2, pp. 73–77.
72. Kurenkov, V.F., Baiburdov, T.A., and Stupen'kova, L.L., in *Khimiya i tekhnologiya elementoorganicheskikh soedinenii i polimerov* (Chemistry and Technology of Organoelement Compounds and Polymers), Kazan: Kazan. Khim.-Tekhnol. Inst., 1985, pp. 47–51.
73. Golubev, S.V., Tikhonova, Z.A., Semchikov, Yu.D., and Trubina, I.V., *Vysokomol. Soedin., Ser. A*, 1987, vol. 29, no. 11, pp. 1762–1767.
74. Myagchenkov, V.A., Krikunenko, O.V., Yunusov, O.A., *et al.*, *Dokl. Akad. Nauk SSSR*, 1992, vol. 324, no. 4, pp. 826–830.
75. Myagchenkov, V.A. and Krikunenko, O.V., *Vysokomol. Soedin., Ser. A*, 1995, vol. 37, no. 1, pp. 44–49.
76. Kurenkov, V.F., Orlova, I.B., and Myagchenkov, V.A., *Vysokomol. Soedin., Ser. A*, 1986, vol. 28, no. 6, pp. 1186–1191.
77. Bekturov, E.A., Myagchenkov, V.A., and Kurenkov, V.F., *Polimery i sopolimery stirolsul'fokisloty* (Styrenesulfonic Acid Polymers and Copolymers), Alma-Ata: Nauka, 1989.
78. Myagchenkov, V.A., Kurenkov, V.F., Karachev, N.A., and Frenkel', S.Ya., *Dokl. Akad. Nauk SSSR*, 1976, vol. 226, no. 4, pp. 869–871.
79. Shipova, L.M., Radical Emulsion Copolymerization of Acrylamide with Sodium 2-acrylamido-2-methylpropanesulfonate and Potassium *p*-Styrenesulfonate, *Cand. Sci. Dissertation*, Kazan, 1998.
80. Kurenkov, V.F., Len'ko, O.A., Snigirev, S.V., and Lobanov, F.I., *Zh. Prikl. Khim.*, 2002, vol. 75, no. 7, pp. 1164–1168.
81. Kabanov, V.A. and Topchiev, D.A., *Polimerizatsiya ionizuyushchikhsya monomerov* (Polymerization of Ionizable Monomers), Moscow: Nauka, 1975.
82. Kurenkov, V.F. and Myagchenkov, V.A., *Zh. Prikl. Khim.*, 1999, vol. 72, no. 6, pp. 881–890.
83. Krikunenko, O.V., Ultrasonic Degradation of Random Acrylamide–Sodium Acrylate Copolymers in Aqueous and Aqueous-Salt Solutions, *Cand. Sci. Dissertation*, Kazan, 1996.
84. Nikolaev, A.F. and Okhrimenko, G.I., *Vodorastvorimye polimery* (Water-Soluble Polymers), Leningrad: Khimiya, 1979.
85. Krikunenko, O.V., Galyamov, A.Sh., and Myagchenkov, V.A., *Plast. Massy*, 1996, no. 5, pp. 18–20.

Russian Journal of Applied Chemistry, Vol. 75, No. 7, 2002, pp. 1051–1054. Translated from Zhurnal Prikladnoi Khimii, Vol. 75, No. 7, 2002, pp. 1069–1071.
Original Russian Text Copyright © 2002 by Skripkin, Chernykh, Stepakova, Samokhvalova.

INORGANIC SYNTHESIS AND INDUSTRIAL INORGANIC CHEMISTRY

Effect of Alkali Metal Chlorides on the Solubility in Ternary Water–Salt Systems Containing Copper Monochloride

M. Yu. Skripkin, L. V. Chernykh, L. V. Stepakova, and V. A. Samokhvalova

St. Petersburg State University, St. Petersburg, Russia

Received January 24, 2002

Abstract—Solubility in the systems of CuCl–LiCl–H_2O and CuCl–CsCl–H_2O at 25°C was studied by the method of isothermal removal of oversaturation. The results were examined in terms of the competition between hydration and complex formation processes in water–salt systems.

Copper monohalides find growing application in chemistry and chemical technology. They are used as catalysts for a number of reactions, primarily for radical-cation processes involving aromatic compounds (production of phenol and aniline from aryl halides), reactions of diazo compound (Sandmeyer reaction), isomerization of unsaturated compounds, polymerization of alkynes, oxidation of carbon(II) oxide, etc. However, the efficiency of using these compounds is limited by the low solubility of copper monohalides and consequently by difficult homogenization of the reaction mixture. Therefore, it is urgent to search for ways to solubilize copper(I) compounds.

It is known that a second salt component added to a solution often significantly affects the solubility of the starting compound. Examination of the solubility data for systems containing copper monohalides [1] shows that reliable and consistent experimental data on solution–solid phase equilibria are available only for the CuCl–KCl–H_2O system. Therefore, we have studied systematically the solubility in the CuCl–MCl–H_2O system (M is an alkali metal). Data on the solubility in the CuCl–NaCl–H_2O system at 25°C were published previously [2]. Here we report experimental data on the solubility in the CuCl–LiCl–H_2O and CuCl–CsCl–H_2O systems at 25°C.

We used lithium and cesium chlorides (both ultrapure grade) and copper(I) chloride recrystallized from hydrochloric acid. The solubility was determined by the method of isothermal oversaturation removal. Solutions were heated to completely dissolve the solid phases and then were thermostated for two days at 25 ± 0.1°C with continuous stirring. The experiment was performed in darkened vessels to avoid photoinitiated disproportionation of copper(I).

Samples were treated with nitric acid (ultrapure grade), after which the concentration of copper(II) ions was determined by complexometric titration, and that of chloride ions, by mercurimetric titration. The accuracy of the analyses was ±0.5%. The concentration of the alkali metal chloride was calculated as the difference. The compositions of the solid phases were determined by the Schreinemachers method. The results are shown in the figure and table.

It was shown earlier that the solubility in the

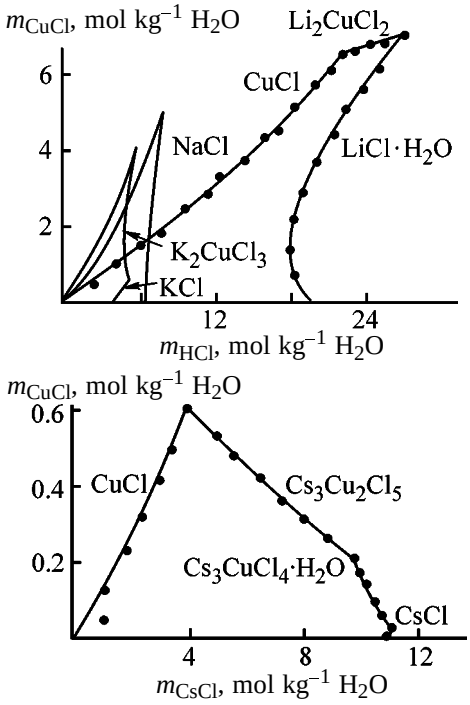

Solubility m_{MCl} at 25°C in the systems CuCl–LiCl–H_2O, CuCl–CsCl–H_2O (data of this work), CuCl–NaCl–H_2O [2], and CuCl–KCl–H_2O [1].

1070-4272/02/7507-1051$27.00 © 2002 MAIK "Nauka/Interperiodica"

Solubility in the systems CuCl–LiCl–H_2O and CuCl–CsCl–H_2O at 25°C

Liquid phase				Solid phase
c, wt %		*m*, mol kg^{-1} H_2O		
CuCl	MCl	CuCl	MCl	
System CuCl–LiCl–H_2O				
0.01	0.00	1.1×10^{-3}	0.00	CuCl
0.76	2.90	0.08	0.71	″
1.17	8.22	0.13	2.14	″
4.37	16.84	0.56	5.04	″
7.83	22.82	1.14	7.76	″
10.81	27.18	1.76	10.34	″
12.74	30.08	2.25	12.41	″
14.34	31.83	2.69	13.95	″
15.95	33.05	3.16	15.29	″
17.89	33.81	3.74	16.51	″
19.93	35.22	4.49	18.53	″
21.50	35.99	5.11	19.97	″
23.13	36.52	5.79	21.35	″
24.57	36.41	6.36	22.01	CuCl + Li_2CuCl_3
24.53	37.41	6.51	23.19	Li_2CuCl_3
24.31	38.59	6.62	24.54	″
24.01	39.85	6.71	26.01	″
24.02	40.77	6.89	27.32	Li_2CuCl_3 + $LiCl \cdot H_2O$
22.68	40.55	6.23	26.01	$LiCl \cdot H_2O$
20.43	40.49	5.28	24.44	″
18.62	40.14	4.56	22.96	″
15.88	39.17	3.65	21.56	″
13.07	38.37	2.99	20.50	″
9.95	37.92	2.24	19.02	″
6.15	40.80	1.17	18.14	″
2.21	43.36	0.41	18.79	″
0.00	45.89	0.00	20.00	″
System CuCl–CsCl–H_2O				
0.01	0.00	1.1×10^{-3}	0.00	CuCl
0.80	9.65	0.09	0.64	″
1.33	19.68	0.17	1.48	″
1.74	24.84	0.24	2.01	″
2.44	32.81	0.38	3.01	″
3.12	37.43	0.53	3.74	″
3.40	39.33	0.60	4.08	CuCl + $Cs_3Cu_2Cl_5$
2.96	40.64	0.53	4.28	$Cs_3Cu_2Cl_5$
2.62	42.29	0.48	4.56	″
1.79	48.01	0.36	5.68	″
1.41	52.59	0.31	6.79	″
1.21	56.57	0.29	7.96	″
0.94	59.46	0.24	8.92	$Cs_3Cu_2Cl_5$
0.79	61.29	0.21	9.60	$Cs_3Cu_2Cl_5$ + $Cs_3CuCl_4 \cdot H_2O$
0.63	61.75	0.17	9.75	$Cs_3CuCl_4 \cdot H_2O$

Table. (Contd.)

Liquid phase				Solid phase
c, wt %		*m*, mol kg^{-1} H_2O		
CuCl	MCl	CuCl	MCl	
0.48	62.58	0.13	10.06	$Cs_3CuCl_4 \cdot H_2O$
0.36	63.29	0.10	10.34	〃
0.21	64.08	0.06	10.66	〃
0.17	64.57	0.05	10.88	$Cs_3CuCl_4 \cdot H_2O$ + CsCl
0.00	64.61	0.00	10.84	CsCl

$CuCl_2$–MCl–H_2O systems is governed by the competition between hydration and complex formation [3]. As the structure-breaking effect of the cation increases, favoring formation of acido complexes, the transition is observed in the binary electrolytes from the branches of $CuCl_2 \cdot 2H_2O$ and MCl (M^+ = Li^+, and Na^+) salting-out to salting-in. In the case of copper monochloride, the stability constants of acido complexes are higher by several orders of magnitude than those for copper(II) (e.g., β_2 is 1.1×10^6 for $CuCl_2^-$ and 26.2 for $CuCl_2$ [4]). Such a strong acido complex formation results in significant salting-in of copper monochloride on adding alkali metal chlorides (see figure). The factors by which the CuCl solubility in ternary systems m_{max} is higher than in the binary solution m_{bin} are given below for various alkali metal chlorides.

Alkali metal chloride	LiCl	NaCl	KCl	CsCl
m_{max}/m_{bin}	5820	4620	3730	550

Acido complex formation is also responsible for salting-in of alkali metal chlorides on adding copper monochloride. However, the competition of hydration and complex formation in the CuCl–LiCl–H_2O system containing the most strongly hydrated lithium cation results in salting-out–salting-in of $LiCl \cdot H_2O$.

The enhancement of acido complex formation under the action of low-hydrated alkali metal cations, repeatedly discussed in the literature [5], affects the shape of the solubility isotherms of these systems. The intensity of salting-in varies in parallel with the structure-breaking effect of cations: $K^+ > Na^+ > Li^+$, whereas the length of the crystallization branches of the pure components (crystal hydrate in the case of lithium chloride) varies in the opposite direction. However, with cesium the pattern is specific: salting-in in the CuCl–CsCl–H_2O system is weaker than in the CuCl–NaCl–H_2O and CuCl–KCl–H_2O systems (a similar behavior was observed in the $CuCl_2$–CsCl–H_2O system, where salting-in was weaker than in the $CuCl_2$–KCl–H_2O system). This may be due to specific features of the complex formation in the systems containing cesium chloride. It was shown earlier [6] that, owing to the strong association of cesium chloride in binary solutions, Cs^+Cl^- ion pairs can participate along with chloride ions as ligands in the complex formation. Such a process would result in peculiar "hydrophobization" of the forming associates (owing to low-hydrated cesium ions) and, consequently, in their stronger salting-out.

Our results and published data show that, in all the systems except CuCl–NaCl–H_2O, complicated solid compounds are formed. In the CuCl–LiCl–H_2O and CuCl–KCl–H_2O systems, M_2CuCl_3 complex salts are formed. The common formula of these compounds and the absence of water of crystallization in the lithium salt suggest the similar mechanism of their formation, involving complexation of copper(I) with chloride ion. A similar type of salts formed in these systems {in contrast to the corresponding systems containing copper(II) [6]} can be explained by stronger acido complex formation, which dominates in almost the whole concentration range. The weaker complex formation in the system with lithium chloride, as compared to the CuCl–KCl–H_2O system, determines the smaller crystallization area of the complex salt and the shift of its formation area toward higher concentrations.

In the CuCl–CsCl–H_2O system, two complex salts are formed: $Cs_3Cu_2Cl_5$ and $Cs_3CuCl_4 \cdot H_2O$. The different (compared to M_2CuCl_3) compositions of these compounds may be due to different mechanisms of their formation (it is likely that the Cs^+Cl^- associate enters into the inner coordination sphere of the complex-forming cation). As for the absence of complexes

in the CuCl–NaCl–H_2O system, its causes were discussed earlier in detail [2].

Thus, our study of the solubility in the CuCl–MCl–H_2O systems showed that addition of alkali metal chloride results in considerable solubilization of copper monochloride. The dependence of solubility on the nature of the second component, which is similar to that observed earlier in the $CuCl_2$–MCl–H_2O systems, is determined by the prevalence of acido complex formation.

ACKNOWLEDGMENTS

This study was financially supported by the Integation Federal Target Program (project no. A-0146) and by the Russian Foundation for Basic Research (project no. 02-03-32729).

REFERENCES

1. *Solubility Data Series*, vol. 46: *Copper(I) Halides and Pseudohalides*, Fritz, J.J. and Königsberger, A., Eds., Oxford: Pergamon, 1997.
2. Stepakova, L.V. and Skripkin, M.Yu., *Zh. Neorg. Khim.*, 1999, vol. 44, no. 2, pp. 325–326.
3. Skripkin, M.Yu. and Chernykh, L.V., *Zh. Neorg. Khim.*, 1994, vol. 39, no. 10, pp. 1747–1751.
4. Sillen, L.G. and Martell, A.E., *Stability Constants of Metal Ion Complexes*, section 1: *Inorganic Ligands*. London: Pergamon, 1971, pp. 163–168.
5. Yakimov, M.A., in *Problemy sovremennoi khimii koordinatsionnykh soedinenii* (Problems of Modern Coordination Chemistry), Leningrad: Leningr. Gos. Univ., 1975, issue 5, pp. 3–21.
6. Chernykh, L.V. and Skripkin, M.Yu., *Koord. Khim.*, 1996, vol. 22, no. 5, pp. 413–416.

Russian Journal of Applied Chemistry, Vol. 75, No. 7, 2002, pp. 1055–1060. Translated from Zhurnal Prikladnoi Khimii, Vol. 75, No. 7, 2002, pp. 1072–1077.
Original Russian Text Copyright © 2002 by Burkov, Sidorov, Sal'nikov, Kryuchkova.

INORGANIC SYNTHESIS AND INDUSTRIAL INORGANIC CHEMISTRY

Competition of Hydrolysis and Complex Formation in the $Cu(NO_3)_2$, (H^+)–$NH_3 \cdot H_2O$–H_2O System

K. A. Burkov, Yu. V. Sidorov, Yu. I. Sal'nikov, and N. A. Kryuchkova

St. Petersburg State University, St. Petersburg, Russia
Kazan State University, Kazan, Tatarstan, Russia

Received November 15, 2001

Abstract—The concentration regions of prevalence of various chemical interactions in the $Cu(NO_3)_2$, (H^+)–$NH_3 \cdot H_2O$–H_2O system were determined by dilatometry, pH-metry, and electronic spectroscopy of solutions and by X-ray phase and gravimetric analyses of precipitates. The adequacy of the model proposed was confirmed by CPESSP calculations.

Occurrence of equilibria (1) in aqueous ammonia solutions suggests that either ammine complexes or mono- and polynuclear hydroxo complexes, and probably mixed hydroxo ammine complexes can be formed in systems metal ion–ammonia–water:

$$NH_3 + H_2O = NH_3 \cdot H_2O = NH_4^+ + OH^-. \quad (1)$$

The hydrolysis and complex formation can compete. Such reactions, which often take place in heterogeneous systems, result in the precipitation of poorly soluble compounds and, in certain cases, in their subsequent dissolution.

It is often difficult to gain insight into the chemical interactions and state of the components in such complicated systems consisting of both solutions and solids. The subject of this work was the $Cu(NO_3)_2$, (H^+)–$NH_3 \cdot H_2O$–H_2O system. The experimental data were obtained dilatometrically. This method allows highly accurate monitoring of changes in the solution volume due to chemical interactions. Also, we used potentiometric titration and electronic absorption spectroscopy of solutions (after thorough filtration to remove precipitates, which, in turn, were studied by chemical and X-ray phase analyses). The data of the dilatometric titration were treated with a simulating CPESSP program.

Hydrolysis and complex formation of copper(II) with ammonia were extensively studied as separate processes. The hydrolysis of copper(II) ions was studied previously in [1] by potentiometric titration with an alkali (NaOH) at a constant ionic strength, and also in [2], with 3.0 M $NaClO_4$ as supporting electrolyte. It was shown that, along with the dominating binuclear complex $Cu_2(OH)_2^{2+}$, the $CuOH^+$ and $Cu_2(OH)^{3+}$ species are formed in solution. Their hydrolysis constants $\log K_h$, equal to -10.93 ± 0.02, -7.4 ± 0.1, and -6.02 ± 0.02, respectively, were determined, and the stability constants $\log\beta$ were calculated in view of $pK_w = 14.09$ found in [3]: 6.69 for $CuOH^+$, 17.25 for $Cu_2(OH)_2^{2+}$, and 8.07 for $Cu_2(OH)^{3+}$. Several authors also detected the trinuclear species $Cu_3(OH)_4^{2+}$. The most probable hydroxo compounds in the solid state are copper hydroxide $Cu(OH)_2$ and also the binuclear complex $Cu_2(OH)_3NO_3$ characteristic of nitrate systems [4].

In solutions of copper ammines, there are only mononuclear complexes $[Cu(NH_3)_n]^{2+}$, n = 1–4 (however, there are also scarce data on the complexes with n 5 and 6). Their step stability constants were determined by many authors [1]. For example, the following values are given in [5]: $\log k_1 = 4.31$, $\log k_2 = 3.67$, $\log k_3 = 3.04$, and $\log k_4 = 2.30$ (thus, $\log\beta_4 = 13.32$ at 18°C in a 2 N solution of ammonium nitrate).

Attempts were made to gain insight into processes occurring under the action of aqueous ammonia solution on the suspension of copper oxide CuO. Gubeli *et al*. [6], when fitting the CuO solubility curve, suggested the presence of a number of species in the system: Cu^{2+}, $Cu(OH)_n^{2-n}$ (n = 2–4), $Cu(NH_3)_n^{2+}$ (n = 2–4), and also $Cu(NH_3)(OH)^+$, $Cu(NH_3)_3(OH)^+$, and $Cu(NH_3)_2(OH)_2$. At the same time, this conclusion seems doubtful, because the well-known existence of binuclear hydroxo complexes was not included in the model.

Comparison of the published data shows that vari-

1070-4272/02/7507-1055$27.00 © 2002 MAIK "Nauka/Interperiodica"

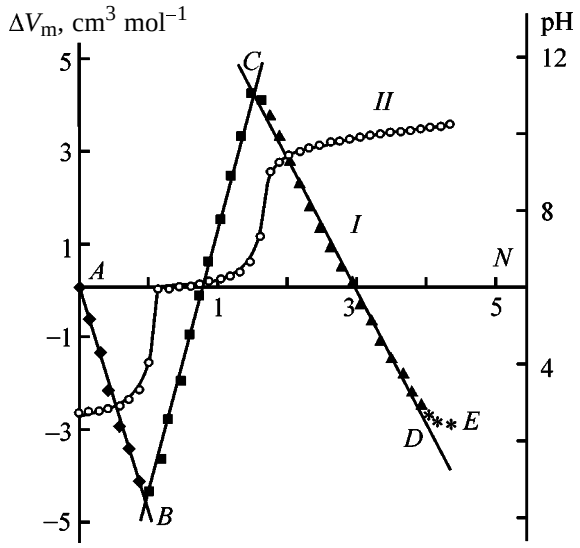

Fig. 1. Curves of (*I*) dilatometric and (*II*) potentiometric titration for the system $Cu(NO_3)_2$, (H^+)–$NH_3 \cdot H_2O$–H_2O. Concentrations, M: copper(II) nitrate 0.091 and ammonia 0.312; ionic strength of solutions 1 M ($NaNO_3$). (ΔV_m) Change in molar volume and (*N*) the number of $NH_3 \cdot H_2O$ moles per mole of Cu(II); the same for Figs. 3 and 5.

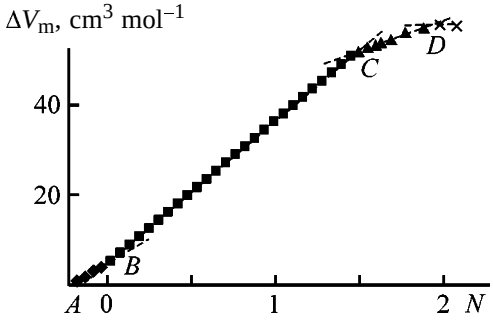

Fig. 2. Dilatometric titration curve for the system $Cu(NO_3)_2$, (H^+)–NaOH–H_2O. Concentrations, M: Cu^{2+} ions 0.228, NaOH 0.330; ionic strength of solutions 1 M ($NaNO_3$). (ΔV_m) Change in the molar volume; N = $[NaOH]/[Cu^{2+}]$.

ous chemical reactions can compete in the system $Cu(NO_3)_2$, (H^+)–$NH_3 \cdot H_2O$–H_2O.

The results of dilatometric and potentiometric titration of copper nitrate solution (with addition of HNO_3 to prevent spontaneous hydrolysis) by an ammonia solution are shown in Fig. 1. The dilatometric curve corresponding to the titration in the system $Cu(NO_3)_2$, (H^+)–NaOH–H_2O, i.e., to the hydrolysis of copper(II) ions without complex formation, is shown in Fig. 2. The dilatometric curves were constructed as the plots of changes in the molar volume ΔV_m ($cm^3\ mol^{-1}$) vs. the number of added moles of a base N per mole of copper ions, N = $[NH_3 \cdot H_2O]/[Cu^{2+}]$ for Fig. 1 and N = $[NaOH]/[Cu^{2+}]$ for Fig. 2.

For more convenient comparison and interpretation, we accepted the starting point of the hydrolysis of Cu^{2+} ions (i.e., point *B*) as the point of zero value of N . Thus, the values $N < 0$ in the beginning of the curve (straight line *AB*) corresponded to the titration region in which the main component [copper(II) ions] yet do not enter into the reaction, and the possible scatter of the starting points *A* in various titration experiments may be due to different amounts of the acid added.

The dilatometric titration curves for such complicated systems as the system under study consist of a number of linear portions, each of which corresponds to various chemical reactions. We have shown earlier [7–9] that the singular points (according to Mendeleev's definition [10]) in the composition–property diagrams correspond to the boundaries of the regions with prevalence of particular types of reactions, depending on *N*. Thus, the change in the solution molar volume ΔV_m for each particular reaction is determined as the slope of the $\Delta V_m = f(N)$ dependence in the dilatometric curve portion under consideration.

A detailed study of the dilatometric titration data for the system $Cu(NO_3)_2$, (H^+)–$NH_3 \cdot H_2O$–H_2O (Fig. 1) in comparison with the data on bulk properties of the system $Cu(NO_3)_2$, (H^+)–NaOH–H_2O (Fig. 2), and also with the data of other methods, allowed us to reveal and interpret the regions of prevalence of the following chemical reactions.

(1) The neutralization of excess nitric acid, which is usually added to the initial solution to prevent the spontaneous hydrolysis of copper(II). The region of the neutralization corresponds to the linear portion *AB* in the dilatometric curves shown in Figs. 1 and 2. A set of facts indicate that specifically neutralization takes place in both systems within boundaries of the *AB* portion. First, point *B* coincides with the calculated equivalence point with respect to the acid. Second, the first equivalence point in the pH-metric curve corresponds to point *B*. Furthermore, after this point, hydroxo compounds start to precipitate.

There is principle difference between the courses of volume changes in neutralization with sodium hydroxide and ammonia aqueous solutions. Reaction (2) involving a strong base and a strong acid (Fig. 2, portion *AB*) is accompanied by an increase in volume

(ΔV_{AB} = 21.06 $cm^3\ mol^{-1}$):

$$NaOH + HNO_3 = H_2O + NaNO_3. \quad (2)$$

The observed positive volume effect agrees well with the published data [9]. The main component of ΔV_{AB} is the partial molar volume of the forming water (V_w = 18.07 $cm^3\ mol^{-1}$ at 25°C). An additional contribution to the volume effect is due to the dehydration of H^+ and OH^- ions and, correspondingly, to their deelectrostriction [11]. Reaction (2) can be written in the ionic form as follows:

$$OH^-_{aq} + H^+_{aq} = H_2O + aq + \Delta V_{AB}, \quad (3)$$

where aq is water in the hydration spheres of ions.

With aqueous ammonia solution (Fig. 1), the pattern of volume changes in the *AB* section is opposite, i.e., the volume of the system decreases. The ΔV_{AB} value for reaction (4) [or (5) in the ionic form] is –4.85 $cm^3\ mol^{-1}$:

$$NH_3 \cdot H_2O + HNO_3 = H_2O + NH_4NO_3, \quad (4)$$

$$NH_{3(aq)} + H^+_{(aq)} = NH^+_{4(aq)}. \quad (5)$$

At first glance, such a difference in the volume effects (as compared to the neutralization with alkali) seems strange, as in both cases water molecules are formed, and dehydration of the acid protons also makes a certain positive contribution. The observed effect is due to specific features of the neutralization with aqueous ammonia (namely, the partial molar volume of the initial ammonia in solution is larger than the partial molar volume of an aquated ammonium ion formed in the reaction [12, 13]).

To confirm additionally the fact that acid is neutralized in the initial stage of the titration (portion *AB*), we titrated a non-acidified solution of copper(II) nitrate with an ammonia solution [the system $Cu(NO_3)_2$–$NH_3 \cdot H_2O$–H_2O]. As expected, the resulting titration curve was similar to the curve under consideration, except for the *AB* portion.

(2) After passing point *B*, a blue precipitate is formed in both systems under consideration, which is accompanied by an increase in volume, suggesting occurrence of a new chemical reaction (Figs. 1 and 2, straight line *BC*) responsible for a sharp change in the molar volume. Point *B* is the starting point for measuring the amount *N* (mol) of a titrant [sodium hydroxide (Fig. 2) or ammonia (Fig. 1)] reacting directly with copper(II). The length of the *BC* section in both cases corresponded to *N* = 1.5 mol. The volume changes describing the *BC* section are ($cm^3\ mol^{-1}$) $\Delta V_{BC}(NaOH)$ = 31.44 and $\Delta V_{BC}(NH_3 \cdot H_2O)$ = 6.04. As found previously for induced hydrolysis of iron(III) ions [8], the hydrolytic polymerization under the action of a strong base is accompanied by an additional positive volume effect, as compared to the first section corresponding to the neutralization of an acid. For the systems under consideration, these additional contributions are as follows ($cm^3\ mol^{-1}$): $\Delta V_{BC}(NaOH)$ – $\Delta V_{AB}(NaOH)$ = 31.44 – 21.06 = 10.38 for NaOH titrant and $\Delta V_{BC}(NH_3 \cdot H_2O)$ – $\Delta V_{AB}(NH_3 \cdot H_2O)$ = 6.04 – (–4.85) = 10.89 for $NH_3 \cdot H_2O$ titrant. This fact allows an important conclusion that, in spite of different nature of the bases in the two titration experiments, the volume effect resulting from the hydrolysis and hydrolytic polymerization remains the same.

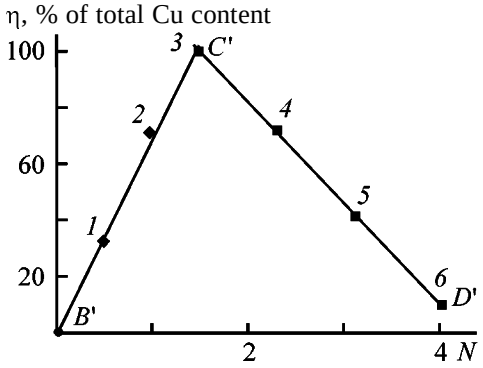

Fig. 3. Plot of the precipitate yield η vs. *N*. *N*: (*1*) 0.5, (*2*) 1.0, (*3*) 1.5, (*4*) 2.3, (*5*) 3.1, and (*6*) 4.0; the same for Fig. 4.

According to X-ray phase analysis, the solid phase is the same in both cases: the known binuclear copper trihydroxonitrate $Cu_2(OH)_3NO_3$. No ammine and mixed hydroxo ammine complexes were detected in the solid phase.

The *B'C'* portion of the plot of the precipitate weight (% of total copper content) vs. *N* in Fig. 3 (in the *B'C'* portion, precipitates were isolated at *N* 0.5, 1.0, and 1.5) is a straight line ascending in parallel to the *BC* portion of the dilatometric curve (Fig. 1). The amount of the precipitate linearly increased, reaching a maximum at *N* = 1.5, i.e., in point *C'*. The electronic absorption spectra (Fig. 4) show that the solutions corresponding to the straight-line portion *BC* of the dilatometric curve contain no Cu(II) ammine complexes (the solutions were prepared by thorough filtration at the same *N* values as the precipitates). The absorption band in the region 600–625 nm, characteristic for copper ammines [14], was absent from the

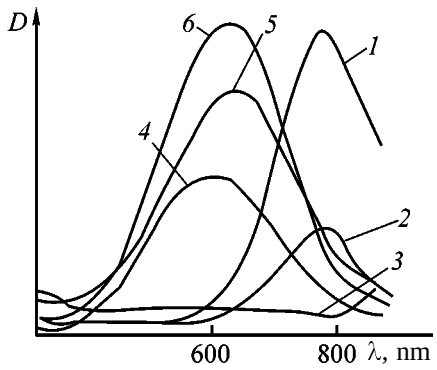

Fig. 4. Electronic absorption spectra of solutions obtained in the system $Cu(NO_3)_2$–$NH_3 \cdot H_2O$–H_2O at various *N* values. (*D*) Optical density and (λ) wavelength.

spectra of solutions corresponding to *N* 0.5, 1.0, and 1.5 (curves *1*, *2*, and *3*, respectively). At the same time, a decrease in the intensity of the absorption band in the region of 800 nm, characteristic for copper(II) aqua complexes [15], was indicative of gradual decrease in the copper amount in the solution. At *N* = 1.5 (singular point *C*), Cu^{2+} ions were almost absent from the solution. Thus, in the range of *N* from 0 up to 1.5 in the system $Cu(NO_3)_2$, (H^+)–$NH_3 \cdot H_2O$–H_2O, the hydrolysis (i.e., interactions also characteristic of the induced hydrolysis under the action of a strong base) prevailed over the formation of ammine complexes.

The following reactions are presumably responsible for the volume changes in the *BC* portions of the dilatometric curves for both systems under consideration:

$$2Cu^{2+} + NO_3^- + 3OH^- = Cu_2(OH)_3NO_3, \quad (6)$$

$$2Cu^{2+} + NO_3^- + 3NH_3 \cdot H_2O = Cu_2(OH)_3NO_3 + 3NH_4^+. \quad (7)$$

Apparently, the hydrolytic transformations described by Eqs. (6) and (7) involve the stages of the formation of copper mono- and polynuclear hydroxo complexes $CuOH^+$, Cu_2OH^{3+}, and $Cu_2(OH)_2^{2+}$, which are precursors of the forming solid phase.

It was shown in [8] that the positive volume effect is due to liberation of water molecules from the hydration shells of the interacting ions upon the hydrolytic polymerization (the molar volume of water in the free state is 18.07 $cm^3\,mol^{-1}$, and in hydration shells of double-charged cations of 3*d* metals it is about 15 [16]). Note that a neutral hydroxo complex was formed from six differently charged species in reaction (6) with liberation of water molecules from the hydration shells of the ions.

The potentiometric titration of the system $Cu(NO_3)_2$, (H^+)–$NH_3 \cdot H_2O$–H_2O (Fig. 1, curve *II*) in the region corresponding to the *BC* portion reveales a slight increase in pH at *N* from 0 to 1.5. The sharp pH increase in the second equivalence point at *N* = 1.5 coincided with singular point *C* in the dilatometric curve. At *N* > 1.5, the pH changed only slightly. Hence, the formation of hydroxo species, with binding of hydroxide ions without noticeable pH change, was complete.

(3) Analysis of the ΔV_{CD}(NaOH) and $\Delta V_{CD}(NH_3 \cdot H_2O)$ values in the *CD* portion (Figs. 1, 2) revealed principal differences in the nature of volume changes and, hence, in chemical reactions in the two systems under consideration (i.e., when sodium hydroxide or aqueous ammonia solution was added). When titrating with sodium hydroxide (Fig. 2), the volume continued to grow up to *N* = 2, with only the value of the volume effect changed [ΔV_{CD}(NaOH) = 13.56 $cm^3\,mol^{-1}$]. The transformations in the system were associated with further hydrolytic reactions whose final solid product was a mixture of copper hydroxide and oxide formed by partial decomposition of $Cu(OH)_2$ (which was also confirmed by X-ray phase analysis). The *CD* portion is located between *N* 1.5 and 2, which apparently corresponds to reaction (8) and parallel partial decomposition (9) of copper hydroxide into copper oxide and water (in the course of the experiment, the precipitate gradually darkens owing to the formation of black copper oxide):

$$Cu_2(OH)_3NO_3 + OH^- = 2Cu(OH)_2 + NO_3^-, \quad (8)$$

$$Cu(OH)_2 = CuO + H_2O. \quad (9)$$

The volume changes are virtually complete in singular point *D* (*N* = 2) owing to the completion of main chemical reactions in the system: after *N* = 2, the titration curve (Fig. 2) flattens out.

At the same time, in titration with aqueous ammonia (Fig. 1), the volume decreased [$\Delta V_{CD}(NH_3 \cdot H_2O)$ = –2.93 $cm^3\,mol^{-1}$], which continued up to *N* = 4.

In the $Cu(NO_3)_2$, (H^+)–$NH_3 \cdot H_2O$–H_2O system, the *CD* section gives one more evidence of competition between the chemical reactions. In contrast to the previous example (titration with alkali), the further titration with ammonia results in the dissolution of the copper hydroxo complex and in its conversion to copper(II) ammines:

$$Cu_2(OH)_3NO_3 + 2nNH_3 \cdot H_2O = 2Cu(NH_3)_n^{2+} + 3OH^- + NO_3^- + 2nH_2O. \quad (10)$$

To examine further changes in m_{Cu} (%), we should note that, according to the plot of the precipitate weight (the precipitates were taken at N 2.3, 3.1, and 4.0) vs. N in the range of N from 1.5 to 4.0 in Fig. 3 (straight line $C'D'$), the precipitate amount decreases, and in poing D' it dissolves almost completely (the course of the dilatometric curve is almost repeated). According to the X-ray phase analysis, the composition of the precipitate $Cu_2(OH)_3NO_3$ remains unchanged in the process. No mixed hydroxo ammine complexes were detected. In the electronic spectra (Fig. 4), instead of the completely disappeaing band at 800 nm, an absorption band appears in the range 600–625 nm (spectra of solutions *4*–*6*), which can be assigned, as mentioned above, to copper ammine complexes.

Thus, the nature of the final solid product of hydrolytic transformations of Cu^{2+} ions in $Cu(NO_3)_2$ solutions depends on the titrating base. In the case of NaOH, it is $Cu(OH)_2$, which is converted to CuO with time and in excess of the base, and, in the case of aqueous ammonia, it is $Cu_2(OH)_3NO_3$, which dissolves in excess ammonia to form copper ammines.

Examining Eq. (10), we can characterize the reaction described by the portion *CD* of the dilatometric curve as reverse of the reaction corresponding to the portion *BC*, i.e., as $Cu_2(OH)_3NO_3$ depolymerization and dissolution. On addition of uncharged molecules of hydrated NH_3 to one molecule of the neutral hydroxo complex, six ions are formed at once, which causes a reduction in the volume at the expense of their hydration.

The fact that, in the course of further titration after passing singular point *D*, the molar volume does not change noticeably (straight line *DE*) is due to the completion of the main chemical reactions in the system.

Dark blue $Cu(NH_3)_2(NO_3)_2$ crystals (identified by X-ray phase analysis) were obtained from the solution at $N > 4$.

The interactions revealed in the system $Cu(NO_3)_2$, (H^+)–$NH_3 \cdot H_2O$–H_2O were confirmed by CPESSP model calculations. The initial model included the dissolved complexes $Cu(OH)^+$, $Cu_2(OH)_2^{2+}$, and $Cu(NH_3)_n^{2+}$ (n = 1–4) with the pK values considered above, and also $Cu_2(OH)_3NO_3$ and $Cu(OH)_2$ precipitates. The resulting distribution of hydroxide and ammine complexes is given in Fig. 5. It follows from the calculations that ammine complexes appear in the solution at N = 1.5. Under the experimental conditions, the hydroxo complex species $Cu(OH)^+$, $Cu_2(OH)^{3+}$, $Cu_2(OH)_2^{2+}$, and also the complex $Cu(NH_3)^{2+}$ are present in the system in minor amounts. Our calculations showed that the volume changes in the system are determined first by neutralization of the acid, then by hydrolytic reactions of copper ions with $Cu_2(OH)_3NO_3$ precipitation, and finally by its dissolution in excess ammonia with the formation of ammine complexes. The calculated ΔV values (Fig. 1, solid line) nicely agree with the experiment.

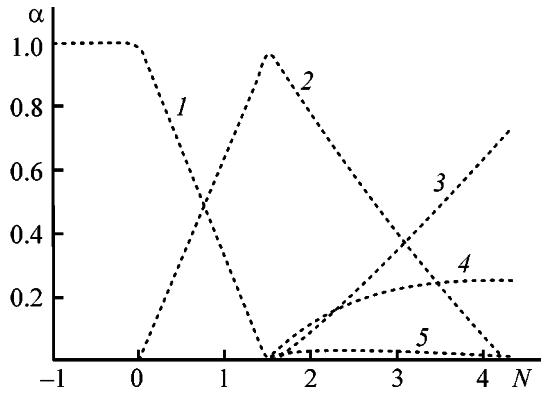

Fig. 5. Distribution of hydroxide and ammine complexes α in the heterogeneous system $Cu(NO_3)_2$, (H^+)–$NH_3 \cdot H_2O$–H_2O as a function of N: (*1*) Cu^{2+}, (*2*) $Cu_2(OH)_3NO_3$(s), (*3*) $Cu(NH_3)_4^{2+}$, (*4*) $Cu(NH_3)_3^{2+}$, and (*5*) $Cu(NH_3)_2^{2+}$.

EXPERIMENTAL

The dilatometric titration was carried out on a precision installation; its scheme and operation principle were described earlier [17]. The volume changes were detected by the shift of the meniscus of a liquid in a calibrated measuring capillary tube 0.4007 mm in diameter. To ensure the stability of the volume changes, a constant temperature of the system (25.00 ± 0.01°C) was maintained with two UT-2/77 ultrathermostats and an air thermostat, connected in series.

For each point of the dilatometric curves, ΔV_m was calculated from the experimental data by the following procedure. We determined the absolute changes in the volume (cm^3) from the shifts s (cm) of the meniscus of a liquid in a calibrated measuring capillary tube by the formula $\Delta V_{abs} = V_{1\,cm}s$ ($V_{1\,cm}$ is the volume corresponding to 1 cm length of the capillary tube, determined by calibration; for the capillary tube in use, $V_{1\,cm}M$ is 1.261×10^{-3} cm^3). For each point, this quantity were converted to ΔV_m, equal to the ratio of ΔV_{abs} to the number of moles of the component being titrated, namely, Cu^{2+} ions.

The pH-metric titration in the system $Cu(NO_3)_2$–

$NH_3 \cdot H_2O$ was carried out on an EV-74 pH meter with a glass electrode. The electronic absorption spectra of solutions were recorded on a Specord UV-VIS spectrophotometer in the range 400–900 nm.

To obtain quantitative characteristics of changes in the volume corresponding to step complex formation, we performed a mathematical simulation using the CPESSP program [18, 19]. The model for processing dilatometric data is based on an additive scheme, which is given in [20], as applied to volume properties.

The basis included the simple species Cu^{2+}, H^+, OH^-, NH_3, and NO_3^-, and the complex species NH_4^+, $Cu(OH)^+$, Cu_2OH^{3+}, $Cu_2(OH)_2^{2+}$, $Cu(NH_3)_n^{2+}$ (n = 1–4), $Cu_2(OH)_3NO_3$, and $Cu(OH)_2$. The distribution of the complexes as a function of N is given in Fig. 5, and the comparison with the experimental data, in Fig. 1.

CONCLUSION

By comprehensive analysis of the data obtained for the system $Cu(NO_3)_2$, (H^+)–$NH_3 \cdot H_2O$–H_2O by several physicochemical methods, we have determined the ranges of N corresponding to prevalence of various chemical reactions. At $N < 0$, excess acid is neutralized. The volume effects of the neutralization with an alkali and with an ammonia solution differ significantly, which is due to specific chemical features of ammonia. At N from 0 to 1.5, the hydrolytic polymerization occurs, yielding the poorly soluble complex $Cu_2(OH)_3NO_3$ with both bases. At $N > 1.5$, the chemical transformations with the two bases are different: in titration with NaOH, solid binuclear copper trihydroxonitrate is converted to copper hydroxide and oxide, and in titration with $NH_3 \cdot H_2O$, it is converted into soluble copper ammines $Cu(NH_3)_n^{2+}$.

ACKNOWLEDGMENTS

The authors are sincerely grateful to I.I. Kozhina for performing the X-ray phase analyses.

REFERENCES

1. Sillen, L.G., *Stability Constants of Metal-Ion Complexes*, section 1: *Inorganic Ligands*, London: Chemical Society, 1964.
2. Burkov, K.A., Bus'ko, E.A., Lilich, L.S., and Ivanova, I.N., *Zh. Neorg. Khim.*, 1982, vol. 27, no. 6, pp. 1455–1459.
3. Burkov, K.A., Bus'ko, E.A., and Zinevich, N.I., *Vestn. Leningr. Gos. Univ., Fiz., Khim.*, 1975, no. 1, pp. 144–145.
4. Effenberger, H., *Z. Kristallogr.*, 1983, vol. 165, nos. 1–4, pp. 127–135.
5. Bjerrum, J., *Metal Ammine Formation in Aqueous Solution. Theory of Reversible Step Reactions*, Copenhagen: P. Haase, 1957.
6. Gubeli, A.O., Hebert, J., Cote, P.A., and Taillon, R., *Helv. Chim. Acta*, 1970, vol. 53, no. 1, pp. 186–197.
7. Smirnova, N.I., Bus'ko, E.A., Wize, G., and Burkov, K.A., *Vestn. Leningr. Gos. Univ., Fiz., Khim.*, 1987, issue 4, no. 25, pp. 83–85.
8. Sidorov, Yu.V., Pykhteev, O.Yu., Burkov, K.A., *et al.*, *Vestn. Sankt-Peterb. Gos. Univ., Fiz., Khim.*, 2000, issue 2, no. 12, pp. 81–86.
9. Burkov, K.A., Bus'ko, E.A., Wize, G., and Smirnova, N.I., *Zh. Neorg. Khim*, 1989, vol. 34, no. 1, pp. 16–19.
10. Mendeleev, D.I., *Rastvory* (Solutions), Moscow: Akad. Nauk SSSR, 1959.
11. Millero, F.J., *Water and Aqueous Solution, Structure, Thermodynamics and Transport Processes*, Horne, R., Ed., New York: Wiley–Interscience, 1972, ch. 13, pp. 519–565.
12. Arat-ool, Sh.M., Chemical Interactions of Phosphonic Acids with Various Bases in Aqueous Solutions, *Cand. Sci. (Chem.) Dissertation*, St. Petersburg, 2001.
13. Stokes, R.H., *Aust. J. Chem.*, 1975, vol. 28, no. 10, pp. 2109–2114.
14. Elliot, H. and Hathaway, B.J., *Inorg. Chem.*, 1966, vol. 5, no. 5, pp. 885–889.
15. Wendling, E., Benali-Baitich, O., and Larrat, J., *Rev. Chim. Miner.*, 1972, vol. 9, no. 4, pp. 607–624.
16. Lo Surdo, A. and Millero, F.J., *J. Phys. Chem.*, 1980, vol. 84, no. 7, pp. 710–715.
17. Wize, G. and Burkov, K.A., *Vestn. Leningr. Gos. Univ., Fiz., Khim.*, 1981, no. 10, pp. 47–52.
18. Sal'nikov, Yu.I., Glebov, A.N., and Devyatov, F.V., *Poliyadernye kompleksy v rastvorakh* (Polynuclear Complexes in Solutions), Kazan. Univ., 1989.
19. Sal'nikov, Yu.I. and Devyatov, F.V., Abstracts of Papers, *Rastvory – elektrolitnye sistemy* (Solutions as Electrolyte Systems), Ivanovo, 1988, pp. 38–41.
20. Sidorov, Yu.V., Sal'nikov, Yu.I., Burkov, K.A., and Arat-ool, Sh.M., *Zh. Obshch. Khim.*, 2002, vol. 72, no. 1, pp. 54–58.

Russian Journal of Applied Chemistry, Vol. 75, No. 7, 2002, pp. 1061–1063. Translated from Zhurnal Prikladnoi Khimii, Vol. 75, No. 7, 2002, pp. 1078–1080.
Original Russian Text Copyright © 2002 by Kozin, Mukhamadiev.

PHYSICOCHEMICAL STUDIES OF SYSTEMS AND PROCESSES

Physicochemical Properties of Binary Solvents Based on Morpholine

V. G. Kozin and A. A. Mukhamadiev

Kazan State Technological University, Kazan, Tatarstan, Russia

Received October 15, 2001; in final form, December 2001

Abstract—The density and viscosity of the binary solvents monoethanolamine–morpholine and monoethylene glycol–morpholine were determined in the entire concentration range at 20, 30, 40, 50, and 60°C. The concentration dependences of the Gibbs energy, enthalpy, and entropy of activation of viscous flow were calculated for these systems.

Binary solvents morpholine–monoethanolamine (MEA) and morpholine–monoethylene glycol (MEG) exhibit high selectivity and solvency [1] and show much promise for separating complex hydrocarbon mixtures in petrochemical industry.

In this work, we studied the physicochemical properties of the binary extractants morholine–MEA and morholine–MEG (systems **I** and **II**, respectively).

Morpholine has a high solvency with respect to both aromatic and saturated hydrocarbons [2]. As a consequence, it has low selectivity and cannot be used straightly. Evidently, the selectivity of this extractant can be increased by addition of highly associated solvents, such as MEA and MEG, which have high selectivity but low solvency [3].

EXPERIMENTAL

The chemicals were repeatedly purified by vacuum distillation and dried over zeolites to attain the density and refractive index coinciding (within the measurement error) with the published data [4]. The density, viscosity, and molar volume measured at 20, 30, 40, 50, and 60°C in the entire concentration range served as structure-sensitive characteristics of the binary solutions. The density ρ_4^T was determined pycnometrically [GOST (State Standard) 18995.1–73], and the kinematic viscosity ν^T, with VPZh-2 and VPZh-3 capillary viscometers (GOST 33–82), with the subsequent recalculation to the dynamic viscosity η^T. The solution temperature was adjusted to within 0.1°C in a thermostat. Experimental data were processed statistically. The experimental densities and dynamic viscosities of systems **I** and **II** over the entire range of component ratios at the temperatures studied are presented in the table. The data are arranged in groups in the order of increasing morpholine concentration c_m in the binary solution.

The table shows that the density of systems **I** and **II** and the viscosity of system **I** decrease monotonically with increasing morpholine content. The concentration dependence of viscosity for system **II** has a pronounced maximum at 20°C, which is probably due to intense intermolecular interaction between morpholine and MEG. The temperature dependences of the density and viscosity for individual and binary solvents are also monotonic.

Data on the concentration and temperature dependences of the density and viscosity of the solvents are of considerable practical importance. However, to gain a better insight into the character of intermolecular interactions in mixing of extractants, we calculated and constructed the isotherms of the deviation from additivity of the density and volume and the isotherms of the deviation of the viscosity from the known Arrhenius equation assuming no interaction between the solution components [5].

The deviations from additivity of the density and molar volume for the binary systems studied are positive and negative, respectively, and differ in the value (Fig. 1). The solution formation in the MEG-containing system is accompanied by a considerably larger compression, which is probably due to more intense intermolecular interaction in this system. For example, the maximal compression at 40°C is 0.3% for system **I** and 1.7% for system **II**. This assumption is supported by the fact that, for system **I**, the dynamic viscosity has positive deviations from the values calculated by

1070-4272/02/7507-1061$27.00 © 2002 MAIK "Nauka/Interperiodica"

Density and dynamic viscosity of MEA–morpholine and MEG–morpholine solutions

c_m, wt %	Density, g cm^{-3}/dynamic viscosity, mPa s, at indicated temperature T, °C				
	20	30	40	50	60
	MEA–morpholine				
0	1.0171/23.38	1.0119/15.34	1.0066/10.02	1.0018/6.88	0.9975/5.07
10	1.0165/21.21	1.0111/13.58	1.0056/8.71	1.0003/6.21	0.9959/4.47
30	1.0142/14.61	1.0086/9.65	1.0028/6.44	0.9970/4.68	0.9921/3.46
50	1.0129/9.19	1.0065/6.31	1.0003/4.57	0.9939/3.36	0.9885/2.57
70	1.0105/5.53	1.0037/3.97	0.9968/2.94	0.9898/2.24	0.9839/1.78
90	1.0050/3.22	0.9980/2.54	0.9915/1.98	0.9839/1.61	0.9777/1.32
100	1.0001/2.12	0.9940/1.74	0.9878/1.45	0.9801/1.21	0.9737/1.06
	MEG–morpholine				
0	1.1142/20.71	1.1098/14.14	1.1053/8.76	1.0981/6.51	1.0947/4.72
10	1.1067/23.22	1.1019/15.77	1.0970/9.66	1.0897/7.00	1.0859/5.02
30	1.0909/24.69	1.0852/16.33	1.0795/10.32	1.0716/7.69	1.0672/5.34
50	1.0740/21.35	1.0665/14.19	1.0601/9.34	1.0520/7.13	1.0470/4.83
70	1.0525/11.83	1.0445/8.07	1.0375/6.02	1.0291/4.41	1.0233/3.12
90	1.0192/3.94	1.0127/2.92	1.0062/2.24	0.9985/1.72	0.9921/1.44
100	1.0001/2.12	0.9940/1.74	0.9878/1.45	0.9801/1.21	0.9737/1.06

the Arrhenius equation over the entire range of temperatures and concentrations. At the same time, the deviations for system **II** are nearly zero and at 60°C become negative over the whole range of mixing, reaching 7.9% (not plotted in Fig. 1).

Thus, the results of the physicochemical analysis of system **II** lead to unambiguous conclusions, whereas, with the results of the volume and viscosity measurements for system **I**, the pattern is not so clear. The presence of electron-donor and electron-acceptor groups in MEG, MEA, and morpholine, along with the data presented in the table and Fig. 1, suggest formation in system **II** of intermolecular hydrogen bonds and supramolecular structures. In system **I**, the components of the solutions most likely interact more weakly, and unstable donor–acceptor complexes are probably formed.

An analysis of the thermodynamic characteristics of viscous flow of the mixed solvents furnishes a more detailed information on the solution structure. The experimentally obtained data on viscosity were additionally treated in terms of the theory of activated complex and the Frenkel molecular-kinetic theory [6], which was possible owing to the linearity of the $\ln\eta = f(1/T)$ isotherms in the examined temperature range. We used the well-known Eyring equation

$$\eta = \frac{hN}{V}\exp\frac{\Delta G_\eta^\#}{RT} = \frac{hN}{V}\exp\left(\frac{\Delta H_\eta^\#}{RT} - \frac{\Delta S_\eta^\#}{R}\right),$$

where η is the dynamic viscosity; h, Planck constant; N, Avogadro number; V, molar volume of the solvent; R, gas constant; T, temperature; $\Delta G_\eta^\#$, $\Delta H_\eta^\#$, and $\Delta S_\eta^\#$, the Gibbs energy, enthalpy, and entropy, respectively, of activation of viscous flow (all values in the equation have IS dimensionality).

The experimental dynamic viscosities and the molar volumes calculated by Eq. (1) for each composition were used to calculate $\Delta G_\eta^\#$ in binary systems **I** and **II** at all the temperatures studied. The $\Delta H_\eta^\#$ values were calculated from the slope of the linear plot of $\ln\eta^T$ vs. reciprocal temperature. This two-parameter dependence was considered for each fixed composition of the solution in five points corresponding to experimental temperatures. The linear correlation coefficient was within 0.996–0.999 for all the solutions studied. Figure 2 shows the concentration dependences of the calculated values of $\Delta G_\eta^\#$, $\Delta H_\eta^\#$, and $\Delta S_\eta^\#$ for systems **I** and **II** at 40°C.

With increasing morpholine concentration in the binary solution, $\Delta G_\eta^\#$ decreases, except the range from 0 to 20–25 mol % morpholine in system **II**, in which $\Delta G_\eta^\#$ increases. The character of these dependences is determined by the ratio of the enthalpy and entropy contributions to the Gibbs energy of activation of viscous flow. As seen from Fig. 2, the main contribution to $\Delta G_\eta^\#$ is made by the enthalpy, whereas the entropy contribution is small and decreases with increasing morpholine concentration in the binary sol-

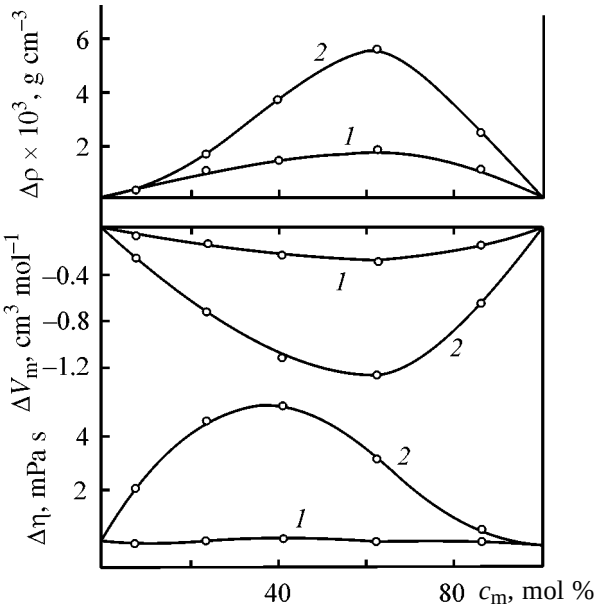

Fig. 1. Deviations of the density $\Delta\rho$ and molar volume ΔV_m from the additivity and of the viscosity $\Delta\eta$ from the Arrhenius equation at 40°C vs. morpholine concentration c_m in binary solutions. Systems: (*1*) MEA–morpholine and (*2*) MEG–morpholine; the same for Fig. 2.

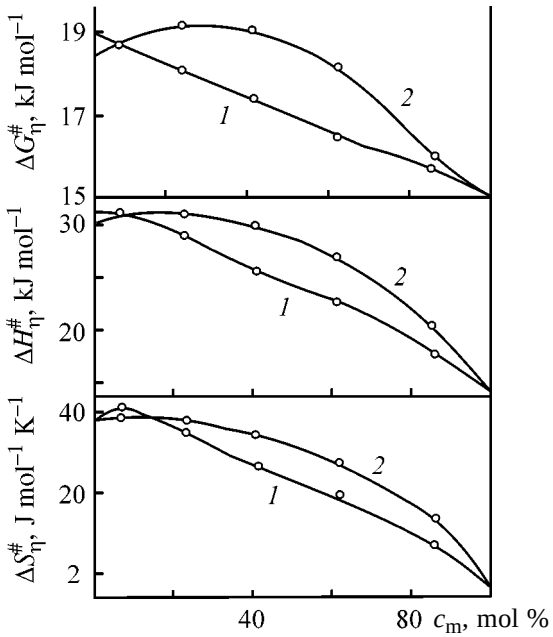

Fig. 2. Gibbs energy $\Delta G_\eta^\#$, enthalpy $\Delta H_\eta^\#$, and entropy $\Delta S_\eta^\#$ of activation of viscous flow for the binary solutions at 40°C vs. morpholine concentration c_m.

vent. The addition of morpholine decreases $\Delta H_\eta^\#$ for both systems. This means that the energy for creation and motion of an activated complex decreases, i.e., the intermolecular interaction in the binary solvents becomes less strong [7]. System **I** is characterized by the lower values of $\Delta H_\eta^\#$, which supports the assumption that interaction in system **II** is stronger (Fig. 2).

The decrease in $\Delta S_\eta^\#$ with addition of morpholine to MEG and MEA shows that the entropy of the initial state increases, i.e., the solution structure becomes less ordered owing to the break of hydrogen bonds between like molecules of MEA and MEG. This fact is apparently responsible for the increase in the solvency of the binary extractants in hand at higher concentrations of morpholine, which is in line with the extraction characteristics of these solvents, studied previously [1]. The disordering effect of morpholine is also confirmed by the negative deviations of the partial derivatives of the thermodynamic functions of viscous flow with respect to morpholine concentration.

CONCLUSIONS

(1) The deviations of the density and molar volume from additivity and the deviations of the viscosity from the values calculated by the Arrhenius equation, in relation to the component ratios, confirm the more intense interaction in the system monoethylene glycol–morpholine.

(2) The addition of morpholine breaks the initial structure of monoethanolamine and monoethylene glycol and increases the solvency of the binary extractants.

REFERENCES

1. Kozin, V.G. and Mukhamadiev, A.A., *Zh. Prikl. Khim.*, 2001, vol. 74, no. 8, pp. 1252–1257.
2. Sharifullin, A.V. and Kozin, V.G., *Neftekhimiya*, 1996, vol. 36, no. 5, pp. 464–468.
3. Bittrich, H.-J., Gaile, A.A., Lempe, D, *et al.*, *Razdelenie uglevodorodov s ispol'zovaniem selektivnykh rastvoritelei* (Separation of Hydrocarbons Using Selective Solvents), Leningrad: Khimiya, 1987.
4. Reichardt, C., *Solvent Effects in Organic Chemistry*, New York: Chemie, 1979.
5. Anosov, V.Ya., Ozerova, M.I., and Fialkov, Yu.A., *Osnovy fiziko-khimicheskogo analiza* (Principles of Physicochemical Analysis), Moscow: Nauka, 1976.
6. Frenkel, Ya.I., *Kineticheskaya teoriya zhidkostei* (Kinetic Theory of Liquids), Leningrad, Nauka, 1945.
7. Shcherbina, A.E., Shcherbina, E.I., and Bashun, T.V., *Zh. Fiz. Khim.*, 1983, vol. 57, no. 4, pp. 946–949.

Russian Journal of Applied Chemistry, Vol. 75, No. 7, 2002, pp. 1064–1068. Translated from Zhurnal Prikladnoi Khimii, Vol. 75, No. 7, 2002, pp. 1081–1085.
Original Russian Text Copyright © 2002 by Yurtov, Murashova.

PHYSICOCHEMICAL STUDIES OF SYSTEMS AND PROCESSES

Gelation in Extraction Systems with Basic Copper(II) and Neodymium(III) Alkyl Phosphates

E. V. Yurtov and N. M. Murashova

Mendeleev Russian Chemical Engineering University, Moscow, Russia

Received February 13, 2002

Abstract—Gelation in extraction systems containing purified or commercial di(2-ethylhexyl) hydrogen phosphate (HDEHP), copper(II) or neodymium(III) hydroxides, hydrocarbon solvent, and water was studied at different ratios of the metal and extractant. The region was determined in which gelation caused by formation of basic neodymium(III) di(2-ethylhexyl) phosphates occurs in decane. Some characteristics of organogels in the HDEHP (commercial)–$Cu(OH)_2$–organic diluent (decane, hexane or toluene)–H_2O extraction systems were studied.

Structure formation in extraction systems affects their main characteristics, such as the distribution and separation factors and the rates of extraction and phase separation. Formation of disperse structures like gels, liquid crystals, amorphous and crystalline precipitates in the bulk of both aqueous and organic phases or at the interface are the factors which, as a rule, deteriorate the extraction process. One of the consequences of the structure formation is appearance of so-called meduses, i.e., stable emulsions, precipitates, or gels located between partially separated organic and aqueous phases [1]. Accumulation of meduses can deteriorate extraction to so significant extent that the extraction process must be interrupted [2, 3]. To prevent this detrimental effect, the region of formation of the disperse structures and their features promoting meduse formation should be studied.

The most attention is given to the structure formation in extraction of metals with di(2-ethylhexyl) hydrogen phosphate (HDEHP) and tributyl phosphate (TBP), which are widely used for recovery, separation, and purification of various organic and inorganic compounds including nonferrous, rare-earth, and radioactive metals. These meduses contain species typical of detergent solutions, e.g., liquid crystals and associates of polymeric metal hydroxides.

Formation of liquid crystals by lanthanide di(2-ethylhexyl) phosphates in CCl_4 was reported in [4]. Liquid crystals were also found in the HDEHP–NaDEHP–decane–H_2O system at high NaDEHP concentration (>90 wt %) [5].

It was reported [6] that, in organic solutions, metals can form oligomeric neutral and acidic di(2-ethylhexyl) phosphates consisting of several alkyl phosphate units [6]. The degree of polymerization of neutral Y(III) and La(III) di(2-ethylhexyl) phosphates in organic solvents reaches 10^2–10^3 [7]. High polymeric species poorly dissolve in both aqueous and organic phases. Therefore, polymeric metal alkyl phosphates can form gels and precipitates in both aqueous and organic phases. It was found that, in extraction of zirconium(IV) and hafnium(IV) with HDEHP, both gels and gel films are formed in the aqueous phase near the interface [8].

In our preliminary study of structure formation in extraction systems containing HDEHP, copper(II) or neodymium(III), hydrocarbon solvent, and water at different ratio of the metal and extractant, neither liquid crystals nor gels were found in the aqueous phase.

In this work we studied gelation in the organic phase of the HDEHP–$Cu(OH)_2$–decane–H_2O and HDEHP–$Nd(OH)_3$–decane–H_2O systems at different metal to extractant ratios. In the experiments, both purified and commercial HDEHP were used.

EXPERIMENTAL

In our experiments we used two different HDEHP samples: HDEHP containing >98% main substance (Merck) and commercial grade HDEHP containing 66% di(2-ethylhexyl) hydrogen phosphate and 19.5% mono(2-ethylhexyl) dihydrogen phosphate, produced by Khimprom Volgograd Joint-Stock Company.

1070-4272/02/7507-1064$27.00 © 2002 MAIK "Nauka/Interperiodica"

Mono(2-ethylhexyl) dihydrogen phosphate (H_2MEHP) was first separated from commercial HDEHP as a water-soluble sodium salt and then converted to H_2MEHP by treatment with sulfuric acid [9]. The other chemicals [decane, $CuSO_4 \cdot 5H_2O$, $Nd(NO_3)_3 \cdot 6H_2O$, and NaOH] were of pure grade. Double-distilled water was prepared by the standard technique.

Copper(II) and neodymium(III) hydroxides were precipitated from aqueous solutions of the corresponding salts by addition of NaOH to pH >10 for Cu(II) and pH > 12 for Nd(III). The $Cu(OH)_2$ precipitate was rapidly separated from the mother liquor by centrifugation and then was washed with double-distilled water to pH 7. The $Nd(OH)_3$ precipitate was kept under mother liquor for 1 h to complete hydrolysis, separated by centrifugation, and washed with double-distilled water to pH 7. Then the prescribed amounts of water and extractant were added to the precipitates of neodymium or copper hydroxide. To obtain an organogel, this mixture was carefully shaken for 30 s. In the Nd(III)–HDEHP and Cu(II)–H_2MEHP systems, gelation occured within several minutes, and in the Cu(II)–commercial grade HDEHP system, within several hours and became complete after keeping at 20°C for a day. Emulsions in these systems were prepared by stirring the aqueous and organic phases at their volume ratio of 3 : 2 with a stirrer at 3000 rpm for 2 min with copper(II) and 30 s with neodymium.

Before measuring the viscosity and evaluating the stability, the emulsions containing copper(II) or neodymium(III) alkyl phosphates were kept for 1 day and 1.5 h, respectively, to ensure completion of structure formation. The period of half-settling of the emulsion in the organic phase was determined by centrifugation at 90*g*. The emulsion viscosity was measured with a Rheotest-2 rotary viscometer with coaxial cylinders within the shear rate interval of 0.167–16.2 s^{-1} at 20°C. The photographs of emulsions were obtained with an optical microscope equipped with a photographic attachment.

The neutral copper(II) and neodymium(III) salts are hydrolyzed in aqueous solutions to form basic salts. Therefore, in extraction of these metals with HDEHP, their basic alkyl phosphates can be formed as intermediate species. We studied the structure formation in the HDEHP–$Cu(OH)_2$–decane–water and HDEHP–$Nd(OH)_3$–decane–water systems at the ratio of the metal and exractant corresponding to the formation of both neutral and basic alkyl phosphates.

In the organic phase, basic neodymium(III) di(2-ethylhexyl) phosphate is present as precipitate and gel.

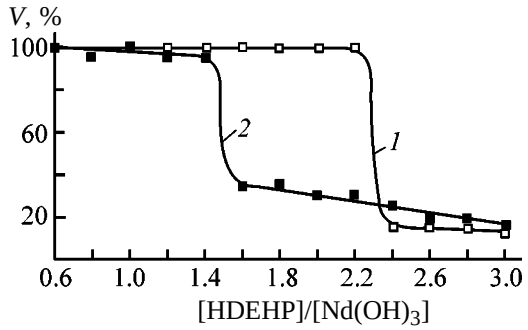

Fig. 1. Apparent precipitate volume *V* (% of the organic phase volume) as a function of the ratio of molar concentrations of HDEHP and neodymium hydroxide. [HDEHP] = 0.3 M; the same for Figs. 3 and 5. HDEHP: (*1*) pure and (*2*) commercial.

The turbid or opalescent gel-like phases do not flow under their gravity. In additional mechanical loading, the structure of these gels is destroyed. Figure 1 shows that, in the HDEHP(pure)–$Nd(OH)_3$–decane–water system at [HDEHP]/[$Nd(OH)_3$] < 2.2, gelation occurs throughout the organic phase. At this ratio of $Nd(OH)_3$ and HDEHP, both mono- and disubstituted basic neodymium(III) di(2-ethylhexyl) phosphates can be formed. With commercial HDEHP contaminated with H_2MEHP, gelation occurs throughout the organic phase at [HDEHP/$Nd(OH)_3$] < 1.4. At higher [HDEHP]/[$Nd(OH)_3$] ratios, either dense precipitate at the water–extract interface or neodymium di(2-ethylhexyl) phosphate solution in decane is formed.

When the concentration of basic neodymium(III) di(2-ethylhexyl) phosphate in organic phase exceeds a certain limit, the gelation in the organic phase starts. At HDEHP concentration > 0.03 M and HDEHP/$Nd(OH)_3$ = 1, the organic phase is completely converted to the gel.

Optical microscopic study of gel-like organic phases containing basic neodymium(III) di(2-ethylhexyl) phosphates failed to reveal any crystal structure. On removal of the solvent from both the gels and precipitate, an amorphous solid is obtained. It is known that neutral lanthanide di(2-ethylhexyl) phosphates form coordination polymers in the organic phase [4, 7]. We believe that basic poorly soluble lanthanide di(2-ethylhexyl) phosphates present in the organic and aqueous phases are also coordination polymers. These polymers build up the three-dimensional network of the organogel.

In the HDEHP (commercial)–$Cu(OH)_2$–decane–water system, gelation occurs within the range of [HDEHP]/[$CuOH)_2$] ratios of 1.0–1.6 (Fig. 2). Under

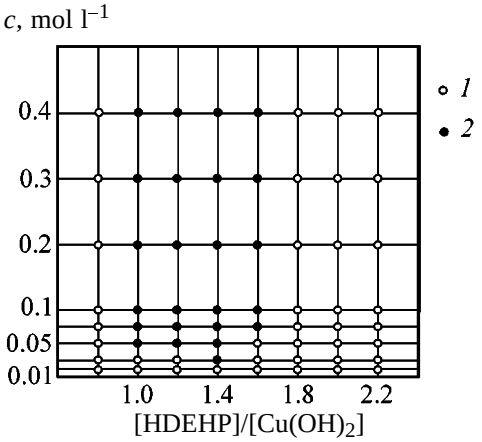

Fig. 2. Gelation in the HDEHP (commercial)–decane–water system at 20°C. (*c*) $Cu(OH)_2$ content. (*1*) No gelation and (*2*) gelation occurs.

these conditions, gelation occurs in the organic phase only, while the aqueous phase is free of the gel. At the ratio of the HDEHP and $Cu(OH)_2$ concentrations outside the gelation region (at excess of HDEHP), the copper alkyl phosphate organic solution is in equilibrium with the aqueous phase. At an HDEHP concentration insufficient for gel formation, a dense crystalline precipitate is formed at the interface.

We found that the gel formation in the systems studied is insensitive to the nature of the nonpolar solvent. Substitution of decane by any other nonpolar solvent results in only minor changes in both the minimal HDEHP concentration and the $[HDEHP]/[CuOH)_2]$ ratio corresponding to the gelation region in the phase diagram. The HDEHP minimal concentration and the ratios of HDEHP and $Cu(OH)_2$ concentrations corresponding to the gelation region in decane, hexane, and toluene are given in the table.

The blue transparent gels initially formed in the HDEHP (commercial)–$Cu(OH)_2$–organic solvent–water system become turbid and whitish on long-term keeping. An optical microscopic study of mature gels showed that their structure is built of fine crystals. On keeping the organogel for several days at 20°C, it becomes turbid owing to increase in the crystal size. The mean size of gel particles in the HDEHP–$Cu(OH)_2$–decane–water system {$[HDEHP]/[Cu(OH)_2]$ = 1.2, [HDEHP] = 0.3 M, T = 20°C} was determined with an optical microscope at 160-fold magnification. These data are given below:

τ, days	1	2	3	4
d, μm	9.4 ± 1.3	18.9 ± 2.5	31.1 ± 4.4	34.9 ± 3.8

On heating above 75°C, the gel is destroyed owing to dissolution of alkyl phosphate crystals. Upon cooling, the structure of the organogel is restored. On mechanical loading, the organogels in the HDEHP (commercial)–$Cu(OH)_2$–decane–water system are irreversibly destroyed.

We found that gelation does not occur in systems containing both commercial HDEHP preliminarily purified as described in [10] and pure HDEHP (Merck) containing more than 98% main substance. In this case, at $[HDEHP]/[Cu(OH)_2] < 1.8$, a dense crystalline substance is precipitated at the interface, which dissolves at $[HDEHP]/[Cu(OH)_2] = 2.0$. These experiments showed that gelation of alkyl phosphates is caused by impurities present in commercial HDEHP.

The main organic impurities present in commercial HDEHP are mono(2-ethylhexyl) dihydrogen phosphate H_2MEHP and 2-ethylhexanol. We found that, on addition of aliphatic alcohols (from butanol to decanol) to pure HDEHP, no gel is formed in the systems concerned. Turbid faintly blue organogels are formed in the H_2MEHP–$Cu(OH)_2$–decane–water systems containing 0.3 M H_2MEHP at $[H_2MEHP]/[Cu(OH)_2] < 2$. Taking into account that H_2MEHP is dibasic acid, both neutral and acidic copper(II) alkyl phosphates can be formed under these conditions. In the region of formation of acidic copper alkyl phosphates, $[H_2MEHP]/[Cu(OH)_2] > 2.0$, two homogeneous liquid phases (aqueous and organic) are formed.

In industrial production of HDEHP, the raw product is washed with NaOH or Na_2CO_3 aqueous solutions to remove H_2MEHP. We found that, after single scrubbing of commercial HDEHP in an organic solvent (0.3 M) with aqueous NaOH, the gelation region is narrowed, and gelation occurs at $[HDEHP]/[Cu(OH)_2]$ 1.6–1.8.

In extraction, a contact between aqueous and organic phases, as a rule, is attained by emulsification of the extraction system at vigorous stirring. We studied

Boundaries of gelation region in the HDEHP (commercial)–$Nd(OH)_3$–organic solvent–water system

Organic solvent	c_{HDEHP}*	[HDEHP]/[Cu(OH)2], mol/mol	
		lower boundary	upper boundary
Decane	0.025	1.0	1.6
Hexane	0.010	1.2	1.8
Toluene	0.050	1.2	2.2

* Minimal HDEHP concentration at which gelation occurred.

the effect of gel formation on the emulsion stability in the HDEHP (commercial)–$Cu(OH)_2$–decane–water and HDEHP (commercial)–$Nd(OH)_3$–decane–water systems. In these systems, emulsions were produced by stirring $Cu(OH)_2$ and $Nd(OH)_3$ precipitates suspended in water with an HDEHP solution in decane. Figure 3 shows how the half-separation time of the emulsion (time of the half-settling of the emulsified organic phase) in the HDEHP–$Nd(OH)_3$–decane–water system depends on the HDEHP/$Nd(OH)_3$ ratio in centrifugation at 90*g*. This figure shows that emulsions are stable only at [HDEHP]/[$Nd(OH)_3$] ratios corresponding to the gelation region. Agitation of the system concerned drastically affects its phase behavior. While no stirring, the gelation occurs in the organic phase only, and in vigorous stirring of the aqueous and organic phases at 3000 rpm, a stable emulsion is formed.

When lanthanide hydroxides suspended in water are stirred with an HDEHP solution in decane, stable emulsions are formed with all the lanthanides. For example, we obtained stable emulsions in the $RE(OH)_3$–HDEHP–decane–water systems (RE = Sm, Dy, Ho, and Yb) at [HDEHP]/[$Ln(OH)_3$] = 1.6 and [HDEHP] = 0.3 M.

In the HDEHP (commercial)–$Cu(OH)_2$–decane–water system, stable emulsions are formed in the range of metal and extractant ratio corresponding to organogel formation. At [HDEHP/[$Cu(OH)_2$] ratios beyond the gelation region (below 1.0 and above 1.6), the emulsions are separated into aqueous and organic phases within 1–2 min.

Figure 4 demonstrates the flow curves of emulsions stabilized with organogels in the HDEHP (commercial)–$Cu(OH)_2$–decane–water and HDEHP (commercial)–$Nd(OH)_3$–decane–water systems. Curves *1* and *2* show that the emulsion viscosity considerably decreases with increasing shear rate. With the subsequently decreasing shear rate (curves *1*' and *2*'), the viscosity of the liquefied emulsions does not return to the initial values, i.e., the initial emulsion structure is not restored. We found that, in mechanically destroyed emulsions, the initial structure is not restored even on keeping for several days. The irreversible breakdown of emulsions under mechanical loading indicates that they are nonthixotropic. Such a behavior correlates with that of organogels of copper(II) and neodymium(III) alkyl phosphates.

The structural features of the emulsions were judged from their viscosity, optical microscopic patterns, and electrolytic conductivity. The miscibility of emulsions with aqueous and organic phases was also

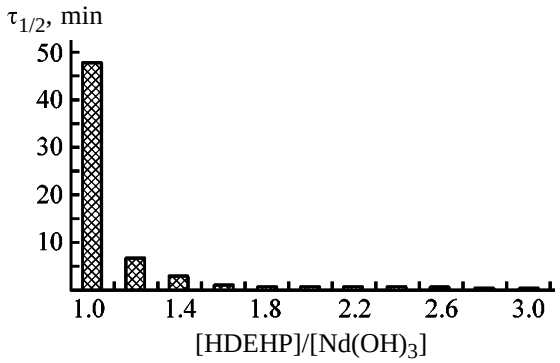

Fig. 3. Time of half-settling of the emulsified organic phase, $\tau_{1/2}$, as a function of the HDEHP and neodymium hydroxide molar ratio in the HDEHP (commercial)–$Nd(OH)_3$–decane–water system.

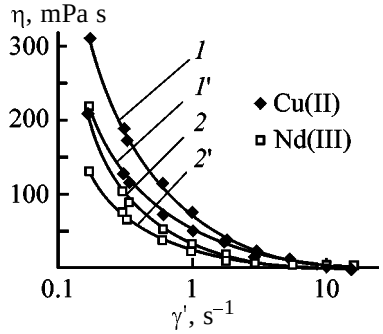

Fig. 4. Effective viscosity η of emulsions stabilized with copper(II) and neodymium(III) organogels as a function of the shear rate γ'. [HDEHP] = 0.3 M, [HDEHP]/[$Nd(OH)_3$] = 1.2 and [HDEHP]/[$Cu(OH)_2$] = 1.2; commercial HDEHP. The viscosity was measured in the course of (*1, 2*) increasing and (*1*', *2*') decreasing the shear rate.

examined. These studies showed that the stability of the emulsion structure is ensured by the organogel network. The photomicrographs of emulsified HDEHP (commercial)–$Cu(OH)_2$–decane–water and HDEHP (commercial)–$Nd(OH)_3$–decane–water mixtures contain light droplets of the liquid phase and darker areas between them. The dark areas correspond to turbid organogels formed by copper(II) mono(2-ethylhexyl) phosphates and basic neodymium(III) di(2-ethylhexyl) phosphates (Figs. 5a, 5b).

Our data on gelation and emulsification in extraction systems containing copper and lanthanide alkyl phosphates allow us to make certain recommendations to prevent the detrimental effect of structure formation. Taking into account that both organogels and stabilized emulsions are irreversibly destroyed under mechanical loading, the mechanical impact can be used for brekdown and removal of meduses.

The removal of H_2MEHP from commercial HDEHP by scrubbing with NaOH aqueous solution

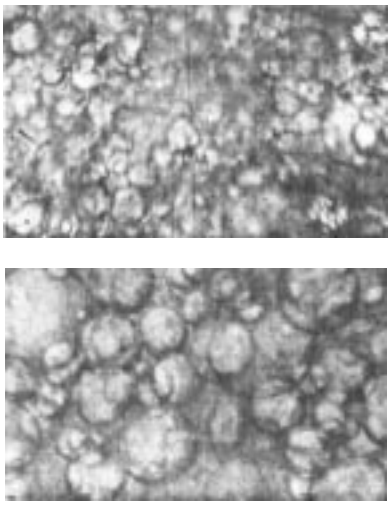

Fig. 5. Photomicrographs of (a) emulsified HDEHP (commercial)–$Cu(OH)_2$–decane–water system with [HDEHP]/[$Cu(OH)_2$] = 1.0 and (b) emulsified HDEHP (commercial)–$Nd(OH)_3$–decane–water system with [HDEHP]/[$Nd(OH)_3$] = 1.0. Scale: 16 mm = 100 μm.

sharply narrows the gelation region in the extraction systems containing copper(II) alkyl phosphates. As a result, purification of the extractant to remove H_2MEHP decreases the probability of meduse formation in the extraction. Under the industrial conditions, the meduse formation is prevented by scrubbing a commercial extractant with Na_2CO_3 aqueous solution. In going from commercial to pure HDEHP, the gelation region of basic neodymium(III) di(2-ethylhexyl) phosphates expands (Fig. 1). Therefore, unlike the cases when, in extraction of metals with commercial HDEHP, gel formation is promoted by organic impurities and, therefore, can be prevented by their removal, in extraction of lanthanides(III) with HDEHP, its purification to remove impurities does not prevent the structure formation.

Our experiments showed that gel formation in the organic phase is caused by basic alkyl phosphates formed at HDEHP deficiency. At sufficiently high acidity suppressing the metal hydrolysis, the meduse formation can be prevented. At low metal concentration and large excess of the extractant, the probability of meduse formation also decreases.

CONCLUSIONS

(1) Conditions of gelation in the basic neodymium di(2-ethylhexyl) phosphate–decane–water system were determined for pure and commercial HDEHP.

(2) The gelation region in the di(2-ethylhexyl) hydrogen phosphate–$Cu(OH)_2$–(decane, hexane or toluene)–water systems was determined at 20°C. A three-dimensional network of organogels is built up by copper(II) mono(2-ethylhexyl) phosphate crystals.

(3) Organogels based on copper(II) mono(2-etylhexyl) phosphate or basic neodymium(III) di(2-ethylhexyl) phosphate promote emulsification in extraction systems.

(4) Different approaches to elimination of the detrimental effect of structure formation in extraction systems containing copper(II) or lanthanide(III) di(2-ethylhexyl) phosphates (e.g., meduse formation) are analyzed.

ACKNOWLEDGMENTS

This work was financially supported in part by the Integration Special Federal Program (project no. A0078/3,5).

REFERENCES

1. Rice, N.M., *Hydrometallugy*, 1981, vol. 7, pp. 177–199.
2. Ritcey, G.M., *Hydrometallugy*, 1980, vol. 5, pp. 97–107.
3. Rozen, A.M., Zakharkin, B.S., Nenarokomov, E.A., *et al*., *At. Energ*., 1992, vol. 72, vol. 5, pp. 436–440.
4. Trifonov, Yu.I., Legin, E.K., and Suglobov, D.N., *Proc. ISEC'90*, Sekine, T., Ed., Tokyo: Elsevier, 1992, pp. 279–284.
5. Yurtov, E.V. and Murashova, N.M., *Proc. Int. Symp. "Extraction Processes in XXI Century"*, Kholkin, A.I. and Yurtov, E.V, Eds., Moscow (Russia), pp. 25–39.
6. Stoyanov, E.S., Mikhailov, V.A., Torgov, V.G., and Us, T.V., *Proc. ISEC'88*, Zolotov, Yu.A. and Spivakov, B.Ya., Eds., Moscow: Nauka, 1988, vol. 1, pp. 195–198.
7. Harada, T., Smutz, M., and Bautista, R.G., *Proc. ISEC'71*, London: Soc. Chem. Ind., 1971, vol. 2, pp. 950–956.
8. Sinegribova, O.A. and Chizhevskaya, S.V., *Zh. Neorg. Khim*., 1997, vol. 42, no. 8, pp. 1397–1400.
9. Peppard, D.F., Ferraro, J.R., and Mason, G.W., *J. Inorg. Nucl. Chem*., 1958, vol, 7, pp. 231–232.
10. McDowell, W.J., Perdue, P.T., and Case, G.N., *J. Inorg. Nucl. Chem*., 1976, vol. 38, pp. 2127–2129.

Russian Journal of Applied Chemistry, Vol. 75, No. 7, 2002, pp. 1069–1074. Translated from Zhurnal Prikladnoi Khimii, Vol. 75, No. 7, 2002, pp. 1086–1091.
Original Russian Text Copyright © 2002 by Ryabtsev, Menzheres, Ten.

SORPTION AND ION-EXCHANGE PROCESSES

Sorption of Lithium from Brine onto Granular $LiCl \cdot 2Al(OH)_3 \cdot mH_2O$ Sorbent under Dynamic Conditions

A. D. Ryabtsev, L. T. Menzheres, and A. V. Ten

Ekostar-Nautekh Private Company, Novosibirsk, Russia

Received January 15, 2001; in final form, December 2001

Abstract—Lithium sorption on, and desorption from sorbent grains of various sizes were studied under dynamic conditions at linear flow velocities in the range 2–34 m h^{-1}.

Many compounds of Group III–VI elements and, in particular, simple hydroxides and difficultly soluble salts of polycharged metals with polybasic salts, such as phosphates of zirconium, titanium, antimony, etc., exhibit selective sorption properties toward lithium ions [1–10]. The most active researchers' interest is attracted by manganese dioxide and composites on its base, whose exchange capacity in alkaline medium is as high as 10 mg-equiv g^{-1}. With decreasing pH, the sorbent capacity decreases to become not higher than 1 mg-equiv g^{-1} in strongly mineralized brines (pH < 7) [7, 8]. Moreover, these sorbents have an expensive matrix, are insufficiently stable, and, in some cases, require that an additional auxiliary sorbent should be present for neutralizing H^+ ions formed in lithium sorption [11, 12].

These disadvantages are not characteristic of a sorbent based on double aluminum lithium hydroxide chloride of the composition $LiCl \cdot 2Al(OH)_3 \cdot mH_2O$ (DALH-Cl), which can selectively recover lithium from highly mineralized chloride brines [5, 6, 13–18]. The sorption properties of this sorbent, which has the layered structure, are based on its capability to release part of LiCl (no more than 40% of the bulk chemical composition) upon treatment with water and recover its initial composition upon treatment with concentrated LiCl solutions or lithium-containing chloride brines, i.e., on its capacity for deintercalation–intercalation of LiCl [19]. A distinctive feature of the sorbent is its unique selectivity, resulting from the fact that only lithium, and no other element, can occupy the site of preliminarily removed lithium in the structure of the compound, which is due to the occurrence of a molecular-sieve effect, as assumed in [19].

It is planned, for the first time in world's practice, to recover lithium from highly mineralized calcium–magnesium chloride brines from the Angara–Lena basin by means of the sorbent in question. For this purpose, we synthesized a large batch of the sorbent and performed its granulation.

Here we report on large-scale laboratory tests of this granular sorbent under dynamic sorption conditions.

EXPERIMENTAL

A DALH-Cl powder was obtained in a mixing apparatus by solid-phase synthesis from a mixture of crystalline LiCl and $Al(OH)_3$, taken in stoichiometric ratio, in the presence of 0.5 mol of water [16]. The powder obtained was activated in a centrifugal apparatus to impart sorption properties to it. The total exchange capacity of the powdered sorbent under static conditions upon 24-h contact with an excess amount of brine was about 7 mg of lithium(I) per 1 g of powder. The powder was granulated using a chlorinated vinyl chloride resin (PVC) of the PSKh-LS brand, soluble in methylene chloride, as a binder [20]. The granulation was carried out in a PSh-45 industrial extruder by extrusion of a paste containing (wt %) DALH-Cl 75.5–75.7, PVC 5.5–6.5, and methylene chloride 18.7–18.9. In terms of dried product, the amount of DALH-Cl in the grains obtained was 92–94%, and that of binder, 6–8%. The exchange capacity of the granular material under static conditions was 5–6 mg g^{-1}.

The dry extrudate of diameter 2 mm was crushed with a rotor; the forming grains were separated on sieves. Grains of the following sizes were chosen as objects of study: $0.63 < l < 1.0$, $1.0 < l < 2.0$, and $l > 2.0$ (mainly 2.5–10), where l is the grain length (mm). The tests were carried out in columns 0.026 m in diameter with the sorbent bed height of 0.49 m.

1070-4272/02/7507-1069$27.00 © 2002 MAIK "Nauka/Interperiodica"

Table 1. TDEC of sorbent of various fractions and average extent of lithium recovery from brine at varied rates of brine feed into the column

Grain size, mm	Brine feed rate, l h^{-1}									
	0.93		1.20		2.55		5.20		5.80	
	TDEC, mg g^{-1}	α, %	TDEC, mg g^{-1}	α, %	TDEC, mg g^{-1}	α, %	TDEC, mg g^{-1}	α, %	TDEC, mg g^{-1}	α, %
$0.63 < l < 1.0$	–	–	–	–	4.85	33.55	3.99	23.0	–	–
$1.0 < l < 2.0$	3.65	31.3	–	–	2.61	26.0	–	–	2.96	23.0
$l > 2.0$	–	–	1.97	19.1	–	–	–	–	2.00	23.0

The weighed portions of sorbent were 165, 180, and 190 g for, respectively, the fractions $0.63 < l < 1.0$, $1.0 < l < 2.0$, and $l > 2.0$. The experiments were mostly performed on two in-series connected columns with the total sorbent weight of about 400 g and total bed height of approximately 1 m. The column dimensions were chosen so that the geometric similarity to columns of the pilot installation constructed for performing pilot tests was observed.

The investigations were carried out with brine from the Znamenskoe deposit (Irkutsk oblast), with density of 1.34 g cm^{-3} and the following composition (g l^{-1}): $CaCl_2$ 341.0, $MgCl_2$ 126.0, KCl 7.0, NaCl 20.0, and LiCl 2.2–2.5 (total salts ~500 g l^{-1}). The brine was used repeatedly after adjusting its density by evaporation and the lithium content by adding lithium chloride. The brine was fed by a Zalimp typ 315 peristaltic pump from bottom upwards. The desorbing solution temperature was maintained to within ±2°C with a WB-2 water bath.

The content of lithium in solutions and solid phases was determined by flame photometry [21] on an SP-9 atomic-absorption spectrophotometer, and the total hardness (in terms of $CaCl_2$) and the content of Al^{3+} and Cl^-, by volumetric titration [22]. The specific surface area of grains was found by thermal desorption of argon [23], and the pore volume, by mercury porosimetry. The density of the swollen sorbent was determined by a simplified method [24], using the formula

$$\rho = (m_1 - m_2)/(V_2 - V_1),$$

where m_1 is the mass of vessel with water; m_2, mass of vessel with sorbent; V_1, initial volume of water in the vessel; and V_2, the total volume of water and sorbent in the vessel. The swellability of sorbent fractions was determined by the method recommended for use with ion-exchange resins [25].

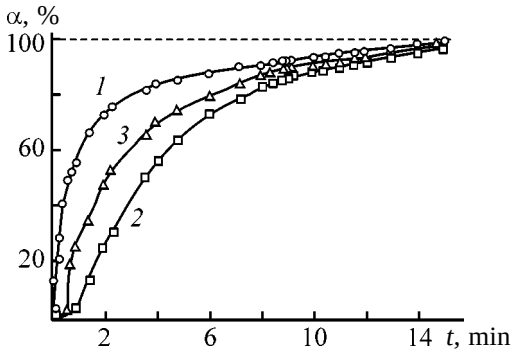

Fig. 1. Extent of lithium(I) recovery, α, from brine vs. sorption duration *t*. Brine feed rate (l h^{-1}): (*1*) 1.2, (*2*) 2.55, and (*3*) 5.2.

Sorption, desorption, and sorbent washing to remove brine were studied with grains of varied size.

Sorption. Comparative data on the extent of lithium(I) recovery from brine indicate that this parameter depends on the sorbent grain size: the smaller the grain, the higher the sorption efficiency. For example, the extent of lithium recovery is 98% for brine passed through the fraction with grain size $0.63 < l < 1.0$ at flow rate of 0.5 l h^{-1} and is nearly 2 times lower for the fraction with $l > 2$ mm. The same is indicated by the output sorption curves (Fig. 1). According to these curves, the exchange capacity of the sorbent is low. Our results show that, in the best case (smallest grains, brine feed rate 2.6 l h^{-1}), only 2 brine volumes per 1 volume of sorbent can be passed before breakthrough. Table 1 shows the total dynamic exchange capacity (TDEC) and average extent of Li^+ recovery from the brine volume passed in relation to the rate of brine feed.

The data of Table 1 also indicate that the TDEC of a sorbent depends not only on its granulometric composition, but also on the brine feed rate. Achieving

Table 2. Physical properties of sorbent

Parameter	Fraction, mm		
	$0.63 < l < 1$	$1 < l < 2$	$l > 2$
Total pore volume, $cm^3\ g^{-1}$	0.18	0.23	0.28
Amount of micropores (diameter ≈2 nm)	5.4	1.3	2.3
Amount of macropores (diameter ≥1000 nm)	65.4	50.0	36.5
Specific surface area of starting material, $m^2\ g^{-1}$	1.6	1.6	2.0
Specific surface area after sorption–desorption cycle, $m^2\ g^{-1}$	27.1	27.0	28.6
Density of swollen sorbent, $g\ cm^{-3}$	1.495	1.424	1.506
Swelling factor	1.06	1.07	1.07

a high TDEC value requires a small sorbent grain size and low brine feed rate corresponding to long contact time. However, even under these conditions, the extent of recovery is not high. Such a dependence of TDEC on the specific load points to the slow sorption kinetics [26], caused by inner-diffusion hindrance to the transport of lithium ions inside the sorbent grains. However, it should be noted that, in accordance with the mercury porosimetry data, the grains have highly developed porosity appearing, in all probability, in solvent removal in the course of grain forming and drying. Table 2 presents data on the physical properties of various sorbent fractions.

The independence of the density from the grain size is presumably accounted for by the irregular shape of grains, their unstable packing, and inhomogeneity of the chemical composition of air-dry samples, since the chemical formula of the sorbent is $LiCl \cdot 2.3Al(OH)_3 \cdot 2.1H_2O$ for the $0.63 < l < 1.0$ fraction and $LiCl \cdot 2.7Al(OH)_3 \cdot mH_2O$ for the other fractions, with m varying from 1.9 for the $1.0 < l < 2.0$ fraction to 2.3 for that with $l > 2.0$.

The data in Table 2 also indicate that the sorbent fractions have a sufficient amount of macro- and intermediate transport pores, whose diameter is incommensurably larger than that of a hydrated lithium ion, equal to 0.107 nm [27], which would seemingly favor fast sorption. Moreover, it can be seen from Table 2 that the specific surface area of the sorbent markedly increases upon pretreatment and a sorption–desorption cycle. Probably, this can be accounted for by the fact that the sorbent synthesized always contains a minor admixture of unreacted LiCl (commonly up to 3–4 wt %), which is washed out in the course of sorbent pretreatment and acts as additional porophore. However, static studies show that, despite this circumstance, the equilibrium state in the system formed by the granular sorbent and strongly mineralized brine is attained rather slowly (in 24 h). It may be assumed that a significant contribution to the deceleration of inner diffusion is made by a film of PVC used as organic binder. The water permeability of such a film is extremely low [28].

Thus, the data obtained indicate that performing the sorption process in a flow-through mode is not optimal for a given sorbent. At the same time, analysis of how the sorbent capacity depends on the time of contact in initial stages of the sorption process ($t <$ 3 h) shows that a higher brine feed rate is preferable for achieving a higher capacity in the same time. Figure 2 presents these dependences for the fraction with $1.0 < l < 2.0$. This behavior is preserved for the other fractions, which indicates that it is advisable to perform sorption in a circulation mode.

The data obtained show that the largest gain in α and, consequently, in the sorbent capacity is ensured in the first 1–2 h of circulation. However, several cycles are necessary since complete recovery of Li^+ is not achieved under these conditions. Data on lithium sorption from brine in this mode at a circulation rate of $5.8\ l\ h^{-1}$ are presented in Table 3 for the fraction with $0.63 < l < 1.0$. The brine volume was 5 l. The brine obtained after completion of the first cycle served as the initial solution for a second cycle. Prior to each cycle, 3.5 mg of lithium per 1 g of sorbent was desorbed.

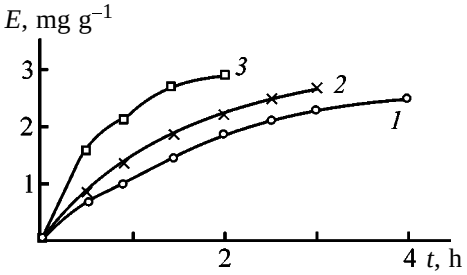

Fig. 2. Sorbent capacity E vs. time t. Fraction $1.0 < l < 2.0$ mm. Brine feed rate ($l\ h^{-1}$): (*1*) 0.93, (*2*) 2.55, and (*3*) 5.80.

Table 3. Li^+ sorption in the circulation mode

Cycle	Time, h	LiCl concentration, g l^{-1}	Extent of recovery		Capacity E, mg g^{-1}	
			in a cycle	total	in a cycle	total
First	0	2.30	0	0	0	0
	0.5	1.68	26.9	26.9	1.54	1.54
	1.0	1.44	37.4	37.4	2.14	2.14
	2.0	1.17	49.1	49.1	2.81	2.81
Second	0	1.17	0	0	0	0
	0.5	0.73	37.6	68.3	1.09	3.90
	1.0	0.52	55.5	77.4	1.62	4.43
	2.0	0.31	73.5	86.5	2.14	4.95
	3.0	0.21	82.0	90.9	2.39	5.20

Table 3 shows that the specified brine volume can be processed in two cycles, with the extent of Li^+ recovery equal to 91% at a total sorption time of 5 h. During this time, the total exchange capacity was 5.2 mg g^{-1}, which is close to the value found under static conditions. It was established experimentally that the optimal range of circulation rates is 5.8–14 l h^{-1} (linear flow velocities 11–27 m h^{-1}). With the circulation rate increasing further, the extent of lithium recovery from brine decreases somewhat.

Analysis of sorption operation parameters shows that the sorbent can recover Li^+ at its any concentration in brine. Figure 3a presents dependences of the sorbent capacity on the LiCl concentration (2.30–0.48 g l^{-1}) in brine. However, as would be expected, the lower the initial concentration of LiCl, the slower the sorption and the lower the sorbent capacity. Since the exchange capacity of the sorbent also decreases with increasing grain size, a greater number of cycles is necessary for complete lithium recovery from brine in the case when grains of the fraction with $l > 2.0$ are used. An extent of Li^+ recovery equal to 92.2% is achieved after four cycles (Fig. 3b).

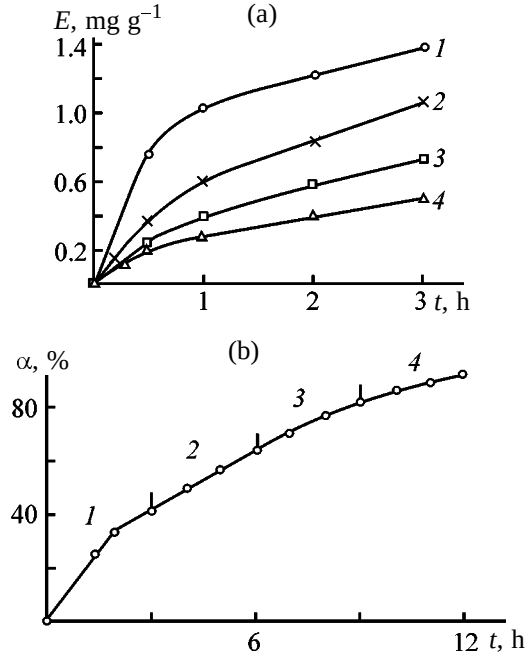

Fig. 3. (a) Sorbent capacity E and (b) extent of lithium(I) recovery from brine, α, vs. duration of sorption, t, in the cyclic mode. Brine volume 4 l. LiCl concentration in cycles *1–4* (g l^{-1}): (*1*) 2.30, (*2*) 1.49, (*3*) 0.86, and (*4*) 0.48.

Thus, dynamic tests of the sorbent demonstrated that the smaller the grain size, the higher the sorption efficiency. However, account should be taken of the fact that the resistance of the sorbent bed grows nearly twofold with decreasing grain size. Therefore, the optimal grain size is 1–2 mm.

Sorbent washing to remove brine. To obtain a purer eluate, it is necessary to wash the sorbent, prior to the desorption stage, to remove brine remaining on the grain surface and in the intergrain space. The study demonstrated that, the larger the sorbent grains, the larger the amount of water required for their washing. In the case of batch feed of water, 1.1–1.2 volumes of water per 1 volume of sorbent is necessary to remove approximately 90% of the remaining salts for the fraction with $0.63 < l < 1.0$. For the fraction with $l > 2.0$, this amount is already 2.2 volumes. With continuous feed of water, the consumption of water is approximately 30% larger than in the case of batch feed at the same process parameters.

In all cases, approximately 20% of sorbed lithium is lost in the washing stage. This is easily removable lithium localized in the surface layer of grains. Use of cooled water (3–5°C) makes it possible to reduce these parameters by 5–8%; however, it is impossible

to eliminate completely the washing loss. In a process cycle of brine treatment, washing water containing, on the average, 125 g l^{-1} of salts (in terms of $CaCl_2$) and 2.8–3.5 g l^{-1} of LiCl can be recycled.

Lithium desorption. It is known [10] that lithium desorption is governed by conditions of sorbent treatment with water and depends on temperature, amount of water used in desorption, and process duration. The desorption is carried out more effectively with water at elevated temperature; however, account should be taken of the fact that partial decomposition of the sorbent is possible at temperatures exceeding 50–60°C, and its sorption properties may be impaired [10]. In lithium desorption with dilute LiCl solutions under the same conditions, the achievable sorbent capacity decreases as compared with the value obtained in desorption with water.

We found that, under dynamic desorption conditions, the concentration of lithium chloride in the eluate depends of the rate of water feed. The lower this rate and, correspondingly, the longer the time of contact between the saturated sorbent and water, the higher the LiCl concentration at the same l : s ratio (Figs. 4a and 4b) and, consequently, the higher the exchange capacity of the sorbent. Figure 4 shows that, for an exchange capacity of about 3 mg g^{-1} to be achieved, the l : s ratio should exceed 5, with the LiCl concentration equal in this case to only 2–3 against 4.5 g l^{-1} at l : s = 2.

In order to obtain higher LiCl concentration in the eluate, we also examined the possibility of carrying out desorption in the circulation mode. We found that raising the linear flow velocity of circulation from 11 to 27 m h^{-1} affects desorption only slightly. After 15 min of water circulation through the sorbent of fraction $0.63 < l < 1.0$, the concentration of LiCl is approximately 3.5–3.7 g l^{-1}, and further lithium desorption is already performed with the resulting solution, which decelerates the desorption process. After 3 h of circulation at a solution flow velocity of 27 m h^{-1}, the LiCl concentration reaches a value of 4.5 g l^{-1}, with the sorbent capacity equal to 1.56 mg g^{-1}. Under these conditions, the capacity of 2.5 mg g^{-1} could be obtained after 10 h of circulation, which is technologically unfeasible. Moreover, this capacity can be achieved much faster by desorption of lithium with fresh portions of water after every 15 min of circulation. However, the LiCl concentration in the eluate decreases steadily in this case. Therefore, the possibility of successive sorbent treatment with portions of eluting solutions with different concentrations was considered with the purpose of

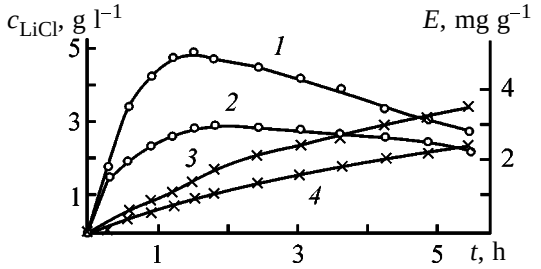

Fig. 4. (*1, 2*) LiCl concentration c_{LiCl} and (*3, 4*) exchange capacity E of the sorbent vs. sorption duration t. Fraction $0.63 < l < 1.0$ mm. Rate of water supply into the column (l h^{-1}): (*1, 3*) 0.64 and (*2, 4*) 1.3.

raising the LiCl concentration in the final eluate. The sorbent was treated with a solution containing about 5 g l^{-1} of LiCl in the first stage, about 3 g l^{-1} in the second, and with pure water in the third. Performing desorption in the circulation mode and lowering the l : s ratio make it possible to raise the content of LiCl in the first portion of the eluate to 9–10 g l^{-1} (Table 4). The first portion of the eluate is regarded as a desorption product, which is then purified to remove impurity salts and processed to obtain various lithium compounds [29]. The remaining portions of the eluate are used as recycle solutions in further desorption cycles.

By varying the l : s ratio and carrying out successive treatment of fresh sorbent portions with recycle LiCl solutions, the concentration of lithium chloride in the eluate can be raised to 12–15 g l^{-1}. At higher concentrations, lithium desorption from the sorbent is strongly suppressed [14]. Desorption from coarser fractions is characterized by the same pattern.

On the whole, it may be concluded that, despite having low dynamic exchange capacity, the sorbent is sufficiently stable in sorption–desorption cycles (i.e., in regeneration). A half-year operation of a column with sorbent of fraction $1.0 < l < 2.0$ demonstrated that the exchange capacity is not impaired, and the decrease in the mass of sorbent discharged from the

Table 4. Desorption of lithium in the circulation mode. Rate of solvent circulation 14.3 l h^{-1}, l : s = 1

Parameter	Treatment		
	first	second	third
c_{LiCl}, g l^{-1}:			
initial	6.00	3.81	0
final	8.77	7.25	4.47
c_{CaCl_2}, g l^{-1}	8.69	3.62	1.54
E, mg g^{-1}	0.45	0.56	0.74

column and dried was approximately 6%. It should be noted here that, in the case of sorbent abrasion in the course of operation, the washed out fine fraction (<0.25 mm) can be used after drying as an additional amount of stock in sorbent granulation and thus can be recycled. In the case of a decrease in the sorbent capacity, it can be easily restored by passing a concentrated LiCl solution (≥50 g l^{-1}) through the column.

CONCLUSIONS

(1) Large-scale laboratory tests of a sorbent based on $LiCl \cdot 2Al(OH)_3 \cdot mH_2O$ showed that it is advisable to perform the sorption–desorption process under dynamic conditions in a circulation mode at linear flow velocities of 10–27 m h^{-1}.

(2) The smaller the sorbent grain size, the higher the efficiency of the sorption–desorption processes. The optimal grain size is 1–2 mm. At the optimal sorption time of 3 h, the dynamic exchange capacity is about 3 mg g^{-1}.

REFERENCES

1. Bortun, A.I. and Khainakov, S.A., *Ukr. Khim. Zh.*, 1990, vol. 56, no. 11, pp. 1160–1163.
2. Ooi, Kenta and Abe, Mitsuo, *Ceram. Jpn.*, 1992, vol. 27, no. 5, pp. 401–405.
3. Shitrakar, R., Tsuji, M., Abe, M., and Hayashi, K., *Bull. Soc. Sea Water Sci.*, 1990, vol. 44, no. 4, pp. 267–271.
4. Van Shuwang, Zhon Hui, and Huang Zhibua, *Ion Exch. Absorb.*, 1994, vol. 10, no. 3, pp. 219–224.
5. US Patent 5389349.
6. US Patent 5599516.
7. Vol'khin, V.V., Khodzhamamedov, A., Dzhumamuradov, B., *et al.*, *Izv. Akad. Nauk Turkmen. SSR, Ser. Fiz., Tekh., Khim. Geol. Nauk*, 1986, no. 4, pp. 99–101.
8. Vol'khin, V.V., Gurtlieva, I.G., and Leont'eva, G.V., *Izv. Akad. Nauk Turkmen. SSR, Ser. Fiz., Tekh., Khim. Geol. Nauk*, 1987, no. 3, pp. 43–45.
9. Onorin, S.A., Vol'khin, V.V., Sesyunina, E.A., and Alpatova, E.V., Abstracts of Papers, *VII Vsesoyuznaya konferentsiya po khimii i tekhnologii redkikh shchelochnykh elementov* (VII All-Union Conf. on Chemistry and Technology of Less-Common Alkali Metals), Apatity, 1988, pp. 101–102.
10. Kotsupalo, N.P., Menzheres, L.T., and Mamylova, E.V., *Zh. Prikl. Khim.*, 1998, vol. 71, no. 10, pp. 1645–1650.
11. USSR Inventor's Certificate no. 1726379.
12. Myasoedov, B.F., Senyavin, M.M., Khamizov, R.Kh., and Rudenko, B.A., *Trudy Vsesoyuznoi nauchno-tekhnicheskoi konferentsii "Perspektivnye napravleniya po sozdaniyu tekhniki i tekhnologii dlya pererabotki mineral'nogo i tekhnogennogo syr'ya"* (Proc. All-Union Scientific and Technical Conf. "Promising Directions for Development of Technology for Processing Mineral Resources and Industrial Wastes"), St. Petersburg, 1991, pp. 218–231.
13. Kotsupalo, N.P., Menzheres, L.T., Mamylova, E.V., and Ryabtsev, A.D., *Khim. Inter. Ustoich. Razv.*, 1999, no. 7, pp. 249–257.
14. Menzheres, L.T. and Kotsupalo, N.P., *Zh. Prikl. Khim.*, 1999, vol. 72, no. 10, pp. 1623–1627.
15. RF Patent 2028385.
16. RF Patent 2113405.
17. Menzheres, L.T., Kotsupalo, N.P., and Mamylova, E.V., *J. Mater. Synth. Process.*, 1999, vol. 7, no. 4, pp. 239–244.
18. Ryabtsev, A.D., Menzheres, L.T., Kotsupalo, N.P., and Serikova, L.A., *Khim. Inter. Ustoich. Razv.*, 1999, no. 7, pp. 343–349.
19. Isupov, V.P., Intercalation Compounds of Aluminum Hydroxide, *Doctoral Dissertation*, Novosibirsk, 1998.
20. RF Patent 2050184.
21. Poluektov, N.S., *Metody analiza po fotometrii plameni* (Methods of Analysis by Flame Photometry), Moscow: Khimiya, 1967.
22. Charlot, G., *Les methods de la chimie analytique. Analyse quantitative minerale*, Paris: Masson, 1961, 4th ed.
23. Buyanova, N.E., Karnaukhov, A.P., and Alabuzhev, Yu.A., *Opredelenie udel'noi poverkhnosti dispersnykh i poristykh materialov* (Determnation of Specific Surface Area in Dispersed and Porous Materials), Novosibirsk: Inst. Kataliza, Sib. Otd. Ross. Akad. Nauk, 1978.
24. Zakharov, E.I., Ryabchikov, B.E., and D'yakov, V.S., *Ionoobmennoe oborudovanie atomnoi promyshlennosti* (Ion-Exchange Apparatus of Nuclear Industry), Moscow: Energoatomizdat, 1987.
25. Polyanskii, N.G., Gorbunov, G.V., and Polyanskaya, N.A., *Metody issledovaniya ionitov* (Methods for Studying Ion-Exchange Resins), Moscow: Khimiya, 1976.
26. Saldadze, K.M., Pashkov, A.B., and Titov, V.S., *Ionoobmennye vysokomolekulyarnye soedineniya* (Ion-Exchange Macromolecular Compounds), Moscow: Goskhimizdat, 1960.
27. Mishchenko, K.P. and Poltoratskii, G.M., *Voprosy termodinamiki i stroeniya vodnykh i nevodnykh rastvorov elektrolitov* (Thermodynamics and Structure of Aqueous and Nonaqueous Electrolyte Solutions), Leningrad: Khimiya, 1968.
28. *Spravochnik khimika* (Chemist's Handbook), Nikol'skii, B.P., Ed., Leningrad: Khimiya, 1971, vols. 1, 2.
29. Kotsupalo, N.P., Menzheres, L.T., and Ryabtsev, A.D., *Khim. Inter. Ustoich. Razv.*, 1999, no. 7, pp. 157–167.

Russian Journal of Applied Chemistry, Vol. 75, No. 7, 2002, pp. 1075–1078. Translated from Zhurnal Prikladnoi Khimii, Vol. 75, No. 7, 2002, pp. 1092–1095.
Original Russian Text Copyright © 2002 by Mamedov.

APPLIED ELECTROCHEMISTRY AND CORROSION PROTECTION OF METALS

Electrodeposition of Thin Lead–Tellurium Alloy Films from Fluoroborate Electrolyte

M. N. Mamedov

Institute of Inorganic and Physical Chemistry, National Academy of Sciences of Azerbaijan, Baku, Azerbaijan

Received October 23, 2001; in final form, March 2002

Abstract—Electrodeposition of lead–tellurium alloys from a fluoroborate electrolyte was studied. Cyclic voltammetry was applied to determine the range of potentials of joint electrodeposition of Pb and Te to form PbTe on the cathode.

Lead telluride, and also solid solutions on its base in the form of thin films are widely used in various fields of semiconductor industry to fabricate thermoelectric transducers, thermoelements, and IR detectors [1].

Thin films of metal chalcogenides, including PbTe, are commonly obtained by vacuum evaporation [2]. This technique is labor-consuming, requires intricate equipment, and involves use of high temperature. Moreover, PbTe dissociates in evaporation into the components, which commonly leads to its fractional distillation and to deposition of compositionally inhomogeneous films. Therefore, the electrochemical technique has been frequently used recently for obtaining thin chalcogenide films [3, 4]. This method is distinguished by simplicity, low material expenditure, and possibility of easily controlling the composition and thickness of the layers obtained.

The first electrochemical syntheses of lead telluride were carried out in [5–7]. The syntheses were based on cathodic dissolution of tellurium and anodic dissolution of the metal whose telluride is being obtained. In the process, interaction between Te^{2-} and Pb^{2+} present in the electrolyte results in the formation of PbTe powder on the electrolyzer bottom.

In [8], thin layers of lead–tellurium alloy were obtained by cathodic deposition from a simple nitrate electrolyte containing $Pb(NO_3)_2$ and TeO_2. However, it is known [9] that high-quality cathodic deposits cannot be always obtained from simple electrolytes, especially in those cases when the standard potentials of the metals being codeposited are strongly different.

The standard potential of the $Te/[TeOOH]^+$ couple in acid media is $+0.551$ V, and that of the Pb/Pb^{2+} couple is -0.126 V. The difference of the standard potentials is 0.677 V.

To make closer the potentials of tellurium and lead deposition, such complex electrolytes were used in which tellurium forms more stable complex ions than lead. In this study, as such an electrolyte we used a fluoroborate lead-plating solution of the composition (g l^{-1}): $Pb(BF_4)_2$ 180, HBF_4 40, H_3BO_3 12.6 and joiner's glue 1.0 (electrolyte no. 1) [10]. In electrolyte no. 1, lead deposition occurs without any noticeable hindrance, whereas in fluorine-containing media, tellurium is present as a complex anion $[Te(OH)_2F_4]^{2-}$ [11], with $Te(OH)_2^{2+}$ ions formed in its dissociation directly involved in the cathodic discharge. According to [11], the discharge of $Te(OH)_2^{2+}$ ions occurs in stages, with each stage of formation of intermediates characterized by a certain equilibrium potential, which becomes more negative in reduction processes. This may also make closer the deposition potentials of tellurium and lead.

EXPERIMENTAL

The electrolysis was performed and polarization curves were measured in a poly(methyl methacrylate) cell. Platinum electrodes coated with tellurium, lead, and tellurium–lead alloy (up to 5 μm) served as cathodes, and platinum plate, as anode. The polarization curves were measured in the potentiodynamic mode at a potential sweep rate of 8 mV s^{-1} with a P-5827M potentiostat and a PDP4-003 self-recorder. As reference served saturated silver chloride electrode. The potentials measured were recalculated to the hydrogen scale. TeO_2 to be added to the lead-plating electrolyte was preliminarily dissolved in HF, since TeO_2 is in-

1070-4272/02/7507-1075$27.00 © 2002 MAIK "Nauka/Interperiodica"

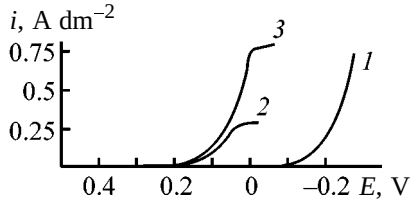

Fig. 1. Cathodic potentiodynamic polarization curves for deposition of (*1*) lead, (*2*) tellurium, and (*3*) lead–tellurium system, obtained in fluoroborate electrolytes of varied composition. (*i*) Current density and (*E*) potential; the same for Figs. 2 and 3. (*1*–*3*) Electrolyte nos. 1–3, respectively.

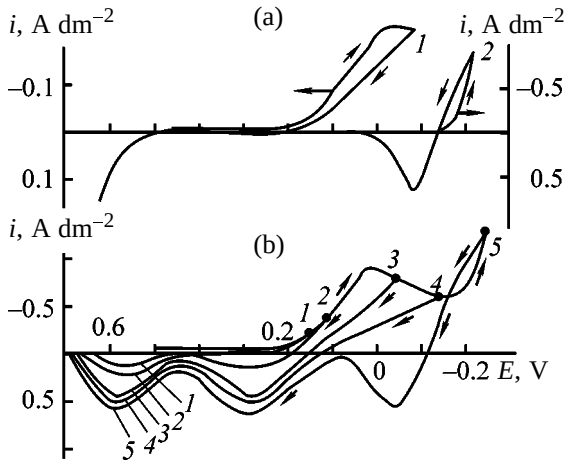

Fig. 2. Cyclic voltammograms of deposition and dissolution of (a) (*1*) tellurium and (*2*) lead and (b) (*1*–*5*) lead–tellurium system, obtained on a platinum electrode. Points *1*–*5* in the curves correspond to end potentials.

soluble in HBF_4. X-ray studies were carried out on a DRON diffractometer (CuK_α radiation). The content of tellurium in an alloy was determined gravimetrically [12], and that of lead, from the difference of masses of the cathodic deposit and tellurium. The cathodic deposits were also analyzed using a Cameca MS-46 X-ray fluorescence analyzer. The outward appearance of the deposits was assessed visually; the type of conduction was determined using a hot probe.

Figure 1 presents the cathodic potentiodynamic curves obtained in fluoroborate electrolytes of various compositions (g l^{-1}): electrolyte no. 2: HBF_4 40, H_3BO_3 12.6, joiner's glue 1.0, and TeO_2 1.0; electrolyte no. 3: $Pb(BF_4)_2$ 180, HBF_4 40, H_3BO_3 12.6, joiner's glue 1.0, and TeO_2 1.0. The stationary potential of Te in electrolyte no. 2 is 0.5 V; deposition of Te is accompanied by high polarization, the deposition overvoltage is 0.34 V at i = 0.05 A dm^{-2} (Fig. 1, curve *2*). The stationary potential of lead in electrolyte no. 1 is –0.12 V, and the deposition overvoltage at i = 0.05 A dm^{-2}, 0.04 V (Fig. 1, curve *1*).

The codeposition of tellurium and lead from electrolyte no. 3 (Fig. 1, curve *3*) occurs at more positive potentials than separate deposition of these metals, i.e., both the components are deposited into the alloy via depolarization. Such an arrangement of polarization curves is observed in those cases when codeposition of components is accompanied by formation of a compound or a solid solution at the cathode [9]. Thus, it may be assumed that codeposition of tellurium and lead at the cathode can be accompanied by formation of PbTe.

To confirm this assumption and determine the potentials at which tellurium and lead are codeposited, cyclic voltammograms were measured on platinum electrode. In this case, it could be expected that current peaks associated with oxidation of products formed during the cathodic half-cycle may appear in the curves of the anodic half-cycle.

As seen from Fig. 2a, deposition of tellurium on the platinum electrode onsets at a potential of 0.18 V (curve *1*), and that of lead, at –0.13 V (curve *2*). The anodic half-cycle of the voltammograms obtained for the individual components shows a single peak of anode current. The current peak is observed at 0.6 V for tellurium and at about –0.1 V for lead. The codeposition curve shows three peaks of anode current (Fig. 2b). The current peaks at 0.6 and –0.1 V are due to oxidation of, respectively, tellurium and lead. The current peak observed at a potential of about 0.3 V may be due to dissolution of PbTe by the reaction

$$PbTe \rightarrow Pb^{2+} + Te + 2e. \quad (1)$$

The anodic half-cycle measured starting with a cathode potential of 0.15 V (Fig. 2b, curve *1*) shows only an anode current peak associated with oxidation of tellurium. Consequently, no codeposition of tellurium and lead occurs at the cathode up to a potential of 0.15 V, and elementary tellurium is the only cathodic product. Codeposition of tellurium and lead onsets at about 0.12 V, which is confirmed by the appearance in the anodic half-cycle (curve *2*) of a second anode current peak associated with PbTe dissolution. This is also confirmed by analysis of deposits obtained under potentiostatic conditions (see table).

The current in the PbTe dissolution peak mainly depends on the end potential, and increases when this potential is shifted to more negative values (curves *3*–*5*). In the anodic half-cycle curve measured on reaching the potential of lead deposition, a third current peak appears, associated with oxidation of lead as

a separate phase (curve *5*). Deposits obtained at potentials more negative than –0.15 V are composed of PbTe and Pb.

It is interesting that, as soon as the platinum electrode is coated with tellurium and a certain potential is reached (0.12 V in the given case), codeposition of lead and tellurium occurs. Tellurium "stimulates" deposition of lead at more positive potentials; the depolarization for lead is –0.25 V.

A similar phenomenon was also observed in codeposition of bismuth and tellurium from a chloride–fluoride electrolyte [13]. This phenomenon is due to the tendency of tellurium to form Te^{2-}. It should be noted that, in contrast to ions of other metals, quadruply charged tellurium tends to undergo six-electron reduction [14] by the reaction

$$Te^{4+} + 6e = Te^{2-}. \quad (2)$$

According to [14], this reaction is possible even at current densities lower than the limiting diffusion current density, with the occurrence of reaction (2) being the more probable, the lower the concentration of quadruply charged ions in solution. In solutions with higher tellurium concentrations, the main energetically favorable cathodic process is the four-electron reduction of Te^{4+} to Te. At low tellurium concentrations in the electrolyte, the region of limiting diffusion current is reached fast. In this case, the four-electron process is hindered through depletion of the near-cathode layer of Te^{4+} ions, and conditions favorable for six-electron reduction are created. Under these conditions, tellurium deposited at the cathode may undergo cathodic dissolution by the reaction

$$Te + 2e = Te^{2-}. \quad (3)$$

Pb^{2+} ions adsorbed on the electrode surface or present in the near-cathode layer may readily interact with the negatively charged surface, and the mechanism of PbTe formation can be described by the scheme

$$Te(OH)_2^{2+} + 4e = Te + 2OH^-, \quad (4)$$

$$Te + 2e + Pb^{2+} = PbTe. \quad (5)$$

To obtain additional data on the influence exerted by tellurium on the codeposition of Te and Pb, voltammetric curves were measured on a tellurium-coated platinum electrode in electrolyte no. 1. The curves were obtained in the potential range from 0.4 to –0.2 V, which ruled out anodic dissolution of tellurium deposited onto platinum. As seen from Fig. 3, deposition of lead on Te(Pt) electrode occurs at more positive potentials than that on Te and Pt electrodes. A noticeable current is seen in the polarization curve at a potential of about 0.1 V (Fig. 3, curve *1*), in good agreement with the onset potential of codeposition of Te and Pb (Fig. 2b). This is indicated by an anode current peak at 0.3 V, corresponding to anodic dissolution of PbTe obtained in codeposition of Te and Pb. When the end potential is shifted to negative potentials, a limiting current region is observed, extending as far as the onset potential of lead deposition (curve *4*). In repeated cycles, the limiting current decreases (curves *2*, *3*). The appearance of the limiting current may be due to either slow motion of charge carriers, i.e., the semiconducting properties of PbTe, or slow motion of tellurium or of lead ions across the PbTe film. At more negative potentials, lead is deposited as a separate phase. This is indicated by the appearance of an anode current peak at a potential of –0.12 V.

Composition and conduction type of films obtained in potentiostatic deposition from electrolyte no. 3. Electrolysis duration 60 min

Deposition potential, V	Phase composition* (Te content, wt %)	Type of conduction
0.1	PbTe, Te (55.6)	*p*
0.05	PbTe, Te (46.3)	*p*
0.00	PbTe, Te (40.2)	*p*
–0.5	PbTe, traces of Te (39.1)	*p*
–0.1	PbTe, traces of Te (38.9)	*p*
–0.15	PbTe, Pb, PbO_2, PbO (36.9)	*n*
–0.2	PbTe, Pb, PbO_2, PbO (30.2)	*n*

* Content of the components, found by chemical analysis.

Thus, in codeposition of tellurium and lead, the primary part in alloying is played by the tendency

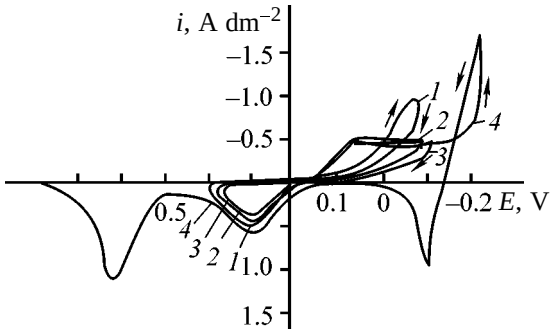

Fig. 3. Cyclic voltammograms obtained successively on a tellurium-coated platinum electrode in electrolyte no. 1. Potential sweep rate 40 mV s^{-1}.

of tellurium to undergo cathodic dissolution to form Te^{2-} ions. In this case, the depolarization in Te deposition into the alloy is associated with alloying (thermodynamic factor), and that in deposition of lead into the alloy, with the low overvoltage of lead deposition on tellurium (kinetic factor).

According to the results of X-ray phase analysis, films containing excess amount of tellurium and obtained at potentials more positive than –0.1 V are composed of two phases, PbTe and Te. The data obtained with a microprobe analyzer demonstrate that Te is mainly present in lower layers of the films (*p*-type conduction). The X-ray patterns of lead-rich films obtained at potentials more negative than –0.15 V contain, in addition to lines related to PbTe and Pb, also those associated with PbO and PbO_2 [15], with lead mainly present in upper layers of the films (*n*-type conduction). Films with composition very close to the compound PbTe are formed at potentials in the range 0.0–0.1 V.

CONCLUSIONS

(1) In electrodeposition of the Pb–Te alloy from a fluoroborate electrolyte, both the components are deposited into the alloy with depolarization due to a thermodynamic factor in deposition of tellurium and to a kinetic factor in that of lead. The range of potentials at which Te and Pb are codeposited was determined.

(2) Tellurium-rich films have *p*-type conduction, and lead-rich films, *n*-type conduction.

REFERENCES

1. Ravich, Yu.I., Efimov, B.A., and Smirnov, I.A., *Metody issledovaniya poluprovodnikov v primenenii k khal'kogenidam PbS, PbSe i PbTe* (Methods for Investigation of Semiconductors for the Example of Chalcogenides), Moscow: Nauka, 1968.
2. Chizhikov, D.M. and Schaslivyi, V.P., *Tellur i telluridy* (Tellurium and Tellurides), Moscow: Nauka, 1966.
3. Patsauskas, E.I., Yanitskii, I.V., and Mitskyavichyus, D.L., *Tr. Akad. Nauk Lit. SSR, Ser. B*, 1970, vol. 3, no. 62, pp. 117–123.
4. Danaher, W.J. and Koyns, L.E., *Aust. J. Chem*., 1984, vol. 37, pp. 688–701.
5. Miles, M.H. and McEwan, W.S., *J. Electrochem. Soc*., 1973, vol. 120, no. 8, pp. 1069–1070.
6. Ugai, Ya.A., Dynnik, A.P., and Ignatevich, S.D., *Elektrokhimiya*, 1976, vol. 12, no. 10, pp. 1626.
7. Dynnik, A.P. and Ignatevich, S.D., in *Fiziko-khimiya poluprovodnikov, materialovedenie* (Physical Chemistry of Semiconductors, Materials Science), Voronezh, 1978, pp. 103–105.
8. Strel'tsov, E.A., Osipovich, N.P., Ivashkevich, L.S., *et al*., *Zh. Prikl. Khim.*, 1997, vol. 70, no. 10, pp. 1735–1737.
9. Fedot'ev, N.P., Bibikov, N.N., Vyacheslavov, P.M., and Grilikhes, S.Ya., *Elektrolitícheskie splavy* (Electrolytic Alloys), Moscow: Mashgiz, 1962.
10. Il'in, V.A., *Luzhenie i svintsevanie* (Tinning and Lead Plating), Moscow: Mashinostroenie, 1971.
11. Bigelis, V.M., Bykova, E.M., and Abrarov, O.A., *Elektrokhimiya*, 1978, vol. 14, no. 8, pp. 1186–1191.
12. Hillebrand, W.F. and Lundell, G.E.F., *Applied Inorganic Analysis with Special Reference to the Analysis of Metals, Minerals, and Rocks*, New York: Wiley, 1953, 2nd ed.
13. Mamedov, M.N., Kuliev, S.A., Alieva, A.G., and Skundin, A.M., *Elektrokhimiya*, 1998, vol. 34, no. 10, pp. 1212–1216.
14. Zhdanov, S.I. and Pats, R.G., *Elektrokhimiya*, 1965, vol. 1, no. 8, pp. 947–955.
15. Mamedov, M.N., Alekperov, A.I., Zeinalova, E.F., and Guseinova, R.G., *Izv. Akad. Nauk SSSR, Neorg. Mater*., 1987, vol. 23, no. 11, pp. 1924–1926.

Russian Journal of Applied Chemistry, Vol. 75, No. 7, 2002, pp. 1079–1081. Translated from Zhurnal Prikladnoi Khimii, Vol. 75, No. 7, 2002, pp. 1096–1098.
Original Russian Text Copyright © 2002 by Ivanova, Gerasimchuk, Vlasenko.

APPLIED ELECTROCHEMISTRY AND CORROSION PROTECTION OF METALS

Kinetics of Copper(II) Electrodeposition from Dilute Electrolytes with a Bipolar Electrode

N. D. Ivanova, A. I. Gerasimchuk, and N. E. Vlasenko

Vernadsky Institute of General and Inorganic Chemistry, National Academy of Sciences of the Ukraine, Kiev, Ukraine

Received December 11, 2001

Abstract—Results obtained in electrodeposition of copper(II) from sulfate solutions with a bipolar electrode are presented.

The principle of operation of the bipolar electrode and its industrial applications are known [1], but this electrode remains unconventional and its possibilities are far from being exhausted.

Noteworthy is the fact that the bipolar electrode allows very high current densities, occasionally exceeding by a factor of several tens those on monopolar electrodes [2]. The kinetics of the electrochemical process on the bipolar electrode has not been studied at all, and, therefore, the aim of this study is to analyze the mass transfer and its components.

The main distinction of the bipolar electrode from the monopolar one is that current is not fed directly to this electrode, being supplied to auxiliary electrodes (Fig. 1).

In studying the mass transfer, we measured stationary polarization curves (by points) with and without a supporting electrolyte (1 M Na_2SO_4 solution). The experimental error did not exceed 3%. As objects of study served dilute solutions which modeled washing water from the copper plating process. The concentration of copper ions was varied between 0.003 and 0.015 M. To our knowledge, the bipolar electrode has not been used in such cases previously, and, therefore, the investigations performed expand its application field.

Figure 2a presents typical stationary polarization curves for electrodeposition of copper. On introducing a supporting electrolyte, the curves virtually coincide in the limiting current range for monopolar and bi-

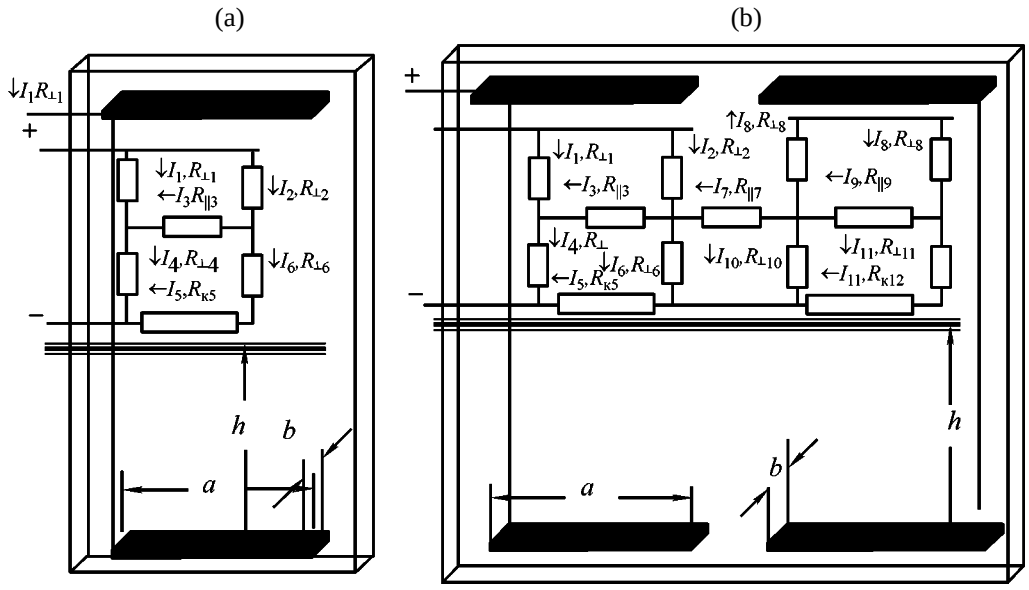

Fig. 1. Schematic arrangement of electrodes and their electrical equivalents. Electrode: (a) monopolar and (b) bipolar.

1070-4272/02/7507-1079$27.00 © 2002 MAIK "Nauka/Interperiodica"

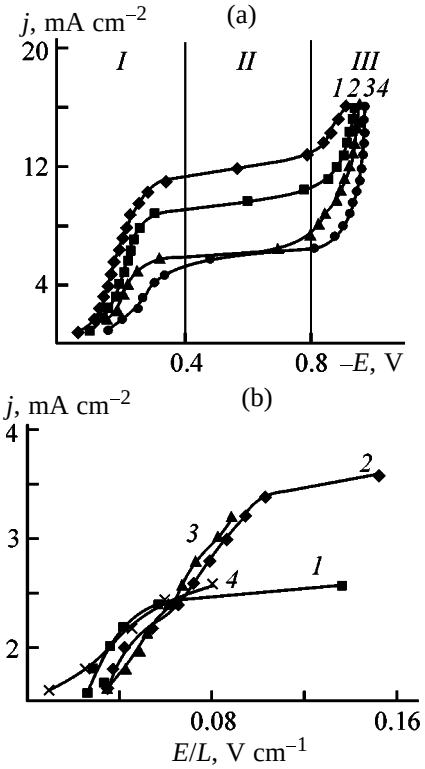

Fig. 2. (a) Stationary polarization curves of copper electrodeposition on electrodes and (b) current density vs. potential gradient for (*1, 4*) monopolar and (*2, 3*) bipolar electrodes. (a) Initial concentration of copper ions 0.078 M and (b) interelectrode spacing L = 5 cm. (*j*) Current density, (*E*) potential, and (*E*/*L*) potential gradient. (a) Electrode: (*1, 3*) bipolar and (*2, 4*) monopolar; (*3, 4*) with supporting electrolyte. (b) Curves: (*1, 2*) experimental and (*3, 4*) calculated.

polar electrodes (curves *3* and *4*), characterizing the limiting diffusion current. Its value is in agreement with the limiting diffusion currents theoretically calculated for the given concentration of metal ions. In calculating the diffusion component, the thickness of the diffusion layer was taken to be 10^{-3}, which corresponds to vertical arrangement of electrodes with account taken of the natural convection [3]. In the absence of a supporting electrolyte, the limiting currents differ widely, with the currents on the bipolar electrode much exceeding those on the monopolar electrode. Hence follows that the migration component makes a major contribution to mass transfer. Under the experimental conditions, this difference of the limiting currents is about 2.8 mA cm^{-2}, or 30%.

When analyzing the polarization curves, we established that not only the limiting currents, but also the electrode potentials are different. All other conditions being the same, the potential of the bipolar electrode is shifted to the electronegative region by 100–150 mV as compared to the potentials of the monopolar electrode. This may serve as evidence in favor of a higher gradient of potential in the case of a bipolar electrode. Indeed, the migration current i_m is described by the equations [3]

$$i_m = -DC\frac{zF}{RT}\operatorname{grad}\varphi, \qquad i_m = -CU^0\operatorname{grad}\varphi,$$

$$U^0 = D\frac{zF}{RT},$$

where U^0 is the absolute velocity of ion motion at unit field strength **E** (V cm^{-1}).

Thus, $\mathbf{E} = -\operatorname{grad}\varphi$. All other conditions (metal ion concentration in solution, solution viscosity, ion mobility) being the same, the larger migration component in the case of a bipolar electrode may by due only to a rise in the electric field strength, i.e., in the potential gradient. This quantity is characterized by the ratio of the voltage applied to the cell to the interelectrode spacing: $\Delta U/L$ [4]. Finding the potential gradient is a complicated task even for the simplest electrochemical cell. In this study, we analyze cells of this kind with mono- and bipolar electrodes (Fig. 1), with the potential gradient determined experimentally and theoretically. In the cell with a bipolar electrode, platinum plates served as auxiliary electrodes, and a copper plate, as the working electrode. The interelectrode spacing L was 5, 7, and 9 cm. The potential difference across the electrodes was measured with a millivoltmeter with high input resistance [5].

The results of measurements are presented in Fig. 2. The $\Delta U/L$ ratio increases with decreasing interelectrode spacing. Hence follows that the matter concerns just the electric field strength, and not the voltage drop in electrolyte or electrode. Otherwise, an inverse relationship would be observed because of the increase in the resistance of the electrolyte and the electrode itself. Furthermore, it is known that the so-called ohmic polarization [6] does not affect the nature or rate of electrochemical processes. At the same time, as shown above, the rate of the process markedly increases in going from a monopolar to a bipolar electrode. The 50 mV cm^{-1} difference between the electric field strengths in the electrodes being compared leads to a rise in the limiting current by approximately 40%.

The electrode polarization results in the appearance in the cells of potential gradients directed perpendicularly to, and in parallel with the cathode (anode) [7]. This gives rise to longitudinal and transverse components of currents and voltages (Fig. 1).

The integral characteristics and estimates of these gradients (and, correspondingly, of the processes occurring in electrochemical cells) are currents and voltage drops in different parts of the cell, which is divided in two. The geometric parameters in the corresponding direction are halved. The electrolyte resistance in the transverse direction

$$R_{\perp} = \rho_e(I)h/(4ab),$$

and in the longitudinal direction,

$$R_{\parallel} = \rho_e(I)a/(2hb),$$

the resistance of the cathode material, which cannot be neglected,

$$R_c = \rho a/(2S_c),$$

where $\rho_e(I)$ is the electrolyte resistivity as a function of the current in the given part of the cell, $\rho = 1/æ$; æ, the electrical conductivity of the electrolyte; a and b, the electrode length and width, respectively; h, the cathode-to-anode distance; and S_c, the cathode cross-section area.

The electrolyte resistivity depends on the current density [8]; however, in the given case, the current density is expressed in terms of the cell parameters:

$$j_{\perp} = 2I_{\perp}/(ab), \qquad j_{\parallel} = I/(hb),$$

We studied the dependence of the average conductivity on current density, represented as a polynomial expression

$$æ_e(j) = (\rho j)^{-1} = \sum_{k=0}^{n} a_k j^k,$$

where j is the current density passing through the electrolyte.

A third-order polynomial was chosen for approximation with the least-squares procedure. It was found that $a_0 = 3.24$, $a_1 = 0.463$, $a_2 = 1.733$, and $a_3 = -0.25$.

The obtained polynomial expression for conductivity is the key formula in calculating a cell of any configuration. The equivalent circuits of the cells (Fig. 1) were used to construct matrices for all the currents I_1, ..., I_N. In the same way were constructed, in accordance with the Kirchhoff law, the matrices for voltages and resistances. Thus, finding the vector of the currents in the cell is reduced to solution of the matrix equation $[R][I] = [U]$.

The nonlinearity of the matrix equations is apparent, and, therefore, the solution is obtained by iteration processes $[I]_{N+1} = [Y]_N[U]$, where N is the number of iteration, and $[Y]$ is a matrix inverse to the matrix of resistances. The bipolar cell has geometric parameters similar to those of the monopolar cell, but with one more equivalent resistance, R_n, introduced. The quantity $I_eR_n(I_e)$ expresses the longitudinal component of the potential gradient between the two parts of the bipolar cell. The resistance R_n is analogous to $R_{\parallel}$ with a certain correction for the intermediate resistance, e.g., of the partition diaphragm. According to the equivalent circuit, the total current in the cells is given by $I = I_1 + I_2$. The resistances in the equivalent circuits, expressed in the matrix form $[R][I] = [U]$, yield the pattern of potential gradient distribution in the mono- and bipolar cells. In the latter case, the electric field strength and, consequently, the potential gradient are much higher. The results of calculation are in satisfactory agreement with the experimental data (Fig. 2b).

CONCLUSIONS

(1) The high rate of mass transfer in the case of a bipolar electrode is due to a major contribution of the migration component. This results from the higher potential gradient compared to the monopolar electrochemical cell. The method proposed for theoretical calculation takes into account the type of electrolyte, cell configuration, and nature of current leads, and well describes the difference in the potential gradients between the mono- and bipolar cells.

(2) The bipolar electrode can be used in electrodeposition of metal from dilute solutions modeling the washing water from electroplating shops.

REFERENCES

1. Bagotskii, V.S., *Osnovy elektrokhimii* (Foundations of Electrochemistry), Moscow: Khimiya, 1988.
2. Ivanova, N.D., Boldyrev, E.I., and Vlasenko, N.E., *Ekotekhnol. Resursosberezh.*, 1999, no. 2, pp. 26–28.
3. Damaskin, B.B. and Petrii, O.A., *Vvedenie v elektrokhimicheskuyu kinetiku* (Introduction to Electrochemical Kinetics), Moscow: Vysshaya Shkola, 1975.
4. Newman, J., *Ind. Eng. Chem. Fundam.*, 1966, vol. 5, no. 4, pp. 525–529.
5. Krasikov, N. and Fadeeva, S., *Izv. Vyssh. Uchebn. Zaved., Khim. Khim. Tekhnol.*, 1995, vol. 38, no. 3, pp. 125–128.
6. Vetter, K.J., *Elektrochemische Kinetik*, Berlin: Springer, 1961.
7. Yavorskii, B.M. and Detlaf, A.A., *Spravochnik po fizike* (Handbook of Physics), Moscow: Nauka, 1990, 3rd ed.
8. Rotinyan, A.L., Tikhonov, K.I., and Shoshina, I.A., *Teoreticheskaya elektrokhimiya* (Theoretical Electrochemistry), Leningrad: Khimiya, 1981.

Russian Journal of Applied Chemistry, Vol. 75, No. 7, 2002, pp. 1082–1086. Translated from Zhurnal Prikladnoi Khimii, Vol. 75, No. 7, 2002, pp. 1099–1103.
Original Russian Text Copyright © 2002 by Rudnev, Lukiyanchuk, Kon'shin, Gordienko.

APPLIED ELECTROCHEMISTRY AND CORROSION PROTECTION OF METALS

Anodic-Spark Deposition of P- and W (Mo)-Containing Coatings onto Aluminum and Titanium Alloys

V. S. Rudnev, I. V. Lukiyanchuk, V. V. Kon'shin, and P. S. Gordienko

Institute of Chemistry, Far-Eastern Division, Russian Academy of Sciences, Vladivostok, Russia

Received February 11, 2002

Abstract—Data of ^{31}P NMR spectroscopy, conductometry, and pH-metry, and results of experiments on Na_2WO_4 replacement with $Na_2H[PW_{12}O_{42}]$ were used to study the relationship between the joint and proportional incorporation of P and W (Mo) into coatings, on the one hand, and the presence of heteropolyoxo anions in the electrolyte, on the other.

It has been shown previously [1] that simultaneous incorporation of phosphorus and vanadium into anodic-spark coatings on aluminum alloys from electrolytes containing $NaVO_3$ and $Na_6P_6O_{18}$ or NaH_2PO_4 is associated with the presence of heteropolyoxo anions (HPA) $[PV_{14}O_{42}]^{9-}$ in the solution bulk. The coatings formed, containing up to 22 wt % vanadium and 12 wt % phosphorus, possess a number of practically important properties. In particular, they decrease 10–100-fold the currents of the corrosion pairs aluminum/titanium, St.3/titanium, etc. in a 3% NaCl solution [2]. Vanadium-, and also tungsten- and molybdenum-containing anodic layers can be used not only in corrosion protection, but also for other purposes, e.g., in catalysis. A wide variety of tungsto- or molybdophosphate HPAs can be formed in aqueous tungstate– or molybdate–phosphate solutions, depending on the relative concentrations of the components, order of their introduction, pH value, and temperature [3]. By analogy with vanadate–phosphate electrolytes, it would be expected that phosphorus and W (Mo) are jointly incorporated into coatings as a result of the involvement of the forming HPA in high-temperature reactions initiated by electric discharges at the anode.

In this work, we studied the relationship between the ionic composition of aqueous electrolytes with PO_4^{3-}, WO_4^{2-}, and MoO_4^{2-} groups, on the one hand, and the elemental composition of coatings formed on anodes made of aluminum and titanium alloys at voltages of spark and microarc electric breakdowns.

EXPERIMENTAL

The electrolytes were prepared using distilled water and commercial chemicals: $NaH_2PO_4 \cdot 2H_2O$ and $Na_2HPO_4 \cdot 12H_2O$ of pure grade, $Na_2H[PW_{12}O_{42}] \cdot 9H_2O$ of chemically pure grade, and $Na_2WO_4 \cdot 2H_2O$ and $Na_2MoO_4 \cdot 2H_2O$ of analytically pure grade. As in phosphate–vanadate solutions [1], the concentration of NaH_2PO_4 in the electrolytes with sodium tungstate and molybdate was 0.3 M. First sodium dihydrogen phosphate, and then sodium tungstate and molybdate were dissolved, with their concentration raised gradually.

The anodic films were formed on electrodes made of technical-grade VT1-0 titanium and AMtsM aluminum alloy at current density of 0.05 A cm^{-2} in the course of 5 min, unless otherwise specified. As a current source served a TER-100/460R-2/2UKhL4 thyristor converter with unipolar pulse shape. Depending on the electrolyte composition, the first visible spark discharges appeared at the anodes 0.5–1.5 min after the beginning of the process.

The elemental composition of the films was determined on an EMAL-2 laser spectrometer and a JXA-5A X-ray fluorescence microprobe analyzer. X-ray phase analysis of coatings on substrates was made on a DRON-3.0 X-ray diffractometer (CuK_α radiation). The electrical conductivity of aqueous solutions was measured with a conductometer. The ^{31}P NMR spectra of aqueous solutions were recorded on a Bruker WP80SY high-resolution spectrometer at a frequency of 32.442 MHz. The chemical shifts are given on the δ scale (ppm) relative to 85% H_3PO_4.

Figure 1 shows the elemental composition of anodic coatings on titanium (Fig. 1a) and aluminum alloy (Fig. 1b) as a function of the Na_2WO_4 concentration in an electrolyte containing 0.3 M NaH_2PO_4. With increasing amount of sodium tungstate in solution,

1070-4272/02/7507-1082$27.00 © 2002 MAIK "Nauka/Interperiodica"

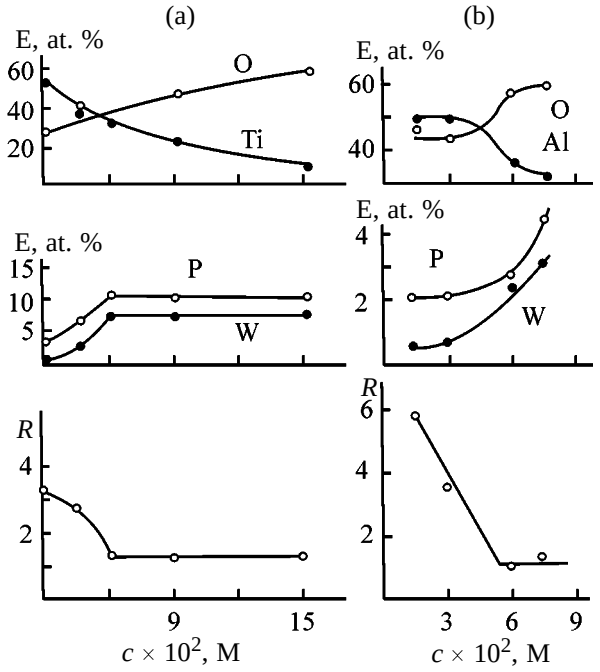

Fig. 1. Elemental composition E and the ratio R of atomic contents of phosphorus and tungsten for coatings on (a) titanium and (b) aluminum alloy vs. concentration c of Na_2WO_4 in 0.3 M aqueous NaH_2PO_4. The coatings were formed in 5 min at a current density of 0.05 A cm^{-2}.

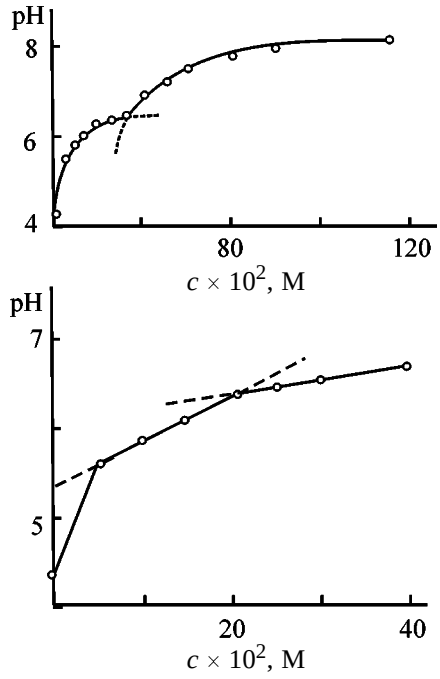

Fig. 2. pH of 0.3 M NaH_2PO_4 solution vs. Na_2WO_4 concentration c.

the content of titanium or aluminum in the coatings decreases, and that of oxygen grows. In the case of titanium, phosphorus and tungsten are incorporated into a film as follows: up to a concentration of 0.06 M, their content increases (phosphorus to 10 at. % and tungsten to 8 at. %) and then remains at this level when further amounts of sodium tungstate are added to the electrolyte. At Na_2WO_4 concentrations exceeding 0.06 M, the ratio of atomic contents of phosphorus and titanium is the same in coatings on both titanium and aluminum alloy and equal to about 1.3.

The sodium tungstate concentration affects the coloration of films formed on the aluminum alloy. At Na_2WO_4 concentrations $c \le 0.045$ M, the films are gray. At $c \ge 0.6$ M, the films are similar in coloration to marble or a kind of enamel, with darker broken lines or spots chaotically scattered on a gray background; the type of sparking at the anode (number per unit surface area, color and size of sparks) changes, and the voltage across the electrodes at a given instant of time decreases. At concentrations $c \ge 0.075$ M, formation of coatings on the AMtsM alloy is hindered. In this case, slow-moving electric discharges appear at the aluminum anode several minutes after the beginning of uniform sparking. These discharges occupy a large surface area and destroy the coating formed before their appearance to bare metal.

Thus, judging from the changes in characteristics of spark discharges and in the formation voltage, color, and elemental composition of the coatings, the concentration of 0.06 M Na_2WO_4 in an electrolyte with sodium dihydrogen phosphate is distinctive. At $c \ge 0.06$ M, the solution acquires yellowish coloration after electrolysis. The coloration becomes more intense with the content of sodium tungstate increasing further. The yellow coloration is characteristic of aqueous solutions of tungstophosphates [3]. The change in the ionic composition is confirmed by the data obtained in measuring the pH value and electrical conductivity (Figs. 2, 3). The curve describing the dependence of the electrical conductivity on concentration exhibits a bend at about 0.05 M, which indicates that the type of charge carriers in solution

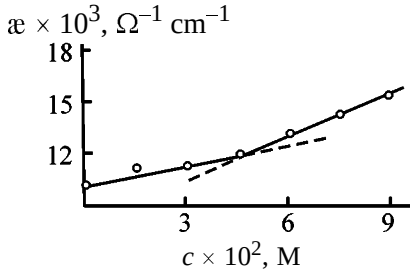

Fig. 3. Electrical conductivity æ of NaH_2PO_4 vs. $Na_2WO_4 \cdot 2H_2O$ concentration c.

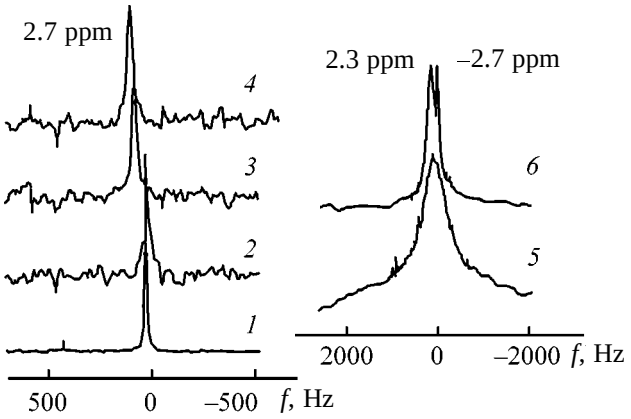

Fig. 4. ^{31}P NMR spectra of aqueous solutions containing 0.03 M NaH_2PO_4. (*f*) Frequency. Na_2WO_4 concentration (M): (*1*) 0, (*2*, *5*) 0.03, (*3*, *6*) 0.15, and (*4*) 0.24. (*1–4*) Before and (*5*, *6*) after formation of anodic-spark coatings.

changes. The variation of all the parameters points to the occurrence of complexation in solution.

Figure 4 presents the ^{31}P NMR spectra of aqueous tungstate–phosphate solutions before and after deposition of anodic-spark coatings onto aluminum alloy. In solutions that were not used for coating formation, addition of Na_2WO_4 in amounts exceeding 0.03 M shifts the ^{31}P resonance line from 0.2 to 2.2–2.7 ppm. This shift may be due to a change in the concentration of the $H_2PO_4^-$, HPO_4^{2-}, and PO_4^{3-} ions in solution with increasing pH value. After electrolysis, the spectra change. In an electrolyte containing 0.03 M Na_2WO_4, the resonance line is broadened, which indicates that the phosphorus(V) speciation in solution is altered. At an Na_2WO_4 concentration of 0.15 M, the resonance line is split in two, with chemical shifts of 2.3 and –2.1 ppm. The resonance line with the chemical shift δ = –2.1 ppm can be assigned to tungstophosphates $[P_2W_5O_{23}]^{6-}$ and $[P_4W_8O_{40}]^{12-}$ [3]. The changes in the ^{31}P NMR spectra upon coating formation presumably result from both electric-breakdown phenomena, accompanied by electrolysis of water [4], and an increase in the content of aluminum and titanium ions in the electrolyte bulk [5] and from a change in the electrolyte parameters in the near-anode and near-cathode spaces. For example, this may be due to acidification and warming-up of the near-anode region of the electrolyte, which creates favorable conditions for formation of HPA differing in structure and composition from those forming in weakly alkaline, neutral, or weakly acidic solutions at room temperature. It is noteworthy that the solutions used are characterized by a significant excess of PO_4^{3-} ions with respect to WO_4^{2-}.

Thus, in phosphate–tungstate electrolytes, as also in phosphate–vanadate electrolytes [1], there is a correlation between complexation processes in the solution bulk (solution color, conductometric and pH-metric measurements, ^{31}P NMR spectra) and changes in the elemental composition of the forming films. As in the case of electrolytes with vanadophosphates, the content of aluminum or titanium in the anodic-spark films decreases, and that of oxygen, phosphorus, and tungsten increases, with the formation of tungstophosphates in solution. The independence of the P/W atomic ratio in the coatings (Fig. 1) from the concentration of sodium tungstate at $c \geq 0.6$ M must be associated with a certain chemical composition of the films formed.

It is noteworthy that coatings containing the crystalline phases of $Al_2(WO_4)_3$, WO_3, and $W_{18}O_{49}$ are formed in a 0.1 M aqueous solution of Na_2WO_4 on an aluminum anode under the action of spark and microarc discharges [6]. In this case, the phase composition depends on the mode of film formation and electrolyte development. In the course of the development (successive formation of coatings on a number of samples), the electrolyte becomes colloidal, and then a precipitate containing $WO_3 \cdot H_2O$ is formed. The coatings obtained on the aluminum alloy in electrolytes containing NaH_2PO_4 and Na_2WO_4 are X-ray amorphous. Such electrolytes are stable and do not change their aggregative state when in use. The sequential processing of a batch of samples results in that the yellow coloration of the solution becomes more intense, which indicates an increase in the concentration of tungstophosphates.

The elemental composition of anodic films obtained on titanium in an electrolyte containing 0.3 M of NaH_2PO_4 and 0.17 M of sodium molybdate is given below (deposition mode: i = 0.05 A cm^{-2}, t = 10 min):

Element	Content, at. %	Element	Content, at. %
C	2.7	P	13.0
N	0.3	Ti	17.7
O	60.1	Mo	5.4

Comparison of the above data with those in Fig. 1 shows that the element contents are virtually the same in Mo- and W-containing coatings. At the same time, the content of carbon is an order of magnitude higher in coatings with phosphorus and molybdenum. The presence of carbon in the coatings is associated with

Effect of electrolyte composition and characteristics on the composition of coatings*

Electrolyte no.	pH	æ × 10^3, Ω^{-1} cm^{-1}	Coatings on aluminum**					Coatings on titanium**				
			U, V	content, wt %			P/W atomic ratio	*U*, V	content, wt %			P/W atomic ratio
				Al	W	P			Ti	W	P	
1	2.2	3.5	324	8.1	43.9	0.4	0.05	74	87.8	0.41	0.03	0.43
2	3	13.2	138	43.3	0.6	3.3	34.9	174	17.5	31.2	5.6	1.1
3	6	16.7	218	37.4	8.2	1.7	1.3	149	18.2	26.7	7.1	1.6
4	6.5	14.2	289	33	14.2	4	1.7	126	18.6	25.8	5.9	1.4

* æ is the electrical conductivity of the solutions, and *U* is the final formation voltage.

** Elemental composition of coatings was found by X-ray fluorescence electron microprobe analysis; the electrolytes and coating formation modes are described in text.

carbon dioxide dissolved in the electrolyte. It may be suggested that synthesis of carbon-containing compounds is caused by the catalytic effect of the whole set of molybdenum and tungsten oxides in high-temperature reactions initiated by electric breakdowns. Carbon is firmly fixed in the coatings, since it remains in the coating subjected to a vacuum with residual pressure of down to 10^{-6} mm Hg in the vacuum chamber of the laser mass spectrometer.

To verify the assumption that HPAs affect the coating composition, an electrolyte containing 0.3 M NaH_2PO_4 and 0.075 M Na_2WO_4 (see table, electrolyte no. 4) was modeled. Sodium tungstate was replaced with $Na_2H[PW_{12}O_{42}]$. Electrolytes of the following compositions were used (M): no. 1: $Na_2H \cdot [PW_{12}O_{42}]$ 0.006; no. 2: $Na_2H[PW_{12}O_{42}]$ 0.006 and NaH_2PO_4 0.29; and no. 3: $Na_2H[PW_{12}O_{42}]$ 0.006, NaH_2PO_4 0.22, and Na_2HPO_4 0.07.

The concentrations of tungsten are the same in electrolyte nos. 1–4, and those of tungsten and phosphorus, in electrolyte nos. 2–4; the pH values are close in electrolyte nos. 3 and 4. Heteropoly blues are formed during anodic-spark oxidation of aluminum and titanium in electrolyte nos. 1–3, with the solutions remaining true. At the same time, the interaction with atmospheric oxygen leads to solution decoloration in the absence of electrolysis. In electrolyte no. 3, formation of reduced forms of HPAs is less pronounced, presumably, because of the higher pH value. During electrolysis, this electrolyte acquires first light blue and then yellowish-greenish color, which is characteristic of electrolyte no. 4.

The coatings formed on the aluminum alloy in electrolyte no. 1 contain the largest amount of tungsten, and the smallest, of phosphorus. X-ray phase analysis shows the presence of tungsten oxide $WO_{2.9}$ in their composition. In anodization of titanium in this electrolyte, the sparking mode cannot be attained in 5 min. As a result, very thin coatings of temper coloration are formed. The coatings formed in electrolyte nos. 2–4 are X-ray amorphous and contain an order of magnitude greater amount of phosphorus. Formation of coatings on the aluminum alloy is hindered in electrolyte no. 2. After 5 min of treatment, aluminum anodes are covered with partly gray anodic-spark film and partly with light gray anodic film. Rough light gray anodic-spark layers are formed on titanium anodes.

Electrolyte no. 3 is the closest in composition and pH value to electrolyte no. 4 being modeled. These electrolytes have close formation parameters (final voltage across the electrodes) and coating compositions on both aluminum and titanium. Thus, model experiments confirm the assumption that the presence of tungstophosphate HPAs in the electrolyte bulk affects the composition of coatings obtained by anodic-spark deposition.

One of the most important stages of an electrochemical process is adsorption. Tungstate ions can protect metals from corrosion by forming a film of isopoly compounds on their surface [7]. In the given case, the incorporation of HPA components into the coatings may result from formation on the oxide surface of an adsorbed HPA layer involved in reactions occurring at, and around, electric breakdowns.

Thus, it follows from the results presented here and data of [1] that the quantitative changes in the elemental composition of anodic-spark layers formed in phosphate–vanadate, phosphate–tungstate, and phosphate–molybdate electrolytes, simultaneous and proportional incorporation of phosphorus and M (M = W, Mo, or V) into coatings, and the decreasing

content of the anode metal correlate with the change in the ionic composition of the electrolytes and the formation of vanado-, tungsto-, and molybdophosphates in them.

The incorporation of the electrolyte components into anodic-spark coatings results from the occurrence of high-temperature reactions on the anode surface, including thermolysis of deposits from the electrolyte in regions adjacent to the breakdown channels. Here, account should be taken of the fact that only those of the compounds synthesized on the anode remain in the coating, which are insoluble in a given electrolyte. The following sequence of stages in which anodic-spark layers are formed in electrolytes with HPAs can be suggested. A layer of oxide of the anode metal is formed in the prespark region. Electrolyte anions are adsorbed on this layer. Sparking is accompanied by additional deposition on the anodes of the salts contained in the electrolyte. Thermolysis of heteropoly compounds results, in certain electric breakdown modes, in the formation of oxides of the constituent elements and products of interaction with the substrate material. If the compounds formed are insoluble in the electrolyte, then and "island" ("nucleus") of the new phase remains in the vicinity of a breakdown.

The results presented here, as well as the data of [1, 2], give reason to believe that, by creating in the electrolyte bulk favorable conditions for formation of HPA of a known composition, one can introduce necessary elements into anodic-spark layers, i.e., purposefully change the composition of the anodic coatings.

CONCLUSIONS

(1) Joint incorporation of phosphorus and tungsten into anodic layers formed on an aluminum alloy and titanium under the action of electric breakdowns from electrolytes containing 0.3 M of NaH_2PO_4 and Na_2WO_4 is due to the presence in the electrolyte of tungstophosphate heteropolyoxo anions.

(2) The P/W atomic ratio in coatings formed on both titanium and aluminum is 1.2–1.6 at an Na_2WO_4 concentration of 0.06 M and more in an electrolyte containing 0.3 M NaH_2PO_4.

(3) Electrolytes containing NaH_2PO_4 and Na_2WO_4 are stable and do not change their aggregative state in electrolysis and coating formation.

(4) The amount of carbon in coatings obtained in anodic-spark deposition on titanium from molybdate–phosphate electrolytes exceeds by an order of magnitude that in the case of tungstate–phosphate electrolytes.

ACKNOWLEDGMENTS

The authors thank A.S. Rudnev (Far-Eastern State University) for assistance in determining the elemental composition of the coatings.

REFERENCES

1. Rudnev, V.S., Gordienko, P.S., Kon'shin, V.V., *et al*., *Elektrokhimiya*, 1996, vol. 32, no. 10, pp. 1242–1246.
2. Gordienko, P.S., Rudnev, V.S., Orlova, T.I., *et al*., *Zashch. Met*., 1993, vol. 29, no. 5, pp. 739–742.
3. Pop, M.S., *Geteropoli- i izopolioksometallaty* (Heteropoly and Isopolyoxo Metallates), Novosibirsk: Nauka, 1990.
4. Ragalyavichus, R. and Yusis, Z., *Chemija* (Lithuania), 1992, no. 2, pp. 45–50.
5. Li, Y., Shimada, H., Sakaizi, M., *et al*., *J. Electrochem. Soc*., 1997, vol. 144, no. 3, pp. 866–876.
6. Rudnev, V.S., Morozova, V.P., Yarovaya, T.P., *et al*., *Zashch. Met*., 1999, vol. 35, no. 5, pp. 524–526.
7. Vas'ko, A.T. and Kovach, S.K., *Elektrokhimiya tugoplavkikh metallov* (Electrochemistry of Refractory Metals), Kiev: Tekhnika, 1983.

Russian Journal of Applied Chemistry, Vol. 75, No. 7, 2002, pp. 1087–1090. Translated from Zhurnal Prikladnoi Khimii, Vol. 75, No. 7, 2002, pp. 1104–1107.
Original Russian Text Copyright © 2002 by Shembel', Apostolova, Nagirnyi, Aurbach, Markovsky.

APPLIED ELECTROCHEMISTRY AND CORROSION PROTECTION OF METALS

Electrolytic Sodium–Vanadium Oxide Compounds in Intercalation Cathodes of Lithium Battery

E. Shembel', R. Apostolova, V. Nagirnyi, D. Aurbach, and B. Markovsky

Ukrainian State University of Chemical Engineering, Dnepropetrovsk, Ukraine
Bar-Ilan University, Ramat-Gan, Israel

Received August 27, 2001; in final form, February 2002

Abstract—Electrolytic mixtures of vanadium(V) oxide and β-$Na_xV_2O_5$ bronze were synthesized and studied by X-ray diffraction and thermal analyses, step galvanostatic titration, IR absorption spectroscopy, mass spectroscopy, and electrochemical methods.

Vanadium oxide compounds (VOCs) obtained by electrolysis of aqueous solutions are used for preparing ballastless cathodes of thin-film lithium batteries [1–3]. Oxovanadium(V) sulfate solutions containing 20 g l^{-1} sodium ions were used to synthesize a monoclinic sodium–vanadium oxide bronze β-$Na_xV_2O_5$ (x = 0.22–0.40) [4–6]. In thin-film cathodes of lithium battery, it provides enhanced discharge characteristics. Since sodium ions increase adhesion of vanadium deposits to a substrate, we continued a study of the electrolytic sodium-containing VOCs (NaVOCs). Some physicochemical and electrochemical characteristics of 5NaVOCs synthesized from solutions of $VOSO_4$ containing 5 g l^{-1} sodium ions were reported in [7].

Here we report new data on electrolytic 5NaVOCs, which show promise as cathode materials for lithium batteries.

EXPERIMENTAL

Electrolytic 5NaVOCs were synthesized by the method [4, 5] developed for β-$Na_xV_2O_5$ bronze, except that the concentration of sodium ions in the electrolyte was decreased to $c \le 5$ g l^{-1}.

The test objects were thin-film "ballastless" cathodes (1–40 mg cm^{-2}) and 5NaVOC composite electrodes prepared with addition of carbon black and fluoroplastic binder (10 wt % each) [2, 4].

The X-ray diffraction analysis and IR absorption study of 5NaVOC samples were performed as described in [4, 5]. Thermal analysis and mass-spectroscopic study were done with a Mettler Toledo Star^C System on 13-mg powdered 5NaVOC samples heated at a rate of 10 deg min^{-1}.

The reversible electrochemical intercalation of lithium ions into the compounds synthesized was studied in the electrolytes containing (i) propylene carbonate (PC), dimethoxyethane (DME) [PC : DME = 2 : 1 (by volume)], and 1 M $LiClO_4$, and (ii) ethylene carbonate (EC), dimethyl carbonate (DMC) [EC : DMC = 1 : 3 (by volume)], and 1 M $LiAsF_6$ [5, 6].

The chemical coefficient of the lithium ion diffusion in the course of electrochemical intercalation was determined by step galvanostatic titration [8], which, as applied to vanadium oxides, was described in detail in [2, 4].

The electrolytic 5NaVOC samples obtained in the form of finely dispersed powder or as compact deposit on stainless steel gauze are finely crystalline black formations of brown shades. They were studied in various heat-treatment modes.

According to the X-ray diffraction analysis, the non-heat-treated 5NaVOC deposits dried at room temperature are a mixture of orthorhombic vanadium(V) oxide and $V_2O_4 \cdot H_2O$. The presence of sodium–vanadium oxide compound in these deposits was confirmed by weak diffuse reflections of NaV_6O_{15}, also present in the diffraction pattern.

The thermal analysis and mass spectrometry of the 5NaVOC powder revealed the presence of water and of impurities of carbonate and sulfate ions. The mass spectrum contains peaks at m/z 16, 18, 39, 44, and 64, probably corresponding to O_2, H_2O, an unidentified compound, CO_2, and SO_2, respectively, released on heating. These compounds are formed by decom-

1070-4272/02/7507-1087$27.00 © 2002 MAIK "Nauka/Interperiodica"

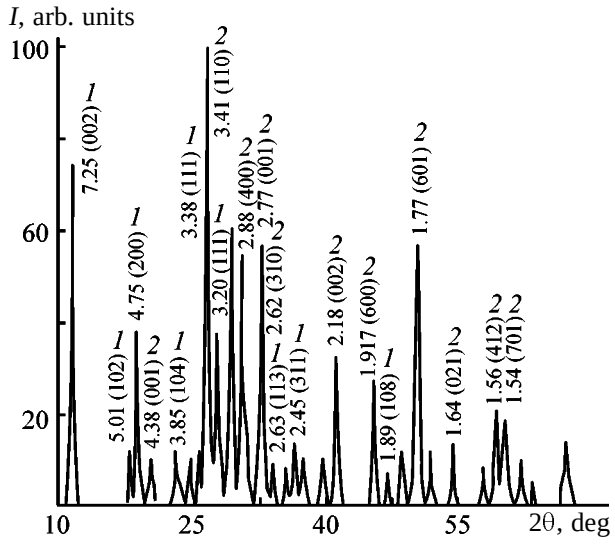

Fig. 1. Diffraction pattern of the 5NaVOC powder. T = 500°C, 7 h, CuK_α radiation. (*I*) Reflection intensity and (2θ) Bragg angle. (*1*) NaV_6O_{15} and (*2*) V_2O_5.

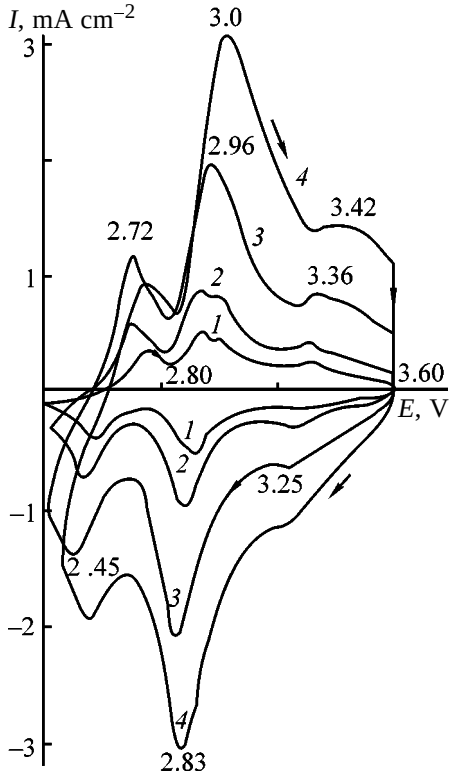

Fig. 2. Cyclic volatmmograms of 4.5 mg cm^{-2} 5NaVOC ballastless cathodes. T_{an} = 300°C; 2.5 h; electrolyte: PC, DME, and 1 M $LiClO_4$. (*I*) Current density and (*E*) potential; the same for Fig. 3. Potential sweep rate (V s^{-1}): (*1*) 10^{-4}, (*2*) 2×10^{-4}, (*3*) 5×10^{-4}, and (*4*) 1×10^{-3}.

position of the vanadium oxide compound, water evaporation, and decomposition of carbonate and sulfate impurity ions.

The presence of carbonates on the surface of 5NaVOCs was established previously by IR Fourier reflection spectroscopy [7]. The carbonates are formed by reaction of 5NaVOCs with atmospheric CO_2. The SO_2 evolution can result from the decomposition of impurity sulfates captured by the electrolytic deposit from the sulfate electrolyte.

The thermogravimetric (TG) curves show that the mass loss of the 5NaVOC sample on heating occurs in two stages in the range 50–400°C. The mass loss in the first stage (50–140°C) is due to evaporation of weakly bound water (0.91 mol mol^{-1} V_2O_5). The mass loss is maximal at 110°C. The second stage (140–400°C) is the evaporation of strongly bound water (0.23 mol mol^{-1} V_2O_5). The total content of water in 5NaVOC was 1.14 mol mol^{-1} V_2O_5. The content of sulfates, as judged from the negligible mass change in the corresponding temperature range (above 500°C), does not exceed trace amounts.

The 5NaVOC deposits heat-treated at high temperature (500°C, 7 h) acquire a light brown color imparted by a mixture of orange orthorhombic vanadium(V) oxide and black β-$Na_xV_2O_5$ bronze. The reflection intensities of these oxide compounds were found in the diffraction pattern of the 5NaVOC powder annealed at 500°C (Fig. 1).

The open-circuit voltage (OCV) of the thin-film ballastless 5NaVOC samples lies within 3.55–3.73 V depending on the heat treatment conditions.

The cyclic voltammograms of 5NaVOC depend on the deposit mass, annealing temperature T_{an}, and potential sweep rate. The voltammograms in the range from OCV to 2.40 V differ in the number of maxima, their positions, and currents.

The maxima for the 5NaVOC electrodes with a deposit mass of 3–4 mg cm^{-2} are more pronounced than for those with a mass of 20–40 mg cm^{-2}. As the potential sweep rate decreases, the current maxima become better resolved. For example, the cyclovoltammograms taken at a potential sweep rate of 10.5×10^{-4} V s^{-1} with the samples annealed at T_{an} = 300°C for 2.5 h have three cathodic current waves and three corresponding anodic current waves. At the lower sweep rate (1×10^{-4} V s^{-1}), the maximum close to 2.80–2.90 V is split in two. As a result, four maxima reflecting phase transitions in 5NaVOC are revealed in the cyclovoltammogram in the course of both intercalation and deintercalation of lithium ions. At lower

sweep rates, the potentials of the anode and cathode maxima become closer, i.e., the lithium ion intercalation becomes more reversible.

At similar values of the deposit mass (4 mg cm^{-2}) and sweep rate (5×10^{-4} V s^{-1}), the voltammograms are determined by the efficiency of the thermal action on the electrolytic deposit. In the cyclovoltammograms obtained with the 5NaVOC electrodes annealed at various temperatures, three current waves corresponding to phase transitions accompanying intercalation of lithium ions are always present: those near 3.20, 2.90, and 2.50 V (Fig. 3). The intensity of the current waves varies down to zero depending on the annealing temperature. As a result, three essentially different cyclovoltammograms are observed (Fig. 3). For example, the nonannealed deposits are characterized by one pronounced cathodic wave and one corresponding anodic wave. The potentials of the cathodic and anodic current maxima are 2.90 and 3.13 V, respectively (Fig. 3*a*). For the nonannealed sample, the second current wave (2.72 V) is weak and not always revealed in the anodic region. As shown above (Fig. 2, curve *3*), the cyclovoltammogram of the deposits annealed at T_{an} = 300°C for 2.5 h (Fig. 3*c*) has three current waves corresponding to intercalation and 3–4 waves corresponding to deintercalation of lithium ions. Increasing annealing temperature to 500°C changes the position of the current maxima and decreases the current value (Fig. 3*b*).

The current decrease can be explained by the crystallization of vanadium oxide compounds incorporated in 5NaVOCs, vanadium(V) oxide and β-bronze, during high-temperature annealing. After crystallization, the morphology of the deposits changes. According to the data of electron microscopy, the electrolytic deposits have a rather rough surface [2, 4]. The 0.5–3.0-μm ordered microformations were observed in the electron micrographs of the oxide compounds annealed at high temperatures. Annealing of the deposits increased their compactness, decreased the tortuosity and relief, and, as a consequence, decreased the specific surface area. Thus, to provide high specific discharge characteristics for 5NaVOC thin-film electrolytic compounds, it is necessary to optimize the thermal treatment conditions with the aim to prepare the cathode material with prescribed compactness, relief, adhesion to the substrate, and chemical composition. Attaining the crystallization and melting temperatures of the synthesized compounds in ballastless electrodes is undesirable. For such electrodes, the optimal annealing temperature is 300°C. The 5NaVOC deposits in the form of thin layers, annealed at 300°C for 2.5–7 h, have high specific discharge characteristics and high Coulombic efficiency of cycling (Fig. 4).

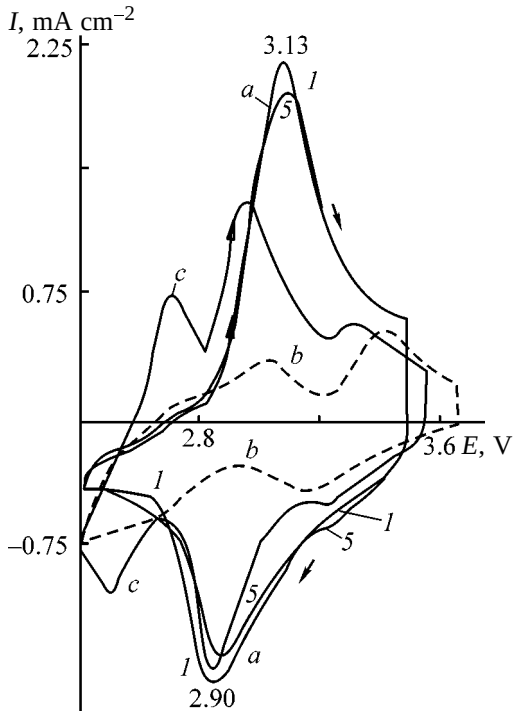

Fig. 3. Cyclic voltammograms of 5NaVOC ballastless electrodes. Potential sweep rate 5×10^{-4} V s^{-1}; Electrolyte: PC, DME, and 1 M $LiClO_4$. Annealing temperature (°C): (*a*) no annealing, (*b*) 500, and (*c*) 300. (*1*, *5*) Number of cycles at room temperature.

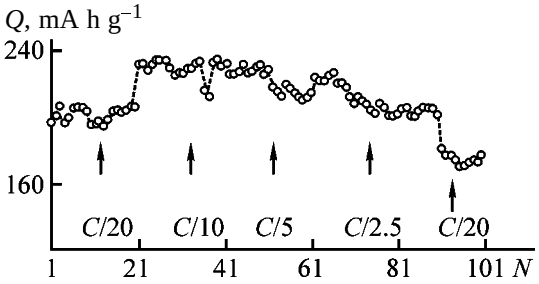

Fig. 4. Discharge capacity Q of the NaVOC ballastless electrode vs. the number of cycles N. T_{an} = 300°C; 2.5 h; electrolyte: EC, DMC, and 1 M $LiAsF_6$; electrode mass 1.1 mg cm^{-2}. $C/20$, $C/10$, $C/5$, and $C/2.5$ are capacities after 20, 10, 5, 2.5 h of discharge, respectively.

The galvanostatic discharge curve of the 5NaVOC electrodes annealed at T_{an} = 300°C depends on the deposit mass. This is due to the kinetic features of intercalation of the sodium ions into the deposit. In the course of electrolysis, sodium ions are intercalated into electrolytic vanadium oxide via the ion-exchange process [9]. For deposits with the 5NaVOC mass equal to or less than 1 mg cm^{-2}, the number of intercalated ions is less than that for the electrodes with

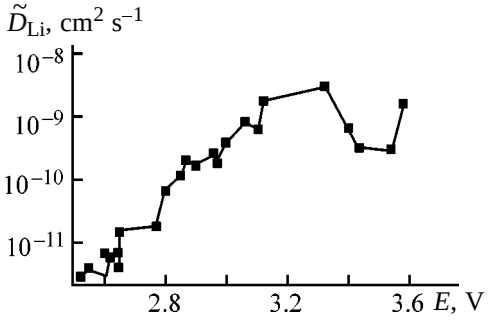

Fig. 5. Chemical coefficient of diffusion $\tilde{D}_{Li}$ for 5NaVOC ballastless electrode vs. electrode potential *E*. Electrolyte: PC, DME, and 1 M $LiClO_4$; electrode mass 1.1 mg cm^{-2}.

the deposit mass equal to or greater than 4 mg cm^{-2}. The galvanostatic discharge curve of the latter compounds is similar to that of electrolytic $Na_xV_2O_5$ β-bronze (three potential plateaus at 3.20, 2.90, and 2.60 V) [4, 5]. However, the potential plateaus for 5NaVOC are weakly pronounced. The discharge curve of the 5NaVOC electrodes with the deposit mass equal to or less than 1 mg cm^{-2} resembles to a greater extent that obtained with electrolytic vanadium(V) oxide [3], whose content exceeds the content of bronze in the 5NaVOC deposit.

Since 5NaVOC is a mixture of vanadium(V) oxide and bronze, the kinetics of intercalation of lithium ions is determined by lithium diffusion and phase formation in this complex system. Some insight into the variations of kinetics in the course of the lithium intercalation into 5NaVOC is given by the dependence of the chemical diffusion coefficient of lithium ions $\tilde{D}_{Li}$ on the electrode potential (Fig. 5). This dependence, obtained by step galvanostatic titration, does not noticeably differ from that obtained by pulsed potentiostatic titration and impedance spectroscopy [7]. The degree of intercalation of lithium ions into 5NaVOC decreases by two–three orders of magnitude after attaining the potential of 2.60 V (the coefficient of the lithium diffusion changes from approximately 10^{-9} to 10^{-12} cm^2 s^{-1}).

The discharge curves of the Li–5NaVOC composite electrodes (T_{an} = 300°C, 2.5 h) operating in the current source 2325 show that, in the course of the intercalation of lithium ions, the potential varies without sharp changes, with smoothly sloping potential plateaus near 3.20, 2.90, and 2.60 V. The smooth run of the discharge curve is well reproduced during the 73rd–100th galvanostatic cycles. The initial discharge capacity Q_1 was 190 mA·h·g^{-1} at the final potential E = 2.50 V and the capacity on the 73rd cycle, Q_{73} = 220 mA h g^{-1} (E = 2.30 V); I_{dis} = 100 μA cm^{-2}.

The high specific discharge characteristics of electrolytic 5NaVOC compounds make them promising as cathode materials for lithium batteries.

CONCLUSIONS

(1) Electrolytic deposits of sodium–vanadium oxide compounds show promise as ballastless electrodes for thin-film lithium batteries, the demand for which is fairly high.

(2) Sodium–vanadium oxide compounds in the form of dispersed powder are new heterogeneous electrode materials and, as composite paste electrodes of lithium batteries, compare well with vanadim(V) oxide.

REFERENCES

1. Shembel', E.M., Nagirnyi, V.M., Apostolova, R.D., and Chaikovskaya, I.M., *Zh. Prikl. Khim.*, 2000, vol. 73, no. 3, pp. 409–412.
2. Shembel, E., Apostolova, R., Nagirny, V., *et al.*, *J. Power Sources*, 1999, vol. 80, nos. 1–2, pp. 90–97.
3. Apostolova, R.D., Shembel', E.M., and Nagirnyi, V.M., *Elektrokhimiya*, 2000, vol. 36, no. 1, pp. 41–48.
4. Shembel, E., Apostolova, R., Nagirny, V., *et al.*, *J. Power Sources*, 1999, vols. 81–82, pp. 480–486.
5. Apostolova, R.D., Shembel', E.M., Nagirnyi, V.M., *et al.*, *Vopr. Khim. Khim. Tekhnol.*, 1999, no. 1, pp. 11–15.
6. Apostolova, R.D., Shembel', E.M., Nagirnyi, V.M., *et al.*, *Elektrokhimiya*, 2000, vol. 36, no. 6, pp. 695–703.
7. Aurbach, D., Markovsky, B., Salitra, G., *et al.*, *J. Power Sources*, 2001, vols. 97–98, pp. 486–490.
8. Weppner, W., and Huggins, R.A., *J. Electrochem. Soc.*, 1979, vol. 126, no. 12, pp. 2258–2266.
9. Apostolova, R.D., Shembel', E.M., Nagirnyi, V.M., *et al.*, *Elektrokhimiya*, 2001, vol. 37, no. 10, pp. 1205–1213.

Russian Journal of Applied Chemistry, Vol. 75, No. 7, 2002, pp. 1091–1094. Translated from Zhurnal Prikladnoi Khimii, Vol. 75, No. 7, 2002, pp. 1108–1111.
Original Russian Text Copyright © 2002 by Kolikova, Barsukova.

APPLIED ELECTROCHEMISTRY AND CORROSION PROTECTION OF METALS

A Possibility of Improving Lead Dioxide Electrode of Lead Battery

G. A. Kolikova and M. M. Barsukova

Istochnik Research Institute of Batteries, Joint-Stock Company, St. Petersburg, Russia

Received January 8, 2002

Abstract—The influence exerted by a reinforcing additive, an aqueous suspension of 4D fluoroplastic (Teflon), on the structural, physicochemical, and service characteristics of the positive electrode of the lead battery was studied. A paste with polymer and carbon additives, extending the service life of the lead dioxide electrode, was developed for industrial use.

Presently, lead batteries constitute about 85% of the entire amount of chemical power cells, and, therefore, further improvement of their service characteristics remains a topical task. One of the most important service characteristics of a lead battery is its service life, which largely depends on the service life of the positive electrode. The failure of a positive electrode is mainly due to corrosion of current leads (grids) and sagging of the active paste, with the shares of these factors being approximately equal.

The problems and methods of improvement of the positive electrode in a lead acid battery were reviewed in considerable detail in [1]. An analysis of the causes and mechanisms of disintegration of the active paste in the lead dioxide electrode revealed their fundamental nature, much hindering the possibility of eliminating this phenomenon [2].

One of ways to extend the service life of lead batteries is to use as a binder in the positive active paste an aqueous suspension of 4D fluoroplastic (Teflon) (VSF4D) [1]. This additive shows high chemical stability with respect to sulfuric acid and resistance to electrochemical oxidation at high anode potentials, which occur at the positive electrode.

However, despite the positive effect of this additive on the service life of lead batteries, it has not found practical use. The reason is that the results obtained are inadequate since no systematic study of the influence exerted by the VSF4D additive on the electrical and physicochemical properties of the lead dioxide electrode has been performed; furthermore, the additive exerts a negative effect on the application characteristics of the paste and the formation process.

To solve these problems, we examined in this work the influence exerted by the VSF4D additive on the structural, physicochemical, and service characteristics of the lead dioxide electrode.

The aqueous suspension of 4D fluoroplastic contained fluoroplastic particles 0.3 μm in diameter, which are in the suspended state because of the addition of a surfactant, have a spherical shape, and are stretched into elastic fibers under mechanical action (in the process of application). The content of fluoroplastic in the suspension is 50–60 wt %. In accordance with the technology developed, the amount of VSF4D introduced into the paste is 0.05–0.15% (in terms of dry substance). Simultaneously, one more additive, a carbon-chain polymeric fiber, can be introduced into the paste in amount of 0.01–0.4 wt % to enhance its strength in electrode fabrication [1].

The present study is concerned with the effect of the reinforcing VSF4D additive and Khlorin fiber on the structure of the positive active paste (porosity, pore tortuosity factor), electrical resistance, and capacity characteristics of the electrode in various modes of its discharge and on its service life.

EXPERIMENTAL

The study was carried out on electrodes of the MT type with the dimensions $62 \times 74 \times 2.65$ mm. Current leads were fabricated from a lead–antimony alloy with antimony content of 6 wt %; the mass of the leads was 35 ± 1 g. Positive pastes were prepared from powdered lead produced with a Chloride mill (PbO content 68.4%, moisture capacity 136 ml kg^{-1}, apparent density 1.48 g cm^{-3}) and sulfuric acid with addition of

1070-4272/02/7507-1091$27.00 © 2002 MAIK "Nauka/Interperiodica"

Table 1. Parameters of positive pastes

Paste no.	Additive, %		Paste density ρ, g cm^{-3}
	VSF4D (in terms of dry substance)	Khlorin fiber	
1	–	–	3.95
2	0.065	–	4.05
3	0.065	0.1	4.05
4	0.1	–	4.05

Table 2. Parameters of formed positive active paste

Paste no.	Content. wt %			Pore tortuosity factor β
	PbO_2	PbO	$PbSO_4$	
1	83.4	13.8	2.2	1.71
2	84.8	12.7	2.2	1.73
3	84.1	13.1	2.4	1.68
4	83.8	13.8	2.4	1.73

a VSF4D solution and Khlorin thread with fiber length of 4–5 mm. The content of sulfuric acid monohydrate in the paste was 36.1 g per gram of powdered lead. The parameters of the pastes studied are listed in Table 1.

Plates with equal dry paste masses of 41 ± 1 g were used in experiments. The plates were formed in a sulfuric acid solution with a density of 1.07 g cm^{-3} (at 15°C), with 0.39 A h of electricity spent per 1 g of paste. The composition of the formed active paste is given in Table 2.

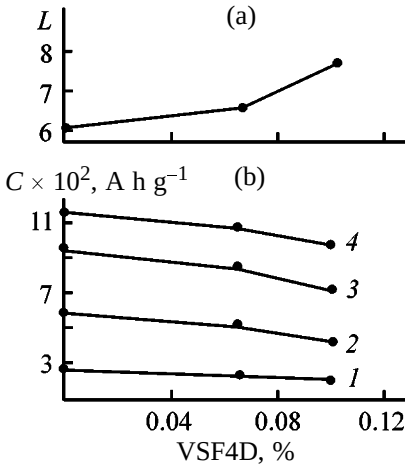

Fig. 1. (a) Relative electrical resistance *L* and (b) specific capacity *C* of lead dioxide electrode in various discharge modes vs. VSF4D content in the active paste. Discharge current density (A dm^{-2}): (*1*) 13.1, (*2*) 2.44, (*3*) 0.74, and (*4*) 0.44.

The relative electrical resistance *L* was measured on a dc setup by the technique proposed by Zhivotinskii [3].

The volume porosity (fraction units) was determined from the difference of masses of dry electrodes and those impregnated for 1 h under vacuum with sulfuric acid with a density of 1.280 g cm^{-3} at 20°C.

The tortuosity factor β, characterizing the pores in the active paste, was calculated from the relative electrical resistance *L* of the electrode and the volume porosity *P* of the active paste by the formula

$$\beta = (LP)^{1/2}.$$

The average values of the pore tortuosity factor of the formed active paste are presented in Table 2.

The capacity characteristics of the electrodes and their service life in cycling were found on prototype batteries comprising one positive and two negative electrodes.

The data in Tables 1 and 2 indicate that introduction of organic additives does not affect noticeably the parameters of the positive and active pastes. Only an insignificant (by 2.5%) increase in the paste density and a minor change in the pore tortuosity factor of the active paste are observed: introduction of VSF4D somewhat raises the pore tortuosity, whereas addition of Khlorin fibers to a VSF4D-containing paste straightens the pores.

Figure 1 presents the relative electrical resistances and capacity characteristics of the electrodes at different discharge currents, which indicate that addition of VSF4D to the positive paste also makes higher the relative electrical resistance of the electrode. With increasing amount of the additive, *L* grows, which leads to a decrease in the electrode capacity. This decrease is particularly noticeable at small discharge rates, when deep layers of the active paste are involved in the process.

Of interest is the fact that addition of Khlorin fiber to the paste changes both the structural parameters of the active paste (porosity, pore tortuosity factor) and the electrical resistance of the electrodes, which affects their capacity characteristics during the initial cycles. For example, the porosity of an active paste with addition of VSF4D and fiber increases in comparison not only with the VSF4D-containing paste, but also with the active paste of the control electrode (Fig. 2). Upon introduction of fiber, the relative elec-

trical resistance of the electrode with VSF4D additive decreases, with its value virtually coinciding with that of the control electrode.

As seen from Fig. 2, the capacity of an electrode with VSF4D and fiber additives occupies an intermediate position between the corresponding values for the control electrode and an electrode with VSF4D additive. Presumably, this is due to the increasing porosity of the active paste and its decreasing relative resistance. It may be assumed that the porosity of the active paste grows because of the formation of more straightened pores oriented along the fibers (Table 2).

As seen from the curves in Fig. 3, describing the variation of the specific capacity of positive electrodes, the capacity of all the electrodes studied grows in the course of cycling. As would be expected, the control electrodes have the highest capacity during the first 40 cycles. After the 70th cycle, the capacity decreases abruptly because of the sag of the active paste. The service life of the control electrodes was 93 cycles. The introduction of the VSF4D additive allowed an increase in this parameter by 20% under free assembly conditions (Fig. 3), which confirms the previously obtained data. Joint introduction of VSF4D and Khlorin fiber into the positive paste raised the discharge capacity of the lead dioxide electrode and lengthened by 40% its service life.

All the batteries failed because of short-circuit at lower edges, caused by sagging of the active paste. The outward appearance of the positive electrodes with VSF4D additive after exhaustion of their service life indicates that more intensive sagging of the active paste is observed without adding the fiber. The totality of elastic adhesive fluoroplastic fibers and rigid carbon-chain polymer fibers forms a three-dimensional skeleton, which keeps the active paste from sagging more reliably.

Thus, the results obtained in studying the structural parameters and electrical characteristics of a positive electrode with organic additives in its active paste revealed the effect of these additives on the operation of the lead dioxide electrode and confirmed the effectiveness of their use to prolong the service life of the lead battery.

Introduction of polymeric additives, which are insulators, impairs the initial capacity characteristics of the electrodes (Figs. 2, 3) and hinders the formation process: a surface layer of lead sulfate is observed on the positive electrodes. Since only the current lead is electrically conducting in the initial stage of formation and the resistance of the paste composed of lead sulfates is very high (10^7–10^{10} Ω), the presence of nonconducting components in the paste complicates the process. Introduction of the electrically conducting additive into the paste must make lower its resistance and improve the process of its formation.

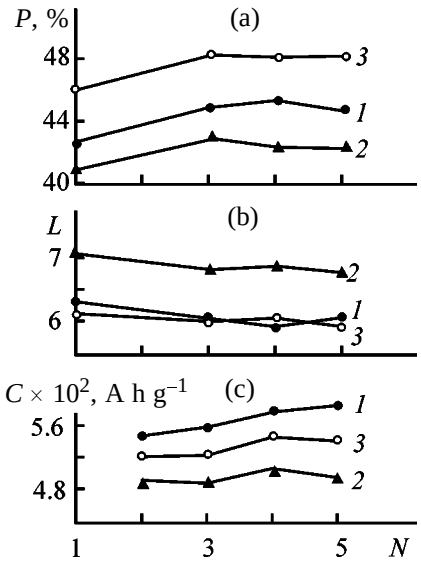

Fig. 2. Variation of (a) porosity *P*, (b) relative electrical resistance *L*, and (c) specific capacity *C* of lead dioxide electrodes with reinforcing additives in initial cycles. (*N*) Cycle number; the same for Fig. 3. Electrode: (*1*) Control, (*2*) with VSF4D additive, and (*3*) VSF4D + fiber; the same for Fig. 3.

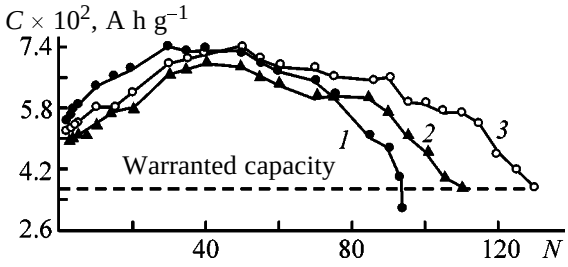

Fig. 3. Specific capacity *C* of lead dioxide electrodes with reinforcing additives in cycling with the current of 1-h discharge mode.

It is known that some carbon materials exhibit high electrical conductivity. Presently, much attention is given to experimental and theoretical studies of recently discovered forms of carbon. These materials possess unique beneficial properties [4] which can be used to compensate for the negative influence of the above-mentioned organic additives.

In this study, we examined the possibility of lowering the electrical resistance of the VSF4D-containing paste and improving its application properties through addition of activated carbon obtained by thermal treatment of graphite of the GL-1 brand. Our study showed

that introduction of 0.01–0.5% activated carbon into the paste with VSF4D additive improves the formation of the lead dioxide electrode, which is indicated by the decrease in the average electrode potential in formation and by the absence of the surface lead sulfate layer.

A study of the electrode microstructure on a JEOL JSM-840A electron microscope (Japan) demonstrated that the active paste with addition of VSF4D and activated carbon has more uniform structure ensuring more stable discharge characteristics of lead dioxide electrodes in cycling.

In addition, it was established that addition of activated carbon, which possesses plasticizing properties, improves the application properties of a paste with VSF4D, i.e., ensures its processability.

Thus, a comprehensive study of the influence exerted by polymer and carbon additives on the physicochemical and electrical characteristics of the lead dioxide electrode allowed a directed modification of its properties, i.e., not only prolonged its service life, but also ensured its stable capacity characteristics and fabricability.

The paste for the positive electrode of a lead battery is protected by a patent [5].

CONCLUSIONS

(1) A study of the structural, physicochemical, and electrical characteristics of a lead dioxide electrode with reinforcing additives in the active paste revealed the effect of these additives on the operation of the electrode and confirmed the effectiveness of their use for extending the service life of the lead battery.

(2) Introduction of activated carbon into the paste with reinforcing VSF4D additive positively addects the structure of the active paste and improves the process of electrode formation.

REFERENCES

1. Rusin, A.I., Kolikova, G.A., Bolotovskii, V.I., *et al.*, *Usovershenstvovanie polozhitel'nogo elektroda svintsovogo akkumulyatora* (Improvement of the Positive Electrode of the Lead Battery), Ser. 22: *Istochniki toka: Obzor informatsii* (Power Sources: Review), Moscow: Informelektro, 1991.
2. Dasoyan, M.A. and Aguf, I.A., *Sovremennaya teoriya svintsovogo akkumulyatora* (Modern Theory of Lead Battery), Leningrad: Energiya, 1975.
3. Zhivotinskii, P.B., *Poristye peregorodki i membrany v elektrokhimicheskoi apparature* (Porous Partitions and Membranes in Electrochemical Apparatus), Leningrad: Khimiya, 1978.
4. Fialkov, A.S., *Uglerod, mezhsloevye soedineniya i kompozity na ego osnove* (Carbon and Intercalation Compounds and Composites on Its Base), Moscow: Aspekt, 1997.
5. RF Patent 2174270.

Russian Journal of Applied Chemistry, Vol. 75, No. 7, 2002, pp. 1095–1100. Translated from Zhurnal Prikladnoi Khimii, Vol. 75, No. 7, 2002, pp. 1112–1117.
Original Russian Text Copyright © 2002 by Grigor'eva, Shainyan, Kaurova, Gracheva, Lesnevskaya, Barabanov.

APPLIED ELECTROCHEMISTRY AND CORROSION PROTECTION OF METALS

Electrochemical Fluorination of Unsaturated Sulfides and Sulfones

A. A. Grigor'eva, B. A. Shainyan, G. I. Kaurova, E. I. Gracheva, N. B. Lesnevskaya, and V. G. Barabanov

Favorskii Irkutsk Institute of Chemistry, Siberian Division, Russian Academy of Sciences, Irkutsk, Russia
Prikladnaya Khimiya Russian Scientific Center, St. Petersburg, Russia

Received May 25, 2001; in final form, January 2002

Abstract—Electrochemical fluorination of some unsaturated sulfides and sulfones and their reactions with anhydrous HF were studied.

Electrochemical fluorination (ECF) of organosulfur compounds in anhydrous HF was studied with saturated or aromatic sulfides, disulfides [1–3], thiols [4–6], sulfoxides [1], and sulfones [7]. On the whole, ECF of S(II) derivativres involves cleavage of one or both S–C bonds. The C–S(O)–C moiety in sulfoxides is not preserved in ECF [1], whereas ECF of sulfones yielded, along with perfluoroalkylsulfonyl fluorides R_fSO_2F, also the corresponding sulfones $R_fSO_2R_f$ [7]. Virtually no data are available, except a single paper [9], on ECF of unsaturated aliphatic or alkenylaromatic sulfides and sulfones.

In this work, we studied ECF of ethyl vinyl sulfide $C_2H_5SCH{=}CH_2$ (**I**), di(1-propenyl) sulfide $(CH_3{-}CH{=}CH)_2S$ (**II**), phenyl vinyl sulfide $C_6H_5SCH{=}CH_2$ (**III**), and phenyl vinyl sulfone $C_6H_5SO_2CH{=}CH_2$ (**IV**), and also reactions of anhydrous HF with **III**, **IV**, and divinyl sulfide $(CH_2{=}CH)_2S$ (**V**). We failed to perform ECF of dichlorovinyl aryl sulfones $ArSO_2{-}CH{=}CCl_2$ (Ar = Ph, *m*-ClC_6H_4, *m*-$NO_2C_6H_4$) because of their insolubility in HF. The compositions and structures of liquid ECF products were determined by GLC, GC–MS, elemental analysis, IR spectroscopy, and ^1H, ^{13}C, and ^{19}F NMR spectroscopy. Gaseous ECF products were analyzed by IR spectroscopy and gas chromatography (GC).

Electrochemical fluorination of sulfide **I** yields gaseous products among which we identified by GC and IR spectroscopy CF_4, C_2F_6, C_3F_8, C_4F_{10}, SF_4, SF_6, SO_2F_2, F_2O, and also liquid low-boiling products (bp 30–35°C) exhibiting no IR absorption in the range above 1350 cm^{-1}, which indicates that these products contain no C=C and C–H bonds. The ^{13}C NMR spectra of liquid ECF products of **I** contain a quartet of triplets at 116 ppm corresponding to the C_2F_5 group. As judged from the boiling points, the major products of ECF of **I** are dodecafluoropentane C_5F_{12} (bp 29.3°C [10]) and pentafluoro(1,1,2,2,2-pentafluoroethyl)-λ^6-sulfane $C_2F_5SF_5$ (the boiling point of the closest homolog, $C_3F_7SF_5$, is 43°C [6]). Formation of dodecafluoropentane was confirmed by the fact that the intensity of ^{19}F NMR signal at –84.2 ppm (CF_3) was equal to the sum of the intensities of the signals at –125.3 (C^3F_2) and –128.9 ppm ($C^{2,4}F_2$), by its refractive index, which was close to the reference value [10], and by the IR spectrum of the distilled product, which coincided with the reference spectrum [11]. The presence of pentafluoro(1,1,2,2,2-pentafluoroethyl)-λ^6-sulfane is confirmed by the substantial (>6%) sulfur content in the liquid products and by the presence in the ^{19}F NMR spectrum of downfield signals at δ_F 46.53 and 64.15 ppm with the intensity ratio of 4 : 1 and J_{FF} 143 Hz. According to [12], the downfield signal belongs to the axial fluorine, and the upfield signal, to equatorial fluorine atoms of the SF_5 group. On the whole, ECF can be described by the equation

$$C_2H_5SCH{=}CH_2 \xrightarrow[HF]{ECF} C_nF_{2n+2}\ (n = 1{-}5) + C_2F_5SF_5 + SF_4 + SF_6 + SO_2F_2 + F_2O. \quad (1)$$

The gaseous products of ECF of sulfide **II** include HF, CF_4, C_2F_6, CO, CO_2, F_2O, and SO_2F_2. CO, CO_2, and SO_2F_2 are formed by electrochemical fluorination of oxygen-containing organic impurities present in the initial compound. Oxygen difluoride OF_2 is the product of electrochemical fluorination of water

1070-4272/02/7507-1095$27.00 © 2002 MAIK "Nauka/Interperiodica"

present in small amounts in liquid HF and in the substrate. The content of sulfur in liquid ECF products is about 2%, and that of hydrogen, about 0.5% (at the level of the determination error); the absence of absorption bands above 1350 cm^{-1} indicates that C=C and C–H bonds are absent. This means that ECF involves substitution of all hydrogen atoms, addition of fluorine to all double bonds, and noticeable removal of sulfur. A GC–MS analysis revealed formation of four products, For all of them, the base peak is that of the CF_3^+ ion, and the other peaks (5–20%) are those of C_bF_m ions (n = 1–6, m = 3–13, odd m). Since perfluorocarbons typically give in the mass spectra the $[M - F]^-$ ion and ions corresponding to successive loss of CF_2 up to formation of CF_3^+, our mass spectra confirm formation of perfluorohexanes. Liquid products were fractionated at 50–86°C. The ^{19}F NMR spectra of all the fractions show signals at –75 to –85 (CF_3), –110 to –130 (CF_2), and –185 to –190 ppm (CF). The presence of several CF_3 signals suggests formation of both linear (CF_3CF_2, δ_{CF_3} –80 to –85 ppm) and branched [$(CF_3)_2CF$, δ_{CF_3} –70 to –75 ppm] perfluoroalkanes; the presence of branched perfluoroalkanes is also confirmed by the CF signal at –185 to –190 ppm. As judged from the boiling points, the major ECF products of **II** are linear and branched perfluoroalkanes C_6–C_7. The downfield region of the ^{19}F NMR spectrum of the fraction with bp 80–85°C contains signals at δ_F 46.62 and 61.20 ppm (intensity ratio 4 : 1, J_{FF} 138.8 Hz) belonging, apparently, to pentafluoro(1,1,2,2,3,3,3-heptafluoropropyl)-λ^6-sulfane $C_3F_7SF_5$. The ^{19}F NMR spectrum of the fraction with bp 100°C contains signals at δ_F 42.82 and 61 ppm (J_{FF} 137.7 Hz), belonging, apparently, to equatorial and axial fluorine atoms of the SF_5 group in $C_5F_{11}SF_5$. The signal at δ_F = 28.09 ppm, characteristic of the SF_4 group [12], belongs, apparently, to tetrafluoro[bis(1,1,2,2,3,3,3-heptafluoropropyl)]-λ^6-sulfane $(CF_3CF_2CF_2)_2SF_4$. These data indicate that ECF involved desulfuration with formation of linear and branched C_6–C_8 perfluorocarbons, and also oxidation of sulfur.

In the experiment on ECF of **III**, we analyzed only the gaseous products by IR spectroscopy. Similar to ECF of **I** and **II**, HF, CF_4, SF_4, SF_6, SOF_2, and SO_2F_2 are formed, i.e., the reaction involves oxidation of sulfur and cleavage of the C–S bonds. Electrochemical fluorination of **IV** occurs with complete saturation and desulfuration and is accompanied by fragmentation, yielding perfluorocarbons of the cyclohexane series:

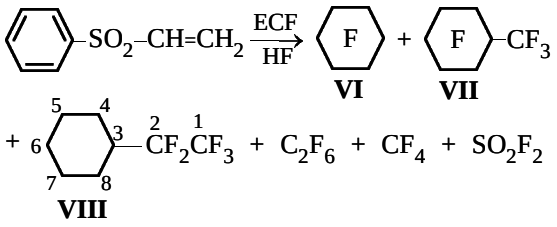

$$+ C_2F_6 + CF_4 + SO_2F_2 + SF_4 + SF_6. \quad (2)$$

Along with the compounds indicated in the scheme, we identified in the gas phase HF, CO, CO_2, and F_2O. The sulfur content in the liquid products is less than 3%, and the hydrogen content, less than 1%. A GC–MS analysis revealed three major products with the fragmentation pattenrs similar to that given for **II**. The ^{19}F NMR spectrum of the products before distillation contained downfield signals at δ_F 65.8 and 61.4 ppm, suggesting formation of R_fSF_5 derivatives, as in ECF of **I** and **II**. The low-boiling (48°C) fraction from distillation of liquid ECF products of **IV** solidifies; its ^{19}F NMR spectrum contains a very broad signal at δ_F –134 ppm. These data confirm formation of perfluorocyclohexane **VI** (mp 51°C, bp 52°C [13]; δ_F –133.25 ppm [14]). The large width of the signal is due to mutual transformations of conformers of **VI** [15]; the signal width varies by two orders of magnitude with temperature [13]. Perfluorocyclohexane **VI** is formed by ECF of various aromatic compounds, including thiophenol [16]. Formation of perfluoroalkylperfluorocyclohexanes **VII** and **VIII** is confirmed by the presence of CF in the ^{13}C NMR spectrum (doublets of multiplets at 96 ppm for **VII** and at 88 ppm for **VIII**) and, in the case of **VIII**, of a quartet of triplets at 116.6 ppm belonging to the CF_3 gorup. The presence of perfluoroethylperfluorocyclohexane **VIII** was confirmed by GLC and by comparison of the ^{13}C and ^{19}F NMR spectra with those of an authentic sample. The content of **VIII** in the product mixture is 19.3%. The ^{19}F NMR spectrum is a complex set of multiplets (see figure). Consideration of the chemical shifts, multiplicities, and integral intensities of signals and comparison with the ^{19}F NMR spectrum of **VII** [17] lead to the following assignments, δ_F, ppm: CF_3 –83.51 d.t.t, 3F, ^2J 2.3, ^3J 14.0, ^3J 12.8 Hz; CF_2 –118.13 t.t, 2F, ^3J 15.8, ^4J 21.5 Hz; CF –187.97 m, 1F, ^3J 15.0 Hz; C^4F_{eq}, C^8F_{eq} –120.67 d.m, 2F, ^2J 303.0 Hz; C^5F_{eq}, C^7F_{eq} –124.11 d.m, 2F, ^2J 288.5 Hz; C^6F_{eq} –126.05 d.m, 1F, ^2J 289.4, ^3J 7.0 Hz; C^4F_{ax}, C^8F_{ax} –131.78 d.m, 2F, ^2J 303.0 Hz; C^5F_{ax}, C^7F_{ax} –141.7 d.m, 2F, ^2J 288.5 Hz; C^6F_{ax} –144.37 d.m, 1F, ^2J 289.4, ^3J 7.0 Hz.

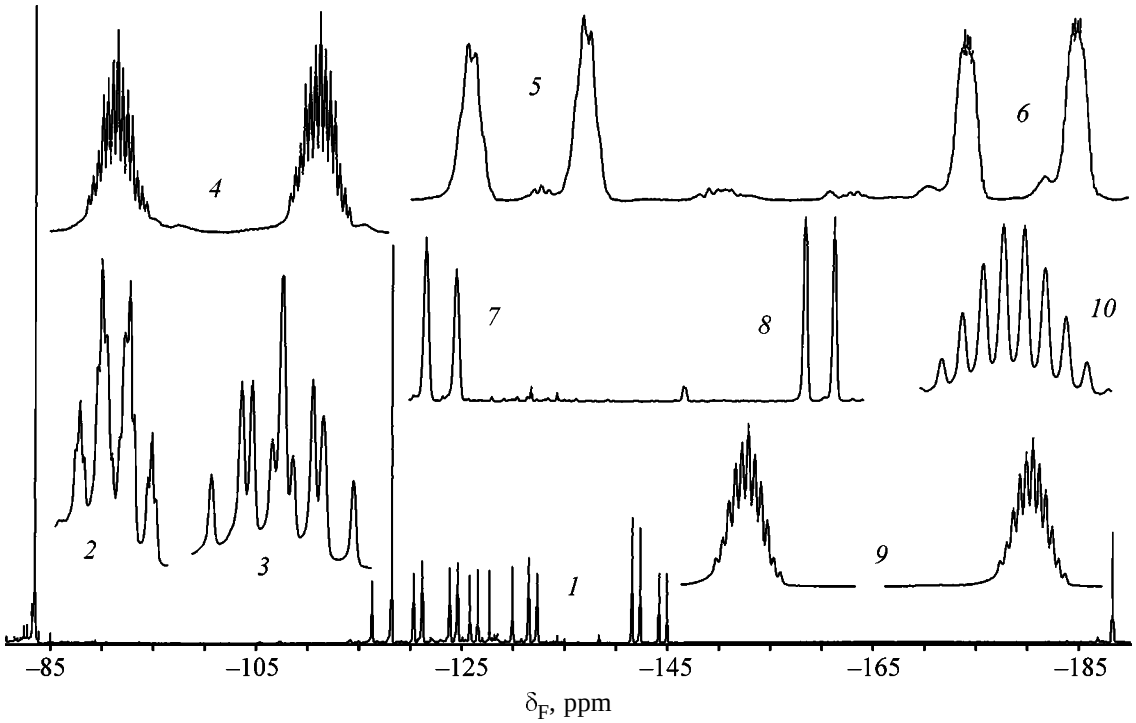

^{19}F NMR spectrum of perfluoroethylperfluorocyclohexane: (*1*) total, (*2*) CF_3, (*3*) CF_2, (*4*) C^6F_{eq}, (*5*) $C^{4(8)}F_{eq}$, (*6*) $C^{5(7)}F_{eq}$, (*7*) $C^{4(8)}F_{ax}$, (*8*) $C^{5(7)}F_{ax}$, (*9*) C^6F_{ax}, and (*10*) CF.

The compounds studied in this work differ from the previously studied alkanethiols, dialkyl sulfides, and dialkyl sulfones in that, in ECF of unsaturated sulfides and sulfones, the yield of sulfur-containing organic compounds is extremely low. For example, in ECF of vinyl sulfides, perfluoroalkyl derivatives of sulfur hexafluoride R_fSF_5 and $R_fSF_4R_f$, which are typical products of ECF of saturated S(II) derivatives [1–6], are formed in minor amounts. As for S(VI) derivatives, it is noted in the literature that the S=O bonds show very high stability in the process, which opens up possibilities for commercial synthesis of trifluoromethanesulfofluoride and, starting from this compound, of the whole class of triflates. However, this is true only for the lower representatives of this series. The yield of perfluoroalkanesulfonyl fluorides R_fSO_2F in ECF oof sulfonyl chlorides RSO_2Cl decreases in the order R = C_1–C_8 from 87 to 25% [18]. In unsaturated sulfones, as shown by the example of **IV**, the ECF products contain virtually no organic sulfonyl detivatives. An increased tendency of unsaturated sulfides and sulfones to undergo desulfuration in ECF is probably due to the fact that the C=C bond is fluorinated more readily than the C–H bond. In the first stage of ECF of S(II) derivatives, S(II) is oxidized to S(VI) [5]. Then, in the case of saturated sulfides, an α-centered radical is formed, and, in the case of unsaturated sulfides, the fluorine atom can add to the α-C atom with subsequent β-scission, which increases the probability of formation of desulfuration products. The general scheme of the process can be represented as follows:

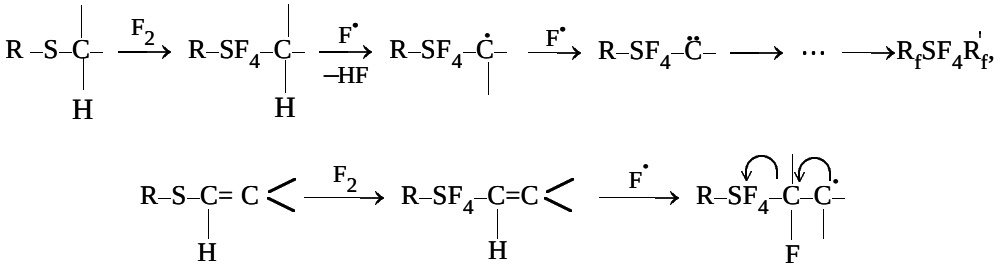

$$\xrightarrow{\beta\text{-Scission}} \dot{R}SF_4 \xrightarrow{F^\cdot} RSF_5 \xrightarrow{F^\cdot} \cdots \rightarrow R_fF + R_fR_f + SF_6,$$
$$\dot{R}SF_4 \xrightarrow{-SF_4} R^\cdot \xrightarrow{F^\cdot} \cdots\rightarrow R_fF + R_fR_f. \qquad (3)$$

To examine the possibility of fluorination of vinyl sulfides and vinyl sulfones on dissolution in HF prior to ECF, compounds **III**–**V** were treated with anhydrous HF. We found that sulfone **IV** in which the vinyl group shows a decreased reactivity toward electrophilic agents due to the electron-withdrawing effect of the sulfonyl group does not react with HF even at 90°C (4 h). At the same time, sulfides **III** and **V**, when brought in contact with anhydrous HF, undergo transformations, probably due to the catalytic effect of HF as acid. For example, divinyl sulfide, when kept in HF at room temperature for several hours, polymerizes to give a light creamy powdered polymer containing 36% sulfur and 5% fluorine; prolonged heating does not change the chemical composition of the polymer, which indicates that the polymer contains chemically bound fluorine rather than adsorbed HF. The polymer is insoluble in organic solvents (benzene, methanol, dichloroethane, CCl_4, DMSO, DMF) and decomposes on heating above 290°C, which suggests its cross-linked structure. We propose the following structure of the polymers (n = 3 on the average):

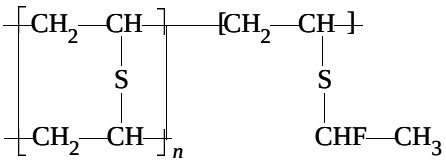

Under similar conditions, phenyl vinyl sulfide gives products containing no vinyl group. After treatment of the reaction mixture with chloroform, removal of excess HF with NaF, distillation of the solvent, and evacuation, we obtained a blue-green viscous oil, from which we isolated by distillation thiophenol, which is probably formed by addition of HF, followed by protonation of sulfur and scission of the C–S bond with the release of volatile fluorocarbons:

$$PhS{-}CH{=}CH_2 \xrightarrow{HF} [PhSCHF{-}CH_3]$$
$$\xrightarrow{H^+} PhS^+(H){-}CHF{-}CH_3 \xrightarrow{F^-} PhSH + [CH_3CHF_2].$$

The residue is a complex mixture; its ^{1}H NMR spectrum contains no signals from vinyl proton of the initial compound but contains complex multiplets in the range of aromatic (7.1–7.8 ppm) and aliphatic (1.0–3.5 ppm) protons, intensity ratio 5 : 4. According to elemental analysis, the product contains no fluorine. These facts suggest oligomerization of the initially formed $[PhSCHCH_3]^+$ ion with the formation of oligomers of the composition close to $(PhSC_2H_4)_n$. We failed to isolate or identify any individual products.

EXPERIMENTAL

The IR spectra of the products in the liquid phase were taken on an IKS-29 spectrometer in a thin film. The ^{1}H, ^{13}C, and ^{19}F NMR spectra were measured on a Bruker DPX 400 spectrometer (400, 100, and 376 MHz, respectively) with neat samples, external reference DMSO-d_6; the chemical shifts are given relative to TMS (^{1}H, ^{13}C) and $CFCl_3$ (^{19}F). The GC–MS analysis was performed with an LKB 2091 device (EI, 70 eV), and GLC analysis, on a Tsvet-100 chromatograph [thermal conductivity detector, carrier gas helium, 3000 × 3-mm columns, stationary phase 20% α,α,α-tris(β-cyanoethyl)acetophenone on Silochrom-80 (France)].

The IR spectra of gaseous electrolysis products were recorded on a Specord-20M spectrometer in a 10-cm Monel metal cell with AgCl windows. The GC analysis was performed with an LKhM-80 chromatograph (thermal conductivity detector, carrier gas helium, 3000 × 3-mm columns, sorbent MgF_2-17, particle diameter 0.25–0.5 mm).

Electrochemical fluorination was performed in a 150 cm^3 cylindrical cell made from St.3 steel and equipped with a reflux condenser and with stopcocks for supplying HF and removing liquid fluorination products; surface area of the nickel anode 54 cm^2. The reflux condenser was kept at –35°C with HCFC 22 as coolant.

Electrochemical fluorination of **I**–**IV** was performed as follows.

Ethyl vinyl sulfide I. An electrochemical cell was filled with 125 ml of anhydrous HF, and 10 g of divinyl sulfide was added. Electrolysis was performed at 14–16°C for 38 h (38 A h) at the anodic current density of 2 A dm^{-2} and cell voltage of 4.4–4.8 V. Electrolysis gases from the reflux condenser were

sampled into an IR cell. IR spectrum of the gas, ν, cm^{-1}: 3700–4000 (HF); 1502, 1269, 848, 885, 925 (O_2F_2); 1300, 1290, 1250, 1120, 715 (C_2F_6); 900, 830, 610 (SF_4, SF_6); 828, 930 (F_2O). Gaseous samples for GC analysis were passed through aqueous KI. The following products were identified by GC: CF_4, C_2F_6, C_3F_8, C_4F_{10}, SO_2F_2, and SF_6. High-boiling fluorination products (1.6 g) were removed through the stopcock on the electrolyzer bottom into a polyethylene vessel filled with water. Found, %: C 19.46, H 0.58, F 70.86, S 6.24. By distillaiton, we isolated a fraction with bp 30–35°C, consisting mainly of dodecafluoropentane, n_D^{20} 1.2805 (bp 29.3°C, n_D^{15} 1.2411 [9]). The IR spectrum is in agreement with published data [10]. ^{19}F NMR spectrum, δ_F, ppm: –84.2 (CF_3), –125.3 ($CF_2CF_2CF_2$), *–128.9 (CF_3CF_2)*. ^{13}C NMR spectrum, δ_C, ppm: 116.2 q.t (*C*F_3CF_2, $^1J_{CF}$ 286.5, $^2J_{CF}$ 34.0 Hz), 109.4 m ($CF_2CF_2CF_2$). The fraction contains a minor amount of pentafluoro(1,1,2,2,2-pentafluoroethyl)-λ^6-sulfane. ^{19}F NMR spectrum, δ_F, ppm: –83.54 [CF_3, J(CF_3–SF_4) 9 Hz], –100.1 [CF_2, J(CF_2–F_{eq}) 13 Hz], 46.53 d (SF_4), 64.15 quintet [J(F_{ax}–F_{eq}) 143 Hz].

Di(propen-1-yl) sulfide II was treated similarly to **I**. Electrolysis was performed with a 30-g portion of **II** at 14–16°C for 122 h (122 A h) at the anodic current density of 2 A dm^{-2} and cell voltage of 5.3–6.8 V. IR spectrum of gaseous electrolysis products, ν, cm^{-1}: 3700–4000 (HF); 1502, 1269, 848, 885, 925 (SO_2F_2); 1300, 1290, 1250, 1120, 715 (C_2F_6); 828, 930 (F_2O); 900, 830, 610 (SF_4, SF_6). CF_4, C_2F_6, CO_2, and SO_2F_2 were identified by GC. Heavy fluorination products (7.35 g) were discharged into a polyethylene vessel filled with water. Found, %: C 21.2, H 0.76, F 62.65, S 2.10. The mixture of liquid products was fractionated. Fraction with bp 50–60°C. ^{19}F NMR spectrum, δ_F, ppm (the most intense signals are given): –74.96, –75.17 (*iso*-CF_3), –83.80, –84.17 (*n*-CF_3), –108.54, –127.64, –128.79 (CF_2), –185.66, –188.70 (CF). Fraction with bp 84–86°C. ^{19}F NMR spectrum, δ_F, ppm: 46.62, 61.20 (SF_5), –73.00, –74.86, –75.09 (*iso*-CF_3), –83.85, –84.07, –84.15 (*n*-CF_3), –114.06, –114.90, –122.75, –124.97, –126.58, –128.39 (CF_2), –184.87, –185.18, –187.46, –188.40 (CF). The ^{13}C NMR spectra of all the fractions contain doublets of multiplets in the range 90–92 ppm (CF), multiplets in the range 104–112 ppm (CF_2), and signals of two types of CF_3 groups: 118.11 q.d [*C*F_3CF, $^1J_{CF}$ 288.8, $^2J_{CF}$ 22.5 Hz] and 116.61 q.t [*C*F_3CF_2, $^1J_{CF}$ 286.5, $^2J_{CF}$ 34.4 Hz].

Phenyl vinyl sulfide III was treated similarly. Electrolysis was performed with a 18-g portion of **III** at 14–16°C for 45 h (45 A h) at the anodic current density of 2 A dm^{-2} and cell voltage of 5.7–7.6 V. IR spectrum of gaseous electrolysis products, ν, cm^{-1}: 3700–4000 (HF); 1502, 1269, 848, 885, 925 (SO_2F_2); 1300, 1290, 1250, 1120, 715 (C_2F_6); 828, 930 (F_2O); 900, 830, 610 (SF_4, SF_6).

Phenyl vinyl sulfone IV. A 20-g portion of phenyl vinyl sulfone was placed in an electrochemical cell, and 125 ml of anhydrous HF was added. Electrolysis was performed at 14–16°C for 64 h (64 A h) at the anodic current density of 2 A dm^{-2} and cell voltage of 5.5–6.6 V. IR spectrum of gaseous electrolysis products, ν, cm^{-1}: 3700–400 (HF); 2320, 2350 (CO, CO_2); 1502, 1269, 848, 885, 925 (SO_2F_2); 1300, 1290, 1250, 1120, 715 (C_2F_6); 828, 930 (F_2O). CF_4, C_2F_6, CO_2, and SO_2F_2 were identified by GC. The heavy fluorination products (8.74 g) were discharged into a polyethylene vessel filled with water. Found, %: C 17.2, H 0.80, F 66.41, S 2.92.

The mixture was separated by fractional distillation. The fraction with bp 38–48°C solidifies on cooling and mainly consists of perfluorocyclohexane **VI**. ^{19}F NMR spectrum, δ_F, ppm: –134 br.s. The fraction with bp 50–70°C contains perfluoromethylperfluorocyclohexane **VII**. ^{19}F NMR spectrum, δ_F, ppm: –188.7 m (CF), ^3J(CF_2–CF) 14.7 Hz. The fraction with bp 68–80°C mainly consists of perfluoroethylperfluorocyclohexane **VIII**. ^{13}C NMR spectrum (DMSO-d_6, δ_C, ppm: 116.26 q.t, CF_3, ^1J 287.12, ^2J 33.17 Hz; 103–112 m, CF_2; 87.42 d.sept, ^2J 218.93, ^3J 25.8 Hz.

Reactions of **III**–**V** with HF were performed as follows.

Phenyl vinyl sulfide III. Into a 100 cm^3 stainless steel autoclave, 3–5 ml of HF was condensed, and 3.0 g of **III** was added. The autoclave was kept at room temperature for 5 h. The mixture was diluted with 50 ml of chloroform and purged with air, after which NaF was added to pH 7.0. The solution was filtered and evaporated. From the resulting green viscous oil, 0.5 g of thiophenol was isolated by vacuum distillation (bp 50°C/23 mm Hg). ^1H NMR spectrum, δ, ppm: 3.54 s (SH, 1H), 7.21 m (*p*-CH, 1H), 7.29 m (*m*-CH, 2H), 7.33 m (*o*-CH, 2H). ^{13}C NMR spectrum, δ_C, ppm: 125.16 (C_p), 128.99 (C_o), 130.44 (C_1). The blue-green residue was analyzed by NMR. Found, %: C 73.10, H 6.74, S 20.66.

Phenyl vinyl sulfone IV. *a.* Similarly to the above procedure, 1.1 g of **IV** was added to HF. The autoclave was heated at 90°C for 4 h. Then 50 ml of chloroform was added, the mixture was purged with air,

and NaF was added to pH 7.0. The solution was filtered and evaporated to dryness, and the residue was vacuum-dried (1 mm Hg). The initial sulfone **IV** (0.8 g) was recovered; its melting point and the ^{1}H and ^{13}C NMR spectra coincided with those of an authentic sample.

b. Gaseous HF was passed for 1.5 h through a solution of 0.84 g of **IV** in 30 ml of dry benzene, cooled with ice to 12–16°C. The mixture was purged with air under stirring, and NaF was added to pH 7.0. The solution was filtered and evaporated to dryness. The initial sulfone **IV** (0.5 g) was recovered; its melting point and the ^{1}H and ^{13}C NMR spectra coincided with those of an authentic sample.

Divinyl sulfide V. Into a stainless steel autoclave, 3–5 ml of HF was condensed, and 4.44 g of cooled sulfide **V** was added. The mixture was kept at room temperature for 24 h. A light creamy powdered polymer (4.48 g) was obtained. Found, %: C 51.35, H 6.72, F 5.90, S 36.02. Found after heating at 50°C for 24 h, %: C 50.33, H 6.52, F 5.10, S 36.34.

CONCLUSIONS

(1) Electrochemical fluorination of vinyl sulfides and sulfones occurs with complete substitution of all the hydrogen atoms by fluorine, addition of fluorine to the double bonds and benzene ring, and considerable desulfuration, yielding perfluorocarbons as major products, and also perfluoroalkyl derivatives of sulfur hexafluoride and fragmentation products.

(2) With no current applied, vinyl sulfones do not react with anhydrous HF even on prolonged heating, whereas vinyl sulfides take up HF (electrophilic addition to the double bond) with the subsequent scission of the C–S bond or polymerization.

REFERENCES

1. Hoffmann, F.W., Simmons, T.C., Beck, R.B., *et al.*, *J. Am. Chem. Soc.*, 1957, vol. 79, no. 13, pp. 3424–3429.
2. Dresdner, R.D. and Young, J.A., *J. Am. Chem. Soc.*, 1959, vol. 81, no. 3, pp. 574–577.
3. Drasdner, R.D., Reed, T.M., III, Taylor, T.E., and Young, J.A., *J. Org. Chem.*, 1960, vol. 25, no. 8, pp. 1464–1466.
4. Abe, T., Nagase, S., and Baba, H., *Bull. Chem. Soc. Jpn.*, 1973, vol. 46, no. 12, pp. 3845–3848.
5. Baba, H., Kodaira, K., Nagase, S., and Abe, T., *Bull. Chem. Soc. Jpn.*, 1977, vol. 50, no. 10, pp. 2809–2810.
6. Baba, H., Kodaira, K., Nagase, S., and Abe, T., *Bull. Chem. Soc. Jpn.*, 1978, vol. 51, no. 6, pp. 1891–1892.
7. Rozhkov, I.N., Bukhtiarov, A.V., and Knunyants, I.L., *Izv. Akad. Nauk SSSR, Ser. Khim.*, 1969, no. 4, pp. 945–947.
8. *Organicheskaya elektrokhimiya* (Organic Electrochemistry), Petrosyan, V.A. and Feoktistov, L.G., Eds., Moscow: Khimiya, 1988.
9. Riyadh, S.M., Ishii, H., and Fuchigami, T., *Tetrahedron Lett.*, 2001, vol. 42, no. 16, pp. 3009–3011.
10. Maksimov, B.N., Barabanov, V.G., Serushkin, I.L., *et al.*, *Promyshlennye ftororganicheskie produkty* (Commercial Organofluorine Products), St. Petersburg: Khimiya, 1996.
11. *Fluorine Chemistry*, Simons, J.H., Ed., New York: Academic, 1950, vol. 1.
12. *Gmelin Handbook of Inorganic Chemistry*, Berlin: Springer, 1987, 8th ed.
13. Gutowsky, H.S. and Chen, F.-M., *J. Phys. Chem.*, 1965, vol. 69, no. 9, pp. 3216–3219.
14. Gordon, A.J. and Ford, R.A., *The Chemist's Companion. A Handbook of Practical Data, Techniques, and References*, New York: Wiley, 1972.
15. Tiers, G.V.D., *Proc. Chem. Soc.*, 1960, pp. 389–390.
16. Inoue, Y., Nagase, S., Kodaira, K., *et al.*, *Repts. Govt. Ind. Res. Inst. Nagoya*, 1973, vol. 22, no. 11, pp. 424–429.
17. Feeney, J. and Sutcliff, L.H., *Trans. Faraday Soc.*, 1960, vol. 56, no. 11, pp. 1559–1569.
18. Gramstad, T. and Haszeldine, R.N., *J. Chem. Soc.*, 1957, no. 6, pp. 2640–2645.
19. Trofimov, B.A. and Amosova, S.V., *Divinilsul'fid i ego proizvodnye* (Divinyl Sulfide and Its Derivatives), Novosibirsk: Nauka, 1983.

Russian Journal of Applied Chemistry, Vol. 75, No. 7, 2002, pp. 1101–1103. Translated from Zhurnal Prikladnoi Khimii, Vol. 75, No. 7, 2002, pp. 1118–1120.
Original Russian Text Copyright © 2002 by Zhaksibaev, Kartonozhkina, Abylkasova, Izdebskaya, Mambetkazieva, Pak.

CATALYSIS

Straight and Modified Copper Catalysts for Stereoselective Hydrogenation of 5,17-Docosadiyne

M. Zh. Zhaksibaev, O. I. Kartonozhkina, G. E. Abylkasova, G. T. Izdebskaya, R. A. Mambetkazieva, and A. M. Pak

Sokol'skii Institute of Organic Catalysis and Electrochemistry, Ministry of Education and Science of Kazakhstan Republic, Almaty, Kazakhstan

Received February 12, 2001; in final form, March 2002

Abstract—Modified copper catalysts providing high rate of 5,17-docosadiyne hydrogenation with 100% yield of *cis,cis*-5,17-docosadiene (gypsy moth attractant) were developed.

Stereoselective hydrogenation of high-molecular-weight acetylene derivatives to corresponding *cis*- or *trans*-olefins is the most complex and the finest stage in the synthesis of attractants and pheromones.[1] Stringent requirements are placed upon hydrogenation products, since even 1% impurities of positional or geometric isomers present in an attractant or pheromone decrease or fully eliminate its biological activity.

It is known that, in hydrogenation of acetylene derivatives, copper catalysts exhibit high selectivity [2–4] and stereospecificity [5, 6] but low activity. The goal of this study was to develop modified copper catalysts for sufficiently fast and stereoselective hydrogenation of diacetylene hydrocarbon 5,17-docosadiyne,[2] with the aim to ensure its complete conversion and quantitative yield of *cis,cis*-diene and fairly high hydrogenation rate.

EXPRERIMENTAL

Copper catalysts (10% Cu) modified with europium and yttrium oxides were prepared by impregnating a support with metal salt solutions [6]. The europium and yttrium content was varied from 1 to 10%.

The catalyst precursors were thermally treated in air at 473 K for 2 h and then reduced in a hydrogen flow in a tubular furnace at 623 K for 3 h.

Hydrogenation was performed in a high-pressure kinetic device (HPKD) by a common procedure. The temperature was varied from 373 to 423 K, and pressure, from 6 to 10 MPa. Hexane was used as a diluent. Hydrogenation was performed until hydrogen uptake ceased after complete conversion of diacetylene derivative into the *cis,cis*-ethylene compound.

The products of 5,17-docosadiyne hydrogenation were analyzed on a Tsvet-500 chromatograph equipped with a $50\,000 \times 0.25$-mm capillary column coated with OV-101 phase. Chromatograms were treated using an internal reference.

The catalysts were studied by X-ray phase analysis on a DRON-4 diffractometer with filtered CuK_α radiation. The catalyst surface area was determined on an Accusorb-2100 device by the BET method from physical adsorption of nitrogen. Temperature-programmed desorption of hydrogen was also performed.

It was found that all catalysts contain metallic copper lattice without any extrinsic atoms. At the same time, no sharp diffraction maxima of the modifier were observed. This may be due to the fact that rare-earth compounds form thin surface films on aluminum and copper oxides, or X-ray amorphous compounds are formed by a solid-phase reaction of the modifier, copper oxide, and aluminum oxide on heating in an air flow. Both the above processes can proceed simultaneously. These suggestions are indirectly confirmed by a decrease in the surface area on introduction of europium and yttrium oxides into the catalyst. Introduction of 1 to 10% europium decreases the catalyst surface area from 68 to 48 $m^2\,g^{-1}$. For the catalyst 10% Cu/γ-Al_2O_3, the surface area is 90 $m^2\,g^{-1}$. With the yttrium content increasing from 1 to 10%, the surface area decreases from 75 to 38 $m^2\,g^{-1}$. The largest amount of hydrogen (2.2 cm^3) is desorbed from the catalyst modified with 5% Eu

[1] Attractants and pheromones of harmful insects allows opportune and efficient use of insecticides, which substantially decreases contamination of the environment [1].

[2] The hydrogenation product of this compound, *cis,cis*-5,17-docosadiene is the hypsy moth attractant.

1070-4272/02/7507-1101$27.00 © 2002 MAIK "Nauka/Interperiodica"

Hydrogenation of 5,17-docosadiyne in hexane on Cu/γ-Al_2O_3 catalysts

Copper content in catalyst, wt %	*P*, MPa	*T*, K	τ, min	Catalyzate composition, %	
				Z,Z-5,17-docosadiene	5,17-docosadiyne
10	4	393	300	–	100
10	6	393	200	86	14
10	8	393	175	100	–
10	4	423	300	–	100
10	6	423	140	100	–
10	8	423	120	100	–
20	4	423	300	–	100
20	6	423	200	100	–
20	8	423	180	100	–
30	4	423	300	–	100
30	6	423	210	100	–
30	8	423	180	100	–

(this catalyst is the most active); it is 2.4 times greater than the amount of hydrogen (0.9 cm^3) desorbed from 10% Cu/γ-Al_2O_3. The increased amount of desorbed hydrogen is probably due to increased hydrogen spillover in copper modified with a rare-earth metal oxide [7]. It is believed [8] that, in some cases, rare-earth metal oxides themselves can generate atomic hydrogen.

In samples modified with yttrium oxide (1% Y), the maximal hydrogen content (1.1 cm^3) is slightly larger than in 10% Cu/γ-Al_2O_3 (0.9 cm^3).

Diacetylene hydrocarbon, 5,17-docosadiyne, is converted into *cis,cis*-5,17-docosadiene with 100% yield on 10% Cu/γ-Al_2O_3 at 393 K and hydrogen pressure of 8 MPa (see table). At a lower pressure (6 MPa), conversion of acetylene hydrocarbon is incomplete at 393 K but becomes complete at 423 K. On 20–30% Cu/γ-Al_2O_3 catalysts at 423 K and hydrogen pressure 6–8 MPa, the initial 5,17-docosadiyne is also completely converted into the single product, *Z,Z*-5,17-docosadiene, after which the reaction stops.

An XPES study showed that mainly metallic copper occurs on the surface of the Cu/γ-Al_2O_3 catalyst; only 5% of Cu occurs as Cu^{2+}. The phase composition of catalysts was refined by X-ray and electron diffraction. It was shown that catalysts consist of metallic copper and a small amount of nonstoichiometric spinel, Cu/γ-Al_2O_3. This conclusion was confirmed by ESR spectroscopy: a weak signal of Cu^{2+} is observed in the spectrum of 10% Cu/γ-Al_2O_3. Electron-microscopic measurements showed that both finely divided (40–60 Å) and dense particles (they are usually 2000–3000 Å in diameter, but sometimes reach microns) occur in all catalyst samples irrespective of the copper content.

The 100% yield of *cis*-olefins in hydrogenation of acetylene derivatives on copper catalysts is attained under appropriate conditions [9–11], but the reaction time is very long. To enhance the activity, modifying additives were introduced into the copper catalysts. It was shown in [12] that, as the donor power of the catalyst increases, the dative electron transfer at adsorption of acetylene derivatives becomes stronger, which loosens the triple bond and increases the selectivity of its hydrogenation.

Rare-earth metal oxides (Eu_2O_3, Y_2O_3), which are strong donors (electronegativity EN: Y 1.2, Eu 1.1) [13], were taken as modifiers.

The most active copper catalyst, 10% Cu/γ-Al_2O_3, was modified at 393 K and hydrogen pressure of 8 MPa. Hydrogenation of 5,17-docosadiyne on the catalyst modified with europium oxide gives 100% yield of *cis,cis*-5,17-docosadiene (GLC). The reaction stops after complete conversion of diacetylene hydrocarbon into *Z,Z*-5,17-docosadiene:

Eu content in the catalyst, wt %	0	1	3	5	7	10
Reaction time τ, min	175	30	40	15	50	50

As seen, the activity of copper catalyst increases after modification. The catalyst containing 5% Eu en-

sures the highest hydrogenation rate and the shortest reaction time. The reaction time decreases by a factor of 11 as compared to Cu/γ-Al_2O_3. For catalysts with 1–3% Eu, the reaction time decreases by a factor of 3.3, and with 7–10% Eu, by a factor of 2.

Hydrogenation of 5,17-docosadiyne at 393 K and hydrogen pressure of 8 MPa on the catalyst 10% Cu/γ-Al_2O_3 modified with 1–10% yttrium oxide proceed with 100% yield of *cis,cis*-5,17-docosadiene (GLC). The reaction stops when formation of *Z,Z*-diene hydrocarbon is complete:

Y content in the catalyst, wt %	0	1	3	5	7	10
Reaction time τ, min	175	40	45	48	50	55

As seen, catalysts containing Y accelerate hydrogenation and correspondingly decrease the reaction time. The shortest reaction time is observed for the catalyst with 1% Y (by a factor of 4.3 shorter than with the yttrium-free catalyst), while for the catalyst with 10% Y this factor is 3.2, e.g., the reaction time increases with increasing yttrium content.

Thus, the developed catalysts 10% Cu + Eu_2O_3/γ-Al_2O_3 and 10% Cu + Y_2O_3/γ-Al_2O_3 not only keep all advantages of copper catalysts (complete conversion of diacetylene derivative, 100% yield of *cis,cis*-diene, reaction completion after dialkyne conversion into *cis,cis*-diene), but also are characterized by higher activity than unmodified catalysts. High selectivity of copper catalysts in dialkyne hydrogenation is mainly caused by low heat of adsorption of ethylene bond on copper, insufficient for its activation [14]. It is known [15] that the limiting stage of hydrogenation on copper catalysts is the dissociative hydrogen chemisorption. Therefore, all factors increasing the amount of sorbed atomic hydrogen should enhance the catalyst activity.

High stereospecificity of copper catalysts is caused by the ability of copper to form dihydride complexes HCuH [16] providing a possibility of simultaneous addition of two hydrogen atoms to a triple bond with formation of a *cis*-olefin.

cis,cis-5,17-Docosadiene obtained by stereoselective hydrogenation of the acetylene derivative was tested as gypsy moth attractant. In an arboretum with a very low population of harmful insects, 5–7 gypsy moth butterflies were found in each catcher with a dispenser containing *cis,cis*-5,17-docosadiene after 7 days.

CONCLUSION

Copper catalysts, both straight and modified with rare-earth metal oxides, can be used in synthesis of gypsy moth attractant.

REFERENCES

1. Lebedeva, K.V., Minyailo, V.A., and Pyatnova, Yu.B., *Feromony nasekomykh* (Insect Pheromones), Moscow: Nauka, 1984.
2. Wehrli, J.T., Thomas, D.J., Wainwright, M.S., and Trimm, D.L., *Appl. Catal.*, 1991, vol. 70, no. 2, pp. 253–261.
3. Wehrli, J.T., Thomas, D.J., Trimm, D.L., *et al.*, *Appl. Catal.*, 1990, vol. 66, pp. 199–208.
4. Stammbach, D.J., Thomas, D.J., Trimm, D.L., and Wainwright, M.S., *Appl. Catal.*, 1990, vol. 58, no. 2, pp. 209–216.
5. Gargano, M., Ravasio, N., Rossi, M., and Santo, J., *Chem. Ind.*, 1987, vol. 69, no. 1, pp. 79–83.
6. Kazakhstan Patent 20877.
7. Bachiller-Baeza, B., Juerrero-Rui, Z.A., and Rodriguer-Ramos, J., Abstracts of Papers, *4th European Congr. on Catalysis*, Rimini (Italy), September 5–10, 1999, P/1/040, p. 240.
8. Sakata, V., Arimoto, T., Kanechika, V., *et al.*, Abstracts of Papers, *4th European Congr. on Catalysis*, Rimini (Italy), September 5–10, 1999, O/10/23, p. 177.
9. Pak, A.M., Kartonozhkina, O.I., Slepov, S.K., and Izdebskaya, G.T., *Izv. Ross. Akad. Nauk, Ser. Khim.*, 1996, no. 5, pp. 1147–1151.
10. Pak, A.M., Kartonozhkina, O.I., Slepov, S.K., and Izdebskaya, G.T., *Zh. Prikl. Khim.*, 1996, vol. 69, no. 7, pp. 1145–1147.
11. Pak, A.M., Kartonozhkina, O.I., and Izdebskaya, G.T., Abstracts of Papers, *2nd Tokyo Conf. on Advanced Catalytic Science and Technology*, Tokyo (Japan), 1994, p. 239.
12. Chuvylkin, N.D., Pak, A.M., and Kazanskii, V.B., *Kinet. Katal.*, 1984, vol. 25, no. 6, pp. 1315–1322.
13. Batsanov, S.S., *Elektrootritsatel'nost' elementov i khimicheskaya svyaz'* (Electronegativity and Chemical Bond), Novosibirsk: Akad. Nauk SSSR, 1962.
14. Zakumbaeva, G.D., *Vzaimodeistvie organicheskikh soedinenii s poverkhnost'yu metallov VIII gruppy* (Interaction of Organic Compounds with Group VIII Metal Surface), Alma-Ata: Nauka, 1978.
15. Gudkov, B.S., Subbotin, A.N., and Yakerson, V.I., *Kinet. Katal.*, 1993, vol. 34, no. 5, pp. 909–912.
16. Efremenko, I.G., Ziberberg, J.K., Zhidomirov, G., and Pak, A.M., *React. Kinet. Catal. Lett.*, 1995, vol. 56, no. 1, pp. 77–79.

Russian Journal of Applied Chemistry, Vol. 75, No. 7, 2002, pp. 1104–1107. Translated from Zhurnal Prikladnoi Khimii, Vol. 75, No. 7, 2002, pp. 1121–1124.
Original Russian Text Copyright © 2002 by Saurambaeva, Sembaev.

CATALYSIS

Effect of Reaction Medium on the Composition of Vanadium–Titanium Catalyst in Oxidative Ammonolysis of Alkylpyridines

L. I. Saurambaeva and D. Kh. Sembaev

Bekturov Institute of Chemical Sciences, Almaty, Kazakhstan

Received July 25, 2001; in final form, January 2002

Abstract—The influence exerted by the concentration of alkylpyridines on the chemical composition of a vanadium–titanium catalyst under oxidative ammonolysis conditions was subjected to a comparative study.

In the course of catalysis, a catalyst undergoes transformations as a result of its interaction with reactants. The steady-state composition of the catalyst, which determines its activity and selectivity, is formed under the influence of the reaction medium. Under the conditions of oxidative ammonolysis, as also in other reactions, the extent to which the medium affects the catalyst depends on numerous factors, among which the relative amounts of air (oxidizing agent) and an organic compound are important. The change in the composition of a catalyst and, in particular, of a vanadium oxide catalyst modified with oxides of titanium(IV), tin(IV), and other metals is due to reduction of vanadium(V) oxide. For example, it has been shown [1–5] that vanadium(V) oxide in a vanadium–titanium catalyst is reduced under the action of the reaction medium, with the result that the ratio of V_2O_5 to the VO_2–TiO_2 solid solution, which determines the activity and selectivity of the catalyst, also changes.

The extent to which the reaction medium affects a catalyst depends on the degree of conversion of an organic substance, which is determined by the nature of this substance [6]. Therefore, in selecting a catalyst and determining the optimal conditions of the oxidative process, account should be taken of the catalyst composition, which is formed in the course of catalysis under the influence of the reaction medium and ensures the stability of the catalyst operation [7].

This study was aimed to reveal how the structure of alkylpyridines affects the composition and, consequently, catalytic properties of the vanadium–titanium oxide catalyst.

EXPERIMENTAL

The starting 2-methyl-5-ethylpyridine (MEP) and β-picoline of pure grade contained no less than 98% main substance.

Experiments on oxidative ammonolysis of alkylpyridines were performed on a flow-through installation with the reaction tube (length 130 mm, diameter 20 mm) made of quartz glass. The reaction products were absorbed with water and analyzed chromatographically with a flame-ionization detector on a column packed with 15% Carbowax 20M on Chromaton N-AW (0.16–0.20 mm). The analytical procedure with programmed heating from 100 to 180°C at a rate of 10 deg min^{-1} enabled determination of pyridine, 3-methylpyridine, 2-methyl-5-ethyl-, 2-methyl-5-vinyl-, 3-cyano-, 2-cyano-5-ethyl-, and 2-cyano-5-vinylpyridines. 2,5-Dicyanopyridine was determined polarographically after its conversion to isocinchomeronic acid by base hydrolysis.

Carbon oxides were analyzed chromatographically with a heat conductivity detector.

The vanadium–titanium catalysts were prepared by mixing vanadium(V) and titanium(IV) oxides of analytically pure grade with subsequent compaction of the stock into pellets and calcination at 800°C in air flow for 2 h.

X-ray phase analysis of the catalysts was carried out on a DRON-0.5 diffractometer with CuK_α radiation. The content of vanadium(V) oxide in the catalysts was determined by IR spectroscopy [8]. Samples for analysis were prepared as KBr pellets.

The oxidative ammonolysis of MEP on a vanadium–titanium oxide catalyst with the molar ratio

1070-4272/02/7507-1104$27.00 © 2002 MAIK "Nauka/Interperiodica"

$V_2O_5 : TiO_2 = 1 : 16$ at $MEP : O_2 : NH_3 : H_2O = 1 : 42 : 25 : 124$, temperature of 380°C, contact time of 0.83 s, and load of 15 g of MEP per 1 l of catalyst per hour (henceforth, g l^{-1} cat. h^{-1}) proceeded to give virtually a single product of partial conversion, 3-cyanopyridine, in 70 mol % yield (Fig. 1, points *a*). Under these conditions, the catalyst operated efficiently and stably for a long time (1200 h). The content of V_2O_5 in the catalyst decreased, compared to that in the initial catalyst, by 51.6 wt %. According to the results of X-ray phase and IR analyses, the catalyst had the form of an oxide system composed of V_2O_5 and a VO_2–TiO_2 solid solution.

Raising the load (MEP) to 27 g l^{-1} cat. h^{-1} caused a minor decrease in the content of vanadium(V) oxide in the catalyst (Fig. 1, point *b*, curve *6*). This led to a decrease in the selectivity of nicotinonitrile formation to 58.6% (curve *4*) and to the appearance in the catalyst of nitriles of 5-ethyl- and 5-vinylpicolinic and pyridine-2,5-dicarboxylic acids (Fig. 1, points *b*, curves *1–3*).

Raising the concentration of dialkylpyridine in the reaction zone further caused an even more significant decrease in the V_2O_5 content and enrichment of the solid solution with the forming vanadium(IV) oxide. As a result, the conversion of the starting compound decreased and the selectivity of formation of 5-ethyl- and 5-vinylpicolinonitriles and 2,5-dicyanopyridine increased to a total of 55% for MEP feed of 68 g l^{-1} cat. h^{-1} (Fig. 1, points *d*).

With a feed of 92 g l^{-1} cat. h^{-1} of MEP, the entire amount of V_2O_5 contained in the catalyst was reduced. On a catalyst in the form of a V_2O_5–TiO_2 solid solution, the conversion of the pyridine base did not exceed 68%, and the major reaction products were nitriles of 5-ethyl- and 5-vinylpicolinic and pyridine-2.5-dicarboxylic acids (Fig. 1, points *e*, curves *1–3*). The intensity of deep oxidation processes decreased dramatically: the selectivity with respect to carbon dioxide did not exceed 3%.

The experimental data presented in Fig. 1 indicate strong changes in the composition of the vanadium-containing catalyst under the influence of the composition of the reaction medium. In the course of vanadium(V) reduction, both the $V_2O_5/(VO_2–TiO_2)$ ratio and the composition of the solid solution changed. At high MEP concentration in the reaction medium, the catalyst was a solid solution. To each composition of the reaction mixture corresponded a certain chemical composition of the catalyst, which determined its activity and selectivity. As a result, the conversion of MEP decreased and the direction

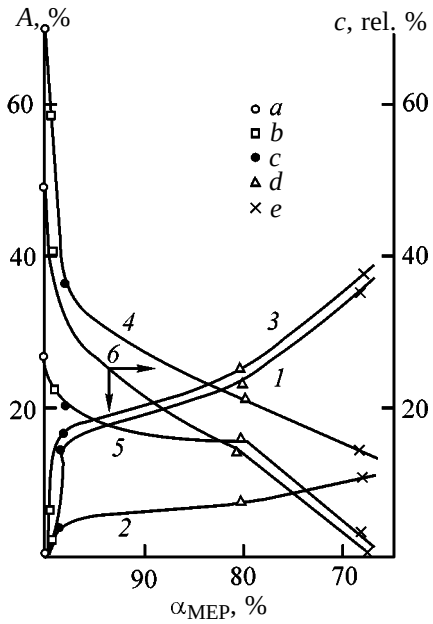

Fig. 1. Effect of conversion α_{MEP} on the selectivity *A* and V_2O_5 content *c* of the catalyst with $V_2O_5 : TiO_2 = 1 : 16$. Temperature 380°C, contact time 0.83 s. MEP feed rate (g l^{-1} cat. h^{-1}): (*a*) 15, (*b*) 27, (*c*) 40, (*d*) 68, and (*e*) 92. Product: (*1*) 2-cyano-5-ethylpyridine, (*2*) 2-cyano-5-vinylpyridine, (*3*) 2,5-dicyanopyridine, (*5*) CO_2, and (*6*) V_2O_5.

of oxidative transformations changed fundamentally:

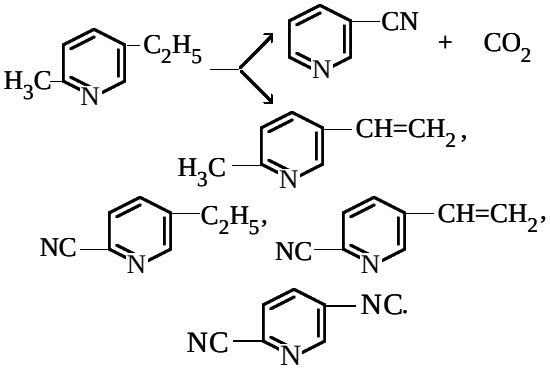

On a catalyst rich in vanadium(V) oxide, oxidative ammonolysis proceeded with oxidative elimination of the methyl group of MEP, and 3-cyanopyridine was the major reaction product. On a catalyst containing a small amount of V_2O_5 (with solid solution the rest), the yield of products with two carbon atoms retained at the pyridine ring increased. These compounds were the major products of the reaction occurring on a catalyst containing minor amounts of V_2O_5 and solid solution.

The results obtained in studying the effect of operation time of a freshly prepared vanadium–titanium

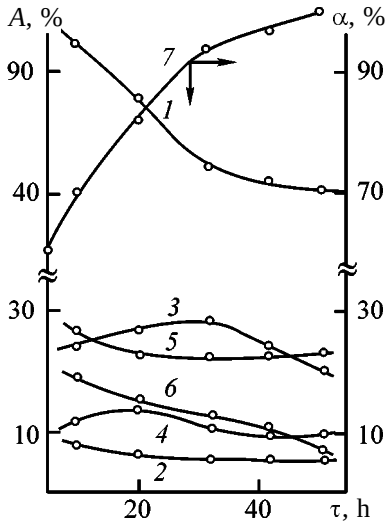

Fig. 2. Effect of the operation time τ of catalyst with $V_2O_5 : TiO_2 = 1 : 16$ on the conversion α of V_2O_5 in the catalyst and on the conversion of MEP and yield of products formed in oxidative ammonolysis of 2-methyl-5-ethylpyridine, *A*. Feed rate: MEP 92, air 1980 l, ammonia 100 g, and water 590 g l^{-1} cat. h^{-1}; temperature 380°C; contact time 0.27 s. (*1*) MEP conversion; yield of products: (*2*) 2-methyl-5-vinylpyridine, (*3*) 2-cyano-5-ethylpyridine, (*4*) 2-cyano-5-vinylpyridine, (*5*) 2,5-dicyanopyridine, and (*6*) 3-cyanopyridine; (*7*) V_2O_5 conversion.

catalyst at high load (MEP) are presented in Fig. 2. An analysis of the catalyzate after 10 h of operation demonstrated that a minor decrease in the V_2O_5 content of the catalyst changed the reaction direction. In this case, 2-methyl-5-vinyl- and 2-cyano-5-ethylpyridines, and also 2-cyano-5-vinyl- and 2,5-ethylpyridines, whose total yield is as high as 70%, became the major reaction products of oxidative ammonolysis of MEP. 3-Cyanopyridine was obtained in a yield as low as 18 mol %.

In prolonged operation of the catalyst (>50 h) under these conditions, the yield of the above-mentioned products changed only slightly. The main reaction products were 2-cyano-5-ethyl- and 2,5-dicyanopyridines. The yield of 3-cyanopyridine was not higher than 7 mol %. The main direction of the oxidative ammonolysis of MEP on a catalyst in the form of a VO_2–TiO_2 solid solution is associated with conversion of one or both alkyl groups into nitrile groups. The share of oxidative elimination of alkyl substituents is low on a catalyst of this kind, which is indicated by the low selectivity of 3-cyanopyridine formation and virtually total absence of CO_2 in the catalyzate.

Effect of 3-methylpyridine load on the yield of products formed in oxidative ammonolysis on catalyst with $V_2O_5 : TiO_2 = 1 : 16$

β-Picoline load, g l^{-1} cat. h^{-1}	β-Picoline conversion	Yield, mol %	
		3-cyanopyridine	CO_2
27.5	98.0	95.0	3.0
49.9	97.8	94.2	3.0
60.0	97.7	94.8	2.8
82.0	97.8	93.8	2.7
100.0	97.7	93.6	2.6

A comparative study of the influence exerted by the reaction medium with varied 3-methylpyridine concentration on the composition of the vanadium–titanium oxide catalyst and on the yield of products formed in oxidative ammonolysis was carried out. The feed rate of the pyridine base was varied between 27.5 and 100 g l^{-1} cat. h^{-1} at constant molar ratio of β-picoline, oxygen, ammonia, and water, equal to 1 : 37 : 8 : 47. The reaction temperature was 380°C, and the contact time, 0.47 s.

The experimental results presented in the table indicate that the reaction medium with widely varied β-picoline feed rate exerts no significant influence on the chemical composition of the catalyst and catalyzate. At a feed of the picoline base at a rate of 100 g l^{-1} cat. h^{-1} for 60 h, the amount of V_2O_5 in the catalyst decreased by 1–2% relative to the initial content, with the conversion of β-picoline decreasing by only 0.2–0.3%, and the yield of 3-cyanopyridine and CO_2, by 1.4 and 0.4%, respectively. Prolonged operation of the catalyst (>200 h) under these conditions did not lead to any new changes in the steady state of the catalyst or in the catalyzate composition.

The data obtained are in agreement with the results of previous experiments on *o*-xylene oxidation into phthalic anhydride on the same catalyst at hydrocarbon load exceeding 100 g l^{-1} cat. h^{-1} [1].

The stronger influence of MEP on the chemical composition of the vanadium–titanium oxide catalyst, compared with that of 3-methylpyridine and *o*-xylene [1, 9], is due to the presence in the molecule of an ethyl group subjected to dehydrogenation, which can be judged from the composition of products formed in oxidative ammonolysis (Figs. 1, 2). The appearance of hydrogen in the catalytic system causes intensive reduction of V_2O_5 to VO_2, which becomes a component of the continuous series of substitutional VO_2–TiO_2 solid solutions [1].

Thus, we found that the extent to which the reac-

tion medium affects the composition of the vanadium–titanium oxide catalyst under the conditions of oxidation reaction depends not only on the reactant ratio, but also on the structure of the organic compound. Therefore, when selecting an effective catalyst and choosing conditions for a particular oxidation reaction, it is necessary to obtain the information about the extent to which the catalyst composition changes under the action of the reaction medium.

CONCLUSIONS

(1) In contrast to 3-methylpyridine, 2-methyl-5-ethylpyridine strongly affects the chemical composition of the vanadium–titanium oxide catalyst, which changes the direction of the dialkylpyridine conversion.

(2) The strong influence of 2-methyl-5-ethylpyridine on the composition of the vanadium–titanium oxide catalyst is due to the presence at the pyridine ring of an ethyl group subjected to dehydrogenation on the catalyst surface.

REFERENCES

1. Sembaev, D.Kh., Suvorov, B.V., Saurambaeva, L.I., and Suleimanov, Kh.T., *Kinet. Katal.*, 1979, vol. 20, no. 3, pp. 750–755.
2. *Vanadievye katalizatory okisleniya geterotsiklicheskikh soedinenii* (Vanadium Catalysts for Oxidation of Heterocyclic Compounds), Shimanskaya, M.V., Ed., Riga: Zinatne, 1990.
3. Andersson, A., *J. Catal.*, 1982, vol. 76, no. 1, pp. 144–156.
4. Grzybowska, B., *Appl. Catal. A: Gener.*, 1997, vol. 157, nos. 1–2, pp. 263–310.
5. Wachs, I.E. and Weckhuysen, B.M., *Appl. Catal. A: Gener.*, 1997, vol. 157, nos. 1–2, pp. 67–90.
6. Suvorov, B.V., *Okislitel'nyi ammonoliz organicheskikh soedinenii* (Oxidative Ammonolysis of Organic Compounds), Alma-Ata: Nauka, 1971.
7. Boreskov, G.K., *Geterogennyi kataliz* (Heterogeneous Catalysis), Moscow: Nauka, 1988.
8. Sembaev, D.Kh., Saurambaeva, L.I., and Kim, S.M., *Zh. Anal. Khim.*, 1978, vol. 33, no. 2, pp. 391–393.
9. Dias, C.R. and Portela, M.F., *Catal. Rev.—Sci. Eng.*, 1997, vol. 39, no. 3, pp. 169–207.

Russian Journal of Applied Chemistry, Vol. 75, No. 7, 2002, pp. 1108–1112. Translated from Zhurnal Prikladnoi Khimii, Vol. 75, No. 7, 2002, pp. 1125–1130.
Original Russian Text Copyright © 2002 by Khimich, Venzel', Drozdova, Koptelova.

CATALYSIS

Trifluoroacetic Acid as a New Effective Catalyst for Preparing Monolithic Silica Gel by the Sol–Gel Process

N. N. Khimich, B. I. Venzel', I. A. Drozdova, and L. A. Koptelova

Grebenshchikov Institute of Silicate Chemistry, Russian Academy of Sciences, St. Petersburg, Russia

Received November 12, 2001

Abstract—Trifluoroacetic acid was proposed as a new effective catalyst for organic sol–gel synthesis. The influence of the solvent (polar or nonpolar, protic or aprotic) on the sol–gel process was studied.

Synthesis of glassy materials by organic sol–gel process involving hydrolysis of silicon alkoxides, polycondensation of the products, drying of the samples, and sintering of the resulting xerogels was extensively studied [1, 2]. These transformations can be described by the following scheme:

$$\equiv Si{-}OR + H_2O \underset{\text{Etherification}}{\overset{\text{Hydrolysis}}{\rightleftharpoons}} \equiv Si{-}OH + ROH, \quad (1)$$

(2)

$$\equiv Si{-}OR + HO{-}Si\equiv \underset{\text{Alcoholysis}}{\overset{\text{Condensation}}{\rightleftharpoons}} \equiv Si{-}O{-}Si\equiv + ROH, \quad (3)$$

(4)

$$\equiv Si{-}OH + HO{-}Si\equiv \underset{\text{Hydrolysis}}{\overset{\text{Condensation}}{\rightleftharpoons}} \equiv Si{-}O{-}Si\equiv + H_2O, \quad (5)$$

(6)

Silicon alkoxides are hydrolyzed to form silanols (1) which can be condensed by two ways [reactions (3) and (5)]. In acidic media, silanols polymerize to form three-dimensionally cross-linked silica gel [3].

As the sol–gel process occurs, the contribution of reverse reactions, silanol etherifications (2) and rupture of siloxane bonds by alcoholysis (4) and hydrolysis (6), increases, which results in degradation of the gel matrix [3]. Therefore, monolithic samples usually crack in the course of their drying.

There are two ways to prevent cracking. The first is controlled drying, i.e., removal of dispersion media from the gel matrix by capillary forces transferring the liquid to the gel surface. Strong stresses arising after gel shrinkage can be decreased by several ways. The simplest but not the best is performing the process for a longer time. Monolithic samples with excellent physicochemical properties were obtained by drying gels for many months (better years) [4]. We will not consider supercritical drying since it is mainly used for preparing aerogels [3]. Optimization of drying by addition of fine SiO_2 powder or treatment of porous articles in a fluidized bed of ceramic powder [5] deserve attention.

The second approach to prepare monolithic silica is introduction of drying control chemical additives (DCCAs) [6, 7] into the sol–gel system. These compounds optimize hydrolysis of silicon alkoxides and polycondensation of the hydrolysis products.

Indeed, the main function of DCCA (in this case, an organic acid amide) in acid hydrolysis of tetramethoxysilane (TMOS) consists in partial neutralization of acid used as catalyst in the sol–gel system [8]. It is known [9] that hydrolysis and polycondensation of TMOS occur at pH < 1 and pH 4–5, respectively. Hence, neutralization of the reaction mixture from pH 0.7–0.9 to pH 1.8–4.5 owing to reaction of the amides with acid protons provides the best conditions for hydrolysis–polycondensation processes and strengthening of the resulting gels, i.e., promotes polycondensation reactions (3) and (5) and suppresses the reverse reactions (4) and (6) of hydrolysis and alcoholysis of the siloxane chain. Under these conditions, the maximal number of siloxane bonds in a unit volume is formed, which prevents cracking of a gel on drying [10].

A substantial disadvantage of xerogels thus prepared is the presence of difficultly volatile organic impurities (5–10% of the SiO_2 weight) in their pores [10]. These impurities are not removed from the gel matrix at 120–150°C, and their pyrolysis at temperatures above 300–400°C is one of the factors causing cracking of monolithic xerogels on sintering. A search for additives to a sol–gel system, which, on the one hand, provide the best conditions for hydrolysis–polycondensation processes and, on the other hand, are

1070-4272/02/7507-1108$27.00 © 2002 MAIK "Nauka/Interperiodica"

Table 1. Solvent properties

Solvent no.	Solvent	M	bp, °C	d_4^{20}, g cm^{-3}	μ, D	ε at 20°C
		Protic				
1	Acetic acid	60.05	117.8	1.049	1.3	6.1
2	*tert*-Amyl alcohol	88.15	101.8	0.809	1.9	12.5
3	Propanol	60.09	97.4	0.803	1.7	20.7
		Aprotic				
4	Dioxane	88.12	101.3	1.034	0	2.2
5	Propionitrile	55.08	97	0.772	3.7	27.0

readily removed on drying, is an urgent problem. One of the ways of its solution is the use of trifluoroacetic acid instead of a strong inorganic acid. Formation of volatile methyl trifluoroacetate provides, on the one hand, the required pH and, on the other hand, the absence of difficultly volatile organic impurities in the gel matrix. Preliminary data on the catalysis with trifluoroacetic acid are briefly reported in [11].

In this work, we studied in detail the influence of the solvent on preparation of monolithic silica gel by the sol–gel process. A solvent is the necessary component of the organic sol–gel system, since alkoxysilane is insoluble in water. In most works, only alcohols (ethanol, methanol, and sometimes 2-methoxyethanol) were used as solvents. Other organic solvents were not studied in this respect. However, the type of the solvent (protic or aprotic, polar or nonpolar) should undoubtedly affect the physicochemical properties of xerogels.

EXPERIMENTAL

TMOS gelation in the presence of various solvents was studied as follows. TMOS (1 equiv) was mixed with a solvent (1 equiv) and then with water (4 equiv). To the resulting solution, on cooling, trifluoroacetic acid (0.1 equiv) was added with vigorous stirring. The solvent-free sol–gel system was prepared by adding dropwise a solution of trifluoroacetic acid (0.1 equiv) in water (4 equiv) to TMOS (1 equiv) with vigorous stirring. Each subsequent drop of the acid solution was added after complete homogenization of the reaction mixture.

The solvents studied in this work were thermally stable under gelation conditions, and their boiling points were close (except for acetic acid). The properties of these solvents are summarized in Table 1.

We studied six solutions. The solutions were placed in hermetically sealed Teflon cylinders 20 mm in diameter (four samples of each system, layer thickness 8–10 mm) and heated for 2 days. Then the hermetic cylinder lids were replaced by lids with 1-mm holes, and samples were dried under the following conditions: heating to 80°C over a period of 2 h, keeping at 80°C for 20 h, heating to 100°C over a period of 4 h, keeping at 100°C for 40 h, heating to 120°C over a period of 4 h, keeping at 120°C for 20 h, heating to 150°C over a period of 3 h, and keeping at 150°C for 20 h.

Six gels were thus prepared. Their numbers correspond to those of the solvent (gel no. 6 was prepared by the solvent-free sol–gel process). Gel no. 7 was prepared from TMOS (1 equiv)–H_2O (4 equiv) mixture containing HCl (0.1 equiv) as catalyst.

The open, W_{open}, and total, W_{tot}, porosities of the samples were determined. The apparent, d_{app}, and true, d_{true}, densities were determined by the Archimede's procedure using toluene and water as saturating and working liquids, respectively. The gel point t (h) was determined as a time required for the sol to become stagnant. The hardness was measured on a PMT-3 microhardness gage. Thermogravimetric analysis was performed on a Q-1500D derivatograph (Hungary) by heating to 1000°C with a rate of 20 deg min^{-1}. The SiO_2 content in the gels was determined thermogravimetrically; the carbon content, from the electrical conductivity of barium hydroxide solutions that absorbed carbon dioxide liberated after combustion of the sample in oxygen; and fluorine content, by a spectrophotometric procedure based on breakdown of the zirconium complex with xylenol orange. The NMR spectra were recorded on a Bruker DPX-300 spectrometer using $CDCl_3$ as the solvent and tetramethylsilane as the internal reference. Electron-microscopic study of the gels was performed on an EM-125 microscope with the accelerating voltage

Table 2. Physicochemical properties of the gels

Sample no.	*t*, h, at 60°C	SiO_2	C	F	d_{app}, g cm^{-3}	W_{open}	W_{tot}	Hardness, kg mm^{-2}
		%				%		
1	1.95	89	0.35	0.015	1.48	15.3	35.6	103
2	4.05	88	0.97	0.14	1.11	45.5	51.6	36
3	5.7	82	6.82	0.07	1.23	30.6	46.7	58
4	15.5	79	0.42	0.1	1.53	9.0	24.0	86
5	5.5	87	1.69	0.19	1.30	16.3	43.6	98
6	2.05	89	0.38	0.38	1.47	26.2	36.1	87
7	5.70	89	0.57	–	1.12	41.0	47.5	49

of 5 kV. For this purpose, cellulose–carbon replicas of fresh chips of the gels were prepared.

Tetramethoxysilane and solvents were purified by distillation on a 10-TP column. The fractions in the range 0.3–0.5°C were collected.

The gels were monolithic transparent disks except for sample nos. 4, 6, and 7 which were partiallty cracked. The physicochemical properties of the gels are given in Table 2.

Trifluoroacetic acid is a strong (pH 0.3) thermally stable organic acid. It forms strong complexes with water and methanol, which complicates its removal from the reaction mixture. Very low fluorine content in the matrix of gel nos. 1–6 dried at 150°C can be only due to chemical transformation of this acid into a more volatile compound. Indeed, the ^{1}H NMR spectrum of the volatile fraction obtained by condensation in a cooled trap of vapor formed on drying of gel no. 6 contains the signals of water (δ = 4.85 ppm), methanol (δ = 3.34 ppm), and methyl trifluoroacetate (δ = 3.98 ppm). To confirm the assignment of the latter signal, methyl trifluoroacetate was prepared from trifluoroacetic acid and methanol in the presence of sulfuric acid [12].

Analysis of the dispersion media of gel nos. 1 and 5 gave the similar results. The spectrum of the condensate contained, along with signals of the solvents (δ = 1.22 and δ = 2.45 ppm for propionitrile and δ = 1.97 ppm for acetic acid), the signals of methanol and methyl trifluoroacetate.

It is interesting that the dispersion medium of the sol–gel process performed in the presence of acetic acid contains one more volatile product, methyl acetate. This is unambiguously indicated by the presence of signals at 3.56 and 1.95 ppm (cf. ethanol).

Thus, the sol–gel process of formation of gel no. 1 involves the reaction

$$CF_3COOH + CH_3OH \rightleftarrows CF_3COOCH_3 + H_2O.$$

In the first steps of the sol–gel synthesis performed in hermetically sealed vessels, this equilibrium is strongly shifted to the left. As a result, the pH of the reaction mixture is ~1, which favors hydrolysis. When the dispersion media is vaporized on drying of the gel matrix, the equilibrium is shifted to the right owing to removal of low-polar highly volatile (bp 43.0–43.5°C) methyl trifluoroacetate. As a results, the acidity of the sol–gel system appreciably decreases, which favors polycondensation of silanol groups [9].

Table 2 demonstrates the influence of the solvent on preparation of monolithic silica gel by sol–gel process. The samples prepared with aprotic nonpolar dioxane are cracked.

When the gelation is performed in the presence of hydrochloric acid, the reaction mixture is constantly acidic (pH < 1). The hardness and density of gel nos. 6 prepared in the presence of trifluoroacetic acid are appreciably higher than those of gel no. 7 prepared in the presence of HCl (Table 2). The structural differences are clearly seen on electron micrographs (Fig. 1). Ordered and uniform structure of gel no. 6 (Fig. 1b) strongly differs from porous and channeled structure of gel no. 7 (Fig. 1a).

However, it is difficult to perform sol–gel process in the absence of solvent, since TMOS is very sparingly soluble in water.

The influence of the solvent on the sol–gel process of formation of monolithic silica gel can be revealed by comparing the physicochemical properties of the samples (Table 2), their electron micrographs (Fig. 1), and the results of thermogravimetric analysis (Fig. 2). Cracked samples with the minimal silica content are formed in the presence of aprotic nonpolar dioxane.

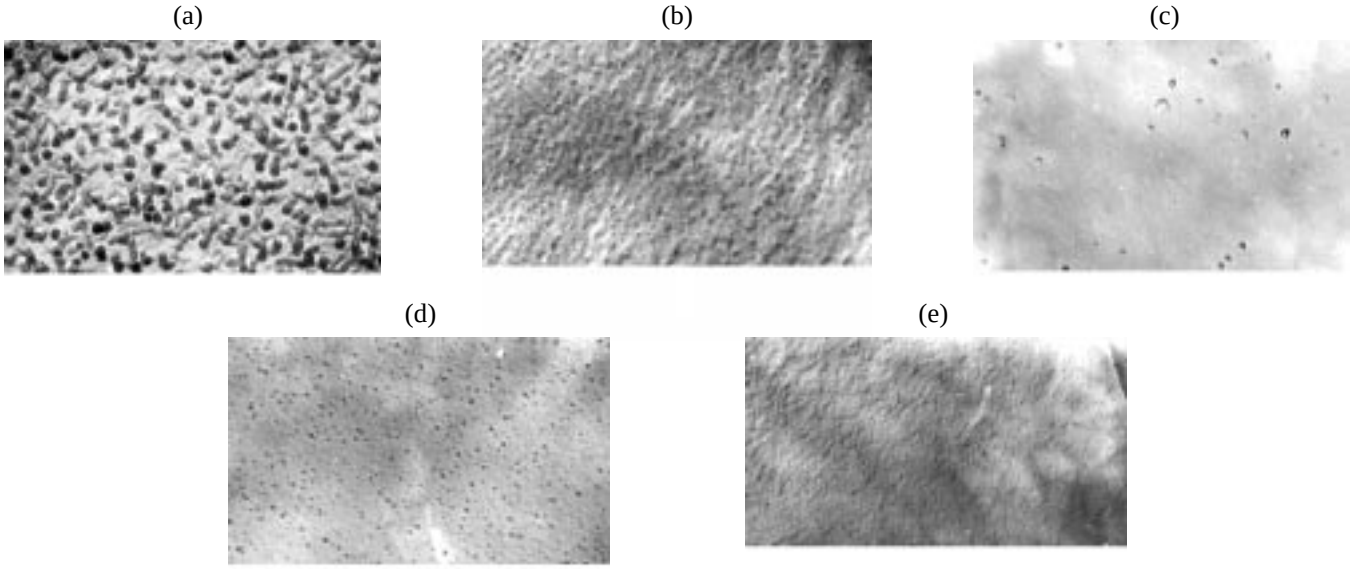

Fig. 1. Electron micrographs of gel nos. (a) 7, (b) 6, (c) 4, (d) 2, and (e) 1. Magnification: (a, b) 60 000 and (c–e) 80 000.

High hardness and density of the gels are due to increased filling of pores with the dispersion media but not to formation of a strong gel skeleton.

The use of alcohols as solvents for the sol–gel synthesis is ineffective. The increased carbon content in the matrix of gel no. 3 prepared with propanol can be due to etherification of silanols formed by TMOS hydrolysis and alcoholysis of the siloxane bonds [13] [Eqs. (2) and (4), respectively]. In *tert*-amyl alcohol, these reactions are sterically hindered. However, although the matrices of the resulting gels are uniform, their density and hardness are low (Fig. 1d).

Acetic acid and propionitrile are promising solvents for the sol–gel process. The density and hardness (Table 2) of the gels prepared with these solvents are the highest. These gels have uniform and microporous structure (Fig. 1e; the structure of gel no. 5 is similar).

As noted above, the reaction of acetic acid with residual methanol suppresses alcoholysis (Eq. 4), thus promoting condensation [Eqs. (3), (5)]. At the same time, transformation of low-volatile acetic acid into the volatile ester reduces the carbon content in the matrix of gel no. 1.

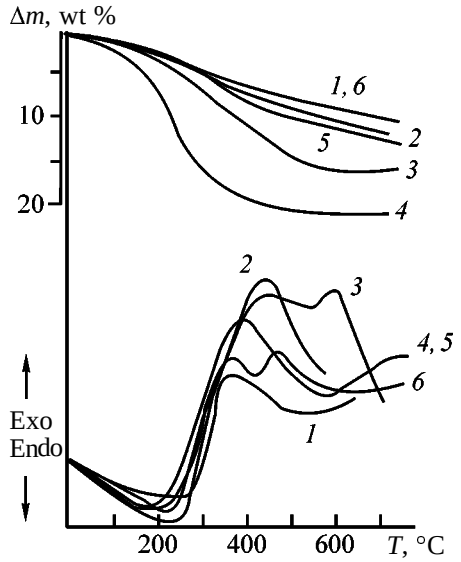

Fig. 2. DTA and TG curves of gel nos. 1–6 (*1–6*, respectively). (Δ*m*) Weight loss and (*T*) temperature.

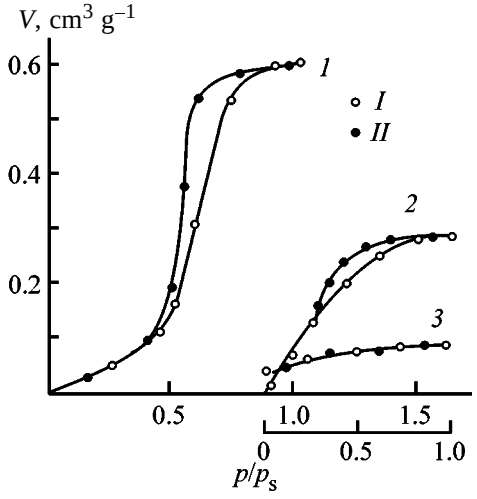

Fig. 3. Adsorption (*I*)–desorption (*II*) isotherms of ethanol on gel nos. (*1*) 7, (*2*) 6, and (*3*) 1 at 18°C. (*V*) Pore volume and (p/p_s) ratio of the ethanol vapor pressure to its saturated vapor pressure.

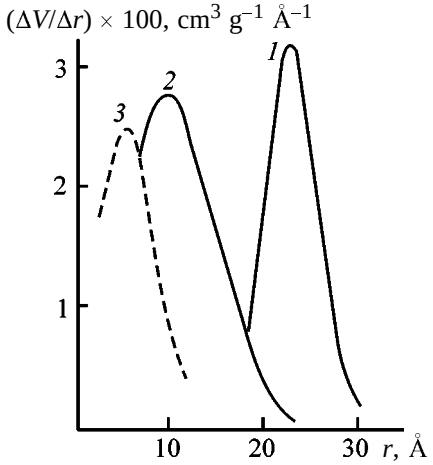

Fig. 4. Distribution of pore volume *V* with respect to pore radius *r* for gel nos. (*1*) 7, (*2*) 6, and (*3*) 1.

It should be noted than macropores of gel nos. 1 and 7 (10–15 and 40–50 nm in diameter, respectively) are not empty. The isotherms of ethanol sorption on gels prepared without solvent (*1*, *2*) and with acetic acid (*3*) are shown in Fig. 3. The size of fine particles filling gel macropores can be estimated from these isotherms. The distribution of pore volume with respect to pore radius is shown in Fig. 4. Since no hysteresis is observed in isotherm *3* for gel no. 1, the volume of pores (smaller than 10 Å) cannot be determined, and curve *1* is shown as dashed line.

Thus, macropores of the gels are filled with more finely divided SiO_2 powder. Although the fact that there are two types of porosity of microporous silica glasses is well known [14], this phenomenon for silica gels is not understood.

CONCLUSIONS

(1) Hydrolysis of tetramethoxysilane and polycondensation of the hydrolysis products were optimized by replacing a strong inorganic acid used as the catalyst by trifluoroacetic acid. The use of trifluoroacetic acid allows the pH of the reaction mixture to be increased from ~1 to almost neutral values owing to removal of trifluoroacetic acid in the form of its volatile methyl ester.

(2) This optimization allows preparation of monolithic gels which do not crack on drying and have high density and hardness.

(3) Difficultly volatile organic impurities formed in the presence of conventional drying control chemical additives are not accumulated in the presence of trifluoroacetic acid, since it is removed from the gel matrix in the form of volatile methyl ester.

(4) The use of propionitrile and acetic acid as solvents for sol–gel process should simplify preparation of gels with the highest hardness and density.

REFERENCES

1. Sakka, S., *J. Sol–Gel Sci. Technol.*, 1994, vol. 1, no. 3, pp. 69–81.
2. Petrovskii, G.T., Shashkin, V.S., and Yakhkind, A.K., *Fiz. Khim. Stekla*, 1997, vol. 23, no. 1, pp. 43–54.
3. Brinker, C.I. and Scherer, G.W., *Sol–Gel Science*, New York: Academic, 1990.
4. Demskaya, E.L., Sokolova, A.P., and Khotimchenko, V.S., *Fiz. Khim. Stekla*, 1991, vol. 17, no. 1, pp. 109–113.
5. Evstrop'ev, S.K., Efimov, A.V., Smirnov, N.V., and Shashkin, V.R., *Steklo Keram.*, 1992, no. 9, pp. 5–7.
6. Hench, L.L., in *Science of Ceramic Chemical Processing*, New York: Wiley, 1986, pp. 52–64.
7. Orcel, G. and Hench, L., *J. Non-Cryst. Solids*, 1986, vol. 79, pp. 177–194.
8. Shul'ts, M.M., Khimich, N.N., Rakhimov, V.I., and Stolyar, S.V., *Dokl. Ross. Akad. Nauk*, 1995, vol. 344, no. 1, pp. 69–71.
9. Pope, E.J.A. and Mackenzie, J.D., *J. Non-Cryst. Solids*, 1986, vol. 87, pp. 185–198.
10. Khimich. N.N. and Stolyar, S.V., *Zh. Prikl. Khim.*, 1998, vol. 71, no. 10, pp. 1590–1595.
11. Khimich. N.N., Venzel', B.I., Drozdova, I.A., and Suslova, L.Ya., *Dokl. Ross. Akad. Nauk*, 1999, vol. 366, no. 3, pp. 361–363.
12. Gryszkiewicz-Trochimowski, E., Sporzynski, A., and Whuk, J., *Recl. Trav. Chim. Pays-Bas*, 1947, vol. 66, p. 413.
13. Peace, B.W., Mayhan, K.G., and Montle, J.F., *Polymer*, 1973, vol. 14, pp. 420–422.
14. Venzel', B.I. and Svatovskaya, L.G., *Fiz. Khim. Stekla*, 1994, vol. 20, no. 4, pp. 523–528.

Russian Journal of Applied Chemistry, Vol. 75, No. 7, 2002, pp. 1113–1116. Translated from Zhurnal Prikladnoi Khimii, Vol. 75, No. 7, 2002, pp. 1131–1134.
Original Russian Text Copyright © 2002 by Dobrynina, Faizullina, Barabanov, Manyurov.

ENVIRONMENTAL PROBLEMS OF CHEMISTRY AND TECHNOLOGY

Coagulation and Flocculation Purification of Fat- and Protein-Containing Disperse Systems

A. F. Dobrynina, G. G. Faizullina, V. P. Barabanov, and I. R. Manyurov

Kazan State Technological University, Kazan, Tatarstan, Russia

Received July 13, 2001; in final form, December 2002

Abstract—Procedure for treatment of wastewater with a coagulant (aluminum sulfate) and anionic flocculants to remove fats and proteins was studied The purification efficiency was evaluated from the flocculation parameters.

Wastewater from dairy, meat-processing, mayonnaise, and other plants of food industry is often a complex disperse mixture of various compounds, among which the most typical are fats and proteins. The parameters of such systems and, in particular, their aggregation and sedimentation stability are determined by the structure of the electrical double layer (DLVO theory) [1, 2], properties of the surrounding boundary layers, and presence of a structural-mechanical barrier (according to Rebinder [3]).

Colloidal-chemical methods involving, in particular, flocculation and coagulation can disturb the aggregation and sedimentation stability of these disperse systems. The mechanisms of particle aggregation occurring in this case were analyzed in detail in [4, 5].

In this work we studied the effect of various factors on the transition of highly dispersed fat- and protein-containing wastewater from the stable into the aggregation-unstable state under the action of a coagulant or its mixture with flocculants.[1]

EXPERIMENTAL

The composition of the product and wastewater characteristics are listed in Tables 1 and 2. First, the wastewater was stored for several hours, then the top layer and precipitate were separated, and the layer containing dispersed proteins, fats, and other impurities was studied.

In our work we used pure grade aluminum sulfate $Al_2(SO_4)_3 \cdot 18H_2O$ [GOST 3758–65] as coagulant, and DKS F40 T1 (Japan Chemical Department) and Praestols 2530TR and 2540TR (Stockhausen GmbH and Co.CG) as flocculants. The characteristics of flocculants are given in Table 3.

The granulometric composition of the untreated

[1] The wastewater from washing of mixers for preparing a crude emulsion of Provansal' mayonnaise was used.

Table 1. Product composition

Component	Content, wt %	GOST*
Vegetable oil	65.4	GOST 1129
Egg powder	5.0	GOST 2859
Skim milk powder	1.6	GOST 10970
Sodium chloride	1.1	GOST 13830
Granulated sugar	1.5	GOST 21
Baking soda	0.05	GOST 2156
Mustard powder	0.75	GOST 18-30877
Acetic acid	0.55	GOST 61
Water	24.05	GOST 2874–73

* State standard.

Table 2. Parameters of industrial wastewater before and after treatment

Parameter	Wastewater		Prescribed limit*
	before treatment	after treatment	
pH	6.5–8.0	6.5–8.0	6.5–8.0
COD, mg l^{-1}	800	200	265
BOD, mg l^{-1}	1250	200	177
Suspended particles, mg l^{-1}	1500	200	186
Fat, mg l^{-1}	1500	1–10	10
Protein, %	0.05	–	–
Detergent, mg l^{-1}	80	8.0	0.5

* Standard concentration of pollutants in wastewater.

1070-4272/02/7507-1113$27.00 © 2002 MAIK "Nauka/Interperiodica"

Table 3. Characteristics of flocculants

Polymer	$[\eta]$, $cm^3\ g^{-1}$	$M_\eta \times 10^{-6}$	Content of monomers in copolymer, mol %	
			acrylamide	sodium acrylate
DKS F40 T1	1970	12.6	81.2	19.8
Praestol 2530 TR	1800	4.46	80	20
Praestol 2540 TR	1600	4.4	72	28

disperse system was studied by optical microscopy (Biolam microscope). Since the disperse phase particles are often of irregular shape, their statistical average radius (R) was evaluated.

To plot the differential curves of the particle size distribution in the dQ_n/dR–R coordinates (Q_n is the particle number in the fraction), 20 series of measurements were carried out. The number of particles in each fraction was calculated at least six times in different sections of the micrometer network. In our calculations we assumed that the radius range in each fraction is equal and comprises a half of the scale factor ($\Delta R = x/2$). For each fraction, the average particle radius was calculated from the following equation:

$$R_i = x(m + 0.5)/2, \quad (1)$$

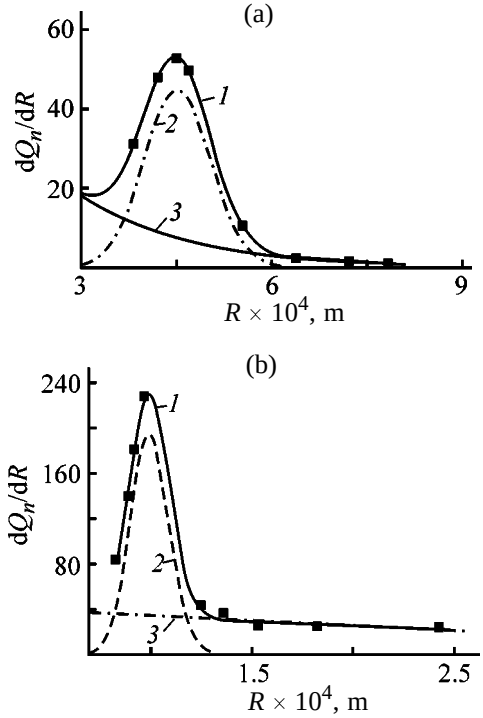

Fig. 1. (*1*) Differential distribution curve of the particle size R in the (a) initial and (b) purified disperse system, and (*2*) normal and (*3*) exponential distributions.

where x is the micrometer scale factor and m is the integer number of the scale factors in the particle diameter for a given fraction.

For each disperse system, we determined (1) the average particle radius

$$R_n = \Sigma N_i R_i / \Sigma N_i, \quad (2)$$

where N_i is the number of particles with radius R_i and ΣN_i is the total number of particles in the system, and (2) weight-average radius

$$R_m = \Sigma N_i R_i^4 / \Sigma N_i R_i^3. \quad (3)$$

The coefficient for polydisperse system $k = R_n/R_m$ was 0.84.

The particle size distribution in the initial disperse system is illustrated in Fig. 1a (curve *1*); the average particle size is 4.6×10^{-6} m.

The differential curve of the particle size distribution is asymmetric and deviates from the normal Gaussian distribution (Fig. 1, curve *2*). Since the system analyzed is multicomponent, we assumed that the total distribution function is a sum of distribution functions of different types. The best approximation is a sum of the normal and exponential distribution functions:

$$dQ_n/dR = A\exp[(R - R_0)^2/\sigma^2] + B\exp(-KR). \quad (4)$$

The parameters A, B, σ, R_0, and K can be calculated from the experimental results using a procedure of nonlinear distribution of the regression analysis [6].

Published data [5, 7] on the aggregation stability of real and model systems suggest the possibility of their destabilization by adding coagulants. Treatment of the disperse system under consideration with coagulants (alumina, aluminum chloride, calcium hydroxide) showed that alumina at pH 6.5–8.0 exhibits the highest coagulation power. The kinetics of the wastewater clarification as influenced by the coagulant

content is illustrated in Fig. 2. The results of 20 experimental series showed that the optimal coagulant concentration is 0.05%.

Data on the optical density and turbidity of the wastewater before purification and after treatment with the optimal dose of alumina indicate that additional treatment with flocculants is required (water turbidity before and after treatment was 3.1 and 2.3 mg l^{-1}, respectively [8]).

The kinetic curves of precipitation of disperse particles on adding optimal doses of the coagulant and its mixtures with flocculants were obtained by sedimentation analysis; they are shown in Fig. 3.

The size distribution curve of the flocculated particles (Fig. 1a), determined by sedimentation analysis using the Stokes equation, suggests the prevalence of coarse particles and essential change in the effective size of the particles as compared to the initial system (from 4.6×10^{-6} to nearly 1.1×10^{-4} m).

Evaluation of the flocculation power of polymers allows us to predict formation of either flocculated or stable colloidal system.

The flocculating power of polymers can be quantitatively evaluated using the dimensionless parameter D [10]:

$$D = V/V_0 - 1 = \tau_{1/2(c=0)}/\tau_{1/2(c)} - 1, \qquad (5)$$

where V and V_0 are the sedimentation rates of the disperse phase in the presence of the polymeric flocculant and without it; $\tau_{1/2(c)}$ and $\tau_{1/2(c=0)}$ are the times of 50% sedimentation of the disperse phase in the presence of flocculant (c) and without it ($c = 0$).

For comparison, we calculated the flocculating activity λ of each additive:

$$\lambda = (\tau_{1/2(c=0)}/\tau_{1/2(c)} - 1)/c_i = D/c_i, \qquad (6)$$

where c_i is the concentration of the polymeric additive.

The flocculation parameters and the size of the resulting aggregates in the presence of various flocculants are shown in Fig. 4 and Table 4.

Our results show that the flocculation power of Praestols 2530 TR and 2540 TR is similar. In the case of DKS, the flocculation activity is two times greater, which is probably due to its higher molecular weight and, thus, larger effective size of macromolecules in solution. This allows efficient use of the DKS flocculant for wastewater treatment at significantly smaller doses as compared to Praestols.

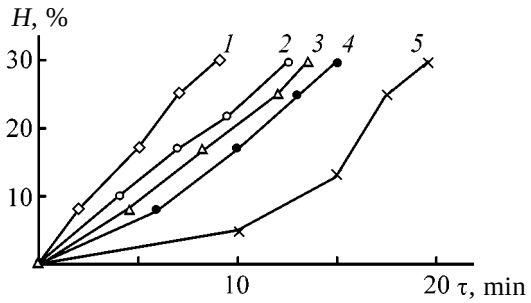

Fig. 2. Clarification degree H in the presence of alumina coagulant as a function of time τ. Alumina content, %: (*1*) 0.05, (*2*) 0.1, (*3*) 0.03, (*4*) 0.15, and (*5*) 0.2.

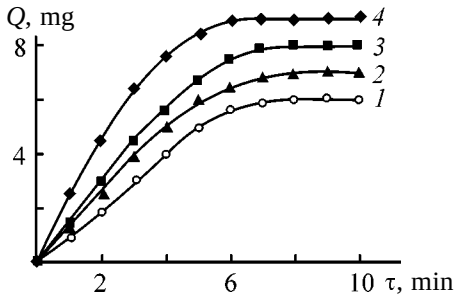

Fig. 3. Kinetic curves of sedimentation of dispersed particles Q at (*1*) optimal dose of coagulant and (*2–4*) in the presence of coagulant and various flocculants. Flocculant content, %: (*2*) Praestol 2540 TR, 2×10^{-4}; (*3*) Praestol 2530 TR, 2×10^{-4}; and (*4*) DKS F40 T1, 4×10^{-6}.

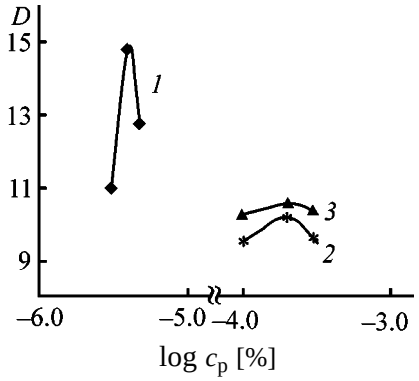

Fig. 4. Flocculation parameter D as a function of the flocculant concentration c_p. Flocculant: (*1*) DKS F40 T1, (*2*) Praestol 2530 TR, and (*3*) Praestol 2540 TR.

It should be noted that the D–$\log c_p$ dependences (Fig. 4) pass through a maximum, the most pronounced in the case of DKS. This is due to the fact [5] that, at low polymer concentrations, the flocculation proceeds through interaction of a single molecule with several particles of the disperse phase ("bridging" flocculation). With increasing polymer concentration, the disperse particles are stabilized by their complete coating with an adsorption layer of the polymer. This

Table 4. Characteristics of the resulting aggregates

Flocculant	c_p, %	D	$\lambda = D/c_p$, $m^3\ kg^{-1}$	$R \times 10^4$, m
DKS F40 T1	3×10^{-6}	11.0	3.7×10^5	1.0
	4×10^{-6}	14.8	3.7×10^5	
	5×10^{-6}	12.6	2.5×10^5	
Praestol 2530 TR	1×10^{-4}	10.2	10.2×10^3	1.2
	2×10^{-4}	10.5	5.3×10^3	
	3×10^{-4}	10.3	3.4×10^3	
Praestol 2540 TR	1×10^{-4}	9.5	9.5×10^3	1.2
	2×10^{-4}	10.1	5.0×10^3	
	3×10^{-4}	9.5	3.2×10^3	

fact should be taken into account when choosing the optimal flocculant dose.

CONCLUSIONS

(1) Fat- and protein-containing disperse system of wastewaters from mayonnaise production contains emulsion particles of the fat with solid inclusions and without them. The average size of the particles is 4.6×10^{-6} m.

(2) Addition of a coagulant or its mixture with flocculants causes flocculation of the particles, with their average size increasing to 1×10^{-4} m.

(3) The flocculating power of the flocculants added at optimal concentration of the coagulant increases in the series Praestol 2540 TR ≈ Praestol 2530 TR < DKS.

REFERENCES

1. Deryagin, B.V., *Teoriya ustoichivosti kolloidov i tonkikh plenok* (Stability Theory of Colloids and Thin Films), Moscow: Nauka, 1987.
2. Deryagin, B.V., Churaev, N.V., and Muller, V.M., *Poverkhnostnye yavleniya* (Surface Phenomena), Moscow: Nauka, 1985.
3. Izmailova, V.N., *Ochistka stochnykh vod ot nefteproduktov, zhirov, belkov* (Treatment of Wastewaters To Remove Petroleum Products, Fats, and Proteins), Petryanov-Sokolov, N.V., Ed., Moscow: VINITI, 1988.
4. Veitser, Yu.I. and Mints, D.M., *Vysokomolekulyarnye flokulyanty v protsessakh ochistki prirodnykh i stochnykh vod* (Macromolecular Flocculants in Purification of Natural and Waste Waters), Moscow: Stroiizdat, 1984.
5. Myagchenkov, V.A., Baran, A.A., Bekturov, E.A., and Bulidorova, G.V., *Poliakrilamidnye flokulyanty* (Polyacrylamide Flocculants), Kazan: Kazan. Gos. Tekhnol. Univ., 1988.
6. Draper, N.R. and Smith, H., *Applied Regression Analysis*, New York: Wiley, 1967.
7. Kurenkov, V.F., Churikov, F.I., and Snigirev, S.V., *Zh. Prikl. Khim.*, 1998, vol. 72, no. 8, pp. 1485–1489.
8. *SanPin* (Sanitary Rules and Regulations) *2.1.4.539–96: Sanitary Requirements to the Quality of Water in the Host System of Water Supply*, Moscow: Goskomepidnadzor, 1996.
9. Voyutskii, S.S., *Kurs kolloidnoi khimii* (Course of Colloid Chemistry), Moscow: Khimiya, 1975.
10. Myagchenkov, V.A. and Proskurina, V.E., *Zh. Prikl. Khim.*, 1999, vol. 72, no. 10, pp. 1704–1709.

Russian Journal of Applied Chemistry, Vol. 75, No. 7, 2002, pp. 1117–1119. Translated from Zhurnal Prikladnoi Khimii, Vol. 75, No. 7, 2002, pp. 1135–1137
Original Russian Text Copyright © 2002 by Tsarev, Dmitriev, Kostrov.

ENVIRONMENTAL PROBLEMS OF CHEMISTRY AND TECHNOLOGY

Synthesis of a Copper-Containing Catalyst for Electrocatalytic Oxidation of Volatile Organic Compounds

Yu. V. Tsarev, A. E. Dmitriev, and V. V. Kostrov

Ivanovo State University of Chemical Engineering, Ivanovo, Russia

Received December 11, 2001; in final form, April 2002

Abstract—The synthesis of a copper-containing catalyst for electrocatalytic oxidation of acetone in exhaust gases was studied. Data on the electrocatalytic oxidation of acetone were analyzed in relation to the CuO content.

Treatment of waste gases to remove volatile organic compounds (VOCs) is an urgent problem of environmental protection. The largest amounts of exhaust VOCs are discharged by oil refining and oil production plants (502 and 202 thousand tons annually), chemical plants, and machine-building plants (89.45 and 43.28 thousand tons annually) [1]. The traditional methods for treatment of waste gases to remove VOCs are thermal afterburning, catalytic oxidation, sorption, and sorption-catalytic treatment [2]. Along with traditional methods, the oxidation of VOCs in barrier discharge plasma became a common method [3]. The thermal afterburning and sorption treatment of VOCs are rather expensive processes. Sorption-catalytic and catalytic treatment (including VOC oxidation) in the non-steady-state mode [4] involve smaller service expenditures. Platinum or less expensive oxide catalysts are used in oxidation. As oxide catalysts are used copper(II) and manganese(IV) oxides [5], and as supports, alumina, titania, and other oxides. In some studies [6, 7], the support was activated carbon. In this study, the main attention is given to the electrocatalytic treatment of hydrocarbon-containing gases on a copper oxide catalyst supported by carbon black.

As support we used PM-750 carbon black. The catalysts were obtained from a mixture of carbon black and copper hydroxycarbonate, to which a plasticizer (10% polyvinyl alcohol solution) was subsequently added. The mixture with the optimal moisture content was pressed into 0.5–1-mm granules, which were then calcined in a CO_2 flow at 350°C. The model gas mixture contained air and acetone (the concentration of the latter was 1–2 g m^{-3}). The acetone concentration in a gas–air mixture was determined nephelometrically on a KFK-2MP photoelectrocolorimeter at λ = 320 nm [8]. The degree of the acetone conversion in the catalyst samples synthesized was determined in an isothermal plug-flow reactor. An ac voltage was applied to the catalyst bed.

The total specific surface area of the catalyst was measured on a Tsvet-211 sorption meter [9]. The surface area of the catalysts was determined by selective low-temperature sorption of helium in pulsed mode at –136°C. The X-ray phase analysis of the catalyst samples was done on a DRON–UM1 diffractometer using a CuK_α X-ray tube (λ = 0.154 nm). The interplanar spacings were calculated on a PC. The compounds were identified by comparison of the interplanar spacings with the reference data [10]. The phase composition of the catalyst samples as influenced by the preparation conditions was evaluated from the intensity of the strongest reflections. The diffraction angle 2θ was calculated from the relation $\lambda = 2d\cos\theta$. The electrocatalytic oxidation products were absorbed with hexane and analyzed on a Saturn-2000R gas chromatograph–mass spectrometer.

The contribution of the acetone sorption on a catalyst to the total process of the electrocatalytic treatment was estimated from the dependence of the degree of the acetone adsorption on time (Fig. 1). It was shown that, at saturations longer than 15 min, the degree of adsorption is virtually zero. Therefore, in determining the degree of acetone oxidation on a catalyst, after the acetone-containing gas is passed through a catalyst bed for 1 h, the sorption can be neglected.

The optimal content of copper oxide in the catalyst samples was determined from the plots of the catalytic activity vs. the CuO percentage in the catalyst for

1070-4272/02/7507-1117$27.00 © 2002 MAIK "Nauka/Interperiodica"

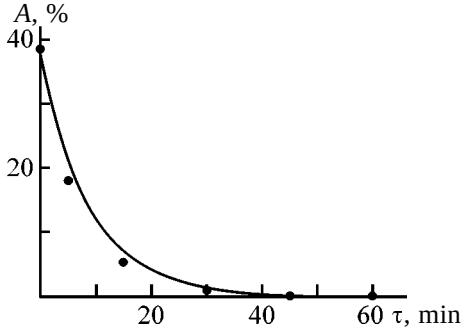

Fig. 1. Degree *A* of acetone adsorption on the catalyst vs. time τ.

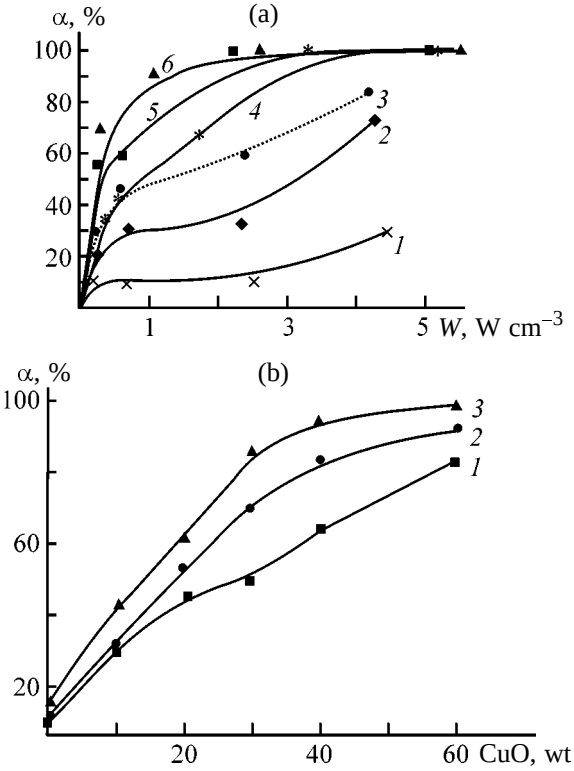

Fig. 2. Degree α of acetone conversion vs. (a) the supplied specific power of electric current *W* and (b) CuO content. (a) CuO content (wt %): (*1*) 0, (*2*) 10, (*3*) 20, (*4*) 30, (*5*) 40, and (*6*) 60. (b) *W* (W cm^{-3}): (*1*) 1.0, (*2*) 2.0, and (*3*) 3.0.

different specific loads of the electric current (Figs. 2a, 2b). The experimental data show that, with the specific load on the catalyst bed increased from 0.6 to 3 W cm^{-3}, the maximal degree of acetone conversion is observed for catalysts containing 40 and 60% copper oxide, respectively. At high specific loads of the electric current (more than 4 W cm^{-3}), the content of the active component in the catalyst only slightly affects the degree of acetone conversion.

The specific surface area of the catalyst samples was determined in the course of the experiment (28–35 $m^2 g^{-1}$). The experimental data show that the specific surface areas of the sample calcined at 350°C and of that calcined at 700°C are similar (28 $m^2 g^{-1}$), i.e., factors other than sintering of the catalyst are responsible for the decreased catalytic activity of the samples calcined at high temperatures. Most probably, the high specific surface area of the catalyst sample containing 60% CuO develops owing to decomposition of $(CuOH)_2CO_3$ whose content in the catalyst is large. The specific surface area of the catalyst sample without copper oxide is equal to that of the initial carbon black (35 $m^2 g^{-1}$), i.e., it is affected by mixing insignificantly.

The experimental data show that, for the specific powers of the supplied electric current less than 2 W cm^{-3}, the degree of acetone conversion on the catalyst decreases with increasing calcination temperature (Fig. 3). Thus, we can conclude that the CuO and Cu_2O phases enhance the effect of the electric current power on the electrocatalytic oxidation of acetone. The metallic copper phase does not affect electrocatalytic oxidation of acetone. At the powers of the supplied electric current higher than 2 W cm^{-3}, the calcination temperature does not affect the degree of acetone conversion on a catalyst. This may be due to the fact that, at high specific powers of supplied electric current, the electrical contribution is dominating.

The phase composition of the catalyst samples was determined by X-ray phase analysis. The test samples containing 20% active component were calcined at 350, 500, and 700°C. The diffraction pattern is shown in Fig. 4. A comparison of the experimental diffraction patterns with the reference data for various compounds revealed crystalline CuO (2θ = 62°) or Cu_2O (2θ = 36°) in the samples synthesized. With increasing calcination temperature, the amount of the crystalline phase decreases, which is manifested as a decrease in the intensity of the strongest reflections attributable to these compounds. Copper oxides undergo reduction, which occurs on the catalyst at high temperature and results in the formation of phase C of metallic copper (2θ 43°, 51°). The diffraction patterns show that the reflections of metallic copper grow in intensity with temperature. The catalyst support, carbon black A, exists in the catalysts in amorphous or weakly crystalline state, which is revealed as a halo corresponding to the diffraction angle 2θ = 25°.

CONCLUSIONS

(1) A study of the conversion of acetone-containing gas in relation to the content of copper(II) oxide

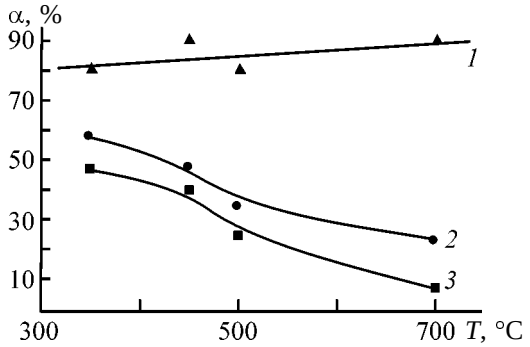

Fig. 3. Degree of acetone conversion α vs. calcination temperature *T*. *W* (W cm^{-3}): (*1*) 4.0, (*2*) 2.0, and (*3*) 0.6.

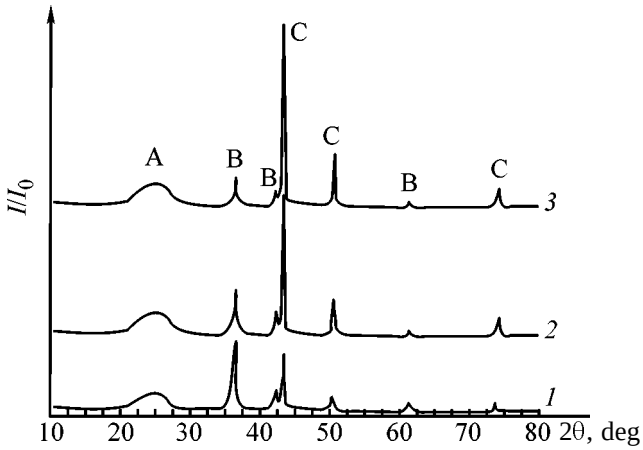

Fig. 4. Diffraction patterns of the catalyst sample containing 20% CuO and calcined at different temperatures. (I/I_0) Relative intensity and (2θ) Bragg angle. Calcination temperature (°C): (*1*) 350, (*2*) 500, and (*3*) 700. (A) Carbon black, (B) CuO (Cu_2O), and (C) metallic copper.

in the catalyst samples showed that the catalyst containing 40–60% copper oxide is the most efficient in electrocatalytic oxidation of acetone.

(2) The X-ray phase analysis showed that the decrease in the catalytic activity of samples with increasing calcination temperature is due to the reduction processes, which occur on the catalyst at high temperatures and result in the formation of metallic copper, inactive in acetone oxidation.

(3) The calcination temperature does not affect the specific surface area of the catalyst samples.

REFERENCES

1. *Gosudarstvennyi doklad "O sostoyanii okruzhayushchei prirodnoi sredy Rossiiskoi Federatsii v 1997 godu"* (Governmental Report "The State of Natural Environment in Russian Federation in 1997"), Moscow: Gos. Tsentr Ekologicheskikh Programm, 1998.
2. Popova, N.M., *Katalizatory ochistki gasovykh vybrosov promyshlennykh proizvodstv* (Catalysts for Treatment of Waste Gases of Industrial Plants), Moscow: Khimiya, 1991.
3. *Ekologiya i kataliz: Sbornik nauchnykh trudov* (Ecology and Catalysis: Coll. of Scientific Works), Novosibirsk: Nauka, 1990.
4. Bugaev, S.P., Kuvshinov, V.A., Sochugov, N.S., and Khryapov, P.A., *Zh. Prikl. Khim.*, 1996, vol. 69, no. 6, pp. 965–969.
5. Oxide Catalysts Withstand Very High Temperatures, *Chem. Eng*. (USA), 1999, Nov., pp. 761–764.
6. Park, B.-J. and Parks, E.-J., *J. Mater. Sci. Lett*., 1999, vol. 18, no. 19, pp. 1607–1609.
7. Vol'fson, V.Ya., Development of Catalysts and Study of the Features of Low-Temperature Catalytic Purification of Gases, *Doctoral Dissertation*, Kiev, 1983.
8. Peregud, E.A., and Gernet, E.V., *Khimicheskii analiz vozdukha promyshlennykh predpriyatii* (Chemical Analysis of Air of Industrial Plants), Leningrad: Khimiya, 1970.
9. Buyanova, N.E., Karnaukhov, A.P., and Alabuzhev, Yu.A., *Opredelenie udel'noi poverkhnosti katalizatora* (Determination of the Specific Surface Area of a Catalyst), Moscow: Khimiya, 1973.
10. *Powder Diffraction File. Data Cards. Inorganic Section*, Sets 1–34, JCPDS, Swarthmore, Pennsylvania (USA), 1948–1984.

Russian Journal of Applied Chemistry, Vol. 75, No. 7, 2002, pp. 1120–1122. Translated from Zhurnal Prikladnoi Khimii, Vol. 75, No. 7, 2002, pp. 1138–1140.
Original Russian Text Copyright © 2002 by Akbalina, Zlotskii, Kabal'nova, Grigor'ev, Kotlyar, Shereshovets.

ORGANIC SYNTHESIS AND INDUSTRIAL ORGANIC CHEMISTRY

Transformations of Cyclic Acetals under the Action of Some Organic and Inorganic Oxidants

Z. F. Akbalina, S. S. Zlotskii, N. N. Kabal'nova, I. A. Grigor'ev, S. A. Kotlyar, and V. V. Shereshovets

Ufa State Petroleum Engineering University, Ufa, Bashkortostan, Russia
Institute of Organic Chemistry, Ufa Scientific Center, Russian Academy of Sciences, Ufa, Bashkortostan, Russia

Received December 19, 2001; in final form, March 2002

Abstract—Liquid-phase oxidation of cyclic acetals and 2,2-disubstituted 1,3-dioxacyclanes with dimethyldioxirane, Caro salt, potassium persulfate, and complex of potassium chlorodiperoxochromate with 15-crown-5 was studied.

Liquid-phase oxidation of cyclic acetals receives much attention as a route to hydroperoxides, peroxides, glycol monoesters, and other valuable organic compounds [1]. Such oxidants as oxygen, ozone, organic hydroperoxides, and nitrogen(II) and (IV) oxides were used [2]; however, search for agents ensuring high selectivity of acetal oxidation remains an urgent problem.

In this work, we studied transformations of cyclic acetals and 2,2-disubstituted 1,3-dioxacyclanes under the action of dimethyldioxirane, Caro salt $K_2SO_4 \cdot 2KHSO_5 \cdot KHSO_4$, potassium persulfate, and complex of potassium chlorodiperoxochromate with 15-crown-5.

EXPERIMENTAL

The initial 1,3-dioxacycloalkanes **I**–**VII** [3, 4], dimethyldioxirane [5], Caro salt [6], and complex of potassium chlorodiperoxochromate with 15-crown-5 [7] were prepared by published procedures. Stable nitroxyl radical, 2,2,5,5-tetramethyl-4-phenyl-3-imidazoline-3-oxide-1-oxyl, was prepared according to [8]. Oxidation with dimethyldioxiane was performed as described in [9].

Oxidation with Caro salt was performed in a 30-ml temperature-controlled glass vessel stirred with a magnetic stirrer. To a solution of 1 mmol of a substrate in 10 ml of chloroform, 3 g of wet alumina was added, and the mixture was heated to 50°C. Caro salt (3 mmol) was added in portions over a period of 1 h, and stirring was continued for 2–5 h. The resulting mixture was cooled to room temperature and filtered. The solvent was removed on a rotary evaporator, and the products were analyzed. Oxidation in the presence of nitroxyl radical was performed similarly.

Oxidation with potassium persulfate and complex of potassium chlorodiperoxochromate with 15-crown-5 was performed in acetonitrile at 60°C for 7 h, molar ratio substrate : oxidant 1 : 3.

The reaction products were identified and analyzed by ^1H and ^{13}C NMR spectroscopy (Bruker 300 spectrometer, 300 and 75 MHz, respectively; reference TMS, solvent $CDCl_3$), GC–MS (Finnigan), and GLC (Chrom-5, 1200 × 3-mm column, stationary phase SE-30), using authentic samples of the monoesters and ketones.

We found that cyclic acetals **I**–**VII** react with dimethyldioxirane with quantitative formation of the corresponding glycol monoesters **VIII**–**XVI**:

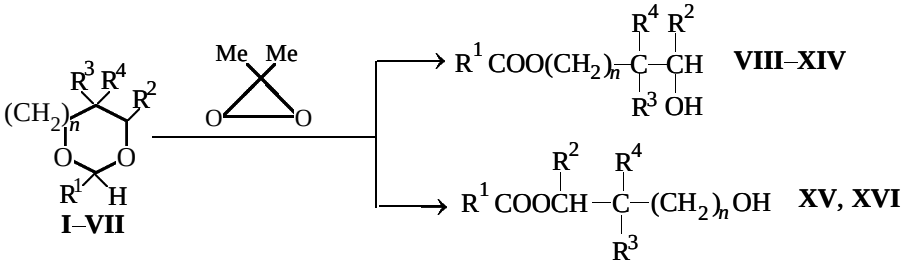

1070-4272/02/7507-1120$27.00 © 2002 MAIK "Nauka/Interperiodica"

where n = 0, R^1 = *i*-Pr (**I**, **VIII**), Ph (**II**, **IX**), R^2 = R^3 = R^4 = H (**I**, **II**, **VIII**, **IX**); n = 1, R^1 = *i*-Pr (**III**, **X**), Ph (**IV**, **XI**), R^2 = R^3 = R^4 = H (**III**, **IV**, **X**, **XI**); R^1 = *i*-Pr (**V**, **XII**, **XV**), Ph (**VI**, **XIII**, **XVI**), R^2 = Me, R^3 = R^4 = H (**V**, **VI**, **XII**, **XIII**, **XV**, **XVI**); R^1 = Ph (**VIII**, **XIV**), R^2 = H, R^3 = R^4 = Me (**VII**, **XIV**).

From **V** and **VI**, both isomeric esters **XII** and **XV**, **XIII** and **XVI** are formed, since the C^2–O^1 and C^2–O^3 bonds are cleaved concurrently. According to the ^{1}H and ^{13}C NMR data, under conditions of our experiments, esters **XII** and **XIII** with the secondary hydroxy group are the major products.

2,2-Disubstituted 1,3-dioxacyclanes **XVII**–**XIX** under the action of dimethyldioxirane decompose to the corresponding ketones **XX**:

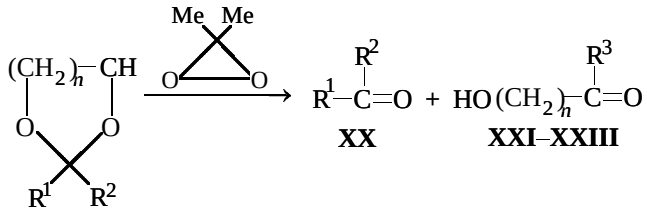

XVII–**XIX** **XX** **XXI**–**XXIII**

where n = 1, R^1 = R^2 = Me, R^3 = H (**XVII**, **XX**, **XXI**); R^1 = R^2 = Me, R^3 = CH_2OH (**XVIII**); n = 2, R^1 = R^2 = R^3 = Me (**XIX**, **XXII**, **XXIII**).

Apparently, in the first stage compounds **XVII**–**XIX** give the corresponding unstable 4-hydroxy-1,3-dioxacyclanes, subsequently decomposing to give ketones **XX**.

It is known [5] that dimethyldioxirane is prepared using Caro salt. We found that this agent oxidizes 2-alkyl-1,3-dioxacyclanes **I** and **III** in the presence of alumina to the corresponding monoesters **VIII** and **X**. However, benzaldehyde derivatives **II** and **VI** under these conditions, along with monoesters **IX** and **XI**, give also benzaldehyde (Table 1).

We found that oxidation of cyclic acetals with Caro salt in the presence of stable nitroxyl radical 2,2,5,5-tetramethyl-4-phenyl-3-imidazoline-3-oxide-1-oxyl **XXIV**

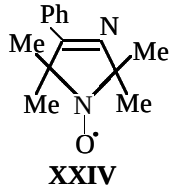

XXIV

allows preparation of monoesters **VIII**–**XI** in quantitative yield (Table 1). The catalytic effect of nitroxyl radicals was noted previously in [10].

Table 1. Oxidation of acetals **I**–**IV** with Caro salt in the presence of alumina (A) or radical **XXIV** (B). Solvent $CHCl_3$, 50°C, 2 h

Acetal	Monoester	Yield of monoester, A (B), %
I	**VIII**	40 (99)
II	**IX**	76* (97)
III	**X**	38 (94)
IV	**XI**	45** (96)

* 13% benzaldehyde. ** 25% benzaldehyde.

Table 2. Oxidation of dioxacycloalkanes **I**–**IV** with the complex $KCrO_5Cl \cdot 2C_{10}H_{20}O_5$ in the absence (A) and in the presence (B) of the radical. Solvent MeCN, 60°C, 2 h; molar ratio substrate : oxidant 1 : 3, substrate : radical 1 : 0.01

Substrate	Product	Product yield, A (B), %
I	**VIII**	55 (≥99)
II	PhCHO	88 (≥99)
III	**X**	≤1 (≥99)
IV	PhCHO	65 (≥99)

In the series of 1,3-dioxacycloalkanes **I**–**VI**, only compounds **I** and **II** are oxidized with potassium persulfate $K_2S_2O_8$ to form, in the first case, ethylene glycol monoisobutyrate **VIII** (yield 45%) and, in the second case, benzaldehyde (yield 25%). In the presence of catalytic amounts of **XXIV**, compounds **I**–**VI** afford esters **VIII**–**XIII** in quantitative yield.

We also studied oxidation of cyclic acetals **I**–**IV** with the complex of potassium chlorodiperoxochromate $KCrO_5Cl$ with 15-crown-5 $C_{10}H_{20}O_5$. We found that acetals **I** and **III** are oxidized with this complex to the corresponding monoesters **VIII** and **X**. At the same time, 2-phenyl derivatives **II** and **IV** are selectively oxidized to benzaldehyde (Table 2). Catalytic amounts of nitroxyl radical **XXIV** provide complete conversions of acetals even in 2 h (Table 2).

Thus, complex of potassium chlorodiperoxochromate with 15-crown-5 can be successfully used for removing acetal protective groups from aromatic aldehydes.

CONCLUSION

Dimethyldioxirane, Caro salt, and complex of potassium chlorodiperoxochromate with 15-crown-5 efficiently oxidize polycyclic acetals to the corre-

sponding glycol moonoesters. 2,2-Disubstituted 1,3-dioxacyclanes under these conditions decompose to the corresponding ketones. Additions of catalytic amounts of the nitroxyl radical increase the reaction yield.

REFERENCES

1. Rakhmankulov, D.L., Karakhanov, R.A., Zlotskii, S.S., *et al.*, *Khimiya i tekhnologiya 1,3-dioksatsiklanov* (Chemistry and Technology of 1,3-Dioxacyclanes), Moscow: VINITI, 1979, vol. 5.
2. Zlotsky, S.S., Rakhmankoulov, D.L., Kouramshin, E.M., and Koulak, L.G., *Int. J. Polym. Mater.*, 1990, vol. 13, no. 7, pp. 117–126.
3. Rakhmankulov, D.L., Zlotskii, S.S., Safarov, O.G., and Siraeva, I.N., *Mezhfaznyi kataliz v khimii 1,3-dioksolanov* (Phase-Transfer Catalysis in the Chemistry of 1,3-Dioxolanes), Moscow: Khimiya, 1993.
4. Ap'ok, I., Bartok, M., Karakhanov, R.A., and Shuikin, N.I., *Izv. Akad. Nauk SSSR, Ser. Khim.*, 1968, no. 10, pp. 2357–2361.
5. Singh, M. and Murray, R.M., *J. Org. Chem.*, 1992, vol. 57, no. 15, pp. 4263–4270.
6. Adam, W. and Hadjiarapoglu, L., *Top. Curr. Chem.*, 1993, vol. 164, no. 1, pp. 45–48.
7. Kotlyar, S.A., Fedorova, G.V., Gorodnyuk, V.P., and Luk'yanenko, N.G., *Zh. Obshch. Khim.*, 1989, vol. 59, no. 12, pp. 2799–2801.
8. Volodarskii, L.B., Grigor'ev, I.A., Dikanov, S.A., *et al.*, *Imidazolinovye nitroksil'nye radikaly* (Imidazoline Nitroxyl Radicals), Novosibirsk: Nauka, 1998.
9. Rakhmankulov, D.L., Zlotskii, S.S., Sheresho-vets, V.V., *et al.*, *Dokl. Ross. Akad. Nauk*, 1998, vol. 361, no. 3, pp. 355–356.
10. De Nooy, A.E.T., Besemer, A.C., and Van Bekkum, H., *Synthesis*, 1996, vol. 10, no. 9, pp. 1153–1174.

Russian Journal of Applied Chemistry, Vol. 75, No. 7, 2002, pp. 1123–1127. Translated from Zhurnal Prikladnoi Khimii, Vol. 75, No. 7, 2002, pp. 1146–1150.
Original Russian Text Copyright © 2002 by O. Fedevich, Levush, E. Fedevich, Kit.

ORGANIC SYNTHESIS AND INDUSTRIAL ORGANIC CHEMISTRY

Oxidation Kinetics of Crotonaldehyde (2-Butenal) at Elevated Oxygen Pressure

O. E. Fedevich, S. S. Levush, E. V. Fedevich, and Yu. V. Kit

L'vivs'ka Politekhnika State University, Lviv, Ukraine
Lviv State Agrarian University, Lviv, Ukraine

Received December 25, 2001; in final form, March 2002

Abstract—Liquid-phase oxidation of crotonaldehyde in ethyl acetate at 285–309 K and oxygen pressure of 1–16 atm was studied. Kinetic equations satisfactorily describing the oxidation kinetics of crotonaldehyde were obtained.

Crotonic acid (CA) and its esters form polymers, which are used in various branches of industry (specialty rubbers, latexes, adhesives, plastics, rubber-modifying agents, etc.). Some CA esters are biologically active compounds exhibiting insecticidal, ascaricidal, and herbicidal properties. Crotonic acid is often prepared by oxidation of crotonaldehyde (CAl) with molecular oxygen at atmospheric pressure. It was found [1, 2] that this process is intensified with increasing pressure. As the partial oxygen pressure is increased from 0.2 to 1 atm, the CAl oxidation accelerates [3], whereas the selectivity of a formation of crotonic and percrotonic (PCA) acids remains virtually constant. The data on the effect of higher oxygen pressures on the CAl oxidation are lacking. In this work, we studied the kinetics of crotonaldehyde oxidation at an oxygen pressure of 1–16 atm.

EXPERIMENTAL

A solution of crotonaldehyde (45 cm^3) in ethyl acetate was placed into a 70-cm^3 stainless steel reactor. Previously we found [4] that ethyl acetate is the best solvent for CAl oxidation. The reactor was sealed and purged with argon (3 atm) three times to remove oxygen. Then the reactor was placed in a water bath temperature-controlled with a thermocouple and a KSP-4 potentiometer. When the required temperature was attained, the excess argon pressure was relieved, and the required oxygen flow of 3.5 $l\,h^{-1}$ through the reactor was set. The reaction mixture was stirred with a magnetic stirrer; it was found that at 1200 rpm the CAl oxidation is kinetically controlled. The reaction products were analyzed by chromatography and IR spectroscopy [5]. Along with the main products of CAl oxidation (CA and PCA), the reaction mixture contained propionic aldehyde, formic and propionic acids, propenyl formate, and epoxypropenyl formate; the total content of by-products did not exceed 15% with respect to reacted CAl. Since the concentration of these by-products in the reaction mixture is low, kinetic study of their formation is rather difficult; thus, we studied only the kinetics of CAl consumption and CA and PCA formation.

The effect of oxygen pressure on the CAl oxidation was studied in the 285–309 K range using ethyl acetate solvent. The kinetic curves of CAl consumption at 309 K at different oxygen pressures (from 1 to 16 atm) are shown as example in Fig. 1. As seen,

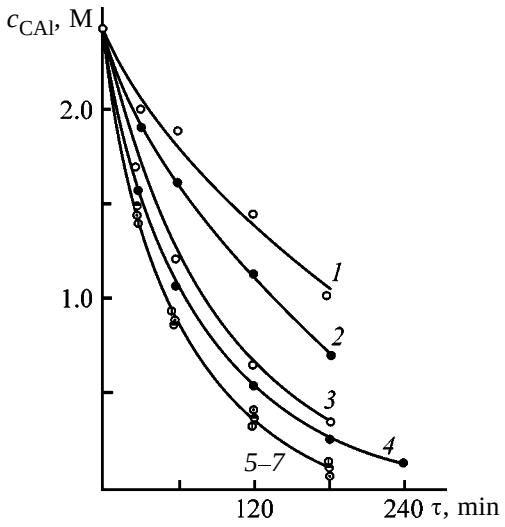

Fig. 1. Kinetics of CAl oxidation at 309 K as a function of the oxygen partial pressure. (C_{CAl}) Concentration of crotonaldehyde and (τ) time. p_{O_2}, atm: (*1*) 1, (*2*) 2, (*3*) 3, (*4*) 4, (*5*) 7, (*6*) 11, and (*7*) 16.

1070-4272/02/7507-1123$27.00 © 2002 MAIK "Nauka/Interperiodica"

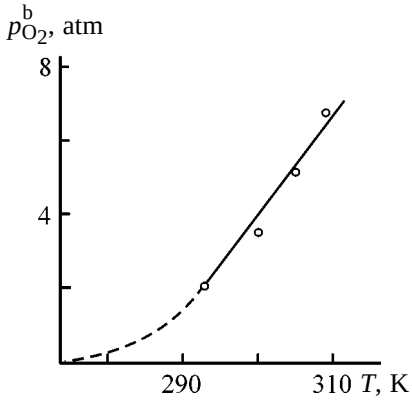

Fig. 2. Boundary oxygen pressure $p^b_{O_2}$ as a function of temperature *T*.

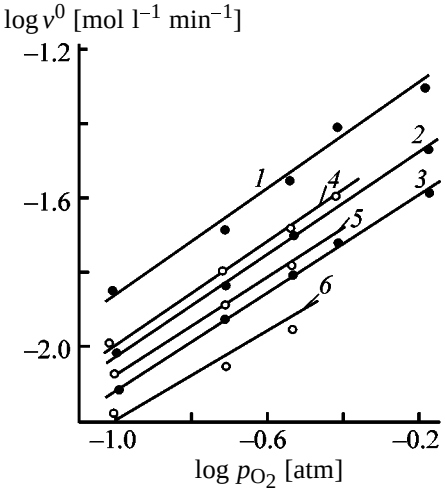

Fig. 3. Initial rate v^0 of (*1*, *4*) CAl oxidation, (*2*, *5*) PCA + CA formation, and (*3*, *6*) PCA formation as a function of the oxygen partial pressure p_{O_2}. C^0_{CAl} = 2.46 M. Temperature, K: (*1*–*3*) 309 and (*4*–*6*) 300.

with increasing pressure to 7 atm, the CAl oxidation is intensified, whereas further increase in p_{O_2} does not noticeably affect the process. Similar phenomenon was observed at the other temperatures studied: at each temperature, above certain boundary pressure of oxygen $p^b_{O_2}$, the oxidation rate becomes independent of the oxygen pressure. Analysis of our experimental data showed that $p^b_{O_2}$ linearly increases with temperature (Fig. 2). Such a trend is probably due to the solubility of oxygen in the reaction medium. With increasing pressure and decreasing temperature, the solubility of gases in liquids increases. Hence, the lower the temperature, the smaller pressure is required to provide certain boundary concentration of dissolved oxygen above which the oxidation rate is independent of its concentration, because the rate of the elementary stages involving dissolved oxygen becomes so high that it does not longer affect the overall reaction rate.

By numerical differentiation, the kinetic dependences $c = f(\tau)$ at 285, 293, 300, and 309 K were transformed into the $v = \varphi(\tau)$ functions. Since the initial CAl concentration in these tests was similar (2.46 M) and in the initial moment there were no by-products in the reaction mixture to affect the process rate, we can determine the kinetic order of reaction with respect to oxygen from the dependences $v = f(p_{O_2})$. Such dependences for the rates of CAl consumption and PCA and PCA + CA accumulation are shown in Fig. 3. Analysis of the experimental data showed that at $p_{O_2} < p^b_{O_2}$ the reaction order with respect to oxygen is similar: 0.6 ± 0.05.

The effect of CAl concentration on the rate of its oxidation and formation of the reaction products was studied at 295 K and p_{O_2} = 2 atm. The experimental results are listed in Table 1. The initial rates of CAl oxidation v^0_{CAl}, PCA formation v^0_{PCA}, and PCA + CA formation $v_{\Sigma A}$ at different initial concentrations of crotonaldehyde were determined by numerical differentiation of the functions $c_i = f(\tau)$. The linear run of the $v^0_i = f(c^0_{CAl})$ curves suggests that the consumption of CAl and formation of PCA and CA are first-order with respect to CAl.

Thus, under the experimental conditions studied, the kinetics of CAl oxidation and PCA and CA formation can be described by the following equations:

$$v_{CAl} = k^{ef}_{CAl} c_{CAl} p^{0.6}_{O_2}, \quad (1)$$

$$v_{PCA} = k^{ef}_{PCA} c_{CAl} p^{0.6}_{O_2}, \quad (2)$$

$$v_{\Sigma A} = k^{ef}_{\Sigma A} c_{CAl} p^{0.6}_{O_2}, \quad (3)$$

where v_{CAl}, v_{PCA}, and $v_{\Sigma A}$ are the rates of CAl consumption and PCA and PCA + CA accumulation, respectively; k^{ef}_{CAl}, k^{ef}_{PCA}, and $k^{ef}_{\Sigma A}$ are the effective rate constants of these reactions.

To analyze the temperature dependences of the reaction rates, we used only the initial rates, which are negligibly affected by the by-product accumulation. Using the initial reaction rates (Table 2) and Eqs. (1)–(3), we calculated the effective rate constants at different temperatures and, using the least-squares procedure, the Arrhenius dependences for the rates of CAl consumption and PCA + CA and CA accumulation:

$$k^{ef}_{CAl} = (1.43 \pm 0.14) \times 10^8 \exp(-60.9 \pm 1.2) \times 10^3/RT, \quad (4)$$

$$k^{ef}_{PCA} = (3.97 \pm 0.59) \times 10^5 \exp(-47.1 \pm 1.2) \times 10^3/RT, \quad (5)$$

$$k^{ef}_{\Sigma A} = (6.34 \pm 0.63) \times 10^7 \exp(-58.6 \pm 1.2) \times 10^3/RT. \quad (6)$$

Table 1. Crotonaldehyde oxidation in ethyl acetate as influenced by its initial concentration; T = 295 K, p_{O_2} = 2 atm

c^0_{CAl}, M	τ, min	c^τ_{CAl}, M	X_{CAl}, %	c_{CA+PCA}	c_{PCA}	$v^0 \times 10^2$, mol l^{-1} min^{-1}			$S_{\Sigma A}$	S_{PCA}
				M		CAl	ΣA	PCA	%	
1.50	60	1.20	20.0	0.26	0.21	0.5	0.48	0.41	86.6	70.0
	120	1.03	31.3	0.40	0.30				85.1	63.8
	180	0.81	46.0	0.58	0.42				84.1	60.9
2.46	30	2.17	11.8	0.24	0.20	0.83	0.73	0.68	82.8	68.3
	60	2.01	18.3	0.38	0.30				84.5	67.6
	120	1.67	32.1	0.66	0.50				83.5	63.3
	180	1.33	45.9	0.94	0.67				83.2	59.3
3.69	30	3.29	10.8	0.32	0.25	1.5	1.12	0.98	80.0	62.5
	60	2.99	18.9	0.58	0.45				82.8	64.2
	120	2.47	33.1	1.00	0.75				82.0	61.5
	180	2.03	45.0	1.33	0.93				80.1	56.0
4.90	30	4.34	11.4	0.43	0.32	1.8	1.48	1.33	77.2	57.2
	60	3.96	19.2	0.75	0.55				79.8	58.6
	120	3.31	32.4	1.26	0.92				79.2	57.9
	180	2.67	45.6	1.72	1.16				77.1	52.0

Table 2. Crotonaldehyde oxidation as influenced by temperature

T, K	p_{O_2}, atm	c^0_{CAl}, M	$v^0 \times 10^2$, mol l^{-1} min^{-1}			$S_{\Sigma A}$,* %	$k^{ef}_{exp} \times 10^2$			$k^{ef}_{theor} \times 10^2$		
			CAl	PCA	CA + PCA		CAl	PCA	CA + PCA	CAl	PCA	CA + PCA
285	1.0	2.46	0.26	0.20	0.20	93.1	0.11	0.08	0.08	0.096	0.075	0.08
293	1.0	2.46	0.48	0.35	0.35	88.6	0.20	0.14	0.14	0.19	0.15	0.15
	1.5	2.46	0.57	0.46	0.46	86.6	0.19	0.14	0.15			
	2.0	2.46	0.66	0.53	0.56	85.3	0.18	0.14	0.15			
295	2.0	1.50	0.48	0.44	0.48	83.5	0.21	0.19	0.21	0.23	0.18	0.19
	2.0	2.46	0.75	0.69	0.74		0.20	0.19	0.20			
	2.0	3.69	1.37	1.00	1.11		0.24	0.18	0.20			
300	1.0	2.46	1.02	0.66	0.85	85.0	0.41	0.27	0.34	0.38	0.24	0.32
	2.0	2.46	1.54	0.89	1.33	83.9	0.41	0.24	0.35			
	3.0	2.46	2.04	1.11	1.67	83.0	0.43	0.24	0.35			
309	1.0	2.46	1.52	0.86	0.97	84.6	0.62	0.35	0.39	0.65	0.35	0.43
	2.0	2.46	2.23	1.18	1.46	83.8	0.60	0.32	0.39			
	3.0	2.46	2.99	1.55	1.96	82.9	0.63	0.33	0.41			
	4.0	2.46	3.78	1.91	2.50	84.0	0.63	0.34	0.44			
	7.0	2.46	4.92	2.50	3.33	82.8	0.62	0.32	0.42			

* 120 min after the reaction start.

The validity of Eqs. (1)–(6) is confirmed by satisfactory agreement of the experimental rate constants determined at various temperatures and partial pressures of oxygen and calculated by Eqs. (1)–(3) with the theoretical values determined from the Arrhenius dependences (4)–(6) (Table 2). The activation energies of CAl oxidation and PCA + CA formation are close: 61.5 and 58.6 kJ mol^{-1}, respectively. The activation energy of PCA accumulation is significantly lower (47.1 kJ mol^{-1}), and with increasing temperature

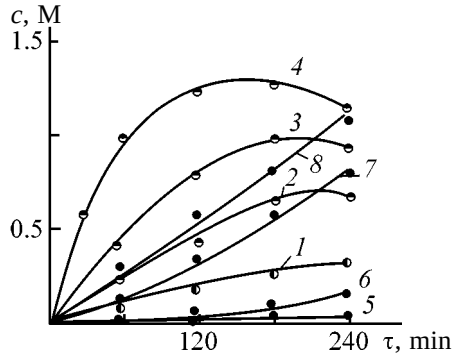

Fig. 4. Kinetics of formation of (*1–4*) PCA and (*5–8*) CA at different temperatures, p_{O_2} 4 atm, c^0_{CAl} 2.46 M. (*c*) Concentration of PCA or CA and (τ) time. Temperature, K: (*1, 5*) 285, (*2, 6*) 293, (*3, 7*) 300, and (*4, 8*) 309.

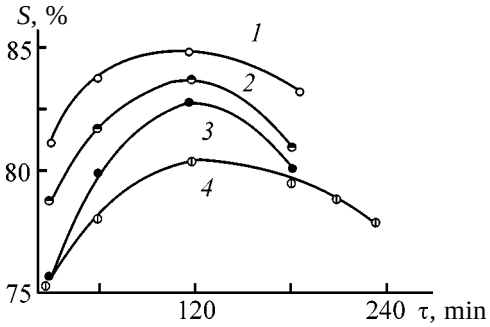

Fig. 5. Total selectivity of PCA + CA formation *S* as influenced by (*1–3*) pressure and (*1, 4*) temperature; c^0_{CAl} 2.46 M. (τ) Time. Temperature, K: (*1–3*) 309 and (*4*) 318. p_{O_2}, atm: (*1, 4*) 1, (*2*) 4, and (*3*) 16.

the selectivity of PCA formation decreases (Table 2).

According to published data [6, 7], oxidation of CAl can be presented by a series of successive and parallel radical and molecular reactions:

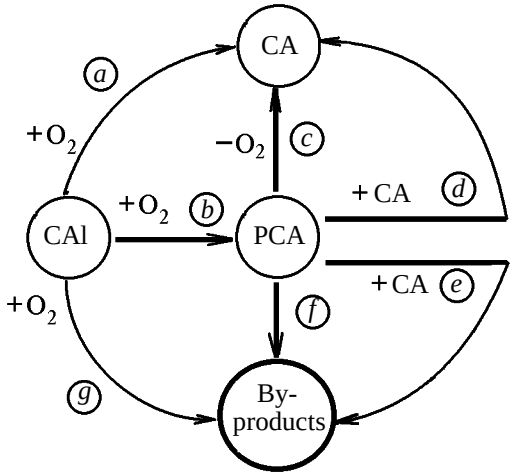

Reactions (1), (2), (6), and (7) are radical reactions and reactions (3)–(5), molecular. As seen from the above scheme, CA can be formed via PCA (reactions *c*, *d*) and directly from CAl (reaction *a*). The kinetic curves of accumulation of CAl oxidation products at different temperatures are similar (Fig. 4). With time, the rate of PCA accumulation decreases and that of CA accumulation grows. Successive formation of CA via PCA is obviously the main process in the kinetic scheme. At low temperatures (285, 293 K), the initial rate of CA formation is close to zero. This suggests that, at $c_{PCA} = 0$, CA is virtually absent in the reaction mixture, and the successive route is the only pathway of CA formation. As seen from Fig. 4, at higher temperatures (300, 309 K), the initial rate of CA formation becomes nonzero and significantly increases with temperature, suggesting that the contribution of the parallel reaction *a* becomes pronounced. This fact is confirmed by decreased selectivity of PCA + CA formation at increased temperature (Table 2).

Thus, PCA is the main intermediate in CA formation. Percrotonic acid is fairly stable, it accumulates in the reaction mixtures in concentrations comparable with the content of crotonic acid and transforms into CA with a high selectivity. Thus, it is advisable to estimate the selectivity of CA formation in the course of oxidation taking into account the total content of PCA and CA and the individual concentration of each acid. While the reaction mixture contains PCA, the selectivity of CA formation will change with time. In most of the published papers, this phenomenon was not taken into account.

Our experimental results show that the total selectivity of PCA + CA formation is independent of the oxygen pressure. As seen from Fig. 5, with increasing oxygen pressure from 1 to 16 atm the selectivity changes by only 2–3%. It should be noted that, in the initial period before accumulation of significant amounts of PCA, the selectivity of PCA + CA formation is lower than in the course of the further process. We believe that, in the initial period, less selective (compared to CA formation) radical reaction *a* is more pronounced, and only with time more selective reaction *d* of CA formation via PCA becomes predominant.

Data on the effect of CAl concentration on the selectivity of its oxidation to acids listed in Table 1 show that, as the initial concentration of CA in ethyl acetate is increased from 1.5 to 4.9 M, the selectivity of CA + PCA formation decreases by 6–8%.

Since the effective activation energy of PCA accumulation is lower as compared to PCA + CA formation, with increasing temperature reactions *e* and *f*

become important, and the selectivity of PCA + CA formation decreases by 8–10% in going from 285 to 309 K (Fig. 5).

The data on the CAl oxidation kinetics were used to optimize CA production. The main optimization factor was the product of CAl conversion X (%) and the selectivity of formation of the target products S (%), i.e., the total yield of crotonic and percrotonic acids B (%). We found that, to attain the maximal yield of the target product at a given temperature, it is advisable to increase the oxygen pressure to $p^{b}_{O_2}$, which allows the oxidation temperature to be decreased and thus the selectivity of formation and yields of PCA and CA to be increased.

CONCLUSION

In oxidation of crotonaldehyde in ethyl acetate, the highest total yield (80%) of crotonic and percrotonic acids is attained at initial crotonaldehyde concentration of 2.5–3.7 M, temperature of 300–309 K, and oxygen pressure of 3–7 atm.

These experimental results were used in the development of a process for production of crotonic acid.

REFERENCES

1. Manzurov, V.D., Morozov, V.M., and Kovalev, L.S., in *Monomery dlya termostoikikh polimerov* (Monomers for Heat-Resistant Polymers), Moscow: Mosk. Gos. Univ., 1085, pp. 30–33.
2. Boboleva, S.P., Bulygin, M.V., Valov, P.I., and Blyumberg, E.A., *Neftekhimiya*, 1990, vol. 30, no. 2, pp. 239–243.
3. Fedevich, O.E., Levush, S.S., and Kit, Yu.V., *Teor. Eksp. Khim.*, 1999, vol. 35, no. 5, pp. 332–337.
4. Fedevich, O.E., Levush, S.S., and Kit, Yu.V., *Visn. Derzh. Univ. L'viv. Politekh., Ser: Khim., Tekhnol. Rech. Ikh Zastos.*, 1998, no. 339, pp. 165–167.
5. Fedevich, O.E., *Visn. Derzh. Univ. L'viv. Politekh., Ser: Khim., Tekhnol. Rech. Ikh Zastos.*, 1997, no. 332, pp. 139–142.
6. Pikh, Z.G., Selective Oxidation of Unsaturated Compounds with Bound Oxygen, *Doctoral Dissertation*, Lviv, 1994.
7. Buzdan, B.I., Study of Autocatalytic Oxidation of Crotonaldehyde to Crotonic Acid, *Cand. Sci. Dissertation*, Lvov, 1969.

Russian Journal of Applied Chemistry, Vol. 75, No. 7, 2002, pp. 1128–1131. Translated from Zhurnal Prikladnoi Khimii, Vol. 75, No. 7, 2002, pp. 1151–1154.
Original Russian Text Copyright © 2002 by Kotomin, Petel'skii, Mashchenko, Yakimchuk, Abramzon.

ORGANIC SYNTHESIS AND INDUSTRIAL ORGANIC CHEMISTRY

Temperature Dependence of the Detergency of Sodium Alkylbenzenesulfonate and Compositions Thereof

A. A. Kotomin, M. B. Petel'skii, E. I. Mashchenko, O. D. Yakimchuk, and A. A. Abramzon

St. Petersburg State Technological Institute, St. Petersburg, Russia

Received January 29, 2002

Abstract—Temperature dependence of the detergency of one of the basic components of synthetic detergents, sodium alkylbenzenesulfonate, and compositions thereof was studied. The influence of the temperature on the detergency equation parameters was elucidated.

The experience of application of synthetic detergents (SDs) shows that the detergency of solutions is temperature-dependent [1, 2]. The temperature affects the solubility of the detergent components and contaminants. The kinetics of diffusion of surfactants to the contaminated surface and of emulsification of the washed off contaminants in a synthetic detergent solution are also temperature-dependent [3]. Rising temperature decreases the viscosity of liquid contaminants and promotes saponification of fat contaminants. In selected cases, however, increased temperatures can exert adverse affect, namely, decrease the surface activity of certain detergents, increase the degree of hydrolysis of soaps, and reduce the stability of emulsions [2]. The temperature dependence of individual properties (solubility, viscosity, surface tension, critical micelle concentration) of surfactants and other components of detergents are widely covered in reference literature and monographs. The quantitative temperature dependence of the detergency of substances is, however, studied inadequately.

Earlier [4, 5] we studied how the qualitative composition of synthetic detergent solutions and concentrations of individual components affect the detergency. For isothermal conditions, the detergency equation was derived:

$$M = \frac{M_{\max} c}{\alpha + c}, \qquad (1)$$

where M is detergency; $M_{\max}$, the maximal detergency; c, the detergent concentration; and α, the coefficient measured in the concentration units, which is a function of the energy parameters of the process. Equation (1) holds for both individual components of synthetic detergents and complex detergents.

The aim of this wirk is to establish the quantitative dependence of the parameters of Eq. (1), $M_{\max}$ and α, on the temperature T and to collect systematized experimental data for developing a physicochemical model of detergency. Also, such data are useful practically, in particular, for optimizing the conditions of using specific synthetic detergents.

We studied the basic component of synthetic detergents, namely, linear sodium alkylbenzenesulfonate C_{10-14}–(C_6H_4)–SO_3Na (SABS), a binary mixture of 30 wt % SABS and 70 wt % inorganic addition, sodium carbonate Na_2CO_3 (for preparing alkaline solution), as well as a complex composition MS-1 comprised of organic and inorganic components, close in composition to commercial synthetic detergents. The MS-1 composition contains, wt %: SABS 20, sodium tripolyphospahte $Na_5P_3O_{10}$ (STPP) 10, sodium hydrosilicate $2SiO_2 \cdot Na_2O \cdot 2H_2O$ 15, sodium sulfate 20, sodium carbonate 14, and sodium salt of carboxymethyl cellulose $[C_6H_7O_2(OH)_{3-x}^-(OCH_2COONa)_x]_n$ 1.

The detergency was studied with white cotton (coarse calico) fabric samples of two types: with dense (for the binary mixture) and loose (for SABS and MS-1) structure. We used solutions of detergents with the practically important concentrations in the range 0.5–10 g l^{-1}.

The detergency was estimated by the accepted [OST (Branch Standard) 6-15-1574–87] method by which we determined the whiteness of 5 × 5 cm fabric samples: initial, contaminated with a standard formulation, and cleansed.

We fixed the rotation rate of the framework stirrer with a fabric sample (200 rpm) and the time of contact

1070-4272/02/7507-1128$27.00 © 2002 MAIK "Nauka/Interperiodica"

with the synthetic detergent (20 min) [4, 5]. The studies were carried out at four temperatures of the detergent solution (30, 50, 70, and 85°C). The lowest temperature corresponds to conditions of careful (manual) washing with thermally unstable biological additions, enzymes. The regime in which the detergent temperature is 50°C is most often used in activator-type washing machines, that with 85°C, in automatic washing machines, and that with 70°C is intermediate.

The degree of whiteness of the fabric samples was estimated with a computer and a scanner, which allowed the error in determining the detergency to be significantly lowered (to 3%).[1]

The detergency, %, was determined by the formula

$$M = \frac{X_3 - X_2}{X_1 - X_2} \times 100, \qquad (2)$$

where X_1, X_2, and X_3 are the whitenesses of the initial (artificially aged), contaminated, and cleansed fabrics, respectively.

Figure 1 presents the plots of the detergency vs. concentration, $1/M$ vs. $1/c$, at various temperatures for all the three investigation objects. The M_{max} and α values obtained by processing these plots are presented in Table 1. It is seen that, for all the systems studied, M_{max} tends to increase with temperature, and α remains virtually unchanged, namely, 1.48 ± 0.02, 0.51 ± 0.04, and 1.78 ± 0.06 for SABS, binary mixture, and MS-1, respectively.

Thus, we found that α is temperature-independent. This can be explained as follows. In [5], we showed that $\alpha = M_{max} \tan\beta$, where β is the slope of the $1/M$ vs. $1/c$ plot. With rising temperature, M_{max} tends to increase, and α remains unchanged (Table 1). Therefore, the growth of M_{max} with temperature is compensated by a decrease in $\tan\beta$, i.e., decrease in the rate of detergency growth with increasing concentration (Fig. 1). The mutual compensation of these two factors may be due to thermodynamic factors. Of all the detergency factors studied [4, 5], the parameter α is affected only by the qualitative composition of the detergent formulation (chemical nature and structure of the detergent components), while M_{max} is affected by the mixture composition and temperature as well.

The detergencies estimated were compared with that of the standard solution M_{st} estimated under identical conditions for a fabric with dense and loose structures. The standard solution satisfied the above-mentioned OST and contained linear SABS (1 g l^{-1}) and sodium tripolyphosphate (2 g l^{-1}).

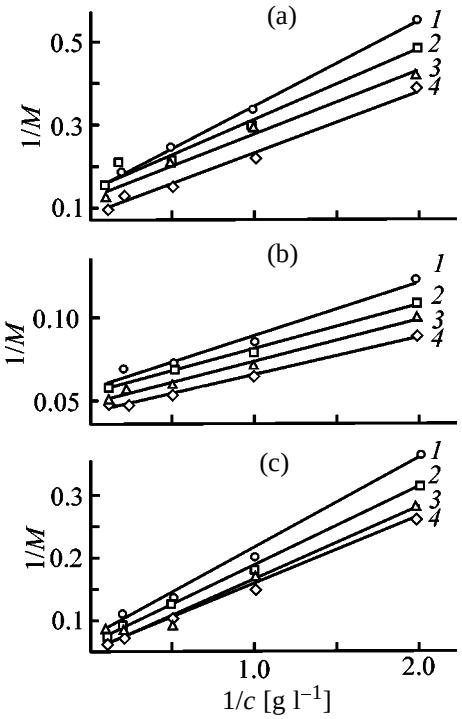

Fig. 1. Detergency M as a function of the detergent concentration c for (a) SABS, (b) SABS + Na_2CO_3, and (c) MS-1. Temperature, °C: (*1*) 30, (*2*) 50, (*3*) 70, and (*4*) 85; the same for Fig. 2.

For smoothing the influence of secondary factors, we used for analyzing the results of our studies the relative detergency of a substance, $\overline{M} = M/M_{st}$. The

Table 1. Parameters M_{max} and α for detergents studied under different temperature regimes

Solution composition	T, °C	M_{max}	α
SABS	30	7.41	1.47
	50	8.16	1.50
	70	9.52	1.49
	85	10.81	1.46
SABS + Na_2CO_3	30	16.88	0.48
	50	18.43	0.47
	70	20.92	0.54
	85	22.89	0.55
MS-1	30	13.33	1.73
	50	14.81	1.72
	70	17.39	1.84
	85	19.05	1.83

[1] The procedure was developed at the St. Petersburg State Technological Institute.

Table 2. Relative detergency of SABS and compositions thereof

T, °C	c_{SABS}, g l^{-1}	$\overline{M}$		
		SABS	SABS + Na_2CO_3	MS-1
30	0.5	0.20	0.64	0.30
	1.0	0.33	0.87	0.63
	2.0	0.46	1.01	0.82
	5.0	0.56	1.06	1.03
	10.0	0.73	–	1.22
50	0.5	0.20	0.65	0.35
	1.0	0.33	0.87	0.60
	2.0	0.44	0.97	0.81
	5.0	0.50	–	1.10
	10.0	0.65	1.07	1.27
70	0.5	0.20	0.58	0.30
	1.0	0.29	0.84	0.50
	2.0	0.39	0.96	0.94
	5.0	0.63	1.01	1.03
	10.0	0.67	1.07	1.25
85	0.5	0.20	0.54	0.30
	1.0	0.37	0.79	0.42
	2.0	0.50	0.96	0.81
	5.0	0.59	1.02	1.12
	10.0	0.76	1.04	1.24

$\overline{M}$ values obtained in the experiment at different concentrations and temperatures are presented in Table 2.

Figure 2 presents the plots of the reciprocal $\overline{M}$ vs. reciprocal concentration at different temperatures for SABS, binary mixture, and MS-1 composition. It is seen that, in the temperature range studied, the plots for each of the objects are straight lines with the correlation coefficients of 0.99, 0.96, and 0.98 for SABS, binary mixture, and MS-1, respectively. The $\overline{M}_{max}$ and α values determined in the $1/\overline{M}$–$1/c$ coordinates from the section cut on the ordinate and the product of $\overline{M}_{max}$ and the slope of the correlation dependence [4], respectively, proved to be constant for a particular washing composition. Thus, $\overline{M}_{max}$ and α are independent of temperature and reflect only the relative detergency of a specific substance of composition. This, in turn, means that the equation of the relative detergency in the form

$$\overline{M} = \frac{\overline{M}_{max} c}{\alpha + c}, \qquad (3)$$

($\overline{M}_{max}$ is the maximal relative detergency) derived by us in [4] for a fixed temperature (80°C) is a general equation for a wide temperature range. Equation (1) is, essentially, the detergency isotherm.

The influence of the temperature on the washing efficiency is illustrated by Fig. 3 showing the temperature dependence of the maximal detergency at a given temperature as referenced to the maximal detergency at a fixed temperature (30°C), M^T_{max}/M^{30}_{max}, for five objects: SABS, SABS + Na_2CO_3, MS-1, and standard solution (1 g l^{-1} SABS + 2 g l^{-1} STPP) for dense and loose cotton fabrics. Mathematical processing of the results presented in Fig. 3 showed that all the

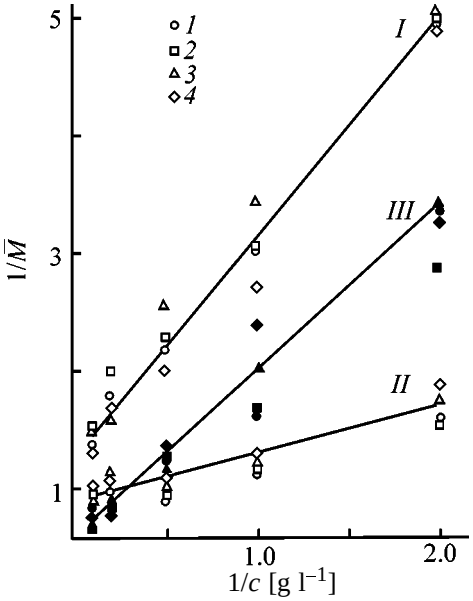

Fig. 2. Relative detergency $\overline{M}$ as a function of the detergent concentration c: (*I*) SABS, (*II*) binary mixture, and (*III*) MS-1 composition.

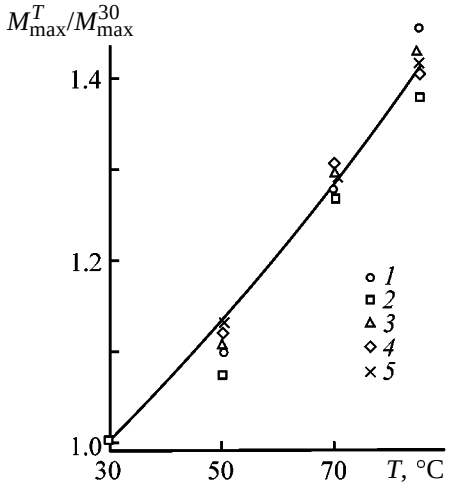

Fig. 3. Maximal detergency M^T_{max} as referenced to the maximal detergency at 30°C M^{30}_{max} as a function of temperature T for (*1*) SABS and (*2–5*) compositions thereof. (*2*) SABS + Na_2CO_3, (*3*) MS-1, and (*4, 5*) standard solution with dense and loose cotton fabrics, respectively.

M^T_{max}/M^{30}_{max} values correspond to the exponential correlation dependence with a correlation coefficient of 0.99:

$$M^T_{max}/M^{30}_{max} = 0.83e^{0.006T}, \quad (4)$$

where T is temperature.

Such an exponential form of equation is characteristic of the temperature dependence of the parameters of various processes: chemical potential, reaction rate constant, solubility, viscosity, etc. Rewriting Eq.(4) in the form

$$M^T_{max} = 0.83M^{30}_{max}e^{0.006T},$$

and analyzing the equation at the boundary conditions $T \to 0$°C and $T \to 100$°C, we obtain for the SABS-based systems studied the maximal detergency varying from $M^0_{max} = 0.83M^{30}_{max}$ to $M^{100}_{max} = 1.52M^{30}_{max}$.

Our results suggest the existence of a common temperature dependence of M_{max} for the basic component of detergents, SABS, and compositions thereof, which is unaffected by the structure of the contaminated fabric. This makes it possible, using formula (5) obtained by substituting the modified equation (4) into Eq. (1), to predict the detergency of such formulations as dependent on both the concentration [4, 5] and temperature of solutions:

$$M^T = \frac{0.83M^{30}_{max}e^{0.006T}c}{\alpha + c}, \quad (5)$$

CONCLUSIONS

(1) The temperature dependence of the detergency was studied for linear sodium alkylbenzenesulfonate and compositions thereof in practically important temperature 30–85°C and concentration 0.5–10 g l^{-1} ranges. For a particular substance or composition, the parameter α in the detergency equation is temperature-independent.

(2) Linear sodium alkylbenzenesulfonate and compositions thereof exhibit a common exponential dependence of the maximal detergency on the temperature. This dependence is unaffected by the structure of the contaminated fabric.

(3) Based on analysis of the experimental data, an equation was proposed for predicting the detergency as dependent on the concentration of the composition and the temperature of the solution.

ACKNOWLEDGMENTS

The authors are grateful to N.P. Shirokov and I.P. Podreshetnikov for assistance in conducting the experiments.

REFERENCES

1. Bukhshtab, Z.I., Mel'nik, A.P., and Kovalev, V.M., *Tekhnologiya sinteticheskikh moyushchikh sredstv* (Technology of Synthetic Detergents), Moscow: Legkaya Prom–st., 1988.
2. Nevolin, F.V., *Khimiya i tekhnologiya sinteticheskikh moyushchikh sredstv* (Chemistry and Technology of Synthetic Detergents), Moscow: Pishchevaya Prom–st., 1971.
3. Abramzon, A.A. and Petel'skii, M.B., *Zh. Fiz. Khim.*, 1997, vol. 71, no. 7, pp. 1240–1243.
4. Abramzon, A.A. and Kotomin, A.A., *Zh. Prikl. Khim.*, 2000, vol. 73, no. 11, pp. 1902–1904.
5. Kotomin, A.A., Petel'skii, M.B., and Abramzon, A.A., *Zh. Prikl. Khim.*, 2001, vol. 74, no. 12, pp. 2038–2042.

Russian Journal of Applied Chemistry, Vol. 75, No. 7, 2002, pp. 1132–1135. Translated from Zhurnal Prikladnoi Khimii, Vol. 75, No. 7, 2002, pp. 1155–1158.
Original Russian Text Copyright © 2002 by Artem'eva, Baklagina, Kukarkina, Kostereva, Samarin, Lavrent'ev, Panov, Kudryavtsev.

MACROMOLECULAR CHEMISTRY AND POLYMERIC MATERIALS

Influence of the Molecular Structure of H Complexes of Dialkyl Dihydrogen Benzophenonetetracarboxylates with Aromatic Diamines on the Viscosity of Their Melts

V. N. Artem'eva, Yu. G. Baklagina, N. V. Kukarkina, T. A. Kostereva, V. P. Samarin, V. K. Lavrent'ev, Yu. N. Panov, and V. V. Kudryavtsev

Institute of Macromolecular Compounds, Russian Academy of Sciences, St. Petersburg, Russia

Received January 9, 2002

Abstract—The possibility of preparing from dialkyl dihydrogen 3,3',4,4'-benzophenonetetracarboxylates and 4,4'-diaminodiphenylmethane or 4,4'-diaminodiphenyl ether H complexes of both amorphous and crystalline structures was elucidated. Methods were proposed for disordering the supramolecular structure of the H complexes, which is technologically essential for reducing the melt viscosity when preparing polyimide carbon-filled plastics and foamed composites.

When aromatic diamines are dissolved in solution of dialkyl dihydrogen tetracarboxylates in alcohol (methanol or ethanol) or in a water–alcohol mixture, complexes with hydrogen bond (H complexes) are formed spontaneously between the amino group of diamine and the ester and carboxy groups of dialkyl dihydrogen carboxylate [1, 2]. Despite high polarity of the solvents used, hydrogen bonds are formed even in solutions with a low concentration of the initial components (0.01% solutions) [1]. In 7–8% solutions, H complexes occur as di- and trimers (n = 2, 3) [3]:

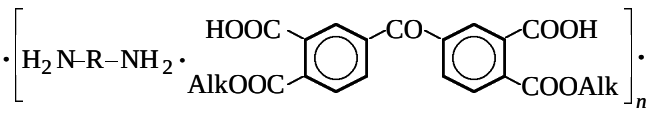

At higher solution concentrations, the n-size of the H complexes increases (n > 5, 6), and the solution gets anisotropic owing to formation of fluctuation domains [3], i.e., an ordered supramolecular packing of such supramolecular structures as H complexes. Even insignificant changes in the concentrations of such solutions cause fluctuations of the orientation ordering factor characterizing the ordering of the H complexes inside the fluctuation domains [4].

Under virtually identical conditions, it is possible to obtain H complexes with different supramolecular structures because of fluctuations of ambient temperature and humidity, solvent purity, etc.

The above-mentioned supramolecular structures can yield polyimide materials such as EPPI foamed polyimides [5], carbon-filled plastics [6], and foamed composites [7] promising for modern aviation and space technology, as well as for ship-building applications. Since all the above-listed materials can be prepared from molten H complexes with low viscosity only, of special importance are data on how the melt viscosity is influenced by the structure of the initial H complexes.

In this work, we proved experimentally that H complexes with amorphous and crystalline supramolecular structures can be obtained by slightly modifying the conditions of their preparation. Also, we studied how the melt viscosity is influenced by the crystallization of H complexes and suggested a method for directed modification of the supramolecular structure of H complexes.

EXPERIMENTAL

Dialkyl dihydrogen 3,3',4,4'-benzophenonetetracarboxylates (BZPMe and BZPEt, respectively) were prepared by refluxing 0.03 mol of 3,3',4,4'-benzophenonetetracarboxylic dianhydride [TU (Technical Specifications) TSR 2159–69; purified by refluxing in acetone; mp 225°C] in 50 ml of the appropriate alcohol or alcohol with addition of 6 vol % water. The H complexes were prepared by dissolving at room temperature equimolar (with respect to BZPMe or BZPEt) amounts of 4,4'-diaminodiphenylmethane (DADPM) or 4,4'-diaminodiphenyl ether (DADPE) (purified by distillation at 1–3 mm Hg; mp 90–92

1070-4272/02/7507-1132$27.00 © 2002 MAIK "Nauka/Interperiodica"

and 190°C, respectively) in solutions of BZPMe or BZPEt in the appropriate alcohol. Solid H complexes were recovered by alcohol evaporation at 1–3 mm Hg and 20–30°C.

X-ray studies of the samples of H complexes were carried out on a DRON-2 diffractometer (nickel-filtered copper radiation). The viscosity of molten H complexes was measured on a PIRSP rheometer (cone–plane working unit; angle at the cone vertex 1°, cone diameter 40 mm) at 95 and 105°C at a shear rate of 0.02 s^{-1} [8].

In most cases, mixing dialkyl dihydrogen benzenetetracarboxylates with aromatic diamines yields H complexes with amorphous structure. Preparation of crystalline H complexes, though practically unpredictable, is rather common. Essential for preparing ordered structures are, typically, seasonal fluctuations of ambient temperature and humidity, uncontrollable changes in the solvent quality, or minor fluctuations of the stoichiometry or concentration of the initial components. Virtually any H complex of any chemical composition can be prepared with amorphous or differently ordered structures.

Figure 1 presents as an example the X-ray diffraction patterns of selected H complexes of various chemical compositions formed in alcohols or aqueous alcohols. It is seen that H complexes with identical compositions BZPEt–DADPE prepared in ethanolic solution (Fig. 1, curves *1*, *1*') can have both amorphous (curve *1*) and low-crystalline structures (curve *1*'). In the case of BZPMe–DADPE H complexes prepared in aqueous methanol, it is possible to obtain supramolecular structures with various degrees of crystallinity (curves *2*, *2*'). With DADPM as amino component, the degree of ordering of the H complexes is also diverse (curves *3*, *3*').

In this connection, it was of interest to elucidate how the crystalline structure of the H complexes affects their viscosity, which governs the preparation of polyimide materials.

Figure 2 shows how the viscosity of molten H complexes with different structures varies with time. Curves *1* and *1*' characterize the variation with time of the viscosity of molten BZPEt–DADPE H complexes, isolated from ethanolic solution, with amorphous (Fig. 1, curve *1*) and low-crystalline (Fig. 1, curve *1*') structures. It is seen that the viscosity of the more highly ordered H complex in the melt is two orders of magnitude higher than that of the amorphous H complex. Curve *2* refers to the BZPMe–DADPE H complex with low-crystalline structure (Fig. 1, curve *2*)

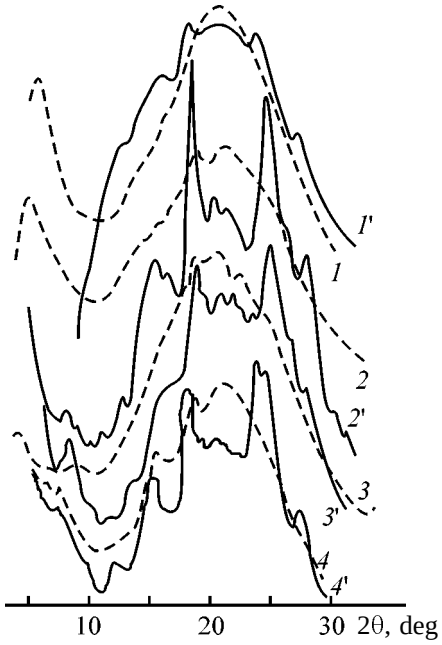

Fig. 1. X-ray diffraction patterns of H complexes (*1*, *1*') BZPEt–DADPE prepared in ethanol, (*2*, *2*') BZPMe–DADPE prepared in aqueous methanol, (*3*, *3*') BZPMe–DADPM prepared in methanol, and (*4*, *4*') BZPEt–DADPM prepared in aqueous ethanol with and without benzimidazole addition, respectively. (2θ) Bragg's angle; the same for Figs. 3 and 4.

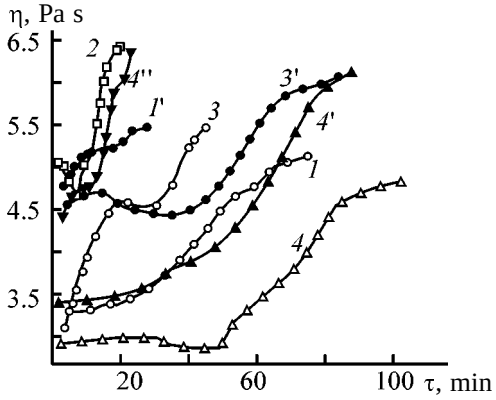

Fig. 2. Variation of the viscosity η with time τ of molten H complexes (*1*, *1*') BZPEt–DADPE prepared in ethanol, (*2*) BZPMe–DADPE prepared in aqueous methanol, (*3*, *3*') BZPEt–DADPM prepared in aqueous ethanol with and without benzimidazole addition, respectively, and (*4*, *4*', *4*'') BZPMe–DADPE prepared in methanol. Temperature, °C: (*1*, *1*', *2*, *3*, *3*', *4*'') 105 and (*4*, *4*') 95.

isolated from aqueous methanol. The BZPMe–DADPE H complex with a high degree of crystallinity (Fig. 1, curve *2*') does not melt at all at 105°C. Thus, the more highly ordered the supramolecular structure of the initial H complex, the higher the melting point

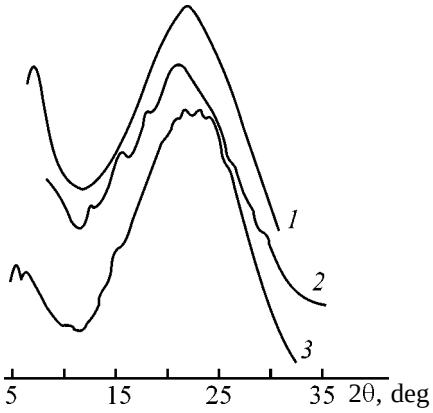

Fig. 3. X-ray diffraction patterns of BZPMe–DADPE H complexes prepared in methanol. Sample nos.: (*1*) 1, (*2*) 2, and (*3*) 3.

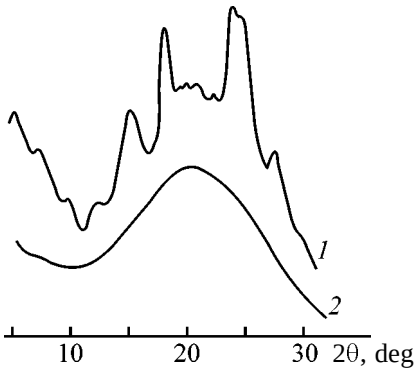

Fig. 4. X-ray diffraction patterns of the BZPEt–DADPM H complex prepared in aqueous ethanol: (*1*) initial and (*2*) after melting at 105°C.

of the H complex and the higher the viscosity of its melt.

As known, in preparing foamed polyamides EPPIs, samples of H complexes are foamed at temperatures above 180°C [5]. Therefore, high viscosities of molten crystalline H complexes at 100±5°C are of no importance for foam formation. However, prepregs for carbon-filled plastics and foamed composites are obtained at temperatures close to 100°C [6, 7]. This makes undesirable the use of crystalline H complexes for these purposes.

In this connection, we suggest a method for disordering the supramolecular structure of H complexes. It was found that adding minor amounts of benzimidazole (3 wt % with respect to dialkyl dihydrogen carboxylate) to the initial reaction mixture yields H complexes with less highly ordered structure, all other conditions being the same. For example, the degree of ordering of the crystalline BZPEt–DADPM H complex prepared from aqueous ethanol (Fig. 1, curve *4*') significantly decreases on adding benzimidazole (Fig. 1, curve *4*). The viscosity of the molten complex decreases, as expected, by two orders of magnitude relative to the crystalline sample (Fig. 2, curves *3*, *3*').

In the case of BZPMe–DADPE H complex isolated from methanolic solution, we succeeded in preparing samples with significantly differing viscosities of melts. Curves *4* and *4*' (Fig. 2) show how the viscosities of melts of these H complexes, as measured at 95°C (sample nos. 1 and 2), vary with time. Curve *4*" refers to sample no. 3 of this H complex at 105°C. At 95°C sample no. 3 does not melt.

The X-ray diffraction patterns of these samples (Fig. 3) show that none of them has highly ordered crystalline structure. Unlike amorphous sample no. 1, however, the X-ray diffraction pattern of sample no. 2 in the region of 2θ = 10°–20° exhibits clear reflections which evidence formation a more ordered structure in it. Sample no. 3 exhibits in the 2θ ~ 18°–27° region low-intensity reflections against the background of an amorphous halo. This suggests formation of ordered domains, similar to crystalline domains in the BZPMe–DADPE sample prepared from aqueous methanol (Fig. 1, curve *2*').

The diffraction patterns (Fig. 3, curves *2* and *3*) suggest that the samples can contain various ordered domains responsible for formation at a later time of both low-crystalline (Fig. 1, curve *1*') and highly ordered crystalline (Fig. 1, curves *2*'–*4*') structures.

Figure 4 presents the X-ray diffraction patterns of the BZPEt–DADPM H complex isolated from aqueous ethanolic solution (curve *1*) and of the sample obtained on melting this H complex at 105°C (curve *2*). It is seen that the initial sample has a crystalline structure. On melting and subsequent cooling, the sample gets amorphous. Similar structural changes were also observed for crystalline H complexes of other compositions.

CONCLUSIONS

(1) The H complexes prepared from dialkyl dihydrogen 3,3',4,4'-benzophenonetetracarboxylates and 4,4'-diaminodiphenylmethane or 4,4'-diaminodiphenyl ether can have both amorphous and crystalline structures. With growing degree of ordering of the H complex, the initial viscosity of its melt tends to increase. The viscosity of molten crystalline H complex exceeds by two orders of magnitude that of amorphous or low-crystalline H complexes with identical chemical compositions.

(2) To obtain low-viscosity melts required for successfully preparing prepregs, it is recommended that minor amounts of benzimidazole, which exerts a disordering effect on the supramolecular structure of the forming H complex, be added to the initial reactant mixture.

REFERENCES

1. Koton, M.M., Artem'eva, V.N., Glumova, T.D., *et al.*, *Zh. Prikl. Spektrosk.*, 1987, vol. 47, no. 4, pp. 623–629.
2. Artem'eva, V.N., Kukarkina, N.V., Samarin, V.P., *et al.*, *Zh. Prikl. Khim.*, 2000, vol. 73, no. 7, pp. 1172–1179.
3. Chupans, P.I., Kallistov, O.V., Artem'eva, V.N., *et al.*, *Izv. Akad. Nauk SSSR, Ser. Khim.*, 1991, no. 6, pp. 1338–1343.
4. Kallistov, O.V., Kalinina, N.A., Silinskaya, I.G., *et al.*, *Izv. Akad. Nauk SSSR, Ser. Khim.*, 1994, no. 9, pp. 1596–1599.
5. RF Patent 1824885.
6. Artem'eva, V.N., Yudin, V.E., Kudryavtsev, V.V., *et al.*, *Plast. Massy*, 1996, no. 5, pp. 3–5.
7. RF Patent 2081134.
8. Vinogradov, G.V., Malkin, A.Ya., Plotnikova, E.P., *et al.*, *Vysokomol. Soedin., Ser. A*, 1978, vol. 20, no. 2, pp. 226–230.

Russian Journal of Applied Chemistry, Vol. 75, No. 7, 2002, pp. 1136–1140. Translated from Zhurnal Prikladnoi Khimii, Vol. 75, No. 7, 2002, pp. 1159–1163.
Original Russian Text Copyright © 2002 by Rashidova, Voropaeva, Mukhamedzhanova, Reshetnikova, Ruban.

MACROMOLECULAR CHEMISTRY AND POLYMERIC MATERIALS

Rheological Properties of Concentrated Solutions of Mixtures of Lemon Pectin with Flexible-Chain Vinyl Polymers

S. Sh. Rashidova, I. L. Voropaeva, M. Yu. Mukhamedzhanova, I. V. Reshetnikova, and I. N. Ruban

Institute of Polymer Chemistry and Physics, Academy of Sciences of Uzbekistan Republic, Tashkent, Uzbekistan

Received March 4, 2002

Abstract—Rheological properties of concentrated aqueous solutions of lemon pectin, polyvinylpyrrolidone, polyvinyl alcohol, and 1 : 1 blends of lemon pictin with these polymers were studied at 25–70°C.

Among polymeric materials with complex composition, growing attention is given to blends of polymers whose specific mechanical and structural features make them suitable for obtaining materials with new properties. Understanding of the mechanism of structure formation in concentrated solutions based on mixtures of linear polymers of different nature, as well as of the factors responsible for the specific complex of properties exhibited by these systems, requires a detailed study of their rheological behavior [1, 2].

Rheological characteristics in certain cases prove to be the most sensitive to changes in the structural parameters of polymers. Molding of almost a half of all polymeric articles proceeds via dissolution. In this case, the relationships in molding are governed by the rheological behavior of concentrated polymer solutions, and the properties of articles originate from the solution proper [3, 4].

In this work, we studied the rheological properties exhibited by concentrated aqueous solutions of blends of linear polymers of different nature: rigid-chain (Kuhn segment 300 Å) polysaccharide lemon pectin (PC) and flexible-chain polymers, polyvinyl alcohol (PVA) and polyvinylpyrrolidone (PVP). These polymers are used in food industry [5] and agriculture. Our studies furnish information about the structure of concentrated solutions of polymers themselves and their blends, as well as about the structural changes in flow.

EXPERIMENTAL

We studied (1) citrus PC prepared from peel and seeds of lemons of the Yalongoch sort, obtained by local selection following the procedure in [6], with molecular weight (MW) of 8.9×10^4 (seeds) and 1.5×10^5 (peel); (2) PVA with MW of 2.2×10^4 containing 1.2 wt % acetate groups and 0.5 wt % sodium acetate (commercial sample); and (3) PVP with MW 10^4 (commercial sample). We studied the rheological properties of concentrated (5%) solutions of polymers and their blends on a Rheotest-2 rotation visometer with a working unit comprised of coaxial cylinders at stresses within 2–380 Pa and shear rates of $(1.5–1.3) \times 10^3$ s^{-1} at 25, 40, 55, and 70°C.

Using the data obtained, we calculated the thermodynamic parameters of the system, namely, enthalpy ΔH_v, entropy ΔS_v, and Gibbs energy ΔG_v of activation of viscous flow [7].

The macromolecules of the PC base, α-*D*-galacturonic acid, are nonuniform in the composition and molecular weight and differ in the degree of esterification of carboxy groups and in the distribution pattern of the methyl groups [8, 9].

The PC macromolecules (α-*D*-galacturonic acid with *D*-rhamnose inclusions) can contain minor amounts of *D*-galactose, *L*-arabinose, and other monosaccharides [10]. Pectin dissolves in water and under certain conditions forms dense gels, which indicates that its macromolecules strongly tend to associate.

The structure of the macromolecules governs the structure of concentrated PC solutions. Aqueous 5% solutions of PC are characterized by higher degrees of structure formation and aggregation of macromolecules than equiconcentrated aqueous solutions of PVA and PVP. When the regular structure of high-molecular-weight associates in concentrated solutions of polymers of different nature is disturbed by mixing,

1070-4272/02/7507-1136$27.00 © 2002 MAIK "Nauka/Interperiodica"

this modifies the structure of solutions, which affects, above all, their viscosity.

The viscosity of solutions of the polymers and their 1 : 1 blends was determined as a function of the shear stress (flow curves) (Figs. 1a, 1b).

The shape of the curves suggests a pseudoplastic non-Newtonian flow. The abnormal viscosity of concentrated polymer solutions is mainly caused by the progressive degradation of the structure with growing shear stress. In concentrated polymer solutions, with their complex system of interacting macromolecules, small shear stresses do not cause deviation from Newtonian flow. This means that the structure of solutions does not change significantly or that flow affects only the bond elements characterized by very short relaxation (restoration) times. At higher shear stresses, the structure of the solutions degrades more profoundly, which disturbs the interchain contacts with relatively long restoration times. This makes the viscosity dependent on τ.

The highest viscosity is exhibited by those aqueous PC solutions whose viscosity anomaly in the flow curves is more pronounced than in the case of solutions of PC–PVA and PC–PVP blends. PVA and PVP solutions themselves exhibit weakly pronounced anomalies of the flow viscosity. Incorporation of these flexible-chain polymers into more structurized systems of aqueous PC solutions reduces the viscosity, but at the PC content in mixtures of 50% the rheological behavior of the systems is the most similar to that of PC solutions.

In the case of associated structures, the kinetic units migrating in flow are chain aggregates, whose size depends on the nature of the solvent, concentration, and temperature, rather than the chains or chain segments [11]. The character of packing of macromolecules into associates and their contacts with each other are determined by the chemical structure of the chains, the ratio between the amounts of different macromolecules in these associates, and the nature of the polymer matrix [12, 13]. With polymer blends, the onset of intensive degradation of the solution structure at different temperatures, as estimated from the flow curves obtained, shifts to lower shear stresses. The reason is that the uniformity of the network of intermolecular contacts is disturbed and decreased by a flexible-chain polymer incorporated into PC associates. It should be noted that PVA macromolecules have a stronger structure-making power than PVP macromolecules, which is explained by a higher molecular weight of the former. The temperature dependence of the viscosity of the studied solutions in the 25–70°C range is described by the Arrhenius–Frenkel relation $\eta = Ae^{\Delta E/RT}$ [3, 4], where ΔE is the viscous flow activation energy.

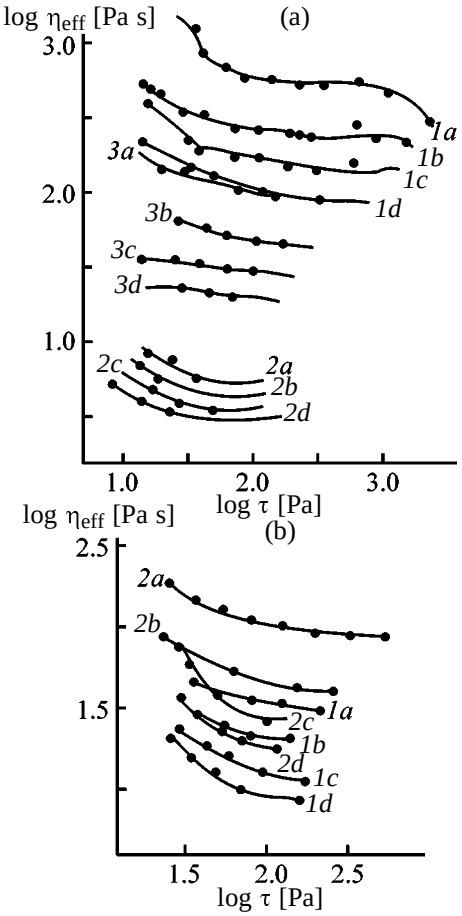

Fig. 1. Flow curves for concentrated (5%) solutions of (*1*) PC, (*2*) vinyl polymer, and (*3*) their blends. (η_{eff}) Viscosity and (τ) stress. Temperature, °C: (*a*) 25, (*b*) 40, (*c*) 55, and (*d*) 70. Polymer: (a) PVP and (b) PVA.

The effective activation energy of viscous flow ΔE is a measure of intensity of intermolecular interaction of macromolecules in solutions (Table 1).

Concentrated aqueous PC solutions are characterized by the highest ΔE values and, hence, the highest stability of the solution structure. When a PC solution is mixed with solutions of flexible-chain polymers, ΔE changes insignificantly. The activation heat of viscous flow is determined by the strength of intermolecular interaction and stability of structural formations in solutions [11, 14]. Thus, formation of more stable structural domains in solution should affect the activation energy more profoundly than formation of a fluctuation network. Presumably, such relationships for ΔE in the case of solutions of PC blends with flexible-chain polymers are explained

Table 1. Effective activation energy of viscous flow ΔE

Composition	ΔE, kJ mol^{-1}
PC	33.0
PVA	25.5
PC : PVA (1 : 1)	29.9
PBP	9.6
PC : PVP (1 : 1)	30.5

by formation of relatively stable structures of intermolecular PC associates with PVA and PVP macromolecules and their associates.

Basing on the rheological data obtained, we estimated the "viscous volumes" V^*, or statistical mean sizes of the kinetic units [15]. The parameter V^* is a qualitative characteristic suitable for estimating the mobility of the structural elements and their sizes for concentrated solutions of PC, PVA, and PVP and their blends (Table 2).

With rising temperature, V^* tends to increase for solutions of PC, PVA, and PVP and their blends, which is explained by unfolding of the macromolecules and facilitation of intermolecular interactions yielding associates. With increasing shear stresses the structural associates gradually degrade for all the systems studied (Table 2).

In the series studied, the smallest V^* is exhibited by PVP solutions, suggesting higher mobility of the structural associates in them. The PVA solution is characterized by a lower mobility of the structural formations owing to higher molecular weights. The structural elements formed in PC solutions are the least mobile and the largest in size.

Interesting V^* data were obtained in going to polymer blends. The V^* parameters (Table 2) for blend solutions exceed those for solutions of PC and flexible-chain polymers, taken separately. Presumably, solutions of PC–PVA and PC–PVP blends undergo rearrangement of the macromolecular associates of PC with flexible-chain polymers and formation of structural elements larger than those in PC solutions and significantly larger than those in PVP solutions. This may be due to the fact that, in the case of blends, the macromolecules (or macromolecular associates) of PC and PVP, as well as those of PC and PVA, form stronger bonds than in the PC : PC, PVP : PVP, and PVA : PVA associates. This yields formations comprised of macromolecular associates of PC surrounded (as if they were enveloped) by macromolecules and macromolecular formations of PVA and PVP. In the case of the PC–PVP blend, this effect is due to hydrogen bonding between the carbonyl (proton-accepting) groups of vinylpyrrolidone and the carboxy (proton-donating) groups of *D*-galacturonic acid >C=O···HOOC–. In the case of PC–PVA blend, hydrogen-bonded are hydroxy groups of *D*-galacturonic acid and PVA (>HC–OH···OH–CH<) or carboxy groups of *D*-galacturonic acid and hydroxy groups of PVA (>HC–OH···HOOC). The occurrence of proton-donating and proton-accepting groups in these polymers governs the nature of the intermolecular bonds responsible for formation of associates between mac-

Table 2. Viscosity volumes V^* at different temperatures and shear stresses τ for PC, PVA, and PVP solutions and their blends

τ, Pa	T, K	$V^* \times 10^{28}$, m^3				
		PC	PVA	PC : PVA	PVP	PC : PVP
1.4	298	7.22	2.63	4.76	3.67	6.18
	313	7.72	2.77	4.99	3.86	6.48
	328	7.84	2.98	5.13	4.04	8.76
	343	8.05	3.09	5.43	4.21	6.97
1.8	298	1.76	1.68	1.85	1.15	1.89
	313	1.78	1.77	1.97	1.23	2.01
	328	1.79	2.61	2.06	1.31	2.11
	343	1.81	2.81	2.15	1.37	2.19
2	298	1.14	1.12	1.20	0.74	1.20
	313	1.21	1.18	1.30	0.78	1.27
	328	1.26	1.24	1.34	0.82	1.33
	343	1.31	1.29	1.39	0.85	1.38

romolecules of polymers of different nature. Our results suggest that the specific features of the structure of concentrated solutions of polymers significantly differing in the nature (MW, chain flexibility, structure of the monomer unit, etc.) in a strongly polar solvent such as water will affect the patterns of variation of the thermodynamic functions of systems with varying shear stress and temperature.

We calculated the Gibbs energy ΔG_v, characterizing the stability of the structures, and the activation entropy of viscous flow ΔS_v, characterizing the degree of ordering of the structures [7].

The parameters ΔS_v and ΔH_v are temperature-dependent. The temperature coefficient of these parameters is the greater, the more highly associated are the systems and the greater is the energy of intermolecular interaction. In this case, the work required for making a "hole" in the liquid is supplemented by the work required for breaking strong intermolecular bonds. With rising temperature, these bonds are degraded by the thermal motion, which causes ΔH_v to decrease [12, 13].

Figures 2a and 2b show that, for systems with pronounced structure formation, the parameters ΔH_v at ordinary temperatures are very high. The reason is the energy spent for degrading the structure of the solution; $\Delta S_v < 0$ suggests a higher degree of ordering in the state characterized by dominating orientation processes owing to unfolding of the macromolecules in a flow. Fairly high ΔH_v and ΔS_v parameters at elevated temperatures suggest fairly stable and ordered structural formations occurring in the initial system in the case of non-Newtonian flow.

High shear stresses radically change the initial structure of the material (Fig. 4). Each stress value corresponds to a particular initial structure of the material. If, after applying an external mechanical field, the initial structure of a concentrated solution gets more highly ordered and more stable, the activation entropy ΔS_v and activation heat ΔH_v should exceed those for small shear stresses. This is the case for aqueous PVA solutions (Fig. 2b). On the contrary, if the structure of the system degrades under shear stress, ΔS_v and ΔH_v tend to decrease. Therefore, decreases in the activation heat and activation entropy with increasing shear stress (Fig. 2b) for solutions of PC, PVA, and PC–PVP and PC–PVA blends suggest that structure degradation processes dominate in flow. For the processes in flow, be they ordering or disordering, the shear stress causes the activation free energy to decrease (Fig. 2b), thereby decreasing the system viscosity.

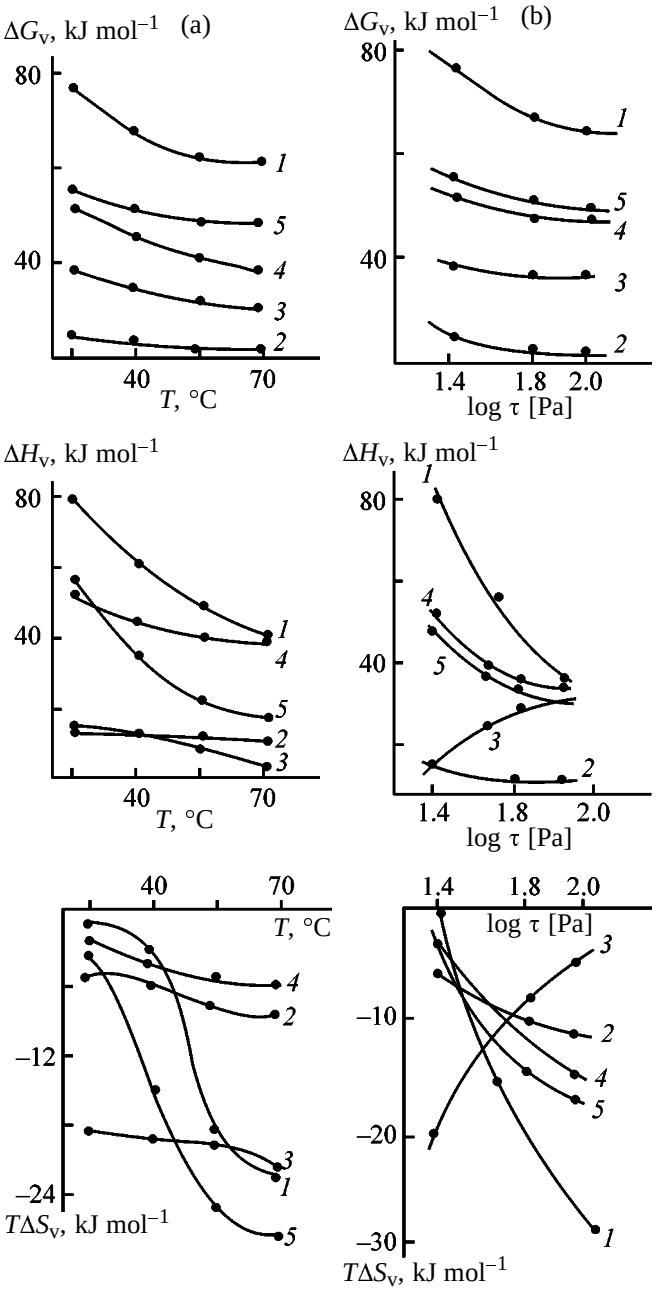

Fig. 2. Gibbs energy ΔG_v, activation heat of viscous flow ΔH_v, and activation entropy of viscous flow $T\Delta S_v$ as functions of (a) temperature T and (b) shear stress τ at 25°C, for solutions of (*1*) PC, (*2*) PVP, (*3*) PVA, (*4*) PC–PVP blends, and (*5*) PC–PVA blends.

Thus, our study of the thermodynamic parameters shows that, for blends of PC with flexible-chain polymers, structure degradation processes dominate in a flow.

Our results can be of importance for developing biodegradable polymeric systems promising for food and other industrial applications. In agriculture, such systems can be used for encapsulating seeds of diverse agricultural crops.

CONCLUSION

Study of the rheological behavior of concentrated solutions and thermodynamic analysis of the properties of PC, PVA, PVP, and their blends shows that these systems are pseudoplastic liquids for which the anomaly of viscous flow is determined by the structure of the associates formed.

REFERENCES

1. Silva, J.A.L. da and Goncalves, M.R., *Carbohydr. Polym.*, 1994, no. 24, pp. 235–245.
2. Silva, J.A.L. da and Rao, M.A., *Food Technol.*, 1995, no. 10, p. 70.
3. Vinogradov, T.V. and Malkin, A.F., *Reologiya polimerov* (Polymer Rheology), Moscow: Khimiya, 1977.
4. Torner, R.V., *Teoreticheskie osnovy pererabotki polimerov* (Theoretical Principles of Polymer Processing), Moscow: Khimiya, 1977.
5. Marshal, L., Fishman, M.L., and Coffin, D.R., *J. Carbohydr. Polym.*, 1998, vol. 35, pp. 195–203.
6. Semenova, L.N., Vasil'eva, S.A., Akhymbetova, G.D., *et al.*, in *Sbornik trudov instituta khimii i fiziki polimerov Akademii Nauk Respubliki Uzbekistan* (Coll. of Works of the Inst. of Polymer Chemistry and Physics, Acad. Sci. of Uzbekistan Republic), Tashkent, 2001, pp. 243–250.
7. Tager, A.A. and Botvinnik, O.G., *Vysokomol. Soedin, Ser. A*, 1974, vol. 16, no. 6, pp. 1284–1288.
8. Rao, M.A., Duren, J.R. van, and Cooley, H.J., *J. Food Sci.*, 1993, no. 58, pp. 173–176, 185.
9. Oakenfull, D.G., *The Chemistry and Technology of Pectins*, Walter, R.H., Ed., New York: Academic, 1991, pp. 87–108.
10. Golubev, V.I. and Shelukhina, N.P., in *Pektin: Khimiya, technologiya, primenenie* (Pectin: Chemistry, Technology, and Application), Moscow: Traktorsel'mash, 1995, p. 75.
11. Drevol', V.E., Studies in the Field of Rheology of Concentrated Solutions of Flexible- and Rigid-Chain Polymers, *Doctoral Dissertation*, Moscow, 1974.
12. Silva, J.A.L. da, Goncalves, M.R., and Rao, M.A., *Carbohydr. Polym.*, 1994, no. 23, pp. 77–87.
13. Silva, J.A.L. da, Goncalves, M.R., and Rao, M.A., *J. Biol. Macromol.*, 1995, no. 17, pp. 25–32.
14. Tager, A.A., Dreval', V.E., Kurbanaliev, M., *et al.*, *Vysokomol. Soedin., Ser. A*, 1968, vol. 10, no. 9, pp. 2044–2057.
15. Kalantarova, T.D., Thermodynamic Characteristics and Structural Features of Polymer Blends Based on Polyvinylpyrrolidone and Methyl Cellulose, *Cand. Sci. Dissertation*, Tashkent, 1997.

Russian Journal of Applied Chemistry, Vol. 75, No. 7, 2002, pp. 1141–1145. Translated from Zhurnal Prikladnoi Khimii, Vol. 75, No. 7, 2002, pp. 1164–1168.
Original Russian Text Copyright © 2002 by Kurenkov, Len'ko, Snigirev, Lobanov.

MACROMOLECULAR CHEMISTRY AND POLYMERIC MATERIALS

Preparation of Partially Degraded Copolymers of Acrylamide with (Acrylamidopropyl)trimethylammonium Chloride in the Presence of Radical Initiators

V. F. Kurenkov, O. A. Len'ko, S. V. Snigirev, and F. I. Lobanov

Kazan State Technological University, Kazan, Tatarstan, Russia
Stockhausen Eurasia Company, Moscow

Received December 5, 2001; in final form, February 2002

Abstract—Chain degradation of copolymers of acrylamide with (acrylamidopropyl)trimethylammonium chloride at 25–50°C in aqueous solutions under the action of radical degradative agents was studied viscometrically. The effiency of controlling the molecular weight of the copolymers was evaluated.

Water-soluble cationic acrylamide (AA) copolymers Praestols (Moscow–Stockhausen–Perm Russian–German Private Company) are successfully used for treating natural and waste waters and for concenrtating and dehydrating sludges. These copolymers have high molecular weight (MW); they are produced as powders and have certain commercial advantages over the analogs produced in other countries. However, in some cases, the MWs of commercial cationic Praestol samples are not optimal for particular applications. This primarily concerns low-molecular-weight cationic copolymers, which can be used as organic coagulants in water treatment with the aim to partially or fully replace mineral coagulants. A promising way to decrease the MW of water-soluble polymers is degradation [1]. Previously we studied some features of degradation of polyacrylamide [2, 3] and its anionic derivatives in aqueous solutions [4, 5] in the presence of various additives [6]. In this work, we studied degradation of high-molecular-weight cationic AA copolymers (Praestols) in aqueous solution under the action of radical degradative agents, with the aim to examine the possibility of preparing low-molecular-weight copolymers with controllable MW.

EXPERIMENTAL

We used commercial samples of cationic Praestols, which are copolymers of AA with (acrylamidopropyl)-trimethylammonium chloride (APTMAC). The sample characteristics are given in the table. The content of APTMAC units in the copolymers was determined mercurimetrically from the concentration of chloride ions [7]. The MW of the copolymers was estimated from their intrinsic viscosity [η] in 0.5 M NaCl at 25°C, using the Mark–Kuhn–Houwink equation.

The radical degradation initiators were potassium persulfate (PP), hydrogen peroxide (HP), and the redox system PP–sodium bisulfite (SB); all chemicals were of chemically pure grade. All the solutions were prepared in double-distilled water.

Degradation experiments were performed in a glass reactor ewuipped with a temperature-control jacket, a magnetic stirrer, a thermometer, a sampling nipple, and a VPZh-3 capillary viscometer (d = 0.56 mm) with which the viscosity of the aqueous solution of the copolymer was monitored in the course of degradation [8]. The viscometer was temperature-controlled with water from a thermostat, flowing through the jacket.

The reactor was charged with an aqueous solution

Characteristics of acrylamide–(acrylamidopropyl)trimethylammonium chloride copolymers

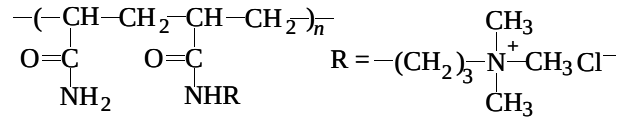

Sample	[η], $cm^3\ g^{-1}$	Content of indicated units, mol %	
		APTMAC	AA
Praestol 644	610	27	73
Praestol 655	440	33	67

1070-4272/02/7507-1141$27.00 © 2002 MAIK "Nauka/Interperiodica"

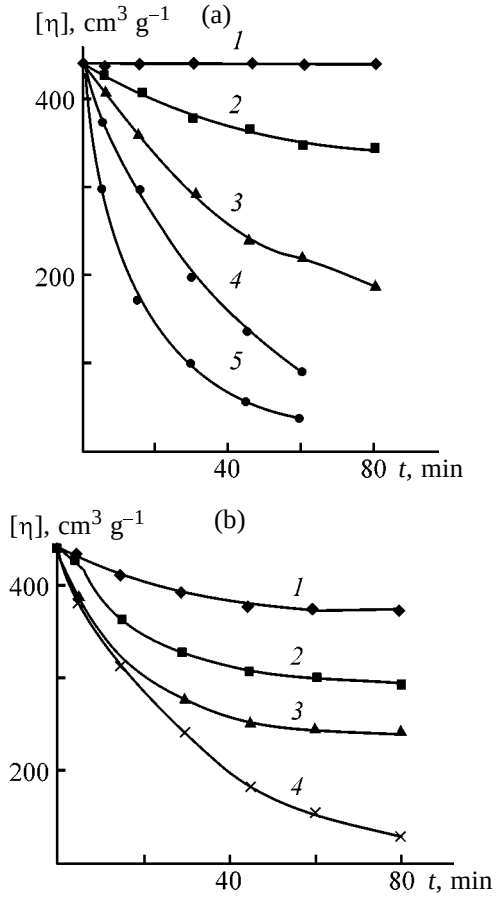

Fig. 1. Variation with time t of [η] of Praestol 655 in the course of degradation at various concentrations of (a) PP and (b) HP. T = 50°C, c_p = 0.1%; the same for Fig. 2. (a) [PP] (% in water): (*1*) 0, (*2*) 0.012, (*3*) 0.02, (*4*) 0.04, and (*5*) 0.06. (b) [HP] (% in water): (*1*) 0.03, (*2*) 0.06, (*3*) 0.09, and (*4*) 0.12.

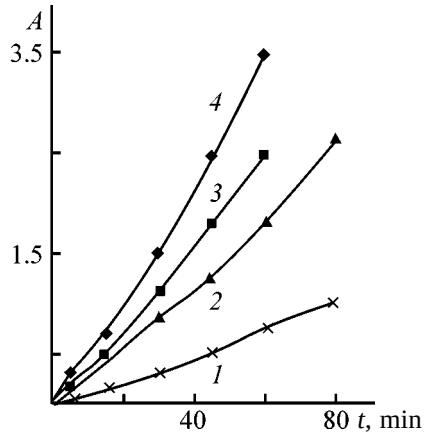

Fig. 2. Number of scissions A per macromolecule as a function of the time t of degradation of cationic Praestol 655 at various PP concentrations. [PP] (% in water): (*1*) 0.01, (*2*) 0.02, (*3*) 0.04, and (*4*) 0.06.

of the copolymer, the required temperature was adjusted, and a radical initiator was added; this moment was considered as the start of degradation. In the course of degradation, the reaction mixture was sampled at regular intervals with a syringe to determine [η]. To do this, NaCl was added to the sample in an amount required to obtain 0.5 M NaCl solution, which was followed by isoionic dilution with 0.5 M NaCl. The viscosity was measured with a VPZh-3 viscometer (d = 0.56 mm) at 25°C. The correction for the kinetic energy did not exceed 2%, and in determinations of the reduced viscosity η_{sp}/c_p it was neglected. The experimental linear dependence $\eta_{sp}/c_p = f(c_p)$ was extrapolated to $c_p = 0$ to determine [η].

Initially, we examined the possibility of degradation of AA–APTMAC copolymer (Praestol 655) under the action of radical degradative agents. Degradation was performed in 0.1% aqueous solutions of the copolymers in the presence of water-soluble initiators PP and HP at 50°C. The results are shown in Fig. 1. It is seen that [η] does not change in time in the absence of an initiator, i.e., the copolymer undergoes no noticeable degradation (Fig. 1a, curve *1*). In the presence of PP (Fig. 1a) and HP (Fig. 1b), [η] decreases with time; this decrease, indicating the occurrence of degradation, is the more pronounced, the higher the initiator concentration.

From data in Fig. 1a, we determined the number of scissions per macromolecule A:

$$A = ([\eta]_0 - [\eta]_t)^{1/\alpha},$$

where $\alpha \approx 1$ for the copolymers in hand, and $[\eta]_0$ and $[\eta]_t$ are the initial (time t = 0) and running intrinsic viscosities, respectively.

The calculated values of A of Praestol 655 are plotted in Fig. 2 vs. degradation time. It is seen that A grows with time; this trend is more pronounced at higher concentrations of a degradative agent (cf. curves *1–4*). The highest value of A attained in 1 h does not exceed 3.5, which excludes formation of low-molecular-weight products under the experimental conditions.

Degradation of AA–APTMAC copolymers is effected by radicals $R^{\bullet}$ generated by decomposition of initiators; the process occurs randomly without depolymerization. Radicals $R^{\bullet}$ abstract a hydrogen atom from the backbone at the initiation centers; at low concentrations of the copolymer in solution, this was followed by scission of abnormally (head-to-head) linked units which had formed by recombination of propagating macroradicals under the copolymerization

conditions. The presence of these structural anomalies in polyacrylamide macromolecules is confirmed in [11]; similar anomalies can apparently be present in macromolecules of AA–APTMAC copolymer. Therefore, the scission of C–C bonds in the backbones of the copolymer macromolecules between the AA and APTMAC units is not excluded.

The degradation of AA–APTMAC copolymer effected by free radicals $R^{\bullet}$ can be described by the following scheme:

Initiation:

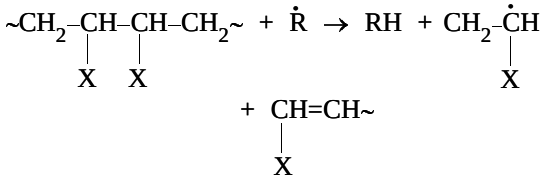

Chain propagation:

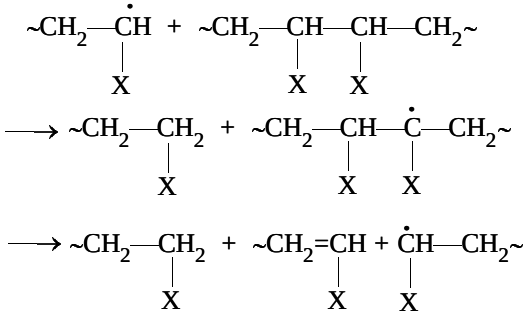

Chain transfer:

Intermolecular

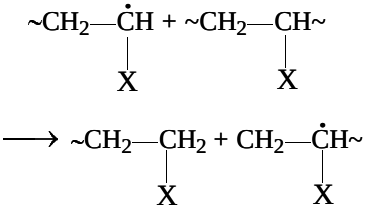

Intramolecular

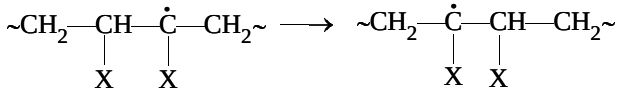

Chain termination:

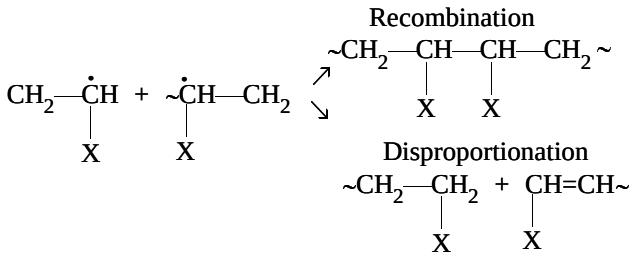

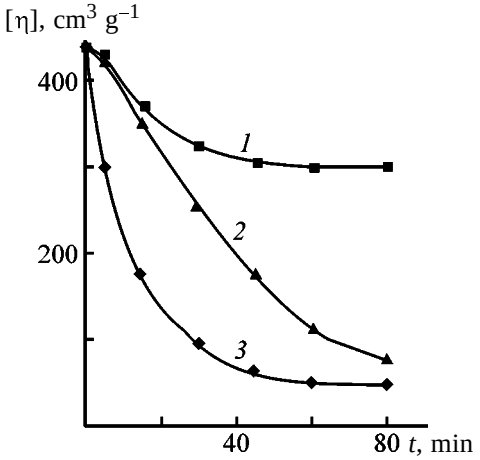

Fig. 3. Plot of [η] of cationic Praestol 655 vs. degradation time t in the presence of various degradative agents. c_p = 0.1%. Degradative agent: (*1*) HP, (*2*) PP + SB, 2 : 1 (by weight), and (*3*) PP. T, °C: (*1*, *3*) 50 and (*2*) 25.

X = $CONH_2$ or $-(CH_2)_3\overset{+}{N}(CH_3)_3Cl^-$.

This scheme is simplified and suggests that various radicals can be involved in initiation of the copolymer degradation (e.g., sulfate radical ions $SO_4^{\bullet-}$ or $HO^{\bullet}$ radicals formed by decomposition of PP in water); it does not exclude participation of these low-molecular-weight radicals in chain termination reactions.

Figure 3 shows how [η] of AA–APTMAC copolymer (Praestol 655) varies with time in the course of degradation effected by various agents: PP, HP, and PP–SB redox system. It is seen that, at 50°C, the initial rate and extent of degradation grow in going from PP to HP (curves *1*, *3*). Figure 5 also demonstrates that the PP–SB redox system ensures efficient degradation of Praestol 655 even at 25°C (curve *2*) when the components taken separately cause no degradation.

We also studied how the degradation of AA–APTMAC copolymer (Praestol 655) is influenced by the copolymer concentration, which was varied in the range 0.1–0.5% (in water). Experiments were performed in the presence of PP at 50°C (Fig. 4). Under these conditions, as seen from Fig. 4, the [η] values noticeably decrease in the course of degradation. Figure 4 also shows that the degradation becomes less intense at increased polymer concentrations. This may be due to increased viscosity of the reaction medium and hence to slower diffusion of the degradative agent and macromolecules in the reaction medium.

We also examined the influence of the MW of AA–APTMAC copolymer on the degradation efficiency. Experiments were performed with samples of Praestols 644 and 655, having similar chemical composi-

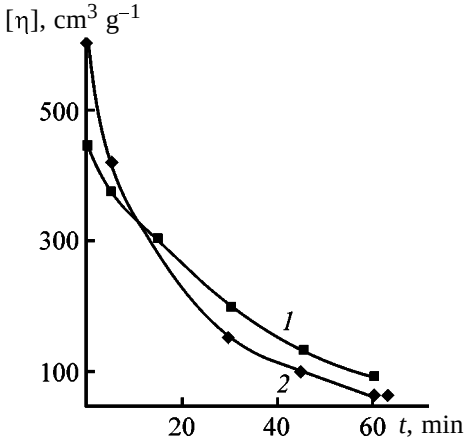

Fig. 4. Plot of [η] of cationic Praestols (*1*) 655 and (*2*) 644 vs. degradation time *t*. T = 50°C, c_p = 0.1%, [PP] = 0.04% (in water).

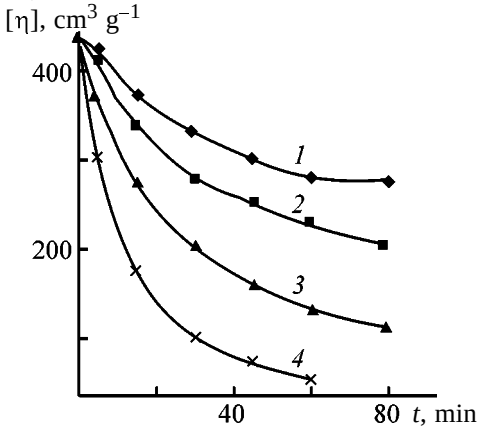

Fig. 5. Plot of [η] of cationic Praestol 655 vs. degradation time t at various concentrations of the copolymer c_p. T = 50°C, [PP] = 0.06% (in water). c_p, % (in water): (*1*) 0.5, (*2*) 0.4, (*3*) 0.3, and (*4*) 0.1.

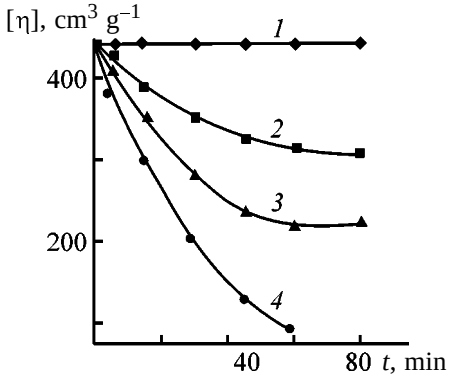

Fig. 6. Plot of [η] of cationic Praestol 655 vs. degradation time t at various temperatures. c_p = 0.1%, [PP] = 0.04% (in water). T, °C: (*1*) 25, (*2*) 30, (*3*) 40, and (*4*) 50.

tion (see table) but differing in the intrinsic viscosity. The reaction was performed under identical conditions; the results are shown in Fig. 5. It is seen that both Praestol samples appreciably degrade under the experimental conditions, with the extent of degradation (variation of [η]) being more pronounced for Praestol 644 whose initial [η] (and hence initial MW, see table) is higher. This trend is due to the fact that the number of probable scission sites is larger in longer macromolecules, which is consistent with the general relationships of the chain degradation of polymers [12]. Furthermore, in higher-molecular-weight samples, [η] should decrease to a greater extent even at the equal number of scission events.

The influence of temperature on degradation of AA–APTMAC copolymer (Praestol 655) in aqueous solutions was estimated in the range 25–50°C and equal other conditions. The results are shown in Fig. 6. At 25°C, no degradation occurs (curve *1*); at higher temperatures, the degradation accelerates (cf. curves *1–4*) owing to faster decomposition of the initiator and accumulation of radicals, causing degradation of the copolymer, in higher effective concentration. As a result, [η] and hence the MW of the copolymer appreciably decrease.

CONCLUSIONS

(1) The molecular weight of the acrylamide–(acrylamidopropyl)trimethylammonium chloride can be varied in a wide range (covering an order of magnitude) by partial degradation of the copolymer in aqueous solutions under the action of radical initiators at 25–50°C.

(2) In the course of degradation, the molecular weight of the copolymer decreases with time. This trend becomes more pronounced with increasing temperature, initiator concentration, and molecular weight of the initial copolymer, decreasing concentration of the copolymer, and in going from hydrogen peroxide to potassium persulfate.

REFERENCES

1. Berlin, A.A., Vol'fson, S.A., and Enikolopyan, N.S., *Kinetika polimerizatsionnykh protsessov* (Kinetics of Polymerization Processes), Moscow: Khimiya, 1978.
2. Myagchenkov, V.A., Kurenkov, V.F., and Akhmed'yanova, R.A., *Vysokomol. Soedin., Ser. B*, 1984, vol. 26, no. 5, pp. 340–344.
3. Kurenkov, V.F. and Tazieva, E.D., *Zh. Prikl. Khim.*, 1994, vol. 67, no. 7, pp. 1162–1166.
4. Kurenkov, V.F., Nagel', M.A., Kosterina, E.N., and Myagchenkov, V.A., in *Khimiya i tekhnologiya elementoorganicheskikh soedinenii i polimerov* (Chemistry and Technology of Organoelement Compounds

and Polymers), Kazan: Kazan. Khimiko-Tekhnol. Inst., 1984, pp. 34–38.

5. Kurenkov, V.F., Orlova, I.B., and Myagchenkov, V.A., *Vysokomol. Soedin., Ser. A*, 1986, vol. 28, no. 16, pp. 1186–1191.
6. Nakonechnyi, I.I., Baiburdov, T.A., and Kurenkov, V.F., *Zh. Prikl. Khim.*, 1991, vol. 64, no. 5, pp. 1062–1065.
7. *Rukovodstvo po khimicheskomu i tekhnologicheskomu analizu vody* (Manual on Chemical and Technological Analysis of Water), Moscow: Stroiizdat, 1973.
8. *Praktikum po khimii i fizike polimerov* (Practical Course of Polymer Chemistry and Physics), Kurenkov, V.F., Ed., Moscow: Khimiya, 1995.
9. Bresler, S.E., Dolgoplosk, B.A., Krol', V.A., *et al.*, *Zh. Obshch. Khim.*, 1956, vol. 26, no. 8, pp. 2201–2209.
10. Dolgoplosk, B.A., Erusalimskii, B.L., Kuren'gina, T.N., and Tinyakova, E.I., *Izv. Akad. Nauk SSSR, Otd. Khim. Nauk*, 1960, pp. 311–316, 2201–2209.
11. Acrus, C.L., *J. Chem. Soc.*, 1949, no. 3, pp. 2732–2736.
12. Grassie, N. and Scott, G., *Polymer Degradation and Stabilisation*, Cambridge: Cambridge Univ., 1985.

Russian Journal of Applied Chemistry, Vol. 75, No. 7, 2002, pp. 1146–1150. Translated from Zhurnal Prikladnoi Khimii, Vol. 75, No. 7, 2002, pp. 1169–1173.
Original Russian Text Copyright © 2002 by Aminova, Manuiko, Litvinenko, D'yakonov, Zolotarev, Filipova, Ignashina, Davydova, Antonova.

MACROMOLECULAR CHEMISTRY AND POLYMERIC MATERIALS

Mechanism of Butadiene Polymerization on Cobalt-Containing Catalyst

G. A. Aminova, G. V. Manuiko, G. I. Litvinenko, G. S. D'yakonov, V. L. Zolotarev, A. G. Filipova, T. V. Ignashina, V. V. Davydova, and O. V. Antonova

Kazan State Technological University, Kazan, Tatarstan, Russia

Received January 22, 2001; in final form, February 2002

Abstract—Based on experimental results and reference data, the main elementary stages of butadiene polymerization on a cobalt-containing catalyst were determined and a mathematical model of the polymerization was developed. The following characteristics of the process were studied using this model: number-average, weight-average, and sedimentation-average degrees of polymerization and branching factor.

SKDK rubber is 1,4-*cis*-polybutadiene prepared with a cobalt-containing catalyst. This rubber, along with titanium (SKD) and rare-earth (SV-22, SV-23) rubbers, is used in production of tires, industrial rubber, industrial asbestos ware, shock-resistant polystyrene, and other items.

To develop a mathematical model of SKDK synthesis, the molecular-kinetic scheme considering the main reactions in the system is required. The synthesis mechanism can be formulated, and its main elementary stages determined, on the basis of reference data and various experimental dependences [1–6], although the structure of active centers of cobalt-containing catalytic systems and their reactivity are not yet clearly understood.

Butadiene polymerization includes some stages. The first of them is initiation, when a catalytic complex with active centers is formed: in the presence of a monomer, it is a π-allyl complex of the transition metal, and in the absence of the monomer, cobalt is reduced to metal [1]:

$$R_3Al + CoCl_2 \rightarrow R_2AlCl + [RCoCl] \rightarrow R_{-H} \downarrow C_4H_6$$

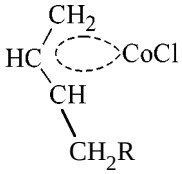

$$+ R_{+H} + Co^0 + CoCl_2.$$

The next stage is chain propagation

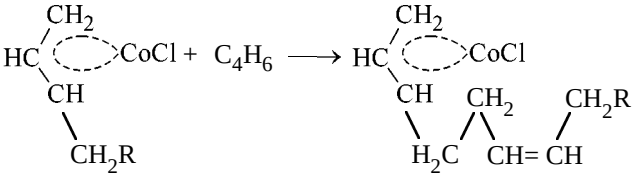

$\rightleftarrows$ $RCH_2–CH=CH–CH_2–CH_2–CH=CH–CH_2CoCl$ etc.

Either *cis* or *trans*- polymers can be formed depending on reaction conditions and composition of the catalytic system.

The chain propagation has certain specific features [1]: the reaction is first-order with respect to the concentration of the monomer and catalyst (cobalt); the overall activation energy amounts to 8.2 kcal mol^{-1}; one active center (per cobalt atom) produces a number of polymeric molecules due to chain transfer to the monomer.

Chain transfer to the monomer and polymer, spontaneous transfer, polymer cross-linking, and chain termination (deactivation) occur simultaneously with chain propagation.

It is believed [1–7] that chain transfer to the monomer consists of two successive spontaneous reactions.

(1) Decomposition of active center and formation of a hydride complex:

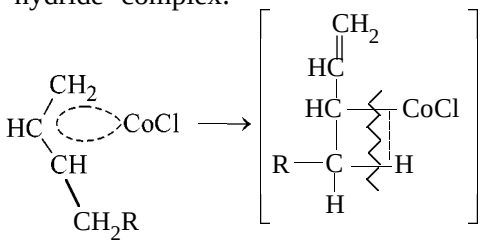

1070-4272/02/7507-1146$27.00 © 2002 MAIK "Nauka/Interperiodica"

$$\rightarrow \text{RCH=CH–CH=CH}_2 + \text{HCoX}.$$

In the process, conjugated double bonds are formed on chain ends [8]. The same bonds are formed by migration of double bonds within molecular chain.

(2) Regeneration of active center, i.e., propagation of a new polymer chain:

$$\text{HCoCl} + \text{C}_4\text{H}_6 \rightarrow \pi\text{-C}_4\text{H}_7\text{CoCl}.$$

In the process, the hydride complex can be deactivated. The same hydride complex can add to a propagating chain with formation of an additional active center, which results in chain branching. Molecules slowly cross-link by reaction of conjugated double bonds with active centers of another molecule. This gives branched polymeric species of various structures. The propagation rate grows with increasing number of active centers in the macromolecule. In turn, the number of centers increases with growth of the macromolecule [8].

In addition, appearance of branched macromolecules is the necessary but insufficient condition for gelation. It is also probable that all monomer molecules polymerize before the formation of macroscopic polymeric three-dimensional network. Gelation is caused by pronounced nonuniformity in the growth of various polymeric chains. As a result, separate strongly branched molecules can grow to macroscopic dimensions even at a low conversion. To determine the gelation conditions, it is necessary to monitor how statistical characteristics of the molecular-mass distribution (MMD) of polymeric chains vary over time. The mechanism of cross-linking of polymeric chains for the case of radical polymerization is described [8]. For anionic polymerization, a particular case of cross-linking of "living" and "dead" macromolecules was considered [9]. Let us consider additionally branching (cross-linking):

$$R(i,l) + R(j,n) \xrightarrow{k_c(in+jl)} R(i+j,\ l+n),$$

where $R(i,l)$ is the concentration of macromolecules with i active centers and l monomeric units, $R(j, n)$ is the concentration of macromolecules with j active centers and n monomeric units, and k_c is the rate constant of macromolecule cross-linking.

The double and conjugated double bonds present in diene polymers can enter into secondary reactions under the action of the components of catalytic systems and catalytic complexes themselves.

The $CoX_2 \cdot H_2O–R_2AlCl$ system contains the components $R_2AlCl–H_2O$ and $RAlCl_2–H_2O$ capable to initiate cationic polymerization. In addition to the above catalysts, hydrogen chloride can be formed in the system as a result of catalyst hydrolysis with a water impurity. For instance, high-molecular-weight *cis*-polybutadiene is comparatively rapidly converted into a gel under the action of $RAlCl_2 \cdot H_2O$. The contribution of the intermolecular reaction will strongly increase with increasing polymer concentration. Organometallic complexes can react with both conjugated and olefin bonds of the polymeric chains.

Taking the above into consideration, we can suggest the following kinetic scheme of polymerization on the cobalt-containing catalyst:

initiation

$$I + M \xrightarrow{k_i} R(1,1);$$

chain propagation

$$R(i,l) + M \xrightarrow{k_p} R(i, l+1);$$

spontaneous chain transfer (in two stages)

(a) transfer proper

$$R(i,l) \xrightarrow{k_{sp}} R(i-1,\ l) + S^*,$$

(b) reinitiation

$$S^* + M \xrightarrow{k_{ri}} R(1,1);$$

chain transfer to monomer

$$R(i,\ l) + M \xrightarrow{k_{tm}} R(i-1,\ l) + R(1,1);$$

chain transfer to polymer

$$R(i,\ l) + R(i',\ l') \begin{cases} \xrightarrow{k_{tp}i'l} R(i+1,\ l) + R(i'-1,\ l'), \\ \xrightarrow{k_{tp}il'} R(i-1,\ l) + R(i'+1,\ l'); \end{cases}$$

polymer cross-linking

$$R(i,l) + R(i',l') \xrightarrow{k_c(il'+i'l)} R(i+i',\ l+l');$$

chain termination

$$R(i,\ l) \xrightarrow{k_t} R(i-1,\ l),$$

where I is the initiator concentration; M, the monomer concentration; S^*, the concentration of the intermediate generated by transfer (probably HCoX); $R(i, l)$, the concentration of macromolecules with i active centers and l monomeric links; k_p, the propagation rate constant; k_i, the initiation rate constant; k_{tm}, the rate constant of chain transfer to monomer; k_{sp}, the rate constant of spontaneous chain transfer; k_{tp}, the rate constant of chain transfer to polymer; k_{ri}, the rate constant of reinitiation; and k_c, the rate constant of macromolecule cross-linking.

The rate of macromolecule cross-linking is proportional to $k_c(in + jl)$, e.g., it depends on the number of the active centers in the reacting molecules and on their length.

In accordance with the kinetic scheme, the system of the equations describing the variation in time of the concentrations of monomer M, active centers R, and propagating chains for a batch process is as follows:

$$dM/dt = -k_p MR, \quad (1)$$

at $t = 0$ $M = M_0$, $R(1, 1) = I_0$, $R(0, 0) = 0$;

$$dR/dt = -k_t R; \quad (2)$$

$$\partial R(i, l)/\partial t = -ik_p M[\partial R(i, l)/\partial l] + [k_{sp} + (k_{tm}M + k_t)][(i + 1)R(i + 1, l) - iR(i, l)] + k_c/2 \sum_{i=0}^{i} \int_0^l [j(l - n) + n(i - j)]R(j, n)R(i - j, l - n)dn - k_c R(i, l) \sum_{i=0}^{\infty} \int_0^{\infty} (in + jl)R(j, n)dn + k_{tp} \sum_{i=0}^{\infty} lj \int_0^{\infty} R(j, n)dn[R(i - 1, l) - R(i, l)] + k_{tp} \sum_{i=0}^{\infty} \int_0^{\infty} nR(j, n)dn[(i + 1)R(i + 1, l) - iR(i, l)] + (k_{sp} + k_{tm}M) I_0 \delta_{i,1} \delta(l), \quad i = 0, 2, \ldots, 0 \le l \le \infty. \quad (3)$$

At $i = 0$ $R(i - 1, l) = 0$.

It is assumed that the initiation and reinitiation proceed instantaneously. Since k_{tm}/k and k_{sp}/k are always much less than unity, the monomer consumption in chain transfer and reinitiation [Eq. (1)] can be neglected. In Eq. (3), the first term of the right-hand part describes the variation of $R(i, l)$ due to propagation; the next five terms describe the variation of $R(i, l)$ due to chain transfer, cross-linking, and termination; and the last term describes the appearance of new short propagating chains at reinitiation.

Equation (3) is wrote for the case of long chains. Equation (2) describes the decay rate of active centers $R = \sum_{i,l}^{\infty} R(i, l)$. It is readily integrated. Using the initial condition, we obtain

$$R = I_0 \exp(-k_t t). \quad (4)$$

After substitution of Eq. (4) in (1), we find the time dependence of monomer conversion $x = (M_0 - M)M_0$:

$$-\ln(1 - x) = \frac{k_p I_0}{k_t}(1 - e^{-k_t t}). \quad (5)$$

In accordance with Eq. (5), at first-order termination the monomer does not transform into the polymer completely. The limiting conversion is

$$x_\infty = 1 - \exp(-k_p I_0/k_t).$$

Thus, if the polymerization kinetics is known, we can determine the propagation rate constant from the initial slope of the first-order dependence of $-\ln(1 - x)$ on time and the termination rate constant from the limiting conversion. It should be noted, however, that, along with deactivation of the active centers by β-elimination, a substantial role can be played by termination on uncontrollable impurities. When there is no deactivation in the system ($k_t = 0$), the number of active centers in the system is constant throughout the process ($R = I_0 e^0 = I_0$). Then, it follows from Eq. (1) that

$$dM/dt = -k_p M I_0,$$

and the equation

$$x = 1 - e^{-k_p I_0 t} \quad (6)$$

is obtained for conversion.

According to preliminary data obtained in the experiments with thoroughly prepared systems, the limiting conversion was close to 100%, although in the other experiments at the same concentrations of cobalt and water the polymerization fully ceased at 50% conversion, which suggests the effect of impurities rather than spontaneous deactivation. Therefore, in this step, when the reliable experimental data are lacking, we will neglect the deactivation reaction

and analyze how chain transfer and cross-linking of macromolecules affect MMD. It follows from the conversion equation that

$$\frac{\partial}{\partial t} = k_p I_0(1 - x)\frac{\partial}{\partial x}, \qquad M = M_0(1 - x).$$

Then, Eqs. (3) can be presented as

$$\partial R(i, l)/\partial x = i\beta[\partial R(i, l)/\partial l] + [\gamma_{sp}/(1 + x) + \gamma_m][(i + 1) \times R(i + 1, l) - iR(i, l)] + [\gamma_{sp}/(1 + x) + \gamma_m] I_0 \delta_{i,1}\delta(l) + 0.5\gamma_c(1 - x)^{-1}\sum_{i=0}^{i}\int_0^l [j(l - n) + n(i - j)]R(j, n) \times R(i - j, l - n)dn + \gamma_c(1 - x)^{-1}[i R(i, l) M_0 x + lR(i, l)I_0] - \gamma_p l[\beta(1 - x)]^{-1}[R(i - 1, l) - R(i, l)] + \gamma_p x(1 - x)^{-1} \times [(i + 1)R(i + 1, l) - iR(i, l)], \quad i = 0, 2, \ldots, \quad (7)$$

where $\beta = M_0/I_0$ is the calculated degree of polymerization, and the parameters $\gamma_m = k_{tm}M_0/k_pI_0$, $\gamma_p = k_{tp}M_0/k_pI_0$, $\gamma_{sp} = k_{sp}/k_pI_0$, and $\gamma_c = k_c/k_pI_0$ characterize the rate of chain transfer to the monomer and polymer, the rate of spontaneous transfer, and the rate of macromolecule cross-linking, respectively.

The system of Eqs. (7) can be combined in one equation by the function $f = \sum_{i=0}^{\infty} s^i \int_0^{\infty} e^{-pl} R(i, l)dl$, which is usually named as producing function:

$$\partial f/\partial x = -\beta sp\,\partial f/\partial x + [\gamma_{sp}/(1 - x) + \gamma_m](s - 1)\partial f/\partial x + [\gamma_{sp}/(1 + x) + \gamma_m]I_0 s - \tilde{\gamma}_c s[(1 - x)\beta I_0]^{-1}(\partial f/\partial s)(\partial f/\partial p) - \tilde{\gamma}_c(1 - x)^{-1}[(xs\partial f/\partial s) - \beta^{-1}(\partial f/\partial p)] + \tilde{\gamma}_p(s - 1)(1 - x)^{-1} \times [\beta^{-1}(\partial f/\partial p) + x(\partial f/\partial s)], \quad (8)$$

where γ_{sp} is the intensity of spontaneous transfer, γ_p is the intensity of chain transfer to polymer, and $\gamma_c = \gamma_c M_0$ is the intensity of cross-linking.

After differentiating Eq. (8) the required number of times with respect to s and p, we obtain the equations for calculating statistical moments of macromolecule distribution with respect to the degree of polymerization l and the number of active centers i. Let us introduce the following designations: $J_{ij} = \left.\frac{\partial^{i+j} f}{\partial s^4 i \partial p^j}\right|_{\substack{s=1,\\ p=0}}$; by definition of MMD moments, $J_{00} = \left. f \right|_{\substack{s=1,\\ p=0}} = \mu_0$ is the total concentration (number) of polymeric chains at the instant t; $J_{10} = \left.\partial f/\partial s\right|_{\substack{s=1,\\ p=0}} = I_0$ is the total concentration (number) of active centers at the instant t; $J_{01} = \left.\partial f/\partial p\right|_{\substack{s=1,\\ p=0}} = -\mu_1 = -M_0 x$ is the concentration of the polymer formed to the instant t (with the opposite sign); and $J_{02} = \left.\partial^2 f/\partial p^2\right|_{\substack{s=1,\\ p=0}} = \mu_2$ and $J_{03} = \left.\partial^3 f/\partial p^3\right|_{\substack{s=1,\\ p=0}} = -\mu_3$ are second- and third-order moments. The system of equations for calculating MMD is as follows:

$$d\mu_0/dx = I_0[\gamma_{sp}/(1 + x) + \gamma_m] - I_0\mu_1[\gamma_c/(1 - x)],$$

$$\mu_1 = M_0 x,$$

$$d\mu_2/dx = -2\beta J_{11} - 2\gamma_c\mu_2 J_{11}/(1 - x),$$

$$dJ_{11}/dx = -\beta I_0 - \beta J_{20} - J_{11}[\gamma_{sp}/(1 - x) + \gamma_m] - [\gamma_c(I_0\mu_2 + J_{11}^2 + J_{20}\mu_2)/(1 - x)] - [\gamma_p(\mu_2\beta^{-1} + xJ_{11})]/(1 - x),$$

$$dJ_{20}/dx = -2J_{20}[\gamma_{sp}/(1 - x) + \gamma_m] - [2\gamma_c(I_0 J_{11} + J_{20}J_{11})/(1 - x)] - [2\gamma_p(J_{11}\beta^{-1} + xJ_{20})/(1 - x)],$$

$$d\mu_2/dx = -3\beta J_{12} - [\gamma_c(3J_{12}\mu_2 - 3J_{11}\mu_3)/(1 - x)],$$

$$dJ_{12}/dx = -2\beta(J_{11} + J_{21}) - J_{12}[\gamma_{sp}/(1 - x) + \gamma_m] - [\gamma_c(2J_{11}\mu_2 - I_0\mu_3)/(1 - x)] - [\gamma_c(2J_{21}\mu_2 + 3J_{11}J_{12} - I_{20}\mu_3)/(1 - x)] - [\gamma_p(\mu_3\beta^{-1} + xJ_{12})]/(1 - x),$$

$$dJ_{30}/dx = -3J_{30}[\gamma_{sp}/(1 - x) + \gamma_m] - [\gamma_c(2J_0 J_{11} + 3J_0 J_{21} + 3J_{30}J_{11} + 3J_{20}J_{21})/(1 - x)] - [3\gamma_p(J_{21}\beta^{-1} + xJ_{30})]/(1 - x).$$

$$dJ_{21}/dx = -2J_{20} - J_{30} - 2J_{21}[\gamma_{sp}/(1 + x) + \gamma_m] - [\gamma_c(6J_{20}\mu_2 + 2I_{12}I_0 + 2J_{30}\mu_2 + 2J_{11} + 3I_{21}J_{11} + 2J_{20}J_{12})/(1 - x)] - [2\gamma_p(J_{12}\beta^{-1} + xJ_{21})]/(1 - x),$$

Initial conditions: $\mu_0 = I_0$ ant $x = 0$, $\mu_1 = \mu_2 = \mu_3 = J_{11} = J_{12} = J_{10} = J_{21} = J_{20} = 0$, $\bar{P}_n = \mu_1/\mu_0$, $\bar{P}_w = \mu_2/\mu_1$, and $\bar{P}_z = \mu_3/\mu_2$.

The results of calculations by the mathematical model proposed are shown in Figs. 1–3.

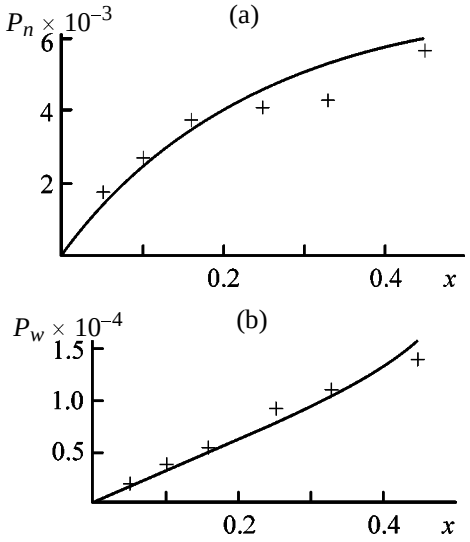

Fig. 1. Comparison of experimental data (points) and calculated curve of (a) number-average, P_n, and (b) weight-average, P_w, degrees of polymerization. k_{sp} = 0.048, k_c = 0.016, k_{tm} = 0, k_p = 297.2, k_{tp} = 0.032, and I_0 = 0.00006; M_0 = 1.85; the same for Figs. 2 and 3. (*x*) Monomer conversion; the same for Figs. 2 and 3.

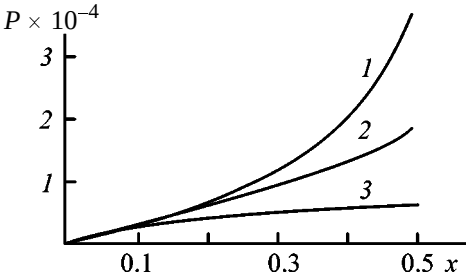

Fig. 2. Comparison of (*1*) sedimentation-average, P_z, (*2*) weight-average, P_w, and (*3*) number-average, P_n, degrees of polymerization.

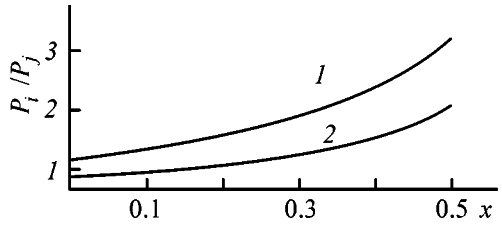

Fig. 3. Polydispersity coefficients (*1*) P_w/P_n and (*2*) P_z/P_w.

The deviation of the calculated data from the experiment amounted to 18.6%, which confirms the proposed mechanism of butadiene polymerization on the cobalt catalyst. The comparison with the experiment showed that the best fitting is attained with k_m = 0, suggesting small contribution of the transfer to the monomer. Probably, spontaneous transfer is sufficient to form conjugated double bonds. In addition, the difference between the chain transfer to the monomer and the spontaneous transfer is manifested only at monomer conversion greater than 30–40%.

Consideration of branching reactions (transfer to polymer and cross-linking) improves agreement between the calculated and experimental data. Figure 3 shows how branching varies with conversion. The polydispersity factor P_w/P_n changes from 1.3 to 3.2, and P_z/P_w, from 0.8 to 2.1, which indicates strong branching at monomer conversion higher than 40%.

CONCLUSIONS

(1) Based on reference and experimental data, the kinetic scheme and mathematical model of SKDK rubber polymerization were developed. The importance of branching reactions, chain transfer to polymer, and cross-linking of macromolecules was demonstrated. Modeling was performed for the case of cross-linking of the "living with living" type.

(2) The model proposed can be used to improve the butadiene polymerization process and optimize properties of SKDK rubber.

REFERENCES

1. Dolgoplosk, B.A. and Tinyakova, E.I., *Metalloorganicheskii kataliz v protsessakh polimerizatsii* (Organometallic Catalysis in Polymerization), Moscow: Nauka, 1958.
2. Korneev, N.N., Popov, A.F., and Krentsel', B.A., *Kompleksnye metalloorganicheskie katalizatory* (Complex Organometallic Catalysts), Leningrad: Khimiya, 1969.
3. Korneev, N.N., *Khimiya i tekhnologiya alyuminiiorganicheskikh soedinenii* (Chemistry and Technology of Organoaluminum Compounds), Moscow: Khimiya, 1979.
4. Coates, G.E., Green, M.L.H., and Wade, K., *Organometallic Compounds*, vol. 2: *The Transition Elements*, London: Methuen, 1969.
5. Krivoshein, V.V., Konovalenko, N.A., Tikhomirova, I.N., *et al.*, *Tsis-1,4-polibutadien "kobal'tovoi" polimerizatsii dlya promyshlennykh plastmass (cis*-1,4-Polybutadiene of "Cobalt" Polymerization for Industrial Plastics), Moscow: TsNIITEneftekhim, 1991.
6. *The Stereo Rubbers*, Saltman, W.M., Ed., New York: Academic, 1950, vol. 1.
7. Smirnova, L.V., Tikhomirov, I.N., Kropacheva, E.N., and Zolotarev, V.L., *Vysokomol. Soedin.*, 1996, vol. 38, no. 6, pp. 458–467.
8. Kuchanov, S.I., *Metody kineticheskikh raschetov v khimii polimerov* (Methods of Kinetic Calculations in Polymer Chemistry), Moscow: Nauka, 1978.
9. Honig, A.J., Cloor, P.E., MacCredon, J.F., and Hamieles, A.E., *J. Appl. Polym. Sci.*, 1987, vol. 3, no. 24, pp. 829–841.

Russian Journal of Applied Chemistry, Vol. 75, No. 7, 2002, pp. 1151–1156. Translated from Zhurnal Prikladnoi Khimii, Vol. 75, No. 7, 2002, pp. 1174–1179.
Original Russian Text Copyright © 2002 by Ragimli, Demir, Bektashi, Bairamov.

MACROMOLECULAR CHEMISTRY AND POLYMERIC MATERIALS

Synthesis and Properties of Oligo(*p*-tolyliminomethyl)phenol

A. V. Ragimli, O. Demir, N. R. Bektashi, and G. K. Bairamov

Institute of Polymeric Materials, National Academy of Sciences of Azerbaijan, Sumgait, Azerbaijan

Received June 19, 2001; in final form, March 2002

Abstract—The conditions and products of oxidative polycondensation of 2-(*p*-tolyliminomethyl)phenol in alkaline aqueous solution in the presence of sodium hypochlorite or atmospheric oxygen were studied. The optimal conditions were found, and procedures for preparing oligo(*p*-tolyliminomethyl)phenols were developed. The composition and structure of the products were determined by chemical and spectroscopic methods.

Thanks to the presence of a system of polyconjugated bonds and of reactive hydroxy groups, oligophenols exhibit a number of specific useful properties: paramagnetism, semiconductor behavior, resistance to radiation, plasma, and high temperatures, reactivity, inhibiting activity, etc. Therefore, they are successfully used for preparing heat-resistant epoxy oligomers and compounds [1, 2], adhesives [3], thermal stabilizing agents [4], plasma-resistant photoresists [5], and antistatic additives [6]. Introduction into oligophenols of additional ionic groups allows preparation of radiation-resistant cation exchangers [7] and high-performance expanding surfactants [8] for pretreatment of lead electrodes.

In this context, we prepared and studied a new oligophenol, oligo(*p*-tolyliminomethyl)phenol, containing a system of conjugated bonds. The structural features of this substance and the presence of two reactive functional groups may make this oligomer suitable not only for the above-mentioned applications, but also for preparation of metal–polymer chain complexes [9], analytical [10, 11] and environmental [12] chemistry, and treatment of industrial wastewater to remove toxic heavy metals [13]. Owing to the presence of radiation-resistant polyconjugated bonds and of active functional groups, oligo(*p*-tolyliminomethyl)phenol can also be used for recovery of radionuclides [14].

The desired product was prepared by oxidative polycondensation of 2-(*p*-tolyliminomethyl)phenol (TIMP) in alkaline aqueous solution in the presence of sodium hypochlorite or atmospheric oxygen, and the properties of the resulting oligomer, OTIMP, were studied.

Under ambient conditions in neutral organic and aqueous solutions, TIMP is not noticeably oxidized with atmospheric oxygen, NaOCl, and H_2O_2. However, addition of an alkali immediately causes red-brown coloration, suggesting oxidation of TIMP to the corresponding phenoxyl radical.

The reaction of 0.8 M of TIMP potassium salt with an equivalent amount of NaOCl in aqueous solution at 50°C for 6 h gives oligomeric products in 42.8% yield (Table 1). With increasing temperature, the conversion of TIMP grows to 47.6% at 60°C, 53.9% at 70°C, 73.1% at 80°C, and 85.0% at 90°C. However, under these conditions, the yield of fractions 2 and 3 (2.8–7.2%) is considerably lower than the yield of fraction 1 (36.9–73.3%). Addition of a double amount of the oxidant under similar conditions results in 97.9% conversion of the monomer, with 25.3% yield of OTIMP-2. At 80°C, $[TIMP]_0 = [KOH]_0 = 0.8$ M, $[NaOCl]_0 = 1.6$ M, and longer (13 h) reaction time, the total yield of reaction products increased to 98.7%, and the yield of OTIMP-2, to 27.9%. In any case, the yield of OTIMP-3 is the lowest (2.8–8.2%). The highest yield of OTIMP-2 (29.3%) is attained with air bubbling (8.5 l h^{-1}, run no. 9).

Replacement of NaOCl with atmospheric oxygen, under equal other conditions, somewhat decreases the TIMP conversion. For example, at 50°C, with air bubbling at a rate of 8.5 l h^{-1}, the conversion in 7 h is 26.9% (with NaOCl, 42.8% in 6 h). At 80°C, the monomer conversion in 17 h is 90.5%, whereas in the presence of NaOCl it reaches 97.9% in 6 h (Table 2).

Oxidative polycondensation of OTIMP-1 with atmospheric oxygen at 80°C for 7 h in alkaline aqueous solution yields 35.1% OTIMP-2 and 19.8% OTIMP-3.

OTIMP-1 is a light brown solid (mp 81°C) solu-

1070-4272/02/7507-1151$27.00 © 2002 MAIK "Nauka/Interperiodica"

Table 1. Oxidative polycondensation of TIMP with sodium hypochlorite in alkaline aqueous solution ($[TIMP]_0$ = $[KOH]_0$ = 0.8 M)

Run no.	$[NaOCl]_0$, M	*T*, °C	τ, h	Total yield, %	Yield of fractions, %		
					OTIMP-1	OTIMP-2	OTIMP-3
1	0.8	50	6	42.8	36.3	3.7	2.8
2	0.8	60	6	47.6	40.1	4.1	3.4
3	0.8	70	6	53.9	45.8	4.4	3.7
4	0.8	80	6	73.1	64.3	4.9	3.9
5	0.8	90	6	85.0	73.3	7.2	4.5
6	1.6	80	6	97.9	66.4	25.3	6.2
7	1.6	80	13	98.7	63.7	27.9	7.1
8	1.6	80	16	97.5	63.8	25.5	8.2
9*	1.6	70	10	78.6	42.2	29.3	7.1
10**	1.6	80	6	57.0	–	42.2	14.8

* Air was bubbled at a rate of 8.6 l h^{-1}.
** OTIMP-1 was taken instead of the monomer.

Table 2. Oxidative polycondensation of TIMP with atmospheric oxygen in alkaline aqueous solution ($[TIMP]_0$ = 0.8 M)

Run no.	$[KOH]_0$, M	V_{air}, l h^{-1}	*T*, °C	τ, h	Total yield, %	Yield of fractions, %		
						OTIMP-1	OTIMP-2	OTIMP-3
1	1.6	8.5	50	7	26.9	21.9	4.2	0.8
2	1.6	8.5	60	7	34.6	26.5	6.6	1.5
3	1.6	8.5	70	7	36.7	28.0	7.1	1.6
4	1.6	8.5	80	7	42.4	32.9	7.6	1.9
5	1.6	8.5	90	7	55.7	44.7	6.7	4.3
6	1.6	8.5	80	5	37.6	30.6	5.4	1.6
7	1.6	8.5	80	12	62.3	47.8	8.9	5.6
8	1.6	8.5	80	17	90.5	65.6	17.6	7.3
9	0.8	8.5	80	7	34.1	27.6	5.3	1.2
10	1.6	6.5	80	7	38.1	30.2	6.8	1.1
11	1.6	1.5	80	7	49.8	36.4	10.9	2.5
12*	1.6	8.5	80	7	54.8	–	35.1	19.8

* OTIMP-1 was taken instead of the monomer.

ble in hot heptane, in chlorinated, aromatic, and polar organic solvents, and also in aqueous alkali and H_2SO_4. OTIMP-2 is a dark brown solid; it does not melt up to 220°C but is soluble in DMF, concentrated H_2SO_4, and aqueous alkali and partially soluble in THF, acetone, and dioxane. OTIMP-3 is a black or dark brown nonmelting solid soluble only in aqueous alkali, concentrated H_2SO_4, and partially in DMSO. Heating of OTIMP-3 in aqueous sodium carbonate solution results in CO_2 evolution, suggesting the presence of acidic groups. Determination of the molecular weight (MW) and molecular-weight distribution (MWD) of TIMP oxidative polycondensation products showed that OTIMP-1 consists of di- and trimers (Fig. 1, Table 3); OTIMP-2, of oligomers with the number-average MW $\overline{M}_n$ = 690–1320 and weight-average MW $\overline{M}_w$ = 1580–1860. The MWD of this fraction has two maxima: the first at $\overline{M}_n$ = 615–620 and $\overline{M}_w$ = 650–760, and the second, weaker peak, at $\overline{M}_n$ = 6610–6780 and $\overline{M}_w$ = 7640–7660. The amounts of the low- and high-molecular-weight fractions are 80–90 and 10–20%, respectively. The MW and MWD of OTIMP-3 are similar to those of OTIMP-2, except that the content of the high-molecular-weight fraction in OTIMP-3 prepared in the presence of NaOCl is higher (26%) than in OTIMP-2 (18%), and the polydispersity of this OTIMP-3 sample is high (3.26).

Table 3. Molecular-weight distribution of products obtained by oxidative polycondensation of TIMP with atmospheric oxygen (run nos. 1–3) and NaOCl (run nos. 4–6)

Run no.	Oligomer	Low-molecular-weight fraction				High-molecular-weight fraction				Overall parameters		
		$\overline{M}_n$	$\overline{M}_w$	$\overline{M}_n/\overline{M}_w$	yield, %	$\overline{M}_n$	$\overline{M}_w$	$\overline{M}_n/\overline{M}_w$	yield, %	$\overline{M}_n$	$\overline{M}_w$	$\overline{M}_n/\overline{M}_w$
1	OTIMP-1	600	650	1.08	100	–	–	–	–	600	650	1.08
2	OTIMP-2	615	760	1.23	82	6610	7640	1.15	18	690	1580	2.29
3	OTIMP-3	590	670	1.13	81	5600	6850	1.22	19	625	1850	2.96
4	OTIMP-1	630	770	1.22	100	–	–	–	–	630	770	1.22
5	OTIMP-2	620	650	1.05	82	6780	7660	1.13	18	1320	1860	1.41
6	OTIMP-3	560	690	1.23	74	5820	7180	1.24	26	750	2440	3.26

The elemental compositions of OTIMP-1 (C 79.49%, N 6.27%) and OTIMP-2 (C 78.13%, N 6.38%) are similar and close to the calculated elemental composition of TIMP (C 80.38%, N 6.69%). This means that the oxidative polycondensation leaves the monomer core intact. The IR spectra of the monomer (Fig. 2) and OTIMP-1 are similar, differing only in the band intensities. Both spectra contain broad absorption bands of OH groups at 3450 and 3427 cm^{-1}, aromatic C–H groups, and aliphatic C–H groups at 2920 and 2865 cm^{-1}. The azomethine groups absorb at 1618–1620 cm^{-1}, and benzene rings give strong bands at 1598, 1568, 1510, and 1496 cm^{-1}. The C–N and C–O stretching vibrations are observed at 1278–1282 and 1182–1184 cm^{-1}, respectively. The bending vibrations of the aromatic C–H groups of TIMP and OTIMP-1 are observed at 850 (weak), 817 (strong), and 758 cm^{-1} (strong). The band at 817 cm^{-1} is due to vicinal C–H bonds in the toluene ring; that at 850 cm^{-1}, to the vicinal C–H bonds in the phenol ring; and that at 758 cm^{-1}, to three adjacent C–H bonds in OTIMP-1 terminal units. Note that the IR spectra of OTIMP-1 samples prepared in the presence of NaOCl and O_2 differ insignificantly. Therefore, the main pathway of TIMP oxidative polycondensation does not depend on the kind of the oxidant.

In the IR spectra of OTIMP-2 and OTIMP-3, some absorption bands overlap owing to the bond conjugation (Fig. 2). Nevertheless, in the range 3200–3600 cm^{-1} we identified the majority of bands characteristic of stretching vibrations of polymer-associated OH groups in OTIMP-2 (maximum at 3387 cm^{-1}). The stretching vibrations of aromatic, azomethine, and methyl C–H bonds give rise to bands at 3033, 2862, and 2920 cm^{-1}, respectively. A number of strong bands are observed at 1618 (azomethine groups),

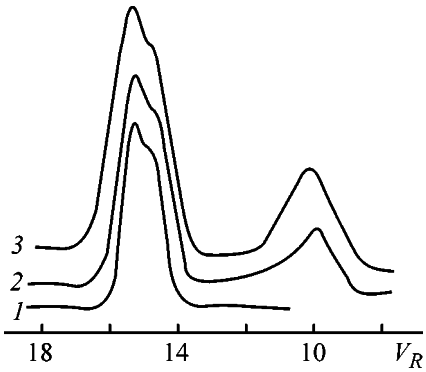

Fig. 1. Molecular-weight distribution of TIMP oxidative polycondensation products. (V_R) Retention volume. (*1*) OTIMP-1, (*2*) OTIMP-2, and (*3*) OTIMP-3.

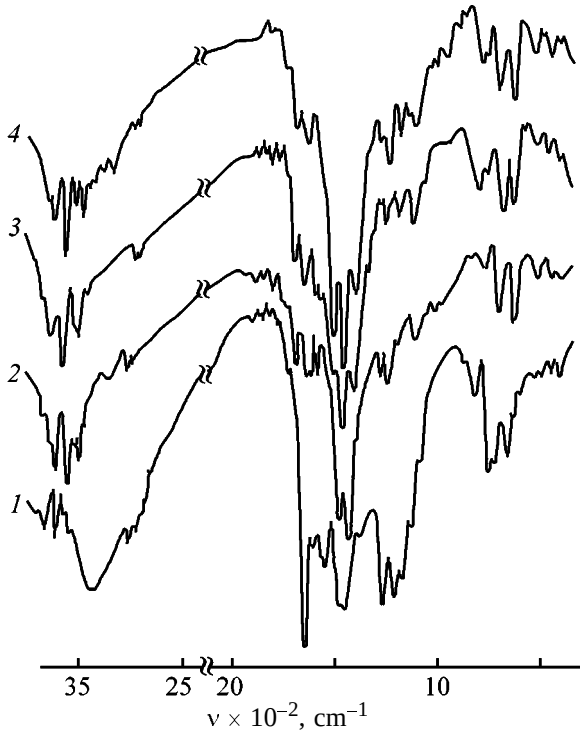

Fig. 2. IR spectra of TIMP and its oxidative polycondensation products. (ν) Wave number. (*1*) TIMP, (*2*) OTIMP-1, (*3*) OTIMP-2, and (*4*) OTIMP-3.

Table 4. ^{1}H NMR spectra of TIMP oxidative polycondensation products

Protons	δ, ppm		
	OTIMP-1	OTIMP-2	OTIMP-3
OH	13.0–13.3 s (1H)	13.1–13.2 s (1H)	13.1–13.3 s (1H)
CH=N	8.8–9.1 s (1H)	8.9–9.1 s (1H)	8.7–8.8 s (1H)
Ar–H	6.9–7.7 m (5H)	6.9–7.7 m (5H)	6.8–7.7 m (5H)
CH_3	2.0–2.6 s (3H)	2.0–2.6 s (3H)	2.0–2.4 s (3H)

1600, 1575, 1512, and 1456 cm^{-1} (aromatic rings and C=C bonds). The C–N and C–O vibrations in OTIMP-2 give rise to bands at 1379 and 1220 cm^{-1}. In the IR spectrum of OTIMP-2, the absorption bands of three (756 cm^{-1}) and two (818 cm^{-1}) adjacent aromatic C–H bonds belong, apparently, to the terminal units and *p*-tolyl saubstituents; a weak band at 857 cm^{-1} is probably due to structural fragments of the oligomer.

In the spectrum of OTIMP-3, as compared to OTIMP-2, the OH absorption bands are stronger and broader, and additional bands appear, originating from vibrations of aldehyde (1653 cm^{-1}) and carboxy (1682–1702 cm^{-1}) groups. These groups are apparently formed in the water-soluble fraction of the oligomer by partial hydrolysis and oxidation of the azomethine groups during the synthesis.

The ^{1}H NMR spectra confirm the structural data derived from the IR spectra. As seen from Table 4, the ^{1}H NMR spectra contain a singlet at 8.7–9.1 ppm belonging to the CH=N proton, a signal of the phenolic OH proton at 13.0–13.3 ppm, singlets of CH_3 protons at 2.0–2.6 ppm, and multiplets of aromatic protons at 6.8–7.7 ppm. The ^{1}H NMR spectrum of OTIMP-3 also contains CHO and COOH proton signals at 12.6 ppm.

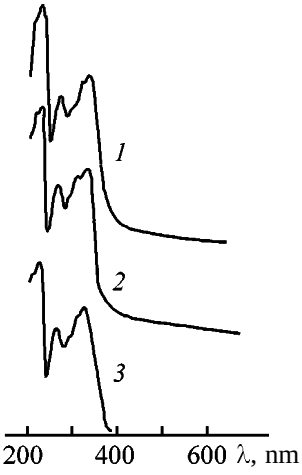

Fig. 3. UV spectra of TIMP and its oxidative polycondensation products. (λ) Wavelength. (*1*) TIMP, (*2*) OTIMP-1, and (*3*) OTIMP-2.

The IR and electronic absorption spectra of TIMP and OTIMP-1 are very similar (Fig. 3). The UV spectrum of the monomer contains the *K* band of phenol rings at 209 nm and a band of the $–C_6H_4N=$ group at 227 nm; in the spectrum of OTIMP-1, these bands coalesce, and an absorption appears at 225 nm. The benzene ring in both substances absorbs at 270 nm. The *R* band, which can be assigned to azomethine groups, is observed at 341 nm. The monomer is fully transparent at $\lambda > 360$ nm, whereas the absorption tail of the di- and trimers extends to 600 nm. Also, the absorption spectrum of OTIMP-1 is noticeably more intense than that of TIMP. This may be due to the longer conjugation system in OTIMP-1.

In the spectra of OTIMP-2 and OTIMP-3, which are very similar, the *K* band is observed at 225–227 nm. Strong bands with peaks at 320 (OTIMP-2) and 307 nm (OTIMP-3) start at 284 nm and extend to 900 nm. These bands are apparently due to interaction of the electronic systems of pendant CH=N groups with the polyconjugated system of the oligophenol macromolecules. Such interaction is also responsible for the brown or black color of these samples.

Thus, our data on the composition, structure, and chemical properties of TIMP oligomers, in combination with published data on the mechanism and products of oxidative polycondensation of hydroaromatic compounds [15–17], suggest that oligophenols prepared by oxidative polycondensation of TIMP mainly consist of the following units:

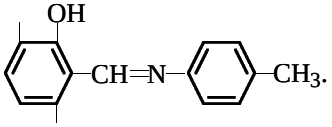

with fraction 3 also containing salicylaldehyde and salicylic acid fragments.

Oligo(*p*-tolyliminomethyl)phenols react under ambient conditions with acetates of some metals (Zn^{2+}, Co^{2+}, Ni^{2+}, Cu^{2+}, Pb^{2+}) to form partially soluble metal–polymer complexes.

The TGA data (Table 5) show that oxidative degradation of OTIMP-2 and OTIMP-3 starts at 130–134°C, with 5 and 50% weight loss occurring at 200–239 and 639–757°C, respectively. Owing to the presence of the polyconjugated systems, the oligomers are considerably more heat-resistant than TIMP. Thermal oxidative degradation of oligo(*p*-tolyliminomethyl)-phenols is a multistage process. This may be due to formation at elevated temperatures of stable macromolecular networks by recombination of phenoxy macroradicals. This suggestion is consistent with formation of a coke residue at high temperatures.

Because of the low stability of COOH groups, OTIMP-3 is less heat-resistant than OTIMP-2. Nevertheless, even this oligomer forms at 1120°C a coke residue (15.9%). In contrast to monomeric TIMP, whose antimicrobial activity is weak, its oligomers, especially their phenolates and onium salts, actively inhibit the growth of 13 test microcultures.

Thus, TIMP reacts with atmospheric oxygen or sodium hypochlorite in alkaline aqueous solutions to form di-, tri-, and oligomers with $\overline{M}_n$ = 615–690 and $\overline{M}_w$ = 650–1860. At equimolar ratios of the reactants, the TIMP conversion at 50–90°C in 6 h is 42.8–85.0%. Increased amount of the oxidant and longer reaction time ensure virtually complete conversion of the monomer. Despite relatively low activity of atmospheric oxygen, compared to NaOCl, in oxidative polycondensation of TIMP, under optimal parameters it also ensures almost complete (90.5%) conversion of the monomer.

The products of TIMP oxidative polycondensation with both oxidants contain (*p*-tolyliminomethyl)-phenol units linked via *o*- and *m*-positions of the phenol ring. A certain fraction of the oligomers also contains minor amounts of CHO and COOH groups originating from partial oxidation and hydrolysis of the azomethine groups.

Oligo(*p*-tolyliminomethyl)phenols show fairly high resistance to thermal oxidation. They decompose by half at 488–757°C and form up to 15.9% coke residue at 1120°C.

The synthesized oligophenols actively react with Zn^{2+}, Co^{2+}, Ni^{2+}, Cu^{2+}, and Pb^{2+} acetates to form partially soluble metal–polymer complexes. Oligo(*p*-tolyliminomethyl)phenols, especially their alcoholates and onium salts, actively inhibit the growth of 13 test microcultures.

Table 5. Parameters of thermal oxidative degradation of TIMP and oligomerization products*

Substance	T_{on}	$T_{5\%}$	$T_{50\%}$	Coke residue, %
	°C			
TIMP	184	243	306	0.3
OTIMP-2	130	239	757	2.9
OTIMP-3	134	200	639	15.9

* (T_{on}) Degradation onset temperature; ($T_{5\%}$, $T_{50\%}$) temperatures of 5 and 50% weight loss, respectively.

EXPERIMENTAL

In experiments and analyses, we used salicylaldehyde, toluidine, KOH, 35% NaOCl solution, 37% HCl, heptane, THF, ethanol, methanol, DMF, and 1,4-dioxane (Merck, Carlo Erba, Analar BDH Chem).

2-(*p*-Tolyliminomethyl)phenol was prepared by condensation of salicylaldehyde with *p*-toluidine in refluxing ethanol [18]; mp 93°C (from ethanol).

Before use in oxidative polycondensation, air was passed through 20% aqueous KOH to remove CO_2.

Oxidative polycondensation of TIMP was performed in a 100-ml three-necked glass flask equipped with a magnetic stirrer, a temperature control unit, a thermometer, and a reflux condenser. In experiments on oxidative polycondensation of phenol with atmospheric oxygen, an air inlet tube was attached.

The flask was charged under stirring with 40 ml of distilled water, 2.24 g (0.04 mol) of KOH, and 8.44 g (0.04 mol) TIMP and was heated to the required temperature. Then air was bubbled at a rate of 8.5 l h^{-1}. After reaction completion, the mixture was neutralized with 37% HCl. The precipitate was separated from water-soluble products (OTIMP-3) on a glass frit, thoroughly washed with hot distilled water to remove inorganic salts, thoroughly washed with heptane to remove unchanged TIMP, and dried at 105°C. Then this product was treated with refluxing heptane to separate the soluble (OTIMP-1) and insoluble (OTIMP-2) fractions and dried at 105°C.

The aqueous solution of the water-soluble products (OTIMP-3) was evaporated to dryness on a water bath and then dried at 105°C for 6 h in an oven. After such a treatment, the major fraction (80–85%) of this product (similar to other oligomers with a system

of conjugated bonds [19]) became water-insoluble. Therefore, it was thoroughly washed with distilled water to remove mineral salts and dried at 105°C to constant weight.

The conversion of TIMP in the course of oxidative polycondensation was monitored by paper chromatography.

Oxidative polycondensation of TIMP with 35% aqueous NaOCl and the subsequent work-up were performed similarly.

The UV and IR spectra were measured in THF solutions and KBr pellets on Shimadzu UV-160A and FT-IR-8300 spectrophotometers. The ^{1}H NMR spectra were recorded on a Varian XL-200 spectrometer (200 MHz) in DMSO-d_6, internal reference TMS.

The molecular weight and MWD of TIMP oligomerization products were determined by exclusion chromatography on a Kovo high-performance liquid chromatograph (Czechia) equipped with a refractometric detector. Two 3.3×150-mm columns were packed with Separon-SGX (particle size 7 μm, porosity 100 Å); eluent DMF, flow rate 0.2 ml min^{-1}.

The thermal analysis was performed on a HiGeH RG 2/5 device at a heating rate of 2 deg min^{-1}.

CONCLUSIONS

(1) Procedures for preparing oligo(*p*-tolyliminomethyl)phenols by oxidative polycondensation of 2-(*p*-tolyliminomethyl)phenol with sodium hypochlorite and atmospheric oxygen were developed and optimized.

(2) The reaction products mainly consist of (*p*-tolyliminomethyl)phenol units linked via *o*- and *m*-positions.

(3) The products consist of low- and high-molecular-weight fractions whose content, depending on the reaction conditions, is about 80 and 20%, respectively. The molecular weight of the oligomers ranges from approximately 600 to 7500.

(4) Oligo(*p*-tolyliminomethyl)phenols show high resistance to thermal oxidation and high inhibiting activity with respect to the growth of 13 test microcultures; these products readily react with transition and heavy metal acetates to form partially soluble metal–polymer complexes exhibiting high heat resistance and high antimicrobial activity.

REFERENCES

1. USSR Inventor's Certificate no. 363720.
2. Mel'nikova, M.A., Mustafaev, R.N., and Ragimov, A.V., *Zh. Prikl. Khim.*, 1991, vol. 64, no. 5, pp. 1930–1934.
3. USSR Inventor's Certificate no. 639910.
4. Anyunene, I.A., Baltushnikas, A.N., Liogonkii, B.I., and Ragimov, A.V., Abstracts of Papers, *26-ya respublikanskaya konferentsiya "Polimernye materialy i ikh issledovanie"* (26th Republican Conf. "Polymeric Materials and Their Study"), Vilnius (Lithuania), 1991, p. 58.
5. USSR Inventor's Certificate no. 731413.
6. USSR Inventor's Certificate no. 946237.
7. Rybalka, K.V., Radzhabov, D.T., and Ragimov, A.V., *Sb. Elektrotekh. Prom–sti*, 1984, vol. 2, no. 95, pp. 20–23.
8. Kiselova, E.D., Chumutov, K.V., Ragimov, A.V., and Berlin, A.A., *Zh. Fiz. Khim.*, 1964, vol. 38, no. 9, pp. 2316–2319.
9. Bayer, E., *Angew. Chem.*, 1957, vol. 69, no. 1, pp. 107–110.
10. Van Griken, R.E., *Anal. Chim. Acta*, 1982, vol. 135, no. 143, pp. 3–8.
11. Hedrickson, L.I., Turner, M.A., and Corecy, K.B., *Anal. Chem.*, 1982, vol. 54, no. 821, pp. 1633–1642.
12. Balto, B.A., *Macromol. Sci. Chem.*, 1980, vol. 14, no. 1, pp. 107–113.
13. Vernon, F., *Hydrometallurgy*, 1979, vol. 4, no. 2, pp. 147–155.
14. Schmuckler, G., *Talanta*, 1965, vol. 12, no. 2, pp. 281–284.
15. Sosin, S.L. and Korshak, V.V., *Izv. Akad. Nauk SSSR, Ser. Khim.*, 1964, no. 5, pp. 970–975.
16. Ragimov, A.V., Ragimov, I.I., and Liogonkii, B.I., *Dokl. Akad. Nauk SSSR*, 1985, vol. 282, no. 6, pp. 1423–1433.
17. Ragimov, A.V., Ragimov, I.I., Mamedov, B.A., *et al.*, *Vysokomol. Soedin., Ser. A*, 1982, vol. 24, no. 10, pp. 2125–2130.
18. Kogan, V.A., Osipov, O.A., Minkin, V.I., and Sokolov, V.R., *Zh. Neorg. Khim.*, 1965, vol. 10, no. 10, pp. 83–86.
19. Berlin, A.A., Geiderikh, M.A., and Davydov, B.E., *Khimiya polisopryazhennykh sistem* (Chemistry of Polyconjugated Systems), Moscow: Khimiya, 1972.

Russian Journal of Applied Chemistry, Vol. 75, No. 7, 2002, pp. 1157–1161. Translated from Zhurnal Prikladnoi Khimii, Vol. 75, No. 7, 2002, pp. 1180–1184.
Original Russian Text Copyright © 2002 by Selivanova, Vyaseleva, Konopleva, Kop'ev, Barabanov.

MACROMOLECULAR CHEMISTRY AND POLYMERIC MATERIALS

Protecting Properties of Composite Fluoroplastic Coatings

N. M. Selivanova, G. Ya. Vyaseleva, A. A. Konopleva, R. A. Kop'ev, and V. P. Barabanov

Kazan State Technological University, Kazan, Tatarstan, Russia

Received September 17, 2001

Abstract—Preparation of protecting fluoroplastic coatings at varied composition of the reaction mixture was studied. Introduction of quarternary pyridinium poly salt and various pigments into the polytrifluorochloroethylene composition allows variation of the process parameters of coating deposition on the cathode and preparation of modified fluoroplastic coatings with good anticorrosive properties.

The most common way to protect metals against corrosion is application of polymeric coatings, with fluoroplastic being the most stable to aggressive media. The properties of polymeric coatings are known [1] to strongly depend on the presence of pigments and fillers. Introduction of pigments in the course of electrodeposition of coatings not only changes the appearance and properties of the coatings but also affects the deposition process, nominal current efficiency, throwing power, and stability of the system as a whole. It is important to determine the protecting properties of electrodeposited coating as influenced by the type of pigment.

EXPERIMENTAL

By the mechanism of protecting action, pigments can be divided into three groups [2]: (1) passivating the metal (Cr_2O_3, ZnO); (2) forming difficultly soluble compounds on the metal surface ($CaHPO_4 \cdot 2H_2O$); and (3) cathodically protecting the metal (Al and Zn powders).

The physicochemical properties of pigments used in electrodeposition are presented in Table 1. The particle size was determined by sedimentometric analysis, and the particle charge, by electroosmosis.

The protecting coatings were deposited from multicomponent dimethylformamide dispersion containing polytrifluorochloroethylene (F-3) and copolymer of quaternary pyridinium salt (CPS) specially synthesized for this purpose (see below).

A CPS macromolecule contains 14.5% *N*-ethyl-2-methyl-5-vinylpyridinium bromide, 8.9% 2-methyl-5-vinylpyridine, and 76.6% butyl acrylate units. The butyl acrylate units make the polymer elastic and enhance adhesion of the polymeric coating to the cathode. Pyridinium functional groups behave as inhibitor. They are converted to 14.5% into pyridiniomethyl bromide groups which readily dissociate in dimethylformamide (DMF) to form polycations. Positively charged pyridinium groups of CPS are sorbed on fluoroplastic particles which become positively charged and are deposited on the cathode [4].

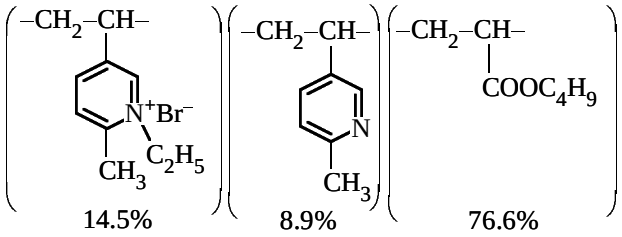

The composition for electrodeposition was prepared as follows. The solid copolymeric salt (0.35 g) was dissolved in DMF (50 ml). The resulting solution (1 ml) was added to fluoroplastic powder wetted with a small amount of DMF (5 ml). The mixture was stirred for a long time with a magnetic stirrer. Then an additional portion of the solvent was added to obtain 7% dispersion. The content of the polymeric salt in the dispersion was 7×10^{-3} g/100 ml.

The deposition process was controlled by varying the dispersion composition, electric parameters, deposition time, and heat treatment conditions. The dispersion composition and electrodeposition conditions are presented in Table 2.

To determine the best pigment concentration, we studied the dependence of the deposit weight on the dispersion composition. The deposit weight was

1070-4272/02/7507-1157$27.00 © 2002 MAIK "Nauka/Interperiodica"

Table 1. Physicochemical properties of pigments*

Pigment	Color	Particle size r, μm	Density ρ, g cm^{-3}	Covering power Y, g cm^{-2}	ζ-Potential, mV
Fe_2O_3	Bordeaux	7.0–8.0	4.8–5.0	3–8	+1.03
Cr_2O_3	Green	4.0–5.0	4.6–5.0	8–12	+0.63
TiO_2	White	5.0–7.0	3.8	25–35	+2.50
Al-powder	Silvery	8.0–10.0	2.5–2.6	10	–2.80
Zn-powder	Gray	3.0–5.0	7.1	–	–
$CaHPO_4 \cdot 2H_2O$	White	1.2–1.3 1.7–1.8	2.3	–	+2.80
ZnO	"	7.5–8.5	5.6	100–120	+11.60

* The particle size was determined by sedimentometric analysis, and the ζ-potential, by electrosmosis; the density and covering power were taken from [3].

Table 2. Electrodeposition conditions from 7% F-3 + 7×10^{-3} g/100 ml CPS + 5% pigment dispersion

Coating no.	Pigment	Electrodeposition		Heat treatment	
		U, V	τ, s	T, °C	τ, min
1	–	110–120	15	250–260	30
2	Cr_2O_3	100–110	15–20	250–260	25
3	$CaHPO_4 \cdot 2H_2O$	120	15–20	250–260	25
4	Zn-powder	120–130	10–15	250–260	25
5	ZnO	80	10	250–260	25
6	Al-powder	120	10–15	250–260	25

maximal at 5–7% pigment content in the dispersion. The thickest coatings with the best properties were formed in the presence of chromium(III) oxide, and the thinnest, in the presence of calcium hydrogen phosphate.

As determined by IR spectroscopy, the pigment content in the deposit differs from that in the electrolytic bath. The pigment : film-forming agent ratio in the deposit is higher than that in the dispersion.

Pigments promote formation of more uniform coating, thus decreasing its electrochemical heterogeneity.

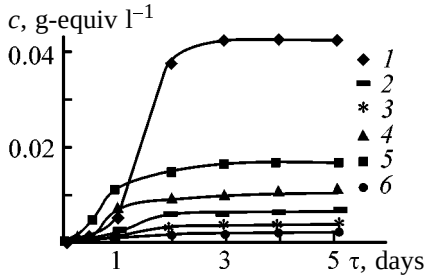

Fig. 1. Concentration c of chloride ions that have diffused through the film as a function of time τ. The figures at the curves correspond to the coating number in Table 2; the same for Figs. 2 and 3.

They increase the electrical resistivity, decelerate the cathodic and anodic processes on passivated support, and plug the channel pores, thus preventing ion diffusion [5].

In this work, we studied the permeability of fluoroplastic coatings filled with various pigments. As seen from Fig. 1, the transfer rate of chloride ions changes with time. Within the first day, the ions transfer is difficult owing to hydrophobic properties of the fluoroplastic. Then the dependence becomes linear, i.e., chloride ions penetrate through the film only by diffusion. In 2–3 days, the ion transfer stops. This is due to both formation of the electrical double layer in film capillaries and the negative film potential appearing owing to the difference in the transference numbers of Na^+ and Cl^-. In the simplest case, the liquid-phase potential can be calculated by the equation

$$\Delta\varphi_z = RT/(zF)(t_{Na^+} - t_{Cl^-}) \ln (c_0/c),$$

where R is the gas constant (J mol^{-1} K^{-1}); T, the temperature (K); F, the Faraday number (C mol^{-1}); z, the charge of the chloride ion; c_0 and c, the concentration of the initial solution and solution in the chamber to which the ions have diffused, respectively (M);

Table 3. Physicochemical properties of chloride ion transfer in the coatings

Coating (Table 1)	Thickness δ, μm	$D \times 10^9$, $m^2\ s^{-1}$	V, g-equiv $l^{-1}\ s^{-1}$	P, $g\ cm^{-2}$	$-\Delta\varphi_z$, V
1	20–25	10.00	2.5×10^{-5}	0.2200	0.0100
2	30–35	2.20	6.8×10^{-8}	0.0420	0.0240
3	40–45	2.26	2.4×10^{-8}	0.0061	0.0250
4	30–35	2.91	7.8×10^{-8}	0.0590	0.0220
5	35–40	2.73	8.1×10^{-8}	0.0830	0.0200
6	45–50	1.85	6.3×10^{-9}	0.0028	0.0299

and $t_{Na^+} = 0.382$, $t_{Cl^-} = 0.618$, the transference numbers.

The liquid-phase potential correlates with the transfer rate v and diffusion coefficients of chloride ions D calculated from the kinetic data (Fig. 1) by the Fick's law.

The film permeability was calculated by the equation [6]

$$P = c\mu V/S,$$

where c is the concentration of diffused chloride ions (g-equiv l^{-1}), determined by titration at time τ (s); μ, the atomic weight of chloride ion; V, the cell volume (l); and S, the surface area of the film.

As seen from Table 3, the liquid-phase potential, diffusion coefficient, transfer rate, and permeability depend on the type of the composite coating. The unfilled fluoroplastic coatings are the most permeable. Introduction of pigments appreciably decreases the film permeability. Finely divided pigment fills the interparticle space of the fluoroplastic matrix. As a result, the coating thickness becomes more uniform and the porosity and hence permeability of the coatings decrease. The coatings filled with Al powder are the least permeable. The diffusion coefficient in these films is 5 times lower than that in the fluoroplastic coatings without the filler.

Polymeric coatings restrict access of reactive compounds to the support surface and affect the electrode processes at the metal–polymer interface, thus protecting the support.

The time dependences of the potential of a coated electrode were measured by chronopotentiometry (Fig. 2). Among the examined coatings, that containing chromium(III) oxide is characterized by the most positive final potential and the smallest difference between the initial and final potentials Δφ.

The rate of chemical reactions occurring on the metal–coating interface cannot be measured directly. However, it can be indirectly estimated from the polarization resistance [7]. The cathodic and anodic polarization curves without the ohmic component are shown in Fig. 3. It should be noted that good anticorrosive properties are determined by high polarization resistance. Among the filled fluoroplastic coatings, the polarizability of the coating with Cr_2O_3 filler is the highest. Polarization of these coatings at low currents indicates the absence of side corrosion processes. The polarizability of all the coatings at cathodic polarization is higher than that at the anodic polarization, i.e., the coatings suppress to a greater extent the cathodic process at the metal–polymer interface. The occurrence of corrosion processes under the film can be also determined by the corrosion currents and their variation with time. The lower the corrosion current, the better the protecting function of the coating. Pigments passivating the metal (Cr_2O_3, ZnO) and forming difficultly soluble compounds ($CaHPO_4 \cdot 2H_2O$) decelerate the cathodic processes, as is indicated by low current, which does not noticeably change with time.

Zinc and aluminum powders plug the channel pores and decrease the permeability. However, corrosion processes are promoted and the corrosion currents increase owing a contact potential difference between iron and the metal powder.

Thus, the type of the pigment strongly affects both

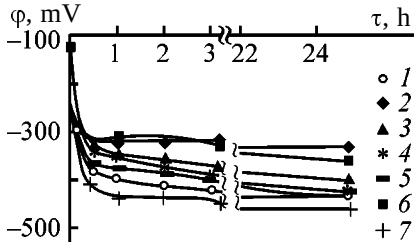

Fig. 2. Chronopotentiograms of coated steel samples in 0.5 M NaCl. (φ) Potential and (τ) time. (*7*) St.3 steel.

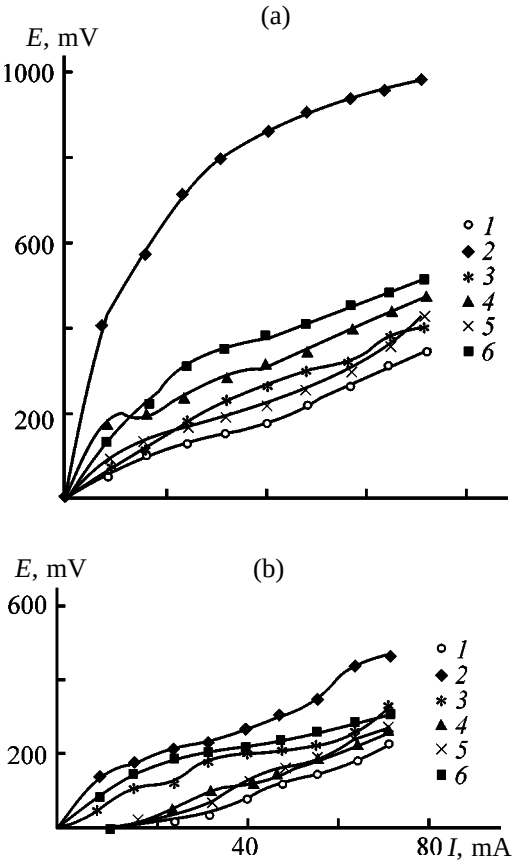

Fig. 3. (a) Cathodic and (b) anodic polarization curves of a coated electrode in 0.5 M NaCl. (*E*) Potential and (*I*) current. (a) $2H^+ + 2e \rightarrow H_2$; (b) $Fe - 2e \rightarrow Fe^{2+}$.

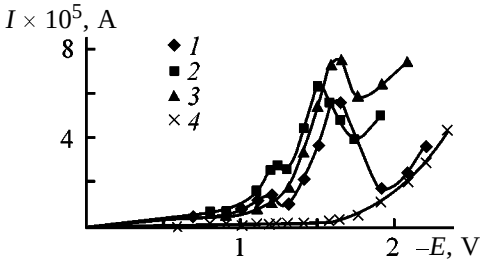

Fig. 4. Voltammogram of reduction of (*1*) poly-NEt2Me5VPBr, (*2*) poly-NEt2Me5VPBr–2Me5VP–BuAcr, (*3*) NEt2Me5VPBr, and (*4*) 0.1 M $NaClO_4$. Concentration 1×10^{-4}, sweeping rate 80 mV s^{-1}; (*I*) current and (*E*) potential.

the electrodeposition and the protecting properties of fluoroplastic coatings. All electrochemical methods used in this work show that cathodic processes are inhibited to a greater extent than anodic processes.

Good protecting properties of the composite coatings are determined mainly by their strong adhesion to the support, which, in its turn, is provided by formation of the first microlayer on the molecular level by electrochemical reduction of pyridinium polyanion sorbed on fluoroplastic and pigment particles.

As determined by chronovoltammetry, pyridinium polycations as well as their monomeric analogs have electroactive centers reducible at cathodic polarization from –0.6 to –1.7 V (Fig. 4). The voltammogram of 2-methyl-5-vinylpyridinium bromide 2Me5VPBr contains only a single current peak due to reduction of the pyridinium ring. In the polycation voltammograms, the current peak splits in two peaks. Along with a strong peak at the potentials close to the potential of monomer reduction, a weak peak or ascending current plateau appears at more positive potentials. The value of the capacitance indicates strong adsorption of the polymeric salt at these potentials [6].

As seen from Fig. 4, the peak potentials of the copolymer salt are shifted to the anodic region as compared to those of the homopolymeric salt. This is due to readier discharge owing to accessibility of the electrode surface to charged chains.

A composite coating is formed by colloid-chemical and electrochemical reactions which make the electrodeposit denser and strengthen the adhesion interaction owing to formation of intermetallic bonds with the metal surface.

The composite fluoroplastic coatings can be used to protect metallic articles from the atmospheric action and as priming coatings protecting from humid and sea atmosphere and saline media.

CONCLUSIONS

(1) The type of the pigment strongly affects electrodeposition and protecting properties of fluoroplastic coatings.

(2) Introduction of aluminum powder into the coatings decreases their permeability and decelerates diffusion of corrosive agents to the support.

(3) Electrochemical studies show that the cathodic processes under the coating are inhibited to a greater extent as compared to the anodic processes.

(4) The electrodeposition mechanism was determined by chronovoltammetry.

REFERENCES

1. Indeikin, E.A., Leibzon, L.N., and Tolmachev, I.A., *Pigmentirovanie lakokrasochnykh materialov* (Pig-

mentation of Paint and Varnish Materials), Leningrad: Khimiya, 1986.

2. Rozenfel'd, I.L. and Rubenshtein, F.I., *Antikorrozionnye gruntovki i ingibirovannye lakokrasochnye pokrytiya* (Anticorrosive Primings and Inhibited Paint and Varnish Coatings), Moscow: Khimiya, 1980.
3. *Entsiklopediya polimerov* (Encyclopedia of Polymers), Moscow: Sov. Entsiklopediya, 1974, vol. 2, pp. 559–600.
4. USSR Inventor's Certificate no. 1 438 215.
5. Krylova, I.A., Kogan, N.D., and Ratnikov, V.I., *Okraska elektroosazhdeniem* (Coloring by Electodeposition), Moscow: Khimiya, 1982.
6. Konopleva, A.A., Vyaseleva, G.Ya, Torsuev, D.M., and Barabanov, V.P., *Zh. Prikl. Khim*., 1998, vol. 71, no. 5, pp. 787–790.
7. Vyaseleva, G.Ya., Rizaeva, M.D., and Barabanov, V.P., *Zashch. Met*., 1987, vol. 23, no. 5, pp. 898–900.

Russian Journal of Applied Chemistry, Vol. 75, No. 7, 2002, pp. 1162–1165. Translated from Zhurnal Prikladnoi Khimii, Vol. 75, No. 7, 2002, pp. 1185–1188.
Original Russian Text Copyright © 2002 by Rakhimov, Vostrikova.

MACROMOLECULAR CHEMISTRY AND POLYMERIC MATERIALS

Polyfluoroalkyl Chlorosulfites as New Polyfluorinating Agents[1]

A. I. Rakhimov and O. V. Vostrikova

Volgograd State Technical University, Volgograd, Russia
Institute of Chemical Problems of Ecology, Russian Academy of Natural Sciences, Volgograd, Russia

Received January 17, 2002

Abstract—The interaction of polyfluorinated alcohols with triethylamine and the kinetics of the reaction of the resulting triethylamine complexes with thionyl chloride were studied, the mechanism of formation of polyfluoroalkyl chlorosulfites was considered, and the optimal reaction conditions were found. The alkylating power of polyfluoroalkyl chlorosulfites was studied in reactions with alkali metal halides (to obtain polyfluorohaloalkanes), in synthesis of acrylic and methacrylic acid esters, and in synthesis of polyfluoroalkyl ethers (with polyfluoroalkyl 1-adamantyl ethers as example).

Polyfluoroalkyl chlorosulfites have been studied poorly. These compounds were prepared by the reaction of perfluoroalkyl hypochlorites with thionyl chloride [1–5]

$$R_FOCl + SOCl_2 \rightarrow R_FOS(O)Cl + Cl_2.$$

In a later study [6], these compounds were prepared by the reaction of polyfluoro alcohols with thionyl chloride in the presence of triethylamine:

$$R_FOH + SOCl_2 \rightarrow R_FOSOCl.$$

In contrast to alkyl chlorosulfites, which are intermediates in reactions of alcohols with thionyl chloride and readily eliminate SO_2 to form chloroalkanes, polyfluoroalkyl chlorosulfites are stable compounds distillable without decomposition.

In this work, we studied the interaction of polyfluorinated alcohols with triethylamine and the reaction of the resulting complexes with thionyl chloride, with the aim to optimize the preparation of polyfluoroalkyl sulfites, which are of interest as polyfluorinating agents in syntheses of polyfluorohaloalkanes and of esters and ethers containing polyfluoroalkyl groups.

EXPERIMENTAL

Calorimetric studies were performed with a DAK-1-2M isothermal differential calorimeter. An ampule-in-ampule glass microreactor was placed in a calorimetric cell equipped with a device for breaking the inner ampule (a thin-walled sphere). After the required temperature was attained, the thin-walled sphere was broken, and the thermokinetic curve was recorded with an LKS 4003 device; this curve was processed to calculate the heat release rate and to determine the rate constants using the kinetic model. The heat of formation of the alcohol–triethylamine complex was determined in the bulk at 30°C and equimolar ratio of the alcohol and amine. Three replicate runs were performed, and the thermokinetic curves were processed by the trapezium method. The error of the calorimetric measurements was 3–5%.

The kinetics of formation of polyfluoroalkyl chlorosulfites was studied at 25, 30, and 35°C. The initial concentrations of the alcohol–amine complex and thionyl chloride were 0.18 M.

Procedures for synthesis and identification of polyfluoroalkyl chlorosulfites are reported elsewhere [7]. The reaction was performed in chloroform; the complex of a polyfluorinated alcohol (0.05 mol) with triethylamine (0.05 mol) was added to a solution of 0.075 mol of thionyl chloride, cooled to –40°C; in the process, the mixture was not allowed to warm up above –15°C. After adding the whole amount of the complex, the mixture was warmed up to 20°C. The precipitate of triethylamine hydrochloride was filtered off, excess thionyl chloride was distilled off at atmospheric pressure, and the residue was vacuum-distilled. The yields and constants of polyfluoroalkyl chlorosulfites obtained by the reaction

[1] Reported at the 3rd International Conference "Chemistry, Technology, and Applications of Fluoro Compounds" (St. Petersburg, July 6–9, 2001).

1070-4272/02/7507-1162$27.00 © 2002 MAIK "Nauka/Interperiodica"

Table 1. Physicochemical characteristics of polyfluoroalkyl chlorosulfites $H(CF_2CF_2)_nCH_2OS(O)Cl$

n	Yield, %	Empirical formula	bp, °C/P, mm Hg	d_4^{20}, g cm^{-3}	n_D^{20}
1	84.2	$C_3H_3F_4SO_2Cl$	61/40	1.611	1.3704
2	82.0	$C_5H_3F_8SO_2Cl$	99/50	1.783	1.3580
3	80.0	$C_7H_3F_{12}SO_2Cl$	101/10	1.787	1.3428

$$H(CF_2CF_2)_nCH_2OH\cdot N(C_2H_5)_3 + SOCl_2$$

$$\rightarrow H(CF_2CF_2)_nCH_2OSOCl + (C_2H_5)_3N\cdot HCl, \quad n = 1\text{–}3,$$

are listed in Table 1.

Polyfluorinated alcohols virtually do not react with thionyl chloride in the absence of triethylamine. If triethylamine is added to a mixture of alcohol and thionyl chloride, the yield of alkyl chlorosulfite does not exceed 15%. The highest yield (80–84%) is attained when the complex of a polyfluorinated alcohol with triethylamine, prepared in advance, is added to thionyl chloride. Therefore, using microcalorimetry and IR and ^{1}H NMR spectroscopy, we studied the interaction of polyfluorinated alcohols with triethylamine.

The thermal effect of the interaction of polyfluorinated alcohols with triethylamine was estimated microcalorimetrically. The heat of interaction with triethylamine is 19.9 kJ mol^{-1} for 2,2,3,3-tetrafluoro-1-propanol (FA1) and 20.7 kJ mol^{-1} for 2,2,3,3,4,4,5,5-octafluoro-1-pentanol (FA2).

Complexation causes significant changes in the IR spectra of polyfluorinated alcohols. The stretching vibration band of the OH group at 3620 cm^{-1} sharply decreases in intensity, and a new medium-intensity band appears at 2600–2700 cm^{-1}, which is split in several bands (Fig. 1). These changes are due to formation of a salt, $H(CF_2CF_2)_nCH_2O^-\,{}^+NH(C_2H_5)_3$.

The conclusions made from the IR spectra are confirmed by the ^{1}H NMR spectra of FA2 solutions in CCl_4. Interaction of FA2 with triethylamine causes a downfield shift of the hydroxyl proton signal by 2.49 ppm. Triethylamine is a stronger proton acceptor than acetone, as with acetone, under similar conditions, the OH proton signal is shifted downfield by only 1.86 ppm. Thus, the complexation is favored by the acid properties of polyfluorinated alcohols and high basicity of triethylamine.

Based on the data on complexation with triethylamine, we optimized the conditions for preparing polyfluoroalkyl chlorosulfite. We suggest the following mechanism of nucleophilic substitution of chlorine in the thionyl chloride molecule:

$$SOCl_2 + R_FO^-[NHEt_3]^+$$

$$\rightleftharpoons \left[R_FO\text{---}\overset{\displaystyle O}{\overset{\|}{S}}\text{---}Cl\right][NHEt_3]^+$$

$$\longrightarrow R_FOS(O)Cl + [NHEt_3]^+Cl^-.$$

This mechanism is confirmed by the kinetic data. Using the kinetic model, we processed experimental heat release curves [8] and determined the rate constants and the effective activation energy of the reaction. For the reaction of thionyl chloride with FA1–triethylamine, the second-order rate constants are as follows (l mol^{-1} s^{-1}): 0.020 at 25°C, 0.025 at 30°C, and 0.027 at 35°C. The effective activation energy is 31.77 kJ mol^{-1}.

We have studied the alkylating power of polyfluo-

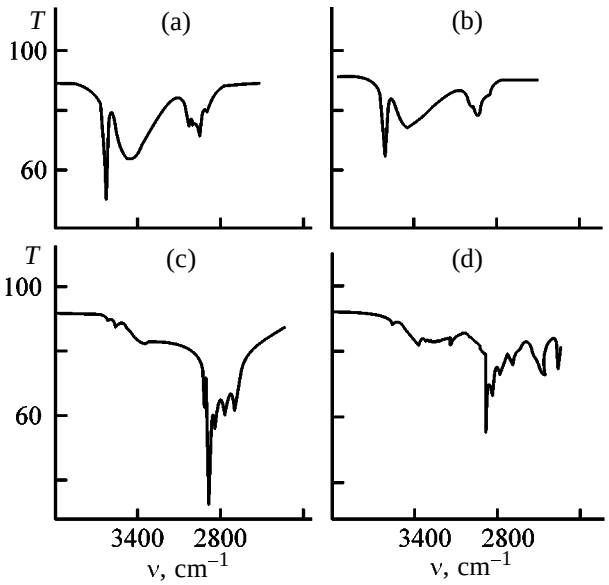

Fig. 1. IR spectra in CCl_4 of (a, b) 2,2,3,3-tetrafluoropropanol and (c, d) 1 : 1 2,2,3,3-tetrafluoropropanol–triethylamine complex. Cell thickness 0.18 mm. (T) Transmission and (ν) wave number. Concentration, M: (a, c) 0.4 and (b, d) 0.2.

Table 2. Polyfluoroalkyl acrylates and methacrylates

R	*n*	Yield, %	bp, °C/*P*, mm Hg	d_4^{20}, g cm^{-3}	n_D^{20}
H	1	76.2	56/60	1.2860	1.3666
		34.0*	75/110	1.2858	1.3668
H	2	76.0	85/40	1.4460	1.3462
		38.5*	84/40	1.4884	1.3460
H	3	76.1	110/40	1.5802	1.3402
		45.2*	107/40	1.5974	1.3400
CH_3	2	76.4	100/40	1.4210	1.3578
		56.0*	87/40	1.4106	1.3580
CH_3	3	76.5	104/20	1.5360	1.3506
		50.8*	112/40	1.5390	1.3500

* Data of [9].

Table 3. Polyfluoroalkyl 1-adamantyl ethers $Ad–OCH_2(CF_2CF_2)_nH$

n	Yield, %	bp, °C/*P*, mm Hg	n_D^{20}	Analytical data, %*		
				C	H	F
1	76	86/2	1.4440	58.02 / 58.65	6.70 / 6.77	28.21 / 28.57
2	75	106/2	1.4233	49.00 / 49.20	4.60 / 4.92	41.03 / 41.53

* Numerator: found; denominator: calculated.

roalkyl chlorosulfites in the reactions with alkali metal halides, carboxylic acid salts, and alcohols.

Polyfluoroalkyl chlorosulfites react with alkali metal halides (KF, LiCl, KBr, KI) in diethylene glycol to form the corresponding polyfluorohaloalkanes in 75–90% yield:

$$H(CF_2CF_2)_nCH_2OS(O)Cl + MX \rightarrow H(CF_2CF_2)_nCH_2X + MCl + SO_2,$$

where n = 1, 2, 3; X = F, Cl, Br, I; M = K, Li, Na.

The advantages of the synthesis of polyfluorohaloalkanes by substitution of the chlorosulfite group in alkyl chlorosulfites are the use of low-toxic chemicals, versatility, and high yield of the reaction products.

By the reaction of alkyl chlorosulfites with potassium (meth)acrylate, we prepared the corresponding polyfluoroalkyl (meth)acrylates:

$$CH_2=C(R)COOH + H(CF_2CF_2)_nCH_2OS(O)Cl \longrightarrow CH_2=C(R)COOCH_2–(CF_2CF_2)_nH,$$

where n = 1, 2, 3; R = H, CH_3.

The yield of acrylates and methacrylates in this case is appreciably higher than in the known procedure [9] (Table 2).

Polyfluoroalkyl chlorosulfites readily react with alcohols in dioxane to form the corresponding ethers. For example, previously unknown polyfluoroalkyl 1-adamantyl ethers were prepared by the reaction of 1-adamantol with polyfluoroalkyl chlorosulfites:

$$Ad–OH + H(CF_2CF_2)_nCH_2OS(O)Cl \longrightarrow Ad–OCH_2(CF_2CF_2)_nH,$$

where n = 1, 2.

Adamantyl polyfluoroalkyl ethers are colorless liquids readily distillable in a vacuum (Table 3). The composition and structure of these compounds were determined by elemental analysis and by IR and ^{1}H NMR spectroscopy.

The IR spectra of the ethers exhibit a very strong absorption at about 2916 cm^{-1} assigned to the stretching vibrations of the methylene and methine groups and at about 1124 cm^{-1} assigned to the ether C–O stretching vibrations.

The ^{1}H NMR data for 1-adamantyl alkyl ethers are given in Table 4.

The ^{1}H NMR spectra of 1-[2,2,3,3-tetrafluoropropoxy]adamantane and 1-[2,2,3,3,4,4,5,5-octafluoropentoxy]adamantane contain characteristic proton signals of the adamantane moiety [10]. The β- (δ 1.56 ppm) and δ-protons (δ 1.68 ppm) give narrow signals. The signal of the γ-protons is broad (δ 2.12 ppm). The signal of the methylene protons in the polyfluoroalkyl moiety is a triplet with a coupling constant of 12 Hz. The proton signal of the hydrofluoromethyl group is a triplet of triplets with a coupling constant of 6 Hz.

According to the predictions of the medicobiological activity, perfluoroalkyl 1-adamantyl ethers show promise as antidepressants and tranquilizers.

CONCLUSIONS

(1) A procedure was developed for synthesis of polyfluoroalkyl chlorosulfites by the reaction of thionyl chloride with complexes of polyfluorinated alcohols with triethylamine.

(2) Complexation in the system polyfluorinated alcohol–triethylamine was studied by microcalorimetry and IR and ^{1}H NMR spectroscopy, and the salt-like structures of the complexes were suggested.

Table 4. ^{1}H NMR spectra of 1-adamantyl alkyl ethers

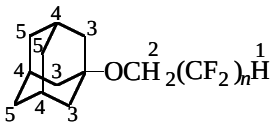

n	Chemical shift δ, ppm					Coupling constant, Hz		
	1	2	3	4	5	J_{HCF}	J_{HCCF}	J_{2HCH}
2	5.78 t.t	3.64 t	1.56 s	2.12 s	1.66 s	52	6	12
4	5.84 t.t	3.74 t	1.56 s	2.12 s	1.68 s	52	6	12

(3) A mechanism of formation of polyfluoroalkyl chlorosulfites was suggested, involving bimolecular nucleophilic substitution of chlorine by the polyfluoroalkoxy group in thionyl chloride in its reaction with the polyfluorinated alcohol–triethylamine complex.

(4) Polyfluoroalkyl chlorosulfites efficiently alkylate carboxylic acid salts (alkyl acrylates and methacrylates were obtained) and alcohols (with 1-adamantol as example); they can also be used for preparing polyfluorohaloalkanes by the reactions with metal halides.

REFERENCES

1. Van Meter, W.P. and Candy, G.H., *J. Am. Chem. Soc.*, 1960, vol. 82, no. 23, pp. 6005–6008.
2. Gould, D.E., Anderson, L.R., Young, D.E., and Fox, W.R., *J. Am. Chem. Soc.*, 1969, vol. 91, no. 6, pp. 1310–1313.
3. Eserrard, V., *J. Chem. Soc.*, 1964, pp. 5480–5482.
4. Young, D.E. and Fox, W.B., *Inorg. Nucl. Chem. Lett.*, 1971, no. 7, pp. 1033–1035.
5. Young, D.E., Anderson, L.R., and Fox, W.B., *Inorg. Chem.*, 1971, vol. 10, no. 12, pp. 2810–2812.
6. De Marco, R.A., Kovacina, T.A., and Fox, W.B., *J. Fluorine Chem.*, 1975, vol. 6, pp. 3–104.
7. Rakhimov, A.I. and Vostrikova, O.V., *Zh. Org. Khim.*, 1999, vol. 35, no. 5, pp. 815–816.
8. Vostrikova, O.V., Synthesis and Properties of Polyfluoroalkyl Chlorosulfites, *Cand. Sci. Dissertation*, Volgograd, 1999.
9. Gol'din, G.S., Averbakh, K.O., Nekrasova, L.A., *et al.*, *Zh. Prikl. Khim.*, 1985, vol. 58, no. 6, pp. 1349–1353.
10. Bagrii, E.I., *Adamantany* (Adamantanes), Moscow: Nauka, 1989.

Russian Journal of Applied Chemistry, Vol. 75, No. 7, 2002, pp. 1166–1169. Translated from Zhurnal Prikladnoi Khimii, Vol. 75, No. 7, 2002, pp. 1189–1192.
Original Russian Text Copyright © 2002 by Chernoberezhskii, Dyagileva, Atanesyan, Leshchenko.

MACROMOLECULAR CHEMISTRY AND POLYMERIC MATERIALS

Influence of the Kraft Lignin Concentration on the Efficiency of Its Coagulation Recovery from Aqueous Electrolyte Solutions

Yu. M. Chernoberezhskii, A. B. Dyagileva, A. A. Atanesyan, and T. V. Leshchenko

St. Petersburg State Technological University of Plant Polymers, St. Petersburg, Russia

Received February 26, 2002

Abstract—The dependence of the aggregation stability of aqueous suspension of kraft lignin on its concentration in the system was studied spectrophotometrically in wide ranges of pH and sodium chloride concentrations.

At present, the main procedure of production of commercial cellulose is kraft cooking of wood [1, 2]. This procedure allows processing of virtually all types of plant raw materials and production of cellulose with high strength characteristics. In addition, kraft cooking has a number of environmental and process advantages. First, this process provides perfect regeneration of chemicals, allowing the use of wood components passing into the cooking liquor as a source of energy. Second, this process allows the most exhaustive treatment of liquor-containing wastewater flows with arrangement of local water-treatment systems at the sites of formation of these concentrated flows. This will decrease the load on the biological treatment plant by preliminary removal of poorly soluble organic impurities and reduction of the color index of wastewaters. These problems cannot be solved by traditional procedures of biological treatment.

High color index and chemical oxygen demand (COD) of this wastewater are caused by a significant concentration of kraft lignin (KL), which is an aromatic compound that is difficult to oxidize biochemically at the wastewater treatment facilities existing at virtually all paper and pulp plants. Therefore, development of procedures of removal of KL from wastewater is an urgent problem. Coagulation recovery of KL can be one of such procedures.

Practically any procedure of wastewater treatment, among them coagulation, includes separation of a phase to be recovered from wastewater so as to prevent secondary contamination of surface and underground water. Therefore, decrease in the amount of the resulting precipitates and their utilization can be of practical interest.

The choice and substantiation of regimes for recovery of poorly soluble part of wastewater (KL) require detailed studies in this field. The results reported here present a part of complex studies of colloid-chemical behavior of KL in aqueous systems.

EXPERIMENTAL

In this work, the aggregation stability of the system water–lignin–electrolyte was studied spectrophotometrically in a wide range of KL and NaCl concentrations and pH. Characteristics of KL, its colloid-chemical properties, and procedures of experiments with "instant mixing" of components were described in [3–5]. The systems for studies with KL concentration from 25 to 1000 mg l^{-1} were prepared from weighed portions of KL by their dissolution in 0.1 M NaOH, dilution with distilled water, and subsequent addition of required amounts of HCl and NaCl. The efficiency of coagulation recovery of KL was determined after settling for 120 min from the residual KL concentration in the solution over the separated phase c_s and in the filtrate c_f. Filtration was carried out through a "blue band" filter. The residual concentration was determined spectrophotometrically (λ = 280 and 480 nm) on an SF-46 spectrophotometer from the optical density of the solution alkalized to pH 11, using the calibrating plot. The residual concentrations of KL in the solution and filtrate were plotted vs. pH of the system.

The pH dependences of the residual concentrations of KL in the solution (Fig. 1a) and filtrate (Fig. 1b) at ionic strength of 10^{-2} M are shown in Fig. 1. Figure 1a showes that at a KL concentration of 25 mg l^{-1} the solution is stable with respect to sedimentation throughout the studied range of pH down to pH 1.5.

1070-4272/02/7507-1166$27.00 © 2002 MAIK "Nauka/Interperiodica"

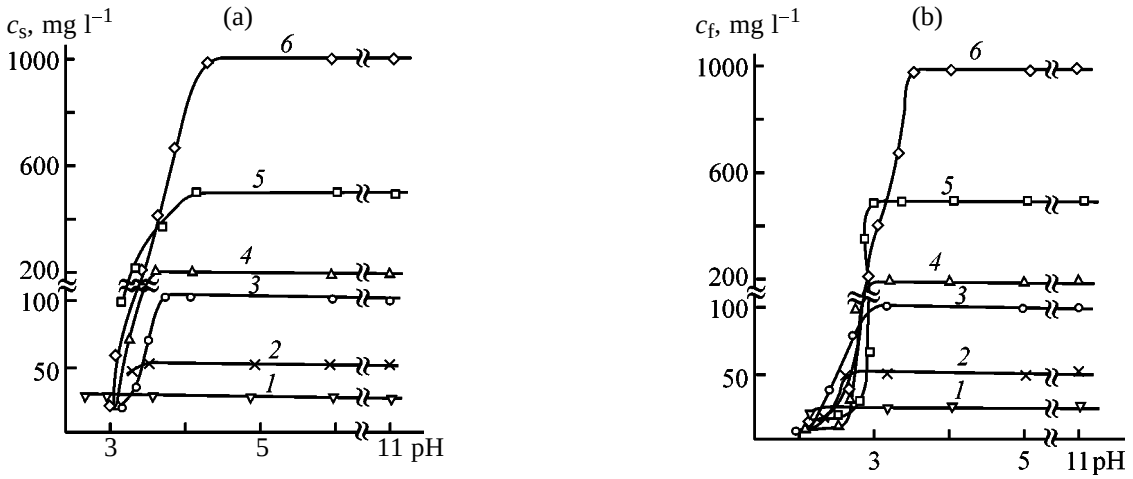

Fig. 1. Residual concentration of KL c (a) in the solution, c_s, and (b) in the filtrate, c_f, as a function of pH. Ionic strength 10^{-2}. Initial concentration of KL (mg l^{-1}): (*1*) 20, (*2*) 50, (*3*) 100, (*4*) 200, (*5*) 500, and (*6*) 1000.

An increase in the initial KL concentration results in the loss of the sedimentation stability of KL. In this case, with increasing the initial KL concentration, pH of the onset of sedimentation is shifted to the less acidic range: from pH 2.5 (50 mg l^{-1}) to 3.2 (1000 mg l^{-1}). A similar pattern is observed with filtered samples (Fig. 1b); however, pH values corresponding to the onset of retention of KL on the filter are somewhat higher (2.6 and 3.3 at KL concentration of 50 and 1000 mg ml^{-1}, respectively), because, in the initial stages of coagulation, finely dispersed slowly sedimending KL aggregates are formed, which, however, can be retained by the filter. Thus, $c_s - c_f$ (the difference between the ordinates of the respective curves in Figs. 1a and 1b) at a certain pH corresponds to the concentration of sedimentation-stable coagulated KL.

The dependences presented in Fig. 1b and also the similar dependences obtained for KL solutions in 0.1 and 1 M NaCl were used to determine the conditions of the onset of KL retention on the filter, corresponding to pH values at which c_f starts to decrease (Fig. 2). As seen from Fig. 2, an increase in KL concentration and ionic strength of the supporting electrolyte results in increased pH value of the onset of KL retention on the filter.

The resulting dependences can be explained as follows. An increase in KL concentration results in increased frequency of particle collisions. Therefore, at a higher concentration of KL, the same coagulation rate should be observed at a higher energy barrier caused, according to the DLVO theory, by the ion–ion electrostatic repulsion forces. Considering the fact that the zero-charge point of KL is at pH 2 [3, 4], at pH > 2 KL particles are negatively charged and their charge and, hence, the ion–ion electrostatic component of the particle interaction energy increases with increasing pH. This should result in a shift of coagulation pH toward lower acidities with increasing KL concentration. The similar effect should be observed with increasing ionic strength of the supporting electrolyte, resulting in weakened ion–ion electrostatic repulsion of KL particles.

Based on the experimental data on the residual KL concentrations after coagulation of the systems under "rigorous conditions" of phase separation (pH 2, zero-charge point of KL), we plotted the concentration dependences of the efficiency of KL recovery by sedimentation (Fig. 3a) and filtration (Fig. 3b) in the absence and in the presence of the supporting electrolyte NaCl. In all cases, an increase in KL concentration results in significant increase in the efficiency of KL recovery. For example, the efficiency of KL recovery (without filtration) in the absence of additional electrolyte increases from approximately zero to

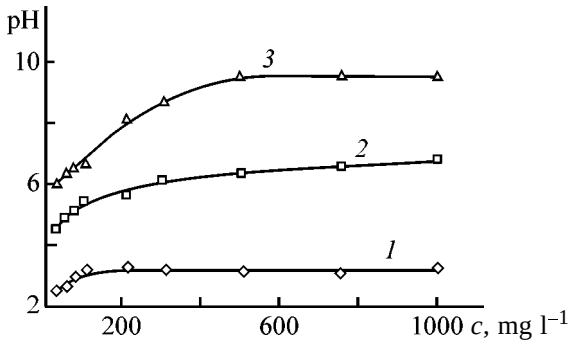

Fig. 2. pH of the onset of lignin retention on the filter as a function of lignin concentration c. NaCl concentration (M): (*1*) 0, (*2*) 0.1, and (*3*) 1.0; the same for Fig. 3.

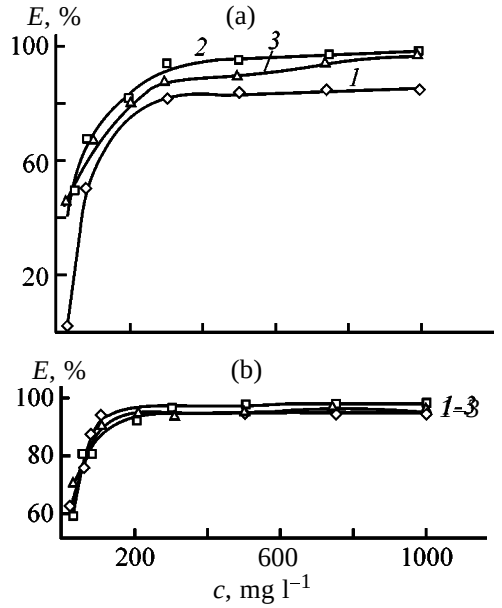

Fig. 3. Efficiency of KL recovery E (a) without filtration and (b) after filtration as a function of KL concentration c at pH 2.0.

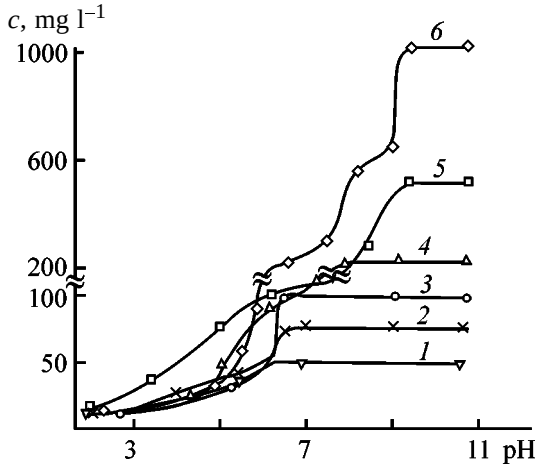

Fig. 4. Residual concentration of KL c as a function of pH after filtration. NaCl concentration 1 M. Initial concentration of KL (mg l^{-1}): (*1*) 50, (*2*) 75, (*3*) 100, (*4*) 200, (*5*) 500, and (*6*) 1000.

85% with the KL concentration increasing from 25 to 1000 mg l^{-1}.

An increase in the concentration of supporting electrolyte in the system also results in significant increase in the efficiency of KL recovery, which reaches 97.5% in 0.1 M NaCl solution at a KL concentration of 1000 mg l^{-1} (Fig. 3a). With separation of coagulated particles by filtration, the efficiency of KL recovery can reach 97–98% (Fig. 3b). It should be noted that in this case addition of supporting electrolyte does not noticeably affect the efficiency of KL recovery. The fact that 2–3% of KL remains in the solution is apparently due to the presence of a low-molecular-weight fraction in KL. This fraction remains aggregation-stable and cannot be recovered by coagulation even at the zero-charge point (pH 2) and high supporting electrolyte concentration.

The pH dependences of the residual concentration of KL (after filtration) at various initial concentrations of KL in the presence of supporting electrolyte NaCl (1 M) are presented in Fig. 4. These data show that, at the initial concentration of KL in the system of 500–1000 mg l^{-1}, in the range of pH 4.5–5.0, the residual concentrations of KL are 25–30 mg l^{-1}, i.e., the degree of its removal from the system is high. The results obtained can be of practical significance.

The natural suppoting electrolyte in the liquors from the kraft process of production of KL-containing cellulose is Na_2SO_4. Washing of cellulose to remove spent cooking liquor is an important process governing proper operation of the main shops and also the amount and degree of contamination of wastewater supplied to a treatment facility. The results of washing are usually estimated from the amount of alkali recalculated to the weight of sodium sulfate or from the degree of withdrawal of dry substances of black liquor from washing to regeneration. Therefore, local recovery of KL from the wastewater of a cooking and washing shop and return of KL in the form of precipitate to the total process flow for regeneration is environmentally and economically attractive.

Since the coagulating powers of NaCl and Na_2SO_4 for negatively charged particles (in our case, KL particles) differ insignificantly, data in Fig. 4 suggest that, with local treatment systems, KL can be recovered to a high degree from liquor-containing flows by their acidification. The higher the concentrations of KL and sodium sulfate, the higher is pH of coagulation recovery of KL. The KL precipitate recovered by this procedure can be supplied to soda-regeneration boilers together with evaporated black liquor, and clarified water with a minimal content of low-molecular-weight fraction of KL from the system of local treatment, to washing of cellulose or to the biological treatment station. After biological treatment, with consideration of dilution and purification, the concentration of organic substances in wastewater will be substantially decreased and will become lower than MPC.

CONCLUSIONS

(1) The pH of coagulation recovery of kraft lignin in filtration of its aqueous solution depends on the concentrations of kraft lignin and supporting electrolyte in the system. An increase in the concentrations

of kraft lignin and NaCl (and, hence, of other Na-containing salts) shifts pH of recovery of kraft lignin to higher values.

(2) Irrespective of the concentrations of kraft lignin and supporting electrolyte NaCl in the initial solution, approximately 2% of the initial amount of kraft lignin remains in the solution after its coagulation treatment. This is due to the presence of low-molecular-weight fraction of kraft lignin unaffected by coagulation recovery.

(3) The results obtained can be used for design of closed-loop systems for water supply in kraft procedure of cellulose production.

REFERENCES

1. Nevolin, V.F. and Korovin, L.K., *Tsellyuloza, Bumaga, Karton*, 1995, nos. 7–8, pp. 29–32.
2. Shvarts, A., *Tsellyuloza, Bumaga, Karton*, 2000, nos. 7–8, pp. 2–4.
3. Chernoberezhskii, Yu.M. and Dyagileva, A.B., *Kolloidn. Zh.*, 1994, vol. 56, no. 2, pp. 287–289.
4. Chernoberezhskii, Yu.M. and Dyagileva, A.B., *Kolloidn. Zh.*, 1995, vol. 57, no. 1, pp. 132–134.
5. Lorentsson, A.V., Chernoberezhskii, Yu.M., and Dyagileva, A.B., *Zh. Prikl. Khim.*, 1999, vol. 72, no. 9, pp. 1496–1498.

Russian Journal of Applied Chemistry, Vol. 75, No. 7, 2002, pp. 1170–1172. Translated from Zhurnal Prikladnoi Khimii, Vol. 75, No. 7, 2002, pp. 1193–1195.
Original Russian Text Copyright © 2002 by Dem'yantseva, Lysogorskaya.

MACROMOLECULAR CHEMISTRY AND POLYMERIC MATERIALS

Colloid-Chemical Characteristics of Aqueous Alkaline Solutions of Organic Components of Pine and Birch Wood

E. Yu. Dem'yantseva and N. P. Lysogorskaya

St. Petersburg State Technological University of Plant Polymers, St. Petersburg, Russia

Received October 15, 2001; in final form, March 2002

Abstract—The surface activity and sedimentation stability of organic substances passing into solution in kraft cooking of pine wood were studied. The data obtained were compared with the corresponding data characteristic of organic components of birch wood.

In kraft cooking of cellulose, resin and fatty acids contained in wood are saponified and pass into solution, black liquor, in the form of sodium salts. Recovery of the resulting sulfate soap from black liquors is governed by its salting-out and settling. Despite the growth of production of sulfate soap and tall oil, the coefficients of their recovery remain low (approximately 50%) [1]. Knowledge of the composition of solutions of wood organic substances passing into the liquor during cooking, their surface activity, and its dependence on the solution temperature can facilitate development of scientific principles of radically new efficient processes for recovery of secondary products formed in kraft cooking. Previously we proved that solutions of organic substances of birch wood in aqueous alkaline medium from kraft cooking are heterogeneous [2, 3]. In this connection, it was of interest to study the sedimentation stability, surface tension, and surface activity of solutions of organic substances of pine wood as a typical coniferous wood and birch as a typical deciduous wood, used in kraft cooking.

Solutions of wood organic substances had pH 12.7, which corresponds to pH of real liquors in kraft cooking. The selected temperature interval (363–293 K) and cooling time (40 min) corresponded to the stage of completion of kraft cooking and separation of black liquor. Precisely this stage is responsible for problems brought about by resins in pulp and paper production [4].

The initial samples of kraft lignin, resinous components, and carbohydrate derivatives were prepared by extraction from wood with various solvents. Lignin was extracted with dioxane, and resin, with diethyl ether. To prepare solutions for the study, the above substances were subjected to the traditional kraft cooking for 1 h at 443 K (liquor ratio 4 : 1). The solution of carbohydrate derivatives was prepared by kraft cooking of holocellulose preliminarily recovered from deresined wood by thorough delignification with peracetic acid. In addition to the solutions of individual components, we used the black liquor (a mixture of organic substances under consideration) recovered after kraft cooking of wood chips. The sedimentation stability of the systems at various temperatures was studied gravimetrically by monitoring of the residual concentration of the substances in the solution during cooling.

The concentration of organic substances of pine and birch wood in aqueous alkaline solution as a function of temperature is plotted in Fig. 1. As seen from Fig. 1a, the amount of dissolved pine wood resin decreases with temperature (curve *1*), which is due to a decrease in the resin solubility and formation of a sedimentation-unstable system. It also follows from Fig. 1 that the rate of sedimentation of the resin particles formed is low. This is due to small difference in the densities of resin particles and liquor, which are 0.95 and 1.15 g cm^{-3}, respectively.

The solutions of kraft lignin and carbohydrate derivatives are sedimentation-unstable. In the case of pine wood, the solutions are somewhat less stable than in the case of birch wood (Figs. 1a and 1b, curves *2* and *3*). The highest sedimentation instability is observed in the solutions of the mixture of organic substances. This is due to a larger size of their particles in comparison with the particle size of individual components [3]. The previously found aggregation instability of the mixture of substances is apparently caused by formation of adsorption ligno-

1070-4272/02/7507-1170$27.00 © 2002 MAIK "Nauka/Interperiodica"

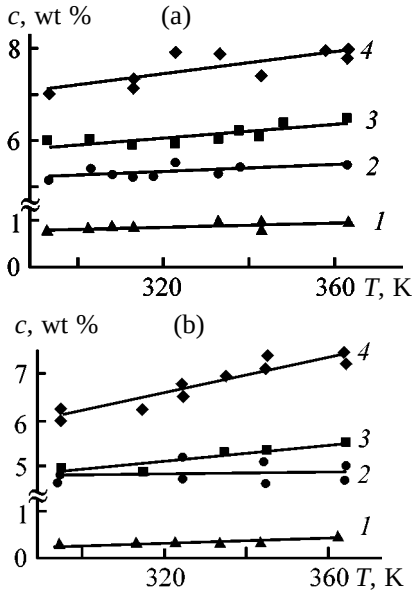

Fig. 1. Concentration of organic substances of (a) pine wood and (b) birch wood in aqueous alkaline solution c as a function of temperature T. (*1*) Resinous substances, (*2*) kraft lignin, (*3*) derivatives of carbohydrate fraction, and (*4*) mixture of organic substances; the same for Fig. 3.

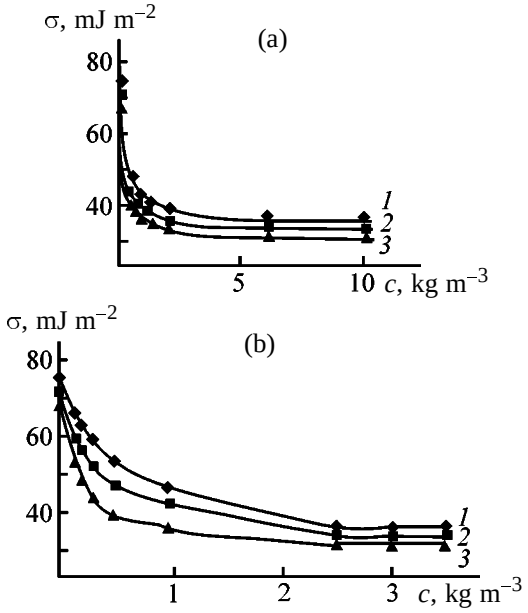

Fig. 2. Surface tension σ of solutions of resinous substances of (a) pine wood and (b) birch wood as a function of solution concentration c at various temperatures T. Temperature (K): (*1*) 293, (*2*) 313, and (*3*) 333.

carbohydrate complexes with resin in cooling of the solutions. It should be noted that the sedimentation instability of the mixture of organic components of birch wood is higher than that of pine wood.

To explain the data obtained, we measured the surface tension of the systems by the ring detachment method [5] at 293, 313, and 333 K, plotted the surface tension isotherms, and evaluated the surface activity G (mJ m kg^{-1}) of the substances by the formula [6]

$$G = \lim \partial\sigma/\partial c, \text{ at } c \to 0,$$

where σ is the surface tension (mJ m^{-2}), and c is the solution concentration (kg m^{-3}).

The surface tension isotherms of the solutions of resinous components of pine and birch wood are shown in Fig. 2. The shapes of the isothermal curves are similar to those of traditional surfactants. With increasing concentration, the surface tension decreases, and in this concentration range the solutions are homogeneous. From a certain concentration of the solutions, the surface tension does not vary noticeably (as for traditional surfactants), which suggests micelle formation and heterogeneity of the solutions. This allows evaluation of the fractions of the homogeneously and heterogeneously dissolved substance. In solutions of resinous substances of birch wood at the initial concentration of the substances of 0.5% and critical micelle concentration c_{CMC} 0.1%, the homogeneously dissolved fraction is 20%. For resinous substances of pine wood at the initial concentration of 1% and c_{CMC} 0.32%, it is 32%.

The surface activities evaluated from the surface tension isotherms are listed in the table.

The table shows that birch extractives are more surface-active. This may be due to high content of fatty acids and phenolic compounds (including sterols) having high surface activity. The surface activities of

Surface activity G of resinous components and kraft lignin in aqueous–alkaline solutions

T, K	G, mJ m kg^{-1}	
	resinous substances	kraft lignin
	Pine wood	
293	11.9	4.8
313	18.6	5.0
333	19.1	5.1
	Birch wood	
293	40.0	3.5
313	74.0	4.3
333	84.0	4.3

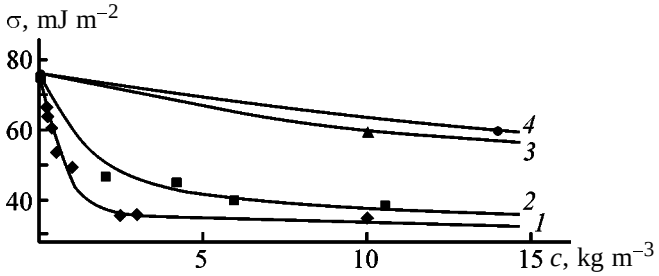

Fig. 3. Surface tension σ of solutions of organic substances of birch wood at 293 K as a function of solution concentration *c*.

pine wood extractives are lower by a factor of 3–4, which is due to lower surface activity of resinous acids mainly contained in the extractive components of pine wood [1]. High surface activity of resinous substances of birch wood suggests their higher hydrophobicity and, hence, higher tendency to aggregate in aqueous solutions. This can explain their higher sedimentation instability described above.

The surface tension isotherms of the other studied solutions of pine wood and birch wood substances are similar. Therefore, Fig. 3 presents the surface tension isotherms only for solutions of organic substances of birch wood. From the surface tension isotherms of kraft lignin solution (curve *2*), the fraction of homogeneously dissolved substance was estimated to be 28% for kraft lignin of birch (substance concentration 5.3%, c_{CMC} 1.5%) and 17% for kraft lignin of pine (substance concentration 6%, c_{KCM} 1%). According to data in the table, the surface activity of solution of kraft birch lignin is lower than that of pine wood, which suggests its higher hydrophilicity and, hence, higher sedimentation stability, as mentioned above.

A comparison of the surface tension isotherms of solutions of resinous components (Fig. 3, curve *1*) and kraft lignin (curve *2*) with the isotherm of the mixture of components (curve *4*) shows that, in the latter case, surface tension does not noticeably decrease. This may be due to the absence of free homogeneously dissolved fraction of resin and lignin, which can be adsorbed at the solution–air interface and decrease the surface tension. Hence, the molecular-dispersed soluble fractions of lignin and resinous substances, found when the individual components are dissolved (Figs. 2, 3), apparently, are not in the free state but are bonded to dispersed particles to form an adsorption complex. This confirms the presumed formation of an adsorption lignocarbohydrate complex with resin in aqueous alkaline solutions of the mixture of organic components.

CONCLUSIONS

(1) The mixture of organic substances of birch and pine wood is less sedimentation-stable in aqueous alkaline solutions than solutions of components of this mixture taken separately.

(2) The fractions of homogeneously and heterogeneously dissolved components in aqueous alkaline solutions were estimated to be 28 and 72% for kraft birch lignin, 17 and 83% for pine lignin, 20 and 80% for resinous substances of birch wood, and 32 and 68% for those of pine wood, respectively.

(3) The surface tension isotherms of solutions of the mixture of organic substances suggest their practical inactivity and possible formation of an adsorption lignocarbohydrate complex with the resin.

REFERENCES

1. Bogomolov, B.D., *Pererabotka sul'fatnykh i sul'fitnykh shchelokov* (Processing of Sulfate and Sulfite Liquors), Moscow: Lesnaya Prom–st., 1989.
2. Dem'yantseva, E.Yu., Lysogorskaya, N.P., Halopenen, I.J., and Jaakkola, P., *Zh. Prikl. Khim.*, 1999, vol. 72, no. 9, pp. 1546–1548.
3. Dem'yantseva, E.Yu., Lysogorskaya, N.P., Klyubin, V.V., and Zaitseva, S.V., *Zh. Prikl. Khim.*, 2002, vol. 75, no. 1, pp. 149–151.
4. Lysogorskaya, N.P., The Fundamentals of Cellulose Deresination with Surfactants, *Doctoral Dissertation*, St. Petersburg, 1993.
5. Abramzon, A.A., *Zh. Prikl. Khim.*, 1999, vol. 72, no. 6, pp. 924–928.
6. Abramzon, A.A., *Poverkhnostno-aktivnye veshchestva* (Surfactants), Leningrad: Khimiya, 1981.

Russian Journal of Applied Chemistry, Vol. 75, No. 7, 2002, pp. 1173–1177. Translated from Zhurnal Prikladnoi Khimii, Vol. 75, No. 7, 2002, pp. 1196–1200.
Original Russian Text Copyright © 2002 by Begak, Syroezhko, Fedorov, Malechkina, Nassonova.

CHEMISTRY OF FOSSIL FUEL

Prediction of the Quality of Petroleum Tars and Bitumens by Infrared Spectroscopic and X-ray Diffraction Methods

O. Yu. Begak, A. M. Syroezhko, V. V. Fedorov, M. N. Malechkina, and M. B. Nassonova

Mendeleev Russian Research Institute of Metrology, St. Petersburg, Russia
St. Petersburg State Technological Institute, St. Petersburg, Russia

Received January 31, 2002

Abstract—The degree of aromaticity of petroleum tars, bitumens, and their fractions is characterized by infrared spectroscopy and X-ray diffraction.

Resinous-asphaltenic matter (RAM) of petroleum tars of West Siberian industrial oil occurs in the substrate as particles with a discrete size distribution [1]. However, their major amount (91%) forms aggregates 2.6–3.2 nm in size. There is only limited information on the supramolecular structure of RAM of bitumens of the indicated oil [2]. It was demonstrated that more structured quality bitumens are characterized by not only more compact chain-packed structure of asphaltenes, but also by closer packing of malthenes around the asphaltenic cores as a result of their higher aromaticity as compared to less thermostable (substandard) bitumens. Malthenes of petroleum tars and bitumens contain a broad spectrum of chemical compounds with different molecular weights, with the structures based on naphthene–aromatic cores with various alkyl substituents. Note that the major amounts of heteroatoms and metal complexes of the petroleum are concentrated in RAM.

Chromatographic group analysis [3] allows separation of petroleum tars and bitumens into cleaner cuts differing in their polarity [naphthenoparaffinic compounds (NPCs), monocycloaromatic compounds (MCACs), bicycloaromatic compounds (BCACs), toluene (TRs) and alcohol–toluene resins (ATRs)]. The supramolecular structure of tars is formed in the course of genesis of the crude oil, and that of bitumens, in the course of oxidation of tars and in the subsequent aging.

After fabrication of bitumen, its structured colloidal system gradually reaches the thermodynamic equilibrium characterized by the fixed distribution of RAM between the dispersed phase (asphaltenes) and the dispersion medium (malthenes). Malthenes of petroleum tars and bitumens contain polar (PCs) and nonpolar components (NPCs). The degree of their structurization is different. In this work we studied the supramolecular structure of the dispersed phase and dispersion medium in petroleum tars and related bitumens (quality and substandard), using chemical analysis, IR spectroscopy, and X-ray diffraction.

EXPERIMENTAL

In the work we studied two samples of petroleum tars (from AVT-6 unit of the KINEF Limited Liability Company) and two samples of bitumens obtained by oxidation of the indicated tar samples. The characteristics of the samples are given in Table 1. It is interesting that the bitumens obtained from the tar samples with a close relative viscosity demonstrate a considerably different thermal stability. One of them (BDUS 70/100) was classified with quality bitumens, as totally meeting the requirements of the technical specifications for bitumens with respect to the softening point, penetration Π_{25}, and elasticity before and after heating in a thin layer at 160°C for 5 h (this test simulates aging of bitumen). The second sample of bitumen (BDUS 60/90) is characterized by a lower thermal stability reflected in an intolerably low penetration and ductility after heat treatment.

Petroleum tars and bitumens were deasphalted by the cool and Holde's hot methods [4, 5] in a Soxhlet apparatus.

Polar components were extracted from malthenes of the tars and bitumens with DMF [6].

Group separation of polar and nonpolar components was performed on silica gel according to the

1070-4272/02/7507-1173$27.00 © 2002 MAIK "Nauka/Interperiodica"

Table 1. Contents of asphaltenes, malthenes, and polar and nonpolar components in petroleum tars and bitumens

Product	Content, wt %			
	malthenes	asphaltenes	PCs	NPCs
Tar, Π_{25} = 305 mm × 0.1, relative viscosity 89 s	89.55	10.45	16.6	83.4
Tar, Π_{25} = 390 mm × 0.1, relative viscosity 92 s	88.62	11.38	15.1	84.9
BDUS 70/100, Π_{25} = 84 mm × 0.1, sp* 46°C, D_{25} = 140 cm	80.7	19.3	21.1	78.9
BDUS 60/90, Π_{25} = 78 mm × 0.1, sp 48°C, D_{25} >150 cm	79.0	21.0	21.4	78.6

* Ring and ball softening point.

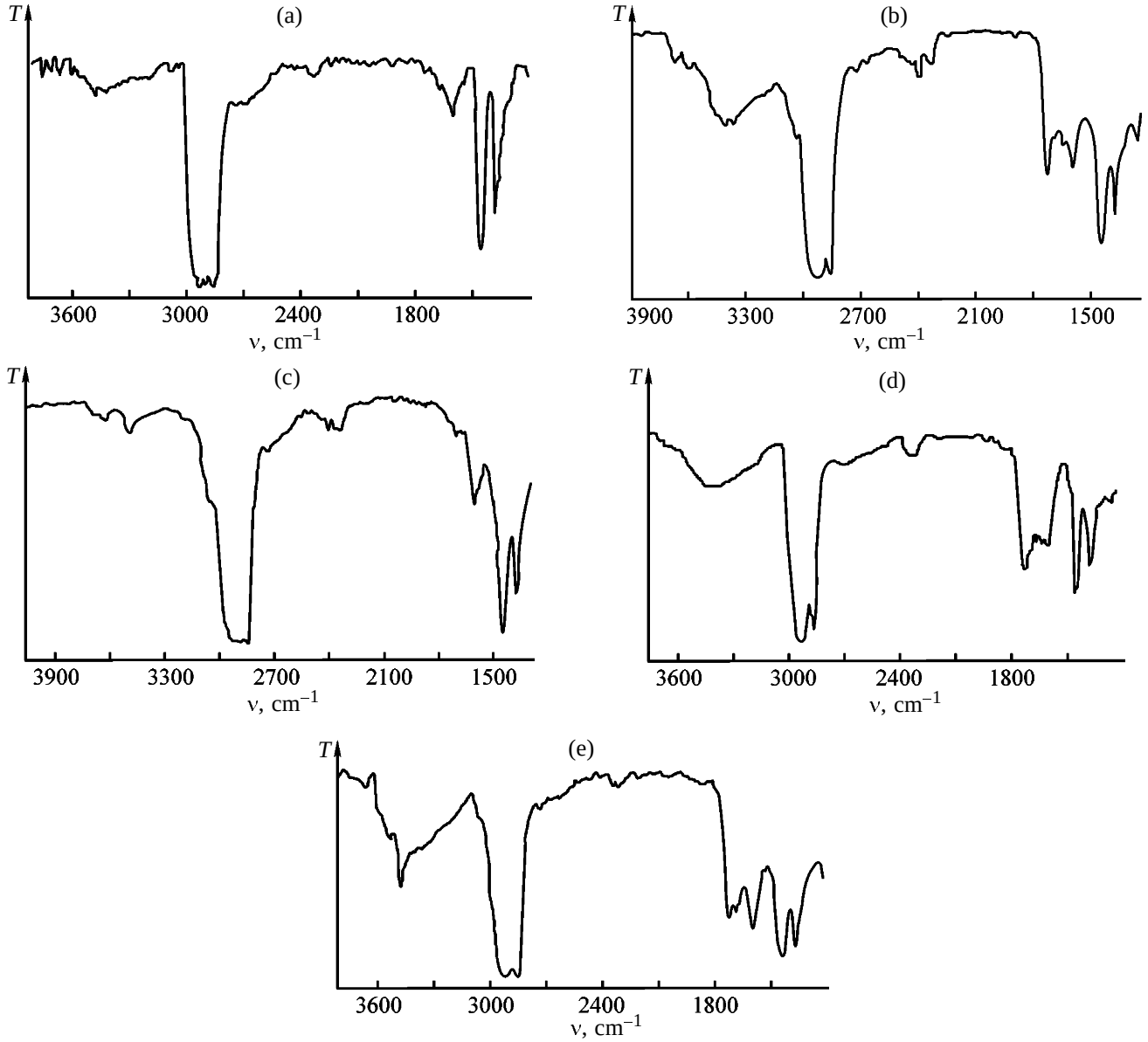

Fig. 1. Infrared spectra: (a) NPCs of BDUS 70/100 bitumen (sp 46°C), (b) MCACs of tar, (c) BCACs of tar, (d) ATRs of BDUS 70/100 bitumen (sp 46°C), and (e) TRs of BDUS 70/100 bitumen (sp 46°C). (b–d) Penetration Π_{25} = 305 mm × 0.1. (*T*) Transmittance and (ν) wave number.

Table 2. IR data for bitumens and tars

Product	ν, cm^{-1}	Intensity, arb. units				
		NPCs	MCACs	BCACs	TRs	ATRs
Nonpolar components of tar, Π_{25} = 305 mm × 0.1	1590	–	33	55	60	78
	3050	–	37	57	60	55
	2930	77	95	115	91	88
	1590/2930	–	0.35 (1)	0.48 (1.37)*	0.66 (1.89)	0.89 (2.54)
	3050/2930	–	0.39 (1)	0.5 (1.28)	0.66 (1.69)	0.63 (1.61)
Polar components of tar, Π_{25} = 305 mm × 0.1	1590	–	49	89	80	57
	3050	–	64	53	52	51
	2930	120	90	94	83	77
	1590/2930	–	0.54	0.95	0.96	0.74
	3050/2930	0.71 (1)	0.56 (0.79)	0.63 (0.89)	0.66 (0.93)	
Nonpolar components of bitumen BDUS 70/100, sp 46°C	1590	–	43	55	89	70
	3050	–	35	50	55	52
	2930	100	100	110	75	73
	1590/2930**	–	0.43 (1)	0.5 (1.16)	1.18 (2.74)	0.96 (2.23)
	3050/2930***	0.35 (1)	0.45 (1.29)	0.73 (2.08)	0.71 (2.02)	

* I_i/I_{MCAC}.
** Ratio of the optical densities of the bands due to CH_{ar} out-of-plane bending vibrations and asymmetric stretching vibrations of CH_2 groups.
*** Ratio of the optical densities of the bands due to CH_{ar} stretching vibrations and asymmetric stretching vibrations of CH_2 groups.

procedure described in [3]. The boundaries of chromatographic zones of the fractions (NPCs, MCACs, BCACs, TRs, and ATRs) were determined by the characteristic luminescence under UV light.

The infrared spectra were recorded on an IKS-29 instrument over the ranges 1100–1800 and 2600–3100 cm^{-1}. The samples were prepared as thin layers or 5% solutions in $CHCl_3$. We analyzed the bending and stretching vibration bands of C–H and C–C bonds in the CH_3 and CH_2 groups and aromatic fragments: the methylene groups in paraffin and six-membered naphthene structures were determined by the bands at 2850 and 2930 cm^{-1}; the bands at 1590 and 3050 cm^{-1} were assigned to the C–C and C–H vibrations in aromatic fragments, respectively; and also we monitored the intensities of the bands at 1378 and 1460 cm^{-1}, to estimate the content of the C–H bonds in the methyl and methylene groups, respectively.

Asphaltenes extracted from petroleum tars and bitumens, the tars and bitumens themselves, and their polar and nonpolar components were also studied by X-ray diffraction using a DRON-2 diffractometer (CuK_α, V = 8.9 kV, λ = 1.544 Å, T = 22°C). We used samples in the form of fine powders (no solvent), to prevent degradation of supramolecular structures. The X-ray diffraction patterns were processed as in [2].

Table 1 shows that the yields of malthenes from both tar samples are very close (88.62 and 89.55%). The same is true for the yields of polar and nonpolar components. After oxidation of the tars into bitumens BDUS 70/100 and BDUS 60/90, the yield of malthenes decreased to 79–80.7%, and the yield of asphaltenes increased.

While the asphaltene content in the initial tars was 10.45–11.38%, that in the corresponding bitumens ranged from 19.3 to 21%. The yield of polar components from the bitumens is higher by 4.3–6.3% than that from the corresponding tars. In this case, the oxidative conversion of the tar with the initial penetration of 390 mm × 0.1 and relative viscosity of 92 s was higher (sp 48°C) as compared to the sample with the initial penetration of 305 mm × 0.1 and relative viscosity of 89 s. The content of polar components in the bitumen having higher softening point increased by 1.8%. Bitumen BDUS 70/100 appeared to be thermostable, and BDUS 60/90, having lower thermal stability, appeared to be substandard (penetration and ductility of this bitumen considerably decreased after heat treatment of a thin layer at 160°C for 5 h).

The typical IR spectra of group components of the tars and bitumens studied are given in Figs. 1a–1e, and their parameters, in Table 2.

For nonpolar and polar components of the tar and bitumen, the ratios I_{1590}/I_{2930} and I_{3050}/I_{2930} increase

Table 3. X-ray diffraction data for tars, bitumens, asphaltenes, and polar and nonpolar components of malthenes

Sample	X-ray diffraction parameters, nm						Asphaltene content in samples, wt %
	d_m	d_γ	L_a	L_s	f_{ar}	M	
Bitumen (sp 46°C)	0.37	0.554	1.56	1.98	0.31	6.35	19.3
Bitumen (sp 48°C)	0.374	0.554	1.44	1.61	0.29	5.3	21
Malthenes of bitumen (mp 46°C)	0.37	0.554	1.57	1.98	0.265	6.35	17.45, heating to 160°C
Tar ($\prod_{25}$ = 305 mm × 0.1)	0.37	0.554	1.25	1.64	0.28	5.43	10.45
Tar ($\prod_{25}$ = 390 mm × 0.1)	0.378	0.554	1.16	1.32	0.27	4.57	1.38
Malthenes of tar ($\prod_{25}$ = 305 mm × 0.1)	0.386	0.554	1.62	1.98	0.23	6.13	7.5, heating to 160°C
Malthenes of tar ($\prod_{25}$ = 390 mm × 0.1)	0.386	0.583	1.48	1.325	0.24	4.43	Not detected
Nonpolar components of tar ($\prod_{25}$ = 305 mm × 0.1)	0.37	0.554	2.02	1.262	0.21	4.42	5.82
Nonpolar components of bitumen (sp 46°C)	0.37	0.554	1.116	0.88	0.35	3.39	20.2
Polar components of bitumen (sp 46°C)	0.37	0.515	1.02	0.88	0.52	3.38	22
Polar components of tar ($\prod_{25}$ = 305 mm × 0.1)	0.37	0.515	2.02	1.10	0.55	3.97	15.8
Asphaltenes of tar ($\prod_{25}$ = 305 mm × 0.1)	0.37	0.504	1.84	1.986	0.36	4.94	Native
Asphaltenes of bitumen (mp 46°C)	0.37	0.554	1.40	1.980	0.395	6.35	Native + secondary
Asphaltenes of nonpolar components of tar ($\prod_{25}$ = 390 mm × 0.1)	0.355	0.651	1.73	1.08	0.44	4.03	Native
Asphaltenes of polar components of tar ($\prod_{25}$ = 390 mm × 0.1)	0.37	0.615	1.162	0.877	0.45	3.37	Native

on passing from MCACs to BCACs and then to TRs, suggesting increase in the degree of aromaticity in this series. Somewhat lower intensity ratio of the indicated bands in the IR spectra of ATRs is consistent with the results of direct determination of the contents of aromatic hydrogen and carbon by ^1H and ^{13}C NMR.

The interplanar spacings d_m in asphaltene blocks and micelles of bitumens, tars, and polar and nonpolar components were estimated according to the procedure described in [7]:

$$d_m = 0.5\lambda/\sin\theta_{002},$$

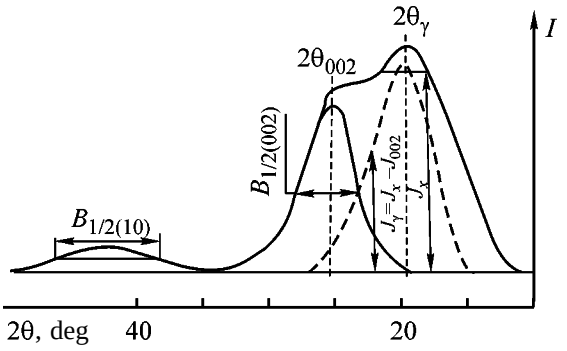

Fig. 2. Typical X-ray diffraction pattern of asphaltenes from bitumen BDUS 70/100 (sp 46°C). (*I*) Peak intensity and (2θ) Bragg angle.

where λ is the wavelength (Å) of the X-ray radiation used.

We analyzed the peak of amorphous carbon at $2\theta_\gamma$ = 18° (Fig. 2). This peak is due to scattering on spatially disordered carbon atoms and heteroatoms. Asphaltene and resin particles forming the ordered stack structure [8] give two broad peaks in the X-ray diffraction patter: a weak peak (10) at $2\theta_{10}$ = 42° due to reflection from planar aromatic layers and also a peak (002) at $2\theta_{002}$ = 21.5°–24°.

From the X-ray diffraction patterns, we estimated [7] the regular spacings between paraffin fragments of the molecules $d_\gamma = 0.625\lambda/\sin\theta_\gamma$ and also the interplanar spacing d_m, size of the condensed aromatic layers L_a, thickness of the stack of aromatic layers L_s, and number of the aromatic layers in the stack M.

From the measured peak halfwidths $B_{1/2}(10)$ and $B_{1/2}(002)$, expressed in the $\sin\theta/\lambda$ units, using the Scherrer equations, we estimated the mean diameter of planar molecular fragments in the stack $L_a = 0.92\,B_{1/2}(10)$ and the mean thickness of the stack $L_c = 0.45\,B_{1/2}(002)$. The mean number of the layers in the stack was estimated as

$$M = (L_c/d_m) + 1.$$

Also we measured the areas under individual peaks (002) and γ (A_{002} and A_γ, respectively) and estimated the aromaticity factor f_{ar} as $f_{ar} = A_{002}/(A_{002} + A_\gamma)$.

The estimated results are summarized in Table 3. It is seen that all the samples studied are considerably different in the parameters of the asphaltene stacks. Asphaltenes, malthenes, and bitumen with sp 46°C appeared to be the most ordered. It is the latter sample that demonstrates the maximal cohesion, which is reflected in the minimal change in its ductility after heat treatment.

CONCLUSIONS

(1) Infrared spectroscopy was used to quantitatively estimate the degree of aromaticity of various polar and nonpolar fractions of malthenes in petroleum tar and quality thermostable bitumen (KINEF Limited Liability Company). The aromaticity increases in the order monocycloaromatic compounds < bicycloaromatic compounds < toluene resins < alcohol–toluene resins.

(2) Parameters of the supramolecular structure of asphaltenes, tars, bitumens, and polar and nonpolar fractions of malthenes were obtained from the X-ray diffraction data. The samples studied are distinguished by parameters of the stack structure of asphaltenes. Asphaltenes, malthenes, and quality bitumen having the maximal cohesion and high thermal stability (minimal change in $\prod_{25}$ and D_{25} after heating under standard conditions) have the most ordered structure.

REFERENCES

1. Khryashchev, A.N., Association of Resinous-Asphaltenic Components of Crude Oil, *Cand. Sci. Dissertation*, Leningrad, 1991.
2. Begak, O.Yu. and Syroezhko, A.M., *Zh. Prikl. Khim.*, 2001, vol. 74, no. 4, pp. 675–678.
3. Kolbanovskaya, A.S., *Tr. Soyuzdornii* (Moscow), 1968, issue 27, pp. 120–125.
4. Korchagina, V.I., Rutman, L.I., and Shnol', F.I., *Neftepererab. Neftekhim.*, 1964, no. 2, pp. 18–21.
5. Antipenko, V.R. and Titov, V.I., *Neftekhimiya*, 1974, vol. 14, no. 4, pp. 505–509.
6. Pechenyi, B.G., *Bitumy I bitumnye kompozitsii* (Bitumens and Bitumen Composites), Moscow: Khimiya, 1990.
7. Begak, O.Yu. and Syroezhko, A.M., *Zh. Prikl. Khim.*, 2001, vol. 74, no. 5, pp. 854–857.
8. Bodan, A.N., *Khim. Tekhnol. Topl. Masel*, 1982, no. 12, pp. 22–24.

Russian Journal of Applied Chemistry, Vol. 75, No. 7, 2002, pp. 1178–1184. Translated from Zhurnal Prikladnoi Khimii, Vol. 75, No. 7, 2002, pp. 1201–1208.
Original Russian Text Copyright © 2002 by Begak, Syroezhko, Fedorov.

CHEMISTRY OF FOSSIL FUEL

Distribution of Elements among Fractions of Petroleum Tars and Bitumens from West Siberian Industrial Oil

O. Yu. Begak, A. M. Syroezhko, and V. V. Fedorov

Mendeleev Russian Research Institute of Metrology, St. Petersburg, Russia
St. Petersburg State Technological Institute, St. Petersburg, Russia

Received January 31, 2002

Abstract—Distribution of C, H, N, S, and O among polar and nonpolar components of malthenes and asphaltenes of initial tars and quality and substandard bitumens obtained from them is studied by chemical and elemental analyses and ^{1}H and ^{13}C NMR.

Improving quality of road asphalts is a topical problem [1]. The heaviest supplier of this material in the Russian Northwest is the KINEF Limited Liability Company refining West Siberian industrial oil. At present, this company manufactures BDUS road bitumens having higher quality as compared to BND tars. However, along with thermostable quality road tars, substandard products are sometimes obtained from particular batches of petroleum tars, which do not meet the requirements of the technical specifications with respect to the thermal stability [ductility of a thin layer of the product after heating at 160°C for 5 h decreases to an intolerably low value ($D_{a.h.}$<100 cm)].

Therefore, the goal of this work was to reveal what characteristics of the initial petroleum tars and resulting road bitumens and their fractions (polar and nonpolar components of malthenes and asphaltenes) may be responsible for the observed differences in the quality of the products.

EXPERIMENTAL

Elemental (C, H, N) analysis was carried out on a Perkin–Elmer-240 analyzer. Sulfur was determined by the Schoeniger microanalysis method.

The ^{1}H NMR spectra were recorded on a Tesla BS-497 instrument (working frequency 100 MHz) against internal HMDS.

Distribution of carbon and hydrogen among fractions of petroleum and road asphalts and polar and nonpolar components of malthenes was studied by ^{1}H and ^{13}C NMR using a Bruker AM-500 instrument (working frequencies 500 and 125 MHz, respectively) at room temperature. In recording ^{1}H NMR spectra, we used 5-μs pulses (30°) (relaxation delay between pulses 15 s; number of scans 32).

The ^{13}C NMR spectra were recorded with inverse gated proton decoupling [to reduce the nuclear Overhauser effect, we used 5-μs pulses (60°) and relaxation delay of 10 s (number of scans 6000)].

In the work, we studied two samples of petroleum tars (from AVT-6 unit of the KINEF Limited Liability Company) and two samples of bitumens obtained by oxidation of the indicated tar samples. In addition, four BDUS samples (two quality and two substandard) were studied by ^{1}H and ^{13}C NMR. The differences between the bitumen samples were that substandard bitumens did not meet the requirements of the technical specifications for bitumens with respect to the ductility after heating in a thin layer at 160°C for 5 h (this test simulates aging of bitumen).

Characteristics of the samples studied were as follows: tar, penetration Π_{25} = 305 mm × 0.1, relative viscosity 89 s; tar, Π_{25} = 390 mm × 0.1, relative viscosity 92 s; BDUS 70/100, Π_{25} = 84 mm × 0.1, sp* 46°C, D_{25} = 140 cm; BDUS 60/90, Π_{25} = 78 mm × 0.1, sp 48°C, D_{25} >150 cm; quality BDUS 70/100, sp 45°C, D_{25} = 147 cm, Π_{25} = 97 mm × 0.1, Π_{25ah}** = 74% of the initial Π_{25}, D_{25ah} = 125 cm; quality BDUS 100/130, sp 43°C, D_{25} = 148 cm, Π_{25} = 103 mm × 0.1, Π_{25ah} = 68% of the initial Π_{25}, D_{25ah} = 140 cm; substandard BDUS 70/100, sp 47°C, D_{25} = 131 cm, Π_{25} = 100 mm × 0.1, Π_{25ah} = 60% of the initial Π_{25}, D_{25ah} = 55 cm; and substandard BDUS 100/130, sp 45°C, D_{25} = 146 cm, Π_{25} =

* Ring-and-ball softening point.
** After heating in a thin layer at 160°C for 5 h.

1070-4272/02/7507-1178$27.00 © 2002 MAIK "Nauka/Interperiodica"

Table 1. Elemental composition of tars, bitumens, their polar and nonpolar components, and asphaltenes

Product	Content, wt %					H/C atomic ratio
	C	H	N	S	O	
Tar (Π_{25} = 305 mm × 0.1, relative viscosity 89 s)	85.56	9.26	0.29	1.40	3.49	1.29
Tar (Π_{25} = 390 mm × 0.1, relative viscosity 92 s)	85.55	8.90	0.41	1.64	3.50	1.25
Polar components of tar (Π_{25} = 305 mm × 0.1)	84.60	8.92	0.60	2.80	3.08	1.26
Nonpolar components of tar (Π_{25} = 305 mm × 0.1)	87.3	9.74	0.27	1.13	1.56	1.34
Polar components of tar (Π_{25} = 390 mm × 0.1)	84.16	9.11	0.86	1.51	4.37	1.30
Nonpolar components of tar (Π_{25} = 390 mm × 0.1)	86.97	9.88	0.36	1.45	1.34	1.37
Asphaltenes of polar components of tar (Π_{25} = 305 mm × 0.1)	83.43	7.58	1.01	3.00	4.98	1.09
Asphaltenes of nonpolar components of tar (Π_{25} = 305 mm × 0.1)	85.45	7.82	0.87	1.40	4.46	1.10
BDUS 70/100	85.35	9.07	0.37	1.56	3.65	1.27
BDUS 60/90	86.00	9.01	0.46	1.73	3.80	1.26
Polar components of BDUS 60/90	84.58	8.88	0.94	2.46	3.14	1.26
Nonpolar components of BDUS 60/90	85.59	10.11	0.31	1.57	2.42	1.42
Polar components of BDUS 70/100	84.60	8.30	0.83	3.06	3.21	1.18
Nonpolar components of BDUS 70/100	87.40	9.98	0.28	1.32	1.02	1.37
Asphaltenes of BDUS 70/100	83.16	7.42	0.94	2.80	5.68	1.07
Asphaltenes of nonpolar components of BDUS 70/100	85.45	7.71	1.05	2.88	2.91	1.08
Asphaltenes of polar components of tar (Π_{25} = 390 mm × 0.1)	86.12	7.95	1.00	2.88	2.05	1.11
Asphaltenes of nonpolar components of tar (Π_{25} = 390 mm × 0.1)	85.54	7.74	0.75	2.62	3.35	1.06

103 mm × 0.1, Π_{25ah} = 67% of the initial Π_{25}, D_{25ah} = 49 cm.

Asphaltenes were separated from the tar and bitumen samples by two methods: exhaustive cool precipitation with petroleum ether and the Holde's hot method in a Soxhlet apparatus [2].

After precipitation of asphaltenes, malthenes of tars and bitumens were separated into polar and nonpolar fractions using DMF [3].

Group separation of malthenes of tars and of the corresponding bitumens into naphtheno–paraffinic compounds (NPCs), monocycloaromatic compounds (MCACs), bicycloaromatic compounds (BCACs) or polycycloaromatic compounds (PCACs), and toluene (TRs) and alcohol–toluene resins (ATRs) was carried out by the procedure described in [4]. The boundaries of chromatographic zones of the indicated fractions were determined by the characteristic luminescence under UV light.

Table 1 shows that the H/C atomic ratio regularly decreases in the order nonpolar components of bitumen (or tar) > tar (or bitumen) > polar components of tar (or bitumen) > asphaltenes. Both tar samples and the corresponding bitumens are characterized by close contents of sulfur and oxygen, but considerably different nitrogen content.

The maximal content of heteroatoms (S, N, O) was found in native asphaltenes extracted from tar or bitumen, and also in heavy fractions of the polar and nonpolar components of the bitumens and tars. It is worth noting that the distribution of the heteroatoms in the polar and nonpolar components of tars and bitumens differs from that in the initial products. The structuring components (asphaltenes) of BDUS 70/100 thermostable bitumen are characterized by the maximal oxygen content (5.68%) and increased contents of sulfur (2.8%) and nitrogen (0.94%) (Table 1).

Table 2 shows that the elemental composition of asphaltenes extracted from the polar and nonpolar components of tars and bitumens differs essentially in the content of heteroatoms (content of heteroatoms in the polar components is higher than that in the nonpolar components).

It is seen that various group components of the tars

Table 2. Elemental composition of polar and nonpolar components of tars and bitumens

Product	Element content, wt %					H/C atomic ratio
	C	H	N	S	O	
Nonpolar components of tar ($\prod_{25}$ = 305 mm × 0.1)						
NPCs	85.62	12.05	–	0.49	1.84	1.69
MCACs	85.70	11.40	–	1.52	1.38	1.60
BCACs	84.31	10.25	–	2.92	2.52	1.46
TRs	83.31	9.85	0.54	2.74	3.56	1.38
ATRs	84.18	9.70	0.74	2.63	2.75	1.38
Polar components of tar ($\prod_{25}$ = 305 mm × 0.1)						
NPCs	85.10	11.32	–	0.70	2.08	1.58
MCACs	85.18	8.85	0.20	2.79	2.98	1.25
BCACs	83.00	8.73	0.31	2.96	5.00	1.26
ATRs	79.5	8.27	1.16	1.92	9.15	1.25
BDUS 70/100 (nonpolar components)						
NPCs	86.66	11.80	–	1.54	–	1.63
MCACs	86.23	9.14	–	1.98	2.65	1.27
BDUS 70/100 (polar components)						
MCACs	85.91	8.48	0.38	2.16	3.07	1.18
BCACs	80.82	8.18	0.95	1.85	8.20	1.21
ATRs	77.97	9.63	1.00	1.80	9.60	1.48
Nonpolar components of tar ($\prod_{25}$ = 390 mm × 0.1)						
NPCs	84.10	11.68	–	0.87	3.35	1.66
MCACs	84.30	10.58	–	1.66	3.46	1.50
BCACs	83.81	9.68	0.24	1.87	4.40	1.39
TRs	83.25	9.36	0.67	2.06	4.66	1.35
Polar components of tar ($\prod_{25}$ = 390 mm × 0.1)						
NPCs	84.63	10.47	–	1.57	3.33	1.49
MCACs	84.97	9.51	0.3	2.03	3.29	1.34
Nonpolar components of BDUS 60/90 (sp 48°C)						
NPCs	85.42	10.83	–	0.86	2.89	1.53
MCACs	85.15	10.28	–	2.12	2.45	1.45
BCACs	83.93	9.90	0.21	1.84	4.12	1.42
TRs	82.94	8.80	0.65	2.19	5.34	1.29
ATRs	81.77	8.95	0.94	2.92	5.42	1.31
Polar components of BDUS 60/90 (sp 49°C)						
NPCs	85.20	10.21	–	1.79	2.80	1.44
MCACs	86.00	9.04	0.38	2.24	2.37	1.26
BCACs	84.60	8.48	0.98	1.94	4.00	1.20
TRs	82.97	8.53	1.04	2.10	5.36	1.23
ATRs	79.40	8.45	1.34	2.23	8.56	1.27

and bitumens differ in the content of not only the base elements (C and H), but also heteroatoms (O, S, N). The H/C atomic ratio regularly decreases in the order NPCs > MCACs > BCACs > TRs ~ ATRs for both the tars and bitumens. Sulfur and oxygen are distributed among all the group components of the tars and bitumens. The sulfur and oxygen contents in the polar components of the tars and the corresponding bitumens are higher than those in the nonpolar components. The oxygen content in resins (TRs and ATRs) is always higher than that in the oil fractions (NPCs, MCACs, and BCACs).

Nitrogen is concentrated essentially in the polar and nonpolar components (BCAs, TRs, and ATRs).

We found some differences in the elemental composition of particular fractions of the polar and nonpolar components of the thermostable (BDUS 70/100) and less thermostable bitumens (BDUS 60/90). In particular, NPCs of BDUS 70/100 contain no oxygen. They contain more sulfur than NPCs of BDUS 60/90. Naphthenoparaffinic compounds of the nonpolar components of BDUS 60/90, on the contrary, contain 2.83% oxygen. Furthermore, the H/C atomic ratios in NPCs of BDUS 70/100 and BDUS 60/90 is also different (1.63 and 1.53, respectively).

MCACs of the nonpolar components of the bitumens under comparison are characterized by similar sulfur and oxygen contents, but different H/C.

The H and O contents in TRs and ATRs of the polar components of the bitumens are comparable (Table 2).

Comparison of the group components of the polar compounds of the bitumens in hand also demonstrates differences not only in the H/C atomic ratio for MCACs, BCACs, and ATRs, but also in the distribution of nitrogen, sulfur, and oxygen among these components. Therefore, we observed differences in the elemental composition not only for particular fractions of the polar and nonpolar components of the initial tars, but also for the bitumens obtained from them. Without question, when interpreting data on the stability of colloidal structures of tars and bitumens, it is necessary to take into account the donor–acceptor power of heteroatoms and microelements as well as the contribution of this factor to the formation of thermostable structures in addition to the aromaticity of asphaltenes, resins, and oils.

In bitumens and tars having close chemical compositions, the course of structurization is governed by such specific features of their structure as the amount, location, and length of alkyl chains; the content of aromatic and naphthenic fragments; the type of condensation of the rings (*peri* or *cata* condensation); the arrangement of heteroatoms and their bonding to microelements (metals); etc.

The colloidal stability of bitumens and their physicochemical properties are controlled not only by the proportion of oils, resins, and asphaltenes in them, but also by their chemical nature. The presence of a fairly large amount of the oil fraction characterized by high carbon content in cyclic structures and aromaticity imparts the colloidal stability and desirable physicochemical characteristics to bitumens. However, in this case they demonstrate relatively higher temperature sensitivity and low elasticity. In the case of an insufficient content of the oil fraction, or when this fraction is of essentially naphtheno paraffinic nature, the colloidal stability of bitumen decreases as well as its ductility and mechanical characteristics.

The condition of the bituminous colloidal system depends not only on the asphaltene to malthene ratio, but also on the aromaticity of asphaltenes (C/H ratio) and solvency of malthenes K_s:

$$K_s = C_{ar} + 1/3\,C_n,$$

where C_{ar} and C_n are the carbon contents (%) in the aromatic and naphthenic structures, respectively.

The stability of the bitumen structure decreases with increasing K_s of the oil fraction and decreasing asphaltene/resin ratio.

The chemical features of the dispersion medium and dispersed phase are characterized by the degree of dispersion D:

$$D = (B + C)/(A + E),$$

where A, E, B, and C are the contents (%) of asphaltenes, saturated and cyclic hydrocarbons, and resins, respectively.

It follows from this relationship that, the higher the asphaltene content in the system (to certain limit), the more ordered the system. In aging initiated by thermal effects, the colloidal state of bitumen changes through aggregation of dispersed particles (free energy of the system decreases). The evolution occurs from a sol with random distribution of particles via a structured sol to a gel. In this case, the orientation ordering of colloid particles increases, and the free energy at the interface decreases. As aging proceeds, micellar aggregates become more compact, the interparticle interaction increases, the volume of the system de-

Table 3. Intensity of signals in the ^{1}H NMR spectra of nonpolar and polar components of bitumens and tars

Product	Fraction	Intensity, %			
		H_a	H_α	H_β	H_γ
Nonpolar components of BDUS 60/90 (sp 48°C)	NPCs	–	–	73.8	26.2
	MCACs	4.7	24	43.3	28
	BCACs	8.02	29	42.28	20.7
	TRs	10.1	26.5	43.8	19.6
	ATRs	8.1	29.9	40.2	21.8
Polar components of BDUS 60/90 (sp 48°C)	NPCs	–	–	75.9	24.1
	MCACs	7	27.6	54.1	11.3
	BCACs	7.9	26.3	46.7	19.1
	TRs	10.6	32.3	45.7	11.4
	ATRs	8.9	33.7	33.3	24.1
Nonpolar components of tar ($\prod_{25}$ = 390 mm × 0.1)	NPCs	–	–	81.4	18.6
	MCACs	4.1	27.9	51.7	16.3
	BCACs	7.5	24	50.5	18
	TRs	11.2	22.2	50.2	16.4
	ATRs	6.3	20.5	51.8	21.4
Polar components of tar ($\prod_{25}$ = 390 mm × 0.1)	NPCs	–	–	60.1	29.9
	MCACs	6.4	31.1	46.0	17.5
	BCACs	8.4	32.1	44.4	15.1
	TRs	9.9	29.7	46.4	14.0
	ATRs	8.2	30.1	46.0	15.4
Polar components of BDUS 70/100 (sp 46°C)	NPCs	–	–	76	24
	MCACs	6.8	26.8	44.0	22.4
	BCACs	8.8	26.9	43.1	21.2
	TRs	10.8	29.2	35.2	24.8
	ATRs	9.0	23.6	45.8	21.6

creases, and the bitumen hardness increases; the elasticity passes through a maximum.

Carbon and hydrogen are the base elements of tars and bitumens, forming the skeletons of their structural fragments (oils, resins, and asphaltenes).

The ^{1}H and ^{13}C NMR data are given in Tables 3–5. In the ^{1}H NMR spectra of tar, bitumen, polar and nonpolar components of asphaltenes, and particular fractions of the polar and nonpolar components, we observed four groups of signals assigned to hydrogen atoms of the aromatic rings (H_{ar}, 6.8–9.2 ppm); hydrogen atoms of CH, CH_2, and CH_3 groups located in the α-position against the aromatic ring (H_α, 2–3.2 ppm); hydrogen atoms in CH_2 and CH groups of the alkyl chains and naphthenic rings located in positions more distant than H_α (H_β, 1.05–2 ppm); and finally, hydrogen atoms in CH_3 groups located in positions more distant than H_α and H_β (H_γ, 0.5–1.0 ppm).

As seen, the quality bitumens and the corresponding tars are characterized by higher degree of aromaticity, as demonstrated by both H_{ar} and the parameter H_{ar}/H_{al}, which is also consistent with data on C_{ar}/C_{al}. Table 4 shows that the quality of bitumen correlates with that of the initial tar. For example, the aromatic hydrogen contents in BDUS 70/100 (sp 46°C) and the initial tar were determined to be 5.9 and 5.5%, respectively. The aromatic hydrogen content in BDUS 60/90 [second after BDUS 70/100 in performance characteristics (thermal stability)] is 5.35%; and that in the initial tar, 3.6%, i.e., the degree of aromaticity of the tar and bitumen is lower in the second case. The nonpolar components of the tar and bitumen are characterized by lower H_{ar} (Table 4). On the contrary, the polar components and asphaltenes are characterized by the highest hydrogen content in the aromatic structures. Comparison of H/C in asphaltenes of the tars and bitumens shows that data on the aromatic hydrogen obtained from the ^{1}H NMR spectra (Table 3) are overestimated. This also follows from results of direct determination of the aromatic carbon in asphaltenes by ^{13}C NMR.

Table 4. Distribution of hydrogen and carbon among structural groups by ^{1}H NMR data

Product or fraction	Intensity, %				H_{ar}/H_{al}	C_{ar}/C_{al}
	H_a	H_α	H_β	H_γ		
Quality BDUS 100/130	6.2	6.96	57.5	29.34	0.066	0.441
Quality BDUS 70/100	5.8	12.0	58.7	23.5	0.0616	0.420
Substandard BDUS 100/130	5.62	10.0	61.5	22.88	0.0595	0.425
Substandard BDUS 70/100	4.95	10.1	61.0	23.95	0.052	0.365
Tar ($\prod_{25}$ = 305 mm × 0.1, relative viscosity 89 s)	5.5	21.9	52.1	20.5	0.058	0.416
BDUS 70/100 (sp 46°C)	5.9	21.8	51.3	21.0	0.0626	0.420
Malthenes of tar ($\prod_{25}$ = 305 mm × 0.1, asphaltene content 7.45%)	6.9	26.6	44.6	21.9	0.074	–
Malthenes of bitumen (sp 46°C, asphaltene content 16.3%)	5.7	26.3	40.0	28	0.060	–
Asphaltenes of tar ($\prod_{25}$ = 305 mm × 0.1)	7.9	24.8	44.6	22.7	0.085	0.74 native
Asphaltenes of BDUS 70/100 (sp 46°C)	8.45	17.9	53.45	20.2	0.092	0.54 native + secondary
BDUS 60/90 (sp 48°C)	5.4	18.1	60.3	16.2	–	–
Tar ($\prod_{25}$ = 390 mm × 0.1)	3.60	18.1	47.1	31.2	–	–
Nonpolar components of tar ($\prod_{25}$ = 390 mm × 0.1)	4.1	27.9	41.5	26.4	–	–
Nonpolar components of BDUS 60/90 (sp 48°C)	3.7	18.0	60.8	25.5	–	–
Polar components of tar ($\prod_{25}$ = 390 mm × 0.1)	10.8	26.8	47.4	15	–	–
Polar components of BDUS 60/90 (sp 48°C)	15.5	36.0	34.3	14.2	–	–
Asphaltenes of tar ($\prod_{25}$ = 390 mm × 0.1)	10.0	27.5	35.4	27.1	–	–
Asphaltenes of BDUS 60/90 (sp 48°C)	16.9	28.6	27.2	27.3	–	–

Table 5. Carbon distribution among structural fragments

Product or fraction	C_{ar}/C_{al}	Content, wt %				
		C_α	C in naphthenes with tertiary C–H bonds	CH_2 groups of naphthenes and alkyls	CH_2 groups of alkyls in position 2	CH_3 groups
Quality BDUS 100/130	0.44	30.6	8.8	42.8	9.8	8.0
Quality BDUS 70/100	0.425	29.8	7.1	45.5	9.2	8.4
Substandard BDUS 100/130	0.427	29.96	9.0	41.6	10.2	9.4
Substandard BDUS 70/100	0.366	26.8	8.3	42.7	10.6	11.6
Tar ($\prod_{25}$ = 305 mm × 0.1)	0.416	29.4	27.5	16.5	17.4	9.2
BDUS 70/100 (sp 46°C)	0.451	31.1	24.6	30.3	10	5.0
Malthenes of tar ($\prod_{25}$ = 305 mm × 0.1)	0.41	29.0	25.4	29.5	11.6	4.5
Malthenes of BDUS 70/100	0.42	29.7	23.4	26.2	15	5.7
Asphaltenes of tar ($\prod_{25}$ = 305 mm × 0.1)	0.74	42.6	19.5	30.1	4.9	2.9
Asphaltenes of BDUS 70/100 (sp 46°C)	0.82	45.2	14.9	25.7	10.5	3.7
BDUS 60/90 (sp 48°C)	0.411	29.2	–	–	–	–
Tar ($\prod_{25}$ = 390 mm × 0.1)	0.382	27.1	–	–	–	–

Evidently, in the ^{1}H NMR spectra (Fig. 1a), the broad signal of the aromatic hydrogen H_{ar} in the polar components and asphaltenes is overlapped with the signal of hydrogen atoms in heteroatomic fragments (pyrrole rings, metal porphyrin complexes, etc.). In the ^{13}C NMR spectra of the tars and bitumens (Fig. 1b), we observed two groups of signals assigned to carbon atoms of aromatic rings (110–155 ppm) and carbon atoms of methylene groups of six-membered naphthenes with one or two alkyl substituents or condensed with aromatic (heteroaromatic) or naphthenic rings (31.94–32.07 ppm). The range 29.4–30.13 ppm

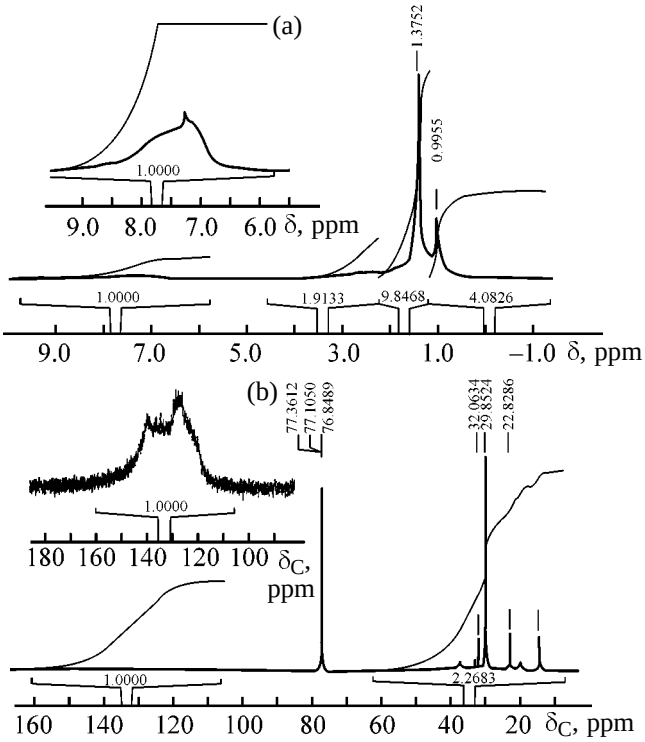

Fig. 1. Typical (a) ^{1}H and (b) ^{13}C NMR spectra of quality bitumen BDUS 70/100 (sp 46°C).

corresponds to the resonance of ^{13}C in the methylene groups of six-membered naphthene rings and distant (at least γ) CH_3 groups of long aliphatic chains. Signals of the methylene groups of aliphatic chains are found at 22.69–22.82 ppm, and those of methyl groups, at 14.11–14.22 ppm. These signals can overlap with signals of the methylene groups at the tertiary C–H bonds in hydroaromatic rings.

The carbon distribution among the structural groups is given in Table 5. The fact that BDUS 60/90 is inferior in quality is due to its lower aromaticity (C_{ar} = 29.2%) as compared to BDUS 70/100 (C_{ar} = 31.1%). Furthermore, the initial tar from which BDUS 60/90 was obtained is characterized by higher oil/resin ratio in both the polar and nonpolar components, and also by lower content of TRs relative to ATRs. It should be pointed out that we observed some differences in the degree of aromaticity of the polar and nonpolar components of the tars and bitumens in all the fractions (MCACs, BCACs, TRs, and ATRs). Also some differences were found in the NPC content in the polar and nonpolar components of both the tars and bitumens studied.

CONCLUSIONS

(1) Various group components of the tars and bitumens differ in the content of not only the base elements (C and H), but also heteroatoms (O, N, S). The H/C atomic ratio decreases in the order naphthenoparaffinic compounds > monocycloaromatic compounds > bicycloaromatic compounds > toluene resins > alcohol–toluene resins for both the tars and bitumens.

(2) The contents of sulfur and oxygen in the polar components of tars and the corresponding bitumens are higher than those in the nonpolar components. The oxygen content in the resinous fraction (toluene and alcohol–toluene resins) is always higher as compared to the oil fractions (naphthenoparaffinic, monocycloaromatic, and bicycloaromatic compounds).

(3) Nitrogen is concentrated essentially in the polar and nonpolar components of bicycloaromatic compounds and alcohol–toluene resins.

(4) Monocycloaromatic compounds of the nonpolar components of BDUS 70/100 quality bitumen and BDUS 60/90 substandard bitumen are characterized by similar sulfur and oxygen contents, but different H/C.

(5) The degree of aromaticity of BDUS quality bitumens and the tars from which these bitumens were obtained is higher than that of substandard (less thermostable) products.

(6) The fact that BDUS 60/90 is inferior in quality to BDUS 70/100 is due to its lower aromaticity (C_{ar} = 29.2 and 31.1%, respectively). The initial tar from which BDUS 60/90 was obtained is characterized by higher oil/resin ratio in both the polar and nonpolar components, and also by lower content of toluene resins relative to alcohol–toluene resins.

(7) Some differences were found in the degree of aromaticity in all the fractions (MCACs, BCACs, TRs, and ATRs) of the polar and nonpolar components of the tars and bitumens. Also some differences were observed in the content of naphthenoparaffinic compounds in the polar and nonpolar components of both the initial tars and resulting quality and substandard bitumens.

REFERENCES

1. Gun, R.B., *Neftyanye bitumy* (Petroleum Bitumens), Moscow: Khimiya, 1989.
2. Pechenyi, B.G., *Bitumy i bitumnye kompozitsii* (Bitumens and Bitumen Composites), Moscow: Khimiya, 1990.
3. Kolbanovskaya, A.S. and Mikhailov, V.V., *Dorozhnye bitumy* (Road Asphalts), Moscow: Transport, 1973.
4. Kolbanovskaya, A.S., *Tr. Soyuzdornii* (Moscow), 1968, issue 27, pp. 120–125.

Russian Journal of Applied Chemistry, Vol. 75, No. 7, 2002, pp. 1185–1187. Translated from Zhurnal Prikladnoi Khimii, Vol. 75, No. 7, 2002, pp. 1209–1211.
Original Russian Text Copyright © 2002 by Vakhula, Yashchishin, Semchuk, Novosad.

BRIEF COMMUNICATIONS

Interaction of Components in Gel-Forming Potassium Silicate Solution

Ya. I. Vakhula, I. N. Yashchishin, O. R. Semchuk, and P. V. Novosad

L'vivs'ka Politekhnika National University, Lviv, Ukraine

Received May 12, 2000; in final form, November 2001

Abstract—X-ray phase analysis was applied to study the phase composition of products formed in reaction between components of silicophosphate solutions obtained on the basis of potassium water glass. The temperature ranges of phase transformations of chemical compounds, occurring in thermal treatment of gels of various compositions, were established.

Low-melting systems containing lead oxide are used in most cases in manufacture of decorative coatings [1, 2]. However, the high toxicity and cost of lead make necessary a search for other glass-forming systems, among which the silicophosphate system shows the most promise [3].

The sol–gel method based on the use of organosilicon compounds is widely used for obtaining glassy coatings [4, 5]. Much fewer papers have been concerned with synthesis of glassy coatings based on soluble silicates or silicic acid sols [6, 7].

The primary stage in using the sol–gel method for obtaining glasses is preparation of a homogeneous solution capable of gel formation. In doing so, it is very important that the forming gels and powders obtained from them should contain low-melting compounds, which do not raise the temperature of melt formation.

The aim of this study was to analyze the processes occurring in formulating a silicate colloid solution based on potassium water glass and to determine the composition of the gel powder used for obtaining decorative coatings in the system K_2O–Al_2O_3–B_2O_3–SiO_2–P_2O_5 and phase transformations of this powder upon heating.

As solution components we used potassium water glass with the silicate ratio M = 3.5, potassium aluminate solution, ammonium hydrogen phosphate $(NH_4)_2 \cdot HPO_4$, boric acid H_3BO_3 of pure grade, and potassium hydroxide KOH of analytically pure grade. The potassium aluminate solution was prepared by dissolving powdered aluminum in an alkali solution.

The products of possible chemical reactions between the solution components were identified by X-ray phase analysis (XPA) on a DRON-3 diffractometer with CuK_α radiation.

Thermal analysis of the powders was made on an MOM Q-1500D derivatograph (Hungary).

The dried water glass is X-ray amorphous. In heating of a powder prepared from the water glass, an exothermic effect is observed, peaked at 180°C (Fig. 1, curve *1*). The X-ray pattern of the resulting product (Fig. 2, curve *1*) and the data of [8] allow its identification as $K_2O \cdot 4SiO_2 \cdot H_2O$ ($KHSi_2O_5$). At 220°C, an intense endothermic effect is observed, which is related to release of adsorbed and molecular water [7, 8].

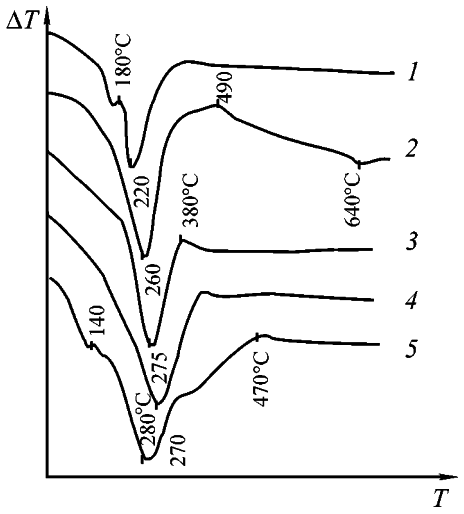

Fig. 1. DTA curves of gel powders. Gel drying temperature 50°C. (*T*) Temperature. System: (*1*) K_2O–SiO_2, (*2*) K_2O–SiO_2–P_2O_5, (*3*) K_2O–SiO_2–P_2O_5–B_2O_3, (*4*) K_2O–SiO_2–P_2O_5–Al_2O_3, and (*5*) K_2O–SiO_2–P_2O_5–B_2O_3–Al_2O_3.

1070-4272/02/7507-1185$27.00 © 2002 MAIK "Nauka/Interperiodica"

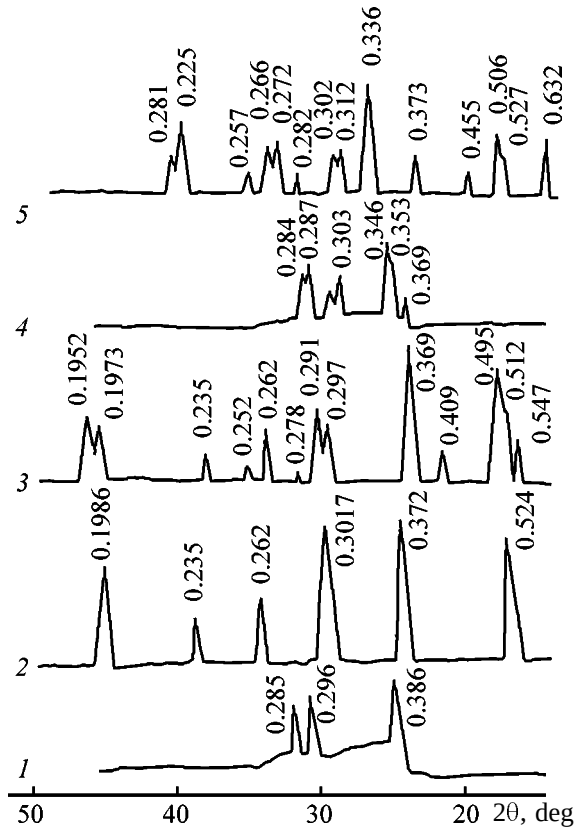

Fig. 2. X-ray diffraction patterns of gel powders. (2θ) Bragg angle. System: (*1*) K_2O–SiO_2, (*2*) K_2O–SiO_2–P_2O_5, (*3*, *4*) K_2O–SiO_2–P_2O_5–Al_2O_3, and (*5*) K_2O–SiO_2–P_2O_5–B_2O_3. Thermal treatment temperature (°C): (*1*) 180, (*2*, *3*) 50, (*4*) 280, and (*5*) 380.

On adding an diammonium hydrogen phosphate solution to water glass, a gel is formed, in agreement with the results of [8]. PO_4^{3-}, K^+, and NH_4^+ ions remain in solution. A crystalline phase is formed in gel drying. This phase is presumably the compound $(0.73NH_4H_2PO_4)\cdot(0.27KH_2PO_4)$ (*d*/*n* 0.524, 0.372, 0.3017, 0.262, 0.235, 0.1986 nm; Fig. 2, curve *2*). Similar lines, characteristic of this compound, are presented in [9]. The presence of potassium dihydrogen phosphate indicates that water glass reacts with $(NH_4)_2HPO_4$. The change in the degree of protonation of phosphate ions in the final products can be accounted for by the occurrence at 50°C of the reaction $(NH_4)_2HPO_4 \rightleftarrows NH_{3(gas)} + NH_4H_2PO_{4(cryst)}$ [10, 11]. No crystalline silicates were found.

To adjust the content of potassium oxide in the system formed by water glass and diammonium hydrogen phosphate, a KOH solution was added. As a result, NH_3 and KH_2PO_4 were formed. In heating (Fig. 1, curve *2*), two endothermic effects are observed at 260 and 640°C, and also an exothermic effect at 490°C. The possible reason for the appearance of the endothermic effect at 260°C is dehydration of the gel powder, and also melting of KH_2PO_4 (T_m = 252.8°C) to give dihydrogen pyrophosphate $K_2H_2P_2O_7$. In further heating of the powder, further dehydration $K_2H_2P_2O_7 \rightarrow 2KPO_3 + H_2O$ occurs at 320–340°C. The $(0.73NH_4H_2PO_4)\cdot(0.27KH_2PO_4)$ phase melts in the range 170–240°C. A minor exothermic effect peaked at 490°C is probably due to partial crystallization of ammonium polyphosphates [12]. The endothermic effect at 640°C can be accounted for by a polymorphic transition of Kurrol's salt KPO_3, melting at 800°C.

Addition of an H_3BO_3 solution to the system $K_2O\cdot 3.5SiO_2$–KOH–$(NH_4)_2HPO_4$ does not change the situation significantly. A single crystalline compound was found in the powder of the mixture obtained. Thermal treatment leads to the appearance in the DTA curve (Fig. 1, curve *3*) of peaks corresponding to an endothermic effect at 275°C and exothermic effect at 380°C. The endothermic effect is due to dehydration processes. Also, H_3BO_3 present in the powder decomposes at 185°C [13]. The appearance of the exothermic effect can be attributed to the formation of BPO_4, confirmed by XPA data (Fig. 2, curve *5*; *d*/*n* 0.632, 0.527, 0.506, 0.455, 0.373, 0.336, 0.312, 0.302, 0.272, 0.266, 0.225, 0.221 nm).

To enhance the chemical stability of the coatings, aluminum ions were introduced into the system $K_2O\cdot 3.5SiO_2$–KOH–$(NH_4)_2HPO_4$. It is known [8] that aluminum salts are completely hydrolyzed in an excess of an alkaline silicate. These reagents form flaky precipitates, composed, in all probability, of aluminum hydroxide. To prevent precipitation, it has been proposed to introduce aluminum in the form of an alkali metal aluminate, which is stable in a strongly alkaline medium [6]. That is why $Al(OH)_3$ additionally precipitates, in accordance with the reaction $K[Al(OH)_4] \rightarrow KOH + Al(OH)_3\downarrow$, after precipitation of H_4SiO_4 and introduction of potassium aluminate. Two crystalline phases, KH_2PO_4 and $AlPO_4\cdot(1.1–1.3)H_2O$ (Fig. 2, curve *3*; *d*/*n* 0.547, 0.512, 0.495, 0.369, 0.278 nm) were identified in a dried gel. In the course of thermal treatment (Fig. 1, curve *4*), an endothermic effect is observed at 280°C, which is due to the same processes as those in the three-component system. A crystalline phase of the composition $3Al_2O_3\cdot 2SiO_2$ (Fig. 2, curve *4*; *d*/*n* 0.369, 0.353, 0.346, 0.297, 0.284 nm) was identified at this temperature.

In industrial manufacture of coatings, account should be taken of both the process parameters of their formation (melt appearance temperature, adhe-

sion) and service characteristics (chemical stability, thermal coefficient of linear expansion).

Of particular interest in this regard is the system $K_2O \cdot 3.5SiO_2$–KOH–$(NH_4)_2HPO_4$–H_3BO_3–$K[Al(OH)_4]$. The chemical reactions occurring in this system in the course of its preparation are similar to those considered above. Only a single crystalline phase, $(0.73NH_4H_2PO_4) \cdot (0.27KH_2PO_4)$, was found in dried gel powder. The DTA curve (Fig. 1, curve *5*) shows exothermic peaks at 140 and 470°C and an intense endothermic peak at 270°C. An X-ray phase analysis confirmed that $(0.73NH_4H_2PO_4) \cdot (0.27KH_2PO_4)$ and KH_2PO_4 are present in the powder at 140°C, with the latter compound crystallized in heating of the starting powder. On raising temperature to above 270°C, the powder becomes totally X-ray amorphous.

Thus, we found that compounds melting below 270°C are formed in the prepared gels of the three-component system in drying. In four-component systems including boric acid and potassium aluminate, high-melting compounds $(0.73NH_4H_2PO_4) \cdot (0.27KH_2PO_4)$ and KH_2PO_4 are formed. In the system K_2O–Al_2O_3–B_2O_3–SiO_2–P_2O_5, low-melting compounds are formed, which favor appearance of the liquid phase at 300°C. The results obtained demonstrate that it is advisable to use solutions of this system for preparing low-melting decorative glassy coatings.

REFERENCES

1. Rienherz, B., *Glass*, 1991, vol. 68, no. 1, pp. 32–33.
2. Bulgarian Inventor's Certificate no. 37899.
3. Pavlushkina, T.K. and Gladushko, O.A., *Steklo Keram.*, 1987, no. 4, pp. 14–15.
4. Dislich, H., Hinz, P., Arfsten, N.-J., and Hubmann, E., *Glastech. Ber.*, 1989, vol. 62, no. 2, pp. 46–51.
5. Petrovskii, G.T., Shashkin, V.S., and Yakhkind, A.K., *Fiz. Khim. Stekla*, 1997, vol. 23, no. 1, pp. 43–54.
6. Yaschyshyn, I.N., Vakhula, Y.I., and Vasijchuk, V.O., in *Fundamentals of Glass Science and Technology*, Växjö, June 9–12, 1997, pp. 181–186.
7. Kuznetsova, L.A., Golubeva, T.Yu., and Khashkovskii, S.V., in Trudy XVII soveshchaniya po temperaturoustoichivym funktsional'nym pokrytiyam (Proc. XVII Meet. on Heat-Resistant Functional Coatings), St. Petersburg, June 1–6, 1997, part 1, pp. 77–80.
8. Korneev, V.I. and Danilov, V.V., *Proizvodstvo i primenenie rastvorimogo stekla* (Manufacture and Use of Soluble Glass), Leningrad: Stroiizdat, 1991.
9. *Set of X-ray Diffraction Data Cards*, Philadelphia, PA: Joint Committee on Chemical Analysis by X-ray Diffraction Methods, 1967.
10. Van Wazer, I.R., *Phosphorus and Its Compounds*, New York: Wiley–Interscience, 1958, vol. 1.
11. Shenkin, Ya.S., in *Issledovaniya v oblasti neorganicheskoi tekhnologii* (Investigations in the Field of Inorganic Technology), Leningrad: Nauka, 1972, pp. 63–66.
12. Lepilina, R.G. and Smirnova, N.M., *Termogrammy neorganicheskikh fosfatnykh soedinenii: Spravochnik* (Thermograms of Inorganic Phosphate Compounds: Reference Book), Leningrad: Nauka, 1984.
13. *Spravochnik khimika* (Chemist's Handbook), Nikol'skii, B.P., Ed., Moscow: Khimiya, 1965, vol. 2.

Russian Journal of Applied Chemistry, Vol. 75, No. 7, 2002, pp. 1188–1190. Translated from Zhurnal Prikladnoi Khimii, Vol. 75, No. 7, 2002, pp. 1212–1214.
Original Russian Text Copyright © 2002 by Vitvitskii.

BRIEF COMMUNICATIONS

Description of the Boiling Curve on the Basis of State Parameters of a Single Point

A. I. Vitvitskii

St. Petersburg State Technological Institute, St. Petersburg, Russia

Received January 28, 2002

Abstract—It is shown for the example of 40 substances that the normal boiling point can be used for approximately describing the entire boiling curve from the triple to critical point.

Data on the equilibrium in single-component two-phase systems gas–liquid are commonly represented in phase diagrams as a boiling curve in the coordinates temperature T (K)–pressure P (Pa) [1, 2]. For all substances, the boiling curve is limited, on the one hand, by the critical state parameters, T_c and P_c, beyond which the two-phase system becomes a single-phase one, and, on the other, by the triple point parameters, T_t and P_t, at which a third phase (crystalline) appears, since boiling, sublimation, and melting curves all run into the triple point. The boiling curve characterizes the temperature dependence of the saturated vapor pressure P_{sv} (Pa) of a substance or the dependence of the boiling point of a substance $T = T_b$ on external pressure P, equal to P_{sv}.

As a rule (except in the case of As, CO_2, C_2H_2, and some other substances [2]), the boiling curve has a point with parameters $P = P_{sv} = P_{st}$ and $T = T_b = T_{b.st}$ (P_{st} is the standard pressure equal to 101 325 Pa; $T_{b.st}$ is the boiling point under standard pressure or normal boiling point), which lies between the triple point (with the parameters $T = T_b = T_t$ and $P = P_{sv} = P_t$) and the critical point ($T = T_b = T_{cr}$ and $P = P_{sv} = P_{cr}$). In a phase diagram plotted in the $\ln P$–$1/T$ coordinates, the boiling, sublimation, and melting curves are virtually straight lines running into the triple point.

The aim of this paper is to demonstrate the possibility of using the point with the parameters $T = T_{b.st}$ and $P = P_{st}$ for describing the entire boiling curve.

It is noteworthy that there is no zero for the parameters P and T in the $\ln P$ and $1/T$ scales. Therefore, it is appropriate to introduce certain constant (initial, standard) state parameters, e.g., P_{st} = 101 325 Pa and T_0 = 298.15 K. Then, representing the temperature dependence of the saturated vapor pressure as an equation of the type

$$\ln(P_{sv}/P_{st}) = A - \Delta H_b/RT \quad (1)$$

[where the dimensionless coefficient A and the heat of boiling ΔH_b (J mol^{-1}) are constant over the entire range of state parameters, from the triple to the critical point; and R is the universal gas constant equal to 8.315 J mol^{-1} K^{-1}], we obtain that, at $\ln(P_{sv}/P_{st}) = 0$ ($P_{sv} = P_{st}$), the heat of boiling (J mol^{-1}) is related for many substances to the normal boiling temperature by the equation

$$\Delta H_b = RT_{b.st}[10.36 + \ln(T_{b.st}/T_0)]. \quad (2)$$

Table 1 lists the results obtained in calculating by Eq. (2) the ΔH_b value for 40 substances differing by a factor of more than 100 in normal boiling points and heats of boiling (e.g., Ne and Au) and by a factor of 62 in the number of atoms in a molecule (from monoatomic molecules to $C_{20}H_{42}$). The average calculation error was 2.3% (for 40 substances) at the maximum error of 6.4% for CH_4.

Using Eq. (2), we can eliminate the heat of boiling in equation of the type (1):

$$\ln(P_{sv}/P_{st}) = [10.36 + \ln(T_{b.st}/T_0)](1 - T_{b.st}/T). \quad (3)$$

Solving Eq. (3) for T, we can obtain the dependence of the boiling point $T_b = T$ on the external pressure P, equal to P_{sv}:

$$T_b = T_{b.st}\left(1 - \frac{\ln(P/P_{st})}{10.36 + \ln(T_{b.st}/T_0)}\right)^{-1}. \quad (4)$$

Table 2 presents the results obtained in calculating by

1070-4272/02/7507-1188$27.00 © 2002 MAIK "Nauka/Interperiodica"

Table 1. Heat of boiling of some liquids

Substance	$T_{b.st}$, K, [3]	ΔH_b, kJ mol^{-1}		Δ, %
		[3]	Eq. (2)	
Ne	27.09	1.79	1.79	0
Ar	87.3	6.50	6.63	–2.0
Kr	119.8	9.05	9.41	–4.0
Xe	165.0	12.63	13.40	–6.0
Hg	629.8	59.23	58.17	1.8
Zn	1179.4 [4]	115.2 [4]	115.1	0.1
Ag	2440 [4]	251 [4]	253	–0.7
Cu	2816 [4]	302 [4]	295	2.3
Au	3150 [4]	331 [4]	333	–0.6
N_2	77.35	5.58	5.80	–3.9
O_2	90.19	6.82	6.87	–0.8
F_2	85.0	6.54	6.44	1.6
Cl_2	239.2	20.42	20.17	1.2
Br_2	331.9	30.56	28.89	5.5
I_2	457.3	41.83	41.02	1.9
CO	81.64	6.07	6.15	–1.4
HF	292.7	25.2	25.2	0
HCl	188.1	16.16	15.48	4.2
HBr	206.4	17.63	17.15	2.7
HI	237.8	19.76	20.04	–1.4
H_2S	212.9	18.67	17.74	5.0
H_2Se	231.8	19.93	19.48	2.2
H_2Te	271.0	23.45	23.13	1.4
HCN	298.8	25.25	25.74	–2.0
ZnF_2	1778.8	185.0	179.6	2.9
PH_3	185.7	14.61	15.27	–4.5
AsH_3	210.7	16.70	17.54	–5.0
SiH_4	161.2	12.43	13.06	–5.1
SnH_4	221.0	18.42	18.49	–0.4
$SnCl_4$	387.0	33.98	34.18	–0.6
CCl_4	349.7	30.02	30.59	–1.9
CCl_2F_2	243.4	20.51	20.56	–0.2
CH_4	111.66	8.19	8.71	–6.3
C_2H_4	169.4 [5]	13.52 [5]	13.80	–2.0
C_6H_6	353.2 [5]	30.77 [5]	30.92	–0.5
$Fe(CO)_5$	375	32.7	33.0	–1.0
B_5H_9	333.15	28.89	29.01	–0.4
$C_4H_8O_2$*	374.2 [5]	31.78 [5]	32.94	–3.7
$Si(C_2H_5)_4$	426.8	39.19	38.04	2.9
$CH_3(CH_2)_{18}CH_3$	618.3 [5]	57.8 [5]	57.0	1.4

* 1,4-Dioxane.

Table 2. State parameters at the triple and critical points

Substance	P_t, kPa [2]	T_t, K		Δ, %	P_{cr}, kPa [3]	T_{cr}, K		Δ, %
		[2]	Eq. (4)			[3]	Eq. (4)	
Ne	43.26	24.54	24.47	0.3	2653	44.40	45.92	–3.4
Ar	68.9	83.81	83.76	0.1	4866	150.65	151.56	–0.6
Hg	3.07×10^{-7}	234.3	227.7	2.8	10 685*	1073.0*	1085.0	–1.1
N_2	12.52	63.14	62.78	0.6	3398	126.19	126.77	–0.5

Table 2. (Contd.)

Substance	P_t, kPa [2]	T_t, K		Δ, %	P_{cr}, kPa [3]	T_{cr}, K		Δ, %
		[2]	Eq. (4)			[3]	Eq. (4)	
O_2	0.156	54.36	52.85	2.8	5046	154.58	157.24	–1.7
Cl_2	1.354	172.1	167.8	2.5	7977	416.9	420.1	–0.8
Br_2	4.655	265.9	256.4	3.6	10 330	584.0	595.0	–1.8
I_2	9.504	386.8	375.0	3.0	11 750	819.3	817.5	0.2
CO	15.37	68.13	67.58	0.8	3500	132.85	134.0	–0.9
HF	0.535	189.8	194.2	–2.3	6480	461.0	489.5	–6.2
HCl	13.7	159.0	156.5	1.6	8260	324.7	338.6	–4.3
H_2S	23.2	187.61	185.60	1.1	8970	373.3	385.2	–3.2
H_2Se	27.3	207.43	205.18	1.1	8850	410.6	415.6	–1.2
PH_3	3.64	139.4	138.9	0.3	6530	325.0	321.0	1.3
AsH_3	2.978	156.23	155.81	0.3	6790	375.0	363.0	3.1
SiH_4	2.8×10^{-2}	88.48	87.57	1.0	4840	269.5	267.2	0.8
$SnCl_4$	6.2×10^{-2}	239.8	228.1	4.9	3840	592.0	588.4	0.6
CH_4	11.54	90.67	90.66	0.0	4600	190.6	188.3	1.2
C_2H_4	0.12	103.94	100.36	3.4	5117 [5]	283.0 [5]	282.5	0.2
B_5H_9	0.453 [6]	226.6 [6]	219.7	3.1	4330	523.0	519.0	0.7

* State parameters below the critical point according to [4].

Eq. (4) the T_b values at extreme points of the boiling curve (at $P = P_t$ and $P = P_{cr}$), at which the calculation error must be the highest. The average calculation error for 20 substances ($T_{b.st}$ value is presented in Table 1) was 1.8% (for 40 values) at the maximum error of 6.2% for HF at the critical point. The average error of the values in Table 2 can be diminished by virtually a factor of 2 by taking the dimensionless coefficient in Eq. (4) to be 10.6, instead of 10.36.

CONCLUSION

The normal boiling point of substances can be used to describe approximately the entire boiling curve in the range of state parameters from the triple to the critical point.

REFERENCES

1. *Khimicheskaya entsiklopediya* (Chemical Encyclopedia), Knunyants, I.L., Ed., Moscow: Sov. Entsiklopediya, 1990, vol. 2.
2. *Khimicheskaya entsiklopediya* (Chemical Encyclopedia), Zefirov, N.S., Ed., Moscow: Bol'shaya Rossiiskaya Entsiklopediya, 1998, vol. 5.
3. Morachevskii, A.G. and Sladkov, I.B., *Fiziko-khimicheskie svoistva molekulyarnykh neorganicheskikh soedinenii (eksperimental'nye dannye i metody rascheta): Spravochnik* (Physicochemical Properties of Molecular Inorganic Compounds (Experimental Data and Calculation Methods): Handbook), St. Petersburg: Khimiya, 1996.
4. *Fizicheskie velichiny: Spravochnik* (Physical Quantities: Handbook), Grigor'ev, I.S. and Meilikhov, E.Z., Eds., Moscow: Energoatomizdat, 1991.
5. *Spravochnik khimika* (Chemist's Handbook), Nikol'skii, B.P., Ed., Leningrad: Khimiya, 1971, vol. 1.
6. *Termicheskie konstanty veshchestv* (Thermal Constants of Substances), Glushko, V.P., Moscow: Akad. Nauk SSSR, 1971, issue 5.

Russian Journal of Applied Chemistry, Vol. 75, No. 7, 2002, pp. 1191–1193. Translated from Zhurnal Prikladnoi Khimii, Vol. 75, No. 7, 2002, pp. 1215–1217.
Original Russian Text Copyright © 2002 by Blinov, Komarova, Polishchuk, Krivosheev, Rybal'chenko.

BRIEF COMMUNICATIONS

Sorption of Lower Alcohols with Activated Charcoals

E. M. Blinov, L. F. Komarova, S. A. Polishchuk, P. A. Krivosheev, and T. A. Rybal'chenko

Polzunov Altai State Technical University, Barnaul, Russia

Received September 10, 2001; in final form, February 2002

Abstract—The features of sorption of ethanol, isopropanol, butanol, isobutanol, and *tert*-butanol with activated charcoals under static conditions were studied.

Lower alcohols are widely used in paint and varnish industry, as chemicals, in production of phenylsiloxanes, photographic films, ascorbic acid, and in other branches [1, 2]. Butanol, isobutanol, *tert*-butanol, and isopropanol are environmental pollutants.

Here we report on the sorption of lower alcohols on activated charcoals produced from birch wood and from a blend of oak and beech wood (Kabardino-Balkar charcoal).[1] The main characteristics of the charcoals were determined previously [3] and are listed in the table.

The characteristics of the sorbents listed in the table demonstrate advantages of birch charcoal. It has lower moisture content, larger pore volume, and higher sorption capacity for iodine. However, in subsequent experiments it was noted that birch charcoal has lower mechanical strength than charcoal produced from a blend of oak and beech wood.

In this work, we studied sorption of butanol, *tert*-butanol, isopropanol, isobutanol, and ethanol from aqueous solutions with the above charcoals. To determine the time required to attain the static sorption capacity of the adsorbent, we studied the alcohol sorption kinetics and sorption isotherms.

The concentrations of aqueous solutions were measured by gas–liquid chromatography on an LKhM-8 MD chromatograph equipped with a heat conductivity detector. Porokhrom was used as a support. Polyethylene glycols with molecular weights of 1000 and 2000 (PEG-1000 and PEG-2000) were used as stationary phases. The mixture composition was calculated using internal reference [4].

Since the solubility limit of butanol, which is the least soluble in water, does not exceed 5.5 wt % (hereinafter, %), to plot the kinetic curves, weighed portions of activated charcoal (1 g) and 100 ml of aqueous solutions (0.8 and 5.5%) of the above alcohols were shaken for 3 h at 20°C. The samples were withdrawn at certain intervals. The results are presented in Fig. 1.

Analysis of the curves shows that the sorption capacity of birch charcoal for practically all alcohols is higher than that of the charcoal produced from a blend of oak and beech wood. Butanol is the most actively sorbed from solutions (0.8 and 5.5%), and the second sorbable is isobutanol. Ethanol is the least actively sorbed from solutions (Figs. 1a, 1b). This is apparently due to this fact that substances readily soluble in water are sorbed on charcoals less efficiently [3].

In sorption from 0.8% solution with charcoal produced from a blend of oak and beech wood, the sorp-

Main characteristics of activated charcoals

Characteristic	Carbon*	
	I	II
Bulk density, kg m^{-3}	224.48	232.87
True density, kg m^{-3}	428.91	450.61
Moisture content, wt %	1.97	4.68
Total pore volume with respect to water, ml per 1 g of charcoal	4.42	4.11
Total pore volume with respect to acetone, ml per 1 g of charcoal	2.18	1.64
pH	9.86	9.83
Total sorption capacity for iodine, g of I_2 per 1 g of charcoal	8.67	5.71
Ash content, %	3.40	2.15

[1] Produced from the wastes of wood working industry and submitted by the ANITIM Joint-Stock Company.

* (I) Birch charcoal and (II) charcoal produced from a blend of oak and beech wood.

1070-4272/02/7507-1191$27.00 © 2002 MAIK "Nauka/Interperiodica"

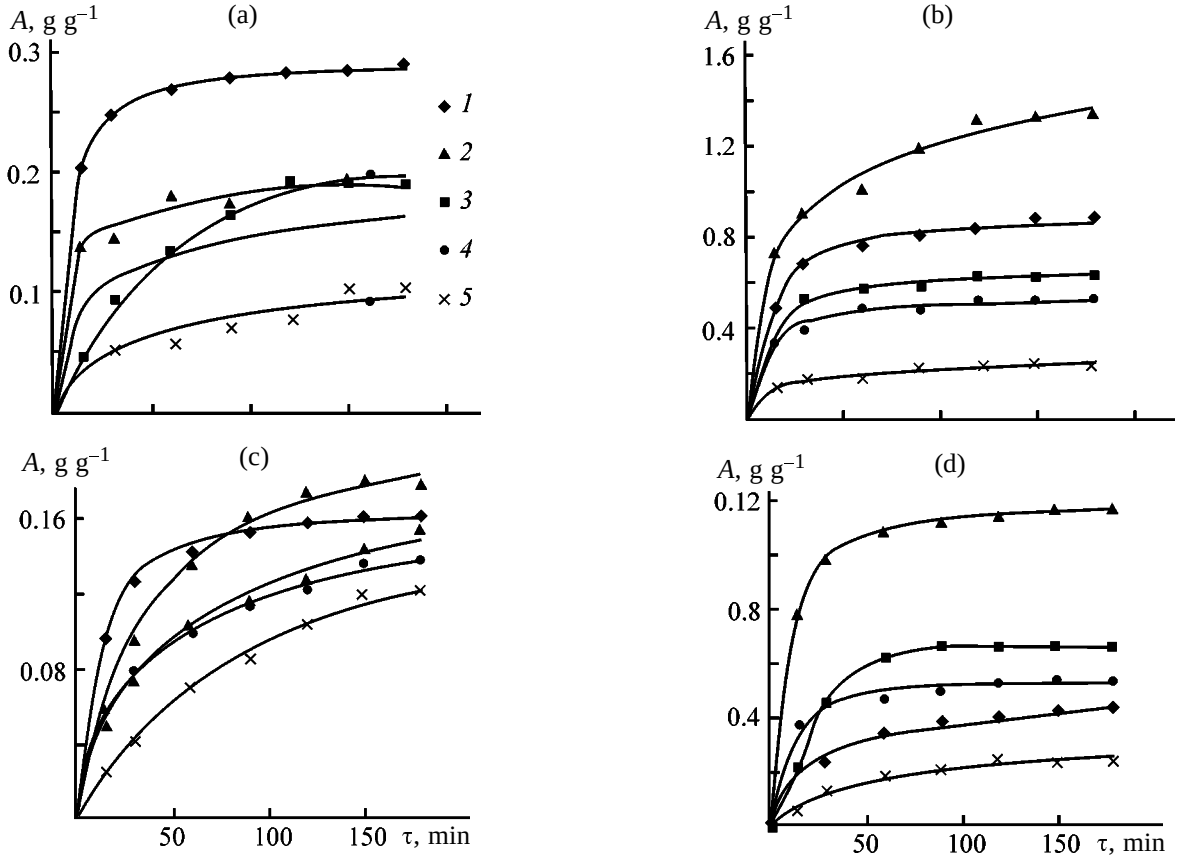

Fig. 1. Kinetic curves of sorption of alcohols with charcoal produced from (a, b) birch wood and (c, d) a blend of oak and beech wood. (*A*) Sorption capacity and (τ) time. (*1*) Butanol, (*2*) isobutanol, (*3*) *tert*-butanol, (*4*) isopropanol, and (*5*) ethanol; the same for Fig. 2. Aqueous solution of alcohol: (a, b) 0.8 and (c, d) 5.5 wt %.

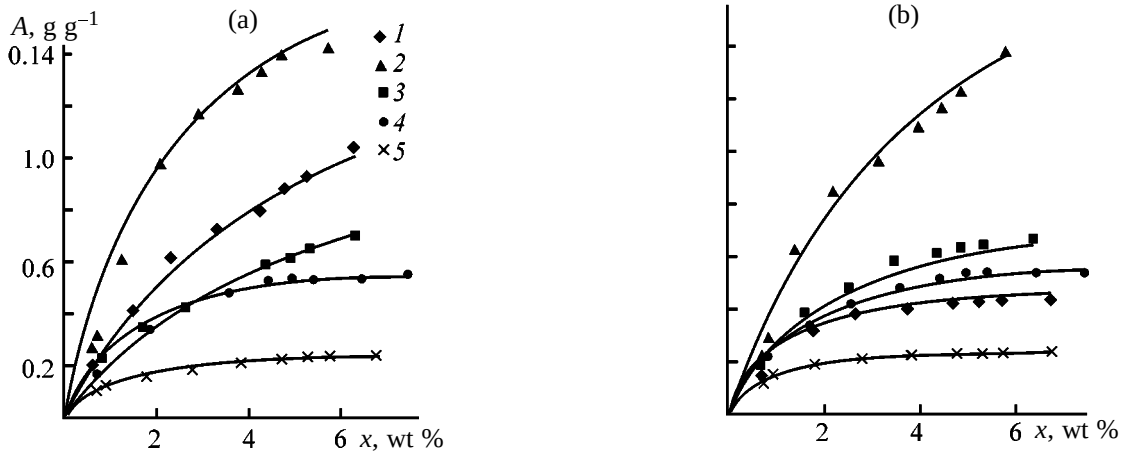

Fig. 2. Isotherms of sorption of alcohols from aqueous solutions with (a) birch charcoal and (b) charcoal produced from a blend of oak and beech wood. (*A*) Sorption capacity and (*x*) equilibrium concentration.

tion efficiency decreases in the order *tert*-butanol > butanol > isobutanol > isopropanol > ethanol. The sorption capacity of these charcoals for the same substances in sorption from 5.5% solutions decreases in the order isobutanol > *tert*-butanol > isopropanol > butanol > ethanol (Figs. 1c, 1d).

The maximal sorption capacity of birch charcoal is reached in 120–180 min for 0.8% solutions of alcohol and in 90–180 min for 5.5% solutions. The maximal sorption capacity of charcoals produced from a blend of oak and beech wood is reached in 150–180 min for solutions of both concentrations.

In study of the sorption isotherms, we used the same procedure as in the study of the kinetic curves, but the concentration was varied from 0.5 to 8%. The analysis was carried out after the equilibrium was reached. The results are shown in Fig. 2. As seen from these data, the absorption capacity of both kinds of charcoal reaches a maximum at a concentration of 5.5–8%.

In preliminary studies of sorption of *tert*-butanol from aqueous solutions (0.4 and 0.8%) with charcoals under dynamic conditions, 99.87% purification was reached. It was found that, in treatment of 0.4% solution, the breakthrough concentration is reached in a shorter time. In addition, charcoal produced from a blend of oak and beech woods has lower dynamic sorption capacity.

From the data obtained, we can conclude that both kinds of charcoal can be used for treatment of wastewater to remove alcohol impurities. Birch charcoal has a higher sorption capacity for alcohol.

REFERENCES

1. *Tekhnologiya spirta* (Production of Alcohol), Yarovenko, B.Ya., Ed., Moscow: Kolos, 1999.
2. Andrianov, K.A. and Khananashvili, L.M., *Tekhnologiya elementoorganicheskikh monomerov i polimerov* (Production of Heteroorganic Monomers and Polymers), Moscow: Khimiya, 1973.
3. Smirnov, A.D., *Sorbtsionnaya tekhnologiya ochistki vody* (Sorption Procedure of Water Purification), Leningrad: Khimiya, 1982.
4. Stolyarov, B.V. and Savinov, I.M., *Rukovodstvo k prakticheskim rabotam po gazovoi khromatografii: Uchebnoe posobie dlya vysshikh uchebnykh zavedenii* (Manual on Gas Chromatography: A Handbook for Higher Institutions), Leningrad: Khimiya, 1978, 2nd ed.

Russian Journal of Applied Chemistry, Vol. 75, No. 7, 2002, pp. 1194–1195. Translated from Zhurnal Prikladnoi Khimii, Vol. 75, No. 7, 2002, p. 1218.
Original Russian Text Copyright © 2002 by Idrisova.

BRIEF COMMUNICATIONS

Inhibitor of Acid Corrosion

S. Sh. Idrisova

Sumgait State University, Sumgait, Azerbaijan

Received July 31, 2001; in final form, January 2002

Abstract—A new inhibitor for steel protection in sulfuric acid solutions, 2,4,6-tribromo-*m*-phenylenediamine, was studied.

It is known that *p*-phenylenediamine is used as inhibitor of acid corrosion of steel. It was of interest to study in this respect 2,4,6-tribromo-*m*-phenylenediamine.

2,4,6-Tribromo-*m*-phenylenediamine was synthesized by oxidative bromination of *m*-phenylenediamine with a mixture of 40% hydrobromic acid and 28% solution of hydrogen peroxide with *m*-phenylenediamine : HBr : H_2O_2 molar ratio of 1 : 3 : 3 at 0–5°C and vigorous stirring for 2 h [2]; yield 99.5%, mp 157°C. Tribromo-*m*-phenylenediamine is a yellow-brown crystalline product identified by IR spectra, in which absorption bands at 650–720 cm^{-1}, characteristic of the C–Br bond, and at 3450 cm^{-1}, characteristic of NH_2 groups, were found.

The inhibiting properties were studied on $30 \times 20 \times$ 2-mm plates made of St.3 low-carbon steel. Prior to experiments, the steel samples were cleaned on a polishing machine to uniform shine of the surface, which was degreased with acetone and then kept in a corrosive medium (0.5, 2.5, or 4 M sulfuric acid solution) at 25–80°C for 1–2 h. The solutions were inhibited immediately before the experiments.

The protection efficiency was evaluated gravimetrically from the weight loss by a steel sample subjected to corrosion for the same period of time in inhibited and uninhibited solutions. The calculations were done on the basis of the results of three replicate runs. The extent of protection of a sample from acid corrosion, *Z*, is presented in the table, whence it is seen that *p*-phenylenediamine exhibits a satisfactory protecting effect.

Introduction of three bromine atoms into the *m*-phenylenediamine molecule much improves the inhibitor performance, presumably by enhancing the adsorption action because of the presence of the Br^- ion.

For comparison, 2,4,6-tribromoaniline was studied as acid corrosion inhibitor under similar conditions.

Protecting properties of 2,4,6-tribromo-*m*-phenylenediamine inhibitor and rate *V* of in-depth corrosion. Inhibitor content 0.2 wt %

Inhibitor*	$c_{H_2SO_4}$, g-equiv l^{-1}	*T*, °C	*V*, mm $year^{-1}$	*Z*, %
p-Phenylenediamine (**I**)	1	25	0.110	34.0
	1	80	0.108	40.0
	5	25	0.105	48.0
	5	80	0.099	52.0
	8	25	0.085	50.0
	8	80	0.102	55.8
2,4,6-Tribromo-*m*-phenylenediamine (**II**)	1	25	0.031	89.7
	1	80	0.030	90.0
	5	25	0.032	85.1
	5	80	0.026	93.8
	8	25	0.023	91.0
	8	80	0.020	98.0
2,4,6-Tribromoaniline (**III**)	1	25	0.089	49.9
	1	80	0.082	51.8
	5	25	0.042	52.4
	5	80	0.032	78.2
	8	25	0.070	68.4
	8	80	0.040	85.4

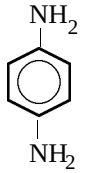

I

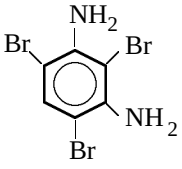

II

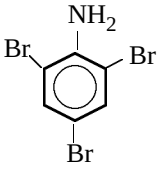

III

1070-4272/02/7507-1194$27.00 © 2002 MAIK "Nauka/Interperiodica"

It was found that its inhibiting action is also lower than that of 2,4,6-tribromo-*m*-phenylenediamine.

Thus, the composition of substituents strongly affects the inhibitor performance.

The protecting effect of 2,4,6-tribromo-*m*-phenylenediamine is also indicated by the fact that samples remain unchanged at 25°C at H_2SO_4 concentrations of 0.5, 2.5, and 4 M, and the steel surface becomes somewhat dull only at 80°C in a 4 M solution.

REFERENCES

1. Altsybeeva, A. and Levin, S., *Ingibitory korrozii metallov* (Inhibitors of Metal Corrosion), Leningrad: Khimiya, 1968.
2. Idrisova, S.Sh., Abstracts of Papers, *Nauchaya konferentsiya aspirantov i molodykh uchenykh "Monomery i polimery"* (Scientific Conf. of Postgraduate Students and Young Scientists "Monomers and Polymers"), Sumgait, 1985, p. 6.

Russian Journal of Applied Chemistry, Vol. 75, No. 7, 2002, pp. 1196–1197. Translated from Zhurnal Prikladnoi Khimii, Vol. 75, No. 7, 2002, pp. 1219–1220.
Original Russian Text Copyright © 2002 by Gorshkov, Kopylov, Markacheva, Polivanov.

BRIEF COMMUNICATIONS

Solvent Regeneration in Direct Synthesis of Alkoxysilanes

A. S. Gorshkov, V. M. Kopylov, A. A. Markacheva, and A. N. Polivanov

State Research Institute of Chemistry and Technology of Organoelement Compounds, State Scientific Center of the Russian Federation, Moscow, Russia

Received July 6, 2001; in final form, April 2002

Abstract—A procedure was developed for regeneration of Termolan, solvent used in synthesis of alkoxysilanes, involving its treatment with ethanol to remove alkoxysilanes.

Alkoxysilanes are synthetic precursors of various organosilicon products. They are used for preparing organosilicon oligomers, carbofunctional products, compounds, high-purity silicon dioxide for fiber optics, etc. Triethoxysilane is also used for producing monosilane and semiconductor-grade silicon. Tetraethoxysilane and ethyl silicate prepared from it are used as binders in fabrication of molds for precision casting [1, 2].

Direct synthesis of alkoxysilanes is based on the reaction of silicon with alcohols. With copper chloride as catalyst, the major products are trialkoxysilanes [3, 4]:

$$Si + 3ROH \rightarrow SiH(OR)_3 + H_2. \quad (1)$$

With base catalysts and with copper or silver salts as cocatalysts, tetraalkoxysilanes $Si(OR)_4$ are formed [5] (R is an alkyl group).

The reaction is performed in a high-boiling solvent, e.g., in polyaromatic oils, alkylbenzene, etc. [6, 7]. In this work, direct synthesis of triethoxysilane was performed in alkylated naphthalene (Termolan [8], an analog of Therminol 59 and Therminol 60 [6, 9]).

Direct synthesis of alkoxysilanes is accompanied by side processes yielding water, which inhibits the main reactions and hydrolyzes alkoxysilanes:

$$(n + 1)Si(OR)_4 + nH_2O \rightarrow Si_{n+1}O_n(OR)_{n+2} + 2nROH, \quad (2)$$

where $n > 1$.

The occurrence of reaction (2) results in the accumulation of oligoethoxysiloxanes. They should be removed from the solvent at regular intervals for its regeneration and reuse.

Procedures are known for the solvent regeneration by treatment with boron derivatives [9, 10] or organic acids [11]. However, in this procedure, oligoethoxysiloxanes decompose to form solid silicon compounds.

Here we propose an extraction procedure for solvent regeneration to remove ethoxysiloxanes after the direct synthesis. The siloxanes were extracted with ethanol. The procedure was optimized using model systems alcohol–ethoxysiloxanes–Termolan. As a source of ethoxysiloxanes we used ethyl silicate from which the low-boiling fraction was preliminarily removed by distillation. The silicon content in the initial ethoxysiloxanes was 14–22%.

First, we prepared a solution of siloxanes in the solvent, and then added alcohol. The contents were thoroughly mixed, with the subsequent phase separation. The siloxanes passed to the alcohol fraction. Experiments were performed at 20°C.

The results are shown in the figure. It is seen that, at the initial concentration of ethoxysilanes in Termolan of up to 30%, the alcohol/Termolan volume ratio of 0.6–0.8 is sufficient to virtually completely remove the siloxanes from the solvent by extraction.

The density of siloxanes is higher than that of the initial Termolan, and at low amounts of alcohol added for extraction the concentration of siloxanes in the alcohol becomes fairly high, with the density of the alcohol phase becoming higher than the density of the solvent phase. In this case, the lower layer was an alcoholic solution of siloxanes, and the upper layer was the regenerated solvent. With a larger amount of alcohol taken for extraction, the concentration of siloxanes in the alcohol phase was lower, and the alcohol phase having lower density formed the upper layer, and the regenerated solvent, the lower layer.

The suggested regeneration procedure was tested

1070-4272/02/7507-1196$27.00 © 2002 MAIK "Nauka/Interperiodica"

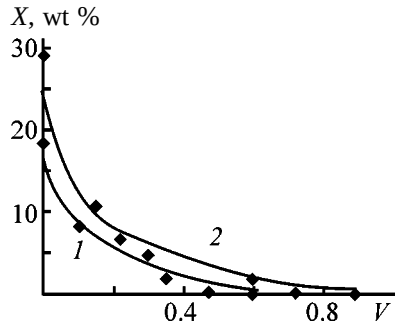

Concentration of ethoxysilozanes in Termolan *X* as a function of the volume ratio of the extractant (alcohol) to Termolan *V*. Initial concentration of ethoxysilanes in Termolan X_0, wt %: (*1*) 18.5 and (*2*) 30.

with the solvent after the direct synthesis of triethoxysilane. It was shown that oligoethoxysiloxanes are recovered by extraction, and the solvent becomes suitable for further syntheses. This procedure can be efficiently used in commercial production of alkoxysilanes. Oligoalkoxysiloxanes recovered from the solvent can be used as components of plugging formulations and for other purposes.

REFERENCES

1. Adrianov, K.A., *Metody elementoorganicheskoi khimii. Kremnii* (Methods of Organometallic Chemistry. Silicon), Moscow: Goskhimizdat, 1968.
2. Khananashvili, L.M., *Khimiya i tekhnologiya elementoorganicheskikh monomerov i polimerov* (Chemistry and Technology of Organoelement Monomers and Polymers), Moscow: Khimiya, 1998.
3. US Patent 4323690.
4. RF Patent 2152775.
5. USSR Inventor's Certificate no. 1658617.
6. US Patent 5783720.
7. Lewis, K.M., Yu, H., Eng, R.N., *et al.*, Abstracts of Papers, *31rd Symp. on Organosilicone*, New Orleans, Louisiana: Tulane Univ., May 29–30, 1998, report B-11.
8. Margulis, M.A., Anpilogov, Yu.E., and Chernykh, S.P., *Khim. Prom–st.*, 1993, no. 5, pp. 53–56.
9. US Patent 5166384.
10. Lewis, K.M., Yu, H., Eng, R.N., *et al.*, Abstracts of Papers, *33rd Organosilicone Symp.*, Saginaw, Michigan: Saginaw Valley State Univ., April 6–8, 2000, report C-5.
11. US Patent 6090965.

Russian Journal of Applied Chemistry, Vol. 75, No. 7, 2002, pp. 1198–1199. Translated from Zhurnal Prikladnoi Khimii, Vol. 75, No. 7, 2002, pp. 1221–1222.
Original Russian Text Copyright © 2002 by Rozental', Ivanova.

BRIEF COMMUNICATIONS

Prediction of Properties of Asphalt Oil in Asphaltic Concrete

D. A. Rozental' and E. S. Ivanova

St. Petersburg State Technological Institute, St. Petersburg, Russia

Received February 26, 2002

Abstract—Evolution of characteristics of asphalt oil in contact with mineral ballast in the course of long-term storage of asphaltic concrete at room temperature is studied. Data on the effect of the preparation time of mix asphalt on the structure and properties of asphalt oil in asphaltic concrete are analyzed.

Asphalt oils are widely used in road construction as materials for asphaltic concrete pavement. Asphalt oils in asphaltic concrete play a role of an organic binder for the mineral fraction. When manufacturing asphaltic concrete, asphalt oil is mixed with mineral ballast at 160°C for 20 min. Physical interaction of asphalt oil with the mineral filler is accompanied by formation of adsorption layers of the binder on the filler grains. This process includes many adsorption–desorption stages, until reaching the equilibrium. This is a selective process, resulting in extraction of the most readily adsorbed components from asphalt oil, which, in its turn, distorts the thermodynamic equilibrium in the colloidal system of asphalt oil. As a result, the system is transformed, approaching new equilibrium state corresponding to given conditions. Finally, transformation of the asphalt oil structure changes its characteristics.

The factors influencing adsorption of asphalt oil on the mineral filler surface are as follows [1–3]: heating temperature, heating time τ, the kinds of mineral ballast and asphalt binder, and, finally, the ballast grading.

The goal of this work was to predict the evolution of characteristics of asphalt oil in asphaltic concrete. Therefore, we studied the effect of the time of heating of mix asphalt at 160°C on the adherence of asphalt oil to mineral ballast. As mineral ballast we used granite with a grading of 3–5 mm. The heating time was varied from 20 min to 4 h. In experiments we used BND 40/60 asphalt oil produced by the KINEF Production Association, Limited Liability Company from a mixture of West Siberian oils. The adhesion was measured by the hot centrifugation method [4], followed by determination of the performance characteristics of the extracted product.

With increasing heating time, the amount of asphalt oil retained on the mineral ballast surface increases, saturating at τ = 3 h (see figure).

Evolution of the performance characteristics (penetration Π_{25} and softening point T_s) of asphalt oil extracted from mix asphalt by centrifugation is given below.

τ, h	0	1/3	2/3	1	2	3	4
Π_{25}, mm × 0.1	59	58	55	34	32	30	28
T_s, °C	51	54	56	67	70	72	73

With increasing τ, the softening point considerably increases, and the penetration abruptly decreases. At τ = 3 h these parameters approach their saturated values.

The observed evolution of the softening point and penetration is well consistent with data on the adhesion of asphalt oil to the mineral ballast, suggesting that establishment of the adsorption equilibrium in mix asphalt takes about 3 h.

In asphaltic concrete in service, asphalt oil occurs in the cold state. Our results obtained at room temperature allow prediction of the behavior of asphalt oil in asphaltic concrete pavements.

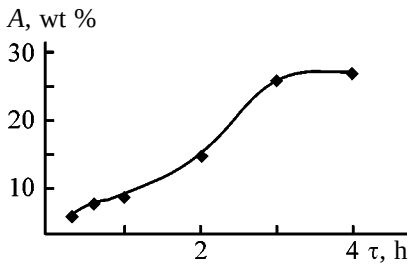

Effect of the heating time τ of mix asphalt at 160°C on the adherence of asphalt oil to mineral ballast *A*.

1070-4272/02/7507-1198$27.00 © 2002 MAIK "Nauka/Interperiodica"

Evolution of characteristics of asphalt oil in storage after heating of mix asphalt for 1 h

Storage time	Adherence, wt %	T_s, °C	Π_{25}, mm × 0.1
0	(27)*	67 (72)	34 (30)
1/3	12 (9)	49 (51)	54 (52)
2/3	12 (9)	51 (55)	52 (42)
1	12 (9)	52 (55)	48 (36)
2	10 (10)	55 (56)	42 (34)
3	8 (10)	56 (57)	39 (33)
4	8 (25)	57 (59)	38 (33)
5	8 (25)	57 (61)	37 (32)
6	8 (25)	58 (63)	37 (32)
7	8 (25)	58 (63)	37 (32)

* Data for mix asphalt after 3-h heating are given in parentheses.

We studied the evolution of characteristics of asphalt oil separated by hot centrifugation from mix asphalt after long-term storage (from 10 days to 7 months) at room temperature (18°C). The results are given in the table.

Initially mix asphalt was heated at 160°C for 1 and 3 h. The results show that establishment of the adsorption equilibrium requires at least 3-h heating. Thus, it is seen how the initial heating time influences the characteristics of asphalt oil in asphaltic concrete.

The temperature drop from 160 to 18°C in mix asphalt initiates a considerable change in the structure and characteristics of asphalt oil (see table). However, in the course of subsequent storage of mix asphalt in the cold state, these changes decay as a result of a large number of adsorption–desorption events. It follows from the table that the equilibrium established after heating for a fixed time is practically identical to that after the subsequent storage at room temperature. Therefore, data on evolution of characteristics of asphalt oil in the course of heating in contact with mineral ballast allows prediction of the behavior of this material in asphaltic concrete.

REFERENCES

1. Rozental', D.A. and Syroezhko, A.M., *Khim. Tekhnol. Topl. Masel*, 2000, no. 4, pp. 41–43.
2. Rozental', D.A., *Zh. Prikl. Khim*., 1995, vol. 68, no. 7, pp. 1057–1066.
3. Rozental', D.A., Golovanova, T.A., and Narubina, S.P., *Khim. Tekhnol. Topl. Masel*, 1998, no. 4, pp. 48–49.
4. Khudyakova, T.S., Rozental', D.A., Mashkova, I.A., *et al*., *Khim. Tekhnol. Topl. Masel*, 1987, no. 6, pp. 35–36.

Russian Journal of Applied Chemistry, Vol. 75, No. 7, 2002, pp. 1200–1203. Translated from Zhurnal Prikladnoi Khimii, Vol. 75, No. 7, 2002, pp. 1223–1225.
Original Russian Text Copyright © 2002 by Morachevskii.

HISTORY OF CHEMISTRY AND CHEMICAL TECHNOLOGY

Academician German Ivanovich Hess (on the 200th Anniversary of His Birthday)

Academician German Ivanovich Hess (Germain Henri Hess) made an outstanding contribution to the development of chemical science and teaching of chemistry in higher school institutions of St. Petersburg in the first half of the XIX century. He carried out comprehensive studies in inorganic and organic chemistry, chemical technology, and mineralogy, and was the first to formulate fundamental concepts of thermochemistry, one of the most important branches of physical chemistry.

G.I. Hess was born on July 26 (August 7), 1802, in Geneva. However, soon after his father, and then the whole family, moved to Russia (1805), where G.I. Hess's parents worked as family tutors. German Hess was well educated at home. His Swiss-born mother, who had a perfect command of German and French, paid much attention to bringing up her son. In 1817, Hess moved to Derpt (Tartu), where he went to a private school for two years, and then to Derpt Gymnasium, which he finished in 1822. In autumn of the same year he became a student of the Faculty of Medicine at Derpt University. One of the largest not only in Russia, but in Europe, too, this oldest university was again opened, after a long break, in 1802, and in the 1820s–1830s, up to 600 students were taught at the university, with, however, no specialists in chemistry trained there till 1850. The chair of chemistry, organized in 1804, satisfied the needs of medicine and pharmacy only. The teaching was in German. During the time when Hess was a student, chemistry (inorganic, organic, and analytical) was taught by Professor G.W. Osann (1797–1866), later (since 1828) a professor at Würzburg University in Germany, a versatile scientist, author of investigations in various fields of chemistry and chemical technology and physics. He studied, in particular, Ural platinum ore and wrote the first volume of a manual of theoretical chemistry (1827). Under Osann's supervision, Hess carried out chemical analyses. Hess was much interested in lectures delivered by Professor of Physics G.F. Parrot (1767–1852), the first rector of the university and academician of the St. Petersburg Academy of Sciences (since 1826), and also lectures given by Professor of Mineralogy M. Engelhardt (1779–1842).

Hess graduated with honors from Derpt University and, having defended the dissertation "Something about Curative Waters, Especially Those in Russia," received the degree of a doctor of medicine. By application of Professors Osann and Engelhardt, Hess was sent on a business trip abroad, to Sweden, to visit one of the best-known chemists of that time, J.J. Berzelius (1779–1848), professor of the Medical-Surgery Institute in Stockholm, member of the Royal Swedish Academy of Sciences (since 1808), and honored member of the St. Petersburg Academy of Sciences (since 1820). Berzelius was a prominent specialist in chemical analysis; he determined the atomic weights of 45 chemical elements and discovered cerium (1803), selenium (1817), and thorium (1828). He was the first to obtain in free state silicon, titanium, tantalum, and zirconium; he studied the phenomenon of catalysis and introduced the notion of allotropy. Berzelius and Hess became good friends. Berzelius highly appreciated the gifted nature and potentialities of his disciple, and was in correspondence with him for many years [2, 3].

After four months in Stockholm, Hess returned to

1070-4272/02/7507-1200$27.00 © 2002 MAIK "Nauka/Interperiodica"

Russia and took part in Professor Engelhardt's expedition to the Urals. When being a student, Hess received a stipend and, according to the regulations of that time, had to serve after having graduated from the University. He was appointed a doctor at Irkutsk and came there in August 1826. In addition to his direct duties, Hess paid much attention, when in Irkutsk, to chemical investigations and studies of the nature of this richest territory. He analyzed local hot mineral waters, a number of minerals, studied impurities in common salt mined in Irkutsk guberniya, recommended a method for impurity removal, and launched several expeditions during which he conducted geological surveys. Later, Hess composed a geological review of a part of Transbaikalia.

In October 1828, by recommendation of Academician Parrot and (by letter) Berzelius and Osann, Hess was elected, at the age of 26, an adjunct in chemistry of the St. Petersburg Academy of Sciences. By that time, the Academy lost such well-known chemists and natural scientists as E. Laksman (1737–1796), T.E. Lovits (1757–1804), and V.M. Severgin (1765–1826), and there was no chemical laboratory any more.

In the late March 1829, Hess came to St. Petersburg from Irkutsk and immediately commenced active work. First, he equipped a laboratory in a room of his flat, and later the Academy of Sciences satisfied Hess's request for organization of a chemical laboratory of the Academy, and this laboratory was opened on February 10, 1830, in a house situated near the main building of the Academy on the Neva River embankment.

German Ivanovich continued his investigations of natural waters and minerals. His works became increasingly known and impressed everybody with the diversity of objects studied. He was elected extraordinary academician in 1830, and ordinary academician in 1834. In these years, Hess started intensive teaching activities. In October 1831, the St. Petersburg Practical Technological Institute was opened in order to "train people having sufficient theoretical and practical knowledge to manage plants or parts of these" [4]. The course of training was intended to be three years. Hess accepted an invitation to become an inspector of classes (deputy director) at this institute. He composed curricula and invited the best specialists from other civilian and military educational institutes of St. Petersburg to teach the basic disciplines. A chemical laboratory was organized in accordance with Hess's recommendations and under his supervision. The fulfillment of the curricula at the institute was checked both by Hess himself and by the specially organized Technical Committee, also serving to control all practical studies.

In 1832, Hess was elected an ordinary professor of chemistry and technology of the Chief Pedagogical Institute (1832–1847). Hess also delivered lectures at the Institute of Ways of Communications and Artillery Mikhail College. Particularly intensive were pedagogical activities of German Ivanovich at the Mining Institute (1832–1849). He organized there a chemical laboratory, introduced practical training in chemistry for students, and paid much attention to studying the analytical chemistry and qualitative and quantitative analyses. Hess emphasized the importance of teaching the students to carry out experimental work. Owing to Hess's efforts, the chemical laboratory of the Mining Institute became a prominent scientific and pedagogical center in the field of analytical chemistry in Russia.

In 1831, Hess published his fundamental work *Osnovaniya chistoi khimii* (Foundations of Pure Chemistry). In the book, practical evidence and theoretical concepts are closely interconnected, and the Russian chemical terminology is introduced for the first time. As experiments are described, their theoretical substantiation, possible at that time, is given. The book was approved by the Academy of Sciences and ran into 7 editions in 18 years. The book was the basic textbook in chemistry in the 1830s–1840s and exerted a strong influence on the formation of scientific outlook in subsequent generations of Russian chemists, among which were such well-known scientists as A.A. Voskresenskii (1809–1880), N.N. Zinin (1812–1880), N.N. Beketov (1827–1911), A.M. Butlerov (1828–1886), and D.I. Mendeleev (1834–1907). Voskresenskii, who graduated from the Chief Pedagogical Institute in 1836, attended Hess's lectures. In his turn, Mendeleev entered the Chief Pedagogical Institute in 1850 and was taught chemistry by Professor Voskresenskii.

Much success was achieved by A.I. Khodnev (1818–1883), Hess's disciple at the Chief Pedagogical Institute. His pedagogical and scientific activities were considered in detail by Figurovskii and Solov'ev in [5] and in monograph [6]. To representatives of Hess's school formed at the Mining Institute belong P.I. Evreinov, N.A. Ivanov, P.P. Shubin, and K.I. Raevskii [7, 8].

Hess's scientific investigations carried out in St. Petersburg were still concerned with mineral resources and practically important processes. He was the first to describe and analyze four minerals, named

vertite (1830), uvarovite (1832), hydroboracite (1833), and volborthite (1834). German Ivanovich also studied the mineral, silver telluride, named hessite after him, and proposed a method for recovering tellurium from this mineral.

In a practical study, Hess came to a conclusion that use of hot blast in blast furnaces must "save a lot of combustible materials." He studied comprehensively the technique for processing of raw platinum and proposed methods for its analysis. Hess was among the first to study the ability of platinum black to accelerate the reaction between oxygen and hydrogen.

German Ivanovich also carried out a number of investigations in the field of organic chemistry. He studied the composition of gas from oil fields near Baku and the process of pyrolysis of oil and wood tars. In one of his studies, Hess isolated a new acid, named "saccharic" by him, and determined its composition.

Despite the great number of various investigations in the field of applied chemistry, technological analysis, and metallurgy, Hess expressed in his public lectures and letters to colleagues, beginning already in 1830, a desire to contribute to solution of the fundamental problem of chemistry, the problem of chemical affinity. German Ivanovich started from the presumption that any chemical addition event is accompanied by heat release. He started experimental determinations of heat effects in 1834, using a specially constructed calorimeter. However, Hess wrote as far back as in the first edition of his book *Osnovaniya chistoi khimii* that "It may be assumed that the stronger the mutual affinity, the larger the amount of heat released." After the beginning of his own calorimetric measurements, he wrote in a letter to Berzelius more categorically: "...I have no doubt concerning the fundamental issue: the heat released is a measure of affinity... My aim is to demonstrate to the scientific community the large amount of work required by this new standpoint and thereby to induce the possibly greater number of researchers to take part in the development of thermochemistry" [6, 9].

In 1840, based on a vast body of experimental data, Hess formulated the thermoneutrality law: in mixing of two salt solutions having the same temperature and forming two new salts through exchange decomposition, the temperature of the mixture remains unchanged. This law was exhaustively substantiated only by the theory of electrolytic dissociation developed by S. Arrhenius (1859–1927) in 1887 and served as one of its verifications. German Ivanovich was also the first to observe that strong acids and strong bases always release the same amount of heat when neutralized in equivalent amounts.

Simultaneously (in 1840), Hess formulated a fundamental law of thermochemistry, named after him, the law of constant heat summation: "The heat evolved in the formation of a chemical compound is the same whether the compound is formed in one or in several steps." This law and other thermochemical investigations of Hess were analyzed in detail in [3, 6, 9, 10].

Germam Ivanovich Hess, state counselor of the 4th class, ordinary academician, member of the Scientific Committee of the Corps of mining engineers, and bearer of other honorary titles died of severe illness on November 30 (December 12), 1850 in St. Petersburg. He was only 48. Hess was buried at Smolenskoe Lutheran cemetery.

The life and pedagogical and scientific activities of Hess have been the subject of a great number of publications. Among these, particular mention should be made of the monograph by Yu.I. Solov'ev [3], paper by A.F. Kapustinskii "German Ivanovich Hess and His Role in the Creation and Development of Thermochemistry" [9], and articles [11, 12]. Biographic information about Hess was included in books [13, 14].

Hess's works, his pedagogical activities were exceedingly important for training of highly educated chemists in Russia. We have every reason to mention his name among the names of other Russian chemists known all over the world.

REFERENCES

1. Martinson, Kh.R. and Martinson, K.A., *Khimiki – vospitanniki Tartuskogo universiteta do 1917 g.* (Chemists Graduated from Tartu University before 1917), Tallinn: Inst. Istorii Akad. Nauk Est. SSR, 1978.
2. Solov'ev, Yu.I., *Vopr. Istor. Estestvozn. Tekh.*, 1958, issue 6, pp. 166–175.
3. Solov'ev, Yu.I., *German Ivanovich Hess*, Moscow: Akad. Nauk SSSR, 1962.
4. *150 let Leningradskogo tekhnologicheskogo instituta im. Lensoveta* (Lensovet Technological Institute in Leningrad is 150), Leningrad: Khimiya, 1978.
5. Figurovskii, N.A. and Solov'ev, Yu.I., *Tr. Inst Istor. Estestvozn. Tekh.*, 1954, vol. 2, pp. 19–45.
6. Solov'ev, Yu.I., *Istoriya khimii v Rossii* (History of Chemistry in Russia), Moscow: Nauka, 1985.
7. Sheptunova, Z.I., *Tr. Inst. Istor. Estestvozn. Tekh.*, 1958, vol. 18, pp. 75–103.
8. *Leningradskii gornyi institut i Akademiya nauk SSSR*

(Leningrad Mining Institute and the Academy of Sciences of the USSR), Leningrad: Leningr. Gornyi Inst., 1978.

9. Hess, G.I., *Termokhimicheskie issledovaniya* (Thermochemical Investigations), Kapustinskii, A.F., Ed. and Author of Introductory Article, Moscow: Akad. Nauk SSSR, 1958.
10. Kipnis, A.Ya., *Razvitie khimicheskoi termodinamiki v Rossii* (The Development of Chemical Thermodynamics in Russia), Moscow: Nauka, 1964.
11. *Gorn. Zh.*, 1851, part 1, book 1, pp. 228–240.
12. Blokh, M.A., *Priroda*, 1941, no. 3, pp. 103–111.
13. Musabekov, Yu.S. and Chernyak, A.Ya., *Vydayushchiesya khimiki mira* (Outstanding Chemists of the World), Moscow: Kniga, 1971.
14. Balezin, S.A. and Beskov, S.D., *Vydayushchiesya russkie uchenye-khimiki* (Outstanding Russian Chemists), Moscow: Prosveshchenie, 1972.

A. G. Morachevskii

Russian Journal of Applied Chemistry, Vol. 75, No. 7, 2002, pp. 1204–1205. Translated from Zhurnal Prikladnoi Khimii, Vol. 75, No. 7, 2002, pp. 1226–1227.
Original Russian Text Copyright © 2002 by Morachevskii.

BOOK REVIEWS

Bulanova, M.V., Buyanov, Yu.I., and Sidorko, V.R., *Vzaimodeistvie redkozemel'nykh metallov so svintsom* (Interaction of Rare-Earth Metals with Lead)

Kiev: Inst. Problem Materialovedeniya im. I.N. Frantsevicha, Nats. Akad. Nauk Ukrainy, 2001, 107 pp.

In continuation of previous publications concerning the interaction of Group IV elements with rare-earth metals,[1] the reference book under consideration discusses alloys of rare-earth metals (REMs) with lead.

In a brief introduction, the authors mention that compounds of REMs with lead, plumbides, have been studied to a lesser extent compared to their Group IV analogs: silicides, germanides, and stannides. This may be due both to the lack among plumbides of compounds with any practically important properties and to severe experimental difficulties encountered in studying the rather reactive R–Pb alloys (where R is a rare-earth metal). Compounds of rare-earth metals with lead are insufficiently stable against the action of atmospheric moisture and oxygen, possess increased brittleness, and therefore can be, probably, used only in multicomponent formulations. In accordance with the position of lead in the periodic table, its alloys with REMs must be closer in their structural, physical, and chemical properties to REM alloys with tin, than to alloys with silicon and germanium. Comparison of the properties of stannides and plumbides confirms this conclusion.

The book by M.V. Bulanova, Yu.I. Buyanov, and V.R. Sidorko presents, with varied extent of completeness and reliability, data on phase diagrams and crystal structure of compounds, and thermodynamic properties of alloys with lead of scandium, yttrium, lanthanum, and all lanthanides, from cerium to lutetium. Of the 17 possible R–Pb phase diagrams, relatively reliable evidence based on experimental studies is available for nine systems (alloys of lead with Sc, Y, La, Pr, Eu, Gd, Dy, Yb, Lu). Less reliable are data on phase diagrams and compositions of compounds in the systems Ce–Pb and Sm–Pb. For the remaining 6 systems (alloys of lead with Nd, Pm, Tb, Ho, Er, Tm) hypothetical phase diagrams are constructed using mathematical simulation. The method is based on various correlations, which allow the authors to evaluate the composition of compounds, their melting and decomposition points, composition and temperature of eutectic mixtures, and position of the liquidus line.

The thermodynamic properties of the R–Pb alloys were studied using various kinds of the emf method, calorimetric measurements, and, in some cases, by measuring the saturated vapor pressure. The emf method was applied to study, to a greater or lesser extent, 15 systems (data are lacking only for the systems Pm–Pb and Tm–Pb). However, evidence on the thermodynamic properties of liquid alloys is, as a rule, lacking. The emf measurements were used in many systems to evaluate the thermodynamic properties of plumbides with the general formula RPb_3 and to determine the solubility of rare-earth elements in liquid lead. To evaluate the enthalpies of compound formation, model concepts were used together with the results of experimental determinations.

The refereed publication is very convenient in use. The material is presented in the book successively for all the systems considered in order of increasing REM number in the periodic table. Data on crystallographic characteristics of intermediate phases, nonvariant equilibria, thermodynamic properties, and, in some cases, liquid phases are presented in the form of tables, and the phase diagrams, in the form of figures. For some systems, data on the specific heat of compounds, REM solubility in liquid lead, and limiting thermodynamic characteristics (partial molar excess Gibbs energies and enthalpies of REM mixing at infinite dilution) are available. In all cases, references to relevant publications are given, with a total of 132 published sources used. There is no escape from mentioning that specialists in thermodynamics of alloys, working at the Institute of Materials Science Problems, National Academy of Sciences of the Ukraine, possess a vast experience in expert assess-

[1] For reviews, see *Zh. Prikl. Khim.*, 1998, vol. 71, no. 7, p. 1229 and *Zh. Prikl. Khim.*, 1999, vol. 72, no. 10, p. 1757.

1070-4272/02/7507-1204$27.00 © 2002 MAIK "Nauka/Interperiodica"

ment of various kinds of experimental studies and in analysis and prognostication of phase diagrams.

Based on the material presented, the authors revealed a number of fundamental aspects of the interaction between rare-earth metals and lead. Intermetallic compounds, whose number varies between 2 for the Sc–Pb system and 7 for Pr–Pb, are formed in all the R–Pb systems. All the compounds can be conditionally classed with constant-composition phases, with narrow homogeneity regions (up to 2 at. %) found only for the compounds Y_5Pb_3, Gd_5Pb_3, and Dy_5Pb_3. The highest-melting compounds in all the R–Pb systems are those of the type R_5Pb_3. Certain patterns are revealed regarding the structural types of compounds in the R–Pb systems.

The book by Bulanova and co-authors contains extensive and useful reference data. It is, undoubtedly, of interest to a wide audience of specialists working in the field of inorganic materials science and chemistry of rare-earth metals.

A. G. Morachevskii

Russian Journal of Applied Chemistry, Vol. 75, No. 7, 2002, p. 1206. Translated from Zhurnal Prikladnoi Khimii, Vol. 75, No. 7, 2002, p. 1228.
Original Russian Text Copyright © 2002 by Zaikov.

INFORMATION

X Korshak Symposium

X Korshak Symposium was held on February 13, 2002 at the Nesmeyanov Institute of Organoelement Compounds (INEOS), Russian Academy of Sciences (RAS) (Moscow). The symposium was organized by the Russian Academy of Science (Scientific Council on Macromolecular Compounds at the Department of General and Technical Chemistry), INEOS, and the Mendeleev Russian University of Chemical Engineering (Moscow).

The symposium was opened by Yu.N. Bubnov (Moscow) who outlined that Academician V.V. Korshak (1909–1988) was one of the pioneers in the polymer chemistry of the XX century, and that his school is one of the largest in the world.

The symposium participants were 150 scientists from 25 institutions of RAS, universities of the Ministry of Higher Education of the Russian Federation, and applied research institutions.

The symposium program included five plenary lectures under the general topic *The Korshak's Concepts are Alive and Flourishing*. The lectures emphasized that the Korshak's concepts are developed at present, being realized in new scientific lines and significant practical applications.

The first lecture given by E.M. Sul'man (Tver) was devoted to nano-scale metal–polymer catalysts in hydrogenation and oxidation. The reported results were obtained by INEOS in cooperation with some German research centers.

The second lecture on polymerization with atom transfer and also on synthesis of amphiphilic block copolymers was given by Yu.A. Kabachii (Moscow). The background of this line was founded by Cristoff Matisevski (Poland). Then his works were successfully developed by Korshak's disciples.

V.I. Sidorenko and I.I. Ponomareva (Moscow) in their lecture reported on a new generation of polyheteroarylene-based binders for highly heat-resistant composite materials. The authors obtained unique polymeric materials for aircraft industry, which are stable to 400–450°C. Such materials are used, in particular, in construction of skin of extrasupersonic airplanes and in manufacture of engines (e.g., turbine blades). Note that the preparation procedure of the binder proposed by the authors is very simple.

The lecture given by A.P. Petrova and P.M. Valetskii (Moscow) was devoted to development of special polymeric materials based on carborane derivatives, suitable for exploitation at temperatures of up to 1000°C. Under such conditions, polymers based on carborane-containing compounds degrade with formation of a coke with good mechanical characteristics. The authors successfully used novolac resins as binders for composites with good mechanical properties. Phenol–rubber and polyurethane adhesives found wide application as binders also. The resulting materials can be exploited not only at very high, but also at very low temperatures (to –200°C).

The composites proposed can operate without deterioration of their performance characteristics for 10000 h at 600°C (for example, they were used to seal joints on the skin of the Soviet shuttle Buran).

The last lecture entitled *The Lessons of V.V. Korshak* was given by P.M. Valetskii. He outlined the Korshak's scientific activities. A special emphasis was made on the fact that he easily entrusted young researchers with important pieces of theoretical and practical works, including those by request of the USSR Defense Ministry.

All the lectures were followed by lively discussions. Particularly, Academician N.A. Plate, vice-president of RAS, and Academician V.A. Kabanov, the Secretary of the Department of General and Technical Chemistry of RAS, participated in the discussions.

The next XI Korshak Symposium will be held at INEOS RAS in 2004.

E. G. Zaikov

1070-4272/02/7507-1206$27.00 © 2002 MAIK "Nauka/Interperiodica"

Russian Journal of Applied Chemistry, Vol. 75, No. 8, 2002, pp. 1207–1210. Translated from Zhurnal Prikladnoi Khimii, Vol. 75, No. 8, 2002, pp. 1233–1236.
Original Russian Text Copyright © 2002 by Dvoretskii, Anikanova, Malysheva, Koshel'.

INORGANIC SYNTHESIS AND INDUSTRIAL INORGANIC CHEMISTRY

Kinetic Parameters of Dissolution of Iron(III) Oxides of Varied Thermal and Chemical Prehistory in Hydrochloric Acid

N. V. Dvoretskii, L. G. Anikanova, Z. G. Malysheva, and G. N. Koshel'

Yaroslavl State Technical University, Yaroslavl, Russia

Received November 1, 2001; in final form, February 2002

Abstract—The kinetic parameters of dissolution in hydrochloric acid of Fe_2O_3 (hematite) samples of varied thermal and chemical prehistory are calculated in terms of Delmon's model of instantaneous nucleation on the surface of a solid reagent.

A finely crystalline structure (FCS) is one of the major structural characteristics of a sample, determining its activity in reactions (ferrite formation, dissolution in acids, etc.) [1]. It is characterized by such parameters as the coherent domain size, level of residual microdistortions, and possibility of stacking fault formation.

The aim of the study was to establish a correlation between the kinetic parameters of dissolution in hydrochloric acid and the FCS characteristics of Fe_2O_3 samples of varied thermal and chemical prehistory.

EXPERIMENTAL

"Carbonate" iron(III) oxide was obtained by thermal decomposition of iron(II) carbonate at 830–850 and 870–890 K for 180 min; "sulfate" iron(III) oxide, by thermal decomposition of iron(II) sulfate at 920–940 and 940–960 K for 180 min; and Fe_2O_3, by thermal decomposition of Mohr's salt, $(NH_4)_2Fe(SO_4)_2 \cdot 6H_2O$, at 960–980 K for 120 min.

X-ray diffraction analysis data were used to calculate the FCS parameters by the method of the fourth central moments [2]. The kinetics of dissolution was studied on homogeneous fractions of Fe_2O_3 samples, with particle size R_0 = 140–150 μm. A 0.5-g portion of the oxide was introduced into a temperature-controlled reactor containing 2 l of a 1 M aqueous solution of hydrochloric acid. The diffusion hindrance was avoided by stirring the water–dispersion mixture at a rate of 400–500 rpm. The tests were performed at temperatures of 300, 310, and 320 K maintained within (±1 K). Systems deoxygenated by bubbling nitrogen through the reactor for 1.5 h before sample introduction were used in the study. The concentration of Fe^{3+} ions in filtrate samples taken at regular intervals from the reactor through a Schott filter was determined by photocolorimetry [3].

The rate of dissolution of metal oxides is determined by the number of active centers on their surface [4, 5]. The kinetics of formation and dissolution of active centers of iron(III) oxide samples of varied thermal and chemical prehistory, brought in contact with an aqueous solution of hydrogen chloride was studied using Delmon's model of nucleation on the surface of a solid reagent [6].

We used in experiments Fe_2O_3 samples obtained by thermal decomposition of various iron(II) salts. Thermolysis followed by quenching is a method for sample treatment, which differs from the reaction under study and creates potential nuclei before the beginning of dissolution. Hence, the nucleation is localized at strictly specified points. The creation of nuclei before the start of the process studied is named artificial nucleation. Processes of artificial nucleation belong to reactions caused by instantaneous nucleation [6]. For this reason, the mathematical analysis of dissolution, performed here, is based on the model of instantaneous nucleation.

To describe the instantaneous nucleation mathematically, it is necessary to assume the existence of a function, $g_{t''}(\theta, \nu_0)$, that expresses the nucleation rate at different instants of time, θ, close to the start time. This function, which is nonzero only during a very

1070-4272/02/7508-1207 $27.00 © 2002 MAIK "Nauka/Interperiodica"

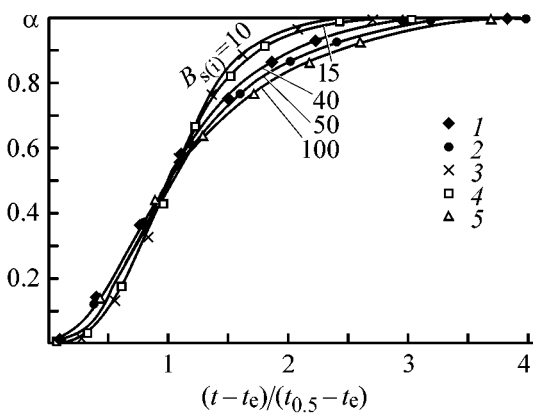

Fig. 1. Degree of Fe_2O_3 transformation, α, vs. reduced time $(t - t_e)/(t_{0.5} - t_e)$. Digits *1*–*5* correspond to sample numbers in Table 1.

short time interval t'', is chosen so that the sum of $g_{t''}(\theta, \nu_0)d\theta$, equal to the number of nuclei appearing during a time dθ, is equal to the concentration of nuclei at the initial instant of time.

In the case when the nucleation occurs at the potential nuclei, the concentration of nuclei at the initial instant time is equal to the initial concentration ν_0 of active centers.

The model of instantaneous nucleation can be conveniently described using the following reduced parameters:

$$B_{s(i)} = \pi \nu_0 a_0^2, \quad (1)$$

$$\tau = (k_i/a_0)t, \quad (2)$$

$$\varepsilon = x/a_0, \quad (3)$$

where $B_{s(i)}$ is a parameter characterizing reactions initiated on samples consisting of spherical grains (subscript "s") by instantaneous nucleation (subscript "i"); τ is reduced time; a_0 is the initial radius of a spherical grain; and x is the distance between the surface of the spherical layer and the grain surface (layer depth).

$B_{s(i)}$ is a dimensionless parameter equal to a quarter of the average number of nuclei on each sphere. The reduced time τ changes from zero to unity within a time necessary for an initial nucleus to reach the center of the sphere corresponding to a solid particle. The τ value becomes equal to 2 when the growth of the given nucleus leads to complete transformation of the entire grain.

According to Delmon's model [6], the dissolution rate is determined by the kinetic parameter k_i, which is the velocity of interface motion or the rate of nucleus growth. The degree of transformation α (or the extent of the reaction) is related to the reduced time τ by the equations:

$$\alpha = 1 - (1-\tau)^3 - 3\int_0^{\tau}(1-\varepsilon)^2 \exp\left(-B_{s(i)}\frac{\tau^2-\varepsilon^2}{1-\varepsilon}\right)d\varepsilon, \quad (4)$$

$$0 \le \tau \le 1;$$

$$\alpha = 1 - (1-\tau)^3\exp(-4B_{s(i)}) - 3\int_0^{2-\tau}(1-\varepsilon)^2\exp\left(-B_{s(i)}\frac{\tau^2-\varepsilon^2}{1-\varepsilon}\right)d\varepsilon,$$

$$1 \le \tau \le 2; \quad (5)$$

$$\alpha = 1 - \exp(-4B_{s(i)}), \quad \tau \ge 2. \quad (6)$$

The kinetic parameters were calculated from the tabulated values of the $B_{s(i)}$ function. The k_i value was determined by superimposing the experimental data plotted in the coordinates α–$(t - t_e)/(t_{0.5} - t_e)$ ($t_{0.5}$ is time necessary for the degree of transformation to become 50%, and t_e is the induction period) on a grid of theoretical curves plotted in the same coordinates at different $B_{s(i)}$ values. Figure 1 shows kinetic curves of dissolution of Fe_2O_3 samples in hydrochloric acid. Points represent the experimental data on dissolution of samples of different prehistories, and solid lines, the graphical solution to the equation.

Comparison of the experimental data and the results of theoretical calculations shows that $B_{s(i)}$ is within 10–100, depending on the sample prehistory. The induction period was calculated in terms of the instantaneous nucleation model by the formula:

$$\alpha^{1/3} = \text{const} \times (t - t_e). \quad (7)$$

In the case of artificial nucleation the induction period t_e is commonly negative (Table 1) and corresponds to the time necessary for natural nuclei to reach the size of the artificial nuclei. Thus, the artificial nuclei have a considerable size even at zero time, i.e., at the beginning of dissolution.

The rate constant of interface motion or nucleus growth at each active center was determined from the relation:

$$\alpha = 2B_{s(i)}\frac{k_i^3}{a_0^3}(t - t_e)^3. \quad (8)$$

Table 1. Kinetic parameters of iron(III) oxide dissolution in sulfuric acid

Sample no.	Prehistory		$-t_e$, min, 330 K	$t_{0.5}$, min			$B_{s(i)}$	k_i, nm min^{-1}
	initial Fe(II) salt	thermal decomposition at T, K		330 K	340 K	350 K		
1	Sulfate	910–920	532	664.2	627	581	50	0.21
2	"	940–960	696	725.0	689	653	40	0.19
3	Carbonate	830–850	385	370	323	281	10	0.49
4	"	870–890	511	561	524	482	15	0.25
5	Morh's salt	960–980	744	733	717	702	100	0.18

Table 2. FCS parameters of iron(III) oxide samples of varied prehistory

Sample no.	Prehistory		D_{300}, nm	$\sqrt{\langle\varepsilon^2\rangle_{300}}$	$\alpha_1\times10^4$	$\alpha_2\times10^4$	$\beta_1\times10^4$
	initial Fe(II) salt	thermal decomposition at T, K					
1	Sulfate	910–920	79	8.3	0	1	220
2	"	940–960	82	7.9	0	3	238
3	Carbonate	830–850	42	15.6	0	227	0
4	"	870–890	79	9.3	25	95	0
5	Morh's salt	960–980	100	3.6	0	31	42

The parameters obtained are presented in Table 1.

The rate of dissolution of various samples of dispersed solid phases with the same chemical composition and crystal structure depends on their dispersity and pore structure, on the area of the reaction surface formed by various crystal faces, and on the type and extent of defectiveness of their lattice defects, i.e., on the real structure of the phases. In the course of dissolution, the initial particle-size and particle-shape distributions undergo changes that virtually cannot be predicted, as also the corresponding changes in the dissolution rates. It was shown that at stirrer rotation rates exceeding 400 rpm the stirring intensity does not affect the dissolution rate, which means that the process passes to the kinetic region in which the interaction at the interface is the rate-determining stage. It was found that the samples of dispersed phases with the same composition and crystal structure, but different prehistories, are always characterized by more or less different curves. Any curve of this kind can be represented as a sum of kinetic curves characterizing the dissolution of separate particles forming a sample. Analysis of the dissolution pattern of various iron(III) oxide samples shows that the run of a kinetic curve varies depending on the sample prehistory. The parameters determining the shape of the kinetic curve (Table 1) are directly related to the FCS of the sample (Table 2).

The fact that the highest rate of nucleus growth is observed in dissolution of "carbonate" Fe_2O_3 results from the large value of root-mean-square microdistortions and presence of exceedingly small mosaic blocks, being also, possibly, associated with the high probability of propagation of quaternary and half-dislocations (Tables 1, 2). Raising the temperature of sample preparation makes the coherent domains larger and the amount of microdistortions lower, which is due to deceleration of nucleus growth.

Hematite obtained from Fe(II) sulfate has low k_i value. Samples of this iron(III) oxide contain rather large mosaic blocks and only high-temperature stacking faults. With increasing temperature, the coherent domains grow in size dramatically and the microdistortions are rather intensively annealed out, which accounts for the very low k_i value and the long period of half-transformation. The Fe_2O_3 sample obtained from Morh's salt contains few defects and large mosaic blocks, being, therefore, characterized by low k_i value.

Thus, the data on the hematite FCS are in agreement with the results obtained in dissolution in hy-

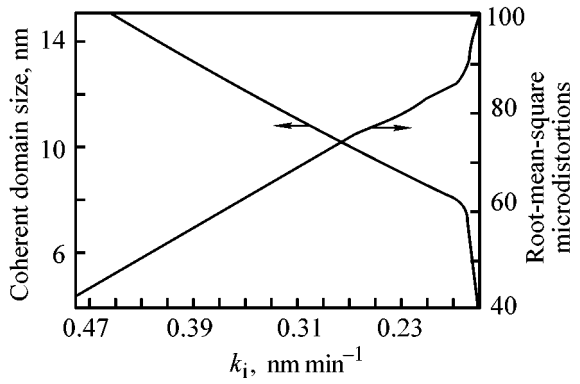

Fig. 2. Relation between the coherent domain size, root-mean-square microdistortions, and kinetic parameter k_i.

drochloric acid of Fe_2O_3 samples of different thermal and chemical prehistories. The relationship between the FCS characteristics and the kinetic parameter k_i for hematite samples is shown in Fig. 2.

CONCLUSIONS

(1) The size of coherent domains and the root-mean-square microdistortions can be determined graphically from the revealed kinetic dependences of dissolution in hydrochloric acid of iron(III) oxide samples.

(2) The kinetics of dissolution in acids can be recommended as a method for evaluating the parameters of finely crystalline structure of hematite samples.

REFERENCES

1. Tret'yakov, Yu.D., *Tverdofaznye reaktsii* (Solid-Phase Reactions), Moscow: Khimiya, 1978.
2. Fadeeva, V.I., and Panchenko, L.A., *Izv. Akad. Nauk, Neorg. Mater.*, 1982, vol. 18, no. 8, pp. 1399–1401.
3. *GOST* (State Standard) *10555–75. Reagents and Special-Purity Substances: Colorimetric Determination of the Content of Iron Impurity*, Moscow: Izd. Standartov, 1988.
4. Gorichev, I.G., Malov, L.V., and Dukhanin, V.S., *Zh. Fiz. Khim.*, 1978, vol. 52, no. 5, pp. 1195–1198.
5. Gorichev, I.G., Dukhanin, V.S., and Gorsheneva, V.F., *Zh. Fiz. Khim.*, 1989, vol. 63, no. 4, pp. 892–895.
6. Delmon, B., *Introduction a la cinetique heterogene*, Paris: Technip, 1969.

Russian Journal of Applied Chemistry, Vol. 75, No. 8, 2002, pp. 1211–1215. Translated from Zhurnal Prikladnoi Khimii, Vol. 75, No. 8, 2002, pp. 1237–1241.
Original Russian Text Copyright © 2002 by Ryabkov, Lekanova, Morozova, Grass.

INORGANIC SYNTHESIS AND INDUSTRIAL INORGANIC CHEMISTRY

Effect of Oxide Preparation Prehistory on Reduction in the System Al_2O_3–TiO_2–*n*C and Properties of Al_2O_3–TiC Powder Formulation

Yu. I. Ryabkov, T. L. Lekanova, E. G. Morozova, and V. E. Grass

Institute of Chemistry, Komi Scientific Center, Ural Division, Russian Academy of Sciences, Syktyvkar, Komi, Russia

Received December 21, 2001

Abstract—The influence exerted by the dispersity and composition of the starting powder and by the temperature and time of treatment on the properties of Al_2O_3–TiC powder formulation was studied.

Al_2O_3–TiC formulations find wide application in cutting tools and heaters and can be used to manufacture abrasives [1, 2]. Studies concerned with joint reduction of titanium and aluminum oxides for obtaining an Al_2O_3–TiC composite powder are few in number [3]. This process can give an active powdered formulation with high degree of homogeneity, which allows intensification of sintering and compaction of oxide–carbide formulations and enables synthesis of a material with high mechanical characteristics without the expensive stage of hot pressing.

To obtain high-strength pore-free composites with a ceramic matrix, powders of high dispersity and purity are necessary. The use of chemical methods for preparing powders of this kind, e.g., joint precipitation of the components in the form of hydroxides or salts, enables application of inexpensive and accessible reagents and simple apparatus. The technique mentioned is employed by numerous researchers for obtaining Al_2O_3-based compounds. Methods for precipitation of individual hydrated aluminum and titanium oxides have been described in the literature [4]; however, carrying out joint precipitation of the hydroxides requires special investigations and choice of optimal conditions. Compared with the conventional technique used in stock preparation by mechanical grinding, namely, mixing of the components, chemical methods ensure formation of particles much less than 1 μm in size. Moreover, the structure-forming phases of the materials are synthesized at much lower temperatures.

Morrow and co-authors [5] were the first to report a method for obtaining an ultrafine Al_2O_3–TiO_2 powder (surface area by BET 330 $m^2 g^{-1}$) from titanium and aluminum isopropoxides in a benzene solution. By now, tens of studies have been published, part of which were analyzed in a review [6] concerned with the development of this method. However, the high cost of the starting organic derivatives of titanium and aluminum necessitates a search for new, less expensive techniques. A scheme closely similar to that employed in the present study was described in [7]. According to this scheme, an Al_2O_3–TiO_2 powder is also prepared from an aqueous solution of a mixture of aluminum and titanium sulfates, but by direct evaporation of water in a vacuum evaporator (without precipitation of hydroxides) with the subsequent calcination of the residue to oxides.

To achieve a high homogeneity of finely dispersed powder formulations, conditions are chosen, ensuring simultaneous precipitation of all the necessary components from solution, e.g., in the form of hydroxides.

Thus, the aims of the present study were as follows: (1) to obtain powdered mixtures of titanium and aluminum oxides with strongly different degrees of dispersity by joint precipitation of the corresponding hydroxides (JPH) from solutions of inorganic salts of these elements (oxide products with specific surface area $S_{sp} > 100$ $m^2 g^{-1}$) and mechanical grinding (MG) of the oxides ($S_{sp} < 5$ $m^2 g^{-1}$); (2) to carry out carbothermic reduction of titanium oxides with different prehistories to titanium carbide in the presence of aluminum oxide; and (3) to determine the influence exerted by the dispersity and composition of the starting powder and by the temperature and time of treatment on the properties of an Al_2O_3–TiC powder formulation.

1070-4272/02/7508-1211 $27.00 © 2002 MAIK "Nauka/Interperiodica"

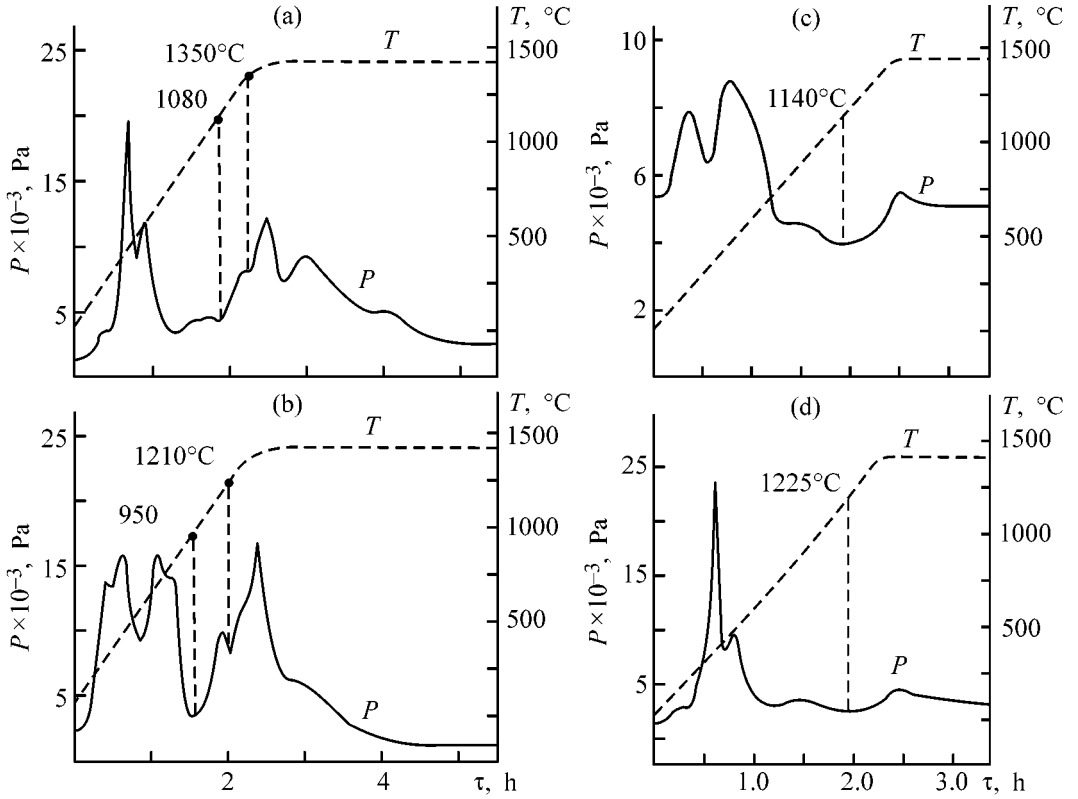

Fig. 1. Thermal treatment mode and curves describing the variation of pressure P in the vacuum chamber for samples prepared (a) by MG, (b) by JPH, (c) via stage of hydroxide precipitation from a solution of an Al(III) salt, and (d) on the basis of standard Al_2O_3 of chemically pure grade. (T) Temperature and (τ) time. Sample composition: (a, b) Al_2O_3–TiO_2–3C and (c, d) Al_2O_3–C.

According to X-ray diffraction analysis data [8], the uncalcined powder of hydrated aluminum and titanium oxides prepared by coprecipitation is X-ray-amorphous. After its isothermal treatment at 1000°C for 2 h, reflections corresponding to corundum and rutile appear in its X-ray diffraction pattern. Beginning with 1300°C, these materials enter into the following solid-state reaction:

$$Al_2O_3 + TiO_2(\text{rutile}) = \beta\text{-}Al_2TiO_5(\text{thialite}). \quad (1)$$

The reaction rate is relatively low at the given temperature: after isothermal treatment for 2 h the reaction is incomplete and X-ray diffraction patterns of the samples contain reflections of thialite and those of corundum with rutile. Raising the temperature to 1500°C results in that the process of aluminotitanate phase formation is complete in 2 h. According to the results of differential-thermal analysis [8], loss of adsorbed and crystal water is observed upon heating to 400°C. Rutile crystallization from coprecipitated hydroxides starts at 800°C, and corundum phase formation, at 1000°C. An endothermic peak corresponding to the reaction of aluminotitanate formation is observed in the interval 1350–1450°C. It should be noted for comparison that, in the case of a mechanically ground Al_2O_3–TiO_2 powder, the temperature of this reaction is shifted to 1450–1500°C.

The specific surface area of the powder obtained by calcination (at 500°C) of coprecipitated aluminum and titanium hydroxides is 130 $m^2\,g^{-1}$ (according to BET), which corresponds to an average equivalent particle radius of about 20 nm. After calcination at 1000°C (surface area by BET 9 $m^2\,g^{-1}$), the average equivalent particle radius increases to 130 nm. Mechanically ground Al_2O_3–TiO_2 powders are characterized by specific surface area of 2 $m^2\,g^{-1}$ and average equivalent particle size of more than 500 nm.

The reduction processes in the system Al_2O_3–TiO_2–nC ($0 \le n \le 4$) are accompanied by release of a large amount of gaseous products. The reduction of titanium dioxide by carbon occurs via formation of lower titanium oxides, with titanium oxocarbide TiO_xC_y or titanium carbide TiC_x being the final products of TiO_2 reduction, depending on temperature, pressure, and composition of the gas phase [9–11]. The intensity of gas formation was monitored by changes in the pressure in the vacuum chamber. Figure 1 shows, in the pressure–time–temperature coordinates, dynamic

curves describing the reduction processes for Al_2O_3–TiO_2–3C samples prepared by MG + carbon (Fig. 1a) and JPH + carbon (Fig. 1b). The observed increase in pressure in the vacuum chamber at low temperatures (below 900°C) is due to liberation of gaseous products formed in pyrolysis of the binder (polyvinyl alcohol) and in degassing of activated carbon. Noticeable reduction onsets at above 950°C, with two peaks of pressure build-up observed in the barograms: peak of medium intensity at 950–1210 (JPH + carbon) and 1080–1350°C (MG + carbon) and a very strong peak at above 1210–1450 (JPH + carbon) and 1350–1450°C (MG + carbon (Figs. 1a and 1b). In the given ranges, the pressure increases until the maximum temperature of isothermal ?keeping is reached and then gradually decreases to the initial values.

According to X-ray phase analysis (XPA) data, reduction of TiO_2 by carbon begins already at 950°C for highly dispersed oxide powders of composition Al_2O_3–TiO_2–3C (JPH + carbon) and at 1080°C for the MG + carbon powder. Carbidization of titanium oxide starts at 1210°C for the JPH + carbon powder and at 1350°C for the MG + carbon powder. Isothermal calcination at 1350°C for 6 h of Al_2O_3–TiO_2–3C powders prepared by both the techniques yields a composite mixture of α-Al_2O_3 and TiO_xC_y. Carbidization of a highly dispersed oxide TiO_2 (JPH + carbon) leads to the formation of a TiC lattice with unit lattice constant ($a = 4.327 \pm 0.004$ Å) virtually coinciding with those of nearly stoichiometric titanium carbide (a = 4.330 Å) [12]. At the same time, treatment of a more coarsely dispersed TiO_2 under the same conditions (MG + carbon) yields TiO_xC_y with lattice constant $a = 4.253 \pm 0.005$ Å. More complete carbidization requires in this case a calcination at higher temperature for a longer time.

Simultaneously with carbothermic reduction of titanium oxide, reduction of aluminum oxide is also observed at temperatures below 1100°C. In carbothermic reduction of aluminum oxide obtained from the hydroxide, this processes begins at a temperature lower by 85°C, which indicates an increase in pressure in the vacuum chamber already at 1140°C (Fig. 1c); for samples containing Al_2O_3 of pure grade and carbon, the onset temperature of gas-forming reactions is 1225°C (Fig. 1d). Although the gas phase composition was not studied, it can be stated on the basis of published data [13, 14] that CO is formed in reduction of metal oxides by carbon in a vacuum. In addition, the gaseous components present at 1140°C in the system studied are Al_2O(g), AlO(g), and also Al(g), which condense to form a loose gray deposit. The condensate contains (according to XPA data) the following phases: Al_2O_3, Al_4O_4C, Al_4C_3, C, and, occasionally, trace amounts of elementary aluminum. The solid residue formed after calcination of the samples at 1600°C for 1 h is only composed of α-Al_2O_3.

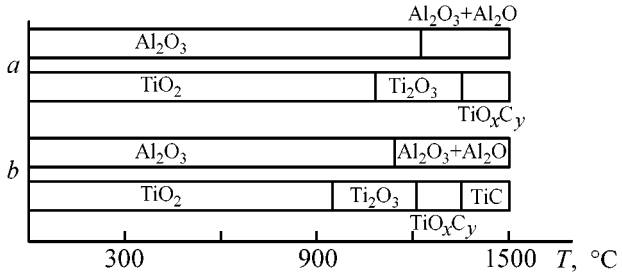

Fig. 2. Changes in the phase composition at various reduction temperatures T for Al_2O_3–TiO_2–3C samples in relation to treatment temperature and prehistory of starting oxides. (*a*) Mechanical grinding of standard oxides with carbon and (*b*) coprecipitation of hydroxides, calcination, and mixing of the oxides with carbon.

To compare the processes of phase formation in Al_2O_3–TiO_2–3C samples obtained using the two methods proposed, Fig. 2 presents histograms of changes in the phase composition at various reduction temperatures in relation to treatment temperature and prehistory of preparation of the oxides. It can be seen that, with coprecipitation of derivative oxides of aluminum and titanium used, the temperature of Ti_2O_3 phase formation can be lowered by 100°C, that of aluminum oxide reduction, by 85°C, and that at which the carbide phase is formed in the oxide system, by 150°C.

Sedimentation analysis shows that a composite micropowder containing α-Al_2O_3–TiC is formed from nanosize precursors (JPH + carbon) of Al_2O_3–TiO_2–3C composition, with the fine fraction (1–3 μm) predominant (>80%) in this micropowder. At the same time, the MG powder is characterized by a broad particle size distribution (5–40 μm).

Also, the nature of phase formation in the system in question was studied in relation to the content of carbon. Figures 3 and 4 present data on the phase composition and mass loss of samples of the Al_2O_3–TiO_2–nC system with carbon content in the range $0 \le n \le 4$ at 1600°C and time of isothermal treatment of 1 h. The amount of gaseous products formed was determined from the difference between the mass of

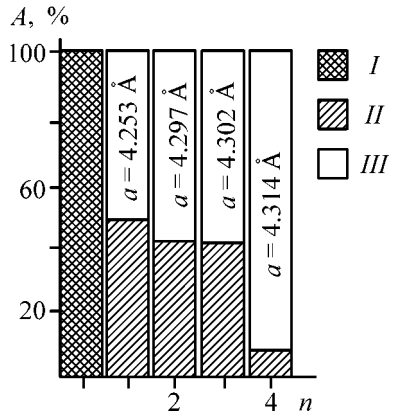

Fig. 3. Phase composition A of solid products of Al_2O_3–TiO_2–nC reduction vs. initial carbon content. T = 1600°C, calcination time 1 h; the same for Fig. 4. (*a*) Lattice constants of titanium oxocarbide TiO_xC_y. (*I*) Al_2TiO_5, (*II*) TiO_xC_y, and (*III*) Al_2O_3.

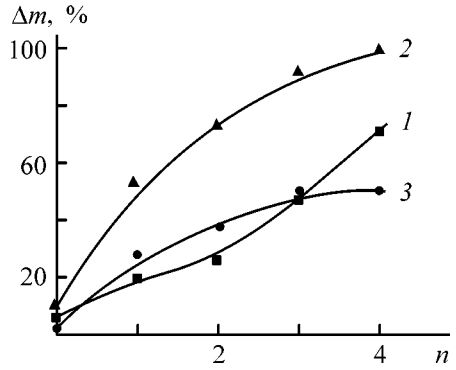

Fig. 4. Mass loss Δm in carbothermic reduction of (*1*) Al_2O_3–TiO_2–nC, (*2*) Al_2O_3–nC, and (*3*) TiO_2–nC systems vs. carbon content of the stock.

the initial reaction mixture and mass of solid reduction products. In the initial portion (carbon content of up to 6 wt % at $n \le 1$), rutile is reduced to TiO_xC_y with lattice constant a = 4.253 Å. The mass loss values recorded can be accounted for by the formation of only CO, since they coincide with experimental loss measured for TiO_2–nC samples containing no aluminum oxide. With 16.5 wt % carbon introduced (n = 3), titanium oxocarbide TiO_xC_y with larger lattice constant a = 4.302 Å is one more reduction product. In the range 6–16.5 wt % C ($1 \le n \le 3$), the mass loss constitutes about 51%, which is mainly due to CO formation. Upon introduction of more than 16.5 wt % C, the loss of mass increases to 70% because of the partial reduction of aluminum oxide to gaseous aluminum suboxides and elementary aluminum [13, 14]. After calcination of the Al_2O_3–TiO_2–4C stock at 1600°C for 1 h, the reduction products contain 10% Al_2O_3 and 90% TiO_xC_y with lattice constant a = 4.314 Å.

EXPERIMENTAL

Joint precipitation of aluminum and titanium hydroxides was carried out with the use of oxotitanium sulfate $TiOSO_4 \cdot 2H_2O$ and aluminum sulfate $Al_2(SO_4)_3 \cdot 18H_2O$, both of pure grade, taken in Al : Ti = 2 : 1 ratio. The precipitation was achieved by adding an equimolar mixture of aluminum and titanium salt solutions to an ammonia solution, taken in excess amount with pH maintained at 7–8 [8].

After drying, hydrated powders of aluminum and titanium oxides were calcined at 1000°C for 2 h in air. As a result, oxides were formed in crystalline state and the specific surface area of the powders decreased. In obtaining Al_2O_3–TiO_2–nC samples ($0 \le n \le 4$), carbon was introduced by mechanical mixing (JPH + carbon).

To reveal the effect of dispersity on the reduction of aluminum and titanium oxides, the starting stocks were also prepared by mechanical grinding. Powdered mechanically ground Al_2O_3–TiO_2–nC samples ($0 \le n \le 4$) were prepared by mixing powdered corundum Al_2O_3 of pure grade and rutile TiO_2 of special-purity grade, taken in a Al : Ti = 2 : 1 ratio, with carbon C of BAU-A grade. The grinding was carried out under wet conditions for 6 h, the aqueous dross was passed through a sieve no. 0050 and then dried at 120°C to constant weight.

Precipitation and mechanical mixing was used to prepare Al_2O_3–C samples from the reagents described above.

The specific surface area of powder samples was measured by BET.

Mixtures for high-temperature treatment were prepared by semidry compaction under pressure of 150 MPa, with 10% aqueous solution of polyvinyl alcohol used as binder. The slugs had the shape of pellets 20 mm in diameter and 5 mm high; the density of compacted samples was 2.0 g cm^{-3}. The thermal treatment of the samples was carried out under dynamic vacuum conditions (P = 10^{-3}–10^{-1} Pa) in an SNVE-1.3.1/16-IZ vacuum electric shaft furnace.

The phase composition of the thermally treated samples was studied by X-ray powder diffractometry on a DRON-3M installation with Cu_{K_α} radiation. The unit cell parameters of TiC were found by the least-squares method for all the unambiguously assigned lines at 2θ reflection angles ranging from 10 to 80°. The error in determining the lattice constants did

not exceed 0.001 Å for titanium carbide and oxocarbide crystallizing in the cubic crystal system.

The powder particle sizes were determined using a Polam R-113 optical polarization microscope at magnification of 400–1100 and JSM-6400 scanning electron microscope at magnification of 2000–10 000 [15].

CONCLUSION

Use of coprecipitation for synthesizing aluminum and titanium oxides makes it possible to lower the onset temperature of their reduction by 100°C and diminish the duration of the high-temperature process in which titanium carbide phases are formed. The reduction of TiO_2 to Ti_2O_3 begins at 950°C for highly dispersed coprecipitated oxide powders and at 1080°C for a powder obtained by mechanical grinding. The final stage of titanium carbidization starts at 1210°C for a powder mixture obtained by coprecipitation and at 1350°C for a powder prepared by mechanical grinding. Further carbidization of highly dispersed mixtures at 1600°C gives TiC with lattice constant $a = 4.327 \pm 0.004$ Å close to that in stoichiometric titanium carbide. Under the same conditions, TiO_xC_y with lattice constant $a = 4.302 \pm 0.005$ Å was obtained from coarser TiO_2. This indicates that the activity of the powders obtained by coprecipitation is retained at high temperature, up to 1600°C.

Processing of nanosize precursors of Al_2O_3–TiO_2–3C composition yields a composite micropowder containing α-Al_2O_3–TiC with predominant (>80%) fine fraction (1–3 μm), whereas the MG powder is characterized by broad particle size distribution (5–40 μm).

REFERENCES

1. US Patent 4 796 134.
2. US Patent 4 549 905.
3. Cutler, R.A., Hurford, A.C., and Virkar, A.V., *Mater. Sci. Eng.*, 1988, A105106, pp. 183–192.
4. Matijevic, E., *Acc. Chem. Res.*, 1981, vol. 14, pp. 22–29.
5. Morrow, M.K., Holcombe, C.E., and Cromer, C.A., *NTIS Report no. Y 1831*, 1972, Oak Ridge Y-12 Plant.
6. Thomas, H.A.J. and Stevens, R., *Br. Ceram. Trans. J.*, 1989, vol. 88, pp. 229–233.
7. Kato, E. and Suyama, Y., *J. Ceram. Soc.*, 1978, vol. 88, p. 212.
8. Lekanova, T.L., Dudkin, B.N., and Sevbo, O.A., Comparative Characteristics of Powders for Preparing Aluminotitanate Ceramics, *Series of Preprints, Russ. Acad. Sci., Ural Div., Komi Sci. Center*, Syktyvkar, 1992.
9. Goroshchenko, Ya.G., *Khimiya titana* (Chemistry of Titanium), Kiev: Naukova Dumka, 1970.
10. Shveikin, G.P. and Perelyaev, V.A., *Izv. Ross. Akad. Nauk, Ser. Khim.*, 1997, no. 2, pp. 233–245.
11. Hiller, R., Berthet, M.P., Bouix, J., and Roche, A., *J. Matter. Sci.*, 1990, vol. 25, pp. 3191–3198.
12. *Powder Diffraction File*, Joint Committee on Powder Diffraction Standards, Swarthmore, Pennsylvania, USA, 6–614.
13. Vodop'yanov, A.G., Serebryakova, A.V., and Kozhevnikov, G.I., *Metally*, 1982, no. 1, pp. 43–47.
14. Ryabkov, Yu.I., Lekanova, T.L., and Sporsheva, T.M., *Zh. Fiz. Khim.*, 2001, vol. 75, no. 7, pp. 21–25.
15. Geller, Yu.A. and Rakhshtadt, A.G., *Materialovedenie* (Materials Science), Metallurgiya, 1989.

Russian Journal of Applied Chemistry, Vol. 75, No. 8, 2002, pp. 1216–1218. Translated from Zhurnal Prikladnoi Khimii, Vol. 75, No. 8, 2002, pp. 1242–1244.
Original Russian Text Copyright © 2002 by Kurbatova, Polupanova, Kurbatov.

INORGANIC SYNTHESIS AND INDUSTRIAL INORGANIC CHEMISTRY

Vanadium(V) Complexes in Hydrochloric Acid Solutions

L. D. Kurbatova, T. I. Polupanova, and D. I. Kurbatov

Institute of Solid State Chemistry, Ural Division, Russian Academy of Sciences, Yekaterinburg, Russia

Received April 19, 2002

Abstract—^{51}V NMR, electronic, and vibrational spectroscopies were applied to study the ionic state of vanadium(V) in hydrochloric acid solutions at c_{HCl} = 1.0–11.3 M and vanadium(V) concentration of 1 M.

In extraction of vanadium(V) with neutral extracting agents (tributyl phosphate and alcohols) from concentrated hydrochloric acid solutions, co-extraction of the mineral acid is possible. Therefore, in selecting the optimal extraction conditions, a knowledge is necessary of the ionic state of vanadium(V) in concentrated hydrochloric acid solutions. It follows from a review of published data that the ionic state of vanadium(V) in concentrated solutions of mineral acids has been studied insufficiently. Previously, the ionic state of vanadium has been studied [1] at $c_V = 2 \times 10^{-4}$ M in concentrated solutions of hydrochloric acid and its mixtures with lithium chloride. Since more concentrated solutions (c_V = 0.1 M), in which vanadium(V) polymerization is possible, are commonly used in extractive recovery of vanadium(V), it is of interest to study the ionic state of vanadium(V) in a wide range of hydrochloric acid concentrations c_{HCl} = 1.0–11.3 M.

The study was carried out using ^{51}V NMR, electronic, and vibrational (IR, Raman) spectroscopies. The working solutions were prepared from chemically pure reagents. ^{51}V NMR spectra were measured on a Bruker MSL-400 spectrometer at a frequency of 105.24 MHz. The chemical shifts were determined relative to $VOCl_3$ (external standard). IR spectra of vanadium(V) solutions in hydrochloric acid were recorded on a Specord IR-75 spectrometer in the range 400–4000 cm^{-1}. The solutions studied were placed between KRS-6 plates. Raman spectra were recorded on an LTN-402 spectrometer (λ = 532 nm). The acid concentration was varied between 1.0 and 11.3 M at a step of 1 M. The concentration range 8–9 M, in which vanadium(V) dioxocation was assumed to be converted into an oxocation, was studied with a step of 0.1 M.

The figure shows selected Raman spectra of vanadium(V) solutions in hydrochloric acid. A Raman spectrum of a chloride solution of vanadium(IV) at a concentration of 0.506 M is shown for comparison.

The Raman spectra of vanadium(V) solutions in hydrochloric acid, presented in the figure, can be divided into two groups. The high-frequency band ν_1 lies at 930–940 cm^{-1} in the first of these and at 1040–1050 cm^{-1} in the second. In the first group of

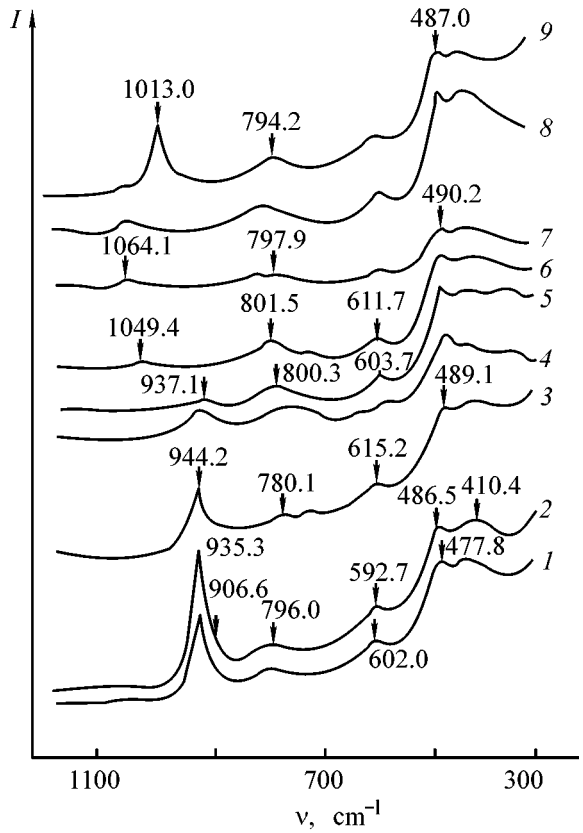

Raman spectra of (*1*–*8*) solutions of the system V(V)–HCl–H_2O and (*9*) $VOCl_2$ complex. (*I*) Intensity and (ν) wave number. c_{HCl} (M): (*1*) 1.0, (*2*) 3.0, (*3*) 7.0, (*4*) 8.0, (*5*) 8.6, (*6*) 8.7, (*7*) 9.5, and (*8*) 11.3.

1070-4272/02/7508-1216 $27.00 © 2002 MAIK "Nauka/Interperiodica"

spectra, the ν_1 band is shifted somewhat to higher frequencies (by up to 10 cm^{-1}) with the acid concentration increasing from 1.0 to 8.6 M and its intensity decreases to the point of its complete disappearance. This is presumably due to a decrease in the concentration of dioxocations VO^{2+} with increasing HCl concentration, similarly to the case of low vanadium(V) concentrations [1]. Three bands were found in the IR and Raman spectra of the first group: 930 [$\nu_s(VO_2)$], 900 [$\nu_{as}(VO_2)$], and 300 [$\delta(VO_2)$] cm^{-1}, characteristic of complexes $VO_2Cl_4^{3-}$ of *cis*-configuration [2]. This suggests that vanadium(V) is present in hydrochloric acid solutions with concentration in the range from 1.0 to 8.6 M in the form of chloride complexes of the vanadium(V) dioxocation. The ^{51}V NMR spectra of vanadium(V) solutions in hydrochloric acid with $c_{HCl} \le 8.6$ M contain a singlet signal with a chemical shift of –(526–540) ppm ($\Delta 1/2$ = 300 Hz), which can be attributed, in accordance with the results of investigations described above, to $VO_2Cl_4^{3-}$ in *cis*-configuration. This is also confirmed by published data. It was shown in [3] that at pH ≤ 1 vanadium(V) exists in solutions as a dioxocation and has, according to Raman studies, a *cis*-dioxo structure and pseudo-octahedral structure of $[VO_2(OH_2)_4]^+$. ^{51}V NMR spectra of vanadium(V) in nitric and chloric acids contain a single broad line with chemical shift of -545 ± 2 ppm ($\Delta 1/2$ = 400 Hz). In acid sulfate and phosphate solutions, the band is markedly broadened ($\Delta 1/2$ = 600–1500 Hz) and has a chemical shift of –(520–580) ppm. It can be seen that the broad lines with chemical shifts within –(520–580) ppm in the ^{51}V NMR spectra of vanadium(V) solutions in chloric, nitric, and sulfuric acids suggest that vanadium(V) also presumably has at $c_{HCl} \le 8.6$ M a pseudo-octahedral structure with a *cis*-dioxo group.

At $c_{HCl} > 8.6$ M the ^{51}V NMR spectra of vanadium(V) solutions show a singlet signal with a chemical shift of –326 ppm ($\Delta 1/2$ = 600 Hz). The strongly differing chemical shift of the ^{51}V signal (by more than 200 ppm) in vanadium(V) solutions at high hydrochloric acid concentrations points to changes in the ligand environment of the first coordination sphere of vanadium(V). The downfield shift of the ^{51}V NMR signal, compared with published data [4], indicates that additional chloride ligands are introduced into the inner coordination sphere of vanadium(V), and the Cl/V(V) ratio increases.

The changes occurring in the inner coordination sphere of vanadium(V) at high hydrochloric acid concentrations ($c_{HCl} \ge 8.6$ M) are also confirmed by Raman spectra. At a hydrochloric acid concentration exceeding 8.60 M (second group of solutions) a low-intensity high-frequency band appears at 1040–1050 cm^{-1}. This band can be assigned [5] to stretching vibrations of the type ν_1 of the oxovanadium(V) cation. If the coordination number of vanadium(V) is preserved equal to six, then further increase in the number of chloride ligands in the inner coordination sphere becomes possible if a pentachloride complex of oxovanadium(V) cation $[VOCl_5]^{2-}$ is formed. In this case, the Cl/V(V) ratio corresponds to 5, which exceeds the value for the $[VO_2Cl_4]^{3-}$ complex.

However, a Raman spectrum of the pentachloride complex of the oxovanadium(V) cation, $(VOCl_5]^{2-}$, different from the Raman spectra of vanadium(V) solutions at high hydrochloric acid concentrations, was described in [6]. This means that complexes of composition $[VOCl_5]^{2-}$ are not formed in concentrated hydrochloric acid solutions. Presumably, at high hydrochloric acid concentrations, not only the vanadium(V) dioxocation is converted into the oxovanadium(V) cation, but also the coordination number of vanadium changes to 5, or even 4, with the formation of complexes of the type $[VOCl_4]^-$ or $[VOCl_3]$. For example, to the stretching vibration ν_1 of the V=O double bond in the complex $[VOCl_3]$ having the coordination number of 4 corresponds the frequency of 1035 cm^{-1} [7].

Comparison of the Raman spectra of vanadium(V) solutions at high hydrochloric acid concentrations (see figure, curves *7* and *8*) with the Raman spectrum of the complex $[VOCl_3]$, presented in [7], reveals their significant difference. This suggests that no complexes of the type $[VOCl_3]$ are formed at high hydrochloric acid concentrations. Under these conditions, vanadium(V) forms complexes of composition $[VOCl_4]^-$ in which the Cl/V(V) ratio exceeds that in the tetrachloride complex of the vanadium(V) dioxocation, $[VO_2Cl_4]^{3-}$. It is this circumstance that leads to a downfield shift of the ^{51}V signal. An identical change in the coordination number with increasing hydrochloric acid concentration was noted in [4] for gallium(III) complexes. A single signal with chemical shift of 0 ppm was observed in ^{71}Ga NMR spectra at c_{HCL} in the range from 0.2 to 5.2 M. At $c_{HCl} \ge 7.0$ M the ^{71}Ga NMR spectrum contains a narrow line with a chemical shift of 248 ppm. The shift of the ^{71}Ga signal was attributed in [4] to conversion of the gallium hexa aqua complex $[Ga(H_2O)_6]^{3+}$ into a tetrachloride complex $[GaCl_4]^-$.

An additional study was carried out to confirm these conclusions. In [8], calculations by the MO

method were performed and an electronic spectrum of a tetrachloride complex of oxovanadium(V) cation, $[VOCl_4]^-$ was presented. Comparison of the electronic spectrum of a vanadium(V) solution with c_{HCl} = 11.3 M, measured in the present study, with the spectrum from [8] shows that both these spectra contain a strong band at 21 500 cm^{-1}, which can be assigned to $b_1(a_2) \rightarrow e\pi^*$ or $e\pi(e) \rightarrow b_2^*$ $(A_1 \rightarrow E)$ transitions. This indicates that, presumably, not only the vanadium(V) dioxocation is converted into the monooxocation at high hydrochloric acid concentrations, but also the coordination number of vanadium(V) changes to 5, with the result that vanadium(V) forms tetrachloride complexes of the oxovanadium(V) cation, $[VOVCl_4]^-$.

A comparative analysis of Raman spectra of vanadium(V) solutions belonging to the first and second groups and hydrochloric acid solutions with the corresponding concentrations was made in the spectral range $\nu < 900$ cm^{-1} where the characteristic vibration frequencies of V–O–V and V–Cl bonds lie. No bands associated with symmetric and asymmetric vibrations of the bridge bonds V–O–V [9, 10] were found in the ranges 750–800 and 480–490 cm^{-1}. This indicates that no polymerization of vanadium(V) polyhedra occurs at high concentrations of vanadium(V) and hydrochloric acid.

Unfortunately, it is impossible to analyze the lowest-frequency range, in which the V–Cl vibrations lie ($\nu < 480$ cm^{-1}), since these vibrations are overlapped by the deformation vibrations of the V–O bond [10].

CONCLUSION

A study of the ionic state of vanadium(V) at c_V = 0.1 M in hydrochloric acid solutions established that the composition of the complexes depends on the hydrochloric acid concentration. Tetrachloride complexes of the vanadium(V) oxocation, $[VO_2Cl_4]^{3-}$, are formed at $c_{HCl} \le 8.6$ M, whereas at $c_{HCl} > 8.6$ M vanadium(V) exists in the form of tetrachloride complexes of the oxovanadium(V) cation, $[VOCl_4]^-$.

REFERENCES

1. Ivakin, A.A., Kurbatova, L.D., and Kruchinina, M.V., *Zh. Neorg. Khim.*, 1987, vol. 32, no. 5, pp. 1065–1068.
2. Griffith, W.P. and Wickins, T.D., *J. Chem. Soc. (A)*, 1968, vol. 2, pp. 400–404.
3. Donnel, S.E.D. and Pope, M.T., *J. Chem. Soc. Dalton. Trans.*, 1976, no. 21, pp. 2290–2297.
4. Korovin, V.Yu., Randarevich, S.B., and Pogorelov, Yu.N., *Zh. Neorg. Khim.*, 1991, vol. 36, no. 1, pp. 205–208.
5. Nakamoto, K., *Infrared Spectra of Inorganic and Coordination Compounds*, New York: Wiley, 1963.
6. Wendling, E. and Rohmer, R., *Bull. Soc. Chim.*, 1967, vol. 45, no. 1, pp. 4–23.
7. Muller, A. and Cousins, L.R., *J. Chem. Phys.*, 1957, vol. 16, no. 2, pp. 329–331.
8. Drake, J.E., Verkis, J.E., and Wood, S.J., *J. Chem. Soc. (A)*, 1969, no. 3, pp. 345–349.
9. Brown, R.G. and Ross, S.D., *Spectrochim. Akta*, 1972, vol. 27B, no. 11, pp. 1424–1427.
10. Brown, R.G. and Ross, S.D., *Spectrochim. Akta*, 1972, vol. 28, no. 10, pp. 1263–1265.

Russian Journal of Applied Chemistry, Vol. 75, No. 8, 2002, pp. 1219–1222. Translated from Zhurnal Prikladnoi Khimii, Vol. 75, No. 8, 2002, pp. 1245–1248.
Original Russian Text Copyright © 2002 by Ostroushko, Mikhalev, Reshetnikova.

INORGANIC SYNTHESIS AND INDUSTRIAL INORGANIC CHEMISTRY

Stability of Polymeric-Salt Gels Used To Synthesize Complex-Oxide Materials

A. A. Ostroushko, D. S. Mikhalev, and N. V. Reshetnikova

Ural State University, Yekaterinburg, Russia

Received October 16, 2000; in final form, November 2001

Abstract—The conditions for stability of polymeric-salt systems based on polyvinyl alcohol, used to synthesize complex-oxide materials containing rare-earth, alkaline-earth, and *d* metals, were studied.

Formulations containing nonionogenic water-soluble polymers of the type of polyvinyl alcohol (PVA) or polyvinyl pyrrolidone and methyl cellulose, and also metal salts (nitrates, acetates, formates, etc.) are used to obtain various complex-oxide materials in the form of powders or coatings [1].

The use of the given method for synthesizing complex oxides containing Mo(VI), W(VI), V(V), rare-earth (REM), alkaline-earth (AEM), and other metals is characterized by a number of specific features associated with the ability of *d* metals contained in these oxides to form oxygen-containing anionic forms. The conventional coprecipitation of components in the form of aqua polycompounds with their subsequent separation from the mother liquor and thermal treatment is frequently hindered by complicated control over the composition of the products being precipitated [2, 3], especially in those cases when two or three different cations are to be introduced into a complex oxide simultaneously.

In the presence of polymers, salts (nitrates, in particular) of REM and AEM can be mixed in solutions with ammonium molybdates, tungstates, and vanadates in such a way that stable dispersed systems (gels or jellies) appear, with homogeneously distributed components. This occurs because of the appearance of three-dimensional (3D) networks in which REM and AEM cations serve as cross-linking agents for fragments of molecular complexes formed by polyanions [4, 5]. Such a method yields homogeneous starting formulations for synthesis of complex oxides of prescribed composition, with the results of synthesis directly dependent on the stability of the corresponding dispersed systems. In the present study, factors determining the stability of dispersed structures are considered and the limits of existence of some of these factors are determined.

EXPERIMENTAL

As starting inorganic reagents served ammonium heptamolybdate tetrahydrate $(NH_4)_6Mo_7O_{24} \cdot 4H_2O$, ammonium vanadate NH_4VO_3, ammonium *para*-dodecatungstate hydrate $(NH_4)_{10}W_{12}O_{41} \cdot nH_2O$, lanthanum trinitrate hexahydrate $La(NO_3)_3 \cdot 6H_2O$, strontium dinitrate tetrahydrate $Sr(NO_3)_2 \cdot 4H_2O$, $RbNO_3$, $(NH_4)_3PO_4$, NH_4HF_2, and HNO_3, all of no less than analytically pure grade. As polymeric component was used PVA with molecular weight M_r 15 000 and 31 000–50 000 (Aldrich Chemical).

The salt and polymeric components were dissolved in distilled water, with heating on water bath when necessary. Then a PVA solution was mixed with solutions of individual salts. The order in which the solutions were poured together was varied depending on the composition of a complex-oxide product to be obtained. Solutions of like components, e.g., those of nitrates of various metals or ammonium vanadate and phosphate were preliminarily mixed, or the components were subjected to joint dissolution in water. Gels or jellies obtained after mixing of the working solutions were allowed to stay in closed tubes for visual inspection of the stability. These formulations were used to obtain by casting and subsequent drying films of thickness ranging from 30 μm to 1 mm on substrates of K8 optical glass. In the case of fluorine-containing compositions, polyethylene substrates were used. The films served for visual inspection under an MIM-7 microscope in reflected light at magnification of up to 100. Films separated from sub-

1070-4272/02/7508-1219 $27.00 © 2002 MAIK "Nauka/Interperiodica"

Stability of gels obtained from lanthanum trinitrate, strontium dinitrate, and ammonium para-dodecatungstate and PVA* [initial concentration of the solutions (M) lanthanum trinitrate 0.1636, strontium dinitrate 0.1266, and ammonium *para*-dodecatungstate 0.004732; pH of the medium in gels 5–7]

n	Concentration of starting PVA solution, wt %			
	5	10	5	10
	M_r = 15 000		M_r = 31 000–50 000	
1	N	LS	S	S
2	LS	S	–	–
3	S	S	S	S
1**	S	S	S	S

* *n* is the number of volumes of the starting PVA solution per one volume of starting salt solutions; N stands for an unstable gel (immediate precipitation), LS denotes a gel with limited stability (precipitation in the course of time, S designates a stable gel (no precipitation, no stratification), and dash means that no experiments were performed in a given case.

** pH 1–2.

strates were subjected to pyrolysis in a muffle furnace and final annealing in air at 600–900°C for 2–24 h. The complex-oxide materials obtained were identified using X-ray phase analysis on a DRON-3M diffractometer with Cu_{K_α} radiation.

The stability of the gels or jellies obtained was assessed by three main criteria: by the absence of (i) stratification with liquid separation in the upper part of the tubes; (ii) compact solid deposits; and (iii) macroscopic separation in the films, with the appearance of nonuniform distribution density of gel or particles discernible under microscope. The requirements to stability were satisfied by gel-forming systems in which the uniformity was not disturbed for any of the characters for at least three weeks. X-ray diffraction analysis of ground films obtained in systems of this kind demonstrated that they contain no individual salt components [4]; complex oxides were most frequently synthesized in thermal treatment directly from the amorphized mass, without intermediate formulation of individual oxides [6, 7].

The stability of dispersed structures is determined by a number of factors and, in particular, by the concentration of a polymer and its molecular weight (see table). The stability of gels is higher for a polymer with larger molecular weight, which forms starting solutions with higher viscosity. Raising the polymer concentration, all other conditions being the same, also stabilizes dispersed systems (Fig. 1). An important factor is the concentration ratio of salts containing cations [lanthanum(III), in particular] and ox-

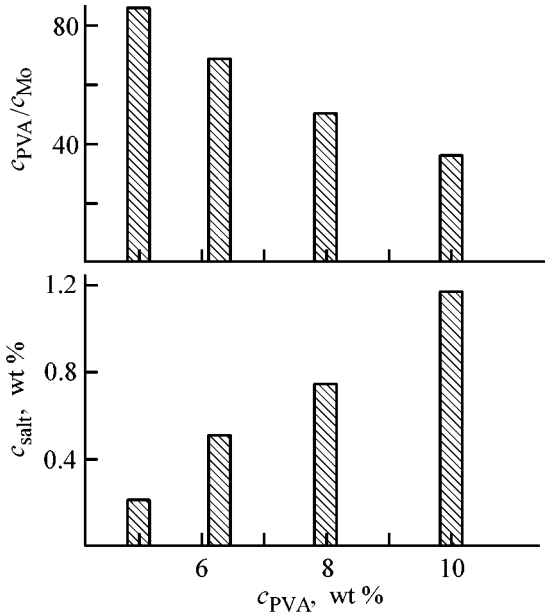

Fig. 1. Concentration dependences of stability of polymeric-salt gels in a system formed by ammonium heptamolybdate and lathanum trinitrate. Atomic ratio La_2O_3 : MoO_3 = 1 : 3. (c_{PVA}/c_{Mo}) Ratio of molar concentrations of PVA (per monomeric unit) and Mo(VI) (in terms of MoO_4^{2-}); (c_{salt}, c_{PVA}) concentrations of salts (total) and PVA (wt %). The region of stable gels is shaded; the same for Fig. 2.

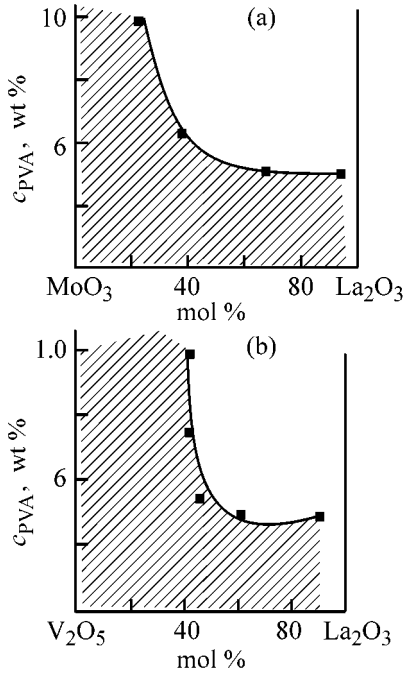

Fig. 2. Stability diagrams of polymeric-salt gels at total salt content of 0.35 wt % in systems formed by (a) ammonium heptamolybdate and lanthanum trinitrate and (b) ammonium vanadate and lanthanum trinitrate. (c_{PVA}) PVA concentration.

ygen-containing anionic forms of *d* metals [molybdenum(VI) and vanadium(V)]. This can be accounted for by the existence, in mixing of polymer-containing salt solutions, of ratios (equivalence points of precipitation titration) corresponding to their maximum binding [4]. For example, in the system comprising ammonium heptamolybdate and lanthanum trinitrate, such a point lies at lanthanum(III) content close to 25 mol % (in terms of La_2O_3). Just at this concentration there occurs a transition from more to less stable gels with higher content of ammonium molybdate (in terms of MoO_3), with the corresponding bend observed in the curve in Fig. 2a. The same circumstance accounts for the dependence of gel stability on the order in which the components are poured together: when this order is changed, the equivalence point is shifted [4]. In particular, for obtaining a stable gel with composition corresponding to that of the compound $LaVO_4$ ($La_2O_3 : V_2O_5 = 1 : 1$), it is necessary to add the ammonium vanadate solution to that of lanthanum trinitrate. In this case, the equivalence point is close to the above ratio, whereas at the inverse order of pouring together it approaches the ratio $La_2O_3 : V_2O_5 = 1 : 3$. It should be noted that use of polymer-containing solutions enables preparation of stable gels in a sufficiently wide concentration range with increasing concentration and molecular weight of the polymer. This circumstance expands the range of applicability of the method, compared with purely salt systems, for synthesizing complex oxides containing the components in amounts differing from their ratios at the equivalence point.

Introduction, together with of REM ions, of AEM or alkaline metal ions impairs the stability of gels because of the higher solubility of the corresponding molybdates, tungstates, and vanadates [4, 8]. In mixed formulations, salts with higher solubility are in the dispersed medium and pass into a liquid that separated from the gel. To prevent stratification of such gels, it is necessary to raise the concentration of a polymer or its molecular weight. One more factor impairing the stability of dispersed systems is the lower charge of AEM ions as compared with REM ions; hence follows their decreased ability to act as cross-linking agents in formation of 3D networks. Nevertheless, it is possible to obtain stable gels by dosing the starting solutions in prescribed proportions (see table). Stable formulations with atomic ratios of the components La(III) : Sr(II) : W(VI), equal to 4 : 1 : 7, 2 : 1 : 1, 2 : 3 : 2, and 2 : 9 : 4, which corresponds to complex oxides or solid solutions $SrLa_4(WO_4)_7$, $SrLa_2WO_7$, $Sr_3La_2W_2O_{12}$, and $Sr_9La_2W_2O_{24}$. Conversely, difficultly soluble aqua polycompounds are occasionally precipitated from gels (see table); in this case, the gel is acidified with nitric acid to improve the stability of dispersed systems. The presence of H^+ ions lowers the concentration of oxygen-containing anionic forms of *d* metals because of their transition to neutral or cationic oxygen-containing forms [2, 4], with their capacity for complexation with the polymer preserved.

Replacing part of vanadium(V) in the system composed of ammonium vanadate and lanthanum trinitrate with phosphorus(V) (which corresponds to $LaV_{1-x}P_xO_4$ solid solutions with x of up to 0.5 [9]) by introduction of ammonium phosphate much improves the stability of gels, to the point of formation of resin-like jellies. These jellies possess a characteristic property of such formations, thixotropy, i.e., the ability to restore geometric shape after removal of mechanical stresses applied. They are even stable upon heating to 80–90°C. In this case, the strength of cross-linking of fragments of molecular complexes into a 3D network is very high, which suggests the influence of the effective charge of the anion per atom of a *d* metal or its substituent, P(V). Vanadate, molybdate, and tungstate anions in solution and in the solid state tend to form strongly condensed polyanions [2, 10] with 4, 7, 12, and more coordination polyhedra of *d* metals associated into a complex polyanion. The bonding between the polyhedra (commonly, distorted octahedra) is effected by common oxygen(II) ions simultaneously belonging to two or three *d* metal atoms. The effective charge per *d* metal atom is equal to, or somewhat greater than unity, e.g., for $V_4O_{12}^{4-}$, $Mo_7O_{24}^{6-}$, and $W_{12}O_{41}^{10-}$ anions. Phosphate ions PO_4^{3-} show less pronounced tendency toward condensation [11], which makes higher the charge state of the formula unit and its capability to be cross-linked into 3D networks by the cations introduced.

The experiments performed yielded gels stable within 1 to several days, corresponding to $La_{1-x}Ca_xVF_yO_{4-y}$ solid solutions (with x of up to 0.7 and $0 \le y \le 0.3$) [9]. The following solid solutions were synthesized: solid solution with monazite structure, $LaV_{1-x}P_xO_4$ (annealing at 700°C for 6 h); $La_{1-x}Rb_xVO_{4-y}$ with x from 0 to 0.5 (4 h at 700°C); $SrWO_4$-based solid solution containing 40 mol % $La_2(WO_4)_3$, with scheelite structure; and $SrLa_4(WO_4)_7$ with perovskite structure (annealing at 800°C for 9 h).

CONCLUSIONS

(1) The stability of polymeric-salt gels and jellies used to synthesize complex-oxide materials containing *d* metals, Mo(VI), W(VI), and V(V), is determined by a number of factors, the most important of which is the nature of the constituents.

(2) The stability of dispersed system is markedly improved by an increase in the effective charge of anions and cations. Presence of cations forming soluble compounds with *d* metals in the anionic form impairs the stability of gels and leads to separation of the liquid part; formation of aqua polycompounds with low solubility product causes precipitation.

(3) All other conditions being the same, higher stability is observed for gels whose composition is close to the equivalence point of precipitation titration of the corresponding salt systems and those with high content of polymer or in the presence of a polymer with high molecular weight.

ACKNOWLEDGMENTS

The study was financially supported in part by the Russian Foundation for Basic Research (project no. 97-03-33 182) and the US Civilian Research and Development Foundation (CRDF project REC-005).

REFERENCES

1. Ostroushko, A.A., *Ross. Khim. Zh.*, 1998, vol. 42, nos. 1–2, pp. 123–133.
2. Mokhosoev, M.V. and Shevtsova, N.A., *Sostoyanie ionov molibdena i vol'frama v vodnykh rastvorakh* (State of Molybdenum and Tungsten Ions in Aqueous Solutions), Ulan-Ude: Buryat. Kn. Izd., 1977.
3. Evdokimov, A.A., Efremov, V.A., Trunov, V.K., *et al., Soedineniya redkozemel'nykh elementov: Molibdaty, vol'framaty* (Compounds of Rare-Earth Elements: Molybdates, Tungstates), Moscow: Nauka, 1991.
4. Ostroushko, A.A., Mogil'nikov, Yu.V., Popov, K.A., *et al., Zh. Neorg. Khim.*, 1999, vol. 44, no. 8, pp. 1402–1408.
5. Ostroushko, A.A., Mogilnikov, Yu.V, and Popov, K.A., Abstracts of Papers, *Int. Symp. on Metastable, Mechanically Alloyed and Nanocryst. Mater. (ISMANAM–98), Wollongong-Sydney, Australia, 7–12 December 1998*, Wollongong-Sydney, 1998, PA35.
6. Ostroushko, A.A., Mogil'nikov, Yu.V., and Popov, K.A., *Neorg. Mater.*, 2000, vol. 36, no. 6, pp. 730–739.
7. Ostroushko, A.A., Mogil'nikov, Yu.V., Vilkova, N.V., and Popov, K.A., *Zh. Prikl. Khim.*, 2000, vol. 73, no. 10, pp. 1604–1611.
8. Lur'e, Yu.Yu., *Spravochnik po analiticheskoi khimii* (Handbook of Analytical Chemistry), Moscow: Khimiya, 1989.
9. *Khimiya redkikh elementov: Silikaty. Germanaty. Fosfaty. Arsenaty. Vanadaty* (Chemistry of Less-common Elements: Silicates, Germanates, Phosphates, Arsenates, Vanadates), Moscow: Nauka, 1983.
10. *Khimiya pyativalentnogo vanadiya v vodnykh rastvorakh* (Chemistry of Pentavalent Vanadium in Aqueous Solutions), Shveikin, G.P., Ed., *Tr. Inst. Khim. Ural'sk. Nauchn. Ts. Akad. Nauk SSSR*, issue 24, Sverdlovsk, 1971.
11. Nekrasov, B.V., *Osnovy obshchei khimii* (Fundamentals of General Chemistry), Moscow: Khimiya, 1973, vol. 1.

Russian Journal of Applied Chemistry, Vol. 75, No. 8, 2002, pp. 1223–1226. Translated from Zhurnal Prikladnoi Khimii, Vol. 75, No. 8, 2002, pp. 1249–1252.
Original Russian Text Copyright © 2002 by Nikolaev, Lebedeva.

INORGANIC SYNTHESIS AND INDUSTRIAL INORGANIC CHEMISTRY

Inorganic Phosphate Curing Agents for Epoxy Composite Materials

P. V. Nikolaev and L. N. Lebedeva

Ivanovo State Academy of Chemical Technology, Ivanovo, Russia

Received March 20, 2002

Abstract—Fundamental aspects of how epoxy polymeric materials are formed on the basis of phosphate curing systems undergoing homopolycondensation were studied. The advisability of using phosphate curing agents in a microheterogeneous colloid-dispersed state was demonstrated.

The wide use of epoxy composite materials (ECM) containing no organic solvents has shown that they have, together with numerous advantages and, occasionally, unique properties, also disadvantages associated with the toxicity of the volatile components (epichlorohydrin, toluene) contained in epoxy oligomers (EO). The assortment of curing agents used in ECM containing no organic solvents is rather narrow. The most widely used at present are aliphatic amines, which allow deposition of polymeric epoxy coatings without heating. As a rule, the amines used are toxic. Important disadvantages of epoxy polymeric systems obtained with the use of most of amine curing agents is their poor thermal stability and high combustibility. In this connection, development of new ecologically safe curing agents improving the thermal stability and lowering the combustibility of epoxy polymeric materials is an urgent task.

Particularly noteworthy is the use of orthophosphoric acid as a curing agent for ECM, since one of the best fire retardants, phosphorus, and an environmentally pure fire retardant, water, are introduced into the material in this case. However, investigations of the systems ⟨epoxy oligomer ED-20⟩–H_3PO_4–H_2O demonstrated that the lifetime of the composites is short, and the degree of their curing strongly depends on the content of water in the acid [1].

In order to make lower the activity of H_3PO_4, to improve the technological properties of the systems being cured, and to enhance their thermal stability and diminish combustibility, a technique for obtaining new phosphate curing agents (PCA) of inorganic origin was developed.

As a raw material for their preparation served large-tonnage commercial products: H_3PO_4, red iron oxide pigment, and talc. The components of phosphate pastes (PP) were mixed without heating. The relative contents of the solid and liquid phases, as a rule, corresponded to acid capacity of the first degree. In the initial state, PCAs are pastes that can spontaneously undergo homopolycondensation without heating of the system. Owing to this circumstance, it is possible not to perform precise dosage of the components in formulating an epoxy composite.

The reactions in which condensed phosphates (PCA prepolymers) are formed in curing agents (homopolycondensation) occur in stages. It is known that H_3PO_4 forms with iron(III) oxide three types of salts: $2Fe(H_2PO_4)_3 \cdot 3H_2O$ (dihydrophosphate), $Fe_2(HPO_4)_3 \cdot 3H_2O$ (hydrophosphate), and $2FePO_4 \cdot 3H_2O$ (orthophosphate). Curing of PPs and their polycondensation yields polymeric phosphate stone.

The intermediate products of homopolycondensation, iron dihydro- and hydrophosphates, are reactive toward EOs and can cure them. The functionality of incomplete phosphates with respect to EO, following from their structure, is 6 and 3 for, respectively, dihydro- and hydrophosphates. This ensures preparation of an epoxy-phosphate organo-inorganic polymeric material with three-dimensional network structure, which may contain $-Fe-O-\underset{|}{P}=O$, $O=\underset{|}{P}-O-CH_2-$. fragments. The final products of homopolycondensation, iron orthophosphate and polymeric inorganic phosphate [2], are inert toward the EO.

In their aggregation state, the curing agents are phosphate pastes of color determined by the presence

1070-4272/02/7508-1223 $27.00 © 2002 MAIK "Nauka/Interperiodica"

Influence exerted by the time of aging of phosphate curing agents on their characteristics

System H_3PO_4 + Fe_2O_3	τ, day	*D*, in Klin units	$c_{Fe^{3+}}$, g l^{-1}	AN, mg KOH/g	$c_{H_3PO_4(fr)}$, %
H_3PO_4 50% (1 mole H_3PO_4,	0	88	0.014	300	100
5.45 mole H_2O, 9.96 mole Fe_2O_3)	5	113	0.025	130	50
	13	140	0.035	20	10
	17	114	0.028	5	3
H_3PO_4 77% (1 mole H_3PO_4,	0	115	0.014	595	100
1.63 mole H_2O, 4.62 mole Fe_2O_3)	5	113	0.033	200	32
	10	92	0.037	50	30
	13	5	0.035	10	5
H_3PO_4 86% (1 mole H_2O,	0	90	0.019	–	–
1.13 mole H_3PO_4, 4.1 mole Fe_2O_3)	5	92	0.027	–	–
	15	100	0.039	–	–
	20	88	0.048	–	–
H_3PO_4 100%	0	120	0.022	Stratification of the system,	
(1 mole H_3PO_4, 2.77 mole Fe_2O_3)	14	125	0.050	loss of processability	
	20	110	0.055		
	30	70	0.062		

of a mixture of iron oxide and talc. It should be noted that such a technological property as the viscosity of PPs prepared from iron oxide and talc first decreases and then, in the course of time, EO turns solid. The time during which this transformation occurs is determined by the concentration of the acid and by the acid/oxide ratio. With decreasing concentration of the acid employed, the "lifetime" of a curing agent becomes shorter. For example, the lifetime of a PP prepared from a 37% solution of H_3PO_4 is only 24 h, and that with a 77% solution, about 1 month.

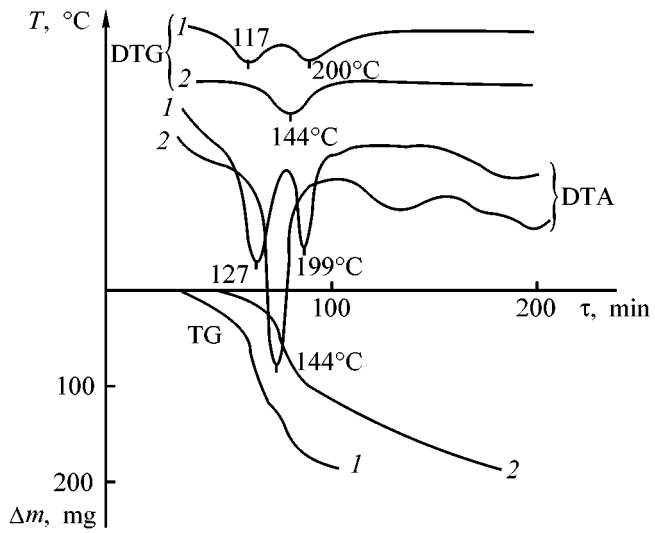

Fig. 1. Thermograms of PCA samples containing 77 wt % H_3PO_4 and red iron oxide pigment. (*T*) Temperature, (Δ*m*) loss of mass, and τ time; the same for Fig. 2. Time of aging of curing agent: (*1*) 30 min and (*2*) 900 h. Rate of temperature rise 5 deg min^{-1} up to 500°C.

The density of the curing agents is 1.29–2.74 g cm^{-3}, with acid number (AN) equal to 150–600 mg KOH/g. The phosphate curing agents are well compatible with liquid EOs or mixtures of these, and also with ECMs, e.g., with EP-0010 epoxy filling and EP-1155 and BEP-1264s epoxy enamels.

To elucidate the nature of the processes occurring in a mixture of a red iron oxide pigment with H_3PO_4 of various concentrations, which ensure a spontaneous conversion of a heterogeneous coarsely dispersed system obtained on mixing powdered oxide with H_3PO_4 into a microheterogeneous colloid-dispersed system, and then into a monolithic solid, the variation of the dispersity *D* of the system, AN, and the content of iron ions, $c_{Fe^{3+}}$, and free H_3PO_4, $c_{H_3PO_4(fr)}$, with the aging time τ of a curing agent was studied (see table).

It can be seen from the table that both the H_3PO_4 content and the AN in the system decrease. This indicates that the acid interacts chemically with the α-oxide of iron(III), with the interaction the more intensive, the lower the acid concentration. However, such characteristics as the content of iron ions and the dispersity vary nonlinearly, which indicates that there occurs homocondensation of the components of the system, and, first, acid iron phosphates and then orthophosphate and polymeric phosphate stone are formed [3].

The phosphate pastes prepared from iron(III) oxide and 77 wt % H_3PO_4 were subjected to thermogravimetric (TG) and differential-thermal (DTA) analyses. Figure 1 presents the results obtained in analysis

of PPs after varied time of aging. It can be seen from the DTA curves that the processes occur in PCAs at moderate temperatures. Two pronounced endothermic peaks in the DTA curves and two regions of mass loss in the TG curves are observed in the temperature interval 120–200°C for a freshly prepared curing agent. These features indicate that the system contains bound and constitution water [4], each removed in a certain temperature range. With increasing time of curing agent aging, the composition of the formulation changes, which is due to the occurrence of a complex physicochemical process accompanied by, e.g., evaporation of the constitution water. The presence of a single endothermic peak and of the corresponding region of mass loss characterizes the loss of the crystal hydrate water by the reaction

$$FePO_4 \cdot 2H_2O \xrightarrow{140–210°C} FePO_4 + 2H_2O\uparrow.$$

A significant difference is also observed in studying the curing of EO with PPs with varied conversion of their components (Fig. 2). The DTA curves exhibit a clear-cut distinction consisting in a strongly pronounced endothermic peak (T_{max} = 408°C) in the case of an aged curing agent, which, in the authors' opinion, indicates a thermal destruction of the organo-inorganic three-dimensional structure formed in curing in the isothermal mode without heating, which does not appear at short aging time. The TG curves show two portions of mass loss. With increasing time of PCA aging, the maximum rate of mass loss is shifted to higher temperatures (from 314 to 372°C), which indicates that the thermal stability of composites with aged curing agents is high. This conclusion is also confirmed by the $T_{0.25}$ values (332 and 362°C for, respectively, the systems with freshly prepared and aged curing agents).

Depending on the H_3PO_4 concentration and time of aging of PP, the content of the curing agent can be varied between 4 and 400 wt % relative to EO. Therefore, the dependence of the relative hardness and degree of curing on the time of aging of phosphate pastes was studied. A decrease in their activity, i.e., an increase in the lifetime of the EO–PCA system, was observed.

The dependences of the content of the gel fraction GF on the time of PP aging are presented in Fig. 3a. The difference in the observed types of behavior is due to the content of acid in the initial PP. The phosphate pastes based on aqueous H_3PO_4 solutions are converted from a heterogeneous coarsely dispersed system of the starting components, by the interaction of these components,

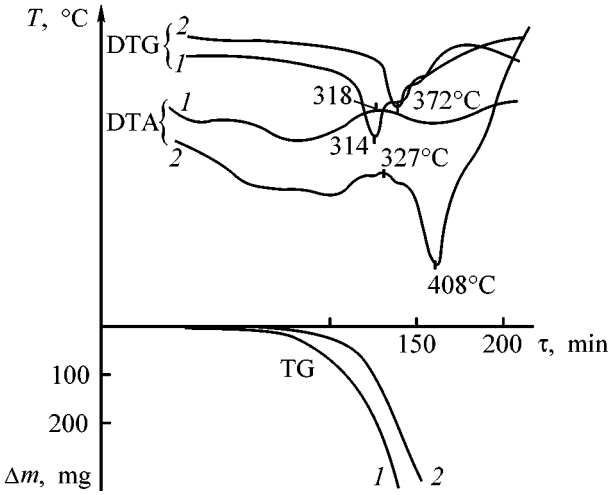

Fig. 2. Thermograms of epoxy composite samples composed of ED-20, phosphate curing agent based on H_3PO_4 (77 wt %), and red iron oxide pigment. Aging time of curing agent: (*1*) 30 min and (*2*) 170 h.

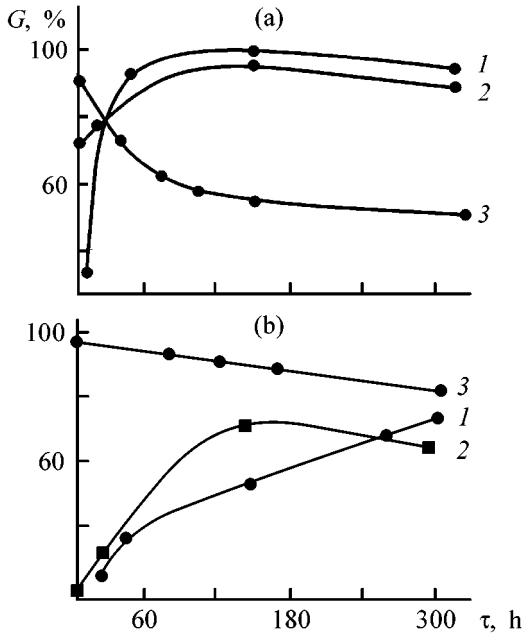

Fig. 3. Gel fraction content G vs. the aging time τ of curing agent before its introduction into ED-20. Composite curing: (a) without heating (at 18°C) for 24 h and (b) stepwise, with 24 h at 18°C and 20 min at 140°C. Fe_2O_3 : H_3PO_4 curing agent: (*1*) 50% H_3PO_4 (1 : 1 by weight), (*2*) 77% H_3PO_4 (1 : 1.4 by weight), and (*3*) 100% H_3PO_4 (1 : 1.7 by weight). Amount of curing agent relative to EO (wt %): (*1*) 60.7, (*2*) 14.4, and (*3*) 9.3.

into a microheterogeneous colloid-dispersed system [4, 5], which contains, together with H_3PO_4 and iron(III) oxides, also products of their reaction, iron phosphates. The pastes based on anhydrous H_3PO_4 become thinner in the course of time and strat-

ify, with no microheterogeneous colloid-dispersed system formed.

The curing agents developed exhibit latent behavior, similarly to H_3PO_4. At moderate temperatures (~140°C) there occurs additional curing of systems formed without heating. The GF content is as high as 98 wt % in some cases (Fig. 3b). For formulations based on anhydrous H_3PO_4, no extremal behavior of the dependences is observed.

It is not impossible, either, that, similarly to the case of ordinary cements, structuring occurs in the system after mixing of PP components and formation of a primary layer of hydrates, owing to molecular interparticle interaction. The resulting iron phosphates are centers of crystallization, and crystals grow through material deposition onto primary miniscule particles, named nuclei [6]. In this case, water plays the part of a component that favors dissolution of the pigment iron(III) oxide and of the forming molecules of iron phosphates, i.e., promotes adhesion of the appearing particles and formation of a solid phosphate stone.

The GF content of cured coatings decreases if the aging time of the curing agent (PP) obtained on the basis of anhydrous H_3PO_4 increases. Chemisorption of the acid on the α-oxide of iron(III) and their chemical reaction in the system containing anhydrous acid also occur. However, these processes are hindered since the surface of iron(III) oxide is more hydrophilic than acidophilic. As a result, a polymer with the maximum GF content is formed at short time of PP aging, when the content of free H_3PO_4 in the PP is high and the amount of iron phosphates and water, as reaction products, is low. The lifetime of the PCA–EO system is at a minimum. In the course of time, the content of free acid in the PP decreases; however, the forming incomplete iron phosphates can only be hydrated by the reaction water whose amount is insufficient to cause dissociation and ionization of salts in the system.

For this reason the intermediate reaction products, incomplete iron phosphates, do not react in the given system with EO without heating and the content of the gel fraction decreases. However, additional curing of ECM occurs at elevated temperature. The content of the gel fraction in the system EO–PCA increases by 5–35%. The effect of additional curing is the most pronounced with PP aged for up 7 days. At 140°C incomplete iron phosphates react, in the first place, with one another and with iron(III) oxide to form an inorganic polymeric phosphate, with reactions involving the epoxy binder being not improbable, either.

The reaction water forms crystal hydrates with iron salts or evaporates, which also favors an increase in the content of the gel fraction, since hydrolysis of tri- and diphosphate esters become less probable.

These features are accounted for by differences between the changes occurring in PPs obtained with diluted and anhydrous H_3PO_4. The presence of water in the acid, and in the PP obtained on its base, favors formation of an organo-inorganic polymeric structure with high degree of cross-linking. It should be noted that the composite obtained contains a substantial amount of unreacted iron(III) oxide and its hydrophosphate.

CONCLUSIONS

(1) Formulas of phosphate curing agents (phosphate pastes) that undergo homopolycondensation and the technology of their use in epoxy composite materials were developed. It was shown that water contained in the starting acid exerts decisive influence on the process of prepolymerization of the system ⟨orthophosphoric acid⟩–Fe_2O_3. This water determines the structure of prepolymers and the lifetime of phosphate curing agents and epoxy composites, and also affects the degree of curing of the polymeric material obtained.

(2) It was shown that phosphate curing agents in microheterogeneous colloid-dispersed state are to be used to obtain an organo-inorganic epoxy polymeric material with high content of the gel fraction.

REFERENCES

1. Nikolaev, P.V., Lebedeva, L.N., and Poltavets, T.A., *Okhrana okruzhayushchei sredy i resursosberezhenie: Mezhvuzovskii sbornik nauchnykh trudov* (Environment Protection and Resource Saving: Intercollegiate Coll. of Sci. Works), St. Petersburg: SPb. Gos. Univ. TD, 1995, pp. 93–98.
2. Van Wazer, I.R., *Phosphorus and its Compounds*, New York: Wiley–Interscience, 1958, vol. 1.
3. Golynko-Vol'fson, S.L., Sychev, M.M., Sudaks, L.G., *et al., Khimicheskie osnovy tekhnologii i primeneniya fosfatnykh svyazok i pokrytii* (Chemical Foundations of the Technology and Use of Phosphate Binders and Coatings), Leningrad: Khimiya, 1968.
4. Kopeikin, V.A., Petrova, A.P., and Rashkovan, I.L., *Materialy na osnove metallofosfatov* (Materials Based on Metal Phosphates), Moscow: Khimiya, 1976.
5. Corbridge, D.E., *Phosphorus. An Outline of its Chemistry, Biochemistry and Technology*, Amsterdam: Elsevier, 1980
6. Sychev, M.M., *Tverdenie vyazhushchikh veshchestv* (Curification of Binders), Leningrad: Stroiizdat, 1974.

Russian Journal of Applied Chemistry, Vol. 75, No. 8, 2002, pp. 1227–1230. Translated from Zhurnal Prikladnoi Khimii, Vol. 75, No. 8, 2002, pp. 1253–1256.
Original Russian Text Copyright © 2002 by Moskvin, Rodinkov, Grigor'ev, Zykin.

SORPTION AND ION-EXCHANGE PROCESSES

Chromatomembrane Gas-Extraction Water Purification To Remove Dissolved Oxygen

L. N. Moskvin, O. V. Rodinkov, G. L. Grigor'ev, and I. A. Zykin

St. Petersburg State University, St. Petersburg, Russia

Received October 8, 2001; in final form February, 2002

Abstract—Fundamental aspects of the process of continuous chromatomembrane gas-extraction purification of water to remove dissolved oxygen are considered. An adequate physicochemical model and mathematical description of the process are proposed. The advantages of the chromatomembrane technology of water deaeration over the conventional methods for removing dissolved oxygen are demonstrated and substantiated.

The problem of effective removal of gas impurities, and dissolved oxygen in the first place, from water is encountered both in various branches of industry, such as nuclear and thermal power engineering, organic synthesis, and manufacture of semiconducting materials, and in laboratory practice, e.g., in carrying out biochemical and electrochemical studies and, in particular, in preparing standard aqueous solutions with prescribed concentrations of these impurities in the stage of calibration of analytical instruments. The efficiency of the most widely used techniques for removing gaseous impurities from aqueous solutions, based on the conventional mass–exchange processes in the gas–liquid system (boiling, bubbling), proves to be insufficient in many cases. Even with the optimal designs of deaerating installations the residual content of oxygen in water exceeds that required by regulations [1]. Membrane methods for extraction of volatile impurities across porous hydrophobic membranes are characterized by relatively low output capacity, which results from hindrances to diffusion processes in membranes [2]. Chemical techniques for removal of dissolved oxygen change the composition of the water medium and, therefore, are not always acceptable for water deaeration.

More promising for deep purification of water to remove volatile impurities and, in particular, dissolved oxygen is the chromatomembrane method for performing mass-exchange processes in the liquid–gas system, proposed by Moskvin [3, 4]. This method combines advantages of chromatographic (high mass-exchange efficiency) and membrane (continuous process mode) techniques of substance separation.

The aim of the present study was to reveal the fundamental aspects of the process of continuous chromatomembrane gas extraction and to evaluate its efficiency in deep purification of water to remove dissolved oxygen.

EXPERIMENTAL

The scheme of the process of continuous chromatomembrane gas extraction is shown in Fig. 1. The mass-exchange between the flows of liquid and gas, leading to gas-extraction removal of dissolved oxygen, occurs in a capillary-biporous medium formed by particles of porous polytetrafluoroethylene (PTFE), which are bound together in sintering. The spaces between the particles form a system of open macropores of arbitrary configuration, through which moves water

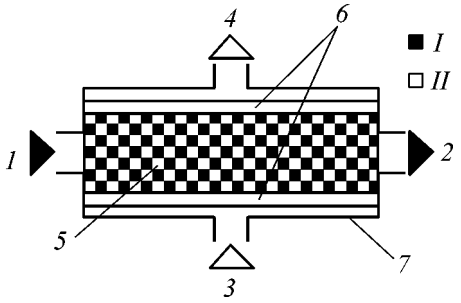

Fig. 1. Scheme of chromatomembrane gas extraction: (*1, 2*) inlet and outlet for liquid, (*3, 4*) inlet and outlet for extracting gas, (*5*) mass-exchange bed of hydrophobic biporous material, (*6*) membranes, and (*7*) case of the chromatomembrane unit. Space in the mass-exchange bed occupied by (*I*) macropores and (*II*) micropores.

1070-4272/02/7508-1227 $27.00 © 2002 MAIK "Nauka/Interperiodica"

being purified to remove dissolved oxygen. The sizes of PTFE particles and, correspondingly, the macropore sizes are set arbitrarily by the technique used to obtain biporous PTFE. The particles themselves contain open pores of micrometer and submicrometer sizes: micropores through which moves extracting gas, whose part was played in the given case by high-purity nitrogen containing less than 0.001 vol % oxygen. Biporous mass-exchange bed is limited from above and below by water-impermeable PTFE membranes through which the flow of the extracting gas is supplied and withdrawn. The inflow of water into micropores of the membranes and the mass-exchange bed is prevented by the negative capillary pressure appearing in the micropores because of the nonwettability of PTFE by water. In its turn, the inflow of the extracting gas into the macropores, in which the capillary pressure is negligibly small, is hindered by the pressure of the liquid, which is maintained higher than the gas pressure according to the experimental conditions. More evidence about the physicochemical essence of chromatomembrane mass-exchange processes and the conditions under which they are to be carried out can be found in [3, 4].

We performed the study on prototype chromatomembrane units (CMU) of our own manufacture, with a mass-exchange bed in the form of a parallelepiped. We analyzed the influence exerted by the ratio of flow rates of water and extracting gas, macropore size in the mass-exchange bed, and bed length on the efficiency of chromatomembrane purification of water to remove dissolved oxygen. For the bed length was taken the extension of the mass-exchange bed in the direction of motion of the liquid being deoxygenated, and for the bed height, the extension of the bed in the direction perpendicular to that of the fluid flow (Fig. 1). The length L of the mass-exchange bed in the CMU prototypes studied was varied within 1–10 cm at constant height and width of 0.8 cm. The macropore diameter, for which was taken the average size of PTFE particles forming the mass-exchange layer, was varied within 0.25–1.5 mm.

A flow of distilled water saturated with atmospheric oxygen was fed into the inlet of a CMU under study. To evaluate the efficiency of the chromatomembrane purification and determine the residual concentration of dissolved oxygen, the flow of water from the CMU under study was directed into a chromatomembrane cell (CMC) of similar design and smaller size, which ensured, as shown by results of independent tests, at least 99% deoxygenation oxygen because of the higher flow rate of the extracting gas. The flow of the extracting agent outflowing from the analytical CMC was directed through a drier with indicator silica gel into the dosing loop of an LKhM-80 gas chromatograph equipped with heat conductivity detector and a column packed with CaA zeolite, and analyzed for the content of oxygen. As carrier gas in gas-chromatographic analysis served helium of B brand, containing less than 0.001 vol % oxygen. The oxygen content in the carrier gas was determined using the method of absolute calibration against standard gas mixtures of oxygen in nitrogen. The residual mass concentration of oxygen, c, in air after chromatomembrane purification was calculated using the formula [4]

$$c = c_g W_g^*/W_l,$$

where c_g is the mass concentration of oxygen in the flow of the extracting gas at the CMC outlet, found by gas-chromatographic analysis; W_g^* and W_l are the volumetric flow rates of the extracting gas and water through the CMC (ml min^{-1}).

The gas-chromatographic technique described allows determination of the residual concentration of dissolved oxygen beginning with 15 μg l^{-1}, with relative error not exceeding 20%.

The admissible pressure gradients in fluid and gas phases and, correspondingly, the maximum velocities of motion of these phases across the mass-exchange bed in carrying out chromatomembrane processes are determined by the capillary pressure, which is inversely proportional to the radius of micropores in the capillary-porous medium [4]. However, the decrease in the micropore radius makes lower the permeability of the porous medium. As shown previously [4], there exists the optimal range of micropore radii (1–10 μm), which ensures the maximum flow velocity of the extracting agent and thereby creates necessary prerequisites for raising the degree of fluid purification to remove volatile substances.

Another opportunity for raising the total flow rate of the extracting gas through a CMU consists in making larger the cross-sectional area of the mass-exchange bed in the direction perpendicular to the gas flow and lowering its height. In this regard, the most appropriate scheme of the extraction process is two-dimensional, with the flows of the fluid and the extracting agent moving at an angle of 90°. The two-dimensional scheme of chromatomembrane gas extraction allows, all other conditions being the same, variation of the flow rate of the extracting gas in much wider range, compared with the counterflow scheme in which the flows of fluid and gas move in opposite directions.

Taking into account the fact that the mass-exchange bed is elongated along the direction of the fluid flow, which is necessary for ensuring the maximum flow rates of the extracting gas through the unit, we can assume that the pattern of the extraction process corresponds in the given case to the model of the so-called cross-extraction [5, 6]. According to this model, the mass-exchange bed of the CMU can be represented as a number of in-series connected identical stages (equivalent theoretical plates), through which passes a fluid flow, with a flow of pure gas passed through each stage in the perpendicular direction. In this case, the flow rate of the extracting agent through each plate is W_g/n, where W_g is the flow rate of the extracting agent through the CMU and n is the number of equivalent theoretical plates in the unit. The relationship between the component concentration in the aqueous phase at the inlet, c_0, and outlet, c, of the cross-extraction system was established in [5, 6]. In terms of the accepted notation system, this relationship is reflected by the equation

$$c = \frac{c_0}{(1 + KW_g/nW_l)^n}, \quad (1)$$

where K is the distribution coefficient of a component between the gas and liquid phases, equal to the ratio of the mass or molar concentration of the component in the gas phase to its concentration in the liquid phase in equilibrium.

As follows from Eq. (1), the main factors affecting the efficiency of gas-extraction purification are the component distribution coefficient, ratio of volumetric flow rates of the extracting gas and the liquid phase, and the efficiency of the mass-exchange process, characterized by the number of equivalent theoretical plates existing within the mass-exchange bed.

The table lists the oxygen distribution coefficients in the gas–liquid system in relation to temperature. The K values presented in the table were calculated by the procedure described in [7] from the known data on oxygen solubility in water [8]. The relatively low solubility of oxygen in water and the correspondingly high K values enable high-efficiency gas-extraction purification of water to remove dissolved oxygen. Raising the number of theoretical plates by improving the efficiency of the exchangeprocess itself or by making longer the mass-exchange bed must lead to a significant decrease in the residual content of the component being extracted.

Comparison of experimentally established dependences of the relative residual content of oxygen dissolved in water on the ratio of flow rates of the extracting gas and water with those calculated by Eq. (1) (Fig. 2) indicates a high level of adequacy of the cross-extraction model to the real process at small W_g/W_l ratios. In this case, the height of the equivalent theoretical plate is 2–3 cm. At the same time, at $W_g/W_l > 1$ the experimental dependence significantly differs from the theoretical one. The decrease in the efficiency of the chromatomembrane process in this range can be accounted for by a substantial decrease in the ratio of the geometric volumes of the liquid and gas phases in the mass-exchange bed with increasing flow rate of the extracting gas, which necessarily entails raising the pressure of the extracting gas [9].

Coefficients of oxygen distribution between the gas and water phases in relation to temperature

T, °C	K	T, °C	K
10	26.5	22	34.5
12	27.8	24	35.9
14	29.1	26	37.3
16	30.4	28	38.7
18	31.8	30	40.2
20	33.1		

At one and the same ratio of flow rates of the extracting gas and water being purified, raising the absolute values of these flow rates leads to a decrease in the residual concentration of oxygen dissolved in water (Fig. 3). The possible reason is that the ratio of the geometric volumes of phases in the mass-exchange bed changes as a result of the compressibility of the extracting gas. Since, at one and the same W_g/W_l ratio, the efficiency of chromatomembrane water purification to remove oxygen is the higher, the greater the flow rate of the liquid being purified, it becomes possible to develop high-throughput instal-

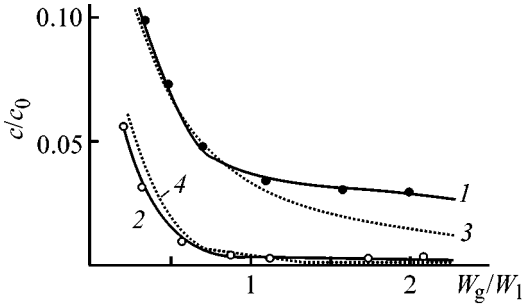

Fig. 2. Relative concentration of oxygen dissolved in water at the CMU outlet, c/c_0, vs. the ratio of flow rates of the extracting gas and water, W_g/W_l. Water flow rate 10 ml min^{-1}. Dependence: (*1*, *2*) experimental and (*3*, *4*) calculated. Length of mass-exchange bed (cm): (*1*) 2.4 and (*2*) 5.0. Number of theoretical plates: (*3*) 1 and (*4*) 2.

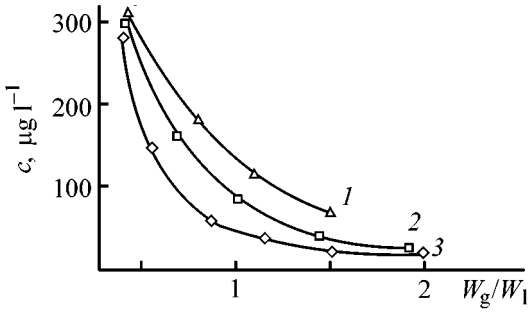

Fig. 3. Residual concentration of oxygen dissolved in water, *c*, at the CMU outlet vs. the ratio of flow rates of the extracting gas and water phase, W_g/W_l. Length of mass-exchange bed 5.0 cm. Flow rate of water (ml min^{-1}): (*1*) 3.3, (*2*) 5.0, and (*3*) 10.0.

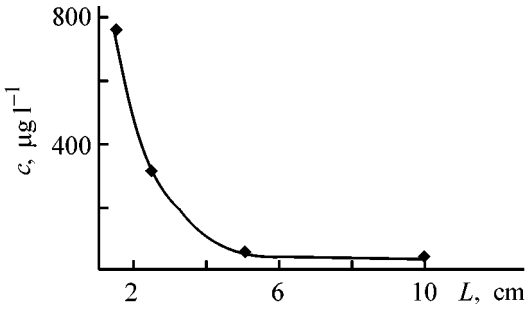

Fig. 4. Residual concentration of oxygen dissolved in water, *c*, at the CMU outlet vs. the length *L* of the mass-exchange bed. Flow rates of extracting gas and water 5 ml min^{-1}.

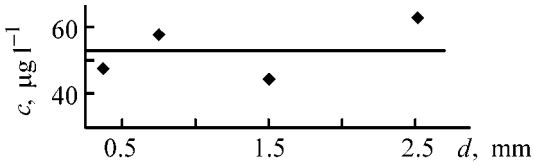

Fig. 5. Residual concentration of oxygen dissolved in water, *c*, at the CMU outlet vs. the average diameter of macropores in the mass-exchange bed, *d*. Length of mass-exchange bed 5.0 cm, flow rates of extracting gas and water 5 ml min^{-1}.

lations for continuous chromatomembrane purification of water to remove gaseous impurities and, in particular, dissolved oxygen.

The effect of the mass-exchange bed length on the efficiency of chromatomembrane removal of oxygen is reflected by Fig. 4. It can be seen that making the bed longer than 5 cm has no practical importance since the residual concentration of dissolved oxygen changes only slightly at lengths exceeding this value. This fact can be well accounted for in terms of the plate theory of chromatography and follows from Eq. (1).

Our study of the influence exerted by the size of pores in the mass-exchange bed on the efficiency of chromatomembrane gas extraction (Fig. 5) makes it possible to state that this parameter affects the efficiency of this process only slightly. Presumably, this can be attributed to the key influence exerted by longitudinal diffusion in the gas phase, which is known to be weakly dependent on the pore size [10], to the broadening of the zone corresponding to the substance being extracted [4]. This circumstance makes appropriate use of CMUs with coarser macropores, which ensure higher permeability of the mass-exchange bed to the liquid phase, in chromatomembrane purification of water to remove dissolved oxygen.

CONCLUSION

It was established that chromatomembrane gas extraction enables continuous purification of water to remove dissolved oxygen to residual concentrations of less than 50 μg l^{-1} at 1 : 1 ratio of the volumetric flow rates of water being purified and extracting gas. The output capacity of the technique can be estimated at about 0.6 l h^{-1} per 1 cm^3 of the volume of the mass-exchange unit.

ACKNOWLEDGMENTS

The authors are grateful to the Ministry of Education of the Russian Federation and to the Ministry of Nuclear Industry of the Russian Federation for the support of the study carried out in the framework of the program of innovation cooperation (grant no. 8-14).

REFERENCES

1. Butler, I.B., Schoonen, M.A.A., and Rickard, D.T., *Talanta*, 1994, vol. 41, pp. 211–214.
2. Kuban, V. and Dasgupta, P.K., *Anal. Chem.*, 1991, vol. 63, pp. 2210–2216.
3. Moskvin, L.N., *Dokl. Ross. Akad. Nauk*, 1994, vol. 334, no. 5, pp. 599–603.
4. Moskvin, L.N., *Ross. Khim. Zh.*, 1996, no. 1, pp. 67–76.
5. Treybal, R.E., *Liquid Extraction*, New York: McGraw Hill, 1963.
6. Gindin, L.M., *Ekstraktsionnye protsessy i ikh primenenie* (Extraction Processes and Their Application), Moscow: Nauka, 1984.
7. Rodnikov, O.V. and Moskvin, L.N., *Zh. Anal. Khim.*, 1995, vol. 50, no. 2, pp. 164–166.
8. Lur'e, Yu.Yu., *Analiticheskaya khimiya promyshlennykh stochnykh vod* (Analytical Chemistry of Industrial Wastewater), Moscow: Khimiya, 1984.
9. Moskvin, L.N., Rodnikov, O.V., Katruzov, A.N., *et al.*, *Talanta*, 1995, vol. 42, pp. 1707–1710.
10. Giddings, J.C., *Dynamics of Chromatography*, part 1, *Principles and Theory*, New York: Marcel Dekker Inc., 1965.

Russian Journal of Applied Chemistry, Vol. 75, No. 8, 2002, pp. 1231–1233. Translated from Zhurnal Prikladnoi Khimii, Vol. 75, No. 8, 2002, pp. 1257–1259.
Original Russian Text Copyright © 2002 by Potapova, Volkovinskaya, Soldatov, Egiazarov.

SORPTION AND ION-EXCHANGE PROCESSES

Fe–Ethylenediamine Tetraacetate Complexes Immobilized on Fibrous Anionite and Their Catalytic Activity in H_2S Oxidation

L. L. Potapova, T. V. Volkovinskaya, V. S. Soldatov, and Yu. G. Egiazarov

Institute of Physicoorganic Chemistry, Belarussian National Academy of Sciences, Minsk, Belarus

Received December 18, 2000; in final form, January 2002

Abstract—The effect of the complexonate solution pH on the nature and amount of ethylenediamine tetraacetate complexes of iron, immobilized on a FIBAN A-5 fibrous anionite, and their catalytic activity in H_2S oxidation by molecular oxygen was studied.

Purification of gas mixtures to remove hydrogen sulfide is commonly carried out by sorption or oxidation techniques with the use of solid or liquid sorbents and catalysts. High activity in liquid-phase oxidation of H_2S by molecular oxygen to sulfur is exhibited by ethylenediamine tetraacetate complexes of iron (Fe–EDTA) [1–4].

Previously (5–7), catalytic systems with Fe–EDTA complexes immobilized on some fibrous anionites have been synthesized and the effect of various factors on their activity has been studied. The catalysts were prepared using a complexonate solution obtained by mixing solutions containing stoichiometric amounts of an iron salt and a disodium salt of ethylenediamine tetraacetic acid (Trilon B). The complexonate solution was strongly acidic (pH ~0.5) and contained, together with complex anions, NO_3^- or Cl^- anions. All other conditions being the same, the presence of competing anions in the system puts limitation on the content of complexes immobilized on the fibrous anionite, which is associated with the ion-exchange equilibrium. Therefore, it was of interest to obtain a solution of iron complexonate without foreign ions and to study the effect of the complexonate solution pH on the content and nature of Fe–EDTA complexes immobilized on the ionite and also on the catalytic activity of the samples obtained.

EXPERIMENTAL

Iron(III) hydroxide and iron(III) complexonate were prepared using conventional procedures. An iron(III) chloride solution was prepared by dissolving 24.3 g of $FeCl_3 \cdot 6H_2O$ in 50 ml of H_2O. The resulting solution was acidified with 2 ml of conc. HCl and heated to 80–90°C, with 30 ml of a 25% NH_4OH solution added dropwise under constant stirring. Then 50 ml of hot water was added to the $Fe(OH)_3$ precipitate formed, the mixture was stirred and allowed to stay for 1 h for particle coagulation to occur, and the precipitate was separated by filtration.

To obtain iron complexonate, 32 g of Trilon B was placed in a beaker, 150 ml of water was added, and the mixture was heated on a water bath, with $Fe(OH)_3$ paste gradually added at 80–90°C. The obtained complexonate solution (of brown color) was filtered to remove a minor amount of unreacted hydroxide and then a complex salt was precipitated. For this purpose, dimethylacetamide was added to the complexonate solution (1 : 2 : 5 by volume) and the mixture was heated on a water bath. The dark yellow crystals precipitated at 60–90°C were separated by filtration and dried in air. The yield of the product was 90% of the theoretically calculated value (~30 g).

The complexonate synthesized was used to prepare a 0.1 M solution for treatment of ionite samples: 11.6 g of complexonate in 300 ml of solution, pH 6–6.5. To vary the solution pH within the prescribed limits (2.5–10.5), concentrated NH_4OH or HCl solutions were added.

The catalysts were prepared from the chloride form of the FIBAN A-5 anionite, which is an ionite with weakly basic tertiary amino groups and low content of carboxy groups (exchange capacity 4.3 mg-equiv g^{-1}, that of carboxy groups 0.6 mg-equiv g^{-1}). The an-

1070-4272/02/7508-1231 $27.00 © 2002 MAIK "Nauka/Interperiodica"

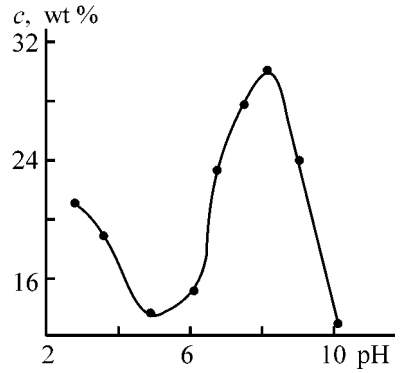

Fig. 1. Content of Fe–EDTA complexes in anionite, *c*, vs. complexonate solution pH.

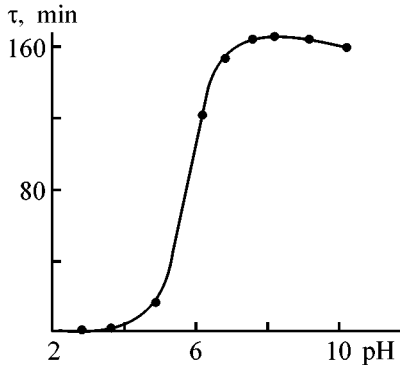

Fig. 2. Working life of samples, τ, vs. complexonate solution pH.

ionite was obtained on the basis of a polyacrylonitrile fiber with *N*,*N*-dimethylaminopropylamine used as aminating agent. Approximately 2 g of anionite swollen in water and squeezed on filter paper (~0.8 g of air-dry fiber) was poured over with 15 ml of a solution with prescribed pH value, kept for 30 min, and then removed from the solution and squeezed on filter paper. The treatment was repeated several-fold, until the ionite was saturated with the complex. The amount of the complex in the fiber was determined gravimetrically: by burning a weighed portion of the sample (1000°C, 1 h) and weighing the Fe_2O_3 formed.

Experiments on oxidation of hydrogen sulfide with molecular oxygen were carried out in a flow-through reactor at room temperature. Composition of the reaction mixture (vol %): H_2S 0.4, O_2 12.2, and N_2 the rest. The sample weight in swollen state was 0.21 g (cross-sectional area of the catalyst bed 0.6 cm^2, bed height 1 cm), and the flow rate of the gas mixture, 27 ml min^{-1}. To evaluate the efficiency of a catalytic system (relative activity), the working life of the samples till H_2S breakthrough, which was recorded chromatographically, was determined.

It can be seen that the dependence of the amount of the complex immobilized on the samples (wt %) on the solution pH is complex: with increasing pH, the amount of the complex decreases from 21 to 13 wt % in the pH interval 3–5, then increases steeply at pH 6–8, and again decreases at pH > 8 (Fig. 1).

The working life till H_2S breakthrough of the catalysts synthesized also depends on the pH of the complexonate solution (Fig. 2). It can be seen that samples obtained from a sufficiently acid solution (pH 3–4) are low-active: H_2S breakthrough is observed in the very first minutes of experiment. Higher catalytic activity is exhibited by samples obtained at pH > 5, and the highest activity, by those prepared at solution pH 7–8.5. With the pH increasing further, to 10, the sample activity decreases somewhat. Noteworthy is the fact that a sample obtained at complexonate solution pH equal to 3 shows low activity despite the relatively high content of the complex (21 wt %).

It should be kept in mind in interpreting the results obtained that the complexonate solution pH simultaneously affects the following factors: composition and degree of ionization of the functional groups of the anionite, composition and charge of ethylenediamine tetraacetate complexes with iron and their quantitative relationship, and the degree of dissociation of hydrogen sulfide molecules.

The known constants of the acid-base equilibria [8, 9] allow calculation of the fractions of various forms of the starting reagents at 20°C:

$$\text{Fe–HEDTA} + OH^- \rightleftarrows [\text{Fe–EDTA}(H_2O)]^-,$$
$$K_1 = 0.5 \times 10^{13}\ M^{-1};$$

$$[\text{Fe–EDTA}(H_2O)]^- \rightleftarrows [\text{Fe–EDTA(OH)}]^{2-} + H^+,$$
$$K_2 = 2.88 \times 10^{-8}\ M;$$

$$[\text{Fe–EDTA(OH)}]^{2-} + OH^- \rightleftarrows [\text{Fe–EDTA}(OH)_2]^{3-},$$
$$K_3 = 3.47 \times 10^{4}\ M^{-1};$$

$$H_2S \rightleftarrows HS^- + H^+, \quad K_4 = 0.91 \times 10^{-7}\ M;$$

$$HS^- \rightleftarrows H^+ + S^{2-}, \quad K_5 = 0.11 \times 10^{-11}\ M.$$

The results of the calculations were used to plot the dependences of the fraction of acid-base forms of the reagents on the pH of the medium (Fig. 3). It can be seen that the degree of hydroxylation of the complexes and their charge grow with increasing pH. At pH equal to 4, 8.5, and 12, the solution contains the maximum amounts of, respectively, single-, double-, and triple-charged anions of iron ethylenediamine tet-

raacetate. According to the electroselectivity rule, an increase in the charge of the complex favors a rise in its content in the anionite. At the same time, the degree of ionization of the functional groups decreases with increasing complexonate solution pH. As a result, the absorption of the complex anion decreases.

In the pH range 3–5, only a hydrated single-charged complex $[Fe–EDTA(H_2O)]^-$ is present in solution (Fig. 3), and the decrease in the content of the complex introduced by ion exchange (Fig. 1) is apparently due to a decrease in the degree of ionization of the functional groups of the ionite. At pH 6–8.5, an increase in the content of the supported complex is observed, which correlates with the increase in the fraction of the hydroxylated double-charged complex ion $[Fe–EDTA(OH)]^{2-}$, and at solution pH 8.5–10.5 the content of the complex in the anionite decreases. Apparently, the charge of the counter ion affects more strongly the ion-exchange equilibrium in the first case (region of transition from weakly acid to weakly alkaline medium), whereas in the second case (strongly alkaline medium) stronger influence is exerted, conversely, by the decrease in the content of ionized functional groups of the anionite, which results from the increase in the concentration of OH^- ions.

Hydrogen sulfide virtually does not dissociate in the acid medium (pH 3–5), and, therefore, the system is low-active, irrespective of the amount and composition of the complex introduced into the anionite. With increasing pH, the H_2S dissociation becomes more pronounced (Fig. 3, curves 5 and 6) and, correspondingly, the activity of the catalytic system grows. It is noteworthy that the content of the complex anion in the ionite falls markedly (from 30 to 13 wt %, Fig. 1) at pH 8.5–10.5, whereas the working life of the samples to H_2S breakthrough decreases only slightly (Fig. 2). The latter indicates that the activity of the $[Fe–EDTA(OH)]^{2-}$ and $[Fe–EDTA(OH)_2]^{3-}$ hydroxo complexes in oxidation of hydrogen sulfide is sufficiently high and dissociation of hydrogen sulfide, rather than HS^- oxidation on active centers of the catalyst, is the rate-limiting stage of the process.

CONCLUSIONS

(1) The amount of Fe–EDTA complexes immobilized on a fibrous anionite depends on the charge of the complex anion and the degree of ionization of the functional groups.

(2) Catalytic activity in oxidation of H_2S by molecular oxygen is exhibited by the complex anions $[Fe–EDTA(OH)]^{2-}$ and $[Fe–EDTA(OH)_2]^{3-}$.

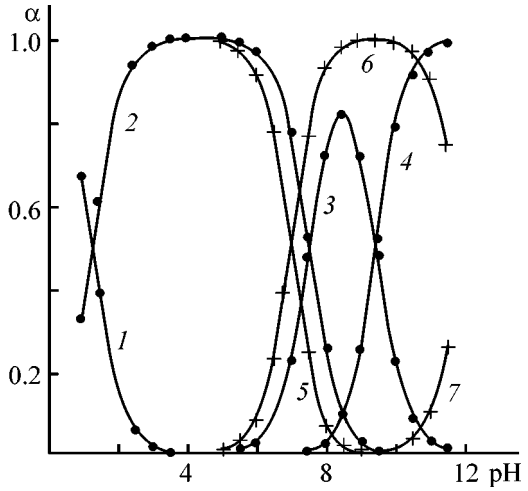

Fig. 3. Fraction of acid-base forms of the reagents, α, vs. the pH of the medium. (*1*) HFe–EDTA, (*2*) $[Fe–EDTA(H_2O)]^-$, (*3*) $[Fe–EDTA(OH)]^{2-}$, (*4*) $[Fe–EDTA(OH)_2]^{3-}$, (*5*) H_2S, (*6*) HS^-, and (*7*) S^{2-}.

(3) The necessary condition for effective operation of the catalytic systems studied is high degree of H_2S dissociation to form the hydrosulfide ion, which can be achieved at pH 8–10.

REFERENCES

1. US Patent 4 014 983.
2. US Patent 4 278 646.
3. Gritsenko, A.I., Galanin, I.A., Zinov'eva, L.M., and Murin, V.I., *Ochistka gazov ot sernistykh soedinenii pri ekspluatatsii gazovykh mestorozhdenii* (Gas Purification To Remove Sulfides in Exploitation of Gas Fields), Moscow: Nedra, 1985.
4. Martell, A.E., Motekaitis, R.J., Chen, D., *et al.*, *Canad. J. Chem.*, 1996, vol. 74, no. 10, pp. 1872–1879.
5. Potapova, L.L., Egiazarov, Yu.G., Soldatov, V.S., and Elinson, I.S., *Dokl. Nats. Akad. Navuk Belarusi*, 1998, vol. 42, no. 3, pp. 54–57.
6. Potapova, L.L., Shunkevich, A.A., Akulich, Z.I., and Egiazarov, Yu.G., *Zh. Prikl. Khim.*, 2000, vol. 73, no. 5, pp. 780–784.
7. Yegiazarov, Yu.G., Soldatov, V.S., Radkevich, V.Z., *et al.*, *Proc. 16th Mendeleev Congr. on General and Applied Chemistry*, St. Petersburg, 1998, vol. 2, p. 292.
8. Neyaglov, A.A., Digurov, N.G., Bukharkina, T.V., *et al.*, *Kinet. Kataliz*, 1991, vol. 32, no. 3, pp. 548–552.
9. Dyatlova, N.M., Temkina, V.Ya., and Popov, K.I., *Kompleksony i kompleksonaty metallov* (Complexones and Complexonates of Metals), Moscow: Khimiya, 1988.

Russian Journal of Applied Chemistry, Vol. 75, No. 8, 2002, pp. 1234–1236. Translated from Zhurnal Prikladnoi Khimii, Vol. 75, No. 8, 2002, pp. 1260–1262.
Original Russian Text Copyright © 2002 by Medvedev, Makrushin.

APPLIED ELECTROCHEMISTRY AND CORROSION PROTECTION OF METALS

A Study of the Kinetics of Tin Electrodeposition from Sulfate Electrolyte with Organic Additives

G. I. Medvedev and N. A. Makrushin

Novomoskovsk Institute, Mendeleev Russian University of Chemical Technology, Novomoskovsk, Tula oblast, Russia

Received January 15, 2002

Abstract—The method of Faraday impedance was applied to study the kinetics of tin electrodeposition from a sulfate electrolyte in the simultaneous presence of syntanol DS-10, formalin (37% solution), and benzyl alcohol.

Previously, the kinetics of tin electrodeposition from a sulfate electrolyte in the presence of syntanol DS-10 has been studied [1]. Dull tin coatings have been obtained in this electrolyte. It has been shown that the kinetics of tin electrodeposition depends on the electrode potential and is gaverned by a heterogeneous and a homogeneous chemical reactions.

In [2], the electrodeposition of tin from a sulfate electrolyte in the presence of syntanol, formalin (37% solution), and benzyl alcohol was studied. It was shown that that, with these organic substances present simultaneously in an electrolyte subjected to stirring, shining coatings are formed at i_c = 4–12 A dm^{-2}.

It was of interest to study the kinetics of tin electrodeposition in the presence of these organic substances. This was done, as in [1], using the Faraday impedance method. The differential capacitance was measured during electrolysis with an R-5021 ac bridge at frequencies in the range 200 Hz–20 kHz on an electrode made of tin-coated platinum wire (S = 0.126 cm^2), placed at the center of a platinum-black-coated platinum cylinder. Electrochemical measurements were carried out using a P-5878 potentiostat in an electrolyte stirred with a magnetic stirrer.

A tin layer 10 μm thick was deposited onto the surface of the working electrode. The electrode surface was refreshed before making a measurement at each potential. The discrepancy between the results of measurements in different series did not exceed 5%. The potentials are given relative to a standard hydrogen electrode. The differential capacitances in electrolytes with organic additives are given with account of the roughness factor f. The procedure for determining f was described in [3].

The results obtained in measurements of the differential capacitance C at different electrode potentials show that C decreases with increasing frequency and is constant in the range 30–50 kHz. It was assumed on the basis of this fact that the differential capacitance measured at these frequencies is the capacitance of the electrical double layer (EDL).

The measurements were done using a series equivalent circuit. The C_b and R_b values obtained with an ac bridge were recalculated to C_s and R_s values [4]. The equivalence of the circuit was verified using the procedure described in [5]. The electrode impedance components R_s and $1/\omega C_s$ were studied in relation to $\omega^{-1/2}$.

The results obtained in measuring the cathode current density and EDL capacitance as functions of the electrode potential demonstrate that organic additives inhibit tin electrodeposition (Fig. 1, curves *1* and *2*). At potentials in the range –0.3…–0.4 V the EDL

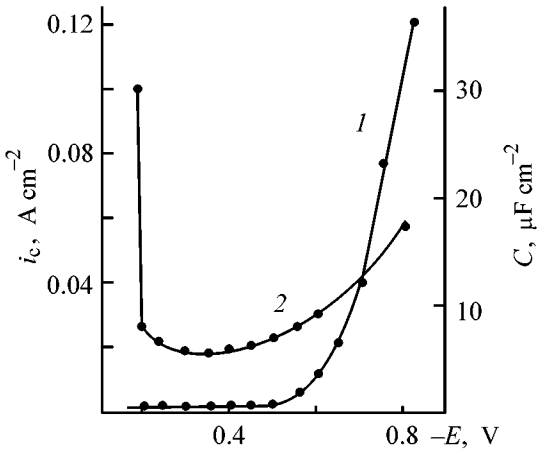

Fig. 1. (*1*) Cathode current density i_c and (*2*) differential capacitance of the electrical double layer, C, at 30 kHz vs. the electrode potential E. Electrolyte composition (g l^{-1}): $SnSO_4$ 30, H_2SO_4 100, syntanol 2; formalin and benzyl alcohol 6 ml l^{-1} each; mechanical stirring.

1070-4272/02/7508-1234 $27.00 © 2002 MAIK "Nauka/Interperiodica"

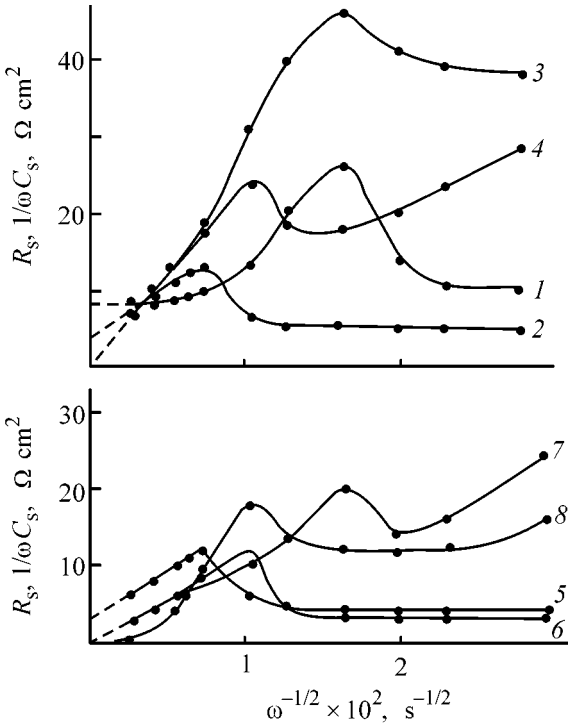

Fig. 2. Electrode impedance components (*1*, *2*; *5*, *6*) R_s and (*3*, *4*; *7*, *8*) $1/\omega C_s$ vs. $\omega^{-1/2}$ at different electrode potentials. Potential (V): (*1*, *4*) –0.3, (*2*, *3*) –0.4, (*5*, *7*) –0.6, and (*6*, *8*) –0.7.

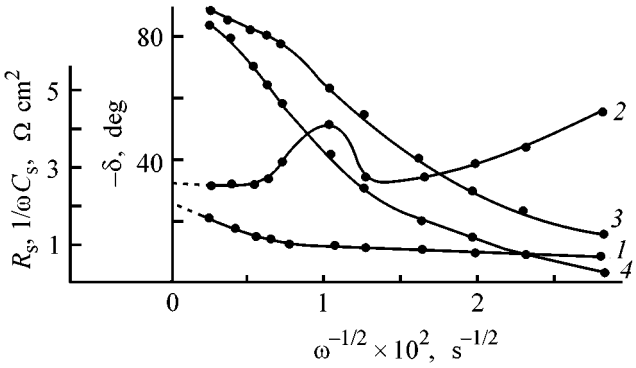

Fig. 3. Electrode impedance components (*1*) R_s and (*2*) $1/\omega C_s$ and (*3*, *4*) phase shift vs. $\omega^{-1/2}$ at different electrode potentials. Potential (V): (*1*, *2*) –0.8; (*3*) –0.3 and –0.6; and (*4*) –0.4, –0.7, and –0.8.

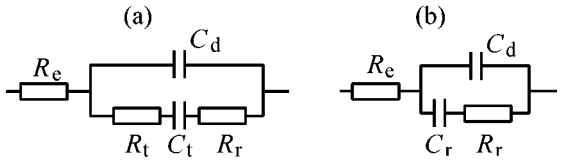

Fig. 4. Equivalent electric circuits of the process of tin deposition from a sulfate electrolyte with organic additives at different potentials. R_e is the electrolyte resistance; C_d, capacitance of the electrical double layer; R_t, the transition resistance; and C_r and R_r, the capacitance and resistance of a heterogeneous chemical reaction. Potential (V): (a) –0.3, –0.4, and –0.8; (b) –0.7 and –0.8.

capacitance is 5.9–6.1 μF cm^{-2}. At $E < -0.54$ V the EDL capacitance and the electrodeposition rate increase. The inhibition of the process in the electrolyte with organic substances is due to their adsorption and formation on the electrode surface of a dense adsorption layer, which starts to disintegrate at $E < -0.4$ owing to desorption of molecules of the organic substances [6]. Dull coatings are obtained at potentials in the range –0.2…–0.6 V, and shining coatings, at –0.7…–0.83 V. With account of these data, the Faraday impedance was measured at potentials of –0.3, –0.4, –0.6, –0.7, and –0.8 V. The dependences of R_s and $1/\omega C_s$ on $\omega^{-1/2}$ are presented in Figs. 2 and 3, curves *1* and *2*, whence it can be seen that R_s at 200 Hz varies within the interval 1–10 Ω cm^2 at all the potentials studied. At –0.3, –0.4, and –0.6 V, R_s grows gradually with increasing frequency and passes through a maximum to reach a constant value after that at a frequency of 20 kHz (Fig. 2, curves *1*, *2*, and *5*). At $E = -0.8$ V, R_s varies in the range 0.9–1.2 Ω cm^2 with frequency increasing in the interval 200–3000 Hz; at higher frequencies R_s increases to 1.6 Ω cm^2 (Fig. 3, curve *1*). Extrapolation of R_s values to higher frequencies yields the ?transition resistance R_t. At E equal to –0.3, –0.4, and –0.6 V, R_t is, respectively, 8.5, 4, and 3 Ω cm^2 (Fig. 2, curves *1*, *2*, and *5*). At a potential of –0.7 V, R_s passes through a maximum with increasing frequency and then tends to zero (Fig. 2, curve *6*). The capacitive components of the impedance, $1/\omega C_s$, much exceed R_s. At a frequency of 200 Hz and potentials equal to –0.3, –0.4, –0.6, and –0.7 V, $1/\omega C_s$ varies in the interval 16–40 Ω cm^2 (Fig. 2, curves *3*, *4*, *7*, and *8*). With increasing frequency, $1/\omega C_s$ decreases, passes through a maximum at a certain frequency, and then tends to zero. The only exception is the potential of –0.8 V at which the $1/\omega C_s$–$\omega^{-1/2}$ dependence shows a decrease from 4.2 to 2.5 Ω cm^2 after the maximum (Fig. 3, curve *2*).

Analysis of the results of impedance measurements suggests that the impedance dependences correspond to equivalent electric circuits with in-series connection of the transition resistance R_t, capacitance C_t and resistance R_r of a heterogeneous chemical reaction at $E = -0.3$, –0.4, and –0.8 V (Fig. 4a); and to in-series connection of the capacitance C_r and resistance R_r of a heterogeneous chemical reaction at $E = -0.7$ and –0.8 V (Fig. 4b).

Thus, it may be concluded that the process kinetics is governed by a transition reaction and a heterogeneous chemical reaction in obtaining dull coatings,

and by a heterogeneous chemical reaction in depositing shining coatings. The transition resistance at $E = -0.3$, -0.4, and -0.6 V is due to the hindered stage of discharge of tin ions. The heterogeneous chemical reaction is of varied nature, depending on the electrode potential.

At the potential of maximum adsorption, $E = -0.3$ and -0.4 V) the heterogeneous chemical reaction is determined by the stage of tin ion penetration to the electrode surface across the adsorption layer. In this case, the process kinetics is governed by the so-called "penetration overvoltage" [7].

At $E = -0.6$ and -0.7 V, when the adsorption layer starts to disintegrate because of the desorption of organic substances from the electrode surface, the heterogeneous reaction is the chemical reaction of tin atoms adsorbed on the electrode surface with organic substances or products of their reduction. The heterogeneous chemical process occurring at $E = -0.8$ V is crystallization, with the transition resistance $R_t = R_{cr}$ (crystallization resistance), $R_{cr} = 2\ \Omega\ cm^2$.

As already noted, at $E = -0.8$ V the capacitive component of the impedance reaches a constant value after passing through a maximum. Extrapolation of $1/\omega C_s$ to higher frequencies yields a value $1/\omega C_{cr}$, where C_{cr} is the crystallization capacitance. According to the data of [5]

$$C_{cr} = z^2F^2C_{ad}/RT,$$

where C_{ad} is the concentration of adatoms on the electrode surface, z is the charge of tin cations, and F is the Faraday number.

The calculations performed demonstrate that $C_{ad} = 2.6 \times 10^{-14}$ mol cm^{-2} for tin. The assumption that heterogeneous reactions occur depending on the electrode potential is also confirmed by measurements of the phase shift δ. The phase shift was calculated in accordance with [5]. With account of the ω_{max} value found from the dependence $1/\omega C_s$–$\omega^{-1/2}$, the reaction rate constant k was determined. For a heterogeneous reaction, $\omega_{max} = k$ and $\tan\delta = -\omega/k$, $\delta \to -90°$. The results of calculations are presented in Fig. 3, curves *3* and *4*. It can be seen that the phase shift does approach –90° at potentials of $-0.3\ldots-0.8$ V.

To conclude, it should be noted that the experimental data on the kinetics of tin electrodeposition from sulfate electrolytes with organic additives, obtained in [1] and in the present study, indicate that, in depositing dull coatings, the rate of the process is determined by a transition reaction and a heterogeneous and homogeneous chemical reactions. At the same time, when shining coatings are deposited, the kinetics of the electrodeposition process is determined by a heterogeneous chemical reaction, which has varied nature depending on the electrode potential.

CONCLUSIONS

(1) A study of the kinetics of tin electrodeposition from a sulfate electrolyte in the presence of syntanol DS-10, formalin (37% solution), and benzyl alcohol by the method of the Faraday impedance established that the kinetics of the process in the range of potentials at which dull tin coatings are formed is determined by a transition reaction and a heterogeneous chemical reaction.

(2) In the range of potentials at which shining coatings are formed, the process rate is determined by a heterogeneous chemical reaction.

(3) It was shown that the part of the transition reaction is played by the hindered reaction of discharge of tin ions, and the heterogeneous reaction has varied nature, depending on the electrode potential. At potentials of -0.3 and -0.4 V, when a dense adsorption layer is formed on the electrode surface, the hindered stage of the process is penetration of tin ions across the adsorption layer.

(4) At more electronegative potentials (E = –0.6, –0.7 V), when the adsorption layer starts to disintegrate as a result of desorption of organic substances from the electrode surface, the role of the heterogeneous reaction is played by the interaction of metal atoms adsorbed on the electrode surface with organic substances or products of their reduction, and at E = –0.8 V, by crystallization.

REFERENCES

1. Medvedev, G.I. and Trubnikova, O.N., *Elektrokhimiya*, 1984, vol. 20, no. 6, pp. 846–849.
2. Medvedev, G.I. and Makrushin, N.A., *Zh. Prikl. Khim.*, 2001, vol. 74, no. 11, pp. 1787–1790.
3. Medvedev, G.I. and Fursova, N.Yu., *Elektrokhimiya*, 2000, vol. 36, no. 6, pp. 899–901.
4. Damaskin, B.B., *Printsipy sovremennykh metodov izucheniya elektrokhimicheskikh reaktsii* (Principles of Modern Techniques for Studying Electrochemical Reactions), Moscow: Mos. Gos. Univ., 1965.
5. Vetter, K.J., *Electrochemische Kinetik*, Berlin: Springer, 1961.
6. Loshkarev, M.A., Sotnikova, V.I., and Kryukova, A.A., *Zh. Fiz. Khim.*, 1997, vol. 21, no. 2, pp. 219–225.
7. Kabanov, B.N., *Elektrokhimiya metallov i adsorbtsiya* (Electrochemistry of Metals and Adsorption), Moscow: Nauka, 1966.

Russian Journal of Applied Chemistry, Vol. 75, No. 8, 2002, pp. 1237–1239. Translated from Zhurnal Prikladnoi Khimii, Vol. 75, No. 8, 2002, pp. 1263–1265.
Original Russian Text Copyright © 2002 by Turygin, Smetanin, Khudenko, Tomilov.

APPLIED ELECTROCHEMISTRY AND CORROSION PROTECTION OF METALS

Electrochemical Synthesis of Arsenic Acid

V. V. Turygin, A. V. Smetanin, A. V. Khudenko, and A. P. Tomilov

State Research Institute of Organic Chemistry and Technology, Moscow, Russia

Received November 26, 2001

Abstract—The possibility of oxidizing arsenic(III) oxide to arsenic acid in quantitative yield in the presence of hydrochloric or hydrobromic acid as a catalyst was studied.

Arsenic acid and arsenic(V) oxide are used to synthesize dyes and pharmaceuticals, to manufacture optical glass, etc. Commonly, arsenic acid is prepared by oxidation of As_2O_3 with nitric acid [1]. A shortcoming of the method is that toxic wastes are formed. Of interest in this connection is the possibility of performing this process electrochemically. As is known, As_2O_3 oxidizes on a rotating platinum electrode in acid medium at a potential of about 1.3 V [2, 3]. The oxidation rate is the highest in a sulfate solution at pH < 1 [4].

A procedure for preparing arsenic acid by oxidation of As_2O_3 suspension on a tin dioxide anode in a 1% sulfuric acid solution containing 1% Na_2SO_4 was described in [5]. However, this technique fails to yield pure, impurity-free arsenic acid.

Much more attention has been given to oxidation of As_2O_3 in an alkaline solution to obtain reagent-grade arsenates, e.g., those of sodium [6] and lithium [7].

The aim of this study was to develop a method for synthesis of pure arsenic acid.

EXPERIMENTAL

We used in the study reagent-grade arsenic(III) oxide containing 99% main substance. Other reagents were of chemically pure grade.

The experiments were performed in a filter-press electrolyzer with platinum or ruthenium oxide anode and a tungsten or titanium plate as a cathode. The anode and cathode spaces were separated by a MF–4SK or Nafion cation-exchange membrane. The anolyte was circulated at a rate sufficient for maintaining As_2O_3 in the form of a suspension with a centrifugal pump. The working area of the anode was 30 cm^2.

In a typical run, 0.5M HCL solution (60 ml) was fed into the cathode chamber of the filter-press electrolyzer equipped with tungsten cathode and ruthenium oxide anode, and 0.5 M HCL solution (70 ml) and 15 g As_2O_3 (0.15 mole As), into the anode chamber. The electrolysis was performed with a current of 6.0 A (current density i = 0.2 A cm^{-2}) for 1.5 h (110% of the theoretically necessary quantity of electricity, Q). In the course of the experiment, the anolyte temperature increased from 20 to 45°C. The catholyte volume increased by 18 ml owing to electrophoresis. H_3AsO_4 was found in the catholyte in amount of 0.0012 mol, i.e., 0.8% of the initial As_2O_3.

The anolyte was evaporated until dry, together with the wash water from the anode chamber, and calcined at 250°C. The resulting dry residue (18.2 g) contained 92.7% As_2O_5. Arsenic acid was obtained by dissolving the residue in water. The yield of the arsenic acid by substance was 97%, and the current efficiency by the acid, 88%.

First, we checked the possibility of oxidizing an aqueous suspension of As_2O_3 on platinum or graphite without addition of any supporting electrolytes. As is known, arsenic(III) oxide is poorly soluble in water and is present in aqueous solutions in the form of a weak arsenous acid, responsible for low electrical conductivity of the solution. The results of these experiments are presented in Table 1.

It can be seen that the voltage across the electrolyzer is high at the beginning of the process and then gradually decreases owing to accumulation of the stronger arsenic acid, which raises the electrical conductivity of the solution. The oxidation is slow, and a nearly sixfold current excess is necessary for oxidizing only half the feed at the Pt anode.

1070-4272/02/7508-1237 $27.00 © 2002 MAIK "Nauka/Interperiodica"

Table 1. Oxidation of aqueous suspension of As_2O_3 in the absence of supporting electrolyte (tungsten cathode; MF–4SK membrane; anolyte 5 g As_2O_3 and 100 ml H_2O; catholyte 0.5 M H_2SO_4 solution)

Anode	Electrolysis conditions			Q,* % of theoretical value	As(V) yield, %	Current efficiency by As(V), %
	i, A cm^{-2}	U, V	T, °C			
Pt	0.33	12.0 → 4.5	22–50	550	40	7
Graphite	0.17	20.0 → 8.0	22–25	140	53	38

* Q is quantity of electricity.

Table 2. Oxidation of aqueous suspension of As_2O_3 in the presence of electrically conducting additives (tungsten cathode; MF–4SK membrane; anolyte 5 g As_2O_3 and 100 ml supporting electrolyte; catholyte 0.5 M H_2SO_4 solution)

Supporting electrolyte, M	Electrolysis conditions			Q, % of theoretical value	As(V) yield, %	Current efficiency by As(V), %
	A cm^{-2}	U, V	T, °C			
H_2SO_4, 1.0	0.07–0.03	3.9–3.2	17–19	450	83	18
H_3AsO_4, 1.0	0.03	4.0–3.7	20–23	300	81	27
HCl, 1.0	0.067	3.7–3.8	23–28	110	~100	90
HBr, 0.5	0.033	3.2	25–28	110	98	88

Table 3. Influence of current density on As_2O_3 oxidation (tungsten cathode, Pt anode; MF–4SK membrane; anolyte feed: As_2O_3 (10 g) and 0.5M HCl solution (100 ml); catholyte 0.5 M HCl solution)

i A cm^{-2}	Electrolysis conditions		Q, % of theoretical value	As(V) yield, %	Current efficiency by As(V), %
	U, V	T, °C			
0.033	3.3–3.5	25–29	120	~100	83
0.067	3.9–4.4	25–30	120	~100	80
0.10	5.1–5.3	20–26	120	~100	85
0.15	6.7–6.8	23–25	120	~100	83
0.20	7.9–8.6	20–27	110	~100	90

In view of the aforesaid, we performed runs with introduction of electrically conducting additives, such as arsenic, sulfuric, hydrochloric, and hydrobromic acids. The results obtained in this series of experiments are presented in Table 2.

It can be seen that As(III) oxidation is slow in solutions of arsenic and sulfuric acid, and much faster in the presence of hydrohalic acids. Probably, the increase in rate of anodic oxidation is due to the fact that free halogens liberated at the anode in this case act as catalysts and transporting agents, namely: free halogen released at the anode

$$2Hal^- - 2e \rightarrow Hal_2,$$

oxidizes As_2O_3 by the reaction

$$As_2O_3 + 2Hal_2 + 5H_2O \rightarrow 2H_3AsO_4 + 4HHal.$$

Since the results obtained for HCl and HBr were about the same, further experiments were done with the cheaper and more readily available hydrochloric acid. Runs were performed with a 0.5 M HCl solution at different current densities. The results obtained demonstrated that the oxidation is fast and can be performed at current densities of up to 0.2 A cm^{-2} (Table 3). It is appropriate, however, for economical reasons, to perform oxidation at current densities not exceeding 0.1 A cm^{-2}, since at higher densities the electrolyzer voltage increases essentially.

The control runs showed that the efficiency of arsenic(III) oxidation is about the same for ruthenium oxide and platinum anodes. Therefore, further experiments on the influence exerted by the hydrochloric acid concentration were performed with a ruthenium oxide anode (Table 4). It was found that raising the hydrochloric acid concentration to 4.0 M has virtually

Table 4. Influence of HCl concentration on As_2O_3 oxidation (Ag cathode, ruthenium oxide anode; Nafion membrane; 10 g As_2O_3; current density 0.1 A cm^{-2})

c_{HCl}, M	Electrolysis conditions		Q, % of theoretical value	H_3AsO_4 yield, %	Current efficiency by H_3AsO_4 %	As transfer into catholyte %	Current efficiency by O_2 %
	U, V	T, °C					
0.5	5.3–5.6	22–23	110	94	85	2.2	9.6
1.0	5.0–5.2	22–27	102	98	96	1.7	3.4
2.0	4.5	23–27	102	98	98	1.4	1.5
3.0	4.3	24–26	102	93	91	1.0	0.7
4.0	4.0–4.3	23–27	102	99	97	0.7	0.8

no effect on the oxidation, but diminishes somewhat the loss of arsenic for its migration into the cathode space. However, it is inappropriate, for technological reasons, to make the concentration of hydrochloric acid in the anolyte higher than 1.0 M.

Finally, we studied the possibility of preparing a concentrated solution of arsenic acid in a single run. For this purpose, we carried out an experiment in which fresh portions of arsenic(III) oxide were fed into the anodic space at regular intervals. The test was performed at a current density of 0.2 A cm^{-2} in a 0.5 M HCl solution, to which As_2O_3 (50 g) was gradually added. As a result, a 5.0 M H_3AsO_4 solution was obtained in 96% yield at a current efficiency of 81%. The loss of arsenic for its migration into the cathode space was 3.7%.

CONCLUSIONS

(1) The study yielded a simple and efficient method for oxidation of arsenic(III) oxide to arsenic acid. The advantage of this technique is the feasibility of preparing sufficiently pure arsenic acid in a single stage.

(2) Hydrogen chloride present in the anolyte is completely removed upon solution evaporation. The HCl-containing distillate is used for preparing a fresh portion of the anolyte. This opens up the possibility of organizing a nearly waste-free production.

REFERENCES

1. Remy, H., *Lehrbuch der anorganischen Chemie*, Leipzig: Geest und Portig, 1960.
2. Zakharov, V.A., and Songina, O.A., *Zh. Fiz. Khim.*, 1964, vol. 38, no. 4, pp. 767–770.
3. Alimarin, L.P., and Terin, S.I., *Zavod. Lab.*, 1954, vol. 20, no. 18, pp. 18–24.
4. JPN Patent Application 9174.
5. USSR Inventor's Certificate, no. 223068.
6. Shul'gin, L.P., and Kuz'min, Yu.A., *Tsvetn. Met.*, 1971, no. 4, pp. 36–39.
7. USSR Inventor's Certificate, no. 542772.

Russian Journal of Applied Chemistry, Vol. 75, No. 8, 2002, pp. 1240–1247. Translated from Zhurnal Prikladnoi Khimii, Vol. 75, No. 8, 2002, pp. 1266–1273.
Original Russian Text Copyright © 2002 by Sokolov, V. Naraev, Murin, Pronkin, A. Naraev.

APPLIED ELECTROCHEMISTRY AND CORROSION PROTECTION OF METALS

Electrochemical Study of Glasses in the System Na_2O–B_2O_3

I. A. Sokolov, V. N. Naraev, I. V. Murin, A. A. Pronkin, and A. V. Naraev

St. Petersburg State Technical University, St. Petersburg, Russia
St. Petersburg State Technological Institute, St. Petersburg, Russia
St. Petersburg State University, St. Petersburg, Russia

Received October 18, 2001; in final form, May 2002

Abstract—The steady-state electrical conductivity and microhardness of glasses in the system Na_2O–B_2O_3 was studied. IR spectroscopy was applied to determine the content of impurity hydrogen in the glasses studied.

Inorganic materials find wide application in various fields of science and technology: as highly conducting ("superionic") solid electrolytes in chemical power cells, in fabrication of electrochemical energy storage units (ionistors), in highly sensitive ion-selective chemical sensors, etc. [1–5].

It has been noted in the literature that the electrical conductivity of glassy solid electrolytes exceeds the conductivity of crystalline solids of the same composition by 1–2 orders of magnitude, with the following postulated: the electrical conductivity of both crystalline and glassy solid electrolytes is due to migration of ions of the same sign. Owing to their high chemical stability, simplicity of fabrication of articles of varied complexity by the conventional glass technology, low sensitivity to impurities, and high ionic conductivity, solid electrolytes attract researchers' attention and more and more frequently find use in various electrochemical devices.

It should be noted that publications concerned with rigorous determination of the nature of charge carriers and mechanisms of their migration in various classes of inorganic solid glasses are scarce in both the domestic and the foreign literature. There is no unified standpoint in the literature, concerning the nature of effects associated with migration of charged particles even in the best-studied borate and silicate glasses. According to common theoretical concepts, anions, cations, electrons, or various combinations of these may be electric current carriers in a solid. At present, there are, presumably, no published results of systematic investigations of migration processes in glasses, which are characterized by a change of the type and nature of a charge carrier.

With account of the aforesaid, we studied the concentration dependence of the electrical conductivity and determined the nature of charge carriers and the dependence of their transport numbers on the composition of glasses in the system Na_2O–B_2O_3.

EXPERIMENTAL

The glasses were synthesized in crucibles made of SU-2000 glassy carbon in a laboratory electric furnace in an atmosphere of argon. As starting reagents were used boric acid and sodium carbonate of analytically pure grade. Boric acid was preliminarily dehydrated at about 450°C to constant weight by a procedure described in [6]. However, it should be noted that removal of chemically bound hydrogen, which can be present in the glass structure in various forms, e.g., $>B–O^{\delta-}\cdots H^{\delta+}$, $\geq B–O^{-}H^{+}$, etc., is difficult, and, therefore, only crystallization water can be removed by calcination at 450°C.

The stock was poured in preheated crucibles at the synthesis temperature. Molten glass was cast into preheated metallic molds and then the billets were placed in a muffle furnace for annealing and kept there for about 60 min at a temperature lower than T_g by 10–15°. Then the samples were allowed to cool together with the muffle furnace to room temperature. The quality of annealing was checked by the polarization-optical method on a PKS-500 polariscope. The billets obtained were used to fabricate samples for further investigation. Selective chemical analysis demonstrated that the content of boron and sodium in the glasses corresponded to the calculated values to within ±1%. The analytical procedure was described in [7].

1070-4272/02/7508-1240 $27.00 © 2002 MAIK "Nauka/Interperiodica"

The electrical conductivity and density were measured on disc-shaped samples 20 mm in diameter and 1.5 mm thick. The samples were plane-parallel to within 0.01 mm. The surface and roughness of the samples corresponded to class 8 according to GOST (State Standard) 2789–79. The surface of the samples for transport number and microhardness measurements was polished. The quality of surface processing corresponded in this case to class 14, and the surface finish to R1-10, with the total error not exceeding two interference rings. The high quality of surface processing enabled optical contact and gave rise to intermolecular interaction forces over the entire surface of contacting samples and thereby ensured unhindered passage of migrating ions across the interface in the course of electrolysis.

We measured in the present study the steady-state dc electrical conductivity with the use of active electrodes. The voltage applied to the samples corresponded to an electric field strength not exceeding 10 kV cm^{-1}, which ensured that the Ohm law was observed. According to [8], glasses in the system $Na_2O–B_2O_3$ show electrolytic conduction, and, therefore, use of active electrodes (sodium amalgam) in dc electrical conductivity measurements prevents electrochemical polarization. An ED-05M dc electrodynamic amplifier was used as measuring instrument. The voltage was supplied from a PI-50-1.1 potentiostat. The measurements were done in heating and cooling modes, with no hysteresis detected. A linear dependence, $\log\sigma = f(1/T)$, where σ is the electrical conductivity, was observed in the range from room temperature to 350°C. The measurement error was about 7%. The activation energy of electrical conductivity, E_σ, was calculated using the equation $\sigma = \sigma_0\exp(E_\sigma/2kT)$.

The density of the glasses was determined by hydrostatic weighing both with samples from the same melting [with the results reproduced to within $(1–5)\times10^{-3}$ g cm^{-3}] and with samples from parallel meltings (reproducibility $\pm1\times10^{-2}$ g cm^{-3}).

The microhardness was measured on PMT-3 and PMT-5 instruments by impressing a diamond pyramid with square base (angle formed by pyramid faces 136° ± 30') into a polished glass surface (Vickers method).

The nature of charge carriers and their transport numbers were determined using the Hittorf method, for which purpose a complete chemical analysis of near-electrode and middle glass samples was made before and after electrolysis. An experiment was considered correct if the composition of the middle glass sample remained unchanged during electrolysis. The nature of species involved in charge transport was determined from changes in the composition of glasses subjected to electrolysis. Tubandt proposed that changes in glass composition are to be judged from a change in their mass as a result of electrolysis, instead of using a complicated chemical analysis. The Tubandt technique is only correct if the nature of charge carriers is established experimentally. The electrolytic nature of conduction in the glasses studied was evaluated by the observance of the Faraday law, by comparing the amount of sodium deposited at the cathode with the amount that should have been deposited in accordance with the Faraday law. A coincidence of the amount of sodium deposited at the cathode as a result of electrolysis with the theoretical value was regarded as evidence in favor of a unipolar conduction associated with migration of sodium cations, and discrepancy of these values, as an indication that some other positively charged species or electrons are involved in transport processes.

The quantity of electricity passed in the course of electrolysis through samples of the glasses under study was measured with in-series connected silver-thallium coulometer and Kh-603 electric-current integrator.

The samples were weighed on VLAO-100/1 semimicroanalytical balance with accuracy of $\pm5\times10^{-5}$ g.

In addition to verifying the observance of the Faraday law, the electronic component of conductivity was evaluated with the use of the Liang–Wagner polarization method [9–11]. This technique also enables evaluation of the contribution of the electronic component to the total electrical conductivity. The electronic component of conductivity is found from current–voltage characteristics of the electrochemical cell M | solid electrolyte | E in which one of the electrodes is reversible (M) and the other is ideally polarizable (E); the solid electrolyte is, in our case, a sample of a glass under study. The cell is polarized in such a way that no Faraday processes occur at the inert electrode. Then the cell is blocked with respect to the ionic current and the current passing through the cell is due to migration of electrons or holes in the solid electrolyte. In the general case, the current strength is given by the equation

$$I = I_n + I_p = \frac{RT}{lF}\left\{\sigma_n^0\left[1-\exp\left(-\frac{EF}{RT}\right)\right] + \sigma_p^0\left[\exp\left(-\frac{EF}{RT}\right)-1\right]\right\},$$

where σ_n^0 and σ_p^0 are, respectively, the electron or hole conductivity of the solid electrolyte, E is applied voltage, and l is the sample thickness.

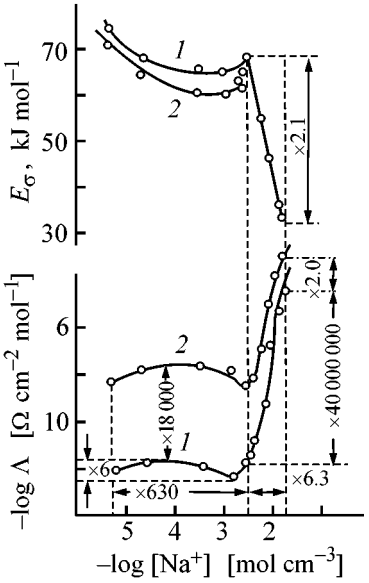

Fig. 1. Dependences of the equivalent electrical conductivity $\Lambda = \sigma/C$ and activation energy E_σ on the concentration of sodium ions in glass, plotted in the $\log \Lambda = f(\log [Na^+])$ and $E_\sigma = \varphi(\log [Na^+])$ coordinates. Temperature (°C): (*1*) 200 and (*2*) 300 [24].

Analysis of this equation shows that, in the case of $\sigma_n^0 > \sigma_p^0$, the current–voltage characteristic levels off at

$$I = I_n = \frac{RT}{lF}\sigma_n^0.$$

At $\sigma_n^0 < \sigma_p^0$, an exponential dependence of the current density on applied voltage is observed:

$$I = I_p = \frac{RT}{lF}\sigma_p^0\left[\exp\left(-\frac{EF}{RT}\right) - 1\right]\Bigg\}.$$

The applied voltage should be lower than the decomposition potential of the solid electrolyte. Analysis of the experimental dependence of the current strength on voltage allows evaluation of the sign and concentration of charge carriers (electrons or holes) in the solid electrolyte. For example, at a temperature of about 320°C the electronic component of the electrical conductivity of glassy borax ($33.3Na_2O \cdot 66.7B_2O_3$, mol %) does not exceed $(1–3) \times 10^{-10}$ Ω^{-1} cm^{-1}, which constitutes less than 10^{-3}% of the total electrical conductivity.

As is known, structurally bound hydrogen is always present in the glass bulk as an impurity. The position of hydrogen ("water") in the glass structure was considered in [12]. The content of structurally bound hydrogen in glass samples of the system Na_2O–B_2O_3 was determined by IR spectroscopy from the absorption band of OH groups at 2.8–2.9 μm by the procedure described in [13, 14]. The absorption spectra were measured with a Specord IR-75 instrument on plane-parallel polished samples about 1.5 mm thick. The extinction coefficients reported in these papers were used in our calculations.

The structure of boron oxide in glassy state and glasses on its base has been studied in detail [15, 16]. Despite certain discrepancies in minute details, most of the authors regard the structure of glassy B_2O_3 as a continuous three-dimensional skeleton composed of tetra- and tricoordinated boron [17–19]. Tetracoordinated boron forms polar $[BO_{4/2}]^-$, and tricoordinated boron, nonpolar $[BO_{3/2}]$ structural-chemical units. Hydrogen is always present as impurity in glassy boron oxide and glasses on its base. It was shown in [20, 21] that crystal hydrate water contained in crystalline borax can be removed by heating. However, hydrogen incorporated into the glass structure in the form

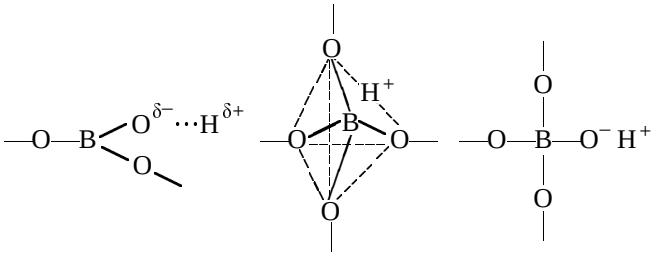

and similar fragments is retained in the melt and cannot be removed by heating. The firmness of hydrogen fixation in structural-chemical fragments of this kind varies, and hydrogen itself strongly affects the coordination of boron.

In [22], a review of studies concerned with the electrical conductivity and other physicochemical properties of alkali-rich oxide glasses was presented. Also considered were experimental data on their electrolysis. Warburg was, presumably, the first to prove that the amount of sodium transferred during electrolysis from anode to cathode through a glass with high content of M_2O obeys the Faraday law with high precision. These data served as a basis for the conclusion that alkaline oxide glasses are electrolytes with unipolar alkali conduction, irrespective of the M_2O concentration, and their electrical conductivity is determined by the concentration of alkali metal ions.

It was shown in [23] that introduction of an alkali oxide into boron oxide is accompanied by a change in the coordination number of boron from 3 to 4, with the number of bridging oxygen atoms also increasing:

$$BO_{3/2} + Na_2O + BO_{3/2} \rightarrow 2[BO_{4/2}]^-Na^+.$$

The stability of the structure increases because of the incorporation into the newly formed borate tetra-

hedron of one more bridging atom of oxygen. Thus, the structural-chemical network of glasses belonging to the system $Na_2O–B_2O_3$ is mainly composed of polar $Na^+[BO_{4/2}]^-$ and nonpolar $[BO_{3/2}]$ structural-chemical units. It is the ratio of these concentrations and also the concentration of polar structural-chemical units that determine the physicochemical properties of glasses in this system.

In [23, 24], it was demonstrated that the concentration dependences of the electrical conductivity of alkali oxide glasses are similar. Figure 1 presents the results obtained in studying the concentration dependence of the electrical conductivity of glasses belonging to the system $Na_2O–B_2O_3$, according to [24].

It is commonly accepted that charge is carried by alkali metal ions in the entire range of sodium oxide concentrations. As seen from the experimental data presented in Fig. 1, with the sodium ion concentration increasing from 0 to 8×10^{-3} mol cm^{-3} ($\log [Na^+] = -2.09$, the molar electrical conductivity remains virtually unchanged. With the concentration of Na^+ ions increasing further (from 8×10^{-3} to 24×10^{-3} mol cm^{-3}; $-1.62 \geq \log[Na^+] \geq -2.09$), the molar electrical conductivity grows exponentially (by more than 7 orders of magnitude). In Muller's opinion [23, 24], such an increase in conductivity is due to the E_σ value. It can be seen from Fig. 1 that there are two clearly delimited portions in the $E_\sigma = f(\log Na^+])$ dependence: at low concentrations of alkali ions E_σ is relatively high, whereas at $[Na^+] > 8 \times 10^{-3}$ its value decreases dramatically. Such a behavior of the $E_\sigma = f(\log Na^+])$ dependence can be accounted for as follows. In the first region, the electrical conductivity is limited by the fact that alkali ions formed in dissociation of polar structural-chemical units have to migrate in the medium of nonpolar chemical-structural units. In the second region, sodium ions migrate in the medium of polar structural-chemical units $Na^+[BO_{4/2}]^-$. This circumstance enabled Muller to suggest that the dissociation energy of alkali ions exceeds the energy of activated displacement: $E_{dis} > E_a$, whence follows that $E_\sigma \sim E_{dis}$. Figure 2 shows schematically the relationship between these quantities.

To characterize the critical concentration of polar chemical-structural units, at which occurs their merging and, consequently, migration of dissociated sodium ions passes from the nonpolar medium ($[BO_{3/2}]$ chemical-structural units) to the polar medium ($Na^+[BO_{4/2}]^-$ structural-chemical units), Muller introduced the function γ equal to the concentration ratio of nonpolar and polar structural-chemical units:

$$\gamma = \frac{[\text{Nonpolar structural-chemical units}]}{[\text{Polar structural-chemical units}]}.$$

At concentration of sodium ions, equal to, or exceeding 8×10^{-3} mol cm^{-3}, the blocking of polar structural units by nonpolar units is disrupted and migration of alkali ions, which are charge carriers, occurs in the medium of polar structural-chemical units, with the degree of blocking $\gamma \leq 6$.

The experimental results obtained in studying the dependence of the electrical conductivity of glasses in the system $Na_2O–B_2O_3$ on temperature and concentration, presented in Fig. 3 and Table 1, are in satisfactory agreement with published data [15]. The differences in the activation energies of electrical con-

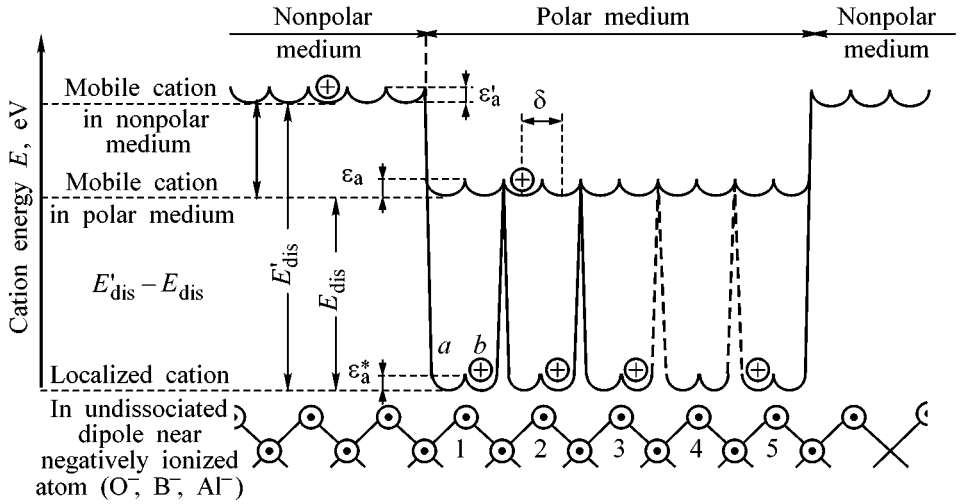

Fig. 2. Dissociation energy of polar structural units: E_{dis}, for cation passing into interstitial positions in polar medium; E'_{dis}, for cation passing into interstitial positions in nonpolar medium. Activation energy in unit displacements of cations: ε'_a, in interstitial positions of nonpolar medium; ε_a, in interstitial positions of polar medium; ε^*_a, via vacancies [31].

Table 1. Volume concentration of alkali ions and electrical properties of glasses in the system $Na_2O–B_2O_3$

Na_2O content, mol %	Density d, g cm^{-3}	$[Na^+] \times 10^3$, mol cm^{-3}	$-\log \sigma$ [Ω^{-1} cm^{-1}]		$-\log \sigma_0$ [Ω^{-1} cm^{-1}]	E_σ, eV
			200°C	300°C		
2.0	1.92	1.10	14.5	10.9	6.15	3.88
3.0	1.92	1.66	14.0	10.55	5.8	3.72
5.0	1.97	2.85	13.6	10.7	3.05	3.13
8.0	2.02	4.65	12.75	10.15	0.2	2.81
10.0	2.06	5.98	11.9	9.8	2.2	2.27
12.5	2.10	7.65	10.95	9.0	0.25	2.10
15.0	2.13	9.60	10.2	8.35	0.4	1.99
20.0	2.21	13.20	8.35	6.65	1.4	1.83
25.0	2.29	16.90	7.3	5.75	1.6	1.67
30.0	2.35	20.80	6.5	5.05	1.8	1.56
33.3	2.37	23.61	6.3	5.0	1.3	1.43
35.0*	2.38	24.80	5.75	4.65	0.8	1.24

* According to chemical analysis data, the content of Na_2O in the glass is 34.2 mol % (31.5 mol %).

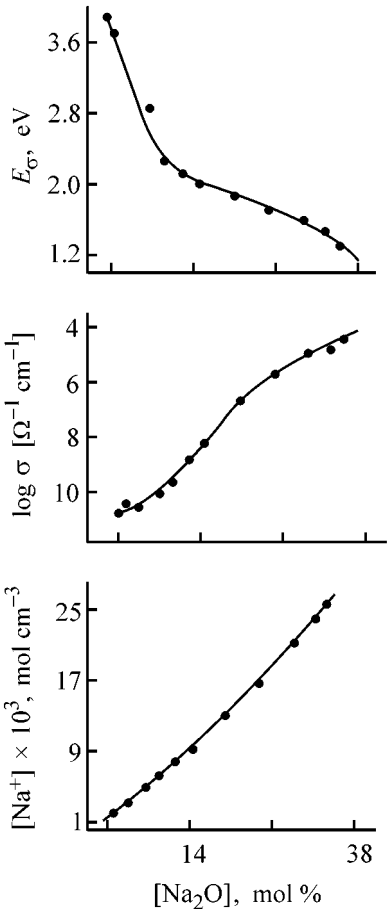

Fig. 3. Activation energy E_σ of electrical conductivity, electrical conductivity σ at 300°C, and volume concentration $[Na^+]$ of sodium ions in glasses of the system $Na_2O–B_2O_3$ vs. the content of sodium oxide, $[Na_2O]$.

ductivity and the conductivity itself at low concentration of Na^+ ions are due to differences in synthesis conditions (compare Figs. 1 and 3).

As already mentioned, the structure and physicochemical properties of borate glasses have been studied in detail. However, studies concerned with the nature of charge carriers are virtually lacking. Conclusions about the type of charge carriers in alkali-free borate glasses were made on the basis of circumstantial evidence [25], and those concerning alkali-borate glasses, on the basis of results obtained in studying electrolysis of alkali-rich glasses [22]. Based on the results of electrolysis, Ostroumov postulated that charge carriers in sodium borax glasses are sodium ions [8]. Using Tubandt's technique he demonstrated that the true sodium ion transport numbers are close to unity ($\eta_{Na^+} \to 1$).

Some researchers believe, on the basis of circumstantial evidence, that charge carriers in alkali-free glasses are either impurity alkali ions or ions of alkaline-earth metals, or electrons [26–28]. In some publications, attention is drawn to the effect of impurity water on the physicochemical properties of glasses. In [25], it was, presumably for the first time, confirmed experimentally that charge carriers in alkali-free, including borate glasses are ions (mainly protons) formed in dissociation of structural-chemical fragments including impurity hydrogen. Therefore, it would be expected that introduction of alkali metal oxides into glassy B_2O_3 is accompanied by a change from protonic conduction to that associated with migration of alkali ions.

Table 2. True transport numbers of sodium ions, η_{Na^+}, in glasses of the system $Na_2O–B_2O_3$

Na_2O content, mol %	η_{Na^+}
15.0	0.96 ± 0.03
20.0	1.00 ± 0.03
25.0	1.00 ± 0.02
33.3	1.01 ± 0.03
33.3	1.00 ± 0.02 [8]
35.0	1.03 ± 0.05

Table 4. Effect of thermal treatment on microhardness of glassy boron oxide and borax

Time of oxygen bubbling, h	Microhardness $H_\mu \times 10^{-2}$, MPa
Glassy B_2O_3 synthesized at 1400°C	
–	14.3 ± 0.9
2	18.1 ± 0.8
6	22.0 ± 1.2
12	29.0 ± 1.4
Glassy $Na_2B_4O_7$ synthesized at 1270°C	
–	36.30 ± 1.7
2	38.2 ± 2.0
4	45.0 ± 2.1

Table 3. Content of structurally bound water in glasses of the system $Na_2O–B_2O_3$

Na_2O content, mol %	H_2O content	
	wt %	mol %
2.0	0.44	1.70
3.0	0.39	1.52
8.0	0.30	1.13
12.5	0.26	0.97
15.0	0.23	0.85
20.0	0.21	0.77
25.0	0.22	0.80
30.0	0.18	0.67
33.3	0.19	0.70
35.0	0.19	0.70

Table 5. Microhardness of glasses in the system $Na_2O–B_2O_3$

B_2O_3 content mol %	Microhardness $H_\mu \times 10^{-2}$, MPa	B_2O_3 content mol %	Microhardness $H_\mu \times 10^{-2}$, MPa
100	19.2	85	37.4
98	20.1	80	44.4
95	20.6	75	45.9
92	24.3	66.5	45.1
87.5	31.0		

Table 2 lists the results obtained in a study of the nature of charge carriers and their transport numbers in glasses of the system $Na_2O–B_2O_3$. It can be seen that unipolar sodium conduction is achieved in glasses of this system at $[Na_2O] > 15$ mol % ($\eta_{Na^+} = 1.01 \pm 0.02$), in good agreement with the data of [8], with, however, a discrepancy going beyond the experimental error observed for the glass $0.15Na_2O–0.85B_2O_3$.

The content of impurity hydrogen incorporated into the structure of glasses belonging to the system $Na_2O–B_2O_3$ is given in Table 3. As seen from these data, 1.5–1.7 mol % H_2O is contained in the structure of glasses in the region with low sodium oxide content. With the concentration of sodium oxide increasing to approximately 12 mol % and more, the content of "water" stabilizes at the level of 0.7–0.9 mol % H_2O. The volume concentration of hydrogen is, in this case, about 4.4×10^{-3} mol cm^{-3}, with the degree of blocking of hydrogen-containing structural fragments $\gamma \approx 9$. Therefore, it would be expected that impurity hydrogen exerts strong influence on the physicochemical properties of borate glasses. The hydrogen incorporated into the structure of glasses affects the coordination of boron, as also metal cations do, and is in thermodynamic equilibrium with atmospheric moisture:

$$H^+[BO_{4/2}]^- \rightleftarrows [BO_{3/2}] + H_2O.$$

As already mentioned, it is impossible to remove thermally the hydrogen incorporated into the glass structure. However, thermal treatment combined with, e.g., bubbling of dried oxygen through the melt, leads to changes in the physicochemical properties of glasses. Table 4 presents the results of microhardness measurements for glassy B_2O_3 and $Na_2B_4O_7$. The microhardness was measured on a fire-polished surface. It can be seen that the microhardness of the glasses grows with increasing time of oxygen bubbling (at T = const). The most probable reason for the rise in microhardness is that the position of hydrogen changes as a result of a change in boron coordination, $B^{III} \rightarrow B^{IV}$, by the scheme

$$>B–O^{\delta-}\cdots H^{\delta+} + 1/2\,O_2 \rightarrow H^+[BO_{4/2}]^-.$$

This assumption is supported by the results obtained in studying the concentration dependence of the microhardness of glasses in the system $Na_2O–B_2O_3$ (Table 5).

Hydrogen forms in the structure of glassy boron oxide, together with other structural-chemical units, also polar fragments of the type $H^+[BO_{4/2}]^-$. Therefore, it would be expected that introduction of alkali oxides into B_2O_3 is accompanied by reactions of the type

$$2H^+[BO_{4/2}]^- + Na_2O \rightleftarrows 2Na^+[BO_{4/2}]^- + H_2O\uparrow.$$

This assumption is supported by the data in Table 3. Indeed, the content of hydrogen decreases with increasing content of alkali ions (to ~10 mol %) and then levels off at 0.7–0.9 mol %.

Comparison of the concentration dependence of sodium ion transport numbers with the content of impurity hydrogen indicates that unipolar alkali conduction is achieved in Na_2O–B_2O_3 glasses at Na_2O content in the glasses of 17–20 mol %, with the content of impurity water equal to 0.8–0.9 mol %. At sodium oxide content lower than 17 mol %, protons are involved in charge transport together with sodium cations.

CONCLUSIONS

(1) A study of the nature of charge carriers in glasses of the system Na_2O–B_2O_3 revealed that protons are involved in charge transport together with sodium ions, at low content of sodium oxide.

(2) It was shown that the contribution of the electronic component to the total conductivity is at the level of sensitivity of the Liang–Wagner method and does not exceed 10^{-3}%.

(3) A study of true transport numbers of sodium ions, η_{Na^+}, demonstrated that unipolar alkali conduction is observed in glasses of this system only at $[Na_2O] > 17$ mol %. At $0 \le [Na_2O] \le 17$ mol %, protons are involved in charge transport together with Na^+ ions.

(4) The dependence of the electrical conductivity on temperature and concentration was interpreted in terms of a microheterogeneous glass structure.

REFERENCES

1. *Proc. 9th Int. Conf. on Solid State Ionics, J. Solid State Ionics*, 1994, vols. 70–71, part 1, pp. 3–696.
2. *Proc. 10th Int. Conf. on Solid State Ionics, J. Solid State Ionics*, 1996, vols. 86–88, pp. 1–689.
3. *Proc. 11th Int. Conf. on Solid State Ionics, J. Solid State Ionics*, 1998, vols. 113–115, pp. 1–747.
4. *Proc. 12th Int. Conf. on Solid State Ionics*, Thessaloniki, Greece, June 6–12, 1999, Abstr., pp. 3–846.
5. *Vserossiiskaya konferentsiya s mezhdunarodnym uchastiem "Sensor 2000" Sankt-Peterburg, 21–23 iyunya 2000 g.* (All-Russian Conf. with Int. Participants "Sensor-2000," St. Petersburg, June 21–23, 2000), St. Petersburg, 2000, pp. 9–303.
6. Sokolov, I.A., Naraev, V.N., Nosakin, A.A., and Pronkin, A.A., *Fiz. Khim. Stekla*, 2000, vol. 26, no. 4, pp. 548–557.
7. Hillebrand, W.F. and Lundell, G.E.F., *Applied Inorganic Analysis with Special Reference to the Analysis of Metals, Minerals and Rocks*, Lundel, G.E.F., Bright, H.A., and Hoffman, J.I., Eds., New York: Wiley, 1963, second ed.
8. Ostroumov, G., *Zh. Obshch. Khim.*, 1949, vol. 19, no. 3, pp. 407–411.
9. Wagner, C., *Proc. 7th meeting of the I.C.E.T.K.*, London: Butterworth, 1957, pp. 361–389.
10. Liang, C.C., *J. Electrochem. Soc.*, 1973, vol. 120, no. 10, pp. 1289–1292.
11. Pronkin, A.A., Naraev, V.N., Murin, I.V., and Sokolov, I.A., *Fiz. Khim. Stekla*, 2000, vol. 26, no. 3, pp. 385–392.
12. Scholze, H., *Glass Industry*, 1959, vol. 40, no. 6, pp. 301–303, 338–341.
13. Franz, H. and Scholze, H., *Glasstechn. Ber.*, 1963, vol. 36, no. 9, pp. 347–356.
14. Kanchieva, O.N., Komarova, N.V., Nemilov, S.V., and Tagantsev, D.K., *Fiz. Khim. Stekla*, 1980, vol. 6, no. 4, pp. 408–414.
15. Mazurin, O.V., Strel'tsina, M., and Shvaiko-Shvaikovskaya, T.P., *Svoistva stekol i stekloobrazuyushchikh rasplavov* (Properties of Glasses and Glass-forming Melts), vol. 1, *Odnokomponentnye i dvukhkomponentnye okisnye nesilikatnye sistemy* (Single- and Two-component Nonsilicate Systems), Leningrad: Nauka, 1975.
16. Mazurin, O.V., Strel'tsina, M.V., and Shvaiko-Shvaikovskaya, T.P., *Svoistva stekol i stekloobrazuyushchikh rasplavov* (Properties of Glasses and Glass-forming Melts), vol. 3, part 1, *Trekhkomponentnye silikatnye sistemy* (Three-component Silicate Systems), Leningrad: Nauka, 1977.
17. Strong, S.L. and Karpo, W.R., *Acta Cryst.*, 1968, vol. 24B, part 8, pp. 1032–1036.
18. Silver, A.M. and Bray, P.J., *J. Chem. Phys.*, 1958, vol. 29, no. 5, pp. 954–990.
19. Krogh-Moe, I., *Phys. Chem. Glasses*, 1965, vol. 6, pp. 46–54.
20. Franz, H., *J. Am. Ceram. Soc.*, 1966, vol. 49, no. 9, pp. 1–8.
21. Fedulov, S.A., Bychkov, V.Z., and Klyueva, G.R., *Izv. Akad. Nauk SSSR, Neorg. Mat.*, 1983, vol. 19, no. 3, pp. 493–495.
22. Eitel, W., *The Physical Chemistry of Silicates*, Chicago: Chicago Univ., 1954.

23. Myuller, R.L., *Elektroprovodnost' stekloobraznykh veshchestv: Sbornik trudov* (Electrical Conductivity of Glassy Substances: Coll. of Sci. Works), Leningrad: Len. Gos. Univ., 1968.
24. Shukarev, S.A. and Myuller, R.L., *Zh.Fiz. Khim.*, 1930, vol. 1, no. 6, pp. 625–661.
25. Sokolov, I.A., Murin, I.V., Naraev, V.H., and Pronkin, A.A., *Fiz. Khim. Stekla*, 1999, vol. 25, no. 5, pp. 593–613.
26. Evstrop'ev, K.K., *Diffuzionnye protsessy v stekle* (Diffusion Processes in Glass), Leningrad: Stroiizdat, 1970.
27. Pavlova, G.A., *Izv. Vyssh. Uchebn. Zaved., Khim. Khim. Tekhnol.*, 1958, no. 5, pp. 82–89.
28. Deshkovskaya, A.A., A Study of the Mechanism of Electrical Conduction in Some Alkali-free Glasses, *Cand. Sci. Dissertation*, Minsk, 1969.
29. Namikawa, H. and Asahara, Y., *J. Ceram. Assoc.*, Japan, 1966, vol. 74, no. 6, pp. 205–212.
30. Milness, G.S. and Isard, J.O., *Phys. Chem. Glasses*, 1962, vol. 3, no. 5, pp. 157–163.
31. Myuller, R.L., *Zh. Vses. Khim. O–va im. D.I. Mendeleeva*, 1963, vol. 8, no. 2, pp. 197–205.

Russian Journal of Applied Chemistry, Vol. 75, No. 8, 2002, pp. 1248–1251. Translated from Zhurnal Prikladnoi Khimii, Vol. 75, No. 8, 2002, pp. 1274–1277.
Original Russian Text Copyright © 2002 by Pisanenko, Pogrebova.

APPLIED ELECTROCHEMISTRY AND CORROSION PROTECTION OF METALS

Synthesis and Corrosion-Protecting Power of Quaternary Ammonium Salts Based on 2-Acetylallyl Chloride

D. A. Pisanenko and I. S. Pogrebova

Kiev Polytechnic Institute, Ukrainian National Technical University, Kiev, Ukraine

Received July 18, 2001; in final form, March 2002

Abstract—Quaternary ammonium salts were synthesized at a 62.5–98% yield by quaternization with 2-acetylallyl chloride of pyridine and its α-methyl and γ-benzoyl derivatives; tributyl-, triethanol-, and dimethylbenzylamines; *N*-methylpiperidine; quinoline; *N,N*-dimethylaniline and its *p*-bromo and *p*-methyl derivatives. The inhibiting activity of these salts against corrosion of 08 KP steel and TsO zinc in sulfuric acid solution was studied.

It is well known that a number of industrial inhibitors of acid corrosion of metals are based on aromatic amine salts, whose protective action is due both to the positive charge on the nitrogen atom and to the π-electron interaction of the aromatic system with a metal [1]. The inhibiting activity is also demonstrated by some carbonyl compounds and ammonium salts with alkenyl radicals [2, 3], whose adsorption on the metal surface involves electrons of the oxygen atom and multiple bonds. It would be expected that simultaneous presence of all the indicated adsorption centers in an ammonium salt could enhance the protective effect of a corrosion inhibitor in acid solutions.

To study the inhibiting activity of compounds of this type, we synthesized a series of quaternary ammonium salts by the reaction

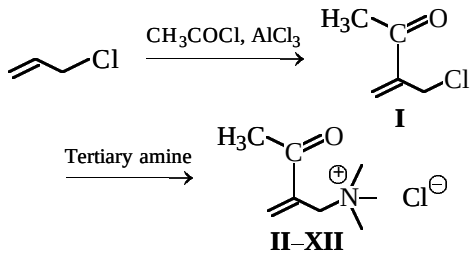

where N is the nitrogen atom of the tertiary amine molecule (Table 1).

Table 1. Quaternary ammonium salts **II**–**XII**

Compound no.	Amine	Yield, %	mp, °C	Found, %		Empirical formula	Calculated, %	
				N	Cl		N	Cl
II	Pyridine	90.0	Hygroscopic	6.85	17.70	$C_{10}H_{12}ClNO$	7.09	17.97
III	Tributylamine	89.0	″	4.52	11.55	$C_{17}H_{34}ClNO$	4.61	11.70
IV	*N*-Methylpiperidine	93.7	″	6.35	16.18	$C_{11}H_{20}ClNO$	6.44	16.32
V	Quinoline	76.7	88	5.55	14.24	$C_{14}H_{14}ClNO$	5.66	14.34
VI	*N,N*-Dimethylaniline	82.1	Hygroscopic	5.77	14.61	$C_{13}H_{18}ClNO$	5.85	14.82
VII	Triethanolamine	78.2	190	5.14	13.17	$C_{11}H_{22}ClNO_4$	5.23	13.27
VIII	*N,N*-Dimethylbenzylamine	98.0	Hygroscopic	5.66	13.18	$C_{14}H_{20}ClNO$	5.52	14.00
IX	γ-Benzoylpyridine	89.3	91	4.59	11.66	$C_{17}H_{16}ClNO_2$	4.64	11.77
X	*N,N*-Dimethyl-*p*-bromoaniline	86.6	78	4.43	11.15	$C_{13}H_{17}ClBrNO$	4.39	11.25
XI	*N,N*-Dimethyl-*p*-toluidine	83.5	55	5.61	13.87	$C_{14}H_{20}ClNO$	5.52	14.00
XII	α-Picoline	62.5	Hygroscopic	6.69	16.60	$C_{11}H_{14}ClNO$	6.62	16.78

1070-4272/02/7508-1248 $27.00 © 2002 MAIK "Nauka/Interperiodica"

Table 2. Corrosion of 08 KP steel in 0.5 M H_2SO_4 at 20°C in the presence of compounds **II**–**XII**

Compound no.	Concentration, g l^{-1}								
	0.1			0.5			1.0		
	γ	Z, %	ΔE_f, mV	γ	Z, %	ΔE_f, mV	γ	Z, %	ΔE_f, mV
II	2.0	50.0	11	2.5	60.0	16	3.0	66.7	19
III	1.7	41.2	8	2.0	50.0	10	2.2	54.6	13
IV	2.1	52.6	12	3.6	72.3	21	4.3	76.8	26
V	2.4	58.4	16	4.5	77.8	26	5.7	82.5	28
VI	1.9	47.4	12	2.5	60.0	16	3.0	66.7	17
VII	1.7	41.2	8	2.1	52.6	11	2.4	58.4	13
VIII	1.9	47.4	12	2.4	58.4	14	3.0	66.7	20
IX	1.9	47.4	11	2.0	50.0	11	2.3	56.6	13
X	2.0	50.0	12	2.4	58.4	12	2.9	65.5	17
XI	2.1	52.6	12	2.8	64.3	17	3.5	71.5	21
XII	2.3	56.6	14	3.9	74.4	23	5.1	80.4	27

As an alkylating agent for quaternization of tertiary amines we used 2-acetylallyl chloride (**I**) obtained by acylation of allyl chloride [4]. The yield of the ammonium salts was 62.5–98% (Table 1). To characterize the corrosion resistance of salts **II**–**XII**, we studied their action against corrosion of 08 KP steel and TsO zinc in sulfuric acid solutions. We determined the inhibition coefficient γ, protective efficiency Z, and free-corrosion potential shift in the presence of inhibitors ΔE_f.

EXPERIMENTAL

2-Acetylallyl chloride was obtained by acylation of allyl chloride with acetyl chloride in CCl_4 in the presence of $AlCl_3$ [4]. The tertiary amines used were of chemically pure grade.

Quaternary ammonium salts II–XII. A mixture of halide **I** (0.05 mol), acetonitrile (25 ml), and a tertiary amine (0.05 mol) was refluxed with stirring for 10–12 h. Then the solvent and unreacted compounds were removed in a vacuum (residual pressure 20 mm Hg) using a rotary evaporator, and chloride in the residue was determined by argentometric titration. The resulting salts were viscous hygroscopic liquids or crystals. Their yields and properties are summarized in Table 1.

Corrosion tests were carried out by the gravimetric method with 08 KP steel and TsO zinc foil (working surface areas 7.2×10^{-4} and 8.4×10^{-4} m^2, respectively). The testing times for the steel were 24 h (20°C), 2 h (40°C), and 0.5 h (50 and 70°C), and for zinc, 1 h (20°C). The polarization curves were registered in the potentiodynamic mode at a scan rate of 2 mV s^{-1} with a steel electrode in the initial and inhibited sulfuric acid solutions.

The results showed that salts **III** and **VII**, having aliphatic radicals in their structure, are low-efficient corrosion inhibitors for 08 KP steel in 0.5 M H_2SO_4 at 20°C (Table 2). Compounds with aromatic radicals and nitrogen-containing heterocycles demonstrate higher performance (with the exception of **IV**), with salts **II**, **V**, and **XII** containing unsaturated heterocycles being the best. These salts, taken in a concentration of 1 g l^{-1}, provide an inhibition coefficient of 3.0–5.7 for the steel in 0.5 M H_2SO_4 at 20°C (Table 2). In the presence of 2 g l^{-1} of the salts (3 M H_2SO_4, 20°C), the inhibition coefficient was found to be 5.4–9.5 (Table 3). With increasing temperature, the performance of **VII** containing aliphatic radicals decreases steadily, while salts **V** and **XII** with unsaturated heterocycles preserve their high performance

Table 3. Corrosion of 08 KP steel in 3 M H_2SO_4 in the presence of compounds **II**, **IV**, **V**, **XII**, and **XIII**

Compound no.	20°C		40°C	
	γ	Z, %	γ	Z, %
II	9.5	89.5	13.7	92.7
IV	6.2	83.9	9.1	89.1
V	5.9	83.1	15.5	93.6
XII	5.4	81.5	17.5	94.3
XIII	9.6	89.6	2.2	54.5

Table 4. Corrosion of 08 KP steel and TsO zinc in 0.5 M H_2SO_4 in the presence of compounds synthesized and their mixtures with KI (salt concentrations, g l^{-1}: 0.5 for the steel and 2 for zinc; KI concentration 2.0 g l^{-1})

Compound no.	08 KP steel				TsO zinc 20°C		Compound no.	08 KP steel				TsO zinc, 20°C	
	20°C		40°C					20°C		40°C			
	γ	*Z*, %	γ	*Z*, %	γ	*Z*, %		γ	*Z*, %	γ	*Z*, %	γ	*Z*, %
II	2.5	60.0	3.0	66.7	2.5	60.0	**VII**	2.2	54.6	1.7	41.2	1.1	9.1
II + KI	3.5	71.5	12.5	92.0	18.9	94.7	**VII** + KI	3.2	68.8	6.7	85.1	6.3	84.2
IV	3.6	72.3	1.9	47.4	2.2	54.6	**XII**	3.9	74.4	4.4	87.3	1.2	16.7
IV + KI	3.9	74.4	9.3	89.3	10.7	91.0	**XII** + KI	3.9	74.4	15.1	93.4	15.1	93.4
V	4.5	77.8	4.9	79.6	1.3	23.1	KI	2.0	50.0	2.0	50.0	1.5	33.4
V + KI	4.0	75.0	17.3	94.3	22.3	95.5							

up to 40°C (it decreases only at 50–70°C) (Fig. 1). This is consistent with the known concept of specific π-electron interaction of unsaturated heterocycles with a corroded metal surface [2].

The presence of the 2-acetylallyl radical in a quaternary ammonium salt molecule has a considerable

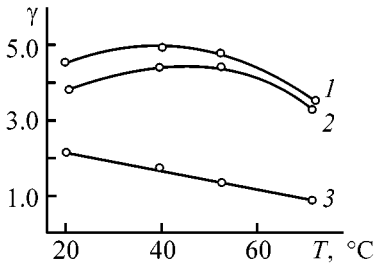

Fig. 1. Inhibition coefficient γ vs. the temperature in corrosion of 08 KP steel in 0.5 M H_2SO_4 in the presence of (*1*) **V**, (*2*) **XII**, and (*3*) **VII**. Salt concentration 0.5 g l^{-1}.

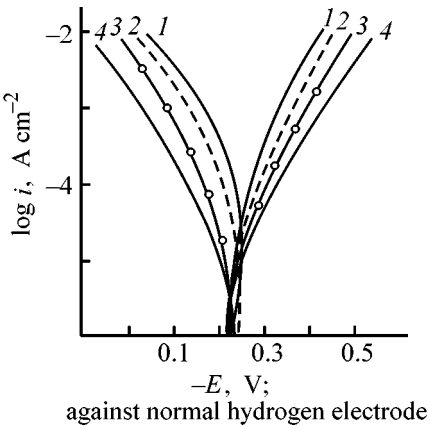

Fig. 2. Polarization curves of the steel electrode in 0.5 M H_2SO_4 at 20°C in the presence of the salts synthesized. Salt concentration 2 g l^{-1}. (*i*) Current density and (*E*) potential. (*1*) Supporting electrolyte solution, (*2*) **VII**, (*3*) **II**, and (*4*) **V**.

effect on the corrosion inhibition of steel. With temperature increasing from 20 to 40°C, the inhibiting coefficient for 08 KP steel in 3 M H_2SO_4 in the presence of 0.01 M pyridinium chloride (**XIII**) decreased from 9.6 to 2.2, and the protective efficiency, from 89.5 to 54.5%, while in the presence of the same concentration of *N*-(2-acetylallyl)pyridinium chloride (**II**), γ increases from 9.5 to 13.7, and *Z*, from 89.4 to 92.7 (Table 3) This is probably due to specific interaction of the steel surface with the C=C bond and carbonyl group of the 2-acetylallyl radical, which increases with the solution temperature.

It is known that the presence of multiple bonds and active π electrons favors adsorption of organic compounds on transition metals, thus enhancing the corrosion resistance [2]. For nontransition metals this effect is considerably less pronounced. In our case, this is manifested in relatively low inhibiting activity of the salts obtained with respect to corrosion of zinc in 0.5 M H_2SO_4 at 20°C (Table 4). Addition of KI in amount of 2 g l^{-1} to the salt solutions enhances their inhibiting activity, which is particularly pronounced in the case of zinc. The inhibition coefficients γ determined in the presence of such mixtures for corrosion of zinc exceed the product of the γ values estimated for their individual components, suggesting occurrence of the synergistic effect [5].

The voltammetric results showed that the salts obtained are corrosion inhibitors of a mixed type. They inhibit both cathodic and anodic corrosion of steel, the anodic process being more strongly affected. The slopes of the cathodic and anodic polarization curves are only slightly sensitive to the presence of these salts (Fig. 2), and the free corrosion potential shifts toward more positive values, i.e., $\Delta E_f > 0$ (Table 2).

The corrosion inhibition coefficients estimated on the basis of Antropov's formalism [6, 7] from γ and

ΔE_f (Table 2) on assumption that $\theta = 0$ are close to the experimental values obtained in the presence of the salts studied. This suggests an energy-related mechanism of the inhibiting action of the salts studied, as well as an insignificant contribution of the blocking effect to inhibition of corrosion. Such a mechanism of inhibiting action of the salts in hand is caused by the positive charge on the nitrogen atom, which results in the formation of a positive adsorption jump of potential in their presence.

REFERENCES

1. Antropov, L.I., Makushin, E.M., and Panasenko, V.F., *Ingibitory korrozii metallov* (Metal Corrosion Inhibitors), Kiev: Tekhnika, 1981.
2. Reshetnikov, S.M., *Ingibitory kislotnoi korrozii metallov* (Inhibitors of Acid Corrosion of Metals), Leningrad: Khimiya, 1986.
3. Rafaelyan, D.G., Melikyan, T.R., Babayan, Zh.R., *et al.*, *Arm. Khim. Zh.*, 1988, vol. 41, no. 7, pp. 443–445.
4. Olah, G., *Friedel-Crafts and Related Reactions*, New York: Interscience, 1964, vol. 2, parts 1, 2.
5. Pogrebova, I.S., *Ukr. Khim. Zh.*, 1982, vol. 48, no. 12, pp. 1275–1280.
6. Antropov, L.I. and Pogrebova, I.S., *Itogi Nauki, Ser.: Korroz. Zashch. Korroz.*, 1973, vol. 2, pp. 27–112.
7. Antropov, L.I., *Zashch. Met.*, 1977, vol. 13, no. 4, pp. 387–399.

Russian Journal of Applied Chemistry, Vol. 75, No. 8, 2002, pp. 1252–1255. Translated from Zhurnal Prikladnoi Khimii, Vol. 75, No. 8, 2002, pp. 1278–1281.
Original Russian Text Copyright © 2002 by Shchurin, Baev, Tishevich.

CATALYSIS

Zeolite Modification with Aluminum and Efficiency of Gas Purification

V. N. Shchurin, A. K. Baev, and V. I. Tishevich

Minsk Research Institute of Materials for Radio Engineering, Minsk, Belarus
Belarussian State Technological University, Minsk, Belarus

Received May 24, 2001; in final form, December 2001

Abstract—A method for modifying the NaX zeolite with aluminum via decomposition of an organoelement compound at low temperature was developed. The basic parameters of gas purification with the modified zeolite were determined.

Efffective methods for gas purification to remove water vapor and oxygen rely upon heterogeneous reactions characterized by high reactivity of the reactants and by an endothermic reverse reaction. Therefore, particular importance in a search for new techniques for gas purification to remove oxygen and water vapor impurities is acquired by zeolites modified with metals. Since zeolite contains aluminum oxide, which is a good dehumidifier of gas mixtures [1] to remove the drop moisture, and the enthalpy of dissociation of the zeolite is extremely high, aluminum is particularly important in zeolite modification. However, this problem has not emerged previously because, in the case of modification with aluminum, the possibility of using the conventional techniques seems to be unrealistic owing to the difficult reduction of its oxide. This issue is complicated by the fact that aluminum melts at relatively low temperature, and, therefore, even implementation of the process of Al_2O_3 reduction fails to yield highly reactive aluminum with developed surface on porous materials.

The most promising is modification of the zeolite surface with aluminum by decomposing an organoelement compound with high volatility and low decomposition temperature. Since Al(III) is present on the surface of a zeolite treated at above 673 K, the decomposition of the organoelement compound must result in good adhesion of aluminum to the surface. To compounds promising in the gas-phase method of aluminum film preparation belong alkyl compounds. Our investigations of the kinetics of thermal decomposition of trimethylaluminum [2] confirmed the formation of aluminum on zeolite and made it possible to choose conditions of zeolite modification. NaX-TB-1235 synthetic zeolite was chosen as adsorbent.

The installation for depositing aluminum onto the adsorbent and its activation is shown schematically in the figure. The installation comprises a device with adsorbent *1*, feeder *2*, manometer *3*, hydroseal *4*, cylinder *5* with argon, laboratory autotransformer *6*, instrument *7* for monitoring the temperature in the device, and cocks *8–12*. The device with adsorbent is also intended for activating the adsorbent with the deposited aluminum. The design of the device is identical to that described previously [3]. It is equipped with a 0.5-kW electric heater. The hydroseal serves to control the flow rate of the carrier gas and to neutralize vapors of organoelement compounds. The feeder is used to obtain a gas-and-vapor mixture of the carrier gas and the vapor of an organoelement compound. Since the process of zeolite modification with aluminum is based on decomposition of an organoelement compound at elevated temperature and occurs with metal formation on the surface, the zeolite was preliminarily thoroughly treated to remove adsorbed moisture and OH functional groups. With account of the fact that the adsorbed moisture is removed at lower temperature than OH groups, the device with zeolite was initially heated to 400 K in an argon flow (1 h) and then kept at 773 K for 6–8 h. The zeolite was modified in a flow of argon under atmospheric pressure, and, therefore, the temperature of the evaporator with trimethylaluminum and the flow rate of the inert gas were maintained constant. The amounts of trimethylaluminum passed through the zeolite and the metal formed were determined from the volume of inert gas, which contained the organoelement compound in a constant concentration, passed through the zeolite and from the change in the zeolite mass. The forming volatile organic products of trimethylaluminum decomposition were removed from the re-

1070-4272/02/7508-1252 $27.00 © 2002 MAIK "Nauka/Interperiodica"

action zone together with argon. After being cooled to room temperature, the device with modified zeolite was connected to the experimental setup described in [3], without letting-in gas and air with excess pressure of 0.1 MPa.

Argon was purified to remove water vapor and oxygen with a zeolite modified with aluminum at a gas flow rate of 30 l h^{-1} at an excess pressure of 0.105–0.115 MPa. The argon used in the study contained (vol %): O_2 1.0×10^{-3} and H_2O 2.5×10^{-4}. The content of water vapor was determined with a G-2-72 condensation hygrometer, and the content of oxygen in the gas, with KhTM-73NL automated chromatograph. The chromatograph operates on the adsorption in an accumulation column at liquid nitrogen temperature and of the impurities to be monitored their subsequent desorption in the stationary gas-chromatographic mode. The results of analysis and measurement errors were calculated using the procedure recommended by the instrument manufacturer. The oxygen detection limit was 0.56×10^{-7} vol %, the total measurement error did not exceed 25 rel. % in the concentration range 1×10^{-5}–1×10^{-7} vol %.

The results of the investigations performed are presented in Table 1. It can be seen that passing the gas leads initially to a gradual depression of the dew point, with the lowest dew point (–100°C) only achieved after passing 1 m^3 of argon. Passing of additional 3 m^3 of argon does not lead to any changes in the dew point. Consequently, the capacity of the zeolite modified with aluminum is not exhausted. The achieved degree of purification exceeds the level corresponding to the first grade. Similar data have been obtained for a zeolite modified with iron, nickel, and palladium [4]. Thus, the given experimental fact is due to the zeolite, rather than to the behavior of metal on the adsorbent. Since the silica gel component of the zeolite loses its OH groups at above 673 K, activation of the zeolite above this temperature makes lower the number of these groups per unit surface area. Therefore, passing the carrier gas initially equilibrates the zeolite with respect to OH groups which favor more complete absorption of water vapor. Naturally, the saturation of the zeolite with OH groups is accompanied by purification of the carrier gas. However, the effective operation of the zeolite is only achieved after passing 1 m^3 of gas with initial water vapor content of 1×10^{-3} vol %. At higher content of water vapor in the gas to be purified its volume that can saturate the zeolite with OH groups decreases. By contrast, lowering the content of water vapor in the carrier gas leads to an increase in its volume capable of saturating the initial zeolite with OH groups and thereby makes the zeolite more efficient, with the result that the extent of purification becomes higher. At the outlet of an adsorber packed with aluminum-modified zeolite the content of oxygen in argon does not exceed 5×10^{-7} vol %. The dynamic capacity for moisture of such a zeolite containing 115 g of aluminum is 18 g/100 g under the given adsorbent activation conditions. In the case of hydrogen purification to remove oxygen and moisture, the content of impurity oxygen becomes 1×10^{-6} vol % the dynamic capacity for moisture 1.5 g/100 g, and the dew point –85°C

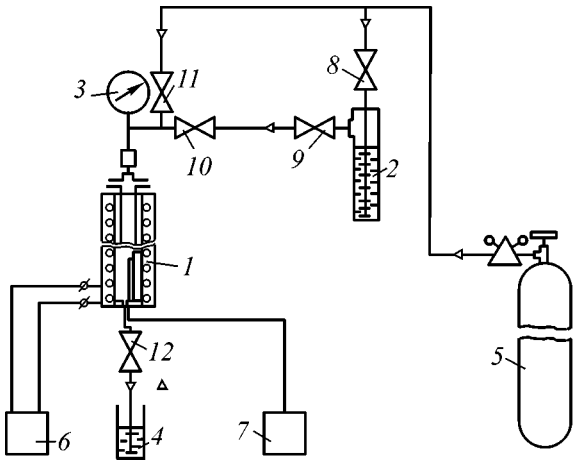

Schematic of installation for zeolite modification with aluminum.

Table 1. Results of argon purification with aluminum-modified zeolite

τ, h	Volume of gas passed, dm^3	Dew point, °C	τ, h	Volume of gas passed, dm^3	Dew point, °C
0		–60	672	19527	–100
9	254	–77	694	20116	–100
24	552	–82	718	20861	–100
42	822	–82	790	22889	–100
47	1308	–84	814	23518	–100
120	3444	–90	838	24070	–100
144	4183	–92	862	24641	–100
167	4882	–93	886	25196	–100
192	5695	–93	984	25958	–100
215	6373	–93	1007	26495	–100
287	2493	–98	1039	27168	–100
311	9208	–97	1064	27888	–100
335	9907	–97	1088	28564	–100
456	13303	–100	1160	29102	–100
482	13756	–100	1208	30091	–100
505	14440	–100	1232	30601	–100
624	18217	–100	1256	31095	–100
648	19010	–100			

Table 2. Results of gas purification to remove water vapor and oxygen

M*	Content in gas, vol %		Volume of purified gas, m^3
	H_2O	O_2	
Nitrogen purification			
Fe	$\frac{3.9 \times 10^{-4}}{1.0 \times 10^{-6}}$**	$\frac{4.0 \times 10^{-4}}{1.0 \times 10^{-5}}$	173.1
Ni	$\frac{4.0 \times 10^{-4}}{9.0 \times 10^{-6}}$	$\frac{6.2 \times 10^{-4}}{1.0 \times 10^{-5}}$	176.4
Pd	$\frac{3.2 \times 10^{-4}}{1.3 \times 10^{-5}}$	$\frac{5.1 \times 10^{-4}}{1.2 \times 10^{-5}}$	154.0
Al	$\frac{2.5 \times 10^{-4}}{-102°C}$	$\frac{1.0 \times 10^{-3}}{5.0 \times 10^{-7}}$	1.0
Hydrogen purification			
Fe	$\frac{4.1 \times 10^{-4}}{4.0 \times 10^{-6}}$	$\frac{3.4 \times 10^{-4}}{8.0 \times 10^{-6}}$	191.0
Ni	$\frac{3.4 \times 10^{-4}}{7.0 \times 10^{-6}}$	$\frac{3.4 \times 10^{-4}}{7.0 \times 10^{-6}}$	26.7
Pd	$\frac{5.1 \times 10^{-4}}{6.0 \times 10^{-6}}$	$\frac{3.0 \times 10^{-4}}{6.0 \times 10^{-6}}$	269.2
Al	$\frac{-62°C}{-106°C}$	$\frac{1.4 \times 10^{-4}}{3.0 \times 10^{-7}}$	1.0
Ga–In–Al–Ca alloy	$\frac{4.0 \times 10^{-4}}{5.0 \times 10^{-5}}$	$\frac{3.2 \times 10^{-4}}{5.0 \times 10^{-6}}$	0.5

* M, metal modifying the zeolite.

** Numerator: content in the initial gas; denominator: that in purified gas; –102, –62, and –106°C, the dew points.

under similar conditions of purification. Consequently, the zeolite modified with aluminum is characterized by high dynamic capacity for moisture, purification to remove oxygen to a level as low as 5×10^{-6} vol %, and low dew point (–100°C). This allows its use for gas purification to a level better than that corresponding to first-grade purity.

The results [3, 4] obtained in studying purification of hydrogen, nitrogen, and argon to remove water vapor and oxygen impurities with a NaX zeolite modified with iron, aluminum, nickel, or palladium allow evaluation of their efficiency. The essence of purification of hydrogen and inert gases to remove oxygen consists in fundamentally different processes occurring on metals. The results obtained in studying hydrogen and nitrogen purification to remove water vapor and oxygen impurities with a zeolite modified with various metals and gallium-based liquid solutions of metals (gallam) are presented in Table 2. It can be seen that the methods developed for purification of the gases under consideration allow higher depth of purification, compared with the first-grade requirements. The commercial diffusion installations of the ODV type can yield hydrogen with oxygen and water vapor content of, respectively, 1×10^{-4} and 5×10^{-4} vol %, whereas OST (All-Union Standard) 11.050.003–83 MEP requires that the volume fraction of impurities in technological gases should not exceed 1×10^{-5} vol %. The data obtained not only satisfy these requirements, but also indicate that the technique we developed markedly outperforms all the previously known methods for purification of hydrogen, nitrogen, and argon.

Indeed, the metal hydride method yields gas with residual pressure of water vapor of up to 5×10^{-5} vol %. This requires 35 kg of a $Ti \cdot Fe \cdot Cr$ alloy or 50 kg of $Ti \cdot Fe_{0.86} \cdot Mn_{0.14}$ [5–8]. In the case of a gallium alloy Ga (100 g)–In (10 g)–Al (12 g), hydrogen and nitrogen of volume 1.5 m^3, containing 0.1 vol % water, were purified to humidity level of 5×10^{-5} vol % [9]. Catalytic hydrogenation on platinum or palladium yields hydrogen with oxygen content of 1×10^{-4} vol %. Such a purification level cannot be always achieved. The content of water is 5×10^{-4} vol % upon purification on $7Al_2O_3 \cdot 3H_2O$ alumogel, and 1×10^{-4} and 1×10^{-5} vol % on silica gel [1, 10]. With 3A zeolite used, moisture content as low as 3.5×10^{-5} vol % can be obtained. However, gas could not be purified to this level in practice. In the case of molecular sieves, a gas with moisture content as low as 1×10^{-4} vol % can be obtained in the first two days of purification. Then the content of moisture in the gas being purified levels-off [11].

It follows from the data in Table 2 that the maximum depth of hydrogen purification to remove oxygen, to 5.0×10^{-6} vol %, is achieved with alloy of composition Ga (300 g)–In (30 g)–Al (8.1 g)–Ca (3.4 g), whereas NaX zeolite modified with aluminum ensures purification to 5.0×10^{-6} vol %. The level to which the alloy removes water vapor from hydrogen is an order of magnitude poorer (5.0×10^{-5} instead of 6.0×10^{-6} vol %). The maximum depth of purification to remove impurities at equal, but somewhat higher initial content was achieved on a zeolite modified with aluminum by means of gas-phase decomposition of an organoelement compound of aluminum. The given adsorbent is the most effective. This method yielded hydrogen with oxygen content of 3×10^{-7} vol %, instead of 6.0×10^{-6} vol % on a zeolite modified with palladium at enhanced depth

of purification to remove water vapor (dew point –101°C). The depth of nitrogen purification to remove water vapor and oxygen by the methods developed, with the use of zeolites modified with iron, nickel, or palladium, is in the range 1×10^{-5}–1×10^{-6} vol % for each of these impurities, which has not been achieved previously, either. However, the NaX zeolite modified with aluminum with the use of organoaluminum compounds ensures purification of inert gases to remove oxygen to 5×10^{-7} and water vapor to 1.3×10^{-6} vol % (dew point –102°C). This opens up prospects for obtaining a titanium-modified zeolite with the use of an organoelement compound, which will ensure deeper purification to remove oxygen.

CONCLUSIONS

(1) A method was developed for modifying NaX zeolite with aluminum by thermal decomposition of an organoelement compound in a flow of nitrogen. The method is characterized by high efficiency and depth of purification to remove oxygen (5×10^{-6} vol %) and moisture (dew point –100°C). In purification of 29400 dm^3 of hydrogen, the level of purification to remove oxygen is 3×10^{-7} vol % at dew point of –100°C.

(2) Ga–In–Al–Ca alloy and NaX zeolite modified with iron, nickel, palladium, or aluminum, and conditions of zeolite activation, are characterized by high dynamic capacity and depth of purification of inert gases to remove water vapor and oxygen impurities, which cannot be achieved with other techniques described in the literature.

REFERENCES

1. Sokolov, B.K., *Gazy osoboi chistoty* (Special-Purity Gases), Moscow: Znanie, 1981.
2. Baev, A.K., Shchurin, V.N., and Tishevich, V.I., Abstracts of Papers, *Vserossiiskaya konferentsiya po metalloorganicheskoi khimii* (All-Union Conf. on Organometallic Chemistry), Nizhnii Novgorod, 1995, p. 254.
3. Shchurin, V.N., Baev, A.K., and Tishevich, V.I., *Zh. Prikl. Khim.*, 1997, vol. 70, no. 1, pp. 55–60.
4. Shchurin, V.N., Baev, A.K., and Tishevich, V.I., *Zh. Prikl. Khim.*, 2000, vol. 73, no. 2, pp. 184–187.
5. Andreev, B.M. and Perevezentsev, A.I., *Vysokochist. Veshchestva*, 1990, no. 2, pp. 23–39.
6. Bao Deyou, Sou Langyin, and Lui Fangjie, *Hydrogen Syst.*, vol. 2, Pap. Present: *Int. Hydrogen Syst. Beijing*, Oxford, 1986, pp. 335–338.
7. Yin Enhua, Yang Xuezhen, Lan Wenhui, and Yu Fenglai, *Hydrogen Syst.*, vol. 2, Pap. Present: *Int. Hydrogen Syst. Beijing*, Oxford, 1986, pp. 339–343.
8. Yan-Min Wu, *Hydrogen Energy Progr. VII, 6th World Hydrogen Energy Conf., Moscow, September 25–29, 1988*, New York, 1988, vol. 2, pp. 1559–1571.
9. Shealy, J.R. and Woodall, J.M., *Appl. Phys. Lett.*, 1982, vol. 41, no. 1, pp. 88–91.
10. Goloto, I.D., Dokuchaev, B.P., and Kolmogorov, G.D., *Chistota v proizvodstve poluprovodnikovykh priborov i integral'nykh skhem* (Cleanness in Manufacture of Semiconductor Devices and Integrated Circuits), Moscow: Energiya, 1975.
11. Kirsh, S.I., Fomicheva, T.M., Karabanov, N.T., and Abakumov, V.Ya., *Zavod. Lab.*, 1986, no. 11, pp. 15–17.

Russian Journal of Applied Chemistry, Vol. 75, No. 8, 2002, pp. 1256–1261. Translated from Zhurnal Prikladnoi Khimii, Vol. 75, No. 8, 2002, pp. 1282–1287.
Original Russian Text Copyright © 2002 by Alimardanov, Velieva, Tairova.

CATALYSIS

Kinetics and Mechanism of Oxidative Dehydrodisproportionation of Methylcyclohexane on Modified High-Silica Zeolite H-TsVM

Kh. M. Alimardanov, F. M. Velieva, and L. A. Tairova

Institute of Petrochemical Processes, National Academy of Sciences of Azerbaijan, Baku, Azerbaijan

Received December 17, 2001; in final form, April 2002

Abstract—The kinetics of oxidative dehydrodisproportionation of methylcyclohexane in the presence of H-TsVM zeolite ($SiO_2 : Al_2O_3 = 30$) modified with gallium and gadolinium oxides was studied. A kinetic model fairly adequately describing this process in a wide temperature range was proposed. The kinetic constants of some oxidation reactions were determined.

In contrast to dehydrogenation, proceeding without changes in the number of carbon atoms in the molecule, oxidative dehydrodisproportionation of alicyclic hydrocarbons is a poorly studied catalytic process involving heterogeneously bound oxygen atoms [1–4]. This reaction allows polyalkylbenzenes and naphthenic hydrocarbons, whose content in straight-run naphtha is fairly high, to be involved in basic organic synthesis along with low-molecular-weight aromatic hydrocarbons [5–9].

Single-stage oxidative dehydrodisproportionation of methyl- and ethylcyclohexane in polyalkylbenzenes is thermodynamically feasible and yields a limited number of products [10, 11]. The kinetic data on these reactions are important for mathematical simulation and optimization of the process.

In this work, we studied the kinetics of oxidative dehydrodisproportionation of methylcyclohexane (MCH) to form xylene isomers in the presence of H-TsVM zeolite modified with gallium and gadolinium oxides.

EXPERIMENTAL

The initial MCH was prepared by hydrogenation of chemically pure toluene; according to gas–liquid chromatography (GLC), its purity was 99.3–99.5%, bp 100–101°C, $n_D^{20} = 1.4244$, $d_4^{20} = 0.7720$.

To prepare the required catalyst, the H-TsVM zeolite ($SiO_2 : Al_2O_3 = 30$) was modified with gallium and gadolinium oxides [10]; the content of metal oxides was 3 wt %.

The experiments were performed in a laboratory unit with a nongradient reactor at 773–813 K and MCH space velocity of 108–432 h^{-1}; the initial partial pressures of MCH and oxygen were 11.8–33.2 and 12.3–17.5 kPa, respectively. The gas mixture was diluted with nitrogen or water vapor. The size of catalysis grains was varied within 0.5–0.8 mm; the plunge pulsation frequency in the reactor was 25 and 50 Hz. Such experimental conditions eliminate the effect of the outer- and pore-diffusion hindrance on the reaction rate.

The liquid and gaseous reaction products were analyzed on Tsvet-31 and KhL-3 chromatographic units using bis(-2-cyanoethyl) sulfide (12 wt %) on Chromosorb W for liquid products or triethylene glycol butyrate (TEGB, 15 wt %) on INZ–600 brick for gaseous products.

The reaction products mainly consisted of xylene isomers, toluene, benzene, cyclohexane, CO_2, water vapor, and minor amounts of C_2–C_5 aliphatic hydrocarbons. In some runs, isomers of tri- and tetramethylbenzene, methylcyclohexene, cyclopentadiene, CO, and hydrogen were identified. However, due to the low concentration of these compounds in the catalyzate, their correct quantitative analysis was impossible and thus they were disregarded in the kinetic simulation of the process. In the catalyzate residue (after distillation of liquid reaction products and condensed water; 0.5–0.8% of the total product weight), we identified by GLC and IR spectroscopy oxygen-containing compounds, such as saturated and unsaturated ketones, aldehydes, and acids [12].

The main experimental results obtained with a catalyst of steady-state activity are listed in Table 1. As seen from these data, under the above conditions, MCH is predominantly involved in oxidative dehy-

1070-4272/02/7508–1256 $27.00 © 2002 MAIK "Nauka/Interperiodica"

Table 1. Accumulation rate of reaction products ω_i as influenced by the initial partial pressures of MCH and oxygen and by the space velocities v of MCH vapor (Ga–Gd–O-modified H-TsVM catalyst, p_{H_2O} = 0.1 kPa)

T_0, kPa		ω_i, mol l_{cat}^{-1} h^{-1}					
MCH	O_2	C_2–C_5	MCH	benzene	toluene	xylene isomers	CO_2
			v = 108 h^{-1}, T = 793 K				
33.2	12.3	0.1976	2.4177	0.2024	1.3685	0.5156	0.1349
25.5	14.15	0.2118	2.5066	0.2166	1.4006	0.5343	0.1396
20.67	15.3	0.2311	2.6253	0.2456	1.4541	0.5441	0.1493
15.0	16.67	0.2649	2.9333	0.2746	1.6138	0.5973	0.1831
13.2	17.1	0.2840	3.0836	0.3033	1.6561	0.6355	0.2022
11.8	17.5	0.2986	3.1505	0.3179	1.6711	0.6501	0.2119
			v = 144 h^{-1}, T = 793 K				
33.2	12.3	0.2441	2.9977	0.2569	1.6891	0.6358	0.1734
25.5	14.15	0.2502	3.1103	0.2695	1.7194	0.6737	0.1925
20.67	15.3	0.2825	3.2247	0.2954	1.7399	0.6870	0.2055
15.0	16.67	0.3115	3.4094	0.3532	1.7726	0.7321	0.2376
13.2	17.1	0.3530	3.5207	0.3659	1.7907	0.7374	0.2503
11.8	17.5	0.3467	3.5452	0.3724	1.7977	0.7705	0.2568
			v = 216 h^{-1}, T = 793 K				
33.2	12.3	0.3083	3.3695	0.2986	1.8876	0.6551	0.2216
25.5	14.15	0.3369	3.4249	0.3081	1.8483	0.6738	0.2503
20.67	15.3	0.3467	3.5654	0.3371	1.8874	0.7225	0.2696
15.0	16.67	0.3950	3.8332	0.3854	1.9365	0.7997	0.3180
13.2	17.1	0.4333	4.0201	0.4140	1.9738	0.8473	0.3467
11.8	17.5	0.4527	4.3167	4.4334	2.0034	0.8765	0.3564
			v = 432 h^{-1}, T = 793 K				
33.2	12.3	0.5202	5.7595	0.5587	3.3525	1.0019	0.3275
25.5	14.15	0.5583	5.8486	0.5776	3.3115	1.0589	0.3273
20.67	15.3	0.6355	6.0329	0.6163	3.2356	1.1749	0.3659
15.0	16.67	0.7130	6.2404	0.6552	3.1793	1.2717	0.4239
13.2	17.1	0.7510	6.3456	0.6740	3.1196	1.3287	0.4621
11.8	17.5	0.7705	6.3602	0.6742	3.0822	1.3485	0.4817
			v = 432 h^{-1}, T = 773 K				
33.2	12.3	0.3854	4.3314	2.4469	0.4239	0.7707	0.3083
25.5	14.15	0.4043	4.5585	2.5414	0.4428	0.8278	0.3273
20.67	15.3	0.4621	4.8387	2.5808	0.5462	0.9053	0.4045
15.0	16.67	0.5780	5.0074	2.3122	0.5781	1.0598	0.4818
13.2	17.1	0.6355	5.2865	2.2723	0.7124	1.1362	0.5199
11.8	17.5	0.6742	5.3199	2.1576	0.7705	1.1944	0.5201
			v = 432 h^{-1}, T = 813 K				
33.2	12.3	0.5780	9.5712	1.0983	4.7398	2.6974	0.4624
25.5	14.15	0.6546	9.7763	1.2129	4.6207	2.7724	0.5006
20.67	15.3	0.7126	9.8272	1.2905	4.4683	2.8312	0.5971
15.0	16.67	0.7900	10.0748	1.4066	4.3740	2.9481	0.5588
13.2	17.1	0.8280	10.0854	1.4443	4.2749	3.0618	0.5584
11.8	17.5	0.8476	10.2323	1.4640	4.2381	3.1015	0.5779

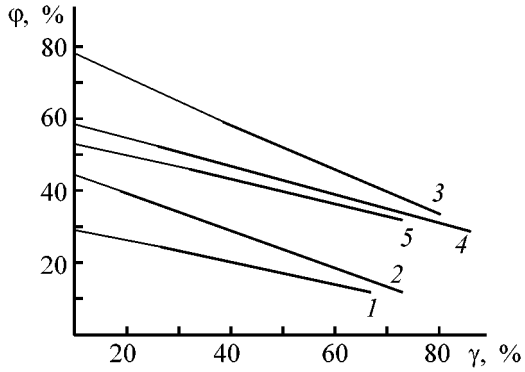

Fig. 1. Selectivity φ of the reaction with respect to xylene isomers vs. MCH conversion γ. Temperature, °C: (*1*) 753, (*2*) 773, (*3*) 803, (*4*) 823, and (*5*) 873.

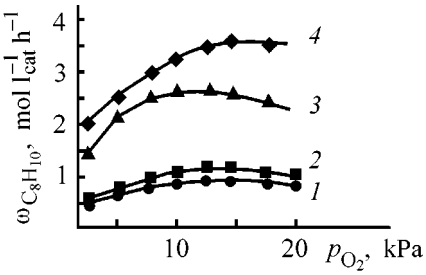

Fig. 2. Rate of oxidative dehydrodisproportionation of MCH vs. the oxygen partial pressure p_{O_2}. p_{MCH} = 33.2 kPa, v_{MCH} = 432 h^{-1}. ($\omega_{C_8H_{10}}$) Rate of accumulation of xylene isomers. Temperature, °C: (*1*) 773, (*2*) 793, (*3*) 813, and (*4*) 843.

drodisproportionation, dehydrogenation, dehydrodemethylation, and destructive oxidation. The oxidative dehydrodisproportionation of MCH leads to accumulation of benzene and xylene isomers in the catalyzate; benzene is also formed in oxidative dehydrodemethylation. The "conversion curves" (dependences of the process selectivity on MCH conversion) at various temperatures (Fig. 1) show that, at MCH conversion close to zero, the selectivity of the process with respect to xylene isomers is lower that 100%, which suggests a parallel-consecutive reaction pattern.

Based on the experimental data, we included in our model the following series of independent reaction pathways:

$$2C_7H_{14} + 3O_2 \rightarrow C_6H_6 + C_8H_{10} + 6H_2O, \quad (1)$$

$$C_7H_{14} + 1.5O_2 \rightarrow C_7H_8 + 3H_2O, \quad (2)$$

$$C_7H_{14} + 3O_2 \rightarrow C_6H_6 + CO_2 + 4H_2O, \quad (3)$$

$$C_7H_{14} + 1.5O_2 \rightarrow C_4H_8 + C_2H_4 + CO_2 + H_2O, \quad (4)$$

$$C_7H_8 + 1.5O_2 \rightarrow C_6H_6 + CO_2 + H_2O, \quad (5)$$

$$C_8H_{10} + 1.5O_2 \rightarrow C_7H_8 + CO_2 + H_2O. \quad (6)$$

Reaction (1) describes oxidative dehydrodisproportionation of MCH into benzene and xylene isomers; reaction (2) is dehydrogenation of MCH into toluene; reactions (3), (5), and (6) correspond to oxidative dehydrodemethylation of the initial hydrocarbon and resulting alkylaromatic compounds, and reaction (4) describes destructive oxidation of MCH. These parallel-consecutive transformations of the initial hydrocarbon and products of its primary conversion proceed at different active centers of the catalyst [13]. The effect of the surface heterogeneity of oxide-modified zeolite catalysts was studied previously in [14].

The above model does not include the reactions of deep oxidation of MCH and coke formation, because our calculations showed that the contribution of these processes is negligibly small.

To determine the formal reaction orders with respect to MCH and oxygen, we plotted the rate of oxidative dehydrodisproportionation of MCH against the partial pressures of hydrocarbon (p_{O_2} = 12.3 kPa) and oxygen (p_{MCH} = 33.2 kPa). The results obtained show that the formal reaction orders with respect to MCH and O_2 are about 2 and 1, respectively. Hence, the rate of the main reaction (1) can be given as follows:

$$r_{C_8H_{10}} = Kp_{C_7H_{14}}^2 p_{O_2}, \quad (7)$$

where $r_{C_8H_{10}}$ is the rate of reaction (1) and $p_{C_7H_{14}}$ and p_{O_2} are the partial pressures of MCH and O_2, respectively.

With account taken of the stage scheme, in the steady state, the sum of the active centers with different oxidation states is 1:

$$Z + ZO + ZO_2 = 1, \quad (8)$$

where ZO and ZO_2 are represented, in accordance with the stage scheme (Table 2), the by equations

$$ZO_2 = K_\beta [Z] p_{O_2}, \quad (9)$$

$$ZO = K_\alpha [ZO_2]^{0.5} [Z]^{0.5} = K_\beta K_\alpha [Z] p_{O_2}^{0.5}, \quad (10)$$

where K_α is the constant of dissociative adsorption of O_2 and K_β is the equilibrium constant of O_2 adsorption.

According to the kinetic data (Figs. 2, 3), at partial pressures of oxygen and water vapor of 2.0–17.5 and 0.1–10 kPa, respectively, the rate of formation of xylene isomers decreases with increasing concentration of both oxygen and water vapor, and this dependence is rather complex. At low partial pressures of oxygen and water vapor, the rate of formation of

Table 2. Stage scheme of oxidative dehydrodisproportionation of MCH

Stage	Stoichiometric number of stages in indicated pathways					
	1	2	3	4	5	6
$C_7H_{14} + ZO \rightarrow C_7H_{13}ZOH$	2	1	1	0	0	0
$C_7H_{13}ZOH + ZO \rightarrow C_7H_{11}ZOH + Z + H_2O$	2	0	0	0	0	0
$C_7H_{11}ZOH + ZO \rightarrow C_7H_9ZOH + Z + H_2O$	2	0	0	0	0	0
$2C_7H_9ZOH + ZO \rightarrow C_6H_6 + C_8H_{10} + 2Z + 2H_2O$	1	0	0	0	0	0
$C_7H_{13}ZOH + ZO \rightarrow C_7H_{11}ZOH + Z + H_2O$	0	1	1	0	0	0
$C_7H_{12}ZOH + ZO \rightarrow C_7H_{10}ZOH + Z + H_2O$	0	1	1	0	0	0
$C_7H_{10}Z + ZO \rightarrow C_7H_8Z + Z + H_2O$	0	1	1	0	0	0
$C_8H_{10} + ZO_2 + ZO \rightarrow C_7H_8Z + CO_2 + H_2O + Z$	0	0	0	0	0	1
$C_7H_8Z \rightarrow C_7H_8 + Z$	0	1	1	0	0	1
$C_7H_8 + ZO_2 + ZO \rightarrow C_6H_6Z + CO_2 + H_2O + Z$	0	0	1	0	1	0
$C_6H_6Z \rightarrow C_6H_6 + Z$	0	0	1	0	1	0
$C_7H_{14} + ZO_2 + ZO \rightarrow C_4H_8Z + C_2H_4Z + CO_2 + H_2O$	0	0	0	1	0	0
$C_4H_8Z \rightarrow C_4H_8 + Z$	0	0	0	1	0	0
$C_2H_4Z \rightarrow C_2H_4 + Z$	0	0	0	1	0	0
$Z + O_2 \rightarrow ZO_2$	3	1.5	2	0.5	0.5	0.5
$Z + ZO_2 \rightarrow 2ZO$	3	1.5	2	0.5	0.5	0.5

xylene isomers increases. However, with increasing volume fraction of oxygen and water vapor, the rate of xylene formation sharply decreases. Thus, stoichiometric amounts of oxygen and water vapor are probably effective agents restoring the active centers which provide dehydrogenation of the initial hydrocarbon and disproportionation of the intermediate carbanions. Taking into account the above considerations and substituting Eqs. (8)–(10) in Eq. (7), we obtain the following kinetic equation:

$$r_{C_8H_{10}} = \frac{k_1 p_{C_7H_{14}}^2 p_{O_2}}{1 + K_\alpha^{0.5} p_{O_2}^{0.5} + K_\beta p_{O_2} + K_\gamma p_{H_2O}}, \quad (11)$$

where $r_{C_8H_{10}}$ is the rate of reaction (1), k_1 is the rate constant of reaction (1) in the steady state, and K_γ is the equilibrium constant of H_2O adsorption.

The kinetic constants were determined by least-squares method, using the random search procedure and taking into account the main and side reactions of hydrocarbon conversion [schemes (1)–(6)]. Our experimental values are fairly adequately described by the following kinetic equations.

$$r_1 = \frac{k_1 [p_{C_7H_{14}}]^2 [p_{O_2}]}{1 + K_\alpha [p_{O_2}]^{0.5} + K_\beta [p_{O_2}] + K_\gamma [p_{H_2O}]}, \quad (12)$$

$$r_2 = \frac{[k_2 p_{C_7H_{14}} + k_6 p_{C_8H_{10}}][p_{O_2}]}{1 + K_\alpha [p_{O_2}^{0.5}] + K_\beta [p_{O_2}] + K_\gamma [p_{H_2O}]}, \quad (13)$$

$$r_3 = \frac{[k_1 [p_{C_7H_{14}}] + k_3][p_{C_7H_{14}}][p_{O_2}^{0.5}]}{[1 + K_\alpha p_{O_2}^{0.5} + K_\beta p_{O_2} + K_\gamma p_{H_2O}]}, \quad (14)$$

$$r_4 = \frac{k_4 [p_{C_7H_{14}}][p_{O_2}]}{1 + K_\alpha [p_{O_2}^{0.5}] + K_\beta [p_{O_2}] + K_\gamma [p_{H_2O}]}, \quad (15)$$

where k_1–k_6 are the rate constants of the corresponding reactions and r_1–r_4 are the rates of hydrocarbon accumulation ($r_1 = r_{C_8H_{10}}$, $r_2 = r_{C_7H_8}$, $r_3 = r_{C_6H_6}$, and $r_4 = r_{C_4H_8}$) in stoichiometric reactions (1)–(4).

Based on the data of additional experiments and analysis of the reaction products, the rates of oxidative demethylation of xylene isomers into toluene and of toluene into benzene were assumed to be zero.

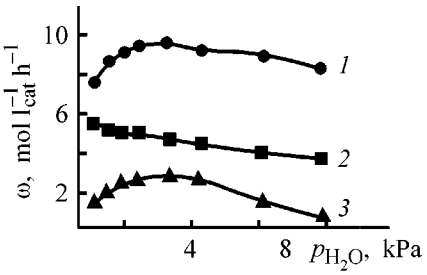

Fig. 3. Rates ω of (*1*) MCH conversion and of accumulation of (*2*) toluene and (*3*) xylene isomers vs. the water vapor partial pressure p_{H_2O}. p_{MCH} = 33.2 kPa, T = 813 K.

The rates of conversion of the initial hydrocarbon and accumulation of the reaction products by the above pathways were calculated using the following expressions:

$$\omega_{C_7H_{14}} = -2r_1 - r_2 - r_3 - r_4, \quad (16)$$

$$\omega_{C_8H_{10}} = r_1 - r_6, \quad (17)$$

$$\omega_{C_6H_6} = r_1 + r_3 + r_5, \quad (18)$$

$$\omega_{C_7H_8} = r_2 - r_5 + r_6, \quad (19)$$

$$\omega_{C_2-C_4} = 2r_4, \quad (20)$$

$$\omega_{CO_2} = r_3 + r_4 + r_5 + r_6, \quad (21)$$

where $\omega_{C_7H_{14}}$, $\omega_{C_8H_{10}}$, $\omega_{C_6H_6}$, $\omega_{C_7H_8}$, $\omega_{C_2-C_4}$, and ω_{CO_2} are the experimental reaction rates given in Table 1.

The best agreement between the rates of oxidative dehydrodisproportionation of MCH and experimental values was obtained with the following rate constants for reactions (1)–(6):

$$k_1 = 5.94 \times 10^3 \exp(-97453.146/RT),$$

$$k_2 = 3.4572 \times 10^4 \exp(-62211.432/RT),$$

$$k_3 = 4.275 \times 10^3 \exp(-70818.8/RT),$$

$$k_4 = 7.18 \times 10^8 \exp(-158352.43/RT),$$

$$k_5 = k_6 = 0,$$

$$K_\alpha = 5.21 \times 10^3 \exp(-164450/RT),$$

$$K_\beta = 9.04 \times 10^{-11} \exp(135523.98/RT),$$

$$K_\gamma = 4.21 \times 10^{-7} \exp(119199.546/RT)$$

(R is the universal gas constant, 8.3144 J mol^{-1} K^{-1}). The root-mean-square deviations of the calculated rates [Eqs. (6)–(21)] from the experiment were 14.5% for main reaction (1), 18–22% for reactions (2)–(4), and 21–25% for reactions (5) and (6). Zero values of k_5 and k_6 suggest that toluene and benzene are predominantly formed by reactions (1)–(3).

The second order of the reaction with respect to MCH and the maximum in the dependence of the disproportionation rate on the partial pressure of water vapor indicate that the limiting stage is the reaction of two intermediate radicals, followed by their disproportionation, whereas adsorption of MCH and elimination of the hydrogen atom with nucleophilic surface oxygen are fast. In this stage, electron passes from the hydrocarbon to the catalyst. The carbocations formed are converted in two competitive reactions to form toluene (dehydrogenation) and xylene isomers (dehydrodisproportionation). The first reaction order with respect to MCH in stage (2) suggests that the dehydrogenation rate is rather high.

The destructive oxidation of MCH can proceed by two independent pathways: (1) by heterogeneous–homogeneous conversion of hydrocarbons to form cycloalkyl radicals and carbocations (after electron transfer from the radical to the catalyst) on the catalyst surface, their subsequent passing into the gas phase, and oxidation with molecular oxygen, and (2) heterogeneous conversion of MCH at the active centers of the catalyst providing oxidative dehydrodisproportionation (strong acid–base centers). In this case, the destructive oxidation on the surface proceeds by the separate interaction mechanism through dissociative adsorption of hydrocarbons, accompanied by the formation of strongly bound hydroxy group from the oxygen ion with localized negative charge, stabilization of hydrocarbon radical on the metal cation linked with oxygen, and reactions of the oxygen molecule from the gas phase with a surface radical. Both mechanisms of oxidative degradation can operate simultaneously.

In the analysis of the reaction mechanism, we used the stage scheme given in Table 2, involving a number of stoichiometric reactions whose sequence determines the rates of realization of independent runs.

According to the stage scheme (Table 2), the stage of reaction of oxygen from the gas phase with the reduced center of the catalyst ($Z + O_2 \rightarrow ZO_2$) is assumed to be irreversible, and the stage of dissociative adsorption of oxygen ($Z + ZO_2 \rightarrow 2ZO$), reversible. Hence, the rate of oxidative dehydrodisproportionation strongly depends on the partial pressure of MCH ($r_{C_7H_{14}} \approx p^2_{MHC}$) and is inhibited by oxygen at its content exceeding the stoichiometric amount.

Our kinetic model of oxidative dehydrodisproportionation of MCH fairly adequately describes the system of chemical transformations proceeding in the reaction scheme in a wide range of experimental parameters and can be used for mathematical simulation of the process.

CONCLUSIONS

(1) The kinetic features of oxidative dehydrodisproportionation of methylcyclohexane in benzene and xylene isomers in the presence of H-TsVM zeolite modified with gallium and gadolinium oxides were studied.

(2) At 773–813 K, methylcyclohexane is involved in oxidative dehydrogenation, dehydrodisproportionation, and dehydrodemethylation. The kinetic model of the process, fairly adequately describing the experimental results in a wide temperature range, was proposed. The rate constants for some reaction pathways were calculated.

(3) Reaction of the products of partial dehydrogenation of methylcyclohexane (namely, methylcyclohexyl and methylcyclohexenyl radicals), with their subsequent disproportionation and dehydrogenation into benzene and xylene isomers, is the limiting stage of the process.

REFERENCES

1. Alimardanov, Kh.M., *Kinet. Katal.*, 1994, vol. 35, no. 6, pp. 841–845.
2. Alimardanov, Kh.M., Suleimanova, E.T., Shakhtakhtinskaya, A.T., and Abdullaev, A.F., Abstracts of Papers, *II Mezhdunarodnaya neftekhimicheskaya konferentsiya posvyashchennaya pamyati Yu.G. Mamedalieva* (II Int. Petrochemical Conf. Dedicated to the Memory of Yu.G. Mamedaliev), Baku, 1996, p. 175.
3. Dadashev, I.B., Abasov, S.I., and Zul'fugarov, Z.G., *Dokl. Akad. Nauk Az.SSR*, 1986, vol. 42, no. 10, pp. 46–49.
4. Tagiev, D.B. and Dadashev, I.B., *Neftekhimiya*, 1990, vol. 30, no. 6, pp. 756–763.
5. Isakov, Ya.I., Isakova, T.A., Minachev, Kh.M., and Lipkind, B.A., *Neftekhimiya*, 1986, vol. 26, no. 3, pp. 335–342.
6. Isakov, Ya.I., *Neftekhimiya*, 1998, vol. 38, no. 6, pp. 404–438.
7. Yushchenko, V.V., Wang Syaoyui, and Romanovskii, B.V., *Neftekhimiya*, 1999, vol. 39, no. 3, pp. 197–202.
8. Ponomareva, O.A., Moskovskaya, I.F., and Romanovskii, B.V., *Neftekhimiya*, 1999, vol. 39, no. 2, pp. 101–106.
9. Nowak, S., Keil, G., and Zimmermann, G., *Hung. J. Ind. Chem. Veszprem.*, 1978, vol. 6, no. 1, pp. 105–109.
10. Alimardanov, Kh.M., Akhverdiev, R.B., Suleimanova, E.T., *et al.*, *Neftekhimiya*, 1997, vol. 37, no. 6, pp. 523–531.
11. Alimardanov, Kh.M., Abstracts of Papers, *Konferentsiya "Tonkii organicheskii sintez i kataliz"* (Conf. on Fine Organic Synthesis and Catalysis), Baku, 1999, pp. 19–20.
12. Alimardanov, Kh.M., *Neftekhimiya*, 1991, vol. 31, no. 1, pp. 24–31.
13. Kuperman, S.L., in *Osnovy khimicheskoi kinetiki v geterogennom katalize* (Fundamentals of Chemical Kinetics in Heterogeneous Catalysis), Moscow: Khimiya, 1979, pp. 157–168.
14. Alimardanov, Kh.M., Suleimanova, E.T., and Shakhtakhtinskaya, A.T., *Neftekhimiya*, 1991, vol. 31, no. 3, pp. 342–349.

Russian Journal of Applied Chemistry, Vol. 75, No. 8, 2002, pp. 1262–1264. Translated from Zhurnal Prikladnoi Khimii, Vol. 75, No. 8, 2002, pp. 1288–1290.
Original Russian Text Copyright © 2002 by Vlasenko, Chernobrivets.

ENVIRONMENTAL PROBLEMS OF CHEMISTRY AND TECHNOLOGY

Catalytic Purification of Gases to Remove Vinyl Chloride

V. M. Vlasenko and V. L. Chernobrivets

Institute of Sorption and Endoecology, National Academy of Sciences of Ukraine, Kiev, Ukraine

Received March 13, 2002

Abstract—The catalytic purification on spinel-like catalysts containing no noble metals of ventilation exhaust gases formed in manufacture of PVC film was studied in the thermal and sorption modes.

Ventilation exhaust gases from numerous industrial plants manufacturing or reprocessing polyvinylchloride are contaminated with a considerable amount of vinyl chloride (C_2H_3Cl). The high toxicity of this substance, whose maximum permissible concentration (MPC) in the atmosphere is strictly limited by pollution control regulations, requires that efficient and reliable methods for its removal from exhaust gases should be developed. A promising method for removal of chlorinated organic compounds, including vinyl chloride, from gas mixtures is based on deep catalytic oxidation of these compounds to nontoxic compounds (CO_2 and H_2O) and neutralization of chlorine and hydrogen chloride formed in the process. The high output capacity, continuity, and simplicity of heterogeneous-catalytic processes constitute a pronounced advantage of catalytic purification methods over other techniques.

The catalytic purification can be implemented in a number of variants, depending on the concentration of an impurity to be removed.

Heating the reaction mixture on a catalyst to temperatures at which the impurity oxidation is complete is appropriate at C_2H_3Cl concentrations of a few percent. The sorption-catalytic purification is more efficient for ventilation exhaust gases containing no more than 20 mg cm^{-3} of vinyl chloride. This method consists in sorption of a contaminant on a catalyst at room temperature and, after the catalyst is saturated, removal of the sorbate by deep oxidation under short heating [1].

The catalysts for oxidation of organochlorine substances commonly contain noble metals. Deep oxidation of vinyl chloride is achieved on catalysts containing platinum-group metals [2]. Ruthenium [3] and platinum–ruthenium [4] catalysts have been proposed for this purpose. Recently, efficient catalysts without noble metals have also been developed. They are based on binary oxide systems of spinel structure, possess high chemical and thermal resistance, and ensure complete oxidation of organochlorine compounds at moderate temperatures. A catalyst ensuring efficient oxidation of chlorinated hydrocarbons to CO_2, H_2O, HCl, and Cl_2 at temperatures below 400°C has been developed on the basis of copper(II) and cobalt(II) chromites on γ-Al_2O_3 support [5]. It has been established that high catalytic properties are also exhibited by catalysts based on chromium(III) oxides.

All the above-mentioned catalysts, both with and without noble metals, cannot be used for sorption-catalytic purification of gases because of their poor sorption capacity for substances to be removed. Catalysts-sorbents that can be recommended for use in sorption-catalytic purification have only been obtained after the development of methods for preparing oxide catalysts with enhanced sorption capacity for chlorinated hydrocarbons. The highest efficiency was achieved with a γ-Al_2O_3-supported catalyst based on chromium(III) oxides, treated with 0.5 vol % HCl. This catalyst exhibits high sorption capacity for vinyl chloride and is sufficiently active in its oxidation [6].

Laboratory studies carried out with a mixture containing 2.6 vol % C_2H_3Cl in air demonstrated that oxidation of vinyl chloride on a catalyst containing 35 wt % Cr_2O_3 on γ-Al_2O_3 support is complete even at 350°C volumetric flow rate not exceeding 1000 h^{-1}. A similar effect is observed on a catalyst containing 20 wt % copper chromite and an equal amount of cobalt chromite on the same support. The sorption

1070-4272/02/7508-1262 $27.00 © 2002 MAIK "Nauka/Interperiodica"

capacity of the chromium oxide catalyst for C_2H_3Cl at 70–75°C does not exceed 10 mg m^{-3}. Regeneration of this catalyst at 350–400°C in an air flow restores completely its sorption capacity.

It is known that, under real conditions, waste gases may contain, in addition to vinyl chloride, other contaminants, such as hydrogen chloride, carbon(II) oxide, etc. In the case of manufacture of PVC articles, waste gases also contain plasticizers (dibutyl phthalate). The presence of these substances in gases may strongly complicate the purification process. To evaluate the efficiency of oxide catalysts containing no noble metals and of methods for gas purification, developed on their basis, the catalysts were tested with ventilation exhaust gases discharged from industrial plants manufacturing the PVC film. The results obtained are presented in this communication.

The purification processes were studied in both thermal-catalytic and sorption-catalytic modes. The average composition of the contaminating impurities was as follows (mg m^{-3}): vinyl chloride up to 5, dibutyl phthalate up to 4, and carbon(II) oxide 1.6–1.8. The study was performed in a flow-through glass reactor of diameter 18 mm, with external heating. The reactor was charged with 40 cm^3 of a catalyst in the form of 5-mm irregular grains.

The content of vinyl chloride in the mixture was determined by its burning on an incandescent platinum coil of a PSU device, followed by absorption of the combustion products with alkaline solution and nephelometric determination of chloride ions in a reaction with silver nitrate [7]. The analysis for dibutyl phthalate was based on hydrolyzing this compound with sulfuric acid to butyl alcohol and determining the alcohol colorimetrically from the product of its condensation with paradimethylaminobenzaldehyde [8]. The CO content in the gas mixture was found by oxidizing it with I_2O_5 to CO_2 and absorbing the latter with barium hydroxide [7].

In the thermal-catalytic mode of purification, two types of catalysts were tested: copper–cobalt–chromium catalyst (20 wt % $CoCl_2O_4$ and $CoCl_2O_4$ each on γ-Al_2O_3) and chromium oxide catalyst (35 wt % Cr_2O_3 on γ-Al_2O_3). In the course of the study, the reactor with the catalyst was heated to 400°C at a volumetric flow rate of waste gases of 1000 h^{-1}. After the prescribed mode was attained, it was maintained for 1 h, and the mixture was analyzed at the inlet and outlet of the reactor. The installation was maintained in the working state for 24 h. The next day, samples were taken for analysis 60 min after the process conditions were stabilized. The results obtained in a continuous test of the copper–cobalt–chromium catalyst for 50 h are presented in Table 1 (c_{VC} and c_{DBPh} are, respectively, the concentrations of vinyl chloride and dibutyl phthalate, and τ is the experiment duration).

Table 1. Degree of oxidation, X, of vinyl chloride and dibutyl phthalate on copper–cobalt–chromium catalyst at volumetric flow rate of 1000 h^{-1}

T, °C	τ, h	c_{VC}, at inlet,* mg m^{-3}	c_{DBPh}, mg m^{-3}		X_{DBPh}, %
			inlet	outlet	
400	1	1.5	2.5	0.5	80
		2.0	3.0	1.0	67
	24	1.5	3.0	0.8	73
		2.0	3.5	1.0	72
	25	1.5	2.5	0.5	80
		2.0	3.0	1.0	67
420		0.6	2.4	0	100
		0.5	2.6	0	100
	50	0.6	2.5	0	100
423		0.4	1.0	0	100
		0.6	1.5	0	100
		0.5	1.5	0	100

* The concentration c_{VC} is zero at the outlet, and X_{VC} is 100%, in all runs.

It can be seen that, when present together in a gas mixture, vinyl chloride and dibutyl phthalate are oxidized on this catalyst at 400–423°C. The oxidation of vinyl chloride is complete under any of the above conditions, and that of dibutyl phthalate, only above 420°C.

The chromium oxide catalyst was tested with industrial ventilation exhaust gases by a similar procedure at 425°C and volumetric flow rate of 1000 h^{-1}. Since waste gases contained CO in this case, we first checked the possibility of carbon(II) oxide oxidation on the catalyst in question. It was found that, under the given conditions, the oxidation of CO at its concentrations of up to 10 mg m^{-3} is complete even at 300°C. A study of waste gase purification to remove vinyl chloride, dibutyl phthalate, and CO on the chromium oxide catalyst at 425°C and volumetric flow rate of 1000 h^{-1} showed that, under the given conditions, the oxidation is complete for all the abovementioned toxic substances, present in waste gases formed in manufacture of the PVC film.

c_{VC}, mg m^{-3}	0.9	1.1	1.3
c_{DBPh}, mg m^{-3}	3.5	3.5	3.5
c_{CO}, mg m^{-3}	4.0	4.0	4.5
X, %	100	100	100

Table 2. Degree of purification X of ventilation exhaust gases to remove vinyl chloride and dibutyl phthalate on chromium oxide catalyst-sorbent in sorption-catalytic mode

T, °C	τ, h	c_{VC} at inlet,* mg m^{-3}	c_{DBPh} at inlet,* mg m^{-3}	T, °C	τ, h	c_{VC} at inlet,* mg m^{-3}	c_{DBPh} at inlet,* mg m^{-3}	T, °C	τ, h	c_{VC} at inlet,* mg m^{-3}	c_{DBPh} at inlet,* mg m^{-3}
72	1	1.0	5.0	74	145	0.5	–	After regeneration			
73	1	0.8	7.0	74	169	0.7	2.0				
73	1	1.1	5.0	74	169	0.4	2.5	76	22	0.6	3.0
73	25	0.9	1.0	74	169	0.4	2.0	76	22	0.6	6.0
73	25	0.7	5.0	73	217	0.6	3.0	76	22	0.6	5.0
73	49	0.6	3.0	73	217	0.7	2.5	75	46	1.0	5.5
73	49	0.5	2.0	73	217	0.6	2.5	75	46	0.8	6.5
73	49	0.6	2.5	76	337	0.5	3.5	75	46	0.8	6.0
72	145	0.8	–	76	337	0.6	–				
74	145	0.6	–	76	337	0.5	–				

* The concentrations c_{VC} and c_{DBPh} at the outlet are zero, and X_{VC} and X_{DBPh}, 100%, in all runs.

The concentrations c_{VC}, c_{DBPh}, and c_{CO} at the outlet were zero, and the degrees of purification X_{VC}, X_{DBPh}, and X_{CO} were 100%, in all tests.

The sorption-catalytic purification was studied on a chromium oxide catalyst composed of 35 wt % Cr_2O_3 supported on γ-Al_2O_3 and treated with 0.5 vol % HCl. According to the results of a laboratory study, this catalyst exhibits high sorption capacity for C_2H_3Cl. The tests were performed at a temperature of 70–75°C, ensuring chemisorption of vinyl chloride at a gas flow rate of 1000 h^{-1}. In the course of the study, the catalyst was preheated in air at 350°C for 2 h. After that the temperature was lowered to 75°C, and the reaction mixture was fed into the reactor. The results of these tests are presented in Table 2.

It can be seen that at 72–76°C and volumetric flow rate of 1000 h^{-1} the chromium oxide catalyst-sorbent effectively sorbed both vinyl chloride and dibutyl phthalate for 337 h, thus ensuring the absence of toxic impurities in the gas mixture at the reactor outlet.

The catalyst was regenerated in an air flow on heating to 400°C for 2 h, with CO_2 determined at the reactor outlet. After regeneration, the temperature in the reactor was lowered to 75°C, and the study of purification was continued. The data characterizing the operation of a regenerated catalyst are also presented in Table 2. These data confirm the efficiency of operation of the regenerated catalyst-sorbent in the sorption-catalytic mode. With a gas mixture containing up to 1 mg m^{-3} of vinyl chloride and up to 6.5 mg m^{-3} of dibutyl phthalate, these impurities were completely removed from the gas.

CONCLUSIONS

(1) The thermal-catalytic and sorption-catalytic methods for purification of ventilation exhaust gases formed in manufacture of the PVC film were studied on spinel-type catalysts containing no noble metals.

(2) The treatment of gases to remove vinyl chloride, dibutyl phthalate, and CO by oxidation on chromium(III) oxide catalysts is efficient at 400–425°C and volumetric flow rate of 1000 h^{-1}. For catalysts composed of copper(II) and cobalt(II) chromites the purification conditions are similar.

(3) In the chemisorption mode, gases are effectively purified to remove vinyl chloride and dibutyl phthalate at 70–75°C on a chromium oxide catalyst composed of 35 wt % Cr_2O_3 supported on γ-Al_2O_3 and treated with 0.5 vol % HCl solution.

REFERENCES

1. Vlasenko, V.M., *Teor. Eksp. Khim.*, 1993. vol. 29, no. 6, pp. 482–500.
2. Mukhutdinov, R. Kh., Bezrukova, N.A., and Peremetina, V.T., *Prom. San. Ochistka Gazov*, 1984, no. 6, pp. 15–16.
3. US Patent 4059675.
4. US Patent 4059676.
5. USSR Inventor's Certificate, no. 1191107.
6. USSR Inventor's Certificate, no. 1674933.
7. Peregud, E.A., and Gernet, E.V., *Khimicheskii analiz vozdukha promyshlennykh predpriyatii* (Chemical Analysis of Air at Industrial Plants), Moscow: Khimiya, 1973.

Russian Journal of Applied Chemistry, Vol. 75, No. 8, 2002, pp. 1265–1268. Translated from Zhurnal Prikladnoi Khimii, Vol. 75, No. 8, 2002, pp. 1291–1294.
Original Russian Text Copyright © 2002 by Kravchenko, Rudnitskii, Nesterenko, Kublanovskii.

ENVIRONMENTAL PROBLEMS OF CHEMISTRY AND TECHNOLOGY

Purification of Wastewater Containing Color Developers and Silver Ions under Conditions of Low-Temperature Plasma Electrolysis

A. V. Kravchenko, A. G. Rudnitskii, A. F. Nesterenko, and V. S. Kublanovskii

Ukrainian State University of Chemical Engineering, Dnepropertovsk, Ukraine

Vernadskii Institute of General and Inorganic Chemistry, National Academy of Sciences of Ukraine, Kiev, Ukraine

Received July 25, 2001; in final form, November 2001

Abstract—The action of glow discharge on aqueous solutions containing color developers and silver ions was studied. The influence of the main processing parameters, such as treatment time, current efficiency, current density, reaction zone pressure, and cathode material, was considered.

Some types of plasma, generated in glow discharge and other kinds of discharge, initiate, while acting upon aqueous solutions, various reactions whose main active agents are hydroxy and hydrogen radicals formed upon decay of water molecules. Plasma-induced oxidation is especially strong and occurs without any additional oxidizing agents. Unlike plasma reactions in the gas phase, these plasma-initiated reactions are reliably controllable. Chemical reactions caused by glow discharge plasma in aqueous solutions cannot be carried out by conventional methods.

Previously, the influence of glow discharge on liquid-phase systems containing silver and thiosulfate ions has been studied [1]. The main kinetic relationships for recovery of silver ions and decomposition of sodium thiosulfate in wastewater have been obtained. It has been shown [2, 3] that the glow discharge plasma efficiently affects decomposition of nonionic surfactants in solutions. It was of interest to consider the efficiency of glow discharge in decomposition of color developers contained in wastewater of photographic and motion-picture production.

EXPERIMENTAL

We used in the study a glow-discharge setup described in [1–3]. As objects of study served aqueous solutions containing 50 or 10 mg l^{-1} of color developer and 500 mg l^{-1} of Ag^+, modeling the real sewage.

Figure 1 shows how the color developer concentration varies with the time of glow discharge treatment. It can be seen that the concentration for the most part decreases at the beginning of the process. After a certain period of time the decomposition rate decreases dramatically.

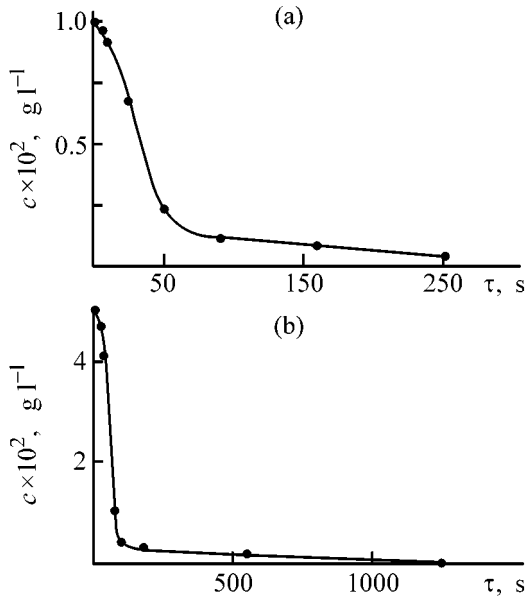

Fig. 1. Kinetic curves of consumption of color developers in aqueous solutions. (c) Concentration and (τ) time. Initial color developer concentration (mg l^{-1}): (a) 10 and (b) 50.

1070-4272/02/7508-1265 $27.00 © 2002 MAIK "Nauka/Interperiodica"

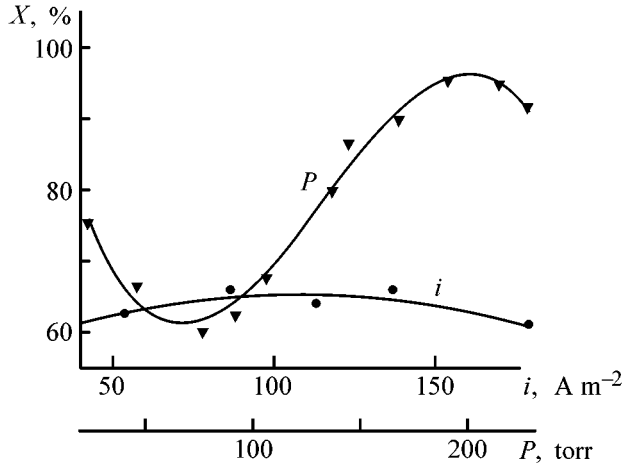

Fig. 2. The degree of purification, *X*, of aqueous solutions to remove color developers vs. current density *i* and pressure *P* in the reaction zone.

It should be noted that treatment with glow discharge changes the color of solutions containing color developers. This suggests that the reaction yields a colored intermediate. In the process, the colorless solution turns pink and then again colorless. This indicates that the oxidation is complicated by a number of subsequent chemical reactions, which was considered in detail for phenylenediamines in [4–5].

Published data and the experimental results obtained suggest that the initial substance, *p*-aminodiethylaniline sulfate, interacts with free electrons at the interface between the liquid and the ionized gas in the anode region (R = C_2H_5–):

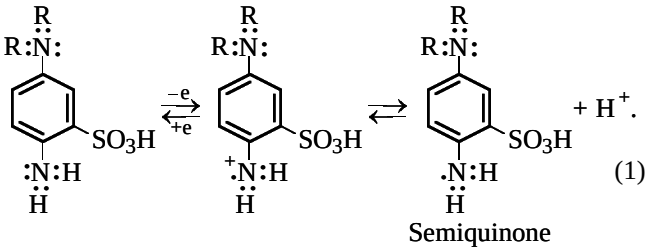

(1)

Then, loosing one more electron, semiquinone can be oxidized further to quinonediimine [6]:

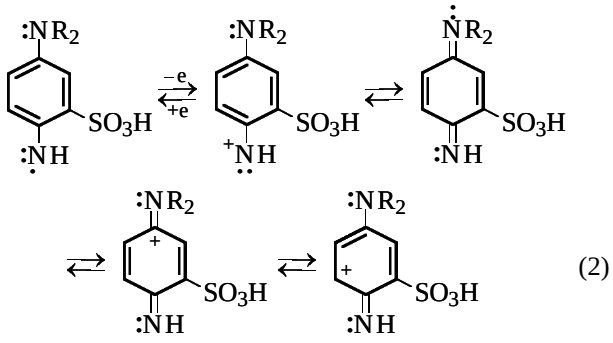

(2)

Reactions (1) and (2) are fast and cannot be the rate-determining stages. The limiting stage is transformation of quinonediimine into quinonemonoimine:

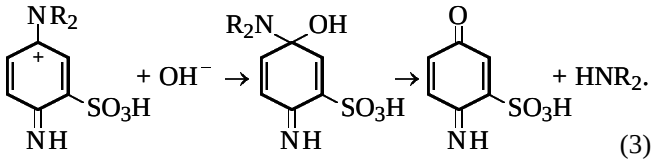

(3)

The initial imine group can be eliminated solely in an acid medium, since a doubly charged quinonediimine cation is the active species in the given reaction.

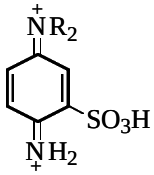

(4)

The qualitative analysis presented indicates the considerable potentialities of the method under consideration. These data are, however, insufficient for substantiating the choice of reactor. They can serve solely as a criterion for qualitative assessment of the systems presented. To describe the processes of nonequilibrium plasmochemical treatment in more detail, it is necessary to determine the dependence of the efficiency of these transformations on the reaction mass temperature, height at which the anode is placed over the liquid surface, discharge current, and pressure in the reaction zone.

Because all the reactions considered occur at the electrode–solution and electrode–gas phase interfaces, the process rate may depend on the current density per cathode area at constant current in the circuit and residual pressure in the reaction zone.

The results obtained in the study are presented in Fig. 2. It can be seen that variation of the current density within the permissible limits affects the degree of solution purification to remove color developers only slightly. The optimal current density is within 10–130 A m^{-2}. Beyond this range, the degree of purification decreases. Figure 2 also illustrates the influence exerted by the reaction zone pressure on the degree of color developer decomposition. The degree of solution purification is at a maximum at a pressure of 150–200 torr. With the pressure decreasing to 70 torr, the purification efficiency decreases, and

then increases upon further decrease in pressure. Apparently, such an unambiguous effect of pressure is due to concurrent reactions of dissipative absorption of the glow discharge energy by the gas phase and formation in it of active radicals captured by the liquid and initiating chemical reactions there.

Because the purification efficiency depends not only on the processes occurring at the gas–liquid interface, but is also affected by processes occurring on the cathode submerged in the solution, it was of interest to study the effect of the cathode material on the degree of purification. In this case, the choice of the cathode material may strongly affect the final result in purification of wastewater from motion-picture and photographic production. Figure 3 demonstrates the influence of the cathode material on the purification efficiency. Analysis of the data in Fig. 3 shows that the most acceptable cathode materials in decomposition of color developers are tin, braze, and steel.

As already mentioned, we studied the recovery of silver ions from wastewater formed in motion-picture and photographic production. The degree of Ag^+ recovery from aqueous solutions is presented in Fig. 4a as a function of the reaction zone pressure. It can be seen that the degree of purification grows markedly with pressure increasing to a certain value (110 torr) and then the process of silver ion deposition becomes slower. It is believed that the increasing pressure activates physicochemical effects associated with the growing amount of elementary events in both the gas phase and the liquid. At pressures above 110 torr the normal glow discharge transforms first into an abnormal glow discharge and then into an arc discharge. The potential distribution between the surface of the aqueous solution and the anode becomes uniform, which adversely affects the purification efficiency because of the considerable increase in the voltage across the electrodes. Below we show how the separation L between the liquid surface and the anode and the pressure P in the reaction zone affect the electrode voltage in recovery of silver ions from aqueous solutions:

P, torr	7.6	38	76	114	152
U, V	600	680	780	890	960
$L \times 10^3$, m	4	9	15	19	25
U, V	600	630	700	800	900

The distance through which the anode is raised above the reagent in deposition of silver ions from solution produces a similar effect (Fig. 4b), with, however, the working voltage across the discharge gap being somewhat lower. The dependence of the rate of nonequilibrium plasmochemical processes on interelectrode spacing is accounted for by the fact that this parameter is responsible for the forming anode and

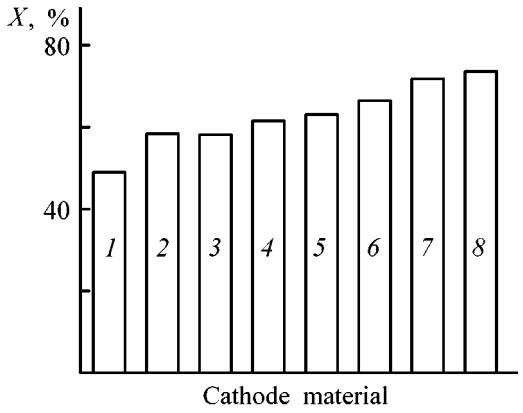

Fig. 3. Dependence of the degree of purification, X, on cathode material. Cathode: (*1*) copper, (*2*) carbon, (*3*) titanium, (*4*) aluminum, (*5*) lead, (*6*) steel, (*7*) brass, and (*8*) tin.

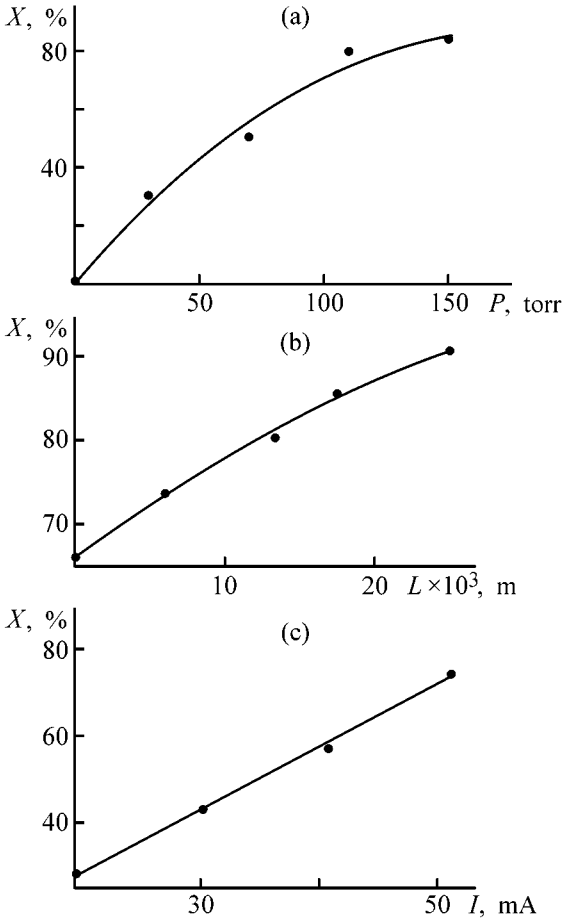

Fig. 4. Degree of purification, X, of solutions to remove silver ions vs. (a) reaction zone pressure P, (b) distance L between the anode and the liquid surface, and (c) current I.

cathode zones and determines their dimensions. The space charge is mainly located near the cathode, where the charge particle concentration is also at a maximum [7]. Consequently, the efficiency of the processes considered is determined by chemical transformations in this region. As the anode is moved away from the solution surface, the above-mentioned discharge zone is formed and the chemical processes associated with the contact action of glow discharge on the liquid are accelerated.

The main parameter ensuring deposition of heavy metal ions in plasmochemical treatment of waste-water, is the current strength in the glow discharge region. The dependence of the rate of the chemical reactions on the discharge current is shown in Fig. 4c. It can be seen that the degree of purification of the liquid also increases linearly with the current. It should be noted that the current can only be raised to 150 mA. Further increase in current results in the appearance of an arc and a drastic decrease in the process efficiency.

A sedimentation analysis of inhomogeneous liquid systems was made to determine the dispersity of the deposits obtained. A weighed portion of the deposit was dissolved in 0.1×10^{-3} m^3 of water. When necessary, the solution was dispersed with ultrasound in a UZDN-2T device and then poured into a FES-112 cuvette. The minimal fraction that can be detected by the device was 5–10 μm. The number of particles was recorded by a photosensitive element. In the given case, the size distribution of the particles was as follows (%): 5–10 μm 44, 10–25 μm 53, and >100 μm 3. Consequently, the recovered silver and its compounds mainly have particles 5–25 μm in size, and only their minor amount exceeds 100 μm or is less than 5 μm. The data presented here show convincingly that the dispersity of particles of the deposits formed exceeds somewhat that of deposits recovered from wastewater by the known technologies and qualified as "compressible."

It should be noted that the deposits formed in the course of the tests have composition and properties inviting additional theoretical and experimental investigation. In this communication, only some characteristics of the recovered solid phase are presented.

CONCLUSIONS

(1) The efficiency of low-temperature plasma electrolysis for purification of wastewater formed in photographic production is demonstrated.

(2) The main technological parameters determining the process intensity are the treatment time, reaction zone pressure, and distance from the anode to the phase boundary.

(3) It is suggested that the decomposition of color developers proceeds via formation of quinonemonoimines.

REFERENCES

1. Kravchenko, A.V., Barskii, B.D., Rudnitskii, A.G., *et al.*, *Zh. Prikl. Khim.*, 1998, vol. 72, no. 3, pp. 447–450.
2. Kravchenko, A.V., Rudnitskii, A.G., Nesterenko, A.F., and Kublanovskii, V.S., *Ukr. Khim. Zh.*, 1995, vol. 60, no. 11, pp. 749–752.
3. Kravchenko, A.V., Rudnitskii, A.G., Nesterenko, A.F., and Kublanovskii, V.S., *Gal'vanotekhn. Obrab. Poverkhn.*, 1996, vol. 4, no. 3, pp. 49–54.
4. Adams, R.N., *Electrochemistry at Solid Electrodes*, New York: Dekker, 1969.
5. *Organicheskaya elktrokhimiya* (Organic Electrochemistry), Petrosyan, V.A. and Feoktistov, L.G., Eds., Moscow: Khimiya, 1988, vol. 1.
6. Tohg, L.K.J. and Glesmann, M.C., *J. Am. Chem. Soc.*, 1957, no. 79, p. 583.
7. Bugaenko, L.T., Kuz'min, M.G., and Polak, L.S., *Khimiya vysokikh energii* (High-Energy Chemistry), Moscow: Khimiya, 1988.

Russian Journal of Applied Chemistry, Vol. 75, No. 8, 2002, pp. 1269–1274. Translated from Zhurnal Prikladnoi Khimii, Vol. 75, No. 8, 2002, pp. 1295–1300.
Original Russian Text Copyright © 2002 by Pashkevich, Mukhortov, Alekseev, Asovich.

ORGANIC SYNTHESIS AND INDUSTRIAL ORGANIC CHEMISTRY

Production of Fluorinated Ethanes Using Elemental Fluorine[1]

D. S. Pashkevich, D. A. Mukhortov, Yu. I. Alekseev, and V. S. Asovich

Prikladnaya Khimiya, Russian Research Center, St. Petersburg, Russia

Received January 17, 2002

Abstract—Scientific principles of industrial gas-phase fluorination of fluoroethanes with elemental fluorine were developed. Conditions for fluorination of low-fluorinated ethanes without rupture of the C–C bond were determined.

Fluorinated ethanes (FEs), such as 1,1-difluoroethane (1,1-DFE), 1,1,2-trifluoroethane (1,1,2-TFE), 1,1,1,2-tetrafluoroethane (1,1,1-2-TFE), pentafluoroethane (PFE), and hexafluoroethane (HFE), are widely used in modern industry as refrigerants, propellants, fire-extinguishing agents, gaseous insulators, reagents for plasmochemical preparation of very large-scale integrated circuits, etc. [1]. The annual consumption of these compounds by the world industry is about tens thousand tons.

Modern industrial production of FEs is based on catalytic fluorination of fluorochloroethanes and fluorochloroethylenes with HF. This process involves chlorine-containing ozone-infriendly compounds whose manufacture should be stropped in accordance with the Montreal protocol. In addition, this process yields large amounts of hydrogen chloride waste and requires replacement of environmentally hazardous chromium-magnesium fluoride catalyst at regular intervals, followed by its utilization. Hence, development of new procedures for producing fluoroethanes is an urgent problem. One of these procedures is gas-phase fluorination of low-fluorinated enthanes with molecular fluorine.

Fluorine is a commercially available product and can be used for production of fluorine-containing compounds.

The first experiments on gas-phase fluorination of ethane with molecular fluorine were performed by Prof. Bigelow's group in 1940–1950 [2–5]. In particular, the possibility of preparing HFE was demonstrated. However, this method has not been used for industrial production.

Production of highly fluorinated ethanes, such as PFE and HFE, by the conventional procedure is the most difficult. Hence, to develope a process for industrial production of highly fluorinated ethanes by fluorination with elemental fluorine of fluoroethanes with lower fluorine content we studied first the kinetics of 1,1,1,2-TFE fluorination. We found that this is a degenerate branched chain reaction terminated by the surface. The reaction order with respect to fluorine is 0.8. The activation energy and the pre-exponential factor in the Arrhenius equation are 50 kJ mol^{-1} and 2.8×10^5 s^{-1}, respectively [6, 7].

The thermal parameters of 1,1,1,2-TFE-F_2 system, calculated from these kinetic data by equation of the combustion theory, show that the steady-state thermal conditions are unsuitable for industrial synthesis [8].

These results stimulated us to study 1,1,1,2-TFE fluorination under non-steady-state thermal conditions, when the reaction temperature is close to the adiabatic temperature. To estimate the fluoroethane stability, we performed a number of experiments under conditions of thermal explosion. The results are presented in Table 1. At fluorine concentration lower than 30 vol %, the major reaction product is PFE and the yield of fluoromethanes is very low. At higher fluorine concentration the C–C bond is ruptured, with fluoromethanes formed.

To provide continuous production, the synthesis should be performed under the conditions of a steady-state self-propagating thermal wave.

In bench experiment, the reactant mixture was fed from a mixer into a reactor equipped with an elec-

[1] Reported at the Third International Conference "Chemistry, Technology, and Application of Fluorine Compounds," St. Petersburg, June 6–9, 2001.

1070-4272/02/7508-1269 $27.00 © 2002 MAIK "Nauka/Interperiodica"

Table 1. Composition of products of 1,1,1,2-TFE fluorination under conditions of thermal explosion

c_{F_2}, vol %	Composition, vol %					
	$C_2H_2F_4$	C_2HF_5	C_2F_6	CF_4	CHF_3	CH_2F_2
14.1	84.6	14.5	0.9	–	–	–
18.0	80.4	18.2	1.4	–	–	–
27.9	66.8	27.6	5.1	1.3	0.5	–
33.5	61.8	23.2	8.9	2.7	1.8	1.4
41.7	51.0	18.4	12.6	8.8	6.0	3.2
48.4	30.6	5.4	15.3	42.3	4.3	2.1
55.1	22.3	1.7	4.2	66.0	3.9	1.9

tric heater. As determined from the temperature of the gas flow, a steady-state self-propagating reaction front is formed at the fluorine concentration exceeding 20 vol %. This wave is initiated by the heated wall, rises along the flow, and is stabilized in the zone of reverse flows at the reactor inlet [8].

The composition of the reaction products is shown in Fig. 1a. At fluorine concentration lower than 30 vol %, the main product is PFE, and the 1,1,1,2-TFE conversion is 35%. At fluorine concentration exceeding 40 vol %, the content of fluoromethanes becomes high [9, 10].

Among FEs, production of HFE by the conventional procedure is the most difficult. In this work we studied formation of HFE from PFE in the wave fluorination mode. The composition of the reaction products is shown in Fig. 1b. At fluorine concentration of up to 30 vol %, the yield of fluoromethanes is very low and the main product is HFE [8–10].

In addition, we studied gas-phase fluorination of 1,1-DFE in the wave mode; the results are presented in Table 2.

Tables 1, 2 and Fig. 1a–1d show that rupture of the C–C bond of fluoroethane molecules (1,1,1,2-TFE, 1,1-DFE, and PFE) in the wave fluorination mode becomes appreciable at fluorine concentration exceeding 25–30 vol % [11].

The kinetic study of gas-phase fluorination of 1,1,1,2-TFE showed that this reaction is autocatalytic, with liberated HF being the catalyst [7].

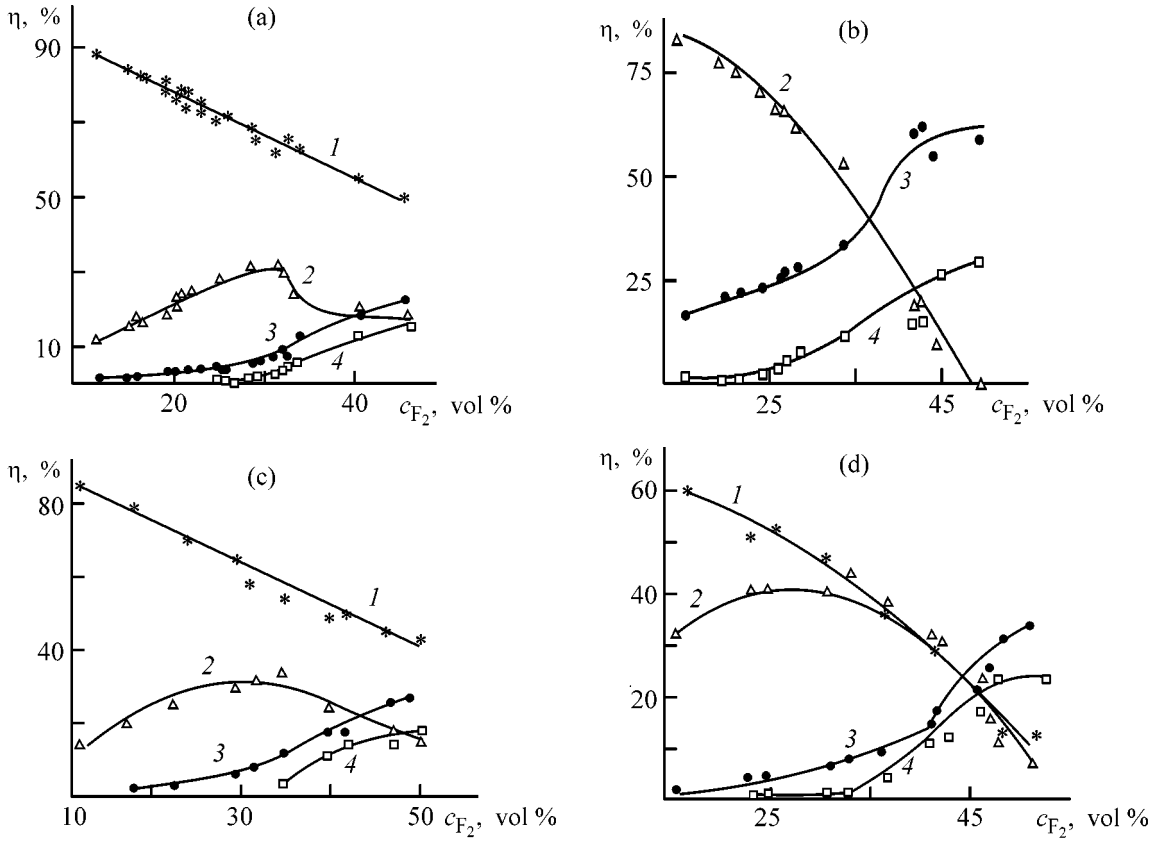

Fig. 1. Composition of the products of gas-phase fluorination in the wave mode of (a) 1,1,1,2-TFE, (b) PFE, (c) a mixture of 1,1,1,2-TFE with 5–10 vol % HF, and (d) a mixture of 32 vol % PFE with 68 vol % 1,1,1,2-TFE. (η) Conversion and (c_{F_2}) F_2 concentration. (*1*) 1,1,1,2-TFE, (*2*) PFE, (*3*) HFE, and (*4*) total content of fluoromethanes.

Table 2. Composition of the fluorination products of a 1,1-DFE (20 vol %)–1,1,1,2-TFE (80 vol %) mixture, obtained in the wave mode

c_{F_2}, vol %	Composition, vol %									
	CF_4	CHF_3	CH_2F_2	C_2F_6	C_2HF_5	CF_3CH_2F	CHF_2CHF_2	CF_3CH_3	CHF_2CH_2F	CHF_2CH_3
10.3	0.32	–	0.04	0.09	6.11	75.6	0.5	1.7	2.3	13.4
12.7	0.46	0.02	0.05	0.10	6.18	75.9	0.4	1.6	2.2	13.1
16.9	0.48	–	0.04	0.15	7.68	74.2	0.6	1.9	2.3	12.0
19.3	0.42	–	0.03	0.25	10.1	74.7	0.8	1.8	2.3	8.9
24.7	0.65	–	0.09	0.45	10.5	71.1	0.9	2.1	2.6	11.2
32.5	0.56	–	0.06	0.38	11.4	71.1	0.9	2.3	2.7	10.6

Table 3. Composition of the products of 1,1,1,2-TFE fluorination under conditions of self-propagating thermal wave in reactors with various diameters

Reaction conditions				Composition, vol %			
d, mm	u_m, m s^{-1}	Re	α, W m^{-2} K^{-1}	$C_2H_2F_4$	C_2HF_5	C_2F_8	FM*
10	1.0	572	25.6	62.4	31.0	5.5	1.1
4	1.5	368	64.1	64.1	30.1	4.9	0.9
3	1.4	140	85.6	64.1	30.0	5.1	0.8
2	1.2	147	128.2	63.8	30.2	5.2	0.8

* FM the total content of fluoromethanes in the reaction products.

We studied 1,1,1,2-TFE fluorination in the wave mode in the presence of 5–10 vol % HF [11]. In these experiments, the features of wave fluorination were similar to those observed with pure fluorine [11]. As seen from Fig. 1c, introduction of 5–10 vol % of HF has no effect on the composition of the products of the wave synthesis. Hence, the crude gas from electrolytic fluorine production can be used for the fluorination in the wave mode without additional purification.

To develop the process for industrial fluorination of fluoroethanes, the scaling principles for gas-phase fluorination in the wave mode should be determined. One of the features of combustion process is that the thickness of the reaction front in the laminar flare is tenths of a millimeter. In a turbulent flare of a tunnel burner, 80% conversion is reached within the length of five crater diameters [12]. This suggests that the compound is converted mainly at the temperature close to the adiabatic temperature. Then the composition of wave-mode fluorination products must be independent of the diameter of the reaction unit and of the gas flow rate in it.

To confirm the assumption that the composition of wave-mode fluorination products is independent of the reactor diameter, we performed the fluorination in reactors 10, 4, 3, and 2 mm in diameter at such a flow rate of the cold mixture which provides the same linear velocity of the gas [13]. The conditions of these experiments (reactor diameter d, flow rate of cold gas mixture u_m, Re number, and the coefficient of convective heat transfer from the reaction zone to the wall α) and the composition of the reaction products are presented in Table 3. The fluorine concentration in all the experiments was 30 vol %.

The composition of the products of wave-mode fluorination is independent of the coefficient of convective heat transfer α in the range 25–130 W m^{-2} K^{-1}, which confirms the absence of heat exchange in the reaction zone of fluorine with 1,1,1,2-TFE and allows prediction of the the synthesis results upon changing reactor size at the same initial fluorine concentration.

Thus, the fluorine concentration is the only parameter affecting the composition of wave-mode fluorination products, which simplifies construction and operation of the reactor [13].

The ignition parameters of 1,1,1,2-TFE-F2 mixture were calculated by the equations of the thermal theory of ignition in a gas flow [12]. These equations allow calculation of the wall temperature providing formation of self-propagating thermal wave from the kinetic

Table 4. Composition of the wave-mode fluorination products of a 1,1-DFE (14 vol %)–HFE (85 vol %) mixture at different fluorine concentrations

c_{F_2}, vol %	Composition, vol %									
	CHF_2–CH_3	CHF_2–CH_2F	CF_3–CH_3	CHF_2–CHF_2	CF_3–CH_2F	C_2HF_5	C_2F_6	CF_4	CHF_3	CH_2F_2
15.4	6.7	3.2	3.2	1.3	1.0	0.20	83.8	–	0.47	0.15
18.8	4.6	2.8	3.0	1.2	1.3	0.71	85.8	–	0.41	0.08
19.4	4.8	3.7	3.3	1.2	1.8	1.08	83.1	–	0.36	0.12
22.1	4.4	3.4	3.3	1.6	1.7	1.11	83.3	0.64	0.44	0.13
23.0	4.1	3.5	3.1	2.0	2.0	1.48	82.6	0.78	0.36	0.17
23.6	4.1	2.2	2.4	1.2	1.3	1.21	85.5	1.37	0.41	0.31
24.3	3.3	2.1	2.0	1.1	1.3	1.08	86.7	1.46	0.41	0.36
28.6	2.9	2.0	1.7	1.2	1.3	1.32	86.0	2.17	0.47	0.69
31.7	2.1	1.4	1.3	0.8	1.0	1.34	86.4	2.88	0.72	1.42

Table 5. Composition of wave-mode fluorination products of 1,1,1,2-TFE diluted with argon at different compositions of the initial mixture.

Initial mixture, vol %			Composition of reaction products, vol %					
Ar	F_2	$C_2H_2F_4$	$C_2H_2F_4$	C_2HF_5	C_2F_6	CF_4	CHF_3	CH_2F_2
84.4	13.9	1.72	–	1.1	97.6	–	0.4	0.9
88.1	10.1	1.80	0.5	0.9	97.3	–	–	1.3
90.7	7.4	1.85	3.9	6.0	88.0	–	–	3.2
90.6	6.6	2.79	3.8	14.6	76.6	–	2.1	2.8

parameters of the reaction and the parameters of the gas flow. At Re ~10^5 the temperature of the reactor wall should be 150–200°C. Under these conditions, a stable thermal wave is formed and detonation processes are ruled out. In addition, permissible flow rates not exceeding the rate of the thermal wave were calculated for different reactor diameters and Re = 35 000. These calculation show that 100 t of PFE can be annually produced from 1,1,1,2-TFE in a reactor 100 mm in diameter [8].

The predicted operation parameters were checked on a pilot unit with a reactor 20 mm in diameter. The fluorine concentration ranged from 22 to 28 vol %. The main reaction product of the wave synthesis was PFE [8].

One of the disadvantages of the wave mode is that synthesis should be performed at substoichiometric fluorine concentration. As noted above, for the content of fluoromethanes in the reaction products to be not higher than 1–2%, the maximal permissible fluorine concentration should be about 30%. Under these conditions, the conversion is relatively low.

To increase the conversion, the following operations should be performed. First, the sabstance to be fluorinated can be partially replaced by HFE, which is not involved noticeably in the reaction at the fluorine concentration lower than 30 vol %, or by other inert compound. Second, a sequence of series-connected wave reactors with intermediate cooling of the reaction products can be used. Third, intermediate fluorination products can be separated from the reaction products and recycled [12].

To illustrate the first approach, we studied fluorination of 1,1-DFE to trifluoroethanes in the wave mode (Table 4). Hexafluoroethane was used as the inert compound. The 1,1-DFE concentration in the initial mixture was 14%. This compound was contaminated with 0.35% CHF_3 and 0.49% CF_3CH_3. The 1,1-DFE conversion was as high as 80%; the selectivity of trifluoroethane formation was 50%. However, at the fluorine concentration exceeding 20 vol %, the TFM yield was relatively high. This is probably due to rupture of the C–C bond in the HFE molecule under the conditions of fluorination in the wave mode.

The first approach was also illustrated by wave-mode fluorination of 1,1,1,2-TFE to HFE, with argon used as a diluent of the reaction mixture. The conditions of these experiments and the composition of the reaction products are summarized in Table 5. In

the presence of argon diluent and at a fluorine excess, the conversion of the initial compound was almost quantitative and the selectivity of HFE formation was about 97%. The yield of fluoromethanes was low. It should be noted that the temperature of the reactor wall was 200–250°C. We failed to generate a thermal wave of gas-phase fluorination at the temperature of the reactor wall of 10°C.

To simulate the operation of a sequence of two series-connected wave reactors, we studied the synthesis of PFE from 1,1,1,2-TFE by fluorination of a PFE (32 vol %)-1,1,1,2-TFE (68 vol %) mixture in the wave mode (Fig. 1b).

The content of PFE formed under these conditions is maximal (43 vol %) at the fluorine concentration of 27 vol %. The HFE content is 6 vol % and fluoromethanes are virtually absent.

The ratio of the rate constants of fluorination of 1,1,1,2-TFE and PFE was estimated from the data presented in Fig. 1 b. At the fluorine concentration of 25 vol % (adiabatic temperature in the reaction zone 1000 K) the rate constant of 1,1,1,2-TFE fluorination is higher than that of PFE by a factor of 1.5. In this calculation, we assumed that 1,1,1,2-TFE is converted only into PFE, and PFE only into HFE. The activation energy of PFE fluorination was estimated to be 53 kJ mol^{-1}. We assumed that the activation energy of 1,1,1,2-TFE fluorination is 50 kJ mol^{-1} [7].

The activation energy of high-temperature fluorination of 1,1-DFE, estimated from the data presented in Table 2, is 44 kJ mol^{-1}. In this calculation, we assumed that 1,1-DFE is converted only into 1,1,1-TFE, 1,1,2-TFE, 1,1,1,2-TFE, and 1,1,2,2-TFE, and 1,1,1,2-TFE, only into PFE and HFE [11].

Based on the experimental data on wave-mode fluorination of 1,1,1,2-TFE, PFE, and their mixtures, we proposed a kinetic model of this process. Formation of both the substitution products and fluoromethanes is taken into account in this model. We suggested that the ratio of the activation energies of hydrogen substitution and degradative fluorination is equal to the ratio of the energies of the C–H and C–C bonds [14, 15].

Parameters of 1,1-DFE fluorination to a mixture of PFE and HFE in the ratio 3 : 1 in two-step and three-step wave reactors were calculated by this model, refined using the experimental data on 1,1-DFE fluorination. The fluorine concentration in each step was 23 vol %. Intermediate tetra- and trifluoroethanes were recycled.

Our calculations show that 1,1-DFE conversion in a series of three wave reactors with recycling of intermediate fluorination products can reach 90% [11].

EXPERIMENTAL

In the bench experiments were used the following chemicals: commercial 1,1,1,2-TFE (ICI company, UK); PFE, HFE, and 1,1-DFE produced by Prikladnaya Khimiya Russian Research Center on a pilot installation for enthylene fluorination with cobalt trifluoride; commercial hydrogen fluoride (Khimprom Joint-Stock Company); and commercial argon (Lentekhgaz plant).

To determine the kinetic parameters of 1,1,1,2-TFE fluorination under the steady-state thermal conditions, a mixture of 1,1,1,2-TFE and fluorine was passed through a 2-mm copper tube thermostat in which the temperature was maintained in the range from 105 to 148°C. The reaction time was controlled by varying the flow rate of the initial mixture and the tube length. The fluorine concentration in the initial mixture was 4–10 vol %, which provided fluorination under the isothermal conditions. Gas samples were taken at the tube outlet, neutralized, and analyzed chromatographically. The reactor scheme and experimental procedure were described in detail in [7].

Fluorination of 1,1,1,2-TFE was performed in a 25-mm steel ampule 150 mm long under the conditions of thermal explosion. An ampule was purged with a 1,1,1,2-TFE–F_2 mixture so as to provide tenfold gas exchange. Then the inlet and outlet valves were closed and the ampule was immersed in a heat-transfer agent heated to 100°C. The thermal explosion was monitored with the aid of a 200 μm Chromel–Copel thermocouple fixed inside the ampule without protective covers. The gaseous samples for chromatographic analysis were taken with a medical syringe.

The bench experiments on wave-mode fluorination of fluoroethanes were performed as follows. A fluoroethane-fluorine mixture was fed in a reactor, which was, unless otherwise noted, a steel tube 300 mm long and 10 mm in diameter. An electric heater initiating the wave process was fixed on the reactor surface in the vicinity of the outlet. A thermal wave rose from the heated region counter to the flow and was stabilized in the region of reverse flows at the reactor inlet. The reactor surface in this region was cooled with water to 10°C. Three Chromel–Copel thermocouples 200 μm in diameter were fixed without protective covers inside the reactors. The thermocouple junctions

were in line with the reactor axis. propagation of the thermal wave counter to the flow and its stabilization in the region of reverse flows was monitored, and the gas temperature in the reaction zone measured with the aid of the thermocouples. Gas samples for chromatographic analysis were taken at the reactor outlet and neutralized with chemical lime absorbent. The laboratory unit was also described in [8, 10].

The initial gaseous mixtures and neutralized reaction products were analyzed chromatographically on an LKhM-80 gas chromatograph (thermal conductivity detector, flow rate of the carrier gas, helium, 30 $cm^3\ min^{-1}$) at 50°C. A 6-m column was packed with Polisorb-10.

CONCLUSIONS

(1) The kinetics of gas-phase fluorination of fluoroethanes with molecular fluorine was studied.

(2) Our calculations demonstrated that the steady-state thermal conditions of gas-phase fluorination of fluoroethanes with fluorine are unsuitable for industrial synthesis.

(3) Gas-phase fluorination of fluoroethanes with fluorine under non-steady-state thermal conditions (thermal explosion and self-propagating thermal wave) was studied. The main process parameters were determined. This process can be industrially used.

(4) Based on the fact that the wave reaction zone is adiabatic, the principles for scaling of the gas-phase wave reactor were developed.

(5) The methods for increasing both conversion of the initial compounds and selectivity of formation of the target product formed in the wave reactor were proposed and the process parameters were calculated and studied experimentally.

REFERENCES

1. *Promyshlennye ftororganicheskie produkty: Spravochnik* (Commercial Fluorinated Organic Products: Handbook), Maksimov, B.N., Barabanov, V.G., Serushkin, I.L., *et al*. Eds., St. Petersburg: Khimiya, 1996.
2. Fukuhara, N. and Bigelow, L.A., *J. Am. Chem. Soc.*, 1941, vol. 63, pp. 2792–2796.
3. Gilbert, A. and Bigelow, L.A., *J. Am. Chem. Soc.*, 1950, vol. 72, pp. 4879–4882.
4. Robson, P., McLoughlin, V.C.R., Hynes, J.B., and Bigelow, L.A., *J. Am. Chem. Soc.*, 1961, vol. 83, p. 5010–1014.
5. Tyczkowski, E.A. and Bigelow, L.A., *J. Am. Chem. Soc.*, 1955, vol. 77, pp. 3007–3012.
6. Pashkevich, D.S., Mukhortov, D.A., Podpalkina, E.A., and Barabanov, V.G., Abstracts of Papers, *2-ya Mezdunarodnaya konferentsiya "Khimiya, tekhnologiya i primenenie ftorsoedinenii"* (Second Int. Conf. "Chemistry, Technology, and Application of Fluorine Compounds"), St. Petersburg, September 23–26, 1997, p. 53.
7. Pashkevich, D.S., Muhortov, D.A., Podpalkina, E.A., and Barabanov, V.G., *J. Fluorine Chem.*, 1999, no. 6, pp. 3–5.
8. Pashkevich, D.S., Alekseev, Yu.I., and Mukhortov, D.A., *Zh. Prikl. Khim.*, 1999, vol. 72, no. 12, pp. 2000–2007.
9. Pashkevich, D.S., Mukhortov, D.A., Alekseev, Yu.I., and Ryleev, G.I., Abstracts of Papers, *2-ya Mezdunarodnaya konferentsiya "Khimiya, tekhnologiya i primenenie ftrosoedinenii" (Second Int. Conf. "Chemistry, Technology, and Application of Fluorine Compounds")*, St. Petersburg, Sptember 23–26, 1997, p. 54.
10. RF Patent 2115645.
11. Pashkevich, D.S., Mukhortov, D.A., Alekseev, Yu.I., *et al.*, *Zh. Prikl. Khim.*, 2001, vol. 74, no. 7, pp. 1120–1125.
12. Khitrin, L.N., *Fizika goreniya i vzryva* (Physics of Combustion and Explosion), Moscow: Mosk. Gos. Univ., 1957.
13. Pashkevich. D.S., Muhortov, D.A., and Alekseev, Yu.I., Abstracts of Papers, *XV Int. Conf. on Chemical Reactors*, Helsinki (Finland) 2001, p. 178.
14. Millward, G.E. and Tschuikow-roux, E., *J. Phys. Chem.*, 1972, vol. 76, no. 3, pp. 292–295.
15. Tschuikow-roux, E., *J. Phys. Chem.*, 1971, vol. 75, no. 3, pp. 295–300.

Russian Journal of Applied Chemistry, Vol. 75, No. 8, 2002, pp. 1275–1279. Translated from Zhurnal Prikladnoi Khimii, Vol. 75, No. 8, 2002, pp. 1301–1305.
Original Russian Text Copyright © 2002 by Fokanov, Pavlov, Semenov, Maksimov, Morozov.

ORGANIC SYNTHESIS AND INDUSTRIAL ORGANIC CHEMISTRY

Photolysis of Perfluoropropylene-Methanol Mixture in Vacuum Ultraviolet[1]

V. P. Fokanov, A. B. Pavlov, V. N. Semenov, B. N. Maksimov, and A. V. Morozov

Prikladnaya Khimiya, Russian Research Center, St. Petersburg, Russia

Received January 17, 2002

Abstract—The products of reaction of C_3F_6 with CH_3OH, initiated by vacuum ultraviolet, were determined. The kinetics scheme of the process was proposed. The parameters of the kinetic processes were calculated. The feasibility of photochemical preparation of 2,2,3,4,4,4-hexafluoro-1-butanol was analyzed.

One of methods for introducing perfluoroalkyl groups in molecules of organic compounds is addition of these groups to unsaturated hydrocarbons in the course of radical telomerization [1, 2]. Many fluorinated organic compounds exhibit absorption only in the range of vacuum ultraviolet (VUV). A great number of compounds with required properties can be prepared by photoreactions of fluorinated organic compounds under exposure to VUV. In this work, we examined a new route to polyfluorinated 1-butanol: irradiation of a C_3F_6–CH_3OH mixture with 185-nm light.

Perfluoroolefins, as well as lower alcohols, do not absorb in the range above 200 nm. Photolysis of C_2F_4 in VUV was studied in [3, 4]. Continuous absorption of C_3F_6 in VUV, determined in our works, suggests radical photolysis of this compound. Reactions of fluoroolefins with alcohols, usually initiated by peroxides or γ-radiation, yield telomers [5]. Photochemical initiation, unlike these methods, allows control of the process owing to selective activation of definite bonds. The aim of this study was do develop a new photochemical synthesis procedure. In particular, we studied possible reaction pathways, determined the yield of the reaction products and the irradiation efficiency, and constructed a mathematical model of the photolysis.

EXPERIMENTAL

Photochemical studies were performed in a cylindrical quartz reactor. A 70 W low-pressure mercury lamp [6] 0.9 m long was fixed at the reactor axis. The power of this lamp, measured at 185 and 254 nm, was 1 and 20 W, respectively. The photoreactor was equipped with a vacuum system used to fill the reactor with the initial reagents and to sample the reaction mixture. The photolysis products were analyzed on an HP5972 chromato–mass spectrometer with an HP-PLOT capillary column coated with Al_2O_3. The mass spectra were assigned with the aid of WILEY.138.L library.

To understand the kinetics of synthesis of polyfluorinated 1-butanol, we studied perfluoropropylene photolysis. Initially we studied C_3F_6 photolysis at a pressure of 4 kPa and exposure time of 15 min. Under these conditions, C_3F_6 is quantitatively converted into perfluorocyclobutane derivatives (up to 45%) and perfluoroparaffin isomers.

Formation of perfluoromethylcyclobutane, 1,2-, and 1,3-bisperfluoromethylcyclobutane (in the ratio 1.6 : 1.4 : 1) can be described by the following scheme:

$$C_3F_6 + h\nu \rightarrow C_3F_6^*(+M) \rightarrow :CF_2 + CF_3CF:,$$

$$C_3F_6^* + (M) \rightarrow C_3F_6,\ 2:CF_2 \rightarrow C_2F_4,$$

$$CF_3CF: + (M) \rightarrow C_2F_4,$$

$$C_2F_4 + h\nu \rightarrow C_2F_4^*(+M) \rightarrow 2:CF_2,$$

$$C_2F_4^* + (M) \rightarrow 2:C_2F_4,$$

$$C_2F_4 + C_3F_6^* \rightarrow C_5F_{10}\ \text{(perfluoromethylcyclobutane)},$$

$$C_2F_4^* + C_3F_6 \rightarrow C_5F_{10},$$

$$C_3F_6 + C_3F_6^* \rightarrow C_6F_{12}\ \text{(perfluorodimethylcyclobutane isomers)},$$

where perfluoropropylene in the electronically excited state is marked with an asterisk. This is probably the

[1] Reported at the Third International Conference "Chemistry, Technology, and Application of Fluorine Compounds", St. Petersburg, June 6–9, 2001.

1070-4272/02/7508-1275 $27.00 © 2002 MAIK "Nauka/Interperiodica"

Table 1. Chromatogram* of the products of C_3F_6 photolysis and calculated component concentrations *c*

τ_{ret}, min	*S*, %	Component	*c*, %
2.99	0.192	C_2F_6	1.28
3.71	0.751	C_2F_4	0
5.99	1.087	C_3F_8	0.65
15.39	5.312	*i*-C_4F_{10}	8.0
15.47	4.082	C_4F_{10}	
17.45	12.537	C_5F_{10} (methylcyclobutane)	12.0
18.55	0.015	$CF_3CF{=}CFCF_3$	0
19.49	4.521	*i*-C_5F_{12}	8.9
19.54	3.486	C_5F_{12}	
19.66	10.734	C_6F_{12} (1,2-dimethylcyclobutane)	18.2
19.97	7.774	C_6F_{12} (1,3-dimethylcyclobutane)	
22.11	17.820	$C_2F_5CF_2CF(CF_3)CF_3$	30.1 (Sum of C_6F_{14} isomers)
22.19	5.945	C_6F_{14}	
22.28	5.898	$CF_3CF(CF_3)CF(CF_3)CF_3$	
25.09	3.644	$CF_3CF(CF_3)CF_2CF(CF_3)CF_3$	9.2 (Sum of C_7F_{16} isomers)
25.27	6.241	$C_2F_5CF_2CF_2CF(CF_3)CF_3$	
25.39	0.154	$C_2F_5CF_2CF(CF_3)C_2F_5$	
25.47	2.608	C_7F_{16}	
30.26	0.688	$CF_3CF(CF_3)CF_2CF(CF_3)C_2H_5$	4.8 (Sum of C_8F_{18} isomers)
30.57	2.189	$C_2F_5CF_2CF_2CF_2CF(CF_3)CF_3$	
30.93	2.337	$C_2F_5CF_2CF_2CF(CF_3)C_2F_5$	
31.41	1.169	C_8F_{18}	
36.57	0.764	Σi-C_9F_{20}	2.8

* (τ_{ret}) Retention time and (*S*) peak area.

triplet state that is involved in deactivation, predissociation degradation into radicals, and reactions with other molecules, ultimately resulting in cyclodimerization.

The presence of trace amounts of perfluoro-2-butene (~0.01%) and C_2F_4 (<1%) in the reaction mixture agrees with the reaction scheme, since C_2F_4 is converted incompletely and the perfluoro-2-butene formation by recombination of methylcarbene radical is considerably slower than the C_2F_4 formation. "Biradical" formation was detected in C_3F_6 pyrolysis [7], i.e., at significantly lower excitation energy of perfluoropropylene. Although cyclodimerization proceeds mainly by degradation of compounds containing a double bond to form saturated compounds and is typical of C_3F_6 pyrolysis (*T* ~200°C), it occurs in the course of C_3F_6 photolysis too.

Photolysis of C_2F_4 under the same conditions occurs simslarly. The main product, perfluorocyclobutane, is formed after irradiation of perfluoroethylene for 3 min (the C_2F_4 conversion is ~15%). The process can be described by the above kinetic scheme, since, in both cases, predissociation degradation yields difluorocarbene. However, C_3F_6 photolysis is a more complex process and yields a series of paraffin isomers, from perfluoropropane to perfluorononane. This process involves an additional pathway initiated by the $:CF_2$ biradical and atomic fluorine formed in the primary photolysis step.

The weakest bonds of a molecule excited by a VUV quantum are ruptured owing to energy redistribution after molecular collisions. Several pathways of $C_3F_6^*$ dissociation are possible. The excess energy of photodissociation products was estimated on the basis of the energy balance and analysis of fluorocarbon fragments of saturated polyfluorinated products of C_3F_6 photolysis performed at a large excess of hydrocarbon. Based on the results of this estimation, we suggest the following scheme of $C_3F_6^*$ dissociation:

$$C_3F_6^* + (M) \rightarrow \cdot CF{=}CFCF_3 + \cdot F,\ E_{exc}\ 22 \text{ and } 158 \text{ kJ mol}^{-1}, \text{ respectively,}$$

$$C_3F_6^* + (M) \rightarrow \cdot CF{=}CF_2 + \cdot CF_3,\ E_{exc}\ 31 \text{ and } 36 \text{ kJ mol}^{-1}, \text{ respectively.}$$

The secondary processes can involve reactions with "hot" radicals $\cdot CF_3'$ and $\cdot F'$, with subsequent photodegradation of the fragments formed. The first photolysis step can be described by a superposition of the above reactions:

$$C_3F_6 + h\nu \rightarrow C_3F_6^*(+M) \rightarrow \cdot CF_3 + \cdot F + C_2F_2,$$

which agrees well with the kinetic scheme of formation of fluoroparaffin isomers presented in Table 1.

Subsequent transformations involve addition of fluorine atom to double bonds to form $\cdot R_F$ radicals ($\cdot R_F$, $\cdot C_3F_7$, $\cdot C_2F_5$, and $\cdot CF_3$) recombining to give a series of paraffin isomers. The rate constants of radical recombination decrease appreciably in going from linear to branched structures and with increasing number of carbon atoms [8]. Therefore, recombination of branched radicals, $\cdot C_4F_9$ and higher, was disregarded in the kinetic scheme. The C_7–C_9 isomers may arise in the photolysis products in the step of formation of methylcyclobutanes, when $\cdot R_F$ radicals recombine with the $:C_6F_{12}$ biradical, which has no time to form a four-membered ring.

Photolysis of C_3F_6 to form detectable products is initiated to the same extent by difluorocarbene and atomic fluorine generated in primary photolysis steps. Generally C_3F_6 is photolyzed under the conditions when the rate of reactions of excited $C_3F_6^*$ molecules is comparable with that of predissociation degradation followed by secondary and tertiary radical reactions, which strongly complicates the photolysis mechanism. To understand the photolysis mechanism, mathematical modeling can be used.

A mathematical model of C_3F_6 photolysis was developed by comparing experimental and calculated data on the composition of the reaction products. The kinetics scheme includes 50 reactions whose constants were taken from the literature or were estimated by extrapolation of the known rate constants of homologs, taking into account the steric factors. A system of differential kinetic equations of these reactions was constructed and integrated by the Gear procedure [9].

The time dependeces of the concentration of the photolysis products are adequately described by the kinetic model (Table 1). The calculations show that C_3F_6 is completely decomposed after 100s of irradiation. The convergence of the calculated and experimental concentrations can be improved by varying the rate constants of the reactions and quantum yields of the products and by recording more exactly the absorption spectra of the radical products. A model calculation confirmed the occurrence of the main reactions of C_3F_6 photodissociation.

Synthesis of polyfluorinated 1-butanol by continuous irradiation of a C_3F_6–CH_3OH mixture with VUV for 15 min was studied. Synthesis was performed at three ratios of the partial pressures of the components C_3F_6 : CF_3OH = 4 : 0.8, 4 : 4, and 0.8 : 4. Under these conditions, the ratio of the absorption coefficients of C_3F_6 and CH_3OH at 185 nm are 75, 15, and 3, respectively. This allows evaluation of the effect of the CH_3OH photolysis on the formation of the target product.

The fact that the chromatograms of the photolysis products of C_3F_6 and the initial mixture C_3F_6 : CH_3OH = 4 : 0.8 are similar indicates that CH_3OH is not involved appreciably in the radical process and is converted mainly by addition to the double bond

$$C_3F_6^* + CH_3OH \rightarrow CF_3CHFCF_2CH_2OH.$$

The yield of 2,2,3,4,4,4-hexafluoro-1-butanol is 20%. This reaction is responsible for formation of about 90% of the photolysis products. Telomerization of $C_3F_6^*$ with CH_3OH is more intense than C_3F_6 dimerization. Side recombination reactions yield up to 1.5% fluorinated ethers [$(C_3F_6 + \cdot F) + CH_3O\cdot \rightarrow C_3F_7OCH_3$, $(C_3F_6 + \cdot CF_3) + CH_3O\cdot \rightarrow C_4F_9OCH_3$] and up to 6.2% R_FH ($\cdot R_F = \cdot CF_3$, $\cdot C_4F_9$, $\cdot C_5F_{11}$, $\cdot C_6F_{13}$). Compounds R_FH are formed mainly by recombination with the $\cdot CHF_2$ radical

$$\cdot CHF_2 + (C_3F_6 + \cdot F) \rightarrow C_4HF_9,$$

$$\cdot CHF_2 + (C_3F_6 + \cdot CF_3) \rightarrow C_5HF_{11},$$

$$\cdot CHF_2 + (C_3F_6 + \cdot C_2F_5) \rightarrow C_6HF_{13},$$

$$(C_3F_6 + \cdot H) + (C_3F_6 + \cdot F) \rightarrow C_6HF_{13}.$$

This system of three-step consecutive reactions accounts for the absence of C_2HF_5 and C_3HF_7 in the photolysis products. The radical $\cdot CHF_2$ is effectively formed by the reactions $:CF_2 + \cdot H \rightarrow \cdot CHF_2$, $:CF_2 + CH_3O\cdot \rightarrow \cdot CHF_2 + CH_2O$. Formation of C_2HF_3 traces is due to the reactions $C_2F_2 + \cdot F \rightarrow \cdot C_2F_3$, $\cdot C_2F_3 + CH_3OH \rightarrow C_2HF_3 + CH_3O\cdot$, or $\cdot CF_3' + CH_3O\cdot \rightarrow C_2HF_3 + H_2O$. CH_3CF_3 is formed by the reactions $\cdot CF_3 + \cdot CH_3 \rightarrow CH_3CF_3$ or $\cdot CF_3' + CH_3O\cdot \rightarrow CH_3CF_3 + O:$ ($\cdot CF_3'$ is "hot" radical). Methanol is involved in photolysis and in reactions with fluorine radicals:

$$CH_3OH + h\nu \rightarrow \cdot H + CH_3O\cdot \ (79\%),$$

$$CH_3OH + h\nu \rightarrow CH_2O\ H_2 \ (20\%),$$

$$CH_3OH + h\nu \rightarrow \cdot CH_3 + \cdot OH \ (1\%) \ [10],$$

$$\cdot R_F + CH_3OH \rightarrow R_FH + CH_3O\cdot \ (85\%),$$

$$\cdot R_F + CH_3OH \rightarrow R_FH + \cdot CH_2OH \ (15\%) \ [11].$$

The main reactions competing with the formation of the fluornated alcohol are cyclodimerization of C_3F_6 and predissociation decomposition of C_3F_6. Photolysis of CH_3OH has virtually no effect on the synthesis. Chromatograms of the products formed in photolysis of the C_3F_6–CH_3OH system are presented in Table 2 in order of increasing retention time.

The yield of 2,2,3,4,4,4-hexafluoro-1-butanol decreases to 11.5% with increasing CH_3OH content in the initial mixture (C_3F_6 : CH_3OH = 4 : 4). The total content of the products of chemical reactions of the photolysis products increases to 60%, and the selectivity of the alcohol formation decreases from 90 to 19%. Among the photolysis products, 2,2,3,4,4,4-

Table 2. Chromatograms of identified products of photolysis of C_3F_6–CH_3OH mixture at various partial pressures of the components

τ_{ret}, min	Composition, %, at indicated C_3F_6 : CH_3OH ratio, kPa : kPa		
	4 : 0.8	4 : 4	0.8 : 4
5.67		$CH_2=CF_2$ (3.2%)	
14.21	C_2HF_3 (0.13%)	C_2HF_3 (3.9%)	
14.74	CHF_3 (0.27%)	CHF_3 (2.3%)	CHF_3 (6.9%)
16.52	CF_3CH_3 (0.13%)	$C_2H_3F_3$ (3.1%)	$C_2H_3F_3$ (12.1%)
17.13	$C_3F_7OCH_3$ (0.32%)		
19.35	C_4HF_9 (1.65%)	C_4HF_9 (10%)	C_4HF_9 (+$C_3H_2F_6$) (8.1%)
19.38		$CF_3CHFCF_2C(O)H$ (30.7%)	
19.63		$C_2F_5CH_3$ (4.6%)	$C_3H_3F_5$ (13%)
20.02		$CF_2=CFCHF_2$ (1.5%)	
20.24	$C_4F_9OCH_3$ (1.25%)		
20.38		$CH_2=CFCF_3$ (2%)	
21.60	C_5HF_{11} (1.2%)	C_5HF_{11} (4.9%)	C_5HF_{11} (5%)
21.62	$CF_3CHFCF_2CH_3$ (0.6%)	$C_4H_4F_6$ (1.1%)	
22.22		$C_3F_7CH_3$ (3.4%)	$C_4H_3F_7$ (6.7%)
22.30			$CHF_2CF_2CH_2F$ (5%)
22.35	$CF_3CHFCF_2CH_2OH$ (90.8%)	$C_4H_4F_6O$ (19%)	
23.77			$CHF_2CF_2CH_3$ (10.5%)
23.84	C_6HF_{13} (3.1%)	C_6HF_{13} (6.5%)	C_6HF_{13} (11.2%)
24.40	$CHF_2CF_2CF(CF_3)CHF_2$ (0.5%)	$C_5H_2F_{10}$ (3.5%)	
25.75			$CH_3CF_2CF_2CH_3$ (10.7%)

hexafluorobutanal is characterized by the maximal yield (30%). As the temperature increases, this compound can be formed by the reaction

$$C_3F_6^* + CH_3OH \rightarrow CF_3CHFCF_2C(O)H + H_2$$

or the secondary reaction

$$C_3F_6^* + CH_2O \rightarrow CF_3CHFCF_2C(O)H.$$

The number of the products of radical reactions increases by approximately a factor of 5. The total content of R_FH compounds increases to 24%. New compounds R_FCH_3 with total content of up to 12% are formed instead of ethers by recombination $\cdot R_F + \cdot CH_3 \rightarrow R_FCH_3$, where $\cdot CH_3$ is generated by the reaction $\cdot H + CH_3OH \rightarrow \cdot CH_3 + H_2O$. These compounds can also be formed by reactions $\cdot R_F + CH_3O\cdot \rightarrow R_FCH_3 + O{:}$. The contribution of these reactions increases with temperature. The heating of the reaction mixture is due to a stronger absorption in the system owing to an increase in its optical density. The increase to approximately 10% in the content of polyolefins ($CF_2=CFCHF_2$, $CH_2=CFCF_3$, $C_2H_2F_2$, C_2HF_3 formed in reactions like $\cdot CF_3 + CH_3 \rightarrow C_2H_2F_2 + HF$) that were not subjected to photolysis is due to intensification of the pyrolytic processes. The kinetic model of the process becomes severely complicated, since CH_3OH photolysis and some temperature-dependent reactions should be taken into account.

No products of addition to the double bond of C_3F_6 were detected in the reaction mixture of photolysis at C_3F_6 : CH_3OH = 0.8 : 4. All the products of the reaction of C_3F_6 with CH_3OH are formed by radical reactions initiated by the photolysis products of C_3F_6 and CH_3OH. The content of R_FH and R_FCH_3 increases to 31 and 32%, respectively. The other products are polyfluorinated paraffins and olefins. Trace amounts of CH_2O, CO_2, HF, H_2O, CF_3OCF_3, etc. are also formed. The chromatograms of the main reaction products are presented in Table 2.

CONCLUSIONS

(1) Photolysis of perfluoropropylene by vacuum ultraviolet was studied. The photolysis products were determined. The kinetic scheme of the process was proposed.

(2) Irradiation of a C_3F_6 : CH_3OH mixture (4 : 0.8) with vacuum ultraviolet yields 2,2,3,4,4,4-hexafluoro-1-butanol in 20% yield. The yield of this compound decreases with increasing CH_3OH content in the mixture. The calculated composition of photolysis prod-

ucts agrees well with the composition of the products formed in the photochemical reactor.

REFERENCES

1. Furin, G.G., *Usp. Khim.*, 2000, vol. 69, no. 6, pp. 538–571.
2. Meubdoerffer, V.J.N. and Niederprum, H., *Chem. Ztg.*, 1980, vol. 104, no. 2, pp. 45–51.
3. Dacey, J.R., Disc. Faraday Soc., 1953, no. 12, pp. 84–89.
4. Furin, G.G., *Zh. Org. Khim.*, 1997, vol. 33, no. 9, pp. 1287–1319.
5. Freidlina, R.F., Velichko, F.K., Zlotskii, S.S., *et al.*, *Radikal'naya telomerizatsiya* (Radical Telomerization), Moscow: Khimiya, 1988.
6. *Spravochnaya kniga po svetotekhnike* (Handbook on Illumination Engineering), Aizenberg, Yu.B., Ed., Moscow; Energoatomizdat, 1983.
7. Buravtsev, N.N. and Kolbanovskii, Yu.A., *Materialy 3-i Mezhdunarodnoi konferentsii "Khimiya, teknologiya i primenenie ftorsoedinenii - CTAF-2001"* (Proc. Third Int. Conf. "Chemistry, Technology, and Application of Fluorinated Compounds - CTAF-2001"), St. Petersburg, June 6–9, 2001, p. 123.
8. Calvert, J.G. and Pitts, J.N., *Jr., Photochemistry*, New York: Willey, 1966,
9. Polak, L.S., Gol'denberg, M.Ya., and Levitskii, A.A., *Vychislitel'nye metody v khimicheskoi kinetike* (Calculation Procedures in Chemical Kinetics), Moscow: Nauka, 1984.
10. Bunsenges, B., *J. Phys. Chem.*, 1968, vol. 72, no. 4, pp. 138–153.
11. Kondrat'ev, V.N., *Konstanty skorosti gazofaznykh reaktsii: Spravochnik* (Rate Constants of Gas-Phase Reactions: Handbook), Moscow: Nauka, 1970.

Russian Journal of Applied Chemistry, Vol. 75, No. 8, 2002, pp. 1280–1282. Translated from Zhurnal Prikladnoi Khimii, Vol. 75, No. 8, 2002, pp. 1306–1308.
Original Russian Text Copyright © 2002 by Nadim, Guseinova, Magerramov, Allakhverdiev.

ORGANIC SYNTHESIS AND INDUSTRIAL ORGANIC CHEMISTRY

Synthesis and Antimicrobial Properties of Fluorinated 1,2-Aminopropanethiols

Kh. Kh. Nadim, A. T. Guseinova, A. M. Magerramov, and M. A. Allakhverdiev

Baku State University, Baku, Azerbaijan

Kuliev Institute of Chemistry of Additives, Azerbaijan Academy of Sciences, Azerbaijan

Received March 28, 2002

Abstract—Reactions of 1,2-aminopropanethiols with methyl trifluoropyruvate were studied, and the antibacterial and fungicidal activity of the resulting trifluoromethyl derivatives as additives to lubricants was examined.

Proceeding with investigations on synthesis of 1,2-aminopropanethiols and their derivatives [1–7], we performed in this study the reactions of 1,2-aminopropanethiols with methyl trifluoropyruvate with the aim to prepare the corresponding trifluoromethyl derivatives. The reaction of various aromatic amines with methyl trifluoropyruvate was comprehensively studied in [8–10]. The reaction involves alkylation of the aromatic ring of the amines and yields the corresponding trifluoromethyl derivatives. However, this reaction has not been performed previously with *N*-aryl-substituted 1,2-aminopropanethiols. Owing to the presence of the reactive NH and SH groups in their molecules, several reaction pathways may be possible along with C-alkylation, such as S-alkylation and cyclization under the action of strongly electrophilic methyl trifluoropyruvate.

We found that 1,2-aminopropanethiols **I**–**V** react with methyl trifluoropyruvate along a single pathway, alkylation of the aromatic ring at the *p*-position relative to the NH group:

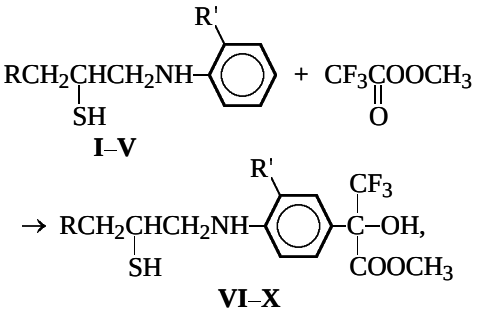

I–**V** → **VI**–**X**

where R = H, R' = H (**VI**), CH_3 (**VII**), CH_3O (**VIII**); R = CH_3O, R' = CH_3 (**IX**), CH_3O (**X**).

Table 1. Yields, constants, and elemental analyses of trifluoromethyl-substituted 1,2-aminopropanethiols

Comp. no.	Yield, %	n_D^{20}	R_f	C	H	N	F	S	Empirical formula
				found, % / calculated, %					
VI	51	1.4950	0.23	48.16 / 48.29	4.85 / 4.99	4.22 / 4.33	17.74 / 17.63	9.77 / 9.92	$C_{13}H_{16}NO_3F_3S$
VII	49	1.4990	0.14	49.96 / 49.84	5.25 / 5.38	4.26 / 4.15	16.73 / 16.89	9.33 / 9.50	$C_{14}H_{18}NO_3F_3S$
VIII	55	1.5660	0.19	47.46 / 47.59	5.02 / 5.13	3.80 / 3.96	16.01 / 16.13	8.92 / 9.07	$C_{14}H_{18}NO_3F_3S$
IX	53	1.6067	0.16	49.16 / 49.04	5.62 / 5.49	3.62 / 3.81	15.34 / 15.51	8.59 / 8.73	$C_{15}H_{20}NO_4F_3S$
X	44	1.5990	0.18	47.11 / 46.93	5.07 / 5.26	3.49 / 3.65	14.99 / 14.87	8.48 / 8.36	$C_{15}H_{20}NO_5F_3S$

1070-4272/02/7508-1280 $27.00 © 2002 MAIK "Nauka/Interperiodica"

The initial aminopropanethiols **I**–**V** were prepared by the reactions of 1,2-epithiopropane and 1,2-epithio-3-methoxypropane with appropriate aromatic amines.

The physicochemical constants of **VI**–**X** are listed in Table 1.

The structure of **VI**–**X** was proved by IR and ^{1}H NMR spectroscopy, and the purity, by elemental analysis and thin-layer chromatography.

The IR spectra of **VI**–**X** contain a strong band at 1730–1740 cm^{-1}, characteristic of esters. A very weak SH band is observed at 2530–2570 cm^{-1}. The overlapping bands of the OH and NH groups are observed at 3350–3370 cm^{-1}. The bands at 1140 and 970 cm^{-1} correspond to stretching vibrations of the C–F bonds in the CF_3 group.

The ^{1}H NMR spectra of **VI**–**X** contain signals of methyl (1.25–1.30 ppm), NCH_2, and methine (3–4 ppm) protons. The CH_3Ar protons give a singlet at about 2.3 ppm, and the ester methyl protons, a singlet at 3.7–3.8 ppm.

The CH_3OAr protons in **VIII** and **X** give signals at 3.65 ppm. The downfield multiplets at 6.2–7.1 ppm in the spectra of all the compounds correspond to nonequivalent protons of the benzene ring.

Fluorinated 1,2-aminopropanethiols **VI**–**X** were tested as antimicrobial additives to Vaseline oil according to GOSTs (State Standards) 9.052–88 and 9.085–78. Tests were performed with *Pseudomonas aeruginosa* bacteria and *Aspergillus niger* and *Candida tragicalic* fungi.

The results of the tests are listed in Table 2. Straight Vaseline oil shows poor biological resistance and degrades under the action of these microorganisms.

Compounds **VI**–**X** exhibit pronounced fungicidal and antibacterial activity at low concentrations (0.1–1.3%); they are readily soluble in Vaseline oil and do not stimulate corrosion. Compounds **VI**–**X** are more effective than a commercial antimicrobial additive, butyl salicylate, used as reference. As seen from Table 2, compounds **VIII** and **X** are the most active. With these compounds, the suppression zone width for fungi is 2.4 cm, whereas with butyl salicylate it is considerably smaller: 0.7 cm.

Table 2. Antimicrobial activity of **VI**–**X**

Comp. no.	*c*, %	Zone of microbial growth suppression, cm	
		mixture of bacteria (MPA medium)	mixture of fungi (mash–agar medium)
VI	0.5	1.3–1.5	1.2–1.4
	1.0	1.7–1.8	1.9
VII	0.5	1.4–1.7	2.1
	1.0	1.8–2.0	2.0–2.2
VIII	0.5	1.6–1.8	2.1–2.3
	1.0	2.1–2.3	2.4
IX	0.5	1.4–1.6	1.8–1.9
	1.0	2.1–2.2	2.3–2.5
X	0.5	1.4–1.6	1.9–2.1
	1.0	1.6–1.8	2.4
XI*	0.5	0.3–0.4	0.3–0.4
	1.0	0.5–0.7	0.5–0.7

* **XI** = 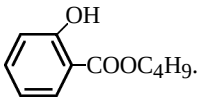 .

EXPERIMENTAL

The IR spectra of 1,2-aminopropanethiols **I**–**V** and their derivatives **VI**–**X** were taken on a Specord 75-IR spectrophotometer (3600–400 cm^{-1}, liquid films, KBr and NaCl prisms) under standard conditions. The frequencies were determined with an accuracy of ±5 cm^{-1}.

The ^{1}H NMR spectra were recorded on a Varian T-60 spectrometer (60 MHz, internal reference TMS, solvent CCl_4). The chemical shifts δ were measured with an accuracy of ±0.03 ppm.

The purity of the compounds was determined by gas–liquid chromatography on a Tsvet-104 instrument equipped with a 200 × 0.3-cm column. The column temperature was 210°C. The moisture content of the carrier gas was P_{H_2O} = 0.2 mg cm^{-2}. The sample volume was 0.1 μl. The stationary phase was SE-301, 5% on Chromaton N-A, 0.5–0.15 mm.

Thin-layer chromatography was performed on Silufol UV-254 plates, with ethanol–hexane (1 : 5) as eluent. In all cases, development with iodine vapor revealed a single spot.

1-[4-(1-hydroxy-1-methoxycarbonyl-2,2,2-trifluoroethyl)phenyl]aminopropane-2-thiol VI. A three-necked flask was charged with 3.3 g (0.02 mol) of 1-(phenylamino)propane-2-thiol **I**, 20 ml of anhydrous tetrachloromethane, and 3.1 g (0.02 mol) of methyl trifluoropyruvate. The mixture was vigorously stirred for 16 h at room temperature. Then the solvent was distilled off, and the product was isolated by column chromatography (alumina, Brockmann grade II, eluent CCl_4–acetone, 10 : 1). A viscous yellow liquid

was obtained; yield 3.3 g (51%), n_D^{20} = 1.4950, R_f = 0.20.

Found, %: C 48.48, H 5.19, N 4.13, F 17.84, S 10.07.

$C_{13}H_{16}NO_3F_3S$.

Calculated, %: C 48.29, H 4.99, N 4.33, F 17.63, S 9.92.

Compounds **VII**–**X** were prepared similarly; the physicochemical constants of **VI**–**X** are listed in Table 1.

CONCLUSIONS

(1) Methyl trifluoropyruvate alkylates 1,2-aminopropanethiols exclusively at the aromatic ring.

(2) Trifluoromethyl derivatives of 1,2-aminopropanethiols added to lubricants exhibit antibacterial and fungicidal activity.

REFERENCES

1. Allakhverdiev, M.A., Farzaliev, V.M., Khalilova, A.Z., *et al., Zh. Org. Khim.*, 1986, vol. 22, no. 1, pp. 90–93.
2. Allakhverdiev, M.A., Farzaliev, V.M., Khalilova, A.Z., *et al., Zh. Org. Khim.*, 1986, vol. 22, no. 11, pp. 2288–2292.
3. Allakhverdiev, M.A., Guseinova, A.T., Farzaliev, V.M., *et al.*, *Neftekhimiya*, 1990, vol. 30, no. 4, pp. 570–573.
4. Allakhverdiev, M.A., Guseinova, A.T., Farzaliev, V.M., *et al.*, *Neftekhimiya*, 1989, vol. 29, no. 2, pp. 275–278.
5. Allakhverdiev, M.A., Farzaliev, V.M., Guseinova, T.M., *et al., Zh. Prikl. Khim.*, 1994, vol. 67, no. 11, pp. 1872–1877.
6. Allakhverdiev, M.A., Farzaliev, V.M., Guseinova, T.M., *et al., Zh. Org. Khim.*, 1995, vol. 31, no. 4, pp. 532–536.
7. Allakhverdiev, M.A., Farzaliev, V.M., Khalilova, A.Z., and Kurbanov, K.B., *Azerb. Khim. Zh.*, 1997, nos. 1–4, pp. 26–29.
8. Zelenin, A.E., Chkanikov, N.D., Kolomiets, A.F., and Galakhov, M.V., *Izv. Akad. Nauk SSSR, Ser. Khim.*, 1985, no. 4, pp. 931–934.
9. Chkanikov, N.D., Sviridov, V.D., Kolomiets, A.F., Zelenin, A.E., *et al., Izv. Akad. Nauk SSSR, Ser. Khim.*, 1992, no. 8, pp. 1820–1831.
10. Osipov, S.N., Chkanikov, N.D., Kolomiets, A.F., and Fokin, A.V., *Izv. Akad. Nauk SSSR, Ser. Khim.*, 1986, no. 6, pp. 1384–1387.

Russian Journal of Applied Chemistry, Vol. 75, No. 8, 2002, pp. 1283–1289. Translated from Zhurnal Prikladnoi Khimii, Vol. 75, No. 8, 2002, pp. 1309–1314.
Original Russian Text Copyright © 2002 by Krivonogov, Afzaletdinova, Sivkova, Kozlova, Murinov, Abdrakhmanov.

ORGANIC SYNTHESIS AND INDUSTRIAL ORGANIC CHEMISTRY

Synthesis and Extractive Power of Polycyclic Pyrimidine Derivatives

V. P. Krivonogov, N. G. Afzaletdinova, G. A. Sivkova, G. G. Kozlova, Yu. I. Murinov, and I. B. Abdrakhmanov

Institute of Organic Chemistry, Ufa Scientific Center, Russian Academy of Sciences, Ufa, Bashkortostan, Russia

Received December 19, 2001; in final form, February 2002

Abstract—A procedure was developed for synthesis of polycyclic pyrimidine derivatives by the reaction of 2,2'-dichlorodicyclohexyl sulfide with uracil, 6-methyluracil, or 5-fluorouracil in the presence of K_2CO_3, followed by oxidation of the resulting products with sodium metaperiodate and hydrogen peroxide. Two of the synthesized compounds were tested in extraction of Ir(IV) from hydrochloric acid solutions.

Functionally substituted acyclic and cyclic sulfides and their oxidized derivatives are valuable as immunostimulants and antiphlogistics [1–6], and also as metal extractants and complexing agents [7].

Previously, a new class of low-toxic nonsteroid antiphogistics has been prepared by the reactions of SCl_2 with cyclohexene [3], cyclooctadiene [4], and cyclododecatriene [5], followed by treatment of the resulting 2,2'-dichlorodicyclohexyl sulfide, 2,6-dichloro-9-thiabicyclo[3.3.1]nonane, and 2,9-dichloro-13-thiabicyclo[8.2.1]-*cis*-tridec-5-ene with secondary amines: morpholine and piperidine. The resulting amino derivatives of dicyclohexyl sulfide, 9-thiabicyclo[3.3.1]nonane, and 13-thiabicyclo[8.2.1]-*cis*-tridec-5-ene showed high antiphlogistic activity in inflammations caused by carragenin and Formalin. The extractive power of amino sulfides has been studied, and fast recovery of iridium with these agents containing N,S-functionalities was reported [8].

In this study, we prepared polycyclic pyrimidine derivatives and tested them in extraction of iridium from hydrochloric acid solutions. As a continuation of our studies concerned with synthesis of potential immunotropic, antiphogistic, membrane-stabilizing, and antiradical agents, and also of extractants for noble metals, we developed a route to previously unknown polycyclic pyrimidine derivatives, involving the reactions of *trans*-2,2'-dichlorodicyclohexyl sulfide with pyrimidine derivatives (uracil, 6-methyluracil, 5-fluorouracil):

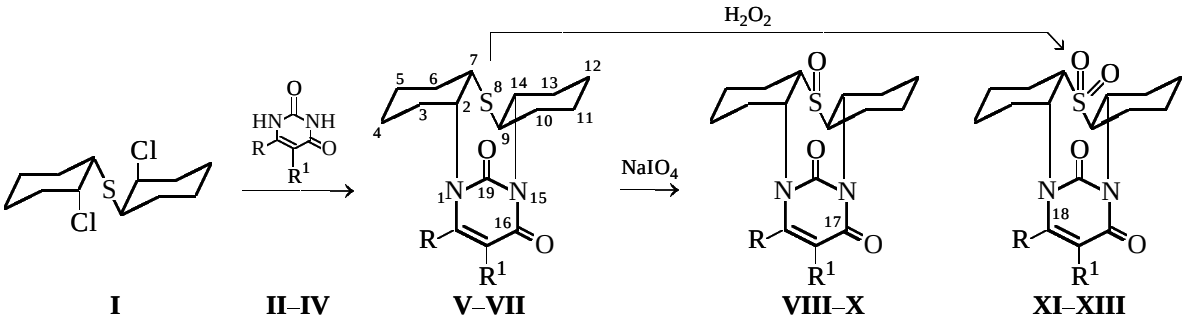

I **II–IV** **V–VII** **VIII–X** **XI–XIII**

R = R' = H (**II**, **V**, **VIII**, **XI**); R = CH_3, R' = H (**III**, **VI**, **IX**, **XII**); R = H, R' = F (**IV**, **VII**, **X**, **XIII**).

It is known that the reaction of SCl_2 with cyclohexene initially yields the *a,e*-dichloro sulfide, which irreversibly isomerizes into stable *e,e,e,e*-dichloro sulfide **I** [8].

1070-4272/02/7508-1283 $27.00 © 2002 MAIK "Nauka/Interperiodica"

The reactions of **I** with uracil **II**, 6-methyluracil **III**, and 5-fluorouracil **IV** in the presence of K_2CO_3 occurred at 80°C within 5 h, yielding sulfur-containing polycyclic pyrimidine derivatives **V**–**VII**. Oxidation of **V**–**VII** with sodium metaperiodate in aqueous alcohol at room temperature for 4 h yielded sulfoxides **VIII**–**X**, which were isolated by extraction with chloroform. Oxidation of **V**–**VII** with hydrogen peroxide gave sulfones **XI**–**XIII**. These products are readily soluble in water, chloroform, alcohol, benzene, acetone, and ether and insoluble in hexane.

The purity and structure of the products were confirmed by IR, UV, and ^{1}H and ^{13}C NMR spectroscopies, and also by elemental analysis. IR spectra of all the compounds contain absorption bands in the ranges 1620–1730 cm^{-1}, characteristic of the pyrimidine moiety [ν(C=O, =NC=O)], 640–690 cm^{-1}, belonging to the C–S bons, and, in the case of **VIII**–**X**, also 1060–1080 cm^{-1} (SO stretching vibrations). The SO_2 group gives bands at about 1175, 1220, and 1320 cm^{-1}. The spectra of **V**–**XIII** also contain absorption bands in the ranges 1120–1200 cm^{-1}, typical of tertiary nitrogen (–N=) derivatives, and 3320–3400 cm^{-1}, belonging to OH stretching vibrations.

In the ^{1}H NMR spectra of sulfoxides VIII–X, the signals of protons of the α-carbon atoms ($C^{7,9}$) are shifted downfield by 0.1 ppm relative to the sulfides, whereas the signals of protons of the β-carbon atoms ($C^{6,10}$) are shifted downfield by 0.8 ppm, and those of protons of $C^{2,14}$, by 1–1.5 ppm. In the spectra of **II**, **V**, **VIII**, and **X**, the signals of protons in 5- and 6-positions of uracil are doublets with *J* 7–7.1 Hz.

In the ^{13}C NMR spectra of sulfoxides **VIII**–**X** and sulfones **XI**–**XIII**, the signals of the α-carbon atoms ($C^{7,9}$) are shifted downfield by 20–23 ppm, whereas the signals of the β-carbon atoms ($C^{6,10,2,14}$) are shifted upfield by 10–15 ppm.

The ^{1}H and ^{13}C NMR spectra were recorded with 1% (^{1}H) or 10–20% (^{13}C) solutions in $CDCl_3$ on a Bruker AM 3000 spectrometer (^{1}H, 300 MHz; ^{13}C, 75.7 MHz). The proton chemical shifts are given relative to TMS (δ, ppm). The IR spectra were recorded on a UR-20 spectrophotometer with NaCl and LiF prisms. The melting point was measured with a Boetius device. The analytical data are consistent with the suggested compositions. The UV spectra (1×10^{-5}% solutions in DMSO) were measured with a Specord M-400 spectrophotometer.

Iridium(IV) was taken in the form of K_2IrCl_6. The working solutions were prepared by diluting the initial solution of Ir(IV) in 2 M HCl with the acid of appropriate concentration. It should be noted that, in the examined range of HCl concentrations, Ir(IV) occurs in the form of the anions $[Ir(OH)Cl_5]^{2-}$, $[IrCl_5(H_2O)]^-$, and $[IrCl_6]^{2-}$ [9]. The total Ir(IV) content in solutions was determined spectrophotometrically [10]. The extraction was performed at room temperature and 1 : 1 ratio of the aqueous and organic phases. Stirring was performed with an R-3 magnetic stirrer. The electronic absorption spectra were taken on a Specord M-40 spectrophotometer with glass and quartz cells.

8-Thia-1,15-diazatetracyclo[13.3.1.$0^{2,7}$.$0^{9,14}$]nonadec-17-ene-16,19-dione V. To a solution of 8.2 g (0.031 mol) of **I** in 100 ml of dimethyl sulfoxide, we added 8.6 g (0.062 mol) of K_2CO_3, 3.47 g (0.031 mol) of uracil **II**, and 2.3 g of the catalyst (tetrabutylammonium bromide, TBAB). The mixture was stirred at 40–70°C for 4 h and left overnight. The next day, 50 ml of water was added, and the mixture was extracted with chloroform (3 × 50 ml). After solvent evaporation, the residue (9.5 g) was dissolved in a minimal amount of acetone (50 ml) and purified by column chromatography (silica gel, 40/100 mesh). Yield of **V** 8 g (84%). The compound is soluble in methanol, acetone, and chloroform and insoluble in hexane and water. TLC: R_f 0.61. IR spectrum, ν, cm^{-1}: 640, 800 (C–S); 1120–1200 (=N–); 1660–1700 [ν(C=O,=NC=O)]; 3400 [ν(OH)]. UV spectrum: λ_{max} 262.5 nm (DMSO). ^{1}H NMR spectrum ($CDCl_3$), δ, ppm: 1.5–2.0 m (16H, $C^{3,4,5,6,10,11,12,13}H_2$), 2.37 m (1H, C^7H), 2.6 m (1H, C^9H), 3.4 q (1H, C^2H, *J* 7 Hz), 4.08 m (1H, $C^{14}H$), 5.7 d (1H, $C^{17}H$, *J* 7.6 Hz), 7.3 s (1H, $C^{18}H$, *J* 7.6 Hz). ^{13}C NMR spectrum ($CDCl_3$), δ_C, ppm: 21.93 (C^{12}), 25.00 ($C^{5,11}$), 25.04 (C^4), 26.79 (C^{10}), 28.70 (C^{13}), 29.63 (C^3), 33.1 (C^6), 54.92 (C^9), 61.41 (C^7), 60.16 (C^{14}), 64.23 (C^7), 126.05 (C^{17}), 144.15 (C^{18}), 147.77 (C^{19}), 159.27 (C^{16}).

Found, %: C 59.1, H 7.85, N 8.30, S 9.42.

$C_{16}H_{22}N_2O_2S \cdot H_2O$.

Calculated, %: C 59.23, H 7.46, N 8.63, S 9.88.

18-Methyl-8-thia-1,15-diazatetracyclo[13.3.1.-$0^{2,7}$.$0^{9,14}$]nonadec-17-ene-16,19-dione VI. A flask was charged with 12.6 g (0.1 mol) of 6-methyluracil **III**, 30 g (0.2 mol) of K_2CO_3, 10 g of the catalyst, and 300 ml of DMF. The mixture was stirred at room temperature for 2 h and left overnight. The next day, 26.7 g (0.1 mol) of 2,2'-dichlorodicyclohexyl sulfide

I was added. The mixture was stirred on a boiling water bath for 5 h. After cooling, 200 ml of water was added to dissolve the crystals, and the mixture was extracted with chloroform (3 × 70 ml). The extract was washed with water (50 ml), and the solvent was distilled off. Compound **VI** was obtained (37.9 g) as a viscous liquid readily soluble in chloroform, ethanol, and methanol and insoluble in hexane and water. IR spectrum, ν, cm^{-1}: 640, 800 (C–S); 1120–1200 (=N–); 1660–1700 [ν(C=O, =NC=O)]; 3400 [ν(OH)]. UV spectrum: λ_{max} 262.5 nm (DMSO). ^1H NMR spectrum ($CDCl_3$), δ, ppm: 1.5–2.0 m (16H, $C^{3,4,5,6,10,11,12,13}H_2$), 2.05 s (3H, $C^{18}CH_3$), 2.35–2.76 m (2H, $C^{7,9}H$), 3.48–4.08 m (2H, $C^{2,14}H$), 5.68 s (1H, $C^{17}H$). ^{13}C NMR spectrum ($CDCl_3$), δ_C, ppm: 15.06 (C^{18}–CH_3), 21.93 (C^{12}), 25.00 ($C^{5,11}$), 25.04 (C^4), 26.79 (C^{10}), 28.71 (C^{13}), 29.90 (C^6), 30.10 (C^3), 54.92 (C^9), 60.01 (C^2), 60.16 (C^{14}), 68.93 (C^7), 99.15 (C^{17}), 147.97 (C^{18}), 159.24 (C^{19}), 161.93 (C^{16}).

Found, %: C 55.92, H 7.97, N 7.37, S 8.95.

$C_{17}H_{24}N_2O_2S \cdot 2.5H_2O$.

Calculated, %: C 55.87, H 8.00, N 7.65, S 8.77.

17-Fluoro-8-thia-1,15-diazatetracyclo[13.3.1.-$0^{2,7}$.$0^{9,14}$]nonadec-17-ene-16,19-dione VII. To a solution of 8.5 g (0.032 mol) of **I** in 100 ml of dimethyl sulfoxide, we added 9 g (0.065 mol) of K_2CO_3, 4.2 g (0.031 mol) of fluorouracil **IV**, and 1 g of the catalyst. The mixture was heated to 70°C, stirred at the same temperature for 8 h, and left overnight. The next day, 100 ml of water was added, and the mixture was extracted with chloroform (3 × 50 ml). After evaporation of the solvent the residue (11.6 g) was dissolved in acetone and refluxed with activated carbon. The product, however, remained dark; therefore, it was dissolved in a minimal amount of acetone (50 ml) and purified by column chromatography (silica gel, 40/100 mesh). Yield of **VII** 6.4 g (61.7%); the product is soluble in methanol and acetone and insoluble in hexane and water. TLC: R_f 0.69; mp 129–131°C. IR spectrum, ν, cm^{-1}: 990, 1010 [ν(C=C)]; 1150–1250 (=N–); 1590, 1660–1715 [ν(C=O,=NC=O)]; 3400 [ν(OH)]. UV spectrum: λ_{max} 272.3 nm (DMSO). ^1H NMR spectrum ($CDCl_3$), δ, ppm: 1.35–1.9 m (16H, $C^{3,4,5,6,10,11,12,13}H_2$), 2.2 m (1H, C^7H), 2.63 s (1H, C^9H), 3.45 m (1H, C^2H), 4.2 m (1H, $C^{14}H$), 7.3 d (1H, $C^{18}H$, J_{HF} 9.0 Hz). ^{13}C NMR spectrum ($CDCl_3$), δ_C, ppm: 21.93 (C^{12}), 25.00 ($C^{5,11}$), 26.79 (C^{10}), 27.84 (C^4), 28.70 (C^{13}), 29.63 (C^3), 32.21 (C^6), 61.16 (C^{14}), 61.41 (C^2), 64.23 ($C^{7,9}$), 134.15 d (C^{18}, J_{CF} 26 Hz), 139.70 (C^{17}, J_{CF} 238 Hz), 147.77 (C^{19}), 159.27 d (C^{16}, J_{CF} 32 Hz).

Found, %: C 56.00, H 6.80, F 5.20, N 8.00, S 9.00.

$C_{16}H_{21}FN_2O_2S \cdot H_2O$.

Calculated, %: C 56.12, H 6.77, F 5.55, N 8.18, S 9.36.

8-Oxo-8λ^4-thia-1,15-diazatetracyclo[13.3.1.$0^{2,7}$-$0^{9,14}$]nonadec-17-ene-16,19-dione VIII. A solution of 0.5 g (0.00245 mol) of $NaIO_4$ in 50 ml of water was added dropwise over a period of 10 min to a solution of 0.5 g (0.0016 mol) of **V** in a mixture of alcohol (10 ml) and water (10 ml), cooled with cold water. Then the mixture was stirred for 4 h at room temperature and left overnight. The next day, the mixture was extracted with chloroform (3 × 50 ml). The solvent was distilled off, and the residue was dried by azeotropic distillation with acetone. Yield of **VIII** 0.4 g (73%). The compound is a viscous liquid readily soluble in alcohol, acetone, chloroform, and benzene and insoluble in water and hexane. TLC: R_f 0.29. IR spectrum, ν, cm^{-1}: 640, 800 (C–S); 1040, 1060 (SO); 1188–1224 (=N–); 1643, 1688, 1710 [ν(C=O, =NC=O)]; 3330 [ν(OH)]. UV spectrum: λ_{max} 265 nm (DMSO). ^1H NMR spectrum ($CDCl_3$), δ, ppm: 1.6–2.0 m (12H, $C^{3,4,5,11,12,13}H_2$), 2.48 t (1H, C^7H, *J* 7 Hz), 2.69 m (4H, $C^{6,}$ $10H_2$), 2.88 t (1H, C^9H, *J* 7.1 Hz), 4.82 q (1H, C^2H, *J* 7 Hz), 5.5 q (1H, $C^{14}H$, *J* 7.1 Hz), 5.74 d (1H, $C^{17}H$, *J* 7.3 Hz), 7.96 d (1H, $C^{18}H$, *J* 7.3 Hz). ^{13}C NMR spectrum ($CDCl_3$), δ_C, ppm: 16.86 (C^{10}), 21.93 (C^{12}), 23.08 ($C^{5,11}$), 24.38 (C^6), 27.24 (C^{13}), 27.60 (C^3), 28.41 (C^4), 59.50 (C^{14}), 61.10 (C^2), 78.02 (C^9), 84.00 (C^7), 126.05 (C^{18}), 144.15 (C^{18}), 147.97 (C^{19}), 159.24 (C^{16}).

Found, %: C 56.6, H 7.28, N 8.6, S 9.25.

$C_{16}H_{22}N_2O_3S \cdot H_2O$.

Calculated, %: C 56.45, H 7.11, N 8.23, S 9.42.

18-Methyl-8-oxo-8λ^4-thia-1,15-diazatetracyclo-[13.3.1.$0^{2,7}$.$0^{9,14}$]nonadec-17-ene-16,19-dione IX was prepared similarly to **VIII** from 3.2 g (0.01 mol) of **VI** in a mixture of alcohol (50 ml) and water (50 ml) and 2.6 g (0.012 mol) of $NaIO_4$ in 100 ml of water. A viscous liquid (3 g, 89%) was obtained, readily soluble in alcohol, acetone, chloroform, and benzene and insoluble in water and hexane. TLC: R_f 0.50. IR spectrum, ν, cm^{-1}: 550, 640, 820 (C–S); 980,

1000 [ω(C=C)]; 1060 (SO); 1120, 1200 (=N–); 1380 [δ^s(CH_3)]; 1460 (CH_2, CH_3); 1620, 1730 [ν(C=O, =N-C=O)]; 3320 [ν(OH)]. UV spectrum: λ_{max} 263 nm (DMSO). ^{1}H NMR spectrum ($CDCl_3$), δ, ppm: 1.5–2.0 m (12H, $C^{3,4,5,11,12,13}H_2$), 2.05 s (3H, $C^{18}CH_3$), 2.46 q (1H, C^7H, *J* 7 Hz), 2.48 t (2H, C^6H_2, *J* 7.1 Hz), 2.69 t (2H, $C^{10}H_2$, *J* 7.1 Hz), 2.88 q (1H, C^9H, *J* 7 Hz), 4.50 q (1H, C^2H, *J* 7 Hz), 5.50 q (1H, $C^{14}H$, *J* 7 Hz), 5.68 s (1H, $C^{17}H$). ^{13}C NMR spectrum ($CDCl_3$), δ_C, ppm: 15.06 ($C^{18}CH_3$), 16.86 (C^{10}), 19.97 (C^6), 21.93 (C^{12}), 23.08 ($C^{5,11}$), 25.04 (C^4), 27.24 (C^{13}), 27.60 (C^3), 59.41 (C^2), 59.50 (C^{14}), 78.02 (C^9), 85.00 (C^7), 99.15 (C^{17}), 147.97 (C^{18}), 159.24 (C^{19}), 161.93 (C^{16}).

Found, %: C 60.40, H 7.00, N 8.50, S 9.10.

$C_{17}H_{24}N_2O_3S$.

Calculated, %: C 60.69, H 7.19, N 8.33, S 9.53.

17-Fluoro-8-oxo-8λ^4-thia-1,15-diazatetracyclo-[13.3.1.0^{2,7}.0^{9,14}]nonadec-17-ene-16,19-dione X was prepared similarly to **IX** from 1.4 g (0.0043 mol) of **VII** in a mixture of water (20 ml) and alcohol (20 ml) and 1.34 g (0.0062 mol) of $NaIO_4$ in 50 ml of water. Compound **X** was obtained in quantitative yield (1.5 g) after evaporation of the solvents. IR spectrum, ν, cm^{-1}: 640, 800 (C–S); 1040–1068 (SO); 1180–1224 (=N–); 1643, 1672, 1688, 1710 [ν(C=O, =NC=O)]; 3400 [ν(OH)]. UV spectrum: λ_{max} 273.55 nm (DMSO). ^{1}H NMR spectrum ($CDCl_3$), δ, ppm: 1.5–2.0 m (16H, $C^{3,4,5,6,10,11,12,13}H_2$), 2.6 m (1H, C^7H), 3.0 m (1H, C^9H), 4.45 q (1H, C^7H, *J* 7 Hz), 5.16 m (1H, $C^{14}H$), 7.27 d (1H, $C^{18}H$, J_{HF} 9 Hz). ^{13}C NMR spectrum ($CDCl_3$), δ_C, ppm: 16.86 (C^{10}), 21.93 (C^{12}), 23.08 ($C^{5,11}$), 23.38 (C^6), 27.24 (C^{13}), 27.60 (C^3), 27.81 (C^4), 60.50 (C^{14}), 61.80 (C^2), 78.02 (C^9), 84.00 (C^7), 134.15 d (C^{18}, J_{CF} 25 Hz), 139.60 d (C^{17}, J_{CF} 237 Hz), 147.97 (C^{19}), 159.24 d (C^{16}, J_{CF} 29 Hz).

Found, %: C 56.8, H 6.39, F 5.30, N 8.00, S 9.60.

$C_{16}H_{21}FN_2O_3S$.

Calculated, %: C 56.45, H 6.22, F 5.58, N 8.23, S 9.42.

8-Dioxo-8λ^6-thia-1,15-diazatetracyclo[13.3.1.-0^{2,7}.0^{9,14}]nonadec-17-ene-16,19-dione XI. To a solution of 0.5 g (0.0016 mol) of **V** in 10 ml of acetic acid, heated on a boiling water bath, 1.5 ml (2.2 g) of 28% hydrogen peroxide was added dropwise. The mixture was stirred for 4 h, while heated on a boiling water bath, and left overnight. The next day, the solvent was distilled off, 10 ml of water was added, the crystals were filtered off, the filtrate was extracted with chloroform (2 × 25 ml), and the solvent was distilled off. Compound **XI** (0.4 g, 73%) was obtained as a viscous liquid readily soluble in organic solvents and insoluble in hexane and water. IR spectrum, ν, cm^{-1}: 640, 800 (C–S); 1120–1200 (=N–); 1175, 1220, 1320 (SO_2); 1624, 1656, 1700 [ν(C=O, =NC=O)]; 3400 [ν(OH)]. UV spectrum: λ_{max} 268 nm (DMSO). ^{1}H NMR spectrum ($CDCl_3$), δ, ppm: 1.5–2.0 m (16H, $C^{3,4,5,6,10,11,12,13}H_2$), 2.7 q (1H, C^7H, *J* 7 Hz), 3.16 q (1H, C^9H, *J* 7.1 Hz), 4.3 q (1H, C^2H, *J* 7 Hz), 4.8 q (1H, $C^{14}H$, *J* 7.1 Hz), 5.7 d (1H, $C^{17}H$, *J* 7.3 Hz), 7.9 d (1H, $C^{18}H$, *J* 7.3 Hz). ^{13}C NMR spectrum ($CDCl_3$), δ_C, ppm: 21.63 (C^{10}), 21.93 (C^{12}), 25.63 ($C^{5,11}$), 26.04 (C^4), 28.41 (C^3), 28.56 (C^6), 29.70 (C^{13}), 45.77 (C^2), 59.80 (C^{14}), 76.05 (C^9), 81.10 (C^7), 126.08 (C^{17}), 144.15 (C^{18}), 147.97 (C^{19}), 159.24 (C^{16}).

Found, %: C 57.00, H 6.81, N 8.00, S 9.57.

$C_{16}H_{22}N_2O_4S$.

Calculated, %: C 56.79, H 6.55, N 8.28, S 9.47.

18-Methyl-8-dioxo-8λ^6-thia-1,15-diazatetracyclo-[13.3.1.0^{2,7}.0^{9,14}]nonadec-17-ene-16,19-dione XII was prepared similarly to **XI** from 5 g (0.0156 mol) of **VI** in 20 ml of acetic acid and 2.2 g (0.06 mol or 8 ml) of 28% hydrogen peroxide. Compound **XII** (4 g, 71%) was obtained as a viscous liquid. TLC: R_f 0.63. IR spectrum, ν, cm^{-1}: 640, 800 (C–S); 980–1010 [ν(C=C)]; 1170–1250 (=N–); 1650, 1670, 1720 [ν(C=O, =NC=O)]; 3430 [ν(OH)]. UV spectrum: λ_{max} 268 nm (DMSO). ^{1}H NMR spectrum ($CDCl_3$), δ, ppm: 1.5–1.9 m (16H, $C^{3,4,5,6,10,11,12,13}H_2$), 2.05 s (3H, $C^{18}CH_3$), 2.76 q (1H, C^7H, *J* 7 Hz), 3.16 q (1H, C^9H, *J* 7.1 Hz), 4.2 q (1H, C^2H, *J* 7.0 Hz), 4.8 t (1H, $C^{14}H$, *J* 7.1 Hz), 5.68 s (1H, $C^{17}H$). ^{13}C NMR spectrum ($CDCl_3$), δ_C, ppm: 15.06 ($C^{18}CH_3$), 21.93 (C^{12}), 25.00 ($C^{5,11}$), 25.04 (C^4), 26.79 (C^{10}), 28.71 (C^{13}), 29.90 (C^6), 30.17 (C^3), 54.92 (C^9), 60.01 (C^2), 60.16 (C^{14}), 76.05 (C^9), 83.03 (C^7), 99.15 (C^{17}), 147.97 (C^{18}), 159.24 (C^{19}), 161.93 (C^{16}).

Found, %: C 57.60, H 6.80, N 7.97, S 8.95.

$C_{17}H_{24}N_2O_2S$.

Calculated, %: C 57.93, H 6.86, N 7.95, S 9.10.

17-Fluoro-8-dioxo-8λ^6-thia-1,15-diazatetracyclo-[13.3.1.0^{2,7}.0^{9,14}]nonadec-17-ene-16,19-dione XIII was prepared similarly to **XII** from 0.5 g (0.0015 mol) of **IV**, 10 ml of acetic acid, and 0.8 ml of 28% hydrogen peroxide in quantitative yield (0.53 g); mp 120–123°C. The crystals are readily soluble in alcohol, acetone, chloroform, and DMF and insoluble in hexane and water. TLC: R_f 0.73. IR spectrum, ν, cm^{-1}: 640, 852 (C–S); 1120–1200 (=N–); 1220, 1320 (SO_2); 1624, 1680–1700 [ν(C=O, =NC=O)]; 3400 [ν(OH)]. UV spectrum: λ_{max} = 276 nm (DMSO). ^{1}H NMR spectrum ($CDCl_3$), δ, ppm: 1.46–2.0 m (16H, C^{3,4,5,6,10,11,12,13}H$_2$), 2.7 q (1H, C^{7}H, *J* 7 Hz), 3.16 q (1H, C^{9}H, *J* 7 Hz), 4.29 q (1H, C^{2}H, *J* 7 Hz), 5.1 q (1H, C^{14}H, *J* 7 Hz), 7.2 d (1H, C^{18}H, J_{HF} 8.8 Hz). ^{13}C NMR spectrum ($CDCl_3$), δ_C, ppm: 21.63 (C^{10}), 21.93 (C^{12}), 25.63 (C^{5,11}), 27.64 (C^6), 27.85 (C^4), 29.37 (C^{13}), 30.20 (C^3), 46.77 (C^2), 59.80 (C^{14}), 76.05 (C^9), 81.81 (C^7), 134.98 d (C^{18}, J_{CF} 16 Hz), 139.70 d (C^{17}, J_{CF} 228 Hz), 147.77 (C^{19}), 159.24 d (C^{16}, J_{CF} 26 Hz).

Found, %: C 54.13, H 6.30, F 5.0, N 7.38, S 8.65.

$C_{16}H_{21}FN_2O_4S$.

Calculated, %: C 53.92, H 6.94, F 5.33, N 7.86, S 9.00.

Compounds **VI** and **IX** were tested in extraction of Ir(IV) from hydrochloric acid solutions. First, we examined how the recovery of Ir(IV) with **VI** and **IX** depends on the phase contact time τ_c. We found that, with solutions of Ir(IV) in 0.2 and 1.0 M HCl, the extraction equilibrium is attained within 5 min. Therefore, further experiments were mostly performed with this contact time (Fig. 1). Below are given the Ir(IV) distribution factors *D* obtained at various contact times [aqueous phase: c_{HCl} 0.2 and $c_{Ir(IV)}$ 4×10^{-4} M; organic phase (chloroform): $c_{\mathbf{VI}}$ 0.06 or $c_{\mathbf{IX}}$ 0.05 M]:

τ_c, min	5	10	15	20	30
$D^*_{\mathbf{IX}}$	2.4	2.4	2.4	2.4	2.4
$D^{**}_{\mathbf{VI}}$	3.3	3.3	3.3	3.3	3.3

* Reagent **IX**. ** Reagent **VI**.

We studied how the Ir(IV) distribution factor is influenced by the HCl concentration. When calculating the distribution factor, we took into account the formation of Ir(III) in the aqueous phase. The Ir(IV) recovery decreases with increasing HCl concentration.

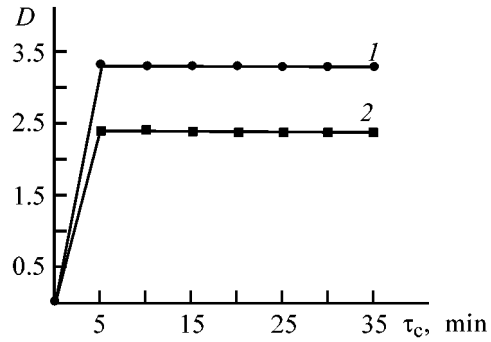

Fig. 1. Iridium(IV) distribution factor *D* vs. contact time τ_c. $c_{\mathbf{VI}}$ or $c_{\mathbf{IX}}$ 0.06 (in chloroform), $c_{Ir(IV)}$ 0.00032, c_{HCl} 0.2 M. (*1*) **VI** and (*2*) **IX**; the same for Fig. 2.

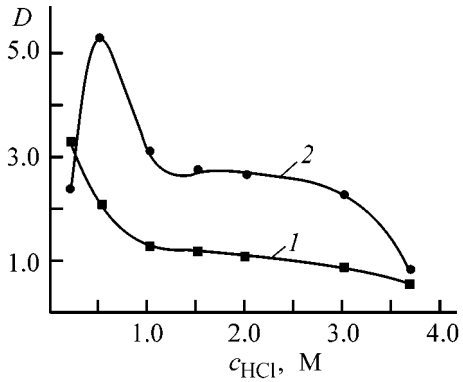

Fig. 2. Iridium(IV) distribution factor *D* vs. HCl concentration c_{HCl}. $c_{\mathbf{IX}}$ 0.06 or $c_{\mathbf{VI}}$ 0.05 M (in chloroform); $c_{Ir(IV)}$ 4×10^{-4} M.

The experimental results [$c_{\mathbf{IX}}$ 0.06 or $c_{\mathbf{VI}}$ 0.05 M in chloroform; $c_{Ir(IV)}$ 4×10^{-4} M] are listed below:

c_{HCl}, M	0.2	0.5	1.0	1.5	2.0	3.0	3.7
$D_{\mathbf{IX}}$	2.4	5.3	3.1	2.9	2.7	2.3	0.9
$D_{\mathbf{VI}}$	3.3	2.1	1.3	1.2	1.1	0.9	0.6

With **IX**, the maximal recovery is observed from 0.5 M HCl. The decreased iridium recovery at increased HCl concentration may be due to the prevalence of the nonextractable iridium species $[IrCl_6]^{2-}$ and to suppression of the extraction by similarly charged chloride ions (Fig. 2).

We also studied how the Ir(IV) recovery with **VI** and **IX** is influenced by the chloride ion concentration, at fixed c_{HCl} = 0.2 M. With increasing chloride ion concentration, the extraction is suppressed.

To confirm the mechanism of iridium extractive recovery, we examined the influence of hydrogen ion concentration at [NaCl] + [HCl] = 1 M. The slope of the plot $\log D = f(c_{H^+})$ is close to zero (0.3), which suggests that the extractable species are neutral.

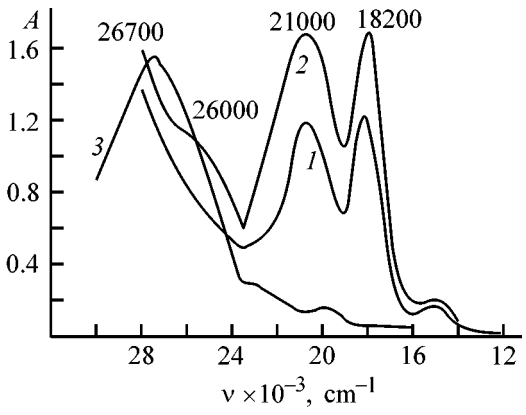

Fig. 3. Electronic absorption spectra of Ir(IV) extracts obtained with **VI**: (*A*) extinction coefficient and (ν) wave number; the same for Fig. 4. Phase contact time, min: (*1*) 1, (*2*) 5, and (*3*) 10.

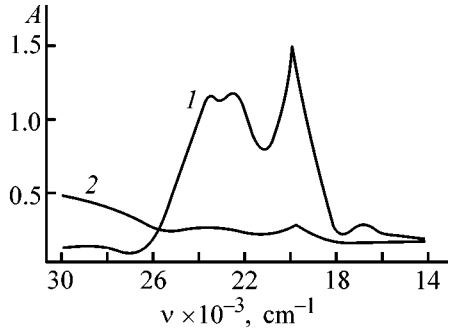

Fig. 4. Electronic absorption spectra of the aqueous phase after extraction of iridium with **VI**. Phase contact time, min: (*1*) 1 and (*2*) 5.

Apparently, in acid solutions, the extractants are protonated at the amide groups. Therefore, initially Ir(IV) is probably recovered from acid solutions in the form of ionic associates (interphase anion exchange). However, this reaction is very fast, and its kinetics cannot be monitored, probably owing to the labilizing effect of the amide nitrogen atoms. It has been shown previously [8, 11] that the amine nitrogen atoms in amino sulfides and amino keto sulfides exert a labilizing effect in recovery of Ir(IV) from acid solutions. It is known that sulfides and sulfoxides recover Ir(IV) only upon prolonged phase contact with heating. The compounds studied here recover Ir(IV) fast and without heating.

Figure 3 shows the electronic absorption spectra of Ir(IV) extracts with **VI**, obtained at various phase contact times: from 1 (curve *1*) to 10 min (curves *2*, *3*). The electronic absorption spectra show that, at longer phase contact times, the extraction occurs by the complexation mechanism: sulfur atoms of the ligands replace chloride ions from Ir(IV) acido complexes. Figure 4 shows the electronic absorption spectra of the aqueous phase after extraction of Ir(IV) with **VI** for 1 and 5 min. It is seen that the extraction is accompanied by gradual accumulation of Ir(III) in the aqueous phase. Reduction was also observed in extraction of Ir(IV) with amino sulfides.

In extraction of Ir(IV) with **IX**, the electronic absorption spectra of the aqueous and organic phases vary with time similarly, suggesting that, in this case, the extraction is also accompanied by redox reactions.

In the course of extraction, sulfide sulfur is probably oxidized to sulfoxide, and sulfoxide, to sulfone. It is yet unclear whether iridium is reduced in the organic or aqueous phase.

Our experimental results suggest that iridium is extracted with VI and IX in the form of the complexes $IrCl_4 \cdot 2L$.

The coordination of iridium by the sulfur atoms of the ligands is also confirmed by the fact that the largest coordination shift in the ^1H NMR spectra is observed for protons of the methylene groups bound to sulfur ($\Delta\delta$ 1.3 ppm).

CONCLUSIONS

(1) Previously unknown polycyclic pyrimidine derivatives were prepared by reactions of 2,2'-dichlorodicyclohexyl sulfide with uracil, 6-methyluracil, and 5-fluorouracil. The resulting products **V**–**VII** were oxidized with sodium metaperiodate to sulfoxides **VIII**–**X** and with hydrogen peroxide to sulfones **XI**–**XIII**, respectively.

(2) Compounds **VI** and **IX** were tested in extraction of Ir(IV) from hydrochloric acid solutions. The optimal conditions of iridium recovery (contact time 5 min, HCl concentration 0.2–0.5 M) were found. The iridium recovery decreases with increasing HCl concentration.

REFERENCES

1. Krivonogov, V.P., Tolstikov, G.A., Murinov, Yu.I., *et al.*, *Khim.-Farm. Zh.*, 1993, vol. 27, no. 11, pp. 41–44.
2. Krivonogov, V.P., Tolstikov, G.A., Murinov, Yu.I., *et al.*, *Khim.-Farm. Zh.*, 1996, vol. 30, no. 4, pp. 39–41.
3. Krivonogov, V.P., Tolstikov, G.A., Murinov, Yu.I., *et al.*, *Khim.-Farm. Zh.*, 1994, vol. 28, no. 9, pp. 29–33.
4. Krivonogov, V.P., Tolstikov, G.A., Murinov, Yu.I.,

et al., *Khim.-Farm. Zh.*, 1997, vol. 31, no. 8, pp. 26–29.

5. Tolstikov, G.A., Krivonogov, V.P., Galimov, B.I., *et al.*, *Khim.-Farm. Zh.*, 1995, vol. 29, no. 10, pp. 14–16.
6. Tolstikov, G.A., Krivonogov, V.P., Galimov, B.I., *et al.*, *Khim.-Farm. Zh.*, 1995, vol. 29, no. 4, pp. 38–40.
7. Krivonogov, V.P., Afzaletdinova, N.G., Murinov, Yu.I., *et al.*, *Zh. Prikl. Khim.*, 1998, vol. 71, no. 5, pp. 828–834.
8. Afzaletdinova, N.G., Khisamutdinov, R.G.A., Murinov, Yu.I., *et al.*, *Zh. Neorg. Khim.*, 1990, vol. 35, no. 5, p. 1327.
9. Buslaeva, T.M. and Simanova, S.A., *Koord. Khim.*, 2000, vol. 26, no. 6, p. 403.
10. *Sintez kompleksnykh soedinenii metallov platinovoi gruppy: Spravochnik* (Synthesis of Coordination Compounds of Platinum Metals: Handbook), Moscow: Nauka, 1964, p. 97.
11. Murinov, Yu.I., Maistrenko, V.N., and Afzaletdinova, N.G., *Ekstraktsiya metallov S,N-organicheskimi soedineniyami* (Extraction of Metals with S,N-Donor Organic Compounds), Moscow: Nauka, 1993

Russian Journal of Applied Chemistry, Vol. 75, No. 8, 2002, pp. 1290–1295. Translated from Zhurnal Prikladnoi Khimii, Vol. 75, No. 8, 2002, pp. 1315–1319.
Original Russian Text Copyright © 2002 by Filimonova, Nikulin.

ORGANIC SYNTHESIS AND INDUSTRIAL ORGANIC CHEMISTRY

Processing of Acetophenon Bottoms from Distillation of Styrene with Maleic Acid

O. N. Filimonova and S. S. Nikulin

Voronezh State Technological Academy, Voronezh, Russia

Voronezh State Forestry Engineering Academy, Voronezh, Russia

Received December 26, 2001; in final form, March 2002

Abstract—The kinetic features of dehydration of maleic acid during preparation of a copolymer based on the styrene distillation bottoms from joint production of styrene and propylene oxide were studied. The potential application fields for the copolymer synthesized were analyzed.

Processing and utilization of waste and by-products from chemical, petrochemical, and other industries receive now much attention both in Russia and abroad. These allow both mitigation of the environmental pollution and preparation of new materials with a set of valuable properties. Of the greatest importance among the wide variety of waste products are those from styrene production, namely, styrene distillation bottoms (SDB). One of the best ways of SDB utilization is processing into polymeric products by copolymerization with other monomers, most often, maleic anhydride (MA).

Reactions of styrene and its oligomers with maleic anhydride and widely covered in literature [1–5]. It has been shown that this copolymer can yield good paint and varnish materials. Application of maleic anhydride is, however, not always advisable because of its short supply and high price. At the same time, it should be noted that maleic anhydride production yields large amounts of maleic acid (MAc) as by-product, which is suitable for copolymerization with styrene instead of maleic anhydride. This, undoubtedly good alternative allows integrated processing of the waste. However, the behavior of maleic acid in copolymerization still remains to be understood. The use of this waste requires extensive studies of both the copolymerization process and its mechanism and the quality of the resulting polymeric product and its behavior in various composite materials.

Therefore, elucidation of the kinetic features of dehydration of maleic acid in the course of copolymer preparation is of both theoretical and applied importance.

The kinetics of the maleic acid dehydration by the reaction

$$\mathrm{MAc} \underset{k_{-1}}{\overset{k_1}{\rightleftarrows}} \mathrm{MA} + \mathrm{H_2O}$$

can be described by the following mathematical model:

$$dc_{MAc}/dt = -k_1 c_{MAc} + k_{-1} c_{MA} c_W. \qquad (1)$$

Here, c_{MAc}, c_{MA}, and c_W are the concentrations of maleic acid, maleic anhydride, and water at instant of time t, respectively, and k_1 and k_{-1} are the rate constants of the forward and back reactions, respectively.

In our experiments, dehydration of maleic acid involved permanent removal of water from the reaction mixture. Thus, c_W can be regarded as a function slowly varying with time. For theoretical analysis, c_W = const and, hence, $k_{-1W} = k_{-1} c_W$ = const was taken.

According to the stoichiometry of the reaction, $c_{MA} = c_{MAc0} - c_{MAc}$, where c_{MAc0} is the maleic acid concentration at the initial moment, and $c_{MAc0} = c_{MAc}$ at $t = 0$.

With the new parameters substituted, Eq. (1) takes the form

$$dc_{MAc}/dt + (k_1 + k_{-1W}) c_{MAc} = k_{-1W} c_{MAc0}. \qquad (2)$$

Differential equation (2) can be solved analytically

1070-4272/02/7508-1290 $27.00 © 2002 MAIK "Nauka/Interperiodica"

$$c_{MAc} = \left(c_{MAc0} - \frac{k_{-1W}c_{MAc0}}{k_{-1} + k_{-1W}}\right)e^{-(k_1 + k_{-1W})t} + \frac{k_{-1W}c_{MAc0}}{k_{-1} + k_{-1W}}. \quad (3)$$

Equation (3) represents the mathematical model of the maleic acid dehydration kinetics. To check the suitability of the model for both theoretical and practical applications, it is necessary to solve the inverse kinetic problem on determining k_1 and k_{-1}.

We studied dehydration of maleic acid at 110, 130, and 150°C in acetophenone at initial maleic acid concentration of 0.442 M by monitoring the variation of the maleic anhydride content in the process by IR spectroscopy.

To determine the kinetic constants k_1 and k_{-1}, we used Eq. (2) in the integral form

$$Y = A_0 + A_1X_1 + A_2X_2, \quad (4)$$

where $Y = c_{MAc}$, $A_0 = c_{MAc0}$, $A_1 = -(k_1 + k_{-1W})$,

$$A_2 = k_{-1}c_{MAc0}c_W = k_{-1W}c_{MAc0}, \quad (5)$$

$$X_1 = \int_0^t c_{MAc}\,dt, \quad X_2 = t. \quad (6)$$

The X_1 parameter was calculated by a numerical procedure from the experimental data. The results are presented in Table 1, along with the maleic acid concentrations (designated as Y).

The coefficients A_0, A_1, and A_2 were determined by solving the problem by the least-squares method for the equation in the matrix form

$$XA = Y, \quad (7)$$

where X is a matrix, and A and Y are vectors.

The matrix X is constructed using the X_1 and X_2 parameters for different instants of time. Using the experimental data from Table 1 for 110, 130, and 150°C, we obtained

$$X = \begin{vmatrix} 1 & 0 & 0 \\ 1 & 6.29 & 15 \\ 1 & 11.8 & 30 \\ 1 & 16.7 & 45 \\ 1 & 21.4 & 60 \\ 1 & 25.6 & 75 \\ 1 & 29.3 & 90 \\ 1 & 32.55 & 105 \end{vmatrix}, \quad X = \begin{vmatrix} 1 & 0 & 0 \\ 1 & 3.74 & 10 \\ 1 & 6.66 & 20 \\ 1 & 9.03 & 30 \\ 1 & 10.8 & 40 \\ 1 & 12.2 & 10 \\ 1 & 13.3 & 60 \end{vmatrix}, \quad X = \begin{vmatrix} 1 & 0 & 0 \\ 1 & 0.83 & 2 \\ 1 & 1.55 & 4 \\ 1 & 2.17 & 6 \\ 1 & 2.75 & 8 \\ 1 & 3.29 & 10 \\ 1 & 3.83 & 12 \end{vmatrix},$$

For the same temperatures,

$$Y = [0.442\ \ 0.396\ \ 0.336\ \ 0.318\ \ 0.314\ \ 0.248\ \ 0.239\ \ 0.195]^T,$$

$$Y = [0.442\ \ 0.305\ \ 0.280\ \ 0.195\ \ 0.158\ \ 0.127\ \ 0.097]^T,$$

$$Y = [0.442\ \ 0.388\ \ 0.330\ \ 0.296\ \ 0.277\ \ 0.268\ \ 0.264]^T.$$

The vector $A = [A_0A_1A_2]^T$, whose elements are coefficients including the kinetic constants, is to be determined. Using formulas (5), we calculated $k_{-1W} = A_2$ and $k_1 = -(A_1 + A_2)$. The results are presented in Table 2. It is seen that the experimental and calculated kinetic data are in good agreement. Thus, the model proposed is adequate to the real system.

The equilibrium pseudoconstant for maleic acid dehydration was calculated by the formula

Table 1. Experimental data on maleic acid dehydration

T, °C	t, min	c_{MAc}, M	$X = \int_0^t c_{MAc}\,dt$
110	0	0.442	0.000
	15	0.396	6.289
	30	0.336	11.782
	45	0.318	16.691
	60	0.314	21.434
	75	0.248	25.647
	90	0.239	29.294
	105	0.195	32.546
130	0	0.442	0.000
	10	0.305	3.735
	20	0.280	6.661
	30	0.195	9.032
	40	0.158	10.792
	50	0.127	12.212
	60	0.097	13.331
150	0	0.442	0.000
	2	0.338	0.831
	4	0.330	1.549
	6	0.296	2.174
	8	0.277	2.747
	10	0.268	3.292
	12	0.264	3.827

Table 2. Kinetic constants k_1 and k_{-1W} and equilibrium constants K_{eq}

T, °C	k_1, min^{-1}	k_{-1W}, $dm^3\ mol^{-1}\ min^{-1}$	K_{eq}, M
110	5.57×10^{-3}	0	∞
130	2.75×10^{-2}	7.54×10^{-4}	36.5
150	1.54×10^{-1}	4.90×10^{-2}	3.14

$$K_{eq} = k_1/k_{-1W}. \quad (8)$$

The results are presented in Table 2 as well. The pseudoconstant tends to decrease with rising temperature, which suggests heat evolution in the reaction [6, 7]. In view of the shift to maleic anhydride formation with lowering temperature, $k_1 >> k_{-1W}$ holds at a certain temperature. Equation (3) suggests that, in a certain time period,

$$c_{MAc} = c_{MAc0}e^{-k_1t}$$

or, in the differential form,

$$dc_{MAc}/dt = -k_1c_{MAc}.$$

This means that maleic acid dehydration can be regarded as an irreversible first-order reaction.

Our data suggest that maleic acid is 90% converted to maleic anhydride within 5.5 and 2 h at 110 and 130°C, respectively. At 150°C, equilibrium is attained within 0.3 h at 50% conversion.

The content of maleic anhydride in the reqaction mixture was determined with an IKS-22 spectrophotometer. To this end, we developed a procedure for quantitative determination of maleic anhydride from the IR absorption spectra. Maleic anhydride is characterized by an intense absorption band near 1840 cm^{-1}, due to stretching vibration of anhydride groups ν(CO–O–CO). This band does not overlap with those of other components and, hence, was chosen for determining the content of maleic anhydride [8].

Thus, we studied the kinetics of maleic acid dehydration into maleic anhydride and showed that, in the initial stage of the combined processing of acetophenone SDB and maleic acid, the temperature should not exceed 130°C, as under these conditions the whole of maleic acid is converted to maleic anhydride, and formation of the product (styrene copolymer with maleic anhydride) is highly probable. Since preparation of a film-forming copolymer at 120–170°C takes no less than 10 h, chemical conversion of acetophenone SDB below 150°C predominantly involves the reaction with maleic anhydride. With temperature increasing at the beginning of the reaction to above 150°C, the equilibrium of maleic acid dehydration shifts to the left, and the content of maleic anhydride participating in the copolymerization tends to decrease. These results are important both from the technological standpoint and for assessing the end product quality (at elevated temperatures maleic acid can directly participate in the chemical process).

At the same time, the most promising line of application of polymeric materials prepared from petrochemical waste and by-products still remains to be chosen. This is due, above all, to essential drawbacks of these polymeric materials, such as low stability of the polymer composition governing the structure and properties of macromolecules, high chromaticity, opalescence, etc., which significantly limits their application field.

The aforesaid suggests that the most promising application line is that posing not very strict requirements on the properties of the resulting polymeric materials and allowing their use despite the above-listed drawbacks. One line can be protection of wood and wood articles against unfavorable factors. Modifying compositions intended for wood protection should satisfy a number of requirements, namely, be available and nontoxic, not deteriorate the principal properties of the material, and easily penetrate into it. Expensive protective agents significantly increase the cost of wood articles, which makes reasonable the use of readily available cheap petrochemical waste and by-products and materials thereof. Also, the SDB-based copolymer contains a large amount of carboxy and anhydride groups which can react with wood components to form chemical bonds.

The available gel-chromatographic data show that the SDB copolymer has a relatively low molecular weight ($\overline{M}_n$ = 1900, $\overline{M}_v$ = 17000, $\overline{M}_w$ = 26500, $\overline{M}_z$ = 252000, $\overline{M}_w/\overline{M}_n$ = 13.8, $\overline{M}_z/\overline{M}_w$ = 9.5). Evidently, polymer molecules with low molecular weights are small in size and, hence, can easily penetrate into the wood structure [9, 10].

We studied the protective properties of the SDB copolymer with 10 × 10 × 20-mm birch wood samples dried to 8–10% moisture content.

The samples were weighed, immersed in a solution of SDB copolymer, and kept there for appropriate time. The impregnated birch samples were taken from the bath, dried, quenched, and weighed. The copolymer content in the samples was estimated gravimetrically, from the mass gain.

The penetrability of a SDB copolymer solution is strongly dependent on its concentration and impregnation temperature. The influence exerted by these factors deserves consideration, as at low tem-

Table 3. Experimental design

A	B			
	$b_1 = 20$	$b_2 = 40$	$b_3 = 60$	$b_4 = 80$
$a_1 = 3$	$c_1 = 1,\ d_1 = 90$ y_1, y_1', y_1''	$c_2 = 3,\ d_2 = 120$ y_2, y_2', y_2''	$c_3 = 5,\ d_3 = 150$ y_3, y_3', y_3''	$c_4 = 7,\ d_4 = 180$ y_4, y_4', y_4''
$a_2 = 8$	$c_2 = 3,\ d_3 = 150$ y_5, y_5', y_5''	$c_1 = 1,\ d_4 = 180$ y_6, y_6', y_6''	$c_4 = 7,\ d_1 = 90$ y_7, y_7', y_7''	$c_3 = 5,\ d_2 = 120$ y_8, y_8', y_8''
$a_3 = 13$	$c_3 = 5,\ d_4 = 180$ y_9, y_9', y_9''	$c_4 = 7,\ d_3 = 150$ $y_{10}, y_{10}', y_{10}''$	$c_1 = 1,\ d_2 = 120$ $y_{11}, y_{11}', y_{11}''$	$c_2 = 3,\ d_1 = 90$ $y_{12}, y_{12}', y_{12}''$
$a_4 = 18$	$c_4 = 7,\ d_2 = 120$ $y_{13}, y_{13}', y_{13}''$	$c_3 = 5,\ d_1 = 90$ $y_{14}, y_{14}', y_{14}''$	$c_2 = 3,\ d_4 = 180$ $y_{15}, y_{15}', y_{15}''$	$c_1 = 1,\ d_3 = 150$ $y_{16}, y_{16}', y_{16}''$

Note: (y_i) Water absorption, %; (y_i') radial swelling, %; and (y_i'') tangential swelling, %.

peratures (10–30°C) and high concentrations (over 60 wt %) the impregnating solution based on SDB copolymer is highly viscous, which complicates its use. Raising the temperature decreases the viscosity and significantly improves the penetrability of impregnating solutions into the wood structure. However, at SDB copolymer concentrations above 80%, even elevated temperatures do not afford high impregnation efficiency. The SDB copolymer solution was prepared using a mixed 4 : 1 xylene–acetone solvent. The optimal concentration of the SDB copolymer solution is not higher than 60 wt % [11]. This affords favorable properties of the impregnating solutions and their penetration into wood via diffusion. In view of the aforesaid, we fixed the SDB copolymer concentration at 43 wt % and varied the impregnation temperature from 20 to 80°C. The main relationships in impregnation of the birch wood samples were studied by the fouth-order Greek–Latin square design [12]. As the principal factors most strongly affecting the properties of the resulting modified wood we chose impregnation time, min (factor A); impregnation temperature, °C (factor B); heat treatment time, h (factor C); and heat treatment temperature, °C (factor D) of the samples being impregnated. The above-cited factors are presented in Table 3.

After computer processing of the experimental data, we obtained the regression equations (9)–(14) describing the water resistance of the birch samples treated with the SDB copolymer solutions as influenced by the main process parameters of impregnation. The regression equations for the response functions y, y', and y'', %, have the following form: after a 1-day period

for water resistance

$$y = 3.726 \times 10^{-5}(36.9 - 0.638a)(43.9 - 0.254b) \times (38.9 - 1.98c)(18.0 + 0.0913d), \quad (9)$$

for radial swelling

$$y' = 5.278 \times 10^{-3}(6.78 - 0.0958a)(6.06 - 0.00605b) \times (6.79 - 0.254c)(5.34 + 0.003d), \quad (10)$$

for tangential swelling

$$y'' = 2.262 \times 10^{-3}(8.64 - 0.0952a)(8.62 - 0.0192b) \times (8.51 - 0.217c)(8.35 - 0.054d), \quad (11)$$

and after a 30-day period,

$$y = 2.868 \times 10^{-6}(73.6 - 0.306a)(71.2 - 0.0156b) \times (72.0 - 0.399c)(73.7 + 0.0246d), \quad (12)$$

$$y' = 1.656 \times 10^{-3}(9.38 - 0.087a)(8.53 - 0.0016b) \times (9.47 - 0.249c)(8.49 + 0.0003d), \quad (13)$$

$$y'' = 8.267 \times 10^{-4}(12.2 - 0.144a)(10.7 - 0.0007b) \times (10.7 + 0.0005c)(11.4 - 0.0055d). \quad (14)$$

The calculated and experimental data for the modified birch wood samples are presented in Table 4.

Our results show that the optimal conditions for birch wood modification are as follows: impregnation

Table 4. Experimental and calculated water resistance

A	B							
	b_1		b_2		b_3		b_4	
	found	calculated	found	calculated	found	calculated	found	calculated
	1-day treatment Water absorption, %							
a_1	57.3	48.9	39.1	41.9	29.7	34.4	18.7	26.5
a_2	46.2	48.0	37.4	50.7	18.9	22.3	46.7	23.4
a_3	35.5	41.3	52.9	28.5	44.8	32.6	6.2	21.7
a_4	10.9	26.6	45.1	24.3	36.1	30.8	23.8	26.1
	Radial swelling, %							
a_1	9.0	7.5	7.5	6.9	4.1	6.2	6.4	5.6
a_2	6.2	6.6	6.4	7.1	4.9	5.1	7.3	5.6
a_3	4.8	5.6	7.0	4.9	6.6	6.2	3.5	5.5
a_4	3.5	4.5	5.8	4.8	6.0	5.4	5.9	5.6
	Tangential swelling, %							
a_1	11.5	10.2	9.5	9.0	5.6	7.9	7.2	6.9
a_2	8.5	8.7	8.0	8.6	7.2	7.3	9.4	7.2
a_3	7.2	7.6	9.8	6.9	8.0	8.0	5.0	7.3
a_4	4.9	7.0	9.0	7.2	6.7	6.8	7.6	7.0
	30-day treatment Water absorption, %							
a_1	80.6	80.3	70.3	79.9	67.1	79.4	71.0	78.9
a_2	72.8	79.3	68.1	80.6	68.3	75.4	78.1	76.6
a_3	65.3	77.4	79.0	75.5	77.3	77.0	61.9	75.1
a_4	60.0	73.4	74.5	73.3	69.9	75.9	65.9	75.7
	Radial swelling, %							
a_1	10.8	10.1	9.5	9.5	7.9	8.9	8.4	8.4
a_2	9.3	9.1	8.5	9.6	8.2	8.0	8.9	8.5
a_3	7.7	8.2	8.9	7.6	9.6	9.1	7.2	8.5
a_4	6.1	7.2	8.0	7.7	8.8	8.1	8.5	8.6
	Tangential swelling, %							
a_1	12.9	12.1	11.9	11.9	10.8	11.7	11.8	11.5
a_2	10.9	11.0	10.2	10.9	12.1	11.4	10.7	11.2
a_3	9.6	10.2	12.1	10.3	10.9	10.5	9.0	10.6
a_4	8.2	9.8	10.7	9.9	9.8	9.4	10.0	9.6

time 18 min, impregnation temperature 80°C, and heat treatment temperature and time 150°C and 7 h, respectively.

CONCLUSIONS

(1) A study of the kinetics of the reactions between styrene distillation bottoms and maleic acid showed that, in the examined temperature range, dehydration of maleic acid into maleic anhydride dominates. The resulting maleic anhydride participates in copolymerization.

(2) With the copolymer as impregnating composition, wood can be efficiently protected against moisture and water, since most of the macromolecules con-

tained in the copolymer have significantly smaller sizes than wood micropores and easily penetrate into the wood structure during impregnation.

REFERENCES

1. Nikolaev, A.F. and Gal'perin, M.V., *Vysokomol. Soedin., Ser. B*, 1969, vol. 11, no. 1, pp. 15–21.
2. JPN Patent 56–55 410.
3. USSR Inventor's Certificate, no. 755 801.
4. USSR Inventor's Certificate, no. 622 819.
5. USSR Inventor's Certificate, no. 1 452 812.
6. Denisov, E.T., *Kinetika gomogennykh khimicheskikh reaktsii* (Kinetics of Homogeneous Chemical Reactions), Moscow: Vysshaya Shkola, 1988.
7. Godnev, I.I., Krasnov, K.S., Vorob'ev, N.K., *et al.*, *Fizicheskaya khimiya* (Physical Chemistry), Moscow: Vysshaya Shkola, 1982.
8. Cross, A.D., *An Introduction to Practical Infra-Red Spectroscopy*, London: Butterworths, 1960.
9. Ugolev, B.N., *Drevesinovedenie s osnovami lesnogo tovarovedeniya* (Wood Science with Wood Merchandizing Basics), Moscow: Lesnaya Promyshlennost', 1986.
10. Perelygin, L.M., *Stroenie drevesiny* (Wood Structure), Moscow: Lesnaya Promyshlennost', 1954.
11. Sakhokiya,I.A., Nikulin, S.S., and Dmitrenkov, A.I., *Proizv. Ispol'z. Elastom.*, 2000, no. 3, pp. 20–23.
12. Akhnazarova, S.L. and Kafarov, V.V., *Optimizatsiya eksperimenta v khimii i khimicheskoi tekhnologii* (Experiment Optimization in Chemistry and Chemical Technology), Moscow: Vysshaya Shkola, 1978.

Russian Journal of Applied Chemistry, Vol. 75, No. 8, 2002, pp. 1296–1303. Translated from Zhurnal Prikladnoi Khimii, Vol. 75, No. 8, 2002, pp. 1320–1328.
Original Russian Text Copyright © 2002 by Syroezhko, Proskuryakov, Begak.

ORGANIC SYNTHESIS AND INDUSTRIAL ORGANIC CHEMISTRY

Mechanism of Cyclohexane Ozonolysis

A. M. Syroezhko, V. A. Proskuryakov, and O. Yu. Begak

St. Petersburg State Technological Institute, St. Petersburg, Russia

Mendeleev Russian Research Institute of Metrology, State Unitary Enterprise, St. Petersburg, Russia

Received March 15, 2002

Abstract—A mathematical model of cyclohexane ozonolysis was developed. The reaction rate constants were found experimentally or by fitting.

Experiments on reactions of ozone with saturated hydrocarbons revealed a nonlinear dependence of the rate constant on the hydrocarbon concentration [1]. At substrate concentrations less than 0.1 M, the reaction was bimolecular.

These results were rationalized [2] by assuming the formation of an intermediate complex RH···O_3. At the same time, Korotkova [3] denies formation of ozone–hydrocarbon complexes under these conditions.

Experiments on ozonolysis of cyclohexane and methylcyclohexane show (Figs. 1–3) that, with increasing substrate concentration, the apparent rate constant decreases.

For ozonolysis of cyclohexane under static conditions, Galimova [4] found the following empirical relationship between the rate constant and the ozone and substrate concentrations:

$$k_{app} = 3.2 \times 10^{-3} + 0.3\sqrt{[O_3]_0/[RH]} = k_0 + bK_0'. \quad (I)$$

According to [4], at oxygen content in the reaction solution of 4.4×10^{-2}, $[O_3] = (4.3–6.0) \times 10^{-4}$, and [RH] = 9.25 M, $k_{app} = 9.5 \times 10^{-3}$ l mol^{-1} s^{-1}.

In contrast to [5], it was shown in [4, 6, 7] that the rate constant of hydrocarbon ozonolysis is an apparent quantity taking into account the consumption of ozone in nonchain and chain reactions:

$$-d[O_3]/dt = k_0[RH][O_3] + b[RH]^{1/2}[O_3]^{3/2} = W_0 + W_0'. \quad (II)$$

The experimental data (Fig. 2) show that the expression for the ozone consumption rate must include not only terms corresponding to nonchain and chain reactions of ozone with the initial hydrocarbon, but also those corresponding to further ozonolysis of the reaction products such as cyclohexyl hydroperoxide, cyclohexanol, hydroxycyclohexyl peroxide, cyclohexanone, and ε-caprolactone. The reactivities of neat hydrocarbons, alcohols, and ketones toward ozone are comparable (Table 1).

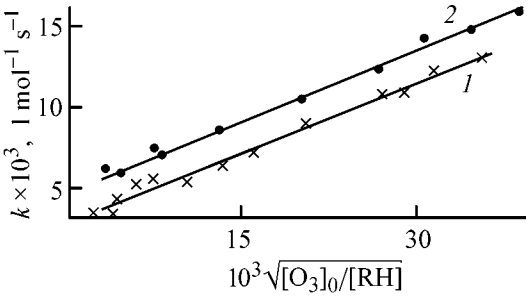

Fig. 1. Apparent rate constant k of hydrocarbon ozonolysis at 22°C vs. reactant concentrations (measured spectrophotometrically): (*1*) cyclohexane and (*2*) methylcyclohexane. [RH], M: (*1*) 1.3–9.25 and (*2*) 0.8–7.8.

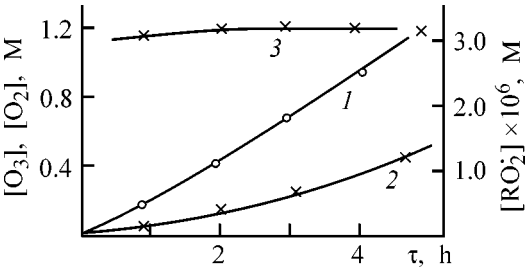

Fig. 2. Kinetic curves of (*1*) ozone consumption, (*2*) oxygen accumulation, and (*3*) variation of the concentration of peroxide radicals $RO_2^{\cdot}$ in the course of cyclohexane ozonolysis. (τ) Time; the same for Fig. 3.

1070-4272/02/7508-1296 $27.00 © 2002 MAIK "Nauka/Interperiodica"

In nonassociated dilute solutions in CCl_4 and cyclohexane, alcohols react with ozone considerably faster than hydrocarbons [8].

It should be noted that the mechanism of ozonolysis of organic compounds appreciably depends on the concentrations of the substrate, ozone, and oxygen, on the extent of the reaction (effect of reaction products), and on the hydrodynamic conditions (mass exchange).

According to [9, 10], for slow reactions of ozonolysis of saturated compounds (k 10^{-3}–10 l mol^{-1} s^{-1}), performed in a bubbled vessel, the rate of ozone bubbling is not rate-determining, i.e., the reactions are kinetically controlled.

The ozonolysis of cyclohexane to small conversions was studied in [11]. It was shown that cyclohexanol, cyclohexanone, organic peroxides, and cyclohexene are accumulated in parallel. The $RO_2^{\bullet}$ radicals not only recombine but also react with ozone. No less than 70% of $R^{\bullet}$ and $OH^{\bullet}$ radicals formed in the initiation event recombine to give an alcohol.

The initial steps in reactions of ozone with saturated hydrocarbons (*n*-alkanes, cycloalkanes), generating radical species, may be different:

$$RH + O_3 \rightarrow RO^{\bullet} + HO^{\bullet} + 91\ \text{kJ mol}^{-1}, \quad \text{(III)}$$

$$RH + O_3 \rightarrow [R^{\bullet} + HO_3^{\bullet}]_{cl} \rightarrow R^{\bullet} + HO_3^{\bullet}$$
$$\rightarrow R^{\bullet} + HO^{\bullet} + O_2 - 127\ \text{kJ mol}^{-1}, \quad \text{(IV)}$$

$$RH + O_3 \rightarrow R^{\bullet} + HO^{\bullet} + O_2 - 75\ \text{kJ mol}^{-1}. \quad \text{(V)}$$

An alternative pathway is a molecular reaction yielding unstable hydrotrioxide:

$$RH + O_3 \rightarrow ROOOH - 19\ \text{kJ mol}^{-1}. \quad \text{(VI)}$$

Reaction (III) is strongly exothermic, but it does not account for the actual composition of cycloalkane oxidation products. With this reaction, the major products must be alcohols and hydrogen peroxide, whereas actually only insignificant amounts of hydrogen peroxide (Table 2) were detected in reaction mixtures from ozonolysis of cyclohexane and methylcyclohexane [12].

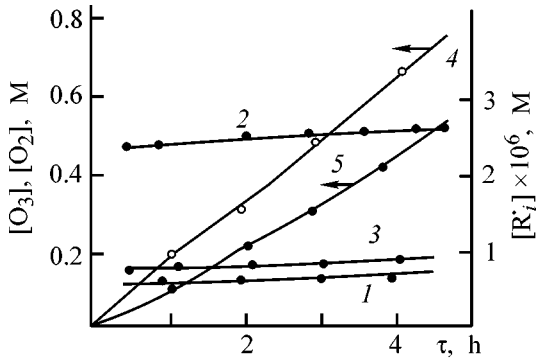

Fig. 3. Kinetic curves of (*1*–*3*) variation of radical concentration [$R_i^{\bullet}$] [(*1*) $HO_2^{\bullet}$, (*2*) $RO_2^{\bullet}$, and (*3*) 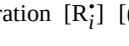], (*4*) consumption of ozone, and (*5*) accumulation of oxygen in ozonolysis of cyclohexane (20°C).

The major product accumulated in ozonolysis of cyclohexane is the ketone rather than alcohol. As for hydrotrioxide, it is unstable and its analytical detection is only possible at low temperatures.

Comparison of the thermal effects of the possible endothermic radical reactions of hydrotrioxide decomposition suggests that reaction (V)

$$ROOOH \rightarrow RO^{\bullet} + HO_2^{\bullet} - 83.5\ \text{kJ mol}^{-1} \quad \text{(VII)}$$

is preferable. Assuming that the preexponential factor in the expression for the rate constant of this reaction is 10^{14}, we obtain for the rate constant of hydrotrioxide decomposition into radicals a value of 6.3×10^{-2} s^{-1} (22°C).

Table 1. Apparent rate constants of the reactions of ozone with saturated hydrocarbons and intermediate oxidation products in a bubbled vessel (20°C, 4 vol % O_3)

Substrate	k, l mol^{-1} s^{-1}	Substrate	k, l mol^{-1} s^{-1}
Cyclohexane*	0.00183	Cyclohexanol*	0.00355
Cyclohexanol*	0.432	Cyclohexanone*	0.0287
Cyclohexylperoxy radical**	1.385×10^3	Cyclohexan-1-ol-2-one	21.11
Cyclohexyl hydroperoxide	1.419	2-Hydroperoxycyclohexanone	1.39
Hydroxycyclohexyl hydroperoxide	0.149	Methylcyclohexane*	0.0086
ε-Caprolactone	0.0461	1-Methylcyclohexyl hydroperoxide	0.019

* Neat substance (cyclohexane, 9.25 M; cyclohexanol, 9.64 M; cyclohexanone, 9.65 M; methylcyclohexane, 7.8 M).

** Solution in cyclohexane.

Table 2. Functional composition of cyclohexane ozonolysis products

T, °C	τ, h	Conversion, %	Yield based on converted cyclohexane, mol %					
			cyclohexanone	cyclohexanol	esters, ethers	acids	hydroperoxides*	H_2O_2
				$[O_3]$ = 4 vol %				
40	1	3.1	70	9.1	0.9	6.1	12.2	1.7
	2	5.6	71.6	5.4	3.5	7.2	10.8	1.5
	3	8.2	73.1	4.1	5.6	6.6	9.6	1.0
	4	9.6	72.6	2.9	7.4	7.4	9.1	0.6
	5	10.9	68.6	1.8	10.0	10.4	8.8	0.4
60	1	4.2	65.1	6.5	3.9	4.2	18.2	2.1
	2	7.9	71.3	5.0	6.9	6.6	8.8	1.4
	3	10.5	72.7	3.0	6.3	9.7	5.4	0.9
	4	11.6	70.3	1.7	11.8	11.8	3.8	0.6
	5	3.1	64.3	1.1	14.8	14.8	2.9	0.5
				$[O_3]$ = 2 vol %				
40	1	0.6	32.7	36.4	0	12.7	18.2**	–
	2	1.2	38.5	28.3	7.0	10.5	17.5	–
	3	1.9	41.4	23.0	8.1	10.3	17.2	–

* Including hydroxycyclohexyl hydroperoxide.

** Including hydroxycyclohexyl hydroperoxide and hydrogen peroxide.

The relative stabilities of secondary and tertiary hydroperoxides formed by oxidation of, respectively, cyclohexane and methylcyclohexane suggest that detection of 1-methylcyclohexyl hydrotrioxide is more probable than that of cyclohexyl hydrotrioxide. The activation energy of the overall ozonolysis reaction is 60 ± 2 kJ mol^{-1} for cyclohexane and 53.7 ± 2.8 kJ mol^{-1} for methylcyclohexane [12].

These energy parameters are considerably lower than the values expected for thermal decomposition of hydrotrioxide into radicals. In ozonolysis of saturated hydrocarbons, hydrotrioxide can form only in low amounts, which was subsequently confirmed by calculations:

$$\mathrm{ROOOH} \rightarrow \mathrm{RO}^{\bullet} + \mathrm{HO}_2^{\bullet} - 83.5\ \mathrm{kJ\ mol}^{-1}, \quad \text{(VIII)}$$

$$\mathrm{ROOOH} \rightarrow \mathrm{RO}_2^{\bullet} + \mathrm{HO}^{\bullet} - 117\ \mathrm{kJ\ mol}^{-1}, \quad \text{(IX)}$$

$$\mathrm{ROOOH} \rightarrow \mathrm{R}^{\bullet} + \mathrm{HO}_3^{\bullet} - 280\ \mathrm{kJ\ mol}^{-1}. \quad \text{(X)}$$

By contrast, in ozonolysis of polar oxygen-containing substrates (alcohols, ketones), the occurrence of the reaction via hydrotrioxide is more probable. The reaction of hydrotrioxide with ozone (XI) is exothermic, whereas reaction (XII) and the reaction with hydrocarbon (XIII) are endothermic:

$$\mathrm{ROOOH} + \mathrm{O_3} \rightarrow \mathrm{RO}^{\bullet} + \mathrm{HO}_3^{\bullet} + \mathrm{O_2} + 80\ \mathrm{kJ\ mol}^{-1}, \quad \text{(XI)}$$

$$\mathrm{ROOOH} + \mathrm{O_3} \rightarrow \mathrm{RO}_2^{\bullet} + \mathrm{HO}_2^{\bullet} + \mathrm{O_2} - 25\ \mathrm{kJ\ mol}^{-1}, \quad \text{(XII)}$$

$$\mathrm{ROOOH} + \mathrm{RH} \rightarrow \mathrm{RO}^{\bullet} + \mathrm{H_2O} + \mathrm{R}^{\bullet} - 22\ \mathrm{kJ\ mol}^{-1}. \quad \text{(XIII)}$$

It is not improbable also that ozone reacts with hydrotrioxide to form ketone and $HO_2^{\bullet}$ and $HO_3^{\bullet}$ radicals. Even experimental detection of hydrotrioxide among the reaction products cannot be considered an evidence of the single-stage process [13] [reaction (IV)].

In view of the composition of the reaction products and ESR data [1, 11, 14], the primary initiation, most probably, occurs by schemes (IV) and (V), yielding $R^{\bullet}$ and $HO^{\bullet}$ radicals and molecular oxygen. Oxygen-containing products are accumulated by the reactions of ozone with hydrocarbons and radicals; the radicals can also react with oxygen. The contribution of the chain reaction can be judged from the ratio of the oxygen content in oxidation products of a hydrocarbon (cyclohexane, methylcyclohexane) to the amount of the ozone consumed.

As shown in [13, 15], in developed ozonolysis of methylcyclohexane and cyclohexane, oxygen is involved in the process along with ozone. For ozonolysis of cyclohexane, the initiation rate W_i at 20°C was estimated to be 1.318×10^{-5} mol l^{-1} s^{-1}. The chain

length is 3.6 units, which is consistent with published data [2, 16, 17].

Previous studies [6, 16] have shown that, under the conditions of low-temperature ozonolysis of cyclohexane, the reaction of $RO_2^{\bullet}$ with the substrate can be neglected. A significant part of alcohols and ketones are formed by recombination of peroxy radicals. The whole set of the experimental data [18–26] and reference information [27] allow us to propose a mechanism of cyclohexane ozonolysis to large (10%) conversions.

The initial events are radical (generating $R^{\bullet}$, $OH^{\bullet}$) and molecular reactions yielding unstable hydroperoxide (ROOOH), alcohol (ROH), and oxygen.

We took into account the possible formation of an intermediate hydrocarbon–ozone complex, consistent with the experimentally observed decrease in the apparent rate constant with increasing concentration of the saturated substrate [28].

The possible transformation pathways of intermediates (cyclohexyl hydroperoxide, ROOH; cyclohexanol, R–OH; cyclohexanone, R=O; hydroxycyclohexyl hydroperoxide; ε-caprolactam) under these conditions were confirmed by experiments in a bubbled vessel, allowing the reaction to be performed to large conversions, with reliable quantitative determination of the products.

In the fitting procedure, we used the constants determined spectrophotometrically [12] and the estimated values based on published data for related reactions [11, 27]. Then these constants were refined by comparing the experimental and calculated concentrations of products in the course of ozonolysis. Fitting was performed until the deviations of the calculated concentrations from the experiment became lower than the chosen level.

We included the following initial substances A_1–A_3 and final products A_4–A_{13}:

A_1, ; A_2, O_3; A_3, O_2; A_4, 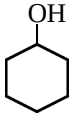 ; A_5, 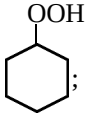 ;

A_6, H_2O_2; A_7, H_2O; A_8, ozonide;

A_9, 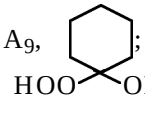 ; A_{11}, 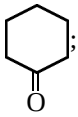 ; A_{12}, 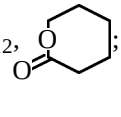 ; A_{13}, adipic acid.

The following intermediates were included:

X_1, ROOOH; X_2, ; X_3, $^{\bullet}OH$; X_4, $HO_2^{\bullet}$; X_5, $HO_3^{\bullet}$;

X_6, 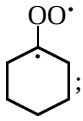 ; X_7, 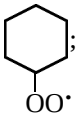 ; X_8, 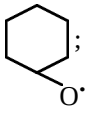 ; X_9, 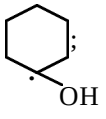 ;

X_{10}, 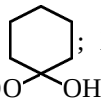 ; X_{11}, 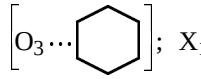 ; X_{12}, $\dot{C}H_2(CH_2)_4C(=O)O^{\bullet}$;

X_{13}, $\dot{C}H_2(CH_2)_4COOH$; A_{14}, $H-\underset{\underset{O}{\|}}{C}-(CH_2)_4C(=O)OH$;

A_{10}, .

The concentrations of the intermediates can be determined from the Bodenstein–Semenov principle of steady state [29, 30]:

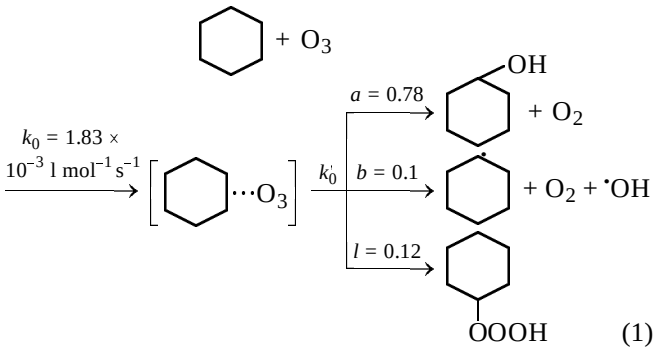

(1)

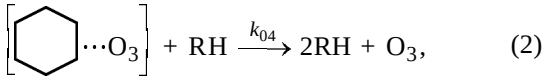

(2)

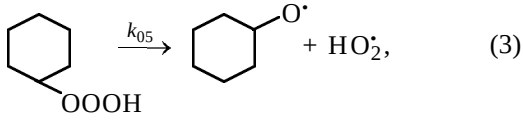

(3)

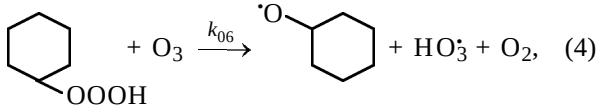

(4)

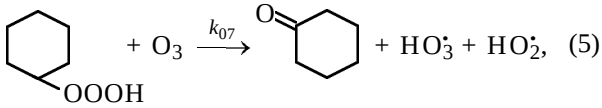

(5)

(6)

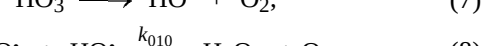

(7)

(8)

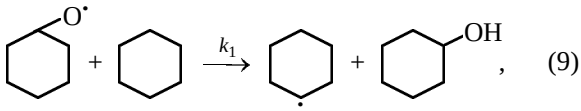

(9)

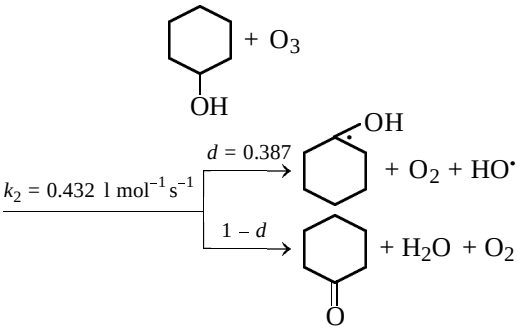

(10)

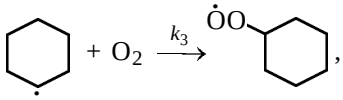

(11)

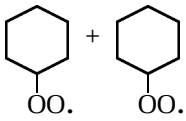

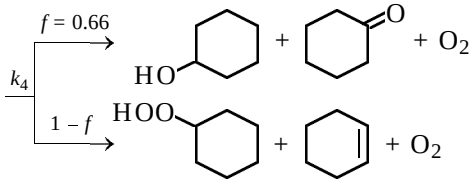

(12)

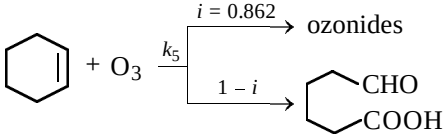

(13)

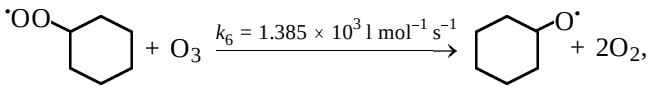

(14)

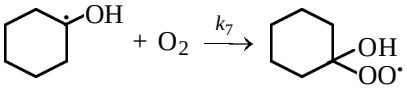

(15)

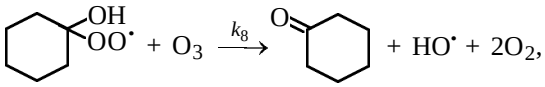

(16)

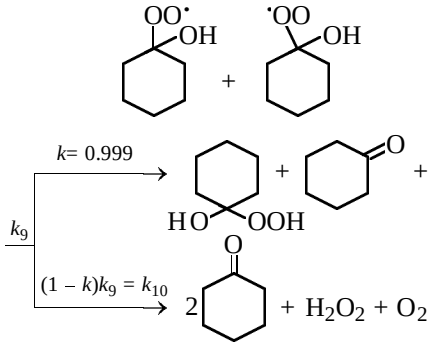

(17)

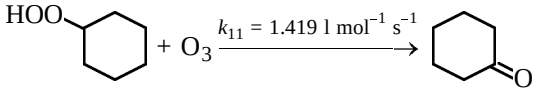

+ 2HO• + O_2, (18)

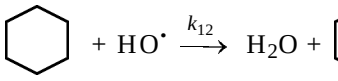

(19)

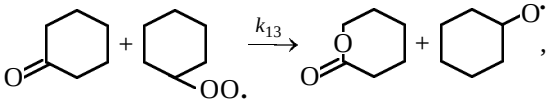

(20)

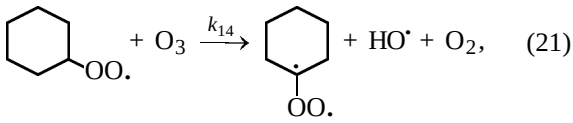

(21)

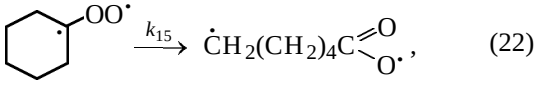

(22)

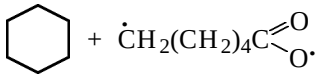

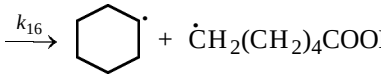

(23)

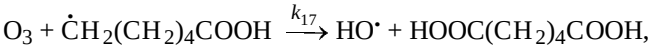

(24)

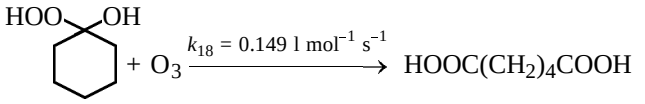

(25)

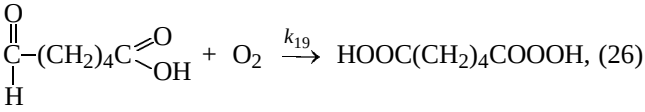

(26)

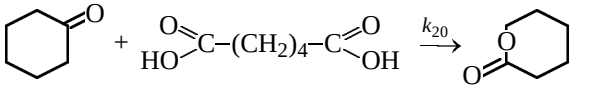

(27)

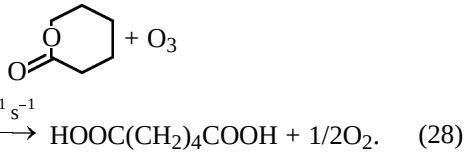

(28)

Along with the recombination of peroxy radicals, we took into account transformations of the alcohol,

ketone, cyclohexyl hydroperoxide, cyclohexene, hydroxycyclohexyl hydroperoxide, and hydrotrioxide. These compounds are very reactive (Table 1). We also took into account the recombination of hydroxyperoxy radicals, formation of a biradical, and its transformation into acids with ring opening, and also the most probable reactions of lactone ozonolysis and reactions of the $HO_2^{\cdot}$, $HO_3^{\cdot}$, $HO^{\cdot}$, and radicals with the reaction medium.

For the rates R_i of ith reactions, we can write

$R_0 = K_0[A_1][A_2]$, $R'_0 = [X_{11}]k'_0$, $R_{04} = [X_{11}][A_1]k_{04}$, $R_{05} = k_{05}[X_1]$, $R_{06} = k_{06}[X_1][A_2]$, $R_{07} = k_{07}[X_1][A_2]$, $R_{08} = k_{08}[X_5][A_2]$, $R_{09} = k_{09}[X_5]$, $R_{010} = k_{010}[X_4]^2$, $R_1 = k_1[X_8][A_1]$, $R_2 = k_2[A_2][A_4]$, $R_3 = k_3[X_2][A_3]$, $R_4 = k_4[X_7]^2$, $R_5 = k_5[A_2][A_{10}]$, $R_6 = k_6[X_7][A_2]$, $R_7 = k_7[X_9][A_3]$, $R_8 = k_8[X_{10}][A_2]$, $R_9 = k_9[X_{10}]^2$, $R_{11} = k_{11}[A_5][A_2]$, $R_{12} = k_{12}[X_3][A_1]$, $R_{13} = k_{13}[X_7][A_{11}]$, $R_{14} = k_{14}[X_7][A_2]$, $R_{15} = k_{15}[X_6]$, $R_{16} = k_{16}[X_{12}][A_1]$, $R_{17} = k_{17}[X_{13}][A_2]$, $R_{18} = k_{18}[A_9][A_2]$, $R_{19} = k_{19}[A_{14}][A_3]$, $R_{20} = k_{20}[X_{14}][A_{11}]$, $R_{21} = k_{21}[A_{12}][A_2]$.

The concentrations of radicals X_i of cyclohexene and adipic acid monoaldehyde can be determined from the steady-state condition $d[X_i]/dt = 0$. Let us introduce the following designations:

$k_{04}/k'_0 = Z_1$, $k_{08}/k_{09} = Z_2$, $k_{06}/k_{05} = Z_3$, $k_{07}/k_{06} = Z_4$, $l = y_1$, $y_2 = 1/(1 + Z_1[A_1])$, $Z_5 = y_1y_2/\{1 + [A_2](Z_3 + Z_4)\}$, $Z_6 = Z_5[A_2]Z_3$, $Z_7 = Z_5[A_2]Z_4$, $y_3 = Z_1[A_1]y_2R_0$.

Then, we take into account that

$R_{14} = R_{15} = R_{16} = R_{17}$, $R_7 = dR_2$, $R'_0 = R_0/(1 + Z_1[A_1])$, $R_{04} = R_0Z_1[A_1]/(1 + Z_1[A_1]$, $R_{05} = Z_5R_0$, $R_{06} = Z_6R_0$, $R_{07} = Z_7R_0$, $R_5 = (1 - f)R_4$, $R_{19} = (1 - i)R_5$.

From the steady-state condition for each kind of radicals, it follows that

$R_1 = R_{05} + R_{06} + R_6 + R_{13}$, $R_{09} = (R_{06} + R_{07})/(1 + Z_2[A_2])$, $R_{08} = (R_{06} + R_{07})Z_2[A_2]/(1 + Z_2[A_2])$, $R_{010} = 0.5(R_{05} + R_{07})$, $R_1 = (Z_5 + Z_6)R_0 + R_6R_{13}$, $R_{010} = 0.5R_0(Z_5 + Z_7)$, $R_{09} = (Z_6 + Z_7)R_0/(1 + Z_2[A_2])$, $R_{08} = (Z_6 + Z_7)RZ_2[A_2]/(1 + Z_2[A_2])$, $R_{12} = bR_0/(1 + Z_1[A_1]) + dR_2 + 2R_{11} + (Z_6 + Z_7)R_0 + R_8 + 2R_{14}$, $R_3 = (Z_5 + 2Z_6 + Z_7)R_0 + R_6 + dR_2 + 2bR_0/(1 + Z_1[A_1]) + 2R_{11} + R_8 + 3R_{14} + R_{13}$, $d[X_7]/dt = (Z_5 + 2Z_6 + Z_7)R_0 + dR_2 + 2bR_0/(1 + Z_1[A_1]) + R_8 - R_{13} + 2R_{14} - 2k_4[X_7]^2 = 0$, $d[X_{10}]/dt = dR_2 - R_8 - 2k_9[X_{10}]^2 = 0$.

In the equation for $d[X_7]/dt$ and the corresponding equations for consumption and accumulation of the initial and final products, the rates R_8, R_{13}, and R_{14} are considerably lower than the other rates and can be neglected. For the same reason, the rate R_8 can be neglected in the equation for $d[X_{10}]/dt$.

For the rates of consumption and accumulation of the initial and final products of cyclohexane ozonolysis, we obtain first-order differential equations:

$d[A_1]/dt = (-by_2 - 1 - Z_5 - Z_7 - 2Z_6)R_0 + y_3 - k_6[A_2][X_7] - dR_2 - R_8 - 2R_{11} - R_{13}\ 3R_{14}$, $d[A_4]/dt = (ay_2 + Z_5 + Z_6)R_0 - R_2 + k_6[A_2][X_7] + f[X_7]^2k_4 - R_{14}$, $d[A_5]/dt = (1 - f) \times [X_7]^2k_4 - R_{11}$, $d[A_6]/dt = 0.5(Z_6 + Z_7)R_0 + (1 - k)0.5dR_2$, $d[A_7]/dt = (Z_6 + Z_7 + by_2)R_0 + R_2 + R_8 + 2R_{11} + 2R_{14} + R_{18}$, $d[A_8]/dt = iR_5$, $d[A_9]/dt = 0.5kdR_2 - R_{18}$, $d[A_{11}]/dt = Z_7R_0 + [f(2 - i) + (1 - i)][X_7]^2k_4 + (1 - 0.5kd)R_2 + R_8 + R_{11} + R_{13}$, $d[A_{12}]/dt = (1 - i)(1 - f)[X_7]^2k_4 + R_{13} - R_{21}$, $d[A_{13}]/dt = (1 - i)(1 - f)[X_7]^2k_4 + R_{14} + R_{18} + R_{21}$.

The rate of ozone consumption[1]

$$-W_{O_3} = Z_9R_0 + (1 + d - fd)R_2 + (3 - 2f)R_{11} + k_6[A_2][X_7] + 2R_{14} + R_{18} + R_{21},$$

where $Z_9 = (1 - Z_1[A_1])/(1 - Z_1[A_1]) + (Z_6 + Z_7) \times \{1 + 1/(1 + Z_2[A_2])\} + (1 - f)(Z_5 + 2Z_6 + Z_7 + 2by_2)$.

The rate of oxygen accumulation

$$W_{O_2} = Z_{10}R_0 + (1 - 2d - kd/2)R_2 + (2.5 + k/2)R_8 + R_6 - 1.5R_{13} - R_{14} + 0.5(R_{18} + R_{21}),$$

where $Z_{10} = ay_2 + \{(Z_6 + Z_7)/(1 + Z_2[A_2])\}(1 + 2.5Z_2[A_2])$.

Thus, the problem is reduced to a search for adequate values of the constants k_0, k_2, k_{11}, k_6, k_{18}, and k_{21}, ratios of the constants Z_1–Z_4, and stoichiometric coefficients a, l, d, f, i, and k. The constant $k_4 = 1.6 \times 10^6$ l mol^{-1} s^{-1} was taken from the literature [31].

This system of differential equations was integrated numerially by the modified Euler method [32] with an ES-10 22 computer. The calculated, c_{calc}, and experimental, c_{exp}, running concentrations of the cyclohex-

[1] In most cases, only one of the three oxygen atoms in the ozone molecule is involved in the reaction (see the scheme of the mechanism).

Table 3. Experimental and calculated data on cyclohexane ozonolysis (20°C; $[O_3] = 1.3 \times 10^{-3}$, $[O_2] = 5.6 \times 10^{-3}$, [RH] = 9.25 M)

τ, h	Concentration, M								
	$[A_1]$	$[A_4] \times 10^3$	$[A_5] \times 10^4$	$[A_6] \times 10^3$	$[A_7]$	$[A_9] \times 10^2$	$[A_{11}]$	$[A_{12}] \times 10^3$	$[A_{13}] \times 10^3$
1	9.110*	34	23.0	2.0	0.10	1.0	0.08	2.0	5.2
	9.110	43.1	21.6	4.39	0.077	0.85	0.076	1.33	4.0
2	8.940	39	26.0	4.2	0.24	2.0	0.21	4.5	19.0
	8.936	52.3	26.0	8.71	0.243	1.87	0.21	2.98	16.55
3	8.74	37	25.0	6.0	0.40	2.5	0.32	6.1	35.0
	8.756	53.7	26.6	12.9	0.416	2.49	0.35	4.39	35.40
4	8.60	35	25.1	8.2	0.55	3.0	0.48	8.0	60.0
	8.577	63.3	26.4	17.1	5.93	2.80	0.49	5.50	57.70
5	8.40	36	25.0	10.0	0.75	3.0	0.60	9.0	80.0
	8.401	52.5	26.0	21.2	0.76	2.93	0.63	6.34	81.70

* Numerator: experiment; denominator: calculation.

ane ozonolysis products were compared, and the target function F was minimized:

$$F = \sqrt{\left\{\sum_{j=1}^{m}\sum_{i=1}^{n}[(c_{i\,\mathrm{exp}} - c_{i\,\mathrm{calc}})/\varepsilon_i]^2\right\}/mn} \times 100,$$

where n is the number of components monitored, m is the number of experimental points for each component, and ε_i is the absolute error of the experimental determination of the concentration of ith component.

The rate constants and the corresponding coefficients were refined using the complex method [32, 33]. The results are listed in Table 3 and in the scheme of the cyclohexane ozonolysis mechanism.

Table 3 shows that the calculated running concentrations of the reaction participants reasonably agree with the experiment. Hence, the above scheme of differential equations can be considered a mathematical model of cyclohexane ozonolysis, and the calculated constants describe adequately the whole set of the experimental data.

The calculated reaction selectivity with respect to the target product, cyclohexanone, is 70.8%, at hydrocarbon conversion of 9%. We found that the contribution from formation and transformation of the ozone–cyclohexane adduct is insignificant ($Z_1 = 0.00895$). At the same time, a significant role is played by formation and transformation of hydrotrioxide ($L = 0.12$, $Z_3 = 7.1$, $Z_4 = 137.8$). The reaction occurs by the radical chain mechanism. However, 78% of the R$^\bullet$ and OH$^\bullet$ radicals generated in the primary initiation stage [reaction (1)] recombine in a cage to form cyclohexanol. Alkyl radicals are generated in reactions (1), (9), (19), and (23) with rate constants k_0, k_1, k_{12}, and k_{16}, involving ozone and the radicals RO$^\bullet$, $^\bullet$OH, and $^\bullet CH_2(CH_2)_4COO$. Peroxy radicals are consumed by recombination and reactions with ozone and cyclohexanone.

Alkoxy radicals are fairly active and react with the initial hydrocarbon with rate constants of 10^{-4}–10^5 l mol^{-1} s^{-1}. The $^\bullet$OH radical is also characterized by high rate constants of hydrogen abstraction from the substrates. The parallel formation of acids and neutral oxidatiomn products (20°C) from the very beginning of the process is, most probably, due to reaction of the peroxy radical to form a biradical, with the subsequent ring opening. As the hydrocarbon conversion increases, new precursors of adipic acid appear, such as hydroxycyclohexyl hydroperoxide, adipic acid monoaldehyde, or ε-caprolactam. We performed special experiments on ozonolysis of these compounds.

The high selectivity with respect to cyclohexanone is due to its formation by reactions (5), (10), (12), and (16)–(18), characterized by the rates R_{07}, R_2, R_4, R_8, R_9, and R_{11}. The rates R_2, R_4, R_9, R_{11} are determining. Cyclohexanone is relatively slowly (rates R_{13} and R_{20}) consumed by reactions (20) and (27). A significant role in the cyclohexane ozonolysis mechanism is played by such fast reactions as selective oxidation of cyclohexanol to the ketone ($k_2 = 0.432$ l mol^{-1} s^{-1}) and reaction of peroxy radical with ozone ($k_6 = 1.385 \times 10^3$ l mol^{-1} s^{-1}).

The kinetic model proposed ensures good agreement with the experiment for all the products of cyclohexane ozonolysis.

CONCLUSIONS

(1) A mathematical model was developed for low-temperature ozonolysis of cyclohexane in a bubbled vessel to large conversions.

(2) The high efficiency of chemical systems for selective low-temperature ozonolysis of saturated hydrocarbons with equivalent C–H bonds into carbonyl compounds is mainly determined by fast oxidation of secondary alcohols and hydroperoxides with ozone, recombination of secondary radicals $RO_2^{\bullet}$, their destructive disproportionation in reaction with ozone to give alkoxy radicals, and relatively slow consumption of ketones by reactions with ozone. The $RO^{\bullet}$ radical can also be generated from hydrotrioxide.

REFERENCES

1. Razumovskii, S.D. and Zaikov, G.E., *Izv. Akad. Nauk SSSR, Ser. Khim.*, 1973, vol. 6, no. 11, pp. 2444–2446.
2. Varkonu, N., Rass, S., and Mazur, U., *J. Chem. Soc., Chem. Commun.*, 1974, vol. 11, pp. 437–438.
3. Aleksandrov, Yu.A., Tarunin, B.I., and Perepletchikov, M.L., *Kinet. Katal.*, 1976, vol. 17, no. 5, pp. 1162–1165.
4. Galimova, L.G., Mechanism of Cyclohexane Oxidation with Ozone, *Cand. Sci. Dissertation*, Ufa, 1975.
5. Razumovskii, S.D. and Zaikov, G.E., *Ozon i ego reaktsii s organicheskimi soedineniyami* (Ozone and Its Reactions with Organic Compounds), Moscow: Nauka, 1974.
6. Komissarov, V.D., Gerchikov, A.Ya., Galimova, L.G., and Denisov, E.T., *Dokl. Akad. Nauk SSSR*, 1973, vol. 213, no. 4, pp. 881–883.
7. Ruban, L.V., Rakovski, S.K., and Popov, A.A., *Izv. Akad. Nauk SSSR, Ser. Khim.*, 1976, no. 9, pp. 1950–1956.
8. Korotkova, N.P., Syroezhko, A.M., and Proskuryakov, V.A., *Zh. Prikl. Khim.*, 1981, vol. 54, no. 3, pp. 660–665.
9. Razumovskii, S.D., Kefeli, A.A., Trubnikov, G.R., and Zaikov, G.E., *Dokl. Akad. Nauk SSSR*, 1970, vol. 192, no. 6, pp. 1313–1316.
10. Lisitsyn, D.M., Poznyak, T.I., and Razumovskii, S.D., *Kinet. Katal.*, 1976, vol. 17, no. 4, pp. 1049–1056.
11. Denisov, E.T., Mechanism of Liquid-Phase Homolysis of Molecules, *Itogi Nauki Tekh., Ser.: Kinet. Katal.*, 1981, vol. 9.
12. Syroezhko, A.M. and Proskuryakov, V.A., *Zh. Prikl. Khim.*, 1998, vol. 71, no. 7, pp. 1168–1173.
13. Korotkova, N.P., Oxidation of Cyclohexane and Some Oxygen-Containing Compounds with Ozone–Air Mixtures, *Cand. Sci. Dissertation*, Leningrad, 1978.
14. Geiseler, G., Asinger, F., and Wien, H., *Chem. Ber.*, 1959, vol. 92, pp. 958–970.
15. Vikhorev, A.A., Syroezhko, A.M., and Proskuryakov, V.A., *Zh. Prikl. Khim.*, 1977, vol. 50, no. 3, pp. 698–699.
16. Komissarov, V.D., Galimova, L.G., and Denisov, E.T., *Kinet. Katal.*, 1974, vol. 15, no. 4, pp. 1063–1065.
17. Komissarov, V.D., Galimova, L.G., Komissarova, I.N., *et al., Dokl. Akad. Nauk SSSR*, 1977, vol. 235, no. 6, pp. 1350–1352.
18. Vikhorev, A.A., Syroezhko, A.M., Proskuryakov, V.A., and Yakovlev, A.S., *Zh. Prikl. Khim.*, 1978, vol. 51, no. 11, pp. 2568–2572.
19. Vikhorev, A.A., Syroezhko, A.M., and Proskuryakov, V.A., *Zh. Prikl. Khim.*, 1976, vol. 49, no. 7, pp. 1592–1597.
20. Korotkova, N.P., Syroezhko, A.M., and Proskuryakov, V.A., *Zh. Prikl. Khim.*, 1989, vol. 62, no. 4, pp. 885–889.
21. Korotkova, N.P., Syroezhko, A.M., and Proskuryakov, V.A., *Zh. Prikl. Khim.*, 1981, vol. 54, no. 4, pp. 861–867.
22. Vikhorev, A.A., Syroezhko, A.M., and Proskuryakov, V.A., *Zh. Prikl. Khim.*, 1975, vol. 48, no. 9, pp. 2059–2062.
23. Vikhorev, A.A., Syroezhko, A.M., and Proskuryakov, V.A., *Zh. Prikl. Khim.*, 1976, vol. 49, no. 3, pp. 588–592.
24. Vikhorev, A.A., Syroezhko, A.M., and Proskuryakov, V.A., *Izv. Vyssh. Uchebn. Zaved., Khim. Khim. Tekhnol.*, 1976, vol. 19, no. 10, pp. 1499–1503.
25. Vikhorev, A.A. and Syroezhko, A.M., *Khim. Prom–st.*, 1977, no. 12, pp. 896–898.
26. Syroezhko, A.M., Korotkova, N.P., Vikhorev, A.A., and Proskuryakov, V.A., *Zh. Prikl. Khim.*, 1978, vol. 51, no. 12, pp. 2743–2754.
27. Denisov, E.T., *Konstanty skorosti gomoliticheskikh zhidkofaznykh reaktsii* (Rate Constants of Liquid-Phase Homolytic Reactions), Moscow: Nauka, 1971.
28. Razumovskii, S.D., Kefeli, A.A., Trubnikov, G.R., and Zaikov, G.E., *Dokl. Akad. Nauk SSSR*, 1970, vol. 192, no. 6, pp. 1313–1316.
29. Emanuel', N.M., Denisov, E.T., and Maizus, Z.K., *Tsepnye reaktsii okisleniya uglevodorodov v zhidkoi faze* (Chain Reaction of Liquid-Phase Oxidation of Hydrocarbons), Moscow: Nauka, 1965.
30. Denisov, E.T. and Kovalev, G.I., *Okislenie i stabilizatsiya reaktivnykh topliv* (Oxidation and Stabilization of Jet Fuels), Moscow: Khimiya, 1983.
31. Maslennikov, S.I., Galimova, L.G., and Komissarov, V.D., *Izv. Akad. Nauk SSSR, Ser. Khim.*, 1979, no. 3, pp. 631–634.
32. Bezdenezhnykh, A.A., *Inzhenernye metody sostavleniya uravnenii skorostei reaktsii i rascheta kineticheskikh konstant* (Engineering Methods for Constructing Reaction Rate Equations and Calculating Kinetic Constants), Leningrad: Khimiya, 1973.
33. Sautin, S.N. and Punin, A.E., *Issledovanie i optimizatsiya khimiko-tekhnologicheskikh protsessov s pomoshch'yu aktivnogo eksperimenta* (Study and Optimization of Processes in Chemical Technology by Active Experiment), Leningrad: Khimiya, 1982.

Russian Journal of Applied Chemistry, Vol. 75, No. 8, 2002, pp. 1304–1307. Translated from Zhurnal Prikladnoi Khimii, Vol. 75, No. 8, 2002, pp. 1329–1333.
Original Russian Text Copyright © 2002 by Klyuev, Prokopchuk, Shostak, Skakovskii, Tychinskaya, Udarov, Stromskii.

ORGANIC SYNTHESIS AND INDUSTRIAL ORGANIC CHEMISTRY

Resistance to Thermal Oxidative Degradation of Paraform-Modified Rosin and Its Derivatives

A. Yu. Klyuev, N. R. Prokopchuk, L. M. Shostak, E. D. Skakovskii, L. Yu. Tychinskaya, B. G. Udarov, and A. S. Stromskii

Belarussian State Technological University, Minsk, Belarus

Institute of Chemistry of New Materials, National Academy of Sciences of Belarus, Minsk, Belarus

Institute of Physical Organic Chemistry, National Academy of Sciences of Belarus, Minsk, Belarus

Received April 4, 2002

Abstract—The resistance to thermal oxidative degradation of paraform-modified rosin and its derivatives (esters and salts) was studied. The modified rosin esters can be used as components of thermoplastic formulations, and modified salts, as heat-resistant additives to cutting fluids.

Rosin and its derivatives are widely used as components of formulations prepared or applied in a wide temperature range, from 50 to 300°C and higher. At high temperatures, rosin products undergo thermal oxidative degradation, which deteriorates the performance of the material. Therefore, data on heat resistance of secondary rosin products are necessary for the development of new formulations.

In this work, which continues our previous studies [1–3], we evaluated the resistance to thermal oxidative degradation of paraform-modified oleoresin rosin and its derivartives (esters and salts).

EXPERIMENTAL

For the experiments, we took commercial pine oleoresin rosin (POR) containing 96.0 wt % resin acids and 4.0 wt % high-boiling unsaponifiable substances. The resin fraction of POR contained 75.0% resin acids with conjugated double bonds (abietic levopimaric, palustric, neoabietic) and 25.0% pimaric-type acids (pimaric, isopimaric, sandaracopimaric), and also saturated and aromatic acids (dehydroabietic, dihydroabietic).

Modification of POR with paraform (PF) was performed at 140–180°C for 1.5–4 h with the subsequent vacuum distillation of residual PF and unsaponifiable substances [PF = $(CH_2O)_n$, n = 6–12, mp 64°C]. The PF-modified rosin (FPOR) was esterified with ethylene glycol (bp 198–200°C, d_4^{20} 1.1088), diethylene glycol (bp 244.6°C, d_4^{20} 1.1177), *d*-sorbitol (mp 89–93°C), glycerol (bp 290°C, d_4^{20} 1.2604), and pentaerythritol (mp 260.5°C).

Rosin esters were prepared by treatment of FPOR at 265–290°C with alcohols, followed by vacuum evaporation of residual alcohols, water formed in the reaction, and unsaponifiable substances. The alcohol was taken in the amount of one hydroxyl equivalent per mole of resin acid. The reaction progress was monitored by variation of the acid number (AN) of the reaction mixture. The reaction was stopped when AN did not change further for 1 h. The softening point T_s and AN were determined as described in [4]. The group composition of POR, FPOR, and its esters was determined according to [4, 5]. The qualitative and quantitative composition of POR and FPOR and its esters was determined by NMR spectroscopy and GLC. The ^{1}H NMR spectra were measured by standard procedures with a BS-567A spectrometer, using 10% solutions in $CDCl_3$ and TMS as internal reference. The ^{13}C NMR spectra were measured with a BS-587A spectrometer using 20% solutions in $CDCl_3$ and standard 10-mm ampules. The procedures allowed quantitative analysis of the samples. Chromium tris-acetylacetonate was used as relaxant.

The physicochemical properties and compositions of the products are listed in Table 1.

FPOR salts (sodium, ethanolammonium, diethanolammonium, triethanolammonium) were prepared in aqueous solutions by treatment of FPOR with the corresponding bases under heating, followed by evaporation.

1070-4272/02/7508-1304 $27.00 © 2002 MAIK "Nauka/Interperiodica"

Table 1. Properties and compositions of rosin products

Sample*	Reaction conditions			Physicochemical characteristics		Group composition, wt %		
	T, °C	agent						
		formula	M	T_s, °C	AN, mg KON g^{-1}	resin acid esters	resin acids	unsaponifiable substances
POR	–	–		72.5	165.0	–	96.0	4.0
$FPOR_2$	140–180	$(CH_2O)_n$		86.0	162.0	–	98.0	2.0
$FPOR_4$	140–180	–		87.0	160.0	–	98.0	2.0
$FPOR_6$	140–180	–		88.0	158.0	–	98.0	2.0
$FPOR_8$	140–180	–		89.0	155.0	–	98.0	2.0
$FPOR_{10}$	140–180	–		87.0	154.0	–	97.0	3.0
DEFPOR	265	$HOCH_2CH_2OCH_2CH_2OH$	106.12	85.6	18.0	87.5	10.0	2.5
EEFPOR	265	$HOCH_2CH_2OH$	62.07	98.5	15.3	90.0	9.0	1.0
SEFPOR	275	$HOCH_2(CHOH)_4CH_2OH$	182.17	120.0	14.0	90.8	7.2	2.0
GEFPOR	290	$HOCH_2CHOHCH_2OH$	92	125.0	10.0	93.0	6.0	1.0
PEFPOR	290	$C(CH_2OH)_4$	136.15	130.0	9.0	94.8	4.2	1.0

* $FPOR_i$, POR modified with i wt % PF; esters of PF-modified POR: DEFPOR, diethylene glycol ester; EEFPOR, ethylene glycol ester; SEFPOR, sorbitol ester; GEFPOR, glycerol ester; and PEFPOR, pentaerythritol ester.

The bases were added in amounts necessary for full neutralization of all the carboxy groups in FPOR.

The parameters of thermal oxidative degradation of rosin products were determined by dynamic and isothermal thermogravimetry [6]. Since FPOR esters, except resin esters and resin acids that remained unchanged after esterification with polyhydric alcohols, contained physically bound water, residual alcohol, and unsaponifiable substances (boiling in the range 100–220°C), the weight loss started at relatively low temperatures. Therefore, the heat resistance was judged from the temperature of degradation onset T_d^{DTG} and T_d^{DTA}, rather than from the temperatures of 5% weight loss $T_{5\%}$ [7].

To fully characterize the stability of FPOR and its esters, we used isothermal TG. Samples of FPOR or its esters (0.5–1.3 g each) were heated at 240°C for 4, 8, and 12 h in a muffle furnace in air. The initial POR was used as reference. The weight loss was determined with an analytical balance.

Data on thermal oxidative degradation of FPOR and of its esters and salts are listed in Tables 2 and 3. The names and abbreviations of FPOR esters are given in Table 1.

As seen from Table 1, as the extent of rosin modification with PF is increased (from 2 to 10 wt %), the softening point increases from 72.5 to 87.0°C, and the AN decreases from 165 to 154 mg KOH g^{-1}. The best results are attained with 6–8 wt % PF: T_s 89.0°C, AN 158–155 mg KOH g^{-1}. At a higher (10 wt % PF) degree of POR modification, the rosin quality decreases: T_s 87.0°C, AN 154 mg KOH g^{-1}.

The $FPOR_6$ sample was esterified with polyhydric alcohols. As seen from Table 1, PEFPOR has the highest (130°C), and DEFPOR, the lowest (85.6°C) softening point. The physicochemical characteristics of the esters depend on the alcohol used. All the FPOR esters, except the corresponding resin acid esters, contain free resin acids and unsaponificable substances. The higher T_s of PEFPOR, compared to the other FPOR esters, may be due to higher reactivity of pentaerythritol. Comparison with our previous data [2] shows that T_s of FPOR esters considerably exceeds T_s of POR esters.

The quantitative and qualitative composition of the main POR components was determined by ^1H and ^{13}C NMR. Oleoresin rosin contains the following acids (%): abietic 39, levopimaric 17, palustric 10, neoabietic 9, dehydroabietic 6, dihydroabietic 1, pimaric 7, isopimaric 9, and sandaracopimaric 2.

The ^1H and ^{13}C NMR data are nicely consistent with the results of the GLC analysis.

The spectra of FPOR show that it is a mixture of organic compounds with resin acids as major components, as judged from the high intensity of the signals of carboxyl hydrogen (δ 9.4 ppm) in the ^1H NMR spectrum and carboxyl carbon (δ_C 185.5 ppm) in the ^{13}C NMR spectrum. The PF-modified rosin samples appreciably differ in quantitative and qualitative composition. After treatment of POR with para-

Table 2. Heat resistance of PF-modified rosin and of its esters and salts (data of thermal analysis)

Sample	T_d^{DTG}	T_d^{DTA}	T_d^{av*}	$T_{5\%}$	$T_{10\%}$	$T_{50\%}$	E_d, kJ mol^{-1}
	°C						
Rosin							
POR	280	280	280	268	286	353	72
$FPOR_2$	302	303	302	282	302	370	86
$FPOR_4$	304	306	305	284	305	370	93
$FPOR_6$	310	308	309	290	312	372	98
$FPOR_8$	303	301	302	282	306	370	88
$FPOR_{10}$	300	300	300	280	304	362	86
Rosin esters							
SEFPOR	340	300	320	305	334	400	86
DEFPOR	350	318	334	327	360	404	100
EEFPOR	350	326	338	340	364	410	102
GEFPOR	366	322	344	340	370	410	108
PEFPOR	366	326	346	345	376	440	110
Rosin salts**							
EAFPOR	320	320	320	–	–	–	–
DAFPOR	335	325	330	–	–	–	–
TAFPOR	342	338	340	–	–	–	–
NaFPOR	379	381	380	–	–	–	–

* $T_d^{av} = (T_d^{DTG} + T_d^{DTA})/2$; E_d is the activation energy of thermal oxidative degradation.

** $FPOR_6$ salts: EAFPOR, ethanolammonium salt; DAFPOR, diethanolammonium salt; TAFPOR, triethanolammonium salt; and NaFPOR, sodium salt.

form, the content of the major component, abietic acid, does not change noticeably, whereas the content of levopimaric acid decreases from 17 to 3%. It is logical to assume that levopimaric acid reacts with formaldehyde by the scheme given in [8], with isomerization of conjugated double bonds and addition of the formaldehyde molecule to form the CH_2OH group. The formation of this group is confirmed by the appearance of the ^1H NMR signals at δ 4.2–3.2 ppm, absent in the spectra of POR. In the ^{13}C NMR spectrum, a broad maximum appears at about 65 ppm.

The treated product contains no neoabietic acid. Dehydroabietic and pimaric acid, similarly to abietic acid, do not react with paraform, and their content remains unchanged. Isopimaric acid is, by contrast, completely converted to other substances.

The ^1H and ^{13}C data suggest that some of the resin acids become linked via the $–CH_2–$ group [9]. This is indicated by the appearance of signals attributable to a methylene group located between double bonds (^1H, δ 2.9 ppm; ^{13}C, δ_C 26 ppm). This is consistent with an appreciable growth of T_s of modified rosins: from 72.5 to 89°C. Also, a ^{13}C NMR signal appearing at about 178 ppm suggests the presence in modified rosin of esters (~15%) along with the acids.

Thus, the NMR spectra show that modified rosin is mainly a mixture of resin acids, some of which additionally contain the $–CH_2OH$ group and some are linked via the $–CH_2–$ group. However, additional studies are required to fully understand the reaction of PF with rosin.

The NMR spectra of products formed in reactions of polyhydric alcohols with FPOR suggest that these products are mixtures of esters. In particular, the ^{13}C NMR signal at 178 ppm is characteristic of carboxy groups.

Table 2 shows that, as judged from all the criterial parameters (T_d^{DTG}, T_d^{DTA}, T_d^{av}, $T_{5\%}$, $T_{10\%}$, $T_{50\%}$), the resistance to thermal oxidative degradation increases upon modification with FP, with the $FPOR_6$ sample being the most stable (T_d^{av} 309°C). The activation energy of thermal oxidative degradation of FPOR samples, calculated from the dynamic TG data by the Broido method [10], increases from 86 to 98 kJ mol^{-1} in going from $FPOR_2$ to $FPOR_8$.

Treatment of $FPOR_6$ with alcohols enhances its resistance to thermal oxidative degradation. For example, the T_d^{av} values increase, on the average, by 11, 25, 29, 35, and 37°C in going from $FPOR_6$ to SEFPOR, DEFPOR, EEFPOR, GEFPOR, and PEFPOR, respec-

tively. The most resistant is PEFPOR (T_d^{av} 346°C), and the least resistant, SEFPOR (T_d^{av} 320°C). The activation energy E_d in the series SEFPOR–PEFPOR increases from 86 to 110 kJ mol^{-1}. FPOR esters are more resistant to thermal oxidative degradation than their analogues prepared from the initial POR [2].

For FPOR esters, a linear correlation is observed between the parameters characterizing the onset of thermal oxidative degradation and T_s: these temperatures vary in the same direction.

As seen from the isothermal TG data (Table 3), the largest weight loss in 4–12 h at 240°C is observed with SEFPOR and DEFPOR, and the smallest weight loss, with PEFPOR, GEFPOR, and EEFPOR.

Our dynamic and isothermal TG studies revealed the general trends in the resistance of FPOR esters to thermal oxidative degradation. The lower the molecular weight of a monohydric alcohol and the larger the number of hydroxy groups in it, the higher the resistance of FPOR ester to thermal oxidative degradation. With respect to this characteristic, FPOR esters can be ranked in the following order: PEFPOR > GEFPOR > EEFPOR > DEFPOR > SEFPOR.

The FPOR esters can be recommended as components of new thermoplastic formulations instead of the less thermostable esters of the initial POR.

The high heat resistance of FPOR opens up possibilities for preparing heat-resistant additives to cutting fluids instead of the traditionally used sodium and ethanolammonium salts of oleoresin rosin.

Therefore, we prepared from $FPOR_6$ its ethanolammonium, diethanolammonium, triethanolammonium, and sodium salts and examined their resistance to thermal oxidative degradation by dynamic TG.

Table 2 shows that, as judged from all the criterial parameters (T_d^{DTG}, T_d^{DTA}, T_d^{av}), the resistance to thermal oxidative degradation grows in going from EAFPOR to NaFPOR. Treatment of FPOR with ethanolamine, diethanolamine, triethanolamine, or NaOH enhances its heat resistance. For example, T_d^{av} increases, on the average, by 11, 21, 31, and 71°C in going from $FPOR_6$ to EAFPOR, DAFPOR, TAFPOR, and NaFPOR, respectively. The T_d^{av} of FPOR salts increases with approximately equal increments in going from monoethanolamine (molecular weight 61.08) to di- and then to triethanolamine (149.18), and the sodium salts are still more stable. All these substances are more heat-resistant than their analogues prepared from the initial POR and can therefore be recommended as heat-resistant additives to cutting fluids.

Table 3. Weight loss Δm of rosin products on isothermal heating at 240°C

Sample	Δm, wt %, in indicated time, h		
	4	8	12
POR	24.3	41.2	46.4
$FPOR_6$	15.0	30.0	35.0
SEFPOR	10.0	14.0	16.0
DEFPOR	7.5	9.0	12.0
EEFPOR	1.2	2.8	3.0
GEFPOR	1.0	2.6	2.8
PEFPOR	0.9	2.4	2.6

CONCLUSION

The heat resistance of rosin is considerably enhanced by its treatment with paraform. The process is simple and waste-free; its product, paraform-modified pine oleoresin rosin, can be converted to more heat-resistant products, in particular, esters and salts.

REFERENCES

1. Klyuev, A.Yu., Shlyashinskii, R.G., Prokopchuk, N.R., *et al.*, *Vestsi Akad. Navuk Bel., Ser. Khim. Navuk*, 2001, no. 1, pp. 84–88.
2. Klyuev, A.Yu., Shlyashinskii, R.G., Prokopchuk, N.R., *et al.*, *Zh. Prikl. Khim.*, 1999, vol. 72, no. 2, pp. 288–292.
3. Klyuev, A.Yu., Shlyashinskii, R.G., Prokopchuk, N.R., *et al.*, *Zh. Prikl. Khim.*, 2000, vol. 73, no. 6, pp. 1018–1024.
4. Vershuk, V.I. and Gurich, N.A., *Metody analiza syr'ya i produktov kanifol'no-skipidarnogo proizvodstva* (Methods for Analysis of Raw Materials and Products of Rosin and Turpentine Industry), Moscow: Goslesbumizdat, 1960.
5. Bardyshev, I.I., Shlyashinskii, R.G., and Bulgakov, A.N., *Vestsi Akad. Nauk Bel. SSR, Ser. Khim. Navuk*, 1976, no. 1, pp. 84–87.
6. Wendlandt, W.Wm., *Thermal Methods of Analysis*, New York: Interscience, 1964.
7. Prokopchuk, N.R., *Vestsi Akad. Navuk Bel., Ser. Khim. Navuk*, 1984, no. 4, pp. 119–121.
8. Parkin, B.A. and Hedrick, G.W., *J. Org. Chem.*, 1965, vol. 30, no. 7, pp. 2356–2358.
9. Sacchi, R., Addeo, F., and Paolillo, L., *Magn. Reson. Chem.*, 1997, vol. 35, pp. 133–145.
10. Broido, A. and Semple, A., *J. Polym. Sci., Part A2*, 1969, vol. 7, no. 10, pp. 1761–1772.

Russian Journal of Applied Chemistry, Vol. 75, No. 8, 2002, pp. 1308–1311. Translated from Zhurnal Prikladnoi Khimii, Vol. 75, No. 8, 2002, pp. 1334–1337.
Original Russian Text Copyright © 2002 by Shtennikova, Bushin, Kolbina, Khotimskii, Litvinova, Chirkova.

MACROMOLECULAR CHEMISTRY AND POLYMERIC MATERIALS

Hydrodynamic Conformation Properties of Poly(1-Trimethylsilylpropyne) Molecules Obtained on $NbCl_5$ Catalyst

I. N. Shtennikova, S. V. Bushin, G. F. Kolbina, V. S. Khotimskii, E. G. Litvinova, and M. V. Chirkova

Institute of Macromolecular Compounds, Russian Academy of Sciences, St. Petersburg, Russia

Topchiev Institute of Petroleum Chemical Synthesis, Moscow, Russia

Received January 28, 2002

Abstract—Hydrodynamic properties of 10 samples of poly(1-trimethylsilylpropyne) of various molecular weights, obtained with $NbCl_5$ catalyst and containing 60–70% *cis* C=C bonds, were studied by sedimentation, translation diffusion, and viscometry techniques. The equilibrium rigidity of the polymer molecules was estimated from the viscometric data using the formalism of the intrinsic viscosity theory as applied to the worm-like coil model with excluded-volume effects. For the polymer macromolecules, the Kuhn segment length, thermodynamic parameter ε, and hydrodynamic diameter of the chain *d* were estimated.

A study of molecular properties of disubstituted polyacetylenes [1] and aromatic polyamides [2] revealed that even insignificant differences in the monomeric unit structure, including those in the alternation of double bonds in the backbone chain [1] or side substituents, can have a considerable effect on properties of the polymer molecule as a whole. Also of vital importance for properties of a polymer can be the arrangement (regular or random) of *cis* and *trans* C=C bonds in the backbone chain [3].

Presently, disubstituted silicon-containing polyacetylenes are intensively studied as promising materials for gas-separating membranes [1, 4, 5].

In this connection, a study of properties of polymers of this class at the molecular level is a topical task [1–3, 5]. It is known that, depending on the synthetic procedure, macromolecules of the disubstituted polyacetylene, poly(1-trimethylsilylpropyne) (PTMSP), can have different relative amounts of the *cis* and *trans* C=C bonds in the backbone chain. It was demonstrated that PTMSP obtained with a $TaCl_5$-based catalyst is characterized by a *cis*/*trans* ratio of 40/60. This polymer is readily soluble in a number of solvents, and its molecular conformation has an increased equilibrium rigidity [1, 5].

To elucidate the effect of the *cis*/*trans* ratio in the backbone chain on the conformation features of the macromolecules, we studied in this work such hydrodynamic parameters as the intrinsic viscosity [η], translation diffusion coefficient *D*, and flotation coefficient (–*s*) of the PTMSP samples obtained on the $NbCl_5$ catalyst, which are characterized by increased *cis*/*trans* ratios (60/40 and 70/30).

EXPERIMENTAL

In the work we used PTMSP synthesized with $NbCl_5$ as a catalyst [4]. Depending on the synthesis conditions, PTMSP samples of various molecular weights were obtained. First, the samples were characterized by gel permeation chromatography (GPC) on a Waters chromatograph with two HP PL columns (particle size 10 μm, pore size 10^4–10^5 Å, 50°C). To obtain initial data on the molecular weight of the samples, we used 0.2 wt % solutions of the polymers in toluene. The flow rate was 1 ml min^{-1}. The PTMSP samples obtained with $NbCl_5$ demonstrated a narrow molecular-weight distribution, which allowed their use without further fractionation.

The *cis*-*trans* microstructure of the polymer macromolecules was studied by ^{13}C NMR in $CDCl_3$ used as internal reference. The spectra were registered on a Bruker MSh-300 instrument (75.47 MHz, solution concentration 20%, integration time 12 h). The spectra of PTMSP show four characteristic doublets corre-

1070-4272/02/7508-1308 $27.00 © 2002 MAIK "Nauka/Interperiodica"

sponding to the four carbon atoms of the monomeric unit $-[C(-Me)=C(-Si(-Me)_3]_n-$ of the macromolecule. The doublet structure of the signals of the carbon atoms suggests the presence of the *cis* and *trans* C=C bonds in the backbone chain of the polymer. The relative intensities of the peaks in the doublets reflect the *cis*/*trans* ratio. The spectra were processed using the ACD:CNMR version 1.1 program pack (product from the ACD Inc. Company). The mean content of the *cis* C=C bonds was estimated to be $65 \pm 5\%$.

For PTMSP **I** we determined the intrinsic viscosity [η], translation diffusion coefficient *D*, and flotation coefficient (–*s*).

We used the Swedberg method to determine the absolute molecular weights of PTMSP **I** samples with [η] ranging from 48.6 to 10^4 cm^3 g^{-1}. For this purpose, we measured the flotation coefficients (–*s*) of five samples of PTMSP **I** in chloroform as a good solvent for ultracentrifugation (viscosity $\eta_0 = 0.542 \times 10^{-2}$ P, density $\rho_0 = 1.485$ g cm^{-3}, 25°C). Centrifugation was carried out with an MOM Model 3170/B ultracentrifuge (Hungary) equipped with a polarization–interferometric unit with 0.3-mm spar split) [3]; rotor speed 40 000 rpm; solution concentration $c \leq (0.1–0.2) \times 10^{-2}$ g cm^{-3}. The time dependence of ln *x* (*x* is the abscissa of the maximum of the sedimentation curve) is presented in Fig. 1. The flotation coefficient was estimated from the slope of this dependence for each of the five PTMSP samples by the equation $(-s) = \omega^{-2}\,\Delta(\ln x)/\Delta t$, where ω is the rotor speed.

The translation diffusion coefficients *D* in chloroform at 25°C were determined with a polarization diffusometer [3] at solution concentrations below 0.1×10^{-2} g cm^{-3}. The diffusion curves were processed using data on the areas under the curves and on the peak ordinates [3]. Fifure 2 shows the variance of the diffusion curves $\langle\Delta^2\rangle$ as a function of the diffusion time *t*.

The absolute molecular weights M_{sD} were estimated by the Swedberg equation (1).

$$M_{sD} = (s/D)RT/(1 - \bar{\nu}\rho_0), \qquad (1)$$

where $\bar{\nu} = 0.94$ cm^3 g^{-1} is the partial specific volume of the polymer determined by the bottle method in chloroform at 25°C; and $(1 - \bar{\nu}\rho_0) = 0.392$ is the flotation factor.

The [η], *D*, (–*s*), and M_{sD} of the PTMSP samples are given in the table.

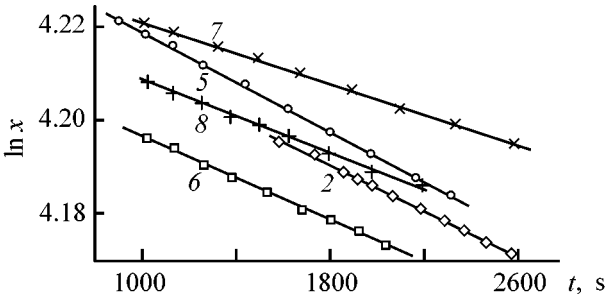

Fig. 1. ln *x* vs. time *t*. The numbers at the curves correspond to the PTMSP sample numbers; the same for Fig. 2.

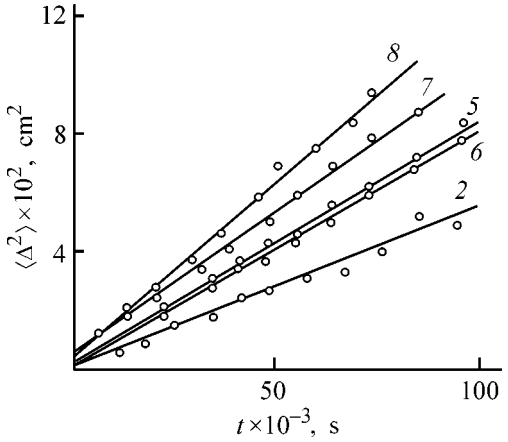

Fig. 2. Variance of the diffusion curves $\langle\Delta^2\rangle$ vs. the diffusion time *t*.

The logarithmic dependence of the intrinsic viscosity [η] of the PTMSP **I** samples, measured in toluene at 21°C, on M_{sD} is given in Fig. 3. This de-

Hydrodynamic characteristics and molecular weights of PTMSP **I** samples

Sample no.	[η], cm^3 g^{-1} (toluene, 21°C)	Chloroform, 24°C		$M \times 10^{-5}$
		$(-s) \times 10^{13}$, s	$D \times 10^7$, cm^2 s^{-1}	
1	138	–	–	5.62*
2	104	14.7	2.8	3.34
3	90	–	–	2.72*
4	83.6	–	–	2.40*
5	70	15.4	4.2	2.35
6	71.4	12.8	4.1	2.00
7	59.9	9.5	4.9	1.23
8	48.6	11	6.1	1.15
9	50	–	–	1.00*
10	32	–	–	0.47*

* Estimated from [η] in toluene by Eq. (3).

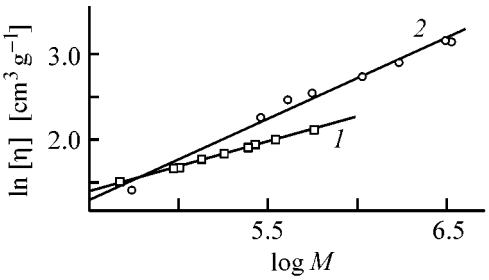

Fig. 3. log [η] vs. log *M*: (*1*) PTMSP **I** fractions in toluene and (*2*) PTMSP **II** fractions in heptane. Temperature 21°C.

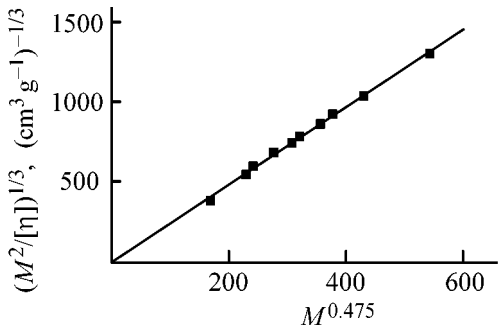

Fig. 4. $(M^2/[\eta])^{1/3}$ vs. $M^{(1-\varepsilon)/2}$ at $\varepsilon = 0.05$.

pendence was approximated by the Mark–Kuhn–Houwink equation (2) (MKH) (Fig. 3, curve *1*).

$$[\eta] = 5.7 \times 10^{-2} M_{sD}^{0.59}. \quad (2)$$

Slight increase in the exponent *a* in Eq. (2) (0.59 against the theoretical value of 0.5) is due to the bulk swelling effect, as for the previously studied PTMSP **II** synthesized on $TaCl_5$/BuLi [1], whose swelling was studied in heptane. At the same time, [η] of PTMSP **II** (Fig. 3, curve *2*) exceeds that of PTMSP **I** at the same *M* (curve *2* in Fig. 1 lies above curve *1*). This suggests that, at any molecular weight, the statistical size of the PTMSP **II** molecules is larger than that of PTMSP **I**, which indirectly suggests the lower equilibrium rigidity of PTMSP **I**.

The molecular weights of the other PTMSP **I** samples were estimated by Eq. (3).

$$M = ([\eta]/0.057)^{1.7}. \quad (3)$$

The estimated results are given in the table.

The equilibrium rigidity of the PTMSP **I** molecules was estimated from the viscometric data using the formalism of the intrinsic viscosity theory as applied to the worm-like coil model with excluded-volume effects. The solvent effect on the dependence of [η] on *M* can be accounted for using Eq. (4) [6–9].

$$(M^2/[\eta])^{1/3} = \Phi_\infty^{-1/3}\left[(1-\varepsilon)(1-\varepsilon/3)\right]^{-1}\left[M_L^{(1+\varepsilon)/2}/A^{(1-\varepsilon)/2}\right] M^{(1-\varepsilon)/2} + M_L P_\infty (3\pi\Phi)^{-1}[\ln(A/d) + 1 + \Psi(\varepsilon)], \quad (4)$$

where ε is the parameter characterizing the thermodynamic quality of the system polymer–solvent; $\Phi_\infty = 2.2 \times 10^{23}$ mol^{-1}, the Flory constant [8]; $P_\infty = 5.11$, the translation friction theory constant [9]; *A*, the Kuhn segment length; *d*, the hydrodynamic diameter of the chain; and Ψ(ε), the tabulated function [9].

The weight of the unit length of the outstretched molecular chain $M_L = M_0/\lambda$, where $M_0 = 112$ is the molecular weight of the monomeric unit and λ is the length of the monomeric unit projection along the direction of the outstretched molecular chain. The λ values are close for the *cis* and *trans* conformations of the monomeric unit (2.32×10^{-8} and 2.12×10^{-8} cm, respectively) [5]. Using Eq. (5),

$$\lambda = 2.321 \times 10^{-8} p + 2.12 \times 10^{-8}(1 - p), \quad (5)$$

we obtained the mean $\lambda = 2.18 \times 10^{-8}$ cm (for *trans*/*cis* = 30/70).

The experimental dependence $(M^2/[\eta])^{1/3}$ vs. $M^{(1-\varepsilon)/2}$ is presented in Fig. 4 at $\varepsilon = 0.05$, close to that obtained previously for PTMSP **II** [5]. The dependence was approximated by a straight line using Eq. (4). From the slope of this dependence, equal to

$$\Phi_\infty^{-1/3}\left[(1-\varepsilon)(1-\varepsilon/3)\right]^{-1}\left[M_L^{(1+\varepsilon)/2}/A^{(1-\varepsilon)/2}\right] = 2.44, \quad (6)$$

we obtained the Kuhn segment length $A = 33 \times 10^{-8}$ cm. This value is half that for PTMSP **II**, determined from hydrodynamic data ($A = 70 \times 10^{-8}$ cm) [2, 5]. Note that the *trans*/*cis* ratio is higher in PTMSP **II** than that in PTMS **I** (60/40 and 40/60, respectively). The difference in the *cis*/*trans* ratio at strongly different equilibrium rigidity suggests a different organization of the *cis* and *trans* structures in the polymers obtained with different catalysts, specifically, different extension of continuous sequences of units having the same conformation (*cis* or *trans*). The higher equilibrium flexibility of PTMSP **I** is caused by the longer flexible *cis* sequences or the shorter *trans* sequences.

The absolute term in Eq. (4), estimated from the position of the approximating straight line (Fig. 4) to be

$$M_L P_\infty (3\pi\Phi)^{-1}[\ln(A/d) + 1 + \Psi(\varepsilon)] = -3.701, \quad (7)$$

gives us the hydrodynamic diameter of the chain $d = 10 \times 10^{-8}$ cm at $\Psi(\varepsilon) = -2.58$ ($\varepsilon = 0.05$). This value is consistent with the chemical structure of the polymer, being virtually coincident with that obtained previously for PTMSP **II** [5].

CONCLUSIONS

(1) Comparison of the hydrodynamic parameters of poly(1-trimethylsilylpropyne) (polymers **I** and **II**) shows that, at the same molecular weight, the molecular size of polymer **I** synthesized with $NbCl_5$ as a catalyst is smaller that that of polymer **II** obtained with $TaCl_5$/BuLi.

(2) The Kuhn segment length of polymer **I** is half that of **II**, suggesting a higher flexibility of the macrochains of **I**.

(3) The higher equilibrium flexibility of PTMSP **I** is caused by the longer flexible *cis* sequences or the shorter *trans* sequences.

ACKNOWLEDGMENTS

The work was financially supported by the Integration Federal Target Program (project AO147).

REFERENCES

1. Shtennikova, I.N., Kolbina, G.F., Khotimskii, V.S., *et al., Vysokomol. Soedin., Ser. A*, 1998, vol. 40, no. 10, pp. 1569–1576.
2. Shtennikova, I.N., Filipova, T.V., Volokhina, A,V., and Lavrenko, P.N., *Vysokomol. Soedin., Ser. A*, 1996, vol. 38, no. 8, pp. 1320–1327.
3. Tsvetkov, V.N., Eskin, V.E., and Frenkel', S.Ya., *Struktura makromolekul v rastvorakh* (Structure of Macromolecules in Solutions), Moscow: Nauka, 1964.
4. Chirkova, M.V., Litvinova, E.G., Rebrov, A.I., *et al.*, Abstracts of Papers, *Vtoroi rossiiskii karginskii simpozium: Khimiya i fizika v nachale XXI veka* (Second Russian Kargin Symp.: Chemistry and Physics in the Beginning of the 21th Century), Chernogolovka, May 29–31, 2000, part 2, pp. 4–7.
5. Shtennikova, I.N., Kolbina, G.F., Yakimanskii, A.V., *et al., Vysokomol. Soedin., Ser. A*, 1998, vol. 40, no. 12, pp. 1973–1978.
6. Shtennikova, I.N., Bushin, S.V., Kolbina, G.F., and Yakimanskii, A.V., *Vysokomol. Soedin., Ser. A*, 2000, vol. 42, no. 9, pp. 1537–1546.
7. Bushin, S.V., Tsvetkov, V.N., Lysenko, E.B., and Emel'yanov, V.N., *Vysokomol. Soedin., Ser. A*, 1981, vol. 23, no. 11, pp. 2494–2503.
8. Sharp, P. and Bloomfield, V.A., *J. Chem. Phys.*, 1968, vol. 48, no. 5, pp. 2149–2155.
9. Gray, H.B., Bloomfield, V.A., and Hearst, J.E., *J. Chem. Phys.*, 1967, vol. 46, no. 4, pp. 1493–1498.

Russian Journal of Applied Chemistry, Vol. 75, No. 8, 2002, pp. 1312–1314. Translated from Zhurnal Prikladnoi Khimii, Vol. 75, No. 8, 2002, pp. 1338–1340.
Original Russian Text Copyright © 2002 by Elchueva, Tabachkov.

MACROMOLECULAR CHEMISTRY AND POLYMERIC MATERIALS

Thiouretane Formation from Polyoxyalkylene Oligomers

A. D. Elchueva and A. A. Tabachkov

Kazan State Technological University, Kazan, Tatarstan, Russia

Received January 14, 2002

Abstract—Thiouretane formation in compounds based on polyoxyalkylenethiols and polyoxyalkylene isocyanates in the presence of catalysts was considered.

At present, polysulfide (PSO) and isocyanate-containing oligomers (ICO) and their mixtures with other reactive oligomers (ROs) are cured by the ionic mechanism in the presence of amine catalysts [1].

EXPERIMENTAL

The developed thiourethane polymer compounds TURELAST are prepared from ROs in the presence of phenolic Mannich bases; they combine advantages of Thiokol and polyurethane materials. Stabilized polyoxyalkylene isocyanate (POAI), the adduct of isocyanate and polyoxyalkylened polyol (POAP), synthesized in the presence of acidic stabilizing agents [2], was used as ICO. Data on variation of the content of isocyanate group in the synthesized prepolymers, depending on the type of the stabilizing agent, are listed in Table 1.

Both catalyzed and uncatalyzed thiouretane formation (TUF) reactions are described by a second-order kinetic equation with respect to concentrations of thiol and isocyanate groups. In this case, the rate constant of the reaction is determined by graphical solution of the equation

$$\frac{1}{x_0 - y_0} \log \frac{y_0}{x_0} \frac{x}{y} = -k\tau, \qquad (1)$$

where x_0 and y_0 are the initial, and x and y, the current concentrations of the reacting groups (M); τ is time.

At the equimolar ratio of ROs, the rate constant of the reaction [3] was determined from Eq. (2):

$$\frac{1}{x} \frac{1}{x_0} = -k\tau, \qquad (2)$$

The kinetic curves of consumption of terminal groups of Thiokol and oligoisocyanate in uncatalyzed TUF and the results of their linearization are shown in Fig. 1.

The efficiency of thiourethane cross-linking is affected by the structure of oligothiol. Comparison of the curing kinetic curves for compounds containing PSO (Thiokol) and polyoxyalkylenethiol (POAT), a thiopolyether, shows that the rates of the reaction of oligothiols with toluylene isocyanate, determined by pulse NMR at room temperature, are almost the same, while the final relaxation time T_2 for the compound based on Thiokol is significantly shorter (Fig. 2). The transverse nuclear magnetic relaxation time T_2 was measured by the Hahn method on a relaxometer operating at 17.5 MHz with restoration time of the transmitting-receiving unit of 50 μs. Thus, with more polar Thiokol of molecular weight 3000, the forming polymer is denser than with thiopolyether of molecular weight 4500.

It has been established previously [4] that phenolic hydroxyl in 2-(methylaminomethyl)phenol (**I**) (MAP) is usually involved in intramolecular or intermolecular hydrogen bonds (**A**) and (**B**), respectively:

Table 1. Variation of the content of isocyanate group in prepolymers in relation to the type of the stabilizing agent

Stabilizing agent	Content of isocyanate group, M	
	immediately after synthesis, x_0	after 3 years, x
Acetylacetone	2.28	1.94
Dinonyl phosphite-chloridite	2.57	1.79
Hydrochloric acid	2.28	1.96

1070-4272/02/7508-1312 $27.00 © 2002 MAIK "Nauka/Interperiodica"

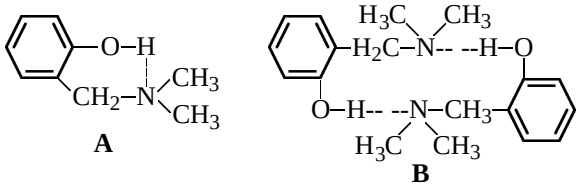

A **B**

I

The terminal thiol group is more acidic than the hydroxy group of aminophenlol **I**. This results in activation of aminophenol **I** by the scheme

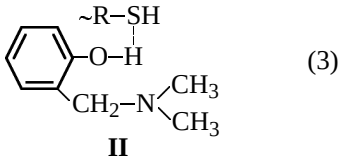

(3)

II

The lone electron pair of the nitrogen atom of the isocyanate group facilitates the attack of the methylene group of the catalyst **II** to give **III**):

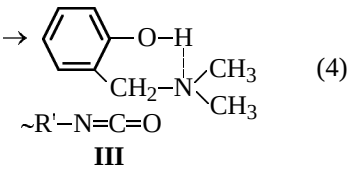

(4)

III

According to the kinetic curves for the reaction of oligoisocyanate with the catalyst (Fig. 3), with the concentration of 2-(dimethylaminomethyl)phenol **I** increasing by a factor of 2, the rate constant of the reaction increases from 8.7×10^{-4} to 23.8×10^{-4} l mol^{-1} s^{-1}, i.e., when aminophenlol **I** molecule adds to oligocyanate, its catalytic activity decreases. The results obtained were used for forecasting the storage life of the prepolymer–catalyst mixture:

$$\frac{d[OH]}{d\tau} = k_{OH}[NCO][OH]^2 = 8.7 \times 10^{-3} \times 1.4[OH]^2 = 1.21 \times 10^{-2}[OH]^2, \quad (5)$$

$$\frac{1}{[OH]} - \frac{1}{[OH]_0} = 1.21 \times 10^{-2}\tau. \quad (6)$$

In sealing compounds, the catalyst is used in an amount of 1.7×10^{-3} mol kg^{-1}. For 90% consumption of hydroxy groups, we can determine the time in which the catalyst loses its activity:

$$\frac{1}{0.1[OH]_0} - \frac{1}{[OH]_0} = \frac{10-1}{[OH]_0} = \frac{9}{[OH]_0} = 1.21 \times 10^{-2}\tau, \quad (7)$$

$$\tau = \frac{9}{1.21 \times 10^{-2} \times 1.7 \times 10^{-3}} = 130 \text{ h} \approx 5.5 \text{ days}. \quad (8)$$

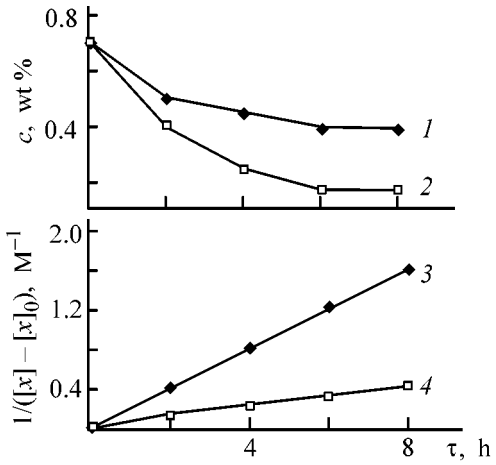

Fig. 1. Kinetic curves of consumption of terminal groups of (*1*) Thiokol and (*2*) prepolymer in uncatalyzed TUF and (*3*, *4*) curves *1* and *2*, respectively, in the linearized form. (*c*) Concentration of terminal groups; (τ) time; (x_0, x) initial and current concentrations of the reacting groups, respectively.

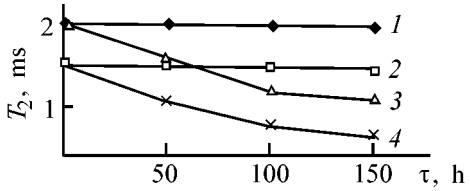

Fig. 2. Influence of the structure of oligothiols on variation of the spin–spin relaxation time T_2 of compounds of (*1*) thiopolyether, (*2*) Thiokol, (*3*) a mixture of thiopolyether with toluylene diisocyanate, and (*4*) a mixture of Thiokol with toluylene diisocyanate. (τ) Time.

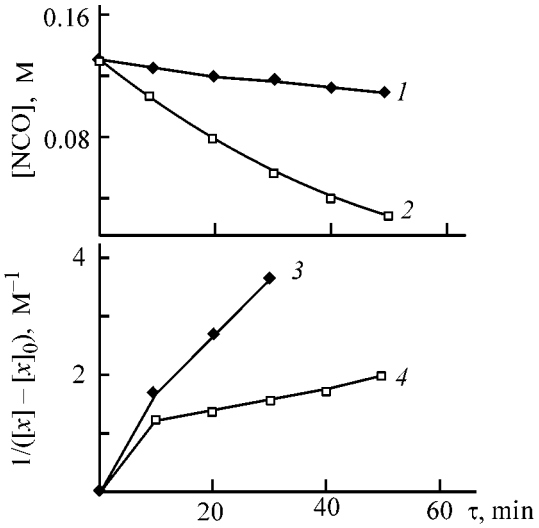

Fig. 3. (*1*, *2*) Kinetic curves for the reaction of oligoisocyanate with (*1*, *2*) (dimethylaminomethyl)phenol (**I**) and (*3*, *4*) curves *1* and *2*, respectively, in the linearized form. ([NCO]) Concentration of isocyanate groups (M), (τ) time, (x_0, x) initial and current concentrations of the reacting groups. Catalyst concentration (M): (*1*) 0.1 and (*2*) 0.2.

Table 2. Degree of conversion of oligomers with various catalysts

Catalyst	Degree of conversion, wt %, with indicated catalyst in indicated amount, wt %							
	Thiokol				thiopolyether			
	20	30	40	50	20	30	40	50
–	27.4	37.6	45.6	50.4	13.5	17.5	21.6	25.0
2-(Dimethylaminomethyl)phenol	64.8	67.2	68.7	70.4	61.7	65.6	68.0	69.6
2,4-Bis(dimethylaminomethyl)phenol	66.0	69.6	72.0	74.4	62.8	69.2	72.0	73.0
2,4,6-Tri(dimethylaminomethyl)phenol	67.5	72.7	75.0	79.5	64.0	72.0	76.0	79.2

Table 3. Physicomechanical characteristics of Thiokol-prepolymer and thiopolyether–prepolymer compounds

Characteristic	Catalyst content recalculated to Thiokol or thiopolyether, wt %							
	Thiokol–prepolymer				Thiopolyether–prepolymer			
	0.2	0.4	0.6	0.8	0.2	0.4	0.6	0.8
Working life, h	4	3	2	1	3	2	2	0.5
Nominal tensile strength, MPa	1.5	2.4	2.2	2.0	1.8	1.7	1.6	1.5
Relative elongation, %	150	210	200	180	440	500	600	700

The working life of the compound increases from 2 to 18 h.

The higher nucleophilicity of the sulfur atom in the oligothiol in comparison with the nitrogen atom in isocyanate group favors predominance of TUF over cyclotrimerization of the prepolymer.

The degree of conversion of oligomers grows with increasing basicity of (dimethylaminomethyl)phenols (Table 2). Irrespective of the catalyst type, the rate constants of the reaction of the oligocyanate with the thiopolyether are higher.

Based on the above data, we considered how the catalyst structure affects the main characteristics of filled compounds at the ratio Thiokol : prepolymer = 1.0 : 0.8. When the optimal amount of the catalyst is exceeded (0.4 wt parts), the deformation characteristics are deteriorated, which suggests the prevalance of oligocyanate cyclization over its copolymerization with Thiokol.

With polar thiopolyether, the elastic characteristics of the composites are significantly better, while the nominal strength is approximately the same (Table 3). This is caused by additional cross-linking of oligomers in the reaction of intramolecular hydroxy groups of oligothiol with isocyanate groups of the prepolymer along with the terminal mercaptan groups.

CONCLUSION

Thiourethane compounds TURELAST based on polyoxyalkylenethiol and stabilized polyoxyalkylene isocyanate (produced by Nizhnekamskneftekhim Joint-Stock Company) can be recommended for industrial use. A combination of elasticity, cohesion strength, impact resistance, and adhesion to various substrates make these materials extremely promising for use as elastic, corrosion-resistant, and sealing coatings and as impregnating agents.

REFERENCES

1. Elchueva, A.D., Sealants Based on Reactive Oligothiols, *Cand. Sci. Dissertation*, Kazan, 1989.
2. Nazipov, M.M., Tabachkov, A.A., Elchueva, A.D., and Liakumovich, A.G., *Zh. Prikl. Khim.*, 2001, vol. 74, no. 1, pp. 143–146.
3. *Praktikum po fizike i khimii vysokomolekulyarnykh soedinenii* (A Practical Guide for Physics and Chemistry of Macromolecular Compounds), Kazan: Kazan Khim.-Tekhnol. Inst., 1977.
4. Tabachkov, A.A., Urethane Isocyanurates as Cross-Linking Agents for Polyurethanes, *Cand. Sci. Dissertation*, Kazan, 1987.

Russian Journal of Applied Chemistry, Vol. 75, No. 8, 2002, pp. 1315–1319. Translated from Zhurnal Prikladnoi Khimii, Vol. 75, No. 8, 2002, pp. 1341–1345.
Original Russian Text Copyright © 2002 by Stepanenko, Novikova, Sergeeva, Shtompel', Chernobai.

MACROMOLECULAR CHEMISTRY AND POLYMERIC MATERIALS

Structure and Properties of Polyurethane Ionomer Blends with Polyaminourethane

L. V. Stepanenko, T. I. Novikova, L. M. Sergeeva, V. I. Shtompel', and A. A. Chernobai

Institute of Macromolecular Chemistry, Ukrainian National Academy of Sciences, Kiev, Ukraine

Received December 29, 2001; in final form, April 2002

Abstract—Binary blends of segmented polyetherurethanes were prepared from oligooxytetramethylene glycol, toluylene diisocyanate, and a chain extender (*p*-hydroxybenzoic acid magnesium salt or *N*-methyldiethanolamine). The nature of intermolecular interactions in the blends of various compositions was studied by IR spectroscopy. Depending on the formulation of the blends, various kinds of microstructural organization exist (as demonstrated by low-angle X-ray scattering data), strongly influencing the mechanical characteristics of polyurethane blends.

Ionomers and their blends attract researcher's attention in view of the possibility of development on their basis of new adhesives, coatings, binders, membranes, and other materials having high performance characteristics [1–5]. By now, a series of binary blends and interpenetrating polymer networks containing ionic groups in one or both components of the blend have been obtained and characterized [6–10]. Polyurethane ionomers and their blends have been studied to a lesser extent [11–14]. At the same time, introduction of ionic groups in polyurethanes, which have a highly developed physically bonded network, forms an additional ionic network, considerably influencing the structural features and other properties of these systems. It was demonstrated that introduction of ionic groups in one of the components of polyurethane–polyurethane systems has a considerable effect on the microphase structure [15] as well as on the thermodynamic and adhesion properties [16].

In this work, we studied binary blends of polyurethanes in which one of the component contains ionic groups, and another component, tertiary amino groups. Study of the intermolecular interactions and phase structure of these systems is a necessary step on the way to directed synthesis of composite materials on their basis.

EXPERIMENTAL

We prepared polymer blends of a linear polyurethane ionomer (LPI) and a linear polyaminourethane (PAU).

The individual LPI and PAU were synthesized in two steps, using the standard procedure described in [12]. Initially we obtained a prepolymer by the reaction of oligooxytetramethylene glycol (MW 1000) with 2,4(or 2,6)-toluylenediisocyanate at a molar ratio of the reacting groups OH/NCO = 1/2. Then the prepolymer was extended by using *p*-hydroxybenzoic acid magnesium salt (for LPI) or *N*-methyldiethanoleamine (for PAU). The molecular weight M_η of LPI was 40 000, and that of PAU, 50 000.

The blends were prepared at room temperature by the method of chemical mixing of the two polymers [6]. To a PAU solution in DMF, the initial prepolymer and chain extender for LPI were added, so that LPI was formed in the PAU solution. The films were formed by casting on Teflon supports with subsequent removal of the solvent and drying at 85°C for 5–7 days. As a result, we obtained a series of samples of polyurethane blend films at various component ratios (from 1 to 95% PAU).

The samples were studied by IR spectroscopy and low-angle X-ray scattering. Also the samples were characterized by the strength and elongation at break.

IR spectra were recorded on a Specord M-80 spectrometer in the range 600 – 4000 cm^{-1}, using the KBr technique.

X-ray diffraction study was made with a KRM-1 low-angle X-ray camera (Cu_{K_α} radiation monochromated using a Ni filter; slit collimation of the initial X-ray beam was performed by Kratky's method

1070-4272/02/7508-1315 $27.00 © 2002 MAIK "Nauka/Interperiodica"

[17]). The experimental X-ray scattering curves were normalized to the scattering volume of the samples, taking into account the attenuation of the initial beam.

LPI and PAU are segmented polyetherurethanes, whose flexible segments (or blocks) are formed by the same oligoether, oligooxytetramethylene glycol, and rigid blocks are formed by the reaction of the terminal isocyanate groups of the prepolymer with the chain extender. In this case, the backbone chains of the polyurethanes contain the Mg-dicarboxylate groups (LPI) or tertiary amino groups (PAU). The general formula of the polyurethanes obtained can be represented as

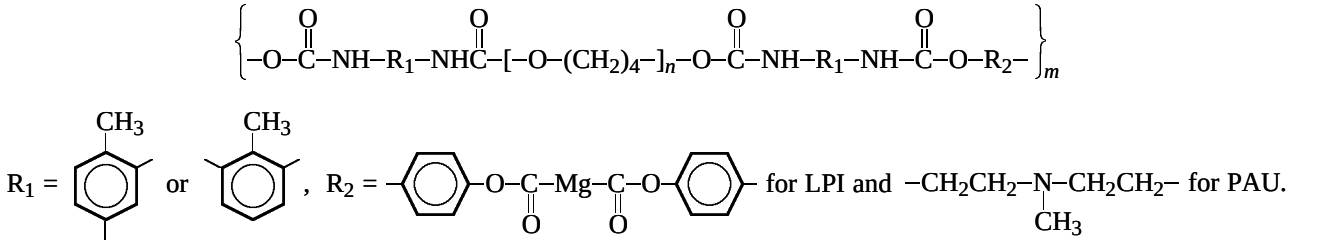

The structure of the molecular chains of the individual polyurethanes used allows various types of intermolecular interactions, including hydrogen bonding and ion–molecule interaction, which control to a considerable extent the properties of polyurethanes [13, 18–20]. These interactions can be studied by IR spectroscopy [3, 13, 21, 22].

A comparison of the IR spectra of LPI, PAU, and their blends showed noticeable differences in the range of stretching vibrations of carbonyl groups in various moieties (urethane, ester, and ionic) of the backbone chains. The IR spectra of the individual polyurethanes and several blends in the range 1800–1500 cm^{-1} are shown in Figs. 1 and 2.

The spectrum of PAU (Fig. 2, spectrum *1*) shows a distinct band at 1730 cm^{-1}, due to vibrations of free C=O groups, and a shoulder at 1710 cm^{-1}, assigned to carbonyl groups involved in H bonding with the NH groups of the urethane fragments. This suggests that a network of intermolecular bonds between the urethane groups exists in the PAU structure, which is typical of segmented polyurethanes [13, 19, 20].

In the range of stretching vibrations of carbonyl groups, the spectrum of LPI (Fig. 1, spectrum *1*) shows the bands of H-bonded carbonyls of the urethane groups and, additionally, the bands at 1675 and 1630 cm^{-1}. It is known that, in polymers, metal cations having high effective charge and polarizability

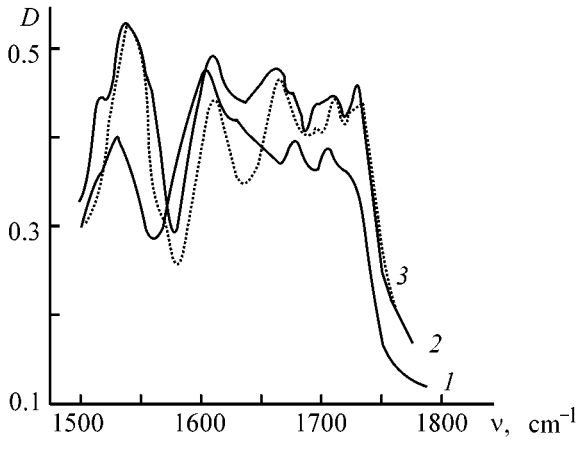

Fig. 1. IR spectra of (*1*) LPI, (*2*) LPI + 10% PAU, and (*3*) LPI + 30% PAU. (*D*) Optical density and (ν) wave number; the same for Fig. 2.

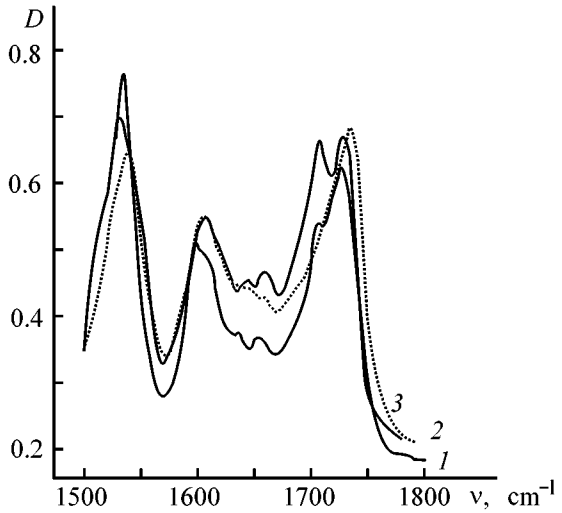

Fig. 2. IR spectra of (*1*) PAU, (*2*) LPI + 70% PAU, and (*3*) LPI + 50% PAU.

can form ion–molecule bonds with the carbonyl groups, resulting in a low-frequency shift of the carbonyl bands [23]. Presumably, the band at 1675 cm^{-1} characterizes the ion–molecule bonds of the carbonyls of the urethane groups with magnesium cations of the ionic fragments $C{=}O\cdots Mg^{2+}$. The shoulder at 1630 cm^{-1} is assigned to vibrations of the carboxylate groups $RCOO^-$ coordinated to the metal [22]. The observed noticeable increase in the relative intensity of the bands in the range 1600–1610 cm^{-1} in the spectrum of LPI, compared to PAU, is due to the absorption of nonassociated $RCOO^-$ groups.

Comparison of the IR spectra of the polyurethane blends studied shows that the nature of absorption of the carbonyl groups strongly depends on the component ratio (Figs. 1, 2). For example, in the spectrum of a blend containing 10% PAU (Fig. 1, spectrum *2*), the intensity of the band at 1730 cm^{-1} increases as compared to that in the spectrum of LPI; a new band is found at 1664 cm^{-1}; and the intensities of the bands at 1610 and 1630 cm^{-1} considerably decrease. This fact suggests that the nature of the intermolecular interactions changes on passing from one system to another. Specifically, the fraction of the nonassociated and metal-coordinated $RCOO^-$ groups decreases, and there occur ion–molecule interactions of the $COO^-\cdots NH$ type involving the protons of the urethane groups of PAU and carboxylate anions of LPI. Such ion–molecule interactions in polyurethanes are more energetically favorable (by a factor of 1.4) as compared to H bonding between the urethane groups [13]. Evidently, small concentration of PAU (up to 20%) in a polyurethane blend initiates reorganization of the intermolecular bonds with preferential realization of ion–molecule interactions between the LPI and PAU macromolecules.

An increase in the PAU concentration to 30% is accompanied by the appearance of a band at 1675 cm^{-1} ($C{=}O\cdots Mg^{2+}$), which is found as a shoulder at the band 1664 cm^{-1} ($COO^-\cdots NH$). In this case, the intensity of the band at 1664 cm^{-1} decreases (Fig. 1, spectrum *3*) and the intensity of absorption bands of H-bonded carbonyls in the urethane groups increases. These facts suggest that ion–molecule bonds between the LPI and PAU polymer chains partly break down, and the contribution of the hydrogen and ion–molecule bonds formed by only the individual LPI and PAU molecules increases. In the spectrum of a blend containing 50% PAU, we found no absorptions at 1664 and 1675 cm^{-1}, as well as in the range of absorption of the H-bonded carbonyls of the urethane groups (Fig. 2, spectrum *3*). Therefore, specific interactions between LPI and PAU do not occur in a blend of this composition.

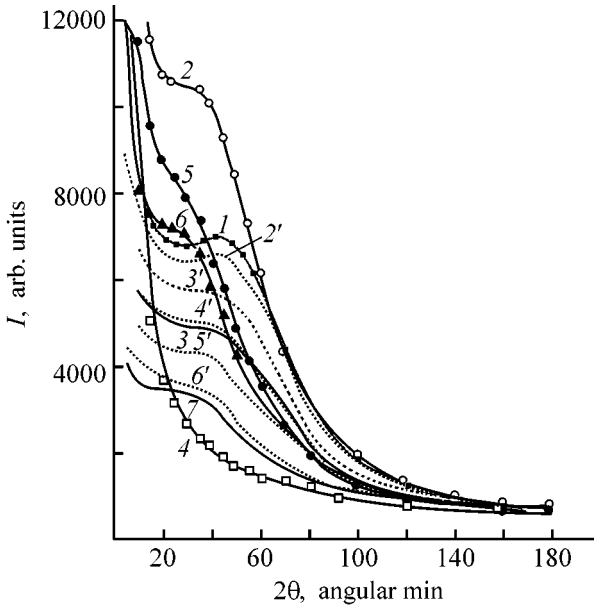

Fig. 3. Low-angle scattering curves of (*1*) LPI, (*2*) LPI + 10% PAU, (*3*) LPI + 30% PAU, (*4*) LPI + 50% PAU, (*5*) LPI + 70% PAU, (*6*) LPI + 90% PAU, and (*7*) PAU. (*I*) Intensity and (2θ) scattering angle. (*2*′–*6*′) Additive curves.

In the IR spectra of the blends with high PAU concentration (70% and more) (Fig. 2, spectrum *2*), we mainly observed the absorption bands of carbonyls of the urethane groups at 1710–1730 cm^{-1} (the band at 1664 cm^{-1} is very weak). It should be suggested that, in this case, the intermolecular interactions are occur primarily via the urethane groups of the polymeric components.

The interrelation between the nature of intermolecular interactions and the microphase structure in the polyurethane blends investigated can be elucidated by analysis of the low-angle X-ray scattering data. Figure 3 shows such data obtained for the initial polyurethanes and their blends.

The results (Fig. 3, curves *1*, *7*) suggest that the individual LPI and PAU both have the rigid-block domain structure, but of different degrees of perfection. A distinct interference peak in curve *1* is an indication of the occurrence in the LPI structure of a three-dimensional macroscopic lattice formed by uniformly sized rigid domains (major domain period L is equal to 105 Å). The presence of ionic groups, actively participating in formation of intermolecular bonds, in the rigid blocks of LPI favors association of these blocks [14], resulting in fairly high degree of their segregation ($\alpha_{seg} = 0.60$). The estimate for this parameter was made by Bonart's method [24]. Curve *7* in Fig. 3 demonstrates a broad peak,

Mechanical properties of polyurethane blends

Component content, wt %		Tensile strength, MPa	Elongation at break, %	Modulus of elasticity, MPa	Hardness, arb. units
LPI	PAU				
100	–	21.0	300	7.0	10
–	100	18.0	800	2.0	5
99	1	24.5	340	7.2	13
98	2	28.8	350	8.1	18
95	5	34.1	365	9.3	22
90	10	37.0	330	11.2	25
85	15	39.2	275	14.3	21
80	20	36.0	220	16.4	18
70	30	28.5	160	17.8	12
60	40	18.7	130	14.4	7
50	50	13.9	110	12.6	3
30	70	20.4	350	6.0	7
20	80	26.0	385	4.7	8
10	90	27.8	490	2.9	15
5	95	25.2	540	3.9	11

reflecting a distorted structure of the rigid-domain superlattice ($L \approx 160$ Å), as well as a relatively low level of block segregation ($\alpha_{seg} = 0.27$). The low scattering intensity near the interference peak in curve *7* is an indication of a small density of packing of the rigid blocks in domains, which is a result of the effect of the side bulky substituents at the nitrogen atom [14]. Therefore, the highly developed network of intermolecular bonds in LPI (concluded from the IR spectra) implies the formation of a perfect domain structure. PAU has a domain structure, characterized by low degree of segregation of blocks and low density of their packing.

Let us consider the microstructure of LPI–PAU binary blends. In addition to the experimental curves, Fig. 3 also shows the theoretical additive curves (curves *2*'–*6*') estimated for the polyurethane blends, assuming the physical ideality. Significant deviation of the experimental curves from the ideality gives additional evidence in favor of the existence of a system of intermolecular interactions between the polymers in their blends, which is consistent with the IR data.

In the composition range 10–20% PAU, the X-ray scattering curves show distinct interference peaks and, simultaneously, the highest scattering intensities (see, e.g., curve *2*). It follows from the IR spectra that, in this composition range, more energetically favorable ionmolecule bonds are formed between the polymeric components. The low-angle X-ray scattering data demonstrate that formation of these bonds controls the microstructure in polyurethane blends, providing high ordering of the domain structure in the bulk of the polymers with high level of segregation of flexible and rigid blocks and density of their packing into the domains.

With the PAU content in a blend increasing to 30 wt %, the scattering intensity near the interference peak decreases and the peak shifts toward the primary X-ray beam (curve *3* in Fig. 3). According to the IR spectrum, the fractions of ion–molecule bonds and associated anionic groups in this sample are decreased, which results in disordering of the rigid-block domain structure, as demonstrated by the scattering data. In this case, a tendency is observed toward extension of the superlattice formed by these domains ($L = 117$ Å) and decrease in the degree of segregation of rigid blocks ($\alpha_{seg} = 0.37$) and in the density of packing of these blocks into domains.

The lack of the interference peak in the scattering curve of the sample with 50% PAU (Fig. 3, curve *4*) implies total breakdown of the rigid domains and existence of a quasihomogeneous structure, which is consistent with the IR spectroscopic data showing the lack of intermolecular interaction in this blend.

Raising the percentage of PAU to 70 wt % is accompanied by the appearance of an interference peak in the scattering curve (curve *5*), suggesting that the superlattice formed in the bulk of this polymer blend contains rigid domains nonuniform in size. Furthermore, the high intensity of scattering on this sample reflects an increased packing density of the rigid blocks in the domains. With the percentage of PAU increasing further to 90% (curve *6*), the interference peak in the scattering curve becomes more distinctly pronounced, which is accompanied by certain decrease in the scattering intensity. Evidently, in PAU-rich blends, when PAU becomes a matrix-forming component, especially at an LPI content of 5–10 wt %, the ionic group concentration in the system is insufficient to formation realization of a highly developed network of ion-ion and ion–molecule bonds. Nevertheless, small addition of the ion-containing polyurethane plays a significant role, as providing conditions for formation of the domain structure (as demonstrated by the low-angle X-ray scattering data), typical of segmented polyurethanes with high degree of segregation and packing density of rigid blocks [14].

The nature of intermolecular interactions controlling the microphase structure in the polyurethane

blends directly influences their mechanical characteristics. Mechanical properties of the polyurethane blends of various compositions are given in the table.

The results show that the strength properties pass through a maximum at a PAU content of 5–20 wt %, i.e., in the composition range where, as demonstrated above, the system of ion–molecule bonds between LPI and PAU is the most developed, providing formation of a perfect domain structure in the polymer blends.

Raising the PAU content to 30 wt % makes worse the mechanical characteristics of the polymer blends. Only the modulus of elasticity of the blends remains relatively high, compared to that of the individual polymers.

In the polymer blends containing 50–5 wt % LPI, the strength properties pass through a maximum at low LPI contents (10–20%). However, their absolute values are lower than those in the blends with low PAU content. The plausible reason is that H bonds between the urethane groups, similar to those in ordinary segmented polyurethanes, rather than ion–molecule interactions, are preferentially formed in this composition range, as supported by the IR spectra.

Polyurethane blend samples of the intermediate composition (50/50), in which, as follows from the IR spectrum and low-angle X-ray scattering curve, a network of intermolecular bonds cannot be formed and the domain structure is not formed, demonstrate the worst mechanical characteristics.

CONCLUSIONS

(1) A network of intermolecular bonds is formed in binary blends of polyurethanes, which is typical of segmented and ion-containing polyurethanes.

(2) In the range of high concentrations (95–80%) of the linear polyurethane ionomer, where a system of essentially ion–molecule bonds is formed to give a quite perfect domain structure, the polyurethane blends demonstrate the best strength parameters.

(3) With small additions (10–20%) of the linear polyurethane ionomer, a network is formed in polyurethane blends mainly via H bonding, which is accompanied by formation of a less perfect domain structure. In this case, the blend samples are inferior in quality.

(4) Polyurethane blend samples in which a network of intermolecular bonds is not formed and the domain structure cannot be formed (at intermediate concentration of the linear polyurethane ionomer of 50%) demonstrate the worst mechanical characteristics.

REFERENCES

1. Lipatov, Yu.S. and Sergeeva, L.M., *Usp. Khim.*, 1986, vol. 40, no. 12, pp. 2086–2106.
2. Tannenbaum, R., Rutkowska, M., and Eisenberg, A., *J. Polym. Sci., Part B: Polym. Phys.*, 1987, vol. 25, pp. 663–671.
3. Hsieh, K.H. and Chou, L.M., *J. Appl. Polym. Sci.*, 1989, vol. 38, pp. 645–654.
4. Vilenskii, V.A., Kercha, Yu.Yu., Shtompel', V.I., *et al., Vysokomol. Soedin., Ser. A*, 1990, vol. 32, no. 7, pp. 1511–1516.
5. Alice Ng, C.-W. and MacKnight, W.J., *Macromolecules*, 1996, vol. 29, no. 12, pp. 2421–2429.
6. Sperling, L.H., *Interpenetrating Polymer Networks and Related Materials*, New York: Plenum, 1981.
7. Rutkowska, M. and Eisenberg, A., *J. Polym. Sci.*, 1987, no. 5, pp. 2835–2838.
8. Sakurai, K., Douglas, E., and MacKnight, W.J., *Macromolecules*, 1993, vol. 26, pp. 208–212.
9. Chen, H., *Macromolecules*, 1996, vol. 29, p. 4919.
10. Kercha, Yu.Yu. and Shtompel', V.I., *Dopov. Nats. Akad. Nauk Ukr.*, 1997, no. 11, pp. 142–147.
11. Miller, J.A., Hwang, K.S., and Cooper, S.L., *J. Macromol. Sci. Ed. Phys.*, 1983, vol. 22, no. 2, pp. 321–341.
12. Stepanenko, L.V., Kolodnitskaya, Z.A., Brovko, A.A., *et al., Kompoz. Polim. Mater.*, 1990, issue 45, pp. 31–36.
13. Khranovskii, V.A., Lipatov, Yu.S., and Maslyuk, A.F., *Dokl. Akad. Nauk SSSR, Ser. A*, 1985, vol. 285, no. 2, pp. 406–410.
14. Shtompel', V.I. and Kercha, Yu.Yu., *Ukr. Khim. Zh.*, 1997, vol. 63, no. 11, pp. 53–56.
15. Lipatov, Yu.S., Shilov, V.V., Bogdanovich, V.A., *et al., J. Polym. Sci., Part B: Polym. Phys.*, 1987, vol. 25, pp. 43–55.
16. Brovko, A.A. and Sergeeva, L.M., *Advances in Urethane Ionomers*, Xiao, H.X. and Frish, K.S., Eds., Lancaster, PA: Technomic, 1995, pp. 147–163.
17. Kratky, O.L. and Leopold, H., *Makromol. Chem.*, 1964, vol. 75, pp. 69–74.
18. Sung, C.S.P. and Schneider, N.S., *Macromolecules*, 1975, vol. 8, no. 1, pp. 68–73.
19. Vilkov, V.P., Nel'son, K.V., Sotnikova, E.N., *et al., Zh. Prikl. Spektrosk.*, 1982, vol. 36, no. 5, pp. 787–792.
20. Kercha, Yu.Yu., *Fizicheskaya khimiya poliuretanov* (Physical Chemistry of Polyurethanes), Kiev: Naukova Dumka, 1979.
21. Szalinska, H. and Pietrsak, M., *Metal-Containing Polymers*, Lodz (Poland): Inst. of Applied Radiation Chemistry, Technical Univ., 1983, pp. 107–163.
22. Pomogailo, A.D. and Savost'yanov, V.S., *Metallsoderzhashchie monomery i polimery na ikh osnove* (Metal-Containing Monomers and Polymers on Their Basis), Moscow: Khimiya, 1988.
23. Lirova, B.I., Smolyanskii, A.L., Tager, A.A., *et al., Vysokomol. Soedin., Ser. A*, 1975, vol. 17, no. 4, pp. 731–737.
24. Bonart, R. and Muller, E.N., *J. Macromol. Sci. Phys., Ser. B*, 1974, vol. 10, no. 1, pp. 177–189.

Russian Journal of Applied Chemistry, Vol. 75, No. 8, 2002, pp. 1320–1324. Translated from Zhurnal Prikladnoi Khimii, Vol. 75, No. 8, 2002, pp. 1346–1350.
Original Russian Text Copyright © 2002 by S. Butrim, Bil'dyukevich, N. Butrim, Yurkshtovich.

MACROMOLECULAR CHEMISTRY AND POLYMERIC MATERIALS

Heterogeneous *O*-Nitration of Carboxy Starch

S. M. Butrim, T. D. Bil'dyukevich, N. S. Butrim, and T. L. Yurkshtovich

Research Institute of Physicochemical Problems, Belarussian State University, Minsk, Belarus

Received January 14, 2002; in final form, April 2002

Abstract—The effect of various factors on preparation of carboxy starch nitrate esters was examined. The ester samples were characterized by IR spectroscopy and chemical analysis.

Growing efforts in the modern carbohydrate chemistry are aimed at development of synthetic routes to biologically active polymers and of new materials for medicine, based on modified polysaccharides [1].

Although certain data are available on nitration of carboxyl-containing polysaccharides [2], the effect of various factors on this reaction has not been studied systematically. Carboxy starch nitrate ester (CSN) prepared by successive polymer-analogous transformations of starch (oxidation with NO_2 in an inert solvent and *O*-nitration) is essentially a random copolymer containing units of different structures. The sodium salt of CSN exhibits appreciable antiaggregation, anticoagulation, and antiarythmic activity [3].

In this work, we studied the effect of various factors (temperature, reaction time, bath ratio, nitrating mixture composition, carboxy group content in oxidized starch) on the esterification of carboxy starch. The modification products were also studied by IR spectroscopy.

EXPERIMENTAL

The characteristics of potato starch used in this study were as follows: amylose content 23.8 wt %, degree of polymerization $\overline{P}_w$ 1760, ash residue 0.31%, phosphorus content 0.22%, moisture content 12.5%, and acidity 15.5 (determined according to [4]). Phosphoric acid (87.6%) and phosphoric anhydride were of pure grade. Fuming (98–99%) nitric acid was prepared by distillation of 61.7% nitric acid mixed (1 : 1 by volume) with concentrated sulfuric acid; the fraction with $T_b \le 94$°C was collected. Oxidation of starch to attain varied content of carboxy groups was performed as described in [5]. *O*-Nitration of carboxy starch was performed with a mixture of nitric acid, phosphoric acid, and phosphoric anhydride at various component ratios by the following procedure. A prescribed volume of the nitrating mixture preliminarily thermostated at 0, 18, or 35°C was added to a sample of carboxy starch, preliminarily pulverized and dried to constant weight. The mixture was kept at a prescribed temperature for a prescribed time. After that, CSN was separated from the nitrating mixture by squeezing on a glass frit and washed with large amount of cold distilled water to neutral reaction; then it was dried in a vacuum oven at 50°C over phosphoric anhydride. The extent of chemical modification of starch was qualitatively monitored by IR spectroscopy (Specord IR-75 spectrometer, 400–4000 cm^{-1}, KBr pellets). The content of nitrogen in nitrate ester groups and of carboxy groups in CSN was determined by the modified Devarda method [6] and with barium acetate [7], respectively. The degree of substitution (DS) with COOH and ONO_2 groups in CSN was calculated by the formulas

$$DS_{COOH} = \frac{162.15\,c_{COOH}}{4500 - 14\,c_{COOH} - 144.64\,c_N},$$

$$DS_{ONO_2} = \frac{162.15\,c_N}{1400 - 4.36\,c_{COOH} - 45\,c_N},$$

where 162.15 is the molecular weight of the anhydroglucopyranose unit, c_{COOH} is the content of carboxy groups (wt %), and c_N is the content of nitrogen in nitrate ester groups (wt %).

To choose the optimal conditions for preparing water-soluble salts of highly substituted nitrate esters of carboxy starch, we examined the effect of *O*-nitration conditions on the composition and properties of the resulting products. As seen from Fig. 1, nitration occurs more slowly at low temperatures. For example, the maximal nitrogen content is attained

1070-4272/02/7508-1320 $27.00 © 2002 MAIK "Nauka/Interperiodica"

at 35°C already in 2–3 min, whereas at 0°C this takes 20–30 min. However, reaction temperatures of 20°C and higher cannot be recommended because of the significant degradation. The highest content of nitrogen in the products obtained by nitration of carboxy starch (DS_{COOH} 0.51) with a mixture of HNO_3, H_3PO_4, and P_2O_5 is 8.50–9.45% (DS_{ONO_2} 1.40–1.64). The relatively low degree of nitration may be due to several factors: steric hindrance produced by bulky carboxy groups, decreased content of primary hydroxy groups in carboxy starch (and, correspondingly, decreased total content of OH groups, which are the most reactive in acid solutions), and also the presence in the glucopyranose unit of a certain amount of carbonyl groups formed by oxidation of starch with NO_2. Furthermore, a part of reactive hydroxy groups in carboxy starch react with carboxy groups to form lactone rings and ester cross-links [8], which also decreases the possible content of nitrate ester groups. The formation of lactone rings and ester cross-links is suggested by the effect exerted on the properties of nitrate esters by carboxy groups, even in small amounts. For example, the solubility of all the carboxy starch nitrate esters with low content of carboxy groups (0.5–3 wt %) is considerably decreased, and the nitrate esters derived from starch with 6–15% substitution of hydroxy groups by carboxy groups are insoluble in organic solvents commonly used for dissolving carbohydrate nitrate esters (amyl acetate, acetone, alcohol–ether mixture, etc.). Owing to the formation of a fairly strong three-dimensional network of ester bonds, these products show only limited swelling in the above solvents at –20 to 60°C.

The influence of the content of COOH groups in carboxy starch on the degree of nitration is shown in Fig. 2. It is seen that, as the content of carboxy groups in the polysaccharide is increased, the content of nitrate ester nitrogen decreases steadily. It should be noted that the total degree of substitution, DS_{tot}, with ONO_2 and COOH groups decreases also (from 2.40 to 1.73) with increasing content of carboxy groups, which confirms the assumption that COOH and OH groups react to form ester bonds, decreasing the amount of OH groups subject to nitration.

A kinetic study of the nitration (Fig. 3) showed that the nitration rate is different with carboxy starch samples differing in the content of carboxy groups, which may be due to different accessibilities of OH groups to the nitrating agent. The highest esterification rate is observed in the samples with high content of COOH groups (DS_{COOH} 0.74), whose grains underwent profound structural transformations, with significant breakdown of ordered regions and of the hydrogen bond system in the course of oxidation. With this sample, the limiting degree of nitration is attained within 3–5 min. By contrast, in low-oxidized samples, the limiting stage is the diffusion of the nitrating agent to active centers, and the reaction is complete in much longer time (~2.5 h). Carboxy starch samples with low content of COOH groups get strongly hardened after oxidation and drying in air, which also considerably decreases their reactivity.

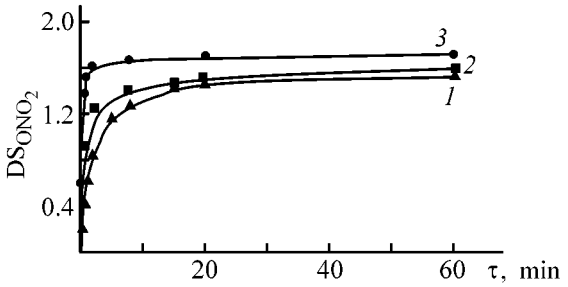

Fig. 1. Accumulation of nitrate ester groups, DS_{ONO_2}, with time τ of esterification of carboxy starch (DS_{COOH} 0.51) with the nitrating mixture $HNO_3 : H_3PO_4 : P_2O_5$ 66.8 : 28.2 : 5; bath ratio 1 : 5; the same for Figs. 2 and 3. *T*, °C: (*1*) 0, (*2*) 18, and (*3*) 35.

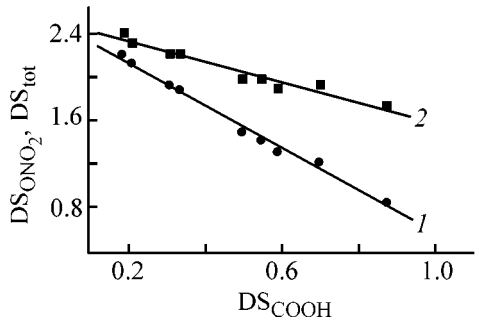

Fig. 2. (*1*) Degree of nitration, DS_{ONO_2}, and (*2*) total degree of substitution with COOH and ONO_2 groups, DS_{tot}, in nitration of carboxy starch vs. content of carboxy groups, DS_{COOH}, in the initial starch. 18°C; τ = 2.5 h.

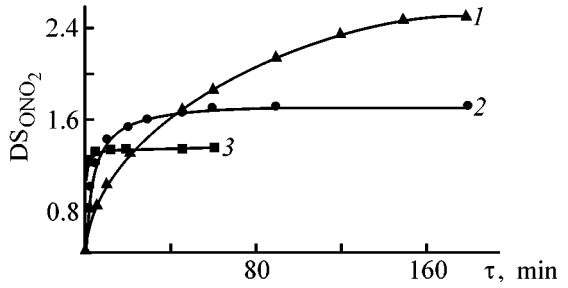

Fig. 3. Content of nitrate ester groups, DS_{ONO_2}, vs. time τ of esterification of carboxy starch with nitrating mixture at 18°C. c_{COOH}, wt %: (*1*) 1.08, (*2*) 12.68, and (*3*) 19.21. DS_{COOH}: (*1*) 0.04, (*2*) 0.48, and (*3*) 0.74.

Table 1. Conditions of *O*-nitration of carboxy starch (DS_{COOH} 0.55, c_{COOH} 14.65 wt %) and composition of reaction products (18°C, 15 h)

Composition of nitrating mixture, wt %	Bath ratio	c_N, wt %	DS_{ONO_2}	c_{COOH}, wt %	Yield, % of theory
$HNO_3 : H_3PO_4 : P_2O_5$:					
66.8 : 28.2 : 5	1 : 30	8.57	1.44	10.69	87.9
	1 : 50	8.78	1.48	10.52	87.1
	1 : 100	8.80	1.48	10.48	86.0
40 : 55 : 5	1 : 50	8.59	1.44	10.69	90.4
20 : 75 : 5	1 : 50	7.30	1.16	11.21	96.7
66.8 : 33.2 : 0	1 : 50	8.70	1.46	10.58	86.9
$HNO_3 : H_3PO_4 : H_2O$:					
66.8 : 28.2 : 5	1 : 50	6.54	1.01	11.57	77.8
40 : 55 : 5	1 : 50	6.49	0.99	11.59	80.5
20 : 75 : 5	1 : 50	3.57	0.49	12.97	82.5
66.8 : 23.2 : 10	1 : 50	5.30	0.77	12.15	80.1
66.8 : 18.2 : 15	1 : 50	3.84	0.53	12.84	76.3

Table 1 shows how the degree of nitration and the product yield and properties are influenced by the composition of the nitrating mixture and the bath ratio. It is known that the major factor governing the degree of nitration is the water content in a nitrating mixture. Table 1 shows that, with increasing water content, the nitrogen content in the product decreases. The presence of water in the nitrating mixture affects not only the degree of nitration of carboxy starch, but also its other properties. At increased water content, more soluble nitration products are formed, but their yields are lower. This is due to the increased hydrolytic and oxidative effect produced on starch by water-rich nitrating mixtures. A decrease in the HNO_3 content from 66.8 to 40 wt % has virtually no effect on the content of nitrate ester nitrogen; the degree of nitration considerably decreases only when nitration is performed with mixtures containing 20 wt % HNO_3 (both anhydrous and aqueous). This may be due to insufficient swelling of modified starch in viscous phosphoric acid and slow diffusion of the nitrating mixture inside the polysaccharide grains. Furthermore, experiments showed that the nitration is the more active, the higher the HNO_3 content in the bath. As seen from Table 1, the best bath ratio is 1 : 50; it ensures high degree of substitution and saving of chemicals. It should be noted that, under any nitration conditions tested, phosphorylation of carboxy starch was insignificant: the phosphorus content in the final products did not exceed 0.15%.

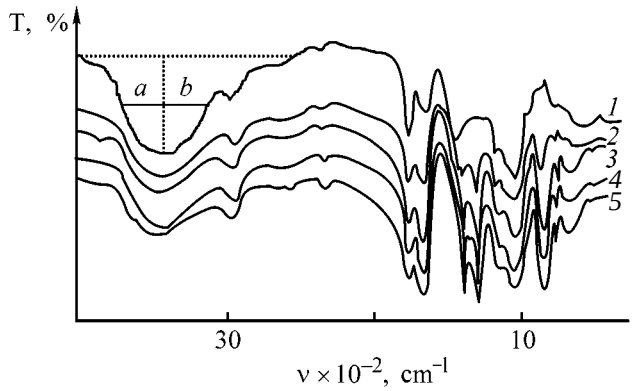

Fig. 4. IR spectra (400–4000 cm^{-1}) of (*1*) carboxy starch with DS_{COOH} 0.51 and (*2*–*5*) its nitration products with varied content of nitrato groups. (T) Transmission and (ν) wave number. DS_{ONO_2}: (*2*) 0.54, (*3*) 1.08, (*4*) 1.32, and (*5*) 1.64.

Figure 4 shows IR spectra of carboxy starch and its nitrate esters with varied content of nitrato groups. The most significant changes in the IR spectrum of CSN, compared to carboxy starch, are due to vibrations of nitrato groups manifested at 1700–1600, 1260–1310, 800–900, and 600–750 cm^{-1}. The IR spectra of all the nitrated samples contain a strong band of antisymmetric stretching vibrations ν_a(N=O) at 1650 cm^{-1} and a band of the symmetric mode ν_s(N=O) at 1280 cm^{-1}. These bands are highly characteristic and are independent of the localization of nitro groups and of the degree of substitution. A broad strong band at 838 cm^{-1} is mainly due to N–O stretching vibrations, with a certain contribution of O–N=O bending vibrations. Also, the IR spectra of CSN contain bands at 747, 675, and 827 cm^{-1}, belonging to the bending modes of the CCO, CON, and O–N=O groups. The IR spectra of CSN samples with any content of nitrogen and carboxy groups contain a band at 1375 cm^{-1}, absent in the spectra of nitro starch. Its intensity grows with increasing degree of nitration. Ivanova *et al.* [9] believe that this band is due to

vibrations of free NO_2 groups. It is quite probable that this band originates from vibrations of the NO_3^- ion (1350–1390 cm^{-1}), since one of the decomposition products of the nitrate esters is nitric acid. Presumably, all the CSN samples contain certain amounts of free or weakly bound NO_2 and HNO_3 molecules. This is, most probably, due to gradual local acid hydrolysis of nitrato groups, promoted by carboxy groups of the polysaccharide; their acidity in air-dry samples is sufficient to cause slow saponification of the nitrato groups. Experiments showed that, the higher the content of COOH and ONO_2 groups in the modified starch macromolecule, the faster the hydrolysis with the release of decomposition products and the greater its extent. Prolonged storage of such samples results in complete degradation of the polysaccharide with the formation of water-soluble oligomeric products. Therefore, for the subsequent biological activity tests, the samples were converted to salts by dissolution in 5% $NaHCO_3$ (pH 8.2), followed by dialysis against distilled water and isolation of the product by lyophilic drying. The sodium salt of CSN can be stored for a long time without noticeable changes.

In the range 3100–3700 cm^{-1}, the IR spectra contain broad bands of irregular shape, belonging to ν(OH) stretching vibrations. These bands are due to H-bonded hydroxy groups in modified starch. The most probable proton acceptors are nitrato groups, other OH groups, COOH groups, and O(5) oxygen atoms of pyranose rings. As seen from Fig. 4, the OH band with a peak at 3400 cm^{-1} decreases in intensity upon esterification of carboxy starch, as the content of nitrato groups increases. In the IR spectrum of CNS (DS_{ONO_2} 1.64), an additional band appears with a maximum at about 3650 cm^{-1}, characteristic of free hydroxy groups.

Carboxy starch should be considered a mixture of granules differing in accessibility to reactive agents. In the course of a heterogeneous reaction, the accessible regions of the modified polysaccharide grains are esterified first. Hence, as the reaction proceeds, the distribution of hydroxy groups with respect to hydrogen bonding energy must change. In heterogeneous nitration of carboxy starch, the most accessible hydroxy groups involved in the weakest hydrogen bonds react first. As these groups are consumed, the relative amount of OH groups involved in stronger hydrogen bonds increases. In this case, the symmetry index a/b (Fig. 4) must decrease, since the relative absorption from the low-frequency side (associated with the parameter b) must increase. At the same time, the progress of substitution and introduction of nitrato groups in place of hydroxy groups must cause the strength of hydrogen bonds between the remaining groups to decrease, owing to steric hindrance. This, in turn, must shift the OH absorption maximum in the IR spectrum [ν(OH)] toward higher frequencies.

Table 2. Absorption frequency of OH groups and the band symmetry at various degrees of nitration of carboxy starch (DS_{COOH} 0.51)

c_N, wt %	DS_{ONO_2}	Symmetry index of OH band, a/b	ν_{OH}^{max}, cm^{-1}
Carboxy starch (DS_{COOH} 0.51)	–	0.87	3385
3.90	0.54	0.83	3415
6.94	1.08	0.81	3415
8.11	1.32	0.78	3430
9.45	1.64	0.50	3485

The parameters of the OH band in the IR spectra of nitrated carboxy starch samples are listed in Table 2. It is seen that, with increasing degree of substitution, the absorption peak shifts toward higher wave numbers, which was previously interpreted as a gradual increase in the content of hydroxyls involved in weak hydrogen bonds. Along with this trend, the OH band becomes more asymmetric (up to DS_{ONO_2} 1.64), which suggests existence of hydroxy groups that are involved in strong hydrogen bonds and remain intact in the reaction. This is quite natural, in view of the above reasoning.

Thus, carboxy starch is structurally nonuniform, and this nonuniformity affects the course of *O*-nitration and the composition of the resulting products.

CONCLUSIONS

(1) The *O*-nitration rate can be considerably increased by raising the temperature from 0 to 35°C. A decrease in the COOH content in the initial carboxy starch and an increase (to 40 wt %) in the nitric acid concentration (in both anhydrous and aqueous nitrating mixtures) result in appreciably higher content of nitrato groups in the final product.

(2) The results of this work allow prediction of conditions necessary for obtaining carboxy starch nitrate esters with prescribed composition in high yield.

(3) The nitrated carboxy starch samples were characterized by IR spectroscopy; free NO_2 and/or NO_3^- species were detected, originating from acid hydrolysis of ONO_2 groups, promoted by carboxy groups of

the polysaccharide. The content of these groups grows with increasing content of ONO_2 groups in nitrated carboxy starch samples.

REFERENCES

1. Belyaev, E.Yu., *Khim.-Farm. Zh.*, 2000, vol. 34, no. 11, pp. 36–41.
2. Yul'chibaev, B.A., Shomirzaev, S.T., Azimbaeva, G.E., *et al.*, Abstracts of Papers, *Vsesoyuznaya konferentsiya "Problemy ispol'zovaniya tsellyulozy i ee proizvodnykh v meditsinskoi i mikrobiologicheskoi promyshlennosti"* (All-Union Conf. "Applications of Cellulose and Its Derivatives in Medical and Microbiological Industry"), Tashkent, 1989, p. 64.
3. Samal', A.B., Kolyadko, M.G., Yurkshtovich, T.L., *et al.*, *Khim.-Farm. Zh.*, 1996, vol. 30, no. 10, pp. 19–21.
4. Richter, M., Augustat, S., and Schierbaum, F., *Ausgewählte Methoden der Stärkechemie*, Leipzig: Fachbuchverlag, 1968.
5. Butrim, S.M., Bil'dyukevich, T.D., and Yurkshtovich, T.L., *Zh. Prikl. Khim.*, 2001, vol. 74, no. 12, pp. 2046–2050.
6. Sarybaeva, R.I. and Shchelokhova, L.S., *Khimiya azotnokislykh efirov tsellyulozy* (Chemistry of Cellulose Nitrate Esters), Frunze: Ilim, 1985.
7. Kaputskii, V.E., Yurkshtovich, T.L., and Balabaeva, M.D., *Vestn. Bel. Gos. Univ. im. V.I. Lenina, Ser. 2*, 1978, no. 1, pp. 15–18.
8. Ermolenko, I.N., *Spektroskopiya v khimii okislennykh tsellyuloz* (Spectroscopy in Chemistry of Oxidized Celluloses), Minsk: Nauka i Tekhnika, 1959.
9. Ivanova, N.V., Korolenko, E.A., Zhbankov, R.G., *et al.*, *Zh. Prikl. Spektrosk.*, 1991, vol. 54, no. 2, pp. 201–206.

Russian Journal of Applied Chemistry, Vol. 75, No. 8, 2002, pp. 1325–1329. Translated from Zhurnal Prikladnoi Khimii, Vol. 75, No. 8, 2002, pp. 1351–1356.
Original Russian Text Copyright © 2002 by Gogotov, Parilova, Khaliullin.

MACROMOLECULAR CHEMISTRY AND POLYMERIC MATERIALS

New Effective Binary Formulations for Inhibiting Thermal Polymerization of Styrene

A. F. Gogotov, M. V. Parilova, and A. K. Khaliullin

Angarsk Petrochemical Joint-Stock Company, Angarsk, Irkutsk oblast, Russia

Favorskii Institute of Chemistry, Siberian Division, Russian Academy of Sciences, Irkutsk, Russia

Received February 6, 2002

Abstract—Synthesis of effective formulations for inhibiting thermal polymerization of styrene, based on sterically hindered phenols, is reported.

Styrene, like many other commercially significant monomers, extremely readily polymerizes upon heating; therefore, its distillation should be performed with addition of inhibitors. Undesirable polymerization in the course of distillation impairs the economical parameters of the process and results in frequent interruptions of the process to remove polymer deposits. In Russia, the most widely used inhibitor of styrene thermal polymerization is *p*-quinone dioxime (QDO) [1, 2], a typical scavenger of alkyl radicals, in combination with various synergistic additives. In the US, Europe, and Japan, have long been using, styrene-producing plants use soluble inhibiting systems based on more effective inhibitors, including inhibitors of the latest generation, nitroxyl radicals [3]. In particular, Nalco Exxon (the US) and Kurita (Japan) produce a wide range of inhibiting formulations containing nitroxyl radicals. In Russia, unfortunately, components of many modern inhibiting systems are not produced commercially (there are only a few patents on this matter [4, 5]); therefore, efforts are still being made to improve commercially used formulations based on QDO with the aim to enhance their performance and decrease the consumption of the main inhibitors. The well-known drawbacks of QDO are low solubility in aromatic hydrocarbons and high toxicity. Therefore, development of effective QDO-free inhibiting formulations is an urgent problem.

The goal of this study is to extend the range of soluble QDO-free inhibiting formulations and enhance their inhibiting effect on thermal polymerization of styrene in the course of its distillation from process solutions.

EXPERIMENTAL

The performance of the inhibiting formulations was evaluated under laboratory conditions with pure freshly distilled styrene or with styrene-containing process solutions, with access of air (no purging with inert gas). The testing procedure consisted in determination of the polystyrene yield after heating of the freshly vacuum-distilled monomer at 120°C for 2–7 h, because polymerization of styrene is considerably slower at temperatures lower than 115–118°C.

Styrene (100 cm^3, 90.6 g) was placed in an autoclave, and weighed portions of the inhibiting formulation components were added. The autoclave was sealed and placed in a thermostat heated to 119 ± 1.5°C. After the first 2 h of heating, samples were taken every hour. The samples were distilled on a boiling water bath at 20 mm Hg. The inhibition efficiency was judged from the amount of the polymeric residue (% of the sample weight). With styrene-containing process solutions, the inhibiting components were taken in proportions corresponding to the styrene content in these solutions.

One of the ways to enhance the performance of inhibiting formulations is to use, in combibation with QDO, various phenolic coinhibitors acting as synergistic additives [6]. Experiments show that, when taken in larger amounts, the coinhibitors can be sufficiently effective not only in combination with QDO but also without it. As examples can serve systems QDO + Ionol + TBPC [7] and Ionol + TBPC [8]; QDO + MB + PNP [2] and MB + PNP [9]; QDO + MB + PCF [10] and MB + PCF [11] {MB, Mannich

1070-4272/02/7508-1325 $27.00 © 2002 MAIK "Nauka/Interperiodica"

Table 1. Performance of inhibiting systems based on MB with respect to styrene and industrial process solutions at 120°C

Run no.	Composition, wt % relative to styrene	Polymer yield, %, in indicated heating time, h					
		2	3	4	5	6	7
	Styrene						
1	MB (0.045) + PNP (0.06) [9]	0.43	0.49	0.65	1.08	5.16	14.3
2	MB (0.06) + PCF (0.06)	0.18	0.22	0.38	0.49	0.62	0.78
3	MB (0.06) + SA* (0.06) [12]	0.43	0.49	0.65	0.98	5.30	13.4
4	[MB (0.06) + SA(0.03)] + PCF (0.03)	0.19	0.36	0.46	0.85	4.59	10.6
5	MB (0.06) + TBPC (0.06)	0.22	0.30	0.36	0.46	0.50	0.60
6	MB (0.045) + TBPC (0.06)	0.21	0.30	0.38	0.43	0.45	0.64
7	MB (0.03) + TBPC (0.06)	0.21	0.28	0.29	0.51	0.54	0.65
8	MB (0.03) + TBPC (0.045)	0.21	0.31	0.34	0.45	0.54	0.63
9	MB (0.06) + PCF (0.03)	0.223	0.29	0.52	0.81	1.08	1.30
10	MB (0.03) + PCF (0.06)	0.21	0.25	0.33	0.53	0.57	0.67
11**	MB (0.03) + TBPC (0.06)	0.12	0.12	0.13	0.14	0.15	0.18
12**	MB (0.03) + PCF (0.06)	0.14	0.15	0.16	0.19	0.21	0.23
13***	MB (0.03) + TBPC (0.06)	0.06	0.08	0.11	0.12	0.13	0.14
	Industrial process solution						
14	MB (0.03) + TBPC (0.06)	0.25	0.34	0.34	0.35	0.35	0.38
15	MB (0.03) + PCF (0.06)	0.21	0.26	0.29	0.32	0.36	0.40
16**	MB (0.03) + TBPC (0.06)	0.18	0.23	0.24	0.25	0.30	0.30
17***	MB (0.03) + TBPC (0.06)	0.16	0.23	0.26	0.28	0.29	0.30

* Stearic acid. ** At 100°C. *** At 90°C.

base (Agidol-3, *N,N*-dimethyl-3,5-di-*tert*-butyl-4-hydroxybenzylamine); PCF, pyrocatechol fraction (a mixture of dihydric coal-tar phenols); PNP, *p*-nitrophenol; Ionol (Agidol-1, A-1), 2,6-di-*tert*-butyl-4-methylphenol, also its dinuclear analog, Agidol-2 [A-2, 2,2'-methylenebis(6-*tert*-butyl-4-methylphenol)], was tested; TBPC, 4-*tert*-butylpyrocatechol}.

Table 2. Composition of the pyrocatechol fraction

PCF component	Content, wt %
Phenol	2.5
o-, *m*-, *p*-Methylphenols (Σ)	2.7
Dimethylphenols + ethylphenols (*o*-, *m*-, *p*-)	0.9
Pyrocatechol	11.3
3-Methyl-1,2-dihydroxybenzene	7.6
4-Methyl-1,2-dihydroxybenzene	13.8
4-*tert*-Butyl-1,2-dihydroxybenzene	1.5
1,3-Dihydroxybenzene + 1,4-dihydroxybenzene	8.6
Isomeric dimethyl-1,4-dihydroxybenzenes	4.3
Isomeric methyl-1,3-dihydroxybenzenes	14.8
Isomeric dimethylethyl-1,3-dihydroxybenzenes	13.7

Based on these results, we attempted to develop a binary inhibiting formulation consisting of MB and a known phenolic inhibitor, TBPC, instead of PNP, which showed poor performance in other formulations. Along with TBPC, we tested as a dihydric phenolic coinhibitor the so-called pyrocatechol fraction of dihydric phenols from the coal-tar plant of the Angarsk Petrochemical Company. The formulations of MB with PCF and TBPC show similar performance, as suggested by the results of laboratory tests (Table 1).

Table 1 shows that the proposed inhibiting formulation (MB + dihydric phenols; run nos. 2, 7) is considerably more effective than the known formulation (run no. 3) [12]. Partial replacement of stearic acid with a dihydric phenol (run no. 4) decreases the formation of the polymer, and full replacement of the aliphatic acid with a pyrocatechol derivative (run nos. 2, 5) sharply (by a factor of about 20) suppresses the formation of the polymer under similar conditions.

Partial decrease in the MB content (by 25%, run no. 6, or 50%, run nos. 7, 10), compared to run no. 3 [12], does not impair the performance. A decrease in

Table 3. Composition of industrial styrene-containing process solution

Compound	Content, wt %	Compound	Content, wt %
Benzene	1.16	*m*- and *p*-Xylenes	0.32
Toluene	3.24	Styrene	50.59
Ethylcyclohexane	0.04	1,2,3,5-Tetramethylcyclohexane	0.25
Ethylbenzene	44.08	α-Methylstyrene	0.13

Table 4. Performance of inhibiting systems based on sterically hindered phenols at 120°C

Run no.	Composition, wt % relative to styrene	Polymer yield, %, in indicated heating time, h					
		2	3	4	5	6	7
18	A-1 (0.03) + TBPC (0.045)	0.16	0.31	0.36	0.41	0.47	0.58
19	A-1 (0.025) + TBPC(0.045)	0.13	0.20	0.42	0.61	0.71	0.84
20	A-2 (0.03) + TBPC (0.045)	0.21	0.25	0.33	0.47	0.57	0.57
21	A-2 (0.045) + TBPC (0.06)	0.20	0.25	0.31	0.35	0.46	0.57
22	A-2 (0.03) + TBPC (0.06)	0.16	0.27	0.35	0.40	0.48	0.60
23	A-2 (0.025) + TBPC (0.045)	0.17	0.26	0.33	0.46	0.55	0.63
24*	A-2 (0.03) + TBPC (0.06)	0.14	0.15	0.16	0.19	0.21	0.23
25*	A-2 (0.03) + TBPC (0.045)	0.15	0.16	0.18	0.21	0.23	0.28
26**	A-1 (0.03) + TBPC (0.06)	0.06	0.08	0.11	0.12	0.13	0.14
27**	A-2 (0.03) + TBPC (0.045)	0.10	0.12	0.13	0.14	0.15	0.17

* At 100°C. ** At 90°C.

the content of dihydric phenols by a factor of 2 impairs somewhat the performance (run no. 9). Change in the OM : PCF ratio from 1 : 1 (run no. 2) to 1 : 2 (run no. 10) enhances somewhat the inhibiting activity of the formulation.

An individual dihydric phenol, TBPC (run no. 5), shows somewhat higher performance than a mixture of phenols (PCF, by-products from coal-tar plants, run no. 2; for the composition of PCF, see Table 2; the sample used contained ~45% pyrocatechol and hydroquinone derivatives and ~30% resorcinol derivatives).

At lower heat-treatment temperatures (100°C, run nos. 11, 12; 90°C, run no. 13), the inhibiting power of the formulation proposed remained high, and the polymerization was almost fully suppressed.

In industry, styrene is distilled from a mixture consisting approximatelly by half of alkyl-substituted aromatic hydrocarbons (for the composition, see Table 3). The inhibiting formulations based on dihydric phenols and MB were tested with this crude mixture and efficiently inhibited thermal polymerization of styrene in the course of its distillation (run nos. 14–17).

It has been noted previously that the inhibiting effect of MB-containing formulations is associated with the acid–base interaction of protons of an organic acid with the lone electron pair of the nitrogen atom of benzylamine [13]. It is quite probable that pyrocatechols, in which phenolic hydroxyl protons are fairly labile, can efficiently replace organic acids in MB-containing formulations; however, such acid–base interactions are typical of aqueous, rather than hydrocarbon solutions. Apparently, the longer inhibiting effect of the binary formulation, compared to its components taken separately, may be due to regeneration of MB by the reaction of the phenoxyl radical formed from it with TBPC. In the process, TBPC transforms into monoradical and then *o*-quinone; furthermore, in the quinoid form it scavenges alkyl radicals. It is quite possible that, as noted in [14], the pyrocatechol derivative and MB form an activated complex which deactivates variable-valence metals in rubbers and radical species in our system.

Along with the systems MB–TBPC and MB–PCF [11], we also tested formulations consisting of a monohydric phenol (Agidol-1) or bisphenol (Agidol-2) and TBPC (1 : 1.5 or 1 : 2 ratio; Tables 4, 5).

Table 5. Performance of systems consisting of Ionol or Agidol-2 and TBPC or PCF in inhibition of thermal polymerization of styrene and industrial styrene-containing process solutions at 120°C

Run no.	Composition, wt % relative to styrene	Polymer yield, %, in indicated heating time, h					
		2	3	4	5	6	7
	Industrial process solution						
28	A-2 (0.03) + TBPC (0.06)	0.25	0.34	0.34	0.35	0.35	0.38
29*	A-2 (0.03) + TBPC (0.06)	0.18	0.23	0.24	0.25	0.30	0.30
30**	A-2 (0.03) + TBPC (0.06)	0.16	0.23	0.25	0.26	0.27	0.28
	Styrene						
31	A-1 (0.03) + PCF(0.06)	0.07	0.28	0.33	0.41	0.53	0.61
32	A-2 (0.03) + PCF (0.06)	0.10	0.28	0.34	0.39	0.45	0.59
33	A-2 (0.03) + PCF (0.045)	0.21	0.26	0.29	0.32	0.36	0.43
	Industrial process solution						
34	A-2 (0.03) + PCF (0.06)	0.36	0.39	0.42	0.52	0.54	0.56
35	A-2 (0.03) + PCF (0.06)	0.42	0.43	0.47	0.50	0.53	0.59

* At 100°C. ** At 90°C.

Table 6. Performance of the inhibiting formulation VB + TBPC

Run no.	VB	TBPC	Polymer yield, %, in indicated heating time, h					
	wt % relative to styrene		2	3	4	5	6	7
34	0.03	0.045	0.32	0.40	0.50	0.75	0.85	0.88
35	0.0225	0.045	0.26	0.36	0.45	0.63	0.7	0.94
36	0.015	0.045	0.40	0.48	0.67	1.07	1.30	1.80
37	0.0125	0.045	0.23	0.26	0.51	0.52	0.63	0.97
38	0.01	0.045	0.23	0.44	0.48	0.65	0.94	1.23
39	0.007	0.045	0.21	0.41	0.52	0.48	0.63	0.86
40	0.005	0.045	0.53	0.57	0.64	0.92	0.94	1.37
41	0.03	0.04	0.27	0.29	0.55	0.80	0.86	0.90
42	0.03	0.035	0.30	0.42	0.61	0.65	0.78	1.00
43	0.0225	0.035	0.32	0.35	0.71	0.6	0.74	0.92
44	0.0225	0.04	0.33	0.3	0.61	0.56	0.76	0.83

Tables 4 and 5 indicate that bisphenols (by the example of Agidol-2) show higher inhibiting power than mononuclear phenols (Ionol) [15].

Thus, virtually any inhibiting formulation containing QDO can be reformulated with elimination of QDO. This preliminary conclusion can be illustrated by the following example. Previously, we proposed an effective formulation for inhibiting thermal polymerization of styrene, consisting of QDO and vanillin barbiturate (VB) [16]. As noted in [17], VB taken separately possesses no inhibiting properties. However, a QDO-free mixture of VB with TBPC effectively inhibits thermal polymerization of styrene in the course of its heating at 120°C for several hours (Table 6).

Table 6 shows that the 1 : (1.5–2.0) ratio of mono- and dihydric phenols in inhibiting formulations for thermal polymerization of styrene, which proved to be optimal for sterically hindered phenols (Ionol, Agidol-2, MB), is also appropriate with methoxylated phenols such as VB (run nos. 34, 35 and 43, 44). Run nos. 39 and 41 also gave satisfactory results,

Table 7. Comparison of various inhibiting formulations

Formulation no.	Composition	Inhibitor content, wt %	*T*, °C	Heating time, h	Polymer yield, wt %
1	Sinoms-5	0.11	120	6	1.1
		0.082	120	6.5	2.88
2	Sinoms-6	0.11	120	6.5	0.74
		0.082	120	6	1.2
3	QDO + hydroquinone	0.05	120	6.5	1.3
4	QDO + PNP	0.05	120	6	2.5
5	MB + PNP	0.1	120	6	3.88
		0.075	100	6	1.1
6	Naugard 1-5	0.1	120	6	1.6
7	Naugard 1-31	0.1	120	6	0.49
8	MB + TBPC	0.075	120	6	0.54
9	MB + PCF	0.105	120	6	0.45
10	MB + TBPC	0.090	100	6	0.30

despite the fact that the component ratios in the inhibiting formulation were not optimal.

Our results are a step forward in the development of effective inhibitors based on 4-*tert*-butylpyrocatechol [18–20]. The proposed formulations MB + PCF and MB + TBPC (Table 7) were compared in performance and total consumption of the inhibitor with the previously tested systems inhibiting thermal polymerization of styrene.

As seen from Table 7, the inhibiting formulations proposed (nos. 8–10) well compete in performance with actively advertised formulations like Naugard (nos. 6, 7) and contain no toxic components.

Thus, we have developed fairly effective soluble inhibiting formulations for styrene production, based on mixtures of mono- and dihydric sterically hindered phenol derivatives.

CONCLUSIONS

(1) A series of hydrocarbon-soluble formulations for inhibiting thermal polymerization of styrene, based on mono- and dihydric sterically hindered phenols and containing no *p*-quinone dioxime, were developed.

(2) Coinhibitors used in combination with *p*-quinone dioxime can also be used in dioxime-free formulations; however, to preserve the high inhibiting power, these compounds should be taken in larger amounts.

REFERENCES

1. USSR Inventor's Certificate, no. 441263.
2. USSR Inventor's Certificate, no. 968041.
3. Jones, C., *Chem. Week*, 1996, vol. 158, no. 49, p. 32.
4. RF Patent 2106331.
5. RF Patent 2128171.
6. Denisov, E.T. and Kovalev, G.I., *Okislenie i stabilizatsiya reaktivnykh topliv* (Oxidation and Stabilization of Jet Fuels), Moscow: Khimiya, 1983.
7. RF Patent 2129112.
8. CSSR Inventor's Certificate, no. 259635.
9. USSR Inventor's Certificate, no. 562092.
10. RF Patent 2152377.
11. RF Patent 2149153.
12. USSR Inventor's Certificate, no. 819078.
13. Tolstikov, G.A., Pantukh, B.N., Tuktarova, L.A., *et al., Prom–st. Sint. Kauchuka: Nauch.-Tekh. Sb.*, 1983, no. 8, pp. 8–10.
14. USSR Inventor's Certificate, no. 681040.
15. Karakuleva, G.I., Vinogradova, I.V., Belyaev, V.A., *et al., Ingibirovanie polimerizatsii diolefinov v protsessakh ikh vydeleniya i khraneniya* (Inhibition of Diolefin Polymerization in the Course of Isolation and Storage), Moscow: TsNIITEneftekhim, 1974.
16. RF Patent 2138473.
17. Gogotov, A.F., Batura, I.I., Voitik, V.S., *et al., Neftepererab. Neftekhim.*, 1999, no. 12, pp. 22–26.
18. US Patent 4409408.
19. EP Patent Appl. 0403672.
20. Gogotov, A.F., Parilova, M.V., Amosov, V.V., and Khaliullin, A.K., *Proizv. Ispol'z. Elastom.*, 2001, no. 5, pp. 8–11.

Russian Journal of Applied Chemistry, Vol. 75, No. 8, 2002, pp. 1330–1335. Translated from Zhurnal Prikladnoi Khimii, Vol. 75, No. 8, 2002, pp. 1357–1362.
Original Russian Text Copyright © 2002 by Ginzburg, Shibaev, Kireenko, Shepelevskii, Baidakova, Sitnikova.

MACROMOLECULAR CHEMISTRY AND POLYMERIC MATERIALS

Antiwear Effect of Fullerene C_{60} Additives to Lubricating Oils

B. M. Ginzburg, L. A. Shibaev, O. F. Kireenko, A. A. Shepelevskii, M. V. Baidakova, and A. A. Sitnikova

Institute for Problems of Mechanical Engineering, Russian Academy of Sciences, St. Petersburg, Russia
Institute of Macromolecular Compounds, Russian Academy of Sciences, St. Petersburg, Russia
Ioffe Physicotechnical Institute, Russian Academy of Sciences, St. Petersburg, Russia

Received April 25, 2002

Abstract—The protective film (≤1000 Å thick) formed on the copper foil surface upon friction of a steel roller lubricated with industrial oil containing 5% fullerene C_{60} was studied by optical and electron microscopy, X-ray diffraction (XRD) analysis, hardness measurements, and mass spectrometry. This protective film is probably a fullerene-polymer network formed by fullerene C_{60} and covalently bound fragments of hydrocarbon chains released in the course of mechanochemical degradation of the lubricating oil. The film exhibits elevated hardness and antiwear properties, and increases the load-carrying power of the tribotechnical unit. Chemical mechanisms of tribopolymerization were analyzed.

Even the first data on the antiwear properties of fullerenes [1–3] showed that this material is promising for tribotechnical applications. At the same time, fullerenes and their modifications did not decrease significantly the friction coefficient in the case of dry and boundary sliding friction of solids. However, systematic study of tribological properties of fullerenes and materials based on them was continued in [4–6]. It was found that the addition of fullerene-containing materials to lubricating oils significantly improves the antiwear and antiscuff properties of tribotechnical units and expands the allowable pressure range by a factor of 1.5–2. Boundary sliding friction of a steel roller on a copper foil lubricated with an oil containing 5% C_{60} gives almost smooth shining friction surface. It was assumed that, during friction treatment, a thin antiwear film is formed on the copper surface. The effect of fullerene additives on I-40A industrial oil was studied by mass-spectrometric thermal analysis (MTA) in [7]. The results showed that fullerene C_{60} reacts with naphthene and paraffin components of the oil in the course of heating or friction; samples of the copper foil after their friction treatment with I-40A oil containing C_{60} were also analyzed [7]. In the presence of fullerene, the major peaks in the mass spectra were shifted toward lower temperatures, which was attributed to covalent linking of hydrocarbon radicals to fullerenes with the formation of a weak β-bond. Such an interpretation was based on published data for fullerene C_{60} with grafted polymeric chains [8]. Hence, it was suggested that the antiwear structure on the copper surface is a tribopolymeric hydrocarbon network in which the fullerene molecules occur predominantly at the network points. It was also concluded [7] that, in the course of friction and thermal treatment, fullerene acts as a trap for free radicals arising from mechanochemical degradation of naphthene and paraffin molecules and initiates polymerization of the fragments of the above hydrocarbons.

In this work, we studied the friction surface structure of the copper foil formed in the presence of fullerene C_{60} and analyzed possible chemical mechanisms of formation of the tribopolymeric network with the participation of C_{60} and atmospheric oxygen contacting the friction surfaces.

We used fullerene C_{60} (99.7%)[1] and I-40A industrial oil. To prepare the required 5% lubrication compositions, finely dispersed fullerene was added to the oil and stirred.

The tribological properties were tested on a 2070 SMT-1 friction machine according to the roller–shoe scheme. A mobile roller (46 mm diameter, 16 mm width) was prepared from 18Kh2N4MA chromium-

[1] Khromotron project, Russian Scientific and Technical Program "Fullerenes and Atomic Clusters," 1994.

1070-4272/02/7508-1330 $27.00 © 2002 MAIK "Nauka/Interperiodica"

nickel-molybdenum wear-resistant steel; the speed of rotation was 400 min^{-1} (1 m s^{-1} linear velocity). The shoe was crimped with a 200-μm commercial copper foil (10 mm width, 2 cm^2 nominal contact area). An oil drop (0.5 g) was placed on the foil surface, and the pressure on the tribotechnical system was increased stepwise to 4–6 MPa.

The XRD patterns were registered on a Dmax-RC (Rigaku) single-crystal diffractometer (Cu_{K_α} radiation, Ni filter). The friction surfaces were studied using a CamScan 4-88DV-1000 scanning electron microscope (accelerating voltage 15 kV), an EM-420 transmission electron microscope (accelerating voltage of up to 100 kV), and an MIM-8 metallographic microscope.

In our experiments, we analyzed copper foils (1) before their treatment; (2) after friction treatment with I-40A lubricant, including the mode of elevated wear resistance [9] attained by slowly increasing the pressure on the tribotechnical unit; and (3) after treatment in the presence of the lubricant containing 5% C_{60}. The surfaces of failure of the copper foils, obtained in the course of stretching in liquid nitrogen of preliminarily notched samples, were also studied. Owing to low temperature of stretching, structural distortions due to plastic deformations were eliminated.

Tribological tests. Two most typical dependences of the friction momentum on time are shown in Fig. 1. Curve *1* is observed for straight I-40A oil in which the friction momentum, providing scuffing, starts to increase at rather small loads (300–600 N), whereas the tribotechnical unit with the lubricant containing C_{60} (curve *2*) operates for a long time in the 800–1200 N load range. In the latter case, the friction coefficient is as low as 0.015–0.030; this level is not attained with straight oil or its mixtures with other carbon additives (graphite, carbon black, and fullerene black after extraction of the main fullerene fraction). In the presence of C_{60} in the lubricating oil, almost entire friction surface of copper becomes smooth and bright, and no copper traces and wear particles are observed on the steel roller, in the lubricant, and on the friction surface. Further rubbing of the roller or substitution of the modified lubricant with straight oil does not affect stable operation of the tribotechnical unit, and the friction coefficient remains as low as in the presence of C_{60}. This suggests the formation of the antifriction antiwear structure on the copper friction surface.

Optical microscopy. The surface of the initial foil exhibits grooves oriented in the rolling direction (Fig. 2a). After friction with the lubricating oil, these

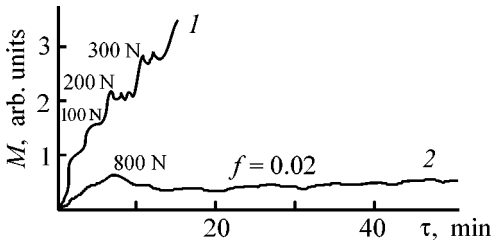

Fig. 1. Friction momentum of the steel roller on the copper foil with (*1*) I-40A lubricant and (*2*) I-40A + 5% C_{60} at stepwise loading of the friction system. (*M*) Friction momentum, (τ) time, and (*f*) friction coefficient.

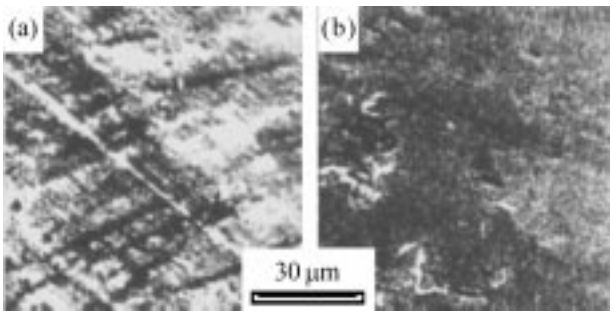

Fig. 2. Photomicrographs of the copper foil surface (a) in the initial state and after treatment with lubricant I-40A + 5% C_{60} and (b) after friction treatment with straight I-40A oil.

groves disappear, the surface becomes fairly uniform, and visual determination of the directions of rolling and even friction becomes impossible (Fig. 2b). After friction with the lubricant containing fullerene C_{60}, the initial grooves are retained, but a protective film is formed on the surface (Fig. 2a).

Scanning electron microscopy (SEM). The SEM data on the surface relief of the copper film are similar to those of yielded by optical microscopy: in the presence of fullerene, the initial surface relief is retained and the surface is coated with a thin film, whereas operation in the straight lubricating oil (even in the elevated wear resistance mode) significantly modifies the material structure.

Additional data on the structure of surface layers were obtained with the samples ruptured in liquid nitrogen. After the fullerene-free friction, the area near the foil rupture exhibits fragments of the surface layer with changed structure, and, as seen at large magnifications (Fig. 3a), the surface layer consists of spherical submicrometer particles (region A). It should be noted that no analogous surface layers were observed in the initial copper samples ruptured in liquid nitrogen, i.e., it is formed in the course of friction treatment. In the case analyzed, the thickness of this layer reaches nearly 3 μm, and its structure signi-

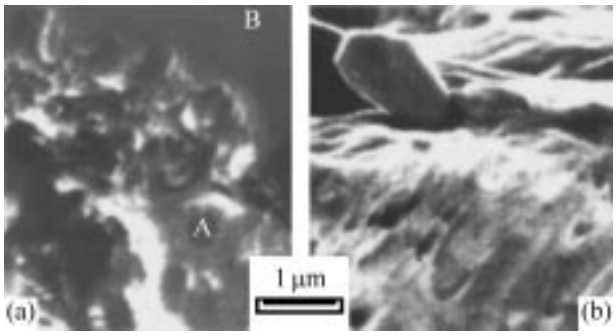

Fig. 3. Electron micrographs of the low-temperature rupture of copper foil after its friction treatment in the presence of (a) I-40A lubricant in the wear-resistant mode and (b) I-40A+5% C_{60} (surface is coated with the protective film formed in the course of treatment) (A) Surface layer consisting of submicron spherical particles and (B) relief-free layer.

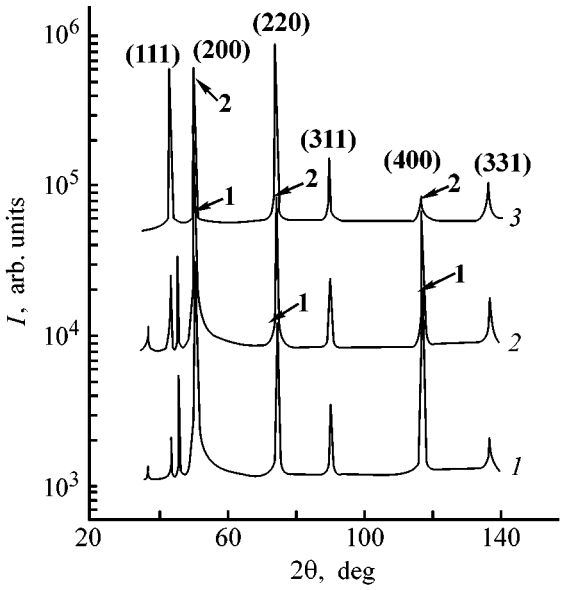

Fig. 4. XRD patterns of the copper foil (*1*) before treatment and after friction treatment with steel roller in the presence of (*2*) I-40A+C_{60} lubricant and (*3*) straight I-40A lubricating oil. (*I*) Intensity and (2θ) Bragg angle. The crystallographic indices of the copper lattice planes are given over the reflections. *Bold figures* **1** and **2** denote the peak apices in the respective curves.

ficantly differs from the structure of the deeper lying coarse-grained material. Moreover, there are no grooves formed during rolling or friction treatment of the surface, which is coated with very thin smooth layer (region B) with the thickness ≤100 nm. This confirms our conclusion that the surface structure of the copper foil changes after its operation with the straight lubricating oil.

After friction in the presence of C_{60} we found no fragment of the surface layer whose structure differed from the initial structure. As seen (Fig. 3b), the friction surface near the foil rupture zone exhibits micrometer surface irregularities whose surface is coated with a film worsening the micrograph contrast. The resulting surface differs from the friction surface formed during treatment in the presence of straight I-40A oil. The layer formed on the copper surface looks like a polymeric film, it is broken in the rupture area and often dangles from the fracture edge; no structural modifications of the surface copper layers or formation of dispersed particles are observed (cf. Fig. 3a).

XRD data. The protective properties of the resulting film are confirmed by wide-angle X-ray diffraction analysis (Fig. 4). The initial structure of the foil (curve *1*) remains unchanged after friction treatment for several hours in the presence of a lubricating oil containing C_{60} (curve *2*). After treatment with the straight lubricant, the surface structure changes sharply (curve *3*): peak 111 increases, and peaks 200 and 400 decrease in relative intensity, with peak 200 becoming smaller than peak 220 (in the initial samples, the pattern was inverse).

Due to the small thickness, the resulting film itself does not noticeably affect the X-ray diffraction; we failed to exfoliate the protective film from the foil and directly study its structure. This film did not dissolve in toluene and other organic solvents. Hence, we used another approach.

Transmission electron microscopy (TEM). The direct confirmation of the presence of a protective film and some data on its structure were obtained by TEM. The foil was treated by ion etching (from the back side) until formation of a hole with a shape of truncated cone (Fig. 5a). Different sections of the material profile formed in this procedure were studied against dark and light background in combination with electron diffraction. The direction of the electron beam coincided with that of the etching ion beam. The pattern of the hole edge in the foil operating with fullerene-free lubricant in the wear-resistant mode [9] is shown in Fig. 5b. In this case, a protective film, which is observed at the hole edge, is formed too. This film has an amorphous structure (no reflections on the corresponding electron diffraction patterns are observed), it thickness reaches 100 Å, and it is fairly resistant to the electron beam. The surface layer has fine structure with crystallite size of 0.1 μm, which agrees with the SEM

data [9]. As seen from Fig. 5b', this layer consists of copper crystallites with admixture of Cu_2O particles.

After friction treatment in the presence of C_{60}, no fragmentation of the surface copper layer was found (Fig. 5c). The resulting surface film is also amorphous and its thickness is an order of magnitude thicker (1000 Å) than in the case of fullerene-free friction and thus is revealed in the electron diffraction patterns. This may be due to the reduced energy of β-bonds in the hydrocarbon chains covalently bound to C_{60} [7] and to decreased heat transfer through the thicker film. The electron diffraction pattern of the film and surface layer corresponds to a textured lattice of Cu_2O [111] with interlayer spacing of 2.45 Å. In the dark-background pattern of the film in the light of reflections 200 [copper(I) oxide] and 111 (metallic copper), nearly overlapping with each other, particle inclusions of 100–1000 Å size are seen, which are obviously the wear particles formed in the initial moment from the oxidized surface material. There are no reflections of crystalline fullerene C_{60} and its derivatives in the diffraction patterns. This fact does not mean that fullerene does not participate in the film formation. The results of tribological studies and the data on the surface structures registered in the case of straight fullerene and its 5% additives to the lubrication oil are the same. Nearly equal positive effect of small fullerene additives (0.5–0.75%) confirms our assumption that C_{60} initiates tribochemical polymerization of hydrocarbons present in petroleum oils, which promotes formation of a protective film of increased thickness.

Chemical mechanisms of tribopolymerization. First of all, we should determine whether the concentration of C_{60} is enough to a form continuous layer on the friction surface. The area of the friction surfaces of the samples in question was nearly 2 cm^2, and the real gap between them was 1 μm. At 5% concentration of fullerene in the lubricating oil, the total amount of the molecules in the gap is 0.8×10^{16}. At hexagonal close packing of fullerene, each C_{60} molecule occupies 100 $Å^2$, and thus the molecules present in the gap can form 40 monolayers with compact packing of the molecules in them over the entire friction surface. The thickness of 40 monolayers reaches nearly 400 Å and reasonably agrees with electron-microscopic data on the protective film thickness (≤1000 Å). Thus, the concentration of fullerene C_{60} is enough to form a continuous film. The resulting film is insoluble in toluene; hence it consists of components other than unmodified molecular fullerene.

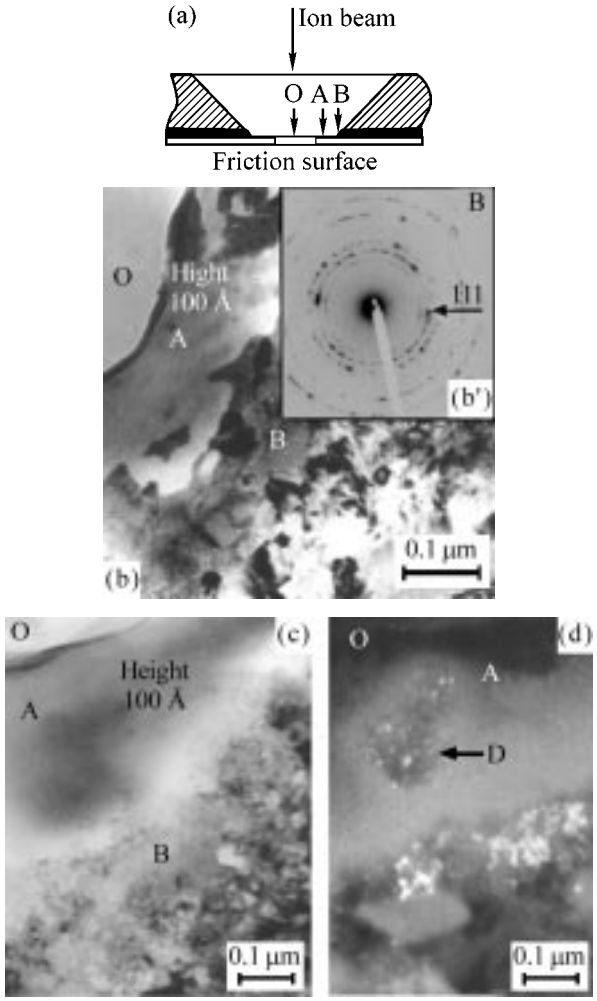

Fig. 5. TEM patterns of an etched hole in the copper foil. (a) Scheme of the hole profile: (O) through hole, (A) tribochemical film, and (B) surface copper layer. (b) Copper film after friction treatment in the presence of I-40A oil in the wear-resistant mode: (O) image of the etched hole against the light background and neighboring conic section (150 000× magnification), (A) 100-Å surface tribofilm, and (B) block structure with 0.1-μm crystallites in the surface layer. (b') Diffraction pattern of the block structure, which is a superposition of the diffraction patterns typical of Cu and Cu_2O crystal lattices. (c) the same as in Fig. 5b, but after treatment in the presence of I-40A + 5% C_{60} lubricant: (O) through hole, (A) 1000-Å surface film, and (B) surface copper layer with no block structure. (d) Dark-background patterns of film A in the light of reflections 200 (Cu_2O) and 111 (Cu); (D) wear particle inclusions.

Let us consider possible differences in the chemical mechanisms of tribochemical polymerization of industrial oil components in the presence and absence of

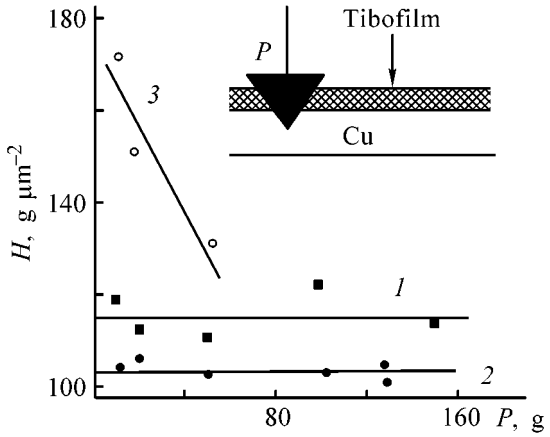

Fig. 6. Microhardness *H* of the copper foil surface vs. the indentor load *P*. The scheme of experiment is shown in the inset. Foil surface: (*1*) initial and after friction treatment in the presence of (*2*) I-40A and (*3*) I-40A + 5% C_{60} lubricants.

C_{60}. Fullerene is an effective scavenger of free organic radicals. This suggests its activity with respect to the radicals formed in the course of mechanochemical degradation of naphthene and paraffin molecules present in the oil. Each fullerene C_{60}, molecule can add up to 6 macroradical chains [10] forming a point of a three-dimensional tribopolymeric network. At the same time, in the absence of C_{60} analogous network points are formed in the course of multiple bond scission, chain transfer, and recombination of several radicals in a small volume, which requires considerably longer time.

It is known that, at elevated temperatures and pressures, C_{60} can from polymeric chains [11, 12]. The shear deformation activates various chemical processes in the region of mechanical contact [13], which suggests that it would promote polymerization of fullerene C_{60} at lower temperatures and pressures. Oil components can act as agents promoting formation of polyfullerenes. Let us analyze this mechanism for the example of naphthene molecules (molecular weight 140). In the course of friction, this molecule can degrade (energy of the C–C bond 260–270 kJ mol^{-1}), e.g., according to the following scheme:

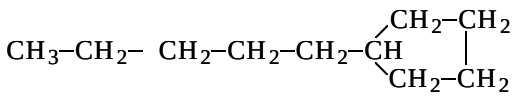

The resulting two radicals can react with a fullerene molecule by the following reactions with low activation energy (≈12–20 kJ mol^{-1}):

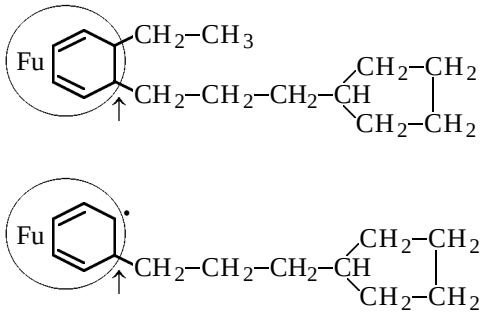

or

The β-bond denoted by an arrow has a dissociation energy 40 kJ mol^{-1} lower than that in the ordinary C–C bond and thus it can be broken at lower temperature and smaller mechanical impact. The scission of β-bonds results in the formation and accumulation of fullerene C_{60} radicals. Two such radicals can recombine [14] (with nearly zero activation energy) to form a dimer:

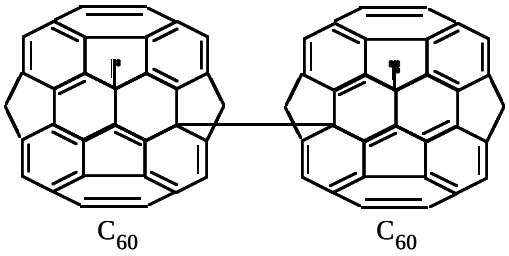

Formation of oligomeric or polymeric fullerene chains and also of two- or three-dimensional fullerene or fullerene-polymeric networks can be described similarly. The capability of C_{60} molecules to react with several macroradical chains obviously ensures accelerated self-restoration of the polymeric tribofilm damaged in the course of mechanochemical degradation. It should be noted that friction can change the density of points in the network and its mechanical and adhesion properties. Since friction treatment proceeds in air, oxygen must play a significant role in tribopolymerization. According to thermogravimetry, thermal oxidation of C_{60} proceeds at the highest rate at 400–600°C [15]. Oxygen reacts with fullerene at lower temperatures, and with the fullerene radical at the same temperature as in the case of the organic radical. For example, the reaction of alkyl radicals with oxygen at 20°C proceeds with nearly zero activation energy [16]:

$$R^{\bullet} + O_2 \rightarrow ROO^{\bullet} \begin{cases} + H \rightarrow ROOH \rightarrow RO^{\bullet} + {}^{\bullet}OH \\ + R_1 \rightarrow ROOR_1 \rightarrow 2RO^{\bullet} \end{cases}$$

$$R^{\bullet} + C_{60} \rightarrow RC_{60}^{\bullet} \begin{cases} + RO^{\bullet} \rightarrow RC_{60}OR \\ + O_2 \rightarrow RC_{60}OO^{\bullet} \begin{cases} + H \rightarrow RC_{60}OOH \\ + R \rightarrow RC_{60}OOR \end{cases} \end{cases}$$

etc.

The tribofilm obviously contains some oxygen. However, due to high reactivity of oxygen with respect to fullerene, the thermal-oxidation stability of the tribopolymeric film increases owing to extra-chain inhibition of the oxidation of the hydrocarbon film [17], which prolongs its operation life. Thus, the presence of C_{60} in the lubricating oil significantly affects the mechanism of chemical processes occurring under the conditions of tribopolymerization and thus changes the mechanical properties of the tribofilm.

Microhardness data. In the analysis of changes in the microhardness of the friction surface of a copper foil, we should note two main factors (Fig. 6). First, the microhardness of the surface layer after friction treatment in the presence of C_{60} is significantly higher (curve *3*) as compared to the initial sample or to the foil after its treatment with straight lubricating oil (curve *2*). Second, after the friction treatment in the presence of C_{60}, the dependence of the microhardness on the load (i.e., in the course of indentor penetration into the material bulk) is descending, showing that the surface layer is harder than the bulk of the material.

It is known that, at elevated temperatures and pressures and/or under the conditions of shear deformation, fullerene can yield several compounds with high hardness: diamond, amorphous carbon (amorphous diamond), and various polyfullerenes with two- and three-dimensional networks. Fragments of the above compounds are probably formed on the friction surface, which, in combination with tribopolymers bound with fullerenes and its modifications, causes its elevated hardness.

CONCLUSIONS

At boundary sliding friction of a steel roller over a copper rider in the presence of small additives of fullerene C_{60} in the lubricating oil, a film (≤1000 Å thick) is formed on the copper foil surface, which exhibits antiwear properties, enhances the bearing strength of the tribotechnical unit, and stabilizes its operation at fairly low friction coefficient. The data of physical and physicochemical methods suggest that this film is a fullerene-polymer network, which is formed by fullerene C_{60} and fragments of the hydrocarbon chains of the oil released during mechanochemical degradation.

REFERENCES

1. Bhushan, B., Gupta, B.K., Van Cleef, G.W., *et al.*, *Tribol. Trans.*, 1993, vol. 36, no. 4, pp. 573–580.
2. Gupta, B.K. and Bhushan, B., *Lubr. Eng.*, 1994, vol. 50, no. 7, pp. 524–528.
3. Ginzburg, B.M., Kozyrev, Yu.P., Kireenko, O.F., and Tochil'nikov, D.G., in *Elektrodiagnostika: Sbornik trudov 1-oi Mezhdunarodnoi konferentsii "Elektrodiagnostika"* (Electrodiagnosis: Collection of Works of the 1st Int. Conf. on Electrodiagnostics), vol. 3: *Tribologiya* (Tribology), Moscow, September, 1995, pp. 173–194.
4. Ginzburg, B.M., Tochil'nikov, D.G., Kireenko, O.F., and Bulatov, V.P., *Pis'ma Zh. Tekh. Fiz.*, 1995, vol. 21, no. 22, pp. 62–66.
5. Ginzburg, B.M., Kireenko, O.F., Tochil'nikov, D.G., and Bulatov, V.P., *Pis'ma Zh. Tekh. Fiz.*, 1995, vol. 21, no. 23, pp. 38–42.
6. Ginzburg, B.M., Tochil'nikov, D.G., and Bulatov, V.P., *Trenie Iznos*, 1997, vol. 18, no. 2, pp. 235–239.
7. Shepelevskii, A.A., Shibaev, L.A., Ginzburg, B.M., and Bulatov, V.P., *Zh. Prikl. Khim.*, 1999, vol. 72, no. 7, pp. 1198–1203.
8. Shibaev, L.A., Antonova, T.A., Vinogradova, L.V., *et al.*, *Zh. Prikl. Khim.*, 1998, vol. 71, no. 5, pp. 835–841.
9. Kireenko, O.F., *Trenie Iznos*, 1993, vol. 14, no. 1, pp. 85–97.
10. Hirsch, A., *Topics in Current Chemistry*, vol. 199: *Fullerenes and Related Structures*, Hirsch, A., Ed., Berlin: Springer, 1998, pp. 1–65.
11. Marques, L., Hodeau, J.-L., Nunnez-Regueiro, M., and Perroux, M., *Phys. Rev. B*, 1996, vol. 54, no. 18, pp. 12 633–12 636.
12. Isakina, A.P., Lubenets, S.V., Natsik, V.D., *et al.*, *Fiz. Nizk. Temp.*, 1998, vol. 24, no. 12, pp. 1192–1201.
13. Zhorin, V.A., Livshits, L.D., and Enikolopyan, N.S., *Dokl. Akad. Nauk SSSR*, 1981, vol. 258, no. 1, pp. 110–112.
14. Morton, J.R., Preston, K.F., Krusic, P.J., *et al.*, *J. Am. Chem. Soc.*, 1992, vol. 114, no. 13, pp. 5454–5455.
15. Ginzburg, B.M., Shibaev, L.A., and Ugolkov, V.L., *Zh. Prikl. Khim.*, 2001, vol. 74, no. 8, pp. 1293–1302.
16. Benson, S.W., *Thermochemical Kinetics. Methods for the Estimation of Thermochemical Data and Rate Parameters*, New York: Wiley, 1968.
17. Shibaev, L.A., Ginzburg, B.M., Antonova, T.A., *et al.*, *Vysokomol. Soedin., Ser. A*, 2002, vol. 44, no. 5, pp. 815–823.

Russian Journal of Applied Chemistry, Vol. 75, No. 8, 2002, pp. 1336–1338. Translated from Zhurnal Prikladnoi Khimii, Vol. 75, No. 8, 2002, pp. 1363–1365.
Original Russian Text Copyright © 2002 by Leonovich, Kovrizhnykh, Korneev, Bodoyavlenskaya, Medvedeva.

MACROMOLECULAR CHEMISTRY AND POLYMERIC MATERIALS

Silicon Dioxide Sol as a Component of Urea-Formaldehyde Adhesive

A. A. Leonovich, L. P. Kovrizhnykh, V. I. Korneev, G. A. Bodoyavlenskaya, and I. N. Medvedeva

St. Petersburg State Forestry Engineering Academy, St. Petersburg, Russia

St. Petersburg State Technological Institute, St. Petersburg, Russia

Received February 8, 2002

Abstract—The possibility of combining an inorganic polymer, silicon dioxide sol, with urea-formaldehyde resins, was studied with the aim to prepare a binding agent for producing nontoxic chip boards. The kinetic characteristics of formaldehyde binding with silicon dioxide during complex binder curing were determined.

Urea-formaldehyde (UF) resins are widely used in chip board production. At present, the application of chip boards is, however, limited by the rather high emission of formaldehyde CH_2O. Formaldehyde can be bound with sorbents compatible with UF polymer, in particular, with silicon dioxide SiO_2 sol having large specific surface area [1]. As shown in [2], SiO_2 sol can be used as part of urea-formaldehyde binder (UF adhesive) in production of chip boards widely applied in furniture production, interior finishing, and construction. Stringent requirements imposed on the free formaldehyde content in chip boards make reasonable introducing SiO_2 sol into the UF adhesive formulation as a sorbent. For example, CH_2O emission from class E1 chip board should not exceed 10 mg per 100 g of the chip board.

The approach we took to preparing nontoxic efficient adhesive based on UF resin and SiO_2 sol is underlain by the physicochemical properties of silicon-containing compounds and the specific features of interaction of polymeric silicon dioxide with other polymers. We had to take advantage of combining the two mutually complementing components of the adhesive in chip board production.

Our study was concerned with 65% aqueous UF oligomer (UF resin) and SiO_2 sol. Sol characterization: $SiO_{2\,total}$ 21.02, Na_2O 0.51, and α-SiO_2 (relative to $SiO_{2\,total}$) 0.305 wt %; specific surface area 256 $m^2\,g^{-1}$; and particle diameter 10.7 nm.

It is found that, in the course of cross-linking, SiO_2 sorbs and strongly retains up to 15 wt % CH_2O. Therefore, the sorbing power of the sol can be utilized in absorption of CH_2O evolving during UF oligomer curing. The sorption of CH_2O was studied with a combined adhesive containing 85% UF resin and 15 wt % sol (in terms of dry substance). The UF resin containing no sol served as reference. The UF resin was cured in the presence of a catalyst and free CH_2O contained in the resin [3]. We monitored variation of the CH_2O content in the cured adhesive during its heat treatment simulating the hot pressing of boards. The rate constants for various stages of the CH_2O binding were determined using the formal-kinetics method.

The plot showing how the temperature in the reaction mixture varies in the course of curing of the UF resin–sol system, combined with the independently obtained plot showing how the CH_2O content varies in the course of curing under identical conditions revealed three stages corresponding primarily to the following processes: (a) reaction of the CH_2O contained in the resin and yielded by condensation of hyrdoxymethyl groups, as well as by breakdown of methylene ether bonds, with unsubstituted hydrogen atoms in amino groups of the oligomer; (b) sorption of CH_2O with SiO_2 sol during gelation; and (c) reaction between the residual CH_2O in the system and unsubstituted hydrogen atoms in amino groups of the polymer.

Table 1 presents the temperature ranges of the processes studied. These data are supplemented with the results of thermogravimetric (TG) and differential thermal (DTA) analyses, which also evidenced three stages of the process in the temperature ranges in-

1070-4272/02/7508-1336 $27.00 © 2002 MAIK "Nauka/Interperiodica"

Table 1. CH_2O binding in the course of curing of the adhesive as divided into individual stages

Curing stage	Stage characterization		Bound CH_2O, wt %	k,* $dm^3\ mol^{-1}\ s^{-1}$
	τ, s	T, °C		
UF resin curing (a)	50–84	87–92	0.15	0.15
Sol gelation (b)	84–113	92–95	0.10	0.55
Final curing of UF resin	113–130	95–97	0.05	1.11
Initial UF resin (reference)	50–90	82–98	0.21	0.23

* (k) Rate constant of the CH_2O binding reaction.

Table 2. Physicochemical properties of UF adhesive

Parameter	Parameter value at indicated SiO_2 sol content in adhesive, wt %			
	0	10	15	20
pH of binder:				
initial	7.1	8.2	8.2	8.5
cured*	3.6	3.8	3.9	4.0
Gelation time at 100°C, s	74	95	110	160
Free CH_2O in cured adhesive,* %	0.05	0.03	0.02	0.03
Water-soluble substances in cured adhesive, %	16.6	16.0	13.1	15.2

* Curing temperature 100°C, curing time 5 min.

dicated. This allowed quantitative estimation of the contribution from SiO_2 sol to CH_2O binding in the course of curing: 30% of free CH_2O occurring in the system is sorbed by the sol.

The degree of formaldehyde binding in the course of curing of the initial resin was estimated at 0.21 wt %, and that in the course of curing of the combined binder, at 0.30 wt %, of which almost one-third of free CH_2O (0.10 wt %) is bound with the sol.

Taken together, these data allowed the rate constants for various stages of CH_2O binding and the contribution from the SiO_2 sol to the CH_2O binding reaction in the course of curing to be estimated by the formal-kinetics method. The rate of the CH_2O binding reaction for the sol significantly differs from that for the reference resin: 0.55 against 0.23 $dm^3\ mol^{-1}\ s^{-1}$.

Our results (Table 2) show that the SiO_2 sol in the cured adhesive tends to decrease the content of free CH_2O and of the water-soluble substances characterizing the degree of curing of the UF oligomer. The minimal effect corresponds to 15% SiO_2 sol; at this concentration the gelation time slightly increases, evidently, due to the system dilution with water making about 78.5 wt % of the sol.

The amount of free CH_2O contained in the combined adhesive is reduced by its sorption by colloidal SiO_2 particles, which significantly reduces the CH_2O emission as estimated under standard condition by the Brunner method [4], namely, 1.0 against 3.0 μg g^{-1} in the reference UF resin. This also reduces the CH_2O emission from chip boards based on the cured adhesive to 6–8 mg per 100 g of board against 15–20 for the reference sample.

The SiO_2 sol improves the glueing power of the adhesive under comparable conditions (Table 3). Pre-

Table 3. Influence of SiO_2 sol on the shear strength of adhesive joints, σ_{shear}, of the initial wood and that pretreated with sol

Sol in adhesive, wt %	σ_{shear} (MPa) at indicated glueing temperature, °C			
	105		160	
	initial	treated with sol	initial	treated with sol
10	5.0	5.3	5.7	7.5
15	6.1	6.4	5.9	9.0
20	6.9	7.3	7.1	9.1
25	6.7	6.9	8.5	8.8
30	6.1	6.5	9.0	8.0
No sol (reference)	4.6	6.0	5.3	6.4

treatment of the wood surface with SiO_2 sol, followed by glueing of the treated surfaces with UF resin, additionally increases the adhesive strength. The data in Table 3 refer to 0.5 g m^2 of the sol spent, which must afford a monolayer of SiO_2 particles coating the wood sample. This is due to the fact that the formation of siloxane bonds between the colloidal SiO_2 particles of the combined adhesive involves the SiO_2 particles occurring on the wood surface, which, in turn, participate in hydrogen bonding with hydroxy groups of the wood components.

The enhanced strength of the adhesive joint with the combined adhesive is also due to increased cohesion strength of the adhesive proper. This is evidenced by the rupture tests with model samples of filter paper as adhesive carrier, whose intrinsic strength is 8 MPa. After curing at 105°C, the strength of the samples of the filter paper impregnated with sol-containing UF adhesive increased, compared to the samples impregnated with UF resin, from 34.1 to 44.0 MPa. This evidences the cross-linking effect of the SiO_2 sol on the UF oligomer. It can be assumed that simultaneous curing of UF resin and SiO_2 sol yields a composite with a different, stronger supramolecular structure with interpenetrating networks [5].

Thus, we substantiated the beneficial effect of the SiO_2 sol on the properties of UF adhesive and its suitability for producing wood boards characterized by the class E1 formaldehyde emission.

EXPERIMENTAL

We studied colloidal silicon dioxide (SiO_2 sol) available from the Cherepovets Metallurgy Combine (TI 105-ST.PS–0.1.89) and UF resin of the KF-MT-15 [GOST (State Standard) 14231–86] brand.

The total content of $(SiO_2)_n$ in the sol was estimated spectrophotometrically, and the Na_2O content, by titration with 0.1 M HCl solution [6]. The fraction of monomeric α-SiO_2 was estimated from the reaction with molybdic acid. The average particle size for $(SiO_2)_n$ was calculated from the specific surface area of the sol, which was estimated by the Sears method [6].

The UF resin was analyzed by the procedure from [7]. The amount of the CH_2O bound with the sol was determined after keeping the sol in 10% Formalin at 100°C for 2 h, as the difference between the initial and final CH_2O concentrations (estimated by potentiometric titration with hydroxylamine).

The CH_2O biding kinetics in curing of UF adhesive with and without sol were monitored by the CH_2O content in the samples taken in curing the adhesive at 100°C with 10-min intervals. The glueing power of the adhesive was estimated from the ultimate shear strength of adhesive joints for birch samples; the amount of the adhesive spent was 25 g m^{-2}.

Thermal analysis was carried out on an MOM derivatograph (Hungary).

CONCLUSIONS

(1) Inorganic polymer, silicon dioxide sol, can be combined with urea-formaldehyde resins with the aim to produce nontoxic boards (medium-density chip and wood-fiber boards). The silicon dioxide sol converts to gel and thus can bind the formaldehyde contained in the resin and evolving in the course of curing.

(2) The kinetic characteristics of the formaldehyde binding in the course of curing of the combined adhesive were determined. The rate constant of formaldehyde sorption by silicon dioxide sol was estimated at 0.55 dm^3 mol^{-1} s^{-1}.

(3) Silicon dioxide sol significantly improves the glueing power of the adhesive, compared to the reference, urea-formaldehyde resin, especially when the wood sufrace being glued is additionally treated with the sol.

REFERENCES

1. Korneev, V.I. and Danilov, V.V., *Zhidkoe i rastvorimoe steklo* (Water Glass), St. Petersburg: Stroiizdat, 1996.
2. RF Patent 2 132 272.
3. Williams, L.L., Updegraff, I.H., and Petropoulos, G.G., *Appl. Polym. Sci.*, 1985, no. 6(65), pp. 1101–1115.
4. Roffael, E., *Die Formaldehyd Abgabe von Spanplatten und anderen Werkstoffen*, Stuttgart: Enke, 1982.
5. Leonovich, A.A, Kovrizhnykh, L.P., and Nikol'skii, S.A., in *Problemy khimicheskoi pererabotki drevesnogo syr'ya: Sbornik trudov Sankt-Peterburgskoi lesotekhnicheskoi akademii* (Problems of Wood Raw Material Processing: Coll. of Works of the St. Petersburg Forest Engineering Academy), St. Petersburg, 2000, pp. 108–114.
6. Iler, R.K., *The Chemistry of Silica*, New York: Wiley-Interscience, 1979.
7. Kalinina, L.S., Motorina, M.A., Nikitina, N.I., and Khachapuridze, N., *Analiz kondensatsionnykh polimerov* (Analysis of Condensation Polymers), Moscow: Khimiya, 1984.

Russian Journal of Applied Chemistry, Vol. 75, No. 8, 2002, pp. 1339–1344. Translated from Zhurnal Prikladnoi Khimii, Vol. 75, No. 8, 2002, pp. 1366–1370.
Original Russian Text Copyright © 2002 by E. Nefed'ev, Rakhmatullin, Orlinskii, Petrov, S. Nefed'ev, Yagudin.

MACROMOLECULAR CHEMISTRY AND POLYMERIC MATERIALS

The Nature of Copper(II) Complexes in the Transition Layer of Thiokol Sealant–Brass Adhesive Joint

E. S. Nefed'ev, R. M. Rakhmatullin, S. B. Orlinskii, O. V. Petrov, S. E. Nefed'ev, and Sh. G. Yagudin

Kazan State Technological University, Kazan, Tatarstan, Russia
Kazan State University, Kazan, Tatarstan, Russia

Received November 5, 2001; in final form, April 2002

Abstract—Copper(II) complexes formed in the interphase area between Thiokol–epoxy adhesive and brass support were studied using the method of the envelope of modulation of the electron spin echo.

Brass plating is a well-known and widely used method of strengthening adhesive joints between a metal and a rubber. High strength of rubber–brass adhesive joints is due to the interaction of macromolecules with a sulfide (Cu_xS, Zn_xS) film formed at the brass surface owing to chemisorption of sulfur added either as a vulcanizer or as an adhesive additive. The nature of this interaction is not yet fully understood. Some researches assume that the high adhesive strength is mainly caused by chemical bonds formed between rubber and surface sulfides, whereas others assume adsorption bonding, facilitated by the high specific surface of the sulfide film [1, 2]. In any case, the necessary component of the rubber stock is sulfur, since without sulfur the adhesion of rubber to the brass surface is poor.

Here we consider one of the factors governing the adhesion strength of such systems, namely, complex formation at the interface of brass and sealant based on polysulfide oligomer (liquid Thiokol). Previous studies have shown that, in contact of Thiokol sealant with the brass surface, paramagnetic copper(II) complexes are formed, and their concentration varies in parallel with the content of free sulfur added as an adhesive additive to the mixture [3, 4]. It has been suggested [3] that the ligands are organic and are coordinated via sulfur atom.

A more detailed study of the forming copper complexes is required in view of the established relationship between their concentration and the adhesion (Fig. 1). Additional data on the structure of ligands would give a possibility of directed control over adhesion characteristics of a sealant by varying its formula. In addition, these data are useful for development of theoretical concepts of the adhesion mechanism.

EXPERIMENTAL

The sealant composition was based on liquid Thiokol of the LP-977 brand (100 wt parts)

$$\begin{array}{l} CH_2{-}R_n{-}SH \\ | \\ CH{-}R_m{-}SH \\ | \\ CH_2{-}R_k{-}SH \end{array}$$

where $k + n + m = 12–14$ and R is $SSC_2H_4OCH_2OC_2H_4–$, and epoxy resin of E-40 brand (20 wt parts).

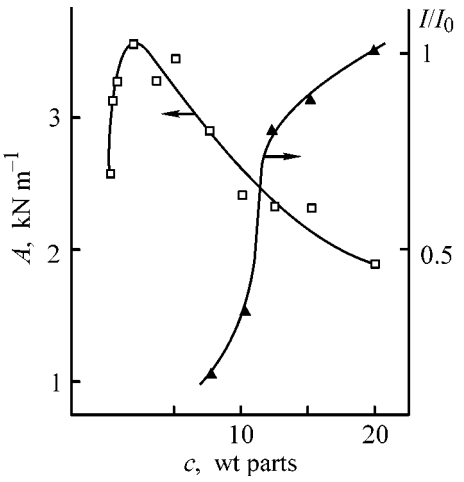

Fig. 1. Adhesion A and relative intensity I/I_0 of the ESR signal vs. sulfur content c.

1070-4272/02/7508-1339 $27.00 © 2002 MAIK "Nauka/Interperiodica"

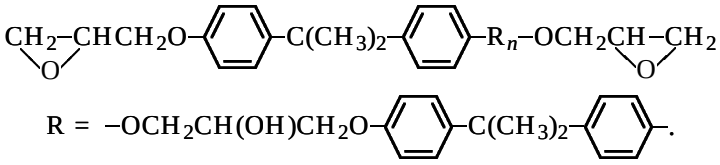

The copolymerization was initiated with a mixture of 2- and 2,6-dimethylaminomethylphenol (phenol Mannich bases, MB-1 and MB-2, respectively; 1.5 wt parts):

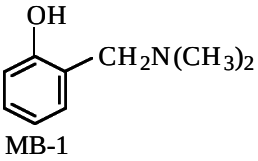

MB-1

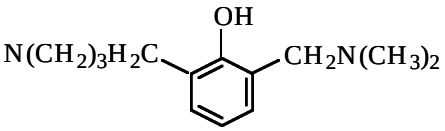

MB-2

The mechanism of copolymerization of Thiokol and epoxy resin in the presence of MB has been discussed previously [5]. Polymeric sulfur S_8 (α-form) in the amount of 0 to 30 wt parts was used as an adhesive additive. Brass plates with relative copper content of 52.6% were used as supports. A mixture applied to the support was cured for 24 h under heating with hot air (80°C) [GOST (State Standard) 12.812–80)].

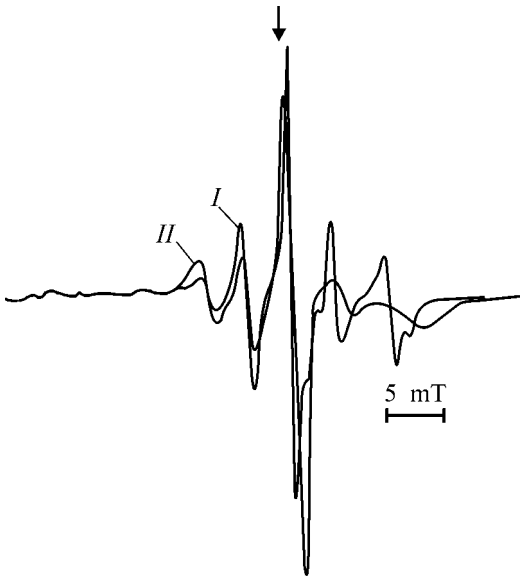

Fig. 2. (*I*) ESR spectrum of the copper complex in a sample containing 20 wt parts of sulfur. The arrow indicates the component excited in the experiments with ESE. (*II*) Spectrum of copper(II) dibutyldithiocarbamate $Cu(Budtc)_2$ in $Zn(Budtc)_2$.

ESR measurements were performed with thin sealant layers (<0.5 mm) cut close to the brass surface. The ESR spectra were recorded on a Bruker ESP 300E spectrometer at room temperature. The experiments on electron spin echo (ESE) were carried out on a Bruker ESP 380 spectrometer at 18 K, using the two-pulse technique (primary ESE) [5].

The ESR spectrum of the sample is shown in Fig. 2 (spectrum *I*). The sample was a thin layer of the sealant in direct contact with the brass surface. The sealant bulk gave no ESR signal. The spin Hamiltonian

$$h = g_{\|}\beta H_z S_z + g_{\perp}\beta(H_x S_x + H_y S_y) + A_{\|} I_z S_z + A_{\perp}(I_x S_x + I_y S_y),$$

corresponding to this spectrum has the following parameters: spin $S = 1/2$; nuclear spin $I = 3/2$ (copper); components of the hyperfine coupling (HFC) tensor $|A_{\|}| = 15.67$ mT, $|A_{\perp}| = 3.77$ mT, $|a| = (|A_{\|}| + 2|A_{\perp}|)/3 = 7.74$ mT; components of the *g*-factor tensor: $|g_{\|}| = 2.086$, $|g_{\perp}| = 2.027$, $g = (|g_{\|}| + 2|g_{\perp}|)/3 = 2.047$.

The coordination of the complex is difficult to elucidate from this spectrum, since broad components of the ESR lines bear little information on ligands. To identify the complex, we recorded the ESR spectra of copper(II) dibutyldithiocarbamate $Cu(Budtc)_2$, a paramagnetic chelate of the following structure

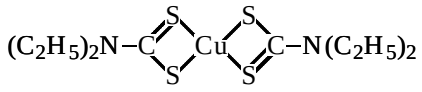

In ether solution, $Cu(Budtc)_2$ gives a spectrum consisting of four lines due to isotropic HFC of unpaired electron with the copper nucleus ($I = 3/2$) with the parameters $|a| = 8.43$ mT and $|g| = 2.046$, which are close to the parameters of the complex in hand. In addition, according to published data [7], the components of the anisotropic HFC tensor for copper(II) thiocarbamates meet the conditions $T_{\|} < 0$ and $T_{\perp} < 0$, which is also in good agreement with the parameters of our complex at appropriate choice of signs of the HFC tensor components ($A_{\|} < 0$, $A_{\perp} > 0$). In a diamagnetic matrix [with addition of diamagnetic $Zn(Budtc)_2$ with subsequent removal of the solvent], $Cu(Budtc)_2$ gives the spectrum practically identical to the spectrum of our complex (Fig. 2, spectrum *II*).

The identity of the spectra and especially the correspondence of their magnetic resonance parameters suggest that the nearest environment of the copper ion consists of four sulfur atoms with the square planar geometry. In terms of the valence bond theory, this configuration is formed when hydridized dsp^2 orbitals of the copper(II) ion overlap with the σ orbitals of the sulfur atom [in the case of $Cu(Budtc)_2$ these are sp^2-hybrids]. Furthermore, there is good reason to believe that, similarly to copper(II) dithiocarbamate, the resulting species is a chelate compound. In particular, this follows from the equality of *g*-factors, whose values are extremely sensitive to the ligand charges.

More detailed data on the environment of copper(II) ion were obtained from analysis of the modulation of ESE envelope, due to HFC of unpaired electron with the magnetic nuclei of ligands [6]. According to [8], the envelope of the initial ESE $\langle V(\tau)\rangle$, averaged over the ensemble of systems containing one electron and one nuclear spin $I = 1/2$, has the form

$$\langle V(\tau)\rangle = 1 - \frac{3T_\perp}{10\nu^2} \times [2 - 4F(T_\perp\tau)\cos(2\pi\nu\tau) + \cos(4\pi\nu\tau) + F(2T_\perp\tau)], \quad (1)$$

$$F(T_\perp\tau) = \frac{15}{4}\int_0^\pi \{\cos^2\theta \sin^2\theta \cos[\pi T_\perp\tau(1-3\cos^2\theta)]\sin\theta\}\, d\theta,$$

where $T_\perp$ is the perpendicular component of the anisotropic HFC tensor; ν is the NMR frequency; τ is the time interval between pulses exciting ESE; θ is the angle between the magnetic field direction and *z* axis in the molecular coordinate system.

It is seen from expression (1) that, in disordered systems, HFC results in oscillation of the ESE envelope at frequencies ν and 2ν.

For quantitative description of modulation of the ESE envelope, we selected the dimensionless parameter

$$\lambda(\tau) = \frac{V_{max}(\tau) - V_{min}(\tau)}{V_{max}(\tau)},$$

where $V_{max}(\tau)$ and $V_{min}(\tau)$ are the extremum values of the ESE envelope.

This parameter is the degree of modulation and can be easily determined from experimental data. For low values of $T_\perp\tau$, expansion of $\lambda(\tau)$ in a series shows a linear dependence of $\lambda(\tau)$ on τ^2 [9]. When an electron interacts with *N* nuclei, the modulation of the ESE signal $V^N(\tau)$ is governed by the product of modulations $V^N(\tau)$ due to HFC with each particular nucleus. In this case, we can write the following equation for the parameter $\lambda(\tau)$:

$$1 - \lambda^{(N)} = \prod_{i=1}^{N}\left[1 - \lambda_i^{(1)}\right],$$

where $\lambda^{(N)}$ and $\lambda^{(1)}$ are the degrees of modulation due to HFC with *N* nuclei and one nucleus, respectively.

When nuclei are nonequivalent and form different coordination spheres containing N_j nuclei each, one can expect that several linear portions would be observed in the experimental dependence of λ on τ^2 according to the number of these coordination spheres. Commonly, nuclei localized in no more than two coordination spheres are distinguished, and more distant nuclei are considered matrix nuclei. By subtracting the contribution of matrix nuclei, as well as the component at the combination frequency 2ν, from the experimental dependence $\lambda(\tau)$, we can determine the dependence $\lambda_j^{(N)}(\tau)$ for neighboring coordination spheres. Then, using the expression obtained from the expansion of $\lambda(\tau^2)$ in terms of $\tau T_\perp$ [9]:

$$\lambda_j^{(1)}(0) = \frac{2\lambda_j'}{2a\nu^2\delta\lambda_j(\ln\delta\lambda_j) + \lambda_j'}, \quad (2)$$

we determine the degree of modulation $\lambda_j^{(1)}$ due to HFC with each nucleus of *j*th individual coordination sphere. In expression (2),

$$\lambda_j' = \frac{d}{d\tau^2}\lambda_j^{(N)}\Big|_{\tau=0}, \quad \delta\lambda = 1 - \lambda_j^{(N)}(0), \quad a = \frac{5\pi^2}{42}.$$

Knowing $\lambda_j^{(1)}$, it is possible to determine the number of nuclei N_j entering into *j*th coordination sphere:

$$N_j = \frac{\ln[1 - \lambda_j^{(N)}(0)]}{\ln[1 - \lambda_j^{(1)}(0)]}, \quad (3)$$

and the transverse component of the anisotropic HFC

$$T_\perp = \sqrt{\frac{5\nu^2\lambda_j^{(1)}(0)}{12}}, \quad (4)$$

which, in turn, allows determination of the distance *r* from the ion to nuclei of the coordination sphere, using approximation for interaction of point dipoles

$$T_\perp = \frac{\mu_0}{4\pi}\frac{g_e g_n \beta_e \beta_n}{r^3 h}, \quad (5)$$

where g_e and g_n are electron and nuclear *g*-factors, β_e is Bohr's magneton, β_n is the nuclear magneton, and *h* is the Planck constant.

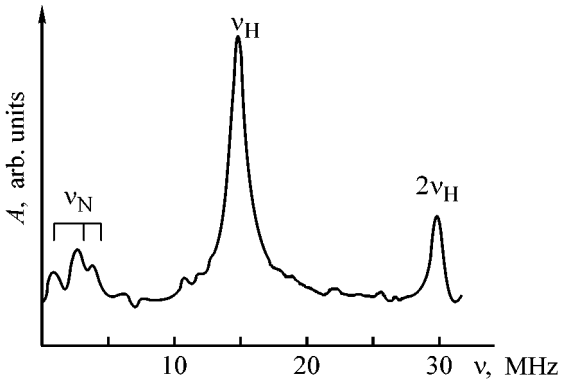

Fig. 3. Fourier image of the ESE envelope $V(\tau)$. (A) Amplitude and (ν) frequency.

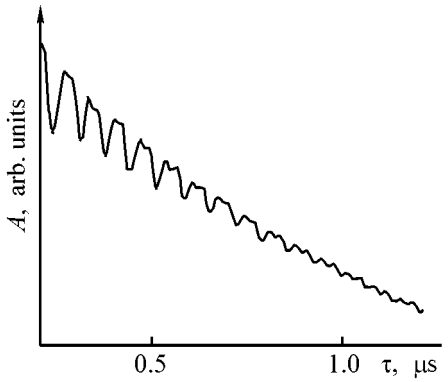

Fig. 4. ESE envelope restored after subtraction of the component at the frequency $2\nu_H$. (A) Amplitude and (τ) time interval between exciting pulses.

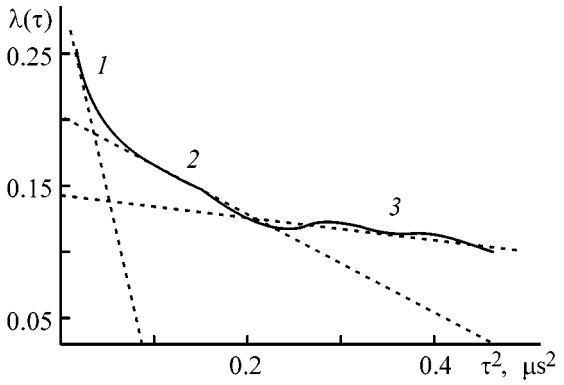

Fig. 5. Degree of modulation $\lambda(\tau)$ vs. τ^2. (τ) Time interval between exciting pulses.

The Fourier image of the envelope of the initial ESE $V(\tau)$, obtained in excitation of the strongest component of the ESR spectrum of the complex (Fig. 2), is shown in Fig. 3. It contains two peaks at the frequencies $\nu_H = 15$ and $2\nu_H = 30$ MHz corresponding to the Zeeman proton frequency and its doubled value, respectively, and three lines in the low-frequency range. After subtraction of the peak at 30 MHz and reverse Fourier transform, the envelope $V(\tau)$ takes the form shown in Fig. 4. The dependence $\lambda(\tau^2)$ found from this envelope (Fig. 5, *solid line*) is a superposition of three contributions, which, based on the preceding, can be referred to HFC with protons of the first and second coordination spheres and matrix (Fig. 5, *dashed lines 1–3*). Using this dependence and formulas (2)–(5), we found $N \approx 2$ and $r \approx 0.3$ nm for the first sphere and $N \approx 4$ and $r \approx 0.4$ nm for the second sphere.

The lines at $\nu_0 = 0.980$, $\nu_- = 2.696$, and $\nu_+ = 3.676$ MHz (Fig. 3) are assigned to ^{14}N nuclei in initiator molecules participating in copolymerization of Thiokol and epoxy resin [7]. With large distance between ^{14}N nucleus and copper ion assumed, the observed frequencies can be assigned to the ^{14}N NQR frequencies.

$$\nu_- = 2K\eta,\ \nu_0 = K(3 - \eta),\ \nu_+ = K(3 + \eta)$$

with the quadrupole coupling constant $K \approx 1.06$ MHz and asymmetry parameter $\eta \approx 0.461$.

The results obtained prove that the ligands in the complex are organic; apparently, these are sulfur-containing fragments of macromolecular chains of the Thiokol–epoxy copolymer. Formation of these complexes can be regarded as including three successive stages: (1) breakdown of the crystal lattice of brass, (2) successive ionization of copper atoms, and (3) coordination of copper ion with ligands incorporated in the polymer matrix. Extraction of copper from iodide and copper-chloride aqueous solutions with organic sulfides and sulfoxides is a classic example demonstrating this scheme [10]. For this process to occur, the matrix should contain, firstly, components acting as acceptor of electrons released in ionization of metal (oxidizing agent), and, secondly, ligands capable of formation of strong coordination bonds. Apparently, disulfide fragments in the main chain of Thiokol can serve as such ligands. These fragments are more reactive with respect to copper than sulfides, since the activity of sulfur-containing compounds with respect to copper decreases in the order elemental sulfur > thiols > disulfides > sulfides [11]. It is evident that free sulfur used as adhesive additive acts in this case as oxidizing agent withdrawing electrons from the metal, which is required for metal–ligand coordination bonding. This can be represented as the scheme

$$xCu + S \rightarrow Cu_xS,$$

$$Cu_xS + S \rightarrow 2Cu_{x/2}S,$$

$$Cu_2S + S \rightarrow 2CuS,$$

$$CuS + 4L \rightarrow [CuL_4] + S,$$

where 2L is RSSR'.

It is assumed that, with increasing concentration of sulfur in the interphase layer, the formal oxidation state of copper grows to +1 or even +2 at a fairly high amount of sulfur. This is quite possible, since, as shown previously [12], the appreciable chemisorption effect of sulfur at the brass surface must result in enrichment of the surface layer of brass with sulfur. The final stage of the reaction in this scheme is coordination of Cu^{2+} ions with sulfur-containing fragments of Thiokol molecules as a result of nucleophilic cleavage of disulfide bonds –S–S– in Thiokol under the action of forming sulfides [13, 14].

The proposed mechanism of formation of copper(II) organic complexes explains adequately the dependence of the intensity of the ESR signal of complexes on the sulfur content, presented in Fig. 1. Addition of more than 5 wt parts of sulfur results in an abrupt increase in the content of paramagnetic copper (II) complexes owing to the formation of the required amount of CuS. At the same time, an excess of CuS (and ZnS) not bound to metallic support must exert a negative effect on the adhesion strength (Fig. 1).

Thus, we believe that the complexes under consideration serve as a peculiar indicator of formation of copper(II) sulfides and do not apparently play any significant role in the formation of the adhesion bond proper, which, as in the case of natural rubber, is governed predominantly by adsorption of macromolecules on the sulfide film having a large specific surface area. However, it is evident that the presence of such metals as copper or zinc, in the form of complex ions or inorganic sulfides, in transition layers of an adhesive joint significantly affects the course of chemical reactions governing the structure and physicochemical characteristics of transition layers. In this relation, mention should be made of a paper [15] concerning Thiokol sealant filled with carbon black. In that work, the concentration of carbon free radicals on the filler surface was found as a function of the distance from the brass support. It was assumed that their decreased concentration directly at the brass surface is due to the presence of copper and zinc cations promoting binding of Thiokol with the filler surface, which results in strengthening of the transition layer and contributes to the adhesion.

CONCLUSION

With respect to magnetic resonance parameters, the copper(II) complex under consideration is similar to copper(II) dibutyldithiocarbamate, with the nearest environment consisting of four sulfur atoms. The presence of protons in the coordination sphere suggests that the ligands are organic, namely, sulfur-containing fragments of Thiokol. Based on the dependence of the intensity of the ESR signal on the concentration of elementary sulfur and also on the correlation of the concentration with the adhesion; a mechanism of formation of the complexes was proposed. This mechanism includes three stages: chemisorption of elemental sulfur at brass surface with the formation of surface copper sulfides, successive ionization of copper atoms, and their coordination with sulfur-containing fragments of Thiokol. The potentialities of electron spin echo as a method for studying these systems were demonstrated.

REFERENCES

1. Van Ooij, W.J., *Proc. Int. Rubber Conf., IRC'96*, Kobo, 1996, pp. 107–110.
2. Rongu, J., Vanlan, J., Vingkuan, S., *et al.*, Abstracts of Papers, *Int. Conf. on Caoutchouc and Rubber, IRC'94*, Moscow: Naucho-Issled. Inst. Shinnoi Prom–sti, vol. 3, pp. 352–361.
3. Nefed'ev, E.S., Mirakova, T.Yu., Averco-Antonovich, L.A., *et al., J. Adhesion Sci. Technol.*, 1991, no. 5, pp. 691–694.
4. Nefed'ev, E.S., Silaev, V.A., Mirakova, T.Yu., *et al., Polymer*, 1992, vol. 33, pp. 3911–3915.
5. Nefed'ev, E.S., Zyablikova, T.A., Silaev, V.A., *et al., Khim. Fiz.*, 1992, vol. 11, no. 10, pp. 1371–1374.
6. Salikhov, K.M., Semenova, A.G., and Tsvetkov, Yu.D., *Elektronnoe spinovoe ekho i ego primenenie* (Electron Spin Echo and Its Application), Moscow: Nauka, 1976.
7. Kivelson, D. and Neiman, R., *J. Chem. Phys.*, 1961, vol. 35, pp. 149–154.
8. Diakonov, S.A., and Tsvetkov, Yu.D., *Electron Spin Echo Envelope Modulation (ESEEM) Spectroscopy*, Boca Raton, Florida: CRC, 1992.
9. Astashkin, A.V. and Tsvetkov, Yu.D., *Appl. Magn. Reson.*, 1994, no. 6, p. 411.

10. Chekushin, V.S. and Borbat, V.F., *Ekstraktsiya blagorodnykh metallov sul'fidami i sulfoksidami* (Extraction of Noble Metals with Sulfides and Sulfoxides), Moscow: Khimiya, 1984.
11. Ando, W., Sugimoto, K., and Oae, S., *Bull. Chem. Soc. Jpn*, 1963, vol. 36, no. 4, pp. 477–479.
12. Nefed'ev, E.S., Structure, Characteristics, and Mechanism of Formation of Thiokol–Epoxy Polymers from the Evidence of Magnetic Spectroscopy, *Doctoral Dissertation*, Kazan, 1991.
13. Averko-Antonovich, L.A., Kirpichnikov, P.A., and Smyslova, R.A., *Polisul'fidnye oligomery i germetiki na ikh osnove* (Polysulfide Oligomers and Sealants Based on Them), Leningrad: Khimiya, 1983.
14. Oae, S., *Khimiya organicheskikh soedinenii sery* (Chemistry of Sulfur-Containing Organic Compounds), Moscow: Khimiya, 1975.
15. Nefed'ev, E.S., Musin, K.M., Mirakova, T.Yu., *et al.*, *Appl. Magn. Res.*, 1996, no. 11, pp. 115–123.

Russian Journal of Applied Chemistry, Vol. 75, No. 8, 2002, pp. 1345–1348. Translated from Zhurnal Prikladnoi Khimii, Vol. 75, No. 8, 2002, pp. 1371–1374.
Original Russian Text Copyright © 2002 by Gladun, Gagarin.

CHEMISTRY OF FOSSIL FUEL

IR-Spectroscopic Determination of the Maceral Composition of Coal

T. G. Gladun and S. G. Gagarin

Institute of Fossil Fuels, Moscow, Russia

Received March 28, 2002

Abstract—The maceral composition of coal was determined from the IR spectra by factor analysis. Simulated spectra were obtained.

The mathematical and statistical method of factor analysis is successfully used in computer processing of the IR spectra of polymer substances [1]. It operates with eigenvalues and eigenvectors of matrices of the coefficients of correlation between the intensities of spectra of various polymer samples. For example, Kim *et al.* [2] applied this method to estimating the amounts of the crystalline and amorphous phases in vinylidene fluoride and trifluoroethylene. We used this method for estimating the quality of chitin-based biopolymer sorbents [3].

In this study, we analyzed the suitability of factor analysis for estimating the amounts of the main groups of macerals (high-molecular-weight organic microcomponents) in fossil coals on the basis of IR spectra of coal samples with varied maceral (petrographic) composition. This was paralelled by simulating the model spectra of selected groups of macerals. This allows subsequent decomposition of the IR spectra of new coal samples, aimed at determining their maceral composition. Our study was concerned with low-metamorphized long-flame coal from Vesta site (Canada), which was characterized in [4, 5].

EXPERIMENTAL

Photoacoustic IR spectra of nine coal fractions of varied density were recorded without fillers at the Coal Research Centre, Devon, on a Bruker IFS 88 FTIR spectrophotometer in the 4000–400 cm^{-1} range (MTEC-200 PA cell, resolution 2 cm^{-1}). For each sample we performed two runs with 100 scannings each. The primary processing of the spectra, carried out on an interfaced PC, involved averaging of the scans, making corrections for the dependence of the intensity on the excitation frequency, and accounting for the background and electronic light absorption [6].

Coal fractions of varied density were isolated both manually and by flotation and density gradient methods. This allowed the maceral composition to be widely varied within 0–76, 5–98, and 0–95% ranges for the major groups, liptinite (L), vitrinite (Vt), and inertinite (I), respectively (Table 1). The reliability of the calculation procedure was assessed using the available petrographic characteristics.

As known [7], the content of hydrogen decreases steadily and the degree of aromaticity of the macromolecules of the organic matter increases in the maceral group order L, Vt, I. Therefore, the IR spectra of

Table 1. Density and maceral composition of coal fractions

Fraction no.*	Density d, g cm^{-3}	Composition, %					
		experiment			calculation		
		L	Vt	I	L	Vt	I
1	1.19	76	24	0	73.9	25.7	0.4
2	1.26	57	40	3	59.8	37.6	2.6
3	1.31	1	95	4	0.6	94.2	5.2
4	1.33	4	91	5	4.6	89.5	5.9
5	1.35	0	98	2	0	96.4	3.6
6	1.36	0	36	64	0	38.4	61.6
7	1.41	1	77	22	0.8	78.8	20.4
8	1.66	2	48	50	2.5	50.9	46.6
9	1.71	0	5	95	0	1.5	98.5

* Fraction nos. 1, 5, and 9 were taken manually; fraction nos. 4, 7, and 8, by flotation; and fraction nos. 2, 3, and 6, by the density gradient method.

1070-4272/02/7508-1345 $27.00 © 2002 MAIK "Nauka/Interperiodica"

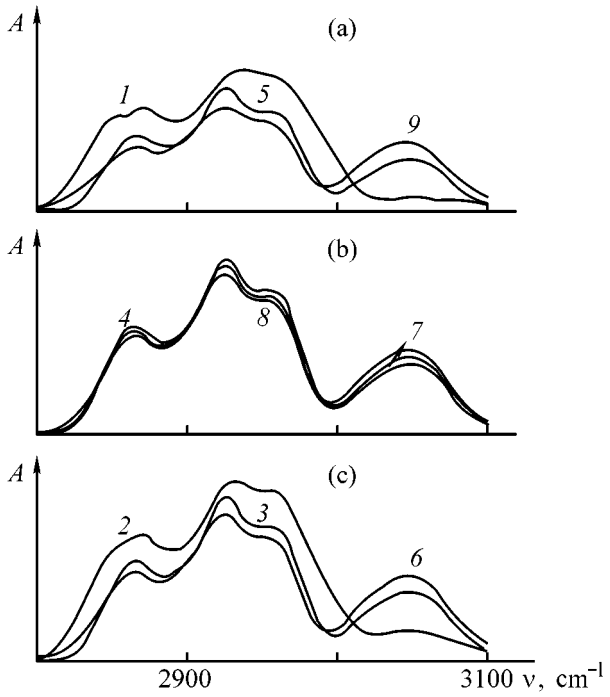

Fig. 1. IR spectra of the coal fractions isolated (a) manually, (b) by flotation, and (c) by the density gradient method. (*A*) Absorption intensity and (ν) wave number; the same for Figs. 2 and 3. Figures at curves correspond to fraction nos. in Table 1.

the maceral groups differ to the greatest extent in the 2800–3100 cm^{-1} region corresponding to the stretching vibrations of the C–H bonds in the aliphatic and naphthene moieties of the organic matter of coal (with the contribution from the stretching vibrations of hydroxy groups subtracted [5, 8]). Therefore, this region was chosen for subsequent computer analysis. The corresponding IR spectra of the nine fractions are shown in Fig. 1.

When represented in the point-by-point manner (with a step $\Delta\nu = 2$ cm^{-1}), the spectra are described by the matrix $A(i, j)$; $i = 1, ..., m$; $j = 1, ..., n$; where $m = 9$ and $n = 151$. When factor analysis is used, these data are utilized for constructing a symmetric quadratic matrix of the correlation coefficients R (with the dimensionality $m \times m$) between the spectra of individual coal fractions. The matrix R is presented in Table 2 (here and hereinafter, the values obtained by computer processing are rounded). Naturally, the largest correlation coefficients are typical of the spectra of the fractions with close petrographic compositions (e.g., sample nos. 3 and 5), and the smallest, of the spectra of the fractions significantly differing in the maceral content (e.g., sample nos. 1 and 9).

Similar to [3], the eigenvalues λ and eigenvectors **V** of the matrix of the correlation coefficients governing the structure of the integrated factors were calculated by the Jacobi method. The parameters λ and the variances corresponding to these factors are presented in Table 3. This table also contains the Fisher *F*-statistics, which, along with total variance, were used for determining the number of the statistically significant factors, and also the components of eigenvectors for factors 1–3. The parameters F are the ratios of the variances corresponding to the given factor, k, to the sum of the variances corresponding to less significant factors $k + 1, ..., m$.

Table 3 shows that factors 1–3 are the key ones, since specifically these factors virtually fully determine the total variance and, unlike other factors, are statistically significant according to the Fisher test F (at significance level $\alpha = 0.01$ [9]). The existence of only three key factors evidences that the IR spectra of coal are determined by three main maceral groups.

In the next stage of data processing, the IR spectra of these maceral groups are constructed, and the maceral composition of each coal fraction is determined. This requires determining the quasi-spectra of the key

Table 2. Matrix of the coefficients of correlation between the IR spectra of coal fractions

Fraction no. (Table 1)	1	2	3	4	5	6	7	8	9
1	1	0.9937	0.8304	0.8462	0.8267	0.7359	0.8096	0.7765	0.6667
2	0.9937	1	0.8874	0.9005	0.8843	0.8063	0.8700	0.8417	0.7440
3	0.8304	0.8874	1	0.9996	0.9999	0.9838	0.9990	0.9932	0.9577
4	0.8462	0.9005	0.9996	1	0.9994	0.9793	0.9975	0.9904	0.9508
5	0.8267	0.8843	0.9999	0.9994	1	0.9844	0.9991	0.9935	0.9586
6	0.7359	0.8063	0.9838	0.9793	0.9844	1	0.9909	0.9979	0.9938
7	0.8096	0.8700	0.9990	0.9975	0.9991	0.9909	1	0.9975	0.9698
8	0.7765	0.8417	0.9932	0.9904	0.9935	0.9979	0.9975	1	0.9845
9	0.6667	0.7440	0.9577	0.9508	0.9586	0.9938	0.9698	0.9845	1

Table 3. Results of factor analysis of the IR spectra of the coal fractions

Factor	λ	Variance, %		*F*	Eigenvector of factors		
		partial	total		1	2	3
1	8.383	93.15	93.15	13.6	0.2961	–0.6644	0.2512
2	0.597	6.63	99.78	30.6	0.3141	–0.5375	0.1507
3	0.019	0.22	100	11000	0.3446	0.0586	–0.3684
4	5×10^{-7}	6×10^{-6}		0.4	0.3450	0.0216	–0.3268
5	3×10^{-7}	3×10^{-6}		0.3	0.3444	0.0665	–0.3967
6	1×10^{-7}	1×10^{-6}		0.1	0.3380	0.2629	0.2391
7	2.5×10^{-9}	3×10^{-9}		<0.01	0.3440	0.1096	–0.2028
8	3×10^{-7}	3×10^{-6}		0.5	0.3419	0.1833	0.0999
9	6×10^{-7}	6×10^{-6}		<0.01	0.3285	0.3229	0.6373

statistical factors ("eigenspectra" of the problem Λ) which can be written in the matrix form as

$$\Lambda^t = A^t(\mathbf{V}^*)^t, \quad (1)$$

here, t is the transposition sign; A is the total spectral matrix; and $\mathbf{V}^*$ is the submatrix of eigenvectors corresponding to factors 1–3.

The matrix dimensionalities in (1) are as follows: Λ^t, $(n \times 3)$; A^t, $(n \times m)$; and $(\mathbf{V}^*)^t$, $(m \times 3)$. Figure 2 presents graphically the eigenspectra. The quasispectra of insignificant factors are at the "noise" level (e.g., that of factor 4 in Fig. 2).

As known [1], factors are certain linear combinations of the sought-for variables, which are in our case, the fractions of the macerals in the coal composition. Therefore, the rows in the matrix Λ can be regarded as linear combinations of the IR spectra of individual macerals. In other words, the sought-for spectra M $(3 \times n)$ are bound to Λ $(3 \times n)$ by the matrix relation

$$M\mathrm{t} = \Lambda^t T, \quad (2)$$

where T (3×3) is the transformation matrix.

The numerical values of the matrix T elements were determined by the iteration algorithm, with the initial approximations chosen according to a certain information known *a priori* [2]. In this study, we used as such information the well-known fact that light coal fractions are usually enriched in liptinite, those with intermediate densities, in vitrinite, and the heaviest ones, in inertinite [7]. This can, undoubtedly, be supported by the data in Table 1, but the actual composition of the fractions is taken as unknown in solving the actual problem. Nevertheless, we can take as the initial approximation the *a priori* known fact that the fractions with densities of 1.19, 1.31, and 1.71 g dm^{-3} correspond to maceral groups L, Vt, and I, respectively. Finally, the iteration process yields

$$T = \begin{bmatrix} 0.2838 & 0.3476 & 0.3305 \\ -0.9309 & 0.0466 & 0.3899 \\ 0.4924 & -0.4326 & 0.6584 \end{bmatrix}$$

The IR spectra of the macerals calculated by formula (2) are shown in Fig. 3. Through matrix inversion by transformation, we can also determine the maceral composition of each coal fraction. It will be represented as a matrix X $(3 \times m)$ with rows corresponding to coal fractions and columns, to

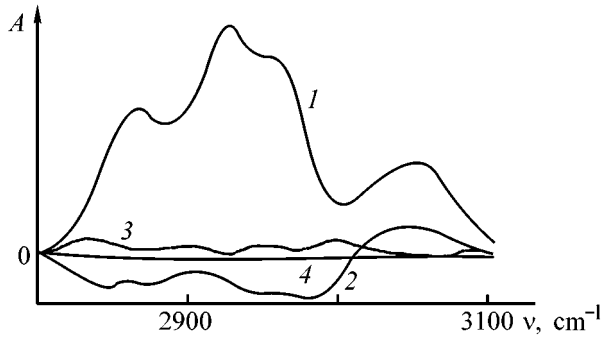

Fig. 2. IR spectra characterizing statistical factors 1–4.

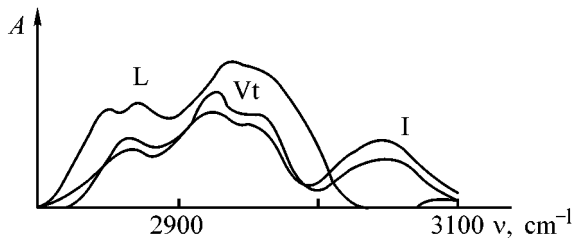

Fig. 3. Calculated IR spectra of the main groups of coal macerals: (L) liptinite, (Vt) vitrinite, and (I) inertinite.

Table 4. Maceral composition of coal as determined from the IR spectra of coal and macerals

Sample	Maceral	Given, %	Found, %		
			range	average	σ
1	L	15	14.75–16.04	14.98	0.16
	Vt	65	59.29–65.97	64.93	0.77
	I	20	19.24–24.67	20.09	0.63
2	L	11	10.84–11.20	11.02	0.09
	Vt	82	81.08–82.68	81.86	0.34
	I	7	6.46–7.98	7.12	0.27
3	L	6	5.92–6.11	6.00	0.05
	Vt	40	39.70–40.30	39.36	0.15
	I	54	53.78–54.25	54.04	0.12

the maceral proportions in their composition. This matrix is given by the equation

$$X = T^{-1}\mathbf{V}^{*}. \quad (3)$$

Since the calculations by formulas (1)–(3) utilize a truncated matrix of eigenvectors of the general problem, the columns in the matrix X need to be normalized to unity for retaining the physical meaning (the possible minor negative values of the fractions of any maceral are replaced by zeros). The corresponding solution of the problem is demonstrated in Table 1, with the calculated data compared with the actual maceral composition determined independently by the coal petrographic method.

The IR spectra of the individual maceral groups, obtained by factor analysis, were used for constructing the spectra of model mixtures with different maceral compositions:

$$A_{M}(\nu) = A_{L}(\nu)x_{L} + A_{Vt}(\nu)x_{Vt} + A_{I}(\nu)x_{I}, \quad (4)$$

where $A_{M}(\nu)$ is the intensity as a function of the wave number ν for a maceral group M (M = L, Vt, I), and x_{M} is the fraction of the group M in the composition of the coal organic matter.

Next, we determined x_{M} by least-squares fitting of the given spectrum $A(\nu)$.

Table 4 presents the starting and found x_{M} values for the three model mixtures. The search followed the Monte-Carlo scheme with randomly chosen initial composition in 100 versions of the calculation for each mixture. Table 4 shows that, with IR spectra of macerals available, it is possible to determine with sufficient precision the maceral composition of coal from its IR spectrum. With data for macerals lacking, elucidating the composition and predicting the individual IR spectra of the components require a factor analysis.

CONCLUSION

The maceral composition of various coal samples was determined from their IR spectra by factor analysis, which allows the amounts of macerals in individual samples to be determined and the model spectra of selected macerals to be obtained. The spectra of macerals, in turn, afford reliable evaluation of their content in coals of any petrographic composition.

REFERENCES

1. Kim, J.-O. and Mueller, Ch.W., *Factor Analysis: Statistical Methods and Practical Issues*, 1968; Kleeka, W.R., *Discriminant Analysis*, 1986; Aldenderfer, M.S. and Blashfield, R.K., *Cluster Analysis*, 1985.
2. Kim, K.J., Reynolds, N.M., and Hsu, S.L., *Macromolecules*, 1989, vol. 22, no. 12, pp. 4395–4401.
3. Gagarin, S.G. and Gladun, T.G., *Zh. Prikl. Khim.*, 1996, vol. 69, no. 4, pp. 591–597.
4. Gagarin, S.G., Friesen, V.I., Mikaelan, K.Kh., and Gladun, T.G., *Khim. Tverd. Topl.*, 1996, no. 3, pp. 43–51.
5. Korolev, Yu.M., Gagarin, S.G., Friesen, V.I., and Mikaelan, K.Kh., *Koks Khim.*, 1997, no. 12, pp. 2–8.
6. Michaelian, K.H., *Vibrational Spectra and Structure*, Amsterdam: Elsevier, 1990, pp. 81–126, vol. 18.
7. Eremin, I.V., Lebedev, V.V., and Tsikarev, D.A., *Petrografiya i fizicheskie svoistva uglei* (Petrography and Physical Properties of Coals), Moscow: Nedra, 1980.
8. Gagarin, S.G., Gladun, T.G., Friesen, V.I., and Mikaelan, K.Kh., *Koks Khim.*, 1993, no. 4, pp. 6–9.
9. Nalimov, V.V., *Primenenie matematicheskoi statistiki pri analize veshchestva* (Application of Mathematical Statistics in Substance Analysis), Moscow: Fizmatgiz, 1960.

Russian Journal of Applied Chemistry, Vol. 75, No. 8, 2002, pp. 1349–1353. Translated from Zhurnal Prikladnoi Khimii, Vol. 75, No. 8, 2002, pp. 1375–1380.
Original Russian Text Copyright © 2002 by Sharipov, Faizrakhmanov.

CHEMISTRY OF FOSSIL FUEL

Some Properties of Petroleum Sulfoxides Suitable for Extraction in Hydrometallurgy

A. Kh. Sharipov and I. S. Faizrakhmanov

Institute of Petrochemistry and Catalysis, Bashkortostan Academy of Science and Ufa Scientific Center, Russian Academy of Sciences, Ufa, Bashkortostan, Russia

Bashkir Research and Planning Institute of the Building Materials Industry, Ufa, Bashkortostan, Russia

Received February 7, 2001

Abstract—Several fractions of diesel fuel recovered from Arlan crude oil were treated with hydrogen peroxide, and the sulfoxides formed by oxidation of petroleum sulfides were isolated with aqueous sulfuric acid. The water solubility of these sulfoxides and their limiting extraction capacity with respect to neodymium nitrate were determined. Correlations between several characteristics of the petroleum sulfoxides [water solubility, limiting extraction capacity with respect to neodymium(III) nitrate, phase separation time under standard conditions, and viscosity] and the boiling range of corresponding petroleum fractions were analyzed.

As noted in [1], sulfoxides find growing application as extractants in hydrometallurgy. The most important parameters of extractants used for recovery of metals from aqueous solutions are their water solubility R, limiting extraction capacity [in particular, with respect to neodymium(III) nitrate] E_{lim}, phase separation time τ_{sep} under standard conditions, and viscosity η [2].

In this work, we studied the correlation between the properties of petroleum sulfoxides and the boiling ranges of the petroleum fractions used for their preparation.

EXPERIMENTAL

The sulfoxides were prepared from a diesel fraction of the Arlan crude oil. The initial and final boiling points of this fuel were 211 and 360°C, respectively. The total sulfur content was 2.2 wt %, including 1.15% sulfide sulfur. The composition of sulfides contained in the diesel fuel was determined on an Finnigan-402 gas chromatograph-mass spectrometer [3]. The sulfide sulfur content S_s was determined iodometrically [4]. The sulfides mainly include monocyclic and bicyclic thiaalkanes.

The initial diesel fuel was fractionated on a high-performance distillation tower at 4–5 torr and the reflux ratio equal to 5. To prepare sulfoxides, these petroleum fractions were oxidized with 30% hydrogen peroxide [GOST (State Standard) 177–88].

The oxidative conversion of sulfides to sulfoxides was performed by the technique described in [5]. The resulting sulfoxides were isolated by extraction with 62% aqueous sulfuric acid [6]. This aqueous sulfuric acid containing sulfoxides was neutralized with aqueous sodium carbonate, washed with aqueous sodium sulfate, and then kept under reduced pressure (80–100 torr) to remove emulsified and dissolved water. The following characteristics of dehydrated sulfoxides RR'SO were determined: the sulfoxide sulfur content S_{SO}, by potentiometric titration [7]; molecular weight $M_{RR'SO}$, cryoscopically [8]; and water solubility R, by a technique developed by us. Namely, a sulfoxide sample (10 ml) was added to distilled water (60 ml) placed in a separatory funnel and this mixture was shaken for 15 min. The resulting emulsion was centrifuged (3000 rpm) for 20 min. The centrifuged aqueous solution (25 ml) was sampled, and petroleum sulfoxides were extracted by successive threefold contact with fresh portions of chloroform (20 ml).

All chloroform extracts were collected in a 100-ml round-bottomed flask. This flask was heated on a water bath to remove chloroform and trace amounts of water. Chloroform was removed at atmospheric pressure, and water, under 100–200 torr. The nonvolatile

1070-4272/02/7508-1349 $27.00 © 2002 MAIK "Nauka/Interperiodica"

bottoms were dissolved in *m*-xylene (or any other high-boiling organic solvent), the resulting organic solution was quanitatively transferred into a 25-ml volumetric flask, and then the organic solvent was added to make the total volume equal to 25 ml. The sulfoxide sulfur content S_{SO} in this solution was determined by potentiometric titration. Based on these data, the water solubility of sulfoxides R (g l^{-1}) was calculated by the equation

$$R = \frac{S_{SO} V d M_{RR'SO} \times 1000}{32 \times 100 \times 25},$$

where d is the solvent (*m*-xylene) density (g cm^{-3}), is the sulfur atomic weight of 32, 25 is the volume of the equilibrium aqueous phase taken for analysis (ml), and V is the volume of sulfoxide solution in *m*-xylene (ml).

The accuracy and sensitivity of sulfoxide analysis were evaluated using organic solutions containing known amounts of thoroughly recrystallized diisobutyl and diamyl sulfoxides.

The sensitivity of sulfoxide determination in our experiments was 0.1 g l^{-1}. The accuracy of determination of sulfoxides in mixtures containing diisobutyl or diamyl sulfoxides taken in amount of 1.0 to 4.0 g l^{-1} did not exceed 5%. This accuracy was accepted by us as the actual accuracy in determination of the water solubility of petroleum sulfoxides.

As the result of analysis was taken the arithmetic mean of two parallel determinations at a standard deviation less than 5% and confidence probability of 0.95.

Apart from the water solubility, we determined the phase separation time τ_{sep} and the limiting extraction capacity E. For this purpose, a mixture consisting of *m*-xylene (5 ml), petroleum sulfoxides (5 ml), and aqueous neodymium(III) nitrate solution (10 ml) was placed in a separatory funnel (100 ml). The separatory funnel was shaken for 5 min, and the phase separation time was registered with a stopwatch. After complete phase separation, the aqueous phase was poured into a beaker and pH was measured with a pH meter. If pH was beyond the range 3.0 ± 0.1, it was adjusted to 3 ± 0.1 by adding aqueous NH_4OH or HNO_3 and then the contact with the organic phase was repeated until pH remained at the level of 2.9–3.1. All contacts were carried out under similar conditions. The phase separation time τ_{sep} was determined as the time within which a distinct interface between the organic and aqueous phases appeared at pH 3.0 ± 0.1. After pH adjustment, the equilibrium aqueous and organic phases were analyzed for neodymium. Prior to analysis, the aqueous phase was diluted in a volumetric flask and its aliquot was analyzed. The organic phase was poured into a centrifuge test tube and centrifuged for 10–15 min at 2500–3000 rpm. The centrifuged organic solution (3 ml) was placed in a separatory funnel and neodymium was backwashed by threefold treatment with 0.1 M HNO_3. The resulting aqueous solutions were collected in a beaker. The neodymium(III) content in the backwash was determined complexometrically with Na_2EDTA. An aliquot of the backwash was placed in a 200-ml beaker and distilled water was added to a volume sufficient for immersing pH meter electrodes. While stirring this solution with a magnetic stirrer, pyridine (8 drops) was added, pH was adjusted to 6.2–6.25 by adding aqueous HNO_3 and NH_4OH, xylenol orange (6–8 drops) was added, and then neodymium was titrated with 0.05 M Na_2EDTA until the initial violetblue color changed to yellow. The neodymium concentration C was calculated by the equation

$$C = \frac{VM \times 168.3n}{a},$$

where C is the neodymium nitrate concentration in the organic or aqueous phase, recalculated to $NdO_{1.5}$, g l^{-1}; V is the Na_2EDTA volume consumed in titration (ml); M is the Na_2EDTA molar concentration determined by titration of standard aqueous yttrium nitrate prepared from a precisely weighed portion of Y_2O_3; 168.3 is the $NdO_{1.5}$ formula weight; a is the volume of organic or aqueous phases taken for analysis (ml); and n is the dilution factor.

The neodymium nitrate content (g l^{-1}, recalculated to $NdO_{1.5}$) in the organic phase is the extraction capacity E of sulfoxides. At the working solution concentration of 400 ± 10 g l^{-1} (recalculated to $NdO_{1.5}$) and pH 3.0 ± 0.1, petroleum sulfoxides exhibit the maximal (limiting) extraction capacity E_{lim}. We found that the sum of the neodymium nitrate content in the organic and aqueous phases is equal to the neodymium nitrate amount taken for extraction, i.e., in our systems a balance with respect to neodymium is observed.

Several characteristics of sulfoxides prepared by oxidation of different petroleum fractions are listed in Table 1.

These results show that the water solubility of petroleum sulfoxides noticeably depends on the boiling range of the petroleum fractions taken for oxidation. For example, the water solubility of sulfoxide prepared from the petroleum fraction 211–360°C with the lowest initial boiling point is 10.6 g l^{-1}. In passing

Table 1. Characteristics of sulfoxides* prepared from petroleum fractions with different boiling ranges

Boiling range, °C	S_S, wt %	$M_{RR'SO}$	R, g l^{-1}	E_{lim}, g l^{-1}	S_{SO}, wt %	E_{lim}/S_{SO}	τ_{sep}	η, mm^2 s^{-1}
211–360	1.5	207	10.6	86.9	10.7	8.1	1.5	71.9
220–360	1.12	209	9.9	86.0	10.3	8.1	1.5	78.7
240–340	1.12	209	9.2	92.6	11.4	8.1	1.4	74.4
240–360	1.14	210	8.9	85.6	10.7	8.0	1.8	81.8
260–340	1.13	211	8.1	90.2	11.3	7.9	1.5	85.4
260–360	1.11	212	7.8	84.4	10.6	7.9	1.8	88.9
265–360	1.11	214	7.7	85.6	10.5	8.1	2.0	90.4
275–360	1.00	217	7.1	80.1	10.1	7.9	2.0	119.7
300–360	0.92	221	5.6	77.6	9.5	8.1	2.1	158.8

* The limiting extraction capacity of sulfoxides with respect to neodymium(III) E_{lim} was determined with 50% sulfoxide solution in *m*-xylene. For comparison, E_{lim} of neat TBP with respect to neodymium nitrate is 144.4 g l^{-1}.

to fractions with higher initial boiling point (for example, to fractions 275–360 and 300–360°C), the water solubility decreases to 7.1 and 5.6 g l^{-1}, respectively. Figure 1 shows that the water solubility of the sulfoxides prepared from the petroleum fractions with similar final boiling points, linearly decreases with increasing initial boiling point. Thus, to prepare poorly water-soluble sulfoxides, the high-boiling petroleum fractions should be used.

To estimate possible losses of sulfoxides in the course of extraction under industrial conditions, we studied changes in the water solubility of sulfoxides on repeated contact of the organic phase with fresh portions of water. In these experiments, equal volumes of the organic and aqueous phases were placed in a separatory funnel and vigorously shaken for 15 min. The resulting emulsion was centrifuged. After phase separation, samples of the organic and aqueous phases were taken for analysis. The remaining volume of the organic phase was measured and contacted with an equal volume of fresh water ($V_{org} : V_{aq} = 1$). After several repeated contacts (third, sixth, tenth, etc.), the equilibrium organic and aqueous phases were analyzed. All sulfoxides used in our experiments were prepared from the diesel fraction of Arlan crude oil (boiling range 260–360°C). Distilled water acidified to pH 3 was used as an aqueous phase.

Figure 2 shows that, with increasing number of repeated contacts, the water solubility of sulfoxides gradually decreases. The largest decrease in the water solubility occurs in the first contacts. In further contacts, the water solubility curve flattens out. We believe that this is caused by multicomponent composition of the petroleum sulfoxides. On contact with water, the most water-soluble low-molecular-weight sulfoxides dissolve first. The remaining higher-molecular-weight are less soluble.

After 24 successive contacts for six hours in total, the sulfoxide content in the organic phase decreases

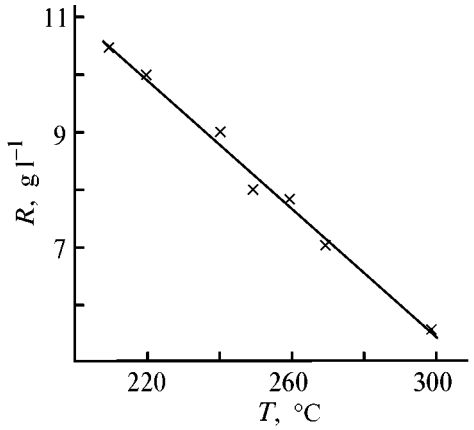

Fig. 1. Water solubility of petroleum sulfoxides R vs. the initial boiling point of the petroleum fractions T.

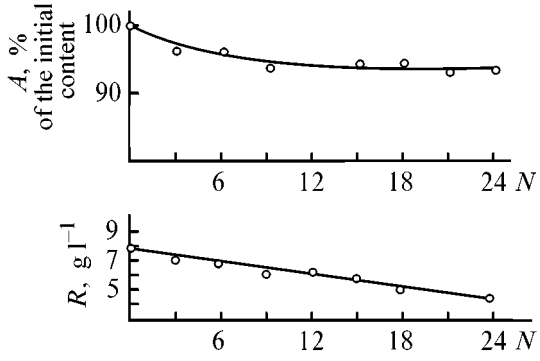

Fig. 2. (A) Sulfoxide content in the organic phase and (R) sulfoxide solubility in acidified water vs. the number N of repeated contacts of the organic and aqueous phases.

Table 2. Sulfoxide characteristics as influenced by the degree of petroleum sulfide oxidation

Sulfoxide sulfur content in oxidized petroleum fraction, wt %	Degree of sulfide conversion to sulfoxides, %	Sulfoxide yield, wt %, based on petroleum fraction	S_{SO}	$S^*_{SO_2}$	η, $mm^2\ s^{-1}$	Acidity recalculated to H_2SO_4, $g\ l^{-1}$	τ_{sep}, min	E_{max}, $g\ l^{-1}$
			wt %					
0.45	39.1	3.38	10.5	–	81.8	1.68	1.75	83.8
0.61	53.0	4.75	10.6	0.65	88.4	2.68	1.50	85.0
0.73	63.4	5.64	10.8	0.10	88.6	1.59	1.82	84.2
0.79	68.7	6.41	10.6	1.42	88.9	0.97	1.75	84.4

* (S_{SO_2}) Sulfone content.

by 7.5% of the initial amount, and the water solubility of sulfoxides decreases from 7.8 to 4.6 $g\ l^{-1}$.

The limiting extraction capacity of the sulfoxides decreases with increasing initial boiling point of the petroleum fraction. For example, in passing from sulfoxide prepared from the petroleum fraction 211–360°C to that prepared from the fraction 300–360°C, the limiting extraction capacity decreases from 86.9 to 77.6 $g\ l^{-1}$.

In determination of the extraction capacity, the phase separation time was approximately similar for all sulfoxides studied (1.5–2.1 min). The extraction capacity of sulfoxides suitable for hydrometallurgy should be no less than 50–55 $g\ l^{-1}$, and the phase separation time, no more than 3 min [9].

In our experiments, the limiting extraction capacity of sulfoxides with respect to neodymium nitrate was determined for 50% sulfoxide solution in *m*-xylene. Data for neat tributyl phosphate are given in Table 1 for comparison.

The extraction capacity of sulfoxides prepared from different petroleum fractions correlates with the sulfoxide sulfur content in these reagents. For the sulfoxides prepared from the petroleum fraction 211–360°C, the sulfoxide number is 10.7 wt %. In passing to sulfoxides prepared from the petroleum fractions with higher initial boiling point, 275–360 and 300–360°C, the sulfoxide number decreases to 10.1 and 9.5 wt %, respectively. We believe that this is caused by the fact that, with increasing molecular weight of the oxidized products, the content of the extraction-active >S=O functional groups decreases. Our further studies showed that the extraction capacity of sulfoxides is in direct proportion to the sulfoxide sulfur content in them. For all the sulfoxides, the average ratio of the limiting extraction capacity to the sulfoxide sulfur content E_{lim}/S_{SO} is 8.0. This ratio varies from 7.9 to 8.1, i.e., within the limits of the error in determination of both the extraction capacity and the sulfoxide sulfur content. Therefore, in some cases, the content of sulfoxide sulfur, being the simpler determinable factor, can be used instead of the limiting extraction capacity.

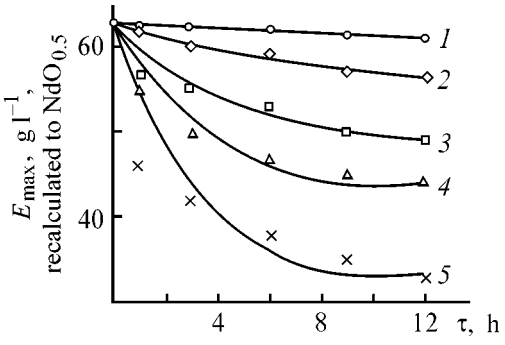

Fig. 3. Limiting extraction capacity of petroleum sulfoxides with respect to $Nd(NO_3)_3$ E_{lim} vs. heating time τ. Temperature (°C): (*1*) 90, (*2*) 110, (*3*) 130, (*4*) 150, and (*5*) 170.

To meet the requirements to extractants suitable for a hydrometallurgical processes, the sulfoxide viscosity η must be no more than 200 $mm^2\ s^{-1}$ at 20°C. Table 1 shows that, with increasing initial boiling point of the petroleum fraction, the sulfoxide viscosity grows. In passing from sulfoxides prepared from the petroleum fraction 220–360°C to those prepared from fractions with higher initial boiling points (275–360°C and 300–360°C), the viscosity increases from 78.7 to 119.7 and 158.8 $mm^2\ s^{-1}$, respectively.

We also studied how the degree of petroleum sulfide oxidation affects the quality of the resulting sulfoxides. Experiments were performed with the petroleum fraction 260–360°C. To vary the degree of sulfide conversion to sulfoxide, hydrogen peroxide was added in different amounts corresponding to 60, 80, 100, and 120% of the stoichiometry. As seen from Table 2, the increase in the degree of conversion from 39.1 to 68.7 % does not affect appreciably the limiting

Table 3. Thermal stability of sulfoxides

T, °C	S_{SO}	S_S	S_{SO_2}	Elemental composition, wt %			
	wt %			C	H	S	O
Before thermal treatment	7.9	2.1	0.6	63.35	10.78	13.75	8.12
90	7.9	2.4	0.6	70.45	10.75	11.90	6.90
110	7.1	2.8	0.4	71.60	10.60	11.71	6.09
130	6.3	3.9	0.5	71.70	10.48	11.61	6.21
150	5.6	5.1	0.8	73.16	10.58	11.90	4.36
170	4.4	5.6	0.6	72.8	10.65	11.69	4.86

extraction capacity of sulfoxide, i.e., the main parameter of the sulfoxide quality. Table 2 shows also that, with increasing degree of conversion, the sulfone content increases to 1.42%. The minor variations in viscosity and extraction capacity of sulfoxides under these conditions are within the limits of the determination accuracy.

To elucidate whether the petroleum sulfoxides can be used as extractants in high-temperature hydrometallurgical processes, we studied the thermal stability of these reagents. For this purpose, a sulfoxide sample was placed in a temperature-controlled three-necked flask equipped with stirrer, thermometer, and reflux condenser. The sulfoxide was kept at a prescribed temperature for 1, 3, 6, or 9 h, and, after each temperature interval, a portion of sulfoxide was taken from a flask for analysis. The remaining amount was also analyzed after heating for 12 h. Portions of sulfoxide were treated with sodium chloride, filtered and analyzed for sulfoxide sulfur. The viscosity of sulfoxides at 20°C and their extraction capacity were also determined. The remaining amount was analyzed for sulfoxides and sulfones and its elemental composition was determined (Table 3). We found that, with increasing temperature and time of heating, the content of sulfoxide sulfur and, as a consequence, the extraction capacity decrease (Fig. 3). Heating to above 130°C causes liberation of sulfur dioxide and hydrogen sulfide. At 150°C and higher temperatures, SO_2 predominates in the gas phase, while the H_2S content is minor. The influence of the heating time on sulfoxide viscosity is governed by thermal degradation of sulfoxides. On heating to 150°C and higher temperatures, the sulfoxide viscosity sharply decreases. Our results showed that, at temperatures higher than 100°C, the petroleum sulfoxides are unstable. Thus, both high temperature and prolonged heating deteriorate the performance of sulfoxides.

CONCLUSIONS

(1) The petroleum sulfoxides prepared from several fractions of diesel fuel with different boiling ranges considerably differ in water solubility, limiting extraction capacity with respect to neodymium(III) nitrate, and viscosity.

(2) Correlations between the boiling ranges of the petroleum fractions used for sulfoxide preparation and some performance characteristics of the resulting sulfoxides allow approximate prediction of the sulfoxide loss in extraction under industrial conditions and enable a choice of best crude oil for production of sulfoxide extractants suitable for hydrometallurgy.

REFERENCES

1. Nikitin, Yu.E., Murinov, Yu.I., and Rozen, A.M., *Usp. Khim.*, 1976, vol. 45, no. 12, pp. 2233–2238.
2. Treybal, R.E., *Liquid Extraction*, New Uork: McGraw–Hill, 1963.
3. Masagutov, R.M., Kruglov, E.A., Popov, I.N., *et al.*, Abstracts of Papers, *10th Symp. on the Organic Chemistry of Sulphur.*, Bangor: Univ. College of North Wales, 1982, p. 129.
4. Gal'perin, G.D., Girina, G.P., and Luk'yanitsa, V.G., *Metody analiza organicheskikh soedinenii nefti, ikh smesei i proizvodnykh* (Technique for Analysis of Petroleum Organic Compounds, Their Mixtures, and Derivatives), Moscow: Nauka, 1969.
5. Sharipov, A.Kh., Masagutov, R.M., Suleimanova, Z.A., and Faizrakhmanov, I.S., *Neftekhimiya*, 1989, vol. 29, no. 4, pp. 551–555.
6. Karaulova, E.N., *Khimiya sul'fidov nefti* (Chemistry of Petroleum Sulfides), Moscow: Nauka, 1970.
7. Wimer, D.C., *Anal. Chem.*, 1958, vol. 30, no. 12, pp. 2060–2065.
8. Rybak, B.M., *Analiz nefti i nefteproduktov* (Analysis of Petroleum and Petroleum Products), Moscow: Gostoptekhizdat, 1962.
9. Mikhailichenko, A.I., Sokolova, N.P., and Reznichenko, L.A., *Nauchn. Tr. GIREDMET*, 1978, vol. 83, pp. 44–49.

Russian Journal of Applied Chemistry, Vol. 75, No. 8, 2002, pp. 1354–1356. Translated from Zhurnal Prikladnoi Khimii, Vol. 75, No. 8, 2002, pp. 1381–1383.
Original Russian Text Copyright © 2002 by Ostanova, Chubarov, Drozdov, Patrushev.

BRIEF COMMUNICATIONS

Oxidation of Zinc Sulfide in the System HNO_3–$Fe(NO_3)_3$–H_2O

S. V. Ostanova, A. V. Chubarov, S. V. Drozdov, and V. V. Patrushev

Institute of Chemistry and Chemical Technology, Siberian Division, Russian Academy of Sciences, Krasnoyarsk, Russia

Received October 10, 2001; in final form, February 2002

Abstract—The behavior of zinc sulfide in the system HNO_3–$Fe(NO_3)_3$–H_2O at 25, 55, and 80°C was studied using the simplex-lattice design method.

Data on reactions of certain metal sulfides with mineral acids are well known; however, the range of systems under study is rather narrow. The system HNO_3–$Fe(NO_3)_3$–H_2O has been studied insufficiently [1].

This system was studied to analyze reactions of zinc sulfide in the ternary system HNO_3–$Fe(NO_3)_3$–H_2O at various HNO_3 and $Fe(NO_3)_3$ concentrations and to obtain data on the composition of precipitates formed in redox reactions at 25, 55, and 80°C.

EXPERIMENTAL

Zinc sulfide was synthesized by the technique described in [2] and identified by X-ray phase analysis; its specific surface area S_{sp} = 4.1 $m^2 g^{-1}$ was determined by BET. Chemically pure iron(III) nitrate and nitric acid, and also distilled water, were used in the study. The experiments were carried out in a temperature-controlled system (the accuracy of temperature measurements was ±0.1°C) in the course of 2 h (preliminary experiments showed that the concentration of Zn^{2+} ions in solution remains unchanged after 2-h contact of zinc sulfide with the solution) with permanent stirring and initial s : l ratio of 1 : 5.

The concentration of Zn^{2+} ions in the liquid phase was determined by titrimetry and atomic-absorption spectrophotometry [3, 4], and that of nitric acid, by titrimetry [4]. After filtration, the solid phase was washed with water and ethanol to remove the solution, dried, and subjected to X-ray phase analysis.

The results obtained were processed by means of the simplex-lattice design [5]. The following components were the vertices of the concentration triangle: X_1, H_2O (55.56 M); X_2, $Fe(NO_3)_3$ (1.8 M); and X_3, HNO_3 (3.2 M). As functions served the extents to which Zn^{2+} passes from ZnS into solution.

A simplex-lattice design for the incomplete cubic model used to describe the system under study is presented in the table. These data were used to calculate the regression equations for 25, 55, and 80°C:

$$Y_{25} = 0.05X_1 + 21.79X_2 = 49.44X_3 + 30.95X_1X_2 + 24.16X_1X_3 + 96.34X_2X_3 + 113.09X_1X_2X_3,$$

$$Y_{55} = 0.08X_1 + 12.46X_2 + 37.31X_3 + 74.42X_1X_2 + 37.16X_1X_3 + 49.70X_2X_3 - 176.91X_1X_2X_3,$$

$$Y_{80} = 0.07X_1 + 50.00X_2 + 55.22X_3 + 22.53X_1X_2 - 98.05X_1X_3 - 19.40X_2X_3 + 237.98X_1X_2X_3.$$

The root-mean-square error was 3%. It was found that these equations describe adequately the data obtained in control experiments nos. 8–10, with 97% probability. The equations were used to construct phase diagrams for the temperatures under study (Figs. 1a–1c).

The increase in the degree of Zn^{2+} leaching is directed toward the HNO_3–$Fe(NO_3)_3$ system in all the diagrams, with the most complete extraction of about 62% achieved at 25°C. The same behavior is observed at 55 and 80%, but the degree of leaching of zinc ions is lower (40 and 55%, respectively). Addition of nitric acid to the solution promotes the oxidation reaction, with an increase in acidity favoring sulfide break-

1070-4272/02/7508-1354 $27.00 © 2002 MAIK "Nauka/Interperiodica"

Simplex-lattice design for incomplete cubic model*

Experiment no.	X_1	X_2	X_3	Y_{e25}	Y_{c25}	Y_{e55}	Y_{c55}	Y_{e80}	Y_{c80}
	M			%					
1	1	–	–	0.05	0.05	0.08	0.08	0.07	0.07
2	–	1	–	21.79	21.79	12.46	12.46	50	50
3	–	–	1	49.44	49.44	37.31	37.31	55.22	55.22
4	0.5	0.5	–	18.66	18.66	24.85	24.85	19.40	19.40
5	0.5	–	0.5	30.78	30.78	27.99	27.99	3.13	3.14
6	–	0.5	0.5	59.70	59.70	37.31	37.31	47.76	47.76
7	0.33	0.33	0.33	44.78	44.78	27.99	27.99	28.36	28.36
8	0.15	0.15	0.7	53.01	53.01	36.01	36.01	37.10	37.07
9	0.15	0.7	0.15	38.36	38.37	25.41	25.41	40.43	40.43
10	0.7	0.15	0.15	20.43	20.45	17.57	17.57	6.47	6.48

* Y_{e25}, Y_{e55}, Y_{e80}, Y_{c25}, Y_{c55}, and Y_{c80} are the experimental and calculated degrees of zinc extraction at 25, 55, and 80°C.

down, as seen from the figures. At 80°C, the concentrations of Fe^{3+} and HNO_3 ions hardly affect the degree of leaching, which falls within the range 50–55%. When temperature is lowered, the oxidation process is shifted to higher nitric acid concentrations, although the highest degree of zinc extraction is observed in the concentration ranges 1.92–2.4 M of HNO_3 and 0.72–0.45 M of $Fe(NO_3)_3$.

According to X-ray phase analysis data, undecomposed ZnS and elementary sulfur are present in the solid phases. As shown by an analysis of the precipitates after breakdown, the content of elementary sulfur at 25°C is much lower than that at elevated temperatures. This suggests that S(–2) → S(0) → S(+6) conversion occurs in the course of the reaction of nitric acid and iron(III) nitrate with ZnS. Raising the temperature results in faster ZnS oxidation and evolution of gaseous reaction products (evolution of NO and NO_2). Such a behavior of the system under study seems to be related to the screening of the reaction surface of the material by elementary sulfur, which is the reason for the poorer extraction of zinc ions at elevated temperatures.

The reaction of ZnS with the oxidizing system $Fe(NO_3)_3$–H_2O depends only on the concentration of the reactants in virtually the entire temperature range under study. Such a behavior suggests that the presence of Fe^{3+} ions in solution promotes zinc sulfide oxidation, and further increase in the concentration of nitric acid results in faster oxidation of the sulfide sulfur to elementary sulfur and in the screening of the reaction surface. By varying the dispersity, one can pass from leaching to complete dissolution of zinc sulfide.

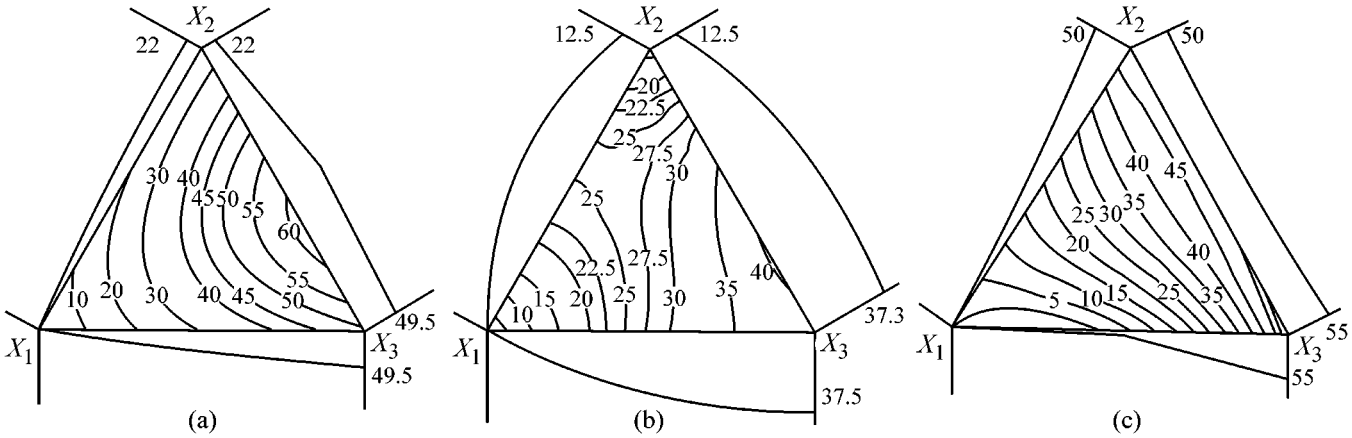

Fig. 1. Zn^{2+} extraction from ZnS (%) at (a) 25, (b) 55, and (c) 80°C.

CONCLUSIONS

(1) The degree of Zn^{2+} leaching grows with increasing concentrations of nitric acid and iron(III) nitrate, and an increase in temperature hardly affects the leaching.

(2) At 25°C the solid phase contains a lesser amount of elementary sulfur than that at elevated temperatures.

(3) In the course of the ZnS reaction with nitric acid and iron(III) nitrate a $S(-2) \rightarrow S(0) \rightarrow S(+6)$ conversion takes place.

(4) Equations describing the degree of Zn^{2+} extraction at 25, 55, and 80°C were obtained, and the corresponding diagrams were constructed on their basis.

REFERENCES

1. Lochmann, J. and Pedlik, M., *Hydrometallurgy*, 1995, vol. 37, pp. 89–96.
2. Karyakin, Yu.V. and Angelov, I.I., *Chistye khimicheskie veshchestva* (Pure Chemical Substances), Moscow: Khimiya, 1974.
3. Fainberg, S.Yu. and Filippova, R.A., *Analiz rud tsvetnykh metallov* (Analysis of Ores of Nonferrous Metals), Moscow: Metallurgizdat, 1963.
4. Alekseev, V.I., *Kolichestvennyi analiz* (Quantitative Analysis), Moscow: Khimiya, 1972.
5. Akhnazarova, S.L. and Kafarov, V.V., *Optimizatsiya eksperimenta v khimii i khimicheskoi tekhnologii* (Optimization of Experiments in Chemistry and Chemical Technology), Moscow: Vysshaya shkola, 1978.

Russian Journal of Applied Chemistry, Vol. 75, No. 8, 2002, pp. 1357–1359. Translated from Zhurnal Prikladnoi Khimii, Vol. 75, No. 8, 2002, pp. 1384–1386.
Original Russian Text Copyright © 2002 by Lebedev, Rudenko.

BRIEF COMMUNICATIONS

On Production of Cerium Dioxide

V. N. Lebedev and A. V. Rudenko

Tananaev Institute of Chemistry and Technology of Rare Elements and Minerals, Kola Scientific Center, Russian Academy of Sciences, Apatity, Russia

Received March 11, 2002

Abstract—The possibility of obtaining cerium dioxide by recovery of Ce(IV) phosphate from acid nitrate solutions with subsequent conversion of Ce(IV) phosphate to Ce(III) oxalate was studied.

Cerium is the most widespread and demanded representative of rare-earth elements (REE). Its content in most of the concentrates being refined exceeds 50 wt %. As a rule, Ce(III) is isolated from an REE mixture through its oxidation to Ce(IV) and subsequent separation by extraction or precipitation with account of differences in the pH of precipitation of mixture components [1, 2].

It is impossible to completely separate cerium(IV) from other REEs by precipitation techniques owing to the close pH values of their precipitation and the considerable adsorptivity of the resulting precipitates. Purer cerium compounds can be obtained by precipitation of Ce(IV) phosphate, which is precipitated at higher acidity than triply charged REEs. Processes of this kind have been proposed for recovery of cerium from monazite [3] and a phosphate concentrate from apatite [4]. A drawback of the phosphate procedure is the complexity of phosphorus(V) removal.

A procedure for processing REE phosphates, based on their conversion to oxalates, has been proposed earlier [5, 6]. Its applicability to the production of cerium dioxide was assessed in the present study.

EXPERIMENTAL

Cerium was oxidized in an acid nitrate medium on a platinum anode. A solution prepared from loparite was used for oxidation. It contained 300 g l^{-1} of Ln_2O_3 and 164 g l^{-1} of Ce_2O_3. After the oxidation the solution contained Ce(IV) in the form of CeO_2 (42 g l^{-1}). The cerium(IV) content in solutions was determined by titration with Mohr's salt $(NH_4)_2Fe(SO_4)_2$. Cerium(IV) phosphate was precipitated from 2–3 N HNO_3 solution by addition of ammonium hydrophosphate $(NH_4)_2HPO_4$. Almost complete precipitation was attained by addition of one mole of PO_4^{3-} per one mole of CeO_2, which corresponds to precipitation of basic phosphate $CeOHPO_4$. This precipitate was filtered off, washed by repulping in 1 N HNO_3 at a solid-to-liquid phase ratio (s : l) of 1 : 3 and treated with oxalic acid in 1.5 N HNO_3 at 80°C for 1 h (s : l = 1 : 3). The conversion to the oxalate occurs by the following reaction:

$$2Ce(OH)PO_4 \cdot nH_2O(s) + 4H_2C_2O_4(l) \rightarrow Ce_2(C_2O_4)_3 \cdot 10H_2O(s) + 2H_3PO_4 + 2H_2O + 2CO_2.$$

Precipitated oxalates were isolated, washed with 1 N HNO_3, and calcined at 900°C. The impurities in cerium dioxide were determined by X-ray fluorescent analysis. The results of the experiments are presented in the table.

As a rule, 75–90% concentrates are produced by single-stage precipitation of Ce(IV) hydroxide, carbonate, or basic nitrate [3]. Cerium samples obtained by precipitation of Ce(IV) phosphate are significantly

Composition of cerium dioxide obtained by recovery of $CeOHPO_4$

Recovery conditions		Impurity content, wt %				
HNO_3, M	Repulping	La_2O_3	Pr_6O_{11}	Nd_2O_3	Sm_2O_3	P_2O_5
2	1	2.2	0.6	1.2	0.12	0.1
2	2	0.78	0.34	0.58	nd*	0.11
3	1	1.86	0.52	1.12	〃	nd*
3	2	0.66	0.26	0.58	〃	〃

* Not determined.

1070-4272/02/7508-1357 $27.00 © 2002 MAIK "Nauka/Interperiodica"

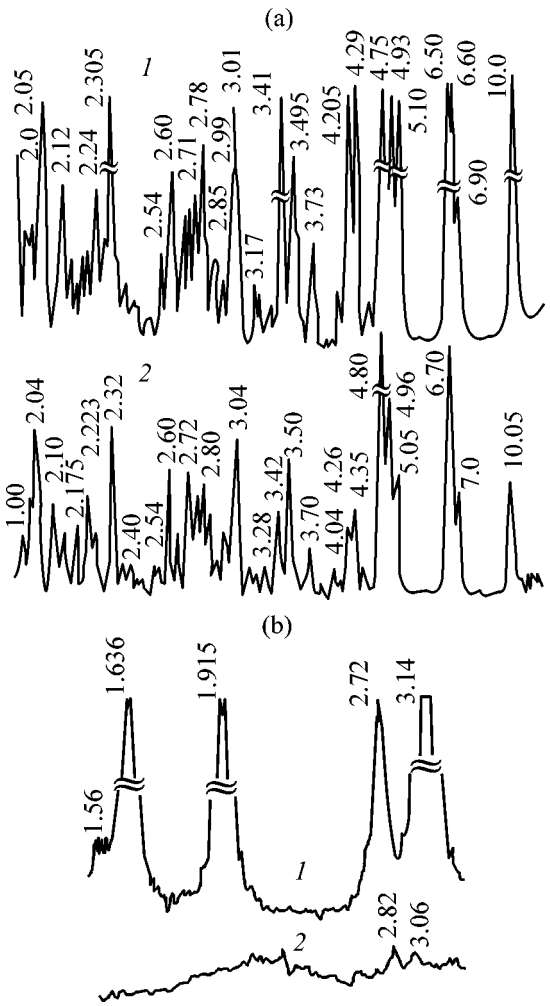

Fig. 1. X-ray diffraction patterns of oxalate samples obtained by conversion of (*1*) Ce(IV) and (*2*) Ce(III) phosphates. Sample: (a) initial and (b) after heat treatment at 250°C for 3 h.

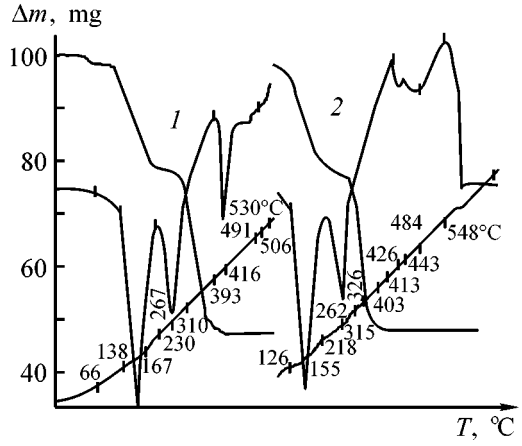

Fig. 2. DTA and weight-loss (Δ*m*) curves for oxalates samples obtained by conversion of (*1*) Ce(IV) and (*2*) Ce(III) phosphates. (*T*) Temperature.

purer and can be used in various fields of technology. A required purity of cerium phosphate can be achieved by its reprecipitation, which can be used for recovery of cerium(IV) from acid solutions after its electrolytic oxidation, since the precipitation procedures involve solution neutralization. At the same time, the extraction recovery entails a considerable loss of the extractant because of its decomposition by Ce(IV), which is a strong oxidizing agent, and by hydrogen peroxide used for the reextraction.

It was found that oxalates obtained from Ce(IV) phosphate differ from those prepared by conversion of Ce(III) orthophosphate in their thermal behavior. Samples of Ce(III) oxalates were synthesized under similar conditions. The content of P_2O_5 in the samples under study was not greater than 0.1%. Although both kinds of oxalate samples have identical X-ray diffraction patterns (Fig. 1a) and thermogravimetric characteristics (Fig. 2), the oxalate obtained from Ce(IV) phosphate is converted to bright yellow cerium dioxide under heating at 250°C for 3 h, whereas the oxalate obtained from Ce(III) phosphate only loses water and becomes X-ray-amorphous (Fig. 1b) under the same conditions. It is converted to dioxide only at 410°C [7], and cerium(III) oxide is shown to form at 370°C [8].

Low-temperature forms of cerium dioxide are likely to be of practical importance, e.g., in catalysis [9, 10]. On the whole, the technology of cerium dioxide production with preliminary recovery of Ce(IV) phosphate is well applicable, because phosphate ions and most of oxalic acid can be recycled. Naturally, treatment of bulk precipitates of Ce(IV) phosphate presents difficulty, but advantages of the method are also obvious.

CONCLUSION

It was shown that cerium dioxide can be produced through preliminary recovery of Ce(IV) phosphate from acid nitrate solutions and its subsequent conversion to Ce(III) oxalate.

Differences in thermal behavior between cerium oxalates obtained by conversion of Ce(IV) and Ce(III) phosphates were found. In the first case, the product decomposes at low temperature (250°C) to form CeO_2.

REFERENCES

1. Bol'shakov, K.A., *Tekhnologiya redkikh i rasseyannykh elementov* (Technology of Rare and Scattered Elements), Moscow: Vysshaya Shkola, 1969, vol. 2.

2. Mikhailichenko, A.I., Mikhlin, E.B., and Patrikeev, Yu.B., *Redkozemel'nye metally* (Rare-Earth Metals), Moscow: Metallurgiya, 1987.
3. Serebrennikov, V.V., *Khimiya redkozemel'nykh elementov* (scandii, ittrii, lantanidy) (Chemistry of Rare-Earth Elements (Scandium, Yttrium, Lanthanides), Tomsk: Tomsk. Univ., 1961, vol. 2.
4. GDR Patent 240 366.
5. RF Patent 2 148 019.
6. RF Patent 2 151 206.
7. Komissarova, L.N., Shatskii, V.M., Pushkina G.Ya., *et al.*, *Soedineniya redkozemel'nykh elementov: Karbonaty, oksalaty, nitraty i titanaty* (Compounds of Rare-Earth Elements: Carbonates, Oxalates, Nitrates, and Titanates), Moscow: Nauka, 1984.
8. Grigor'eva, Z.M. and Smagina, E.I., *Scientific Proc. of GIRIDMET* (State Institute of Rare Metals), 1978, vol. 83, pp. 89–95.
9. Mikhailichenko, A.I. and Krylova, A.V., Abstracts of Papers, *Vserossiiskaya konferentsiya po tekhnologii neorganicheskikh veshchestv* (All-Russia Conference on the Technology of Inorganic Substances), Kazan, 2001, pp. 156–158.
10. Protsenko, T.V., Mikhailichenko, A.I., Karataeva, E.Yu., and Nefedova, N.V., Abstracts of Papers, *Vserossiskaya konferentsiya po tekhnologii neorganicheskikh veshchestv* (All-Russia Conference on the Technology of Inorganic Substances), Kazan, 2001, pp. 158–162.
11. Kagan, B.I. and Skripka, I.P., *Redkie elementy: Syr'e i ekonomika* (Rare Elements: Raw Materials and Economics), Moscow: Inst. of Mineralogy, Geochemistry, and Crystal Chemistry of Rare Elements, 1973, issue 8, pp. 3–57.

Russian Journal of Applied Chemistry, Vol. 75, No. 8, 2002, pp. 1360–1361. Translated from Zhurnal Prikladnoi Khimii, Vol. 75, No. 8, 2002, pp. 1387–1388.
Original Russian Text Copyright © 2002 by Pavlov, Makhamatkhanov, Kutepov, Kudasheva, Lebedev.

BRIEF COMMUNICATIONS

Synthesis of Mordenite with the Use of Aluminum Sulfate Solutions

M. L. Pavlov, R. A. Makhamatkhanov, B. I. Kutepov, F. Kh. Kudasheva, and Yu. A. Lebedev

Institute of Petrochemistry and Catalysis, Academy of Sciences of Bashkortostan Republic and Ufa Scientific Center of Russian Academy of Sciences, Ufa, Bashkortostan, Russia

Received October 15, 2001; in final form, January 2002

Abstract—A procedure has been developed for synthesis of a mordenite-type zeolite with high phase purity and high dispersity of crystals. The procedure is based on hydrothermal crystallization of aluminum-silicon hydrogels prepared from aluminum sulfate solutions serving as a source of Al(III).

Commonly, a mordenite-type zeolite is obtained using sodium aluminate solutions with Al_2O_3 and Na_2O concentrations of 150–200 and 200–230 g l^{-1}, respectively, as aluminum-containing reagents. However, the metastability of these solutins results in that the desired results are not always obtained. The composition of the reaction mixture can be disturbed in storage or upon dilution with water owing to the precipitation of aluminum hydroxide [1]. Coarse grains of aluminum hydroxide can play the part of foreign heterogeneous crystallization centers, which deteriorates the phase purity and the dispersion composition of the resulting zeolite. Furthermore, a separate unit for preparation of sodium aluminate solutions is required in commercial production of the zeolite.

In this communication, an industrially promising version of mordenite-type zeolite synthesis, with aluminum sulfate solutions as aluminum-containing raw material, is proposed.

EXPERIMENTAL

The synthesis was carried out in an autoclave with a stirrer and a sampler. The degree of crystallization and the type of the resulting zeolite were determined by X-ray phase analysis. The procedure for obtaining and studying zeolites is described in [2] in more detail.

Preliminary experiments have shown that mordenite-type zeolite can be synthesized from reaction mixtures containing (mol): $(1.8–7.1)Na_2O \cdot Al_2O_3 \times (12–30)SiO_2 \cdot (250–600)H_2O$, which were prepared by mixing aqueous solutions of sodium silicate and hydroxide, and also aluminum sulfate. The kinetics of solid phase crystallization was studied for this range of reaction mixture compositions at 125–170°C.

Kinetic curves describing mordenite crystallization at 130°C are presented in Fig. 1. They are S-shaped, which is characteristic of kinetic curves describing the crystallization of zeolites.

Approximately 35 h is necessary for mordenite with high degree (~100%) of crystallinity to be formed (Fig. 1, curve *1*). Raising the Na_2O/Al_2O_3 ratio (mol : mol) in the reaction mixture from 1.8 to 3.0 leads to

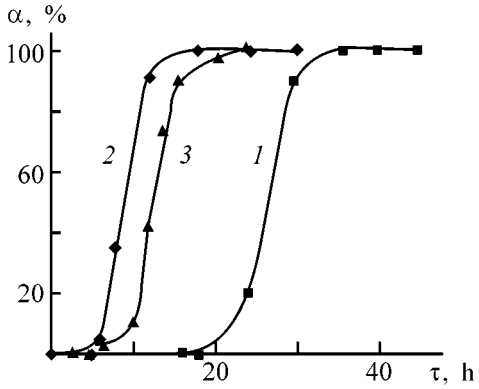

Fig. 1. Dependence of the degree of sample crystallinity, α, on the time τ of crystallization at 130°C of reaction mixtures obtained with the use of aluminum sulfate solution. Reaction mixture (mol): (*1*, *2*) $xNa_2O \cdot Al_2O_3 \cdot 12SiO_2 \times 250H_2O$ and (*3*) $7.1Na_2O \cdot Al_2O_3 \cdot 30SiO_2 \cdot 600H_2O$. *x*: (*1*) 1.8, (*2*) 3.0.

1070-4272/02/7508-1360 $27.00 © 2002 MAIK "Nauka/Interperiodica"

a twofold decrease in the duration of the induction period and in the total duration of the mordenite synthesis (Fig. 1, curve *2*).

A higher degree of dispersion is characteristic of mordenite crystals formed with the use of aluminum sulfate solutions, compared with those obtained using of sodium aluminate solutions. In the first case, the predominant crystal size is 4–5 μm, compared with 6–8 μm in the second [2].

An electron micrograph of mordenite crystals synthesized with the use of aluminum sulfate solutions is shown in Fig. 2. It is evident that the crystals are close in size, which seems to be associated with the formation of the main amount of crystallization centers in the nucleation stage, owing to the use of a true aluminum sulfate solution, instead of a colloidal sodium aluminate solution. This assumption is also confirmed by higher rate of mordenite formation. For example, the duration of synthesis of a mordenite with nearly 100% crystallinity from a $3Na_2O \cdot Al_2O_3 \cdot 12SiO_2 \cdot 300H_2O$ alumina-silica gel prepared using a sodium aluminate solution, is about 40 h at 135°C [2]. When mordenite is crystallized from an alumina-silica hydrogel with similar composition, prepared using an aluminum sulfate solution, the time of synthessis decreases to 18 h (Fig. 1, curve *2*), although the temperature of synthesis is 5°C lower in the second case.

The mordenite-type zeolite obtained using this method has an adsorption capacity of 0.14–0.15 and 0.08–0.09 $cm^3\ g^{-1}$ for, respectively, water and heptane vapor. Close values are characteristic of the mordenites described in [2].

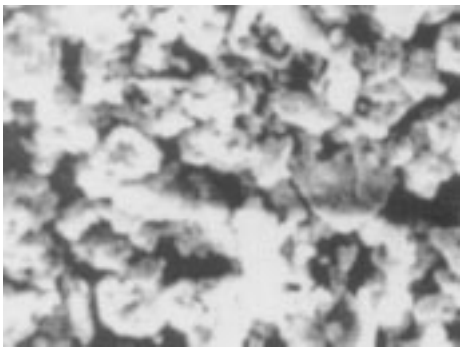

Fig. 2. Electron micrograph of a mordenite-type zeolite. (Magnification 1500).

CONCLUSION

A procedure has been developed for synthesis of finely dispersed mordenite with high phase purity and high degree of crystallinity (close to 100%). The procedure is based on crystallization at 125–170°C of an alumina-silica hydrogel prepared by mixing of gel-forming solutions of sodium silicate, sodium hydroxide, and aluminum sulfate in the ratio (mol) $(1.8–7.1)Na_2O \cdot Al_2O_3 \cdot (12–30)SiO_2 \cdot (250–600)H_2O$.

REFERENCES

1. Eremin, N.I., Naumchik, A.N., and Kazakov, V.G., *Protsessy i apparaty glinozemnogo proizvodstva* (Processes and Apparatus of Alumina Production), Moscow: Metallurgiya, 1980.
2. Pavlov, M.L., Makhamatkhanov, R.A., Kutepov, B.I., and Dzhemilev, U.M., *Zh. Prikl. Khim.*, 2001, vol. 74, no. 2, pp. 328–329.

Russian Journal of Applied Chemistry, Vol. 75, No. 8, 2002, pp. 1362–1363. Translated from Zhurnal Prikladnoi Khimii, Vol. 75, No. 8, 2002, pp. 1389–1390.
Original Russian Text Copyright © 2002 by Bannyi, Makarevich, Pinchuk, An.

BRIEF COMMUNICATIONS

Radio-Frequency Method for Measuring the Water Content of Liquids

V. A. Bannyi, A. V. Makarevich, L. S. Pinchuk, and B. G. An

Belyi Institute for Mechanics of Metal-Polymer Systems, Belarussian National Academy of Sciences, Gomel, Belarus

Korean Institute of Ceramics Technology, Seoul, Korea

Received March 20, 2002

Abstract—The method for radio-frequency measurements of water content in nonaqueous liquids is improved, and a procedure for measuring the concentration of water emulsified in oils and diesel fuels is described. Correlations between the composition of emulsions studied and the attenuation of the energy of electromagnetic radiation passing through the emulsions are revealed.

Emulsified water admixtures contained in nonaqueous technological liquids and fuels for machinery impair their service characteristics. For example, presence of water in transformer oil causes electric breakdown of the dielectric medium (oil) and short-circuiting of transformer windings. Water accumulated in motor oils in engine operation affects the functional properties of oils: their lubricating ability decreases, tendency toward sludge formation grows, etc. [1]. When minor amounts of water find their way into diesel fuels, the throughput capacity of fuel filters decreases and the corrosion rate of fuel tanks and lines increases. Determining quantitatively the content of water in nonaqueous technological liquids is an important task, which poses a serious technological problem.

Various methods are used in technology for measuring the water content. These methods differ in complexity, sensitivity, precision, and cost. Some techniques for determining the water content of liquid working media employ electromagnetic fields [2–6]. In particular, the radio-frequency (RF) method [5] relies upon the influence exerted by electromagnetic radiation (ER) of the microwave range with nonthermal intensity upon a liquid sample placed in the waveguide of a measuring instrument. The parameter measured in this case is the ER reflection coefficient for the surface of the liquid at its interface with air.

The aim of the present study was to improve the existing methods for RF water content measurements and to reveal and explain in terms of physical chemistry correlations between the water content of liquids and attenuation of the energy of ER passed through the liquids. The point is that the attenuation of the energy of ER passed through a liquid layer is used as the main recorded parameter, instead of the reflection coefficient. This makes it possible to reduce the volume of a sample being analyzed, with the sensitivity of the method preserved, and to use it for media with high content of water. For this purpose, a special cell for small-volume liquid samples and an original system for its fixation in the waveguide were designed.

As objects of study served nonaqueous technological liquids: diesel fuel, automotive ($M6_312G_1$) and transformer oils containing emulsified water. The emulsions were obtained by intensive mechanical dispersion of water in oil media. The content of water in the emulsions was determined using R2-61 standing-wave and ER-attenuation meter assembled in accordance with the attenuation measurement scheme (Fig. 1). Cell *1* was filled with the liquid under study

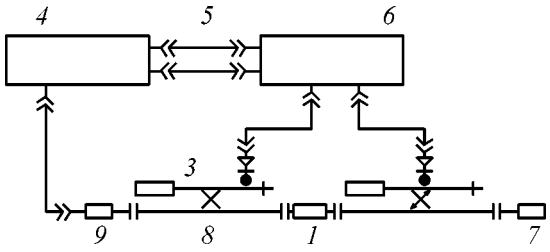

Fig. 1. Setup for measuring the attenuation of the energy of ER passing through a liquid being analyzed. (*1*) Cell with liquid, (*2*, *3*) detectors of incident and passed wave, (*4*) microwave generator, (*5*) connecting cables, (*6*) indicator of energy attenuation, (*7*) matched load, (*8*) waveguide, and (*9*) waveguide-to-coaxial adapter.

1070-4272/02/7508-1362 $27.00 © 2002 MAIK "Nauka/Interperiodica"

(layer thickness 3 cm) and placed between the detectors *2* and *3* of incident and passed ER. The parameter *S* of ER attenuation was measured at a fixed frequency and the water content was found from the calibration concentration dependences *S*–*c* for reference liquids.

Analysis of the data in Figs. 2a and 2b shows that the intensity of ER interaction with the dispersed liquid–liquid systems under study depends on, at least, several factors. Of fundamental importance is the dielectric constant of the dispersed medium, which is higher in diesel fuel, compared with oils [7]. Other important factors changing the conditions of absorption and scattering of the ER energy are the concentration *c* and particle size of the dispersed phase (water).

The dependences of *S* on *c* are exponential (Fig. 2b). At concentration *c* in the range from 3 to 20 vol % they are virtually linear and have high slope, which predetermines the high sensitivity of the method. The main contribution to the attenuation of the energy of the passing ER comes in this case from dielectric losses, which markedly grow with increasing content of water, which is characterized by high dielectric constant. The measurement results are also affected by the energy loss for ER scattering at the interface between the dispersed phase and dispersion medium. With the concentration of water increasing to above 20 vol %, the run of the *S*–*c* curves changes, with only a small rise in *S* corresponding to large increments Δc. It is believed that, at high content of water in oil emulsions, ER mainly interacts with the dispersed (aqueous) phase whose particles become coarser as a result of coagulation.

The resolving power of the proposed RF method for measuring the water content of liquids is 0.5–1.0 vol %.

CONCLUSIONS

(1) A radio-frequency technique for water content measurements is proposed. This technique belongs to physicochemical methods for studying colloid systems with the use of microwave electromagnetic radiation and is based on the difference between the dielectric properties of the components of the systems under study.

(2) The technique proposed ensures simplicity, accessibility, and reliability analysis of liquids for water content and can be used to study coagulation processes in colloid systems.

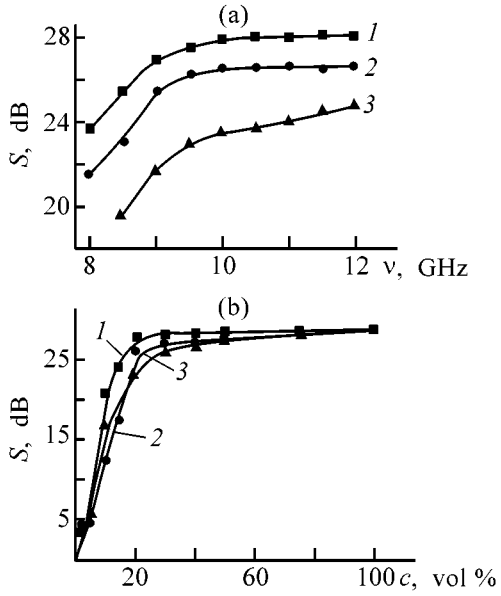

Fig. 2. Parameter *S*, characterizing ER energy attenuation, vs. (a) ER frequency ν and (b) concentration *c* of water in samples under study. (a) Content of water in technological liquid 20 vol % and (b) ER frequency 10 GHz. (*1*) Diesel fuel, (*2*) transformer oil, and (*3*) automobile oil.

REFERENCES

1. Boltanina, M.A., Shor, G.I., Fuks, I.G., *et al.*, *Khim. Tekhnol. Topl. Masel*, 2001, no. 4, pp. 49–51.
2. RF Patent 2 011 185.
3. RF Patent 2 084 877.
4. RF Patent 2 073 852.
5. RF Patent 2 096 768.
6. RF Patent 2 132 051.
7. *Fizika, Bol'shoi entsiklopedicheskii slovar'* (Physics: Comprehensive Encyclopedia), Prokhorov, A.M., Ed., Moscow: Bol'shaya Ross. Etsiklopediya, 1999.

Russian Journal of Applied Chemistry, Vol. 75, No. 8, 2002, pp. 1364–1366. Translated from Zhurnal Prikladnoi Khimii, Vol. 75, No. 8, 2002, pp. 1391–1393.
Original Russian Text Copyright © 2002 by Suvorova, Tishchenko, Iozep, Passet.

BRIEF COMMUNICATIONS

Influence of the Solution Acidity and pK_a of the Amine on the Reaction of Dextran Polyaldehyde with Amines

O. B. Suvorova, E. V. Tishchenko, A. A. Iozep, and B. V. Passet

St. Petersburg State Academy of Pharmaceutical Chemistry, St. Petersburg, Russia

Received March 7, 2002

Abstract—The influence exerted by the solution pH and pK_a of the amine on the reaction of dextran polyaldehyde with aromatic and aliphatic amines was studied.

As shown previously [1], the solution pH strongly influences the reactions of polysaccharide aldehydes with amines; the pH values at which the maximal degrees of substitution are attained correlate with the acidity constants of the amines. In this context, our goal was to study the influence exerted by the solution acidity on the yield of the target product in the reaction of dextran polyaldehyde (DPA) with aromatic and aliphatic amines.

The chemical modification of DPA was performed by the scheme

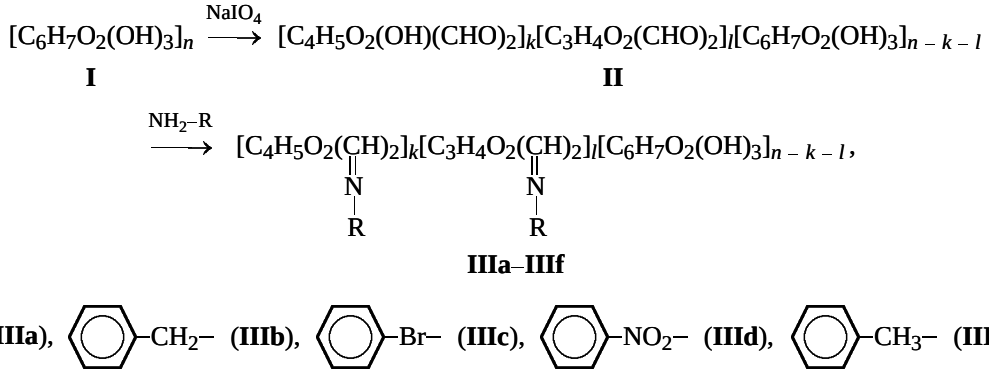

R = ⬡– (**IIIa**), ⬡–CH_2– (**IIIb**), ⬡–Br– (**IIIc**), ⬡–NO_2– (**IIId**), ⬡–CH_3– (**IIIe**), OH (**IIIf**).

Dextran **I** was activated by periodate oxidation in an acetate buffer solution (pH 4.1). The metaperiodate consumption was monitored spectrophotometrically at 222.5 nm, and the amount of the formic acid released was determined by volumetric titration. After oxidation completion, the reaction mixture was dialyzed to remove low-molecular-weight substances, and the polyaldehyde was precipitated with ethanol after concentrating the solution in a vacuum at 60°C.

DPA samples were characterized by the degree of substitution C_{sa} (number of aldehyde groups per monosaccharide unit of the polymer), which was determined by the oxime and hydroxamic procedures [2]. In the samples used, C_{sa} varied from 0.73 to 1.

The reactions of DPA with amines were performed for 2 h at 18–20°C; the reactant ratio was 3 mol of aromatic or 2 mol of aliphatic amine per mole of aldehyde groups. The solution pH was varied from 0.5 to 10. After reaction completion, the mixture was diluted with 10 volumes of alcohol, and the precipitated products were filtered off, washed with alcohol and ether, and vacuum-dried (60°C, 20–25 mm Hg) for 2 h. The absence of low-molecular-weight impurities in the samples was confirmed by thin-layer chromatography.

The polymeric azomethines synthesized were characterized by the degree of substitution C_s (number of amine fragments per monosaccharide unit), which was

1070-4272/02/7508-1364 $27.00 © 2002 MAIK "Nauka/Interperiodica"

calculated from the analytical data and results of conductometric titration of the samples hydrolyzed with 0.1 N HCl; the extent of the reaction with amines was characterized by the degree of conversion of aldehyde groups C_{ca} (%), defined as $C_{ca} = (C_s/C_{sa}) \times 100$.

The samples are white, light creamy, yellow, or orange amorphous powders insoluble in water, alcohol, ether, acetone, and most of other organic solvents.

The IR spectra of the reaction products contain absorption bands at 1600, 690, and 750 cm^{-1}, characteristic of monosubstituted benzene, at 1640–1660 cm^{-1}, belonging to C=N stretching vibrations, and (for *p*-substituted benzene derivatives) also at 810 cm^{-1}. The product of the reaction of DPA with *p*-nitroaniline also exhibits absorption at 1560 cm^{-1}, characteristic of the NO_2 stretching vibrations.

In accordance with the reaction mechanism, the rate of transformation of the aldehyde groups into azomethine groups depends on the nucleophilicity of the amine. There is no common nucleophilicity scale, and we assume the nucleophilicity of primary amines to be proportional to the quantity pK_a, characterizing their basicity.

Indeed, if the reactions with primary amines are performed under similar conditions at the same pH, there is a linear correlation between the degree of conversion of DPA aldehyde groups into azomethines and the pK_a value of the amine (Table 1):

$$C_{ca(pH\ 7)} = 20.5\,pK_a - 13.16\ (n = 5,\ R^2 = 0.986).$$

Also, C_{ca} linearly correlates with the σ_p constants of substituents in the aromatic ring (Table 1). This fact shows that C_{ca} correlates with the reaction rate. For *p*-substituted amines, the correlation between C_{ca} and the Hammett constants is as follows: $C_{ca} = -87.14\sigma_p + 79.06$ ($n = 5$, $R^2 = 0.996$). Electron-withdrawing substituents decrease, and electron-donor substituents enhance the reactivity of amines toward DPA.

As expected, the acidity of the reaction mixture strongly affects the yield of the products in reactions of DPA with amines. The optimal pH at which the degree of conversion of DPA aldehyde groups reaches a maximum correlates with pK_a of the amine (Fig. 1, Table 2).

For each amine, there is a certain pH at which the rate of its reaction with DPA is the highest. With strong (benzylamine) and very weak (*p*-nitroaniline) nucleophiles, the yield of the target product decreases by a factor of 1.5–2 when the pH of the reaction mixture differs from the optimum by ±1.5 units; with aniline and *p*-bromoaniline, the pH dependence of the conversion of DPA aldehyde groups is less pronounced. With less nucleophilic amines (*p*-nitroaniline, *p*-bromoaniline, aniline), a catalytic effect of the acid is required for the reaction to occur. Stronger bases (*p*-toluidine, hydroxylamine, benzylamine), by contrast, better react with DPA in neutral and alkaline solutions.

Table 1. Degree of conversion of aldehyde groups into azomethine groups in reactions of DPA with aromatic amines in relation to pK_a of the amine and the Hammett constant σ_p (pH 7, 20°C, 3 mol of amine per mole of aldehyde groups)

Amine	pK_a	σ_p	C_{ca}, %
p-Nitroaniline	1.02	0.778	10
p-Bromoaniline	3.91	0.232	61
Aniline	4.63	0	81
p-Toluidine	5.12	–0.170	91
p-Phenetidine	5.25	–0.268	100

Table 2. pH values at which the conversion of DPA aldehyde groups in reactions with amines reaches a maximum (15–20°C, 2 h, 3 mol of amine per mole of aldehyde groups)

Amine	pK_a of amine	pH
p-Nitroaniline	1.02	1.03
p-Bromoaniline	3.91	4.6
Aniline	4.63	5.88
p-Toluidine	5.12	6.6
Hydroxylamine	5.97	7.45
Benzylamine	9.33	10.45

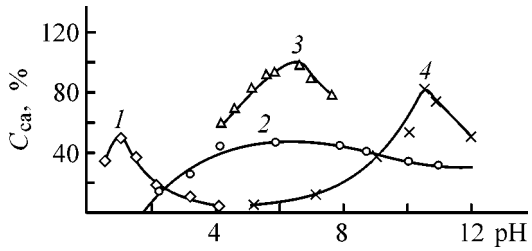

Fig. 1. Degree of conversion, C_{ca}, of DPA aldehyde groups in reactions with (*1*) *p*-nitroaniline, (*2*) aniline, (*3*) *p*-toluidine, and (*4*) benzylamine vs. pH.

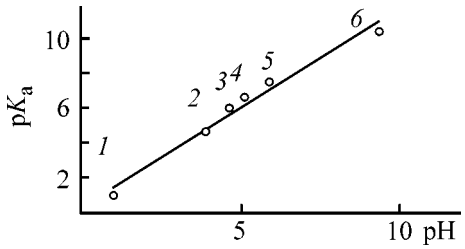

Fig. 2. Correlation of the optimal pH for the reactions of DPA with (*1*) *p*-nitroaniline, (*2*) *p*-bromoaniline, (*3*) aniline, (*4*) *p*-toluidine, (*5*) hydroxylamine, and (*6*) benzylamine with pK_a of the amine.

Based on these data, we plotted the optimal pH values against the basicity (pK_a) of the amine (Fig. 2).

We found that the correlation between these quantities is linear: pH = 1.47 pK_a + 0.28 (n = 6, R^2 = 0.9822). That is, the more basic the amine, the higher the optimal pH value.

Using this correlation, we can estimate *a priori* the optimal pH values for the reactions of DPA aldehyde groups with other amines, which will significantly simplify development of procedures for modification of polyaldehydes with biologically active substances.

CONCLUSION

In reactions of dextran polyaldehyde with amines, the highest rate is attained at certain optimal pH values, which correlate with pK_a of the amine: pH = 1.47 pK_a + 0.28. This correlation allows the *a priori* estimation of the optimal reaction conditions.

REFERENCES

1. Suvorova, O.B., Iozep, A.A., and Passet, B.V., *Zh. Prikl. Khim.*, 2001, vol. 74, no. 6, pp. 988–992.
2. Iozep, A.A., Suvorova, O.B., Iozep, L.I., and Passet, B.V., *Zh. Prikl. Khim.*, 1998, vol. 71, no. 7, pp. 1202–1205.

Russian Journal of Applied Chemistry, Vol. 75, No. 8, 2002, pp. 1367–1368. Translated from Zhurnal Prikladnoi Khimii, Vol. 75, No. 8, 2002, pp. 1394–1395.
Original Russian Text Copyright © 2002 by Aliskerov, Aliev, Kharlamova.

BRIEF COMMUNICATIONS

Reaction of Chlorine in Aqueous Solution with Hydrolysis Lignin under Elevated Pressure

A. R. Aliskerov, Z. M. Aliev, and T. A. Kharlamova

Dagestan State University, Makhachkala, Dagestan, Russia
Moscow State University of Food Industry, Moscow, Russia

Received October 4, 2001; in final form, April 2002

Abstract—Chlorination and oxidation of hydrolysis lignin with chlorine in aqueous solution under elevated pressure was studied with the aim to intensify the process.

Chlorination is one of promising ways to modify technical-grade lignins, a large-tonnage waste from hydrolysis, pulp-and-paper, and sulfite-and-alcohol industry. Chemical chlorination of hydrolysis lignin has been studied in sufficient detail [1–3]. Chlorination involves substantial activation of lignin macromolecules owing to incorporation of chlorine and oxidation, accompanied by an increase in the content of carbonyl and carboxy groups.

The goal of this study was to prepare chlorinated lignins with high content of chlorine and other functional groups under elevated pressure.

EXPERIMENTAL

Experiments were performed with coniferous hydrolysis lignin. Chlorination of lignin saturated with chlorine under elevated pressure (0.1 to 0.6 MPa) was performed in an autoclave made of a titanium alloy and lined with fluoroplastic. Gaseous chlorine from a cylinder was purified by passing through distilled water in an intermediate vessel and then was fed into the autoclave containing 50 g of hydrolysis lignin suspended in 0.5 l of distilled water. The contents were stirred for 2–3 h on a laboratory magnetic stirrer to attain the phase equilibrium (monitored with a manometer). Chlorination was performed at approximately 20°C for 3 h. The experimentally determined solubility of Cl_2 is 0.72 g per 100 g of water (with increasing temperature, it decreases to 0.56 g of Cl_2 per 100 g of water). The resulting chlorinated lignin was filtered through a paper filter, washed to negative reaction for chloride ions, and dried first in air and then at 40°C in a vacuum desiccator to constant weight. The content of functional groups was determined as described in [4], and that of chlorine, according to [5]. The UV spectra were taken with a Specord UV VIS spectrophotometer [6].

Data on the content of chlorine and functional groups in chlorinated lignins prepared under various pressures are listed in the table.

It is seen that, with increasing pressure, the content of chlorine and of carbonyl and carboxy groups increases, and the content of methoxy and hydroxy groups decreases.

Elevated pressures favor chlorination of lignin because of the increased content in solution of the chlorinating agent, molecular chlorine. Its solubility grows, and the degree of its hydrolysis decreases [7–9].

The aromatic rings in lignin macromolecules are chlorinated first. This is confirmed by the fact that the chlorine content in chlorinated lignins does not noticeably decrease after their saponification with 5% NaOH. The generally accepted mechanism of

Content of chlorine and functional groups in chlorinated lignins as influenced by the pressure in the autoclave

P, MPa	Content, %				
	–Cl	$-OCH_3$	=CO	–COOH	–OH
Initial lignin	–	10.8	3.1	1.0	9.2
0.1	26.9	6.2	15.9	16.3	8.2
0.3	30.1	4.1	21.5	20.1	8.8
0.5	31.9	3.2	24.7	24.3	8.1
0.6	32.5	2.7	25.0	24.9	7.8

1070-4272/02/7508-1367 $27.00 © 2002 MAIK "Nauka/Interperiodica"

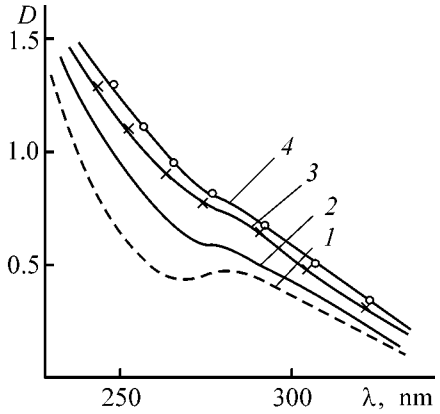

UV spectra of solutions of (*1*) initial hydrolysis lignin and (*2*–*4*) chlorinated lignin prepared at pressures of (*2*) 0.1, (*3*) 0.5, and (*4*) 0.6 MPa. (*D*) Optical density and (λ) wavelength.

chlorination of aromatic rings in lignin is shown below:

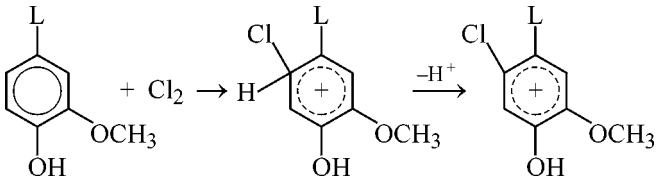

Further chlorination involves side chains of lignin macromolecules:

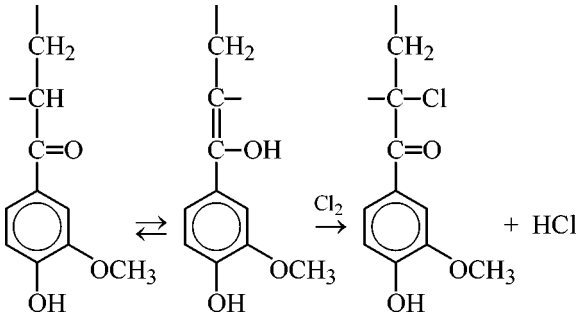

It is known [1] that chlorination under atmospheric pressure decreases the content of methoxy groups; since the chlorine content in lignin increases with chlorine pressure, elevated pressures apparently favor demethoxylation.

The demethoxylation usually yields phenolic groups. However, our experiments show that the content of phenolic hydroxyls in chlorinated lignin prepared under elevated pressure is lower than that in the initial lignin. Probably, chlorination under elevated pressure is accompanied by oxidation of hydroxy derivatives to carbonyl compounds. *o*-Benzoquinones are formed, which are oxidized further, as indicated by the increased content of carboxy groups originating from degradation of lignin with breakdown of aromatic rings to dicarboxylic acids. The breakdown of the aromatic rings is clearly seen in the UV spectra of chlorinated lignins (see figure): A clear maximum at 280 nm, characteristic of hydrolysis lignin, transforms into an ill-defined shoulder even at low pressures. In the spectra of chlorinated lignins prepared under higher pressures (0.5, 0.6 MPa), this peak is virtually lacking, which suggests decreased content of guaiacyl and syringyl structures.

CONCLUSION

With increasing chlorine pressure, the chlorine content in chlorinated lignins grows, with the extent of oxidation and degradation of lignin macromolecules increasing.

REFERENCES

1. *Lignins: Occurrence, Formation, Structure, and Reactions*, Sarkanen, K.V. and Ludwig, C.H., Eds., New York: Wiley, 1971.
2. Nikitin, V.M., Obolenskaya, A.V., and Shchegolev, V.P., *Khimiya drevesiny i tsellyulozy* (Chemistry of Wood and Cellulose), Moscow: Lesnaya Prom–st., 1978.
3. Grushnikov, O.P. and Shorygina, N.N., *Khim. Drev.*, 1971, no. 7, pp. 3–29.
4. Zakis, G.F., Mozheiko, L.N., and Telysheva, G.M., *Metody opredeleniya funktsional'nykh grupp lignina* (Methods for Determination of Functional Groups in Lignin), Riga: Zinatne, 1975.
5. *Houben–Weyl, Methoden der organischen Chemie*, vol. 2: *Analytische Methoden*, Stuttgart: Thieme, 1953.
6. Moiseeva, D.P., Sokolova, A.A., Likhushina, L.K., and Semakova, L.A., *Khim. Drev.*, 1975, no. 4, p. 72.
7. Gupalo, A.P., Teodorovich, R.E., and Vatamanyuk, N.M., *Sintez galogenirovannykh ligninov i ikh gidroliz* (Synthesis and Hydrolysis of Halogenated Lignins), Moscow: Gidroliznaya i Lesokhimicheskaya Prom–st., 1975.
8. Smirnov, V.A., Aliev, Z.M., Karapysh, V.V., and Gurchin, I.I., *Zh. Fiz. Khim.*, 1974, vol. 48, no. 5, pp. 1241–1243.
9. Smirnov, V.A. and Aliev, Z.M., *Zh. Fiz. Khim.*, 1976, vol. 50, no. 5, pp. 1132–1135.

Russian Journal of Applied Chemistry, Vol. 75, No. 8, 2002, pp. 1369–1370. Translated from Zhurnal Prikladnoi Khimii, Vol. 75, No. 8, 2002, pp. 1396–1397.
Original Russian Text Copyright © 2002 by V. Maslosh, Kotova, O. Maslosh.

BRIEF COMMUNICATIONS

Effect of Acetylacetone on the Residual Content of Formaldehyde in Urea–Formaldehyde Resin

V. Z. Maslosh, V. V. Kotova, and O. V. Maslosh

Institute of Applied Chemistry, Ministry of Education and Science of Ukraine, Rubezhnoe, Lugansk oblast, Ukraine

Received March 25, 2002

Abstract—The effect of small additions of acetylacetone and ammonia to urea–formaldehyde resin is considered. The occurring processes, involving the formation of 2,6-dimethyl-3,5-diacetyl-1,4-dihydropyridine and condensation of this compound and acetylacetone with terminal methylol groups of the resin, are discussed.

Stringent environmental requirements are imposed upon the quality of urea–formaldehyde resins (UFRs), which are widely used as binders and are produced on large scale in many countries.

The major drawback of UFRs is their toxicity, resulting from the presence of free formaldehyde. The toxicity can be decreased by improving the production process or introducing special additives that bind free formaldehyde. Numerous additives have been patented for this purpose [1–7], such as urea, thiourea, melamine, higher aldehydes and ketones, aliphatic amines, some inorganic compounds, etc. However, the problem of decreasing the content of free formaldehyde in UFRs remains topical.

The poor performance of the majority of additives may be due to the fact that they react with formaldehyde relatively slowly and reversibly. Thus, the following requirements to the additives can be formulated *a priori*: They should react with formaldehyde fast and irreversibly in the absence of strong acids, bases, and oxidants degrading UFRs or causing their premature curing. Furthermore, the additives and products of their reactions with formaldehyde should be well compatible with UFRs.

Despite the fact that the formaldehyde chemistry has been extensively studied [8, 9], there are only a few reactions meeting these requirements. One of them is the reaction of formaldehyde with β-diketones and ammonia, yielding pyridine derivatives [10]. This reaction is fast at room temperature, even at very low concentration of formaldehyde.

In this study, we examined the possibility of using this reaction to decrease the content of free formaldehyde in UFR.

EXPERIMENTAL

We used a commercial sample of KFMP-15 resin containing 0.5% free formaldehyde; 99% pure acetylacetone; and 25% aqueous ammonia, pure grade.

A glass beaker was charged with 100 g of the resin, and 3.36 g of acetylacetone and aqueous ammonia containing 0.57 g of NH_3 were added. The mixture was stirred at room temperature for 30 min, after which the content of free formaldehyde and the conventional viscosity (VZ-4 viscometer) were determined. Samples were placed in a hermetically sealed vessel, and their viscosity and free formaldehyde content were determiend daily [11, 12].

Experiments were performed with the simplest β-diketone, acetylacetone. Addition to UFR of a mixture of acetylacetone and ammonia (molar ratio 2 : 1) in amount of about 3 wt % fully eliminates free formaldehyde. Monitoring of the sample for 9 days showed that no free formaldehyde appeared in UFR. In a control sample (without addition of acetylacetone and ammonia), the content of free formaldehyde varied within 0.3–0.7%. After adding acetylacetone and ammonia, the resin appearance changed: Within 30 min, the resin became orange-yellow, and the color grew in intensity in the course of 9-day storage at room temperature. Three days after preparing the mixture, the characteristic acetylacetone odor disap-

1070-4272/02/7508-1369 $27.00 © 2002 MAIK "Nauka/Interperiodica"

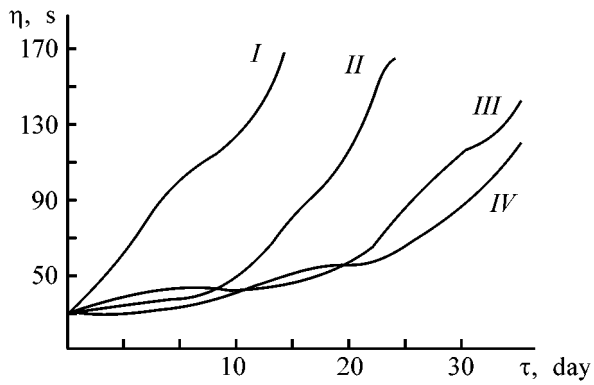

Conventional viscosity η of urea–formaldehyde resin vs. storage time τ. Acetylacetone : ammonia molar ratio: (*I*) 1 : 0.5, (*II*) 1 : 1, and (*III*) 1 : 1.5; (*IV*) control sample without additives.

peared. In the course of 9-day storage, the resin viscosity rapidly increased (to 150 s), after which the resin became unsuitable for use (see figure), whereas the viscosity of the control sample remained virtually constant within this period. The rapid growth of the viscosity can be avoided by increasing the amount of ammonia added from 0.5 to 1.3 mol per mole of acetylacetone. Such a concentration increases the working life of the resin to 29 days (see figure); throughout this period, no free formaldehyde was detected in the resin.

Let us discuss the possible mechanism of formaldehyde binding. It is known that acetylacetone reacts with acetone and formaldehyde (Hansch reaction [10]) to give 2,6-dimethyl-3,5-diacetyl-1,4-dihydropyridine.

$$CH_3COCH_2COCH_3 + CH_2O + NH_4OH$$

$$\xrightarrow[-H_2O]{} \begin{array}{l} H_3C{=}COCH_3 \\ HN \\ H_3C{=}COCH_3 \end{array}$$

The formation of this product is confirmed by the appearance of a characteristic yellow-orange color (λ_{max} = 410 nm). However, the role of acetylacetone is not limited to this reaction. The disappearance of the acetylacetone odor and the growth of the viscosity suggest a reaction of acetylacetone with reactive groups of the resin and incorporation of acetylacetone into the polymer chain. The most probable pathway of acetylacetone binding may be its reaction with terminal *N*-methylol groups of the resin (Mannich reaction [13]):

$$-CO-NHCH_2OH + CH_3COCH_2COCH_3$$

$$\rightarrow -CO-NH-CH_2-\underset{\displaystyle COCH_3}{\overset{\displaystyle COCH_3}{CH}} + H_2O.$$

Acetylacetone is very reactive in Mannich reactions [14]. Since it contains several active hydrogen atoms in the methylene and methyl groups, it can react as a polyfunctional monomer.

2,6-Dimethyl-3,5-diacetyl-1,4-dihydropyridine can also enter the Mannich reaction via methyl groups bound to the heteroring and carbonyl carbon atoms; it can react as a polyfunctional monomer also. Therefore, the increase in the resin viscosity may be due to the presence of polyfunctional monomers capable of forming cross-linked structures. Indeed, heating of the resin with the additives to 100°C in the absence of acid catalysts causes formation of a solid nonmelting polymer within several minutes. The control sample of the resin is not cured in the absence of acid catalysts.

Our results demonstrate that UFR containing no free formaldehyde can be prepared by adding acetylacetone and ammonia.

REFERENCES

1. Melcerová, A., Melcer, I., and Vomelová, S., in *Zb. Pr. Drev. Fak. Vysk. Šk. Les. Drev. Zlovene, 1985–1986*, Bratislava, 1987, pp. 123–161.
2. JPN Patent 48–17 755.
3. French Patent Appl. 2575-754.
4. Mladenov I. and Vladnova T., *Khim. Ind.*, 1987, vol. 59, no. 1, pp. 16–17.
5. UK Patent 1 598 338.
6. JPN Patent 52–36 129.
7. Wirpza, Z., *Polimerytwozz. Wielkocracfeczk.*, 1972, vol. 17, no. 18, pp. 416–419.
8. Walker, J.F., *Formaldehyde*, New York: Am. Chem. Soc., 1953, 2nd ed.
9. Ogorodnikov, S.K., *Formal'degid* (Formaldehyde), Leningrad: Khimiya, 1984.
10. *Kratkaya khimicheskaya entsiklopediya* (Concise Chemical Encyclopedia), Knutyants, I.L., Ed., Moscow: Sov. Entsiklopediya, 1961, p. 806.
11. *TU* (Technical Specifications) *6-06-12–88: Urea–Formaldehyde Resin of KF-MT-15 Brand*, Item 3.5: *Determination of the Weight Fraction of Formaldehyde.*
12. *GOST* (State Standard) *8420–74: Determination of Conventional Viscosity with a VZ-4 Viscometer.*
13. Weygand–Hilgetag, *Organisch-chemische Experimentierkunst*, Leipzig: Johann Ambrosius Barth, 1964, 3rd ed.
14. *Organic reactions*, Adams, R., Ed., New York: Wiley, 1942, vol. I.

Russian Journal of Applied Chemistry, Vol. 75, No. 8, 2002, pp. 1371–1372. Translated from Zhurnal Prikladnoi Khimii, Vol. 75, No. 8, 2002, pp. 1398–1400.
Original Russian Text Copyright © 2002 by Kovalets, Aleinikova, Derbisher.

BRIEF COMMUNICATIONS

Synthesis of Diperoxy Acetals and Their Use in Production of Latexes for Textile Finishing

I. Yu. Kovalets, T. P. Aleinikova, and V. E. Derbisher

Volgograd State Technical University, Volgograd, Russia

Received February 14, 2002

Abstract—Conditions of synthesis of hydroxyl-containing mono- and diperoxy acetals by the reactions of α-chloroethyl *tert*-butyl peroxide with triethylene glycol and glycerol were determined. These compounds were used for preparing latexes.

The diversity of existing and new requirements to peroxides used in polymer synthesis and processing makes it necessary to extend their assortment and functionality, improve preparation processes, study comprehensively their physicochemical properties, optimize conditions for radical generation, and find conditions of their use in polymer synthesis.

Dialkyl peroxides and their derivatives are of interest in this respect, especially from the viewpoint of their functionality, since these compounds, when decomposing, generate not only alkoxy but also alkyl radicals, which actively initiate radical polymerization. Among such peroxides are, in particular, peroxy acetals containing peroxy and alkoxy groups separated by a carbon atom. Experiments on vulcanization of siloxane, ethylene–propylene, and liquid carboxyl-containing rubbers with functionally substituted peroxy acetals demonstrated their high performance, e.g., in cross-linking of saturated elastomers [1]. These compounds also show promise as initiators of high-temperature radical additions across C=C bonds [2]. Owing to their high thermal stability, low sensitivity to shocks and friction, and low toxicity, peroxy acetals can be widely used to initiate not only polymerization, but also some high-temperature radical processes in various branches of chemical industry.

It should be noted that the available data on synthesis of peroxy acetals are insufficient for setting up their commercial production. In this study, we prepared peroxy acetals by the reactions of α-chloroethyl *tert*-butyl peroxide (α-CETBP) with triethylene glycol (TEG) and glycerol (GL):

$$\begin{array}{l} CH_2{-}OH \\ | \\ R_1 \\ | \\ CH_2{-}OH \end{array} + Cl{-}CH(CH_3){-}O{-}O{-}C(CH_3)_3$$

$$\xrightarrow{-HCl} \begin{array}{l} CH_2{-}O{-}CH(CH_3){-}O{-}O{-}C(CH_3)_3 \\ | \\ R_1 \\ | \\ CH_2{-}OH \end{array} \quad (1)$$

$$\begin{array}{l} CH_2{-}OH \\ | \\ CH{-}OH \\ | \\ CH_2{-}OH \end{array} + 2Cl{-}CH(CH_3){-}O{-}O{-}C(CH_3)_3$$

$$\xrightarrow{-2HCl} \begin{array}{l} CH_2{-}O{-}CH(CH_3){-}O{-}O{-}C(CH_3)_3 \\ | \\ CH{-}O{-}CH(CH_3){-}O{-}O{-}C(CH_3)_3 \\ | \\ CH_2{-}OH \end{array} \quad (2)$$

where $R_1 = (CH_2{-}O{-}CH_2)_2$.

In view of the fact that the initial chloro peroxides are readily hydrolyzed, the chemicals used in the synthesis were thoroughly dried.

Hydrogen chloride was removed from the reaction mixture by purging the reactor with dry nitrogen or argon. It is advisable to perform the reaction at 65°C for 2.5 h. Higher temperatures or longer reaction times are not appropriate, as leading to a decreased content of available oxygen. The diperoxy acetals synthesized were purified by common procedures and analyzed.

The structure of the products was confirmed by IR spectroscopy, titrations, and elemental analysis (see table), and their purity, also by thin-layer chromatography. The ether groups give an absorption band in the range 1000–1300 cm^{-1}; the peroxy groups, a broad band at 820–890 cm^{-1}; also, absorption is observed in the range 2500–3600 cm^{-1}. A broad band at 1160–1190 cm^{-1} is due to C–O vibrations. Broad bands originating from stretching vibrations of alkyl-substituted hydroxy groups are observed at about 3400 cm^{-1}.

1070-4272/02/7508-1371 $27.00 © 2002 MAIK "Nauka/Interperiodica"

Experimental and calculated characteristics of peroxy acetals

Product	Available oxygen content		Hydroxyl number		Found		Calculated	
	%							
	experiment	calculation	experiment	calculation	C	H	C	H
Monoperoxy acetal	5.97	6.02	6.10	6.39	56.3	9.43	56.5	9.9
Diperoxy acetal	9.73	9.85	4.95	5.26	43.5	9.5	43.7	9.7

Peroxy acetals were tested without isolation as initiators for preparing butadiene–styrene, butadiene–acrylonitrile, polyvinyl chloride, polyacrylate, and polystyrene latexes. In the last case, sodium dibutylnaphthalenesulfonate (Nekal') mixed (1 : 1) with nonionic surfactant OP-10 (6.5 wt parts per 100 wt parts of the monomer) was used as emulsifier. The concentrations of the polymers in the latexes were 16–18%.

The latexes prepared were used for impregnation of various textile fabrics (polymer content on the fiber 1.6–1.8%) containing natural and manmade fibers by the procedure accepted in textile finishing [3]. The most interesting results were obtained with polyacrylate and butadiene–styrene latexes: The durability, strength, and resistance to wet-heat treatments of the finished textile materials increased by 90–170%.

EXPERIMENTAL

α-Chloroethyl *tert*-butyl peroxide. Technical-grade *tert*-butyl hydroperoxide was purified by treatment with sodium carbonate, followed by vacuum distillation. Chloroform used as solvent was purified according to [4]. A reactor equipped with a stirrer, a thermometer, and a bubbler was charged with a solution of 9.6 g (0.23 mol) of acetaldehyde in 50 ml of chloroform and 18 g (0.20 mol) of *tert*-butyl hydroperoxide. Dry hydrogen chloride (8.0–8.5 g, 0.22–0.24 mol) was passed at 263–268 K. After phase separation, the aqueous layer was removed, and the organic layer was dried over sodium sulfate. The product was isolated by vacuum distillation (bp 298–299 K at 3 mm Hg). Yield of α-CETBP 21.4 g (70%); n_D^{20} 1.4194.

Monoperoxy acetals. A reactor equipped with a stirrer, a thermometer, and a reflux condenser was charged with 0.2 mol of α-CETBP, to which 40 ml of dry chloroform and 15 g (0.1 mol) of TEG were added. The HCl released was removed with a flow of a dry inert gas and absorbed with an NaOH solution placed in a stirred bubbler. Then the reaction mixture was washed with 15% aqueous $NaHCO_3$ and water to neutral reaction. The resulting solution was dried over sodium sulfate. After removal of the solvent, the product was analyzed. Yield 53% based on the initial chloro peroxide; n_D^{20} 1.4278, d^{20} 1.4938.

Diperoxy acetals were prepared similarly using glycerol instead of TEG. A reactor was charged with 40 ml of chloroform, 6.2 g (0.07 mol) of glycerol, and 30.5 g (0.21 mol) of α-CETBP. The mixture was worked up as described above. Yield 67% based on the initial chloro peroxide; n_D^{20} 1.4465, d^{20} 1.3389.

The IR spectra were taken on a Specord M82 spectrophotometer.

Active oxygen was determined by iodometric titration [5], and hydroxyl number, according to [6].

CONCLUSIONS

(1) Hydroxyl-containing peroxy acetals were prepared by reactions of α-chloroethyl *tert*-butyl peroxide with polyhydric alcohols.

(2) Peroxy acetals were successfully tested as initiators of radical polymerization in preparation of latexes for textile finishing.

REFERENCES

1. Pestov, A.G., Cross-Linking of SKEP Rubber with α-Hydroxyalkyl Peroxides and Their Functional Derivatives, *Cand. Sci. Dissertation*, Volgograd, 1975.
2. Khardin, A.P. and Navrotskii, V.A., in *Khimiya organicheskikh peroksidov: Sbornik nauchnykh trudov VPI* (Chemistry of Organic Peroxides: Coll. of Scientific Works of Volgograd Polytechnic Inst.), Volgograd, 1982, pp. 35–45.
3. Krichevskii, G.E., Korchagin, M.V., and Senakhov, A.V., *Khimicheskaya tekhnologiya tekstil'nykh materialov* (Chemical Technology of Textiles), Moscow: Legprombytizdat, 1985.
4. Gordon, A.J. and Ford, R.A., *The Chemist's Companion. A Handbook of Practical Data, Techniques, and References*, New York: Wiley, 1972.
5. Aleinikova, T.P., Brailovskaya, A.A., and Kargina, L.V., *Zh. Anal. Khim.*, 1984, vol. 39, no. 6, pp. 1120–1123.
6. Kalinina, L.S., *Kachestvennyi analiz polimerov* (Qualitative Analysis of Polymers), Moscow: Khimiya, 1975.

Russian Journal of Applied Chemistry, Vol. 75, No. 8, 2002, p. 1373. Translated from Zhurnal Prikladnoi Khimii, Vol. 75, No. 8, 2002, p. 1401.
Original Russian Text Copyright © 2002 by Morachevskii.

BOOK REVIEWS

Chernov, Ya.B., Afinogenov, A.I., and Shurov, N.I., *Borirovanie stalei v ionnykh rasplavakh* (Boronizing of Steels in Ionic Melts), Yekaterinburg: Ur. Otd. Ross. Akad. Nauk, 2001, 223 pp.

Systematic studies of steel boronizing with the use of ionic melts have been carried out at the Institute of High-Temperature Electrochemistry, Ural Division, Russian Academy of Sciences, since 1965. The investigations were commenced by professor N.G. Ilyushchenko and are continued now by his pupils. The primary attention has been given to deposition of boride coatings on steels by liquid electroless diffusion boronizing. The monograph presents the physicochemical foundations of this method and the technology of coating deposition, and discusses the properties of boride coatings and promising fields of their use. The book comprises an introduction, seven chapters, and list of references.

The introduction (pp. 3–7) notes that the diffusion boronizing is one of the most effective and promising methods for surface strengthening of machinery and tools. This procedure improves their wear resistance, surface hardness, and fatigue strength. The authors give a classification of the boronizing methods. The first chapter (pp. 8–23) is concerned with the physicochemical foundations of the liquid boronizing technique. Various viewpoints concerning the mechanism of electroless boron transfer in ionic melts are analyzed. The authors note that boron transfer processes are based on the same electrochemical reactions involving boron ions in lower oxidation states. The very small second chapter (pp. 24–28) considers boronizing in halide and halide-oxide melts. Their main disadvantage is the relatively high volatility of boron halides and oxyhalides. The third chapter (pp. 29–63) discusses boronizing in oxide melts. The main component of the electrolyte is sodium tetraborate, to which various compounds and, in particular, boron carbide B_4C are added. The material presented in the chapter is predominantly of formulation nature.

The fourth chapter (pp. 54–79) summarizes evidence concerning the influence of various factors on the boronizing kinetics, formation of the surface boride layer, and its thickness. It is, in particular, mentioned that raising the content of carbon and alloying elements in steels hinders the diffusion of boron and leads to its accumulation in the surface layer. Some alloying elements are incorporated into the composition of borides, which makes higher their hardness and wear resistance; however, alloying, as a rule, lowers the rate of boronizing, leads to build-up of internal stresses, and enhances the tendency toward flaking-off of the boronized layer. The fifth chapter (pp. 80–113) describes the technology of liquid boronizing, developed at the Institute of High-Temperature Electrochemistry, Ural Division, Russian Academy of Sciences, with the participation of the authors of the monograph. The electrolyte contains (wt %): sodium tetraborate 79, sodium chloride 15, amorphous boron 6. The process temperature lies within 850–950°C. Data on how the thickness of the diffusion layer on steels of various brands depends on temperature and time of boronizing are presented.

The sixth chapter (pp. 132–180) is devoted to the properties of boride coatings: their structure, microhardness, residual stresses, wear resistance, and corrosion resistance. The seventh chapter (pp. 181–205) lists plants employing the technology of liquid boronizing. The bibliography (pp. 206–221) contains references to 270 publications and patents, mainly by domestic authors.

On the whole, the monograph has a technological orientation. It includes various kinds of evidence concerning processes of boronizing and, in the first place, the results of the studies performed at the Institute of High-Temperature Electrochemistry, Ural Division, Russian Academy of Sciences. In our opinion, the book pays insufficient attention to the theory of electroless boronizing, to which were devoted comprehensive and original investigations of Ilyushchenko and co-workers, among whom were the authors of the monograph. Thermodynamic analysis of the process virtually escaped the attention of the authors. Nevertheless, there is good reason to believe that the book will promote wider use of boronizing techniques at machine-building plants of the country. The authors present the technology of the process with exhaustive completeness.

A. G. Morachevskii

1070-4272/02/7508-1373 $27.00 © 2002 MAIK "Nauka/Interperiodica"

Russian Journal of Applied Chemistry, Vol. 75, No. 8, 2002, pp. 1374–1375. Translated from Zhurnal Prikladnoi Khimii, Vol. 75, No. 8, 2002, pp. 1402–1403.
Original Russian Text Copyright © 2002 by Morachevskii.

BOOK REVIEWS

Moiseev, G.K. and Vatolin, N.A., *Nekotorye zakonomernosti izmeneniya i metody rascheta termokhimicheskikh svoistv neorganicheskikh soedinenii* (Some Patterns of Variation and Methods for Calculation of Thermochemical Properties of Inorganic Compounds), Yekaterinburg: Inst. Metall. Ur. Otd. Ross. Akad. Nauk, 2001, 136 pp.

In the last two decades, much attention has been given to compiling and supplementing of databases of thermodynamic quantities for inorganic compounds. Among important sources furnishing new information and allowing revision of the existing data are various calculation methods. Investigations in this field have been carried out at the Institute of Metallurgy, Ural Division, Russian Academy of Sciences, under general supervision of V.A. Vatolin, academician of the Russian Academy of Sciences, for quite a number of years. These investigations were aimed to reveal patterns of variation of the thermodynamic properties of various groups of inorganic compounds, establish the corresponding correlations, and develop methods for evaluation of the basic thermodynamic characteristics of the compounds: standard enthalpy of formation, ΔH^0_{298}; standard entropy, S^0_{298}; specific heat, $C^0_{p,298}$; and temperature of congruent melting, T_m.

The book presents new evidence concerning the thermochemical properties of several tens of inorganic substances of varied complexity, which allowed the authors to substantially supplement the previously compiled database[1] and carry out various computer simulations. The arrays of reference data were analyzed and correlations were revealed using the method of thermodynamic modeling, developed in previous works of the same authors. It should be particularly emphasized that the given publication presents information concerning exclusively the studies of its authors and does not pretend to give a complete review of methods for calculating the quantities in question.

[1] Moiseev, G.K., Vatolin, N.A., Marshuk, L.A., and Il'inykh, N.I., *Temperaturnye zavisimosti privedennoi energii Gibbsa nekotorykh neorganicheskikh veshchestv: Al'ternativnyi bank dannykh ASTRA, OWN* (Temperature Dependences of Reduced Gibbs Energy of Some Inorganic Substances: Alternative Database Astra, OWN), Yekaterinburg: Ur. Otd. Ross. Akad. Nauk, 1997.

The book comprises six chapters, conclusion, and a common bibliographic list for the entire monograph. The first chapter (pp. 5–38) discusses fundamental aspects of how ΔH^0_{298} varies for related substances in binary and quasi-binary inorganic systems. The possibility of evaluating the standard enthalpies of formation of oxides, double oxides, intermetallic compounds, carbides, phosphides, borides, and chlorides are considered.

The second chapter (pp. 39–53) is devoted to application of the model of ideal solutions of reaction products to evaluation of the standard thermodynamic characteristics of copper-containing ceramic semiconductors. The third chapter (pp. 54–57) presents an analysis of the variation pattern of the standard entropy S^0_{298} in some classes of inorganic compounds. The numerical equations proposed by the authors on the basis of the pattern revealed can be used to revise the known, and find unknown S^0_{298} values for binary compounds. Data on standard entropy are analyzed for 380 compounds: phosphides, arsenides, selenides, tellurides, and bismuthides, and their reliability is assessed.

The fourth chapter (pp. 68–92) is concerned with calculation of the standard thermodynamic characteristics of double oxides. The authors demonstrate that the procedure proposed is applicable to calculation of ΔH^0_{298}, S^0_{298}, and $C^0_{p,298}$ for binary oxides, with precision achieved in physical experiments, from the results of a single computer simulation in terms of the model of ideal solution of reaction products. The fifth chapter (pp. 93–117) analyzes the dependences of the standard enthalpies of formation of intermetallic compounds on the atomic radius of one of components and on the numbers of the constituent elements in the periodic table. In the sixth chapter (pp. 118–125), the authors summarize the results of their studies concerned with evaluation of the standard thermo-

1070-4272/02/7508-1374 $27.00 © 2002 MAIK "Nauka/Interperiodica"

dynamic characteristics of inorganic compounds of various classes.

In a brief conclusion (pp. 126, 127), it is, in particular, noted that the known data on ΔH^0_{298}, S^0_{298}, and $C^0_{p,298}$ for approximately 1335 binary and quasi-binary compounds are subjected in the book to a critical review with the use of the numerical evaluation methods proposed. For 20–25% of the substances the deviations of the calculated values from the known data are found to exceed 15%. Based on this fact, the authors conclude that only 75–80% of the reference and previously accepted data on the thermodynamic properties of inorganic compounds are reliable and can be used in calculations.

The bibliographic list contains references to 166 publications, of which about 30% belong to the authors of the book.

The monograph was published with the financial support of the Russian Foundation for Basic Research. It is of indubitable interest, although its manner of presentation is intended for rather advanced readers. In our opinion, the authors use, when not absolutely necessary, too large a number of various abbreviations, without giving their meaning in a single place. The book is very well printed.

A. G. Morachevskii

Russian Journal of Applied Chemistry, Vol. 75, No. 9, 2002, pp. 1377–1383. Translated from Zhurnal Prikladnoi Khimii, Vol. 75, No. 9, 2002, pp. 1409–1416.
Original Russian Text Copyright © 2002 by Rakhmankulov, Shavshukova, Latypova, Zorin.

REVIEWS

Laboratory and Industrial Applications of Microwave Techniques

D. L. Rakhmankulov, S. Yu. Shavshukova, F. N. Latypova, and V. V. Zorin

Research Institute of Low-Tonnage Chemical Products and Reagents, Ufa, Bashkortostan, Russia
Ufa State University of Petroleum Engineering, Ufa, Bashkortostan, Russia

Abstract—The use of microwave techniques in scientific research is reviewed. Also some semicommercial-scale microwave units are examined.

The microwave range of the electromagnetic spectrum covers the ultrahigh frequencies from 30 GGz to 300 MHz [1]. Radiation from this range is used in radiolocation, satellite TV communication systems, radio navigation, biology, chemistry, and medicine. For the unification sake, the working frequencies of 915, 2450, 5800, and 22 125 MHz were accepted by the International Agreement as the working frequencies for industrial and scientific microwave facilities [2, 3]. The frequency of 2450 MHz (working frequency of home microwave ovens) is most often used in research practice.

At present the term microwave radiation (MWR) is commonly used in Western literature, and the term ultrahigh frequency (UHF), in the Russian-language literature.

The first device for generation of microwaves was invented in the Birmingham University in the Second World War time in the framework of the program on development of radar systems. This device called magnetron was manufactured in large amounts in the wartime in collaboration with the United States [3, 4]. It was known even at that time that microwaves can heat up water very rapidly.

In the middle 1950s, microwave heating became the custom with microwave ovens, and later it was used in food industry for drying of macaroni foods [5], corn [6], fruits and berries [7], etc.

At present, microwave heating is more and more frequently used for drying industrial goods. For example, the Ford Motors uses a microwave unit for drying ceramic molds used in manufacture of automotive engines [8]. International Standard Electric Co. and Special Metals Co. use MWR in production of refractory and ceramic products [9]. Microwave units were developed for drying and splicing of wood and for acceleration of hardening of concrete [10]. The Institute of Mines of the Russian North and the St. Petersburg Mining Institute developed microwave units for softening of frozen grounds [11]. Also microwave radiation finds use for drying processed films [12, 13].

After 1986, when the first works were published on the use of MWR in organic synthesis [14, 15], great interest has been expressed by chemists in this method, since many reactions proceed considerably more rapidly in the MWR field, providing higher yields of the products as compared to the traditional heating methods. Although the effect of MWR on the reaction mechanism has not been demonstrated in these first works, such indisputable advantages of the method as high heating rate, power control without inertia, and the possibility of bulk heating gave impetus to further investigations in this field.

Despite active research performed in recent years in Russia [16–21] and other countries [22–30] in the reviewed area, the progress in the microwave chemistry is somewhat limited by hardware implementation problems.

The most researchers conducted their experiments in home microwave ovens equipped, if necessary, with a stirrer and also a reflux condenser arranged outside the irradiation zone [3, 16, 21, 24]. In such a system, it is needed to avoid escape of the radiation at the joints between the reaction flask with a stirrer and a pipe for withdrawal of the reagent vapor. Mingos [3] in his experiments protected the withdrawal pipes at the outlet from the case using copper pipes at least 12 cm long, which should have good contact with the case. In any case, a microwave unit should be equipped with an escaping radiation detector. According to the existing Sanitary Regulations, the radiation power density should not exceed 1 mW cm^{-2} at a distance of 5 cm from the oven (ANSI US Standard) and 0.01 mW cm^{-2} at a distance of 50 cm from the

1070-4272/02/7509-1377$27.00 © 2002 MAIK "Nauka/Interperiodica"

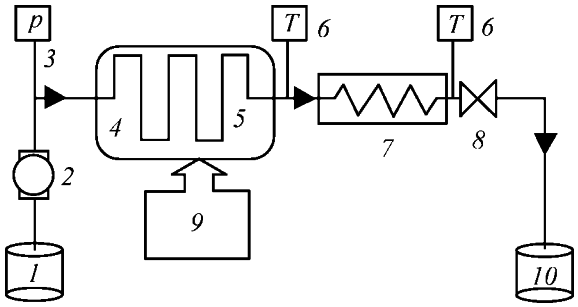

Fig. 1. Schematic of a continuous microwave reactor: (*1*) reaction mixture, (*2*) proportioning pump, (*3*) pressure transducer, (*4*) microwave chamber, (*5*) coil pipe, (*6*) temperature gage, (*7*) heat exchanger, (*8*) pressure control valve, (*9*) microprocessor-based controller, and (*10*) product receiver.

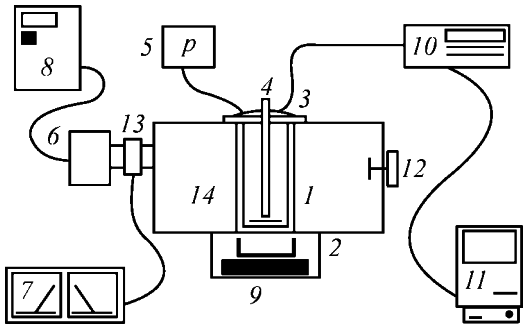

Fig. 2. Schematic of a microwave batch reactor: (*1*) reaction vessel, (*2*) casing, (*3*) flange, (*4*) cooling pipe, (*5*) pressure transducer, (*6*) magnetron, (*7*) input and output wattmeters, (*8*) ac source, (*9*) stirrer, (*10*) fiber-optic thermometer, (*11*) personal computer, (*12*) load control system, (*13*) waveguide, and (*14*) microwave chamber.

radiation source (European and Russian Standards) [31].

A home microwave oven is of little use for chemical experimentation. It is not designed to be operated under conditions of explosions and action of aggressive media. Rotary tables and bottoms of home ovens are unsuitable for chemical reaction vessels. The known information about explosions of reaction vessels in the MWR field [15, 22] demonstrate the necessity in installation of a temperature and pressure control and regulation system, which appears to be rather difficult with a home oven.

This and other problems arising with home microwave ovens initiated the researchers to begin development of microwave systems specially designed for chemical experiments [32, 33]. For example, Cablewski *et al*. [32] developed a laboratory microwave continuous reactor (MCR) (Fig. 1) with a power of 600–800 W. In this reactor, the reaction mixture is fed under pressure to a coil pipe arranged in the microwave heating zone and then through a heat exchanger to the product receiver. The setup is equipped with temperature and pressure control devices, a pressure regulating valve, and a microprocessor-based controller for setting such process parameters as the reagent feed rate and heating and cooling temperatures, which can be varied in the course of the process. The coil is made from perfluoroalkoxy Teflon. The system can operate at temperature of up to 200°C and pressure of up to 1400 kPa. Cablewski *et al*. [32] reported the results for 26 reactions, whose rates were higher by a factor of 3 on the average as compared to the reference data. Among these reactions were nucleophilic substitution, esterification, ester interchange, acetylation, acid and base hydrolysis, isomerization, decarboxylation, and elimination. However, MCR is not a universal setup. It cannot be used in the cases of solid or highly viscous substances and also of microwave-incompatible substances (metals and compounds having no dipole moment).

Strauss and Trainor in their review [33] described a 1200-W microwave batch reactor (MBR) (Fig. 2). Its performance characteristics are as follows: volume 20–100 ml, temperature up to 260°C, and pressure up to 10 MPa. The reactor is equipped with a device for determination of the absorbed and reflected energy, a load control system providing the optimal heating, a system for direct measurement of the temperature and pressure, a stirrer, and a system for feeding and withdrawal of the reaction mixture in the course of heating. The reactor has chemically inert walls. It is designed so as to provide the possibility of conducting a reaction at atmospheric pressure in air or under inert gas.

To prevent back irradiation of the magnetron, the reflected microwave power is controlled. With increasing reflected power, the input power is decreased through the load control system. Continuous control of the temperature, pressure, and radiation power, stirring, and the presence of cooling pipe and emergency valve—all these provide safe and efficient operation of the system.

With an example of heating of a 100-ml sample of 1,3-propanediol, Strauss and Trainor demonstrated the high rate of establishment of the desired temperature in MBR: bp 214°C was reached in 2 min, whereas that in an autoclave, only in 14 min [33].

An additional advantage of microwave heating over the traditional methods is in exclusion of the effect of vessel walls. However, the most of the reaction vessels for conducting microwave-stimulated reactions

Table 1. Characteristics of microwave digests

Characteristic	Closed multimode system	Monomode system	
		open	closed
Type	Floyd ovens	Digests 301, A301, 401, MX 350, MX 4350	Superdigests
Operation under pressure	Yes	No	Yes
Automated addition of reactants	No	Yes	No
Mineralization mode	Up to 12 samples simultaneously	From 4 to 16 samples simultaneously, depending on the model	Up to 4 samples simultaneously
Use of acids with bp above 200°C	No	Yes	No
Use of acids with bp below 200°C	Yes	Yes	Yes
Reaction vessel material	PTFE*	PTFE, quartz, borosilicate glass	Quartz
Sample weight	0.25–0.8 g	0.1–5 g	0.1–1 g
Bringing to dry residue	No	Yes	No
Main fields of application	Dissolution of biological and geological samples (nonexplosive)	Analysis of plastic materials, petroleum products, composites, environmental objects, mineral samples, and agricultural, food, and sea products; determination of COD** in water (MX 4350 Model only)	Determination of trace amounts of volatiles, hydrolysis, and dissolution of ceramic materials

* Poly(tetrafluoroethylene).
** Chemical oxygen demand.

under pressure are made from heat-insulating materials, so that cooling after completion of the reaction takes a long time. In CMR the problem of rapid cooling is solved by arranging the heat exchanger just at the outlet of the radiation zone, i.e., the reaction mixture is cooled under pressure, to prevent loss of volatiles and decomposition of thermally unstable compounds.

In MBR, a cooling pipe filled with a coolant is used, whose end is arranged immediately in the reaction mixture, thus increasing the cooling efficiency. Furthermore, cooling can be started, if needed, even in the course of irradiation. It is also important that, in the course of heating and cooling, the reaction vessel is inside the microwave reactor, so that there is no access to it until its content is under pressure. Therefore, MBR and CMR are particularly efficient in synthesis of thermally unstable compounds.

The energy distribution throughout the microwave chamber can be both multi- and monomode. In a multimode reactor, as a home microwave oven is, the energy is randomly distributed as a result of multiple reflections from the oven walls.

Microwave digests provide an example of a monomode reactor. They are designed for sample preparation for atomic absorption spectroscopy, spectrocalorimetry, ICP, ion-exchange chromatography, polarography, and also for nitrogen determination by the Kjeldahl method. In these reactors, MWR is input as a focused beam to the bottom of the reaction vessel. The performance characteristics of Prolabo digests (France) are given in Table 1 [34].

The digest units are equipped with a reagent feed pump and a programming block for control of the process parameters (reagent feed rate, temperature, and irradiation power and time). The unit can include several digest modules.

Other manufacturers of microwave facilities for analysis are Milestone Inc. and CEM Corp. Among their products one may find open- and closed-vessel systems, moisture analyzers, microwave extraction systems, and accessories and vessels for microwave systems [35].

Loupy [36] proposed to use a Maxidigest MX-350 microwave analyzer (Prolabo) for chemical syntheses. The advantage of this instrument over a home oven is

Table 2. Comparative data on heating of diethyl benzylmalonate in decarboxylation

Heating mode	Power, temperature	Reaction time	Yield, %
Reactor:			
multimode	600 W	10 min	50
monomode	60 W	10 min	90
Thermal heating	160°C	4 h	90

in the single-mode microwave type characterized by high output power at decreased power consumption and also in excellent reproducibility of the results. Particularly, the author made a comparative analysis of the efficiency of the two types of reactors (Table 2) with an example of decarboxylation.

$$PhCH_2CH(CO_2Et)_2 \xrightarrow[-CO_2]{} PhCH_2CH_2CO_2Et.$$

In performing chemical syntheses under elevated pressure in the microwave zone, the reaction vessels should be chemically inert, transparent for microwaves, and thermally and barostable. Researchers most frequently used sealed pressure tubes of borosilicate or Pyrex glass, placed into a heat-insulating medium (vermiculite) [15, 37] or into a Parr bomb [3] for the safety sake in the case of explosion or failure of the vessel. Pyrex tubes were also used for conducting reactions at the atmospheric pressure [16–20]. Parr [38] and the CEM Corp. [39] developed specially designed acid-proof screw-top vessels.

Temperature monitoring is a difficult problem in microwave experiments, since the traditional methods are unsuitable under conditions of high-frequency electric field. Giguere [15] measured the temperature in sealed tubes using capillaries filled with reference compounds (with known mp) attached to the reaction vessel. This method is not universal. It provides no information about the temperature evolution in the course of the process. It is more reliable to use fiber-optic devices [33, 40, 41]. Abramovitch [22] monitored the temperature of the closed-vessel system using a gold-coated thermocouple in a thick quartz casing, but he did not describe technical details. Daminev [42] improved the temperature monitoring capabilities by eliminating undesired arcing at temperatures near 500°C in the thermocouple quartz well by isolation of this unit and shielding of the thermocouple. The shield was a metal well of corrosion-resistant steel, isolated from the case via ceramics or fluoroplastic and grounded.

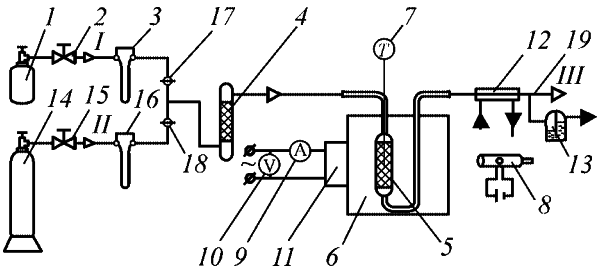

Fig. 3. Schematic of a laboratory microwave dehydrogenation unit: (*1, 14*) cylinders with butenes and nitrogen, respectively, (*2, 15*) fine control reducers, (*3, 16*) rheometers, (*4*) dehumidifier, (*5*) reactor, (*6*) cavity, (*7*) thermocouple, (*8*) optical pyrometer, (*9*) ammeter, (*10*) voltmeter, (*11*) microwave generator, (*12*) cooler, (*13*) safety valve, (*17, 18*) cocks, and (*19*) gas withdrawal to the gasometer. (*I*) Raw material (butenes), (*II*) diluent (nitrogen), and (*III*) contact gas.

Several microwave units of various purposes were developed at the Ufa State University of Petroleum Engineering [42–46].

Daminev *et al*. [42, 43] studied the effect of microwave radiation on catalytic dehydrogenation of 1- and 2-butenes into 1,3-butadiene. A microwave reactor for performing heterophase endothermic reactions and a laboratory unit for dehydrogenation of butanes were designed on the basis of the results obtained. The essence of the technique proposed is that the cold raw material (1- and 2-butenes) is passed through a catalyst, which, in its turn, is an absorber of microwave radiation. Therefore, the catalyst serves as a thermal energy source for dehydrogenation, preserving, however, the function of the ordinary heterogeneous catalyst in the gas-phase process.

In the laboratory dehydrogenation unit (Fig. 3), a gas mixture of the butenes and nitrogen (gas-diluent) is fed via a dehumidifier to the reactor partly filled with the catalyst. The reactor is arranged in the cavity of the microwave generator. The temperature of the reaction zone is monitored using a thermocouple, and the temperature of the outer side of the reactor, by a pyrometer. The power consumed by the microwave generator is controlled with an ammeter and a voltmeter.

The microwave generator (1300 W) consists of a power supply, a waveguide, a ventilation unit, and a control station. The magnetron transforms electric current into electromagnetic radiation (2450 MHz), which passes to the cavity through the waveguide. The control station provides the magnetron switch on and switch off and the time control using an automatic timer. The cavity represents a case made from sheet steel with a door at one side and process holes at

the other side. To prevent escape of the microwave radiation, copper tubes are fixed to the holes from the outside. In the top of the cavity, a scatterer (device for uniform dissipation of the electromagnetic energy throughout the bulk) is arranged. The reactor (quartz tube 170 cm long and 30 mm i.d.) is equipped with a quartz well for the thermocouple and a quartz net for arranging the catalyst.

The reactor of the setup for conducting thermocatalytic reactions serves as a resonator of the microwave generator (Fig. 4) [42]. Its upper cover plays a role of an emitting antenna. The raw material is fed to the top of the reactor, and the contact gas is taken off from the bottom. The coupling chamber in the outlet unit is meant for utilization of the residual radiation which is absorbed by water. The circulator is arranged in the waveguide to prevent the entry of the reflected radiation to the magnetron.

Bikbulatov *et al*. [43] optimized the process with K-16u industrial catalyst: temperature 600°C, raw material to nitrogen volume ratio 1 : 10, and raw material space velocity 800 h^{-1}. With these conditions and at a catalyst bed of 73 mm, the radiation at the bottom of the reactor is practically lacking.

Shulaev [44] proposed thermodynamic methods for designing a reactor for heterophase catalytic processes with the use of a new mode of heat supply to the reaction zone. The mathematical relationship between the MWR parameters and reactor characteristics obtained in this work provides the possibility of optimizing and controlling the operation mode of electrodynamic reactors.

Energy calculations made for the microwave reactor demonstrated that its efficiency is more than twice that of an industrial adiabatic reactor [42]. The use of microwaves eliminates the need in water vapor as a heat carrier, which, in its turn, eliminates atmospheric pollution with toxic materials formed as a result of firing in superheaters, and water is used only for absorption of the excess radiation in the closed line. Therefore, the new method for heat supply to the reaction zone shows promise in the economic and environmental respects.

In [45] one can find a description of Elektronika KIE-501 laboratory microwave unit (2.5 kW, 2450 MHz) designed for thermal treatment of dielectric materials, particularly grounds, and for research purposes. Also stationary (industrial) and portable (for field works) semicommercial-scale microwave units for heat strengthening of grounds were described. Heat treatment with these units involves three stages:

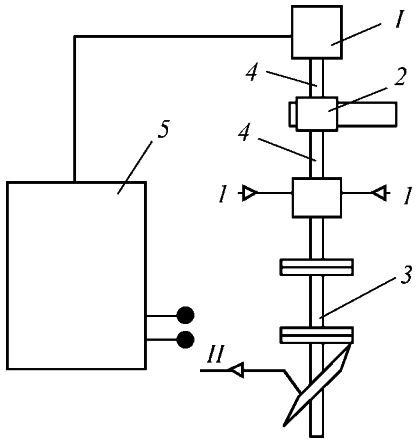

Fig. 4. Laboratory unit for performing thermocatalytic reactions in the microwave field: (*1*) microwave generator, (*2*) microwave circulator, (*3*) reactor, (*4*) waveguide, and (*5*) power supply. (*I*) Raw material (butenes) and (*II*) contact gas.

heating (supplied heat entirely goes to heating of ground to 100°C); drying; and roasting (heating to 1100°C).

The laboratory microwave unit is assembled on a specially designed elevating platform on a laboratory table. It includes an MWR source, waveguide system, working chamber, control system (direct and reflected power wattmeters and thermocouple), and ventilation and cooling systems.

Two versions of the stationary units were designed: one for one-side treatment of ground blocks and another, for two-side treatment. The first version includes an electric heating unit, since in one-side treatment it is impossible to ensure uniform warming of the entire body of ground. In the second version, only microwave heating is used.

The stationary units include three basic blocks: energy, working, and safe (for protection of the personnel against stray radiation). The energy block includes a microwave generator, waveguide system, power dividers, transmitters, and a medium for absorbing excess radiation. It is arranged on a mobile platform, which moves by a sinusoidal trajectory along the ground block surface, to provide the estimated energy density. The base element of the working block is a kiln. Protection of the personnel against radiation is provided by a heat-retention lagging, metallic shield of the kiln, and airtight doors.

A ground block on a small cart goes from the molding shop to the first channel, moving in the direction of the transmitters. It is heated to 950–1100°C, and then it goes to the second channel, to be further

Table 3. Characteristics of semicommercial-scale microwave units for thermal strengthening of grounds

Characteristic	Unit			
	stationary one-side	stationary two-side	mobile	mobile unit for operation just at deposition site
Maximal total output power of MWR sources, kW	500	1000	500	500
Unit capacity, m^3 $year^{-1}$	7500	12 100	6500	3500
Specific power consumption, MJ m^{-3}	2637	2513	2012	3668
Application area	Manufacture of heavers for stabilization of pipelines			Manufacture of anchor stabilizers for pipelines; construction of foundations

heated with the electric heaters. At the final section of the second channel, the block is cooled.

The two-side stationary unit has two energy blocks and a Z-shaped kiln. In the first channel, a ground block is heated to 500–600°C, in the initial section of the second channel, to 950–1100°C, and in the end section, it is cooled.

The mobile microwave unit for manufacture of heat-treated ground blocks is intended for the pipe run conditions. It includes a molding machine and a kiln, which are arranged on mobile platforms. The unit is equipped with power and movement facilities, automatic control system, and a radiation protection block. A molded ground block goes to a roll-table of the kiln, where it is dried and heated to 950–1100°C, and then to a receiver.

The mobile microwave unit for heat treatment of grounds just at their deposition site is based on KrAZ-250 truck. Its energy block includes an MWR source, waveguide and transmitter systems, and also a rotating gear for the waveguide sections to revolve on their axis. Characteristics of the semicommercial-scale units are given in Table 3.

The strengthening of grounds with microwaves, compared with other methods (chemical and physicochemical), provides better mechanical characteristics of grounds after treatment and reduces the transport charges. The temperature distribution across the ground body with firing in a well is close to that with microwave heating at 915 MHz. However, the heating time in the first case is 40 h, and in the second case, only 8 h [46].

Finally, the use of microwaves shows promise for improving technical, cost, and environmental parameters of the most important physicochemical processes, particularly, for accelerating chemical reaction and increasing yields of target products in organic synthesis. By now, techniques are developed for microwave enhancement of various processes under both laboratory and industrial conditions.

REFERENCES

1. *Sovetskii entsiklopedicheskii slovar'* (Soviet Encyclopedia), Moscow: Sov. Entsiklopediya, 1987.
2. Metaxis, A.C. and Meredith, R.J., *Industrial Microwave Heating*, London: Peregrinus, 1998.
3. Mingos, D.M.P. and Baghurst, D.R., *Chem. Soc. Rev.*, 1991, vol. 20, pp. 1–47.
4. Harvey. A.F., *Microwave Engineering*, New York: Academic, 1963.
5. *Resource and Development*, 1988, Jan., p. 54.
6. Janos, B., *Drying Technol.*, 1999, vol. 17, nos. 7–8, pp. 1339–1410.
7. Venkatachalaphy, K. and Radhavon, G.S.V., *Drying Technol.*, 1999, vol. 17, nos. 4–5, pp. 837–853.
8. Knyazhevskaya, G.S., Firsova, M.G., and Kil'keev, R.Sh., *Vysokochastotnyi nagrev dielektricheskikh materialov* (Microwave Heating of Dielectric Materials), Leningrad: Mashinostroenie, 1989.
9. Syrovets, P.A., *Printsip. Novye Tekhnol. Proizvod.*, 1990, issue 2, pp. 64–69.
10. *Microwave Power Engineering*, Okress, E.C., Ed., New York: Academic, 1968, vol. 2.
11. Misnik, Yu.M., *Osnovy razuprochneniya merzlykh porod SVCh-polyami* (Principles of Softening of Frozen Rocks in Microwave Field), Leningrad: Leningr. Gos. Univ., 1982.
12. Arkhangel'skii, Yu.S. and Satarov, I.K., *Elektron.*

Tekh., Ser.: Elektronika SVCh, 1979, no. 1, pp. 79–80.

13. Rozental', F.A., Vinogradova, V.A., Polonskaya, F.M., *et al.*, *Tekh. Kino Televid.*, 1974, no. 4, pp. 38–40.
14. Gedue, R.N., Smith, F.E., Westway, K.C., *et al.*, *Tetrahedron Lett.*, 1986, vol. 27, no. 3, pp. 279–282.
15. Giguere, R.J., Bray, T.L., Duncan, S.M., *et al.*, *Tetrahedron Lett.*, 1986, vol. 27, no. 41, pp. 4945–4948.
16. El'tsov, A.V., Martynova, V.P., Sokolova, N.B., *et al.*, *Zh. Obshch. Khim.*, 1994, vol. 64, no. 9, pp. 1581–1582.
17. El'tsov, A.V., Martynova, V.P., Sokolova, N.B., *et al.*, *Zh. Obshch. Khim.*, 1995, vol. 65, no. 3, pp. 511–513.
18. Grigor'ev, A.D., Dmitrieva, N.M., El'tsov, A.V., *et al.*, *Zh. Obshch. Khim.*, 1997, vol. 67, no. 6, pp. 1042–1043.
19. El'tsov, A.V., Sokolova, N.B., Dmitrieva, N.M., *et al.*, *Zh. Obshch. Khim.*, 1995, vol. 65, no. 9, pp. 1581–1582.
20. El'tsov, A.V., Sokolova, N.B., Dmitrieva, N.M., *et al.*, *Zh. Obshch. Khim.*, 1997, vol. 67, no. 2, pp. 314–318.
21. Zorin, V.V., Maslennikov, S.I., Shavshukova, S.Yu., *et al.*, *Zh. Org. Khim.*, 1998, vol. 34, no. 5, pp. 768–769.
22. Abramovitch, R.A., *Org. Prep. Proc. Int.*, 1991, vol. 23, no. 6, pp. 683–711.
23. Raner, K.D., Strauss, C.R., Vyskos, F., *et al.*, *J. Org. Chem.*, 1993, no. 58, pp. 950–953.
24. Baghurst, D.R. and Mingos, D.M.P., *J. Organomet. Chem.*, 1990, no. 384, pp. 57–59.
25. Matsura-Inoue, T., Tanabe, N., Miname, T., *et al.*, *Chem. Lett.*, 1994, no. 12, pp. 2443–2446.
26. Bose, A.R., Manhas, M.S., Ghosh, M., *et al.*, *Heterocycles*, 1990, no. 30, pp. 741–745.
27. Ali, M., Bond, S.P., Mbogo, A., *et al.*, *J. Org. Chem.*, 1989, vol. 54, pp. 11–13.
28. Sabitha, G., Subba Reddy, B.V., Babu, R.S., *et al.*, *Chem. Lett.*, 1998, no. 4, pp. 773–775.
29. Laurent, R., Laporterie, A., Dubac, J., *et al.*, *J. Org. Chem.*, 1992, vol. 57, pp. 7099–7102.
30. Lescovsec, S., Smidovnik, A., and Koloni, T., *J. Org. Chem.*, 1994, vol. 59, pp. 7433–7436.
31. Sapunov, G.S., *Remont mikrovolnovykh pechei* (Repair of Microwave Ovens), Moscow: Solon-R, 2000.
32. Cablewski, T., Faux, A.F., and Strauss, C.R., *J. Org. Chem.*, 1994, vol. 59, pp. 3408–3412.
33. Strauss, C.R. and Trainor, R.W., *Aust. J. Chem.*, 1995, vol. 48, pp. 1665–1692.
34. *Pribory, reaktivy i oborudovanie Prolabo* (Instruments, Chemicals, and Facilities from Prolabo), Moscow: Reaktiv, 1995.
35. *The Pittsburgh Conf. on Analytical Chemistry and Applied Spectroscopy* (Pittcon-99), Pittsburgh (the United States), 1999.
36. Loupy, A., *Rev. Spectra Anal.*, 1993, vol. 175, pp. 1–16.
37. Jones, G.B. and Chapman, B.J., *J. Org. Chem.*, 1993, vol. 58, pp. 5558–5559.
38. *Parr Instrument Company*, Moline, Illinois, 61265, the United States.
39. *CEM Corporation*, Matthews, North Carolina, 28106, the United States.
40. Baghurst, D.R. and Mingos, D.M.P., *J. Chem. Soc.*, 1992, pp. 1151–1165.
41. Jahngen, E.G.E., Lentz, R.R., Pesheck, P.S., *et al.*, *J. Org. Chem.*, 1990, vol. 55, pp. 3406–3409.
42. Daminev, R.R., Catalyzed Dehydrogenation in Microwave Field, *Cand. Sci. Dissertation*, Ufa, 1997.
43. Bikbulatov, I.Kh., Daminev, R.R., Shulaev, N.S., and Shulaev, S.N., *Bashkir. Khim. Zh.*, 1997, vol. 4, no. 2, pp. 11–13.
44. Shulaev, S.N., Dehydrogenation of Hydrocarbons C_4–C_5 with Catalytic Transformation of Microwave Energy, *Cand. Sci. Dissertation*, Ufa, 1999.
45. USSR Inventor's Certificate no. 1807587.
46. Spektor, Yu.I., Novel Techniques in Pipeline Construction, Based on Engineered Soil Development, *Doctoral Dissertation*, Ufa, 1996.

Russian Journal of Applied Chemistry, Vol. 75, No. 9, 2002, pp. 1384–1388. Translated from Zhurnal Prikladnoi Khimii, Vol. 75, No. 9, 2002, pp. 1417–1421.
Original Russian Text Copyright © 2002 by Tolchev, Kleshchev, Lopushan.

INORGANIC SYNTHESIS AND INDUSTRIAL INORGANIC CHEMISTRY

Effects of Mechanochemical Activation and α-Fe_2O_3 Addition on the Formation of Corundum in Thermal Transformations of γ-$Al(OH)_3$

A. V. Tolchev, D. G. Kleshchev, and V. I. Lopushan

Chelyabinsk State Pedagogical University, Chelyabinsk, Russia

Received January 28, 2002; in final form, May 2002

Abstract—Transformations of hydrargillite γ-$Al(OH)_3$ during mechanochemical activation in various grinding mills and further calcination of activated samples at 200–1300°C were studied. The effects of mechanochemical activation and additions of iron(III) oxide compounds on the temperature of corundum formation and on its crystal size distribution were studied.

Finely crystalline corundum α-Al_2O_3 with the crystal size less than 1 μm is a promising polishing material [1]. One of procedures for preparing corundum is heat treatment of γ-$Al(OH)_3$ (hydrargillite) in air. The sequence of transformations in the course of its calcination, the temperatures of formation of intermediate and equilibrium phases, and the size distribution and habit of corundum crystals depend on a number of factors, e.g., on the chemical composition and particle size distribution of the initial aluminum hydroxide [1, 2], its purity [2–5], presence of structure defects [6–8], etc. The formation of α-Al_2O_3 is preceded by the formation of a number of intermediates, and, according to [2, 7–10], the general scheme of the transformations can be presented as follows:

$$\gamma\text{-}Al(OH)_3 \begin{cases} \xrightarrow{300^\circ C} \text{X-ray amorphous } Al_2O_3 \xrightarrow{500-800^\circ C} æ\text{-}Al_2O_3 \xrightarrow{1200^\circ C} \alpha\text{-}Al_2O_3 \\ \xrightarrow{180^\circ C} \gamma\text{-AlOOH} \xrightarrow{300-500^\circ C} \gamma\text{-}Al_2O_3 \xrightarrow{850-1000^\circ C} \theta\text{-}Al_2O_3 \xrightarrow{1200^\circ C} \alpha\text{-}Al_2O_3 \end{cases} \quad (1)$$

As believed in [2, 8], the existence of two directions of phase and chemical transformations results from the fact that X-ray amorphous Al_2O_3 is always formed along with the γ-AlOOH (boehmite) phase in the thermolysis of γ-$Al(OH)_3$ in air, with further phase transitions of X-ray amorphous Al_2O_3 occurring independently. The consequence of this fact is high polydispersity of α-Al_2O_3, which makes it unsuitable as a polishing material. It is known [11–14] that mechanochemical activation of hydrated oxides promotes the formation of finely dispersed powders on calcination, and admixtures of oxides isostructural with α-Al_2O_3 reduce the temperature of the corundum formation.

In this work we studied phase and chemical transformations of hydrargillite in the course of mechanochemical activation in grinding mills of various types and of the further calcination in air at 200–300°C. Also, we examined the effect of mechanochemical activation and additions of iron(III) oxides on the temperature of formation and crystal size distribution of corundum.

EXPERIMENTAL

We used technical-grade aluminum hydroxide (irregular-shaped platelike crystals 1–5 μm in diameter and 10–15 nm thick). According to the data of X-ray phase and thermogravimetric analyses, the sample was single-phase γ-$Al(OH)_3$; its empirical composition $Al_2O_3 \cdot 3.1H_2O$ was close to the stoichiometric composition. As additions we used Fe(II) or Fe(III) com-

1070-4272/02/7509-1384$27.00 © 2002 MAIK "Nauka/Interperiodica"

pounds in the form of $FeSO_4 \cdot 7H_2O$, α-FeOOH, and α-Fe_2O_3 in amounts of 1–10 wt % (recalculated on Fe_2O_3), which were added to hydrargillite before mechanochemical activation and uniformly distributied by stirring. Hydrargillite samples mixed with iron compounds (e.g., α-FeOOH) were mechanochemically activated in laboratory grinding mills under various energy conditions. The duration of the activation was 2–10 min in planetary mills; 15, 30, and 60 min in vibratory mills; and 0.5–3 h in ball mills. Isothermal calcination of samples was carried out at 200–300°C for 2 h.

The phase composition and particle size distribution of samples were evaluated by X-ray phase analysis (DRON-3 diffractometer, filtered CoK_α radiation) and by transmission electron microscopy (UEMV-100K), and the chemical composition, by volumetric chemical analysis and thermogravimetry (MOM derivatograph, Hungary; heating rate 10 deg min^{-1}). The unit cell parameters *a* and *c* of compounds with the corundum structure were determined by the standard technique [15] from the reflections (226) and $10\bar{1}0$). The average crystal size *d* was calculated from physical broadening $\Delta 2\theta$ of diffraction peaks [15].

According to the thermogravimetric data, the weight loss in the initial hydrargillite sample occurs within a broad temperature range, 200–500°C (Fig. 1, curve *a*). The DTA curve contains three endothermic peaks at 215, 310, 480°C and one exothermic peak at 850°C. According to the published data [2, 3] and the data of X-ray phase analysis (Fig. 2) for samples subjected to isothermal calcination at the above-mentioned temperatures, the first endothermic effect results from chemical transformation of a part (~15 wt % by the thermogravimetric data) of γ-$Al(OH)_3$ to the γ-AlOOH (boehmite) phase; the second (310°C), from chemical transformation of the remaining hydrargillite to X-ray amorphous Al_2O_3; and the third (480°C), from chemical transformation of γ-AlOOH to γ-Al_2O_3. The exothermic effect at 850°C results from the crystallization of X-ray amorphous alumina into finely crystalline (~7 nm) θ-Al_2O_3. The formation of the equilibrium corundum phase during the isothermal calcination in air is macroscopically manifested starting from 1100°C (Fig. 2, curve *e*). According to the electron microscopic data, the single-phase sample of α-Al_2O_3 obtained by calcination of γ-$Al(OH)_3$ at 1300°C is polydisperse and consists of isometric or oval corundum crystals of size from 0.2 to 6.0 μm, sintered into larger aggregates of size 2–5 μm (Fig. 3a).

The mechanochemical activation of the initial hydragillite resulted in changes in its structure and chemical composition, with the extent of these changes being proportional to the energy of the mechanochemical action. Thus, redistribution of the relative intensities of the diffraction peaks was observed in the X-ray patterns of a sample subjected to mechanochemical activation in a ball mill for 3 h. For example, the ratio of intensities of reflections β with Miller indices (002) and (110) ($\beta = I_{002}/I_{110}$, where I_i are the integral intensities of the corresponding reflections) increases from 3 [initial γ-$Al(OH)_3$] to 10. Also, hydrargillite samples became moist after milling. No changes in the shape and size of γ-$Al(OH)_3$ crystals

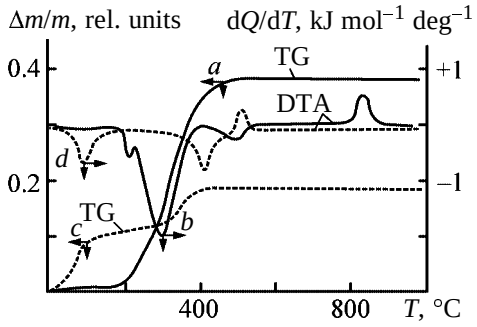

Fig. 1. Thermograms of hydrargillite samples: (*a*, *b*) initial and (*c*, *d*) mechanochemically activated in a planetary grinding mill. ($\Delta m/m$) Weight loss during calcination, (dQ/dt) enthalpy change, and (T) calcination temperature.

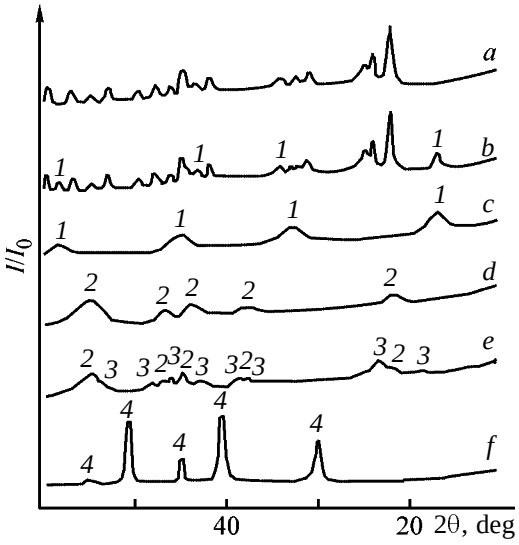

Fig. 2. Fragments of X-ray diffraction patterns of (*a*) initial hydrargillite and (*b*–*f*) products of its calcination under isothermal conditions in air for 2 h. (I/I_0) Relative intensity of diffraction maxima and (2θ) diffraction angle. Calcination temperature (°C): (*b*) 240, (*c*) 300, (*d*) 550, (*e*) 1000, and (*f*) 1300. Phase: (*1*) γ-AlOOH, (*2*) γ-Al_2O_3, (*3*) θ-Al_2O_3, (*4*) α-Al_2O_3, and (no mark) γ-$Al(OH)_3$.

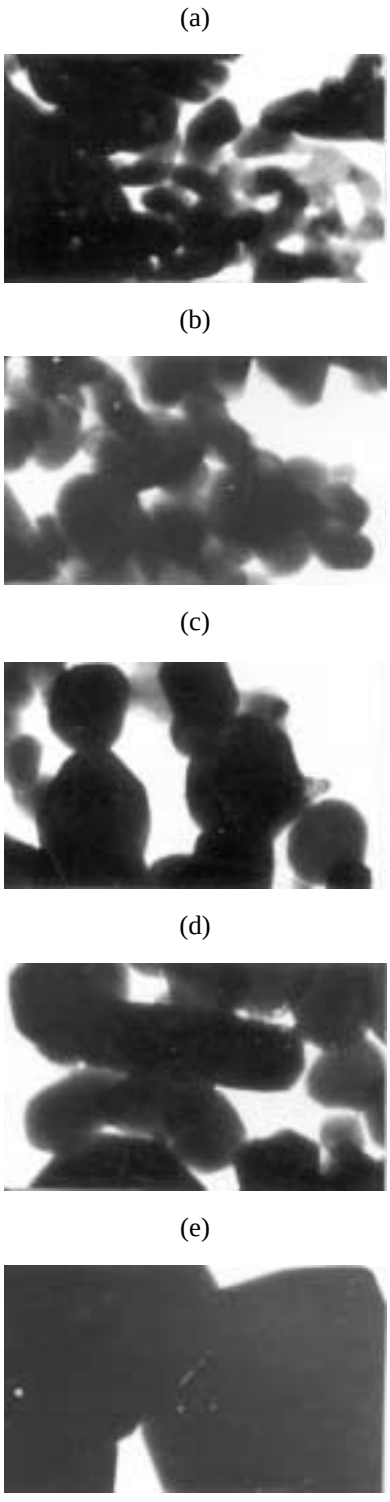

Fig. 3. Electron micrographs of α-Al_2O_3 samples obtained by isothermal calcination at 1200°C for 2 h of (a) initial hydrargillite, (b) hydrargillite mechanochemically activated in a planetary grinding mill for 10 min, and (c–f) hydrargillite mechanochemically activated in a ball mill for 3 h. Contents of added Fe_2O_3 in samples (wt %): (a, b) 0, (c) 1, (d) 5, and (e) 8. Magnification 20000.

were observed after mechanochemical activation in a ball mill.

In addition to the redistribution of the relative intensities of reflections in the X-ray patterns of hydrargillite samples mechanochemically activated in a vibratory mill, the half-widths of the reflections increased with the grinding time τ. In particular, when τ increased from 0 to 1 h, the half-width $\Delta 2\theta$ of the (002) reflection of hydrargillite increased approximately twice. As compared to the mechanochemical activation in a ball mill, moistening of samples was more pronounced. When γ-$Al(OH)_3$ was ground in a planetary mill, which exerts the strongest mechanochemical effect on samples as compared to the other mills [11], along with strong moistening observed alreay within 10 min, the crystalline structure of hydrargillite was completely destroyed. This is proved by the absence of γ-$Al(OH)_3$ reflections in the X-ray patterns. However, diffuse diffraction maxima were detected, assignable to the boehmite phase in accordance with the data of [16] and Fig. 2 (curve *c*).

There are two maxima and one minimum at 105, 410, and 520°C, respectively, in the DTA curve of a hydrargillite sample activated in a planetary mill (Fig. 1, curve *c*). Comparison of the data [1, 7, 10] on the boehmite dehydration with the results of the X-ray phase analysis of samples subjected to isothermal calcination at the above-mentioned temperatures shows that the endothermic effect at 105°C is due to the removal of approximately 11 wt % of physically adsorbed water (Fig. 1, curve *d*); the second endothermic effect (410°C), to the chemical transformation of finely crystalline γ-AlOOH to γ-Al_2O_3 accompanied by the removal of the remaining (~15 wt %) constitutional water; and the exothermic effect at 510°C, apparently, to crystallization of γ-Al_2O_3. The presence of a considerable amount (~11 wt %) of physically adsorbed water in the mechanochemically activated hydrargillite sample shows that the crystal structure of the γ-$Al(OH)_3$ phase is partially (in ball and vibratory mills) or completely (in planetary mill) destroyed during the activation. As a result, a part of constitutional water (OH^- groups in hydrargillite) is released (activated hydrargillite dehydration), which results in moistening of the sample during the activation. The highest degree of γ-$Al(OH)_3$ dehydration is reached in a planetary mill as compared to the other mills and is probably responsible for the formation of the γ-AlOOH phase. We emphasize that the conversion of compounds based on hydrated oxides of various metals to the amorphous state and their phase and chemical transformations in the course of mechanochemical activation were mentioned in numerous pub-

lications [6, 11–13], where the possibility of the transformation of crystallization water into adsorbed water was confirmed. If adsorbed water is not taken into account, the composition of the hydrargillite sample mechanochemically activated in a planetary mill corresponds to the formula $Al_2O_3 \cdot 1.1H_2O$, which is close to the boehmite stoichiometric composition.

The X-ray phase analysis shows that, in calcination of mechanochemically activated hydrargillite samples, corundum starts to form from at about 1100°C. Its content reaches 100 wt % in samples calcined at 1200°C. According to the electron microscopy data, α-Al_2O_3 samples obtained by calcination of activated hydrargillite at 1200°C are characterized by narrow particle size distribution and consist of isometric or oval crystals of size 0.3–0.5 μm (Fig. 3b). When the temperature of heat treatment is increased to 1300°C, separate corundum crystals are sintered to form aggregates.

Heat treatment of activated γ-$Al(OH)_3$ in a mixture with Fe(II) or Fe(III) compounds results in a decrease in the temperature of corundum formation to approximately 900°C; however, apart from a set of reflections characteristic of the α-Al_2O_3 phase (their half-width $\Delta 2\theta$ is 0.3°), weak maxima are observed in the X-ray patterns, which, according to [16], should be assigned to the α-Fe_2O_3 phase. The relative intensity of these reflections changes in parallel with the weight fraction of iron(III) oxide added to hydrargillite. The pink color of samples calcined at 900°C, characteristic of hematite, also suggests the existence of the individual α-Fe_2O_3 phase. The increase in the calcination temperature to 1100°C results in the formation of single-phase samples with the corundum structure. Their color depends on the weight fraction C of added iron(III) compounds and changes from white ($C \leq$ 1 wt %) to light yellow. As the weight fraction of Fe_2O_3 in samples increases, the unit cell parameters a and c of the phase with the corundum structure increase from $a = 0.4760 \pm 0.0002$ and $c = 1.2987 \pm 0.0005$ nm ($C = 0$) to $a = 0.4790 \pm 0.0002$ and $c = 1.3025 \pm 0.0005$ nm ($C = 10$ wt %). This suggests formation of a solid solution of Fe_2O_3 in α-Al_2O_3 under these conditions.

According to the electron microscopic data, the size of corundum crystals depends on the amount of added Fe_2O_3. In particular, the corundum sample obtained at 1200°C and containing 1 wt % Fe_2O_3 is monodisperse and consists of crystals 0.3–0.4 μm in size with approximately hexagonal faces (Fig. 3c). At the Fe_2O_3 content in samples increased to 5 wt %, larger corundum crystals are formed (approximately 1 μm, Fig. 3d), and the crystal size in samples containing more than 5 wt % Fe_2O_3 can reach 2 μm (Fig. 3e).

Let us examine possible causes of the formation of monodisperse corundum samples upon the heat treatment of hydrargillite. As already noted, the chemical transformations of hydrargillite in the range 200–400°C can occur by two independent pathways shown in scheme (1). Therefore, along with γ-AlOOH, X-ray amorphous aluminum oxide is always formed by dehydration of γ-$Al(OH)_3$. At higher temperatures, phase and chemical transformations of boehmite and X-ray amorphous Al_2O_3 give rise to various nonequilibrium forms of aluminum oxide differing in the crystal structure and temperature ranges of their existence, which is the main cause of the polydispersity of the final product of hydrargillite phase and chemical transformations, namely, α-Al_2O_3. In this case, most probably, large (up to 5 μm) aggregates are formed from finely crystalline α-Al_2O_3, i.e., from the product of phase transformation of amorphous aluminum oxide, owing to activation of sintering and coalescence processes in the finely crystalline system upon heat treatment, whereas isometric corundum crystals are formed by the second pathway via γ-Al_2O_3. During mechanochemical activation, hydrargillite completely or partially transforms into boehmite (in the latter case, formation of nuclei of the γ-AlOOH phase should be assumed), which promotes phase and chemical transformations during calcination of activated hydrargillite predominantly (or completely) by the pathway involving formation of the γ-Al_2O_3 phase and its further transformations. This ultimately results in formation of monodisperse α-Al_2O_3 samples.

The effect of added iron oxides on the temperature of corundum formation and its particle size distribution is probably due to the following facts. On the one hand, small α-Fe_2O_3 crystals formed at relatively low (~700°C) temperatures play the role of corundum crystal seed, as they are isostructural with α-Al_2O_3, which decreases the temperature of α-Al_2O_3 formation. On the other hand, an increase in the calcination temperature leads to the formation of a Fe_2O_3 solid solution in α-Al_2O_3, which, according to the phase diagram of the Fe_2O_3–Al_2O_3 system [17], decreases the melting point of the solid solution $\alpha(Fe_xAl_{1-x})_2O_3$ from 2044 ($x = 0$) to 1700°C ($x = 0.1$). Therefore, the intensity of mass transfer in the finely crystalline system varies in parallel with x, which is manifested as an increase in the average size of crystals and as formation of crystal faces.

CONCLUSIONS

(1) In the course of mechanochemical activation, depending on its energy, γ-$Al(OH)_3$ is partially or completely dehydrated to form the γ-AlOOH phase, which subsequently promotes the formation of monodisperse finely crystalline α-Al_2O_3 on calcination.

(2) The presence of an α-Fe_2O_3 admixture, which is isostructural with α-Al_2O_3, reduces the temperature of corundum formation approximately by 100°C and affects the average size of its crystals. The factors responsible for a decrease in the temperature of formation of corundum crystals and for the formation of their faces were revealed.

ACKNOWLEDGMENTS

The work was financially supported by the Russian Foundation for Basic Research (project no. R 2001 Urchel 03-03).

REFERENCES

1. RF Patent 2 109 026.
2. Garshin, A.P., Gropyanov, V.M., and Lagunov, Yu.V., *Abrazivnye materialy* (Abrasives), Leningrad: Mashinostroenie, 1983.
3. Kalinina, A.M., in *Khimiya i tekhnologiya glinozema: Trudy IV Vsesoyuznogo soveshchaniya* (Chemistry and Technology of Alumina: Proc. IV All-Union Meet.), Novosibirsk: Nauka, 1971, pp. 360–369.
4. Oberbach, T., Gunter, C., Werner, G., *et al*., *Thermochim. Acta*, 1996, vol. 271, pp. 155–162.
5. Khanamirova, A.A., Adimosyan, A.R., and Apresyan, L.P., *Zh. Prikl. Khim*., 1998, vol. 71, no. 3, pp. 356–361.
6. Khanamirova, A.A., Adimosyan, A.R., and Apresyan, L.P., *Zh. Prikl. Khim*., 1998, vol. 71, no. 2, pp. 198–204.
7. Khanamirova, A.A., Oganesyan, P.L., Adimosyan, A.R., and Apresyan, L.P., *Zh. Prikl. Khim*., 1998, vol. 71, no. 10, pp. 1600–1603.
8. Wells, A.F., *Structural Inorganic Chemistry*, Oxford: Clarendon, 1984, 5th ed.
9. Freim, J., McKittric, J., Katz, J., and Sickafus, K., *Nanostruct. Mater*., 1994, vol. 4, no. 4, pp. 371–385.
10. Sato, T., *J. Therm. Anal*., 1987, vol. 32, no. 2, pp. 67–70.
11. Il'in, A.P., Shirokov, Yu.G., and Prokof'ev, V.Yu., *Izv. Ross. Akad. Nauk, Neorg. Mater*., 1995, vol. 31, no. 7, pp. 933–936.
12. Karagedov, G.R. and Lyakhov, N.Z., *Izv. Ross. Akad. Nauk, Neorg. Mater*., 1997, vol. 33, no. 7, pp. 817–821.
13. Mendelovici, E., Villalba, R., and Sagarzazy, A., *Mater. Res. Bull*., 1982, vol. 17, no. 2, pp. 241–243.
14. Cirilli, V., *Gazz. Chim. Ital*., 1950, vol. 80, p. 347.
15. Umanskii, Yu.S., Skakov, Yu.A., Ivanov, A.N., and Rastorguev, L.N., *Kristallografiya, rentgenografiya i elektronnaya mikroskopiya* (Crystallography, X-ray Diffraction, and Electron Microscopy), Moscow: Metallurgiya, 1982.
16. *Powder Diffraction File: Search Manual*, Swarthmore, Pennsylvania (the United States): Joint Committee on Powder Diffraction, 1977, card nos. 7-324, 10-425, 11-517, 11-661, 21-1307.
17. *Mineraly: Diagrammy fazovykh ravnovesii: Spravochnik* (Minerals: Diagrams of Phase Equilibria: Handbook), Chukhrov, F.V., Lapin, V.V., and Ovsyannikova, N.I., Eds., Moscow: Nauka, 1974, issue 2.

Russian Journal of Applied Chemistry, Vol. 75, No. 9, 2002, pp. 1389–1393. Translated from Zhurnal Prikladnoi Khimii, Vol. 75, No. 9, 2002, pp. 1422–1426.
Original Russian Text Copyright © 2002 by Maiorov, Nikolaev, Kopkov.

INORGANIC SYNTHESIS AND INDUSTRIAL INORGANIC CHEMISTRY

Extraction of Tantalum(V) Impurities from Niobium(V) Fluoride Solutions with Octanol

V. G. Maiorov, A. I. Nikolaev, and V. K. Kopkov

Tananaev Institute of Chemistry and Technology of Rare Elements and Mineral Resources, Kola Scientific Center, Russian Academy of Sciences, Apatity, Murmansk oblast, Russia

Received April 22, 2002

Abstract—Fine purification of niobium(V) to remove tantalum(V) by extraction was studied at various compositions of solutions and ratios of phase volumes. Washing of tantalum(V) and niobium(V) extracts with aqueous solutions of their fluorides was considered.

Preparation of niobium(V) compounds with a minimal content of tantalum(V) is a complicated problem in the extraction technology of tantalum(V) and niobium(V). Such a problem arises in processing of rare-metal raw materials with high Nb(V)/Ta(V) ratios (e.g., pyrochlore*) or in extraction flowsheets based on joint revovery of tantalum(V) and niobium(V) with their subsequent separation in the backwashing stage. In the latter case, as a rule, the niobium backwash is contaminated with tantalum(V). Whereas in pyrochlore processing addition of sulfuric acid to the extraction system for improving tantalum(V) and niobium(V) separation [2] is possible (though undesirable because of complicated utilization of spent fluoride solutions), in refining of the niobium backwash introduction of an additional reagent is unacceptable, as the backwash purified to remove tantalum(V) is immediately directed to the precipitation of niobium hydroxide. This limitation imposed on the extraction system composition additionally complicates separation of Ta from Nb. If the content of tantalum(V) is sufficiently high and commercial production of tantalum products is economically feasible, a necessity arises in treating the tantalum-containing organic phase (after processing of niobium solutions) to remove niobium(V).

We studied earlier [1, 3] the removal of tantalum(V) impurities from niobium(V) using tributyl phosphate (TBP) as extractant. Conditions were found for efficient separation of these elements at low volume ratios of the organic and aqueous phases $V_o : V_a$ both in the absence and in the presence of sulfuric acid. However, a significant drawback of TBP is its hydrolysis in contact with process solutions, which leads to contamination of niobium–tantalum products with phosphorus(V) and other elements [2]. Additional drawbacks of TBP are its toxicity and high density, which impedes phase separation of emulsions and increases the size and cost of the equipment.

Octanol is a promising extractant finding growing application in the extraction technology of tantalum(V) and niobium(V) [4–11]. It was used in production of high-purity tantalum(V) and niobium(V) compounds by processing tantalite–columbite concentrates [5–9] and in the isolation of pure pentoxides of these elements from titanium fluoride solutions containing up to 500 g l^{-1} TiO_2, according to one of versions of processing loparite (rare-earth titanoniobate) [4, 10]. It was shown in [5] that, in extraction power, octanol compares well with methyl isobutyl ketone, which is usually used in other countries to extract tantalum(V) and niobium(V); however, in contrast to octanol, methyl isobutyl ketone is dangerously explosive and noticeably soluble in aqueous solutions.

In this work we used 1-octanol $CH_3(CH_2)_6CH_2OH$ (OCL). We found previously that OCL and other octanol isomers (2-octanol and 2-ethylhexanol) have similar extraction properties; these extractants are commercially available and relatively cheap. 1-Octanol is resistant to prolonged action of fluoride–sulfate solutions; for example, after a contact with a solution of 4 M HF and 5 M H_2SO_4 for 280 days ($V_o : V_a$ = 1 : 1), OCL remains usable. Under the same conditions, TBP forms a homogeneous solution in 70 days, which determines the stability limit of this extractant [8, 12]. The physicochemical properties of OCL are

* Pyrochlore of the Belaya Zima field (one of samples) contains 30.6 wt % Nb_2O_5 and 0.32 wt % Ta_2O_5 [1].

1070-4272/02/7509-1389$27.00 © 2002 MAIK "Nauka/Interperiodica"

Table 1. Effect of HF_{free} concentration and $V_o : V_a$ ratio on extraction of tantalum(V) and niobium(V). Content in solution, M: Ta(V) 0.45 or Nb(V) 0.75

$c_{HF_{free}}$, M	$V_o : V_a$	Extraction, %	
		Ta(V)	Nb(V)
0	1 : 1	27.5	9.8
1	1 : 1	32.5	–
2	1 : 1	33.4	24.4
4	1 : 1	–	22.5
0	4 : 1	53.3	15.8
1	4 : 1	54.6	–
2	4 : 1	49.9	29.8
4	1 : 1	–	26.6

Table 2. Influence of niobium(V) concentration on its purification to remove tantalum(V). Initial molar ratio Ta(V) : Nb(V) = 1 : 1660 (0.1 wt % Ta_2O_5 in Nb_2O_5), $c_{HF_{free}} \sim 0$ M

$c_{Nb(V)}$, M	$V_o : V_a$	Extraction, %	
		Ta(V)	Nb(V)
2.0	0.9 : 1	60.3	15.8
2.0	1.2 : 1	72.2	18.5
2.7	0.9 : 1	61.7	24.4
2.7	1.2 : 1	76.2	27.2
4.0	0.9 : 1	49.5	34.7
4.0	1.2 : 1	60.8	38.5

described in [8, 12], and the techniques of operation with aggressive fluoride solutions and the corresponding analytical control are given in detail in [13].

The distribution of tantalum(V) and niobium(V) extracted from solutions of these elements taken separately is shown in Table 1 in relation to the phase volume ratio $V_o : V_a$ and HF_{free} content. Here and hereinafter, HF_{free} is the calculated nominal HF content in excess of its content in the complexes $HTa(Nb)F_6$, H_2TiOF_4, H_2SiF_6, etc. (according to [13, 14], these complexes dominate in the extraction system under study). It should be noted that, as opposed to tantalum(V), niobium(V) is relatively poorly extracted from solutions containing HF only, even at high $V_o : V_a$ ratios. This drawback of OCL is attributable to its low basicity. Furthermore, it follows from the obtained data that the best separation of Ta(V) and Nb(V) can be achieved for solutions with low $c_{HF_{free}}$.

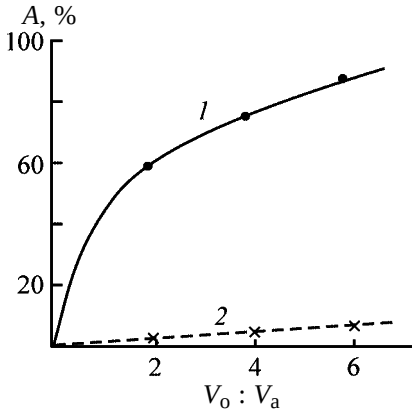

Fig. 1. Influence of the $V_o : V_a$ ratio on the extraction of (*1*) Ta(V) and (*2*) Nb(V) from a solution containing 0.3 M Ta(V) and 0.5 M Nb(V). (*A*) Recovery; the same for Fig. 2.

We have studied the effect of the $V_o : V_a$ ratio on the separation of tantalum(V) and niobium(V) from mixed solutions of these elements with low HF_{free} content (Fig. 1) and found that tantalum(V) is extracted much better in the presence of niobium(V). It is known [2] that neutral organic solvents, including OCL, extract tantalum(V) and niobium(V) from fluoride-containing solutions as complexes of fluorometallic acids HMF_6 whose extraction increases with the H^+ concentration in the system. In the case of HF deficiency, niobium(V), as opposed to tantalum(V), is not noticeably extracted; however, the presence of the readily dissociating acid $HNbF_6$ increases the acidity of the system and promotes the tantalum(V) extraction. Under the experimental conditions (Fig. 1), the extraction of Ta(V) in one stage is 80–90, and that of Nb(V), only 5–8%. A calculation by Cremser's formula [14] shows that, when the Ta(V) recovery in one stage is 90% ($V_o : V_a \approx 7 : 1$), only six equilibrium steps are sufficient to obtain Nb_2O_5 containing less than 0.001 wt % Ta_2O_5 in a continuous counterflow process.

The above-found conditions for the extraction and separation of tantalum(V) and niobium(V) from solutions containing HF without additions of other inorganic acids were used to find conditions for the removal of tantalum(V) impurity, which may be as large as several weight percents of Ta_2O_5 in Nb_2O_5 [2], from niobium(V) backwash. The data on the influence of the Nb(V) content on its purification to remove Ta(V) are given in Table 2. As the Nb(V) concentration (i.e., the content of $HNbF_6$) increases, the extraction of both Nb(V) and Ta(V) into the organic phase grows. However, at high Nb(V) contents (more than 2.7 M), the extraction of Ta(V) decreases, apparently owing to competition with Nb(V) for the organic phase. In the examined range of process conditions, the optimal Nb(V) concentration ensuring fairly complete extraction of Ta(V) with relatively low coextraction of Nb(V) is about 2.2 M.

Table 3. Removal of niobium(V) impurities from tantalum(V) extract ($V_o : V_a = 10 : 1$, $c_{HF_{free}} \approx 0$ M)

Molar ratio Ta(V) : Nb(V) in extract	Ta(V) concentration in scrubbing solution, M	Degree of Nb(V) washout, %	Total extraction of Ta(V) to scrubbed extract, %
1 : 110	0.18	86.1	92.4
1 : 110	0.36	72.7	117.2
1 : 10	0.18	87.3	96.0
1 : 10	0.36	84.4	109.4
1 : 1.1	0.18	74.1	94.8
1 : 1.1	0.36	64.9	114.3

We studied in detail the effect of various process parameters on the extraction of Ta(V) impurities from solutions containing 2.2 M Nb(V) (Fig. 2). The extraction of Ta(V) only weakly depends on the Ta(V) : Nb(V) ratio, which suggests the possibility of fine purification of Nb(V) to remove Ta(V) in a continuous counterflow process. As expected, the extraction weakly increases with increasing $V_o : V_a$ ratio and decreases with increasing HF_{free} content. These data suggest that niobium backwashes should be purified at $c_{HF_{free}} \geq 0$ M and $V_o : V_a \geq 1.8 : 1$. A calculation by Cremser's formula [14] shows that, when about 80% of Ta(V) is extracted in one stage, four equilibrium steps are necessary to decrease the content of Ta_2O_5 in Nb_2O_5 from 3 to 0.01 wt %, and six steps, to decrease it to 0.001 wt %.

The niobium backwash purified to remove tantalum(V) is sent to the precipitation of niobium hydroxide, whereas the organic phase should be treated to recover both Nb(V) and Ta(V), with Ta(V) being in the form of a commercial product. The Ta(V) extract can be scrubbed to remove Nb(V) with water or (Table 3) with a Ta(V) solution. In the latter case, addition of Ta(V) to a scrubbing solution increases its content in the extraction system and, correspondingly, promotes displacement of impurities from the organic phase into the aqueous phase. The introduction of one of components to be separated into a scrubbing solution is successfully used, e.g., in separation of cobalt(II) and nickel(II) [15]. The backwash or a solution obtained by dissolving Ta(V) oxide in HF can be used as such scrubbing solution. A solution containing 0.18 M Ta(V) appeared to be efficient for Nb(V) purification at Nb(V) : Ta(V) ratios in the extract varying a wide range (Table 3). The increase in the Ta(V) content to 0.36 M leads to an increase in the acidity of the scrubbing solution (owing to $HTaF_6$ dissociation) and, correspondingly, to less complete removal of Nb(V). In a continuous counterflow scrubbing process with 6–8 equilibrium steps, the Nb_2O_5 content in Ta_2O_5 is reduced to values less than 0.001–0.01 wt %. Tantalum(V) is readily backwashed with water from the scrubbed extract at $V_o : V_a \approx 3 : 1$ [9], and OCL is returned to the extraction of Ta(V) impurity.

The scheme of extraction treatment of niobium(V) to remove tantalum(V) is shown in Fig. 3. The initial solution, e.g., niobium(V) backwash, is evaporated to the Nb(V) concentration of about 2.2 M, which is the best for the efficient extraction of Ta(V) impurities. The evaporation also makes it possible to reduce as much as possible the HF_{free} content and the volume of process streams. The spent solution after scrubbing the tantalum(V) extract is combined with the initial solution to prevent losses of rare metals. Using main process stages of this scheme, we have prepared niobium(V) oxide containing less than 0.005 wt % Ta_2O_5, as shown by mass spectrometry.

We have considered niobium(V) treatment to remove tantalum(V) without adding other inorganic acids, e.g., sulfuric acid, into the extraction system. Of great practical interest is the recovery of tantalum(V)

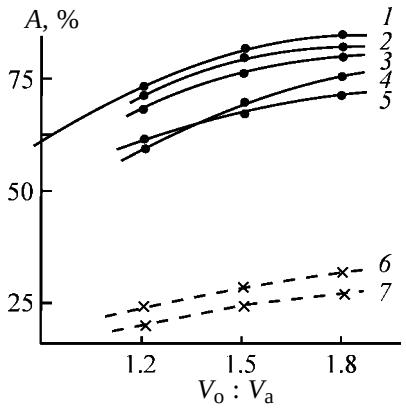

Fig. 2. Influence of the $V_o : V_a$ ratio on the extraction of (*1–5*) Ta(V) and (*6, 7*) Nb(V) from 2.2 M solution of Nb(V). HF_{free} content, M: (*1–3, 7*) 0 and (*4–6*) 2. Molar ratio Ta(V) : Nb(V): (*1*) 1 : 1660, (*2, 4*) 1 : 570, and (*3, 5*) 1 : 140.

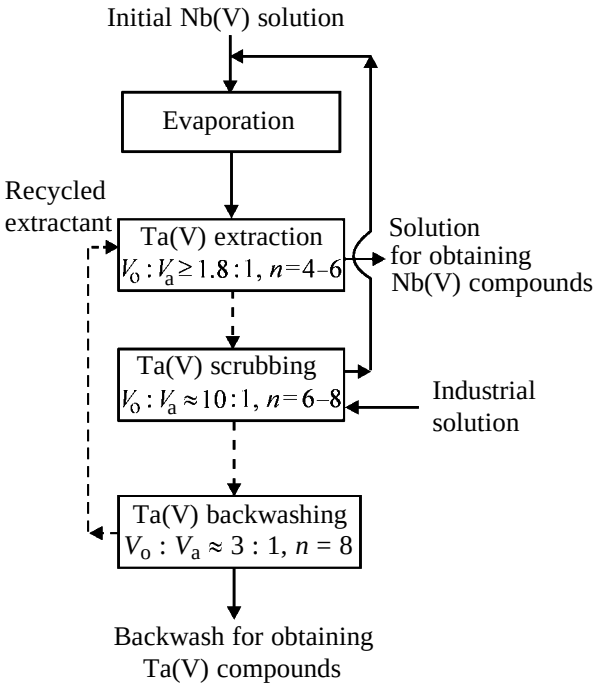

Fig. 3. Flowsheet of treatment of Nb(V) solution (backwash) to remove Ta(V). (*n*) Number of extraction steps.

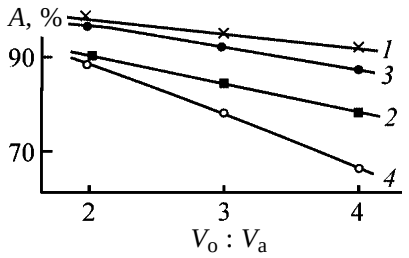

Fig. 4. Influence of the $V_o : V_a$ ratio on Nb(V) backwashing from extracts by water. (*A*) Degree of backwashing. Composition of extracts (M): Nb(V) (*1, 2*) 0.3 and (*3, 4*) 0.75; HF_{free} (*1, 3*) 0 and (*2, 4*) 1.5.

and niobium(V) from solutions obtained in pyrochlore processing, which have a high Nb(V) : Ta(V) ratio close to that in niobium backwash. When pyrochlore is broken down with hydrofluoric acid without adding other acids [2, 3], pure tantalum(V) is readily recovered by a scheme similar to that shown in Fig. 3, and niobium(V) can be utilized for obtaining ferroniobium. However, if production of pure niobium(V) compounds is intended, a necessity arises in its transfer into the organic phase to remove concomitant impurities. With OCL as extractant, niobium(V) is efficiently extracted only on adding other inorganic acids. According to [9], when niobium(V) is extracted with OCL, the concentration of H_2SO_4 should be 5–6 M. Our experiments showed that fluoride solutions of niobium(V) can be successfully used to remove impurities from its extracts. When an extract [0.7 M Nb(V)] is scrubbed with an 1.9 M Nb(V) solution [$c_{HF_{free}} \approx 0$ M, $V_o : V_a = (6–8) : 1$], the degree of titanium(IV) removal (the most difficult-to-remove impurity [2]) is more than 90% in one step. Niobium(V) is readily backwashed with water from the scrubbed organic phase (Fig. 4): at $V_o : V_a = 4 : 1$, 66–92% of Nb(V) passes into the aqueous phase in one step depending on the Nb(V) and HF_{free} contents in the extract. The best parameters of niobium(V) backwashing were obtained, as expected, at low Nb(V) and HF_{free} concentrations (Fig. 4): in this case, backwashing can be performed at a ratio $V_o : V_a \geq 5 : 1$. Thus, our study has confirmed the efficiency of using octanol as extractant in tantalum(V) and niobium(V) hydrometallurgy.

CONCLUSIONS

(1) The optimal conditions for the removal of tantalum(V) impurity from niobium(V) backwash are as follows: Nb(V) content in the initial solution 2.2 M and low $c_{HF_{free}}$.

(2) The applicability of the developed technology to pyrochlore processing was demonstrated.

ACKNOWLEDGMENTS

The work was financially supported by a grant of Leading Scientific Schools (project no. 00-15-97364).

REFERENCES

1. Nikolaev, A.I., Maiorov, V.G., and Kopkov, V.K., *Tsvetn. Met.*, 1999, no. 3, pp. 83–85.
2. Babkin, A.G., , Maiorov, V.G., and Nikolaev, A.I., *Ekstraktsiya niobiya i tantala i drugikh elementov iz ftoridnykh rastvorov* (Extraction of Niobium and Tantalum and Other Elements from Fluoride Solutions), Leningrad: Nauka, 1988.
3. Maiorov, V.G., Nikolaev, A.I., and Kopkov, V.K., *Zh. Prikl. Khim.*, 1994, vol. 67, no. 2, pp. 329–331.
4. Maiorov, V.G., Sklokin, S.I., and Nikolaev, A.I., Abstracts of Papers, *XI Rossiiskaya konferentsiya po ekstraktsii* (XI Russian Conf. on Extraction), Moscow, June 21–27, 1998, p. 188.
5. Hydrometallurgical Extraction of Tantalum and Niobium in China, *Bulletin of Tantalum–Niobium International Study Center (T.I.C.)*, 1998, no. 93, pp. 1–6.
6. Travkin, V.F., Agulyanskii, A.I., Glubokov, Yu.M.,

and Karamushko, E.V., *Tsvetn. Metall*., 1998, nos. 8–9, pp. 18–22.

7. Travkin, V.F., Agulyanskii, A.I., Glubokov, Yu.M., and Karamushko, E.V., *Tsvetn. Metall*., 1999, no. 4, pp. 19–22.
8. Maiorov, V.G., Nikolaev, A.I., and Kopkov, V.K., *Zh. Prikl. Khim*., 2001, vol. 74, no. 3, pp. 357–360.
9. Maiorov, V.G., Nikolaev, A.I., Kopkov, V.K., *et al*., in *Khimiya i tekhnologiya ekstraktsii: Sbornik nauchnykh trudov RKhTU im. D.I. Mendeleeva* (Chemistry and Technology of Extraction: Coll. of Scientific Works of the Mendeleev Russian University of Chemical Engeneering), Moscow, 2001, vol. 2, pp. 19–26.
10. Maiorov, V.G., Nikolaev, A.I., Sklokin, S.I., *et al*., in *Razvitie redkometal'noi promyshlennosti v Rossii na baze loparita: Trudy IV nauchnoi konferentsii* (Development of Rare-Metal Industry in Russia on the Basis of Loparite: Proc. IV Scientific Conf.), St. Petersburg, May 22–24, 2001, pp. 179–180.
11. Glubokov, Yu.M., Travkin, V.F., Il'in, E.G., *et al*., *Tsvetn. Metall*., 2001, no. 10, pp. 23–27.
12. Maiorov, V.G., Baklanova, I.V., Nikolaev, A.I., and Safonova, L.A., *Zh. Prikl. Khim*., 2000, vol. 73, no. 10, pp. 1636–1640.
13. Maiorov, V.G., Nikolaev, A.I., and Kopkov, V.K., *Zh. Prikl. Khim*., 1999, vol. 72, no. 6, pp. 929–932.
14. Alders, L., *Liquid–Liquid Exraction. Theory and Laboratory Practice*, Amsterdam: Elsevier, 1959.
15. Ritcey, G.M. and Ashbrook, A.W., *Solvent Extraction. Principles and Applications to Process Metallurgy*, Amsterdam: Elsevier, 1979.

Russian Journal of Applied Chemistry, Vol. 75, No. 9, 2002, pp. 1394–1398. Translated from Zhurnal Prikladnoi Khimii, Vol. 75, No. 9, 2002, pp. 1427–1430.
Original Russian Text Copyright © 2002 by Sharygin.

INORGANIC SYNTHESIS AND INDUSTRIAL INORGANIC CHEMISTRY

Preparation of Globular Zirconium(IV) Hydroxide by Sol–Gel Process

L. M. Sharygin

Termoksid Production and Research Company, Zarechnyi, Sverdlovsk oblast, Russia

Received January 25, 2001; in final form, February 2002

Abstract—The sol–gel process of the preparation of globular zirconium(IV) hydroxide is described, which involves formation of zirconium(IV) hydroxide sol by electrolysis of zirconium(IV) chloride solution in a one-compartment cell to a Cl/Zr atomic ratio of less than 0.6, gelation of sol droplets in aqueous ammonia, treatment of gel spheres to remove electrolytes, and drying.

Zirconium(IV) hydroxide is used as inorganic sorbent in radiochemistry for concentrating and separating radionuclides, in chemical industry for preparing ultrapure substances, in medicine, and in other fields.

Zirconium(IV) hydroxide is an amphoteric ion exchanger; its properties have been studied by many researchers [1–4]. It is a cation exchanger in neutral and alkaline solutions and an anion exchanger in acid solutions. With multiple-charged anions and cations, ion exchange is complicated by chemical interaction between the sorbate and sorbent, yielding sparingly soluble surface compounds. Therefore, zirconium hydroxide in neutral solutions is selective to multiple-charged anions (phosphates, silicates, molybdates, arsenates, and other anions) and cations [lead(II), copper(II), cobalt(II), and other cations].

The requirements to the content of toxic impurities in tap water become at present more and more stringent. For example, the maximum permissible concentration of silicon is 10 mg dm^{-3}. The high chemical stability of zirconium(IV) hydroxide in neutral aqueous solutions and the high selectivity to multiple-charged anions and cations make this compound promising as a sorbent for local systems of tap water treatment.

Also, zirconium(IV) hydroxide is used for preparing zirconium(IV) oxide powders, which, in turn, are used for the manufacture of ceramics, refractory materials, and catalysts [5].

Globular zirconium(IV) hydroxide is prepared by gel or sol–gel process [1–10]. The gel process involves precipitation of zirconium(IV) hydroxide from the solution of its salt, followed by washing and dehydration of the gel precipitate [1–6]. The sol–gel process consists of the following main stages: formation of a metal hydroxide hydrosol, gelation of sol droplets, washing of sol spheres, and drying [9, 10]. In the sol–gel process, the stages of sol and gel formation are separated in time. As a result, gel spheres are formed from the initial particles after their formation and have high mechanical strength and elastic skeleton, which allows their shape to be retained in the subsequent stages of washing and drying. All this allows preparation of metal hydroxides in the form of mechanically strong spheres of prescribed size with reproducible properties.

Here we report on a sol–gel process for the preparation of globular zirconium(IV) hydroxide, which involves formation of sol by electrolysis of zirconium(IV) chloride solution, gelation of sol droplets in aqueous ammonia, and washing and drying of gel spheres.

Among many methods for preparing zirconium(IV) hydroxide hydrosols, direct electrochemical synthesis attracts the most attention [9, 11, 12]. The method is based on removal of hydrochloric acid, which is the product of the salt hydrolysis, from aqueous solutions of metal chlorides by decomposing it on the electrodes into chlorine and hydrogen on passing electric current. Owing to the hydrolysis, the dissolution of zirconium(IV) oxide dichloride, $ZrOCl_2$, in water yields hydrochloric acid. The concentration of free hydrochloric acid is approximately equal to the molar concentration of zirconium in the solution [6, 13]. The decrease in the hydrochloric acid concentration during electrolysis of zirconium chloride solution promotes further hydrolysis and polymerization of zirconium(IV) hydroxo complexes and results in the forma-

1070-4272/02/7509-1394$27.00 © 2002 MAIK "Nauka/Interperiodica"

tion of zirconium hydroxide as a sol. The electrolysis can be performed in a one-compartment cell using platinum, graphite, titanium, zirconium, and other electrodes resistant to hydrochloric acid.

The hydrolysis and polymerization of zirconium ions in aqueous solutions were studied in numerous works [4–6, 14]. It was shown by different physical methods that, in solid salts and aqueous solutions, zirconyl ions are absent, and the main structural unit in these compounds is a tetranuclear hydroxo complex $[Zr_4(OH)_8(H_2O)_{16}]^{8+}$. The X-ray scattering, Raman spectroscopy, and other methods [14–18] showed that, upon dissolution of zirconium oxide dichloride in water, the complex $[Zr_4(OH)_8(H_2O)_{16}]^{8+}$ as the main structural unit is preserved. The hydrolysis and polymerization of this hydroxo complex determine further behavior of zirconium in solution. These processes are considered in more detail in [6]. The degree of polymerization of hydroxo complexes can be characterized by the fraction α of bridging zirconium ions. In the limiting case, when polymerization is 100% complete, there will be four bridging bonds per hydroxo complex consisting of four zirconium atoms. Therefore, the degree of polymerization of zirconium hydroxo complexes can be found from the relationship $\alpha = (n/4) \times 100$, where n is the number of bridging bonds per tetranuclear complex.

In [18] we used the methods of electrical conductivity, Raman spectroscopy, and determination of the solution viscosity in relation to shear stress for studying formation of zirconium hydroxide sol in the course of electrolysis of zirconium oxide dichloride solution in a one-compartment cell. The dependences of the electrical conductivity and the relative content of bridging zirconium ions on the Cl/Zr atomic ratio in the course of the electrolysis of 1 M $ZrOCl_2$ solution are shown in Fig. 1. It is seen that, with decreasing Cl/Zr ratio, the fraction of bridging zirconium ions increases, which shows that hydroxo complexes polymerize as hydrochloric acid is removed from the solution. The polymerization is also confirmed by the Raman spectra of the solutions taken in the course of the electrolysis. At Cl/Zr = 0.55, the fraction of bridging zirconium ions is 54%. Reinten [6] found that, in a $ZrOCl_2$ solution neutralized with alkali with formation of zircomium(IV) hydroxide, the fraction of bridging zirconium ions is the same (52–56%). This shows that, in the course of the electrolysis of zirconium chloride solution to a Cl/Zr atomic ratio less than 0.6, a colloidal solution (sol) of zirconium(IV) hydroxide is formed, with the degree of polymerization being maximal for colloidal particles of this size. Further decrease in the Cl/Zr ratio in a solution is not accompanied by the polymerization and involves neutralization of surface chloride ions and free hydrochloric acid and coagulation of colloidal particles. The electron diffraction [9] showed that the colloidal particles are amorphous.

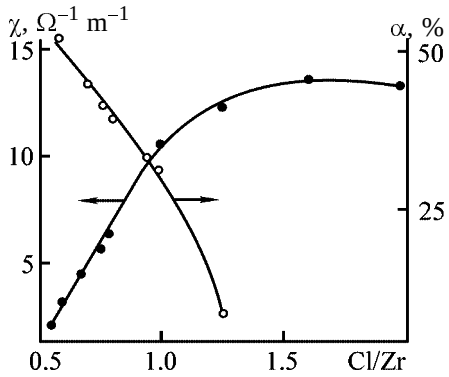

Fig. 1. Electrical conductivity χ and fraction α of bridging zirconium ions vs. Cl/Zr atomic ratio in the course of the electrolysis [18].

The chemical composition of the colloids can be conventionally described by the formula $\{Zr(OH)_4\} \cdot Zr(OH)_{4-x}^{x+} \cdots x Cl^-$, where $2 < x < 4$. The particle core is formed by zirconium(IV) hydroxide, and the surface layer, by zirconium hydroxochloride. The chloride ions are not bonded directly to zirconium, but instead are arranged in the outer coordination sphere and neutralize the positive charge of colloids. Experimental data on the electrical conductivity show that, e.g., at Cl/Zr = 0.55 the concentration of free hydrochloric acid is 0.055 M, which corresponds to only about 10% of the amount chloride ions present in the system. The remaining 90% of ions are bound in polymeric complexes as counterions. Therefore, the chemical composition of sol colloids, e.g., at Cl/Zr = 0.5 is $\{Zr(OH)_4\}Zr(OH)_3^+ \cdots Cl^-$.

The solution viscosity in the course of the zirconium chloride electrolysis to Cl/Zr = 1.0 does not noticeably vary. Decreasing the above ratio increases viscosity, with the increase being especially pronounced at a Cl/Zr ratio less than 0.6. In rheological properties, solutions with Cl/Zr > 0.6 are Newtonian liquids, and those with Cl/Zr < 0.6 are weakly structured colloidal systems.

In the course of the electrolysis of zirconium chloride solution, the following processes occur:

at the cathode,

$$2H^+ + 2e \rightarrow H_2\uparrow, \quad (1)$$

$$2H_2O + 2e \rightarrow H_2\uparrow + 2OH^-; \quad (2)$$

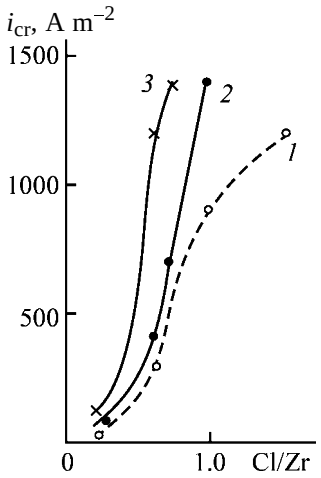

Fig. 2. Critical current density i_{cr} vs. Cl/Zr atomic ratio [20]. Temperature (°C): (*1*) 25, (*2*) 40, and (*3*) 60.

and at the anode,

$$2Cl^- - 2e \rightarrow Cl_2\uparrow, \quad (3)$$

$$2H_2O - 4e \rightarrow O_2\uparrow + 4H^+. \quad (4)$$

Evolution of chlorine and oxygen at the anode by reactions (3) and (4) in chloride melts was extensively studied previously [19]. In [20], we recorded the cathodic polarization curves on platinum as functions of the current density, Cl/Zr atomic ratio in solution, and temperature within 25–80°C with the aim to study the cathodic evolution of hydrogen in the course of electrolysis of 1 M $ZrOCl_2$ solution. The cathodic polarization in solutions with the Cl/Zr ratio varied from 2.0 to 1.6 is weak. With decreasing Cl/Zr ratio, i.e., concentration of hydrochloric acid in solution, the character of the polarization curves changes. At a certain current density, which can be referred to as critical density i_{cr}, the slope of the curves changes. A sharp increase in the cathode polarization is due to impeded diffusion of hydrogen ions toward the cathode and by the discharge of water molecules. The hydrogen evolution by reaction (2) results in the alkalization of the near-cathode space, formation of basic zirconium salts, and spontaneous termination of the process. At higher temperatures, the above diffusion hindrance appears at smaller Cl/Zr ratios, which is due to accelerated hydrolysis of the salt. At 80°C, the critical current density is not observed even for Cl/Zr = 0.86. The dependences of the critical current density on the Cl/Zr ratio are shown in Fig. 1. As the Cl/Zr ratio in solution is decreased, the critical current density decreases also; this trend is the most pronounced at the Cl/Zr ratios from 1.0 to 0.6.

The temperature dependence of the critical current density is also significant. Elevated temperatures accelerate hydrolysis and decrease the solution viscosity. As a result, the hydrogen discharge overvoltage decreases, and i_{cr} grows. Thus, for preparing a zirconium(IV) hydroxide sol with Cl/Zr < 0.6, the electrolysis of zirconium chloride solution should be performed at a cathodic current density not exceeding the critical value. From the start of the electrolysis to a moment of attaining the ratio Cl/Zr ≈ 1.4, the current efficiency by chlorine is more than 100%, which is due to removal of a part of hydrochloric acid from the solution with gaseous electrolysis products. As the Cl/Zr ratio is decreased, the current efficiency by chlorine decreases also. For the electrolytic method of sol preparation, the average current efficiency by chlorine is about 80%.

The second stage of the sol–gel process is dispersion of the zirconium hydroxide gel in aqueous ammonia. The diffusion of ammonia into sol droplets neutralizes free hydrochloric acid and chloride ions bound to colloids and causes gelation of sol droplets into spheres. The gelation conditions (the properties of sol and gelating medium) are chosen so as to prevent breakdown of gel spheres and preserve their shape after transformation of sol droplets, and also to ensure high mechanical strength of the gel spheres, sufficient to withstand the subsequent stages of washing off electrolytes and drying. The chemical processes occurring upon the sol–gel transformation of zirconium(IV) hydroxide can be presented by the following equation:

$$\{Zr(OH)_4\}Zr(OH)_{4-x}Cl_x + xNH_4OH$$
$$= 2Zr(OH)_4 + xNH_4Cl.$$

The gel spheres consist of a three-dimensional network of primary particles separated by water-filled pores. Conventionally, the moisture content of the gel spheres is within 60–80% depending on the sol concentration. Therefore, gel spheres are fairly diluted finely dispersed porous substances. Their chemical composition corresponds to zirconium(IV) hydroxide. According to an electron-microscopic study [6], the particle size is about 3 nm. Similar to the majority of hydroxides, zirconium(IV) hydroxide has a layered structure. The layer consists of tetrameric ions bound with each other by hydroxy groups arranged above and below the plane of the layer [4]. As a result, each zirconium atom is surrounded by eight hydroxy groups in the form of a distorted cube.

The gel spheres are washed to remove excess am-

monia and electrolytes and dried at a temperature from 20 to 150°C. Since zirconium(IV) hydroxide is a cation exchanger in alkaline media, the gel spheres after washing contain certain amount of ammonium ions. To exhaustively remove ammonium ions, gel spheres are washed with dilute hydrochloric acid. Drying gel spheres decreases several-fold their volume and results in the formation of the adsorbent pore structure. According to the most popular concept [21, 22], the gel skeleton is compressed upon drying under the action of capillary forces whose value depends on the capillary radius. The strength of the gel skeleton, increasing upon drying, resists the capillary compressive forces. The final pore structure of the adsorbent is fixed when the counteractive forces come in equilibrium. Therefore, the equilibrium pore structure of the sorbent formed upon drying the gel depends not only on the drying conditions (temperature, water vapor pressure, surface tension of water, and other factors), but also on the procedures of gel formation and treatment [21, 22]. Since in the final stages of drying the capillary radii of porous substances are fairly small, the capillary forces attain high values (several kilobars). The chemical reactions in solids are considerably activated by mechanical stress [23]. Therefore, the chemical transformation of hydroxide into oxide may occur even in the course of drying of gel spheres.

Drying of gel spheres at 100–150°C results in the formation of globular, mechanically strong amorphous products classed with microporous sorbents [24, 25] according to Dubinin's classification. The chemical composition of the xerogel strongly depends on the drying conditions, first of all, on temperature. There is still no common opinion in the literature on the chemical composition of the xerogel. However, the majority of researches [4, 6] consider it as oxohydroxide $ZrO_x(OH)_{4-2x}$, where x varies from 0 to 2. Upon calcination of xerogel, the hydroxide is converted into oxohydroxide and oxide, which can be conventionally represented by the following scheme:

$$Zr(OH)_4 \xrightarrow{\Delta} ZrO_x(OH)_{4-2x} + xH_2O \xrightarrow{\Delta} ZrO_2 + (2 - x)H_2O.$$

The chemical reactions are complete at temperatures below 350°C and are accompanied by dehydration, pore structure transformation, and changes in the phase composition and other physicochemical properties of the product [25].

CONCLUSIONS

(1) Electrolysis of zirconium(IV) chloride solution in a one-compartment cell is accompanied by hydrolysis and polymerization of four-membered zirconium hydroxo complexes, and at a Cl/Zr ratio less than 0.6 zirconium hydroxide is formed in the form of stable sol. The preparation of zirconium hydroxide sol by electrolysis is limited by cathodic evolution of hydrogen.

(2) When the sol is dispersed in aqueous ammonia, free hydrochloric acid and chloride ions bound to colloids are neutralized, and gelation of sol droplets with formation of gel spheres takes place.

REFERENCES

1. Amphlett, C.B., *Inorganic Ion Exchangers*, Amsterdam: Elsevier, 1964.
2. Blumenthal, W.B., *The Chemical Behavior of Zirconium*, New York: Van Nostrand, 1958.
3. Boichinova, E.S., in *Ionnyi obmen i ionometriya* (Ion Exchange and Ionometry), Leningrad: Leningr. Gos. Univ., 1984, issue 4, pp. 76–82.
4. Clearfield, A., Nancollas, G.H., and Blessing, R.K., *Ion Exch. Solvent Extr*., 1973, vol. 5, no. 1, pp. 1–120.
5. Strekalovskii, V.N., Polezhaev, Yu.M., and Pal'guev, S.F., *Oksidy s primesnoi razuporyadochennost'yu* (Oxides with Impurity Disordering), Moscow: Nauka, 1987.
6. *Physical and Chemical Aspects of Adsorbents and Catalysts*, Linsen, B.G., Ed., London: Academic, 1970. Transolated under the title *Stroenie i svoistva adsorbentov i katalizatorov*, Moscow: Mir, 1973, pp. 332–384.
7. Makarov, V.M., Skotnikov, A.S., Zhiboedov, V.G., *et al*., *Radiokhimiya*, 1976, vol. 18, no. 5, pp. 773–783.
8. Pospelov, A.A., Krylov, V.N., Rakov, N.A., *et al*., in *Khimiya i tekhnologiya neorganicheskikh sorbentov* (Chemistry and Technology of Inorganic Sorbents), Perm: Perm. Politekh. Inst., 1979, pp. 85–91.
9. Sharygin, L.M., Gonchar, V.F., and Moiseev, V.E., in *Ionnyi obmen i ionometriya* (Ion Exchange and Ionometry), Leningrad: Leningr. Gos. Univ., 1986, issue 5, pp. 9–29.
10. Vol'khin, V.V., in *Ionnyi obmen i ionometriya* (Ion Exchange and Ionometry), Leningrad: Leningr. Gos. Univ., 1996, issue 9, pp. 3–23.
11. Sharygin, L.M., Shtin, A.P., Tret'yakov, S.Ya., *et al*., *Kolloidn. Zh*., 1981, vol. 43, no. 4, pp. 812–816.
12. Karpachev, L.G., Belenok, T.M., and Mityakin, P.L., *Sib. Khim. Zh*., 1992, no. 4, pp. 100–104.

13. Ermakov, A.N., Marov, I.N., and Belyaeva, V.K., *Zh. Neorg. Khim.*, 1963, vol. 8, no. 7, pp. 1623–1633.
14. Solovkin, A.S., and Tsvetkova, Z.N., *Usp. Khim.*, 1962, vol. 31, no. 11, pp. 1394–1409.
15. Clearfield, A. and Vaughan, P.A., *Acta Crystallogr.*, 1956, vol. 9, no. 7, pp. 555–558.
16. Muha, G.H., and Vaughan, P.A., *J. Chem. Phys.*, 1960, vol. 33, no. 1, pp. 194–199.
17. Burkov, K.D., Kozhevnikova, G.V., Lilich, L.S., *et al.*, *Zh. Neorg. Khim.*, 1982, vol. 27, no. 6, pp. 1427–1432.
18. Sharygin, L.M., Galkin, V.M., Vovk, S.M., *et al.*, *Kolloidn. Zh.*, 1985, vol. 47, no. 1, pp. 120–125.
19. Fedot'ev, N.P., Alabyshev, A.F., Rotinyan, A.L., *et al.*, *Prikladnaya elektrokhimiya: Uchebnoe posobie* (Applied Electrochemistry: Textbook), Fedot'ev, N.P., Ed., Leningrad: Goskhimizdat, 1962.
20. Sharygin, L.M., Korenkova, A.V., Shtin, A.P., *et al.*, *Zh. Prikl. Khim.*, 1985, vol. 58, no. 8, pp. 1771–1776.
21. Neimark, N.E., *Usp. Khim.*, 1956, vol. 25, no. 6, pp. 748–764.
22. Sharygin, L.M., *Zh. Fiz. Khim.*, 1979, vol. 53, no. 3, pp. 703–709.
23. Avvakumov, V.G., *Mekhanicheskie metody aktivatsii khimicheskikh protsessov* (Mechanical Activation of Chemical Processes), Novosibirsk: Nauka, 1979.
24. Sharygin, L.M., Galkin, V.M., and Shtin, A.P., *Izv. Akad. Nauk SSSR, Neorg. Mater.*, 1979, vol. 15, no. 11, pp. 2051–2054.
25. Sharygin, L.M. and Galkin, V.M., *Adsorb. Adsorb.* (Kiev), 1983, no. 11, pp. 40–44.

Russian Journal of Applied Chemistry, Vol. 75, No. 9, 2002, pp. 1399–1405. Translated from Zhurnal Prikladnoi Khimii, Vol. 75, No. 9, 2002, pp. 1431–1437.
Original Russian Text Copyright © 2002 by Reva, Vorob'eva.

INORGANIC SYNTHESIS AND INDUSTRIAL INORGANIC CHEMISTRY

Photostimulated Oxidation of Sn(II) in Aqueous Solutions: Spectral Sensitivity and Quantum Yield

O. V. Reva and T. N. Vorob'eva

Research Institute of Physicochemical Problems, Belarussian State University, Minsk, Belarus

Received November 9, 2001; in final form, June 2002

Abstract—The spectral sensitivity of Sn(II) complexes in acid and alkaline solutions of $SnCl_2$ in photostimulated oxidation with oxygen was studied. The reaction mechanism was revealed. A spectrophotometric method for prompt monitoring of the composition of $SnCl_2$ solutions was proposed.

Tin(II) compounds have pronounced reductive properties and can be oxidized even with atmospheric oxygen, both in solutions and in the solid phase, as, e.g., in films of Sn(II) hydroxo compounds [1–4]. The oxidation can be considerably accelerated by UV irradiation [5–8]. This specific feature of chemistry of Sn(II) compounds has found application in photoforming, i.e., manufacture of selective thin-film structures using photochemical processes. These processes occur upon irradiation of films of Sn(II) hydroxo compounds adsorbed on the surface of dielectrics [1–3, 8–11]. After treating samples in $PdCl_2$ solutions, the Sn(II) hydroxo compounds that remained intact in the regions not subjected to irradiation reduce adsorbed Pd(II) with the formation of catalytically active centers. These centers may initiate deposition of metals from solutions in which spontaneous reduction of these metals from complex compounds is kinetically hindered. This results in selective deposition of conducting film components.

Despite a great deal of papers on the metal plating of dielectrics using Sn(II) and Sn(IV) compounds [1, 2], in most of them the transformation of tin and palladium has been considered only schematically. In [12–17], the photostimulated oxidation of Sn(II) compounds was studied without taking into account a number of important factors, such as a change in the solution composition upon storage owing to mutual influence of dark oxidation and hydrolysis of tin(II) compounds, and formation, coagulation, and sedimentation of colloidal particles. The influence of all the above factors on the efficiency of participation of Sn(II) compounds in photoforming processes was not considered. Unfortunately, specific methods of controlling properties of tin-containing films and coatings prepared from $SnCl_2$ solutions are found only empirically.

It is known that the light-sensitive tin species in photostimulated oxidation are tin oxo- and hydroxochlorides such as $Sn_4(OH)_6Cl_2$ and $Sn_2Cl_{16}(OH)_{14}O_6$ incorporated into island films [10, 11]. However, the rate and mechanism of oxidation of Sn(II) complexes and the sensitivity of Sn(II) compounds in both solution and condensed phase have not been analyzed in detail.

Based on experimental data on the order of photostimulated oxidation with oxygen of Sn(II) complexes in $SnCl_2$ aqueous solutions, a chain oxidation mechanism was proposed [12–14, 17] in which $Cl^{\bullet}$ and $HO_2^{\bullet}$ radicals and H_2O_2 and O_2 molecules are oxidants, Sn(III) is an intermediate, and Sn(IV) is the final product.

A molecular mechanism of photostimulated oxidation of Sn(II) with participation of polydentate organic compounds, described in [15, 16], is confirmed in experiments with isotopically substituted water:

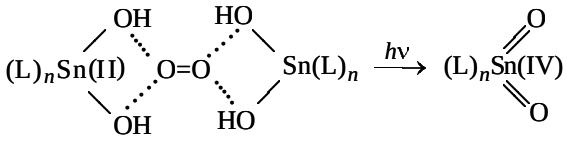

$$+ H_2O \rightarrow (L)_nOSn(OH)_2.$$

The published works do not take into account how the composition of Sn(II) complexes in $SnCl_2$ solutions with various pH affects the pathways and rate of photostimulated reactions and the formation of colloidal particles in solutions. The spectral sensitivity of Sn(II) compounds was not analyzed; no data are available on the quantum yields of photochemical

1070-4272/02/7509-1399$27.00 © 2002 MAIK "Nauka/Interperiodica"

oxidation in relation to the radiation wavelength and composition of the irradiated solution, which, in turn, depends on the completeness of oxidation, hydrolysis, and formation of colloidal particles. The same is true about the spectral sensitivity of Sn(II) compounds differing in the composition.

In this work, we studied the total and spectral photosensitivity of Sn(II) compounds in photostimulated oxidation of Sn(II) with oxygen in $SnCl_2$ solutions and the effect exerted on the quantum yield by the concentration of H^+, OH^-, and Cl^- ions and by the presence of ligands. These data are important for development of the theory of photostimulated oxidation of Sn(II) compounds, and also for practical applications (photochemical activation of dielectrics, choice of materials for phototemplates, determination of exposure conditions in the course of production of conducting thin-film structures of a prescribed configuration). First of all, they are of interest for manufacturing printed-circuit boards and integrated circuits for electronic engineering.

EXPERIMENTAL

We studied $SnCl_2$ solutions in which tin(II) ions occur as chloride complexes (acid solutions containing excess chloride ions) or as hydroxo complexes coexisting with tartrate or EDTA complexes (alkaline solutions) (M): no. 1, $SnCl_2$ 0.11 and HCl 0.11; no. 2, $SnCl_2$ 0.11 and HCl 0.06; no. 3, $SnCl_2$ 0.11, HCl 0.11, and KCl 1.60; no. 4, $SnCl_2$ 0.11 and HCl 0.66; no. 5, $SnCl_2$ 0.11, HCl 0.66, and KCl 1.60 (acid solutions); no. 6, $SnCl_2$ 0.22, NaOH 1.40, and EDTA 0.1; no. 7, $SnCl_2$ 0.22, NaOH 1.50, and NH_3 0.4; no. 8, $SnCl_2$ 0.22 and NaOH 2.50; and no. 9, $SnCl_2$ 0.22, NaOH 1.00, and $KNaC_4H_4O_6$ 0.28 (alkaline solutions). The compositions of these solutions correspond to those used for activating the surface of dielectrics [1, 2, 5–9]. The binding of ions into complexes is used to prevent hydrolysis and stabilize $SnCl_2$ solutions. Special calculations showed that different complex ions always coexist in equilibrium in the solutions studied, with some of them prevailing. The major components are as follows: solution no. 1, hydroxochlorides; solution no. 2, aqua and hydroxo complexes; solution nos. 3–5, chloride complexes; and solution nos. 6–9, hydroxo complexes. The content of Sn(II) in the solutions was determined by iodometric titration to within ± 0.0025 M [18]. The solutions were analyzed before and after irradiation. Because the composition of $SnCl_2$ solutions is affected by the Sn(II) oxidation and hydrolysis in the course of storage [10, 12], both fresh solutions and those stored for 1–30 days at 18–20°C were studied.

The absorption spectra of the solutions were measured in the range 200–1600 nm on an SF-4A spectrophotometer in a 1-cm quartz cell against distilled water.

The photochemical oxidation of Sn(II) with dissolved oxygen was initiated with a DRT-1000 mercury–quartz lamp as a source of UV radiation with linear spectrum. We used for irradiation both the total spectrum and single spectral lines cut with glass filters from a DOST 9411–75 kit and with chemical light filters [12, 19]. The incident light intensity, determined with a $K_3[Fe(C_2O_4)_3]$ chemical actinometer, was 1.07×10^{-2} J einstein^{-1} [19].

The $SnCl_2$ test solutions were irradiated in a glass cell with darkened bottom and side walls. The cell was open from the top when irradiated within the total spectrum and covered by a light filter when irradiated at a specific wavelength. The contact area of solutions with glass was 10.2 cm^2, which is important for taking into account tin adsorption on the cell walls. The solution thickness (1.3 cm) ensured the minimal UV absorption upon irradiation. Photostimulated oxidation of Sn(II) with atmospheric oxygen was performed with free access of air (10^5 Pa) to the solution at 20 ± 2°C. The decrease in the Sn(II) concentration upon irradiation did not exceed 20 at. %, and the oxygen consumption for oxidation was compensated by its free diffusion into solution. Using the reference data [20] on the diffusion coefficient of oxygen in water at 20°C, the first Fick law, and laws of mass transfer in aqueous solution and through the air–solution interface, and taking into account the volume of the irradiated solution, we can estimate the time in which the solution in the cell is saturated with oxygen (2 min). In determination of the quantum yield, the irradiation time was no less than 3–6 min. This suggests that the concentration of oxygen in the $SnCl_2$ solutions was approximately constant. Because stirring strongly affects the adsorption and diffusion rates and is dufficult to control in small cells, the solutions were not stirred during irradiation, which allowed us to obtain more or less reproducible results.

The number of Sn(IV) atoms formed by the photostimulated reaction with oxygen was determined from the decrease in the Sn(II) concentration in solution and then corrected for the dark oxidation and adsorption of Sn(II) and Sn(IV) compounds on the cell walls, as well as for the formation of colloidal particles owing to hydrolysis. The above correction for the dark

oxidation was found from analysis of reference solutions placed in darkened cells in the vicinity of the irradiated samples.

The quantum yield Φ of the Sn(IV) formation was calculated from the ratio of the number of tin(IV) atoms, ΔnSn(IV), formed in the solution of a given volume and concentration in a certain time to the number of absorbed photons by the formula (19]

$$\Phi\text{Sn(IV)} = [\Delta n\text{Sn(IV)}] : [n_{\text{abs.phot}}],$$

where $\Delta n\text{Sn(IV)} = 6.02 \times 10^{23} V_{\text{exp}} \Delta\text{Sn(II)} : 1000$; $n_{\text{abs.phot}} = I_0 t S(1 - T_1^h)$; V_{exp} is the irradiated solution volume (ml); I_0, incident radiation intensity (phot s^{-1} cm^{-2}); t, exposure time (s); S, cell area (cm^2); $1 - T_1^h$, absorption of irradiated solution of thickness h; and T_1, transmission of 1-cm-thick solution (experimental).

To determine the photosensitivity of Sn(II) compounds, we synthesized $Sn_6O_4(OH)_4$ and $Na[Sn(OH)_3]$ according to [21–23]. To preparing $Sn_6O_4(OH)_4$, a saturated solution of Na_2CO_3 was gradually added to a solution of $SnCl_2$ in 10% hydrochloric acid containing phenolphthalein indicator to weak pinkish color [21, 22]. The precipitate was washed by decanting four times with 5% Na_2CO_3 solution and twice with distilled water. $Na[Sn(OH)_3]$ was synthesized in two stages [23]. First, $Sn(OH)_2$ was synthesized from colloidal milk-white aqueous solution of $SnCl_2$ by adding a 10% solution of $NH_3 \cdot H_2O$. The $Sn(OH)_2$ precipitate was filtered off on a Büchner funnel and repeatedly washed with distilled water. Then, the pasty $Sn(OH)_2$ precipitate was placed in a flask with a 50% NaOH solution at 50–60°C. Reduced pressure in the flask was provided by a water-jet pump. $Sn(OH)_2$ dissolved with formation of $Na[Sn(OH)_3]$ upon shaking. The Sn(II) concentration in the solution was determined by titration. A small amount of the SnO_2 precipitate was filtered off. The $Na[Sn(OH)_3]$ solution and the $Sn_6O_4(OH)_4$ suspension were irradiated similarly as $SnCl_2$ solutions. In the course of irradiation, the suspension was shaken mechanically.

The results of titrimetric determination of Sn(II) in $SnCl_2$ acid solutions (nos. 1–5) irradiated with the total UV spectrum for different times show that the irradiation causes a a rapid decrease in the Sn(II) concentration (Fig. 1a). The Sn(II) loss is the fastest during the first 5–10 min of irradiation (0.10–0.18 mol l^{-1} h^{-1}), and then it decelerates, probably as a result of decrease in the Sn(II) concentration due to oxidation, hydrolysis, and formation of colloidal particles. The mean rate of photostimulated oxidation of

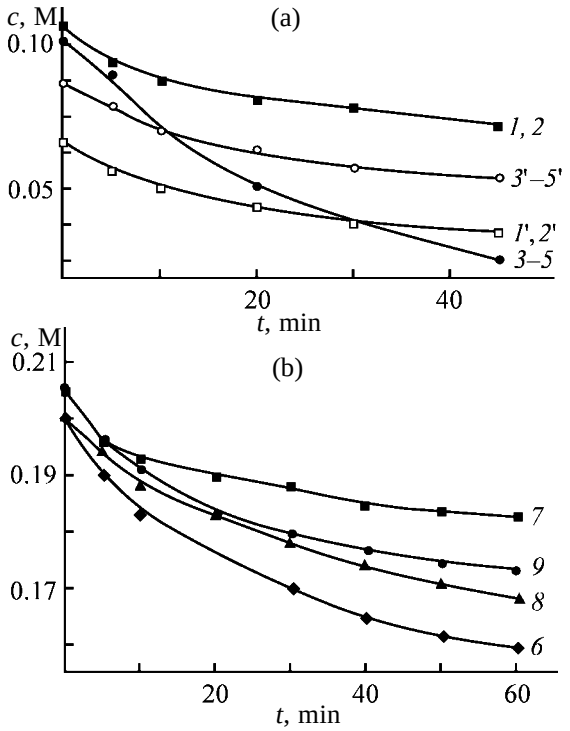

Fig. 1. Sn(II) concentration c in (a) acid and (b) alkaline solutions of $SnCl_2$ vs. irradiation time t with the total spectrum of a DRT-1000 UV lamp. Storage time, days: (*1*–*9*) 0 and (*1'*–*5'*) 12. Curve numbers are solution numbers; the same for Figs. 2c and 3.

Sn(II) in acid solutions in the range of linear variation of the concentration with time is about 0.030–0.075 mol l^{-1} h^{-1}. In the solutions stored in the dark, at the similar concentration of dissolved oxygen determined by the solution temperature, the mean oxidation rate was 0.6×10^{-4}–1.9×10^{-4} mol l^{-1} h^{-1} [6].

We studied how the composition of fresh $SnCl_2$ solutions affects the rate of the photostimulated oxidation of Sn(II). We found that, in solution no. 1 containing hydroxochloride complexes as major species and in solution no. 2 with prevailing aqua and hydroxo complexes, the Sn(II) concentration decreases considerably more slowly than in solution nos. 3–5 with chloride complexes as major species (Fig. 1). Comparison of the dependences of the Sn(II) concentration on the irradiation time for $SnCl_2$ solutions stored for 12 days and then irradiated with a total spectrum of a mercury–quartz lamp shows that, irrespective of solution composition, the Sn(II) oxidation rate in the first 10 min of irradiation approaches the minimal value of ~0.10 mol l^{-1} h^{-1} characteristic of solution no. 1.

The hydrolysis in $SnCl_2$ solutions upon storage decreases the content of chloride complexes [10,

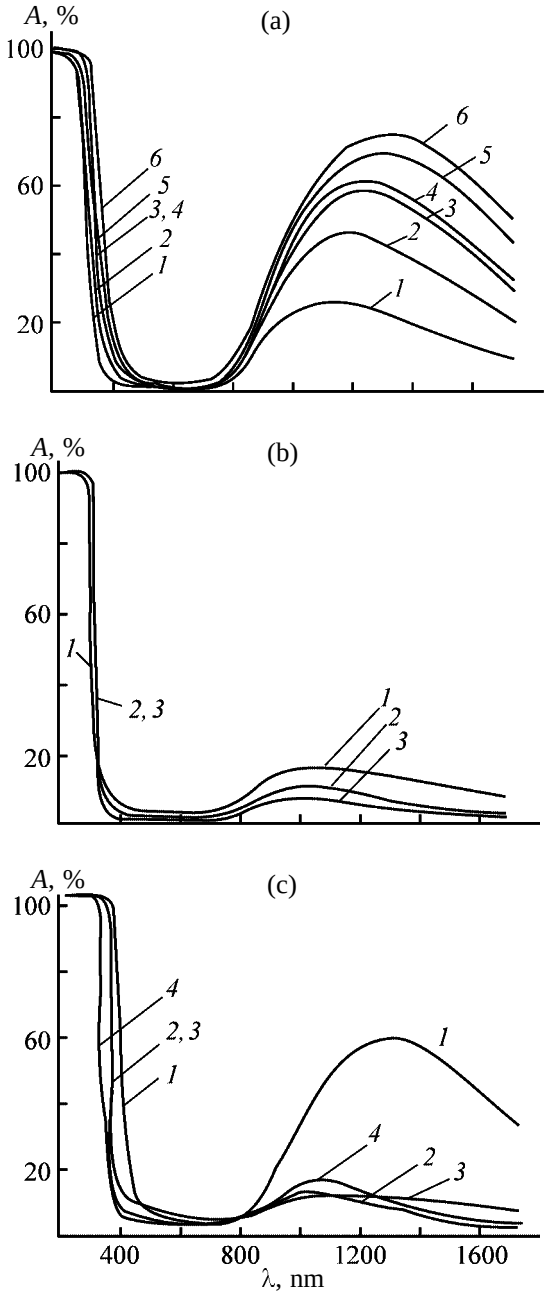

Fig. 2. Absorption spectra of $SnCl_2$ solutions: (a) no. 1, (b) no. 3, and (c) acid solutions. (*A*) Absorption and (λ) wavelength; the same for Fig. 3. Storage time (h): (a) (*1*) 1, (*2*) 24, (*3*) 48, (*4*) 96, (*5*) 190, and (*6*) 212; (b) (*1*) 1, (*2*) 48, and (*3*) 96; and (c) 48.

11]. The experimental data obtained show that the chloride-containing Sn(II) complexes are oxidized faster than hydroxo compounds.

The results of studying photostimulated oxidation of Sn(II) in the volume of $SnCl_2$ solutions showed that, under the similar conditions of irradiation with the total spectrum of a DRT-1000 lamp, the oxidation rate in alkaline solution (0.015–0.040 mol l^{-1} h^{-1}) is somewhat lower than in acid solution (Fig. 1b). This may be due to the lower photosensitivity of Sn(II) hydroxo complexes, which are major species in these solutions, as compared to chloride complexes in acid solutions.

To determine the UV photosensitivity of the individual Sn(II) compounds, a fresh solution of $Na[Sn(OH)_3]$ and an $Sn_6O_4(OH)_4$ suspension were irradiated with the total spectrum of a DRT-1000 lamp. It was found that the decrease in the Sn(II) concentration in these solutions does not go beyond the experimental error of titration and does not exceed the concentration change upon dark oxidation of Sn(II). Taking into account the experimental error, we can state that, in contrast to $Sn_4(OH)_6Cl_2$ and related compounds, Sn(II) hydroxo compounds containing no chloride ions are virtually insensitive to UV radiation. Therefore, in irradiation of $SnCl_2$ solutions, the contribution of Sn(II) hydroxo compounds to photostimulated oxidation can be neglected.

Data on the radiation absorption by $SnCl_2$ acid solutions in a wide spectral range, from 200 to 1600 nm, allow us to distinguish three ranges of the spectrum (Figs. 2a–2c). In the range λ = 200–300 nm, total absorption is observed (the absorption coefficient $A > 99.5\%$). In the range from 300 to 350–450 nm, the absorption sharply decreases to A = 3–5% for most solutions. In the visible range, the solutions are nearly totally transparent (A = 2–5%). In the range from 750 to 1800 nm, the absorption passes through a flat broad maximum; its value appreciably depends on the solution composition and storage time.

For the solutions stored for the similar time, the positions of the UV absorption edge differ only slightly (within 30–100 nm). This is apparently indicative of the fact that the first stage of photostimulated oxidation is similar for all the photosensitive Sn(II) compounds. As suggested in [13], the first stage of chemical activation of the Sn(II) complexes is scission of the Sn–Cl bond with the formation of the $Cl^{\bullet}$ radical and Sn(III) ion. Following this hypothesis, the position and smearing of the right edge of the UV absorption band for each specific Sn(II) complex would be determined by the energy of the Sn–Cl bond.

A drastic decrease in the absorption intensity within 300–400 nm is characteristic of solution nos. 3–5 with high concentrations of H^+ and Cl^- ions and of fresh solution no. 1 containing a small amount of aqua and hydroxo complexes and Sn(II) chloride complexes as major species (Figs. 2a–2c). At longer storage time, the absorption band edge becomes less steep and

shifts toward visible region, to 410 nm and even longer waves (Figs. 2a, 2b). This may be due to the accumulation and polymerization of hydroxo complexes on storage.

It is known that the near IR absorption is mainly due to the interaction of electromagnetic waves with groups of atoms and small particles. Not only the IR absorption but also the scattering take place, with the scattering increasing with growing particle size. Moreover, following the Mie theory, with increasing particle size the absorption coefficient also increases and the absorption maximum shifts toward longer wavelengths [24]. Therefore, it may be suggested that the character of the IR absorption of $SnCl_2$ solutions is governed by the presence of colloidal particles accumulated in storage (Figs. 2a–2c). The absorption spectra of $SnCl_2$ solutions stored for different times, in combination with electron-microscopic data on the size and concentration of colloidal particles formed in the solutions [25–27], show that the higher the particle concentration, the higher the IR absorption coefficient. The experimental data also show that the larger colloidal particles, the longer the IR absorption wavelength.

The absorption spectra of $SnCl_2$ alkaline solutions stored for different times show that, with storage time, the absorption band edge shifts from the UV to visible range; this trend is similar to that observed with acid solutions (Figs. 3a, 3b).

A previous electron-microscopic study of $SnCl_2$ solutions showed that colloidal particles in alkaline solutions are larger by an order of magnitude than those in acid solutions (100–150 nm against 5–10 nm) and that the number of particles in alkaline solutions is very small [21]. Correspondingly, the absorption maximum in the IR region, clearly pronounced in the spectra of acid solutions, is absent for alkaline solutions.

Thus, the UV absorption edge in the spectra of $SnCl_2$ solutions becomes more diffuse and shifts toward visible region in storage accompanied by Sn(II) hydrolysis and oxidation. With accumulation and growth of colloidal particles, the IR absorption maximum becomes stronger and shifts toward longer wavelengths. These facts allow the UV and IR absorption spectra of $SnCl_2$ solutions to be used for prompt monitoring of their composition and formation of colloidal particles.

The efficiency of photostimulated oxidation with oxygen of Sn(II) compounds in $SnCl_2$ solutions was quantitatively estimated from the quantum yield Φ of oxidation, taking into account, as noted above, a decrease in the $SnCl_2$ concentration due to dark processes. Note that, in determination of Φ, the irradiation time (3–6 min) did not exceed the value at which the Sn(II) concentration decreases linearly with exposure (Fig. 1). The experimentally determined quantum yields of the photostimulated Sn(II) oxidation in $SnCl_2$ solutions are given in the table. Despite a con-

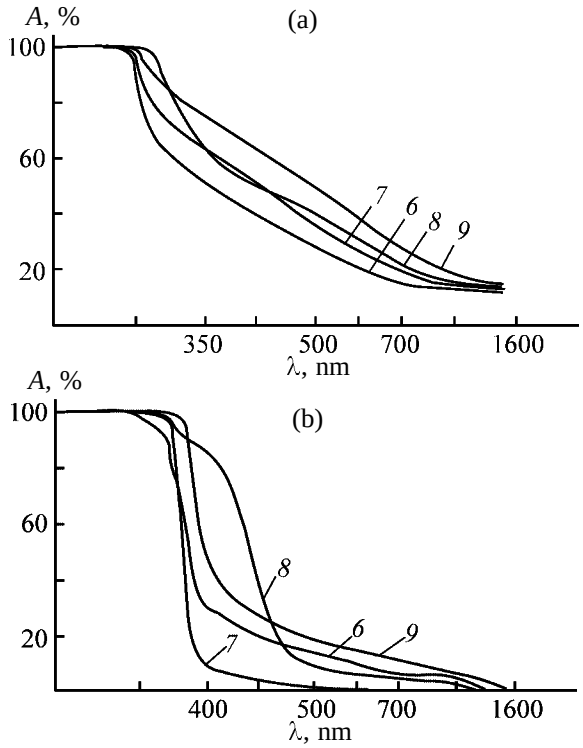

Fig. 3. Absorption spectra of $SnCl_2$ alkaline solutions stored for (a) 1 h and (b) 15 days.

Quantum yield Φ of photostimulated oxidation of Sn(II) in acid and alkaline $SnCl_2$ solutions irradiated at various UV wavelengths ($\Delta\Phi = 0.5$)

Solution no.	Φ at indicated λ, nm				
	total spectrum	253.7	312.6	365	435.8
Acid solutions					
1	2.8	3.0	2.2	0.8	0.2
3	5.0	4.7	4.5	1.3	0.4
4	3.2	2.8	2.6	0.9	0.2
5	3.5	3.1	2.9	1.1	0.3
Alkaline solutions					
6	1.4	–	–	–	–
7	0.9	–	–	–	–
8	0.3	–	–	–	–
9	0.2	–	–	–	–

siderable experimental error ($\Delta\Phi = \pm 0.5$), comparison of the Φ values for the solutions with prevailing complex species of given chemical composition, irradiated at specific wavelengths in a wide spectral range (250–440 nm) and with the total spectrum of the UV source, allows quite reliable conclusions.

We found that the average quantum yields for the solutions irradiated within the total spectrum lie within 0.2–5.0; the highest quantum yield Φ is observed in acid solutions containing Sn(II) chloride complexes as major species (nos. 3, 5). The photosensitivity of Sn(II) compounds in all alkaline solutions is comparatively low. For example, owing to the low UV sensitivity of tin hydroxo compounds, the quantum yield of the photostimulated oxidation of Sn(II) in all alkaline solutions could be determined only upon irradiation within the total spectrum of a DTR–1000 lamp (see table). Among alkaline solutions, the quantum yield Φ is the highest for solution nos. 6 and 7 containing hydroxo complexes as major species and, probably, Sn(II) hydroxo chloride complexes as minor species. For solution nos. 8, 9 containing virtually no hydroxochloride complexes, in which Sn(II) is in the form of hydroxo, tartrate, and EDTA complexes, the Φ value is lower by an order of magnitude than in $SnCl_2$ acid solutions. As follows from the experiment, these complexes have virtually no photosensitivity, irrespective of the procedure for solution preparation (dissolution of $SnCl_2$ in NaOH solution or synthesis of individual compounds).

The dependence of Φ in photostimulated oxidation of Sn(II) on the incident radiation wavelength showed that the quantum yield is the highest in the region of far UV ($\lambda = 253.7$ nm), which is in agreement with the published data [8, 9]. We found that, with increasing incident radiation wavelength, Φ sharply decreases. Nonetheless, for solutions with high concentration of Sn(II) chloride complexes the quantum yield is 0.2–0.4 even at $\lambda = 435.8$ nm and decreases to zero only at longer λ (~450 nm). This fact confirms once again the published data [8, 9] on the spectral range of photosensitivity of Sn(II) compounds and also explains the possibility of exposing island films based on tin compounds using Dacron phototemplates, which almost totally absorb the UV radiation but are transparent in the visible range [2]. As indicated above, such processes are used in photochemical activation of substrates intended for selective metal deposition.

The fact that the quantum yield of the photostimulated oxidation of Sn(II) in $SnCl_2$ solutions is sometimes considerably larger than unity (see table) is confirmed quite reliably ($\Phi \gg \Delta\Phi$) and is indicative of occurrence of a chain process. The quantum yields of photostimulated oxidation of Sn(II) compounds in $SnCl_2$ solutions show that the chain reaction mechanism is characteristic of solutions containing Sn(II) chloride complexes as major component. This mechanism is not realized in solutions containing Sn(II) hydroxo or tartrate complexes as major species (nos. 7–9). Consequently, the Φ value and, correspondingly, the mechanism of photostimulated oxidation strongly depend on the composition of the irradiated solution. With increasing λ the quantum yield decreases, which is in accordance with the published data on the photosensitivity of Sn(II) compounds.

CONCLUSIONS

(1) A correlation was established between the absorption spectra of $SnCl_2$ solutions and the composition of major Sn(II) complex species in them. A method was proposed for prompt qualitative monitoring of the composition of $SnCl_2$ solutions, based on the absorption spectra.

(2) For $SnCl_2$ solutions irradiated with the total spectrum of a mercury–quartz lamp with an intensity of 1.07×10^{-2} J einshtein^{-1}, the rate of the photostimulated oxidation of Sn(II) with oxygen is higher by two orders of magnitude than the rate of the dark oxidation. The rate of photostimulated oxidation depends on the chemical composition of tin compounds and irradiation wavelength. The oxidation rate and the quantum yield are the highest for Sn(II) chloride complexes; the oxidation efficiency for the hydroxo compound is lower by several orders of magnitude. The photostimulated oxidation of the chloride complexes occurs by a chain mechanism ($\Phi > 1$).

(3) The radiation at a wavelength shorter than 350 nm ensures the highest efficiency of initiation of Sn(II) oxidation. At $\lambda = 400-435$ nm, the oxidation also occurs, but at a considerably lower rate.

REFERENCES

1. Shalkauskas, M. and Vashkyalis, A., *Khimicheskaya metallizatsiya plastmass* (Electroless Metal Plating of Plastics), Leningrad: Khimiya, 1985, 3rd ed.
2. Sviridov, V.V., Vorob'eva, T.N., Gaevskaya, T.V., and Stepanova, L.I., *Khimicheskoe osaszhdenie metallov iz vodnykh rastvorov* (Electroless Deposition of Metals from Aqueous Solutions), Sviridov, V.V., Ed., Minsk: Universitetskoe, 1987.
3. Schlesinger, M. and Feldstein, N., *J. Electrochem. Soc.*, 1973, vol. 120, pp. 236–241.

4. Dressik, W.J., Dulcey, C.S., Georger, J.H., *et al.*, *J. Electrochem. Soc.*, 1994, vol. 141, no. 1, pp. 210–220.
5. Putten, A.M.T. van der and Bakker, J.W.G. de, *J. Electrochem. Soc.*, 1993, vol. 40, no. 8, pp. 2221–2228.
6. Reva, O.V. and Vorob'eva, T.N., *Vestsi Akad. Navuk Bel., Ser. Khim. Navuk*, 1995, no. 3, pp. 100–115.
7. Sard, R., *J. Electrochem. Soc.*, 1970, vol. 117, pp. 864–870.
8. Cohen, R.L., D'Amico, I.F., and West, K.W., *J. Electrochem. Soc.*, 1971, vol. 118, pp. 2042–2046.
9. Sharp, D.J., *Plating*, 1971, vol. 58, no. 8, pp. 786–790.
10. Reva, O.V., Vorob'eva, T.N., and Sviridov, V.V., *Zh. Nauchn. Prikl. Fotogr. Kinematogr.*, 1999, vol. 44, no. 4, pp. 20–26.
11. Reva, O.V. and Vorob'eva, T.N., *Zh. Prikl. Khim.*, 1998, vol. 71, no. 3, pp. 498–502.
12. Atkins, P.W., *Physical Chemistry*, Oxford: Oxford Univ. Press, 1994, 3rd ed.
13. Kutner, E. and Matseevskii, B., *Kinet. Katal.*, 1969, vol. 10, no. 5, pp. 997–1003.
14. Zakharov, I., Karasevich, E., Shilov, A., and Shteinman, A., *Kinet. Katal.*, 1975, vol. 14, no. 5, pp. 1151–1157.
15. Berentsveig, V., Pleskach, N., and Rudenko, A., *Zh. Fiz. Khim.*, 1980, vol. 54, no. 12, pp. 222–236.
16. Razinkin, M., Berentsveig, V., and Rudenko, A., *Vestn. Mosk. Gos. Univ., Ser. Khim.*, 1990, issue 31, no. 1, pp. 75–87.
17. Petrite, L.I., Solutions of Palladium and Tin Compounds and Their Use in Electroless Metal Plating, *Cand. Sci. Dissertation*, Vilnius, 1981.
18. Paul, R.C., Sooch, K.S., Vaidya, O.S., and Narula, S.P., *Anal. Chim. Acta*, 1969, vol. 46, no. 1, pp. 131–137.
19. Calvert, J.G. and Pitts, J.N., *Photochemistry*, New York: Wiley, 1966.
20. *Spravochnik khimika* (Chemist's Handbook), Nikol'skii, B.P., Ed., Moscow: Khimiya, 1966, vol. 5.
21. Klyuchnikov, N.G., *Rukovodstvo po neorganicheskomu sintezu* (Manual on Inorganic Synthesis), Moscow: Khimiya, 1965.
22. Baudler, M., Brauer, J., Feher, F., *et al.*, *Handbuch der präparativen anorganischen Chemie*, Stuttgart: Enke, 1975. Translated under the title *Rukovodstvo po neorganicheskomu sintezu*, Moscow: Mir, 1985, vol. 3, pp. 669–1056.
23. *Khimicheskaya entsiklopediya* (Chemical Encyclopedia), Knunyants, I.L., Ed., Moscow: Bol'shaya Ross. Entsiklopediya, 1988, vol. 3.
24. Bohren, C.E. and Huffman, D.R., *Absorption and Scattering of Light by Small Particles*, New York: Wiley, 1983.
25. Reva, O.V., Chemical, Electrochemical, and Photochemical Transformations of Tin Compounds in Heterogeneous Systems, *Cand. Sci. Dissertation*, Minsk, 1999.
26. Vorob'eva, T.N., Barkovskaya, L.V., Stepanova, L.I., and Rukhlya, V.A., *Vestsi Akad. Navuk Bel. SSR, Ser. Khim. Navuk*, 1991, no. 5, pp. 106–111.
27. Vorob'eva, T.N., Reva, O.V., Rukhlya, V.A., *et al.*, *Vestsi Akad. Navuk Bel., Ser. Khim. Navuk*, 1994, no. 2, pp. 94–100.

Russian Journal of Applied Chemistry, Vol. 75, No. 9, 2002, pp. 1406–1410. Translated from Zhurnal Prikladnoi Khimii, Vol. 75, No. 9, 2002, pp. 1438–1442.
Original Russian Text Copyright © 2002 by G. Mikhailov, V. Mikhailov, Reva, Ryabchuk.

PHYSICOCHEMICAL STUDIES OF SYSTEMS AND PROCESSES

Correlation Equations for Predicting the Temperature Depression in Boiling of Aqueous Solutions of Nonvolatile Substances

G. M. Mikhailov, V. G. Mikhailov, L. S. Reva, and G. V. Ryabchuk

Volgograd State Technical University, Volgograd, Russia

Received May 27, 2002

Abstract—Three-constant correlation equations describing the boiling point of aqueous solutions of nonvolatile substances and temperature depression in boiling of the solutions under normal and arbitrary pressures are considered. The three constants appearing in the correlation equations are tabulated for aqueous solutions of 19 nonvolatile substances, and formulas for determining these constants for other aqueous solutions of nonvolatile substances from experimental data are presented.

In calculating evaporation installations, especially those with multiple casings, a necessity arises for repeatedly determining the boiling point of water as a function of pressure, pressure as a function of the boiling point of water, and temperature depression as a function of solute concentration and pressure. In doing so, the temperature depression Δ at various pressures is defined in terms of the normal temperature depression Δ_n [1–3]. With the effect of the differential heat of dehydration disregarded because of its being weak or unknown for a given solution, the following equation is proposed [2]:

$$\Delta = r_n T^2 \Delta_n / (T_n^2 r), \quad (1)$$

where r, T, r_n, and T_n are the current values of r and temperature and their corresponding normal values.

When Eq. (1) is used, a necessity arises for using three experimental tables, namely, tabulated dependences of T and r on pressure and that of Δ_n on solute concentration. This creates severe difficulties, especially when account is taken of the fact that an interpolation procedure is to be carried out each time. Not without reason, it was proposed in [3] to tabulate $r_n T^2/(T_n^2 r)$ values in relation to pressure.

Furthermore, Eq. (1) is approximate and, at large deviations of pressure from the normal value, is in strong disagreement with the Babo rule, which is a particular case of the fundamental Kirchhoff law [1] at zero dehydration heat, assumed in Eq. (1). For example, at Δ_n = 30°C and pressure P = 10 atm, Δ = 46.76°C according to the Babo rule and Δ = 49.24°C in accordance with Eq. (1). The discrepancy is 2.57°C. Such an error in prediction of the temperature depression in calculating an evaporator apparatus intended to operate at a useful temperature difference ΔT_u = 10°C leads to an error exceeding 25% in prediction of the necessary heat-exchange surface area.

The lack of correlation equations describing the concentration dependences of the normal temperature depression makes it necessary to use, in working with the tables, linear interpolation leading in some cases to errors of about several degrees. For example, normal temperature depressions Δ_{n1} = 126.5 and Δ_{n2} = 190.3°C were reported in [4] for a KOH solution with x_1 = 70 and x_2 = 80 wt %. For a concentration x_3 = 75.76 wt %, linear interpolation gives Δ_{n3} = 163.25°C, which exceeds by 3.25°C the value Δ_{n3} = 160°C reported for x_3 = 75.76 wt % in [2]. Unhappy combination of this error with the above-mentioned inexactness of Eq. (1) may lead to considerable errors in prediction of the required heat-exchange surface area.

The aim of this study was to derive a correlation equation for predicting the temperature depression in boiling of aqueous solutions of nonvolatile substances in relation to pressure and solute concentration. Such an equation would make unnecessary repeated use of experimental tables and the related repeated interpolation.

For correlating the boiling point of water and pressure, compact interconvertible equations have been proposed previously [4]:

$$T = 100\frac{11.693 + 2.279\ln(P/P_n)}{11.693 - \ln(P/P_n)}, \quad (2)$$

1070-4272/02/7509-1406$27.00 © 2002 MAIK "Nauka/Interperiodica"

$$P = P_n \exp[11.693(T - 100)/(T + 227.9)], \quad (3)$$

where T is temperature, and P_n is the pressure under normal conditions.

In the pressure range P = (0.04–50) atm, deviations of values yielded by Eq. (1) from reference data are lower than 0.1°C, and those for Eq. (2) do not exceed 0.2%.

As regards both the applicability range and correlation accuracy, Eqs. (2) and (3) are quite satisfactory for practical calculations of evaporator apparatus.

The dependences of the normal temperature depression on the concentration x

$$\Delta_n = f(x) \quad (4)$$

for solutions of various nonvolatile substances are so strongly diverse that no correlation equation describing these dependences has been found until now, despite some effort in this direction [5].

Being aware of the complicatedness of correlating directly the dependences (4) with a single equation, even if with numerous coefficients dependent on the solute nature, we found that the following dependences have the same character for different solutions:

$$\ln(P_{equiv.n}/P_n) = f(z), \quad (5)$$

where $z = x/(1 - x)$ is the relative solute concentration, P_n is the normal pressure, and $P_{equiv.n}$ is the equivalent pressure at normal pressure in the apparatus.

The term equivalent is used here for the saturated vapor pressure of water (solvent) at the solution boiling point.

The dependences (5) are well correlated with the equation

$$\ln(P_{equiv.n}/P_n) = Az + Bz^2 + Cz^3. \quad (6)$$

Substitution of this equation into (2) gives an equation for predicting the solution boiling point under normal pressure

$$T_{b.s.n} = 100\frac{11.963 + 2.279(Az + Bz^2 + Cz^3)}{11.963 - (Az + Bz^2 + Cz^3)}. \quad (7)$$

Since $\Delta_n = T_{b.s.n} - 100$, the following equation is obtained for predicting the normal temperature depression:

$$\Delta_n = 100\left[\frac{11.963 + 2.279(Az + Bz^2 + Cz^3)}{11.963 - (Az + Bz^2 + Cz^3)} - 1\right]$$

or, after some transforms,

$$\Delta_n = 327.9[11.693/(Az + Bz^2 + Cz^3) - 1]^{-1}. \quad (8)$$

It can be shown by simple transforms that the best (least-squares) fitting of the experimental data by Eq. (8) is provided with the coefficients given by

$$C = \frac{\alpha_1/\beta_1 - \alpha_2/\beta_2}{\gamma_1/\beta_1 - \gamma_2/\beta_2}, \qquad B = \frac{\alpha_1 - C_1}{\beta_1},$$

$$A = (E_1 - BB_1 - CC_1)/A_1 \quad (9)$$

at

$$\alpha_1 = E_1/A_1 - E_2/A_2, \ \beta_1 = B_1/A_1 - B_2/A_2,$$

$$\gamma_1 = C_1/A_1 - C_2/A_2;$$

$$\alpha_2 = E_2/A_2 - E_3/A_3, \ \beta_2 = B_2/A_2 - B_3/A_3,$$

$$\gamma_2 = C_2/A_2 - C_3/A_3,$$

where

$$A_1 = \sum_{i=1}^{n} (\Delta_{n_i} + 327.9)^4 z_i^2, \qquad B_1 = A_2;$$

$$A_2 = \sum_{i=1}^{n} (\Delta_{n_i} + 327.9)^4 z_i^3, \qquad B_2 = A_3;$$

$$A_3 = \sum_{i=1}^{n} (\Delta_{n_i} + 327.9)^4 z_i^4, \qquad B_3 = \sum_{i=1}^{n} (\Delta_{n_i} + 327.9)^4 z_i^5;$$

$$C_1 = A_3, \qquad E_1 = 11.693 \sum_{i=1}^{n} (\Delta_{n_i} + 327.9)^3 \Delta_{n_i} z_i;$$

$$C_2 = B_3, \qquad E_2 = 11.693 \sum_{i=1}^{n} (\Delta_{n_i} + 327.9)^3 \Delta_{n_i} z_i^2;$$

$$C_3 = \sum_{i=1}^{n} (\Delta_{n_i} + 327.9)^4 z_i^6,$$

$$E_3 = 11.693 \sum_{i=1}^{n} (\Delta_{n_i} + 327.9)^3 \Delta_{n_i} z_i^3;$$

Table 1 presents the coefficients of Eqs. (6)–(8) for solutions of some salts and alkalis, found from the experimental data reported in [2, 6].

Table 2 compares the values calculated using Eq. (8) with the experimental normal temperature

Table 1. Coefficients of Eqs. (6)–(8), (12), and (13), found from experimental data [2, 6]

Solute	*M*	*A*	*B*	*C*	Applicability limit *x*
NH_4NO_3	80.054	0.35539	–0.038867	0.0018811	≤0.8
$(NH_4)_2SO_4$	132.154	0.22639	0.023441	0.0084854	≤0.5
NH_4Cl	53.497	0.54399	0.27418	–0.26985	≤0.47
$FeSO_4$	151.910	0.080249	0.12026	–0.13557	≤0.35
KNO_3	101.107	0.25488	–0.043002	0.0029882	≤0.8
K_2CO_3	138.21	0.20896	0.40180	–0.12136	≤0.6
KCl	74.55	0.36282	0.43950	–0.28904	≤0.35
$Ca(NO_3)_2$	164.094	0.43354	–0.21280	0.12825	≤0.5
	164.094	0.20783	0.17267	–0.032318	$0.5 \le x \le 0.8$
$CaCl_2$	110.98	0.48884	1.0753	–0.56598	≤0.55
	110.98	1.1886	–0.2240	0.02487	$0.55 \le x \le 0.76$
$MgSO_4$	120.37	0.094574	0.64733	–0.42599	≤0.43
$MgCl_2$	95.21	0.61987	1.1474	0.69196	≤0.36
$CuSO_4$	159.61	0.041081	0.18426	–0.017624	≤0.45
$NaNO_3$	84.997	0.38315	–0.033788	–0.0010743	≤0.7
Na_2SO_4	142.04	0.26781	–0.29392	0.49946	≤0.31
Na_2CO_3	105.99	0.35114	–0.065123	0.099615	≤0.35
NaCl	58.44	0.47309	1.02646	0.76790	≤0.25
$ZnSO_4$	161.43	0.12376	0.059773	0.033545	≤0.4615
KOH	56.11	0.61604	1.1781	–0.38250	≤0.649
	56.11	1.9668	–0.28020	0.013940	$0.649 \le x \le 0.816$
NaOH	40	0.78530	1.5828	–1.0365	≤0.5
	40	1.6272	–0.29791	0.0090152	$0.5 \le x \le 0.7$

Table 2. Comparison of calculated normal temperature depressions Δ_n^{calc} with experimental values Δ_n^{exp}

NH_4NO_3					K_2CO_3				
x, kg kg^{-1}	Δ_n^{exp}, °C		Δ_n^{calc}	δ	*x*, kg kg^{-1}	Δ_n^{exp}, °C		Δ_n^{calc}	δ
	[4]	[2]	°C			[4]	[2]	°C	
0.0909	1	–	0.99	–0.01	0.100	–	0.8	0.79	–0.01
0.1000	–	1.10	1.10	–0.00	0.1031	1	–	0.82	–0.18
0.1666	2	–	1.96	0.04	0.1837	2	–	1.86	–0.14
0.2000	–	2.5	2.44	–0.06	0.2000	–	2.2	2.13	–0.07
0.2308	3	–	2.92	–0.08	0.2424	3	–	2.94	–0.06
0.2908	4	–	3.95	–0.05	0.2857	4	–	3.98	–0.02
0.3000	–	4.0	4.13	0.13	0.3000	–	4.4	4.37	–0.03
0.3421	5	–	4.97	–0.03	0.3224	5	–	5.05	0.05
0.3500	–	5.1	5.14	–0.04	0.3500	–	6	6.00	0.00
0.4000	–	6.3	6.29	–0.01	0.3769	7	–	7.06	0.06
0.4253	7	–	6.96	–0.04	0.4000	–	8	8.10	0.10
0.4500	–	7.5	7.63	0.13	0.4397	10	–	10.20	0.20
0.5000	–	9.1	9.18	0.08	0.4500	–	10.9	10.82	–0.08
0.5192	10	–	9.84	–0.16	0.5000	–	14.6	14.32	–0.28
0.5500	–	11.0	11.01	0.01	0.5086	15	–	15.02	0.02
0.6000	–	13.2	13.18	–0.02	0.5500	–	19.0	18.80	–0.20
0.6324	15	–	14.83	–0.17	0.5604	20	–	19.86	–0.14
0.7000	–	19.0	19.03	0.03	0.6000	–	24.0	24.34	0.34
0.7126	20	–	19.96	–0.04	0.6040	25	–	24.82	–0.18
0.7711	25	–	24.99	–0.01	–	–	–	–	–
0.8	–	28	28.00	0.00	–	–	–	–	–

Table 3. Comparison of temperature depressions found using the equations and the Babo rule (BR)

P, atm	NH_4NO_3, x = 0.8 kg kg^{-1}, Δ_n = 28°C					$CaCl_2$, x = 0.55 kg kg^{-1}, Δ_n = 36.5°C				
	BR, Δ	(1)		(13)		BR, Δ	(1)		(13)	
		Δ_{calc}	δ	Δ_{calc}	δ		Δ_{calc}	δ	Δ_{calc}	δ
	°C									
0.1	19.27	19.36	0.09	19.28	0.01	25.07	25.23	0.16	25.00	–0.07
0.2	21.40	21.43	0.03	21.42	0.02	27.81	27.94	0.13	27.81	0.00
0.5	24.82	24.82	0.00	24.84	0.02	32.30	32.35	0.05	32.30	0.00
1.0	28.00	28.00	0.00	28.00	0.00	36.50	36.50	0.00	36.47	–0.03
2.0	31.80	32.00	0.20	31.82	0.02	41.58	41.71	0.13	41.50	–0.08
4.0	36.44	37.08	0.64	36.46	0.02	47.78	48.33	0.55	47.66	–0.12
6.0	39.65	40.75	1.10	39.67	0.02	52.04	53.12	1.08	51.91	–0.13
10.0	44.30	46.41	2.11	44.35	0.05	58.20	60.50	2.30	58.14	–0.06
12.0	46.20	48.79	2.59	46.22	0.02	60.64	63.60	2.96	60.63	–0.01
15.0	48.63	52.04	3.41	48.68	0.05	63.81	67.83	4.02	63.91	0.10

depressions for solutions of some nonvolatile substances, reported in [2, 6]. The deviations of the calculated values from the experimental data very rarely exceed 0.2°C. This is to be considered quite satisfactory, if account is taken of the fact that, in some cases, even greater discrepancies are observed between two independent experimental values [2, 6].

According to the Kirchhoff law [1], at zero differential heat of dehydration

$$P_{equiv}/P = P_{equiv.n}/P_n = \text{const}, \quad (10)$$

i.e., the Babo rule is valid. Consequently, with the effect of the differential dehydration heat neglected, we can write for any arbitrary pressure

$$P_{equiv}/P = Az + Bz^2 + Cz^3. \quad (11)$$

According to (2), the boiling point of a solution is given by

$$T_{b.s} = 100\,\frac{11.693 + 2.279\ln(P_{equiv}/P_n)}{11.693 - \ln(P_{equiv}/P_n)}$$

$$= 100\,\frac{11.693 + 2.279[\ln(P/P_n) + \ln(P_{equiv}/P_n)]}{11.693 - \ln(P/P_n) - \ln(P_{equiv}/P_n)}$$

or, with account of (11),

$$T_{b.s} = 100\,\frac{11.693 + 2.279[\ln(P/P_n) + Az + Bz^2 + Cz^3]}{11.693 - [\ln(P/P_n) - Az + Bz^2 + Cz^3]}. \quad (12)$$

It can be readily seen that the last equation transforms into (7) at $P = P_n$.

Since the boiling point of water under pressure P is given by Eq. (2), the temperature depression under pressure P can be found from the equation

$$\Delta = 100\,\frac{11.693 + 2.279[\ln(P/P_n) + Az + Bz^2 + Cz^3]}{11.693 - [\ln(P/P_n) - Az + Bz^2 + Cz^3]} - 100\,\frac{11.693 + 2.279\ln(P/P_n)}{11.693 - \ln(P/P_n)}$$

or, after some rearrangements,

$$\Delta = 3834[11.693 - \ln(P/P_n)]^{-1}\left[\frac{11.693 - \ln(P/P_n)}{Az + Bz^2 + Cz^3} - 1\right]^{-1}. \quad (13)$$

Naturally, the last equation turns into (8) at $P = P_0$.

Table 3 compares the temperature depressions found from Eqs. (1) and (13) with the values determined using the Babo rule.

It can be seen that the approximate equation (1) is in strong disagreement with the Babo rule at pressures much exceeding the normal pressure, especially at high normal temperature depressions. The small but systematic deviation of Eq. (13) from the values found using the Babo rule can be accounted for by the experimental deviations of the normal temperature depressions used in calculations based on the Babo rule from the true concentration dependence of the normal

temperature depression. Therefore, the temperature depressions found using Eq. (13) are more reliable than those determined from the Babo rule.

CONCLUSIONS

(1) An equation is proposed for analytical prediction of the solution boiling point in relation to the solute concentration, and its constants are calculated.

(2) Equations for analytical prediction of the normal temperature depression in relation to the solute concentration, boiling point of solution in relation to pressure and concentration, and temperature depression in relation to pressure in apparatus and concentration are derived. When data on the equation constants are lacking, these constants can be found from experimental data using the equations proposed.

REFERENCES

1. Gel'perin, N.I., Ainshtein, V.G., and El'gart, B.M., *Khim. Prom–st.*, 1988, no. 7, pp. 32–33.
2. *Osnovnye protsessy i apparaty khimicheskoi tekhnologii: Posobie po proektirovaniyu* (Basic Processes and Apparatus of Chemical Technology: Designing Manual), Dytnerskii, Yu.I., Ed., Moscow: Khimiya, 983.
3. Shur, V.A., *Khim. Prom–st.*, 1982, no. 11, p. 677.
4. Mikhailov, G.M., Reva, L.S., Mikhailov, V.G., and Kondakova, L.A., *Reologiya, protsessy i apparaty khimicheskoi tekhnologii: Sbornik nauchnykh trudov* (Rheology, Processes and Apparatus of Chemical Technology: Coll. of Sci. Works), Volgograd: Volgogr. Gos. Tekh. Univ., 1999.
5. Planovskii, A.N. and Nikolaev, P.I., *Protsessy i apparaty khimicheskoi i neftekhimicheskoi tekhnologii* (Processes and Apparatus of Chemical and Petrochemical Technology), Moscow: Khimiya, 1972, 2nd ed.
6. Pavlov, K.F., Romankov, P.G., and Noskov, A.A., *Primery i zadachi po kursu protsessov i apparatov khimicheskoi tekhnologii* (Praxis and Problems for the Course of Processes and Apparatus of Chemical Technology), Leningrad: Khimiya, 1970, 7th ed.

Russian Journal of Applied Chemistry, Vol. 75, No. 9, 2002, pp. 1411–1415. Translated from Zhurnal Prikladnoi Khimii, Vol. 75, No. 9, 2002, pp. 1443–1447.
Original Russian Text Copyright © 2002 by Kartel', Gerasimenko, Strelko.

SORPTION AND ION-EXCHANGE PROCESSES

Influence of Combined Treatment before Activation on the Development of Pore Structure of Anthracite

N. T. Kartel', N. V. Gerasimenko, and V. V. Strelko

Institute of Sorption and Endoecological Problems, National Academy of Sciences of Ukraine, Kiev, Ukraine

Received January 23, 2002

Abstract—The influence of surface oxidation of anthracite with humid air, followed by impregnation with alkali metal compounds and calcination in inert atmosphere before activation, on the efficiency of steam–gas activation and on the development of the pore structure of the resulting carbon adsorbents was studied.

Coals are a major raw material for preparing various carbon adsorbents [1, 2]. Among them, the most attractive is anthracite because of increased content of carbon and low ash residue; furthermore, activated carbon prepared from it has high mechanical strength.

At the same time, the activation of anthracite for preparing sorbents is impeded by its low reactivity in high-temperature contact with traditional gaseous activators, superheated steam and carbon dioxide. This is due to the high degree of metamorphism of anthracite (well-organized supramolecular structure with short-range and partly long-range order). Therefore, direct gas–steam activation of anthracite often fails to develop its pore structure and attain the high specific parameters of porosity.

It is also known that alkali metal (AM) compounds catalyze activation of carbon-containing materials. Using published basic data [3, 4] and the results of our studies, including quantum-chemical calculations [5–9], we suggested the possibility of formation of layered intermediate compounds by intercalation of a metal into the interlayer space of carbon planes (graphite-like clusters) of microcrystallites; this factor is responsible for the increased reactivity of the microcrystallites in oxidative gas activation.

Indeed, in the course of high-temperature (600–800°C) treatment of carbon materials impregnated with AM ions (thermochemical modification), these ions can be reduced to zero oxidation state. The metal being formed penetrates into slitlike pores of graphitic microcystallites, donating its valence *s* electrons to the π-conjugated systems of condensed aromatic rings. As a result, structural radical anions are formed, which are highly reactive in contact with electron-acceptor molecules.

The formation of the interphase of carbide-like compounds with essentially ionic M–C bonds and low hydrolytic resistance is also responsible for the increase in the reactivity of a carbon material under the above conditions and facilitates activation with superheated steam.

In any case, the activation efficiency should depend on the impregnation procedure, which should ensure the required content of alkali metal ions and their uniform distribution and deep penetration in the carbon matrix. It seemed promising to perform impregnation by ion exchange in contact of a solution of an AM compound with preliminarily oxidized anthracite samples.

In this work, we studied how the extent of oxidation of anthracite after impregnattion with alkali metal compounds and heat treatment affects the efficiency of the subsequent activation with steam and the transformation of the resulting pore structure.

The initial material was weakly activated A grade anthracite (Sverdlovantratsit Production Association, Donets coal fields). The initial raw material contained (wt %) 90 carbon, 3–4 ash, 6–7 volatiles, and less than 2 sulfur. Its particle size was 0.25–1.0 mm. The oxidative treatment of the anthracite samples was performed at 360–400°C in humid air. The total number of proton-donor (phenolic and carboxy) groups on the surface of anthracite was determined by titration with 0.1 N NaOH solution and by calculation of the static exchange capacity (SEC). In the course of the oxidation, we obtained samples differing in the extent of oxidation (with SEC 0.6, 1.0, 1.4, and 1.8 mg-equiv g^{-1}).

The impregnation of samples with AM salt (preac-

1070-4272/02/7509-1411$27.00 © 2002 MAIK "Nauka/Interperiodica"

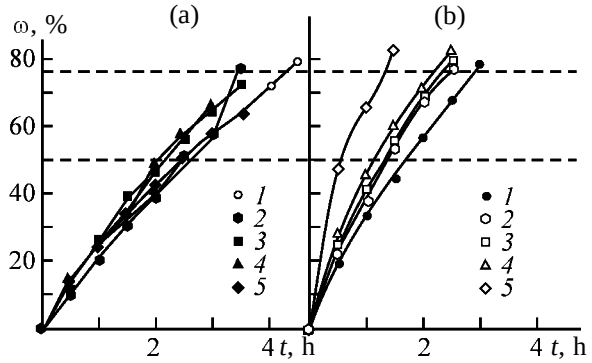

Fig. 1. Kinetic curves of burn-out ω of anthracite samples activated by different procedures. (τ) Time. (a) (*1*) Direct activation; activation of heat-treated oxidized samples with SEC (mg-equiv g^{-1}) (*2*) 0.6, (*3*) 1.0, (*4*) 1.4, and (*5*) 1.8. (b) Activation of heat-treated samples impregnated with sodium nitrate: (*1*) initial; oxidized to SEC (mg-equiv g^{-1}): (*2*) 0.6, (*3*) 1.0, (*4*) 1.4, and (*5*) 1.8.

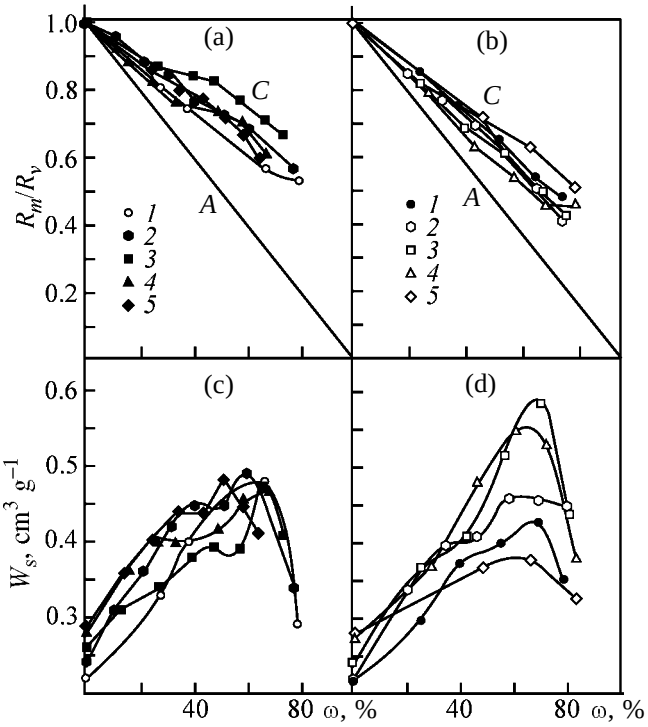

Fig. 2. (a, b) Activation index R_m/R_v and (c, d) sorption pore volume by benzene W_s vs. burn-out ω for anthracite samples activated by different procedures. (a, c) (*1*) Direct activation; activation of heat-treated oxidized samples with SEC (mg-equiv g^{-1}) (*2*) 0.6, (*3*) 1.0, (*4*) 1.4, and (*5*) 1.8. (b, d) Activation of heat-treated samples impregnated with sodium nitrate: (*1*) initial; oxidized to SEC (mg-equiv g^{-1}): (*2*) 0.6, (*3*) 1.0, (*4*) 1.4, and (*5*) 1.8.

tivation heat treatment) was performed in the similar mode. Oxidized anthracite samples were impregnated with a 5 wt % solution of sodium nitrate at a liquid-to-solid volume ratio of 1 : 1 and kept for 5–6 h at 120°C to complete drying. Then, the impregnated samples were placed in a quartz reactor in a horizontal furnace and calcined at 900°C for 1 h in argon. After that, the samples were activated with steam at the same temperature. The flow rate of steam (0.1 l h^{-1}) ensured a 8–9-fold excess of water with respect to stoichiometry in gasification of condensed carbon.

To reveal the effect of oxidative treatment combined with the subsequent impregnation with sodium nitrate and heating, we also performed direct activation of anthracite (without treatment before activation) and activation of anthracite samples oxidized to the above values of SEC and heat-treated in Ar before activation.

In all stages of the study, variation of the pore structure of the samples was monitored by measuring the pore volume by benzene [10]. The radius distribution of macro- and mesopores was determined by the mercury porosimetry on a Pore-Sizer 9300 device (Cultronix, France). In the course of the activation, the sample yield with respect to mass and volume, R_m and R_v, the bulk density Δ, and the degree of burn-out ω were determined.

The kinetic curves of burn-out of anthracite samples prepared by different procedures in the course of the steam activation at 900°C are shown in Fig. 1. As seen, for the initial anthracite sample subjected to direct activation, the kinetic curve approaches the linear dependence. In this case, 50 and 75% burn-out was attained in 2.5 and 4.25 h, respectively. The preliminary oxidation to SEC from 0.6 to 1.8 mg-equiv g^{-1} and subsequent heating in argon at 900°C before activation do not noticeably affect the burn-out dynamics (Fig. 1a). The corresponding kinetic curves are close, within insignificant scatter of experimental data, to the dependence obtained for direct activation of anthracite at the initial burn-out rate of about 20% h^{-1}.

Thus, the oxidative treatment of anthracite does not affect the rate of activation with superheated steam.

At the same time, impregnation of the initial anthracite with sodium nitrate followed by heating in argon at 900°C before activation considerably enhances the reactivity of condensed carbon (Fig. 1b). The initial rate of the anthracite burn-out increases two-fold (~40% h^{-1}), and 50 and 75% burn-out is attained in a considerably shorter time (1.75 and 3 h, respectively).

The reactivity increased to a still greater extent when preliminarily oxidation was followed by impregnation with $NaNO_3$ and calcination in inert

Porometric characteristics of anthracite samples activated by different procedures to 70% burn-out

Anthracite	V^{Hg}	V^{Hg}_{ma}	$V^{Hg} - V^{Hg}_{ma}$	ρ, g cm^{-3}	V_Σ	$V_\Sigma - \Sigma V^{Hg}$
	cm^3 g^{-1}				cm^3 g^{-1}	
Direct activation						
Initial	0.20	0.16	0.04	0.847	0.68	0.48
Oxidized to SEC 1.0 mg-equiv g^{-1}	0.22	0.10	0.12	0.890	0.62	0.40
Activation of samples impregnated with $NaNO_3$ and calcined in Ar						
Initial	0.30	0.15	0.15	0.940	0.56	0.26
Oxidized to SEC, mg-equiv g^{-1}:						
0.6	0.26	0.11	0.15	0.990	0.51	0.25
1.0	0.29	0.11	0.18	0.898	0.61	0.32
1.4	0.42	0.16	0.26	0.796	0.76	0.34

atmosphere before activation. The initial rate of the activation exceeds 50% h^{-1}, reaching 70% h^{-1} at a high burn-out. In this case, 50% and 75% burn-out is attained within 0.5–1.25 and 1.25–2.5 h, respectively. It is interesting that oxidation of samples to SEC within 0.6–1.4 mg-equiv g^{-1} ensured approximately similar increase in the carbon reactivity. Only at fairly large extents of oxidation (SEC 1.8 mg-equiv g^{-1}), the carbon skeleton underwent rapid weight loss in the course of activation; the process resembled combustion rather than pore formation.

It is important to know how the activation index and the sorption volume by benzene vary with the degree of burn-out of the samples (Fig. 2). The variation of R_m/R_v ratio shows that the oxidized anthracite samples show stronger tendency to combustion than samples obtained by direct activation of the initial anthracite (Fig. 2a). This is due to the removal of CO and CO_2 from the surface oxides during activation. Upon activation of anthracite and its oxidized modifications impregnated with sodium nitrate, the pore formation always dominates over combustion (Fig. 2b, lines *A* and *C*, resectively). The only exception is the strongly oxidized sample with SEC 1.8 mg-equiv g^{-1}, for which the contribution of combustion also considerably increases. Apparently, this is due to the extremely high content of surface oxides present on anthracite and replacement of a part of protons in protono-donor groups by sodium ions. For all other modifications of anthracite activated with sodium nitrate, the curves virtually coincide to 65% burn-out and deviate toward combustion only at higher degrees of burn-out.

The sorption volume by benzene is virtually similar for samples obtained by direct activation and for those activated after oxidation (Fig. 2c). In this case, W_s by benzene is maximal, 0.5 cm^3 g^{-1}, at 50–75% combustion. The impregnation with sodium nitrate (Fig. 2d) results in somewhat lower values of W_s for nonoxidized anthracite samples and considerably increased values, for oxidized samples. In this case, W_s passes through a maximum with increasing amount of oxygen-containing groups. For samples with SEC 1.0 mg-equiv g^{-1}, W_s of 0.6 cm^3 g^{-1} and higher is attained at 60–75% burn-out. Anthracite samples oxidized to SEC 1.0–1.4 mg-equiv g^{-1} are the best from the viewpoint of development of the sorption pore volume. Apparentlty, at further oxidation the reactivity of the matrix sharply increases, which intensifies combustion and facilitates formation of macropores, in particular, by destruction of walls of micro- and mesopores.

Our results show that the SEC values within 1.0–1.4 mg-equiv g^{-1} are optimal for anthracite oxidation.

The results of studying the samples by mercury porosimetry (see table) confirm our assumptions concerning the character of development of the anthracite pore structure upon different activations. For example, the data of the table show that the volume V^{Hg} of the mercury being pressed is minimal for the sample obtained by direct activation, is markedly higher for that activated after oxidation, and is also higher (by a factor of 1.5) for the sample impregnated with sodium nitrate. Upon combined treatment (oxidation, impregnation, and heat treatment) before activation, V^{Hg} grows with increasing SEC. At SEC 1.4 mg-equiv g^{-1}, the volume of Hg-filled pores increases twofold as compared to direct activation.

At the same time, the growth of the macropore

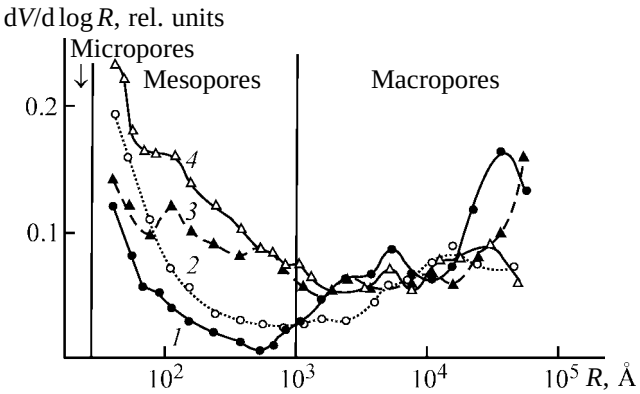

Fig. 3. Differential curves of the pore volume distribution $dV/d\log R$ with respect to equivalent radii R for anthracite samples activated by various procedures. Activation: (*1*) direct, (*2*) heat-treated sample oxidized to SEC 1.0 mg-equiv g^{-1}; (*3*) heat-treated initial sample impregnated with sodium nitrate; and (*4*) heat-treated sample oxidized to SEC 1.0 mg-equiv g^{-1} and impregnated with sodium nitrate.

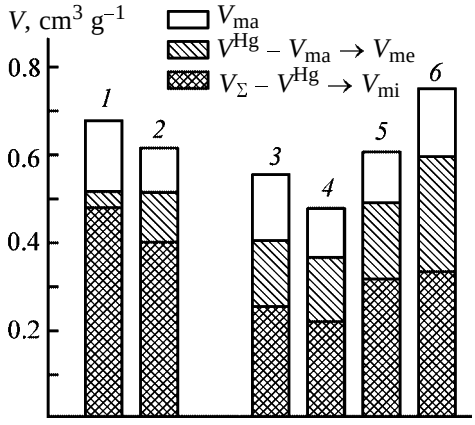

Fig. 4. Histogram of the ratio of micro-, meso-, and macropores in anthracite samples activated by different procedures. (V) Pore volume. Activation: (*1*) direct; (*2*) heat-treated sample oxidized to SEC 1.0 mg-equiv g^{-1}; (*3*) heat-treated initial sample impregnated with sodium nitrate; and (*4–6*) heat-treated oxidized samples (SEC 0.6, 1.0, and 1.4 mg-equiv g^{-1}, respectively) impregnated with sodium nitrate.

volume was not noticeably affected by activation. In this case, the difference $V^{Hg} - V^{Hg}_{ma}$, which is close to the absolute mesopore volume, V_{me}, increases, which shows that the combined treatment before activation results in efficient development of the mesopore structure.

At the same time, the anthracite sample obtained by direct activation has one of the lowest apparent densities by mercury ρ. As a rule, the activated anthracite samples subjected to preliminary oxidation, impregnation with sodium nitrate, or combined treatment have a higher apparent density. And only after fairly deep oxidation (to SEC 1.5 mg equiv g^{-1}) the apparent density attains the values similar to, or lower than those yielded by direct activation. Correspondingly, the comparable and even larger total pore volume V_Σ is attained under these conditions. Thus, preactivation treatment of samples shifts the ratio of the micro-to-mesopore volume toward formation of mesopores. This is clearly illustrated by the differential curves of pore distribution with respect to equivalent radius (Fig. 3) and also by the ratios of the pore volumes for all types of pores developed in the anthracite samples activated by different procedures (Fig. 4). Indeed, whereas the anthracite sample obtained by direct activation contains insufficient amount of transition (meso-) pores (micro- to mesopore ratio 5 : 1), the proposed combined treatment before activation allows the activation to be shifted toward formation of mesopores (micro- to mesopore ratio 3 : 2). In the process, the sorption volume $V_{mi} + V_{me}$ in the resulting samples at comparable burn-out can be increased by 20–25% compared to direct activation. The specific surface area of such sorbents with polymodal pore structure, as estimated from thermal desorption of argon, reaches 900–1000 $m^2 g^{-1}$.

CONCLUSIONS

(1) The preliminary oxidative treatment followed by impregnation with alkali metal compounds and treatment in an inert gas before activation allow the reactivity of anthracite to be increased 2–3-fold. The sorption pore volume of the resulting samples is larger than in the case of direct activation, and the mesopore structure is formed.

(2) In the course of the anthracite activation, the catalytic effect of alkali metal compounds increases when oxygen-containing groups (including proton-donor groups) are present on the surface of the carbon matrix. The optimal degree of the anthracite oxidation, ensuring the largest pore volume upon activation, corresponds to the static exchange capacity of 1.0–1.4 mg-equiv g^{-1}.

REFERENCES

1. Parra, J.B., Pis, J.J., Sousa, J.C. de, *et al.*, *Carbon*, 1996, vol. 34, p. 783.
2. Parra, J.B., Sousa, J.C. de, Pis, J.J., *et al.*, *Carbon*, 1995, vol. 33, p. 801.
3. Babenko, V.S., and Buyanov, R.A., *Khim. Tverd. Topl.*, 1990, no. 4, pp. 33–38.

4. Kucherenko, V.A., Sapunov, V.A., Zubova, T.I., *et al*., *Khim. Tverd. Topl*., 1992, no. 4, pp. 96–101.
5. Strelko, V.V., Gerasimenko, N.V., and Kartel', N.T., *Teor. Eksp. Khim*., 1999, vol. 35, no. 5, pp. 306–310.
6. Gerasimenko, N.V., Strelko, V.V., and Kartel, N.T., Abstracts of Papers, *1st World Conf. on Carbon (Eurocarbon 2000)*, Berlin (Germany), July 9–13, 2000, vol. 2, pp. 599–600.
7. Strelko, V.V., Gerasimenko, N.V., and Kartel', N.T., *Teor. Eksp. Khim*., 2001, vol. 37, no. 1, pp. 48–52.
8. Strelko, V.V., Kuts, V.S., and Khanasyuk, J.P., Abstracts of Papers, *23rd Biennial Conf. on Carbon (Carbon'97)*, Pennsylvania (the United States), July 18–23, 1997, pp. 431–432.
9. Strelko, V.V. and Kuts, V.S., Abstracts of Papers, *World Conf. on Carbon (Carbon'98)*, Strasbourg (France), July 5–9, 1998, pp. 773–775.
10. Kel'tsev, N.V., *Osnovy adsorbtsionnoi tekhniki* (Principles of Adsorption Technology), Moscow: Khimiya, 1984.

Russian Journal of Applied Chemistry, Vol. 75, No. 9, 2002, pp. 1416–1419. Translated from Zhurnal Prikladnoi Khimii, Vol. 75, No. 9, 2002, pp. 1448–1451.
Original Russian Text Copyright © 2002 by Girchene, Matulenis.

APPLIED ELECTROCHEMISTRY AND CORROSION PROTECTION OF METALS

Exfoliation of Coatings from Silicon Crystals Electroless-Plated with Nickel and Electroplated with Gold

O. Girchene and E. Matulenis

Institute of Chemistry, Vilnius, Lithuania

Received February 19, 2002

Abstract—The microhardness and content of carbon in electroplated gold coatings were studied as influenced by the operation time of citrate and citrate–phosphate gold-plating electrolytes. Such physicomechanical properties as porosity, microhardness, internal stress, plasticity, and microstructure of electroless-plated and electroplated nickel coatings were studied and analyzed.

Electroplated gold coatings [1–3] are widely used in semiconductor industry owing to chemical stability, small and constant contact resistivity, high soldering ability, and formation of low-melting eutectic with silicon, which provides prolonged safe operation of electronics. In special cases gold is deposited to protect the nickel ohmic contacts in the course of further treatment of the silicon crystals with aggressive etching agents and to improve soldering of the electric contacts. Such electroplated coatings should exhibit high adhesion to nickel support and minimal porosity.

According to the preparation procedure of the ohmic contacts, electroplating with gold is preceded by electroless deposition of the second nickel layer on silicon plates electroless-plated with nickel. For uncertain reasons, in some cases, exfoliation of coatings is observed when cutting silicon plates. In the course of electrolysis, anodic oxidation of citrates in gold-plating electrolytes occurs, and its products can be incorporated in the gold coatings [4]. Electroless-plated nickel can also contain impurities, whose content depends on the solution pH, temperature, and some other factors [5]. Therefore, during coating of silicon plates with nickel and gold, even slight changes in the plating mode can affect the physicomechanical properties of the coatings and cause low adhesion at the Au–Ni and Ni–Ni interfaces.

The goals of this work were to reveal factors responsible for exfoliation of coatings from silicon crystals at their cutting and to develop the optimal preparation procedure providing high adhesion at the Au–Ni and Ni–Ni interfaces. The dependences of microhardness and content of carbon in electroplated gold coatings as influenced by the operation time of citrate and citrate–phosphate gold-plating electrolytes were studied, and various physicomechanical properties of electroless-plated and several electroplated nickel coatings were determined.

EXPERIMENTAL

All the solutions for gold plating and for electroless and electrolytic nickel plating were prepared by dissolution of appropriate chemically pure grade and analytically pure grade chemicals in distilled water. The compositions of the resulting solutions are listed in Tables 1 and 2.

The samples were coated with metals in 0.2-l electrolyzers equipped with a magnetic stirrer. A platinized titanium plate was used as an anode in gold electroplating.

The content of carbon in the electroplated gold coatings was determined on an AN-7529 express carbon analyzer. The microstructure of the nickel coatings was studied on a JXA-50A electron microscope-microanalyzer. The microhardness H_μ (kgf mm^{-2}) of the electroplated coatings with thickness $d \geq 10$ μm at 20-g load was registered on a PMT-3 microhardness meter according to the Vickers procedure [6]. The plasticity of the nickel coatings was tested by bending at right angles; the bending areas were examined with a microscope.

To determine the porosity of nickel coatings, they were deposited on a 1 cm^2 copper plate. On this plate (acting as anode), we put a photographic paper treated with a fixer and impregnated with a 1% NH_4NO_3 solution (the emulsion-coated side toward the coat-

1070-4272/02/7509-1416$27.00 © 2002 MAIK "Nauka/Interperiodica"

Table 1. Gold-plating electrolytes and physicomechanical properties of gold coatings

Parameter	Electrolyte						
	no. 1	no. 2	no. 2a	no. 2b	no. 2c	no. 3	no. 3a
Electrolyte composition, g l^{-1}:							
Au {in form of $K[Au(CN)_2]$}	10	10	10	10	10	10–13	10–13
H_3PO_4, d = 1.7 g cm^{-3}	19.6–21	19.6–21	19.6–21	19.6–21	19.6–21	–	–
citric acid	100	100	100	100	100	30–33	30–33
NH_4Cl	23.8–25	23.8–25	23.8–25	23.8–25	23.8–25	–	–
Tl (in form of Tl_2SO_4)	–	0.002–0.005	0.002–0.005	0.002–0.005	0.002–0.005	–	–
potassium hydrocitrate	–	–	–	–	–	75–80	75–80
pH	6	6	6	6	6	4.7	4.7–5
Temperature, °C	50	50	50	50	50	60–65	60–65
Current density i_c, A dm^{-2}	0.25	0.25	0.25	0.25	0.25	0.25	0.25
Electrolyte operation time, A h l^{-1}	0	0	20	50	150	0	100
Content of carbon in electroplated gold coating	0.0097	0.0108	0.0095	0.0106	0.0100	0.0072	0.0107
Microhardness of electroplated gold coating H_μ, kgf mm^{-2}	65	65	70	85	80	70	75

Table 2. Nickel-plating electrolytes and physicomechanical properties of nickel coatings

Parameter	Electrolyte			
	no. 1, electroless-plated Ni	no. 2, sulfamic Ni	no. 3, Watts	no. 4, lustrous Ni
Electrolyte composition, g l^{-1}:				
$NiSO_4 \cdot 7H_2O$	10	–	280	280
$NiCl_2 \cdot 6H_2O$	–	5	35	35
$Ni(NH_2SO_3)_2 \cdot 4H_2O$	–	400	–	–
H_3BO_3	–	30	30	30
sodium lauryl sulfate	–	0.5	–	–
saccharin	–	–	–	0.15
sodium acetate	10	–	–	–
acetic acid	To pH 4.5	–	–	–
NaH_2PO_2	10	–	–	–
pH	4.5	3.5–4.5	3.5–5.5	3.5–5.5
Temperature, °C	80	25–30	20–40	20–40
i_c, A dm^{-2}	–	1	1	1
H_μ, kgf mm^{-2}	300	175	210	295
Internal stress IS, kgf mm^{-2}	610	790	960	370

ing), over which an aluminum cathode was placed. The resulting assembly was pressed (1 MPa) and treated with an electric current (5 mA cm^{-2}) for 0.5–1.0 min. Then, the photographic paper was developed in a 1% solution of dimethylglyoxime. The through pores in the nickel coating were observed as brown-green spots [7].

The internal stress IS in the nickel coatings was measured by a flexible cathode procedure [6]. The coating was deposited on a brass plate (0.46 mm thick); it was fixed in a special holder preserving its position on a test desk. The cathode bend was determined from the difference of measurements before and after coating. The IS values were calculated from

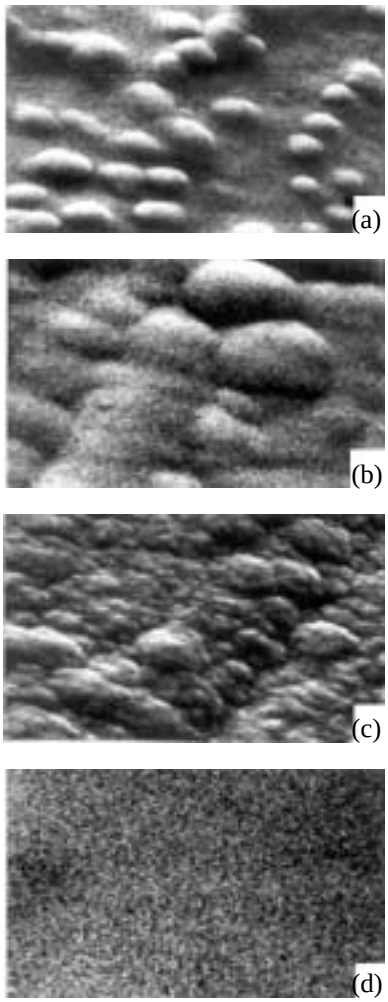

Fig. 1. Microstructure of nickel coatings deposited form electrolyte nos.: (a) 1, (b) 2, (c) 3, and (d) 4. Magnification $\times 3000$.

the following equation [6]:

$$IS = (Ed^2 z)/(3gl^2),$$

where E is the Young's modulus (kg cm^{-2}); d, the plate thickness (cm); z, the cathode deviation (cm); g, the coating thickness (cm); and l, the plate length (cm).

The measurement error was ±5%.

Coating of the nickel-plated silicon plates with gold was performed from citrate (99.9% Au) and citrate–phosphate (99.9% Au) electrolytes (Table 1, nos. 3, 3a, 1, 2, and 2a–2c, respectively). Since gold anodes are insoluble in such electrolytes, we used as anodes platinized titanium plates. In the course of electrolysis, oxidation of citrates at the anode is observed [4]. The oxidation products are accumulated in solution and can be incorporated into the gold coating, affecting its physicomechanical properties [4].

We determined the content of carbon in the gold coatings electroplated from freshly prepared solutions and from those used for a long period (Table 1, nos. 1–3 and 2a–2c, 3a, respectively). It was found that, in the case of citrate electrolyte (nos. 3, 3a), with increasing operation time from 0 to 100 A h l^{-1} the content of carbon increases from 0.72×10^{-2} to 1.07×10^{-2}% (Table 1). In the gold coatings prepared in citrate–phosphate electrolytes, with increasing operation time to 150 A h l^{-1}, the content of carbon remains approximately constant and varies from 0.95×10^{-2} to 1.08×10^{-2}% (Table 1, electrolyte nos. 1, 2, 2a–2c). With increasing operation time, the microhardness of the gold coatings obtained from all the electrolytes studied increases by only 6–10% (Table 1).

These data show that H_μ and content of carbon in the gold coatings do not change significantly with increasing operation time of gold electrolytes to 150 A h l^{-1}.

In the preparation of the ohmic contacts, the first fine layer of nickel is electroless-plated on the silicon plate, and the second layer of nickel is electroless-plated directly before gold electroplating. As seen from published data [1, 5, 8], when hypophosphite is used as a reducing agent, nickel electroless-plated from acidic and alkali solutions contains 6–15 and 3–7 wt % phosphorus, respectively. Phosphorus in the coating is distributed nonuniformly, causing layered structure of the nickel coatings. It is often considered that freshly prepared electroless-plated nickel coatings are the supersaturated solid solutions of phosphorus in nickel. As shown in [1], the Ni–P solid solution is susceptible to passivation and it should be soldered directly after deposition. The plasticity of electroless-plated nickel is low. The IS values of the electroless-plated nickel coatings depend on the conditions of their deposition [5], and variations in the deposition procedure can affect the physicomechanical properties of the resulting coatings. Taking into account the above facts, we studied and analyzed physicomechanical properties (porosity, microhardness, internal stress, plasticity, and microstructure) of the electroless-plated and several electroplated nickel coatings deposited from various nickel-plating electrolytes [9, 10]. The compositions of the nickel-plating electrolytes and physicomechanical properties of the resulting nickel coatings are listed in Table 2.

Analysis of the microstructure showed that the coatings deposited from electrolyte nos. 1 and 2 (Figs. 1a, 1b) are similar. In the electroless deposition of coatings from nickel-plating solutions, ellipsoidal spherical aggregates of up to 2 μm size are formed (Fig. 1a), whereas in deposition from Watts solution

no. 2 coarser aggregates of up to 5 μm size appear (Fig. 1b). When nickel coatings are deposited from sulfamic electrolyte no. 3, a fine-grained precipitate is formed, and separate crystallites and concretions are observed (Fig. 1c). From electrolyte no. 4, finely crystalline and lustrous nickel coating is deposited (Fig. 1d). Our tests showed that all the nickel coatings of 0.3 μm thickness are porous. With increasing thickness of nickel coatings to 1 μm, their porosity decreases, and at 3 μm they become poreless. As seen from the comparison of 1-μm coatings, the nickel coating prepared by electroplating from electrolyte nos. 2 and 3 are less porous and simultaneously the most plastic.

One of the most important characteristics of nickel coatings is their internal stress. Significant internal stresses cause fracture of the deposit and its exfoliation from the support. It is known that the internal stresses in the nickel coatings depend on the presence of anions of the nickel salts used in the synthesis. According to [10], the IS value grows in the following order: sulfamates < bromides < fluoroborates < sulfates < chlorides.

With increasing solution temperature, IS decreases [5]. The data on IS and H_μ listed in Table 2 show that the smallest internal stresses are typical for the coatings deposited from electrolyte solutions containing saccharin (lustrous no. 4). This fact agrees with published data [11], where small additives of saccharin or 1,4-butynediol in nickel-plating electrolytes are recommended to reduce IS. The H_μ values of the electroless-plated and lustrous electroplated nickel coatings are similar (Table 2, electrolyte nos. 1, 4).

Our experimental and published [1, 5, 8] data suggest that the electrolytic nickel coatings in some properties (plasticity, porosity, and internal stress) are even more appropriate for deposition of the second nickel layer. Moreover, electroless-plated nickel coatings contain phosphorus and other impurities, which may cause exfoliation of the coatings from silicon crystals when cutting the plates.

To study the possibility of replacement of the electroless-plated nickel coatings by electroplated samples, a series of silicon plates were electroplated with nickel (layer thickness of 3 μm) using electrolyte nos. 2–4 (Table 2) with subsequent deposition of the gold coatings. The entire series successfully passed the industrial tests, and no exfoliation of the coatings was observed. This confirms our assumption that exfoliation of the coatings from silicon crystals at their cutting is due to changes in the physicomechanical properties of the electroless-plated nickel coatings, which deteriorates adhesion at the Ni–Ni and Ni–Au interfaces. We recommend to substitute the second layer of electroless-plated nickel with an electroplated coating (nearly 3 μm thick) deposited from electrolyte of the following composition, g l^{-1}: 280 $NiSO_4 \cdot 7H_2O$, 35 $NiCl_2 \cdot 6H_2O$, and 30 H_3BO_3; pH 3.5–5.5 (Table 2, electrolyte no. 3). This electrolyte contains no organic additives which could be incorporated into the nickel coatings.

CONCLUSIONS

(1) With increasing operation time of the gold-plating electrolytes from 0 to 150 A h l^{-1}, the content of carbon in the gold coatings and H_μ change insignificantly.

(2) To exclude exfoliation of coatings from the crystals at cutting, the second layer of electroless-plated nickel should be substituted with electroplated coating (nearly 3 μm thick) deposited from electrolyte of the following composition, g l^{-1}: 280 $NiSO_4 \cdot 7H_2O$, 35 $NiCl_2 \cdot 6H_2O$, and 30 H_3BO_3; pH 3.5–5.5.

REFERENCES

1. Grilikhes, S.Ya. and Tikhonov, K.I., *Elektroliticheskie i khimicheskie pokrytiya* (Electrolytic and Electroless-Plated Coatings), Leningrad: Khimiya, 1990.
2. Kaiser, H., Beeh, G., Blosch, P., *et al*., *Galvanotechnik*, 1998, vol. 89, no. 3, pp. 757–764.
3. Kaiser, H., Beeh, G., Blosch, P., *et al*., *Galvanotechnik*, 1999, vol. 90, no. 3, pp. 665–671.
4. Molchadskite, O., Butkyavichus, Yu., and Vishomirskis, R., Abstracts of Papers, *Konferentsiya "Issledovaniya v oblasti elektroosazhdeniya metallov"* (Conf. on Metal Electroplating), Vilnius, 1976, pp. 144–149.
5. Shalkauskas, M. and Vashkyalis, A., *Khimicheskaya metallizatsiya plasmass* (Electroless Metal Plating of Plastics), Leningrad: Khimiya, 1972.
6. Vagramyan, A.T. and Petrova, Yu.S., *Fiziko-khimicheskie svoistva elektroliticheskikh osadkov* (Physico-Chemical Properties of Electrolytic Deposits), Moscow: Akad. Nauk SSSR, 1960.
7. Socha, J., *Zlocenie galwaniczne*, Warsaw: Inst. Mechaniki Precyzyjnej, 1979.
8. Gyanutune, I.K., Lunyatskas, A.M., and Butkyavichus, Yu.P., *Tr. Akad. Nauk Lit. SSSR, Ser. B*, 1988, vol. 2(81), pp. 15–22.
9. Kurbediene, R. and Jankauskiene, R.D., *Chem. Technol.* (Lithuania), 1995, no. 2, pp. 6–12.
10. Kushner, J. B., *Metal Finish.*, 1958, vol. 56, pp. 82–87.
11. Schmitz, J.H.A. and Wyngaarden, S.V., *Galvanotechnik*, 1986, vol. 77, no. 1, pp. 61–63.

Russian Journal of Applied Chemistry, Vol. 75, No. 9, 2002, pp. 1420–1423. Translated from Zhurnal Prikladnoi Khimii, Vol. 75, No. 9, 2002, pp. 1452–1455.
Original Russian Text Copyright © 2002 by Ivanova, Ivanov, Boldyrev, Sokol'skii, Makeeva.

CATALYSIS

High-Performance Manganese Oxide Catalysts for CO Oxidation

N. D. Ivanova, S. V. Ivanov, E. I. Boldyrev, G. V. Sokol'skii, and I. S. Makeeva

Vernadsky Institute of General and Inorganic Chemistry, National Academy of Sciences of Ukraine, Kiev, Ukraine

National Aviation University, Kiev, Ukraine

Received September 4, 2001; in final form, April 2002

Abstract—The catalytic activity of manganese dioxide samples in oxidation of CO and decomposition of hydrogen peroxide was studied. The promise of manganese dioxide obtained from fluorine-containing electrolytes as a catalyst for carbon monoxide oxidation was considered.

Carbon(II) oxide is one of the most toxic components of industrial waste gases and exhaust gases of automobiles; also, it is formed in regeneration of hydrocarbon cracking catalysts [1–3]. Its maximum permissible concentration is 3 mg m^{-3}. Despite active research in this field, the problem of CO conversion into CO_2 remains topical.

Oxidation of carbon monoxide is accompanied by a considerable decrease in the Gibbs energy (ΔG^0_{298} = –242 kJ mol^{-1}). However, no CO_2 is formed without a catalyst at temperatures below 923 K. As catalysts for CO oxidation, both metals and oxides MnO_2, Co_3O_4, and CuO are used [1]. With some oxides, the process temperature can be decreased to 393–423 K.

It is known that such structural factors as phase composition, size and orientation of crystallites, dispersity of the material, presence of various kinds of defects, and the extent to which the composition of a compound deviates from the stoichiometry determine its chemical properties [4, 5]. It has also been shown that the catalytic activity of a material grows when its structure becomes disordered [4–6]. An interesting object in this regard is manganese dioxide. Only β-MnO_2 is a stoichiometric compound. The composition of other manganese oxides is commonly represented as MnO_x, where $1.7 < x < 2.0$ [7–9]. Account should also be taken of the fact that manganese dioxide is one of the most common and least expensive oxide materials. The structure of this compound depends very strongly on a method by which it is obtained. Electrochemical manganese dioxide is distinguished by more disordered structure, compared with the chemically synthesized compound.

The aim of this study was to analyze oxidation of carbon monoxide in the presence of various samples of manganese dioxide.

It was shown previously [10, 11] that the use of fluorine-containing electrolytes to obtain manganese dioxide allows control over its composition and properties. In this connection, we made a comparative study of the catalytic activity of various kinds of manganese dioxide, including those prepared electrochemically from fluorine-containing electrolytes (see table, sample nos. 1 and 2).

EXPERIMENTAL

The model reaction of hydrogen peroxide decomposition is frequently used in choosing catalysts for oxidation reactions. Being carried out in aqueous solutions at room temperature, it is very convenient. The reaction progress was monitored by the volume of evolved oxygen, and the activity of manganese dioxide was evaluated from the reaction rate constant:

$$W = kc^nS, \quad (1)$$

where W is the reaction rate; k, the rate constant of the reaction (s^{-1}); n, the reaction order; and S, the specific surface area ($m^2\ g^{-1}$).

The time reckoning was from the instant when the catalyst and a solution were brought in contact. The weighed portion of the catalyst was 10 mg. Experiments were performed with a 30% solution of analytically pure grade hydrogen peroxide whose concentration was checked by titration with 0.1 N $KMnO_4$ solution by the standard procedure [11]. The concentration and volume of the H_2O_2 solution in the reaction vessel

1070-4272/02/7509-1420$27.00 © 2002 MAIK "Nauka/Interperiodica"

Manganese dioxide samples studied

Sample no.	Electrolyte	Mn(IV), wt %	OH_{tot}, wt %	x in MnO_x	$k^* \times 10^5$, s^{-1}	S_{sp}, $m^2\ g^{-1}$
	Electrolytic manganese dioxide					
	Fluorine-containing, c_{HF}, M:					
1	0.1	50.8	4.0	1.95	21.7	140–160
2	0.3	49.7	6.9	1.94	18.1	40–60
3	Sulfate, EDM-2, Georgia [OST (Branch Standard) 6-22-34–76]	58.0	3.2	1.97	10	20–30
	Chemical manganese dioxide					
4	Ultrapure grade reagent	62.1	0.4	1.99	3	1
5	Dnieper Chemical Plant, Ukraine [TU (Technical Specifications) U 14312708.174–94]	61.0	2.3	1.98	18.1	20–30

* Rate constant of catalytic decomposition of H_2O_2.

were 4.92 M and 25 ml. The measurements were done without stirring. The temperature of the hydrogen peroxide solution was maintained at $25 \pm 1°C$ with a U-10 thermostat.

The oxidation of carbon monoxide was studied in a flow-through reactor. The gas flow rate was 1.67×10^{-6} $m^3\ s^{-1}$, the weighed portion of the catalyst was 0.5 g, and the carrier gas was helium. The temperature of the catalyst bed was measured with a Chromel–Alumel thermocouple. The mixture of reactants (O_2, CO, CO_2) was analyzed with an LKhM-8MD chromatograph in which this mixture was separated at 355 K in a column packed with activated carbon impregnated with nickel sulfate. This analytical procedure detects O_2, CO, and CO_2 in amounts of 0.01 vol % with accuracy of 10%. The sample volume subjected to analysis was 1.3 ml. Composition of the reaction mixture (vol %): carbon monoxide 1, oxygen 20, and helium 79. The specific rate of the reaction, W_{sp} ($mol\ s^{-1}\ m^{-2}$), was calculated by the formula

$$W_{sp} = (cU)/(gS), \quad (2)$$

where c is the CO concentration at the reactor outlet ($mol\ m^{-3}$), g is the weighed portion of the catalyst (kg), and S is the specific surface area of the catalyst ($m^2\ kg^{-1}$).

The reaction order with respect to reagent concentrations was found from the slope of a plot constructed in the $\ln W_{sp}$–$\ln c$ coordinates.

The X-ray phase analysis of manganese dioxide was carried out on a DRON-3 instrument with MoK_α radiation.

The chemical analysis of manganese dioxide was made in accordance with GOST (State Standard) 25823–23. The content of manganese(II) was found using the procedure described in [12]. Data on the content of low-charged manganese ions were recalculated to Mn(II) and Mn(III). The x value was calculated for all of the samples studied from the content of differently charged manganese ions [13]:

$$x = (2 + 1.5R)/(1 + R), \quad (3)$$

where $R = [Mn(III)]_s/[Mn(IV)]_s$.

Thermogravimetric measurements were done on an OD-2 derivatograph (Hungary) with Al_2O_3 reference under heating (20–600°C) in air. The sample weight was 250 mg, and the heating rate, 5 and 10 deg min^{-1}. The content of OH groups was found from the mass loss (thermogravimetric curve) in the following temperature ranges: surface OH groups at 130–200°C and total OH groups (with the exception of physically adsorbed water) up to 400°C.

The specific surface area was determined by high-temperature adsorption of argon, using samples with the known surface area as reference [14]. The measurements were carried out on an LKhM-8MD chromatograph (model 1). The working mixture contained 12% argon and 88% helium. The reference adsorbent was Al_2O_3 with the specific surface area of 26 $m^2\ g^{-1}$. The use of the chromatographic technique gave an error of 10%.

The ESR spectra were measured at room temperature on a Radiopan SE/x-2547 microwave spectrom-

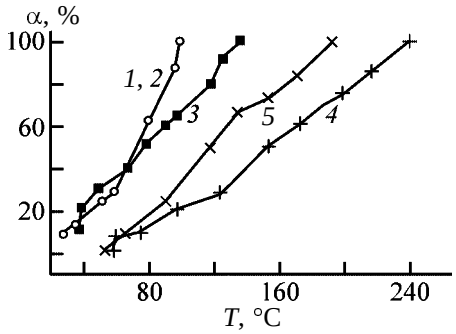

Fig. 1. Degree of catalytic conversion of carbon monoxide, α, vs. temperature *T* for the manganese dioxide samples studied. Digits at curves correspond to sample numbers in the table.

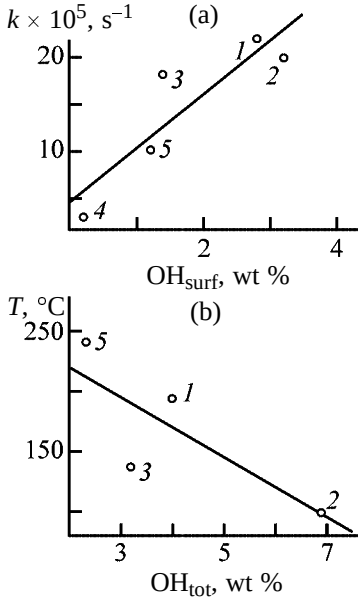

Fig. 2. (a) Catalytic activity in hydrogen peroxide decomposition and (b) temperature *T* of 100% conversion of carbon monoxide vs. content of surface OH groups, OH_{surf}, and total content of OH groups, OH_{tot}, in manganese dioxide samples studied. (*k*) Reaction rate constant. Digits at points correspond to sample numbers in the table; the same for Fig. 3.

eter (3 cm) equipped with a computerized spectral analyzer.

The results obtained in determining the catalytic activity in hydrogen peroxide decomposition, acidity, and specific surface area of several manganese dioxide samples are presented in the table. It can be seen that the difference in composition between the samples is reflected in the rate constant of H_2O_2 decomposition.

With all of the samples studied, hydrogen peroxide decomposition is a first-order reaction. Therefore, the rate constant was found as the slope of the curve in the $\log c$–τ coordinates. The highest catalytic activity was observed for nonstoichiometric manganese dioxide (sample no. 1) obtained from fluorine-containing electrolytes, and the lowest, for stoichiometric manganese dioxide (sample no. 4).

Figure 1 presents the degree of catalytic conversion of carbon monoxide as a function of temperature. It can be seen that the temperature of full CO conversion increases in the following order of manganese dioxide samples studied: nos. 1, 2 < 3 < 5 < 4.

When the temperature is lowered, which corresponds to the reverse run of the dependence (Fig. 1), all the samples exhibit hysteresis; namely, the degree of conversion in heating of a sample exceeds that in cooling. This catalytic reaction is also first-order, which is indicated by the linear dependence of the rate of catalytic oxidation of carbon monoxide on its concentration.

The lowest temperature of full conversion of CO at its concentration of 1% is characteristic of sample no. 2 obtained from a fluorine-containing electrolyte. The working temperature of this catalyst is about 100°C. It should be noted that this catalyst can be used at even lower temperature, e.g., at 90°C, with the degree of conversion being still sufficiently high: about 80%.

The activation energy of the reaction at constant reactant concentrations was found in the range 40–100°C. The lowest activation energy was observed for sample no. 2 with the lowest temperature of full CO conversion into CO_2. The activation energy of hydrogen peroxide decomposition was determined using the isothermal method from the rate constants of the catalytic reaction at 25, 30, 35, and 40°C. The activation energies calculated for both catalytic processes are close, in the range from 15 to 30 kJ mol^{-1}. According to the results obtained, the catalytic decomposition of hydrogen peroxide can be used as model reaction in studying catalytic oxidation reactions.

In [15], data on catalysis of various reactions on manganese dioxide were summarized and correlated with structural parameters of the material. Here we made an attempt to consider in the same terms the problem of carbon monoxide conversion and hydrogen peroxide decomposition on manganese dioxide.

According to X-ray diffraction patterns, two-phase sample nos. 1 and 2 (γ-MnO_2 with impurity of the α-phase), sample no. 4 (with well-formed structure of β-MnO_2), and sample nos. 3 and 5 (structure of the γ-MnO_2 type) can be distinguished.

A relationship is observed between the activity of

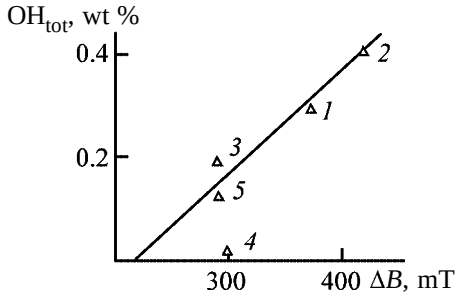

Fig. 3. Correlation between the ESR signal broadening ΔB and the total content of OH groups, OH_{tot}, in the samples studied.

the samples in both the catalytic reactions and their structural disorder.

One of the most important criteria of nonstoichiometry of manganese dioxide is the presence of OH groups. These groups ensure electroneutrality in the case of cationic vacancies of manganese in the lattice and provide charge stabilization of differently charged manganese ions Mn(III)/Mn(IV) in the structure of this oxide. Mention should be made of the dependence of the activity on the number of surface OH groups in catalysis of hydrogen peroxide decomposition (Fig. 2a). The relationship between the temperature of full conversion of carbon monoxide and the content of surface OH groups, revealed in the samples studied, demonstrates that catalytic oxidation of CO is governed by the defectiveness of the catalyst structure (Fig. 2b).

Important information about the defectiveness of the manganese dioxide structure is furnished by ESR spectroscopy. According to the data obtained, the observed broadening of the ESR signal indicates an intensive exchange interaction between differently charged manganese ions in the lattice. This quantity correlates satisfactorily with the content of differently charged manganese ions and OH groups in the structure [16] (Fig. 3). The stoichiometric sample falls out of this dependence, presumably because of differences in the structure (β-MnO_2) and in the mechanism of compensation of the charge of defects.

Thus, the defects, including OH groups and differently charged manganese ions, govern the catalytic activity of the manganese dioxide samples studied.

CONCLUSIONS

(1) The catalytic properties of manganese dioxide can be improved significantly by changing the method of its preparation. Manganese dioxide obtained from fluorine-containing electrolytes is a promising catalyst for CO oxidation.

(2) The activity of the samples is governed by the defectiveness of their structure, which can be judged from the concentration of OH groups.

REFERENCES

1. Thomas, J.M. and Thomas, W.J., *Introduction to the Principles of Heterogeneous Catalysis*, New York: Academic, 1967.
2. Mardanova, N.M., Akkhverdiev, R.B., Talushinskii, R.M., *et al.*, *Kinet. Katal.*, 1996, vol. 37, no. 1, pp. 84–86.
3. Boreskov, G.K. and Marshneva, V.I., *Dokl. Akad. Nauk SSSR*, 1973, vol. 213, no. 1, pp. 112–115.
4. Tret'yakov, Yu.D., *Khimiya nestekhiometricheskikh okislov* (Chemistry of Nonstoichiometric Oxides), Moscow: Mosk. Gos. Univ., 1974.
5. Tret'yakov, Yu.D., *Tverdofaznye reaktsii* (Solid-Phase Reactions), Moscow: Khimiya, 1978.
6. Trasatti, S., *Croat. Chem. Acta*, 1990, vol. 63, no. 3, pp. 313–329.
7. Ivanova, N.D., Kirillov, S.A., and Mishchenko, A.B., *Electrochim. Acta*, 1993, vol. 38, no. 15, pp. 2305–2307.
8. Buzova, Z.M. and Sobolev, R.P., *Elektrotekh. Prom–st. Khim. Fiz. Istochn. Toka*, 1982, issue 1(82), pp. 6–8.
9. Wells, A.F., *Structural Inorganic Chemistry*, Oxford: Clarendon, 1984. 5th ed.
10. USSR Inventor's Certificate no. 1 332 869.
11. Ivanova, N.D., Boldyrev, E.I., Pimenova, K.N., *et al.*, *Zh. Prikl. Khim.*, 1998, vol. 71, no. 7, pp. 1209–1210.
12. Babko, A.K. and Pyatnitskii, I.V., *Kolichestvennyi analiz* (Quantitative Analysis), Moscow: Vysshaya Shkola, 1968.
13. Kozawa, A. and Powers, R.A., *J. Electrochem. Soc.*, 1966, vol. 113, pp. 870–873.
14. Kholyavenko, K.M., in *Problemy teorii i praktiki issledovanii v oblasti kataliza* (Problems of Theory and Practice of Research in the Field of Catalysis), Kiev: Naukova Dumka, 1971, pp. 44–71.
15. Kotur, M.G., *Teor. Eksp. Khim.*, 1998, vol. 34, no. 5, pp. 324–327.
16. Kakazey, M., Ivanova, N., Sokolsky, G., and Gonzalez-Rodriguez, *Electrochem. Solid-State Lett.*, 2001, vol. 4, no. 5, pp. J1–J4.

Russian Journal of Applied Chemistry, Vol. 75, No. 9, 2002, pp. 1424–1426. Translated from Zhurnal Prikladnoi Khimii, Vol. 75, No. 9, 2002, pp. 1456–1458.
Original Russian Text Copyright © 2002 by Kopeikina, Vodyankina, Golovko, Kurina.

CATALYSIS

Oxidation of Ethylene Glycol on Oxide Catalysts

L. Yu. Kopeikina, O. V. Vodyankina, A. K. Golovko, and L. N. Kurina

Institute of Petroleum Chemistry, Siberian Division, Russian Academy of Sciences, Tomsk, Russia
Tomsk State University, Tomsk, Russia

Received March 13, 2001; in final form, June 2002

Abstract—The catalytic activity of a series of metal oxides in oxidation of ethylene glycol was studied.

Transformations of alcohols into lower aliphatic carbonyl compounds are performed in industry on a large scale [1]. These reactions are catalyzed by *d*-metal oxides (V_2O_5, MoO_3, etc.) and complex systems based on them [2].

Partial oxidation of lower alcohols (methanol, ethanol) into carbonyl compounds on oxide catalysts has been extensively studied [3–5]. However, only scarce data are available on oxidation of dihydric alcohols on oxide catalysts. In particular, for oxidation of ethylene glycol (EG) on complex molybdenum-containing catalysts, only the composition of the reaction products was reported [6], without detailed discussion. In this work, we studied selective oxidation of EG on a series of individual oxide catalysts.

EXPERIMENTAL

We tested as catalysts V_2O_5, MoO_3, WO_3, CuO, and Cr_2O_3. This choice was governed by the following factors. According to published data on catalytic oxidation of monohydric alcohols to carbonyl compounds [7], these individual oxide catalysts exhibit acid properties, i.e., they readily adsorb alcohols. Furthermore, the oxygen binding energy in the crystal lattice of these oxides is high, which favors partial oxidation of organic compounds [2, 7]. It is also known that addition of Cr_2O_3 or WO_3 to vanadium catalytic systems appreciably enhances the catalytic activity of V_2O_3 in oxidation of methanol into formaldehyde [8, 9]. Supported copper oxide catalyst is fairly active in oxidation of EG to glyoxal [10, 11].

The catalysts were prepared as follows: WO_3, by decomposition of $(NH_4)_2WO_4$ at 600°C for 4 h; MoO_3, by decomposition of $(NH_4)_6Mo_7O_{24}$ at 350–400°C; V_2O_5, by decomposition of NH_4VO_3 at 450°C for 3 h; and Cr_2O_3 and CuO, by decomposition of the corresponding hydroxides, $Cr(OH)_3$ and $Cu(OH)_2$, precipitated with NH_4OH from metal nitrate solutions, followed by drying of the precipitates at 200°C and calcination at 450–500°C for 3 h. The specific surface area of the resulting oxide systems was 7.6, 5.0, 7.6, and 20.0 $m^2 g^{-1}$ for WO_3, MoO_3, V_2O_5, and Cr_2O_3, respectively.

Experiments were performed in a flow quartz reactor (d = 20 mm) with a fixed bed of a catalyst (bed height 1 cm). The contact time of the reaction mixture with the catalyst was 0.1 s, and the content of EG in air, 3.5 vol %. Liquid reaction products were analyzed with a Chrom-5 chromatograph (flame ionization detector, 1.6-m column, stationary phase 15% Reoplex-400 on Chromaton N, carrier gas nitrogen; flow rates, ml min^{-1}: nitrogen 25, hydrogen 40, and air 500; temperatures, °C: column 146, vaporizer 200, and detector 190). Analyses were performed by the procedure described in [12] for determination of glyoxal in scrubber waters in the form of quinoxaline.

Gaseous reaction products were analyzed on an LKhM-80 chromatograph (thermal conductivity detector; 2-m column packed with silica gel or 3-m column packed with CaA molecular sieves; carrier gas argon; temperature, °C: columns 80 and detector 150; detector current 120 mA) [13].

Figure 1 shows that the EG conversion increases with temperature on all the catalysts tested, reaching 100% at 350°C (except MoO_3, on which the conversion, though growing with temperature, does not reach 100% even at 400–450°C).

With respect to the product composition, the oxide systems can be subdivided into the following groups: (1) CuO and Cr_2O_3, on which EG is oxidized to CO_2; (2) V_2O_5 and WO_3, on which EG undergoes partial oxidation to formaldehyde, formic acid, methyl formate, and CO; and (3) MoO_3, on which EG undergoes polycondensation to give polyethylene glycols.

Deep oxidation of EG to CO_2 on the first group of

1070-4272/02/7509-1424$27.00 © 2002 MAIK "Nauka/Interperiodica"

oxide catalysts (Cr_2O_3, CuO) is due to the presence on their surface of molecular weakly bonded oxygen responsible for deep oxidation of organic compounds [14]. Figure 2a shows experimental data on the catalytic activity of Cr_2O_3. At low temperatures (~200°C), the EG conversion on Cr_2O_3 is low (~10%), with the main product being formaldehyde. As the temperature is increased to 250°C, the conversion of EG increases to 60%, with formation of CO_2 becoming prevalent. At 300–350°C, the EG conversion reaches 100%.

The low activity of Cr_2O_3 at 200°C may be due to rapid reduction of the catalyst surface to Cr(II) under the action of the reaction medium [15]. Under such conditions, transformation of EG is limited by reoxidation of the surface, and the process attenuates with time. Since the main product of EG conversion on Cr_2O_3 is formaldehyde, the active centers of partial oxidation of EG are, presumably, Cr^{2+} ions [16]. At 350–400°C, the catalyst surface is reoxidized faster, and deep oxidation of EG to CO_2 becomes prevalent (Fig. 2a). The yield of CO passes through a maximum (12%) at approximately 300°C. At higher temperatures, the CO yield decreases to 4%, which may be due to the fact that CO is formed from formaldehyde in a consecutive process; note that the yield of formaldehyde passes through a maximum at 250–300°C.

Figure 2b illustrates the activity of V_2O_5 in EG oxidation. With increasing temperature, the yields of formaldehyde and CO_2 pass through a maximum at 250–300°C. The yield of formic acid decreases with temperature, which is due to its further oxidation to CO_2. The consecutive-parallel reaction pattern includes the initial formation of formaldehyde (by scission of the C–C bond in EG), whose secondary adsorption on the catalyst surface is followed by oxidation to formic acid and CO_2. The yield of CO monotonically increases with temperature, which may be due to thermal decomposition of formaldehyde.

Among all the oxide systems studied, V_2O_5 is the most selective with respect to formation of formaldehyde and formic acid. The yield of HCOOH reaches 10% (Fig. 2b). The major product of EG oxidation at elevated temperatures is CO.

At low temperatures (~200–250°C), up to 5% of glyoxal is formed. The low yield of glyoxal may be due to structural features of EG, which mainly exists in the conformation with an intramolecular hydrogen bond and *cis* location of the hydroxy groups at the C–C bond [16]. In the excited state, the *cis* configuration of glyoxal is the most stable [17]. The distance between the vanadium cations in the V_2O_5 lattice varies from 4.369 (the longest distance, perpendicular

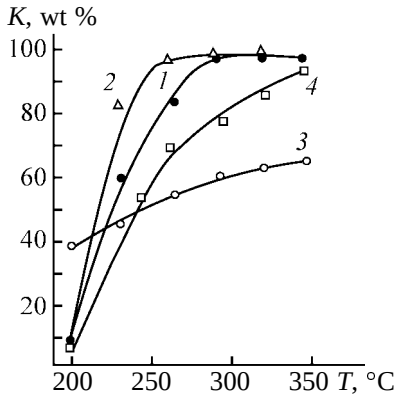

Fig. 1. Temperature dependence of EG conversion *K* in vapor-phase oxidation on oxides: (*1*) Cr_2O_3, (*2*) V_2O_5, (*3*) MoO_3, and (*4*) WO_3.

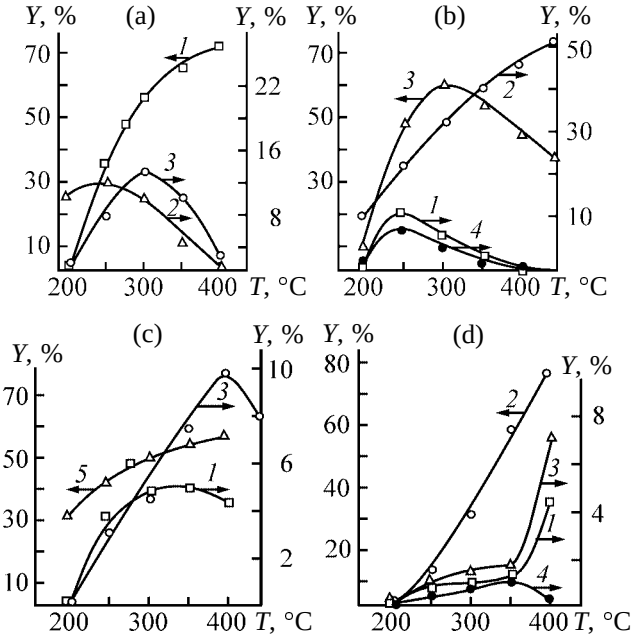

Fig. 2. Oxidation of EG on (a) Cr_2O_3, (b) V_2O_5, (c) MoO_3, and (d) WO_3. (*Y*) Yield and (*T*) temperature. (*1*) CO_2, (*2*) H_2CO, (*3*) CO, (*4*) HCOOH, and (*5*) EG ethers.

to the plane of the bipyramid network layer) to 3.42 Å (along cogged chains formed by distorted VO_4 tetrahedra) [18]. In view of preferableness of EG adsorption on paired centers [19], it can be presumed that, in the precatalysis stage, EG and its carbonyl derivatives are adsorbed via two hydroxy (or aldehyde) groups, extending the C–C bond whose length is 1.54 and 1.47 Å in EG and glyoxal, respectively. Stabilization of the system should involve scission of the C–C bond and formation of formaldehyde as the major product of vapor-phase oxidation of EG.

These assumptions are supported by the fact that the yield of glyoxal decreases with increasing temper-

ature. It is interesting that, at 350–400°C, glycolaldehyde is formed (i.e., only one functional group is oxidized). Dehydration in the course of EG oxidation can be ruled out, since no olefins were detected in the gas phase.

Experimental data on the temperature dependence of the catalytic activity of MoO_3 are shown in Fig. 2c. The major products of EG conversion are di- and triethylene glycols. MoO_3 is less active than the other oxides tested (Fig. 1). The EG conversion at 400°C is as low as 60%. The activity of MoO_3 in partial oxidation of monohydric alcohols (methanol, ethanol) is also low [5, 20], but the selectivity reaches 90%. It is known [21] that WO_3 and MoO_3 effect fast isomerization of 1-butene, which is the model process for determining the surface acidity function. However, the necessary condition for high activity of a catalyst is low strength of oxygen bonding with the catalyst surface, Q_s. In pure MoO_3, on the contrary, Q_s is fairly high. In WO_3, Q_s is somewhat lower but still not optimal for the process [7]. Since etherification involves proton transfer, the strong surface acidity of MoO_3 and WO_3 presumably results in predominant polycondensation of EG to form polyethers.

The activity of WO_3 is illustrated by Fig. 2d. The major products of EG oxidation are formaldehyde and CO. The yield of formic acid passes through a maximum at 300–350°C. Presumably, HCOOH is formed after readsorption of formaldehyde on the catalyst surface. With increasing temperature, the yield of partial oxidation products decreases, and the yield of EG condensation products grows.

CONCLUSIONS

(1) With respect to the activity in partial oxidation of ethylene glycol, oxide catalysts can be ranked in the following order: $V_2O_5 > WO_3 > MoO_3 > Cr_2O_3 > CuO$. The major products are formaldehyde and formic acid.

(2) The low (~5%) yield of glyoxal on V_2O_5 is presumably due to scission of the C–C bond upon adsorption of ethylene glycol on the catalyst surface.

REFERENCES

1. Golodets, G.I., *Probl. Kinet. Katal.*, 1985, vol. 19, pp. 28–58.
2. Margolis, L.Ya., *Geterogennoe kataliticheskoe okislenie uglevodorodov* (Heterogeneous Catalytic Oxidation of Hydrocarbons), Moscow: Khimiya, 1967.
3. Boreskov, G.K., Popov, B.I., Bibin, V.N., and Kozishnikova, E.S., *Kinet. Katal.*, 1968, vol. 9, no. 4, pp. 796–803.
4. Ai, M., *J. Catal.*, 1983, vol. 3, no. 1, pp. 141–150.
5. Allakhverdova, N.Kh., Kerimov, Kh.M., and Alkhazov, T.G., *Kinet. Katal.*, 1992, vol. 33, no. 3, pp. 586–590.
6. Volkov, V.L., Skobeleva, V.D., Buldakova, L.Yu., and Zakharova, G.S., *Zh. Obshch. Khim.*, 1989, vol. 59, no. 10, pp. 2307–2310.
7. Golodets, G.I., *Teor. Eksp. Khim.*, 1982, vol. 18, no. 1, pp. 37–45.
8. Ediseeva, O.N. and Kurina, L.N., *Kinet. Katal.*, 1973, vol. 14, no. 1, pp. 267–270.
9. Kurina, L.N. and Sterligova, T.I., *Kinet. Katal.*, 1972, vol. 13, no. 4, pp. 942–948.
10. Bohmfalk, J.F., *Ind. Eng. Chem.*, 1951, vol. 43, no. 4, pp. 786–794.
11. Ioffe, I.I., Brodskii, M.S., and Tishchenko, A.I., *Metody proizvodstva monomerov* (Methods for Production of Monomers), Moscow: Nauka, 1964, p. 205.
12. Medonos, V., Ruzicka, V., Kalina, Y., and Marnoln, A., *Coll. Czech. Chem. Commun.*, 1968, vol. 33, no. 12, pp. 4393–4395.
13. Vodyankina, O.V. and Galanov, S.I., *Zavod. Lab.*, 1995, no. 8, pp. 12–13.
14. Popovskii, V.V., in *Mekhanizmy geterogenno-kataliticheskikh reaktsii okisleniya* (Mechanisms of Heterogeneous-Catalytic Oxidation Reactions), Novosibirsk: Inst. Kataliza, Sib. Otd. Ross. Akad. Nauk, 1993, pp. 37–48.
15. Kurina, L.N., Koval', L.M., and Kotenko, N.F., *Zh. Fiz. Khim.*, 1975, vol. 49, no. 6, pp. 1494–1497.
16. Strelkova, L.F. and Ginzburg, I.M., *Zh. Obshch. Khim.*, 1986, vol. 56, no. 8, pp. 1884–1887.
17. Le Khyu Kho and Tyulin, V.I., *Zh. Strukt. Khim.*, 1975, vol. 16, no. 1, pp. 63–70.
18. Fotiev, A.A., Glazyrin, M.P., Volkov, V.L., *et al.*, *Issledovaniya kislorodnykh vanadievykh soedinenii* (Studies of Oxygen Compounds of Vanadium), Sverdlovsk: Ural. Otd. Akad. Nauk SSSR, 1970.
19. Vodyankina, O.V., Kurina, L.N., Sudakova, N.N., *et al.*, *Zh. Fiz. Khim.*, 1998, vol. 72, no. 3, pp. 521–524.
20. Osipova, N.A., Kurina, L.N., Belousova, V.N., *et al.*, *Zh. Fiz. Khim.*, 1984, vol. 58, no. 4, pp. 1000–1003.
21. Golodets, G.I. and Roiter, V.A., *Ukr. Khim. Zh.*, 1963, vol. 29, no. 7, pp. 667–685.

Russian Journal of Applied Chemistry, Vol. 75, No. 9, 2002, pp. 1427–1429. Translated from Zhurnal Prikladnoi Khimii, Vol. 75, No. 9, 2002, pp. 1459–1461.
Original Russian Text Copyright © 2002 by Baksanova, Val'tsifer, Budnikov, Kondrashova.

ENVIRONMENTAL PROBLEMS OF CHEMISTRY AND TECHNOLOGY

Gas-Chromatographic Determination of Acrylic Acid in Aqueous Solutions

L. E. Baksanova, V. A. Val'tsifer, V. I. Budnikov, and N. B. Kondrashova

Institute of Technical Chemistry, Ural Division, Russian Academy of Sciences, Perm, Russia

Received April 22, 2002

Abstract—A procedure was developed for determining acrylic acid in aqueous solutions at its concentration within 0.5–20 MPC.

Analysis of water from reservoirs and especially wastewater for the content of microimpurities of harmful substances is a complicated problem, because, first, the substances to be determined have low maximum permissible concentrations (MPC), and, second, the analysis results can be affected by numerous concomitant impurities present in wastewater from both a given enterprise and neighboring plants.

In the past years, the production and consumption of acrylic monomers, polymers, and composites based on them considerably increased; new applications arose, and new countries became involved in the production. Therefore, environmental control of plants producing these substances is an urgent problem.

At the majority of plant laboratories, wastewater is analyzed using unified procedures. However, as the requirements to potable water and to wastewater treatment became more stringent, it appeared necessary to develop advanced analytical procedures with low detection limits for determining impurities of highly toxic substances. Major attention is given to reducing the time required for analysis, since at many plants the composition of natural water and especially wastewater varies with time.

The most widely used procedure for determining trace amounts of organic substances in multicomponent mixtures is gas chromatography. To determine organic pollutants, such methods are recommended as capillary gas chromatography, high-performance liquid chromatography, supercritical fluid chromatography, IR spectroscopy, and exclusion chromatography [1, 2].

Aqueous solutions containing more than 10% organic acids can be, in principle, chromatographed without pretreatment. However, analysis of aqueous solutions of polar compounds such as free acids is complicated by sorption; this is a serious problem not only with traces but even with macroamounts of acids. Gas-chromatographic determination of organic acids is also complicated by their low volatility, requiring the use of high temperatures, close to the limiting working temperatures of the majority of available stationary phases; furthermore, acids tend to associate in the vapor phase. To overcome these difficulties, especially in analysis of trace amounts, acids are converted to more volatile and less polar derivatives, most often to esters [3]. This increases the analysis sensitivity and eliminates interferences caused by adsorption. However, lower acids, in contrast to their higher homologs, cannot be esterified quantitatively.

High-molecular-weight acids can be efficiently recovered and concentrated from sea and ground waters by extraction with organic solvents [4]. Extraction of acids with diethyl ether in the presence of a salting-out agent allows the acid detection limit to be decreased. However, this concentrating procedure is time- and labor-consuming.

All these problems pertain equally to chromatographic determination of traces of acrylic acid (AA) in wastewater.

Traditional methods for preliminary concentration of a sample (sorption on solid adsorbents, extraction followed by solvent evaporation, distillation, headspace analysis) show poor efficiency in concentrating AA from aqueous solutions and do not ensure the required sensitivity of analysis [5–7].

The goal of this work was to develop a simple, reliable, and highly sensitive procedure for determination of AA microimpurities in aqueous solutions.

1070-4272/02/7509-1427$27.00 © 2002 MAIK "Nauka/Interperiodica"

Results of acrylic acid determination (introduced–found, $n = 6$, $P = 0.95$)

Introduced	Found	Confidence range ε	Relative standard deviation S_r
mg l^{-1}			
0.3026	0.2605	0.0472	0.1466
0.5612	0.521	0.0894	0.1382
0.8850	0.781	0.1179	0.1216
1.6413	1.5625	0.1967	0.1014
2.0064	1.953	0.2790	0.1006
2.7756	2.539	0.2720	0.08625
4.9024	5.078	0.3580	0.0568
7.8312	7.5515	0.4714	0.05028
10.316	10.564	0.5302	0.04043

EXPERIMENTAL

Determinations were performed with an LKhM-80 gas chromatograph (flame ionization detector, 100 × 0.3-cm steel column, stationary phase 10 wt % polyethylene glycol on Polysorb-1, 0.025–0.05 cm).

The optimal chromatographing conditions are as follows: column temperature 165°C, vaporizer temperature 190°C, detector temperature 170°C, and carrier gas (nitrogen) flow rate 30 $cm^3\ min^{-1}$. The measured peak areas were recalculated to the electrometer scale of 50×10^{-12} A. To suppress sorption of acrylic acid by the surface of the sorbent and pipelines, the carrier gas was saturated with formic acid vapor [8].

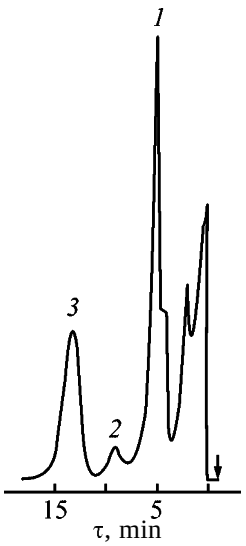

Chromatogram of impurities in wastewater from acrylate production. Packed 1000 × 3-mm steel column; stationary phase polyethylene glycol, 10% on Polysorb-1 (0.25–0.5 mm). (τ) Time. Acid: (*1*) acrylic, (*2*) methacrylic, and (*3*) isovaleric (internal reference).

Acrylic acid was converted to a salt, the salt solution was evaporated to dryness, and the resulting concentrate was subjected to analysis.

Quantitative determination was performed by the graphical method of internal reference. A series of calibrating solutions containing AA in amount of 0.5–20 MPC were prepared from accurately weighed portions of chemically pure grade AA by successive dilution. As internal reference we chose isovaleric acid. With this method, it is not necessary to strictly reproduce the dosage; furthermore, the components of a mixture to be analyzed can be determined irrespective of the presence or absence of other peaks in the chromatogram.

The analytical procedure was as follows. A sample, after adding a known amount of the reference and converting acrylic and isovaleric acids into salts with an alkali (phenolphthalein indicator), was evaporated to dryness in a porcelain cup. The dry residue was dissolved in 1 ml of 0.5 M HCl. The solution was transferred in a volumetric vessel, and a 5-μl sample was injected into a chromatograph. The AA concentration in the sample was determined from the calibration function. Solutions were evaporated on a water bath or, for quicker analysis, on a glycerol bath at 120°C. Experiments were performed in the presence of butyl acrylate and butanol, which may be present in amounts of up to 20 MPC in the wastewater being analyzed. We found that, in the presence of alkali, butyl acrylate was hydrolyzed to 1-butanol and AA. 1-Butanol in amounts of up to 20 MPC does not interfere with the chromatographic analysis by our procedure, as it fully volatilizes in the course of evaporation. We also found that, under the analysis conditions, butyl acrylate, when present in wastewater in amounts of up to 100 MPC, does not interfere with the determination of AA because of the low (<10%) degree of its hydrolysis and partial volatilization during evaporation.

The results of analysis of artificial mixtures (introduced–found, see table) demonstrate the feasibility of determining AA in aqueous solutions in the range 0.5–20 MPC. The relative error of the chromatographic determination for the ranges 0.5–5, 5–10, and 10–20 MPC is 17, 10, and 7%, respectively. The analysis time, including the concentration stage, does not exceed 2 h.

The proposed procedure for AA determination in aqueous solutions was tested with real wastewater samples from acrylate production (see figure). In

chromatographic analysis of impurities in wastewater, major attention should be given to their identification, since identification of microamounts by the retention parameters is not always reliable, especially when a sample contains substances of different classes. In our procedure, identification was based on comparing, under the same conditions, the retention times of particular substances which were added to the solution both separately and as model mixtures. This is associated with the fact that the retention times of the acids appeared to be strongly dependent on the substance amount in the sample.

CONCLUSION

The procedure developed for analysis of natural water and wastewater is suitable for assessing the efficiency of wastewater treatment facilities at plants producing acrylic polymers, for revealing discharge sources, and for evaluating their impact on water reservoirs. The sample preparation procedure is simple, and the analysis is performed with equipment series-produced in Russia.

REFERENCES

1. Rudenko, B.A., *Partn. Konkur.*, 2000, no. 12, pp. 32–39.
2. Yashin, Ya.I. and Yashin, A.Ya., *Zh. Anal. Khim.*, 1999, vol. 54, no. 9, pp. 949–956.
3. *MUK* (Methodical Instructions) *4.1.616–96: Determination of Concentrations of Chemical Substances in Household Potable Water of Centralized Supply*, Moscow: Minzdrav Rossii, 1997.
4. Ushakova, V.A. and Rzhavskaya, F.M., *Gigiena Sanit.*, 1987, no. 3, pp. 69–70.
5. Dmitriev, M.T. and Komrakova, E.A., *Gigiena Sanit.*, 1986, no. 2, pp. 44–45.
6. Sukharev, Yu.G. and Litvinov, N.R., *Plast. Massy*, 1986, no. 2, pp. 45–46.
7. Dmitriev, M.T. and Komrakova, E.A., *Gigiena Sanit.*, 1986, no. 1, pp. 32–33.
8. Komrakova, E.A., in *Gigiena truda i okhrana okruzhayushchei sredy v khimicheskoi promyshlennosti: Sbornik nauchnykh trudov* (Professional Hygiene and Environmental Protection in Chemical Industry: Coll. of Scientific Works), Nizhni Novgorod: Nauchno-Issled. Inst. Gigieny Truda i Profzabolevanii, 1991, pp. 126–130.

Russian Journal of Applied Chemistry, Vol. 75, No. 9, 2002, pp. 1430–1433. Translated from Zhurnal Prikladnoi Khimii, Vol. 75, No. 9, 2002, pp. 1462–1465.
Original Russian Text Copyright © 2002 by Zakharov, Mukhametzyanova, Takhavutdinov, D'yakonov, Minsker.

PROCESSES AND EQUIPMENT OF CHEMICAL INDUSTRY

Preparation of Homogeneous Emulsions in Tubular Turbulent Apparatus of Diffuser–Confuser Design

V. P. Zakharov, A. G. Mukhametzyanova, R. G. Takhavutdinov, G. S. D'yakonov, and K. S. Minsker

Baskir State University, Ufa, Bashkortostan, Russia
Kazan State Technological University, Kazan, Tatarstan, Russia

Received October 23, 2001; in final form, March 2002

Abstract—Changing the design of small-size tubular turbulent apparatus of diffuser–confuser design and the hydrodynamic mode of moving dispersed flows allows effective control over the quality of emulsions obtained from two immiscible fluids.

There are a great number of heterophase processes occurring under phase-separation conditions in a fluid–fluid system. To these belong, in particular, sulfation of α-olefins with sulfuric acid in an organic solvent, emulsion (co)polymerization of divinyl with α-methylstyrene, decomposition and washing of electrophilic catalysts and Ziegler–Natta catalytic systems in synthesis of stereoregular isoprene and divinyl rubbers, sulfuric acid alkylation of isoparaffins with olefins, etc. [1]. A specific feature of heterophase processes is the necessity for substance (reagent) transfer from one phase into another, with the efficiency of the process as a whole and quality of the products obtained depending on the specific surface area of phase contact, F [2, 3]. The mass transfer is complicated in systems in which rather fast chemical reactions occur (characteristic time of chemical reaction $\tau_{ch} < 0.01–0.001$ s). In this case, one of the most effective ways to form heterophase disperse systems fluid–fluid with developed phase boundary is intensification of the degree of turbulence in the flow mixing zone, which, simultaneously, much intensifies the chemical process. For example, in the case of α-olefin sulfation with concentrated sulfuric acid in a solution of a saturated hydrocarbon, the reaction mixture stratifies because of the significant difference in density and viscosity between the flows of the starting reagents ($\rho_{H_2SO_4} : \rho_{\alpha\text{-olefin}} = 2.63$; $\eta_{H_2SO_4} : \eta_{\alpha\text{-olefin}} = 75.1$) in their introduction into an apparatus in classical volume stirred or plug-flow reactors. This leads to a dramatic decrease in the phase contact area and retards the chemical reaction, despite that this reaction can be classed with fast chemical processes [1]. In this case, an increase in the degree of turbulent mixing in the reaction zone makes the chemical reaction faster (Fig. 1) and, correspondingly, allows shorter residence time of the reactants in the reactor, τ_r. As a result, the yield of the target products, monoalkyl sulfates, increases and the contribution of side processes yielding undesirable dialkyl sulfates decreases.

Thus, of primary importance in performing fast heterophase chemical reactions is preparation of homogeneous finely dispersed emulsions with developed phase contact surface. According to [4], the best results are obtained with small-size tubular turbulent apparatus with local hydrodynamic resistances of the diffuser–confuser design because of the possibility of attaining in this case a strongly turbulent mode at moderate fluid flow rates.

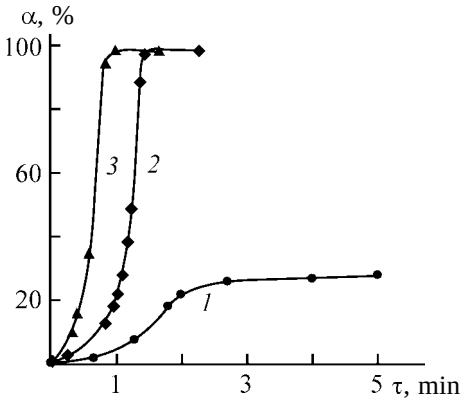

Fig. 1. Conversion curves for sulfation of α-olefins of the $C_8–C_{16}$ fraction (~97 wt %) with concentrated (~95 wt %) sulfuric acid in volume well-stirred apparatus. α-Olefins/H_2SO_4 = 3.9 (v : v), T = 298 K. (α) Conversion and (τ) time. Stirring rate (rpm): (*1*) 100, (*2*) 500, and (*3*) 1000.

1070-4272/02/7509-1430$27.00 © 2002 MAIK "Nauka/Interperiodica"

The aim of this study was to analyze experimentally the fundamental aspects of emulsion formation from two immiscible fluid flows in tubular turbulent apparatus of the diffuser–confuser design with varied channel geometry.

For this purpose, an experimental setup was assembled, shown schematically in Fig. 2. We used glass six-section (N_s = 6) tubular turbulent apparatus of the diffuser–confuser design [4] with varied geometry of the stirring mode (see table).

The frequency curves of the size distribution of drops of the dispersed phase were obtained by video recording in high-intensity transmitted light with a Hitachi VM2980E video camera (12/1 focus). Rapid video recording minimizes the influence exerted by drop image smearing because of the high drop motion velocity. To account for image distortions because of the curved shape of the apparatus casing, zinc-plated calibration threads of a known diameter (0.2, 0.5, and 1 mm) were introduced into the apparatus volume [5]. The calculations performed were based on the central part of the apparatus cross section with dimensions $0.74 \times d_d$, in which the discrepancy between the real dimensions of the calibration threads and their values calculated from the images obtained was less than 1%. This technique also ruled out image distortion associated with the influence exerted by the refractive index of the glass casing of the apparatus and took into account systematic errors. Since rather small volumes of the dispersed phase were used [flow rate of the dispersed phase was 1–1.5 ml s^{-1}, and that of the dispersion medium (V), 40–200 ml s^{-1}], images of all particles in the flow cross section were obtained.

A frame-by-frame inspection of a computer-synthesized image of moving dispersed systems (24 frames per second) with tenfold magnification, with linear dimensions of particles of the dispersed phase (all particles were spherical in the chosen range of flow rates) compared with the linear size of the calibration threads, allows calculation of the true drop size (or, more precisely, the projection area of a spherical drop). The drops were counted in the following ranges (mm): 0–0.4, 0.4–0.6, 0.6–0.8, 0.8–1.0, 1.0–1.5, 1.5–2.0, and more than 2. To estimate the experimental error, eight images of some part of the flow were chosen. The experimental data obtained were used to evaluate the distribution variance s^2:

$$s^2 = (N - 1)^{-1} \sum_{1}^{N} (d_i - d)^2, \quad (1)$$

where N is the number of measurements, d_i is the drop diameter in a chosen interval, and d is the average drop diameter.

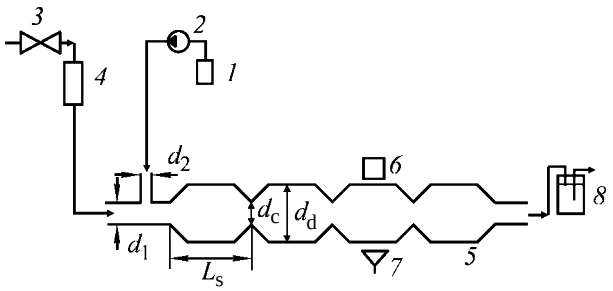

Fig. 2. Schematic of the experimental setup: (*1*) vessel for the dispersed phase (hexane, ρ = 0.66 g cm^{-3}, η = 0.3 mPa s), (*2*) peristaltic pump, (*3*) feed line for delivery of the dispersion medium (water), (*4*) rotameter, (*5*) tubular turbulent apparatus of the diffuser-confuser design (d_1 = 10 mm, d_2 = 5 mm), (*6*) video camera, (*7*) light source, and (*8*) receiver.

The standard error Δ at confidence probability α = 0.95 was calculated as $\Delta = \pm 2.4 s N^{-1/2}$. The average measurement error was ±7%.

The dispersion process in a fluid–fluid system in turbulent flows for the hydrodynamic operation mode of tubular apparatus of the diffuser–confuser design can be conveniently described using the volume–surface diameter of drops of the dispersed phase, d_{32} [6]:

$$d_{32} = \frac{\sum m_i d_i^3}{\sum m_i d_i^2}, \quad (2)$$

related to the specific surface area F of the spherical particles of the dispersed phase by

$$F = \frac{6}{d_{32}} = \frac{6 \sum m_i d_i^2}{\sum m_i d_i^3}, \quad (3)$$

where m_i is the number of drops of ith fraction, and d_i is the drop diameter in ith fraction.

Characteristics of diffuser–confuser apparatus* (d_d = 24 mm)

Apparatus no.	d_c, mm	d_d/d_c	L_s, mm	L_s/d_d
1	15	1.6	48	2
2	12	2	48	2
3	8	3	48	2
4	15	1.6	72	3

* d_d and d_c are the diameters of, respectively, the diffuser and confuser parts of the apparatus; L_s is the length of the diffuser–confuser section.

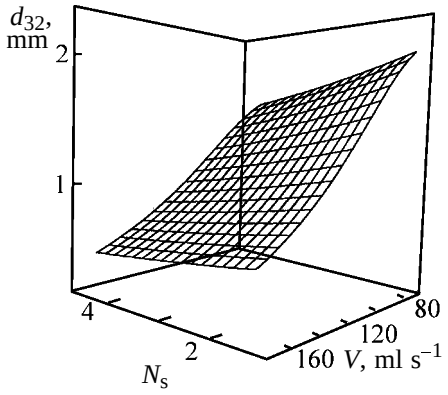

Fig. 3. d_{32} vs. flow rate V of a heterophase flow and number N_s of diffuser–confuser sections for apparatus no. 1 (see table).

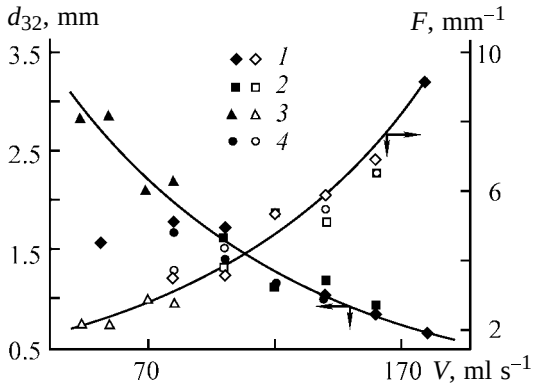

Fig. 4. Variation of the volume–surface diameter d_{32} of particles in the dispersed phase and the specific phase boundary surface area F with the design of a tubular turbulent apparatus and flow rate. (*1–4*) Apparatus nos. (see table). Points, experimental data; lines, calculation by Eqs. (3) for F and (5) for d_{32}.

As in the case of small-size tubular turbulent apparatus of the cylindrical design ($d_d/d_c = 1$, $L/d_d \approx 40$) [4], the size distribution of drops in the dispersed phase in the diffuser–confuser channels becomes narrower with increasing flow rate V of immiscible fluid flows, and the curves are shifted to the region in which homogeneous finely dispersed systems are formed [7, 8].

On the basis of experimental data, we obtained equations relating the efficiency of emulsification (percentage n of drops with diameter $d \le 0.8$ mm in the dispersed phase) in tubular channels of the diffuser–confuser design to the flow rate V of the flows (R is the correlation coefficient):

$$\begin{aligned} n &= 0.78V - 51.0 \quad \text{(apparatus no 1, } R = 0.96\text{)},\\ n &= 0.88V - 58.2 \quad \text{(apparatus no 2, } R = 0.98\text{)},\\ n &= 0.90V - 30.1 \quad \text{(apparatus no 3, } R = 0.99\text{)},\\ n &= 0.72V - 35.6 \quad \text{(apparatus no 4, } R = 0.97\text{)}. \end{aligned} \tag{4}$$

Raising the flow rate V of the flows and the number of diffuser–confuser sections N_s from 1 to 4 makes the volume–surface diameter of drops smaller and the specific interface area, correspondingly, larger (Fig. 3). This, in the case of fast chemical reactions, intensifies the chemical process as a whole. The inexpedience of using tubular turbulent apparatus with number N_s of diffuser–confuser sections exceeding 4 makes these devices compact (with length not exceeding 8–10 diameters: $L/d_d \le 8$–10) and simple in fabrication and operation.

Figure 4 presents the dependence of d_{32} on the flow rate of heterophase flows in diffuser–confuser channels of varied design. Statistical processing of the experimental data obtained for $d_d = 24$ mm yielded an equation approximating this dependence:

$$d_{32} = 4.74\,e^{-0.011V}. \tag{5}$$

Comparison of the experimentally obtained data with the calculated values shows (Fig. 4) that relation (5) describes with satisfactory accuracy the influence exerted by V on the particle size d_{32} in the dispersed phase (average deviation 6%). At the same time, there exists a certain range of rates of heterophase flows to which corresponds a diffuser–confuser channel with the optimal d_d/d_c ratio. This range is bounded by the zone of stratified flow [9] from below, and by energy loss associated with increasing pressure drop at apparatus ends in accordance with the relation $\Delta p \sim V^2$, from above. In particular, the interval $44 < V < 80$ ml s^{-1} corresponds to the ratio $d_d/d_c = 3$, and $80 < V < 180$ ml s^{-1}, to $d_d/d_c = 1.6$. Apparently, further increase in the flow rate of the dispersed system ($V > 180$ ml s^{-1}) makes necessary further decrease in the d_d/d_c ratio (Fig. 4), down to $d_d/d_c = 1$, in which case small-size tubular apparatus of cylindrical design are rather effective. The same restrictions govern the boundary conditions of applicability of the dependences (4). In accordance with Eq. (3), a characteristic change in the specific phase boundary surface area is observed (Fig. 4), which determines the intensity of the mass-exchange process.

Thus, in tubular turbulent apparatus of the diffuser–confuser design, as compared with apparatus with cylindrical channels, a flow in which particles of the dispersed phase are uniformly distributed over the apparatus volume is formed at lower flow rates of the dispersed system, and the decrease in the required V value is the greater, the larger the d_d/d_c ratio.

Another important quantity characterizing the quality of the emulsions obtained is the polydispersity

factor k [10]:

$$k = \frac{\sum m_i d_i^3 \sum m_i d_i}{\sum m_i d_i^4 \sum m_i}. \quad (6)$$

For monodisperse systems $k = 1$, and for polydisperse systems $k < 1$, with the parameter k being the smaller, the wider the scatter of the particle sizes. As also in the case when dispersions with volume–surface diameter d_{32} are obtained (Fig. 4), the L_s/d_d ratio has virtually no effect on the polydispersity of the emulsions obtained. With increasing d_d/d_c ratio, the scatter of particle size in the dispersed phase becomes more pronounced, with rather homogeneous emulsions formed in the diffuser–confuser channel of a tubular apparatus with $d_d/d_c = 1.6$. In particular, for L_s/d_d = 2–3, the k value is 0.72–0.75 at $d_d/d_c = 1.6$ and decreases to 0.63 and 0.41 at d_d/d_c ratios equal to, respectively, 2 and 3.

Thus, use of small-size tubular turbulent apparatus of the diffuser–confuser design allows effective dispersion in fluid–fluid systems and makes it really possible to increase the specific surface area of spherical particles belonging to the dispersed phase. Varying the flow rate V of fluid flows in tubular apparatus and the d_d/d_c ratio is virtually the only, but quite effective way to affect the nature of the dispersion process and the quality of the emulsions obtained. This enables easy control over rather fast heterophase chemical and mass-exchange physical processes occurring in emulsions. The relationships revealed make it possible to obtain, when necessary, fine homogeneous dispersions in the fluid–fluid systems without any technical difficulty and to use small-size tubular turbulent apparatus of simple diffuser–confuser design for intensifying the chemical and mass-exchange physical processes. This can be done, in the first place, because of the formation of finely dispersed emulsions under the optimal conditions at a minimum time of reactant residence in the mixing zone. Tubular turbulent apparatus of the diffuser–confuser design can be recommended for industrial use both as a basic reactor for performing fast heterogeneous chemical reactions and as a prereactor for formation of fine homogeneous emulsions and their subsequent delivery in volume stirred vessels. This technology will apparently be able to diminish the time necessary for heterophase processes to occur in fluid–fluid systems.

CONCLUSIONS

(1) Raising the flow rate of a dispersed system and the number of diffuser-confuser sections from 1 to 4 leads to an increase in the specific interface area in tubular turbulent apparatus, which allows use of mixers with length equal to 8–10 diameters.

(2) Raising the d_d/d_c ratio in tubular turbulent apparatus of the diffuser–confuser design makes lower the flow rate of the dispersed system, necessary for obtaining a flow with uniform distribution of the dispersed phase. In this case, the polydispersity of the forming emulsions is higher at comparable output capacities of the apparatus, all other conditions being the same.

(3) Emulsions with comparable specific interface areas F and polydispersities k are formed in tubular turbulent apparatus at L_s/d_d = 2–3.

REFERENCES

1. Berlin, Al.Al., Minsker, K.S., and Dyumaev, K.M., *Novye unifitsirovannye energo- i resursosberegayushchie vysokoproizvoditel'nye tekhnologii povyshennoi ekologicheskoi chistoty na osnove trubchatykh turbulentnykh reaktorov* (New Unified Energy- and Resource-Saving High-Output-Capacity Technologies of Enhanced Environmental Safety, Based on Tubular Turbulent Reactors), Moscow: NIITEKhIM, 1996.
2. Lebedev, N.N., Manakov, M.I., and Shvets, V.F., *Teoriya tekhnologicheskikh protsessov osnovnogo organicheskogo i neftekhimicheskogo sinteza* (Theory of Processes of Basic Organic and Petrochemical Synthesis), Moscow: Khimiya, 1975.
3. Ivanets, V.N., Al'brekht, S.N., and Ivanets, G.E., *Zh. Prikl. Khim.*, 2001, vol. 74, no. 3, pp. 451–455.
4. Minsker, K.S., Zakharov, V.P., and Berlin, Al.Al., *Teor. Osn. Khim. Tekhnol.*, 2001, vol. 35, no. 2, pp. 172–177.
5. Ramm, V.A., *Absorbtsiya gazov* (Absorption of Gases), Moscow: Khimiya, 1976.
6. Blaznov, A.N., Kunichan, V.A., and Chashchilov, D.V., *Zh. Prikl. Khim.*, 2001, vol. 74, no. 4, pp. 621–624.
7. Krekhova, M.G., Minsker, S.K., Prochukhan, Yu.A., and Minsker, K.S., *Teor. Osn. Khim. Tekhnol.*, 1994, vol. 28, no. 3, pp. 271–273.
8. Krekhova, M.G., Minsker, S.K., and Minsker, K.S., *Teor. Osn. Khim. Tekhnol.*, 1995, vol. 29, no. 5, pp. 496–499.
9. Nadler, M. and Mewes, D., *Int. J. Multiphase Flow*, 1997, vol. 23, no. 1, pp. 55–68.
10. Shchukin, E.D., Pertsov, A.V., and Amelina, E.A., *Kolloidnaya khimiya* (Colloid Chemistry), Moscow: Mosk. Gos. Univ., 1982.

Russian Journal of Applied Chemistry, Vol. 75, No. 9, 2002, pp. 1434–1437. Translated from Zhurnal Prikladnoi Khimii, Vol. 75, No. 9, 2002, pp. 1466–1469.
Original Russian Text Copyright © 2002 by Koshchii.

ORGANIC SYNTHESIS AND INDUSTRIAL ORGANIC CHEMISTRY

Optimization of Synthesis of Mono-*O*-methylglycerol Isomers

S. V. Koshchii

Institute of Problems of Cryobiology and Cryomedicine, National Academy of Sciences of Ukraine, Kharkov, Ukraine

Received January 23, 2002

Abstract—Parameters were refined for synthesis of glycerol 1-monomethyl ether by methylation of glycerol with dimethyl sulfate in the presence of alkali; a gas–liquid chromatographic procedure was proposed for identification of structural isomers of mono-*O*-methylglycerol.

Procedures for preparing glycerol 1-monomethyl ether (1-MG) are diverse and are summarized in reviews [1–4]. These procedures give relatively low (compared to other glycerol monoalkyl ethers) yield of the target product, are multistage, and require large (up to tenfold) excess of methanol and sodium metal [5, 6]. Only Fairbaurne [7] reported on preparation of noticeable amounts of the second isomer, glycerol 2-monomethyl ether (2-MG), with the major product being 1-MG.

Glycerol monomethyl ether is a promising cryoprotector in low-temperature preservation of blood cells, bone marrow, and reinoculated cell cultures [8, 9]. In view of the necessity of producing pilot batches of 1-MG for large-scale biological tests and with the aim to reveal the effect of isomerism on the cryoprotective properties, we performed experiments to refine the conditions for preparing 1-MG and 2-MG. Our goal was to find the method and conditions ensuring the highest yield of the target products, with the procedure being as simple as possible. As the route to 1-MG and 2-MG, we chose methylation of glycerol with dimethyl sulfate (DMST) in the presence of alkali. Fairbaurne [7] reported on synthesis of sodium glycerate from excess glycerol and aqueous NaOH; its methylation with DMST, after removing water under reduced pressure, yielded a mixture of 1-MG and 2-MG. Cross and Jacobs [5] reported on another convenient procedure involving preparation of sodium glycerate from equimolar amounts of anhydrous glycerol and powdered NaOH, followed by alkylation with alkyl halides to obtain glycerol 1-monoalkyl ethers. It seemed appropriate to refine the effect of the synthesis parameters (molar ratio of components, concentration of aqueous alkali) on the yield and isomeric composition of the product. To this end, we tested several procedures based on Fairbaurne's method [7] (Table 1).

EXPERIMENTAL

Run no. 1. Synthesis of 1-MG and 2-MG involved the following stages [7]: (1) mixing of glycerol with 47% aqueous NaOH in the molar ratio glycerol : NaOH = 3 : 1; (2) distillation of water under reduced pressure (40 mm Hg) on an oil bath, with the bath temperature gradually increased to 150°C; (3) addition of DMST to the resulting sodium glycerate (GONa) at 120–125°C over a period of 1 h in the molar ratio GONa : DMST = 1 : 0.5; (4) removal of Na_2SO_4 from the reaction mixture; (5) distillation of a mixture of 1-MG and 2-MG from the bottoms at 140°C/2 mm Hg; and (6) separation of 1-MG and 2-MG by repeated vacuum distillation on a column with cutting 1°C fractions in the range 91–140°C/2 mm Hg. The total yield of the isomers was 45%, with the isomer ratio 1-MG : 2-MG = 6 : 1.

Run no. 2 was performed similarly to run no. 1, except that NaOH was taken as 69% solution (instead of 47% solution) to reduce the time for water distillation under reduced pressure. The total yield of the isomers was 41%, with the isomer ratio 1-MG : 2-MG = 8 : 1.

Run no. 3. Sodium glycerate was prepared as described in [5] by heating anhydrous glycerol and powdered NaOH with vigorous stirring, with the molar ratio glycerol : NaOH = 2 : 1. The temperature in the oil bath was raised to 120–145°C. After removal of water, the temperature was decreased to 110–115°C, with the stirring continued, and 0.5 mol of DMST was added dropwise. The resulting Na_2SO_4 was filtered off. After distillation of the bottoms in a vacuum

1070-4272/02/7509-1434$27.00 © 2002 MAIK "Nauka/Interperiodica"

Table 1. Ratio of reactants and reaction products in methylation of glycerol with DMST in the presence of NaOH

Molar ratio of reactants				Total yield of isomers, %	1-MG : 2-MG ratio
glycerol	NaOH	DMST	H_2O		
3	1	0.5	2.5	45	6 : 1
3	1	0.5	1	41	8 : 1
2	1	0.5	–	33	10 : 1
3	1	0.5	–	63	15 : 1

(up to 140°C/5 mm Hg) and repeated fractionation, 1-MG and 2-MG were obtained in a 10 : 1 ratio; total yield 33%.

Run no. 4. The procedure ensuring the highest content of 1-MG was as follows. A three-necked flask equipped with a stirrer and a thermometer and purged with an inert gas was charged with equimolar amounts of purified anhydrous glycerol and powdered NaOH. The mixture was heated to 145°C with continuous vigorous stirring. At 120°C, release of water formed in the synthesis started, and the mixture warmed up to 145°C with foaming. After short stirring at this temperature, a uniform paste formed. The temperature was decreased to 90°C, and, with the stirring continued, anhydrous glycerol was added over a period of 30 min to dissolve the resulting sodium glycerate; the final molar ratio glycerol : NaOH was 3 : 1. Then, 0.5 mol (relative to NaOH) of DMST was added from a dropping funnel, with the temperature maintained within 90–100°C. In the course of reaction, white fumes liberated, the mixture slightly warmed up, and Na_2SO_4 precipitated. The precipitate was filtered off. 1-MG was isolated by vacuum distillation at 92–93.5°C/5 mm Hg; yield 59%. Along with 1-MG, a small (3–5%) amount of 2-MG was obtained.

Run no. 5. 1-MG was prepared by an independent procedure: reaction of glycerol 1-monochlorohydrin (1-MCHG) with sodium methylate in a tenfold excess of absolute methanol [6]. The synthesis involved the following stages: (1) preparation of sodium methylate; (2) reaction of 1-MCHG with sodium methylate; (3) filtration to remove the NaCl precipitate; (4) distillation of excess methanol under reduced pressure; and (5) isolation of 1-MG. Yield 42%. The necessity of performing this labor-consuming and fire-hazardous procedure was dictated by the need in obtaining a 1-MG sample free of its isomer, 2-MG. The sample was used for identification of structural isomers of glycerol monomethyl ether.

The structures of the products were confirmed by molecular refraction and IR spectroscopy. The spectra are discussed in detail in [10]. The refractive index n_D^{20} was determined with a URL-M1 refractometer. The IR spectra were recorded on a Specord 75-IR spectrophotometer (thin film between KBr plates).

The molecular weight of 1-MG and 2-MG was determined by gel permeation chromatography on a Waters GPC-200-1 Model 200 gel chromatograph under the following conditions: eluent tetrahydrofuran; three styrogel columns 200, 500, and 1000 Å; 25°C; flow rate 1.2 ml min^{-1}. Samples (2 ml) contained about 0.2 wt % of the substance. The product purity was checked by GLC (LKhM-80 chromatograph, 1000 × 3-mm column, stationary phase 20% Carbowax 20M on Chromaton N-Super, flame ionization detector, carrier gas He, flow rate 50 ml min^{-1}, programmed column heating from 60 to 280°C). A 0.1-g sample was dissolved in 0.2 ml of purified anhydrous pyridine, and 0.4 ml of hexamethyldisilazane and 0.1 ml of trimethylchlorosilane were added. The mixture was allowed to stand for 2–3 h and then injected into the chromatograph vaporizer. The main constants of the products are listed in Table 2 together with published data.

The IR spectra contain the following characteristic absorption bands (cm^{-1}): 3385, 3395 (OH); 2928, 1465 (CH_2); 2830 (OCH_3); 1360 (CH_3); 1190 (COC).

The isomers are difficult to separate and identify, as their have close physicochemical parameters (except n_D^{20}) and similar IR spectra. In the gel chromatogram, both compounds give a narrow symmetrical peak with the same retention volume V_R corresponding to M 106. Their separation by vacuum distillation requires repeated thorough fractionation with collection of close-cut (1–2°C) fractions; the isomer percentage in the fractions gradually changes with increasing temperature. Fairbaurne [7] suggested to identify isomers by refractive indices. However, examination using an LKhM-80 chromatograph and the procedure developed in [12] showed that, even at the same n_D^{20}, samples may contain 1-MG and 2-MG in

Table 2. Physicochemical characteristics of 1-MG and 2-MG at 25°C (molecular weight of 1-MG and 2-MG 106)

Compound*	bp, °C/*p*, mm Hg	n_D^{20}	d_4^{20}	Molecular refraction	
				experimental	calculated
1-MG	92–95/5	1.4444	1.1169	25.23	25.37
		1.4445 [11]	1.1163 [11]	25.28	25.37
2-MG	109–110/4	1.4480	1.1311	25.12	25.37
		1.4456 [7]	1.124 [7]	25.16	25.37

* Structural formulas: 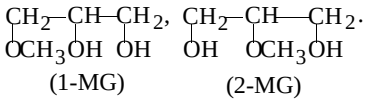

Table 3. Results of GLC analysis of 1-MG–2-MG fractions from run no. 1

Fraction	bp, °C	n_D^{20}	Content, %		Impurities, %
			1-MG	2-MG	
I	92–93.5	1.4444	99.9	–	0.1
II	93.5–95	1.4444	96.1	3.4	0.5
III	95–97	1.4444	83.6	16.4	–
IV	97–99	1.4446	57.0	43.0	–
V	99–101	1.4450	57.9	45.1	–
VI	101–104	1.4454	22.4	77.6	–
VII	104–106	1.4464	20.8	79.2	–
VIII	106–108	1.4476	19.1	80.9	–
IX	108–109	1.4478	18.4	80.3	1.3
X	109–110	1.4480	–	99.0	1.0

different ratios. The chromatograms contain two major narrow symmetrical peaks. The isomer ratio was evaluated from the peak areas. The scheme of fractionation of structural isomers obtained in run no. 1 is given in Table 3.

Table 3 shows that the first three fractions have the same refractive index, n_D^{20} = 1.4444, but differ in the isomeric composition by up to 15%. The refractive index of fraction IV is very close, n_D^{20} = 1.4446, at the isomer ratio 1-MEG : 2-MEG = 57 : 43. Comparison of these data shows that the refractive index n_D^{20} is unsuitable for identifying 1-MG and 2-MG in synthesis of glycerol methyl ethers by methylation of glycerol with DMST in the presence of aqueous alkali (run nos. 1, 2). Run nos. 1–4 show that variation of the reactant ratio (Table 1) and the use of aqueous alkali as solvent result in formation of products containing different ratios of 1-MG and 2-MG. The highest content of 1-MG was obtained in run no. 4. Heating of glycerol with equimolar amount of powdered NaOH, followed by addition of excess glycerol (to the ratio glycerol : NaOH = 3 : 1) to dissolve the resulting sodium glycerate ensure increased yield of 1-MG (59%). Excess glycerol (run no. 3) complicates fast removal of water from sodium glycerate, which is hygroscopic and moisture-sensitive [5]. It is also known that prolonged heating of glycerol in the presence of alkali favors formation of polyglycerol [13]. Apparently, these facts are responsible for the low yield of 1-MG in run no. 3. The synthesis under conditions of run no. 4 is simpler, because no water is added (cf. run nos. 1, 2) and hence the stage of water removal under reduced pressure after the completion of sodium glycerate formation and before isolation of 1-MG is eliminated. Furthermore, under conditions of run no. 4 the by-product 2-MG is formed in a small amount and does not appreciably complicate isolation of 1-MG.

At the same time, if 2-MG is the target product, the conditions of run no. 1 are preferable. The use of water as solvent in the reaction of glycerol with aqueous alkali favors formation of appreciable amount of

2-MG along with 1-MG. As the water content in the NaOH solution is decreased from 63 (run no. 1) to 31% (run no. 2), the content of 2-MG decreases (Table 1), and with anhydrous glycerol and dry NaOH (run no. 4) it becomes as low as 3%. More dilute NaOH solutions were not tested because of more difficult isolation of the reaction product.

CONCLUSIONS

(1) The procedure for preparing glycerol 1-monomethyl ether by methylation of glycerol with dimethyl sulfate in the presence of NaOH was optimized by varying the reactant ratio; the yield of the target product was increased to 59%, and the isolation procedure was simplified.

(2) The highest yield of glycerol 2-monomethyl ether is attained when methylation of glycerol with dimethyl sulfate is performed using 47% NaOH.

REFERENCES

1. Edgar, S., *Manuf. Chem. Aeros. News*, 1981, vol. 52, no. 10, pp. 63–65.
2. Fairbaurne, A., Gibson, G., and Stephens, D., *Chem. Ind.*, 1930, vol. 49, pp. 1021–1023.
3. Malinovskii, M.S. and Vedenskii, V.M., *Zh. Obshch. Khim.*, 1953, vol. 23, no. 2, pp. 219–221.
4. Koshchii, S.V., Lugovoi, V.I., and Kompaniets, A.M., *Probl. Kriobiol.*, 1999, no. 3, pp. 46–53.
5. Cross, C.F. and Jacobs, J.M., *J. Soc. Chem. Ind.*, vol. 3020, no. 10, pp. 1026–1030.
6. Kimsanov, B.Kh. and Ishanova, Kh.Kh., *Izv. Akad. Nauk Tadzh. SSR, Otd. Fiz.-Mat., Khim. Geol. Nauk*, 1981, no. 2, pp. 102–104.
7. Fairbaurne, A., *J. Chem. Soc.*, 1931, pp. 445–458.
8. USSR Inventor's Certificate no. 1298203.
9. Shuaff-Werner, P. and Miler, U., *Cryobiology*, 1988, vol. 25, pp. 487–491.
10. Atovmyan, E.G., Koshchii, S.V., and Fedotova, T.N., *Zh. Prikl. Spektrosk.*, 1988, vol. 48, no. 2, pp. 287–290.
11. Eremenko, L.T. and Korolev, A.M., *Izv. Akad. Nauk SSSR*, 1977, no. 2, pp. 285–288.
12. Ukrainian Patent 33887A.
13. Allaberdiev, Kh. and Kovan'ko, Yu.A., *Zh. Prikl. Khim.*, 1987, vol. 60, no. 6, pp. 1327–1331.

Russian Journal of Applied Chemistry, Vol. 75, No. 9, 2002, pp. 1438–1440. Translated from Zhurnal Prikladnoi Khimii, Vol. 75, No. 9, 2002, pp. 1470–1472.
Original Russian Text Copyright © 2002 by Islamgulova, Shitova, Akhmerova, Tomilov.

ORGANIC SYNTHESIS AND INDUSTRIAL ORGANIC CHEMISTRY

Improvement of a Process for Synthesis of Thioglycolic Acid

V. R. Islamgulova, E. N. Shitova, S. G. Akhmerova, and A. P. Tomilov

Research and Technological Institute of Herbicides and Plant Growth Regulators with Pilot Plant, Ufa, Bashkortostan, Russia

State Research Institute of Organic Chemistry and Technology, Moscow, Russia

Received November 26, 2001; in final form, June 2002

Abstract—An environmentally clean process was proposed for synthesis of thioglycolic acid by condensation of monochloroacetic acid with sodium disulfide, followed by electrochemical reduction of the resulting mixture.

Thioglycolic acid (TGA) and its derivatives are used in production of polymers, drugs, pesticides, dyes, flotation agents, and perfumes [1].

The known routes to TGA are based on reactions of monochloroacetic acid (MCAA) in the form of sodium salt with various sulfur derivatives. MCAA reacts with sodium hydrosulfide in one stage under H_2S pressure of 5–50 atm; yield of TGA 81.0–90.8% [2–5]. The reaction of MCAA with sodium thiosulfate yields sodium 5-carboxymethyl thiosulfate; its hydrolysis in the presence of oxidants affords TGA, yield 92–96% [6–8]. The reaction is sensitive to oxidants, whose presence results ion formation of dithiodiglycolic acid (DTDGA) as impurity [8]. DTDGA can be prepared in a reasonable yield by the reaction of sodium disulfide with sodium monochloroacetate [9] and can be subsequently reduced to TGA (yield 98–99%) on hydrogenation catalysts at 140°C and hydrogen pressure of 50 atm [10]. DTDGA can also be reduced electrochemically (yield 80%) [11].

Thus, the known procedures for preparing TGA either involve the use of high pressures or require thorough protection of the reaction mixtures from atmospheric oxygen. Taking into account published data and the availability of starting compounds for commercial synthesis, we chose the route based on the reaction of MCA with sodium disulfide, followed by electrochemical reduction of the resulting DTDGA.

MCA reacts with sodium disulfide as follows:

$$Na_2S_2 + 2ClCH_2COOH \rightarrow HOOCCH_2SSCH_2COOH + 2NaCl.$$

First, we determined the optimal conditions for this reaction: 70–80°C, 30 min. Below 70°C the reaction takes much longer time, and above 80°C by-products start to form. Under the optimal conditions, the yield of DTDGA is nearly quantitative.

Electrochemical reduction of DTDGA occurs with the consumption of $2F$ of electricity per mole:

$$HOOCCH_2SSCH_2COOH + 2e + 2H^+ \rightarrow 2HSCH_2COOH.$$

According to published data, the reaction occurs with a high yield in a sulfuric acid solution on a lead anode; however, the process was not optimized.

For the success of the electrochemical synthesis, TGA should be stable under the electrolysis conditions. We have studied the behavior of pure TGA in aqueous sulfuric acid at 25–30°C and current density of 200 A m^{-2}. The amount and purity of TGA remained unchanged after passing $2F$ of electricity per mole. Similar results were obtained when a double amount of electricity was passed in the course of electroreduction of DTDGA (see figure). The maximal amount of TGA formed remains unchanged after passing 200% amount of electricity relative to the stoichiometry, with the optimal amount being 140–150%.

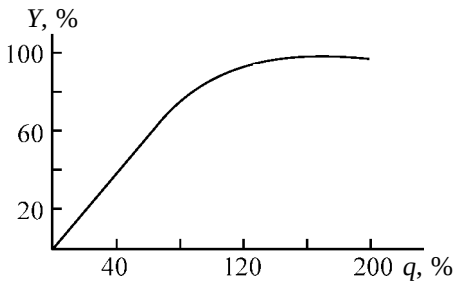

TGA yield Y as a function of the amount of electricity passed q (relative to stoichiometry). 20–25°C; current density 200 A m^{-2}.

1070-4272/02/7509-1438$27.00 © 2002 MAIK "Nauka/Interperiodica"

Table 1. Influence of the current density on the yield and quality of TGA. 20–25°C; 0.3 mol of DTDGA loaded; amount of electricity passed 11.3 A h (140% relative to stoichiometry)

Run no.	i, A m^{-2}	Obtained, mol		DTDGA conversion, %	TGA yield, %	Current efficiency, %	Content in isolated product, %	
		TGA	DTDGA				TGA	DTGA
1	100	0.291	0.003	99.0	96.9	69.2	96.0	1.0
2	300	0.288	0.008	97.3	96.1	68.6	95.3	2.7
3	500	0.286	0.010	96.7	95.2	68.0	94.7	3.3
4	700	0.283	0.014	95.3	94.3	67.4	93.3	4.7
5*	500–600	0.290	0.005	98.3	96.7	69.1	96.0	1.7

* Gradual decrease in the current density.

Table 2. Influence of temperature on the TGA yield and DTDGA conversion. Current density 200 A m^{-2}; 0.3 mol of DTDGA loaded; amount of electricity passed 140% relative to stoichiometry

Run no.	T, °C	Obtained, mol		TGA yield, %	Current efficiency, %	DTDGA conversion, %
		TGA	DTDGA			
1	20–23	0.289	0.008	96.3	68.8	97.71
2	40–43	0.290	0.007	96.7	69.0	97.3
3	60–62	0.288	0.007	96.0	68.6	97.7
4	70–75	0.285	0.005	95.1	67.9	98.3

To find the optimal parameters of the electrochemical synthesis of TGA, we studied the cathodic reduction of pure DTDGA in 2 N sulfuric acid. The influence of the current density on the yield of TGA is illustrated by Table 1.

As seen from Table 1, with increasing current density the DTDGA conversion and the current efficiency by TGA decrease, which is due to water decomposition with the release of hydrogen. Electrolysis at a low (100 A m^{-2}) or gradually decreased (from 500 to 100 A m^{-2}) current density affords higher yield and purity of TGA. At low current density, the electrolysis takes longer time; therefore, the gradual decrease of the current density is preferable.

We have studied how the reaction temperature affects the process parameters and the quality of TGA in the range 20–80°C (Table 2).

Table 2 shows that variation of temperature in the range 20–75°C has no appreciable effect on the TGA yield. Slightly decreased yield at elevated temperatures may be due to self-esterification of TGA. Thus, the optimal conditions for the electrochemical reduction of DTDGA are as follows: i_c = 100–400 A m^{-2}, T = 20–40°C, and amount of electricity 140–150% relative to stoichiometry.

We have studied under the same conditions the electrochemical reduction of mixtures from the reaction of MCA sodium salt with sodium disulfide. The yield of TGA in the process was 92–97% based on MCA, and the purity, 94–98%; the amount of wastewater was 2–2.5 times lower as compared to published procedures for TGA synthesis.

EXPERIMENTAL

The content of TGA in the reaction mixture and finished product was determined by iodometric titration, and the total content of TGA and DTDGA, by bromatometric titration in the presence of KBr in acid solution. The DTDGA content in reaction mixtures and isolated products was determined from the difference.

Electrochemical reduction was performed in a glass electrolyzer with a ceramic diaphragm, equipped with a stirrer and a heat-exchange jacket. A lead cathode was used; working surface area 120 cm^2. Solutions were prepared in double-distilled water.

A solution of 11 g (0.1 mol) of sodium disulfide in 60 ml of water was addded to an aqueous solution of 23.3 g (0.2 mol) of sodium monochloroacetate in 26 ml of water, heated to 70–80°C. The resulting

solution was stirred for 30 min, according to [9]. To the cooled reaction mixture, 19.6 g (0.2 mol) of concentrated sulfuric acid was added, and the solution was subjected to electrochemical reduction at 20–45°C and current density gradually decreased from 500 to 100 A m^{-2}; 8 A h of electricity was passed. After the electrolysis completion, the catholyte was extracted with ethyl acetate, and the solvent was evaporated; 17.8 g of 95.2% pure TGA was obtained. Yield 92.0%. The waste was a solution of 11.7 g (0.2 mol) of NaCl and 14.9 g (0.1 mol) of Na_2SO_4 in 80 ml of water.

CONCLUSION

The optimal parameters were determined and a process was developed for the synthesis of thioglycolic acid from sodium monochloroacetate and sodium disulfide without isolation of intermediates. The yield of the target product is as high as 92–97%, with the amount of wastewater being considerably reduced.

REFERENCES

1. Mirskova, A.N., Levkovskaya, G.G., and Bel'kova, A.N., *Zh. Prikl. Khim.*, 1996, vol. 69, no. 12, pp. 2038–2041.
2. JPN Patent 68-17564.
3. JPN Patent 47-114529.
4. FRG Patent Appl. 2711867.
5. JPN Patent Appl. 55-145663.
6. US Patent 2413361.
7. US Patent 2594030.
8. USSR Inventor's Certificate no. 1014829.
9. Almeida, P. de, *Trib. Farm.*, 1974, vol. 442, nos. 1–2, pp. 40–42.
10. JPN Patent 13066.
11. Larsson, E., *Ber.*, 1928, vol. 61, pp. 1439–1442.

Russian Journal of Applied Chemistry, Vol. 75, No. 9, 2002, pp. 1441–1443. Translated from Zhurnal Prikladnoi Khimii, Vol. 75, No. 9, 2002, pp. 1473–1475.
Original Russian Text Copyright © 2002 by Smirnov, Kalinina.

ORGANIC SYNTHESIS AND INDUSTRIAL ORGANIC CHEMISTRY

Thermodynamic Analysis of High-Temperature Transformations of *p*-Diethylbenzene

B. Yu. Smirnov and I. P. Kalinina

Samara State Technical University, Samara, Russia

Received February 22, 2002

Abstract—Analysis of the maximum efficiency of complex chemical transformations of *p*-diethylbenzene was performed by computer simulation. Major pathways of *p*-diethylbenzene transformations were determined depending on the process conditions.

Isomeric divinylbenzenes are important precursors in the synthesis of a wide assortment of ion-exchange resins, synthetic rubbers, sorbents, membranes, and other polymeric materials [1–4]. Due to stability of their carbon skeleton to the action of acids, alkalis, radiation, and heating and high reactivity in copolymerization, they are widely used as cross-linking agents in various polymeric materials. It is known that *p*-divinylbenzene is the most efficient in this respect [5].

The modern process of preparation of isomeric divinylbenzenes is based on catalytic dehydrogenation of the corresponding diethylbenzenes at high temperatures and high dilution of the initial dialkylbenzene with steam and is accompanied by formation of a series of by-products. Dehydrogenation of commercial diethylbenzene, which is a mixture of *ortho*, *meta*, and *para* isomers, yields a difficultly separable mixture of divinylbenzene isomers [6–8].

The preferred synthesis of individual *p*-divinylbenzene became possible starting from *p*-diethylbenzene, which, in turn, is synthesized by alkylation of ethylbenzene with ethylene in the presence of zeolite catalysts [9, 10]. Increase in the completeness and selectivity of the raw material conversion in the process is urgent from both economical and environmental viewpoint. For this purpose, it is necessary to study equilibrium transformations of *p*-divinylbenzene, which was the goal of this work. Earlier, such a study was performed only with respect to the target reaction [11].

Based on published data [12, 13] and preliminary estimation of the Gibbs energies of reactions, we proposed the following scheme of successive-parallel transformations of *p*-diethylbenzene:

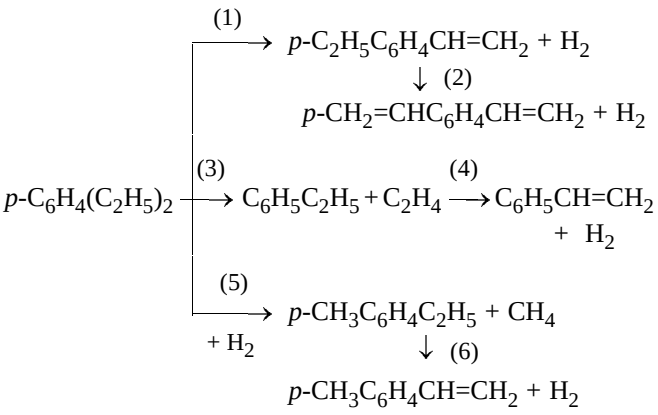

The system of equations for the equilibrium constants of the individual reactions, composed on the basis of the mass action law, was used as a mathematical model. The algorithm of solving this system is the direct thermodynamic problem, whose solution is the equilibrium composition of products and equilibrium degree of raw material conversion [14]. The calculated equilibrium constants were used in a computer experiment based on the program for realization of the above algorithm. It should be noted that the calculated equilibrium constants of reaction (1) are in good agreement with the experimental values found in [11].

Calculations were performed for the 700–1000 K range and degree of dilution of diethylbenzene with water vapor from 0 to 80 mol/mol. The above intervals cover the traditional industrial ranges of these parameters.

The results obtained show that higher temperatures and stronger dilutions increase the equilibrium con-

1070-4272/02/7509-1441$27.00 © 2002 MAIK "Nauka/Interperiodica"

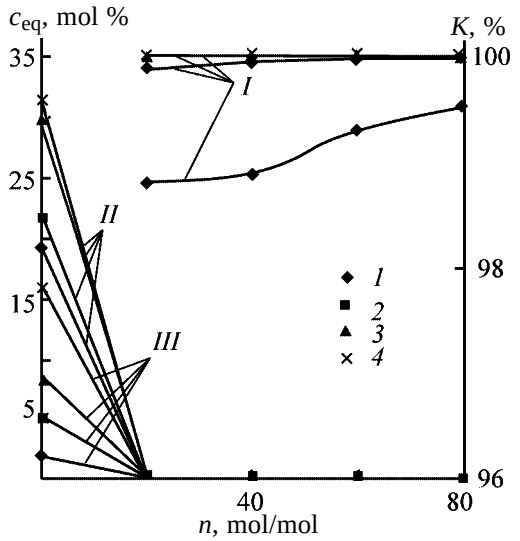

Fig. 1. Dependence of (*I*) *p*-diethylbenzene equilibrium conversion *K* and equilibrium concentrations c_{eq} of (*II*) *p*-ethyltoluene and (*III*) methylstyrene on the dilution degree *n* at various temperatures. Temperature (K): (*1*) 700, (*2*) 800, (*3*) 900, and (*4*) 1000; the same for Figs. 2 and 3.

version of *p*-diethylbenzene, and virtually complete conversion of the initial alkylbenzene can be attained (Fig. 1).

Without diluent, the equilibrium shifts to formation of *p*-ethyltoluene and *p*-methylstyrene [reactions (5) and (6)] (Fig. 1). Introduction of water vapor strongly affects the direction of the prevalent transformation of *p*-diethylbenzene: ethylbenzene (at 700 K) and styrene (at 1000 K) become the main products (Fig. 2). This is probably caused by the fact that the equilibrium of reaction (5) is independent of the inert component, while the equilibria of the other reactions shift to formation of the corresponding products with dilution.

With increasing temperature from 800 to 1000 K, in the presence of the diluent, the styrene concentration gradually decreases (Fig. 2), and the contribution of reactions (1) and (2) leading to substantial increase in the content of *p*-divinylbenzene becomes noticeable (Fig. 3). This increase is limited by 40–50-fold water vapor excess at 800–900 K and 20-fold excess at 1000 K. This dependence allows preliminary evaluation of the appropriate degree of diethylbenzene dilution with water vapor at various temperatures.

CONCLUSIONS

(1) The thermodynamic analysis of the assumed reactions of *p*-diethylbenzene allows determination of the major pathways of its transformation under various conditions. This analysis can be the basis for developing a scheme of catalytic transformations of *p*-diethylbenzene, predicting its behavior in the precatalytic zone of the reactor in the process of *p*-divinylbenzene production, and estimating the working parameters of the reaction apparatus.

(2) Because of the above-noted high styrene content in the equilibrium reaction mixture, it is thermodynamically feasible and attractive to perform joint dehydrogenation of *p*-diethylbenzene and ethylbenzene with the aim to produce *p*-divinylbenzene,

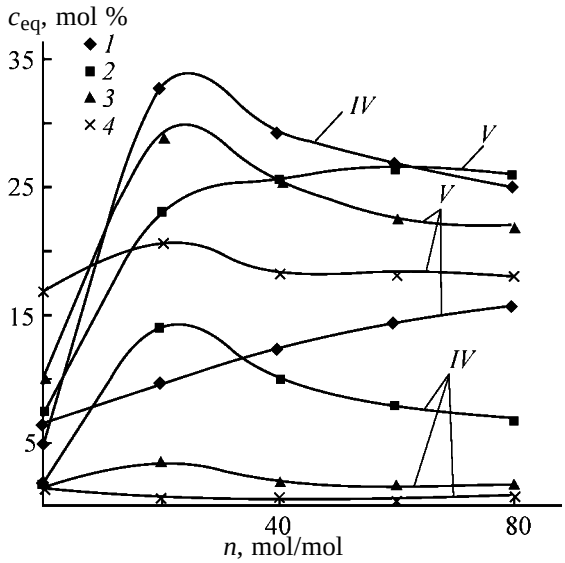

Fig. 2. Dependence of the equilibrium concentrations c_{eq} of (*IV*) ethylbenzene and (*V*) styrene on the dilution degree *n* at various temperatures.

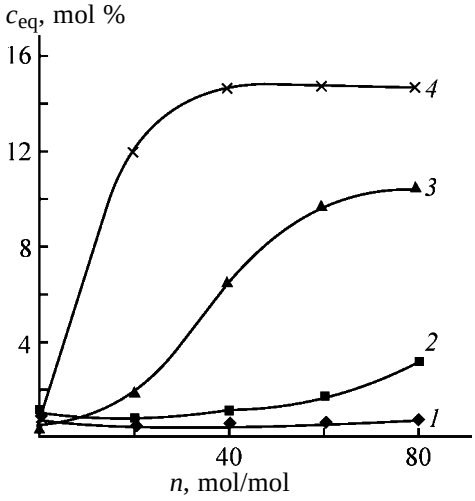

Fig. 3. Dependence of the equilibrium concentration c_{eq} of *p*-divinylbenzene on the dilution degree *n* at various temperatures.

styrene, and their required mixtures depending on the market demands.

REFERENCES

1. Kalinina, I.P. and Smirnov, B.Yu., *Divinilbenzol i polimery na ego osnove* (Divinylbenzene and Derived Polymers), available from VINITI, Ross. Akad. Nauk, Moscow, 2000, no. 2693-V00.
2. Kolarz, B.N. and Bartkowiak, D., *High Technol. Lett*., 1997, vol. 3, no. 2, pp. 76–77.
3. Aleksandrova, I. and Iordanov, G., *J. Polym. Sci*., 1996, no. 2, pp. 2285–2288.
4. Strauix, G.B., *J. Org. Chem*., 1997, vol. 62, no. 26, pp. 8987–8993.
5. Zubakova, L.B., Tevlina, A.S., and Davankov, A.B., *Sinteticheskie ionoobmennye materialy* (Synthetic Ion-Exchange Materials), Moscow: Khimiya, 1978.
6. Murzin, D., Smeds, S., and Salmi, T., *React. Kinet. Catal. Lett*., 1997, vol. 60, no. 1, pp. 57–64.
7. Volkov, R.N. and Yanchuk, V.A., *Prom–st. Sint. Kauchuka, Shin, Rezino-Tekh. Izdel*., 1984, no. 2, pp. 7–9.
8. Romanian Patent 81 032.
9. US Patent 4 982 030.
10. Kaeding, W.W., *J. Catal*. 1985, vol. 95, no. 2, pp. 512–519.
11. Lebedev, N.N., Rozhkov, V.I., and Odabashyan, G.V., *Neftekhimiya*, 1983, vol. 23, no. 4, pp. 508–510.
12. Sidnev, V.B., Smirnov, A.Yu., Sidnev, E.S. *et al*., *Zh. Prikl. Khim*., 1988, vol. 61, no. 11, pp. 2586–2589.
13. Rozhkov, V.I., Lebedev, N.N., Odabashyan, G.V., and Zaidman, O.A., *Izv. Vyssh. Uchebn. Zaved., Khim. Khim. Tekhnol*., 1984, vol. 27, no. 8, pp. 915–919.
14. Safronov, V.S., Bogomolova, G.Ya., Bogomolov, Yu.I., and Morozov, A.V., *Neftekhimiya*, 1982, vol. 22, no. 3, pp. 312–316.

Russian Journal of Applied Chemistry, Vol. 75, No. 9, 2002, pp. 1444–1447. Translated from Zhurnal Prikladnoi Khimii, Vol. 75, No. 9, 2002, pp. 1476–1479.
Original Russian Text Copyright © 2002 by Fokanov, Pavlov, Semenov, Morozov.

ORGANIC SYNTHESIS AND INDUSTRIAL ORGANIC CHEMISTRY

Photochemical Reactions in Gaseous Mixtures of C_2F_4 and CF_3I[1]

V. P. Fokanov, A. B. Pavlov, V. N. Semenov, and A. V. Morozov

Prikladnaya Khimiya Russian Scientific Center, St. Petersburg, Russia

Received January 17, 2002

Abstract—Products of photochemical reactions occurring in gaseous mixtures of C_2F_4 and CF_3I under vacuum-UV irradiation were studied. The major photolysis products are linear perfluoroparaffins C_nF_{2n+2} and linear perfluoroalkyl iodides $C_nF_{2n+1}I$. The product ratio is consistent with the suggested kinetic scheme of chain reactions of telomers.

Radical or homolytic telomerization is a convenient route to homologous series of compounds of various classes and is of much promise for practice [1–4]. The products of these reactions are, in particular, iodofluoroalkane telomers, which are used in syntheses of many important products: fluorinated surfactants, rubbers, chemically resistant lubricants and heat carriers, drugs, etc.

Formation of telomers in the reaction medium is initiated by free radicals, which are generated by three main methods: heating (thermal initiation), addition of radical-generating compounds (chemical initiation), and irradiation (photo- or radiation initiation).

With thermal initiation, the heat released in the process results in the temperature and pressure rise, and telomers with a broad molecular-weight distribution are obtained. With chemical initiators, telomerization can be performed under controllable conditions, with the formation of telomers with relatively narrow molecular-weight distribution. However, contamination of the resulting telomers with initiator fragments is a serious drawback of this procedure. Photochemical initiation is free of the above drawbacks. The process parameters can be readily controlled and varied in the course of the reaction. Proper choice of the irradiation spectrum allows variation of the reaction pathways in the same mixture and, correspondingly, the control over the product composition. Vacuum-UV (VUV) irradiation can produce telomerization initiators that cannot be generated by other methods. In this connection, it is interesting to study telomerization in mixtures of fluoroolefins with iodofluoroalkanes.

[1] Reported at the 3rd International Conference "Chemistry, Technology, and Applications of Fluorine Compounds," St. Petersburg, June 6–9, 2001.

EXPERIMENTAL

Irradiation of C_2F_4 and a mixture of C_2F_4 with CF_3I was performed in a closed reactor. The reactor was a quartz tube, with a low-pressure mercury lamp arranged along its axis. The distance from the lamp surface to tube walls was about 4 mm. The cell was evacuated to a pressure of 1.3 Pa. In the course of the experiment (3 min), the pressure increased to 26 Pa. The lamp output was 70 W, of which UV radiation at λ = 254 nm made up 30%. The VUV radiation at λ = 185 nm made up only 5% of the output at λ = 254 nm.

Tetrafluoroethylene used in the experiments contained less than 1% impurities. Photolysis was performed both with pure C_2F_4 and with 10 : 1 and 1.5 : 1 mixtures of C_2F_4 and CF_3I (total pressure 3.7–5.7 kPa). Photolysis products were studied by gas chromatography–mass spectrometry and analyzed on the basis of the developed kinetic model. The following reaction scheme was assumed:

$$C_2F_4 + h\nu\ (\lambda = 185\ \text{nm}) = C_2F_4(S), \quad (1)$$

$$C_2F_4(S) = C_2F_4, \quad (2)$$

$$C_2F_4(S) = :CF_2 + :CF_2, \quad (3)$$

$$C_2F_4(S) + C_2F_4 = \text{cyclo-}C_4F_8, \quad (4)$$

$$:CF_2 + :CF_2 = C_2F_4, \quad (5)$$

$$C_2F_4 + :CF_2 = C_3F_6, \quad (6)$$

$$CF_3I + h\nu\ (\lambda = 254\ \text{nm}) = {\cdot}CF_3 + I^*, \quad (7)$$

$$I^* + M(I_2, C_2F_4) = I + M(I_2, C_2F_4), \quad (8)$$

1070-4272/02/7509-1444$27.00 © 2002 MAIK "Nauka/Interperiodica"

$$\cdot CF_3 + I = CF_3I, \quad (9)$$

$$\cdot CF_3 + \cdot CF_3 = C_2F_6, \quad (10)$$

$$I + I + M(C_2F_4) = I_2 + M(C_2F_4), \quad (11)$$

$$C_2F_4 + \cdot CF_3 = \cdot C_3F_7, \quad (12)$$

$$\cdot C_3F_7 + I = C_3F_7I, \quad (13)$$

$$\cdot CF_3 + :CF_2 = \cdot C_2F_5, \quad (14)$$

$$\cdot C_2F_5 + I = C_2F_5I, \quad (15)$$

$$C_2F_5I + h\nu\ (\lambda = 254\ \text{nm}) = \cdot C_2F_5 + I^*, \quad (16)$$

$$\cdot C_2F_5 + C_2F_4 = \cdot C_4F_9, \quad (17)$$

$$C_3F_7I + h\nu\ (\lambda = 254\ \text{nm}) = \cdot C_3F_7 + I^*, \quad (18)$$

$$\cdot C_3F_7 + \cdot C_3F_7 = C_6F_{14}, \quad (19)$$

$$\cdot C_3F_7 + \cdot C_4F_9 = C_7F_{16}, \quad (20)$$

$$\cdot C_3F_7 + C_2F_4 = \cdot C_5F_{11}, \quad (21)$$

$$\cdot C_4F_9 + I = C_4F_9I, \quad (22)$$

$$C_4F_9I + h\nu\ (\lambda = 254\ \text{nm}) = \cdot C_4F_9 + I^*, \quad (23)$$

$$\cdot C_5F_{11} + I = C_5F_{11}I, \quad (24)$$

$$\cdot C_5F_{11}I + h\nu\ (\lambda = 254\ \text{nm}) = \cdot C_5F_{11} + I^*, \quad (25)$$

$$\cdot C_4F_9 + C_2F_4 = \cdot C_6F_{13}, \quad (26)$$

$$\cdot C_5F_{11} + C_2F_4 = \cdot C_7F_{15}, \quad (27)$$

$$I_2 + h\nu\ (\lambda = 185\ \text{nm}) = I + I, \quad (28)$$

$$\cdot CF_3 + \cdot C_2F_5 = C_3F_8, \quad (29)$$

$$\cdot CF_3 + \cdot C_3F_7 = C_4F_{10}, \quad (30)$$

$$\cdot CF_3 + \cdot C_4F_9 = C_5F_{12}, \quad (31)$$

$$\cdot C_2F_5 + \cdot C_2F_5 = C_4F_{10}, \quad (32)$$

$$\cdot C_2F_5 + \cdot C_3F_7 = C_5F_{12}, \quad (33)$$

$$\cdot C_2F_5 + \cdot C_4F_9 = C_6F_{14}, \quad (34)$$

$$\cdot CF_3 + I_2 = CF_3I + I, \quad (35)$$

$$\cdot C_2F_5 + I_2 = C_2F_5I + I, \quad (36)$$

$$\cdot C_3F_7 + I_2 = C_3F_7I + I, \quad (37)$$

$$\cdot C_4F_9 + I_2 = C_4F_9I + I, \quad (38)$$

$$\cdot C_5F_{11} + I_2 = C_5F_{11}I + I, \quad (39)$$

$$C_2F_5I + C_2F_4(S) = C_3F_7I + :CF_2, \quad (40)$$

$$C_2F_5I + C_2F_4(S) = C_4F_9I, \quad (41)$$

$$C_3F_7I + C_2F_4(S) = C_4F_9I + :CF_2, \quad (42)$$

$$C_3F_7I + C_2F_4(S) = C_5F_{11}I, \quad (43)$$

$$C_4F_9I + C_2F_4(S) = C_5F_{11}I + :CF_2, \quad (44)$$

$$C_4F_9I + C_2F_4(S) = C_6F_{13}I, \quad (45)$$

$$\cdot C_nF_{2n+1} + C_2F_4 = \cdot C_{n+2}F_{2n+5}, \quad n = 5, 16, \quad (46)$$

$$\cdot C_nF_{2n+1} + \cdot C_mF_{2m+1} = C_{n+m}F_{2(n+m)+2},$$
$$n = 5, 16, \quad m = 1, 2, 3, \quad (47)$$

$$\cdot C_nF_{2n+1} + :CF_2 = \cdot C_{n+1}F_{2n+3}, \quad n = 5, 17. \quad (48)$$

Photodissociation of CF_3I results in the generation of $\cdot CF_3$ radicals [reaction (7), absorption cross section $\sim 5 \times 10^{-19}$ cm^2] and excited iodine $I^*(^2P_{1/2})$. $\cdot C_2F_5$, $\cdot C_3F_7$, $\cdot C_4F_9$, and related radicals are formed by secondary reactions with C_2F_4 and $:CF_2$ [reactions (12), (14), (17), (21), (26), (27), (46), (48)], and also by photodissociation of C_2F_5I, C_3F_7I, and C_4F_9I [reactions (16), (18), (23), (25)].

Irradiation of C_2F_4 at $\lambda = 185$ nm generates excited $C_2F_4(S)$ molecules (probably singlet), which either emit quanta or dissociate into $:CF_2$ radical [5]. The $:CF_2$ radicals participate in chain propagation reactions $\cdot C_nF_{2n+1} + :CF_2 = \cdot C_{n+1}F_{2n+3}$. The addition reactions $CF_3I + :CF_2 = C_{n+1}F_{2n+3}I$ and $C_nF_{2n+2} + :CF_2 = C_{n+1}F_{2n+4}$ were taken into account in the preliminary calculations, but their contribution to the overall process appeared to be insignificant. Reaction of excited $C_2F_4(S)$ with ground-state C_2F_4 yields cyclo-C_4F_8 [reaction (4)]. Chains are terminated by recombination of radicals [reactions (9), (10), (19), (20), (29)–(39), (47)]. We also included in the calculation scheme the reactions of excited $C_2F_4(S)$ with perfluoroalkyl iodides (CF_3I, C_2F_5I, C_3F_7I, C_4F_9I) yielding higher-molecular-weight perfluoroalkyl iodides and $:CF_2$ radicals [reactions (40)–(45)].

The system of ordinary differential equations constructed according to the above-given kinetic scheme was integrated by the Gear method [6, 7]. The rate constants of chemical reactions were taken from [8–10] or determined by extrapolation in the homologous

Products identified after irradiation of the gaseous mixture of C_2F_4 with CF_3I

Photolysis products	Content, %			
	C_2F_4 (3325 Pa), CF_3I (2261 Pa)		C_2F_4 (3325 Pa), CF_3I (399 Pa)	
	experimental	calculated	experimental	calculated
C_2F_4*	13	32.6	19.7	80.8
cyclo-C_4F_8*	1.8	2.6	3.3	8.3
CF_3I	26	22.9	10.5	1.65
C_2F_5I	14	8.85	8	1.15
C_3F_7I	24	20.8	14.8	4.1
C_4F_9I	6.7	5.4	9.7	1.51
$C_5F_{11}I$	1.4	3.2	2.8	1.15
C_2F_6	1.6	0.5	0.5	0.02
C_3F_8	0.8	0.11	0.7	0.004
C_4F_{10}	1.8	0.47	2.2	0.03
C_5F_{12}	0.8	0.19	2.4	0.016
C_6F_{14}	0.7	0.51	2.8	0.07
C_7F_{16}	0.3	0.09	2.6	0.014
C_8F_{18}	0.1	0.097	2	0.015
C_9F_{20}	–	0.02	1.4	0.003

* For C_2F_4 (3990 Pa) and CF_3I (0 Pa), the experimental and calculated values are as follows, %: C_2F_4, 90 and 90.2; cyclo-C_4F_8, 8 and 9.3, respectively.

series, taking into account steric factors. The experimental and calculated data on the composition of the gaseous mixture after irradiation are given in the table.

In the photolysis products of a mixture of C_2F_4 with CF_3I, we detected small amounts of C_2F_3I and C_3F_5I, which may originate from background reactions of fluorine elimination. Fluorine may arise from photodissociation of perfluoroalkyl iodides under the influence of the irradiation with λ = 185 nm [11] (absorption cross section 3×10^{-20}–1.5×10^{-19} cm^2 depending on particular compound).

As the irradiation time is increased, the process shifts toward formation of higher-molecular-weight perfluoroalkyl iodides. The amounts of such components as determined from the gas composition may be underestimated because of condensation on the reactor walls, especially for compounds containing more than 15 carbon atoms.

As seen from the table, stepwise telomerization is the main process occurring upon UV and VUV irradiation of a gaseous mixture of C_2F_4 with CF_3I. Two interrelated radical chain processes occur simultaneously in the system: telomerization of tetrafluoroethylene with the telogen CF_3I and telomerization of C_2F_4 with the arising telomer T_1 (C_3F_7I). This is indicated by the increase in the content of T_1 and T_2 ($C_5F_{11}I$) in the reaction products as the reaction time is increased from 1 to 3 min. The following reaction is mainly responsible for initiation:

$$R_FI + h\nu\ (\lambda = 254\ \text{nm}) = R_F + I^*,$$

where R_F = $^{\cdot}CF_3$, $^{\cdot}C_2F_5$, $^{\cdot}C_3F_7$, etc.

Under conditions of VUV irradiation, this major process is accompanied by formation of $:CF_2$ and, apparently, IF, as judged from the composition of the reaction products. The following reactions probably occur in the system:

$$C_2F_4 + h\nu\ (\lambda = 185\ \text{nm}) = 2{:}CF_2,$$

$$CF_3I + h\nu\ (\lambda = 185\ \text{nm}) = {:}CF_2 + IF,$$

$$IF + C_2F_4 = C_2F_5I.$$

They give rise to a new telogen which subsequently participates in telomerization; however, this pathway was not taken into account in the kinetic scheme.

As seen from the table, for the C_2F_4–CF_3I mixture, the calculation results reasonably agree with the experiment only at $C_2F_4 : CF_3I = 1.5 : 1$. This may be due to considerable excess rotation, vibration, and forward motion energy, sufficient to induce additional reactions that were not taken into account in the calculations.

CONCLUSIONS

(1) Telomers $C_nF_{2n+1}I$ and C_nF_{2n+2} can be prepared from a mixture of tetrafluoroethylene and trifluoromethyl iodide under conditions of UV and VUV initiation. On longer irradiation, the process shifts toward formation of higher-molecular-weight perfluoroalkyl iodides. At decreased concentration of CF_3I, the yield of telomers C_nF_{2n+2} grows.

(2) When photolysis of a C_2F_4–CF_3I mixture is performed with VUV radiation, new reactions may be promoted, accelerating telomerization and involving a new telogen, C_2F_5I, in the process.

(3) At comparable concentrations of CF_3I and C_2F_4, the calculated yields of telomeric photolysis products reasonably agree with the experiment.

REFERENCES

1. Freidlina, R.F., Velichko, F.K., Zlotskii, S.S., *et al.*, *Radikal'naya telomerizatsiya* (Radical Telomerization), Moscow: Khimiya, 1988.
2. Sheppard, W.A., Sharts, C.M, *Organic Fluorine Chemistry*, New York: W.A. Benjamin, 1969.
3. Rakhmanov, A.I., *Khimiya i tekhnologiya ftororganicheskikh soedinenii* (Chemistry and Technology of Organofluorine Compounds), Moscow: Khimiya, 1988.
4. Calvert, J.G. and Pitts, J.N., *Photochemistry*, New York: Wiley, 1965.
5. Belinger, G. and Landorty, C., *Chem. Phys. Lett.*, 1969, vol. 3, no. 9, pp. 661–664.
6. Polak, L.S., Gol'denberg, M.Ya., and Levitskii, A.A., *Vychislitel'nye metody v khimicheskoi kinetike* (Calculation Methods in Chemical Kinetics), Moscow: Nauka, 1984.
7. Arushanyan, O.B. and Zaletkin, S.F., *Chislennoe reshenie obyknovennykh differentsial'nykh uravnenii na fortrane* (Numerical Solution of Ordinary Differential Equations in Fortran), Moscow: Mosk. Gos. Univ., 1990.
8. Kondrat'ev, V.N., *Konstanty skorosti gazofaznykh reaktsii: Spravochnik* (Rate Constants of Gas-Phase Reactions: Handbook), Moscow: Nauka, 1970.
9. Okabe, J., *Photochemistry of Small Molecules* (Photochemistry of Small Molecules), New York: Wiley, 1978.
10. Andreeva, T.L., Dzyabenko, O.V., Kuznetsova, S.V., and Maslov, A.I., *Kvant. Elektron.*, 1995, vol. 22, no. 5, pp. 479–484.
11. Pravilov, A.M., *Kvant. Elektron.*, 1980, vol. 8, no. 7, pp. 1397–1424.

Russian Journal of Applied Chemistry, Vol. 75, No. 9, 2002, pp. 1448–1452. Translated from Zhurnal Prikladnoi Khimii, Vol. 75, No. 9, 2002, pp. 1480–1484.
Original Russian Text Copyright © 2002 by Syroezhko, Proskuryakov, Begak.

ORGANIC SYNTHESIS AND INDUSTRIAL ORGANIC CHEMISTRY

Mechanism of Cyclohexane Ozonolysis Considering Alternative Pathways

A. M. Syroezhko, V. A. Proskuryakov, and O. Yu. Begak

St. Petersburg State Technological Institute, St. Petersburg, Russia
Mendeleev Russian Research Institute of Metrology, Federal State Unitary Enterprise, St. Petersburg, Russia

Received March 15, 2002

Abstract—Ozonolysis of cyclohexane was considered taking into account the alternative pathway of recombination of peroxy radicals to form cyclohexanol and cyclohexanone. The rate constants of the reactions involved were determined experimentally or by calculations (optimization of the process model).

The mechanism of cyclohexane ozonolysis [1] taking into account formation of unstable hydrotrioxide (ROOOH) and recombination of peroxy radicals to form alcohol and ketone, and also cyclohexene and cyclohexyl hydroperoxide was substantiated in [1].

However, an alternative mechanism of cyclohexane ozonolysis can be considered, with different pathways of recombination of peroxy radicals, formation of cyclohexyl hydroperoxide, and transformations of cyclohexanol.

According to [2], disproportionation of peroxy radicals yields only cyclohexanol and cyclohexanone, without formation of cyclohexene and cyclohexyl hydroperoxide.

In this case, the experimentally detected cyclohexyl hydroperoxide originates, most probably, from recombination of $HO_2^{\bullet}$ and $RO_2^{\bullet}$ radicals.

The mechanism of cyclohexane ozonolysis that we discuss does not include the reaction of the adduct $RH\cdots O_3$ with the hydrocarbons for the reason given above.

Transformation of cyclohexanol was supplemented by the pathway of formation of unstable hydrotrioxide, in conformity with the overall kinetic scheme of cyclohexanol ozonolysis established in [2].

The kinetic scheme under consideration includes only major (but not all) pathways of transformation of cyclohexanol into cyclohexanone.

The rate constants of elementary reactions of the mechanism of cyclohexane ozonolysis were refined on the basis of the mathematical model and results of optimizing the scheme of cyclohexanol and cyclohexanone ozonolysis [3].

Taking into account data in [1], the alternative mechanism of cyclohexane ozonolysis at high degrees of conversion includes 29 reactions:

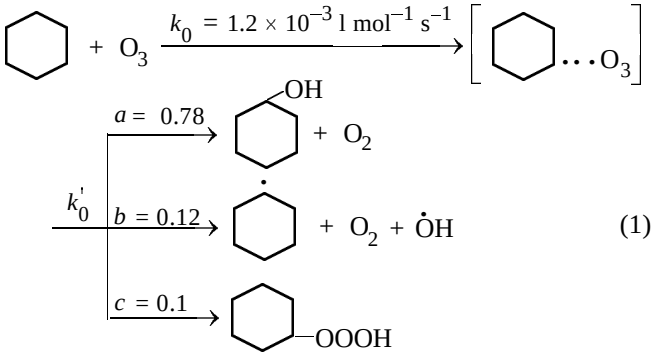

(1)

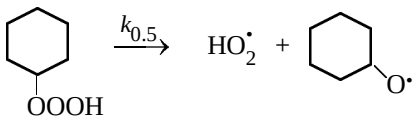

(2)

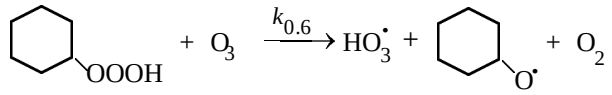

(3)

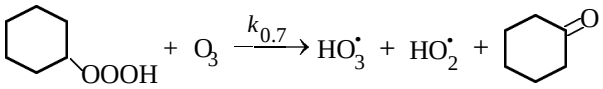

(4)

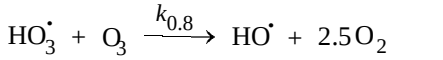

(5)

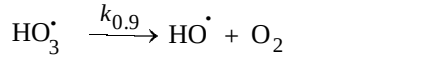

(6)

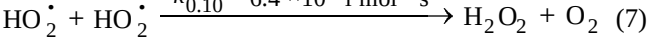

(7)

* Estimated values of k [reactions (7), (15), (16)].

1070-4272/02/7509-1448$27.00 © 2002 MAIK "Nauka/Interperiodica"

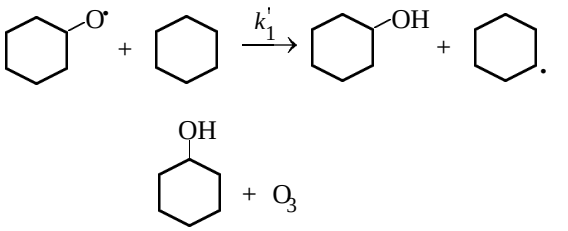
(8)

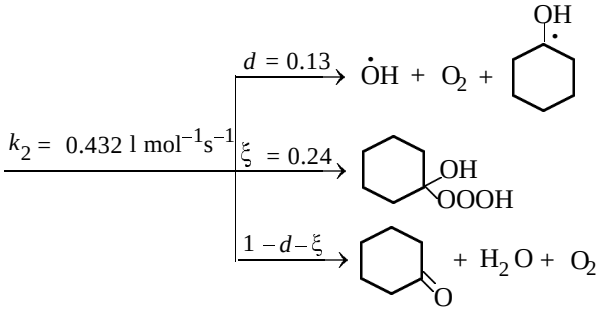
(9)

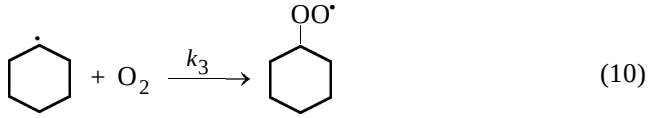
(10)

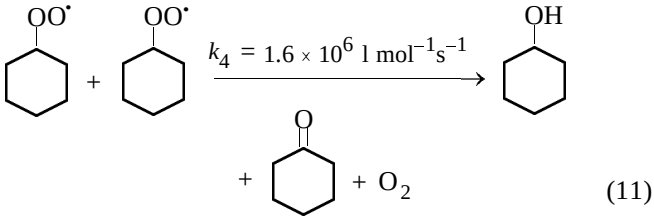
(11)

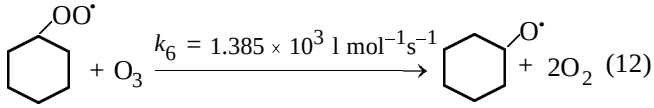
(12)

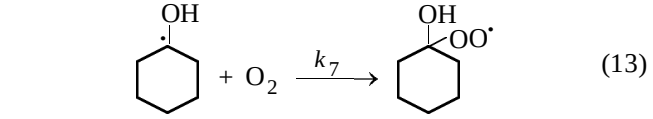
(13)

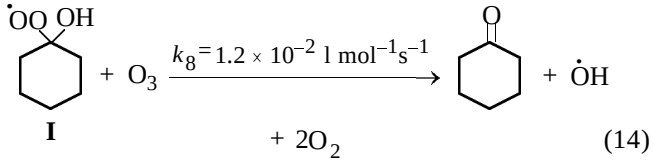
(14)

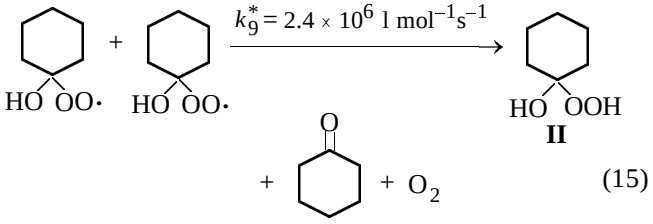
(15)

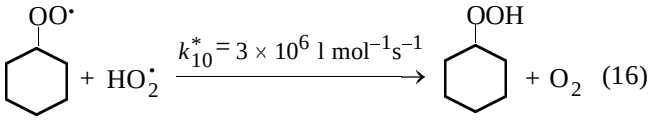
(16)

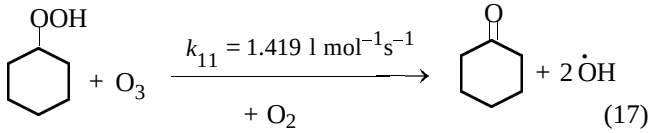
(17)

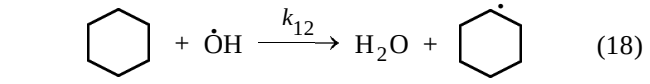
(18)

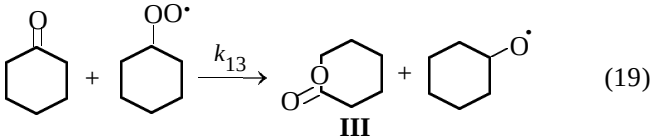
(19)

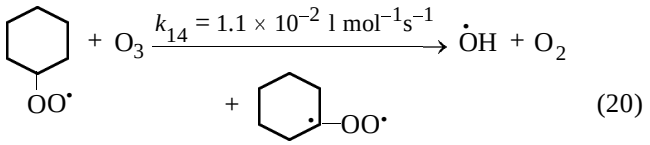
(20)

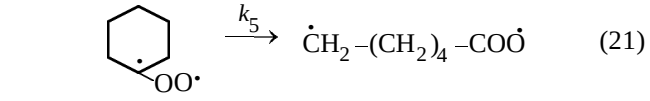
(21)

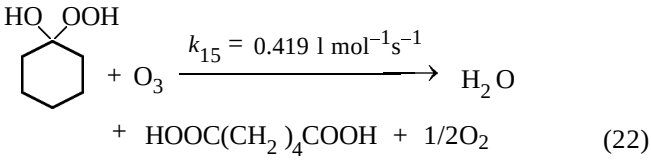
(22)

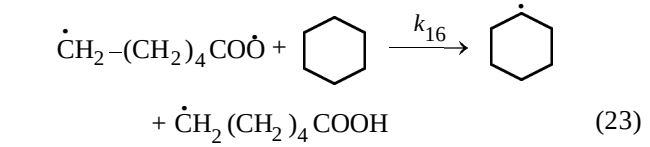
(23)

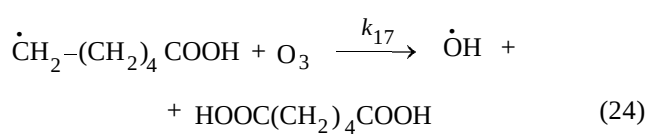
(24)

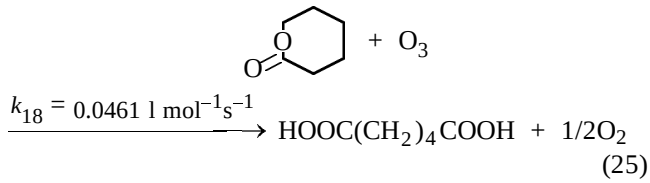
(25)

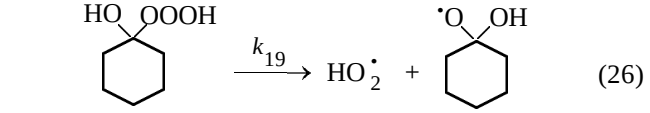
(26)

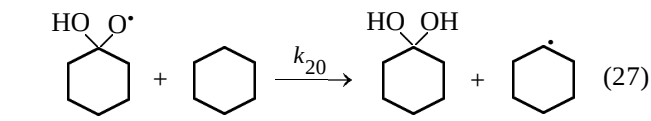
(27)

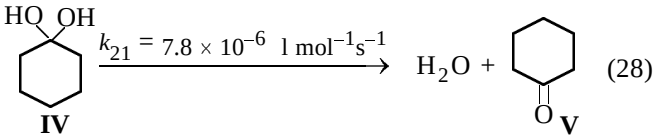

IV **V** (28)

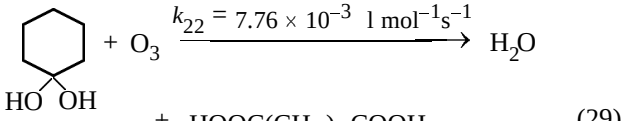

+ $HOOC(CH_2)_4COOH$ (29)

The concentrations x_i of ith radical, cyclohexane hydrotrioxide, or cyclohexanol hydrotrioxide are determined from the condition of steady state, $dx_i/dt = 0$. Let us introduce the following ratios of constants:

$$k_0/k_{05} = Z_1,\ k_{08}/k_{09} = Z_2,\ k_{06}/k_{05} = Z_3,\ k_{07}/k_{05} = Z_4,$$

$$k_6/k_{14} = Z_5,\ k_{13}/k_{14} = Z_6,\ k_4/k_{14} = Z_7,\ \ k_8/k_9 = Z_8.$$

Let us take into account that

$$R_0'c = R_{05} + R_{06} + R_{07},$$

$$R_3 = 2R_4 + R_6 + R_{10} + R_{13} + R_{14} = R_0'b + R_1 + R_{12} + R_{16} + R_{20},$$

$$R_{12} = bR_0' + dR_2 + R_{08} + R_{09} + 2R_{11} + R_8 + R_{14} + R_{17},$$

$$R_{06} + R_{07} = R_{08} + R_{09},\qquad R_{05} + R_{07} + R_{19} = 2R_{010} + R_{10},$$

$$dR_2 = R_7 = R_8 + 2R_{09},\qquad R_{14} = R_5 = R_{16} = R_{17},$$

$$\xi R_2 = R_{19} = R_{20},$$

$$2R_4 + R_{10} - 2R_{14} = (\xi + d)R_2 + 2bR_0 + R_{05} + R_{06} + R_{08} + R_{09} + R_8 + 2R_{11}.$$

The system of differential equations for the rates of consumption of the hydrocarbon and ozone and accumulation of ozonolysis products is as follows:

$$\frac{d[RH]}{dt} = (1 + b)R_0 + \left[\frac{c + c[O_3](2Z_3 + Z_4)}{1 + [O_3](Z_3 + Z_4)}\right]R_0 + R_6[1 + ([R{=}O]Z_6)/([O_3]Z_5) + 3/Z_5)] + (\xi + d)R_2 + R_8 + 2R_{11},$$

$$\frac{d[ROH]}{dt} = a + \left[\frac{c(1 + [O_3]Z_3)}{1 + [O_3](Z_3 + Z_4)}\right]R_0 + R_6[1 + ([R{=}O]Z_6)/([O_3]Z_5)] - R_2 + R_4,$$

$$d[ROOH]/dt = R_{10} - R_{11},$$

$$d[H_2O]/dt = R_{010} = 0.5R_0\left[\frac{c(1 + [O_3]Z_4)}{1 + [O_3](Z_3 + Z_4)}\right] + 0.5(\xi R_2 - R_{10}),$$

$$\frac{d[H_2O]}{dt} = \left[b + \frac{c[O_3](Z_3 + Z_4)}{1 + [O_3](Z_3 + Z_4)}\right]R_0 + (1 - \xi)R_2 + R_8 + 2R_6/Z_5 + 2R_{11} + R_{15} + R_{21} + R_{22},$$

$$d[\mathbf{II}]/dt = R_9 - R_{15},$$

$$\frac{d[R{=}O]}{dt} = \frac{c[O_3]Z_4}{1 + [O_3](Z_3 + Z_4)}R_0 + (1 - d/2 - \xi)R_2 + R_4 + R_{8/2} + R_{11} + ([R{=}O]Z_6R_6)/([O_3]Z_5) + R_{21},$$

$$d[\mathbf{III}]/dt = ([R{=}O]Z_6R_6)/([O_3]Z_5) - R_{18},$$

$$d[HOOC(CH_2)_4COOH]/dt = R_6/Z_5 + R_{15} + R_{18} + R_{22},$$

$$d[\mathbf{II}]/dt = \xi R_2 - R_{21} - R_{22}.$$

Rate of ozone consumption:

$$W_{O_3} = \left[1 + \frac{c[O_3](Z_3 + Z_4)}{1 + [O_3](Z_3 + Z_4)}\right]R_0 + R_2 + R_6(1 + 2/Z_5) + R_8 + R_{11} + R_{15} + R_{22}.$$

Rate of oxygen accumulation:

$$W_{O_2} = \left[a + b + \frac{c[O_3]Z_3}{1 + [O_3](Z_3 + Z_4)}\right]R_0 + 2.5R_0\left[\frac{c[O_3]^2Z_2(Z_3 + Z_4)}{\{1 + [O_3](Z_3 + Z_4)\}([O_3]Z_2 + 1)}\right] + R_0\left[\frac{c[O_3](Z_3 + Z_4)}{\{1 + [O_3](Z_3 + Z_4)\}([O_3]Z_2 + 1)}\right] + R_{010} + (1 - \xi)R_2 - R_4 + R_6[1 - ([R{=}O]Z_6R_6)/([O_3]Z_5)] - R_2 + 2R_8 + R_9 + 2R_{11} + 0.5(R_{15} + R_{18}),$$

The above differential equations include the rates R_0, R_2, R_4, R_6, R_8–R_{11}, R_{15}, R_{18}, R_{21}, and R_{22}. To

calculate the rates R_4, R_6, R_8, R_9, R_{010}, and R_{10}, it is necessary to know the concentrations of the radicals $RO_2^{\bullet}$, $HO_2^{\bullet}$, and **I**.

The sought-for rates R_0–R_{22} are determined from the expressions

$$R_0 = [RH][O_3]k_0,\ R_2 = [ROH][O_3]k_2,\ R_4 = [RO_2^{\bullet}]^2k_4,$$

$$R_6 = [RO_2^{\bullet}],\ R_8 = [\mathbf{I}][O_3]k_8,\ R_9 = [\mathbf{I}]^2k_9,$$

$$R_{010} = [HO_2^{\bullet}]k_{010},\ R_{10} = [HO_2^{\bullet}][RO_2^{\bullet}]k_{10},$$

$$R_{11} = [ROOH][O_3]k_{11},\ R_{15} = [\mathbf{II}][O_3]k_{15},$$

$$R_{18} = [\mathbf{III}][O_3]k_{18},\ R_{21} = [\mathbf{IV}]k_{21},\ R_{22} = [\mathbf{IV}][O_3]k_{22},$$

$$R_{05} = \left[\frac{c}{1 + [O_3](Z_3 + Z_4)}\right]R_0,$$

$$R_{06} = \frac{c[O_3]Z_3}{1 + [O_3](Z_3 + Z_4)}R_0,$$

$$R_{07} = \frac{c[O_3]Z_4}{1 + [O_3](Z_3 + Z_4)}R_0,$$

$$R_{08} = \frac{c[O_3]^2Z_2(Z_3 + Z_4)}{\{1 + [O_3](Z_3 + Z_4)\}([O_3]Z_2 + 1)}R_0,$$

$$R_{09} = \frac{c[O_3](Z_3 + Z_4)}{\{1 + [O_3](Z_3 + Z_4)\}([O_3]Z_2 + 1)}R_0,$$

$$R_4 = [RO_2^{\bullet}]^2k_6Z_7/Z_5 = R_6^2Z_7/[O_3]^2k_6Z_5,$$

$$R_{13} = [\mathbf{V}]Z_6R_6/([O_3]Z_5),\ R_{14} = R_6/Z_5.$$

The concentrations of the radicals $RO_2^{\bullet}$, $HO_2^{\bullet}$, and **I** are

$$[HO_2^{\bullet}] = f[RO_2^{\bullet}] = \left[\frac{R_{05} + R_{07} + R_{19}}{2k_{010} + k_{10}/f}\right]^{1/2},$$

$$f = \frac{-[k_{10}(D - P)] + \{[k_{10}(D - P)]^2 + 16DPk_{010}k_4\}^{1/2}}{4Dk_{010}},$$

$$P = R_{05} + R_{07} + R_{19},$$

$$D = (\xi + d)R_2 + R_{05} + R_{06} + R_{08} + R_{09} + 2bR_0 + R_8 + 2R_{11},$$

$$[RO_2^{\bullet}] = (-[HO_2^{\bullet}]k_{10} - 2[O_3]k_{14})/4k_4 + \{([HO_2^{\bullet}]k_{10} - 2[O_3]k_{14})^2 + 8k_4D\}^{1/2}/4k_4,$$

$$[\mathbf{I}] = \frac{-k_9[O_3]Z_8 + \{(k_9[O_3]Z_8)^2 + 8k_9dR_2\}^{1/2}}{4k_9}.$$

The system of differential equation was integrated on a computer using the standard DERE program, PL/1 language. The system was solved by the method of rational extrapolation, based on discrete approximation when calculating the concentration of *i*th product. The parameters Z_1–Z_8 are as follows: $Z_1 = 0.027$, $Z_2 = 2.27 \times 10^7$, $Z_3 = 7.1$, $Z_4 = 137.8$, $Z_5 = 1.27 \times 10^5$, $Z_6 = 54.5$, $Z_7 = 1.45 \times 10^8$, and $Z_8 = 5 \times 10^{-9}$. The calculation results are given in the table and in the scheme of the mechanism of cyclohexane ozonolysis.

Comparative analysis of the table shows that the largest discrepancy between the calculations and experiment is observed for hydrogen peroxide, hydroxycyclohexyl hydroperoxide, and adipic acid, whereas for the other products the agreement is much better. Both calculated and experimental kinetic curves of the hydrocarbon consumption become straight lines in the semilog coordinates. The differential equation for the hydrocarbon consumption includes the rates R_0, R_2, R_6, R_{11}, and R_8. These rates (except R_8) are comparable and vary insignificantly in the steady-state mode of the process. The rates vary in the following ranges: R_0, $(1.42–1.32) \times 10^{-5}$; R_2, $(2.03–2.78) \times 10^{-5}$; R_6, $(0.422–0.468) \times 10^{-5}$; and R_{11}, $(0.427–0.562) \times 10^{-5}$ mol l^{-1} s^{-1} (τ = 1–5 h). The hydrocarbon is consumed in a bimolecular reaction with ozone and by a chain pathway (reaction of the peroxy radical with ozone). In the developed process, an appreciable contribution is made by bimolecular reactions of cyclohexanol and cyclohexyl hydroperoxide with ozone.

In the differential equation of the ozone consumption, the terms corresponding to each reaction contain the ozone concentration to the first power, except the term

$$R_0\{1 + c[O_3](Z_3 + Z_4)/[1 + [O_3](Z_3 + Z_4)]\}.$$

Substituting in the above expression the values $Z_3 = 7.1$ and $Z_4 = 137.8$ found by mathematical analysis of the model, we obtain

$$c[O_3](Z_3 + Z_4)/\{1 + [O_3](Z_3 + Z_4)\} \ll 1.$$

Actually, there are no noticeable deviations from the first order with respect to ozone. Ozone is con-

Experimental and calculated data for cyclohexane ozonolysis*

Time, h	Product concentrations, M								
	A_1	$A_4 \times 10^3$	$A_5 \times 10^4$	$A_6 \times 10^3$	A_7	$A_9 \times 10^2$	A_{11}	$A_{12} \times 10^3$	$A_{13} \times 10^3$
1	9.14	36.3	23.2	7.10	0.60	0.225	0.064	0.108	0.75
	9.11	34.0	23.0	2.0	0.10	1.0	0.08	2.0	5.2
2	8.99	46.4	28.9	17.9	0.17	0.52	0.177	0.665	4.18
	8.94	39	26	4.2	0.24	2.0	0.21	4.5	19
3	8.84	49.0	30.3	29.6	0.299	0.714	0.303	1.74	10.2
	8.74	37	25	6.0	0.40	2.5	0.32	6.1	35
4	8.68	49.6	30.5	41.6	0.431	0.823	0.432	3.25	18.37
	8.60	35	25.1	8.2	0.55	3.0	0.48	8.0	60
5	8.52	49.6	30.4	53.47	0.565	0.879	0.561	5.12	28.14
	8.40	36	25	10.0	0.75	3.0	0.60	9.0	80

* Numerator: calculated; denominator: experimental.

sumed in bimolecular reactions with cyclohexanol, cyclohexyl hydroperoxide, cyclohexanone, 1-hydroxycyclohexyl hydroperoxide, and peroxy radical. Calculations show that only 0.67 mol of oxygen is released per mole of consumed ozone (usually, only one of three oxygen atoms in the ozone molecule is involved in oxidation). Comparison of the total amounts of oxygen incorporated in the reaction products, ozone consumed, and oxygen released shows that the reaction involves not only oxygen generated in the event of reaction of ozone with the reaction medium, but also oxygen continuously fed to the reactor as a component of the ozone–oxygen mixture.

CONCLUSION

A mathematical model was developed for low-temperature selective ozonolysis of cyclohexane to cyclohexanone. The reaction selectivity is due to recombination of peroxy radicals with formation of cyclohexanol and cyclohexanone, fast oxidation of cyclohexanol and cyclohexyl hydroperoxide to cyclohexanone, and relatively slow oxidation of cyclohexanone to acids and ε-caprolactone.

REFERENCES

1. Syroezhko, A.M., Proskuryakov, V.A., and Begak, O.Yu., *Zh. Prikl. Khim.*, 2002, vol. 75, no. 8, pp. 1320–1328.
2. Maslennikov, S.I., Galimova, L.G., and Komissarov, V.D., *Izv. Akad. Nauk SSSR, Ser. Khim.*, 1979, no. 3, pp. 631–634.
3. Korotkova, N.P., Oxidation of Cyclohexane and Some Oxygen-Containing Compounds with Ozone–Air Mixtures, *Cand. Sci. Dissertation*, Leningrad, 1978.

Russian Journal of Applied Chemistry, Vol. 75, No. 9, 2002, pp. 1453–1457. Translated from Zhurnal Prikladnoi Khimii, Vol. 75, No. 9, 2002, pp. 1485–1489.
Original Russian Text Copyright © 2002 by Solov'ev, Ryadnova, Shataeva.

MACROMOLECULAR CHEMISTRY AND POLYMERIC MATERIALS

Modification of Poly(Ethylene Terephthalate) Track Membranes by Sorption of Poly(Ethylene Glycol)

A. Yu. Solov'ev, I. Yu. Ryadnova, and L. K. Shataeva

Institute of Macromolecular Compounds, Russian Academy of Sciences, St. Petersburg, Russia

Received January 15, 2002

Abstract—Sorption of poly(ethylene glycol) on poly(ethylene terephthalate) track membranes was studied at different pH. The hydrophilic-hydrophobic properties of the intact membranes and those modified with poly(ethylene glycol) are compared. The membrane–aqueous human serum albumin and membrane–aqueous insulin adhesive tensions were determined for modified membranes. The competitive sorption of human serum albumin and poly(ethylene glycol) from aqueous solution on the track membranes is analyzed.

Poly(ethylene terephthalate) (PET) track membranes (TMs) are widely used for microfiltration to separate filterable viruses, fractionation of colloid solutions, and plasmophoresis to separate blood corpuscules of a donor blood from its plasma [1]. However, relatively high hydrophobicity of the surface of these membranes [2] results in nonselective sorption of proteins from aqueous solutions, resulting in plugging of membrane pores and microfiltration deceleration. There are diverse techniques for chemical modification of PET surface [3] to decrease the nonselective sorption. Poly(ethylene terephthalate) track membranes can be modified by immobilization of hydrophilic groups on the pore surface via covalent bonding. Such modification, as a rule, results in significant pore narrowing [4]. Track membranes can also be hydrophilized by immobilization of hydrophilic nonionic substances, e.g., nonionic surfactants, on the surface of membrane pores by the sorption mechanism. Track membranes can be modified with poly(ethylene glycol) (PEG), which is amphiphilic biocompatible polymer widely used in biochemistry, molecular biology, and medicine [5]. It is known that the chemical grafting of PEG decreases the nonselective sorption of blood plasma proteins on the surface of track membranes [6–8]. The immobilization of PEG on TM surface by the sorption mechanism also decreases the sorption of serum albumin from model aqueous solutions [6].

In this work we studied the sorption of PEG on the TM surface and the influence of PEG sorption on the hydrophilicity of the track membranes and their sorption power with respect to various biopolymers.

EXPERIMENTAL

In our experiments we used 10 μm thick microfiltration poly(ethylene terephthalate) track membranes with the nominal pore diameter d = 0.35 μm and the specific porosity $N = 1.2 \times 10^8$ pore cm^{-2}. A plasmophoretic setup manufactured by Plazmofil'tr Research and Production Association (St. Petersburg, Russia) was equipped with microfiltration track membrane modules with the filtering surface of area 480 cm^2. Track membranes with the nominal pore diameters of 0.05 and 0.03 μm were also used in our experiments. The porosity of these membranes was not precisely determined by the manufacturer (Joint Institute for Nuclear Research, Dubna, Russia).

The track membrane surface was modified by sorption of PEGs with the average molecular weights M of 3 and 40 kDa (Ferak). The influence of such modification on the nonspecific sorption of proteins was studied in the following solutions: 0.02 M human serum albumin HSA (Reanal, Czechia) in phosphate buffer, pH 5.7; 0.05 M crystalline insulin in phosphate buffer, pH 6.8; and 5% HSA for perfusion (Lipetsk, Russia) in distilled water.

Sorption of PEG from different aqueous solutions on track membranes was performed under static conditions for 24 h at 25°C. In these experiments, the following aqueous PEGs were used: $(1–125) \times 10^{-6}$ M PEG (M = 3 and 40 kDa) in distilled water at pH 6.2; $(25–400) \times 10^{-6}$ M PEG (M = 3 kDa) in distilled water at pH 6.2; $(1–20) \times 10^{-6}$ M PEG (M = 40 kDa) in the acetate buffer at pH 8.5; and PEGs of the same molecular weights and concentrations as for the

1070-4272/02/7509-1453$27.00 © 2002 MAIK "Nauka/Interperiodica"

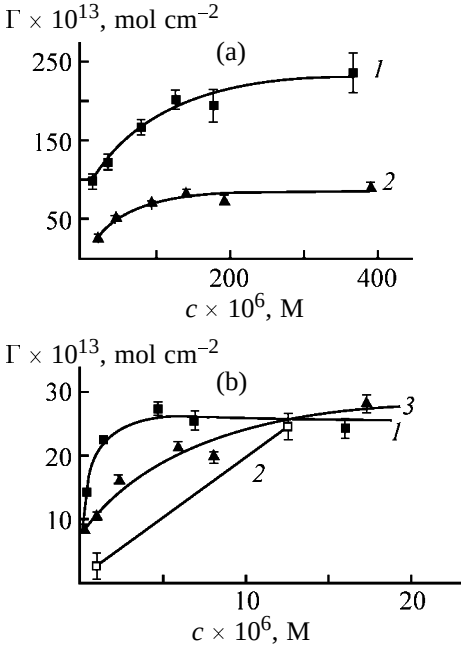

Fig. 1. Sorption of PEG on poly(ethylene terephthalate) track membranes with the pore diameter of 350 nm. (*c*) PEG concentration and (Γ) membrane sorption capacity. M_{PEG} (kDa): (a) 3 and (b) 40. pH: (*1*) 2.8, (*2*) 6.2, and (*3*) 8.5.

above-noted systems in 1% aqueous acetic acid at pH 2.8.

To obtain the PEG sorption isotherms, a weighed portion of a track membrane (1.5–2.0 g) preliminarily treated by the technique reported in [2] was immersed in aqueous PEG (15 ml). The PEG concentration in the equilibrium aqueous phase was determined by the optical absorption of a PEG molecular complex with iodine. Prior to determination, an I_2 + KI saturated solution was diluted with water by a factor of 100 to obtain the working solution. 1 ml of aqueous $BaCl_2$ (5%) and 1 ml of the working I_2 + KI solution were added to 2 ml of the solution to be analyzed. After the lapse of 2 min, the optical density of the solution was measured at 535 nm against water. The calibration curve was obtained with aqueous PEG solutions of the concentrations similar to those in the sorption experiments. The difference between the initial and final PEG amount in the liquid phase was accepted as the PEG amount sorbed on the track membrane. After completion of the sorption experiment, the track membranes were washed with distilled water and air-dried. The presence of sorbed PEG on the track membrane surface was confirmed with modified Dragendorff reagent [9]. To characterize the wettability of the modified membranes, the contact angles θ (the flowing angles) were determined with a VT-500 torsion balance by the Wilhelmi plate method [2]. The contact angle was calculated by the equation

$$\cos\theta = \frac{m - m_0 + V(\rho - \rho_0)g}{\Pi\gamma}, \quad (1)$$

where m_0 and m are the weights of the dry membrane and that partly immersed in the liquid phase, respectively; V, the volume of the membrane part immersed in a liquid: P, the perimeter of the membrane–liquid contact; γ and ρ, the surface tension and the density of the liquid, respectively; ρ_0, the membrane density; and g, the free fall acceleration. The mean error in measuring cos θ was about 10%, which corresponds to scattering of the contact angles within ±3° for the contact angles exceeding 80°.

Because of lack of the data on the HSA and insulin surface tension, the wetting power of these proteins with respect to the track membrane surface was characterized by the adhesive tension [10]:

$$A = \gamma\cos\theta = \frac{m - m_0 + V(\rho - \rho_0)g}{\Pi}. \quad (2)$$

The adhesive tension is defined as the difference between the surface tension at the solid surface–vapor phase contact and that at the solid surface–equilibrium liquid phase contact. Therefore, the adhesive tension reflects the energy of interactions between a solid surface and a solution at the constant vapor pressure of the solvent.

In our experiments, the track membranes were wetted with distilled water, and the water–membrane contact angle characterized the influence of PEG sorption on the hydrophobicity of the membrane surface.

A membrane microfiltration module was modified by recirculating aqueous PEG (M = 40 kDa) for 7 days, an then the module was washed with distilled water. 5% aqueous HSA (100 ml) was pumped through both the modified and control (intact) modules. The second control module was not contacted with aqueous HSA. After completion of microfiltration of aqueous HSA, the modules were disassembled, and the hydrophilicity of the track membranes (hereinafter denoted as MTM) was determined.

The isotherms of sorption on track membranes of PEG with different molecular weights from aqueous solutions of different pH are shown in Figs. 1a and 1b. These isotherms show that acidity of solutions significantly affects the sorption isotherms. For low-molecular-weight PEG (M = 3 kDa), passing from

acidic (pH 2.8) to neutral (pH 6.2) solutions decreases the membrane sorption capacity. A similar pattern is observed with PEG of higher molecular weight, M = 40 kDa.

One of the stages of preparation of poly(ethylene terephthalate) track membranes is their treatment with aqueous alkali solutions to etch the initial radiation tracks in a PET matrix. In so doing, carboxy and hydroxy groups arise on the sorbing surface of the membrane pores. Along with these new hydrophilic sites, hydrophobic sites also remain on the surface [11]. Therefore, amphiphilic surfactants can be sorbed on both hydrophilic and hydrophobic sites of the track membrane surface. The effect of pH on sorption of PEG on track membranes shows that PEG macromolecules are sorbed by the mechanism of hydrogen bonding with the hydrophilic sites. It is known that, in hydrogen bonding, PEG macromolecules are the electron acceptors only. Therefore, sorption of PEG from acidic solution occurs by the hydrogen bonding between oxygen atoms of its ether groups (proton acceptors) and the carboxy and hydroxy groups (proton donors) located on the pore surface. With increasing acidity of solution, the protonation of the hydrophilic groups on the surface of track pores increases, and, as a result, the hydrogen bonding is strengthened. The number of such hydrogen bonds increases with increasing PEG molecular weight.

The degree of saturation of the pore surface with PEG macromolecules was evaluated from the average pore surface area per PEG macromolecule (M = 3 and 40 kDa).

The specific pore surface area (specfic sorbing surface area) of track membranes was calculated by the equation

$$S_{sp} = \pi dN/r_0, \quad (3)$$

where d is the pore diameter, N is the pore number per unit filtering surface area, and ρ_0 is the TM density (1.21 g cm^{-3}).

In our experiments we used the membranes with the specific pore surface area of 1.09 m^2 g^{-1}.

Using the reference data on the intrinsic viscosity of aqueous PEG [12] (7.5 and 32.0 cm^3 g^{-1} for PEG with M = 3 and 40 kDa, respectively) and assuming that these values are the exclusion volumes of the hydrated PEG macromolecules, we can calculate the average area of the projection of the hydrated macromolecule onto the sorbing surface. These calculations show that PEG molecules with M = 3 and 40 kDa occupy the surface area of 11 and 165 nm^2, respectively. We found that, at the limiting sorption of these PEGs on the membranes, the total surface area occupied by the PEG macromolecules exceeds the specific sorption surface area of the membranes by a factor of 1.5–2.0. These results are indicative of the dense occupation of the sorbing surface by PEG macromolecules and their certain dehydration.

Table 1. Characteristics of PEG sorption on the track membranes with the pore diameter of 0.35 μm

M_{PEG}, kDa	K			W, kJ mol^{-1}		
	at indicated pH					
	2.8	6.2	8.5	2.8	6.2	8.5
3×10^3	17	7	–	7.0	4.8	–
4×10^4	133	20	33	12.1	7.4	8.7

The PEG sorbability to the pore surface can be qualitatively estimated from the distribution factor calculated from the slope of the initial portion of the sorption isotherm. In the systems under consideration, the PEG macromolecules are distributed between the bulk of the liquid phase and the membrane surface layer whose volume cannot be determined experimentally. For simplification, we can assume that PEG is distributed between the bulk of the aqueous solution, in which the PEG concentration can be determined, and the pore solution. The amount of pore solution in the membranes used in our experiments was 0.09 cm^3 g^{-1}. The distribution factor K was calculated by the equation

$$K = c/c_s, \quad (4)$$

where c is the PEG concentration in the porous solution and c_s is the PEG concentration in the equilibrium liquid phase.

The distribution factor K of a macromolecule allows estimation of the work of its sorption W by the equation [10]

$$W = RT\ln(c/c_s). \quad (5)$$

The experimental distribution factors of PEGs and the corresponding W values calculated by Eq. (5) are listed in Table 1. These results show that the work of sorption of PEG with M = 40 kDa exceeds that of PEG with M = 3 kDa. This difference reflects the fact that, with increasing PEG molecular weight, the number of the molecular contacts between PEG and the pore surface increases.

The hydrophilicity of the polymer surface is com-

Table 2. Membrane–water contact angles θ for intact and modified membranes

d_{TM}, μm	θ, deg		
	intact TM	TM modified with PEG	
		M = 3 kDa	M = 40 kDa (from water)
0.03	65	54	–
0.05	72	69	68
0.35	82	75	73

Table 3. Membrane (MTM)–water contact angles (θ) and membrane–aqueous HSA (A_{HSA}) and membrane–aqueous insulin (A_{ins}) adhesive tensions for modified membranes of microfiltration module

Membrane	θ, deg	A_{HSA}		A_{ins}		
		mN m^{-1} at indicated protein concentration, mg ml^{-1}				
		0.5	4.0	3.0	6.5	13.0
MTM + PEG	74	8.5	23.0	46.5	44.0	42.0
MTM + PEG + HSA	64	39.7	34.0	–	–	–
MTM + HSA	65	31.5	29.3	39.0	40.0	42.0

monly estimated by the polymer–water contact angle. The smaller the contact angle, the more hydrophilic is the solid surface. As a rule, sorption of nonionic surfactant on a hydrophilic surface results in its hydrophobization, whereas sorption of a nonionic surfactant on a hydrophobic surface causes its hydrophilization [13]. To elucidate how sorption of PEG affects the hydrophilicity of the membrane surface, we measured the contact angles (θ) for both the intact membranes and those modified by sorption of PEG. Along with the TMs with the pore diameter of 0.35 μm, whose sorption power with respect to PEG was thoroughly studied, the contact angles were also determined for membranes with the pore size of 0.05 and 0.03 μm whose specific porosity was not characterized. Table 2 shows that, for all the membranes, regardless of their characteristics, the sorption of PEG decreases the contact angle. Thus, the sorption of PEG makes the membrane surface more hydrophilic. This effect is apparently caused by formation of a hydrate shell around the sorbed PEG macromolecules [14]. These results also show that hydrophilization of the track membranes increases as the pore diameter is increased from 0.03 and 0.05 to 0.35 μm.

It is known that an increase in the hydrophilicity of track membranes substantially decreases sorbability of biologically active macromolecules [7, 8]. We studied the effect of hydrophilization of the track membranes with PEG on their wettability with aqueous HSA and insulin solutions of widely varied concentrations.

The membranes were modified with PEG (M = 40 kDa) by recirculation of aqueous PEG (M = 40 kDa) through a membrane module for 7 days, after which the membrane module was washed with water.

We found that the rate of microfiltration of water through a membrane module modified by sorption of PEG decreased, on the average by 5–12% as compared to the intact module. Thus, the hydrodynamic resistance of the modified module exceeds that of the intact modules. This fact shows that PEG is sorbed on the pore surface and, therefore, narrows the effective pore diameter. The similar increase in the hydrodynamic resistance was observed in microfiltration of HSA through both the intact and modified membranes. In view of the fact that PEG and HSA can be sorbed not only on the membrane surface but also on the other parts of a module, our experiments show only a tendency in the effects of macromolecule sorption on microfiltration.

Upon completion of passing 5% aqueous HSA through both the intact and modified modules, these were disassembled and the membrane (MTM)–water contact angles (θ) and membrane–aqueous HSA (A_{HSA}) and membrane–aqueous insulin (A_{ins}) adhesive tensions were determined (Table 3). The membrane–water contact angles θ show that sorption of HSA makes the TM surface more hydrophilic than sorption of PEG. Therefore, the (MTM + PEG + HSA) membrane–water and the (MTM + HSA) control membrane–water contact angles are similar within the limits of the experimental error. The qualitative analysis of the (MTM + PEG + HSA) membrane for PEG with Dragendorff reagent has not revealed these macromolecules. Most likely that, on contact of (MTM + PEG) membrane with 5 wt % aqueous HSA, this protein displaces PEG from the sorption layers. It should be noted that the replacement of PEG is not observed at lower HSA concentrations (0.1, 0.2, and 0.5 wt %). These facts show that HSA replaces PEG not by the mechanism of competitive sorption of separate macromolecules, but by a colloidal mechanism involving replacement of PEG macromolecules by an HSA solution with the lower surface tension.

Figure 2 shows the plot of the membrane–liquid adhesive tension vs. the surface tension of different liquids [10, 15]. As seen from this plot, the mem-

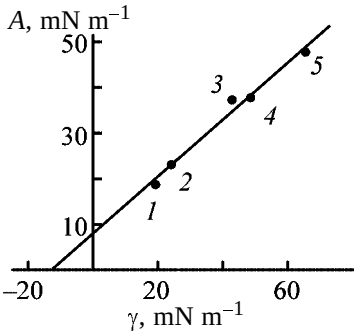

Fig. 2. Membrane–liquid adhesion tension A as a function of the surface tension of liquid γ for (*1*) hexane, (*2*) ethanol, (*3*) chloroform, (*4*) ethylene glycol, and (*5*) glycerol.

brane–liquid adhesive tension correlates with the membrane–liquid contact angle [2].

Therefore, the membrane–aqueous protein adhesive tension qualitatively characterizes their surface tension. For an example, with increasing HSA concentration, the adhesive tension decreases to a level corresponding to liquids with low surface tension. This effect shows that HSA is a strong surfactant. As opposed to HSA, aqueous insulin apparently exhibits higher surface tension and, therefore, cannot displace PEG from the sorption layer. By the same reason, PEG immobilized on the TM surface is not displaced by aqueous mineral salts but is desorbed only by liquids with a low surface tension, e.g., by chloroform.

CONCLUSIONS

(1) Sorption of poly(ethylene glycol) with the molecular weight of 3 and 40 kDa on track membranes was studied at different pH. The sorbability of poly(ethylene glycol) and selectivity of its sorption increase with decreasing pH.

(2) The water–membrane contact angles were measured for both intact track membranes and those modified with poly(ethylene glycol). Sorption of poly(ethylene glycol) on the track membranes decreases the membrane–water contact angle, indicating the increased hydrophilicity of the membrane surface.

(3) The membrane–aqueous human serum albumin and membrane–aqueous insulin adhesive tensions show that, as opposed to insulin, human serum albumin makes the track membranes more hydrophilic than poly(ethylene glycol) does.

(4) Owing to relatively low surface tension, 5 wt % aqueous human albumin completely displaces poly(ethylene glycol) from the surface of the modified track membranes.

REFERENCES

1. Mchedlishvili, B.V., and Flerov, G.P., *Zh. Vses. Khim. O–va im. D.I. Mendeleeva*, 1987, vol. 32, no. 6, pp. 641–647.
2. Shataeva, L.K., Ryadnova, I.Yu, and Nechaev, A.N., *Kolloidn. Zh.*, 2000, vol. 62, no. 1, pp. 126–132.
3. Kochkodan, V.M. and Bryk, M.T., *Dokl. Akad. Nauk Ukr. SSR, Ser. B*, 1986, no. 8, pp. 29–31.
4. Kochkodan, V.M., Bryk, M.T., and Mchedlishvili, B.V., *Ukr. Khim. Zh.*, 1987, vol. 53, no.1, pp. 100–103.
5. Topchieva, I.N., *Usp. Khim.*, 1980, vol. 49, no. 3, pp. 494–517.
6. Kochkodan, V.M., Bryk, T.M., and Tsapyuk, E.A., *Khim. Tekhnol.*, 1987, no. 1, pp. 45–50.
7. Jeon, S.I. and Andrade, J.D., *J. Colloid Interface Sci.*, 1991, vol. 142, no. 1, pp. 159–166.
8. Lee, J.H., Kopeckova, P., Kopecek, J., and Andrade, J.D., *Biomaterials*, 1990, vol. 11, no. 7, pp. 455–464.
9. Buerger, K., *Ann. Chem.*, 1963, vol. 196, no. 2, pp. 251–259.
10. Adamson, A.W., *Physical Chemistry of Surfaces*, New York: Wiley, 1976. Translated under the title *Fizicheskaya khimiya poverkhnostei*, Moscow: Mir, 1979, pp. 35–50.
11. Thom, V., Ulbricht, M., and Jonsson, G., *Acta Polytech. Scand.*, 1997, no. 247, pp. 35–50.
12. Bailey, F.E. and Koleske, J.K., *Poly(Ethylene Oxide)*, New York: Academic, 1976.
13. Churaev, N.V., *Kolloidn. Zh.*, 1994, vol. 56, no. 5, pp. 707–723.
14. Baran, A.A., Solomentseva, I.M., and Mank, V.V., *Dokl. Akad. Nauk SSSR*, 1972, vol. 207, no. 2, pp. 363–366.
15. *Poverkhnostno-aktivnye veshchestva: Spravochnik* (Surfactants: Handbook), Abramzon, A.A. and Gaevskii, G.M., Eds., Leningrad: Khimiya, 1979.

Russian Journal of Applied Chemistry, Vol. 75, No. 9, 2002, pp. 1458–1461. Translated from Zhurnal Prikladnoi Khimii, Vol. 75, No. 9, 2002, pp. 1490–1493.
Original Russian Text Copyright © 2002 by Ershov, Gavrilova, Panarin.

MACROMOLECULAR CHEMISTRY AND POLYMERIC MATERIALS

Modification of Vinylformamide by Michael Addition to Methyl Acrylate and Methyl Vinyl Ketone, and Copolymers Derived from the Resulting Products

A. Yu. Ershov, I. I. Gavrilova, and E. F. Panarin

Institute of Macromolecular Compounds, Russian Academy of Sciences, St. Petersburg, Russia

Received June 18, 2002

Abstract—Vinylformamide reacts with methyl acrylate and methyl vinyl ketone under conditions of base catalysis, following the Michael addition pattern, to give methyl 3-(vinylformylamino)propionate and previously unknown 4-(vinylformylamino)-2-butanone. Radical copolymerization of these compounds with vinylformamide and *N*-vinylpyrrolidone was studied.

Targeted transport of a physiologically active substance to a definite organ, cell, or tissue of a living body is an important problem in modern pharmacology. Efficient carriers for such transport can be water-soluble copolymers derived from *N*-vinylamides, which show enhanced affinity for proteins owing to the presence of similar amide groups and other functional moieties.

Polymers derived from *N*-vinylpyrrolidone and *N*-vinylacetamide and its *N*-alkyl analogs were studied previously [1–3]. Introduction of hydrophobic alkyl radicals into side chains of such polymers opens up possibilities for control of their conformational state and increases the probability of their binding with hydrophobic sections of cell membranes.

In this work, with the aim to develop new copolymers based on vinylformamide (VF) and containing functional fragments in pendant chains, we studied modification of VF by the reactions with methyl acrylate (MA) and methyl vinyl ketone (MVK) under conditions of base catalysis, following the Michael addition pattern:

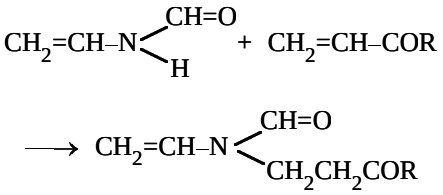

Ia, Ib

where R = OCH_3 (**Ia**), CH_3 (**Ib**).

We found that the reaction occurs within 24 h at room temperature without a solvent in the presence of catalytic amounts of an alkali. The products are liquids readily distillable in a vacuum. The physicochemical characteristics of the compounds are listed in Table 1.

The ^1H NMR spectra of **Ia** and **Ib** fully confirm their structure. In particular, the spectra (Fig. 1a) contain a characteristic *ABX* pattern of vinyl protons (4.5 and 6.5 ppm) and two multiplets of methylene protons (2.5 and 4.0 ppm, CH_2CH_2N). Some signals are doubled because of braked rotation of the formyl group about the C–N bond (Table 2).

Thus, Michael addition of vinylformamide to com-

Table 1. Physicochemical characteristics of **Ia** and **Ib**

Compound	bp, °C/*P*, mm Hg	Found, %			Formula	Calculated, %			Yield, %
		C	H	N		C	H	N	
Ia	93–96/2	53.54	6.97	8.87	$C_7H_{11}NO_3$	53.49	7.05	8.91	70
Ib	98–104/1	59.60	7.79	9.88	$C_7H_{11}NO_2$	59.56	7.85	9.92	75

1070-4272/02/7509-1458$27.00 © 2002 MAIK "Nauka/Interperiodica"

Table 2. ^{1}H NMR spectra of **Ia** and **Ib** in $CDCl_3$

Compound	Conformational composition, %	δ, ppm					
		CH_3, s	CH_2CO, m	CH_2N, m	CH_2=, m	CH=, m	CH=O, s
Ia	*E*, 75	3.62	3.80	4.51	6.51	7.18	8.23
	Z, 25	3.62	3.80	4.51	6.49	6.90	8.18
Ib	*E*, 80	2.07	2.63	4.41	6.50	7.11	8.20
	Z, 20	2.07	2.63	4.41	6.49	6.91	8.18

pounds containing an activated C=C bond (MA, MVK) is a convenient route to modified vinylformamide derivatives, which are of interest as monomeric precursors of water-soluble copolymers containing a functionally substituted vinylamide moiety:

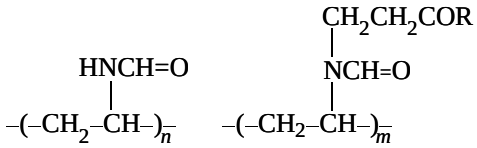

IIa, IIb

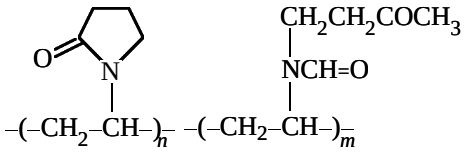

III

where R = OCH_3 (**IIa**), CH_3 (**IIb**).

Copolymerization of VF and VP with modified VF analogs, methyl 3-(vinylformylamino)propionate (VFMA) and 4-(vinylformylamino)-2-butanone (VFVMK) was performed by heating of the monomers dissolved in isopropanol at 60°C in glass ampules under nitrogen, with azobis(isobutyronitrile) initiator (1 wt % relative to comonomers). The conditions for preparing copolymers **IIa**, **IIb**, and **III** and their intrinsic viscosities [η] are listed in Table 3. The procedure allows preparation of random water-soluble copolymers in high yields.

The compositions of the copolymers were determined from the integral intensities of the characteristic ^{1}H NMR signals, namely, of those of H–C=O (8 ppm) and CH_2 (2.8 ppm) groups in the case of **IIa** and **IIb** (Fig. 1b, Table 4) and of H–C=O group (8 ppm) and H^5 atom in the pyrrolidone ring in the case of copolymer **III** derived from VP. The measurement error was ±3–5%.

Copolymers **IIa** were hydrolyzed to vinylamine–3-(vinylamino)propionic acid copolymers (in the form of hydrochlorides, **IV**) by heating in 10% HCl at 120°C for 24 h; the products were isolated by precipitation into acetone.

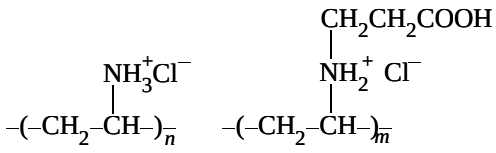

IV

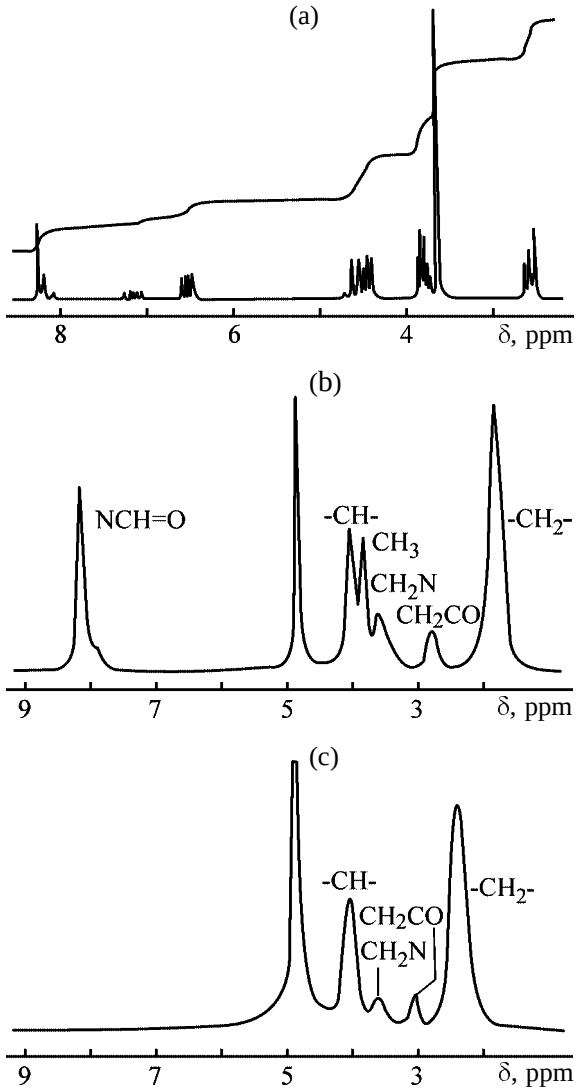

Fig. 1. ^{1}H NMR spectra of (a) **Ia** in $CDCl_3$, (b) **IIa** in D_2O, and (c) **IV** in D_2O. (δ) Chemical shift.

Table 3. Copolymerization conditions and characteristics of copolymers

Compound	Content of initial monomers, mol %		Yield, %	Copolymer composition, mol %		[η], dl g^{-1}
	VF or VP	VFMA or VFVMK		VF or VP	VFMA or VFVMK	
IIa	85	15	90	85	15	0.27
	50	50	60	60	40	0.18
	25	75	50	35	65	0.17
IIb	80	20	95	84	16	0.40
	65	35	70	62	38	0.18
III	80	20	98	82	18	0.21
	70	30	75	75	25	0.13
IV	85	15	65	85	15	0.15
	50	50	75	60	40	0.12
	25	75	70	35	65	0.10

Table 4. ^{1}H NMR spectra of copolymers in D_2O

Compound	δ, ppm					
	$-CH_2-$	–CH–	H–C=O or H^3, H^4, H^5	CH_2CO	CH_2N	CH_3
IIa	1.97	4.02	8.12 (H–C=O)	2.76	3.56	3.78
IIb	1.98	4.12	8.20 (H–C=O)	3.08	3.61	2.46
III	2.03	3.97	2.24 (H^4), 2.48 (H^3), 3.53 (H^5)	3.13	3.44	2.41
IV	2.21	4.04	–	3.13	3.64	–

The degree of hydrolysis was evaluated from the Cl^- content, determined by conductometric titration with 0.01 M $AgNO_3$, and also from the ^{1}H NMR spectra (disappearance of the formyl proton signal at 8.0 ppm and of the methoxy group signal at 2.8 ppm; Fig. 1c). The conditions for synthesis of copolymers **IV** and their intrinsic viscosities are given in Table 3.

Thus, Michael addition of vinylformamide to compounds containing an activated double bond is a convenient route to modified derivatives of this monomer. The procedure allows introduction into pendant chains of ester and carbonyl groups for subsequent modification by functional binding of physiologically active substances.

EXPERIMENTAL

Elemental (C, H, N) analysis was performed with a Hewlett–Packard 185B analyzer. The ^{1}H NMR spectra were recorded on a Bruker AC 200 spectrometer. Titration was performed with a TV-6L-1 conductometer. The intrinsic viscosity was measured with an Ubbelohde viscometer in water at 25°C. Compound **Ia** was prepared as described in [4].

4-(Vinylformylamino)-2-butanone Ib. A 35-g (0.5-mol) portion of VF was added dropwise with cooling (the temperature was maintained within 20–25°C) to a mixture of 40 g (0.55 mol) of freshly distilled MVK, 0.56 g of KOH, and 0.01 g of hydroquinone in 10 ml of methanol. The mixture was left overnight at room temperature and, after addition of 0.5 g of sodium acetate, distilled in a vacuum.

CONCLUSIONS

(1) Michael addition of vinylformamide to methyl acrylate and methyl vinyl ketone, yielding new monomers, methyl 3-(vinylformylamino)propionate and 4-(vinylformylamino)-2-butanone, was studied.

(2) Copolymers of these monomers with vinylformamide and *N*-vinylpyrrolidone were prepared, and their acid hydrolysis was studied. The *N*-formyl and ester groups can be quantitatively removed with the

formation of vinylamine–3-(vinylamino)propionic acid copolymers in the form of hydrochlorides.

ACKNOWLEDGMENTS

The study was financially supported by the Russian Foundation for Basic Research (project no. 02-03-33110).

REFERENCES

1. Ershov, A.Yu., Gavrilova, I.I., and Panarin, E.F., *Zh. Prikl. Khim.*, 1995, vol. 68, no. 9, pp. 1522–1526.
2. Ershov, A.Yu., Gavrilova, I.I., and Panarin, E.F., *Zh. Prikl. Khim.*, 1998, vol. 71, no. 11, pp. 1852–1855.
3. Pavlov, G.M., Korneeva, E.V., Zhumel', K., *et al.*, *Zh. Prikl. Khim.*, 2000, vol. 73, no. 6, pp. 992–996.
4. US Patent 5463110.

Russian Journal of Applied Chemistry, Vol. 75, No. 9, 2002, pp. 1462–1464. Translated from Zhurnal Prikladnoi Khimii, Vol. 75, No. 9, 2002, pp. 1494–1496.
Original Russian Text Copyright © 2002 by Shaglaeva, Lebedeva, Mikhaleva, Pirogova, Sultangareev, Chipanina, Gavrilova.

MACROMOLECULAR CHEMISTRY AND POLYMERIC MATERIALS

Copolymerization of 1-Vinyl-4,5,6,7-tetrahydroindole with Vinyl Chloride in the Presence of a Radical Initiator

N. S. Shaglaeva, O. V. Lebedeva, A. I. Mikhaleva, G. A. Pirogova, R. G. Sultangareev, N. N. Chipanina, and G. A. Gavrilova

Favorskii Irkutsk Institute of Chemistry, Siberian Division, Russian Academy of Sciences, Irkutsk, Russia

Received March 21, 2002

Abstract—Copolymerization of 1-vinyl-4,5,6,7-tetrahydroindole with vinyl chloride in the presence of azobis(isobutyronitrile) occurs as a two-step process. The copolymer is initially formed by the radical mechanism. Then, the eliminated hydrogen chloride initiates cationic oligomerization of 1-vinyl-4,5,6,7-tetrahydroindole, enriching the copolymer with units of this monomer.

N-Vinylpyrroles, which became accessible after the discovery and comprehensive study of pyrrole synthesis from ketoximes and acetylene [1, 2], are a subject of active research as monomers for preparing new macromolecular compounds with a set of valuable properties. *N*-Vinylpyrroles are used for preparing special semiconductors, synthetic dyes [1], photosensitive materials, and biologically active compounds [4, 5].

Introduction of functional groups into *N*-vinylpyrrole polymers will extend applications of pyrrole-containing polymers. Owing to the potential modifying effect of *N*-vinylpyrroles on polymers prepared by radical polymerization, growing attention is given to radical copolymerization of these monomers with commercial monomers such as vinyl chloride, vinyl bromide, vinylidene chloride, methyl methacrylate, acrylamide, and acrylonitrile.

For example, heterocyclic nitrogen-containing compounds are used for enhancing the adhesive properties of vinyl chloride (VC) homo- and copolymers and for stabilizing them against light and heat [6].

In this work, we studied radical copolymerization of *N*-vinyl-4,5,6,7-tetrahydroindole (VTHI) with VC in the presence of azobis(isobutyronitrile) (AIBN). The results are listed in the table.

Copolymers are formed in the entire examined range of the monomer ratios and are enriched in VTHI units as compared to the initial monomer mixture. As the VTHI content in the monomer mixture is increased, the yield of the copolymer grows and its viscosity decreases. The compositions of the obtained copolymers were calculated from elemental analyses.

Determination of the content of VC units from the weight fractions of chlorine and nitrogen gives different results. This fact suggests occurrence of dehydrochlorination:

Copolymerization of VTHI with VC (1.5 wt % AIBN, 60°C, 6 h)

Mole fractions of monomers		Mole fractions of monomer units, calculated from N and Cl content				$[\eta]$, dl g^{-1}	Yield, %
		N		Cl			
VTHI	VC	VTHI	VC	VTHI	VC		
0.23	0.77	0.49	0.51	0.51	0.49	0.18	7.0
0.39	0.61	0.64	0.36	0.68	0.32	0.09	12.2
0.52	0.48	0.73	0.27	0.82	0.18	0.08	36.4
0.72	0.28	0.85	0.15	0.91	0.09	0.07	56.5
0.88	0.12	0.90	0.10	0.98	0.02	0.05	63.0

1070-4272/02/7509-1462$27.00 © 2002 MAIK "Nauka/Interperiodica"

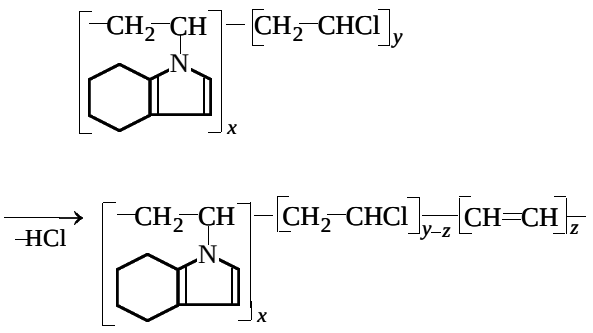

The released HCl can initiate cationic oligomerization of VTHI and protonate the pyrrole ring in the macromolecular chain.

We found that passing HCl through VTHI monomer at 22°C results in instantaneous formation of the oligomer. Its IR spectrum (Fig. 1b) is similar to the spectrum of the cationic VTHI oligomer (Fig. 1a) prepared in the presence of $ClSiEt_3$ [7]. The spectrum of the VTHI–VC copolymer (Fig. 1c) is, on the whole, similar to the spectra of the oligomers (Figs. 1a, 1b). This fact suggests the presence of blocks formed by cationic oligomerization of VTHI under the action of the eliminated HCl. The rate of cationic oligomerization of VTHI is considerably higher than the rate of radical copolymerization of VTHI with VC.

In block copolymerization of VTHI with VC in the presence of AIBN at 60°C, the viscosity of the medium growth only slightly even after 10 h: initial mixture, η_{rel} = 0.08; after 10 h, η_{rel} = 0.10. At the same time, HCl converts monomeric VTHI into an insoluble solid within 5–10 min at 22°C. The higher activity of VTHI as compared to VC, in contrast to the published data that VTHI is characterized by low rate of radical polymerization [8, 9], may be due to fast cationic polymerization of VTHI in the presence of HCl, resulting in enrichment of the copolymer with VTHI units.

Cationic oligomerization of VTHI in the course of copolymerization does not yield a separate product, as indicated by the results of turbidimetric titration (Fig. 2) and TLC.

Thus, initially copolymerization of VTHI with VC occurs by the radical mechanism. Then, the released HCl initiates oligomerization of VTHI resulting in grafting of short blocks of the cationic oligomer to the backbone of the VTHI–VC copolymer:

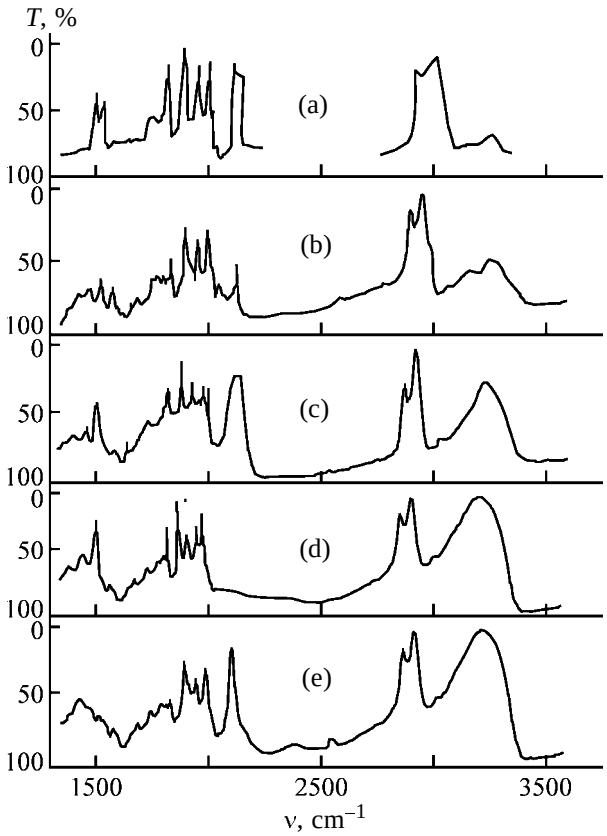

Fig. 1. IR spectra of (a) VTHI oligomer prepared in the presence of $ClSiEt_3$; (b) VTHI homopolymer prepared in the presence of dry HCl; (c) VTHI–VC copolymer; (d) VTHI homopolymer prepared by the radical mechanism; and (e) the same, after treatment with dry HCl. (*T*) transmission and (ν) wave number. (a) Thin film and (b–e) KBr pellets.

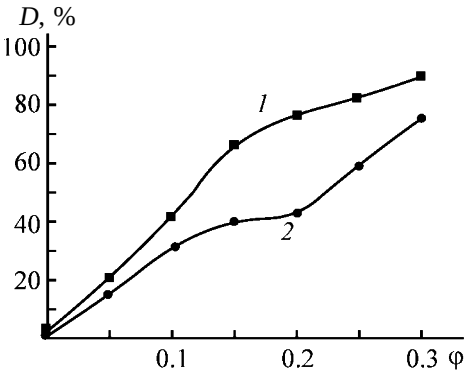

Fig. 2. Turbidimetric titration curves of (*1*) VTHI–VC copolymer and (*2*) a blend of VTHI and VC homopolymers. (*D*) Absorption and (φ) volume fraction of substance.

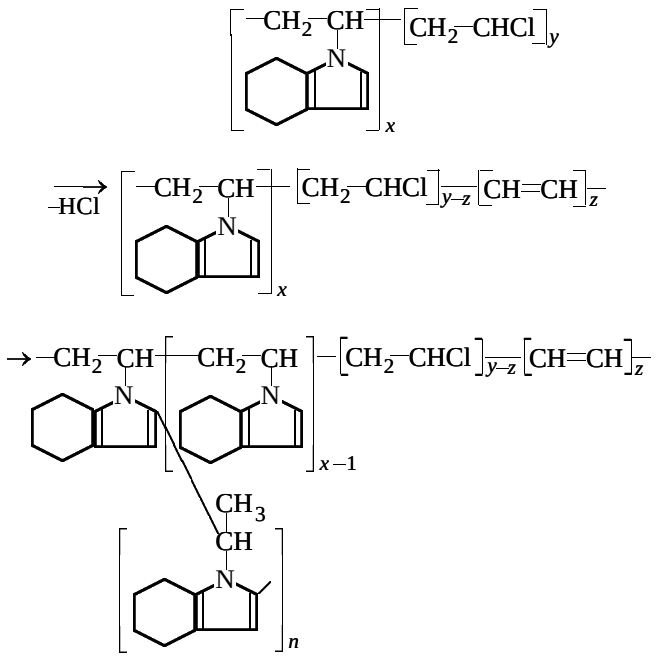

Also, the eliminated HCl partially protonates the tetrahydroindole moieties in the macromolecule. This conclusion follows from comparison of the IR spectra of the VTHI homopolymer obtained by AIBN-initiated radical polymerization (Fig. 1d) and of its protonated form (Fig. 1e). In the IR spectra of both the protonated form of the homopolymer and the VTHI–VC copolymer, an immonium absorption band appears at 1680 cm^{-1} [10]:

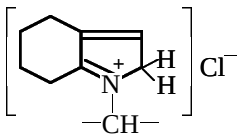

EXPERIMENTAL

N-Vinyl-4,5,6,7-tetrahydroindole was prepared as described in [2]. Copolymerization was performed in sealed ampules at 60°C in the presence of AIBN under argon.

The reaction mixture was dissolved in benzene, and the copolymer was precipitated with heptane. The copolymers were reprecipitated from benzene solution into heptane and vacuum-dried to constant weight.

The VTHI homopolymer was prepared by AIBN-initiated radical polymerization. Protonation was performed by passing dry HCl through VTHI or a solution of the homopolymer. The products were filtered off and washed.

The IR spectra were recorded on a Specord 751-IR spectrophotometer. Turbidimetric titration was performed with a KFK-2 photocolorimeter (solvent benzene, precipitant hexane). TLC was performed on Silufol UV-254 plates (eluent hexane–ether, 2 : 1; developer I_2).

CONCLUSION

Radical copolymerization of 1-vinyl-4,5,6,7-tetrahydroindole with vinyl chloride is accompanied by polymer-analogous transformations, namely, by dehydrochlorination and graft cationic oligomerization of 1-vinyl-4,5,6,7-tetrahydroindole.

REFERENCES

1. Trofimov, B.A. and Mikhaleva, A.I., *N-Vinilpirroly* (*N*-Vinylpyrroles), Novosibirsk: Nauka, 1984.
2. Trofimov, B.A., Mikhaleva, A.I., and Morozova, L.V., *Usp. Khim.*, 1985, vol. 54, pp. 1034–1050.
3. Morozova, L.V., Mikhaleva, A.I., Korostova, S.E., and Filimonova, I.L., in *Elektronika organicheskikh materialov* (Electronics of Organic Materials), Moscow: Nauka, 1985, pp. 305–307.
4. Trofimov, B.A., Minakova, T.G., Morozova, L.V., *et al.*, *Vysokomol. Soedin., Ser. B*, 1980, vol. 22, no. 11, pp. 803–805.
5. Annenkov, V.V., Lebedeva, O.V., and Danilovtseva, E.N., *Vysokomol. Soedin., Ser. B*, 2001, vol. 43, no. 9, pp. 1560–1564.
6. Minsker, K.S. and Fedoseev, G.G., *Destruktsiya i stabilizatsiya polivinilkhlorida* (Degradation and Stabilization of Polyvinyl Chloride), Moscow: Khimiya, 1972.
7. Trofimov, B.A., Morozova, L.V., Sigalov, M.V., *et al.*, *Makromol. Chem.*, 1987, vol. 188, pp. 2251–2257.
8. Kruglova, V.A., Izykenova, G.A., Kalabina, A.V., *et al.*, *Vysokomol. Soedin., Ser. B*, 1982, vol. 24, no. 9, pp. 691–694.
9. Danilovtseva, E.N., Annenkov, V.V., and Mikhaleva, A.I., *Vysokomol. Soedin., Ser. B*, 1998, vol. 40, no. 2, pp. 366–368.
10. Sigalov, M.V. and Trofimov, B.A., *Zh. Org. Khim.*, 1995, vol. 31, no. 6, pp. 801–826.

Russian Journal of Applied Chemistry, Vol. 75, No. 9, 2002, pp. 1468–1472. Translated from Zhurnal Prikladnoi Khimii, Vol. 75, No. 9, 2002, pp. 1500–1504.
Original Russian Text Copyright © 2002 by Grishin, Pavlovskaya, Kolyakina, Semenycheva.

MACROMOLECULAR CHEMISTRY AND POLYMERIC MATERIALS

Radical Polymerization of Methyl Methacrylate in the Presence of Aromatic Nitroso Compounds

D. F. Grishin, M. V. Pavlovskaya, E. V. Kolyakina, and L. L. Semenycheva

Research Institute of Chemistry, Nizhni Novgorod State University, Nizhni Novgorod, Russia

Received March 26, 2002

Abstract—Features of radical polymerization of methyl methacrylate in the presence of various aromatic nitroso compounds (nitrosobenzene, nitrosodurene, 2,4,6-tribromonitrosobenzene) as potential sources of stable nitroxyl radicals controlling the chain propagation were studied.

Polymerization under conditions of reversible inhibition attracts growing researchers' attention both in Russia and in other countries. Within a short period, these processes have occupied a prominent place among nontraditional methods of polymer synthesis, primarily are to the fact that controllable radical polymerization allows synthesis of polymers with preset properties. The most widely used chain-terminating agents are sterically hindered stable nitroxyl radicals, e.g., 2,2,6,6-tetramethylpiperidin-1-oxyl (TEMPO) and its substituted analogs, which show high performance in the temperature range 120–140°C and, as a rule, are used in polymerization of styrene and its deriva tives [1–8].

It was proposed previously to use spin traps, in particular, *C*-phenyl-*N*-*tert*-butylnitrone [9] and 2-methyl-2-nitrosopropane (MNP) [10], for controlling polymerization under conditions of radical initiation. It was found that these compounds as potential sources of stable radicals allow controllable synthesis of polymers at lower temperatures (50–70°C) and can be successfully used for preparing not only polystyrene, but also polymethacrylates.

With the aim to find new chain-terminating agents, it is interesting to study radical polymerization of methyl methacrylate (MMA) initiated with azobis(isobutyronitrile) (AIBN) in the presence of various aromatic nitroso compounds: nitrosodurene (ND), 2,4,6-tribromonitrosobenzene (TBNB), and nitrosobenzene (NB).

EXPERIMENTAL

Methyl methacrylate was purified as described in [11] by repeated washing with 5–10% alkali solution, followed by washing with distilled water to neutral reaction, drying over $CaCl_2$, and distillation under reduced pressure. ND and NB were prepared as described in [12–14], and TBNB, as described in [15]. The physicochemical constants of the compounds agree with published data. The polymerization kinetics was monitored gravimetrically, dilatometrically [16], and calorimetrically [17]. Samples were prepared as follows: The monomer was placed in glass ampules, degassed three times, and polymerized at residual pressure of 1.3 Pa. The molecular weight M of polymethyl methacrylate (PMMA) was determined viscometrically at 25°C in chloroform [18]. The molecular-weight distribution (MWD) of PMMA was analyzed by gel permeation chromatography (GPC) using a set of five styrogel columns with the pore diameter of 1×10^5, 3×10^4, 1×10^4, 1×10^3, and 250 Å (Waters, the United States). An R-403 differential refractometer (Waters) was used as detector; the eluent was tetrahydrofuran. Close-cut polystyrene (PS) references were used for calibration [19]. Recalculation of M from polystyrene to PMMA was performed by the formula $\log M_{PMMA} = 1.019 \log (0.644 M_{PS})$. The ESR spectra were recorded with an AE-4700 radiospectrometer. In the magnetic field calibrations, Mn^{2+} ions in the MgO lattice were used as reference.

We found that aromatic nitroso compounds appreciably affect the MMA polymerization kinetics (Fig. 1). In particular, addition of NB, TBNB, or ND in the presence of AIBN initiator shifts the gel effect to higher conversion and decreases its intensity. These changes are the more pronounced, the higher the nitroso compound concentration. When taken in amounts of 0.01–0.03 mol %, the nitroso compounds fully suppress the effect of polymerization autoacceleration.

1070-4272/02/7509-1468$27.00 © 2002 MAIK "Nauka/Interperiodica"

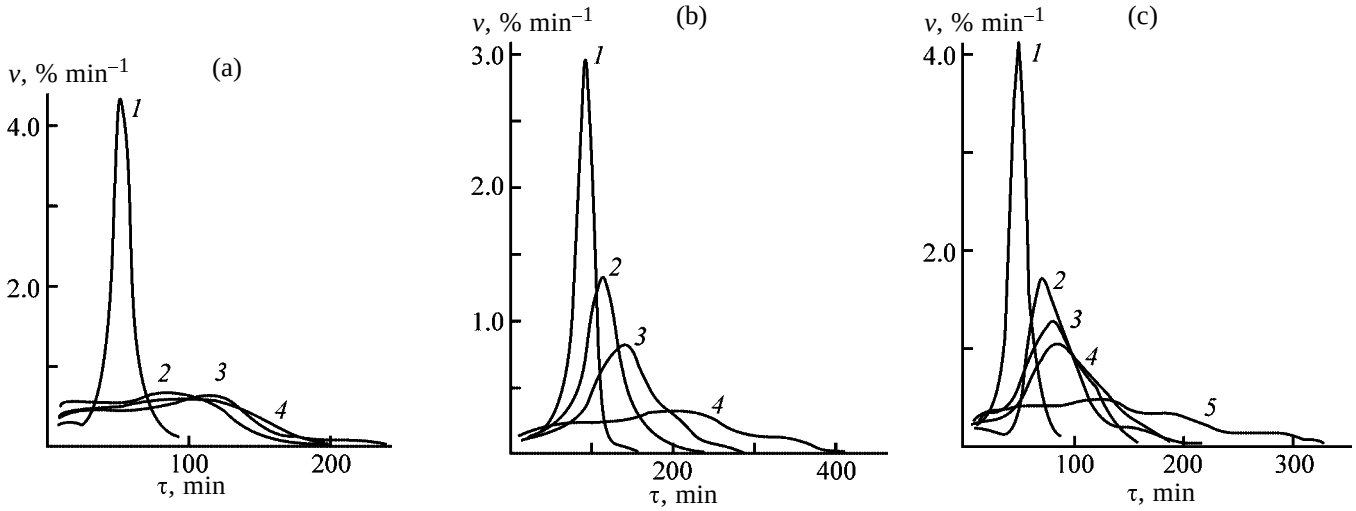

Fig. 1. Differential kinetic curves of MMA polymerization in the presence of aromatic nitroso compounds at (a, c) 70 and (b) 65°C. Initiator AIBN, 0.1 mol %. (*v*) Polymerization rate and (τ) time. Additive: (a) NB, (b) ND, and (c) TBNB; the same for Figs. 2 and 3. Concentration of the additive, mol %: (a) (*1*) 0, (*2*) 0.01, (*3*) 0.02, and (*4*) 0.03; (b) (*1*) 0, (*2*) 0.005, (*3*) 0.01, and (*4*) 0.025; (c) (*1*) 0, (*2*) 0.005, (*3*) 0.015, (*4*) 0.01, and (*5*) 0.03.

It should be noted that, in the presence of NB, ND, or TBNB, as in the case of TEMPO, an induction period is observed, with its duration depending on the structure and concentration of the additive and ranging from 20 min to several hours (Table 1). It should be noted that, with any of the aromatic nitroso compounds, the induction period is somewhat longer than with their aliphatic analogs, e.g., MNP [10], which may be due to differences both in the rate constants of scavenging of propagating radicals with aliphatic and aromatic nitroso compounds and in the stability of the resulting nitroxyl spin adducts:

$$\sim P_n^{\bullet} + R\text{–}N{=}O \rightarrow \sim P_n\text{–}N\underset{(T^{\bullet})}{(O^{\bullet})}\text{–}R, \qquad (1)$$

where $\sim P_n$ is the propagating radical; R = phenyl, 2,4,6-tribromophenyl, 2,3,5,6-tetramethylphenyl (duryl), or *tert*-butyl.

Formation of the above spin adducts in the course of MMA polymerization in the presence of nitroso compounds was detected by ESR. In particular, the ESR spectra contains triplets with the hyperfine coupling constants a_N of 13.5 and 15.4 Oe in the case of ND and TBNB, respectively, or a triplet (a_N = 12.4 Oe) additionally split due to coupling with protons (a_H = 1.9 and 0.9 Oe) in the case of NB.

The nitroxyl spin adducts subsequently participate in the chain propagation stage by reversibly reacting with the propagating radicals $P^{\bullet}$ to form a labile bond, following the reversible inhibition pattern:

$$\wedge\!\wedge\!\wedge P\text{–}T \underset{k_c}{\overset{k_d}{\rightleftarrows}} \wedge\!\wedge\!\wedge \overset{\frown}{P}^{\bullet} + {}^{\bullet}T. \qquad (2)$$

A similar propagation scheme in polymerization of styrene in the presence of phosphorus-containing nitroxyl spin adducts (analogs of TEMPO) was proposed in [20].

As expected from the constants of radical scavenging with ND and TBNB [21], with ND the induction

Table 1. Kinetic parameters of MMA polymerization at 50°C in the presence of nitroso compounds (AIBN initiator, 0.1 mol %)

Additive, mol %	Induction period, min	$V_p \times 10^4$, mol l^{-1} s^{-1}
–	–	1.2
ND:		
0.010	60	0.9
0.025	110	0.6
0.050	180	0.5
TBNB:		
0.005	20	1.2
0.010	30	0.8
0.030	60	0.6
MNP:*		
0.050	25	0.5
0.100	180	0.4

* Data of [10].

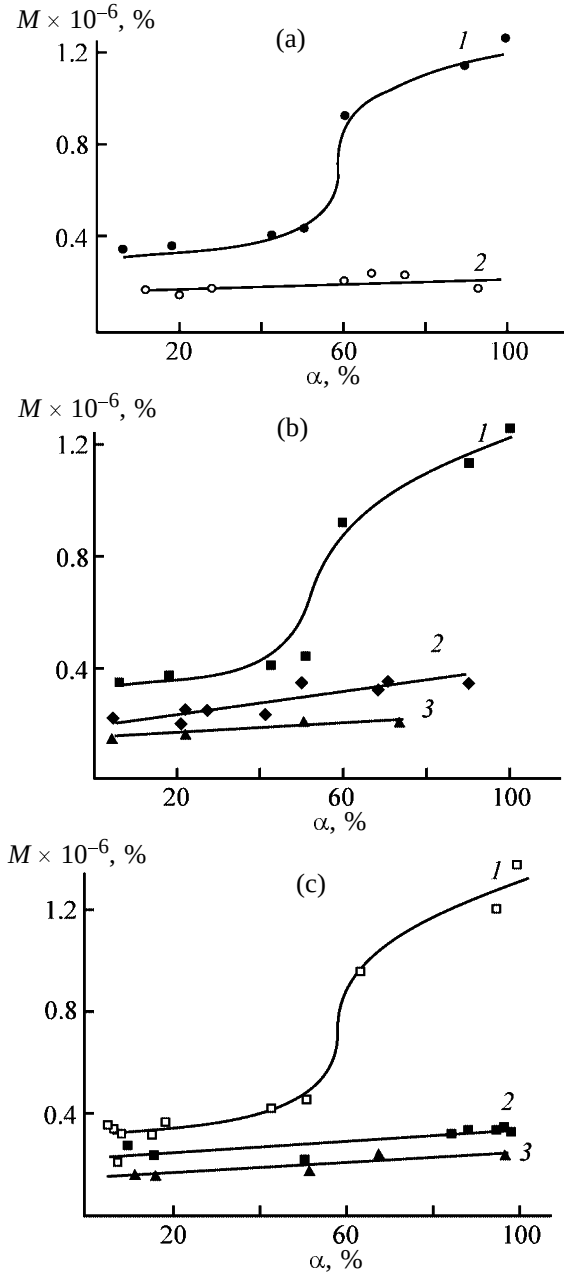

Fig. 2. (*1*, *2*) Viscosity-average and (*3*) number-average molecular weights *M* of PMMA as functions of conversion α. AIBN initiator, 0.1 mol %; 70°C; the same for Fig. 3. Concentration of the additive, mol %: (a) (*1*) 0 and (*2*) 0.03; (b) (*1*) 0 and (*2*, *3*) 0.025; (c) (*1*) 0 and (*2*, *3*) 0.03.

period in MMA polymerization is somewhat longer than with TBNB. Table 1 shows that, as the nitroso compound concentration is increased, the induction period becomes longer, and the MMA polymerization (as compared to the process performed with a common radical initiator without additives) decelerates. However, it is important for practice that the polymerization deceleration is less significant than with

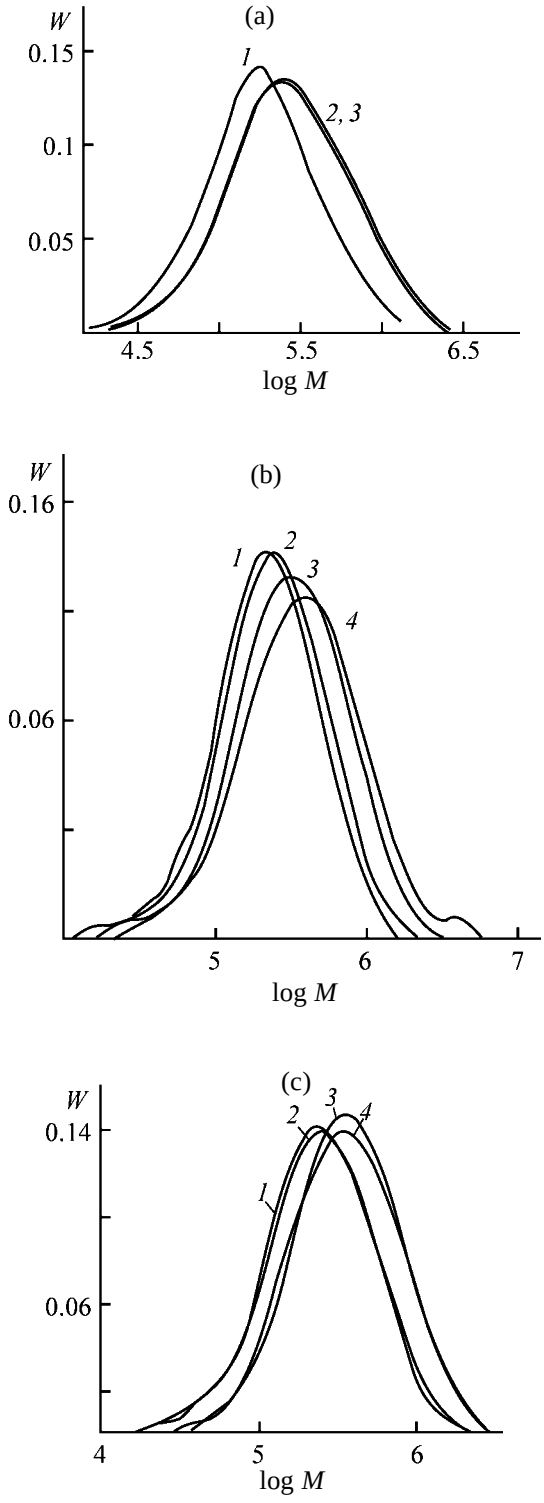

Fig. 3. MWD curves for PMMA samples with various MMA conversions: (*W*) wt fraction and (*M*) molecular weight. Concentration of the additive, mol %: (a, c) 0.03 and (b) 0.025. Conversion, %: (a) (*1*) 12, (*2*) 60, and (*3*) 93; (b) (*1*) 4.8, (*2*) 22.0, (*3*) 50.7, and (*4*) 74.0; (c) (*1*) 16.1, (*2*) 10.8, (*3*) 96.3, and (*4*) 67.7.

TEMPO and its analogs [1–8] with which the polymerization rate decreases by an order of magnitude and more.

Thus, the kinetic study shows that NB, ND, and TBNB efficintly control the kinetic parameters of MMA polymerization. It should be noted that the effect is only slightly dependent on substituents in the aromatic nitroso compound.

Examination of the molecular-weight characteristics of the polymers prepared confirms the conclusions based on the kinetic data. As seen from Figs. 2a–2c (curves *1*), in polymerization of MMA with no nitroso compounds added, a gel effect with an abrupt growth of the molecular weight is observed. Addition of NB, ND, or TBNB suppresses the polymerization autoacceleration, and both viscosity-average and number-average molecular weights linearly increase with conversion (Figs. 2a–2c, curves *2* and *3*, respectively).

Figure 3 shows the MWD curves for PMMA synthesized in the presence of additives at various MMA conversions. It is seen that, on adding NB (Fig. 3a), ND (Fig. 3b), and TBNB (Fig. 3c), the unimodal MWD curves uniformly shift toward higher M with increasing conversion. For PMMA prepared in the presence of aromatic nitroso compounds, the polydispersity coefficients are relatively low, within 1.8–2.0, and do not change noticeably in the course of polymerization. The MMA polymer prepared under comparable conditions (but without additive) has a considerably higher polydispersity coefficient, 2.4 (Table 2). It should be noted that the strongest changes in the molecular weight of the polymer are observed with TBNB (Table 2). This may be due to considerably smaller participation of this additive in chain transfer, as compared to NB and ND [21]. This data also show that the polymeric chain grows in the controllable mode.

Table 2. Molecular-weight characteristics of PMMA prepared at 70°C (0.1 mol % AIBN)

Additive, mol %	Conversion, %	$M_w \times 10^{-3}$	$M_n \times 10^{-3}$	M_w/M_n
–	51	894	368	2.43
NB, 0.03	12	223	124	1.80
	60	339	170	1.99
	93	342	174	1.96
TBNB, 0.03	16	299	158	1.89
	37	362	189	1.91
	96	444	234	1.90
ND, 0.03	5	266	147	1.81
	22	303	162	1.87
	51	419	208	2.01

CONCLUSIONS

(1) Polymerization of methyl methacrylate at 65–70°C, initiated with azobis(isobutyronitrile) and performed in the presence of aromatic nitroso compounds as sources of stable nitroxyl radicals, exhibits the main features of controllable radical polymerization: the absence of gel effect, uniform increase in M of the polymer and shift of unimodal molecular-weight distribution curves toward higher molecular weights with increasing conversion, and relatively low polydispersity coefficients of the resulting polymer.

(2) On adding nitrosobenzene, 2,4,6-tribromonitrosobenzene, or nitrosodurene, the polymerization time increases by a factor of no more than 2 as compared to the process without additives; the weaker decelerating effect is an advantage of these additives over 2,2,6,6-tetramethylpiperidine-1-oxyl and its analogs traditionally used for performing polymerization in the "living" chain mode.

(3) The structure of substituents in aromatic nitroso compounds has no noticeable effect on their performance.

ACKNOWLEDGMENTS

The study was financially supported by the Competitive Center for Basic Natural Science at the Ministry of Education of the Russian Federation and by the Russian Foundation for Basic Research (project no. 02-03-32427).

REFERENCES

1. Smirnov, B.R., *Vysokomol. Soedin., Ser. A*, 1990, vol. 32, no. 3, pp. 583–589.
2. Veregin, R.P.N., Odell, P.G., Michalak, L.M., and Georges, M.K., *Macromolecules*, 1996, vol. 29, no. 8, pp. 2746–2754.
3. Matyjaszewski, K., *Controlled Radical Polymerization*, Oxford: Oxford Univ. Press, 1998.
4. Otsu, T. and Matsumoto, A., *Adv. Polym. Sci.*, 1998, vol. 136, pp. 75–127.
5. Korolev, G.V. and Marchenko, A.P., *Usp. Khim.*, 2000, vol. 69, no. 5, pp. 447–475.
6. Matyjaszewski, K., *Controlled/Living Radical Polymerization*, Oxford: Oxford Univ. Press, 2000.

7. Grishin, D.F. and Semenycheva, L.L., *Usp. Khim.*, 2001, vol. 70, no. 5, pp. 486–510.
8. Zaremskii, M.Yu. and Golubev, V.B., *Vysokomol. Soedin.*, 2001, vol. 43, no. 9, pp. 1689–1728.
9. Grishin, D.F., Semenycheva, L.L., and Kolyakina, E.V., *Vysokomol. Soedin., Ser. A*, 1999, vol. 40, no. 4, pp. 609–614.
10. Grishin, D.F., Semionicheva, L.L., and Koliakina, E.V., *Mendeleev Commun.*, 1999, no. 6, pp. 250–252.
11. *Analytical Chemistry of Polymers*, Kline, G.M., Ed., New York: Interscience, 1959.
12. Makarova, L.G. and Nesmeyanov, A.N., *Metody elementoorganicheskoi khimii: Rtut'* (Methods of Organometallic Chemistry: Mercury), Moscow: Nauka, 1965.
13. Smith, L.J. and Taylor, F.L., *J. Am. Chem. Soc.*, 1935, vol. 57, no. 8, pp. 2461–2463.
14. *Organic Synthesis*, Gilman, H. and Blatt, A.H., Eds., New York: Wiley, 1946, coll. vol. 2.
15. Holmes, R.R. and Bayer, R.P., *J. Am. Chem. Soc.*, 1960, vol. 82, p. 3454.
16. *Praktikum po khimii i fizike polimerov* (Practical Course of Polymer Chemistry and Physics), Moscow: Khimiya, 1990, pp. 218–220.
17. Arulin, V.I. and Efimov, L.I., *Tr. Khim. Khim. Tekhnol.* (Gor'kii), 1970, no. 2, pp. 74–77.
18. Rafikov, S.R., Pavlov, S.A., and Tverdokhledova, I.I., *Metody opredeleniya molekulyarnykh vesov i polidispersnosti vysokomolekulyarnykh soedinenii* (Methods for Determining Molecular Weights and Polydispersity of Macromolecular Compounds), Moscow: Khimiya, 1963.
19. Belen'kii, B.G. and Vilenchik, L.Z., *Khromatografiya polimerov* (Polymer Chromatography), Moscow: Khimiya, 1978.
20. Le Mercier, C., Lutz, J.-F., Marque, S., *et al.*, *Controlled Radical Polymerization*, Matyjiaszewski, K., Ed., *ACS Symp. Ser. 768*, Washington, DC: Am. Chem. Soc., 2000, ch. 8, pp. 109–122.
21. Zubarev, V.E., *Metod spinovykh lovushek* (Method of Spin Traps), Moscow: Mosk. Gos. Univ., 1984.

Russian Journal of Applied Chemistry, Vol. 75, No. 9, 2002, pp. 1465–1467. Translated from Zhurnal Prikladnoi Khimii, Vol. 75, No. 9, 2002, pp. 1497–1499.
Original Russian Text Copyright © 2002 by Kudyshkin, Abdurakhmanova, Bozorov, Voropaeva, Ruban, Rashidova.

MACROMOLECULAR CHEMISTRY AND POLYMERIC MATERIALS

Radical Polymerization of *N*-Vinylcaprolactam in Isopropanol

V. O. Kudyshkin, T. R. Abdurakhmanova, N. I. Bozorov, N. L. Voropaeva, I. N. Ruban, and S. Sh. Rashidova

Institute of Polymer Chemistry and Physics, Academy of Sciences of Uzbekistan Republic, Tashkent, Uzbekistan

Received January 17, 2002

Abstract—Radical polymerization of *N*-vinylcaprolactam in isopropanol, initiated with azobis(isobutyronitrile), was studied with the aim to prepare polyvinylcaprolactam of controllable molecular weight. The rate and degree of polymerization are influenced by the reaction mixture composition.

A set of unique properties of polyvinylcaprolactam (PVCL) make it promising for microbiology, medicine, and agriculture. The properties of this polymer in solutions are largely governed by its molecular weight *M*. Therefore, development of simple and efficient procedures for preparing PVCL of required *M* is a key problem in the chemistry of this type of polymers [1]. It is known that, in polymerization of vinylpyrrolidone (VP), isopropyl alcohol (IPA) can be used as chain-transfer agent, and in some cases it is preferred as a means for controlling *M* [1]. In this connection, the goals of this work were to study radical polymerization of *N*-vinylcaprolactam (VCL) in IPA and reveal the advantages and shortcomings of this approach as compared to VCL polymerization in the presence of allyl compounds [2, 3].

EXPERIMENTAL

Polyvinylcaprolactam was prepared by radical polymerization in glass ampules in the presence of AIBN initiator. Air was removed by repeated freeze–pump–thaw cycles in a vacuum to a residual pressure of 0.13 Pa. The polymers were reprecipitated into diethyl ether. The intrinsic viscosity ($cm^3\ g^{-1}$) of the polymers was determined in dimethylformamide at 25°C. The molecular weights of PVCL samples were estimated from the Mark–Kuhn–Houwink equation, $[\eta] = 0.0743M^{0.53}$. This equation was derived from the dependence of the intrinsic viscosity on the number-average increment of *M*, evaluated previously from the MWD curves of PVCL [3]. The polymerization kinetics at 60°C were studied dilatometrically. The initiation rate was evaluated from the induction period of polymerization in the presence of a stable nitroxyl radical, tetramethylpiperidine-1-oxyl (TEMPO). The induction period was linearly dependent on the TEMPO concentration in the system.

The polymerization rate was studied in relation to the reaction mixture composition, VCL/IPA. It is known that, in classical radical polymerization, the reaction is first-order with respect to the monomer. In our case, when the monomer concentration was decreased by a factor of 15, at a constant AIBN concentration of 10^{-2} M, the polymerization rate decreased by a factor of only 7.9. As a result, the reduced polymerization rate $V_p[VCL]^{-1}$ grows with increasing content of IPA, until the IPA : VCL ratio of approximately 8 : 1 is reached. Such a dependence shows that the effect of IPA on the polymerization kinetics is significant. Similar dependences were observed previously for radical polymerization of VP in water and ethanol [4]. The solvent effect is also confirmed by experiments on radical polymerization of VCL in a mixture of IPA with dioxane. We found that, at a constant concentration of the monomer and initiator, the polymerization rate grows with increasing content of IPA in the reaction mixture (Fig. 1). Isopropyl alcohol is not an inert solvent in radical polymerization of VCL. It is known that, in protic solvents, vinyllactam molecules can form hydrogen bonds with the solvent. The hydrogen bonding increases the polarity of the vinyl C=C bond owing to its conjugation with the C=O group via nitrogen atom. This is characteristic of polymerization of both VP and VCL [1, 5]. Apparently, IPA can also form hydrogen bonds with VCL molecules. As a result, we actually deal with copolymerization of the free and solvated monomer species, differing in the polarization of the double bond.

We have examined the dependence of the initiation

1070-4272/02/7509-1465$27.00 © 2002 MAIK "Nauka/Interperiodica"

Kinetic parameters of VCL polymerization in IPA and molecular weights of the polymer samples

Concentration, M		Yield, %	$v_p \times 10^5$, mol l^{-1} s^{-1}	$(K_t K_p^{-2})(v_p M^{-2}) \times 10^3$	[η], dl g^{-1}	$M_\eta \times 10^{-3}$	P_η
IPA	VCL						
12.4	0.37	12.5	1.4	1.96	–	–	–
11.7	0.74	9.4	2.7	1.23	0.11	12.4	89
10.5	1.48	10.6	5.7	0.81	0.16	25.2	181
9.8	1.85	8.3	6.3	0.91	0.20	38.4	276
6.5	3.71	8.6	10.3	0.77	0.25	58.5	421
3.9	5.55	9.7	11.0	0.73	0.41	149.0	1072

rate v_{in} on the reaction mixture composition (Fig. 2). With increasing VCL content in solution, v_{in} grows. This may be due, among other things, to increased initiation efficiency at high monomer concentrations [6]. From the initiation and polymerization rates, we calculated the ratios of the propagation and termination constants, $K_p K_t^{-0.5}$. This parameter increases with dilution of the reaction mixture, which confirms the assumption that the free and solvated monomer species have different reactivity (Fig. 2). The viscosity-average molecular weights M_η of PVCL synthesized at various VCL : IPA ratios are listed in the table. This parameter decreases with dilution of the reaction mixture. The chain-transfer constant was $C_s \sim 6 \times 10^{-4}$. As noted previously [1], in radical polymerization of VP in IPA the main reaction limiting M is the chain transfer to IPA [1]. Analysis of the equation

$$P^{-1} = (K_t K_p^{-2})(v_p[M]^{-2}) + C_s[S][M]^{-1},$$

where [M] and [S] are the concentrations of, respectively, the monomer and chain-transfer agent (IPA), shows that, in our case, at high concentrations of the monomer the first and second summands are comparable, and the chain transfer to IPA becomes a decisive factor limiting M in polymerization of VCL in dilute IPA solutions.

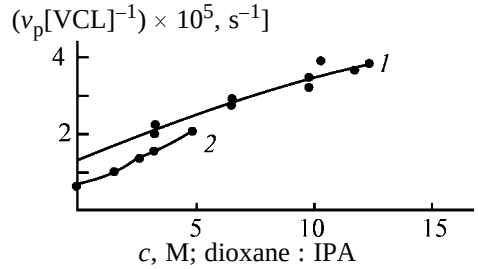

Fig. 1. Reduced rate of VCL polymerization, $v_p[VCL]^{-1}$, as a function (*1*) of IPA concentration c in IPA–VCL mixtures ratios and (*2*) of dioxane : IPA ratio at a constant VCL concentration of 3.71 M. AIBN concentration 10^{-2} M; the same for Fig. 2.

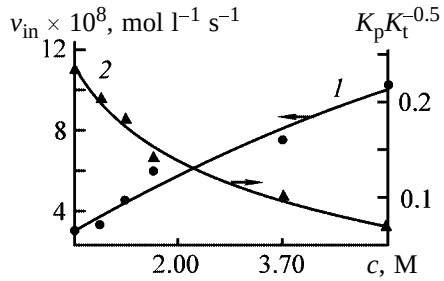

Fig. 2. (*1*) Initiation rate v_{in} and (*2*) parameter $K_p K_t^{-0.5}$ as functions of the VCL concentration in IPA c.

Comparison of theses results with previous data on polymerization of VCL in the presence of allyl compounds [2, 3] shows that both approaches allow preparation of low-molecular-weight PVCL, but the control mechanisms are different. With allylbenzene and allylcaprolactam, the main reaction limiting M of PVCL is degradation chain transfer; its specific feature is that the allyl radical formed by the chain transfer is stabilized by conjugation; therefore, it is low-active and virtually incapable of reacting with the double bond of the monomer. Such chain transfer is essentially equivalent to monomolecular termination. In polymerization of VCL in IPA, an ordinary chain transfer occurs, with bimolecular termination. With allylbenzene and allylcaprolactam, the chain-transfer constants are considerably higher [2, 3] than with IPA. From this viewpoint, IPA has no advantages over allyl compounds. Polyvinylcaprolactam with low M can be prepared only in dilute solutions of the monomer in IPA. At the same time, it should be noted that IPA can be readily removed from the reaction mixture after reaction completion, whereas removal of unchanged allyl chain-terminating agents is a serious problem. Furthermore, by performing polymerization of VCL in IPA, it is feasible to prepare oligomers with terminal hydroxy groups, which may be of particular interest.

Growing attention is given today to synthesis of biodegradable polymers. It is known that polyvinyl-

lactams undergo biodegradation difficultly. The problem can be solved by introducing groups capable of chemical or enzymatic hydrolysis into the backbone [7]. Apparently, one of possible routes to such polymers is the use of VCL oligomers with terminal hydroxy groups as macromonomers capable of reaction with bifunctional compounds to form polymers with heteroatoms in the backbone.

CONCLUSION

Isopropyl alcohol can be used for controlling *M* of polyvinylcaprolactam in radical polymerization. Because of relatively small constant of chain transfer to isopropyl alcohol, low-molecular-weight polymers can be prepared in dilute solutions of vinylcaprolactam in isopropyl alcohol. The observed deviations of the polymerization kinetics from the classical relationships (variation of the parameter $K_pK_t^{-0.5}$ with increasing content of isopropyl alcohol in the reaction mixture) are due to hydrogen bonding of the monomer with the solvent and the presence of free and solvated monomer species, differing in the polarization of the double bond.

REFERENCES

1. Kirsh, Yu.E., *Polivinilpirrolidony i drugie poli-N-vinilamidy* (Polyvinylpyrrolidones and Other Poly-*N*-vinylamides), Moscow: Nauka, 1998.
2. Kudyshkin, V.O. and Mukhitdinova, N.A., *Zh. Prikl. Khim.*, 1999, vol. 72, no. 10, pp. 1742–1744.
3. Kudyshkin, V.O., Abdurakhmanova, T.R., and Kadyrkhanov, M.R., *Zh. Prikl. Khim.*, 2000, vol. 73, no. 9, pp. 1522–1525.
4. Karaputadze, T.M., Shumskii, V.I., and Kirsh, Yu.E., *Vysokomol. Soedin., Ser. A*, 1978, vol. 20, no. 8, pp. 1854–1859.
5. Alimov, A.Kh., Karaputadze, T.M., Rashidova, S.Sh., and Kirsh, Yu.E., *Uzb. Khim. Zh.*, 1981, no. 5, pp. 29–30.
6. Odian, G., *Principles of Polymerization*, New York: McGraw-Hill, 1970.
7. Maiboroda, V.B., Loseva, S.V., Klyagina, M.V., *et al.*, Abstracts of Papers, *Mezhdunarodnaya konferentsiya "Biodegradiruemye polimery, podkhody k sintezu"* (Int. Conf. "Biodegradable Polymers: Synthetic Approaches"), Tashkent, 2001, pp. 18–19.

Russian Journal of Applied Chemistry, Vol. 75, No. 9, 2002, pp. 1473–1476. Translated from Zhurnal Prikladnoi Khimii, Vol. 75, No. 9, 2002, pp. 1505–1508.
Original Russian Text Copyright © 2002 by Amirova, Andrianova, Bukharaev, Fomin.

MACROMOLECULAR CHEMISTRY AND POLYMERIC MATERIALS

Preparation of Polymeric Films with a Gradient of Composition and Properties across the Thickness from Limitedly Compatible Epoxy Oligomers

L. M. Amirova, K. A. Andrianova, A. A. Bukharaev, and V. P. Fomin

Tupolev Kazan State Technical University, Kazan, Tatarstan, Russia
Zavoiskii Kazan Physicotechnical Institute, Kazan Scientific Center, Russian Academy of Sciences, Kazan, Tatarstan, Russia

Received April 12, 2002

Abstract—Preparation of films from a blend of limitedly compatible epoxy oligomers was considered. The composition and structure of the films were studied by IR spectroscopy and scanning power microscopy, and the film asymmetry was demonstrated. The influence exerted by the composition and curing conditions on the phase separation of the compounds and the structure of the films was revealed.

Polymer–polymer composite coatings structurally nonuniform across the thickness find growing application owing to the possibility of controlling the surface, interface, and bulk properties of the films [1].

These goals are commonly accomplished by multilayer coating with paint-and-varnish materials differing in the composition and purpose. However, preparation of such coatings is time- and labor-consuming; furthermore, additional problems often arise with a poor adhesion between the layers. Self-segregating films based on thermodynamically incompatible or limitedly compatible polymer–polymer, polymer–oligomer, or oligomer–oligomer compounds are free of all these drawbacks [2]. Problems related to preparation of asymmetric films from water-dispersible, soluble, and latex formulations are discussed in [3–5].

Of particular interest in this respect are active glycidyl diluents, which are widely used in commercial production of epoxy lacquers and paints [6]. To obtain asymmetric films, it is necessary to use diluents that are limitedly compatible with the epoxy oligomer and provide controllable distribution of components in the coatings (e.g., due to different densities).

In this work, we examined the possibility of preparing such asymmetric films from E-40 epoxy–4,4'-isopropylidenediphenol (Dian) oligomer and glycidyl esters of phosphorus acids. These esters, as shown in [7, 8], are high-performance active diluents of epoxy oligomers and allow preparation of polymers with a high level of service properties (adhesion, softening point, heat and fire resistance, etc.).

EXPERIMENTAL

Experiments were performed with E-40 epoxy–Dian oligomer and the following glycidyl esters of phosphorus acids (GEPs): triglycidyl phosphate **I**, diglycidyl methyl phosphate **II**, and diglycidyl methylphosphonate **III**; their characteristics are listed in Table 1. As curing agent we used monocyanoethyldiethylenetriamine UP-0633M (stoichiometric coefficient 0.92, viscosity 0.2 Pa s at 25°C, density 1.1 g cm^{-3}).

The compatibility of ED-40 with GEPs was evaluated microinterferometrically with an MI-2 device [9], and the phase diagrams were constructred. The surface tension was determined by the Du Nouy method from the force of detachment of a platinum ring. The size and size distribution of emulsion droplets were evaluated from the turbidity spectra [10, 11]. Optical measurements were performed with an SF-26 spectrophotometer. The viscosity of epoxy oligomer mixtures was measured with a Hoeppler viscometer.

Coatings from E-40–GEP compounds, 80–100 μm

Table 1. Characteristics of epoxy oligomers*

Oligomer	EN, %	*M*	ρ, g cm^{-3}
E-40	14.1	800	1.178
I	48	266	1.3673
II	38	224	1.3140
III	41	208	1.2789

* (EN) Epoxy number, (*M*) molecular weight, and (ρ) density.

1070-4272/02/7509-1473$27.00 © 2002 MAIK "Nauka/Interperiodica"

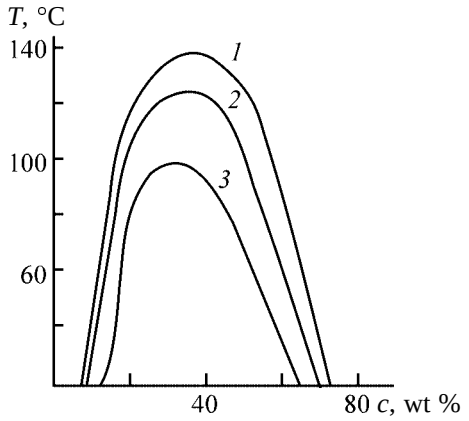

Fig. 1. Phase diagram of the system E-40–GEP: (*T*) temperature and (*c*) GEP concentration. GEP: (*1*) **I**, (*2*) **II**, and (*3*) **III**.

Table 2. Surface tension of E-40–GEP solutions

GEP content, wt %	Surface tension, mN m^{-1}		
	I	**II**	**III**
10	49	49	49
30	49	49	49
40	49	49	49
60	49	49	49
80	52	51	50
100	57	56	55

Table 3. Particle-size distribution in the system E-40–GEP

GEP content, wt %	Particle size, nm		
	I	**II**	**III**
20	108 ± 18	105 ± 14	84 ± 10
30	125 ± 25	121 ± 19	107 ± 12
35	151 ± 29	148 ± 24	125 ± 18
40	127 ± 23	122 ± 16	104 ± 11
50	110 ± 16	108 ± 13	79 ± 8

Table 4. Gel time of the E-40–GEP–UP0633 compound

GEP content, wt %	Curing temperature, °C	Gel time, min		
		I	**II**	**III**
30	20	100	120	150
35	20	80	105	130
40	20	60	90	100
30	30	50	80	90
35	30	30	60	70
40	30	15	45	55

thick, were prepared on various supports (glass, Teflon). The coating structure was examined by scanning power microscopy (SPM) with a Solver P47-SPM microscope in the semicontact mode. For this purpose, we made brittle chips of coatings on glass cooled in liquid nitrogen.

The IR ATIR spectra of the upper and lower surfaces of the coatings on Teflon were recorded with a Bruker IFS-66 V/S Fourier transform spectrometer using KRS-5 prisms (45°).

Figure 1 shows the phase diagram of the systems in hand. It is seen that all the GEPs are limitedly compatible with E-40; however, the incompatibility range contracts in going from **I** to **III**, and the upper critical solution temperature decreases.

In the insolubility range, all the compounds form fairly stable emulsions. This may be due to close surface tensions of the mutually saturated E-40 and GEP phases (Table 2).

The particle size distribution in emulsions is given in Table 3. Gradient coatings are formed by settling of the heavier phase (GEP saturated with E-40) and floating-up of the less dense phase (E-40 saturated with GEP). According to the Stokes equation, the settling or floating-up rate of emulsion particles is determined by their size and by the difference between the phase densities. Owing to broad particle-size distribution of emulsion particles and, correspondingly, broad distribution with respect to settling (or floating-up) rates, the composition changes gradually across the layer thickness.

The settling sharply decelerates as the viscosity of the compounds grows in the course of curing. The curing rate depends on the composition and temperature of the medium. The gel time was determined from the viscosity growth curves in the course of cross-linking of the oligomeric systems. The gel times for various compounds and temperatures are listed in Table 4. It is seen that increased content of GEP and elevated temperatures accelerate gelation and "freeze" settling. Curing of compounds of different compositions at different temperatures allows preparation of coatings with variable gradient of the component concentrations and hence with controllable structure and properties.

The structures of these samples were studied by SPM. Figure 2 shows as example the SPM images of a coating based on E-40–**I** (content of **I** 30 wt %, curing temperature 20°C), made at different heights. It is seen that, in going from the upper to the lower surface, the polymer structure gradually changes from

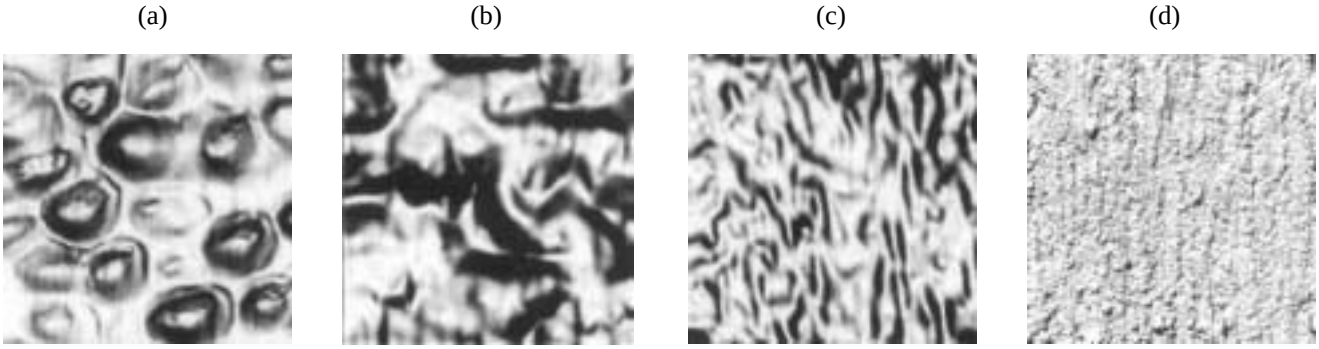

Fig. 2. SPM images of a chip of a coating based on E-40–**I** at various heights. Scanned area 500 × 500 nm; height, μm: (a) 1, (b) 20, (c) 40, and (d) 80.

globular, typical of cured E-40 resin, to nonglobular, typical of densely cross-linked polymer based on **I**. Similar images were taken for all the examined systems at various GEP concentrations and various curing temperatures. We found that, at higher curing temperatures, the coating structure varies more gradually. At lower curing temperatures, the gel time is longer, settling occurs to a greater extent, and the transition from the globular to nonglobular structue is sharper. With decreasing concentration of GEP, the polymer layer with the globular structure becomes thicker.

The concentration ratio of E-40 and GEP in the upper and lower layers of the coatings can be determined from the IR ATIR spectra of the upper and lower surfaces (Fig. 3). The concentration ratio was evaluated from the intensity ratio of the absorption bands of the benzene ring (1610 cm^{-1}, E-40) and phosphoryl or phosphate group (1250 and 1025 cm^{-1}, respectively; GEP). With a 45° KRS-5 prism, the effective penetration thickness was 2.0 ± 0.5 μm depending on the analytical band and the refractive index of the compound. The calculated ratios of E-40 and GEPs in the upper and lower layers of the coatings of different gross composition, cured at different temperatures, are listed in Table 5. It is seen that the GEP content in the upper layer corresponds to its maximal solubility in E-40 (Fig. 1), and the lower layer is the GEP-based phase containing dissolved E-40 in the saturation concentration.

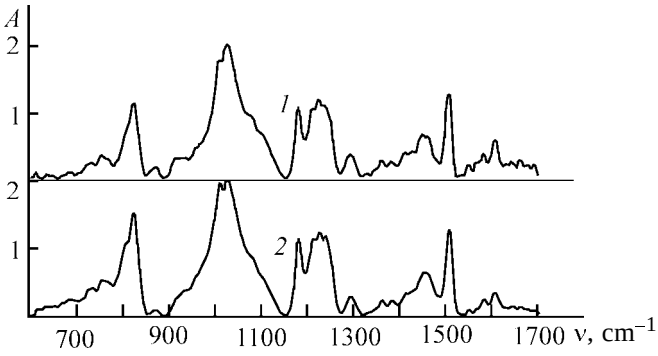

Fig. 3. IR ATIR spectra of the (*1*) upper and (*2*) lower surfaces. (*A*) normalized absorption and (ν) wave number.

Table 5. Relative content of E-40 and GEPs in coating layers at various concentrations of GEPs in compounds and various curing temperatures

Layer	c_{GEP}, wt %	T_{cur}, °C	Content, wt %		
			I	**II**	**III**
Upper	30	20	8	9	13
		30	9	10	15
	35	20	8	9	13
		30	9	10	15
	40	20	8	9	13
		30	9	10	15
Lower	30	20	72	71	65
		30	70	68	62
	35	20	72	71	65
		30	70	68	62
	40	20	72	71	65
		30	70	68	62

CONCLUSIONS

(1) Asymmetric films with a compositional and structural gradient across the film thickness were prepared.

(2) The phase separation is affected by the nature and concentration of the oligomeric components and by the curing temperature.

REFERENCES

1. Sergeeva, L.M. and Gorbach, L.A., *Usp. Khim.*, 1996, vol. 65, no. 4, pp. 367–376.

2. Verkholantsev, V.V., *Lakokras. Mater.*, 1998, nos. 2–3, pp. 12–16.
3. Verkholantsev, V.V., *Lakokras. Mater.*, 1990, no. 4, pp. 13–21.
4. Verkholantsev, V.V. and Krylova, V.V., *Vysokomol. Ssoedin., Ser. A*, 1988, vol. 30, no. 8, pp. 1653–1660.
5. Pavlyuchenko, V.N., Primachenko, O.N., and Khaikin, S.Ya., *Zh. Prikl. Khim.*, 2001, vol. 74, no. 7, pp. 1142–1147.
6. Dzhavadyan, E.A., Ivanova-Muzhmieva, V.G., Gorbatkina, Yu.A., *et al., Vysokomol. Soedin., Ser. A*, 1994, vol. 36, no. 8, pp. 1349–1352.
7. Amirova, L.M., Stroganov, V.F., and Sakhabieva, E.V., *Int. J. Polym. Mater.*, 2000, vol. 47, no. 1, pp. 43–60.
8. Amirova, L.M., Saifutdinov, R.Kh., Magsumova, A.F., *et al., Zh. Prikl. Khim.*, 2001, vol. 74, no. 11, pp. 1881–1884.
9. Chalykh, A.E., Gerasimov, V.K., and Mikhailov, Yu.M., *Diagrammy fazovogo sostoyaniya polimernykh sistem* (Phase Diagrams of Polymeric Systems), Moscow: Yanus-K, 1998.
10. Klenin, V.I., Shchegolev, S.Yu., and Lavrushin, V.I., *Kharakteristicheskie funktsii svetorasseyaniya dispersnykh sistem* (Characteristic Light Scattering Functions of Disperse Systems), Saratov: Saratov. Univ., 1977.
11. Klenin, V.I., *Termodinamicheskie sistemy s gibkotsepnymi polimerami* (Thermodynamic Systems with Flexible-Chain Polymers), Saratov: Saratov. Univ., 1995.

Russian Journal of Applied Chemistry, Vol. 75, No. 9, 2002, pp. 1477–1480. Translated from Zhurnal Prikladnoi Khimii, Vol. 75, No. 9, 2002, pp. 1509–1512.
Original Russian Text Copyright © 2002 by Ostrovidova, Makeev.

MACROMOLECULAR CHEMISTRY AND POLYMERIC MATERIALS

Directed Regulation of Biological Activity of Multicomponent Polymeric Structures

G. U. Ostrovidova and A. V. Makeev

St. Petersburg State Technological Institute, St. Petersburg, Russia

Received November 29, 2001; in final form, April 2002

Abstract—Biological activity of multicomponent polymeric films based on polyvinyl alcohol, polyvinylpyrrolidone, and lactic acid, containing trypsin and kanamycin, is studied. The degrees of degradation and biodegradation of multicomponent film coatings can be controlled by introduction of polyvinylpyrrolidone or lactic acid and also by variation in their electroforming parameters.

Searching for and developing materials destined for operating in contact with tissues and biological liquors of a living body have attracted growing attention, with a special emphasis made on the structure and composition of the surface, biocompatibility, biodegradation, and antimicrobial action [1, 2].

The existing methods for modification of various materials with biologically active compounds (BACs) not always provide the whole combination of desired properties as well as the prolonged effect of immobilized BACs [3–6]. For example, polyvinyl alcohol (PVA) films with immobilized protease C and polyhexamethyleneguanidine hydrochloride, obtained on the basis of forming solutions of various compositions by the impregnation method, practically lose their enzymatic (in 2–3 h) and antimicrobial activities (in 24 h) [6].

Polymeric structures demonstrating a directional physiological action may be obtained by electroforming on the surface of various materials [7].

EXPERIMENTAL

As polymeric matrices for BACs we used hydrogels obtained on the basis of PVA, polyvinylpyrrolidone (PVP) (content of opened lactam rings ~1%) [7], lactic acid (LA), or their mixtures. To improve the biocompatibility and antimicrobial activity, we introduced a proteolytic enzyme (trypsin) and an antibiotic (kanamycin) in the coating formula. The polymeric matrices were formed on the surface of the composite support (CS) [graphite-extended polydimethylsiloxane rubber (SKTV-med)] or silicon wafers. Properties of the coatings are strongly affected by the working composition formula and forming procedure (in the electric field or by impregnation) [8]. The optimal conditions of forming of multicomponent hydrogel coatings are realized in performing the process in the electric field (field strength 25–30 V cm^{-1}, time 0.5–4 min). In this case, the basic structure-forming components of the polymeric matrix are PVA and boric acid. Electroforming was performed at pH 4.5–6 (in this pH range, PVP molecules are positively charged by virtue of the presence of opened lactam rings). The degree of cross-linking and degradation of the polymeric structures were characterized by the difference in the sample weight upon exposure to water. The adhesive strength of the coatings was determined by the lattice cut method according to GOST (State Standard) 15140–78. Heating of the samples at 50–60°C for 1 h increased the degree of cross-linking of a PVA gel and the adhesive strength and decreased its degradation. To improve the ductility of the coatings formed, glycerol (3 wt %) was added to the working composition.

The concentration and proteolytic activity of trypsin were determined spectrophotometrically (λ = 280 nm) with a casein solution as a substrate [9]. The hemocompatibility of the materials was characterized *in vitro* using the procedure described in [10]. The antimicrobial action of the antibiotic immobilized on the polymeric film was determined by the biological method (diffusion to agar) with *Staphylococcus citreus* culture as a probe [11].

High biocompatibility of the individual polymeric components (PVA, PVP) [7, 12] suggests that the polymeric structure obtained on their basis will be also sufficiently biocompatible with tissues and blood

1070-4272/02/7509-1477$27.00 © 2002 MAIK "Nauka/Interperiodica"

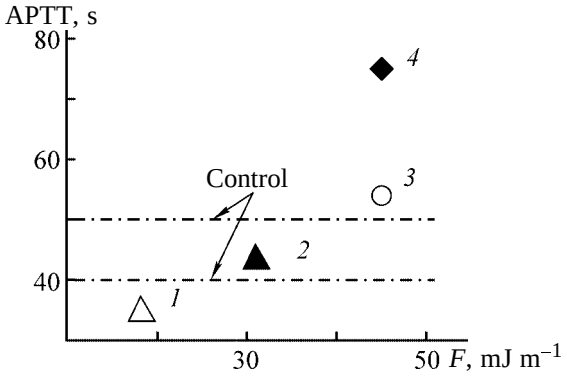

Fig. 1. Effect of hydrogel film coatings on the thromboresistant properties of the material surface. (APTT) Activated partial thromboplastin time and (*F*) free surface energy. (*1*) SKTV-med, (*2*) SKTV-med + graphite composite material; hydrogel coatings: (*3*) PVA and (*4*) PVA + trypsin.

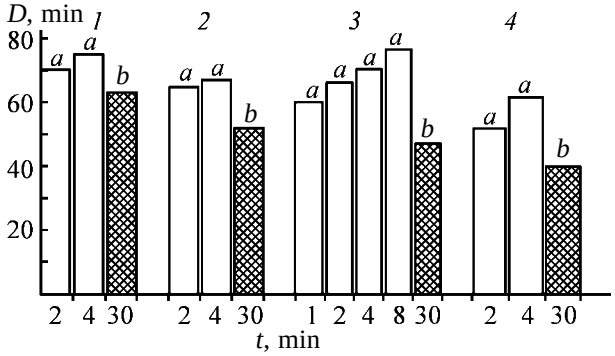

Fig. 2. Antimicrobial activity of polymeric structures. Component ratio 1 : 1; the same for Fig. 4. (*D*) Growth suppression zone and (*t*) time. Composition formula: (*1, 2*) PVA, (*3*) PVA + PVP, and (*4*) PVA + lactic acid. Kanamycin concentration in the initial composite (%): (*1*) 1.5 and (*2–4*) 1. Forming method: (*a*) electroforming and (*b*) impregnation.

cells of a living body. Hemocompatibility tests (monitoring of the coagulation rate of normal human plasma in contact with the surface of the tested materials) showed that materials with the hydrogel coating do not initiate processes resulting in thrombosis (Fig. 1). For example, SKTV-med produced only slight coagulation, and the presence of a hydrophilic surface structure reduces this effect, thus improving the hemocompatibility. This fact demonstrates a favoring effect of PVA-based electroformed polymeric systems on the interaction of the material with blood. The biocompatibility, particularly hemocompatibility of a material can be improved by introducing a proteolytic enzyme in the coating formula (Fig. 1).

The use of trypsin as a proteinic molecular probe for characterization of the biocompatibility of the electroformed coatings is based on the sensitivity of the most of enzymes to inactivating effects of the environment [13, 14]. For example, some of the fibrillation factors are associated with alterations in the tertiary structure of protein globules, which cause irreversible transformation of fibrinogen into insoluble fibrin grumes. The power and nature of the effect of the multicomponent polymeric matrix on the trypsin molecule were estimated from the difference in its activity. The experimental results showed that the composite hydrogels based on PVA and PVP have no considerable inactivating effect on immobilized trypsin (see table).

In the electric field of an infralow frequency (meander-line signal), all the components are simultaneously involved in formation of the polymeric system. A PVA–borate hydrogel network is formed at the negative electrode. Its structure may include PVP or LA molecules. In this case, the interaction between PVA and PVP is of the physical (nonspecific) nature. Since the trypsin (amphoteric polyelectrolyte) and kanamycin molecules are positively charged under the experimental conditions [13, 15], the amount of immobilized BACs on the negatively charged support surface can be varied (from 1 to 10 wt %) by changing the process time, which, in its turn, allows control of the enzymatic activity and antimicrobial action. It follows from the results obtained (table, Fig. 2) that increasing immobilization time in the electric field increases the amount of immobilized BACs, which is accompanied by slightly decreasing proteolytic activity of the enzyme. This can be attributed to strengthening of the intermolecular interaction. The electric field strength can affect the enzymatic activity also, as demonstrated in [8, 16]. Data on the amount and activity of immobilized bioactive compounds in the hydrogel coatings based on PVA, PVP, and lactic acid showed that electrical immobilization ensures an effective and controllable concentration of active compounds in the polymeric hydrogel layer (see table and Fig. 2). The amount of immobilized active compounds was found to be well comparable with that obtained in their chemical fixation on polymeric supports [17, 18]; however, the activity of electroimmobilized BACs appeared to be considerably higher. The observed high activity of the coatings obtained is due to the fact that in the electric field, when the enzyme molecules are exposed to simultaneous and specific effect of the adsorption, electrostatic, and dispersion forces, the rate of enzyme immobilization in the hydrogel matrix formed increases by an order of magnitude, as compared to impregnation (see table). With the experimental parameters of the electric field, denaturation of protein molecules is excluded. Formation of the complexes protein–polymeric matrix becomes more favorable in the presence of a hydro-

Bioactive properties of polymeric structures

Forming conditions		Trypsin concentration, mg cm^{-2}				Proteolytic activity of trypsin, % of native value			
material of support; forming procedure	τ, min	PVA	PVA + PVP	PVA + LA	PVP	PVA	PVA + PVP	PVA + LA	PVP
CS, electric field 30 V cm^{-1}	0.5	0.18	–	–	–	90	–	–	–
	1	0.30	0.20	–	–	90	92	–	–
	1.5	0.38	–	–	–	82	–	–	–
CS, impregnation	60	0.06	0.10	–	–	82	82	–	–
CS; electric field 25 V cm^{-1}	2	0.43	0.34	0.20	0.17	74	80	68	91
	4	0.45	0.49	0.28	0.21	68	78	62	85
Silicon; impregnation	60		<0.05		0.13	74	78	50	87

philic environment, since in this case the free energy is not consumed to compensate the loss in the translational and rotational entropy of the enzyme globule in its adsorption on the hydrogel matrix. As a result, the degree of inactivation decreases. These factors make electroimmobilization of BACs on hydrogel structures highly efficient, preventing denaturation of the enzyme.

Biological tests performed by the method of diffusion to agar [10] showed that the hydrogel structures with the immobilized antibiotic, obtained in the electric field for 2–4 min, have an enhanced antimicrobial activity, as compared to the coatings prepared by impregnation. The zone of growth suppression of the test microorganisms was no less than 40 mm for all the composites studied (Fig. 2). The coatings based on PVA and PVC + PVP demonstrate the most pronounced and prolonged (at least 10 days) antimicrobial action (Fig. 3).

Lactic acid has a considerable effect on the degradation rate. It is known that lactic acid acts as a condensing agent in gelation in aqueous PVA solutions. It is also used to accelerate disintegration of PVA-based goods [12]. Thanks to its tendency to hydrolytic decomposition under the action of biological fluids (blood, saliva, etc.) [19], it is advisable to use lactic acid as a component of PVA-based matrices for controlled release of bioactive agents. Lactic acid is a weaker cross-linking agent for PVA than boric acid, since it forms weaker bonds with hydroxy groups of PVA. Data on degradation of hydrogel structures (Fig. 4) demonstrate that lactic acid totally leaves the polymeric coating in 2 days, favoring gradual degradation of the hydrogel network and release of the antibiotic (Fig. 3). Variation of the lactic acid content in the hydrogel coating allows control of the degradation rate and, therefore, the period of antimicrobial and enzymatic activity. At the same time, introduction of lactic acid in a high concentration (above 50%) results in considerable decrease in the proteolytic

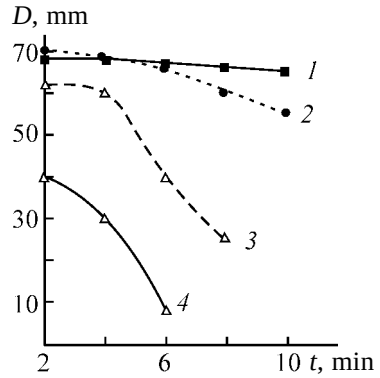

Fig. 3. Kinetic curves of biodegradation of polymeric film antimicrobial structures. Component ratio 1 : 1; kanamycin concentration in the initial composition 1 wt %. (*D*) Growth suppression zone and (*t*) time. (*1*) PVA, (*2*) PVA + PVP, (*3*) PVA + LA (electroforming for 4 min), and (*4*) PVA + lactic acid (impregnation for 30 min).

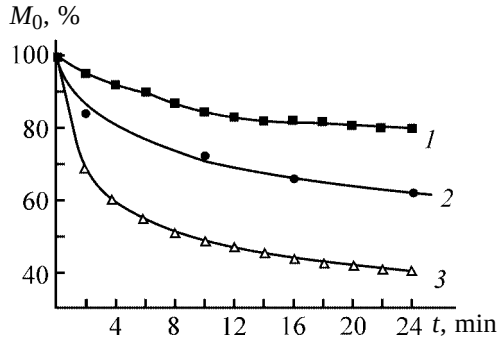

Fig. 4. Kinetic curves of degradation of polymeric film structures formed in the electric field. (M_0) Weight of the film and (*t*) time. (*1*) PVA, (*2*) PVA + PVP, and (*3*) PVA + LA.

activity of the immobilized enzyme, trypsin. Therefore, the use of neutral and basic enzymes in coatings containing lactic acid is inadvisable.

CONCLUSIONS

(1) Electroforming of multicomponent film structures based on the hydrogels studied allows effective control of their enzymatic and antimicrobial activities.

(2) At the electric field strength of 20–30 V cm^{-1}, a film containing 1–4 mg cm^{-2} kanamycin and 0.18–0.49 cm^{-2} trypsin is formed in 1–4 min on the surface of material under modification, providing high antimicrobial and proteolytic activities in the course of at least 10 days.

(3) Introduction of such components as polyvinylpyrrolidone or lactic acid and also variation of the electroforming parameters allow directional control of the degradation rate of the resulting film coatings. The degree of degradation in 24 h of the hydrogel structures based on polyvinyl alcohol and composites of polyvinyl alcohol with polyvinylpyrrolidone or lactic acid is 20, 38, and 60%, respectively.

(4) Depending on the formulation of the composite consisting of polyvinyl alcohol, polyvinylpyrrolidone, and lactic acid, its antimicrobial activity is preserved for 4–10 days.

ACKNOWLEDGMENTS

The authors are grateful to M.M. Shamtsyan for help in study of the antimicrobial properties of multicomponent polymeric coatings. The work was financially supported by INTAS FOOD (project no. 00-876).

REFERENCES

1. San Roman, J., in *Proc. 5th Eur. Polymer Federation Symp. on Polymeric Materials*, Basel (Switzerland), October 9–12, 1994, pp. 171–173.
2. Hocher, H., in *Proc. 5th Eur. Polymer Federation Symp. on Polymeric Materials*, Basel (Switzerland), October 9–12, 1994, pp. 149–152.
3. Virnik, A.D., Skokova, I.F., and Yudanova, T.N., *Zh. Org. Khim.*, 1996, vol. 32, no. 6, pp. 615–619.
4. Polyak, M.S., Bukhvalova, L.A., and Pavlova, L.M., *Eksperimental'noe izuchenie lechebnykh svoistv immobilizovannogo terrilitina* (Experimental Study of Therapeutic Properties of Immobilized Terrilytin), Leningrad: Med. Prom–st, 1982.
5. Plate, N.A., Valuev, L.I., and Chupov, V.V., *Vysokomol. Soedin., Ser. A*, 1980, vol. 22, no. 9, pp. 1963–1972.
6. Yudanova, T.N., Skokova, I.F., Aleshina, E.U., and Gal'braikh, L.S., *Khim. Volokna*, 2001, no. 1, pp. 19–22.
7. Kirsh, Yu.E., *Poli-N-vinilpirrolidon i drugie poli-N-vinilamidy: Sintez i fiziko-khimicheskie svoistva* (Poly-*N*-vinylpyrrolidone and Other Poly-*N*-vinylamides: Synthesis and Physicochemical Properties), Moscow: Nauka, 1998.
8. Ostrovidova, G.U., Makeev, A.V., and Zamyslov, E.V., *Zh. Prikl. Khim.*, 2000, vol. 73, no. 5, pp. 830–833.
9. Aleinikova, T.L. and Rubtsova, G.V., *Rukovodstvo k prakticheskim zanyatiyam po biologicheskoi khimii* (Practical Manual on Biochemistry), Moscow: Vysshaya Shkola, 1988.
10. Bueva, O.A., Zamyslov, E.V., and Ostrovidova, G.U., in *Patofiziologiya mikrotsirkulyatsii i gemostaza* (Pathophysiology of Microcirculation and Hemostasis), St. Petersburg: Sankt-Peterburg. Gos. Med. Univ., 1998, pp. 447–453.
11. Belikov, V.G., *Farmatsevticheskaya khimiya* (Pharmaceutical Chemistry), Moscow: Vysshaya Shkola, 1993.
12. Ushakov, S.N., *Polivinilovyi spirt i ego proizvodnye* (Polyvinyl Alcohol and Its Derivatives), Moscow: Akad. Nauk SSSR, 1960, vols. 1, 2, p. 812.
13. Berezin, I.V., Klyachko, N.L., Levashov, A.V., *et al.*, *Immobilizovannye fermenty* (Immobilized Enzymes), Moscow: Vysshaya Shkola, 1987.
14. Landau, M.A., *Molekulyarnye mekhanizmy deistviya fiziologicheski aktivnykh soedinenii* (Molecular Mechanisms of Action of Physiologically Active Compounds), Moscow: Nauka, 1981.
15. Mashkovskii, M.D., *Lekarstvennye sredstva* (Pharmaceutical Substances), Kharkov: Torsing, 1998, vol. 2.
16. Ostrovidova, G.U., Chechot, M.I., and Ivanova, E.N., *Prikl. Biokhim. Mikrobiol.*, 1990, no. 2, pp. 209–213.
17. Plate, N.A. and Valuev, L.I., *Zh. Vsesoyuzn. Khim. O–va*, 1985, vol. 30, no. 4, pp. 402–410.
18. Plate, N.A., Valuev, L.I., Chulak, V.V., and Burdygina, I.F., *Vopr. Med. Khim.*, 1985, no. 4, pp. 43–47.
19. Lipinsky, E.S. and Sinclair, R.G., *Chem. Eng. Progr.*, 1986, vol. 8, pp. 26–32.

Russian Journal of Applied Chemistry, Vol. 75, No. 9, 2002, pp. 1481–1484. Translated from Zhurnal Prikladnoi Khimii, Vol. 75, No. 9, 2002, pp. 1513–1516.
Original Russian Text Copyright © 2002 by Gribanov, Mokeev, Sazanov.

MACROMOLECULAR CHEMISTRY AND POLYMERIC MATERIALS

Structural Features of Carbonization of Copolyimides

A. V. Gribanov, M. V. Mokeev, and Yu. N. Sazanov

Institute of Macromolecular Compounds, Russian Academy of Sciences, St. Petersburg, Russia

Received June 20, 2002

Abstract—The influence of nitrogen-containing heterocycles on the main parameters of carbonization of aromatic copolyimides was considered for aromatic copolyimides containing phenylquinoxaline units as an example. The structural characteristics of intermediates and final products of carbonization were determined.

It is well known that polyimides occupy a very important place among polymeric materials operating under severe thermal conditions [1–3]. In some cases, these conditions result in a certain thermochemical transformation of the polyimide structure to the carbonized structure; the mechanism of this transformation was studied previously [4, 5]. It was found that the nitrogen atom of the benzimide ring of polyimides plays a decisive role in formation of carbonized products. In addition, other nitrogen atoms entering into the composition of polymer composites with polyimide participate in thermochemical cross-linking of the composites and copolymers, imparting qualitatively new characteristics to these materials. For example, copolyimides produced from standard polyimide PM and compounds containing pyrimidine rings have higher strength and heat resistance than polyimide PM and give a larger amount of the coke residue in carbonization [6].

Since the cyclic structure of pyrimidine contains two nitrogen atoms conjugated by the main chain with the benzimide structure, it was of some interest to examine their influence on the copolyimide characteristics as compared to the characteristics of another copolyimide containing two nitrogen atoms in the comonomer, namely, polyphenylquinoxaline (PQO). For this purpose, we used copolyimides of phenylquinoxaline and aromatic polyimide polyimidophenylquinoxaline (PIPQ), polynaphthylimidophenylquinoxaline (PNIPQ), and polyamidophenylquinoxaline (PAPQ) of the general formula

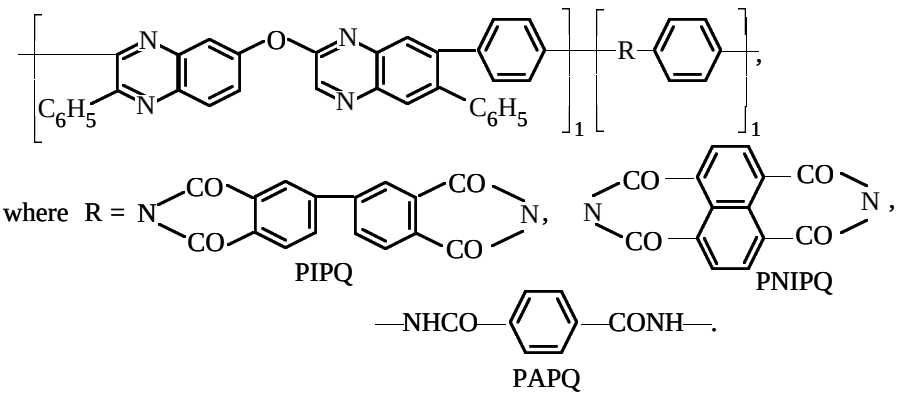

(1)

where R =

PIPQ

PNIPQ

PAPQ

In addition, PQO with the structure corresponding to the left part of formula (1) was carbonized under the similar conditions.

EXPERIMENTAL

The copolymers were produced by the procedure described in [7]. Thermal analysis was carried out on a derivatograph in the self-generated medium at a heating rate of 10 deg min^{-1} with weighed portions of 50 mg. Thermolysis of the samples was carried out on a device for thermal volumetric analysis [8]. High-resolution ^{13}C NMR spectra in solids were recorded at room temperature on a Bruker CXP-100 spectrometer using MAS and cross-polarization. The ^{13}C NMR

1070-4272/02/7509-1481$27.00 © 2002 MAIK "Nauka/Interperiodica"

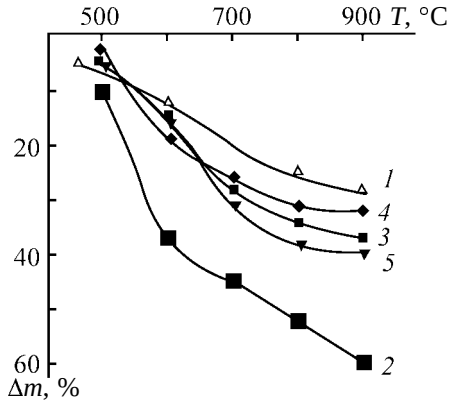

Fig. 1. TGA curve for the initial stage of carbonization of copolyimides. (Δ*m*) Weight loss and (*T*) temperature; the same for Fig. 3. (*1*) PI-PM, (*2*) PAPQ, (*3*) PIPQ, (*4*) PQO, and (*5*) PNIPQ.

spectra were run at 25.18 MHz, the rotation frequency of the samples was 3000–4000 rpm. Chemical shifts (ppm) were referred to TMS (tetramethylsilane).

As known, one of the main criteria of carbonization is the amount of coke residue (CR). The curves for weight loss under the conditions of vacuum thermolysis of the film samples in comparison with polyimide PM are shown in Fig. 1. It is evident that, in the initial stage of carbonization in the range 500–600°C, the weight loss noticeably differs depending on the polymer structure. Even at 600°C, the CR values for copolyimides containing naphthylimide units are lower by only 3–5% than those for polyimide PM. For the PQO sample, these values are lower by a factor of 2 than those for polyimide PM. As regards the PAPQ sample, at 600°C it loses almost 40% of the initial weight. The ratio between the CR values remains approximately the same at higher (up to 900°C) temperatures. With variation of the carbonization conditions (decrease in the heating rate and increase in the keeping time at stepwise heating), in the range 500–600°C, the CR values varied in some cases. To elucidate distinctions in the carbonization kinetics depending on the chemical structure of copolyimides and also to determine the structural features of the products of their carbonization, we studied high-resolution ^{13}C NMR spectra in solids using dipole decoupling.

The high-resolution ^{13}C NMR spectrum of PQO obtained by the standard MAS procedure and cross-polarization (Fig. 2, spectrum *1*) corresponds completely to the structure of its elementary unit. This spectrum consists of the signals at 160 (carbon atoms of aromatic rings at ether bond), 155 (external carbon atoms of pyrimidine rings), 140 (carbon atoms of pyrimidine ring and carbon atoms of other benzene rings directly bonded to them), and 129 ppm (all other carbon atoms of aromatic structures). With proton decoupling, the spectrum changes so that only the signals of carbon atoms not directly bonded to hydrogen atoms remain. The spectra of the intermediates of PQO carbonization at 500 and 600°C (Fig. 2, spectra *3* and *4*) do not differ significantly from the spectrum of the initial product. This suggests that, despite significant weight loss (approximately 20% at 600°C),

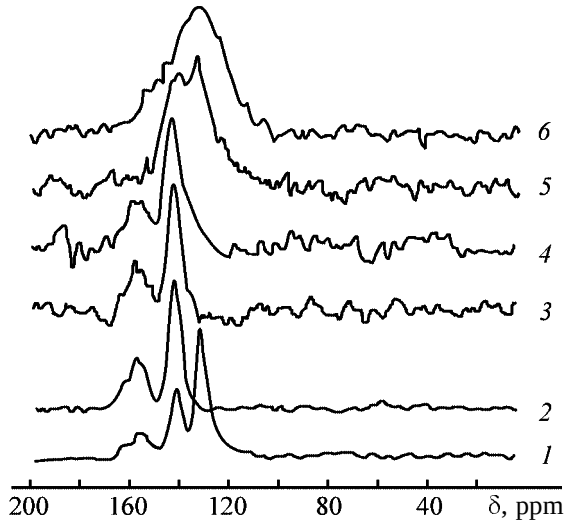

Fig. 2. High-resolution ^{13}C NMR spectra of PQO. (δ) Chemical shift. (*1*) Initial polymer; (*2*) decoupling technique; products of PQO carbonization at *T* (°C): (*3*) 500, (*4*) 600, (*5*) 700, and (*6*) 800°C; the same for Fig. 4.

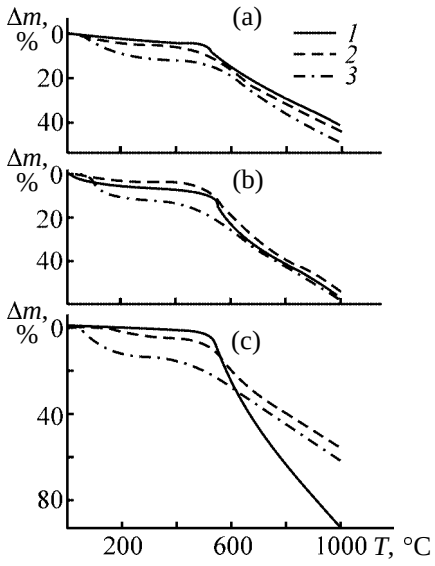

Fig. 3. TGA curves of preheated samples. Preheating temperature (°C): (*1*) 500, (*2*) 600, and (*3*) 900. Sample: (a) PQO, (b) PIPQ, and (c) PNIPQ.

the main structure of the polymer remains the same. As regards the weight loss at the above temperature, it can be assigned to phenyl groups that are side substituents at pyrimidine rings of PQO, and also to some low-molecular-weight fragments formed by rupture of the ether bond at the ends of PQO macromolecules. Such a direction of thermochemical transformations of this polymer is confirmed by the absence of weight loss up to 600°C for the PQO samples preheated to 500°C and 600°C (Fig. 3a). The spectrum of the sample heated in a vacuum to 700°C (Fig. 2, spectrum *5*) is indicative of significant transformation of the structure. There is only a signal at 140 ppm, suggesting high thermal stability of phenylquinoxaline ring; its decomposition starts only above 800°C with appearance of a signal at 128 ppm, showing the onset of formation of a polyheteroaromatic structure (Fig. 2, spectrum *6*). With further heating to 900°C, only the signal at 128 ppm remains. This rearrangement is also reflected in the shape of the TG curve of the sample preheated to 900°C (Fig. 3a). The weight loss at 100–300°C, caused by removal of low-molecular-weight products of thermal degradation, is well pronounced.

The ^{13}C NMR spectrum of PIPQ (Fig. 4a, spectrum *1*) is also in good agreement with the proposed structure of the unit (signals at 168, 155, and 140 ppm). The spectra of the pyrolysis products obtained with proton decoupling (Fig. 4a, spectrum *2*) vary insignificantly up to 600°C. The polymer structure does not vary appreciably, and the appearance of weak signals in the range 170–150 ppm can be explained by degradation of polymeric chains, in particular, by the above changes in the structure of the phenylquinoxaline fragment and also the onset of thermal degradation of the imide ring. As expected, with further heating in the temperature range 600–700°C, the decomposition of the imide ring mainly proceeds with the release of carbon oxides. By the end of this period, the signals of carbon atoms bonded to oxygen atoms disappear completely. Above 700°C, approximately 50% of pyrimidine rings remain in the resulting carbonized products, and the signals corresponding to the mixed heteroaromatic structures formed, similar to the products of thermal degradation of straight polyimide, grow in intensity. As in the case of PQO, for PIPQ preheating to 500–900°C affects the rate of weight loss (Fig. 3b).

The spectrum of the initial PNIPQ obtained by the standard CP MAS technique (Fig. 4b) is consistent with the structure of this polymer. However, this spectrum has poor information content.

In the spectrum obtained with proton decoupling

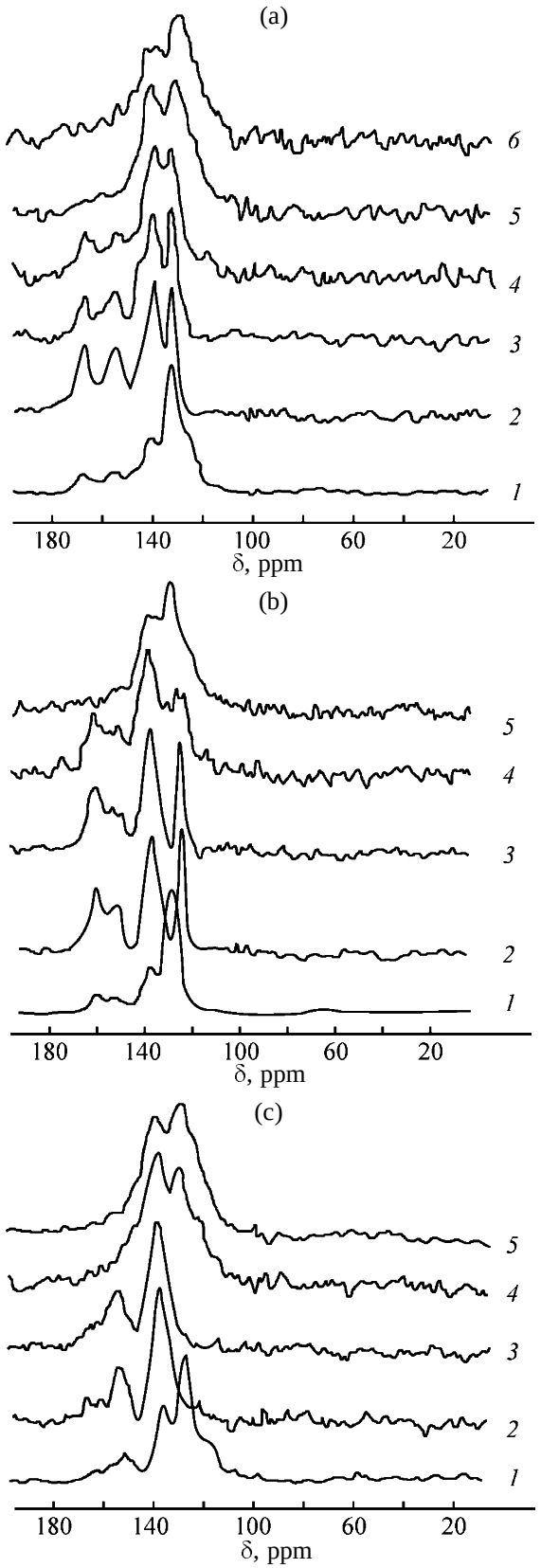

Fig. 4. Hihg-resolution ^{13}C NMR spectra of (a) PIPQ, (b) PNIPQ, and (c) PAPQ.

(Fig. 4b, spectrum *2*), there is a separate relatively narrow signal at 127 ppm assigned to the group of carbon atoms in symmetrical diimidonaphthalenetetracarboxylic dianhydride (hydrogen-free carbon atoms). In this case, the narrow signal is in good agreement with the concept that this group in the above polymer has a planar structure, which is a center of "oriented" carbonization. This structure remains fairly stable up to 600°C and is essentially the dominant of formation of heteroaromatic rings at further heating. The spectral feature of the carbonized product of this copolymer is the presence of a weak narrow signal corresponding to the diimidonaphthalene group at the background of extremely broad (more than 40 ppm) signal of aromatic carbons.

This suggests extremely high thermal stability of this fragment and, evidently, its incomplete incorporation into the resulting polyheteroaromatic structure of the carbonized product. The shape of TG curves (Fig. 3c) also suggests the presence of this structural heterogeneity. The difference in thermal degradation of ordered and disordered domains of PNIP carbonized at various temperatures is also evident from these curves. If carbonized PNIP sample is considered as some turbostratic structure in which the most ordered domain is formed by planar aggregates of diimidonaphthalenetetracarboxylic acid and quinoxaline structures, the disordered linking units are cleaved first in thermal treatment. Low-molecular-weight products of their thermolysis determine the difference in the weight loss in the entire temperature range (Fig. 3c).

The spectrum of PAPQ obtained with proton decoupling (Fig. 4b, spectrum *2*) has the highest information content. It is characterized by fairly early (at 500°C) decrease in the intensity and, later on, disappearance of the signal of amide carbonyl carbon. The other fragments show fairly high thermal stability. Formation of a polyaromatic structure starts at 600°C. The final product of carbonization is also characterized by the presence of a significant amount of heteroaromatic rings (signal at 140 ppm). However, as expected, the presence of labile amide bonds limits the stability of this polymer, which is evident from Fig. 1 (weight loss more than 40%).

CONCLUSIONS

(1) Carbonization of polyphenylquinoxalines and their copolymers with imides and amides proceeds by the mechanism of homolytic and heterolytic thermally induced cross-linking involving nitrogen atoms of the heterocycles.

(2) Contrary to polyimides, introduction of nitrogen atoms into the phenylquinoxaline fragments causes neither adequate enhancement of the thermal stability of the polymers nor significant increase in the amount of the coke residue after thermolysis.

(3) The decisive role of nitrogen-containing rings in formation of stable carbonized structures of turbostratic organization was established.

REFERENCES

1. Koton, M.M., *Zh. Prikl. Khim*., 1995, vol. 68, no. 5, pp. 822–826.
2. Srooq, C.E., *Prog. Polym. Sci*., 1991, vol. 16, pp. 561–694.
3. Sazanov, Yu.N., *Zh. Prikl. Khim*., 2001, vol. 74, no. 8, pp. 1217–1234.
4. Gribanov, A.V., Sazanov, Yu.N., Beloborodova, E.V., and Fedorova, G.N., *Zh. Prikl. Khim*., 1999, vol. 72, no. 2, pp. 467–473.
5. Gribanov, A.V. and Sazanov, Yu.N., *Zh. Prikl. Khim*., 2000, vol. 73, no. 10, pp. 1705–1709.
6. Sazanov, Yu.N., Artem'eva, V.N., Mikhailova, G.M., *et al*., *Zh. Prikl. Khim*., 1999, vol. 72, no. 6, pp. 975–982.
7. Korshak, V.V., Krongauz, E.S., Belomoina, N.M., and Kashutina, L.L., *Vysokomol. Soedin., Ser. A*, 1977, vol. 19, no. 12, pp. 2760–2766.
8. Sazanov, Yu.N. and Sysoev, V.A., *Eur. Polym. J*., 1974, vol. 10, pp. 867–869.

Russian Journal of Applied Chemistry, Vol. 75, No. 9, 2002, pp. 1485–1488. Translated from Zhurnal Prikladnoi Khimii, Vol. 75, No. 9, 2002, pp. 1517–1520.
Original Russian Text Copyright © 2002 by V. Myagchenkov, Chichkanov, Proskurina, A. Myagchenkov.

MACROMOLECULAR CHEMISTRY AND POLYMERIC MATERIALS

Thoms Effect as Influenced by the Concentration and Molecular Parameters of the Cationic Copolymer of Acrylamide

V. A. Myagchenkov, S. V. Chichkanov, V. E. Proskurina, and A. V. Myagchenkov

Kazan State Technological University, Kazan, Tatarstan, Russia

Received May 13, 2002

Abstract—The Thoms effect observed with water-soluble cationic copolymer of acrylamide was studied in relation to the concentration, molecular weight, and molecular weight polydispersity of the polymeric additive, with its composition and composition polydispersity being constant.

The Thoms effect, i.e., a decrease in the apparent viscosity of turbulently flowing liquids (aqueous media change from laminar to turbulent flow at Reynolds numbers $Re \geq 2 \times 10^3$) due to minor additions of polymers with high molecular weight *M*, is widely used in diverse branches of economy. For example, the Thoms effect underlays measures aimed to increase the velocity of high-speed ships, submarines, and torpedos, accelerate well drilling, and decrease the power consumed by driving systems in various stages of oil extraction and transportation, as well as to increase the hitting range of water jets of fire pumps in putting out severe fires [1, 2]. The Thoms effect depends on a large number of system parameters, above all, on the molecular characteristics and concentration *c* of the polymeric component. It should be noted that many aspects of assessing the Thoms effect as dependent on the molecular characteristics of copolymers require in-depth understanding and more precise determination, as the effect generally depends on both the molecular weight *M* and the composition α of the copolymer. Most of the works devoted to the Thoms effect observed in the presence of copolymers did not take into account these major complications in interpreting the experimental data.

Among the most promising and fairly inexpensive turbulence "quenchers" are (co)polymers of acrylamide (AA) [3]. The major body of information on the Thoms effect as dependent on the molecular characteristics refers to nonionic and anionic derivatives of polyacrylamide [4–8]. For cationic copolymers of AA, the data on the Thoms effect are fragmentary, and the results are not discussed comprehensively [3, 4].

In this work, we correctly estimated the Thoms effect as influenced by the molecular characteristics (*M* and polydispersity in *M*) of water-soluble ionic (cationic) random copolymers of AA with dimethylaminoethyl methacrylate hydrochloride (for all the copolymers studied, the content of ionic units α was 16.3 wt %). Account should be taken of the fact that, for nonionic AA copolymers, most of physical and physicochemical characteristics (in particular, Thoms effect) of the copolymers and compositions thereof are much more strongly dependent on α and chemical heterogeneity (polydispersity in α) than for nonionic AA copolymers [9]. This is due mainly to the fact that the conformation of the macromolecules of ionic copolymers strongly depends on α and polydispersity in α.

To *a priori* ensure constant α and polydispersity in α for the copolymers studied, we chose a nonconventional method of their preparation, namely, random scission of backbone C–C bonds in the macromolecules.

EXPERIMENTAL

As the initial (basic) copolymer for degradation we used high-molecular-weight cationic copolymer of AA with dimethylaminoethyl methacrylate hydrochloride ($M = 2.3 \times 10^6$) of the structural formula

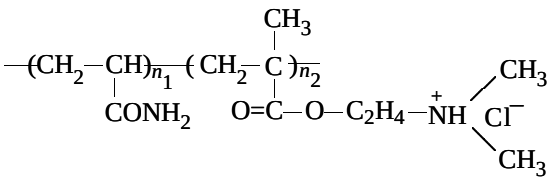

1070-4272/02/7509-1485$27.00 © 2002 MAIK "Nauka/Interperiodica"

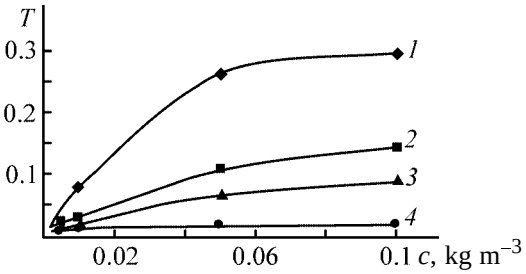

Fig. 1. Thoms effect as a function of the copolymer concentration c. $M \times 10^{-6}$: (*1*) 2.3, (*2*) 0.69, (*3*) 0.24, and (*4*) 0.025.

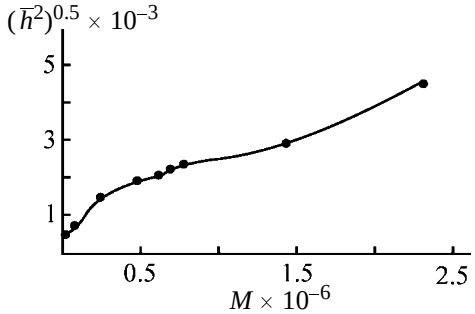

Fig. 2. Root-mean-square distance between the ends of the macromolecule $(\bar{h}^2)^{0.5}$ as a function of the molecular weight of the copolymer M.

Degradation in 0.1% aqueous solution, effected by a radical initiator ($K_2S_2O_8$, 1% of the copolymer mass), was carried out under mild conditions (45–60°C, 6 h). Current monitoring of the degradation kinetics was based on viscometry. We obtained nine samples of cationic copolymers with identical α and polydispersity in α and with strongly (by two orders of magnitude) differing molecular weights M (maximal $M = 2.3 \times 10^6$, minimal $M = 2.5 \times 10^4$). The constancy of α and polydispersity in α for the samples studied can be most easily proven by analyzing the simplified scheme of the copolymer degradation

$$-(A)_n-(B)_m + \dot{R} \rightarrow -(A)_{n-n'}-(B)_{m-m'} + -(A)_{n'}-(B)_{m'} + \dot{Z},$$

where A and B are fragments of AA and ionic monomer, respectively, and $\dot{Z}$ are inactive (toward scission of the backbone bonds of the macromolecules) radicals.

According to Enikolopyan's theory [10, 11], comparative analysis of the molecular characteristics of macromolecular "fragments" does not necessarily require knowing the detailed mechanism of the totality of radical multistage reactions of macromolecule degradation. It is sufficient to be certain that degradation occurs randomly without depolymerization. In our work, these requirements were satisfied, as evidenced by a number of special experiments, in particular, by gravimetric analysis.

For all the copolymer samples studied in this work (even those with the lowest molecular weight, $M = 2.5 \times 10^4$), the degrees of polymerization $(n' + m')$ and $(n + m - n' - m')$ were much greater than 100. Thus, the equality

$$\frac{n}{n + m} = \frac{n'}{n' + m'} = \frac{n - n'}{n + m - n' - m'} \quad (1)$$

holds, as suggested by the general theory of copolymerization [9, 12]. This proves the validity of the previously assumed identity of all the nine samples of the copolymers in both α and polydispersity in α.

The Thoms effect in a turbulent flow of aqueous media was studied by the following scheme. A special pump forced the polymer solutions at a constant pressure through a 0.5×38-mm capillary. Under these conditions, the Reynolds number for water was 5.2×10^3. The Thoms effect was quantitatively characterized by the dimensionless parameter T:

$$T = \frac{m - m_0}{m_0}, \quad (2)$$

where m and m_0 are, respectively, the masses of the copolymer solution and distilled water that passed through the capillary within the time $t = 30$ s.

We measured m_0 and m on an AND (Japan) automatic one-arm electronic balance. Figure 1 shows that the Thoms effect is strongly dependent on the concentration c and molecular weight M of the cationic copolymers of AA. The $T = f(M)$ and $T = f(c)$ plots run in parallel: The Thoms effect increases with M and c. It is convenient to analyze the $T = f(M)$ dependence by comparing the T values for fixed copolymer concentrations. The experimentally observed $T = f(M)$ dependence can be fairly simply explained as follows. Growing M tends to increase the apparent size of the macromolecular coils, which is responsible for their enhanced efficiency in turbulence wave quenching both in the immediate vicinity of the capillary walls and in the course of wave propagation deep inside the liquid [13].

Figure 2 shows how the size of the macromolecules varies with M. The root-mean-square distances between the ends of the macromolecule $(\bar{h}^2)^{0.5}$ with different molecular weights M were calculated under

the assumption that aqueous solutions of cationic copolymers adhere (to a first approximation) to the Flory equation [14]:

$$(\bar{h}^2)^{3/2}\Phi = M[\eta], \quad (3)$$

where $[\eta]$ is the intrinsic viscosity, $cm^3\,g^{-1}$, and $\Phi = 2.8 \times 10^{23}$ is the Flory constant.

The generally accepted views on the role played by the polymeric component in decreasing the effective viscosity of liquids flowing in the turbulent mode agree well, in principle, with the experimentally observed $T = f(c)$ dependences (for fixed M values): The more macromolecules participate in turbulence quenching, the greater T (Fig. 1).

To assess more rigorously the contribution from each new portion of the dosed polymer to the cumulative effect, it is convenient to change from T to reduced Thoms effect T/c. Figure 3 shows that, for fixed M values, the reduced Thoms effect decreases with increasing c, which suggests a decrease in the specific efficiency of quenching the flow turbulence for higher doses. This should be taken into account when choosing the optimal concentration of the (co)polymer c_{opt} for a liquid to be transported through a pipe in the turbulent mode. Clearly, the choice of c_{opt} should take into account, along with M, the costs of the additive and the target product, transportation costs, etc. [2]. The mentioned complex pattern of variation of the reduced Thoms effect with c and M stimulates experiments on assessing the Thoms effect for copolymer mixtures with different molecular weights M. Figure 4 presents the concentration dependence of T for 1 : 1 (by weight) copolymer mixtures including copolymer samples most strongly differing in M ($M_1 = 2.3 \times 10^6$ and $M_2 = 2.5 \times 10^4$). Dashed line is the theoretical dependence (with additive scheme assumed). For this curve we calculated individual points for fixed c values by the formula

$$T_{calc}(c) = \omega_1 T_1(c) + \omega_2 T_2(c), \quad (4)$$

where T_1, T_2 and ω_1, ω_2 are the Thoms effects and the weight fractions of the copolymers with molecular weights M_1 and M_2, respectively.

It should be specified that, in our case, $\omega_1 = \omega_2 = 0.5$. Figure 4 shows that the mixture components exert a synergistic effect, namely, mutually enhance their turbulence quenching powers.

Comparison of the calculated and experimental data for mixtures of cationic copolymers with different molecular weights M suggests that the Thoms effect depends not only on M but also on the polydispersity in M. To prove (or reject) this assumption, we used copolymer samples with different M (and identical α and polydispersity in α) for preparing mixtures with fixed average molecular weight $\bar{M} = 6.1 \times 10^5$ and with *a fortiori* different polydispersities in M. We will illustrate the formulation procedure taking a simple binary mixture of copolymers with $M_a > \bar{M}$ and $M_d < \bar{M}$ as an example. The weight fraction of the component with $M = M_a\omega_a$ was determined from the relation

$$\omega_a M_a + (1 - \omega_a)M_d = \bar{M}, \quad (5)$$

The polydispersity in M for the compositions of copolymer samples with different molecular weight M_i (i = 1–9) was quantitatively characterized by the Schulz parameter F [14]:

$$F = \bar{M}_w/\bar{M}_n - 1 = \sum_{i=1}^{k} \omega_i M_i \sum_{i=1}^{k} \omega_i/M_i - 1, \quad (6)$$

where $\bar{M}_w$ and $\bar{M}_n$ are the weight-average and number-average molecular weights of the mixtures,

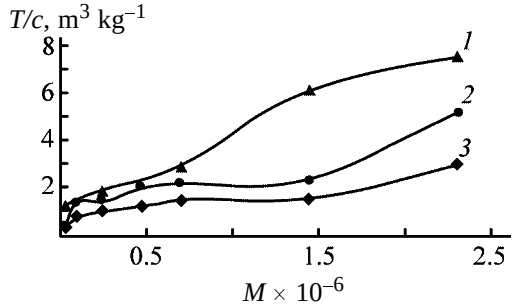

Fig. 3. Reduced Thoms effect T/c as a function of the molecular weight of the copolymer M. $c \times 10^2$, $kg\,m^{-3}$: (*1*) 1, (*2*) 5, and (*3*) 10.

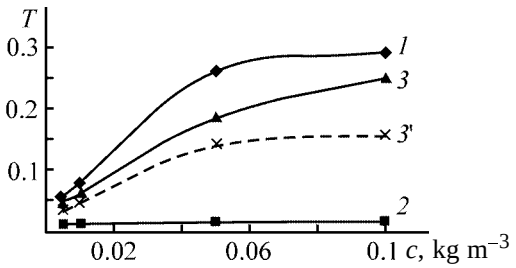

Fig. 4. Thoms effect T as a function of the concentration c of (*1*, *2*) copolymers with different molecular weights and (*3*, *3'*) 1 : 1 mixture of these copolymers. $M \times 10^{-6}$: (*1*) 2.3 and (*2*) 0.025. (*3*) Experiment and (*3'*) calculation by the additive scheme.

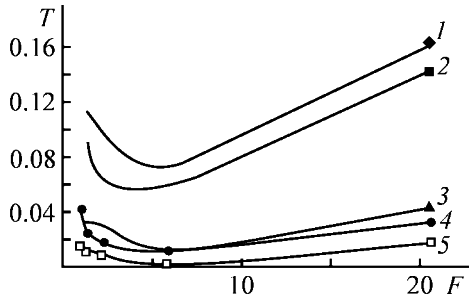

Fig. 5. Thoms effect T as a function of the Schulz parameter F for mixtures of copolymers with $\overline{M} = 6.1 \times 10^5$. $c \times 10^3$, kg m^{-3}: (*1*) 100, (*2*) 50, (*3*) 10, (*4*) 5, and (*5*) 1.

respectively, and ω_i and M_i are the content (weight fraction) and the molecular weight of *i*th polymeric component in the mixtures.

The larger the Schulz parameter F, the greater the polydispersity in M for a composition. The Enikolopyan's theory [11] states that, for each copolymer sample prepared by random scission without depolymerization, the Schulz parameter F is to be taken as unity. Figure 5 shows that the Thoms effect depends on the polydispersity in M for all the copolymer concentrations studied. The maximal Thoms effect corresponds to the largest Schulz parameters F. This, in principle, agrees with the synergistic effect exerted by the components of the mixture of copolymers with the molecular weights M_1 and M_2 (see Fig. 4), as specifically this system is characterized by the largest Schulz parameter (F = 23.5). The minimum in the $T = f(F)$ plot (Fig. 5) and the mentioned synergistic effect exhibited by the copolymer mixture components (Fig. 4) suggest that the contributions from individual fractions of cationic copolymers of AA with different molecular weights M to the cumulative Thoms effect are not additive. Without touching upon the complex and, in many respects, disputable theories concerning the Thoms effect in the case of mixed polymeric additions, we will assume the following. The relationships for the Thoms effect revealed in this work are due to the changes in the local concentrations and in the ratio of the mixture components in a thin layer of the liquid adjacent to the liquid–solid interface in the close proximity to the capillary walls [15].

CONCLUSIONS

(1) Cationic copolymers of acrylaminde exhibit a minimum in the plot of the Thoms effect vs. the polydispersity in the molecular weight, provided that the composition and polydispersity in the composition of the copolymer are constant.

(2) The components of a binary mixture of copolymers with strong polydispersity in the molecular weight exhibit a synergistic effect in flow turbulence quenching.

REFERENCES

1. Nikolaev, A.F. and Okhrimenko, G.I., *Vodorastvorimye polimery* (Water-Soluble Polymers), Leningrad: Khimiya, 1979.
2. Mastobaev, B.N., Dmitrieva, T.V., and Movsumzade, E.M., *Neft. Khoz.*, 2000, vol. 11, pp. 107–108.
3. Abramova, L.I., Baiburdov, T.A., Grigoryan, E.P., *et al.*, *Poliakrilamid* (Polyacrylamide), Moscow: Khimiya, 1992.
4. Escudier, M.P., Presti, F., and Smith, S., *J. Non-Newton Fluid Mech.*, 1999, vol. 81, no. 3, pp. 197–213.
5. Movsumzade, E.M., Mastobaev, B.N., and Dmitrieva, T.V., *Proizv. Ispol'z. Elastom.*, 2000, no. 2, pp. 15–19.
6. Wojs, K., *Inz. Chem. Processowa*, 1997, vol. 18, no. 2, pp. 309–319.
7. Brestkin, Yu.V., Frenkel', S.Ya., Zoolshoev, Z.F., *et al.*, *Vysokomol. Soedin., Ser. A–B*, 1994, vol. 36, no. 8, pp. 1281–1286.
8. Mumick, P.S., Hester, R.D., and McCormick, C.L., *Polym. Eng. Sci.*, 1994, vol. 34, no. 18, pp. 1429–1439.
9. Myagchenkov, V.A. and Frenkel', S.Ya., *Kompositsionnaya neodnorodnost' polimerov* (Compositional Heterogeneity of Copolymers), Leningrad: Khimiya, 1988.
10. Berlin, Al.Al., Khakimdzhanova, M.A., Karmilova, L.V., and Enikolopyan, N.S., *Vysokomol. Soedin.*, 1968, vol. 10, no. 7, pp. 1496–1501.
11. Berlin, Al.Al., Vol'fson, S.A., and Enikolopyan, N.S., *Kinetika polimerizatsionnykh protsessov* (Kinetics of Polymerization Processes), Moscow: Khimiya, 1978.
12. Kuchanov, S.I., *Metody kineticheskikh raschetov v khimii polimerov* (Methods of Kinetic Calculations in Polymer Chemistry), Moscow: Khimiya, 1978.
13. Ait-Cady, A., Carrean, P., and Chauveteau, G., *J. Rheol.*, 1987, vol. 31, no. 7, pp. 537–561.
14. Bartenev, G.M. and Frenkel', S.Ya., *Fizika polimerov* (Polymer Physics), Leningrad: Khimiya, 1990.
15. Rabinovich, E.Z., *Gidravlika* (Hydraulics), Moscow: Nedra, 1980.

Russian Journal of Applied Chemistry, Vol. 75, No. 9, 2002, pp. 1489–1493. Translated from Zhurnal Prikladnoi Khimii, Vol. 75, No. 9, 2002, pp. 1521–1524.
Original Russian Text Copyright © 2002 by Kurenkov, Kolesnikova, Antonovich.

MACROMOLECULAR CHEMISTRY AND POLYMERIC MATERIALS

Degree of Binding of Double-Charged Cations in Solutions of 2-Acrylamido-2-Methylpropanesulfonate Copolymers

V. F. Kurenkov, I. Yu. Kolesnikova, and O. A. Antonovich

Kazan State Technological University, Kazan, Tatarstan, Russia

Received December 11, 2001; in final form, April 2002

Abstract—The degree of binding of Mg^{2+}, Ca^{2+}, Sr^{2+}, and Ba^{2+} cations with polysulfonate anions in aqueous solutions of 2-acrylamido-2-methylpropanesulfonate polymers and their binary mixtures with acrylamide and *N*-vinylpyrrolidone with various molecular characteristics was studied by the Terayama–Wall viscometric procedure.

Water-soluble polymers of salts of 2-acrylamido-2-methylpropanesulfonic acid (H-AMS) and their binary copolymers with acrylamide (AA) and *N*-vinylpyrrolidone (VP) are effective structure-forming agents and regulators of rheological properties of solutions for drilling and petroleum production [1, 2], flocculants [3–5], adhesives, and antistatic agents [6]. The nature of cation strongly affects the preparation and properties of the (co)polymer solutions. For example, the effect of double-charged cations in H-AMS salts was found previously in the course of their polymerization [7] and copolymerization with AA [8] and VP [9, 10]. The qualitative dependences of the counterion association in polyelectrolyte solutions were determined previously in [11]. In this work, the degree of binding of Mg^{2+}, Ca^{2+}, Sr^{2+}, and Ba^{2+} cations in solutions of salts of poly-H-AMS (H-PAMS) and binary copolymers of H-AMS salts with AA and VP was quantitatively evaluated by the Terayama–Wall viscometric procedure, which is important for monitoring the radical copolymerization of H-AMS salts in aqueous solutions and for controlling the properties of aqueous (co)polymer solutions.

EXPERIMENTAL

In our work, we used samples of Na-PAMS and copolymers of Na-AMS with AA and VP prepared by radical polymerization [7] and copolymerization [8, 9] in aqueous solutions. The polymers were recrystallized from aqueous solutions in acetone, washed with acetone, and dried in a vacuum desiccator at room temperature to constant weight. The properties of the polymers studied are listed in Table 1. The viscosity-average molecular weight M_η of Na-PAMS was calculated from the following equation [13]:

$$[\eta] = 1.95 \times 10^{-5} M_\eta^{0.83},$$

where the intrinsic viscosity $[\eta]$ ($cm^3\ g^{-1}$) was determined in 0.5 M NaCl solution at 25°C.

The intrinsic viscosity $[\eta]$ of copolymer solutions was measured with an Ubbelohde viscometer (d_c = 0.56 mm). The content of ionic groups in the copoly-

Table 1. Characteristics of polymers and copolymers studied

Sample*	$[\eta]$, $cm^3\ g^{-1}$	$M_\eta \times 10^{-6}$	Content of ionic groups, mol %		
			N-VP	AA	H-AMS
A	421	2.04	–	–	100.0
B	497	–	–	12.6	87.4
C	100	–	–	52.9	47.1
D	215	–	–	7.8	92.2
E	96	–	50.8	–	49.2
F	69	–	17.4	–	82.6

* Structural formulas of macromolecules

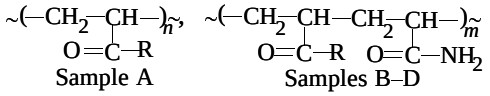

Sample A — Samples B–D

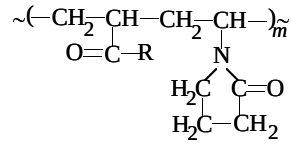

Samples E, F

where R –NH–C(CH$_3$)$_2$–CH$_2$–SO$_3$Na.

1070-4272/02/7509-1489$27.00 © 2002 MAIK "Nauka/Interperiodica"

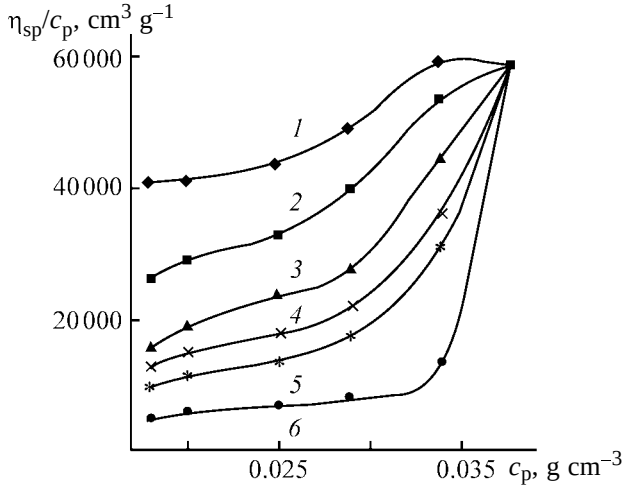

Fig. 1. Reduced viscosity η_{sp}/c_p of aqueous solutions of Na-AMS-AA copolymer (sample B) as a function of the copolymer concentration c_p at isoionic dilution with NaCl solution. c_e/c_p: (*1*) 0.46, (*2*) 1.38, (*3*) 2.31, (*4*) 4.61, (*5*) 23.1, and (*6*) 32.4.

mers was determined from the content of sulfur [14]. In our work we used chemically pure grade reagents. To study the counterion association, samples of Na-PAMS and binary copolymers of Na-AMS with AA and VP were converted into the hydrogen form by ion exchange on KU-2 × 8 sulfonic acid cation exchanger, which was pretreated according to the procedure given in GOST (State Standard) 10896–78. The salts of polyelectrolytes with double-charged cations were prepared by potentiometric titration, with cooling and stirring, of solutions of H-PAMS and binary copolymers of H-AMS with AA and VP to pH 7 using a solution of NaOH or suspensions of $Mg(OH)_2$, CaO, SrO, and $Ba(OH)_2$, with subsequent removal of the insoluble residue.

The intrinsic viscosity $[\eta]$ of copolymer solutions was measured at 30°C using a VPZh-3 viscometer (d_c = 0.56 mm). The kinetic energy correction was as low as 2% and thus was not taken into account in the evaluation of the reduced viscosity of the solutions η_{sp}/c_p, where c_p is the polymer concentration.

The potentiometric titration was performed using a pH-121 pH-millivoltmeter equipped with an ESL-63-07 working glass electrode and an EVL 1M-3 silver chloride reference electrode.

The degree of binding of counterions, which can be used as a criterion of interaction of cations with anions in polyelectrolyte solutions, is determined by the following expression:

$$\alpha_b = 1 - \alpha_f,$$

where α_f is the fraction of free counterions.

To determine α_b of metal cations with polysulfonate anions derived from H-AMS salts, we used the Terayama–Wall viscometric procedure [12]. This method is based on the analysis of the $\eta_{sp}/c_p = f(c_p)$ curves registered in the course of isoionic dilution of a polyelectrolyte solution with a solution of a low-molecular-weight electrolyte with a similar cation. The conformation of the polyanion in the polyelectrolyte solution is determined by its charge, and, according to the Terayama–Wall assumption, the isoionic dilution of the polyelectrolyte solution (in which the polymer conformation is retained) can be used to determine α_b. These conditions correspond to the linear dependence $\eta_{sp}/c_p = f(c_p)$; in this case, $\alpha_f = c_e/c_p$, where c_e is the concentration of low-molecular-weight electrolyte at which the $\eta_{sp}/c_p = f(c_p)$ is a linear function. Commonly, the $\eta_{sp}/c_p = f(c_p)$ dependence passes through a minimum at high c_e and a maximum at small c_e. Thus, the shape of the $\eta_{sp}/c_p = f(c_p)$ curve allows evaluation of the electrolyte concentration c_e at which the dependence studied will be linear. The values of α_b for K^+ cations in solutions of potassium salts of cellulose sulfate [12] agree with the data of electrochemical analysis. As found in [15], α_b for Cd^{2+} in solutions of poly-*p*-styrenesulfonic acid determined by the Terayama–Wall method and by polarography are in good agreement.

The $\eta_{sp}/c_p = f(c_p)$ curves registered at isoionic dilution of Na-AMS–AA copolymer (sample B) with an NaCl solution are shown in Fig. 1. No linear sections of the $\eta_{sp}/c_p = f(c_p)$ dependence were found in a wide range of NaCl concentrations, which makes evaluation of α_b impossible. Similar phenomenon was found for solutions of Na-PAMS and Na-AMS–VP copolymer. The fact that the Terayama–Wall procedure is inapplicable for quantitative evaluation of α_b for Tl^+ in poly-*p*-styrenesulfonic acid solutions was mentioned previously in [15].

To assess the possibility of the viscometric evaluation of α_b for double-charged cations in solutions of polyelectrolytes in question, we recorded the $\eta_{sp}/c_p = f(c_p)$ curves for the homopolymers (Mg-, Ca-, and Sr-PAMS) in the presence of respective salts ($MgCl_2$, $CaCl_2$, and $SrCl_2$). In all the above cases, we determined the optimal c_e at which the $\eta_{sp}/c_p = f(c_p)$ curves becomes linear. The $\eta_{sp}/c_p = f(c_p)$ dependence at isoionic dilution of Mg-PAMS solution (sample A) with $MgCl_2$, which becomes linear at c_e/c_p = 0.41, is shown in Fig. 2 as example. As seen from Table 2, in

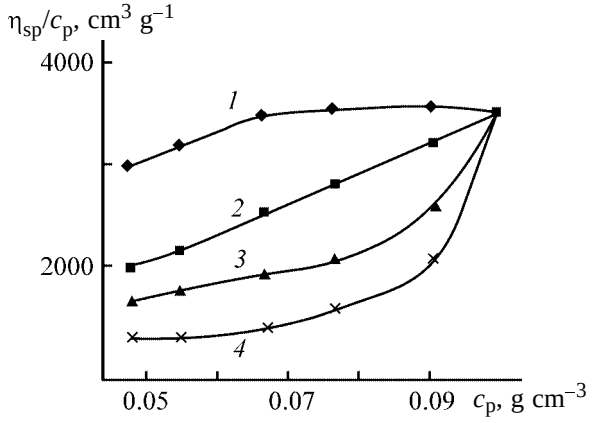

Fig. 2. Reduced viscosity η_{sp}/c_p of aqueous solutions of Mg-PAMS polymer (sample A) as a function of the polymer concentration c_p at isoionic dilution with $MgCl_2$ solution. c_e/c_p: (*1*) 0.30, (*2*) 0.41, (*3*) 0.61, and (*4*) 0.81.

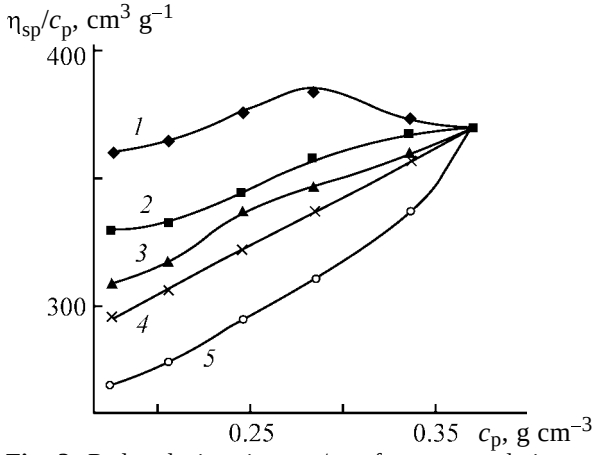

Fig. 3. Reduced viscosity η_{sp}/c_p of aqueous solutions of Ca-AMS copolymer with AA (sample C) as a function of the copolymer concentration c_p at isoionic dilution with $CaCl_2$ solution. c_e/c_p: (*1*) 0.06, (*2*) 0.11, (*3*) 0.14, (*4*) 0.22, and (*5*) 0.23.

the case of homopolymers (H-PAMS salts, sample A), α_b decreases in the order $Sr^{2+} > Ca^{2+} > Mg^{2+}$.

This dependence agrees with the effect of strontium, calcium, and magnesium cations on the η_{sp}/c_p values at c_p = const for solutions of H-PAMS in the presence of $MgCl_2$, $CaCl_2$, and $SrCl_2$ [11], and published data for the salts of poly-*p*-styrenesulfonic and polyvinylsulfonic acids, obtained by conductometry, osmometry, dilatometry, and IR spectroscopy [16, 17].

We analyzed binding of Mg^{2+}, Ca^{2+}, Sr^{2+}, and Ba^{2+} cations with polysulfonate anions of H-AMS salt copolymers with AA (samples C, D). The copolymers differed in [η] and in the chemical composition (Table 1). The resulting linear dependences $\eta_{sp}/c_p = f(c_p)$ (see, e.g., Fig. 3, curve *4*) allowed evaluation of α_b and α_f, which are presented in Table 2. For copolymers with various molecular characteristics α_b decreases (at c_p = const) in the order $Mg^{2+} > Ca^{2+} > Ba^{2+}$ (Sr^{2+}).

The binding of cations with polysulfonate anions was also successfully evaluated for copolymers of Mg-, Ca-, Sr-, and Ba-AMS with VP (samples E, F). As seen from Fig. 4, the $\eta_{sp}/c_p = f(c_p)$ curve becomes linear at c_e/c_p = 0.74 (curve *3*); the resulting α_b values are listed in Table 2. These data show that, similar to the case of H-AMS salt copolymers with AA, for H-AMS salt copolymers with VP α_b decreases in the following order: $Mg^{2+} > Ca^{2+} > Sr^{2+}$ (Ba^{2+}).

The data given in Table 2 indicate that the binding efficiency of double-charged cations with polysulfonate anions in copolymers varies in the opposite direction as compared to homopolymers (H-PAMS salts). This is true for H-AMS salt copolymers with both AA and VP, irrespective of the variations in the molecular weight (determined from [η]) and chemical composition of the polymer macromolecules (Table 1). Similar inversion of the binding efficiency of double-charged cations with polyanions on passing from homopolymers to copolymers with the same polyanions was found previously in [11]. Such variation in α_b for copolymers as compared to homopolymers is probably due to the interaction of sulfonate and amide groups of binary copolymers of H-AMS salts with VP [18] and AA [19] in aqueous solutions.

Our study showed that the above dependences in

Table 2. Degree of cation binding with polyanions in solutions of polyelectrolytes based on H-AMS salts

Sample	c_p, %	Cation	$\alpha_b = 1 - \alpha_f$
A	0.100	Mg	0.59
		Ca	0.67
		Sr	0.96
C	0.371	Mg	0.81
		Ca	0.78
		Ba	0.22
D	0.008	Mg	0.23
		Ca	0.17
		Sr	0.09
E	0.623	Mg	0.84
		Ca	0.78
		Ba	0.26
F	0.210	Mg	0.64
		Ca	0.55
		Sr	0.13

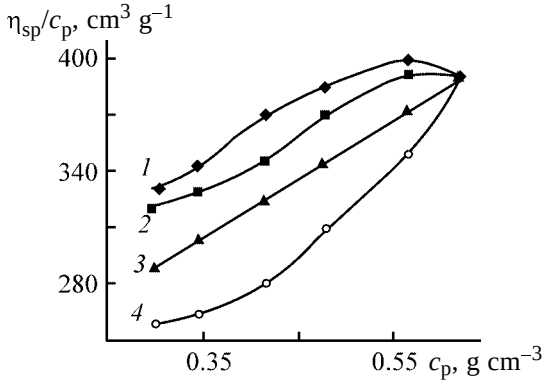

Fig. 4. Reduced viscosity η_{sp}/c_p of aqueous solutions of Ba-AMS copolymer with VP (sample E) as a function of the copolymer concentration c_p at isoionic dilution with $BaCl_2$ solution. c_e/c_p: (*1*) 0.41, (*2*) 0.57, (*3*) 0.74, and (*4*) 0.82.

binding of double-charged cations with polysulfonate anions are general, because they were determined for (co)polymers with equal molecular weight and at c_p = const (Table 1), and the reverse order in variation of α_b depending on the double-charged cation radius (Mg^{2+}, Ca^{2+}, Sr^{2+}, and Ba^{2+}) for copolymers (as compared to homopolymers) was found for the samples with different molecular properties (molecular weight, chemical composition, and nature of nonionic groups) and in a wide concentration range (0.006–0.6%). The dependences of the counterion association can be useful for interpretation of specific features of solutions of strong polyelectrolytes based on H-AMS and for their direct synthesis in aqueous solutions, because they explain the effect of the cation on the kinetics of homopolymerization of H-AMS salts [7] and their copolymerization with AA [8] and VP [9, 10]. This fact is probably due to the effect of the degree of cation binding with polyanions on the intensity of electrostatic interactions and on the conformation state of growing macroradicals, which affect the reactivity of the ionic monomers and their macroradicals in radical reactions [20, 21].

CONCLUSIONS

(1) The Terayama–Wall viscometric procedure can be used for quantitative evaluation of the degree of binding of cations in solutions of binary (co)polymers of magnesium, calcium, strontium, and barium 2-acrylamido-2-methylpropanesulfonates with acrylamide and *n*-vinylpyrrolidone, but it is inapplicable to the (co)polymers of sodium 2-acrylamido-2-methylpropanesulfonate.

(2) The degree of binding decreases in the order $Sr^{2+} > Ca^{2+} > Mg^{2+}$ for polymeric salts of 2-acrylamido-2-methylpropanesulfonic acid, and in the reverse order, $Mg^{2+} > Ca^{2+} > Sr^{2+}$ (Ba^{2+}), for binary copolymers of metal 2-acrylamido-2-methylpropanesulfonates with acrylamide and *N*-vinylpyrrolidone with various molecular properties.

REFERENCES

1. McCormick, C.L., *J. Macromol. Sci. Chem., Ser. A*, 1985, vol. 22, nos. 5–7, pp. 955–982.
2. Lisovtsev, V.V., Rostokin, G.A., and Kulikova, A.E., in *Khimicheskaya promyshlennost': Akrilaty i polivinilkhlorid* (Chemical Industry: Acrylates and Polyvinyl Chloride), Moscow: NIITEKhIM, 1984, pp. 1–20.
3. Kurenkov, V.F., Safin, A.G., and Merkanina, O.N., *Zh. Prikl. Khim.*, 1998, vol. 71, no. 9, pp. 1015–1018.
4. Kurenkov, V.F. and Shipova, L.M., *Zh. Prikl. Khim.*, 1997, vol. 70, no. 1, pp. 153–157.
5. Kurenkov, V.F., Sharapova, Z.F., and Khairulin, M.R., *Zh. Prikl. Khim.*, 1999, vol. 72, no. 8, pp. 1374–1378.
6. Shevtsova, S.A., Zaitseva, O.A., and Kurenkov, V.F., *Vestn. Kazan. Tekhnol. Univ.*, 2000, nos. 1–2, pp. 126–128.
7. Kurenkov, V.F., Safin, A.G., and Almazova, E.I., *Zh. Prikl. Khim.*, 1998, vol. 71, no. 10, pp. 1704–1708.
8. Kurenkov, V.F., Zaitseva, O.A., Vazeeva, D.G., and Solov'ev, D.A., *Zh. Prikl. Khim.*, 2001, vol. 74, no. 5, pp. 789–792.
9. Kurenkov, V.F., Zaitseva, O.A., and Isaeva, N.V., *Zh. Prikl. Khim.*, 2001, vol. 74, no. 10, pp. 1684–1687.
10. Kurenkov, V.F., Zaitseva, O.A., Hartan, H.-G., and Lobanov, F.I., *Vestn. Kazan. Tekhnol. Univ. (Suppl.)*, 2001, pp. 199–214.
11. Kurenkov, V.F., Kolesnikova, I.Yu., and Solov'ev, D.A., *Zh. Prikl. Khim.*, 2001, vol. 74, no. 3, pp. 490–493.
12. Terayama, H. and Wall, F.T., *J. Polym. Sci.*, 1955, vol. 16, pp. 357–365.
13. Fisher, L.W., Soher, A.R., and Tan, J.S., *Macromolecules*, 1977, vol. 10, pp. 949–954.
14. Charlot, G., *Les methods de la chimie analytique. Analyse quantitative minerale*, Paris: Masson, 1961, 4th ed.
15. Lapanje, S. and Leskovsek, H., *Z. Phys. Chem. Neue*

Folge, 1964, vol. 42, nos. 1–2, pp. 1–12.

16. Marina, N.G. and Monakov, Yu.B., in *Khimiya vysokomolekulyarnykh soedinenii* (Chemistry of Macromolecular Compounds), Ufa: Inst. Khim., Bashk. Filial Akad. Nauk SSSR, 1976, pp. 116–146.
17. Bekturov, E.A., Myagchenkov, V.A., and Kurenkov, V.F., *Polimery i sopolimery stirolsul'fokisloty* (Polymers and Copolymers of Stryrenesulfonic Acid), Alma-Ata: Nauka, 1989.
18. Olson, K.G. and Butler, G.B., *Macromolecules*, 1984, vol. 17, pp. 2486–2498.
19. Valueva, S.V., Kipper, A.I., Lyubina, S.Ya., *et al*., *Vysokomol. Soedin., Ser. A*, 1992, vol. 34, no. 12, pp. 35–44.
20. Kabanov, V.A. and Topchiev, D.A., *Polimerizatsiya ionizuyushchikhsya monomerov* (Polymerization of Ionizable Monomers), Moscow: Nauka, 1975.
21. Kurenkov, V.F. and Myagchenkov, V.A., *Zh. Prikl. Khim*., 1999, vol. 72, no. 6, pp. 881–890.

Russian Journal of Applied Chemistry, Vol. 75, No. 9, 2002, pp. 1494–1496. Translated from Zhurnal Prikladnoi Khimii, Vol. 75, No. 9, 2002, pp. 1525–1528.
Original Russian Text Copyright © 2002 by Davletbaev, Davletbaeva, Galyametdinov, Kalachev.

MACROMOLECULAR CHEMISTRY AND POLYMERIC MATERIALS

Effect of Metal Complex Binding on the Properties of Polymethyl Methacrylate

R. S. Davletbaev, I. M. Davletbaeva, Yu. G. Galyametdinov, and K. E. Kalachev

Kazan State Technological University, Kazan, Tatarstan, Russia

Received January 18, 2002; in final form, March 2002

Abstract—Coordination binding of polymethyl methacrylate with copper(II) ions was studied by IR spectroscopy and viscometry.

Metal complex modification of polymers is a promising way to affect macrochain conformation, their structure, formation of supramolecular structures, and, ultimately, the performance of the materials produced. Metal-complex binding, along with cross-linking action, imparts new specific properties to polymers (magnetic, electric, nonlinear-optical, catalytic, etc.). Coordination binding of macrochains may proceed in solutions and melts of polymers and in the course of their synthesis [1, 2].

Synthesis and properties of metal-coordinated polyurethanes (MCPU) are described in [3–5]. Preparation of MCPU involves preliminarily synthesis of metal complexes and their introduction into the urethane-forming reaction system. It was found that metal complex modification of polyurethanes changes their physicomechanical properties and sharply (by 4–5 orders of magnitude) decreases the volume and surface electrical resistivity. The physicomechanical properties of MCPU pass through several extrema. The first maximum lies in the region of very small metal ion concentrations. Studies performed showed that these phenomena are caused by formation of additional intermolecular interactions due to coordination binding of electron-donor groups.

Therefore, it was interesting to study the effect of metal complex binding on the properties of the other polymers whose macrochains contain electron-donor groups. In this work, we chose polymethyl methacrylate (PMMA). It contains ester groups capable of coordination binding, has a linear structure, and is well soluble in polar organic solvents. In addition, methyl methacrylate, similar to methyl acrylate, is the initial reagent for synthesis of paramagnetic mesomorphic comb-shaped metal-coordinated polymers [6]. The features of metal complex binding of PMMA can serve as a model for the further study of coordination binding of comb-shaped polymers. The product of the reaction between $CuCl_2$ and *N*,*N*'-diethylhydroxylamine (DEHA) was used as a metal complex modifier. In this reaction, the oxidation degree of a part of copper(II) ions decreases, DEHA is oxidized to nitrone, and polynuclear complexes in which both copper(I) and copper(II) ions are bound by chloride bridges [7] are formed. It was found that copper(I, II) binds heteroatoms of the macrochain with substitution of labile chloride bridges by electron-donor groups. To confirm this mechanism, copper(II) chloride was also used in metal complex modification of PMMA.

To prepare modified samples, $CuCl_2$–DEHA or $CuCl_2$ were introduced into a solution of PMMA in acetone. The resulting polymer was examined as acetone solution or as films. In the IR spectrum of the product of PMMA interaction with a $CuCl_2$–DEHA mixture, the band at 1730 cm^{-1} belonging to stretching vibrations of the PMMA carbonyl groups becomes narrower as compared to the initial PMMA, and a new strong band at 1630 cm^{-1} appears (Fig. 1). According

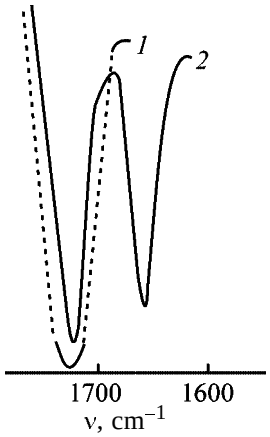

Fig. 1. IR Spectra of (*1*) PMMA and (*2*) product of PMMA reaction with $CuCl_2$–DEHA mixture. (ν) Wave number.

1070-4272/02/7509-1494$27.00 © 2002 MAIK "Nauka/Interperiodica"

to [5, 8], these changes result from coordination binding of PMMA carbonyl groups. They are not observed when straight Cu(II) chloride is added to PMMA. This confirms the main role of chloride bridges in coordination binding between the metal ion and electron-donor groups of macrochains.

The influence of metal complex binding on conformation of PMMA chains was studied by viscometry. As seen from Fig. 2, the dependence of the intrinsic viscosity on the $CuCl_2$ concentration has two maxima. The twofold increase in the intrinsic viscosity indicates that two adjacent PMMA molecules coordinate with Cu(II) via their carbonyl groups. As a result, the macromolecules get unrolled and increase in size.

The intrinsic viscosity of a PMMA solution in acetone and of this solution modified with a $CuCl_2$–DEHA mixture decreases similarly with temperature rise (Fig. 3). This shows that the coordination binding of macrochains is preserved on heating. At the same time, the intrinsic viscosity of solutions containing PMMA and $CuCl_2$ changes insignificantly as compared to that of the initial PMMA solution (Fig. 2). In this case, measurements were performed within a narrow range of $CuCl_2$ concentrations because of the low $CuCl_2$ solubility in acetone. Since the IR spectra of films prepared from a PMMA solution and a solution containing both PMMA and $CuCl_2$ are similar, we can suggest that PMMA macrochains are located in the outer coordination sphere of the Cu(II) ion. In parallel with increase in the intrinsic viscosity of PMMA modified with $CuCl_2$–DEHA, the hardness and luster of films obtained from solutions noticeably increase (Fig. 4). Such effect of metal complex binding on the mechanical properties of PMMA films can be caused by additional interactions between PMMA macrochains, which are preserved after solvent evaporation. On the contrary, the hardness of films obtained from PMMA–$CuCl_2$ solutions somewhat decreases.

The comparison of the concentration dependences of the mechanical properties of MCPU [5], hardness of modified PMMA samples, and intrinsic viscosity of their solutions shows that the properties of these polymers as functions of the $CuCl_2$ content in the $CuCl_2$–DEHA modifying system also pass through extrema. For example, the MCPU hardness in the region of small $CuCl_2$ contents has a maximum. For PMMA, the intrinsic viscosity of solutions and hardness of solid films pass through maxima.

The decrease in the volume resistivity by 4–5 orders of magnitude is the most substantial effect in

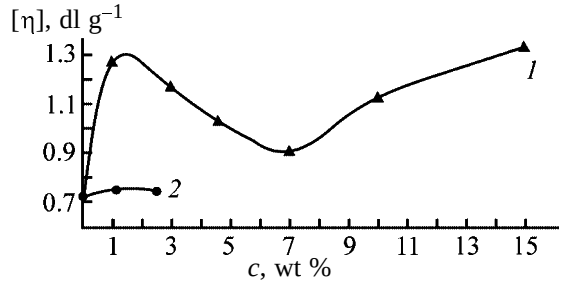

Fig. 2. Intrintic viscosity [η] as a function of $CuCl_2$ concentration c for PMMA solutions modified with (*1*) $CuCl_2$–DEHA mixture and (*2*) $CuCl_2$.

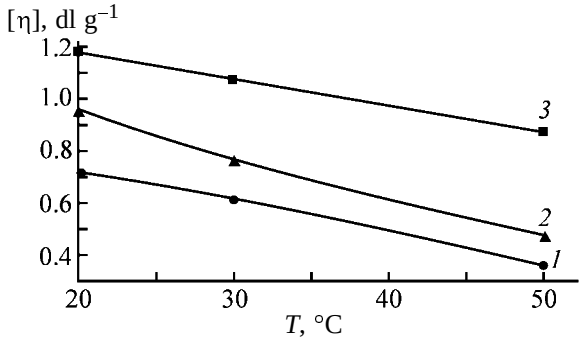

Fig. 3. Intrinsic viscosity [η] of PMMA solutions in acetone modified with $CuCl_2$–DEHA mixture as a function of temperature T. $CuCl_2$ concentration (wt %): (*1*) 0, (*2*) 3, and (*3*) 5.

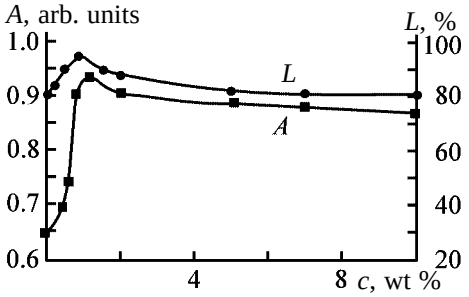

Fig. 4. Hardness A and luster L of films obtained from acetone solutions of PMMA modified with $CuCl_2$–DEHA mixture as functions of $CuCl_2$ concentration c.

metal complex binding of polyurethanes. It decreases jumpwise within the $CuCl_2$ concentration range 0.1–0.3% depending on the nature of the flexible polyurethane chains. As the content of metal complex modifier is increased further, the specific volume resistivity slightly increases. The main role in the mechanism of charge transfer in MCPU belongs to electron-donor groups of the polyurethane matrix and to the presence of copper ions in two oxidation states (I) and (II). In this connection, we studied electrophysical properties of PMMA modified with the $CuCl_2$–DEHA system.

It follows from Fig. 5 that the volume resistivity of films of modified PMMA sharply decreases in the

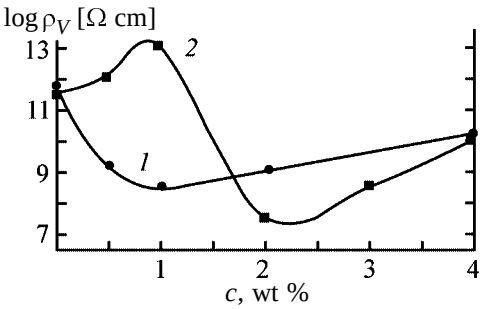

Fig. 5. Volume resistivity ρ_V of PMMA films modified with (*1*) $CuCl_2$–DEHA mixture and (*2*) $CuCl_2$ as a function of $CuCl_2$ concentration *c*.

region of small copper(II) chloride concentrations. At higher $CuCl_2$ concentrations, the volume resistivity somewhat increases. For PMMA modified with $CuCl_2$ only, a decrease in the resistivity after its initial increase occurs at higher $CuCl_2$ concentrations. This is probably due to appearance of Cu(II)–Cu(I) exchange pairs because of partial copper(II) reduction in acetone solutions [9]. As a whole, the experimental dependences obtained allow us to rule out the ionic mechanism of the electrical conductance and to follow the electronic model of charge transfer, previously proposed for MCPU [3].

EXPERIMENTAL

N,N'-Diethylhydroxylamine was distilled at 48°C and 13 hPa. Pure grade $CuCl_2 \cdot 2H_2O$ was dehydrated by heating for 5–6 h at 110°C. Copper(II) chloride was dissolved in DEHA at a molar ratio of 1 : 1.

The IR spectra were recorded on a Perkin-Elmer 16 C FT-IR Fourier spectrometer. The error in determination of the IR frequency was ±1 rel. %. Films prepared from acetone solutions were used as samples.

The intrinsic viscosity was measured with an Ubbelohde viscometer at 20°C. The film hardness was determined on an M-3 pendulum device. The luster was measured with an FB-2 photoelectric device. The volume resistivity of films was measured on an E6-13A teraohmmeter with a 2.5% error. Films were cast on a conducting glass, which was placed into a special measuring cell.

CONCLUSIONS

(1) In reaction of polymethyl methacrylate with $CuCl_2$–*N,N'*-diethylhydroxylamine mixture, the polymethyl methacrylate ester groups coordinate with copper ions, which results in cross-linking of adjacent macrochains. As a result, the intrinsic viscosity of polymethyl methacrylate increases (twofold), and its films become harder. Modification of PMMA with straight copper(II) chloride does not produce similar effects.

(2) Metal complex binding of PMMA decreases the volume resistivity by four orders of magnitude. The charge transfer has electronic but not ionic mechanism.

ACKNOWLEDGMENTS

The work was supported by the Ministry of Education of the Russian Federation (project no. T-00-9.2-2106) and Russian Foundation for Basic Research (project no. 01-03-32 280).

REFERENCES

1. Pomogailo, A.D. and Savost'yanov, V.S., *Metallsoderzhashchie monomery i polimery na ikh osnove* (Metal-Containing Monomers and Derived Polymers), Moscow: Khimiya, 1988.
2. Pomogailo, A.D., *Polimernye immobilizovannye metallokompleksnye katalizatory* (Polymeric Immobilized Coordination Catalysts), Moscow: Nauka, 1988.
3. Davletbaeva, I.M., Parfenov, V.V., Dorozhkin, V.P., and Kirpichnikov, P.A., *Vysokomol. Soedin., Ser. A*, 1989, vol. 31, no. 6, pp. 1215–1220.
4. Davletbaeva, I.M., Rakhmatullina, A.P., Kirpichnikov, P.A., and Kuzaev, A.I., *Vysokomol. Soedin., Ser. B*, 1998, vol. 40, no. 4, pp. 667–671.
5. Davletbaeva, I.M., Kirpichnikov, P.A., Atova, R.A., *et al.*, *Zh. Prikl. Khim.*, 1994, vol. 67, no. 2, pp. 258–262.
6. Haase, W., Griesar, K., Soto Bustamante, E.A., and Galyamedtinov, Y., *Metal-Containing Polymeric Materials*, Pittman, C.U., Ed., New York: Plenum, 1995, pp. 287–299.
7. Davletbaeva, I.M., Ismagilova, A.I., Tyut'ko, K.A., *et al.*, *Zh. Obshch. Khim.*, 1998, vol. 68, no. 6, pp. 1021–1027.
8. Vatulev, V.N., Laptii, S.V., and Kercha, Yu.Yu., *Infrakrasnye spektry i struktura poliuretanov* (Infrared Spectra and Structure of Polyurethanes), Kiev: Naukova Dumka, 1987.
9. Kukushkin, Yu.N., *Reaktsionnaya sposobnost' koordinatsionnykh soedinenii* (Reactivity of Coordination Compounds), Leningrad: Khimiya, 1987.

Russian Journal of Applied Chemistry, Vol. 75, No. 9, 2002, pp. 1497–1500. Translated from Zhurnal Prikladnoi Khimii, Vol. 75, No. 9, 2002, pp. 1529–1532.
Original Russian Text Copyright © 2002 by Kislenko, Oliinyk.

MACROMOLECULAR CHEMISTRY AND POLYMERIC MATERIALS

Reaction of Copper(II) with Polyacrylic Acid and Its Copolymers in Dilute Solutions

V. N. Kislenko and L. P. Oliinyk

L'viv'ska Politekhnika National University, Lviv, Ukraine

Received April 19, 2002

Abstract—The effect of the concentration of copper(II) and polyacrylic acid (or its copolymers) and of pH on the amount of bound copper in precipitation of copper salts with poly acids was studied.

Carboxyl-containing polymers find growing application for precipitation [1] and separation [2] of heavy metals. This requires further study of interaction between metal ions and polymeric acids in aqueous solutions. Mandel and Leyte [3] showed that copper(II) nitrate reacts with polymethacrylic acid to form complexes with one and two carboxy groups of the polymer. In the latter case, the reaction proceeds in two stages. At high copper(II) concentrations, 1 : 1 complexes and, at low concentrations, 2 : 1 complexes are formed [4]. Viscosimetric study showed that each copper(II) ion can react with one, two, and four carboxy groups of polymethacrylic acid [5, 6]. In the presence of Cu(II), the molecular weight of polymethacrylic acid increases, which suggests formation of bridges between two macromolecules [6, 7]. It follows from the kinetic study that the activation energy of Cu(II) chelation with polymethacrylic acid is fairly low and amounts to 24–28 kJ mol^{-1}, the activity of isotactic polymethacrylic acid being 1.5 times higher than that of the syndiotactic acid [8]. At the same time, it should be noted that colloid-chemical features of formation of copper(II) precipitates with poly acids are studied insufficiently.

Polyacrylic acid reacts with copper(II) sulfate in dilute solutions to give insoluble copper polyacrylates. The concentration of bound copper(II) ions in the reaction mixture decreases with increasing polyacrylic acid concentration and reaches a minimum at the molar ratio of carboxy groups to bound copper ions equal to 2 (Fig. 1, curve *1*). This confirms published data [5, 6] that chelates are formed in which the copper ion binds two carboxy groups of the poly acid.

The concentration of bound copper increases with decreasing the initial concentration of the poly acid. This is probably due to increase in pH. The dependence between the amount of bound copper and pH is linear (Fig. 1, curve *2*). Probably, polyacrylic acid favors precipitation of copper(II) basic salts formed by hydrolysis of copper(II) sulfate in dilute aqueous solutions. Indeed, at the constant concentration of polyacrylic acid, the concentration of bound copper(II) ions linearly increases with increasing the initial concentration of copper sulfate (Fig. 2).

The curves of titration of freshly precipitated copper hydroxide suspension with polyacrylic acid have a plateau at pH ~ 5 (Fig. 3, curves *1, 2*) indicating salt formation. The molar ratio of copper to carboxy groups equal to 1 suggests formation of copper(II) basic salts with polyacrylic acid within the pH range 4.5–5.0. An increase in the initial concentration of polyacrylic acid decreases the plateau length, probably due to changes in the size of macromolecule globules in the solution. This is confirmed by the shape of the curve of titration of a copper(II) hydroxide suspension with a dispersion of acrylic acid–acrylonitrile copolymer (Fig. 3, curve *3*). In this case, the plateau is absent, since the reaction proceeds only between the

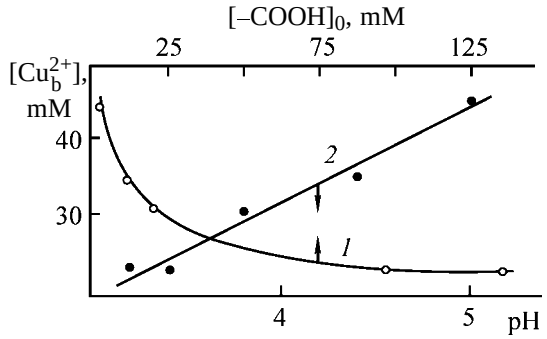

Fig. 1. Concentration of bound copper(II) ions, $[Cu_b^{2+}]$, as a function of the (*1*) initial concentration of polyacrylic acid carboxy groups $[–COOH]_0$ and (*2*) pH. Initial concentration of copper(II) sulfate 62 mM.

1070-4272/02/7509-1497$27.00 © 2002 MAIK "Nauka/Interperiodica"

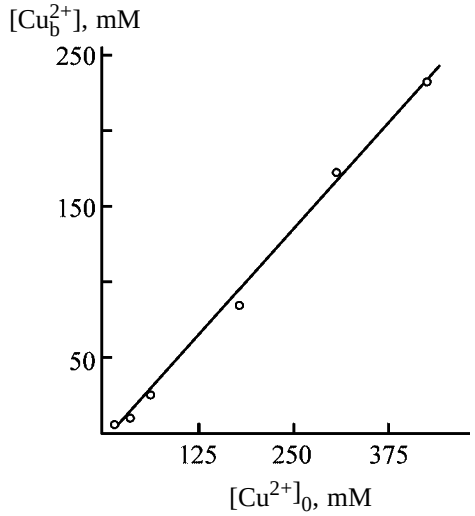

Fig. 2. Concentration of bound copper(II) ions, [Cu$_b^{2+}$], as a function of the initial concentration of copper(II) sulfate, [Cu^{2+}]. Initial concentration of polyacrylic acid 1.4 g l^{-1}.

surface carboxy groups of copolymer particles and copper(II) hydroxide groups located on the surface of dispersion particles. As a result, insoluble basic salts formed on the surface of the reacting particles stop the reaction.

Then we studied the reaction of copper ammine complexes with ammonium polyacrylates at decreasing pH. Titration of ammonium polyacrylate with hydrochloric acid showed that, at pH close to 6, there is an inflection in the titration curve, probably caused by conformational transitions in the polyacrylic acid macromolecule (Fig. 4, curve *1*). At pH 2.5–3.0 polyacrylic acid precipitates. The titration curve of the copper ammine complex has two plateaus (Fig. 4, curve *2*). The first plateau at pH ~8 probably corresponds to formation of chloride salts of the copper ammine complex, and the second plateau at pH 5.0–5.5, to complete decomposition of the complex and formation of a copper hydroxide precipitate. At pH decreased further, the precipitate dissolves with formation of copper(II) chloride. Titration with hydrochloric acid of a mixture of ammonium polyacrylate and copper ammine complex showed that initially, at pH ~8, salts of the copper ammine complex with polyacrylic acid are formed. At the further decrease in pH, copper ammine complex completely decomposes, and basic copper salts with polyacrylic acid are formed. Copper polyacrylates precipitate only at pH 3.0–3.5. Light green color of the solution over the precipitate at pH 3 shows that copper(II) chloride is partially formed. Similar titration curves are obtained when mixtures of the copper ammine complex and ammonium salts of acrylic acid–acrylonitrile copolymers are titrated with hydrochloric acid. A decrease in the concentration of carboxy groups in the copolymer increases pH of the copper salt precipitation.

As seen from Fig. 5, an increase in the ratio of the initial molar concentrations of the carboxy groups of poly acids and copper ions decreases the copper ion concentration in the solution after precipitate formation. Thus, a decrease in the acrylic acid content in the copolymer allows more complete binding of copper ions and hence decrease in their concentration in the solution over the precipitate. This is probably due to

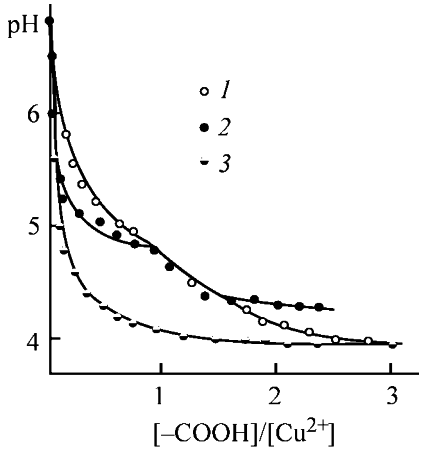

Fig. 3. Titration of copper(II) hydroxyde suspension with (*1, 2*) polyacrylic acid and (*3*) acrylic acid–acrylonitrile copolymer PAAN-1. Initial concentration of copper(II) hydroxide in the suspension 6.3 g l^{-1}. Concentrations (g l^{-1}): polyacrylic acid (*1*) 22 and (*2*) 11; PAAN-1 copolymer (*3*) 31.

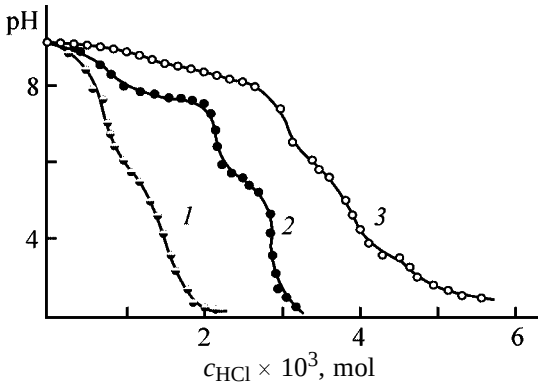

Fig. 4. Titration of (*1*) ammonium polyacrylate, (*2*) copper(II) ammine complex, and (*3*) their mixture with 0.1 M hydrochloric acid. Initial concentrations: polyacrylic acid carboxy groups 60 mM and copper(II) ions 12 mM. (c_{HCl}) HCl amount.

the fact that the copper salt with the acrylic acid–acrylonitrile copolymer is formed at higher pH (up to pH 5.0 for PAAN-3 copolymer). This favors formation of copper(II) hydroxide, which precipitates together with basic copper polyacrylates.

An attempt to calculate complex formation constants of copper with polyacrylic acid and its copolymers with acrylonitrile failed, probably because of colloid-chemical features of the process, which is accompanied by two parallel reactions: formation of insoluble copper salts with poly acids and formation of copper(II) hydroxide at pH close to 5. Copper polyacrylate forms a shell around copper hydroxide particles, which prevents $Cu(OH)_2$ dissolution during titration with hydrochloric acid. At the same time, the dependence of the concentration of bound copper ions on the initial concentration of the copper ammine complex and ammonium polyacrylate is well approximated by a straight line in the logarithmic coordinates [Fig. 6, Eq.(1)]:

$$\log([Cu_b^{2+}]) = \log A + K\log([COOH]_0/[Cu^{2+}]_0). \quad (1)$$

The correlation coefficients and constants of copper salt formation with poly acids, calculated by Eq. (1), are presented below:

Polymer	R	$\log A$	K
PAA	0.911	0.9 ± 0.5	0.84 ± 0.18
PAAN-1	0.982	-2.4 ± 0.2	0.70 ± 0.08
PAAN-2	0.926	-3.1 ± 0.4	0.52 ± 0.16

Equation (1) and the constants found allow calculation of the amounts of polyacrylic acid and its copolymers with acrylonitrile that should be added to the copper ammine complex to decrease the copper ion concentration in the solution to the required level (at pH ~ 3 for polyacrylic acid and 4 for acrylic acid–acrylonitrile copolymer).

EXPERIMENTAL

Chemically pure grade anhydrous copper(II) sulfate and freshly distilled acrylic acid and acrylonitrile were used. Polyacrylic acid and its copolymers were prepared by polymerization initiated with potassium persulfate. The monomer conversion, which was determined by the bromide–bromate method, in all cases exceeded 99.5%. Acrylic acid–acrylonitrile copolymers were obtained as dispersions stabilized with ammonia. The content of acrylic acid in copolymers was determined by potentiometric titration in dimethylformamide. The molar ratio of acrylic acid to acrylonitrile in the copolymers was 3.43 (PAAN-1), 1.22 (PAAN-2), and 0.78 (PAAN-3). The molecular weight of polyacrylic acid, measured viscometrically, was 1.6×10^5. The intrinsic viscosity of polyacrylic acid and its copolymers, determined in dimethylformamide at 26°C, was 1.303 (acid), 1.324 (PAAN-1), 1.436 (PAAN-2), and 1.275 (PAAN-3). Copper hydroxide dispersion was prepared by precipitation with sodium hydroxide and was washed with distilled water to negative reaction for sulfate ions.

The copper(II) concentration in the solution after separation of the copper salt precipitate was determined spectrophotometrically at 448 nm (absorption of the copper ammine complex). The concentration of

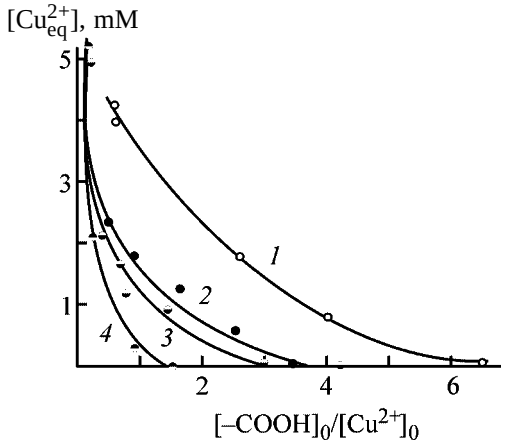

Fig. 5. Effect of the initial concentration ratio of the carboxy groups of poly acid ammonium salt and copper(II) in ammine complex $[-COOH]_0/[Cu^{2+}]_0$ on the copper ion concentration in the solution $[Cu_{eq}^{2+}]$ after precipitation of copper salts with (*1*) polyacrylic acid, (*2*) PAAN-1, (*3*) PAAN-2, and (*4*) PAAN-3. pH: (*1*) 3.0, (*2*, *3*) 4.0, and (*4*) 5.0.

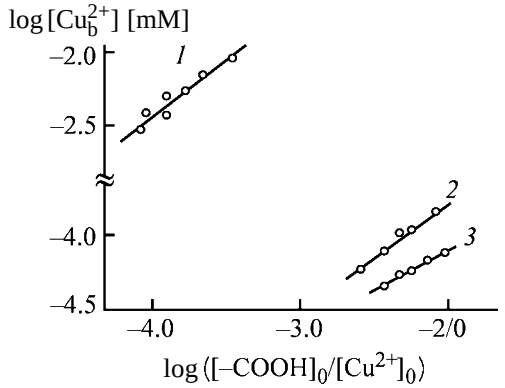

Fig. 6. Concentration of bound copper(II) ions, $[Cu_b^{2+}]$, vs. the initial concentration ratio of carboxy groups $[-COOH]_0$ belonging to ammonium polyacrylates and copper(II) ions $[Cu^{2+}]_0$ in the ammine complex after precipitation of copper salts with (*1*) polyacrylic acid, (*2*) PAAN-1, and (*3*) PAAN-3. Coordinates of Eq. (1). pH: (*1*) 3 and (*2*, *3*) 4.

bound copper was determined as difference between the initial copper concentration and the copper ion concentration after the precipitate separation.

CONCLUSION

The influence of colloid-chemical factors on the amount of bound copper during precipitation of copper salts with poly acids was characterized.

REFERENCES

1. Esumi, K., Ogihara, K., and Meguro, K., *Bull. Soc. Chem. Jpn.*, 1984, vol. 57, no. 3, pp. 1202–1207.
2. Olinikova, M., Muraviev, D., and Valiente, M., *Anal. Chem.*, 1999, vol. 71, pp. 4866–4873.
3. Mandel, M. and Leyte, J.C., *J. Polym. Sci., Part A*, 1964, vol. 2, no. 6, pp. 2883–2899.
4. Kolawole, E.G., and Bello, M.A., *Eur. Polym. J.*, 1980, vol. 16, no. 4, pp. 325–332.
5. Kolawole, E.G. and Mathieson, S.M., *J. Polym. Sci., Polym. Chem. Ed.*, 1977, vol. 15, no. 10, pp. 2291–2301.
6. Kolawole, E.G. and Mathieson, S.M., *J. Polym. Sci. Polym., Chem. Lett. Ed.*, 1979, vol. 17, no. 9, pp. 573–578.
7. Marinsky, J.A. and Ansapach, W.M., *J. Phys. Chem.*, 1975, vol. 9, no. 5, pp. 439–444.
8. David, C., Panw, A.D., and Geuskens, G., *J. Polym. Sci., Part C-1*, 1968, no. 22, pp. 319–327.

Russian Journal of Applied Chemistry, Vol. 75, No. 9, 2002, pp. 1501–1505. Translated from Zhurnal Prikladnoi Khimii, Vol. 75, No. 9, 2002, pp. 1533–1537.
Original Russian Text Copyright © 2002 by Bobashova, Dudkina, Nikolaeva.

MACROMOLECULAR CHEMISTRY AND POLYMERIC MATERIALS

Formation of Hydrogen Bonds in the System Polyamidine–Low-Molecular-Weight Dye

A. S. Bobashova, M. M. Dudkina, and M. N. Nikolaeva

Institute of Macromolecular Compounds, Russian Academy of Sciences, St. Petersburg, Russia

Received May 13, 2002

Abstract—The interaction of poly-1,10-decamethyleneacetamidine with some low-molecular-weight additives was studied. It was shown by nuclear magnetic relaxation and IR spectroscopy that linear dyes of the bis-hydroxyalkanone type form hydrogen bonds with amidine groups of the polymer, and the strength of these bonds depends on the degree of dissociation of the dye.

Amidines are widely used in medicine and technology; also, they are the subjects of active research in organometallic chemistry. At present, low-molecular-weight amidines are well known, while polymers containing amidine groups, which are of interest for many applications, are not adequately studied [1]. The structure and characteristics of these polymers were studied by ^{1}H, ^{15}N, and ^{13}C NMR both in solids and in solutions, and also by thermal gravimetric analysis [1–3]. Polyamidines have the general formula –NH–CR=N–, where R is an aliphatic or aromatic group.

It is known [4] that polymeric networks of polyamidines, formed by hydrogen bonds with dyes, are capable of nonlinear optical (NLO) behavior. As regards production of complexes with NLO behavior, polyamidines show much promise, which is due to high basicity of amidine groups [5]. In this work, we studied the structure of complexes of ionogenic comb-shaped polymers, namely, poly-1,10-decamethyleneacetamidine, with the functional group in the main chain and low-molecular-weight polyconjugated NLO dyes of the bis-hydroxyalkanone type. It was shown previously [4] that poly-1,10-decamethyleneacetamidine can form fairly heat-resistant, stable for a long time (more than 1 year) film-forming polymeric complexes with dyes, capable of efficient generation of the third harmonic. However, the relationship between the chemical structures formed by polyamidine with NLO dyes and macroscopic characteristics of the resulting associates has not been adequately studied [6].

Here we paid attention to variation of the characteristics of the polymers as a result of formation of comb-shaped structures and their possible supramolecular ordering. It was important to study the mechanism of formation of supramolecular polymer structure upon addition of the dye and the mechanism of rupture of the existing hydrogen-bonded polymer network. In addition, it is believed that the relationship between the acidity of the low-molecular-weight compound and the basicity of the polyamidine should significantly affect the structure of the complexes. To confirm this assumption, the compounds having similar structure but different dissociation constants pK_a were selected as low-molecular-weight additives. The aim of this work was also to determine the temperature range of existence of hydrogen bonds in the system polyamidine–low-molecular-weight additive and to elucidate changes in the supramolecular structures with time.

Formation of hydrogen bonds in the above systems was studied by NMR relaxation and IR spectroscopy. IR spectroscopy is widely used for analysis of systems forming hydrogen bonds [7]. NMR relaxation allows monitoring of the mobility of polymer chains and determination of structural changes of molten systems in time.

In this work we studied the interaction of poly-1,10-decamethyleneacetamidine (hereinafter, polyamidine)

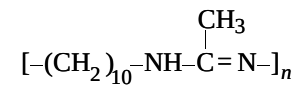

I

with the following additives: 4,4'-dihydroxydiphenyl

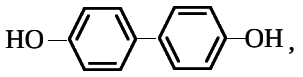

II

1070-4272/02/7509-1501$27.00 © 2002 MAIK "Nauka/Interperiodica"

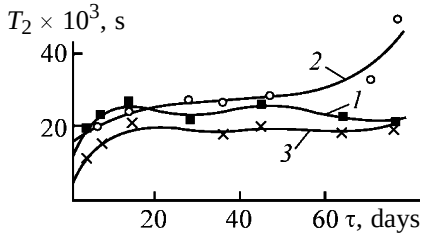

Fig. 1. Spin–spin relaxation time T_2 as a function of the experiment duration τ. (*1*) Polyamidine; polyamidine with 15% addition of (*2*) 4,4'-dihydroxydiphenyl and (*3*) bis-(4-hydroxybenzylidene)acetone at 90°C.

bis(4-hydroxybenzylidene)acetone

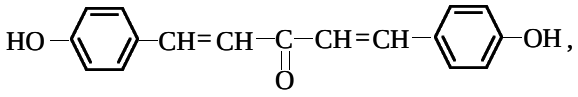

III

(4-hydroxy-4'-methoxybenzylidene)acetone

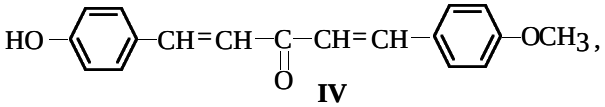

IV

and phenolphthalein

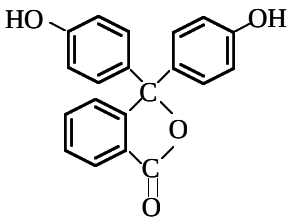

V

Apparently, the characteristics of the resulting polymer networks will depend on the number of deprotonated hydroxy groups. The choice of the first three low-molecular-weight additives is based on the fact that the negative logarithms of the dissociation constants pK_a of these compounds are different. Considering the possibility of deprotonation of hydroxy groups of dyes **III** and **IV**, we can assume that deprotonation takes place and these hydroxy groups form hydrogen bond with the amidine group of the polymer, since the pK_a values for these dyes are lower than for polyamidine (pK_a 10.8 [5]): for dye **III**, pK_a is 8.6 [8], and for dye **IV**, 9.2. In the case of dye **III**, both hydroxy groups can be deprotonated, but to a different degree, since their dissociation constants are different. Therefore, in spite of possible formation of hydrogen-bonded network, the ionicity of the resulting bonds at different pK_a should be different: the lower pK_a, the more ionic are the bonds and, hence, the higher is their strength. This is also apparently true for the molecules of the other dyes. With dye **IV**, whose acidity is close to the acidity of dye **III**, only comb-shaped structures can be formed. 4,4'-Dihydroxydiphenyl, having low acidity (pK_a ~ 13), is not, most likely, deprotonated in a mixture with polyamidine and, probably, forms weak hydrogen bonds with the functional groups of the polyamidine. Thus, the basicity of polyamidine must be sufficient for deprotonation of molecules of **III** and **IV**, while dye **II** should remain protonated. Possible effect of the steric structure of the dye on formation of the polymer network was studied with complexes of polyamidine with phenolphthalein having nonlinear structure.

EXPERIMENTAL

The spin–spin relaxation time T_2 for polyamidine and a mixture of polyamidine with low-molecular-weight chromophores was measured in the temperature range 70–180°C. The measurements were carried out in melts on an RRP-1 relaxometer.

The melting point of polyamidine is approximately 70°C, and that of dye **III**, approximately 245°C. As a result of heating of the polymer with dyes, melts are formed, and the color of the system changes. The spin–spin relaxation times T_2 increased with time for all mixtures of substances, reaching some stable level (Fig. 1).

The increase in T_2, shown in Fig. 1 for 90°C, is also characteristic of other temperatures at which the experiments were carried out.

The results obtained refer to the first type of sample heating (from 80°C gradually to 180°C). In the second case, to obtain the relaxation dependences for polyamidine and its mixture with chromophores, the samples were heated to 180°C, kept at this temperature for 15 min, cooled to 80°C, and then heated again to 180°C.

The concentration of the dyes was 15 mol %. The choice of this concentration is due to the fact that the maximum capacity of polymer with respect to the dye is 20 mol %.

The IR spectra of the above mixtures, polyamidine, and dye **III** were recorded on a Bruker IFS 88 spectrophotometer in KBr pellets (in the case of individual dye) and in films (in the case of polyamidine and a mixture of polyamidine with dye).

It is known [1] that polyamidine molecules form stable interchain hydrogen bonds. Addition of a dye should result in competition of the functional groups of the dye and polymer for formation of hydrogen

bonds. As seen from comparison of the IR spectra (Fig. 2a), a hydrogen bond is formed between the polymer and dye **III**. Since the NMR relaxation method used in the experiments furnishes information on the proton mobility, variation of the relaxation rate in the samples also suggests variation of the bond strength between the components.

The data obtained from relaxation measurements allow a conclusion that the energy of the hydrogen bond between the polymer and low-molecular-weight additives in the melts of their mixtures and also in straight polyamidine varies in time. Since the time dependences of the spin–spin relaxation time were obtained at varied temperature, we can assume that the apparent increase in T_2 is caused by the presence of crystalline and amorphous phases of polyamidine. On heating, the fraction of the amorphous component of the polymer increases, and the polymer structure returns to the initial structure within several months. In addition to increase in T_2 with time, T_2 also varied depending on the particular additive (Figs. 1, 3). It is well known that, with increasing viscosity, the spin–spin relaxation time T_2 decreases [9] and, with increasing temperature, the trend is usually reverse [9]. Since the melt viscosity should not vary significantly with addition of substances with close molecular weights, we can conclude that the shorter relaxation time for a mixture of poyamidine with **III** as compared to its mixture with **II** suggests formation of stronger bonds for a mixture with dye **III**. One of the possible mechanisms of the interaction of the polyamidine with the additives is deprotonation of the OH group of the dye and formation of a hydrogen bond with the amidine group of the polymer with the degree of ionicity depending on the degree of deprotonation.

Deprotonation of hydroxy groups of low-molecular-weight dyes can result in formation of a structure of the quinoid type, which is confirmed by the appearance of absorption bands in the range 480–530 nm. For example, in a mixture of polyamidine with dye **III** this absorption band appears at 500 nm [6]. For dye **III** this quinoid structure has the form

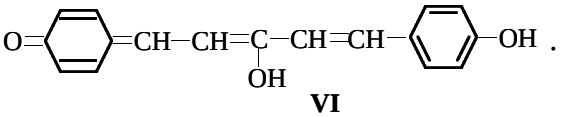

VI

The deprotonated nonquinoid structure has the form

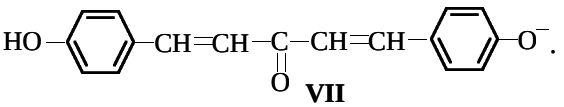

VII

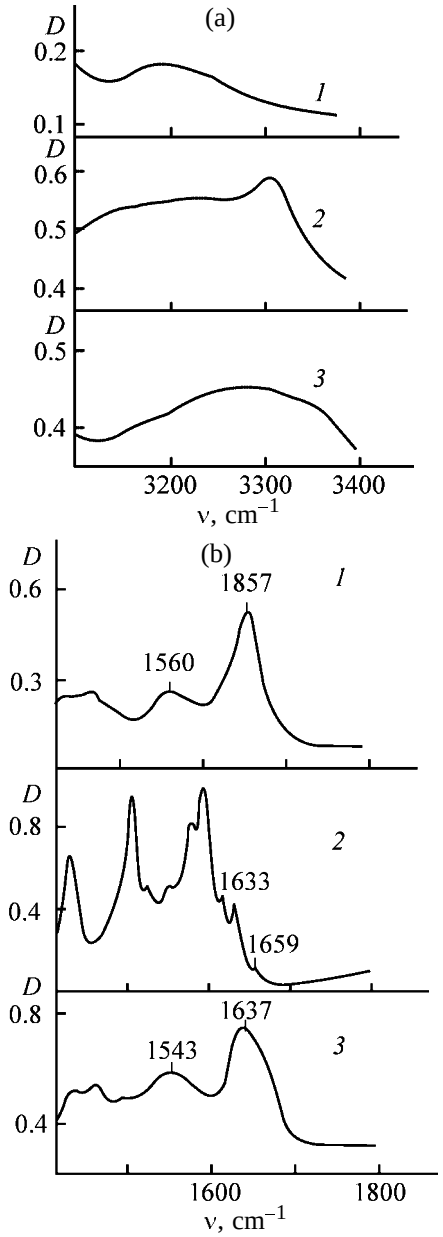

Fig. 2. IR spectra of (*1*) polyamidine, (*2*) bis(4-hydroxybenzylidene)acetone, and (*3*) a mixture of polyamidine with 15% of bis(4-hydroxybenzylidene)acetone in the range of (a) hydrogen and (b) double bonds. (*D*) Optical density and (ν) wave number.

As follows from NMR data, in a mixture of polyamidine with dye **III** in deuterated methanol the content of quinoid structures is approximately 10% [6]. Deprotonation of dye **III** in a mixture with the polyamidine is evident from the ^{13}C CPMAS spectra; in this case, the degree of deprotonation increases with increasing polymer concentration in the mixture.

The absorption band of the C=N stretching modes in the polyamidine is observed at approximately

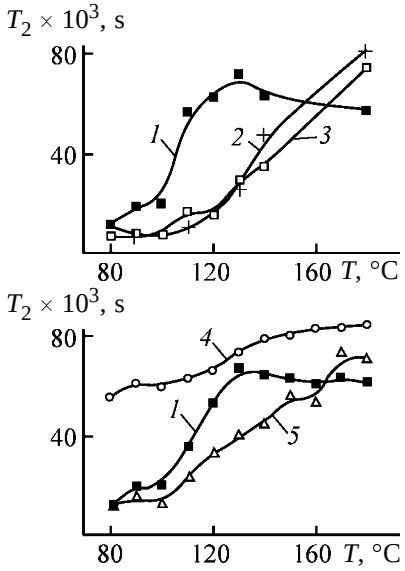

Fig. 3. Spin–spin relaxation time T_2 as a function of temperature T for (*1*) polyamidine and (*2*–*5*) polyamidine with various additives. Additive (15%): (*2*) bis(4-hydroxybenzylidene)acetone, (*3*) (4-hydroxy-4′-methoxybezylidene)acetone, (*4*) dihydroxydiphenyl, and (*5*) phenolphthalein.

1650 cm^{-1}, while the absorption band of the keto groups is usually observed at a higher frequency [10]. The absorption band of the keto group of dye **III** in the solids is significantly shifted toward low frequencies (Fig. 2b; 1633 and 1659 cm^{-1}), which suggests the formation of an intramolecular hydrogen bond. This assumption is confirmed by theoretical calculations [6] and X-ray diffraction data [2]. The absorption bands of the C=N bond are shifted, which suggests participation of this group in the bonding. Comparison of the two main peaks (Fig. 2b) in the spectra of the polyamidine and a mixture of polyamidine with dye **III** shows appearance of shoulders in the spectrum of the mixture. These shoulders are absent in the spectrum of straight polyamidine. This suggests the presence of two forms of the amidine group in the system: bonded to dye and free amidine group.

In addition, in a mixture of the polymer with dye **III**, the bands of the stretching modes of the benzene ring are shifted (absorption bands at approximately 1500, 1600, and 3030 cm^{-1}). The positions of these bands are governed by the substitution pattern; therefore, this shift can be explained by the interaction of hydroxy groups of dye **III** with the polyamidine. It is evident that, in the system polyamidine–dye **III**, several types of hydrogen bonds can coexist. This is confirmed by the fact that, in the spectrum of a mixture of polymer with dye **III**, the absorption bands assigned to hydrogen bonds differ from those in the spectrum of straight dye **III** (Fig. 2a). Hydrogen bonds are formed between polyamidine molecules [1, 11] and between polyamidine and dye **III** molecules both via the peripheral hydroxy group of the dye and via the lateral hydroxy group of the quinoid form of the dye or the keto group of its major form [8]. Formation of hydrogen bonds in the examined mixtures of the polyamidine with additives of various chemical structures via peripheral oxygen atoms of the dye and the resulting noticeable changes in the mobility of polymer chains can be assumed from the NMR relaxation data (Fig. 3).

The relaxation time T_2 of a mixture of polyamidine with 15% of both dyes **III** and **IV** is shorter than T_2 for the straight polyamidine (Fig. 3), which suggests decreased mobility of the polymer chains.

Addition of **II** to the polymer increases the relaxation time of the mixture (Fig. 3), since the mobility of the polymer chains increases. This suggests that, in this case, contrary to the complexes of dyes **III** and **IV** forming ionic bonds with the polymer, a strong bond between the components is not formed. It should be noted that the difference in the spin–spin relaxation time of polyamidine complexes with **III** and **IV** is insignificant, despite close pK_a values (the difference is approximately 0.6). This may be caused by the fact that molecules of these dyes form, to a large extent, the bonds with the polymer via keto groups, which, to a some extent, levels out the influence of formation of network structures. This assumption is consistent with the results of quantum-chemical calculations [6] suggesting distribution of the negative charge between the oxygen atom in dye **III** in the ratio enol : phenolate 3 : 7.

The theoretical calculations of thermodynamic compatibility were carried out for polyamidine with addition of **II** and **III** by the procedure described in [12]. These calculations, considering both van der Waals and specific interactions (among them, formation of a hydrogen bond), showed that dye **III** has a higher solubility parameter than **II**, i.e. it is better compatible with polymer.

It was found that addition of phenolphthalein decreases the mobility of the polymeric chains of the polyamidine, but to a lesser extent than addition of chromophores **III** and **IV**, evidently, owing to their nonlinear structure. This is manifested in a longer spin–spin relaxation time T_2 for the most of temperatures, as compared to the relaxation time obtained with the above additives (Fig. 3).

For all cases, T_2 increases with temperature, since

the mobility of protons in melts increases with temperature.

CONCLUSIONS

(1) The IR data show that linear dyes of the bis-hydroxyalkanone type form comb-shaped structures with poly-1,10-decamethyleneamidine owing to formation of hydrogen bonds between molecules of the low-molecular-weight dye and amidine groups of the polymer.

(2) The NMR relaxation data show that the mobility of polymeric chains varies on adding low-molecular-weight dyes: the strength of the bond between poly-1,10-decamethyleneacetamidine and dye depends on the degree of dissociation of the dye.

(3) The bond between the dye and poly-1,10-decamethyleneacetamidine can be formed at a temperature not exceeding 160°C.

REFERENCES

1. Bohme, F., Klinger, C., Komber, H., *et al*., *J. Polym. Sci., Part A: Polym. Chem*., 1998, vol. 36, pp. 929–938.
2. Komber, H., Klinger, C., and Bohme, F., *Macromolecules*, 1997, vol. 30, pp. 8066–8068.
3. Komber, H., Klinger, C., and Bohme, F., *Polymer*, 1997, vol. 38, no. 11, pp. 2603–2608.
4. Ten'kovtsev, A.V., Yakimanskii, A.V., Lukoshkin, V.N., *et al*., *Fiz. Tverd. Tela*, 2000, vol. 42, no. 11, pp. 2099–2102.
5. Bohme, F., Haubler, L., Tenkovtsev, A.V., and Yakimansky, A.V., *Polym. Prepr*., 1999, vol. 40, no. 2, pp. 1140–1141.
6. Tenkovtsev, A.V., Yakimansky, A.V., Dudkina, M.M., *et al*., *Macromolecules*, 2001, vol. 34, no. 20, pp. 7100–7107.
7. Pimentel, G.C. and McClellan, A.L., *The Hydrogen Bond*, Pauling, L., Ed., San Francisco: Freeman, 1960.
8. Bohme, F., Tenkovtsev, V.A., Haussler, L., and Komber, H., *Macromol. Symp*., 1998, vol. 128, p. 102.
9. Chizhik, V.I., *Yadernaya magnitnaya relaksatsiya* (Nuclear Magnetic Relaxation), Leningrad: Leningr. Gos. Univ., 1991.
10. Bellamy, L.J., *The Infra-Red Spectra of Complex Molecules*, London: Methuen, 1954.
11. Bohme, F., Kunert, C., Klinger, C., and Komber, H., *Macromol. Symp*., 1998, vol. 128, p. 183.
12. Askadskii, A.A., *Struktura i svoistva teplostoikikh polimerov* (Structure and Characteristics of Heat-Resistant Polymers), Moscow: Khimiya, 1981.

Russian Journal of Applied Chemistry, Vol. 75, No. 9, 2002, pp. 1506–1509. Translated from Zhurnal Prikladnoi Khimii, Vol. 75, No. 9, 2002, pp. 1538–1541.
Original Russian Text Copyright © 2002 by Baranov, Zheleznov.

MACROMOLECULAR CHEMISTRY AND POLYMERIC MATERIALS

Influence of *n*-Alkanes on Hardening and Selected Properties of Gelatin Shells of Microcapsules

A. V. Baranov and K. N. Zheleznov

Institute of Chemistry of Solutions, Russian Academy of Sciences, Ivanovo, Russia

Received May 13, 2002

Abstract—The influence of aliphatic hydrocarbons encapsulated in gelatin shells on hardening and heat resistance of these shells was studied by linear dilatometry, gravimetry, and pH-metry.

Microencapsulation attracts now particular attention owing to the fact that microcapsules of functional substances, obtained by such technologiles, endow conventional and new articles, products, and materials with a set of valuable properties and new benefits. Of greatest importance in storage, processing, and utilization of microcapsules are heat resistance, mechanical strength, and permeability of the shells, i.e., characteristics governed by the shell structure [1].

The performance characteristics, in particular, thermophysical properties, of gelatin shells of microcapsules are largely determined by the course of their hardening. Therefore, the conditions of this process are of decisive importance. It should be noted that, despite a great number of papers devoted to microencapsulation technologies and the properties of the resulting microcapsules, the influence exerted by the core substance on hardening of the shells and their properties still remains to be understood.

In this work, we studied the influence of aliphatic hydrocarbons C_6–C_{10} on hardening and selected properties of gelatin shells of microcapsules.

EXPERIMENTAL

As core substances we used homologs of saturated hydrocarbons (*n*-alkanes) C_nH_{2n+2} (n = 6–10). The shell material for microcapsules was active, brand A, low-viscosity photographic gelatin [OST (Branch Standard) 6-17-421–84] with the isoelectric point p*I* 4.7. Microencapsulation was performed by simple coacervation of gelatin dissolved in water at 50–55°C using sodium sulfate (see [2]). The dispersion of the microcapsules with primary coacervation shells was cooled and subjected to chrome–syntane–tannide hardening [3]. This involved two-stage successive treatment with solutions of chromium–potash alums $CrK(SO_4)_2 \cdot 12H_2O$ and synthetic hardening agent no. 2 (syntane no. 2). The latter is the product of condensation of phenol and formaldehyde, sulfonated with sulfuric acid. The aqueous dispersions of the microcapsules were washed to remove the chemicals until the washing and initial waters had identical pH. The microcapsules were hardened, washed, and dried at room temperature. The encapsulation product was a friable powder containing microcapsules with the average diameter of 70 μm. The hydrocarbon content in the capsules was 82–87 wt %.

To study the properties of the shells, we withdrew microcapsules in various stages of the process, and dried and opened them mechanically, whereupon the contents (core) was left to evaporate.

Model samples were fluoroplastic-supported films prepared from the initial gelatin solutions. Selected samples were kept in *n*-alkanes and hardened by chrome–syntane–tannide procedure [3].

The behavior of the initial gelatin, its coacervate, and microcapsule shells on heating was studied by linear dilatometry, which is particularly sensitive to changes in the mobility of the molecules and structural elements in polymeric systems. We used a specially designed setup shown schematically in Fig. 1. The setup was equipped with a balance producing a minimal mechanical effect on the sample, which is very important for studying polymers transforming to devitrified state during heating. The samples studied were shaped as cylinders 5 mm in diameter and 20 mm in length made from the shell material. The sample heating rate was 5 deg min^{-1}.

Figure 2 presents the temperature dependences of the linear dimensions for the initial gelatin, gelatin

1070-4272/02/7509-1506$27.00 © 2002 MAIK "Nauka/Interperiodica"

coacervate, microcapsule shells subject to chrome hardening with hexane as the core, and microcapsule shells that passed the full hardening cycle, with alkane as the core. The resulting dilatometric curves show that the initial gelatin, coacervate, and shells that passed the chrome hardening only tend to grow in linear size and, therefore, to expand. The onset temperature for expansion of the sample of the initial gelatin is 125°C, which is the middle of the temperature range 80–180°C, corresponding to melting of less heat-resistant crystalline zones in the structure of this polymer [4]. More heat-resistant crystalline zones melt at 200°C. In the case of coacervate, the expansion onset temperature for the sample decreases to 90°C. This is due to the specific action of inorganic salt on an aqueous gelatin solution and, therefore, to the specific structure of the coacervate. As shown in [5, 6], adding a neutral salt into a homogeneous solution of the protein favors coagulation of the macromolecules, thus facilitating the coil–helix transition, which is specifically responsible for gelatin coacervation. As a result, dried coacervate differs from the initial gelatin by a much larger proportion of the macromolecules taking the helical form (α form of gelatin). The vitrified α form of gelatin has a significantly lower density and, therefore, a significantly lower cohesion energy than the collagen-like β form [7]. This difference in the cohesion energy is specifically responsible for the fact that the molecular mobility of the coacervate is manifested in the course of heating at a lower temperature compared to the initial gelatin.

Figure 2 (curve *3*) shows that hardening with chrome hardener enhances the heat resistance of the coacervate, but the onset temperature of the sample expansion remains unchanged. This suggests that certain domains in the microcapsule shell material contain no hardener.

Complete treatment cycle, i.e., two-stage hardening of microcapsules, imparts to them a strong tendency to thermal contraction (Fig. 2, curves *4*–*9*). Notably, the onset temperatures for thermal expansion and contraction are almost identical (curves *1*–*9*), which suggests identical character of molecular mobility in gelatin.

Figure 2 shows that, with increasing concentration of syntane no. 2 in the hardening solution and the hardening time (curves *8*, *9*), the contractibility of the shells tends to increase. These factors beneficially affect the sorption of the hardener, as confirmed by the pattern of variation of pH in solution during hardening (Fig. 3). The observed sharp decrease in pH of the hardening solution is due to deprotonation of the $-NH^{3+}$ groups of gelatin by hydrogen bonding with –OH groups of the hardener. Under favorable conditions, the functional groups of the hardener and gelatin approach each other and get covalently bound,

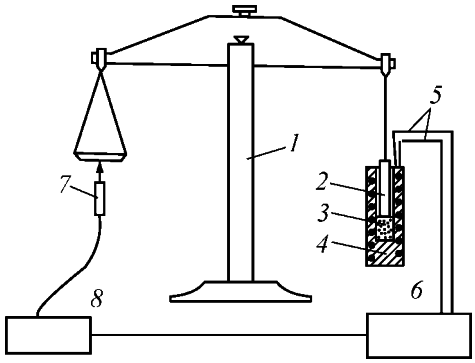

Fig. 1. Schematic of linear dilatometer: (*1*) balance, (*2*) rod, (*3*) sample, (*4*) thermal unit, (*5*) thermocouple, (*6*) two-coordinate potentiometer, (*7*) electromechanical sensor of linear displacement, and (*8*) instrument for measuring microdisplacements.

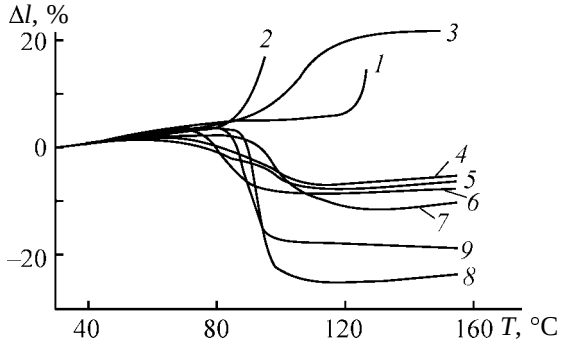

Fig. 2. Variation of the linear dimensions of gelatin-based materials Δl as a function of the temperature T. (*1*) Initial gelatin, (*2*) coacervate, (*3*) coacervate after chrome hardening; (*4*–*9*) microcapsule shell after chrome–syntane–tannide hardening. *n*-Alkane: (*4*) nonane, (*5*) octane, (*6*) decane, (*7*) heptane, and (*8*, *9*) hexane. Hardener concentration, wt %: (*3*) 0.6, (*4*–*8*) 2.6, and (*9*) 1.3. Hardening time, h: (*3*) 1, (*4*–*8*) 4, and (*9*) 2.

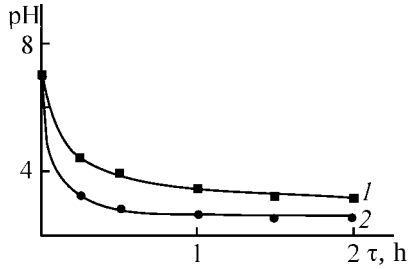

Fig. 3. Kinetic curves of variation of pH of the aqueous dispersion of nonane microcapsules during hardening with syntane no. 2. (τ) Time. Hardener concentration, wt %: (*1*) 1.3 and (*2*) 2.6.

Gelatin film thickness as influenced by the pretreatment conditions and hardening mode

Sample no.	Pretreatment conditions and hardening mode	Film thickness change, %
1	Chrome hardening without pretreatment in *n*-alkane	–11
2	Chrome hardening after 5-min treatment in water and 15-min treatment in nonane	+3
3	Chrome–syntane–tannide hardening without pretreatment in *n*-alkane	+120
4	Chrome–syntane–tannide hardening after 24-h treatment in nonane	+158
5	Chrome–syntane–tannide hardening after 5-min treatment in water and 15-min treatment in nonane	+207
6	Chrome–syntane–tannide hardening after 20-min treatment at the water–nonane interface	+177

eliminating water molecules. It should be noted that, along with the hardener molecules chemically bound to gelatin, the microcapsule shells contain weakly bound hardener occurring as associates, which can be extracted during washing. The correlation established between sorption of syntane no. 2 and thermal contraction of gelatin shells of microcapsules proves indirectly that contraction is due to pores created by extraction of syntane no. 2 weakly bound by gelatin, during washing of the microcapsules.

A study of gelatin shell hardening as influenced by the core substance showed that the capability of the shells for thermal contraction strongly depends on the nature of the core. In view of the fact that *n*-alkanes are unable of specific interaction with gelatin and hardener, we can suggest that the difference in the thermal behavior of shells is due to different amounts of *n*-alkane contained in the shell material. We carried out isothermal drying of the samples of films pretreated in *n*-alkanes at room temperature for 20 h and examined the compatibility between the hydrocarbons and gelatin, which proved to widely vary (Fig. 4): The plot of the compatibility vs. the molecular weight of *n*-alkane has a maximum corresponding to octane. Such a plot is indicative of the clathrate mechanism of dissolution of *n*-alkanes in gelatin, when sorption occurs in voids inside the associates of the polymeric material.

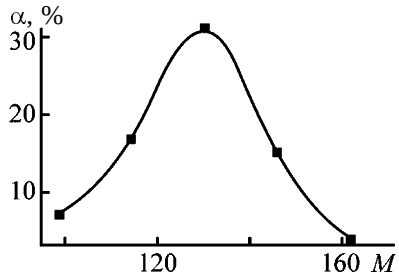

Fig. 4. Compatibility α of *n*-alkane with gelatin film as a function of the molecular weight *M* of *n*-alkane.

The *n*-alkane occurring in gelatin affects substantially the degree of swelling of the gelatin film and, hence, the accessibility of the polymer interior for syntane no. 2 molecules, as well as the gelatin hardening efficiency. The table shows how the alkane incorporated into gelatin film and the conditions of its incorporation into gelatin prior to hardening affect the film thickness as measured after hardening, washing with distilled water, and drying. It is seen that, unlike chrome hardening, which results in a minor thickening of the sample, hardening with syntane no. 2 significantly increases the film thickness. The film thickening is due to the selectivity of sorption of syntane no. 2 from aqueous solution. As noted above, syntane no. 2 is not entirely bound covalently by the active centers of gelatin and, thus, is partially extracted during washing. This affords a certain porosity of the gelatin shell. The alkane occurring in the microcapsule shells strongly hinders chrome hardening of the shell and, thus, affects its swelling and, correspondingly, the accessibility of the gelatin interior for the hardener molecules. Also, the alkane occurring in the shell affects the thermodynamic affinity of syntane no. 2 for the shell material and the ratio between the amounts of the syntane no. 2 bound to gelatin and sorbed. Evidently, the porosity of the shells is the largest in the case when a high sorption power of the shell with respect to syntane is combined with a low degree of fixing of the hardener on the active centers of the polymer. The strongest capability for thermal contraction, exhibited by the shells in the case of hexane (Fig. 2), suggests that, when in minor amounts in the shell material, hexane makes the interior of the shell material accessible for the hardener and does not substantially decrease the affinity for gelatin of syntane no. 2. By contrast, large amounts of heptane, octane, and nonane in the shell material shield the functional groups of gelatin, thus decreasing the selectivity of sorption of syntane no. 2 and, hence, the degree of hardening of the shells.

CONCLUSION

A study of hardening and selected properties of gelatin shells as influenced by aliphatic hydrocarbons C_6–C_{10} showed that chrome hardening enhances the heat resistance of the gelatin coacervate. Treatment (chrome–syntane–tannide hardening) endows the microcapsule shells with a prominent capability for thermal contraction. Increases of the concentration of the hardening solution of syntane no. 2 and of the hardening time tend to increase the thermal contraction of the shells, depending on the *n*-alkane homolog encapsulated. The plot of the gelatin–*n*-alkane compatibility vs. the molecular weight of *n*-alkane has a maximum.

REFERENCES

1. Solodovnik, V.D., *Mikrokapsulirovanie* (Microencapsulation), Moscow: Khimiya, 1980.
2. USSR Inventor's Certificate no. 1 636 035.
3. Metelkin, A.I. and Belobrova, L.V., *Proizvodstvo yufti i ee svoistva* (Production and Properties of Yuft (Russian Leather)), Legkaya i Pishchevaya Prom–st., 1988.
4. Andrianova, G.P., Shestakova, I.S., Kutsidi, D.A., *et al*., *Khimiya i fizika vysokomolekulyarnykh soedinenii v proizvodstve iskusstvennoi kozhi, kozhi i mekha: Uchebnik dlya vuzov* (Chemistry and Physics of Macromolecular Compounds in Artificial Leather, Leather, and Fur Production: Handbook for Higher Educational Institutions), Moscow: Legbytpromizdat, 1987.
5. Dubinovskii, M.Z. and Chistyakova, N.V., *Tekhnologiya kozhi* (Leather Technology), Moscow: Legprombytizdat, 1991.
6. Boiy, H.Z. and Bungenberg de Jong, H.G., *Biocolloids and Their Interaction*, Wien: Springer, 1956.
7. Nikolaeva, S.S., Pchelin, V.A., and Mikhailov, A.N., *Vysokomol. Soedin., Ser. B*, 1978, vol. 20, no. 7, pp. 521–523.

Russian Journal of Applied Chemistry, Vol. 75, No. 9, 2002, pp. 1510–1512. Translated from Zhurnal Prikladnoi Khimii, Vol. 75, No. 9, 2002, pp. 1538–1541.
Original Russian Text Copyright © 2002 by Kon'shin, M. Chemeris, N. Chemeris, Zevakov.

MACROMOLECULAR CHEMISTRY AND POLYMERIC MATERIALS

Determination of the Content of Bound Carboxylic Acids in Mixed Cellulose Esters

V. V. Kon'shin, M. M. Chemeris, N. A. Chemeris, and A. G. Zevakov

Polzunov Altai State Technical University, Barnaul, Russia

Received May 14, 2002

Abstract—A method was proposed for differential determination of bound carboxylic acids in mixed cellulose esters containing residues of acetic and higher carboxylic (capric, lauric, myristic, palmitic) acids.

Mixed cellulose esters containing residues of acetic and higher carboxylic acids (e.g., capric, lauric, myristic, palmitic) show promise as compounds exceeding cellulose acetate in solubility, hydrophobicity, and resistance to acid and base hydrolysis [1].

Study of such mixed cellulose esters requires development of reliable analytical methods. The existing methods of analysis of cellulose esters [2–4] containing lower acyl groups are unsuitable for joint determination of acetyl and higher acyl groups in mixed cellulose esters. Here we propose a simple method for differential determination of these groups.

A mixed cellulose ester is saponified with a titrated KOH solution. Potentiometric titration of excess KOH with HCl allows determination of the alkali consumed for formation of potassium carboxylates in the course of saponification:

$$[(C_6H_7O_2)(OCOCH_3)_x(OCOC_{2n}H_{2n+1})_y(OH)_{3-x-y}]_m + mH_2O \xrightarrow{(x+y)KOH} [C_6H_7O_2(OH)_3]_m + xCH_3COOK + yC_nH_{2n+1}COOK,$$

where n = 9–15.

Determination of higher carboxylic acids is based on the well-known property of these acids and their soluble salts, distinguishing them from lower carboxylic acids, to form insoluble salts in reaction with $Ca(NO_3)_2$ [5]:

$$2C_nH_{2n+1}COOK + Ca(NO_3)_2 \rightarrow (C_nH_{2n+1}COO)_2Ca\downarrow + 2KNO_3.$$

The content of higher carboxylic acids was calculated from the results of titrating excess Ca^{2+} with Na_2EDTA (murexide indicator). The content of bound acetic acid was determined from the difference between the total acid content (saponification with KOH) and the content of higher acids (precipitation of Ca^{2+}).

EXPERIMENTAL

Highly substituted mixed cellulose esters were prepared by treatment of dispersed cellulose (α-cellulose content 95.5–96.0%) with acylating mixture consisting of acetic anhydride, higher carboxylic acid, and trifluoroacetic acid (TFAA) [6, 7]. Preparation of mixed esters can be described as follows:

$$[C_6H_7O_2(OH)_3]_m + mx\,(CH_3CO)_2O + my\,C_nH_{2n+1}COOH \xrightarrow{CF_3COOH} -mxCH_3COOH \downarrow [C_6H_7O_2(OCOCH_3)_x(OCOC_nH_{2n+1})_y(OH)_{3-x-y}]_m.$$

The synthesis procedure is given in [7].

The content of bound carboxylic acids in mixed cellulose esters was determined as follows. A 100-ml conical flask was charged with a 0.35 ± 0.01-g portion (weighed with an accuracy of 0.0002 g) of mixed cellulose ester. Then 10 ml of ethanol was added, and the flask was stoppered and placed for 15 min in a thermostat heated to 56–57°C for better swelling. After that, 10 ml of 0.5 M KOH was added, and the sample was saponified (55–60°C, 1 day). The resulting mixture was titrated potentiometrically with 0.5 M HCl (glass indicator electrode, silver chloride refer-

1070-4272/02/7509-1510$27.00 © 2002 MAIK "Nauka/Interperiodica"

ence electrode). After titration completion, 2 M KOH (to pH 12.5–13.0) and then 10 ml of 0.1 M $Ca(NO_3)_2$ were added. The precipitated calcium salts of higher carboxylic acids, together with the saponified product, were filtered off on a Büchner funnel in a water-jet-pump vacuum. The precipitate was washed with four 10-ml portions of water. Then the filtrate was quantitatively transferred into a 250-ml Erlenmeyer flask (the Bunsen flask was rinsed with 10-ml portions of water, which were combined with the filtrate). To the resulting solution, murexide was added, and excess $Ca(NO_3)_2$ was titrated with 0.1 M Na_2EDTA until the indicator changed color from pink to violet.

The content of bound higher carboxylic and acetic acids was determined by the formulas

$$P_1 = \frac{(k_1 - 0.1V_1)M_1 \times 100}{1000g},$$

$$P_2 = \frac{(5k_2 - 0.5V_2) \times 100}{1000g} - (P_1M_2)/M_1,$$

where P_1 is the content of bound higher carboxylic acid, %; P_2, content of bound acetic acid, %; k_1, correction for the titer of 0.1 M $Ca(NO_3)_2$ solution; k_2, correction for the titer of 0.5 M KOH solution; V_1, volume of 0.1 M Na_2EDTA solution consumed for back-titration of excess $Ca(NO_3)_2$, ml; V_2, volume of 0.5 M HCl solution consumed for back-titration of excess alkali, ml; M_1, molar weight of higher carboxylic acid, g mol^{-1}; M_2, molar weight of acetic acid (60.0), g mol^{-1}; and g, weight of the sample of mixed cellulose ester, g.

The analytical procedure was checked with artificial mixtures containing acetic and higher carboxylic acids (Table 1).

As seen from Table 1, the method ensures fairly high repeatability of the results.

In our procedure for analysis of mixed cellulose esters, particular attention should be given to the completeness of their saponification. The saponification completeness was judged from the IR spectra of the saponified hydrated cellulose (absence of the carbonyl stretching band at 1720–1740 cm^{-1}). Experiments showed that the esters under consideration are completely saponified under the following conditions: saponification time 20 h, KOH concentration 0.5 M, temperature ≥55°C.

The main metrological characteristics of the method, determined from the results of analysis of cellulose acetopalmitate as example (Table 2), are as follows (for bound acetic and palmitic acids, respectively): variance S^2 0.057, 1.29; standard deviation of the average S_r 0.119, 0.568; confidence range ε_p 0.379, 1.807; accuracy Δ 1.095, 4.563%. For analysis of cellulose acetomyristate, acetolaurate, and acetocaprate, the metrological characteristics are similar.

Table 1. Analysis of artificial mixtures of acetic (AA) and palmitic (PA) acids

Mixture composition, wt %		Found, wt %	
AA	PA	AA	PA
0	100.0	0	99.96
10.0	90.0	9.93	89.94
20.0	80.0	20.05	80.05
40.0	60.0	39.94	60.15
60.0	40.0	60.14	39.84
80.0	20.0	79.95	19.90
100.0	0	99.95	0

Table 2. Chemical analysis of cellulose acetopalmitate. Acylation conditions: 50°C; 20 g of TFAA per gram of cellulose; 0.5 ml of palmitic acid per mole of acetic anhydride

Run no.	Content of bound acid, wt %	
	AA	PA
1	34.42	38.41
2	34.43	38.86
3	34.93	40.15
4	34.58	40.87
Result	34.6 ± 0.4	39.6 ± 1.8

Table 2 demonstrates good reproducibility of the results; the procedure is suitable for analysis of mixed cellulose esters in a wide range of concentrations of bound acetic and higher carboxylic acids (Table 3).

The results of analysis for the content of bound carboxylic acids in various mixed cellulose esters prepared under comparable conditions are listed in Table 4.

CONCLUSION

A procedure was developed for determination of the content of bound carboxylic acids in mixed cellulose esters. The results of determination of bound acetic and higher carboxylic acids in mixed cellulose

Table 3. Analysis of products of cellulose acylation with an acetic anhydride (AAn)–palmitic acid–trifluoroacetic acid mixture. AAn amount 4.5 mol per glucopyranose unit of cellulose

PA, mol mol^{-1} AAn	TFAA, g g^{-1} cellulose	Acylation temperature, °C	Content of bound acid, wt %	
			PA	AA
0.2	15	40	25.0 ± 1.2	44.8 ± 0.3
–	–	50	21.5 ± 0.9	47.4 ± 0.2
–	–	60	18.0 ± 1.1	50.0 ± 0.3
–	20	40	22.1 ± 1.0	46.4 ± 0.4
–	–	50	22.1 ± 1.6	47.1 ± 0.2
–	25	40	19.2 ± 1.2	48.1 ± 0.2
–	–	50	22.8 ± 1.3	46.9 ± 0.2
0.6	15	40	31.5 ± 1.1	40.2 ± 0.4
–	–	50	29.6 ± 1.7	41.9 ± 0.3
–	–	60	27.6 ± 1.9	43.6 ± 0.2
–	20	40	32.7 ± 1.2	39.0 ± 0.3
–	–	50	32.7 ± 1.1	39.9 ± 0.3
–	25	40	33.9 ± 0.9	37.8 ± 0.3
–	–	50	35.9 ± 1.2	37.5 ± 0.5
1.0	15	40	38.0 ± 1.5	35.6 ± 0.3
–	–	50	37.6 ± 1.6	36.4 ± 0.2
–	–	60	37.2 ± 1.1	37.2 ± 0.2
–	20	40	43.3 ± 0.7	31.5 ± 0.4
–	–	50	43.3 ± 1.2	32.2 ± 0.2
–	–	60	43.3 ± 1.6	32.9 ± 0.3
–	25	40	48.6 ± 1.0	27.4 ± 0.4
–	–	50	49.1 ± 1.0	28.0 ± 0.5

Table 4. Analysis of mixed cellulose esters for the content of bound carboxylic acids. Acylation conditions: 50°C; 1.5 h; 20 g of TFAA per gram of cellulose; 0.6 mol of higher carboxylic acid (HCA) per mole of acetic anhydride

Cellulose ester	Content of bound acid, wt %	
	AA	HCA
Acetocaprate	34.4 ± 0.3	36.6 ± 0.9
Acetolaurate	35.0 ± 0.4	36.5 ± 0.8
Acetomyristate	37.4 ± 0.2	34.8 ± 1.1
Acetopalmitate	38.9 ± 0.3	33.2 ± 1.0

esters and the metrological characteristics of the method are presented.

REFERENCES

1. Rogovin, Z.A., *Khimiya tsellyulozy* (Cellulose Chemistry), Moscow: Khimiya, 1972.
2. Nikitin, V.M., Obolenskaya, A.V., and Shchegolev, V.P., *Khimiya drevesiny i tsellyulozy* (Chemistry of Wood and Cellulose), Moscow: Lesnaya Prom–st., 1978.
3. *Entsiklopediya polimerov* (Polymer Encyclopedia), Kargin, V.A., Ed., Moscow: Sov. Entsiklopediya, 1972, vol. 1.
4. Mironov, D.P., Grishin, E.P., Malinina, L.P., and Mironov, V.N., in *Khimiya i khimicheskaya tekhnologiya efirov tsellyulozy* (Chemistry and Chemical Technology of Cellulose Ethers and Esters), Vladimir, 1974, pp. 30–34.
5. *Organicheskaya khimiya* (Organic Chemistry), Petrov, A.A., Ed., Moscow: Vysshaya Shkola, 1981.
6. USSR Inventor's Certificate no. 1 650 649.
7. Kon'shin, V.V., Chemeris, M.M., Mus'ko, N.P., *et al.*, *Izv. Vyssh. Uchebn. Zaved., Lesn. Zh.*, 2000, nos. 5–6, pp. 165–171.

Russian Journal of Applied Chemistry, Vol. 75, No. 9, 2002, pp. 1513–1516. Translated from Zhurnal Prikladnoi Khimii, Vol. 75, No. 9, 2002, pp. 1545–1548.
Original Russian Text Copyright © 2002 by Andreeva, Burkova, A. N. Grebenkin, A. A. Grebenkin.

MACROMOLECULAR CHEMISTRY AND POLYMERIC MATERIALS

IR Spectroscopic Study of Prepurified Flax

O. A. Andreeva, L. A. Burkova, A. N. Grebenkin, and A. A. Grebenkin

Institute of Macromolecular Compounds, Russian Academy of Sciences, St. Petersburg, Russia
St. Petersburg State University of Technology and Design, St. Petersburg, Russia

Received March 15, 2001; in final form, June 2002

Abstract—Flax fiber treated by conventional and ultrasonic procedures was studied. IR spectroscopic procedures were developed to estimate the degree of fiber decontamination from lignin and noncellulose fractions and to study supramolecular transformations of cellulose.

Flax fiber recovered from flax bast should be chemically treated before spinning [1, 2]. This treatment increases the degree of separation of crude fiber and hence enhances its spinning properties. The fiber rigidity is believed [3, 4] to be due to lignin present in the cell walls and middle plates. The agglutination of fibers is determined by the presence on the fiber surface of noncellulose polysaccharides and low-molecular-weight celluloses, which in total are termed as readily hydrolyzable polysaccharides (RHP) [5]. Hence, to prepare flax fiber with good spinning properties, crude fiber is boiled in alkali solution at elevated pressure for many hours and bleached by different procedures to partially destroy the middle plates and to remove lignin from the cell walls of the fibers. However, mechanical treatment can initiate mechanochemical reactions and result in degradation and amorphization of polymers [6]. Various mechanical treatments such as rolling, crushing, grinding, combing, etc. are used in industrial processing of polymers.

In this work we studied finishing of crude flax fiber by ultrasonic treatment. It is known [7] that regions with developed cavitation in the form of pulsation and oscillation of vapor gas bubbles are formed in the bulk of liquids at the intensity of an unltasonic field higher than 0.3 W cm^{-2}. This phenomenon is used for a long time to clean surfaces and to disperse films and coating in metallurgy and mining. In addition, the collapse of bubbles in the compression phase is accompanied by strong adiabatic heating of gas in the bubbles and its ionization, which can initiate chemical reactions. Probably, these processes can affect the structure of flax bast fiber by destroying the middle plates, removing fat films, and increasing the solubility of the concomitant compounds.

In this work we performed comparative IR spectroscopic study of structural transformations of bast fibers treated by ultrasonic and conventional chemical [1] procedures.

Ultrasonic treatment was performed in an aqueous solution of surfactant [laundry soap, GOST (State Standard) 7696–55, 5 g l^{-1}] at room temperature for 20, 60, 100 min in a bath of a standard UZU-0.25 ultrasonic unit operating at 18 kHz. The intensity of ultrasonic vibrations did not exceed 0.5 W cm^{-2}. After the treatment, the fiber was thoroughly washed with running water and dried in air in the free state. The IR spectra were recorded on an IR-75 spectrophotometer in KBr pellets. For the whole spectrum, the baseline corresponding to the window transparency was drawn.

To compare the efficiency of various procedures for removing lignin and RHP from flax, reliable methods should be developed for estimating the degree of decontamination of the initial flax and suitability of the flax for commercial purposes. In this work we propose an IR spectroscopic procedure for estimating the degree of flax decontamination from lignin and RHP. The IR spectra of the initial bast and the bast treated by the conventional and ultrasonic procedures for 20 min are shown in Figs. 1a and 1b, respectively. In the spectrum of the initial sample, two narrow bands at 2920 and 2855 cm^{-1} are observed against the background of a broad band of stretching vibrations of the CH_2 and CH groups of cellulose. Based on the results of [8], these bands are assigned to antisymmetrical and symmetrical stretching vibrations of the CH_2 groups of RHP (Fig. 1a). In the spectrum of the treated samples, the bands at 2920 and 2855 cm^{-1} are weaker, and the band at 2900 cm^{-1} of the stretching vibrations of the CH_2 groups of cellulose becomes well-defined. The changes in the other region of spec-

1070-4272/02/7509-1513$27.00 © 2002 MAIK "Nauka/Interperiodica"

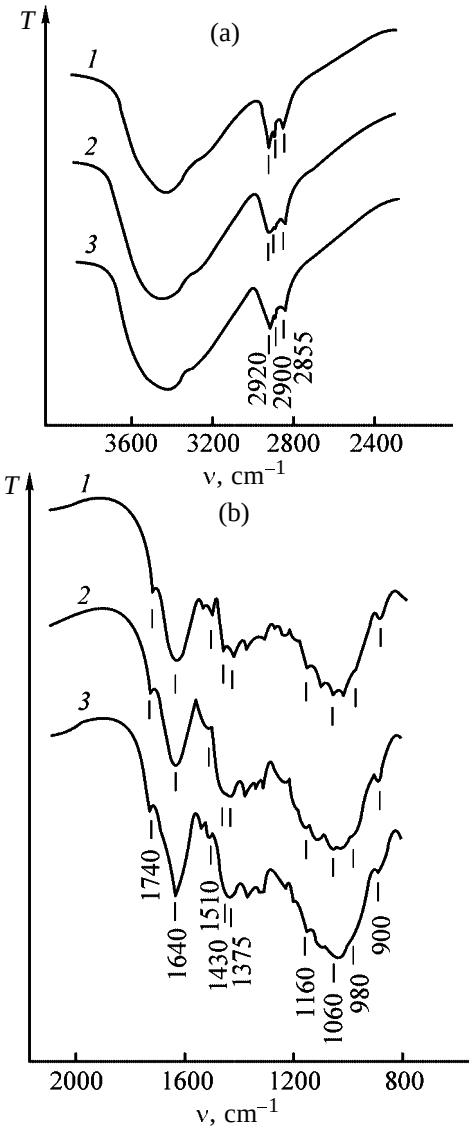

Fig. 1. IR spectra of flax fiber in the range (a) 2400–4000 and (b) 800–2000 cm^{-1}. Sample: (*1*) initial, (*2*) treated by the conventional procedure, and (*3*) ultrasonically treated for 20 min. (*T*) Transmission and (ν) wave number (cm^{-1}).

trum are less pronounced and require quantitative estimation (Fig. 1b).

To estimate quantitatively the spectral transformation, the internal reference, i.e., a band remaining unchanged after the treatment, should be chosen. Taking into account the results of [9], we used the band at 2900 cm^{-1} as the internal standard. Although in the spectrum of the initial sample this band appears only as a shoulder on the RHP band at 2920 cm^{-1}, the RHP bands, as noted above, are narrow enough to determine the optical density of this band with small error, even in the spectrum of the initial sample. The optical densities of some RHP and lignin bands normalized to the density of the band at 2900 cm^{-1} are presented in Table 1. The degree of lignin decontamination from RHP was estimated using the bands at 2920, 2855 (stretching vibrations of CH_2 groups), 1460 (bending vibrations of CH_2 groups), and 1740 cm^{-1} (vibrations of carboxy groups formed by hydrolysis of polysaccharides). The characteristic bands of lignin are the bands of skeletal vibrations of the aromatic ring at 1510 and 1600 cm^{-1}. However, the band at 1600 cm^{-1} is a constituent, along with the bands at 1660 and 1640 cm^{-1} of a complex band with a maximum at 1640 cm^{-1}. The band at 1660 cm^{-1} is assigned to the C=O groups of lignin. The strongest band at 1640 cm^{-1} is due to the bending vibrations of the OH groups of water present in all the samples. Thus, only a single band at 1510 cm^{-1} can be used to estimate the degree of flax decontamination from lignin.

As seen from Table 1, the intensities of the bands at 2920, 1740, and 510 cm^{-1} located in the transparence range of cellulose decrease after conventional and ultrasonic treatments to the similar extent: by 22 and 18%, respectively. This fact indicates that the internal reference was chosen correctly. This relationship does not hold for the bands at 2855 and 1460 cm^{-1} overlapping with strong cellulose bands. As seen from Fig. 1b, in the spectra of the treated samples the complex band at 1640 cm^{-1} is appreciably narrowed, which indicates a decrease in the content of lignin absorbing at the wings of this band.

Thus, the degree of flax decontamination from RHP and lignin can be estimated using the bands at 2920, 1740, and 1510 cm^{-1}. We propose as the estimation parameter the relative change of the optical density at the maxima of these bands. The degree of decontamination from lignin estimated by this method agrees with the data of Lebedeva and Shibaeva [10], confirming the correctness of the proposed criteria. In should be noted in conclusion that, since the degree of decontamination does not noticeably increase at longer ultrasonic treatment of the initial bast, we present in Table 1 only the data for the shortest treatment (20 min).

It was of interest to study the structural transformations of cellulose under different treatments of the initial fiber and manifestation of these transformations in the IR spectra. Several parameters were proposed for evaluation of supramolecular structural changes of polymeric chains and degree of cellulose mercerization in the course of purification of the crude fiber. To estimate the information content of these parameters, we present in Table 2 the optical densities of

Table 1. Normalized optical densities of the bands of lignin and RHP in the spectrum of bast treated by different procedures

ν, cm^{-1}	D_1/D_{2900}	D_2/D_{2900}	D_3/D_{2900}	$(D_1 - D_2)/D_1$	$(D_1 - D_3)/D_1$
2920	1.41	1.11	1.16	0.21	0.18
2855	1.07	0.96	0.96	0.10	0.10
1740	0.76	0.59	0.62	0.22	0.18
1510	1.01	0.86	0.89	0.22	0.19
1460	1.41	1.45	1.33	–0.03	0.06

* D_1, D_2, and D_3 are, respectively, the optical densities in the spectrum of the initial bast and of bast treated by the conventional procedure and ultrasonically for 20 min; the same for Table 2.

Table 2. Normalized optical densities of some cellulose bands in the spectrum of bast treated by different procedures

ν, cm^{-1}	D_1/D_{2900}	D_2/D_{2900}	D_3/D_{2900}	$(D_2 - D_1)/D_1$	$(D_3 - D_1)/D_1$
900	1.20	1.42	1.34	0.18	0.12
980	1.80	2.11	2.03	0.17	0.13
1060	2.06	2.28	2.30	0.11	0.11
1160	1.68	1.94	1.89	0.16	0.12
1375	1.49	1.65	1.49	0.11	0.00

the strongest cellulose bands normalized to the optical density of the band at 2900 cm^{-1}.

It is known that cellulose is mercerized by phase transition of cellulose 1 to cellulose 2 in the course of boiling of bast in an alkali solution. The structure of native cellulose 1 is formed by the system of intermolecular hydrogen bonds stabilizing a definite conformation of the polymeric chains. At elevated temperature, these bonds are ruptured, which allows partial rotation of the macromolecules around the glucoside bonds. As a result, a new network of mainly intramolecular hydrogen bonds stabilizing the new macromolecule conformation in the structure of cellulose 2 is formed. In the IR spectra, this phase transition should be manifested by a change in the optical densities of the bands of glucoside bridge and of OH groups involved in the hydrogen bonding.

There are two bands of glucoside bridge at 1060 [ν_a(COC)] and 900 cm^{-1} [ν_s(COC) + $\delta(C_1H)$] [12]. The bending vibrations of OH groups contribute to almost all bands located in the range lower than 1300 cm^{-1}. Among them, the strongest are 1160 [δ(OH) + $\delta(CH_2)$] and 980 cm^{-1} [δ(OH) + δ(CH)]. The relative optical densities of all the above bands are summarized in Table 2. The degree of cellulose mercerization is estimated from the change in the optical densities of the bands at 900 and 980 cm^{-1} [12]. As seen from Table 2, the changes in the optical densities of these bands are similar. The estimated degree of mercerization of samples treated by the conventional and ultrasonic procedures is 18 and 12%, respectively. It should be noted that the degree of mercerization can also be estimated using the band at 1160 cm^{-1}. The band at 1060 cm^{-1} strongly overlaps with adjacent bands and cannot be used for this purpose.

The degree of crystallinity of the initial fiber can change after boiling of the fiber in polar solvents. Since recrystallization is usually accompanied by phase transitions, the degree of crystallinity should be evaluated from the ratio of the optical densities of the bands that are insensitive to the crystal lattice type. As the crystallinity index, Nelson and O'Connor proposed the ratio of the optical densities of the bands at 1375 and 2900 cm^{-1} [9]. The degree of crystallinity estimated by this index slightly increases for the samples treated by the conventional procedure (Table 2) and remains the same for the samples treated by ultrasonic procedure. It is interesting to check whether this phenomenon will be observed for other samples, since a decrease in the fiber rigidity is very important for spinning process. The fiber rigidity does not appreciably decrease after boiling of the fiber with alkali and bleaching, although lignin is removed after this treatment. The causes of this phenomenon are unclear. Our data show that the rigidity of treated fiber may be due to crystallization of cellulose during treatment in a hot liquid. Ultrasonic treatment may leave the

degree of crystallinity unchanged, since in this case the polymer is subject to only local and short heating.

The time dependence of lignin removal from the fiber during ultrasonic treatment flattens out. This is due to the fact that the maximal dispersity of flax fiber complexes at the given power of ultrasonic radiation is reached within 20 min. In the process, lignin is removed only from destroyed middle plates but not from the cell walls of the fibers. To remove lignin from the cell walls, the fiber should be divided to microfibrils, which requires higher energies.

CONCLUSIONS

(1) An IR spectroscopic procedure was developed to determine the degree of flax decontamination from lignin and readily hydrolyzed polysaccharides after pretreatment of crude fiber and to estimate the degree of crystallinity and mercerization of cellulose.

(2) The degree of decontamination of the fiber ultrasonically treated for 20 min is comparable to that obtained by the conventional procedure.

(3) In the course of the both treatments cellulose is mercerized without an additional crystallization.

REFERENCES

1. RF Inventor's Certificate no. 3638332/28-05.
2. Melikuziev, Sh., *Khimicheskaya modifikatsiya tsellyulozosoderzhashchikh tekstil'nykh materialov* (Chemical Modification of Cellulose-Containing Textiles), Tashkent: Mekhnat, 1989.
3. Grushnikov, O.P. and Elkin, V.V., *Dostizheniya i problemy khimii lignina* (Advances and Problems of Lignin Chemistry), Moscow: Nauka, 1973.
4. Ivanov. A.N., *Izv. Vyssh. Uchebn. Zaved., Tekhnol. Tekstil. Prom–sti*, 1990, no. 3, pp. 14–17.
5. Darevskii, Yu.S., in *Sovershenstvovanie tekhnologicheskikh protsessov l'nyanoi i pen'ko-dzhutovoi promyshlennosti* (Improvement of Processes of Flax and Hemp Jute Industry), Moscow: TsNIITEIlergprom, 1985, pp. 106–108.
6. Grassie, N. and Scott, G., *Polymer Degradation and Stabilization*, Cambridge: Cambridge Univ. Press, 1985.
7. Agranat, B.A., *Ul'trazvukovaya teknologiya* (Ultrasonic Technology), Moscow: Metallurgiya, 1986.
8. Karyakin, L.B., Murav'eva, L.F., Osipova, N.N., and Bashilova, T.G., in *Sovershenstvovanie tekhnologicheskikh protsessov l'nyanoi i pen'ko-dzhutovoi promyshlennosti* (Improvement of Processes of Flax and Hemp Jute Industry), Moscow: TsNIITEIlergprom, 1985, pp. 18–23.
9. Nelson, M.L. and O'Connor, R.T., *J. Appl. Polym. Sci.*, 1964, no. 3, vol. 8, pp. 1325–1341.
10. Lebedeva, V.I. and Shibaeva, S.Yu., *Izv. Vyssh. Uchebn. Zaved., Tekhnol. Tekstil. Prom–sti*, 1990, no. 3, pp. 66–69.
11. Nelson, M.L. and O'Connor, R.T., *J. Appl. Polym. Sci.*, 1964, no. 3, vol. 8, pp. 1311–1324.
12. Dechant, J., Danz, R., Kimmer, W., *et al.*, *Ultrarotspektroskopische Untersuchungen an Polymeren*, Berlin: Akademie, 1972.

Russian Journal of Applied Chemistry, Vol. 75, No. 9, 2002, pp. 1517–1521. Translated from Zhurnal Prikladnoi Khimii, Vol. 75, No. 9, 2002, pp. 1549–1554.
Original Russian Text Copyright © 2002 by Bochek, Zabivalova, Shamolina, Grishanov.

MACROMOLECULAR CHEMISTRY AND POLYMERIC MATERIALS

Isolation of Pectins from Flax Pedicels and Fibers and Their Characterization

A. M. Bochek, N. M. Zabivalova, I. I. Shamolina, and S. A. Grishanov

Institute of Macromolecular Compounds, Russian Academy of Sciences, St. Petersburg, Russia
St. Petersburg State University of Technology and Design, St. Petersburg, Russia

Received May 13, 2002; in final form, June 2002

Abstract—Isolation of pectins form flax pedicels and fibers was studied. Isolated pectins and flax fibers treated by various chemical procedures were studied by IR spectroscopy. The morphology of fascicles of flax fibers was studied by electron microscopy as influenced by chemical treatment.

Linen clothes, among various cellulose materials produced from plant fibers, have good consumer's properties owing to peculiar fine structure and morphology of flax fibers and the presence of concomitant compounds. Linen clothes are characterized by good durability and physicomechanical properties; an increased comfort provided by linen wear is due to permeability of flax fibers to air, their low electifiableness, and strong sorption of moisture [1, 2]. The physicomechanical properties of fibers and the consumer's properties of linen clothes depend on impurities present in them. Fats, lignin, pectins, and hemicellulose weaken the surface tension of the fiber as compared to purified cotton fiber [3] and increase the hygroscopicity of the fibers [1, 4]. Pectin impurities decrease the resistance of the fiber to the action of microorganisms [5]. One of disadvantages of mechanical cottonizing of flax fiber is relatively high yield of fairly thick and rigid fibers. Compounds, including pectins, that accompany cellulose are removed in the course of mechanical cottonizing. The pectin content in flax straw exceeds 4–5 wt %, whereas in recovered fibers it is as low as 0.25–0.35%. Thus, hemicelluloses including pectins are removed in the course of recovery of flax fibers and their finishing. Combination of mechanical and chemical cottonizing of fibers allows production of fibers with improved spinning properties and recovery of valuable polysaccharides such as pectins.

Flax pectins, unlike pectins contained in fruits and vegetables, are poorly studied. To determine the potential fields of application of these pectins and practicable (efficient) procedures for recovering them, a comparative study of physicochemical and biological properties of pectins should be performed.

The aim of this work was to study recovery of flax pectins from flax straw and short fibers. Flax straw was used as experimental raw material for pectin recovery.

EXPERIMENTAL

Flax straw and short flax fibers produced at Nevel' flax processing plant (Russia) were used as the initial material. Isolated pectin was characterized by IR spectroscopy (Specord M80 spectrometer, KBr pellets).

The chemical composition of short fibers and flax straw was determined (Table 1). The cellulose content was determined by the Kürschner–Hoffer's procedure [6]; the lignin content, by the Komarov's procedure; the contents of fat, ash, and moisture, by the procedure in [6, 7]; and the pectin content, by the calcium pectate procedure [7].

Table 1. Chemical composition of flax pedicels and fibers

Component	Content, wt %	
	flax straw	short fibers
Fats and waxes	2.9	1.5
Lignin	39.4	5.2
Ash	1.5	1.4
Cellulose and hemicelluloses including:	48.8	87.5
cellulose	37.2	71.1
pectin	2.2	1.6
other hemicelluloses	9.4	14.8
Moisture content	7.4	4.4

1070-4272/02/7509-1517$27.00 © 2002 MAIK "Nauka/Interperiodica"

Table 2. Isolation of pectin from straw and short flax fiber by different procedures

Run no.	Initial material	Treatment conditions of plant material	Conditions of pectin isolation from solutions	Pectin yield, %
1	Flax straw	Treatment with 0.03 N HCl, washing with hot water, treatment with 1% ammonium citrate solution, washing with water	Neutralization of solution and saponification of pectin in the solution with 4% NaOH, acidification with CH_3COOH to pH 6.0, precipitation of pectin with 44% $CaCl_2$ solution, washing of the precipitate with 0.5% $CaCl_2$ solution and water	2.15
2.1	″	Treatment with 0.03 N HCl, washing with hot water	″	1.3
2.2	Flax straw treated with HCl solution and washed with water	Treatment with 1% ammonium citrate solution, washing with water	Saponification of pectin in the solution with 4% NaOH, acidification with CH_3COOH to pH 6.0, precipitation of pectin with 44% $CaCl_2$ solution, washing of the precipitate with 0.5% $CaCl_2$ solution and water	0.85
3	Flax straw ″	Treatment with 0.03 N HCl, washing with hot water	Alkalization with aqueous ammonia to pH 6.0, evaporation of pectin solution on a rotary evaporator, precipitation of pectin with 50% aqueous ethanol, washing of the precipitate with ethanol and acetone	2.7
4	″	″	Alkalization with aqueous ammonia to pH 6.0, evaporation of pectin solution on a rotary evaporator, precipitation of pectin with acetone, washing of the precipitate with acetone	2.95
5	″	″	Addition of saturated CaO solution to pH 6.0; evaporation of pectin solution on a rotary evaporator, precipitation of pectin with acetone, washing of the precipitate with acetone	2.7
6	Short flax fiber	Treatment with 0.03 N HCl, washing with hot water, treatment with 1% ammonium citrate solution, washing with water	Saponification of pectin in the solution with 4% NaOH, acidification with CH_3COOH to pH 6.0, precipitation of pectin with 44% $CaCl_2$ solution, washing of the precipitate with 0.5% $CaCl_2$ solution and water	1.6
7	″	Treatment with 0.03 N HCl, washing with hot water	Alkalization with aqueous ammonia to pH 6.0, evaporation of pectin solution on a rotary evaporator, precipitation of pectin with 50% aqueous ethanol, washing of the precipitate with ethanol and acetone	1.43

As seen from Table 1, the pectin content in the fibers is 1.6%, which agrees well with the results of other works [2, 8].

There are several methods for recovering pectins from plant materials [7–10]. One of classical methods is the calcium pectate procedure. It is based on hydrolysis of pectic acid with dilute HCl, followed by treatment with ammonium citrate to form soluble complexes. Then dissolved pectin is hydrolyzed with an NaOH solution to form polygalacturonic acid; its calcium salt is precipitated with aqueous $CaCl_2$ [7].

To improve pectin extraction, the initial flax straw was preliminarily milled in an MN-250 knife mill. Isolation of pectins from straw and fibers was performed by various methods. Prior to isolation, all samples of straw and fibers were treated with an alcohol–benzene mixture to remove grease and waxes [6]. The isolation conditions and the pectin yields are presented in Table 2.

Isolation of pectin in the form of calcium pectate was performed in two steps: treatment with 0.03 N HCl with subsequent washing with hot water and an

ammonium citrate solution (Table 2, run no. 1). From an industrial standpoint, the number of treatments should be minimized. In addition, it is not appropriate to use food citric acid for recovering another food substance, polysaccharide. Analysis of the pectin yield (Table 2, run nos. 1, 2.1, 2.2) shows that the major portion (60% of the isolated pectins) of pectins passes into the solution in the course of treatment with an HCl solution. The remaining 40% of pectins is dissolved when flax straw is treated with a ammonium citrate solution. Hence, the latter step involving the food reagent is not necessary. Saponification of polygalacturonic acid in solution, followed by its precipitation with a $CaCl_2$ solution, is time-consuming. It is difficult to filter off and wash the precipitate of calcium pectate. To overcome this difficulties, we studied isolation of pectin from a solution by precipitation of polygalacturonic acid with an organic solvent from evaporated working solutions. To suppress hydrolysis of polygalacturonis acid in the course of evaporation on a rotary evaporator at 80°C, these solutions were neutralized with aqueous ammonia to pH 6.0.

As seen from Table 2, pectin and a fraction of hemicelluloses (run no. 3) are precipitated with ethanol from concentrated (evaporated) pectin solutions. The precipitate amount is higher than that in the conventional procedure (run no. 1). The highest amount of pectins and hemicelluloses (2.95%) is isolated by precipitation with acetone (run no. 4), which is due to coprecipitation of chlorides insoluble in acetone. The presence of chloride ions in the precipitate was confirmed by reactions with $AgNO_3$.

Removal of chloride ions from the precipitate by washing is a labor- and time-consuming procedure. To exclude the presence of chloride ions, we used a CaO solution for isolation of pectins (Table 2, run no. 5). We suggested that insoluble calcium polygalacturonate would be formed, as in the case of $CaCl_2$. However, calcium oxide is only sparingly soluble in water. The volume of the CaO solution was 3 times larger than that of the initial (not evaporated) pectin solution. The precipitate amount (2.7%) formed after evaporation of the solution and precipitation of pectin with acetone is higher than that in the calcium pectate procedure. Probably, calcium oxide is partially precipitated during evaporation of the pectin solution, which makes the pectin content overestimated. This is the case in isolation of pectins from fibers (Table 2, run nos. 6, 7).

It should be noted that the amount of the precipitate formed by treatment of flax fiber with 0.03 N HCl, followed by evaporation of the resulting pectin solution and precipitation of pectin with ethanol (run no. 7), is 89% of the yield of pectin prepared by the conventional procedure (run no. 6). We suggest that hemicelluloses that passed into the solution during treatment of the fibers with dilute HCl partially coprecipitate with pectins. Unlike wood, flax pedicels and fibers have high content of hemicelluloses which pass into the solution during boiling in 0.03 N HCl.

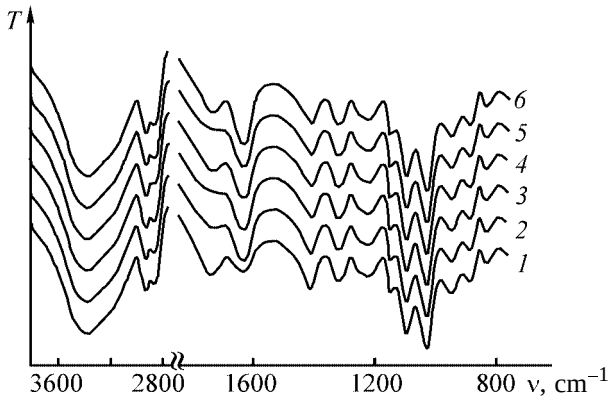

Fig. 1. IR spectra of (*1*) apple pectin and (*2*–*4*) pectins isolated by different procedures. (*T*) transmission and (ν) wave number; the same for Fig. 2. Run no. (Table 2): (*2*) 1, (*3*) 2.1, (*4*) 3, (*5*) 6, and (*6*) 7.

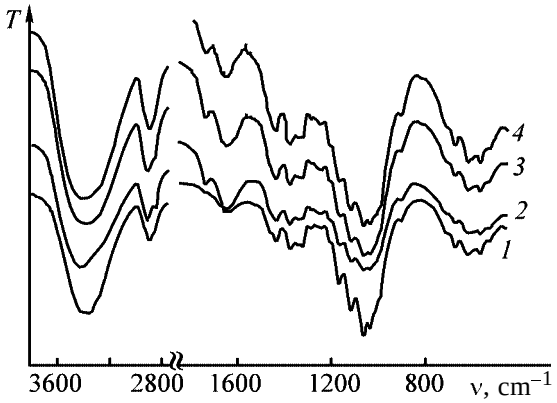

Fig. 2. IR spectra of (*1*) cotton cellulose, (*2*) initial flax fiber, and flax fiber treated to remove (*2*) fats and waxes and (*3*) fats, waxes and pectins.

The IR spectra of isolated pectins are shown in Fig. 1. Apple pectin was used as the reference.

The IR spectra of pectins contain characteristic absorption bands of free COOH groups of polygalacturonic acid at 1740 cm^{-1} and the bands of symmetric and asymmetric vibrations of COO^- groups at 1615 and 1410 cm^{-1}, respectively. In the range 2850–2950 cm^{-1}, a single broad band or two bands at 2875 and 2925 cm^{-1} assigned to stretching vibrations of CH_2 and CH groups can appear [9].

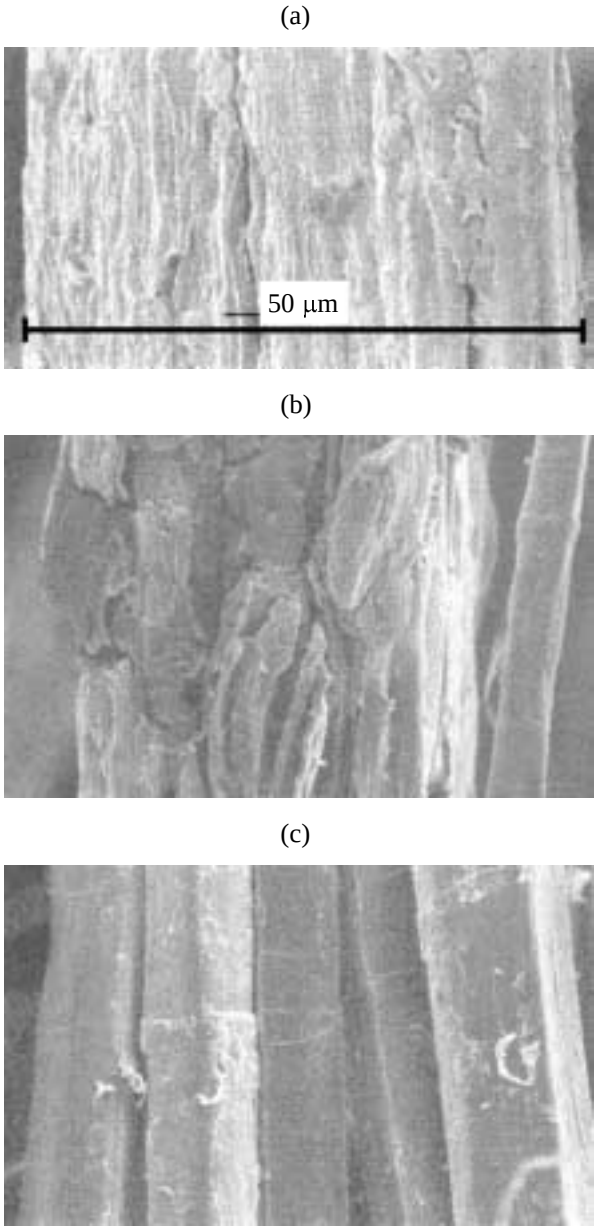

Fig. 3. Electron micrographs of flax fibers: (a) crude fibers and fibers treated to remove (b) fats and waxes and (c) fats, waxes, and pectins. Magnification ×1500.

The presence of strong bands at 1410 and 1615 cm^{-1} in the IR spectra of pectins isolated by the calcium pectate procedure from flax pedicels and fibers (Fig. 1, curves *2*, *3*, and *5*) indicates that the most of carboxy groups of the pectin are ionized. A weak band at 1740 cm^{-1} appears as a shoulder. An increased absorption at 1740 cm^{-1} in the spectrum of pectins prepared by evaporation of solutions (without saponification of pectin) followed by precipitation with ethanol and acetone is due to an increase in the fraction of free COOH groups (spectra *4*, *6*). The intensity of the bands at 1740 and 2900 cm^{-1} in the spectra of pectins isolated under the same conditions from straw and fibers by evaporation of solutions and precipitation with ethanol differ. We suggest that, in this case, the additional absorption, especially at 2875 cm^{-1}, is due to a contribution of hemicelluloses which pass with pectin into the solution and then precipitate.

Sobolev and Krasivskaya [8] noted that pectins are incompletely removed from flax fibers in the course of treatment with solutions of HCl and ammonium citrate. To determine the completeness of pectin removal, we recorded the IR spectra of flax fiber after removal from them of fats and waxes and then pectins (Fig. 2). The IR spectrum of bleached cotton linter was recorded as a reference.

The IR spectrum of purified cotton cellulose contains the following characteristic bands: a broad band in the range 3000–3700 cm^{-1} of free OH groups and OH groups involved in intra- and intermolecular hydrogen bonds; the band of CH_2 and CH groups at 2900 cm^{-1}, which is symmetrical in the spectrum of pure cellulose [12].

The IR spectrum of crude wood cellulose and cellulose isolated from flax pedicels contain characteristic lignin bands at 1600, 1500, and 850 cm^{-1} [11, 12]. Thus, the impurity content in cellulose samples can be qualitatively estimated by IR spectroscopy.

As seen from Fig. 2, in the spectrum of crude flax fibers the band at 1740 cm^{-1} and a broader band in the range 1650–1600 cm^{-1}, as well as the bands at 2925 and 1875 cm^{-1}, indicate the presence of pectins. It should be noted that the vibrations of CH_2 and CH groups of fatty acids (i.e., fats and waxes) can additionally contribute to the absorption in the region of 2900 cm^{-1}. The presence of lignin can be determined by comparing the IR spectra of crude flax fibers and bleached cotton cellulose (Fig. 2, curves *1* and *2*). Broadening of the band in the range 1650–1600 cm^{-1} in the spectrum of flax fiber can be due to the presence of lignin (1600 cm^{-1}) and pectin (1615 cm^{-1}). The IR spectra of all flax samples, unlike the cotton spectra, contain the lignin band at 850 cm^{-1}.

Fatty acids are removed by treatment with a benzene–ethanol mixture (Fig. 2, curve *3*), which is indicated by the decrease in the absorption at 2900 cm^{-1} and the sharper shape of the lignin bands. A shoulder at 1500 cm^{-1} and a sharp band at 850 cm^{-1} appear. The band at 2900 cm^{-1} becomes more symmetrical after removal of fats and pectins (Fig. 2, curve *4*),

although the pectin bands at 2925 and 2875 cm^{-1} appear as shoulders on this band. The characteristic lignin band at 850 cm^{-1} is also observed.

Pectins are contained not only in intercellular layers but also in primary walls of a single fiber. To remove pectins binding single flax fibers in fascicles, more rigid conditions are required. Under these conditions, cellulose can appreciably degrade.

The distinctions in the morphology of fiber fascicles are seen in the electron micrographs of flax fibers treated under different conditions (Fig. 3). Comparison of the micrographs shows how each chemical treatment affects, on the one hand, the contamination of the surface of flax fiber fascicles with concomitant compounds and, on the other hand, the degree of rupture of bonds between single fibers in fascicles, i.e., the degree of fiber cottonizing.

The surface of untreated flax fibers isolated from bast is contaminated with the following substances: parenchyma, pectins, and other components of external pedicel layer in which the fascicles of bast fibers were incorporated. After removal of fats and waxes (Fig. 3b), the relief of pectin residues on the fibers as well as defects on the surface of single fibers and fascicles become more pronounced. The content of residual substances on the fibers remains high. These substances are removed and the fibers in fascicles are separated (FIg. 3b) after treatment of the fibers with an ethanol–benzene mixture and removal of pectins with solutions of HCl and ammonium citrate. At the same time, relatively large amount of noncellulose components remain on the fiber surface, and complete separation of fibers (their cottonizing) is not observed.

Thus, pectins are incompletely removed from flax fibers by treatment with solutions of HCl and ammonium citrate. The most part of pectins (up to 90% of the total amount) is removed from the fibers with dilute HCl. Hemicelluloses of flax fiber entering into the composition of polycarbohydrate complex of flax fiber cellulose partially passes with pectins into the solution. Pectins isolated by evaporation of the solution with subsequent precipitation with organic solvent contain ionized and free carboxy groups. The degree of separation of fibers in fascicles increases after the treatment of flax fibers to remove fats, waxes, and pectins.

CONCLUSIONS

(1) Methods for isolating pectins from flax pedicels and fibers were studied.

(2) Pectins isolated from flax pedicels and fibers by chemical treatment were studied by IR spectroscopy. The ratio of free and ionized carboxy groups in isolated pectins depends on the isolation procdure. Hemicellulose entering into the composition of polycarbohydrate complex of flax fiber cellulose partially passes with pectins in the solution.

(3) Flax fibers chemically treated by different procedures were studied by IR spectroscopy and electron microscopy. The surface of fibers in fascicles is cleaned and the degree of separation of fibers increases after the treatment of flax fibers to remove fats, waxes, and pectins.

REFERENCES

1. Kuleshova, L.N., Komarova, N.V., Osipova, N.N., *et al.*, *Khim. Drev.*, 1988, no. 4, pp. 92–94.
2. *Pryadenie l'na i khimicheskikh volokon: Sparvochnik* (Spinning of Linen and Chemical Fibers: Handbook), Karyakin, L.B. and Ginzburg, L.N., Eds., Moscow: Legprombytizdat, 1991.
3. Van Hazendonk, J.M., Van der Putten, J.C., and Keurentjes, J.T.F., *Cellulose and Cellulose Derivatives: Physico-Chemical Aspects and Industrial Application*, Kennedy, J.F., Phillips, G.O., Williams, P.O., and Piculell, L., Eds., Cambridge (England): Woodhead, 1995, pp. 107–114.
4. Kuleshova, L.N., Osipova, N.N., Taraskina, N.G., *et al.*, *Khim. Drev.*, 1989, no. 5, pp. 19–24.
5. Piven', T.V. and Khodyrev, V.I., *Khim. Drev.*, 1988, no. 1, pp. 106–111.
6. *Prakticheskie raboty po khimii drevesiny* (Practical Course of Wood Chemistry), Nikitin, V.M., Ed., Moscow: Lesnaya Prom–st., 1965.
7. *Spravochnik khimicheskoi tekhnologii obrabotki l'nyanykh tkanei* (Handbook on Chemical Treatment of Linen Fabrics), Fridlyand, G.I., Ed., Moscow: Legkaya Industriya, 1973.
8. Sobolev, M.A. and Krasivskaya, A.A., *Tekstil. Prom–st.*, 1954, no. 7, pp. 39–41.
9. Aimukhammedova, G.B., Alieva, Dzh.E., and Shelukhina, N.P., *Svoistva i primemenie pektinovykh sorbentov* (Properties and Application of Pectin Sorbents), Frunze: Ilim, 1984.
10. Reznikov, V.M., Matusevich, L.G., and Seliverstova, T.S., *Khim. Drev.*, 1982, no. 2, pp. 108–113.
11. *Cellulose and Cellulose Derivatives*, Bikales, N.M. and Segal, L., Eds., New York: Wiley–Interscience, 1971.
12. Zhbankov, R.G., *Infrakrasnye spektry tsellyulozy i ee proizvodnykh* (IR Spectra of Cellulose and Its Derivatives), Minsk: Nauka i Tekhnika, 1964.

Russian Journal of Applied Chemistry, Vol. 75, No. 9, 2002, pp. 1522–1524. Translated from Zhurnal Prikladnoi Khimii, Vol. 75, No. 9, 2002, pp. 1555–1558.
Original Russian Text Copyright © 2002 by Okhotnikov, Valuev.

MACROMOLECULAR CHEMISTRY AND POLYMERIC MATERIALS

Kinetics of Dinitrile Dioxide Curing of Polyurethanes Containing Double Bonds in the Chain

M. A. Okhotnikov and V. I. Valuev

Research Institute of Synthetic Rubber, Federal State Unitary Enterprise, St. Petersburg, Russia

Received May 30, 2002

Abstract—The kinetics of cross-linking of highly plasticized polyurethanes conrtaining C=C bonds in the chain with a low-temperature dinitrile dioxide curing agent was studied by IR spectroscopy and gel permeation chromatography.

Dinitrile dioxide vulcanizing agents came recently into use for curing polyurethanes containing unsaturated bonds in the chain. Therefore, kinetic and mechanistic studies of this process are urgent. Nitrile oxide groups of a curing agent react with double bonds of a polyurethane in two stages, following the 1,3-dipolar cycloaddition pattern and giving five-membered isoxazoline rings [1]:

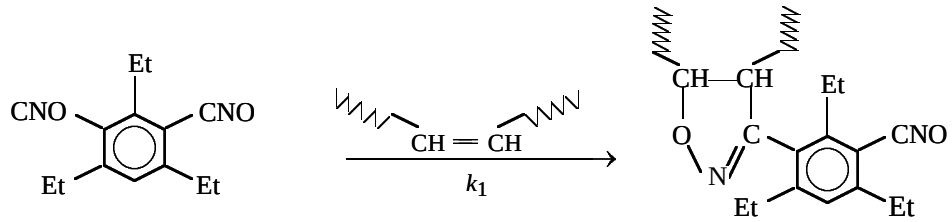

(P1)

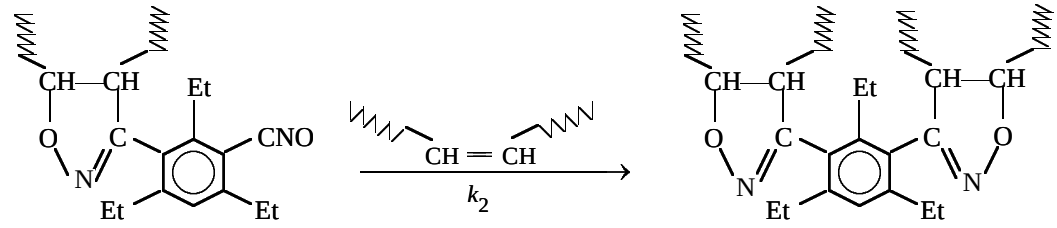

(P2)

One of the major advantages of curing agents of this type, as compared to other curing agents, is their capability to cross-link polyurethanes at relatively low temperatures, 30–40°C, which is due to high reactivity of nitrile oxide groups in [3+2]-cycloadditions [2].

In this work, using IR spectroscopy and gel permeation chromatography (GPC), we studied the kinetics of the reaction of nitrile oxide groups of the curing agent with C=C bonds of polyurethane, including calculation of the rate constants of the main curing stages, and examined the effect exerted by temperature and polymer structure on the rate constants.

EXPERIMENTAL

Experiments were performed with linear polyurethane rubbers of ester structure, containing C=C bonds (M_w = 5000–60000), and with 2,4,6-triethyl-1,3-benzenedi(nitrile oxide) as curing agent.

The IR spectra were taken on a Specord IR-75 spectrophotometer. Samples for recording the spectra were prepared as a microlayer between CaF_2 plates. The kinetics of polyester urethane curing with nitrile oxides was monitored by IR spectroscopy, namely, by the intensity of the ν(C≡N) band of the nitrile oxide

1070-4272/02/7509-1522$27.00 © 2002 MAIK "Nauka/Interperiodica"

group at 2290 cm^{-1}. One of the plasticizer bands was used as internal reference.

The IR spectra furnished comprehensive information on the kinetics of the polymer reaction with the curing agent as influenced by temperature and the polymer structure. Nevertheless, IR spectroscopy has certain limitations. In particular, the process kinetics cannot be monitored in thin film at high (>40%) conversions of the functional groups of the curing agent, because the gel point is attained. Furthermore, it is impossible to determine the rate constant of the reaction of C=C bonds in the polymer with the CNO groups incorporated into the macromolecular fraction in the first stage of curing, i.e., the rate constant of cross-linking proper. The combined use of IR spectroscopy and GPC allows solution of problems that cannot be solved by these methods used separately. These methods are mutually supplementing: IR spectroscopy allows monitoring of the total concentration of nitrile oxide groups, and GPC, monitoring of the content of the free curing agent in the system, decreasing owing to incorporation into the macromolecular fraction.

Polymeric compounds were chromatographed on a Waters-244 module-type gel chromatograph. Three columns packed with styrogel (pore size 100, 500, and 1×10^3 Å) were used. The eluent was tetrahydrofuran (flow rate 1 ml min^{-1}), and the detector, UV spectrophotometer (working wavelength 255 nm).

Experimental data show that the calculated rate constants of the reaction of CNO groups with the polyurethane C=C bonds, as determined by IR spectroscopy and GPC, at ~15% conversion of the curing agent agree within the instrumental error (Table 1). This fact suggests that, at low conversions of the curing agent, the major process is the reaction of nitrile oxide groups of the free curing agent with C=C bonds of the polymer (rate constant k_1). With increasing conversion of dinitrile dioxide, the differences between the rate constants determined by IR spectroscopy and GPC become more pronounced, with suggests the occurrence of cross-linking by the reaction of the second CNO group with the C=C bond (rate constant k_2).

The activation energy of the reaction between the functional groups of the polymer and curing agent, determined from the Arrhenius plot (Fig. 1), is relatively low, 42 ± 4 kJ mol^{-1}, which confirms the concerted reaction mechanism.

The differences between the kinetic parameters determined by IR spectroscopy (combination of k_1 and k_2) and GPC (k_1 only) allow determination of the concentration of cross-links (P2) in the system before the gel point.

Table 1. Rate constants of the reaction of the curing agent with double bonds of the polymer (IR and GPC data)

T, °C	$k_1 \times 10^4$, l mol^{-1} s^{-1}	
	IR	GPC
18	0.041	0.038
40	0.210	0.223
60	1.425	1.408
70	2.382	2.286

Let us denote the total concentration of CNO groups, determined by IR spectroscopy, as c_{IR}, and the concentration of the free curing agent, determined by GPC, as c_{GPC}. Since in the first stage the free curing agent becomes incorporated in fragment P1, the decrease in the concentration of the free curing agent is presumably equivalent to the increase in the concentration of P1. The concentration of P1 units, assuming that they do not react with C=C bonds of the polyurethane to form cross-links P2, is found from the formula

$$c_{P1(GPC)} = c_{0GPC} - c_{\tau GPX},$$

where c_{0GPC} and $c_{\tau GPC}$ are the concentrations of free dinitrile dioxide at the initial instant and in time τ after the start of curing, respectively.

However, actually formation of P1 fragments is accompanied by their reaction with C=C bonds. Since the quantity c_{IR} includes the concentrations of CNO groups in the free curing agent (equal to $2c_{GPC}$) and CNO groups incorporated in P1, the concentration of P1 fragments can be determined by subtracting $2c_{GPC}$ from c_{IR}:

$$c_{P1} = c_{IR} - 2c_{GPC}.$$

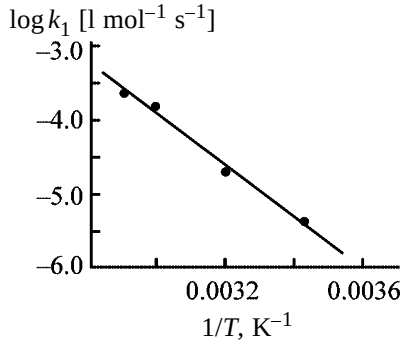

Fig. 1. Temperature dependence of the rate constant k_1.

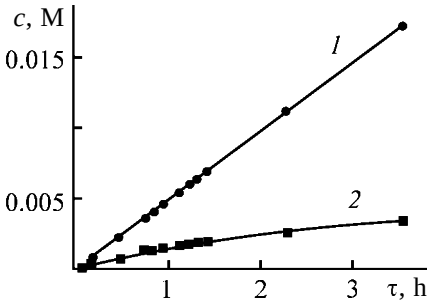

Fig. 2. Kinetic curves of accumulation of fragments (*1*) P1 and (*2*) P2 in the initial stage of curing (60°C): (*c*) concentration and (τ) time.

Finally, knowing the actual concentration of P1 fragments and their expected concentration in the absence of cross-linking, we can determine the concentration of cross-links:

$$c_{P2} = c_{P1(GPC)} - c_{P1}.$$

We found that, in the initial stage of curing, cross-linking is insignificant (Fig. 2), i.e., the curing occurs as essentially two-stage process, with predominant formation of P1 fragments in the first stage.

Table 2. Differences in the reactivity of internal (randomly located in the chain) and terminal double bonds

T, °C	$k_1 \times 10^4$, l mol^{-1} s^{-1}	
	internal double bonds	terminal double bonds
18	0.04	0.80
40	0.21	2.05
60	1.42	8.32
70	2.38	10.74

Table 3. Influence of M_w of polyurethane on the kinetics of its reaction with the curing agent

T, °C	$k_1 \times 10^4$, l mol^{-1} s^{-1}, at indicated M_w	
	5200	22 600
18	0.78	0.80
40	2.14	2.05
60	8.40	8.32
70	10.63	10.74

The rate constant k_2 was calculated from the kinetic curve of accumulation of P2 fragments. We found that the constant k_2 is by a factor of 2 lower than k_1 (k_2 = 0.73×10^{-4}, 60°C), which is apparently due to steric shielding of CNO groups in P1 by bulky polymeric chains.

Examination of the influence exerted by the structure of polyurethanes on the curing kinetics revealed significant differences in the reactivity of internal and terminal double bonds in the macromolecules with respect to the CNO groups (Table 2). This result may also be due to the steric factor, namely, to stronger shielding of internal double bonds as compared to the terminal bonds.

With the aim to reveal the influence of the polyurethane molecular weight on the kinetics of its curing, we performed curing of two polyurethane samples containing terminal double bonds, with M_w 5200 and 22 600. The results are listed in Table 3. They show that, within the examined range, the influence of the chain length on the reactivity of the double bonds is insignificant.

CONCLUSIONS

(1) The curing kinetics of polyester urethanes containing double bonds in the chain with 2,4,6-triethyl-1,3-benzenedi(nitrile oxide) was studied by IR spectroscopy and gel permeation chromatography. A procedure was proposed for determining the content of cross-links in the compound in the course of curing from the data furnished by these two methods.

(2) The rate constants of the reactions of the CNO groups of the curing agent with terminal double bonds are several times higher than those of the reactions with the internal double bonds in the polymeric chain.

(3) Within the examined range of molecular weights of polyurethane (M_w = 5000–23 000), the reactivity of terminal double bonds is independent of the length of the polymeric chain.

REFERENCES

1. Bianchi, G., De Micheli, C., and Gandolfi, R., *The Chemistry of Double-Bonded Functional Groups*, Patai, S., Ed., New York: Interscience, 1977, suppl. A, part 1, ch. 6, pp. 369–532.
2. Grundmann, C. and Grunanger, P., in *The Nitrile Oxides*, Berlin: Springer, 1971, ch. 5, pp. 85–139.

Russian Journal of Applied Chemistry, Vol. 75, No. 9, 2002, pp. 1525–1528. Translated from Zhurnal Prikladnoi Khimii, Vol. 75, No. 9, 2002, pp. 1559–1562.
Original Russian Text Copyright © 2002 by Syroezhko, Begak, Fedorov, Proskuryakov, Semenova.

CHEMISTRY OF FOSSIL FUEL

Modification of Paving Asphalts with an Elastoplastic

A. M. Syroezhko, O. Yu. Begak, V. V. Fedorov, V. A. Proskuryakov, and E. B. Semenova

St. Petersburg State Technological Institute, St. Petersburg, Russia
Mendeleev Russian Research Institute of Metrology, State Unitary Enterprise, St. Petersburg, Russia

Received January 9, 2002

Abstract—BND 60/90 and BND 89/130 paving asphalts were modified by addition of DST-30 elastoplastic and petroleum plasticizers. Their performance at temperatures from –(32–35) to +(90–95)°C was examined in comparison with that of commercial unmodified asphalts, which are efficient at temperatures from –(23–27) to +(44–50)°C.

Petroleum asphalts are the main binding material in pavements. About 80% of the produced asphalt is used for paving; the remainder is used in production of roofing materials, house building, erection of various hydraulic structures, laying of pipings; it is also used in electrical engineering, chemical industry, and some other fields [1, 2].

The durability of an asphalt concrete pavement depends not only on the quality of the bed preparation and of mineral fillers used, but also on the asphalt quality.

In north-western Russia, the main supplier of asphalts is Kirishinefteorgsintez Production Association. Because of specific features of tars from commercial West-Siberian crude oil (increased content of paraffinic and naphthenic compounds), used for producing paving asphalts, the asphalts do not always have the required performance and quality characteristics (softening point, penetration before and after standard heat treatment, ductility, brittle point).

Since, in the forecastable future, oil refineries producing asphalt by oxidation of petroleum tar with air will have no ways of significantly improving their consumer's characteristics, one of the promising ways to obtain high-quality materials is compounding of asphalts with polymers [2].

In this work, we examined the possibility of improving the quality of oxidized paving asphalts by adding rubber. As noted in [2], asphalt–rubber compounds are considerably more durable than common asphalts [3].

In modification of a paving asphalt, it is desirable to increase its softening point, make penetration less temperature-dependent, make asphalt less susceptible to elastic reverse deformation, increase the ductility (especially at low temperatures), enhance the adhesion of the asphalt to mineral fillers of asphalt concrete, and extend the range of working temperatures.

To this end, it is first necessary to ensure good compatibility of rubbers with asphalts. However, elastoplastics are not all compatible with asphalts. Their compatibility depends on the chemical composition of both asphalts and elastoplastics. It is known that high-molecular-weight rubbers to be compounded with asphalt require, for swelling and subsequent dissolution, larger amount of oils than that contained in paving asphalts. Furthermore, these rubbers (elastoplastics) can induce coagulation of asphaltenes, which are the major structuring components of asphalts; this is inadmissible in production of high-performance paving asphalts.

Therefore, in this work, we examined how the properties of rubber-modified paving asphalts are affected by addition of not only elastoplastics but also available and relatively cheap plasticizers.

EXPERIMENTAL

Experiments were performed with commercial paving asphalts BND 60/90 and BND 90/130 (Kirishinefteorgsintez). As modifier we used DST-30 divinyl–styrene elastoplastic rubber [Voronezh Synthetic Rubber Plant, TU (Technical Specifications) 38-40365–76], as the most economically acceptable. This elastoplastic is well soluble in asphalt.

As plasticizers we used commercial products: second vacuum gas oil (SVG) from AVT-2 installation

1070-4272/02/7509-1525$27.00 © 2002 MAIK "Nauka/Interperiodica"

(Kirishinefteorgsintez), density 912 kg m^{-3}, boiling range 390–499°C (50% distillation at 455°C), flash point 254°C, and polyalkylbenzene (PAB) from LAB-LABS installation, boiling range 315–480°C. Alkyl substituents in PAB are linear aliphatic chains containing 12–14 carbon atoms.

Polymer–asphalt compounds were prepared as follows. To the asphalt heated to 180–200°C, we added DST-30 rubber, and the blend was stirred for 1.5 h at 1250 rpm. The rubber amount was varied in steps from 1 to 6 wt % relative to the asphalt. Then, maintaining the temperature at 180–200°C, we added a plasticizer (SVG or PAB) in amount of 3, 5, 10, 15, or 20 wt % with vigorous stirring; the resulting compound was stirred for 15 min.

The performance characteristics of the resulting modified compounds were measured as prescribed by the corresponding standards for paving asphalts: the ring-and-ball softening point, according to GOST (State Standard) 11506–73; penetration at 25°C, P_{25}, according to GOST 11505–75; Fraas brittle point, according to GOST 11507–78 on a VRAZ device (Petrotest); and ductility, D_{25} (mm), according to GOST 11505–75 on a laboratory ductilometer.

The component composition of the initial and modified asphalts was determined with an IATRO-ACAN-5 device (Japan).

The component composition (wt %) of asphalts was as follows: BND 60/90, paraffinic and naphthenic compounds (PNCs) 9.34, arenes 46.65, resins 24.85, and asphaltenes 19.16; BND 90/130 (softer and more plastic asphalt), PNCs 10.03, arenes 47.85, resins 25.23, and asphaltenes 16.88. It is seen that harder BND 60/90 asphalt contains more resins and asphaltenes, whereas more plastic BND 90/130 asphalt contains more saturated and aromatic hydrocarbons (oils).

It is known that properties of asphalt compounds are improved at good compatibility of an asphalt with a rubber.

BND 60/90 asphalt having higher softening point is worse compatible with DST-30 elastoplastic than BND 90/130 asphalt. Rubber molecules swell in malthenes, altering the dispersion medium of the compound, since, in the course of swelling, they adsorb polar aromatic hydrocarbons and also heteroatomic components from the oil fraction of the asphalt.

The main characteristics of compounds based on BND 60/90 and BND 90/130 asphalts, as influenced by the plasticizer content, are listed in Figs. 1a and 1b. Figure 1a shows that, on adding DST-30 in proportion with a plasticizer, the softening point of the compound increases. Apparently, swollen rubber forms in the bulk of asphalt an elastic network, and the plasticizer facilitating uniform distribution of the rubber decreases the softening point to the greater extent, the higher its content in the compound. For BND 60/90 asphalt, according to GOST 22245–90, the softening point should be no lower than 47°C.

The effect of SVG plasticizer on the penetration of the compounds based on BND 60/90 asphalt is also seen from Fig. 1a. The penetration is an approximately linear function of the plasticizer content, i.e., increased content of the plasticizer enhances the solubility not only of the elastoplastic, but also of the resins and asphaltenes. The alkylaromatic plasticizer (PAB) decreases the viscosity (and hence increases the penetration) to the greater extent, i.e., in this case the structure of the compound is more plastic and mobile than with SVG. According to GOST 22245–90 for BND 60/90 asphalt, the penetration P_{25} should be within 60–90 mm. The following formulations meet these requirements: (1) 1 wt % DST-30, (2) 1 wt % DST-30 and 3 wt % SVG or PAB, (3) 3 wt % DST-30 and 3–5 wt % PAB or 3–10% SVG, and (4) 6 wt % DST-30 and 10–15 wt % SVG.

Asphalts modified with DST-30 and SVG differ from the initial asphalt not only in the softening point, penetration, and ductility, but also in the brittle point. The lower brittle point (down to –32°C) and higher softening point (up to 95°C) extend the working temperature range of the asphalt, which is important for territories with, respectively, cold and hot climate.

The softening points sharply decrease on adding 0–3% plasticizer and more gradually, with further additions.

The ductility of rubber–asphalt compounds varies differently depending on the formulation. For example, for the compounds based on BND 60/90, the ductility in most cases increases on adding SVG, but in the case of the compound with 1 wt % DST-30, it starts to decrease when the amount of the added SVG exceeds 3%. That is, the cohesion of the three-dimensional network formed by the asphalt, elastoplastic, and plasticizer becomes lower than that of the initial asphalt. Addition of the tested plasticizers decreases the brittle point in all the cases. Generally, PAB is a better plasticizer than SVG.

Similar trends are observed with compounds based on BND 90/130 (Fig. 1b). The softening point of this asphalt, according to GOST, should be now lower than 43°C; this requirement is met by all the compounds except that containing 1 wt % DST-30 and

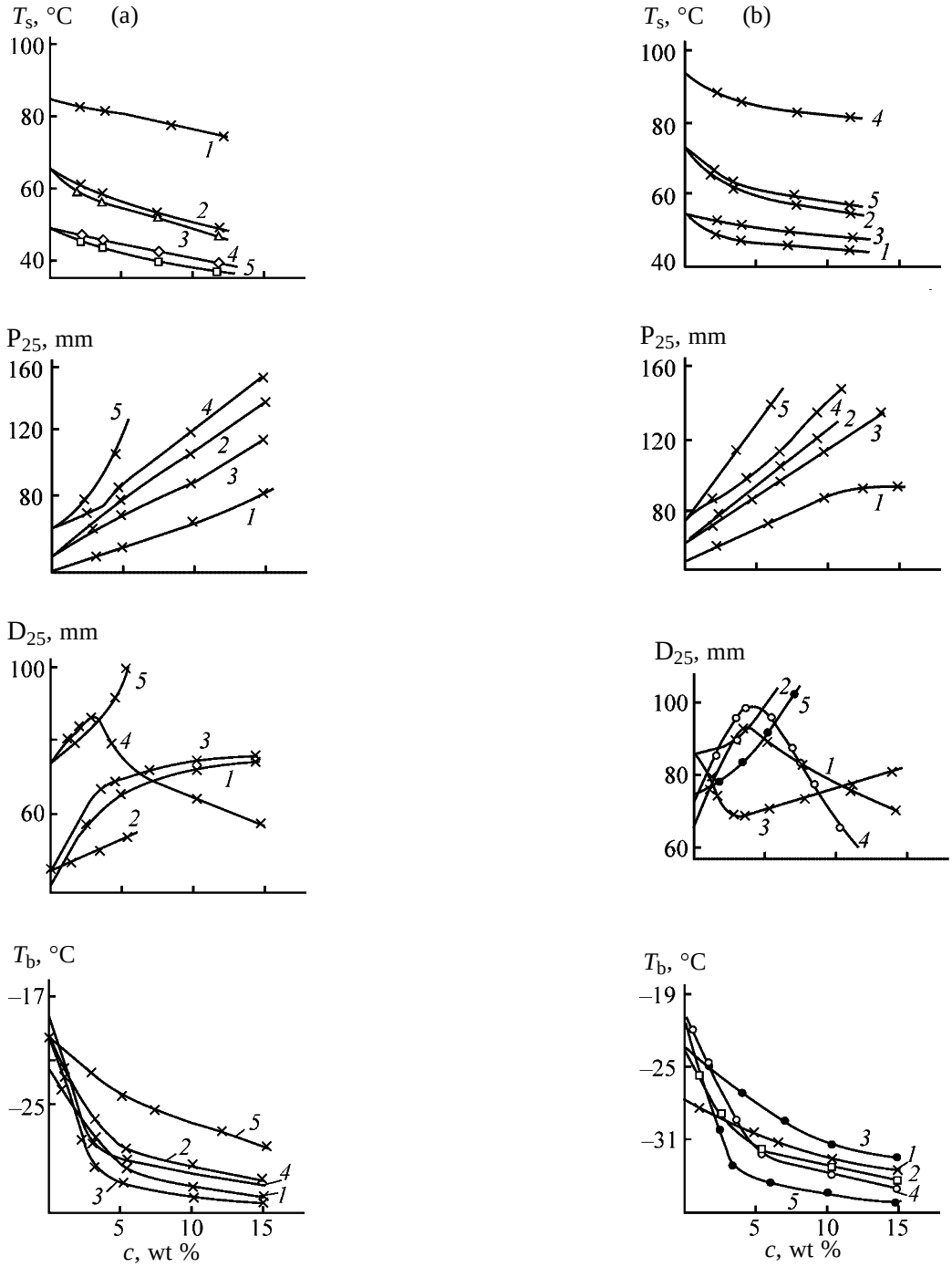

Fig. 1. Softening point T_s, penetration P_{25}, ductility D_{25}, and brittle point T_b of compounds based on (a) BND 60/90 and (b) BND 90/130 as functions of the plasticizer content c at various concentrations of DST-30 rubber. Plasticizer: (*1*, *3*, *4*) SVG and (*2*, *5*) PAB. DST-30 content, wt %: (*1*) 6, (*2*, *3*) 3, and (*4*, *5*) 1.

15 wt % SVG. As for penetration, the requirements of the standard are met by the following compounds: (1) 1 wt % DST-30 and 3 wt % PAB; (2) 3–5 wt % SVG and 1 wt % DST-30; (3) 3 wt % DST-30 and 10–15 wt % SVG or 3–5 wt % PAB; and (4) 6 wt % DST-30 and 10–15 wt % SVG.

The effect of the modifying additives on the ductility of BND 90/130 asphalt is also ambiguous. Addition of the elastoplastic sharply decreases the stretchability of the asphalt into a thread (by a factor of 1.5–2). However, on adding SVG, the ductility passes through an extremum at approximately 3 wt % content

of the plasticizer. Since the rubber does not react chemically with bitumen components (oils, resins, asphaltenes), it is, most likely, dispersed in the asphalt; on adding a plasticizer, the structure becomes more coarsely dispersed.

According to the standard, the stretchability of BND 90/130 asphalt should be no less than 65 cm. All the compounds meet this requirement, except the compounds containing 1 wt % DST-30 + 15 wt % SVG and 3 wt % DST-30 + 3 wt % SVG.

Figure 1b shows that addition of the elastoplastic increases the brittle point of the binary compound owing to formation of an elastic network structure. However, on adding a plasticizer, such structures become more stable, with PAB additions decreasing the brittle point to a greater extent. Thus, combined modification of oxidized petroleum paving asphalts BND 60/90 and BND 90/130 with DST-30 elastoplastic and SVG or PAB plasticizer appreciably extends the working temperature range of the asphalt (from the brittle point to the softening point), which will extend possible applications of the modified asphalts.

CONCLUSION

Modification of BND 60/90 and BND 90/130 paving asphalte with DST-30 elastomer (1–6 wt %) and petroleum plasticizers (polyalkylbenzene, 3–5 wt %; vacuum gas oil, 3–15 wt %, boiling range 390–499°C) extends the working range of the compounds [from –(32–35) to +(90–95)°C], as compared to unmodified asphalts [from –(25–27) to +(44–50)°C].

REFERENCES

1. Kolbanovskaya, A.S. and Mikhailov, V.V., *Dorozhnye bitumy* (Paving Asphalts), Moscow: Transport, 1973.
2. Pechenyi, B.G., *Bitumy i bitumnye kompozitsii* (Asphalts and Asphalt Compounds), Moscow: Khimiya, 1990.
3. *Primenenie polimerno-bitumnogo vyazhushchego pri stroitel'stve dorozhnykh, mostovykh i aerodromnykh asfal'tobetonnykh pokrytii: Uchebnoe posobie* (Use of a Polymer–Asphalt Binder for Asphalt Concrete Paving of Roads, Bridges, and Airports: Textbook), Tarasenko, I.E., Ed., Moscow: Soyuzdornii, 1979.

Russian Journal of Applied Chemistry, Vol. 75, No. 9, 2002, pp. 1529–1531. Translated from Zhurnal Prikladnoi Khimii, Vol. 75, No. 9, 2002, pp. 1563–1565.
Original Russian Text Copyright © 2002 by Tolstoi, Tolstobrov.

BRIEF COMMUNICATIONS

Synthesis of Highly Oriented α-PbO_2 Layers on the Surfaces of Single-Crystal Silicon and Quartz by Successive Ionic Layer Deposition

V. P. Tolstoi and E. V. Tolstobrov

St. Petersburg State University, St. Petersburg, Russia

Received January 2, 2002

Abstract—Conditions for the synthesis of α-PbO_2 layers on silica surfaces by successive ionic layer deposition were determined. These layers were studied by X-ray spectral microanalysis, X-ray diffraction, IR Fourier spectroscopy, UV-Vis spectroscopy, and ellipsometry.

Layers of Pb(IV) oxides are used in electrochemical current sources as precursors in the synthesis of Li-conducting solid electrolytes, high-temperature superconductors, etc.

The synthesis of such layers by successive ionic layer deposition technique (SILD) is the aim of this work. Earlier this technique was applied to the syntheses of layers of other oxides, hydroxides, and peroxides of metals, e.g., of $SnO_2 \cdot nH_2O$ [1], FeOOH [2], and $CeO_{2+x} \cdot nH_2O$ [3]. This method allows precise adjustment of the thickness of the synthesized layer (at the level of fractions of nanometer or several nanometers) and synthesis on the surface of a complex-shape support.

EXPERIMENTAL

Fused quartz of KU (quartz for ultraviolet region) brand and [100] silicon single crystal of KEF-7.5 brand polished to grade 14 were used as supports. Quartz supports were washed in acetone and were kept for 10 min in concentrated HNO_3 at 90–100°C and then rinsed with water, a KOH solution (pH 9), and again water. After etching in HF, single-crystal silicon supports were treated with concentrated HNO_3 at 90–100°C for 0.5 h, rinsed with distilled water, a KOH (pH 9) solution, and again water.

Nanolayers of α-PbO_2 were synthesized as follows. After a standard treatment, supports were fixed in holders of a computer-aided installation for syntheses and were immersed in various solutions in the sequence according to a scheme corresponding to an elementary ILD cycle, namely, in a $Pb(NO_3)_2$ solution (c = 0.01 M, pH ~5.8, in the presence of CH_3COONa), distilled water, $KMnO_4$ solution (c = 0.005 M, pH ~9.5 was adjusted by adding KOH), and in distilled water again. These reagents were chosen on the basis of considerable experimental work, which included tests of a number of other lead salts and solutions of oxidants, in particular, H_2O_2 and NaClO solutions. However, these experiments showed that the best conditions for SILD were attained with $Pb(NO_3)_2$ solutions containing CH_3COONa and alkalized $KMnO_4$ solutions. The duration of the treatment with each reagent was 0.5 min. As a result of the above-mentioned process sequence, one nanolayer of lead oxide was formed on the support surface. The subsequent nanolayers were synthesized by multiple repetition of SILD cycles.

As experimental methods we used UV-Vis and IR Fourier transmission spectroscopy, ellipsometry, X-ray diffraction, and X-ray spectral microanalysis. The transmission spectra of the synthesized layers were recorded in the UV and Vis ranges on a Perkin–Elmer Lambda-9 spectrophotometer (scanning rate 50 nm min^{-1}, slit program 2 nm), and the IR Fourier transmission spectra, on a Perkin–Elmer 1760X spectrophotometer at a resolution of 4 cm^{-1}. Ellipsometric measurements were carried out on an ellipsometer with an incidence angle of 45° and wavelength of 632.8 nm. The X-ray patterns were obtained on a DRON-3.0 diffractometer with CuK_α radiation. The X-ray spectral microanalysis was carried out on a CAMSCAN-4 scanning electron microscope (accelerating voltage 20 kV) integrated with an AN-10000 semiconductor spectrometer of characteristic

1070-4272/02/7509-1529$27.00 © 2002 MAIK "Nauka/Interperiodica"

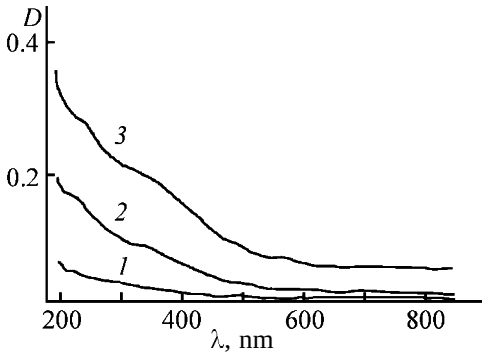

Fig. 1. Transmission spectra of α-PbO_2 layers synthesized on quartz surface by SILD: (*D*) optical density and (λ) wavelength. Number of SILD cycles: (*1*) 10, (*2*) 20, and (*3*) 30.

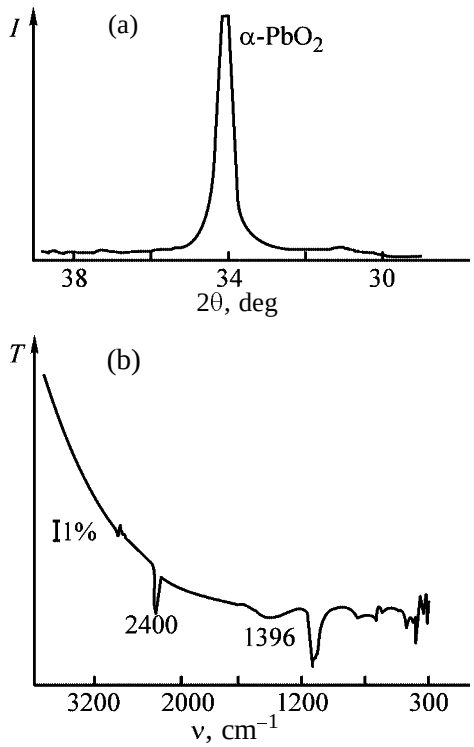

Fig. 2. (a) X-ray pattern and (b) FTIR transmission spectrum of an α-PbO_2 layer synthesized on the silicon surface by 40 SILD cycles and heated in air at 100°C for 0.5 h. (a) (*I*) Intensity and (2θ) Bragg angle; (b) (*T*) transmission and (ν) wave number.

X-ray radiation. Layers synthesized on single-crystal silicon served as samples for the X-ray spectral microanalysis, X-ray diffraction, ellipsometry, and FTIR spectroscopy, and layers on the quartz surface, for UV-Vis transmission spectroscopy. The support was chosen so as to ensure the highest efficiency of each method. The point is that the layers synthesized by SILD are very thin, and thus they can be studied only under conditions of the highest sensitivity of each method. Such conditions are attained when silicon and quartz supports are used in studies by FTIR and UV-Vis spectroscopy, respectively, because of their transparency in these spectral regions. The X-ray spectral method is the more efficient with a silicon support owing to its higher conductivity and smaller amount of surface charges. X-ray diffraction and ellipsometry are more efficient in studying layers on a silicon surface: the first method, owing to the higher intensity of the useful signal, and the second, owing to the wider range of the linear dependence of the ellipsometric parameters on the layer thickness.

When a quartz plate is subjected to 10, 20, and 30 SILD cycles, a broad absorption band appears in its UV-Vis transmission spectrum in the range 200–450 nm (Fig. 1); its integral intensity grows with increasing number of cycles. According to ellipsometric measurements, the thickness of a layer formed in one cycle is 0.45 nm. The X-ray spectral analysis showed that the layer consists of lead and oxygen atoms. No manganese and potassium ions pass into the layer from the solution. The X-ray pattern (Fig. 2a) suggests that the layer has the crystal structure of rhombic α-PbO_2 (a = 0.4038, b = 0.503, c = 0.5486 nm), with the c axis being normal to the support surface. The layer also contains OH groups, which can be identified by their bending band at 1356 cm^{-1} in the FTIR spectrum (Fig. 2b). It should be noted that the presence of OH groups is consistent with the structure model of the α-PbO_2 layer accepted, e.g., in [4].

The following model offers the most probable explanation of our results. The treatment of the support with a $Pb(NO_3)_2$ solution results in adsorption of Pb^{2+} or $PbOH^+$ ions [5]. Then excess $Pb(NO_3)_2$ is removed from the surface in the stage of washing with water. In the subsequent stage, the support containing a sorbed layer of Pb^{2+} ions is treated with an alkalized $KMnO_4$ solution, which results in the oxidation of Pb(II) to Pb(IV) and the reduction of Mn(VII), apparently to Mn(V) which subsequently reacts with excess $KMnO_4$ to form MnO_4^{2-}. We believe that such a process is the most probable, since specifically the MnO_4^{2-} ions can be removed most readily from the surface in the stage of washing off excess $KMnO_4$ from the support. The process is repeated in each subsequent SILD cycle. This scheme also allows us to explain the high crystal-chemical perfection of the synthesized layer, as in each SILD stage the reaction products are removed from the surface, which reduces steric hindrances to the layer growth.

CONCLUSION

The possibility of preparing α-PbO_2 layers by successive ionic layer deposition on silicon and quartz surfaces was shown. The thickness of the resulting layers is precisely specified by the number of ionic deposition cycles.

ACKNOWLEDGMENTS

This work was financially supported by the Russian Foundation for Basic Research (project no. 01-03-32427).

REFERENCES

1. Tolstoi, V.P., *Zh. Neorg. Khim.*, 1993, vol. 38, no. 7, pp. 1146–1148.
2. Tolstoi, V.P., *Zh. Prikl. Khim.*, 1999, vol. 72, no. 8, pp. 1259–1261.
3. Tolstoi, V.P. and Ehrlich, A.G., *Thin Solid Films*, 1997, vol. 307, pp. 60–64.
4. Chelani, N., Zerroual, L., Hammouche, A., *et al.*, *Solid State Ionics*, 1996, vol. 91, pp. 289–294.
5. Tsukanova, V.M. and Tikhomolova, K.P., *Kolloidn. Zh.*, 1995, vol. 57, no. 6, pp. 878–884.

Russian Journal of Applied Chemistry, Vol. 75, No. 9, 2002, pp. 1532–1534. Translated from Zhurnal Prikladnoi Khimii, Vol. 75, No. 9, 2002, pp. 1566–1568.
Original Russian Text Copyright © 2002 by Krivosheeva, Zhukova, Kagan.

BRIEF COMMUNICATIONS

Electrochemical Synthesis of 3-Methoxycarbonyl-2,2,5,5-tetramethylpyrrolidine

S. N. Krivosheeva, I. Yu. Zhukova, and E. Sh. Kagan

South-Russian State Technical University (Novocherkassk Polytechnic Institute), Novocherkassk, Rostov oblast, Russia

Received April 15, 2002

Abstract—Electrochemical halogenation of 4-oxo-2,2,6,6-tetramethylpiperidine (triacetonamine) in the electrolytes triacetonamine–KX–CH_3ONa (X = Cl, Br, I) was studied, and a procedure was developed for preparing 3-methoxycarbonyl-2,2,5,5-tetramethylpyrrolidine by this reaction.

Compounds of the 2,2,5,5-tetramethylpyrroline and 2,2,5,5-tetramethylpyrrolidine series are used for preparing spin markers in studies of polymers, biopolymers, and drugs [1]; however, synthesis of these compounds is difficult. 3-Methoxycarbonyl-2,2,5,5-tetramethylpyrrolidine **II** is an important synthetic precursor of nitroxyl radicals of the pyrrolidine series [2]. It is prepared from 4-oxo-2,2,6,6-tetramethylpiperidine (triacetonamine, TAA, **I**) in several steps [3]. In this work we developed a procedure for preparing **II** by electrochemical halogenation of **I**.

Electrochemical halogenation of **I** in a sodium methylate solution is accompanied by the Favorskii rearrangement [4] and yields a mixture of **II** with 3-methoxycarbonyl-2,2,5,5-tetramethylpyrroline **III**. Apparently, the reaction occurs via mono- and dihalo derivatives of TAA. The process involves the following transformations:

at the anode: $2Br^- - 2e \rightarrow Br_2$,

at the cathode: $2CH_3OH + 2e \rightarrow 2\ CH_3O^- + H_2$,

in solution:

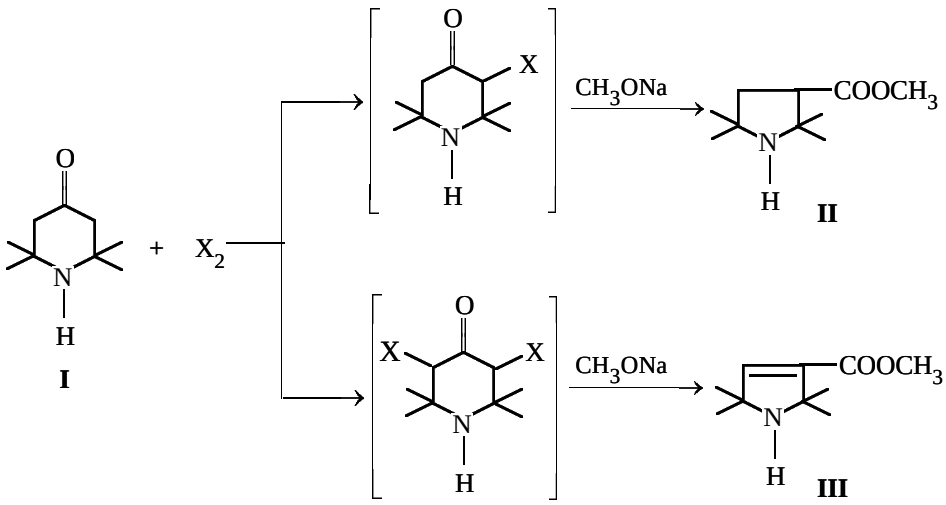

where X = Cl, Br, I.

As sources of halide ions, we used KCl, KBr, and KI. The ratio of **II** and **III**, determined by gas–liquid chromatography (GLC), depended mainly on the halide ion. The total yield of **II** and **III** was 80–87% irrespective of the halide ion. Pure 3-methoxycarbonyl-2,2,5,5-tetramethylpyrrolidine **II** was prepared by reduction of a mixture of **II** and **III** with sodium amalgam.

1070-4272/02/7509-1532$27.00 © 2002 MAIK "Nauka/Interperiodica"

Influence of electrolysis conditions on the yield of **II** and **III** in electrochemical halogenation of TAA. Electrolyte: TAA–KX–CH_3ONa (X = Cl, Br, I)

Halide ion	Q, F mol^{-1}	TAA conversion	Yield of **II** + **III**	Mixture composition, %	
		%		**II**	**III**
Cl^-	2	21	86	7	14
	4	62	84	12	50
	8	100	80	16	84
Br^-	2	24	87	6	18
	4	72	85	20	52
	8	100	85	38	62
I^-	2	18	84	8	10
	4	69	81	30	39
	8	100	82	46.8	53.2

EXPERIMENTAL

Chromatographically pure TAA was purchased from Sintez Joint-Stock Company (Tambov, Russia); organic solvents were of pure grade. Gas chromatography was performed with an LKhM-8MD chromatograph (thermal conductivity detector; sensitivity 1 : 3; carrier gas helium, flow rate 0.4 ml s^{-1}; stationary phase PEG-4000 on Chromaton N-AW; temperatures: vaporizer 270, detector 200, and column 150; 1500 × 3-mm column).

Electrochemical halogenation of **I** was performed in a sodium methylate solution. Electrolysis was performed in a 200-ml diaphragmless electrolyzer equipped with a magnetic stirrer, a reflux condenser, and an electrode stack (anode: platinum plate, surface area 7.5 cm^2; cathode: two stainless steel plates of the same surface area; distance between the anode and cathode 3 mm). The electrolyzer was charged with 6 g (0.038 mol) of TAA, 0.067 mol of a potassium halide, and 100 ml of methanol containing 2.3 g (0.1 mol) of dissolved sodium. Electrolysis was performed under vigorous stirring with a current of 1 A (current density 0.1 A cm^{-2}). The reaction completion was judged from disappearance of **I** (TLC, Al_2O_3, Brockmann grade II, eluent CH_2Cl_2, development with I_2 vapor). After electrolysis completion, the solvent was distilled off, 50 ml of water was added, and the products were extracted with CH_2Cl_2 (3 × 30 ml). The extract was evaporated in a rotary evaporator, and the oily residue was distilled in a vacuum; the fraction boiling within 80–85°C/3 mm Hg was collected. The composition of the mixture was determined by GLC from the peak areas, assuming equal sensitivity of the detector to **II** and **III**. The peak areas were measured with an accuracy of 5 rel. %.

Compound **III** was reduced to **II** with sodium amalgam. Synthesis was performed in a diaphragm electrolyzer made of a 200-ml battery housing. The cathode was mercury added in an amount sufficient to fully cover the bottom. The surface area of the mercury electrode was 38.5 cm^2. Current was fed with a copper wire insulated with Teflon, except the tip (0.3 cm) immersed in mercury [5]. The anode was a platinum spiral (surface area 10 cm^2).

The cathodic compartment was charged with 50 ml of 7% NaOH, and the anodic compartment, with 5% alkali. Electrolytic preparation of the amalgam was performed at a current of 5.2 A (current density 0.1 A cm^{-2}) at 30–40°C with stirring. The electrolysis was completed after passing 2.2 F mol^{-1} (0.9 A h) of electricity. After the electrolysis completion, the alkali solution was removed, and the electrolyzer was charged with a solution of a mixture containing 2 g (0.011 mol) of **II** + **III** and 30 ml of methanol. The reaction completion was judged from disappearance of **III** (TLC, Al_2O_3, Brockmann grade II, eluent CH_2Cl_2, development with I_2 vapor). After the reaction completion, the solvent was removed, and 1.8 g (90%) of **II** was obtained; oily substance, melting point of the picrate 124–126°C. Mixing the picrate sample obtained with an authentic sample gave no melting point depression [6].

CONCLUSION

Electrochemical halogenation of triacetonamine in a sodium methylate solution is accompanied by the Favorskii rearrangement, giving in a high yield a mixture of 3-methoxycarbonyl-2,2,5,5-tetramethylpyrroline and 3-methoxycarbonyl-2,2,5,5-tetramethylpyr-

rolidine; a procedure was developed for the reduction of 3-methoxycarbonyl-2,2,5,5-tetramethylpyrroline to 3-methoxycarbonyl-2,2,5,5-tetramethylpyrrolidine with sodium amalgam.

REFERENCES

1. Zhdanov, R.I., *Paramagnitnye modeli biologicheski aktivnykh soedinenii* (Paramagnetic Models of Biologically Active Compounds), Moscow: Nauka, 1981.
2. Rozantsev, E.G., *Svobodnye iminoksil'nye radikaly* (Free Iminoxyl Radicals), Moscow: Khimiya, 1970.
3. Sosnovsky, G. and Zhen-Wei Cai, *J. Org. Chem.*, 1995, vol. 60, no. 11, pp. 3414–3418.
4. Kagan, E.Sh., Zhukova, I.Yu., Pozhidaeva, S.A., and Kovalenko, E.I., *Elektrokhimiya*, 1996, vol. 32, no. 1, pp. 100–104.
5. Smirnov, V.A., *Vosstanovlenie amal'gamami* (Reduction with Amalgams), Leningrad: Khimiya, 1970.
6. Krinitskaya, L.A. and Volodarskii, L.B., *Izv. Akad. Nauk SSSR, Ser. Khim.*, 1982, no. 2, pp. 443–446.

Russian Journal of Applied Chemistry, Vol. 75, No. 9, 2002, pp. 1535–1536. Translated from Zhurnal Prikladnoi Khimii, Vol. 75, No. 9, 2002, pp. 1569–1571.
Original Russian Text Copyright © 2002 by Illarionova, Kalinina, Khokhlova, Vainburg, Chufarovskaya, Shtyagina.

BRIEF COMMUNICATIONS

Alginate Fibers with Controllable Calcium Content

E. L. Illarionova, T. N. Kalinina, V. A. Khokhlova, V. M. Vainburg, T. I. Chufarovskaya, and L. M. Shtyagina

St. Petersburg State University of Technology and Design, St. Petersburg, Russia

Received April 24, 2002

Abstract—A procedure was developed for preparing alginate fibers with controllable calcium content. The effect of ethonium and Katamin AB on desorption of calcium ions from the alginate fiber was studied.

Alginate fibers are used in medicine and in food and textile industries. Alginate fibers prepared by the existing process contain about 10–12% calcium ions (0.25–0.30 mol per 100 g of fiber).

Alginate fibers show promise as dressings and resolving materials in medicine; also, soluble alginate fibers give useful effect in textile industry. In these cases, the calcium content on the fiber should not exceed 2–6% (0.05–0.15 mol per 100 g of fiber), depending on particular application. To prepare alginate fibers containing 2–6% Ca^{2+}, the initial fiber was subjected to multistep time-consuming treatments [1, 2]. The fiber was treated for 20 min with a sodium hypochlorite solution, which was followed by successive washing with an aqueous solution of sodium thiosulfate, water, and calculated amount of hydrochloric or another acid for 30 min. After that, the fiber was again washed with water and neutralized with alcoholic NaOH. Finally, it was treated with 95% methanol.

Experiments on preparation of alginate fibers with antimicrobial activity showed that treatment of alginate fibers with some nitrogen-containing antimicrobial agents considerably reduces the calcium content on the fiber, even when performed under common conditions [3]. Data on the content of calcium ions on alginate fiber after treatment under static conditions with 1% aqueous solutions of agents (1 h, 20°C) and, for comparison, with distilled water are listed in the table.

The best results were obtained with agents containing a quaternary nitrogen atom. Ethonium contains two quaternary nitrogen atoms per formula unit, and Katamin AB, only one; correspondingly, ethonium is more effective. These two agents were chosen for further experiments aimed at controlling the Ca^{2+} content on the alginate fiber.

Detailed study of calcium removal as influenced by the concentrations of the nitrogen-containing agents (Fig. 1) showed that the optimal concentration of ethonium is 5% (85 mM), and that of Katamin AB, 3% (70 mM). Treatment with such solutions reduces the Ca^{2+} content to 0.102 (4.0%) and 0.140 mol per 100 g of fiber (5.6%), respectively. In the course of treatment, the solution pH increases from 3.8–4.0 to 5.0–5.3. The ratio of the optimal concentrations of the agents correlates to some extent with the ratio of their critical micelle concentration: ethonium, 3.2; Katamin AB, 2.5 mM [4], although our experiments were performed at considerably higher concentrations of these agents.

Apparently, the extremum in the curves, when further additions of the nitrogen-containing agent decrease its performance, is due to active micelle formation. Data on the content of free carboxy groups on

Content of calcium ions on alginate fiber after its treatment with solutions of nitrogen-containing agents. Initial content of calcium ions 0.277 mol per 100 g of fiber

Agent for treament	Ca^{2+} content, mol per 100 g of fiber
Distilled water	0.230
Ethonium, 1,2-[*N*,*N*,*N*',*N*'-tetramethyl-*N*,*N*'-bis(decyl acetate)]ethylenediammonium dichloride	0.177
Dioxidine, 2,3-bis(hydroxymethyl)-quinoxaline *N*,*N*'-dioxide	0.205
Katamin AB, alkylbenzyldimethylammonium chloride	0.185
Chlorhexidine, 1,6-bis[5-(*p*-chlorophenyl)biguanido]hexane	0.190
Iodopyrone, a complex of polyvinylpyrrolidone iodide with potassium iodide	0.200

1070-4272/02/7509-1535$27.00 © 2002 MAIK "Nauka/Interperiodica"

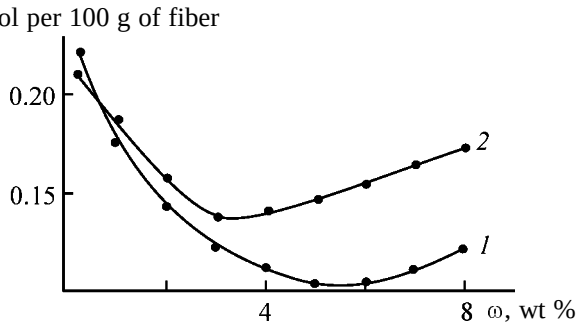

Fig. 1. Content of calcium ions *c* on alginate fiber as a function of concentration ω of (*1*) ethonium and (*2*) Katamin AB in solution. 20°C; the same for Fig. 2.

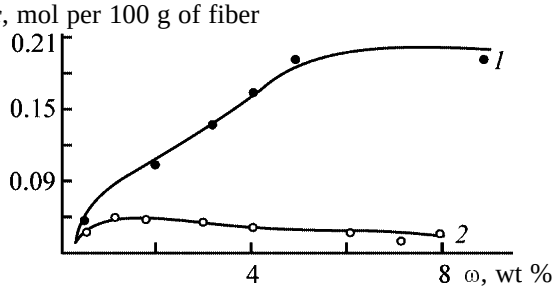

Fig. 2. Content of free carboxy groups *c* on alginate fiber as a function of concentration ω of (*1*) ethonium and (*2*) Katamin AB in solution.

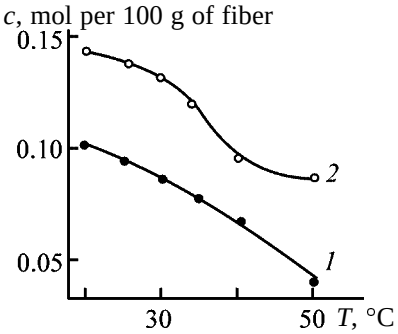

Fig. 3. Content of calcium ions *c* on alginate fiber as a function of temperature *T* of treatment with (*1*) 5% ethonium solution and (*2*) 3% solution of Katamin AB. Treatment time 1 h.

the fiber can be interpreted from the same standpoint (Fig. 2). With ethonium, the curve first linearly ascends and then flattens out, whereas with Katamin AB a short linearly ascending portion is followed by a slow descent. These curves are resultant of two processes: release of carboxy groups due to removal of Ca^{2+} ions and their reaction with quaternary ammonium compounds. Bulky ethonium ion reacts with carboxy groups very slowly, whereas Katamin AB reacts actively. This is indirectly confirmed by data on their antimicrobial activity. The diameter of the growth suppresion zone for *Staphylococcus aureus 209* is 25 mm with ethonium-treated alginate fiber and 42 mm with the Katamin AB treated fiber.

The Ca^{2+} content on the fiber can be controlled still more efficiently by varying the treatment temperature (Fig. 3). In this case, the Ca^{2+} content on the fiber can be reduced to 0.05 mol per 100 g of fiber (2%), which is very important for medicine. The treatment temperature should not exceed 50°C, since at higher temperatures the fiber undergoes irreversible deformations.

The developed procedure allows preparation of alginate fiber with preset and well-reproducible calcium content. The fluctuations of the calcium content do not exceed 3%, whereas in treatment with sodium hypochlorite, because of the multistep procedure, they reach 10%.

EXPERIMENTAL

An accurately weighed 1-g portion of calcium-containing alginate fiber was placed in an aqueous solution containing a prescribed amount of a nitrogen-containing agent; liquid-to-solid ratio 30. After the treatment, the fiber was washed with distilled water (liquid-to-solid ratio 1000), squeezed with filter paper, and air-dried.

To determine the calcium content on alginate fiber, an accurately weighed 0.3-g portion of the fiber was placed in a porcelain cup, 5 ml of 2.0 M HCl was added, and the cup was placed on a boiling water bath. The solution was evaporated by half with stirring, and an additional 5 ml of HCl was added. The hydrochloric acid extract was quantitatively transferred onto a filter, with collection of the filtrate and wash waters. To the solution, 12.5 ml of 2.0 M NaOH was added dropwise with stirring, and the solution was titrated with Na_2EDTA.

The content of free carboxy groups in the alginate fiber was determined as follows. To an accurately weighed fiber sample (0.3 g), we added 30 ml of 0.1 M NaOH, kept for 1 h until the sample completely dissolved, and titrated with 0.05 M sulfuric acid (phenolphthalein indicator).

REFERENCES

1. US Patent 3879168.
2. UK Patent 1231506.
3. RF Patent 1819923.
4. Abramzon, A.A., Bocharov, V.V., Gaevoi, G.M., *et al.*, *Poverkhnostno-aktivnye veshchestva: Spravochnik* (Surfactants: Handbook), Abramzon, A.A. and Gaevoi, G.M., Eds., Leningrad: Khimiya, 1979, pp. 292–295.

Russian Journal of Applied Chemistry, Vol. 75, No. 9, 2002, pp. 1537–1538. Translated from Zhurnal Prikladnoi Khimii, Vol. 75, No. 9, 2002, pp. 1572–1573.
Original Russian Text Copyright © 2002 by Davletbaeva, Ten'kovtsev, Bylinkin, Lukoshkin, Parfenov.

BRIEF COMMUNICATIONS

Influence of Metal Complexing on the Nonlinear-Optical Properties of Compounds with High Molecular Symmetry

I. M. Davletbaeva, A. V. Ten'kovtsev, R. A. Bylinkin, V. A. Lukoshkin, and V. V. Parfenov

Kazan State Technological University, Kazan, Tatarstan, Russia
Institute of Macromolecular Compounds, Russian Academy of Sciences, St. Petersburg, Russia
Ioffe Physicotechnical Institute, St. Petersburg, Russia
Kazan State University, Kazan, Tatarstan, Russia

Received April 4, 2002

Abstract—Coordination bonding of 1,5-diphenylpentadienone was studied with the aim to prepare compounds exhibiting third-order nonlinear optical properties. The volume resistivity of these compounds was studied as influenced by the third-order nonlinear susceptibility tensor.

Preparation of materials exhibiting nonlinear optical (NO) effects, in particular, third-order nonlinear susceptibility, is today one of the most promising lines of research. These effects find application in fiber-optics communication systems. The structural features of compounds exhibiting NO effects are the presence of a system of conjugated bonds and the polarizability and capability for uniaxial orientation of their molecules.

The known approach to preparing nonlinear isotropic media involves synthesis of highly oriented metal complex oligomeric systems. In particular, Bubeck [1] synthesized oligomers in which complexes of ruthenium with phthalocyanines were bound into "stacks" by *p*-phenylene diisocyanate bridges. It was assumed that the optical properties of such oligomers are primarily determined by the two-dimensional π-conjugation system of the phthalocyanine moieties. These oligomers have one of the largest known third-order nonlinear susceptibility tensor $\chi^{(3)}$ (3.7×10^{-12} CGSE units).

We showed in [2] that 1,5-bis(4-hydroxyphenyl)-1,4-pentadien-3-one (HPPD) and 1,5-bis(4-hydroxy)-3-methoxyphenyl)-1,4-pentadien-3-one (HMPPD) can exhibit third-order NO effects:

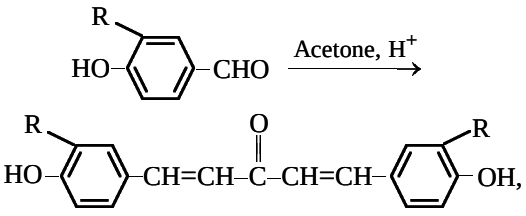

where R = H (HPPD) (**I**) and CH_3O (HMPPD) (**II**). With this specific chemical structure, these compounds can have the following resonance structures:

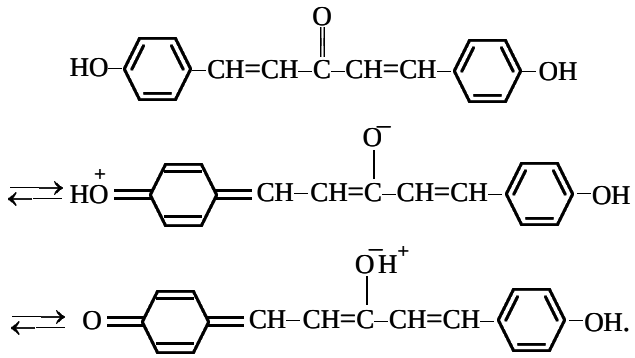

The structures of HPPD and HMPPD suggest that the NO response of their derivatives can be increased by enhancing the degree of polarization of the conjugation system and orientation of the HPPD and HMPPD macromolecules by coordination bonding. The choice of coordination compounds based on chlorides of 3*d* metals ($CoCl_2$, $CuCl_2$, $MnCl_2$) and monoethanolamine (MEA) or *N*,*N*'-diethylhydroxylamine (DEHA) as complexing agents was based on the previously revealed [3, 4] capability for self-organization of oligomers containing electron-donating (in particular, carbonyl) groups with the formation of liquid-crystalline compounds.

For the reaction products of HPPD and HMPPD with metal complexes, we measured the third-order nonlinear susceptibility tensors $\chi^{(3)}$ and the volume resistivity ρ_v (see figure).

1070-4272/02/7509-1537$27.00 © 2002 MAIK "Nauka/Interperiodica"

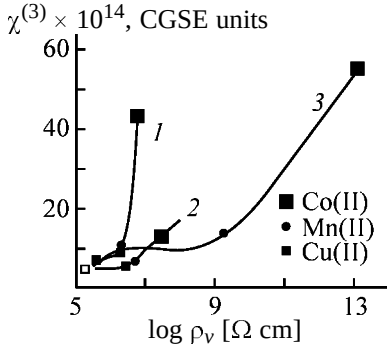

Variation of the third-order nonlinear susceptibility tensor $\chi^{(3)}$, CGSE units, with the volume resistivity ρ_v, Ω cm, for the products of the reactions between HPPD and metal complexes.

A combined study of the electrical and optical properties of the synthesized metal complexes revealed a correlation between their volume resistivity and nonlinear optical susceptibility: $\chi^{(3)}$ increases in parallel with ρ_v, and both these parameters are strongly influenced by the nature of the coordination center.

Our results can be explained by coordination bonding of the metal ion with the carbonyl group, which disturbs the conjugation system in HPPD and HMPPD, thus increasing ρ_v.

The ρ_v increment depends on the nature of the 3*d* ion. For example, with Cu(II), Mn(II), and Co(II) as coordination centers, ρ_v increases by one, four, and eight orders of magnitude, respectively.

These profound changes in ρ_v suggest that the strength of coordination bonding affects the electron density redistribution in the resonance structures of HPPD and HMPPD. For example, the greatest coordination power and, hence, the strongest disturbance of the π-electron system delocalization in compounds **I** and **II** is characteristic of the Co(II) ion, and the smallest, of the Cu(II) ion.

The coordination power of metal complexes with respect to HPPD and HMPPD is also suggested by IR spectra. For example, the absorption bands near 1650 cm^{-1}, corresponding to vibrations of the carbonyl group in HPPD, get significantly broadened, and the intensity and width of the absorption bands at 1600 cm^{-1}, corresponding to stretching vibrations of C=C double bonds, remain unchanged.

Our studies showed that increase in $\chi^{(3)}$ is due, above all, to enhanced polarizability of the HPPD and HMPPD molecules owing to changes in the electronic structure of the carbonyl group resulting from its coordination.

CONCLUSIONS

(1) Metal ions coordinated to the carbonyl group in 1,5-bis(4-hydroxyphenyl)-1,4-pentadien-3-one draw off the lone electron pair from the oxygen atom, thus disturbing the conjugation system of this compound. This increases the volume resistivity of the films from 10^5 to 10^{14} Ω cm. Increase in ρ_v tends to increase the third-order nonlinear susceptibility tensor $\chi^{(3)}$ from 5×10^{-14} to 6×10^{-13} CGSE units.

(2) The ρ_v increment is strongly influenced by the nature of the 3*d* ion. With Cu(II), Mn(II), and Co(II) as the coordination centers, ρ_v increases by one, four, and eight orders of magnitude, respectively.

ACKNOWLEDGMENTS

This work was financially supported by the Ministry of Education of the Russian Federation (project no. T 00-9.2-2106) and by the Russian Foundation for Basic Research (project no. 01-03-32 294).

REFERENCES

1. Bubeck, C., in *Nonlinear Optical Properties of Oligomers*, 1998, pp. 449–478.
2. Agrinskaya, N.V., Lukoshkin, V.A., Ten'kovtsev, A.V., and Yakimanskii, A.V., *Fiz. Tverd. Tela*, 1997, vol. 39, no. 9, pp. 1687–1689.
3. Davletbaeva, I.M., Khairutdinov, A.R., Bylinkin, R.A., and Parfenov, V.V., *Zh. Prikl. Khim.*, 2001, vol. 74, no. 5, pp. 805–808.
4. Davletbaeva, I.M., Kirpichnikov, P.A., and Rakhmatulina, A.P., in *Macromolecular Symp. on Nano-Structures in Polymer Systems*, 1996, vol. 4, pp. 87–90.

Russian Journal of Applied Chemistry, Vol. 75, No. 9, 2002, pp. 1539–1540. Translated from Zhurnal Prikladnoi Khimii, Vol. 75, No. 9, 2002, pp. 1574–1575.
Original Russian Text Copyright © 2002 by Grigor'eva, Kutepov, Makhamatkhanov, Bikbaev, Khazipova, Kovtunenko.

BRIEF COMMUNICATIONS

Oligomerization of α-Methylstyrene in the Presence of Mordenite Type Zeolite

N. G. Grigor'eva, B. I. Kutepov, R. A. Makhamatkhanov, R. T. Bikbaev, A. N. Khazipova, and I. A. Kovtunenko

Institute of Petrochemistry and Catalysis, Bashkortostan Academy of Sciences and Ufa Scientific Center, Russian Academy of Sciences, Ufa, Bashkortostan, Russia

Received October 15, 2001; in final form, January 2002

Abstract—The activity and selectivity of coarse-porous H-mordenite in synthesis of cyclic and linear dimers of α-methylstyrene were studied.

Numerous homogeneous and heterogeneous acid catalysts are used to synthesize dimers and trimers of α-methylstyrene; these include sulfuric, phosphoric, chloroacetic, and *p*-toluenesulfonic acids, cation-exchange resins [1, 2], metal oxides [3], and zeolite-like aluminophosphates [4]. However, data on the effect of zeolites in this reaction are scarce. Synthesis of linear dimers of α-methylstyrene in CH_2Cl_2 solution in the presence of zeolites Y with various Brønsted acidities was studied in [5]. Utilization of a solvent in this case requires additional stage of distillation, which complicates the process and deteriorates its feasibility characteristics.

In this work we studied oligomerization of α-methylstyrene in the presence of mordenite type zeolite.

EXPERIMENTAL

Oligomerization of α-methylstyrene was performed in a batch reactor at atmospheric pressure in the 20–140°C range. The reaction products were analyzed by gas–liquid chromatography (GLC).

The mordenite type zeolites were prepared from aqueous solutions of sodium aluminate, sodium hydroxide, and white black (samples I, II) or the waste from production of crystalline silicon (sample III) [6, 7]. The SiO_2/Al_2O_3 molar ratio in the resulting samples was 12.2 (I), 9.8 (II), and 10.0 (III). Sample I was a fine-porous (static capacity for benzene vapor 0.02 $cm^3\ g^{-1}$), and samples II and III, coarse-porous (static capacity for benzene vapor 0.11 and 0.12 $cm^3\ g^{-1}$, respectively) modifications of mordenite.

To prepare catalysts in the H form, the samples were treated with NH_4NO_3 solutions to the residual content of Na_2O ≤0.1 wt % and then calcined in air for 4 h at 540°C.

As in the case of the other acid catalysts [1–5], oligomerization of α-methylstyrene on mordenite yields the cyclic dimer c-D (1,1,3-trimethyl-3-phenylindane), linear dimers α-D and β-D (4-methyl-2,4-diphenyl-1-pentene and 4-methyl-2,4-diphenyl-2-pentene), trimers, and tetramers. The composition of the reaction products is determined by the catalyst properties and reaction conditions.

As seen from Table 1, Na-mordenite is inactive in this reaction, whereas the H-form exhibits a catalytic activity strongly depending on the pore size in the mordenite crystal lattice. No conversion of α-methylstyrene occurs at 120–140°C in 6 h with fine-porous mordenite I (10–20 wt % relative to the feed), and significant conversion *K* is observed only in the presence of 50–60 wt % of this catalyst, which suggests that the reaction proceeds predominantly at the outer zeolite surface.

In the presence of coarse-porous catalysts II and III, a mixture of α-methylstyrene oligomers is formed, and in the case of catalyst III the content of trimers and tetramers reaches 30 wt %.

Mordenite II is the most active and selective catalyst providing conversion of α-methylstyrene into the linear dimers α-D and β-D. The data on oligomerization of α-methylstyrene in the presence of this catalyst at various temperatures are listed in Table 2. The reaction starts even at a low content of catalyst II (1–2 wt %) at 60°C, with the selectivity *S* of formation of dimers α-D and β-D being 61.4%; however, the

1070-4272/02/7509-1539$27.00 © 2002 MAIK "Nauka/Interperiodica"

Table 1. Oligomerization of α-methylstyrene in the presence of mordenite type zeolite

Catalyst	c_{cat}, wt %	*T*, °C	τ, h	*K*, %	Composition, wt %			
					c-D	α-D	β-D	trimers
Na-II	1	120	10	0	–	–	–	–
	20	100	8	0	–	–	–	–
I	10	120	6	0	–	–	–	–
	20	140	6	0	–	–	–	–
	50	120	4	82.2	1.8	64.0	0.4	16.0
II	10	100	0.5	83.5	3.4	73.1	1.1	5.9
III	10	100	6	62.0	2.1	41.3	0.5	18.1
	20	120	7	94.0	17.3	31.2	19.7	25.8

Table 2. Dimerization of α-methylstyrene in the presence of mordenite II

c_{cat}, wt %	*T*, °C	τ, h	Composition, wt %				*K*, %	*S*, %
			c-D	α-D	β-D	trimers		
1	120	6	2.0	10.0	0.2	–	12.2	83.6
2	60	5	4.7	8.5	0.1	0.7	14.0	61.4
5	100	3	2.8	57.5	4.0	14.3	78.6	78.2
10	80	1	2.0	65.6	1.3	5.1	74.0	90.4
		2	3.2	70.8	2.1	11.3	87.4	83.4
10	100	0.25	3.3	64.9	0.8	5.8	74.8	87.8
		1.0	3.7	71.8	2.2	6.1	83.8	88.3
10	110	0.25	9.8	61.7	2.0	8.0	81.5	78.2
		2.0	14.6	52.7	15.8	12.7	96.8	71.2
15	100	1	4.9	78.2	0.6	8.1	91.8	85.8
20	100	1	10.2	59.6	16.3	11.2	97.3	78.0
20	140	1	93.3	–	–	6.7	100.0	–

monomer conversion is relatively low. With increasing content of the catalyst to 10–15 wt %, at 80–110°C, the conversion of α-methylstyrene reaches 97%, with 80–90% selectivity. Under the more rigid conditions, the yield of the cyclic dimer increases, and at 140°C and 20 wt % content of mordenite II the yield of c-D is 93.3 wt %.

It should be noted that mordenites II and III, having similar characteristics, differ in the catalytic properties: The conversion of α-methylstyrene and selectivity in the presence of catalyst II are significantly higher as compared to catalyst III. This is probably due to the different composition of the initial silicon-containing materials used in the mordenite preparation.

CONCLUSION

The coarse-porous H-mordenite prepared from the aqueous solutions of sodium aluminate, sodium hydroxide, and white black with the subsequent removal of cations and annealing at 540°C exhibits high activity and selectivity in oligomerization of α-methylstyrene.

REFERENCES

1. *The Chemistry of Cationic Polymerization*, Plesch, P.H., Ed., Oxford: Pergamon, 1963.
2. Chaudhuri, B. and Sharma, M.M., *Ind. Eng. Chem. Res.*, 1989, no. 28, pp. 1757–1763.
3. Kawakami, Y., Toyshima, N., Ando, T., and Yamashita, Y., *Polym. J.*, 1981, vol. 13, no. 10, pp. 947–953.
4. Isakov, Ya.I., Minachev, Kh.M., Sharf, V.Z., *et al.*, *Neftekhimiya*, 1999, vol. 39, no. 4, pp. 278–283.
5. Talzi, V.P., Doronin, V.P., Sorokina, T.P., *et al.*, *Zh. Prikl. Khim.*, 2000, vol. 73, no. 5, pp. 787–790.
6. RF Patent 2160228.
7. Pavlov, M.L., Makhamatkhanov, R.A., Kutepov, B.I., *et al.*, *Zh. Prikl. Khim.*, 2001, vol. 74, no. 2, pp. 328–330.

Russian Journal of Applied Chemistry, Vol. 75, No. 9, 2002, pp. 1541–1542. Translated from Zhurnal Prikladnoi Khimii, Vol. 75, No. 9, 2002, pp. 1576–1577.
Original Russian Text Copyright © 2002 by Morachevskii.

HISTORY OF CHEMISTRY AND CHEMICAL TECHNOLOGY

Professor Vladimir Fedorovich Alekseev (on 150th Anniversary of His Birthday)

Vladimir Fedorovich Alekseev, a prominent Russian physical chemist of the end of the XIX century, carried out a number of classical experimental investigations in the theory of solutions and heterogeneous equilibria involving liquid phases.

V.F. Alekseev was born on October 12, 1852, in St. Petersburg. He received secondary education at the Second St. Petersburg Military College. In 1867, he entered the Mining Institute and graduated from the institute as a mining engineer in 1873. Alekseev started his studies in chemistry already when being a student, under supervision of Prof. K.I. Lisenko (1836–1903), a known scientist working in the field of technical chemistry. In 1873–1877, Alekseev worked as laboratory assistant at the chemical laboratory of the Mining Institute and conducted research in preparative organic chemistry and mutual solubility of liquids. In 1877–1879, he held the position of assistant assayer at the Mint, without terminating his studies of solutions. In 1879, Vladimir Fedorovich defended his dissertation *On Mutual Solubility of Liquids* at the Mining Institute and became an adjunct at the chair of chemistry of the same institute. This was the beginning of the twenty years of Alekseev's pedagogical activities at the Mining Institute.

During his work on the dissertation, the young scientist established for the first time the existence of a temperature at which two liquid layers mix with each other in any proportion to form a homogeneous mixture. The author proposed a rather simple and original optical method for determining the mutual solubility of liquids.

The first Russian chemist to become interested in the mutual solubility of liquids was D.N. Abashev (1829–1880), a graduate from St. Petersburg University (1851) and, later, a professor of Kiev and Novorossiya (Odessa) Universities. In 1858, he defended his master's dissertation *Studies of Mutual Solubility of Liquids.* Abashev's experiments became the starting point for extensive investigations carried out in this field by Alekseev. Using the method developed by him, he obtained systematic data on the mutual solubility of a wide variety of liquids, with many of these data still found in reference books. As noted by

N.S. Kurnakov (1860–1941), "V.F. Alekseev was the first to present the facts for constructing full solubility diagrams for binary systems characterized by formation of two liquid layers" [1]. Alekseev was also the first to present experimental data on the mutual solubility in the form of graphical phase diagrams, published first geometric images of phase diagrams for liquid systems, and indicated the homogeneity and phase separation regions.

One more thing is associated with Alekseev's name, the "rectilinear diameter rule," according to which the arithmetic mean of the composition (presented in wt %) of equilibrium liquid phases varies linearly with temperature, and the point of intersection of the straight line expressing this dependence with the boundary of the phase separation region (binodal curve) corresponds to the critical solution temperature, which is a critical point [2, 3]. A detailed analysis of the history of this discovery and the evidence of Alekseev's priority have been presented [4] by S.A. Pogo-

1070-4272/02/7509-1541$27.00 © 2002 MAIK "Nauka/Interperiodica"

din, a known physical chemist and historian of chemistry.

Alekseev's active investigations into various properties of solutions and heterogeneous equilibria involving such solutions were carried out since 1875 until 1886. During this period of time, he published 17 papers and made 31 reports at meetings of the Russian Physicochemical Society. To elucidate the nature of solutions, the scientist studied a wide variety of their properties: specific heat, heats of mixing, saturated vapor pressure, and surface tension. In contrast to the standpoint of D.I. Mendeleev (1834–1907), Alekseev believed that chemical interaction is not a necessary condition for dissolution. Later, I.F. Shreder (1858–1918), also a professor of the St. Petersburg Mining Institute, considered solutions with the minimum extent of chemical interaction between their components as a special group of solutions. Alekseev believed that the fundamental aspects of behavior are the same for widely diverse classes of solutions, including metal alloys. However, alloys were the subject of only a single Alekseev's paper concerned with the mutual solubility of bismuth and mercury. A detailed analysis of Alekseev's works in the field of mutual solubility of liquids and solution properties can be found in a paper by Ya.I. Gerasimov [5] and monograph by A.Ya. Kipnis [6].

Together with studying various solutions, Alekseev paid much attention to general problems of the chemical thermodynamics of that time. In 1884, he published an interesting "Treatise of the Present State of Chemical Mechanics" [*Gornyi Zhurnal* (Journal of Mining), 1884] devoted to the theory of chemical equilibrium. The treatise, in particular, read: "Chemical mechanics plays an exceedingly important role in applied chemistry, and clear understanding of at least such fundamental processes as, e.g., the evergreen Bessemer process and blast-furnace melting is impossible without it" [7]. Here, the works of H. Saint-Clair Deville (1818–1881), a French chemist, in the field of thermal dissociation and theory of chemical equilibrium are meant in the first place. The same treatise presented, for the first time in the Russian chemical literature, the notion of entropy and also gave an account of J. Gibbs' (1839–1903) equilibrium principle.

In 1886, Alekseev ceased studies of solutions and devoted himself entirely to problems of applied chemistry. In Kurnakov's opinion [1], "... the reason why this occurred is V.F.'s passionate and not always balanced temper, a financial position that became complicated, and changes in his social standpoint under the influence of Leo Tolstoy's concepts." Alekseev started to study coals and peat and developed methods for testing these. In 1895, he published his fundamental work "Fossil Coals of the Russian Empire and Their Composition" (St. Petersburg, 1895). To achieve an efficient use of peat deposits in northern regions of Russia, Alekseev founded a special laboratory in St. Petersburg and a peat plant in Tver Province.

After 25 years of service at State institutions, Alekseev ceased teaching at the Mining Institute and retired. Beginning in 1901, he lived at his Sosno manor in the Vyshni Volochek District of Tver Province, where he did farming, studied problems of peatery, and was engaged in social activities. He died on September 12, 1919. The obituary written by Academician Kurnakov read: "The general chemistry and its new field, physicochemical analysis, lost in V.F. Alekseev's person an outstanding researcher, whose works will undoubtedly grow in importance for the understanding of the fundamental properties of equilibrium systems with the development of science" [1]. Later (in 1928), he noted: "Three chemists, V.F. Alekseev, D.P. Konovalov, and I.F. Shreder, originating from the chemical laboratory of the Mining Institute, had great impact on the development of such a field of general chemistry as physicochemical analysis" [8].

REFERENCES

1. Kurnakov, N.S., *Izv. Inst. Fiz.-Khim. Anal.*, 1922, vol. 2, pp. 1–4.
2. Gerasimov, Ya.I., Dreving, V.P., Eremin, E.N., *et al.*, *Kurs fizicheskoi khimii* (A Course of Physical Chemistry), Moscow: Goskhimizdat, 1963, vol. 1.
3. Anosov, V.Ya., Ozerova, M.I., and Fialkov, Yu.Ya., *Osnovy fiziko-khimicheskogo analiza* (Fundamentals of Physicochemical Analysis), Moscow: Nauka, 1978.
4. Pogodin, S.A., *Usp. Khim.*, 1950, vol. 19, no. 1, pp. 125–127.
5. Gerasimov, Ya.I., *Materialy po istorii otechestvennoi khimii* (Materials on the History of Domestic Chemistry), Moscow: Akad. Nauk SSSR, 1950, pp. 52–62.
6. Kipnis, A.Ya., *Razvitie khimicheskoi termodinamiki v Rossii* (The Development of Chemical Thermodynamics in Russia), Moscow: Nauka, 1964.
7. Solov'ev, Yu.I., *Ocherki po istorii fizicheskoi khimii* (Studies of the History of Physical Chemistry), Moscow: Nauka, 1964.
8. Solov'ev, Yu.I., *Nikolai Semenovich Kurnakov: 1860–1941*, Moscow: Nauka, 1986.

A. G. Morachevskii

Russian Journal of Applied Chemistry, Vol. 75, No. 9, 2002, pp. 1543–1544. Translated from Zhurnal Prikladnoi Khimii, Vol. 75, No. 9, 2002, pp. 1578–1579.
Original Russian Text Copyright © 2002 by Andreikov.

BOOK REVIEWS

Volkov, V.L., Zakharova, G.S., and Bondarenka, V.M., *Kserogeli prostykh i slozhnykh polivanadatov* (Xerogels of Simple and Complex Polyvanadates)

Yekaterinburg: Inst. Khimii Tverdogo Tela, Ural. Otd., Ross. Akad. Nauk, 2001, 194 pp.

The appearance of this book has been stimulated not only by achievements in the understanding of the nature of hydrated vanadium(V) oxide, but, to no lesser extent, by success in use of its unique properties for creating practically important materials. The present level in this field has been attained mainly owing to fruitful investigations of several research groups, one of which is constituted by the authors of the monograph in question, well familiar with the object of study.

The monograph generalizes the results of investigations of synthesis procedures, chemistry, and physicochemical properties of simple and complex polyvanadates with vanadium(V) oxide structure and possible ways of their use. The book comprises 5 chapters, 67 figures, 35 tables, and a list of 411 references.

The first chapter presents results of X-ray diffraction and structural studies of hydrated and anhydrous vanadium(V) and (VI) oxides, and also data on synthesis and structure of a xerogel of vanadium(V) oxide, which is a solid polyvanadic acid $H_2V_{12}O_{31-\delta}\cdot nH_2O$. The structure of vanadium(V) oxide xerogel forms a basis for polyvanadate xerogels, compounds in which part of vanadium atoms in vanadium–oxygen layers are replaced by elements of Groups IV–VI or interlayer protons are displaced by other cations.

The second chapter considers xerogels of polyvanadates of mono-, di-, and trivalent metals. These compounds are represented as hydrated interstitial alloys of variable composition, isostructural to polyvanadic acid. The state of vanadium and oxygen–hydrogen groups in xerogels have been studied using ESR, ^{1}H NMR, and XPE spectroscopy.

The third chapter generalizes the results obtained in studying xerogels of complex polyvanadates obtained through substitution of vanadium ions in $V_2O_5\cdot nH_2O$ xerogels by tetra-, penta-, and hexavalent ions. The best studied were xerogels of polyvanadomolybdic acid and polyvanadomolybdates of alkali metals, for which thermal dehydration patterns, structural characteristics, and evidence concerning the valence state of vanadium and molybdenum ions have been obtained. Data on xerogels obtained by substitution of vanadium by tungsten, selenium, rhenium, titanium, silicon, germanium, and antimony are presented. Also considered are closely related layered compounds isostructural to vanadium phosphates, obtained through introduction of metal cations and of organic and organometallic compounds into the interlayer space of phosphovanadates.

The fourth chapter considers physicochemical properties of polyvanadate xerogels, which are governed by the properties of both the basic polymeric vanadium–oxygen lattice and cations and molecules introduced into the interlayer space. Readily obtainable as films, xerogels have layered structure with weak interaction between layers, into which both metal cations and organic or organometallic molecules can be intercalated. Intercalation of organic compounds may be accompanied by redox reactions, which are of interest as means of obtaining oligomers and polymers of such compounds as pyrrole, aniline, and ethylene oxide, with unique electrical properties. The chapter presents thermodynamic data characterizing the state in xerogels of water molecules with different types of chemical bonding with the matrix, and also that of hydrogen and lithium ions.

The chapter also describes investigations of the electrical conductivity of polyvanadate xerogels, including those in the form of films, whose electrical properties exhibit clearly pronounced anisotropy. The conductivity of compounds studied is constituted by electronic and protonic components, and is determined both by their chemical composition and by the content of water, which, in turn, depends on the moisture content of the medium. The possibility of widely varying the physicochemical properties of xerogels by changing the chemical composition of both the main lattice and the interlayer components enables control over the semiconducting, optical, magnetic, and inter-

1070-4272/02/7509-1543$27.00 © 2002 MAIK "Nauka/Interperiodica"

calation properties of xerogels, which creates prerequisites for their practical use.

The fifth chapter considers directions of practical application of polyvanadate xerogels. The high mobility of lithium ions in the interlayer space of polyvanadates stimulated their studies as cathode materials for chemical power cells with lithium anode. The specific energy of lithium incorporation into electrode materials was 1137 W h kg^{-1} for V_2O_5 xerogel. Polyvanadate xerogels are of interest as solid electrolytes with ionic conduction and as electrochromic and sensor materials.

Vanadium oxide gels show promise as precursors of supported vanadium catalysts obtainable by the sol–gel method, which makes it possible to achieve deposition uniformity, highest homogeneity, and good adhesion to substrate of nanoparticles of the active component.

Polyvanadate xerogels can also serve as starting compounds for "mild" synthesis (at temperatures below 500°C) of vanadium oxide compounds, including structures that cannot be obtained at higher temperatures. Recent studies in this field have been concerned with application of the given process to synthesis of vanadium oxide nanotubes.

In conclusion, the authors emphasize that the achieved level of fundamental knowledge in the field of vanadate xerogels and the development of simple methods for their synthesis in the form of finely dispersed powders and films provide a basis for their wide practical application. The book will undoubtedly be of interest both to specialists in inorganic and solid-state chemistry and to researchers using vanadium compounds in various fields of science and technology.

E. I. Andreikov

Russian Journal of Applied Chemistry, Vol. 75, No. 9, 2002, pp. 1545–1546. Translated from Zhurnal Prikladnoi Khimii, Vol. 75, No. 9, 2002, pp. 1580–1581.
Original Russian Text Copyright © 2002 by Morachevskii.

BOOK REVIEWS

Kedrinskii, I.A. and Yakovlev, V.G., *Li-ionnye akkumulyatory* (Li-Ion Batteries)

Krasnoyarsk: Platina, 2002, 268 pp.

In the last 3 decades, R&D work in the field of lithium power cells has led to appreciable positive results. This is largely associated with the unique technical characteristics of lithium power cells, higher energy density as compared to the conventional chemical power cells, wide range of working temperatures, and use of relatively inexpensive and readily available materials. However, the development of secondary lithium power cells encountered difficulties in ensuring reversible operation of the lithium electrode, which are associated with the high chemical activity of lithium toward the electrolyte solutions employed. For primary lithium power cells, the formation of a passivating film on the lithium surface has a positive effect: it protects the metal from corrosion in the solvent. At the same time, passivation is a serious obstacle in development of lithium batteries on the basis of aprotic organic solvents.

In the 1990s, secondary lithium power cells using no metallic lithium in their design have been widely recognized. These cells employ as electrode materials various compounds of transition metals (oxides, chalcogenides), graphite, and other materials that can intercalate and deintercalate lithium ions. When a battery of this kind is being charged, lithium ions are deintercalated from the cathode and reversibly intercalated into the anode material. Discharge involves deintercalation of lithium from the anode and its intercalation into the cathode. Chemical power cells of this kind have been named lithium-ion batteries. Much has been done for promotion of these batteries at the world market by Japanese companies. The book by A.I. Kedrinskii and V.G. Yakovlev is the first domestic monograph concerned with lithium-ion batteries.

The book comprises 17 relatively small chapters, each with its own reference list. The brief introduction (pp. 5–9) explains the principle of operation of Li-ion batteries and presents a list of abbreviations and designations. The following types of Li-ion batteries are distinguished: batteries with liquid electrolyte (LiIB) and those with solid or thickened electrolyte with a polymeric basis, organic or inorganic (PLi-IB). The book is mainly concerned with batteries of the first type (Li-IB).

Chapter 1 (pp. 10–18) gives general characterization of Li-ion batteries. Their main rivals, Ni–Cd and Ni–MH batteries, have a voltage of 1.25 V and energy densities of 40–60 and 60–80 W h kg^{-1}, respectively. For Li-IA, these highly important characteristics are 3.6 V and 100–150 W h kg^{-1}.

Chapters 2 (pp. 19–22), 3 (pp. 23–30), and 4 (pp. 31–41) describe, respectively, the mechanism of Li-IB operation, the intercalation process, and the crystal structure of the electrode materials. Chapter 5 is primarily concerned with analysis of components of the equilibrium electrode potential of the intercalate. The authors put emphasis on the specificity of its nature. Chapters 6 (pp. 59–81) and 7 (pp. 82–102) discuss the charging of Li-IB and kinetic characteristics of the intercalation and deintercalation processes. Chapters 8 (pp. 103–115) and 9 (pp. 136–158) analyze the requirements imposed on the materials for the positive and negative electrodes of a battery. Chapter 10 (pp. 159–174) considers the electrolyte properties. Chapter 11 (pp. 175–193) briefly describes basic physical (X-ray phase analysis, various spectroscopies) and electrochemical (chronopotentiometry, cyclic voltammetry, impedance measurements) techniques for studying processes and materials related to Li-IB. Chapter 12 presents methods for studying and testing both separate electrodes and batteries as a whole under laboratory and industrial conditions. A small chapter 13 (pp. 213–215) outlines the history of development of Li-IB. Chapter 14 (pp. 216–232) describes the assortment and characteristics of commercial articles manufactured by leading foreign companies. The undeniable priority in manufacture of Li-IB for domestic appliances belongs to Japan. The leading position in development and manufacture of industrial batteries belongs to France. Chapters 15 (pp. 233–251), 16 (pp. 252–264), and 17 (p. 265) are devoted to analysis of the world market of Li-IB,

1070-4272/02/7509-1545$27.00 © 2002 MAIK "Nauka/Interperiodica"

promising theoretical and applied research aimed to improve Li-ion batteries, and investigations carried out in this field in Russia and CIS countries.

The book has a peculiar structure: each chapter is, in fact, an independent review of the present state of affairs concerning one or another problem. The chapters come in a certain logically substantiated order, but there is no close relationship between them. This makes the monograph more a reference book, as regards the manner of presentation. The authors of the book made a major contribution to investigations of lithium power cells in our country, they could combine the rather high scientific level of presentation with simplicity for a wide audience of readers.

A. G. Morachevskii

Russian Journal of Applied Chemistry, Vol. 75, No. 10, 2002, pp. 1547–1556. Translated from Zhurnal Prikladnoi Khimii, Vol. 75, No. 10, 2002, pp. 1585–1593.
Original Russian Text Copyright © 2002 by Ertseva, Tsymbulov.

REVIEWS

On Transformations of Iron, Nickel, and Cobalt Arsenides and Sulfoarsenides under Thermal Treatment in Various Media

L. N. Ertseva and L. B. Tsymbulov

Institut Gipronikel' Joint-Stock Company, St. Petersburg, Russia

Abstract—Published data on phase transformations of iron, nickel and cobalt arsenides and sulfoarsenides under thermal treatment are reviewed.

Arsenide and sulfoarsenide minerals constitute a major part of ores in a number of technologically important cobalt deposits in Morocco (Bou-Azzer), Canada (Werner Lake), US (Sunshine), and Russia (Tuva) [1–3]. Possible products of their high temperature treatment are highly toxic arsenic compounds. In this context, evidence concerning transformations of main arsenic-containing minerals of nickel, cobalt, and iron under thermal treatment is necessary in studying the behavior of arsenide and sulfoarsenide minerals in ore raw materials [4].

The present review systematizes and analyzes the relevant published data.

1. EQUILIBRIUM DIAGRAMS

Transformations occurring when a complex compound is heated are largely determined by phase equilibria in the corresponding systems at a particular temperature. There is a vast body of published data on double (M–As) and more complex (M(M')–As–S) equilibrium diagrams. The most complete review of binary and ternary phase diagrams, with reference to original sources, was made in [5], with the studies reviewed aimed in the first place at analysis and prognostication of mineral-formation in ore deposits and, therefore, emphasis placed upon the agreement or disagreement of the real mineral associations with the phase associations of the equilibrium system.

According to results of various studies [6–20], the following compounds exist in the systems Co–As, Fe–As, Ni–As: Co_2As, Co_3As_2, CoAs, $CoAs_2$ (natural analogue safflorite), $CoAs_{3-x}$ (natural analogue skutterudite), Fe_2As, FeAs, Fe_3As_2, $FeAs_2$ (natural analogue loellingite, $NiAs_2$ (natural analogues rammelsbergite and pararammelsbergite), $Ni_{5-x}As$, $Ni_{11}As_8$ (natural analogue maucherite), $Ni_{1\pm x}As$ (natural analogue nickeline), and Ni_2As with parameters close to those of orsellite mineral.

In the systems Co–Fe–As, Co–Ni–As, and Fe–Ni–As, an extended region of a ternary solid solution formed by $CoAs_{3-x}$ and $FeAs_3$ (up to 24 wt %) has been established. The compound $CoAs_2$ corresponds to the end member of the safflorite $(Co,Fe)As_2$ mineral series. The solid solution of $CoAs_2$ and $FeAs_2$ is complete when a temperature of 800°C is reached. A large region of ternary solid solutions of $CoAs_{3-x}$ and $NiAs_3$ (up to 65 wt %) at 800°C and complete solubility between $NiAs_2$ and $CoAs_2$ in solid state has been found. A ternary phase, $(Fe,Ni)As_{3-x}$, corresponding to skutterudite stable at 800°C in the range 49.5–76 wt % $NiAs_3$, has been demonstrated. The mutual solubility of $NiAs_2$ and $FeAs_2$ is incomplete: it covers compositions from $FeAs_2$ to ~70 wt % $NiAs_2$ and from $NiAs_2$ to ~6 wt % $FeAs_2$. A second ternary phase, $(Fe,Ni_2)As$, corresponding to oregonite mineral has been synthesized. The Fe–As–S system has an only ternary compound, arsenopyrite FeAsS. The only ternary phase in the Ni–As–S system, corresponding to the gersdorffite mineral with commonly accepted formula NiAsS, shows widely varying As/S ratio. It is homogeneous from $NiAs_{1.77}S_{0.23}$ to $NiAs_{0.77}S_{1.23}$ at 700°C. With increasing M/(As + S) ratio, there exist a continuous series of solid solutions of $Ni_{1\pm x}As$ and $Ni_{1-x}S$ (700°C) with general formula Ni(As,S). The decomposition temperature of this solid solution into $Ni_{1\pm x}As$ and $Ni_{1-x}S$ at varied As/S ratio has been established. In contrast to Fe–As–S and Ni–As–S, the system Co–As–S has been studied insufficiently. The section CoS_2–$CoAs_2$ has been analyzed in part in studying the stability of cobaltine and alloclasite in the systems Co–As–S and Co–Ni–As–S. The composition of cobaltine on the $CoAs_2$ side corresponds to the formula CoAsS, whereas the boundary on the CoS_2 side has not been determined. It has been

1070-4272/02/7510-1547 $27.00 © 2002 MAIK "Nauka/Interperiodica"

established that sulfur cannot be substituted by arsenic in the cobaltine lattice at any temperature without structural transformations. Replacement of cobalt by nickel must stabilize the cobaltine structure at arsenic content higher than that in CoAsS. It has been established that any metal replacements to form solid solutions are possible between FeS_2, CoS_2, NiS_2, CoAsS, and NiAsS. The extension of these solutions in the system FeAsS–CoAsS–NiAsS has been determined.

2. PHASE TRANSFORMATIONS UNDER THERMAL TREATMENT

2.1. Nickel Arsenides and Sulfoarsenides. First publications concerning the thermal stability of arsenide minerals of nickel appeared in the early 1960s. In [21], DTA curves obtained in air for nickeline (two deposits) and gersdorffite were reported. The heating rate was 500 deg h^{-1}, and the grain size of the material, 300 μm. It was established that, in nickeline oxidation, exothermic effects occur in the temperature range 450–700°C and are represented by triple overlapping peaks (with the second peak weakly pronounced), and in the case of gersdorffite, at 350–650°C, also with a triple exothermic peak (with the second, poorly pronounced peak). The authors attributed the appearance of several peaks to the existence of successive transformation stages (as yet unknown). It was shown that the heat of oxidation of the minerals studied, calculated in curve processing, can be found to a first approximation on the basis of their chemical composition. The presence of NiO and Fe_2O_3 in products obtained at temperatures higher than the oxidation temperature was obseved. In [9], DTA curves obtained in air for three compounds: orsellite, maucherite, and nickeline, were presented in describing a new mineral—orsellite. The richer a mineral in the metal, the higher the onset temperature of the effects: 400°C for nickeline (a total of three effects), 575°C for maucherite (two effects), and 600°C for orsellite (a single effect). Comparison of the obtained DTA curves with mass loss (TG) curves suggests that the oxidation occurs in two stages. The first stage, characterized by loss of mass as a result of partial removal of arsenic(IV), is accompanied by enrichment with the metal:

$$\mathrm{NiAs} \rightarrow \mathrm{Ni_{1.2}As} \rightarrow \mathrm{Ni_{1.5}As\,(maucherite)} \rightarrow \mathrm{Ni_2As\,(orsellite)}. \quad (1)$$

The second stage is characterized by mass gain caused by the formation of a mixture of Ni(II) oxide and diarsenate:

$$\mathrm{Ni_2As + O_2 \rightarrow NiO + Ni_2As_2O_7}. \quad (2)$$

A detailed study of the behavior of arsenides, sulfides, and sulfoarsenides in thermal analysis in air was reported in [22]; DTA was applied to classify oxidation reactions of 19 minerals, including nickeline, gersdorffite, cobaltine, and skutterudite (heating rate in air 12 deg min^{-1}, grain size of material −400 + 200 μm). All the exothermic effects revealed in the DTA curves have been attributed to oxidation [22]. After each thermal effect, the reaction products formed were identified by X-ray phase (XPA) and chemical analyses. It was established that the reactions of nickeline and gersdorffite oxidation are of different types. In nickeline oxidation, there occurs partial oxidative removal of the nonmetal, with a single or several metal-enriched arsenides remaining in the residue. At 500°C, nickeline is converted into maucherite, which is further transformed into orsellite at 680°C; then, the metal is oxidized. The scheme of nickeline oxidation is as follows.

$$\mathrm{NiAs + O_2 \rightarrow Ni_{11}As_8 + As_2O_3(g) \rightarrow Ni_2As + Ni_3As_2O_8 + NiO + As_2O_3(g)}^{1} \rightarrow \mathrm{Ni_3As_2O_8 + NiO + As_2O_3(g)}. \quad (3)$$

For gersdorffite, there occurs complete oxidation and removal of arsenic, with sulfur remaining in the residue—sulfide (400–450°C).

$$\mathrm{NiAsS + O_2 \rightarrow NiS + As_2O_3(g) \rightarrow NiO + SO_2(g)}. \quad (4)$$

Domestic investigations [23–25] have been aimed to reveal specific features of DTA of minerals, including gersdorffite, arsenopyrite, and cobaltine. The final objective of these studies was to use DTA for identification of these minerals and to find conditions for their selective oxidation. The authors analyzed the behavior of the minerals heated in an inert medium with protection from oxidation. The heating rate was 10–15 deg min^{-1}, and the grain size of the materials, about 0.05 mm. The products were identified by XPA and chemical analysis.

---

[1] One of the main characteristics of any equilibrium between a condensed phase and vapor is the change in the composition of equilibrium phases in the course of evaporation. Analysis of reactions in which As_4S_4, As_4O_6, and As_2O_3 are formed not always makes clear their aggregative state. Commonly, the formula As_2O_3 characterizes the solid state, and the formula As_4O_6, the gaseous state. We ventured to give the schemes and reaction equations as it was done by the authors of [22].

In the case of heating in an inert medium, the authors noticed an endothermic effect at 800–860°C and presented the following scheme of gersdorffite transformations:

$$(Ni,Fe)AsS \rightarrow NiAs + (Ni,Fe)_9S_8 + Fe_{1-x}S + As_4S_4 + As_4. \quad (5)$$

Chunaeva and co-authors have studied the thermal stability of synthetic gersdorffite and cobaltine in an inert medium [26–28]. A tentative scheme of gersdorffite decomposition at 830°C was suggested [26]

$$20NiAsS \rightarrow Ni_9S_8 + Ni_{11}As_8 + 3As_4S_4(g) \quad (6)$$

and an opinion was voiced that more complete removal of arsenic requires higher temperature, vacuumization, or addition of a sulfidizing agent.

In [27], stages of gersdorffite decomposition were considered:

$$8NiAsS \xrightarrow{750-770^\circ C} 4NiAs + 4NiS + As_4S_4(g) \quad (7)$$

and, further,

$$36NiAs + 36NiS \rightarrow 4Ni_{11}As_8 + 4Ni_7S_6 + As_4S_4(g) + 4S_2 \quad (8)$$

with $Ni_{11}As_8$ considered molten.

The overall reaction is as follows

$$72NiAsS \xrightarrow{800^\circ C} 4Ni_{11}As_8 + 4Ni_7S_6 + 6As_4S_4(g) + 8As_2S_3.^2 \quad (9)$$

The authors made a conclusion that the process occurs in two stages: (1) decomposition proper and (2) interaction of decomposition products whose phase composition was determined by XPA.

In our opinion, the presence of NiAs and NiS in the products formed at 750–770°C is in the first place due to decomposition of the solid solution M(As, S) [14], formation of $Ni_{11}As_8$ is accounted for by decomposition of nickeline [9, 22], and conversion $NiS \rightarrow Ni_7S_6$ is associated with partial removal of sulfur. Thus, the interaction of the products formed in decomposition of gersdorffite by reaction (9) seems to be unlikely, and the final composition is determined by successive transformations of the products formed in the first stage of decomposition.

Wilson and Mikhail's work [30], one of later and more detailed studies, is devoted to dissociation and oxidation of nickeline. The authors compare the results obtained in [9, 21, 22], attributing some data discrepancy to the uncertainty of composition of compounds in the system Ni–As. The dissociation of nickeline (synthetic and natural) in an inert medium and the effect of particle size and partial pressure of oxygen on the oxidation process was studied by DTA, TG, XPA, spectral, and chemical analyses. Heating rate, 6–7 deg min^{-1}; grain size of synthetic and natural nickeline, –90 + 74 μm and –38, –53 + 45, –105 + 74 μm, respectively; partial pressure of oxygen, 0.05, 0.21, 0.50, and 1.0 atm.

Wilson and Mikhail identified successively NiAs, $Ni_{11}As_8$, and Ni_5As_2 in products of dissociation of synthetic nickeline (according to the DTA curve showing an endothermic effect at around 850°C) and suggested the following scheme of thermal decomposition

$$11NiAs \rightarrow Ni_{11}As_8 + \frac{3}{4}As_4, \quad (10)$$

$$5Ni_{11}As_8 \rightarrow 11Ni_5As_2 + \frac{9}{2}As_4. \quad (11)$$

The loss of mass begins for natural nickeline at a temperature approximately 40°C higher than that in the case of the synthetic compound; further, the rate at which mass is lost by natural NiAs is lower than that of the synthetic material. Dissociation is independent of grain size within the limits 45–105 μm.

The liquid phase may appear in the system at $T > 800^\circ C$ [8]; the authors of [30] name three possible causes of melting: $[Ni_{5-x}As_2 + Ni_{11}As_8]$, eutectic reaction at 818 ± 5°C; incongruent melting of $Ni_{11}As_8$ (830 ± 5°C); overall melting at $T > 818^\circ C$.

The most probable of these is the first one.

In oxidizing heating of natural nickeline in pure oxygen, steplike oxidation was revealed (four exothermic peaks and three steps of mass change):

$$11NiAs + \frac{9}{4}O_2 \rightarrow Ni_{11}As_8 + \frac{3}{4}As_4O_6, \quad (12)$$

$$5Ni_{11}As_8 + \frac{27}{2}O_2 \rightarrow 11Ni_5As_2 + \frac{9}{2}As_4O_6, \quad (13)$$

$$Ni_5As_2 + 4O_2 \rightarrow 5NiO + \frac{1}{2}As_4O_6, \quad (14)$$

$$3Ni_5As_2 + 17O_2 + As_4O_6 \rightarrow 5Ni_3As_2O_8. \quad (15)$$

[2] It should be noted that representation of As_2S_3 in the gas phase by this formula is conventional, the true composition of the vapor of this compound being complex [29].

Reactions (12) and (13) may occur in two stages, including thermal dissociation of arsenide to give As_4 and oxidation of As_4 to As_4O_6(g).

The authors of [30] have presented dependences of the intensity and position of endothermic peaks (oxidation stages) on particle size and partial oxygen pressure. The particle size determines the intergranular spaces filled with oxidation products; the partial pressure governs the extent of formation of impermeable oxide layers hindering the oxidation reaction and the extent of nickel arsenate formation. The results obtained indicate that complete removal of arsenic from ores in their calcination in inert and oxidizing atmospheres is unattainable.

In monograph [29], it was noted that higher nickel arsenides dissociate in inert and reducing atmospheres, whereas in oxidizing atmosphere, they are oxidized to give arsenic(III) oxide and thermally stable arsenates $NiO \cdot As_2O_5$; however, the book contains no reference to concrete investigations concerned with this issue.

When carrying out [31, 32], we were not aware of a part of investigations mentioned above; however, the use of direct techniques for determining the composition of the transformation products, electron microscopy and microprobe analysis, allowed us to suggest a scheme of nickeline oxidation

$$NiAs + O_2 \rightarrow Ni_{11}As_8 \rightarrow Ni_5As_2 \rightarrow NiO \rightarrow Ni_3(AsO_4)_2 \quad (16)$$

totally coinciding with those presented in most of the reports cited.

It has also been established that thermal dissociation of gersdorffite occurs to give a solid solution M(As, S) with As/S ratio of about unity

$$MAsS \rightarrow M(As,S) + \frac{1}{4}As_4S_4(g), \quad (17)$$

with further solid-phase decomposition into MAs and MS.

According to the data obtained in [32], formation of some or other products of gersdorffite oxidation is determined both by the temperature and time of calcination and by conditions under which the material interacts with the gas phase and its oxidizing capacity. Under the conditions used in experiments, a number of products are formed successively, of which the primary is the solid solution M(AsS) with A/S ≈ 0.1–0.3:

$$MAsS + O_2 \begin{cases} \rightarrow M_2(AsO_4)_3 \\ \rightarrow M(AsS) \rightarrow MS \rightarrow MSO_4 \rightarrow MO. \end{cases} \quad (18)$$

The results obtained confirm the fact that arsenic is mainly removed from gersdorffite in oxidizing calcination, established in [22].

2.2. Cobalt Arsenides and Sulfoarsenides. Thermal dissociation of higher cobalt arsenides has been studied in sufficient detail; however, there has been no common opinion regarding the temperatures, stages, and products of transformations.

Isabaev and co-authors [33] have analyzed the available data on thermal stability of $CoAs_2$ and presented experimental results obtained in studying the decomposition of synthetic safflorite (heating rate 8–10 deg min^{-1}):

$$8CoAs_2 \xrightarrow{870°C} 4Co_2As_3 + As_4, \quad (19)$$

$$4Co_2As_3 \xrightarrow{940°C} 8CoAs + As_4. \quad (20)$$

The product composition was confirmed by XPA.

In [34], the thermal behavior of synthetic higher arsenides $CoAs_2$ and $CoAs_3$ was studied with the gas (N_2) flow rate varied between 35 and 65 ml min^{-1} and heating rate of 5–4 deg min^{-1}. Analysis of TG curves revealed a two-stage decomposition of $CoAs_3$ (gas flow rate 50 ml min^{-1}):

$$CoAs_3 \xrightarrow{500–850°C} CoAs_2 + \frac{1}{4}As_4, \quad (21)$$

$$CoAs_2 \xrightarrow{750–950°C} CoAs + \frac{1}{4}As_4 \quad (22)$$

and single stage decomposition of $CoAs_2$

$$CoAs_2 \xrightarrow{550–950°C} CoAs + \frac{1}{4}As_4. \quad (23)$$

The onset of decomposition is independent of the heating rate, and the temperature of process completion grows with increasing heating rate.

DTA was performed at a heating rate of 20 deg min^{-1}. The DTA curve for $CoAs_3$ shows two endothermic peaks at 830 and 980°C, and that for $CoAs_2$, a single peak at 980°C, which correspond to decomposition to, respectively, $CoAs_2$ and CoAs. The starting material at 450°C and products sampled at 590, 700, 730, 810, and 878°C were analyzed. Only a single intermediate, $CoAs_2$, was found between $CoAs_3$ and CoAs. At 878°C, trace amounts of Co_2As, the presumed product of CoAs decomposition at temperatures below 940°C (the lower stability limit of Co_3As_2), were found.

The following results have been obtained in studying the oxidizing heating of cobalt arsenides. Asensio and Sabatier [21] presented DTA curves measured in

air for skutterudite from two deposits. The curves show a single exothermic peak at about 600–650°C. Cobalt oxides were identified in the products, and the oxidation heat of the material was calculated.

In [22], a single endothermic peak was also found at around 600°C in the DTA curve measure in air for natural skutterudite of composition $(Co_{0.6}Ni_{0.3}Fe_{0.1})As_3$. The reaction products contain a complex arsenate or a mixture of arsenates of general formula $5(CoO \cdot NiO \cdot FeO) \cdot 2As_2O_5$. The authors noted the lack of data that can be used to completely identify the X-ray diffraction pattern. Thus, arsenic is partly removed only in the form of As_2O_3. No other data on oxidation of cobalt arsenides could be found in the literature.

Oxidation-free heating of natural cobaltine has been studied by Shlyapkina [24], and a decomposition scheme of iron-containing cobaltine was suggested

$$(Co,Fe)AsS \xrightarrow{885-905^\circ C} CoS_2 + Fe_{1-x}S + As_4S_4 + As_4 + S_2. \quad (24)$$

Noteworthy is the fact that the decomposition products contain no cobalt arsenides.

Dissociation of synthetic CoAsS was studied in [26, 33, 35], and the following decomposition schemes were presented in [26]:

$$2CoAsS \xrightarrow{870^\circ C} CoS_2 + CoAs_2, \quad (25)$$

$$4CoS_2 + 4CoAs_2 \xrightarrow{950^\circ C} 4CoS + 4CoAs + As_4S_4(g) \quad (26)$$

and further refined in [33, 35]:

$$8CoAsS \xrightarrow{850^\circ C} 4CoS + 4CoAs + As_4S_4(g). \quad (27)$$

In the authors' opinion, the forming Co_2As_3 reacts, in the initial stage of cobaltine dissociation, with sulfur:

$$16CoAsS \rightarrow 8CoS + 4Co_2As_3 + As_4S_4 + 2S_2, \quad (28)$$

$$4Co_2As_3 + 2S_2 \rightarrow 8CoAs + As_4S_4. \quad (29)$$

Further,

$$48CoS + 42CoAs \xrightarrow{890^\circ C} 12Co_4S_3 + Co_3As_2 + 3As_4S_4 + \frac{1}{2}As_4. \quad (30)$$

The overall reaction is as follows:

$$96CoAsS \rightarrow 12Co_4S_3 + 6CoS + 14Co_3As_2 + 15As_4S_4(g) + \frac{1}{4}As_4. \quad (31)$$

Since the authors used in study the same investigation techniques—DTA, XPA, and chemical analysis, the results obtained are questionable, since CoS_2 and $CoAs_2$ or CoAs and CoS are named as dissociation products at the same temperatures (850–870°C).

Pashinkina and co-authors [36] have calculated the chemical equilibria in the systems Co–As–S at 973 K and Co–As–S–O at 1200 K and constructed partial pressure diagrams. The results obtained account for the specific features of thermal dissociation and oxidation of CoAsS. The authors believe that the equilibrium MAsS → MS + 1/4 As_4 is not monovariant in the system Co–As–S, and, therefore, it is difficult to judge the thermal stability of cobaltine on the basis of the data of [25]. The run of equilibrium curves in the partial pressure diagram of the system Co–As–S (923 K) in the coordinates $\log P_{S_2}$–$\log P_{As_4}$ points to a higher thermal stability of CoAsS with respect to liberation of arsenic, compared with that of arsenopyrite, but CoAsS is less stable with respect to reactions associated with liberation of sulfur. At equilibrium between cobaltine and higher cobalt arsenides, the content of As_4S_4 in the gas phase is higher than that in the equilibrium FeAsS–$FeAs_2$. Thus, the scheme (24) of CoAsS decomposition could be only operative (with account of the higher temperatures) in the case of selective removal of arsenic (with increasing $P_{As_4S_4}$, P_{S_2} and decreasing P_{As_4}), and scheme (31), in the case of a simultaneous decrease in P_{S_2}, P_{As_4}, and $P_{As_4S_4}$, i.e., with simultaneous removal of sulfur and arsenic. As for CoAsS oxidation, it follows from the diagram obtained for a part of the system Co–As–S–O (P_{SO_2} = 0.5 atm) that cobalt arsenates can only be formed via the stage of CoO formation:

$$CoAsS + O_2 \rightarrow CoO \rightarrow 3CoO \cdot As_2O_5 \rightarrow 2CoO \cdot As_2O_5. \quad (32)$$

Asensio and Sabatier [21] have established, when performing DTA of natural cobaltite in air, the presence of a double thermal effect at 750–850°C, but did not identify the products formed.

Maurel [22] has also established the stage nature of oxidation of natural cobaltite (with even a third weak peak present) at 750–850°C and reported the oxidation products

$$CoAsS + O_2 \rightarrow Co_3As_2O_8 + CoO + As_2O_3(g) + SO_2. \quad (33)$$

In the author's opinion, the nature of a metal plays an important part in the appearance of various oxidation reactions (cf. selective oxidation of arsenic in gersdorffite).

In [37], an assumption was made, with the results of [36] invoked, that arsenate formation can be precluded if As_4O_6 is removed from the system. The authors studied the effect of pressure (100–26.6 kPa), air flow rate ($1.2-4.8^{-8}$ $m^3\,h^{-1}$), and temperature (650–800°C) on the rate of oxidation of synthetic cobaltine. It was established that, when pressure is lowered at an oxygen consumption factor $\alpha = 0.5$, the formation of CoO and arsenates decreases and the deceleration of sulfur oxidation to SO_2 makes higher the rate of dissociation processes; $CoAs_2$, CoAs, and the starting product were found among the products. By contrast, at $\alpha = 1–1.5$ products contain arsenates and CoO, with sulfur removed completely:

$$4CoAsS + 9O_2 \rightarrow 4CoO + 4SO_2(g) + As_4O_6(g), \quad (34)$$

$$6CoO + 0.5As_4O_6 + O_2 \rightarrow Co_6As_2O_{11}, \quad (35)$$

$$Co_6As_2O_{11} + 0.5As_4O_6 + O_2 \rightarrow 2Co_3As_2O_8. \quad (36)$$

Thus, the calcination of cobaltine is characterized by simultaneous oxidation of sulfur and arsenic, with sulfur removed completely, and arsenic, partly, into the gas phase and thermally stable arsenates formed in the final products.

2.3. Iron Arsenides and Sulfoarsenides. Studies of the thermal dissociation and oxidation of iron arsenides and sulfoarsenides are due to the necessity for, first, improving the technology of gold-bearing arsenious concentrates for ecologically safe removal of arsenic, and, second, obtaining high-purity arsenic in a vacuum.

Thermal dissociation of synthetic iron arsenides FeAs and $FeAs_2$ was studied in [38] at heating rate of 10 deg min^{-1} under pressure of 0.08 mm Hg, with grain size of the material of 0.074–0.14 mm. It was found that, upon grinding, the extent and rate of decomposition of the material increases approximately twofold. The authors present the following decomposition scheme of arsenides:

$$FeAs_2 \xrightarrow{>700^\circ C} FeAs \xrightarrow{>900^\circ C} Fe_2As. \quad (37)$$

The maximum extent of decomposition is observed at 790 and 960°C, respectively.

To determine the optimal conditions of arsenic recovery from FeAsS, FeAs, and Fe_2As, Mil'ke and Spivak [39] sulfidized the arsenides with sulfur, with the mixtures heated under inert conditions. It was found that Fe_2As reacts with sulfur at 300–400°C to form FeAs and then

$$2FeAs + S \rightarrow FeAs_2 + FeS \quad (38)$$

the products are sulfidized. $FeAs_2$ starts to react with sulfur at 400°C to give $Fe_{1-x}S$, FeAsS, and FeS_2. A mixture of arsenic sulfides was found in the sublimates formed.

The behavior of iron arsenides is of interest to researchers, since it is with their decomposition that the completeness of arsenic removal from raw materials is associated. However, published data on the dissociation kinetics of arsenides are extremely scarce. One of goal-seeking works is a study of how synthetic $FeAs_2$ dissociates in a vacuum by Khrapunov a co-authors [40] at a heating rate of 10 deg min^{-1}, grain size of 0.1 mm, and pressure of 3.5×10^2 Pa. The following process scheme was established:

$$FeAs_2 \xrightarrow{>510-690^\circ C} FeAs_{1.62} \xrightarrow{690-805^\circ C} FeAs \xrightarrow{>805^\circ C} FeAs_{0.57} \xrightarrow{>1200^\circ C} Fe_2As + Fe. \quad (39)$$

The first mention of results of oxidizing heating of loellingite can be found in [21]. The DTA curve measured in air for two natural $FeAs_2$ samples show only a single exothermic peak at 550–700°C. This was explained by Maurel [22], who confirmed the peak position and identified the following oxidation products:

$$FeAs_2 + O_2 \rightarrow Fe_2O_3 + As_2O_3(g). \quad (40)$$

One of the first domestic reports on studies of neutral heating of arsenopyrite was that by Zhuchkov and co-authors [41], in which the following scheme of FeAsS (grain size $-0.15 + 0.10$ mm) decomposition was presented:

$$4FeAsS \rightarrow 4FeS + As_4 \quad (41)$$

with the iron sulfide formed as troilite, which is confirmed by XPA. The arsenic vapor pressure becomes equal to 1 atm at 730°C, the decomposition starts at about 600°C to reach a maximum at 750°C.

Isakova and co-authors [42] have pointed to the presence of As_4, As_4S_4, S_2, and As_2S_3 in products

of arsenopyrite decomposition. The same authors [43] have studied the phase composition of FeAsS decomposition in a vacuum and revealed the formation of pyrrotine ($Fe_{1-x}S$) and $FeAs_2$.

Slyapkina [23–25] has presented a decomposition scheme of natural arsenopyrite in an inert medium, differing from that suggested in [41], despite that the investigations were carried out under identical conditions.

$$FeAsS \xrightarrow{670-740^\circ C} FeAs_2 + Fe_{1-x}S + As_4S_4(g) + As_4. \quad (42)$$

The reasons for the difference between the reaction products require separate discussion.

Mil'ke and co-authors [44] believe that natural arsenopyrite decomposes in a neutral medium by the reactions

$$68FeAsS \xrightarrow{700-720^\circ C} 4Fe_{16}S_{17} + 4FeAs_2 + 15As_4, \quad (43)$$

$$2Fe_{16}S_{17} + 2FeAs_2 \xrightarrow{870-900^\circ C} 34FeS + As_4. \quad (44)$$

Thus, removal of arsenic from arsenopyrite occurs in two stages, with FeS and As_4 as final products.

In all probability, some authors describe the products formed in the first stage of arsenopyrite decomposition, and others, the final products. We are not aware of any explanation why the second stage (if at all present) is not observed.

Of indubitable interest in studying the arsenopyrite decomposition are the results obtained by Pashinkin and co-authors [36, 45–48], who calculated the chemical equilibria in the systems Fe–S–As and Fe–As–O and constructed the phase diagram of Fe–As–S in the coordinates $\log P_{As_4}$–$\log P_{S_2}$ at 923 K [45]. They determined the dissociation pressure of an arsenopyrite of composition $FeAs_{0.96}S_{1.04}$ (595–696°C) and proposed a scheme of its decomposition

$$FeAs_{0.96}S_{1.04} \rightarrow FeS + 0.23As_4(g) + 0.01As_4S_4(g). \quad (45)$$

In [47], they ascertain, with account of the data on phase equilibria from [13], that the dissociation of arsenopyrite is determined by the equilibrium FeAsS + $Fe_{1-x}S$ + L + V, i.e., confirm the scheme they suggested.

A similar diagram for a temperature of 800 K has been constructed by Spivak and co-authors [49], who used it for developing a technology for synthesis of arsenopyrite.

In [46, 48], a diagram of partial pressures of Fe–As–O at 923 and 1200 K is given

$$FeAs_2 + O_2 \rightarrow Fe_3O_4 + O_2 \rightarrow Fe_2O_3 + As_4O_6(g) \rightarrow Fe_2O_3 \cdot FeAsO_4 \rightarrow FeAsO_4, \quad (46)$$

$$FeAs + O_2 \rightarrow FeO \rightarrow Fe_3O_4 \rightarrow Fe_2O_3. \quad (47)$$

Thus, formation of iron arsenides is possible at the given temperature via the stage of formation of iron oxides. The authors believe that, with intensive removal of As_4O_6, the scheme presented may end in Fe_2O_3 formation. Presumably, the author of [22] did not test products for iron arsenate.

It was noted in a study concerned with the thermal behavior of arsenopyrite [50] that only iron sulfides were found in final dissociation products in some investigations, and iron sulfides and arsenides, in others. The dissociation pressures of natural arsenopyrite, found by different methods, do not coincide, which is due to the wide homogeneity region of arsenopyrite, presence of pyrite admixtures, and difficulties in identification of the vapor composition. The authors studied heating of natural and synthetic arsenopyrite in a vacuum and inert (He) medium in the temperature range 300–1200°C by Mossbauer spectroscopy and mass spectrometry. The natural arsenopyrite was found to contain 1.5 wt % FeS_2. The heating rate was 10 deg min^{-1}. The products formed upon heating in a vacuum and inert medium are identical, with only the rate of processes being higher in the vacuum; no differences in behavior between the synthetic and natural materials were observed. The authors identified $Fe_{1-x}S$, FeS, and $FeAs_2$ in the products and represented the process as occurring in two stages: decomposition of arsenopyrite to troilite (550–800°C) and dissociation of troilite (>1100°C). The reactions occur successively:

(a) $$2FeAsS \xrightarrow{>300^\circ C} FeAs_2 + FeS_2,$$

(b) $$FeAs_2 \xrightarrow{520-680^\circ C} FeAs_{1.5} + \frac{1}{8}As_4,$$

(c) $$FeAs_{1.5} \xrightarrow{680-850^\circ C} FeAs + \frac{1}{8}As_4,$$

(d) $$2FeAs \xrightarrow{850-950^\circ C} Fe_2As_{1+x} + \frac{1-x}{2}As_2,$$

(e) $$Fe_2As_{1+x} \xrightarrow{1100-1200^\circ C} Fe_2As_{1-y} + \frac{x+y}{2}As_2,$$

(f) $$FeS_2 \xrightarrow{620-800^\circ C} FeS + \frac{1}{2}S_2,$$

(g) $$FeS \xrightarrow{>1100^\circ C} FeS_{1-x} + \frac{x}{2}S_2$$

and concurrently

(a) $2FeAs_2 + S_2 \rightleftarrows 2FeS + As_4$,

(b) $4FeAs + 2S_2 \rightleftarrows 4FeS + As_4$,

(c) $4Fe_2As + 4S \rightleftarrows 8FeS + As_4$,

(d) $\frac{n}{4}As_4 + \frac{m}{2}S_2 \rightleftarrows As_nS_m$.

Thus, the solid products of decomposition are the following

$$FeAsS \rightarrow FeS_2 + FeAs_2 \rightarrow FeS_{1-x} + Fe_2As. \quad (48)$$

To confirm the possibility that iron oxides can react with sulfur, the authors heated natural FeAs with and without sulfur vapor [50] (750°C, 1.33 kPa). In the experiments without sulfur, the residue contained (as found by X-ray fluorescence microanalysis) pyrrotine of composition $FeS_{1.03–1.04}$ and arsenide of composition $FeAs_{0.91–0.94}$; in experiments with sulfur, no arsenides were found and a pyrrotine of composition $FeS_{1.14–1.18}$ was identified.

As for the oxidizing heating of arsenopyrite, it was first mentioned in [21], where a single endothermic peak was observed (500–650°C) in DTA of natural arsenopyrite (mispickel), but the composition of the products was not indicated. The temperature range of the conversion was confirmed in [22], and an oxidation scheme was presented:

$$FeAsS + O_2 \rightarrow Fe_2O_3 + SO_2 + As_2O_3(g). \quad (49)$$

An opinion has been put forward [22] that loellingite and arsenopyrite oxidize by a widely occurring type, with complete removal of nonmetals and formation of metal oxides. The absence of iron arsenates in the products may be due to removal of $As_4O_6(g)$ from the system.

Oxidation of natural arsenopyrite (grain size –0.15 + 0.10 μm) was studied in the temperature range 20–1000°C and a scheme of transformation was presented (XPA, IR spectroscopy, high-temperature X-ray diffraction analysis) in [51]:

$$FeAsS \begin{cases} \xrightarrow{480–540^\circ C} FeS \xrightarrow{500–600^\circ C} Fe_3O_4 \xrightarrow{600–700^\circ C} \gamma\text{-}Fe_2O_3 \rightarrow \alpha\text{-}Fe_2O_3, \\ \xrightarrow{500–800^\circ C} \Phi_1 \xrightarrow{750–900^\circ C} Fe_4As_2O_{11} \xrightarrow{850–950^\circ C} \Phi_2 \xrightarrow{>940^\circ C} Fe_2O_3 + As_2O_3(g), \end{cases} \quad (50)$$

where Φ_1 and Φ_2 are arsenates of unidentified formula.

In [51], formation of dense melted structures of the eutectic type as a result of the possible interaction of oxidation products was noted.

In studying the behavior of arsenic-containing concentrates in the course of calcination [52], partial pressure diagrams have been calculated and constructed for the system Fe–As–S–O at 798 and 973 K. These modifications of diagrams were used to calculate the results of heating of natural and synthetic arsenopyrite in inert, reducing, and oxidizing atmospheres created by mixing CO, CO_2, He, and O_2 in various proportions. The experimental results demonstrated that the reducing and oxidizing atmospheres are more effective in arsenic removal than the inert one. The largest amounts of arsenic are removed in the oxidizing atmosphere to give As_4O_6, which readily volatilizes from $As_2O_5(s)$, or $FeAsO_4$ if the pressure P_{As_4} is high. When heating is done in an inert atmosphere, sulfur is also released, and arsenic sulfides constitute the main form of arsenic removal.

Oxidation of arsenopyrite under normal and lowered pressure has been studied by Potselueva and coauthors [53]. The effect of temperature (400–700°C), pressure (6.6 kPa, 1 atm), and air flow rate [$(3.6–28.8) \times 10^{-4}$ m^3 h^{-1}] on the extent and rate of oxidation of natural arsenopyrite (grain size –0.174 + 0.074 mm) was analyzed. It was found that raising the temperature from 400 to 700°C makes the oxidation 2 times faster, as also does lowering the pressure to 6.6 kPa. Raising the airflow rate accelerates the process 6-fold at 700°C (6.6 kPa). No mention was made of the reaction products.

CONCLUSIONS

Summarizing published data, we can make the following conclusions. The sequence of nickeline and gersdorffite transformations in inert and oxidizing calcination has been studied in sufficient detail, but there is no evidence concerning transformations in the reducing medium. Data on transformation of higher nickel arsenide—$NiAs_2$—rammelsbergite (pararammelsbergite) are lacking in the literature. Dissociation of higher cobalt arsenides has been studied extensively, but there is no common opinion about the products formed in dissociation of natural compounds. Oxidation and reduction of synthesized and natural cobalt

arsenide have virtually not been studied at all. There are no reliable published data on products formed in dissociation and reduction of natural cobaltine, its oxidation has been studied insufficiently, and there is no common opinion concerning the composition of products formed in the process. Evidence concerning the kinetics and products of neutral and oxidizing heating of arsenopyrite are exceedingly contradictory, and the body of data on reducing heating is insufficient.

Thermodynamic data and dissociation pressures of nickel, cobalt, and iron arsenides and sulfoarsenides, in particular, obtained by different authors are frequently contradictory and require special consideration.

REFERENCES

1. *Cobalt News*, 2000, no. 4, p. 9.
2. *Cobalt News*, 1993, no. 2, p. 14.
3. *Cobalt News*, 2000, no. 2, p. 6.
4. Tsymbulov, L.B., Tsemekhman, L.Sh., Klement'ev, V.V., *et al.*, *Vestn. Gorn.-Metal. Sektsii Ross. Akad. Estestv. Nauk, Otd. Metal.*, Novokuznetsk, 1996, pp. 43–52.
5. Kullerud, G., *Review and Evaluation of Recent Research on Geologically Significant Sulfide Type Systems, Fort. Mineral.*, vol. 41, no. 2, Stuttgart, April, 1964.
6. Elliott, R.P., *Constitution of Binary Alloys*, New York: McGraw–Hill, 1965.
7. Heyding, R.D. and Calvert, L.D., *Canad. J. Chem.*, 1960, vol. 38, no. 2, pp. 313–316.
8. Yund, R.A., *Econ. Geol.*, 1961, vol. 56, pp. 1273–1296.
9. Caillere, S., Avias, J., and Falgueirettes, J., *Bull. Soc. franc. Miner. Crist.*, 1961, vol. 84, no. 1, pp. 9–12.
10. Roseboom, E.H., *Am. Miner.*, 1962, vol. 47, pp. 310–327.
11. Radcliffe, D. and Berry, L.G., *Am. Miner.*, 1968, vol. 53, pp. 1856–1881.
12. Buseck, P.R., *Carnegie Inst. Wash., Year Book*, 1962, vol. 61, pp. 152–154.
13. Clark, L.A., *Econ. Geol.*, 1960, vol. 55, pp. 1345–1381, 1631–1652.
14. Yund, R.A., *Am. J. Sci.*, 1962, vol. 260, pp. 761–782.
15. Darmon, R. and Wintenberger, M., *Bull. Soc. franc. Miner. Crist.*, 1966, vol. 89, pp. 213–215.
16. Maurel, C. and Picot, P., *Bull. Soc. franc. Miner. Crist.*, 1973, vol. 96, pp. 292–297.
17. Maurel, C. and Picot, P., *Bull. Soc. franc. Miner. Crist.*, 1974, vol. 97, pp. 251–256.
18. Klemm, D.D., *Neues Jahrbuch fur Mineralogie, Geologie und Palaontologie Abhandlungen, Abt. A, Mineralogie*, 1965, vol. 103, pp. 205–255.
19. Vaughan, D.J. and Craig, J.R., *Mineral Chemistry of Metal Sulfides*, Cambridge: Cambridge Univ., 1978.
20. *Geochemistry of Hydrothermal Ore Deposits*, Barnes, H.L., Ed., New York: Wiley, 1979.
21. Asensio, I. and Sabatier, G., *Bull. Soc. franc. Miner. Crist.*, 1958, vol. 81, no. 1, pp. 12–15.
22. Maurel, C., *Bull. Soc. franc. Miner. Crist.*, 1964, vol. 87, no. 3, pp. 377–385.
23. Shlyapkina, E.N. and Berg, L.G., *Izv. Vyssh. Uchebn. Zaved., Khim. Khim. Tekhnol.*, 1970, vol. 13, no. 6, pp. 831–836.
24. Shlyapkina, E.N., Termographic Characteristics of Sulfide Minerals, *Cand. Sci. Dissertation*, Kazan, 1972.
25. Berg, L.G. and Shlyapkina, E.N., *Thermal. Anal.*, 1975, vol. 8, pp. 417–426.
26. Chunaeva, V.D., Muldagalieva, F.A., Isabaev, S.M., *et al.*, Abstracts of Papers, *III Vsesoyuznoe soveshchanie po khimii i tekhnologii khal'kogenov i khal'kogenidov* (III All-Union Symp. on Chemistry and Technology of Chalcogens and Chalcogenides), Karaganda, 1986, p. 212.
27. Chunaeva, V.D., Muldagalieva, F.A., Isabaev, S.M., *et al.*, *Kompleks. Ispol'z. Miner. Syr'ya*, 1990, no. 1, pp. 76–79.
28. Muldagalieva, F.A., Chunaeva, V.D., Isabaev, S.M., *et al.*, *Kompleks. Ispol'z. Miner. Syr'ya*, 1990, no. 4, pp. 84–85.
29. Isabaev, S.M., Pashinkin, A.S., Mil'ke, E.G., *et al.*, *Fiziko-khimicheskie osnovy sul'fidirovaniya mysh'yaksoderzhashchikh soedinenii* (Physicochemical Foundations of Sulfidizing of Arsenic-containing Compounds), Alma-Ata: Nauka, 1986.
30. Wilson, L.J. and Mikhail, S.A., *Thermochim. Acta*, 1987, vol. 112, pp. 197–213.
31. Tsymbulov, L.B. and Ertseva, L.N., *Metally*, 1998, no. 5, pp. 3–7.
32. Tsymbulov, L.B. and Ertseva, L.N., *Metally*, 2000, no. 3, pp. 25–30.
33. Isabaev, S.M., Polukarov, A.N., Chunaeva, V.D., *et al.*, *Thermal Stability of CoAsS, CoS_2, and $CoAs_2$*, Available from VINITI, 1988, no. 7705-V88.
34. Mikhail, S.A., Turcotte, A.M., and Bowman, W.S., *Thermochim. Acta*, 1989, vol. 153, pp. 287–296.
35. Chunaeva, V.D., Muldagalieva, R.A., Isabaev, S.M., *et al.*, *Izv. Vyssh. Uchebn. Zaved., Tsvetn. Metall.* 1990, no. 1, pp. 31–33.
36. Pashinkin A.S., Malkova A.S., Fedorov V.A. *Vysokochist. Veshchestva*, 1991, no. 1, pp. 155–160.
37. Potselueva, A.D., Spivak, M.M., Isakova, R.A., *et al.*, *Kompleks. Ispol'z. Miner. Syr'ya*, 1992, no. 10, pp. 47–50.
38. Tkach, M.A., Tkachenko, O.B., Isakova, R.A., *et al.*, *Sbornik trudov Instituta metallurgii i obogashcheniya Akad. Nauk KazSSR* (Coll. of Works of the Inst. of Metallurgy and Ore Dressing), 1977, vol. 52, pp. 54–60.

39. Mil'ke, E.G. and Spivak, L.F., Abstracts of Papers, *III Vsesoyuznoe soveshchanie po khimii i tekhnologii khal'kogenov i khal'kogenidov* (III All-Union Symp. on Chemistry and Technology of Chalcogens and Chalcogenides), Karaganda, 1986, p. 213.
40. Khrapunov, V.E., Isakova, R.A., Spivak, M.M., *et al.*, *Zh. Neorg. Khim.*, 1993, vol. 38, no. 4, pp. 784–785.
41. Zhuchkov, I.A., Lodeishchikov, V.V., and Skobeev, I.K., *Zh. Prikl. Khim.*, 1967, vol. 40, no. 12, pp. 2703–2710.
42. Isakova, R.A., Ugryumova, L.E., Chelokhsaev, L.S., *et al.*, *Vakuumnye protsessy v tsvetnoi metallurgii* (Vacuum Processes in Nonferrous Metalurgy), Alma-Ata: Nauka, 1967, vol. 26, pp. 57–67.
43. Isakova, R.A., *Izv. Akad. Nauk KazSSR, Ser. Khim.*, 1977, no. 4, pp. 11–14.
44. Mil'ke, E.G., Polukarov, A.N., and Isabaev, S.M., *Khimiya i tekhnologiya soedinenii mysh'yaka i sur'my* (Chemistry and Technology of Compounds of Arsenic and Antimony), Alma-Ata: Nauka, 1980, pp. 69–74.
45. Pashinkin, A.S., Fedorov, V.A., Zviadadze, G.N., *et al.*, *Zh. Prikl. Khim.*, 1979, vol. 52, no. 5, pp. 1085–1091.
46. Pashinkin, A.S., Malkova, A.S., and Fedorov, V.A., *Vysokochist. Veshchestva*, 1990, no. 4, pp. 102–109.
47. Pashinkin, A.S., Muratova, V.A., Fedorov, V.A., *et al.*, *Zh. Neorg. Khim.*, 1990, vol. 35, no. 11, pp. 2951–2954.
48. Pashinkin, A.S. and Fedorov, V.A., *Neorg. Mater.*, 1995, vol. 31, no. 5, pp. 592–603.
49. Spivak, M.M., Skosyrev, N.T., and Fedulov, I.O., *Kompleks. Ispol'z. Miner. Syr'ya*, 1989, no. 3, pp. 11–12.
50. Khrapunov, V.E., Spivak, M.M., and Spitsyn, V.A., *Zh. Neorg. Khim.*, 1991, vol. 36, no. 11, pp. 2786–2790.
51. Zhuchkov, I.A. and Smagunov, V.I., *Zh. Prikl. Khim.*, 1971, vol. 44, no. 8, pp. 1680–1688.
52. Chakraborti, N. and Lynch, D.C., *Met. Trans. B*, 1983, vol. 14, no. 2, pp. 239–251.
53. Potselueva, A.D., Isakova, R.A., Spivak, M.M., *et al.*, *Kompleks. Ispol'z. Miner. Syr'ya*, 1990, no. 9, pp. 56–59.

Russian Journal of Applied Chemistry, Vol. 75, No. 10, 2002, pp. 1557–1561. Translated from Zhurnal Prikladnoi Khimii, Vol. 75, No. 10, 2002, pp. 1594–1597.
Original Russian Text Copyright © 2002 by Aparnev, Yukhin, Malinovskaya, Egorov.

INORGANIC SYNTHESIS AND INDUSTRIAL INORGANIC CHEMISTRY

Synthesis and Study of Mixed Tin and Antimony Oxides

A. I. Aparnev, Yu. M. Yukhin, T. D. Malinovskaya, and Yu. P. Egorov

Institute of Solid State Chemistry and Mechanochemistry, Siberian Division, Russian Academy of Sciences, Novosibirsk, Russia

Siberian Physicotechnical Institute, Tomsk, Russia

Received February 6, 2002; in final form, June 2002

Abstract—Coprecipitation of tin(II, IV) and antimony(III) from chloride solutions was studied by X-ray phase analysis, thermogravimetry, IR spectroscopy, and elemental analysis.

Tin-antimony oxide materials of the $Sn_{1-x}Sb_xO_2$ solid solution type find wide application as catalysts in organic synthesis, semiconducting elements in chemical sensors, and components of thick-film resistors [1–3]. These solid solutions, which contain up to 20–30 at.% antimony, are obtained both by coprecipitation of tin(II, IV) and antimony(III) from chloride or nitrate solutions, with subsequent calcination of their hydrolyzed forms, and by heat treatment of mixtures of the corresponding metal oxides [2, 4].

Synthesis of tin and antimony oxide materials is based, as a rule, on coprecipitation of tin and antimony ions from hydrochloric acid solutions of Sn(IV) and Sb(III) or Sb(V) chlorides in their neutralization with aqueous ammonia solution to pH > 5, followed by precipitate drying at 120°C and calcination at 500–1000°C [1]. Variants have been proposed for synthesizing the materials by separate treatment of metallic tin and antimony with nitric acid solutions, mixing the resulting precipitates, their washing with water, drying, and calcination [1, 5–7]. The possibility of synthesizing tin and antimony materials by adding water to a mixture of SnO and Sb_2O_5 oxides, stirring the paste obtained for 16 h, and subsequent drying and calcination at 540°C has been demonstrated [8].

Synthesis conditions have a profound impact on the properties of the tin and antimony materials. The catalysts prepared by coprecipitation of tin(II, IV) and antimony(III) from chloride solutions are characterized by high activity and selectivity in organic syntheses. We emphasize that, in the synthesis of tin and antimony oxide materials from metals by the nitrate scheme, the stage of their treatment with nitric acid is accompanied by release of toxic nitrogen oxides into the atmosphere [1]. When tin(II, IV) and antimony(III) are coprecipitated by adding an alkali reagent to their chloride solutions, the precipitate contains antimony(III) as oxo chloride, and its calcination results in partial sublimation of antimony as a chloride, which disrupts the stoichiometry of the material and also leads to pollution during calcination.

This communication presents the results obtained in studying the influence exerted by the pH of the medium on the extent of Sn(II), Sn(IV), and Sb(III) precipitation from hydrochloric acid solutions and on the composition of the resulting precipitates, and also the effect of calcination temperature on the phase composition of tin and antimony oxide compounds.

EXPERIMENTAL

The starting solutions of antimony(III) chloride were prepared by dissolving analytical-grade antimony(III) oxide in 9 M hydrochloric acid solution (special-purity grade 20-4); those of tin (IV) chloride, by dissolving $SnCl_4 \cdot 5H_2O$ (pure grade) in the 1 M hydrochloric acid solution; and those of tin(II) chloride, by dissolving $SnCl_2 \cdot 2H_2O$ (pure grade) in 1 M hydrochloric acid solution. Also, solutions obtained by dissolving pure-grade metallic tin in 9 M hydrochloric acid solution were used.

Sn(II, IV) and Sb(III) were precipitated by adding an aqueous solution of an alkali reagent (3–6 M NH_4OH, or 1–3 M NaOH, or 1–2 M Na_2CO_3) to tin- and antimony-containing solutions, with the following com-

1070-4272/02/7510-1557 $27.00 © 2002 MAIK "Nauka/Interperiodica"

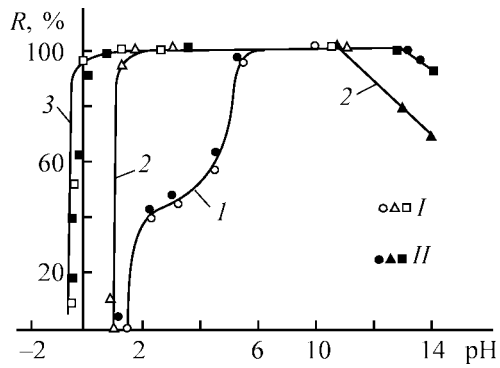

Fig. 1. Degree of precipitation, *R*, of (*1*) Sn(II), (*2*) Sn(IV), and (*3*) Sb(III) from chloride solutions vs. pH of the medium and nature of the alkali reagent. (*I*) NH_4OH and (*II*) NaOH.

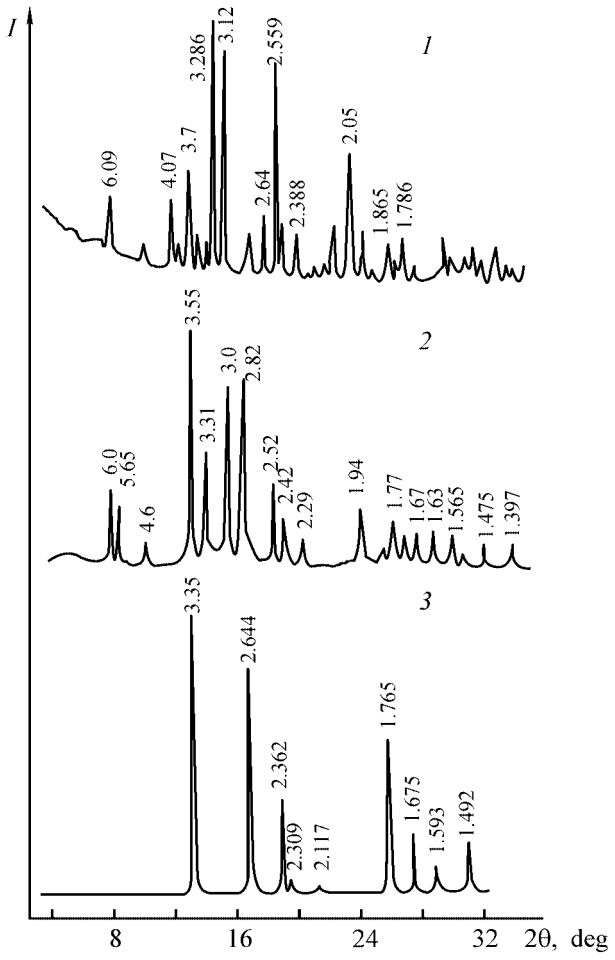

Fig. 2. X-ray diffraction patterns of (*1*) $Sb_4O_5Cl_2$ synthesized by hydrolysis of tin(III) chloride at pH 1.6, (*2*) $Sn_3O_2(OH)_2$ precipitated from Sn(II) chloride at pH 7, and (*3*) product of coprecipitation of Sn(IV) and Sb(III) from chloride solutions at pH 7. Initial Sb(III) content 20 at.%; the same for Fig. 3. (*I*) Signal intensity and (2θ) Bragg angle.

positions (g l^{-1}): Sn(IV) 150, Sn(II) 100, Sb(III) 100, and free hydrochloric acid 70, 35, and 210, respectively. The experiments were carried out in fluoroplastic containers with stirrers. The sludge was stirred for 1 h. After settling for 2 h, the precipitate was filtered off, washed with distilled water on a filter, and dried in air. The X-ray phase analysis (XPA) was carried out on a DRON-3 diffractometer with Cu_{K_α} radiation at counter rotation rate of 0.5 deg min^{-1}. The curves of differential thermal (DTA) and thermogravimetric (TGA) analyses of the samples under study were recorded on an MOM derivatograph (Hungary) at a heating rate of 10 deg min^{-1}. The IR absorption spectra were recorded on a Specord IR-71 spectrophotometer in the frequency range 400–4000 cm^{-1}. The samples were prepared as pellets with calcined KBr. The ammonia concentration and the solution pH were measured on an OP-264/1 pH-meter (Hungary) with a renewable electrode [9]. Macroscopic amounts of bound antimony and tin in the liquid and solid phases were determined by iodometric titration, and their microscopic amounts, by the atomic-absorption method on a Saturn-2M spectrophotometer.

A study of antimony(III) precipitation from chloride solutions with aqueous solutions of ammonia or sodium hydroxide showed (Fig. 1, curve *3*) that the degree *R* of antimony(III) extraction into the precipitate strongly depends on the nature of an alkaline reagent. With increasing pH, the degree of antimony(III) extraction into the precipitate grows to become 99.75% at 1 M acidity of the medium, and the residual concentration of Sb(III) is 10–15 mg l^{-1}. In the pH range 0.5–13, antimony(III) precipitates almost completely (*R* ~99.98%), with the residual concentration of Sb(III) in the solution being approximately 1–3 mg ml^{-1}. The pH value increases to 13.3–13.5 on adding a sodium hydroxide solution (the residual concentration of NaOH in the solution is about 0.15 M), which leads to a decrease in *R* owing to the formation of sodium antimonite Na[$(Sb(OH)_4]$ [Sb(III) concentration in solution becomes as high as 1.2–1.4 g l^{-1}]. According to XPA (Fig. 2, curve *1*) and IR spectral data (Fig. 3, curve *1*), the product of hydrolysis of an antimony(III) chloride solution at pH 1.6–1.8 is an oxo chloride of composition $Sb_4O_5Cl_2$. The X-ray diffraction patterns of the samples obtained at pH 2–7 show lower fraction of $Sb_4O_5Cl_2$ reflections. In this case, diffraction peaks appear, with *d*/*n* of 4.57, 3.494, 3.142, 2.65, 2.456, 2.058, 1.929, 1.805, 1.675, 1.572, and 1.523 Å, which correspond to antimony oxide Sb_2O_3 [10]. The IR spectra of the sam-

ples reveal vibrations at 420, 495, 605, 725, and 840 cm^{-1}, related to only the antimony–oxygen bond [11]. The product of hydrolysis at pH 7 is antimony(III) oxide, with the residual content of chloride ions not exceeding 1%.

When tin(IV) is precipitated from chloride solutions, the degree of its extraction into the precipitate first grows with increasing pH, to become 99.9% at pH 1.0–10.6 [residual concentration of Sn(IV) in solution is 5–20 mg l^{-1}]. Further increase in pH results in a decrease in *R*, and, at pH 14, the concentration of Sn(IV) in the solution is approximately 9.8 g l^{-1}. This is due to the fact that Sn(IV) precipitates from chloride solutions as an X-ray-amorphous hydrated tin dioxide or α-stannic acid, which easily dissolves in an alkaline medium to give salts containing $[Sn(OH)_6]^{2-}$ complex ions. The composition of hydrated tin dioxide is represented as $\{SnO_2\}Sn(OH)_4$ [6, 12].

The precipitation of Sn(II) from chloride solutions occurs in the pH range 1.2–5.5, being complete (*R* ~99.98%) at pH ~6 [the residual concentration of Sn(II) in solution is 0.5–1.0 mg l^{-1}]. With the pH value increasing to 12–13, a minor decrease in *R* is observed [residual concentration of Sn(II) in solution is about 17–20 mg l^{-1}]. The X-ray diffraction pattern of the Sn(II) precipitate contains peaks with *d*/*n* of 3.55, 3.31, 3.00, 2.82, 2.52, 1.92, and 1.77 Å (Fig. 2, curve *2*), typical of hydrated tin dioxide with composition $Sn_3O_2(OH)_2$ [10].

Thus, depending on the pH of solution, coprecipitation of Sn(IV) and Sb(III) is possible in the pH range 1–10, and that of Sn(II) and Sb(III), only at pH 5.5–11. In this case, the tin/antimony molar ratio in the precipitates may vary widely.

According to the XPA data, an X-ray-amorphous product containing 5 to 20 at.% antimony(III) is formed in coprecipitation of tin(IV) and antimony(III) from chloride solutions upon addition of an alkaline reagent to make pH 7. Thermal treatment of these samples initiates structural phase transformations. Calcination of the precipitates at 250–600°C results in loss of mass and is accompanied by an endothermic effect (Fig. 4, curve *1*) associated with dehydration of hydrated tin dioxide. The X-ray diffraction patterns contain peaks with *d*/*n* of 3.35, 2.644, 1.765, 1.675, 1.595, and 1.498 Å (Fig. 2, curve *3*), related to tin dioxide with rutile structure [10]. No formation of antimony compounds is observed. Raising the calcination temperature further, to 1000°C, leads to higher degree of crystallinity and results in the formation of

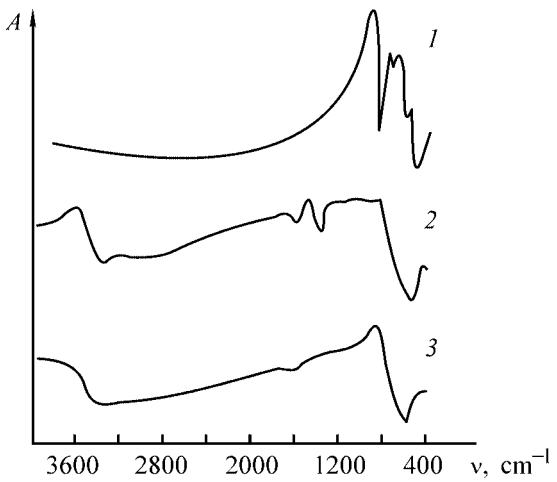

Fig. 3. IR spectra of (*1*) $Sb_4O_5Cl_2$ synthesized by hydrolysis of antimony(III) chloride at pH 1.6 and of products of coprecipitation of (*2*) Sn(IV) and Sb(III) and (*3*) Sn(II) and Sb(III) from chloride solutions at pH 7. (*A*) Absorption and (ν) wave number.

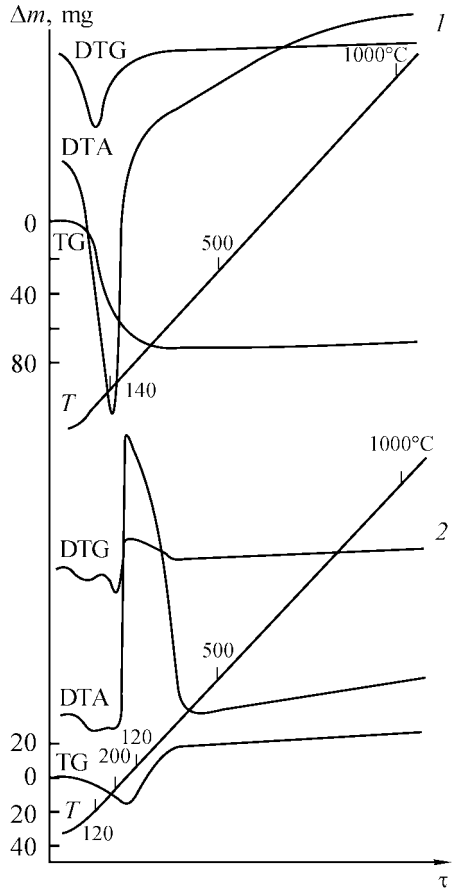

Fig. 4. Thermograms of products formed in coprecipitation of (*1*) Sn(IV) and Sb(III) and (*2*) Sn(II) and Sb(III) at pH 7. Initial Sb(III) content 20 at.%, sample weight 500 mg. (Δ*m*) Mass change, (τ) time, and (*T*) temperature.

Lattice parameters *a* and *c* of tin(IV) oxide with various initial concentrations of Sb_2O_x (calcination temperature 1000°C)

Sb_2O_x, mol %	*a*	*c*
	Å	
0	4.738	3.188
5	4.741	3.191
10	4.745	3.192
15	4.750	3.193

isotype solid solutions of antimony in tin dioxide. In this case, chemical analysis shows the presence of Sb(III) and Sb(V) ions in the samples. The ionic radii of Sn^{4+} (0.067 nm), Sb^{3+} (0.090 nm), and Sb^{5+} (0.062 nm) allow them to be incorporated in the same lattice. The formation of solid solutions of antimony in tin dioxide is confirmed by X-ray studies of SnO_2 unit cell parameters. The experimental data presented in the table show that the parameters *a* and *c* grow with the content of Sb_2O_x increasing to 15 at.%, with the period *c* changing only slightly. The increase in the volume of SnO_2 unit cells can be attributed to introduction of antimony(III) ions, having a somewhat greater ionic radius than Sn(IV).

The IR spectra of dried samples, containing up to 20 at.% Sb(III) show only bands of dried hydrated tin dioxide: bands at 3400, 1620, and 1405 cm^{-1}, related to stretching and bending vibrations of water molecules, and a broad absorption band below 600 cm^{-1} with a shoulder at 620 cm^{-1} and a slightly diffuse maximum at 570 cm^{-1}, related to Sn–O stretching vibrations (Fig. 3, curve *2*).

The IR spectra of the samples containing up to 20 mol % Sb_2O_x and calcined at 1000°C show absorption bands at 560 and 600 cm^{-1} (shoulder corresponding to SnO_2). The absorption band at 645 cm^{-1}, related to the Sn–O stretching vibrations, is shifted to lower frequencies:

Sb_2O_x, mol %	0	5	10	20
ν, cm^{-1}	645	640	625	615

This shift, determined by the content of antimony, is attributed to the formation of a solid solution based on SnO_2, since the character of the IR spectrum of tin(IV) oxide is preserved.

The X-ray diffraction patterns of samples obtained by coprecipitation of Sn(II) and Sb(III) from a hydrochloric acid solution with Sb(III) content of up to 20 at.% upon addition of an alkali reagent, to make pH 7 contain peaks with *d*/*n* 5.68, 3.55, 3.31, 3.00, 2.82, 2.52, 1.92, 1.77, and 1.56 Å corresponding to a hydrated tin(II) oxide of composition $Sn_3O_2(OH)_2$. The IR spectra of samples dried in air and containing up to 20 at.% Sb(III) show only bands of hydrated tin(II) oxide (Fig. 3, curve *3*). With increasing content of Sb(III) in the mixture, the absorption band at 540 cm^{-1}, associated with Sn–O stretching vibrations, is shifted to higher frequencies:

Sb(III), at.%	0	5	10	15	20
ν, cm^{-1}	540	550	570	580	590

In thermal treatment of the products of Sn(II) and Sb(III) coprecipitation, the following processes occur successively: dehydration (endothermic effects at 100 and 220°C) associated with loss of water molecules and Sn(II) oxidation to Sn(IV) (exothermic effect at 270–320°C) (Fig. 4, curve *2*). The X-ray diffraction patterns of samples calcined at temperatures above 400°C contain peaks related to tin dioxide with rutile structure, whereas diffraction peaks associated with $Sb_2O_{4\pm1}$ phases are absent. Therefore, a conclusion can be made that thermal treatment at temperatures higher than 400°C results in the formation of structures based on tin dioxide alloyed with antimony, of the type of $Sn_{1-x}Sb_xO_2$ solid solutions.

CONCLUSIONS

(1) It is established that coprecipitation of tin(IV) and antimony(III) from chloride solutions at pH 1–10, and of tin (II) and antimony(III) at pH 5.5–11, makes it possible to obtain precipitates containing these elements in various proportions.

(2) Whatever the nature of the initial reagents, solid solutions of antimony oxide in tin dioxide are formed upon calcination of precipitates containing up to 20 at.% Sb. Use of Sn(II) as a starting reagent makes it possible to lower the temperature of solid solution formation from 800–1000°C [with Sn(IV) used in the starting mixture] to 500–600°C.

REFERENCES

1. Lemberanskii, R.A., Annenkova, I.B., and Bakhshieva, Z.A., *Usp. Khim.*, 1992, vol. 61, no. 1, pp. 124–138.

2. Vlasova, M.V., Dyshel', D.E., and Kakazei, N.G., *Neorg. Mater.*, 1990, vol. 26, no. 7, pp. 1486–1490.
3. Orlik, D.R., Ivanovskaya, M.I., and Gurlo, A.Ch., *Zh. Anal. Khim.*, 1997, vol. 52, no. 1, pp. 69–73.
4. Pyke, D., Reid, R., and Tilley, J.J., *J. Chem. Soc. Faraday I*, 1980, vol. 75, pp. 1174–1182.
5. Cooper, R.B., Advani, G.N., and Jordan, A.G., *J. Electron. Mater.*, 1981, vol. 10, no. 3, pp. 455–472.
6. Capehart, T. and Chang, S., *J. Vac. Sci. Technol.*, 1981, vol. 18, no. 2, pp. 393–397.
7. UK Patent 876 446.
8. UK Patent 864 666.
9. Kletenik, Yu.B., Bek, R.Yu., Kiryushov, V.N., *et al.*, *Zh. Anal. Khim.*, 1982, vol. 37, no. 3. pp. 534–538.
10. *Powder Diffraction File*, Swarthmore: Joint Commitee on Powder Diffraction Standard, USA, Pennsylvania, 1985.
11. Petrov, K.I., Golovin, Yu.M., and Fomochev, V.V., *Zh. Anal. Khim.*, 1973, vol 18, no. 11, pp. 2922–2924.
12. Sharygin, L.M., Denisova, T.A., Vovk, S.M., *et al.*, *Zh. Neorg. Khim.*, 1985, vol. 30, no. 8, pp. 1968–1973.

Russian Journal of Applied Chemistry, Vol. 75, No. 10, 2002, pp. 1562–1565. Translated from Zhurnal Prikladnoi Khimii, Vol. 75, No. 10, 2002, pp. 1598–1601.
Original Russian Text Copyright © 2002 by Belova, Uritskaya, Kitaev.

INORGANIC SYNTHESIS AND INDUSTRIAL INORGANIC CHEMISTRY

Kinetics of Lead Sulfide Precipitation from Citrate Solutions of Thiourea

N. S. Belova, A. A. Uritskaya, and G. A. Kitaev

Ural State Technical University, Yekaterinburg, Russia

Received May 7, 2001; in final form, March 2002

Abstract—The kinetics of lead sulfide precipitation with thiourea from alkaline solutions at 30, 40, and 50°C under conditions of spontaneous nucleation of the solid phase in the solution bulk was studied.

Lead sulfide is a material widely used to fabricate semiconductor devices operating in the IR spectral range [1]. At present, a chemical method of lead sulfide precipitation in the form of deposits and thin films on a solid surface is widely employed. The properties of the precipitated material strongly depend on the technology of its preparation.

This study is concerned with the kinetics of lead sulfide precipitation from alkaline solutions containing citrate lead(II) complexes and thiourea.

Upon introduction of sodium citrate into an aqueous solution of a lead(II) salt in an alkaline medium, the following complex ions are formed [2]:

$$Pb^{2+} + Cit^{3-} \rightleftarrows PbCit^{-},\ \beta_1 = 3.07 \times 10^6;$$

$$Pb^{2+} + 2Cit^{3-} \rightleftarrows Pb(Cit)_2^{4-},\ \beta_{1,2} = 3.03 \times 10^8;$$

$$Pb^{2+} + Cit^{3-} + OH^- \rightleftarrows Pb(OH)Cit^{2-},\ \beta'_1 = 5.25 \times 10^{13};$$

$$Pb^{2+} + OH^- \rightleftarrows Pb(OH)^+,\ \beta''_1 = 7.95 \times 10^6;$$

$$Pb^{2+} + 2OH^- \rightleftarrows Pb(OH)_2,\ \beta''_{1,2} = 6.28 \times 10^{10};$$

$$Pb^{2+} + 3OH^- \rightleftarrows Pb(OH)_3^-,\ \beta''_{1,2,3} = 1.99 \times 10^{13},$$

where β_i are the formation constants of the complex ions.

The analytical concentration of lead(II) in solution is given by

$$c_{Pb} = [Pb^{2+}] + [PbCit^{3-}] + [Pb(Cit)_2^{4-}] + [Pb(OH)Cit^{2-}] + [Pb(OH)^+] + [Pb(OH)_2] + [Pb(OH)_3^-]. \quad (1)$$

The partial mole fraction of each complex ion can be calculated with account of the above formation constants [3, 4], e.g., as follows:

$$\alpha_{Pb^{2+}} = [Pb^{2+}]/c_{Pb} = \{1 + \beta_1[Cit^{3-}] + \beta_{1,2}[(Cit)^{3-}]^2 + \beta'_1[OH^-][Cit^{3-}] + \beta''_1[OH^-] + \beta''_{1,2}[OH^-]^2 + \beta''_{1,2,3}[OH^-]^3\}^{-1}. \quad (2)$$

The calculated partial mole fractions of lead ions and complex ions in solution are presented in Table 1 in relation to the pH of the medium and concentration of free sodium citrate.

It can be seen that mainly the $Pb(OH)Cit^{2-}$ complex exists in alkaline solutions at pH 10.5–12.5, and the $Pb(OH)_3^-$ complex, at pH > 13.

In aqueous solution, thiourea undergoes hydrolysis to form weak dibasic acids, hydrosulfuric acid H_2S and cyanamide H_2NCN [5]:

$$(NH_2)_2CS \rightleftarrows H_2S + H_2NCN. \quad (3)$$

Table 1. Partial concentrations of lead(II) in a sodium citrate solution ($[Cit^{3-}] = 25 \times 10^{-3}$ M)

pH value	Partial content of Pb(II), mol fraction		
	$\alpha_{Pb^{2+}}$	$\alpha_{Pb(OH)Cit^{2-}}$	$\alpha_{Pb(OH)_3^-}$
10.5	3×10^{-9}	1	8.49×10^{-6}
11.0	9.53×10^{-10}	1	8.49×10^{-5}
11.5	3.01×10^{-10}	0.999	8.48×10^{-4}
12.0	9.44×10^{-11}	0.991	8.42×10^{-3}
12.5	2.77×10^{-11}	0.921	0.078
13.0	5.14×10^{-12}	0.54	0.458
13.5	3.17×10^{-13}	0.105	0.894

1070-4272/02/7510-1562 $27.00 © 2002 MAIK "Nauka/Interperiodica"

The equilibrium constant of reaction (3) was determined experimentally in [5].

Upon introduction of thiourea into an alkaline solution of a complex salt of lead(II), the clear solution turns turbid because of the formation of a solid phase, PbS, by the reaction

$$Pb(OH)Cit^{2-} + N_2H_4CS + OH^- = PbS + Cit^{3-} + H_2NCN + 2H_2O. \quad (4)$$

The rate of this heterogeneous reaction is determined by reactant concentrations, pH value, temperature, and the surface area of the PbS solid phase nucleating in the initially homogeneous system and changing in the course of the process because of the growth of particles in the solution bulk and as a result of their coagulation and sedimentation. To prevent sedimentation, we carried out the process with stirring, which maintained the particles in the suspended state.

We studied the process kinetics by sampling the solution. The concentration of lead(II) in a sample was determined by direct complexometric titration at pH 5 with visual indication of the end point with Xylene Orange indicator [6, 7].

The experiments were carried out at 303, 313, and 323 K. We prepared the working solutions in volumetric flasks by pouring together appropriate volumes of the starting solutions in the following order: 1 M solution of sodium citrate, 1.0 M solution of lead acetate, 3.9 M solution of alkali, 0.5 M solution of thiourea, and distilled water. The experimental data obtained are presented in Table 2 and Fig. 1.

As it can be seen from Fig. 1, the typical kinetic curve is S-shaped, which is characteristic of heterogeneous autocatalytic processes, in which the surface of the forming solid phase acts as a catalyst. In this case, the rate of lead sulfide formation in the system must be proportional to the surface area of the solid phase nucleating in the reaction mixture bulk and to the concentrations of the main reactants, complex salt of lead and thiourea. Therefore, we described the reaction rate with the equation, which, in our opinion, can be named model:

$$\omega = \frac{d(c_{0,A} - c_A)}{d\tau} = k_{exp}(c_{0,A} - c_A)^{2/3} c_A c_B, \quad (5)$$

where $c_{0,A}$ and c_A are the concentrations of the complex salt of lead (M) at, respectively, $\tau = 0$ and $\tau > 0$; $c_{0,B}$ and c_B are the concentrations of thiourea (M) at $\tau = 0$ and $\tau > 0$; $(c_{0,A} - c_A) = (c_{0,B} - c_B) = x$ is the amount of lead sulfide (M) formed during a time τ from the beginning of the reaction; $(c_{0,A} - c_A)^{2/3} = x^{2/3}$ is a quantity proportional to the surface area of PbS particles nucleated in a homogeneous solution.

Table 2. Kinetic characteristics

τ, min	$c_{Pb} \times 10^3$, M	τ, min	$c_{Pb} \times 10^3$, M	τ, min	$c_{Pb} \times 10^3$, M
$[N_2H_4CS] = 0.05$ M, $T = 313$ K					
$[Cit^{3-}] = 0.03$ M		$[Cit^{3-}] = 0.06$ M		$[Cit^{3-}] = 0.10$ M	
0	10.0	0	10.0	0	10.0
9	9.3	11	9.1	9	9.5
19	8.3	21	7.8	25	7.7
34	5.1	36	5.0	39	5.5
49	0.8	47	2.1	54	2.3
$[N_2H_4CS] = 0.025$ M, $T = 323$ K					
pH 12.00		pH 12.25		pH 12.50	
0	5.0	0	5.0	0	5.0
10	4.6	9	4.5	9	4.3
23	3.7	25	3.4	17	1.9
30	3.5	38	2.4	26	0.3
40	3.0	51	1.4	33	0.2
55	2.5	63	0.5	–	–
75	1.9	73	0.1	–	–
120	1.0	–	–	–	–

We assume that the particles of the nucleating solid phase have the shape of sphere of radius r, their number N remains constant, and the mass and surface area of each particle increase in the course of the process [8].

Let us express the surface area S of the solid phase in terms of the number of particles, N, and the surface area of a single particle, $s_0 = 4\pi r^2$, which can be found from the volume of a particle, $v_0 = 4/3\pi r^3$:

$$S = N_{s_0} = (36\pi N)^{1/3}(v_0 N)^{2/3}.$$

Let us define the volume $v_0 N$ of the solid phase by the time elapsed τ from the beginning of the reac-

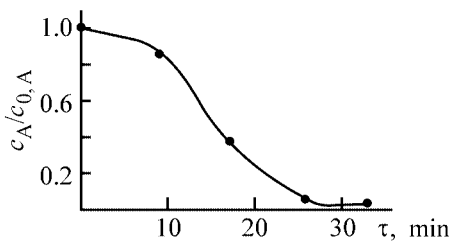

Fig. 1. Kinetic curve. $T = 323$ K; pH 12.5; $[Cit^{3-}] = 0.02$, $[Pb^{2+}] = 0.005$ M; the same for Fig. 2. $(c_A/c_{0,A})$ Relative concentration and τ time.

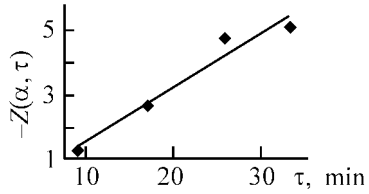

Fig. 2. Graphic representation of Eq. (6).

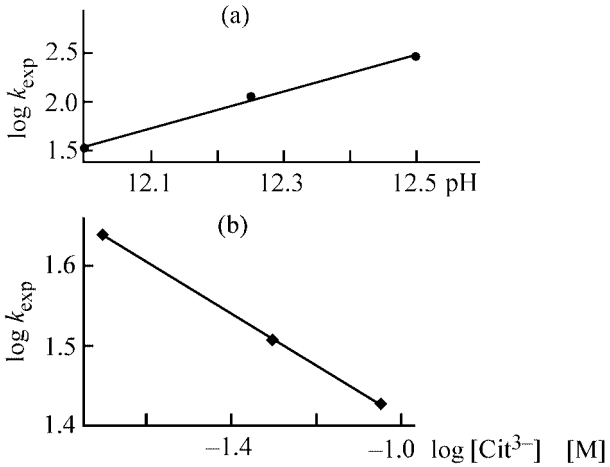

Fig. 3. Graphic determination of the reaction order with respect to concentration of (a) OH^- ions and (b) citrate ions. (k_{exp}) Reaction rate constant. (a) T = 323 K; [Cit^{3-}] = 0.025, [Pb^{2+}] = 0.005 M. (b) T = 313 K; pH 12.77, [Pb^{2+}] = 0.005 M.

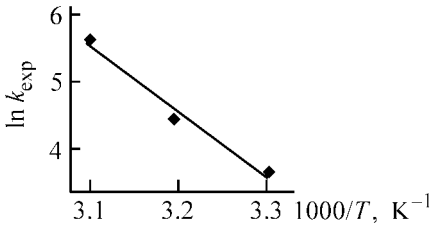

Fig. 4. Determination of the activation energy from the Arrhenius equation. [Pb^{2+}] = 0.005, [Cit^{3-}] = 0.025, [N_2H_4CS] = 0.025 M. (k_{exp}) Reaction rate constant and (T) temperature.

tion in terms of the molar mass M_{PbS}, density ρ_{PbS}, and number of moles, n_{PbS}:

$$v_0 N = (n_{PbS} M_{PbS})/\rho_{PbS},$$

by expressing n_{PbS} in terms of the initial, $c_{0,A}$, and running, c_A, concentrations of the lead salt in a reaction mixture of volume V. Then

$$S = B(c_{0,A} - c_A)^{2/3},$$

where B is a constant incorporated in the rate constant k_{exp} in Eq. (5) and equal to

$$B = \sqrt{36\pi N M_{PbS}^2 V^2/\rho_{PBS}^2}.$$

Let us integrate Eq. (5) by reducing it to a tabulated integral [9]. Upon introduction of the dimensionless quantities $\alpha = c_A/c_{0,A}$ and $\beta = c_{0,B}/c_{0,A}$, the equation takes the form

$$Z(\alpha,\tau) = \frac{1}{2}\ln\frac{[1-(1-\alpha)^{1/3}]^3}{\alpha} - \frac{1}{2\beta^{2/3}}\ln\frac{[\beta^{1/3}-(1-\alpha)^{1/3}]^3}{\beta-(1-\alpha)}$$

$$- \sqrt{3}\,\mathrm{arctg}\frac{2(1-\alpha)^{1/3}+1}{\sqrt{3}} + \frac{\sqrt{3}}{\beta^{2/3}}\,\mathrm{arctg}\frac{2(1-\alpha)^{1/3}+\beta^{1/3}}{\beta^{2/3}\sqrt{3}}$$

$$- \frac{\sqrt{3}\,(1-\beta^{2/3})}{\beta^{2/3}}\,\mathrm{arctg}\frac{1}{\sqrt{3}} = c_{0.A}^{5/3}(1-\beta)k_{exp}\tau. \quad (6)$$

A graphic representation of Eq. (6) in the coordinates $Z(\alpha, \tau)$–τ is a straight line (Fig. 2) whose slope K_{exp} is used to calculate from $K_{exp} = c_{0,A}^{5/3}(1-\beta)k_{exp}$ the experimental rate constant k_{exp} of the process. This constant depends on temperature and yields information about the influence exerted on it by all substances involved in the process and about the number N of nucleated particles.

The experimental data obtained were processed using MathCAD 2000 Professional software package. The results obtained make it possible to determine the reaction orders with respect to each of reactants from the experimental reaction rate constants at different initial ligand and thiourea concentrations and pH value. The kinetic orders of the reaction with respect to the components were calculated using the equation

$$\ln k_{exp} = \ln k_i + n_i \ln c_i, \quad (7)$$

whose graphic solution is presented in Figs. 3a and 3b. The reaction orders n_i with respect to the components are given below:

Reactant	$Pb(OAc)_2$	N_2H_4CS	OH^-	Cit^{3-}
n_i	1.0	1.0	1.85	–0.33

Using the experimental reaction rate constants obtained by processing the kinetic curves in terms of Eq. (6) at 303, 313, and 323 K, the activation energy of the process was found using the Arrhenius equation (Fig. 4) to be 83000 J mol^{-1}. The pre-exponential of the Arrhenius equation was calculated from the rate constant k_0 of reaction (4), related to unit concentration of the reaction mixture components (with account of the reaction order with respect to the components):

$$k_0 = \frac{k_{exp}}{c_{OH^-}^{1.85} c_{Cit^{3-}}^{-0.33}} = 1.37 \times 10^{17}. \quad (8)$$

Our study of lead sulfide precipitation with thiourea in alkaline citrate solutions yielded a kinetic equation that can be used to set process conditions necessary for obtaining a required process rate, on which depends the morphology of the deposit and of the lead sulfide film:

$$\frac{dx}{d\tau} = 1.37 \times 10^{17} \exp\left(-\frac{83000}{8.314T}\right) x^{2/3} c_{Cit^{3-}}^{-0.33} c_{OH^-}^{1.85} \times (c_{0,A} - x)(c_{0,B} - x). \quad (9)$$

CONCLUSIONS

(1) A model equation was proposed for describing the kinetics of lead sulfide preparation in aqueous alkaline solutions of thiourea.

(2) Reaction orders with respect to thiourea, alkali, and ligand (citrate ion) were determined. The activation energy and the pre-exponential of the Arrhenius equation were calculated.

REFERENCES

1. Butkevich, V.G., Globus, E.R., and Zalevskaya, L.N., *Prikl. Fiz.*, 1999, no. 2, pp. 96–101.
2. Lur'e, Yu.Yu., *Spravochnik po analiticheskoi khimii* (Handbook of Analytical Chemistry), Moscow: Khimiya, 1989.
3. Butler, J.N., *Ionic Equilibrium* (A Mathematical Approach), Reading, Massachusetts: Addison–Wesley, 1964.
4. Beck, M.T., *Chemistry of Complex Equilibria*, Chalmers, R.A., Transl. Ed., Budapest: Akad. Kiado, 1970.
5. Kitaev, G.A., Bol'shchikova, T.P., Fofanov, G.M., *et al.*, *Kinetika i mekhanizm obrazovaniya tverdoi fazy* (Kinetics and Mechanism of Solid Phase Formation), Sverdlovsk: Ural'sk. Politekhn. Inst., 1968, issue 170, pp. 113–126.
6. Přibil, R., *Analytical Applications of EDTA and Related Compounds*, Oxford: Pergamon, 1972.
7. Polyanskii, N.K., *Svinets* (Lead), Moscow: Nauka, 1986, p. 115.
8. Delmon, B., *Introduction á la Cinétique Hétérogene*, Paris: Technip, 1969.
9. Dwight, H.B., *Tables of Integrals and Other Mathematical Data*, New York: Macmillan, 1961.

Russian Journal of Applied Chemistry, Vol. 75, No. 10, 2002, pp. 1566–1571. Translated from Zhurnal Prikladnoi Khimii, Vol. 75, No. 10, 2002, pp. 1602–1607.
Original Russian Text Copyright © 2002 by Dresvyannikov, Kolpakov.

INORGANIC SYNTHESIS AND INDUSTRIAL INORGANIC CHEMISTRY

Kinetics of Fe(III) → Fe(0) Reduction on Aluminum in Aqueous Solutions

A. F. Dresvyannikov and M. E. Kolpakov

Kazan State Technological University, Kazan, Tatarstan, Russia

Received February 19, 2002

Abstract—The reduction of iron(III) ions by dispersed aluminum in chloride-containing aqueous solutions and the influence exerted by the initial iron(III) ion concentration and the degree of aluminum dispersion on the kinetics of the process were studied.

Spent industrial solutions (solutions for etching, electrolytes for iron plating, etc.) contain a great amount of iron, which is mainly in the oxidation state (III). Therefore, these solutions can be considered potential sources of metallic iron.

Recovery of metallic iron from aqueous solutions with the use of such conventional reducing agents as hydrogen, calcium hydride, and potassium or sodium borohydride, and also by means of electrolysis of solutions, is not always sufficiently effective. This is due to specific features of the reduction process Fe(III) → Fe(0) and also to the great number of equilibrium forms of iron, which hampers its isolation in certain cases. It is necessary to note that, in contrast to other metals, which can be reduced from aqueous solutions of their salts, the polarization observed in electrochemical reduction of iron is high. Iron electroreduction is characterized, along with high overvoltage, by low densities of the exchange current (10^{-8}–10^{-9} A cm^{-2} [1–3]) and a noticeable shift of the stationary potential from the equilibrium value, which is caused by the irreversibility of the process $M^{2+}_{aq} + 2e \rightleftarrows M$.

When iron is electrodeposited, iron ions are discharged together with proton donors [4], which changes the solution pH near the electrode. The joint discharge of iron ions and proton donors leads to the formation of difficultly soluble basic compounds, which not only promote formation of finely crystalline structure of iron precipitates through their adsorption onto the cathode, but also enter into the deposit composition themselves.

The possibility of using metallic aluminum for reducing iron ions in aqueous solutions was mentioned in [5, 6]; however, no detailed studies were carried out. In this connection, the question concerning the kinetics of reduction of iron(III) ions with aluminum remains open. Meanwhile, essential differences between the properties of compact and dispersed aluminum, including its reactivity, have been reported [7, 8].

The aim of this study was to analyze the influence exerted by the size of aluminum particles on the kinetics of iron(III) reduction in aqueous solutions and to consider the possibility of reducing iron(III) ions to iron(0) with aluminum. The processes occurring in interaction of an iron(III) salt solution with aluminum samples of varied dispersity are to be investigated.

EXPERIMENTAL

We used in the experiments narrow-fractionated samples of dispersed aluminum (with purity of no less than 99.0%) and A-999 aluminum foil 100 μm thick. As the main reagent served $FeCl_3 \cdot 6H_2O$ (analytically pure grade) without additional purification. We maintained the reaction mixture pH at 0.5 by adding appropriate amounts of hydrochloric acid to the initial solution in the process of its dilution. In doing so, we used a glass temperature-controlled vessel equipped with an electric stirrer. Preliminarily purified argon was bubbled through the solution to remove dissolved oxygen. Preliminary experiments carried out with inert gas bubbling and with natural aeration demonstrated that the presence of atmospheric oxygen has little effect on the rate of the iron(III) reduction by aluminum. For this reason, the experiments were carried out in part under natural aeration. The process kinetics was studied by taking samples at fixed intervals of time and their subsequent potentiometric titration to determine iron(II) by dichromatometry and iron(III) by

1070-4272/02/7510-1566 $27.00 © 2002 MAIK "Nauka/Interperiodica"

by complexometry [9]. The equivalence points were indicated with a specially designed differentiating device [10]. The total iron in solution was additionally monitored by X-ray fluorescent analysis on a Carl Zeiss VRA-20L instrument.

The initial aluminum samples and the products formed were studied by X-ray phase analysis on a DRON-3M installation with Co_{K_α} radiation and by electron microscopy on a REMMA-202M installation. The X-ray diffraction patterns obtained were identified using a JCPDS data file. In addition, the X-ray diffraction patterns were processed with MAUD software.

Prior to analysis, part of deposits were kept in an alkali to remove the excess amount of aluminum, washed with twice-distilled water to neutral reaction and then with ethanol, and dried in a vacuum at 60°C.

As shown by the experiments performed, solutions of iron(III) chloride react with aluminum differently, depending on the size of aluminum particles, initial concentration of iron(III) solutions, and other factors (temperature and pH). When a solution of iron(III) chloride reacts with compact aluminum, iron(II) ions are mainly accumulated, whereas with dispersed aluminum, the process yields free iron. In the latter case, a brown solution turns colorless with blue tint upon iron(III) reduction, and ferromagnetic particles are formed. A more detailed study has shown that the reaction occurs in two successive stages: 1) reduction of iron(III) ions to iron(II) and 2) reduction of iron(II) to iron(0).

Replacement of the iron(III) chloride solution with a solution of iron(III) sulfate leads to complete termination of Fe(0) formation. In all probability, this is due to the ability of chloride ions to migrate across an oxide film to the metal (via defective sites, in the first place) [11]. Filling of the film with anions raises the cationic conductivity, and the passivating film gains the capacity to pass a high current density. Furthermore, chloride ions can be adsorbed on the oxide layer with the formation and subsequent dissolution of chloride "islands" catalyzing the dissolution of the film [11]. Sulfate ions are much larger than chloride ions, and, therefore, their migration across the oxide layer on the aluminum surface is hindered [5]. The microstructure of the oxide surface layer on aluminum particles is characterized by the presence of a number of cracks and defects, which may appear due to high stresses in oxide film, resulting from the considerable difference in molar volumes between the metal and oxide, and also by the different densities of amorphous and crystalline oxides [12, 13]. This facilitates migration of chloride ions across the oxide layer to the metal surface, and, correspondingly, the intensity of aluminum ionization increases. These features of dispersed aluminum are responsible for the nature of its reaction with solutions containing iron(III) ions. The temperature and pH of a medium strongly affect the reactions considered above. It was found that, with a compact metal (as pellets or plates), mainly the process Fe(III) → Fe(II) occurs, whereas use of dispersed aluminum allows the second stage, Fe(II) → Fe(0), to be clearly detected. Since this process can be classified with consecutive reactions, it can be described in terms of a model based on the classical formal kinetics.

Using the graphical and Ostwald–Neues methods, we found that the decrease in the concentration of iron(III) ions in solution in presence of an excess amount of aluminum is described by a first-order (or pseudo-first-order) kinetic equation. In this connection, we assume all stages of the process to fit such equations. The experimental data suggest that the redox process involves the following stages

$$\mathrm{Fe(III)} \underset{k_2}{\overset{k_1}{\rightleftarrows}} \mathrm{Fe(II)} \underset{k_4}{\overset{k_3}{\rightleftarrows}} \mathrm{Fe(0)}.$$

Formally, they can be represented as

$$\mathrm{Fe(H_2O)_6^{3+}} + \mathrm{e} \underset{k_2}{\overset{k_1}{\rightleftarrows}} \mathrm{Fe(H_2O)_6^{2+}}, \quad (1)$$

$$\mathrm{Fe(H_2O)_6^{2+}} + 2\mathrm{e} \underset{k_4}{\overset{k_3}{\rightleftarrows}} \mathrm{Fe^0} + 6\mathrm{H_2O}. \quad (2)$$

Here k_1–k_4 are the respective rate constants.

The stage of the process, which is characterized by the constant k_4 of reaction (2), may result from several side reactions, e.g.,

$$2\mathrm{Fe(H_2O)_6^{3+}} + 6\mathrm{H_2O} + \mathrm{Fe^0} \rightarrow 3\mathrm{Fe(H_2O)_6^{2+}}, \quad (3)$$

$$\mathrm{Fe^0} + \mathrm{H_3O^+} + 5\mathrm{H_2O} \rightarrow \mathrm{Fe(H_2O)_6^{2+}} + 1/2\mathrm{H_2}. \quad (4)$$

Our calculation demonstrated that the rate constant k_2 of reaction (1) is very small as compared with the other constants ($\sim 10^{-5}$ s^{-1}), and, therefore, it can be neglected. In this context, we further consider the following scheme of the process:

$$\mathrm{Fe(III)} \xrightarrow{k_1} \mathrm{Fe(II)} \underset{k_4}{\overset{k_3}{\rightleftarrows}} \mathrm{Fe(0)},$$

which can be described in terms of formal kinetics by the following set of equations

$$\frac{dc[\mathrm{Fe(III)}]}{d\tau} = -k_1 c[\mathrm{Fe(III)}], \quad (5)$$

$$\frac{dc[\mathrm{Fe(II)}]}{d\tau} = -k_1 c[\mathrm{Fe(III)}] - k_3 c[\mathrm{Fe(II)}] + k_4 c[\mathrm{Fe(0)}], \quad (6)$$

$$\frac{dc[\mathrm{Fe(0)}]}{d\tau} = -k_3 c[\mathrm{Fe(II)}], - k_4 c[\mathrm{Fe(0)}]. \quad (7)$$

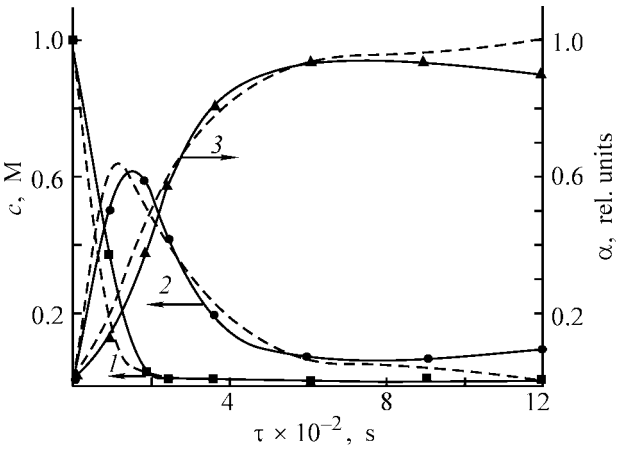

Fig. 1. Kinetic curves of iron(III) reduction by dispersed aluminum. (*c*) Concentration, (α) degree of α-iron transformation, and (τ) time. Size of aluminum particles 71–100 μm, initial $FeCl_3$ concentration 1 M, temperature 298 K; the same for Fig. 3. Compound: (*1*) Fe(III), (*2*) Fe(II), and (*3*) Fe(0). (*1–3*) experiment; *dashed lines*, calculation by Eqs. (8), (13), and (15).

The solution of system (5)–(7) results in the following expressions:

$$c[\mathrm{Fe(III)}] = c_0[\mathrm{Fe(III)}]\exp(-k_1\tau), \quad (8)$$

$$c[\mathrm{Fe(II)}] = \frac{c_0[\mathrm{Fe(III)}]}{K_{eq} + 1}[1 - \exp(-k_1\tau)], \quad (9)$$

$$c[\mathrm{Fe(0)}] = \frac{c_0[\mathrm{Fe(III)}]K_{eq}}{K_{eq} + 1}[1 - \exp(-k_1\tau)]. \quad (10)$$

Here $K_{eq} = k_3/k_4$.

Since Fe(0) is in the nonionic state, we replace c[Fe(0)] with m[Fe(0)]:

$$m[\mathrm{Fe(0)}] = \frac{m_0[\mathrm{Fe(III)}]K_{eq}}{K_{eq} + 1}[1 - \exp(-k_1\tau)]. \quad (11)$$

Hence, introducing a degree of transformation, α, we obtain

$$\alpha = \frac{m[\mathrm{Fe(0)}]}{m_0[\mathrm{Fe(III)}]} = \frac{K_{eq}}{K_{eq} + 1}[1 - \exp(-k_1\tau)]. \quad (12)$$

However, a comparison of the calculated characteristics with the experimental data demonstrated that Eqs. (9) and (12) disagree somewhat with the experimental data. A detailed analysis revealed that $k_4 << k_3$, and, therefore, k_4 can be neglected. As a result, we obtain

$$\mathrm{Fe(III)} \xrightarrow{k_1} \mathrm{Fe(II)} \xrightarrow{k_3} \mathrm{Fe(0)}.$$

Analysis of this scheme gives

$$c[\mathrm{Fe(II)}] = \frac{c_0[\mathrm{Fe(III)}]k_1}{k_3 - k_1}[\exp(-k_1\tau) - \exp(-k_3\tau)], \quad (13)$$

$$m[\mathrm{Fe(0)}] = m_0[\mathrm{Fe(III)}] \times \left[1 - \frac{k_3}{k_3 - k_1}\exp(-k_1\tau) + \frac{k_1}{k_3 - k_1}\exp(-k_3\tau)\right], \quad (14)$$

$$\alpha = \frac{k_3}{k_3 - k_1}\exp(-k_1\tau) + \frac{k_1}{k_3 - k_1}\exp(-k_3\tau). \quad (15)$$

Changes in the concentration c[Fe(III)] are calculated using Eq. (8). The experimental and calculated kinetic curves are shown in Fig. 1. Their satisfactory agreement indicates that the kinetics of Fe(III) reduction by dispersed aluminum can be described by Eqs. (8), (13), and (15).

Deviations of c[Fe(II)] and α, calculated using Eqs. (13) and (15), from the experimental values corresponding to the initial and final periods of the reaction are attributable to imperfection of the model proposed. In particular, it disregards the diffusion and adsorption processes, and also other specific features of the reactions occurring at the interface. The calculated and experimental data quite satisfactorily coincide in the time interval 0–600 s after the beginning of the process. Further, deviations appear, caused, in all probability, by the above-mentioned factors and also by the intensification of dissolution of deposited iron(0). This intensification occurs virtually from the very beginning of Fe(III) ion reduction when compact aluminum is used, and also in the case of dispersed aluminum (particles greater than 200 μm) under the following conditions: elevated temperature, low concentrations of the initial solution, and long duration of the process (>600 s after its beginning).

The rate of the process, and also the yield of α-iron grow with increasing concentration of iron(III) solutions (Fig. 2a), with the yield reaching a value of 99% at $c \geq 2.0$ M. It is necessary to note that the process under consideration is not isothermal, and its exothermic effect becomes more pronounced with increasing concentration of iron(III) chloride. Elevating the temperature also accelerates iron deposition, with, however the yield of iron decreasing in this case. Most likely, a rise in temperature essentially accelerates side reactions (3) and (4).

The size of aluminum particles strongly affects relative the rates of the redox stages under consideration (Fig. 2b). An increase in the particle size leads, on passing a certain conditional boundary of ~200 μm, to a sharp decrease in k_1 and k_3 and, correspondingly, in the iron(0) yield. This is attributable to a difference in structure and physicochemical properties of surface oxide layers between compact and dispersed alumi-

num. The film on the surface of particles of finely dispersed aluminum is not ideally smooth and shows a shallow profile in the form of folds, pits, and bulges. We assume that the profile on oxide layers originates from volume shrinkage of the metal in transition from a melt to the solid state, and also from the difference in thermal expansion coefficients between the metal and the oxide (by approximately a factor of 4) [14]. Stresses arising in the surface oxide layers of aluminum particles are rather substantial, which may be due to the significant difference in modulus of elasticity between the metal and the oxide phase [14, 15].

The crystalline oxide formed in dry air or upon high-temperature heating of powders stretches the metal lattice at room temperature and compresses it at elevated temperatures [16]. The appearance of shearing stresses, which are more or less uniformly distributed throughout the particle volume, results from differences in structure and thermal expansion between aluminum and its oxide. Trace amounts of crystalline aluminum oxide mono- and trihydrates were detected in the oxide layers of aluminum powders, except in those obtained at high temperatures [12, 17]. The formation of hydroxides on the particle surface is due to hydration of the amorphous oxide and finely dispersed γ-Al_2O_3 in storage with access of air containing water vapor. Ultramicroscopic quantities of a foreign phase (e.g., Si, Fe, Zn, K, Mg, etc.) are also present in the surface layers.

Thus, the surface microstructure of the oxide layer on aluminum particles is characterized by the presence of a large number of microcracks [16–19]. Furthermore, the oxide films on particles have a great number of structural defects [12, 14]. These features of dispersed aluminum predetermine the nature of its reaction with solutions containing iron(III) ions.

The aforesaid suggests the following course of the process: when iron(III) chloride is dissolved, it undergoes hydrolysis, which leads to liberation of a certain amount of hydrochloric acid; however, in strongly acid or concentrated solutions the hydrolysis of iron ions does not result in the formation of difficultly soluble basic compounds. The liberated Cl^- anions are depassivators, being adsorbed to displace or partially replace the passivating oxygen on the metal surface to give a surface complex [11] that can further pass into solution. Chloride ions play a double role [20]: they depassivate the electrode and are involved in the kinetic stage of aluminum ionization.

The oxidation of aluminum in the course of corrosion is accompanied by reduction of proton donors

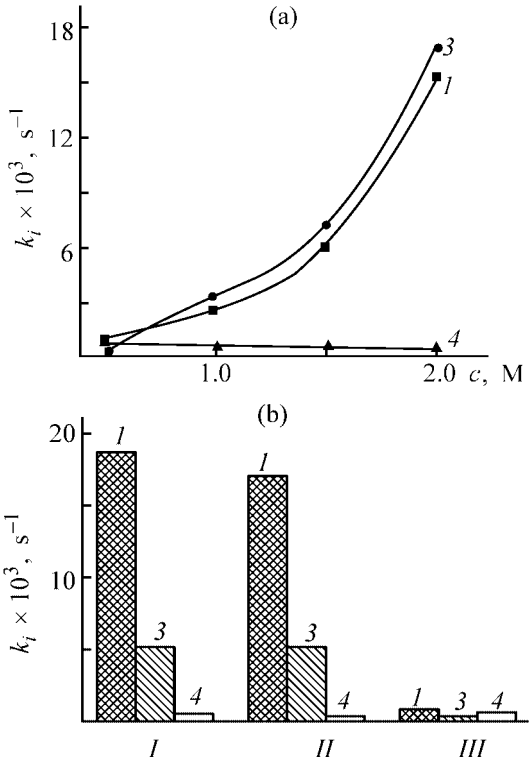

Fig. 2. Effects of (a) initial $FeCl_3$ concentration c and (b) size of aluminum particles on the rate constants k_i of various stages of iron(III) reduction. Temperature 298 K, (b) initial $FeCl_3$ concentration 1 M. *Digits 1, 3,* and *4* correspond to k_1, k_3, and k_4, respectively. Size of aluminum particles (μm): (*I*) 71–100, (*II*) 140–250, and (*III*) 250–400.

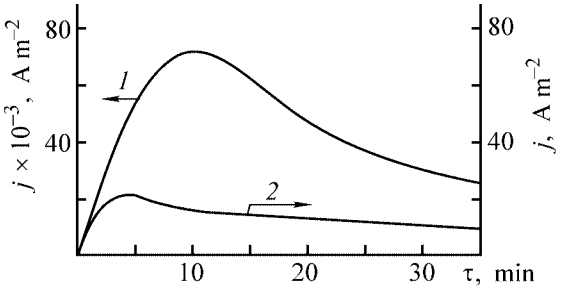

Fig. 3. Rates j of (*1*) iron deposition and (*2*) hydrogen evolution on aluminum microparticles vs. time τ.

(hydrogen depolarization) and iron ions (oxidizing agent). As shown above, the latter process includes two stages and culminates in precipitation of α-iron.

The conjugate deposition of iron and hydrogen evolution on aluminum is illustrated in Fig. 3. It is necessary to note that the rate of hydrogen liberation is, in this case, lower than that of iron precipitation by more than 3 orders of magnitude. Such a disagreement

with the data presented above is attributable to the following: difference in the nature of the supporting metal; hydrogen liberation only on the metal being deposited, owing to an essential difference between the overvoltages of hydrogen liberation on aluminum and iron [21]; and high rate of metal deposition, resulting from a developed aluminum surface and nonisothermal character of the process (exothermic effect). In this case, the solution pH grows essentially, by approximately two pH units.

Since basic compounds of iron are formed in its deposition, it makes sense to determine qualitatively and quantitatively the composition of deposits formed on aluminum. According to X-ray phase analysis and local microanalysis, samples obtained with the use of dispersed aluminum (71–100-μm fraction) are formed by a mechanical mixture of crystals of α-iron and aluminum. We found that a deposit kept in a concentrated NaOH solution (3.0 M) consists of a single phase of α-iron. It is necessary to note that the size of mosaic iron blocks obtained by reduction of $FeCl_3$ solutions with dispersed aluminum is 24.569 nm. Correspondingly, the lattice constant a is 0.28662 ± 0.00001 nm, in agreement with reference data [22, 23] (a = 0.28665 nm). Some parameters of crystallites of the α-iron obtained are given below:

h	*k*	*l*	Crystallite size, nm	Microstrain
1	1	1	24.569	0.00402
2	0	0	13.791	0.00419
2	1	1	24.569	0.00402
2	2	0	24.569	0.00402

When a deposit is not kept in an alkali, an amorphous phase, most likely pseudoboehmite, appears in the deposit. In the course of time, bayerite crystals formed from metastable products of aluminum dissolution also appear.

The resulting iron particles are spherical or nearly so and have different sizes. Large particles (40–50 μm) bear on their surface spherical subparticles 0.5–5 μm in size and an open-work network of thread-like nuclei in microcracks and pores.

CONCLUSIONS

(1) It is established for the first time that reduction of iron(III) ions by dispersed aluminum in chloride-containing aqueous solutions may occur in two successive stages Fe(III) → Fe(II) → α-Fe, with α-Fe yield as high as 99%. In this case, the rate of iron deposition exceeds that of conjugate hydrogen liberation by approximately 3 orders of magnitude.

(2) The decisive influence on the kinetics of this process is exerted by the initial concentration of iron(III) ions and the degree of aluminum dispersity.

(3) It is established by X-ray fluorescent and X-ray phase analyses and electron microscopy that the deposits formed in this process are formed of α-iron (crystallographic Miller indexes 110, 200, 211, and 220) with a minor amount of admixtures.

REFERENCES

1. Skorcheletti, V.V., *Teoreticheskaya elektrokhimiya* (Theoretical Electrochemistry), Leningrad: Khimiya, 1974.
2. Antropov, L.I., *Teoreticheskaya elektrokhimiya* (Theoretical Electrochemistry), Moscow: Vyshaya Shkola, 1984.
3. Roiter, V.A., Yuza, V.A., and Poluyan, E.S., *Zh. Fiz. Khim.*, 1939, vol. 13, no. 5, pp. 605–620.
4. Lainer, V.I. and Kudryavtsev, N.T., *Osnovy gal'vanostegii* (Fundamentals of Electroplating), Moscow: Metallurgizdat, 1957.
5. Wernik, S. and Pinner, R., *The Surface Treatment and Finishing of Aluminium and its Alloys*, Teddington: R. Draper Ltd, 1972, 4th ed.
6. Riegel, E.R. and Schwartz, R.D., *Analyt. Chem.*, 1952, vol. 24, no. 11, pp. 1803–1806.
7. Lepin', L.K., *Izv. Akad. Nauk LatvSSR, Ser. Khim.*, 1975, no. 2, pp. 155–168
8. Lepin', L.K., *Izv. Akad. Nauk LatvSSR, Ser. Khim.*, 1981, no. 1, pp. 12–25
9. *Praktikum po fiziko-khimicheskim metodam analiza* (Practical Works on Physicochemical Methods of Analysis), Petrukhin, O.M., Ed., Moscow: Khimiya, 1987.
10. Dresvyannikov, A.F., Fomin, A.V., and Rusetskii, O.I., *Zavod. Lab.*, 1990, vol. 56, no. 3, pp. 19–21.
11. Kolotyrkin, Ya.M., *Metall i korroziya* (Metal and Corrosion), Moscow: Metallurgiya, 1985.
12. Lokenbakh, A.K., Zaporina, N.A., and Lepin', L.K., *Izv. Akad. Nauk LatvSSR, Ser. Khim.*, 1981, no. 1, pp. 45–49.
13. Zhilinskii, V.V., Lokenbakh, A.K., and Lepin', L.K., *Izv. Akad. Nauk LatvSSR, Ser. Khim.*, 1986, no. 2, pp. 151–155.
14. Ivanov, A.S. and Borisov, S.A., *Poverkhnost': Fiz., Khim., Mekh.*, 1983, no. 10, pp. 31–35.
15. Akimov, A.G. and Makarychev, Yu.B., *Poverkhnost': Fiz., Khim., Mekh.*, 1983, no. 5, pp. 88–96.

16. Petrov, Yu.I., *Fiz. Tverd. Tela*, 1963, vol. 5, no. 9, pp. 2461–2476.
17. Lokenbakh, A.K., Strod, V.V., Nekrasova, N.V., *et al.*, *Izv. Akad. Nauk LatvSSR, Ser. Khim.*, 1984, no. 5, pp. 627–628.
18. Lokenbakh, A.K., Strod, V.V., Lepin', L.K., *et al.*, *Izv. Akad. Nauk LatvSSR, Ser. Khim.*, 1981, no. 1, pp. 50–58.
19. Petrov, Yu.I. and Bibilashvili, R.Sh., *Zh. Fiz. Khim.*, 1964, vol. 38, no. 11, pp. 2614–2624.
20. Barteneva, O.I., Bartenev, V.V., and Grigor'ev, V.P., *Elektrokhimiya*, 2000, vol. 36, no. 11, pp. 1337–1342.
21. *Spravochnik po elektrokhimii* (Handbook of Electrochemistry), Sukhotin, A.M., Ed., Leningrad: Khimiya, 1981.
22. Mirkin, L.I., *Spravochnik po rentgenostrukturnomu analizu polikristallov* (Handbook of X-ray Structural Analysis of Polycrystals), Moscow: Fizmatgiz, 1961.
23. *The Rietveld Method*, Young, R.A., Ed., New York: Oxford Univ., 1993.

Russian Journal of Applied Chemistry, Vol. 75, No. 10, 2002, pp. 1572–1576. Translated from Zhurnal Prikladnoi Khimii, Vol. 75, No. 10, 2002, pp. 1608–1611.
Original Russian Text Copyright © 2002 by Lokshin, Vershkova, Vershkov, Tareeva.

INORGANIC SYNTHESIS AND INDUSTRIAL INORGANIC CHEMISTRY

Efficiency of Sulfuric Acid Leaching of Lanthanides in Relation to Quality of Phosphosemihydrate Obtained from Khibiny Apatite Concentrate

E. P. Lokshin, Yu. A. Vershkova, A. V. Vershkov, and O. A. Tareeva

Tananaev Institute of Chemistry and Technology of Rare Elements and Mineral Raw Materials, Kola Scientific Center, Russian Academy of Sciences, Apatity, Russia

Received May 13, 2002

Abstract—Reasons for a decrease in recovery of lanthanides by sulfuric acid leaching from separate lots of phosphosemihydrate produced by Voskresenskie Mineral'nye Udobreniya joint-stock company were studied.

Khibiny apatites are one of the most promising Russian raw sources of lanthanides [1, 2]. The sum of lanthanides in the apatite concentrate (AC) obtained from ores mined at the Khibiny field is about 1 wt % [3], with the relative contents of elements being close to the optimal in the pattern of consumption [4].

In 1996, more than 80% of the 4.82 million tons of AC supplied to Russian plants were processed by the sulfuric acid technology. This technology was implemented in the form of semihydrate and dihydrate processes, which produce as a recrement, together with H_3PO_4, either "phosphosemihydrate" $2CaSO_4 \cdot H_2O$ (PSH) or "phosphodihydrate" $CaSO_4 \cdot 2H_2O$ (PDH), respectively.

The semihydrate process is used at two largest Russian fertilizer plants: Ammofos joint-stock company (Cherepovets) and Voskresenskie Mineral'nye Udobreniya joint-stock company (Voskresensk, Moscow oblast). This method is more economical and will gradually replace the dihydrate process at other Russian plants. With the semihydrate process, up to 95% of lanthanides is extracted to PSH from the apatite concentrate [5, 6].

An efficient technology for recovery of lanthanides from PSH has been developed at the Ammofos joint-stock company [7–15]. According to this scheme, the same H_2SO_4 solution is used for leaching of several PSH portions. In each leaching stage, concentrated sulfuric acid (93.5 wt %) is added to the solution to maintain its concentration. Lanthanides are extracted from the sulfate solution by ionic flotation.

In the case of acid leaching, only lanthanides forming independent phases in PSH can pass into solution. Part of lanthanides in PSH do not crystallize isomorphically with hydrated calcium sulfate, but form independent phases precipitating on celestine ($SrSO_4$) grains. The most probable compounds of lanthanides in these phases are phosphates and binary sulfates of rare-earth and alkali metals [16].

Some authors [17] believe that the limiting concentration of lanthanides in solutions (1.1–1.2 g l^{-1}) is determined by the salting-out action of H_2SO_4, which lowers the solubility of lanthanide sulfates. However, the solubility of lanthanide sulfates is an order of magnitude higher in H_2SO_4 solutions with the concentrations under study, compared with that reached in leaching solutions.

Phosphoric acid is accumulated in leaching solutions [7, 9, 17] because of the dissolution of lanthanide and calcium phosphates in H_2SO_4 and also because of its inflow from unwashed PSH.

The solubility of lanthanide orthophosphates in acid sulfate-phosphate solutions grows with increasing concentration of sulfuric acid and falls with increasing concentration of orthophosphoric acid [13]. The use of more concentrated acidic sulfate solutions allowed the sum of lanthanides in the leaching solution to be raised to 3 g l^{-1} and more [13]. As a result, the volume of solutions decreased to a level permitting their utilization in manufacture of fertilizers without disturbing the water balance and carrying out their concentration by evaporation.

1070-4272/02/7510-1572 $27.00 © 2002 MAIK "Nauka/Interperiodica"

When working with PSH, the Voskresenskie Mineral'nye Udobreniya joint-stock company found that previously obtained data on leaching of lanthanides with H_2SO_4 solutions could not be reproduced for separate lots of the product.

The aim of this study was to analyze the reasons for the decrease in recovery of lanthanides by leaching from PSH with H_2SO_4.

EXPERIMENTAL

The following methods and instruments were used in analyzing the products: oxalic gravimetry (lanthanides, calcium, and strontium); atomic–emission spectrometry with inductively coupled plasma, Perkin Elmer Plasma 400 instrument (lanthanides, calcium, strontium, and titanium); X-ray fluorescence analysis (lanthanides and phosphorus); atomic–absorption spectrometry in an acetylene-air flame, Carl Zeiss AAS-30 (Jena) instrument (sodium and potassium); and spectrophotometry (phosphorus, fluorine, and silicic acid) [18, 19].

The results obtained in analyzing solutions suggest that increased content of sodium and potassium hexafluorosilicates in PSH can hinder accumulation of lanthanides in solution. Sodium and potassium ions, which pass into an acidic sulfate solution, must bind lanthanides into poorly soluble binary sulfates $MLn(SO_4)_2$ by the reaction

$$M_2SO_4 + Ln_2(SO_4)_3 = 2MLn(SO_4)_2 \ (M = Na, K).$$

Calculations with the use of the data of [20] on the solubility of binary sulfates of lanthanides in water demonstrated the following.

(1) With increasing concentration of sulfuric acid, the solubility of binary sulfates of rare-earth and alkali metals decreases substantially, especially for potassium. With increasing content of water-soluble compounds of sodium and potassium in PSH, binary sulfates may form and precipitate.

(2) The solubility of binary sulfates of lanthanum, cerium, and alkali metals, whose total content in the "apatite sum" exceeds 70%, is particularly small [21]. This accounts for the observed [7] increase in the content of yttrium-group lanthanides in the sum of lanthanides leached out by sulfuric acid from PSH, compared with their content in the initial PSH.

It is not improbable that fluoride ion passing into solution together with Na_2SiF_6 and K_2SiF_6 and also upon decomposition of apatite remainder, can hinder lanthanides from passing into solution. The rather low solubilities of Na_2SiF_6 and K_2SiF_6 [22] predetermine the difficulty of their removal in washing PSH with water on revolving filters. Although lanthanide fluorosilicates are readily soluble in inorganic acids [23], fluoride ions are formed in solution through SiF_6^{2-} hydrolysis. They can bind lanthanides into poorly soluble fluorides LnF_3 [24].

It is known [24] that the solubility of lanthanide fluorides grows with increasing acidity, and at pH ~1 it falls in the range 0.17–0.4 g l^{-1} (in terms of Ln_2O_3) for various lanthanides. Further increase in the solution acidity seems to raise the solubility of lanthanide fluorides.

The probability of formation of lanthanide fluorides in sulfuric acid leaching solutions is estimated below. When SiF_4 is absorbed by sulfuric acid with concentration of 62.5 wt % and lower, silicic acid is formed by the reaction [25]

$$SiF_6^{2-} + 2H_2O = SiO_2 + 4H^+ + 6F^-. \qquad (1)$$

The equilibrium constant of reaction (1) has been found by different researchers to fall in the range $n \times 10^{-27}$–$n \times 10^{-28}$ [25]. For our calculations we adopted the maximal value of 2.3×10^{-27}, since in this case, the equilibrium content of fluoride ions in solution will be the highest.

We assumed in our calculations that the Na_2SiF_6 solubility in sulfuric acid, as also that in water, is 0.7 wt % and the ion activities are equal to their concentrations. The estimated concentrations of F^- ions in acidic sulfate solutions are given below:

$c_{H_2SO_4}$, wt %	2	4	6	8	10	20
c_{F^-}, mg l^{-1}	1.10	0.69	0.54	0.44	0.38	0.24

These data show that the concentration of F^- ions in acidic sulfate solutions is several orders of magnitude lower than it follows from the data [24] on the solubility of lanthanide fluorides in acidic solutions, i.e., lanthanide fluorides must not precipitate.

As mentioned above, solutions containing 3 g l^{-1} and more of lanthanides were obtained by processing four portions of PSH (from Ammofos joint-stock company) with average extraction of 32.6–38.7%, using the same H_2SO_4 solution, to which new portions of the acid were successively added to maintain its concentration. In this case, one leaching cycle with 2–6% solution of sulfuric acid within 1 h resulted in that 150–160 mg l^{-1} of Na_2O and 94 mg l^{-1} of K_2O passed into solution.

Table 1. Leaching of lanthanides from PSH (0.45wt % Ln_2O_3 in PSH) with 6% H_2SO_4 solution (V_l : V_s = 3 : 1) (duration of leaching 0.5 h, 3% H_2SO_4 added in each of cycles 2–4)

Stage	Concentration in solution, g l^{-1}				Ln_2O_3 recovery, %
	Na_2O	K_2O	P_2O_5	Ln_2O_3	
1	0.36	0.076	1.46	0.44	29.3
2	0.41	0.084	2.23	0.73	19.3
3	0.42	0.11	2.72	0.91	12.0
4	0.47	0.096	3.36	1.162	16.8

Table 2. Efficiency of sulfuric acid leaching of lanthanides (V_l : V_s = 3 : 1) in the case of PSH washing with water (V_l : V_s = 2 : 1, duration of leaching 1 h, duration of washing 0.5 h)

Stage	Concentration in solution,		Ln_2O_3 recovery, %
	H_2SO_4, wt %	Ln_2O_3, g l^{-1}	
Without washing			
1	6	0.478	25.2
2	6 + 3	0.576	5.2
After washing with water			
1	6	1.28	67.37
2	6 + 3	2.36	56.84
3	6 + 3 + 3	3.14	41.05

Table 3. Leaching of lanthanides with nitric acid from unwashed PSH (V_s : V_l = 1 : 3) (leaching duration 1 h, Ln_2O_3 content in the concentrate 0.43 wt %)

Concentration in solution			Recovered, %	
HNO_3, wt %	Ln_2O_3, g l^{-1}	Ca(Sr)O, g l^{-1}	Ln_2O_3	Ca(Sr)O
2	0.76	3.81	53.0	2.96
4	1.10	5.97	76.7	4.64
6	1.15	7.87	80.2	6.11
8	1.20	8.10	83.7	6.3

Table 4. Leaching of lanthanides from PSH with multiple recycling of HNO_3 solution (V_s : V_l = 1 : 3) (duration of leaching 1 h, Ln_2O_3 content in the concentrate 0.53 wt %)

Stage	Concentration in solution			Extracted, %	
	HNO_3, wt %	Ca(Sr)O, g l^{-1}	Ln_2O_3, g l^{-1}	Ca(Sr)O	Ln_2O_3
1	4	5.52	0.8	4.29	45.3
2	4 + 1	5.92	1.34	0.31	30.5
3	4 + 1 + 1	6.28	1.82	0.28	27.2
4	4 + 1 + 1 + 1	6.77	2.14	0.38	18.1

We found that the efficiency of lanthanide leaching sharply decreased when working with certain PSH samples manufactured by Voskresenskie Mineral'nye Udobreniya joint-stock company (Table 1). The concentration of lanthanides in solution increased somewhat starting from the second stage (probably, yttrium and medium lanthanides, whose solubility as binary sulfates is high and the content in the sum of lanthanides in PSH is low, continued to dissolve). The concentrations of sodium and potassium ions remained virtually unchanged.

In some cases, washing of such a PSH with water resulted in a sharp increase in recovery of lanthanides into leaching solutions (Table 2).

The experiments demonstrated that, with washing for 0.5 h at V_l : V_s = 2 : 1, the main part of sodium and potassium ions is washed out of PSH by water. However, when the washing water is reused for processing the subsequent PSH portions, the efficiency of washing in solution much decreases, although the concentration of sodium and potassium ions in solution is much less than that corresponding to the equilibrium solubility of Na_2SiF_6 and K_2SiF_6.

However, in the case of certain PSH lots manufactured at the Voskresenskie Mineral'nye Udobreniya joint-stock company, even washing with water increased the efficiency of sulfuric acid leaching only slightly. As a rule, the content of lanthanides in these lots was too low for PSH, namely, no more than 0.43 wt %, instead of the usual 0.57 wt %. When such PSH lots were treated with HNO_3 solutions with various concentrations (Table 3), effective leaching of lanthanides was achieved in the first stage, a significant amount of PSH being dissolved in this case. The greatest increase in the REE extraction was obtained with 4–6% HNO_3 solution, with 4.64–6.11% of PSH passing into solution.

When HNO_3 solution is used for successive leaching of several portions of such a PSH, the efficiency of rare-earth leaching decreases sharply even upon addition of nitric acid to maintain its concentration (Table 4).

We were able to transfer in solution 96.28 % of rare-earth elements by twofold leaching of a single portion of such a PSH with fresh portions of nitric acid (Table 5). This fact confirms the data of [16],

Table 5. Processing of a single PSH portion with two successive portions of fresh HNO_3 ($V_s : V_l = 1 : 3$) (duration of leaching 1 h, Ln_2O_3 content in the concentrate 0.43 wt %)

Stage	Concentration in solution			Extracted, %	
	HNO_3, wt %	Ca(Sr)O, g l^{-1}	Ln_2O_3, g l^{-1}	Ca(Sr)O	Ln_2O_3
1	4	5.04	1.03	3.91	71.86
2	4	5.04	0.35	3.91	24.42

according to which the main part of lanthanides in the PSH studied is not isomorphically crystallized with $2CaSO_4 \cdot H_2O$ (bassanite) and 10.1 % Ca(Sr)O contained in PSH.

The data of Tables 4 and 5 suggest that the PSH lots most difficultly leached with sulfuric acid were obtained with violations of the semihydrate technology (by a "mixed" process) and are, in fact, PSH grains with a PDH crust. The solubility of calcium sulfate in fresh nitrate solutions is rather high, and crusts hindering the access of the acid to rare-earth-containing grains are dissolved. In this case, lanthanides are leached by nitric acid. After the acidic nitrate solution is saturated with calcium sulfate, it becomes difficult for lanthanides to pass into solution.

CONCLUSIONS

(1) Increased content of soluble compounds of sodium and potassium (Na_2SiF_6 and K_2SiF_6) in the phosphosemihydrate and(or) production of phosphosemihydrate in a mixed semihydrate-dihydrate process lead to a sharp decrease in the extent of recovery of lanthanides in their sulfuric acid leaching from phosphosemihydrate.

(2) Loss of lanthanides in sulfuric acid leaching of phosphosemihydrate is less probable owing to the formation of poorly soluble fluorides.

(3) It has been established experimentally that the main part of lanthanides do not crystallize isomorphically with phosphosemihydrate.

ACKNOWLEDGMENTS

The study was supported financially supported by the program "Leading Scientific Schools" (project no. 00-15-97364).

REFERENCES

1. Lebedev, V.N., Lokshin, E.P., Masloboev, V.A., *et al.*, *Tsvetn. Met.*, 1997, no. 8, pp. 46–51.
2. Kudrin, V.S., Usova, T.Yu., Chistov, L.B., *et al.*, *Redkozemel'nye metally Rossii: sostoyanie, perspektivy osvoeniya i razvitiya mineral'no-syr'evoi bazy* (Rare-Earth Metals of Russia: State, Prospects for Use and Development of Mineral Resources), Moscow: VIMS (Fedorovski All-Russia Institute of Mineral Resources), 1999.
3. Mineev, D.A., *Lantanoidy v rudakh* (Lanthanides in Ores), Moscow: Nauka, 1974.
4. Kudrin, V.S., *Mineral'n. Resursy Rossii*, 1996, no. 5, pp. 6–12.
5. Lebedev, V.N., Masloboev, V.A., Popova, L.A., and Serkova, L.P., *Problemy effektivnogo ispol'zovaniya mineral'nogo syr'ya Kol'skogo poluostrova* (Problem of Effective Utilization of Mineral Resources of the Kola Peninsula), Apatity: KNTs RAN (Kola Scientific Center, Russian Academy of Sciences), 1993, pp. 43–49
6. Kazak, V.G., Angelov, A.I., and Zaitsev, P.M., *Khim. Prom–st.*, 1995, no. 9, pp. 11–19.
7. Lebedev, V.N., Smirnova, I.P., Masloboev, V.A., *et al.*, *Fiziko-khimicheskie i tekhnologicheskie problemy pererabotki syr'ya Kol'skogo poluostrova* (Physicochemical and Technological Problems of Processing of Raw Materials from the Kola Peninsula), St. Petersburg: Nauka, 1993, pp. 56–60.
8. Vershkov, A.V. and Masloboev, V.A., *Tsvetn. Met.*, 1995, no. 2, pp. 58–59.
9. Lokshin, E.P., Vershkov, A.V., and Vershkova, Yu. A., Abstracts of Papers, *XVI Mendeleev Congress on General and Applied Chemistry*, Moscow, 1998, vol. 2, p. 111.
10. Lokshin, E.P., Vershkov, A.V., Vershkova, Yu.A., and Masloboev, V.A., *Kompleksnaya pererabotka khibinskikh apatito-nefelinovykh rud* (Complex Processing of Khibiny Apaptite-Nepheline Ores), Apatity: KNTs RAN (Kola Scientific Center, Russian Academy of Sciences), 1999, pp. 84–89.
11. Lokshin, E.P., Vershkov, A.V., Vershkova, Yu.A., *et al.*, *Tsvetn. Met.*, 2000, no. 10, pp. 44–48.
12. Lokshin, E.P., Vershkov, A.V., Vershkova, Yu.A., and Masloboev, V.A., *Nekotorye kineticheskie kharakteristiki ionnoi flotatsii redkozemel'nykh elementov iz rastvorov pererabotki khibinskogo apatitovogo kontsentrata* (Some Kinetic Characteristics of Ionic Flotation of Rare Earths from Solutions Produced in Processing of Khibiny Apatite Concentrate), 2000, Available from VINITI, Apatity, no. 941–V00.
13. Lokshin, E.P., Vershkov, A.V., and Vershkova, Yu.A., Metally, 2001, no. 1, pp. 42–50.
14. RF Patent 2167105.
15. RF Patent 2172719.
16. Lokshin, E.P., Vershkov, A.V., and Vershkova, Yu. A., *et al.*, Abstracts of Papers, *Nauchnaya konferentsiya "Khimiya i khimicheskaya tekhnologiya v osvoenii prirodnykh resursov Kol'skogo poluostrova"* (Sci.

Conf. "Chemistry and Chemical Technology in Development of Natural Resources of the Kola Peninsula"), Apatity, 1998 pp. 31–32.

17. Vorob'ev, N.I., Teterevkov, A.I., and Zyk, V.V., *Vestsy Akad. Navuk Belarusi, Ser. Khim. Navuk*, 1998, no. 2, pp. 103–106.
18. Fritz, J.S. and Schenk, G.H., *Quantitative Analytical Chemistry*, Boston: Allyn and Bacon, 1974.
19. Charlot, G., *Les Methods de la Chemie Analytique. Analyse quantitative Minerale*, Quatrieme Edition, Paris: Masson, 1961.
20. Komissarova, L.N., Pushkina, G.Ya., Shatskii, V.M., *et al.*, *Soedineniya redkozemel'nykh elementov: Sul'faty, selenaty, telluraty, khromaty* (Compounds of Rare Earths: Sulfates, Selenates, Tellurates, Chromates), Moscow: Nauka, 1986.
21. Masloboev, V.A. and Lebedev, V.N., *Redkozemel'noe syr'e Kol'skogo poluostrova i problemy ego kompleksnoi pererabotki* (Rare Earth Raw Materials from the Kola Peninsula and Problems of Its Integrated Processing), Apatity: KNTs AN SSSR (Kola Scientific Center, Academy of Sciences of the USSR), 1991.
22. Kirgintsev, A.N., Trushnikova, L.N., and Lavrent'eva, V. G., *Rastvorimost' neorganicheskikh veshchestv v vode: Spravochnik* (Solubility of Inorganic Substances in Water: Reference Book), Leningrad: Khimiya, 1972.
23. Serebrennikov, V.V., *Khimiya redkozemel'nykh elementov* (Chemistry of Rare Earths), Tomsk: Tomsk. Univ., 1959.
24. Menon, M.P., and James, J., *J. Chem. Soc. Faraday Trans.*, 1989, vol. 85, no. 9, pp. 2683–2694.
25. Ryss, I.G., *Khimiya ftora i ego neorganicheskikh soedinenii* (Chemistry of Fluorine and Its Inorganic Compounds), Moscow: Goskhimizdat, 1956.

Russian Journal of Applied Chemistry, Vol. 75, No. 10, 2002, pp. 1577–1579. Translated from Zhurnal Prikladnoi Khimii, Vol. 75, No. 10, 2002, pp. 1612–1614.
Original Russian Text Copyright © 2002 by Brykov, Danilov, Korneev, Larichkov.

INORGANIC SYNTHESIS AND INDUSTRIAL INORGANIC CHEMISTRY

Effect of Hydrated Sodium Silicates on Cement Paste Hardening

A. S. Brykov, V. V. Danilov, V. I. Korneev, and A. V. Larichkov

St. Petersburg State Technological Institute, St. Petersburg, Russia

Received April 29, 2002

Abstract—The hydration of cement clinker minerals occurs at a high rate in the presence of sodium silicates owing to a decrease in the initial pH of pore solutions of cement pastes and to intensive formation of calcium hydrosilicates.

We have attempted earlier [1] to find an explanation for the accelerated setting and hardening of portland-cement pastes with addition of hydrated sodium silicates (hydrosilicate powders, or HSP). According to the mechanism suggested in [1] for the case of simultaneous dissolution of a part of clinker phases and HSP, OH^- ions formed in clinker dissolution interact in the liquid phase with polymeric silicate anions originating from HSP. The consequence of this process is a high rate of hydration, whereas in the case of HSP-free portland cement pastes, a prolonged induction period begins almost immediately.

In the present study, we measured the pH of pore solutions of cement pastes with HSP additives. These data supplement the concepts put forward in [1].

EXPERIMENTAL

Hydrated sodium silicates under study are characterized in Table 1. Pastes were prepared from a PTs500 DO cement (Oskoltsement) with the following phase composition (wt %): $3CaO \cdot SiO_2$ 52–55, $2CaO \cdot SiO_2$ 20–22, $3CaO \cdot Al_2O_3$ 20–22, and gypsum 5. The pH values of pore solutions were measured on a pH-673.M pH-meter.

The pastes were prepared as follows. Hydrosilicate powders 2.0 and 2.8 were mixed with the cement in amounts of 1, 3, and 5% relative to the cement weight for each powder. The resulting composition was mixed with water. The water-dried cement ratio (water-to-cement ratio) was 0.35. The HSP hydration water was disregarded.

The $Na_2SiO_3 \cdot 5H_2O$ compound was mixed with cement in amounts of 1 and 5% relative to the cement weight (in terms of $Na_2O \cdot SiO_2$). The metasilicate hydration water was taken into account in such a way that this water and water added to the cement (tempering water) ensured a water-to-cement ratio of 0.35.

The intrinsic pH values of solutions of sodium silicates in cement tempering water are presented in Table 2.

Table 1. Physicochemical properties of powders of hydrated sodium silicates

Characteristic	Sodium silicate		
	$Na_2SiO_3 \cdot 5H_2O$	HSP 2.0	HSP 2.8
Outward appearance	White powder		
SiO_2, wt %	28.5	55.0	58.6
Na_2O, wt %	28.7	29.0	21.4
Silica modulus n*	1.0	2.0	2.8
H_2O, wt %	42.8	16.0	20.0
Particle size, mm	0.65–0.90	<0.25	<0.25
Dissolution time, min	<5	10	5

* $n = \dfrac{SiO_2,\ wt\ \%}{Na_2O,\ wt\ \%} \dfrac{Mr(Na_2O)}{Mr(SiO_2)}$.

Table 2. pH values of solutions of sodium silicates in cement tempering water

Sodium silicate	pH of solutions containing sodium silicates, wt %		
	1	3	5
Na_2SiO_3	13.1	–	13.5
HSP 2.0	12.1	12.2	12.35
HSP 2.8	11.3	11.35	11.4

1070-4272/02/7510-1577 $27.00 © 2002 MAIK "Nauka/Interperiodica"

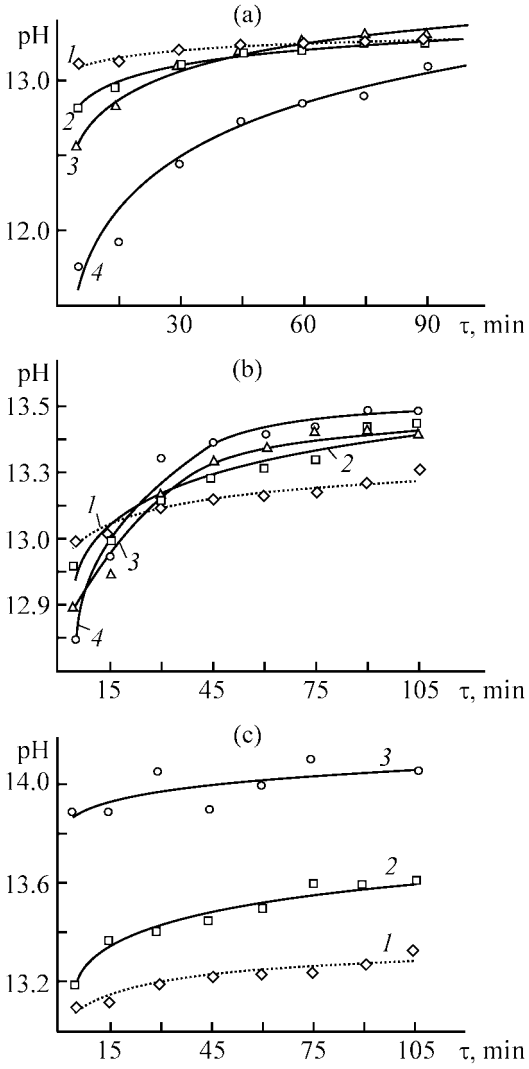

Fig. 1. pH of pore solutions of cement pastes with sodium hydrosilicates having silica modulus of (a) 2.8 and (b) 2.0, and (c) with sodium metasilicate vs. time τ. Addition of sodium hydrosilicate (% relative to cement weight): (*1*) 0 (pure paste), (*2*) 1, (*3*) 3, and (*4*) 5.

Within 5 min after mixing the cement formulation with water, the first paste sample was taken, filtered, and the pH of the obtained pore solution (filtrate) was measured. Further paste samples were taken every 10–15 min during 1.5 h. The data obtained are shown in Figs. 1a–1c.

During the period under study, the hydration of alite, $3CaO \cdot SiO_2$, is the main process in the cement solution free of alkaline silicates. Within about 10 min after mixing cement with water, OH^- and Ca^{2+} ions and a minor amount of SiO_2 are present in the pore solution in the following concentrations (M): SiO_2 $(4–5) \times 10^{-5}$; OH^- 2.0×10^{-2}, and CaO 3×10^{-2}. At the resulting solution alkalinity (as seen from Figs. 1a–1c, pH is about 13 for the pure, HSP-free paste) soluble silica species are predominantly in the form of dimeric anions with a certain average degree of ionization [2].

The initial hydration results in the formation of a thin layer of calcium silicates on the surface of clinker grains, and after that a 2-h induction period starts. Then the hydration rate increases to reach a maximum within approximately 10 h. Throughout the experiment, the pore solution concentrations change only slightly as compared with the initial values, which gives no way of distinguishing the induction and active periods of hydration on the basis of pH measurements.

In the case of simultaneous hydration of clinker and dissolution of HSP (whose solution has, in the concentration range under study, a pH of 11.3–11.4, which is lower than the pH of the pure, HSP-free paste) OH^- ions liberated as a result of hydration react with silicate ions of HSP by the reactions:

$$\equiv Si{-}OH + OH^- \rightarrow H_2O + \equiv SiO^-, \quad (1)$$

$$\equiv Si{-}O{-}Si\equiv + OH^- \rightarrow \equiv SiOH + \equiv SiO^-, \quad (2)$$

It follows from these data that cement pastes with high-modulus (silica modulus higher than 1.5–2.0), i.e., low-alkaline, silicates must have lower pH than the pure cement paste. The decrease in pH must occur at least in the initial period, after mixing cement and water. Since cement is in excess with respect to HSP, reactions (1) and (2) can proceed until a pH value close to the pH of the cement paste is attained in solution. Throughout this time, clinker minerals are hydrated at a high rate. A certain polymeric composition of the solution with respect to silica must correspond to the attained pH value. As noted above, dimeric SiO_2 species ionized in accordance with this pH value are the most probable forms.

A different type of behavior in the pore solution must be observed for low-modulus sodium silicate (metasilicate), since the pH values of its own solutions (13.1–13.5) are higher than, or comparable with the pH of the pure cement paste. If sodium metasilicate is added to the paste, the pore solution must turn highly alkaline almost instantly.

Calcium ions, which appear in the solution at the instant when the cement starts to react with water, and silicate ions passing into solution from HSP or sodium silicate form difficulty soluble calcium sil-

Table 3. Calculated and experimental pH values of pore solutions

Sodium silicate	pH values at indicated content of HSP additive, wt %					
	1		3		5	
	calculated	experimental	calculated	experimental	calculated	experimental
Na_2SiO_3	13.51	13.6	–	–	14.23	14.1
HSP 2.0	13.27	13.46	13.72	13.44	13.95	13.5
HSP 2.8	13.16	13.3	13.60	13.33	13.83	13.25

icate. For example, for the simplest monomeric silicate anions, the salt can be formed by the scheme:

$$Ca(OH)_2 + 2NaH_3SiO_4 \rightarrow Ca(H_3SiO_4)_2 + 2NaOH. \quad (3)$$

In this case, an equivalent amount of NaOH appears in the solution. Consequently, final pH values higher than those in the case of pure cement pastes would be expected.

It is evident from Figs. 1a and 1b that, during the initial period after mixing the formulations with water, the pH values of the cement pastes with HSP (2.0 and 2.8) are lower than those of the pure paste. In the case under consideration, the pH of the pure paste is 13.1, i.e., is higher than the value reported in the monograph [2]. Possibly, this is due to the high content of alkalis in the cement clinker. Raising the amount of HSP added to the paste results in a more pronounced decrease in pH. The time required for the pH to restore to about 13 is 15, 30, and 100 min for HSP 2.8 added in amounts of 1, 3, and 5%, respectively (Fig. 1a). With increasing silicate modulus, the initial pH values become lower (Figs. 1a and 1b).

According to Figs. 1a and 1b, pastes with HSP 2.0 and sodium metasilicate become more alkaline than the pure cement paste. In the case of HSP 2.0, this occurs not immediately, but only after an initial decrease in pH to 12.8–13.0, whereas in the case of sodium metasilicate, a highly alkaline medium is created, as expected, very fast.

Thus Figs. 1a–1b reflect the concepts presented above and in the preceding publication [1].

Table 3 lists the pH values calculated for pore solutions of cement pastes with HSP for the case of complete precipitation of silicate anions with calcium ions, when an equivalent amount of free alkali is formed in the solution by reaction (3). The experimental pH values (Figs. 1a–1c) are shown in Table 3 for comparison.

The data of Table 3 suggest that silicate-ions are precipitated in almost all of the cases studied, though at different rates depending on the type and amount of an HSP additive. It is clear that the higher alkalinity of the medium, the easier reaction (3) occurs. For example, addition of any sodium silicate in amount of 1% results in the maximal pH value corresponding to complete precipitation of calcium silicate during the time of experiment. If 5% HSP is added, the maximal pH value can be attained only with sodium metasilicate. For the pastes with HSP 2.8, the final pH value exceeds that of the pure paste only slightly.

Thus, HSP silicate ions are actively bound in the paste by calcium cations passing into the pore solution. It can be shown that the amount of SiO_2 introduced into a paste with HSP additive may be as high as 20% relative to the SiO_2 content in $3CaO \cdot SiO_2$. If we assume that silica from HSP is entirely consumed for the formation of calcium hydrosilicates by reaction (3), this amount may be quite sufficient for the cementation to start. In any case, the induction period does not begin while calcium hydrosilicates are formed intensively.

When sodium silicates with SiO_2/Na_2O ratio of about 2 and higher are added to the paste before, or simultaneously with, the precipitation of calcium hydrosilicates, there occurs depolymerization of low-polymeric silica acids, involving hydroxide ions present in the pore solution. This depolymerization significantly accelerates the hydration process. Thus, after mixing cement with water in the presence of HSP the hydration occurs at a high rate until high pH values, typical of the pure cement paste, are attained. This is indicated by the dependence of the paste setting time on the silicate modulus of HSP added [1].

REFERENCES

1. Aborin, A.V., Brykov, A.S., Danilov, V.V., and Korneev, V.I., *Tsement i ego primenenie* (Cement and Its Applications), 2001, no. 3, pp. 40–42.
2. Taylor, H.F.W., *Cement Chemistry*, London: Academic, 1990.

Russian Journal of Applied Chemistry, Vol. 75, No. 10, 2002, pp. 1580–1584. Translated from Zhurnal Prikladnoi Khimii, Vol. 75, No. 10, 2002, pp. 1615–1619.
Original Russian Text Copyright © 2002 by Morachevskii, Maiorova.

PHYSICOCHEMICAL STUDIES OF SYSTEMS AND PROCESSES

Thermodynamic Analysis of Interaction between Components in the System Potassium–Sulfur

A. G. Morachevskii and E. A. Maiorova

St. Petersburg State Polytechnical University, St. Petersburg, Russia

Received May 13, 2002

Abstract—Thermodynamic properties of the system potassium–sulfur in molten and solid state are compared and discussed.

The phase diagram of the system potassium–sulfur has been repeatedly studied [1]. According to refined data [2], potassium and sulfur form six congruently melting compounds: K_2S (mp 948 ± 20°C), K_2S_2 (487°C), K_2S_3 (302°C), K_2S_4 (154°C), K_2S_5 (206°C), and K_2S_6 (189°C) (Fig. 1). Thermal analysis of the potassium–sulfur system is difficult because of the tendency of the alloys toward supercooling. Potassium monosulfide, having the highest melting point among polysulfides, is characterized by considerable fraction of ionic bonding. The available data on the melting point of K_2S are rather controversial. For example, T_{mp} is 835°C according to [3]. A review [2] presented Dworkin and Bredig's experimental data [4]. For other potassium polysulfides, the error in determining the melting point does not probably exceed ±5%. Apart from thermal analysis, differential scanning calorimetry (DSC) [5, 6] and the electromotive force (EMF) method [7–9] have been used to obtain data on the position of the liquidus line and boundaries of the stratification region in the sulfur-rich part of the system. The upper critical temperature in the K–K_2S system is 900°C, and the monotectic horizontal lies at 883°C [10].

Potassium and sulfur start to interact with considerable heat effects even upon weak heating. Data on the enthalpy of formation of the compounds and on the standard entropies and enthalpies of melting are summarized in Table 1. In [3], separate data available to the authors were used to calculate the enthalpy of K_2S formation. In [11], the enthalpies of formation of potassium polysulfides were estimated from the heat effects of their interaction with a 0.1 N solution of H_2SO_4 at 25°C. In reference book [13], these values were only recalculated with account of more recent data on thermodynamic properties of substances involved in the process. In [12], the enthalpy of K_2S formation was obtained using the method of fluorine calorimetry.

The standard entropies were estimated in reference book [13] for compounds K_2S, K_2S_2, K_2S_3, and K_2S_4 by Latimer's method [17]. For K_2S, a method proposed by Voronin [14] was also used. A closely similar S^0_{298} value (117 J mol^{-1} K^{-1}) was calculated for this compound by Kelly's method [18]. For the com-

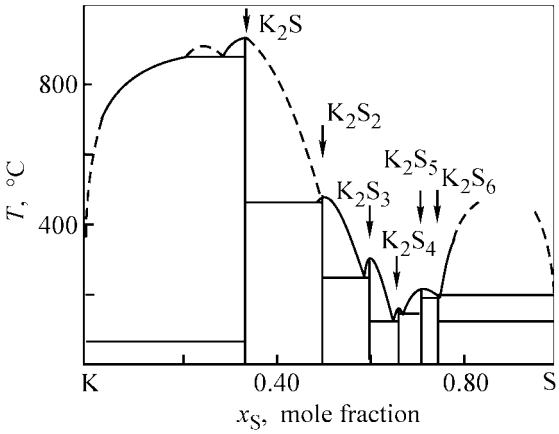

Fig. 1. Phase diagram of the K–S system. (T) Temperature and (x) sulfur content in the system.

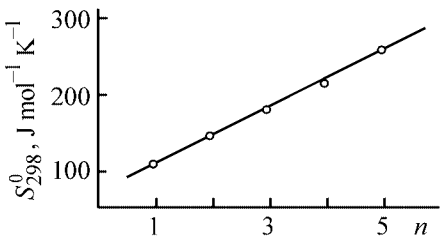

Fig. 2. Standard entropy S^0_{298} vs. number n of sulfur atoms in a potassium polysulfide molecule K_2S_n.

1070-4272/02/7510-1580 $27.00 © 2002 MAIK "Nauka/Interperiodica"

Table 1. Thermodynamic characteristics of potassium polysulfides, according to data of different authors

Compound	ΔH^0_{298}, kJ mol^{-1}	S^0_{298}, J mol^{-1} K^{-1}	ΔH_{mp}, kJ mol^{-1}	Compound	ΔH^0_{298}, kJ mol^{-1}	S^0_{298}, J mol^{-1} K^{-1}	ΔH_{mp}, kJ mol^{-1}
K_2S	–428.0 [3]	113.6 ± 12.6 [13]	16.1 [4]	K_2S_4	–465.7 ± 2.1 [11]	213.4 ± 20.9 [13]	8.31* [15]
	–381.0 ± 3.8 [11]	113.0 [14]			–472.0 ± 2.1 [13]		14.2** [15]
	–406.2 ± 2.9 [12]						11.6 [5]
	–387.0 ± 3.8 [13]			K_2S_5	–496.0 ± 2.1 [11]	256.8 ± 2.5 [16]	7.2* [15]
	–377.0 [2]				–475.3 ± 1.7 [13]		25.1** [15]
K_2S_2	–431.0 ± 2.9 [11]	146.4 ± 20.9 [13]	11.5* [15]				27.0 [5]
	–436.8 ± 2.9 [13]		18.3 [5]	K_2S_6	–468.2 ± 2.9 [11]	(285 ± 5)***	25.9* [15]
K_2S_3	–467.8 ± 2.1 [11]	179.9 ± 20.9 [13]	16.2* [15]		–474.5 ± 2.9 [13]		26.4** [15]
	–473.6 ± 5.0 [13]		14.6** [15]				27.6 [5]

* Calorimetric data. ** DTA data. *** Data obtained in the present study by extrapolation.

pound K_2S_5, S^0_{298} was calculated from the experimental heat capacities C_p in the temperature range 10–298 K [16]. The S^0_{298} value calculated by Latimer's method is equal to 248.5 J mol^{-1} K^{-1}. Figure 2 shows the standard entropy for potassium polysulfides as a function of the number of sulfur atoms in a polysulfide molecule. The S^0_{298} value for K_2S_6 in Table 1 was obtained by graphical extrapolation.

In [15], the calorimetric ("throwing-in") method was used to determine the H^0_T–H^0_{298} values for a number of potassium polysulfides in the temperature range 298–804 K and to estimate the enthalpies of their melting. In the same study, the enthalpies of mixing were obtained by DTA. The results of both methods are in rather satisfactory agreement for K_2S_3 and K_2S_6 and differ strongly for K_2S_4 and K_2S_5 (Table 1). The DTA values are higher by 70–250% than those obtained in a calorimetric experiment. Probably, this is due to common difficulties encountered in studying phase transformations in substances subject to supercooling and vitrification. The enthalpies of melting of potassium polysulfides were also determined in [5, 6] by the DSC method (Table 1). In Janz and Rogers' opinion [5, 6], the vitrification in the potassium–sulfur system is the most pronounced in the composition range K_2S_4–K_2S_5. The chemical properties and preparation of potassium polysulfides are considered in detail in a monograph [1].

The thermodynamic properties of melts in the system potassium–sulfur were studied in [7–9] by the EMF method with solid glassy or ceramic electrolytes. The EMF of the following cells ($0.023 \le x_K \le 0.293$, 12 compositions, 354–450°C, x_K is the molar fraction of potassium in the alloy) was measured in [7].

$$(-)\ \mathrm{K}\ |\ \text{Glass}\ |\ \text{Salt melt}\ |\ \text{Glass}\ |\ \mathrm{K, S}\ (+) \qquad (1)$$

The experiments were carried out with a commercial C-48-1 glass containing 3.8 wt % K_2O. As intermediate electrolyte served the eutectic mixture KCl–$ZnCl_2$ (mp 228°C). As shown previously [19], such cells are suitable for studying thermodynamic properties of potassium-based liquid alloys. At 450°C, the following results were obtained:

x_K	E, V	ΔG_K, kJ mol^{-1}	a_K
0.023	2.345	–226.3	4.47×10^{-17}
0.054	2.348	–226.6	4.25×10^{-17}
0.061	2.345	–226.3	4.47×10^{-17}
0.077	2.347	–226.5	4.32×10^{-17}
0.086	2.349	–226.7	4.18×10^{-17}
0.099	2.342	–226.0	4.69×10^{-17}
0.137	2.343	–226.1	4.62×10^{-17}
0.156	2.337	–225.5	5.10×10^{-17}
0.215	2.322	–225.0	5.54×10^{-17}
0.269	2.182	–210.6	6.08×10^{-17}
0.280	2.170	–209.4	7.43×10^{-16}
0.293	2.128	–205.4	1.44×10^{-15}

where ΔG_K is the partial molar Gibbs energy, and a_K is the potassium activity in an alloy.

The EMF of the cell is constant (2.345 ± 0.003 V) within the stratification region. The average values of ΔG_K and a_K in this range are -226.3 ± 0.3 kJ mol^{-1} and 4.47×10^{-17}, respectively. Estimating the partial molar entropy of a component in the heterogeneity region is always difficult [20]. However, the temperature coefficient (dE/dT) of EMF is negative, i.e., the EMF of the potassium–sulfur cell increases with decreasing temperature.

More recently, Grosbie [8] studied, using EMF method with β"-alumina solid electrolyte exhibiting ionic conduction by potassium ions, the thermodynamic properties of liquid alloys of the system K–S

Table 2. EMF of K | Solid electrolyte | K, S cells according to [8]

x_K	EMF (V) at indicated temperature, °C				
	225	250	275	300	325
0.274	2.393	2.385	2.380	2.372	2.367
0.333	2.259	2.250	2.242	2.233	2.229
0.364	2.112	2.107	2.103	2.094	–
0.385	–	–	2.038	2.029	–
0.400	–	–	–	1.990	1.977
0.412	–	–	–	–	1.929

Table 3. Thermodynamic characteristics of melts of the potassium–sulfur system at 325°C

x_K	a_K	ΔG_K	ΔH_K	ΔG	ΔH
		kJ mol^{-1}			
0.05	8.68×10^{-21}	–229.7	–231.9	–11.3	–11.6
0.10	8.68×10^{-21}	–229.7	–232.0	–22.8	–23.1
0.15	8.68×10^{-21}	–229.7	–232.2	–34.3	–34.6
0.20	8.68×10^{-21}	–229.7	–232.7	–45.7	–46.3
0.25	1.33×10^{-20}	–227.6	–232.8	–57.2	–57.9
0.30	8.25×10^{-20}	–218.5	–227.7	–68.2	–69.4
0.35	1.11×10^{-18}	–205.5	–219.4	–78.4	–80.4
0.40	7.25×10^{-17}	–189.3	–208.9	–87.5	–90.7

($x_K \le 0.412$, 225–325°C). In the stratification region at 250°C (phase region S–K_2S_6), EMF is 2.414 V [8]. For potassium-richer alloys the EMF values were estimated at various temperatures in this study on the basis of data on ΔG_K from [8] (Table 2).

In a more recent study [9], both glass and potassium-containing β-alumina were used as solid electrolytes with ionic conductivity in analyzing the thermodynamic properties of liquid alloys of potassium and sulfur ($0.065 \le x_K \le 0.412$, 230–330°C). Since the commercial brands of glasses are characterized by relatively low content of potassium and high electrical resistivity, it is difficult to use them as solid electrolyte below 400°C. For this reason, a glass with high content of potassium oxide, having the following composition (wt %): K_2O 31–34, SiO_2 56–58, and B_2O_3 9–11 [21], was synthesized in a special experiment. A ceramic solid electrolyte based on potassium polyaluminate was obtained by replacing sodium ions in the crystal lattice of sodium polyaluminate with potassium ions. A test tube made of sodium-containing β-alumina was alternately treated with sodium chloride vapor and molten potassium nitrate [22]. The content of potassium in the polysulfide melts was determined by flame photometry. The EMF of the following cells was measured.

$$(-)\ \mathrm{K}\ |\ \text{Solid electrolyte}\ |\ \mathrm{K, S}\ (+) \qquad (2)$$

In both cell (1) and cell (2), the EMF values measured were the same when temperature was raised and then lowered within a temperature range. As noted previously [9], a small systematic discrepancy between EMF values measured in cells with glass and ceramic electrolytes is observed at 325°C. The discrepancy is the strongest in the stratification region, but, even in this case, it does not exceed 2.5% of measured value. Analysis and comparison of the data obtained in [7, 9] makes it possible to recommend the averaged values of such basic thermodynamic functions (Table 3) as potassium activity a_K, partial molar Gibbs energies and enthalpies of mixing for potassium, and also integral molar Gibbs energies and enthalpies of mixing (ΔG_K, ΔH_K, ΔG, and ΔH) for characterization of the potassim–sulfur system at 325°C.

Since a value of –377 kJ mol^{-1} was reported for the enthalpy of K_2S formation under standard conditions, ΔH^0_{298}, in the most recent review [2] citing reference books published in 1985 and 1989, it is this value that was used to calculate the standard Gibbs energy of formation of K_2S from elements at 598 K (ΔG^0_{598}).

The ΔG^0_T value at 598 K, calculated for the reaction

$$2\mathrm{K(l)} + \mathrm{S(l)} = \mathrm{K_2S(s)} \qquad (3)$$

with account of the H_{598}–H_{298} and S_{598}–S_{298} values for all the reagents, is –341 kJ. Correspondingly, for a mole of $K_{0.667}S_{0.333}$, this value is –113.7 kJ mol^{-1}. Calculation of ΔG^0_T for reaction (3) by the equation

$$\Delta G^0_T = \Delta H^0_{298} - T\Delta S^0_{298} \qquad (4)$$

with heat capacities of the components disregarded, yields the following: ΔG^0_{598} = –346 kJ mol^{-1}, which is rather close to the above value (–341 kJ mol^{-1}).

The standard Gibbs energy of formation of solid K_2S_2 from pure liquid components by reaction

$$2\mathrm{K(l)} + 2\mathrm{S(l)} = \mathrm{K_2S_2(s)} \qquad (5)$$

was estimated using Eq. (4). The ΔG_{598} value is –406.1 kJ mol^{-1}; for a mole of $K_{0.5}S_{0.5}$, ΔG_{598} = –101.5 kJ mol^{-1}.

Based on the experimental data ($x_S \le 0.60$) and calculations performed, the dependences of the integral molar Gibbs energy (Fig. 3) and partial molar Gibbs energy of potassium (Fig. 4) at 325°C on composition were plotted. ΔG_K values at 325°C were reported in [8] for a number of composition, which allows their comparison with the recommended values of ΔG_K (Table 3). According to the data of [8]:

Potassium polysulfide	Molar fraction of sulfur, x_S	ΔG_K, kJ mol^{-1}
$K_2S_{5.3}$	0.726	–228.4
K_2S_4	0.666	–215.1
K_2S_3	0.600	–190.8
$K_2S_{2.86}$	0.588	–186.2

As seen from Fig. 4, the ΔG_K values are in good agreement with the recommended dependence.

In [8], experimental data on the integral molar Gibbs energy at 250°C were presented for some potassium polysulfides. In particular, ΔG_{523} is –460.7 kJ mol^{-1} for potassium polysulfide K_2S_4, which melts at 154°C [8]. Calculation using Eq. (4) and the data of Table 1 for the reaction

$$2K(l) + 4S(l) = K_2S_4(s) \quad (6)$$

yields for ΔG at 250°C a value of –460.8 kJ mol^{-1}. In this case, the enthalpy of formation, ΔH_{298}, is taken from [13], and the enthalpy of K_2S_4 melting, from [5]. As in preceding calculations, account is taken of the enthalpies and entropies of melting of potassium and sulfur.

The aforesaid suggests that rather satisfactory and correlated data on the thermodynamic properties of liquid and solid phases in a relatively broad temperature range are presently available for the composition range K_2S–S in the potassium–sulfur system.

There is good reason to believe that the electrochemical behavior of potassium polysulfides in the molten state is similar to that of other potassium-containing ionic melts. This assumption was confirmed by studies of the cathodic polarization of antimony in a number of nitrate–nitrite molten systems (KNO_2–KNO_3–$CsNO_3$, KNO_2–KOH, and KNO_2–KNO_3–KOH) [23] and in molten polysulfide K_2S_4 [24]. A number of two-phase regions, which are formed successively, in accordance with the phase diagram of the system, on the antimony electrode at 240°C, which is reflected on the potential–current curve. First, a layer with Sb + KSb_2 intermetallic compound with the lowest content of metal being deposited is formed on the anode. Further, two-phase

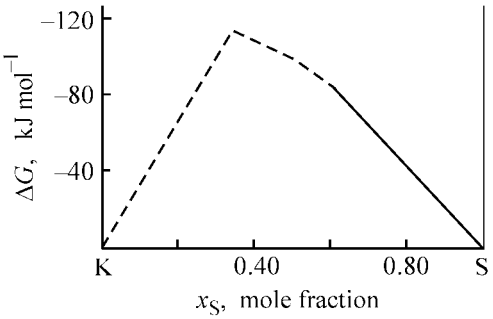

Fig. 3. Integral molar Gibbs energy ΔG vs. composition of the potassium–sulfur system at 325°C. (x_S) Sulfur content; the same for Fig. 4.

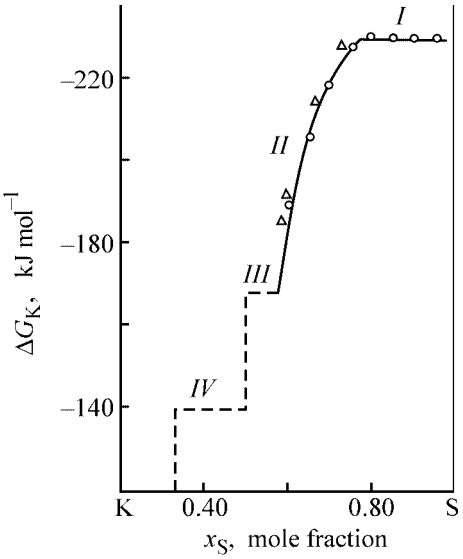

Fig. 4. Partial molar Gibbs energy of potassium ΔG_K in the potassium–sulfur system at 325°C in different phase regions. Region: (*I*) two liquid phases, (*II*) liquid phase, (*III*) K_2S_2(s) + liquid phase, and (*IV*) K_2S_2(s) + K_2S(s).

regions with other intermetallic compounds of potassium and sulfur, such as KSb, K_5Sb_4, and K_3Sb, are formed stratification. The discharge of potassium ions and the alloy formation constitute a single electrochemical event. As shown in [23, 24], the potentials of phase boundaries in the formation of the alloys in nitrate–nitrite melts and in molten potassium polysulfide coincide rather nicely. The same has been observed for the cathodic polarization of bismuth in salt mixtures and polysulfide melts [25].

CONCLUSION

The values of the basic thermodynamic functions for solid and liquid phases of the system potassium–sulfur in the K_2S–S composition range are recommended on the basis of an analysis and comparison of the available experimental and reference data.

REFERENCES

1. Morachevskii, A.G., Beloglazov, I.N., and Kasymbaev, B.A., *Kalii: Svoistva, proizvodstvo, primenenie* (Potassium: Properties, Manufacture, and Application), Moscow: Ruda Metally, 2000.
2. Sangster, J. and Pelton, A.D., *J. Phase Equilibria*, 1997, vol. 18, no. 1, pp. 82–88.
3. Rasch, R., *Sprechsaal Keram., Glass, Email, Silikate*, 1970, no. 3, pp. 117–130.
4. Dworkin, A.S. and Bredig, M.A., *J. Phys. Chem.*, 1968, vol. 72, no. 4, pp. 1277–1281.
5. Janz, G.J. and Rogers, D.J., *J. Chem. Eng. Data*, 1983, vol. 28, no. 3, pp. 331–335.
6. Janz, G.J. and Rogers, D.J., *Proc. Electrochem. Soc.*, 1984, vol. 84, no. 2, pp. 322–334.
7. Maiorova, E.A., Thermodynamic Properties of Dilute Solutions of Sodium or Potassium in Various Liquid Metals and Chalcogenides, *Cand. Sci. Dissertation*, Leningrad, 1977.
8. Grosbie, G.M., *J. Electrochem. Soc.*, 1982, vol. 129, no. 12. pp. 2707–2711.
9. Morachevskii, A.G., Sharivker, V.S, Klebanov, E.B., and Maiorova, E.A., *Zh. Prikl. Khim.*, 1988, vol. 61, no. 10, pp. 2311–2314.
10. Dworkin, A.S. and Bredig, M.A., *J. Phys. Chem.*, 1967, vol. 71, no. 3, pp. 764–765.
11. Letoffe, J.M., Joly, R.D., Thourey, J., *et al.*, *J. Chim. Phys.*, 1974, vol. 71, no. 3, pp. 427–430.
12. Johnson, G.K. and Steele, W.V., *J. Chem. Thermodyn.*, 1981, vol. 13, no. 10, pp. 985–990.
13. *Termicheskie konstanty veshchestv* (Thermal Constants of Substances), Glushko, V.P., Ed., no. 10, part 2, Moscow: VINITI Akad. Nauk SSSR, 1981.
14. Voronin, G.F., *Zh. Fiz. Khim.*, 1970, vol. 44, no. 12, pp. 3013–3017.
15. Bousquet, J., Letoffe, J.-M., and Diot, M., *J. Chim. Phys.*, 1974, vol. 71, no. 9, pp. 1180–1184.
16. Diot, M., Letoffe, J.-M., Prost, M., and Bousquet, J., *Bull. Soc. chim. France*, 1972, no. 12, pp. 4490–4493.
17. Latimer, W.M., *The Oxidation States of the Elements and Their Potentials in Aqueous Solutions*, New York: Prentice-Hall, 1952.
18. Morachevskii, A.G. and Sladkov, I.B., *Termodinamicheskie raschety v metallurgii* (Thermodynamic Calculations in Metallurgy), Moscow: Metallurgiya, 1993.
19. Morachevskii, A.G., and Bykova, M.A., *Ionnye rasplavy* (Ionic Melts), Kiev: Naukova Dumka, 1974, issue 2, pp. 46–65.
20. Gerasimov, Ya.I., and Geiderikh, V.A., *Termodinamika splavov* (Thermodynamics of Alloys), Moscow: Mos. Gos. Univ., 1980.
21. USSR Inventor's Certificate, no. 1 041 923.
22. Crosbie, G.M., and Tennenhouse, G.J., *J. Am. Ceram. Soc.*, 1982, vol. 65, no. 4, pp. 187–191.
23. Klebanov, E.B., Shesterkina, I.I., and Morachevskii, A.G., *Izv. Vyssh. Uchebn. Zaved., Tsvet. Metal.*, 1987, no. 4, pp. 35–37.
24. Morachevskii, A.G., Klebanov, E.B., Sharivker, V.S., and Erofeeva, G.I., *Elektrokhimiya*, 1989, vol. 25, no. 10, pp. 1392–1393.
25. Morachevskii, A.G., Klebanov, E.B., and Sharivker, V.S., *Rasplavy*, 1988, vol. 2, no. 3, pp. 117–118.

Russian Journal of Applied Chemistry, Vol. 75, No. 10, 2002, pp. 1585–1590. Translated from Zhurnal Prikladnoi Khimii, Vol. 75, No. 10, 2002, pp. 1620–1625.
Original Russian Text Copyright © 2002 by Egorova, Revina, Rumyantsev, Smirnov, Toidze, Shishkov.

PHYSICOCHEMICAL STUDIES OF SYSTEMS AND PROCESSES

Stable Silver Nanoparticles in Aqueous Dispersions Obtained from Micellar Solutions

E. M. Egorova, A. A. Revina, B. V. Rumyantsev, O. K. Smirnov, Z. G. Toidze, and D. I. Shishkov

Frumkin Institute of Electrochemistry, Russian Academy of Sciences, Moscow, Russia
BIONANOKhIM Research-and-Production Company, Moscow, Russia
VITA EKO Ltd., Moscow, Russia

Received January 14, 2002

Abstract—Two methods for obtaining aqueous dispersions of silver nanoparticles, stable during several months, from their reverse micellar solutions in an organic solvent: (i) centrifugation of a two-phase system formed by micellar solution and water and (ii) mixing of micellar solution with water, followed by settling.

One of the main directions in the development of modern nanotechnology is chemical synthesis of metal nanoparticles, with ultradispersed metal particles obtained by reducing the corresponding ions in solution [1–9]. A most important task in this field is to make longer the lifetime of such metal sols, since real ways of their practical use is only possible at their sufficiently high stability in ultradispersed state.

The most widely used variants are those based on chemical synthesis in aqueous solutions with the use of known reducing agents (hydrazine, sodium borohydride, etc.) [1, 6–9] or solvated electrons (radiochemical synthesis) [2–5] and nanoparticle stabilization with special additives (commonly polymer solutions). However, the lifetime of such particles does not exceed several days. Recently, successful synthesis of nanoparticles in a two-phase system formed by water and organic solvent has been reported [10]. This method can be used to obtain longer-lived metal sols in an organic solvent without special stabilizing agents, with particle stabilization achieved by using metal salts with long-chain organic anions. More efficient from the standpoint of nanoparticle stability is chemical synthesis in reverse micelles—in a ternary system formed by $M(H_2O)$, surfactant, and nonpolar solvent [11, 12]. In this case, the part of a stabilizing agent is played by surfactant molecules constituting a micelle shell in which nanoparticles are formed. Here, the same chemical reducing agents are used as in the other variants of synthesis, mentioned above.

In the present communication, two new methods for synthesis in reverse micelles are proposed. As reducing agents in these methods serve solvated electrons [4] or biologically active substances belonging to flavonoids (biochemical synthesis) [13, 14]. These methods yield a reverse-micelle solution of silver nanoparticles in an organic solvent (further, micellar solution), in which they are stable from several months to a year and more. Owing to such a high stability, it became possible to study the adsorption of nanoparticles from solution onto solid materials [15]. Introduction of micellar solutions of silver nanoparticles into some liquid-phase systems allows production of paintwork materials with stable antimicrobial activity with respect to a number of pathogens and viruses [16]. Studies of the catalytic activity of copper nanoparticles obtained by biochemical synthesis in a micellar solution and on solid supports demonstrated their high efficiency as catalysts for isomerization of dichlorobutenes [15].

In developing various nanoparticle applications, it is important to obtain their stable dispersions not only in organic solvents (hydrocarbons, in particular), but also in a polar medium, water in the first place. For example, use of silver nanoparticles in the form of an aqueous dispersion is preferable for obtaining aqueous dispersion paints or new makeup preparations with bactericidal properties. Aqueous dispersions are also more convenient for developing technologies aimed to create solid materials with deposited silver nanoparticles, which can be used in water purification to re-

1070-4272/02/7510-1585 $27.00 © 2002 MAIK "Nauka/Interperiodica"

move bacterial contaminants, e.g., in various tanks or filter units [17]. There is good reason to believe that stable metal nanoparticles in aqueous dispersions can find use in biotechnology and medicine [1].

The present communication reports the possibility of obtaining stable aqueous dispersions of silver nanoparticles from their micellar solutions. Two procedures for preparing such dispersions are described: (i) centrifugation of a two-phase system constituted by a micellar solution and water and (ii) mixing a micellar solution with water and its subsequent settling. The optical properties of nanoparticles in solutions were monitored by optical absorption spectra; the particle size distribution in the micellar solution and aqueous dispersions was determined by photonic correlation spectroscopy.

EXPERIMENTAL

Silver nanoparticles in reverse micelles were obtained by a previously described biochemical technique [14]. First, a reverse micellar solution of quercetin (Qr) flavonoid, a system composed of Qr, AOT, and saturated hydrocarbon, where AOT is a surfactant forming the shell of a micelle (with polar heads directed inwards, and nonpolar tails, outwards) is prepared; as saturated hydrocarbon serve heptane, octane, or isooctane. Then, an aqueous solution of $AgNO_3$ is introduced into the reverse micellar solution to make the concentration of the silver salt in the latter, $c(AgNO_3)$ = 3 mM. Nanoparticles are formed as a result of reduction with quercetin of Ag^+ ions to atoms and subsequent aggregation of silver atoms and ions in the water core of a reverse micelle formed upon introduction of an aqueous solution of the silver salt. The nanoparticle size is mainly determined by the diameter of the water core, which depends on the degree of hydration $w = [H_2O]/[AOT]$. In the present study, nanoparticles were obtained at w = 3.7. Aqueous dispersions were prepared from micellar solutions of silver nanoparticles, which attained a steady state (with constant optical density in the absorption band peak) and demonstrated a sufficiently high intensity of light scattering, which made it possible to measure particle sizes. The system came to a steady state 10–14 days after being synthesized.

Aqueous dispersions of silver nanoparticles were obtained by centrifuging a two-phase system composed of a micellar solution of nanoparticles (organic phase) and water (aqueous phase). In both cases, deionized water with conductivity of $(5–10) \times 10^{-8}$ S, obtained using a Khimpribor Vodolei instrument, was used, and equal amounts (commonly 3 + 3 or 4 + 4 ml) of the organic and aqueous phases were taken. The centrifuging was done on a T52.I.MLW laboratory centrifuge (Germany) in test tubes 14 mm in diameter. First, water was poured into the test tubes and then a micellar solution was slowly introduced from above, until a system with sufficiently distinct phase boundary was formed. The parameters of a centrifuging stage are as follows: rotation speed, 5300 rpm; time, 15 min.

The formation of nanoparticles and changes in their concentration in the liquid phase were monitored spectrophotometrically, with optical absorption spectra measured in the spectral range 230–900 nm on a Specord M40 spectrophotometer in quartz cells with optical path l = 1 mm. The particle size in solution was determined by photonic correlation spectroscopy on a Coulter Electronic Coulter N4 MD laser spectrometer (US). This method makes it possible to determine the size of reverse micelles [18, 19] or other particles present in solution. For small micelles (several nanometers in diameter), measurements give the size of their water core, d_w, as the difference $d_m - 2r$, where d_m is the micelle diameter, and r is the length of the surfactant molecule forming the micelle shell [18]. The diameter of the water core can be regarded as the upper limit to nanoparticle diameter. In the case in question, the water core diameter coincides with the silver nanoparticle diameter in reverse micellar systems, found by electron microscopy.

Optical absorption spectra of the starting micellar solution and aqueous dispersions of silver nanoparticles obtained upon centrifuging of the two-phase system composed of the micellar solution and water are shown in Fig. 1. The micellar solution of nanoparticles has intense red-brown color, with the absorption band peaked at 420–430 nm, in agreement with published data for silver nanoparticles in reverse micelles [3, 18]. The optical density at the absorption band peak, D_{max}, can be used to determine the degree of conversion of Ag^+ ions in nanoparticle formation.

With the use of the published value of the extinction coefficient of silver nanoparticles in a reverse micellar system, $\varepsilon = 7.2 \times 10^3$ M^{-1} cm^{-1} [20], it is found for the micellar solution in Fig. 1 that the concentration of silver ions present in the form of nanoparticles (and the concentration of the silver salt, numerically equal to the ionic concentration), $c(AgNO_3) = D_{max}/(\varepsilon l) = 2.16$ mM. At a total concentration of the silver salt in the micellar solution, $c(AgNO_3)$ = 3 mM, the degree of conversion of silver ions is 2.16/3 = 0.72 (i.e., the yield of nanoparticles is 72%). In addition to the characteristic absorption band associated

with nanoparticles, λ_{max} = 420 nm, the spectrum of the micellar solution contains a less intense band with λ_{max} = 295 nm, presumably related to the presence in solution of either minor clusters of silver or large complexes of Qr molecules with silver clusters [21, 22].

After centrifuging, the lower (aqueous) phase turns yellowish brown because nanoparticles pass into it from the micellar solution. An 3–5-mm-thick AOT layer is formed at the phase boundary, and the adjacent water layer turns slightly turbid because of the formation of colloid particles (aggregates) from AOT. A dark brown precipitate, readily soluble in water, is formed at the test tube bottom. To measure absorption spectra and particle size and to perform subsequent tests for stability, the middle (transparent) layer of the aqueous phase was sampled. After a single centrifuging, only a minor part of nanoparticles present in the micellar solution pass into water. To make higher the concentration of nanoparticles, the obtained aqueous solution of nanoparticles can again be subjected to centrifuging, with fresh portions of the micellar solution used as the organic phase.

Figure 1 shows optical spectra of aqueous dispersions, measured 1–2 h after one-, two-, and three-stage centrifuging. On the assumption that the extinction coefficients of nanoparticles are the same in micellar and aqueous solutions, the extent to which nanoparticles pass into the aqueous phase can be evaluated from the ratio of optical densities at absorption band peaks; this parameter equals 15–30 (one stage), 30–40 (two stages), and 50–60% (three stages) relative to their concentrations in the micellar solution. The absorption band of nanoparticles is shifted in the aqueous dispersion relative to that in the micellar solutions. A similar shift of bands was observed in [20] in extraction of silver nanoparticles from a micellar solution by a similar centrifuging procedure, with the reasons for such a shift not discussed. Probably, this may be due to a change in the polarity of the medium near the surface of a particle passing into the aqueous phase (penetration of water molecules into the micelle core).

The resulting aqueous dispersions of nanoparticles proved to be stable for a long time (no less than 1 month) when stored in air at room temperature. As an example, Fig. 2 shows how optical absorption spectra of aqueous dispersions prepared by two-stage centrifuging vary with time. It can be seen that the position of the band associated with nanoparticles remains unchanged during a month. The optical density at the band peak increases by 20–30% (not shown)

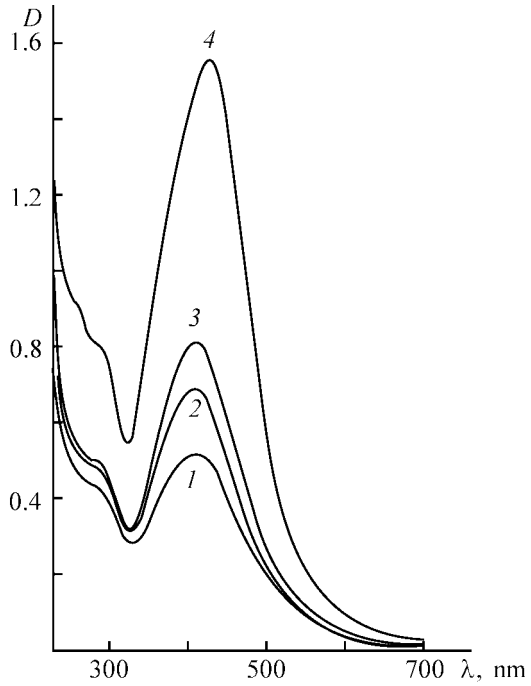

Fig. 1. Optical absorption spectra of aqueous dispersions of silver nanoparticles, measured 1.5–2 h after centrifuging in (*1*) one, (*2*) two, and (*3*) stages, and (*4*) spectrum of the micellar solution. (*D*) Optical density and (λ) wavelength; the same for Figs. 2 and 5.

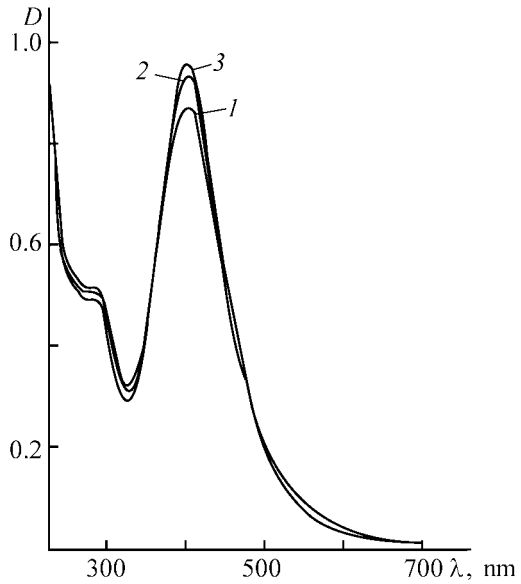

Fig. 2. Optical absorption spectra of aqueous dispersions of silver nanoparticles (*1*) 8, (*2*) 17, and (*3*) 35 days after two-stage centrifuging.

during the first weak, with the band half-width simultaneously decreasing somewhat. Then the system reaches its steady state, and D_{max} changes by no more than 10% during the following three or four weeks. An increase in D_{max} in storage was observed for all

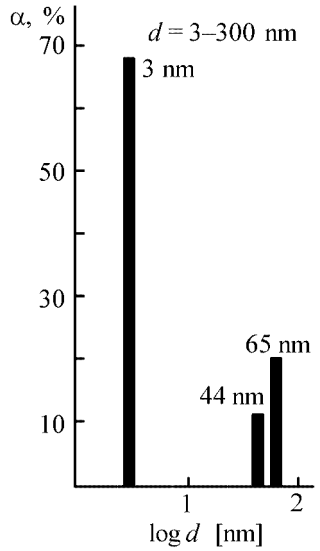

Fig. 3. Histogram of silver nanoparticle size distribution in micellar solution. (α) Fraction of particles and (*d*) particle diameter; the same for Figs. 4 and 6.

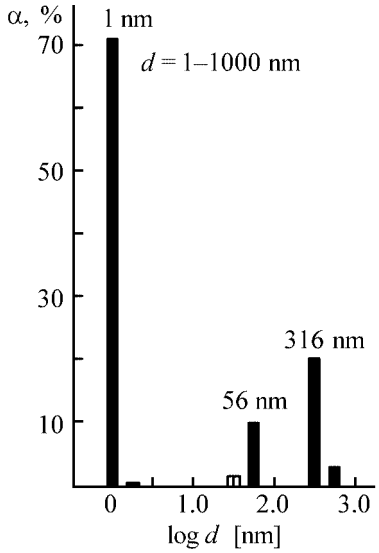

Fig. 4. Histogram of particle size distribution for aqueous dispersion of silver nanoparticles 5 days after single-stage centrifuging.

of the samples studied after centrifuging in one, two, or three stages. Such a change in D_{max} in the steady state may be due to a minor increase in nanoparticle concentration as a result of water evaporation.

Typical particle size distributions in micellar solution and aqueous dispersion are shown in Figs. 3 and 4.[1]

[1] The size of 1–3 nm, obtained in light scattering measurements by analyzing the correlation function by means of the CONTIN software, should be understood in the given case not literally, but only as an indication of the presence in solution of fine particles about several nanometers in size.

Correlation between the optical absorption spectra and particle size distributions in micellar solutions suggests that it is fine micelles that contain silver nanoparticles. Moreover, the solutions also contain particles 30–70 nm in size. It may be assumed that these particles are either formed through aggregation of fine micelles or reflect the initial stage of nanoparticle oxidation, which eventually leads to appearance of silver oxide crystals of micrometer dimensions [8].

The histogram for an aqueous dispersion of nanoparticles shows, during the first several hours after centrifuging, large particles 300–600 nm in size. With account of the fact that, at the chosen AOT concentration in the micellar solution, its concentration in water may be high enough for a lamellar phase to be formed [22], it may be assumed that large particles are fragments of AOT lamellas, formed when AOT passes into water from the micellar solution. These particles are unstable and disintegrate in 1 or 2 days, and after that fine particles predominate in the solution during the entire time of storage. Possibly, disintegration of AOT aggregates is responsible for the change in the absorption spectra during the first days after centrifuging. The particle size distribution in the aqueous dispersion in the stationary stage is shown in Fig. 4. It can be seen that the ratio of concentrations of fine micelles and larger particles is similar to that in the starting micellar solution; a minor "admixture" of particles about 300 nm in size is, probably, the remainder of AOT aggregates. It is noteworthy that, in the given case, fine micelles must have a shell composed of two, rather than one monolayer of the surfactant, since its molecules must have polar heads facing both water and nanoparticles. In other words, the nanoparticles have, in the given case, shells composed of a bilayer, rather than a monolayer, of AOT molecules.

A stable aqueous dispersion of silver nanoparticles can also be obtained by simply mixing a micellar solution of nanoparticles with water and subsequent settling until separation into the organic and aqueous phases. In this case, the concentration of nanoparticles in water is much higher than in the case when nanoparticles pass into water under centrifugation. As seen from Fig. 5, the aqueous dispersion of nanoparticles obtained by mixing equal volumes of water and micellar solution has optical density at the peak of the band associated with nanoparticles close to that of the micellar solution. The halfwidth of the band in the aqueous dispersion is much narrower in the given case, compared with that in the micellar solution: $\Delta\lambda_{1/2}$ (mic.sol.) = 117.4 nm, and $\Delta\lambda_{1/2}$ (aq.disp.) = 86.1 nm. In storage in air, the intensity of the band

in the aqueous dispersion remains virtually unchanged for no less than 1–1.5 months. As also in the case of extraction by centrifuging, the position of the nanoparticle-related band in the aqueous dispersion is shifted toward the UV region by 10–15 nm, compared with that in the micellar solution.

The evolution of particle dimensions in a dispersion of this kind is similar to that observed after centrifuging: large particles, initially present in great number, gradually disintegrate, so that that the fraction of small micelles several nanometers in size increases, and then the system reaches its steady state and the size distribution stabilizes. However, large particles are now bigger (300–3000 nm) and, in contrast to the preceding case, the contribution from these particles remains in the steady state more significant that that from small micelles (Fig. 6). This may result from the fact that the AOT concentration in the aqueous phase after mixing exceeds that after centrifuging. As a result, larger part of nanoparticles are "enclosed" in AOT lamellas and cannot be recorded in light-scattering measurements as fine micelles. At the same time, these nanoparticles strongly absorb light, with no band broadening or increased long-wavelength absorption, both of these characteristic of nanoparticle aggregation to form fractal clusters [23], observed in the spectrum (Fig. 5). Hence follows that the average distance between the nanoparticles in lamellas is rather large, so that they absorb light as isolated particles.

Thus, both methods yield aqueous solutions of silver nanoparticles, which are stable for a long time. It is planned that, after appropriate tests for antimicrobial activity, solutions of this kind will be proposed as bactericidal additives to various materials. Deposition of silver nanoparticles from aqueous solutions onto solid supports can give modified solid materials applicable as filtering elements for purification of water or other liquids to remove bacterial contaminants.

CONCLUSIONS

(1) Two methods for obtaining aqueous dispersions of silver nanoparticles from their micellar solutions: (i) centrifuging of a two-phase system composed of a micellar solution and water and (ii) mixing of a micellar solution with water with subsequent settling are proposed.

(2) It is shown that nanoparticles remain stable in aqueous dispersions for a long time, which enables their use as bactericidal additives or coatings.

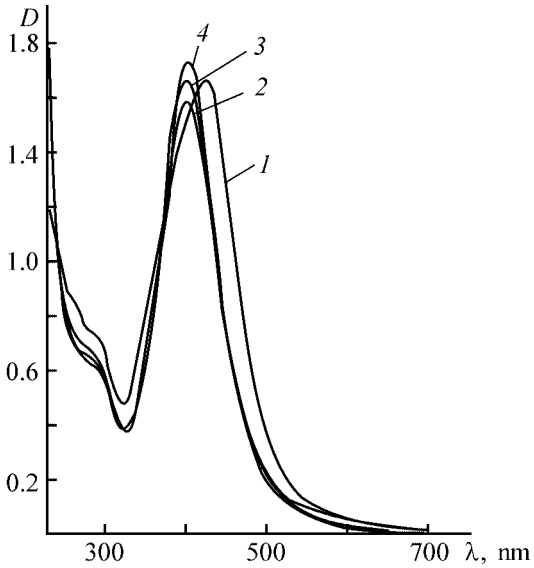

Fig. 5. Optical absorption spectra of (*1*) micellar solution and (*2–4*) aqueous dispersion of silver nanoparticles, obtained by mixing equal volumes of micellar solution and water. Time elapsed after mixing (days): (*2*) 7, (*3*) 25, and (*4*) 32.

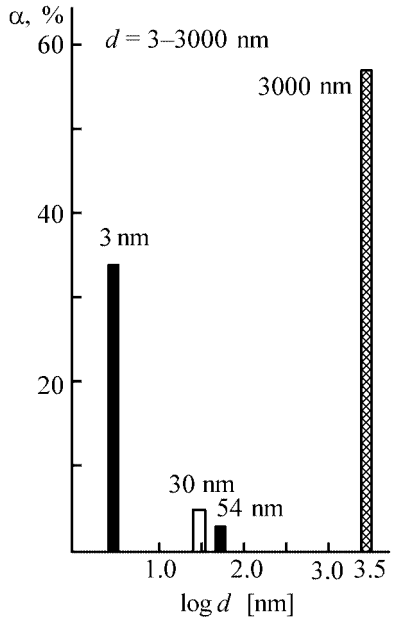

Fig. 6. Histogram of silver nanoparticle size distribution in aqueous dispersion obtained 17 days after mixing of micellar solution and water.

ACKNOWLEDGMENTS

The study was supported by the Russian Foundation for Basic Research (project no. 01-03-32783) and integrated program of the Russian Academy of Sciences "Nanomaterials and Supramolecular Systems."

REFERENCES

1. Pomogailo, A.D., Rozenberg, A.S., and Uflyand, M.E., *Nanochastitsy metallov v polimerakh* (Metal Nanoparticles in Polymers), Moscow: Khimiya, 2000.
2. Henglein, A., *Chem. Phys. Lett.*, 1989, vol. 154, no. 5, pp. 473–476
3. Ershov, B.G., Sukhov, N.L., and Troitskii, D.A., *Izv. Akad. Nauk SSSR*, 1989, no. 8, pp. 1930–1931.
4. Dokuchaev, A.G., Myasoedova, T.G., and Revina, A.A., *Khim. Vys. Energ.*, 1997, vol. 31, no. 5, pp. 353–356.
5. Treuger, M., de Cointer, C., Remita, H., *et al.*, *J. Phys. Chem. B*, 1998, vol. 102, no. 22, pp. 4310–4321.
6. Brichkin, S.B., Razumov, V.F., and Spirin, M.G., *Kolloidn. Zh.*, 2000, vol. 62, no. 1, pp. 12–17.
7. Butenko, A.V., Chubakov, P.A., Danilova, Yu.E., *et al.*, *Z. Phys. D*, 1990, vol. 17, no. 2, pp. 283–289.
8. Huang, Z.-Y., Mills, G., and Hajek, B., *J. Phys. Chem.*, 1993, vol. 97, no. 44, pp. 11542–11550.
9. Toporko, A.V., Tsvetkov, V.V., Yagodovskii, V.D., *et al.*, *Zh. Fiz. Khim.*, 1995, vol. 69, no. 5, pp. 867–870.
10. Vorobyova, S.A., Sobal, N.S., and Lesnikovich, A.I., *Colloid Surf. A*, 2001, vol. 176, no. 2–3, pp. 273–277.
11. Robinson, B.H., Khan-Lodhi, A.N., and Towey, T., *Structure and Reactivity in Reverse Micelles*, Pileni, M., Ed., Amsterdam: Elsevier, 1989, pp. 198–219.
12. Pileni, M.P., *Langmuir*, 1997, vol. 13, no. 13, pp. 3266–3276.
13. RF Patent 2147487.
14. Egorova, E.M. and Revina, A.A., *Colloid Surf. A*, 2000, vol. 168, no. 1, pp. 87–96.
15. Egorova, E.M., Revina, A.A., Rostovshchikova, T.N., and Kiseleva, O.I., *Vestn. Mos. Gos. Univ., Ser. 2, Khim.*, 2001, vol. 42, no. 5, pp. 433–439.
16. Revina, A.A., Egorova, E.M., and Kudryavtsev, B.B., *Khim. Prom–st.*, 2001, no. 4, pp. 28–32.
17. RF Patent 13949.
18. Day, R.A. and Robinson, B.H., *J. Chem. Soc. Far. I*, 1979, vol. 75, no. 1, pp. 132–139.
19. Zulauf, M. and Eicke, H.-F., *J. Phys. Chem.*, 1979, vol. 83, no. 3, pp. 480–486.
20. Petit, C., Lixon, P., and Pileni, M.P., *J. Phys. Chem.*, 1993, vol. 97, no. 49, pp. 12974–12983.
21. Revina, A.A., Egorova, E.M., and Karataeva, A.D., *Zh. Fiz. Khim.*, 1999, vol. 73, no. 10, pp. 1897–1904.
22. Coppola, L., Mazzalupo, R., Ranieri, G.A., *et al.*, *Langmuir*, 1995, vol. 11, no. 4, pp. 1116–1121.
23. Karpov, S.V., Bas'ko, A.L., Popov, A.K., *et al.*, *Kolloidn. Zh.*, 2000, vol. 62, no. 6, pp. 773–789.

Russian Journal of Applied Chemistry, Vol. 75, No. 10, 2002, pp. 1591–1593. Translated from Zhurnal Prikladnoi Khimii, Vol. 75, No. 10, 2002, pp. 1626–1628.
Original Russian Text Copyright © 2002 by Bychkova, Rodzivilova, Panova, Artemenko.

SORPTION AND ION-EXCHANGE PROCESSES

Adsorption of Fire Retardant from Dilute Aqueous Solutions onto Viscose Fiber

E. V. Bychkova, I. S. Rodzivilova, L. G. Panova, and S. E. Artemenko

Saratov State Technical University, Saratov, Russia
Technological Institute, Engels, Saratov oblast, Russia

Received February 5, 2001; in final form, April 2002

Abstract—The adsorption isotherms of the product of transesterification of dimethyl methylphosphonate (ZG-2), used as fire retardant, from dilute solutions on viscose fiber were determined experimentally at various temperatures. The parameters of pore structure of the fibrous sorbent were estimated using the general equation of the theory of volume filling of micropores.

Impregnation of finished fiber with a solution of fire retardant (FR) is the most promising method of fire protection of viscous fibers [1]. The mechanism by which fibers react with FR is affected not only by the chemical structure of the fiber, but also by their pore structure, which governs sorption characteristics of fibrous sorbents. To explain sorption phenomena, thermodynamic methods can be used [2].

Studies of sorption processes are always focused on determining the pore structure parameters (micropore volume and prevalent pore diameter). The conventional methods for studying the pore structure require complicated equipment and have a number of limitations [3, 4].

The present study is concerned with adsorption of FR from dilute aqueous solutions onto viscose fiber (VF) with the aim to estimate the pore structure parameters.

Chemical fibers can be subdivided into two groups according to the classification of adsorbents proposed by Dubinin [5]: macroporous fibers [which are, in some cases, adequately approximated by the equation of micropore filling theory (MFT) at $n = 1$], and mesoporous and microporous fibers, on which the sorption is described by the MFT equation with $n = 2$ or $n = 3$.

Analysis of published data [6–8] shows that VFs can be regarded as microporous sorbents, whose pore structure parameters can be estimated using the general equation of MFT

$$n_i^1 = n_{i0}^1 \exp[(A/E)^n - \alpha(T - T_0)],$$

where n_i^1 is the amount of sorption (mmol g^{-1}) at a temperature T; n_{i0}^1, the limiting sorption (mmol g^{-1}) at temperature T_0; $A = RT\ln(c_s/c)$, the differential molar work (J mol^{-1}); E, the characteristic sorption energy (J mol^{-1}); n, the order of the MFT equation; $\alpha = -(\mathrm{d}\ln n_i^1/\mathrm{d}T)_{\Delta G}$, the thermal coefficient of sorption; c, the equilibrium concentration (mM); and c_s, the saturation concentration (mM).

The product of transesterification of dimethyl methylphosphonate (ZG-2) containing 25 wt % phosphorus was used as an FR.

For studying sorption isotherms, we used interferometry. A weighed portion of the sorbent was placed in a tightly stoppered flask, and 10 ml of aqueous FR solution of a definite concentration was added. From the direct relationship between the scale readings of the interferometer compensator and the concentration, determined by calibration with the initial solution, we evaluated the composition of the equilibrium solution and the transesterification adsorption, n_i^1 (mmol g^{-1}):

$$n_i^1 = (c_{in} - c_{eq})V/m,$$

were c_{in} and c_{eq} are the initial and equilibrium concentrations of the solution (mM); V, the solution volume (ml); and m, the weighed portion of the sorbent (g).

The experimental and calculated isotherms of FR adsorption on VF at various temperatures are shown in Fig. 1. This shape of isotherms is characteristic of the adsorption onto microporous sorbents [8].

To estimate the pore structure parameters for the sorbents, we used the MFT equation in the linear form

$$\log n_i^1 = \log n_{i0}^1 - (0.434/E^n)A^n.$$

1070-4272/02/7510-1591 $27.00 © 2002 MAIK "Nauka/Interperiodica"

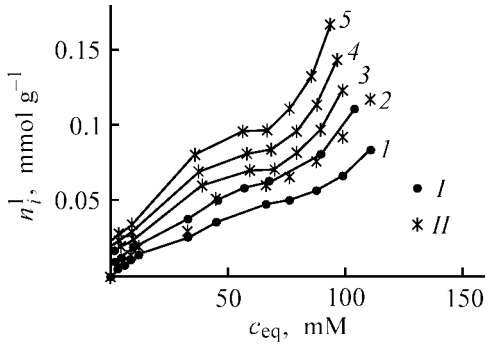

Fig. 1. Isotherms of FR adsorption from dilute solutions onto VFs. (n_i^1) Amount of adsorption and (c_{eq}) equilibrium concentration of FR. Temperature, °C: (*1*) 20, (*2*) 40, (*3*) 50, (*4*) 60, and (*5*) 70. Data: (*I*) experimental and (*II*) calculated.

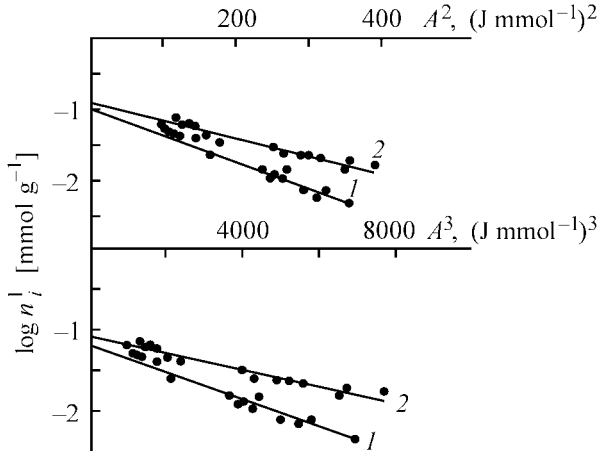

Fig. 2. Linear isotherms of FR adsorption from dilute solutions onto VFs. (n_i^1) Amount of adsorption and (A) differential molar work. Temperature, °C: (*1*) 20 and (*2*) 40.

The MFT equation was tested at parameter n equal to 2 and 3.

The isotherms of FR adsorption onto viscous fiber, ploted in the coordinates in which the MFT equation is linear, are shown in Fig. 2. It is seen that the MFT equation describes the experimental data adequately at $n = 3$.

The limiting adsorbed volume W_0 was evaluated from the molecular weight of FR, its density, and the limiting adsorption. To estimate the limiting adsorbed volume, we assumed that the FR density in the adsorbed state is the same as in the solution.

The pore half-width X was evaluated with the use of the Stackley equation [9]

$$2X = 10.8/(E - 11.4),$$

were E is the characteristic energy of sorption (J mol^{-1}). The correlation of the calculated data is 3–5%.

The calculated limiting values of adsorption n_{i0}^1, limiting adsorbed volumes W_0, characteristic energy E, and pore half-width X (our and published data) are listed in the table.

From the experimental data on the adsorption of FR from aqueous solutions onto VFs, we evaluated the thermal adsorption coefficient $\alpha = -\mathrm{d}\ln n_{i0}^1/\mathrm{d}T$, used then for calculating the adsorption of FR from solutions at other temperatures (Fig. 1) by the equation

$$n_i^1 = n_{i0}^1 \exp[-\alpha(T - T_0)].$$

As seen from Fig. 1, the experimental and calculated data are in good agreement.

A small rise in the FR adsorption with increasing temperature and, hence, also the temperature coefficient of adsorption are governed by the structures of the solvent, FR, and adsorbent. All these factors result in small positive values of FR adsorption from dilute solutions. It seems likely that, in this adsorption system, interaction of solvent molecules with the adsorbent becomes weaker with increasing temperature, and the competing effect of the solvent molecules becomes less pronounced.

The adsorption isotherms carry no information on the true pattern of adsorption on the surface of a fibrous sorbent. Therefore, thermodynamic analysis of the adsorption equilibrium is of interest. For thermodynamic consideration of adsorption systems, we used the Gibbs method of excess quantities [11]. This method allows evaluation of the main thermodynamic characteristics of sorption systems as a whole on the basis of the excess values of adsorption determined in the experiments.

According to [11], the change in the chemical potential of the sorbent was calculated using the equation

Parameters of pore structure of VFs evaluated from the MFT equation (system FR–H_2O–VF)

VF at T, °C	n_{i0}^1, mmol g^{-1}	$E \times 10^{-3}$, J mol^{-1}	W_0, cm^3 g^{-1}	X, nm
25	0.063	27.4	0.011	0.34
40	0.070	27.6	0.014	0.34
[5, 8, 10]	0.066	15–30	0.016–0.039	0.37

$$\Delta\Phi = RT\int_0^{x_1}\frac{n_i^1}{x_1x_2}dx_1,$$

where $\Delta\Phi$ is the change in the chemical potential of the sorbent upon wetting with a binary solution ($J\,g^{-1}$), x_1 and x_2 are the mole fractions of FR and the solvent, and n_i^1 is the adsorption value ($mmol\,g^{-1}$).

Calculation of $\Delta\Phi$ was carried out using graphical integration, by evaluating the area under the curve:

$$n_i^1/(x_1x_2) = f(x_1).$$

The change in the Gibbs energy of the sorption system as a result of wetting of the sorbent with the solution of concentration x was calculated by the equation

$$-\Delta G = -\Delta\Phi - \Sigma n_i(\mu_{i0} - \mu_i),$$

where $(\mu_{i0} - \mu_i)$ is the change in the chemical potential of a component.

Analysis of the concentration dependences of $\Delta\Phi$ and ΔG (Fig. 3) shows that the largest changes in the chemical potential of the sorbent and Gibbs energy of the system as a result of sorbent wetting with FR solution take place at low x_1. This may be due to the specific features of interaction between the components, caused by the fact that FR molecules can penetrate into amorphous and defective regions of the fiber, enhancing the sorption by the fibrous surface.

The adsorption equilibria in the FR–H_2O–fiber systems studied here allow evaluation of the structural characteristics of the fiber and, on their basis, prediction of the features of interaction between the components.

CONCLUSION

Use of the theory of micropore volume filling for describing adsorption equilibria in the systems fire retardant–H_2O–fiber allows description of adsorption onto viscous fiber at various temperatures and evaluation of the pore structure parameters of fibers, using the general equation of this theory.

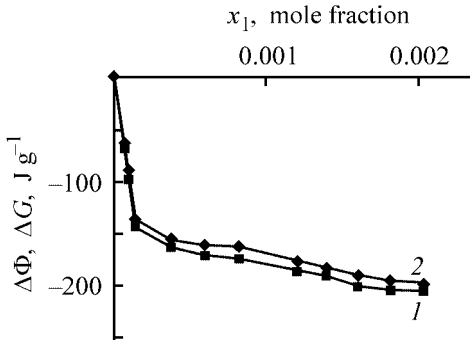

Fig. 3. Change in (*1*) the chemical potential $\Delta\Phi$ of the sorbent and (*2*) Gibbs energy ΔG of the system FR–H_2O–fiber vs. the FR mole fraction in solution, x_1.

REFERENCES

1. Artemenko, S.E., Panova, L.G., Besshaposhnikova, V.I., and Khalturinskii, N.A., *Vysokomol. Soedin., Ser. A*, 1999, vol. 33, no. 8, pp. 1768–1774.
2. *Svoistva i osobennosti pererabotki khimicheskikh volokon* (Characteristic and Specific Features of Recovery of Chemical Fibers), Pakshver, A.B., Moscow: Khimiya, 1975.
3. Gregg, S.J., *Adsorption, Surface Area, and Porosity*, London: Academic, 1982.
4. Kiselev, A.V., *Mezhmolekulyarnoe vzaimodeistvie v adsorbtsii i khromatografii* (Intermolecular Interaction in Adsorption and Chromatography), Moscow: Vysshaya Shkola, 1986.
5. Grebennikov, S.F. and Kynin, A.T., *Zh. Prikl. Khim.*, 1982, vol. 55, no. 10, pp. 2299–2303.
6. Grebennikov, S.F. Grebennikova, O.D., and Serpinskii, V.V., *Izv. Akad. Nauk SSSR, Ser. Khim.*, 1980, no. 2, pp. 453–456.
7. El'tekova, N.A. and El'tekov, Yu.A., *Zh. Fiz. Khim.*, 1992, vol. 66, no. 4, pp. 1014–1019.
8. Rodzivilova, I.S., Ovchinnikova, G.P., Artemenko, S.E., *et al., Zh. Prikl. Khim.*, 1999, vol. 72, no. 1, pp. 75–78.
9. Konovalova, L.Ya., Negodyaeva, G.S., Monastyrskaya, E.G., *et al., Khim. Volokna*, 1993, no. 2, pp. 40–41.
10. Perepelkin, K.E., *Struktura i svoistva volokon* (Structure and Charactristics of Fibers), Moscow: Khimiya, 1985.
11. Larionov, O.G., Chmutov, K.V., and Shayusupova, M.M., *Zh. Fiz. Khim.*, 1979, vol. 53, no. 3, pp. 734–736.

Russian Journal of Applied Chemistry, Vol. 75, No. 10, 2002, pp. 1594–1597. Translated from Zhurnal Prikladnoi Khimii, Vol. 75, No. 10, 2002, pp. 1629–1631.
Original Russian Text Copyright © 2002 by Zakharchenko.

SORPTION AND ION-EXCHANGE PROCESSES

Recovery with Calcium Oxide Sorbent of Conversion Products of Rhodium Catalyst for Ammonia Oxidation

N. I. Zakharchenko

Zhukovsky National Aerospace University, Kharkov, Ukraine

Received June 4, 2002

Abstract—The chemical aspects of recovery with a calcium oxide sorbent of rhodium lost in high-temperature oxidation of ammonia were studied. The physicochemical properties of this compound and conditions of its formation were considered.

Catalytic oxidation of ammonia to nitrogen(II) oxide underlies the industrial method for manufacture of nitric acid [1]. Industrial catalysts (Pt, Rh, and Pd alloys) undergo physicochemical transformations in technological processes, with the surface structure and the chemical composition of the catalysts changed [1–6]. A set of such transformations of platinoid catalysts leads to loss of deficient and expensive metals of the platinum group. An effective way to diminish the loss of platinum metals is their partial recovery by sorption masses mainly based on calcium oxide [1, 7–17].

The mechanism of platinum recovery with calcium-containing sorbents and the chemical aspect of the process are rather extensively covered in the scientific literature [1, 7–20]. At the same time, there is no evidence concerning the mechanism of recovery of rhodium, entering into the composition of industrial catalysts for ammonia oxidation (alloy nos. 1 and 5), with a calcium oxide sorbent; there are no data, either, on what kind of chemical compounds are formed in interaction between the products of conversion of rhodium catalysts and sorbents [1].

The present communication reports the results obtained in studying the recovery with a calcium oxide sorbent of rhodium lost in high-temperature oxidation of ammonia.

As a starting compound for preparing the sorbent was used calcium oxide of chemically pure grade. The reagent was ground and treated with a 70% aqueous solution of ethynol (2–3% relative to the sorbent mass) and compacted into pellets under pressure of 150 MPa. After thermal treatment of the mass in air at 473, 673, 873, and 1253 K (2 h at each temperature), the sorbent was crashed into grains and a fraction with grain size of 2×3 mm was selected.

Since recovery of lost metals and their compounds is mainly effected by the surface layer of sorbents [1, 7–16, 18–20], the sorbent grains were ground after every 40 h of operation and subjected to repeated forming and thermal treatment in an inert medium (Ar) in accordance with the scheme considered above.

The catalytic process of ammonia oxidation was carried out in a flow-through installation with quartz reactor 50 cm in diameter. As a catalyst served rhodium in the form of a package of five grids with thread diameter of 0.06 mm. The 17-cm-high bed of sorbent grains was placed at a distance of 0.8 cm from the catalyst grids.

The temperature of ammonia oxidation was 1253 K; the pressure in the system, 0.101 MPa; the content of ammonia in the ammonia–air mixture, 11.5 vol %; and the linear flow velocity of the mixture, 0.40 m s^{-1}. The time of catalyst operation and absorption mass testing was 600 h. An X-ray phase analysis of the compounds was made on a Siemens D-500 diffractometer with $Cu_{K\alpha}$ radiation. A differential-thermal analysis was done on an MOM Q-derivatograph (Hungary). The heating rate was 5 deg min^{-1} in the temperature range 293–1773 K.

During reactor shutdowns, the system was purged with dried argon and isolated from air with moisture absorbers. After being discharged from the reactor, the sorbent was stored in hermetically sealed vessels filled with dried argon.

The X-ray phase analysis of the sorbent demonstrated that it contains CaO and a rhodium compound

1070-4272/02/7510-1594 $27.00 © 2002 MAIK "Nauka/Interperiodica"

of unknown composition (Fig. 1). To eliminate the effect of unreacted sorbent on the X-ray diffraction patterns obtained, the sorbent was dissolved in 25% HNO_3 of chemically pure grade at 308 K. In doing so, account was taken of the fact that rhodium compounds do not dissolve in HNO_3 of this concentration at moderate temperatures [21]. The liquid phase was separated from the solid phase and removed. The solid phase was thoroughly and repeatedly washed with hot twice-distilled water (antil no Ca^{2+} and NO_3^- ions were contained in washing water) and subjected to thermal treatment in an inert medium (Ar) at 473–523 K to constant weight.

The X-ray diffraction patterns of the solid residue contained only lines characteristic of the compound $CaRh_2O_4$ (Fig. 1). The parameters of the X-ray patterns of this compound are presented in the table.

The set of lines in the diffraction patterns (interplanar spacings d and intensities I) is in good agreement with data from the ASTM file [22], which indicates that the chemical compound $CaRh_2O_4$, having rhombic lattice (a = 0.9169, b = 1.0747, c = 0.3087 nm) of the $CaFe_2O_4$ structural type with Pnam space group, is formed in the sorbent.

The composition of the $CaRh_2O_4$ compound was confirmed by X-ray phase and chemical analyses [23].

A thermogram of the compound $CaRh_2O_4$ is presented in Fig. 2.

When the substance is heated in an inert medium (argon) to prevent high-temperature oxidation of Rh and its sublimation in the form of rhodium(III) oxide [21, 23] in the temperature range 1713–1763 K, loss of mass (15.49%) is observed, associated with endothermic decomposition of the compound by the equation

$$2CaRh_2O_4 = 2CaO + 4Rh + 3O_2. \quad (1)$$

The products of dissociation are calcium oxide, rhodium metal, and oxygen, which is characteristic of double oxides including a noble metal [23]. The X-ray diffraction patterns of products of $CaRh_2O_4$ decomposition, cooled in an inert medium (Ar), contain, in addition to reflections related to calcium oxide (0.276, 0.239, 0.169, 0.1447, 0.1383, 0.1203, 0.1072, 0.0980 nm), also reflections from metallic rhodium (0.2196, 0.1902, 0.1345, 0.1147, 0.1098, 0.0951, 0.0872, 0.0850 nm). An endothermic peak appears in the DTA curve at 1743 ± 10 K.

For the $CaRh_2O_4$ compound, the loss of mass in decomposition virtually did not exceed the expected

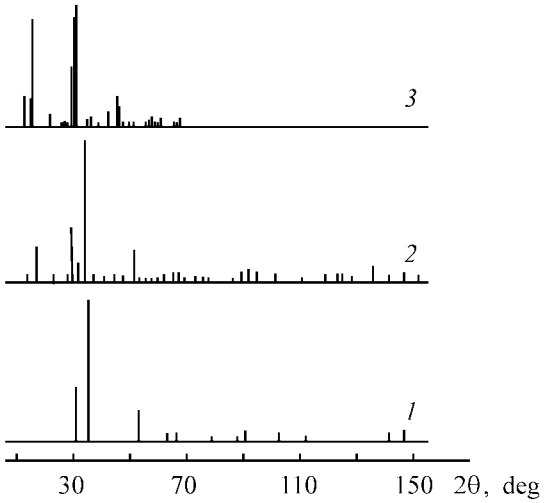

Fig. 1. X-ray diffraction patterns of the sorbents and products of rhodium recovery. (2θ) Bragg angle. (*1*) Initial sorbent, (*2*) sorbent after 600 h of catalyst operation, and (*3*) product of interaction between the sorbent and rhodium compounds ($CaRh_2O_4$).

value calculated using Eq. (1), which indicates that the inert medium rules out any influence of rhodium sublimation in the form of rhodium(III) oxide [21, 23].

The formation of $CaRh_2O_4$ in the sorbent can be accounted for on the basis of a comparative analysis of the conditions under which the products of rhodium catalyst conversion are recovered and the conditions of synthesis of the given compound.

The authors of [24] synthesized $CaRh_2O_4$ by prolonged (for no less than 150°C) heating in air

Characteristics of X-ray diffraction patterns of the $CaRh_2O_4$ compound found in the sorbent

d, nm	I, %	d, nm	I, %
0.5373	12	0.1978	17
0.4617	24	0.1850	34
0.4515	49	0.1823	25
0.3456	8	0.1797	7
0.3329	1	0.1711	8
0.2972	3	0.1664	10
0.2822	3	0.1624	3
0.2686	49	0.1546	16
0.2626	91	0.1539	9
0.2569	100	0.1527	13
0.2551	43	0.1508	22
0.2308	7	0.1497	11
0.2265	11	0.1340	9
0.2114	4	0.1277	7
0.2001	9		

(T = 1173–1373 K, P = 0.101 MPa) of a mixture of rhodium(III) oxide (or rhodium metal) with calcium oxide (carbonate). Under these conditions, metallic rhodium is converted into rhodium(III) oxide [21, 23, 24].

In high-temperature oxidation of ammonium, the rhodium catalyst undergoes a number of physicochemical transformations [1, 25] in accordance with the reaction equations

$$4Rh_{(c)} + 3O_{2(g)} = 2Rh_2O_{3(c)}, \quad (2)$$

$$Rh_{(c)} = Rh_{(g)}, \quad (3)$$

$$4Rh_{(c)} + 3O_{2(g)} = 2Rh_2O_{3(g)}, \quad (4)$$

$$4Rh_{(g)} + 3O_{2(g)} = 2Rh_2O_{3(g)}. \quad (5)$$

At a process temperature of 1253 K rhodium sublimates predominantly in the form of rhodium(III) oxide [21, 26]. However, in the gas phase too, rhodium is readily oxidized by the oxygen present in the reaction medium to rhodium(III) oxide. Rhodium(III) oxide dissociates at 1333 K [21], being, therefore, stable at the reaction temperature.

The forming products of reactions (2)–(5), Rh and Rh_2O_3, carried away by the flow of the reaction mixture, are starting compounds in processes yielding the $CaRh_2O_4$ compound on the sorbent surface in accordance with the reaction equations

$$Rh_2O_3 + CaO = CaRh_2O_4, \quad (6)$$

$$4Rh + 3O_2 + 2CaO = 2CaRh_2O_4. \quad (7)$$

Thus, the products of conversion of the rhodium catalyst in high-temperature oxidation of ammonia are bound by the calcium oxide sorbent into the compound $CaRh_2O_4$. This fact is to be taken into account when using industrial catalysts for ammonia oxidation (with sorbents based on calcium oxide) containing rhodium. In rhodium recovery from calcium-containing sorbents, account should be taken of the high thermal and chemical stability of the $CaRh_2O_4$ compound [24], and the appropriate temperature and reagents should be used.

CONCLUSIONS

(1) The products of conversion of rhodium lost in high-temperature oxidation of ammonia are bound by the calcium oxide sorbent into the $CaRh_2O_4$ compound.

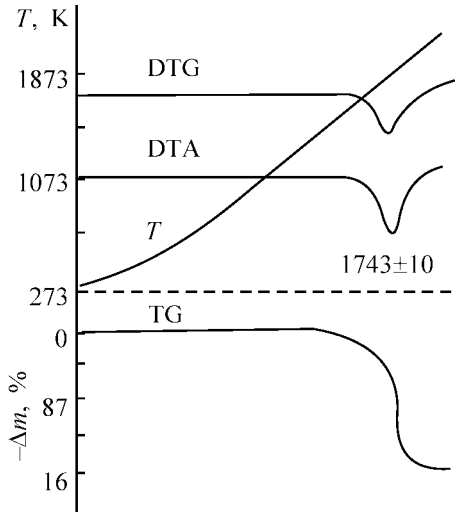

Fig. 2. Thermogram of $CaRh_2O_4$. Substance mass 100 mg, heating rate 5 deg min^{-1}. (T) Temperature and (Δm) mass change.

(2) Data on chemical aspects of recovery with the calcium oxide sorbent of rhodium lost in high-temperature oxidation of ammonia can be used in developing theoretical foundations for creation of effective sorption masses.

REFERENCES

1. Karavaev, M.M., Zasorin, A.P., and Kleshchev, N.F., *Kataliticheskoe okislenie ammiaka* (Catalytic Oxidation of Ammonium), Moscow: Khimiya, 1983.
2. Karavaev, M.M., Mumchyan, E.G., Arutyunyan, V.A., *et al.*, *Azot. Prom–st.*, 1974, no. 5, pp. 26–29.
3. Phillips, W. Z., *Trans. ASM*, 1964, vol. 57, no. 1, pp. 33–37.
4. Schäfer, V.H. and Tebben, A.Z., *Z. anorg. allgem. Chem.*, 1960, vol. 304, nos. 3–4, pp. 317–321.
5. Holzmann, H., *Platinum Metals Rev.*, 1969, vol. 13, no. 1, pp. 2–8.
6. Kozub, P., Gryn, G., and Goncharov, I., *Platinum Metals Rev.*, 2000, vol. 44, no. 2, pp. 74–84.
7. Atroshchenko, V.I., Loboiko, A.Ya., Sedashova, E.G., *et al.*, *Izv. Vyssh. Uchebn. Zaved., Khim. Khim. Tekhnol.*, 1974, vol. 17, no. 10, pp. 1587–1590.
8. Sikora, H. and Blasiak, E., *Przem. Chem.*, 1967, vol. 46, no. 1, pp. 31–37.
9. *Kataliticheskie i massoobmennye protsessy pod davleniem v tekhnologii neorganicheskikh veshchestv* (Catalytic and Mass-Exchange Processes Carried out Under Pressure in Technology of Inorganic Substances), Loboiko, A.Ya., Ed.,. Kharkov: Osnova, 1993.
10. Janiczek, W., Krawiec, Z., Gajewski, A., and Ka-

rolewicz, S., *Przem. Chem.*, 1967, vol. 46, no. 9, pp. 547–550.

11. Darling, A., Selman, G., and Rushforth, R., *Platinum Metals Rev.*, 1970, vol. 14, no. 2, pp. 54–60.
12. Karavaev, M.M., Mumchan, E.G., Solei, E.M., *et al.*, *Khim. Prom–st.*, 1975, no. 2, pp. 116–117.
13. Blasiak, E., Lugowska, M., and Swerczak, R., *Chemicne stosow*, 1971, vol. 15, no. 2, pp. 225–230.
14. Sikora, H. and Blasiak, E., *J. Am. Ceram. Soc.*, 1972, vol. 55, no. 8, pp. 426–427.
15. Atroshchenko, V.I., Loboiko, A.Ya., Sedashova, E.G., *et al.*, *Khim. Prom–st.*, 1976, no. 1, pp. 73–75.
16. Karavaev, M.M., Pal'mova, N.A., Telyatnikova, T.V., *et al.*, *Khim. Prom–st.*, 1978, no. 3, pp. 198–200.
17. Kozub, P., Trusov, N., Gryn, G., and Prezhdo, V., *J. Chem. Techol. Biotechnol.*, 2001, vol. 76, no. 2, pp. 147–152.
18. Lavrenko, A.A., Kozub, P.A., Grin', G.I., *et al.*, *Vestn. Nats. Tekhn. Univ. "KhPI"*, 2001, issue 3, pp. 108–110.
19. Zakharchenko, N.I., *Zh. Prikl. Khim.*, 2002, vol. 75, no. 3, pp. 413–418.
20. Shushura, O.S., Goncharov, I.I., Loboiko, A.Ya., *et al.*, *Vestn. Kharkov. Gos. Politekhn. Univ.*, 1999, issue 39, pp. 44–47.
21. *Blagorodnye metally: Spravochnik* (Noble Metals: Reference Book), Savitskii, E.M., Ed., Moscow: Metallurgiya, 1984.
22. *Powder diffraction data file, ASTM, Joint Committee in Powder Diffraction Standards*, Philadelphia, 1967.
23. Shaplygin, I.S., *Zh. Neorg. Khim.*, 1985, vol. 30, no. 12, pp. 3038–3041.
24. Lazarev, V.B. and Shaplygin, I.S., *Zh. Neorg. Khim.*, 1978, vol. 23, no. 2, pp. 291–303.
25. Holzmann, H., *Chemie Ingenieur Technik.*, 1967, no. 2, pp. 89–95.
26. Kazenas, E.K. and Chizhikov, D.M., *Davlenie i sostav para nad okislami khimicheskikh elementov* (Vapor Pressure and Composition over Oxides of Chemical Elements), Moscow: Nauka, 1976.

Russian Journal of Applied Chemistry, Vol. 75, No. 10, 2002, pp. 1598–1604. Translated from Zhurnal Prikladnoi Khimii, Vol. 75, No. 10, 2002, pp. 1632–1638.
Original Russian Text Copyright © 2002 by Yakovleva, Yakovlev, Finaenov.

APPLIED ELECTROCHEMISTRY AND CORROSION PROTECTION OF METALS

Electrochemical Synthesis of Thermally Expandable Graphite Compounds in Nitrate Electrolyte

E. V. Yakovleva, A. V. Yakovlev, and A. I. Finaenov

Saratov State Technical University, Saratov, Russia

Technological Institute, Engels, Saratov oblast, Russia

Received April 19, 2002

Abstract—The influence of potential and time of anodic treatment of dispersed graphite in an HNO_3 solution on the intercalation rate and possible concurrent reactions was studied.

Graphite intercalation compounds (GIC) and products of their hydrolysis, whose volume may increase manyfold upon fast heating (thermal expansion) are widely used for manufacture of graphite foil, pressed carbon articles, fireproof materials and coatings, and various-purpose composites [1, 2]. Industrial production of thermally expandable graphite (TEG) is mainly based on chemical synthesis of such GIC as graphite hydrosulfate and nitrate [3]. The chemical synthesis involves interaction of graphite with concentrated acids containing an additional oxidant. The action of the oxidant on graphite gives rise to a distributed positive charge on polyarene networks, after which spaces between carbon planes are successively, in accordance with the step-by-step model [4], filled with anions and molecules of the acid to give a GIC of general formula [5]:

$$C^{+}_{24n}A^{-} \cdot (2\text{–}2.5)HA,$$

where A is HSO^{-}_{4} (graphite hydrosulfate) or NO^{-}_{3} (graphite nitrate), and n = 1, 2, 3, is intercalation step.

In HNO_3 solutions with concentration higher than 15 M, intercalation occurs spontaneously without any additional oxidant. HNO_3 molecules act simultaneously as an oxidant, intercalating component (intercalate), and a source of solvate ligands [6]. In a 17–18 M HNO_3 solution, graphite nitrate of the second step is formed, with the decrease in concentration leading to lower content of the intercalate in the interlayer spaces (the step number increases). In a 15 M HNO_3 solution, no intercalation reactions are observed. The composition of graphite nitrate synthesized by liquid-phase chemical method [7] is determined by the redox-potential of an oxidizing solution, whose being lowered to 0.995 V (silver chloride electrode) stops the intercalation.

GIC can also be prepared with acids by anodic oxidation of graphite [8–11]. A considerable body of data on electrochemical synthesis has been obtained with pyrolytic graphite plate electrodes in galvanostatic polarization mode, using concentrated acids [12–14]. The system graphite–H_2SO_4 has been studied to a greater extent. Publications devoted to anodic oxidation of graphite nitrate appear irregularly [15–17]. Unlike liquid-phase spontaneous intercalation, the electrochemical synthesis ensures the first step of intercalation [18, 19] and allows the HNO_3 concentration to be lowered to 15 M, i.e., to a value at which GIC of composition $C^{+}_{48}NO^{-}_{3} \cdot 2HNO_3$ can be formed. The chemical and electrochemical syntheses of GIC with acids proceed by the same mechanisms [7]. This conclusion is based on the dependences of the CIG formation kinetics and step of intercalation on the type and concentration of the oxidant in a reagent mixture in the chemical method (redox-potential) [7] and on the potential and quantity of electricity supplied in anodic treatment of graphite in the electrochemical method [18]. Undoubtedly, the electrochemical method allows the potential of carbon material to be varied more widely, with the maximal potential limited by involvement of water in the electrode processes. When graphite is polarized anodically in HNO_3 solutions with sufficient content of water, a set of reactions occurs [20, 21]. For example, the intercalation is preceded by charging of the electrical double layer and oxidation of surface functional groups (SFG), which involves water and is accompanied by an increase in

1070-4272/02/7510-1598 $27.00 © 2002 MAIK "Nauka/Interperiodica"

the content of oxygen in SFG. Depending on the acid concentration and polarization potential, the electrochemical intercalation

$$24C + 3HNO_3 = C_{24}^{+}NO_3^{-} \cdot 2HNO_3 + H^+ + e \quad (1)$$

may be accompanied by SFG peroxidation [20]

$$C_{24}^{+}NO_3^{-} \cdot 2HNO_3 + 3HNO_3 \rightarrow 2C_{12}^{+}NO_3^{-} \cdot 2HNO_3 + H^+ + e, \quad (2)$$

formation of graphite oxide [20]

$$8C + 4H_2O \rightarrow C_8O_2(OH)_2 + 6H^+ + 6e, \quad (3)$$

or by complete or incomplete hydrolysis of graphite nitrate [20]

$$C_{24}^{+}NO_3^{-} \cdot 2HNO_3 + H_2O \rightarrow C_{24}^{+}OH^{-} \cdot 2H_2O + 3HNO_3. \quad (4)$$

In the final stage of synthesis, or simultaneously with bulk reactions (1)–(3), oxygen may be evolved if a necessary potential is attained, in the form of CO, CO_2, and O_2 [21]:

$$=\overset{|}{C}-\underset{|}{\overset{|}{C}}=O + H_2O \rightarrow =\overset{|}{C}-H + CO_2 + 2H^+ + 2e, \quad (5)$$
$$\quad\quad\quad

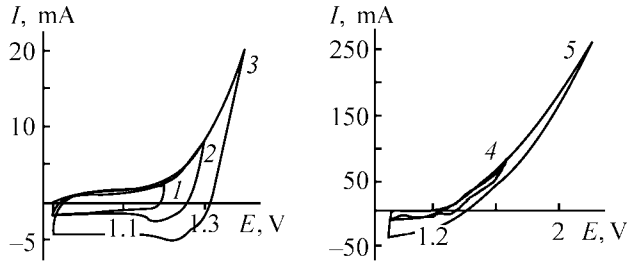

Fig. 1. Cyclic potentiodynamic curves (10th cycle) for GSM-1 graphite in a 13.5 M HNO_3 solution at various reverse potentials E_{rev}. V = 20 mV s^{-1}, T = 20°C. (*I*) Current and (*E*) potential. E_{rev} (V): (*1*) 1.20, (*2*) 1.30, (*3*) 1.40, (*4*) 1.65, and (*5*) 2.2.

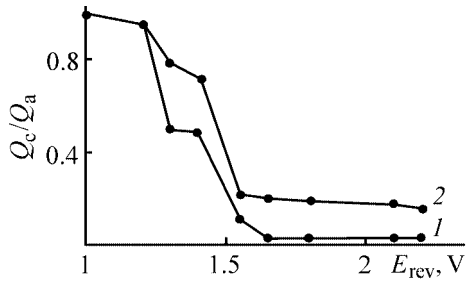

Fig. 2. Q_c/Q_a ratio vs. reverse potential E_{rev} of cyclic potentiodynamic curves measured on a GSM-1 graphite electrode in a 13.5M HNO_3 solution. Cycle: (*1*) 1st and (*2*) 10th.

cyclic potentiodynamic curve, Q_a, grows steadily with increasing E_a, but decreases in cycling (Fig. 1, Table 1). Since the graphite electrode area is virtually constant, the higher anodic currents in the first cycles are due to the possibility of intercalation of all interlayer spaces; it is not improbable that terminal carbon atoms and defects of the graphite matrix may be oxidized by reaction (6) at higher E_a. The quantity of electricity consumed in the reverse cycles in the cathodic region will be determined by the reduction currents of SFG, GIC, and, in part, graphite oxide and adsorbed oxygen. With extending range of potential sweep, as well as in the course of cycling, Q_c increases. The Q_c increase in cycling at a simultaneous decrease in Q_a can be accounted for solely by the increased contribution to the total current of the intercalation–deintercalation bulk reactions, which is apparently due to the ordering of the carbon material structure. The degree of reversibility of the occurring processes can be estimated from the Q_c/Q_a ratio. Regarding the degree of reversibility of the anodic reactions, the potential range studied can be conventionally divided into three regions (Fig. 2). In the range from E_{st} to 1.2 V, where no GIC is formed, the anodic processes are virtually completely reversible (Q_c/Q_a = 0.99–0.96), which also indicates that no reactions occur with gas evolution.

Table 1. Anodic Q_a and cathodic Q_c quantities of electricity in cyclic potentiodynamic curves for graphite in a 13.5 M HNO_3 solution in relation to E_{rev} and cycle number (V = 20 mV s^{-1}, T = 20°C)

E_{rev}, V	Cycle	Q_a	Q_c
		mA h	
1.20	1–10	0.0036	0.0033
1.30	1	0.014	0.007
	7–10	0.009	0.008
1.40	1	0.042	0.021
	7–10	0.031	0.023
1.55	1	0.222	0.024
	7–10	0.133	0.029
1.65	1	1.833	0.055
	7–10	0.453	0.091
2.20	1	4.047	0.162
	7–10	2.022	0.324

In the transition region E_a = 1.2–1.6 V, the Q_c/Q_a ratio decreases steeply (Fig. 2), which may be due to the irreversibility of intercalation reactions or to acceleration of surface reactions (5)–(7). It should be noted that, in this range of potentials, the rate of GIC formation grows, since the currents in the cathodic region, which are mainly due to deintercalation, also increase. At higher potentials (E_a > 1.6 V) the Q_c/Q_a ratio ceases to vary, the revealed tendencies in the influence of cycling are retained, and the deintercalation currents increase further.

To confirm the assumptions concerning the nature of the processes occurring at various anodic polarization potentials, potentiostatic syntheses of GIC were performed, and the properties of the resulting carbon compounds were assessed by means of XPA and heat treatment, with bulk density of TEG determined.

The X-ray diffraction patterns of the samples synthesized samples contain broad diffuse reflections corresponding to defective graphite (d_{002} = 3.4–3.5 Å), i.e., reveal no graphite nitrate. At the same time, the compounds obtained can be thermally expanded. To confirm the occurrence of bulk intercalation reactions under the potentiostatic treatment of graphite, the variation of current with time was measured simultaneously with the thickness of a carbon material layer (Fig. 3). In the course of formation of graphite intercalation compounds, graphite undergoes structural transformations caused by an increase in the interplanar spaces *a* [1]. For example, *a* increases from 3.35 to 8.2 Å in graphite nitrate [7] and may increase

Table 2. Effect of potential and time of TEGC synthesis in a 13.5 M HNO_3 solutions on the rate of the anodic reactions, quantity of electricity passed, and properties of the compounds synthesized

E_a, V	τ, h	I_i^*	I_{av}^*	I_f^*	Q, mA h g^{-1}	B_C, %	d_{TEG}, g dm^{-3}	K_{te}, ml g^{-1}
		mA g^{-1}						
1.3	2.0	98	0.5	0.2	1	100	–	0
1.4	2.0	100	2	1.6	4	100	–	0
1.5	2.0	128	4	3.2	8	100	–	0
1.6	2.0	300	38	28	75	100	59.2	8
1.7	2.0	360	60	52	120	99	9.2	80
1.8	2.0	390	65	55	140	99	8.0	110
1.9	0.5	390	70	60	35	99	16.0	56
	1.0	380	65	60	65	98	10.0	78
	1.5	400	77	60	115	97	8.0	100
	2.0	400	80	70	160	95	6.0	132
2.0	2.0	460	107	86	214	97	3.71	210
2.1	0.5	620	160	114	80	97	5.5	146
	1.0	580	140	100	140	96	3.5	230
	1.5	600	130	100	195	95	2.7	300
	2.0	560	140	90	280	94	2.4	340
2.2	2.0	660	160	100	320	92	2.4	330
2.3	2.0	720	180	130	360	90	2.4	310

* I_i, I_{av}, and I_f are, respectively, the initial, average, and final currents in the potentiodynamic curve; I_{av} is calculated from Q and synthesis time.

to 6.6 Å in graphite oxide [28]. As a result, the thickness of a graphite layer must increase in the course of the GIC formation.

The potentiostatic curves I–τ are of classical shape (Fig. 3). A sharp rise in the current is observed at the beginning of the process, whose magnitude tends grow with increasing potential of the anodic polarization (Fig. 3, Table 2). The decrease in current is caused by charging of the electrical double layer and by SFG oxidation. Further run of the curve is characterized by a number of inflections corresponding to successive formation of GIC belonging to different steps (Daumas–Herold model [4]). Then, the current virtually ceases to change with time.

Similar intervals of time can also be distinguished in the curves of piston displacement (Fig. 3, Δl–τ). A zero or, in some cases, negative change in the graphite layer thickness corresponds to a fast decrease in the current, which indicates that only surface reactions proceed during this interval of time. Thus, it was demonstrated experimentally that the intercalation is preceded by the induction period during which the composition of SFG on the graphite surface changes. Previously, the induction period has been mentioned as an assumption in [12, 28]. According to Fig. 3, the time of graphite matrix preparation for intercalation decreases steadily with increasing E_a, since the initial currents I_i (Table. 2) in the potentiostatic curves grows, and the necessary quantity of electricity supplied to graphite during the induction period must be the same.

It should be noted that the system used to measure the change in the graphite layer thickness shows time lag because of the piston-loading pressure and friction

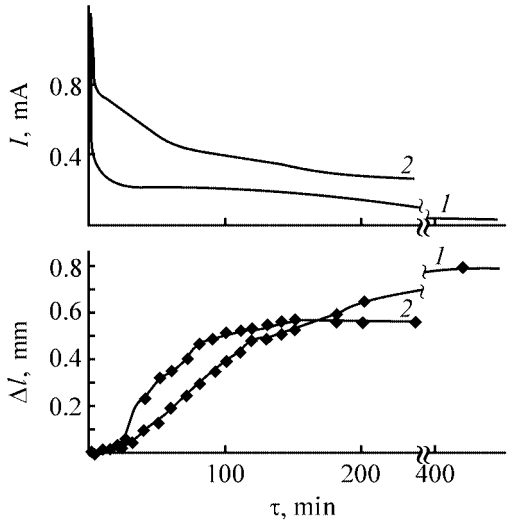

Fig 3. Current I and thickness Δl of the graphite electrode vs. time τ of anodic treatment with the same quantity Q = 450 mA h g^{-1} of passed electricity. (*1*) E_a = 1.75 V, d_{TEG} = 2.2 g dm^{-3}; (*2*) E_a = 2.1 V, d_{TEG} = 1.8 g dm^{-3}.

Table 3. Variation of thickness Δl of a graphite layer with time in anodic potentiostatic treatment in a 13.5 M HNO_3 solution

E_a, V	Δl (%) for indicated time, min				
	50	100	150	250	420
2.1	25	40	44	44	44
1.75	11	29	40	52	61

forces. For this reason, bends in the Δl–τ curves may be shifted along the time axis relative to those in the potentiostatic curves, especially at the beginning of synthesis.

As predicted previously, the bulk reactions of electrochemical intercalation do entail an increase in the graphite layer thickness (Fig. 3), with the entire time during which the piston goes up divided into two portions with different piston displacement velocities. The Δl curves (Fig. 3) show that the layer thickness grows faster at the beginning of the process and the piston motion slows down. Similar changes are characteristic of the I–τ curves. Such a run of the curves is due to deceleration of the electrochemical intercalation processes, caused by diffusion hindrance increasing upon intercalate penetration into the graphite clusters.

After the intercalation is complete, and the volume of the graphite anode stops to increase, the potentiostatic curves continue to show currents, which may be due to peroxidation of the already formed GIC or to surface reactions, with the piston at rest.

With increasing anode potential, the current grows in all the three stages of TEGC synthesis, distinguished here (Fig. 3, Table 2). At higher positive E_a, the piston velocity grows with graphite converted into GIC. At the same time, the highest values of Δl are, conversely, attained at lower anodic polarization (Fig. 3, Δl–τ). This can be understood with account

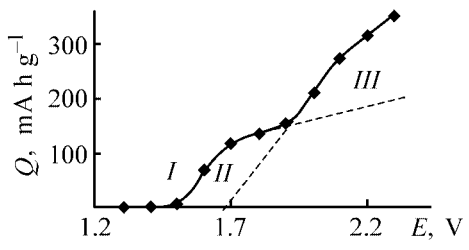

Fig. 4. Amount of electricity Q passed through graphite anode for 2 h vs. potential E of anodic potentiostatic treatment in a 13.5 M HNO_3 solution.

of the fact that the possibility of graphite oxide formation becomes higher with increasing anode potential. The theoretically possible (judging from a values) increase in the graphite volume in formation of graphite nitrate must be 30% higher than that in graphite conversion into graphite oxide. The experimentally observed discrepancy of Δl is also about 30% (Fig. 3, Table 3). Consequently, it may be assumed that the main product of synthesis at E_a = 1.75 V is graphite nitrate undergoing hydrolysis, whereas at E_a = 2.1 V compounds similar to graphite oxide are formed.

The assumptions made are also indirectly confirmed by the data on the TEG density. Despite that the quantity of passed electricity is the same and the volume expansion is smaller, the TEG compounds formed by anodic treatment at E_a = 2.1 V have smaller bulk density (1.8 g dm^{-3}) than samples synthesized at E_a = 1.75 V (d_{TEG} = 2.2 g dm^{-3}). This is in agreement with published data [12], whence follows that graphite oxide has larger coefficient of thermal expansion.

The data of Table 2 show that the thermal expandability of the compounds synthesized depends on the E_a value and is determined by the quantity of electricity passed through the carbon material. With increasing Q, d_{TEG} decreases steadily, whereas K_{te} increases. If the Q–E_a dependence is regarded as a stationary polarization curve of the overall electrode process, three main potential ranges can be distinguished (Fig. 4). In range I (up to 1.5 V), no electrochemical intercalation occurs, with reversible GIC oxidation reactions being predominant. This assumption is confirmed experimentally. Prolonged (20 h) anodic treatment of graphite at E_a = 1.3 V does not lead to any increase in the graphite layer thickness in electrolysis or TEGC formation. Treatment at E_a = 1.5 for the same time yields samples with K_{te} of up to 20–30. Consequently, the threshold potential of GIC formation in a 13.5 M HNO_3 solution is within 1.4–1.5 V. In range II (Fig. 4) the electrochemical intercalation reactions are predominant. However, the XPA and the high degree of irreversibility of the electrode reactions (Fig. 2) show that graphite nitrate formed by reaction (1) undergoes fast hydrolysis or reoxidation. Both the products of reactions (2) and (4) are less electrochemically reversible, compared with graphite nitrate, because of the formation of covalent bonds between the intercalate and the carbon layers. In range III, the run of the polarization curve reveals a new electrode process, which onsets at E_a = 1.6–1.7 V, as shown by extrapolation to the potential axis (Fig. 4). A rise in current is observed in the potentiodynamic curves in this potential range, confirmed by the data of Table 1. At the same time, the Q_c/Q_a remains vir-

tually unchanged (Fig. 2). Consequently, the contribution of surface reactions (5)–(7), which are already possible thermodynamically [20, 23], is insignificant. It is therefore appropriate to conclude that the nature of the electrochemical intercalation of graphite changes. Presumably, the intercalation process occurs in range III to give mainly GIC of the type of graphite oxide. These assumptions are consistent with published data [28], which show that graphite oxide is formed at potentials more positive by 200–700 mV, compared with those in the case of GIC, and a decrease in the width of this interval with increasing water content in the electrolyte would be expected. The absence of intensive oxidation of carbon to CO and CO_2 is also confirmed by the rather high current efficiencies by carbon (Table 2).

To ensure a considerable thermal expandability of GIC synthesized under the experimental conditions, the quantity of electricity to be passed through the graphite anode should be 150 mA h and more per 1 g of graphite. It is reasonable, in this case, to perform synthesis at potentials of 2.0–2.1 V, which not only considerably accelerates intercalation, but also results in the formation of TEGC with the highest K_{te} (Table 2), as mentioned above. Further increase in E_a and also passing more than 250 mA h g^{-1} of electricity through a graphite sample do not decrease the TEGC density, with the thermal expansion coefficient even decreasing somewhat. Under the given conditions, the partial contribution of reactions (5) and (6) to the total current of the electrode process increases, which results in the aggravation of defects of the graphite matrix and makes removal of intercalate from the interlayer spaces in heat treatment inefficient. The experiments performed revealed the fundamental aspects of the potentiostatic synthesis of TEGC in a 13.5 M HNO_3 electrolyte with the use of a dispersed carbon material. The possibility of obtaining compounds with prescribed coefficient of thermal expansion by controlling the potential and time of anodic treatment of graphite was demonstrated.

CONCLUSIONS

(1) Electrochemical studies and measurements of the change in the thickness of a dispersed graphite layer in anodic polarization in a 13.5 M HNO_3 electrolyte showed that the threshold potential of intercalation is 1.3–1.4 V relative to a silver chloride reference electrode. At lower potentials, reversible electrode reactions involving surface functional groups occur. At potentials higher than 1.7 V, intercalation compounds like graphite oxide can be formed. The intercalation is preceded by an induction period involving oxidation of surface groups of the graphite matrix.

(2) XPA data and cyclic potentiodynamic curves showed that the graphite intercalation compounds formed are hydrolyzed or reoxidized owing to the high content of water in the electrolyte. The compounds obtained may undergo effective thermal expansion upon heating.

(3) The influence exerted by the potential of potentiostatic anodic treatment and by the quantity of electricity passed through graphite electrode on the thermal expansion coefficient of the compounds synthesized was determined. For example, to ensure a less than 3 g dm^{-3} density of thermally expanded graphite, the synthesis should be performed at 2.1 V for 1.5–2 h with 200–280 mA h g^{-1} of electricity passed.

REFERENCES

1. Ubbelohde, A.R. and Lewis, F.A., *Graphite and Its Crystal Compounds*, Oxford: Clarendon Press, 1960.
2. Setton, R., *Synth. Met.*, 1988, vol. 23, pp. 519–524.
3. Avdeev, V.V., Sorokina, N.E., Nikol'skaya, I.V., *et al.*, *Neorg. Mater.*, 1997, vol. 33, no. 6, pp. 699–702.
4. Daumas, N. and Herold, A., C. R. *Acad. Sci. Paris, Ser. C*, 1969, vol. 268, no. 5, pp. 373–375.
5. Rudorff, W. and Hofmann U., *Z. anorg. allgem. Chem.*, 1938, vol. 238, no. 1, pp. 1–50.
6. Yaroshenko, A.P., Popov, A.F., and Shapranov, V.V., *Zh. Prikl. Khim.*, 1994, vol. 67, no. 2, pp. 204–211.
7. Avdeev, V.V., Sorokina, N.E., Tverezovskaya, O.A., *et al.*, *Neorg. Mater.*, 1999, vol. 35, no. 4, pp. 435–439.
8. Metrot, A., *Synth. Met.*, 1983, vol. 7, no. 3, pp. 177–184.
9. Fudzi, R., *Osaka koge gidzyutsu sikense khkoku*, 1978, vol. 353, pp. 1–66.
10. Apostolov, S.P., Krasnov, V.V., Avdeev, V.V., and Finaenov A.I., *Izv. Vyssh. Uchebn. Zaved., Khim. Khim. Tekhnol.*, 1997, vol. 40, no. 1, pp. 113–117.
11. Apostolov, S.P., Krasnov, V.V., and Finaenov A.I., *Zh. Prikl. Khim.*, 1997, vol. 70, no. 4, pp. 602–607.
12. Shapranov, V.V. and Yaroshenko, A.P., *Khim. Fiz. Uglya*, Kiev, 1991, pp. 56–74.
13. Beck, F., Krohn, H., and Junge, H., *Ber. Bunsenges. Phys. Chem.*, 1980, no. 84, pp. 1023–1026.
14. Metrot, A., Willmann, P., Meral, T., and Herold A., *Carbon*, 1979, vol. 17, no. 2, pp. 182–183.
15. Scharff, P. and Stump, E., *Ber. Bunsenges. Phys. Chem.*, 1995, no. 1, pp. 58–61.
16. Scharff, P., Xut, Z.-Y., Stump, E., and Barteczko, K., Carbon, 1991, vol. 29, no. 1, pp. 31–37.

17. Scharff, P., Stump, E., Barteczko, K., and Xut Z.-Y., *Ber. Bunsenges., Phys. Chem.*, 1994, pp. 568–573.
18. Avdeev, V.V., Tverezovskaya, O.A., Sorokina, N.E., *et al.*, *Neorg. Mater.*, 2000, vol. 36, no. 3, pp. 276–281.
19. Sorokina, N.E., Maksimova, N.V., and Avdeev, V.V., *Neorg. Mater.*, 2001, vol. 37, no. 4, pp. 1–7.
20. Tarasevich, M.P., *Elektrokhimiya uglerodnykh materialov* (Electrochemistry of Carbon Materials), Moscow: Nauka, 1984.
21. Shapranov, V.V., Yaroshenko, A.P, and Kucherenko, V.A., *Elektrokhimiya*, 1990, vol. 26, no. 9, pp. 1130–1135.
22. Yakovlev, A.I. and Finaenov, A.I., *Zh. Prikl. Khim.*, 1999, vol. 72, no. 1, pp. 88–91.
23. Yakovlev, A.V., Finaenov A.I., Nikitina, L.E., and Apostolov, S.P., *Zh. Prikl. Khim.*, 1999, vol. 72, no. 4, pp. 589–593.
24. Ukr. Patent no. 18187.
25. Vasil'ev, Yu.B., Kanevskii, L.S., Lushnikov, V.I., and Skundin, A.M., *Elektrokhimiya*, 1997, vol. 13, no. 3, pp. 440–443.
26. Kanevskii, L.S., Lushnikov, V.I., and Skundin, A.M., *Elektrokhimiya*, 1977, vol. 13, no. 11, pp. 1728–1731.
27. Skolunov, A.V., Varshavskii, V.Ya., and Monastyrskaya, E.G., *Elektrokhimiya*, 1995, vol. 31, no. 6, pp. 594–597.
28. Fialkov, A.S., *Uglerod, mezhsloevye soedineniya i komposity na ego osnove* (Carbon, Interlayer Compounds and Composites on Its Base), Moscow: Aspekt, 1997.

Russian Journal of Applied Chemistry, Vol. 75, No. 10, 2002, pp. 1605–1608. Translated from Zhurnal Prikladnoi Khimii, Vol. 75, No. 10, 2002, pp. 1639–1642.
Original Russian Text Copyright © 2002 by Boguta, Rudnev, Yarovaya, Kaidalova, Gordienko.

APPLIED ELECTROCHEMISTRY AND CORROSION PROTECTION OF METALS

On Composition of Anodic-Spark Coatings Formed on Aluminum Alloys in Electrolytes with Polyphosphate Complexes of Metals

D. L. Boguta, V. S. Rudnev, T. P. Yarovaya, T. A. Kaidalova, and P. S. Gordienko

Institute of Chemistry, Far-Eastern Division, Russian Academy of Sciences, Vladivostok, Russia

Received April 25, 2002

Abstract—Anodic layers containing M(II) phosphates, e.g., $Mg_3(PO_4)_2$, $Mn_2P_2O_7$, $Mn(PO_3)_2$, and $NaZnPO_4$, were obtained.

Anodic coatings containing electrolyte components have been formed on aluminum, its alloys, and titanium in electrolytes with M(II) and M(III) polyphosphate complexes (MPC) at sparking voltages [1–6]. The elemental composition of the coatings depends on the MPC concentration and the [polyphosphate]/metal cation] molar ratio in an electrolyte. A possible mechanism of incorporation of the electrolyte components into coatings is thermolysis in near-breakdown regions of hydrated metal polyphosphates being deposited onto anode [1]. However, the phase composition of coatings has not been determined.

This study is concerned with the phase composition of anodic-spark coatings on aluminum alloys with phosphorus(V) and magnesium(II), manganese(II) or zinc(II).

EXPERIMENTAL

The electrolytes were prepared using commercial reagents $Na_6P_6O_{18}$ (pure grade) and $Mg(CH_3COO)_2 \cdot 4H_2O$, $Mn(CH_3COO)_2 \cdot 4H_2O$, $Zn(CH_3COO)_2 \cdot 2H_2O$ (all chemically pure grade). The electrolyte preparation, electrochemical cell, and power source were similar to those described in [2–4].

The coatings were formed on samples made of AD1 alloy at a constant current density $j = 0.05$ A cm^{-2} in the course of 10 min. The first sparking discharges appeared on the anode surface during the first minute of the process. After anodization, the samples were washed with distilled water and dried in air at 70–80°C.

The samples were in the form of a 30-cm^2 foil bent as an "accordion," with the coating partially peeling off when the accordion is stretched.

The phase composition of the coatings separated from a support was determined from X-ray diffraction patterns obtained on a DRON–2.0 diffractometer with Cu_{K_α} radiation. The coating material was annealed in air for 30 min.

Figure 1 shows the content of aluminum(III), phosphorus(V), and zinc(II) in coatings on an AMtsM aluminum alloy in relation to the $n = [P_6O_{18}^{6-}]/[Zn^{2+}]$ molar ratio in the electrolyte bulk. Similar dependences have been obtained for coatings formed in the electrolytes containing $Na_6P_6O_{18}$ or $Na_5P_3O_{10}$ and other M(II), M(III) salts [1–4]. Analysis of these data shows that the electrolyte elements are incorporated

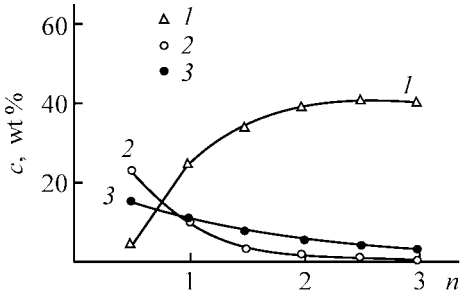

Fig. 1. Content c of (*1*) aluminum(III), (*2*) zinc(II), and (*3*) phosphorus(V) in the coatings vs. the molar ratio $n = [P_6O_{18}^{6-}]/[Zn^{2+}]$. Coatings formed on the AMtsM aluminum alloy in an electrolyte containing 0.05 M $Na_6P_6O_{18}$ and $Zn(CH_3COO)_2 \cdot 2H_2O$ at a current density $j = 0.05$ A cm^{-2} for 10 min.

1070-4272/02/7510-1605 $27.00 © 2002 MAIK "Nauka/Interperiodica"

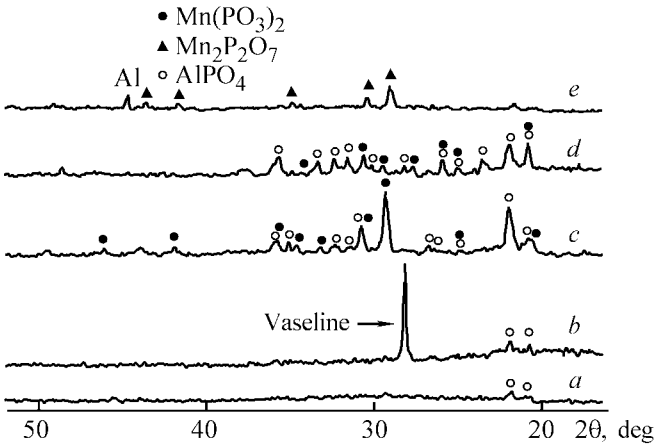

Fig. 2. X-ray diffraction patterns of coatings formed on the AD–1 aluminum alloy in an electrolyte containing 0.05 M $Na_6P_6O_{18}$ and $Mn(CH_3COO)_2 \cdot 4H_2O$ with n = 0.5, subjected to annealing at different temperatures and detached from the support. (2θ) Bragg angle; the same for Figs. 3 and 4. (*a*) Initial sample; Calcination conditions: (*b*) 300°C, 30 min; (*c*) 800°C, 30 min; (*d*) 1000°C, 1.5 h; and (*e*) sample on substrate obtained in the decreasing power mode in an electrolyte with n = 0.6.

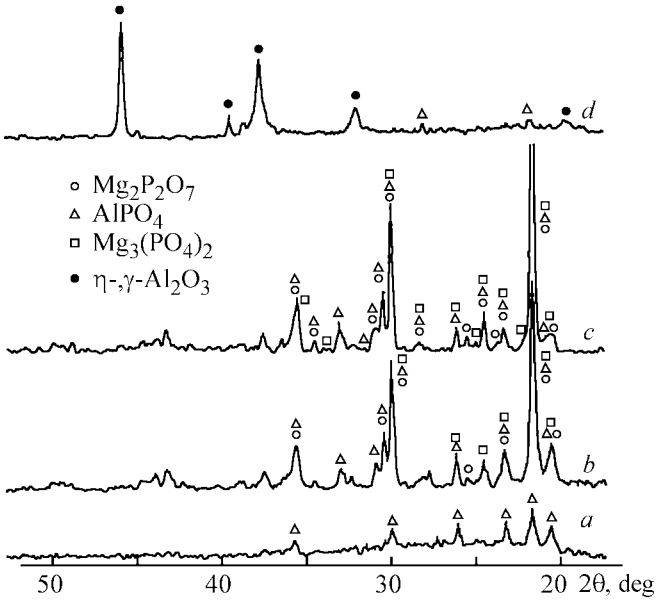

Fig. 3. X-ray diffraction patterns of coatings formed on AD-1 aluminum alloy in an electrolyte containing 0.05 M^{-1} $Na_6P_6O_{18}$ and $Mg(CH_3COO)_2 \cdot 4H_2O$ with n = 0.5, subjected to annealing at different temperatures and detached from the support. (*a*) Initial sample; Calcination conditions: (*b*) 800°C, 30 min and (*c*) 1000°C, 1.5 h; (*d*) the sample formed in the electrolyte with n = 2.

into coatings in noticeable amounts when n is less than a certain value n_0. For zinc coatings $n_0 \approx 3$. Coatings formed in electrolytes with $n < n_c$, where n_c characterizes the transition of an electrolyte into a colloid state, consist virtually solely of the electrolyte components and oxygen. For the system considered in Fig. 1, $n_c \approx 1$. It has also been shown [4] that the content of the electrolyte components in the coating is only slightly affected by presence of alloying additives in the aluminum alloy. Therefore, it is appropriate to compare the elemental composition of coatings on AMtsM alloy (Fig. 1) with the phase composition (described below) of coatings on the AD1 alloy.

The initial coatings formed in the electrolyte with $Na_6P_6O_{18}$ and $Mn(CH_3COO)_2 \cdot 4H_2O$ at n = 1 contain $AlPO_4$, Al_2O_3, and $Mn(PO_3)_2$ phases, and those formed at n = 0.5, $AlPO_4$. After annealing, the crystallinity of the coatings increases (Fig. 2), and, in the coating formed in the electrolyte with n = 0.5, the $Mn(PO_3)_2$ phase crystallizes (Fig. 2). It should be noted that, in the initial coatings formed in the given electrolyte in the decreasing power mode at U_0 = 440 V, a $Mn_2P_2O_7$ phase is present (Fig. 2, curve *e*). This is probably due to large current densities passing through the sample at the beginning of coating formation in the given mode, and, consequently, to different thermal conditions on the anode surface in near-breakdown regions.

The coatings formed in the electrolytes with $Na_6P_6O_{18}$ and $Mg(CH_3COO)_2 \cdot 4H_2O$ at a 0.5 molar ratio of the components, also contain the $AlPO_4$ crystalline phase. Annealing of this coating results in the crystallization of the $Mg_2P_2O_7$ and $Mg_3(PO_4)_2$ phases (Fig. 3). Coatings formed in a similar electrolyte at n = 2, which corresponds to lower concentrations of phosphorus and M(II) in them (Fig. 1), contain η- and γ-Al_2O_3 (Fig. 3, curve *d*).

Coatings formed in a polyphosphate electrolyte with $Zn(CH_3COO)_2 \cdot 2H_2O$ at n = 0.5 contain, along with $AlPO_4$, also double orthophosphate $NaZnPO_4$ (Fig. 4). Annealing of this coating at 750°C makes higher the intensity of reflections related to these phases and leads to crystallization of $ZnAl_2O_4$ spinel and orthophosphate $Zn_3(PO_4)_2$.

To confirm the assumption that the electrolyte components are incorporated into a coating in the sparking mode as a result of the thermolysis of a deposit from the electrolyte in near-breakdown regions, the following experiment was performed: sediments were isolated from solutions containing $Na_6P_6O_{18}$ and the Mg(II) and Mn(II) acetates at $[P_6O_{18}^{6-}]/[M^{2+}]$ = 0.33, which corresponds to hexametaphosphates of composition $M^{II}_3P_6O_{18}$, after 1 day of settling at room temperature, filtered off, and dried in air at about 60°C for 1 h. Then, the sediments were suc-

Phase composition of deposits annealed at different temperatures [electrolyte: 0.05 M $Na_6P_6O_{18}$, $M(CH_3COOH)_2 \cdot 4H_2O$, $n = 0.33$]

M(II)	Phase composition at indicated T, °C				
	initial	450	650	800	950
Mg(II)	X_{ra}^*	$Na_2Mg(PO_3)_4$	$Mg(PO_3)_2$, $(NaPO_3)_x$	$Na_2(PO_3)_4$, $Mg_2P_2O_7$	$Na_2Mg(PO_3)_4$, $Mg(PO_3)_2$, $Mg_2P_2O_7$
Mn(II)	X_{ra}	$Mn_2P_2O_7$, $Mn(PO_3)_2$, $NaMn(PO_3)_2$	$Mn_2P_2O_7$, $Mn(PO_3)_2$, $NaMn(PO_3)_2$	$Mn_2P_2O_7$, $Mn(PO_3)_2$, $NaMn(PO_3)_2$	$Mn_2P_2O_7$

* (X_{ra}) X-ray-amorphous sample.

cesively annealed for 30 min at temperatures ranging from 450 to 950°C. The results obtained are presented in the table.

The deposits separated were always X-ray-amorphous. In the course of the annealing, various polyphosphates, including double polyphosphate, crystallize. The final products of thermolysis are M(II) meta- and diphosphates.

Comparison of the calcination products of the sediments obtained from solutions with the compounds incorporated into coatings shows that the components of the electrolyte containing M(II) polyphosphate complexes are incorporated into the coatings through thermolysis of hydrated M(II) polyphosphates

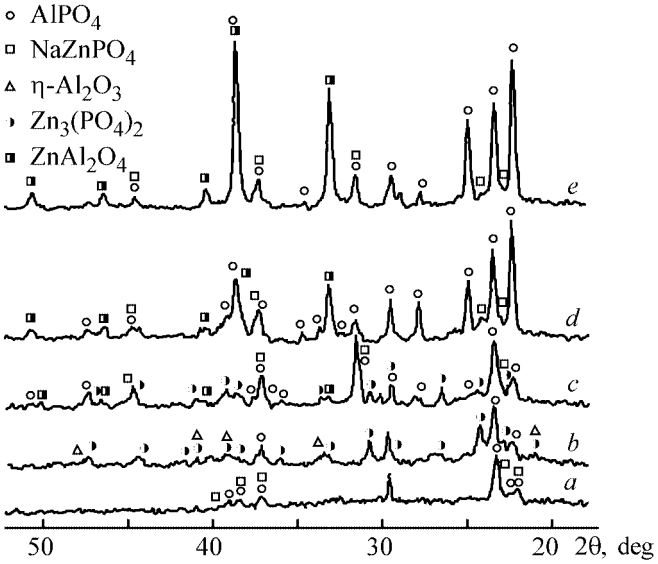

Fig. 4. X-ray diffraction patterns of coatings formed on AD–1 aluminum alloy in an electrolyte containing 0.05 M $Na_6P_6O_{18}$ and $Zn(CH_3COO)_2 \cdot 2H_2O$ with $n = 0.5$, subjected to annealing at different temperatures and detached from the support. (*a*) Initial sample; Calcination conditions: (*b*) 500°C, 30 min; (*c*) 750°C, 30 min; (*d*) 900°C, 30 min; and (*e*) 1000°C, 1.5 h.

in the near-breakdown regions on the anode. Owing to the conditions existing in the near-breakdown regions (electric field, sharp drops of temperature and pressure, presence of aluminum substrate, Al_2O_3, etc.), the thermolysis of a deposit in the course of coating formation occurs in a somewhat different way than that in calcination of a sediment in a crucible.

Thus, the coatings formed on aluminum alloy under the action of electric discharges in electrolytes with MPC contain high-temperature M(II) phosphates. Depending on the type of M cation, the phosphates can be used in the following, widely diverse fields: as phosphate grounds and protecting-decorative layers [7], in catalysis [8], as solid lubricants [9], as bioinert coatings [10, 11], and in luminescent and cathodoluminescent devices [12]. It is noteworthy that the coatings formed in electrolytes with MPC and containing P(V) and Zn(II), Pb(II) or Cd(II) show a marked biocide effect.

CONCLUSIONS

(1) Anodic layers formed at electric breakdown voltages on aluminum alloy in aqueous electrolytes with M(II) polyphosphate complexes [M(II) is Mn, Mg, and Zn] contain M(II) phosphates, e.g., $Mn(PO_3)_2$, $Mg_2P_2O_7$, $NaZnPO_4$, and $AlPO_4$.

(2) The phase composition of the coatings depends on the n = [polyphosphate]/[M cation] molar ratio in an electrolyte.

(3) Phosphorus(V) and metal ions are incorporated into coatings from an electrolyte owing to thermolysis of hydrated metal polyphosphates on the anode in near-breakdown regions.

REFERENCES

1. Gordienko, P.S., and Rudnev, V.S., *Elektrokhimicheskoe formirovanie pokrytii na alyuminii i ego splavakh*

pri potentsialakh iskreniya i proboya (Electrochemical Formation of Coatings on Aluminum and Its Alloys at Sparking and Breakdown Potentials), Vladivostok: Dal'nauka, 1999.

2. Boguta, D.L., Rudnev, V.S, Yarovaya, T.R., *et al.*, *Zh. Prikl. Khim.*, 2000, vol. 73, no. 8, pp. 1296–1300.
3. Rudnev, V.S., Yarovaya T.R., Boguta D.L., *et al.*, *J. Electroanal. Chem.*, 2001, vol. 497, no. 1–2, pp. 150–158.
4. Rudnev, V.S., Yarovaya, T.R., Boguta, D.L., *et al.*, *Elektrokhimiya*, 2000, vol. 36, no. 12, pp. 1457–1462.
5. Tananaev, I.V., *Zh. Neorg. Khim.*, 1984, vol. 29, no. 2, pp. 467–483.
6. Lazarevski, E.V., Kubasova, L.V., Chudinova, N.N., Tananaev, I.V., *et al.*, *Izv. Akad. Nauk SSSR, Neorg. Mater.*, 1980. vol. 16, no. 1, pp. 120–125.
7. RF Patent, no. 9531587 PCT, Cl C23C 22/12.
8. Baba, G.P., Ganguly, P., Metcalfe, K., *et al.*, *J. Mater. Chem.*, 1994, vol. 4, no. 2, pp. 331–336.
9. Gulyaev, G.N., Sergeev, V.V., Evsyukova, G.A., and Chernyi, V.N., *Stal'*, 1995, no. 12, pp. 51–54.
10. Ishizawa, H., and Ogino, M., *J. Biomed. Mater. Res.*, 1995, vol. 29, pp. 1071–1079.
11. Ishizawa, H., and Ogino, M., *J. Biomed. Mater. Res.*, 1995, vol. 29, pp. 65–72.
12. JPN Patent 05320638.
13. Rudnev, V.S., Yarovaya, T.R., Morozova, V.P., *et al.*, *Zashch. Met.*, 2001, vol. 37, no. 1, pp. 79–84.

Russian Journal of Applied Chemistry, Vol. 75, No. 10, 2002, pp. 1609–1613. Translated from Zhurnal Prikladnoi Khimii, Vol. 75, No. 10, 2002, pp. 1643–1647.
Original Russian Text Copyright © 2002 by Ovcharenko, Frolov.

APPLIED ELECTROCHEMISTRY AND CORROSION PROTECTION OF METALS

Electrodialysis of Hydrosols of Ultradispersed Diamonds

A. G. Ovcharenko and A. V. Frolov

Biisk Technological Institute, Polzunov Altai State Technical University, Biisk, Altai Krai, Russia

Received November 2, 2001; in final form, April 2002

Abstract—The electrical conductivity of hydrosols of ultradispersed diamonds was studied. The electromembrane method for cleaning and concentrating of ultradispersed diamonds in hydrosols was considered. The influence exerted by the concentration of the dispersed phase on the electrical characteristics of the cleaning process was analyzed. A mathematical relation making it possible to evaluate the output characteristics of the process and to determine the geometrical characteristics of the apparatus was proposed.

Ultradispersed diamonds (UDD) formed in detonation synthesis are used in composite electrochemical metal-diamond coatings, finishing and superfinishing polishing formulations, grinding materials, resins, antiwear additives to lubricants, and components for fabrication of magnetic recording media [1]. After being prepared, UDD contain a large amount of undesirable impurities classed into several types [2]: water-soluble ionized (free electrolytes), water-insoluble (salts and oxides of various metals), adsorbed and chemically bound (functional surface groups), and those incorporated in the crystal lattice and encapsulated. For UDD to be usable in the above technologies, a dry diamond powder or a diamond hydrosol must be characterized by high degree of purity, determining its physicochemical properties.

The electromembrane method is proposed as the most efficient technique for cleaning of UDD hydrosols, which not only removes undesirable impurities, but also yields a diamond concentrate.

The aim of this study was to analyze the behavior of the given ultradispersed system under the action of an electric field and to determine its electrical properties.

EXPERIMENTAL

The study was carried out on an electrodialysis cell in a periodic mode with ion exchange membranes (Fig. 1). The cell case *1* comprises two fluoroplastic plates attached to each other with stainless steel studs. Each plate of the case has two connecting pipes for inlet of distilled water and outlet of brine. Graphite electrodes *2*, to which dc voltage is applied, are mounted in the cell. Between the case and the central frame *3*, anion- *4* and cation-exchange *5* membranes are fixed on rubber gaskets *6*. The working interelectrode chamber *7* is filled with water suspension of diamond with varied concentration of the solid phase. The distilled water in the brine chambers is circulated by a peristaltic pump. The volume of each chamber is 100 ml, the intermembrane spacing is 5 mm, and the active surface area of the membranes is 130 cm^2. The dialysis chamber is separated from the brine chambers by ion-exchange membranes MA-40 and MK-40.

The main stage of the process of UDD cleaning after synthesis is acid treatment [2]. As a result of oxidation, the surface of UDD particles possesses a large number of oxygen-containing groups (carboxy, carbonyl, hydroxy), which impart to this surface in an aqueous solution a charge whose sign and magnitude are determined by the concentration of these groups, solution pH, and concentration of the supporting electrolyte. The adsorption of H^+ and OH^- ions, resulting from dissociation of the surface groups and adsorption of potential-determining ions in the case of an indifferent electrolyte, was determined by potentiometric titration enabling direct measurement of the surface charge. The adsorption Γ, g-equiv g^{-1} (total number of oxygen-containing groups), was found using the formula

$$\Gamma = \frac{c\Delta V}{m}, \quad (1)$$

where c is the concentration of alkali added (g-equiv cm^{-3}); $\Delta V = V_2 - V_1$ is the difference of, respectively, alkali volume added to achieve a given pH value in titration of a supporting electrolyte and

1070-4272/02/7510-1609 $27.00 © 2002 MAIK "Nauka/Interperiodica"

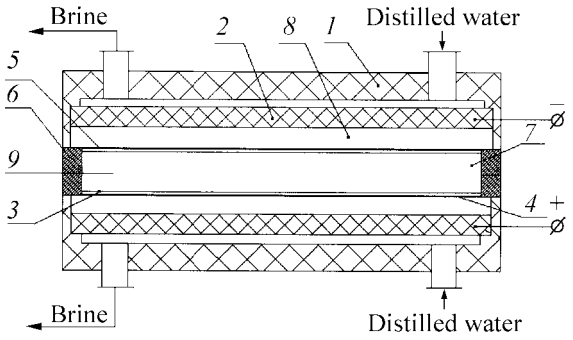

Fig. 1. Electromembrane cell: (*1*) case, (*2*) graphite electrode, (*3*) central frame, (*4*) anion-exchange membrane, (*5*) cation-exchange membrane, (*6*) gasket, (*7*) dialysis chamber, (*8*) brine chamber, and (*9*) UDD hydrosol.

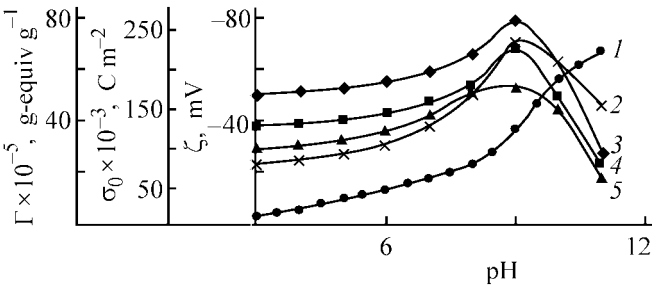

Fig. 2. (*1*) Adsorption Γ, (*2*) specific surface charge σ_0, and (*3–5*) ζ-potential vs. the pH of the medium. Ionic strength: (*1*, *2*) 0, (*3*) 0.0001, (*4*) 0.001, and (*5*) 0.01.

that added in the presence of a sample (cm^3); and *m* is the sample weight (g).

The specific surface charge σ_0 ($C\ m^{-2}$) was found using the formula

$$\sigma_0 = \frac{\Gamma F}{S}, \qquad (2)$$

where *F* is the Faraday number, and *S* is the specific surface area of a particle ($m^2\ g^{-1}$).

The mechanism by which the surface charge is formed is reflected by the dependence of the electrophoretic mobility or electrokinetic potential (ζ-potential) on the pH value. The ζ-potential, which depends on the number of counter ions in the diffusion layer of a particle, in fact determines its charge.

The required pH value was attained using a KOH solution in distilled water. To maintain constant the ionic strength, a KCl solution of appropriate concentration was introduced into the hydrosol. The experimental results are presented in Fig. 2. The particles acquire a negative charge at pH 3–11. When the pH values are shifted to the alkaline region, the dependences of Γ and σ_0 on pH become stronger, which can be accounted for by an increasing degree of dissociation of surface functional groups. It is believed that mainly carbonyl groups dissociate at pH < 8, carboxy groups, at pH 8–10, and hydroxy groups, at pH > 10. The increase in the magnitude of the negative ζ-potential and, consequently, in the electrophoretic mobility of particles with increasing pH is apparently due to ionization of functional groups. It can be seen from Fig. 2 that the ionic strength of the electrolyte affects only the magnitude of the ζ-potential and has virtually no effect on the type of the ζ-pH dependence. Further decrease in the ζ-potential is presumably due to specific adsorption of the K^+ counter ion and to compression of the electrical double layer of a particle with increasing concentration of OH ions. The presence of a negative charge forces the particles toward the anode and, when a solution passes across the membrane, UDD is concentrated and accumulated. When ionexchange membranes are used, there occurs an additional process of electrodialysis of soluble impurities and those adsorbed on the surface of diamond particles.

The main elements contained in insoluble impurities in a UDD hydrosol are the following (wt %): Ca 0.17, Fe 0.26, Si 0.25, S 0.15, Ti 0.08, K 0.08, and trace amounts (sum total less than 0.1 wt %) Al, P, Na, Cu, and Zn.

The electromembrane method gives no way of carrying out complete cleaning of the ultradispersed system to remove all of these elements and compounds of these. Therefore, a combined technology was proposed, consisting in the following stages: acid cleaning of UDD to remove metals; dilution of the system to neutral system; and electrochemical cleaning to remove P, S, Na, K, and acid residues.

The amount of incombustible (sol) impurities after acid treatment is 0.7–0.9 wt %. The subsequent electrochemical treatment can decrease this value to 0.12–0.15 wt %. The time of electrochemical treatment can be made shorter because of the use of simultaneous concentrating and cleaning of UDD in a single apparatus [3]; in addition, the stages used in the basic technology (alkaline treatment, concentrating on an ultrafiltration installation) are excluded. As a result of electrochemical treatment, the UDD hydrosols acquire enhanced aggregative and sedimentation stability in a wide range of UDD concentrations, since the concentration of ions in the ultradispersed system do not exceed 3×10^{-5} $g\ l^{-1}$.

The dependences of the current density on the time of cleaning, *j*–τ, and of the current density on the concentration of electrolyte in the ultradispersed system,

j–*c*, were obtained in the study. The dependences *j*–τ for a UDD hydrosol with concentration of 0.1 wt % at varied concentration of the supporting electrolyte and *j*–τ for an electrolyte containing no dispersed phase are presented in Fig. 3.

The key contribution to the total electrical resistance of the electrodialyzer comes from the dialysis chamber. The run of the dependences of current density on time is determined by changes in the resistance of the whole cell in the course of electrodialysis. Comparison of the dependences (*1*–*3*) and (*1*'–*3*') shows that the initial current densities are lower in the second case. This can be accounted for by the difference between the electrical conductivities of the ultradispersed system and the supporting electrolyte and by accumulation of a UDD sediment on the anion-exchange membrane, which makes the rate of ion permeation across the membrane lower and the total time of cleaning longer.

Since no data on the electrical conductivity of aqueous UDD suspensions are available in the literature, experiments were performed for determining the conductivity in relation to the concentrations of the solid phase and the supporting electrolyte. The measurements were done in a glass cell with platinum electrodes, connected to a slide-wire bridge. As seen from Fig. 4, the electrical conductivity of the system $æ_s$ exceeds that of the electrolyte, æ, at low concentrations *c*. At an electrolyte concentration of 0.2 g l^{-1}, the $æ_s$ and æ values are close, and, with the concentration increasing further, $æ > æ_s$. Since the solid particles are nearly spherical and electrically nonconducting, the electrical conductivity of a dispersed system with volume fraction of the dispersed phase, $p = 3 \times 10^{-4} << 1$, is described by the well-known Maxwell formula [4]

$$\Delta æ_s = 3/2 p æ, \quad (3)$$

$$æ_s = æ - \Delta æ_s. \quad (4)$$

The dependence of æ on *c* can be understood as follows. According to the data of [4],

$$æ_s/æ = \alpha/F, \quad (5)$$

where α is the efficiency factor, $1 \le \alpha \le F$; and *F* is the coefficient of structural resistance.

At high electrolyte concentrations, when the influence of the surface conductivity is insignificant, the right-hand side of the equation is equal to 1/*F*. The decrease in the electrical conductivity of UDD suspensions is due to the nature of diamond particles,

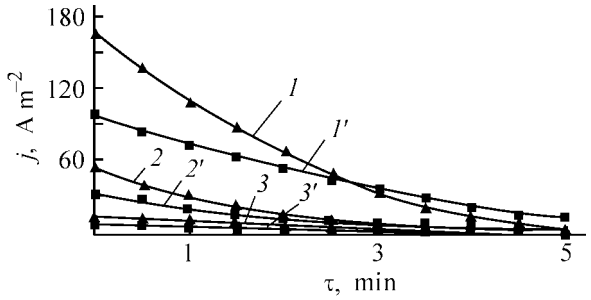

Fig. 3. Current density *j* vs. time τ of electrochemical treatment of (*1*–*3*) KNO_3 electrolyte and (*1*'–*3*') ultradispersed system 0.1 wt % UDD + KNO_3. Electric field strength $E = 16$ kV m^{-1}. KNO_3 concentration (g l^{-1}): (*1*, *1*') 0.4, (*2*, *2*') 0.1, and (*3*, *3*') 0.02.

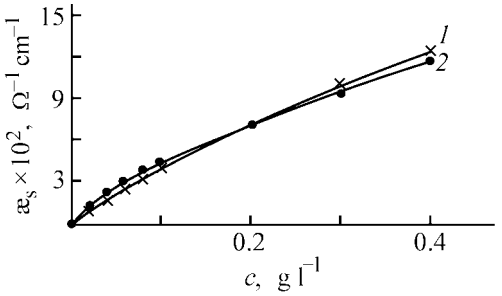

Fig. 4. Electrical conductivity $æ_s$ vs. concentration *c* of the supporting electrolyte KNO_3. (*1*) KNO_3 and (*2*) 0.1 wt % UDD + KNO_3.

which have large specific surface area and a developed electrical double layer. When salt ions are added to the hydrosol, these ions are partly captured by the outer layer of the particles. The resulting decrease in the number of unbound ions in the suspension makes the electrical conductivity lower.

When an electric field is applied to the system, the lines of current round the surface of nonconducting particles, which is equivalent to a decrease in the electrical conductivity of the system.

With decreasing electrolyte concentration, the conductivity deficiency in the system is compensated for by the increasing influence of the surface conductivity of UDD particles. At a certain electrolyte concentration the electrical conductivity of the ultradispersed system is equal to the conductivity of the equilibrium electrolyte. Measurements demonstrated that the electrical conductivity of the system is independent of the volume fraction of the dispersed phase at the isoconductivity point. At concentrations lower than that corresponding to the isoconductivity point the ultradispersed system has, despite the decrease in the effective cross-section for a current to flow through, higher electrical conductivity than the equilibrium electrolyte because of the surface conductivity of UDD particles.

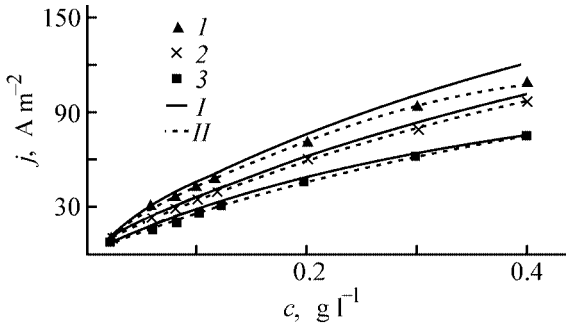

Fig. 5. Current density j vs. concentration c of the supporting electrolyte KNO_3 in a dispersed system with 0.1 wt % UDD. Electric field strength E (kV m^{-1}): (*1*) 20, (*2*) 16, and (*3*) 12. (*I*) Calculated curves and (*II*) experimental data.

The results obtained in an experimental study of the initial electrical properties of the ultradispersed system made it possible to propose a mathematical description of the process occurring in a cell to which an electric field is applied. Two processes, electrodialysis of dissolved salts and electrophoresis of UDD particles, occur in the cell simultaneously. The task to be accomplished consisted in obtaining a relation that could be used in design calculations of installations for electrochemical cleaning of ultradispersed systems with account of the influence exerted by the solid UDD phase on the characteristics of the electrodialysis process.

The solution consisted in describing the process of electrodialysis for a model system characterizing the dispersion medium and correcting the expressions obtained with account of the dispersed phase introduced into the system.

The system under study was considered for the following conditions: maximum concentration of the supporting electrolyte not exceeding 0.4 g l^{-1}; electrochemical treatment at current density higher than the limiting value, which much improves the output capacity and the degree of cleaning; batch mode of the process; permanent washing of side chambers with distilled water, which allows the initial salt concentration in the chambers to be considered constant.

In deriving the equation describing the dependence of the current density on the electrolyte concentration, account was taken of the Nernst–Planck film theory, and an equation for the total voltage drop across an electrochemical cell was used. The following assumptions were made: a constant voltage is applied to the system, the thickness of the diffusion layer on the eluate side is constant, and the electrolyte concentration along the chambers is invariable. The following semiempirical relation was obtained:

$$j = \frac{U_e - \frac{RT}{F}\left(\ln\frac{c_b}{c_d} - \varphi_{el}\right)}{R_a + R_c + \frac{\rho_d\delta_d\left[K_1\left(\frac{\nu}{D}\right)^{1/3} + 2K_2\frac{\delta_b}{\delta_d} + 1\right]}{1 + 0.02(T + 18)}}, \quad (6)$$

where R_a and R_c are the membrane resistivities (Ω m^2); ρ_d is the electrical resistivity of the diluate chamber (Ω m); δ_d and δ_b are the chamber widths (m); ν is the kinetic viscosity of the medium (m^2 s^{-1}); D is the diffusion coefficient (m^2 s^{-1}); c_b and c_d are the salt concentrations in the chambers (g l^{-1}); U_e is the cell voltage (V); φ_{el} is the electrode potential (V); T is temperature (K); $K_1 = 25$; $K_2 = 30$.

The coefficients K_1 and K_2, obtained by carrying out a set of experiments to make corrections to the equation, determine the effect of diffusion on the concentration of ions in side chambers and in the boundary layer.

After introduction of the UDD solid phase into the model system, the obtained relation was corrected. The following assumptions were made: the concentration of the solid phase is less than 1 wt % since larger amount leads to an increase in the specific hydraulic resistance of the sediment and, as a result, to lower desalting rate. It was also assumed that the layer of diamond particles on the membrane surface prevents formation of a boundary layer since it controls, by virtue of its adsorbing capacity, the transport of ions across the membrane, which prevents depletion of the near-membrane layer. Subject to the condition that the sedimentation of particles onto the membrane is complete, a coefficient K_3 is introduced, which accounts for changes in the electrical resistivity of the sediment, depending on the electrical resistivity of the electrolyte in the dialysis chamber. With account of the aforesaid, the following expression was obtained for UDD hydrosols

$$j = \frac{U_e - \frac{RT}{F}\left(\ln\frac{c_b}{c_d} - \varphi_{el}\right)}{R_a + R_c + \frac{\rho_d\left[K_1\frac{\delta_d}{2}\left(\frac{\nu}{D}\right)^{1/3} + 2K_2\delta_b + K_3\delta_s + \delta_d\right]}{1 + 0.02(T + 18)}}, \quad (7)$$

where δ_s is the sediment layer thickness (m), and $K_3 = 17000$.

Equations (6) and (7) make it possible to determine, from the current densities measured, the ion concentration in the dialysis chamber and to take into

account the electrical and geometric parameters of the apparatus, and enable determination of the desalting time.

To verify calculations by the equations obtained, experiments with a three-chamber electromembrane cell were carried out. The experimental results obtained confirm the calculated data (Fig. 5). The difference between the calculated and experimental values does not exceed 15% at field strengths lower than 16 kV m^{-1}. Previous studies of how the electric field strength depends on the cleaning time have shown that, with the field strength increasing to more than 16 kV m^{-1}, the energy expenditure grows, but the time of treatment decreases only slightly. At the same time, on lowering the field strength to 8 kV m^{-1} the cleaning time increases severalfold. This allowed the electric field strength of 16 kV m^{-1} to be recommended as the value optimal for operation of the electrochemical cleaning apparatus.

The results obtained found use in developing an engineering procedure for calculating a pilot-industrial installation for cleaning and thickening of a UDD hydrosol [3].

CONCLUSIONS

(1) It was established that the electrical conductivity of hydrosols of ultradispersed diamonds depends on the volume fraction of the solid phase. The isoconductivity point of the dispersed system was determined.

(2) It was found that addition of the solid phase to the dispersed system makes lower the initial current densities, all other conditions being the same. The weakening of the dependence of the current density on the treatment time is determined by changes in the electrical conductivity of the ultradispersed system.

(3) A design equation was obtained, which makes it possible to evaluate the output characteristics of the electrochemical cleaning process and determine the geometrical parameters of a cleaning apparatus. The equation was used in developing a procedure for engineering calculations of electrochemical cleaning apparatus.

REFERENCES

1. Sakovich, G.V., Brylyakov, P.M., Gubarevich, V.D., *et al., Zh. Vses. Khim. O–va im. D.I. Mendeleeva*, 1990, vol. 35, no. 5, pp. 600–602.
2. Gubarevich, T.M., Kostyukova, N.M., Larionova, I.S., *et al., Sverkhtverd. Mater.*, 1991, no. 5, pp. 21–23.
3. RF Patent 1815933.
4. Dukhin, S.S., *Elektroprovodnost' i elektrokineticheskie svoistva dispersnykh sistem* (Electrical Conductivity and Electrokinetic Properties of Dispersed Systems), Kiev: Naukova Dumka, 1975.

Russian Journal of Applied Chemistry, Vol. 75, No. 10, 2002, pp. 1614–1616. Translated from Zhurnal Prikladnoi Khimii, Vol. 75, No. 10, 2002, pp. 1648–1650.
Original Russian Text Copyright © 2002 by Valiotti, Abakumova.

APPLIED ELECTROCHEMISTRY AND CORROSION PROTECTION OF METALS

Cobalt Porphyrin–based Solid-Contact Electrode Sensitive to Pyridine Concentration

A. B. Valiotti and R. A. Abakumova

St. Petersburg State University, St. Petersburg, Russia

Received October 26, 2001; in final form, March 2002

Abstract—A solid-contact electrode based on cobalt tetraphenyl porphin, sensitive to pyridine concentration, was studied. The properties of this electrode were analyzed.

Extracoordination of various compounds, including nitrogen-containing heterocycles, with metal porphyrins has been extensively studied recently [1–3]. The present communication demonstrates the possibility of fabricating a potentiometric sensor for determining the concentration of pyridine, which is based on a redox system composed of cobalt(III) tetraphenyl porphin [$Co(III)TPP^+$] and cobalt(II) tetraphenyl porphin [Co(II)TPP].

It is known [4] that this redox system can enter into various electrochemical reactions, with the result that (1) reversible change in the formal oxidation level of the central metal ion

$$Co(III)TPP^+ + e \rightarrow Co(II)TPP$$

and (2) reversible or irreversible partial disruptions of conjugation in the porphyrin ring may occur.

The present consideration takes into account the redox reaction involving only the central metal (cobalt) atom. Cobalt porphyrins can be involved in extracoordination reactions with various ligands. As ligands may act species able to form σ-donor and π-acceptor bonds. The capacity of cobalt porphyrins for extracoordination of pyridine was used to create a molecular-selective potentiometric sensor for determining the pyridine concentration. For this purpose, a solid-contact electrode was designed. Electrodes of this kind were fabricated from a graphite rod and graphite powder (dispersity ~70 mesh), which ensured the electronic conduction. As potential-determining system served the redox system Co(II)TPP–$Co(III)TPPClO_4$ in 1 : 1 molar ratio. The graphite rods were used to fabricate electrodes in the form of pellets with shallow depressions drilled out on their edges. Then copper conductors were glued into these depressions to serve as current leads. After that the pellets were fixed in standard PVC tubes with an epoxy adhesive.

Membranes for the solid-contact electrodes were prepared as follows. Weighed portions of cobalt porphyrins and graphite powder were dissolved in the minimum possible amount of chloroform, and then the solvent was removed by evaporation to obtain uniform distribution of cobalt porphyrins over the surface of graphite grains. Then weighed portions of PVC and a plasticizer (dibutyl phthalate, DBP) were dissolved under heating in tetrahydrofuran (THF) and the graphite powder with porphyrin was added to the solution. The mixture obtained was deposited onto a cleaned graphite surface of the electrode. After THF was evaporated, the process was repeated, in all, 5 or 6 times. The cobalt porphyrin : PVC : plasticizer : graphite mass ratios were varied between 1 : 1 : 0 : 0 and 1 : 2 : 8 : 8.

The potential of the solid-contact electrode was found by measuring the emf of the electrochemical cell

Cu | Ag | AgCl, KCl (sat.) | Working solution | Membrane | Graphite | Cu

The pH of a solution under study was determined using a glass electrode preliminarily calibrated with standard buffer solutions. The emf of the galvanic cells was measured with a pH-121 pH-meter-millivoltmeter whose output signal was delivered to an in-series connected KSP-4 printing unit. The solid-contact electrode under study operates on the reaction of electron transfer between the oxidized and reduced

1070-4272/02/7510-1614 $27.00 © 2002 MAIK "Nauka/Interperiodica"

forms of CoTPP under the conditions of complexation with pyridine.

The heterogeneous redox reaction occurring in the system under study at the interface between the electrode and the external solution in the absence of a ligand can be represented as

$$Co(III)TPP^{+}_{(s)} + A^{-}_{(s)} + e = Co(II)TPPL_{(s)} + A^{-}, \quad (1)$$

with the index *s* referring henceforth to the solid phase, and A^- being a counter ion, ClO_4^- in the given case.

Writing the redox reaction in this way assumes that the electrode-active substance Co(III)TPPA is in the totally dissociated state. Then the expression for the potential of the given solid-contact electrode, which is of the redox type, has the form

$$E = E^0 + 2.3\frac{RT}{F}\log\frac{c^{s}_{Co(III)TPP^{+}}c^{s}_{A^-}}{c^{s}_{Co(II)TPP}c_{A^-}}. \quad (2)$$

In the presence of pyridine in the working solution, complexation is possible by the scheme

$$Co(II)TPP_{(s)} + L = Co(II)TPPL_{(s)}, \quad (3)$$

where L is an extra ligand, pyridine in the given case.

The complexation constant K^R is defined by

$$K^R = \frac{c^{s}_{Co(II)TPPL}}{c^{s}_{Co(II)TPP}c_L}. \quad (4)$$

For the oxidized form

$$Co(III)TPP^{+}_{(s)} + L = Co(III)TPPL^{+}_{(s)}, \quad (5)$$

$$K^0_1 = \frac{c^{s}_{Co(III)TPPL^{+}}}{c^{s}_{Co(III)TPPL^{+}}c_L}, \quad (6)$$

$$Co(III)TPPL^{+}_{(s)} + L = Co(III)TPPL^{+}_{2(s)}, \quad (7)$$

$$K^0_2 = \frac{c^{s}_{Co(III)TPPL^{+}_2}}{c^{s}_{Co(III)TPPL^{+}}c_L}. \quad (8)$$

With account of (3)–(8), Eq. (2) is transformed into

$$E = E^0 + 2.3\frac{RT}{F}\log\frac{c^{OX}}{c^{RED}} + 2.3\frac{RT}{F}\log(1 + K^Rc_L) - 2.3\frac{RT}{F}\log(1 + K^0_1c_L + K^0_1K^0_2c^2_L) + 2.3\frac{RT}{F}\log\frac{c^{s}_{A^-}}{c_{A^-}}, \quad (9)$$

where

$$c^{OX} = c^{s}_{Co(III)TPP^{+}} + c^{s}_{Co(III)TPPL^{+}} + c^{s}_{Co(III)TPPL^{+}_2},$$

$$c^{RED} = c^{s}_{Co(II)TPP} + c^{s}_{Co(II)TPPL}.$$

With the coefficient $2.3RT/F$ denoted by ϑ, Eq. (9) takes, at $c^{OX} = c^{RED}$ and $c^{s}_{A^-}/c_{A^-} = \text{const}$, the form

$$E = E^{0'} + \vartheta\log(1 + K^Rc_L) - \vartheta\log(1 + K^0_1c_L + K^0_1K^0_2c^2_L), \quad (10)$$

where

$$E^{0'} = E^0 + 2.3\frac{RT}{F}\log\frac{c^{s}_{A^-}}{c_{A^-}}.$$

Analysis of Eq. (10) in the general form is difficult; however, in the ranges of predominance of certain complex forms of cobalt porphyrin, the equation is simplified. At low ligand concentrations, when the inequalities $K^Rc_L << 1$ and $(K^0_1c_L + K^0_1K^0_2c_L) << 1$ hold true, Eq. (10) takes the form $E = E^{0'}$. Under these conditions, the forms $Co(III)TPP^+$ and Co(II)TPP are predominant, and the oxidation potential is independent of the ligand concentration ($\partial E/\partial pc_L = 0$). With increasing pyridine concentration in the external solution, the inequalities $K^Rc_L << 1$ and $1 << K^0_1c_L >> K^0_1K^0_2c^2_L$ become good and Eq. (10) takes the form $E = E^{0'} - \vartheta\log(K^0_1c_L)$. In this case, the compounds $Co(III)TPPL^+$ and Co(II)TPP predominate and the dependence of E on pc_L is expressed by the equation $\partial E/\partial pc_L = \vartheta$ (at 25°C ϑ = 59 mV). With the pyridine concentration increasing further, the inequalities $K^Rc_L << 1$ and $1 << K^0_1c_L << K^0_1K^0_2c^2_L$ hold true. In this case, Eq. (10) takes the form $E = E^{0'} - \vartheta\log(K^0_1K^0_2c^2_L)$. Under these conditions, the complex forms Co(III)TPPL and Co(II)TPP predominate. The dependence of E on pc_L is described by the equation $E = E^{0'} + \vartheta\log(K^Rc_L) - \vartheta\log(K^0_1K^0_2c^2_L)$, whence follows $\partial E\partial pc_L = \vartheta$. Analysis of Eq. (10) shows that the curve describing the dependence of $\partial E\partial pc_L$ when the above inequalities hold true must consist of several straight portions with slopes equal to 0, ϑ, 2ϑ, and ϑ, connected by smooth bent curves.

A study of the properties of a solid-contact electrode consisted in determining the dependence of its potential on the pyridine concentration in the external solution at constant pH of the working solution (7.0). The buffer capacity was maintained using the sodium salt of *N*,*N*-piperazinebis(ethanesulfonic acid) (PIPES). As supporting electrolyte served 0.1 M KCl solution. All measurements were done at 20 ± 1°C.

The experiment was carried out on a solid-contact electrode with a membrane of composition cobalt porphyrin : PVC : plasticizer : graphite = 1 : 2 : 4 : 8. It was shown that the electrodes of this composition are

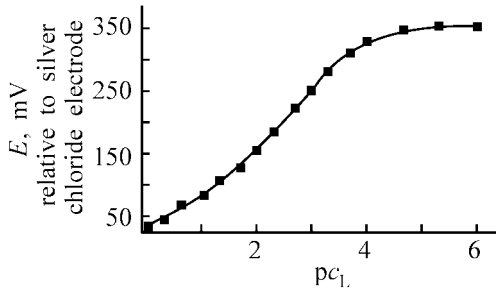

Potential E of the solid-contact electrode vs. pc_L.

favorably distinguished by high sensitivity to pyridine concentration and fast stabilization of electrode potentials. Furthermore, these electrodes exhibit to a lesser extent the so-called "cathode response," i.e., a short-time rise in potential on passing to concentrated pyridine solutions, which is due to diffusion of pyridine into the membrane phase.

The experimental data obtained are represented in the figure as a dependence of the electrode potential on the pyridine concentration pc_L. The E–pc_L curve shows no clearly pronounced straight portions, which indicates that the constants K_1^0, K_2^0, and K^R are close. However, the run of the curve and the manner in which the derivative $\partial E/\partial pc_L$ varies suggest that the following complex forms of cobalt porphyrin predominate in the membrane phase with increasing pyridine concentration: Co(III)TPPL$^+_{(s)}$, Co(III)TPPL$^+_{2(s)}$, and Co(II)TPPL$_{(s)}$. The respective complexation constants calculated by fitting with the help of Eq. (10) are as follows:

$$\log K_1^0 = 4.3 \pm 0.2, \quad \log K_2^0 = 3.3 \pm 0.2, \quad \log K^R = 2.0 \pm 0.2.$$

CONCLUSIONS

(1) A study of a solid-contact electrode based on cobalt tetraphenylporphin demonstrated that the potential E of the electrode depends on the pyridine concentration in solution, and this dependence is satisfactorily described by the E–pc_L equation presented.

(2) The experimental data obtained can serve as a basis for developing a potentiometric sensor for determining the pyridine concentration.

REFERENCES

1. Berezin, B.D., *Koordinatsionnye soedineniya porfirinov i ftalotsianina* (Coordination Compounds of Porphyrins and Phthalocyanine), Moscow: Nauka, 1978.
2. *Porfiriny: struktura, svoistva, sintez* (Porphyrins: Structure, Properties, and Synthesis), Enikolopyan, N.S., Ed., Moscow: Nauka, 1985.
3. Falk, J.E., *Porphyrins and Metalloporphyrins*, Amsterdam: Elsevier, 1964.
4. Fuhrhop, J.H., *Str. Bond.*, 1974, vol. 18, pp. 1–67.

Russian Journal of Applied Chemistry, Vol. 75, No. 10, 2002, pp. 1617–1620. Translated from Zhurnal Prikladnoi Khimii, Vol. 75, No. 10, 2002, pp. 1651–1654.
Original Russian Text Copyright © 2002 by Pak, Sukhanov, Gavronskaya.

APPLIED ELECTROCHEMISTRY AND CORROSION PROTECTION OF METALS

Electrical Conductivity of Carbon in Porous Glasses

V. N. Pak, S. V. Sukhanov, and Yu. Yu. Gavronskaya

Herzen Russian Pedagogical University, St. Petersburg, Russia

Received March 5, 2002

Abstract—The electrical conductivity of carbon-containing porous glasses obtained by gas-phase treatment of sodium–borosilicate glasses with a mixture of *n*-hexane and carbon tetrachloride at 480°C was studied.

To indubitable advantages of porous glasses obtained by acid–base etching of liquating glasses of the sodium–borosilicate system [1–4] belong widely controllable parameters of the porous structure, narrow pore radius distribution, and availability in the form of mechanically strong articles of various configurations (wafers, tubes), rather than as powders only. Making porous glasses electrically conducting opens up new possibilities of their use in electrocatalysis, electrosorption purification, concentration, and membrane separation. Among possible variants is chemical modification of porous glasses with carbon. "Passing" from the silica surface of glasses to a carbon surface allows fabrication of articles differing both in the spatial-geometric structure and in the content of carbon distributed over walls of through channels in supports. The methods for synthesizing carbon layers on the surface of solids, reported in the literature, mainly involve high-temperature processes [5]. At the same time, with porous glasses used as supports, the deposition temperature should be limited (< 500°C) to prevent support caking. The temperature of carbon formation can be lowered to within the above limits by using a gaseous reaction mixture of hydrocarbons and their chloro derivatives, and CCl_4 in particular [6–8]. The results obtained in testing one of the possible variants of carbon synthesis in bulk porous glasses and in measuring the electrical conductivity of the compounds obtained are presented in this communication.

Porous glasses with parameters listed in the table were obtained in the form of 10 × 10 × 1 mm plates by varying modes of preliminary thermal treatment and conditions of the subsequent acid–base etching of DV-1 sodium–borosilicate glass [1–4]. As components of the reaction mixture for preparing carbon served [8] *n*-hexane and carbon tetrachloride, taken in molar ratio $C_6H_{14}/CCl_4 = 0.07$. These substances were delivered by the dosing unit of the evaporator into an evacuated reactor in which the glass plates to be treated were mounted perpendicularly to the reagent flow. With account of the characteristic kinetic features of carbon growth in porous glasses [8], the time of treatment at 480°C was varied between 5 and 200 min. The excess amounts of reagents and gaseous reaction products were caught with a zeolite trap cooled with liquid nitrogen. After synthesis was complete, the samples obtained were cooled in a vacuum. The amount q_C of carbon deposited into porous glasses was determined gravimetrically, and the adsorption-structural parameters of the starting and carbon-containing porous glasses (CPG), by the known techniques [2–4, 9]: the specific surface area S_{sp} was found from low-temperature adsorption of argon; pore volume δ, from moisture capacity in a saturated water vapor; and pore radii r_p, from parameters of the hysteresis loop in isotherms of water adsorption and by mercury porosimetry. The currents flowing along the pore walls in CPG (across the plates) and voltage drops across the samples were measured in the dc mode with a P136 stabilized power supply and V7-27A/1 voltammeter. To eliminate the possible leaks,

Parameters of the porous structure

r_p, nm	S_{sp}, $m^2\ g^{-1}$	δ, $cm^3\ g^{-1}$
4.1	60.7	0.1597
8.2	73.0	0.4651
16.3	23.1	0.2750
32.6	24.2	0.3621
47.3	21.9	0.4438
68.7	17.3	0.3622

1070-4272/02/7510-1617 $27.00 © 2002 MAIK "Nauka/Interperiodica"

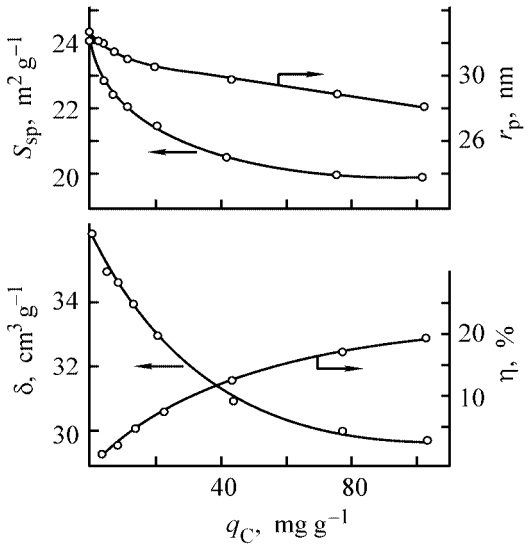

Fig. 1. Specific surface area S_{sp}, pore radius r_p, pore space volume δ, and degree of its filling, η, vs. content q_C of carbon synthesized in porous glasses.

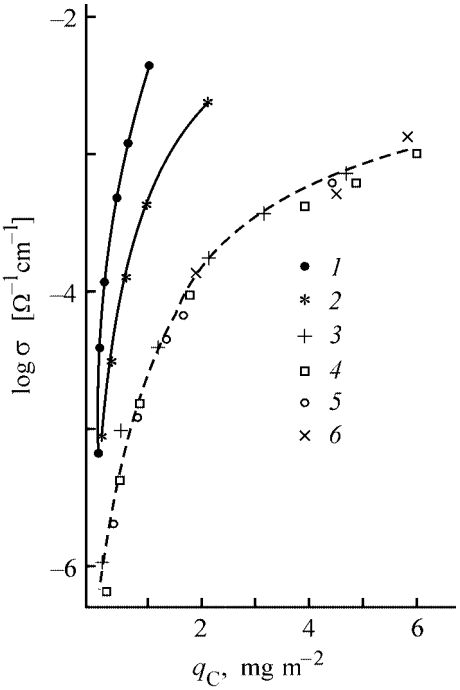

Fig. 2. Electrical conductivity σ of CPG vs. amount of carbon, q_C, synthesized in porous glass. Pore radius r_p (nm): (*1*) 4.1, (*2*) 8.2, (*3*) 16.3, (*4*) 32.6, (*5*) 47.3, and (*6*) 68.7.

the lateral parts of CPG plates were preliminarily ground off. Pressure contacts (pressed with constant force of 200 g cm^{-3}) in the form of polished copper discs with silver-plated surface were employed [10]. The electrical conductivity σ was calculated, to a first approximation, with account of the real dimensions of the CPG plates. The thus obtained values characterize the behavior of a sample as a whole; relating them to the conducting component requires model estimates of the effective cross-section and length of carbon inclusions, which is beyond the scope of the present study.

In all cases, the increase in the carbon content was accompanied by a gradual decrease in the specific surface area, volume, and effective radius of pores. Figure 1 presents this change in porous structure parameters for a number of CPGs obtained on a support with initial r_p = 32.6 nm. One more quantitative characteristic of carbon distribution within CPG is the degree of pore space filling with carbon, η (%), (Fig. 1), calculated as

$$\eta = \frac{\delta - \delta^*}{\delta} \times 100, \quad (1)$$

where δ^* and δ are, respectively, the pore volumes of a CPG sample and initial (pure) porous glass.

The characteristic monotonic run of the dependences of the structural parameters on the carbon content q_C up to substantial (η = 20%) degrees of pore space filling with carbon (Fig. 1) points to favor of a uniform distribution of the growing layer over the entire silica surface of the support. If it is assumed that carbon is mainly formed on the outer, open surface of a porous glass and in mouths and possible constrictions of pores, then a relatively small amount of carbon would be sufficient for a significant decrease in measured values of S_{sp} and δ because of a decrease in the accessibility of the internal volume of CPG. It is not improbable that important factors in carbon structure formation are the well-pronounced electron-acceptor ability of silica [11] and lateral interactions ensuring, taken together, a predominantly layer-by-layer growth. It is very important in this context that the pore radius decreases nearly linearly with increasing q_C (Fig. 1), which disproves the assumption that porous carbon has island structure. The data obtained and their interpretation are in good agreement with the previously studied [8] specific features of the carbonization kinetics of porous glasses and with changes in the isotherms of water adsorption onto CPG with increasing q_C.

The through (measured across the plates) electrical conductivity of CPG is due to carbon distributed over channel walls; the resistivity of the initial porous glasses is beyond the possibilities of measurement (R > 10 GΩ). The absence of polarization and the linearity of current–voltage characteristics for all the CPG samples point to the electronic nature of conduction. Figure 2 shows the conductivity σ as a func-

tion of carbon content reduced to unit surface area of the conducting channels. It is important to note that a dramatic increase in σ is observed in the earliest stages of synthesis, when the amount of the conducting component is much smaller than that necessary for a solid conducting layer to be formed. For example, in the range q_C = 0.1–0.5 mg m^{-2}, where a pronounced rise in electrical conductivity is observed, the average number of carbon atoms per unit area of 100 $Å^2$ changes from 5 to 25. It should be noted that the carbon packing "density" in layers of the hexagonal lattice of graphite is 42 atoms per 100 $Å^2$ [12]. The feature revealed suggests that extended carbon chains with high degree of delocalization of π-electrons can be formed even at very low degrees of filling of the surface of the porous glass, which are far from those for a conventional graphite-like monolayer. It may be assumed that that these chains are gradually jointed in the course of synthesis, to give a two-dimensional conducting layer of carbon. This growth mechanism is promoted both by the increasing conjugation area and by the electron-acceptor effect of silica [11], with these two factors leading to predominance of the layer-by-layer mechanism of carbon condensation.

Before comparing the electrical conductivities of CPGs with different in spatial-geometric characteristics, an attempt is to be made to evaluate the density d_C of the carbon synthesized, using the relation

$$d_C = q_C/(\delta^* - \delta). \quad (2)$$

The determinations performed demonstrate that only a weak tendency for d_C to grow with increasing mass of synthesized carbon is observed in each CPG sample: the densification does not exceed 5% in all the q_C ranges. This indicates that the carbon structure is determined by synthesis conditions and by the orienting action of silica supports, being mainly preserved (reproduced) in the process of growth. A more interesting and important factor is that the carbon density depends on pore radii in porous glasses. The d_C values presented in Fig. 3, averaged over CPG samples, grow more than twofold with r_p increasing from 4.1 to 68.7 nm. With account taken of the identical chemical nature of the porous glass surface in all cases, the established specific feature should be related to the effect of the dimension factor: steric hindrance to fixation of a dense carbon layer is created in narrow pores with strong surface curvature. Moreover, the run of the curve in Fig. 3 indicates that the main change in d_C occurs in the pore radius range studied, with further rise in r_p leading, in all probability, to only a minor increase in the carbon density. On the whole, the specificity of porous glasses as supports and the synthesis conditions employed ensure formation of carbon structures with low density.

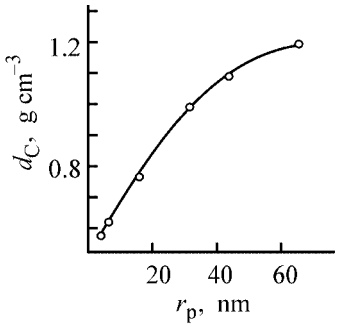

Fig. 3. Averaged density d_C of carbon synthesized in porous glass vs. pore radius r_p of the supports.

Reverting to the results presented in Fig. 2, it should be emphasized that the electrical conductivity of equal amounts of carbon is the highest in pores of small radius, despite its lowest density (the relative σ values of CPG samples are the same when the dimension of q_C is mg g^{-1}). It is rather difficult to explain unambiguously the observed behavior of the systems under study. It is not improbable, however, that the decrease in r_p to about several nanometers predetermines a substantial increase in the average length of conducting carbon chains in the direction of the applied electric field (along the channels) and makes smaller the number of breaks between the chains. It is significant that a 2–4-fold increase in pore radius is accompanied by a pronounced decrease in the σ values measured for pore carbon, but σ remains virtually unchanged with r_p increasing further (r_p = 16.2–68.7 nm) (Fig. 2). The manifestation of the dimension factor in the electrical conductivity of CPG is, therefore, limited to a narrow range of pore radii. It may be assumed that the decrease in channel wall curvature, occurring in porous glasses beyond this range, results in the predominance of the radial (along the channel perimeter) component of carbon growth. This leads to the observed rise in carbon density (Fig. 2), but favors an increase in the through electrical conductivity to a lesser extent.

CONCLUSIONS

(1) A number of carbon-containing porous glasses were synthesized by gas-phase treatment of silica supports with a mixture of *n*-hexane and carbon tetrachloride at 480°C. The nature of changes in the porous structure parameters of carbon-containing porous glasses, which accompany carbon growth, indicates

that carbon is uniformly distributed over walls of through channels in porous glasses.

(2) A substantial increase in the electrical conductance of carbon-containing porous glasses at small degrees coverage of silica surface with carbon and the dependence of the electrical conductivity δ on pore radius in a narrow range r_p = 4.1–16.3 nm were established.

(3) The use of porous glasses with small pore radii predetermined the increased electrical conductivity of carbon deposited into these pores, with carbon density being much lower in this case. An assumption is made that the orienting action of narrow pores favors an increase in the length of conducting carbon chains.

REFERENCES

1. Molchanova, O.S., *Natrievoborosilikatnye i poristye stekla* (Sodium-Borosilicate and Porous Glasses), Moscow: Oborongiz, 1961.
2. Roskova, G.P. and Tsekhomskaya, T.S., *Fiz. Khim. Stekla*, 1981, vol. 7, no. 5, pp. 513–534.
3. Zhdanov, S.P., Koromal'di, E.V., and Smirnova, L.G., *Izv. Akad. Nauk SSSR, Neorg. Mater.*, 1973, vol. 9, no. 10, pp. 1852–1853.
4. Burkat, T.M. and Dobychin, D.P., *Fiz. Khim. Stekla*, 1991, vol. 17, no. 1, pp. 160–164.
5. Tesner, P.A., *Obrazovanie ugleroda iz uglevodorodov gazovoi fazy* (Formation of Carbon from Hydrocarbons in the Gas Phase), Moscow: Khimiya, 1972.
6. Mozgunov, V.I, Bogomolov, N.A., and Smirnov, E.P., *Zh. Prikl. Khim.*, 1987, vol. 60, no. 3, pp. 639–640.
7. Bogomolov, N.A., Gordeev, S.K., and Smirnov, E.P., *Dokl. Akad. Nauk SSSR*, 1985, vol. 281, no. 4, pp. 876–880.
8. Gavronskaya, Yu.Yu., Kopylov, V.B., and Pak, V.N., *Zh. Prikl. Khim.*, 1993, vol. 66, no. 9, pp. 2001–2005.
9. *Eksperimental'nye metody v adsorbtsii i khromatografii* (Experimental Techniques in Adsorption and Chromatography), Nikitin, Yu.S., Ed., Moscow: Mos. Gos. Univ., 1990.
10. Verezhinskaya, R.L., Burkat, T.M., and Pak, V.N., *Fiz. Khim. Stekla*, 1999, vol. 25, no. 6, pp. 688–692.
11. Chuiko, A.A., *Teor. Eksp. Khim.*, 1987, vol. 23, no. 5, pp. 597–620.
12. Chernysh, I.G., Karpov, I.I., Prikhod'ko, G.P., and Shai, V.M., *Fiziko-khimicheskie svoistva grafita i ego soedinenii* (Physicochemical Properties of Graphite and Its Compounds), Kiev: Naukova Dumka, 1990, p. 26.

Russian Journal of Applied Chemistry, Vol. 75, No. 10, 2002, pp. 1621–1624. Translated from Zhurnal Prikladnoi Khimii, Vol. 75, No. 10, 2002, pp. 1655–1658.
Original Russian Text Copyright © 2002 by Berezhnaya, Ekilik, Tugolukova.

APPLIED ELECTROCHEMISTRY AND CORROSION PROTECTION OF METALS

Anodic Dissolution of Ni50Zn Alloy in the Presence of Mixtures of Organic Additives with Sodium Chloride

A. G. Berezhnaya, V. V. Ekilik, and E. A. Tugolukova

Rostov State University, Rostov-on-Don, Russia

Received April 26, 2001; in final form, June 2002

Abstract—Electrochemical behavior of nickel and nickel–zinc alloy in an acidic perchlorate media was studied as influenced by some organic additives, sodium chloride, and their binary mixtures.

Nickel-zinc alloys with low or medium content of nickel [Ni], used to prepare Raney catalysts, are promising in replacement of cadmium coatings. The stability of these alloys grows with increasing nickel content above 50 wt %, and, similarly to pure nickel, they are inclined to undergo passivation [1]. Data on the effect of individual organic compounds on the electrochemical behavior of the Ni50Zn alloy ([Ni] = [Zn] = 50 wt %) are scarce. Only its selective and uniform dissolution, predominantly in chloride media, has been investigated [2, 3]. In this study, we analyze the electrochemical behavior and passivation of the Ni50Zn alloy in perchlorate media as influenced by some organic additives, sodium chloride, and their mixtures.

The alloy reinforced in Teflon was trimmed with an abrasive paper with decreasing grain size and degreased with ethanol. The potentiostatic measurements were carried out in a three-electrode cell with separated cathodic and anodic volumes at 25°C in a 0.1 M $HClO_4$ + 0.1 M $LiClO_4$ solution (preliminarily deaerated with argon). The resulting electrode potentials E are given with respect to a saturated silver chloride reference electrode.

As inhibitors we used 1,2-dimethyl-3-octyloxymethyl-5-methoxybenzimidazolium chloride (**I**), 1-heptyl-2-immonio-3-(2-methoxyethyl)benzimidazoline chloride (**II**), 1-methyl-4,6-di(4-ethoxycarbonylmethoxyphenyl)pyrylium perchlorate (**III**), sodium chloride, and their mixtures.

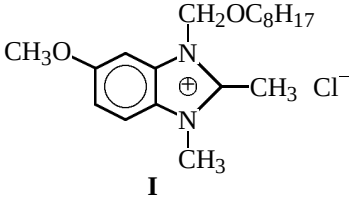

I

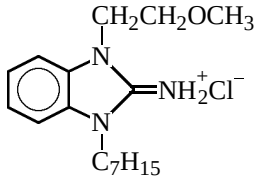

II

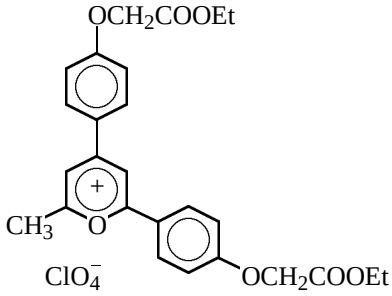

III

The working concentration c_s of surfactants **I**–**III** was varied within 2×10^{-5}–10^{-4} M. The effect of surfactants was evaluated by the inhibition coefficient $\gamma = i_0/i_a$, where i_0 and i_a are the rates of alloy dissolution in electrolyte with and without additive, respectively.

The alloy dissolves uniformly. The polarization curves of the alloy and metallic nickel are similar. They dissolve in the active state up to E = –0.20V, and at $E \geq 0.05$ V they occur in the passive state. The critical current i_{cr} and the current of complete passivation i_{cp} of the alloy, are, respectively, 200 and 30 times greater than those of metallic nickel.

The effects of additives **I**–**III** on the cathodic evolution of hydrogen i_H on the alloy and nickel are different. The dependence of γ on the concentration and

1070-4272/02/7510-1621 $27.00 © 2002 MAIK "Nauka/Interperiodica"

Table 1. Inhibition coefficient γ is relation to *E* and organic additive

–*E*, V	γ at indicated $c_s \times 10^5$, M											
	2	6	8	10	2	4	8	10	2	4	6	8
	I				**II**				**III**			
0.50	1.6	1.0	1.0	0.9	2.1	1.5	2.2	2.0	0.7	0.7	0.7	0.5
0.40	1.7	0.8	0.8	0.6	1.5	1.9	1.8	0.7	0.7	0.8	0.3	0.4
0.24	2.8	1.7	1.4	1.2	4.6	6.1	3.8	4.3	0.8	0.6	0.5	0.4
0.15	1.8	1.1	0.8	0.6	1.3	1.5	0.3	0.3	1.0	1.2	1.3	1.1
0.00	2.1	1.9	1.7	0.9	1.2	1.6	0.4	0.3	1.8	3.4	3.1	3.1
–0.4	0.8	0.9	1.0	0.9	0.8	0.7	0.6	0.5	0.9	1.1	0.9	0.7

nature of organic additive obtained, for the alloy, is partially illustrated in Table 1.

Compound **II** acts as inhibitor in the entire concentration range studied, its effects on i_H for both alloy and metallic nickel are similar, and, depending on c_s and *E*, γ varies within the range 1.2–3.4, decreasing with increasing *E*. Compound **I** inhibits hydrogen evolution at the lowest c_s, whereas at higher c_s it accelerates this process. Sodium chloride and compound **III** make i_H higher in the entire concentration range studied. Comparison of the effect of compounds **I**, **II**, and NaCl on the cathodic process suggests that, taking into account different types of influence exerted by organic cations and the chloride anion on the ψ-potential, the effect of the cation is predominant in the case of **II** (i_H decreases at any content of surfactant c_s), whereas for **I**, the anion effect is predominant and i_H increases, especially at high c_s. The stronger influence exerted by the anion in surfactant **II** is probably due to the effect of the third nitrogen atom (position 2 in benzimidazole), which must increase both the effective charge on the nitrogen atom and the contribution of physical adsorption. In accordance with [4], the stimulating effect of the pyrylium cation is due to its sorption on the surface regions free of sorbed hydrogen or on regions of energetically nonuniform alloy surface with the minimal metal–hydrogen bonding energy (E_{M-H}), which makes higher the average E_{M-H} and facilitates the cathodic process. This is possible when the metal–surfactant system is characterized by specific interaction or chemisorption. The pyrylium cations tend to be chemisorbed on transition metals, including nickel.

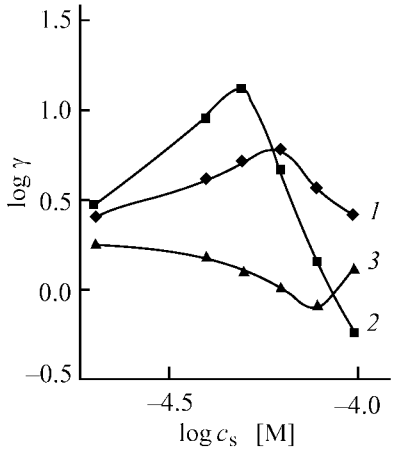

Fig. 1. Protective effect of additives on Ni50Zn alloy in relation to their concentration: (*1*) **I**, (*2*) **II**, and (*3*) **III** (E = –0.26 V). (γ) Inhibition coefficient and (c_s) surfactant concentration.

Compounds **I** and **II** decelerate the alloy dissolution in the active region, and the dependence of γ on c_s passes through a maximum (Fig. 1). They differ only in the effect on the critical potential E_{cr} and passivation current i_{cr}. Depending on concentration, compound **I** shifts E_{cr} by 0.05–0.1 V toward the anodic region and makes i_{cr} lower by a factor of 1.1–5.6. Compound **II** also raises E_{cr} by 0.1–0.2 V, but makes i_{cr} higher by a factor of 1.1–6.2. Compound **III** does not affect E_{cr} and dissolution of the alloy in the active region, but inhibits its ionization in the transition region. The coefficient γ varies from 1.2 to 3.0, depending on *E* and inhibitor concentration. Sodium chloride does not affect noticeably the alloy dissolution in the active region, promotes ionization in the transition region, and raises i_{cr} by a factor of 2.0–6.0, whereas E_{cr} remains unchanged. At low concentrations, all the additives studied do not affect the process, whereas at higher c_s the rate of the alloy dissolution in the passivation region increases by a factor of 1.2–2.0, i.e., the organic compounds studied hinder formation of a passive film. At equal concentrations, γ decreases in the order **II** > **I** > **III** > NaCl (Fig. 2). As seen, NaCl and compound **I** show no similarity in the effect on i_H. Hence, certain role in the protective effect

Table 2. Coefficient of mutual effect χ in relation to E and nature and concentration of organic additive ($c_{NaCl} = 2 \times 10^{-5}$ M)

–E, V	χ at indicated $c_s \times 10^5$, M											
	2	6	8	10	2	4	8	10	2	4	6	8
	I				**II**				**III**			
0.50	0.3	0.4	0.4	0.4	0.3	0.3	0.1	0.3	1.2	0.6	0.7	1.9
0.40	0.3	0.4	0.4	0.3	0.2	0.1	0.1	0.3	1.2	0.6	1.0	1.4
0.26	0.1	0.1	0.1	0.5	0.1	0.3	0.3	0.3	6.2	2.5	3.5	12.2
0.15	0.3	0.2	0.6	0.9	0.2	0.2	0.1	0.4	1.7	1.2	0.9	2.4
–0.4	2.8	1.4	0.3	1.0	3.7	3.3	2.6	2.7	4.0	4.3	4.0	4.6

Table 3. Inhibition coefficient γ and coefficient of mutual effect χ as influenced by concentration of sodium chloride and E ($c_{\mathbf{III}} = 10^{-4}$ M)

–E, V	γ and χ at indicated $c_{NaCl} \times 10^5$, M							
	4		6		8		10	
	γ	χ	γ	χ	γ	χ	γ	χ
0.50	2.2	4.0	1.2	2.7	1.2	3.4	1.7	4.2
0.40	2.1	4.8	1.0	3.1	0.8	3.3	1.3	6.2
0.26	85	202	5.1	12	4.4	15	2.4	13
0.15	1.4	2.4	0.8	2.1	0.7	1.8	1.0	2.6
–0.4	2.7	6.7	2.2	4.4	2.9	15	2.8	2.3

of **I** and **II** belongs to the organic cation, whose sorption on the positively charged alloy surface must be hindered. Adsorption of organic cation in **II** is weaker than that of the cation in **I**, in accordance with their structural, which is manifested in their different effects on E_{cr} and i_{cr}. The chloride anion in compounds **I** and **II** probably acts as a bridge and favors an increase in the contribution of physical adsorption.

Addition of NaCl to organic additives **I**–**III** changes their behavior. In the cathodic potential range and in the case of active dissolution, mixtures of **I** and **II** with NaCl accelerate the process, whereas in the passive region, the inhibiting effect is observed. The mixture of **III** with NaCl decelerates the process in the entire potential range studied. The coefficient of mutual effect, χ, calculated from the equation $\chi = \gamma_m/\gamma_i\gamma_{NaCl}$, where γ_m, γ_i, and γ_{NaCl} are the inhibition coefficients of the mixture and components, i = **I**–**III**, shows the follows. In mixtures of chloride-containing organic additives with constant concentration of sodium chloride, the effect is mainly antagonistic, and with additive **III** it is synergistic at any of the anodic potentials studied (Table 2).

At constant concentration of salt **III** and varied concentration of sodium chloride, their mixtures exert protective influence with mutual enhancement observed at all potentials except E = 0 (Table 3).

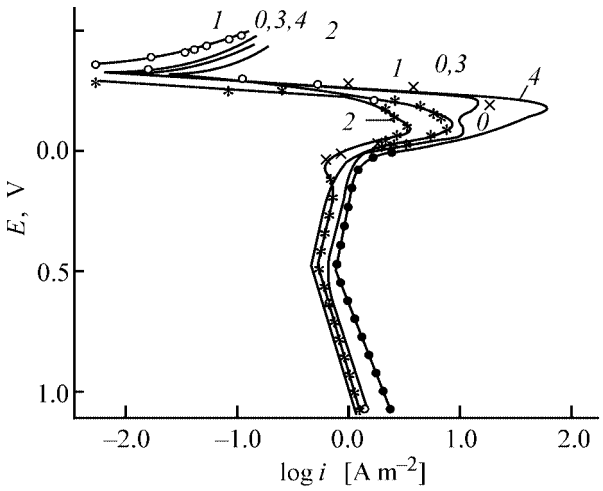

Fig. 2. Polarization curves of the alloy in the presence of additives: (*0*) none, (*1*) **I**, (*2*) **II**, (*3*) **III**, and (*4*) NaCl. (*E*) Electrode potential and (*i*) process rate.

CONCLUSIONS

(1) 1,2-Dimethyl-3-octyloxymethyl-5-methoxybenzimidazolium chloride and 1-heptyl-2-immonio-3-(2-methoxyethyl)benzimidazoline chloride inhibit active dissolution of Ni50Zn alloy and this effect is almost completely eliminated in the presence of NaCl. Mixtures are effective in dissolution of the alloy under study in the passivation region.

(2) The dependence of the protective influence exerted by the individual organic additives on their concentration passes through a maximum.

(3) The protective effect of 1-methyl-4,6-di(4-ethoxycarbonylmethoxyphenyl)pyrylium perchlorate is insignificant, it is strongly enhanced in the presence of sodium chloride.

REFERENCES

1. Ekilik, V.V., Berezhnaya, A.G., and Fevraleva, V.A., *Elektrokhimiya*, 1990, vol. 26, no. 5, pp. 288–293.
2. Ekilik, V.V., Berezhnaya, A.G., and Fevraleva, V.A., *Zashch. Met.*, 1990, vol. 26, no. 3, pp. 367–371.
3. Ekilik, V.V., Fevraleva, V.A., and Berezhnaya, A.G., *Zashch. Met.*, 1990, vol. 26, no. 5, pp. 842–847.
4. Reshetnikov, S.M., *Ingibirovanie kislotnoi korrozii metallov* (Inhibition of Acidic Corrosion of Metals), Izhevsk: Udmurtiya, 1980.

Russian Journal of Applied Chemistry, Vol. 75, No. 10, 2002, pp. 1625–1633. Translated from Zhurnal Prikladnoi Khimii, Vol. 75, No. 10, 2002, pp. 1659–1667.
Original Russian Text Copyright © 2002 by Moiseeva, Rashevskaya.

APPLIED ELECTROCHEMISTRY AND CORROSION PROTECTION OF METALS

Effect of pH Value on Corrosion Behavior of Steel in CO_2-containing Aqueous Media

L. S. Moiseeva and N. S. Rashevskaya

Scientific-Engineering Center, Lukoil Oil Company, Moscow, Russia
Dneprodzerzhinsk State Technical University, Dneprodzerzhinsk, Ukraine

Received October 29, 2001; in final form, February 2002

Abstract—The dependence of the pH of the medium on the partial pressure of CO_2 and temperature in the system constituted by low-carbon steel and NaCl (3%) and the effect of pH variation on the corrosion rate were studied. The mechanism of carbonic acid corrosion of ferrous metals in oxygen-free mineralized aqueous media was analyzed. The possibility of prognosticating the rate of steel corrosion on the basis of partial pressure of CO_2 and pH value was considered.

The corrosion activity of mineralized aqueous media is determined by the content of dissolved carbon dioxide causing intensive corrosion of oil-and-gas production equipment. The mechanism of metal corrosion under the action of CO_2 still remains the matter of discussion, despite numerous investigations in this field.

The aim of the present study was to discuss further the mechanism of carbonic acid corrosion of ferrous metals in oxygen-free mineralized media [1, 2].

Commonly, the effect of CO_2 is related to acidification of the medium [2–7]. As is known, the pH of the medium and, in the end, the corrosion danger are determined by the concentration of carbon dioxide in the stratal water, which, in turn, depends on the partial pressure of CO_2, p_{CO_2}, in the system. In this case, the following reactions are common to all aqueous media in the working range of p_{CO_2}:

$$CO_2 + H_2O \rightleftarrows H^+ + HCO_3^- \rightleftarrows H_2CO_{3(sol)}, \quad (1)$$

in solution [8] and

$$CO_{2(sol)} = CO_{2(ads)}, \quad (2)$$

$$CO_{2(ads)} + H_2O \rightarrow RH_2CO_{3(ads)} \quad (3)$$

on active centers on the metal surface [9].

With increasing p_{CO_2} and varying pH of the medium, the total and relative concentrations of the molecular and ionic forms (HCO_3^-, CO_3^{2-}, H_2CO_3) in the solution bulk and in adsorbed state change. As is known [10–12], the possible depolarizers in oxygen-free aqueous media saturated with CO_2 are, in addition to hydroxonium ion, H_2CO_3, HCO_3^-, and $CO_2 \cdot H_2O$.

Using the known nomograms [8, 13–15] describing the dependence of the equilibrium relation between H_2CO_3, HCO_3^-, and CO_3^{2-} on pH, the form (molecular or ionic) in which carbonic acid is present in solution can be determined. In [16], equilibrium constants of chemical reactions occurring in CO_2 dissolution in water were used to plot dependences of the share of each species in the analytically determined total concentration c_{CO_2} of carbonic acid on solution pH:

$$c_{CO_2} = [CO_2 \cdot H_2O] + [H_2CO_3] + [HCO_3^-] + [CO_3^{2-}].$$

In media with pH < 5, dissolved carbon dioxide is present virtually in the molecular form, 99.5% H_2CO_3 (25°C) [8], and, therefore, carbonic acid acts under these conditions mainly as a depolarizer:

$$H_2CO_{3(ads)} + e = H_{(ads)} + HCO_{3(ads)}^-. \quad (4)$$

When the cathode process occurs in accordance with Eq. (4), regeneration of carbonic acid proceeds simultaneously [9, 17]:

$$HCO_{3(ads)}^- + H_3O^+ = H_2CO_{3(ads)} + H_2O. \quad (5)$$

In this case, hydroxonium ions, also involved in the cathode process, may be formed both in the solu-

1070-4272/02/7510-1625 $27.00 © 2002 MAIK "Nauka/Interperiodica"

tion bulk and in adsorbed state, as a result of hydrolysis of carbonic acid [9]:

$$H_2CO_{3(ads)} + H_2O = H_3O^+_{(ads)} + HCO_3^-. \quad (6)$$

Presumably, with increasing concentration of hydroxonium ions in the adsorption and near-surface layers, the part played by competing reactions in the cathode process becomes more important:

$$H_3O^+ + e \rightleftarrows H_{(ads)} + H_2O, \quad (7)$$

$$H_3O^+_{(ads)} + e \rightleftarrows H_{(ads)} + H_2O. \quad (7a)$$

At pH ~6.5, about 30% H_2CO_3 and 70% HCO_3^- are present in solution [8]. In this case, the cathode process may occur by several pathways simultaneously [Eqs, (4), (7), (7a), (8), and (8a)]:

$$HCO^-_{3(sol)} + e \rightarrow H_{(ads)} + CO_3^{2-}, \quad (8)$$

$$HCO^-_{3(ads)} + e \rightarrow H_{(ads)} + CO_3^{2-}, \quad (8a)$$

$$2H^+_{(ads)} \rightarrow H_2\uparrow.$$

With increasing p_{CO_2} in the system, the share of reactions (7a) and (8a) in the overall cathode process will, presumably, grow.

At pH > 6.8 up to 99% HCO_3^- is contained in aqueous media [8]. Under these conditions, depolarization is mainly effected by HCO_3^- ions from solution in accordance with Eq. (8).

The increase in the concentrations of carbonic acid and HCO_3^- ion makes higher the rate of the cathode process, but does so only until the layer of corrosion products formed on the steel surface as a result of the concurrent anode process reaches its critical thickness.

At pH ≥ 7, reaction (9) becomes important, in addition to Eq. (8), in the cathode process [3, 4, 6]:

$$2H_2O + 2e \rightarrow H_2\uparrow + 2OH^-. \quad (9)$$

Accumulation of OH^- ions in solution creates favorable conditions for formation of carbonate ions by the reaction

$$HCO_3^- + OH^- \rightarrow H_2O + CO_3^{2-}. \quad (10)$$

As a result, the CO_3^{2-} concentration in solution grows, which favors formation of $FeCO_3$ and gives rise to a protective layer of siderite, lowering the total rate of the corrosion process, on the metal surface. However, the danger of local corrosion is preserved because of the local acidification of the medium within pores of corrosion products via, in particular, reaction (6).

In the general case, the rate of the cathode reaction in CO_2-containing media is given by the known relation [7, 9]

$$i_c = K_c c_{CO_2} \exp[-\alpha FE/(RT)].$$

The reversible potential of the cathode reactions considered depends on pH and is described by the equation

$$E_{rev} = -0.059\,pH - 0.295 \log p_{H_2}.$$

The total pressure in the system is in fact a sum of partial pressures of gases present (under the conditions of the experiment, these are pumped-in CO_2 and H_2 formed in the cathode process). Therefore, it may be concluded that the rate of the cathode process will grow with increasing total or partial CO_2 pressure in the system only to a certain critical value p_{CO_2}, above which the rate starts to decrease because of the hindrance to electrode processes associated with hydrogen evolution.

It is believed [9–11, 16] that depolarizer reduction proceeds in carbonate corrosion of ferrous metals depending on conditions of activation and diffusion control. The control is, as a rule, of activation type in the initial stage on a clean metal surface, and of diffusion type in the presence of a layer of corrosion products on the surface.

The anode process is intimately associated with the cathode process. Analysis and generalization of a wide variety [6, 9–12, 17–24] of schemes describing the anode process in aqueous media with CO_2 and without O_2 suggest the following. The overall anode electrochemical reaction for ferrous metals is as follows

$$Fe + 2H_2O \rightarrow Fe(OH)_{2(s)} + 2H^+ + 2e. \quad (11)$$

In media with pH < 5, a competing process is direct reaction of iron with the acid

$$Fe + 2H_2CO_3 \rightarrow Fe(HCO_3)_2 + H_2\uparrow. \quad (12)$$

Hydrocarbonates are unstable and, in the course of time, decompose to give carbonates:

$$Fe(HCO_3)_2 \rightarrow Fe^{2+} + 2HCO_3^-, \quad (13)$$

$$HCO_3^- \rightarrow H^+ + CO_3^{2-}. \quad (14)$$

Fe^{2+} ions formed in this stage interact with CO_3^{2-} by the reaction

$$Fe^{2+} + CO_3^{2-} \rightarrow FeCO_{3(s)}. \quad (15)$$

This leads, in the end, to formation of a siderite layer on the metal surface and to hindrance to both the cathode and anode processes.

In media with high HCO_3^- (pH > 6.8), iron carbonate may be formed by direct reaction of HCO_3^- with iron

$$Fe + HCO_3^- \rightarrow FeCO_{3(s)} + H^+ + 2e \quad (16)$$

and iron(II) hydroxide formed in an earlier stage of the process by reaction (11):

$$Fe(OH)_2 + HCO_3^- \rightarrow FeCO_{3(s)} + H_2O + OH^-. \quad (17)$$

Iron carbonate, in its turn, reacts with HCO_3^- to give a soluble complex compound:

$$FeCO_{3(s)} + HCO_3^- \rightarrow [Fe(CO_3)_2]^{2-} + H^+. \quad (18)$$

This, presumably, accounts for the fact that the siderite-hydroxide film loses its protective properties in media with higher HCO_3^- content, and the medium is acidified, eventually catalyzing the process.

It should be noted that all the reactions described above, and the related formation of the film and a deposit of corrosion products proceed in the course of time.

Another important factor determining the rate and mechanism of carbonic acid corrosion is temperature [9, 11, 18–24]. In contrast to the case of acid corrosion, the temperature dependence of carbonate corrosion is ambiguous: with the temperature increasing to 40–60°C, the corrosion rate grows, and then the process is hindered [9–12, 17–19]. This was attributed in [9–11, 18] to a change of mechanism. At 25°C, an unstable, porous oxide-hydroxide film of corrosion products, occasionally with inclusions of iron carbonate, is formed. The film is permeable to the depolarizer. The rate of the process is determined by the stage of H_2CO_3 and HCO_3^- discharge [Eqs. (4) and (8)]. At a temperature of about 60°C, the film of corrosion products becomes denser and acquires protective properties [23, 24]. This is due to the formation of films of another composition: carbonate-hydrocarbonate and purely carbonate (with inclusion of cementite) films are formed instead of oxide-hydroxide films at high temperature (>100°C), with the nature of the rate-determining stage changed. The solubility and permeability of corrosion products become key factors controlling the corrosion rate, which, in turn, is governed by the stage of chemical dissolution of siderite $FeCO_3$. It is known [13, 15, 16] that the solubility of siderite grows with increasing p_{CO_2}, and falls when pH or temperature become higher.

The concepts presented above can account for the phenomena observed in carbonic acid corrosion. First, the damage to production equipment much exceeds that expectable only on the basis of the effect of acidification of the medium by carbon dioxide. Second, the opinion that at pH > 7 there is virtually no danger of steel corrosion under the action of CO_2 in mineralized media is erroneous. Previously, it has been shown for low-carbon steel in carbonate-hydrocarbonate buffer solutions with free access of oxygen [1, 2] that the danger of local corrosion is preserved in the alkaline region. The present study considers in terms of the above-described mechanism of CO_2 action on the metal the variation of the pH of mineralized water (without access of oxygen) with increasing partial pressure of CO_2 in the system or temperature and the influence exerted by this variation on corrosion of low-carbon steel. Attention is also paid to another practically important question concerning the possibility of prognostication of the steel corrosion rate on the basis of partial values of CO_2 and pH in the system.

EXPERIMENTAL

Tests were performed in a 3% solution of NaCl by the procedure accepted in oil and gas industries [25, 26] under steady-state conditions in 6-l autoclaves whose bottom part was filled with 500 ml of the solution. The autoclaves were hermetically isolated from the atmosphere, and purged with nitrogen to remove air and then with a mixture of N_2 and CO_2 under pressure of 0.7–1.0 MPa. The autoclave was thermostated at a temperature of (25–80) ± 2°C. The total duration of an experiment was 96 h. Three 2-cm^2 cylindrical samples of St.3 low-carbon steel were placed in the solution in special holders. Prior to experiments the samples were polished with no. 3–0 sandpaper, degreased with ethanol, and kept in a desiccator over calcined CaO for 24 h. After tests the sample surface was inspected visually under a microscope at 400× magnification and washed with water, corrosion products were removed from the surface with a rubber, and then the samples were weighed. The pH of a 3% aqueous solution of NaCl, stationary potential E_{st}, and corrosion rate V_c were recorded in relation to the time of sample tests in solution at various partial pressures (p_{CO_2} = 0.7–1.0 MPa) and temperature.

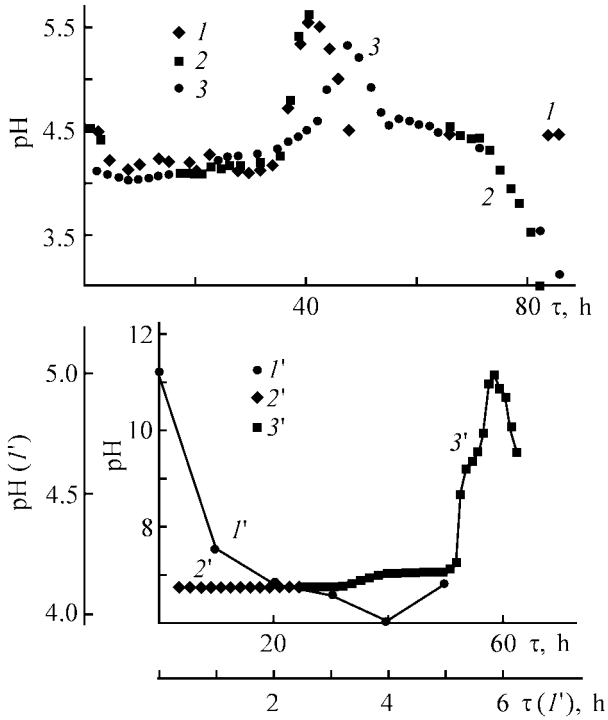

Fig. 1. PH of 3% NaCl solution vs. test time τ. p_{CO_2} (MPa): (*1*) 0.7, (*2*, *3*') 0.8, (*3*) 0.9, and (*1*', *2*') 1.0. *T* (°C): (*1–3*, *1*') 25 and (*2*', *3*') 80.

The corrosion rate was evaluated from the loss of sample mass during an experiment [25]. Changes in the stationary potentials were recorded with a PI-50-1 potentiostat connected to an LKD-4-003 XY recorder. A silver chloride electrode served as reference. The potential was recalculated relative to the standard hydrogen electrode.

Variation of p_{CO_2} in the range 0.7–1.0 MPa strongly affects, as also does the duration of tests, the pH of an aqueous NaCl solution. At a comparatively low p_{CO_2} (0.7 MPa) the pH values are somewhat higher. However, with increasing partial pressure, the solution pH decreases (Fig. 1) only during the initial stage of tests. For example, a rather low pH value of 4.3 is attained at 25°C in tests with duration of up to 5 h in the p_{CO_2} range studied (Fig. 1, curve *1*') because of the occurrence of reactions (1)–(3). The shift of pH to the acid region at 25°C with time (>40 h) (Fig. 1, curves *1–3*) is presumably due to parallel occurrence of reactions (16) and (18). This means that, when the metal is kept in solution for a long time, the solution pH starts to be determined by electrochemical and chemical reactions proceeding on the metal surface and in the near-surface layer.

Table 1. pH of 3% NaCl solution

T, °C	pH value at indicated p_{CO_2}, MPa	
	0.8	1.1
25	4.23	4.06
40	6.91	7.00
60	6.60	6.75
70	6.71	6.75
80	6.74	6.75
90	6.76	6.76

The longer the action of dissolved CO_2 upon the metal, or the more intensive this process, e.g., under the influence of temperature, the larger the amount of corrosion products formed both on the metal surface and in the solution bulk. Accumulation of oxidation products on the metal surface and their subsequent dissolution under the action of HCO_3^- ions [reaction (18)] changes the pH of the medium and enables occurrence of other reactions and reaction (17), in particular. At 80°C and $p_{CO_2} \geq 0.8$ MPa, a higher pH value (6.8–7.0) is observed. This value remains virtually unchanged during 24 h, with subsequent abrupt shift into the alkaline region to pH 11 on keeping the metal in solution for more than 2 days (Fig. 1, curves *2*' and *3*'), which can be regarded as resulting from the occurrence of reaction (17).

It should be noted that, previously, no equally high pH values have been observed in these same systems, modeling the carbon dioxide media at oil and gas fields, on keeping samples in the medium for a shorter time [3, 12, 21]. These data indicate that at least one of the conditions for formation of a protective siderite film is lacking. This means that there is no changeover of corrosion mechanism at 80°C, suggested in [9–11, 18]. It is known [9, 12, 16] that conditions for siderite formation are created at $T > 60$°C, with the film of corrosion products improving its protective properties. Indicative in this regard are the data in Table 1. A characteristic abrupt change in pH is observed at 40°C; beginning with 60°C, raising the temperature has virtually no effect on the pH value, which is presumably due to the change of reactions governing the pH of the medium, occurring at 40–60°C.

The thermodynamic conditions for formation of a dense siderite film are as follows: pH range 6–8, temperature interval 60–100°C, range of potentials –0.5…–0.6 V. Only the first two of these are satisfied in the experiment. In particular, on keeping the electrode for a long time (60–67 h) at $p_{CO_2} \geq 0.8$ MPa and temperature of 80°C, the pH value was 11, and the stationary electrode potential, –0.419 V. The sta-

tionary electrode potential coincides with the potential of γ-Fe_2O_3 oxide formation by the equation [14–16]

$$2Fe_3O_4 + H_2O = 3\gamma\text{-}Fe_2O_3 + 2H^+ + e. \quad (19)$$

The presence of Fe_3O_4 in the oxide film can apparently be attributed to the preceding decomposition of $Fe(OH)_2$ by the reaction

$$3Fe(OH)_2 \rightarrow Fe_3O_4 + 2H_2O + H_2. \quad (20)$$

The stationary potential in the pH ranges 5–6.3 (25°C) and 7–11 (80°C) is described by the equation $E_{rev} = 0.09 - 0.06pH$, which points to the possibility of occurrence of the reaction

$$Fe + CO_3^{2-} \rightarrow FeCO_3 + 2e. \quad (21)$$

The shift of stationary electrode potential at 25°C and p = 0.9 MPa during 10-h tests toward the positive region, from –0.34 to –0.23 V (Fig. 2, curve *3*), may indicate that the ratio of the oxide-hydroxide and carbonate components changes as a result of a change of the order of the occurring reactions (11)–(18). Further stabilization of the potential on keeping the electrode in the medium for a long time might indicate the completion of protective layer formation. However, no stabilization is observed under the experimental conditions: by contrast, at 25°C the stationary potential oscillates with a certain amplitude relative to the horizontal line at E = –0.22 V.

At 80°C the electrode potential shifted from –0.35 to –0.42 V, with increasing partial pressure of CO_2 in the system, and the amplitude of oscillations grew higher in the course of time (Fig. 2, curve *2*'). This points to activation of, in the first place, the cathode process because of the occurrence of reactions (4) and (7), and the related anode process [reaction (18)], changing the film composition, impairing its protective properties, and raising its permeability.

More positive values of the stationary potential, established at 25°C, and the nature of its variation with increasing p_{CO_2} may point to existence of a critical partial CO_2 pressure in the system, above which the concentration of depolarizers in the system does not change. For the system under study this critical pressure is, presumably, 0.8 MPa.

It has been noted previously [11] that a characteristic feature of passivation processes occurring on the iron surface in carbonate corrosion is the existence of a relatively high "corrosivity" threshold, which is to be overcome for a certain corrosion rate to be reached.

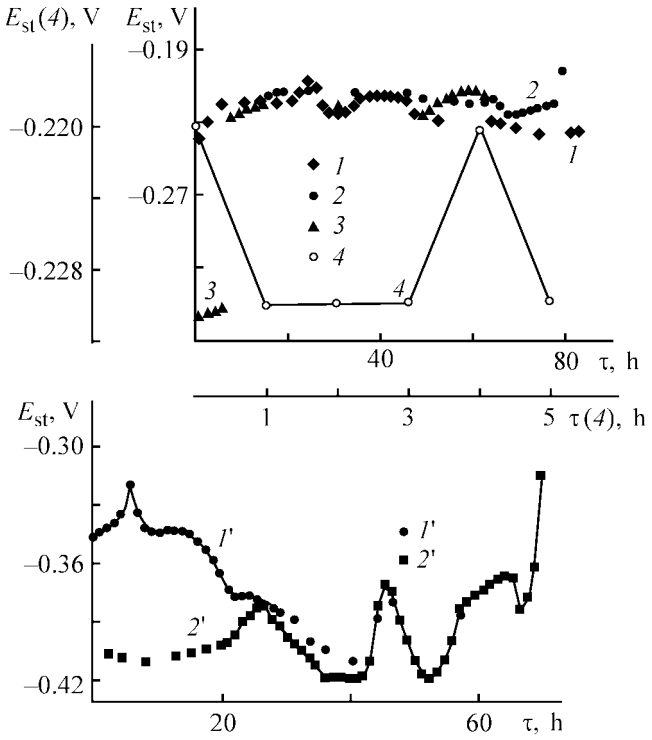

Fig. 2. Stationary potential E_{st} of St.3 steel vs. time τ of tests in 3% NaCl solution. p_{CO_2} (MPa): (*1*, *1*') 0.7, (*2*) 0.8, (*3*) 0.9, and (*4*, *2*') 1.0. T (°C): (*1*–*4*) 2.5 and (*1*', *2*') 80.

This threshold is determined by the "critical corrosion potential," above which a protective layer of deposits starts to be formed. The good solubility of corrosion products makes higher the critical corrosion potential required for the so-called pseudopassive state to be achieved [9, 11]. Presumably, the observed behavior of E_{st} with time at a temperature of 25°C can be related to the onset of the pseudopassivation state, which is not achieved at 80°C.

The positive shift of the stationary electrode potential in the initial period and its decrease and oscillations in the course of time are due to the occurrence of the chemical and electrochemical reactions considered above both directly on the metal surface and in the solution bulk, which leads to growth and subsequent dissolution of carbonate-oxide films on the steel surface. A vast body of data on the nature of films formed on steel in CO_2-containing solutions, summarized in Table 2, has been accumulated [3, 4, 9–17]. Analysis of published data and comparison of these with the results obtained under the experimental conditions shows the following. Films formed on the metal surface in the system under study at 25 and 80°C differ in outward appearance and, presumably, composition. In the course of time, changes in the out-

Table 2. Composition, properties, and formation conditions of films formed on iron and low-carbon steels in CO_2-containing aqueous media

Composition, outward appearance, and properties of a film	Formation conditions	Determination method	Reference
Amorphous phase $FeO \cdot FeCO_3$ (corrosite). Poorly soluble black compound, loose, easily permeable, electrically nonconducting, with magnetic properties	Condensation water of gas-condensate wells, distilled water; as a result of reactions occurring within the adsorption layer and on the metal surface	Analytical	[7]
$FeCO_3$ (siderite). Light gray compound, dense, impermeable, with protective properties	Condensation water of gas-condensate wells, distilled water; as a result of deposition from the near electrode layer	"	[7]
FeC_3 (cementite). Phase with cubic (spinel) structure isomorphic to siderite structure	Synthetic stratal water, g l^{-1}: 17.0 NaCl, 0.14–0.20 $CaCl_2$, 0.20 $MgCl_2$, 0.10–0.80 $NaHCO_3$; p_{CO_2} = 0.4–101 MPa; as a result of reactions occurring within the adsorption layer and on the metal surface	Microprobe X-ray fluorescence analysis, X-ray phase analysis	[20]
Cementite layer	1 M NaCl, pH 3.7–6.2, 70°C, τ = 24 h, p_{CO_2} = 1 bar, E = –0.675 V (standard calomel electrode); as a result of reactions on metal surface	Energy-dispersive X-ray diffraction (EDX)	[23]
Matrix of insoluble steel cementite, filled with siderite	In 1% solutions of NaCl, p_{CO_2} = 1×10^5 Pa, 50°C; as a result of reactions on metal surface	"	[21]
Oxyhydroxide $FeO_x(OH)_{3-2x}$ (as small inclusions in a two-layer film), gray-brown. Intermediate product of α-FeOOH formation. Forms in large amounts at room temperature, and medium amounts at 95°C	Tap water, p_{CO_2} = 0.83 MPa, 95°C; 4% solution of NaCl + 1–14 mg l^{-1}, p_{CO_2} = 0.83 MPa	Micrographic method (SEM)	[22, 23]
Hematite α-Fe_2O_3. Paramagnetic, insulator. Color from brick-red to black	3% solution of NaCl (pH 3.7); 0.55 M NaCl, 0.013 M $CaCl_2$, 0.0062 M $MgCl_2$, 0.005 M $NaHCO_3$ (pH 5), $T \geq 80$°C	Electron-probe microanalysis (EPMA), SEM, EDX	[10, 26]
Lepidocrocite γ-FeOOH. Paramagnetic, insulator. Brown. Transforms into α-FeOOH	3% solution of NaCl (pH 3.7); 0.55 M NaCl, 0.013 M $CaCl_2$, 0.0062 M $MgCl_2$, 0.005 M $NaHCO_3$ (pH 5); τ = 20 h, p_{CO_2} = 0.1 MPa, E = –0.60 V; –0.65 V (SCE); 23, 65, 80°C	"	[10, 26]
Layer of siderite $FeCO_3$. Formed in large amounts at 90°C, and in medium amounts at room temperature. Dense, protective films. Paramagnetic, insulator. Color from yellow to black	1 M NaCl + 3 M $NaHCO_3$ (acidified with HCl), pH 4–6.2, $Fe^{2+} < 5$ mg $^{-1}$, 70°C, 68 h, p_{CO_2} = 1 bar. Tap water p_{CO_2} = 0.83 MPa, 20–90°C; ~100°C, above 150°C	EPMA, SEM, ESCA, EDX	[23, 26]
α-$Fe_2O_3 \cdot H_2O$; magnetite Fe_3O_4 (as inclusions). Ferromagnetic, electrically conducting	Water saturated with CO_2, at T > 180°C; 0.5 M NaCl (pH 3.7); 0.5 M NaCl + 0.0062 M $MgCl_2$ + 0.005 M $NaHCO_3$ (pH 5.0), 80°C; as a result of surface reaction	ESCA	[10, 26]

Table 3. Experimental and calculated corrosion rates V_c and pH of 3% solution of NaCl

p_{CO_2}, MPa	T, °C	pH value			V_c, mm yr^{-1}			
		experiment	calculation by equation		calculation by equation		experiment	reference
			(25)	(26)	(22)	(23)		
0.7	25	4.6	4.2	–	4.0	1.3	25	–
0.8	25	4.0	4.2	–	4.4	1.5	24	96* [12]
0.9	25	4.4	4.1	–	4.7	1.6	25	–
1.0	25	4.1	4.1	–	5.0	1.8	26	–
0.8	80	7.0	–	4.5	36	4.8**	33	50* [12], 4.6 [7]
1.0	80	6.8	–	4.4	42	5.6**	33	5.6 [7]

* 4% solution of NaCl. ** Calculation by Eq. (24).

ward appearance and protective properties, as indicated by stationary potentials and corrosion rates, are observed even at one and the same temperature. The samples are covered, after being kept in the medium for 96 h at 25°C, with a solid black film of corrosion products, probably of oxide-carbonate nature (corrosite), and, after 72 h at 80°C, with a brown-black film of, presumably, hematite or oxide-hydroxide nature, as follows from analysis of the data in Table 2. The solution contains a suspension of brown corrosion products.

It is indicative that the experimental average corrosion rates obtained in the tests are rather high (even at pH 10–11) over the entire range of partial pressures of CO_2 and temperatures. In this case, an increase in p_{CO_2} has virtually no effect on the total corrosion rate of low-carbon steel, found gravimetrically. The insignificant variation of the experimental corrosion rates with partial pressure of CO_2 at constant temperature possibly indicates that there occur no substantial changes in the protective properties of the film. Contrary to expectations, raising the temperature from 25 to 80°C does not exert strong influence on the rise in total rate of steel corrosion in the carbon dioxide medium. Insignificant differences may indicate that, contrary to expectations, a film formed at high temperature has no protective properties and does not prevent activator and depolarizer from penetrating to the metal surface. This is also indicated by the above-mentioned potential oscillations. Thus, with account of the high corrosion rates, values of stationary potential and its oscillations with time, and the outward appearance of the samples, it may be concluded that, under the experimental conditions, no protective film of siderite is formed on the steel surface.

The data obtained on how the corrosion rate varies with time at different partial pressures and pH values furnish an opportunity to consider the problem of prognostication of the corrosion rate of ferrous metals at different p_{CO_2} and pH values for the example of a simple model system. For this purpose, the corrosion rate and pH were calculated for the system under study by the equations proposed previously. In particular, then best-known of these is the de Waard–Milliams equation [18]

$$\log V_c = 7.96 - \frac{2320}{273.2 + T} - \frac{5.55T}{1000} + 0.67 \log p_{CO_2}, \quad (22)$$

where V_c is the average rate of metal corrosion in terms of the corrosion depth factor (mm yr^{-1}), p_{CO_2} is the partial pressure of carbon dioxide (bar), and T is temperature (°C).

Kuznetsov [7] proposed equations for calculating the rate of corrosion, V_c, in the condensation water of gas and gas-condensate wells in the presence of CO_2

$$\log V_c = 0.7493 \log p_{CO_2} - 0.5060, \quad 25°C; \quad (23)$$

$$\log V_c = 0.7493 \log p_{CO_2}, \quad 80°C, \quad (24)$$

and the pH of condensation water

$$\log \mathrm{pH} = 0.6902 - 0.792 \log p_{CO_2}, \quad 25°C, \quad (25)$$

$$\log \mathrm{pH} = 0.7410 - 0.0986 \log p_{CO_2}, \quad 80°C, \quad (26)$$

where p_{CO_2} is the partial pressure of carbon dioxide (bar).

A calculation of the corrosion rate by Eqs. (22)–(24) demonstrated a discrepancy of the calculated and experimental corrosion rates at 25°C, with the former being an order of magnitude lower than the latter.

Only at 80°C, calculation by the de Waard–Milliams equation gives values close to the experimental corrosion rates. At the same time, a satisfactory agreement between the experimental and calculated values at low temperature is obtained for the pH (Table 3). At high temperature the calculated values are lower than the experimental values. Presumably, Eqs. (23), (24), and (26) disregard the influence of corrosion products accumulated on the metal surface and in solution in the case of keeping the metal in the medium for a long time at elevated temperature.

In [11], the problem associated with deposit formation and stabilization of the rate of carbonate corrosion in time was considered. An equation was proposed, relating the initial (V_0) and final (V) corrosion rates to the thickness l of a film on the metal surface

$$\tau = \frac{2l}{R(V + V_0)}, \quad (27)$$

where τ is the test duration, R is "the ratio of molar volumes of iron in the metal and in deposits," depending on the type of deposit (3 for $FeCO_3$ below 60°C, and 4.3 for $FeCO_3$ above 60°C).

Equation (27) disregards changes in p_{CO_2} and pH in the system, but allows calculation of the initial corrosion rate at constant pH and CO_2 pressure from the film thickness and final corrosion rate. With the film thickness taken to be 1 mm [9], calculations by Eqs. (23) and (24) for 25 and 80°C yield for both 25 and 80°C an initial corrosion rate of 25 mm yr^{-1}, i.e., the calculated initial rate of corrosion coincides with the average experimental rate of corrosion (Table 3). In this connection, it should be noted that that the corrosion rate attained in the course of tests is determined by its initial value.

As already noted, an opinion has been formed that the pH range 10–11 is safe as regards corrosion. However, according to the results obtained in the present study, even average values of the total corrosion rate at 25–80°C in aqueous oxygen-free carbon dioxide media remain rather high at p_{CO_2} = 0.7–1.0 MPa and pH 4–11. Previously [1, 2], a high rate of local corrosion has been observed in carbonate–hydrocarbonate buffer solutions at high pH values (10–11).

CONCLUSIONS

(1) The mechanism of the corrosion process occurring on the steel surface in mineralized aqueous media under the action of CO_2 is considered in terms of variation of the pH of the medium.

(2) It is shown that changing the temperature and time of testing in a corrosive medium affects more strongly the variation of the pH of the medium and the rate of steel corrosion, than changing the partial pressure of CO_2 does.

(3) It is demonstrated that high total rates of corrosion of low-carbon steel, determined by the initial rate, are observed in a 3% solution of NaCl at $p_{CO_2} >$ 0.8 MPa and T = 25–80°C. A steel kept at high temperature in the model oxygen-free carbon dioxide medium for a long time is in the active state, with no protective film formed on its surface and danger of corrosion under the action of dissolved CO_2 persisting.

(4) The experimental rates of St.3 steel corrosion in the carbon dioxide medium under study are much higher than those predicted by equations disregarding the growth of a film of corrosion products on the metal surface. This indicates that it is difficult to use these equations for prognosticating the rate of low-carbon steel corrosion on the basis of p_{CO_2} for real systems with metal kept in the corrosive medium for a long time.

(5) The possibility of calculating the pH from the known partial pressure of CO_2 in aqueous oxygen-free media at low temperature is shown.

ACKNOWLEDGMENTS

The authors thank A.E. Chalykh for critical remarks in manuscript preparation.

REFERENCES

1. Moiseeva, L.S. and Kuznetsov, Yu.I., *Zash. Met.*, 1996, vol. 32, no. 6, pp. 565–572.
2. Moiseeva, L.S. and Kuznetsov, Yu.I., *Zh. Prikl. Khim.*, 1998, vol. 71, no. 6, pp. 950–955.
3. Saakiyan, L.S. and Efremov, A.P., *Zashchita neftegazopromyslovogo oborudovaniya ot korrozii* (Corrosion Protection of Oil-and-Gas-producing Equipment), Moscow: Nedra, 1982.
4. Rozenfel'd, I.L., *Ingibitory korrozii* (Corrosion Inhibitors), Moscow: Khimiya, 1977.
5. Gonik, A.A., *Korroziya neftepromyslovogo oborudovaniya i mery ee preduprezhdeniya* (Corrosion of Oil-and-Gas-producing Equipment and Measures for Its Protection), Moscow: Nedra, 1976.
6. Bregman, J.I., *Corrosion Ingibitors*, New York: The Macmillan Company; London: Collier-Macmillan, 1963.
7. Kuznetsov, V.P. and Chernaya, N.G., *Korroziya i zashchita v neftegazovoi promyshlennosti* (Corrosion

and Protection in Oil-and-Gas Industry), RNTS, Moscow: VNIIOENG, 1980, issue 8, p. 2.

8. Remy, H., *Lehrbuch der anorganischen Chemie*, Bd. 2, Leipzig: Akademische, 1961.
9. Valand, T. and Sjowall, P.A., Electrochim. Acta, 1989, vol. 34, no. 2, pp. 273–281.
10. Schmitt, G., *Advanced Materials in CO_2 Corrosion*, Houston, TX: NACE, 1984, vol. 1, pp. 1–7.
11. Crolet, J.-L., *10th Eur. Corrosion Congress*, Barcelona, Spain, 1993, Paper no. 270.
12. Markin, A.N., *Zashch. Met.*, 1996, vol. 32, no. 5, pp. 497–501.
13. Bulakh, A.G.and Bulakh, K.G., *Fiziko-khimicheskie svoistva mineralov i komponentov gidrotermal'nykh rastvorov* (Physicochemical Properties of Minerals and Components of Hydrometallurgical Solutions), Leningrad: Nedra, 1978.
14. Butler, J.N., *Ionic Equilibrium (A Mathematical Approach), Reading*, Massachusetts: Addison–Wesley, 1964.
15. Garrels, R.M. and Christ, Ch.L., *Christ, Solutions, Minerals, and Equilibria*, New York: Harper and Row, 1965.
16. Mitina, A.P., Gorichev, I.G., Khoroshilov, A.V., and Konichev, V.S., *Teoreticheskie osnovy karbonatnoi korrozii stali* (Theoretical Foundations of Carbonate Corrosion of Steel), Moscow: VNIIEgazprom, 1992.
17. Schmitt, G. and Rothman, B., *Werkst. Korros.*, 1978, vol. 29, pp. 98–103; 237–241.
18. De Waard, C. and Milliams, D.E., *Corrosion*, 1975, vol. 31, no. 5, pp. 177–183.
19. *Corrosion Handbook: Corrosion Agents and Their Interaction with Materials*, New York: VCH, 1990.
20. Markin, A.N. and Legezin, N.E., *Zashch. Met.*, 1993, vol. 29, no. 3, pp. 452–456.
21. Nesic, S., Solvi, G.T., and Energhaug, V., *Corrosion*, 1995, vol. 51, no. 10, pp. 773–778.
22. Jasinski, R., *Corrosion*, 1987, vol. 43, no. 4, pp. 215–218.
23. Videm, K., *Corrosion*, 1993, Paper no. 21; Paper no. 83.
24. Videm, K. and Dugstad, A., *Corrosion*, Houston, 1988, Paper no. 186.
25. *OST* (All-Union Standard) *39-099–79, Corrosion Inhibitors: Method for Evaluating the Efficiency of Protection by Corrosion Inhibitors in Oil-Production Wastewater*.
26. Ostrovskii, V.V., Osminin, V.S., and Brusov, K.N., *Tekhnologii i materialy dlya zashchity ot korrozii i ee posledstvii* (Technologies and Materials for Protection from Corrosion and Its Consequences), St. Petersburg: Nauka, 1992.

Russian Journal of Applied Chemistry, Vol. 75, No. 10, 2002, pp. 1634–1638. Translated from Zhurnal Prikladnoi Khimii, Vol. 75, No. 10, 2002, pp. 1668–1672.
Original Russian Text Copyright © 2002 by Novgorodov, Trukshin, Blyum, Tokareva, Dmitriev.

CATALYSIS

Calculation Procedure for Compositional Optimization of Supported Catalysts[1]

V. N. Novgorodov, I. G. Trukshin, M. M. Blyum, T. V. Tokareva, and A. V. Dmitriev

Prikladnaya Khimiya Russian Scientific Center, St. Petersburg, Russia

Received January 17, 2002

Abstract—A set of equations, describing the dependence of the activity of supported catalysts on the content of the active component, specific surface area of the support, and preparation method, is proposed. The model is applied to optimize the composition and preparation method of chromium-magnesium-fluoride catalyst for hydrofluorination of chlorohydrocarbons.

A search for new catalyst formulations is commonly conducted by performing a thorough experimental study of their activity in relation to the content of the active components (AC) and specific surface of a support at a chosen preparation procedure. This search can be much accelerated by employing a calculation procedure allowing prognostication of the relationships of interest.

This can be done using Zaidman's [1, 2] inversely proportional dependence of the dispersity of AC, equal to the ratio of the number N_s of its surface atoms responsible for catalysis to their total number N, on the surface concentration c_s ($g_{AC}\ m_{sup}^{-2}$, i.e., the AC concentration related to unit surface area of the support S_{sup} ($m^2\ g_{sup}^{-1}$):

$$1/D = N/N_s = 1 + K_t c_s = 1 + K_t n/S_{sup}, \quad (1)$$

where K_t is the crystallization constant ($m_{sup}^2\ g_{AC}^{-1}$), D is the dispersity, and n is the mass fraction of AC in the catalyst ($g_{AC}\ g_{cat}^{-1}$).

The applicability of this relation has been demonstrated for widely diverse catalysts, Ni, Pt, Pd, Fe, etc., supported by aluminum, silicon, and chromium oxides, with the AC concentration varied widely, between (0.2–2.0) and (0.4–50)%.

However, the calculation of the surface concentration by the formula $c_s = n/S_{sup}$ in [1, 2] disregarded the variation of the fraction of the support itself in the catalyst with the AC concentration. For this reason, the specific surface area of the AC and, consequently, its activity too would have increased steadily with the AC concentration increasing up to 100%. Therefore, as noted in [2], Eq. (1) is valid "at not too high AC concentrations."

However, this dependence commonly shows a maximum for supported catalysts [1–3]. When the maximum is reached, the tendencies for the specific surface area of AC to increase because of its increasing concentration and for the same area to decrease because of the decreasing AC dispersity cancel out each other. Therefore, the model proposed in [4] is based on the equation

$$1/D = 1 + K_t n/[(1 - n)S_{sup}], \quad (2)$$

This model, applying Eq. (2) to supported metallic catalysts, allows, as shown in [4, 5], prognostication of how the specific surface area of a sample and its dispersity, and, consequently its activity too, depend on the AC content of the sample, on the basis of the specific surface area of metal in the sample. However, measuring the AC dispersity (at relatively low AC content of less than 10 wt %) with sufficient accuracy is rather problematic for supported acid-base catalysts, to which belong, for example, hydrofluorination catalysts (chromium hydroxo chlorofluorides) for khladon synthesis. Therefore, a modified version of the given method for prognostication of properties of such catalytic systems is proposed, and its essence is as follows.

Catalyst samples with varied AC content are prepared on the same support with known specific surface area, and their activity is measured. Then the expected dependence of a activity of a catalyst on its AC content is calculated on the basis of the following considerations.

In accordance with the model of [4], the variation of the activity W ($mol\ g_{cat}^{-1}\ s^{-1}$) of the catalyst with the content of AC in it is described by the equation

[1] Reported at 3rd International Conference "Chemistry, Technology, and Use of Fluorine Compounds," St. Peterburg, June 6–9, 2001.

1070-4272/02/7510-1634 $27.00 © 2002 MAIK "Nauka/Interperiodica"

$$W = W_s S_{AC} = W_s S_{max} n/\{1 + K_t n/[(1 - n)S_{sup}]\}, \quad (3)$$

where W_s is the specific catalytic activity of a unit surface area of AC (mol m_{AC}^{-2} s^{-1}), S_{AC} is the specific surface area of AC (m_{AC}^2 g_{cat}^{-1}), and S_{max} is the maximum possible specific surface area of an AC with unit dispersity (m_{AC}^2 g_{AC}^{-1}),

$$S_{max} = 6.02 \times 10^{23}\omega/M_{AC}. \quad (4)$$

Here ω is the surface area of crystallographic face per molecule (or atom) of AC (m^2 $molecule^{-1}$), and M_{AC} is the molecular (or atomic) mass of AC (g mol^{-1}).

The surface area of the crystallographic face is found from X-ray structural data [6] or approximately calculated using the formula

$$\omega = \{[M_{AC}/(d_{AC} \times 6.02 \times 10^{23})]^{1/3}/100\}^2, \quad (5)$$

where d_{AC} is the true density of AC (g_{AC} cm_{AC}^{-3}).

In linearized coordinates, Eq. (3) takes the form

$$n/W = 1/(S_{max} W_s) + [K_t/(S_{sup} S_{max} W_s)][n/(1 - n)]$$
$$= A[n/(1 - n)] + B, \quad (6)$$

$$A = K_t/(S_{sup} W_s S_{max}), \quad (7)$$

$$B = 1/(S_{max} W_s). \quad (8)$$

Provided that W_s (G.K. Boreskov's rule) and the specific surface area of the support are constant, Eq. (6) must be linear.

From the intercept on the ordinate axis in the coordinates of Eq. (6), the coefficient B is calculated and, in its turn, used to calculate in accordance with Eq. (8) the W_s value, which is substituted in Eq. (7) to find K_t.

The results of mathematical processing of experimental data obtained for a wide variety of catalyst in CO_2 hydrogenation on a nickel-chromium catalyst [3], liquid-phase hydrogenation of unsaturated sulfone on an aluminum-palladium catalyst [7], dehydrogenation of cyclohexane on aluminum-molybdenum [8] and aluminum-platinum catalysts [9] are presented in Figs. 1a–1e, respectively. It can be seen that the cal-

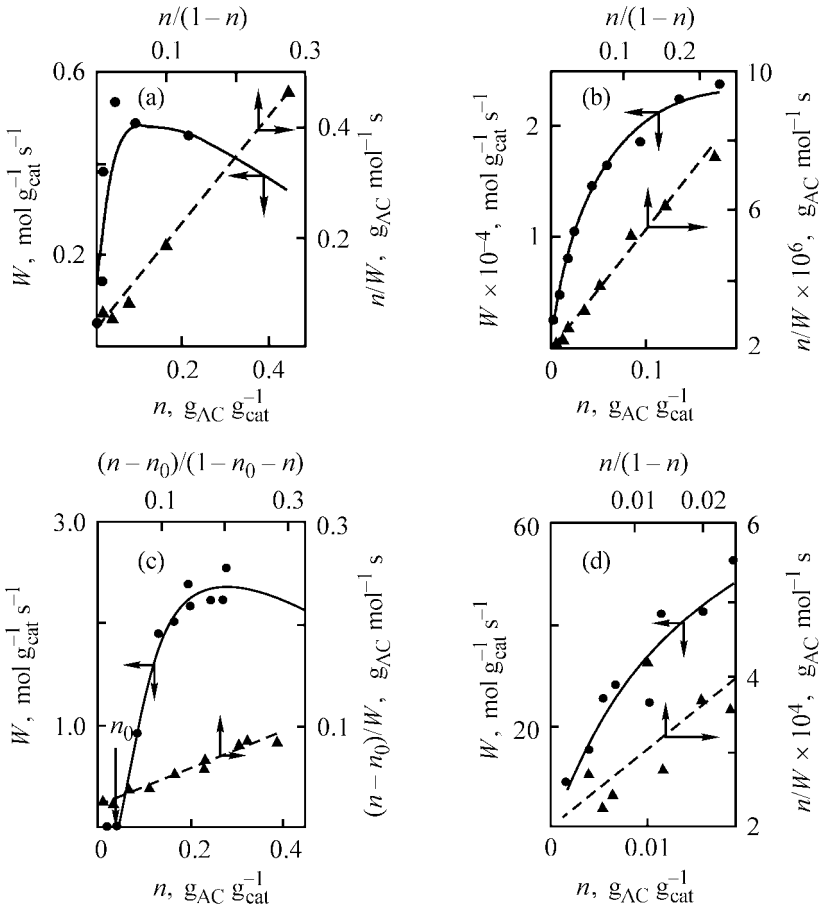

Fig. 1. AC activity W vs. AC concentration n, plotted in the coordinates of Eqs. (3) and (6), in reactions of (a) CO_2 hydrogenation [3], (b) liquid-phase hydrogenation of unsaturated sulfone [7], and (c, d) dehydrogenation of cyclohexane [8, 9]. Catalyst: (a) nickel-chromium, (b) aluminum-palladium, (c) aluminum-molybdenum, and (d) aluminum-platinum.

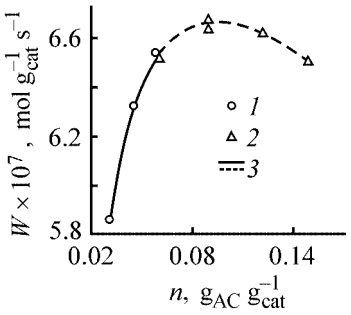

Fig. 2. Activity *W* of chromium-magnesium-fluoride catalyst in hydrofluorination of perchloroethylene vs. AC content *n* in the catalyst. Catalyst preparation method: (*1*) wet mixing [10] and (*2*) method under study; (*3*) calculation by Eq. (3).

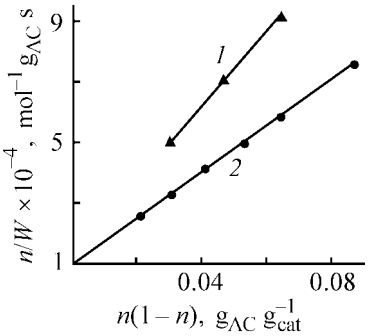

Fig. 3. Activity *W* of chromium-magnesium-fluoride catalyst prepared by the technology described previously in [10] in hydrofluorination of (*1*) polychloroethylene and (*2*) TCP vs. AC concentration *n* ?in the catalyst, plotted in the coordinates of Eq. (6).

culated and experimental values are in good agreement, which furnished an opportunity to apply this optimization method also to chromium-magnesium-fluoride catalysts obtained by the so-called "wet" mixing technique [10, 11]. It should be noted that this technique cannot be used to introduce more than 6.0–6.5 wt % Cr(III) because of the limited solubility of chromium chloride in water.

Results of tests of chromium-magnesium-fluoride catalysts prepared on MgF_2 in synthesis of khladons from polychloroethylene (temperature 380°C, pressure 0.3 MPa, molar ratio HF : C_2Cl_4 = 10 : 1, S_{MgF_2} = 95 m^2 g^{-1})

C(III), mass fraction	*Q*, $g_{C_2Cl_4}$ l_{cat}^{-1} h^{-1}	$\alpha_{C_2Cl_4}$, %	$W \times 10^7$, $mol_{C_2Cl_4}$ g_{cat}^{-1} s^{-1}
3.0	503	69.5	5.86
4.5	506	74.6	6.32
6.0	510	76.6	6.55

Hydrofluorination of perchloroethylene was carried out on these catalysts to obtain khladons 123, 124, and 125.

The catalyst activity *W* (mol g_{cat}^{-1} s^{-1}) was calculated by the formula

$$W = Q\alpha/(\Delta M_{C_2Cl_4} \times 3600 \times 100), \quad (9)$$

where *Q* is the load ($g_{C_2Cl_4}$ l_{cat}^{-1} h^{-1}), α is the conversion of C_2Cl_4 (%), Δ is the bulk density of the catalyst (kg l^{-1}), and $M_{C_2Cl_4}$ is the molecular weight of perchloroethylene.

The results obtained in testing the catalysts in synthesis of khladons by hydrofluorination of perchloroethylene are presented in the table and Fig. 2.

It can be seen from Fig. 2 that, with the above technique used to produce the catalyst, its activity steadily grows with increasing AC content, but does not reach the maximum value.

Processing of the experimental data obtained (see table), plotted in the coordinates of linearized Eq. (6) (Fig. 3), yields the following values of the constants: $B = 1.32 \times 10^4$, $W_s = 1.04 \times 10^{-7}$ mol m_{AC}^{-2} s^{-1} and $A = 1.23 \times 10^6$, $K_t = 8825$ m_{sup}^2 g_{AC}^{-1}.

The optimal content of the active component, n_{max}, in a catalyst, which ensures its maximum activity W_{max}, is found by differentiating Eq. (3):

$$dW_{AC}/dn = S_{max} W_s [1 - 2n - n^2(b-1)]/[1 + n(b-1)]^2, \quad (10)$$

where $b = K_t/S_{sup}$.

At the point of maximum, $dW_{AC}/dn = 0$ and, since $S_{max} \neq 0$ and $W_s \neq 0$,

$$n_{max} = 1/[1 + (K_t/S_{sup})^{1/2}] = 0.094 \ (9.4 \text{ wt \%}). \quad (11)$$

With Eq. (11) substituted into (3), the maximum activity of the catalyst can be calculated by the equation

$$W_{max} = W_s S_{max} n_{max}^2. \quad (12)$$

The calculations performed established that, with a support having a specific surface area of 95 m^2 g^{-1}, the catalyst activity must be at a maximum upon introduction 9.4% Cr(III), which cannot be ensured by the wet mixing method. In this context, it became necessary to develop another way to produce highly concentrated chromium-magnesium-fluoride catalysts.

The tests of catalysts produced by the new technique confirmed the results of calculations (Fig. 3). The use of the model proposed for prognosticating the

properties of supported catalysts allowed prediction and implementation of the possibility of raising their activity. More than that, it was found that the new, more concentrated catalysts have a longer service life because of the possibility of a greater number of regenerations, during which AC is partially lost in the form of volatile compounds of chromium(VI).

Another way to raise the activity of a catalyst is to vary the porous structure of its support, e.g., by making larger the specific surface area of the support.

Figure 4 presents the calculated dependence of the maximum possible relative activity of the catalyst on the specific surface area of the support at the optimal content of chromium fluoride for each value of the specific surface area. For example, raising the specific surface area of the support (magnesium fluoride, in the case in question) from 100 to 200 $m^2\ g^{-1}$ by, e.g., changing the method of its preparation, or raising its thermal stability, may lead to nearly a twofold increase in activity.

This makes understandable the reason for the decrease in the activity of the chromium-magnesium-fluoride catalyst during its operation, which is associated, in the first place, with caking of magnesium fluoride, which lowers the specific surface area under the action of high temperature, especially in the course of regeneration.

The pattern revealed makes it possible to assess the nature of variation of the specific surface area of the AC itself and its dispersity with the catalyst composition. Equation (3) and the W_s value obtained for chromium fluoride were used to calculate its specific surface area S_{CrF_3} ($m^2\ g_{cat}^{-1}$) in relation to the catalyst composition by the formula

$$S_{CrF_3} = W/W_s. \quad (13)$$

The specific surface area of chromium fluoride itself, S'_{CrF_3} ($m^2_{CrF_3}\ g^{-1}_{CrF_3}$), dispersity D, and crystallite size d_{cr} of chromium fluoride (nm) were calculated by the formulas

$$S'_{CrF_3} = S_{CrF_3}/n, \quad (14)$$

$$D = S'_{CrF_3}/S_{max}, \quad (15)$$

$$d_{cr} = 5 \times 10^3/(S'_{CrF_3} d_{CrF_3}). \quad (16)$$

The calculated data are presented in Figs. 5 and 6, whence it can be seen that, with increasing content of the AC in the catalyst, the specific surface area of chromium fluoride itself decreases steadily because of its decreasing dispersity and increasing crystallite size. At the same time, the specific surface area of chromium fluoride (Fig. 5) and its activity (Fig. 2), both related to unit catalyst mass, are the highest at

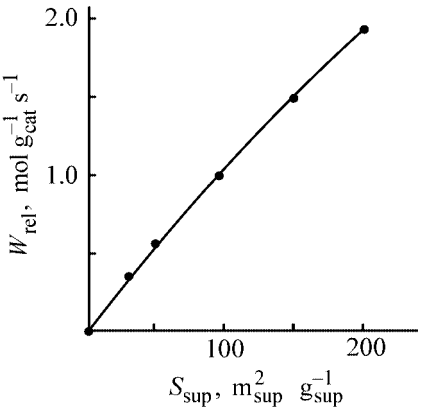

Fig. 4. Relative activity $W_{rel} = W_{max}/W_{max(S_{sup} = 95\ m^2\ g^{-1})}$ of chromium-magnesium-fluoride catalyst vs. specific surface area of magnesium fluoride, S_{sup}, at the optimal content of AC for each value of the specific surface area of the support.

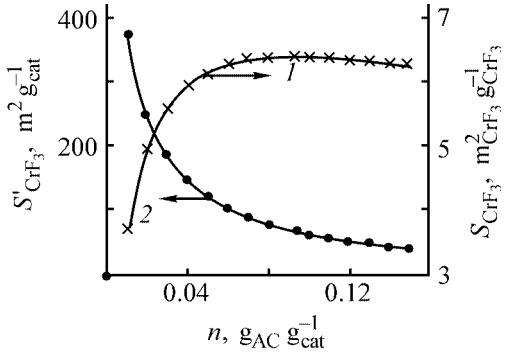

Fig. 5. Specific surface area of chromium fluoride, related to (*1*) unit catalyst mass, S_{CrF_3}, and (*2*) unit mass of chromium fluoride, S'_{CrF_3}, vs. AC content n.

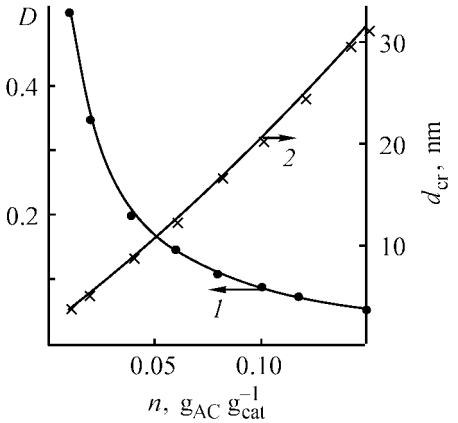

Fig. 6. (*1*) Dispersity D of chromium fluoride and (*2*) size d_{cr} of its crystallites vs. the AC content n of the chromium-magnesium-fluoride catalyst.

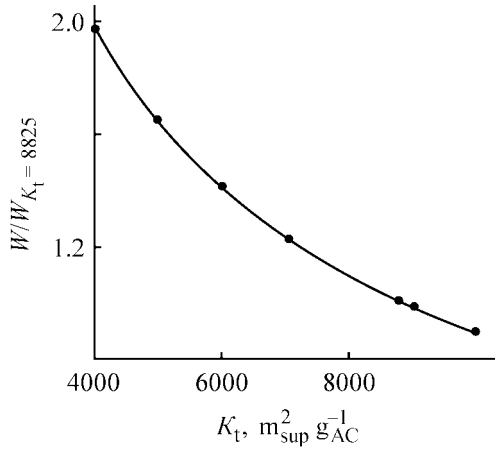

Fig. 7. Relative activity of the chromium-magnesium-fluoride catalyst vs. its crystallization constant K_t for n = 9.4 wt % Cr(III) and S_{sup} = 95 $m^2\ g^{-1}$.

one and the same optimal content of AC, equal to 9.4 wt % Cr(III).

The dispersity of chromium fluoride at its optimal content in the catalyst produced on a standard support with specific surface area of 95 $m^2\ g^{-1}$ is 0.09 (Fig. 6). Thus, only 9% of all the AC atoms are involved in khladon synthesis. Hence follows that the catalyst activity can be raised significantly by making higher the dispersity of magnesium fluoride on the catalyst, e.g., by introducing dispersants into the active phase.

The catalyst preparation conditions may also strongly affect the dispersity and, consequently, the activity of AC. The key factor is the crystallization constant and, whenever possible, it is appropriate to lower it to the minimum (Fig. 7). It can be seen that lowering K_t by half must raise the activity by no less than a factor of 1.5.

Similar dependences were obtained on the same catalyst samples in hydrofluorination of 1,1,1,3-tetrachloropropane (TCP) to trifluoropropene (Fig. 3).

The catalysts were tested in a flow-through reactor under the following conditions: catalyst mass 25–26 g; consumption of TCP and hydrogen fluoride 0.003 and 0.03 mol min^{-1}, respectively; and synthesis temperature 250°C.

The obtained values, K_t = 8694 $m^2_{sup}\ g^{-1}_{AC}$ and optimal AC content of 9.6%, are close to those found previously in studying hydrofluorination of perchloroethylene. This means that the model proposed for prognostication and optimization of the properties of supported catalysts is adequate.

CONCLUSIONS

(1) A calculation procedure for optimizing the composition of supported catalysts with constant specific catalytic activity and prognosticating the dependence of their activity, specific surface area of the active component, and for its dispersity on composition, specific surface area of the support and catalyst preparation method was proposed.

(2) The applicability of the model was demonstrated for the example of supported aluminum-palladium, aluminum-platinum, nickel-chromium, and aluminum-molybdenum catalysts.

(3) Processing the experimental dependences of the activity of the chromium-magnesium-fluoride catalyst in hydrofluorination of hydrocarbons on its composition made it possible to calculate the optimal composition of the catalyst, find a new method for its preparation, and determine how the dispersity of the active component varies with its increasing concentration.

REFERENCES

1. Zaidman, N.M., *Kinet. Katal.*, 1973, vol. 13, no. 4, pp. 1012–1019.
2. Zaidman, N.M. and Savostin, Yu.A., *Kinet. Katal.*, 1973, vol. 14, no. 6, pp. 1544–1547.
3. Dzis'ko, V.A., *Usp. Khim.*, 1974, vol. 43, no. 6, pp. 977–1005.
4. Novgorodov, V.N., Gaidei, T.P., Parfenova, L.V., and Tyuryaev, I.Ya., in *Razrabotka i issledovanie katalizatorov organicheskogo sinteza* (Development and Study of Catalysts for Organic Synthesis), Tyuryaev, I.Ya. and Gaidei, T.P., Eds., Leningrad: Gos. Inst. Prikl. Khim., 1981, pp. 60–67.
5. Gaidei, T.P., Novgorodov, V.N., and Tyuryaev, I.Ya., *Zh. Prikl. Khim.*, 1994, vol. 67, no. 1, pp. 22–24.
6. Karnaukhov, A.P., *Adsorbtsiya, tekstura dispersnykh i poristykh materialov* (Adsorption and Texture of Dispersed and Porous Materials), Novosibirsk: Nauka, 1999, p. 177.
7. Kulishkin, N.T., Mashkina, A.V., Buyanova, N.E., *et al.*, *Kinet. Katal.*, 1971, vol. 12, no. 6, pp. 1539–1543.
8. Kharlampova, R.N., Zaidman, N.M., Karnaukhov, A.P., *et al.*, *Kinet. Katal.*, 1973, vol. 14, no. 6, pp. 1538–1543
9. Zaidman, N.M., Dzis'ko, V.A., Karnaukhov, A.P., *et al.*, *Kinet. Katal.*, 1968, vol. 9, no. 4, pp. 863–869.
10. RF Patent 2005539.
11. Kramerova, G.E., Dul'tseva, Z.A., and Yurchenko, E.N., *Zh. Prikl. Khim.*, 1994, vol. 67, no. 4, pp. 30–36.

Russian Journal of Applied Chemistry, Vol. 75, No. 10, 2002, pp. 1639–1642. Translated from Zhurnal Prikladnoi Khimii, Vol. 75, No. 10, 2002, pp. 1673–1676.
Original Russian Text Copyright © 2002 by Radkevich, Egiazarov.

CATALYSIS

Activity of Palladium Catalysts Based on FIBAN K-1 Fibrous Sulfonic Cation Exchanger in Reaction of Hydrogen Oxidation

V. Z. Radkevich and Yu. G. Egiazarov

Institute of Physical Organic Chemistry, Belarussian National Academy of Sciences, Minsk, Belarus

Received January, 10, 2002

Abstract—For palladium catalysts based on FIBAN K-1 fibrous sulfonic cation exchanger (Li^+, Na^+, Rb^+, Cs^+, Mg^{2+}, Ca^{2+}, Ba^{2+} forms) the dispersity and depth distribution of palladium metal in the fiber and the activity of the catalyst in hydrogen oxidation were studied in relation to the conditions of the synthesis and activation.

We have shown previously that physicochemical and ion-exchange properties of fibrous sulfonic cation exchangers strongly depend on the exchanging cation [1, 2] and that the palladium catalysts based on FIBAN K-1 sulfonic cation exchanger (barium form) exhibit high activity in hydrogen oxidation [3, 4]. However, the effect of the exchanging cation on the reactivity of metal-containing catalysts applied to sulfo cationites has been studied insufficiently.

In this study, we prepared palladium catalysts applied to sulfonic cation exchangers with various exchanging cations and analyzed how the exchanging cation and activation conditions affect the degree of reduction, dispersity, and depth distribution of palladium metal in the fiber and the activity of the catalyst in hydrogen oxidation.

EXPERIMENTAL

FIBAN K-1 fibrous sulfonic cation exchanger (H form) was prepared by radiation-induced bulk grafting of styrene (98%) and divinylbenzene (2%) copolymer to propylene stapel, followed by sulfonation of the resulting matrix with concentrated sulfuric acid [5].

The completely substituted M^{z+} forms of K-1 (M^{z+} = Li^+, Na^+, Rb^+, Cs^+, Mg^{2+}, Ca^{2+}, Ba^{2+}) were prepared from the H form by passing 1 N solution of an appropriate metal chloride (taken in excess amount) through a column packed with the ion exchanger until the pH of the filtrate became equal to the pH of the starting solution. After the exchange was complete, the ion exchanger was washed with distilled water until the wash water became free of Cl^- and dried in air at room temperature for 12 h and then at 40°C for 4 h. The sample swelling was determined by centrifugation.

The Li^+, Na^+, Rb^+, Cs^+, Mg^{2+}, Ca^{2+}, Ba^{2+} cations were replaced with $[Pd(NH_3)_4]^{2+}$ ion by treating an ion exchanger sample with a calculated volume of a solution of palladium(II) tetrammine chloride (0.001 N), which provided uniform depth distribution of metal in the fiber. The weighed portions of the initial ion exchanger were varied depending on the equivalent weight at a constant volume of the contacting solution, so that, after exchange, the content of palladium(II) tetrammine cations amounted to 1.5% of the exchange capacity in all the samples.

The samples of the ion exchanger were preliminarily kept in distilled water for 30 min (up to complete swelling); then the exchange was performed by addition of a calculated volume of palladium(II) tetrammine chloride with vigorous stirring at room temperature for 30 min. In the process, the pH of the contacting solution was maintained within 8.0–8.5 {$[Pd(NH_3)_4]^{2+}$ is stable in aqueous ammonia at pH ≥ 8.0 [6]}.

The Pd(II) concentration before and after the exchange was monitored spectrophotometrically [7]. Catalysts were reduced with a 10% aqueous solution of hydrazine hydrate (40°C, 30 min), washed with water to neutral reaction, and dried in air at room temperature for 12 h and then at 40°C for 4 h.

The degree of palladium(II) reduction in the cationite samples was monitored by treatment with an excess amount of 1 N NaCl to complete transfer of exchangeable palladium ions into the solution, followed by determination of the palladium(II) content in the solution.

The depth distribution of palladium in the fiber was determined by X-ray fluorescence microanalysis on

1070-4272/02/7510-1639 $27.00 © 2002 MAIK "Nauka/Interperiodica"

Composition and physicochemical properties of catalysts synthesized (T_r = 40°C, 0.5 h)

Catalyst, wt %	Radius of exchanging cation, Å	Degree of ion exchanger swelling, wt %	Degree of Pd(II) reduction, %	A, $cm^3\ g_{red.Pd}^{-1}\ s^{-1}$
0.245 Pd/Li–K-1	0.68	130	92	3.5
0.230 Pd/Na–K-1	0.98	97	98	15.4
0.197 Pd/Rb–K-1	1.49	61	98	21.2
0.176 Pd/Cs–K-1	1.65	59	98	21.4
0.240 Pd/Mg–K-1	0.74	91	92	8.4
0.235 Pd/Ca–K-1	1.04	65	97	18.5
0.205 Pd/Ba–K-1	1.38	55	98	20.3

an MS-46F Cameca instrument. An X-ray phase analysis (XPA) was performed on a DRON-1 X-ray diffractometer with Cu_{K_α} radiation. For analysis, reference samples containing 1.0 wt% Pd were prepared.

The hydrogen oxidation in the presence of catalysts synthesized was performed in a flow-type glass reactor (inner diameter 20 mm) with automatically controlled electric heating. A 12-cm^3 portion of a compacted catalyst was charged into the reactor (the bed height and weight were 40 mm and 0.9–1.2 g, respectively).

The catalysts were tested as follows. The reaction mixture was fed into the reactor at room temperature, the temperature was raised to 100°C at a rate of 5 deg min^{-1} and kept at this level for 15–20 min, and after that the catalytic activity was determined.

The hydrogen conversion was calculated as the difference between its content in the gas flow before and after the reactor; the hydrogen content was monitored with a Gazokhrom-31 chromatograph.

The specific activity A ($cm^3\ g_{Pd}^{-1}\ s^{-1}$) of palladium was calculated by the formula

$$A = V_{H_2}\alpha/m_{Pd},$$

where V_{H_2} is the rate of hydrogen feed ($cm^3\ g_{cat}^{-1}\ s^{-1}$), α is hydrogen conversion (vol. fraction), and m_{Pd} is the content of reduced palladium in the catalyst ($g_{red.Pd}\ g_{cat}^{-1}$).

The table shows that the content of palladium(II) in catalysts based on ion exchangers with various cations amounts to 0.176–0.250 wt % [the palladium(II) content in one equivalent of the ion exchanger is the same for all samples].

The catalysts are characterized by high degree of Pd(II) reduction (92-98%), but noticeably differ in catalytic activity (see table). Since the degree of palladium reduction is similar in all the samples, this is probably due to different sizes of reduced palladium particles.

Since traditional methods are unsuitable for determining the palladium particle size in catalysts based on organic ion exchangers, the degree of palladium crystallinity was measured by XPA. These data allow estimation of the relative metal dispersity.

The X-ray diffraction pattern of a 1% Pd/Li–K-1 catalyst exhibits sharp narrow reflections with d = 2.234, 1.958, 1.367, and 1.166 Å, characteristic of the crystalline phase of palladium metal. For 1% Pd/Mg–K-1 and 1% Pd/Na–K-1, the reflections are broader, which indicates lower crystallinity of the metal. Cesium, rubidium, calcium, and barium-containing samples are X-ray-amorphous, i.e., palladium is characterized by higher dispersity in these catalysts.

Presumably, the different palladium dispersities are due to the fact that, in the bulk of ion exchangers with different cations, conditions for migration of finely dispersed palladium clusters formed by reduction of the catalyst with an aqueous solution of hydrazine hydrate are different. We believe that the cation size is the major factor. Large cations hinder migration of palladium clusters more strongly than small cations do. In the latter case, the clusters formed can migrate faster to the fiber periphery and aggregate into particles of varied size and degree of crystallinity, depending on the ion exchanger form.

This assumption is confirmed by X-ray fluorescence microanalysis. It follows from Fig. 1a that palladium(II) tetraammine cations in the 1.0% Pd/Ba–K-1 catalyst before reduction are uniformly distributed across the fiber. After reduction, the metal concentration in the fiber periphery increases slightly (Fig. 1b). After activation in a hydrogen flow (100°C, 30 min),

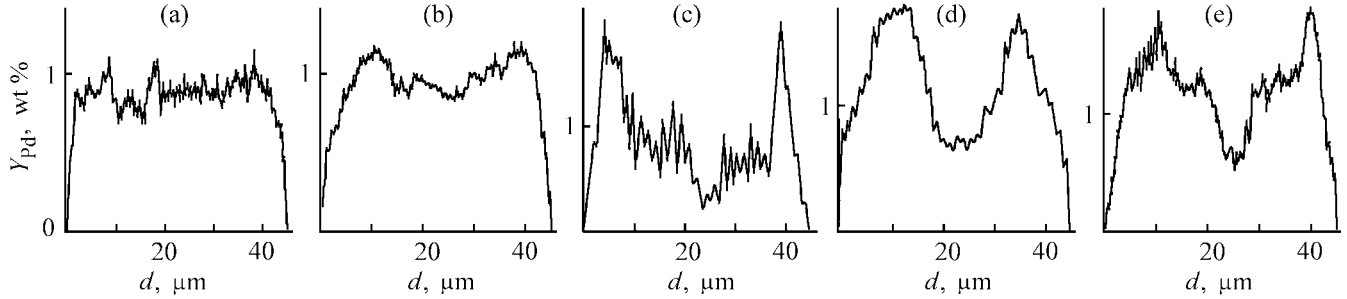

Fig. 1. Depth distribution of palladium in fibers of FIBAN K-1 sulfonic cation exchanger. (Y_{Pd}) Palladium content and (d) coordinate across the fiber. Catalyst based on the Ba form of the ion exchanger: (a) before reduction, (b) after reduction with hydrazine hydrate, and (c) after activation in a hydrogen flow; catalyst based on the Li form of the ion exchanger: (d) after reduction with hydrazine hydrate and (e) after activation in a hydrogen flow.

the main part of palladium concentrates in the ~10 μm surface layer of the fiber (Fig. 1c). Catalysts based on Ca, Rb, and Cs forms of the ion-exchanger behave similarly. Another pattern is observed with a 1.0% Pd/Li–K-1 catalyst. After its reduction with a hydrazine hydrate solution, the major part of palladium is concentrated in the 15–20-μm peripheral layer of the fiber (Fig. 1d). Activation in a hydrogen flow causes no significant changes (Fig. 1e). Similar palladium distribution patterns were obtained for catalysts based on Mg and Na forms of the ion exchanger.

Thus, the data obtained confirm our assumption that the migration of finely dispersed palladium clusters in ion exchangers with small exchanging cations is intense already in the stage of catalyst reduction with hydrazine hydrate solution.

We have shown previously [1] that catalysts containing finely dispersed palladium in the thin surface layer of the fiber exhibit the highest activity in hydrogen oxidation. It follows from the aforesaid that such palladium distribution is characteristic of catalysts based on ion exchangers with relatively large exchanging cations.

The dependence of the catalyst specific activity on the radius of the exchanging cation (Fig. 2) is complex. On the whole, the catalyst activity grows with increasing cation radius. However, a sharp break divides this dependence in two linear portions. This is obviously due to the fact that, along with cation radius, another factor (most likely, the degree of swelling) affects the intensity of migration and aggregation of finely dispersed palladium clusters.

The size of cations and their amount and charge affect the degree of ion exchanger swelling. It follows from the table that the degree of swelling decreases with increasing cation size at the same amount of alkali metal cations. The amount of alkaline-earth metal cations in the ion exchanger is half that of alkali metal ions, which must decrease the volume occupied by them and, hence, make higher the degree of swelling. At the same time, double-charged cations can bind sulfonic groups of different polystyrene chains of the ion exchanger, which must decrease the degree of swelling.

As seen from the table, samples of the ion exchanger in the Li, Mg, and Na forms are characterized by relatively high degree of swelling (130, 91, and 97%, respectively), while for the Ca, Ba, and Cs forms it is substantially lower (from 55 to 65%).

Thus, for the first group of catalysts, based on ion exchangers with small exchanging cations, the high degree of swelling favors more intense migration of palladium clusters, while, for the second group, the low swelling inhibits migration and aggregation, which results in a sharp bend in the activity-cation radius dependence.

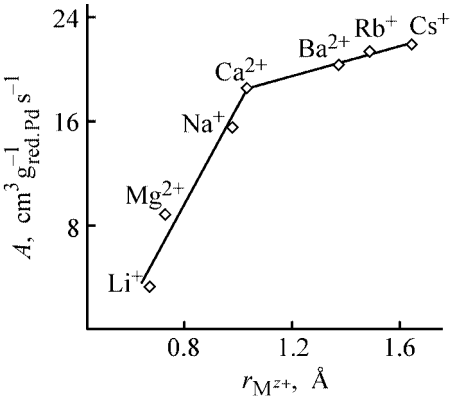

Fig. 2. Specific activity A of catalysts based on various cationic forms of the ion exchanger as a function of cation radius $r_{M^{z+}}$.

CONCLUSIONS

(1) In the stage of reduction with hydrazine hydrate of palladium catalysts based on Li, Na, and Mg forms of the sulfonic cation exchanger, finely dispersed palladium clusters migrate and aggregate into relatively large particles with low activity in hydrogen oxidation. In reduction of the catalysts based on the Ca, Ba, and Cs forms of the ion exchanger, palladium migration is virtually absent.

(2) Activation of reduced catalysts based on the Ca, Ba, and Cs forms of the ion exchanger at 100°C in a hydrogen flow is accompanied by migration of palladium clusters to the periphery of the fiber and formation of highly active particles of finely dispersed metal.

(3) The palladium dispersity and depth distribution in the fiber, which depend on the exchanging cation radius and the degree of the ion exchanger swelling, affect the catalyst activity in hydrogen oxidation.

REFERENCES

1. Radkevich, V.Z., Shunkevich, A.A., Kistanova, I.E., *et al.*, *Zh. Prikl. Khim.*, 2000, vol. 73, no. 11, pp. 1861–1864.
2. Radkevich, V.Z., Kistanova, I.E., Soldatov, V.S, and Egiazarov, Yu.G., *Zh. Prikl. Khim.*, 2001, vol. 74, no. 9, pp. 1407–1409.
3. Egiazarov, Yu.G., Soldatov, V.S, Radkevich, V.Z., *et al.*, Abstracts of Papers, *XVI Mendeleevskii s"ezd po obshchei i prikladnoi khimii* (XVI Mendeleev Congress on General and Applied Chemistry), St. Petersburg, May 25–29, 1998, Moscow, 1998, vol. 2, p. 292.
4. Yegiazarov, Yu.G., Radkevich, V.Z., Jurgen, J., *et al.*, *React. Funct. Polym.*, 2000, vol. 44, pp. 145–152.
5. Soldatov, V.S., Pokrovskaya, A.I., and Martsinkevich, R.V., *Zh. Prikl. Khim.*, 1984, vol. 57, no. 9, pp. 2030–2034.
6. Zamanova, L.P., Aleksandrova, I.L., and Khadzhiev, S.N., Abstracts of Papers, *II Vsesoyuznaya konferentsiya, "Primenenie tseolitov v katalize"* (II All-Union Conf. "Use of Zeolites in Catalysis"), Moscow, 1981, pp. 277–280.
7. Veshtort, V.Z., Shingel', I.A., Savchits, M.F., and Egiazarov, Yu.G., *Zavod. Lab.*, 1989, no. 10, pp. 6–8.

Russian Journal of Applied Chemistry, Vol. 75, No. 10, 2002, pp. 1643–1645. Translated from Zhurnal Prikladnoi Khimii, Vol. 75, No. 10, 2002, pp. 1677–1679.
Original Russian Text Copyright © 2002 by Galanov, Mutas, Kurina, Popov.

CATALYSIS

Tin-containing Systems as Catalysts for Deep Oxidation of Hydrocarbons

S. I. Galanov, I. N. Mutas, L. N. Kurina, and V. N. Popov

Tomsk State University, Tomsk, Russia

Received January 30, 2001

Abstract—MO_x–SnO_y (M = Zn, Cu, Co, Mn, Ce) systems were studied in the reaction of deep oxidation of propane and butane.

The development of new methods for full oxidation of hydrocarbons (reverse process, which enables accumulation of the heat of oxidation and catalytic burning of hydrocarbon fuels) imposes strict requirements upon catalysts [1, 2]. A catalyst must (a) induce combustion of a fuel–air mixture at as low a temperature as possible, (b) have activity sufficient for full oxidation to occur at the lowest initial temperature and highest velocity of the gas–air flow, (c) retain its activity at elevated temperature during long service life, and (d) show stable operation in stoichiometric hydrocarbon–air mixtures (containing no excess of oxygen). Catalysts based on platinum metals satisfy the above requirements, being, however, labor consuming in manufacture and expensive, which makes topical a search for active and thermally stable catalytic oxide systems containing no noble metals.

EXPERIMENTAL

The study is concerned with catalysts based on tin dioxide, with equimolar MO_x : SnO_2 ratio, where M = Zn, Cu, Co, Mn, or Ce, obtained by mixing tin(IV) hydroxide and appropriate metal nitrates, drying at 200°C, and calcination in air at 600°C for 3 h. Tin(IV) hydroxide was obtained from a 1 M $SnCl_4 \cdot 5H_2O$ solution by precipitation with 25% aqueous ammonia and subsequent washing to remove chloride ions.

The catalytic properties of the samples obtained were studied on flow-through and flow-through-circulatory catalytic installations with fixed catalyst bed at 100–850°C. The reaction products were analyzed chromatographically on a Tsvet-100 instrument with flame-ionization detector and LKhM-80 chromatograph with katharometer as detector.

The volumetric flow rate of the feed mixture was varied in the range 10 000–20 000 h^{-1}, the concentration of a hydrocarbon (propane or butane) was 1 vol % at stoichiometric content of oxygen and oxygen excess factor α = 1.1, with nitrogen the rest. The thermal stability of the samples was determined by comparing the activities of systems kept in a reaction mixture flow at 600 and 800°C for 100 min.

It is known that tin-containing systems promoted with metals of basic nature are thermally stable catalysts for oxidative dimerization of methane at $T \approx$ 800–850°C [3, 4]. It may be assumed that introduction of metals with variable oxidation state into the SnO_2 structure can give active catalytic systems for deep oxidation of hydrocarbons, which would retain their high catalytic activity at elevated temperature. Mn, Ce, Cu, Co, and Zn oxides, both in individual state and combined with other oxides, are known as active catalysts for full oxidation of hydrocarbons and CO [5, 6], which predetermined their being chosen for synthesis of tin-containing catalysts. As a criterion served, in addition to the high activity, preservation of the catalytic properties of the systems at high temperature (600–800°C) and in operation with mixtures characterized by low content of oxygen.

Pretreatment of tin-containing catalysts with a hydrocarbon–oxygen mixture at 600–800°C changes their activity: the temperatures of 50 and 100% conversion of propane increase (Fig. 1) and the rate of butane oxidation decreases (see table) for Co-, Zn-, and Cu-containing systems. Thermal treatment of Ce- and Mn-containing catalysts changes their specific surface area only slightly, but their activity in oxidation of hydrocarbons grows (see table and Fig. 1), i.e., the catalysts are thermally activated. A similar effect has been observed in full oxidation on manganese ox-

1070-4272/02/7510-1643 $27.00 © 2002 MAIK "Nauka/Interperiodica"

Effect of temperature treatment in the reaction mixture for 100 min on specific surface area S_{sp} and rate of butane oxidation, W (concentrations: butane, 1.0 vol %, oxygen, 6.6 vol %; reaction temperature 250°C for Zn–SnO_x, Co–SnO_x, and Mn–SnO_x, and 300°C for Cu–SnO_x and Ce–SnO_x)

M–SnO_x catalyst	Freshly prepared		After calcination at indicated temperature, °C			
			600		800	
	S_{sp}, $m^2\ g^{-1}$	$W \times 10^{-8}$, mol CO_2 $g^{-1}\ s^{-1}$	S_{sp}, $m^2\ g^{-1}$	$W \times 10^{-8}$, mol CO_2 $g^{-1}\ s^{-1}$	S_{sp}, $m^2\ g^{-1}$	$W \times 10^{-8}$, mol CO_2 $g^{-1}\ s^{-1}$
Zn	23.0	4.6	30.0	3.3	30.0	0.05
Cu	18.6	116.8	15.8	42.2	7.7	6.5
Co	25.1	587.3	16.9	65.5	8.3	60.1
Mn	6.8	41.3	8.0	76.8	8.0	85.1
Ce	24.0	21.2	24.0	355.0	16.0	283.5

ides supported by aluminum or zirconium oxide, because of the thermal dispersion of the forming oxides. An increase in the activity of Sr–SnO_x-containing systems as a result of decomposition of strontium orthostannates to give strontium metastannates and oxide has also been observed in oxidative dimerization of methane. Manganese orthostannates formed in preparing catalysts based on the tin–manganese system decompose at elevated temperatures in the reaction medium to give finely dispersed manganese oxides distributed over the surface, which may improve the catalytic activity of the systems [8]:

$$Mn_2SnO_4 \xrightarrow{T} MnSnO_3 + Mn$$

$$\xrightarrow{O_2} MnSnO_3 + Mn_2O_3 + Mn_3O_4.$$

Similar processes may occur in Co- and Cu-containing systems, but the copper and cobalt oxides formed undergo caking at temperatures above 600°C, which makes smaller the specific surface area of the catalysts and impairs their catalytic activity [5, 9].

Together with the maximum conversion of hydrocarbons, achieved at low temperature, factors characterizing the efficiency of catalysts of burning include release of the minimum amount of incomplete combustion products in the reaction. Deep oxidation of hydrocarbons, especially in the case of equimolar mixtures with oxygen, commonly occurs via destruction of an oxidized molecule to give compounds with smaller molecular weight, and their subsequent additional oxidation to CO_2 and H_2O [5].

As seen from Fig. 2, temperature treatment of a Mn-containing system affects its catalytic properties and the extent of butane oxidation. On a sample not treated with the reaction mixture, C_2-hydrocarbons (ethane and ethylene) and methane accumulate in the reaction products with increasing reaction temperature and butane conversion; and only when the 100% conversion of butane is reached, the concentration of C_2-hydrocarbons decreases to zero. Full oxidation of the forming methane only occurs at temperatures exceeding 650°C. Treatment of the catalyst with the reaction mixture at 600°C makes higher the selectiv-

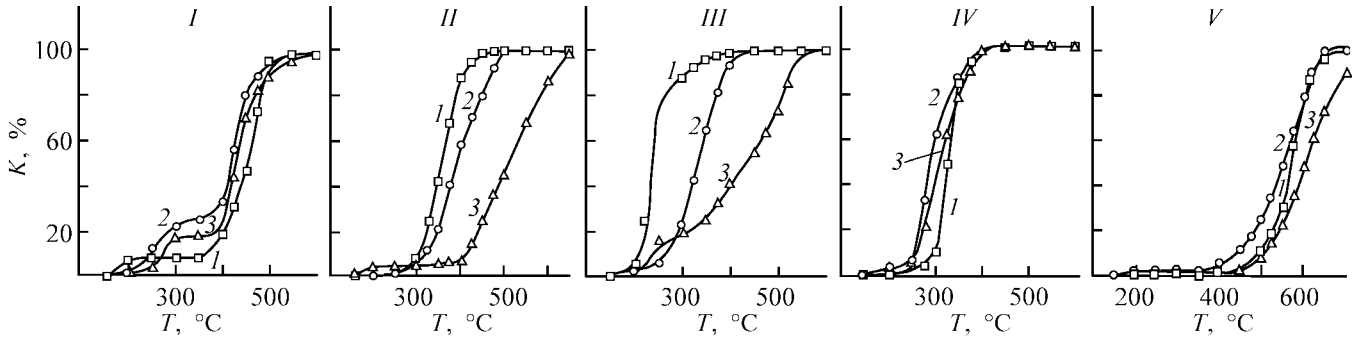

Fig. 1. Effect of calcination temperature T on the propane conversion K. Volumetric flow rate of the mixture 20 000 h^{-1}, $c_{C_3H_8}$ = 1.0 vol %. M–SiO_x catalyst: (*1*) calcined in air at 600°C; and that after treatment with propane–oxygen mixture for 100 min at (*2*) 600 and (*3*) 800°C. M: (*I*) Ce, (*II*) Cu, (*III*) Co, (*IV*) Mn, and (*V*) Zn.

Fig. 2. Effect of temperature T on (*1*) conversion K of butane and (*2–4*) concentration c of incomplete combustion products. Catalyst Mn–SnO_x, volumetric flow rate of the mixture 20 000 h^{-1}, $c_{C_4H_{10}}$ = 1.0 vol %. Catalyst: (*I*) calcined in air at 600°C and that treated with a butane–oxygen mixture for 100 min at (*II*) 600 and (*III*) 800°C. (*2*) Ethylene, (*3*) methane, and (*4*) ethane.

ity of deep oxidation of butane: the content of ethane in the mixture decreases to a minimum, and methane undergoes afterburning at lower temperature. However, the content of ethylene in the reaction products is rather high in the range 300–400°C. Raising the treatment temperature to 800°C (Fig. 2) improves the oxidizing properties of the system, the content of destruction products decreases, and full oxidation is observed at 550°C. Thus, high-temperature treatment of Mn-containing systems, together with making higher their activity (see table), improves the selectivity of full oxidation of hydrocarbons.

In most of catalytic processes for deep oxidation, the highest working temperature is 700–800°C [5, 9], in which context Mn- and Ce-containing systems may be promising catalysts for multipurpose catalytic devices, with the activity of these catalysts increasing in the course of operation.

CONCLUSION

Operation in a stoichiometric hydrocarbon–oxygen mixture at 600–800°C improves the catalytic activity of Mn- and Ce-containing systems.

REFERENCES

1. Gogin, L.L., Matros, Yu.Sh., and Ivanov, A.G., *Ekologiya i kataliz* (Ecology and Catalysis), Novosibirsk: Nauka, 1990.
2. Prasad Ravi, A. Kennedy Lawrence, and Ruckenstein Eli, *Catal. Rev. Sci. Eng.*, 1984, vol. 26, no. 1, pp. 1–86.
3. Galanov, S.I. and Kurina, L.N., *Zh. Prikl. Khim.*, 2000, vol. 73, no. 6, pp. 948–951.
4. Yang, W.-M., Yan, Q.-J., and Fu, X.-C., *React. Kinet. Catal. Lett.*, 1995, vol. 54, no. 1, pp. 21–27.
5. Alkhazov, T.G. and Margolis, L.Ya., *Glubokoe okislenie organicheskikh veshchestv* (Deep Oxidation of Organic Substances), Moscow: Khimiya, 1985.
6. Vodyankin, A.Yu., Galanov, S.I., and Kurina, L.N., *Zh. Prikl. Khim.*, 1995, vol. 68, no. 6, pp. 1021–1023.
7. Tsikoza, L.T., Ismagilov, Z.R., Shkrabina, R.A., *et al.*, *Sbornik trudov seminara pamyati V.V. Popovskogo "Zakonomernosti glubokogo okisleniya organicheskikh veshchestv na tverdykh katalizatorakh"* (Proc. Symp. in Memory of V.V. Popovskii "Fundamental Aspects of Deep Oxidation of Organic Substances on Solid Catalysts"), Novosibirsk, 2000, pp. 276–281.
8. Tsyrul'nikov, P.G., Shitova, N.B., Kudrya, E.N., and Savel'eva, G.G., *Sbornik trudov seminara pamyati V.V. Popovskogo "Zakonomernosti glubokogo okisleniya organicheskikh veshchestv na tverdykh katalizatorakh"* (Proc. Symp. in Memory of V.V. Popovskii "Fundamental Aspects of Deep Oxidation of Organic Substances on Solid Catalysts"), Novosibirsk, 2000, pp. 282–288.
9. *Problemy kinetiki i kataliza* (Problems of Kinetics and Catalysis), Krylov, O.V., Ed., 1982, vol. 18.

Russian Journal of Applied Chemistry, Vol. 75, No. 10, 2002, pp. 1646–1649. Translated from Zhurnal Prikladnoi Khimii, Vol. 75, No. 10, 2002, pp. 1680–1683.
Original Russian Text Copyright © 2002 by Erofeev, Shabalina, Koval', Minakova.

CATALYSIS

Conjugate Conversion of a Broad Fraction of Light Hydrocarbons and Methanol on Zeolite-Containing Catalysts

V. I. Erofeev, L. B. Shabalina, L. M. Koval', and T. S. Minakova

Management of Scientific and Technical Development, Tomsk Petrochemical Plant, Open Joint-Stock Company, Tomsk, Russia

Tomsk State University, Tomsk, Russia

Received February 19, 2002

Abstract—The effect of modification of ZSM-5 type high-silica zeolites on their acidity and selectivity in formation of lower olefins and arenes in conjugate conversion of propane-butane fraction and methanol was studied.

Low-molecular-weight alkanes convert into higher hydrocarbons at high temperatures (700–850°C) on high-selective catalysts with endothermic effect [1]. By contrast, methanol converts into hydrocarbons on zeolite-containing catalysts with considerable heat evolution, which severely complicates the process design [2]. The process temperature and heat release can be decreased by introduction of methanol into the reaction mixture and choice of a selective catalyst [3]. The zeolite acidity can be controlled by isomorphous substitution of Si atoms in the zeolite skeleton with atoms with effective charge other than 4. Variation of the substituting cation allows construction of acid-base centers with varied strength and selectivity [4].

In this context, the study and development of a process for conjugate conversion of methanol and a broad fraction of light hydrocarbons (BFLH) into olefins and arenes on zeolite-containing catalysts are of interest.

EXPERIMENTAL

High-silica zeolites (HSZ) with silicate ratio SiO_2/Al_2O_3 = 30 and elementoaluminosilicates (EAS) with $SiO_2/(Al_2O_3 + E_nO_m)$ = 30 were prepared hydrothermally from alkaline aluminosilicate gel with introduction of structure-forming organic cation by the method described in [5]. In the EAS synthesis, a part of Al(III) was substituted with B(III), P(V), and Fe(III) and samples B-Al-HSZ, P-Al-HSZ, and Fe-Al-HSZ, respectively, were prepared. The samples of HSZ and EAS were converted into the H form by treatment with a 25% aqueous solution of NH_4Cl for 2 h at 90°C, dried at 110°C, and calcined for 8 h at 550°C (Na_2O content less than 0.1%). An H-B-HSZ sample was prepared by impregnation of HSZ H form with a boric acid solution; the boron content amounted to 2 wt % in terms boron oxide. According to IR spectral and X-ray phase analysis (Mo anode, Ni filter), the HSZ and EAS synthesized were zeolites of ZSM-5 type with 90–95% crystallinity.

As raw material served commercial methanol (produced by Metanol Ltd.) and BFLH containing (wt %): ethane 1.7, propane 61.4, *n*-butane 32.4, and isobutane 4.5. They were converted in a flow-type catalytic device containing a quartz reactor with fixed catalyst bed (5 cm^3, 1–2 mm grains). The overall experimental cycle included three stages: catalyst activation, conjugate conversion of methanol and BFLH, and catalyst regeneration.

The zeolite activation and regeneration were performed in air flow under similar conditions. Preliminary experiments showed that, in the presence of H-HSZ, the optimal methanol : BFLH weight ratio at which the yield of lower olefins is the highest, amounts to 4 : 1. The subsequent experiments were carried out at this ratio. The conjugate conversion of methanol and BFLH was studied within the 500–650°C temperature range. At temperatures higher than 650°C, the yields of CO, CH_4, and coke increase sharply. The initial substances and products were analyzed on an LKhM-80 chromatograph equipped with a thermal conductivity detector.

The acidity of silicates was studied by temperature-programmed ammonia desorption at linear heating

1070-4272/02/7510-1646 $27.00 © 2002 MAIK "Nauka/Interperiodica"

Table 1. Composition of products of conjugate conversion of propane-butane fraction (PBF) and methanol on zeolite-containing catalysts (methanol space velocity is 2 h^{-1}; weight ratio methanol : PBF = 4 : 1)

Catalyst	*T*, °C	Yield (based on the feed passed), wt %							C_2–C_4 alkene content in the gas, rel. %
		total of H_2, CO, CH_4	alkanes C_2–C_4	alkenes C_2–C_4			gas formation	arenes	
				ethylene	propene	butenes			
H-HSZ	500	6.2	49.1	3.6	4.5	3.5	66.6	31.8	17.4
	550	7.4	40.7	8.1	9.5	5.7	71.1	26.7	32.8
	600	10.3	25.8	13.7	13.1	6.6	68.6	29.0	48.7
	650	20.7	19.9	14.8	14.2	4.0	70.7	25.8	46.7
B-Al-HSZ	500	3.6	47.8	6.1	7.5	6.2	71.0	26.3	27.9
	550	5.3	35.2	8.9	14.6	8.9	72.6	23.5	44.6
	600	8.7	23.2	17.6	17.9	7.8	74.8	22.1	57.9
	650	15.5	15.8	19.6	18.3	5.4	72.8	24.0	59.5
H-B-HSZ	500	3.4	46.4	5.3	7.5	7.6	70.2	25.5	29.1
	550	5.0	39.6	9.2	11.5	8.5	73.5	22.6	39.7
	600	7.5	32.8	14.1	15.3	7.1	76.5	20.6	47.7
	650	12.2	28.2	17.4	18.0	6.1	80.9	16.5	51.3
P-Al-HSZ	500	3.5	49.6	6.4	7.8	5.8	72.9	24.6	27.4
	550	5.4	39.3	12.2	12.9	6.4	76.1	21.5	41.4
	600	7.3	32.9	16.5	16.0	6.3	78.6	19.3	49.4
	650	11.3	25.7	18.4	17.5	4.6	76.7	21.5	52.8
Fe-Al-HSZ	500	1.5	45.5	4.7	7.2	9.7	68.5	19.5	31.5
	550	8.1	24.8	8.9	11.2	9.7	62.1	31.0	48.0
	600	13.0	34.8	7.9	7.0	2.3	63.3	34.5	27.2
	650	19.3	34.6	6.9	5.0	1.1	63.7	33.0	20.4

rate of 10 deg min^{-1} [6]. The yields of conversion products and the amount of the acid centers in the catalysts were determined chromatographically with a ±2.5 % error.

It follows from Table 1 that, as the temperature increases from 500 to 650°C, the ethylene and propylene yields grow on all the zeolites studied except iron aluminosilicate, for which the temperature dependences of the ethylene and propylene yields pass through a maximum. The maximal yield of C_2–C_4 alkenes is achieved at 550°C, when their content amounts to 48.0%. The temperature dependence of the yield of butenes has a maximum at 550°C for all of the catalysts studied (Table 1).

B-Al-HSZ show the maximal activity with respect to the yield of C_2–C_4 alkenes: their content reaches almost 60% at 650°C (Table 1). No acetylene and diene hydrocarbons are present in gaseous products of conjugate conversion of methanol and BFLH, which indicates that diene and triene hydrocarbons are hydrogenated into the corresponding olefins in the presence of HSZ and EAS. The low hydrogen yield (less than 0.5 wt %) confirms this suggestion.

As seen, catalysts modified with nonmetals B and P exhibit higher catalytic activity and selectivity in formation of C_2–C_4 alkenes as compared to the initial Pentasil. For instance, at 650°C the ethylene and propylene yield on B-Al-HSZ is higher by 4.8 and 4.1 wt %, respectively, than that on H-HSZ. With H-B-HSZ sample prepared by impregnation, the ethylene and propylene yields increase by 2.6 and 3.8 wt %, respectively, which is comparable with the activity of phosphorus-containing EAS.

With Fe-Al-HSZ, the alkene yield is lower; however, this catalyst exhibits enhanced aromatizing power. The yield of arenes on Fe-Al-HSZ is about 34.5% at 600°C. This is probably caused by formation of new catalytic centers containing iron cations [7]. They can participate in oligomerization of alkenes formed and in further conversion of the oligomers into aromatic hydrocarbons [8].

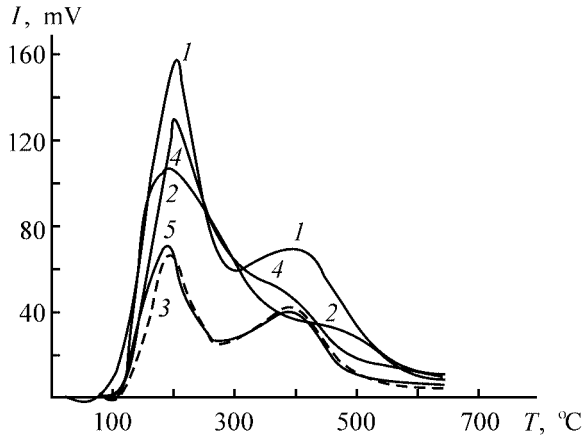

Temperature-programmed desorption spectra of ammonia adsorbed on various HSZ at 100°C: (*I*) intensity and (*T*) temperature. Catalyst: (*1*) H-HSZ, (*2*) Fe-Al-HSZ, (*3*) B-Al-HSZ, (*4*) H-B-HSZ, and (*5*) P-Al-HSZ.

Such a difference in the catalytic action of the Pentasils studied may be associated with their acid properties. A study of the acid properties of zeolites by temperature-programmed ammonia desorption showed that the temperature-programmed desorption curve obtained with the initial H-HSZ contains two peaks corresponding to two adsorption forms of ammonia: low-temperature form I, corresponding to weak Lewis acid centers with peak temperature T_{max} of 208°C, and high-temperature form II with T_{max} of 411°C, corresponding to strong Brønsted acid centers (see figure). The concentrations of acid centers, determined from the amount of desorbed ammonia, are 683 and 532 μmol g^{-1} for forms I and II, respectively (Table 2).

Nonmetals B(III) and P(V) introduced into the zeolite matrix in the synthesis stage (samples B-Al-HSZ and P-Al-HSZ, respectively) decrease T_{max} of both forms I and II, especially for the boron-containing sample. The concentration of acid centers also sharply decreases, especially that of weak acid centers (form I).

Table 2. Acidity of zeolite-containing catalysts

Catalyst	T_{max} of peak, °C		Amount of acid centers, μmol g^{-1}		
	form I	form II	form I	form II	total
H-HSZ	208	411	683	532	1215
B-Al-HSZ	196	396	259	271	530
H-B-HSZ	208	401	616	308	923
P-Al-HSZ	198	398	210	240	450
Fe-Al-HSZ	201	464	630	237	867

Impregnation of the initial H-HSZ with boric acid changes the shape of the ammonia temperature-programmed desorption spectrum. The H-B-HSZ zeolite gives a spectrum with a pronounced maximum at 208°C and a shoulder at 401°C. Impregnation of the initial H-HSZ with boric acid also lowers the total acidity of HSZ, but mainly due to a decrease in the amount of strong acid centers. Substitution of a part of Al(III) with Fe(III) shifts T_{max} of form I to lower temperature (201°C), and that of form II, to higher temperature (464°C). In this case, the amount of acid centers decreases, especially that of strong acid centers (by more than a factor of two).

Thus, B(III) and P(V) introduced into the zeolite in the stage of hydrothermal synthesis make the strength and concentration of the acid centers lower and the yield of low-molecular-weight alkenes higher. This may be due to a decrease in the acidity of strong Brønsted acid centers of zeolite (form II), on which lower alkenes mainly oligomerize and transform into aromatics. By contrast, iron-containing EAS has sufficiently strong acid centers (form II) able to catalyze formation of aromatic hydrocarbons. It should be noted that the higher selectivity of B-Al-HSZ, compared with HHSZ, with respect to formation of C_2–C_4 alkenes may be due to a change not only in acid properties, but also in the lattice parameters, since the radius of the B atom is substantially smaller than that of the Al atom [9]. It is established that Brønsted centers lying within the zeolite channels [8] play the decisive role in oligomerization and aromatization of olefins. Then, narrower channels make B-AlHSZ more selective with respect to alkene synthesis.

CONCLUSIONS

(1) A relationship was revealed between the acid and catalytic properties of catalysts based on ZSM-5 type zeolites in conjugate conversion of the propane-butane fraction and methanol.

(2) B(III) and P(V) introduced into ZSM-5 zeolites in the stage of the synthesis decrease the strength and concentration of the acid centers and increase the yield of lower olefins C_2–C_4. By contrast, Fe(III) introduced into the zeolite makes the strength of strong Brønsted acid centers higher, which increases the selectivity of formation of aromatic hydrocarbons in conjugate conversion of lower alkanes and methanol.

REFERENCES

1. Minachev, Kh.M. and Dergachev, A.A., *Usp. Khim.*, 1990, vol. 59, pp. 1522–1554.
2. Kapustin, M.A. and Nefedov, B.K., *Tekhnologicheskie protsessy polucheniya vysokooktanovogo benzina iz metanola* (Technology of Production of High-Octane Gasoline from Methanol), Moscow: TsNIITEneftekhim, 1982.
3. Novak, Z., Gunschel, G., Lantsch, I., and Anders, K., *Neftekhimiya*, 1987, vol. 27, no. 6, pp. 736–749.
4. Ione, K.G., Salakhutdinov, N.F., Testova, N.V., and Nikhtyanin, O.V., *Khim. Prom–st.*, 1996, no. 4, pp. 275–280.
5. RF Patent 1527154.
6. Vosmerikov, A.V. and Erofeev, V.I., *Zh. Fiz. Khim.*, 1995, vol. 69, no. 5, pp. 787–790.
7. Volodin, A.M., Sobolev, V.I., and Zhidomirov, G.M., *Kinet. Katal.*, 1998, vol. 39, no. 6, pp. 844–858.
8. Dergachev, A.A., *Khim. Tverd. Topl.*, 1998, no. 6, pp. 7–22.
9. Wendlandt, K.P., Unger, B., and Becker, K., *Appl. Catal.*, 1990, vol. 66, no. 1, pp. 111–122.

Russian Journal of Applied Chemistry, Vol. 75, No. 10, 2002, pp. 1650–1652. Translated from Zhurnal Prikladnoi Khimii, Vol. 75, No. 10, 2002, pp. 1684–1686.
Original Russian Text Copyright © 2002 by Zykova, Panov, Makashova, Baigel'dinov.

ENVIRONMENTAL PROBLEMS OF CHEMISTRY AND TECHNOLOGY

Fundamental Aspects of Heavy Metal Absorption by Activated-Sludge Microorganisms

I. V. Zykova, V. P. Panov, T. G. Makashova, and A. K. Baigel'dinov

St. Petersburg University of Technology and Design, St. Petersburg, Russia

Received May 29, 2002

Abstract—Patterns of heavy metal absorption by activated-sludge microorganisms were studied, and the possible mechanisms of the process were considered.

Biological treatment of process wastewater contaminated with heavy metals involves accumulation of these latter by activated sludge microorganisms. Understanding of the quantitative aspects of accumulation of heavy metal ions by activated sludge microorganisms is necessary for controlling the treatment process and efficiently extracting heavy metals from excess activated sludge intended for agricultural utilization [1].

A large proportion of the ions accumulated is bound by active segments of cell membranes, and only an insignificant proportion permeates inside the cell. Copper, selenium, aluminum, and iron ions are accumulated on the surface of *Micrococcus*, *Pseudomonas*, *Mycobacterium*, *E. Coli*, and other bacteria. About 90% of the silver ions absorbed are localized in the shell and cytoplasm membrane fractions of *Micrococcus luteus* and *Azotobacter* cultures, and 99% of lead ions, in the cell wall and membrane fraction. Mercury ions, unlike other ions, are bound by a small number of active segments on the cell wall, but these bonds are highly specific [2].

Ions can permeate through a membrane by the mechanisms of facilitated diffusion [Ca(II), Mg(II), Co(II), Mn(II), Cu(II), Ag(I)], primary active transport, or secondary active transport [3, 4].

It has been reported previously [5] that the energy of adenosine triphosphate (ATP) can be spent for transport of Mg(II), Mn(II), and other double-charged ions [5].

However, the available systematic data on the influence of physicochemical factors on the accumulation by microorganisms of metal ions and, in particular, that from process wastewater are insufficient, which motivated this study.

The objects of our investigation were *Pseudomonas* and *Micrococcus* genus microorganisms dominant in the biocenosis of activated sludge from biological treatment plants. We used suspensions of *Micrococcus* and *Pseudomonas* microorganisms containing 1.134×10^8 and 1.017×10^8 cells per liter, respectively. We studied model solutions containing, along with the suspension, Cu(II), Co(II), or Cr(III) ions in appropriate concentrations. The parameters varied were pH, temperature, process time, and initial concentration of metal ions in the model solution. After the experiment, a suspension of microorganisms was separated on a glass frit with pore size of 5–10 μm. The process was monitored by recording the pattern of variation of the metal ion concentration in the aqueous phase, which was determined on a Perkin-Elmer atomic-absorption spectrophotometer by standard procedures.

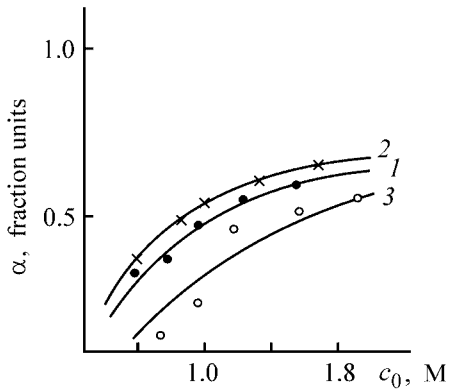

Fig. 1. Degree of absorption of the metal ions α, by *Pseudomonas* genus microorganisms vs. the initial concentration of metal ions in the aqueous phase c_0. Metal ion: (*1*) Co(II), (*2*) Cu(II), and (*3*) Cr(III); the same for Figs. 2 and 3.

1070-4272/02/7510-1650 $27.00 © 2002 MAIK "Nauka/Interperiodica"

The microorganisms are saturated with metal ions within 40 min in amounts depending on the initial concentration of the absorbed ions in the model solution. The higher the initial concentration of metal ions, the greater the amount absorbed by the microorganisms within the same period (Fig. 1).

Under the experimental conditions, the metal ions are absorbed by microorganisms to a certain residual concentration varying insignificantly with their initial concentration in water (Fig. 2). Similar results were obtained with *Micrococcus* microorganisms.

We calculated the averaged rate of the metal ion extraction by microorganisms and found that it is at a maximum in the first minutes of the process. The longer the phase contact time, the slower the extraction. The metal ion extraction tends to accelerate with the initial concentration increasing to 60 mg l^{-1}, whereupon raising the concentration of metal ions in the aqueous phase ceases to accelerate their removal by microorganisms.

The primary stage in the extraction of metal ions by microorganisms is their absorption by active segments of the cell surface. Taking this into account, we used our experimental results for plotting the isotherms of adsorption by *Pseudomonas* microorganisms as an example (Fig. 3). The experimental data on the metal ion adsorption by *Micrococcus* microorganisms are presented in Table 1.

The adsorption isotherms suggest that the amount of the metal ions adsorbed, a (mmol m^{-2}), can be described by the Freundlich equation for *Pseudomonas* and *Micrococcus* microorganisms.

$$a = Kc_p^{1/n}.$$

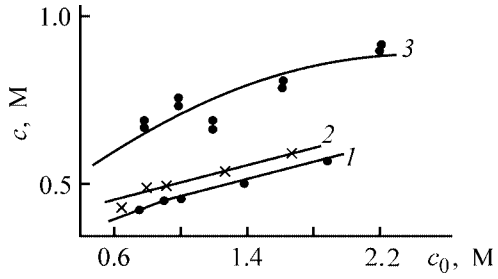

Fig. 2. Residual concentration of metal ions in the aqueous phase, c, vs. initial concentration c_0, in adsorption by *Pseudomonas* microorganisms.

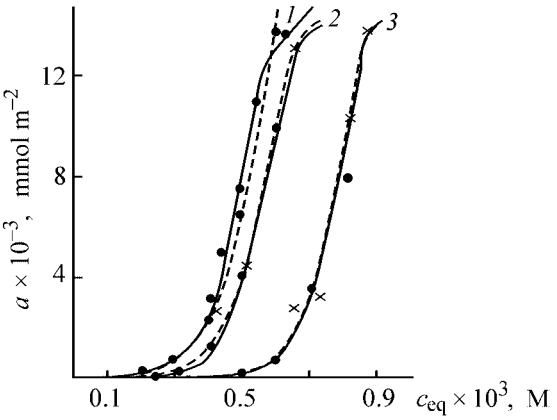

Fig. 3. Isotherms of metal ions adsorption by *Pseudomonas* genus microorganisms at pH 6 and T = 293 K. (a) Adsorption and (c_{eq}) equilibrium concentration.

Here, c_{eq} is the equilibrium (residual) concentration of the metal ion; n and K are constants; K determines in vivo the degree of affinity of the metal for microorganisms [6]. Table 2 lists the coefficients n and K at 293 K and pH 6.0.

Table 1. Metal ion adsorption by *Micrococcus* genus microorganisms at pH 6, T = 293 K

Co(II)		Cu(II)		Cr(III)	
$c_{eq} \times 10^3$, M	$a \times 10^{-3}$, mmol m^{-2}	$c_{eq} \times 10^3$, M	$a \times 10^{-3}$, mmol m^{-2}	$c_{eq} \times 10^3$, M	$a \times 10^{-3}$, mmol m^{-2}
0.400	2.41	0.403	1.96	0.677	0.80
0.450	3.46	0.456	2.86	0.750	1.83
0.428	5.12	0.463	4.17	0.715	3.80
0.502	7.41	0.554	6.11	0.831	6.13
0.373	11.47	0.598	8.46	0.808	9.67

Table 2. Coefficients in Freundlich equation*

Coefficient	Cu(II)	Co(II)	Cr(II)	Coefficient	Cu(II)	Co(II)	Cr(II)
K	1.5×10^5 / 5.62×10^4	1.4×10^5 / 1.45×10^5	3.7×10^4 / 5.01×10^4	n	0.188 / 0.245	0.227 / 0.231	0.147 / 0.141

* Numerator is the coefficient for *Pseudomonas*, and denominator, that for *Micrococcus* microorganisms.

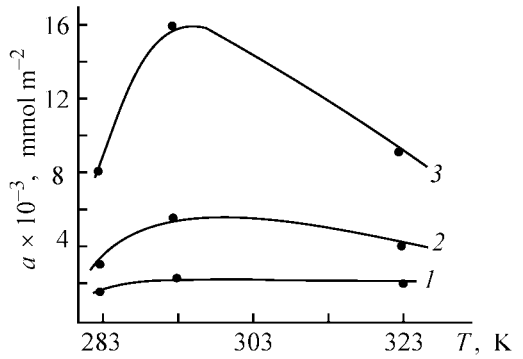

Fig. 4. Metal ion adsorption a by *Pseudomonas* genus microorganisms vs. temperature T. Equilibrium concentration of Cu(II) ions, mM: (*1*) 0.3, (*2*) 0.5, and (*3*) 0.7.

The theoretical adsorption isotherms plotted using the coefficients we determined agree well with the experimental data for both *Pseudomonas* and *Micrococcus* microorganisms in the metal ion concentration range studied, namely, up to 100 mg l^{-1} (Fig. 3, dashed lines). We failed to describe the process by the above-given equation at high *Pseudomonas* concentrations. This may be due to cell lysis with increasing metal ion concentration in the aqueous phase (>100 mg l^{-1}) or to metal ion sorption by *Pseudomonas* microorganisms by other (energy-dependent) mechanisms. *Micrococcus* microorganisms did not exhibit such a phenomenon, evidently, owing to the different structures of the cell shell of Gram-positive and -negative bacteria [7].

As shown by the constants calculated, the metal ions can be ranked, with respect to their affinity for the microorganism surface, in the following order: Cu(II) > Co(II) > Cr(III) for *Pseudomonas* and Co(II) > Cu(II) > Cr(III) for *Micrococcus* microorganisms.

Taking Cu(II) and *Pseudomonas* microorganisms as an example, we studied the accumulation as influenced by temperature varied within 283–323 K, and pH, within 3–9. Using the experimental data, we determined the constants for the Freundlich equation

T	283	293	323
K	3.7×10^4	1.5×10^5	7.3×10^4
n	0.262	0.188	0.184
pH	3	6	9
K	1.1×10^5	1.5×10^5	3.7×10^4
n	0.227	0.188	0.173

A decline in the metal ion adsorption by microorganisms with increasing pH (particularly prominent at pH 6–9) at high concentrations of metal ions in the aqueous phase is evidently due to formation of metal hydroxide species. At pH 3–7, complex metal ions such as $[Cu(H_2O)_3OH]^+$, $[Co(H_2O)_5OH]^+$, etc. are formed, and at pH above 7, formation of precipitates and colloids of metal hydroxides is possible.

The plot of the metal adsorption by microorganisms against temperature has a maximum (Fig. 4) owing to the change in the living conditions for *Pseudomonas* and *Micrococcus* mesophylls.

The results of the experimental study of the patterns of accumulation of Cu(II), Cr(III), and Co(II) ions by activated sludge microorganisms as influenced by various physicochemical parameters allows process control with the aim to achieve the maximal or minimal accumulation of heavy metals by activated sludge microorganisms.

CONCLUSIONS

(1) Microorganisms are saturated with metal ions within 40 min, and the amount of metal ions adsorbed depends on their initial concentration in the model solution.

(2) The primary stage in the extraction of metal ions by microorganisms consists in their adsorption by active segments of the cell surface. This makes it possible to describe the amounts of the adsorbed metal ions by the Freundlich equation for both *Pseudomonas* and *Micrococcus* microorganisms at metal ion concentrations in the aqueous phase within 1–100 mg l^{-1}.

(3) With Cu(II) ions and *Pseudomonas* microorganisms as an example, we studied the accumulation process as influenced by temperature within 283–323 K and pH within 3–9. The optimal conditions for accumulation are T = 293 K and pH 6–7.

REFERENCES

1. Zykova, I.V., Alekseeva, E.A., and Panov, V.P., *Zh. Prikl. Khim.*, 2001, vol. 74, no. 11, pp. 1901–1903.
2. Ilyaletdinov, A.A., *Mikrobiologicheskoe prevrashchenie metallov* [Microbiological Transformation of Metals], Alma-Ata: Nauka, 1975.
3. Kotyk, A. and Janaček, K, *Membrane Transport: An Interdisciplinary Approach*, New York: Plenum, 1977.
4. Rubin, A.B., *Biofiizika* {Biophysics), vol. 2: *Biofizika kletochnykh protsessov* (Biophysics of Cell Processes), Moscow: Universitet, 2000.
5. Antonov, V.F., *Lipidy i ionnaya pronitsaemost' membran* (Lipids and Ion Permeability of Membranes), Moscow: Nauka, 1982.
6. Hashimoto, S. and Fujima, M., *Hakko Kogaku Zisshi*, 1969, vol. 16, no. 3, pp. 263–269.
7. Gromov, B.V., *Stroenie bakterii* (Structure of Bacteria), Leningrad: Lening. Gos. Univ., 1985.

Russian Journal of Applied Chemistry, Vol. 75, No. 10, 2002, pp. 1653–1659. Translated from Zhurnal Prikladnoi Khimii, Vol. 75, No. 10, 2002, pp. 1687–1693.
Original Russian Text Copyright © 2002 by Yablonskii, Ryabchuk.

PROCESSES AND EQUIPMENT OF CHEMICAL INDUSTRY

Modeling of the Concentration Field of Solid Phase in a Hydrocyclone in Suspension Separation by Pressure Flotation

V. O. Yablonskii and G. V. Ryabchuk

Volgograd State Technical University, Volgograd, Russia

Received October 12, 2001; in final form, February 2002

Abstract—A mathematical model of suspension separation by pressure flotation in a hydrocyclone was developed. The continuity equation was solved numerically for a flux of particles of the solid phase in a flow of a non-Newtonian suspension in a hydrocyclone. The concentration field of solid particles was determined. The effect of the defining similarity criteria on the distribution of concentrations was studied.

Hydrocyclones are used to separate heterogeneous systems in chemical and other industries. Carrying out separation processes in a centrifugal field allows their significant intensification. At present, development of mathematical models of separation processes in a centrifugal field is necessary in order to substantiate theoretically their optimal modes. Modeling of the concentration field in a hydrocyclone for obtaining theoretically substantiated and experimentally verified results should be carried out with the flow hydrodynamics calculated using complete Navier-Stokes equations or equations of rheodynamics of a non-Newtonian fluid.

In [1], the flow structure and separation processes in a hydrocyclone were studied numerically on the basis of Navier–Stokes equations. The transfer of the dispersed-phase momentum was described in terms of the theory of multiple-velocity continuum. It was noted that separation processes in a hydrocyclone with a freely formed surface of the liquid phase had not been described by that time.

At present, pressure flotation is widely used for separation of heterogeneous systems. This process can be carried out most intensively in a centrifugal field. Carrying out the pressure flotation in a centrifugal field in a film flow mode raises the efficiency of separation of finely dispersed suspensions. This was substantiated in [2], where the dependence of the number of possible collisions between particles and bubbles on the centrifugal acceleration was demonstrated and a conclusion was made that the centrifugal field is a factor making greater the number of collisions between particles and bubbles, with the result that the rate of the flotation process becomes higher.

In [3, 4], a procedure for calculating separation characteristics of a hydrocyclone-flotator by solving the equation for the radial motion of a particle–bubble system was proposed. However, these studies disregarded the flow of a suspension being separated in a hydrocyclone with freely formed surface, with the calculation of separation characteristics being only approximate. The flow hydrodynamics of a film of a non-Newtonian suspension in a cylindrical direct-flow hydrocyclone was modeled with the use of complete rheodynamics equations in [5]. The rheological properties of the suspension were described in terms of Ostwald de Ville's power-law rheological equation. Dependences of the fluid film thickness on the axial component, and the velocity and pressure fields in the apparatus at different values of the defining similarity criteria and rheological properties of the suspension were found.

In [6, 7], a conclusion was made that the rheological equation of state of a non-Newtonian fluid, commonly written in the form of Ostwald de Ville's exponential equation, is applicable to multiphase heterogeneous systems. Consequently, the field of solid particle concentrations can be modeled and the basic characteristics of separation by pressure flotation in a hydrocyclone can be calculated using the results obtained in [5] in modeling the flow hydrodynamics of a non-Newtonian suspension in a hydrocyclone with the use of a power rheological law.

To find the concentration distribution of solid particles in a hydrocyclone, analytical expressions were

1070-4272/02/7510-1653 $27.00 © 2002 MAIK "Nauka/Interperiodica"

obtained for the axial and circumferential velocity components (the radial velocity component was neglected, its calculated values being two orders of magnitude smaller than the axial velocity component), together with an expression describing how the suspension film thickness depends on the axial component at certain values of similarity criteria and rheological properties of the suspension. For this purpose, the results of calculations were approximated with analytical expressions in the whole range of variation of the rheological properties of the suspension and of the similarity criteria characterizing the flow.

The approximating dependences for the axial and circumferential flow velocity components were found in the following form:

$$\left.\begin{aligned} H(\bar{r},\bar{z}) &= H_{\max}(\bar{z})\left[1-\left(1-\frac{1-\bar{r}}{\bar{\delta}}\right)^{m}\right] \\ \varphi(\bar{r},\bar{z}) &= \varphi_{\max}(\bar{z})\left[1-\left(1-\frac{1-\bar{r}}{\bar{\delta}}\right)^{l}\right] \end{aligned}\right\} \quad (1)$$

where $H(\bar{r}, \bar{z}) = V_z/U_0$, $\varphi(\bar{r}, \bar{z}) = V_\varphi/U_0$ are the dimensionless axial and circumferential flow velocity components; V_z and V_φ are the axial and circumferential flow velocity components ($m\ s^{-1}$); U_0 is the mean flow velocity in the inlet pipe of the hydrocyclone ($m\ s^{-1}$); $H_{\max}(\bar{z})$ and $\varphi_{\max}(\bar{z})$ are the maximum dimensionless axial and circumferential flow velocities; $\bar{z} = z/R$ and $\bar{r} = r/R$ are the axial and circumferential coordinates; $\bar{\delta} = \delta/R$ is the dimensionless thickness of a suspension film; δ is the film thickness (m); R is the hydrocyclone casing radius; m and l are exponents found by processing the radial profiles of the axial and circumferential flow velocity components by the method of selected points with the subsequent piecewise-linear approximation of the dependences of m and l on the axial coordinate $\bar{z}$.

The approximating dependences for determining $H_{\max}(\bar{z})$ and $\varphi_{\max}(\bar{z})$ have the form of fourth-order polynomials. $H_{\max}(\bar{z})$ and $\varphi_{\max}(\bar{z})$ were calculated using the least-squares method.

To approximate the dimensionless thickness $\bar{\delta}$ of the suspension film as a function of the axial component $\bar{z}$ by integrating the dependence approximating the distribution of the axial flow velocity component along the radial coordinate, a formula was obtained allowing calculation of $\bar{\delta}$ at known $H_{\max}(\bar{z})$ and m for a given cross-section on the basis of the condition that the fluid flow rate is invariable in the axial direction:

$$\bar{\delta} = \frac{m(m+2) - \sqrt{[m(m+2)]^2 - [(m+2)(m+1)-2](m+2)(m+1)\dfrac{\bar{Q}}{H_{\max}(\bar{z})}}}{(m+2)(m+1)-2}, \quad (2)$$

$$\bar{Q} = Q/(\pi R^2 U_0) = (bh)/(\pi R^2). \quad (3)$$

Here $\bar{Q}$ is the dimensionless flow rate, Q is the flow rate of the suspension being separated ($m^3\ s^{-1}$), h is the height of the inlet pipe of the hydrocyclone (m), b is the radial dimension of the inlet pipe (m), and g is the acceleration of gravity ($m\ s^{-2}$).

The axial and circumferential velocity components found by approximating all the quantities appearing in (1) were in good agreement with the results of numerical calculations at arbitrary axial and radial coordinates in that part of the flow for which the calculations were done. The maximum discrepancy of the calculated and approximating values did not exceed 3% for the axial and 5% for the circumferential flow velocity components.

The obtained approximating dependences of the suspension film thickness on the axial coordinate, and of the flow velocity components on the axial and radial coordinates, form a basis for modeling the concentration field in a hydrocyclone and for calculating the principal separation parameters.

The pressure flotation in a centrifugal field can be used to manufacture protein-vitamin concentrates (paprin, gaprin, meprin), obtain suspensions of biomass, syrup, and SiC_3, and purify wastewater to remove oil, grease, and other substances.

The pressure flotation occurs as follows: a preliminarily aerated suspension is fed under elevated pressure (up to 0.8 MPa) into a hydrocyclone tangentially, along the generatrix, through the inlet pipe in the upper part of the hydrocyclone. Inside the hydrocyclone, the suspension flows down circling along its walls, being characterized by the circumferential V_φ, axial V_H, and radial V_r velocity components. When the pressure is lowered to its atmospheric value, the suspension becomes supersaturated with dissolved air and "boils-up." Solid particles move under the action of the centrifugal force to the wall of the hydrocyclone casing, and air bubbles, in the opposite

direction, toward the film surface. Collisions of solid particles with air bubbles give floated complexes carrying solid particles to the film surface into the froth, removed through the upper pipe of the hydrocyclone. The amount of floated complexes formed and their transport toward the film surface are determined by hydrodynamic parameters of the preliminarily swirled suspension film flowing down the vertical cylindrical wall of the hydrocyclone casing under the action of the gravity force and pressure created by the centrifugal force, which, in the end, determines the efficiency of pressure flotation. Clarified suspension is removed from the apparatus through the bottom discharge. The height of the working zone of the hydrocyclone, for which the velocity and pressure fields were calculated in [5], is 30 apparatus casing diameters. According to [5], the swirling motion of the suspension terminates at this distance in all hydrocyclone operation modes and the thickness of the flowing-down film becomes invariable.

The problem was formulated mathematically under the following assumptions [8]: (1) monodispersed air bubbles of equal size, distributed uniformly throughout the film volume, are evolved when aerated suspension is fed into the hydrocyclone; (2) the bubbles are formed along a negligibly small part of the hydrocyclone height during an equally short period of time; (3) there is no coalescence of air bubbles; (4) particles of the substance being extracted are distributed uniformly within the inlet pipe of the hydrocyclone and their concentration at the hydrocyclone inlet is c_{h0}.

The concentration field in separation of finely dispersed suspensions by pressure flotation is modeled mathematically using continuity equations for the fluxes of solid particles and air bubbles. These equations can be written as follows

$$\left.\begin{aligned} V_{rh}\frac{\partial c_h}{\partial r} + V_{zh}\frac{\partial c_h}{\partial z} &= -J_h \\ V_{rg}\frac{\partial c_g}{\partial r} + V_{zg}\frac{\partial c_g}{\partial z} &= -J_g \end{aligned}\right\} \qquad (4)$$

where V_{rh} and V_{zh} are the radial and axial components of the particle motion velocity (m s^{-1}); V_{rg} and V_{zg} are the radial and axial components of the bubble motion velocity (m s^{-1}) c_h and c_g are the concentrations of particles and bubbles in the suspension (m^3 m^{-3}); $J_h = K_h c_g c_h$, $J_g = K_g c_g c_h$ are the intensities of the bulk discharge of particles and bubbles (s^{-1}); K_h and K_g are the kinetic constants of the pressure flotation process (s^{-1}), determined by the number of collisions between solid particles and air bubbles (depending on the solid particle and air bubble diameters and physical properties of solid particles, air bubbles, and dispersion medium) and found, according to [9], under the condition that monoflotation process occurs in the apparatus, i.e., one particle is extracted by one bubble; r and z are the radial and axial coordinates (m); the indices mean the following: h, solid particles; l, dispersion medium; g, gas bubbles.

The system of partial differential equations (4) was solved for two practically important cases.

(1) The concentration of air bubbles much exceeds that of solid particles: $c_g > c_h$. In this case, the second equation in the system (4) can be excluded by taking c_g = const, and the system is reduced to a single equation. In view of the fact that pressure flotation is the most efficient at insignificant difference in density between solid particles and dispersion medium, it can be assumed with sufficient exactness that solid particles move in the axial direction without inertia, i.e., the axial velocities of solid particles and the dispersion medium coincide, $V_{zh} = V_{zl}$. Under this assumption the equation has the form

$$V_{rh}\frac{\partial c_h}{\partial r} + V_{zl}\frac{\partial c_h}{\partial z} = -K_h c_g c_h, \qquad (5)$$

where V_{zl} is the axial component of the flow velocity of the dispersion medium.

(2) The concentrations of gas bubbles and solid particles are equal: $c_g = c_h$. In this case, the first and second equations of the system (4) are equivalent and the system is also reduced to a single equation with account of the fact that $V_{zh} = V_{zl}$:

$$V_{rh}\frac{\partial c_h}{\partial r} + V_{zl}\frac{\partial c_h}{\partial z} = -K_h c_h^2. \qquad (6)$$

The boundary condition for the differential equations (5) and (6) has the form

$$z = 0, \quad R - b \le r \le R, \quad c_h = c_{h0}. \qquad (7)$$

The velocity of radial sedimentation of a particle was found by the formula [10]

$$V_{rh} = \left[\frac{2}{9}\left(\frac{d_h}{2}\right)^{n+1}(\rho_h - \rho_l)V_{\varphi l}^2\frac{\psi(n)}{rk}\right]^{1/n}, \qquad (8)$$

where $V_{\varphi l}$ is the circumferential component of the flow velocity of the dispersion medium; n is the nonlinearity factor of the flow curve for a non-Newtonian dispersion medium described by Ostwald de Ville's law; k is the thickness index (Pa s^n); d_h is the solid particle diameter (m); ρ_h is the density of solid par-

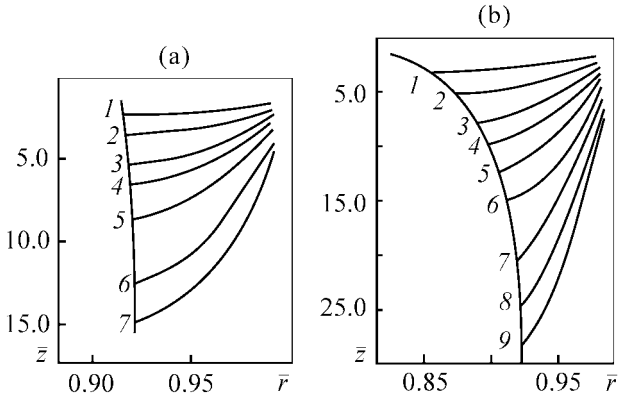

Fig. 1. Distribution of solid particle concentration in suspension film at $Re_n = 4000$, $\bar{Q} = 3.98 \times 10^{-2}$. $(\bar{z}, \bar{r})$ Dimensionless axial and radial coordinates; the same for Figs. 2–5. Fr: (a) 32.6 and (b) 293.6. Isoconcentration lines at $\bar{c}$: (*1*) 0.8, (*2*) 0.6, (*3*) 0.4, (*4*) 0.3, (*5*) 0.2, (*6*) 0.1, (*7*) 0.05, (*8*) 0.02, and (*9*) 0.01.

ticles, and ρ_l, that of the dispersion medium (kg m^{-3}); $\psi(n)$ is the correction factor found from the data presented in [11].

Bringing the differential equations to the dimensionless form with account of formula (8) yields:

$$\frac{\partial \bar{c}_h}{\partial \bar{r}} + \frac{H(\bar{r}, \bar{z})}{\mathrm{Re}_n^d [\varphi(\bar{r}, \bar{z})]^{2/n} \bar{r}^{-1/n}} \frac{\partial \bar{c}_h}{\partial z} = -\frac{1}{F_g [\varphi(\bar{r}, \bar{z})]^{2/n} \bar{r}^{-1/n}} \bar{c}_h, \tag{9}$$

for the $\bar{c}_g > \bar{c}_h$ case, with $\bar{c}_g$ assumed to be constant, and

$$\frac{\partial \bar{c}_h}{\partial \bar{r}} + \frac{H(\bar{r}, \bar{z})}{\mathrm{Re}_n^d [\varphi(\bar{r}, \bar{z})]^{2/n} \bar{r}^{-1/n}} \frac{\partial \bar{c}_h}{\partial z} = -\frac{1}{F_h [\varphi(\bar{r}, \bar{z})]^{2/n} \bar{r}^{-1/n}} \bar{c}_h^2, \tag{10}$$

for $\bar{c}_g = \bar{c}_h$. Here $\bar{c}_h = c_h/c_{h0}$ is the dimensionless concentration of solid particles in a suspension flow; $\mathrm{Re}_n^{sed} = \left[\frac{2}{9}\left(\frac{d_h}{2}\right)^{n+1}(\rho_h - \rho_l)\frac{\psi(n)}{Rk}\right]^{1/n} U_0^{\frac{2-n}{n}}$ is the Reynolds number characterizing the sedimentation of a solid particle in a centrifugal field in a non-Newtonian dispersion medium; $F_g = \frac{\mathrm{Re}_n^{sed} U_0}{A_g R}$, $F_h = \frac{\mathrm{Re}_n^{sed} U_0}{A_h R}$ are dimensionless complexes; $A_g = k_h c_g$, $A_h = k_h c_{h0}$ are the modified kinetic constants of pressure flotation (s^{-1}).

The first-order partial differential equations (9) and (10) were solved using the method of characteristics, which reduces a partial differential equation to an equivalent system of ordinary differential equations [12]. This yielded for the case $\bar{c}_g > \bar{c}_h$, under assumption that $\bar{c}_g$ = const, the following

$$\left.\begin{aligned} \frac{\partial \bar{r}}{\mathrm{Re}_n^{sed} [\varphi(\bar{r}, \bar{z})]^{2/n} \bar{r}^{-1/n}} &= \frac{\partial \bar{z}}{H} \\ d\bar{r} &= -F_g [\varphi(\bar{r}, \bar{z})]^{2/n} \bar{r}^{-1/n} \frac{\partial \bar{c}_h}{\bar{c}_h} \end{aligned}\right\} \tag{11}$$

For the case $\bar{c}_g = \bar{c}_h$

$$\left.\begin{aligned} \frac{\partial \bar{r}}{\mathrm{Re}_n^{sed} [\varphi(\bar{r}, \bar{z})]^{2/n} \bar{r}^{-1/n}} &= \frac{\partial \bar{z}}{H} \\ d\bar{r} &= -F_h [\varphi(\bar{r}, \bar{z})]^{2/n} \bar{r}^{-1/n} \frac{\partial \bar{c}_h}{\bar{c}_h^2} \end{aligned}\right\} \tag{12}$$

The boundary condition (7) for the systems of ordinary differential equations (11) and (12) has the form

$$\bar{z} = 0, \quad 1 - \bar{b} \le \bar{r} \le 1, \quad \bar{c}_{h0} = 1, \tag{13}$$

where $\bar{c}_{h0} = 1$ is the dimensionless concentration of solid particles in the inlet pipe of the hydrocyclone; $\bar{b} = b/R$ is the dimensionless radial dimension of the inlet pipe.

The first equations in the systems (11) and (12) define the trajectory of particle motion in the suspension, which depends on the place of particle entry into the apparatus, i.e., specify the direction of the characteristic, and the second equations determine the values of the function, i.e., the concentrations of solid particles.

The systems of differential equations (11) and (12) were solved by the Runge–Kutta method.

Based on modeling of the velocity and pressure fields in a flow of a non-Newtonian suspension in a hydrocyclone [5] and subsequent approximation of the results obtained, the field of solid particle concentrations in suspension purification in a hydrocyclone by pressure flotation was modeled by solving the systems (11) and (12) of differential equations numerically under the boundary conditions (13) at widely varied values of the defining criteria. The suspension flow in the hydrocyclone was characterized by the centrifugal Froude criterion (separation factor) [5], an analogue of the Reynolds criterion for power fluids, Re_n, and also by the dimensionless flow rate $\bar{Q}$.

The results of mathematical modeling of the concentration field in a hydrocyclone, presented here, refer to the case of $c_g > c_h$ under assumption that c_g = const.

Figures 1a and 1b present the distribution of solid particle concentrations in suspension separation by pressure flotation in a swirling film flowing down

along the hydrocyclone wall at Fr criteria of, respectively, 32.6 and 293.6.

Analysis of Fig. 1a shows that the concentration of solid particles in the suspension being separated decreases along the apparatus axis with increasing distance from the inlet pipe, with the steepest decrease observed near the apparatus wall, which is accounted for by the most complete extraction of particles by air bubbles moving in the opposite direction in the field of centrifugal forces. Along the free surface of the film, the concentration of solid particles also decreases with increasing distance from the inlet pipe, but does so less steeply. The concentration of solid particles also decreases in the radial direction, from the free surface toward the apparatus wall, which is accounted for by capture of particles by air bubbles, to form floated complexes, and their transportation to the free surface. This pattern is preserved at any value of the defining similarity criteria.

When the Fr criterion becomes larger, which is accompanied by an increase in the suspension film thickness [5], the concentration of solid particles in the suspension film grows. This is due to an increase in the number of solid particles per unit length of the film in the axial direction as a result of a rise in the hydrocyclone throughput at higher mean velocity of the suspension, U_0, in the inlet pipe.

The increase in the Fr criterion causes a simultaneous rise in the velocity of radial sedimentation of solid particles and the corresponding increase in the number of collisions of particles with air bubbles and in the number of floated complexes formed, which results in the corresponding increase in the number of solid particles extracted from the suspension [9]. The interaction of these contrary factors predetermines the insignificant change in the concentration of solid particles at the lower boundary of the region for which the calculations are performed and in the extent of recovery upon a change in the separation factor. With the separation factor in the hydrocyclone increased by raising the rate of suspension feed into the apparatus, the flow rate of the suspension being separated and the hydrocyclone throughput can both be made higher. With the separation factor raised by diminishing the radius of the hydrocyclone casing, the apparatus can be made more compact.

Figures 2a and 2b present the distribution of solid particle concentration in the suspension film at Re_n criteria of, respectively, 2260 and 18070. With increasing Re_n, the suspension film thickness [5] decreases because of a decrease in its effective viscosity characterized by the thickness index k. The axial component of the flow velocity grows, and the concentration of solid particles in the suspension film at the lower boundary of the flow region being calculated becomes higher, which is due to the decreasing residence time of solid particles in the separation zone. Consequently, higher extents of recovery can be achieved in separation of suspensions with higher effective viscosity.

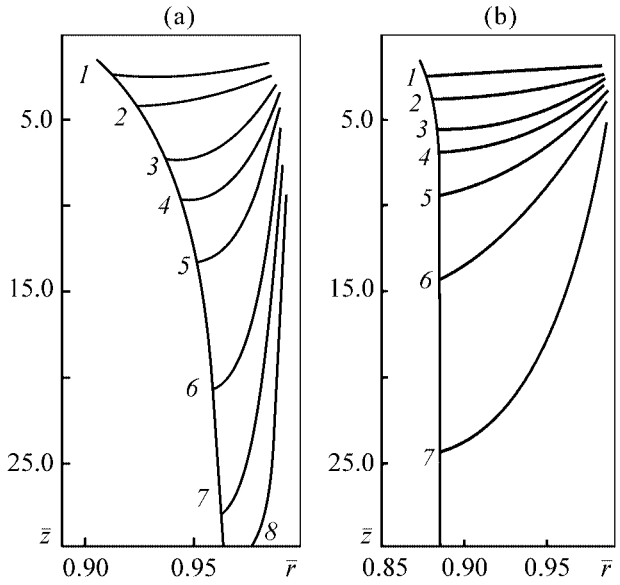

Fig. 2. Distribution of solid particles in suspension film at Fr = 73.4, $\bar{Q} = 3.98 \times 10^{-2}$. Re_n: (a) 2260 and (b) 18070. Isoconcentration lines at $\bar{c}$: (*1*) 0.8, (*2*) 0.6, (*3*) 0.4, (*4*) 0.3, (*5*) 0.2, (*6*) 0.1, (*7*) 0.05, and (*8*) 0.02.

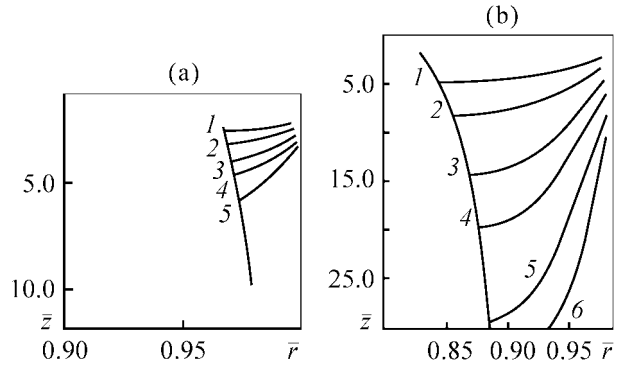

Fig. 3. Distribution of solid particles in suspension film at Fr = 73.4, Re_n = 4000. $\bar{Q} \times 10^3$: (a) = 3.09 and (b) 99.0. Isoconcentration lines at $\bar{c}$: (a) (*1*) 0.7, (*2*) 0.3, (*3*) 0.1, (*4*) 0.05, and (*5*) 0.01; (b) (*1*) 0.7, (*2*) 0.5, (*3*) 0.3, (*4*) 0.2, (*5*) 0.1, and (*6*) 0.05.

Figures 3a and 3b present the distributions of solid particles in a suspension film at dimensionless flow rates $\bar{Q}$ of, respectively, 3.09×10^{-3} and 99.0×10^{-3}. When $\bar{Q}$ grows, with a simultaneous increase in

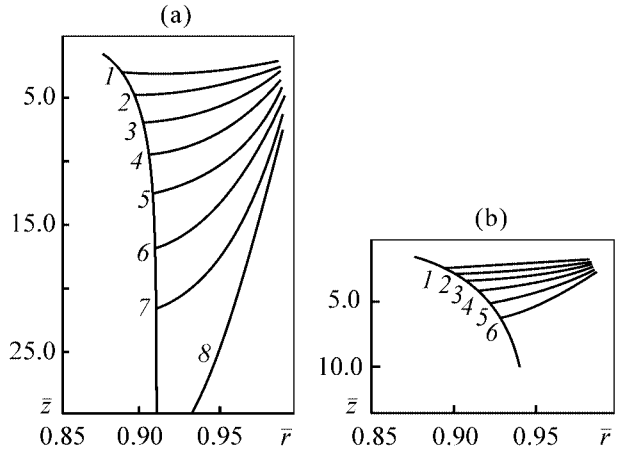

Fig. 4. Distribution of solid particles in suspension film at $F_g = 4.12 \times 10^{-1}$, Fr = 73.4, $Re_n = 4000$, $\bar{Q} = 3.98 \times 10^{-2}$ Re_n^{sett}: (a) 0.763×10^{-3} and (b) 0.970×10^{-2}. Isoconcentration lines at $\bar{c}$: (a) (*1*) 0.9, (*2*) 0.8, (*3*) 0.7, (*4*) 0.6, (*5*) 0.5, (*6*) 0.4, (*7*) 0.3, and (*8*) 0.2; (b) (*1*) 0.5, (*2*) 0.3, (*3*) 0.2, (4) 0.1, (*5*) 0.05, and (*6*) 0.02.

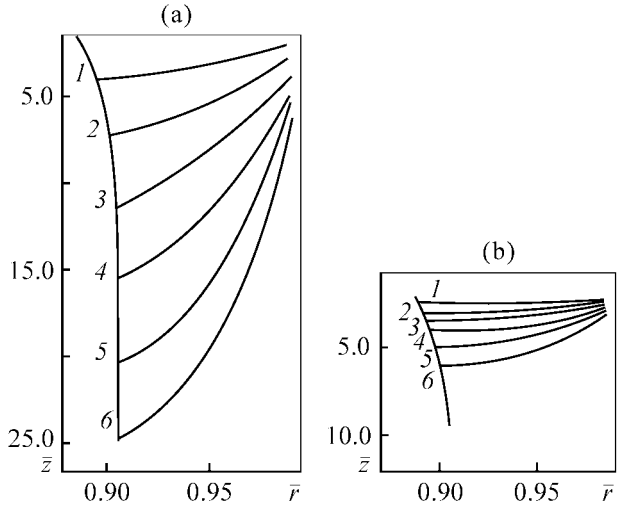

Fig. 5. Distribution of solid particles in suspension film at $Re_n^{sett} = 2.24 \times 10^{-3}$, Fr = 73.4, $Re_n = 4000$, $\bar{Q} = 3.98 \times 10^{-2}$. F_g: (a) 1.35 and (b) 8.98×10^{-3}. Isoconcentration lines at $\bar{c}$: (a) (*1*) 0.99, (*2*) 0.97, (*3*) 0.95, (*4*) 0.93, (*5*) 0.91, and (*6*) 0.89; (b) (*1*) 0.6, (*2*) 0.4, (*3*) 0.2, (*4*) 0.1, (*5*) 0.05, and (*6*) 0.02.

the suspension film thickness [5] (resulting from an increasing ratio of the cross-sectional area of the inlet pipe to that of the apparatus casing), the concentration of solid particles in the suspension becomes higher. This is due to an increase in the number of solid particles per unit suspension film length in the axial direction, resulting from the increasing film thickness. As seen from the calculated data, the necessary height of the working zone of the hydrocyclone is determined by the dimensionless flow rate $\bar{Q}$, characterizing the ratio of the basic geometric dimensions of the inlet pipe and the apparatus casing, and by the desired extent of recovery at the exit from the working zone of the hydrocyclone. This is so because analysis of Figs. 1–3 shows that the strongest change in the field of solid particles in the suspension film is observed when varying the dimensionless flow rate $\bar{Q}$.

In addition to the criteria characterizing the flow hydrodynamics, the process of separation of a non-Newtonian suspension in a hydrocyclone by pressure flotation is characterized by the Reynolds criterion Re_n^{sed} describing solid particle sedimentation in a non-Newtonian fluid and by dimensionless complexes F_g for the case $\bar{c}_g > \bar{c}_h$, $\bar{c}_g$ = const and F_h for the case $\bar{c}_g = \bar{c}_h$, characterizing the kinetics of pressure flotation.

Figures 4a and 4b presents the distributions of solid particle concentration in the suspension film at Re_n^{sed} of, respectively, 0.763×10^{-3} and 0.970×10^{-2}. Comparison of the concentration distributions shows that, with increasing criterion Re_n^{sed}, which characterizes the ratio of the centrifugal inertia force acting on solid particles to viscous friction forces, the concentration of solid particles in the suspension film decreases. This is accounted for by the fact that, with the velocity of radial sedimentation of solid particles growing because of the increase in the centrifugal inertia force or decrease in viscous friction forces, the particles travel to a longer distance in the fluid in unit time and, as a result, the number of their collisions with air bubbles becomes greater. Thus, with increasing diameter and density of solid particles and with decreasing effective viscosity of the dispersion medium, the extent of particle extraction at the lower boundary of the calculated flow region grows.

Figures 5a and 5b present the distributions of solid particle concentration in a suspension film at F_g complexes of, respectively, 1.35 and 8.98×10^{-3}. Comparison of the concentration distributions shows that, with decreasing complex F_g characterizing the kinetics of pressure flotation, the concentration of solid particles in the suspension film decreases owing to the growing number of collisions between solid particles and air bubbles. This occurs because of an increase in the modified rate constant of the process of pressure flotation, A_g, which characterizes the number of collisions of particles and bubbles in unit time or an increase in the Re_n^{sed} criterion appearing in the complex F_g. The influence of this criterion on the concentration field was analyzed above. Consequently, the rate of suspension input into the hydrocyclone in pressure flotation, appearing in the complex F_g and determin-

ing the throughput of the apparatus, must be determined by the rate constant of the process, which depends on a number of factors characterizing the process [9], and by the necessary extent of recovery at the exit from the working zone of the hydrocyclone.

According to the calculated data obtained, the same basic patterns of variation of the solid particle concentration on changing the defining similarity criteria (at higher concentrations of solid particles) are valid for the case $c_g = c_h$, which is accounted for by lower concentration of air bubbles in unit suspension volume and the resulting formation of a smaller number of floated complexes. Consequently, the height of the working zone in the hydrocyclone should be raised in this case compared with the case of $\bar{c}_g > \bar{c}_h$, $\bar{c}_g$ = const.

CONCLUSIONS

(1) A mathematical model of pressure flotation of a non-Newtonian suspension in a centrifugal field, based on continuity equations for fluxes of solid particles and air bubbles in a flow of a film of a non-Newtonian suspension with free surface in a hydrocyclone, was developed.

(2) For two practically important cases, which occur depending on the ratio of concentrations of solid particles and air bubbles, the effect of defining similarity criteria on the distribution of solid particle concentration in the film of a non-Newtonian suspension was studied.

REFERENCES

1. Dik, I.G., Matvienko, O.V., and Neesse, T., *Teor. Osn. Kim. Tekhnol.*, 2000, vol. 34, no. 5, pp. 478–488.
2. Orlov, S.L., *Razvitie metodov mekhanicheskoi i biologicheskoi ochistki stochnykh vod: Trudy in–ta VODGEO* (Development of Methods for Mechanical and Biological Purification of Wastewater), Moscow, 1982, pp. 131–136.
3. Lagutkin, M.G. and Pavlovskii, G.V., *Khim. Prom–st.*, 1997, no. 8, pp. 556–558.
4. Kutepov, A.M., Lagutkin, M.G., and Pavlovskii, G.V., *Teor. Osn. Kim. Tekhnol.*, 1999, vol. 33, no. 5, pp. 571–577.
5. Yablonskii, V.O., *Zh. Prikl. Khim.*, 2000, vol. 73, no. 1, pp. 95–99.
6. Romankov, P.G., *Teor. Osn. Kim. Tekhnol.*, 1972, vol. 6, no. 6, pp. 855–871.
7. Vainshtein, I.A., *Inzh.-Fiz. Zh.*, 1983, vol. 45, no. 4, pp. 602–608.
8. Alekseev, V.I., Myasnikov, I.N., and Naidenko, V.V., *Nauchnye issledovaniya v oblasti fiziko-khimicheskoi ochistki promyshlennykh stochnykh vod: Tekhnologiya, avtomatizatsiya i analiz: Trudy in–ta VODGEO* (Research in Physicochemica; Purification of Industrial Wastewater: Technology, Automation, and Analysis), Moscow, 1980, pp. 87–95.
9. Tyabin, N.V., Dakhina, G.L., Golovanchikov, A.B., and Mamakov, A.A., *Teor. Osn. Kim. Tekhnol.*, 1979, vol. 13, no. 6, pp. 880–884.
10. Shchukina, A.G., Mathematical Modeling of Separation of Heterogeneous Systems with non-Newtonian Dispersion Medium, *Cand. Sci. Dissertation*, Volgograd, 1996.
11. Vinogradov, G.V., Vachagin, K.D., Zakirov, E.N., *et al.*, *Inzh.-Fiz. Zh.*, 1975, vol. 28, no. 3, pp. 435–438.
12. Matveev, N.M., *Differentsial'nye uravneniya*. Minsk: Vysheisha Shkola, 1976.

Russian Journal of Applied Chemistry, Vol. 75, No. 10, 2002, pp. 1660–1664. Translated from Zhurnal Prikladnoi Khimii, Vol. 75, No. 10, 2002, pp. 1694–1698.
Original Russian Text Copyright © 2002 by Pinko, Terakh, Gorokh, Nikulina, Prosenko, Grigor'ev.

ORGANIC SYNTHESIS AND INDUSTRIAL ORGANIC CHEMISTRY

Synthesis and Antioxidant Properties of Unsymmetrical Sulfides Based on ω-(3,5-Di-*tert*-butyl-4-hydroxyphenyl)alkanethiols

P. I. Pinko, E. I. Terakh, E. A. Gorokh, V. V. Nikulina, A. E. Prosenko, and I. A. Grigor'ev

Novosibirsk State Pedagogical Institute, Novosibirsk, Russia

Vorozhtsov Novosibirsk Institute of Organic Chemistry, Siberian Division, Russian Academy of Sciences, Novosibirsk, Russia

Received January 10, 2002

Abstract—Unsymmetrical sulfides were prepared by reactions of ω-(3,5-di-*tert*-butyl-4-hydroxyphenyl)-alkanethiols with various alkyl halides, and their antioxidant activity with respect to thermal autooxidation of lard was studied in relation to their structure.

SO-3 antioxidant {bis[3-(3,5-di-*tert*-butyl-4-hydroxyphenyl)propyl] sulfide} is a well-known high-performance versatile inhibitor of oxidative degradation of organic and bioorganic substrates [1–4]. It is a bifunctional antioxidant; its molecule contains two phenolic moieties exhibiting antiradical activity and one sulfide moiety with antiperoxide activity. It has been shown previously that, with respect to some model systems, the antioxidant activity (AOA) of SO-3 is lower than that of its structural analogs containing the same number of sulfide and phenolic fragments [4–6]. In this connection, we prepared from ω-(3,5-di-*tert*-butyl-4-hydroxyphenyl)alkanethiols **I** and alkyl halides a series of unsymmetrical sulfides **II** and compared their antioxidant power with respect to oxidation of lard as a model reaction:

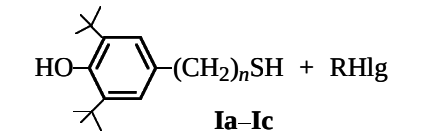

Ia–**Ic**

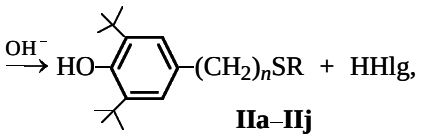

IIa–**IIj**

where n = 2 (**Ia**), 3 (**Ib**), 4 (**Ic**); n = 2, R = Bu (**IIa**); n = 3, R = Me (**IIb**); n = 3, R = Et (**IIc**); n = 3, R = Pr (IId); n = 3, R = Bu (**IIe**); n = 3, R = *s*-Bu (**IIf**); n = 3, R = *t*-Bu (**IIg**); n = 3, R = $C_{18}H_{37}$ (**IIh**); n = 3, R = CH_2Ph (**IIi**); n = 4, R = Bu (**IIj**).

The initial thiols **Ia**–**Ic** were prepared from the corresponding alkyl halides as described in [7]. The reactions of thiols **I** with primary and secondary alkyl halides were performed in ethanol in the presence of NaOH at approximately equimolar ratio of the reactants. The yields of sulfides **IIa**–**IIf** and **IIh**–**IIj** were 72–86%.

There were certain problems with synthesis of the *tert*-butyl sulfide **IIg**. This compound could not be prepared from **Ib** and 2-chloro- or 2-bromo-2-methylpropane under the above-described conditions because of vigorous dehydrohalogenation and evolution of 2-methylpropene. Sulfide **IIg** could be prepared in 43% yield only in the absence of bases at 150°C and elevated pressure (sealed ampules).

The composition and structure of all the compounds **II** were confirmed by elemental analysis and spectroscopy.

The relationship between the structure and the antioxidant power was studied for sulfides **II** with thermal autooxidation of lard as a model reaction. As references we used SO-3, Ionol (2,6-di-*tert*-butyl-4-methylphenol), and a 1 : 1 mixture of Ionol with didodecyl sulfide. The rate of lard oxidation was monitored by accumulation of primary oxidation products (hydroperoxides), and the AOA was judged from the induction period τ (time in which the lard was oxidized to a peroxide number of 0.1). The results are obtained listed in the table.

All the sulfides **II** synthesized exhibited pronounced AOA, surpassing that of both Ionol and its mixture with didodecyl sulfide. The striking lack of synergistic effect in this mixture is most probably due to specific features of lard as oxidation substrate.

1070-4272/02/7510-1660 $27.00 © 2002 MAIK "Nauka/Interperiodica"

It is known [9] that lard contains a large amount of unsaturated fatty acid residues [in particular, oleic (41–54%), linoleic (5–16%), and linolenic and arachidonic (up to 2%)] whose hydroperoxide derivatives are thermally unstable. Because of the relatively high oxidation temperature in our model system, the rate of decomposition of hydroperoxides appears to be considerably higher than the rate of their reaction with didodecyl sulfide; as a result, the antioxidant effect of didodecyl sulfide is not manifested, and AOA of the synergistic mixture of Ionol and dodecyl sulfide is determined essentially by the antiradical activity of Ionol. Since neither SO-3 nor its structural analogs surpass Ionol in the antiradical activity [10], their high AOA can be accounted for only by the internal synergism (bifunctional antioxidant activity).

The internal synergism of SO-3, sulfides **II**, and their structural analogs [11, 12] is probably due to the favorable steric arrangement of the phenolic and sulfide moieties, owing to which the hydroperoxide molecule formed by reaction of the generated radical with the phenolic group of the inhibitor is activated by the sulfide moiety, having no time to escape to the bulk of the substrate:

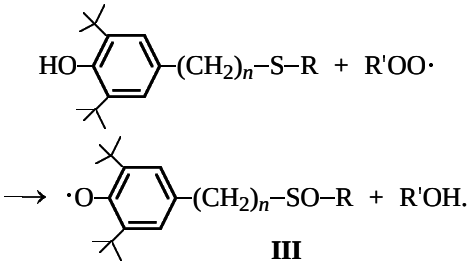

III

Thus, the reaction of the antioxidant with an active radical yields a thermally stable alkanol instead of hydroperoxide acting as a chain-branching agent.

According to the generally accepted mechanism of the effect of phenolic antioxidants, phenoxyl **III** can react with peroxy radical to form quinoid peroxide **IV** or quinone **V**, with the former pathway presumably being preferable [13]:

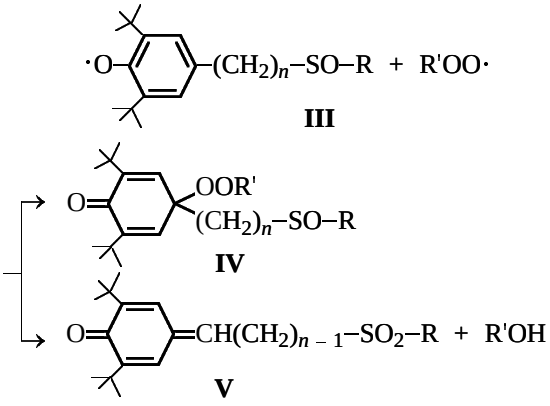

III

IV

V

Induction period in lard oxidation inhibited with phenolic antioxidants (1 μmol per gram of lard, 130°C)

Antioxidant*	τ, min
$R(CH_2)_2SC_4H_9$ (**IIa**)	254
$R(CH_2)_3SCH_3$ (**IIb**)	271
$R(CH_2)_3SC_2H_5$ (**IIc**)	296
$R(CH_2)_3SC_3H_7$ (**IId**)	290
$R(CH_2)_3SC_4H_9$ (**IIe**)	282
$R(CH_2)_3SCH(CH_3)C_2H_5$ (**IIf**)	297
$R(CH_2)_3SC(CH_3)_3$ (**IIg**)	321
$R(CH_2)_3SC_{18}H_{37}$ (**IIh**)	284
$R(CH_2)_3SCH_2C_6H_5$ (**IIi**)	266
$R(CH_2)_4SC_4H_9$ (**IIj**)	350
RCH_3 (Ionol)	169
$C_{12}H_{25}SC_{12}H_{25}$	34
$RCH_3 + C_{12}H_{25}SC_{12}H_{25}$ (synergistic mixture)	169
$R(CH_2)_3S(CH_2)_3R$ (CO-3)	290
Control	34

* R = 3,5-di-*tert*-butyl-4-hydroxyphenyl.

In this connection, the oxidative transformations of sulfides **II** and SO-3 in reactions with peroxy radicals can be represented by schemes (1) and (2), respectively:

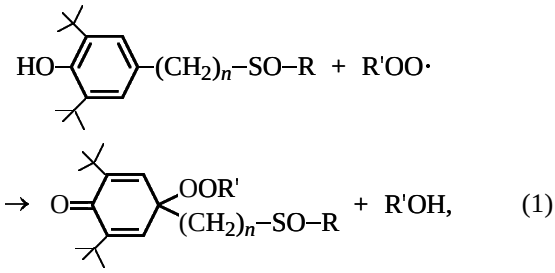

(1)

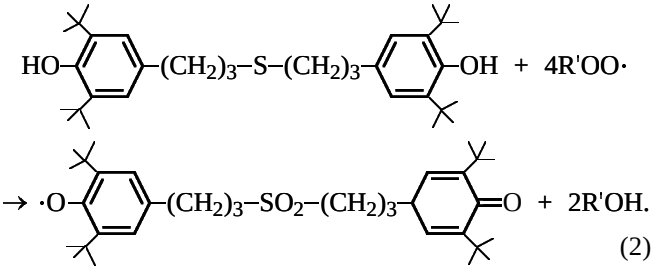

(2)

Under the conditions chosen by us for oxidation of lard, the antioxidant activities of SO-3 and sulfides **II** are similar (the induction periods differ by no more than 20%), which is quite consistent with the assumed mechanism [reactions (1), (2)]. Despite the lower sulfur content in SO-3, its sulfide moiety, similar to

that in unsymmetrical sulfides **II**, is capable of deactivating all the hydroperoxide molecules formed with the participation of the phenolic groups of the antioxidant. Therefore, SO-3 and sulfides **II** exhibit similar degrees of internal synergism. The capability of sulfoxide **IV** to reduce a second hydroperoxide molecule formed in the substrate without participation of the antioxidant does not contribute noticeably to the inhibiting effect, as shown by data on the antioxidant activity of didodecyl sulfide (see table).

Among sulfides **II**, sulfide **IIj** appeared to be the most effective as inhibitor of lard oxidation; AOA grew in the order **IIa**–**IIe**–**IIj**, i.e., with increasing number of methylene units linking phenolic and sulfide moieties [10]. The effect of alkyl substituent R on AOA of sulfides **II** is most probably determined by its electron-donor power. For example, there is a reliably detected trend toward an increase in the antioxidant activity in the order **IIe**–**IIf**–**IIg** and in going from **IIb** to **IIc**, i.e., with an increase in the electron density on the sulfur atom and, hence, in the reactivity of the sulfide moiety toward hydroperoxides.

On the whole, sulfides **IIa**–**IIj** can be considered effective polyfunctional antioxidants.

EXPERIMENTAL

The ^{1}H NMR spectra were taken on a Bruker spectrometer (500 MHz, $CDCl_3$, external reference TMS), and the IR spectra, on a Vektor 22 Fourier spectrometer [neat samples, CCl_4 solutions, or KBr pellets (150 : 1).

The melting points were determined with a PTP device.

Butyl 2-(3,5-di-*tert*-butyl-4-hydroxyphenyl)ethyl sulfide IIa. 1-Chlorobutane (1.9 ml, 18.3 mmol) was added dropwise at room temperature to a solution of 4.5 g (16.9 mmol) of thiol **Ia** and 0.71 g (17.7 mmol) of NaOH in 25 ml of ethanol. The mixture was refluxed for 2 h, cooled, and treated with toluene. The extract was washed with water and dried over Na_2SO_4; the solvent was distilled off, and the residue was vacuum-distilled. Yield of sulfide **IIa** 4.03 g (74%), bp 159–161°C (1 mm Hg). ^{1}H NMR spectrum ($CDCl_3$), δ, ppm: 1.01–1.04 t (3H, $CH_2\underline{Me}$), 1.51–1.53 m (2H, $C\underline{H}_2Me$), 1.55 s (18H, *t*-Bu), 1.68–1.69 m (2H, $C\underline{H}_2Et$), 2.63–2.66 t (2H, $SC\underline{H}_2Pr$), 2.87–2.90 m [4H, $Ar(C\underline{H}_2)_2S$], 5.17 s (1H, OH), 7.12 s (2H, Ar–H). IR spectrum (KBr), ν_{max}, cm^{-1}: 3646 (PhOH).

Found, %: C 74.63, H 10.78, S 10.17.
$C_{20}H_{34}OS$.
Calculated, %: C 74.47, H 10.62, S 9.94.

Methyl 3-(3,5-di-*tert*-butyl-4-hydroxyphenyl)propyl sulfide IIb was prepared similarly to **IIa** from 5 g (17.8 mmol) of thiol **Ib** and 1.2 ml (19.2 mmol) of iodomethane; yield 4.11 g (78%), bp 145°C (1 mm Hg). ^{1}H NMR spectrum ($CDCl_3$), δ, ppm: 1.40–1.43 s (18H, *t*-Bu), 1.89–1.90 m (2H, $ArCH_2C\underline{H}_2$), 2.10 s (3H, S–Me), 2.51–2.54 t (2H, $CH_2S\underline{Me}$), 2.61–2.64 t (2H, $ArC\underline{H}_2$), 5.04 s (1H, OH), 6.98 s (2H, Ar–H). IR spectrum (KBr), ν_{max}, cm^{-1}: 3644 (PhOH).

Found, %: C 73.47, H 10.32, S 11.06.
$C_{18}H_{30}OS$.
Calculated, %: C 73.41, H 10.27, S 10.89.

Ethyl 3-(3,5-di-*tert*-butyl-4-hydroxyphenyl)propyl sulfide IIc was prepared similarly to **IIa** from 5 g (17.8 mmol) of **Ib** and 1.5 ml (18.5 mmol) of iodoethane; yield 4.0 g (73%), bp 150–151°C (1 mm Hg). ^{1}H NMR spectrum ($CDCl_3$), δ, ppm: 1.23–1.26 t (3H, $CH_2\underline{Me}$), 1.43 s (18H, *t*-Bu), 1.85–1.91 m (2H, $ArCH_2C\underline{H}_2$), 2.53–2.57 m (4H, CH_2SCH_2), 2.61–2.63 t (2H, $ArC\underline{H}_2$), 5.03 s (1H, OH), 6.98 s (2H, Ar–H). IR spectrum (thin film), ν_{max}, cm^{-1}: 3645 (PhOH).

Found, %: C 73.84, H 10.51, S 10.55.
$C_{19}H_{32}OS$.
Calculated, %: C 73.97, H 10.45, S 10.39.

Propyl 3-(3,5-di-*tert*-butyl-4-hydroxyphenyl)propyl sulfide IId was prepared similarly to **IIa** from 5 g (17.8 mmol) of thiol **Ib** and 2 ml (22.6 mmol) 1-chloropropane; yield 4.32 g (75%), bp 155–157°C (1 mm Hg). ^{1}H NMR spectrum ($CDCl_3$), δ, ppm: 0.96–0.99 t (3H, $CH_2\underline{Me}$), 1.39–1.47 s (18H, *t*-Bu), 1.58–1.62 m (2H, $C\underline{H}_2Me$), 1.86–1.89 m (2H, $ArCH_2C\underline{H}_2$), 2.47–2.55 m (4H, CH_2SCH_2), 2.61–2.64 t (2H, $ArC\underline{H}_2$), 5.03 s (1H, OH), 6.98 s (2H, Ar–H). IR spectrum (thin film), ν_{max}, cm^{-1}: 3645 (PhOH).

Found, %: C 74.61, H 10.78, S 9.83.
$C_{20}H_{34}OS$.
Calculated, %: C 74.47, H 10.62, S 9.94.

Butyl 3-(3,5-di-*tert*-butyl-4-hydroxyphenyl)propyl sulfide IIe was prepared similarly to **IIa** from 5 g (17.8 mmol) of thiol **Ib** and 1.9 ml (18 mmol) of 1-chlorobutane; yield 4.68 g (78%), bp 165°C (1 mm Hg). ^{1}H NMR spectrum ($CDCl_3$), δ, ppm: 0.89–0.92 t (3H, $CH_2\underline{Me}$), 1.38–1.42 m (2H, CH_2Me), 1.43 s (18H, *t*-Bu), 1.53–1.59 m (2H, CH_2Et), 1.86–1.91 m (2H, $ArCH_2C\underline{H}_2$), 2.50–2.52 t (2H, $SC\underline{H}_2Pr$), 2.53–2.55 t (2H, $C\underline{H}_2SBu$), 2.61–2.64 t (2H, $ArCH_2$), 5.03 s (1H, OH); 6.98 s (2H, Ar–H). IR spectrum (thin film), ν_{max}, cm^{-1}: 3646 (PhOH).

Found, %: C 75.08, H 10.85, S 9.69.
$C_{21}H_{36}OS$.
Calculated, %: C 74.94, H 10.78, S 9.53.

***sec*-Butyl 3-(3,5-di-*tert*-butyl-4-hydroxyphenyl)propyl sulfide IIf** was prepared similarly to **IIa** from 5 g (17.8 mmol) of thiol **Ib** and 2 ml (18.3 mmol) of 2-bromobutane; yield 4.33 g (72%), bp 151°C (1 mm Hg). ^{1}H NMR spectrum ($CDCl_3$), δ, ppm: 0.96–0.99 t (3H, $CH_2\underline{Me}$), 1.24–1.26 d (3H, $SC\underline{H}Me$), 1.43 s (18H, *t*-Bu), 1.51–1.61 m (2H, $C\underline{H}_2Me$), 1.87– 1.89 m (2H, $ArCH_2C\underline{H}_2$), 2.53–2.56 t (2H, $C\underline{H}_2S$), 2.61–2.63 t (2H, $ArC\underline{H}_2$), 2.68–2.69 m (1H, $SC\underline{H}$), 5.03 s (1H, OH), 6.98 s (2H, Ar–H). IR spectrum (thin film), ν_{max}, cm^{-1}: 3647 (PhOH).

Found, %: C 74.98, H 10.89, S 9.72.
$C_{21}H_{36}OS$.
Calculated, %: C 74.94, H 10.78, S 9.53.

***tert*-Butyl 3-(3,5-di-*tert*-butyl-4-hydroxyphenyl)propyl sulfide IIg.** A 120-ml ampule was charged with 5 g (17.8 mmol) of thiol **Ib** and 30 ml (270 mmol) of 2-bromo-2-methylpropane and kept at 150°C for 3 h in a thermostat equipped with a shaker, after which it was cooled. The reaction mixture was treated with benzene. The extract was washed with water and dried over Na_2SO_4; the solvent was distilled off. The product was purified by column chromatography (silica gel, hexane). Yield 2.60 g (43%), bp 157–160°C (1 mm Hg). ^{1}H NMR spectrum ($CDCl_3$), δ, ppm: 1.31 s (9H, S–*t*-Bu), 1.43 s (18H, Ar–*t*-Bu), 1.87 m (2H, $ArCH_2C\underline{H}_2$), 2.57 t (2H, $C\underline{H}_2S$), 2.66 t (2H, $ArC\underline{H}_2$), 5.03 s (1H, OH), 6.98 s (2H, Ar–H). IR spectrum (KBr), ν_{max}, cm^{-1}: 3632 (PhOH).

Found, %: C 74.87, H 10.91, S 9.94.
$C_{21}H_{36}OS$.
Calculated, %: C 74.94, H 10.78, S 9.53.

Octadecyl 3-(3,5-di-*tert*-butyl-4-hydroxyphenyl)propyl sulfide IIh was prepared similarly to **IIa** from 5 g (17.8 mmol) of thiol **Ib** and 6.16 g (18.5 mmol) of 1-bromooctadecane (synthesis time 8 h); yield 7.45 g (78%), mp 48–50°C. ^{1}H NMR spectrum ($CDCl_3$), δ, ppm: 0.87–0.89 t (3H, $(CH_2)_{17}\underline{Me}$), 1.26–1.30 s [30H, $(CH_2)_{15}\underline{Me}$], 1.43 s (18H, *t*-Bu), 1.57 m (2H, $C\underline{H}_2C_{16}H_{33}$), 1.88 m (2H, $ArCH_2C\underline{H}_2$), 2.50–2.56 m (4H, CH_2SCH_2), 2.61–2.69 t (2H, $ArC\underline{H}_2$), 5.03 s (1H, OH), 6.98 s (2H, Ar–H). IR spectrum (KBr), ν_{max}, cm^{-1}: 3645 (PhOH).

Found, %: C 78.84, H 12.23, S 6.21.
$C_{35}H_{64}OS$.
Calculated, %: C 78.88, H 12.10, S 6.02.

Benzyl 3-(3,5-di-*tert*-butyl-4-hydroxyphenyl)propyl sulfide IIi was prepared similarly to **IIa** from 5 g (17.8 mmol) of thiol **Ib** and 2.15 ml (18.7 mmol) of benzyl chloride (synthesis time 0.5 h); yield 5.73 g (86%), mp 75–76°C. ^{1}H NMR spectrum ($CDCl_3$), δ, ppm: 1.42 s (18H, *t*-Bu), 1.85 m (2H, $ArCH_2C\underline{H}_2$), 2.42–2.45 t (2H, CH_2S), 2.57–2.60 t (2H, $ArC\underline{H}_2$), 3.69 s (2H, $C\underline{H}_2Ph$), 5.03 s (1H, OH); 6.94 s (2H, Ar–H); 7.26–7.28 m (5H, Ph). IR spectrum (KBr), ν_{max}, cm^{-1}: 3574 (PhOH).

Found, %: C 77.91, H 9.19, S 8.79.
$C_{24}H_{34}OS$.
Calculated, %: C 77.78, H 9.25, S 8.65.

Butyl 4-(3,5-di-***tert*-butyl-4-hydroxyphenyl)butyl sulfide IIj** was prepared similarly to **IIa** from 5.7 g (19.3 mmol) of thiol **Ic** and 2.2 ml (21.3 mmol) of 1-chlorobutane (synthesis time 4 h); yield 4.88 g (72%), bp 168–170°C (1 mm Hg). ^{1}H NMR spectrum ($CDCl_3$), δ, ppm: 0.92–0.95 t (3H, $CH_2\underline{Me}$), 1.42–1.42 m (2H, $C\underline{H}_2Me$), 1.46 s (18H, *t*-Bu), 1.56–1.62 m (2H, $C\underline{H}_2Et$), 1.71 m [4H, $ArCH_2(C\underline{H}_2)_2$], 2.55–2.56 m (4H, CH_2SCH_2), 2.64 t (2H, $ArC\underline{H}_2$), 5.03 s (1H, OH), 6.99 s (2H, Ar–H). IR spectrum (KBr), ν_{max}, cm^{-1}: 3645 (PhOH).

Found, %: C 75.61, H 11.09, S 9.32.
$C_{22}H_{38}OS$.
Calculated, %: C 75.36, H 10.92, S 9.15.

Lard was oxidized at 130°C in an oxidation cell with bubbling oxygen, as described in [14]. The amount of lard placed in the cell was 50 g, and the concentration of antioxidants, 1 μmol per gram of lard. The progress of oxidation was monitored

by accumulation of peroxide compounds whose concentration was determined iodometrically [15] and expressed in peroxide numbers. The initial peroxide number of the lard was 0.002% iodine. The induction periods were determined graphically from the kinetic curves.

CONCLUSIONS

(1) The alkyl ω-(3,5-di-*tert*-butyl-4-hydroxyphenyl)alkyl sulfides synthesized exhibit high inhibiting activity, which is due to the bifunctional mechanism of the antioxidant effect and to the internal synergism.

(2) Under the conditions of the model reaction used in this study, the antioxidant activity of the sulfides grows with increasing length of the hydrocarbon chain linking the phenolic and sulfide moieties and with increasing electron-donor power of the aliphatic substituent.

(3) The compounds synthesized are of interest as antioxidants preventing development of oxidation processes in fats.

ACKNOWLEDGMENTS

The authors are grateful to the Russian Foundation for Basic Research for the access to STN International data bases (project no. 00-03-32 721) via the Novosibirsk STN center at the Novosibirsk Institute of Organic Chemistry, Siberian Division, Russian Academy of Sciences.

REFERENCES

1. RF Patent 1 072 420.
2. RF Patent 1 007 405.
3. Rezvukhin, A.I., Krysin, A.P., and Shalaurova, I.Yu., *Vopr. Med. Khim.*, 1995, no. 3, pp. 37–39.
4. Prosenko, A.E., Terakh, E.I., Kandalintseva, N.V., *et al., Zh. Prikl. Khim.*, 2001, vol. 74, no. 11, pp. 1839–1843.
5. USSR Inventor's Certificate, no. 1 123 284.
6. USSR Inventor's Certificate, no. 1 154 296.
7. USSR Inventor's Certificate, no. 1 074 865.
8. US Patent 4 021 468.
9. Bezzubov, A.P., *Khimiya zhirov* (Chemistry of Fats), Moscow: Pishchevaya Prom–st., 1975.
10. Prosenko, A.E., Kandalintseva, N.V., and Tolstikov, G.A., *Kinet. Katal.*, 2002, vol. 43, no. 1, pp. 29–33.
11. Pinko, P.I., Terakh, E.I., Prosenko, A.E., and Grigor'ev, I.A., *Zh. Prikl. Khim.*, 2001, vol. 74, no. 11, pp. 1843–1847.
12. Prosenko, A.E., ω-(4-Hydroxyaryl)haloalkanes and Sulfur-Containing Antioxidants Derived from Them, *Cand. Sci. Dissertation*, Novosibirsk, 2000.
13. Roginskii, V.A., *Fenol'nye antioksidanty: Reaktsionnaya sposobnost' i effektivnost'* (Phenolic Antioxidants: Reactivity and Performance), Moscow: Nauka, 1988.
14. Shishkina, L.N., in *Issledovanie sinteticheskikh i prirodnykh antioksidantov in vivo i in vitro* (*In vivo* and *in vitro* study of Synthetic and Natural Antioxidants), Moscow: Nauka, 1992, pp. 26–30.
15. Zinov'ev, A.A., *Khimiya zhirov* (Chemistry of Fats), Moscow: Pishchepromizdat, 1952.

Russian Journal of Applied Chemistry, Vol. 75, No. 10, 2002, pp. 1665–1672. Translated from Zhurnal Prikladnoi Khimii, Vol. 75, No. 10, 2002, pp. 1699–1706.
Original Russian Text Copyright © 2002 by Evlampieva, Yakimanskii, Pavlov, Zaitseva, Ryumtsev.

MACROMOLECULAR CHEMISTRY AND POLYMERIC MATERIALS

Electrooptical and Conformational Properties of Poly(1-Trimethylsilyl-1-Propynes) with Different Chain Microstructures

N. P. Evlampieva, A. V. Yakimanskii, G. M. Pavlov, I. I. Zaitseva, and E. I. Ryumtsev

Institute of Physics, St. Petersburg State University, St. Petersburg, Russia
Institute of Macromolecular Compounds, Russian Academy of Sciences, St. Petersburg, Russia

Received March 29, 2002; in final form June, 2002

Abstract—The methods of the Kerr effect and solution hydrodynamics were applied to study the electrooptical and hydrodynamic properties of samples of disubstituted polyacetylenes, poly(1-trimethylsilyl-1-propynes), prepared by polymerization of 1-trimethylsilyl-1-propyne with $NbCl_5$ and $TaCl_5$/BuLi as catalysts. The experimental electrooptical characteristics of polymers were compared with those calculated by PM3 semiempirical quantum-chemical method.

1,2-Disubstituted polyacetylenes catalytically synthesized from the corresponding derivatives of acetylenes [1–3] are used in new membrane technologies [4, 5] and show promise for establishing the microstructure–properties correlation in polymer physics. The reason is that synthesis of these compounds can yield *cis* or *trans* blocks of regular sequences of double carbon–carbon bonds, since the main chain of these polymers is built from alternating ordinary and double bonds $–[–C(CH)_3=C(R)–]_n$. Masuda *et al.* [1, 2, 6] showed that halides of Group V and VI elements are suitable as catalysts for preparing organometallic disubstituted polyacetylenes, in particular, poly(1-trimethylsilyl-1-propynes) (PTMSPs) with $R = –Si(CH)_3$, which are the subjects of this study. It was found that different catalysts yield polymers differing in the solubility in organic solvents, as well as in the molecular weight *M*, heat resistance, and glass transition temperature [6]. This variability of the physical properties of PTMSPs motivated a study of the microstructural features of the chains of these polymers as dependent on the synthesis conditions. However, traditional approaches to solving this problem proved hardly applicable. For example, X-ray diffraction analysis of films with the aim to determine the stereoregular structural elements was found to be inefficient. This is due to the fact that PTMSP samples synthesized using various catalytic systems are noncrystallizing polymers with virtually identical percentages of *cis–trans* configurations of the C=C bonds in the chains [4, 7].

Revealing the microstructural features of the PTMSP molecules required a method sensitive to the degree of intramolecular ordering of the chemical bonds in polymer chains. In polymer physics, such experimental methods include those involving measurements of the induced optical anisotropy of polymers in solutions. These methods show good performance in studying the physical properties of stereoregular polymers with different tacticities [8].

In this work, we studied the optical anisotropy induced by an external electric field (electrooptical Kerr effect) in solutions of PTMSP samples prepared using tantalum and niobium salts as catalysts. Also, we compared the conformational characteristics of these polymers, on the basis of the results obtained in diffusion and sedimentation analysis of their solutions.

The PTMSP samples were synthesized by the procedure described in [6]. Table 1 summarizes the conditions of catalytic synthesis, *M*, and the *cis–trans* ratio for C=C bonds in the PTMSP samples synthe-

Table 1. Conditions of synthesis of PTMSP-1 and PTMSP-2 samples

Sample	Catalytic system	*cis–trans* ratio for C=C bonds	$M \times 10^3$
PTMSP-1	$NbCl_5$	60 : 40	159
PTMSP-2	$TaCl_5$/BuLi	40 : 60	1340

1070-4272/02/7510-1665 $27.00 © 2002 MAIK "Nauka/Interperiodica"

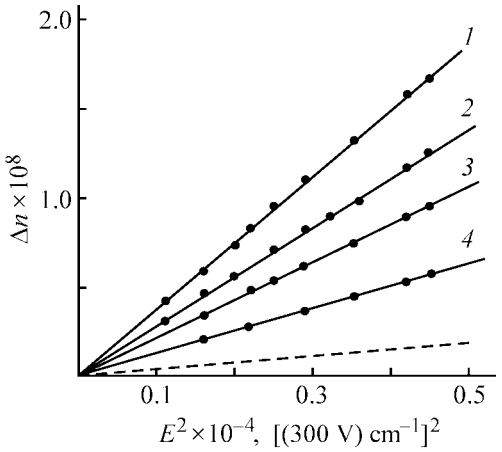

Fig. 1. Birefringence Δn vs. squared field intensity E^2 for PTMSP-1 fraction no. 1 in CCl_4. Solution concentration $c \times 10^2$, g cm^{-3}: (*1*) 1.317, (*2*) 0.92, (*3*) 0.653, and (*4*) 0.332. *Dashed straight line*: data for the pure solvent.

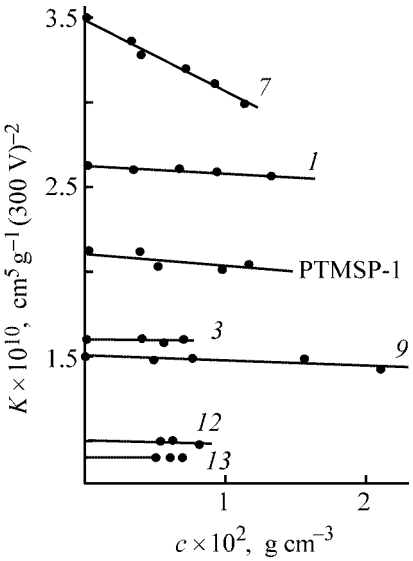

Fig. 2. Specific Kerr constant K for PTMSP-1 fractions and for nonfractionated PTMSP-1 sample in CCl_4 vs. concentration c. Curve numbers are fraction numbers in Table 2.

sized. The average *cis–trans* C=C ratio was estimated by ^{13}C NMR spectroscopy from the intensity ratios of the signals of carbon atoms from C=C bonds with different configurations [solutions in $CDCl_3$, MSh-300 (Bruker) spectrometer, 75.47 MHz]. The molecular weight M of the samples was determined from the data on diffusion and sedimentation in solutions of cyclohexane (CH) (for PTMSP-1 sample) and heptane (for PTMSP-2 sample) [9].

The initial samples were subjected to fractional precipitation from solution in a 1 : 1 toluene–CCl_4 mixture in the case of PTMSP-1 and from toluene solution in the case of PTMSP-2. Ethanol served as the precipitant. Fractionation yielded 13 fractions of PTMSP-1 and 5 fractions of PTMSP-2. In view of the fact that silicon-containing disubstituted polyacetylenes are selectively soluble in organic solvents [1, 6], a study of the molecular properties of such polymers required selecting a polymer–solvent system dissolving all the isolated fractions of the initial samples. Therefore, we studied the electrooptical properties of the PTMSP-1 fractions in CCl_4, and those of PTMSP-2 fractions, in toluene.

The electrooptical Kerr effect [9] was studied in pulsed electric field; the duration of the rectangular pulse was 1–2 ms at a voltage applied to the Kerr cell of up to 1 kV. The measurements were carried out in a glass cell with 2-cm-long parallel-plate titanium electrodes separated by 0.05 cm. The optical birefringence of the polymer solution was recorded photoelectrically, by the compensation procedure used to measure the Kerr effect [9]. The light source was a He–Ne laser ($\lambda = 6328 \times 10^{-8}$ cm); a thin mica plate with intrinsic phase difference of $0.01 \times 2\pi$ served as compensator.

In this study, we discuss the equilibrium (i.e., independent of the electric pulse repetition frequency and duration) electrooptical properties of polymers. These are conventionally characterized by the specific Kerr constant K defined by

$$K = \lim_{\substack{E\to 0 \\ c\to 0}} [\Delta n - \Delta n_0)/E^2 c], \qquad (1)$$

where, $\Delta n - \Delta n_0$ is the difference between the field-induced birefringences in a solution of the substance under investigation (with concentration c) and in the solvent, respectively, and E is the electric field intensity.

In PTMSP solutions, we observed a positive (in sign) electrooptical effect, which was proportional to the squared electric field intensity and exceeded the contribution to the observed birefringence from the solvent.

Figure 1 shows a typical plot of the birefringence Δn vs. the squared electric field intensity E^2 for solutions of PTMSP-1 fraction no. 1 in CCl_4. Figure 2 presents the concentration dependences of the specific Kerr constant for PTMSP-1 fractions in CCl_4. By extrapolating these plots to $c = 0$, we estimated the constant K.

The hydrodynamic characteristics of the fractions and of the nonfractionated PTMSP-1 sample were measured in cyclohexane solutions. Cyclohexane afforded the maximal refractive index increment dn/d_c =

Table 2. Hydrodynamic and electrooptical characteristics of PTMSP-1 fractions

Fraction no.	$[\eta]/k'$ ($[\eta]$, $cm^3\ g^{-1}$)		$D_0 \times 10^7$, $cm^2\ s^{-1}$	$S_0 \times 10^{13}$, s	$M_{SD} \times 10^{-3}$ (CH)	$K \times 10^{10}$, $cm^5\ g^{-1}\ (300\ V)^{-2}$ (CCl_4)
	CCl_4	CH				
1	91/0.22	90/0.72	2.01	–	197	2.6
2*	103/0.21	–	–	–	186	1.6
3	85/0.33	100/0.44	1.95	3.11	172	2.0
4	–	53/0.21	3.28	2.57	84	–
6*	64/0.23	–	–	–	92	1.5
7	–	88/0.43	2.04	3.32	175	3.5
8*	48/0.22	–	–	–	60	1.0
9	68/0.06	74/0.44	2.71	2.55	101	1.5
11*	18/0.11	–	–	–	14	1.0
12	58/0.10	50/0.54	3.58	2.23	67	1.0
13	54/0.10	40/0.46	4.11	2.15	56	0.9

* The M_{SD} parameter for fraction nos. 2, 6, 8, and 11 of the PTMSP-1 sample were estimated using the relationship $[\eta]_{CH} = 2.59 \times 10^{-2}\ M_{SD}^{0.68 \pm 0.07}$ which was experimentally determined for this homologous series; the $[\eta]_{CCl_4}/[\eta]_{CH}$ ratio was taken equal to 1.04 for the fractions on the average.

0.16 for the polymer–solvent system, ensuring appropriate precision of methods based on optical and polarization-optical techniques [9, 10]. Shtennikova *et al.* [11] studied the hydrodynamics of PTMSP-2 molecules for the homologous series of its fractions.

Accelerated sedimentation was studied on an MOM 3180 analytical ultracentrifuge in a one-sector cell at rotor rotation rate $n = 40 \times 10^3$ rpm. For details of the procedure for recording sedimentation boundary and of the method for measuring the translational diffusion used in this work, see [10]. The sedimentation coefficients S were calculated by the formula

$$S = \omega^{-2}(\Delta \ln X/\Delta t),$$

where ω is the angular velocity; X, the position of the sedimentation boundary at instant of time t; and $(\Delta \ln X/\Delta t)$, the rate of displacement of the sedimentation boundary with time, determined experimentally from the slope of the time dependence of $\Delta \ln X$.

The translational diffusion was studied in a Tsvetkov's diffusometer by the classical method for forming the solution–solvent boundary whose position was recorded at certain time intervals using a polarization interferometer [9, 10]. The diffusion interferograms were processed by the method of maximal ordinate and area [10]. The diffusion coefficient $D = (1/2)(d\sigma^2/dt)$ was calculated from the slope of the experimental dependence of the diffusion boundary variance σ^2 on experiment duration t. The S and D parameters estimated for several concentrations were extrapolated to zero concentration of the solutions. Therefore, we provided with subscripts 0 the diffusion and sedimentation coefficients to be used below (D_0 and S_0, respectively).

The molecular weights of the PTMSP-1 and PTMSP-2 samples and fractions were calculated by the Svedberg formula [9, 10]

$$M_{SD} = [RT/(1 - \nu\rho_0)](S_0/D_0), \qquad (2)$$

where R is the universal gas constant; T, the absolute temperature; ν, the specific partial volume of the polymer in solution; and ρ_0, the solvent density.

The specific partial volume ν of the nonfractionated PTMSP-1 sample in cyclohexane was estimated picnometrically to be 0.995 $cm^3\ g^{-1}$ [10].

The intrinsic viscosities $[\eta]$ of nonfractionated samples and fractions were determined from the Huggins plots [10]

$$\eta_{sp}/c = [\eta] + k'[\eta]^2 c,$$

where $\eta_{sp} = (\eta - \eta_0)/\eta_0 = (t - t_0)/t_0$; η and η_0, the solution and solvent viscosities, respectively; t and t_0, the outflow times for, respectively, the solution and solvent in an Ostwald viscometer; and k', the Huggins constant.

Table 2 presents the hydrodynamic characteristics of the PTMSP-1 fractions studied. The viscometric

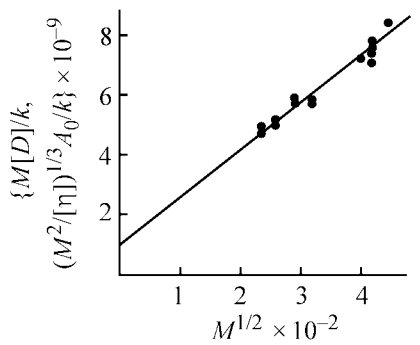

Fig. 3. Plot of $M[D]/k$ and $(M^2[\eta])^{1/3}A_0/k$ vs. $M^{1/2}$ for PTMSP-1 fractions and nonfractionated PTMSP-1 sample in cyclohexane. Both dependences for seven fractions and nonfractionated PTMSP-1 sample were approximated by the same curve for estimating A and d.

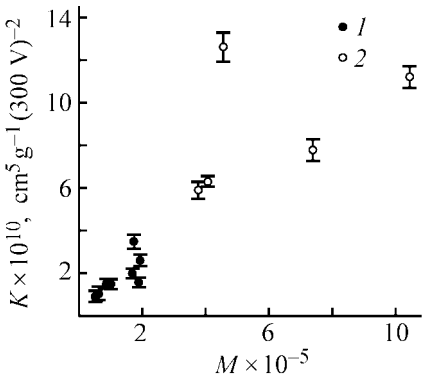

Fig. 4. Specific Kerr constant K in the Gaussian region of M for (*1*) PTMSP-1 fractions in CCl_4 and (*2*) PTMSP-2 fractions in toluene. The experimental inaccuracies in determining K are significantly smaller than the scatter in the K values for individual fractions of PTMSP-1 and PTMSP-2.

and diffusion measurements were carried out at 25 ± 0.1°C, and fractionation and electrooptical measurements, at 21 ± 0.1°C.

One of our goals was to estimate the equilibrium rigidity (or the length of the Kuhn statistical segment A [10]) of the PTMSP-1 molecules. The conformations of the PTMSP-2 molecules were characterized in [11]. The equilibrium rigidity of the chains of the PTMSP-2 molecules A was estimated to be 90 ± 10 Å, and the hydrodynamic chain diameter d, to be 7.5 ± 0.5 Å [11].

The equilibrium rigidity of the PTMSP-1 molecules was estimated in terms of the theoretical model of translational friction of persistent chains, as it was done previously for PTMSP-2 [11]. Figure 3 shows the plot constructed for the relation

$$[S]N_A = M_{SD}[D]/k = (M_{SD}^2/[\eta])^{1/3}A_0/k$$
$$= P_0^{-1}(M_L/A)^{1/2}M_{SD}^{1/2} + (M_L/3\pi)[\ln(A/d) - \varphi(0)], \quad (3)$$

where $[S] = S_0\eta_0/(1 - \nu\rho_0)$; $[D] = D_0\eta_0/T$; N_A is the Avogadro number; k, the Boltzmann constant; P_0 = 5.11 [9, 10]; $A_0 = 3.31 \times 10^{-10}$ g cm^2 s^{-2} deg^{-1} mol$^{-1/3}$, the average experimental hydrodynamic invariant [9] for this series of fractions; M_L, the weight of the chain length unit; $\varphi(0)$ = 1.056 [12]; and $\varphi(0)$ = 1.431 [13].

Relation (3) was used for estimating the length of the Kuhn statistical segment A and the hydrodynamic chain diameter d of the PTMSP-1 molecules in terms of the theory of translational friction of polymer chains modeled by worm-like cylinders [12] or a worm-like necklace [13]. The slope of the curve extrapolating the dependence of the hydrodynamic characteristics MD_0 or $(M^2/[\eta])^{1/3}$ on $M^{1/2}$ can be used for estimating the Kuhn segment length, and the intercept on the ordinate axis, for estimating the hydrodynamic diameter of the polymer chain [9].

The Kuhn segment length A for PTMSP-1 molecules was estimated to be 67 ± 7 Å both from the experimental data on the translational mobility and intrinsic viscosity of the fractions of this sample and by substituting $M_L = 44.8 \times 10^8$ g mol^{-1} cm^{-1} from [11] in relation (3). The parameter A for PTMSP-1 molecules is smaller than that for PTMSP-2 molecules. Using the plot from Fig. 3, the hydrodynamic diameter d of the PTMSP-1 molecules was estimated to be 4 ± 2 Å in [12] and 3 ± 1.5 Å in [13]. These values disagree with the calculated value, but, in our case, this can be attributed to the small number of the members in the homologous series of fractions and to only fourfold variation range of their M, which is responsible for significant inaccuracy in determining the conformational parameters of the polymer chains [9, 10].

Thus, the hydrodynamic behavior of the PTMSP samples prepared with different catalysts interpreted in terms of the same model, showes that the conformational characteristics of their chains are different and that the equilibrium rigidity of the PTMSP-1 molecules ($NbCl_5$ catalyst) is smaller than that of the PTMSP-2 molecules ($TaCl_5$/BuLi catalyst).

A study of the equilibrium electrooptical properties of the PTMSP-1 and PTMSP-2 fractions showed the following. First, the Kerr effect for solutions of PTMSP-2 fractions exceeds several times that for PTMSP-1 fractions (Fig. 4). Second, in both fraction

series the specific Kerr constant K is variable for fractions with M belonging to the Gauss region of properties, which is absolutely untypical of polymer homologs [9]. The fact that the specific Kerr constant is independent of M in the region where the polymer chains are described by the Gauss statistics has been confirmed theoretically for a number of models and experimentally for various polymer classes [9]. With nonfractionated PTMSP samples as an example, it has been shown that the above-mentioned feature of the electrooptical properties of PTMPS cannot be attributed to the solvent effect, since the difference in the K values for samples is independent of the thermodynamic quality of the polymer–solvent system. All the above-mentioned facts suggest that the isolated fractions are, evidently, nonhomologous in their microstructures, e.g., in the average number of the monomeric units constituting the regularly structured blocks. The different degrees of the intramolecular ordering of the bonds may be responsible for differences in the optical and dipole characteristics of the macromolecules of individual fractions of PTMSP-1, 2.

The possible differences in the conformational characteristics of the PTMSP chains as dependent on the presence of *cis* or *trans* stereo blocks in the polymer chains were analyzed for decameric chain fragments by the PM3 semiempirical quantum-chemical method [14, 15]. We found that, for both all-*cis* and all-*trans* decamers, the most energetically advantageous are coiled conformations. Specifically, for all-*trans* decamer this is a 4_1 coil, in which four monomeric units constitute the coil pitch, and for the all-*cis* decamer, a more strongly folded 3_1 coil in which the chain segment of the length identical with 4_1 coil accommodates a larger number of monomeric units (Fig. 5). By calculating the polarity and anisotropy of the optical polarizability of such chains, it is possible to reveal the specific features of the PTMSP molecules essential for the electrooptical properties.

Table 3 presents the calculated dipole moments μ of the propagating chain of the all-*cis* and all-*trans* decamers of PTMSP. It is seen that, in the case of coiled conformation, the longitudinal components of the dipole moments tend to accumulate (add) with each new coil turn along the chain propagation direction and the corresponding perpendicular components of the dipole moments of the PTMSP monomeric units almost totally cancel out each other. The reason is that the dipole moment component along the chain propagation direction, μ_x, is much greater than μ_y and μ_z. Therefore, the most polar coiled segments of the PTMSP chain must be oriented by the external

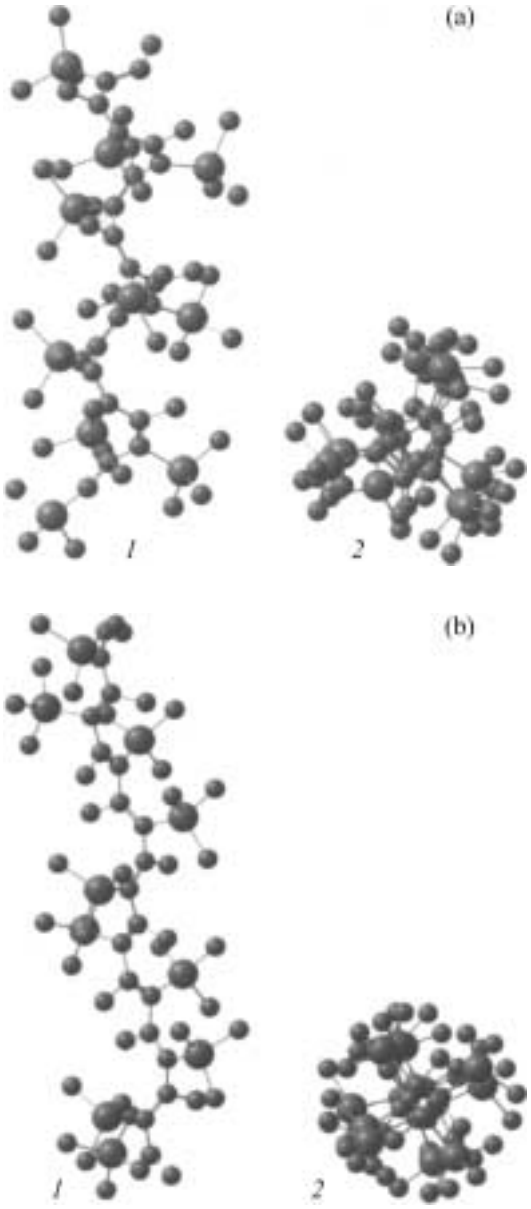

Fig. 5. Two projections of the conformations of (a) 3_1 coil of the decameric fragment of the all-*cis* PTMSP chain and (b) 4_1 coil of the decameric fragment of the all-*trans* PTMSP chain as optimized by the PM3 method. (*1*) Lateral view and (*2*) view along the coil axis. Hydrogen atoms in methyl groups are not shown.

electric field to a greater extent than noncoiled (randomly folded) segments for which the total dipole moment will be significantly smaller and the μ_x, μ_y, and μ_z components will be in another proportion. Thus, the PTMSP segments assuming the coiled conformation with the total dipole oriented along the coil axis, evidently, make the major contribution to the observed electrooptical effect owing to their orientation induced by the pulsed electric field.

Table 3. Dipole moment μ components and anisotropy of the optical polarizability, Δα, for all-*cis* and all-*trans*-*n*-mer of PTMSP H-[–C(CH_3)=C(Si(CH_3)$_3$)–]$_n$–H (n = 1–100),* calculated by the PM-3 method

n	μ_x	μ_y	μ_z	$\lvert\mu\rvert$	β, deg	Δα, Å^3	*n*	μ_x	μ_y	μ_z	$\lvert\mu\rvert$	β, deg	Δα, Å^3
	D							D					
	All-*cis* *n*-mer of PTMSP							All-*trans* *n*-mer of PTMSP					
1	0.034	0.332	0.035	0.335	84.2	3.961	1	0.070	0.165	0.004	0.180	67.1	3.563
2	0.548	0.230	0.342	0.686	37.0	4.830	2	0.550	0.017	0.216	0.591	21.5	3.799
3	0.083	0.468	0.137	0.495	80.3	1.831	3	0.935	0.000	0.147	0.946	8.7	6.484
4	0.553	0.488	0.384	0.832	48.3	1.174	4	1.117	0.061	0.127	1.126	7.2	8.075
5	1.237	0.074	0.046	1.240	4.0	8.293	5	1.466	0.138	0.147	1.479	7.8	10.837
6	1.601	0.231	0.359	1.657	14.9	10.589	6	1.821	0.165	0.208	1.840	8.2	16.120
7	2.197	0.209	0.318	2.230	9.9	16.389	7	2.282	0.301	0.058	2.302	7.6	22.021
8	2.716	0.170	0.080	2.723	4.1	20.317	8	2.609	0.088	0.076	2.612	2.7	27.294
9	3.350	0.169	0.138	3.357	3.7	27.244	9	3.038	0.117	0.098	3.042	2.9	31.795
10	3.933	0.236	0.374	3.958	6.4	34.916	10	3.413	0.133	0.314	3.430	5.7	37.668

* The conformations of *n*-mers are fully optimized and represented by 3_1 coils (for $n \geq 3$, *cis* *n*-mer of PTMSP) and 4_1 coils for $n \geq 4$ (*trans* *n*-mer). The *x* axis corresponds to the longitudinal coil axis.

According to the calculated data (Table 3), the polarity of the regular segment of the PTMPS chain is directly related to its length. This fact is of decisive importance for electrooptical properties of this class of polymers, since the specific Kerr constant K is related to the constant dipole moment of the independently oriented chain unit as [9]

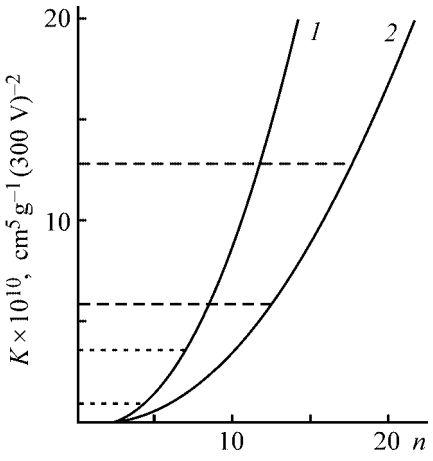

Fig. 6. Variation of the calculated Kerr constant K with the number of monomeric units, n, in independently oriented (*1*) all-*cis* and (*2*) all-*trans* fragments of the PTMSP chain. *Dashed straight lines* indicate the variation ranges for the experimental Kerr constants K of the fractions of PTMSP-1 (CCl_4 as solvent) and PTMSP-2 (toluene as solvent) samples studied.

$$K = \frac{2\pi N_A (n_0 + 2)^2 (\varepsilon_0 + 2)^2 \rho_0}{1215 kT n_0 M} \Delta\alpha \times \left[2\Delta\alpha + \frac{\mu^2}{kT}(3\cos^2\beta - 1)\right], \quad (4)$$

where M is the molecular weight of the independently orienting chain unit; Δα and μ, the anisotropy of optical polarizability and constant dipole moment, respectively; β, the angle between the dipole moment direction and the axis of the largest optical polarizability of the isolated chain fragment, respectively: n_0, ε_0, and ρ_0, the refractive index, dielectric permittivity, and density of the solvent, respectively.

Figure 6 shows how the Kerr constant K calculated for the polymeric chain of PTMSP varies with the number of monomeric units; it was assumed that its chain fragment independently oriented in the electric field corresponds to a *cis* stereo block comprising 3–10 monomeric units or to a *trans* stereo block comprising 4–10 monomeric units. In calculations, we used formula (4) and the μ, Δα, and β values from Table 3. The experimentally determined and calculated Kerr constants K agree well for the PTMSP-1 and PTMSP-2 fractions studied (Fig. 6). This suggests that these fractions can constitute polar stereo blocks of variable length, whose orientation in the electric field is responsible for the observed difference in their electrooptical properties.

Table 4. Geometric parameters* and parameters characterizing the polarity and polarizabilty anisotropy of the chains for all-*trans* and all-*cis* PTMSP decamers (PM3 calculations)

Decamer	l_{coil}	d_{coil}	μ, D	Δα, Å^3	β, deg
	Å				
trans-PTMSP, 4_1 coil	9.3	8.2	3.4	37.7	4.4
cis-PTMSP, 3_1 coil	5.4	9.5	4.0	34.9	6.5

* l_{coil} is the coil period, and d_{coil}, the coil diameter.

Table 4 lists the calculated geometric parameters and the parameters characterizing the polarity and anisotropy of the optical polarizability for the fully optimized *cis* and *trans* decamers of the PTMSP chain. It is seen that the dipole moments μ and the anisotropy of optical polarizability, Δα, for both types of regular decameric fragments of the PTMSP chains are close (despite the difference in the geometry of the 3_1 and 4_1 coils). This must be manifested in closely similar electrooptical properties of the PTMSP samples containing coiled fragments of both all-*cis* and all-*trans* chains with close numbers of their constituent double carbon-carbon bonds (see in Table 3 the characteristics of the PTMSP chains with identical numbers of the monomer units). Clearly, the observed difference in optical birefringence in the electric field between solutions of PTMSP-1 and PTMSP-2 fractions must be only due to the difference in the lengths of the polar regular sequences of the C=C bonds assuming the coil conformations which are part of the chains of these polymers.

The variation ranges for the experimentally determined constant K for PTMSP-1 fractions in CCl_4, $(0.9–3.5) \times 10^{-10}$ cm^5 g^{-1} (300 V)$^{-2}$, and for PTMSP-2 fractions in toluene, $(5.9–12.6) \times 10^{-10}$ cm^5 g^{-1} (300 V)$^{-2}$, were compared with the corresponding calculated constants K (Fig. 6). The comparison showed that PTMSP-1 fractions may contain regular *cis* or *trans* sequences of C=C bonds comprising 4–7 monomer units, and the fractions of the PTMSP-2 sample may contain longer regular blocks comprising 11–18 monomer units.

The fact that the PTMSP-2 chains contain longer, compared to the PTMSP-1 chains, coiled (and thus more rigid) fragments is consistent with the enhanced equilibrium rigidity of the PTMSP-2 macromolecules, compared to PTMSP-1, as suggested by the hydrodynamic data.

CONCLUSIONS

(1) Electrooptical and hydrodynamic properties of the fractions of samples of poly-(1-trimethylsilyl-1-propynes)-1 and -2 samples with close average *cis–trans* ratios for C=C bonds were studied. The molecular characteristics of these polymers in solutions are governed by the presence in their chains of rather long coiled regular sequences of C=C bonds, strongly differing in the polarity and rigidity from randomly folded chain segments.

(2) The microstructure of the chains of poly-(1-trimethylsilyl-1-propynes) depends on the catalyst used for polymerizing the initial monomer, 1-trimethylsilyl-1-propyne.

(3) The electrooptical characteristics of the fractions of poly-(1-trimethylsilyl-1-propynes)-1 and -2 vary in the Gaussian region of molecular weights. This suggests a significant polydispersity of the samples with respect to the length of regular *cis* or *trans* sequences of C=C bonds (stereo blocks) and uniformity of their distribution in the chains of poly-(1-trimethylsilyl-1-propynes) synthesized using the above-mentioned catalysts.

ACKNOWLEDGMENTS

The authors are grateful to V.S. Khotimskii for providing samples of poly-(1-trimethylsilyl-1-propynes) for fractionation and the data on the average *cis–trans* ratio for C=C bonds in their composition.

REFERENCES

1. Masuda, T. and Higashimura, T., *Acc. Chem. Res.*, 1984, vol. 17, pp. 51–68.
2. Masuda, T. and Higashimura, T., *Adv. Polym. Sci.*, 1987, vol. 81, pp. 121–159.
3. Khotimskii, V.S., Chirkova, M.V., Litvinova, E.G., *et al., Vysokomol. Soedin., Ser. A*, 2001, vol. 43, no. 6, pp. 949–956.
4. Odani, H. and Masuda, T., *Polymer for Gas Separation*, Toshima, N., Ed., New York: VCH, 1991.
5. Plate, N.A., Antipov, E.M., Teplyakov, V.V., *et al., Vysokomol. Soedin., Ser. A*, 1990, vol. 32, no. 6, pp. 1123–1138.
6. Masuda, T., Isobe, E., and Higashimura, T., *Macromolecules*, 1985, vol. 18, pp. 841–845.
7. Plate, N.A., Bokarev, A.K., Kaliuzhnii, N.E., *et al., J. Membr. Sci.*, 1991, vol. 60, no. 1, pp. 13–18.

8. *New Methods of Polymer Characterization*, Ke, B., Ed., New York: Interscience, 1964.
9. Tsvetkov, V.N., *Zhestkotsepnye polimernye molekuly* (Rigid-Chain Polymer Molecules), Leningrad: Nauka, 1986.
10. Tsvetkov, V.N., Eskin, V.E., and Frenkel', S.Ya., *Struktura makromolekul v rastvorakh* (Structure of Macromolecules in Solutions), Moscow: Nauka, 1964.
11. Shtennikova, I.N., Kolbina, G.F., Khotimskii, V.S., *et al.*, *Vysokomol. Soedin., Ser. A*, 1998, vol. 40, no. 10, pp. 1569–1576.
12. Yamakawa, H. and Fudjii, M., *Macromolecules*, 1974, vol. 7, no. 1, pp. 128–134.
13. Hearst, J.E. and Stockmayer, W., *J. Chem. Phys.*, 1962, vol. 37, no. 7, pp. 1425–1432.
14. Stewart, J.J.P., *J. Comput. Chem.*, 1989, vol. 10, pp. 209–220.
15. Kurtz, H.A., *Int. J. Quant. Chem. Quant. Chem. Symp.*, 1990, vol. 24, pp. 791–798.

Russian Journal of Applied Chemistry, Vol. 75, No. 10, 2002, pp. 1673–1677. Translated from Zhurnal Prikladnoi Khimii, Vol. 75, No. 10, 2002, pp. 1707–1711.
Original Russian Text Copyright © 2002 by Kurenkov, Antonovich, Khusainova.

MACROMOLECULAR CHEMISTRY AND POLYMERIC MATERIALS

Copolymerization of Acrylamide with Sodium 2-Acrylamido-2-methylpropanesulfonate in Aqueous Salt Solutions

V. F. Kurenkov, O. A. Antonovich, and A. F. Khusainova

Kazan State Technological University, Kazan, Tatarstan, Russia

Received April 8, 2002

Abstract—The kinetics of radical copolymerization of acrylamide with sodium 2-acrylamido-2-methylpropanesulfonate in water and in 1 M NaCl solutions at pH 9 and 30–50°C was studied. The kinetic data were interpreted with account of the state of the ionic groups and conformations of growing polymeric chains in the reaction mixtures.

Owing to high resistance to salts and heat, and high thickening and flocculating power, water-soluble copolymers of acrylamide (AA) with sodium 2-acrylamido-2-methylpropanesulfonate (Na-AMS) are widely used in drilling, petroleum production, and water treatment [1, 2]. The practical importance and specific features of copolymerization of ionic monomers in ionizing solutions [3, 4] invite a study of copolymerization of AA with Na-AMS in various media. The copolymerization of these monomers in aqueous solutions has been studied previously [5–7], but data on copolymerization in aqueous salt solutions are scarce [8]. In this work, we studied the kinetics of radical copolymerization of acrylamide with sodium 2-acrylamido-2-methylpropanesulfonate in aqueous salt solutions in the range 30–50°C as influenced by the state of the ionic groups and conformations of growing polymeric chains in the reaction mixtures.

EXPERIMENTAL

In our work we used acrylamide purchased from Mitsubishi Chem. Ind. Ltd. (Japan) (mp 84.5°C), H-AMS purchased from Lubrizol Corp. (United Kingdom) (mp 185°C), and other reagents of chemically pure grade. Sodium 2-acrylamido-2-methylpropanesulfonate was prepared by potentiometric titration of aqueous H-AMS solutions with aqueous solution of NaOH to pH 9; the resulting salt was used as aqueous solution.

The copolymerization procedure was similar to that described in [6]. The reaction at 50°C was initiated with potassium persulfate ([PP] = 5.9×10^{-3} M); the effect of temperature on the copolymerization in the 30–50°C range was studied using the PP–sodium hydrosulfite (SHS) redox initiating system ([PP] = 5.2×10^{-4} M, [SHS] = 3.5×10^{-4} M).

The process kinetics was monitored dilatometrically. Copolymerization was performed in 7-ml glass dilatometers; the shift of the meniscus of the reaction mixture in a dilatometer capillary in the course of reaction was monitored with a KM-8 cathetometer. The conversion of monomers into copolymer x (%) was calculated from the following expression:

$$x = \Delta V/(VK) \times 100,$$

where V and ΔV are the initial volume of the reaction mixture in the dilatometer and its change with time, respectively; and K is the contraction factor of copolymerization,

$$K = K_1\omega + K_2(100 - \omega).$$

Here K_1 and K_2 are the contraction factors for homopolymerization of Na-AMS and AA, respectively, and ω is the content of Na-AMS in the initial monomer mixture.

The factors of K_1 and K_2 were determined using the equation

$$K_1,\ K_2 = (\rho_p - \rho_m)/\rho_p,$$

where ρ_p and ρ_m are the densities of the polymer and monomer, respectively.

1070-4272/02/7510-1673 $27.00 © 2002 MAIK "Nauka/Interperiodica"

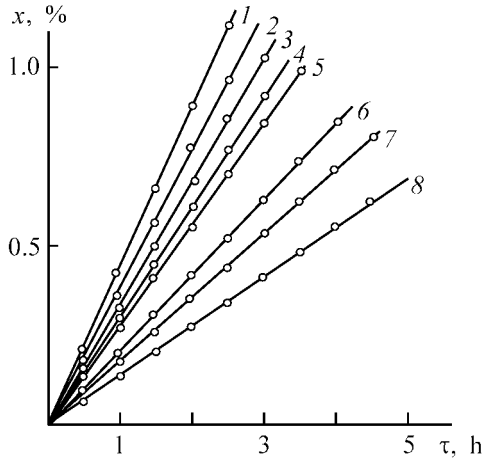

Fig. 1. Initial portions of the kinetic curves of copolymerization of AA with Na-AMS; $[M_1] + [M_2] = 10\%$. (x) Conversion and (τ) time. Mole fraction of AA in the initial monomer mixture M_1: (*1*) 0.8, (*2*) 0.7, (*3*) 0.6, (*4*) 0.5, (*5*) 0.4, (*6*) 0.3, (*7*) 0.2, and (*8*) 0.1.

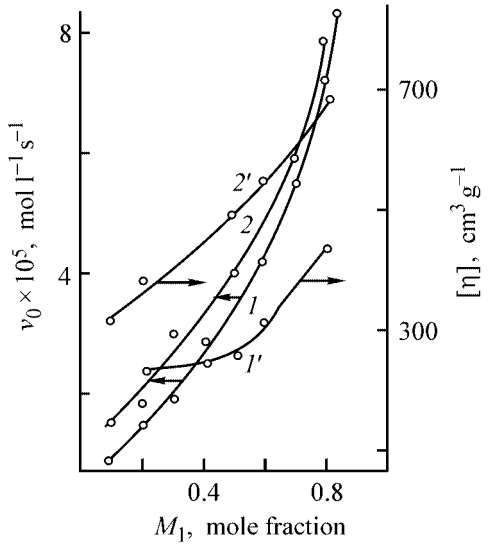

Fig. 2. (*1*, *2*) Initial copolymerization rate v_0 and (*1*′, *2*′) intrinsic viscosity of solutions [η] of AA copolymers with Na-AMS (τ = 2 h) vs. AA mole fraction in the initial monomer mixture M_1. $[M_1] + [M_2]$ = 15 wt %, [PP] = 5.92×10^{-3} M. Medium: (*1*, *1*′, *2*′) water and (*2*) 1 M aqueous NaCl. Temperature, °C: (*1*, *1*′, *2*) 50 and (*2*′) 30.

The conversion was calculated using the correction factor:

$$K = K[1 + \alpha_m(T_1 - T_2)],$$

where α_m is the volume expansion coefficient of the monomer solution; and T_1 and T_2 are, respectively, the temperatures at which the experiment was performed and the dilatometer was filled.

After copolymerization, the resulting polymers were precipitated from aqueous solutions (containing unchanged monomers) with acetone, filtered off, washed with acetone, and dried to constant weight in a vacuum. The yield of the copolymers was determined gravimetrically. The content of Na-AMS units in the copolymers was determined from the content of sulfur [9].

The molecular weight of copolymers was evaluated from the intrinsic viscosity [η] of their solutions, which was measured in a 0.5 M NaCl solution at 25°C using a VPZh-3 viscometer (d_c = 0.43 mm).

The solution acidity was measured with a pH-121 pH-millivoltmeter equipped with an ESL-63-07 working glass electrode and an EVL 1M-3 silver chloride reference electrode.

Copolymerization of AA (M_1) with Na-AMS (M_2) was carried out in concentrated solutions ($[M_1] + [M_2]$ = 10–15%) of the monomers in water and 1 M NaCl at pH 9. Maintaining pH 9 during copolymerization with PP initiator and PP-SHS initiating system [10] is necessary to provide the constant rates of initiation at changing ionic strength μ (due to changes in the Na-AMS concentration and at NaCl addition [11]) and to hinder imidization of the amide groups [12] and hydrolysis of Na-AMS [13].

Our preliminary experiments confirmed the absence of copolymerization without initiator. In the presence of initiators, copolymerization in water and in 1 M NaCl solution proceeded under the homogeneous conditions at any conversions, owing to high solubility of both copolymer and monomers.

The influence exerted by the composition of the initial monomer mixture on copolymerization was studied at $[M_1] + [M_2]$ = 10%, all other experimental conditions being the same. The initial portions of the kinetic curves of copolymerization in water, obtained by the dilatometric procedure, are shown in Fig. 1. Using the kinetic data at low conversions (x < 4%), we determined the initial copolymerization rates v_0, which are plotted in Fig. 2. As seen, v_0 of copolymers grows with increasing concentration of AA in the reaction mixture both in water (Fig. 2, curve *1*) and in 1 M aqueous NaCl (Fig. 2, curve *2*). Such a shape of the kinetic dependences $v_0 = f(M_1)$ indicates a higher reactivity of AA in the course of copolymerization as compared to Na-AMS. The higher reactivity of AA is, apparently, responsible for the increase in the copolymer yield with increasing AA content in the initial monomer mixture. The effect of AA content (M_1) on the yield of its copolymer with Na-AMS in copoly-

merization for 2 h ($[M_1] + [M_2] = 30\%$, [PP] = 5.92×10^{-3} M) is illustrated below:

M_1, mole fraction	0.1	0.2	0.3	0.4	0.7
Yield, %	67	69	90	96	93

Figure 2 shows that (a) with increasing content of AA in the initial mixture, both v_0 and [η] grow (curve *1'*); (b) higher-molecular-weight copolymers are obtained in mixtures enriched in AA; and (c) with μ increasing upon addition of NaCl, v_0 grows in a wide range of compositions of the initial monomer mixture (passing from curve *1* to curve *2*).

To explain the observed trends in copolymerization of Na-AMS with AA, we consider the ionization equilibrium of the ionic groups in Na-AMS and its units in the macroradicals in aqueous salt solutions:

$$\underset{\text{I}}{A^-X^+} \rightleftarrows A^- \parallel \underset{\text{II}}{X^+} \rightleftarrows \underset{\text{III}}{A^-} + X^+, \qquad (1)$$

where A^- is the anion of the monomer or macroradical; X^+ is the cation; and I, II, and III are the contact ion pairs, ion pairs separated with a solvent, and free ions, respectively.

As known, the ionic groups in Na-AMS and its units in the copolymer chain are completely ionized in aqueous solutions. On adding NaCl, μ and the degree of binding of Na^+ cations with polysulfonate anions increase, shifting the ionization equilibrium (1) to the left. This changes the content of various ionic species in the reaction mixture, decreases the electrostatic interaction, and affects the conformation state of the growing chains and, thus, the reactivity of ionic monomers and their macroradicals in copolymerization. In should be noted that, in the system studied, the reactivity of AA and the corresponding radical is virtually independent of μ in the course of copolymerization [14].

In copolymerization of AA with Na-AMS, raising μ decreases the electrostatic repulsion between similarly charged species in chain propagation (in reaction of Na-AMS with a macroradical containing the terminal Na-AMS unit) or termination (in reaction between macroradicals with terminal Na-AMS units), and thus increases the constants of chain propagation k_p and termination k_t. In this case, the greater increase in k_p as compared to k_t, which is confirmed by the increase in the molecular weight of the resulting copolymers (Fig. 2, curve *1'*), causes an increase in v_0 with growing μ.

The effect of μ on the conformation of macroradicals is confirmed by viscometric data for solutions

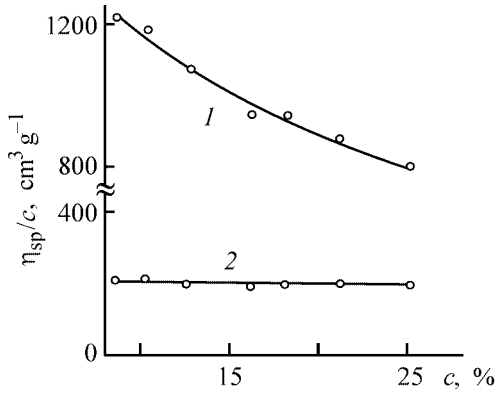

Fig. 3. Reduced viscosity η_{sp}/c of AA copolymer with Na-AMS vs. its concentration c in (*1*) water and (*2*) 1 M NaCl at 30°C. [η] = 225 cm^3 g^{-1}, 75% Na-AMS units, the same for Fig. 6.

of AA copolymer with Na-AMS (Fig. 3). Upon dilution of the copolymer solution with pure water, the $\eta_{sp}/c = f(c)$ dependence has a shape typical of polyelectrolytes (curve *1*), which is due to the increasing size of macromolecular globules as a result of stronger electrostatic repulsion of fixed charges along the polymer chain at higher degrees of ionization of the ionic groups. The increase in μ on addition of NaCl decreases the electrostatic repulsion between the sulfonate anions of the macromolecules shielded by Na^+ counterions and thus decreases the size of the polymer aggregates. In this case, the $\eta_{sp}/c = f(c)$ dependence can be described by the Huggins equation [15] (curve *2*). Hence, with increasing μ, the decrease in the chain charge and aggregate size (passing from curve *1* to curve *2*, Fig. 3) probably results in higher local concentration of Na-AMS monomer near the active centers in the course of copolymerization and thus in increased k_p and v_0.

The influence exerted by the composition of the initial monomer mixture on the instantaneous composition of copolymers was evaluated at ($[M_1] + [M_2]$ = const), other experimental conditions being the same. As seen from Fig. 4, in a wide range of the compositions of the initial monomer mixture, copolymerization in water (curve *1*) and 1 M NaCl (curve *2*) yields the copolymers enriched in AA units. This corresponds to the case when $r_1 = k_{11}/k_{12} > 1$ for AA and $r_2 = k_{21}/k_{22} < 1$ for Na-AMS, which is well consistent with published data [5]. The dependence in Fig. 4 indicates a higher reactivity of AA in copolymerization as compared to Na-AMS; with increasing AA content in the monomer mixture, the content of AA units in the copolymer grows. This suggests that, for given $[M_1]/[M_2]$ ratios, the content of Na-AMS units in the copolymer increases on adding NaCl (passing

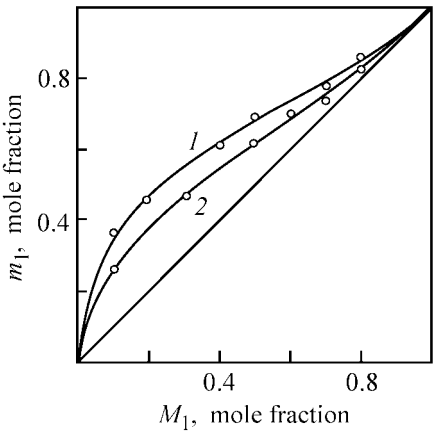

Fig. 4. Mole fraction of AA units in copolymer m_1 at x < 3% vs. conversion AA mole fraction in the initial monomer mixture M_1 at copolymerization of AA and Na-AMS in (*1*) water and (*2*) 1 M aqueous NaCl.

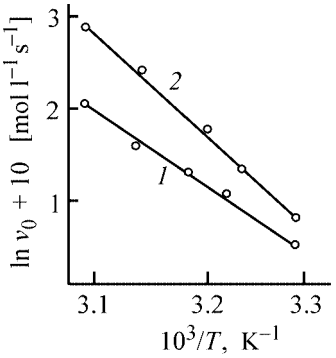

Fig. 5. Initial rate of copolymerization v_0 of AA with Na-AMS in (*1*) water and (*2*) 1 M NaCl vs. temperature T. Initial molar composition: $[M_1]/M_2] = 7:3$; $[M_1] + [M_2] = 15\%$.

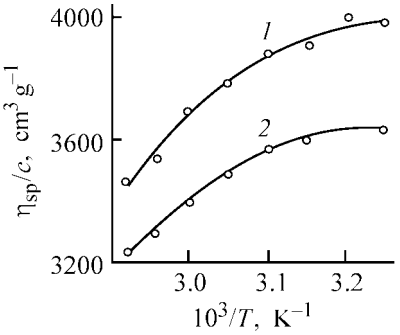

Fig. 6. Reduced viscosity η_{sp}/c of aqueous solutions of AA copolymer with Na-AMS vs. temperature T. c, %: (*1*) 0.18 and (*2*) 0.25.

from curve *1* to curve *2*), probably owing to an increase in μ. In this case, the rate constant of one of the four elementary reactions of chain propagation k_{22} (addition of Na-AMS to macroradical with terminal Na-AMS unit) increases, and a copolymer enriched in ionic units is formed. It should be noted that r_1 and r_2 in the system studied were not determined. This is due to the nonisoionic copolymerization conditions (changing μ), resulting from variation of the concentration of the ionic monomer in the initial reaction mixture and in the course of copolymerization, which affects the copolymerization constants r_1 and r_2. As a result, the process cannot be described by the classical equations [4].

The effect of temperature on copolymerization of AA and Na-AMS in water and in 1 M NaCl was studied in the range 30–50°C at $[M_1] + [M_2]$ = const and $[M_1]/[M_2]$ = const, all other conditions being the same. The experimental data, given in the Arrhenius coordinates (Fig. 5), correspond to an effective overall activation energy of copolymerization E_a of 57.4 and 79.7 kJ mol^{-1} in water and 1 M NaCl, respectively. It should be noted that the changes in the conformational state of the macroradical with temperature affect the above values, which is confirmed by viscometry (Fig. 6). As seen from Fig. 6, the linear size of macromolecules decreases with increasing temperature, which is due to the weakening of electrostatic repulsion of fixed charges along the chain with decreasing ionization of the ionic groups. This, in turn, results in that the local concentration of Na-AMS near the active centers and, hence, v_0 increase with temperature. Figure 5 also shows that on passing from water to 1 M NaCl (curves *1*, *2*), E_a increases too. This is probably due to changes in the electrostatic interaction of the reacting species and conformational state of macroradicals in the course of copolymerization. With increasing temperature, [η] of the polymers prepared decreases in a wide range of concentrations of the initial monomer mixtures (Fig. 2, curves *1'*, *2'*), in agreement with common trends observed in radical copolymerization.

CONCLUSIONS

(1) The copolymerization rate v_0, yield, and intrinsic viscosity [η] of copolymers grow with increasing concentration of acrylamide in the initial monomer mixture.

(2) The v_0 values increase with temperature and on adding NaCl, [η] grows with decreasing temperature.

(3) Copolymers enriched in acrylamide units are formed in a wide range of compositions of the initial monomer mixture, and their content grows with increasing initial concentration of acrylamide and on passing from 1 M NaCl to water.

REFERENCES

1. Lisovtsev, V.V., Rostokin, G.A., and Kulikova, A.E., in *Khimicheskaya promyshlennost'. Akrilaty i polivinilkhlorid* (Chemical Industry. Acrylates and Polyvinyl Chloride), Moscow: NIITEKhIM, 1984, pp. 1–20.
2. McCormik, C.L., *J. Macromol. Sci. Chem., Ser. A*, 1985, vol. 22, nos. 5–7, pp. 955–982.
3. Kabanov, V.A. and Topchiev, D.A., *Polimerizatsiya ionizuyushchikhsya monomerov* (Polymerization of Ionizable Monomers), Moscow: Nauka, 1975.
4. Kurenkov, V.F. and Myagchenkov, V.A., *Zh. Prikl. Khim.*, 1999, vol. 72, no. 6, pp. 881–890.
5. McCormik, C.L. and Chen, G.S., *J. Polym. Sci., Polym. Chem. Ed.*, 1982, vol. 20, no. 3, pp. 817–838.
6. Kurenkov, V.F., Khairulin, M.R., and Utikeeva, A.R., *Zh. Prikl. Khim.*, 1999, vol. 72, no. 7, pp. 1177–1181.
7. Kurenkov, V.F., Zaitseva, O.A., and Kudryashova, G.N., *Zh. Prikl. Khim.*, 2002, vol. 75, no. 4, pp. 655–658.
8. Kurenkov, V.F. and Utikeeva, A.R., *Vysokomol. Soedin., Ser. A*, 2000, vol. 42, no. 4, pp. 587–593.
9. Charlot, G., *Les methods de la chimie analytique. Analyse quantitative minerale*, Paris: Masson, 1961. Translated under the title: *Metody analiticheskoi khimii*, Moscow: Khimiya, 1969, pp. 988–989.
10. Kholodnova, L.V., Pavlyuchenko, V.N., Alekseeva, Z.M., and Andreeva, A.I., in *Kataliticheskie i initsiiruyushchie sistemy dlya sinteza i modifikatsii polimerov* (Catalytic and Initiating Systems for Synthesis and Modification of Polymers), Leningrad: Plastpolimer, 1984, pp. 90–104.
11. Kolthoff, I.M. and Miller, I.K., *J. Am. Chem. Soc.*, 1951, vol. 73, no. 7, pp. 3055–3059.
12. USSR Inventor's Certificate, no. 235997.
13. *2-Acrylamido-2-methylpropane Sulfonic Acid Monomer*, Wickliffe, Ohio (USA): Lubrizol, 1994, pp. 1–18.
14. Topchiev, D.A., Shakirov, R.Z., Kalinina, L.P., *et al.*, *Vysokomol. Soedin., Ser. A*, 1972, vol. 14, no. 3, pp. 581–586.
15. Morawetz, H., *Macromolecules in solution*, New York: Wiley & Sons, 1965.

Russian Journal of Applied Chemistry, Vol. 75, No. 10, 2002, pp. 1678–1682. Translated from Zhurnal Prikladnoi Khimii, Vol. 75, No. 10, 2002, pp. 1712–1716.
Original Russian Text Copyright © 2002 by Nud'ga, Petrova, Klishevich, Litvinova, Babenko, Shelegedin.

MACROMOLECULAR CHEMISTRY AND POLYMERIC MATERIALS

Synthesis and Microbiological Stability of Graft Copolymers of *N*-Vinylpyrrolidone and Chitosan

L. A. Nud'ga, V. A. Petrova, N. V. Klishevich, L. S. Litvinova, A. Yu. Babenko, and V. N. Shelegedin

Institute of Macromolecular Compounds, Russian Academy of Sciences, St. Petersburg, Russia
St. Petersburg State Technological University of Plant Polymers, St. Petersburg, Russia
St. Petersburg State Polytechnic University, St. Petersburg, Russia

Received May 31, 2002

Abstract—The kinetics of homogeneous graft polymerization of *N*-vinylpyrrolidone on chitosan, initiated by ammonium peroxodisulfate, was studied in relation to the reactant concentrations. The reaction orders with respect to the monomer, initiator, and matrix polymer were determined. The compositional nonuniformity and microbiological stability of the copolymer were evaluated.

Poly-*N*-vinylpyrrolidone (PVP) is a hemocompatible water- and plasma-soluble synthetic polymer exhibiting a wide spectrum of biological activity; it is used in clinical practice. The natural polymer chitosan (CAN) is biocompatible; it causes no allergic reactions and exhibits antimicrobial effect, lacking in the case of PVP. Chitosan films are used in surgery for treating wounds, in particular, those originating from burns. Such films not only mechanically protect the wound from the environment, but also stimulate regeneration of the damaged tissue, favoring formation of fibroblasts, histiocytes, and immunocompetant cells. As a result, the wounds heal faster, with decreased formation of fibrous tissue [1]. Combination of the properties of PVP and CAN in single compound would be useful for developing multifunctional biomaterials for wound healing and carriers for various drugs. The most convenient way of combining PVP and CAN is to prepare graft copolymers.

Graft copolymers of PVP and acrylic monomers are used for preparing fiber-forming materials [2]. In this case, polymerization is performed under homogeneous conditions (heating in the presence of peroxide initiators). Copolymers with grafted pendant PVP chains are prepared under heterogeneous conditions in aqueous solutions of *N*-vinylpyrrolidone (*N*-VP), with radiation or redox initiation. Copolymers of this kind with cellulose exhibit good dyeability [3]. Grafting of PVP to polymethylsiloxane with the aim to prepare new complexing materials was performed in toluene (AIBN initiator). The process started in solution, with transition to a two-phase disperse system. The content of PVP in the graft copolymer reached 50% [4].

Copolymerization of CAN with various monomers is performed to improve the elastic properties of films [5], prepare microspheres with incorporated drugs [6], and enhance the mechanical characteristics of membranes [7]. Cerium compounds, redox systems, or peroxo salts are used as initiators. The possibility of formation of PVP–CAN copolymers in the course of radical polymerization of *N*-VP in the presence of CAN was mentioned in [8], but neither the course of graft polymerization nor composition of the copolymers were reported.

In this work, we studied graft polymerization of *N*-VP on CAN in acetic acid solution in the presence of ammonium peroxodisulfate initiator in relation to the reactant concentrations and examined the compositional nonuniformity and microbiological stability of the copolymers.

EXPERIMENTAL

N-Vinylpyrrolidone was distilled in a vacuum; the fraction with bp 81.1–81.5°C (5 mm Hg) was taken. Ammonium peroxodisulfate (APS) was recrystallized from water. Chitosan was isolated from North Sea crimp shells; degree of deacetylation 0.88, molecular weight 1.87×10^5. Graft polymerization was performed under homogeneous conditions at 333 K without stirring. The reaction mixture was prepared from appropriate amounts of CAN (4% solution in 2% ace-

1070-4272/02/7510-1678 $27.00 © 2002 MAIK "Nauka/Interperiodica"

tic acid) and monomer, which were stirred with a magnetic stirrer; the initiator was added last, after which the mixture was transferred into a temperature-controlled Hoeppler viscometer. The reaction time was measured from the moment when the temperature of the reaction mixture reached 333 K. The reaction kinetics in relation to the concentrations of *N*-VP, APS, and CAN was monitored by variation of the bromine number in samples taken at regular intervals and by the dynamic viscosity of the reaction mixture. The viscosity was measured in parallel experiments.

The compositional nonuniformity was studied by successive extraction of films prepared from the reaction mixture with water and chloroform, and also by thin-layer chromatography. Separation was performed with TLC plates on Polygram MN 300 DEAE supports (Masherey-Nagel, Germany). The spots of CAN, PVP, and the copolymer were developed with a solution of iodine in chloroform. The homopolymers and copolymer were separated by step chromatography in a chamber filled with nitrogen; the first eluent was ethanol (up to a height of 8 cm), and the second eluent, 2% acetic acid (additional 5 cm). Under these conditions, PVP moves with the ethanol front, and CAN, with the acetic acid front. A compound whose adsorption properties differ from those of the homopolymers, i.e., the copolymer, remains at the start.

The microbiological stability of the copolymers was tested with respect to *E. coli K 12*, *Vibrio spp. X*, *Serratia marcescens*, and *Bacillus subtillus SHgw* bacteria using 0.35% copolymer solutions. Solutions of test samples (5 ml) were seeded with appropriate amounts of bacteria and incubated at 298 K for 7 days. The bacterial growth was judged from the growth of the optical density of the medium as compared to the initial medium.

Preliminary blank experiments on measurement of the dynamic viscosity of 1% CAN solutions in PVP (molecular weight 12×10^3) in the presence of the initiator showed that the viscosity of the CAN solution decreases with time, whereas that of the PVP solution remains unchanged. This fact reflects the sensitivity of bonds in the polymer backbones to degradation in the presence of APS; the glycoside bonds between the CAN monomeric units are cleaved, whereas the C–C bonds in PVP are stable under the reaction conditions.

Figure 1 shows how the dynamic viscosity varies with time in reaction mixtures containing CAN, *N*-VP, and their mixtures in various proportions, with various amounts of APS initiator added. It is seen that, in copolymerization experiments, the viscosity

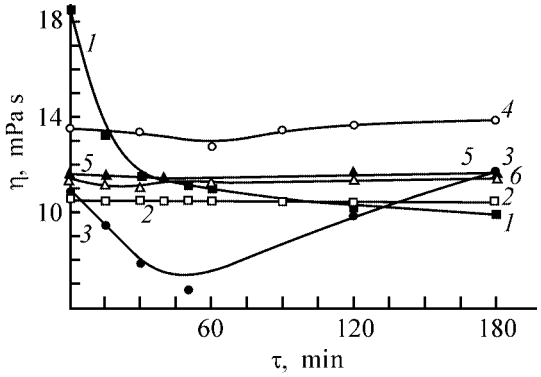

Fig. 1. Variation with time τ of the dynamic viscosity η of the reaction medium at 333 K. [CAN], M: (*1*, *3*–*6*) 0.06 and (*2*) 0. [APS], mM: (*1*, *2*, *4*, *6*) 1.2, (*3*) 3.6, and (*5*) 2.4. [*N*-VP], M: (*1*) 0, (*2*) 1.0, (*3*, *4*) 1.19, and (*5*) 2.38.

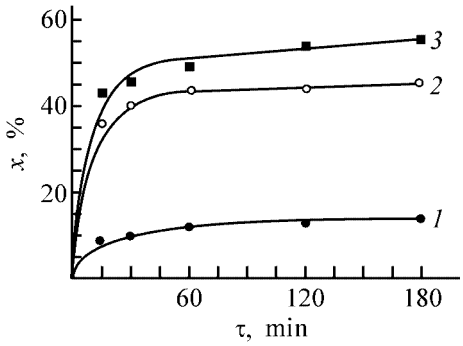

Fig. 2. Kinetic curves of graft polymerization of *N*-VP on CAN at 333 K and [CAN] = 0.06 M. [*N*-VP] = 1.19 M. [APS], mM: (*1*) 1.2, (*2*) 2.4, and (*3*) 3.6. (*x*) Conversion and (τ) time; the same for Figs. 3 and 4.

passes through a minimum at a time depending on the concentrations of the initiator and monomer and corresponding to the induction period. Radicals arising from decomposition of APS initiate both degradation of CAN and polymerization of *N*-VP. These processes exert opposite effects on the viscosity of the reaction mixture; the viscosity minimum corresponds to the moment when polymerization of *N*-VP starts to prevail over degradation. This moment can be considered the end of the induction period, although the bromine number of the reaction system starts to decrease even within 15 min after the reaction temperature is attained.

However, the reaction kinetics cannot be monitored by variation of the dynamic viscosity, because the variations are noticeable only in the initial period, and after 60 min either the viscosity flattens out or gelation occurs. Therefore, the reaction kinetics was monitored in further experiments by variation of the bromine number of the reaction mixture.

Figure 2 shows the kinetic curves of graft polymerization of *N*-VP at constant concentrations of

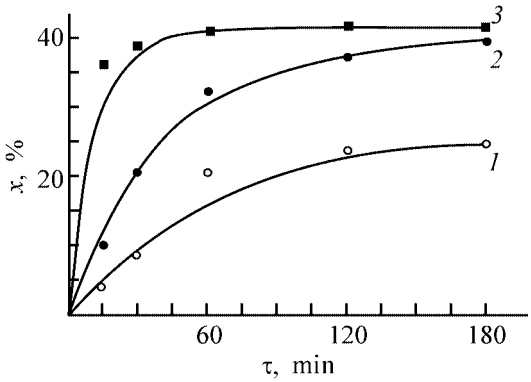

Fig. 3. Kinetic curves of graft polymerization of *N*-VP on CAN at 333 K, [CAN] = 0.06 M, and [APS] = 2.4 mM. [*N*-VP], M: (*1*) 1.19, (*2*) 1.78, and (*3*) 2.38.

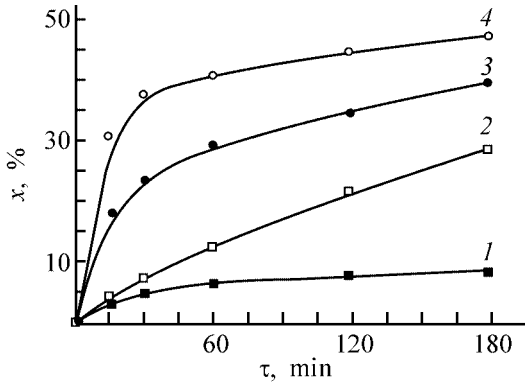

Fig. 4. Kinetic curves of graft polymerization of *N*-VP on CAN at 333 K, [*N*-VP] = 1.19 M, and [APS] = 2.4 mM. [CAN], M: (*1*) 0.03, (*2*) 0.06, (*3*) 0, and (*4*) 0.12.

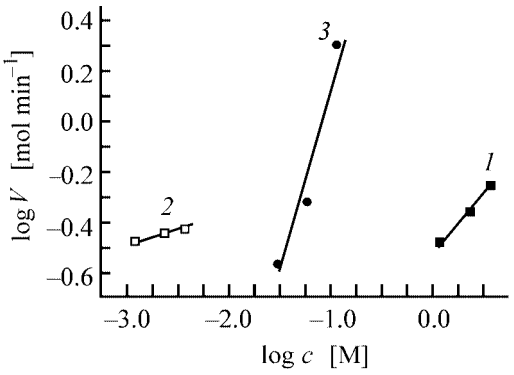

Fig. 5. Rate *V* of graft polymerization of *N*-VP on CAN at 333 K vs. concentrations *c* of (*1*) *N*-VP, (*2*) APS, and (*3*) CAN (log–log plots).

CAN and *N*-VP and different concentrations of the initiator. It is seen that the initial reaction rate and the final conversion of the monomer grow with increasing concentration of the initiator. The maximal conversion, equal to 53%, is attained at [APS] = 3.6 mM.

As the *N*-VP concentration is increased, the initial reaction rate grows, but the limiting conversion is reached faster, i.e., increased concentrations of *N*-VP favor chain termination reactions. Apparently, propagating PVP chains are mainly terminated by disproportionation. This is indicated by increased yield of the homopolymer at high [*N*-VP]. The limiting conversion of the monomer is attained in 120 min at [*N*-VP] = 1.19 M, 60 min at [*N*-VP] = 1.78 M, and 30 min at [*N*-VP] = 2.38 M (Fig. 3).

Increased concentrations of CAN, under equal other conditions, cause both the initial reaction rate and the final conversion of the monomer to increase (Fig. 4). The reaction reaches the steady-state mode within 30 min at any CAN concentrations. However, the promoting effect of CAN amino groups, noted in [9] for grafting of vinyl acetate on CAN, becomes appreciable only at [CAN] = 0.12 M. Only at this CAN concentration the initial rate and final conversion of the monomer become higher than those in polymerization of *N*-VP in the absence of CAN (Fig. 4, curve *3*). Apparently, deceleration of the polymerization of *N*-VP at low concentrations of chitosan is due to the consumption of radical ions generated by decomposition of APS for oxidation and cleavage of the CAN polymer chains, which levels out the activating effect of amino groups on the double bond in *N*-VP. Only at [CAN] = 0.12 M the loss of radicals in the system is compensated for.

On the whole, it should be noted that the monomer conversion remains low at all the reactant concentrations tested. The final product is a transparent viscous solution or (at [APS] = 3.6 mM) a gel. The 3D structure of the gel is formed by recombination of the propagating grafted PVP chains, which becomes possible when the number of growth points on the matrix polymer becomes sufficiently large. Such conditions are provided at high concentration of the initiator (in our system, at [APS] = 3.6 mM).

From the kinetic curves, we calculated the initial rates of graft polymerization at various concentrations of the reactants, constructed the log–log plots of these rates vs. reactant concentrations (Fig. 5), and determined from their slopes the reaction orders with respect to each of the reactants. We found that graft polymerization of *N*-VP on CAN is described by the equation

$$V = k[N\text{-VP}]^{0.46}[\text{APS}]^{0.11}[\text{CAN}]^{1.45},$$

where k is a coefficient.

Results of microbiological stability tests for PVP and CAN samples

Sample	CAN content, %	Variation of optical density, ΔD_{535}			
		Vibrio sp.X	*Esherichia coli K12*	*Serratia marcescens 218*	*Bacillus subtilis SHgw*
PVP	0	0.131	0.165	0.240	0.217
CAN	100	0.059	0.027	0.017	0.025
PVP–CAN mixture	30	0.077	0.028	0.019	0.034
PVP–CAN copolymer	25	0.089	0.047	0.038	0.045
PVP–CAN copolymer	10	0.103	0.066	0.055	0.073

Comparison with a similar dependence for grafting of vinyl acetate (VA) on CAN under comparable conditions [9],

$$V = k[\mathrm{VA}]^{1.03}[\mathrm{APS}]^{0.14}[\mathrm{CAN}]^{-0.08}$$

shows that, with *N*-VP, the reaction order with respect to the monomer is lower by a factor of 2, the orders with respect to the initiator are the same, and the orders with respect to CAN differ cardinally. This means that the matrix polymer affects grafting of VA and *N*-VP differently. Increased CAN concentrations negatively affect all the parameters of VA grafting, whereas grafting of *N*-VP is intensified by increased concentrations of CAN and, at certain [CAN], the rate of graft polymerization becomes higher than the rate of *N*-VP polymerization under comparable conditions in the absence of CAN.

From the reaction mixtures, we prepared transparent elastic films by drying in air in Petri dishes. Evidences of phase separation were detected neither in solutions nor in films. This indicates that PVP, CAN, and their copolymers are well compatible both in solution and in the solid phase.

Determination of the compositional nonuniformity of films by extraction with chloroform and water showed that the reaction mixtures contain both PVP homopolymer and CAN–PVP copolymer. Thin-layer chromatography also revealed these (and no other) components. The efficiency of graft polymerization did not exceed 50%. This means that homopolymerization and graft polymerization occur simultaneously with similar rates.

The results of microbiological tests of samples containing CAN as a mixture or copolymer with PVP are listed in the table.

Microbiological tests of solutions of CAN–PVP copolymers and equiconcentrated solutions of CAN, PVP, and their mixture showed that bacteria do not grow noticeably in the CAN solution but actively propagate in the PVP solution. A 70/30 mixture of PVP and CAN behaves similarly to straight CAN, i.e., it does not support the bacterial growth. In the copolymers containing 25 and 10% CAN, the bacteria propagate more slowly than in the PVP solution but faster than in the solutions of straight CAN and 70/30 mixture of PVP and CAN. These tests suggest that the microbiological stability of the copolymer or mixture under consideration depends on the CAN content and is independent of the PVP state (free or covalently bound).

CONCLUSIONS

(1) 1% CAN solutions undergo at 333 K oxidative degradation under the action of APS, whereas equiconcentrated PVP solutions are stable under these conditions.

(2) The kinetics of homogeneous graft polymerization of *N*-vinylpyrrolidone on chitosan, initiated with ammonium peroxodisulfate, was studied in relation to the concentrations of the monomer, initiator, and matrix polymer. The reaction orders with respect to each of the reactants were determined.

(3) Tests of the microbiological stability of aqueous solutions of chitosan, polyvinylpyrrolidone, and their mixture and copolymers with respect to a series of bacteria showed that the bacterial resistance of the preparations is determined by the content of chitosan in the mixture or copolymer, irrespective of the presence of a chemical bond between chitosan and polyvinylpyrrolidone.

ACKNOWLEDGMENTS

The study was supported by the Federal Target Program “Integration” (project no. A0143).

REFERENCES

1. Kifune, K., Yamaguchi, Y., and Kishimoto, S., *Trans. Soc. Biomat.*, 1988, no. 11, pp. 216–222.
2. Sidel'kovskaya, F.P., *Khimiya vinilpirrolidona i ego sopolimerov* (Chemistry of Vinylpyrrolidone and Its Copolymers), Moscow: Nauka, 1970.
3. Mal'tseva, T.A., Virnik, F.D., Pestereva, G.F., and Rogovin, Z.A., *Izv. Vyssh. Uchebn. Zaved., Tekhnol. Tekstil. Prom–sti*, 1966, no. 4, p. 92.
4. Terent'eva, L.M., Dolgoplosk, S.B., Erenburg, E.G., *et al.*, *Vysokomol. Soedin., Ser. A*, 1988, vol. 18, no. 3, pp. 482–487.
5. Wei Deging *et al.*, *Gaofenzi Xuebao*, 1995, no. 4, pp. 427–433.
6. Shauta, R.X., Baba, U., and Rao, K.P., *Eur. Polym. J.*, 1995, vol. 31, no. 4, pp. 377–382.
7. Kweon, D.K., Kaug, D.W., and Kim, W.K., *Pollimo*, 1995, vol. 19, no. 2, pp. 153–160.
8. Mukhina, V.R., Smirnova, L.A., and Semchikov, L.D., Abstracts of Papers, *Mezhdunarodnaya konferentsiya "Fundamental'nye problemy nauki o polimerakh" (k 90-letiyu akademika V.A. Kargina)* (Int. Conf. "Basic Problems of Polymer Science" dedicated to 90th anniversary of Acad. V.A. Kargin's birthday), Moscow, January 21–23, 1997, pp. 2–63.
9. Nud'ga, L.A., Petrova, V.A., Lebedeva, M.F., and Petropavlovskii, G.A., *Zh. Prikl. Khim.*, 1996, vol. 69, no. 7, pp. 1194–1199.

Russian Journal of Applied Chemistry, Vol. 75, No. 10, 2002, pp. 1683–1687. Translated from Zhurnal Prikladnoi Khimii, Vol. 75, No. 10, 2002, pp. 1717–1721.
Original Russian Text Copyright © 2002 by Zamyatin, Makovetskii, Milyavskii.

MACROMOLECULAR CHEMISTRY AND POLYMERIC MATERIALS

A Procedure for Measuring the Viscosity of Formulations Based on Oligourethane Acrylates for UV-Curable Protective Coatings of Fiber Light Guides

A. A. Zamyatin, A. N. Makovetskii, and Yu. S. Milyavskii

Institute of Radio Engineering and Electronics, Russian Academy of Sciences, Fryazino, Moscow oblast, Russia

Received June 18, 2002

Abstract—A capillary viscometric procedure was developed for measuring the viscosity of formulations based on oligourethane acrylates for UV-curable protective coatings of fiber light guides. The temperature dependences of the viscosities of these formulations were studied. The moduli of elasticity of fibers prepared from these formulations after UV curing were measured. These formulations can be stably applied, using a die, to the surface of fiber light guides in the course of their drawing at a drawing rate of up to 100–120 m min^{-1}.

It is known that, to preserve the initial mechanical strength of quartz fiber light guides (FLGs), their drawing should be combined with application of protective coatings (one- or two-layered), in particular, of polymeric coatings. Preparation of a protective coating includes two steps: application, using a die, of a liquid thermosetting or UV-curable (polymerizable) compound on the FLG surface and curing of this film in an oven or by UV irradiation.

In this work, we studied the viscosity characteristics of some UV-curable formulations for FLG protective coatings. Their study is of practical interest, since the viscosity largely governs the choice of the FLG drawing conditions. For example, the maximal drawing rate in the case of a die with liquid outflowing under gravity is restricted by the limiting shear rate in the die channel; if this rate is exceeded, the "meniscus" in the die tube is disrupted, which results in nonuniform thickness and rough surface of the coating [1, 2]. On the other hand, the minimal drawing rate is determined by the kinetics of the so-called capillary disintegration of the applied liquid film and also depends on the properties of the liquid formulation (viscosity and surface tension) [3].

Several methods have been developed for measuring the viscosity of liquids: that based on using various types of plastometers, falling ball method, and vibratory method. The corresponding devices (viscometers) are available for industrial purposes and scientific research. The oldest and the most widely used method is capillary viscometry; there are several modifications of this method suitable for various viscosity ranges [4]. Here we developed a new capillary viscometric procedure based on monitoring the movement of a liquid column in a capillary under the action of applied rarefaction.

THEORY

Consider the movement of an incompressible Newtonian liquid in a capillary under the action of rarefaction created, e.g., with a vacuum pump (Fig. 1). Let us introduce the following designations: $l(t)$, height of the liquid column at instant of time t from the start

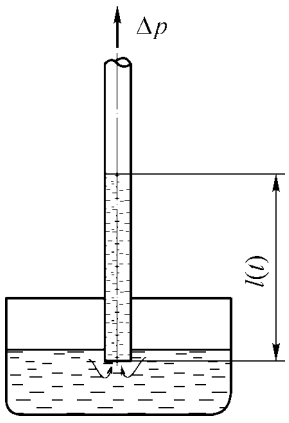

Fig. 1. Scheme of the liquid rise in a capillary under the action of applied rarefaction.

1070-4272/02/7510-1683 $27.00 © 2002 MAIK "Nauka/Interperiodica"

of the movement; μ and ρ, dynamic viscosity and density of the liquid, respectively; R, inner diameter of the capillary; Δp, rarefaction inside the capillary; and g, acceleration of gravity.

According to the Poiseuille formula, the instantaneous flow rate of a liquid $Q(t)$ at time t is given by

$$Q(t) = \frac{\pi}{8}\frac{\Delta p(t)}{l(t)}\frac{R^4}{\mu}, \quad (1)$$

where $\Delta p(t) = \Delta p - \rho g l(t)$ is the pressure in the capillary column at time t. The increment in liquid volume, $\Delta V(t)$, in the capillary in time Δt can be expressed as $\Delta V(t) = Q(t)\Delta t$. At the same time, $\Delta V(t) = \pi R^2 \Delta l(t)$, where $\Delta l(t)$ is the increment in the liquid column in time Δt. Equating both expressions for $\Delta V(t)$, we obtain

$$\Delta l(t) = \frac{1}{8}\frac{\Delta p - \rho g l(t)}{l(t)}\frac{R^2}{\mu}\Delta t. \quad (2)$$

Dividing both sides of Eq. (2) by Δt, we obtain at $\Delta t \to 0$ a differential equation for $l(t)$:

$$l'(t) = \frac{1}{8}\frac{\Delta p - \rho g l}{l}\frac{R^2}{\mu}, \quad (3)$$

which can be supplemented with the initial condition

$$l(0) = 0. \quad (4)$$

The solution to (3) and (4) is given as an implicit function of time:

$$l(t) + \frac{\Delta p}{\rho g}\log\left(1 - \frac{\rho g l(t)}{\Delta p}\right) + \frac{\rho g R^2}{8\mu}t. \quad (5)$$

Note that, for practically significant cases, Δp = 0.2–0.9 atm, ρ = 1.0–2.0 g cm^{-3}, and l = 10–20 cm.

The pressure of the liquid column $\rho g l$ is much less than the rarefaction Δp, i.e., $\rho g l/\Delta p << 1$. Using the asymptotic expansion of the function $\ln(1 + x) = x - x^2/2 + o(x)$ at $x \to 0$, we can simplify Eq. (5) and finally bring it to the following form:

$$l(t) \cong \frac{R}{2}\sqrt{\frac{\Delta p}{\mu}}\,t. \quad (6)$$

From Eq. (6) follows the formula for estimating the viscosity of an incompressible Newtonian liquid:

$$\mu \cong \left(\frac{R}{2}\right)^2 \Delta p t. \quad (7)$$

Thus, to estimate μ, it suffices to measure the time t in which a liquid rises in a capillary of radius R to a chosen level l under the action of Δp, and then to calculate the viscosity by formula (7).

Note that, if a liquid wets the capillary in an actual experiment, the pressure due to the surface tension forces acts on the liquid column in the same direction as the applied rarefaction Δp does. This pressure is given by the Laplace formula $P_L = 2\sigma\cos Q/R$, where σ is the surface tension and Q, the wetting angle. Therefore, generally speaking, the Laplace pressure should be added to the applied rarefaction in formulas (1)–(5). However, for the liquids under consideration, as will be shown below, P_L was actually always much less than Δp and was therefore neglected.

EXPERIMENTAL

The procedure was tested in experiments on measuring the viscosity of formulations for UV-curable FLG coatings.

As starting substances we used oligourethane acrylates mixed with the monomer, propylene glycol acrylate (PGA) [5]. Depending on the length of the chain linking the functional groups, oligomers are subdivided into low-molecular-weight and high-molecular-weight substances. Among low-molecular-weight oligomers, the best is bis(3-acryloyloxypropyl) 2,4-toluylenediurethane (APT), and among high-molecular-weight oligomers, OUA-2000T (molecular weight 2718). Depending on the ratio of OUA-2000T and APT, the materials are suitable for primary (soft), single-layer (intermediate-modulus), and secondary (hard) coatings. Formulations with the ratio of OUA-2000T to APT from 90 : 10 to 98 : 2 are used for primary FLG coatings; those with the ratio of OUA-2000T to APT from 15 : 85 to 25 : 75, for secondary coatings; and those with intermediate ratios, for single-layer coatings.

Propylene glycol monoacrylate (APG) is used as active diluent making lower the viscosity of formulations and thus accelerating application of coatings. APG is added to the oligomers in the ratio from 3.0 : 1 to 7.5 : 1, with the optimal ratio ranging from 4.0 : 1 to 5.0 : 1.

In the process, aromatic ketones generating free radicals in photolysis are used as photoinitiators. In this study, we used 2,2'-dimethoxy-2-phenylacetophenone (DMAP); its content was 2–3%, which is the best for curing the formulations at drawing rates of up to 100–120 m min^{-1}.

To measure the viscosity of liquids by our procedure, we assmebled a setup shown in Fig. 2. An NVR-5D roughing pump *1* created rarefaction in a vacuum tube *2* at closed valve *4* connecting the tube to the capillary *3*. The rarefaction was varied in the range

0.1–0.9 atm with reducer *5* and was monitored with manometer *6*. The end of the vacuum tube with the connected capillary was fixed on adjustment stage *7* with the aid of which the tip of the capillary was submerged in a test liquid.

The measurements were performed as follows. First, a prescribed rarefaction was created in the vacuum tube at valve *4* closed. Then, using the adjustment stage, the tip of the capillary was submerged by 0.5–1.0 mm in a test liquid, after which valve *4* was opened simultaneously with starting a stopwatch. The resulting rarefaction in the capillary was determined with the manometer and used in calculations. After the liquid column in the capillary reached a certain level *l*, the time *t* was registered. Then valve *4* was closed, and air was admitted into the capillary through valve *8*. The filled capillary was removed from the vessel with the liquid and detached from the vacuum tube.

Preliminary experiments were performed for selecting R, Δp, and l for one of formulations (no. 3) for single-layer coating. It was found that, for the range of measured viscosities from 1.0 to 50.0 Pa s, the optimal ranges of rarefaction, capillary radius, and liquid column height are Δp = 0.3–0.8 atm, R = 0.2–0.5 mm, and l = 40–100 mm; the measurement time under these conditions is 10–300 s. The choice of l is governed by the necessity for attainment of the steady-state mode of the liquid flow, and the chosen ranges of Δp and R ensure fairly high accuracy of measuring t.

As an illustration, we present below the results obtained in measuring the viscosity of formulation no. 3 for single-layer coating at various l (Δp = 0.285 atm, R = 0.245 mm):

l, mm	30	40	50	60	70	80	90
t, s	24.5	41.5	65.5	94.5	128.5	164.5	207.5
μ, Pa s	11.35	10.84	11.0	11.0	11.0	10.8	10.8

It is seen that the results of single measurements differ from the mean value by no more than ±3.5%.

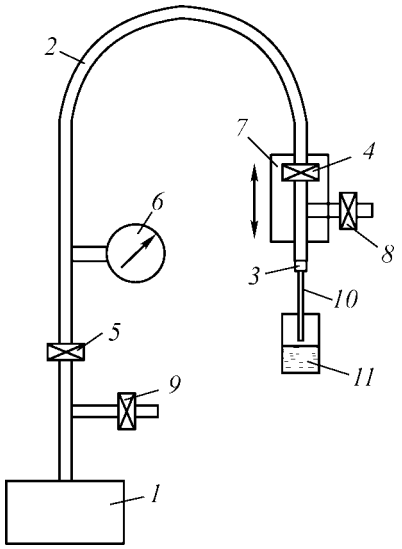

Fig. 2. Scheme of experimental setup for measuring the viscosity of liquids: (*1*) NVR-5D vacuum pump, (*2*) vacuum tube, (*3*) fitting for vacuum-tight connection of the capillary to the vacuum tube, (*4*) valve for detaching the capillary volume from the vacuum pump, (*5*) reducer for controlling the rarefaction, (*6*) OMBI1-160 manometer, (*7*) adjustment stage for submerging the capillary in a test liquid, (*8*) valve for admitting air into the capillary, (*9*) valve for admitting air into the vacuum pump, (*10*) capillary, and (*11*) vessel with a test liquid.

The results obtained in measuring the viscosity of the initial components (OUA-2000T, APT, APG) and several formulations based on them for primary (pr. no. 1), single-layer (s.l. nos. 1–5), and secondary (sec. nos. 1 and 2) coatings at room temperature (20°C) are listed in the table, together with the results for DS-5471-3-14 formulation (DeSolite) for single-layer coating (for comparison).

As seen from the table, although the viscosities of the initial components differ by 4–5 orders of magnitude, the viscosities of the formulations for primary, single-layer, and secondary FLG coatings vary in a relatively narrow range, 4.0–18.0 Pa s. Thus, the conditions for applying these coatings will be similar,

Measured the viscosity of the initial substances and coating compounds

Parameter	OUA-2000T	APT	APG	Pr. no. 1	S.l. no. 1	S.l. no. 2	S.l. no. 3	S.l. no. 4	S.l. no. 5	Sec. no. 1	Sec. no. 2	DS-5471-3-14
R, mm	0.238	0.413	0.144	0.24	0.44	0.43	0.43	0.425	0.445	0.51	0.48	0.49
Δ*p*, atm	0.30	0.60	0.1	0.3	0.3	0.31	0.30	0.30	0.295	0.32	0.31	0.3
l, mm	100	8	110	100	100	100	100	100	100	100	100	100
t, s	134.5	307.5	3.4	144	28	54	94	91	295	39.5	101	73
μ, Pa s	5.6	12050	0.014	6.1	4.0	7.8	10.8	12.1	42.0	8.05	17.7	12.9

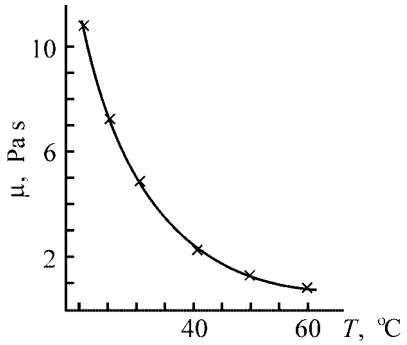

Fig. 3. Temperature dependence of the viscosity of compound no. 3 for single-layer coating of FLGs: (μ) viscosity and (*T*) polymer temperature.

which is favorable for preparing high-quality protective coatings on FLGs.

To evaluate the accuracy of our procedure, we measured the viscosity of glycerol at room temperature (20°C); the resulting value, 1.3 Pa s, is in reasonable agreement (within 15%) with the tabulated value of 1.5 Pa s [6].

Our procedure is also suitable for measuring the viscosity at varied temperature. We have studied the $\mu(T)$ dependences for several formulations. For this purpose, a cell with a test liquid was placed, together with the measuring capillary, in a quartz tubular furnace with with a coil-type heater; the motion of the liquid column in the capillary could be observed through the coil. The temperature *T* inside the furnace was maintained with an accuracy of ±0.2°C using an RTP-3M automatic temperature control unit. Figure 3 shows as an example a $\mu(T)$ plot for single-layer formulation no. 3 in the temperature range 20–60°C. For the other formulations, the $\mu(T)$ dependences were similar.

Figure 3 shows that, as the temperature is increased from 20 to 60°C, the viscosity of single-layer formulation no. 1 decreases by an order of magnitude, from 10.8 to 0.83 Pa s. At room temperature (20°C), this formulation can be successfully applied onto the FLG surface with an open die at drawing rates of up to 30 m min^{-1}. When extrusion is performed at elevated pressure and temperature (40–50°C), the drawing rate can be increased to 100–120 m min^{-1}.

Note that the capillaries filled in viscosity measurements were used for preparing fiber samples from the UV-cured formulations. For this purpose, the liquid in the capillaries was cured in a four-lamp UV irradiator used for curing FLG coatings. We used DRT-230 tubular mercury arc lamps; the lamp current I_l was about 2 A, and the exposure time, 5–10 s. After curing of the liquid core, the thin-walled capillary (50–60 μm) was broken, and the surface of the cured core was cleaned to remove glass crumb.

The thus prepared fiber samples were used for measuring the Young modulus as one of the main mechanical parameters of the coating material. The results of the measurements for a series of cured formulations at 2.5% relative elongation are listed below:

Young modulus of materials of cured formulations

Material	Pr. no. 1	S.l. no. 1	S.l. no. 2	S.l. no. 3	S.l. no. 4	S.l. no. 5	Sec. no. 1	Sec. no. 2	DS-5471-3-14
E, MPa	5.1	25.7	33.2	70.0	145.0	160.0	1700	1900	53.0

Let us comment on the effect of the surface tension σ on the results of viscosity measurements. We did not measure μ directly but evaluated the Laplace pressure in the capillary P_L from the height of the liquid rise *h*: $P_L = \rho gh$. For example, for single-layer formulation no. 3 ($\rho \approx 1.2$ g cm^{-3}) at $T = 20$°C and $R = 0.24$ mm, $h = 27$ mm, which corresponds to $P_L \approx 118$ Pa, whereas the rarefaction used in the experiment was $\Delta p \approx 29400$ Pa (0.3 atm). Thus, the contribution of the Laplace pressure can be neglected.

Let us estimate the flow shear rates in the liquids under consideration in the course of viscosity measurements. For a steady-state flow of a Newtonian liquid in a capillary, the shear rate is the highest at the capillary walls and is determined by the formula $\gamma_m = (P/L)(R/2\mu)$, where *P* and *L* are the applied pressure and the capillary length, respectively. In our case, the flow is not steady, especially in the initial period. Therefore, it is appropriate to average the shear rate over the measurement time:

$$\langle\gamma_m\rangle = \frac{l}{t}\int_0^t \gamma_m(\tau)\,d\tau. \quad (8)$$

After substituting $P \to \Delta p$ and $L \to l(t)$ [formula (6)] in the integrand and performing integration, we obtain

$$\langle\gamma_m\rangle = 2\sqrt{\frac{\Delta p}{\mu t}}. \quad (9)$$

Estimation of $\langle\gamma_m\rangle$ for the case of our viscosity measurements gives a value of 10–100 s^{-1}.

CONCLUSIONS

(1) A fast capillary procedure was developed for estimating the viscosity of Newtonian liquids, which does not require large sample volumes and washing of the viscometer in going from one sample to another; the measurement requires only 1–3 ml of a test liquid and a 15–20-cm-long capillary with an inner diameter of 200–1000 μm.

(2) By this procedure, the viscosity characteristics of UV-curable formulations based on oligourethane acrylates for protective coatings on fiber light guides were evaluated; formulations were found for primary (soft), single-layer (intermediate-modulus), and secondary (hard) FLG protective coatings, which can be stably applied with a die at FLG drawing rates of up to 100–120 m min^{-1}.

REFERENCES

1. Pack, U.C., *J. Lightwave Technol.*, 1986, vol. 4, no. 8, pp. 1048–1060.
2. Chido, K., Kimura, T., and Wagatsuma, M., *Rev. Electr. Commun. Lab.*, 1984, vol. 32, no. 3, pp. 425–431.
3. Pack, U.C. and Schroeder, C.M., *Fiber Integr. Opt.*, 1979, vol. 2, nos. 3–4, pp. 287–298.
4. Malkin, A.Ya. and Chalykh, A.E., *Diffuziya i vyazkost' polimerov: Metody izmereniya* (Diffusion and Viscosity of Polymers: Measurement Procedures), Moscow: Khimiya, 1979.
5. USSR Inventor's Certificate, no. 1662089.
6. *Spravochnik khimika* (Chemist's Handbook), Nikol'skii, B.P., Ed., Leningrad: Khimiya, 1971, vol. 1, p. 170.

Russian Journal of Applied Chemistry, Vol. 75, No. 10, 2002, pp. 1688–1691. Translated from Zhurnal Prikladnoi Khimii, Vol. 75, No. 10, 2002, pp. 1722–1725.
Original Russian Text Copyright © 2002 by Lazareva, Shinkareva.

MACROMOLECULAR CHEMISTRY AND POLYMERIC MATERIALS

Rheological and Electrophysical Characteristics of Solutions of Polyvinyl Alcohol and Water-Soluble Carboxymethyl Cellulose

T. G. Lazareva and E. V. Shinkareva

Institute of General and Inorganic Chemistry, Belarussian National Academy of Sciences, Minsk, Belarus

Received December 5, 2001; in final form, March 2002

Abstract—The flow and viscosity curves of solutions of polyvinyl alcohol and water-soluble carboxymethyl cellulose of various brands, and also of their mixtures are studied over the temperature range 30–70°C.

Water-soluble polymer and, in particular, polyvinyl alcohol (PVA) and carboxymethyl cellulose (Na-CMC) are widely used in the pulp-and-paper, varnish-and-paint, and other branches of industry. In the pulp-and-paper works, their 1–5% solutions are used for paper sizing. In this context, it is of interest to compare rheological characteristics of such solutions, as dependent on the polymer brand and concentration and the solution temperature. A study of the flow and viscosity curves as influenced by the temperature and electric and magnetic fields is necessary to evaluate the operational capacity of polymer solutions [1, 2]. The rheological properties of polymer solutions are also of interest for elucidating their structural features related to the system of intermolecular interactions, conformational transformations, and stereoregularity. Finally, the initial parameters of polymer solutions largely control the mechanical and performance characteristics of the resulting products (coatings, fibers, special-purpose paper, paints, etc.) [3].

Here we report generalized data on the rheological properties of polyvinyl alcohol and water-soluble carboxymethyl cellulose of various brands and formulations on their base.

EXPERIMENTAL

Rheological measurements were carried out with a Rheotest-2 rotary viscometer over wide the shear rate (D_r from 1 to 1350 s^{-1}) and temperature ranges (from 30 to 80°C). Mechanical action on the polymer solutions was effected by rotation of the inner cylinder of the rotary cell of the viscometer. The electrical conductivity æ and dielectric loss tangent tan δ were determined on an E7-15 instrument at a frequency of 1 kHz.

It was demonstrated experimentally that, in PVA solutions, the shear stress τ_v linearly depends on the shear rate D_r over the concentration range 1–20 wt %. Such a dependence, known as the flow curve, is one of the main rheological characteristics of fluid media. The flow curves allow classification of liquids with Newtonian or non-Newtonian fluids. For ordinary (Newtonian) fluids, the dependences of the viscosity η and shear stress τ_v on the shear rate D_r are linear, and η is independent of the shear rate and shear stress. The viscosity of non-Newtonian fluids is not constant, being dependent on the shear rate or stress [4].

In PVA solutions, the plots of η vs. D_r are different in shape, depending on the PVA brand (Fig. 1). For PVA manufactured in Japan, η at 30°C initially increases and then level off (Fig. 1, curve *1*). At 70°C, the flow curves are similar in shape. It may be suggested that, under shearing load at low shear rate,

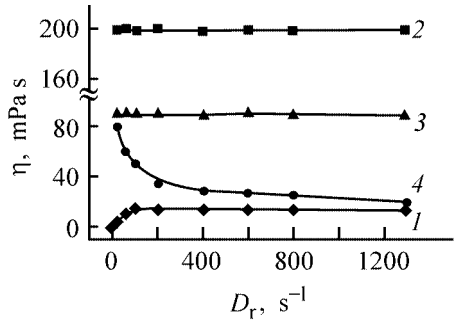

Fig. 1. Viscosity η vs. shear rate D_r in 16% PVA solutions. PVA manufacture: (*1*) in Japan and (*2–4*) in Russia (16/1). Temperature (°C): (*1*, *2*) 30, (*3*) 45, and (*4*) 70.

1070-4272/02/7510-1688 $27.00 © 2002 MAIK "Nauka/Interperiodica"

structural transformation of the macromolecules proceeds via rearrangement of the system of intermolecular interactions, resulting in an increase in viscosity. Such a trend is typical of non-Newtonian dilatant fluids, e.g., highly concentrated suspensions prepared by mixing a PVC emulsion with some liquid plasticizers (to obtain a paste) [5]. Other examples are electro- and magnetorheological media based on dispersions of polymers and metal oxides in oils or polymeric binders [1, 2].

Solutions of PVA 16/1 (Russia) demonstrate no dilatant behavior at low temperatures (30–45°C). In this temperature range, the viscosity is independent of the shear rate (Fig. 1, curves *2*, *3*). However, with the solution temperature increasing to 70°C, the dynamic viscosity decreases with increasing shear rate (Fig. 1, curve *4*). In this case, the liquid becomes readily structured, acquiring some plastic properties, as well as the capability of orientation ordering at certain shear rates.

Figure 2 shows the temperature dependences of the dielectric loss tangent. In the PVA 16/1 solutions, tan δ increases at temperatures above 60°C, which can be attributed to weakening of hydrogen bonding in the system, and, therefore, to increasing molecular flexibility of the macromolecules. As a result, the liquid becomes more readily structured, which is reflected in a change in the shape of the flow curves at the corresponding temperature (Fig. 1, curve *4*).

The structure of aqueous PVA solutions strongly depends on the polymer concentration. There are several concentration intervals characterized by specific solution structures (see table). The effect of concentration on the viscosity is more clearly pronounced in highly viscous solutions of PVA 16/1: the viscosity only slightly changes at concentrations below 5 wt %; within the concentration range 5–10 wt %, the viscosity initially grows rapidly and then more slowly again; in the PVA concentration 15–20 wt %, the viscosity increases rapidly.

The results obtained suggest that 1–20% PVA solutions can be classified with structures intermediate between Newtonian and non-Newtonian fluids. For these structures, the shear stress is still independent of the shear rate, but some anomalies are already observed in the flow curves. Evidently, the anomalous behavior is associated with structural effects occurring with increasing temperature or polymer concentration. In dilute solutions, the macromolecules are not associated. With increasing concentration, a network of hydrogen bonds is formed. Therefore, the system of intermolecular interactions and, quite possibly, the physical structure of the macromolecules [3] depend on the solution concentration, which is reflected in the features of the solution flow in the mechanical field.

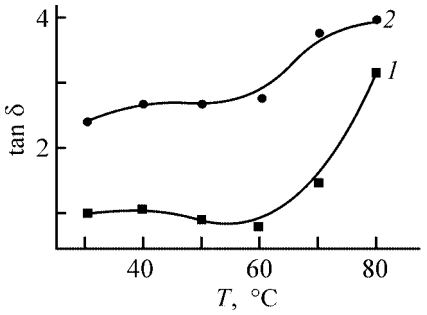

Fig. 2. Dielectric loss tangent tan δ vs. the temperature T in (*1*) 1% and (*2*) 5% PVA (16/1) solutions.

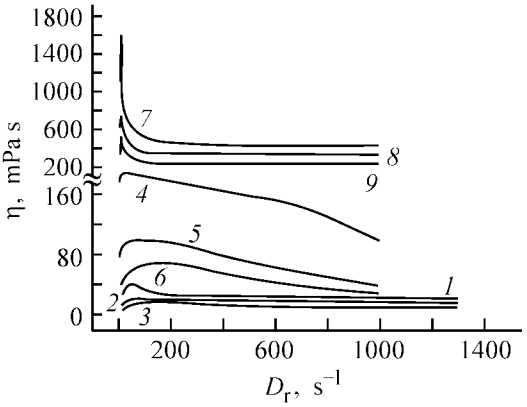

Fig. 3. Viscosity η vs. shear rate D_r in 1% Na-CMC solutions. Na-CMC grade: (*1–3*) 7MF, (*4–6*) 9M31F, and (*7–9*) 7HOF. Temperature (°C): (*1, 4, 7*) 30, (*2, 5, 8*) 50, and (*3, 6, 9*) 70.

Let us analyze the dependences of the viscosity on the shear rate for Na-CMC solutions. The flow curves considerably depend on the Na-CMC grade and solution temperature. The dependences of the viscosity at various temperatures on the shear rate for 1 wt % Na-CMC 7MF (low-viscosity grade) are given in Fig. 3 (curves *1–3*). In these curves, there is a portion of increasing viscosity at low shear rates; with increas-

Viscosity of PVA solutions of various concentrations (30°C, shear rate 81–729 s^{-1})

PVA, manufactured	Concentration range	c_{PVA}, wt %	η, mPa s
Japan	I	1–5	0.1–0.2
	II	5–12	0.2–4
	III	14–20	5–20
16/1, Russia	I	1–5	15–20
	II	5–10	20–60
	III	15–20	100–450

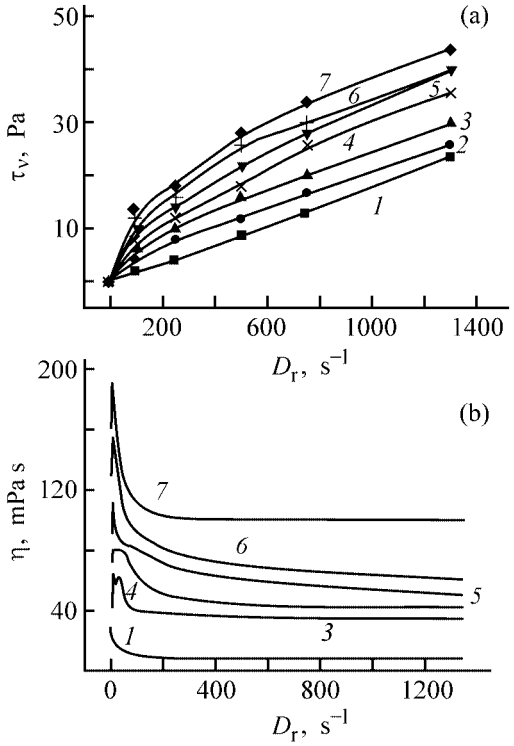

Fig. 4. (a) Shear stress τ_v and (b) viscosity η vs. shear rate D_r in solutions obtained from 10% PVA and 1% Na-CMC at 30°C. PVA : Na-CMC (wt % : wt %): (*1*) 100 : 0, (*2*) 95 : 5, (*3*) 90 : 10, (*4*) 80 : 20, (*5*) 70 : 30, (*6*) 50 : 50, and (*7*) 40 : 60.

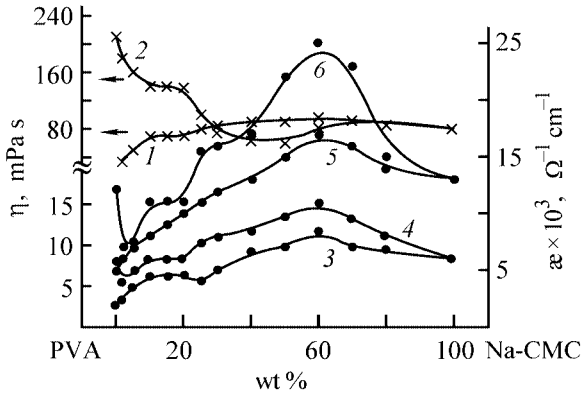

Fig. 5. (*1, 2*) Viscosity η and (*3–6*) conductivity æ vs. polymer weight ratio in mixtures obtained from (*1, 3, 4*) 5% or (*2, 5, 6*) 10% PVA and 1% Na-CMC. (*1, 2*) D_r = 16.2 s^{-1}. Temperature (°C): (*1–3, 5*) 30 and (*4, 6*) 80.

ing temperature, the viscosity maxima shift toward higher D_r (Fig. 3, curves *2*, *3*). The flow curves for Na-CMC of medium viscosity, specifically Na-CMC 9M31F, are shown in Fig. 3 (curves *4–6*). They are characterized by a diffuse peak in the range 1–1000 s^{-1}. For more viscous Na-CMC 7HOF, a strong peak is observed at low D_r, followed by rapid decrease in the viscosity (Fig. 3, curves *7–9*).

The results obtained suggest that the mechanical shear load has a considerable effect on the structure and properties of the Na-CMC solutions. With Na-CMC of low- and medium-viscosity brands, at a shear rate from 1 to 1000 s^{-1}, the initial system of intermolecular interactions can change under the action of the mechanical field with the formation of new supramolecular structures. With increasing solution viscosity, such processes occur at lower shear rates, and, at a shear rate of about 1 s^{-1}, an afterflow portion is already observed in the flow curve, as a result of the orientation of macromolecular aggregates.

The rheological properties of mixtures of PVA with water-soluble Na-CMC were studied. The mixtures were prepared from 5 or 10% PVA (16/1) and 1% Na-CMC (86/600) solutions.

It is known [3] that structures of three types can be distinguished in mixed polymer solutions. At low concentrations, the solution consists of a mixture of free macromolecules of both polymers. At higher concentrations, the solution consists of two phases, being a mixture of associated macromolecules. The effect of one polymer on the degree of association or, in other words, on the short-range order of the other polymer is reflected in structural transformation of each polymeric phase in the mixture, which is accompanied by change in the crystallization temperature, glass transition temperature [6, 7], and density of the mixture [8].

Complexes can be formed on mixing polymers with different functional groups, e.g., of PVA with polyacrylic (PAA) and polymethacrylic acids or CMC (both in the acidic and salt forms). PVA can form complexes of various structures with polyacids through hydrogen bonding. For example, Chatterjee and Malhotra [9] suggested several possible mechanisms for their formation:

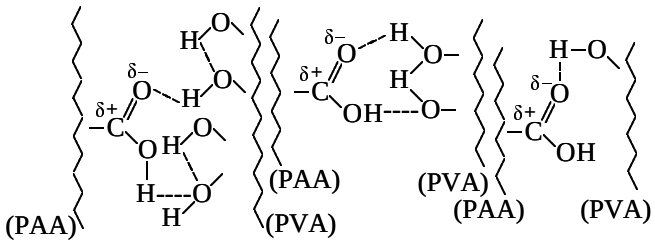

Complexation is followed by formation of associates with definite arrangement of polymer macromolecules.

In Fig. 4a, the shear stress is plotted as a function of the shear rate for mixtures prepared from 10% PVA and 1% Na-CMC. Introduction of even small concentrations of Na-CMC (PVA : Na-CMC = 95 : 5; Fig. 4a, curve *2*) changes the initial flow curve of PVA.

The resulting mixture demonstrates a behavior typical of non-Newtonian fluids. Even stronger effect of Na-CMC addition is observed in the dependence of the viscosity on the shear rate (extension of the afterflow portion) (Fig. 4b).

In Fig. 5, the viscosity η and conductivity æ of mixtures prepared from 5% or 10% PVA (16/1) and 1% Na-CMC are plotted against the polymer weight ratio. In the mixtures studied, anomalous behavior (deviation from the additive model) of the viscosity was observed, which is the most clearly pronounced at low shear rates. The anomalous behavior is reflected in the appearance of peaks and dips in the viscosity curves. The anomalies are also observed in the dependences of the electrical conductivity (Fig. 5).

The results obtained can be interpreted in terms of the concept of complexation between PVA and Na-CMC macromolecules [9]. The extension of the afterflow portion in the viscosity curves is associated with orientation of the macromolecules in the mechanical field, suggesting the formation of anisotropic structures from macromolecular associates.

CONCLUSIONS

(1) Solutions of polyvinyl alcohol and carboxymethyl cellulose of various brands differ in the nature of the viscosity and flow curves, demonstrating pseudoplastic and dilatant properties.

(2) Complexation between PVA and Na-CMC macromolecules controls the viscosity and flow behavior, as well as the electrophysical and rheological characteristics of the mixed polymer solutions. In a mechanical field, the solution acquires properties of a non-Newtonian fluid. The deviation of the electrophysical and rheological properties from the additive model is associated with the formation of anisotropic structures from macromolecular associates.

REFERENCES

1. Lazareva, T.G., Kabisheva, I.V., and Prodan, S.A., *Proc. 4th European and 2nd MIMR Conf.*, Harrogate (UK), July 6–8, 1998, pp. 149–150.
2. Lazareva, T.G., Shitik, I.G., and Gaiduk, Yu.S., *Vestsi Nats. Akad. Navuk Bel., Ser. Khim. Navuk*, 1998, no. 3, pp. 34–38.
3. Kuleznev, V.N., *Smesi polimerov* (Polymer Blends), Moscow: Khimiya, 1980.
4. Fridrikhsberg, D.A., *Kurs kolloidnoi khimii* (Course of Colloid Chemistry), Leningrad: Khimiya, 1984.
5. Schramm, G., *A Practical Approach to Rheology and Rheometry*, Karlsruhe: Gebrueder HAAKE, 1994.
6. Vinogradov, G.V., Yanovskii, Yu.G., Kuleznev, V.N., and Ivanenko, T.A., *Kolloidn. Zh.*, 1966, vol. 28, no. 5, pp. 640–644.
7. Manahe, S., Marokomi, R., and Takoynagi, M., *J. Polym. Mater.*, 1971, vol. 2, no. 1, pp. 47–73.
8. Kuleznev, V.N. and Igosheva, K.M., *Vysokomol. Soedin., Ser. A*, 1962, vol. 4, no. 12, pp. 1858–1862.
9. Chatterjee, S.K. and Malhotra, A., *Angew. Makromol. Chem.*, 1984, vol. 126, pp. 153–161.

Russian Journal of Applied Chemistry, Vol. 75, No. 10, 2002, pp. 1692–1695. Translated from Zhurnal Prikladnoi Khimii, Vol. 75, No. 10, 2002, pp. 1726–1729.
Original Russian Text Copyright © 2002 by Lazareva, Yakovleva, Shinkareva.

MACROMOLECULAR CHEMISTRY AND POLYMERIC MATERIALS

Rheological and Electrophysical Characteristics of Polyvinyl Alcohol Solutions Containing Copper and Cobalt Chlorides

T. G. Lazareva, O. V. Yakovleva, and E. V. Shinkareva

Institute of General and Inorganic Chemistry, Belarussian National Academy of Sciences, Minsk, Belarus

Received April 4, 2002

Abstract—Rheological and electrical properties of polyvinyl alcohol solutions containing copper(II) and cobalt(II) chlorides are studied. Anomalous behavior of these properties is associated with complex formation, depending on the component ratio and temperature.

Polyvinyl alcohol–based composites with transition metals, such as Cu, Co, etc., can find use for preparation of materials for various purposes (polymerization catalysts, membranes, thermochromic materials, paints, and fibers) [1]. Inorganic coordination chemistry of copper, cobalt, and iron has been quite thoroughly studied [2], while the chemistry of hybrid organo-inorganic complexes became a subject of extensive investigation only recently.

It is known [2] that Cu^{2+} can form both cationic and anionic octahedral complexes (coordination number 6). For example, blue aqua complexes $[Cu(H_2O)_6]^{2+}$ are formed in dissolution of copper(II) salts in water or by reaction of CuO or $Cu(OH)_2$ with acids. Copper(II) crystal hydrates are also mostly blue, e.g., $Cu(NO_3)_2 \cdot 6H_2O$. But they may be green and deep brown too. In this case, the coordination sphere of the cation includes both water molecules and anions. For example, in green $CuCl_2 \cdot 2H_2O$, copper atoms are surrounded by two water molecules and four chloride anions:

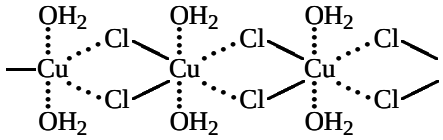

With addition of water to $CuCl_2 \cdot 2H_2O$, the solution changes its color to blue as a result of the formation of the aqua complex $[Cu(H_2O)_6]^{2+}$.

Complexation in the system polyvinyl alcohol (PVA)–Cu^{2+} has been studied in a number of works. Chelate complexes PVA–Cu^{2+} have been synthesized by adding $Cu(NO_3)_2$ and NaOH to a dilute aqueous PVA solution [3–7]. Complexation of PVA with Cu^{2+} in the presence of ammonia and *n*-alkylamines has also been studied. In this case, ammonia is believed to act not only as a deprotonating agent for PVA, but also as a complex-forming agent. Godard [1] suggested three possible structures for PVA–Cu^{2+} complexes obtained by deprotonation.

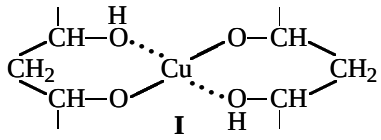

I

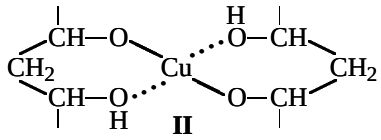

II

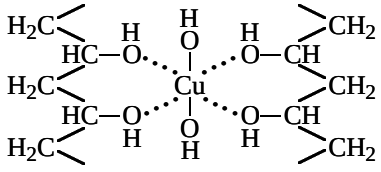

III

Moneva and Ivanova [8] studied complexation and gelation in the PVA–Cu^{2+} system. It was demonstrated that complexation includes two stages with the formation of a positively charged blue complex and a green deprotonated complex. The green complex is formed through loss of two protons, which is accompanied by transition to a compact conformation. The pH and free energy of the conformation transition were determined.

1070-4272/02/7510-1692 $27.00 © 2002 MAIK "Nauka/Interperiodica"

Previously, we studied the rheological and electrophysical properties of PVA-based composites with copper(II) chloride and orthophosphoric acid [9]. It was suggested that complexation may occur in such materials at certain component ratios. The present study is concerned with the rheological and electrical properties of PVA-based composites with copper(II) and cobalt(II) chlorides.

EXPERIMENTAL

In the experiments we used composites prepared at room temperature from 5 or 10% aqueous PVA 16/1 solutions and copper(II) and cobalt(II) chlorides at various component ratios. The rheological characteristics were determined with a Rheotest-2 rotary viscometer at 30–80°C in the range of the shear rates from 3 to 1.3×10^3 s^{-1}. The electrical characteristics of the fluid composites (electrical conductivity æ and dielectric loss tangent tan δ) were measured with an E7-15 instrument at a frequency of 1 kHz.

The viscosity η in the PVA–$CuCl_2$ system at a shear rate of 16.2 s^{-1} is shown in Fig. 1 as a function of the component ratio. The composites were prepared by dissolution of copper(II) chloride in 5 or 10% aqueous PVA solutions. The experimental curves deviate from the additive model; peaks and dips are observed in certain concentration ranges. In 5% PVA, at 30 and 70°C, the peaks are found at 15, 35, and 60 wt % $CuCl_2$; and in 10% PVA, at 25, 40, and 60 wt % $CuCl_2$.

In Fig. 2, the viscosity η at 30°C of the PVA–$CuCl_2$ system of various compositions is plotted against the shear rate $\dot{\gamma}$. As seen, the viscosity is strongly dependent on the shear rate, which is typical of non-Newtonian fluids. The viscosity rapidly increases at low shear rates (up to 10 s^{-1}) and then decreases.

In Fig. 3, the electrical characteristics (dielectric loss tangent tan δ and electrical conductivity æ) are given as functions of the system composition. In the composition range where æ shows maxima, tan δ, quite the contrary, takes the minimal values.

The results show that complexation in the PVA–$CuCl_2$ system strongly influences the rheological behavior and electrical characteristics. The viscosity curves suggest that complexes of various compositions are formed in the system, depending on the component ratio.

We obtained similar results for the PVA–$CoCl_2$ system, too. Figure 4 shows the viscosity as a function of the cobalt chloride concentration in 5 and 10% PVA. The anomalous behavior of the viscosity is reflected in the appearance of extrema in the curves. In 5% PVA (30°C), peaks are observed at 10,

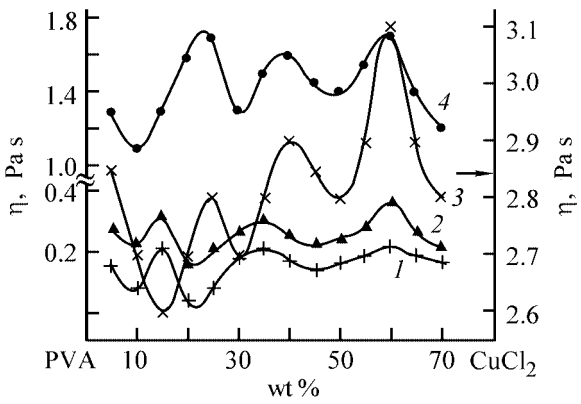

Fig. 1. Viscosity η vs. the composition of the PVA–$CuCl_2$ system based on (*1*, *2*) 5 and (*3*, *4*) 10% PVA solutions. Shear rate 16.2 s^{-1}; solution temperature (°C): (*1*, *3*) 30 and (*2*, *4*) 70; the same for Fig. 4.

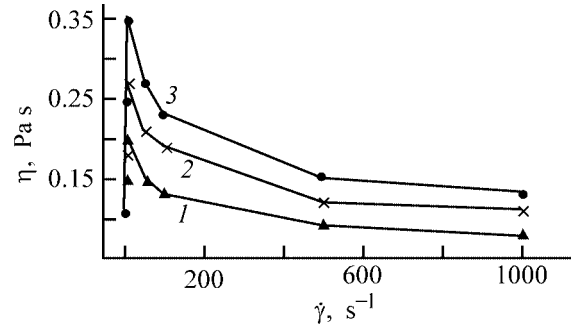

Fig. 2. Viscosity η vs. the shear rate $\dot{\gamma}$ in the PVA–$CuCl_2$ system based on 5% PVA solution. Temperature 30°C. Copper chloride concentration (wt %): (*1*) 15, (*2*) 40, and (*3*) 60.

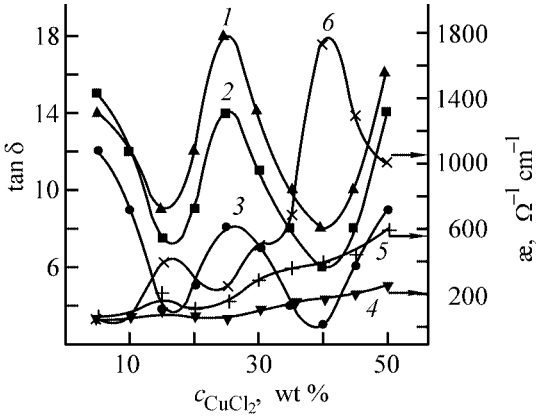

Fig. 3. (*1*–*3*) Dielectric loss tangent tan σ and (*4*–*6*) electrical conductivity æ vs. the $CuCl_2$ concentration c_{CuCl_2} in the PVA–$CuCl_2$ system based on 10% PVA solution. Temperature (°C): (*1*, *4*) 30, (*2*, *5*) 50, and (*3*, *6*) 80.

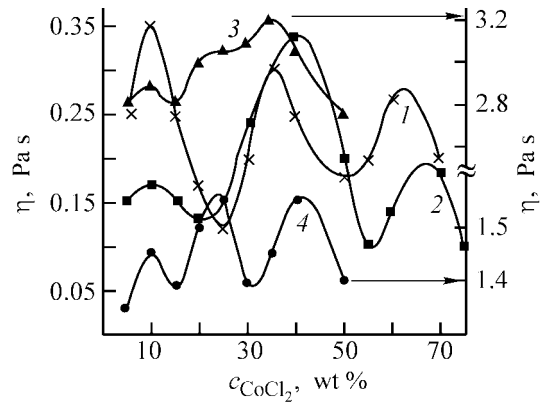

Fig. 4. Viscosity η vs. the $CoCl_2$ concentration c_{CoCl_2} in the PVA–$CoCl_2$ system based on (*1*, *2*) 5 and (*3*, *4*) 10% PVA solutions.

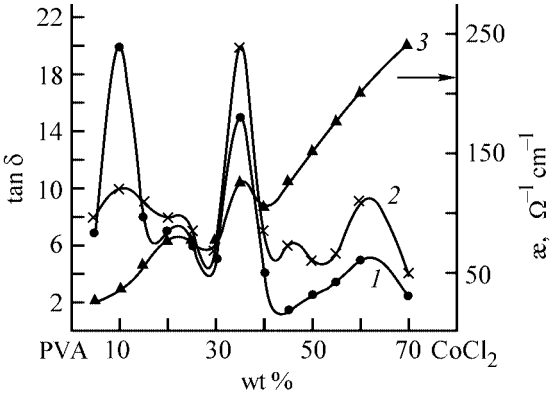

Fig. 5. (*1*–*2*) Dielectric loss tangent tan δ and (*3*) electrical conductivity æ vs. the composition of the PVA–$CoCl_2$ system based on 10% PVA solution. Temperature (°C): (*1*, *3*) 30 and (*2*) 70.

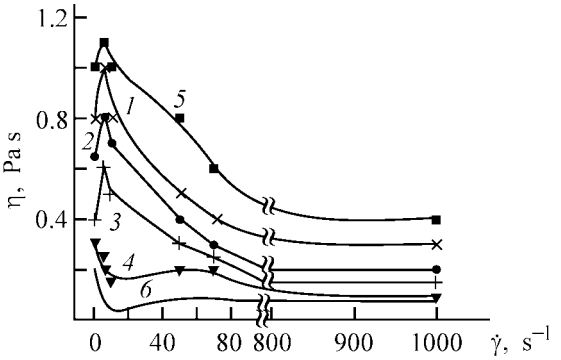

Fig. 6. Viscosity η vs. the shear rate $\dot{\gamma}$ in the PVA–$CoCl_2$ system based on 5% PVA solution. Cobalt chloride concentration (wt %): (*1*, *4*) 10, (*2*) 30, (*3*, *6*) 60, and (*5*) 40. Temperature (°C): (*1*–*3*) 30 and (*4*–*6*) 70.

35, and 65 wt % $CoCl_2$ (curve *1*). Raising the temperature to 70°C changes somewhat the viscosity pattern. The peak at 40 wt % $CoCl_2$ becomes stronger than that at 10 wt %, and a weak peak at 70 wt % appears instead of that at 65 wt % (curve *2*).

For the system PVA–$CoCl_2$ prepared from 10% PVA (30°C), we observed a weak peak at 10 wt % $CoCl_2$ and a broad peak at 20–40 wt % (Fig. 4, curve *3*). With this system, again, raising the temperature to 70°C alters the shape of the viscosity curve. In this case, three peaks at 10, 25, and 40 wt % $CoCl_2$ are observed (curve *4*).

In Fig. 5, the dielectric loss tangent tan δ and electrical conductivity æ are shown as functions of the system composition. At 30°C, two weak peaks are found in the æ curve at 20–25 and 35 wt % $CoCl_2$ (curve *3*), and three peaks in the tan δ curve at 10, 35, and 60 wt % (curve *1*). Raising the temperature to 70°C weakens the effect at 10 wt % and strengthens that at 35 and 60 wt % (curve *2*).

In Fig. 6, the viscosity of the 5% PVA–$CoCl_2$ system is plotted against the shear rate for various $CoCl_2$ contents. At a $CoCl_2$ content of 10, 30, and 60 wt % (30°C, curves *1*–*3*) and of 40 wt % (70°C, curve *5*) peaks are found at low shear rates, followed by monotonic smooth decrease with the shear rate increasing further. At a $CoCl_2$ content of 10 and 60 wt % (70°C, curves *4*, *6*), we observed an anomalous behavior of the viscosity. The peaks and dips in the flow curves can be interpreted as being due to structural reorganization of the polymer macromolecules in the mechanical field. It may be suggested that, in the indicated composition ranges, the structural organization of the solution is optimal for fluid flow to occur under the action of the mechanical shear load provided by rotation of the inner cylinder of the measuring cell. In this case, we can find in the flow curve a clearly pronounced portion of afterflow (flow of readily structured anisotropic solution), followed by a portion corresponding to the flow of associates oriented in the mechanical field. Note that, for the initial PVA, the flow curves behave similarly in the temperature range near 70°C [10–12].

The optical characteristics of 10% PVA (16/1) containing various concentrations of $CoCl_2$ are listed in the table below. It is seen that the optical density *D* and absorption peak area *S* depend on the $CoCl_2$ concentration nonlinearly.

The solution acidity grows with increasing $CoCl_2$ concentration. Below is given the dependence of pH of 10% PVA solutions on the $CoCl_2$ concentration.

c_{CoCl_2}, %	10	20	30	50	60
pH	6.08	6.06	5.84	5.41	5.19

Optical characteristics of 10% PVA solutions containing $CoCl_2$

c_{CoCl_2}, %	λ_{max}	Optical density D	Peak area S
10	507	0.926	108.37
20	509	1.338	153.341
30	510	2.025	224.32
50	522	3.0	437.239
60	537	3.0	417.107

The results suggest the interaction between PVA and the salt additive.

Complex formation between PVA and MCl_2 affects the rheological and electrical properties of PVA solutions, resulting in an anomalous behavior. It is clear that addition of the salt additives changes the structural organization of the polymer macromolecules. Applying a mechanical field causes further reorganization of the solution structure, as demonstrated by the appearance of peaks at low shear rates (up to 10 s^{-1}) and of the afterflow portion in the viscosity curves.

CONCLUSIONS

(1) The anomalous behavior of the rheological and electrical properties in PVA solutions containing Cu^{2+} and Co^{2+} ions is associated with complex formation in the systems studied.

(2) The long-range order in PVA solutions and their flow behavior depend on the content of copper(II) and cobalt(II) chlorides in the system.

REFERENCES

1. Godard, P., *Polym. Eng. Sci.*, 1989, vol. 29, no. 2, pp. 127.
2. Akhmetov, N.S., *Neorganicheskaya khimiya* (Inorganic Chemistry), Moscow: Khimiya, 1968.
3. Saito, S. and Okuyama, H., *Kolloid. Z.*, 1954, vol. 139, p. 150.
4. Norden, B., *Acta Chem. Scand.*, 1971, vol. 25, p. 3545.
5. Kuhn, W., Toth, I., and Kuhn, H., *Makromol. Chem.*, 1963, vol. 60, p. 77.
6. Hojo, N., Shiroi, H., and Hayashi, S., *J. Polym. Sci.*, 1974, vol. 47, p. 299.
7. Sumito, O., Fukuda, A., and Kuze, E., *J. Polym. Sci., Polym. Phys. Ed.*, 1978, vol. 16, p. 1801.
8. Moneva, L.I. and Ivanova, Kh.R., *Vysokomol. Soedin., Ser. A*, 1990, vol. 32, no. 10, pp. 2142–2148.
9. Lazareva, T.G. and Il'yushchenko, I.A., *Vestsi. Akad. Navuk Bel., Ser. Khim. Navuk* 1996, no. 2, pp. 70–73.
10. Zhilenko, N.P., Serdyukova, L.P., and Rudenko, A.P., Abstracts of Papers, *XII Vsesoyuznoe soveshchanie po khimii kompleksnykh soedinenii* (XII All-Union Meet. On Coordination Chemistry), Krasnoyarsk (Russia), June 16–18, 1987, part 2, p. 578.
11. Lazareva, T.G. and Vashuk, E.V., *Proc. 5th Int. Conf. on Electro-Rheological Fluids, Magneto-Rheological Suspensions, and Associated Technology*, Sheffield (UK), July 10–14, 1995, pp. 149–155.
12. Yakobson, E. and Faitel'son, L.A., *Mekh. Kompoz. Mater.*, 1997, vol. 36, no. 6, pp. 821–839.

Russian Journal of Applied Chemistry, Vol. 75, No. 10, 2002, pp. 1696–1699. Translated from Zhurnal Prikladnoi Khimii, Vol. 75, No. 10, 2002, pp. 1730–1732.
Original Russian Text Copyright © 2002 by Chernoberezhskii, Mineev, Dyagileva, Lorentsson, Belova.

MACROMOLECULAR CHEMISTRY AND POLYMERIC MATERIALS

Recovery of Kraft Lignin from Aqueous Solutions with Oxotitanium Sulfate, Aluminum Sulfate, and Their Mixture

Yu. M. Chernoberezhskii, D. Yu. Mineev, A. B. Dyagileva, A. V. Lorentsson, and Yu. V. Belova

St. Petersburg State Technological University of Plant Polymers, St. Petersburg, Russia

Received April 24, 2002

Abstract—Coagulation recovery of kraft lignin from aqueous solutions with oxotitanium sulfate, aluminum sulfate, and a composite coagulant based on their mixture was studied in a wide range of coagulant concentrations and solution pH values.

Wastewater from kraft cellulose production is characterized by high contamination level and multicomponent composition. One of the main contaminants is kraft lignin (KL), imparting to water deep color and high chemical oxygen demand (COD). Wastewater from kraft cellulose production is usually supplied to centralized biological treatment. However, biological treatment fails to remove KL and completely thus to decrease the coloration and COD of wastewater to the prescribed level. To achieve the permissible concentrations of KL in the discharged water, additional physicochemical treatment of wastewater is required [1, 2]. Among the procedures for physicochemical treatment, the most widely used are coagulation and flocculation. In wastewater treatment, aluminum sulfate is commonly used as a coagulant [3–5]. The treatment process can be intensified and its efficiency can be raised by using modified (prehydrolyzed) coagulants (e.g., OKhA) [6] and composite coagulants (a mixture of salts of aluminum, iron, and other metal) [7]. Recently, the use of coagulants based on Ti(IV) salts, having some advantages over aluminum and iron salts, for water and wastewater treatment has been reported [8–16]. However, these reports do not describe the composition of these coagulants and the mechanism of their interaction with contaminants.

In this work, we studied coagulation of KL with oxotitanium sulfate $TiOSO_4 \cdot 2H_2O$, aluminum sulfate $Al_2(SO_4)_3 \cdot 18H_2O$, and their mixture (composite coagulant) in a wide range of coagulant concentrations and pH values.

EXPERIMENTAL

KL was taken from the Solombal' Paper and Pulp Combine and was purified to remove substances insoluble in alkali (pH 12). The model wastewater was a solution of KL in 0.01 N NaOH (100 mg l^{-1}). A solution of $TiOSO_4$ and $Al_2(SO_4)_3$ in 0.01 N H_2SO_4 was used as a mixed coagulant. The concentrations of Ti(IV) and Al(III) in the initial solution were 2.5 and 1 M, respectively. The pH was adjusted with 0.1 N solutions of H_2SO_4 and NaOH. Mixing of the model wastewater with coagulant solutions and with the composite coagulant components was performed instantaneously. All the chemicals were of analytically pure grade. The efficiency of KL recovery was determined from the residual concentration of KL in the solution, c_s, and in the filtrate, c_f. Filtration was carried out through blue-band paper filters. The concentration of KL in solution was determined spectrophotometrically with an SF-46 spectrophotometer at a wavelength of 480 nm and pH 11. The experimental procedure was described in more detail in [1, 2].

To elucidate the processes occurring in recovery of KL from the model wastewater under the action of a mixed coagulant, we first studied the behavior of KL in the presence of $TiOSO_4$ or $Al_2(SO_4)_3$, taken separately, in a wide range of their concentrations and pH values.

The pH dependences of the residual concentration of KL in the presence of $TiOSO_4$ before and after

1070-4272/02/7510-1696 $27.00 © 2002 MAIK "Nauka/Interperiodica"

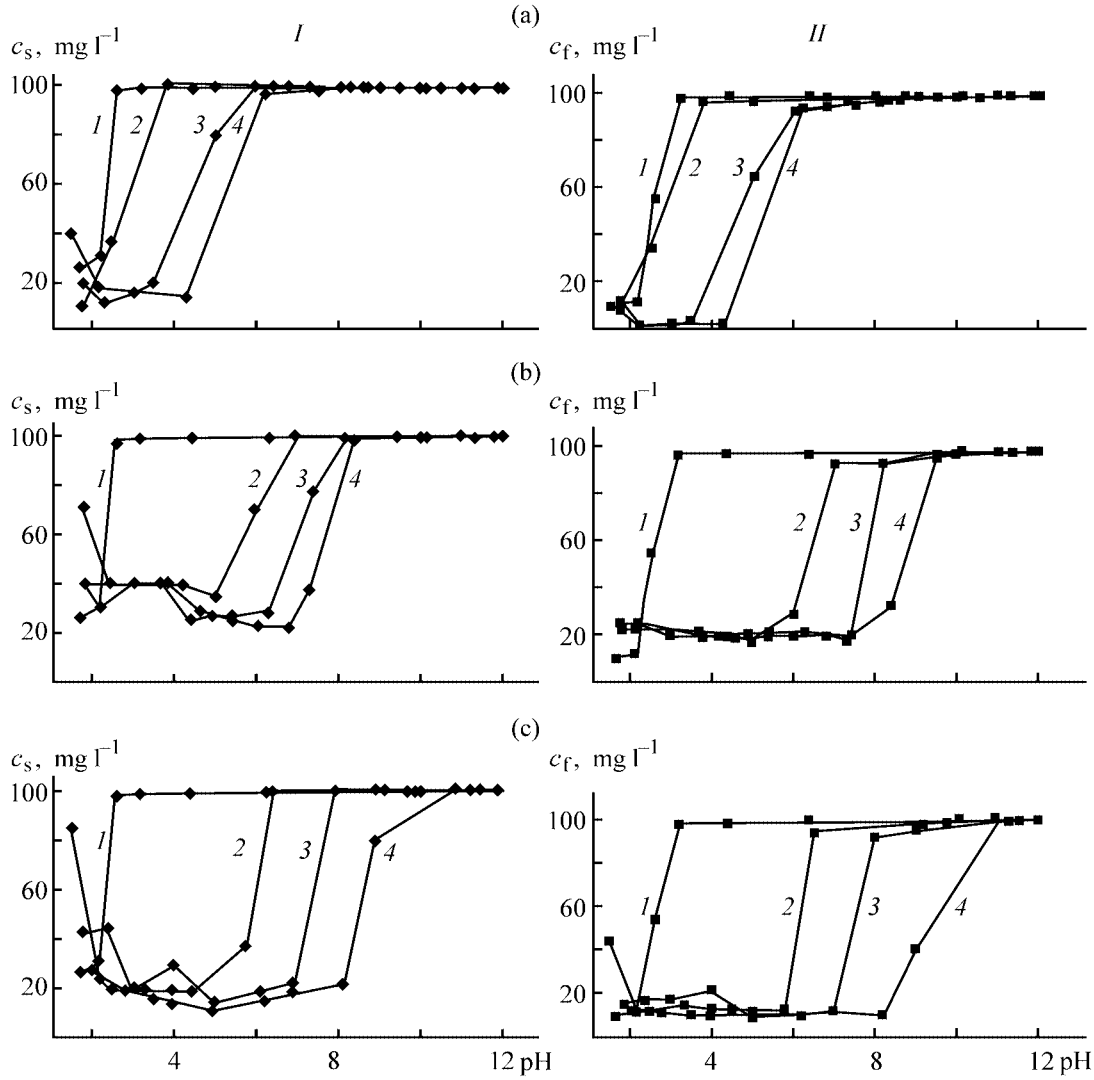

Fig. 1. Residual concentration of KL in the systems (a) KL–$TiOSO_4$, (b) KL–$Al_2(SO_4)_3$, and (c) KL–$TiOSO_4$–$Al_2(SO_4)_3$ (*I*) before filtration, c_s, and (*II*) after filtration, c_f, vs. pH. (a) $TiOSO_4$ concentration, M: (*1*) 0, (*2*) 10^{-4}, (*3*) 5×10^{-4}, and (*4*) 10^{-3}. (b) $Al_2(SO_4)_3$ concentration, M: (*1*) 0, (*2*) 10^{-4}, (*3*) 5×10^{-4}, and (*4*) 10^{-3}. (c) Concentrations of $TiOSO_4$ and $Al_2(SO_4)_3$, M: (*1*) 0, (*2*) 10^{-4}, (*3*) 5×10^{-4}, and (*4*) 10^{-3}.

filtration are shown in Fig. 1a. The pH at which the coagulation recovery of KL starts in the absence of a coagulant is approximately 3.1 (Fig. 1a, *II*, curve *1*), in good agreement with published data [17, 18]. This value was defined as pH at which the residual concentration of KL in the solution after its filtration starts to decrease. The presence of 10^{-4} M $TiOSO_4$ shifts the pH of the onset of coagulation recovery of KL to a less acidic range (approximately to pH 3.7). However, the maximal efficiency of KL removal remains virtually the same as that in the absence of $TiOSO_4$ (Fig. 1a, *II*, curves *1* and *2*). Raising the concentration of $TiOSO_4$ to 5×10^{-4} M and then to 10^{-3} M results in a regular shift of the pH of the onset of KL recovery to approximately 6.2; in this case, the efficiency of sedimentation recovery of KL in the range pH 2.1–4.2 increases to 90%, and upon filtration, to virtually 100% (Fig. 1a, *II*, curve *4*).

According to published data, the recovery of KL in the presence of $TiOSO_4$ proceeds by the heterocoagulation mechanism as a result of interaction of KL particles with the products of $TiOSO_4$ hydrolysis (PTH). Since the KL particles are negatively charged, the heterocoagulation is the most active at low pH (at low negative values of ζ-potential of KL and PTH particles). This can account for the narrow pH range of KL recovery observed in the experiments.

The dependences of the residual KL concentration on pH in the presence of $Al_2(SO_4)_3$ before and after

filtration are shown in Fig. 1b. As seen, the efficiency of KL removal at pH 2–7 reaches 80% in the case of filtration. The mechanisms of KL recovery with aluminum sulfate have been considered and discussed previously [18]. It should be noted that, in contrast to $TiOSO_4$, KL is recovered most completely in the presence of $Al_2(SO_4)_3$ in a wider pH range 2–7 (curves *2*–*4*). This is due to the fact that, in contrast to the KL–$TiOSO_4$ system, KL particles and hydrolysis products of $Al_2(SO_4)_3$ have opposite charges in this pH range [18, 19].

Our results show that, with $TiOSO_4$ as a coagulant, KL can be recovered virtually completely, but in a narrow pH range 2–4. The working pH range for aluminum sulfate is significantly wider; however, the use of aluminum sulfate allows recovery of KL from the model wastewater with an efficiency not exceeding 80%.

The treatment efficiency was must improved and the working pH range made significantly wider by using $TiOSO_4$ and $Al_2(SO_4)_3$ in combination. The dependence of the residual concentration of KL on pH before and after filtration, with $TiOSO_4$ and $Al_2(SO_4)_3$ present simultaneously, is shown in Fig. 1c. It is seen that, at concentration of the salts of 10^{-4} and 5×10^{-4} M (curves *2* and *3*), the pH range in which the mixed coagulant is the most effective is the same as in the case of $Al_2(SO_4)_3$. At metal concentrations of 10^{-3} M (curve *4*), this range is wider (pH 2–8) than that with $Al_2(SO_4)_3$ taken alone (pH 2–7). Furthermore, addition of the mixed coagulant results in ~10% higher efficiency of coagulation recovery of KL than with $Al_2(SO_4)_3$ taken alone, which corresponds to a decrease in the residual concentration of KL in solution by a factor of 2 (from 20 to 10 mg l^{-1}). The apparent enhancement of the coagulation effect of the mixed coagulant as compared to $Al_2(SO_4)_3$ widely used in practice is due to parallel occurrence of several heterocoagulation processes in the resulting multicomponent disperse system containing negatively charged particles of KL and PTH and positively charged hydrolysis products of the aluminum salt.

CONCLUSIONS

(1) Oxotitanium sulfate has high coagulation power with respect to aqueous solutions of kraft lignin. However, the pH range in which it is effective is rather narrow (pH 2–4).

(2) The use of a mixed coagulant based of oxotitanium sulfate and aluminum sulfate significantly expands the pH range (pH 2–8) in which kraft lignin can be effectively (to an extent of up to 90%) recovered from aqueous solution.

ACKNOWLEDGMENTS

The study was financially supported by the Ministry of Education of the Russian Federation, project "Basic Research at Higher School in the Field of Natural Science and Humanities. Russian Universities" (project no. UR.05.01.044).

REFERENCES

1. Chernoberezhskii, Yu.M., Lorentsson, A.V., and Dyagileva, A.B., *Zh. Prikl. Khim.*, 1999, vol. 72, no. 9, pp. 1496–1498.
2. Chernoberezhskii, Yu.M., Lorentsson, A.V., and Dyagileva, A.B., *Zh. Prikl. Khim.*, 1999, vol. 72, no. 9, pp. 1498–1501.
3. Kul'skii, L.A., *Teoreticheskie osnovy i tekhnologiya konditsionirovaniya vody* (Theory and Technology of Water Conditioning), Kiev: Naukova Dumka, 1983.
4. Babenkov, E.D., *Ochistka vody koagulyantami* (Water Treatment with Coagulants), Moscow: Nauka, 1977.
5. Zapol'skii, A.G. and Baran, A.A., *Koagulyanty i flokulyanty v protsessakh ochistki vody: Svoistva. Poluchenie. Primenenie* (Coagulants and Flocculants in Water Treatment: Characteristics. Synthesis. Application), Leningrad: Khimiya, 1987.
6. Shut'ko, A.P., Sorochenko, V.F., Kozikovskii, Ya.B., *et al.*, *Ochistka vody osnovnymi khloridami alyuminiya* (Water Treatment with Basic Aluminum Chlorides), Kiev: Tekhnika, 1984.
7. French Patent Appl. 2 705 661.
8. Beloskurskaya, G.I., *Zdravookhr. Kazakh.*, 1976, no. 4, pp. 51–54.
9. Davydov, V.D., Osipova, G.Ya., Osipov, P.V., Kocheva, L.S., *Tr. Komi Nauchn. Tsentra Ural. Otd. Ross. Akad. Nauk*, 1993, no. 129, p. 121.
10. Stremilova, N.N., Abstracts of Papers, *XVI Mendeleevskii s"ezd po obshchei i prikladnoi khimii* (XVI Mendeleev Congr. on General and Applied Chemistry), Moscow, 1998, vol. 3, p. 244.
11. Stremilova, N.N., Abstracts of Papers, *III Mezhdunarodnyi kongress "Voda: Ekologiya i tekhnologiya"* (III Int. Congr. "Water: Ecology and Technology"), Moscow, 1998, p. 311.
12. Stremilova, N.N., Abstracts of Papers, *Pervaya mezhdunarodnaya nauchnaya konferentsiya "Ekologicheskaya adaptatsiya na postsovetskom prostranstve"* (First Int. Scientific Conf. "Ecological Adaptation in After-Soviet Area"), St. Petersburg, 1999, pp. 214–215.

13. Stremilova, N.N., Abstracts of Papers, *IV Mezdunarodnyi kongress "Ekvatek-2000"* (IV Int. Congr. "Equatech-2000"), Moscow, 2000, p. 421.
14. Stremilova, N.N., Abstracts of Papers, *Int. Conf. "International Association for Great Lakes Research (IAGLR-2000),"* Canada, 2000, p. 187.
15. Stremilova, N.N., Viktorovskii, I.V., and Zagel', V.V., Abstracts of Papers, *III Mezhdunarodnaya konferentsiya "Akvaterra-2000"* (III Int. Conf. "Aquaterra-2000"), St. Petersburg, 2000, p. 182.
16. Stremilova, N.N., Viktorovskii, I.V., and Zagel', V.V., *Zh. Obshch. Khim.*, 2001, vol. 71, no. 1, pp. 21–24.
17. Lindstrom, T., *Colloid Polym. Sci.*, 1979, vol. 257, pp. 277–285.
18. Chernoberezhskii, Yu.M. and Dyagileva, A.B., *Kolloidn. Zh.*, 1993, vol. 55, no. 6, pp. 138–139.
19. Nazarenko, V.A., Antanovich, V.P., and Nevskaya, E.M., *Gidroliz ionov metallov v razbavlennykh rastvorakh* (Hydrolysis of Metal Ions in Dilute Solutions), Moscow: Atomizdat, 1979.

Russian Journal of Applied Chemistry, Vol. 75, No. 10, 2002, pp. 1700–1704. Translated from Zhurnal Prikladnoi Khimii, Vol. 75, No. 10, 2002, pp. 1733–1738.
Original Russian Text Copyright © 2002 by Sidorovich, Baklagina, Khripunov, Bursian, Denisov, Lavrent'ev, Praslova, Kuznetsov, Kruchinina, Shtykova, Sukhanova.

MACROMOLECULAR CHEMISTRY AND POLYMERIC MATERIALS

Structure and Transport Properties of Films of Mixed Cellulose Esters

A. V. Sidorovich, Yu. G. Baklagina, A. K. Khripunov, A. E. Bursian, V. M. Denisov, V. K. Lavrent'ev, O. E. Praslova, Yu. P. Kuznetsov, E. V. Kruchinina, E. V. Shtykova, and T. E. Sukhanova

Institute of Macromolecular Compounds, Russian Academy of Sciences, St. Petersburg, Russia

Institute of Crystallography, Russian Academy of Sciences, Moscow, Russia

Received May 21, 2002

Abstract—Cellulose acetomyristates of varied composition were studied. The sample volume abnormally increases in high-temperature stretching and after swelling in benzene. Cellulose acetomyristates can be used as membranes for separating aromatic and aliphatic hydrocarbons.

Natural polysaccharides, in particular cellulose, attract growing attention. Polymorphism of cellulose and its derivatives has been extensively studied [1–5]. Of special interest are determination of the ratio of I_α and I_β modifications and conditions of phase transition of metastable I_α modification into I_β, II, III_I, III_{II}, IV_I, and IV_{II} phases [2, 4].

It is known [6, 7] that the properties of cellulose derivatives are determined not only by the structure of the initial cellulose and degree of its ordering but also, and to a greater extent, by the structure of substituents and the number of residual free hydroxy groups.

As determined by IR spectroscopy [6], free hydroxy groups of highly substituted cellulose derivatives are involved, irrespective of the nature and volume of the substituents, in intramolecular hydrogen bonding and stabilize the shape and rigidity of the glucoside skeleton, not affecting the mobility of substituents of any size. Hence, it is possible to prepare, by gradual substitution of hydroxy groups, cellulose homologs with various amphiphilic, physical and chemical properties, which can be used in various branches of nanotechnology, including the Langmuir–Blodgett process [7–9]. More reliable interpretation of the structural data requires a systematic study of macro- and Langmuir–Blodgett films of mixed cellulose esters, acetomyristates (CAM), with account of their polymorphic nature [9, 10].

A comprehensive study of celluloses with different composition is a topical task, since both Langmuir–Blodgett and macrofilms can be used in pervaporation and gas separation [11, 12].

In this work, we studied the structural, thermomechanical and mass exchange properties of three CAM derivatives prepared from natural cellulose and containing residues of acetic (indicated in the numerator) and myristic (indicated in the denominator) acids: CAM 290/10, CAM 275/25, and CAM 250/50. Cellulose diacetate (CDA) was also studied.

EXPERIMENTAL

Cellulose acetomyristate was prepared by acylation of linter cellulose with a mixture of acetic and myristic acid in trifluoroacetic acid. Trifluoroacetic acid anhydride was added to induce formation of acid anhydrides and to promote their reaction with cellulose [13]. The molecular weight of the samples, estimated by sedimentation and diffusion procedures, was $(350 \pm 30) \times 10^2$ [14].

The degree of esterification of cellulose with acetic and myristic acids was determined by ^{1}H NMR spectroscopy. The ^{1}H NMR spectra were recorded in $CDCl_3$–10% CD_3OD solutions on a Bruker AC-200 spectrometer operating at 200 MHz. CAM films 25–100 μm thick were prepared by casting a chloroform solution of the celluloses on a glass support with subsequent drying at room temperature.

1070-4272/02/7510-1700 $27.00 © 2002 MAIK "Nauka/Interperiodica"

To determine the thermomechanical properties, the linear sizes of free and uniaxilly stretched samples were measured in a forevacuum with heating from 20 to 400°C at a rate of 5 deg min^{-1} [15]. The absolute measurements error was 10 μm. The samples were film strips 30 mm long, 4 mm wide, and 24–25 μm thick.

To determine the influence of the repeated thermomechanical treatment on the density and structure of CAM, the size of a single sample was measured after the following treatments at the softening point: (a) primary stretching of the initial samples at a stress σ = 2.9 kg cm^{-2}; (b) repeated heating of the samples after removing the load; and (c) repeated stretching at a load equal to that in the first experiment. The volume change (V_1/V_0, where V_0 and V_1 are the volumes before and after stretching) caused by the thermomechanical treatment was determined from the linear sizes measured after the primary and the secondary stretching.

The X-ray diffraction study was performed on a DRON-2.0 diffractometer using Cu_{K_α} radiation. The samples were stacks of 10–20 film strips. Low-angle X-ray scattering patterns were obtained on an Amur-K diffractometer with a position-sensitive detector.

The transport properties of 20–25-μm films were studied in an self-contained laboratory cell for studying membranes with working surface area of 13 cm^2. In this cell, the mixture being separated or pure compounds were stirred at definite temperatures. The residual pressure under the membrane was 0.2 mbar. The permeate vapor (flow passed through the membrane) was condensed in a receiver cooled with liquid nitrogen. The membrane throughput was calculated from the weight of the condensate. The composition of the permeate formed in separation of a benzeneheptane mixture was determined by refractometry or chromatography (Reoplex column). The selectivity coefficient was calculated by the equation

$$\alpha = \frac{X_A/X_B}{Y_A/Y_B},$$

where X_A and X_B are, respectively, the weight of benzene and heptane in the permeate; and Y_A and Y_B are, respectively, the weights of benzene and heptane in the initial mixture.

The thermomechanical curves of CAM films are shown in Fig. 1. Curve *1* measured in primary stretching of a CAM film contains the following portions:

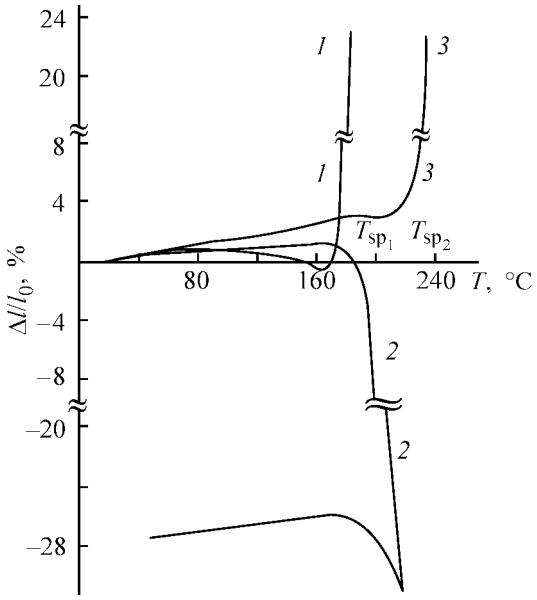

Fig. 1. (*1*, *3*) Thermomechanical curves and (*2*) curve of free contraction of a CAM film. ($\Delta l/l_0$) Deformation and (T) temperature; (T_{sp_1}, T_{sp_2}) softening points. (*1*) Primary stretching, σ = 2.9 kg cm^{-2}; (*2*) heating to 210°C and cooling to 40°C in the unloaded state; (*3*) secondary stretching, σ = 2.9 kg cm^{-2}.

thermal expansion of a solid film, slight contraction owing to disappearance of the residual stresses developed when the film was dried on the support, and the steep (almost vertical) portion due to sample softening at the softening point T_{sp_1} = 168°C. Curve *2* was measured with heating to 210°C of unloaded samples subjected to primary stretching and subsequent cooling to 40°C. Up to 160°C, thermal expansion of the sample is observed. On further heating, the samples sharply contract owing to the disappearance of the orientation stretching, which indicates a highly elastic deformation under primary stretching. In the first cooling step, abnomal elongation is observed. Only below 160°C, the samples contracts with decreasing temperature, which is presumably due to its structural ordering. Polymers with semirigid fragments of macromolecular chains behave similarly at low degrees of stretching. Bel'nikevich *et al.* observed self-orientation processes in films and fibers of some highly substituted cellulose derivatives [16]. In our case, an insignificant orientation of the film, retained upon heating up to 210°C, could result in structural transformation and self-ordering upon cooling. The softening point of the sample subjected to the secondary stretching under the same stress (curve *3*) is higher (T_{sp_2} = 222°C). Negligible contraction is observed at temperatures from 180°C to the onset of the steep ascent.

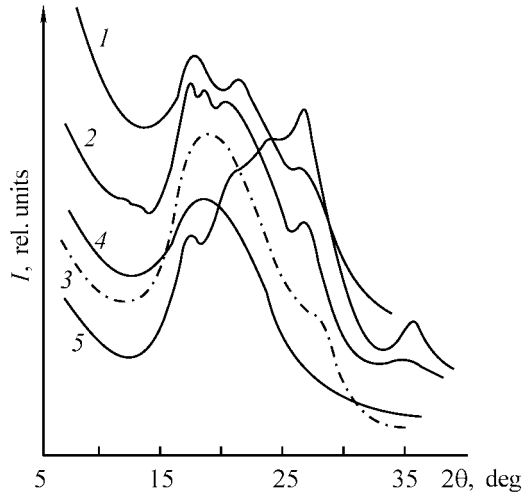

Fig. 2. X-ray diffraction patterns of (*1–3*) unoriented and (*4*, *5*) oriented CAM 275/25 films. (*I*) intensity and (2θ) Bragg's angle. (*1*) Initial sample; (*2*, *3*) films swollen in benzene for 1 h; (*4*, *5*) equatorial and meridional scattering regions of the sample stretched in benzene (λ = 1.8).

The presence of this portion in curve *3* confirms the proposed interpretation of abnomal thermal expansion (curve *2*) upon cooling from 210 to 160°C. This unusual behavior upon heating to above 200°C is due to disordering of the structure formed on cooling.

After the primary stretching the volume of a CAM film increased by 25%. No cracking was observed under this strong deformation. As determined by optical microscopy, the film surface remained smooth after the first stretching and contained no visible defects. A negligible turbidity was probably due to development of film porosity. The film volume did not change after contraction of the unloaded film. Strong densification, reaching 17% (V_1/V_0 = 0.83), was observed under repeated stretching. This indicates a two-step structural transformation of the film in the course of high-temperature stretching. Loose structure formed in the first step becomes denser after repeated stretching.

Appreciable loosening of the film under deformation may be due to development of microporous structure. To confirm this assumption, the thickness and weight of a CAM film swollen in benzene for 1 h were determined in the course of drying of the film at 30°C for 7 days. The swollen film 5, 15, and 30 min after removal from benzene was thicker than the initial film by 54, 30, and 27%, respectively. In the equilibrium state, attained in 2 h, the film thickness corresponded to a 24% increase in the film volume. Since, by this time the film weight returned to the initial value owing to almost complete removal of benzene, the increased volume of the sample was due to structural transformations. These data agree quantitatively with the thermomechanical curves measured in primary stretching.

Analysis of the shape of low-angle X-ray scattering patterns of CAM 275/25 before and after swelling in benzene shows that the interplanar spacing increases from 2.4 to 2.9 nm after swelling, the size of the ordered regions decreases, and the degree of disordering of the polymer increases. These structural transformations indicate, on the whole, an increase in the free volume of the sample swollen in benzene.

The structural transformations of oriented and unoriented (λ = 1.8) CAM films with varied thickness (20–130 μm) were studied by X-ray diffraction. The X-ray diffraction pattern of the initial thin film (Fig. 2, curve *1*) contains weak reflections with 2θ 17°–18°, 21°–22°, and 26°–27° against the background of an amorphous halo. The X-ray diffraction pattern remains virtually the same after heating the samples to 150, 200, and 250°C. The reflections of the swollen samples, corresponding to *d* 0.514, 0.336, and 0.256 nm are sharper than those of the initial thin film (Fig. 2, curve *2*). By contrast, 100–130-μm films swollen in benzene for 20 h become X-ray amorphous (Fig. 2, curve *3*).

The meridional and equatorial regions of the X-ray diffraction pattern (Fig. 2, curves *4*, *5*) of the oriented film swollen in benzene for 10–15 min were analyzed. The sharpest meridional reflections with *d* 0.514, 0.336, and 0.256 nm may be due to 002, 003, and 004 planes with a period *c* = 1.04 nm along the stretching axis. This spacing is close to the lattice parameter *c* of two polymorphous forms of cellulose triacetate (CTA) [5]. However, the X-ray diffraction patterns of CAM, unlike those of highly ordered CTA-I and CTA-II, also contain a 003 reflection (2θ = 26.5°). This is due to the fact that the skeleton of the CAM macromolecule loses 2_I symmetry, i.e., the twofold screw axis disappears. The loss of the 2_I symmetry of CTA-II macromolecule because of the high conformation mobility of the side groups was taken into account in calculation of the structural parameters of CTA [5]. However, the lack of odd 001 reflections along the stretching axis indicates the preservation of the 2_I screw axis in crystalline regions of CTA-II, which is typical of ordered natural cellulose. An amorphous halo is observed in the equatorial region (2θ = 17°–22°) of the X-ray diffraction pattern of oriented CAM (Fig. 2, curve *4*).

The presence of sharp meridional reflections and an equatorial amorphous halo indicates that the rigid

Transport properties of homogeneous CAM membranes at 40°C

Sample no.*	Membrane	Flow, kg m^{-2} h^{-1}		Benzene–heptane mixture (50/50) wt %		
		benzene	heptane	flow, kg m^{-2} h^{-1}	C_6H_6 content in permeate, wt %	$\alpha_{benzene}$
1	CDA	0.1	Traces	0.05	89	8.1
	CAM:					
2	290/10	1.3	0.007	0.17	85	5.7
3	275/25	2.4	0.02	0.33	79	3.8
4	250/50	5.5	0.19	2.7	57	1.3
5	275/25	2.4	–	–	–	–
		–	–	1.4	77	3.3
6	275/25	2.4	–	–	–	–
		–	0.33–0.59	–	8–10	–
7	275/25	–	–	0.85	75	3
8	275/25	–	0.02	–	–	–

* Sample nos. 5 and 6 were activated with benzene for 30 min; sample no 7 is undried sample no. 6 after passing of heptane; sample no. 8 is sample no. 7 dried in the cell at 50°C for 1 h.

fragments of the macromolecules are strongly ordered along the stretching direction and the recurrent fragments of this chain are azimuthally disordered [17]. In CAM films, side acetate and myristate fragments are randomly distributed relative to the skeleton of the cellulose chain, thus favoring formation of a mesomorphous structure (so-called amorphous texture [17]).

Let us turn to interpretation of the results of mechanochemical and X-ray diffraction studies and the solvent effect on swelling of CAM films. Absorption of some solvents by films and fibers of CDA, CTA, and mixed cellulose esters does not obey Fick's law [18, 19]. These processes are characterized by unusual swelling curves. Structural transformations of polymers in these systems involve both ordering and spontaneous shrinkage of the samples. Intramolecular bonds restricting the mobility of the macromolecules are ruptured after absorption of a small amount of the solvent. As a result, filaments and films of not only highly substituted CDA and CTA, but also mixed cellulose esters of varied composition are spontaneously elongated owing to ordering of their macromolecules [16, 18]. A similar effect was observed when cellulose acetates were cooled to the glass transition temperature [18].

The reflections assigned to the ordering along the polymeric chain become sharper in the X-ray diffraction patterns of unoriented CAM samples swollen in benzene, which points to long-range ordering in this direction. Bel'nikevich *et al.* [16] found that the abnormal sorption kinetics results in rupture of intermolecular bonds, which favors formation of new intermolecular interactions. Since myristate fragments are highly mobile, a new structure is formed upon even negligible changes in the initial intermolecular bonds during swelling or thermal treatment. Indeed, the volume of 24–25-μm CAM films increases by 20–25% during the thermomechanical measurements. CAM films of thickness 100–130 μm become amorphous after swelling in benzene for 1 h and subsequent drying to constant weight at 30°C.

The direction of selective mass transfer during pervaporation correlates, as a rule, with the equilibrium swelling of the membrane material in the pure components of the mixtures to be separated. In going from CDA to CAM 290/10, 275/25, and 250/50 the swelling in benzene increases from 10 to 38%; the heptane absorption ranges from trace amounts to 5%, respectively. At a higher content of the myristate fragments in CAM, the equilibrium swellings in benzene and heptane sharply increase and approach each other. For this reason, CAM films containing more than 50% myristine fragments are unsuitable for separation of a benzene–heptane mixture by pervaporation.

The transport properties of CDA and CAM membranes with respect to benzene, heptane, and their mixture (50/50 wt %) at 40°C (sample nos. 1–4) are presented in the table. As seen from the table, the permeability of the membranes increases monotonically and the selectivity of the separation decreases with increasing content of myristate fragments. These results correlate with data on equilibrium swelling of the membranes. Clearly, the deterioration of the separating properties of the membranes is mainly due to their plasticization with benzene having higher thermodynamic affinity for the CAM examined than heptane.

At the same time, as shown above, the membrane permeability may increase owing to supramolecular structural transformations of CAM. This is confirmed by results of successive pervaporation experiments with a CAM 275/25 membrane (table, sample nos. 5 and 6) activated by stationary diffusion of benzene for 30 min. The permeability of this membrane to benzene at 40°C was 2.4 kg m^{-2} h^{-1} (sample no. 3). The permeability of the activated membrane (absorbed benzene was not removed from the samples) to heptane and a heptane–benzene mixture was studied in the pervaporation cell (sample nos. 5–7). Under these conditions, the permeability to heptane (sample no. 6) and its mixture with benzene (sample nos. 5 and 7) increases as compared to the initial values (sample no. 3).

It should be noted that the benzene content in heptane passed through the activated membrane was constant (8–10%) within 3 h. This suggests that benzene in the activated membrane is partially bound to the macromolecules. This assumption is confirmed by stabilization of the volume of the CAM sample after its swelling in benzene and drying in air. Similarly, both free and bound solvent is present in the ethyl acetate–nitrocellulose system [20]. The ethyl acetate diffusion in this system is believed [20] to be abnormal and to be controlled by relaxation of the nitrocellulose structure. Clearly, the presence of bound benzene in CAM promotes formation of diffusion channels. This is confirmed by the fact that not only the permeabilities but also the α parameters of membranes 3 and 5 differ. At the same time, the permeability to heptane of the activated membrane dried in the evacuated cell at 40°C for 1 h (sample no. 8) returns to the initial values, which is clearly due to complete removal of benzene from the membrane and the resulting restoration of the initial structure of the sample.

CONCLUSIONS

(1) The volume of cellulose acetomyristate films increases abnormaly (by 25%) after primary high-temperature stretching. After secondary stretching, the structure of the sample becomes denser. A similar transformation is observed on drying a sample swollen in benzene.

(2) Cellulose acetomyristate membranes show promise for pervaporation separation of benzene–heptane mixtures.

ACKNOWLEDGMENTS

This work was financially supported by the Russian Foundation for Basic Research (project no. 01-03-33158), NWO (047.009.015), and the program of the St. Petersburg Research Center of the Russian Academy of Sciences (2001, grant no. 2-31).

REFERENCES

1. Glasser, W.G., *Cellulose*, 2000, pp. 211–212.
2. O'Sullivan, A.C., *Cellulose*, 1997, vol. 4, pp. 173–207.
3. Brown, R.M., *J.M.S.-Pure Appl. Chem.*, 1996, vol. 33, no. 10, pp. 1345–1373.
4. Kroon-Batenburg, R.M.J. and Kroon, J., *Carbohydr. Eur.*, 1995, vol. 12, May, pp. 15–19.
5. Roche, E., Chanzy, H., Boudeulle, M., *et al.*, *Macromolecules*, 1978, vol. 11, no. 1, pp. 86–94.
6. Zhbankov, P.G. and Kozlov, P.V., ?*Minsk: Nauka Tekhnika*, 1983, ch. 2, pp. 98–180.
7. Stepina, N.D., Tolstikhina, A.L., Klechkovskaya, V.V., *et al.*, *Izv. Ross. Akad. Nauk, Ser. Fiz.*, 1998, vol. 62, no. 3, pp. 492–495.
8. Tsvetkov, N.V., Khripunov, A.K., Astepenko, E.P., *et al.*, *Vysokomol. Soedin., Ser. A*, 1995, vol. 37, no. 8, pp. 1306–1313.
9. Khripunov, A.K., Baklagina, Yu.G., Stepina, N.D., *et al.*, *Kristallografiya*, 2000, vol. 45, no. 2, pp. 352–356.
10. Vada, M., Okano, T., and Sugiyama, J., *Cellulose*, 1997, vol. 4, pp. 221–232.
11. Kuznetsov, Yu.P., Kruchinina, E.V., Revel's-kaya, L.G., *et al.*, Abstrcats of Papers, *Vserossiiskaya nauchnaya konferentsiya "Membrany-98"* (Russian Scientific Conf. "Membranes-98"), October 5–10, 1998, p. 105.
12. Gainutdinov, R.V., Zanaveskina, I.S., Stepina, N.D., *et al.*, Abstracts of Papers, *Rossiiskii simpozium REM-2001* (Russian Symp. REM-2001), Chernogolovka, June 4–6, 2001, p. 174.
13. Khripunov, A.K., Koz'mina, O.P., Shtennikova, I.N., *et al.*, *Zh. Prikl. Khim.*, 1970, vol. 43, no. 11, pp. 2581–2583.
14. Bushin, S.V., Astapenko, E.P., Belyaeva, E.V., *et al.*, *Vysokomol. Soedin., Ser. A*, 1992, vol. 34, no. 6., pp. 1021–1026.
15. Raglis, V.V., Sidorovich, A.V., and Efanova, N.V., *Mekh. Polim.*, 1978, no. 2, pp. 361–362.
16. Bel'nikevich, N.G., Bolotnikova, L.S., Kramarenko, L.N., *et al.*, *Vysokomol. Soedin., Ser. B*, 1978, vol. 20, no. 1, pp. 37–38.
17. Kazaryan, L.G. and Tsvankin, D.Ya., *Vysokomol. Soedin., Ser. A*, 1965, vol 7, no. 1, pp. 80–87.
18. Shipovskaya, A.B. and Timofeeva, G.N., *Vysokomol. Soedin., Ser. A*, 2001, Vol. 43, no. 7, pp. 1237–1244.
19. Fridman, O.A., Naimark, N.I., Malinin, L.N., *et al.*, *Vysokomol. Soedin., Ser. A*, 1982, vol. 24, no. 3, pp. 512–516.
20. Popova, E.D. and Chalykh, A.E., *Vysokomol. Soedin., Ser. A*, 1991, vol. 33, no. 12, pp. 2574–2584.

Russian Journal of Applied Chemistry, Vol. 75, No. 10, 2002, pp. 1705–1708. Translated from Zhurnal Prikladnoi Khimii, Vol. 75, No. 10, 2002, pp. 1739–1742.
Original Russian Text Copyright © 2002 by Primachenko, Sorochinskaya, Pavlyuchenko, Ivanchev, Skrifvars, Koskinen, Karna, Laamanen.

MACROMOLECULAR CHEMISTRY AND POLYMERIC MATERIALS

Compound Latexes for Antistatic Coatings

O. N. Primachenko, O. V. Sorochinskaya, V. N. Pavlyuchenko, S. S. Ivanchev, M. Skrifvars, J. Koskinen, T. Karna, and H. Laamanen

St. Petersburg Branch, Boreskov Institute of Catalysis, Siberian Division, Russian Academy of Sciences, St. Petersburg, Russia

Neste Chemicals Oy, Porvoo, Finland

Received June 3, 2002

Abstract—Compound latexes based on amine-containing styrene–acrylate copolymers and hollow particles of a polystyrene-based copolymer as a filler were studied. With this filler, it is possible to prepare antistatic pigmented coatings with increased surface hardness, decreased density, and surface resistivity ρ_s of the order of 10^8 Ω.

We have shown previously [1, 2] that film-forming cationic amine-containing styrene–acrylate latexes can form antistatic coatings with surface resistivity ρ_s within 10^7–10^{11} Ω on the surface of insulators; the antistatic properties of the coatings are preserved for a long time. The process and environmental advantages of polymeric coatings based on aqueous latexes are obvious. Certain limitations are associated with the low glass transition point (T_g) of the polymer, which results in decreased surface hardness of the coating and sometimes in its stickiness. At the same time, with latexes based on high-T_g polymers, elevated temperatures are required to obtain a high-quality coating.

The problem can be solved by adding a finely dispersed filler to enhance the hardness and eliminate stickiness of the coatings; furthermore, fillers can impart to the coating certain specific properties. Of special promise is the use of solid polymeric fillers in the form of a latex. In this case, the procedure for introducing a filler into an antistatic coating is very simple (mixing of two low-viscous latexes), and uniform distribution of filler particles in the polymeric binder is provided.

In this study, we used as filler a latex with hollow solid particles of polystyrene-based copolymers. We expected that such a filler would not only enhance the coating hardness, but also impart to it additional useful properties. The presence of voids (~400 nm in diameter) in the filler decreases the density of the material and simultaneously imparts a white color to the coating because of the intensive light scattering on voids filled with air. It is known [3, 4] that hollow submicron polymeric particles are effective polymeric pigments and can substitute titania and other inorganic pigments.

The goal of this study was to develop a procedure for compounding a cationic amine-containing latex with a hollow-particle latex (HPL) and to study the properties of antistatic coatings prepared from the compound latex. The major the difficulty originated from the fact that the most of commercially available latexes, including HPLs, are anionic, and their mixing with cationic latexes, as a rule, results in partial or complete coagulation of the system. As for cationic HPLs, they are known, but the reported procedure for their preparation [5] is unsatisfactory because of the formation of a large amount of coagulum, which results in decreased content of the dry matter in the latex and makes preparation of concentrated compound latexes from these HPLs impossible. Therefore, we chose another approach based on recharging of an anionic HPL with a cationic surfactant, followed by mixing with a cationic latex of an amine-containing copolymer.

EXPERIMENTAL

Cationic latexes were prepared from copolymers of styrene, *n*-butyl acrylate, and *N*,*N*-dimethylaminoethyl methacrylate as described in [2]. Latex particles were uniform or had a core–shell morphology (to enrich the surface layers of the particles with amino groups ensuring the antistatic effect of the coatings). The characteristics of the latexes are listed in Table 1.

1070-4272/02/7510-1705 $27.00 © 2002 MAIK "Nauka/Interperiodica"

Table 1. Composition and properties of cationic amine-containing styrene–acrylate latexes

Latex	Copolymer composition,* wt %							Latex characteristics			
	core			shell			core : shell (by weight)	dry residue, wt %	particle diameter, nm	Brookfield viscosity, cP	ζ-potential, mV
	ST	BA	EGDMA	ST	BA	DMAEMA					
2a	47.3	52.3	0.4	38	42	20	33.3	50.8	260	37.2	+15
2b	–	–	–	4.5	40	15	–	44.8	150	30.0	+36
2c	47.3	52.3	0.4	40.5	40.5	19	33.4	41.8	200	76.9	+21

* ST, styrene; BA, *n*-butyl acrylate; EGDMA, ethylene glycol dimethacrylate; DMAEMA, dimethylaminoethyl methacrylate.

As HPL we used commercially available (Rorm & Haas, the United States) anionic styrene–acrylate latex Ropaque HP-543. The experimentally determined characteristics of the latex are as follows: dry residue 30.6 wt %, particle diameter 500 nm, relative volume of the void 43 vol %, Brookfield viscosity 13 cP, and ζ-potential of particles –42 mV. The geometric parameters of the particles were determined by electron microscopy.

To recharge HPL, we used cationic surfactants purchased from Fluka Chemie AG: trimethyldodecylammonium chloride (TMDAC) and trimethyldodecylammonium bromide (TMDAB). Recharging was performed in a 0.2–0.5-l glass vessel by adding aqueous solutions of cationic surfactants to the latex over a definite period of time with vigorous stirring (800–1000 rpm) at room temperature. The content of dry matter in the latex was determined according to GOST (State Standard) 25709–83; the coagulum content, according to GOST 24923–81; the Brookfield viscosity of latexes and their compounds, with an LVDV-I$^+$ Brookfield viscometer (spindle no. 2, rotation rate 50 rpm, 20°C); the relative hardness, by the pendulum method according to GOST 5233–89; and the surface resistivity ρ_s, according to GOST 20214–74. The density of a polymeric coating was determined for a free latex film from its weight and size (area and thickness). The covering power of the hollow pigment in coatings was determined according to GOST 8784–75. The ζ-potential was measured by macroelectrophoresis using a Barton cell suitable for latexes. As side liquid we used 0.025 N aqueous potassium chloride. Measurements were performed at a 7 wt % concentration of a polymer in a latex. The ζ-potential was calculated by the Helmholtz–Smoluchowski equation

$$\zeta = 4\pi\eta U_0/D,$$

where η and D are, respectively, the viscosity and dielectric permittivity of the dispersion medium (water), and U_0 is the electrophoretic mobility of particles, calculated by the formula

$$U_0 = Ul/E,$$

in which U is the velocity of the latex–side liquid boundary in electrophoresis; l, interelectrode distance; and E, voltage difference.

The most complicated problem in recharging of particles is to maintain the colloidal stability of a latex system when passing through the isoelectric state in which the particles lose their electric charge. The possibility of recharging of negatively charged particles is determined by several factors, the most important of which are concentration of the cationic surfactant and the rate of its addition to anionic HPL. To avoid strong dilution of HPL and, ultimately, of the system formed by HPL and the amine-containing latex, we used concentrated surfactant solutions. The advisability of using latexes with high content of dry matter for preparing highperformance coatings has been shown previously [1, 2].

The figure shows how the ζ-potential of HPL particles varies with the amount (35–50 wt %) of added aqueous solution of TMDAB. It is seen that the isoelectric state occurs at a surfactant content of about 2 wt % relative to the polymer. At a surfactant content of 3 wt %, the particles become positively charged, with a ζ-potential of +20 mV. However, the recharged latex acquires colloidal stability only at a ζ-potential of about +30 mV, which corresponds to 7 wt % content of TMDAB relative to the polymer. The necessity of adding this amount of surfactant to the latex is determined by the maximum observed in the plot of HPL viscosity vs. TMDAB concentration. As seen from Table 2, the HPL viscosity increases drastically at lower amounts of the surfactant, which complicates its compounding with the amine-containing latex.

As already noted, the most important factor is the rate of introduction a cationic surfactant into the latex.

Table 2. Recharging conditions and properties of recharged Ropaque HP-543 latex

Latex	Surfactant	Concentration of aqueous solution, wt %	Amount for recharging, wt %	Rate of addition of cationic surfactant,* wt % s^{-1}	Properties of recharged latex			
					dry residue, wt %	coagulum, wt %	Brookfield viscosity, cP	ζ-potential, mV
1a	TMDAC	36.5	4.0	0.13	–	100	–	–
1b	〃	10	4.0	0.13	–	100	–	–
1c	〃	36.5	4.0	0.80	22.4	27	180	+29
1d	〃	36.5	4.0	2.00	30.8	None	317	+31
1e	TMDAB	50.0	5.0	2.50	31.2	〃	250	+30.5
1f	〃	50.0	7.0	3.50	31.2	〃	65	+27
1g	TMDAC	36.5	9.0	4.50	30.8	〃	70	+27

* Relative to dry polymer of the latex.

Table 3. Properties of compound latexes and antistatic coatings prepared from them

Latex	Compound composition			Properties of compound latex		Temperature of coating formation, °C	Coating properties			
	cationic amine-containing latex	recharged HPL	weight ratio of amine-containing copolymer to hollow polymer	dry residue, wt %	Brookfield viscosity, cP		ρ_s, Ω (RH* = 65%)	relative hardness	density, g cm^{-3}	
									found	calculated**
2a	**2a*****	–	–	–	–	50	2.0×10^8	0.42	1.16	–
2b	**2b**	–	–	–	–	70	8.7×10^7	0.49	1.14	–
2c	**2c**	–	–	–	–	50	2.5×10^8	0.39	1.16	–
3a	**2a**	**1d*****	74.1 : 25.9	41.5	180	70	4.0×10^9	0.58	0.87	0.96
3b	**2a**	**1d**	95.3 : 4.7	49.2	50	50	2.4×10^8	0.50	1.12	1.13
3c	**2c**	**1g**	83.3 : 16.7	39.0	91	70	2.2×10^8	0.46	0.99	1.03
3d	**2c**	**1g**	90.9 : 9.1	40.2	82	70	1.9×10^8	0.44	1.10	1.09
3e	**2b**	**1f**	95.3 : 4.7	43.8	30	50	1.8×10^8	0.52	1.12	1.13
3f	**2a**	**1d**	66.7 : 33.3	40.3	23	70	1.9×10^{13}	0.60	0.80	0.88

* Relative humidity.

** Assuming that the density is an additive quantity and the apparent density of hollow particles is 0.66 g cm^{-3}.

*** The designations are the same as in Tables 1 and 2.

This rate determines the time in which the system passes the isoelectric state. If this time is too long, the latex particles have time to come in coagulation contact, and the system loses stability. This is illustrated by data in Table 2. At slow surfactant addition, the latex undergoes complete or partial coagulation, despite the fact that the amount of the surfactant added is quite sufficient to attain the required ζ-potential. At a rate of surfactant addition increased to 2.0 wt % s^{-1} (relative to the dry latex polymer), no coagulum is formed at all.

Recharged HPLs were readily compounded with cationic amine-containing latexes without any decrease in the colloidal stability of the system, to form compound latexes for preparing antistatic coatings containing hollow latex particles as filler. The compositions of the compound latexes and the properties of coatings prepared from them are listed in Table 3. As expected, addition of hollow solid particles to a polymeric binder enhances the coating hardness and decreases its density. It should be noted that, at low content of hollow particles, the coating density is approximately equal to the calculated value, whereas at a high content of hollow particles the deviations from the calculated values are appreciable and negative, suggesting the formation of a porous coating (insufficiently close packing of particles). Furthermore, at a high content of hollow particles the antistatic properties of the coating are drastically impaired.

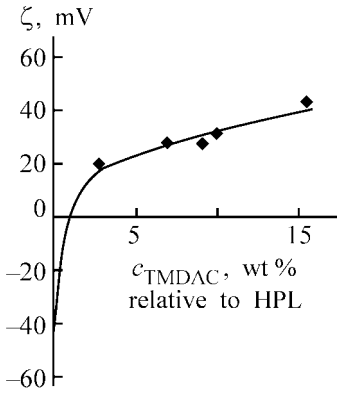

Variation of the ζ-potential of HPL on adding TMDAC.

Our results show that the content of hollow particles in the filled coatings should not exceed 20 wt %. In this case, the viscosity of the compound latex is close to that of the latex of the amine-containing copolymer, and the filled coatings have good antistatic properties (close to those of the unfilled coatings). The stickiness of the coatings is eliminated even on adding small amounts of the filler. From the viewpoint of light scattering, the optimal size of the voids is about 400 nm; in this case, the covering power of the coating is as high as 40–50 g m^{-2} in terms of dry pigment.

CONCLUSIONS

(1) A procedure was developed for preparing compound latexes for antistatic coatings by compounding cationic amine-containing styrene–acrylate latexes and anionic latexes with hollow particles acting as a white polymeric pigment and filler, with the aim to decrease the density and enhance the surface hardness of the coatings.

(2) The necessary condition for avoiding coagulation in compounding is preliminary recharging with a cationic surfactant of the anionic latex consisting of hollow particles.

(3) Compound latexes containing 40–50 wt % dry matter were prepared. The density of the resulting coatings is 0.80–1.16 g cm^{-3}; relative hardness, 0.4–0.6; and covering power, 40–50 g m^{-2} recalculated to dry "hollow" pigment. At the optimal content of the "hollow" pigment of 20 wt %, the surface resistivity ρ_s of the coating is 2×10^8 Ω.

ACKNOWLEDGMENTS

The authors are grateful to Neste Chemicals Oy for financial support.

REFERENCES

1. Primachenko, O.N., Pavlyuchenko, V.N., Gagarina, K.A., *et al.*, *Zh. Prikl. Khim.*, 2000, vol. 73, no. 10, pp. 1713–1719.
2. RF Patent 2128671.
3. Pavlyuchenko, V.N., Sorochinskaya, O.V., Ivanchev, S.S., *et al.*, *J. Polym. Sci., Part A: Polym. Chem.*, 2001, vol. 39, no. 9, pp. 1435–1449.
4. PCT WO Patent Application 98/39372.
5. US Patent 4469825.

Russian Journal of Applied Chemistry, Vol. 75, No. 10, 2002, pp. 1709–1710. Translated from Zhurnal Prikladnoi Khimii, Vol. 75, No. 10, 2002, pp. 1743–1744.
Original Russian Text Copyright © 2002 by Ananichev, Voronova, Blinov.

BRIEF COMMUNICATIONS

Thermal Expansion of Arsenic

V. A. Ananichev, A. E. Voronova, and L. N. Blinov

St. Petersburg State Technical University, St. Petersburg, Russia

Received April 15, 2002

Abstract—The temperature dependence of molar volume of arsenic was studied in the range 293–1410 K.

It is commonly believed that the systematic decrease, with increasing atomic number, in the density drop upon melting of Group V elements is due to the growing metallization of the melt [1–3].

Phosphorus can exist at atmospheric pressure in several modifications, among which white phosphorus has been studied in most detail. White phosphorus has a cubic structure [4] and melts at 317 K. The increase in the molar volume upon melting is 0.593 $cm^3\ mol^{-1}$ [4], and the decrease in density, 3.3% [3]. The structure of the white phosphorus melt has been studied at 319 and 499 K [5]. At these temperatures, the atomic radial distribution function (ARDF) shows peaks at 2.25, 3.9, and 5.9 Å, at $Z_1 = 3$. It was concluded that pyramidal P_4 molecules are structural elements of the melt.

Arsenic has a rhombohedral structure at atmospheric pressure. It melts under elevated pressure at 1090 K [4]. The change in the molar volume upon melting has not been determined experimentally. The value calculated from the Clapeyron equation is 0.8 $cm^3\ mol^{-1}$ [4]. The calculated decrease in density is 5.4%, which is questionable [6]. The structure of As in the liquid state is unknown [5].

Antimony has at atmospheric pressure a rhombohedral structure, similar to that of arsenic, and melts at 903 K [4]. The experimental change in the molar volume upon melting is 0.2 $cm^3\ mol^{-1}$. The value calculated by the Clapeyron equation has the opposite sign and is equal to $-0.11\ cm^3\ mol^{-1}$ [4]. The relatively small decrease in the Sb density upon melting (0.95% [6]) was attributed in [3] to incomplete metallization of the melt. The structure of liquid antimony was described in detail in [5]. A study of the intensities of X-ray scattering by liquid and crystalline antimony revealed a similarity, even if incomplete, of short-range orders in Sb in the crystalline and molten state. Analysis of experimental data on the short-range atomic order suggests [5] that melting of antimony is accompanied by rupture of covalent bonds between atoms in layers of the crystal lattice to give a short-range order whose main structural properties can be described in terms of a diffuse primitive cubic lattice. This melt structure is stable over a wide temperature range. The packing density of atoms in an antimony melt is higher than that in a crystal, but lower than that in liquid metals.

Bismuth has at atmospheric pressure a rhombohedral structure similar to that of As and Sb. It melts at 544 K [4]. The volume drop upon melting, calculated by the Clapeyron equation ($\Delta V = -0.84\ cm^3\ mol^{-1}$), and its experimentally determined value ($\Delta V = -0.85\ cm^3\ mol^{-1}$) [3, 6] are in good agreement. The increase in density upon melting (3.42%) was attributed in [1, 3] to a decrease in the covalent component of the chemical bond in Group V elements, which results in metallization of the Bi melt. Heating the melt to 1087 K leads to an increase in the coordination number to 9.4 and to broadening of peak II in the ARDF curve [5]. At 1103 K the distribution of atoms in the melt becomes quasi-uniform. With account taken of the structural similarity between semimetals in the molten and crystalline states, it has been concluded [5] that groups with short-range order isostructural to that in crystalline bismuth are present among various atomic groups in the melt.

In this study, the molar volume of As at 293–1410 K was determined experimentally and a correlation between the numerical value of the volume change upon melting and the change in the nature of the interatomic bond in Group V elements was established.

Measurements were performed on an installation of design similar to that used for measuring the coefficient β of volume thermal expansion [7]. The dif-

1070-4272/02/7510-1709 $27.00 © 2002 MAIK "Nauka/Interperiodica"

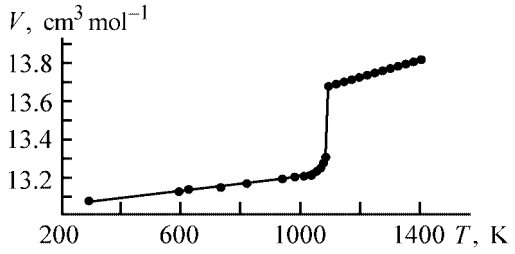

Molar volume V of an As vs. temperature in the range 293–1410 K.

ference was as follows: an ampule with As was placed on a balance arm at an angle of 45°. The total length of the ampule was 60 mm; its inner diameter, about 8 mm; and the column of the As melt in the ampule, approximately 50 mm high. The sample volume at 298 K was 1 cm^3. The ampule with As was heated to 1410 K and kept at this temperature for 5–10 min. The measurements were done under cooling or heating at a rate of 0.3–0.5 deg min^{-1}. The upper part of the ampule was maintained at a temperature higher by 60 ± 5 K than the temperature of the bottom part. Under these conditions, the pressure in the free part of the ampule at the melting point of As was 50–100 bar [4]. The temperature in the middle part of the ampule was taken as the sample temperature. The sample volume was calculated by identically equating expression (1) from [8]

$$\beta = (V_2 - V_1)/V_1(T_2 - T_1)$$

(where V_2 and V_1 are the sample volumes at T_2 and T_1) to expression (1) from [7]

$$\beta = \gamma(P_2 - P_1)/P(T_2 - T_1),$$

where γ is the vessel constant; P_1 and P_2 are balance readings at T_1 and T_2, respectively; and P is the sample mass.

The temperature dependence of the change in the molar volume of an As sample is presented in the figure.

Most probably, the sample volume increases within the range 293–1030 K owing to thermal expansion of As. For the given temperature range, the bulk thermal expansion coefficient of arsenic, averaged over three crystalline samples, $\beta = (14.5 \pm 0.1) \times 10^{-6}$ K^{-1}, in good agreement with the data of [7].

A marked increase in the volume at 1030–1089 K has not been explained unambiguously so far. Arsenic melting at 1089 ± 2 K is accompanied by a stepwise increase in volume by $2.8 \pm 0.1\%$.

Further heating of As to 1410 K is accompanied by a steady increase in volume, which is probably due to thermal expansion of the melt. In the range 1090–1410 K, the bulk thermal expansion coefficient of As $\beta = (33.9 \pm 0.1) \times 10^{-6}$ K^{-1} and it is virtually pressure independent.

The linear thermal expansion coefficient of Group V elements with rhombohedral structure grows steadily with increasing principal quantum number, as is readily seen from comparison of its values for P, As, Sb, and Bi ($\alpha_P = 124.5 \times 10^{-6}$, $\alpha_{As} = 4.7 \times 10^{-6}$, $\alpha_{Sb} = 8.5 \times 10^{-6}$, and $\alpha_{Bi} = 13.4 \times 10^{-6}$ K^{-1} [7]). The coefficient of linear thermal expansion of white phosphorus (having cubic structure) is higher by an order of magnitude than that of As, Sb, and Bi, and, therefore, falls out of this sequence.

The drop in the molar volume of Group V elements upon melting (cm^3 mol^{-1}): 0.59 for P[6], 0.39 for As [this study], 0.2 for Sb [6], and –0.84 for Bi [6], decreases steadily with increasing principal quantum number.

Analysis of the data presented shows that the chage in volume with increasing temperature is governed in As, Sb, and Bi by their crystal structure and the nature of interatomic bonds, which is determined for *p*-elements by both covalent and metallic components.

REFERENCES

1. Regel', A.R., and Glazov, V.M., *Periodicheskii zakon i fizicheskie svoistva electronnykh rasplavov* (The Periodic Law and Physical Properties of Electronic Melts), Moscow: Nauka, 1979.
2. Samsonov, G.V., *Fiz. Khim. Obrab. Mater.*, 1975, no. 6, pp. 43–52.
3. Stankus, S.V., *Izmenenie plotnosti elementov pri plavlenii: Obshchie zakonomernosti* (Density Change of Elements upon Melting: General Trends), Novosibirsk: Inst. Teplofiz. Sib. Otd. Akad. Nauk SSSR, 1991.
4. Tonkov, E.Yu., *Fazovye diagrammy elementov pri vysokom davlenii* (Phase Diagrams of Elements at Elevated Pressure), Moscow: Nauka, 1979.
5. Poltavtsev, Yu.G., *Struktura poluprovodnikovykh rasplavov* (The Structure of Semiconductor Melts), Moscow: Metallurgiya, 1984.
6. Stankus, S.V., *Izmenenie plotnosti elementov pri plavlenii: Metody i eksperimental'nye dannye* (Density Change of Elements upon Melting: Methods and Experimental Data), Novosibirsk: Inst. Teplofiz. Sib. Otd. Akad Nauk SSSR, 1991.
7. Emsley, J.W., *The Elements*, Oxford: Clarendon Press, 1991.
8. Novikova, S.I., *Teplovoe raschirenie tverdykh tel* (Thermal Expansion of Solids), Moscow: Nauka, 1974.

Russian Journal of Applied Chemistry, Vol. 75, No. 10, 2002, pp. 1711–1712. Translated from Zhurnal Prikladnoi Khimii, Vol. 75, No. 10, 2002, pp. 1745–1746.
Original Russian Text Copyright © 2002 by Efanov, Dudkin, Galochkin.

BRIEF COMMUNICATIONS

Production of Nitrogen-containing Sorbents from Wood Waste

M. V. Efanov, D. V. Dudkin, and A. I. Galochkin

Altai State University, Barnaul, Russia

Received January 14, 2002

Abstract—The sorption capacity for Fe(II), Cu(II), Cd(II), and Zn(II) ions of nitrogen-containing derivatives of birch wood, obtained by different variations of oxidative ammonolysis, was studied.

Nitrogen-containing derivatives of lignin exhibit ion-exchange properties and can be used as sorbents of heavy metal ions and organic dyes [1]. The main drawbacks of these products are their relatively low exchange capacity and low mechanical strength.

To produce nitrogen-containing sorbents in quantitative yield, hydrolyzed lignin has been treated with ammonia solution of ammonium peroxodisulfate under mild conditions at 20°C for 1–5 days [2]. Along with hydrolyzed lignin, poor wood (aspen or birch) can be used as an accessible raw material for production of nitrogen-containing sorbents.

Nitrogen-containing sorbents based on sawdust of aspen wood have been obtained mechanochemically by reaction with ammonia solution of ammonium peroxodisulfate, and their sorption capacity for certain heavy metal ions has been studied [3]. It was found that the resulting nitrogen-containing derivatives of wood exhibit enhanced sorption capacity for the metal cations studied.

In this communication, we present results of a comparative study of nitrogen-containing derivatives of birch wood, produced mechanochemically by oxidation of wood with an ammonia solution of ammonium peroxodisulfate and atmospheric oxygen in an ammonia medium.

Nitrogen-containing sorbents were obtained from secondary waste of wood in two ways. According to the first procedure, the sawdust of birch wood, combined with ammonium peroxodisulfate (0.2 g of available oxygen per 1 g of wood), was subjected to intensive mechanical crushing in a ball mill in 25% aqueous ammonia (0.9 g of NH_3 per 1 g of wood) for 10–100 min. According to the second, the sawdust combined with aqueous ammonia (0.9 g of NH_3 per 1 g of wood) was subjected to intensive mechanical crushing in a ball mill under air pressure of 3 atm for 10–100 min.

The content of nitrogen in the products obtained was determined by Kjeldahl's semimicromethod [4], and the number of carboxy groups, by back conductometric titration [5].

The sorption capacity of the resulting products was studied by the static method [6]. Nitrate solutions of appropriate metals, with concentration of 0.01–0.1 g-equiv dm^{-3}, were taken as starting solutions. When the equilibrium was attained (in 24 h), the concentration of the corresponding cation in solution was determined complexometrically. The exchange capacity of the sorbents was calculated by the formula:

$$\mathrm{SEC} = (c_0 - c_e)V/1000g,$$

where SEC is the static exchange capacity (mg-equiv g^{-1}); c_0, the concentration of metal ions in the starting solution (g-equiv dm^{-3}); c_e, the concentration of metal ion in equilibrium solution (g-equiv dm^{-3}); V, the volume of equilibrium solution (cm^3); and g, the sorbent mass (g).

Comparison of the functional compositions of the products obtained by oxidative ammonolysis of wood (procedures 1 and 2) shows that, in the case of an ammonia solution of ammonium peroxodisulfate, the oxidation is more complete and the amount of nitrogen and the number of carboxy groups in the wood derivatives obtained is larger (Table 1).

The results of the experiments performed show that the nitrogen-containing wood derivatives obtained by procedures 1 and 2 have high sorption capacity for the metal ions studied (Table 2). Their exchange capacity, depending on the content of nitrogen and the number

1070-4272/02/7510-1711 $27.00 © 2002 MAIK "Nauka/Interperiodica"

Table 1. Content of nitrogen and number of carboxy groups in nitrogen-containing derivatives of birch wood, obtained by procedures 1 and 2

t, min	Content, %	
	N	COOH
10	1.76/1.10*	3.63/1.72*
50	3.11/1.17	5.47/2.88
100	5.32/1.38	16.3/6.7

* Procedure 1/procedure 2; the same for Table 2.

Table 2. Influence of the concentration of metal ion in solution on the sorption capacity of nitrogen-containing derivatives of birch wood, obtained by procedures 1 and 2

c_0, g-equiv dm^{-3}	SEC, mg-equiv g^{-1}			
	Cu(II)	Cd(II)	Zn(II)	Fe(II)
0.01	5.88/4.22	5.27/3.47	4.17/3.11	3.08/2.06
0.05	5.95/4.25	5.34/3.54	4.26/3.13	3.16/2.09
0.1	6.13/4.29	5.36/3.56	4.32/3.16	3.24/2.14

of carboxy groups incorporated into them, is comparable with that in oxycellulose (Tables 1, 2), in agreement with published data [3].

It was found that the sorption capacity of the nitrogen-containing derivatives of birch wood, obtained by oxidative ammonolysis, is somewhat higher in the case of procedure 1, compared with that for procedure 2 [3.1–6.1 and 2.1–4.3 mg-equiv g^{-1}, respectively (Table 2)].

The sorption capacity of sorbents obtained by oxidative ammonolysis of wood for the metal ions studied depends on their concentration only slightly, increasing in the order Fe(II) < Zn(II) < Cd(II) < Cu(II) (Table 2). The absorption of metal ions by nitrogen-containing wood derivatives from solutions makes lower the pH value of aqueous solutions obtained after their sorption. The decrease in the pH value of the filtrates after sorption and the high content of carboxy groups in nitrogen-containing wood sorbents suggests that mobile hydrogen cations incorporated into them can be substituted by heavy metal ions, i.e., the obtained sorbents bind metal cations by the ion-exchange mechanism.

CONCLUSIONS

(1) The sorption capacity of nitrogen-containing derivatives of birch wood, obtained by oxidative ammonolysis of wood, is somewhat higher in the case of procedure 1, compared with procedure 2 (3.1–6.1 and 2.1–4.3 mg-equiv g^{-1}, respectively).

(2) The sorption capacity of nitrogen-containing derivatives of birch wood, obtained by various procedures, for heavy metal ions depends on their concentration only slightly and increases in the order Fe(II) < Zn(II) < Cd(II) < Cu(II).

(3) Sorption of the metal cations studied by nitrogen-containing wood sorbents from aqueous solutions makes lower the solution pH, thus indicating the ion-exchange mechanism of sorption.

REFERENCES

1. Yaunzems, V.R., Mozheiko, L.N., and Sergeeva, V.N., *Khim. Drev.*, 1968, no. 2, pp. 115–118.
2. USSR Inventor's Certificate, no. 363710.
3. Efanov, M.V. and Klepikov, A.G., *Zh. Prikl. Khim.*, 2001, vol. 74, no. 2, pp. 340–342.
4. Klimova, V.A., *Osnovnye mikrometody analiza organicheskikh soedinenii* (Basic Micromethods for Analysis of Organic Compounds), Moscow: Khimiya, 1975.
5. Mozheiko, L.N., Sergeeva, V.N., Yaunzems, V.R., *et al.*, *Khim. Drev.*, 1969, no. 3, pp. 139–142.
6. Garkusha, D.G., Kuznetsov, P.M., and Fogileva, R.S., *Zh. Anal. Khim.*, 1974, no. 11, pp. 2295–2298.

Russian Journal of Applied Chemistry, Vol. 75, No. 10, 2002, pp. 1713–1714. Translated from Zhurnal Prikladnoi Khimii, Vol. 75, No. 10, 2002, pp. 1747–1748.
Original Russian Text Copyright © 2002 by Kabanov, Perelygin.

BRIEF COMMUNICATIONS

Electrodeposition of Palladium–Zinc Alloy from Aminoacetic Electrolyte

S. V. Kabanov and Yu. P. Perelygin

Penza State University, Penza, Russia

Received April 4, 2002

Abstract—The influence of the electrolysis conditions and electrolyte composition on the cathodic current efficiency by the alloy and on the alloy composition was studied for electrodeposition of the palladium–zinc alloy from an aminoacetic electrolyte.

The industrial use of palladium alloys with nickel, indium, and some other metals in coatings is due to lower consumption of the noble metal and enhanced physicomechanical and chemical properties of the coatings [1, 2]. The metallurgical palladium–zinc alloy is a complex system comprising a solid solution at zinc content of less than 6% and several chemical compounds at higher zinc content [3].

The possibility of obtaining a palladium–zinc alloy with up to 8% zinc from ammonia–trilonate electrolyte has been shown previously [4]. Since intermetallic compounds have enhanced physicomechanical properties [1–3], it is of certain practical and theoretical interest to obtain the given alloy with higher content of zinc.

The alloy was electrodeposited from an aminoacetic solution in a 100-ml rectangular glass bath with graphite anodes. The content of zinc in the alloy was determined by complexometric titration after separating palladium in the form of palladium dimethylglyoximate [5].

Preliminary experiments showed that quality coatings are formed solely in a saccharin-containing electrolyte. Addition of 0.25–1 g l^{-1} saccharin considerably decreases (from 10 to 2.5 MPa) the internal stresses in deposits and increases somewhat (by 1–2%) the content of zinc in a coating.

The influence of the electrolysis conditions and electrolyte composition on the cathodic current efficiency (CE) by the alloy and on the alloy composition was studied at 30°C, current density of 0.5 A dm^{-2}, and pH 7 from a solution containing (g l^{-1}): palladium chloride 20, zinc chloride 3 (in terms of metal), ammonium chloride 20, aminoacetic acid 40, and saccharin 0.5.

With increasing zinc concentration $c_{Zn^{2+}}$ in an electrolyte, zinc content in a coating, c_{Zn}, grows and the cathodic CE by the alloy falls:

$c_{Zn^{2+}}$, g l^{-1}	0.5	1	2	3
c_{Zn}, %	7.7	9	12.8	15.8
CE, %	88.5	84	82	77

The ratio of metal contents in the alloy as a function of the ratio of concentrations of their ions in the electrolyte is described by the equation [6]:

$$\log\frac{[Pd]}{[Zn]} = 0.37 + 0.457\log\frac{[Pd^{2+}]}{[Zn^{2+}]}.$$

The correlation coefficient of the equation is $R = 0.987$.

With zinc concentration in the electrolyte increasing further to 5 g l^{-1}, the current efficiency by the alloy decreases from 77 to 65%, and the content of zinc in the coating increases to 20%. Lowering the palladium concentration in the electrolyte under these conditions results in deterioration of the deposit quality.

When the cathode current density is lowered from 0.25 to 1 A dm^{-2}, the CE by the alloy falls from 90.5 to 72% (Fig. 1, curve *1*), with the zinc content decreasing only slightly (from 15.8 to 17%). At higher current densities the coating quality deteriorates because of the cracking resulting from the build-up of considerable internal stresses.

1070-4272/02/7510-1713 $27.00 © 2002 MAIK "Nauka/Interperiodica"

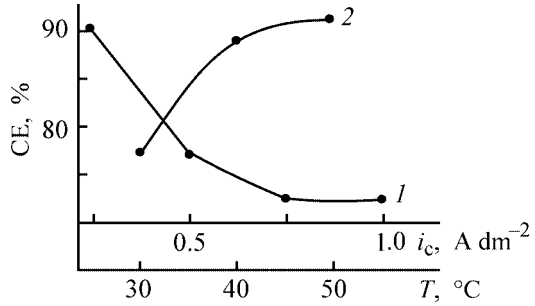

Fig. 1. Current efficiency CE by the alloy vs. (*1*) cathode current density i_c and (*2*) temperature T.

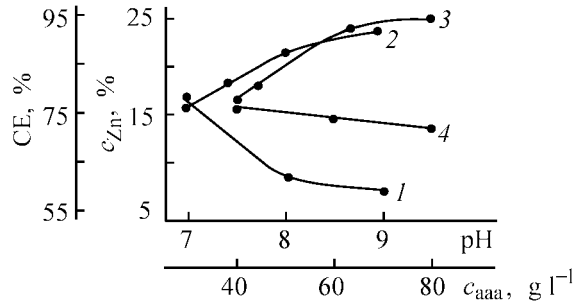

Fig. 2. (*1, 3*) Current efficiency CE by the alloy and (*2, 4*) content of zinc in the alloy, c_{Zn}, vs. (*1, 2*) pH and (*3, 4*) concentration c_{aaa} of aminoacetic acid.

Raising the temperature from 30 to 50°C leads to an increase in CE from 77 to 91% (curve *2*). In this case, the composition of the alloy is virtually unaffected, and the coating quality is improved. Owing to the high internal stresses, high-quality deposits cannot be obtained at temperatures below 30°C.

On changing the solution pH from 7 to 9, the CE by the alloy decreases from 77 to 58% (Fig. 2, curve *1*) and the zinc content increases from 15.8 to 24% (curve *2*). In this case, the quality of the coating is deteriorated somewhat.

Raising the aminoacetic acid concentration from 40 to 80 g l^{-1} (Fig. 2, curve *3*) leads to an increase in the CE by the alloy from 77 to 94% and a decrease in the content of zinc in the coating to 13.5% (curve *4*).

At aminoacetate acid concentrations lower than 40 g l^{-1} the cathodic CE does not exceed 55%.

Changing the ammonium chloride concentration in the electrolyte from 20 to 40 g l^{-1} does not affect significantly the alloy composition and the CE by the alloy.

Thus, for deposition of semilustrous alloy coatings with zinc content from 7 to 16%, an electrolyte containing (g l^{-1}): palladium chloride 20, zinc chloride 0.5–3.0 (in terms of metal), ammonium chloride 20–40, aminoacetic acid 40–80, and saccharin 0.5–1.0 can be recommended. The electrodeposition should be performed at 30–40°C, current density of 0.25–0.5 A dm^{-2}, and pH 7. Under these conditions, the current efficiency by the alloy is 90–77%.

The contact electrical resistance of the alloy with zinc content of 15–16% is 0.038 Ω at a contact load of 0.5 N and decreases to 0.03 Ω with load increasing to 2 H. The microhardness of alloy coatings with zinc content of 7.7 and 15.8% is 220 and 278 kg mm^{-2}, respectively.

The wear resistance of the obtained alloy coating with 15–16% zinc, as measured on an installation described in [7] at a contact load of 2H, is 40 000 switchings, i.e., is 2 times that for pure palladium.

REFERENCES

1. Vinogradov, S.N., *Elektroosazhdenie splavov palladiya* (Electrodeposition of Palladium Alloys), Saratov: Saratov. Univ., 1978.
2. Perelygin, Yu.P., *Elektroosazhdenie, svoistva i oblast' primeneniya indiya i ego dvoinykh splavov* (Electrodeposition, Properties, and Application of Indium and Its Binary Alloys), Penza: Penz. Politekh. Univ., 1993.
3. Savitskii, E.M., Polyakova, V.P., and Tylkina, M.A., *Splavy palladiya* (Palladium Alloys), Moscow: Nauka, 1967.
4. Kabanov, S.V., and Perelygin, Yu.P., *Zh. Prikl. Khim.*, 2001, vol. 74, no. 11. pp. 1895–1897.
5. Budyak, N.F., and Ekimenkova, T.A., *Analiz kontaktnykh i provodnikovykh splavov* (Analysis of Contact and Conductor Alloys), Moscow: Metallurgiya, 1975.
6. Akhumov, E.I., and Rozen, B.Ya., *Dokl. Akad. Nauk SSSR*, 1956, vol. 109, no. 6, pp. 1149–1151.
7. Perelygin, Yu.P., *Gal'vanotekh. Obrab. Poverkh.*, 1993, vol. 2, no. 4, pp. 65–66.

Russian Journal of Applied Chemistry, Vol. 75, No. 10, 2002, pp. 1715–1717. Translated from Zhurnal Prikladnoi Khimii, Vol. 75, No. 10, 2002, pp. 1749–1751.
Original Russian Text Copyright © 2002 by Storozhakova, Efanova, Rakhimov.

BRIEF COMMUNICATIONS

Reactions of Polyfluorinated Telomeric Alcohols with ε-Caprolactam[1]

N. A. Storozhakova, E. Yu. Efanova, and A. I. Rakhimov

Volgograd State Technical University, Volgograd, Russia

Institute of Chemical Problems of Ecology, Russian Academy of Natural Sciences, Volgograd, Russia

Received January 17, 2002

Abstract—The possibility of preparing fluorinated oligomeric derivatives of ε-aminocaproic acid by reaction of polyfluorinated telomeric alcohols $H(CF_2CF_2)_nCH_2OH$ (n = 1–4) with ε-caprolactam under conditions of homogeneous catalysis (triethylamine, dimethylformamide) was examined. The thermal stability of the oligomers was studied in relation to the fluorine content.

Reactions of ε-caprolactam with saturated monohydric alcohols have been studied previously under conditions of heterogeneous (lead oxide, lead powder, zinc powder [1]) and homogeneous (triethylamine, TEA; dimethylformamide, DMF [2]) catalysis. The resulting oligomeric esters are of interest as matrices for preparing substances with biomedical activity [2]. With fluorinated alkoxy groups, these compounds show promise for preparing materials with decreased combustibility [3], enhanced resistance to aggressive media and organic solvents [4], and decreased friction coefficient [5].

The goal of this study was to prepare fluorinated oligomers by reaction of ε-caprolactam with polyfluorinated telomeric alcohols of the general formula $H(CF_2CF_2)_nCH_2OH$, where n = 1 (PFA1), 2 (PFA2), 3 (PFA3), and 4 (PFA4), and to analyze their physicochemical properties.

EXPERIMENTAL

The reaction of ε-caprolactam with polyfluorinated alcohols was performed at a molar ratio ε-caprolactam : alcohol = 1 : 1.2 in the presence of catalytic amounts (0.05 mol) of lead oxide, TEA, or DMF at high temperature (260°C). At lower temperatures, the oligomer yield is low.

Kinetic experiments were performed with PFA2; we monitored the amounts of unchanged ε-caprolactam (as described in [1]) and polyfluorinated alcohol, which was isolated by vacuum distillation. Also, we determined the yield of the oligomer after its isolation by filtration. The oligomer was recrystallized from acetic acid.

The structure of the oligomer was determined by IR and NMR spectroscopy. The IR spectra were recorded with a Specord M82 spectrometer (mulls in mineral oil, NaCl or KBr cells). The ^1H NMR spectra were taken on a Tesla BS487 spectrometer (100 MHz, internal reference HMDS, solvent dimethyl sulfoxide).

The thermal stability of polyfluorinated oligomers was studied with an MOM derivatograph (Hungary). Samples were heated to 500°C over a period of 50 min.

Polyfluorinated telomeric alcohols react with the lactam in the presence of DMF to give esters of alcohols and ε-aminocaproic acid oligomers:

$$H(CF_2CF_2)_nCH_2OH + HN(CH_2)_5C{=}O \rightarrow H[NH(CH_2)_5C(O)]_mOCH_2(CF_2CF_2)_nH,$$

where n = 1–4, m = 2, 3.

The yield of polyfluorinated oligomers increases with decreasing length of the fluorocarbon chain, being 32–41% with PFA1 and PFA2 and 10–13% with PFA3 and PFA4. It is convenient to purify the oligomers by recrystallization from hot acetic acid. Trimers precipitate upon cooling; their melting points (°C) are as follows: PFA1, 192; PFA2, 204. Dimers

[1] Reported at the 3rd International Conference "Chemistry, Technology, and Application of Fluoro Compounds," St. Petersburg, June 6–9, 2001.

1070-4272/02/7510-1715 $27.00 © 2002 MAIK "Nauka/Interperiodica"

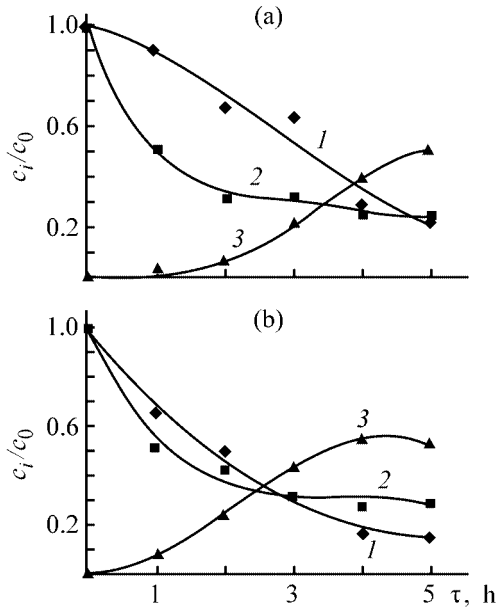

Fig. 1. Variations with time τ of the relative concentrations of reactants, c_i/c_0, in the reaction of caprolactam with octafluoropentanol at 260°C. Catalyst: (a) TEA and (b) DMF. (*1*) Lactam, (*2*) alcohol, and (*3*) oligomer.

are readily soluble in acetic acid, and their melting points (°C) are lower: PFA1, 172; PFA2, 193; PFA3, 185; PFA4, 178–180.

Oligomers have light brown color due to impurities of dehydrofluorination products. The color is the most intense with lead oxide or TEA as catalyst, and the least so with DMF as catalyst. The catalyst was chosen on the basis of kinetic studies. The kinetic curves for the reaction of PFA2 with ε-caprolactam (1 : 1) in the presence of TEA, describing the consumption of polyfluorinated alcohol and ε-caprolactam and accumulation of the oligomer, are shown in Fig. 1a.

It is seen that, in the initial period, polyfluorinated alcohol is consumed considerably faster than lactam. This is due to the side reaction of dehydrofluorination, yielding an unsaturated compound which subsequently polymerizes to give a colored product.

In contrast to the reaction in the presence of TEA, the consumption of PFA2 with DMF as catalyst exceeds only slightly the consumption of ε-caprolactam in the first 2.5 h (Fig. 1b), which indicates that the extent of dehydrofluorination is small.

However, the consumption of the lactam starts to appreciably exceed the consumption of PFA2 after 2.5 h. This is due to the fact that, in this period, formation of the dimer becomes the major reaction pathway:

$$\text{Lactam} + H_2N(CH_2)_5C(O)OCH_2(CF_2CF_2)_2H \rightarrow \underset{\text{(Dimer)}}{H[HN(CH_2)_5C(O)]_2OCH_2(CF_2CF_2)_2H}.$$

After 2.5 h, the accumulation of the oligomer becomes noticeable. Longer (10 h) reaction results in accumulation of trimers:

$$\text{Dimer} + \text{Lactam} \rightarrow H[HN(CH_2)_5C(O)]_3OCH_2(CF_2CF_2)_2H.$$

The IR spectra of esters of polyfluoroalkanols with ε-aminocaproic acid dimer and trimer contain bands originating from stretching vibrations of ester carbonyls [ν(C=O)] at 1733–1750 cm^{-1}, with their frequencies growing with increasing length of the fluorocarbon chain (n = 1, 1733 cm^{-1}; n = 4, 1750 cm^{-1}). The terminal C–H group in the alcohol moieties gives a stretching vibration band at 3055 (n = 1) to 3067 cm^{-1} (n = 4), which is broadened and split owing to hydrogen bonding.

The amide groups [5] give bands at 3300 (NH), 1640 (amide I), and 1545 cm^{-1} (amide II).

In the ^1H NMR spectra, the HCF_2CF_2 group gives a triplet of triplets (δ 6.28 ppm, J 52 and 6 Hz).

Esters of PFA1 and PFA2 with oligomers of ε-aminocaproic acid decompose more slowly than polycaproamide and n-butyl ester of α-aminocaproic acid trimer do. The weight loss in 20 min at 300°C is 4% for the PFA1 ester and about 5% for the PFA2 ester. However, the decomposition rate drastically increases at higher temperatures: at 350°C, the weight loss in 25 min is 12.5% for the PFA1 ester and 10% for the PFA2 ester.

At 400°C, the weight loss in 30 min is 15% for the octafluoropentyl ester, and about 30% for polycaproamide under comparable conditions. The enhanced thermal stability of polyfluorinated esters of ε-aminocaproic acid oligomers is due to less intense intra- and intermolecular decomposition of oligomeric molecules with the release of ε-caprolactam, and also to decreased contribution of hydrolytic cleavage of peptide bonds.

CONCLUSIONS

(1) Fluorinated esters of ε-aminocaproic acid oligomers were prepared by the reaction of polyfluorinated telomeric alcohols $H(CF_2CF_2)_nCH_2OH$ (n = 1–4) with ε-caprolactam in the presence of homogeneous catalysts. The reactivity of the alcohol de-

creases with increasing length of the perfluorinated chain.

(2) Dimethylformamide is a more selective oligomerization catalyst than triethylamine, ensuring smaller contribution of dehydrofluorination processes.

(3) Introduction of fluorinated groups into the oligomer molecule enhances its thermal stability.

REFERENCES

1. Khitrin, S.V. and Bagaev, S.I., *Izv. Vyssh. Uchebn. Zaved., Khim. Khim. Tekhnol.*, 1997, vol. 40, no. 1, pp. 3–7.
2. Storozhakova, N.A., Efanova, E.Yu., and Rakhimov, A.I., *Zh. Org. Khim.*, 2000, vol. 36, no. 12, pp. 1875–1876.
3. Storojakova, N.A., Jeltobruchov, V.F., Rakhimov, A.I., *et al.*, Abstracts of Papers, *7th Eur. Conf. on Fire Retardant Polymers, Society of Chemical Industry*, Univ. of Greenwich (the United Kingdom), 1999.
4. Storozhakova, N.A., Abstracts of Papers, *IX konferentsiya "Destruktsiya i stabilizatsiya polimerov"* (IX Conf. "Degradation and Stabilization of Polymers"), Moscow: Ross. Akad. Nauk, 2001, pp. 192–193.
5. Storozhakova, N.A., Modification with Polyfluorinated Telomeric Alcohols and Properties of Poly-ε-caprolactam, *Cand. Sci. Dissertation*, Volgograd, 1998.

Russian Journal of Applied Chemistry, Vol. 75, No. 10, 2002, pp. 1718–1719. Translated from Zhurnal Prikladnoi Khimii, Vol. 75, No. 10, 2002, pp. 1752–1753.
Original Russian Text Copyright © 2002 by Builov, Popova, Shevchuk, Podgornova.

BRIEF COMMUNICATIONS

Synthesis of *N*-Benzylacrylamide

V. A. Builov, V. V. Popova, A. S. Shevchuk, and V. A. Podgornova

Yaroslavl State Technical University, Yaroslavl, Russia

Received February 11, 2002

Abstract—A procedure was developed for preparing *N*-benzylacrylamide in quantitative yield in a single stage from acrylonitrile and benzyl alcohol.

N-Substituted acrylamides derived from acrylic and methacrylic acids are important monomers [1–4]. One of these, *N*-benzylacrylamide (*N*-BAA), imparts valuable properties to polymeric materials, making them more elastic and more resistant to water, chemicals, and heat and enhancing the adhesion and antistatic properties of polymeric films. Development of new procedures for preparing *N*-BAA is an urgent problem, and study of its physical and chemical properties can reveal new interesting fields of its application in polymer chemistry.

There are numerous patents concerning synthesis of *N*-substituted (meth)acrylamides starting from amides, esters, and chlorides of unsaturated acids [5]. However, the proposed precursors are expensive and difficultly available, and isolation of target products is complicated.

The goal of this study was to develop a procedure for preparing *N*-BAA from cheaper and more available precursors: acrylonitrile (AN) and benzyl alcohol (BA). AN reacts with BA in the presence of an acid catalyst at relatively low temperatures:

$$CH_2{=}CH{-}CN + HO{-}CH_2{-}C_6H_5 \rightarrow CH_2{=}CH{-}CO{-}NH{-}CH_2{-}C_6H_5.$$

Acidic medium and elevated temperatures favor formation of by-products: acrylamide and dibenzyl alcohol. To prevent polymerization, the synthesis is performed in the presence of a polymerization inhibitor, $CuCl_2 \cdot 2H_2O$.

As catalysts, we tested both mineral (H_2SO_4, H_3PO_4, HCl) and organic (acetic, *p*-toluenesulfonic) acids; 3.2 M sulfuric acid proved to be the most effective. At lower acid concentrations, the reaction is slow, and at higher concentrations it is too vigorous, so that the evolved heat cannot be efficiently removed and the reaction is accompanied by polymerization. The influence of temperature on the *N*-BAA yield was studied in the range 20–50°C, at the reaction time of up to 3 h and constant molar ratio AN : BA : H_2SO_4 = 3 : 1 : 1 (see table).

The optimal temperature, at which the maximal yield is attained in 60 min, is 50°C. Higher temperatures are not appropriate because of polymerization.

The AN : BA molar ratio was varied from 0.5 : 1 to 5 : 1 at 40°C, reaction time of 3 h, and constant acid concentration. Experiments showed that the reaction occurs considerably faster with excess AN; at the molar ratio AN : BA = 5 : 1, the maximal yield is attained already in 1 h. However, higher concentrations of AN are not appropriate because of the increased expenses for its utilization.

Thus, we have found the best conditions for preparing *N*-BAA in quantitative yield. *N*-Benzylacrylamide is a white crystalline substance, $C_{10}H_{11}NO$, M = 161.20, mp 64–65°C. Yield based on loaded benzyl alcohol 96.4%; yield based on reacted AN 87.5%. Main substance content 96.6 wt %.

We used technical-grade AN [GOST (State Standard) 11 097–73], which was purified by distillation, bp

Variation of *N*-BAA concentration in the course of synthesis

T, °C	*N*-BAA amount, wt %, in indicated time, min				
	15	30	60	120	180
20	2.83	11.06	16.24	22.68	27.24
30	12.53	16.88	26.75	31.76	31.82
40	22.39	27.61	30.29	33.82	34.75
50	31.70	34.43	35.75	36.05	36.31

1070-4272/02/7510-1718 $27.00 © 2002 MAIK "Nauka/Interperiodica"

78.5–79°C (760 mm Hg), d_4^{20} 1.045, n_D^{20} 1.5396; pure grade sulfuric acid (GOST 4204–77); and pure grade solvents.

Synthesis was performed in a four-necked batch reactor equipped with a stirrer, thermometer, reflux condenser, and dropping funnel. The reactor was charged with the required amount of AN, and the inhibitor was added. The mixture was cooled with stirring to 0°C, after which a mixture of BA with a catalyst was added through a dropping funnel, avoiding warming of the reaction mixture to above 0–1°C. After adding the reactants, the mixture was heated to the required temperature on a water bath. After reaction completion, the mixture was poured into cold water, and the organic layer was separated, washed with 0.5% NaOH, and dried over Na_2SO_4.

The crystalline product was recrystallized from toluene; mp 64–65°C. The reaction mixture was analyzed by gas–liquid chromatography on a Chrom-5 chromatograph (flame ionization detector, 5000 × 3-mm glass column, stationary phase 25 wt % SKTFT-50Kh methylsiloxane trifluoropropyl elastomer on Chromaton N-AW). The calibration coefficients for all the components were determined by standard computer processing of the data for reference mixtures. *N*-Benzylacrylamide was identified by bromination; its molecular weight, ~161.0, was determined by cryoscopy. The IR spectrum of *N*-BAA was recorded on an IKS-14a device (NaCl prism, mull in mineral oil). The IR spectrum contains absorption bands characteristic of various functional groups, ν, cm^{-1}: 700–800, monosubstituted benzene ring; 1240, C–N; 1410, CH_2=CH–; 1500, C_6H_6; 1540, N–H; 1620, C=C; 1650, C=O; 3050, CH=; 3300, N–H; 2950 and 1450, bands of mineral oil. Consistent analytical data were obtained.

CONCLUSION

A procedure was developed for synthesis of *N*-benzylacrylamide in quantitative yield in a single stage by reaction of acrylonitrile with benzyl alcohol (50°C, 1 h, acrylonitrile : benzyl alcohol molar ratio 5 : 1), and also for isolation and purification of the product.

REFERENCES

1. Khalistova, I.D. and Podgornova, V.A., *Zh. Prikl. Khim.*, 1994, vol. 67, no. 8, pp. 1346–1350.
2. Podgornova, V.A., Farafontova, V.I., Borovkova, G.B., and Ustavshchikov, B.F., *Izv. Vyssh. Uchebn. Zaved., Khim. Khim. Tekhnol.*, 1999, vol. 42, no. 5, pp. 58–61.
3. Podgornova, V.A., Farafontova, V.I., and Ustavshchikov, B.F., *Zh. Prikl. Khim.*, 1981, vol. 54, no. 11, pp. 2599–2601.
4. Kazantsev, O.A., Kazakov, S.A., Shirshin, K.V., and Danov, S.A., *Zh. Obshch. Khim.*, 1999, vol. 69, no. 2, p. 348.
5. Podgornova, V.A., Farafontova, V.I., and Khalistova, I.D., *Sintez i primenenie N-zameshchennykh akrilamidov* (Synthesis and Application of *N*-Substituted Acrylamides), Avaliable from ONIITEKhIM, April 2, 1985, Yaroslavl, no. 299 KhP-85.

Russian Journal of Applied Chemistry, Vol. 75, No. 10, 2002, pp. 1720–1722. Translated from Zhurnal Prikladnoi Khimii, Vol. 75, No. 10, 2002, pp. 1754–1756.
Original Russian Text Copyright © 2002 by Morachevskii.

Henri Moissan (To 150th Anniversary of His Birthday)

Professor H. Moissan made an outstanding contribution to the development of quite a number of branches of applied chemistry in the late XIX–early XX century. He obtained fluorine in free state for the first time, studied a number of its compounds, designed an electric arc furnace (having thereby laid the foundation of high-temperature chemistry), synthesized a great number of high-melting compounds, and isolated boron and other elements by reducing their oxides.

Ferdinand Frederic Henri Moissan was born on September 28, 1852, in Paris; his father was a minor official at the Eastern Railroad Company. In 1864, his family moved to a small town Meaux in northern France, Department of Seine-et-Marne, where Henri entered a municipal college. The scientist-to-be revealed strong interest in mathematics and natural sciences, especially chemistry. In 1870, he graduated from the college, and, desiring to become independent as soon as possible, started to work in Paris as apprentice pharmaceutical chemist. In 1872, Moissan transferred to the Museum Natural History, laboratory of Edmond Fremy (1814–1894), a known chemist, member of the Paris Academy of Sciences (since 1857), and a corresponding member of the St. Petersburg Academy of Sciences (since 1856). Fremy's investigations were concerned with a wide variety of problems associated with technical chemistry. In particular, he worked on synthesis of artificial precious stones, development of technology for manufacture of glass, cement, and mineral fertilizers, studied saponification of fats, obtained hydrofluoric acid, made an attempt to isolate fluorine in free state, and established that ozone is an allotropic variety of oxygen. Moissan's stay at Fremy's laboratory was short, but, in our opinion, had impact on his subsequent scientific activities.

Soon after, Moissan transferred, within the same Museum, to the agrochemical laboratory headed by Pierre-Paul Deherain (1830–1902), where he carried out, together with his supervisor, a study in physiology of plants. However, the work concerned with this subject was, in fact, the only one, and the young scientist paid his primary attention to inorganic chemistry and technology. Simultaneously, influenced by

Deherain, Moissan occupied himself with completion of his education. In 1874, he received bachelor's degree, and became Licencie des Sciences in 1877. This, still preserved in France, scientific degree, intermediate between those of bachelor and doctor of science, gave the right of teaching and delivering lectures at higher and secondary school institutions.

In 1879, Moissan was given the rank of first-class pharmaceutical chemist, By 1890, he completed a set of studies in chemistry of iron and chromium oxides and backed his doctoral dissertation devoted to this subject. Young scientist's works received approval and support of leading French chemists of that time, H. Saint-Claire Deville (1818–1881) and H.J. Debray (1827–1888), members of the Paris Academy of Sciences.

In 1879–1883, Moissan occupied the position of an assistant at a higher pharmaceutical school in Paris, and in 1886, he was elected a professor (of toxicol-

1070-4272/02/7510-1720 $27.00 © 2002 MAIK "Nauka/Interperiodica"

ogy); in 1889, he became a professor of inorganic chemistry. Beginning in 1900, he was professor of inorganic chemistry at Paris University.

It is impossible to reflect in full the diversity and scale of experimental investigations carried out by Henri Moissan. More evidence about his life and scientific activities can be found in a detailed communication by German scientist Alfred Stock (1876–1946), who worked for some time at Moissan's laboratory and was well-acquainted with him [1]. Let us mention the basic directions of investigations carried out by the French scientist.

In 1884, Moissan started detailed studies of fluorine compounds. He was the first to synthesize and describe quite a number of fluorine compounds with nonmetals, e.g., PF_5, POF_3, PF_3Br_2. Before Moissan, many researchers, beginning with the outstanding English chemist G. Davy (1778–1829), had made unsuccessful attempts to obtain fluorine. In 1886, Moissan could solve this problem. He isolated fluorine by electrolysis of an anhydrous mixture of hydrofluoric acid and potassium chloride. The electrodes employed were fabricated from a platinum–iridium alloy, and the electrolysis was carried out in a platinum vessel. Much later (1899), Moissan demonstrated the possibility of using cheaper copper apparatus in electrolysis. In cooperation with the English physicist James Dewar (1842–1923), Moissan obtained fluorine in liquid (bp 187°C) and solid (mp 233°C) states.

Moissan synthesized and studied a number of fluorine- and carbon-containing compounds. These included carbon tetrafluoride, methyl fluoride, and isobutyl fluoride. He also obtained organofluoric compounds for the first time.

In 1891–1892, Moissan concerned himself with isolation of boron. By that time, boron had not been isolated in pure form, with the content of boron in formulations obtained not exceeding 70%. Moissan could improve the purity of boron to 95% by reducing boron oxide with magnesium, and to 99% in the case of its reduction with hydrogen.

Since the time when it was shown that diamond is pure carbon, attempts had started to obtain artificial diamonds [2]. The classical investigations in this field belong to Moissan. They were based on Debray's assumption that diamonds had formed in nature at high temperatures and pressures. In addition, reports appeared in 1892 about diamond inclusions contained in a meteorite found in the U.S. Moissan made an attempt to obtain diamonds by fast cooling of iron saturated with carbon at temperatures of up to 3500°C. In this case, a high pressure developed within the ingot. Prolonged chemical treatment of a solidified mass removed iron, graphite, and, possibly, carbides, with only fine crystal particles (up to 0.5 mm in size) remaining in very small amounts. The crystals had very high hardness and were nearly completely burnt out in oxygen, with their density falling within the range 3.0–3.5 g cm^{-3}. The minute dimensions of the crystals gave no way of applying crystallographic methods, and synthesis of artificial diamonds by Moissan cannot be considered a proven fact.

However, the electric arc furnace designed by the scientist for heating iron (1892), have found exceedingly wide application. It became possible for the first time to carry out various high-temperature investigations. Reduction of metal oxides with carbon was used to obtain uranium, tungsten, vanadium, chromium, and manganese (1893); titanium and molybdenum (1895); niobium (1901); tantalum (1902); and thorium (1906). Beginning in 1894, Moissan obtained, using his furnace, 28 carbides, 9 borides, and 6 silicides of various metals [1, 3]. A number of compounds had been unknown before that time. The compounds were synthesized directly from pure components or by reduction of metal oxides with carbon, boron, or silicon. Moissan also developed an industrial technique for obtaining calcium carbide. The scientist studied the chemical properties of carbides and the action of water and acids on them. He also synthesized hydrides of calcium and alkali metals, and pointed to their high reducing capacity. Moissan's pioneering studies attracted to him pupils not only from France, but also from other European countries.

The main Moissan's works are the following *Le four èlectrique* (Paris, 1897), *Le fluor et ses composès* (Paris, 1900), and a five-volume course of organic chemistry *Traite de chemie minèrale*, Paris, vols. 1–5, 1904–1906), written by him with participation of his pupils.

By recommendation of academicians N.N. Beketov and F.F. Bel'shtein, Moissan was elected a foreign corresponding member (department of physics) of the St. Petersburg Academy of Sciences in 1904 [4]. The recommendation written in hand by Beketov read "... Moissan's investigations enriched the science with quite a number of valuable and reliable facts." Earlier, in 1888, the scientist was elected a member of the Academy of Medicine in France and became a member of the Paris Academy of Sciences in 1891. Moissan was also a member of the Royal London, British chemical, German chemical, and many other scientific societies. In 1906, Moissan was awarded the Nobel Prize in chemistry "in recognition of the great services

rendered by him in his investigation and isolation of the element fluorine, and for the adoption in the service of science of the electric furnace called after him" [5]. His presentation by the Swedish Royal Academy of Sciences read "The whole world has admired the great experimental skill with which you have isolated and studied fluorine... With the aid of your electric furnace you have solved the riddle of how diamonds are formed in nature. You have unleashed a mighty wave into the world of technology, a wave which has not yet attained its full height." Before that Moissan had received the Davy medal of the Royal London Society (1896) and the Hoffman medal of the German chemical society (1903). In 1900, the scientist was awarded the Order of the Legion d'Honneur. In 1896 and 1902, Moissan was elected the President of the French chemical society.

Henri Moissan passed away after brief illness on February 20, 1907. Many years' work with toxic substances had affected adversely his health. Moissan himself spoke about this as follows: "Fluorine deprived me of 10 years of life." Brief biographic evidence about the scientist is contained in publications of different years [3, 6–8] and numerous reference books [5, 9–11].

In the beginning of 1907, the world's chemical community suffered severe loss, when such its outstanding representatives as D.I. Mendeleev (2.02.1907), N.A. Menshutkin (5.02), H. Rosebohm (8.02), H. Moissan (20.02), and M. Berthelot (18.03) passed away.

REFERENCES

1. Stock, A., *Ber. Deutsch. Chem. Gesellschaft*, 1908, vol. 4, pp. 5099–5130.
2. Leipunskii, O.I., *Usp. Khim.*, 1939, vol. 8, no. 10, pp. 1519–1534.
3. Samsonov, G.V. and Obolonchik, V.A., *Poroshk. Metall.*, 1972, no. 9, pp. 102–103.
4. *Russko-frantsuzskie nauchnye svyazi* (Russian-French Scientific Relations), Leningrad: Nauka, 1968.
5. *Laureaty Nobelevskoi premii: M–Ya* (Nobel Prize Winners: M–Ya) Moscow: Progress, 1992.
6. Wedekind, E., *Z. Elektrochem.*, 1907, vol. 20, no. 13, pp. 515–517.
7. Kapinus, N.A., *Vopr. Istorii Estestvozn. Tekhn.*, 1974, no. 1(46), pp. 96–98.
8. Sheptunova, Z.I., *Zh. Vses. Khim. O–va im. D.I. Mendeleeva*, 1975, vol. 20, no. 6, p. 618.
9. Blokh, M.A., *Biograficheskii spravochnik: Vydayushchiesya khimiki i uchenye XIX i XX stoletii, rabotavshie v smezhnykh s khimiei oblastyakh nauki* (Reference Book of Biographies: Outstanding Chemists and Scientists of the XIX and XX centuries in Fields of Science Adjoining Chemistry), Leningrad: Nauch. Khim.-Tekhn. Izd., 1931, vol. 2, issue 1.
10. Manolov, K., *Velikie khimiki* (Outstanding Chemists), Moscow: Mir, 1977, vol. 2.
11. *Dictionary of Scientific Biography*, Gillespie, Ch.C., Ed., New York, 1981, vol. 9.

A. G. Morachevskii

Russian Journal of Applied Chemistry, Vol. 75, No. 10, 2002, p. 1723. Translated from Zhurnal Prikladnoi Khimii, Vol. 75, No. 10, 2002, p. 1757.
Original Russian Text Copyright © 2002 by Morachevskii, Beloglazov.

BOOK REVIEWS

Yanko, E.A., *Anody alyuminievukh elektrolizerov* (Anodes of Aluminum Electrolyzers), Moscow: Ruda i Metally, 2001, 670 pp.

Anodes, playing an important part in the technology of aluminum manufacture by electrolysis, affect the energy consumption and the level of environment protection. In the last three decades, the aluminum industry of quite a number of largest countries–aluminum manufacturers has mostly or completely changed over to energy-saving technologies with the maximum possible level of environment protection. The key measure in such a conversion is to install electrolyzers with high power (up to 200–300 kA) with prebaked anodes. This makes it possible to raise somewhat the current efficiency (to 93–95%), make lower the energy expenditure per ton of aluminum by 1500–2000 kW h, and, what is the most important, to resolve with more success the ecological problems. With baked anodes, it becomes possible to diminish to a minimum the discharge of fluorides into the atmosphere and preclude entirely the discharge of aromatic hydrocarbons and tars, including carcinogens. In Russia, up to 90% of aluminum is manufactured with the use of self-baking anodes. In the foreseeable future, reconstruction of the Russian aluminum pants seems to be unlikely. In this connection, a topical task is to improve the technology of operation of electrolyzers with self-baking anodes and to lower the discharge of noxious compounds to admissible levels. E.A. Yanko's monograph, summarizing the experience gained in working with both types of anodes and discussing their advantages and disadvantages, is of indubitable interest for Russian aluminum manufacturers. The book comprises an introduction, 11 chapters, and a list of references.

A brief introduction (pp. 3–8) considers the transport-technological schemes for production of the anode mass for self-baking anodes and for manufacture of baked anodes. It is the analysis of the elements of these schemes that mainly constitutes the monograph, which has purely industrial orientation.

The first chapter (pp. 9–55) describes raw materials for production of the anode mass and anodes—coal-tar pitch and electrode coke. The properties of both the components and requirements to them are presented with exhaustive completeness. The second chapter (pp. 56–125) gives an equally detailed description of coke calcination procedure. By this term is meant coke treatment at high temperature (1150–1350°C) in a reductive atmosphere. Under these conditions, moisture and volatiles are removed, the coke structure becomes denser, and there occurs partial graphitization. Main attention is given to describing the process technology. A small third chapter (pp. 126–139) considers storage coal-tar pitch and its preparation for the technological process, with much attention given to monitoring of its quality and to its aggregative state. The fourth chapter (pp. 140–204) mainly describes the apparatus used in preparing stock for manufacture of the anode mass. All kinds of apparatus for crushing and milling are described in ample detail.

The fifth chapter (pp. 205–250) presents evidence concerning the formulations of the anode mass. Theoretical foundations of the anode structure formation, the optimal granulometric composition of the anode mass, and dosage of stock components are discussed. The sixth chapter (pp. 251–310) considers technologies for anode mass mixing and mixing apparatus. The seventh (pp. 311–353) and eighth (pp. 354–469) chapters describe the processes for forming and baking of the anode units. The ninth chapter (pp. 470–522) describes in detail the procedures used in dismantling worked-out anodes and mounting new ones. The tenth (pp. 523–595) and eleventh (pp. 596–655) chapters compare the advantages, disadvantages, and specific features of baked and self-baking anodes. The author noted, in particular, that electrolyzers with self-baking anodes have not exhausted their potentialities and can be regarded as a promising object of further modernization. In the author's opinion, it is apparently advisable to use electrolyzers of this kind for manufacture of aluminum in regions that are remote from large settlements and are not subject to stringent ecological requirements.

The bibliography (pp. 656–666) contains references to 246 studies by domestic and foreign researchers.

The book contains a vast body of reference material and describes in detail the apparatus and technologies used in manufacture of anodes. Less successful are separate inclusions of physicochemical and electrochemical nature. The book is very well printed.

A.G. Morachevskii, I.N. Beloglazov

1070-4272/02/7510-1723 $27.00 © 2002 MAIK "Nauka/Interperiodica"

Russian Journal of Applied Chemistry, Vol. 75, No. 11, 2002, pp. 1725–1731. Translated from Zhurnal Prikladnoi Khimii, Vol. 75, No. 11, 2002, pp. 1761–1767.
Original Russian Text Copyright © 2002 by Kartsova, Makarov.

REVIEWS

Properties of Carbon Materials and Their Use in Chromatography

L. A. Kartsova and A. A. Makarov

St. Petersburg State University, St. Petersburg, Russia

Received July 24, 2002

Abstract—Sorption properties of graphite, fullerene, and nanotubes were considered, as well as the pattern of variation of the sorption properties of fullerene C_{60} in complexing with various macrocycles. The use of these materials as stationary phase in chromatography and in solid-phase concentration of microimpurities of aromatic hydrocarbons was discussed.

Carbon exists in four allotropic modifications, namely, diamond, graphite, fullerenes, and linear carbon polymer (Karbin). Graphite and diamond were discovered in the nature as early as the XVIII century (the relations between diamond and graphite were studied in detail by French physicists Antoine Loraine Lavoisier and Louis Bernard Guyton de Morveau). Karbin [1] and fullerenes were prepared in laboratories in recent decades. In the 1960s, white Karbin crystals were detected in natural graphite, and in 1992 it was found that the Karelian mineral shungite (amorphous carbon) contains a fullerene impurity (~0.001%). Diamond and graphite had found wide practical application long before their structures were elucidated. However, these structures were established conclusively only after development of the appropriate physicochemical methods (X-ray and electron diffraction analyses, etc.). The situation with Karbin and fullerenes is the opposite: Their structures have been established fairly reliably, but possible applications based on their expected process characteristics are still the matter of discussion rather than commercial implementation. Such allotropic modifications of carbon as diamond, graphite, and Karbin can be regarded as infinite systems with a regular three, two-, and one-dimensional structure, respectively. By contrast, fullerenes form a family of individual polyhedral molecules with a closed structure [2]. The scheme in Fig. 1 shows the hierarchy of the carbon structures.

The IUPAC recommends that fullerenes be defined as closed spherical polyhedra formed exclusively by three-coordinate carbon atoms with 12 pentagonal and (n/2 – 10) hexagonal faces, where $n > 20$. Fullerenes are termed [60]fullerene, [70]fullerene, etc. Any other closed spherical polyhedra formed exclusively by three-coordinate carbon atoms were termed quasifullerenes. The most stable are fullerenes whose structure is described by the isolated pentagon rule, with each pentagon surrounded by five hexagons.

The appearance and the physical and chemical properties of the above-mentioned carbon modifications strongly vary with the type of the bonds between the carbon atoms in the molecules of these substances (Table 1; l is the bond length, and ρ is the density).

Graphite. The sp^2-hybridized carbon atoms in graphite form infinite planes composed of regular hexagons, and in fullerenes they form closed shells including a certain number of atoms. Real graphite bodies contain a certain amount of disordered atoms intercalated in the interlayer space. These atoms can occur in the sp-, sp^2-, or sp^3-hybridized states.

The ideal structure of graphite is, essentially, an infinite series of mutually parallel layers composed of hexagons formed by carbon atoms. Mutual displace-

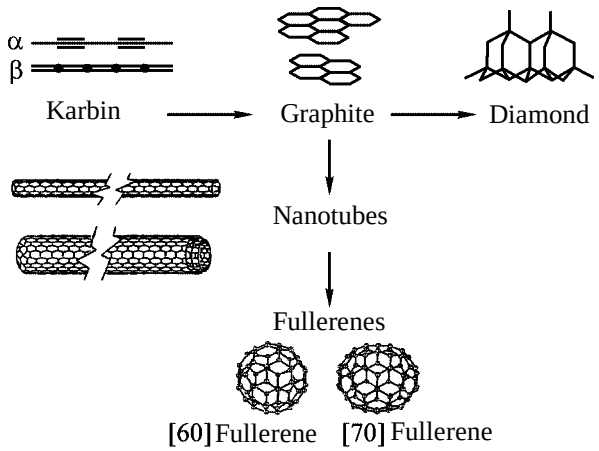

Fig. 1. Hierarchy of carbon structures.

1070-4272/02/7511-1725$27.00 © 2002 MAIK "Nauka/Interperiodica"

Table 1. Properties of the principal carbon modifications

Modification	Hybridization	*l*	ρ, g cm^{-3}	Crystal lattice
Diamond	sp^3	0.148	3.515	Cubic
Graphite	sp^2	0.142 (0.335)*	1.848	Hexagonal
Fullerene	sp^2	0.144/0.139**	1.651	Molecular cubic face-centered
Karbin	*sp*	α: 0.125/0.149***; β: 0.138	1.917	Hexagonal

* Interlayer spacing.
** Pentagon-hexagon/hexagon-hexagon.
*** Triple/ordinary bonds.

ment of these layers by two different modes yield two different forms, hexagonal and rhombohedral. In the former, the layers alternate by the A–B–A–B... scheme, and in the latter, by the A–B–C–A–B–C–... scheme. In naturally occurring graphites, the content of the rhombohedral form can reach 30%, and in artificial, this form is virtually lacking. Any neighboring carbon atoms in the layer plane are separated by 0.142 nm, and the neighboring layers, by 0.335 nm. Each atom in the layer is connected with three neighboring atoms, and the bond angles are 120°. The bonds involve three of the four valence electrons, and the remaining electrons form a common electron cloud. This structure is responsible for anisotropy of the physical properties of graphite, i.e., their difference in directions going parallel and perpendicular to the layers. Graphite ranks among the softest minerals. It should be mentioned that the above-described structure is characteristic of graphite single crystal. Real bodies contain a multitude of areas comprised of the ordered carbon atoms, which have finite dimensions differing by several orders of magnitude for different samples of carbon bodies with graphite or graphite-like structures. The structures of these areas can approach that of the ideal graphite lattice or differ therefrom owing to intralayer distortions and irregular alternation of the layers.

Graphite can form intercalation compounds with certain molecules, when these latter are inserted between the graphite layers. The reactant molecules can be linked to carbon atoms by covalent, coordination, or ionic bonds. These structures involve, in particular, intercalation compounds in which graphite layers (matrix) are separated by alkali metal clusters (matrix-isolated particles). Depending on the type of the forming bonds, the layered compound can preserve or lose the electrical conductivity characteristic of the initial graphite.

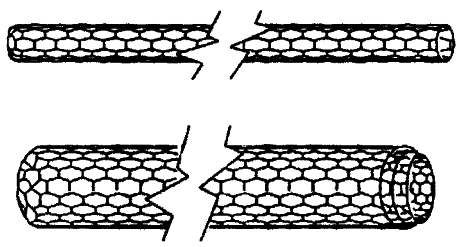

Fig. 2. Single- and multilayer nanotubes.

Nanotubes. Nanotubes (or tubulenes) were first prepared in 1991 by Japanese scientist Sumio Iijima by electric-arc vaporization of graphite under argon. In that experiment, carbon needles 4–30 nm in diameter up to 2 μm long grew on the graphite cathode [3]. In the optimal mode, the yield of nanotubes from the cathodic carbon black is 60%. This class of compounds has diverse structures. Nanotubes consist of two fullerene halves and a cylinder made up by hexagons. The cylinder, in turn, is, essentially, a rolled-up graphite layer. There exist single- and multilayer, open- and closed-ended nanotubes differing in the length and diameter. The interlayer spacing in multilayer tubes is equal to 0.34 nm, like in crystalline graphite. Multilayer graphite nanotubes differ from single-layer nanotubes by a greater diversity of shapes and configurations [4, 5]. Figure 2 shows single- and multilayer nanotubes [6]. An ideal nanotube is, essentially, a graphite plane rolled up in a cylinder, with the surface consisting of regular hexagons. The resulting structure is governed by the orientation angle of the graphite plane with respect to the nanotube axis. The orientation angle governs the chirality of the nanotube (Fig. 3).

The specific structure is responsible for a number of specific features of nanotubes. For example, open-ended nanotubes, when immersed in molten lead, get partially filled with lead (owing to the capillary effect) [7]. Early studies into capillary phenomena revealed a connection between the surface tension of a liquid and the possibility of its drawing into the nanotube channel. Laser vaporization of graphite in the presence

of certain metallic catalysts yields both nanotubes and C_{60} (in particular, those inside nanotubes), as shown by high-resolution electron-microscopic studies.

Observation of capillary effects requires opening nanotubes, which can be done by two ways: annealing at 850°C for several hours in a CO_2 flow (opening 10% of all nanotubes) and keeping in concentrated HNO_3 for 4.5 h at 240°C (80% of nanotubes). Oxidation of nanotubes yields carbonyl and carboxy groups on the nanotube surface.

Isolation of individual nanotubes still remains a fairly complicated task, as most of nanotubes are insoluble in the known solvents. Only single-layer nanotubes form solutions [8].

Fullerene. The spherical structure of fullerene and identity of all the 60 carbon atoms were confirmed by NMR spectroscopic and high-resolution electron-microscopic studies. Only truncated icosahedral structure suggested for C_{60} affords so highly symmetrical arrangement of the carbon atoms that all the strains are distributed uniformly. Of all the possible three-dimensional structures, the C_{60} molecule exhibits the highest symmetry [9]. The accessible interior space has a radius of 1.7 Å. The sphere circumscribed around the fullerene molecule is 7.1 Å in diameter [10, 11].

Fullerene is soluble (though fairly poorly) primarily in organic [12, 13], better aromatic, solvents (Table 2 in [5]).

Study of the solubility of fullerenes in organic solvents is the starting point for their separation and purification. The structures of fullerenes with different compositions differ only slightly, which makes them close in solubility and adsorbability. At the same time, efficient isolation and separation of fullerenes are based specifically on the distinctions in these properties.

The solubility in water for carbon molecules such as C_{60} cannot be high, but it can be improved by "incorporating" the carbon molecules into appropriate water-soluble molecules, e.g., cyclodextrins (CDs). α- and β-CDs cannot accommodate the entire hydrophobic molecule such as C_{60}. When dissolved in excess γ-cyclodextrin, fullerene forms a "host–guest" complex existing as a yellowish colloidal solution [16, 17] (Fig. 4).

Adsorption properties of fullerene-containing materials (FCMs). Samonin and Marakulina [18] found that FCMs can adsorb water (approximately a monomolecular layer) and inorganic ions. Studies of the sorption potential of fullerene C_{60} with respect to various organic and organometallic compounds in aqueous solution showed the following. Fullerene adsorbs *N*-methylcarbamates, phenols, polycyclic aromatic hydrocarbons, and amines with the efficiency of about 60%, depending on the nature of the sorbate. It should be mentioned that, in these applications,

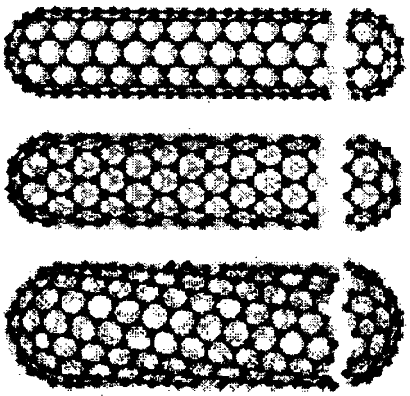

Fig. 3. Nanotubes with different chiralities.

Table 2. Solubility of fullerenes in various solvents

Solvent	Solubility, mg ml^{-1}
n-Pentane	0.005
n-Hexane	0.043–0.052
n-Decane	0.071
Tetradecane	0.126 (303 K)
Decalin	4.60
Cyclohexyl iodide	8.06
trans-1,2-Dibromocyclohexane	14.28
Dichloromethane	0.23–0.25
Tetrachloromethane	0.32–0.45
Chloroform	0.16–0.25
Bromoform	5.64
1,1,2,2-Tetrachloroethane	5.30
1,2,3-Tribromopropane	8.31
Benzene	0.88–1.70
Toluene	0.54–2.90
1,2-Dimethylbenzene	7.35–9.30
1,2,4-Trimethylbenzene	17.90
1,2,3,5-Tetramethylbenzene	20.80
1,2-Dichlorobenzene	7.11–27.00
1,3-Dibromobenzene	13.80
3-Nitrotoluene	2.36
Dimethylnaphthalene	36.00
1-Phenylnaphthalene	50.00
1-Chloronaphthalene	51.00
Ethanol	0.0008–0.001
Tetrahydrofuran	0.00–0.06
Water	1.3×10^{-11}

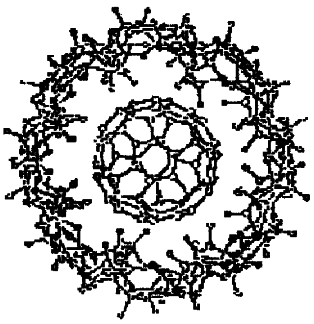

Fig. 4. [60]Fullerene–γ-cyclodextrin intercalation complex.

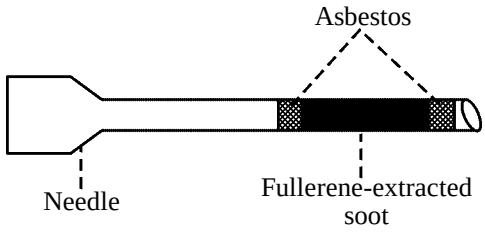

Fig. 5. Scheme of the adapter for SPE.

conventional sorbents such as XAD-2 or foamed polyurethane surpass C_{60} in the sorption efficiency [19]. Nevertheless, organometallic compounds (metallocenes and organic compounds of lead) are quantitatively adsorbed by C_{60}, forming neutral complexes or chelates. A comparative assessment of the adsorption of organometallic complexes on sorbents such as inverted C_{18} phase and silica gel 100 shows the superiority of C_{60} [19].

The fullerene extraction residue (fullerene-extracted soot, FES) was suggested as adsorbent for collecting volatile organic components from ambient air. The retention characteristics of FES were measured for 17 volatile organic components [20].

High affinity of fullerenes for aromatic hydrocarbons and their functional derivatives could be of use for environmental monitoring: When utilized in the solid-phase extraction mode, fullerene could serve for identifying the above-mentioned compounds. For this purpose, we used a specially prepared needle containing a ~7-mm layer of fullerene black (yielded by fullerene production), through which a gas mixture containing benzene, toluene, and *p*-xylene vapors was pumped (Fig. 5). The volume of the gas mixture was varied from 50 to 200 ml. The needle was placed into the vaporizer of a chromatograph, where thermal desorption (for 5–10 min under stopped carrier gas flow) and chromatographic analysis (after resuming the carrier gas flow) were run. It was shown that, despite a high density of the needle filling (which hinders gas passage), the above-described adapter is suitable for concentration in analysis of aromatic compounds.

High filling density poses, however, a number of limitations on application of this device. In particular, it is unsuitable for analyzing aqueous samples whose thermal desorption takes much time.

Use of carbon materials in chromatography. Graphite finds application in chromatography as activated carbons or graphitized thermal carbon blacks (GTCBs). Activated carbons are used primarily for separation of light gases; they are distinguished by highly developed pore structure. One recognizes micropores (1–2 nm), mesopores (5–10 nm), and macropores (>100 nm). The specific surface area of micropores reaches 1000–1200 (sometimes 1800), that of mespores, up to 100, and that of macropores is of the order of 1 $m^2 g^{-1}$. In gas chromatography, preference is given to carbons for which the surface area of micropores is at a maximum [21].

Graphitized thermal carbon blacks are nonspecific adsorbents with a small specific surface area of 6–12 $m^2 g^{-1}$. GTCBs are not very strong mechanically. Hence, to make GTCB handling more convenient and to improve the separation efficiency, the carbon black particles are covered with pyrocarbon by hydrocarbon pyrolysis in a flow of a gas passing through a carbon black layer. This yields fairly strong mechanically macroporous adsorbents, Carbochrome A (from GTCB) and Carbochrome B (from nongraphitized thermal carbon black). The surface properties of these Carbochromes are very close to those of GTCB. Based on a more finely dispersed and chemically heterogeneous channel black, it is possible to prepare by the same procedure Carbochrome C, a mechanically strong adsorbent with a much greater specific surface area of ~80 $m^2 g^{-1}$. Carbochrome C has a fairly uniform and nonspecific surface, especially after an additional treatment with hydrogen [22].

GTCBs and Carbochrome are efficient in separation of isomeric cyclanes, unsaturated and aromatic hydrocarbons, halogenated alkanes, and diverse structural isomers whose molecules contain primary, secondary, and tertiary carbon atoms.

Such properties of fullerene as thermal stability (C_{60} vaporizes at ~800°C and sublimes without decomposition; after heating to 980°C for over 10 min the fullerene crystals degrade into amorphous carbon [23]), resistance to oxidation, spherical shape of the molecule, and capability for donor–acceptor interac-

tions make it a candidate sorbent for gas chromatography.

Fullerene C_{60} was for the first time used in capillary gas chromatography in 1993. The capability of fullerene C_{60} for dispersion interactions was measured.

The free energy of sorption of the methylene unit of *n*-alkanes (Table 3) was estimated and compared with those of other gas-chromatographic phases. This allowed an interesting conclusion, namely, that the operation mode for C_{60} is of the gas–liquid, rather than of the gas-adsorption type. The C_{60}-based stationary phase is close to nonpolar phases, Apiezon and Squalane [24].

The thermodynamic characteristics of adsorption of various organic substances on the surface of crystals of fullerenes C_{60} and C_{70} were determined by gas chromatography. It was shown that adsorption properties of fullerenes differ from those of graphitized carbon black. The surface of fullerene crystals exceeds in polarity that of graphitized carbon black; adsorption on fullerene involves stronger, compared to graphitized carbon black, interaction with electron- and proton-donating molecules [25, 26].

Fullerene-based stationary phase in which C_{60} is chemically immobilized on polysiloxane via the amide bond (Fig. 6) was used in gas chromatography for analyzing substituted aromatic compounds [27, 28].

The fullerene C_{60} grafted chemically to the silica gel phase was used as stationary phase in liquid chromatography for analyzing polycylic aromatic compounds and polychlorinated biphenyls [28], as well as for separating calixarenes (with methanol–water mobile phase), benzene, anthracene, diphenyl, etc.

Gas-chromatographic analyses on columns packed with C_{60} revealed sharp weakening of the dispersion interactions relative to Carbochrome-based stationary phase. By contrast, polar organic compounds exhibit higher retention parameters with C_{60} compared to graphitized carbon black and SE-30. High thermal stability of fullerene allowed operation of the chromatographic column over a wide temperature range, but the selectivity in analysis of mixtures containing fairly volatile low-boiling organic substances was low.

One way to extend the selectivity range is to prepare mixed-composition phases. Surface modification of carbonic sorbents serves to modify the sorbate–sorbent interactions. By choosing appropriate modifier, it is possible to increase the contribution from

Table 3. Free energy of sorption of the methylene unit $\Delta G(CH_2)$ of *n*-alkanes in gas chromatography

Phase	$-\Delta G(CH_2)$, J mol^{-1}	T, °C
Fullerene C_{60}	2018	100
Apiezon L	2124	120
Squalane	2179	120
Acetylene carbon black modified with pyrocarbon (Carbochrome AC)	4914	100
Graphitized carbon black	4511	100

dipole–dipole, donor–acceptor, and π–π interactions, etc. [29].

Modifiers should be fairly strongly retained by the carbon material, so as to decrease its gradual washing off by the carrier gas flow. To this end, covalent linking can be used. Another way is to take advantage of complexes that can be formed by the modifier and the substance being modified. In particular, fullerenes are known to form complexes with certain macrocycles.

Fullerene is capable of complexing with various organic and inorganic molecules, thus acting as electron acceptor [30, 31].

Incorporation of the C_{60} guest into appropriate host molecule is the first step toward synthesis of supramolecules comprising fullerenes. Supramolecular complexes were obtained from cyclic host macromolecules such as cyclodextrins, crown ethers, and cycloveratrylenes, having voids able of accommodating the guest fullerene. It was shown that the properties of such intercalation compounds depend on the

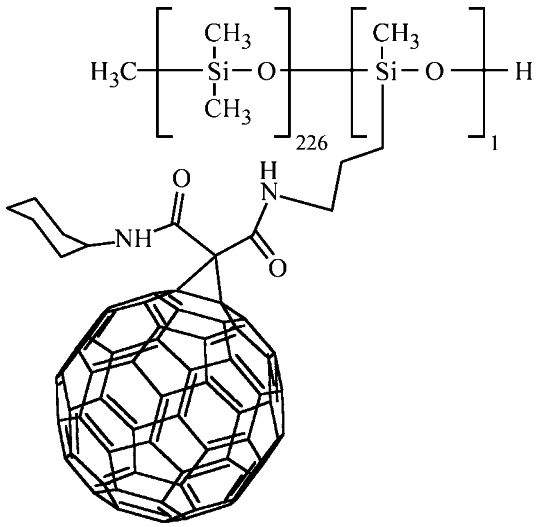

Fig. 6. C_{60}-based stationary phase.

π–π, –OH $\rightarrow$ π, and $\sigma \rightarrow \pi$ interactions. Of great importance is understanding of the interactions between the fullerenes and macromolecules, as this affords preparation of water-soluble complexes for potential biological and medical applications. Also, complexes of this type are suitable for purification and isolation of certain fullerenes from ordinary carbon black for the synthesis of new materials to be used in electronic devices.

The complex formed by C_{60} and γ-cyclodextrin [32–34] was studied by NMR spectroscopy [33] and mass spectrometry [35], as well as by electrochemical and spectrometric methods [36].

Murthy and Geckeler [37] reported on a stable sandwich-type complex formed by β-CD and fullerene C_{60}. Kawaguchi *et al*. [38] discussed the interaction between fullerene and various calix[*n*]arenes. It was found that certain calix[*n*]arenes (n = 5, 6), as well as calix[3]arenes with *tert*-butyl substituents, can interact with C_{60} in solution. The molecules of calixarenes typically take the conical form, and the benzene rings are arranged in a way favorable for intercalation of C_{60} [39, 40]. It was shown that the complex is stabilized by *tert*-butyl or benzyl substituents [41]. Formation of complexes between certain calix[8]arenes and fullerenes C_{60} and C_{70} was proven in [42, 43]. Also, fullerenes can form host–guest complexes with other molecules such as metacyclophane [44] and with dendrimers [45].

It can be assumed that large crown ethers (dibenzo-24-crown-8, dibenzo-30-crown-10), similar to β- and γ-cyclodextrins, can form sandwich-type complexes with [60]fullerene, but this assumption requires independent verification. This should take into account the fact that complexes of fullerene with certain macrocycles are stable only in the solid state [39].

To extend the selectivity range of fullerene-based phases, chromatographic phases of mixed composition were prepared and tested, namely, those containing 10% C_{60} and dibenzo-24-crown-8, or C_{60} and dibenzo-30-crown-10. The polarity of these phases is intermediate between those of fullerene and individual crown ethers. These columns allow highly efficient and highly selective separation of positional isomers and of aliphatic and aromatic organic compounds containing various functional groups (OH, NH_2, NO_2, Cl) and boiling in a wide temperature range without preliminary chemical transformation.

Thus, sorbents based on fullerene and macrocycles allow the advantages of both fullerene itself (thermal stability and high performance) and the macrocycle (high selectivity) to be preserved and realized.

REFERENCES

1. Vol'pin, M. E., *Vestn. Ross. Akad. Nauk.*, 1992, no. 10, pp. 25–32.
2. Sokolov, V.I., *Dokl. Ross. Akad. Nauk*, 1992, vol. 325, no. 5, pp. 991–993.
3. Iijima, S., *Nature* (London), 1991, vol. 354, pp. 56–58.
4. Ebessen, T.W., *J. Phys. Chem. Solids*, 1997, vol. 58, no. 11, pp. 1979–1982.
5. Eletskii, A.V., *Usp. Fiz. Nauk*, 1997, vol. 167, no. 9, pp. 945–972.
6. Withers, J. C., Loutfy, R.O., and Lowe, T.P., *Fullerene Sci. Technol.*, 1997, vol. 5, no. 1, pp. 1–31.
7. Ajayam, P.M. and Iijima, S., *Nature* (London), 1993, vol. 361, pp. 333–334.
8. Chen, J., Hamon, M.A., Hu, H., *et al*., *Science*, 1998, vol. 282, pp. 95–98.
9. Curl, R.F. and Smalley, R.E., *Sci. Am*., 1991, vol. 265, no. 4, pp. 32–41.
10. Letcher, T.M. and English, R.B., *S. Afr. J. Sci*., 1992, vol. 88, nos. 11/12, pp. 540–543.
11. Zharikov, O.V., *Priroda*, 1992, no. 3, pp. 68–73.
12. Ruoff, R.S., Tse, D.S., Malhotra, R., Lorents, D.C., *J. Phys. Chem*., 1993, vol. 97, pp. 3379–3383.
13. Beck, M.T. and Mandi, G., *Fullerene Sci. Technol*., 1997, vol. 5, no. 2, pp. 291–310.
14. Belov, N.N., Sukhov, I.V., Bezmel'nitsin, V.N., *et al*., *Radiokhimiya*, 1994, vol. 36, no. 5, pp. 457–458.
15. Bezmel'nitsyn, V.N., Eletskii, A.V., and Okun', M.V., *Physics—Uspekhi*, 1998, vol. 41, pp. 1091–1114.
16. Andersson, T., Nilsson, K., Sundahl, M., *et al*., *J. Chem. Soc., Chem. Commun*., 1992, no. 8, pp. 604–606.
17. Buvari-Barcza, A., Barcza, L., Braun, T., *et al*., *Fullerene Sci. Technol*., 1997, vol. 5, no. 2, pp. 311–323.
18. Samonin, V.V. and Marakulina, E.A., Abstracts of Papers, *Khimiya poverkhosti i nanotekhnologii* (Surface Chemistry and Nanotechnologies), 1999, St. Petersburg, 1999, p. 149.
19. Ballesteros, E., Gallego, M., and Valcarcel, M., *J. Chromatogr. A*, 2000, vol. 869, nos. 1–2, pp. 101–110.
20. Chen, C., Chen, J., Wang, X., *et al., J. Chromatogr. A*, 2000, vol. 886, pp. 313–317.
21. Lur'e, A.A., *Khromatograficheskie materialy* (Chromatographic Materials), Moscow: Khimiya, 1978, pp. 40–41.
22. Kiselev, A.V. and Yashin, Ya.I., *Adsorbtsionnaya gazovaya i zhidkostnaya khromatografiya* (Gas and Liquid Adsorption Chromatography), Moscow: Khimiya, 1979, pp. 29–47.

23. Stetzer, M.R., Heiney, P.A., Fisher, J.A., and McGhie, A.R., *Phys. Rev. B*, 1997, vol. 55, no. 1, pp. 127–131.
24. Golovnya, R.V., Terenina, M.V., Ruchkina, E.L., and Karnatsevich, V.L., *Mendeleev Commun.*, 1993, no. 6, pp. 231–233.
25. Davydov, V.Ya., Roshchina, T.M., Filatova, G.N., and Khrustaleva, N.M., *Zh. Fiz. Khim.*, 1996, vol. 70, no. 9, pp. 1680–1684.
26. Davydov, V.Ya., Roshchina, T.M., Filatova, G.N., and Khrustaleva, N.M., *Zh. Fiz. Khim.*, 1996, vol. 70, no. 10, pp. 1857–1862.
27. Chen, Y.Y., Fang, P.F., Zeng, Z.R., and Fan, J.H., *Chem. Lett.*, 1999, no. 6, pp. 499–500.
28. Glausch, A., Hirsch, A., Lampartz, I., and Schurig, V., *J. Chromatogr. A*, 1998, vol. 809. pp. 252–257.
29. Bardina, I.A., Kovaleva, N.V., and Nikitin, Yu.S., *Zh. Fiz. Khim.*, 2001, vol. 75, no. 8, pp. 1461–1464.
30. Turanov, A.I. and Kremenskaya, I.N., *Izv. Ross. Akad. Nauk, Ser. Khim.*, 1995, no. 3, pp. 481–483.
31. Sun, Y.-P., Bunker, C.E., and Ma, B., *J. Am. Chem. Soc.*, 1994, vol. 116, pp. 9692–9699.
32. Bourdelande, J.L., Font, J., and Gonzalez-Moreno, R., *J. Photochem. Photobiol. A: Chem.*, 1996, vol. 94, pp. 215–216.
33. Marconi, G., Mayer, B., Klein, Ch.Th., and Kuhler, G., *Chem. Phys. Lett*, 1996, vol. 260, pp. 589–594.
34. Priyadarsini, K.I. and Mohan, H., *J. Photochem. Photobiol. A: Chem.*, 1995, vol. 85, pp. 63–67.
35. Andersson, T., Westman, G., Stenhagen, G., *et al.*, *Tetrahedron Lett.*, 1995, vol. 36, no. 4, pp. 597–600.
36. Li, M.-X., Li, N.-Q., Gu, Z.-N., *et al.*, *Electrochim. Acta*, 1996, vol. 41, no. 18, pp. 2897–2901.
37. Murthy, C.N. and Geckeler, K.E., *Chem. Commun.*, 2001, pp. 1194–1195.
38. Kawaguchi, M., Ikeda, A., and Shinkai, S., *J. Incl. Phenom. Macrocyclic Chem.*, 2000, vol. 37, pp. 253–258.
39. Ikeda, A., Yoshimura, M., and Shinkai, S., *Tetrahedron Lett.*, 1997, vol. 38, no. 12, pp. 2107–2110.
40. Haino, T., Yanase, M., and Fukazawa, Y., *Tetrahedron Lett.*, 1997, vol. 38, no. 21, pp. 3739–3742.
41. Schlachter, I., Höweler, U., Iwanek, W., *et al.*, *Tetrahedron.*, 1999, vol. 55, pp. 14931–14940.
42. Suzuki, T., Makashima, K., and Shinkai, S., *Tetrahedron Lett.*, 1995, vol. 36, no. 2, pp. 249–252.
43. Bourdelande, J.L., Font, J., Gonzalez-Moreno, R., *et al.*, *J. Photochem. Photobiol. A: Chem.*, 1998, vol. 115, pp. 69–71.
44. Martinez Garcia, M., Chavez Uribe, M.I., Bautista Palacios, E., *et al.*, *Tetrahedron*, 1999, vol. 55, pp. 6010–6026.
45. Numata, M., Ikeda, A., Fukumara, C., and Shinkai, S., *Tetrahedron Lett.*, 1999, vol. 40, no. 38, pp. 6945–6948.

Russian Journal of Applied Chemistry, Vol. 75, No. 11, 2002, pp. 1732–1735. Translated from Zhurnal Prikladnoi Khimii, Vol. 75, No. 11, 2002, pp. 1768–1771.
Original Russian Text Copyright © 2002 by Bashkirov, But'ko, Dudchik, Kris'ko, Petrov, Shershavina, Shichkova.

INORGANIC SYNTHESIS AND INDUSTRIAL INORGANIC CHEMISTRY

Formation of the Compound La_2BaCuO_5 ($La_4Ba_2Cu_2O_{10}$)

L. A. Bashkirov, T. A. But'ko, G. P. Dudchik, L. Ya. Kris'ko, G. S. Petrov, A. A. Shershavina, and T. A. Shichkova

Belarussian State Technological University, Minsk, Belarus

Received April 19, 2002

Abstract—Synthesis of the compound La_2BaCuO_5 ($La_4Ba_2Cu_2O_{10}$), whose X-ray diffraction pattern is identical to that available in the literature for the solid solution $La_{3.6}Ba_{2.4}Cu_{1.8}O_{9.6}$, was studied.

The main elements of the phase diagram of the ternary system La_2O_3–BaO–CuO had been obtained [1] before the region of solid solutions $La_{2-x}Ba_xCuO_4$, which become superconducting at 30–35 K, was found in this system in 1986 [2]. After this discovery, intensive search for new oxide superconductors started at numerous research centers all over the world. This search culminated in 1987 in that the compound $YBa_2Cu_3O_{7-\delta}$ with the superconducting transition temperature T_c of 93 K was synthesized [3].

Since the T_c of the compound $YBa_2Cu_3O_{7-\delta}$ much exceeds that of $La_{2-x}Ba_xCuO_4$ solid solutions, the primary attention of researchers has been focused on the system Y_2O_3–BaO–CuO. As a result, phase equilibria in the system La_2O_3–BaO–CuO have been studied to a much lesser extent than those in the system Y_2O_3–BaO–CuO [4–6].

The observed pronounced dissimilarity between the phase diagrams of the systems La_2O_3–BaO–CuO and Y_2O_3–BaO–CuO is, probably, mainly due to difference in size between the La^{3+} and Y^{3+} ions. For example, in the system Y_2O_3–BaO–CuO there exists a nonsuperconducting "green" phase Y_2BaCuO_5 (211 phase) with orthorhombic structure, which plays an important part in solid-phase synthesis of the superconducting compound $YBa_2Cu_3O_{7-\delta}$. No green phase of this kind is formed in the system La_2O_3–BaO–CuO, with solid solutions $La_{4-2x}Ba_{2+2x}Cu_{2-x}O_{10-2x}$ ($0.15 \le x \le 0.25$) crystallizing instead. These solid solutions have tetragonal structure and brown color [1, 7]; they are characterized by a certain deficiency of copper and can be regarded as derivatives of the stoichiometric compound $La_4Ba_2Cu_2O_{10}$ (422 phase) whose formula is doubled in comparison with the La_2BaCuO_5 phase. In [8], the $La_{2-x}Ba_{1+x}CuO_{5-x/2+\delta}$ solid solutions ($0.1 \le x \le 0.8$) were revealed. It has been reported that there exists an $La_4Ba_2Cu_2O_{10}$ phase with the lattice constants *a* and *c* of, respectively, 6.8447 and 5.8637 Å. It has been established [10] that the La_2BaCuO_5 solid phase is formed in incongruent melting of $LaBa_2Cu_3O_{7-y}$ at 1353 K.

The green (211) phase is formed in all R_2O_3–BaO–CuO systems (R is rare earth) except those with R = Nd and Pr [4, 6, 11]. In the system Nd_2O_3–BaO–CuO, as also in La_2O_3–BaO–CuO, there exists a "brown" tetragonal phase, $Nd_{4-2x}Ba_{2+2x}Cu_{2-x}O_{10-2x}$ ($0 \le x \le 0.1$) [4, 12].

It should be noted that the compound $Nd_4Ba_2Cu_2O_{10}$, whose composition corresponds to the simplest formula Nd_2BaCuO_5, has also been obtained in the given system at $x = 0$. The tetragonal crystal structure and some properties of this compound were described in [13, 14].

The goal of this work was to analyze by the method of diffusion pairs the reaction of La_2BaO_4 with La_2CuO_4. It was assumed that mutual diffusion of Ba^{2+} and Cu^{2+} ions would give $La_2Cu_{1-x}Ba_xO_4$ and $La_2Ba_{1-x}Cu_xO_4$ solid solutions based on, respectively, La_2CuO_4 and La_2BaO_4. However, as shown by the results of X-ray fluorescence analysis, the reaction of La_2BaO_4 with La_2CuO_4 gives a phase whose composition is invariable across the diffusion layer and can be expressed by the simplest formula La_2BaCuO_5. Therefore, this compound was also analyzed as a component of mixtures with various oxide phases.

EXPERIMENTAL

The compounds La_2BaO_4 and La_2CuO_4, whose reaction was studied by the method of diffusion pairs, were synthesized by calcining in air at 1223 K for 8 h

1070-4272/02/7511-1732$27.00 © 2002 MAIK "Nauka/Interperiodica"

pellets compacted from mixed powders of $BaCO_3$ + $2La(OH)_3$ and CuO + $2La(OH)_3$. Then the samples obtained were ground in an agate mortar and the resulting finely dispersed powders were compacted into pellets 10 mm in diameter and 5–6 mm high. The pellets were calcined in air at 1273 K for 8 h. The edge surfaces of the sintered La_2BaO_4 and La_2CuO_4 pellets were polished with diamond paste. Pairs of pellets of these two different compounds were put one upon another, with polished faces in contact, placed in an Alundum tube, and introduced, together with the compression unit, into a furnace heated to 1223 K. After 24 h, the entire content of the tube was rapidly removed from the furnace.

After calcining, the diffusion pair was divided into the initial pellets, with the reaction layer remaining on the La_2CuO_4 pellet. This pellet was cut in two, perpendicularly to the edge surfaces, and the cuts were polished with diamond paste.

A Cameca MS-46 electron-microprobe X-ray fluorescence analyzer was used to determine the distribution, across the reaction layer and at a certain distance from it, of characteristic X-ray emission from, simultaneously, two elements: La, Ba and Cu, Ba.

The intensities of characteristic X-ray emission of these elements were invariable across the reaction layer (Fig. 1). Hence follows that the reaction of La_2CuO_4 with La_2BaO_4 yields not the $La_2Cu_{1-x}Ba_xO_4$ solid solution, but a compound whose cationic composition is approximately expressed by a simple formula La_2BaCuO_5.

Figure 2 shows the Gibbs triangle of the ternary system La_2O_3–BaO–CuO, in which point *a* lies in the middle of the straight line connecting points with coordinates corresponding to the compositions of the compounds La_2BaO_4 and La_2CuO_4.

Point *a* corresponds to a solid solution $La_2Ba_{0.5}Cu_{0.5}O_4$, which would be formed if there occurred mutual diffusion of Ba^{2+} ions from the crystal lattice of La_2BaO_4 into that of La_2CuO_4 and of Cu^{2+} ions from the La_2CuO_4 phase into the La_2BaO_4 phase. However, such a solid solution is unstable and, if formed, would decompose into La_2O_3 and La_2BaCuO_5 phases (Fig. 2, point *b*) by the scheme

$$2La_2Ba_{0.5}Cu_{0.5}O_4 \rightarrow La_2O_3 + La_2BaCuO_5.$$

For such a mechanism of the reaction between La_2BaO_4 and La_2CuO_4 to be operative, the reaction layer must consist of two phases. However, this layer is actually single-phase.

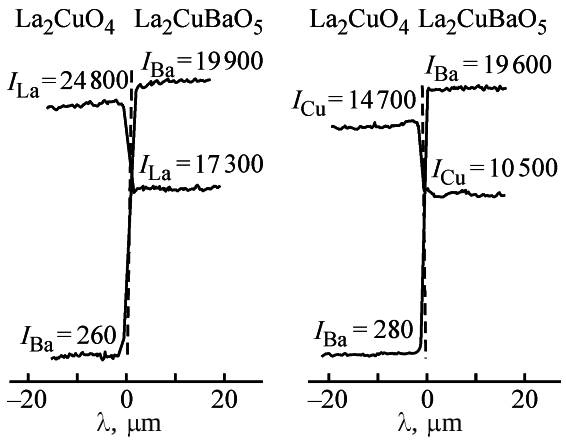

Fig. 1. Intensity distribution of characteristic X-ray emission from (*1*) Ba, (*2*) La, and (*3*) Cu across the reaction layer of the diffusion pair La_2CuO_4–La_2BaO_4 calcined at 1223 K for 24 h. (λ) Coordinate across the layer. The reaction layer is on the La_2CuO_4 pellet. The dashed line denotes the phase boundary between La_2CuO_4 and the reaction layer.

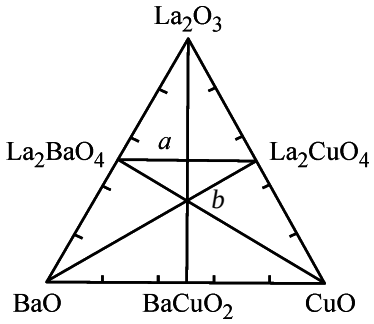

Fig. 2. Gibbs triangle of the system La_2O_3–BaO–CuO.

Consequently, it may be suggested that this single-phase reaction proceeds by the mechanism of one-way diffusion of one of the ions, Ba^{2+} or Cu^{2+}, and electrons of oxygen ions. In view of the fact that the reaction layer is formed on the La_2CuO_4 pellet, it is barium and oxygen ions that diffuse, in all probability, despite the much larger size of Ba^{2+} ions, compared to Cu^{2+} ions, from the crystal lattice of La_2BaO_4 into that of La_2CuO_4. The La_2BaCuO_5 phase is formed from the latter, and lanthanum oxide crystallizes in the porous surface layer of the La_2BaO_4 pellet. This process can be represented as

$$La_2BaO_4 = La_2O_3 + Ba^{2+} + 2e + 1/2O_2$$

(on La_2BaO_4 pellet),

$$La_2CuO_4 + Ba^{2+} + 2e + 1/2O_2 = La_2BaCuO_5$$

(on La_2CuO_4 pellet),

Relative intensity *I* of X-ray reflections, interplanar spacings *d* of the compound obtained, La_2BaCuO_5 ($La_4Ba_2Cu_2O_{10}$), and published data for the phase $La_{3.6}Ba_{2.4}Cu_{1.8}O_{9.6}$

Experimental data		Published data [16]			Experimental data		Published data [16]		
d, Å	*I*, %	*d*, Å	*I*, %	*hkl*	*d*, Å	*I*, %	*d*, Å	*I*, %	*hkl*
3.73	16	3.748	19	111	1.89	12	1.8720	19	222
3.40	8	3.438	3	200	–	–	1.8153	4	113
3.06	28	3.076	21	210	1.74	8	1.7477	9	312
2.95	100	2.966	100	201	1.69	12	1.7008	20	203
2.88	28	2.935	41	002	–	–	1.6678	5	410
2.71	43	2.723	58	211	1.64	15	1.6505	16	213
–	–	2.510	2	112	–	–	1.6203	3	330
2.42	32	2.433	23	220	1.59	15	1.6041	10	411
2.24	8	2.246	3	221	1.56	2	1.5619	9	331
2.17	28	2.175	20	310					
2.12	30	2.122	41	212					
–	–	2.038	3	311					

or

$$La_2BaO_4 = La_2O_3 + Ba^{2+} + O^{2-}$$
(on La_2BaO_4 pellet),

$$La_2CuO_4 + Ba^{2+} + O^{2-} = La_2BaCuO_5,$$
(on La_2CuO_4 pellet)

It is known that the reaction of ferrite $BaFe_2O_4$ with Fe_2O_3, yielding hexaferrite $BaFe_{12}O_{19}$, also proceeds via one-way diffusion of larger Ba^{2+} ions, rather than small Fe^{3+} ions [15]. This fact may serve as circumstantial evidence in favor of the suggested mechanism of the solid-phase reaction between La_2BaO_4 and La_2CuO_4.

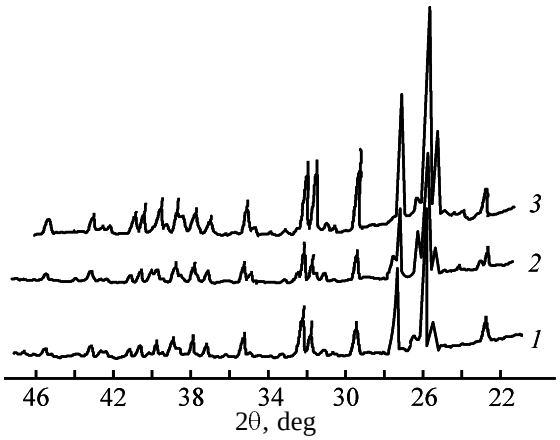

Fig. 3. X-ray diffraction patterns of products formed by reaction at 1373 K for 6 h in mixtures (*1*) La_2BaO_4 + CuO and (*2*) La_2CuO_4 + $BaCO_3$; (*3*) the diffraction pattern of La_2BaCuO_5 ($La_4Ba_2Cu_2O_{10}$) obtained by calcination at 1323 K for 24 h of the mixture $BaCO_3$ + CuO + $2La(OH)_3$. (2θ) Bragg angle.

To confirm the existence of the compound La_2BaCuO_5 ($La_4Ba_2Cu_2O_{10}$), it was also prepared by heating a mixture of $BaCO_3$, CuO, and $La(OH)_3$ powders taken in the molar ratio of 1 : 1 : 2. After thorough mixing in a vibrating mill, the stock was compressed into pellets and calcined at 1223, 1273, and 1323 K for 4, 8, 24, and 48 h at each temperature. The phase state of the calcination products under study was monitored by X-ray phase analysis on a DRON-3 instrument (CuK_α radiation).

The X-ray diffraction patterns obtained demonstrated that a compound with the same X-ray reflections is formed in all cases. The interplanar spacings *d* calculated from these reflections correspond to the values reported in the literature for the $La_{3.6}Ba_{2.4}Cu_{1.8}O_{9.6}$ phase [16] (see table).

Lines corresponding to compositions belonging to three quasi-binary systems La_2BaO_4–CuO, La_2CuO_4–BaO, and La_2O_3–$BaCuO_2$ pass in the Gibbs triangle (Fig. 2) through point *b* corresponding to the compound La_2BaCuO_5. Consequently, this compound can be synthesized by the reaction between two components of each of these systems. In this connection, pellets compacted from powder mixtures of the compositions La_2BaO_4 + CuO, La_2CuO_4 + $BaCO_3$, and $La(OH)_3$ + $BaCuO_2$, thoroughly mixed in a vibrating mill, were calcined in air at 1373 K for 6 h.

The X-ray diffraction patterns of these three calcined mixtures were virtually the same and coincided with that of the compound La_2BaCuO_5, obtained by calcining a mixture of the composition $BaCO_3$ + $2La(OH)_3$ + CuO (Fig. 3).

To study the homogeneity region of La_2BaCuO_5 with respect to the cations, we prepared variable-composition phases $La_{2-x}Ba_{1+x}CuO_5$, $La_{2+x}Ba_{1-x}CuO_5$, $La_{2-x}BaCu_{1+x}O_5$, and $La_{2+x}BaCu_{1-x}O_5$ (x = 0.05, 0.1). The synthesis was done in air at 1373 K from a mixture of powdered $BaCO_3$, $La(OH)_3$, and CuO. As shown by X-ray phase analysis, only samples containing an excess amount of barium(II) at the expense of lanthanum(III) content ($La_{2-x}Ba_{1+x}CuO_5$) were single-phase. Other samples contained minor amounts of other phases.

CONCLUSION

Solid-phase reaction in air at 1223 K in vitrified pellets of double compounds La_2BaO_4 and La_2CuO_4 yields at the $La_2BaO_4 | La_2CuO_4$ phase boundary a layer of the ternary compound La_2BaCuO_5 ($La_4Ba_2 \cdot Cu_2O_{10}$) whose cationic composition is determined with an electron-microprobe X-ray fluorescence analyzer. The reaction occurs via one-way diffusion of Ba^{2+} and O^{2-} ions or electrons from the crystal lattice of La_2BaO_4 into the crystal lattice of the cuprate La_2CuO_4.

The compound can also be synthesized by calcining in air in the temperature interval 1223–1373 K powder mixtures of the compositions $BaCO_3$ + $2La(OH)_3$ + CuO, La_2BaO_4 + CuO, La_2CuO_4 + $BaCO_3$, and $2La(OH)_3$ + $BaCuO_2$. The X-ray diffraction patterns of the final product are the same for all of the mixtures and coincide with published data for the $La_{3.6}Ba_{2.4}Cu_{1.8}O_{9.6}$ phase. The single-phase state of $La_{2-x}Ba_{1+x}CuO_5$ is preserved on raising the content of barium(II) by 10% because of the equivalent decrease in the content of lanthanum(III).

REFERENCES

1. Michel, C., Er-Rakvho, L., and Reveau, B., *J. Solid State Chem.*, 1981, vol. 39, no. 2, pp. 161–167.
2. Bednorz, J.G. and Müller, K.A., *Z. Phys. B*, 1986, vol. 64, no. 1, pp. 189–193.
3. Wu, M.K., Ashburn, J.R., Torng, C.J., *et al.*, *Phys. Rev. Lett.*, 1987, vol. 58, no. 9, pp. 908–910.
4. Fotiev, A.A., Slobodin, B.V., and Fotiev, V.A., *Khimiya i tekhnologiya vysokotemperaturnykh sverkhprovodnikov* (Chemistry and Technology of High-Temperature Superconductors), Yekaterinburg: Ural'sk. Otd. Ross. Akad. Nauk, 1994.
5. *Diagrammy sostoyaniya sistem tugoplavkikh oksidov: Spravochnik* (Phase Diagrams of Systems Composed of High-Melting Oxides: Reference Book), issue 6: *Sistemy keramicheskikh vysokotemperaturnykh sverkhprovodnikov (Systems of Ceramic High-Temperature Superconductors), Grebenshchikov, R.G., Ed., St. Petersburg: Nauka, 1997.*
6. *Tret'yakov, Yu.D. and Gudilin, E.A., Usp. Khim.*, 2000, vol. 69, no. 1, pp. 3–40.
7. Klibanow, D., Sujata, K., and Mason, T.O., *J. Am. Ceram. Soc.*, 1988, vol. 71, no. 5, pp. 267–269.
8. Abbattista, F., Vallino, M., and Mazza, D., *Mater. Chem. Phys.*, 1990, vol. 24, no. 4, pp. 363–372.
9. Ogawa, N., Mizuno, F., Mazuda, H., *et al.*, *Physica B*, 1990, vol. 165–166, no. 2, pp. 1687–1688.
10. Vodalazskaya, I.V., Voronkova, V.I., Gvozdover, R.S., *et al.*, *Physica C*, 1989, vols. 162–164, pp. 1213–1214.
11. Michel, C. and Reveau, B., *J. Solid State Chem.*, 1982, vol. 43, no. 1, pp. 73–80.
12. Dube, D., Champaigne, B., and Le Page, Y., *Mater. Lett.*, 1989, vol. 8, no. 8, pp. 283–285.
13. Klyndyuk, A.I., Petrov, G.S., Masyuk, S.V., and Bashkirov, L.A., *Izv. Ross. Akad. Nauk, Neorg. Mater.*, 1999, vol. 35, no. 10, pp. 1174–1176.
14. Staliok, K. and Wong, W., *Mater. Lett.*, 1990, vol. 9, no. 10, pp. 401–404.
15. Aksel'rod, N.L., Tkachenko, E.V., Buyanova, E.S., and Shapovalov, A.G., *Zh. Neorg. Khim.*, 1984, vol. 29, no. 2, pp. 2775–2779.
16. *Powder Diffraction File*, Swarthmore: Joint Committee on Powder Diffraction Standard, card no. 39-1416.

Russian Journal of Applied Chemistry, Vol. 75, No. 11, 2002, pp. 1736–1739. Translated from Zhurnal Prikladnoi Khimii, Vol. 75, No. 11, 2002, pp. 1772–1775.
Original Russian Text Copyright © 2002 by Obraztsova, Simenyuk, Eremenko.

INORGANIC SYNTHESIS AND INDUSTRIAL INORGANIC CHEMISTRY

Effect of Chemical Modification of Ultradispersed Copper Powders on Electrical Conductivity of Formulations on Their Base

I. I. Obraztsova, G. Yu. Simenyuk, and N. K. Eremenko

Institute of Coal and Coal Chemistry, Siberian Division, Russian Academy of Sciences, Kemerovo, Russia

Received March 13, 2002

Abstract—Ultradispersed powders of copper were obtained by reducing various copper salts with glycerol, and formulations on their base were prepared. The effect of various modifiers on the dispersity, stability, and electrical conductivity of copper powders was examined.

Synthesis and study of ultradispersed powders (UDPs) of metals and development of electrically conducting materials on their base is a topical direction of research in modern science. Recently, increasing attention has been given to copper [1, 2], which is virtually as good as noble metals as regards its electrical conductivity [3–5] and much less expensive. However, copper powders exhibit rather high activity and are oxidized in the course of time, which inevitably impairs the conductivity. This problem can be solved by optimizing the preparation process, modifying the surface of copper UDPs, and creating formulations on their base, whose electrically conducting properties are preserved for a long time. Data on the longevity of electrically conducting formulations are virtually lacking from the literature.

Previously, two methods for obtaining copper UDPs have been developed [6, 7]. These methods are based on reduction of copper sulfate with glycerol. The optimal temperature, time, and reagent concentrations were determined. Also, the influence exerted by organic acids with reducing properties (ascorbic, citric, etc.) on the reaction of copper sulfate with glycerol and on the properties of the copper powders obtained was examined. It was established that additions of these acids accelerate the reaction by a factor of 5–6, allow the process temperature to be decreased by 20–40°C, and ensure enhanced stability and electrical conductivity of the resulting copper UDPs.

It was also found that, upon an appropriate treatment with solutions of hydroquinone and stearic acid in ethanol or pentane, copper UDPs possess increased dispersity (average particle size 20–30 nm), stability, and electrical conductivity. Furthermore, powders treated with pentane can be stored for a long time not only in solution, but also in air.

In this work, we prepared UDPs from various copper(II) salts and examined the influence exerted by chemical modification of copper UDPs on the electrical conductivity and stability of formulations on their base. The data obtained in the study are compared with those published previously [8, 9]. New data on the formulation longevity are presented.

EXPERIMENTAL

Copper UDPs were prepared by reducing various copper salts with glycerol by the method described in [9]. However, it was found that complete reduction of readily decomposing salts (acetate, basic carbonate, and tartrate) requires smaller amount of glycerol, lower temperature T_r, and shorter reaction time τ_r. The results obtained at different copper salt to glycerol mass ratios A are presented in Table 1. It can be seen that the reduction of copper basic carbonate, acetate, and tartrate is the most effective, and their formulations with novolac show high electrical conductivity and are stable for a long time (more than 5 years) without addition of any stabilizers. Here, copper UDP is presumably stabilized in the course of the reaction by glycerol itself.

It also follows from Table 1 that, in reduction of copper(II) sulfate, the electrical conductivity of the resulting formulations falls dramatically when no additional stabilizers are introduced into the resin (experiment no. 1). When, however, modifiers are introduced (experiment no. 2), the formulations obtained

1070-4272/02/7511-1736$27.00 © 2002 MAIK "Nauka/Interperiodica"

Table 1. Conditions of copper UDP preparation from various copper salts and resistivity ρ of novolac formulations based on copper UDPs

Experiment no.	Compound	A	τ_r, min	T_r, °C	$\rho \times 10^4$, Ω cm, at indicated testing time, years							
					1 day	1 month	0.5	1	2	3	4	5
1	$CuSO_4 \cdot 5H_2O$	1 : 10	300	180–190	5.4	8.0	18.2	32.4	48.4	57.6	64.8	72.6
2	$CuSO_4 \cdot 5H_2O$*	1 : 10	300	180–190	1.2	1.2	1.3	1.5	1.7	1.8	1.8	1.9
3	$Cu(OAc)_2 \cdot H_2O$	1 : 3	40	145–155	0.6	1.2	1.2	1.2	1.2	1.2	1.2	1.2
4	$CuCO_3 \cdot Cu(OH)_2$	1 : 4	14	140–145	0.6	0.8	0.9	0.9	0.9	0.9	0.9	0.9
5	$CuTart \cdot 3H_2O$	1 : 5	145	160–165	1.2	1.4	1.4	1.5	1.6	1.7	1.8	1.9
6	$Cu(NO_3)_2 \cdot 3H_2O$**	1 : 10	350	160–170	–	–	–	–	–	–	–	–
7	$CuCl_2 \cdot 2H_2O$***	1 : 10	–	–	–	–	–	–	–	–	–	–

* Formulation stabilized with 1-naphthol and glycerol simultaneously.
** Copper UDPs are rapidly oxidized by reaction products.
*** No copper powder is formed.

compare well in the electrical conductivity and stability with pastes based on copper UDPs produced by reduction of readily decomposing copper salts (experiment nos. 3–5).

In the case of reduction of copper(II) nitrate, the UDP formed is very rapidly oxidized in the course of the reaction, which markedly diminishes the yield of the metallic phase.

In reduction of copper(II) chloride, no metallic copper is formed, even upon addition of an initiator, ascorbic acid (up to 0.5 g per gram of copper). In the reaction with copper chloride, glycerol undergoes extensive tarring to give a black viscous mass solidifying on cooling.

The aforesaid suggests that it is preferable to use copper sulfate for commercial preparation of electrically conducting materials. On the one hand, other copper salts are less readily available and more expensive, and, on the other, $CuSO_4$-based formulations with various modifiers are virtually as good as pastes prepared from other copper salts, as regards their stability and electrical conductivity.

The effect of chemical modification of the surface of copper UDPs was studied in different stages: in synthesis, treatment, storage, and formulation preparation.

It was shown previously [9] that introduction of organic acids with reducing properties (ascorbic, oxalic, citric, and formic) into the reaction mixture much intensifies the reduction process. It was found here that addition of acetylsalicylic acid in amount of 5 wt % relative to copper sulfate pentahydrate makes it possible to diminish the process time even more (10-fold). Furthermore, it was found that the nature of the acid also affects the particle size. For example, the highest dispersity is observed when acetylsalicylic acid is added as initiating agent, since the major part of particles are 10–40 nm in size (according to electron microscopy). In the case when ascorbic acid is used, a minor amount of 100–200-nm aggregates are present together with the highly dispersed phase, and introduction of citric acid leads to formation of 40–300-nm particles. It was found that the dispersity grows with increasing acid concentration. This is due to the following facts: (i) particle agglomeration becomes weaker under milder reaction conditions; (ii) in some cases, introduction of acids instantaneously initiates reduction to give a large number of nuclei of the metallic phase; and (iii) organic acids may enter into the composition of intermediate reaction products, thereby changing the structure of copper UDPs formed on their base.

Prolonged storage of copper UDPs in air or in ethanol may lead to partial oxidation of the surface layer, with the electrical conductivity of formulations decreasing dramatically. It was found that the electrical conductivity can be easily restored in this case by treating the copper UDP with formic acid (1–2 ml of HCOOH per gram of copper). No UDP oxidation is observed in the case of storage in pentane.

The copper UDPs obtained were used to prepare electrically conducting formulations with epoxy or novolac resins. The formulations were cured in accordance with the polymerization mode of the resin employed. A study of the influence exerted by reduction of copper sulfate with glycerol on the electrical conductivity of the formulations demonstrated that the number of conducting chains in formulations with

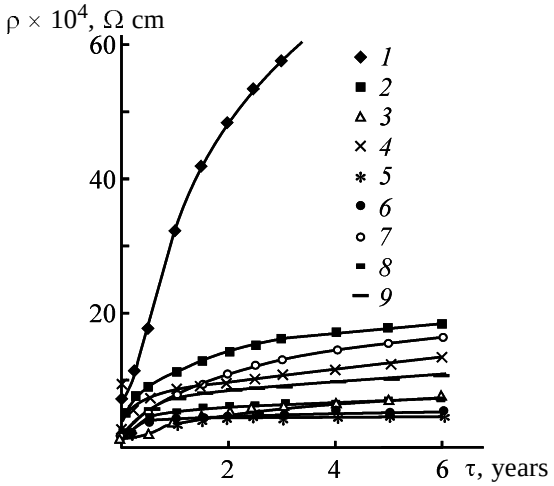

Fig. 1. Electrical resistivity ρ of formulations comprising SF-010 novolac resin, copper UDP, and organic acid vs. testing time τ. Curve nos. are sample nos. in Table 1.

epoxy resin is sufficient for stable electricity transfer even at metal concentration of 55%. In the case of novolac resin, a higher content of metal is necessary (65–70%). However, at a metal content of 75–80% the electrical conductivities of composites based on these resins become comparable.

It was established that copper formulations obtained using different methods and different modifiers markedly differ in the electrical conductivity and stability (Figs. 1, 2). Table 2 lists the results obtained in studying the influence exerted by introduction of a number of organic acids (initiating agents) at different mass ratios B ($CuSO_4 \cdot 5H_2O$: glycerol : initiating agent) on the parameters τ_r and T_r of the copper UDP preparation process.

As follows from Fig. 1 and Table 2, introduction of various organic acids (ascorbic, oxalic, citric, formic, or acetylsalicylic) markedly shortens τ_r of copper reduction with glycerol (by a factor of more than 10 in the case of acetylsalicylic acid) and yields formulations with novolac resin that are characterized by high stability (for more than 6 years) and low resistivity (compared to sample no. 1 prepared without introduction of initiating agents). It can also be seen that the electrical conductivity and stability of the formulations grow with increasing concentration of any of the organic acids (sample nos. 3, 5, 6, and 8).

The effect of various stabilizing additives on the electrical conductivity and stability of formulations with epoxy resin is illustrated in Fig. 2a. It can be seen that all formulations with addition of 1-naphthol or *p*-aminophenol retain unchanged high electrical conductivity for more than 10 years (curves *2*–*6*), and formulations with 1-naphthol have the lowest electrical resistivity of $(0.8–1.2) \times 10^{-4}$ Ω cm, close to that of the metal. Formulations with Diaphene (curve *7*) have high initial electrical conductivity, but, after 4 years, the properties of the formulation deteriorate dramatically. With other stabilizers (curves *8*, *9*), the longevity of formulations was even lower.

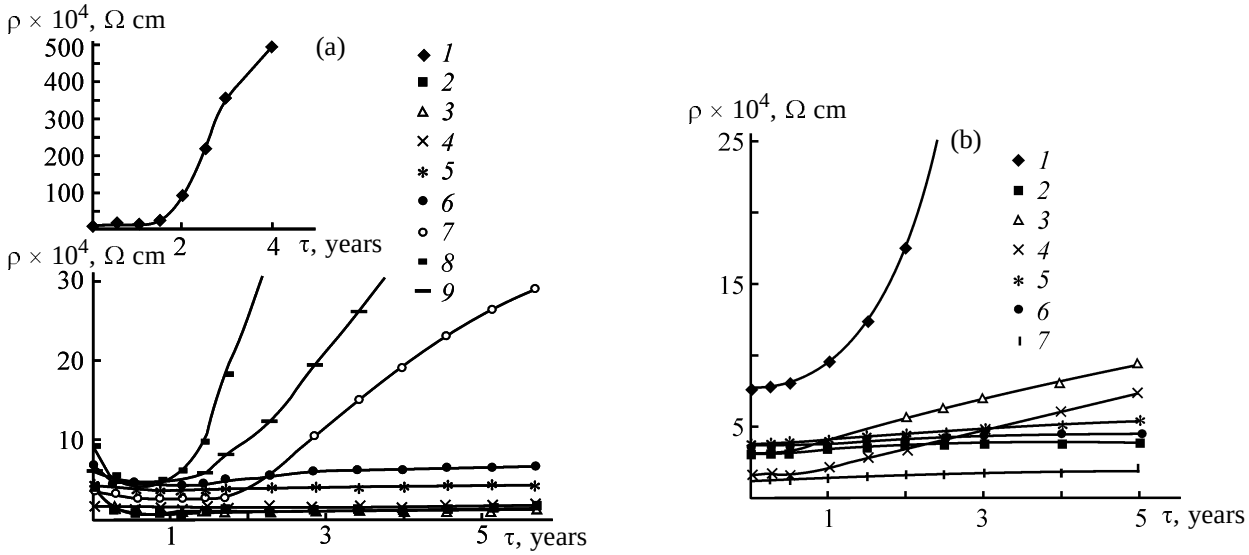

Fig. 2. Effect of stabilizers on the dependence of the electrical resistivity of formulations with (a) EDP epoxy resin and (b) SF-010 novolac resin on the testing time τ. (a) (*1*) Without stabilizer; stabilizer: (*2*–*4*) 1-naphthol, (*5*, *6*) *p*-aminophenol, (*7*) Diaphene, (*8*) *p*-phenylenediamine, and (*9*) 1-naphthylamine. Copper UDP : EDP : stabilizer mass ratio: (*1*) 100 : 40 : 0, (*2*) 100 : 40 : 1.0, (*3*) 100 : 35 : 1.0, (*4*) 100 : 25 : 1.0, (*5*–*7*, *9*) 100 : 30 : 1.0, and (*8*) 100 : 32 : 1.0. (b) (*1*) Without stabilizer; stabilizer: (*2*) 1-naphthol, (*3*) *p*-aminophenol, (*4*) ascorbic acid, (*5*) hydroquinone, (*6*) formic acid, and (*7*) 1-naphthol + glycerol (plasticizer). Copper UDP : SF-010 : stabilizer mass ratio: (*1*) 100 : 25 : 0, (*2*–*5*) 100 : 25 : 1.0, (*6*) 100 : 25 : 5.0, and (*7*) 100 : 25 : 1.0 : 3.0 (3 wt parts of glycerol).

Table 2. Effect of initiator on the conditions of preparation of copper UDPs

Sample no.	*B*	Initiator (acid)	τ_r, min	T_r, °C
1	1 : 10.0 : 0	–	300	180–190
2	1 : 10.0 : 0.003	Ascorbic	85	160–165
3	1 : 7.5 : 0.020	″	40	140–145
4	1 : 5.0 : 0.010	″	40	150–155
5	1 : 7.5 : 0.100	Oxalic	70	160–165
6	1 : 7.5 : 0.060	Citric	100	170–175
7	1 : 7.5 : 0.030	Formic	80	160–165
8	1 : 6.7 : 0.120	″	55	160–165
9	1 : 10.0 : 0.050	Acetylsalicylic	25	155–160

Thus, a conclusion can be made that the best stabilizers for epoxy formulations are 1-naphthol and *p*-aminophenol, which are known [10] to be effective inhibitors of oxidation with molecular oxygen, used to prevent aging of polymers and stabilize jet-engine fuel in prolonged storage.

For formulations with novolac resin, the effect of various stabilizers is illustrated in Fig. 2b. It can be seen that all of the modified samples have lower resistivity and are more stable than the initial sample (curve *1*), with the lowest resistivity observed for the formulation stabilized with a mixture of glycerol and 1-naphthol (curve *7*). The introduction of glycerol, presumably, makes lower the brittleness of the novolac formulations and improves their adhesion characteristics, which makes higher their electrical conductivity. In contrast to [9], where stability data were reported for a time period of only 3 months, we report here the data obtained during the last 5 years. It is clear that not all of the formulations studied possess stable characteristics, but only those stabilized with 1-naphthol (curve *2*), formic acid (curve *6*), hydroquinone (curve *5*), and a mixture of glycerol and 1-naphthol (curve *7*). As in the case of epoxy formulations, the best oxidation inhibitor is 1-naphthol, and addition to this compound of glycerol in 1 : 3 ratio yields formulations comparable in electrical conductivity (resistivity 1.2×10^{-4} Ω cm) with the best samples with epoxy resin (Fig. 2a) and novolac formulations with addition of organic acids (Fig. 1) or those obtained from readily decomposing copper salts (Table 1).

CONCLUSIONS

(1) Ultradispersed powders prepared from readily decomposing copper salts and formulations synthesized on their base retain high electrical conductivity for more than 5 years.

(2) The best stabilizer for ultradispersed copper powders obtained from copper sulfate is 1-naphthol or its mixture with glycerol.

(3) Chemical modification of ultradispersed copper powders results in that epoxy formulations prepared on their base retain their high electrical conductivity for more than 10 years.

(4) The enhanced stability and low cost of these copper-based materials makes them promising for use in modern nanoelectronics instead of composites based on noble metals.

REFERENCES

1. Figlars, M., Ducamp-Sanguesa, C., Fievet, F., and Lagier, J.-P., *Advances in Powder Metallurgy: World Congr.*, San Francisco, California, 1992, vol. 1, pp. 179–192.
2. RF Patent 2043874.
3. Chai Liyuan, Zhong Haiyun, and Wu Haiyun, *Trans. Nonferrous Met. Soc. China*, 1994, vol. 4, no. 1, pp. 33–36.
4. US Patent 5891367.
5. US Patent 5929141.
6. RF Patent 2031759.
7. RF Patent 2115516.
8. Obraztsova, I.I., Efimov, O.A., Eremenko, N.K., and Simenyuk, G.Yu., *Izv. Ross. Akad. Nauk, Neorg. Mater.*, 1995, vol. 31, no. 6, pp. 798–799.
9. Obraztsova, I.I., Simenyuk, G.Yu., and Eremenko, N.K., *Izv. Ross. Akad. Nauk, Neorg. Mater.*, 1999, vol. 35, no. 8, pp. 937–939.
10. *Khimicheskaya entsiklopediya* (Chemical Encyclopedia), Moscow: Sovetskaya Entsiklopediya, 1988, vol. 1, p. 334.

Russian Journal of Applied Chemistry, Vol. 75, No. 11, 2002, pp. 1740–1743. Translated from Zhurnal Prikladnoi Khimii, Vol. 75, No. 11, 2002, pp. 1776–1779.
Original Russian Text Copyright © 2002 by Shibanov, Khadykina, Solov'ev.

INORGANIC SYNTHESIS AND INDUSTRIAL INORGANIC CHEMISTRY

Composition and Stability of a Polynuclear Copper Sulfite Complex

V. N. Shibanov, E. A. Khadykina, and E. M. Solov'ev

Murmansk State Technical University, Murmansk, Russia
Gipronikel' Institute, Joint-Stock Company, St. Petersburg, Russia

Received November 5, 2001; in final form, May 2002

Abstract—Conditions for the formation of a polynuclear copper sulfite complex were studied by spectrophotometry, conductometry, and chemical analysis. The composition of the forming sulfites was determined, and the equilibrium constant of formation of the polynuclear copper sulfite complex and its dissociation constant were calculated.

The reaction between $CuSO_4$ and Na_2SO_3 aqueous solutions results in the precipitation of $Cu_2SO_3 \cdot 4.5H_2O$ at $T \le 40°C$ and $Cu_2SO_3 \cdot CuSO_3 \cdot 2H_2O$ at $T \ge 40°C$ [1]. These sulfites are prepared at the molar ratio $Na_2SO_3(H_2SO_3)/CuSO_4 \approx 1$ (pH ≥7) [1, 2]. However, when copper sulfite is obtained using sulfur dioxide, the residual sulfuric acid acidity of up to 1.05 wt % suggests that copper sulfite can form at lower pH values than it follows from the reaction equation, which is of importance for the removal of copper ions from copper–nickel solutions [4]. The unit cell parameters of $Cu_2SO_3 \cdot CuSO_3 \cdot 2H_2O$ have been determined [5]. The composition and stability of the mononuclear copper(I) sulfite complexes $[CuSO_3]^-$, $[Cu(SO_3)_2]^{3-}$, and $[Cu(SO_3)_3]^{5-}$ in aqueous solutions were studied [6]. However, conditions for the formation of the polynuclear copper complex in aqueous solution and its composition were not studied.

The aim of this work was to find optimal conditions for the formation of the polynuclear copper sulfite complex and to determine its composition and stability.

EXPERIMENTAL

The $CuSO_4$–Na_2SO_3–H_2O system was studied by spectrophotometry and chemical analysis [7]. The experimental technique was described earlier in [8].

To determine the optimal pH of the solution, we measured the optical densities at 790 nm for several solutions of the complex and copper(II) sulfate with equal concentrations but different pH. The maximal difference in optical densities of the complex and copper(II) sulfate was observed in the pH range 2.8–3.2; therefore, subsequent experiments were carried out in this range.

To study the composition of the copper complex with sodium sulfite, we first prepared an isomolar series of solutions with the total concentration of components of 0.140 M and ionic strength of 0.70. The maximal yield of the complex corresponded to the ratio $c_{Cu} : (c_{Cu} + c_{SO_3^{2-}}) = 0.62$; in this case, the optical density reached a maximum of 2.88 (Fig. 1, curve *1*). A minimum of conduction was detected at $c_{Cu}/(c_{Cu} + c_{SO_3^{2-}}) = 0.60$ (Fig. 1). Hence, we can assign the composition $n_{Cu} : n_{SO_3^{2-}} = 3 : 2$ to the complex. However, as shown by N.P. Komar', the ratio of stoichiometric coefficients of a reaction determined by the method of isomolar series is often inconsistent with the formula of the resulting complex compound. It is particularly typical for complexes having an absorption maximum shifted to the left- or the right-

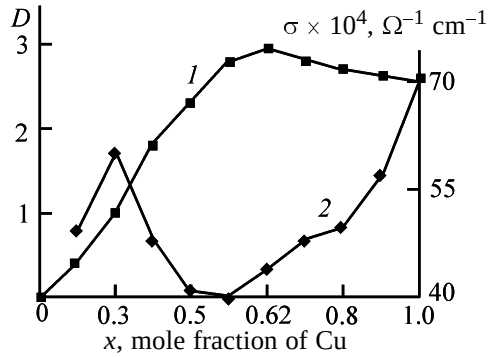

Fig. 1. Dependences of (*1*) optical density *D* and (*2*) conductivity σ on solution composition *x*. $c_{Cu} + c_{SO_3^{2-}} = 0.140$ M, pH 3.12 ± 0.01.

1070-4272/02/7511-1740$27.00 © 2002 MAIK "Nauka/Interperiodica"

Table 1. Experimental data for the calculation of the composition of the complex by the method of molar ratios* (λ = 790 nm)

c_{Cu}	$c_{SO_3^{2-}}$	$c_{Cu}/c_{SO_3^{2-}}$	D	$c_{SO_3^{2-}}$,** M	$c_{SO_3^{2-}}/c_{Cu}$	D
M						
l = 3.0 cm, pH 2.87				l = 2.0 cm, pH 2.97		
0.0110	0.0997	0.11	0.196	0.334	3.34	0.219
0.0254	0.0976	0.26	0.659	0.198	1.98	1.150
0.0426	0.0989	0.43	1.060	0.143	1.43	1.568
0.0578	0.0975	0.59	1.444	0.100	1.00	1.946
0.0631	0.0991	0.64	1.563	0.048	0.48	2.128
0.0784	0.0998	0.78	2.193	0.032	0.32	2.235
0.1198	0.0990	1.21	2.943	0.020	0.20	2.235
0.1362	0.0987	1.38	3.111	0.00	0	2.236
0.1623	0.0978	1.66	3.691			
0.1874	0.0988	1.90	3.700			
0.2030	0.0998	2.03	3.928			
0.3204	0.0990	3.24	4.066			
0.7224	0.1056	6.84	4.233			

* c_{Cu} is the total concentration of copper(I) and copper(II), and $c_{SO_3^{2-}}$ is the total concentration of sulfite ions.
** c_{Cu} = 0.0999 M.

hand side of the isomolar diagram. Therefore, we used additional spectroscopic methods to elucidate reliably the composition of the complex.

The most common technique for studying complex compounds is the method of molar ratios. Our experimental data, used to determine the composition of the complex by this method, are given in Table 1. The breakpoints in the experimental curves (Fig. 2) correspond to the ratio of stoichiometric coefficients, which is equal to the ratio of concentrations of reacting components in the abscissa of the equivalent point. According to curves *1* and *2*, the ratios $c_{Cu}/c_{SO_3^{2-}}$ and $c_{SO_3^{2-}}/c_{Cu}$ are 1.5 and 0.67, respectively. It is evident that the complex with the composition $c_{Cu} : n_{SO_3^{2-}}$ = 3 : 2 is formed.

The data required for the determination of the composition of the complex by Starik–Barbanel' method [10] are given in Table 2. Unlike the method of isomolar series, this method allows determination not of the ratios of the stoichiometric coefficients, but of their absolute values. It is applicable to any stoichiometric reaction. It follows from Table 2 that the maximal yield is observed at $\Delta D/c_{Cu}$ = 9.233, which corresponds to $\Delta D/\Delta D_{lim}$ = 0.67, and at $\Delta D/c_{SO_3^{2-}}$ = –32.2, which corresponds to $\Delta D/\Delta D_{lim}$ = 0.497. The calculation by equations [7] for the complex formation reaction $mM + nM \rightleftarrows M_mR_n$ gives m = 3.04 and n = 1.99.

The reaction of a weak acid with metal ions can be represented for the system under study in the following generalized form:

$$mM^{n+} + pHL^- \rightleftarrows [M_mL_p]^{mn-2p} + pH^+. \quad (1)$$

Therefore, we can write the equilibrium constant for process (1) as

$$K = \frac{c_c[H^+]^p}{(c_M - c_c)^m (c_L - c_c)^p}. \quad (2)$$

where c_c is the equilibrium concentration of the complex; c_M, total concentration of metal ions M^{n+}; c_L,

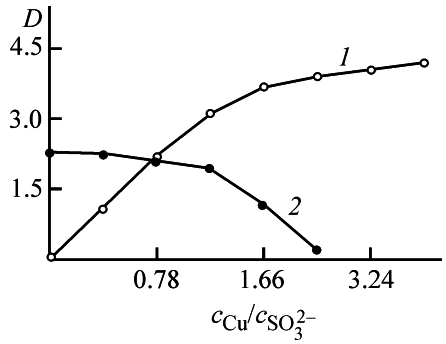

Fig. 2. Dependences of D on the initial concentration ratios (*1*) $c_{Cu}/c_{SO_3^{2-}}$ and (*2*) $c_{SO_3^{2-}}/c_{Cu}$.

Table 2. Experimental data for the calculation of the composition of the complex by Starik–Barbanel' method (λ = 790 nm). $c_{Cu} = \Sigma(c_{Cu^{2+}} + c_{Cu^{+}})$

c_{Cu}, M	D_{comp}	D_{CuSO_4},	ΔD	$\Delta D/c_{Cu}$	$\Delta D/\Delta D_{lim}$	$c_{SO_3^{2-}}$ M	D_{comp}	$D_{SO_3^{2-}}$	ΔD	$\Delta D/c_{SO_3^{2-}}$	$\Delta D/\Delta D_{lim}$
l = 3.0 cm, pH 2.87						l = 2.0 cm, pH 2.97					
0.0631	2.193	2.507	–0.314	–4.976	–0.222	0.2259	0.196	0.011	–2.055	–9.08	0.922
0.0730	2.943	2.667	0.276	3.781	0.195	0.1171	0.219	0.011	–2.028	–17.3	0.907
0.0743	3.111	2.706	0.405	5.451	0.286	0.0343	1.142	0.011	–1.105	–32.2	0.497
0.0770	3.149	2.710	0.439	5.701	0.310	0.0226	1.568	0.011	–0.673	–29.8	0.302
0.1030	3.691	2.740	0.951	9.233	0.672	0.0638	1.946	0.011	–0.290	–4.53	0.130
0.2073	4.066	2.750	1.316	6.358	0.930	0.0298	2.128	0.011	–0.108	–3.62	0.048
0.4050	4.233	2.818	1.415	3.494	1.000	0.0010	2.235	0.011	–0.001	–1.00	0.0004

Table 3. Amount of hydrogen ions displaced by copper ions in the reaction with hydrosulfite ions. λ = 790 nm, l = 3 cm, D_{lim} = 1.368

Run no.	pH	D	$A \times 10^{-10}$	$K_c \times 10^{-3}$	Combination of experiments nos.	p
1	3.73	1.296	24.8	8.58	1, 2	1.98
2	3.48	1.278	8.00	8.77	1, 3	1.99
3	3.17	1.249	1.94	8.84	1, 4	2.00
4	2.95	1.222	0.681	8.57	2, 3	1.99
				Average 8.69	2, 4	2.00
					3, 4	2.03

total concentration of weak acid ions HL^-; and p, amount of displaced hydrogen ions.

Replacing c_c by the equal value $c_M D/D_{lim}$, provided that equimolar solutions of a metal salt and a ligand were taken in the experiments, we transform Eq. (2) to the following form [11]:

$$K = \frac{c_M D/D_{lim}[H^+]^p}{(c_M - c_M D/D_{lim})^m (c_L - c_M D/D_{lim})^p}. \quad (3)$$

Using the notation

$$\frac{c_M D}{D_{lim}(c_M - c_M D/D_{lim})^{m+p}} = A$$

after taking the logarithm of Eq. (3), we obtain Eq. (4).

$$\log K = \log A - p\text{pH}. \quad (4)$$

The solution of Eq. (4) with respect to p for two experiments gives Eq. (5).

$$p = \frac{\log A_i - \log A_k}{\text{pH}_i - \text{pH}_k}. \quad (5)$$

The data calculated by Eqs. (3) and (5) for various pH values are given in Table 3.

It is seen from Table 3 that p is close to two for all the combinations of experiments. Thus, the formula of the compound formed in solution can be represented as $[Cu_3(SO_3)_2]^0$ or $[Cu_3(SO_3)_2]_{aq}$. Alternatively, the equilibrium constant of reaction (1) can be written as

$$K = K_{a_2}/K_i, \quad (6)$$

where K_a is the dissociation constant of HSO_3^- and K_i is the overall instability constant of $Cu_3(SO_3)_2$. Then

$$K_i = K_{a_2}/K. \quad (7)$$

With $K_{a_2} = 6.31 \times 10^{-8}$ [12] we obtain

$$K_i = \frac{(6.31 \times 10^{-8})^2}{8.69 \times 10^3} = 4.58 \times 10^{-19}.$$

The chemical analysis of the resulting yellow-green precipitate has shown that its composition corresponds to the formula $Cu_2SO_3 \cdot 5H_2O$:

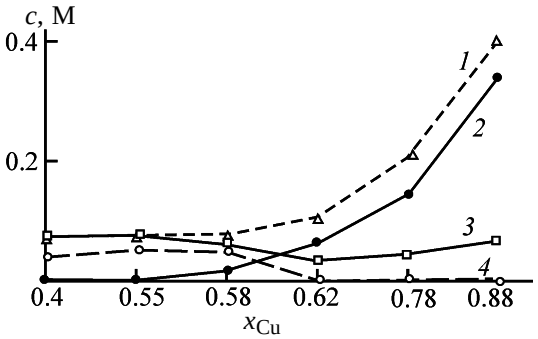

Fig. 3. Dependences of concentrations c of (*1*) Cu_{total} ($Cu^+ + Cu^{2+}$), (*2*) Cu^{2+}, (*3*) Cu^+, and (*4*) SO_3^{2-} on the copper mole fraction x_{Cu}.

Method of determination	Cu^+ content, %	SO_3^{2-} content, %
Analysis	48.2	27.2
Calculation	48.2	26.9

According to the X-ray phase analysis, the salt $Cu_2SO_3 \cdot 5H_2O$ is X-ray amorphous.

It is probable that the complex $[Cu_3(S_2O_3)_2]_{aq}$ formed at 25°C is unstable at low temperatures and decomposes to form the $Cu_2SO_3 \cdot 5H_2O$ precipitate. The dependences of the concentrations of Cu^+, Cu^{2+}, Cu_{total}, and SO_3^{2-} on the copper content x_{Cu} (mole fraction) in solution at a constant initial concentration of sulfite ions are shown in Fig. 3. It is seen that Cu^+ and SO_3^{2-} ions prevail in solution up to $x_{Cu} = 0.55$. Therefore, when the ionic product $[Cu^+]^2[SO_3^{2-}]$ is greater than $SP_{Cu_2SO_3 \cdot 5H_2O}$, only $Cu_2SO_3 \cdot 5H_2O$ is precipitated. In the range $x_{Cu} = 0.55–0.62$, the concentration of Cu^{2+} ions start to increase, but the concentrations of Cu^+ and SO_3^{2-} ions decrease, the latter decreasing much faster, reaching almost zero in the point $x_{Cu} = 0.62$. The ionic product exceeding the solubility product of the corresponding salt ($Cu_2SO_3 \cdot 5H_2O$ or $Cu_2SO_3 \cdot CuSO_3 \cdot 2H_2O$) is reached only for $Cu_2SO_3 \cdot 5H_2O$. Margulis and Rodin [1] qualitatively explained its precipitation by its lower solubility at $T \leq 40$°C compared to $Cu_3(SO_3)_2 \cdot 2H_2O$, which agrees with the data of this work. The corresponding data on SP and K_i are also close to each other, which is attributable to the fact that, for the reaction

$$[Cu_3(SO_3)_2]_s \rightleftarrows [Cu_3(SO_3)_2]_{aq},$$

the following equality is valid:

$$K = [Cu_3(SO_3)_2]_{aq} = SP[Cu_3(SO_3)_2]_s/K_i \approx 1.$$

A certain discrepancy between the numbers of water molecules in the formulas of the precipitates seems to result from different drying conditions. In this work, we dried precipitates in a desiccator over concentrated sulfuric acid at room temperature.

CONCLUSIONS

(1) The reaction of $CuSO_4$ with Na_2SO_3 in aqueous solution at 25°C in the pH range 2.8–3.2 results in the formation of the complex $[Cu_3(SO_3)_2]_{aq}$, which then dissociates to give $Cu_2SO_3 \cdot 5H_2O$.

(2) The equilibrium constant of 8.69×10^3 for the formation of the complex $[Cu_3(SO_3)_2]^0$ was determined. The overall constant of 4.58×10^{-19} for dissociation of $[Cu_3(SO_3)_2]_{aq}$ was calculated.

(3) Copper sulfates under study can be obtained in more acidic medium than it follows from the reaction equation, which opens up new opportunities for removal of copper ions from multicomponent solutions.

REFERENCES

1. Margulis, E.V. and Rodin, N.V., *Zh. Neorg. Khim.*, 1982, vol. 27, no. 2, pp. 374–377.
2. Pesin, Ya.M. and Shabashova, M.L., *Zh. Prikl. Khim.*, 1950, vol. 23, no. 3, pp. 278–284.
3. Shabashova, M.L., Reaction of Sulfur Dioxide with Certain Copper Compounds and Preparation of Blue Vitriol, *Cand. Sci. Dissertation*, Leningrad, 1950.
4. Baimakov, Yu.V. and Zhurin, A.I., *Elektroliz v gidrometallurgii* (Electrolysis in Hydrometallurgy), Moscow: Metallurgiya, 1977.
5. Kierkegaard, P. and Nyberg B., *Acta Chem. Scand.*, 1965, vol. 19, no. 9, pp. 2189–2199.
6. Toropova, V.F., Sirotina, I.A., and Rotanova, V.B., *Uch. Zap. Kazan. Gos. Univ.*, 1955, vol. 115, book 3, pp. 53–60.
7. Bulatov, M.N. and Kalinkin, I.P., *Prakticheskoe rukovodstvo po fotokolorimetricheskim i spektrofotometricheskim metodam analiza* (Manual on Photocolorimetric and Spectrophotometric Analytical Methods), Leningrad: Khimiya, 1972.
8. Shibanov, V.N., Taranenko, V.G., and Tereshkina, M.A., *Zh. Prikl. Khim.*, 1999, vol. 72, no. 9, p. 1581.
9. Komar', N.P., *Zh. Anal. Khim.*, 1965, vol. 20, no. 12, pp. 1299–1305.
10. Barbanel', Yu.A., *Zh. Neorg. Khim.*, 1964, vol. 9, no. 2, pp. 437–446.
11. Salikhov, V.D. and Yampol'skii, Z.Ya., *Zh. Anal. Khim.*, 1965, vol. 20, no. 12, pp. 1299–1305.
12. Rabinovich, V.A. and Khavin, Z.Ya., *Kratkii khimicheskii spravochnik* (Concise Chemical Handbook), Leningrad: Khimiya, 1977.

Russian Journal of Applied Chemistry, Vol. 75, No. 11, 2002, pp. 1744–1747. Translated from Zhurnal Prikladnoi Khimii, Vol. 75, No. 11, 2002, pp. 1780–1783.
Original Russian Text Copyright © 2002 by Sokolovskii, Radion, Rudakov.

INORGANIC SYNTHESIS AND INDUSTRIAL INORGANIC CHEMISTRY

Hydroxo Complex Formation in the Fe^{3+}–Hg^{2+}–NO_3^-–H_2O System

A. E. Sokolovskii, E. V. Radion, and D. A. Rudakov

Belarussian State Technological University, Minsk, Belarus

Received December 8, 2001; in final form, June 2002

Abstract—Hydrolysis of the Fe^{3+}–Hg^{2+}–NO_3^-–H_2O system was studied by spectrophotometry, pH-metric titration, and sorption methods. The mutual influence of the cations on the hydrolytic and sorption behavior was discussed in terms of heteronuclear complex formation.

Iron(III) salts are widely used in water and sewage treatment, e.g., for removal of mercury(II) by coprecipitation with iron(III) hydroxide.

The study of hydrolytic interaction of Fe(III) and Hg(II) ions [1] showed that, during the hydrolysis of Fe^{3+} ions, Hg^{2+} ions precipitate also. The kinetics of the hydrolysis of simultaneously present Fe^{3+} and Hg^{2+} ions was studied, and the parameters of this process were found to differ essentially from the parameters of the hydrolysis of individual ions.

The sorption of Fe^{3+} and Hg^{2+} ions from Fe^{3+}–Hg^{2+}–NO_3^-–H_2O solutions was studied in [2], and the formation of a heteronuclear iron(III)–mercury(II) hydroxo complex was found by dialysis.

In this work, the hydrolysis of cations in the Fe^{3+}–Hg^{2+}–NO_3^-–H_2O system was further studied by spectrophotometry, pH-metric titration, and sorption.

EXPERIMENTAL

Solutions of iron(III) and mercury(II) nitrates were prepared by dissolving metallic mercury and carbonyl iron in chemically pure grade nitric acid. The concentration of metal ions in the Hg^{2+}–NO_3^-–H_2O and Fe^{3+}–Hg^{2+}–NO_3^-–H_2O systems was 0.01 M, in the Fe^{3+}–Hg^{2+}–NO_3^-–H_2O system their total concentration was 0.02 M at the Fe^{3+} : Hg^{2+} molar ratio of 1 : 1; the temperature was 25 ± 0.1°C, and the ionic strength, 0.3 M (KNO_3).

To determine the Fe^{3+} content in solution, we used direct complexometric titration with sulfosalicylic acid in acetate buffer solution [3], The Hg^{2+} content was determined by complexometric back-titration with a zinc salt [3]. The contents of simultaneously present Fe^{3+} and Hg^{2+} were determined by complexometric back-titration of the sum of the two ions followed by displacement of Hg^{2+} ions from the complex with potassium iodide and titration of the released ethylenediaminetetraacetate (EDTA) with a zinc salt [3]. The content of free HNO_3 in the starting solutions was determined by potentiometric titration in the presence of EDTA [4]. The error of concentration determination was 0.9%.

Solutions of iron(III), mercury(II), and iron(III)–mercury(II) with various OH/M molar ratios were prepared from the stock solutions of iron(III) and mercury(II) nitrates. From the determined concentrations of metal ions and free nitric acid, we calculated the amount of KOH necessary to neutralize the free acid and to fix a particular OH/M ratio, and the amount of KNO_3 necessary to maintain the constant ionic strength. Then we mixed the calculated amounts of the starting metal solutions, 0.2 M KOH, and 1 M KNO_3. When the free acid was neutralized partially, we designated the OH/M molar ratio with the negative sign. After preparation, we thermostated the solutions for 7 days to reach an equilibrium and then measured the equilibrium pH of each solution.

To study the hydrolysis, we used pH-metric titration, spectrophotometry, and sorption. The pH values were measured on an I-160 pH-meter equipped with a microprocessor and a temperature-controlled pH-metric cell connected to a UTU-2.84 universal ultrathermostat. We used an ESL-43-07 glass electrode as an indicator electrode and an EVL-1M1 silver chloride electrode as a reference electrode. Absorption spectra were recorded on an SF-46 spectrophotometer with a microprocessor.

We used KU-2-8chS cation exchanger (ultrapure

1070-4272/02/7511-1744$27.00 © 2002 MAIK "Nauka/Interperiodica"

KU-2 cation exchanger containing 8% divinylbenzene) and KB-4P-2 cation exchanger in the H^+ form. The resins were pretrated by the generally accepted procedure [5], and their moisture content was determined [6]. We studied the sorption at 25 ± 0.1°C under static conditions and always proved the attainment of the equilibrium of metal ion distribution between the solution and the resin. The solution–resin contact time was 7 days. We calculated the sorption *S* of metal ions by the resins (mmol per gram of resin dried to constant weight at 105°C) from the results of chemical analysis of equilibrium solutions.

The absorption spectra of mercury(II) solutions with various OH^-/Hg^{2+} molar ratios are shown in Fig. 1. In all the curves in the UV range, an edge of a medium-intensity absorption band is observed (at λ = 255 nm ε ~ 150). This band was assigned to charge transfer [7]. As the OH^-/Hg^{2+} ratio (i.e., pH) increases, the absorption band is shifted bathochromically, suggesting the occurrence of equilibria involving protons [7]. In the pH range under study (1.86–2.67 [8]), mercury(II) exists in the form of aqua ions and $HgOH^+$ and $Hg(OH)_2$ hydroxo complexes. Correspondingly, changes occurring in the spectra as pH increases are attributable to the formation of hydrolyzed mercury(II) species.

In the absorption spectra of Fe^{3+}–NO_3^-–H_2O solutions (Fig. 2, curves *3–7*) an edge of a strong absorption band is observed, which is usually assigned to activated iron(III) ions and is accounted for by the ligand-to-metal charge transfer H_2O–Fe(III) [7]. In the spectra of the solutions with the OH^-/Fe^{3+} ratio from –1 to 0.5 (pH 1.93–2.27), a shoulder is observed in the range of wavelengths 300–320 nm, assignable to mononuclear iron(III) hydroxo complexes [9]. As the OH^-/Fe^{3+} ratio increases to 1 (pH 2.29), the light absorption increases and the shoulder disappears, suggesting formation of polynuclear hydroxo complexes. These data are in good agreement with our previous results and allow us to refine the pH value at which the polynuclear iron(III) complexes in solution start to be manifested in the absorption spectrum.

The light absorption of iron(III) is considerably stronger than that of mercury(II); therefore, we recorded the spectra of Fe^{3+}–Hg^{2+}–NO_3^-–H_2O solutions under the same conditions (*b* = 0.5 mm) as the spectra of Fe^{3+}–NO_3^-–H_2O solutions (Fig. 2, curves *1* and *2*). Since hydroxides were precipitated from solutions at the ratio of $OH/\Sigma M > 0$, only the spectra with $OH/\Sigma M$ –1 and 0 are shown. The light absorption of Fe^{3+}–Hg^{2+}–NO_3^-–H_2O solutions is appreciably lower than that of Fe^{3+}–NO_3^-–H_2O solutions with the same

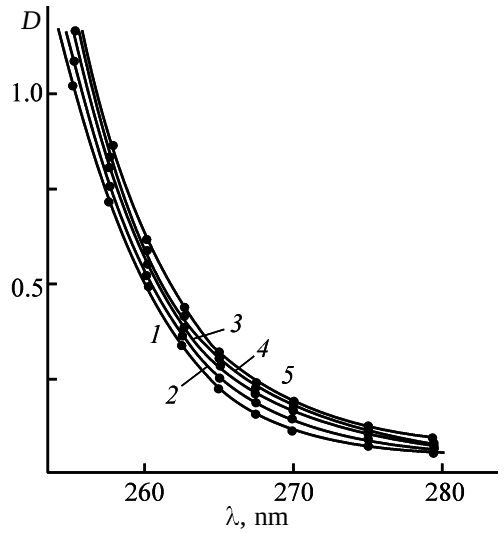

Fig. 1. Absorption spectra of Hg^{2+}–NO_3^-–H_2O solutions: (*D*) optical density and (λ) wavelength; the same for Fig. 2. Molar ratio OH/M: (*1*) –1, (*2*) –0.5, (*3*) 0, (*4*) 0.5, and (*5*) 1.

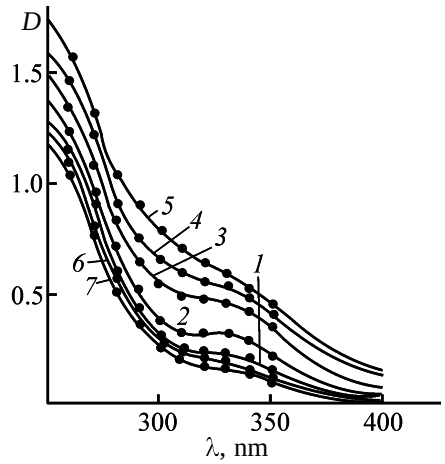

Fig. 2. Absorption spectra of solutions: (*1, 2*) Fe^{3+}–Hg^{2+}–NO_3^-–H_2O and (*3–7*) Fe^{3+}–NO_3^-–H_2O. Molar ratio OH/M: (*1, 3*) –1, (*2, 5*) 0, (*4*) –0.5, (*6*) 0.5, and (*7*) 1.

iron(III) concentration. In this case, the absorption in the region of the shoulder at 330 nm decreases noticeably, suggesting smaller fraction of mononuclear iron(III) hydroxo complexes. Thus, our results indicate that Hg^{2+} ions affect the hydrolysis of Fe^{3+} ions. These data are in good agreement with the previous studies [2], where "weakening" of iron(III) hydrolysis in the presence of mercury(II) was found by dialysis.

When acidified solutions of Fe^{3+}, Hg^{2+}, and Fe^{3+}–Hg^{2+} are titrated with an alkali, free HNO_3 and metal ion hydroxo species are neutralized, and hydroxides precipitate. The curves of pH-metric titration (the titrant was 0.2 M NaOH solution) are given beginning with the ratio $OH/\Sigma M = 0$, since no discontinuities

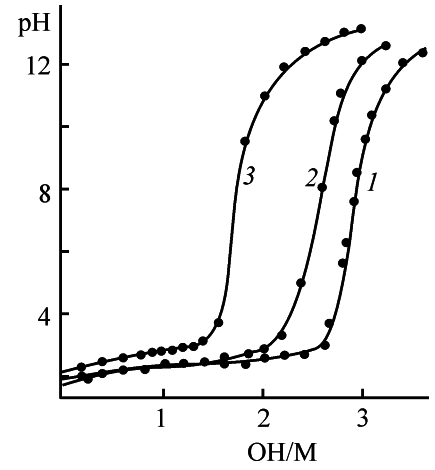

Fig. 3. Curves of pH-metric titration of solutions: (*1*) Fe^{3+}–NO_3^-–H_2O, (*2*) Hg^{2+}–NO_3^-–H_2O, and (*3*) Fe^{3+}–Hg^{2+}–NO_3^-–H_2O.

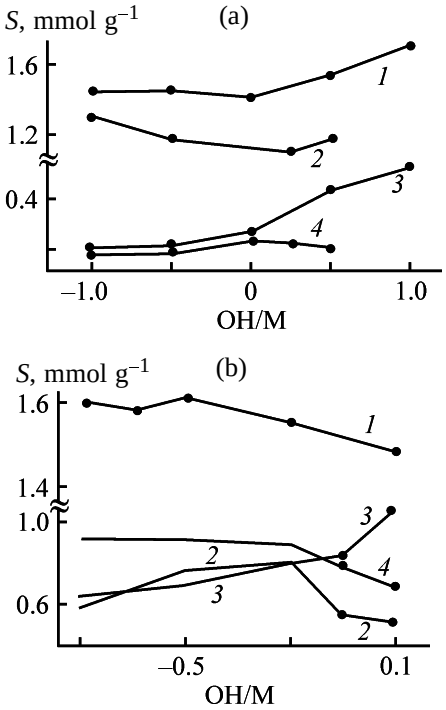

Fig. 4. Sorption *S* of (a) iron(III) and (b) mercury(II) by cation exchangers (*1*, *2*) KU-2-8chS and (*3*, *4*) KB-4P-2. Solution: (a) (*1*, *3*) Fe^{3+}–NO_3^-–H_2O and (*2*, *4*) Fe^{3+}–Hg^{2+}–NO_3^-–H_2O; (b) (*1*, *3*) Hg^{2+}–NO_3^-–H_2O and (*2*, *4*) Fe^{3+}–Hg^{2+}–NO_3^-–H_2O.

were observed in them up to the completion of free nitric acid neutralization (Fig. 3). The pK_a values for $Fe(H_2O)_6^{3+}$ and $Fe(H_2O)_5OH^{2+}$ ions are 2.2 and 3.46, respectively, and for $Hg(H_2O)_6^{2+}$ and $Hg(H_2O)_5OH^+$, 3.4 and 2.77, respectively [8]. Hence, the differentiated titration of these ions and of free HNO_3 is impossible. In all three curves we observed a single titration jump. The equivalence points corresponded to the ratios OH^-/Fe^{3+} = 2.8 (curve *1*) and OH^-/Hg^{2+} = 1.7 (curve *2*). Iron(III) hydroxide began to precipitate at pH ~3, i.e., at the beginning of the jump in the titration curve. The solution of mercury(II) grew turbid at OH^-/Hg^{2+} = 0 and pH ~2. In the titration curve of the Fe^{3+}–Hg^{2+} solution, we also observed a jump with an equivalence point at $OH^-/\Sigma M$ = 2.5. In this case, the precipitation began at $OH^-/\Sigma M$ = 0 as in the case of Hg^{2+}. The obtained data do not allow us to judge the behavior of the simultaneously present ions before hydroxides start to precipitate; however, they indicate that, under the action of alkali, iron(III) and mercury(II) precipitate simultaneously.

The sorption of iron(III) by the KU-2-8chS strongly acidic cation exchanger (Fig. 4a, curve *1*) is almost independent of the OH^-/Fe^{3+} ratio in the range from –1 to 0 and somewhat increases in the range from 0.5 to –1. The KU-2(H^+) resin, as shown previously [10], sorbs all the iron(III) species except polynuclear ions. Therefore, our spectrophotometric data suggest that, in the acidity range under study, the sorbable species are, most probably, iron(III) aqua and mononuclear hydroxo complexes.

The KB-4P-2 weakly acidic carboxylic cation exchanger sorbed iron(III) ions in appreciably smaller amounts, and, as the ratio OH^-/Fe^{3+} increased, the sorption substantially increased (Fig. 4a, curve *3*). The KB-4(H^+) resin, as shown previously [10], selectively sorbs mononuclear iron(III) hydroxo species. The data of this work agree well with each other and with the data of [10]: at the OH^-/Fe^{3+} ratio exceeding 0.5, noticeable increases in the light absorption at 300–320 nm, resulting from the appearance of mononuclear iron(III) hydroxo complexes, and in the sorption occurred simultaneously.

The sorption of Fe(III) ions by the KU-2-8chS cation exchanger from the solutions containing iron(III) and mercury(II) is a little lower than the sorption from the solution containing iron(III) only (Fig. 4a, curves *2* and *1*). In this case, the dependence of sorption on the $OH/\Sigma M$ ratio remained virtually the same. At the same time, the sorption of iron(III) by the KB-4P-2 cation exchanger as a function of the $OH/\Sigma M$ ratio appreciably differs for the Fe^{3+}–NO_3^-–H_2O and Fe^{3+}–Hg^{2+}–NO_3^-–H_2O systems (Fig. 4a, curves *3* and *4*). In the range of $OH/\Sigma M$ from –1 to 0, the curves ran in parallel, whereas at higher $OH/\Sigma M$ ratios the trends became opposite. Since the KB-4P-2 resin absorbed predominantly mononuclear iron(III) hydroxo complexes, a decrease in iron(III) sorption

in the presence of mercury(II) can be accounted for by the fact that, in the presence of Hg(II) ions, as follows from the spectrophotometric data, the concentration of mononuclear Fe(III) hydroxo complexes decreased.

The sorption of Hg(II) ions by the KU-2-8chS cation exchanger somewhat decreased as OH^-/Hg^{2+} increased (Fig. 4b, curve *1*), which seems to result from predominant sorption of mercury(II) aqua complexes, and the sorption by the KB-4P-2 resin increased (Fig. 4b, curve *3*). This fact can be associated only with a change in the state of mercury(II) ions on pH variation, as in the range under study the ionization of the resin carboxy groups is negligible. According to [2], at pH > 2 the fraction of mercury(II) aqua ions in solution decreases at the expense of the formation of polymeric species. Consequently, an increase in the mercury(II) sorption by the KB-4 resin, especially at $OH^-/Hg^{2+} > -0.5$ (pH > 2.01), is determined by the participation of mercury(II) polymeric forms in the process.

In the Fe^{3+}–Hg^{2+}–NO_3^-–H_2O system, the sorption of mercury(II) by the KU-2-8chS cation exchanger noticeably decreased (Fig. 4b, curve *2*), and the character of its sorption by the KB-4P-2 resin changed (Fig. 4b, curve *4*). The sorption of mercury(II) from the Fe^{3+}–Hg^{2+}–NO_3^-–H_2O system on the both resins at $OH/\Sigma M > 0$ noticeably decreased, suggesting an increase in the concentration of nonsorbable polymeric species in the solution.

Thus, in hydrolysis, iron(III) and mercury(II) exert a strong mutual effect, manifested in changes in their absorption spectra and sorption behavior. Starting with $OH/\Sigma M = 0$, a noticeable and parallel decrease in sorption of both ions by both strongly and weakly acidic ion exchangers was observed. Since the strongly acidic KU-2-8chS resin sorbs all iron(III) ionic species except polynuclear ions [10], a noticeable decrease in the iron(III) sorption in the presence of mercury(II) at $OH/\Sigma M > 0$ suggests binding of iron(III) active species into nonsorbable polynuclear complexes. Since this was not observed in pure iron(III) solutions, we suggest formation of iron(III)–mercury(II) heteronuclear hydroxo complexes in the Fe^{3+}–Hg^{2+}–NO_3^-–H_2O solution. At the same time, a decrease in the sorption of mercury(II) by the KB-4P-2 resin in the presence of iron(III) also suggests binding of mercury(II) sorption-active polymeric species into a new compound, which was not sorbed. These data are in good agreement with the data of [2], where the formation of iron(III)–mercury(II) heteronuclear complexes at pH > 2.15 was found by dialysis. Thus, we suggest that these complexes are formed from mononuclear iron(III) hydroxo complexes and homopolynuclear mercury(II) complexes.

CONCLUSIONS

(1) In the Fe(III)-Hg(II) solution, mutual influence of ions on their sorption and hydrolytic behavior takes place, which is determined by their interaction.

(2) The heteronuclear complex formed in the solution is not sorbed by KU-2-8chS and KB-4P-2 ion exchangers.

REFERENCES

1. Bakeev, T.B., Study of Hydrolytic and Reductive Separation of Mercury from Aqueous Solutions, *Cand. Sci. Dissertation*, Karaganda, 1993.
2. Radion, E.V., Zalevskaya, T.L., Baev, A.K., and Sheremet, E.N., *Koord. Khim.*, 1998, vol. 24, no. 5, pp. 339–342.
3. Umland, F., Janssen, A., Thierig, D., und Wünsch, G., *Theorie und praktische Anwendung von Komplexbildnern*, Frankfurt am Main: Akademische, 1971.
4. Bulatov, N.I. and Bulatova, A.A., *Zh. Anal. Khim.*, 1983, vol. 24, no. 5, pp. 339–342.
5. Aivazov, B.V., *Vvedenie v khromatografiyu* (Introduction to Chromatography), Moscow: Vysshaya Shkola, 1983.
6. Ol'shanova, K.M., Potapova, M.A., and Morozova, N.M., *Praktikum po khromatograficheskomu analizu* (Practical Course of Chromatographic Analysis), Moscow: Vysshaya Shkola, 1970.
7. Lever, A.B.P., *Inorganic Electronic Spectroscopy*, Amsterdam: Elsevier, 1984.
8. Nazarenko, V.A., Antonovich, V.P., and Nevskaya, E.M., *Gidroliz ionov metallov v razbavlennykh rastvorakh* (Hydrolysis of Metal Ions in Dilute Solutions), Moscow: Atomizdat, 1979.
9. Radion, E.V., Zalevskaya, T.L., and Baev, A.K., *Vestsi Akad. Navuk Bel., Ser. Khim. Navuk*, 1992, no. 2, pp. 45–48.
10. Radion, E.V., Zalevskaya, T.L., and Baev, A.K., *Vestsi Akad. Navuk Bel., Ser. Khim. Navuk*, 1993, no. 4, pp. 3–7.

Russian Journal of Applied Chemistry, Vol. 75, No. 11, 2002, pp. 1748–1752. Translated from Zhurnal Prikladnoi Khimii, Vol. 75, No. 11, 2002, pp. 1784–1788.
Original Russian Text Copyright © 2002 by Nikolaev, Maiorov, Baklanova.

INORGANIC SYNTHESIS AND INDUSTRIAL INORGANIC CHEMISTRY

Decrease of HF Concentration in Process Solutions before Extractive Separation of Tantalum(V) from Niobium(V)

A. I. Nikolaev, V. G. Maiorov, and I. V. Baklanova

Tananaev Institute of Chemistry and Technology of Rare Elements and Mineral Resources, Kola Scientific Center, Russian Academy of Sciences, Apatity, Murmansk oblast, Russia

Received June 13, 2002

Abstract—To improve separation of tantalum(V) from niobium(V) in their extraction from fluoride solutions, different ways for decreasing the fluoride ion concentration in the aqueous phase were tested. The efficiency of decomposition of rare-metal concentrate in continuous countercurrent process with several equilibrium decomposition stages was studied.

In industrial production of tantalum(V) and niobium(V) compounds, the separation and purification of these metals is mainly performed by extraction. Two types of extraction flowsheets are used. The first type includes joint extraction of tantalum(V) and niobium(V) followed by their separation in the backwashing stage. The second type is based on successive selective recovery of tantalum(V) and niobium(V). The second flowsheet is preferable owing to simpler process control and lower cost of the process [1]. However, for selective recovery of tantalum(V) with its separation from niobium(V), the hydrofluoric acid content in the aqueous phase must be minimized. To improve extractive separation of Ta(V) from Nb(V), an additional mineral acid (as a rule, sulfuric acid) is added into the solution. The H_2SO_4 concentration in this solution should be relatively low, and the lower, the stronger the extractant basicity. However, to ensure complete dissolution of Ta(V) and Nb(V) in decomposition of a rare-metal concentrate, a large excess of acids, especially HF, is required [2]. Therefore, in some cases, to improve the extractive separation of niobium(V) from tantalum(V), the HF concentration in the solution should be decreased. In this work we studied the main approaches to solution of this problem.

The procedures for preparing solutions, performing experiments, analyzing target metals, and safely handling aggressive hydrofluoric acid solutions were reported in detail previously [2, 3]. Separation of Ta(V) from Nb(V) was performed by extraction with *n*-octyl alcohol (OCL) whose main characteristics were reported in [4].

The data on the effect of the HF_{free} concentration and ratio of the organic and aqueous phases $V_o : V_{aq}$ on extractive recovery of Ta(V) and Nb(V) are listed in Table 1. In this table, HF_{free} is the HF concentration calculated as the difference between the total HF concentration and the HF amount combined in the prevailing complexes $HTa(Nb)F_6$, H_2TiOF_4, and H_2SiF_6 formed in the solutions under consideration [3]. The Ta(V) and Nb(V) concentrations in the solutions used in our experiments are close to those in solutions obtained by decomposition of pyrochlore. With increasing HF_{free} concentration by 2 M, the extraction recovery of Ta(V) decreases by 7–8%, whereas the Nb(V) recovery increases by 4–6%. We found that the most efficient separation of these metals is reached at $c_{HF_{free}} \leq 0$ M. The fact that in some cases the $c_{HF_{free}}$ value calculated by us is less than zero shows that, along with above-noted fluoride

Table 1. Extractive separation of Ta(V) from Nb(V) as influenced by the HF_{free} concentration in the aqueous phase. Initial metal concentration, M: Ta(V) 0.016 and Nb(V) 2.26

$c_{HF_{free}}$, M	V_o/V_{aq}	Recovered, %	
		Ta(V)	Nb(V)
0	1.1 : 1	68.5	20.1
2	1.2 : 1	61.1	24.0
0	1.5 :1	76.7	25.0
2	1.5 : 1	68.5	28.6
0	1.8 : 1	80.5	27.5
2	1.8 : 1	72.6	33.5

1070-4272/02/7511-1748$27.00 © 2002 MAIK "Nauka/Interperiodica"

Table 2. Extractive separation of Ta(V) from Nb(V) as a function of the degree of dilution of the initial aqueous solution α

Run no.	Concentration in aqueous solution, M					α	V_o/V_{aq}	Recovered, %	
	HF^*_{tot}	H_2SO_4	Ta(V)	Nb(V)	Ti(IV)			Ta(V)	Nb(V)
1	12	4.1	0.16	0.78	–	–	1 : 1	96.5	74.1
2	12	4.1	0.16	0.78	–	2	1 : 1	93.8	20.0
3	12	4.1	0.16	0.78	–	2	1 : 2	86.0	16.1
4	14	4.5	0.19	0.73	–	–	1 : 2	64.8	62.2
5	14	4.5	0.19	0.73	–	2	1 : 2	68.9	15.0
6	14	4.5	0.19	0.73	–	3	1 : 1	85.4	14.2
7	4.6**	3.6	0.15	0.64	–	2	1 : 1	70.0	16.1
8	34***	–	0.033	0.80	6.3	–	1 : 1.5	98.7	94.4
9	34***	–	0.033	0.80	6.3	–	1 : 3	92.0	80.0
10	34***	–	0.033	0.80	6.3	2	1 : 6	94.0	16.4
11	34***	–	0.033	0.80	6.3	2	1 : 12	87.9	5.1

* Total HF concentration.
** Solution evaporated by 2/3; degree of HF removal in evaporation exceeds 65%.
*** Solution evaporated by half.

complexes, other complexes with a lower content of fluoride ions are formed also. This explanation is consistent with the data reported in [1]. The addition of H_2SO_4 improves separation of Ta(V) from Nb(V). In extraction of these metals with OCL, the optimal sulfuric acid content in the aqueous phase is about 2 M [4]. It was reported [5] that, in extraction with a stronger base, tributyl phosphate, the efficient separation of Ta(V) from Nb(V) can be reached without addition of H_2SO_4 ($c_{HF_{free}} < 0$ M).

The simplest way to decrease the HF_{free} concentration is dilution of the initial solution (Table 2). The initial solutions were prepared by dissolving columbite [2] (Table 2, run nos. 1–7) and hydrated cake (HC) [a mixture of Ta(V), Nb(V) and Ti(IV) hydroxides] obtained by treating loparite concentrate with nitric acid [6] (Table 2, run nos. 8–11). The latter solutions containing a large amount of HF_{tot} and Ti(IV) were also used in the experiments (Tables 3, 4).

In extraction of metals from solutions obtained immediately after columbite decomposition, Ta(V) and Nb(V) are recovered jointly (Table 2, run nos.1 and 4). After dilution of these solutions by a factor of 2–3, Ta(V) is recovered to 85–86%, and Nb(V) to 14–16% (Table 2, run nos. 3 and 6). Such a difference in the extractability of the metals allow the quantitative recovery of Ta(V) in a counterflow mode at minor passing of Nb(V) to the organic phase. Fairly efficient separation of Ta(V) from Nb(V) was reached also in the experiments involving preliminary evaporation of the initial solution to remove excess hydrofluoric acid and subsequent dilution of the remaining solution (Table 2, run nos. 7 and 11).

To decrease the free hydrofluoric acid content in the solutions, we also introduced in them the metal cations capable of binding fluoride ions into poorly soluble compounds or strong complexes (Tables 3, 4). In these experiments, 45 g of HC or LC was added to 200 ml of HF-containing solution with stirring at 60°C. Introduction of these substances significantly decreases the HF_{free} concentration. An especially large effect was observed on treating the solutions with a loparite concentrate LC (rare-earth niobates), which is caused by binding of excess fluoride ions by titanium(IV) and rare-earth elements(III). A drawback of HC, consisting mainly of titanium(IV) hydroxide,

Table 3. Content of the target metals and HF species in the initial solution as influenced by treatment with hydrated cake (HC) and loparite concentrate (LC)

Solution	Concentration, M				
	Ta(V)	Nb(V)	Ti(IV)	HF_{tot}	HF_{free}
Initial solution	0.0168	0.406	3.72	22.7	5.3
After treatment with:					
HC	0.0145	0.093	4.25	17.7	0.1
LC	0.0201	0.381	4.13	17.9	<0.1

Table 4. Precipitation of excess fluoride ions with lanthanum and calcium carbonates*

Run no.	Reagent	Weight, g		Precipitation degree, %				$c_{HF_{free}}$ after precipitation, M
		reagent	precipitate	Ta(V)	Nb(V)	Ti(IV)	F^-	
1	$La_2(CO_3)_3 \cdot 6H_2O$	4.7	3.3	1.0	1.0	–	5.4 (7.1)**	2.2
2	$La_2(CO_3)_3 \cdot 6H_2O$	9.4	6.8	2.6	4.0	3.4	13 (14)	1.2
3	$CaCO_3$	2.5	3.1	1.8	1.4	–	4.9 (3.7)	4.2
4***	$CaCO_3$	2.5	4.2	2.6	1.8	–	6.7 (3.7)	3.7
5	$CaCO_3$	5.0	7.8	6.0	4.9	12.8	13 (7.4)	2.0

* Initial solution, M: run nos. 1 and 2, Ta(V) 0.0152, Nb(V) 0.305, Ti(IV) 2.40, HF_{tot} 14.5, and HF_{free} 3.0; run nos. 3–5, Ta(V) 0.0237, Nb(V) 0.509, Ti(IV) 4.51, HF_{tot} 26.8, and HF_{free} 5.5.

** In parentheses is the degree of precipitation of fluoride anions, calculated assuming that La(III) and Ca(II) are completely converted to LaF_3 and CaF_2, respectively.

*** Precipitated at ~0°C.

is precipitation of Ta(V), and especially Nb(V), caused by binding of fluoride ions into stronger insoluble titanium fluoride complexes [1].

Fluoride anions were precipitated in the form of poorly soluble fluorides of appropriate cations introduced in the solution in the form of their carbonates. Metal carbonates were gradually added with stirring to 50 ml of solution containing fluoride anions. The resulting slurry was kept for several hours and then filtered, washed with water, and dried at 100°C. As seen from Table 4 (run no. 4), with increasing carbonate amount and raising temperature, the degree of precipitation of fluoride anions increases and the HF_{free} content in the solution decreases. On precipitating fluoride ions by adding calcium carbonate, the degree of precipitation of fluoride ions exceeds that expected in the case that CaF_2 is formed only. We found that, under these conditions, the relatively large Ti(IV) amount is precipitated also (Table 4). X-ray phase analysis showed[1] that this precipitate is $CaTiF_6 \cdot 2H_2O$ containing CaF_2 as impurity (Fig. 1b, interplanar spacing 3.16 Å). At the same time, the X-ray pattern (Fig. 1a) shows that, in precipitation of fluoride anions by La(III) carbo- nate, LaF_3 is formed only. An IR study of the precipitates showed that they contain no CO_3^{2-} anions, i.e., fluoride anions completely replace carbonate anions in La(III) and Ca(II) carbonates. The use of $La_2(CO_3)_3$ (actually carbonates of the sum of rare-earth elements from processing of loparite) is preferable, because lanthanide fluorides are compounds of commercial interest. In this process, the loss of Ti(IV) considerably decreases (Table 4).

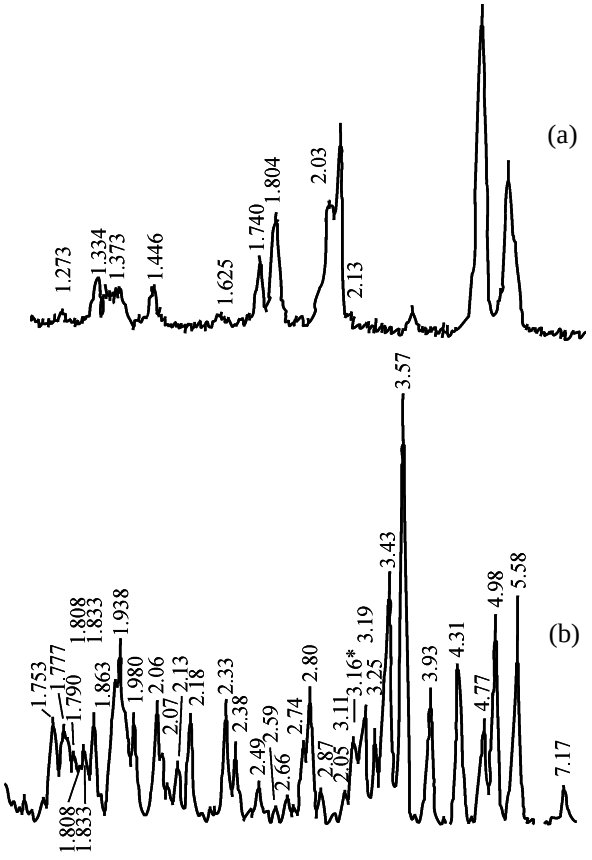

Fig. 1. X-ray diffraction patterns of (a) LaF_3 and (b) $CaTiF_6 \cdot 2H_2O$ (containing CaF_2 impurity) precipitated in treating the process solutions with $La_2(CO_3)_3$ and $CaCO_3$, respectively.

The procedures used for decreasing the free hydrofluoric acid concentration in Nb(V)- and Ta(V)-containing solutions have several drawbacks: increase in process solution volume due to dilution, power consumption in the evaporation stage, filtration of precipitates, and losses of Ta(V) and Nb(V) because of partial precipitation of their poorly soluble fluorides.

[1] X-ray diffraction patterns were obtained and treated by V.Ya. Kuznetsov.

Therefore, decomposition of rare-metal concentrate must be performed in a continuous countercurrent process with several equilibrium stages, similar to multistage continuous countercurrent extraction widely used in processing multicomponent aqueous solutions. The multistage flowsheet provides repeated recovery of the target metals from the intermediate partly decomposed concentrate with fresh portions of the decomposing solution at every decomposition stage. This decomposing solution contains a large excess of acid (hydrofluoric acid or a mixture of hydrofluoric and sulfuric acids). Multistage flowsheet is economically preferable owing to lower reagent consumption, and, what is more, to lower HF_{free} content in the process solution.

Model experiments on decomposition of the rare-metal concentrate using a two-stage batch flowsheet were carried out by the Alders technique [7]. Our results on distribution of Nb(V) and Ta(V) at different stages of the process are noted in the scheme. In experiments on multistage decomposition, we used a tantalite concentrate of the following chemical composition (wt %): Ta_2O_5 19.28, Nb_2O_5 26.26, SiO_2 3.89, WO_3 0.36, SnO_2 21.00, TiO_2 4.30, ZrO_2 0.50, Fe_2O_3 12.44, MnO 4.30, Al_2O_3 0.95, CaO 0.34, and MgO 0.42. Mineralogical analysis showed that the rare-metal concentrate contained also several other minerals as admixtures: columbite, cassiterite, zircon, rutile, monazite, sodium feldspar, and apatite.

Flowsheet of two-stage countercurrent decomposition of the rare-metal concentrate

Filtrate for extraction: 85 ml, 1.36 M Nb(V), 0.52 M Ta(V)	Intermediate filtrate: 117 ml, 0.58 M Nb(V), 0.20 M Ta(V)	Decomposing solution: 113.4 ml, 0 M Nb(V), 0 M Ta(V)
← → Decomposition no. 1	← → Decomposition no. 2	← →
Rare-metal concentrate: 63.0 g, 23.71 wt % Nb_2O_5, 10.47 wt % Ta_2O_5	Precipitate no. 1, intermediate: 35.35 g, 15.15 wt % Nb_2O_5, 13.14 wt % Ta_2O_5	Precipitate no. 2 for washing: 23.31 g, 2.51 wt % Nb_2O_5, 4.38 wt % Ta_2O_5

The rare-metal concentrate was decomposed with a solution containing HF (19.5 M) and H_2SO_4 (2 M). The HF consumption was 90% of the stoichiometric amount. The HF stoichiometric consumption was calculated assuming that the main metals are bound into fluoride complexes $HTaF_6$, $HNbF_6$, FeF_2, MnF_2, H_2SiF_4, AlF_3, and H_2TiOF_4. Taking into account that cassiterite remains virtually unchanged in our process, the HF consumption associated with tin complexing was neglected.

Decomposition of the rare-metal concentrate was carried out in a fluoroplastic vessel equipped with a lid and a mixer at the 1 : 1.8 ratio of the solid and liquid phases. A solution formed in the second decomposition stage was poured into the vessel, and then a fresh portion of the rare-metal concentrate was added at 60°C. After that the mixture was heated to the prescribed temperature and kept for 4 h with stirring. The liquid phase was separated from the precipitate and used for extractive recovery of Nb(V) from Ta(V). To increase the degree of recovery of the target metals, the precipitate remaining after the first decomposition stage was filtered and transferred to the second decomposition stage for treatment with a fresh portion of the $HF–H_2SO_4$ mixture under the conditions identical to those in the first decomposition stage. The final precipitate was washed with water. Under these conditions, a steady state was reached within four cycles.

In the course of decomposition of the rare-metal concentrate, the liquid phase volume decreases due to evaporation. After continuous two-stage counterflow decomposition, the weight of the rare-metal concentrate decreases by 63%. After the first decomposition stage, the washed precipitate contained 35.9% of Nb(V) and 70% of Ta(V) relative to the initial concentrate. After the second decomposition stage, these values decreased to 3.9 and 15.2% for Nb(V) and Ta(V), respectively. Thus, after the two-stage decomposition, 96.1% of Nb(V) and 84.8% of Ta(V) was removed from the concentrate (see flowsheet). Our calculation show that the three-stage decomposition scheme provides more than 99 and 98% recovery of Nb(V) and Ta(V), respectively, which meets the requirements of the industrial process. In passing from one-stage to countercurrent process, the Nb(V) and Ta(V) content in the final solutions increases, whereas the HF_{free} content decreases (<0 M). To increase the degree of recovery of the target metals in the one-stage process, a substantial excess of HF is required.

As reported in [2, 8], in the one-stage decomposi-

tion of the concentrate whose chemical compostion was close to that of the concentrate used in this work, the degree of recovery of Nb(V) and Ta(V) exceeded 97% only at the HF_{free} concentration higher than 1 M, which corresponds 100–120% consumption of HF relative to the stoichiometry. In extractive processing of this solution, Nb(V) and Ta(V) are extracted jointly.

As opposed to solutions formed after one-stage decomposition of the rare-metal concentrate, those formed in multistage decomposition contain the minimal amount of HF_{free} and, therefore, are suitable for selective recovery of Ta(V). For example, Ta(V) was selectively separated from Nb(V) in extraction with OCL at $V_o : V_{aq}$ ratio of 1 : 1. To improve the stability of the process solutions and prevent precipitation of the target metals, the initial solutions were diluted prior to extraction by a factor of 1.4. With increasing ratio of the organic and aqueous phases, the degree of recovery of Ta(V) increases from 82.1 to 88.6% and that of Nb(V), from 6.3 to 8.4%, which shows that the extraction system preserves high separation efficiency. Thus, our experiments showed that continuous countercurrent decomposition of the rare-metal concentrate allows efficient recovery of the target metals at decreased power and reagent consumptions.

CONCLUSION

(1) A decrease of the hydrofluoric acid concentration in the niobium- and tantalum-containing solutions by their dilution, evaporation, or precipitation of poorly soluble metal fluorides allows improvement of the extractive separation of tantalum(V) from niobium(V).

(2) Decomposition of the rare-metal concentrate in the continuous countercurrent mode allows production of the target metal solutions with a minimal content of fluoride anions.

REFERENCES

1. Babkin, A.G., Maiorov, V.G., and Nikolaev, A.I., *Ekstraktsiya niobiya, tantala i drugikh elementov iz ftoridnykh rastvorov* (Extraction of Niobium, Tantalum, and Other Elements from Fluoride-Containing Solutions), Leningrad: Nauka, 1988.
2. Maiorov, V.G., Kopkov, V.K., Baklanova, I.V., *et al.*, *Khim. Tekhnol.*, 2000, no. 7, pp. 23–27.
3. Maiorov, V.G., Nikolaev, A.I., and Kopkov, V.K., *Zh. Prikl. Khim.*, 1999, vol. 72, no. 6, pp. 929–932.
4. Maiorov, V.G., Nikolaev, A.I., and Kopkov, V.K., *Zh. Prikl. Khim.*, 2001, vol. 74, no. 3, pp. 357–360.
5. Maiorov, V.G., Nikolaev, A.I., and Kopkov, V.K., *Zh. Prikl. Khim.*, 1994, vol. 67, no. 2, pp. 329–331.
6. Sklokin, L.I., Zots, N.V., Shestakov, S.V., *et al.*, *Tsvetn. Met.*, 2000, no. 10, pp. 48–53.
7. Alders, L., *Liquid–Liqid Extraction. Theory and Laboratory Practice*, Amsterdam: Elsevier, 1959.
8. Baklanova, I.V., Maiorov, V.G., Kopkov, V.K., *et al.*, *Khim. Tekhnol.*, 2001, no. 2, pp. 28–32.

Russian Journal of Applied Chemistry, Vol. 75, No. 11, 2002, pp. 1753–1759. Translated from Zhurnal Prikladnoi Khimii, Vol. 75, No. 11, 2002, pp. 1789–1795.
Original Russian Text Copyright © 2002 by Lokshin, Vershkova, Vershkov, Tareeva.

INORGANIC SYNTHESIS AND INDUSTRIAL INORGANIC CHEMISTRY

Leaching of Lanthanides from Phosphohemihydrate with Nitric Acid

E. P. Lokshin, Yu. A. Vershkova, A. V. Vershkov, and O. A. Tareeva

Tananaev Institute of Chemistry and Technology of Rare Elements and Mineral Resources, Kola Scientific Center, Russian Academy of Sciences, Apatity, Murmansk oblast, Russia

Received May 29, 2002

Abstract—Factors were examined that determine passing of lanthanides into solution during nitric acid leaching of phosphohemihydrate obtained in the course of production of wet-process phosphoric acid from Khibiny apatite concentrate by the hemihydrate technique. The data obtained were compared to the results of sulfuric acid leaching.

It is known [1, 2] that, in the course of production of wet-process phosphoric acid from Khibiny apatite concentrate by treatment with sulfuric acid, the main part of lanthanides passes to the phase of dihydrate $CaSO_4 \cdot 2H_2O$, whereas in the hemihydrate process they pass to the phase of calcium sulfate hemihydrate $2CaSO_4 \cdot H_2O$. In practice, these calcium sulfates are usually termed phosphogypsum (PDH) and phosphohemihydrate (PHH), respectively, which underlines the fact that they were obtained by processing of phosphate raw material and have increased content of phosphates.

The leaching of lanthanides from them with nitric acid solutions was studied in [3, 4] (Table 1). Table 1 shows that 10–20% solutions of nitric acid (here and hereinafter, the concentrations are given in wt %) efficiently extract lanthanides from PDH; however, their content in the leaching solutions was low. When sulfuric acid was used, the extraction of lanthanides was much lower [5].

On leaching of rare-earth elements from PHH with solutions based on calcium nitrate, their extraction into solution was slightly increased (Table 2), but the REE concentration remained low [4].

The addition of calcium nitrate to nitric acid solutions somewhat increased the extraction and concentration of lanthanides (Table 2), in spite of the fact that the consumption of chemicals much exceeded the stoichiometric amount.

The 79.3% extraction of lanthanides from PHH was reached using a solution containing 60 g l^{-1} (5.8%) of HNO_3 and 70 g l^{-1} of $Ca(NO_3)_2$, l : s = 2–3. In this case, the solution contained (g l^{-1}): Ln_2O_3 1.28, P_2O_5 4.1, and fluoride ions 1.2 [6].

The leaching of lanthanides from precipitates formed by evaporation of wet-process phosphoric acid obtained by dihydrate processing of apatite from Phalaborwa deposit (Republic of South Africa) was studied in [7] (Table 3). The precipitates, which were carefully washed with water to remove phosphoric

Table 1. Conditions and results of lanthanide leaching with nitric acid

c_{HNO_3}, wt %	l : s	$\varepsilon_{Ln_2O_3}$, %	$c_{Ln_2O_3}$ in solution, g l^{-1}
PDH, Ln_2O_3 content 0.3–0.37% [3]*			
5	10	68.3	0.23
10	10	86.7	0.29
15	10	91.8	0.31
20	10	93.1	0.31
25	10	39.8	0.13
30	10	53.0	0.18
35	10	61.0	0.20
40	10	65.5	0.22
45	10	68.0	0.23
PHH, Ln_2O_3 content 0.57% [4]**			
2	1	6.0	0.31
2	2	11.9	0.28
2	3	18.5	0.31
2	4	17.5	0.21
2	5	25.5	0.25
2	10	39.6	0.19

* Leaching temperature and time were not reported.
** Leaching temperature 20°C, time 0.5 h.

1070-4272/02/7511-1753$27.00 © 2002 MAIK "Nauka/Interperiodica"

Table 2. Extraction of lanthanides from PHH (Ammofos Joint-Stock Company, Cherepovets) by leaching with solutions containing calcium nitrate [4]

l : s	Leaching solution, %			
	$Ca(NO_3)_2$, 5		HNO_3, 2 + $Ca(NO_3)_2$, 5	
	$c_{Ln_2O_3}$ in solution, g l^{-1}	$\varepsilon_{Ln_2O_3}$, %	$c_{Ln_2O_3}$ in solution, g l^{-1}	$\varepsilon_{Ln_2O_3}$, %
1	0.52	10.8	0.40	7.5
2	0.29	11.5	0.48	16.2
3	0.24	13.3	–	–
4	0.22	17.8	0.52	34.2
5	0.27	26.9	0.50	38.2
10	0.25	49.5	0.25	50.7

Table 3. Composition of solutions obtained from nitric acid leaching of the precipitate formed by evaporation of dihydrate wet-process phosphoric acid [7]

Leaching solution %		Concentration in solution, g l^{-1}				Ln_2O_3 extracted, %
HNO_3, %	$Ca(NO_3)_2$, M	Ln_2O_3	P_2O_5	Si	F	
6.3–8.8	0.45–0.58	16.3–20.3	12.5–36.9	0.7–1.9	3.8–7.1	65–78
3.6–4.5	1.75–2.50	4.1–6.9	2.3–8.9	1.3–2.2	3.9–8.4	46–76

acid, seem to be products based on anhydrite or PHH containing 2.8–8.3% of the sum of lanthanides. When a solution containing 2 M HNO_3 (11.8 %) and 0.5 M $Ca(NO_3)_2$ was used for leaching at the ratio l : s = 2 and temperature of 20°C, the Ln_2O_3 extraction reached 76%. The extraction increased as the HNO_3 concentration increased from 1 to 3 M, but decreased at the concentration of 4.5 M. The temperature rise from 0 to 100°C reduced the extraction by a factor of more than 13, with the concentrations of Si(IV) and fluoride ions in leaching solution increasing. When temperature was increased from 20 to 100°C, the concentration of Si(IV) increased from 0.12 to 0.20 M, and the concentration of fluoride ions, from 0.64 to 0.97 M. If $Ca(NO_3)_2$ was not added to the solution (<0.5 M), only 33% of lanthanides was extracted at 20°C. In enlarged tests, leaching conditions were considerably changed, but the results did not become worse (Table 3).

Preston *et al*. [7] assumed that the effect of calcium ions consists in binding of fluoride ions present in leaching solutions by the reactions

$$HF = H^+ + F^-, \quad (1)$$

$$SiF_6^{2-} = SiF_4 + 2F^-, \quad (2)$$

$$Ca^{2+} + 2F^- = CaF_2\downarrow, \quad (3)$$

preventing formation of poorly soluble lanthanide fluorides:

$$Ln^{3+} + 3F^- = LnF_3. \quad (4)$$

The addition of aluminum and iron(III) compounds to the nitric acid leaching solution had no effect on the extraction of lanthanides.

Preston *et al*. also proposed another explanation of the increase in the extraction in the presence of calcium ions [7], according to which a high concentration of calcium ions in solution favors the ion-exchange extraction of lanthanides from calcium sulfate in which lanthanides isomorphously substitute calcium ions. However, it does not account for a sharp decrease in the extraction of lanthanides as the leaching temperature is increased to 100°C.

Thus, as a rule, the high extraction of lanthanides in solution was reached at medium concentrations of nitric acid and high l : s ratios, but in this case the resulting solutions were difficult to process further because of their large volumes and low concentrations of lanthanides in them. The extraction of lanthanides from such solutions is rather expensive, being complicated by a high content of calcium ions. The low concentration of lanthanides in leaching solution, the

attainment of reasonable extraction only at high l : s ratios, and also a sharp decrease in the extraction of lanthanides from PDH with increasing concentration of nitric acid from 20 to 25% remain to be explained.

As the hemihydrate process, which is more economically expedient than the dihydrate process, is widely used in Russia, we studied the factors limiting the extraction and concentration of lanthanides in solutions in their nitric acid leaching from PHH. Furthermore, the interest in these studies has increased because, except for higher content of lanthanides in PHH as compared to PDH [1, 2] (Table 4), the sum of lanthanides extracted from PHH is enriched with yttrium and middle-group lanthanides.

EXPERIMENTAL

In the work, we used PHH from Voskresenskie Mineral'nye Udobreniya (Voskresensk Mineral Fertilizers) Joint-Stock Company with the 10–11 wt % moisture content. The content of lanthanides in this product appeared to be lower (0.43–0.53%) than in PHH from Ammofos Joint-Stock Company (0.57%). The experimental technique was described earlier [5].

Treatment of PHH for 1 h with 2% nitric acid (Table 5) resulted in higher extraction and concentration of lanthanides than those reached in [4] (Table 1). Increase in the concentration and extraction of lanthanides were attained when the concentration of nitric acid was increased to 8%; in this case, a considerable amount of PHH passed into solution (as in the case of PDH dissolution in nitric acid [8], the content of CaO and SO_3 corresponded to $CaSO_4$). Fairly high extraction of lanthanides was reached even with 4% HNO_3: in this case, 4.64% of PHH passed into the solution.

Lanthanide nitrates are readily soluble in nitric acid solutions, including highly concentrated solutions [9]. Therefore, we examined the possibility of increasing the concentration of lanthanides by using the same portion of a leaching solution for successive processing of several PHH portions. However, in this case the efficiency of leaching lanthanides sharply decreased, even when nitric acid was added to the solution (Table 6).

The concentration of lanthanides in solution increased and reached 2.14 g l^{-1}. As the solution contained a significant amount of calcium sulfate after the first treatment stage, the dissolution of PHH sharply decreased as the concentration of nitric acid increased only slightly.

Table 4. Composition of the sum of lanthanides extracted in the nitric acid leaching of PDH [3] and PHH [4] obtained from processing of Khibiny apatite concentrate

Oxide	Ln_2O_3 contents, wt %	
	PDH	PHH
Y_2O_3	2.61	5.2–6.7
La_2O_3	28.57	24.1–29.0
Ce_2O_3	46.9	41.2–43.7
Pr_6O_{11}	3.92	Not determined
Nd_2O_3	13.24	Not determined
Sm_2O_3	1.42	1.8–2.5
Eu_2O_3	0.41	0.86–0.90
Gd_2O_3	0.97	Not determined
Tb_4O_7	1.22	Not determined
Dy_2O_3	0.40	1.35–1.49
Ho_2O_3	0.06	Not determined
Er_2O_3	0.21	Not determined
Tm_2O_3	0.011	Not determined
Yb_2O_3	0.049	Not determined
Lu_2O_3	0.005	Not determined

Table 5. Nitric acid leaching of lanthanides from PHH (s : l = 1 : 3, 1 h, Ln_2O_3 content 0.43%)

HNO_3 %	Concentration in solution, g l^{-1}		Extracted, %	
	Ln_2O_3	Ca(Sr)O	Ln_2O_3	Ca(Sr)O
2	0.76	3.81	53.0	2.96
4	1.10	5.97	76.7	4.64
6	1.15	7.87	80.2	6.11
8	1.20	8.10	83.7	6.30

In successive acid leaching of the same PHH portion by fresh portions of nitric acid (Table 7), we were able to transfer into solution a total of 96.28% of REE, but only 7.82% of Ca(Sr)O contained in PHH. This proves the fact that the main part of lanthanides is not cocrystallized isomorphously with PHH [10] and exists in it as independent phases.

Preliminary washing of PHH with water (l : s = 2, 0.5 h) allowed us to increase the extraction of lanthanides in the single-stage leaching with 2–6 wt % solutions of HNO_3 (Table 8). Passing of calcium sulfate into solution increased simultaneously, which is due to the conversion of PHH to PDH in solution during washing with water and, probably, to the higher solubility of PDH in nitric acid solutions.

Grinding of PSH before leaching sharply increased the extraction of lanthanides.

Table 6. Nitric acid leaching of lanthanides from PHH with reuse of leaching solution (l : s = 1 : 3, 1 h, Ln_2O_3 content 0.53%)

Stage	HNO_3, %	Concentration in solution, g l^{-1}					Ln_2O_3 extracted, %
		Na_2O	K_2O	P_2O_5	Ca(Sr)O	Ln_2O_3	
1	4	0.82	0.165	3.38	5.52	0.80	45.3
2	4 + 1	1.46	0.331	6.12	5.92	1.34	30.5
3	4 + 1 + 1	2.14	0.440	8.77	6.28	1.82	27.2
4	4 + 1 + 1 + 1	2.50	0.537	10.63	6.77	2.14	18.1

Table 7. Successive treatment of the same PHH portion with two portions of the fresh acid (l : s = 1 : 3, 1 h, Ln_2O_3 content 0.43%)

Stage	HNO_3, %	Concentration in solution, g l^{-1}		Extracted, %	
		Ca(Sr)O	Ln_2O_3	Ca(Sr)O	Ln_2O_3
1	4	5.04	1.03	3.91	71.86
2	4	5.04	0.35	3.91	24.42

Table 8. Nitric acid leaching of lanthanides from PHH (s : l = 1 : 3, 1 h, Ln_2O_3 content 0.53%)

PHH	HNO_3, %	Concentration in solution, g l^{-1}		Extracted, %	
		Ca(Sr)O	Ln_2O_3	Ca(Sr)O	Ln_2O_3
Initial	2	4.09	0.34	3.0	19.2
	4	5.68	0.65	4.1	36.8
	6	6.86	0.67	5.0	37.9
Washed with water	2	4.42	0.57	3.2	32.3
	4	6.38	0.71	4.6	40.2
	6	8.02	0.77	5.8	43.6
Initial*	6	8.48	1.02	6.2	57.7
Washed with water*	6	8.68	1.49	6.3	84.3

* PHH was preliminarily ground.

We have studied the effects of various additives on the efficiency of the nitric acid leaching (Tables 9, 10).

The expected effect of additives was either salting-out of sodium and potassium hexafluorosilicates with sodium and potassium compounds or binding of fluoride ions in stable complexes and poorly soluble compounds (excess of calcium ions). In this case, we took into account the following series of stability of complex fluorides in solutions: $SiF_6^{2-} < AlF_6^{3-} < BF_4^-$ [11].

Our and published data suggest that, for leaching lanthanides from PHH, it is sufficient to use solutions containing 4–6% HNO_3. Increase in the l : s ratio and also in leaching time favors the extraction. This fact agrees with the data of Kuzina *et al*. [12], who showed that the hydrated orthophosphates of lanthanides (Ce, La, and Nd) slowly dissolve in 1.5–5 M HNO_3.

We can assume that, when $Ca(NO_3)_2$ solutions are used, lanthanides are leached with a dilute solution of nitric acid formed by the reaction of calcium nitrate with sulfuric and phosphoric acids remaining in PHH after washing. It is likely that the leaching of lanthanides from PHH with calcium nitrate can be described by the reactions

$$Ca(NO_3)_2 + H_2SO_4 = 2HNO_3 + CaSO_4\downarrow, \quad (5)$$

$$3Ca(NO_3)_2 + 4H_3PO_4 = 6HNO_3 + Ca(H_2PO_4)_2 + 2CaHPO_4, \quad (6)$$

$$2LnPO_4 \cdot 0.5H_2O + 6HNO_3 = 2Ln(NO_3)_3 + 2H_3PO_4 + H_2O, \quad (7)$$

Table 9. Effect of additives on the efficiency of nitric acid leaching of lanthanides from PHH (s : l = 1 : 3, 1 h, Ln_2O_3 content 0.53%)

PHH	Composition of leaching solution		Concentration in solution, g l^{-1}		Extracted, %	
	HNO_3, %	additive, g l^{-1}	Ln_2O_3	Ca(Sr)O	Ln_2O_3	Ca(Sr)O
Initial	6	–	0.67	6.86	37.9	5.00
Washed with water	6	–	0.77	8.02	43.6	5.84
	6	25 $H_2B_4O_7$	0.77	Not determined	43.6	Not determined
	6	7 $Al(NO_3)_3$	0.7	7.86	39.6	4.21
Washed with water*	6	25 $Na_2B_4O_7$	1.71	8.10	96.8	4.34
Initial	1	3 Na_2SO_4	0.63	4.79	35.7	2.57
	6	3 Na_2SO_4	0.64	6.05	36.2	3.24
	6	51 $Ca(NO_3)_2$	0.82	Not determined	46.4	–
Initial**	6	3 Na_2SO_4	0.79	9.20	44.7	4.93

* PHH was preliminarily ground.
** Leaching time 1.5 h.

$$MeLn(SO_4)_2 + 4HNO_3 = Ln(NO_3)_3 + MeNO_3 + H_2SO_4. \quad (8)$$

Lanthanides were not leached with calcium nitrate solutions from PHH that had been carefully washed with water.

In the case of the single-stage process, lanthanides are leached with nitric acid solutions from PHH or PDH more effeciently than with sulfuric acid solutions [5], as not only lanthanide phosphates, but also their double sulfates (first of all those of lanthanum and cerium) with alkali metals are readily soluble in nitric acid [13]. Furthermore, the solubility of hydrated forms of calcium sulfate in nitric acid is much higher than in sulfuric acid, which facilitated the access of leaching solution to the grains of an REE-enriched phase covered by a PDH or PHH crust. The presence of such crusts is confirmed by the fact that the extraction of lanthanides under similar leaching conditions is much higher from an additionally ground PHH sample, as compared to a sample that was not subjected to such a treatment (Tables 8, 9).

When the same portion of nitric acid solution was used for successive leaching of several portions of PHH, lanthanides were accumulated more slowly than with the use of sulfuric acid solutions. Probable reasons are a decrease in the solubility of lanthanide nitrates in nitric acid solutions in the presence of calcium sulfate; a decrease in dissolution of calcium sulfate in the second and subsequent stages due to saturation of the leaching solution with it even in the first stage; and the lower concentration of nitric acid used in the experiments.

The concentration of calcium sulfate in nitric acid leaching solutions increases with increasing concentration of nitric acid [8]. This hinders the subsequent isolation of lanthanides from the solutions.

It is difficult to explain a sharp decrease in the extraction of lanthanides from PDH at HNO_3 concentration in the leaching solution of about 25% [3]. This is hardly due to precipitation of lanthanides in the form of fluorides [reactions (1), (2), and (4)]. This decrease is attributable to the fact that the process was carried out at elevated temperature (~80–90°C), and it was accompanied by the conversion of PDH to PHH [14], which could make the leaching of lanthanides more difficult.

We have calculated the equilibrium concentrations of fluoride ions in HNO_3 solutions at room temperature assuming that the activity of the ions in solutions is equal to their concentration and that the solubility of Na_2SiF_6 in nitric acid solutions is equal to its solubility (0.7%) in water. We took into account the

Table 10. Effect of potassium salts on the efficiency of nitric acid leaching of lanthanides from "fresh" PHH (s : l = 1 : 3, 1 h, Ln_2O_3 content 0.43%, HNO_3 concentration 4 wt %)

Additive, g l^{-1}	$c_{Ln_2O_3}$ in solution, g l^{-1}	Ln_2O_3 extracted, %
–	1.10	76.8
KCl:		
3	1.18	82.3
5	1.04	72.5
K_2SO_4, 5.8	1.01	70.5

overall reaction of SiF_6^{2-} hydrolysis

$$SiF_6^{2-} + 2H_2O = SiO_2 + 4H^+ + 6F^-.$$

Several authors have found its equilibrium constant to be within 10^{-27}–10^{-28} [15]. In our calculations we accepted the maximal value $K = a_{H^+}^4 a_{F^-}^6 / a_{SiF_6^{2-}} = 2.3 \times 10^{-27}$, as in this case the equilibrium content of fluoride ions in solution is the highest. The calculated data are given below:

c_{HNO_3}, %	1	2	4	6	8	10
c_{F^-}, mg l^{-1}	2.5	0.86	0.54	0.41	0.36	0.29

According to these data, the concentration of fluoride ions formed by hydrolysis of SiF_6^{2-} in nitric acid solutions at room temperature is very small. Comparison with the data of [16] suggests that lanthanide fluorides should not precipitate in the course of nitric acid leaching of PHH or PDH. It is probable that the hydrolysis of SiF_6^{2-} ions increases with temperature to such an extent that the concentration of fluoride ions becomes sufficient for the formation of lanthanide fluorides. This can account for a sharp decrease in the degree of leaching of lanthanides at 50–100°C, which was observed in [7] for nitric acid leaching solutions containing up to 12.2 g l^{-1} fluoride ions at room temperature.

The addition of sodium and potassium salts (sodium and potassium sulfates and potassium chloride), which salt-out sodium and potassium hexafluorosilicates, did not increase the lanthanide leaching efficiency. With sodium and potassium sulfates added, the passing of lanthanides into solution was slightly reduced, apparently at the expense of decreasing solubility of calcium sulfate crusts blocking the grains of lanthanide-rich phases (Tables 9, 10).

An essential increase in the extraction with sodium tetraborate added (Table 9) is attributable to preliminary regrinding of PHH, which made the grains of REE-rich phases accessible for the solution. The addition of boric acid or aluminum nitrate did not change the degree of lanthanide leaching. Addition of calcium nitrate did not noticeably affect the leaching of lanthanides from PHH (in contrast to the data of [7]). Finally, high content of phosphate and fluoride ions in nitric acid leaching solutions, which considerably exceeded their content reached in the sulfuric acid leaching of PHH, did not hinder attainment of a high concentration of lanthanides.

An essential drawback of the nitric acid process of lanthanide extraction is that removal of nitrate ions from phosphogypsum to the required degree is difficult. The permissible content of nitrate ions in nonutilizable waste is much lower than that of sulfate ions. It is also necessary to examine the possibility of reusing nitric acid solutions in leaching of PHH after isolation of lanthanides from them, as these solutions are difficult to utilize at plants processing Khibiny apatite concentrate by the sulfuric acid technique.

CONCLUSION

(1) In the single-stage process, nitric acid leaches lanthanides from phosphohemihydrate more effecient-ly than sulfuric acid. The higher degree of extraction is due to high solubility of double sulfates of lanthanides (first of all, of cerium and lanthanum) with sodium and potassium in nitric acid solutions and also to elevated solubility of calcium sulfate in nitric acid.

(2) The accumulation of lanthanides in the case when the same portion of solution is reused for successive leaching of several PHH portions is less intense in nitric acid solutions than in sulfuric acid solutions.

(3) The impurity composition of phosphohemihydrate (phosphate ions and sodium and potassium hexafluorosilicates) affects the efficiency of lanthanide leaching with nitric acid leaching solutions to a lesser extent than with sulfuric acid solutions.

(4) The efficiency of lanthanide leaching from nitric acid solutions, as well as from sulfuric acid solutions, sharply decreases if grains of the phases enriched with lanthanides are blocked by a calcium sulfate crust. Such a crust seems to be formed owing to unstable course of the hemihydrate decomposition of the apatite concentrate.

ACKNOWLEDGMENTS

The work was financially supported by the Leading Scientific Schools program (project no. 00-15-97364).

REFERENCES

1. Lebedev, V.N., Masloboev, V.A., Popova, L.A., and Serkova, L.P., in *Problemy effektivnogo ispol'zovaniya mineral'nogo syr'ya Kol'skogo poluostrova* (Problems of Efficient Utilization of Mineral Resources of the Kola Peninsula), Apatity: Kol'sk. Nauchn. Tsentr, Ross. Akad. Nauk, 1993, pp. 43–49.
2. Kazak, V.G., Angelov, A.I., and Zaitsev, P.M., *Khim. Prom–st.*, 1995, no. 9, pp. 11–19.

3. Kijkowska, R. and Pawlowska-Kozinska, D., *Prage Nauk. Inst. Techn. Niorg. Nawoz. Mineral. P. Wroch.*, 1986, no. 30, pp. 17–26.
4. Lebedev, V.N., Smirnova, I.P., Masloboev, V.A., and Mikhlin, E.B., in *Fiziko-khimicheskie i tekhnologicheskie problemy pererabotki syr'ya Kol'skogo poluostrova* (Physicochemical and Technological Problems of Processing of Resources of the Kola Peninsula), St. Petersburg: Nauka, 1993, pp. 56–60.
5. Lokshin, E.P., Vershkov, A.V., and Vershkova, Yu.A., *Metally*, 2001, no. 1, pp. 42–50.
6. Kosynkin, V.D., Shatalov, V.V., Selivanovskii, A.K., *et al.*, *Khim. Tekhnol.*, 2001, no. 1, pp. 27–36.
7. Preston, J.S., Cole, P.M., Craig, W.M., and Feather, A.M., *Hydrometallurgy*, 1996, vol. 41, no. 1, pp. 1–19.
8. Karmyshev, V.F., Popova, V.A., and Zakharova, M.I., *Zh. Prikl. Khim.*, 1982, vol. 55, no. 4, pp. 904–905.
9. Protsenko, P.I., Razumovskaya, O.N., and Brykova, N.A, *Spravochnik po rastvorimosti nitritnykh i nitratnykh solevykh sistem* (Handbook on Solubility of Nitrite and Nitrate Salt Systems), Leningrad: Khimiya, 1971.
10. Lokshin, E.P., Vershkov, A.V., Vershkova, Yu.A., *et al.*, Abstracts of Papers, *Nauchnaya konferentsiya "Khimiya i khimicheskaya tekhnologiya v osvoenii prorodnykh resursov Kol'skogo poluostrova"* (Scientific Conf. "Chemistry and Chemical Technology in Development of Natural Resources of the Kola Peninsula"), Apatity: Kol'sk. Nauchn. Tsentr, Ross. Akad. Nauk, September 22–24, 1998, pp. 31–32.
11. Chepelevetskii, M. and Bol'ts, Ts., *Zh. Prikl. Khim.*, 1937, vol. 10, no. 7, pp. 1183–1193.
12. Kuzina, T.I., Slivko, T.A., and Komissarova, L.N., *Izv. Vyssh. Uchebn. Zaved., Tsvetn. Metall.*, 1994, no. 1–2, pp. 68–70.
13. Bobrik, V.M., *Radiokhimiya*, 1977, vol. 19, no. 5, pp. 606–610.
14. Gol'dinov, A.L., Kopylev, B.A., Abramov, O.B., and Dmitrievskii, B.A., *Kompleksnaya azotnokislotnaya pererabotka fosfatnogo syr'ya* (Complex Nitric Acid Processing of Phosphate Raw Materials), Leningrad: Khimiya, 1982.
15. Ryss, I.G., *Khimiya ftora i ego neorganicheskikh soedinenii* (Chemistry of Fluorine and Its Inorganic Compounds), Moscow: Goskhimizdat, 1956.
16. Menon, M.P. and James, J., *J. Chem. Soc., Faraday Trans.*, 1989, vol. 85, no. 9, pp. 2683–2694.

Russian Journal of Applied Chemistry, Vol. 75, No. 11, 2002, pp. 1760–1764. Translated from Zhurnal Prikladnoi Khimii, Vol. 75, No. 11, 2002, pp. 1796–1800.
Original Russian Text Copyright © 2002 by Kalinnikov, Makarov, Tikhomirova, Elizarova, Kuznetsov.

INORGANIC SYNTHESIS AND INDUSTRIAL INORGANIC CHEMISTRY

Hydrofluoride Synthesis of Fluorides of Some Rare-Earth Elements

V. T. Kalinnikov, D. V. Makarov, E. L. Tikhomirova, I. R. Elizarova, and V. Ya. Kuznetsov

Tananaev Institute of Chemistry and Technology of Rare Elements and Mineral Resources, Kola Scientific Center, Russian Academy of Sciences, Apatity, Murmansk oblast, Russia

Received April 15, 2002

Abstract—Thermal gravimetric, X-ray phase, IR spectroscopic, and chemical analyses were applied to study the reaction of yttrium and neodymium oxides with NH_4HF_2.

Fluorides of rare-earth elements (REE) are used in electrochemical recovery of these metals by electrolysis of molten salts and in production of glasses for active and passive waveguides; they are of interest for production of laser media based on complex REE fluorides [1–4].

A study of the reaction of REE oxides with ammonium hydrofluoride, including identification of the intermediates, is of interest not only for controlling the process, but also for developing and optimizing the hydrofluoride synthesis of complex fluorides of the composition $M_mLn_nF_{m+3n}$, where M is an alkali metal and Ln is an REE, to be used as stock for growth of single crystals.

A disadvantage of the conventional method for obtaining REE fluorides by precipitation from solution is the relatively high content of oxygen-containing anionic impurities.

Use of ammonium hydrofluoride as a fluorinating agent has a number of advantages, since NH_4HF_2 is close in reactivity to anhydrous hydrogen fluoride, is inexpensive, and can be readily dehydrated and regenerated from gaseous components, and reactions involving this agent can be carried out without complex equipment [5–7].

Despite extensive published data on hydrofluoride synthesis of REE fluorides, there is no common opinion concerning the scheme of the reactions in the literature. Therefore, we performed in this work a detailed study of reactions of yttrium and neodymium oxides with ammonium hydrofluoride and examined the composition and order of thermal decomposition of the intermediates formed. In addition, the methods for obtaining yttrium, neodymium, and gadolinium fluorides by (a) hydrofluoride synthesis and (b) precipitation from solutions were compared with respect to the concentration of oxygen-containing anionic impurities in the final products.

As starting substances we used REE oxides of analytically pure grade and twice recrystallized NH_4HF_2 of the same grade. Thermogravimetric studies were carried out on a Q-1500D derivatograph in platinum crucibles, with weighed portions of 350–400 mg. As reference served calcined Al_2O_3. Measurements were done in dynamic and quasi-isothermal modes at a heating rate of 5 deg min^{-1}. X-ray phase analysis was carried out on a DRON-3 diffractometer with CuK_α radiation. IR absorption spectra were recorded on a UR-20 spectrophotometer. Chemical analysis for fluoride ions was performed by pyrohydrolysis followed by potentiometric determination (with F^--selective electrode). Analysis for metals was done by flame emission spectrometry. The content of ammonia was determined by the Kjeldahl method. The concentrations of oxygen-containing anionic impurities in the final synthesis products was found using linear voltammetry in halide melts [8]. The measurements were done under isothermal conditions in an argon atmosphere. The fluorides synthesized were introduced into a KCl–KF melt of eutectic composition. A glassy carbon (SU-2000) crucible with the melt was placed in a hermetically sealed stainless steel retort. The crucible simultaneously served as a counterelectrode. Molybdenum was used as material of the quasi-reference electrode. Voltammograms were measured on a glassy carbon (SU-2000) electrode using an Autolab computerized electrochemical

1070-4272/02/7511-1760$27.00 © 2002 MAIK "Nauka/Interperiodica"

complex. The residual current densities found from voltammograms of the supporting melt characterized its purity; for oxygen, these current densities were about 5 mA cm^{-2}.

In [9], complex yttrium fluorides were studied thermogravimetrically, and it was demonstrated that the reaction of Y_2O_3 with NH_4HF_2 starts at 60–80°C to give $NH_4Y_2F_7 \cdot NH_4F$, which dissociates into $NH_4Y_2F_7$ and yttrium trifluoride upon heating. In [10], no formation of $NH_4Y_2F_7 \cdot NH_4F$ in the reaction of Y_2O_3 with NH_4F was observed, but yttrium compounds of the composition $(NH_4)_3Y_2F_9$ and $NH_4Y_2F_7$ were synthesized.

A thermogram of a mixture of Ln_2O_3 with NH_4HF_2 in 1 : 6 molar ratio is shown in Fig. 1a. The reaction is accompanied by a series of exo- and endothermic effects. The endothermic effect at 145°C can apparently be attributed to melting of ammonium hydrofluoride, which intensifies the reaction. At 236°C, excess NH_4HF_2 boils, giving an endothermic peak in the DTA curve. Hydrofluorination is complete at a temperature of about 350°C.

To elucidate the scheme of the reaction between Y_2O_3 and NH_4HF_2, we also performed measurements in the quasi-isothermal mode. Figure 2a shows a typical thermogravigram of a mixture of Y_2O_3 and NH_4HF_2 in 1 : 4.5 molar ratio, in which three plateaus can be observed. An analysis of the experimental Δm values corresponding to each of the plateaus revealed the following scheme of the process:

$$Y_2O_3 + 4.5NH_4NF_2 \rightarrow (NH_4)_3Y_2F_9 + 1.5NH_3 + H_2O, \quad (1)$$

$$(NH_4)_3Y_2F_9 \rightarrow NH_4Y_2F_7 + 2NH_3 + 2HF, \quad (2)$$

$$NH_4Y_2F_7 \rightarrow 2YF_3 + NH_3 + HF. \quad (3)$$

The theoretical weight losses corresponding to each stage of synthesis and amounting to, respectively, 16.5, 31.8, and 39.5 wt % are in good agreement with the experimental values (Fig. 2a).

The products formed at 170, 250, and 350°C were analyzed by the methods mentioned above; the results obtained confirmed the reaction scheme represented by Eqs. (1)–(3).

Figure 3 shows X-ray diffraction patterns of $Y_2O_3 : NH_4HF_2$ mixtures with the molar ratio of 1 : 4.5, measured at different temperatures. The results of X-ray phase analysis of the products formed at 170 and 250°C (Figs. 3a, 3b) are in good agreement with [10] and indicate formation of, respectively,

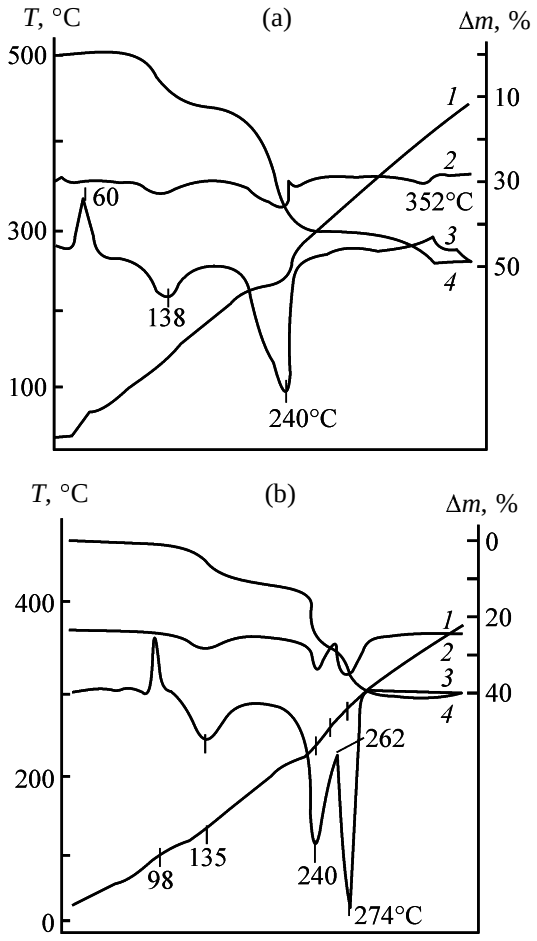

Fig. 1. Thermograms of Ln_2O_3 mixed with NH_4HF_2 in 1 : 6 molar ratio: (T) temperature and (Δm) weight loss; the same for Fig. 2. (a) Yttrium oxide and (b) neodymium oxide.

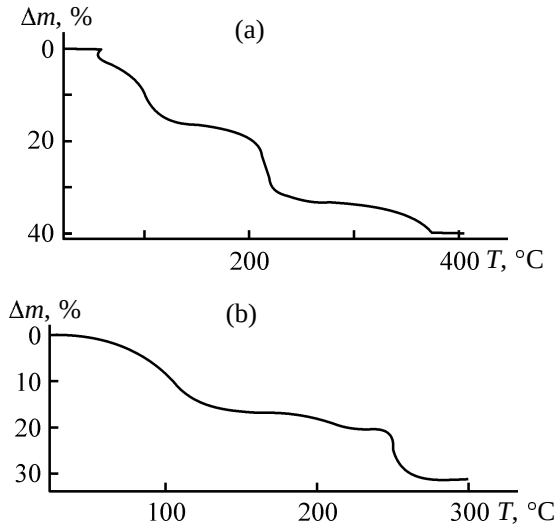

Fig. 2. Thermograms of Ln_2O_3 mixed with NH_4HF_2: (a) yttrium oxide, 1 : 4.5 molar ratio, and (b) neodymium oxide, 1 : 4 molar ratio.

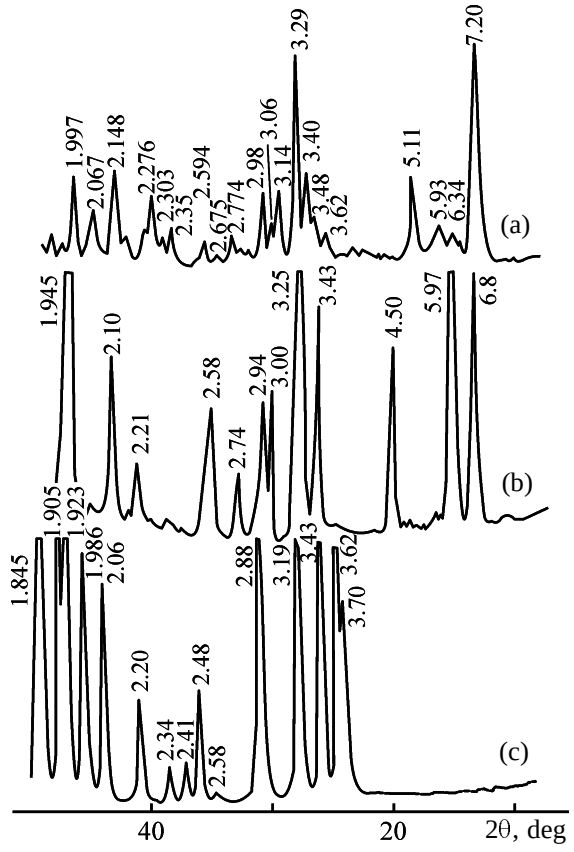

Fig. 3. X-ray diffraction patterns of reaction products formed from a $Y_2O_3 : NH_4HF_2 = 1 : 4.5$ mixture. (2θ) Bragg angle. (a) $(NH_4)_3Y_2F_9$, synthesis temperature 170°C; (b) $NH_4Y_2F_7$, 250°C; and (c) YF_3, 350°C.

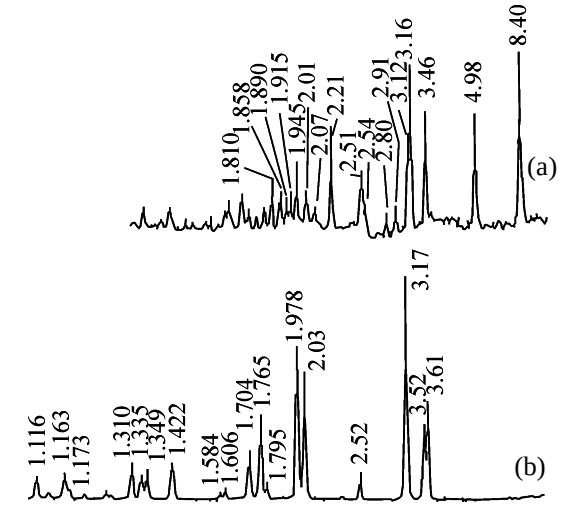

Fig. 4. X-ray diffraction patterns of reaction products formed from an $Nd_2O_3 : NH_4HF_2 = 1 : 4.5$ mixture. (a) NH_4NdF_4, synthesis temperature 150°C, and (b) NdF_3, 250°C.

$(NH_4)_3Y_2F_9$ and $NH_4Y_2F_7$. Figure 3c presents an X-ray diffraction pattern of yttrium trifluoride formed at 350°C.

The results of chemical analysis of intermediate synthesis products also confirm the formation of $(NH_4)_3Y_2F_9$ and $NH_4Y_2F_7$.

Data on the reaction of Nd_2O_3 with ammonium trifluoride were reported in [10], where a compound of the composition NH_4NdF_4 was obtained by keeping a mixture of Nd_2O_3 and NH_4F at 130–150°C for 1–3 days. Rakov presented in his review [6] data obtained by Polish researchers who established that this reaction proceeds in stages to give, in the first stage, the compound $(NH_4)_3NdF_6$, and then, at 350–400°C, NH_4NdF_4, which decomposes at 500°C to yield NdF_3 [6].

A thermogram of a mixture of Nd_2O_3 and NH_4HF_2 in 1 : 6 molar ratio is shown in Fig. 1b. The reaction, accompanied by a series of endo- and exothermic effects, is complete at temperatures higher than 270°C.

The results obtained in studies in the quasi-isothermal mode are presented in Fig. 2b. The thermogravigram of a mixture of Nd_2O_3 and NH_4HF_2 in 1 : 4 molar ratio is characterized by the presence of two plateaus. With account of the experimental values of Δm corresponding to each plateau, the presumed scheme of the process is as follows:

$$Nd_2O_3 + 4NH_4HF_2 \rightarrow 2NH_4NdF_4 + 3H_2O + 2NH_3, \quad (4)$$

$$2NH_4NdF_4 \rightarrow 2NdF_3 + 2NH_3 + 2HF. \quad (5)$$

The theoretical weight losses of 15.6 and 28.7 wt %, corresponding to reactions (4) and (5), are in good agreement with the experimental values (Fig. 2b).

The products of synthesis at temperatures corresponding to the plateaus in the thermogravimetric curve were subjected to X-ray phase analysis. X-ray diffraction patterns of $Nd_2O_3 : NH_4HF_2$ mixtures with the molar ratio of 1 : 4 at 150 and 250°C are shown in Fig. 4. The X-ray diffraction pattern of the product formed at 150°C is in agreement with the results of [10] and indicates the formation of NH_4NdF_4.

As an example of the measurements performed, the table presents the results obtained in determining oxygen in gadolinium fluoride, together with summarized data on the content of oxygen in yttrium and neodymium fluorides prepared by different methods.

With increasing content of gadolinium, neodymium, and yttrium oxides in the melt, the peak corresponding to the oxidation wave of oxygen-containing

Content of oxygen in REE fluorides

Method of LnF_3 synthesis	$(KCl–KF)_{eut}–LnF_3$ melt			Content in LnF_3		
	LnF_3, wt %	j_p^a, mA cm^{-2}	Ln_2O_3, $c \times 10^2$, wt %	Ln_2O_3, wt %	O_2	
					wt %	$c \times 10^4$, mol %
Gadolinium fluoride						
Hydrofluoride:						
in air	0.867	2.042	0.851	0.981	0.129	0.964
in air with repeated fluorination	0.331	0.341	0.116	0.350	0.046	0.343
in inert atmosphere	0.579	0.214	0.073	0.126	0.017	0.124
Precipitation from solution with subsequent calcination in a vacuum	0.708	1.203	0.409	0.578	0.076	0.568
LnF_3 of ultrapure grade	3.376	5.728	1.948	0.577	0.076	0.568
Yttrium fluoride						
Hydrofluoride:						
in air	0.487	1.057	2.736	5.623	1.195	13.124
in air with repeated fluorination	0.699	0.528	1.368	1.956	0.416	4.565
in inert atmosphere	0.848	0.264	0.684	0.807	0.172	1.884
Neodymium fluoride						
Hydrofluoride:						
in air	0.878	27.590	38.680	43.959	6.273	52.942
in air with repeated fluorination	1.239	4.109	5.761	4.642	0.663	5.596
in inert atmosphere	1.960	0.839	1.176	0.600	0.0856	0.723

halide complex of a rare-earth metal in voltammograms measured at polarizing voltage sweep rate of 0.1 V s^{-1} becomes more pronounced. Figure 5a shows a typical family of curves for the above process, measured with gadolinium oxide added to the melt. On reaching the limiting solubility of REE oxide (gadolinium oxide in the given case), the anode current at the peak corresponding to oxidation of the oxygen-containing halide complex levels off (Fig. 5a, curves *5*–*7*). The dependences $j_p^a = f([Ln_2O_3])$ show a portion corresponding to constant j_p^a (Fig. 5b). The initial linear portion (before leveling-off of the anode current) is described by the equations

$$j = 294.020c \text{ for gadolinium oxide,} \quad (6)$$

$$j = 38.617c \text{ for yttrium oxide,} \quad (7)$$

$$j = 71.323c \text{ for neodymium oxide,} \quad (8)$$

where j is the anode current density at the peak corresponding to oxidation of the oxygen-containing ion (mA cm^{-2}), and c is the oxide content of the melt (wt %).

Addition of an REE oxide to a melt under study in amounts *a fortiori* exceeding the maximum soluble

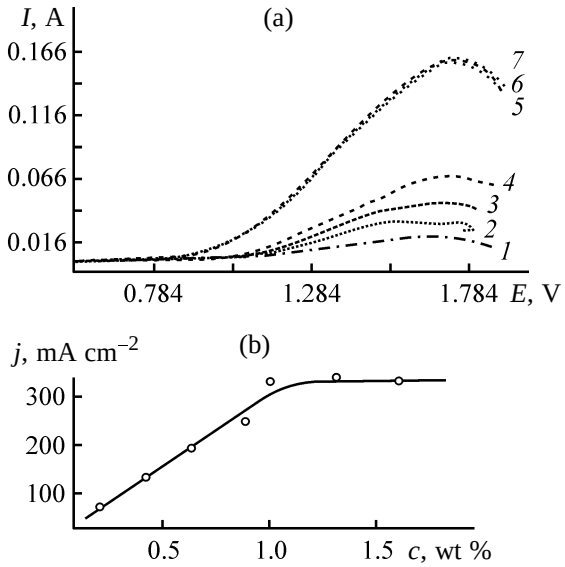

Fig. 5. (a) Voltammograms of oxidation of an oxygen-containing complex of gadolinium in a KCl–KF–Gd_2O_3 melt at 735°C on a glassy carbon electrode relative to a molybdenum quasi-reference electrode and (b) oxidation current j of oxygen-containing gadolinium complex vs. Gd_2O_3 content c in a melt of the KCl–KF eutectic at 735°C. (a) Polarization rate 0.1 V s^{-1}. (*I*) Current and (*E*) potential. Electrode area (cm^2): (*1*–*3*) 0.23 and (*4*–*7*) 0.27. Gd_2O_3 content (wt %): (*1*) 0.21, (*2*) 0.425, (*3*) 0.638, (*4*) 0.896, (*5*) 1.012, (*6*) 1.32, and (*7*) 1.617.

amount (about 5 wt % in the case in question) and sampling for determining the content of Ln_2O_3 made it possible to plot the temperature dependences of the limiting solubility of the REE oxides. The functions obtained are described by the equations

$$c_{lim} = 0.0015T - 0.0794 \text{ for gadolinium oxide,} \quad (9)$$

$$c_{lim} = 0.0136T - 8.4549 \text{ for yttrium oxide,} \quad (10)$$

$$c_{lim} = 0.0139T - 0.2602 \text{ for neodymium oxide,} \quad (11)$$

where c_{lim} is the limiting content of Ln_2O_3 in the melt (wt %), and T is the temperature of the melt (°C).

The use of dependences (6)–(8) and evaluation of the content of oxygen in fluorides of the above-mentioned REEs made it possible to give preference to the hydrofluoride method of LnF_3 preparation in an inert atmosphere [oxygen content of the REE fluoride was $(0.12–1.88) \times 10^{-4}$ mol %].

CONCLUSIONS

(1) Reactions of Y_2O_3 and Nd_2O_3 with ammonium hydrofluoride were studied. Intermediate complex ammonium fluorometallates were isolated and identified.

(2) The content of cationic impurities in the final products, trifluorides of rare-earth elements, was found to be determined by their content in the starting oxides; the content of anionic impurities (oxygen-containing in the first place) can be lowered by creating an inert or fluorinating atmosphere in synthesis. A comparison of various methods for the synthesis of yttrium, gadolinium, and neodymium fluorides as regards the content of oxygen-containing anionic impurities in the final products demonstrated that the best results are obtained with the hydrofluoride method. The content of oxygen was $(0.12–1.88) \times 10^{-4}$ mol %. The use of glassy carbon materials lowered to a minimum the contaminating effect of the apparatus.

ACKNOWLEDGMENTS

The study was carried out in accordance with the project "High-Temperature Chemical and Electrochemical Syntheses of New Compounds Based on Less-Common and Rare-Earth Metals," within the framework of the integrated program of the Russian Academy of Sciences.

REFERENCES

1. *Rare Earth Elements. Technology and Applications*, Villani, F., Ed., New York: Park Ridge, 1980.
2. Churbanov, M.F., Abstracts of Papers, *X Simpozium po khimii neorganicheskikh ftoridov* (X Symp. on Chemistry of Inorganic Fluorides), Moscow: Dialog-MGU, 1998, p. 172.
3. Egorov, V.Yu., Mironov, I.A., Ponomareva, E.A., and Reiterov, V.M., Abstracts of Papers, *X Simpozium po khimii neorganicheskikh ftoridov* (X Symp. on Chemistry of Inorganic Fluorides), Moscow: Dialog-MGU, 1998, p. 50.
4. Zamoryanskaya, M.V., Petrova, M.A., and Semenova, T.S., *Izv. Ross. Akad. Nauk, Neorg. Mater.*, 1998, vol. 34, no. 6, pp. 752–757.
5. Opalovskii, A.A. and Fedotova, T.D., *Gidroftoridy* (Hydrofluorides), Novosibirsk: Nauka, 1979.
6. Rakov, E.G., Ammonium Fluorides, *Itogi Nauki Tekh., Ser.: Neorg. Khim.*, 1988, vol. 15.
7. Rakov, E.G. and Mel'nichenko, E.I., *Usp. Khim.*, 1984, vol. 53, no. 9, pp. 1463–1492.
8. Polyakova, L.P., Kononova, Z.A., Elizarova, I.R., and Polyakov, E.G., *Zh. Anal. Khim.*, 1994, vol. 49, no. 11, pp. 1228–1232.
9. Mikhailov, M.A., Epov, D.G., Sergienko, V.I., *et al.*, *Zh. Neorg. Khim.*, 1973, vol. 18, no. 6, pp. 1508–1512.
10. Rajeshwar, K. and Secco, E.A., *Can. J. Chem.*, 1977, vol. 55, no. 3, pp. 2620–2627.

Russian Journal of Applied Chemistry, Vol. 75, No. 11, 2002, pp. 1765–1769. Translated from Zhurnal Prikladnoi Khimii, Vol. 75, No. 11, 2002, pp. 1801–1805.
Original Russian Text Copyright © 2002 by Morachevskii, Fedorova, Tsymbulov, Tsemekhman.

PHYSICOCHEMICAL STUDIES OF SYSTEMS AND PROCESSES

Thermodynamic Properties of Liquid Alloys of the System Nickel–Copper–Iron

A. G. Morachevskii, N. A. Fedorova, L. B. Tsymbulov, and L. Sh. Tsemekhman

St. Petersburg State Polytechnic University, St. Petersburg, Russia
Gipronikel' Institute, Joint-Stock Company, St. Petersburg, Russia

Received July 2, 2002

Abstract—The integral molar excess Gibbs energy and the enthalpy of mixing of liquid alloys of the ternary system nickel–copper–iron at 1600°C were calculated by various methods from data on boundary binary systems.

The nickel–copper–iron system in a liquid state is of interest for various processes of nonferrous metallurgy. It is a basis of matte obtained in reprocessing of copper–nickel sulfide raw materials. Data on thermodynamic properties of liquid alloys of this ternary system are virtually lacking. Experimental data for a large number of ternary systems with different character of component interaction show that the thermodynamic properties of liquid ternary systems can be estimated with a reliability sufficient for process calculations from data on boundary binary systems using geometric models and polynomials [1–5]. The thermodynamic properties of liquid alloys of the boundary systems nickel–copper, copper–iron, and iron–nickel are fairly well studied.

The phase diagram of the Ni–Cu system is characterized by formation of the solid solutions over the entire composition range and unlimited solubility of the components in the liquid state. Various methods, including emf measurements with molten or solid electrolytes, saturated vapor pressure measurements, and high-temperature calorimetry, were used for studying thermodynamic properties of the Ni–Cu liquid alloys. Published data on this system are analyzed in detail in [6]. In accordance with the phase diagram, the activity isotherms show moderate positive deviations from Raoult's law (Fig. 1a).

The thermodynamic properties of liquid alloys of the system Ni–Cu–Fe were calculated from data [7, 8] on the Ni–Cu system. In [7], the effusion method was used to measure the saturated vapor pressure over liquid alloys of nickel with copper at 1430°C. The saturated vapor pressure of copper exceeds that of nickel by more than two orders of magnitude; therefore, copper is a major evaporating component. Nonetheless, the authors introduced the correction for evaporation of nickel. The nickel activity and the integral thermodynamic properties of the Ni–Cu liquid alloys were calculated using the Gibbs–Duhem equation. In [8], the system Ni–Cu was studied calorimetrically (with a high-temperature isoperibolic calorimeter) at 1480°C. The excess Gibbs energy ΔG^{E} and the enthalpy of mixing ΔH at 1600°C were estimated from data of these works.

In the system copper–iron, the liquidus curve lies nearly horizontally in the central region of compositions, which can be considered as confirmation of the separation tendency. This leads, in turn, to the positive deviations of the component activity isotherms (Fig. 1b), and the enthalpies of mixing are also positive. Data of [10], where both emf measurements with the molten oxide as electrolyte (1460°C) and the high-temperature calorimetry (at 1600 and 1637°C) were used for studying thermodynamic properties of liquid alloys, were recommended for the Cu–Fe system in a handbook [9]. The latter method allowed direct experimental determination of the partial molar enthal-

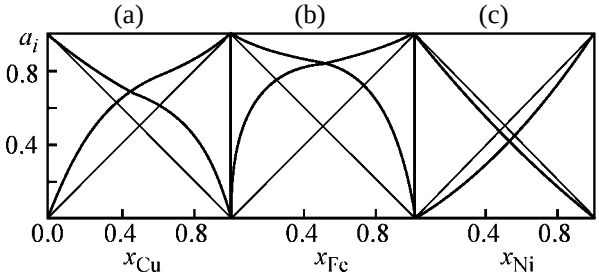

Fig. 1. Isotherms of component activity in the binary liquid systems (a) Ni–Cu, (b) Cu–Fe, and (c) Fe–Ni at 1600°C: (a_i) activity and (x_i) component mole fraction.

1070-4272/02/7511-1765$27.00© 2002 MAIK "Nauka/Interperiodica"

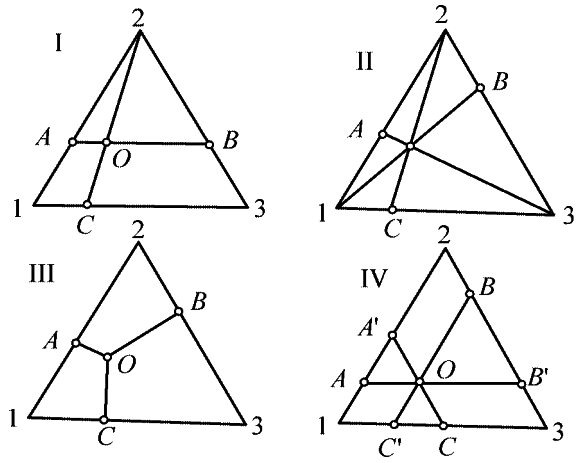

Fig. 2. Geometrical models for calculating integral thermodynamic properties of the ternary systems from data on boundary binary systems. For explanation, see text.

pies of mixing of iron, which made it is possible to recalculate for higher temperature (1600°C) the activities determined by the emf method. Thermodynamic properties of liquid alloys of the system Cu–Fe are also analyzed in [11].

The phase diagram of the iron–nickel system shows that, in the liquid state and in the solid state at high temperatures, except for a very narrow composition range adjacent to iron, the component miscibility is unlimited. A computer calculation of the phase diagram of the Fe–Ni system on the basis of thermodynamic data showed that the solidus and liquidus lines are very close and sometimes virtually coalesce [12]. Such a phase diagram, arising from closeness of the atomic radii of iron and nickel (0.126 and 0.124 nm, respectively), predetermines the minimal deviations of the component activities from the ideal values (Fig. 1c).

Thermodynamic properties of liquid alloys of the system Fe–Ni have been repeatedly studied by various methods [13]. Comparison of the data on the component activity coefficients for liquid alloys of this system obtained by various authors, along with the results of our studies, were reported in [14]. The majority of data refers to 1600°C. Published data on the general character of the concentration dependence of activity, activity coefficients, excess and total Gibbs energy, and on their numerical values are in reasonable agreement. Data on the enthalpies of mixing of liquid alloys are less reliable [15–17]. In calculations we used the values recommended in [13, 18].

Four geometrical models (I–IV) and the Redlich–Kister polinomials (V) were applied to calculating the integral molar thermodynamic characteristics of liquid alloys of the ternary system from data on boundary binary systems. The geometrical models are schematically shown in Fig. 2. Point *O* designates the composition of a ternary alloy (x_1, x_2, x_3) for which the integral thermodynamic property is calculated. Because the models for calculating ΔG^E, ΔG, and ΔH were similar, let us designate any of these thermodynamic functions as $\Delta\Phi$. Points *A*, *B*, and *C* indicate compositions of the boundary binary systems for which the integral quantities $\Delta\Phi_{12}$, $\Delta\Phi_{23}$, and $\Delta\Phi_{31}$ are used in the calculations. The mathematical expressions corresponding to the geometrical models are presented below. Model IV (Colinet's method) allows two calculation procedures: the "left" method and the "right" method using the $\Delta\Phi_{ij}$ values at points *A*, *B*, and *C* or at points *A*', *B*', and *C*', respectively. As a rule, both calculation methods are used simultaneously, with the results averaged (the coefficient 0.5 in the equation for model IV). All the calculations were done along the secants of the concentration triangle at a constant $x_{Ni} : x_{Fe}$ ratio.

Algorithms for calculating integral molar thermodynamic properties of the ternary system from data on boundary binary systems

$$\text{model I: } \Delta\Phi = \left[\frac{x_1}{1-x_2}\Delta\Phi_{12} + \frac{x_3}{1-x_2}\Delta\Phi_{23}\right]_{x_1, x_1/x_3} + (1 - x_2)[\Delta\Phi_{13}]_{x_2=0, x_1/x_3};$$

$$\text{model II: } \Delta\Phi = (x_1 + x_2)[\Delta\Phi_{12}]_{x_1/x_2} + (x_2 + x_3)^2[\Delta\Phi_{23}]_{x_2/x_3} + (x_1 + x_3)^2[\Delta\Phi_{31}]_{x_3/x_1};$$

model III:

$$\Delta\Phi = \frac{4x_1x_3}{(2x_1 + x_2)(2x_3 + x_2)}[\Delta\Phi_{13}]_{x_3 + x_2/2} + \frac{4x_2x_3}{(2x_3 + x_1)(2x_2 + x_1)}[\Delta\Phi_{23}]_{x_2 + x_1/2} + \frac{4x_1x_2}{(2x_2 + x_3)(2x_1 + x_3)}[\Delta\Phi_{12}]_{x_1 + x_3/2};$$

model IV:

$$\Delta\Phi = 0.5\left(\frac{x_1}{1-x_2}[\Delta\Phi_{12}]_{x_2} + \frac{x_2}{1-x_3}[\Delta\Phi_{23}]_{x_3} + \frac{x_3}{1-x_1}[\Delta\Phi_{13}]_{x_1} + \frac{x_2}{1-x_1}[\Delta\Phi_{12}]_{x_1} + \frac{x_3}{1-x_2}[\Delta\Phi_{23}]_{x_2} + \frac{x_1}{1-x_3}[\Delta\Phi_{13}]_{x_3}\right).$$

Table 1. Results of the calculation of ΔG^E and ΔH for the Ni–Cu–Fe ternary system at 1600°C

x_{Cu}	$x_{Ni} : x_{Fe} = 3 : 1$		$x_{Ni} : x_{Fe} = 1 : 1$		$x_{Ni} : x_{Fe} = 1 : 3$	
	ΔG^E	ΔH	ΔG^E	ΔH	ΔG^E	ΔH
0.10	–0.39 ± 0.06	–0.97 ± 0.19	–0.08 ± 0.01	–0.20 ± 0.36	1.33 ± 0.06	2.74 ± 0.35
0.20	1.60 ± 0.08	1.14 ± 0.35	2.10 ± 0.02	2.33 ± 0.45	3.43 ± 0.03	5.49 ± 0.49
0.30	3.15 ± 0.10	2.60 ± 0.38	3.75 ± 0.02	3.79 ± 0.47	5.01 ± 0.04	6.54 ± 0.47
0.40	4.26 ± 0.09	3.51 ± 0.28	4.88 ± 0.02	4.53 ± 0.34	6.00 ± 0.04	6.77 ± 0.35
0.50	4.90 ± 0.10	3.96 ± 0.17	5.48 ± 0.04	4.82 ± 0.25	6.42 ± 0.04	6.49 ± 0.23
0.60	5.05 ± 0.12	3.99 ± 0.08	5.60 ± 0.10	4.85 ± 0.09	6.30 ± 0.05	5.96 ± 0.10
0.70	4.70 ± 0.11	3.66 ± 0.08	5.24 ± 0.13	4.38 ± 0.06	5.77 ± 0.09	5.27 ± 0.03
0.80	3.85 ± 0.08	2.92 ± 0.06	4.35 ± 0.10	3.58 ± 0.07	4.80 ± 0.08	4.30 ± 0.07
0.90	2.38 ± 0.03	1.75 ± 0.02	2.70 ± 0.04	2.20 ± 0.03	2.99 ± 0.03	2.69 ± 0.08

The Toop's method (model I) belongs to asymmetrical methods, i.e., the results of the calculation are to a certain extent dependent on the choice of a specified position of components. The Kohler's, Muggiani's, and Colinet's models (II, III, and IV, respectively) are symmetrical with respect to the numbering of the system components (Fig. 2; see algorithms). The calculation results for all the four geometric models are reasonably consistent. The average values of the integral thermodynamic functions, ΔG^E and ΔH, for the system Ni–Cu–Fe, along with the averaged deviation, are given in Table 1. The analysis shows that none of the four methods is in preference for the given system, and it is unreasonable to consider any of them as inadequate. The lines of the equal values of ΔG^E and ΔH are plotted in Figs. 3a and 3b.

To express analytically the concentration dependence of the integral molar excess Gibbs energy and the enthalpy of mixing in the binary systems Ni–Cu, Cu–Fe, and Fe–Ni at 1600°C, the data were formalized with the following polynomials:

$$\Delta G^E = x_1(1 - x_1)[b + c(2x_1 - 1) + d(2x_1 - 1)^2],$$

$$\Delta H = x_1(1 - x_1)[b' + c'(2x_1 - 1) + d'(2x_1 - 1)^2].$$

Special calculations [19] showed that it is unnecessary to use the higher degrees of the polynomials of this type to describe the thermodynamic properties of liquid binary metal systems with different character of component interaction. For a series of the binary systems considered, the coefficients obtained are given below.

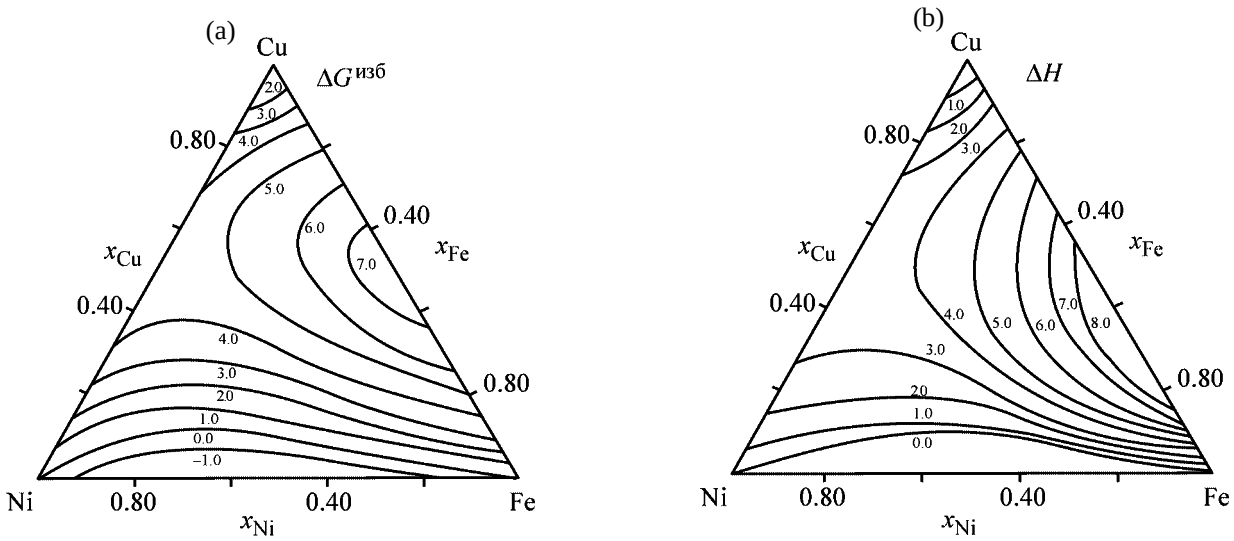

Fig. 3. Lines of the equal values of (a) integral molar excess Gibbs energy ΔG^E and (b) enthalpy of mixing ΔH in the ternary system Ni–Cu–Fe at 1600°C (kJ mol^{-1}).

Table 2. Results of the calculation of ΔG^E and ΔH in the ternary system Ni–Cu–Fe at 1600°C using polynomial expressions

x_{Cu}	$x_{Ni}:x_{Fe} = 3:1$		$x_{Ni}:x_{Fe} = 1:1$		$x_{Ni}:x_{Fe} = 1:3$	
	ΔG^E	ΔH	ΔG^E	ΔH	ΔG^E	ΔH
	kJ mol^{-1}					
0.20	2.17	1.75	2.03	1.76	2.78	3.96
0.40	4.52	3.69	4.85	4.24	5.63	5.20
0.60	5.17	4.05	5.67	4.70	6.31	5.80
0.80	3.79	2.91	4.23	3.53	4.68	4.19

System	b	c	d	r*
Ni–Cu	18.8829	–3.5732	–0.3147	0.9996
Cu–Fe	29.5990	0.2475	6.8151	0.9244
Fe–Ni	–11.3192	5.6692	0.6750	0.9984
System	b'	c'	d'	r
Ni–Cu	15.4828	1.6414	0.1771	0.9999
Cu–Fe	34.9053	22.7298	26.4809	0.9997
Fe–Ni	–17.1611	9.0480	2.5736	0.9973

* Correlation coefficient.

The excess Gibbs energy in the ternary system can be presented as the following sum of independent contributions [1, 2]:

$$\Delta G^E = \Delta G^E_{12} + \Delta G^E_{23} + \Delta G^E_{31} + \Delta G^E_{123}.$$

To estimate the first three contributions, it is necessary to know the coefficients b_{ij}, c_{ij}, and d_{ij} of the corresponding binary systems. Determination of ΔG_{123} needs the minimum amount of data on the ternary system. At the same time, the calculations performed for a number of experimentally studied systems showed that the ΔG^E value for a ternary system can be sufficiently reliably estimated from data on boundary binary systems only [1, 20, 21]. The enthalpy of mixing in ternary systems is estimated similarly. Thus, the final equations for calculating ΔG^E and ΔH in ternary systems contain solely the coefficients entering into the equations for the binary systems:

$$\Delta G^E = x_1x_2[b_{12} + c_{12}(x_1 - x_2) + d_{12}(x_1 - x_2)^2] + x_2x_3[b_{23} + c_{23}(x_2 - x_3) + d_{23}(x_2 - x_3)^2] + x_3x_1[b_{31} + c_{31}(x_3 - x_1) + d_{31}(x_3 - x_1)^2],$$

$$\Delta H = x_1x_2[b'_{12} + c'_{12}(x_1 - x_2) + d'_{12}(x_1 - x_2)^2] + x_2x_3[b'_{23} + c'_{23}(x_2 - x_3) + d'_{23}(x_2 - x_3)^2] + x_3x_1[b'_{31} + c'_{31}(x_3 - x_1) + d'_{31}(x_3 - x_1)^2].$$

The parameters x_1–x_3 in these equations characterize the composition of the ternary alloy. The results of the calculations are given in Table 2. The values obtained are in reasonable agreement with the results of the geometric models. The discrepancies were observed only in the composition region adjacent to the Fe–Ni side, because ΔG^E and ΔH change sign.

CONCLUSION

The calculations of the integral molar excess Gibbs energies and the enthalpies of mixing in liquid alloys of the nickel–copper–iron system at 1600°C by four different geometric models from data on boundary binary systems yield consistent results. The calculation of these functions with polynomials yields, on the whole, similar results.

REFERENCES

1. Morachevskii, A.G., *Termodinamika rasplavlennykh metallicheskikh i solevykh sistem* (Thermodynamics of Molten Metal and Salt Systems), Moscow: Metallurgiya, 1987.
2. Morachevskii, A.G., and Sladkov, I.B., *Termodinamicheskie raschety v metallurgii: Spravochnik* (Thermodynamic Calculations in Metallurgy: Reference Book), Moscow: Metallurgiya, 1993.
3. Hillert, M., *CALPHAD*, 1988, vol. 12, no. 3, pp. 257–259.
4. Chou, K.-Ch., and Chang, Y.A., *Ber. Bunsenges. Phys. Chem.*, 1989, vol. 93, no. 6, pp. 735–741.
5. Azzaoui, M., and Hertz, J., *Z. Metallkunde*, 1995, vol. 86, no. 11, pp. 776–783.
6. Fedorova, N.A., *Termodinamicheskie svoistva sistemy med'–nikel'* (Thermodynamic Properties of the Copper–Nickel System), Available from VINITI, March 6, 2001, no. 591-V.
7. Berezutskii, V.V., and Lukashenko, G.M., *Ukr. Khim. Zh.*, 1987, vol. 53, no. 10, pp. 1029–1032.
8. Turchanin, M.A., Porokhnya, S.V., Belevtsov, L.V., and Kokhan, A.V., *Rasplavy*, 1994, no. 4, pp. 8–12.
9. Belousov, A.A., Bakhvalov, S.G., Aleshina, S.N., *et al.*, *Fiziko-khimicheskie svoistva zhidkoi medi i ee splavov. Spravochnik* (Physicochemical Properties of Liquid Copper and Copper Alloys. Reference Book),

Yekaterinburg: Inst. Metallurgii, Ural. Otd. Ross. Akad. Nauk, 1997.

10. Batalin, G.I., and Sudavtsova, V.S., *Metally*, 1980, no. 2, pp. 45–49.
11. Sorokin, M.L., Andryushechkin, N.A., and Nikolaev, A.G., *Izv. Vyssh. Uchebn. Zaved., Tsvetn. Metall*., 1996, no. 6, pp. 10–14.
12. Tomiska, J., and Vrestal, J., *Thermochim. Acta*, 1998, vol. 314, pp. 155–167.
13. Batalin, G.I., *Termodinamika zhidkikh splavov na osnove zheleza* (Thermodynamics of Liquid Iron Alloys), Kiev: Vishcha Shkola, 1982.
14. Tsemekhman, L.Sh., Alekseeva, N.N., and Parshukova, L.N., *Metally*, 2000, no. 1, pp. 25–29.
15. Predel, B., and Mohs, R., *Arch. Eisenhüttenwes*., 1970, vol. 41, no. 2, pp. 143–149.
16. Batalin, G.I., Minenko, N.N., and Sudavtsova, V.S., *Izv. Akad. Nauk SSSR, Met*., 1974, no. 5, pp. 99–103.
17. Wang, H., Luck, R., and Predel, B., *J. Phase Equil*., 1993, vol. 14, no. 1, pp. 48–53.
18. Hultgren, R. *et al*., *Selected Values of the Thermodynamic Properties of Binary Alloys*, Metals Park, Ohio: Am. Soc. of Metals, 1973.
19. Morachevskii, A.G., and Erofeev, K.B., *Zh. Prikl. Khim*., 2000, vol. 73, no. 6, pp. 1032–1034.
20. Morachevskii, A.G., and Gerasimenko, L.N., *Zh. Fiz. Khim*., 1971, vol. 45, no. 8, pp. 1951–1953.
21. Morachevskii, A.G., in *Termodinamicheskie svoistva metallicheskikh splavov i sovremennye metody ikh issledovaniya* (Thermodynamic Properties of Metal Alloys and Modern Methods of Their Study), Kiev: Naukova Dumka, 1976, pp. 71–78.

Russian Journal of Applied Chemistry, Vol. 75, No. 11, 2002, pp. 1770–1773. Translated from Zhurnal Prikladnoi Khimii, Vol. 75, No. 11, 2002, pp. 1806–1809.
Original Russian Text Copyright © 2002 by Sladkov.

PHYSICOCHEMICAL STUDIES OF SYSTEMS AND PROCESSES

Calculating Density of Molecular Liquids Using Agrawal–Thodos Equation

I. B. Sladkov

St. Petersburg State Polytechnic University, St. Petersburg, Russia

Received November 1, 2001

Abstract—The correlation between the parameters of the Agrawal–Thodos equation and the fundamental constants of a substance are established. A modified equation is proposed, in which the minimum set of easily measurable properties of the substance is used as input data.

The majority of molecular compounds under normal conditions exist in the liquid state. The most important characteristic of such compounds is liquid density. Data on the density are necessary for theoretical calculations and for process development and control, including calculation of heat exchangers, distillation columns, and all the equipment for fluid control.

A number of correlations allowing prediction of the density of molecular liquids on the saturation line in the entire range of existence of the liquid phase have been reported. These include the Mathias [1], Goldhammer [1], Spencer–Danner [2], Campbell–Thodos [3], and Eselev–Krupskii equations [4]. To these correlations also belongs the Agrawal–Thodos equation [5] derived from the following prerequisites.

Based on experimental data on the density of liquid Ar, Ne, H_2, O_2, N_2, CO, and CH_4, Agrawal and Thodos found that the temperature dependence of density, if plotted in the coordinates $\ln(1 - T_{red})$ vs. $\ln(\rho_{red} - 1)$, is the simplest (linear) dependence over the entire region of existence of the liquid phase. Here, $\rho_{red} = \rho/\rho_{cr}$ is the reduced density; $T_{red} = T/T_{cr}$, reduced temperature; and ρ_{cr} and T_{cr}, critical density and temperature, respectively. As a result, the temperature dependence of the liquid density is described by the following equation:

$$\rho = \rho_{cr}[1 + \alpha(1 - T/T_{cr})^{\beta}]. \quad (1)$$

Agrawal and Thodos found that, for the above substances, the temperature dependence of the liquid density can be described with sufficient accuracy by Eq. (1) with properly chosen individual constants α and β. The errors averaged over the whole temperature range (T_m–T_{cr}) were from 0.4 (for Ne) to 1.3% (for CH_4).

The Agrawal–Thodos equation is advantageous over analogous equations, because it allows the temperature dependence of the liquid density to be obtained in a simple and compact form; it does not require data on the vapor density (unlike Mathias–Goldhammer equations), critical pressure (unlike Spencer–Danner equation), or saturated vapor pressure (unlike Eselev–Krupskii equation); as compared to the Campbell–Thodos equation, it contains considerably smaller number of fitting parameters.

All the above shows that the Agrawal–Thodos equation is, without doubt, promising and efficient for predicting the density of molecular liquids. At the same time, the authors' proposal to use the experimental temperature dependence of the liquid density for determining α and β limits practical application of Eq. (1) to a small number of thoroughly studied substances. This equation has practical value and can be applied solely in the case when α and β can be determined from calculation rather than from experimental data on the liquid density.

The goals of this work were (a) to establish a correlation between the parameters α and β and the fundamental constants of a substance and, as a result, to derive equations for calculating the above parameters without data on liquid density, (b) to propose a modification of the Agrawal–Thodos equation allowing prediction of the liquid density from the minimum amount of easily accessible data, and (c) to study potentials of this modified equation on substances belonging to different classes of chemical compounds.

Solving this problem would make the Agrawal–Thodos equation more versatile and applicable to poorly studied substances.

Let us consider the main relationships underlying

1070-4272/02/7511-1770$27.00 © 2002 MAIK "Nauka/Interperiodica"

the method proposed. Basically, the parameters α and β of Eq. (1) can be expressed in terms of the parameters of two reference points: $T = 0$, and, consequently, $\rho = \rho_0$ and $T = T_b$, and, consequently, $\rho = \rho_b$. First, we write Eq. (1) for $T = 0$, then, for $T = T_b$, and, after appropriate transformations, we obtain the following relationships:

$$\alpha = \rho_0/\rho_{cr} - 1, \quad (2)$$

$$\beta = \ln[(\rho_b/\rho_{cr} - 1)/\alpha]/\ln(1 - T_b/T_{cr}). \quad (3)$$

As seen from Eq. (2), determination of α needs data on the ρ_0/ρ_{cr} ratio, where ρ_0 is zero density, i.e, a hypothetical density of a liquid at absolute zero, and ρ_{cr}, critical density. The ρ_{cr} is difficult to determine, and data on ρ_0 are even less accessible. We found that the ρ_0/ρ_{cr} ratio and the boiling point of a substance correlate. For example, for carbon tetrafluoride having T_b = 145.2 K ρ_0/ρ_{cr} = 3.60, whereas for tin tetraiodide having T_b = 622.5 K, ρ_0/ρ_{cr} = 4.02.

By assuming that the correlation between the ρ_0/ρ_{cr} ratio and the boiling point is linear,

$$\rho_0/\rho_{cr} = aT_b + b,$$

we minimized the error in calculating the liquid density by Eq. (1) to derive the parameters of this dependence. For this purpose, we used the experimental data on the temperature dependence of the liquid density. For the temperature range from the melting point to the boiling temperature, such data are available for many molecular inorganic compounds [6]. We chose 50 well-known substances, for which, apart from the liquid density, all necessary data for the calculation by Eq. (1) are available: hydrides CH_4, B_2H_6, GeH_4, SnH_4, NH_3, and N_2H_4; fluorides CH_4, MoF_6, WF_6, and UF_6; chlorides CCl_4, $SnCl_4$, $GeCl_4$, $TiCl_4$, PCl_3, PCl_5, $BiCl_3$, S_2Cl_2, and HCl; bromides BBr_3, PBr_3, and $SnBr_4$; iodides BI_3, SiI_4, and SnI_4; mixed halides CCl_3F, CCl_2F_2, $CClF_3$, CBr_2F_2, $CBrF_3$, $PClF_2$, PCl_2F, $SiBrCl_3$, and $SiBr_2Cl_2$; hydrohalides CH_3Cl, CH_3Br, CH_3I, $CHCl_3$, $CHClF_2$, $SiHCl_3$, and $SiHBr_3$; oxyhalides PCl_3O, PBr_3O, SCl_2O, ClO_3F, and WCl_4O; oxides CO, N_2O, SO_2, and H_2O.

The parameters a and b were determined by the following procedure: For each substance the calculations were performed for 10 temperatures in the range from the melting point to the boiling point, and the relative error was averaged in absolute values over the whole range. Then, the errors obtained were averaged over all the 50 substances. The resulting error, which is the average value over 500 experimental points, is denoted as Δ.

The calculations performed showed that the minimal value of Δ is provided by the equation

$$\rho_0/\rho_{cr} = 1.055 \times 10^{-3}T_b + 3.38, \quad (4)$$

which, taking into account Eq. (2), yields

$$\alpha = 1.055 \times 10^{-3}T_b + 2.38. \quad (5)$$

In what follows, we show that the calculations by Eq. (1), in which α and β are calculated by Eqs. (5) and (3), provide reliable prediction for molecular liquids.

In the next stage, we examined the possibility of using more accessible input data. The above method of calculating density needs comprehensive input data on the substance under study, including boiling point, critical temperature, density of the liquid at boiling point, and critical density. Among these data, critical temperature and critical density are difficult to determine.

Because the boiling-point parameters are more accessible than the critical parameters, we studied the possibility of replacing the critical temperature by the boiling point and the critical density by the liquid density at the boiling point. For this purpose, we studied the relationships [6] between the critical-point and boiling-point parameters:

$$T_{cr} = T_b + 0.89T_b^{0.2\psi + 0.92}, \quad (6)$$

$$\rho_{cr} = \rho_b/(2.69 + 1.067\psi), \quad (7)$$

where ψ is the factor of complexity of intermolecular interaction [6],

$$\psi = 0.1\ln T_b - 0.122\ln V_b + 0.006, \quad (8)$$

where V_b is the molar volume of liquid at boiling point ($cm^3\ mol^{-1}$).

As a result, we obtained the modified Agrawal–Thodos equation based on Eqs. (1), (3), and (5)–(8) with the minimum amount of easily accessible input data (boiling point and molar volume of a liquid at boiling point).

The calculations by the above two procedures were performed on a data set obtained for the 50 abovementioned substances covering a broad range of molecular compounds of different classes, with different types of intermolecular interaction. All numerical values of the physicochemical constants were taken from a handbook [6].

Table 1. Error in calculating liquid density using different sets of input data

Calculation method	Calculation formulas	Input data	Δ, %
1	(1), (3), (5)	T_b, ρ_b, T_{cr}, ρ_{cr}	0.94
2	(1), (3), (5)–(8)	T_b, ρ_b	1.02

Table 2. Average absolute error in calculating density of liquid substances in different temperature ranges

Substance	Δ,* %, in indicated temperature range			
	T_m–T_b		T_b–T_{cr}	
	Δ_1	Δ_2	Δ_1	Δ_2
NH_3	0.9	0.8	2.0	1.1
CF_4	1.0	1.1	2.3	3.2
HCl	0.5	0.3	0.8	0.9
BBr_3	0.3	0.2	0.6	0.6
BI_3	0.8	1.2	1.1	1.2
SiI_4	1.3	1.1	1.1	1.2
SnI_4	1.1	1.1	1.2	1.4
$CHClF_2$	1.1	0.8	0.7	0.8
ClO_3F	0.2	1.2	0.9	0.8
SO_2	0.4	0.5	0.3	1.1

* (Δ_1, Δ_2) Calculation errors for procedures 1 and 2; the same for Tables 3 and 4.

Table 3. Average absolute error in calculating liquid density of organic and organometallic compounds in the temperature range from the melting to boiling point

Substance	Δ_1	Δ_2
$Si(CH_3)_4$	0.8	1.5
$Ge(CH_3)_4$	1.0	1.2
$Si(C_2H_5)_4$	1.5	2.0
$Ge(C_2H_5)_4$	1.2	1.5
$Sn(CH_3)_4$	0.8	0.8
C_2H_5OH	2.7	1.1
CH_3OH	1.2	2.1
C_2F_4	1.2	2.1
C_6H_6	0.3	0.1
$C_6H_5CH_3$	2.1	2.7
Average	1.2	1.5

The calculation accuracy for the set of 50 substances is given in Table 1. The typical results for 10 substances are given in Table 2 for more detailed characterization of different calculation procedures. The choice of substances in Table 2 intended to illustrate the potentials of the calculation procedures was governed by three criteria: the compounds belong to different classes of molecular inorganic compounds; their polarity varies within a wide range; and, finally, experimental data on the density of these compounds over the entire range of existence of the liquid phase are available.

It is seen that both calculation procedures provide sufficient accuracy in calculating the density. In both the low-temperature (from the melting point to the boiling point) and high-temperature (from the boiling point to the critical point) ranges, the accuracy is virtually constant. This shows that both procedures provide reliable prediction of the density over the entire range of existence of the liquid phase.

It is important that the calculation method using boiling-point parameters as input data does not virtually differ in accuracy from that using critical constants. This considerably expands the potential of the Agrawal–Thodos equation for predicting the density of poorly studied substances.

The polarities of the 50 substances chosen vary within a wide range. One of important results is that the accuracy of the proposed modifications of the Agrawal–Thodos equation is polarity independent (Table 2): for strongly polar substances (SO_2, HCl, and NH_3) the error in calculating density is simlar to that obtained for nonpolar substances (CF_4, BBr_3, and SnI_4).

The substances chosen are molecular inorganic compounds. It is known that approximate methods, as applied to different classes of substances [7], can yield different errors in prediction of physicochemical properties. Therefore, it was of interest to study the applicability of the Agrawal–Thodos equation to other classes of molecular substances (including organic and organometallic compounds).

To do this, among the compounds of the above classes we selected 10 well-known substances for which experimental data on the liquid density are available [8–12]. Table 3 shows that, in the temperature range from the melting point to the boiling point, the accuracy of the considered modifications of the Agrawal–Thodos equations is high for both organic and organometallic compounds.

In the high-temperature range ($T > T_b$), procedure 2 can yield higher error for certain organic substances with a marked polarity. This is explained by the fact that, in going to more accessible input data in method 2, we used correlations obtained for inorganic

Table 4. Influence of polarity on the error in calculating the density of organic liquids

T, K	ρ_{exp}	Δ_1, %	Δ_2, %
	C_3F_8		
213.2	1.6935 [13]	–0.1	1.1
223.2	1.6526 [13]	0.1	1.4
236.5*	1.601 [13]	0	0
243.2	1.5745 [13]	–0.1	1.4
253.2	1.5369 [13]	–0.5	1.1
273.2	1.4531 [13]	–1.3	0.4
300.2	1.3119 [13]	–2.6	–0.6
310.2	1.2457 [13]	–3.1	–1.0
320.2	1.1718 [13]	–3.4	–1.8
	C_2H_5OH		
194.7	0.8962 [11]	2.3	0.9
273.2	0.8262 [11]	2.4	1.1
322.6	0.7752 [11]	3.9	0.9
351.6*	0.746 [11]	0	0
377.6	0.7101 [11]	–0.2	–3.8
422.6	0.6419 [11]	–1.4	–5.7
473.2	0.5383 [11]	–2.7	–7.9
488.8	0.4923 [11]	–3.0	–8.4
499.2	0.4524 [11]	–2.9	–8.4

* Boiling point.

compounds. These correlations, when applied to organic compounds, are less accurate and can yield increased error in calculation by method 2. As seen from Table 4, for the nonpolar compound C_3F_8 the error of method 2 in the temperature ranges T_b–T_{cr} and T_b–T_{cr} is virtually the same. At the same time, for strongly polar compound C_2H_5OH the error of method 2 at $T > T_b$ markedly increases and considerably exceeds that of method 1.

CONCLUSIONS

(1) The correlation between the parameters α and β of the Agrawal–Thodos equation and the fundamental constants of the substance is established, allowing calculation of the liquid density using a limited set of experimental data.

(2) The modification of the Agrawal–Thodos equation based on only two easily accessible parameters, boiling point and liquid density at boiling point, is proposed.

(3) The proposed modification considerably extends the applicability of the Agrawal–Thodos equation, making it suitable for predicting the density of poorly studied substances.

REFERENCES

1. Sladkov, I.B., *Metody priblizhennogo rascheta fiziko-khimicheskikh svoistv kovalentnykh neorganicheskikh soedinenii* (Procedures for Approximate Calculation of Physicochemical Properties of Covalent Inorganic Compounds), Leningrad: Leningr. Gos. Univ., 1978.
2. Spencer, C.F., and Danner, R.P., *J. Chem. Eng. Data*, 1978, vol. 23, no. 1, pp. 82–86.
3. Campbell, S.W., and Thodos, G., *Ind. Eng. Chem. Fundam.*, 1984, vol. 23, no. 4, pp. 500–510.
4. Eselev, M.B., and Krupskii, N.P., *Inzh.-Fiz. Zh.*, 1986, vol. 56, no. 2, pp. 333–334.
5. Agrawal, G.M., and Thodos, G., *Phys. Chem. Liq.*, 1971, vol. 2, no. 1, pp. 135–145.
6. Morachevskii, A.G. and Sladkov, I.B., *Fiziko-khimicheskie svoistva molekulyarnykh neorganicheskikh soedinenii* (Physicochemical Properties of Molecular Inorganic Compounds), St. Petersburg: Khimiya, 1996.
7. Sladkov, I.B., and Prokopenko, O.A., *Zh. Prikl. Khim.*, 1997, vol. 70, no. 10, pp. 1606–1611.
8. Maksimov, B.N., Barabanov, V.G., Serushkin, I.L., *et al.*, *Promyshlennye ftoroorganicheskie produkty: Spravochnik* (Commercial Organofluorine Products. Reference Book), Leningrad: Khimiya, 1990.
9. Mamedov, A.M., and Akhundov, T.S., *Tablitsy termodinamicheskikh svoistv gazov i zhidkostei* (Tables of Thermodynamic Properties of Gases and Liquids), issue 5: *Uglevodorody aromaticheskogo ryada* (Aromatic Hydrocarbons), Moscow: Izd. Standartov, 1978.
10. Sladkov, I.B., *Zh. Prikl. Khim.*, 2000, vol. 73, no. 5, pp. 727–732.
11. Zolin, V.S., in *Teplofizicheskie svoistva veshchestv i materialov* (Thermal Properties of Substances and Materials), Moscow: Izd. Standartov, 1983, issue 18, pp. 24–30.
12. Liley, P.E., *Chem. Eng.*, 1982, vol. 89, no. 24, pp. 59–64.
13. Brown, J.A., *J. Chem. Eng. Data*, 1963, vol. 8, no. 1, p. 108.

Russian Journal of Applied Chemistry, Vol. 75, No. 11, 2002, pp. 1774–1779. Translated from Zhurnal Prikladnoi Khimii, Vol. 75, No. 11, 2002, pp. 1810–1815.
Original Russian Text Copyright © 2002 by Prikhod'ko, Vinogradova.

PHYSICOCHEMICAL STUDIES OF SYSTEMS AND PROCESSES

Modeling of Liquid–Vapor Equilibrium in Systems Including a Light Oil–Gas Component and Aromatic and Polyaromatic Hydrocarbons[1]

I. V. Prikhod'ko and I. V. Vinogradova

St. Petersburg State University, St. Petersburg, Russia

Received March 25, 2002

Abstract—The Victorov–Smirnova's hole lattice quasichemical group-contribution model (HM) is used to simulate the vapor–liquid equilibrium in binary and ternary mixtures systems composed by aromatic (benzene, toluene) and polyaromatic (naphthalene, phenanthrene) hydrocarbons and light oil–gas components (carbon dioxide, hydrogen sulfide, nitrogen, methane, ethane, propane). Eighteen binary and two ternary systems are examined. New group parameters for these systems are estimated. The results of modeling are compared with the experimental data and those predicted by the Peng–Robinson equation of state.

Designing of oil-and-gas production and processing requires reliable methods for predicting phase equilibria over wide temperature and pressure ranges in mixtures composed by a lot of components different in their chemical nature. Among the systems frequently occurring in petrochemical and coal-mining industries are binary mixtures of aromatic (or polyaromatic) hydrocarbons with typical light oil–gas components (lower alkanes, nitrogen, carbon dioxide, and hydrogen sulfide).

In design engineering, cubic equations of state (EOS) of the van der Waals type hold much favor. For the above-indicated systems these are the Peng–Robinson and Soave–Redlich–Kwong equations and their multiple modifications. All the equations of the van der Waals type used in practice are insufficiently universal and hardly suitable for description of the systems with long-chain, polar, and associated components. The questions related to developing equations of state and their practical use in modeling fluid phase equilibria are examined in the review [1]. Among the most valid (from the molecular standpoint) equations of state one can distinguish those based on the perturbation and numerical modeling theories and also on the lattice fluid models. One of the up-to-date lattice models was developed by Smirnova and Victorov [2–4]. In practice, the model can be used as its group-contribution modification.

The common in all the group models is that molecules of components are represented as a combination of some chemical groups that are thought to provide additive contributions to thermodynamic characteristics of the system. The appeal of the group-contribution approach is caused by the fact that great diversity of molecules is composed by relatively small amount of chemical groups. As a result, compared to the number of molecules, considerably lesser amount of groups is needed to represent a great number of multicomponent systems occurring in the practice. Just these models are best suited for prediction of thermodynamic properties and phase equilibria in cases when experimental data are lacking.

In this work, we selected the Victorov–Smirnova's hole lattice quasichemical model (HM) and an equation of state derived on its basis. The HM was already successfully tested for modeling systems with specific intermolecular interactions, particularly, for pure and mixed fluids such as various hydrocarbons, alkanols, acetone, acetic acid, water, nitrogen, hydrogen sulfide, and carbon dioxide [2–10]. The model proved to be quite adequate in simulating phase equilibria in diverse binary and multicomponent mixtures. In particular, it appeared to be useful in predicting phase equilibria in ternary systems water–subcritical vapor–organic component [9]. Kuranov *et al*. [11] extended HM to include the electrostatic contribution and modeled the liquid–vapor equilibria at elevated pressure in the ternary systems CO_2–methyldiethanolamine–water and H_2S–methyldiethanolamine–water

[1] Results were presented in part at the IV International Conference on Oil and Gas Chemistry, Tomsk (Russia), October 2–6, 2000.

1070-4272/02/7511-1774$27.00 © 2002 MAIK "Nauka/Interperiodica"

with acid–base reactions in the liquid phase. Hofman *et al.* [12] proposed a simplified version of the Victorov–Smirnova's group-contribution EOS with a smaller number of parameters as compared to the original model. With the modified HM they performed a great body of calculations of the thermodynamic properties and phase equilibria for pure alkanes and ethers and their binary mixtures.

HM was not used till now for systems composed by aromatic (or polyaromatic) hydrocarbons and light oil–gas components, since necessary parameters of the model were not determined. Therefore, the main goal of this work is to describe the vapor–liquid equilibria in the binary systems aromatic hydrocarbon (benzene, toluene)–light oil–gas component (CO_2, H_2S, N_2, CH_4, C_2H_6, C_3H_8) and polyaromatic hydrocarbon (naphthalene, phenanthrene)–light oil–gas component (N_2, CH_4, CO_2) over wide temperature and pressure ranges using HM. Solution of this task included determination of new corresponding group parameters and evaluation of potentialities of the model for predicting phase diagrams of the above-mentioned binary systems and a series of ternary systems. The results of modeling were compared with the experimental data and those predicted by the Peng–Robinson equation of state.

The equation of state derived from HM is written as

$$\frac{pv^*}{RT} = -\ln(1-\rho) + \rho\left(\sum_{i=1}^{n} x_i l_i\right)\left(\sum_{i=1}^{n} x_i r_i\right)^{-1}$$

$$+ 0.5z\left\{1 - \rho\left[1 - \left(\sum_{i=1}^{n} x_i q_i\right)\left(\sum_{i=1}^{n} x_i r_i\right)^{-1}\right]\right\} - z\ln X_0,$$

where p is the pressure; v^*, molar volume per single lattice site; x_i, mole fraction of the ith component; $l_i = -z(q_i - r_i)/2 - (r_i - 1)$, molecular bulkiness factor; z, coordination number of the lattice; r_i and q_i, geometrical parameters characterizing the volume and surface area of the ith molecule which are related to the corresponding values of the groups composing the molecule by $r_i = \Sigma \nu_s r_s$ and $q_i = \Sigma \nu_s q_s$ (ν_s is the number of groups of the s type in the ith molecule); $\tilde{\rho} = v^* \sum_{i=1}^{n} x_i r_i / v$, reduced density ($v$ is the molar volume); and X_0, solution of the system of quasichemical equations $X_s \Sigma \alpha_t X_t \exp[-(\Delta\varepsilon_{st}/kT)] = 1$, where the indices s and t refer to the molecular surface sites (groups) whose interaction is described by the interchange energies $\Delta\varepsilon_{st}$ [$s = 0$ for lattice vacancies (holes)] and α_t is the fraction of the surface area occupied by the groups of the t type in the system.

The $\Delta\varepsilon_{st}$ depends on the temperature:

$$\Delta\varepsilon_{st}/(kT) = w_{st} + h_{st}(T_0 - T)/T + c_{st}[\ln(T_0/T) - (T_0 - T)/T],$$

where w_{st}, h_{st}, and c_{st} are energy parameters of the model (free energy, enthalpy, and interchange heat capacity, respectively) expressed in the kT_0 units and T_0 is some standard temperature.

Therefore, calculations by HM require a set of the geometrical (r_s and q_s) and energy group parameters (w_{st}, h_{st}, and c_{st}).

Here we will not dwell upon the details of HM and calculation procedure by this model, since they are reported in detail in [2, 4]. Note that HM represents a generalized solution of the Barker's lattice model for systems with vacancies, taking into account the size and shape of the molecules composing the system and also the orientation effects associated with energy inhomogeneity of the molecular surface. It should be pointed out that, on the assumption of random distribution of molecules and holes between the points of the quasilattice, the above, complex in appearance, equation of state is reduced to the Sanchez and Lacombe's equation as a particular case [13], and at $p \to 0$, the Victorov–Smirnova's equation is reduced to the equation of state for the ideal gas.

As a first step in modeling liquid–vapor equilibria, it was necessary to select some binary systems for which the experimental data are available. These data were then used for validation of the equations of state and optimization of the model parameters. In making efforts on collection and systematization of experimental data on the phase equilibria in binary and multicomponent mixtures containing oil–gas components, a data bank of phase equilibria in oil–gas systems has been developed.[2] The data bank covers data on more than 1300 binary and multicomponent systems (more than 5000 datasets). Among them are mixtures with *n*- and *iso*-alkanes, benzene, toluene, hydrogen sulfide, carbon dioxide, water, and solutions of subcritical and supercritical components in aqueous–organic solvents. For the indicated systems, the data bank is one of the most complete in the Europe. Note that the bank contains not the experimental data files, but their detailed specification, including references to the literature sources, type of the equilibrium, experimental conditions, and data format in the original

[2] Over a period of years, this work is being intensively conducted at the Laboratiry of Nonelectrolyte Solutions, Chair of Physical Chemistry, St. Petersburg State University.

Table 1. Group parameters and thermodynamic characteristics of pure polyaromatic hydrocarbons

Types of *s* and *t* groups	w_{st}	h_{st}	c_{st}
>C=–CH	–1.1814	–1.5609	1.1863
CH–hole	0.2502	0.2205	0.0475
>C=–hole	0.2502	0.2205	0.0475

r_{CH} = 1.03175, r_C = 0.20473, l_{CH} = 1.0, l_C = 1.0

Hydrocarbon	*T*, K	$\delta\rho^l$	δP, %
Naphthalene	373–633	0.7	0.7
Phenanthrene	373–563	0.5	0.4

source. We intensively used the data bank for estimating parameters of the Victorov–Smirnova's quasichemical model. This allowed selection of the most representative and reliable data. Analysis of all the available data on binary mixtures of oil–gas components revealed specific features of the phase behavior in the indicated systems in the subcritical range.[3]

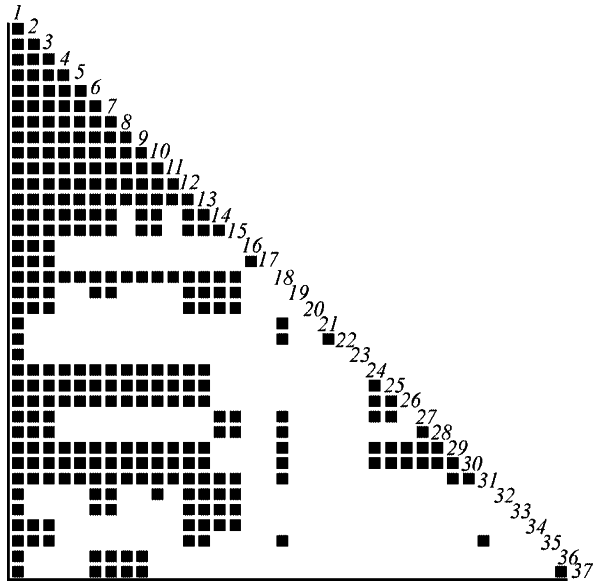

Fig. 1. Matrix of group parameters of HM. Filled elements refer to available parameters. (*1*) Hole, (*2*) CH_2, (*3*) CH_3, (*4*) S (H_2S), (*5*) H (H_2S), (*6*) C (CO_2), (*7*) 2O (CO_2), (*8*) N_2, (*9*) C_1, (*10*) C_2, (*11*) C_3, (*12*) O (H_2O), (*13*) 2H (H_2O), (*14*) O (alkanols), (*15*) H (alkanols), (*16*) CH_3COO, (*17*) H (CH_3COOH), (*18*) ACH (aromatics), (*19*) CH_2=CH(alkenes), (*20*) C≡C (alkynes), (*21*) ACCOO, (*22*) H (ACCOOH), (*23*) CH_3CH_3CH–, (*24*) =CH–, (*25*) C_3H_6 (acetone), (*26*) O= (acetone), (*27*) N (NH_3), (*28*) 3H (NH_3), (*29*) CH_3O (MeOH), (*30*) H (MeOH), (*31*) CCH_3 (toluene), (*32*) C_2H_5 (EtOH), (*33*) C_3H_7 (*i*-PrOH), (*34*) OCH_2CH_2–, (*35*) N– (pyridine), (*36*) CH= (polyaromatics), and (*37*) >C= (polyaromatics).

In the recent decade, researchers gained a great body of experimental data on the liquid–vapor equilibria in the systems aromatic hydrocarbon–light oil–gas component, and considerably lesser, on mixtures of polyaromatic hydrocarbons with oil–gas fluids. These data are mostly either sets of the pressure–composition isothermal data ($P - x$) or data on the solubility of components. Over a wide range of conditions, methane and nitrogen are permanent gases, while the other light oil–gas fluids can occur both in the sub- and supercritical states. In this work we examined 18 binary and two ternary mixtures with attraction of about 110 published experimental datasets.

Following the group-contribution approach used in HM, molecules of the components were divided into groups in the following way: CO_2 and H_2S were divided into two types of groups each (O and C, and H and S); benzene, into six ACH groups; toluene, into five ACH groups and CCH_3–; and naphthalene and phenanthrene were represented as combinations of the CH and >C= groups. It was accepted also that the geometrical parameters of the ACH and CH groups in aromatic and polyaromatic hydrocarbons are the same. The nitrogen and lower alkane molecules were not divided into groups. In HM calculations, the molar volume of the standard segment was accepted to be v^* = 14.244 $cm^3\,mol^{-1}$ and the lattice coordination number, z = 10. For cyclic structures, including those of polyaromatic hydrocarbons, the molecular bulkiness factors were taken equal to unity. The geometrical and energy parameters of groups of the above-indicated components (except for the polyaromatic compounds) were reported earlier [3–5, 8]. For naphthalene and phenanthrene, these parameters of HM were obtained in this work from data on the saturated vapor pressure and density of the liquid phase [14–17]. These data and the saturation line parameters of these compounds are given in Table 1. The number of energy parameters (interchange energies) of the model is smaller than that of the types of contacts between the groups, since some averaged parameters are introduced that refer to only a few nonspecific contact types.

In addition to simulation of the vapor–liquid equilibria in the indicated binary systems, HM was applied to model the phase behavior in these systems, and the results obtained were compared with the experimental data. Figure 1 shows the matrix of group

[3] For brief information on the data bank, see http://www.chem.msu.su/rus/chinfo/fluid/welcom.html. Much work on extension of the bank is being carried out by L.I. Reshetova.

Table 2. Comparative data for the equilibrium pressure in the investigated systems, estimated by the Victorov–Smirnova's hole model and the Peng–Robinson EOS

System	T, K	P, MPa	δP, %	
			HM	PR (k_{ij})
CO_2–benzene	273.2–413.6	0.1–10.5	5.0	5.0 (0.097)
CO_2–toluene	290.8–542.7	0.3–13.6	4.3	3.6 (0.097)
H_2S–benzene	323.2–422.7	0.5–9.8	2.1	1.5 (0.006)
H_2S–toluene	310.9–477.6	0.2–11.6	3.5	4.3 (0.0)
N_2–benzene	303.2–410.9	3.2–35.6	2.8	4.6 (0.201)
N_2–toluene	313.2–548.2	1.5–40.0	6.6	7.9 (0.206)
C_1–benzene	313.2–501.2	1.5–37.4	4.3	8.1 (0.064)
C_1–toluene	313.2–543.2	0.7–42.4	5.4	9.5 (0.058)
C_2–benzene	298.2–415.2	0.8–8.3	1.6	2.9 (0.039)
C_2–toluene	313.1–473.2	0.6–10.2	2.8	4.5 (0.033)
C_3–benzene	310.9–477.6	0.1–5.9	4.2	2.5 (0.036)
C_3–toluene	312.8–473.2	0.3–6.6	3.4	1.5 (0.034)
CO_2–naphthalene	373.2–423.2	1.4–10.5	3.4	3.9 (0.120)
CO_2–phenanthrene	383.2–423.2	1.9–10.6	2.5	4.2 (0.143)
N_2–naphthalene	377.6–410.9	6.2–18.8	1.0	0.9 (0.287)
N_2–phenanthrene	383.2–410.9	10.4–21.4	3.6	3.3 (0.398)
C_1–naphthalene	373.2–423.2	1.9–8.7	2.2	0.6 (–0.119)
C_1–phenanthrene	383.2–423.2	2.0–10.7	2.2	1.1 (–0.097)

parameters of HM obtained in this work and previously, which reflects the specific features of division of the component molecules into separate chemical groups. The list of binary mixtures examined in this work is given in Table 2, also including the binary interaction parameter k_{ij} of the Peng–Robinson equation [18]. This parameter was varied for both every temperature from the experimental dataset and for a wide series of isotherms. Because of its negligible value in the systems H_2S–aromatic hydrocarbon, k_{ij} was accepted to be zero for these systems. In the systems N_2–aromatic hydrocarbon, k_{ij} appeared to be somewhat higher as compared to other binary mixtures. We estimated the vapor composition and equilibrium pressure at fixed temperatures and solution compositions. The vapor–liquid equilibrium simulation results are summarized in Table 2. Some examples of the phase diagrams of binary systems estimated by HM and PR EOS are presented in Figs. 2–4. The energy parameters of HM estimated from the experimental data on the liquid–vapor equilibria in the binary systems are listed in Table 3.

It follows from Table 2 and Figs. 2–4 that both equations of state used are suitable for description of all the binary system of the indicated type over a wide temperature range. We did not include the mean absolute deviation of the experimental vapor composition from the estimated value in Table 2, since the vapor practically totally consists of the light oil–gas component.

Figure 5 shows the vapor pressure in the CO_2–benzene–naphthalene system, predicted by HM and PR EOS, and the experimental values taken from [22].

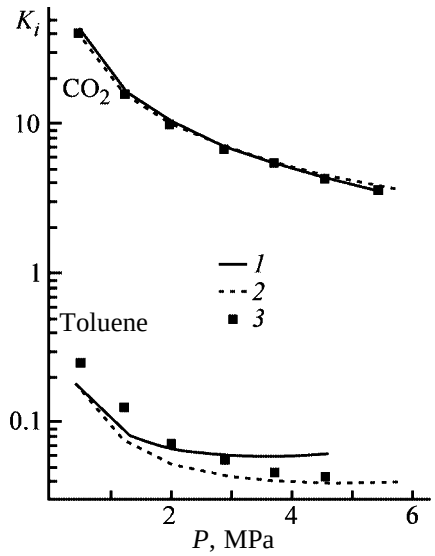

Fig. 2. Comparison of the experimental and predicted distribution coefficients of the components K_i in the system CO_2–toluene at 373.2 K. (P) Pressure. (*1*) HM, (*2*) PR EOS, (*3*) experimental data from [19].

Table 3. Energy parameters of the hole model for mixtures aromatic (or polyaromatic) hydrocarbon–light oil–gas component (T_0 = 298.16 K)

Types of *s* and *t* groups	w_{ss}	h_{st}	c_{st}
$C(CO_2)$–ACH	–0.0941	0.2115	–0.4389
$O(CO_2)$–ACH	–0.0941	0.2115	–0.4389
$C(CO_2)$–CCH_3	–0.1024	0.1658	–0.3585
$O(CO_2)$–CCH_3	–0.1024	0.1658	–0.3585
$S(H_2S)$–ACH	–0.0061	0.3249	–0.1961
$H(H_2S)$–ACH	–0.0061	0.3249	–0.1961
$S(H_2S)$–CCH_3	–0.0095	0.2277	0.4956
$H(H_2S)$–CCH_3	–0.0095	0.2277	0.4956
N_2–ACH	0.0789	0.0948	0.0704
N_2–CCH_3	0.0490	–0.2337	0.8107
C_1–ACH	0.0349	–0.0059	0.1624
C_1–CCH_3	0.0390	0.2757	–0.9173
C_2–ACH	0.0209	0.0310	0.0
C_2–CCH_3	0.0131	0.0564	0.0
C_3–ACH	0.0129	0.0399	0.0
C_3–CCH_3	0.0072	–0.0068	0.0
$C(CO_2)$–CH (polyaromatic)	–0.1315	0.0380	0.0
$O(CO_2)$–CH (polyaromatic)	–0.1315	0.0380	0.0
$C(CO_2)$–>C= (polyaromatic)	–0.1315	0.0380	0.0
$O(CO_2)$–>C= (polyaromatic)	–0.1315	0.0380	0.0
N_2–CH (polyaromatic)	0.0525	0.0521	0.0
N_2–>C= (polyaromatic)	1.8318	4.4115	0.0
C_1–CH (polyaromatic)	0.0264	0.0372	0.0
C_1–>C= (polyaromatic)	0.0264	0.0372	0.0

The results show that HM better reproduces the experimental data than PR EOS. For the CO_2–toluene–naphthalene system, HM provides a reasonable prediction for the liquid–liquid–vapor equilibrium. For example, the heterogeneous region is predicted at T = 308–313 K and P = 7.1–8.0 MPa, which is consistent with the experimental data from [23] (note that there are only a few experimental data on the phase equilibria in ternary systems containing the fluids under consideration).

The simulation results obtained with HM and PR EOS show that the maximal deviations between the theoretical and experimental vapor pressures are observed in the vicinity of the critical point. Note that this is a common drawback of any classical equation of state, including HM and PR EOS. With examples of the systems considered in this work, one cannot draw an unambiguous conclusion what equation of state is the best suited. Nevertheless, it may be stated that HM more precisely reproduces the density of the liquid phase. Furthermore, it was demonstrated that HM gives good results in systems with polar, particularly, associated fluids, where equations of the van der Waals type are mostly unsuitable. A group-contribution version of the hole model, developed by Victorov and Smirnova, demonstrates good predictive potential, as demonstrated by the examples of the binary and ternary systems studied. At the same time, PR EOS is considered essentially as a tool for presentation (correlation) of experimental data. To conclude, the hole lattice group-contribution model can be recommended for practical use as a tool for *a priori* predictions.

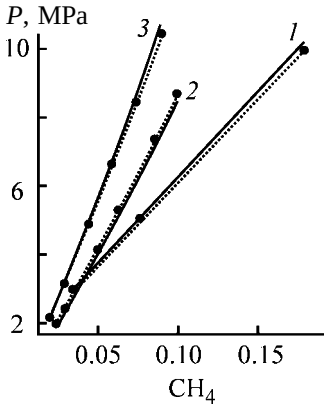

Fig. 3. Equilibrium vapor pressure P as a function of the solution composition for systems (*1*) methane–benzene, (*2*) methane–naphthalene, and (*3*) methane–phenanthrene. (CH_4) Mole fraction of methane. Temperature (K): (*1*) 461.9, (*2*) 373.2, and (*3*) 423.2. (*1*) HM, (*2*) PR EOS, and (*3*) experimental data from [20].

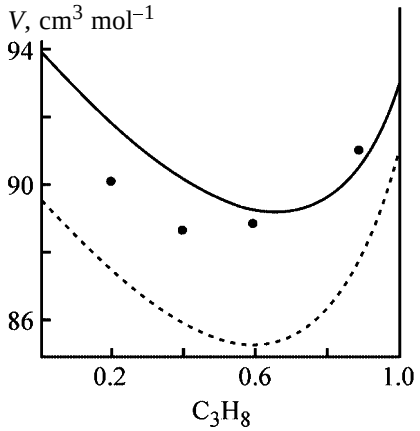

Fig. 4. Molar volume of the liquid phase V as a function of the composition in the system propane–benzene at 311 K. (C_3H_8) Mole fraction of propane. (*1*) HM, (*2*) PR EOS, and (*3*) experimental data from [21].

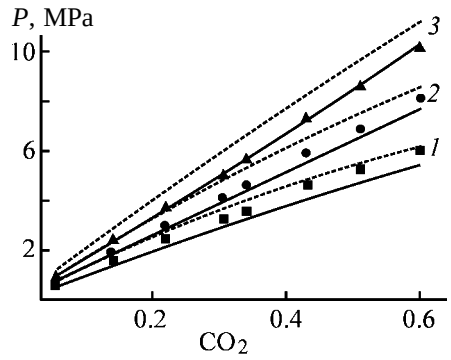

Fig. 5. Experimental and estimated pressure P of the coexisting phases in the CO_2–benzene–naphthalene system. Benzene to naphthalene molar ratio 9 : 3. (CO_2) Mole fraction of CO_2. Temperature (K): (*1*) 313.15, (*2*) 333.15, and (*3*) 353.15. (*1*) HM, (*2*) PR, and (*3*) experimental data from [22].

CONCLUSIONS

(1) The Victorov and Smirnova's hole lattice group-contribution model appeared to be quite applicable to description of some binary and ternary systems containing light oil–gas components and aromatic and polyaromatic hydrocarbons.

(2) The database of group parameters of the model was extended, to simulate phase equilibria in oil–gas systems with the indicated components.

(3) The model allows reasonably accurate prediction of the fluid phase equilibria in the systems under consideration.

ACKNOWLEDGMENTS

The authors are grateful to Professor A.G. Morachevskii for reading the manuscript and valuable discussions.

The work was financially supported by the Russian Foundation for Basic Research (project nos. 00-15-97353 and 02-03-32709).

REFERENCES

1. Viktorov, A.I., Kuranov, G.L., Morachevskii, A.G., and Smirnova, N.A., *Zh. Prikl. Khim.*, 1991, vol. 64, no. 5, pp. 961–978.
2. Smirnova, N.A. and Victorov, A.I., *IUPAC*, vol. 5: *Equations of State for Fluids and Fluid Mixtures*, Sengers, J.V., Kayser, R.F., Peters, C.J., and White, H.J., Eds., Amsterdam: Elsevier, 2000, pp. 255–288.
3. Smirnova, N.A. and Victorov, A.I., *Fluid Phase Equil.*, 1987, vol. 34, pp. 235–263.
4. Morachevskii, A.G., Smirnova, N.A., Piotrovskaya, E.M., *et al.*, *Termodinamika ravnovesiya zhidkost'–par* (Thermodynamics of Liquid–Vapor Equilibria), Leningrad: Khimiya, 1989.
5. Prikhod'ko, I.V., Schmelzer, J., Viktorov, A.I., and Smirnova, N.A., *Zh. Prikl. Khim.*, 1989, vol. 62, no. 12, pp. 2738–2744.
6. Victorov, A.I., Fridensland, Aa., and Smirnova, N.A., *Fluid Phase Equil.*, 1991, vol. 66, pp. 187–210.
7. Deak, A., Victorov, A.I., and de Loos, Th.W., *Fluid Phase Equil.*, 1995, vol. 107, pp. 277–301.
8. Prikhod'ko, I.V., Victorov, A.I., Smirnova, N.A., and de Loos, Th.W., *Fluid Phase Equil.*, 1995, vol. 110, pp. 17–30.
9. Viktorov, A.I., Morachevskii, A.G., Prikhod'ko, I.V., and Smirnova, N.A., *Vestn. Sankt-Peterb. Gos. Univ.*, *Ser. 4*, 1995, issue 3, pp. 24–32.
10. Prikhod'ko, I.V., Letcher, T.M., and de Loos, Th.W., *Ind. Eng. Chem. Res.*, 1997, vol. 36, pp. 4391–4396.
11. Kuranov, G., Rumpf, B., Maurer, G., and Smirnova, N.A., *Fluid Phase Equil.*, 1997, vol. 136, pp. 147–162.
12. Hofman, T., Gonzalez, J., and Casanova, C., *Fluid Phase Equil.*, 1999, vol. 156, pp. 3–20.
13. Sanchez, I.C. and Lacombe, R.H., *J. Phys. Chem.*, 1976, vol. 80, pp. 2568–2580.
14. Vargaftik, N.B., *Spravochnik po teplofizicheskim svoistvam gasov i zhidkostei* (A Handbook of Thermal Characteristics of Gases and Liquids), Moscow: Nauka, 1972.
15. Kudchadker, A.P., Kudchadker, S.A., and Withoit, R.S., *API Monograph Series, Monograph no. 707: Naphthalene*, Washington, DC: Am. Petroleum Inst., 1978.
16. Kudchadker, A.P., Kudchadker, S.A., and Withoit, R.S., *API Monograph Series, Monograph no. 708: Anthracene and Phenanthrene*, Washington, DC: Am. Petroleum Inst., 1979.
17. Ruužička, K., Mokbel, I., Majer, V., *et al.*, *Fluid Phase Equil.*, 1998, vol. 148, pp. 107–137.
18. Peng, D. and Robinson, D.B., *Ind. Eng. Chem. Fundam.*, 1976, vol. 15, pp. 59–64.
19. Kim, C.-H., Vimalchand, P., and Donohue, M.D., *Fluid Phase Equil.*, 1986, vol. 31, pp. 299–311.
20. Malone, P.V. and Kobayashi, R., *Fluid Phase Equil.*, 1990, vol. 55, pp. 193–205.
21. Glanville, J.W., Sage, B.H., and Lacey, W.N., *Ind. Eng. Chem.*, 1950, vol. 42, pp. 508–513.
22. Al-Sahhaf, T.A., Al-Ameeri, R.S., Nashef, I.M., and Hamam, S.E.M., *Fluid Phase Equil.*, 1990, vol. 55, pp. 231–240.
23. Hong, S.-P. and Luks, K.D., *Fluid Phase Equil.*, 1992, vol. 74, pp. 133–144.

Russian Journal of Applied Chemistry, Vol. 75, No. 11, 2002, pp. 1780–1783. Translated from Zhurnal Prikladnoi Khimii, Vol. 75, No. 11, 2002, pp. 1816–1819.
Original Russian Text Copyright © 2002 by Muminov, Gulyamova, Seitova.

SORPTION AND ION-EXCHANGE PROCESSES

Adsorption of Carbon Tetrachloride on Pyridinium Montmorillonite

S. Z. Muminov, D. B. Gulyamova, and E. A. Seitova

Institute of General and Inorganic Chemistry, Academy of Sciences of Uzbekistan, Tashkent, Uzbekistan

Received October 25, 2001; in final form, July 2002

Abstract—Effect of substitution of Na^+ by pyridinium on the surface and pore structures of montmorillonite is studied by CCl_4 vapor adsorption.

Growing practical use of natural mineral sorbents causes the need in the study of these adsorbents, particularly, the features of the surface and pore structure of minerals forming their basis. A special attention is paid to clay sorbents modified with various surfactants, including the effect of the low-molecular-weight cationic surfactants on the sorption and energy characteristics of clay minerals.

Various organo clays were obtained [1]. These materials, particularly organo derivatives of montmorillonite, hold promise, since they can be used as adsorbents, fillers in paints and plastic materials, supports in gas chromatography, and also for deactivation.

Treatment of clay minerals of the layer (montmorillonite, vermiculite, and kaolin) and layer–ribbon structures (palygorskite) with alkylammonium and alkyldiammonium salts strongly modifies their surface structure [2]. The adsorption properties of pyridinium montmorillonite were studied in [3–5]. Berezin [6] reported application of organo montmorillonite of this type for separation of three xylene isomers, and Van Olphen [7] employed it as a model adsorbent, to make a quantitative estimate for hydrocarbon liberation from oil strata.

In this work we studied CCl_4 adsorption on dehydrated pyridinium montmorillonite (PyMt). The data obtained on the adsorption isotherms and the heat of adsorption were compared with those for sodium montmorillonite (NaMt).

The pyridinium montmorillonite was prepared by the method described in [3]. A 2% suspension of Azkamar white bentonite consisting essentially of NaMt was treated with 0.02 N aqueous pyridine hydrochloride. The basal interplanar spacing in PyMt was found by XRD to be 1.327 nm, which corresponds to the distance between the basal silicate layers of the neighboring stacks (Δd_{001}) of 0.367 nm.

The CCl_4 vapor adsorption isotherms were obtained using a McBain balance, and a series of isosteres, on an isosteric experimental setup [8] with a small dead volume. Prior to measuring the adsorption, PyMt was dried and heated in a vacuum at 293, 423, and 523 K; and NaMt, at 423 K to a residual pressure in the system of about 1.3×10^{-3} Pa.

The isotherms of CCl_4 adsorption on NaMt and PyMt are shown in Fig. 1. Adsorption of CCl_4 on NaMt, like that of benzene on this clay mineral, is controlled essentially by its surface. At medium and high CCl_4 relative pressures P/P_s, hysteresis loops are observed in the isotherms, corresponding to formation of polylayers and a capillary condensate of CCl_4 in the secondary pores formed by the platelike mineral

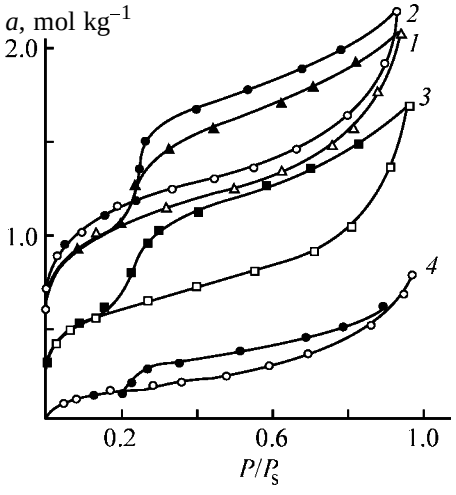

Fig. 1. Isotherms of CCl_4 vapor adsorption at 293 K on heat-treated (*1*–*3*) PyMt and (*4*) NaMt. (*a*) Adsorption and (P/P_s) CCl_4 relative pressure.

1070-4272/02/7511-1780$27.00 © 2002 MAIK "Nauka/Interperiodica"

particles. The width of the hysteresis loops is nearly constant for all the PyMt samples, and that for the NaMt sample is considerably narrower. For PyMt, the adsorption isotherms at low CCl_4 pressure rise steeply, which is typical of microporous adsorbents. At very low CCl_4 pressures, the pyridinium cations in PyMt still tightly fix the aluminosilicate layers, and adsorption of CCl_4 occurs on the outer surface. The interlayer space in PyMt starts to open at $P/P_s > 0.005$ to $\Delta d_{001} = 0.546$ nm as a result of the vertical orientation of the pyridinium cations [4], thus favoring the adsorption of CCl_4.

Keeping PyMt in a vacuum at room temperature (293 K) results in the removal of the major amount of physically adsorbed moisture. In this case, the initial (at low P/P_s) adsorption of CCl_4 considerably increases relative to that on NaMt. Thermal treatment of PyMt at 423 K provides some increase in the adsorption. The sorption capacity of PyMt heat-treated at 523 K significantly decreases because of thermal degradation of the organic component.

Both NaMt and PyMt demonstrate a reversible adsorption at $P/P_s < 0.2$ (initial sections of the isotherms). The shape of the hysteresis loop in the CCl_4 adsorption isotherms can be related to the B type by the De Boer classification [9]. This type of hysteresis can be initiated by adsorption in slotlike micropores open from all sides. At $P/P_s \sim 0.21–0.22$, the desorption isotherms are steeply curved, which is associated with disordering of the thixotropic structure [10] formed upon saturation of the sorbents.

The sorption volumes of the heat-treated PyMt samples with respect to CCl_4 at P/P_s 0.2 (W), 0.4 (W_0), and 1.0 (V_s), and also the mesopore volumes $W_{me} = V_s - W_0$ estimated from the adsorption isotherms are given in the table below. For comparison, we included the sorption data for NaMt dehydrated at 423 K.

It is seen that the micropore volumes W_0 of sample nos. 1 and 2 amount to only 59% of the total pore volume, and that of sample no. 3, to even 44%. With thermal treatment at 293–423 K, W_0 of PyMt increases by about 5% (from 0.116×10^{-3} to 0.122×10^{-3} $m^3\ kg^{-1}$). Thermal treatment of PyMt at 523 K leads to a considerable decrease in the micropore volume. Based on the micro- to mesopore volume ratios, PyMt should be classified with micro-mesoporous adsorbents.

The changes in the surface and pore structure of montmorillonite initiated by substitution of Na^+ by $[C_5H_5NH]^+$ can be judged from data on the heat of CCl_4 adsorption on the initial and modified montmorillonite samples. The heat of adsorption was determined from the temperature dependence of the adsorption, i.e., from the CCl_4 adsorption isosteres obtained over the temperature range 260– 340 K at fillings from fractions of V_s to the saturation (sample nos. 2,

Sorption volumes of PyMt and NaMt

Sample no.	T_d,* K	$W \times 10^3$	$W_0 \times 10^3$	$V_s \times 10^3$	$W_{me} \times 10^3$
		$m^3\ kg^{-1}$			
		PyMt			
1	293	0.106	0.116	0.195	0.079
2	423	0.116	0.122	0.211	0.089
3	523	0.058	0.071	0.162	0.091
		NaMt			
4	423	0.016		0.077	

* (T_d) Dehydration temperature.

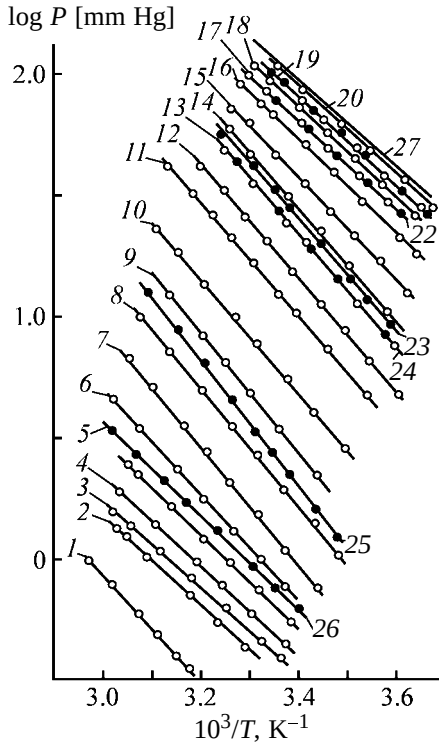

Fig. 2. Isosteres of (*1–20*) adsorption and (*21–26*) desorption of CCl_4 on PyMt (sample no. 2) corresponding to various amounts of adsorbed CCl_4. (P) Pressure and (T) temperature. Adsorption of CCl_4 (mol kg^{-1}): (*1*) 0.25, (*2*) 0.42, (*3*) 0.48, (*4*) 0.54, (*5*) 0.60, (*6*) 0.68, (*7*) 0.73, (*8*) 0.80, (*9*) 0.85, (*10*) 0.91, (*11*) 0.98, (*12*) 1.03, (*13*) 1.08, (*14*) 1.13, (*15*) 1.17, (*16*) 1.26, (*17*) 1.34, (*18*) 1.44, (*19*) 1.66, (*20*) 1.88, (*21*) 1.58, (*22*) 1.40, (*23*) 1.19, (*24*) 1.06, (*25*) 0.79, and (*26*) 0.63; (*27*) $\log P_s–T^{-1}$ for free (not adsorbed) CCl_4.

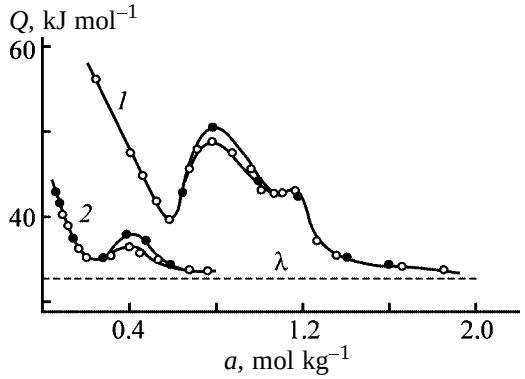

Fig. 3. Differential isosteric heat of adsorption of CCl_4 on (*1*) PyMt and (*2*) NaMt as a function of the amount of adsorbed CCl_4. (Q) Heat of adsorption, (a) adsorption, and (λ) heat of condensation.

4). For example, Fig. 2 shows a series of the CCl_4 adsorption isosteres obtained for sample no. 2 and plotted in the coordinates $\log P$–T^{-1}. The isosteres are fitted by straight lines, indicating that the heat of adsorption is temperature-independent over the experimental range. The upper line gives the dependence of the saturated vapor pressure of bulk CCl_4 on the reciprocal temperature. The slopes of the isosteres depend on the CCl_4 adsorption. The differential isosteric heats of adsorption Q_a and desorption Q_d in the systems CCl_4–PyMt and CCl_4–NaMt were calculated using the Clausius–Clapeyron equation from the slope of the isosteres. The results are presented in Fig. 3.

The dependences of Q_a and Q_d on the CCl_4 adsorption in the systems under consideration steeply decrease to a minimum at low fillings, then increase reaching a maximum at intermediate fillings, and finally decrease gradually, approaching the heat of condensation of the bulk CCl_4 (33.2 kJ mol^{-1}). Over the entire range, the heat of CCl_4 adsorption on PyMt is considerably higher than that on NaMt. The initial decrease in Q at low fillings in both the CCl_4–PyMt and CCl_4–NaMt systems is probably due to inhomogeneity of the outer surface of the adsorbent.

Taking into account the similarity of the initial sections in the $Q = f(a)$ curves for the two systems, it appears reasonable to estimate the heats of CCl_4 adsorption on PyMt and NaMt by extrapolation to zero filling ($\theta = 0$). Such extrapolation gave 74.5 and 45.6 kJ mol^{-1} for PyMt and NaMt, respectively. Comparison of these values suggests higher inhomogeneity of the PyMt outer surface as compared to NaMt. Since the CCl_4 molecules are insensitive to dehydration of, for example, silica [11], it should be assumed that the heat liberation in adsorption of CCl_4 on PyMt is caused essentially by interaction of the adsorbate molecules with $[C_5H_5NH]^+$ and residual Na^+ ions, and that on NaMt, with Na^+ ions. The initial decrease in the heat of adsorption of CCl_4 on PyMt could be even steeper if it were not partly compensated by increase in the heat by virtue of strengthening interaction of the adsorbed molecules. For example, Kiselev *et al.* [12] have demonstrated that the heat of nonspecific adsorption of CCl_4 on graphitized thermal black increases with increasing adsorption as a result of the adsorbate–adsorbate interaction. In the CCl_4–PyMt system, the $Q = f(a)$ dependence shows a minimum (Q_a^{min} ~38.5 kJ mol^{-1}) at a = 0.60 mol kg^{-1} (i.e., at $\theta = a/a_0 = 0.55$, where a_0 is the adsorption at $P/P_s = 0.4$). In the system with NaMt, the minimum (Q_a^{min} ~33.6 kJ mol^{-1}) is observed at a = 0.30 mol kg^{-1}. The minimal value is close to the heat of condensation of the bulk CCl_4. After reaching the minimum, the heat of CCl_4 adsorption on PyMt rapidly rose to a maximum at $\theta = 0.67$ (Q_a^{max} ~47.5 kJ mol^{-1}). In this case, the difference between the minimal and maximal values is 9.0 kJ mol^{-1}.

In another system, the heat of adsorption shows a maximum at a ~0.4 mol kg^{-1} (Q_a^{max} ~36.5 kJ mol^{-1}). With increasing adsorption from 0.3 (a of the minimum) to 0.4 mol kg^{-1}, Q_a increased by 2.9 kJ mol^{-1}, i.e., to a considerably lesser extent than in the CCl_4–PyMt system. Evidently, the increase in Q_a in the CCl_4–NaMt system within the indicated filling range is caused by the interaction between the adsorbate molecules on the outer surface and in the secondary pores of the mineral. Data on the heat of adsorption on PyMt show that, over the indicated filling ranges, the heat of desorption increases to a greater extent than the heat of adsorption, so that the difference $\Delta Q^{max} = Q_d^{max} - Q_a^{max}$ was 4.5 and 1.3 kJ mol^{-1} in the systems CCl_4–PyMt and CCl_4–NaMt, respectively.

With further increasing CCl_4 adsorption on PyMt to 1.01 mol kg^{-1}, Q_a and Q_d decreased to 42.5 kJ mol^{-1} and then remained practically unchanged over the filling range 1.01–1.19 mol kg^{-1}. The constancy of the heats of adsorption and desorption at the adsorption close to the complete filling of the micropores suggests a uniform distribution of the active sites throughout the slotlike micropore structure and also the formation of ion–molecule complexes. At higher CCl_4 adsorption on PyMt and NaMt (a > 1.2 mol kg^{-1} and a > 0.4 mol kg^{-1}, respectively), polylayers and a capillary condensate are formed in the secondary pores of the adsorbent. As a result, the heats of adsorption

gradually approach the heat of condensation of bulk CCl_4.

CONCLUSIONS

(1) The effect of substitution of Na^+ by pyridinium on the adsorption properties of dehydrated montmorillonite clay is studied. The isosteres of CCl_4 vapor adsorption and desorption are obtained. From the changes in parameters of the adsorption equilibrium over a wide occupancy range, the differential isosteric heats of adsorption/desorption are estimated.

(2) Increase in the heat of adsorption of CCl_4 induced by substitution of Na^+ by pyridinium is a result of the formation of a highly developed slotlike micropore structure in the interlayer space of montmorillonite; CCl_4 adsorption on pyridinium montmorillonite occurs essentially in the micropores through formation of ion–molecule complexes.

REFERENCES

1. Grim, R.E., *Clay Mineralogy*, New York: McGraw-Hill, 1953.
2. Barrer, R.M., *Zeolites and Clay Minerals as Adsorbents and Molecular Sieves*, London: Academic, 1988, pp. 407–486.
3. Muminov, S.Z., Aripov, E.A., and Saidova, M.D., *Kolloidn. Zh.*, 1985, vol. 47, no. 4, pp. 813–816.
4. Van Olphen, H., *J. Colloid Interface Sci.*, 1968, vol. 28, nos. 3–4, pp. 370–375.
5. Muminov, S.Z. and Aripov, E.A., *Issledovaniya v oblasti termodinamiki i termokhimii adsorbtsii na glinistykh mineralakh* (Thermodynamics and Thermochemistry of Adsorption on Clay Minerals), Tashkent, 1987.
6. Berezin, V.G., Gavrichev, V.S., Kolomiets, L.N., *et al.*, *Gazovaya khromatografiya v neftekhimii* (Gas Chromatography in Petroleum Chemistry), Moscow: Nauka, 1975, pp. 200–235.
7. Van Olphen, H., *Earth Sci.*, 1965, no. 14, pp. 307–317.
8. Muminov, S.Z., *Uzb. Khim. Zh.*, 1965, no. 6, pp. 58–62.
9. De Boer, J.H., *The Structure and Properties of Porous Materials*, London: Butterworth, 1958, p. 68.
10. Muminov, S.Z. and Aripov, E.A., *Adsorbtsiya i poristost'* (Adsorption and Porosity), Moscow: Nauka, 1976, p. 71.
11. Babkin, I.Yu. and Kiselev, A.V., *Zh. Fiz. Khim.*, 1963, vol. 57, no. 1, pp. 228–231.
12. Kiselev, A.V., Kovaleva, N.V., Korolev, A.D., *et al.*, *Dokl. Akad. Nauk SSSR*, 1959, vol. 124, no. 3, pp. 617–620.

Russian Journal of Applied Chemistry, Vol. 75, No. 11, 2002, pp. 1784–1786. Translated from Zhurnal Prikladnoi Khimii, Vol. 75, No. 11, 2002, pp. 1820–1822.
Original Russian Text Copyright © 2002 by Pechenyuk, Kondakova, and Kashulina.

SORPTION AND ION-EXCHANGE PROCESSES

Dynamics of Copper(II), Nickel(II), and Iron(III) Ion Exchange

S. I. Pechenyuk, A. A. Kondakova, and T. G. Kashulina

Tananaev Institute of Chemistry and Technology of Rare Elements and Mineral Resources, Kola Scientific Center, Russian Academy of Sciences, Apatity, Murmansk oblast, Russia

Received June 18, 2002; in final form, September 2002

Abstract—The degree of utilization of the static exchange capacity of KU-2 × 8 × 12 cation exchanger with respect to copper(II), nickel(II), and iron(III) cations was considered as a function of the solution flow velocity through the column cross section.

Ion exchange is widely used for concentrating elements from aqueous solutions and for treating water [1, 2]. Large-scale ion-exchange processes (especially in industry) are performed in columns under dynamic conditions. It is known that the static exchange capacity (SEC) of ion exchangers cannot be utilized completely under the dynamic conditions. Two dynamic exchange capacities are considered: exchange capacity to breakthrough (DECB) and total dynamic exchange capacity at saturation (DECS). For water treatment, DECB is the most significant. It depends on the properties of the ion (charge, radius, polarizability, hydration) and ion exchanger structure (mainly pore size at swelling). The DEC value can depend of the solution flow velocity, since the ion exchange rate is limited by the diffusion within the ion exchanger grain or through the solution–resin grain boundary. Despite the practical importance of this question, papers in which it is discussed as applied to particular ion exchangers are scarce. A study of the dynamics of copper(II) and nickel(II) sorption and desorption on Amberlite IRC-718 cation exchanger under conditions of water treatment [3] can be such an example. It was found that this chelating resin efficiently recovers copper(II) from water but is inefficient with respect to nickel(II).

In this work, the degree of utilization of SEC of widely used Russian cation exchanger KU-2 × 8 × 12 with respect to Ni^{2+}, Cu^{2+}, and Fe^{3+} was studied at various velocities of the effluent flow through the column cross section.

EXPERIMENTAL

The H form of KU-2 × 8 × 12 cation exchanger (without sieving; prevailing fractions: d = 0.63–1.0 mm 45.5%, 0.4–0.63 mm 47.6%, 0.25–0.4 mm 4.8%) pretreated as described in [2] (equilibrated with water, washed successively with acid, alkali, again acid, and water to neutral reaction, and then washed to remove dust) was used. Two glass columns with a resin bed height l 86 (I) and 66 (II) cm and cross section S 1.13 and 2.00 cm^2, containing 71.5 and 97.5 g of the cation exchanger (calculated for air-dry resin), respectively, were used. Stoichiometric solutions of nickel(II) nitrate, copper(II) sulfate, and iron(III) chloride and a $FeCl_3$ solution acidified with HCl to 1 M were used as eluents. The chemicals were of analytically pure grade, and all the solutions had the same normal concentration of 0.7 g-equiv l^{-1}. SEC of the cation exchanger was determined for each above solution by the known method [2]; it was (mg-equiv g^{-1}) 8.03 [Ni(II)], 9.25 [Cu(II)], 7.47 [Fe(III)], and 6.45 [Fe(III) + HCl].

To determine DECB (Fig. 1), at equal intervals (25 ± 3 min) we took samples of the effluent, determined the content of ions {Ni(II) and Fe(III), spectrophotometrically [4] on an SF-26 spectrophotometer, and Cu(II), by atomic absorption method} in each of them, and calculated the average velocities of the solution flow and the amounts of cations adsorbed. When the concentration of the unsorbed cation began to steadily increase in the effluent, the process was stopped, and the column was washed with water to disappearance of the sorbate in the wash water and regenerated (washed with the acid) for the next experiment. The results obtained are presented in the table and in Figs. 1 and 2.

The shape of the output curve corresponding to column operation in the frontal mode is shown in Fig. 1. Here, the effluent volume V_b corresponds to breakthrough of the cation, V_s, to saturation, i.e.,

1070-4272/02/7511-1784$27.00 © 2002 MAIK "Nauka/Interperiodica"

DECB at various velocities of effluent flow

Cation sorbed	Column	Velocity, cm min^{-1}	DECB, mg-equiv g^{-1}	Degree of SEC utilization, %
Ni(II)	I	0.68	4.28	53.3
	I	0.97	3.56	44.3
	I	3.30	3.82	47.6
	I	17.25	4.10	51.0
	II	1.18	4.85	60.4
	II	2.43	4.48	55.8
Cu(II)	I	1.14	3.58	38.7
	I	3.68	3.15	34.0
	II	1.22	3.15	34.0
	II	4.55	2.87	31.0
Fe(III)	I	1.03	3.55	47.5
	I	3.97	3.05	40.8
Fe(III) + 1 M HCl	I	1.06	2.73	42.3
	I	4.21	1.99	30.8
	II	1.30	2.91	45.1
	II	3.14	2.18	33.8

complete utilization of SEC, and V', V'', and V''', to arbitrary instants in which the experiment was terminated (in the period of steady increase in the unsorbed cation concentration in the effluent). After termination of the experiment, the column was washed with water until concentration of the unsorbed ions decreased practically to zero. This is reflected in Fig. 1 by dashed lines corresponding to V', V'', and V'''. Thus, the output curve has the concentration peak. Usually, the effluent flow was stopped when the cation concentration reached 10–15% of the initial concentration (2–3 g l^{-1}). The shape of the output curves illustrates the steepness of the sorption front. The lower the effluent velocity, the steeper is the sorption front, and vice versa. Smearing of the sorption front is the weakest for nickel(II) cations and the strongest for iron(III) cations in the acidified solution (Fig. 2).

It follows from the table that SEC is different for the ions studied. For the copper(II) and nickel(II) cations, whose radii are 0.74 and 0.8 Å, respectively [5], the SEC is higher than for iron(III) cation with a radius of 0.67 Å. This may be due to the fact that less hydrated nickel(II) and copper(II) cations more readily and deeper penetrate into the resin pores. In addition, their bidentate coordination is less sterically demanding than tridentate coordination of Fe(III). SEC for Fe(III) in the acidified solution is lower than in the stoichiometric solution; this may be due to competition of Fe^{3+} and H^+ cations for the ion-exchanging groups.

In all the cases, the degree of utilization of SEC clearly decreases with increasing solution flow velocity, especially in the case of Fe(III) (see table). This is quite natural taking into consideration the larger size of the hydrated ion Fe^{3+}_{aq} as compared to Ni^{2+}_{aq} and Cu^{2+}_{aq} ions and hence the lower rate of its diffusion.

Since Fe^{3+} is very susceptible to hydrolysis [6], we should consider this factor. The first stage of Fe^{3+} hydrolysis is described by the equation of the acid

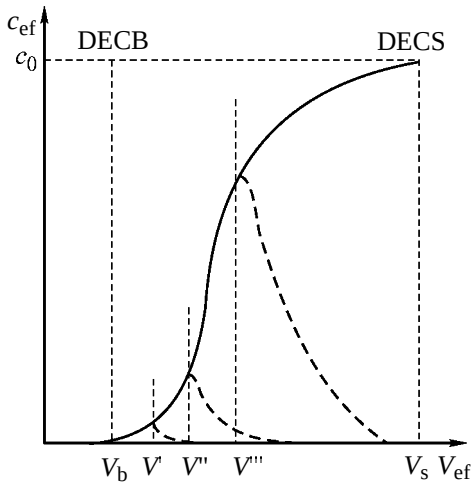

Fig. 1. General view of output curve at frontal mode of ion-exchange column operation. (c_{ef}) Effluent concentration; (V_{ef}) effluent volume; (c_0) initial effluent concentration; (V_b) effluent volume before breakthrough; (V_s) effluent volume at column saturation; and (V', V'', V''') effluent volumes at arbitrarily taken instants between breakthrough and saturation. Dashed lines show decrease in the sorbate concentration when the effluent at the inlet was replaced by water.

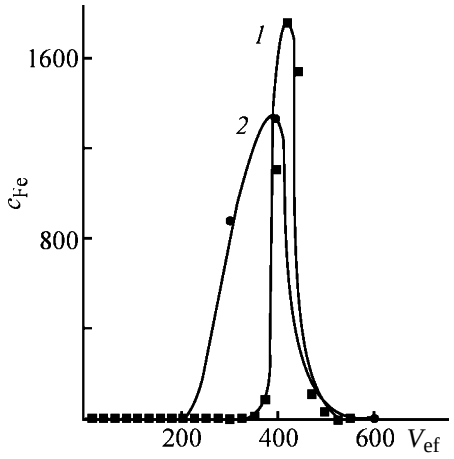

Fig. 2. Output curves of Fe(III) ion-exchange sorption. (c_{Fe}) Iron(III) concentration and (V_{ef}) effluent volume. Flow velocity (cm min^{-1}): (*1*) 1.03 and (*2*) 3.97.

dissociation of the iron(III) hexaaqua ion

$$[Fe(H_2O)_6]^{3+} \rightleftarrows [Fe(H_2O)_5OH]^{2+} + H^+$$

with the equilibrium constant of 10^{-3}. Calculation showed that, in a 0.23 M stoichiometric solution of $FeCl_3$, the degree of the hydrolysis amounts to 15.4%, and in the solution additionally containing 1 M HCl it is 0.66%. In both solutions, $[Fe(H_2O)_6]^{3+}$ is the prevailing species, and thus the hydrolysis should not appreciably affect the ion exchange. The hydrolysis affects the exchange of Ni(II) and Cu(II) cations with hydrolysis constants of about 10^{-3} [7, 8] still more weakly. Therefore, at concentrations higher than 0.2 M, to recover iron(III), we should use lower flow velocity than in recovery of nickel(II) but higher velocity than in recovery of copper(II).

However, with decreasing effluent concentration, the hydrolysis should become more pronounced. To estimate this effect, it is sufficient to calculate the solution composition from data on the first stage of the hydrolysis. For instance, in a 0.023 M solution of $FeCl_3$ the degree of the hydrolysis is 93.6%, e.g., the $[Fe(H_2O)_5OH]^{2+}$ ion is the prevailing species, and the Fe(III) behavior becomes similar to that of double-charged cations. In the acidified solution of $FeCl_3$, degree of the hydrolysis is 0.015%, and the difference in the behavior of the acidified and stoichiometric $FeCl_3$ solutions is very pronounced.

CONCLUSIONS

(1) The dynamic exchange capacity of KU-2 × 8 × 12 cation exchanger for metal cations weakly depends on the flow velocity; however, the degree of utilization of the static exchange capacity does not exceed 60% for nickel(II), 50% for iron(III), and 40% for copper(II) at equal effluent concentrations and flow velocities.

(2) At increased velocities of the effluent flow, the degree of utilization of the static exchange capacity for nickel(II) and copper(II) weakly decreases. For iron(III), this effect is more pronounced as a result of stronger diffusion resistance for the cation with a larger hydration shell.

(3) At concentrations of the cations studied close to 1 g-equiv l^{-1}, the hydrolysis does not affect the ion exchange.

REFERENCES

1. Rieman, W. and Walton, H.F., *Ion-Exchange Chromatography in Analytical Chemistry*, New York: Pergamon, 1970.
2. *Ionoobmennye vysokomolekulyarnye soedineniya* (Macromolecular Ion Exchangers), Saldadze, K.M., Ed., Moscow: Goskhimizdat, 1960.
3. Chen Jia-Ming and Chang Fang-Ching, *Sep. Sci. Technol.*, 2000, vol. 35, no. 8, pp. 1099–1116.
4. Charlot, G., *Les methods de la chimie analytique. Analyse quantitayive minerale*, Paris: Masson, 1961, 4 th ed.
5. Cotton, F.A. and Wilkinson, G., *Advanced Inorganic Chemistry*, New York: Interscience, 1966.
6. Flynn, C.M., *Chem. Rev.*, 1984, vol. 84, no. 1, pp. 31–41.
7. Peshkova, V.M. and Savostina, V.M., *Analiticheskaya khimiya elementov: Nikel'* (Analytical Chemistry of Elements: Nickel), Moscow: Nauka, 1966.
8. Podchainova, V.N. and Simonova, L.N., *Analiticheskaya khimiya elementov: Med'* (Analytical Chemistry of Elements: Copper), Moscow: Nauka, 1990.

Russian Journal of Applied Chemistry, Vol. 75, No. 11, 2002, pp. 1787–1790. Translated from Zhurnal Prikladnoi Khimii, Vol. 75, No. 11, 2002, pp. 1823–1825.
Original Russian Text Copyright © 2002 by Saikova, Panteleeva, Nikolaeva, Pashkov.

SORPTION AND ION-EXCHANGE PROCESSES

Optimal Conditions of Ion-Exchange Synthesis of Cobalt(II) Hydroxide with AV-17-8 Anion Exchanger in the OH Form

S. V. Saikova, M. V. Panteleeva, R. B. Nikolaeva, and G. L. Pashkov

Institute of Chemistry and Chemical Technology, Siberian Division, Russian Academy of Sciences, Krasnoyarsk, Russia
Krasnoyarsk State University, Krasnoyarsk, Russia

Received Oktober 31, 2001; in final form, April 2002

Abstract—Ion-exchange synthesis of cobalt(II) hydroxide by treatment of aqueous solutions of cobalt salts with OH form of AV-17-8 anion exchanger was studied. The influence of time, anion of cobalt salt, number of precipitation stages, and anion exchanger swelling on the degree of cobalt(II) precipitation was examined.

It is convenient to synthesize cobalt-containing substances (including salts) from cobalt(II) hydroxide, which readily dissolves in acids and does not participate in side redox reactions. As a result, pure salts are formed. Traditional preparation of cobalt(II) hydroxide by exchange of cobalt salts with a small excess of alkali gives the product contaminated with anions of the initial cobalt salt and cations of the precipitant, whose removal requires special separation procedures. In a strongly alkaline medium, $Co(OH)_2$ is readily oxidized into cobalt(II, III) hydroxide whose dissolution proceeds under more rigid conditions and is accompanied by redox reactions, which is unacceptable in preparation of certain cobalt-containing substances.

Basing on reference data [1], we assumed that cobalt(II) hydroxide can be prepared using an anion exchanger in the OH form. Because of sufficiently strong binding of anions of cobalt salt with the anion exchanger, $Co(OH)_2$ can be prepared in a weakly alkaline medium, avoiding noticeable oxidation of cobalt(II).

In the case of $CoCl_2$ solution, such a process can be described by the equation

$$2R\text{–}OH + CoCl_2 \rightarrow 2R\text{–}Cl + Co(OH)_2.$$

In [2], we showed that the use of an anion exchanger, indeed, allows the synthesis of cobalt(II) hydroxide at pH 6–7.

We also found that, for efficient precipitation of cobalt(II) hydroxide as a separate phase, it is necessary to use strongly basic anion exchangers, which, in contrast to weakly basic sorbents, have a high Donnan potential (the positive surface charge of the anion exchanger matrix inhibiting penetration of cations). In addition, the sorbent should have gel-like structure containing no macropores. This decreases formation of the $Co(OH)_2$ precipitate in the anion exchanger phase. We found that AV-17-8 anion exchanger exhibits such properties.

The goal of this work is to study the effect of the process time, anion of the initial cobalt(II) salt, number of precipitation stages, and degree of anion exchanger swelling on $Co(OH)_2$ precipitation from cobalt(II) salt solutions with strongly basic anion exchanger AV-17-8 in the OH form.

EXPERIMENTAL

Initially, the AV-17-8 anion exchanger was transformed into the OH form by four 1-h treatments with 2 M NaOH at the volume ratio of the liquid to solid phase of 3 : 1, followed by 1-day treatment under similar conditions. Then, the sorbent was washed with water to pH 6–7 and dried at 60°C,[1] and its total exchange capacity (TEC) was determined by the reaction with excess 1 M HCl (TEC 2.72 mg equiv g^{-1}; determination error ≤2%).

The anion-exchange precipitation of $Co(OH)_2$ was performed by the method described in [2]: A threefold molar excess of the anion exchanger was added to a 0.25 or 0.5 M solution of the cobalt(II) salt. Precipitation proceeded at 20 ± 2°C for the time from 30 min to

[1] In certain experiments, the anion exchanger was not dried; in these cases TEC was related to 1 ml of the swollen anion exchanger.

1070-4272/02/7511-1787$27.00 © 2002 MAIK "Nauka/Interperiodica"

Table 1. Effect of process time τ on the degree of $Co(OH)_2$ anion-exchange precipitation from 0.25 M solution of $CoCl_2$

τ, h	Residual Co(II) concentration in solution, M	χ_{Co} in indicated phase			
		solution	precipitate	ion exchanger	wash water
0.5	0.072	0.29	0.27	0.02	0.38
1	0.060	0.24	0.32	0.02	0.38
3	0.060	0.24	0.35	0.02	0.36
24	0.055	0.22	0.37	0.03	0.38

Table 2. Effect of cobalt(II) salt anion on the degree of $Co(OH)_2$ precipitation. Concentration of the initial Co(II) salt solution 0.25 M, time of precipitation 1 day

Anion	Hydration energy, kJ mol^{-1} [4]	χ_{Co} in indicated phase			
		solution	precipitate	ion exchanger	wash water
Cl^-	84	0.41	0.25	0.02	0.27
NO_3^-	74	0.33	0.33	0.02	0.33
SO_4^{2-}	265	0.26	0.39	0.02	0.32

Table 3. Effect of the time of anion exchanger swelling in water τ_s on the degree of anion-exchange precipitation of $Co(OH)_2$ from 0.5 M solution of $CoCl_2$

τ, h	Residual Co(II) concentration in solution, M	χ_{Co} in indicated phase			
		solution	precipitate	ion exchanger	wash water
0	0.080	0.16	0.51	0.02	0.30
0.1	0.155	0.31	0.31	0.02	0.34
1	0.155	0.31	0.32	0.02	0.35
24	0.125	0.25	0.38	0.02	0.32

1 day. Then, the phases were separated by filtration, initially through a sieve with 0.5-mm mesh (to separate the anion exchanger) and then through a paper filter "blue tape" (to separate the hydroxide). The amount of cobalt in each phase was monitored complexometrically, photocolorimetrically, or by atomic absorption analysis. Then, the mole fraction of cobalt χ_{Co} was calculated as the ratio of the cobalt content in each phase to the total cobalt content in the system.

We have examined the dependences of the degree of cobalt hydroxide precipitation on the time of phase (anion exchanger and solution) contact, anion of the cobalt salt, and degree of preliminary swelling of the anion exchanger. To increase the yield of the precipitate, in certain experiments the synthesis was performed in three stages, since, as shown earlier [2, 3], the degree of cobalt(II) precipitation with anion exchanger from dilute solutions at single phase contact is low. In the three-stage precipitation, the total amount of the anion exchanger used in single-stage precipitation was divided in three portions, and each of them was contacted with a $CoCl_2$ solution (after separation of the preceding portion by filtration) for 1 h. The results as average values of three replicate experiments are listed in Tables 1–5 (relative error <5%).

To explain the effect of the anion on the degree of $Co(OH)_2$ precipitation, we studied the kinetics of Cl^-, NO_3^-, and SO_4^{2-} sorption with AV-17-8 from 0.1 N solutions of HCl, HNO_3, and H_2SO_4, respectively, and of the corresponding sodium salts, and also from mixed solutions of acid (H^+ concentration 0.1 M) and salt (anion concentration 1 M). The static exchange capacity of the anion exchanger SEC for the above anions was related to 1 ml of the swollen anion exchanger.

Table 4. Effect of the number of stages of the anion-exchange synthesis on the degree of $Co(OH)_2$ precipitation from 0.25 M $CoCl_2$ solution

Number of the stage	Residual Co(II) concentration in solution, M	χ_{Co} in indicated phase			
		solution	precipitate	ion exchanger	wash water
1	–	–	0.22	0.02	0.16
2	–	–	0.21	0.01	0.12
3	0.008	0.04	0.11	0.01	0.07
Total		0.04	0.54	0.04	0.35
1*	0.055	0.22	0.37	0.03	0.38

* Single-stage process.

The ion-exchange isotherms for solutions of Na_2SO_4, $NaNO_3$, and NaCl were also measured. The anion concentration was taken within the 0.05–1 M range, since for the efficient anion-exchange synthesis of $Co(OH)_2$ the concentration of the cobalt(II) salt should be higher than 0.1 M [2]. The results are presented in Table 5 and Figs. 1 and 2.

It follows from Table 1 that the anion-exchange synthesis is complete in 3 h. Therefore, this time was taken for the subsequent experiments (Tables 2–4).

The degree of $Co(OH)_2$ precipitation decreases in the series $CoSO_4 > Co(NO_3)_2 > CoCl_2$, which is in agreement with the data on the anion exchange, listed in Table 5 and Figs. 1 and 2. In anion exchange from neutral solutions and solutions with high ionic strength, i.e., under conditions close to $Co(OH)_2$ anion-exchange synthesis, the rate of the exchange and exchange capacity (EC) for sulfate ion are higher than those for nitrate and chloride ions. This fact

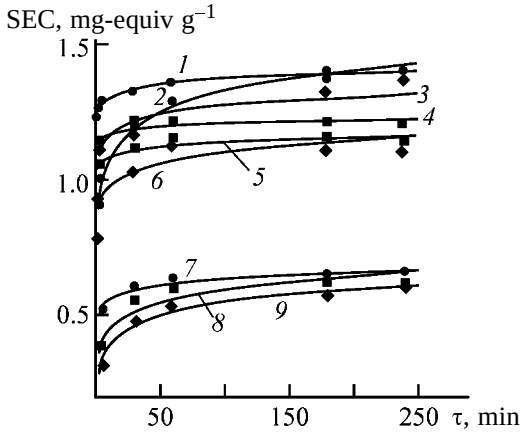

Fig. 1. Rate of anion exchange on AV-17-8 anion exchanger from 0.1 N salt and acid solutions and their mixtures. (SEC) Static exchange capacity and (τ) time. Solution: (*1*) $H_2SO_4 + Na_2SO_4$, (*2*) H_2SO_4, (*3*) HCl + NaCl, (*4*) $HNO_3 + NaNO_3$, (*5*) HNO_3, (*6*) HCl, (*7*) Na_2SO_4, (*8*) $NaNO_3$, and (*9*) NaCl.

Table 5. Effect of anion concentration *c* and pH on SEC of AV-17-8 anion exchanger

c, M	pH	SEC for indicated anion, mg-equiv ml^{-1}		
		Cl	NO_3^-	SO_4^{2-}
0.1	7	0.46	0.51	0.60
	1	1.12	1.17	1.30
1	7	0.51	0.63	0.70
	1	1.20	1.22	1.30

reflects the so-called electroselectivity of ion exchangers (prevalent absorption of anions with the higher charge). The lower EC of Cl^- as compared to NO_3^- may be due to the higher degree of Cl^- hydration (Table 2).

It follows from Table 3 that the amount of the hydroxide precipitate decreases by almost 40% when

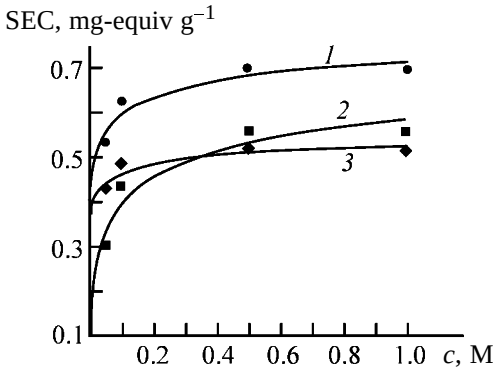

Fig. 2. Isotherms of anion exchange of AV-17-8 anion exchanger with 0.1–1.0 M solutions of (*1*) Na_2SO_4, (*2*) $NaNO_3$, and (*3*) NaCl. (SEC) Static exchange capacity and (*c*) solution concentration.

the swollen anion exchanger is used. When anion exchanger swelled for 1 day (time required for complete unwrapping of chains in the grain), the negative effect was weaker. Three stages are enough to obtain 96% of cobalt(II) as a hydroxide precipitate [the residual Co(II) concentration in the solution is 0.008 M], while in the single-stage procedure, only 80% Co(II) is precipitated at the same consumption of the anion exchanger. In the three-stage synthesis, the amount of the $Co(OH)_2$ precipitate is also larger (by about 20%), with the amount of Co(II) in the anion exchanger phase increasing insignificantly.

CONCLUSIONS

(1) In $Co(OH)_2$ synthesis with AV-17-8 anion exchanger, the degree of cobalt(II) precipitation increases by no more than 6% when the time of phase contact is increased from 3 h to 1 day.

(2) The degree of $Co(OH)_2$ precipitation increases from 59 to 74% in the series $CoCl_2 < Co(NO_3)_2 < CoSO_4$, which coincides with the series of the selectivity of AV-17-8 anion exchanger with respect to these anions.

(3) Performing the process in three stages istead of one stage increases the degree of $Co(OH)_2$ precipitation from 80 to 96%.

ACKNOWLEDGMENTS

The work was financially supported by the Krasnoyarsk Krai Science Foundation.

REFERENCES

1. Vulikh, A.I., *Ionoobmennyi sintez* (Ion-Exchange Synthesis), Moscow: Khimiya, 1973.
2. Pashkov, G.L., Nikolaeva, R.B., Saikova, S.V., and Panteleeva, M.V., *Khim. Inter. Ustoich. Razv.*, 2001, vol. 9, no. 3, pp. 57–60.
3. Panteleeva, M.V., Saikova, S.V., Pashkov, G.L., and Nikolaeva, R.B., *Elektr. Zh. Issled. Ross.*, 2002, vol. 48, pp. 522–533.
4. Vasil'ev, V.P., Zolotarev, E.K., Kapustinskii, A.F., *et al.*, *Zh. Fiz. Khim.*, 1960, vol. 34, no. 8, pp. 1763–1767.

Russian Journal of Applied Chemistry, Vol. 75, No. 11, 2002, pp. 1791–1794. Translated from Zhurnal Prikladnoi Khimii, Vol. 75, No. 11, 2002, pp. 1826–1829.
Original Russian Text Copyright © 2002 by Ergozhin, Chalov, Iskakova, Sarsenov.

SORPTION AND ION-EXCHANGE PROCESSES

Anion Exchangers Based on Glycidyl Derivatives of Aromatic Diamines and Some Allyl Halides

E. E. Ergozhin, A. K. Chalov, R. A. Iskakova, and S. K. Sarsenov

Bekturov Institute of Chemical Sciences, Ministry of Education and Science of Kazakhstan Republic, Almaty, Kazakhstan

Received April 9, 2002

Abstract—Polyfunctional three-dimensional network anion exchangers were prepared by condensation of tetraglycidyl-4,4'-diaminodiphenylmethane with allyl halides and amines. The optimal preparation conditions were determined; the properties of the resulting product as influenced by the nature of the initial monomers were evaluated.

Owing to high static exchange capacity (SEC) and thermal and chemical stability, polyelectrolytes based on nitrogen-containing epoxy compounds are widely used in hydrometallurgy of rare metals, in recovery of metal ions from spent solutions and wastewaters, and in other branches of industry.

Condensation of tetraglycidyl diamines with polyethylenepolyamine (PEPA), polyethylenimine (PEI), polyxylylenepolyamine, and hexamethylenediamine (HMDA) in methanol yielded selective polyfunctional anion exchangers with high exchange capacity [1–3]. Utilization of long-chain aromatic nitrogen-containing epoxy resins in combination with heteroatoms of –S–, SO_2–, or –O– type between phenyl rings improves the sorption and kinetic properties of the resulting sorbents with respect to polyvanadate ions [4, 5].

To obtain ion-exchange materials possessing high thermal and radiation stability, we prepared anion exchangers based on glycidyl derivatives of 4,4'-diaminodiphenyl sulfide, 4,4'-diaminodiphenyl oxide, PEPA, and PEI [6].

The goal of this work was to prepare highly porous three-dimensional network anion exchangers based on tetraglycidyl-4,4'-diaminodiphenylmethane (TGDADPM), allyl halides (AHs), and di- and polyamines.

EXPERIMENTAL

TGDADPM was synthesized according to [7]; the content of the epoxy groups was determined by the procedure given in [8].

The condensation of AH with TGDADPM was performed in dimethylformamide (DMF) at 13–25°C with subsequent curing at 80–120°C. Then, the gel was crushed, sieved, and the fraction with a particle size of 0.25 mm was taken.

The static exchange capacity (mg-equiv g^{-1}), moisture content, swellability γ, and thermal and chemical stability of the resulting anion exchangers were determined by the standard procedures [9].

The IR spectra of the initial and final products (thin films or KBr pellets, 200 mg KBr per 1 mg compound) were recorded on a Specord M 80/M 85 spectrophotometer.

To determine the optimal preparation conditions, we examined the effect of various factors such as the ratio of the initial components, temperature, curing conditions, and process time on the product properties.

The effect of the initial component ratio is of particular importance, because the content of amine in the polymer determines the properties of the resulting product. It was found that, with increasing content of amine, both SEC and swellability increase, and the strongest effect is observed with PEPA, which is probably due to its structure. As seen from the NMR data [10, 11], PEPA contains significant amounts of diethylenetriamine with two primary and one secondary amino groups. Since primary amino groups are the most reactive, they are involve in the reaction first. In the case of PEI, despite significant content of nitrogen (16%), more branched structure of the polyamine causes strong cross-linking and thus hinders accessibility of the corresponding functional groups. Double bonds, a certain fraction of which is cleaved with atmospheric oxygen [2], also strongly affect the

1070-4272/02/7511-1791$27.00 © 2002 MAIK "Nauka/Interperiodica"

Table 1. Physicochemical properties of anion exchangers based on TGDADPM, AB, and amines as influenced by the curing temperature

Amine	SEC,* mg-equiv g^{-1}	γ, ml g^{-1}	SEC,* mg-equiv g^{-1}	γ, ml g^{-1}	SEC,* mg-equiv g^{-1}	γ, ml g^{-1}
	80°C		100°C		110°C	
PEPA	9.4	5.8	8.6	5.1	7.9	4.6
PEI	8.8	3.0	8.6	2.9	8.4	2.9
HMDA	5.2	2.6	5.1	2.6	4.7	2.5
PMVP	5.0	2.8	5.0	2.7	4.7	2.5

* SEC with respect to 0.1 M HCl.

structure of the resulting polyelectrolyte. The optimal ratios of the initial components TGDADPM : allyl bromide (AB) : amine (weight fraction) for the anion exchangers based on PEPA, PEI, and poly-2-methyl-5-vinylpyridine (PMVP) are 1.5 : 1.0 : 2.0, 1.5 : 1.0 : 3.5, and 1.5 : 1 : 3.0, respectively. With increasing HMDA concentration above 1 wt part, soluble products are formed.

It was found that the SEC of anion exchangers based on TGDADPM increases in the order PMVP < HMDA < PEI < PEPA. The capacities of the resulting anion exchangers prepared at the above optimal ratios of the initial components are 5.0, 5.2, 8.8, and 9.4 mg-equiv g^{-1}, respectively. Thus, PEPA and PEI allow preparation of anion exchangers with the exchange capacity of 8–10 mg-equiv g^{-1}. As seen from the experimental data, the anion exchanger with the highest exchange capacity simultaneously exhibits the highest swellability. For example, SEC of the polyelectrolyte based on TGDADPM, AB, and PEPA is 9.4 mg-equiv g^{-1}, and its swellability reaches 5.8 ml g^{-1}, whereas the swellabilities of the anion exchangers based on PEI and PMVP are significantly smaller: 3.0 and 2.8 ml g^{-1}, respectively.

The halogen in allyl compound does not noticeably affect SEC. For example, in the case of allyl chloride, the maximal SEC of anion exchangers based on PEI and TGDADPM is 9.1 mg-equiv g^{-1}.

Our experimental data on the effect of precondensation temperature and time on the SEC of the resulting anion exchanger showed that polyelectrolyte with the highest SEC is formed at 25°C in 40 min; the yield of the product is 90%.

Owing to different reactivity and to concentration and steric effects, polymers resulting from condensation of polyfunctional compounds contain unchanged functional groups. Thus, it is necessary to determine the optimal curing temperature at which all the functional groups in the initial monomers will be involved in the reaction.

As seen from Table 1, increasing curing temperature deteriorates the physicochemical properties of the resulting anion exchanger. In the case of the anion exchanger based on PEPA, SEC decreases to 7.9 mg-equiv g^{-1} at 110°C; at the same time, the exchange capacity and swellability of the anion exchangers based on PEI, HMDA, and PMVP vary insignificantly. Certain decrease in SEC with increasing curing temperature is due to compression of the polymer structure. Strong decrease in the exchange capacity of the anion exchanger based on PEPA is probably due to heterogeneous composition of the amine reagent and increase in the content of low-molecular-weight and soluble amines during polyelectrolyte treatment.

The structure of the initial tetraglycidyl compound and final products was studied by IR spectroscopy. The presence of the epoxy groups in oligomers of polyglycidyl derivatives of aromatic amines is confirmed by characteristic absorption bands at 745, 865, 935, and 970 cm^{-1}. There are no such absorption bands in the spectra of the resulting anion exchangers, which suggests their chemical transformation. At the same time, new absorption bands appear at 3600–3300 and 1650–1550 cm^{-1}, which correspond to the stretching and bending vibrations of the aminogroups of various basicity. The stretching vibrations of the C–N bonds in the aromatic amino groups are observed in the 1350–1300 cm^{-1} range. The absorption bands at 1510 cm^{-1} belonging to the stretching vibrations of the C=C bond and at 3030 cm^{-1} (stretching vibrations of the =C–H bonds in the benzene ring) confirm the presence of aromatic fragments in the resulting compounds. The spectra of the polymers in question also contain the characteristic absorption bands belonging to the antisymmetric (2940 cm^{-1}) and symmetric (2840 cm^{-1}) stretching vibrations of the CH_2

group and to the C–H bending vibrations at 1470–1460 cm^{-1}. The absorption bands at 1600–1560 and 1500 cm^{-1}, characteristic of the stretching vibrations of the C=C and C=N bonds in the pyridine ring, also undergo certain changes.

The functional groups in the anion exchangers are characterized by the degrees of protonation, which depend on several factors, primarily on the solution pH [13, 14]. The functionality and basicity of the resulting three-dimensional network polyelectrolytes were studied by potentiometric titration. The values of pK_a (Table 2) and empirical coefficient *m*, characterizing the interchain interaction in the polymer, were determined from the potentiometric titration curves using the Henderson–Hasselbach equation [15]. The shape of the titration curves determined by the nature of di- and polyamine and concentration of the functional groups in the anion exchanger showed that the compounds in question based on the polyglycidyl amine are polyfunctional.

The thermal and chemical stability was evaluated by variation in the SEC of the anion exchangers in 2.5 M H_2SO_4, 5 M NaOH, and 10% hydrogen peroxide solutions. As seen from Table 3, the anion exchangers based on TGDADPM are chemically stable in concentrated acids and bases; SEC decreases by no more than 6%. The chemical stability of polyelectrolytes decreases in the order: PEI > HMDA > PMVP > PEPA.

Some physicochemical properties of the anion exchangers change after their boiling in water. In this connection, we studied the thermal stability of compounds in the 80–100°C range at a treatment time of 4–12 h. As seen from Table 3, after such treatment the relative SEC decreases by no more than 5%, and the most stable are the anion exchangers based on PEI and HMDA.

Certain increase in the thermal stability of the polymers in question is probably due to the regular structure of the polyelectrolyte and incorporation of the stable aromatic fragments into the polymer structure. The thermal stability of the resulting anion exchangers decreases in the following order: HMDA > PEI > PMVP > PEPA.

The sorption of the transition metal ions was studied by EDTA titration of the residual amounts of copper(II), cobalt, and nickel in the filtrate after a contact with the anion exchanger for 24 h. The dependence of the sorption capacity of the polyelectrolyte on the acidity of the metal salt solutions (Fig. 1) showed that at pH 5–7 the anion exchanger based on

Table 2. pK_a and *m* of the anion exchangers based on TGDADPM, AB, and amines

Amine	pK_a	*m*
PEPA	7.0	2.1
PEI	7.8	2.2
HMDA	6.2	1.9
PMVP	7.4	2.1

Table 3. Relative SEC of the anion exchangers based on TGDADPM, AB, and amines as influenced by the solution composition and heat treatment time

Amine	Relative SEC, %					
	NaOH	H_2SO_4	H_2O_2	4 h	7 h	12 h
PEPA	100	100	94	100	96	95
PEI	100	100	98	100	100	100
HMDA	100	100	97	100	100	100
PMVP	100	100	94	100	100	98

TGDADPM, AB, and PEPA exhibits the highest sorption capacity for copper(II), nickel, and cobalt ions.

The sorption kinetics of copper ions on the anion exchangers based on TGDADPM and AB was studied using 0.05 N solution of copper(II) sulfate. It was found (Fig. 2) that the fastest sorption is observed with the polymer based on PEPA, which sorbs up to 80% of copper in 0.5 h. This is probably due to the formation of the more elastic three-dimensional network, which provides high swellability and makes the functional groups in the polymer bulk more accessible.

CONCLUSIONS

(1) Procedures for preparing thermally and chemically stable polymeric anion exchangers based on allyl

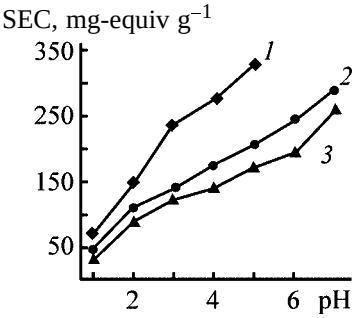

Fig. 1. SEC of the anion exchanger based on TGDADPM, AB, and PEPA for (*1*) Cu^{2+}, (*2*) Ni^{2+}, and (*3*) Co^{2+} as a function of solution pH.

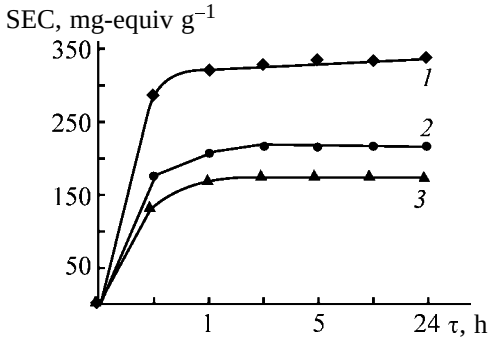

Fig. 2. Kinetics of copper(II) sorption on the anion exchanger based on TGDADPM, AB, and (*1*) PEPA, (*2*) PEI, and (*3*) PMVP. (τ) Time.

halides, tetraglycidyl diaminodiphenylmethane, and some di- and polyamines were developed.

(2) The nature of the amine strongly affects the properties of the resulting anion exchangers. More regular structure of polyethylenimine and introduction of aromatic fragments into the polyelectrolyte structure enhance the thermal and chemical stability of the resulting compounds.

(3) Highly permeable network anion exchangers prepared using the polyglycidyl amine derivative recover up to 80% of copper(II) from 0.05 M copper sulfate solution in 0.5 h.

REFERENCES

1. Ergozhin, E.E. and Menligaziev, E.Zh., *Polifunktsional'nye ionoobmenniki* (Polyfunctional Ion Exchangers), Alma-Ata: Akad. Nauk Kaz. SSR, 1986.
2. Ergozhin, E.E., Tastanov, K.Kh., and Menligaziev, E.Zh., *Izv. Akad. Nauk Kaz. SSR, Ser. Khim.*, 1983, no. 3, pp. 69–78.
3. Menligaziev, E.Zh., Abil'seitov, B.T., and Ergozhin, E.E., *Izv. Akad. Nauk Kaz. SSR, Ser. Khim.*, 1982, no. 3, pp. 29–37.
4. Menligaziev, E.Zh., Ergozhin, E.E., and Abil'seitov, B.T., *Izv. Akad. Nauk Kaz. SSR, Ser. Khim.*, 1982, no. 4, pp. 24–29.
5. Mikhailyuk, E.L., Ergozhin, E.E., Menligaziev, E.Zh., *et al.*, *Izv. Akad. Nauk Kaz. SSR, Ser. Khim.*, 1979, no. 4, pp. 70–71.
6. Nurkhodzhaeva, Z.A., Menligaziev, E.Zh., and Ergozhin, E.E., *Izv. Akad. Nauk Kaz. SSR, Ser. Khim.*, 1988, no. 3, pp. 45–49.
7. US Patent 2951822.
8. Paquin, A.M., *Epoxydverbindungen und Epoxydharze*, Berlin: Springer, 1958.
9. *GOSTs* (State Standards) *10898–84, 10898.2–74, and 10898.5–84.*
10. Klepikova, S.G., Iskakova, R.A., Chalov, A.K., *et al.*, *Izv. Minist. Obraz. Nauki Resp. Kaz., Nats. Akad. Nauk. Resp. Kaz., Ser. Khim.*, 2001, no. 4, pp. 88–90.
11. Ergozhin, E.E., Chalov, A.K., Iskakova, R.A., *et al.*, *Zh. Prikl. Khim.*, 2002, vol. 75, no. 1, pp. 103–106.
12. Salistyi, S.M. and Mironovich, L.M., *Vysokomol. Soedin., Ser. B*, 1994, vol. 36, no. 12, pp. 2092–2095.
13. Saldadze, K.M. and Kopylova-Valova, V.D., *Kompleksooobrazuyushchie ionity (kompleksity)* (Complex-Forming Ion Exchangers), Moscow: Khimiya, 1980.
14. Zarkhina, T.S., Zarkhin, L.S., Zelenetskii, A.N., *et al.*, *Vysokomol. Soedin., Ser. A*, 1982, vol. 24, no. 11, pp. 2429–2442.
15. Grissbach, R., *Austauschadsorption in Theorie und Praxis*, Berlin: Akademie, 1957.

Russian Journal of Applied Chemistry, Vol. 75, No. 11, 2002, pp. 1795–1798. Translated from Zhurnal Prikladnoi Khimii, Vol. 75, No. 11, 2002, pp. 1830–1833.
Original Russian Text Copyright © 2002 by Kartsova, Makarov.

SORPTION AND ION-EXCHANGE PROCESSES

A Mixed Phase C_{60} + Dibenzo-24-crown-8 for Gas Chromatography

L. A. Kartsova and A. A. Makarov

St. Petersburg State University, St. Petersburg, Russia

Received April 24, 2002

Abstract—Stationary phases for gas chromatography were prepared: 10 wt % fullerene C_{60} on Inerton N-AW (deposition from saturated toluene solution) and a mixed phase C_{60} + dibenzo-24-crown-8. These phases were tested in a wide temperature range (40–280°C) with selected organic compounds containing various functional groups and with their mixtures.

Active recent efforts were aimed at searching for new selective chromatographic phases allowing separation in one chromatographic run of multicomponent mixtures of compounds differing in the nature of functional groups, polarity, and boiling point.

Development of an electric-arc procedure for preparing fullerenes in a fairly high yield stimulated active studies of the chemical and physicochemical properties of the new modification of carbon. Chromatographic studies of interactions between fullerenes and organic compounds furnish useful information concerning both the physicochemical properties of fullerenes themselves and their possible use as chromatographic sorbents.

The high hydrophobicity of C_{60} in combination with its thermal stability, resistance to oxidation, and capability for donor–acceptor interactions make this substance promising as a stationary phase for gas chromatography.

The selectivity range in analysis of multicomponent mixtures can be extended by using mixed phases. Combining fullerenes with crown ethers will not only affect the physicochemical characteristics of the carbonaceous stationary phases (solubility, hydrophobicity, capability for various specific interactions with functional groups of components of complex mixtures being separated), but also furnish new data on complexation with macrocycles.

EXPERIMENTAL

Stationary phases were prepared from fullerenes C_{60} and C_{60} + C_{70} (Astrin Joint-Stock Company, St. Petersburg) and dibenzo-24-crown-8 (DB-24-C-8, Reaktiv-Servis Scientific and Production Complex, Limited Liability Company, Moscow).

Fullerene C_{60} tested as stationary phase for gas chromatography was applied onto Inerton N-AW support (grain size 0.20–0.315 mm) in an amount of 10 wt % from toluene. A toluene solution of fullerene was added to Inerton N-AW placed in a porcelain cup in an amount fully covering the solid (0.5-cm layer of the liquid over the solid); the cup was placed on a water bath and carefully stirred until the solvent was fully evaporated. The mass obtained after the solvent evaporation was dried in the air thermostat of a Tsvet-500M gas chromatograph at 100°C for 3 h. Then it was sieved through standard sieves, and the 0.20–0.25-mm fraction was used as packing for a 3000 × 2-mm glass column. The packed column was conditioned in a carrier gas flow (N_2, 30 ml min^{-1}; stepwise heating from 70 to 270°C).

The mixed C_{60} + DB-24-C-8 phase was prepared as follows. Fullerene was applied onto Inerton N-AW (0.20–0.25 mm) as described above, after which 10 wt % DB-24-DC-8 was applied from a chloroform solution (at the reverse application order, i.e., first DB-24-C-8 from chloroform and then C_{60} from toluene, the characteristics of the resulting sorbent were similar). After complete evaporation of the solvents, the packing was dried in the air thermostat of a Tsvet-500M gas chromatograph at 70°C for 3 h. Then it was used as packing for a 3000 × 2-mm glass column. The packed column was conditioned in a carrier gas flow (N_2, 30 ml min^{-1}; programmed heating from 80 to 200°C and keeping at 200°C for 5 h).[1]

[1] Experiments were performed with the participation of I.K. Khmel'nitskii.

1070-4272/02/7511-1795$27.00 © 2002 MAIK "Nauka/Interperiodica"

Mean polarity and performance of stationary phases for gas chromatography, containing C_{60} and DB-24-C-8, and of some commercial phases

Stationary phase	Mean polarity	Performance (HETP), cm	Retention factor *k*
DB-24-C-8	423	0.43	35.8
C_{60}	260	0.12	9.2
DB-24-C-8 + C_{60}	390	0.19	33.3
SE-30	3	0.33	–
Carbowax 20M	462	0.42	31.6
Tricresyl phosphate	284	0.47	39.5

The retention indices were measured with a Tsvet-500M gas chromatograph equipped with a flame ionization detector and a 3000 × 2-mm glass packed column. The column temperature was varied from 60 to 230°C (for the column packed with 10 wt % C_{60} on Inerton N-AW) or from 90 to 180°C (for the column packed with 10 wt % C_{60} + 10 wt % DB-24-C-8 on the same support); the vaporizer temperature was 150–250°C. Carrier gas (nitrogen) was passed at a rate of 20 or 30 ml min^{-1}; auxiliary gases (air, hydrogen) were fed to the flame ionization detector at rates of 30 and 300 ml min^{-1}, respectively. The electrometer working scales in the course of chromatographing model mixtures were varied from 128×10^7 to 32×10^8. The paper feed velocity was 600 mm h^{-1}. Samples (0.2–0.8 μl) were injected with an MSh-1 microsyringe. From the measured retention distances of the organic compounds and appropriate reference *n*-alkanes, we calculated the Kovats retention indices [1]. The reproducibility of the retention indices in replicate experiments was 3–5 units for the retention times exceeding 5 min and 10–15 units for retention times of 2–5 min.

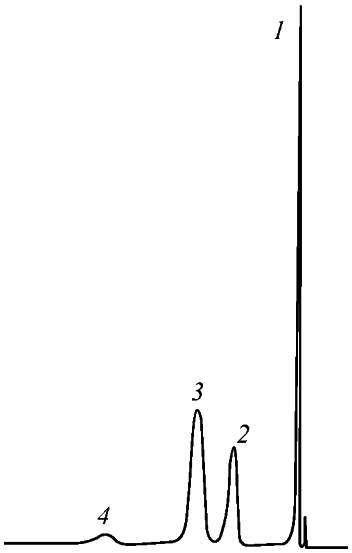

Fig. 1. Chromatogram of a model mixture. Conditions of chromatographic analysis: Tsvet-500M chromatograph, 10 wt % DB-24-C-8 + C_{60} on Inerton N-AW, carrier gas N_2, 30 ml min^{-1}, flame ionization detector; the same for Figs. 2 and 3. Column temperature 150°C. Peaks: (*1*) benzene, (*2*) *N*,*N*-dimethylaniline, (*3*) aniline, and (*4*) phenol.

The polarity of the prepared and studied chromatographic phases was evaluated by the MacReynolds constants using the following test substances: benzene, 1-butanol, nitropropane, pyridine, and 2-pentanone [1].

The mean polarities of our chromatographic phases are compared in the table with those of polyethylene glycol, Carbowax 20M (polar stationary phase), tricresyl phosphate (medium-polarity stationary phase), and SE-30 (nonpolar stationary phase).

The column performance was evaluated by the number of theoretical plates *n*, calculated as

$$n = 5.54(l/\omega_{0.5})^2,$$

where *l* is the retention distance (from the start mark, mm), and $\omega_{0.5}$ is the full width at half-maximum of the chromatographic peak, mm.

The height *H* equivalent to the theoretical plate was calculated by the formula

$$H = L/n,$$

where *L* is the column length, cm.

The performance (with respect to tetradecane) of the columns packed with our phases is compared in the table with that of the selected commercial phases.

To prepare the associate DB-24-C-8 + C_{60}, equimolar amounts of fullerene and DB-24-C-8 were dissolved in the minimal amount of toluene, and the solution was placed in a penicillin vial, which was hermetically sealed and kept at 100°C for 1 h. After cooling, the vial was opened and allowed to stand until the solvent fully evaporated, after which the resulting associate was dried at 120°C for 2 h.

The "fullerene" phase appeared to be more polar than Carbochrome [2] and SE-30 silicone elastomer (see table). Despite the hydrophobic character of C_{60}, the dispersion interactions drastically decreased: The retention times of alkanes were appreciably shorter than those on graphitized carbon black (Fig. 1). On the contrary, polar organic compounds had longer retention times on C_{60} than on graphitized black.

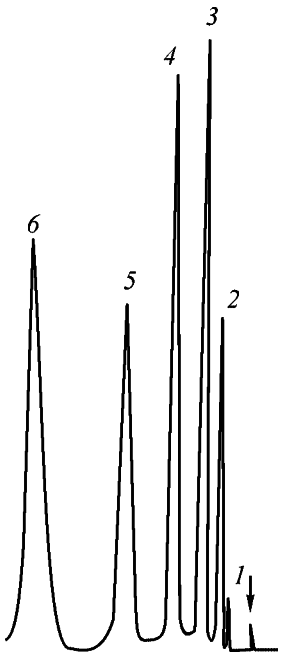

Fig. 2. Chromatogram of a mixture of C_2–C_7 alcohols. Column temperature 120°C; the same for Fig. 3. Peaks: (*1*) ethanol, (*2*) 1-propanol, (*3*) 1-butanol, (*4*) 1-pentanol, (*5*) 1-hexanol, and (*6*) 1-heptanol.

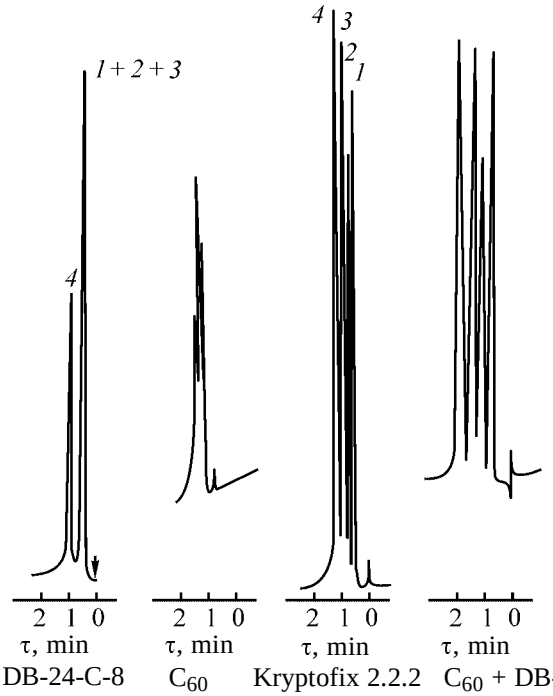

Fig. 3. Chromatogram of a mixture of isomeric butyl alcohols: (*1*) 2-methyl-2-propanol, (*2*) 2-butanol, (*3*) 2-methyl-1-propanol, and (*4*) 1-butanol.

We found that the C_{60} column exhibits increased affinity for aromatic hydrocarbons and their derivatives. The high thermal stability of fullerenes allowed the column to operate in a wide temperature range. The calculated performance of the chromatographic column with the fullerene phase appeared to be higher compared to the other tested phases (see table; the performance is the higher, the lower HETP); however, in analysis of complex mixtures, its selectivity was apparently insufficient.

Thus, our goal was to increase the selectivity with respect to various classes of organic compounds, preserving the obvious advantages of fullerene sorbents (high performance, stability of chromatographic characteristics in a wide temperature range).

The selectivity range can be often extended by using mixed phases. We prepared a mixed phase containing 10 wt % C_{60} + DB-24-C-8 on Inerton N-AW.

Dibenzo-24-crown-8 was tested previously [3] and showed high performance in analysis of highly polar organic compounds: phenols and aromatic amines. The crown ether was applied from chloroform onto the sorbent preliminarily modified with fullerene. The prepared sorbent was tested in the gas-adsorption (90°C) and gas–liquid (120, 150, 180, 200°C) modes.

The mixed chromatographic phase appeared to be suitable for selective analysis of polar and nonpolar organic compounds boiling in a wide temperature range: aliphatic and aromatic hydrocarbons, alcohols, phenols, chlorinated phenols, and aromatic amines (Figs. 1, 2). Many of the above substances are priority ecotoxicants. With respect to the arbitrary mean chromatographic polarity, the mixed stationary phase is inferior only to Carbowax 20M and substantially surpasses SE-30. The mean polarity of C_{60} + DB-24-C-8 is intermediate between the polarities of the stationary phases based on C_{60} and DB-24-C-8 taken separately (see table). The mixed phase showed a high performance characteristic of the C_{60} column. With the C_{60} + DB-24-C-8 phase, it is possible to separate structural and geometric isomers, which is impossible with C_{60} and DB-24-C-8 taken separately, i.e., a synergistic effect is observed. Figure 3 shows the chromatograms of a mixture of isomeric butyl alcohols on several individual phases (Kryptofix 2.2.2 [4], DB-24-C-8, C_{60}, all 10 wt % on Inerton N-AW) and on the mixed phase C_{60} + DB-24-C-8.

The fullerene in the mixed phase may act as support modifier or may form an associate with the crown ether.

It should be also borne in mind that, in thin-layer chromatography with the same elution system, straight silica gel plates and plates modified with different

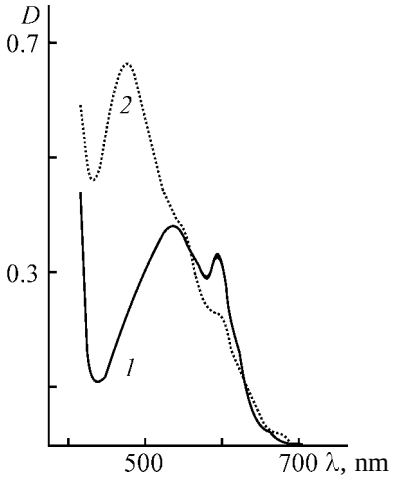

Fig. 4. Absorption spectra of (*1*) C_{60} and (*2*) mixture of C_{60} with DB-24-C-8. (*D*) Optical density and (λ) wavelength.

macrocycles (DB-24-C-8, DB-18-C-6, DB-15-C-5; crown compounds containing labile hydrogen atoms, e.g., diaza-18-C-6) show different performance in separation of a mixture of carbon clusters: stronger sorption and better separation of C_{60} and C_{70} are observed with DB-24-C-8.

In view of these facts, we performed the following experiment in the HPLC mode: Through a chromatographic column packed with a polar sorbent based on silica gel, we passed for a certain period a mobile phase containing DB-24-C-8. The sorbent surface was thus modified with DB-24-C-8. Experiments on separation of a mixture of C_{60} and C_{70} showed that the separation performance of the modified sorbent was appreciably higher than that of the initial sorbent.

A similar trend was observed in [5] with an HPLC column modified with tetraphenylporphyrin. Separation of fullerenes C_{60} and C_{70} was accounted for by formation of a host–guest complex of the porphyrin with fullerene.

To independently detect possible interactions between DB-24-C-8 and C_{60}, we measured the UV/Vis and IR spectra of the individual components and their associate [6]. The UV/Vis spectrum of the mixture (Fig. 4) contains a new absorption band with a maximum at $\lambda = 474$ nm, absent in the spectra of the components taken separately.

CONCLUSION

The mixed C_{60} + DB-24-C-8 stationary phase for gas chromatography shows high selectivity and high performance in separation of mixtures of organic compounds with various functional groups, so that their derivatization is not required.

REFERENCES

1. Stolyarov, B.V., Savinov, I.M., Vitenberg, A.G., *et al.*, *Prakticheskaya gazovaya i zhidkostnaya khromatografiya* (Practical Gas and Liquid Chromatography), St. Petersburg: Sankt-Peterb. Gos. Univ., 1998.
2. Golovnya, R.V., Terenina, M.B., Ruchkina, E.L., and Karnatsevich, E.L., *Mendeleev Commun.*, 1993, no. 6, pp. 231–233.
3. Kartsova, L.A. and Markova, O.V., *Zh. Anal. Khim.*, 1999, vol. 54, no. 3, pp. 256–262.
4. Kartsova, L.A., Markova, O.V., Amel'chenko, A.I., and Ostryanina, N.D., *Zh. Anal. Khim.*, 2000, vol. 55, no. 3, pp. 302–311.
5. Kele, M., Kompton, R.H., and Guiochou, G., *J. Chromatogr. A*, 1997, vol. 786, no. 1, pp. 31–45.
6. Makarov, A.A. and Kartsova, L.A., Abstracts of Papers, *IX Mezhdunarodnaya konferentsiya po teoreticheskim voprosam adsorbtsii i adsorbtsionnoi khromatografii "Sovremennoe sostoyanie i perspektivy razvitiya teorii adsorbtsii"* (IX Int. Conf. on Theoretical Problems of Adsorption and Adsorption Chromatography "Modern State and Prospects of Development of the Adsorption Theory"), Moscow, April 24–28, 2001, p. 176.

Russian Journal of Applied Chemistry, Vol. 75, No. 11, 2002, pp. 1799–1803. Translated from Zhurnal Prikladnoi Khimii, Vol. 75, No. 11, 2002, pp. 1834–1838.
Original Russian Text Copyright © 2002 by Medvedev, Makrushin, Dubenkov.

APPLIED ELECTROCHEMISTRY AND CORROSION PROTECTION OF METALS

Organic Compounds for Preparing Lustrous Tin Coatings

G. I. Medvedev, N. A. Makrushin, and A. N. Dubenkov

Novomoskovsk Institute, Mendeleev Russian University of Chemical Engineering, Novomoskovsk, Tula oblast, Russia

Received February 7, 2002

Abstract—Organic compounds for preparing lustrous tin coatings were selected taking into account their ionization potential. The best electrolyte composition for plating these coatings was determined.

Various organic compounds are added to sulfate electrolytes for tin-plating [1]. To obtain dense finely crystalline dull or lustrous coatings, these electrolytes should contain colloid-forming compounds (glue, gelatin) and wetting agents (e.g., ethylene oxide condensation products) along with other organic compounds. Unsaturated alcohols, ketones, aldehydes, and products of the electrochemical synthesis are used for preparing lustrous tin coatings [1–3]. It should be noted that organic compounds for plating lustrous tin coatings are selected empirically.

Nechaev *et al*. [4–7] showed that the sorption on the surface of tin and other metals is caused by not only electrostatic interactions but also chemical bonding. The chemisorption is maximal when the energy of electronic levels of the metal is similar to that of the molecular orbital of the organic compound, which provides formation of donor–acceptor bonds between the molecules of the additive and the metal surface. Under these conditions the occupied molecular orbitals of the adsorbent and the adsorbate overlap to form a common electronic system. The correlation between the adsorption properties of organic compounds and the energy of the highest occupied molecular orbital (MO) can be quantitatively characterized by the first ionization potential *I*.

According to [4–7], the range of *I* of organic compounds optimal for their sorption on tin is 7.74–7.96 eV. The second maximum is observed at *I* = 9.6 eV. To explain this phenomenon, Nechaev and Volgina suggested [8] that the tin surface consists of pure and oxidized regions. However, the dependence of the adsorption energy on *I*, measured on cathodically polarized tin whose surface is constantly renewed (oxide formation is thermodynamically forbidden), also has two maxima. It was suggested that not only highest occupied MO characterized by the first *I* but also other occupied orbitals are involved in the bonding. Dull finely crystalline tin coatings were plated from sulfate electrolyte containing organic compounds with *I* = 7.8–8.0 eV [4, 5, 10]. Introductions of compounds with *I* = 9.5–9.7 eV makes the coatings compact, uniform, and semilustrous. Organic compounds with *I* other than 7.8–8.0 and 9.5–9.7 eV do not inhibit tin-plating. No high-quality coating are formed in their presence.

In this work, taking into account *I* of organic compounds, we selected such compounds or their mixtures that provide plating of lustrous tin coating from sulfate electrolyte.

For this purpose we mainly used an electrolyte containing 30 g l^{-1} $SnSO_4$ and 100 g l^{-1} H_2SO_4. The coatings were plated at 20–22°C with or without stirring of the electrolyte with a mechanical stirrer.

The tested organic compounds are presented in the table.

Condensation products Syntanol DS-10 (*I* = 9.4 eV), OP-7, OP-10 (*I* = 9.3 eV), OS-20 (*I* = 9.2 eV), VA-20 smoothing agent (*I* = 9.5 eV), hide glue, and gelatin (*I* = 7.5 eV) were also studied.

The ionization potentials of the tested organic compounds ranged from 6.88 to 12.2 eV. The concentration of these compounds was varied from 1 to 15 g l^{-1}. Saturated solutions of difficultly soluble compounds were used. The ionization potentials of organic compounds were taken from [6, 7] or calculated by the PM3 method [11].

The most precise experimental procedure for determining ionization potentials of atoms and molecules is PES [12]. In this work, the *I* values determined by PES were correlated with those calculated quantum-chemically. First, we examined how semiempirical

1070-4272/02/7511-1799$27.00 © 2002 MAIK "Nauka/Interperiodica"

Organic compounds tested and their first ionization potentials

Compound nos.	Compound	*I*, eV	Compound nos.	Compound	*I*, eV
1	Benzidine	6.88	21	Quinoline	8.62
2	*N*,*N*-Dimethylaniline	7.14	22	Piperidine	8.7
3	Diphenylamine	7.25	23	Benzotriazole	8.72
4	α-Naphthylamine	7.3	24	Imidazole	8.8
5	*m*-Toluidine	7.5	25	Furan	8.88
6	Aniline	7.7	26	Benzyl alcohol*	8.95
7	Indole	7.74	27	Coumarin*	8.97
8	β-Naphthol	7.76	28	2-Butene-1,4-diol*	9.13
9	α-Naphthol	7.78	29	Acetic anhydride	9.5
10	Phloroglucinol	7.87	30	Benzenesulfonic acid	9.6
11	Hydroquinone	7.95	31	2-Butyne-1,4-diol*	9.77
12	Pyrogallol	8.0	32	*p*-Phenolsulfonic acid	9.8
13	Pyrocatechol	8.07	33	Propargyl alcohol	10.41
14	Naphthalene	8.2	34	Butane-1,4-diol*	10.43
15	*p*-Cresol	8.24	35	3,5-Dinitrobenzoic acid	10.7
16	Resorcinol	8.31	36	Formaldehyde	10.88
17	*o*-Cresol	8.34	37	Nitromethane	11.18
18	*m*-Cresol	8.37	38	Trinitrobenzoic acid	11.3
19	Phenol	8.5	39	Valeric acid	12.2
20	Triethylamine	8.6			

* Determined in this work.

methods for calculating the electronic structure (MNDO, AM1, and PM3) and *ab initio* methods with STO-3G and 3-21G basis sets describe PES data.

We found that the PM3 method [11] gives the most satisfactory results. In this case, the ionization potentials of organic molecules can be calculated by the equation

$$I = 1.075I_{PM3} - 1.1679. \quad (1)$$

The correlation coefficient is 0.979.

The ionization potentials calculated by Eq. (1) from the PM3 data are given in the table (the corresponding compounds are denoted with asterisks).

The degree of luster of the coatings was measured on an FB-2 photoelectric luster meter. The polarization curves were recorded with a P-5828 potentiostat under the potentiodynamic conditions. In the course of tin-plating, the capacitance of the electrical double layer was measured with a P-5021 ac bridge operating at 30 kHz in the successive substitution mode. Tin coatings 6–9 μm thick were plated on copper supports.

High-quality coatings were obtained in the presence of none of the tested organic compounds whose concentrations were varied in a wide range. The use of the glue and gelatin gave similar results. Dull finely crystalline coatings are formed in the presence of the condensation products in the electrolyte. When both condensation products and the organic compounds given in the table are present in the electrolyte, silvery dull coatings are obtained. Some sulfate electrolytes for plating lustrous tin coatings contain formaldehyde (I = 10.88 eV) along with luster-producing additives [1, 2]. Taking into account this fact, we performed the subsequent studies in electrolyte no. 2 containing 2 g l^{-1} Syntanol and 6 ml l^{-1} Formalin. Dull, semilustrous, and lustrous coatings were plated from these electrolyte in the presence of various organic additives. Depending on the electrolyte composition, lustrous coatings are formed at i_c = 1–12 A dm^{-2}.

The dependence of the luster L (%) of the coating plated from electrolyte no. 2 with mechanical stirring on I of organic additives is shown in Fig. 1. Two maxima in this curve correspond to formation of lustrous coating. The first maximum appears at I = 7.25 eV (diphenylamine). The second maximum is observed in a broader range of ionization potentials (I = 8.95– 10.43 V), i.e., lustrous coatings are plated in the presence of benzyl alcohol, coumarin, 2-butene-1,4-diol, acetic anhydride, benzenesulfonic acid, 2-butyne-1,4-diol, *p*-phenolsulfonic acid, propargyl

alcohol, or butane-1,4-diol [13, 14]. Lustrous coatings are also formed when these additives are present in combination with smoothing agents and formaldehyde. It should be noted that lustrous coatings are plated from electrolyte containing OP-7, OP-10, and OS-20 condensation products and luster-producing agents without addition of formaldehyde [15]. Formaldehyde addition is not required also when luster-producing agents, gelatin (glue), and cresol are present in the electrolyte [3].

Previously we found [16] that formaldehyde in an electrolyte containing gelatin (glue) and cresol starts to exhibit luster-producing properties itself, but only after plating for a definite time.

It should be noted that high-quality lustrous films are plated only from the stirred electrolyte. Without stirring, dull coatings are formed.

The study of cathodic polarization in the electrolyte for tin-plating (Fig. 2) showed that the condensation products inhibit electrodeposition (curves *1, 2*).

The polarization curves flatten out at the limiting current. The polarization ΔE_c decreases (curves *2–4*) in the presence of the condensation products, formaldehyde, and luster-producing agents in the electrolyte.

The polarization also decreases with stirring of the electrolyte (curves *4, 5*). However, when the electrolyte contains condensation products, formaldehyde, and benzyl alcohol, ΔE_c increases (curves *6, 7*).

Probably, organic compounds present in the electrolyte are adsorbed on the electrode surface, thus inhibiting tin-plating. The measured capacitance of the electrical double layer C confirms this assumption. As seen from Fig. 3, the capacitance of the electrical double layer decreases in the presence of the organic compounds in the electrolyte (curves *1–3*). In this case, the C–E curves pass through a minimum at E from –0.3 to –0.4 V. In this potential range, C = 6–10 μF cm^{-2}. At higher potentials, the continuity of the adsorption layer is broken owing to desorption of organic compounds from the cathode surface. As a result, the capacitance of the electrical double layer increases [17].

Thus, to obtain lustrous tin coating, the electrolyte should contain an inhibitor, formaldehyde, and a luster-producing agent or an inhibitor and a luster-producing agent.

An inhibitor decelerates tin-plating and provides formation of dull finely crystalline deposits. Condensation products (Syntanol DS-10, OP-7, OP-10, OS-20), VA-20 smoothing agent, gelatin, and glue

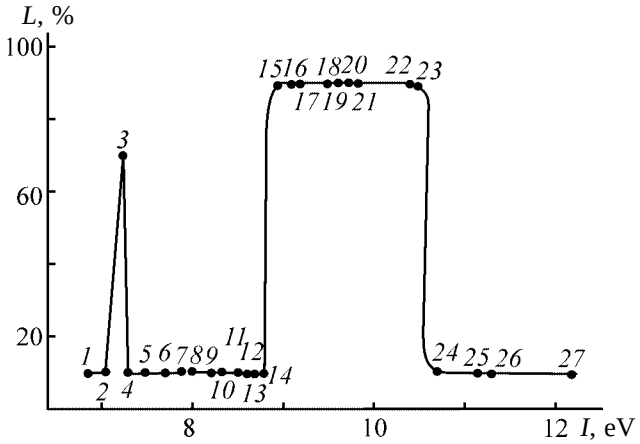

Fig. 1. Luster of tin coatings L as a function of the ionization potential of the organic additives I: (*1*) benzidine; (*2*) *N*,*N*-dimethylaniline; (*3*) diphenylamine; (*4*) α-naphthylamine; (*5*) *m*-toluidine; (*6*) aniline, indole, and (α- and β-naphthols; (*7*) phloroglucinol and hydroquinone; (*8*) pyrogallol and pyrocatechol; (*9*) naphthalene and *p*-cresol; (*10*) resorcinol, *o*-cresol, and *m*-cresol; (*11*) phenol; (*12*) triethylamine and quinoline; (*13*) piperidine and benzotriazole; (*14*) imidazole and furan; (*15*) benzyl alcohol; (*16*) coumarin; (*17*) 2-butene-1,4-diol; (*18*) acetic anhydride; (*19*) benzenesulfonic acid; (*20*) 2-butyne-1,4-diol; (*21*) *p*-phenolsulfonic acid; (*22*) propargyl alcohol; (*23*) butane-1,4-diol; (*24*) 3,5-dinitrobenzoic acid; (*25*) nitromethane; (*26*) trinitrobenzoic acid; and (*27*) valeric acid.

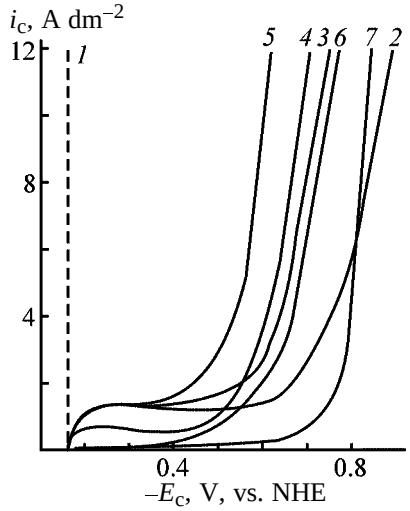

Fig. 2. Cathodic polarization curves recorded in sulfate tin-plating electrolyte no. 1. (i_c) Current density and (E_c) potential. (*1*) Electrolyte no. 1; (*2*) 1 + Syntanol, 2 g l^{-1}; (*3*) *2* + Formalin, 6 ml l^{-1}; (*4*) *3* + propargyl alcohol, 10 ml l^{-1}; (*5*) *4* with stirring; (*6*) *3* + benzyl alcohol, 6 ml l^{-1}; and (*7*) *6* with stirring.

can be used as inhibitors. However, the two latter substances weakly inhibit tin-plating. In this case, cresols (I = 8.24–8.31 eV), phenols (I = 8.5 eV), and naphthols (I = 7.76–7.78 eV) should be added to the elec-

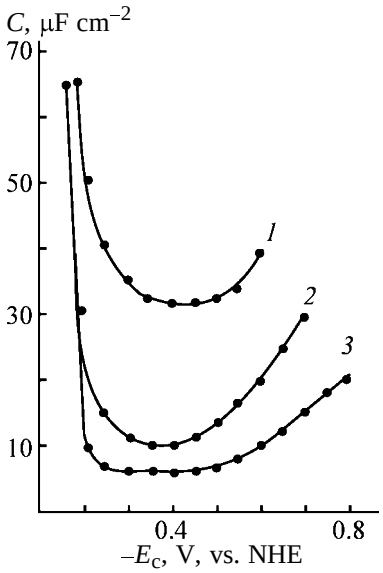

Fig. 3. Capacitance of the electrical double layer C as a function of the cathodic potential E_C: (*1*) electrolyte no. 1; (*2*) *1* + Syntanol, 2 g l^{-1} + Formalin, 6 ml l^{-1} + propargyl alcohol, 10 ml l^{-1}; (*3*) *1* + Syntanol, 2 g l^{-1} + Formalin, 6 ml l^{-1} + benzyl alcohol, 6 ml l^{-1}.

trolyte to obtain high-quality dull coatings [1, 2]. Formaldehyde (I = 10.88 eV) present in the electrolyte is a depolarizer of the process. Organic compounds with I = 7.25 and 8.95–10.43 eV exhibit lister-producing properties.

The fact that lustrous coating are formed only at a definite combination of organic compounds and stirring of the electrolyte suggests that sorption of organic compounds on the cathode surface is necessary but insufficient for obtaining such coatings. In this case, there are other factors affecting the luster of the coatings. Among them are complex physicochemical processes occurring in the catholyte layer [2] and the conditions of diffusion hydrodynamic feeding (or removal) of ions, which change the structure and properties of the absorption layer on the cathode surface [18].

Thus, the proposed approach affords a criterion of selection of organic compounds that, in combination with inhibitors, may provide formation of lustrous tin coatings. However, it does not warrant obtaining such coatings with particular additives *a priori*. Electrolytes for plating lustrous tin coatings are developed on the basis of this principle [13–16, 19, 20].

CONCLUSIONS

(1) Organic compounds promising for plating lustrous tin coatings were selected taking into account their first ionization potential. Lustrous tin coating were plated from the electrolyte containing an inhibitor, formaldehyde, and a luster-producing agent or an inhibitor and a luster-producing agent.

(2) Products of ethylene oxide condensation (Syntanol DS-10, OP-7, OP-10, and OS-20), VA-20 smoothing agent, as well as gelatin and glue in combinations with cresol, phenol, or naphthol can be used as inhibitors.

(3) Diphenylamine (I = 7.25 eV), benzyl alcohol (I = 8.95 eV), coumarin (I = 8.97 eV), 2-butene-1,4-diol (I = 9.13 eV), acetic anhydride (I = 9.5 eV), benzenesulfonic acid (I = 9.8 eV), 2-butyne-1,4-diol (I = 9.77 eV), *p*-phenolsulfonic acid (I = 9.8 eV), propargyl alcohol (I = 10.41 eV), and butane-1,4-diol (I = 10.43 eV) can be used as luster-producing additives to tin-plating electrolyte.

(4) The luster-producing additives allow plating of lustrous coatings from electrolyte containing or not containing formaldehyde, depending on the particular inhibitor. In the presence of gelatin, glue, and cresol, formaldehyde exhibits luster-producing properties.

(5) The proposed approach can be used to select organic compounds that may provide formation of lustrous tin coatings from electrolyte containing inhibitors.

REFERENCES

1. Kudryavtsev, N.G., *Elektroliticheskie pokrytiya metallami* (Metal Electroplating), Moscow: Khimiya, 1979.
2. *Blestyashchie elektroliticheskie pokrytiya* (Lustrous Electrolytic Coatings), Matulis, Yu.Yu., Ed., Vilnius: Mintis, 1969.
3. Medvedev, G.I., Influence of Surfactatns on Electrolytic Tin Plating from Sulfuric Acid Electrolytes, *Cand. Sci. Dissertation*, Moscow, 1992.
4. Nechaev, E.A., Kudryavtsev, N.G., and Medvedev, G.I., *Elektrokhimiya*, 1971, vol. 7, no. 3, pp. 383–386.
5. Kudryavtsev, N.G., Nechaev, E.A., and Medvedev, G.I., *Elektrokhimiya*, 1972, vol. 8, no. 4, pp. 538–541.
6. Nechaev, E.A., *Khemosorbtsiya organicheskikh veshchestv na oksidakh i metallakh* (Chemisorption of Organic Compounds on Oxides and Metals), Kharkov: Vyshcha Shkola, 1989.
7. Nechaev, E.A. and Kuprin, V.P., *Itogi Nauki Tekh., Ser.: Elektrokhimiya*, 1989, vol. 29, pp. 93–152.
8. Nechaev, E.A. and Volgina, V.A., *Elektrokhimiya*, 1978, vol. 14, no. 3, pp. 417–421.

9. Nechaev, E.A. Kuprin, V.P., Shapovalova, I.M., and Zelinskii, A.E., *Elektrokhimiya*, 1989, vol. 25, no. 2, pp. 262–266.
10. Kuprin, V.P., Shapovalova, I.M., and Nechaev, E.A., *Elektrokhimiya*, 1991, vol. 27, no. 5, pp. 845–849.
11. Dewar, M.J.S. and Stewart, J.J.P., *J. Comput. Chem.*, 1989, vol. 10, pp. 210–214.
12. Vilesov, F.I., Kurbatov, B.L. and Terenin, A.N., *Dokl. Akad. Nauk SSSR*, 1961, vol. 132, no. 6, pp. 1329–1333.
13. Medvedev, G.I. and Gorbunova, I.M., *Zh. Prikl. Khim.*, 1990, vol. 63, no. 4, pp. 807–812.
14. Medvedev, G.I. and Mashutina, G.G., *Zh. Prikl. Khim.*, 1992, vol. 65, no. 4, pp. 789–795.
15. Medvedev, G.I., Kudryavtsev, N.G., and Solov'ev, G.S., *Zh. Prikl. Khim.*, 1975, vol. 48, no. 11, pp. 2475–2477.
16. Medvedev, G.I., Solov'ev, G.S., and Dobrydnev, S.V., *Zashch. Met.*, 1976, vol. 12, no. 5, pp. 609–612.
17. Damaskin, B.B., Petrii, O.A., and Batrakov, V.V., *Adsorbtsiya organicheskikh soedinenii na elektrodakh* (Adsorption of Organic Compounds on Electrodes), Moscow: Nauka, 1968.
18. Gorbunova, K.M., Ivanovskaya, T.V., and Shishakov, N.A., *Zh. Fiz. Khim.*, 1951, vol. 25, no. 8, pp. 981–985.
19. Medvedev, G.I. and Makrushin, N.A., *Zh. Prikl. Khim.*, 2001, vol. 74, no. 11, pp. 1787–1791.
20. Medvedev, G.I., Makrushin, N.A., and Dubenkov, A.N., *Zh. Prikl. Khim.*, 2002, vol. 75, no. 2, pp. 227–230.

Russian Journal of Applied Chemistry, Vol. 75, No. 11, 2002, pp. 1804–1807. Translated from Zhurnal Prikladnoi Khimii, Vol. 75, No. 11, 2002, pp. 1839–1842.
Original Russian Text Copyright © 2002 by Kuzina, Bachaev.

APPLIED ELECTROCHEMISTRY AND CORROSION PROTECTION OF METALS

Intensification of Fabrication of Nickel Oxide Metal–Ceramic Electrodes by Chloride Impregnation

T. E. Kuzina and A. A. Bachaev

Nizhni Novgorod State Technical University, Nizhni Novgorod, Russia

Received November 27, 2001; in final form, August 2002

Abstract—The possibility of making shorter the time of fabrication of a nickel oxide electrode by impregnation of the metal–ceramic support with a nickel(II) solution and subsequent treatment with a solution of potassium hydroxide, containing potassium permanganate, was analyzed.

Electrodes on metal-ceramic (MC) supports for alkaline batteries have better specific characteristics than electrodes of other designs [1]. Nickel oxide electrodes (NOEs) of this kind are fabricated by high-temperature impregnation of an MC support in solutions of nickel(II) salts, most frequently nitrates, with high concentration. Several cycles are performed in order to introduce into the support a sufficient amount of nickel(II) compounds, with each cycle involving the entire process chain, including the alkaline treatment of the nickel(II) salts in pores of the support [1]. Fabrication of MC NOE is a time-, power-, and labor-consuming process.

The specific characteristics of MC electrodes are determined by the initial porosity and surface activity of the support, pore structure, concentration of the impregnating solution, activity of the forming nickel(II) hydroxide, and ability of nickel particles in the MC support to react with the impregnating solution to give additional electrochemically active nickel compounds in pores. The opening of blind pores, occurring in the process, is accompanied by development of the reaction surface. In some cases, industrial technologies envisage preliminary etching of supports in a hydrochloric acid solution to open pores and activate the surface of nickel supports [2].

The aim of this study was to analyze the possibility of replacing the commonly used impregnating solution of $Ni(NO_3)_2$ [1] by an $NiCl_2$ solution. The latter possesses a number of advantages over the nitrate solution [3]: the solubility in terms of nickel at 80°C increases from 320 to 380 g l^{-1}, the viscosity of a 30% solution at 80°C decreases from 1.3×10^{-3} to 1.2×10^{-3} Pa s, and the solution has higher corrosive activity. The last factor makes it possible to tackle with the problem of opening of blind pores in the support and activation of its surface in a single process cycle, with the stage of preliminary etching of supports in a hydrochloric acid solution eliminated.

EXPERIMENTAL

MC supports with dimensions of $34 \times 10 \times 0.75$ mm were used in corrosion tests, and those with dimensions of $40 \times 27 \times 1.6$ mm, for determining the change in mass and electrical characteristics. The volume porosity of the supports was 70–75%. The MC supports were filled with nickel(II) hydroxide by the following procedure (with no indication of occasionally used improving additives) [1, 4]: impregnation with $NiCl_2$ solution ($c_{Ni(II)}$ = 290–365 g l^{-1}, pH 3–4, temperature 60–80°C), crystallization in air (30 min), treatment with an alkali solution (c_{KOH} = 300–330 g l^{-1}, T = 60–80°C, τ = 1 h), washing to remove the alkali, and drying (T = 110°C). The content of residual chlorine (Cl^- ions) in the washing water after MC NOE treatment in an alkali solution was found using the procedure described in [5]. The mass gain of MC supports was determined from the difference of masses before impregnation and after drying. To find the amount of nickel oxidized in impregnation of an MC support, the method of selective dissolution of nickel(II) hydroxide from electrodes in a 30% solution of CH_3COOH was used. The difference of MC support masses before impregnation and after selective dissolution corresponded to the amount of oxidized nickel. The amount of nickel dissolved in CH_3COOH, found by complexometric titration [6], corresponded to the total amount of nickel(II) hydroxide formed via pore filling with the salt from the impregnating solution and nickel from the support, oxidized in the

1070-4272/02/7511-1804$27.00 © 2002 MAIK "Nauka/Interperiodica"

course of its impregnation. The optimal conditions for chloride impregnation were found by full factorial experimental design. The process of nickel etching was monitored on a prototype battery in the form of a voltaic cell with relatively large electrodes (S = 14 cm^2), with platinum as cathode and MC support as anode. The cathode and anode spaces in the cell were separated by a porous diaphragm (Khlorin fabric). The cathode space was filled with a solution under study, and the anode space, with an $NiCl_2$ solution. Both the solutions had the same ionic strength, for which purpose KNO_3 and NaCl, respectively, were added. The operation of a short-circuited voltaic cell Ni–Pt only qualitatively models the operation of real cells, since, in the course of nickel etching, microirregularities continuously move over the surface, and, what is more, platinum may exert electrocatalytic effect on the process.

The capacity characteristics of the electrodes fabricated were tested in cells with auxiliary electrodes made of perforated nickel foil with perforated polyvinyl chloride plastic as separator. As electrolyte served KOH solution with a density of 1.19–1.20 g cm^{-3}. In charging, 150% of the theoretical capacity was imparted to the electrodes at a current density of 4.4 mA cm^{-2} [4]. Discharge was done at the same current density until an abrupt change in the working potential.

Nickel dissolves in impregnation of MC supports by the electrochemical mechanism [1]. In $NiCl_2$ solutions, nickel oxidation occurs via reduction of dissolved oxygen and free hydrogen ions. The content of dissolved oxygen in $NiCl_2$ solutions is low (solubility of oxygen at 80°C in a 3–4.5 M $NiCl_2$ solution is 0.3–0.5 $cm^3\ l^{-1}$ [7]). The dissolution of nickel from the MC support (Fig. 1) proceeds with pronounced (96%) cathodic control over the process. Interaction of nickel with an acidic (pH 3–4) $NiCl_2$ solution leads to fast alkalization of the solution in the near-cathode layer with deposition of hydroxide films shielding the metal surface. This hinders the process of nickel dissolution and, presumably, is one of the reasons for lower use factors of MC electrodes in chloride impregnation, compared to electrodes subjected to treatment in a nitrate impregnating solution [4]. However, faster formation of solid products in the case of the chloride impregnation technique [1] must decrease the loss of dissolving nickel through its removal into the external volume of the electrolyte, which points to reserves of the capacitance characteristics of electrodes of this kind.

Up to 16–20% of nickel from the support passes

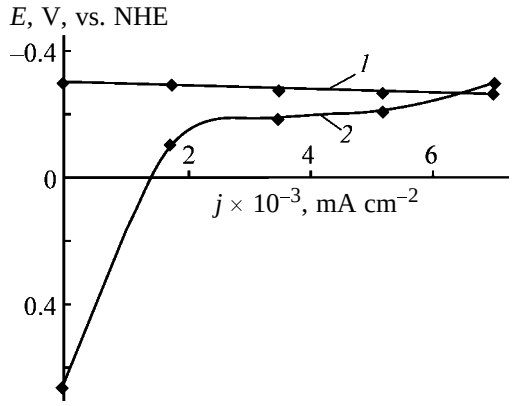

Fig. 1. Variation of the potential E of (*1*) MC support and (*2*) Pt electrode in cell operation in an $NiCl_2$ solution at T = 80°C, $c_{Ni(II)}$ = 360 g l^{-1}. (*j*) Current density.

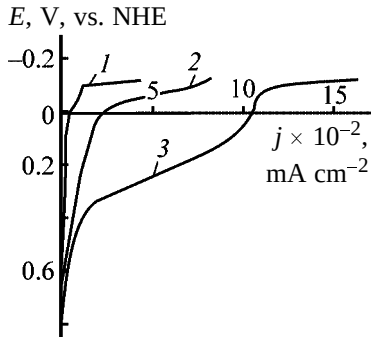

Fig. 2. Cathodic potentiodynamic curves obtained on a Pt electrode in $NiCl_2$ solutions of varied composition. Sweep rate V_s = 2 mV s^{-1}, T = 80°C, $c_{Ni(II)}$ = 290–360 g l^{-1}. (*E*) Potential and (*j*) current density. (*1*) $NiCl_2$, (*2*) $NiCl_2$: $Ni(NO_3)_2$ with 1 : 1 volume ratio of components, and (*3*) $NiCl_2$ + 4.7 g l^{-1} $NaNO_2$.

into the active substance in impregnation of MC supports in an $NiCl_2$ solution containing 0.05–0.1 g l^{-1} $NaNO_2$, [4], and 11–15% in the case of a nitrate impregnating solution [8], which may be due to different oxidizing powers of the nitrate and nitrite ions [1, 4] (Fig. 2).

The forming nickel compounds hinder dissolution of the metal from the support. However, these compounds can be oxidized and act as oxidizing agents in subsequent oxidation.

For example, dry-charged NOE can be obtained using chemical oxidation of finished electrodes with hydrogen peroxide, hypochlorite, persulfate, or hypobromite [9]. The resulting formation of higher nickel hydroxides, which are in contact with nickel in the support, favors dissolution of the latter; in addition, the higher density of higher nickel hydroxides may give rise to porosity in the solid film [7].

Table 1. Relative mass loss, Δm, by MC supports after the first and second cycles of impregnation in an $NiCl_2$ solution and content of chlorine ions c_{Cl^-} in washing water for different types of treatment. $c_{Ni(II)}$ = 320 g l^{-1}, τ = 1 h, T = 60°C

Method of treatment in alkali solution	$\Delta m \times 10^{-2}$, in indicated cycle		c_{Cl^-}, mg l^{-1}
	first	second	
Control	0.45	0.08	81.8
3% $KMnO_4$ (experiment)	0.45	4.0	24.3

In [6], readily available potassium permanganate $KMnO_4$ in an alkali solution was used as oxidizing agent. Reduction of MnO_4^- leads to formation of MnOOH-like structures, which are similar to NiOOH [10]. The close similarity of structures and ionic radii of Mn^{3+} and Ni^{3+} allows the former to be incorporated into the crystal lattice of NiOOH, making higher the concentration of electronic defects, which facilitates the charging of nickel oxide electrodes [10]. Permanganate treatment leads to formation of NiOOH in pores of MC supports, which acts in subsequent impregnation cycles as a depolarizer of nickel dissolution. In operation of an $NiOOH/Ni_{met}$ voltaic couple, the amount of nickel oxidized in MC supports in the second impregnation cycle increased 50-fold, compared to the control (Table 1). The forming nickel(III) oxide has a structure of β-NiOOH, which is indirectly confirmed by the oxidation state of nickel (equal to 3 for the β-NiOOH phase and 3.7 for γ-NiOOH) and by the potential of its reduction, which is more negative than the potential of γ-NiOOH reduction [11].

The most pronounced change in the electrode mass and the highest discharge capacity were achieved under the following conditions of MC support impregnation in $NiCl_2$ solution: $c_{Ni(II)}$ = 360–365 g l^{-1}, T = 65–70°C, and τ = 150 min.

After three impregnation cycles in nickel chloride solutions and subsequent intermediate oxidation, electrodes with perforated foil as current lead changed their mass by 0.76 g cm^{-3} and had the capacity Q = 0.19 A h cm^{-3} (Table 2).

The results obtained in measuring the change in mass and specific discharge capacity were also verified on 1.6-mm-thick MC supports with nickel mesh as current lead.

The change in mass of the electrodes under study after three impregnation cycles is approximately 1.4 times larger for 0.75-mm-thick supports, and 1.8 times larger for 1.6-mm-thick supports (Table 2). The amount of the active substance formed through oxidation of nickel from the support is 35% in the case of permanganate oxidation, and 7% in the control treatment. The change in mass after the first cycle of impregnation with intermediate oxidation is 1.4–2 times that in the control, possibly because of the presence of potassium permanganate reduction products (Table 2).

The electrical characteristics of compacted MC NOE fabricated with intermediate oxidation approach after three cycles of impregnation those of the elec-

Table 2. Effect of the number of impregnation cycles on the mass change of MC NOEs and on their characteristics for different treatment methods* ($c_{Ni(II)}$ = 365 g l^{-1}, T = 70°C, τ = 150 min)

Characteristic	MC NOE thickness, mm			
	0.75		1.6	
	method of alkali treatment			
	control	experiment	control	experiment
Δm, g cm^{-3}, after indicated cycle of MC NOE:				
1st	0.22	0.26	0.3	0.45
2nd	0.17	0.25	0.21	0.42
3rd	0.14	0.25	0.17	0.38
Σ	0.53	0.76	0.68	1.25
Q, A h cm^{-3}	0.13	0.19	0.16	0.29
K_{use}, %	88	88	80	80

* Q is the specific discharge capacity, and K_{use} is the use factor of the active paste.

trodes fabricated by the nitrate technology (0.32–0.37 A h cm^{-3} [8]). However, three cycles of nitrate impregnation take 20–24 h [8], whereas with the method being tested, MC NOE can be fabricated in 15 h, and this is achieved without preliminary etching of MC supports stored for several years.

Use of a $KMnO_4$ additive makes it possible to lower significantly the content of chlorine impurity in the electrodes. In subsequent impregnation of MC electrodes, MnO_2 contained in their pores can oxidize Cl^- ions in acid medium [10]:

$$2Cl^- + 4H^+ + MnO_2 \rightarrow Mn^{2+} + 2H_2O + Cl_2\uparrow.$$

As a result, the content of Cl^- ions in washing waters (serving as a criterion of their content in electrodes) decreased by a factor of approximately 3 (Table 1).

The recommended solution compositions and process modes are as follows: impregnation with $NiCl_2$ solution, $c_{Ni(II)}$ = 360–365 g l^{-1}, T = 65–70°C, τ = 150 min; treatment with alkali solution: c_{KOH} = 300–330 g l^{-1}, c_{KMnO_4} = 25–30 g l^{-1}, T = 60–80°C, τ = 1 h.

CONCLUSIONS

(1) The time required for fabrication of metal–ceramic nickel oxide electrodes is shortened by 25–40% in the case of intermediate oxidation of the active substance in an alkali solution containing $KMnO_4$.

(2) The duration of the process is decreased because of the intensification of anodic dissolution of nickel from metal–ceramic supports by the electrochemical mechanism with cathodic control.

(3) A procedure for chloride impregnation is proposed, which allows fabrication of electrodes of capacity 0.29 A h cm^{-3} without any additional activation of the support.

REFERENCES

1. Pozin, Yu.M. and Shtertser, N.I., *Zh. Prikl. Khim.*, 1970, vol. 43, no. 7, pp. 1482–1486.
2. Pervushin, Yu.N., A Study in Technology of MC NOE Fabrication for an Alkaline Battery, *Cand. Sci. Dissertation*, Novocherkassk, 1968.
3. Zaitsev, I.D. and Aseev, G.G., *Fiziko-khimicheskie svoistva binarnykh i mnogokomponentnykh rastvorov neorganicheskikh veshchestv: Spravochnik* (Physicochemical Properties of Binary and Multicomponent Solutions of Inorganic Substances: Reference Book), Moscow: Khimiya, 1988.
4. Zhdanov, V.V., Poltavchenko, V.S., Tikhonov, K.I., and Pozin, Yu.M., *Zh. Prikl. Khim.*, 1982, vol. 55, no. 3, pp. 694–696.
5. *GOSTs* (State Standards) *4.245–72, 18190–72: Potable Water*, Moscow: Izd. Standartov, 1997.
6. Posypaiko, V.I., *Khimicheskie metody analiza: Uchebnoe posobie* (Chemical Methods of Analysis: Textbook), Moscow: Vysshaya Shkola, 1989.
7. *Spravochnik khimika* (Chemist's Handbook), Nikol'skii, B.P., Ed., Moscow: Khimiya, 1968, vol. 3.
8. Berezin, M.Yu. and Pozin, Yu.M., *Issledovaniya v oblasti elektricheskikh akkumulyatorov: Sbornik nauchnykh trudov* (Investigations in the Field of Electric Batteries: Coll. of Scientific Works), Leningrad: Energoizdat, 1990.
9. Miroshnichenko, A.S., Nikol'skii, V.A., and Pozin, Yu.M., *Sbornik rabot po KhIT* (Coll. of Works on Chemical Power Cells), Nikol'skii, V.A., Ed., Leningrad: Energiya, 1974, issue 9.
10. Hugi-Cleary, D., Rearcly, M.-O., and Stoeckli, H.F., *Chimia*, 1997, vol. 51, nos. 8–9, pp. 645–650.
11. Malandin, O.G. and Ezhov, B.B., *Elektrokhimiya*, 1995, vol. 31, no. 4, pp. 423–427.

Russian Journal of Applied Chemistry, Vol. 75, No. 11, 2002, pp. 1808–1811. Translated from Zhurnal Prikladnoi Khimii, Vol. 75, No. 11, 2002, pp. 1843–1846.
Original Russian Text Copyright © 2002 by Tošković, Rajković, Čirić.

APPLIED ELECTROCHEMISTRY AND CORROSION PROTECTION OF METALS

Corrosion of Tin Plate in Brine Solutions

D. Tošković, M. B. Rajković, and I. Čirić

Technological Faculty, Zvornik, Serbia
Institute of Food Technology, Beograd-Zemun, Serbia, Yugoslavia
Higher School of Chemical Technology, Sabac, Serbia, Yugoslavia

Received June 14, 2001; in final form, January 2002

Abstract—The corrosion behavior at 25°C of tin plate, used for canning, in synthetic and natural brine solutions employed in storage of a number of food products (legumes) was studied.

Some kinds of foodstuff are stored in cans made of tin plate, in NaCl brine solutions. In the course of storage, the brine composition may change. For example, organic acids contained in the product may pass into brine and affect the corrosion of tin. In some cases, oxidizing agents and salts creating an alkaline medium are added to brine solutions.

Previously [1], it has been shown that tin is fairly corrosion-resistant in NaCl brine solutions. Addition of very small amounts of nitrates (up to 0.01 g) leads to acceleration of corrosion in storage of foodstuff with pH < 7. Under these conditions, corrosion processes may occur via reduction of nitrate ions with NH_4^+.

The composition of brine solutions depends on the temperature of product treatment, salt additives used to preserve the commercial value of the product, and storage time. Account should be taken of the influence exerted on the corrosion rate of tin plate by trace amounts of oxygen contained in brine solutions after can sealing.

This study is concerned with the corrosion behavior of electrolytic tin plate in synthetic and natural brine solutions used to store legumes (peas, kidney beans). Synthetic brine solutions were prepared from NaCl with and without addition of $NaNO_3$.

EXPERIMENTAL

The study was performed with samples of E-1 tin plate (manufactured by Sartid 1913 plant, Belye zhesti Joint-Stock Company, Sabac). Legume seeds were stored at 25°C in hermetically sealed containers made of unvarnished tin plate. During storage, natural brine was extracted after 1, 5, 12, and 18 months of storage and electrodes of area 1 cm^2 were cut out of the plate. The nonworking side of the electrodes was insulated with epoxy resin.

Synthetic brine solutions were prepared from chemically pure grade reagents and had concentration commonly used in storage of legumes [peas (I) and kidney beans (II)], namely, 25% NaCl, with and without addition of 0.015% $NaNO_3$.

The current and potential of corrosion were determined potentiometrically by the Evans–Hore galvanostatic technique [2–12] in an electrolytic cell with three electrodes: tin plate as working electrode, armco iron as auxiliary electrode, and calomel electrode as reference.

The measurements were carried out under natural aeration conditions and in an atmosphere of inert gas (nitrogen). To remove dissolved oxygen, nitrogen was passed through the solution. Preliminarily, nitrogen was passed (to remove trace amounts of oxygen) successively through a vessel containing an ammonium metavanadate solution, on whose bottom 25 g of zinc amalgam was placed [13], and through a column containing P_2O_5 with a 3 Å molecular sieve.

The currents and potentials were found graphically from the intersection of polarization curves. The corrosion currents i_{corr} ($\mu A\ cm^{-2}$) were recalculated into the corrosion depth factor V ($mm\ year^{-1}$) by the formula

$$V = \frac{mK}{\rho S \tau} = \frac{M i_{corr} 8.76 \times 10^4}{zF\rho}, \qquad (1)$$

where M is the molar mass of tin ($g\ mol^{-1}$); ρ, the density of tin plate ($g\ cm^{-3}$); F, the Faraday number ($C\ mol^{-1}$); S, the area (cm^2); τ, time (h); z, the num-

1070-4272/02/7511-1808$27.00 © 2002 MAIK "Nauka/Interperiodica"

Table 1. pH of brine solutions studied

Brine solution	pH after tests for indicated time, months				
	1 day	2	7	12	18
Synthetic, %:					
NaCl, 2.5	5.92	–	–	–	–
NaCl, 2.5 + $NaNO_3$, 0.015	5.88	–	–	–	–
Natural:					
for product I	6.24	6.23	6.22	6.21	6.22
for product II	5.45	5.29	5.14	5.18	

ber of electrons; and *K*, the coefficient taking into account the dimension of area and time.

Table 1 presents the results obtained in determining the pH of brine solutions used for storage of products I and II in relation to the testing time.

As seen from Table 1, the pH of brine solutions used to store product I remains virtually unchanged during the time of testing. The high pH value of brines used in storage of product I is due to an increased amount of basic salts added to the solution in the course of product treatment to preserve its commercial value. The rise in the acidity of brine solutions used to store product II with increasing duration of testing may be due to the activity of the methylesterase enzyme, which leads to deesterification of carboxy groups and to their dissociation.

Figure 1 shows corrosion diagrams, which make it possible to find graphically the potential and current of corrosion in air of tin plate in synthetic and natural brine solutions extracted after the first day of tests. It can be seen that the highest current of tin plate corrosion is observed in natural brines used to store product I (curve *1*), and the lowest, in brine solutions used for storage of product II (curve *2*). The tin corrosion in the initial period of time, as a rule, occurs under cathodic control.

The corrosion diagrams reflecting dissolution of tin plate in synthetic and natural brine solutions in an inert atmosphere are presented in Fig. 2, curves *3* and *4*. It can be seen that, in both cases, removal of dissolved oxygen makes lower the current of tin plate corrosion.

Figure 3 shows how the current of tin corrosion in the solutions under study varies with time of testing (a) in air and (b) in an inert atmosphere. In all cases, a steep increase in corrosion current is observed during the first month of tests. Further, the dissolution of tin is hindered somewhat, with this phenomenon observed in both synthetic and natural brine solutions. Addition of $NaNO_3$ suppresses to some extent the corrosion of tin. Possibly this is due to inhibition under the given conditions of tin dissolution. In natural brines used to store product II, the rate of tin corrosion is higher than that in brines used in storage of product I. This is, in the first place, due to the higher temperature of treatment of product II and to introduction into the brine of additives aimed to preserve the commercial quality of the product. All these factors lead to a decrease in the brine pH during storage (Table 1) and to an increase in the rate of tin corrosion.

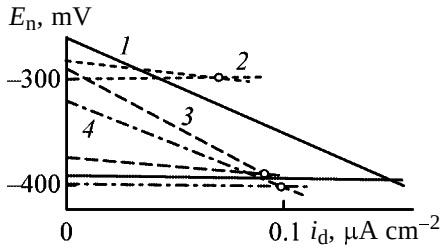

Fig. 1. Relationship between current i_d and potential E_n in polarization of tin plate in air after the first day of storage. (*1*) Liquid content of product I, (*2*) that of product II, (*3*) 2.5% solution of NaCl, and (*4*) 2.5% solution of NaCl + 0.015% Na_2CO_3; the same for Fig. 3.

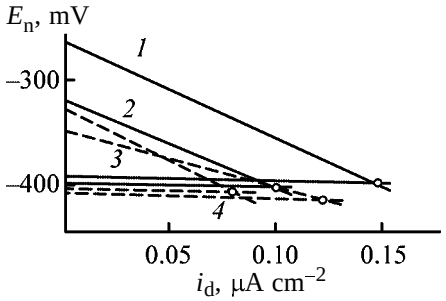

Fig. 2. Relationship between current i_d and potential E_n in polarization of tin plate in liquid content of products I and II in, respectively, (*1, 2*) air and (*3, 4*) nitrogen after the first day of storage.

Table 2. Currents, potentials, and rates of tin plate corrosion in brine solutions

Test duration, months	Parameter	Natural solution				Synthetic solution			
		storage of product I		storage of product II		2.5% NaCl		2.5% NaCl + 0.015% $NaNO_3$	
		air	nitrogen	air	nitrogen	air	nitrogen	air	nitrogen
0	i_{corr}, μA cm^{-2}	0.05	0.035	0.080	0.70	0.040	0.030	0.030	0.020
	E, mV	–402	–404	–380	–390	–400	–395	–305	–350
	$V\times10^3$, mm year^{-1}	2.66	1.85	4.25	3.72	2.12	1.59	1.59	1.05
1	i_{corr}, μA cm^{-2}	0.100	0.080	0.150	0.120	0.900	0.050	0.075	0.045
	E, mV	–400	–405	–395	–410	–395	–400	–302	–390
	$V\times10^3$, mm year^{-1}	5.32	4.25	7.98	6.38	4.79	2.66	3.99	2.39
6	i_{corr}, μA cm^{-2}	0.120	0.110	0.190	0.170	0.135	0.90	0.090	0.068
	E, mV	–402	–410	–390	–405	–390	–405	–308	–385
	$V\times10^3$, mm year^{-1}	6.38	5.85	6.38	90.2	7.18	4.79	4.79	36.2
12	i_{corr}, μA cm^{-2}	0.160	0.140	0.240	0.200	0.160	0.120	0.110	0.075
	E, mV	–405	–411	–398	–416	–398	–401	–318	–360
	$V\times10^3$, mm year^{-1}	8.31	7.45	12.7	10.6	8.52	6.39	5.85	3.99
18	i_{corr}, μA cm^{-2}	0.240	0.200	0.380	0.200	0.200	0.140	0.180	0.125
	E, mV	–400	–418	–388	–402	–306	–407	–340	–348
	$V\times10^3$, mm year^{-1}	12.7	10.6	20.2	10.6	10.6	7.45	9.50	6.60

Table 2 presents corrosion potentials E, corrosion currents i_{corr}, and corrosion rates V in relation to test duration. It can be seen that, during 18 months of tests in all of the solutions studied, the corrosion rate of tin plate increases and the corrosion potential remains virtually unchanged. This indicates that, in the course of time, the corrosion of tin plate starts to proceed under mixed control conditions.

CONCLUSIONS

(1) Corrosion of tin plate in brine solutions becomes more pronounced with increasing test duration.

(2) Addition of $NaNO_3$ to brine solutions hinders the dissolution of tin plate.

(3) The rate of tin plate dissolution in an inert

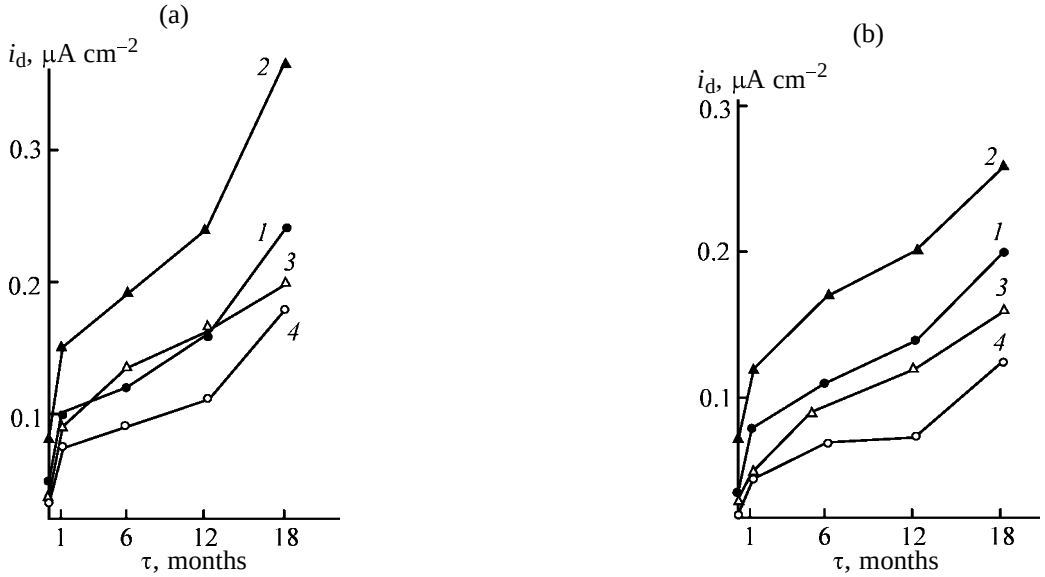

Fig. 3. Corrosion of tin plate vs. time of storage τ in (a) air and (b) nitrogen. (i_d) Corrosion current.

atmosphere is lower than that under natural aeration conditions.

REFERENCES

1. Niketih-Aleksih, G., *Tekhnologija voha i povrha*. Beograd-Zemun: Pol'oprivredni fakultet, 1994.
2. Mansfeld, F., Jean, S.L., and Kending, M.W., *Corrosion Sci*., 1986, vol. 26, p. 735.
3. Oldham, K.B. and Mansfeld, F., *Corrosion*, 1971, vol. 27, no. 10, pp. 434–435.
4. Drazhih, D.M. and Vashchih, V., *Khem. Ind*., 1994, vol. 39, p. 1.
5. Tsurumaru, M., Nunokawa, A., and Suzuki, Y., *2nd Int. Tinplate Conf*., London, October 6–10, 1980, pp. 348–359.
6. Butler, T.J. and Carter, P.R., *Electrochem. Technol*., 1963, vol. 1, no. 1, pp. 22–27.
7. Alby-Yaron, A., Bertchelin, N., Chisten, J.M., and Pagetty, J., *J. Food Technol*., 1979, vol. 14, no. 3, pp. 9–19.
8. Catala, R. and Cadanes, J.M., *Rev. Agroquim. Tecnol. Aliment*., 1981, vol. 21, no. 3, pp. 341–352.
9. *Advances in Electrochemistry and Electrochemical Engineering*, Gerischer, H. and Tobias, Ch.W., Eds., New York: Wiley, 1978, vol. 2, pp. 273–352.
10. Tošković D., Rajković B.M., Lačnjevac Č., *Zašt. Mater*., 1999, vol. 40, no. 2, pp. 13–18.
11. Trassati, S., *J. Electroanal. Chem*., 1971, vol. 33, pp. 351–378.
12. Kamm, G.G. and Willey, A.R., *Corrosion*, 1961, vol. 17, no. 2, pp. 99–106.
13. Nagy, S., Rousffe, R., and Sik-Vune, *J. Agric. Food Chem*., 1980, vol. 28, pp. 1166–1169.

Russian Journal of Applied Chemistry, Vol. 75, No. 11, 2002, pp. 1812–1815. Translated from Zhurnal Prikladnoi Khimii, Vol. 75, No. 11, 2002, pp. 1847–1850.
Original Russian Text Copyright © 2002 by Grigor'eva, Bikbaev, Kutepov, Apkarimova, Makhamatkhanov.

CATALYSIS

Effect of Thermal Treatment on the Acidity and Catalytic Properties of Pentasil-Containing Catalysts

N. G. Grigor'eva, R. T. Bikbaev, B. I. Kutepov, G. I. Apkarimova, and R. A. Makhamatkhanov

Institute of Petrochemistry and Catalysis, Academy of Sciences of the Republic of Bashkortostan and Ural Scientific Center, Russian Academy of Sciences, Ufa, Bashkortostan, Russia

Received May 27, 2002

Abstract—The effect of thermal treatment of zeolite-containing catalysts on their acid and catalytic properties in aromatization of the long distillate of light hydrocarbons was studied.

One of application fields of Pentasil-containing catalysts is conversion of saturated hydrocarbons into aromatic compounds [1, 2]. These processes are carried out at 340–420 (aromatization of benzine fractions) or 500–600°C (conversion of C_3–C_4 alkanes), with the catalyst gradually deactivated by coking. To restore its catalytic properties, the catalyst is subjected to oxidizing regeneration at temperatures exceeding 550°C. During regeneration, zones with higher temperature may appear, and dehydroxylation, dealumination, and even disintegration of the crystalline framework of the zeolite are possible [3–5]. Therefore, one of the most important characteristics of catalysts is their thermal stability, which is largely determined by the SiO_2/Al_2O_3 molar ratio in the zeolite.

This study is concerned with the effect of thermal treatment on the acid and catalytic properties of catalysts synthesized on the basis of Pentasils of varied composition in aromatization of the long distillate of light hydrocarbons (LDLH).

EXPERIMENTAL

The starting zeolites of mixed structure, ZSM-5/11, with SiO_2/Al_2O_3 molar ratios of 30 and 60 were synthesized in the sodium form by crystallization of alkaline aluminosilicate hydrogels under hydrothermal conditions (pressure 5 atm, temperature 130–150°C, duration 94–96 h) using monoethanolamine as an organic template. The samples obtained were dried at 150°C for 3 h and calcined in air at 540°C for 16 h. The hydrogen form of Pentasils was obtained by treating the samples with NH_4NO_3 at 60°C to residual Na_2O content of 0.1 wt % and less, with subsequent conversion of the NH_4 form into the H form (thermal treatment in air flow at 540°C for 4 h). Catalyst samples were prepared by mixing 70 wt % Pentasils obtained with 30 wt % pseudoboehmite in a mixer and paste forming into sticks. It has been shown previously [2] that the presence of up to 40 wt % Al_2O_3 in catalysts of this kind has no noticeable effect on the activity and selectivity of a catalyst in aromatization of hydrocarbons.

To study the thermal stability, the catalyst samples were calcined in air at 600, 650, and 700°C for 6–24 h. The catalyst containing Pentasil with the molar ratio SiO_2/Al_2O_3 = 30 is denoted by TsSK, and that with SiO_2/Al_2O_3 = 60, by TsSK(M).

Transformations of LDLH were studied on a flow-through installation under atmospheric pressure in the temperature range 320–550°C and feed space velocity w of 0.5 h^{-1}. The working cycle comprised a 8-h experiment and 3-h catalyst regeneration with air at 550–580°C. The reaction products formed were analyzed by gas–liquid chromatography.

The LDLH characteristics are as follows: density at 20°C 0.675 g cm^{-3}, initial boiling point 27°C, final boiling point 185°C; content (wt %): *n*-paraffins 36.9, isoparaffins 43.8, naphthenes 16.8, and arenes 2.5.

The acid properties of the catalysts were studied by temperature-programmed desorption of ammonia on a Quarta Chrom instrument. The samples were heated in a helium flow to 600°C, kept at this temperature for 2 h, and then cooled to room temperature and saturated with ammonia. Thermal desorption of NH_3 was done at 100–575°C after removal of physically adsorbed ammonia.

The IR spectra were recorded on a UR-20 instrument. Samples for measurement of IR spectra of the

1070-4272/02/7511-1812$27.00 © 2002 MAIK "Nauka/Interperiodica"

zeolite framework (400–1300 cm^{-1}) were prepared by compaction into pellets with KBr; to study acid properties by adsorption of pyridine, catalyst pellets were pressed. The IR spectra of chemisorbed pyridine were recorded in the range 1400–3800 cm^{-1} after removal of weakly bound base molecules in a vacuum at 200°C.

X-ray diffraction analysis was performed on a DRON-3 diffractometer with monochromated CuK_α radiation (graphite monochromator in reflected beam).

According to the results of X-ray phase analysis, no changes in the crystallinity and pore structure of the catalysts occur after their thermal treatment at 550–700°C for 24 h and also upon 5 reaction–regeneration cycles. The IR spectra associated with framework vibrations of both the catalysts remained virtually unchanged after various treatments, which confirms that no disintegration of the crystal lattice of the zeolites occurs under the conditions studied.

It can be seen from Table 1 that, even after calcination at 700°C for 24 h, the specific surface area and pore volume do not decrease.

The nature of interaction between ammonia and the catalysts depends not only on their composition, but also on treatment conditions. As is known [6], ammonia is adsorbed onto decationized Pentasils in two forms: the peak at 100–350°C characterizes desorption of ammonia from "weak" acid centers, and that at 350–500°C, desorption from "strong" acid centers.

It can be seen from desorption patterns (Fig. 1) that raising the catalyst calcination temperature from 550 to 700°C makes lower the concentrations of both kinds of acid centers, especially that of strong centers. In the case of TsSK subjected to thermal treatment, the decrease in the total concentration of acid centers is much more pronounced compared to TsSK(M), and, as a result, the high-temperature peak characterizing strong acid centers is virtually absent in the desorption pattern of calcined TsSK.

Commonly, the decrease in the concentration of B centers in thermal treatment is related to zeolite dehydroxylation, during which one L center is formed from two B centers [7]. In this case, the IR spectra of pyridine adsorbed on the catalyst surface must show a decrease in the intensity of the absorption band associated with protonated pyridine (1550 cm^{-1}) and an increase in the intensity of the absorption band associated with coordination-bound pyridine (1450 cm^{-1}). However, it follows from the obtained IR spectra of adsorbed pyridine (Fig. 2) that, with increasing catalyst calcination temperature, the intensities of all absorption bands decrease, especially those of the bands at 1550 and 1491 cm^{-1} (at frequencies characterizing pyridine adsorption on both B and L centers, but to a greater extent related to that on B centers). In the spectrum of TsSK calcined at 700°C, these bands are virtually lacking at all. The simultaneous decrease in the intensity of the absorption band at 1450 cm^{-1}, i.e., in the concentration of L centers, suggests that the decrease in the concentration of strong B centers is due not only to dehydroxylation. Indeed, the IR spec-

Table 1. Specific surface area and pore volume of catalysts calcined at varied temperatures

Sample	Thermal treatment conditions		S_{sp}, $m^2\ g^{-1}$	V_{pore}, $cm^3\ g^{-1}$
	T, °C	τ, h		
TsSK	550	4	202	0.64
	600	24	201	0.62
	700	24	198	0.61
TsSK(M)	550	4	321	0.26
	600	24	320	0.25
	700	24	319	0.24

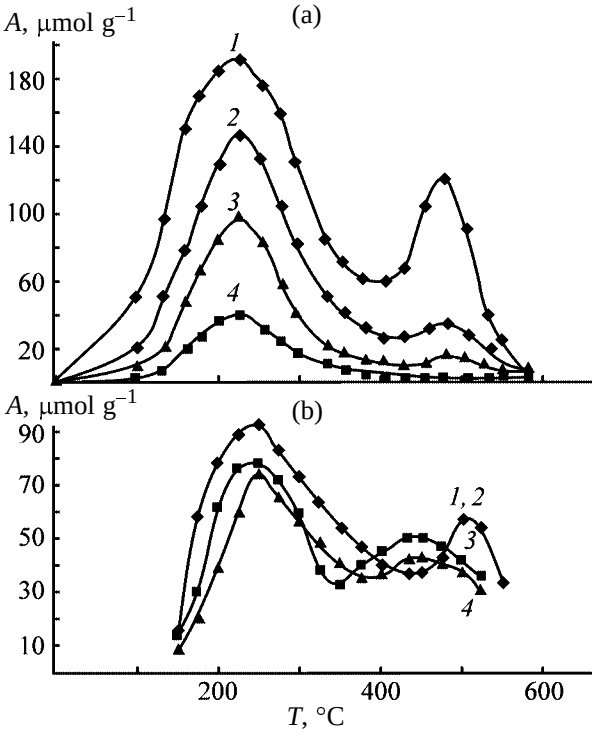

Fig. 1. Desorption of ammonia from the surface of (a) TsSK and (b) TsSK(M) samples heat-treated at different temperatures for 6 h. (*A*) Amount of desorbed ammonia and (*T*) temperature. Heat treatment temperature (°C): (*1*) 550, (*2*) 600, (*3*) 650, and (*4*) 700.

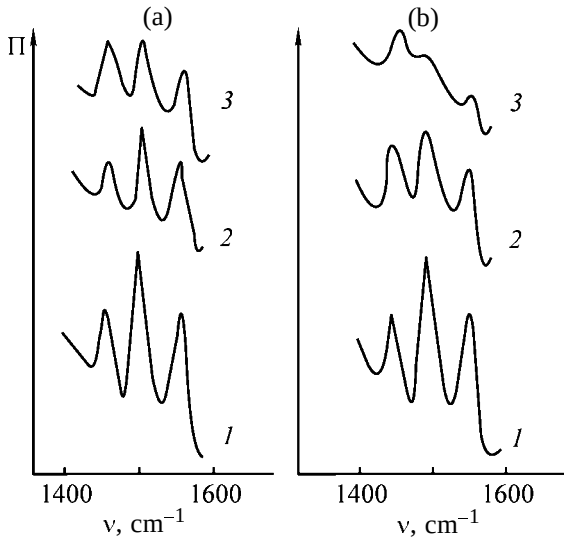

Fig. 2. IR spectra of pyridine adsorbed on TsSK samples calcined for (a) 1 and (b) 4 h. (∏) Absorption and (ν) wave number; the same for Fig. 3. Calcination temperature (°C): (*1*) 600, (*2*) 650, and (*3*) 700.

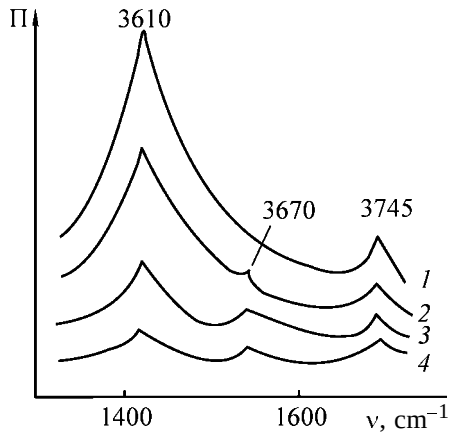

Fig. 3. IR spectra of fundamental vibrations of OH groups in calcined TsSK. Calcination temperature (°C): (*1*) 550, (*2*) 600, (*3*) 650, and (*4*) 700.

tra of catalysts subjected to thermal treatment contain (Fig. 3), together with the absorption bands peaked at 3610 (B centers, acidic bridging hydroxy groups, Si–OH–Al) and 3745 cm^{-1} (nonacidic terminal SiOH groups), also an additional absorption band at 3670 cm^{-1}, which can be assigned to OH groups bound to extra-framework aluminum appearing as a result of dealumination of the aluminosilicate lattice [8].

With increasing treatment temperature T_t, the intensities of the absorption bands at 3610 and 3745 cm^{-1}, associated with hydroxy groups, decrease and that of the band at 3670 cm^{-1} increases. Comparison of the IR spectra of the catalysts suggests that, in the case of TsSK, the extent of the dealumination process much exceeds that for TsSK(M).

Thus, the spectral data indicate that thermal treatment of the catalysts leads to surface rearrangement of the zeolite, during which the concentration and strength of acid centers change. The most typical is a dramatic change in the number of strong B centers. Since it is commonly believed that specifically B centers of Pentasils effect cracking of saturated hydrocarbons and the subsequent reactions with the forming olefins, it would be expected that the decrease in the acidity of thermally treated catalysts must change their catalytic activity in LDLH conversion.

Table 2 presents data on the effect of thermal treatment of the catalysts on the yield and composition of the reaction products obtained from LDLH at 360°C and $\omega = 0.5\ h^{-1}$. Raising the temperature T_t of thermal treatment of the catalysts changes their activity and selectivity: the amount of gaseous products decreases, the yield of the liquid catalyzate grows, and the conversion of paraffins and yield of aromatic hydrocarbons both decrease. In the composition of the gas phase, the content of olefins grows. At T_t = 600°C, TsSK is more active: a 1.6 times larger amount of aromatic hydrocarbons is formed on this catalyst, compared to TsSK(M). This is in agreement with the data on the catalyst acidity (Figs. 1a and 1b, curves *1*), whence follows that the number of strong acid centers on TsSK is 2 times that on TsSK(M).

In the case of TsSK, a noticeable decrease in the conversion of paraffins and in the content of arenes in the product formed is observed already at sample calcination temperature of 650°C, and on a sample calcined at 700°C, the concentration of aromatic hydrocarbons decreases twofold as compared to that at T_t = 600°C. TsSK(M) shows higher thermal stability: with a catalyst treated at 600 and 650°C, liquid products of close composition are obtained, whereas raising the treatment temperature to 700°C makes the conversion of paraffins lower, with the content of arenes decreasing by 5–10%.

CONCLUSIONS

(1) Thermal treatment of Pentasil-containing catalysts TsSK and TsSK(M) at 550–700°C strongly affects their acid and catalytic properties in conversion of the long distillate of light hydrocarbons.

(2) The number of strong B centers decreases to the greatest extent in high-temperature treatment of

Table 2. Effect of high-temperature treatment of catalysts on the yield and composition of reaction products (T = 360°C, ω = 0.5 h^{-1})

Parameter	Temperature of catalyst treatment, °C					
	TsSK			TsSK(M)		
	600	650	700	600	650	700
Yield, wt %:						
of gas	46.6	49.0	34.8	33.9	33.6	30.2
of catalyzate	53.4	56.0	65.2	66.1	66.4	69.8
Composition, wt %						
of gas:						
C_1–C_2	4.6	3.6	2.3	3.1	3.5	2.0
propane	50.7	49.1	45.2	61.4	61.5	61.7
butanes	35.9	38.9	42.4	31.5	31.0	32.2
olefins C_2–C_4	5.6	6.4	8.5	2.3	2.4	2.9
hydrogen	2.2	2.0	1.6	1.7	1.6	1.2
of catalyzate:						
n-paraffins	13.1	18.3	23.2	21.3	21.9	23.5
isoparaffins	45.5	47.1	52.6	48.8	48.6	49.6
naphthenes	10.3	9.8	10.2	11.1	11.3	12.6
aromatic hydrocarbons	31.1	24.8	14.0	18.8	18.2	14.3

the TsSK catalyst (synthesized on the basis of Pentasil with the SiO_2/Al_2O_3 ratio of 30), which impairs its aromatizing activity. In the case of TsSK(M) synthesized on the basis of Pentasil with the SiO_2/Al_2O_3 ratio of 60, dehydroxylation and dealumination proceed to a lesser extent and its catalytic activity decreases only slightly.

REFERENCES

1. Isakov, Ya.I., *Neftekhimiya*, 1998, vol. 38, no. 6, pp. 404–438.
2. Kutepov, B.I. and Belousova, O.I., *Aromatizatsiya uglevodorodov na pentasilsoderzhashchikh katalizatorakh* (Aromatization of Hydrocarbons on Pentasil-Containing Catalysts), Akhmetov, A.F., Ed., Moscow: Khimiya, 2000, p. 95.
3. Minachev, Kh.M., Dergachev, A.A., Bondarenko, T.N., *et al*., *Neftekhimiya*, 1994, vol. 34, no. 1, pp. 9–16.
4. Minachev, Kh.M., Isakova, T.A., Isakov, Ya.I., and Mirskii, Ya.V., *Neftekhimiya*, 1988, vol. 28, no. 2, p. 151.
5. Khusid, B.L., Chukin, G.D., Gullyev, Ch., and Nefedov, B.K., *Kinet. Katal*., 1987, vol. 28, no. 4, pp. 938–942.
6. Vorob'ev, B.L., Koshelev, Yu.N., Khvorova, E.P., *et al*., *Neftekhimiya*, 1991, no. 4, pp. 475–481.
7. Nefedov, B.K., *Khim. Tekhnol. Topl. Masel*, 1992, no. 2, p. 29.
8. Vasina, T.V., Sitnik, V.P., Kustov, L.M., *et al*., *Izv. Akad. Nauk SSSR, Ser. Khim.*, 1989, no. 6, pp. 1234–1239.

Russian Journal of Applied Chemistry, Vol. 75, No. 11, 2002, pp. 1816–1819. Translated from Zhurnal Prikladnoi Khimii, Vol. 75, No. 11, 2002, pp. 1851–1854.
Original Russian Text Copyright © 2002 by Kuznetsova, Dobkina, Nefedova, Lavrishcheva.

CATALYSIS

Vanadium Catalysts Promoted with Magnesium Compounds for Production of Sulfuric Acid

S. M. Kuznetsova, E. I. Dobkina, L. A. Nefedova, and S. A. Lavrishcheva

St. Petersburg State Technological Institute, St. Petersburg, Russia

Received March 6, 2002

Abstract—The feasibility and efficiency of promotion with magnesium compounds of supported and mixed catalysts for sulfuric acid production were studied.

Production of sulfuric acid based on catalytic oxidation of SO_2 on vanadium catalysts is one of the most large-tonnage processes in chemical industry. Efforts to make the production of sulfuric acid more efficient include development of new and improvement of existing processes and catalysts. The catalysts in the existing processes operate in a fairly broad range of temperatures and concentrations. To extend further this range, new flowsheets are developed, allowing gas conversion at a large concentration of sulfur dioxide under pressure. There is no universal catalyst exhibiting equally high performance under different reaction conditions [1–3]. To each range of temperatures corresponds its own optimal catalyst formulation.

Because the state of a catalyst essentially depends on reaction conditions, it should be expected that there should be certain optimal catalyst compositions ensuring the highest performance under different conditions.

For gas conversion at increased concentrations of sulfur (more than 10%), it is advisable to perform the process in a fluidized bed with a wear-resistant finely dispersed catalyst [2, 3].

In catalytic method of the sulfuric acid production, heterogeneous vanadium catalysts are used [3, 4]. Vanadium oxides dissolved in disulfates of alkali metals (promoters) containing more or less SO_3 are active components of all these catalysts [3, 4].

The most widely used promoter in industrial catalysts is readily available and cheap potassium. At the reaction temperature, the active component of the catalysts for sulfuric acid production exists as a molten mixture of the salts over the pore surface of a silicate support [4, 5].

The catalyst for oxidation of gases with increased concentration of SO_2 in a fluidized bed should exhibit activity in a wide temperature range, including $T \sim 380$°C, and low abradability during operation. The first condition is met by catalytic masses containing as promoters, along with alkali metal ions, also magnesium additives [1, 3].

The goal of this study was the development of promoted catalytic masses intended for production of sulfuric acid in fluidized and filtering beds.

EXPERIMENTAL

Because the catalysts in a fluidized bed should exhibit enhanced resistance, it is advisable to apply the active component onto appropriate support. The support should have the necessary strength and chemical composition, whose combination determines the catalyst activity and strength.

In various vanadium catalysts for sulfuric acid production, natural or artificial silicate materials serve as supports [2, 3, 6], in particular, spherical aluminosilicates with a low content of Al_2O_3 [3, 6].

In this study, aluminosilicate with a grain size of 0.4–1.2 mm, containing about 5.5% Al_2O_3, was the catalyst support. This material was subjected to hydrothermal treatment at 450–600°C for 6 h in a fluidized bed. The humidity of air fed for fluidizing ranged from 30 to 40%. The temperature was raised stepwise to 400, 500, 600, and 700°C; the heating time at each temperature was 2 h.

The heat treatment was done to enhance the water resistance of a support. As a result, we obtained aluminosilicates with the following structural characteristics: pore volume 0.6–0.7 $cm^3\,g^{-1}$ at the average pore radius of 5–6 nm and specific surface area of 210–250 $m^2\,g^{-1}$.

1070-4272/02/7511-1816$27.00 © 2002 MAIK "Nauka/Interperiodica"

Table 1. Chemical composition of the catalyst samples

Sample no.	Composition of impregnating solution, g dm^{-3}			Catalyst composition, wt %			
	V_2O_5	K_2SO_4	$MgSO_4 \cdot 7H_2O$	V_2O_5	K_2O	MgO	K/V
1	40	120	–	6.4	12.1	–	3.64
2	60	120	–	9.6	13.1	–	2.64
3	80	120	–	10.0	13.4	–	2.58
4	100	120	–	11.6	13.1	–	2.20
5	50	130	–	7.3	12.6	–	3.35
6	40	120	30	6.6	11.8	0.6	3.46
7	50	130	40	7.3	12.0	0.65	3.20
8	50	130	30	6.8	12.1	0.55	3.41

The impregnation parameters were chosen based on the chemical composition characteristics that should ensure the conversion of concentrated gases, including those under pressure [1, 5, 6]. The amount of vanadium(V) oxide in the contact must be no less that 6 wt % at the ratio K/V > 2.5 and the magnesium oxide content of no more than 1 wt %.

Taking into account the porosity of the support used and data of the previous studies [3, 6], the concentration of the impregnating solution containing potassium vanadate and sulfate, as well as magnesium sulfate, was varied as follows (g dm^{-3}): V_2O_5 from 40 to 100, K_2SO_4 from 120 to 140, and $MgSO_4 \cdot 7H_2O$ from 30 to 40.

The impregnation was performed at the liquid-to-solid ratio of 1.5 for 2 h at 80°C. After the impregnating solution was decanted, granules were dried at 100–120°C and calcined for 2 h at 650°C. The characteristics of the chemical composition of the catalysts are presented in Table 1.

To adjust catalyst composition with respect to major components, i.e., potassium(I) and vanadium(V), sample nos. 1–5 were synthesized without addition of magnesium ions. Then, magnesium ions were added to sample nos. 1 and 5 chosen for further studies.

First, the activity of these samples was tested on a flow-through kinetic installation [3, 7] under standard conditions. In this case, the space velocity V was 4000 h^{-1}, the initial gas mixture contained 10 vol % SO_2 (the remainder was air), and the pressure was equal to atmospheric pressure. The conversion of SO_2 into SO_3 was 56–57% at 420°C and 91–92% at 485°C. At lower temperatures, this catalyst surpasses in activity the similar supported catalysts synthesized previously without addition of magnesium ions. Their activity at 420°C does not exceed 35%. The structural characteristics of the magnesium-containing catalyst (Fig. 1) are as follows:

Bulk density ρ_b, g cm^{-3}	0.74
True density ρ_t, g cm^{-3}	2.14
Apparent density ρ_{ap}, g cm^{-3}	1.1
Total pore volume ΣV, cm^3 g^{-1}	0.4–0.5
Specific surface area S_{sp}, m^2 g^{-1}	20–30
Average pore radius r, nm	80

The kinetic characteristics of sample nos. 5 and 8 were studied under conditions of SO_2 oxidation at elevated pressure (the study was performed at the Institute of Catalysis, Siberian Division, Russian Academy of Sciences, Novosibirsk). The particle size was 0.180–0.315 mm, the gas mixture fed for oxidation contained (vol %) SO_2 12, O_2 12, and the remainder helium; the total gas pressure in a reactor was 8 atm. By varying the space velocity, we established how

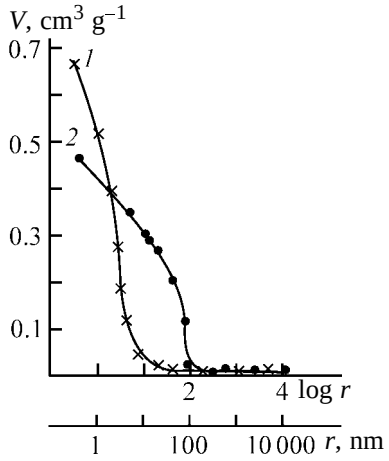

Fig. 1. Integral structural curves of the (*1*) initial support and (*2*) catalyst on its base. (*V*) pore volume and (*r*) pore radius.

Table 2. Activity characteristic of catalyst nos. 5 and 8

Catalyst	V_g, $ncm^3\ s^{-1}$	τ, s	Degree of SO_2 oxidation χ, %
no. 5, ρ_b = 0.65 g cm^{-3}	1.03	0.300	90.1
	1.51	0.204	70.2
	2.62	0.117	44.5
	4.00	0.077	27.0
no. 8, ρ_b = 0.74 g cm^{-3}	1.96	0.137	84.0
	2.88	0.094	62.1
	3.75	0.072	48.2
	4.53	0.060	32.6

Table 3. Characteristics of the catalysts supported on magnesium-containing silicate and diatomite

Catalyst support	χ, %, at indicated temperature, °C		Degree of thermal deactivation, %
	420	485	
New silicate	33.7	89.0	22.0
Diatomite (SVD)	18.0	84.3	26.0

the degree of sulfur dioxide conversion varies with contact time (s):

$$\tau = P/(\rho_b V_g),$$

where P is catalyst mass (g); ρ_b, bulk density, g cm^{-3}; V_g, space velocity of the gas mixture reduced to normal conditions, $ncm^3\ s^{-1}$.

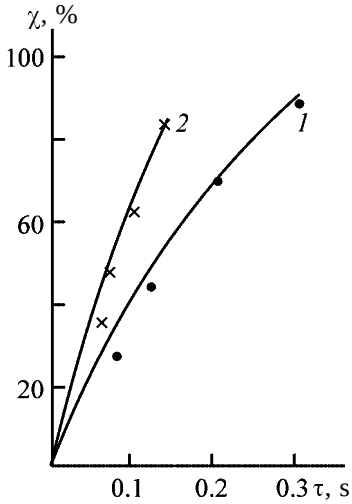

Fig. 2. Degree of SO_2 oxidation χ vs. contact time τ. T = 420°C and P = 8 atm. Gas mixture composition (vol %): SO_2 12, O_2 12, and the remainder helium. Sample: (*1*) no. 5 and (*2*) no. 8 (Table 1).

The results of the study are presented in Table 2 and Fig. 2.

As seen, the sample containing magnesium ions has the high kinetic characteristics over a wide temperature range. This makes it promising for SO_2 conversion at increased concentration and pressure [8].

Introduction of Mg(II) was also of interest in synthesis of filtering-bed catalysts prepared by another process. We chose a "mixed" process commonly used for preparing SVD catalysts for sulfuric acid production [3]. For this purpose, we used for the first time the silicate support containing (wt %) no more than 1–2 Al_2O_3, 0.2–0.3 MgO, and 0.8–1.2 K_2O + Na_2O [9]. This material is relatively cheap. Therefore, its use instead of diatomite seems appropriate. As noted above, in synthesis of the test sample with the new support, the main process parameters were fully reproduced.

The results of studying the kinetic characteristics under the given standard conditions, along with data on the heat resistance of the samples, are presented in Table 3.[1]

The heat resistance was determined by the method involving treatment for 10 h at 700°C with a gas mixture containing 15% SO_2 and 15.75% O_2 and subsequent measurement of the degree of deactivation.

The results obtained show that the catalyst on the new support containing magnesium(II) ions surpasses in activity and heat resistance the commercial SVD catalyst on diatomite. The degrees of the sulfur dioxide oxidation differ by 4–5% at 485°C and by about 15% at 420°C.

Apparently, this is explained by a unique combination of the oxides in both the initial support and the final catalyst. The simultaneous presence of certain amounts of potassium, sodium, and magnesium oxides ensures the strong promotion effect, especially at lower temperatures. This may be due to the lower melting point and lower viscosity of the active component, which are known [4] to facilitate promotion of sulfuric acid catalysts.

CONCLUSIONS

(1) It is appropriate to promote the catalysts of different types for production of sulfuric acid with magnesium compounds.

[1] The study was carried out at the Umpire Physicochemical Research Laboratory, Research Institute of Fertilizers and Insectofungicides (Moscow).

(2) The activity of the supported catalyst in conversion of gases with high concentration of sulfur dioxide was determined in a fluidized bed and at elevated pressure.

(3) It is appropriate to use the magnesium-containing silicate support instead of diatomite for the synthesis of the catalytic masses for SO_2 oxidation in a filtering bed.

(4) The introduction of Mg(II) enhanced the catalyst activity, especially in the low-temperature range.

REFERENCES

1. Bal'zhinimaev, B.S., Belyaeva, N.P., Simonova, L.G., *et al*., *Katalizatory proizvodstva sernoi kisloty* (Catalysts for Production of Sulfuric Acid), Novosibirsk: Inst. Kataliza, Sib. Otd. Ross. Akad. Nauk, 1990.
2. *Kataliz v kipyashchem sloe* (Fluidized Bed Catalysis), Mukhlenov, I.P., Ed., Leningrad: Khimiya, 1971.
3. Mukhlenov, I.P., Dobkina, E.I., Deryuzhkina, V.I., and Soroko, V.E., *Tekhnologiya katalizatorov* (Catalyst Technology), Leningrad: Khimiya 1989.
4. Boreskov, G.K., *Geterogennyi kataliz* (Heterogeneous Catalysis), Moscow: Nauka, 1989.
5. Bal'zhinimaev, B.S., Belyaeva, N.P., Simonova, L.G., and Ivanov, A.A., *Kinet. Katal*., 1989, vol. 30, no. 4, pp. 885–889.
6. Mukhlenov, I.P., Petukhova, T.S., Larionov, A.M., *et al*., *Zh. Prikl. Khim*., 1984, vol. 57, no. 11, pp. 2602–2605.
7. Boreskov, G.K., *Kataliz v proizvodstve sernoi kisloty* (Catalysis in Sulfuric Acid Production), Moscow: Goskhimizdat, 1954.
8. RF Inventor's Certificate no. 1 704 815.
9. RF Patent 2 036 720.

Russian Journal of Applied Chemistry, Vol. 75, No. 11, 2002, pp. 1820–1823. Translated from Zhurnal Prikladnoi Khimii, Vol. 75, No. 11, 2002, pp. 1855–1859.
Original Russian Text Copyright © 2002 by Dobkina, Kuznetsova, Nefedova, Lavrishcheva.

CATALYSIS

Modification of Macrostructure of Silica Gels

E. I. Dobkina, S. M. Kuznetsova, L. A. Nefedova, and S. A. Lavrishcheva

St. Petersburg State Technological Institute, St. Petersburg, Russia

Received January 18, 2002

Abstract—The possibility of physicochemical transformation of porous silica gels is studied.

The macrostructure of solid materials largely determines the intensity of a number of heterogeneous reactions, including catalysis and adsorption. For example, obtaining catalysts with a prescribed porosity is often a difficult problem [1–3]. The catalysts with the pore size considerably larger than that in standard commercial materials (active aluminum oxide, silica gels, and aluminosilicates) are frequently in demand. The structure considered to be macroporous as applied to sorbents may be extremely microporous and unsuitable as applied to many catalysts.

Transformation of aluminosilicate under the action of certain modifiers was considered and possible ways for controlling porosity within a wide range were demonstrated in [4, 5].

Owing to macro- and microstructural properties, aluminosilicates are widely used as sorbents and catalyst supports. Therefore, problems on controlling their porosity are of undoubted interest.

In this work, we used the method applied previously for modification of aluminosilicate in [5]. We pursued two goals: to check the versatility of the method and to transform the silica gel pore structure within a wide range.

EXPERIMENTAL

We used various silica gels: finely porous, medium-porous, and coarsely porous. All silica gels were impregnated with a potassium metavanadate solution and then dried and calcined. The treatment conditions were similar to those reported in [5]. The concentration of the potassium metavanadate solution was 120 g dm^{-3} V_2O_5; particle size, 1.5 mm; calcination temperature, 65°C; and time, 2 h.

The characteristics of the initial silica gels and modified samples are presented in Table 1. As seen, the molar ratio K_2O/V_2O_5 was above unity in all the systems, i.e., in the given case, as in impregnation of aluminosilicate, filling of pores with potassium metavanadate was accompanied by chemisorption of K^+ ions on accessible areas of the weakly acidic surface of the samples.

The integral structural curves for all the modified samples and two initial silica gels are shown in Fig. 1. As seen, all the silica gels undergo structural transformation under the action of potassium metavanadate. Only in the course of the calcination the modification is essential. Before high-temperature treatment, the initial and impregnated samples have very similar structures. The modification character is identical in all the silica gels: in the course of the treatment, the specific surface area decreases, the total pore volume decreases by 45–55%, and the average pore radius increases.

The extent of transformation is different in various silica gels. The most significant changes were ob-

Table 1. Results of the modification of the pore structure of silica gels*

Sample no.	K_2O (wt %)	V_2O_5 (wt %)	K_2O/V_2O_5	S_{sp}, m^2 g^{-1}	ρ_b (g cm^{-3})	ρ_{app} (g cm^{-3})	V_{sp}, cm^3 g^{-1}	r_{av}, Å
1	–/11.4	–/18.2	–/1.2	340/0.7	2.24/2.57	0.61/1.16	1.2/0.5	70.0/11 200
2	–/9.1	–/14.5	–/1.2	520/16.0	2.24/2.30	0.73/1.13	0.92/0.45	35.0/7000
3	–/8.2	–/14.2	–/1.08	650/1.0	2.24/2.33	0.83/1.43	0.76/0.26	23.0/600
4	–/4.2	–/6.2	–/1.33	530/11.9	2.25/2.30	1.35/1.70	0.30/0.16	11.0/150
5	–/8.4	–/12.7	–/1.28	710/1.0	2.25/2.36	0.98/1.43	0.58/0.25	16.0/700

* Data for the initial silica gel and modified sample are given in the numerator and denominator, respectively.

1070-4272/02/7511-1820$27.00 © 2002 MAIK "Nauka/Interperiodica"

served in coarsely porous and medium-porous samples (sample nos. 10 and 2, respectively). The structure of sample nos. 3 and 5 is transformed to a lesser extent. After treatment, their structure is multidispersed, and no pronounced maximum is observed. The pore size in the finest silica gel after modification is 150 Å on the average, i.e., it increased by only an order of magnitude.

Apparently, the structural transformation observed is due to the transformation of the silica gel skeleton, including size, shape, and mutual arrangement of globules [6]. Indeed, the electron-microscopic study of the impregnated and calcined silica gels revealed consolidation of the structural elements and transformation of the globular structure into quasi-globular structure (Fig. 2).

The structural similarity of aluminosilicates and silica gels and the close chemical compositions of the compounds obtained on their basis after impregnation with potassium metavanadate suggest that the mechanism of the porosity transformation in these materials under the action of vanadium(V) compounds at high temperatures is similar [2].

The content of the vanadium(V) compounds in silica gel can be varied by varying the number of impregnations, their time, and the concentration of the impregnating solution. In the tests, the potassium metavanadate concentration in terms of V_2O_5 was 50, 100, and 120 g cm^{-3}, which allowed introduction of different amounts of the modifier into the material. The heat-treatment conditions were always similar: 600°C and 2 h. As example we chose sample no. 1. As shown above, the structural transformations in it are more significant, and, consequently, the transformation pattern is more obvious. The results obtained are presented in Table 2 and Fig. 3.

The experimental data show that, with increasing modifier content in silica gel, the extent of the structural transformation also increases: the average pore radius increases, whereas the total porosity and the specific surface area decrease. Especially dramatic changes were observed in the sample containing 18 wt % V_2O_5 and 11 wt % K_2O (at a concentration of impregnating solution of 120 g dm^{-3} V_2O_5).

For the practice of catalysis, such a considerable increase in the pore radius accompanied by a dramatic decrease in the surface area is of little use. Therefore, it is appropriate to use solutions with a concentration less than 100 g dm^{-3}. Silica gel treated with less concentrated solutions (50 and 100 g dm^{-3} V_2O_5) contains less modifier and undergoes less considerable

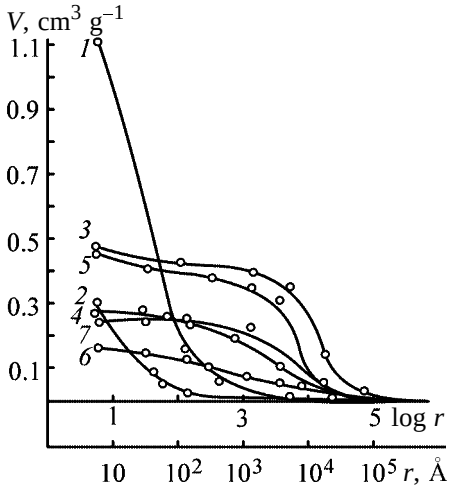

Fig. 1. Integral structural curves of the initial and modified silica gels (Table 1). (*V*) Total specific pore volume and (*r*) average pore radius; the same for Figs. 3–5. Initial silica gel: (*1*) no. 1 and (*2*) no. 4; modified silica gel: (*3*) no. 1, (*4*) no. 3, (*5*) no. 2, (*6*) no. 4, and (*7*) no. 5.

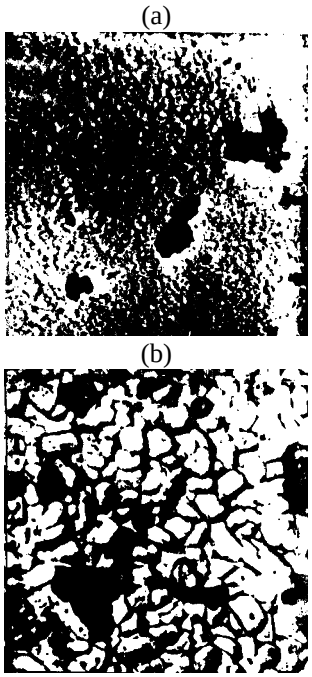

Fig. 2. Structural transformation in sample no. 1. Sample: (a) before and (b) after modification.

structural transformations. Thus, by varying the concentration of the potassium metavanadate impregnating solution, it is possible to finely modify the initial silica gel skeleton within a wide range.

The structural transformations as influenced by the calcination temperature were studied on a series of samples, which were impregnated with a KVO_3 aqueous solution containing 50 and 100 g dm^{-3} V_2O_5 and calcined at different temperatures from 400 to 700°C

Table 2. Transformation of the silica gel structure at different amounts of the modifier

$c_{V_2O_5}$, g dm^{-3}	K_2O	V_2O_5	K_2O/V_2O_5	S_{sp}, m^2 g^{-1}	ρ_b	ρ_{app}	V_{sp}, cm^3 g^{-1}	r_{av}, Å
	wt %				g cm^{-3}			
50	5.3	8.4	1.2	54	2.24	0.89	0.67	500
100	9.1	14.5	1.2	13	2.27	1.02	0.56	650
120	11.4	18.2	1.2	1	2.57	1.16	0.50	11 200

Table 3. Influence of the calcination temperature T_c on the pore structure of silica gel impregnated with KVO_3 solution ($c_{V_2O_5}$ = 50 g dm^{-3})

T_c, °C	S_{sp}, m^2 g^{-1}	ρ_b	ρ_{app}	V_{sp}, cm^3 g^{-1}
		g cm^{-3}		
400	160	2.25	0.82	0.77
500	150	2.23	0.89	0.68
600	54	2.24	0.89	0.67
700	6.2	2.25	0.93	0.64

for 2 h. The data for sample no. 1 are presented in Table 3 and Fig. 4. The pore structure of impregnated silica gel calcined at 400–500°C is similar to that of the initial material. As compared to the initial silica gel, the pore size, specific surface area, and total porosity slightly decrease. Apparently, the above structural transformation is due to deposition of the modifier in the pores of the initial support. As a result, the equivalent pore radius decreases, and a part of small pores becomes filled up.

The heat treatment of impregnated silica gels above 500°C results in dramatic changes in the pore-radius distribution. To each heat-treatment temperature corresponds a particular stable pore structure. With increasing temperature, the specific surface area decreases, but the total porosity varies insignificantly. In the 600–700°C range, the structural transformations are the most significant.

As in the case of aluminosilicate, the essence of the process observed is the formation of an eutectic mixture of the support (silica gel) and potassium vanadate. As the calcination temperature increases, the viscosity of the system decreases, and increasing amount of the support passes to the melt, i.e., the component ratio in the melt changes. The globules gradually increase in size owing to agglomeration. As a result, coarse pores are formed, whereas fine pores disappear.

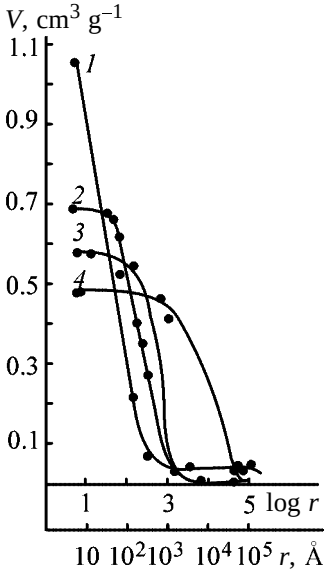

Fig. 3. Influence of the potassium metavanadate concentration on the extent of structural modification. Calcination temperature 600°C; τ = 2 h. (*1*) Initial silica gel; modified samples, V_2O_5 content in solution, g dm^{-3}: (*2*) 50, (*3*) 100, and (*4*) 120.

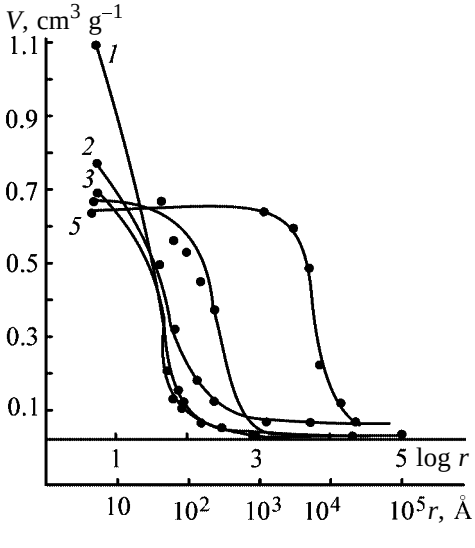

Fig. 4. Influence of the calcination temperture on the pore structure of silica gel (sample no. 1) impregnated with a potassium metavanadate solution. V_2O_5 concentration in solution 50 g dm^{-3}. (*1*) Initial silica gel; calcination temperature, °C: (*2*) 400, (*3*) 500, (*4*) 600, and (*5*) 700.

The irreversibility of transformation of the silica gel macrostructure under the influence of vanadium(V) compounds is the necessary condition for applying them as sorbents and catalyst supports. The second condition is that the content of the modifier in the transformed silica gels should be minimal and should not restrict their further use for catalyst support. The possibility of decreasing the modifier content was studied with sample no. 1 (Table 1), which was impregnated with a potassium metavanadate solution (50 g dm^{-3} V_2O_5) and calcined at 700°C for 2 h.

Based on many experiments, we chose the following conditions of washing off the modifier: liquid (H_2O)-to-solid ratio of 6, with the extractant replaced hourly. After 4 h of washing off, no potassium metavanadate was found in the wash water. The pore structure of the initial sample and that of the impregnated sample washed under the above conditions are characterized in Fig. 5. Washing of the modified silica gel removes about 60% of K_2O and 80% of V_2O_5 from the skeleton. However, the modifier is not removed from silica gel completely. In the wash water, the molar ratio of the extracted components, K_2O/V_2O_5, is 0.9, i.e., it is close to unity and corresponds to the water-soluble vanadium(V) compound KVO_3.

It should be noted that a minor amount of the modifier apparently remaining inside the silica gel globules is probably inactive and, therefore, "nontoxic" for sorbents and catalytically active substances deposited onto such a support.

Potassium oxide K_2O is removed from silica gel more actively than from aluminosilicates. This may be due to the fact that the surface of aluminosilicates is more acidic, and, as a consequence, it chemisorbs oxides, which therefore become difficultly extractable. The mutual influence of aluminum and silicon oxides in the aluminosilicate causes formation of strong acid centers [6, 7].

Treatment of silica gel with water does not noticeably alter the coarsely porous structure. At the same time, at the expense of a considerable amount of the extracted modifier, an additional pore volume is formed, and the specific surface area somewhat increases. Apparently, the increase in the surface area is also due to the fact that the surface of pore walls becomes rough owing to removal of crystals.

CONCLUSIONS

(1) The possibility of irreversible transformation of the pore structure of various silica gels was shown.

(2) The method of physicochemical structural transformation with KVO_3 modifier was chosen for silicate systems.

(3) The correlation of the modifier concentration and calcination temperature with the porosity characteristics was established.

(4) The data obtained can be used for forming the prescribed porosity of sorbents and supports intended for preparing certain catalytic masses.

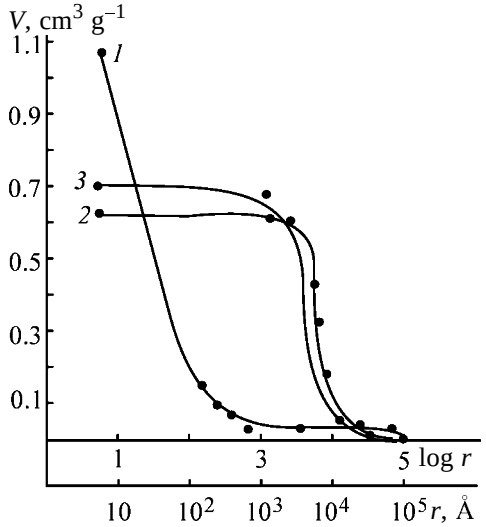

Fig. 5. Structure of the initial and transformed silica gel (sample no. 1) before and after extraction of the modifier. Calcination temperature 700°C. Silica gel: (*1*) initial, (*2*) impregnated and calcined, and (*3*) washed.

REFERENCES

1. Dzis'ko, V.A., *Osnovy metodov prigotovleniya katalizatorov* (Principles of Catalyst Preparation), Novosibirsk: Nauka, 1983.
2. Mukhlenov, I.P., Dobkina, E.I., Deryuzhkina, V.I., and Soroko, V.E., *Tekhnologiya katalizatorov* (Catalyst Technology), Leningrad: Khimiya, 1989.
3. Boreskov, G.K., *Kataliz: Voprosy teorii i praktiki* (Catalysis: Theoretical and Practical Aspects), Novosibirsk; Nauka, 1987.
4. Dobkina, E.I., Kuznetsova, S.M., and Nefedova, L.A., *Nauka Tekhnol. Uglevodorod.*, 2000, no. 2, pp. 49–53.
5. Dobkina, E.I. and Varshavskii, O.M., in *Sbornik nauchnykh trudov OOO "ISMINEF" za 1998– 2000 gg.* (Coll. of Scientific Works of ISMINEF Limited Liability Company Covering the Period 1998–2000), Moscow: TsNIITEneftekhim, 2001, pp. 228–238.
6. Iler, R.K., *The Colloid Chemistry of Silica and Silicates*, Ithaca, NY: Cornell Univ. Press, 1955.
7. Skarchenko, V.K., *Alyumosilikatnye katalizatory* (Aluminosilicate Catalysts), Kiev: Akad. Nauk USSR, 1963.

Russian Journal of Applied Chemistry, Vol. 75, No. 11, 2002, pp. 1824–1827. Translated from Zhurnal Prikladnoi Khimii, Vol. 75, No. 11, 2002, pp. 1860–1863.
Original Russian Text Copyright © 2002 by Panasyugin, Rat'ko, Bondareva.

CATALYSIS

Sorption and Catalytic Activity of Adsorbent–Catalyst Based on Montmorillonite Modified with Cr(III) and Cu(II) Mixed Oxides

A. S. Panasyugin, A. I. Rat'ko, and G. V. Bondareva

Belarussian National Polytechnic Academy, Minsk, Belarus
Institute of General and Inorganic Chemistry, Belarussian National Academy of Sciences, Minsk, Belarus

Received April 5, 2001; in final form, June 2002

Abstract—The sorption properties of mixed adsorbent–catalyst based on high-silica zeolite and montmorillonite modified with mixed oxides of Cr(III) and Cu(II) with respect to organic compounds of various classes were studied, and the optimal dynamic conditions of its operation were determined.

Utilization of organic solvents in industrial production poses a problem of minimization of their environmental hazard. The majority of common procedures of the exhaust treatment are unprofitable; they require special systems of the gas treatment, rather expensive catalysts, and complex equipment for their regeneration. Moreover, these methods are efficient only at fairly high concentration of organic compounds. At the same time, utilization of sorbent–catalysts in the first stage allows concentration of compounds occurring in amounts close to maximum permissible concentration, with their subsequent flameless catalytic oxidation to carbon dioxide and water. Hence, sorption-catalytic treatment of exhaust gases is rather promising due to the absence of regeneration stages, low temperature, and some other features of the process minimizing formation of by-products.

As seen from the published data, sorbent–catalysts based on high-silica zeolites (HSZs) are of particular interest. To perform exhaustive oxidation of organic compounds to CO_2 and water these materials should contain additional catalytic phase supported by layered montmorillonite commonly used as a binder in the zeolite granulation. Such layered materials undergo easy modification based on expansion of aluminosilicate layers at a certain distance by hydroxy complexes of polyvalent metal cations, which after calcination form oxide clusters fixing clay layers and acting as an active catalytic phase [1, 2]. The resulting interlayer spacing is determined by the nature of the metal cation as a complex-forming agent and by the procedure of hydroxy complex preparation. It can reach 2.5 nm, which allows utilization of this material in sorption of large organic molecules [3].

As shown in [4, 5], layered aluminosilicates modified with heteronuclear polyhydroxy complexes exhibit higher catalytic activity as compared to analogous minerals modified with homonuclear polyhydroxy complexes [6, 7]. Among catalys containing no expensive metals, mixed Cr–Cu oxide catalysts show high performance in exhaustive oxidation of organic compounds [8, 9]. This fact determined our choice of chromium–copper systems as intercalating agents.

In this work we studied the sorption and catalytic properties of composites based on high-silica zeolites and montmorillonite intercalated with polyhydroxy complexes of chromium and copper.

EXPERIMENTAL

The required layered-columnar material was prepared from montmorillonite clay from the Askan field. The heteronuclear polyhydroxy complexes were prepared by directed hydrolysis of chromium chloride; for this purpose a 0.2 M NaOH solution was added at a constant rate with stirring to a 0.2 M $CrCl_3$ solution until the OH^-/Cr^{3+} ratio (basicity degree) reached 2.0. The solution was aged for 24 h at 25°C and 0.2 M $CuCl_2$ solution was added in amounts providing equimolar (1 : 1) chromium–copper ratio. Then, after 3-day storage at 25°C, the montmorillonite suspension (3 wt %) was added to the solution of Cr–Cu polyhydroxy complexes to attain the concentration of Cr(III) of 10 mg-equiv per gram of montmorillonite. The mixture was stored for 2 h, and the resulting montmorillonite with fixed Cr–Cu polyhydroxy complexes (Cr : Cu-MM) was separated from the solution by centrifugation and washed with distilled water

1070-4272/02/7511-1824$27.00 © 2002 MAIK "Nauka/Interperiodica"

6–7 times. The resulting compound was thoroughly mixed with zeolite and A-175 brand Aerosil in 1 : 1 : 0.5 ratio. After drying, the resulting loose material was granulated on a tableting machine to obtain cylindrical granules 1–4 mm in diameter, which were dried in air and calcined at 500°C.

The specific surface area S_{sp} of the samples was evaluated from low-temperature sorption of nitrogen using a Micromeritics 2200 express analyzer. The value of the first basal deviation d_{200} of modified clays was determined on a Siemens 5000 diffractometer.

The sorption and catalytic properties of the resulting samples were measured using a gas mixture of the composition similar to that of the gas exhausts of the varnish-and-paint production. As seen from Table 1, the gas mixture prepared from chemically pure and analytically pure grade reagents contains various classes of organic compounds: saturated hydrocarbons, unsaturated hydrocarbons, alcohols, etc.

The concentrations of organic compounds were determined on a Tsvet-100 gas chromatograph equipped with a flame-ionization detector and a capillary column (d = 0.5 mm, l = 60 mm) coated with Carbowax-20; ultrapure grade nitrogen was used as a carrier gas. The content of CO in the waste gases was determined on an HP-5710A gas chromatograph equipped with a katharometer and a Teflon column (d = 3.5 mm, l = 2.5 m) packed with AG-3 activated carbon; carrier gas argon. The resulting chromatograms were interpreted using Multichrom 1.39 software.

The sorption and catalytic properties of the resulting samples were determined in both the static (in a desiccator) and dynamic modes on a pilot unit shown schematically in Fig. 1. Air is injected with blower *1* into a device *3* controlling the flow rate, which is equipped with vessel *2* warranting uniform gas flow. Then, the air passes chamber *5* containing a mixture of organic compounds and becomes saturated with its vapor, whose concentration was 80–100 mg m^{-3}. Organic compounds are sorbed from the air mixture in reactor *6* (d = 35 mm, l = 650 mm) packed with cylindrical granules of the sorbent–catalyst. The volume of this material was 100 ml.

The efficiency of sorption of organic compounds A (%) on the sorbent–catalyst under the dynamic conditions was calculated from the equation

$$A = \frac{c_i - c_o}{c_i} \times 100,$$

where c_i is the total content of organic compounds in the gas mixture at the reactor inlet and c_o is their content at the reactor outlet.

Table 1. Composition of the model gas mixture

Component	Content, wt %
n-Pentane	3.0
n-Decane	1.5
Ethylbenzene	12.0
p-Xylene	12.0
m-Xylene	41.0
o-Xylene	21.0
Isoamyl alcohol	7.0
Cellosolve	2.5

The sorption properties of the mixed sorbent–catalyst and initial compounds (Cr–Cu-MM and high-silica zeolite) with respect to some organic compounds determined under the static conditions are listed in Table 2. As seen, the sorption capacities of the initial compounds are similar. After calcination at 500°C, the sorption capacity for water of the Cr–Cu-MM sample strongly decreases from 7.50 to 4.62 mmol g^{-1}, which is due to the decrease in the volume of micropores [10]. After thermal treatment, the sorption capacity with respect to acetone and ethanol also decreases from 2.64 and 2.26 to 2.10 and 1.67 mmol g^{-1}, respectively. It should be noted that, after calcination, the sorption capacity of Cr–Cu-MM for benzene and toluene increases from 1.05 and 0.62 to 1.20 and 1.09 mmol g^{-1}, respectively. This is probably due to the increase in the average pore width in columnar clays after calcination [7]. This phenomenon

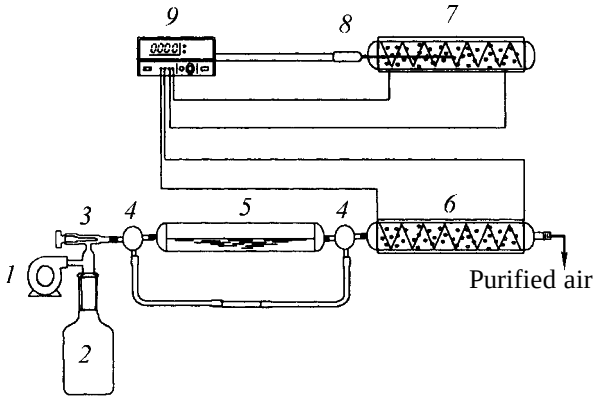

Fig. 1. Scheme of a pilot unit for studying the sorption and catalytic properties of the sorbent: (*1*) blower, (*2*) surge tank, (*3*) gas-flow regulator, (*4*) three-way stopcock, (*5*) vessel with a model organic mixture, (*6*) catalytic thermal reactor, (*7*) reference catalytic thermal reactor, (*8*) thermocouple, and (*9*) control potentiometer.

Table 2. Sorption of organic compounds and water on the sorbent–catalyst and initial compounds

Sample	Calcination temperature	Sorption, mmol g^{-1}				
		water	acetone	ethanol	benzene	toluene
Cr–Cu-MM	120	7.50	2.64 (35)*	2.26 (30)	1.05 (14)	0.62 (8)
	500	4.62	2.10 (45)	1.67 (36)	1.20 (26)	1.09 (24)
HSZ	200	7.80	2.62 (33)	2.30 (29)	1.16 (15)	0.70 (9)
HSZ–Aerosil–Cr–Cu-MM	500	4.46	2.66 (59)	2.54 (57)	1.75 (39)	1.24 (28)

* The ratio of the sorption capacity for the given substance to that for water (%) is given in parentheses.

was found previously at intercalation of montmorillonite with aluminum hydroxy cations, and it is probably a common property of columnar clays [11].

The sorption capacity of the composite sorbent–catalyst calcined at 500°C strongly differs from both Cr–Cu-MM and HSZ, especially with respect to aromatic compounds. For example, its sorption capacity for benzene and toluene is 1.75 and 1.24, whereas the respective sorption capacities of Cr–Cu-MM comprise 1.20 and 1,09 mmol g^{-1}, and those of HSZ, 1.16 and 0.70 mmol g^{-1}.

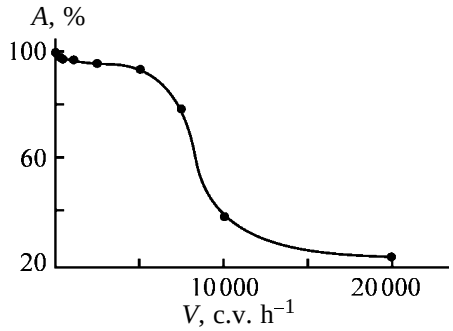

Fig. 2. Efficiency of sorption *A* of organic compounds from the gas mixture as a function of the space velocity *V* of the gas supply through the reactor packed with the sorbent–catalyst.

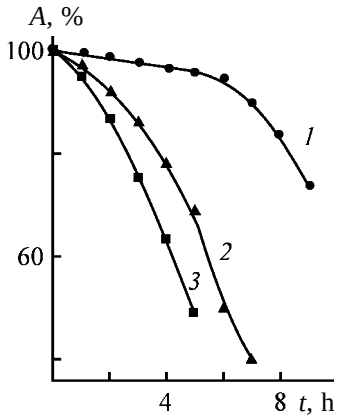

Fig. 3. Efficiency of sorption *A* of organic compounds from the gas mixture as a function of the operation time *t*. Temperature, °C: (*1*) 20, (*2*) 40, and (*3*) 70.

As seen from the ratio of sorption capacities for organic compounds and water (Table 2), the mixed sorbent–catalyst exhibits elevated affinity for organic molecules. This fact, indirectly confirming the selectivity of the sorbent in question, becomes important in sorption of organic compounds from humid air.

When studying the sorption capacity of the mixed sorbent–catalyst under the dynamic conditions, we varied the space velocity of the gas flow and its temperature.

The dependence of the efficiency of sorption of organic compounds *A* by the sorbent–catalyst on the inlet space velocity [column volumes per hour (c.v. h^{-1})] was measured at 20°C. The concentration of organic compounds at the reactor outlet was measured after passing 100 column volumes. As seen, at space velocity less than 500 c.v. h^{-1} the sorption efficiency reaches 95%. With increasing velocity of the gas supply to 10000 c.v. h^{-1}, *A* sharply decreases to 40, and then to 20% at 20000 c.v. h^{-1}.

Variations in the efficiency of sorption of organic compounds on the sorbent–catalyst in question as influenced by the operation time at different temperatures at V = 4800–5000 c.v. h^{-1} are illustrated in Fig. 3. As seen, with increasing temperature of the gas mixture, the operation life of the sorbent strongly decreases. For example, at 20°C the sorption efficiency decreases below 95% after 6 h operation, whereas at 30°C similar decrease in the sorption efficiency is observed in 2 h.

When the total concentration of organic compounds at the reactor outlet exceeded the limit of 5% as compared to the initial mixture, the gas supply was terminated, and the reactor was heated at a constant rate (30 deg min^{-1}) to 200–400°C with an electrical heater placed within the glass reactor. The temperature and the heating rate of the inner reactor volume were

Table 3. Content of organic compounds, a_o, and CO, a_{CO}, in the gas at the outlet from the reactor containing spent sorbent–catalyst after its heating

T, °C	No air supply		With air supply	
	a_o	a_{CO}	a_o	a_{CO}
	mg m^{-3}			
200	43	147	41	43
250	30	133	22	22
300	22	29	12	1
350	11	1	0	0
400	6	0	0	0

controlled with potentiometer *9* (Fig. 1). To monitor the real temperature changes in the reactor and to prevent the breakthrough of the contaminated gas mixture, the thermocouple was placed into a reference reactor *7* similar in size and design to reactor *6* (Fig. 1) and packed with a similar amount of the same sorbent–catalyst.

Heating was performed both with air supply into the reactor and without it. At certain temperatures, air samples were taken at the reactor outlet and analyzed for the content of CO and organic compounds.

As seen from the analytical data (Table 3), with increasing temperature the total amount of organic compounds including those partially oxidized on the catalyst decreases. High content of CO in the sample obtained at 200–250°C (147–133 mg m^{-3}) indicates incomplete oxidation of organic compounds at oxygen deficiency. Our catalyst is the most efficient at 300–400°C. However, even at so high temperatures the exhaust gas along with CO contains insignificant amounts of organic impurities. The air supply even at a low rate (1–2 l min^{-1}) provides exhaustive oxidation of organic compounds to CO_2 at 350°C, and no CO is detected in the outlet gas mixture.

CONCLUSION

A new sorbent–catalyst exhibiting high sorption capacity for organic compounds of various classes and efficient in exhaustive catalytic oxidation of organic compounds was developed. This sorbent–catalyst shows promise for neutralization of harmful impurities in exhaust gases from various branches of industry.

REFERENCES

1. Rozengart, M. I., V'yunova, G.M., and Isagulyants, G.V., *Usp. Khim.*, 1988, vol. 57, no. 2, pp. 204–227.
2. Ming-Yuan, Yt, Zhonghui, Lie, and Enze, Min, *Catal. Today*, 1988, vol. 2, pp. 321–338.
3. Occelli, M.L. and Rennard, R.J., *Prepr. Am. Chem. Soc., Div. Fuel Chem.*, 1984, vol. 29, pp. 30–31.
4. Tzou, M. S. and Pinnavaia, T.J., *Catal. Today*, 1988, vol. 2, pp. 243–259.
5. Volzone, C., *Clays Clay Miner.*, 1995, vol. 43, no. 3, pp. 377–382.
6. Brandly, S.M. and Kydd, R.A., *Catal. Lett.*, 1991, vol. 8, no. 4, pp. 185–198.
7. Wen-Yang, Xu, Xian-mei, Xie, Yi-zhao, Yao, *et al.*, *J. Catal.*, 1991, vol. 12, no. 1, pp. 26–32.
8. Alkhazov, T.G. and Margolis, L.Ya., *Glubokoe kataliticheskoe okislenie organicheskikh veshchestv* (Exhaustive Catalytic Oxidation of Organic Compounds), Moscow: Khimiya, 1985.
9. Rao, R., Dandeker, R., Baker, R.T.K., and Vanice, M.A., *J. Catal.*, 1997, vol. 171, no. 2, pp. 404–419.
10. Sychev, M.V., Kostoglod, N.Yu., Astrelin, I.M., *et al.*, *Kinet. Katal.*, 1998, vol. 39, no. 1, pp. 114–121.
11. Mokaya, R. and Jones, W., *J. Catal.*, 1995, vol. 153, no. 1, pp. 76–88.

Russian Journal of Applied Chemistry, Vol. 75, No. 11, 2002, pp. 1828–1832. Translated from Zhurnal Prikladnoi Khimii, Vol. 75, No. 11, 2002, pp. 1864–1868.
Original Russian Text Copyright © 2002 by Lavrenov, Urzhuntsev, Paukshtis, Duplyakin, Bal'zhinimaev.

CATALYSIS

Promotion of Catalytic Properties of Sulfated Zirconium and Aluminum Oxides with Carbon Tetrachloride

A. V. Lavrenov, G. A. Urzhuntsev, E. A. Paukshtis, V. K. Duplyakin, and B. S. Bal'zhinimaev

Omsk Branch, Boreskov Institute of Catalysis, Siberian Division, Russian Academy of Sciences, Omsk, Russia
Boreskov Institute of Catalysis, Siberian Division, Russian Academy of Sciences, Novosibirsk, Russia

Received July 2, 2002

Abstract— The promoting effect of minor amounts of carbon tetrachloride on the catalytic activity and working life of sulfated zirconium and aluminum oxides is considered for the example of isobutane alkylation with butenes.

Industrial processes for isobutane alkylation with olefins have been carried with sulfuric and hydrofluoric acids as catalysts for more than 60 years and fail to satisfy modern economical and environmental requirements. The development and improvement of technology for manufacture of alkylation gasoline largely rely upon changing to solid acid catalysts [1]. Attention has been rather long given to sulfated oxides of metals (zirconium, iron, titanium, tin, and aluminum) as the most promising catalysts for alkylation of isobutane with butenes. The strong acid properties of these oxides make it possible to carry out the reaction under the same conditions as in the case of the conventional liquid acids [2]. However, industrial use of these catalysts is hindered by the insufficient stability of their catalytic properties.

It is well known that presence of trace amounts of the so-called astoichiometric components in the reaction mixture [8] may exert positive influence on the activity, selectivity, and stability of various catalytic systems. Introduction of halogen-containing organic compounds into the raw material and their interaction with solid acid catalysts directly under the reaction conditions improve the rate and stability of numerous acid–base processes, including alkylation of isobutane with butenes on, e.g., a rare-earth form of the Y zeolite [4]. This approach has been used successfully to maintain the required acidity of aluminoplatinum chlorine-containing catalysts in industrial processes of reforming [5] and skeleton isomerization of paraffins [6].

In this work we performed a comparative study of the influence exerted by minor additions of CCl_4 on the catalytic properties of sulfated zirconium and aluminum oxides in alkylation of isobutane with butenes. The catalytic systems considered occupy extreme positions in the series of increasing activity of sulfated metal oxides in the alkylation [2]: SO_4^{2-}/ZrO_2 > SO_4^{2-}/TiO_2 > SO_4^{2-}/SnO_2 > SO_4^{2-}/Fe_2O_3 > SO_4^{2-}/Al_2O_3.

This will allow a clearer assessment of the extent and efficiency of the promoting effect of carbon tetrachloride.

EXPERIMENTAL

Sulfated zirconium oxide (henceforth SZ) was synthesized as follows: To 400 ml of an ammonia solution (28 wt % NH_3) we added at 80°C in the course of 2.5 h 300 ml of a 223 g l^{-1} (in terms of ZrO_2) solution of oxozirconium(IV) nitrate. The resulting precipitate of zirconium hydroxide was filtered off and washed with ammonia water (pH 9), and then dried in air at room temperature and calcined at 400°C for 4 h. Zirconium oxide was treated with 2 N H_2SO_4, dried at 150°C, and calcined in a flow of dry air at 550°C for 4 h. This yielded a sample with the specific surface area of 188 m^2 g^{-1} and SO_4^{2-} content of 5.8 wt %.

Sulfated aluminum oxide was prepared by adding to γ-Al_2O_3 with the specific surface area of 200 m^2 g^{-1} a 14% H_2SO_4 solution and drying the product obtained at 100°C. Calcination at 600 (sample SA-600) or 700°C (sample SA-700) yielded catalysts containing 8 and 6 wt % SO_4^{2-}, respectively.

The catalytic properties were studied in a 180-ml stainless steel autoclave. As raw material served industrial isobutane (IBF) and butane–butylene (BBF)

1070-4272/02/7511-1828$27.00 © 2002 MAIK "Nauka/Interperiodica"

fraction preliminarily purified over solid alkali and NaA zeolite. The composition of the fraction was as follows:

Component	IBF, wt %	BBF, wt %
Propane	0.01	0.55
Isobutane	99.81	42.64
1-Butene + isobutane	0.15	26.65
n-Butane	0.03	8.76
trans-2-Butene	0.00	12.54
cis-2-Butene	0.00	8.86

To carry out the reaction, the autoclave was charged with 2 g of a catalyst (with particle size of 0.4–1 mm) and 40 g of IBF. In experiments with promotion, the IBF contained 0.02 wt % CCl_4. In the course of the tests, BBF was fed into the autoclave with a syringe pump at a rate of 0.05 to 1 g h^{-1}.

The liquid reaction mixture and the catalyst were stirred with jolt-rammer on which the autoclave was mounted. The alkylation was done at a temperature of 40°C, maintained by passing hot water through the autoclave jacket.

The composition of the reaction mixture in the autoclave was determined every hour by gas–liquid chromatography using a syringe of special design for sampling liquid hydrocarbons under pressure and a Hewlett–Packard 5890 Series II chromatograph with a DB-1 capillary column and a flame-ionization detector. The chromatograms were recorded and processed using the Multikhrom computerized chromatographic system.

To characterize the course of the reaction on the basis of the autoclave tests, the following parameters were determined: conversion of butenes, mass yield of C_{5+} products and *n*-butane based on converted butenes, and their fractional composition. All the parameters were calculated on the basis of a material balance for each hour of the process, minus the starting compounds and reaction products accumulated in the autoclave.

The results of the experiments performed are shown in Figs. 1 and 2 and in the table. A sample of sulfated zirconium oxide is characterized by high initial activity (the yield of C_{5+} products is about 2 g g^{-1} at complete conversion of butenes), which decreases fast when 0.62 to 0.81 g of butenes is supplied per gram of catalyst. The alkylation of isobutane with butenes is nearly always accompanied by redistribution of carbon and hydrogen [7], which leads to formation of isoparaffin hydrocarbons with less than eight carbon atoms, *n*-butane, and high-molecular-weight unsaturated compounds as reaction products. In the case of sulfated zirconium oxide, these processes are the most pronounced during the initial stage of the reaction [8], and deposits of heavy unsaturated products on the

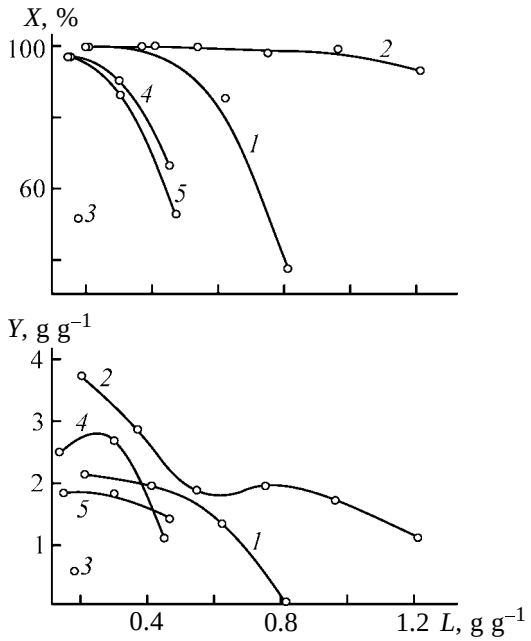

Fig. 1. Conversion of butenes, *X*, and yield of C_{5+} products based on converted butenes, *Y*, vs. mass *L* of butenes supplied per unit mass of catalyst in alkylation with and without adding CCl_4. Sample: (*1*) SZ, (*2*) SZ + CCl_4, (*3*) SA-600, (*4*) SA-600 + CCl_4, and (*5*) SA-700 + CCl_4; the same for Fig. 2.

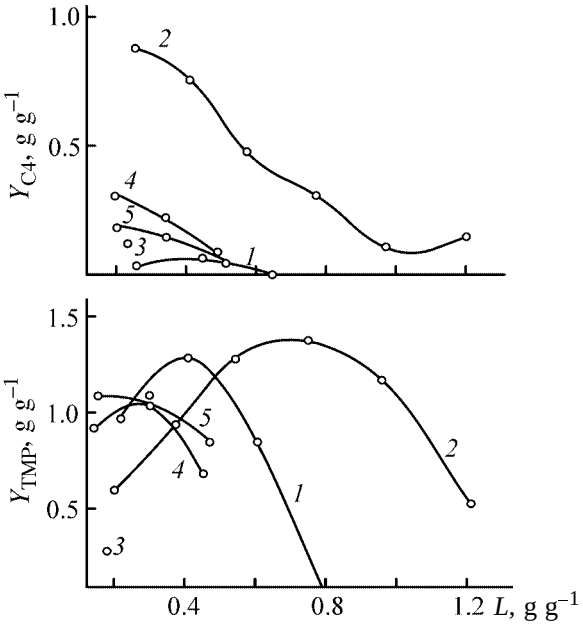

Fig. 2. Yields of *n*-butane, Y_{C4}, and trimethylpentanes, Y_{TMP}, based on converted butenes vs. mass *L* of butenes supplied per unit mass of catalyst in alkylation with and without adding CCl_4.

Effect of CCl_4 additions on the composition of C_{5+} products

Catalyst	CCl_4	L,* g g^{-1}	Composition, wt %						
			i-C_5	*i*-C_6	*i*-C_7	DMH	TMP	other *i*-C_8	C_{9+}
SZ	–	0.21	7.81	6.25	10.9	23.44	45.31	6.25	0.00
		0.41	7.04	2.82	4.23	16.90	64.79	2.82	1.41
		0.62	4.35	2.17	8.70	1.04	56.52	8.70	6.52
		0.81	0.00	0.00	0.00	0.00	0.00	100.00	0.00
SZ	+	0.20	28.17	12.68	13.73	16.20	15.85	12.32	1.06
		0.37	24.10	8.43	12.05	18.07	32.53	2.41	2.41
		0.54	7.27	1.82	3.64	12.73	67.27	3.64	3.64
		0.75	5.80	4.35	2.90	10.14	69.57	0.00	7.25
		0.96	3.13	1.56	4.69	15.63	65.63	3.13	6.25
		1.21	12.77	6.38	8.51	8.51	44.68	0.00	19.15
SA-600	–	0.18	10.53	7.89	7.89	10.53	44.74	2.63	15.79
SA-600	+	0.14	14.47	7.02	10.53	21.93	36.40	9.21	0.44
		0.30	14.10	6.41	10.26	16.67	38.46	6.41	7.69
		0.45	12.00	8.00	8.00	8.00	60.00	0.00	4.00
SA-700	+	0.15	11.89	5.59	5.59	18.88	58.04	0.00	0.00
		0.30	10.42	6.25	10.42	10.42	58.33	0.00	4.17
		0.47	3.45	3.45	6.90	13.79	58.62	6.90	6.90

* L is the catalyst mass.

solid catalyst surface are one of the most probable reasons for fast loss of activity.

The working life of zirconium sulfate catalysts in alkylation (from several minutes to several hours) and, correspondingly, the extent and rate of side processes largely depend both on the preparation conditions of the catalyst and on the conditions and method of catalytic test [8, 10, 11]. The selectivity in alkylation, exhibited by the SZ sample obtained, proved to be satisfactory and was characterized by average-integral mass fraction of trimethylpentanes (TMP) in C_{5+} products equal to 54% and by fraction ratio of TMP to dimethylhexanes (DMH) of about 3.

The interaction of the SZ catalyst with the isobutane–butene raw materials in the presence of CCl_4 intensifies processes involving excessive (for alkylation) consumption of isobutane. With this behavior of the system, the conversion of butenes is not a parameter characterizing the catalyst activity. The depth of conversion of the starting hydrocarbons is in the first place determined by the yield of C_{5+} products, whose values exceed, during the initial stage of the reaction at 100% conversion of butenes, by a factor of 1.4–1.8 the value of 2.04 g g^{-1} corresponding to the stoichiometry of isobutane alkylation with butenes. The forming C_{5+} products are strongly enriched in isopentane, isohexanes, and isoheptanes. Simultaneously, substantial amounts of *n*-butane are formed. However, the average yield of target alkylation products proper, TMP, remains at the same level as that without a promoter, being equal to about 1 g g^{-1}.

In the presence of CCl_4, the working life of the SZ catalyst increases nearly twofold. For example, an SZ sample without promoting additive ensured conversion of 0.67 g of butenes per gram of catalyst, with the conversion decreasing from 100 to 38%. On adding the promoter, the conversion of 1.2 g of butenes per gram of catalyst was achieved, and the conversion was retained at a level of about 90%. However, the joint conversion of isobutane and butenes still remained unstable.

Commonly, the effect of chlorinated compounds on the course of acid–base reactions is attributed to chlorination of catalysts at temperatures exceeding 100°C. Depending on the interaction conditions, states with varied nature of the surface acidity, both Brønsted [12] and Lewis [13], may be generated. At low temperature, there is virtually no surface modification of oxide catalysts, since the chlorination rate turns out to be exceedingly low.

In the case of low-temperature alkylation, the promoting effect of CCl_4 is in all probability associated with intensified generation of active species, such as *tert*-butyl cation, which play a key part in the classical chain mechanism of the reaction [7]. Formally, the main pathway of formation of *tert*-butyl cations in the course of alkylation is detachment of hydride anion from an isobutane molecule, with its subsequent transfer to other positively charged species to give neutral products (*n*-butane and isoparaffins with varied number of carbon atoms). It is this process, the so-called hydride transfer, that determines the stages of chain initiation and transfer in the course of alkylation. In the case of solid acids, the course of the hydride transfer is presumably determined by the presence of Lewis acid centers as electron acceptors. As a rule, all solid catalytic systems exhibiting activity in isobutane alkylation (chlorinated aluminum oxide, zeolites, sulfated metal oxides) are characterized by the presence of both protic and aprotic acid centers.

The C_{sp^3}–Cl bond energy is 59 kJ mol^{-1} lower than the C_{sp^3}–H_{tert} bond energy (344.8 and 403.8 kJ mol^{-1}, respectively [14]). Therefore, it may be assumed that CCl_4 can be much easier, compared with isobutane, activated on the surface of sulfated zirconium oxide. An activated CCl_4 molecule may act as an intermediate in detachment of a hydride anion from the isobutane molecule:

$$[Zr^{\delta+}\cdots Cl^{\delta-}\cdots CCl_3^{\delta+}] + \textit{iso}\text{-}C_4H_{10} \rightarrow [Zr^{\delta+}\cdots Cl^{\delta-}] + CCl_3H + \textit{tert}\text{-}C_4H_9^+.$$

Thus, initiation of the alkylation reaction may also involve catalyst surface sites with weaker acidity, which formally increases the total number of centers responsible for joint conversion of isobutane and butenes, with the strength of these centers growing.

However, as seen from the data obtained, introduction of CCl_4, apparently, not only reduces the activation barriers for isobutane alkylation with butenes, but also leads to development of nonselective transformations in the form of intensive occurrence of the so-called self-alkylation (self-condensation) of isobutane.

In this case, *n*-butenes act as hydrogen acceptors, being converted into *n*-butane, and it is this fact that may account for its high yield, and molecules of C_{5+} products are mainly formed from isobutane. The role of CCl_4 may consist in initiation of multistage processes of hydrogen chloride exchange, with the starting butenes and isobutane involved and products formed, which are identical to those produced in alkylation. As an example may serve the following reactions:

$$\textit{iso}\text{-}C_4H_{10} + CCl_4 \rightarrow \textit{tert}\text{-}C_4H_9Cl + CCl_3H, \quad (1)$$

$$\textit{tert}\text{-}C_4H_9Cl + \textit{iso}\text{-}C_4H_{10} \rightarrow \textit{iso}\text{-}C_8H_{18} + HCl, \quad (2)$$

$$\textit{n}\text{-}C_4H_8 + HCl \rightarrow \textit{sec}\text{-}C_4H_9Cl, \quad (3)$$

$$\textit{sec}\text{-}C_4H_9Cl + \textit{iso}\text{-}C_4H_{10} \rightarrow \textit{tert}\text{-}C_4H_9Cl + \textit{n}\text{-}C_4H_{10}. \quad (4)$$

Indeed, special experiments with large amounts of CCl_4 revealed formation of both chloroform and *tert*- and *sec*-butyl chlorides. Thus, CCl_4 enters into the reaction in quantitative amounts, also playing a part of hydrogen acceptor and ensuring self-alkylation of isobutane, which was observed in [4] when carrying out alkylation on a zeolite catalyst.

As already noted, alkylation and self-alkylation of isobutane are not limited to formation of isoparaffins C_8, being a complex process of redistribution of carbon and hydrogen. The significant increase in the yield of isoparaffins C_5–C_7 (products of destructive processes), observed in the presence of CCl_4, is presumably caused by the surface acidity of the catalyst, which is induced by the promoter and is clearly excessive for the reaction considered here.

In the presence of CCl_4, sulfated aluminum oxide, exhibiting virtually zero inherent activity in alkylation, can be used in the reaction and yields as good results as those obtained in alkylation on sulfated zirconium oxide in the absence of promoter. The calcination temperature (samples SA-600 and SA-700) affects the initial acidity of the catalyst and governs the selectivity of conversion of isobutane and butenes in the presence of promoter. Sample SA-600 is characterized by noticeable superstoichiometric consumption of isobutane and formation of large amounts of *n*-butane, hydrocarbons C_5–C_7, and DMH. At the same time, sample SA-700 is characterized by amount and composition of products, corresponding to a greater extent just to isobutane alkylation. At butene conversion of 97%, the alkylate yield is 1.86 g g^{-1} at a mass fraction of TMP equal to 58% and TMP/DMH ratio of about 3.

The results obtained suggest that, with permanent dosing of minor amounts of CCl_4 into the raw material and the reaction carried out under flow-through conditions, alkylation of isobutane with butenes on common sulfated aluminum oxide may be efficient.

CONCLUSION

The influence of CCl_4 additions on the alkylation of isobutane with butenes on sulfated zirconium and

aluminum oxides is demonstrated. The observed strong promoting effect furnishes additional opportunities for control over industrial processes of alkylation on solid catalysts based on sulfated metal oxides.

REFERENCES

1. Gembicki, S., *Stud. Surf. Sci. Catal*., 2000, vol. 130, pp. 147–155.
2. Comra, A., Martinez, A., and Martinez, C., *Appl. Catal. A*, 1996, vol. 144, no. 2, pp. 249–268.
3. Eidus, Ya.T., *Astekhiometricheskie komponenty kataliticheskikh reaktsii* (Astoichiometric Components of Catalytic Reactions), Moscow: Nauka, 1975.
4. Mortikov, E.S., Chkheidze, G.S., and Gritskov, A.M., *Neftekhimiya*, 1981, vol. 21, no. 5, pp. 662–667.
5. Kravtsov, A.V. and Ivanchina, E.D., *Intellektual'nye sistemy v khimicheskoi tekhnologii i inzhenernom obrazovanii: Neftekhimicheskie protsessy na Pt-katalizatorakh* (Intellectual Systems in Chemical Technology and Engineering Education: Petrochemical Processes on Pt Catalysts), Novosibirsk: Nauka, 1996.
6. Duprat, C. and Minkkinen, A., *Neftepererab. Neftekhim*., 1999, no. 10, pp. 1–56.
7. Dorogochinskii, A.Z., Lyuter, A.V., and Vol'pova, E.G., *Sernokislotnoe alkilirovanie izoparafinov olefinami* (Sulfuric Acid Alkylation of Isoparaffins with Olefins), Moscow: Nauka, 1970.
8. Xiao, X., Tierney, J., and Wender, I., *Appl. Catal. A*, 1999, vol. 183, no. 1, pp. 209–219.
9. Guo, C., Yao, S., Cao, J., and Qian, Z., *Appl. Catal. A*, 1994, vol. 107, no. 2, pp. 229–238.
10. Corma, A., Martinez, A., and Martinez, C., *J. Catal*., 1994, vol. 149, no. 1, pp. 52–60.
11. Das, D. and Chakrabarty, D., *Energy Fuels*, 1998, vol. 12, no. 1, pp. 109–114.
12. Bursian, N.R., Borutskii, P.N., and Dvorova, N.M., *Zh. Prikl. Khim*., 1975, vol. 48, no. 6, pp. 1349–1352.
13. Goupil, J., Poirier, J., and Cornet, D., *Catal. Lett*., 1995, vol. 31, no. 1, pp. 121–131.
14. Dneprovskii, A.S. and Temnikova, T.I., *Teoreticheskie osnovy organicheskoi khimii* (Theoretical Foundations of Organic Chemistry), Leningrad: Khimiya, 1991.

Russian Journal of Applied Chemistry, Vol. 75, No. 11, 2002, pp. 1833–1836. Translated from Zhurnal Prikladnoi Khimii, Vol. 75, No. 11, 2002, pp. 1869–1872.
Original Russian Text Copyright © 2002 by Korenman, Kochetova, Kuchmenko.

ENVIRONMENTAL PROBLEMS OF CHEMISTRY AND TECHNOLOGY

Sensor Analysis of Gases Emitted in Basic Organic Synthesis

Ya. I. Korenman, Zh. Yu. Kochetova, and T. A. Kuchmenko

Voronezh State Technological Academy, Voronezh, Russia

Received October 11, 2001; in final form, May 2002

Abstract—A matrix comprised of eight different sensors based on piezoelectric-crystal resonators was used for analysis of multicomponent gas mixtures. The resonator electrodes were modified with both known and unconventional gas-chromatographic sorbents.

Gas emissions from basic organic synthesis consist of substances belonging to diverse classes, in particular, alcohols, amines, amides, ketones, aldehydes, ethers, esters, and aromatic compounds. Volatile anthropogenic pollutants are able of fast migration to residential areas; many of them are accumulated in the biosphere in concentrations posing hazard to human life. The content of these pollutants should be strictly controlled [1, 2].

Modern methods of analysis should be prompt, mobile, sensitive, cost-effective, and accurate. In this connection, particular attention is now paid to development of gas-analyzing sensors. The operation of these sensors is underlain by transformation of the analytical signal generated by interaction of the sample analyzed with the sensitive coating on the electrodes into a physical signal [3–5].

Sensor selectivity is governed by the nature of the sensitive coating (modifier) of the piezoelectric-crystal resonator. Modifiers should be selective to individual components or groups of related compounds, exhibit adhesion to the electrode surface, and afford accurate determination of pollutants at the levels of their maximum permissible concentrations (MPCs). Repeated use of sensors should not markedly affect the main physical and chemical properties of the modifiers.

The aim of this work was to optimize the detection of multicomponent gas mixtures emitted in basic organic synthesis using sensors based on piezoelectric-crystal resonators.

EXPERIMENTAL

The experimental setup for static determination of volatile organic compounds was assembled at the laboratory from inexpensive units (Fig. 1).

Standard gas mixtures were prepared in a generator, into which samples were injected under permanent stirring of the mixture components with a stirrer. The required amount of saturated vapors of the substances under study was injected into the generator with a syringe via a polyurethane gasket, where the sample was uniformly diluted to appropriate concentrations (MPC, 1/2 MPC, etc.).

The concentrations of the components c, $\mu g\ m^{-3}$, were calculated by the Mendeleev–Clapeyron equation [6]

$$c = 1.22 p_i M \times 10^7/(pT), \quad (1)$$

where 1.22 is the proportionality coefficient; p_i, the saturated vapor pressure, mm Hg; M, the molecular weight; p, atmospheric pressure, Pa; and T, temperature, K.

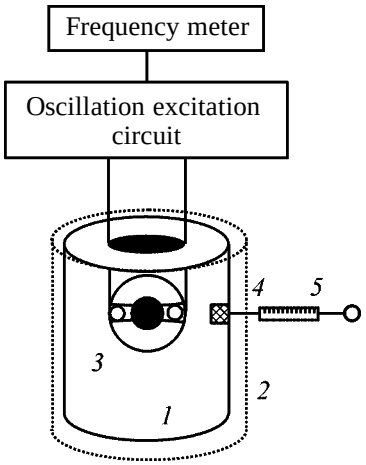

Fig. 1. Schematic of the static sensor device for analysis of gaseous media, involving sample injection: (*1*) detection unit, (*2*) thermostat, (*3*) resonator with two film-coated electrodes, (4) polyurethane gasket, and (*5*) syringe.

1070-4272/02/7511-1833$27.00 © 2002 MAIK "Nauka/Interperiodica"

Table 1. Analytical signal for phenol sorption at different BW masses

$m \pm 2$, μg	ΔF, Hz	S, Hz m^3 mg^{-1}	a	τ, s	S_{rms}
5	24	8000	0.007	10	1.0
10	38	12 700	0.004	15	1.2
20	46	15 300	0.002	30	1.4
30	54	18 000	0.002	60	1.8
40	60	20 000	0.001	75	2.4
50	63	21 000	0.001	90	3.6

Note: $m \pm 2$ is the mass of the film being applied, measured with the accuracy of ±2 μg; and τ is the time of establishment of the equilibrium.

The air sample was introduced into a temperature-controlled detection cell at the sensor electrode height, which significantly decreases the loss of the compounds analyzed by adsorption on the cell walls. Interaction of the gas sample components with the modifier changes the sensor oscillation frequency by ΔF, Hz. The relationship between the analytical signal from the sensor based on a piezoelectric resonator of volume acoustic waves, on the one hand, and the mass of the film coating on the electrodes and the mass of the analytes adsorbed on its surface m_f, on the other hand, is described by the Sauerbrey equation [3]

$$\Delta F = -K_f m_f, \quad (2)$$

where K_f is the proportionality coefficient taking into account the intrinsic characteristics of the piezoelectric-crystal plate and electrodes.

As modifiers of the resonator electrodes we used standard stationary phases utilized in gas chromatography, namely, polyethylene glycol-2000 (PEG-2000), polyethylene glycol succinate (PEGS), polyethylene glycol sebacate (PEGSb), octylpolyethoxyphenol (Triton X-100), dinonyl phthalate (DP), beeswax (BW), and polystyrene (PS) [7]. Also we utilized an unconventional sorbent, bees glue, propolis (PP). The 1 μg μl^{-1} sorbent solutions were uniformly applied with a microsyringe onto the surface of two resonator electrodes. To evaporate the solvent (acetone, toluene, ethanol, chloroform), we kept the sensors for 30–40 min in an oven at 40–45°C. The degree of the solvent removal was estimated from the time stability of the oscillation frequency of the resonator with the coating applied (zero signal drift within 3 Hz min^{-1}).

The quantitative characteristics of the sorption, namely, the sorbent sensitivity to the compound being analyzed S, Hz m^3 mg^{-1}, and the sorption capacity of the modifier a (a dimensionless parameter) [8], were calculated by the equations

$$S = \Delta F/c, \quad (3)$$

$$a = \Delta F/(F_0 - F_f), \quad (4)$$

where F_0 and F_f are the intrinsic oscillation frequencies of the unmodified (10 MHz) and modified piezoelectric crystal-based resonator, respectively.

The root-mean-square deviation S_{rms} was calculated by the equation

$$S_{rms} = \left[\sum_{i=1}^{i=n}(x_1 - x)^2\right](n - 1)^{-1}, \quad (5)$$

where x_i is the result of a single run, and n is the number of replicate runs.

One of the major parameters governing the sensitivity, reliability, and stability of the operation of gas sensors based on mass-sensitive piezoelectric-crystal resonators is the optimal mass of the sorbent [Eq. (2)]. Taking interactions in the phenol–sorbent system as an example, we showed how the analytical signal of the sensor varies with increasing modifier mass (Table 1).

With the sorbent mass increasing to 20–30 μg, the parameter ΔF and, hence, the sensor sensitivity, tend to increase. At m = 30–50 μg the acoustic wave is quenched in the near-electrode sorbent layer, and the effective mass and the sorption capacity of the modifier tend to decrease [9, 10]. Also, increase in the modifier mass decreases the reproducibility of the results by increasing the proportion of the volume-acoustic wave quenching component in the total microweighing error. For all the sorbents studied in this work, the optimal mass is estimated at 20–30 μg.

Table 2 presents the sensitivities of the modifiers (m = 25–30 μg) with respect to the compounds studied at concentrations corresponding to their MPCs. Based on the maximal S value we identified the optimal sorbents for detecting individual compounds. The largest responses from the sensors were obtained with PEG-2000 sensitive film in sorption of ethanol, butyl acetate, and formamide, with PEGS and PEGSb films in the case of phenol and *n*-butanol, with Triton X-100 film in the case of butyl acetate, diethylamine, acetone, toluene, and nitrophenol, and dinitrophenols, and with PP film in the case of 1,4-dioxane.

For prompt and reliable identification of individual

Table 2. Sensitivity of the modifiers of different nature to the compounds under study

Compound	MPC, mg m^{-1}	S of indicated modifier, Hz m^3 mg^{-1}							
		PEG-2000	PEGS	PEGSb	Triton X-100	BW	PP	DP	PS
Ethanol	0.1	2880	420	540	2000	570	640	210	370
n-Butanol	0.1	290	330	450	290	–	120	360	–
n-Butyl acetate	0.1	5880	3220	2600	7360	5280	1740	2110	120
Diethylamine	0.05	4280	3760	7770	17900	2220	17000	13380	1000
1,4-Dioxane	10.0	3	18	34	90	8	90	65	–
Phenol	0.003	17650	30000	30650	21650	15650	20000	18000	400
2-Nitrophenol	5.0	5	9	5	52	7	32	4	3
2,4-, 2,5-, and 2,6-Dinitrophenols	0.5	44	52	30	412	66	174	22	–
Formamide	3.0	33	5	6	6	5	7	6	3
Acetone	0.35	125	63	86	14	91	94	125	–
Ammonia	0.2	320	460	600	370	320	1400	240	115
Toluene	0.6	30	35	50	140	50	65	50	20

Note: The dash means that the analytical signal is indistinguishable from the noise.

compounds, we proposed a graphical procedure which implies no complicated calculations. It consists in the following. The signals from different sensors based on sorbents with the preset properties are converted to a "visual image", namely, a petal diagram with ΔF, Hz, axes. Figure 2 shows the standard diagrams of sorption for the selected compounds. The diagram profile remains unchanged with varying concentrations of the substances in the sample. The content of each component was determined using the calibration plots $\Delta F = f(c)$.

The search for highly selective modifiers suitable for resonator electrodes in analyzing multicomponent gas mixtures using sensors still remains urgent. At the same time, active development of computational facilities for on-line processing of multiple-parameter information allows the use of a group (matrix) of nonselective sensors for analyzing complex mixtures. Multisensor devices provide information (with a certain accuracy) about the qualitative and quantitative composition of the mixture [11].

Sorption diagrams were plotted for multicomponent gas mixtures based on the total responses of the sensors for vapors of individual compounds (Fig. 3a) and mixtures of phenol, nitrophenol, and dinitrophenols (Fig. 3b). The diagram profiles are identical, though the ΔF parameters differ, thus confirming the previously revealed nonadditivity of sorption of the gas mixture components [12].

Data in Table 2 and the "visual images" of sorption make it possible to determine the composition of a gas

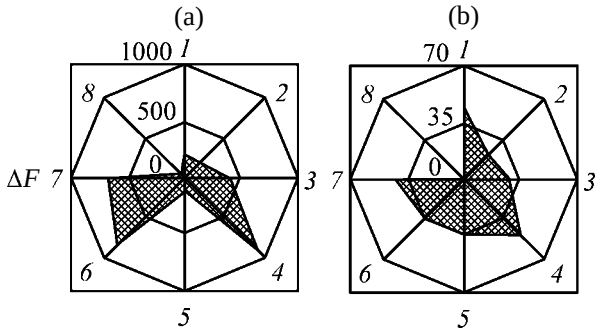

Fig. 2. Standard petal diagrams of sorption of (a) diethylamine and (b) 1,4-dioxane on (*1*) PEG-2000, (*2*) PEGS, (*3*) PEGSb, (*4*) Triton X-100, (*5*) BW, (6) PP, (*7*) DP, and (*8*) PS. (ΔF) Analytical signal from the sensor, Hz; the same for Figs. 3 and 4.

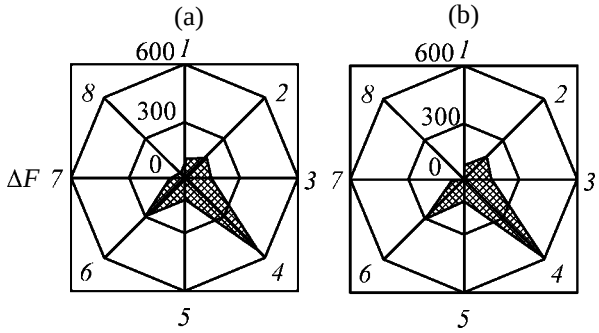

Fig. 3. (a) Calculated (from the sorption responses of individual compounds) and (b) experimental standard sorption diagrams of gas mixtures containing phenol, 2-nitro- and 2,4-, 2,5-, and 2,6-dinitrophenols.

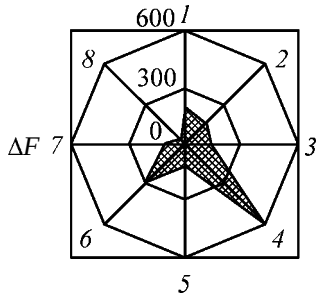

Fig. 4. Petal diagram of sorption of a mixture containing phenol, formamide, 2-nitrophenol, and 2,4-, 2,5-, and 2,6-dinitrophenol vapors.

mixture and the concentrations of its individual components. Increased ΔF parameter in axis *4* (Fig. 3) evidences the presence of nitro- and dinitrophenols in the mixture. The maximum permissible concentration of nitrophenol exceeds several times those of the other mixture components, as indicated in axis *6* (propolis). The ΔF value in axis *7* (DP) confirms the presence of phenol in the mixture. Increase of the content of any compound in the mixture tends to increase in ΔF in the corresponding axis.

The diagram profile changes with introduction into the mixture of concomitant components, e.g., formamide (Fig. 4). Enhanced sensitivity to formamide is exhibited by PEG-200 (axis *1*); in the other axes, ΔF varies insignificantly. By comparing the responses of the sensors to vapors of the mixtures of compounds with those on films with enhanced sensitivity to the individual substances, it is possible to determine the concentrations of individual components. For example, PEG-2000 and beeswax are insensitive to nitrophenol and dinitrophenols (Table 2), which allows determination of the formamide and phenol concentrations in axes *1* and *5*, respectively.

CONCLUSIONS

(1) The optimal masses of sorbents of different nature in determining volatile organic compounds, ensuring significant response, accuracy, and reliability of operation of the piezoelectric crystal-based sensor, were estimated at 20–30 μg.

(2) A new procedure was proposed for identifying the components of multicomponent gas mixtures. It is based on plotting standard petal diagrams of sorption for gas mixtures on different sorbents, electrode modifiers. Comparison of the experimental and standard diagrams allows determination of the composition and concentrations of individual components of multicomponent mixtures.

(3) An unconventional sorbent, propolis, was tested as modifier. It satisfies the requirements posed on modifiers and is suitable as sensitive coating for electrodes of piezoelectric-crystal resonator in detecting gases emitted in basic organic synthesis using sensors prepared therefrom.

REFERENCES

1. Dmitriev, M.T., Kazina, N.I., and Pinigina, N.A., *Sanitarno-khimicheskii analiz zagryaznyayushchikh veshchestv v okruzhayushchei srede* (Hygienic Analysis of Environmental Pollutants), Moscow: Khimiya, 1989.
2. Bespamyatnov, G.P. and Krotov, Yu.A., *Predel'no-dopustimye kontsentratsii khimicheskikh veshchestv v okruzhayushchei srede* (Maximum Permissible Concentrations of Chemical Substances in the Environment), Leningrad: Khimiya, 1985.
3. Malov, V.V., *P'ezorezonansnye datchiki* (Piezoelectric Crystal-Based Sensors), Moscow: Energopromizdat, 1989.
4. King, W.N., Camili, C.T., and Finders, A.F., *Anal. Chem.*, 1968, vol. 40, pp. 1330–1335.
5. Korenman, Ya.I., Tunikova, S.A., Kuchmenko, T.A., and Rajakovic, Lj.V., *Izv. Vyssh. Uchebn. Zaved., Khim. Khim. Tekhnol.*, 1997, vol. 40, no. 5, pp. 86–89.
6. Dorozhkin, L.M., Doroshenko, V.S., Krasilov, Yu.I., and Kuznetsov, N.T., *Zh. Anal. Khim.*, 1995, vol. 50, no. 9, pp. 979–982.
7. Petsev, N. and Kotsev, N., *Nar"chnik po gazova khromatografiya* (A Handbook on Gas Chromatography), Sofia: Nauka i Izkustvo, 1984.
8. Rajakovic, Lj.V., *J. Serb. Chem. Soc.*, 1991, vol. 56, nos. 8–9, pp. 521–534.
9. Korenman, Ya.I., Bel'skikh, N.V., and Kuchmenko, T.A., *Zh. Prikl. Khim.*, 1997, vol. 70, no. 4, pp. 626–630.
10. Koremnan, Ya.I., Tunikova, S.A., and Bel'skikh, N.V., *Zh. Anal. Khim.*, 1997, vol. 50, no. 6, p. 313–318.
11. Craven, M.A., Gardner, J.W., and Bartlett, P. N., *TRAC: Trends Anal. Chem.*, 1996, vol. 15, no. 9, pp. 486–493.
12. Edmons, T.E. and West, T.S., *Anal. Chim. Acta*, 1980, vol. 117, pp. 147–157.

Russian Journal of Applied Chemistry, Vol. 75, No. 11, 2002, pp. 1837–1840. Translated from Zhurnal Prikladnoi Khimii, Vol. 75, No. 11, 2002, pp. 1873–1876.
Original Russian Text Copyright © 2002 by Leont'eva, Konovalov, Karetnikov, Utrobin.

ENVIRONMENTAL PROBLEMS OF CHEMISTRY AND TECHNOLOGY

On the Possibility of Saving Chemicals in Salting-out Processes

A. I. Leont'eva, V. I. Konovalov, S. V. Karetnikov, and A. N. Utrobin

Tambov State Technical University, Tambov, Russia

Received September 10, 2001; in final form, August 2002

Abstract—A reagent charging mode is proposed to reduce the consumption of sodium chloride and water in manufacture of half-products of optical bleaching agents (Belofors).

Salting-out is used in chemical industry to isolate a number of organic substances from solutions [1, 2]. This method involves considerable consumption of sodium chloride (or some other salt) and formation of a large amount of wastewater enriched in this salt (up to 400 kg of NaCl per 1 m^3).

One of important half-products in manufacture of bleaching agents (Belofors) is 4,4'-dinitrostilbene-2,2'-disulfonic acid (DNS). DNS is produced industrially by oxidative dimerization of 4-nitrotoluene-2-sulfonic acid (NTSA) in the presence of atmospheric oxygen. Sodium chloride is used for isolating DNS in the stage of oxidation. To make lower the consumption of sodium chloride, it is necessary to analyze the salting-out mechanism based on the state of molecules and ions in solution.

The equilibria in protic solvents (H_2O and CH_3OH)

$$ArN< + H_3O^+ \underset{H_2O}{\rightleftarrows} ArN^+(H)< + H_2O, \quad (1)$$

$$ROH + H_3O^+ \underset{H_2O}{\rightleftarrows} R^+ + 2H_2O, \quad (2)$$

$$RH + CH_3O^- \underset{CH_3OH}{\rightleftarrows} R^- + CH_3OH, \quad (3)$$

$$ArOH + CH_3O^- \underset{CH_3OH}{\rightleftarrows} ArO^- + CH_3OH, \quad (4)$$

can be shifted to the right (toward larger ions) by adding alkali metal salts. This phenomenon is accounted for by the "drying" effect of salts [2] whose ions are characterized by high charge densities ("hard" anions and cations). Their solvation by protic solvents is very strong [3], and, therefore, the fraction of free solvent molecules decreases, which leads to the corresponding shift of the equilibrium. The magnitude of the effect depends not only on the concentration of a salt added, but also on the chemical composition of the ions constituting the salt. At the same concentration of salt additive in solution, the solvent vapor pressure corresponding to a decrease in the activity of water or methanol may be higher or lower, depending on the chemical composition of the salt. In addition to a decrease in the solvent activity, the drying effect is manifested in an increase in the degree of solvation of ions involved in the equilibria under study. In the reaction mixture, there exists competition between solvation processes for all of the ions present. Beginning with a certain concentration of an alkali metal salt in solution, ions involved in the equilibrium may be totally or partly desolvated:

$$OH \cdot nH_2O + X^-M^+ \rightleftarrows OH \cdot (n-m)H_2O + X^-M^+ \cdot mH_2O, \quad (5)$$

$$H_3O^+ \cdot nH_2O + X^-M^+ \rightleftarrows H_3O^+ \cdot (n-m)H_2O + X^-M^+ \cdot mH_2O. \quad (6)$$

The desolvation of ions is accompanied by an increase in their activity coefficients [2]. The energy of solvation of large ions by protic solvents, and especially that of organic ions with low charge density ("soft" ions) is markedly lower than the energy of solvation of small ions ("hard" ions) such as OH^-, CH_3O^-, and H_3O^+. The stability and, consequently, the activity of such large organic ions depend on desolvation to a lesser extent than the activity of small ions does. It should be noted that salt effects lowering the solvent activity are only clearly pronounced at a sufficiently large (≥ 0.1) salt : solvent ratio. In the existing production of bleaching agents with the use of sodium chloride, this ratio is 0.1875.

There also exists another approach to investigation

1070-4272/02/7511-1837$27.00 © 2002 MAIK "Nauka/Interperiodica"

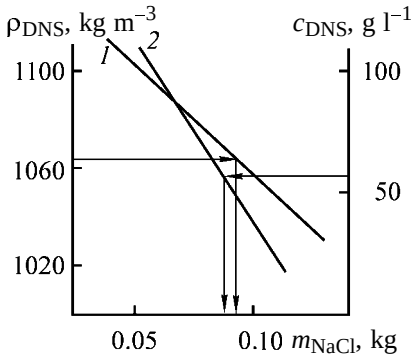

Fig. 1. (*1*) Density ρ_{DNS} and (*2*) concentration c_{DNS} vs. amount of NaCl, m_{NaCl}, to be added to salt-out DNS.

of electrolyte solutions. In this case, of particular importance is coordination in short- and long-range solvation of ions. It has been shown for cations with electronic configuration of noble gases that their coordination numbers are independent of the solvent nature and solution temperature and concentration [4, 5]. Experimental (NMR spectroscopy, gravimetry, X-ray and neutron diffraction analyses, IR spectroscopy, etc.) and calculational (Monte Carlo, molecular dynamics, quantum-chemical) investigation techniques yield information about the coordination of solvent molecules in the first solvation shell. A geometric analysis of the possible structural arrangements demonstrated that the number of solvent molecules directly bound to the ion must be limited. The most frequently occurring coordination numbers are 4, 6, and 8. For cations of small radius, e.g., Li^+, Be^{2+}, the maximum coordination number in a solvent is 4. In the case of large solvent molecules, the coordination number may decrease: e.g., Al^{3+} has 4 hexamethylphosphorotriamide molecules in the first coordination sphere. Cations of larger size, including Ln^{3+}, An^{3+}, may have in solution a coordination number exceeding 6, possibly in the range from 8 to 10 [6]. The coordination numbers in hydrate shells of ions, obtained by different methods, were reported in monograph [6].

The tentative scheme of DNS salting-out with NaCl can be represented as follows:

$$DNS \cdot nH_2O + NaCl \rightarrow DNS + NaCl \cdot nH_2O. \quad (7)$$

Scheme (7) may be valid in a wide range of DNS and NaCl concentrations in solution, since the heat of NaCl hydration is, in all probability, much higher than that of DNS hydration (large organic anion [2]). In this case, it would be expected that there exists a relationship between the amount of salt necessary for salting-out and the DNS concentration in solution.

This dependence was determined experimentally. A 1-l vessel was charged with 5×10^{-4} m^3 of a DNS solution of varied concentration, and then the necessary amount of NaCl was added to make the DNS solution density in the vessel 1150 kg m^{-3}. The precipitated DNS was filtered off, and the DNS content in the filtrate was determined. The amount of the salt necessary for salting-out the DNS was calculated from the material balance equation

$$5 \times 10^{-4}\rho + 2168V = (5 \times 10^{-4} + V) \times 1150, \quad (8)$$

where 5×10^{-4} is the DNS solution volume (m^3); ρ, the initial density of the DNS solution (kg m^{-3}); 2168, the NaCl density (kg m^{-3}) [7]; V, the NaCl volume (m^3); 1150, the final density of the DNS solution with the salt (kg m^{-3}).

As a result, linear relationships were obtained allowing the amount of NaCl required for salting-out DNS to be calculated from the density or concentration of the DNS solution (Fig. 1, straight lines *1* and *2*, respectively). For example, for a solution with a density of 1062 kg m^{-3} (which corresponds to the mass concentration of DNS equal to 54.45 g l^{-1}) the necessary amount of the salt (0.095 kg) is found on the abscissa. If account is taken of the fact that this amount is required for a solution with a volume of 5×10^{-4} m^3, then a value of 7.5 t is obtained for the reactor volume (40 m^3). Carrying out the same calculation procedure for an initial DNS concentration of 54.45 kg m^{-3} gives 7.4 t of sodium chloride.

The discrepancy (3%) between the amounts of NaCl salt to be added to the solution, found from the graphical dependences *1* and *2*, does not exceed the overall error of the methods. For practical purposes, it is simpler to determine the amount of sodium chloride required for salting-out by measuring the DNS solution density.

Analysis of the linear dependences shown in Fig. 1 shows that, with increasing concentration and density of the DNS solution, the amount of NaCl used to salt-out the same amount of DNS decreases. Under industrial conditions, the concentration and, correspondingly, density of the DNS solution can be raised by decreasing the amount of water fed into the reactor.

To check under laboratory conditions how a decrease in the amount of water affects oxidation of NTSA, we assembled a setup shown in Fig. 2. The setup comprises a vessel *1* with the reaction mass, placed in a thermostat *2*. The heating is done with boiler *3*. A blade stirrer is used to agitate the reaction mass. Air is fed through a bubbler integrated with the

bottom part of vessel *1*. The air flow rate is monitored with an RT-1 rotameter. The temperature is measured and controlled with a thermocouple and TR200 device *6*.

The dimerization of NTSA in the laboratory setup was carried out as follows. Vessel *1* was successively charged with water, soap (0.2 g), catalyst (0.08 g), defoaming agent (tributyl phosphate, 0.6 ml), and alkali (45% NaOH, 150 ml). With the stirrer *4* switched-on, air was fed through the bubbler 5 (Q = 0.6 $m^3 h^{-1}$), and a homogeneous NTSA solution (280 ml, density 1186 $kg\,m^{-3}$, acidity 179 $g\,l^{-1}$, concentration 298.5 $g\,l^{-1}$) was added. The alkalinity of the reaction mass was brought to 2% by adding NaOH in 2–5-ml portions. Samples were taken at 1-h intervals and the NTSA, DNS, and dye concentrations were determined spectrophotometrically from the optical densities measured on an SF-26 spectrophotometer.

Three sets of experiments on NTSA oxidation were carried out with the following amounts of water: 1200, 850, and 650 ml. It was found that, with the volume of fed water decreased, a precipitate [intermediate dinitrodibenzylsulfonic acid (DNDB)] is formed in the reaction medium 3–4 h after the beginning of oxidation. The amount of the precipitate depends on temperature and the NTSA and alkali concentrations in the reaction mass. The formal scheme of the reaction, with an intermediate formed, looks like

$$A \rightarrow B \rightarrow C$$

where A is the starting reagent, B is the intermediate, and C is the final product.

By varying the oxidation mode, a condition can be achieved when the DNDB concentration remains constant and does not exceed the saturation concentration in the reaction mass. This can be done by parallel charging of NTSA and NaOH into the apparatus over a long time (5–6 h).

The kinetics of oxidation, observed with the method of reagent charging used in manufacture of bleaching agents and the technique proposed here, is shown in Fig. 3. The parallel charging of NTSA and NaOH is done in five equal batches.

It can be seen from the dependences presented in Fig. 3 that, in the case of batch charging of the components, the maximum concentration of the intermediate (DNDB) (curve *5*) is lower than that with the charging mode used industrially in manufacture of bleaching agents (curve *4*).

To verify the efficiency of batch charging of components under laboratory conditions, experiments were carried out on a setup shown in Fig. 2, using the procedure described above.

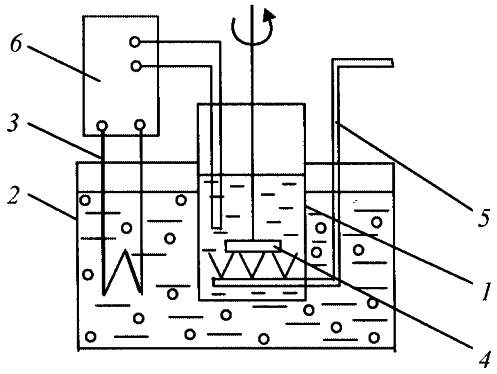

Fig. 2. Schematic of the experimental setup: (*1*) vessel, (*2*) thermostat, (*3*) boiler, (*4*) stirrer, (*5*) bubbler, and (*6*) TR-200 device.

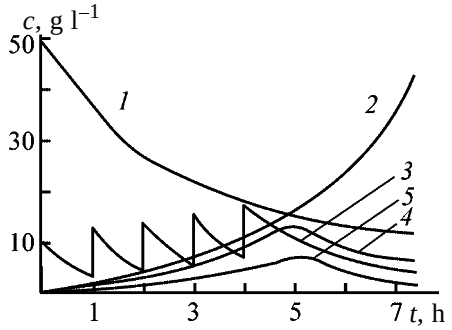

Fig. 3. Kinetics of oxidative dimerization of NTSA in DNS. (*c*) Concentration and (*t*) time. Variation of concentration: (*1*) NTSA with charging in a single portion, (*2*) DNS, (*3*) NTSA with charging extended over time, (*4*) intermediate (DNDB) with charging in a single portion, and (*5*) intermediate (DNDB) with charging extended over time.

The first set of experiments reproduced the process of oxidative dimerization of NTSA used industrially in manufacture of bleaching agents. The reactor was charged with 1200 ml of water, and then 250 ml of a homogeneous solution of NTSA and 100 ml of NaOH were introduced in a single portion.

The second set of experiments reproduced the process of oxidative dimerization of NTSA with batch charging of the components. To verify the assumption that the consumption of water and NaCl decreases in the case of batch charging, a smaller amount of water (850 ml) was fed into the reactor in the second set of experiments. A homogeneous NTSA solution (250 ml) and NaOH (100 ml) were charged as follows: 10 ml of NTSA and 3–4 ml of NaOH every 10 min. In the first charging, the alkalinity of the reac-

tion mass was brought to 2% by adding NaOH in 2–5-ml portions. The alkalinity and temperature were maintained constant (2%, 58°C) during the entire process (12 h).

After the oxidative dimerization of NTSA was complete, DNS was isolated and the amount of NaCl consumed was measured. Below are presented the results of the experimental studies:

V_{H_2O}, ml	m_{DNS}, g	m_{NaCl}, g
1200	54	432
1200	58	471
1200	61	455
850	57	254
850	53	250
850	59	263

It can be seen that, in the case of batch charging of the components, the consumption of water decreases by 30%, and that of the salt, by 40%, with the amount of DNS obtained in the experiment remaining virtually the same.

The proposed method of batch component charging was tested on an industrial installation. The industrial reactor was a 29 m^3 vessel with a jacket. The amount of water used in NTSA oxidation in the existing production of bleaching agents was 15 m^3. The total volume of the reaction mass was 19 m^3 (DNS concentration 54–55 g l^{-1}). This amount of the DNS solution requires 3.8 t of NaCl. With the batch charging of the components used, the reactor was charged with 10 m^3 of water. The total volume of the reaction mass was 14 m^3 (DNS concentration 72–74 g l^{-1}). This amount of the DNS solution required 2.3 t of NaCl.

CONCLUSION

A component charging method with which the consumption of water decreases by 30% and that of NaCl required for isolation of 4,4'-dinitrostilbene-2,2'-disulfonic acid, by 40% was developed experimentally and tested on an industrial installation.

REFERENCES

1. Leont'eva, A.I., Konovalov, V.I., Bryankin, K.V., *et al*., *Zh. Prikl. Khim*., 2000, vol. 73, no. 3, pp. 453–456.
2. Loupy, A. and Tchoubar, B., *Effets de sols en chimie organique et organometallique*, Paris: Bordas, 1988.
3. Basolo, F. and Pearson, R.G., *Mechanisms of Inorganic Reactions. A Study of Metal Complexes in Solution*, New York: Wiley, 1967.
4. Krestov, G.A., Vinogradov, V.I., Kessler, Yu.M., *et al*., *Sovremennye problemy khimii rastvorov* (Present-Day Problems of the Chemistry of Solutions), Moscow: Nauka, 1986.
5. Krestov, G.A., *Termodinamika ionnykh protsessov v rastvorakh* (Thermodynamics of Ionic Processes in Solutions), Leningrad: Khimiya, 1984.
6. Krestov, G.A., Novoselov, N.P., Perelygin, I.S., *et al*., *Ionnaya sol'vatatsiya* (Ionic Solvation), Moscow: Nauka, 1987.
7. *Kratkii spravochnik khimika* (Concise Chemist's Handbook), Perel'man, V.I., Ed., Moscow: Khimiya, 1964.

Russian Journal of Applied Chemistry, Vol. 75, No. 11, 2002, pp. 1841–1844. Translated from Zhurnal Prikladnoi Khimii, Vol. 75, No. 11, 2002, pp. 1877–1880.
Original Russian Text Copyright © 2002 by Tishin, Dorokhov.

PROCESSES AND EQUIPMENT OF CHEMICAL INDUSTRY

Determining the Conditions of Preliminary Mixing in Stirred Vessels

O. A. Tishin and I. N. Dorokhov

Volzhskii Polytechnic Institute, Volgograd State Technical University, Volzhskii, Volgograd oblast, Russia
Mendeleev Russian University of Chemical Engineering, Moscow, Russia

Received February 18, 2002

Abstract—The results of experimental and theoretical studies of the influence exerted by stirring on a chemical reaction are presented. A parameter is proposed for evaluating this influence. The values of this parameter at which the state of preliminary mixing of reactants is achieved are determined.

Stirring strongly affects the integral characteristics (conversion, selectivity, yield) of a chemical process. This influence was first studied by Danckwerts [1, 2] and Zwietering [3], who demonstrated that preliminary mixing of the fed reactants ensures guaranteed conversions. Therefore, conditions corresponding to the state of preliminary mixing are to be created at the reactor inlet in reactor design. However, reactants are fed into the reactor in separate flows, and their stoichiometric ratio is ensured for the entire volume of the medium fed into the reactor. The aim of mixing consists in that the reactants should be brought as fast as possible to a state for which the stoichiometric ratio is observed at any point of the medium, i.e., to the state of preliminary mixing. Of much interest in this context is defining the criteria that can be used to evaluate the state of the starting mixture as regards its mixing. This study makes an attempt to develop a criterion allowing evaluation of the condition of preliminary mixing.

The effect of mixing on the course of a chemical process is manifested, in the first place, in nonuniformity of the concentration of substances involved in the chemical reaction. The effect of concentration nonuniformity can be demonstrated for the example of a second-order reaction proceeding by the scheme

$$A + B \xrightarrow{k} P, \qquad (1)$$

where A, B, and P are reactants and reaction products; k is the rate constant of the chemical reaction ($m^3\ mol^{-1}\ s^{-1}$).

In the case of nonideal mixing, the concentration c ($mol\ m^{-3}$) of the substance can be represented as a sum of its mean value and concentration pulsation:

$$c = \bar{c} + \Delta c. \qquad (2)$$

The effect of stirring nonuniformity can be evaluated using an expansion of the function into a Taylor series. The rate of the chemical reaction, r ($mol\ m^{-3}\ s^{-1}$), in zones with positive and negative deviations of the concentration from its mean value is as follows:

$$\left.\begin{aligned} r(\bar{c} + \Delta c) &= r(\bar{c}) + \frac{dr}{dc}\Delta c + \frac{1}{2}\frac{d^2r}{dc^2}(\Delta c)^2, \\ r(\bar{c} - \Delta c) &= r(\bar{c}) - \frac{dr}{dc}\Delta c + \frac{1}{2}\frac{d^2r}{d^2c}(\Delta c)^2, \end{aligned}\right\} \qquad (3)$$

The volume-average rate of the chemical reaction is given by

$$r = r(\bar{c}) + \frac{1}{2}\frac{d^2r}{dc^2}(\Delta c)^2. \qquad (4)$$

The rate of chemical conversion at equal initial concentrations of the reactants is as follows:

$$r_A = -k\bar{c}_A^2 - k(\Delta c_A)^2. \qquad (5)$$

For a stirred vessel, the deviation of the concentration from its mean value is related to the degree of homogeneity of the mass being stirred by [4]

$$\Delta c_A = \bar{c}_A(1 - \eta). \qquad (6)$$

The dependence of the degree of homogeneity on the volume mass-transfer coefficient is described by the equation

$$1 - \eta = \exp(-k_m\tau), \qquad (7)$$

1070-4272/02/7511-1841$27.00 © 2002 MAIK "Nauka/Interperiodica"

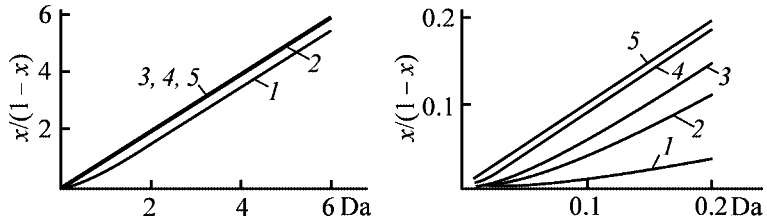

Fig. 1. Complex $x/(1 - x)$ vs. Dammköhler number Da for a batch reactor. *m*: (*1*) 1, (*2*) 5, (*3*) 10, (*4*) 50, and (*5*) ∞.

where k_m is the volume mass-transfer coefficient (s^{-1}), and τ is time (s).

Substitution of (6) and (7) into Eq. (5) gives an equation for calculating the average rate of the chemical reaction:

$$r_A = \frac{dc_A}{d\tau} = -k\bar{c}_A^2[1 + \exp(-2k_m\tau)]. \quad (8)$$

Integration of Eq. (8) with the initial conditions $\tau = 0$ and $c_A = c_{A_0}$ yields a relation for evaluating the reactant conversion in the course of the reaction:

$$\frac{x}{1 - x} = \mathrm{Da} + [\exp(-2m^2\,\mathrm{Da}) - 1]\frac{1}{2m^*}, \quad (9)$$

where $m^* = k_m/kc_{A_0}$ is the stirring parameter, c_{A_0} is the initial concentration of the reactant (mol m^{-3}), $\mathrm{Da} = kc_{A_0}\tau$ is the Dammköhler number, and x is the conversion.

An equation for calculating the conversion at unequal initial concentrations of the reactants can be derived similarly.

Figure 1, demonstrating the results of calculations by Eq. (9), shows that raising the complex m^* can create in the apparatus conditions close to the state of preliminary mixing of reagents. The complex m^* can be regarded as a characteristic of stirring. If the efficiency of mass transfer in the apparatus is high, i.e., $m^* \gg 1$, then stirring has no effect on the course of the chemical reaction; otherwise, the stirring starts to affect the chemical process.

The aim of this study was to determine experimentally the values of the parameter m^* at which the state of preliminary mixing of input flows in a srtirred vessel is ensured.

EXPERIMENTAL

The method of a model reaction was used in the experiments. As the model reaction served the second-order reaction of hydrogen peroxide with sodium thiosulfate [5]:

$$H_2O_2 + Na_2S_2O_3 \xrightarrow{k} \text{Products}, \quad (10)$$

with the rate constant $k = 6.853 \times 10^5 \times \exp(-18\,200/RT)$ l mol^{-1} s^{-1}.

The experiments were carried out on an installation described in [6–8]. As object of study served a 1-l flat-bottom cylindrical vessel 106 mm in diameter. The vessel casing was made of glass, which allowed visual inspection of the process. The reagents were fed into the vessel through standpipes directly to the surface of the reacting mass. The product formed was discharged through a pipe at the vessel bottom.

The conversion in the model reaction was determined as follows. The concentrations of reactant solutions in the feeding vessels were hydrogen peroxide 0.8 M and sodium thiosulfate 0.4 M. In all the experiments, the molar ratio of the reactant concentrations (peroxide : thiosulfate) in the reactor, provided that the substances were uniformly distributed over the entire volume of the apparatus, was 2 : 1, which corresponds to the reaction stoichiometry [5]. The solutions were fed into the reactor by dosing pumps, with the flow rates monitored with rotameters. The volumetric flow rates of the reactants were the same in all the experiments. All measurements were done in the steady state, the conditions for its attainment were established in [6–8]. The temperature was recorded with an electronic measuring and control system. The temperature probe was placed within the reactor outlet (at the reactor bottom). The accuracy of temperature measurements was 0.5°C. The temperature of the input flows was measured with mercury thermometers to within 0.1°C. The experiments were carried out at temperatures of the medium in the apparatus in the range 26–31°C. The heat effect of the reaction in this temperature range was 117 kcal mol^{-1}. The substance conversion was evaluated from the change in temperature within the reactor volume. The reactor operated under nearly adiabatic conditions since the heat removal through the side walls of the reactor did not

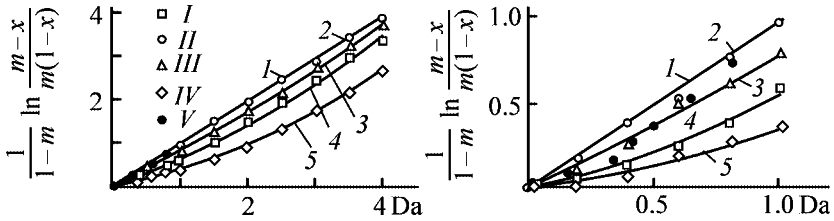

Fig. 2. Complex $(m-1)^{-1}\ln\{[(m-x)[m(1-x)]^{-1}\}$ vs. Dammköhler number Da for a batch reactor. m^*: (*1*) ∞, (*2*) 14, (*3*) 7.2, (*4*) 3.5, and (*5*) 1.75. Data from references: (*I–IV*) [10] and (*V*) [11] (m^* = 20.4).

exceed 1% of the heat carried away from the reactor by the output flow. The conversion of the reactants was calculated by the formula

$$x = \sum_{1}^{2}[\rho C_p(T_f - T_{in})](c_{A_0}\Delta H)^{-1}, \qquad (11)$$

where C_p is the specific heat of the substance (J kg^{-1} deg^{-1}); ΔH, the heat effect of the reaction (J mol^{-1}); T, the final and initial temperatures (deg); ρ, the density of the substance (kg m^{-3}).

The volume mass-transfer coefficient was calculated by the equation [9]

$$k_m = K\bar{V}^{-0.52}(\varepsilon/\nu)^{1/2}[\ln(Sc) - 1.27]^{-1}, \qquad (12)$$

where V is the vessel volume (m^3); Sc = ν/D, the Schmidt number; ε, the power expenditure for stirring of a unit mass of the liquid (m^2 s^{-3}); ν, the kinematic coefficient of viscosity (m^2 s^{-1}); D, the diffusion coefficient (m^2 s^{-1}); the coefficient K is 0.0016 for turbine-type agitators and 0.00047 for blade stirrers.

The numerical values of the coefficients and the dependence of the volume mass-transfer coefficient on the vessel volume were determined in experimental studies of the stirring rate in stirred vessels [10–12].

The distribution of the residence time (DRT) was studied using the tracer (KCl solution) and measuring variation of the electrical conductivity of the output flow. The DRT curves were obtained at varied process parameters (n = 120–625 rpm, τ = 90–200 s). Experimental data processing demonstrated that, in all process modes, the DRT of the vessel corresponds to the ideal mixing model.

The experimental conversion was compared with that possible theoretically, calculated by Eqs. (9) at m^* = ∞ and by the Danckwerts equation [1, 2] for continuous reactors:

$$x = 1 - \int \frac{\exp(-\theta)}{1 + Da\,\theta}d\theta, \qquad (13)$$

where $\theta = \tau/\bar{\tau}$ is the relative residence time; τ, the average residence time of the liquid in the apparatus (s); Da = $kc_{A_0}\bar{\tau}$, the Dammköhler number.

The results obtained in theoretical and experimental studies are shown in Figs. 2 and 3 for batch and continuous reactors, respectively. The results obtained in studying different reactions in vessels of different designs and dimensions are in good agreement. It can be seen from Figs. 2 and 3 that raising the parameter m^* makes it possible to increase the conversion in a reactor.

At $m^* \geq 30$, conditions are ensured at which the conversion achieved is close to the theoretical value under the given process conditions. When the parameter m^* reaches m^*_{cr}, the system passes into the state of preliminarily mixed flows. With the parameter increasing further, the conversion ceases to vary.

Thus, the parameter m^* can serve as a criterion characterizing the transition of the reagents to the preliminary mixing state. In apparatus for which $m^* \geq m^*_{cr}$, the integral characteristics of a chemical process can be calculated by the Danckwerts and Zwietering equations.

CONCLUSION

A theoretical analysis and experimental studies demonstrated that the state of preliminary mixing of

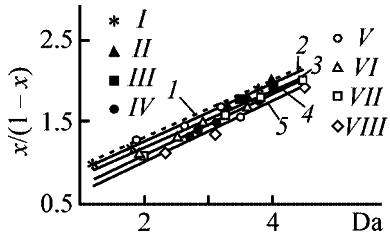

Fig. 3. Complex $x/(1-x)$ vs. Dammköhler number Da for a flow-through reactor. m^*: (*1*) ∞, (*2*) 54, (*3*) 25.4, (*4*) 14.2, and (*5*) 7.98. Saponification of ethyl acetate [6–8], m^*: (*I*) 54, (*II*) 25, (*III*) 14, and (*IV*) 8. Reaction of H_2O_2 with $Na_2S_2O_3$, m^*: (*V*) 39–40, (*VI*) 30–31, (*VII*) 23–25, and (*VIII*) 13–14.

the input flows can be achieved at $m^* \geq 30$ in stirred vessels in the case when the flow structure corresponds to the ideal mixing model.

REFERENCES

1. Danckwerts, P.V., *Chem. Eng. Sci*., 1958, vol. 7, no. 1, pp. 116–117.
2. Danckwerts, P.V., *Chem. Eng. Sci*., 1958, vol. 8, no. 1, pp. 93–102.
3. Zwietering, Th.N., *Chem. Eng. Sci*., 1959, vol. 9, no. 1, pp. 1–15.
4. Vasil'tsov, E.A. and Ushakov, V.G., *Apparaty dlya peremeshivaniya zhidkikh sred: Spravochnoe posobie* (Apparatus for Stirring of Liquid Media: Reference Book), Leningrad: Mashinostroenie, 1979.
5. Worrell, G.R. and Eagleton, L.C., *Can. J. Chem. Eng*., 1964, vol. 8, no. 12, pp. 254–258.
6. Darmanyan, A.P., Tishin, O.A., and Tyabin, N.V., *Zh. Prikl. Khim*., 1985, vol. 58, no. 9, pp. 2046–2050.
7. Darmanyan, A,P., Tishin, O.A., and Tyabin, N.V., Abstracts of Papers, *8-ya Vsesoyuznaya konferentsiya "Khimreaktor-8"* (8th All-Union Conf. "Khimreaktor-8"), Chimkent, October 13–18, 1983, pp. 312–317.
8. Darmanyan, A.P., Tishin, O.A., and Mironov, A.Yu., *Reologiya, protsessy i apparaty khimicheskoi tekhnologii. Sbornik nauchnykh trudov* (Rheology, Processes and Apparatus of Chemical Technology, Coll. of Scientific Works), Volgograd, 1983, pp. 50–58.
9. Pohorecki, P. and Baldyga, J., *Chem. Eng. Sci*., 1983, vol. 38, no. 1, pp. 79–83.
10. Takao, M., Yamamoto, T., Murakami, Y., and Sato, Y., *J. Chem. Eng. Jpn*., 1978, vol. 11, no. 6, pp. 481–486.
11. Miyawaki, O., Tsujikawa, H., and Uraguchi, Y., *J. Chem. Eng. Jpn*., 1975, vol. 8, no. 4, pp. 63–68.
12. Kramers, H., Baars, G.M., and Knoll, W.H., *Chem. Eng. Sci*., 1953, vol. 2, no. 1, pp. 35–41.

Russian Journal of Applied Chemistry, Vol. 75, No. 11, 2002, pp. 1845–1848. Translated from Zhurnal Prikladnoi Khimii, Vol. 75, No. 11, 2002, pp. 1881–1884.
Original Russian Text Copyright © 2002 by A. Levdanskii, Vil'kotskii, E. Levdanskii.

PROCESSES AND EQUIPMENT OF CHEMICAL INDUSTRY

Multistage Mill with Flow-through Classification for Selective Comminution of Sylvinite Ore

A. E. Levdanskii, A. I. Vil'kotskii, and E. I. Levdanskii

Belarussian State Technological University, Minsk, Belarus

Received March 14, 2002

Abstract—The process of sylvinite ore comminution in a multistage flow-through mill is analyzed. The potential applications of the mill in preliminary treatment of the sylvinite ore to prepare it for flotation are considered.

In dressing of mineral ores, comminution occupies a prominent place. The efficiency of ore dressing is largely determined by the extent to which the components are accessible for agents used in dressing. Therefore, the ore is crushed to the required grain size, after which the valuable product is recovered. The flotation technique, based on differences in wettability between minerals, has gained the widest acceptance for recovery of components from ores.

The sylvinite ore contains three main components: potassium chloride, sodium chloride, and halopelite. The valuable recoverable mineral is potassium chloride, and the other two components are dumped. Halopelite contains various combinations of clayey minerals, carbonates, sulfates, chlorides, etc.

The potassium ores from the Starobinsk deposit contain an increased amount of halopelites, with the majority of these found in bands. The thickness of these bands in potassium horizons varies between fractions of a millimeter and several centimeters. In addition, a minor amount of halopelite is contained as microinclusions in rock salt and potassium minerals [1–4]. The composition of the potassium ore varies with the bed attitude, being not constant even within a single bed. In calculations, the following average component contents were adopted for the beds mined at the Starobinsk deposit (wt %): KCl 25, NaCl 69, and halopelite 8 [5].

The potassium ore extracted by plough machines in mines has lumps up to 150 mm in size, it is crushed in impact disintegrators to grain size of 10–15 mm. Since inclusions of potassium chloride in the sylvinite mineral are 0.5–3 mm in size, it is necessary to crush the ore to particle size of less than 3 mm to ensure total recovery of potassium chloride by flotation. For this purpose, the final comminution of the ore is done in rod mills by the wet method. A saturated aqueous solution of NaCl and KCl is used as liquid phase. The grinding is done using the closed system: the material ground in the rod mill is delivered for classification into an arch screen, wherefrom the undersize product is removed from the scheme, and the oversize product is returned into the mill for additional processing. The comminution by this scheme ensures the minimum possible overgrinding of the ore. However, water-insoluble impurities (halopelites) contained in the potassium ore and mainly represented by clayey–carbonate materials tend to swell in aqueous media and, when treated mechanically in a mill, are dispersed into fractions with grain size of less than 0.07 mm.

The presence in the milled ore of a finely dispersed clayey–carbonate sludge affects adversely the flotation of potassium salts [2]. This is accounted for by the fact that minute clay particles have large surface area onto which the flotation agents are adsorbed. The adverse influence of the clayey–carbonate sludge on the flotation is eliminated as follows: (1) mechanical rubbing-away of the sludges with subsequent removal of minute particles in hydrocyclones and hydroseparators; (2) flotation of sludges; (3) depression of sludges with depressing reagents, which, being adsorbed onto the surface of clayey–carbonate particles, preclude adsorption of collectors on these particles.

The scheme with preliminary removal of the major part of halopelite before delivering the ore into the drum mill for final comminution is more acceptable. It was noted in [3] that comminution of the sylvinite ore entails selective size distribution of KCl and halopelite: size grades larger than 3 mm are characterized

1070-4272/02/7511-1845$27.00 © 2002 MAIK "Nauka/Interperiodica"

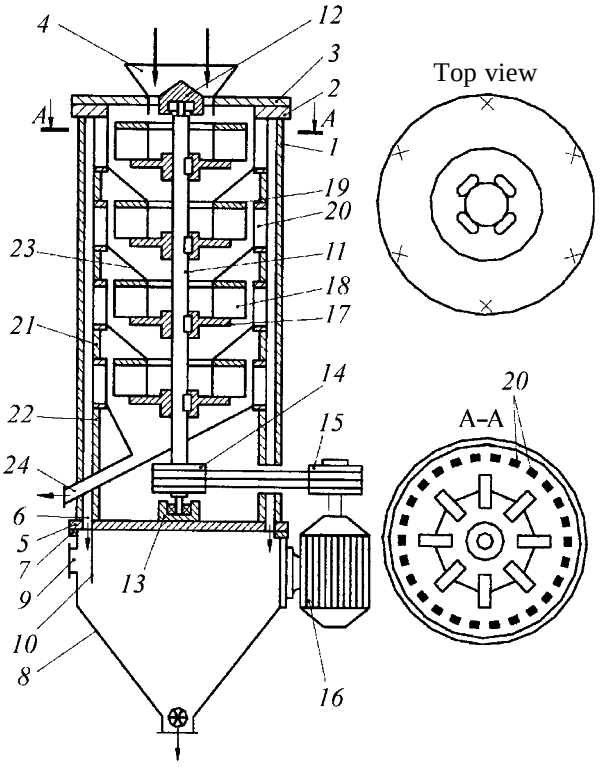

Fig. 1. Multistage rotary-centrifugal mill with flow-through classification of the material: (*1*) casing, (*2*, *7*) flanges, (*3*) cover plate, (*4*) funnel, (*5*) bottom plate, (*6*) annular slits, (*8*) bunker, (*9*) pipe, (*10*) bumper plate, (*11*) shaft, (*12*, *13*) bushing units, (*14*, *15*) pulleys, (*16*) electric motor, (*17*) discs, (*18*) blades, (*19*) rings, (*20*) baffler rods, (*21*) cylindrical collars, (*22*) bottom collar, (*23*) cones, and (*24*) pipe.

by lower content of KCl and higher content of halopelite, whereas fine grades are, conversely, characterized by high content of KCl and lower content of halopelite. It was proposed to process large-grain fractions containing increased amount of halopelite by means of halurgy, and fine fractions, by flotation, thus obtaining a high-quality concentrate. It was mentioned in the monograph [1] that, in dry grinding, the clayey admixtures having higher plasticity than salt minerals tend to accumulate in coarser fractions.

Of practical interest for the case of the potassium ore are the results obtained in tests on a pilot installation employing the dry method [5]. Based on the results obtained, the authors classed NaCl and KCl with easily milled components of the ore, and halopelite, with difficultly milled components. With the use of an installation comprising a unit for drying the material, impact mill, and air classifier, the content of halopelite in the ore can be lowered by 25–30%, with that in the clay–salt residue increasing to 40%. In the authors' opinion, this clay-salt residue can be used in various industries. To carry out investigations, a multistage rotary-centrifugal mill with continuous flow-through classification of the milled material has been developed. The mill design is shown in Fig. 1.

The mill comprises a vertical cylindrical vessel *1*, to whose upper part a cover plate *3* with a funnel *4* is attached with a flange *2*. A bottom plate *5* with annular slits *6* is attached to the lower part of the vessel. A flange *7* fixes a bunker *8* to the bottom. The bunker has on its side wall an outlet pipe *9* for air. To diminish the amount of the finely ground material carried away by air, a bumper plate *10* is mounted opposite the pipe *9*. A shaft *11* with ends fixed in bushings passes through the central part of the cylindrical casing of the mill. The upper bushing is attached to the bushing unit *12* of the upper cover *3*, and the lower, to the bushing unit *13* fixed to the bottom plate *5*. The shaft *11* is set in motion, via pulleys *14* and *15* and cone belts, by electric motor *16*. Coupling dowels and spacer sleeves fix discs *17* carrying blades *18*. The upper parts of the blades are attached to ring *19*. Baffler rods *20* with rectangular cross section are mounted opposite each disc with blades along the ring. The rods are mounted at a certain distance from one another, forming slits for passage of air and the milled material. The annular rows of rods are connected by cylindrical collars *21*. The bottom collar *22* is attached to the mill bottom *5*, so that the rings of baffler rods, collars *21* and *22*, and the shell of the casing *1* form an annular space communicating with the bunker through annular slits *6* in the bottom plate *5*. Cones *23* are mounted within the working space of the mill for delivery of the undermilled material from a higher stage to a lower one. The cone mounted below the last stage ends in a pipe *24* for removal of difficultly milled materials. A funnel *4* is attached to the upper cover for delivery of the material into the mill.

In an operating multistage rotary-centrifugal mill, the electric motor 16 sets in motion, via pulleys *14* and *15* and cone belts, the shaft *11* with discs *17* and blades *18*. The starting material is delivered into the funnel *4* and, passing through the annular slits in the upper cover plate, arrives at the upper disc *17* wherefrom its is thrown by blades *18* toward the baffler rods *20* at a high velocity. Upon impact on the rods, the material is crushed and its fine particles are carried by the air flow through slits between the rods into the annular space, and then move down within this space into the bunker. Coarse particles move down and,

passing through the cone *23*, arrive at the center of an underlying disc where additional comminution of the material occurs. Then the process is repeated. After the last stage, only those particles of the material remain which are difficultly milled, and these particles move within the cone and, further, through the pipe *24* out of the mill. Thus, there are no stagnant zones in the mill, accumulation of the material is ruled out, and the comminution process occurs repeatedly. It is the most appropriate to use this mill to carry out selective comminution based on the unequal extents of grinding of strong and soft rocks. Depending on physicomechanical properties of the minerals constituting the initial lumps, a certain degree of material dressing can be achieved at the outlet by selecting the necessary number of comminution stages and shaft rotation rate. Those components of the material which have low strength are crushed and, passing through slits between the rods, arrive at the bunker, and undermilled particles of a material with higher strength are removed from the mill via pipe *24*.

Thus, the multistage mill of the given design furnishes wider opportunities for carrying out selective comminution of sylvinite in order to recover halopelite to a fuller extent, with the minimum content of potassium chloride in the residue.

To test the working capacity of the new design and carry out preliminary investigations, a four-stage mill of this type with working wheel diameter (measured across the blade ends) of 400 mm was fabricated. The investigation demonstrated that this mill design can be used for selective comminution of multicomponent materials with different strengths of separate constituents. Preliminary studies revealed that the content of halopelite in enriched milled ore, and also the content of KCl and NaCl in the halopelite residue are affected by numerous factors, such as moisture content of the ore, speed of rotor rotation, width of slits between the baffler rods, number of stages in the mill, output capacity in terms of the starting ore, etc. Further, a single-stage mill with stage dimensions equal to those in the multistage mill was used. The unmilled residue, discharged from the bottom part of the mill, was again fed into the mill a necessary number of times. After each passage of the material through the mill, the amount of milled material, unmilled residue, and the content of halopelite in both of the flows were measured. The content of halopelite in the ore was determined by weighing the dry residue after dissolving an ore sample in water three times in succession. A 100-g portion of the ore was placed in a vessel and poured over with 1 l of water. The dissolution was

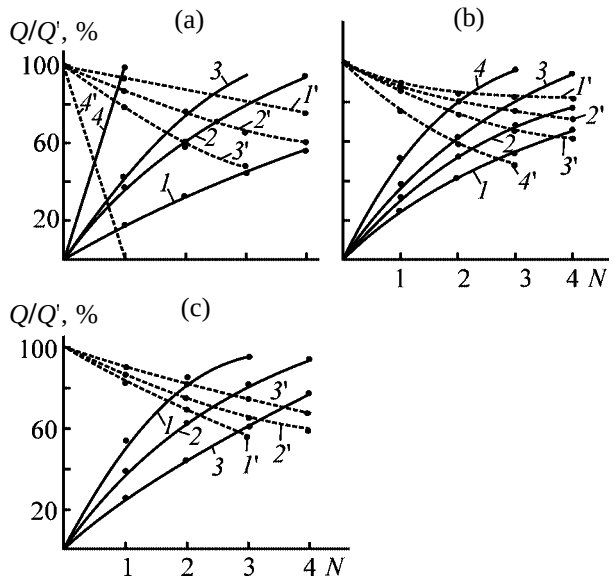

Fig. 2. Variation over stages *N* of (*1*–*4*) the amount *Q* of milled ore and (*1'*–*4'*) that of halopelite in the residue. (a) G = 960 kg h^{-1}, δ = 3 mm; (b) G = 960 kg h^{-1}, n = 1033 pm; and (c) n = 1033 rpm, δ = 3 mm. (a) Speed of rotor rotation, n (rpm): (*1*, *1'*) 710, (*2*, *2'*) 1033, (*3*, *3'*) 1500, and (*4*, *4'*) 3100. (b) Slit width between the rods, δ (mm): (*1*, *1'*) 1, (*2*, *2'*) 2, (*3*, *3'*) 3, and (*4*, *4'*) 4. (*c*) Load on the mill, G (kg h^{-1}): (*1*, *1'*) 480, (*2*, *2'*) 960, and (*3*, *3'*) 1030.

done under vigorous stirring, the sample was allowed to stay for 24 h, and then the aqueous salt solution was decanted. The procedure was repeated two times more, after which the insoluble residue was dried and weighed.

It should be noted that the content of halopelite in several samples taken from a small batch of sylvinite ore differed widely, and, therefore, three samples of each of the starting and milled ore and undermilled residue were taken. In data processing, the results of analysis were averaged over three samples. The experiments demonstrated that recovery of halopelite from the sylvinite ore by selective comminution can only be achieved at its moisture content not exceeding 1%. At moisture content of the ore exceeding 5%, no selective grinding of the ore was observed at all. Therefore, in further experiments, the ore was dried to moisture content of less than 1% and stored prior to experiments in tightly sealed polyethylene bags.

The principal results of the study are shown in Figs. 2a–2c. The solid lines represent the increase in the amount of milled ore (in percent of the initial amount) on its successive passage through the four stages of the mill, and the dashed lines show the decrease in the amount of halopelite (in percent of the initial amount) in the unmilled residue.

Figure 2a shows the results of experiments carried out at different rates of rotor rotation. The load on the mill in terms of the starting ore was 960 kg h^{-1}, and the spacing between the baffler rods, 3 mm. It can be seen that the largest amount of milled ore is removed from the mill in the first and second stages. This is due to the fact that the starting ore, mined with a plough machine and subjected to preliminary crushing, contains a large amount of the fine fraction, which is removed from the grinding zone in the first and second stages of the pilot mill. It can also be seen from Fig. 2a that the rotation speed of the rotor, n = 3100 rpm, which corresponds to a circumferential velocity of the blade ends of 65 m s^{-1}, is unacceptable since the ore comminution, including that of the difficultly milled halopelite, is complete already in the first stage (lines *4* and *4*'). At the same time, at n = 710 rpm, which corresponds to a circumferential velocity of blade ends of 15 m s^{-1}, the ore comminution is incomplete, and, even after the fourth stage, about 40% of the ore is removed from the mill in the form of an unmilled residue, which is economically and environmentally unacceptable. Thus, the acceptable circumferential velocity of blade ends in the rotary-centrifugal mill must be 20–30 m s^{-1}.

The influence exerted by the slits between the baffler rods on the degree of comminution was studied with the slit width varied between 1 and 4 mm. The granulometric composition of the grinding products was determined by sieving. Experiments demonstrated that the comminution product is composed of particles less than 3 mm in size at slit width δ = 4 mm, less than 2.2 mm at δ = 2 mm, and less than 0.6 mm at δ = 1 mm. Figure 2b shows the results of ore comminution for varied number of stages at different widths of slits between the baffler rods. For example, virtually complete ore comminution occurred in three stages at slit width δ = 4 mm. However, a considerable amount (>50%) of halopelite passed into the milled ore (curve *4*). At the same time, at slit widths of 1, and even 2 mm (curves *1* and *2*), the entire amount of the ore could be ground finely on passing four stages, and its considerable part (20 to 40%) was removed from the mill in the form of an unmilled residue. It should be noted that the major part of halopelite (curves *1*' and *2*') also remained in the unmilled part of the ore. The results presented in Fig. 2b demonstrate that, with account of the requirements to the granulometric composition of the ore delivered to flotation, the optimal width of slits between the baffler rods must be 3–3.5 mm.

The effect of the rate of supplying the starting ore, G, on the degree of its comminution over stages of the rotary-centrifugal mill can be seen from Fig. 2c, which shows for the same G how the content of halopelite in the residue decreases after multistage comminution. It follows from the figure that the optimal G value for the given mill dimensions is about 100 kg h^{-1}. In the pilot mill, the height of baffler rods was 70 mm. If these rods are made longer, the throughput will, naturally, increase. For industrial implementation of the mill, it is necessary to carry out industrial tests of a mill of similar design with output capacity of 8–10 t h^{-1}.

CONCLUSION

The study performed demonstrated that a multistage rotary-centrifugal mill can be successfully used instead of a rod mill in flotation manufacture of potassium fertilizers. In the process, more than half of the halopelite contained will be removed from the ore, which will markedly improve the flotation. In addition, impact comminution of the material in the given mill yields a much smaller amount of overmilled ore, which also exerts positive influence on the flotation process.

REFERENCES

1. Aleksandrovich, Kh.M. and Mozheiko, F.F., *Fizikokhimiya selektivnoi flotatsii kaliinykh solei* (Physical Chemistry of the Selective Flotation of Potassium Salts), Minsk: Nauka i Tekhnika, 1983.
2. Kashkanov, O.D. and Sokolov, I.D., *Tekhnologiya kaliinykh udobrenii* (Technology of Potassium Fertilizers), Leningrad: Khimiya, 1978.
3. *Tekhnologiya kaliinykh udobrenii* (Technology of Potassium Fertilizers), Pechkovskii, V.V., Ed., Minsk: Vysheisha Shkola, 1978.
4. *Galurgiya* (Halurgy), Sokolov, I.D., Ed., Leningrad: Khimiya, 1983.
5. Sapeshko, V.V., Nitsenko, V.I., and Tyurikov, V.F., Abstracts of Papers, *Mezhdunarodnaya nauchno-tekhnicheskaya konferentsiya "Resurso- i energosberegayushchie tekhnologii v khimicheskoi promyshlennosti i proizvodstve stroitel'nykh materialov"* (Int. Scientific and Technical Conf. "Resource- and Energy-Saving Technologies in Chemical Industry and in Manufacture of Building Materials," Minsk: Bel. Gos. Tekh. Univ., November 9–10, 2000.
6. Levdanskii, A.E. and Levdanskii, E.I., *Vysokoeffektivnye protochnye protsessy i apparaty* (High-Performance Flow-through Processes and Apparatus), Minsk: Bel. Gos. Tekh. Univ., 2001.

Russian Journal of Applied Chemistry, Vol. 75, No. 11, 2002, pp. 1849–1851. Translated from Zhurnal Prikladnoi Khimii, Vol. 75, No. 11, 2002, pp. 1885–1888.
Original Russian Text Copyright © 2002 by Zhilin, Ilyushin, Tselinskii, Kozlov, Kuz'mina.

ORGANIC SYNTHESIS AND INDUSTRIAL ORGANIC CHEMISTRY

Synthesis and Properties of Tetraamminebis(1-methyl-5-aminotetrazole-N^3, N^4)cobalt(III) Perchlorate

A. Yu. Zhilin, M. A. Ilyushin, I. V. Tselinskii, A. S. Kozlov, and N. E. Kuz'mina

St. Petersburg State Technological Institute, St. Petersburg, Russia
Kurnakov Institute of General and Inorganic Chemistry, Russian Academy of Sciences, Moscow, Russia

Received April 10, 2002

Abstract—Physicochemical and explosive properties of tetraamminebis(1-methyl-5-aminotetrazole-N^3, N^4) cobalt(III) perchlorate were studied. The possibility of using this compound as priming charge was demonstrated.

Previously we showed [1] that high-energy-capacity tetraammine-*cis*-bis(5-nitro-2*H*-tetrazolato-N^2)-cobalt(III) perchlorate (**I**) can be used instead of conventional primers in priming charges (PC). At present complex **I** is used in missile manufacture and mining industry. In this work we prepared and characterized tetraamminebis(1-methyl-5-aminotetrazole-N^3, N^4)cobalt(III) perchlorate (**II**) which has a combustion–detonation transition. The structure of this complex is similar to that of **I**. We studied structural features and detonating properties of **II**.

EXPERIMENTAL

Complex **II** was prepared as follows:

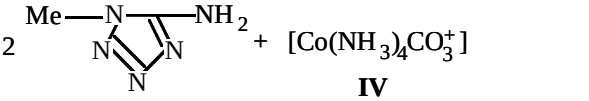

III **IV**

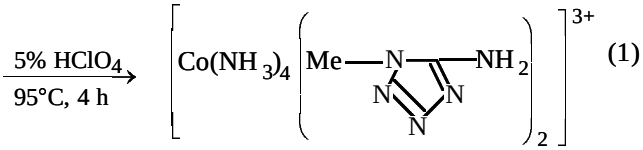

(1)

II

Carbonatotetraamminecobalt(III) perchlorate (IV) was prepared by the procedure in [2]. The yield of the dried compound was 77%. IR, cm^{-1}: 1596 s, 1560 m (C=O, NH_3), 1084 s (ClO_4). ^1H NMR (DMSO-d_6), δ, ppm: 4.40 (12 H, NH3).

Found, %: C 4.6, H 4.7, N 20.1
$CH_{12}ClCoN_4O_7$
Calculated, %: C 4.2, H 4.2, N 19.6

Tetraamminebis(1-methyl-5-aminotetrazole-N^3, N^4)cobalt(III) perchlorate (II). A solution of **IV** (0.5 g) in 5% perchloric acid (10 ml) was filtered. To the filtrate 1-methyl-5-aminotetrazole (**III**) prepared by the procedure in [3] was added. The reaction mixture was heated on a boiling water bath for 4 h and cooled to 15°C. The precipitate was filtered off, washed with ethanol (2 × 5 ml), and recrystallized from 1% perchloric acid. Yield 58%. IR, cm^{-1}: 3316 m, 1334 m 9NH_3, Tz), 1118 m (ClO_4), 1628 m (C=N), 3236 w, 1616 w (NH_2), 2830 w (CH_3). ^1H NMR (DMSO-d_6), δ, ppm: 3.85, 3.90 [9H, NH_3(*eq*)], 3.75, 3.80 [3H, NH_3(*ax*)], 7.12 [2H, NH_2-Tz(ax)], 7.52 [2H, NH_2-Tz(*eq*), 4.03 [3H, CH_3-Tz(*ax*)], 4.22 [3H, CH_3-Tz(*eq*)].

Found, %: C 7.8, H 3.3, N 31.9
$C_4H_{22}Cl_3CoN_{14}O_{12}$
Calculated, %: C 7.7, H 3.6, N 31.5

The IR spectrum of **II** in the form of thin film or Nujol mull was recorded on a Perkin–Elmer M-457 spectrometer; the electronic absorption spectrum was recorded on a Perkin–Elmer LAMBDA 40 spectrometer; the ^1H NMR spectra were recorded in DMSO-d_6 solution on a Bruker AC (300 MHz) spectrometer using hexamethyldisiloxane as internal reference.

Synthesis of **II** was monitored by thin-layer chromatography on Silufol UV-254 plates using 3% sodium perchlorate solution as the eluent.

Thermal gravimetric analysis was performed on an MOM derivatograph (Hungary) in the range 20–500°C with the heating rate of 5 deg min^{-1}. The onset temperature of intense decomposition T_0 was determined on a thermograph at the heating rate of

1070-4272/02/7511-1849$27.00 © 2002 MAIK "Nauka/Interperiodica"

5.3 deg min^{-1}. The sensitivity to shock and fire beam of fuse (SF) was determined by the pile-driving procedure performed in accordance with GOST (State Standard) 1944–80 and OST (Branch Standard) V-84-8892–72, respectively. The minimal primer charge (MPC) of the complexes was determined with respect to hexogen in the bulk of detonating cap (DC) no. 8 (compaction pressures P_p of the compound and hexogen were 121 and 363 kg cm^{-2}, respectively).

The X-ray reflection intensities were collected at room temperature on an Enraf–Nonius CAD-4 automatic diffractometer (graphite monochromator, MoK_α radiation, θ scanning, θ_{max} = 28°). A total of 5268 reflections were registered. The structural parameters were determined and refined using 3222 reflections with $I > 2\sigma(I)$. The calculations were performed with the aid of Shelx-93 software.

The structure of **II** was solved by the direct method and refined by the full-matrix least-squares techniques. Nonhydrogen atoms were refined anisotropically. Hydrogen atoms were located by difference maps and refined with the same thermal parameter (3.948 $Å^2$). The maximal and minimal densities of free electrons on the last *F* map were 0.92 and –0.77 e/$Å^3$, respectively. The structure was refined to *R* 0.048, R_w 0.136, and GOOF 1.119.

Complex **II** is a golden yellow powder soluble in water, DMSO, and DMF and poorly soluble in ethanol, isopropanol, and isobutanol. The physicochemical and explosion properties of **II** as as follows: density ρ_{exp} = 1.90 g cm^{-3}, detonation rate D^0_{calc} = 7.5 km s^{-1}, T_o 234°C, SF (the lower limit of 100% ignition) 2.0 cm, MPC 0.15 g, sensitivity to shock (height 25 cm, load 2 kg, weighted portion of the sample 20 mg) 8%.

To estimate the detonation rate of **II**, a molecule of the complex was separated into the active (perchlorate anion and ligands) and inert (metal cation) parts. The calculation was performed using increments of the structural fragments. The average error was ±140 m s^{-1} [4].

The study of thermolysis of **II** under dynamic conditions at a heating rate of 5 deg min^{-1} showed that this complex is relatively stable thermally (T_o > 230°C). The first step of thermolysis of Co(III) tetraamminetetrazolates is elimination of coordinated ammonia molecule with subsequent decomposition of the residual complex. Then tetrazole ligands are oxidized stepwise with perchlorate counterions [5]. In the case of complex **II**, all the steps overlap in time, and the thermogram contains a single exothermic peak with a maximum at 289°C. The kinetic parameters of thermolysis at T_o were calculated from the results of differential termogravimetry (DTG) and differential thermal analysis (DTA). The preexponential factor of the Arrhenius equation, activation energy (kJ mol^{-1}), and the reaction order are 18.5, 218.3, and 1.0, respectively. The first reaction order indicates that diffusion is not the rate-determining step of the degradation.

The IR spectrum of complex **II** contains the bands of coordinated ammonia, methyl and amino groups of the tetrazole ring, and perchlorate anions. The electronic absorption spectrum of an aqueous solution of this complex is typical for this type of coordination compounds and contains the band of *d–d* ($^1T_{1g} \leftarrow {}^1A_{1g}$) transition at 466 nm ($\varepsilon$ 77 l cm^{-1} mol^{-1}). The other strong band ($^1T_{2g} \leftarrow {}^1A_{1g}$) is obscured by the absorption of the tetrazole ligand. Clearly the molecule of the complex contains the octahedral CoN_6 chromophore. In the ^{1}H NMR spectrum of **II**, the signals of equatorial (downfield) and axial (upfield) ammonia ligands are present in the range 3.5–4.0 ppm. The difference in the location of the singals of equatorial (3.85 and 3.90 ppm) and axial (3.75 and 3.80 ppm) ammonia molecules is consistent with coordination of the heterocyclic ligands via the nitrogen atoms [7]. Spitting of these signals into doublets indicates that the ammine protons are nonequivalent. This spitting is due to coordination of N^3 and N^4 nitrogen atoms of the tetrazole rings.

As determined by single crystal X-ray diffraction, complex **II** crystallizes in the monoclinic system with space group $P2_1/c$, *a* = 13.664(3), *b* = 8.054(3), *c* = 19.880(4) Å, β = 95.07(3)°, *Z* = 4, *V* = 2179.3(9) $Å^3$, *M* = 623.64, ρ_{calc} = 1.90 g cm^{-3}, μ_{Mo} = 1.242 mm^{-1}, *F*(000) 1272.0.

The atomic coordinates and equivalent isotropic thermal parameters are deposited at the Cambridge Crystallographic Data Center. The crystal structure of **II** consists of $[Co(C_2H_5N_5)_2(NH_3)_4]^{3+}$ complex cations and "free" ClO_4^- anions. The octahedral coordination environment of Co is completed by four N atoms of ammonia molecules and two N atoms of 1-methyl-5-aminotetrazole molecules A and B. Molecules A and B are in the axial and equatorial positions, respectively, with the dihedral angle between the planes of the tetrazole rings being 60.2° (Fig. 1). It should be noted that the heterocyclic ligands are coordinated via different nitrogen atoms (N^3 and N^4), whereas in complexes containing several tetrazole molecules these ligands are usually coordinated by similar nitrogen atoms {e.g. complex **I** [8], [pentakis-(1-phenyltetrazole-N^4)-tetrafluoroborato]copper(II) [9]}. The CoN_6 octahedron is virtually undistorted:

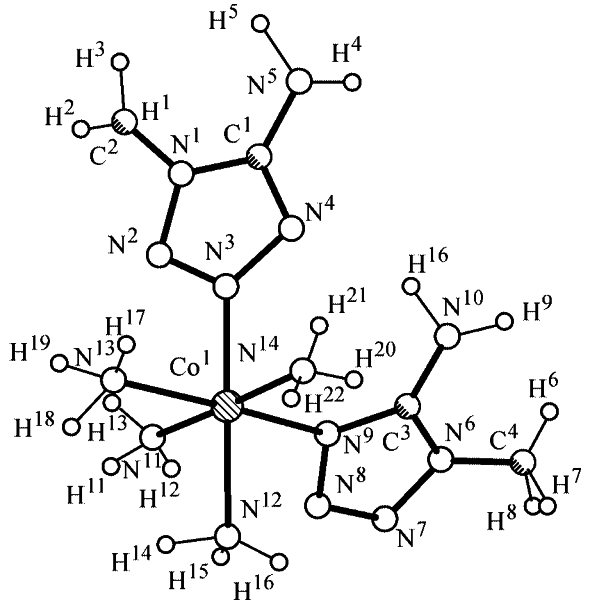

Fig. 1. Molecular structure of the $[Co(C_2H_5N_5)_2(NH_3)_4]^{3+}$ complex cation.

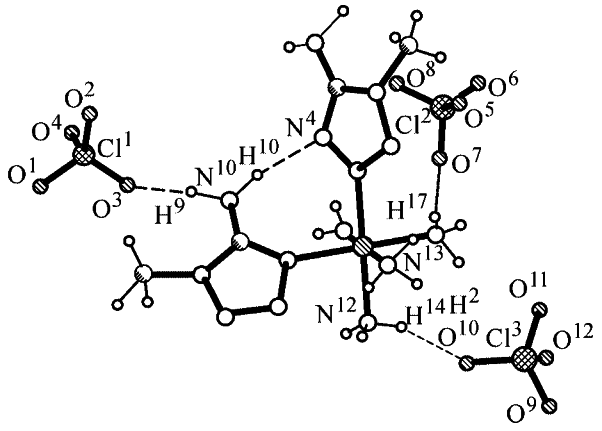

Fig. 2. Hydrogen bonding in the crystal structure of **II**.

the average deviation of nitrogen and cobalt atoms form the equatorial plane is 0.008 Å. The N^3N^{12} axial axis forms an 88.5° angle with this plane. The Co–N distances range from 1.929 to 1.9717 Å. The distance between Co and N^9 atom of the equatorial tetrazole ligand is the longest, and the distance between Co and N^3 of the axial tetrazole ligand is the shortest.

The tetrazole rings of the organic ligands are planar [the average deviation of the atoms form the least-squares plane in molecules A and B is 0.056 and 0.034 Å, respectively]. The interatomic distances and angles in molecules A and B are similar. The main differences are due to different orientation of the NH_2 groups and their hydrogen bonding. The amino group in molecule A is turned relative to the plane of the heterocyclic ring by 28.1°. The N^5 atom is in the flattened pyramidal surrounding (the sum of the bond angles at this atom is 344.1°) and does not form hydrogen bonds (Fig. 2). The NH_2 group of molecule B is almost coplanar with the plane of the heterocyclic ring. It is turned relative to the plane by 7.1°. The N^{10} atom is in trigonal planar surrounding (the sum of bond angles at this atom is 354.7°) and forms H bonds with the N atom of the heterocyclic ring of molecule A and ClO_4^- anion.

Coordinated ammonia molecules are nonequivalent: two of them form weak hydrogen bonds with ClO_4^- anion and two other do not (Fig. 2).

The perchlorate anions in the structure of **II** have typical interatomic distances and angles [10]. High thermal parameters of O atoms of these uncoordinated anions indicate their high mobility.

CONCLUSIONS

(1) 1-Methyl-5-aminotetrazole reacts with Co(III) tetraamminate in perchloric acid to form tetraammine-bis(1-methyl-5-aminotetrazole-N^3,N^4)cobalt(III) perchlorate. The heterocylic ligands are coordinated with the Co atom via different nitrogen atoms and occupy axial and equatorial positions in the coordination sphere.

(2) This complex shows promise as priming explosive which can be used in safe priming facilities operating from an incandescence bridge.

REFERENCES

1. Zhilin, A.Yu., Ilyushin, M.A., Tselinskii, I.V., and Brykov, A.S., *Zh. Prikl. Khim.*, 2001, vol. 74, no. 1, pp. 96–99.
2. Novakovskii, M.S., *Laboratornye raboty po khimii kompleksnykh soedinenii* (Practical Course of Coordination Chemistry), Kharkov: Khar'kov. Univ., 1972.
3. Henry, R.A. and Finnegan, W.C., *J. Am. Chem. Soc.*, 1954, vol. 76, no. 3, pp. 923–926.
4. Ilushin, M.A., Smirnov, A.V., Kotomin, A.A., and Tselynsky, I.V., *Hanneng Cailiao* (Energ. Mater.), 1994, vol. 2, no. 1, pp. 16–20.
5. Zhilin, A.Yu., Ilyushin, M.A., and Tselinskii, I.V., *Zh. Obshch. Khim.*, 2001, vol. 71, no. 5, pp. 710–713.
6. Fronabarger, J., Schuman, A., Chapman, R.D., *et al.*, *AIAA Pap.*, 1995, no. 2858, pp. 1–7.
7. Sheng, D., Ma, F., Sun, F., and Lu, Q., *Hanneng Cailiao* (Energ. Mater.), 2000, vol. 8, no. 3, pp. 100–103.
8. Morosin, B., Dunn, R.G., Assink, *et al.*, *Acta Crystallogr., Sect. C*, 1997, vol. 53, pp. 1609–1611.
9. Palkina, K.K., Kuz'mina, N.E., Lyakhov, A.S., *et al.*, *Zh. Neorg. Khim.*, 2001, vol. 46, no. 10, pp. 1649–1654.
10. Allen, F.H., Kennard, O., and Watson, D.G., *J. Chem. Soc., Perkin Trans. 2*, 1987, suppl. pp. 1–19.

Russian Journal of Applied Chemistry, Vol. 75, No. 11, 2002, pp. 1852–1854. Translated from Zhurnal Prikladnoi Khimii, Vol. 75, No. 11, 2002, pp. 1889–1891.
Original Russian Text Copyright © 2002 by Udarov, Klyuev, Bei, Yuvchenko, Prokopchuk.

ORGANIC SYNTHESIS AND INDUSTRIAL ORGANIC CHEMISTRY

Gas-Chromatographic Analysis of Terpenoid–Maleic Adducts

B. G. Udarov, A. Yu. Klyuev, M. P. Bei, A. P. Yuvchenko, and N. R. Prokopchuk

Institute of New Materials, National Academy of Sciences of Belarus, Minsk, Belarus
Belarussian State Technological University, Minsk, Belarus

Received April 4, 2002

Abstract—Conditions were found for separation of a mixture of terpenoid–maleic adducts and maleic adduct of resin acids in the form of methyl esters by gas–liquid chromatography.

Terpenoid–maleic adducts (TMAs) prepared by the reaction of terpenoids with maleic anhydride, and also their derivatives (esters, imides, heavy metal salts) are used in electrical, paint-and-varnish, rubber, and pulp-and-paper industries [1]. TMAs are complex multicomponent mixtures whose composition is determined by the raw material and preparation conditions [2]. Group analysis of TMAs by physicochemical methods is difficult and labor-consuming. The use of a quicker analytical method, gas–liquid chromatography (GLC), for the analysis of TMAs was limited to chromatography of methyl esters of terpene–maleic adducts [3]; we found no data on the conditions for separation of TMAs containing, along with terpene–maleic adducts, also the resin acid adduct.

The goal of this study was to find conditions for GLC separation of a mixture of terpene–maleic adducts and the maleic adduct of resin acids (in the form of methyl esters).

EXPERIMENTAL

The procedure for preparing dimethyl esters of terpene–maleic adducts [3] is labor-consuming and involves synthesis and use of diazomethane, which is toxic and dangerously explosive [4]. With the aim to eliminate the use of diazomethane, we methylated adducts **I**–**III** by thermolysis of the tetramethylammonium salts of the adducts in the chromatograph vaporizer [5]:

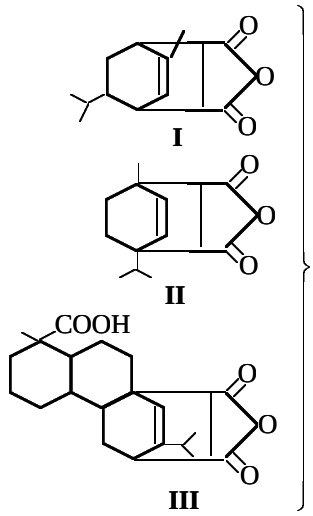

$$+\ n[(CH_3)_4N]OH \xrightarrow{60^\circ C} R[COON(CH_3)_4]_n + n\,H_2O,$$

$$R[COON(CH_3)_4]_n \xrightarrow{250^\circ C} R(COOCH_3)_n + nCH_3)_3N,$$

where n = 2 (**I**, **II**), 3 (**III**); R is the hydrocarbon fragment of the adduct.

The methylation procedure proposed (method 1) involves titration of a sample of **I**–**III** (0.2 ml of a 10% alcoholic solution) with a 3% aqueous solution of tetramethylammonium hydroxide [5] in the presence of phenolphthalein (a drop of 0.1% alcoholic solution) at 60–70°C until appearance of stable pink

1070-4272/02/7511-1852$27.00 © 2002 MAIK "Nauka/Interperiodica"

color. The resulting solution was evaporated almost to dryness, and the residue was dissolved in alcohol (volume ratio from 1 : 1 to 1 : 3) and injected into the chromatograph vaporizer with a microsyringe (0.5 to 1.5 μl).

Compounds **I**–**III** were also methylated with diazomethane (method 2) [6]. A three-necked flask equipped with a dropping funnel, a reflux condenser, and a capillary for feeding inert gas (nitrogen) was charged with 8.4 g of KOH, 2.8 ml of hydrazine hydrate, and 30 ml of methanol; 10 ml of chloroform was placed in the dropping funnel. The flask was deaerated by passing nitrogen at a rate of 20 ml min^{-1}, with the gas outlet through the reflux condenser. After that, the outgoing gas from the flask was fed to a bubbler (25 ml) containing 0.2 g of **I**–**III** in 10 ml of ether–methanol (9 : 1 by volume). Chloroform was added dropwise from the dropping funnel. The evolving diazomethane was transferred with a nitrogen flow to the bubbler with the sample. After the reaction completion, the solvent was removed, and 2 ml of hexane was added. The crystals were separated and used for GLC experiments; their IR spectra were measured.

According to modern views, terpene–maleic adducts prepared from turpentines contain monoadducts consisting of α-phellandrene (**I**) and α-terpinene (**II**) adducts [7].[1]

Maleopimaric acid **III** was prepared from pine oleoresin. Oleoresin (16 g) was dissolved in 40 ml of hexane and kept at 2–3°C for 18 h, after which the solution was separated from the precipitated oxidized substances by decanting. The solution of resin acids in hexane was saponified with 2% aqueous NaOH (100 ml), and the aqueous phase was separated with a separatory funnel. Then the aqueous phase was acidified with 40 ml of 12.5% aqueous acetic acid, and the released acids were extracted with hexane (2 × 30 ml). The extract was dried over $CaCl_2$, and a solution of freshly distilled maleic anhydride (1.6 g) in acetone (2.5 ml) was added dropwise at 45–50°C over a period of 10 min. The mixture was stirred at 45–50°C for 4 h. The precipitated maleopimaric acid was washed with hexane (3 × 30 ml) and hot (60–70°C) water (4 × 125 ml) and dried in a vacuum desiccator over $CaCl_2$. The melting point of maleopimaric acid obtained was 224.5°C.

The IR spectra of adducts **I**–**III** (KBr, UR-20 spectrometer) contained absorption bands at 1784 and 1855 cm^{-1}, characteristic of carbonyl groups of maleic anhydride. The absence of these bands in the spectra of methyl esters of **I**–**III** and appearance of a band at 1750 cm^{-1}, characteristic of the ester carbonyl group, indicate that method 2 ensures exhaustive methylation of **I**–**III**.

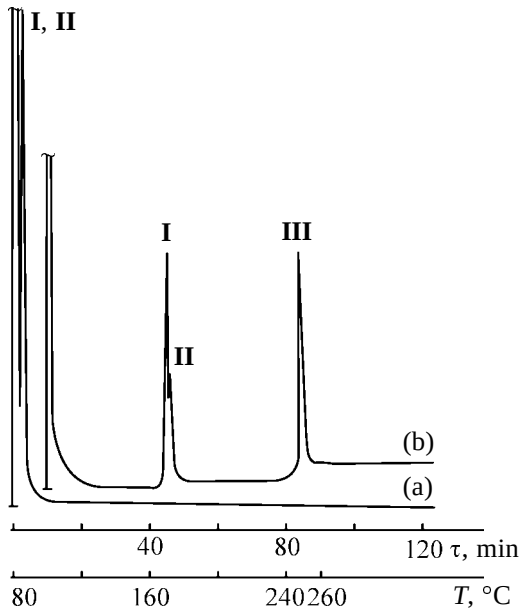

Fig. 1. GLC separation of a mixture of **I**–**III** methylated by method 1: (τ) time and (*T*) temperature; the same for Fig. 2. (a) Isothermal mode, column temperature 190°C, vaporizer temperature 245 ± 5°C, linear velocity of carrier gas (nitrogen) 11 cm s^{-1}; (b) programmed heating from 80 to 260°C at a rate of 2 deg min^{-1}.

GLC separation of **I**–**III** was performed with an LKhM-8MD-5 chromatograph equipped with a flame ionization detector; a stainless steel column (1000 mm long, 3 mm i.d.) was packed with Chromaton N-AW-DMCS + 5 wt % XE-60. With other high-temperature liquid phases (Apiezon L, Apiezon N, E-301, SE-30), separation of methyl esters of **I**–**III** was worse.

The column and vaporizer temperatures were chosen taking into account the fact that methyl esters of **I**–**III** and resin acid adducts tend to decompose at column temperatures higher than 190°C and vaporizer temperatures higher than 215°C [8, 9].

It should be noted that, in separation of methyl esters prepared by thermolysis of tetramethylammonium salts, the vaporizer temperature should be higher, 250°C [5].

Figures 1 and 2 show the chromatograms of the methyl esters of **I**–**III** obtained by methods 1 and 2, respectively.

[1] Samples of α-phellandrene and α-terpinene adducts were kindly submitted by A.I. Pronevich (Belarussian State Technological University).

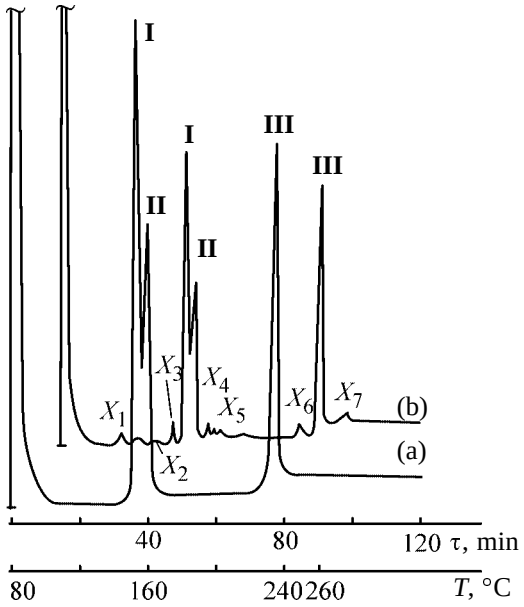

Fig. 2. GLC separation of a mixture of **I**–**III** methylated by method 2. Vaporizer temperature, °C: (a) 210 ± 5 and (b) 245 ± 5. (X_1–X_7) Peaks of decomposition products.

As seen from Fig. 1a, at a column temperature of 190°C in the isothermal mode the dimethyl esters of **I** and **II** are not separated, and the peak of the trimethyl ester of **III** is lacking. Programmed heating from 80 to 260°C at a rate of 2 deg min^{-1} and vaporizer temperature of 245 ± 5°C allowed satisfactory separation of **I** and **II** and elution of **III** as a narrow peak (Fig. 1b). These conditions ensure decomposition of tetramethylammonium salts of **I**–**III** and formation of the methyl esters without their subsequent thermolysis.

As seen from Fig. 2a, separation of a mixture of **I**–**III** methylated by method 2 should be performed at the vaporizer temperature of 210 ± 5°C, since at 245 ± 5°C (Fig. 2b) peaks of decomposition products X_1–X_7 appear in the chromatogram. The chromatograms of mixtures of **I**–**III** methylated by methods 2 (Fig. 2a) and 1 (Fig. 1b) were identical.

CONCLUSION

Conditions were found for separation by gas–liquid chromatography of not only dimethyl, but also trimethyl esters of adducts, with these esters being prepared without using diazomethane. The separation procedure proposed can be used for developing and optimizing processes of production of new terpene–maleic adducts, for revealing relationships between their composition and physicochemical properties, and for studying the mechanism of thermal degradation of terpene–maleic adducts by analysis of their decomposition products.

REFERENCES

1. Klyuev, Yu.P., Klyuev, A.Yu., Shlyashinskii, R.G., and Antonovich, I.V., *Izv. Vyssh. Uchebn. Zaved., Lesn. Zh.*, 1998, no. 5, pp. 107–116.
2. Klyuev, A.Yu., Shlyashinskii, R.G., Titov, A.I., and Antonovich, I.V., *Zh. Prikl. Khim.*, 1997, vol. 69, no. 3, pp. 2056–2060.
3. Lamotkin, A.I., But'ko, T.A., and Turuk, G.S., *Gidrolizn. Lesokhim. Prom–st.*, 1993, vol. 1, pp. 10–11.
4. Becker, H., Berger, W., Domschke, G., *et al.*, *Organikum: Organisch-chemisches Grundpraktikum*, Berlin: Wissenschaften, 1976.
5. Bardyshev, I.I., Bulgakov, A.N., and Udarov, B.G., *Vestsi Akad. Navuk Bel. SSR, Ser. Khim. Navuk*, 1970, vol. 6, pp. 102–104.
6. Standinger, H. and Kupfer, O., *Ber.*, 1912, vol. 45, pp. 501–509.
7. Pronevich, A.N., Preparation, Properties, and Use of Terpene–Maleic Resins, *Cand. Sci. Dissertation*, Minsk, 1999.
8. Lamotkin, A.I., But'ko, T.A., Pronevich, A.N., and Kalennikova, S.I., *Khim. Drev.*, 1991, vol. 1, pp. 109–112.
9. Medyantsev, V.E., Bokov, Yu.P., and Vyakhirov, D.A., *Khim. Drev.*, 1978, vol. 6, pp. 91–95.

Russian Journal of Applied Chemistry, Vol. 75, No. 11, 2002, pp. 1855–1858. Translated from Zhurnal Prikladnoi Khimii, Vol. 75, No. 11, 2002, pp. 1892–1895.
Original Russian Text Copyright © 2002 by Kurenkov, Khabibullina, Zaitseva.

MACROMOLECULAR CHEMISTRY AND POLYMERIC MATERIALS

Radical Copolymerization of Sodium 2-Acrylamido-2-methyl-2-propanesulfonate with *N*-Vinyl-2-pyrrolidone in Water and Aqueous Salt Solutions

V. F. Kurenkov, G. Z. Khabibullina, and N. N. Zaitseva

Kazan State Technological University, Kazan, Tatarstan, Russia

Received May 30, 2002

Abstract—Features of homogeneous radical copolymerization of sodium 2-acrylamido-2-methyl-2-propanesulfonate with *N*-vinyl-2-pyrrolidone in water and aqueous NaCl solutions at pH 9 and 50°C, initiated with the redox system potassium peroxomonosulfate K_2SO_5–sodium pyrosulfite $Na_2S_2O_5$ were studied dilatometrically.

Water-soluble copolymers of salts of 2-acrylamido-2-methyl-2-propanesulfonic acid (H-AMS) with *N*-vinyl-2-pyrrolidone (N-VP) exhibit high thickening, flocculating [1], adhesive, and antistatic activity [2] and complexing power, which makes them undoubtedly promising for medicine, pharmaceutical and cosmetic industry, etc. [3–5]. Data are available on copolymerization of N-VP with sodium salts of ethylenesulfonic acid [6], *p*-styrenesulfonic acid [7], and H-AMS [7, 8]; the effect of the cation on copolymerization of N-VP with Li, Na, K [9, 10], Mg, and Ca [10, 11] salts of H-AMS in aqueous solution was considered. A set of valuable properties and insufficient knowledge of the copolymerization processes make it necessary to study systematically the features of copolymerization of H-AMS salts with N-VP in various media with the aim to prepare copolymers with controllable molecular characteristics and properties. Here we report on features of radical copolymerization of Na-AMS with N-VP in water and aqueous salt solutions.

EXPERIMENTAL

Na-AMS was prepared by neutralization of aqueous solutions of H-AMS (Lubrizol, the United Kingdom; mp 185°C) with an aqueous solution of NaOH to pH 9; N-VP (Merck, Germany) was purified by double distillation in a vacuum from KOH (0.1%); n_D^{20} 1.5119. Potassium peroxomonosulfate (PP) was purified by double recrystallization from water; the main substance content determined by redox titration was 97.8%. All the solutions were prepared in distilled water. Other chemicals were of chemically pure or analytically pure grads.

Copolymerization of Na-AMS (M_1) with N-VP (M_2) was performed in 15% aqueous solutions in the presence of the redox initiating system PP–sodium pyrosulfite (SP) ([PP] = [SP] = 7.4×10^{-5} M) at 50°C for 2 h. All the experiments were performed at pH 9 at which the system PP–SP is effective [12], the initiation rate is independent of the solution ionic strength [13], and Na-AMS [4] and N-VP [5] are not hydrolyzed.

The reaction was performed in 7 cm^3 glass dilatometers and 25 cm^3 weighing bottles. The copolymerization procedure was similar to that described in [8]. The copolymers were reprecipitated from aqueous solurtions into acetone, washed with acetone, and dried in a vacuum oven at 50°C to constant weight.

The yield of the copolymers was determined gravimetrically. The content of ionic units in the N-VP–Na-AMS copolymer

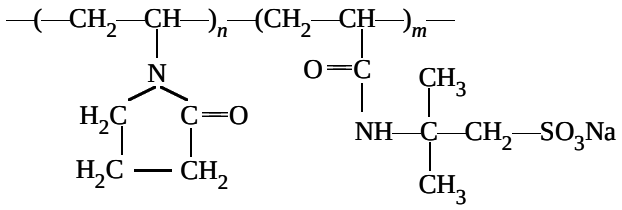

was calculated from the sulfur content determined according to [14]. The molecular weight *M* of the copolymers was evaluated from the intrinsic viscosity

1070-4272/02/7511-1855$27.00 © 2002 MAIK "Nauka/Interperiodica"

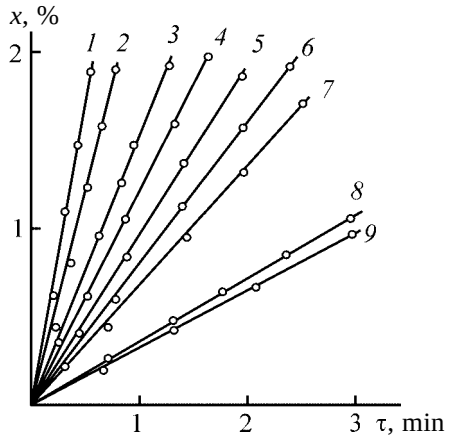

Fig. 1. Initial portions of the kinetic curves of copolymerization of Na-AMS with N-VP in 1 M NaCl at various mole fractions of Na-AMS, M_1, in the initial monomer mixture. (x) Conversion and (τ) time. M_1: (*1*) 0.5, (*2*) 0.6, (*3*) 0.4, (*4*) 0.3, (*5*) 0.2, (*6*) 0.7, (*7*) 0.8, (*8*) 0.9, and (*9*) 0.1.

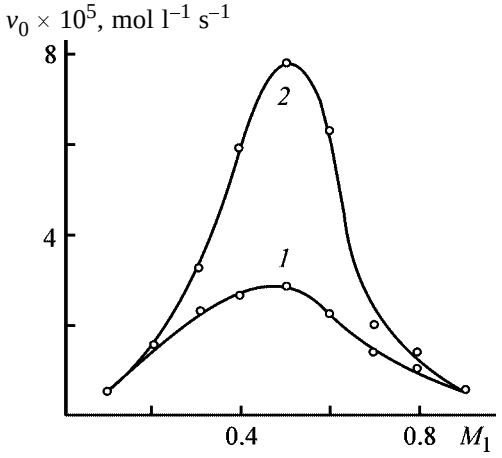

Fig. 2. Initial rate v_0 of copolymerization of Na-AMS with N-VP (*1*) in water and (*2*) in 1 M NaCl, as a function of the Na-AMS mole fraction M_1 in the initial monomer mixture.

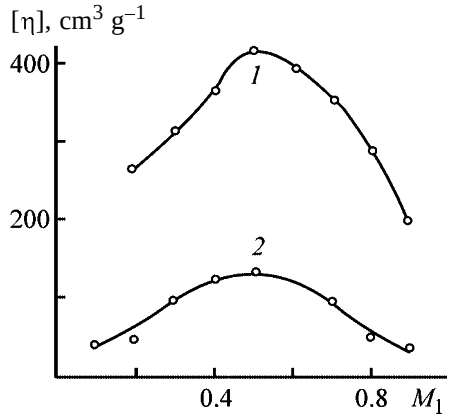

Fig. 3. Intrinsic viscosity [η] of copolymers as a function of Na-AMS mole fraction M_1 in the initial monomer mixture in copolymerization of Na-AMS with N-VP (*1*) in water and (*2*) in 1 M NaCl.

[η], determined with a VPZh-3 viscometer (d_c = 0.56 mm) by isoionic dilution in 0.5 M NaCl at 30°C.

The pH was measured with a pH-121 pH-millivoltmeter equipped with an ESL-63-07 glass working electrode and an EVL-1M3 auxiliary silver chloride electrode.

We found that, under the experimental conditions, the copolymerization of Na-AMS with N-VP occurred under homogeneous conditions, without spontaneous copolymerization. No unusual kinetic effects, characteristic of polymerization of N-VP in aqueous solutions at very high concentrations of the monomer [15], were revealed.

The effect of the composition of the initial monomeric mixture on the copolymerization was estimated at $[M_1 + M_2]$ = const and equal other conditions. Figure 1 shows as example the typical kinetic curves (dilatometric data) of the initial copolymerization stage at various compositions of the initial monomer mixture. In all the runs, the initial portions of the kinetic curves were linear, which allowed determination of the initial copolymerization rate v_0 at low conversions (x < 3%). From the data obtained, we constructed the dependences $v_0 = f(M_1)$, where M_1 is the mole fraction of Na-AMS in the initial monomer mixture (Fig. 2). As seen from Fig. 2, the dependence $v_0 = f(M_1)$ for copolymerization in both water (curve *1*) and 1 M NaCl (curve *2*) passes through a maximum.

The dependence $v_0 = f(M_1)$ is more pronounced in 1 M NaCl. The values of [η] in copolymerization in water (Fig. 3, curve *1*) and 1 M NaCl (Fig. 3, curve *2*) varied in parallel with v_0. Figures 2 and 3 show that the maximal values of v_0 and [η] are attained at the equimolar ratio of the monomers in the initial mixture ($[M_1] : [M_2] = 1 : 1$), which is nicely consistent with the data of [7, 8]. This fact confirms the occurrence of donor–acceptor interaction of Na-AMS with N-VP [16]. Comparison of the data for constant $[M_1]$ shows that, in going from water to 1 M NaCl, v_0 increases but [η] decreases (Fig. 3).

In copolymerization of Na-AMS with N-VP in water and in 1 M NaCl, the copolymer yield increases as the Na-AMS content in the initial monomer mixture is increased (see table). The table also shows that, in going from water to 1 M NaCl, the copolymer yield increases at any monomer ratio.

Figure 4 shows the dependence of the running composition of the Na-AMS–N-VP copolymer at low conversions (x < 3%) on the composition of the initial monomer mixture. For copolymerization in water, the dependence (curve *1*) corresponds to the relative activ-

ities of the monomers $r_1 < 1$ (for Na-AMS), $r_2 < 1$ (for N-VP), and $r_1 > r_2$. These data are nicely consistent with published data [7] ($r_1 = 0.66$ and $r_2 = 0.13$, $r_1 r_2 = 0.086$), confirming that the Na-AMS and N-VP units in the copolymer tend to alternate. According to Fig. 4 (curve *1*), the azeotropic composition of the copolymer is observed at the equimolar ratio of the monomers in the initial mixture ($[M_1] : [M_2] = 1 : 1$).

Comparison of data in Fig. 4 at $[M_1]$ = const shows that, in a wide range of compositions of the initial monomer mixture, the content of ionic units in the copolymer increases in going from water to 1 M NaCl (cf. curves *1* and *2*).

To explain the experimental data, let us consider the ionization equilibrium of the ionic groups in salt solutions:

$$\underset{\text{I}}{A^-X^+} \rightleftarrows \underset{\text{II}}{A^- \,||\, X^+} \rightleftarrows \underset{\text{III}}{A^- + X^+}.$$

where A^- is the anion of the monomer and macroradical; X^+ is the cation; I–III are the contact ion pairs, solvent-separated ion pairs, and free ions, respectively.

It is known that, in aqueous solutions, the sulfonate groups of the monomers and the corresponding units in the copolymers are fully ionized. The above-given ionization equilibrium is largely influenced by the ionic strength of solutions μ, which is determined by the concentration of Na-AMS in the initial mixture in the course of the copolymerization and also depends on the addition of NaCl. The reactivity of nonionic N-VP and of the corresponding propagating radical in polymerization is not affected by μ [17]. The nonisoionic conditions of Na-AMS copolymerization result in changes in the content of various ionic species of the monomer and macroradical in the reaction system. As a result, the intra- and intermolecular electrostatic interactions in the system change, causing variation of the copolymerization "constants" $r_1 = k_{11}/k_{12}$ and $r_2 = k_{22}/k_{21}$, which does not allow the copolymerization to be described by the Mayo–Lewis equation.

An increase in μ in going from water to 1 M NaCl shifted the ionization equilibrium to the left, which weakened the electrostatic repulsion between the similarly charged Na-AMS monomer and the macroradical with the terminal Na-AMS unit, and also between the fixed charges of the macromolecules. This, in turn, affected the conformational state of the propagating chains, which was indirectly confirmed by viscometric data (Fig. 5). These factors affected the reactivity of Na-AMS and its macroradical in copolymerization and resulted in increased v_0; increase in only one of

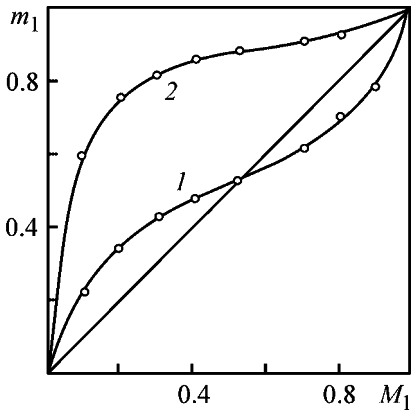

Fig. 4. Mole fraction of Na-AMS units in the copolymer, m_1, at the conversion $x < 3\%$ as a function of the Na-AMS mole fraction in the initial monomer mixture, M_1, in copolymerization of Na-AMS with N-VP (*1*) in water and (*2*) in 1 M NaCl.

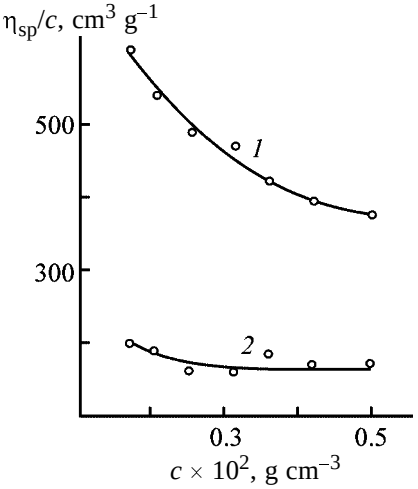

Fig. 5. Reduced viscosity η_{sp}/c of Na-AMS–N-VP copolymer as a function of copolymer concentration c (*1*) in water and (*2*) in 1 M NaCl. $[\eta] = 49$ cm^3 g^{-1}; content of Na-AMS units 34 mol %; $T = 30$°C.

Yield of Na-AMS–N-VP copolymer in copolymerization in various media as a function of the Na-AMS mole fraction M_1 in the initial monomer mixture

M_1	Copolymer yield	
	in water	in 1 M NaCl
0.1	36	64
0.2	47	71
0.3	60	68
0.5	70	98
0.6	70	–
0.7	–	96
0.8	87	98

the four elementary rate constants of chain propagation, k_{11}, describing addition of Na-AMS to the macroradial with the terminal Na-AMS unit, is apparently responsible for the increased content of the ionic units in the copolymer prepared in NaCl solution.

CONCLUSIONS

(1) In radical copolymerization of sodium 2-acrylamido-2-methyl-2-propanesulfonate with *N*-vinyl-2-pyrrolidone in water and 1 M NaCl, v_0 and [η] of the copolymer as functions of the $[M_1] : [M_2]$ ratio pass through a maximum at the equimolar ratio.

(2) The copolymer yield grows with increasing $[M_1] : [M_2]$ (both in water and in 1 M NaCl) and in going from water to 1 M NaCl.

(3) In going from water to 1 M NaCl, v_0 increases but [η] of the copolymer decreases.

REFERENCES

1. Kurenkov, V.F., Sharapova, Z.F., and Khairullin, M.R., *Zh. Prikl. Khim.*, 1999, vol. 72, no. 8, pp. 1374–1378.
2. Shevtsova, S.A., Zaitseva, O.A., and Kurenkov, V.F., *Vestn. Kazan. Tekhnol. Univ.*, 2000, nos. 1–2, pp. 126–128.
3. Lisovtsev, V.V., Rostokin, G.A., and Kulikova, A.E., *Khimicheskaya promyshlennost'. Akrilaty i polivinilkhlorid* (Chemical Industry. Acrylates and Polyvinyl Chloride), Moscow: NIITEKhIM, 1984, pp. 1–20.
4. *2-Acrylamido-2-Methylpropane Sulfonic Acid Monomer*, Wickliffe, Ohio (the United States): Lubrizol, 1994.
5. Sidel'kovskaya, F.P., *Khimiya N-vinilpirrolidona i ego polimerov* (Chemistry of *N*-Vinylpyrrolidone and Its Polymers), Moscow: Nauka, 1970.
6. Kutner, A. and Breslow, D.S., *J. Polym. Sci.*, 1959, vol. 38, no. 133, pp. 274–275.
7. Schulz, D.N., Kitano, K., Danik, J.A., and Kaladas, J.J., *Polym. Mater. Sci. Eng.*, 1987, vol. 57, pp. 149–153.
8. Kurenkov, V.F., Sirotkin, R.O., Beryachkova, E.A., and Khairullin, M.R., *Zh. Prikl. Khim.*, 1999, vol. 72, no. 8, pp. 1533–1537.
9. Kurenkov, V.F., Zaitseva, O.A., and Karyagina, S.V., *Vestn. Kazan. Tekhnol. Univ.*, 2000, nos. 1–2, pp. 121–126.
10. Kurenkov, V.F., Zaitseva, O.A., Khartan, Kh.-G., and Lobanov, F.I., *Vestn. Kazan. Tekhnol. Univ.*, supplement, 2001, pp. 1684–1687.
11. Kurenkov, V.F., Zaitseva, O.A., and Isaeva, N.V., *Zh. Prikl. Khim.*, 2001, vol. 74, no. 10, pp. 1374–1378.
12. Kholodnova, L.V., Pavlyuchenko, V.N., Alekseeva, Z.M., and Andreeva, A.I., in *Kataliticheskie i initsiiruyushchie sistemy dlya sinteza i modifikatsii polimerov* (Catalytic and Initiating Systems for Synthesis and Modification of Polymers), Leningrad: Plastpolimer, 1984, pp. 90–104.
13. Kolthoff, I.M. and Miller, I.K., *J. Am. Chem. Soc.*, 1951, vol. 73, pp. 3055–3059.
14. Charlot, G., *Les methods de la chimie analytique. Analyse quantitative minerale*, Paris: Masson, 1961, 4th ed. Translated under the title *Metody analiticheskoi khimii*, Moscow: Khimiya, 1969, p. 988.
15. Topchiev, D.A., Martynenko, A.I., Kabanova, E.Yu., and Timofeeva, L.M., *Vysokomol. Soedin., Ser. A*, 1997, vol. 39, no. 7, pp. 1129–1139.
16. Olson, K.G. and Butler, G.B., *Macromolecules*, 1984, vol. 18, pp. 2486–2496.
17. Topchiev, D.A., Shakirov, R.Z., Kalinina, L.P., *et al.*, *Vysokomol. Soedin., Ser. A*, 1972, vol. 14, no. 3, pp. 581–587.

Russian Journal of Applied Chemistry, Vol. 75, No. 11, 2002, pp. 1859–1863. Translated from Zhurnal Prikladnoi Khimii, Vol. 75, No. 11, 2002, pp. 1896–1900.
Original Russian Text Copyright © 2002 by Zhubanov, Boiko, Umerzakova.

MACROMOLECULAR CHEMISTRY AND POLYMERIC MATERIALS

N-Monosubstituted Tricyclodecenetetracarboxylic Acid Diimides Containing the Double Bond in the Substituent and Polymers Derived from Them

B. A. Zhubanov, G. I. Boiko, and M. B. Umerzakova

Bekturov Institute of Chemical Sciences, Ministry of Education and Science of Kazakhstan Republic, Almaty, Kazakhstan

Received April 25, 2002

Abstract—N-Monosubstituted tricyclodecenetetracarboxylic acid diimides with allyl- and vinyl-containing substituents, exhibiting antitumor activity, were prepared. Their copolymerization with *N*-vinylpyrrolidone yielded polymers with alicyclic diimide moieties in the pendant chain.

In the modern natural science, new lines of research often arise at the junction of different fields of knowledge. An example is the development of the chemistry of medicobiological polymers at the junction of macromolecular chemistry, medicine, pharmacology, and biochemistry. Its rapid progress resulted in the development of polymeric materials for surgery, public-health items, parts of medical apparatus and tools, dressings, organ and tissue prostheses, blood substitutes, packages, drug shells, etc. [1–5]. One of the important problems in this field was development of polymeric medicinals. Such medicinals create the therapeutic concentration of a drug in the body and maintain it at the required level for a long period, eliminating or reducing the side effects and decreasing the drug consumption for the therapeutic course owing to more complete utilization of the drug.

A number of high-performance polymeric and low-molecular-weight antiblastic agents have been developed; these agents are successfully used for treatment of some kinds of malignant tumors. However, the majority of such drugs oppress physiological regeneration of normal tissues, and tumors quickly become resistant to their effect [6, 7]. Therefore, it became necessary to develop a new generation of antitumor medicinals with increased selectivity, high therapeutic efficiency, and low toxicity.

Previously [8–12], we prepared diimides of alicyclic tetracarboxylic acids and demonstrated their high antitumor activity in the experiments on animals. Here we report on synthesis of N-monosubstituted tricyclodecenetetracarboxylic acid diimides with allyl- and vinyl-containing substituents, on their toxicity and antitumor activity, and on preparation of new polymeric forms of these agents.

EXPERIMENTAL

Tricyclo[4.2.2.0^{2,5}]dec-7-ene-3,4,7,8-tetracarboxylic acid dianhydride (AB) was purified by stirring for 1.5–2 h in hot acetone; the procedure was repeated three or four times, until acetone no longer got colored. The precipitate was filtered off and dried in air and then in a vacuum oven at 30–40°C. Then AB was additionally dehydrated by refluxing for 2–3 h in acetic or propionic anhydride. The dianhydride was filtered off, washed on the filter with acetone, and dried in air and then in a vacuum oven at 30–40°C to constant weight; equivalent weight 68.5 (calculated 68.5), mp 250–252°C (published data [13]: 252°C).

Allylamine was distilled at 56°C/692 mm Hg (reference data [14]: bp 58°C). 1-Vinyloxy-2-aminoethane (monoethanolamine vinyl ether) was distilled at 114°C/692 mm Hg (published data [15]: bp 114.5–115.5°C/710 mm Hg). *N*-Vinylpyrrolidone (VP), pure grade, stabilized with KOH, was distilled in a vacuum (bp 68°C/1.5 mm Hg); n_D^{20} 1.5116 [14]. Azobis(isobutyronitrile, pure grade, was recrystallized from ethanol; mp 103°C (published data [16]: mp 103°C).

Dimethylformamide (DMF), dimethyl sulfoxide (DMSO), and *N*-methylpyrrolidone (MP) were dried over 4 Å molecular sieves and distilled; fractions with the boiling points consistent with reference data [14] were collected.

To prepare tricyclodecenetetracarboxylic acid

1070-4272/02/7511-1859$27.00 © 2002 MAIK "Nauka/Interperiodica"

Table 1. Results of synthesis of N-monosubstituted tricyclodecenetetracarboxylic acid diimides in DMF

R	Stage	Urea : anhydrido imide molar ratio	*T*, °C	τ, h	*c*,* wt %	Yield, %
$CH_2CH=CH_2$	1	–	–(12–15)	4	9	–
	2	2:1	140	5	20	85
$(CH_2)_2OCH=CH_2$	1	–	–(12–15)	4	9	–
	2	2:1	140	5	20	79

* (*c*) Reagent concentration.

N-monoallyldiimide (MADI), a three-necked flask equipped with a stirrer and a dropping funnel was charged with 24.66 g (0.09 mol) of AB, and 284 ml of DMF was added; the flask was submerged in a bath with an ice–salt mixture. To the cooled solution, 5.18 ml (0.09 mol) of allylamine was added dropwise in small portions; the residual amount of allylamine from the dropping funnel was washed into the flask with 20 ml of DMF. After the reaction completion, a part of the solvent (185 ml) was distilled off in a water-jet-pump vacuum, and 10.37 g (0.173 mol) of urea was added. The flask was submerged in a bath preheated to the required temperature. The product was precipitated by adding ethanol, filtered off, washed with diethyl ether, and dried at 30–40°C. Bromine number: found 51.29, calculated 51.22.

Tricyclodecenetetracarboxylic acid *N*-monovinyloxyethyldiimide (MVODI) was prepared similarly. Bromine number: calculated 46.84, found 46.73. The bromine number was determined by the procedure given in [16]. The IR spectra of the initial compounds and synthesized drugs were taken on a Jasco IR-810 spectrometer (Japan) in the range 4000–400 cm^{-1}; samples were prepared as KBr pellets (1 mg substance per 200 mg KBr). Pure KBr pellet was the reference.

Tricyclodecentetracarboxylic dianhydride has an asymmetrical structure, with different reactivity of the anhydride groups [17]. Therefore, it is feasible to involve in condensations either one anhydride group selectively or both anhydride groups [18, 19]. This fact was used for preparing N-monosubstituted diimides of alicyclic tetracarboxylic acids containing unsubstituted and substituted imide rings containing a terminal functional group or double bond, with the aim of subsequent preparation of polymers with pendant alicyclic diimide moieties.

Monosubstituted diimides of tricyclodecenetetracarboxylic acid, containing double bonds in the substituent, were prepared by the reaction

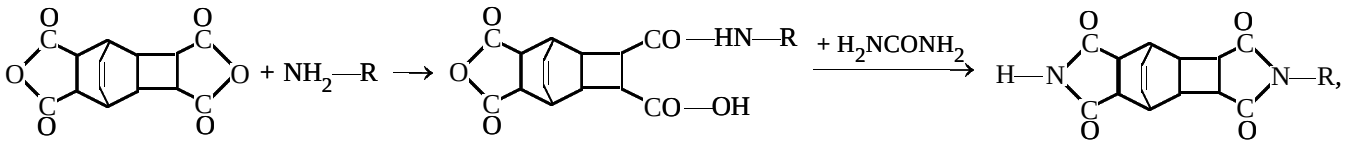

where R = CH_2–$CH=CH_2$, CH_2–CH_2–O–$CH=CH_2$.

Experiments performed to optimize the conditions for the synthesis of tricyclodecenetetracarboxylic acid diimides allowed us to abandon thermal imidization of anhydrido amido acid in a vacuum, described in [18, 19], and prepare N-monosubstituted tricyclodecenetetracarboxylic acid diimides by the reaction of anhydrido amido acid with urea at 130–150°C in amide solvents. The results are given in Table 1.

Monosubstituted tricyclodecenetetracarboxylic acid diimides are moderately (5–10%) soluble in organic solvents; consistent analytical data were obtained. The IR spectra of these compounds contain all the absorption bands characteristic of related substances (Table 2).

The synthesized diimides were tested for the toxicity and antitumor activity.[1] The toxicity data and high values of the maximum bearable dose indicate that these compounds are low-toxic and exhibit a wide range of therapeutic effect.

One of the ways to prepare polymeric medicinals is

[1] Tests were performed at the Kazakh Research Institute of Oncology and Radiology, Ministry of Public Health of the Kazakhstan Republic. The antitumor activity tests show that MADI exhibits moderate antitumor activity against Sarcoma 37 strain (53% at a treatment course dose of 5000 mg kg^{-1}).

Table 2. Characteristics of N-monosubstituted tricyclodecenetetracarboxylic acid diimides

Amine incorporated	Calculated, %			Found, %			mp, °C	ν_{max}, cm^{-1}	Solvent
	C	H	N	C	H	N			
Monoallylamine	65.38	5.13	8.97	65.09	5.08	8.92	294–297	1720–1780 (doublet); 1380, 730 (imide); 1640 (C=C); 3050, 910, 980 (C–H in $CH=CH_2$); 3200 (N–N in unsubstituted imide)	DMSO DMAA DMF MP
2-Vinyloxy-1-aminoethane	64.86	5.10	4.20	64.66	5.22	4.00	262–265	1720–1780 (doublet); 1380, 730 (imide); 1640 (C=C); 3050, 910, 980 (C–H in $CH=CH_2$); 3200 (N–H in unsubstituted imide)	DMSO DMAA DMF MP

polycondensation or polymerization of a low-molecular-weight drug. Since tricyclodecenetetracarboxylic acid *N*-monoallyl- and *N*-mono-2-vinyloxyethyldiimides contain terminal functional unsaturated groups, their polymeric derivatives can be prepared by radical polymerization. A specific feature of such compounds in radical polymerizations is their tendency to degradation chain transfer; as a result, the compounds are low-reactive and form low-molecular-weight polymers [15, 20]. At the same time, vinyl ethers readily undergo radical copolymerization. As the second comonomer we took VP whose copolymers and polymers are widely used in medical practice and pharmacology.

Copolymerization was performed in glass ampules at 1 : 1 ratio of the starting components in the presence of 2 mol % AIBN initiator in DMSO under nitrogen at 70°C for 8 h at the reactant concentration of 15 wt %. The reaction followed the scheme

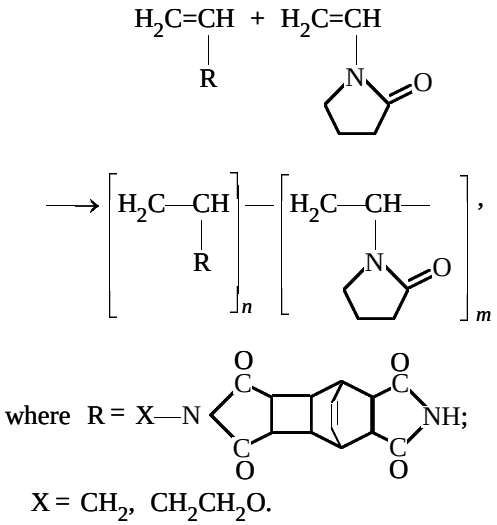

The polymers were obtained as white powders soluble in DMSO and MP; yield 45–48%. The reduced viscosity of the polymers derived from MADI and MVODI was 0.19 and 0.16 dl g^{-1}, respectively.

Elemental analysis shows that the synthesized polymers are enriched iin VP; the content of the active substance is 25–30%. The results are listed in Table 3; the elemental composition of the homopolymers based on VP and N-monosubstituted diimides is given also for comparison.

The IR spectra of the starting compounds and their copolymer (with MADI as example) are shown in the figure. The spectrum of the copolymer contains no absorption bands at 1440 and 1635–1645 cm^{-1} (vibra-

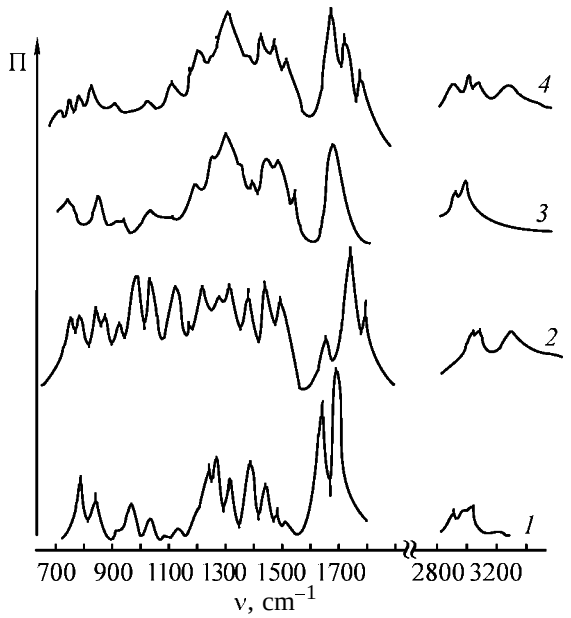

IR absorption spectra: (*1*) VP, (*2*) MADI, (*3*) polyvinylpyrrolidone, and (*4*) VP–MADI copolymer. (П) Absorption and (ν) wave number.

Table 3. Elemental composition of the polymers prepared from N-monosubstituted tricyclodecenetetracarboxylic acid diimides and VP

Starting monomers	Calculated, %			Found, %			Copolymer composition, %	
	C	H	N	C	H	N	diimide	VP
MADI	65.38	5.13	8.97	–	–	–	–	–
MADI + VP	62.25	5.91	9.93	65.03	6.48	10.62	30	70
MVODI	63.16	5.26	8.18	–	–	–	–	–
MVODI + VP	63.58	5.96	9.27	64.00	6.67	10.37	25	75
VP	64.86	8.11	12.61	–	–	–	–	100

tions of the C=C bond) and at about 980 cm^{-1} (vibrations of the vinyl CH bond), but contains the bands at 1720–1780, 1380, 1660, and 3200 cm^{-1}, assignable to the imide rings, amide group, and N–H-unsubstituted imide group.

CONCLUSIONS

(1) N-Monosubstituted tricyclodecenetetracarboxylic acid diimides containing a double bond in the substituent were prepared by the reaction of tricyclodecenetetracarboxylic acid with allylamine and 1-vinyloxy-2-aminoethane. Radical copolymerization of these diimides with *N*-vinylpyrrolidone in dimethyl sulfoxide yielded new polymers with alicyclic diimide moieties in the pendant chain. The compounds were identified by IR spectroscopy and elemental analysis.

(2) The copolymers are enriched in *N*-vinylpyrrolidone; the content of the active substance is 25–30%. Tests for the toxicity and maximum bearable dose show that the compounds are low-toxic and exhibit a wide range of therapeutic effect. Tricyclodecenetetracarboxylic acid *N*-monoallyldiimide inhibits by 53% the growth of Sarcoma 37.

REFERENCES

1. Dimitriu, S., *Polymeric Biomaterials*, New York: Marcel Dekker, 1994, pp. 233–244.
2. El-Nokaly, M.A., Piatt, D.M., and Charpentier, B.A., *Polymeric Delivery Systems: Properties and Applications*, Washington: Am. Chem. Soc., 1993.
3. Lipatova, T.E. and Pkhakadze, G.A., *Polimery v endoprotezirovanii* (Polymers in Endoprosthesis), Kiev: Naukova Dumka, 1983.
4. Plate, N.A. and Vasil'ev, A.E., *Fiziologicheski aktivnye polimery* (Physiologically Active Polymers), Moscow: Khimiya, 1986.
5. Korshak, V.V. and Shtil'man, M.I., *Polimery v protsessakh immobilizatsii i modifikatsii prirodnykh soedinenii* (Polymers in Immobilization and Modification of Natural Compounds), Moscow: Nauka, 1984.
6. Bulkina, Z.P., *Protivoopukholevye preparaty* (Antitumor Agents), Kiev: Naukova Dumka, 1991.
7. *Protivoopukholevaya khimioterapiya: Spravochnik* (Antitumor Chemotherapy: Handbook), Perevodchikova, N.I., Ed., Moscow: Meditsina, 1986.
8. Umerzakova, M.B., Boiko, G.I., and Zhubanov, B.A., Abstracts of Papers, *Turkce konusulan ulkeler 4 polimer sempozyumu*, Istanbul (Turkey), 1996, section 1, p. S22.
9. Zhubanov, B.A., Boiko, G.I., Abdullin, K.A., *et al.*, *Khim.-Farm. Zh.*, 1991, no. 1, pp. 43–44.
10. Umerzakova, M.B., Boiko, G.I., Edygenova, A.K., *et al.*, *Khim.-Farm. Zh.*, 1996, no. 8, pp. 5–6.
11. Boiko, G.I., Abdullin, K.A., Umerzakova, M.B., and Zhubanov, B.A., Abstracts of Papers, *14-i Mendeleevskii s"ezd po obshchei i prikladnoi khimii* (14th Mendeleev Congr. on General and Applied Chemistry), Moscow: Nauka, 1989, no. 1, p. 414.
12. Umerzakova, M.B., Boiko, G.I., and Abdullin, K.A., Abstracts of Short Communications, *Modern Problems of Polymer Science: Int. Research Conf.*, Tashkent, 1995, pp. 42–43.
13. Zhubanov, B.A., Arkhipova, I.A., and Almabekov, O.A., *Termostoikie geterotsiklicheskie polimery* (Heat-Resistant Heterocyclic Polymers), Alma-Ata: Nauka, 1979.
14. *Spravochnik khimika* (Chemist's Handbook), Nikol'skii, B.P., Ed., Leningrad: Khimiya, 1971, vol. 2.
15. Shostakovskii, M.F., *Prostye vinilovye efiry* (Vinyl Ethers), Moscow: Akad. Nauk SSSR, 1952.
16. Toroptseva, A.M., Belogorodskaya, K.V., and Bonda-

renko, V.M., *Laboratornyi praktikum po khimii i tekhnologii vysokomolekulyarnykh soedinenii* (Laboratory Manual on Chemistry and Technology of Macromolecular Compounds), Leningrad: Khimiya, 1972.

17. Zhubanov, B.A., Solomin, V.A., Messerle, P.E., *et al.*, *Vysokomol. Soedin., Ser. A*, 1977, vol. 19, no. 11, pp. 2500–2505.
18. Zhubanov, B.A., Grinina, O.V., and Lyubchenko, N.P., *Vysokomol. Soedin., Ser. B*, 1987, vol. 29, no. 7, pp. 486–489.
19. Zhubanov, B.A., Grinina, O.V., and Lyubchenko, N.P., *Vysokomol. Soedin., Ser. B*, 1987, vol. 29, no. 5, pp. 331–336.
20. Zhubanov, B.A., Shaikhutdinov, E.M., and Osadchaya, E.F., *Prostye vinilovye efiry v radikal'noi polimerizatsii* (Vinyl Ethers in Radical Polymerization), Alma-Ata: Nauka, 1985.

Russian Journal of Applied Chemistry, Vol. 75, No. 11, 2002, pp. 1864–1867. Translated from Zhurnal Prikladnoi Khimii, Vol. 75, No. 11, 2002, pp. 1901–1904.
Original Russian Text Copyright © 2002 by Nud'ga, Petrova, Kever, Makarova.

MACROMOLECULAR CHEMISTRY AND POLYMERIC MATERIALS

Hydrolysis of Chitin–Glucan Complex of *Aspergillus niger* Fungus with Phosphoric Acid

L. A. Nud'ga, V. A. Petrova, E. E. Kever, and T. V. Makarova

Institute of Macromolecular Compounds, Russian Academy of Sciences, St. Petersburg, Russia
St. Petersburg State Technical University of Plant Polymers, St. Petersburg, Russia

Received July 3, 2002

Abstract—The kinetic parameters of hydrolysis of chitin–glucan complex of *Aspergillus niger* fungus with 85% phosphoric acid were studied at three temperatures. The activation energies of hydrolysis of chitin and glucan components of the complex were determined.

Chitin–glucan complex (CGC) is contained in the cell walls of mold fungus *Aspergillus niger*, producer of citric acid used in its industrial biochemical production. The mycelium of *Aspergillus niger* is a large-tonnage waste product of this production, and a search of ways to utilize mycelium or its components is extremely important for development of environmentally harmless and wasteless production. A high sorption power of CGC with respect to heavy metal ions [1] makes it promising for water treatment to remove some ions and also as an enterosorbent in the composition of baked and candy goods [2] for prophylactic food of staff subjected to possible impact of heavy metals.

The presence of chitin in the complex suggests the biological activity of CGC with respect to a number of diseases caused by weakening of the immunity. It is well known that the biological activity of polysaccharides increases with decreasing their molecular weight, and oligosaccharides most often give the maximum effect [3]. To decrease the molecular weight of polysaccharides, destructive methods such as oxidation, ultrasonic treatment, and mechanical and radiation degradation are used. Being highly efficient, these methods, however, involve side processes giving rise to new functional groups or causing cross-linking of macromolecule fragments owing to the arising radicals. Enzymatic methods are mild and selective, but they require certain bacterial cultures [4, 5]. Classic degradation method, acid hydrolysis, has no these drawbacks. However, the use of concentrated HCl and H_2SO_4 results in formation of oligosaccharides with a wide molecular-weight distribution or even in hydrolysis to monosaccharides. The use of 85% H_3PO_4, which is a milder hydrolyzing agent, for hydrolysis of chitosan under mild conditions (at room temperature) gives oligosaccharides with a degree of polymerization (DP) of 17 in 43% yield in 4 weeks or with DP 7 in 12.5% yield in 6 weeks [6]. The use of 85% H_3PO_4 in this work is also caused by the possibility of comparison of the hydrolysis rates of chitin and glucan components of CGC.

EXPERIMENTAL

In the study we used CGC recovered from *Aspergillus niger* mycelium [1]. The composition of CGC was as follows (wt %): chitin 81.6, glucan 15.1, and melanin 3.3.

CGC was hydrolyzed with 85% H_3PO_4 at 293, 323, and 353 K with sampling at certain intervals. In samples, we determined the solubility, absolute viscosity of hydrolyzate, and the amounts of glucose, *N*-acetylglucosamine, and glucosamine. Quantitative analysis of monosaccharides was carried out photocolorimetrically on an SF-46 spectrophotometer from the absorption of chromogens formed in the reactions of glucose with anthranone (absorption at λ = 620 nm) [7], glucosamine with salicylaldehyde (λ = 410 nm) [8], and *N*-acetylglucosamine with *N*,*N*-dimethyl-*p*-aminobenzaldehyde (λ = 585 nm) [9], using calibration curves preliminary plotted for each monosaccharide. The oligosaccharide composition was determined by exclusion gel chromatography with a TSK-PW support. Pullulan with the molecular weight of 1000 was used as a reference, and trifluoroacetate buffer solution, as an eluent.

CGC is dissolved in 85% H_3PO_4 within 5 days at 293 K. In the process, the hydrolyzate viscosity in-

1070-4272/02/7511-1864$27.00 © 2002 MAIK "Nauka/Interperiodica"

creases in the first 3 days owing to increasing solution concentration and then decreases as a result of predominance of the hydrolytic process. At 323 K, CGC passes into solution within 45 min, and at 353 K, within 30 min. In this case, the absolute viscosity of the solutions decreases asymptotically, tending to a constant value of approximately 10 cP (Fig. 1). Curves of this type are characteristic of hydrolysis of cellulose with trifluoroacetic acid: abrupt decrease takes place in the initial period and then the curves flatten out with the viscosity corresponding to the maximum degree of polymerization [10].

In CGC hydrolyzates produced at 293 K, the amount of glucose increases with time, reaching the maximum value, corresponding to the glucan content in CGC within 4 h. The amount of *N*-acetylglucosamine slowly increases, reaching only 2.5% of the amount of the initial polymer, despite the fact that CGC contains 81.6% of chitin. Glucosamine was not found in the samples (Fig. 2a).

At 323 K, the amount of glucose in the samples reaches the limiting value within 45 min, and the maximum amount of *N*-acetylglucosamine in the sample is 8%. Glucosamine was not found in the samples.

At 353 K, hydrolysis proceeds differently: The amount of glucose increases in the first 3 h. *N*-Acetylglucosamine is accumulated in the first 30 min, after which its amount decreases. Simultaneously, glucosamine appears in the samples and its amount increases to 60% by the end of the reaction (Fig. 2b). Glucosamine is formed by elimination of the *N*-acetyl group from *N*-acetylglucosamine, i.e., this is a secondary hydrolysis process occurring only at a high temperature.

Based on kinetic curves for accumulation of glucose and *N*-acetylglucosamine, we evaluated the initial rates of hydrolysis of chitin and glucan components of CGC (Table 1).

It is seen from Table 1 that the hydrolysis rate of the glucan component is higher than that of the chitin component by a factor of 5.3 at 293 K, 1.3 at 323 K, and 1.25 at 353 K. At 353 K, this value does not reflect the true hydrolysis rate of the chitin part, since it does not consider the simultaneous transformation of *N*-acetylglucosamine to glucosamine.

To evaluate the hydrolysis constants, the experimental data on the concentration of monosaccharides were expressed in mM and for 353 K the total concentration of *N*-acetylglucosamine and glucosamine was taken with the correction for molecular weight. Based on the data obtained, the dependences $\log[a/(a - x_i)] = f(\tau)$ were plotted. This dependence at 293 K is shown in Fig. 3. All the dependencies are linear, i.e., hydrolysis is described by a first-order reaction equation, which allows determination of the rate constants of

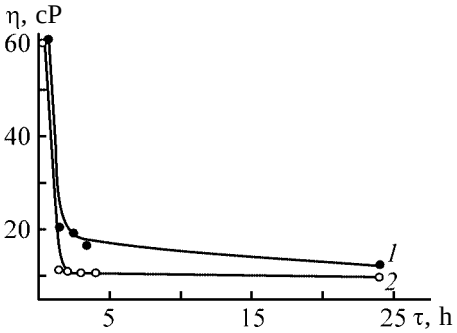

Fig. 1. Variation of the absolute viscosity of hydrolyzates η with time τ at (*1*) 323 and (*2*) 353 K.

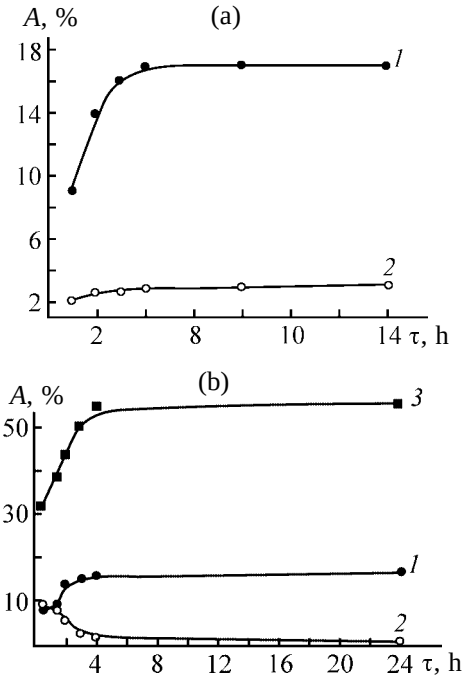

Fig. 2. Variation of the amount *A* of (*1*) glucose, (*2*) *N*-acetylglucosamine, and (*3*) glucosamine in the hydrolyzate in time τ at (a) 293 and (b) 353 K.

Table 1. Initial rate of hydrolysis of chitin and glucan components of CGC

CGC component	Initial rate of hydrolysis, % min^{-1}, at indicated *T*, K		
	293	323	353
Glucan	0.0083	0.1050	0.3000
Chitin	0.0016	0.0830	0.2400

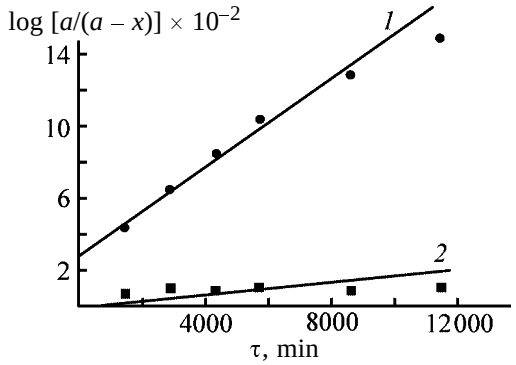

Fig. 3. Determination of the rate constants of hydrolysis of (*1*) glucan and (*2*) chitin components of CGC at 293 K. (τ) Time.

hydrolysis at the studied temperatures from the slopes of the straight lines. The results are listed in Table 2. From the rate constants, using the Arrhenius equation, we evaluated E_a for hydrolysis of chitin and glucan components of CGC.

The E_a values obtained for chitin and glucan components of CGC are significantly lower than those published for chitin, E_a = 106.22 kJ mol^{-1}, and laminarin having the structure of poly-β-1→3-glucopyranoside, i.e., the structure closest to that of glucan part of CGC, E_a = 110.82 kJ mol^{-1} [11]. It is believed that the activation energy of hydrolysis of the glucoside bond is almost independent of the molecular weight and structural features of polysaccharide [11]. However, the influence of supramolecular organization on the hydrolysis energy must not be ruled out. Contrary to chitin and laminarin having highly crystalline supramolecular organization, CGC has a disordered mesomorphic structure in which the system of intermolecular hydrogen bonds is strongly disturbed [12]. A fast change of hydrolysis conditions from heterogeneous to homogeneous relieves the influence of diffusion processes. It is likely that the accessibility of glucoside bond for the hydrolyzing agent is responsible for its low E_a values. In addition, it is not improbable that the branched structure of CGC, in which the main skeleton chain is chitin and the side short chains are 1→3 bonds of glucan, facilitates hydrolysis of both chitin and glucan components.

Table 2. Rate constants and activation energies of hydrolysis of glucan and chitin components of CGC

CGC component	*T*, K	$k \times 10^5$	E_a, kJ mol^{-1}
Glucan	293	1.1428	57.44
	323	100.0	
	353	794.3	
Chitin	293	0.107	89.99
	323	6.667	
	353	87.50	

The above data show that the composition of the hydrolyzed product strongly depends on the temperature and hydrolysis time. Considering the composition of the final hydrolysis products, we can conclude that at 293 K glucose and *N*-acetylglucosamine in the total amount of 20% of CGC taken for hydrolysis are present in the hydrolyzed product and, hence, 80% of CGC transforms into oligosaccharides. At 323 K, the hydrolyzed product contains the same monosaccharides in the amount of 25% of the initial CGC and 75% oligosaccharides. At 353 K, the hydrolyzed product contains 78.7% glucose, *N*-acetylglucosamine, and glucosamine (59.4%) and 21.3% oligosaccharides. Since oligosaccharides are not precipitated from hydrolyzed products with acetone, we can assume that their degree of polymerization does not exceed 10.

The gel-chromatographic analysis of the oligosaccharide composition in the final hydrolysis product at 323 K showed that the main part of oligosaccharides has the degree of polymerization of 5–6. Specifically at this degree of polymerization chitooligosaccharides have the highest biological activity [3].

CONCLUSIONS

(1) The hydrolysis of chitin–glucan complex with 85% phosphoric acid starts under heterophase conditions and passes to homogeneous conditions within a period depending on the process temperature.

(2) The glucan component of the complex is hydrolyzed first.

(3) The study of hydrolysis kinetics allows determination of the rate constants and activation energies of hydrolysis of chitin and glucan components of the complex. It was found that the glucan part is hydrolyzed first, and then the chitin chain is hydrolyzed to form *N*-acetylglucosamine with subsequent deacetylation to glucosamine.

ACKNOWLEDGMENTS

This work was supported by the Integration Federal Target Program, grant no. A0143.

REFERENCES

1. Nud'ga, L.A., Ganicheva, S.I., Petrova, V.A., *et al.*, *Zh. Prikl. Khim.*, 1997, vol. 70, no. 2, pp. 242–246.

2. Kuznetsova, L.I., Kiseleva, N.A., Ganicheva, S.I., and Bystrova, L.S., *Khlebopech. Ross.*, 2000, no. 4, pp. 14–15.
3. Osborn, H. and Khan, T., *Oligosaccharides: Their Synthesis and Biological Roles*, Oxford: Oxford Univ. Press, 2000.
4. Li Tong, Brzezinskii, R., and Beaulicu, C., *Plant Physiol. Biochem.*, 1995, vol. 33, no. 5, pp. 599–603.
5. Ilyina, A.V., Tatarinova, N.Ju., and Varlamov, V.P., *Process Biochem.*, 1999, vol. 34, no. 9, pp. 875–878.
6. Hasegawa, M., Isogai, A., and Onabe, F., *Carbohydr. Polym.*, 1993, vol. 20, no. 4, pp. 279–283.
7. Treveljan, W.J. and Yarrison, J.S., *Biochem. J.*, 1952, vol. 50, pp. 303–305.
8. USSR Inventor's Certificate no. 1273796.
9. *Methods in Carbohydrate Chemistry*, Whistler, R.L. and Wolfrom, M.L., Eds., New York: Academic, 1962–1965.
10. Khripunov, A.K., Plisko, E.A., Laius, L.A., *et al.*, *Vysokomol. Soedin., Ser. B*, 1975, vol. 17, no. 8, pp. 600–603.
11. Konkin, A.A. and Shuralova, E.A., *Zh. Prikl. Khim.*, 1959, vol. 32, no. 5, pp. 1076–1080.
12. Nud'ga, L.A., Petrova, V.A., Ganicheva, S.I., *et al.*, *Novye perspektivy v issledovanii khitina i khitozana: Materialy V konferentsii, Moskva–Shchelkovo, 25–27 maya 1999 g.* (New Prospects in the Study of Chitin and Chitosan: Proc. Vth Conf., Moscow–Shchelkovo, May 25–27, 1999), Moscow: VNIRO, 1999, pp. 242–245.

Russian Journal of Applied Chemistry, Vol. 75, No. 11, 2002, pp. 1868–1872. Translated from Zhurnal Prikladnoi Khimii, Vol. 75, No. 11, 2002, pp. 1905–1909.
Original Russian Text Copyright © 2002 by Pavlovskaya, Kolyakina, Polyanskova, Semenycheva, Grishin.

MACROMOLECULAR CHEMISTRY AND POLYMERIC MATERIALS

Polymerization of Styrene in the Presence of Nitroxyl Radicals Generated Directly in the Course of the Polymer Synthesis (*in situ*)

M. V. Pavlovskaya, E. V. Kolyakina, V. V. Polyanskova, L. L. Semenycheva, and D. F. Grishin

Research Institute of Chemistry, Nizhni Novgorod State University, Nizhni Novgorod, Russia

Received July 13, 2002

Abstract—The features of radical polymerization of styrene in the presence of nitroxyl radicals generated directly in the course of the polymer synthesis (*in situ*) by irreversible reaction of stable organic compounds 2-methyl-2-nitrosopropane, *C*-phenyl-*N*-*tert*-butylnitrone, and nitrosodurene with propagating polymer radicals were studied.

The interest of the majority of researchers in radical polymerization substantially increased in late 1980s–early 1990s, with publication of papers on "pseudoliving" polymerization [1, 2]. Performing polymerization in the "living" chain mode allows control of the polymerization kinetics and molecular-weight characteristics of the macromolecules [3–6]. The mechanism of such a process is based on reversible reaction of stable radicals X$^{\bullet}$ with chain-leading macroradicals R$^{\bullet}$, yielding a labile adduct R–X which decomposes with regeneration of the same propagating macroradical:

$$R^{\bullet} + {}^{\bullet}X \rightleftarrows R\text{–}X \qquad (1)$$

The best studied is pseudoliving polymerization of styrene and its analogs in the presence of 2,2,6,6-tetramethylpiperidine-1-oxyl (TEMPO) and its derivatives [1, 3–7]. It is notable that, both with excess and deficiency of nitroxyl relative to the initiator, the process finally becomes steady-state, with constant concentrations of TEMPO and propagating macroradicals [7]. The major drawback of styrene polymerization in the presence of TEMPO is the low rate: At 120°C (optimal temperature for obtaining narrow-MWD polystyrene) the reaction takes more than two days [3, 6]. Several methods are used to shift the equilibrium of reaction (1) toward higher concentration of active radicals and to accelerate polymerization in the presence of TEMPO. In particular, special agents (e.g., organic acids, aldehydes, etc.) converting a part of nitroxyl radicals into the corresponding hydroxylamine are added [8–11]; high-temperature initiators (cumyl peroxide, *tert*-butyl hydroperoxide, etc.) generating additional radicals accelerating polymerization are introduced; TEMPO is replaced by more stable nitroxyl radicals [14–17] forming more labile adducts R–X. It should be noted that all these methods complicate the formulation and procedure and increase the production cost. Furthermore, the contribution of competing reactions considerably increases; as a result, the molecular-weight characteristics and physicochemical properties of the resulting polymers are appreciably deteriorated.

Here we propose to perform controlled radical polymerization of styrene, initiated with azobis(isobutyronitrile) (AIBN) or benzoyl peroxide (BP), at 70–100°C, in the presence of nitroso compounds, nitrones, and oxytriazenes, which were successfully used previously for controlled synthesis of polymers from (meth)acrylic monomers [18–24].

EXPERIMENTAL

2-Methyl-2-nitrosopropane (MNP), *C*-phenyl-*N*-*tert*-butylnitrone (PBN), *tert*-butyl-3-phenyl-1-oxytriazene (BPT), and nitrosodurene (ND) were prepared by the procedures described in [25–28]. Polymerization was performed at 70°C using AIBN as initiator and at 100°C with BP initiator. Styrene and solvents were purified by standard procedures. The polymerization kinetics was monitored gravimetrically, dilatometrically [29], and thermographically [30]. The molecular weight of the polymer M was determined by viscometry [31] and gel permeation chromatography

1070-4272/02/7511-1868$27.00 © 2002 MAIK "Nauka/Interperiodica"

(GPC); the chromatograph was equipped with a set of five styrogel columns with the pore diameter of 10^5, 3×10^4, 10^4, 10^3, and 250 Å (Waters, the United States). An R-403 differential refractometer (Waters) was used as detector. The eluent was THF. Calibration was performed with close-cut polystyrene references [32].

As noted above, addition of nitroxyl radicals that form with propagating radicals [Eq. (1)] a more labile bond than TEMPO increases the rate of styrene polymerization. Among such nitroxyl radicals are phosphorus-substituted nitroxyls [33], diphenyldialkylpyrrolidone nitroxyl derivatives, etc. [7]. However, the synthesis of such derivatives is labor-consuming; the formulation and procedure are complicated, and the production cost of the polymer grows.

In our studies aimed at performing low-temperature pseudoliving polymerization of styrene at a high rate, we chose the strategy of approaching as much as possible the conditions of commercial synthesis, rather than complicating the process by introducing additional stages or expensive chemicals. In particular, we used traditional radical initiators (azo compounds and peroxides) and chose as chain propagation regulators such organic compounds as nitroso compounds, nitrones, and oxytriazenes, which are stable in storage and generate sterically hindered nitroxyl spin adducts directly in the polymerization system (*in situ*) [34].

Our experiments showed that addition of MNP or BPT in amounts comparable with that of BP initiator suppresses the gel effect in styrene polymerization at 100°C. It is interesting and important for practice that, in polymerization of styrene initiated with AIBN at 70°C, the gel effect is eliminated by additions of PBN and BPT in concentrations that are, respectively, ten and four times lower than the concentration of the initiator (Figs. 1a and 1b show as example the kinetic curves of styrene polymerization in the presence of MNP and ND, respectively). It should be noted that, when the gel effect is fully suppressed, the polymerization time increases, as compared to the process without the additive, by a factor of no more than 2, whereas polymerization of styrene in the presence of TEMPO at 100°C lasts for more than two days [7].

Thus, the additives proposed allow control of the kinetic parameters of styrene polymerization under conditions of radical initiation and eliminate gelation in the course of polystyrene synthesis.

As expected, nitroso compounds, PBN, and BPT strongly affect the molecular-weight characteristics of the polymer (see table). The viscosity-average and

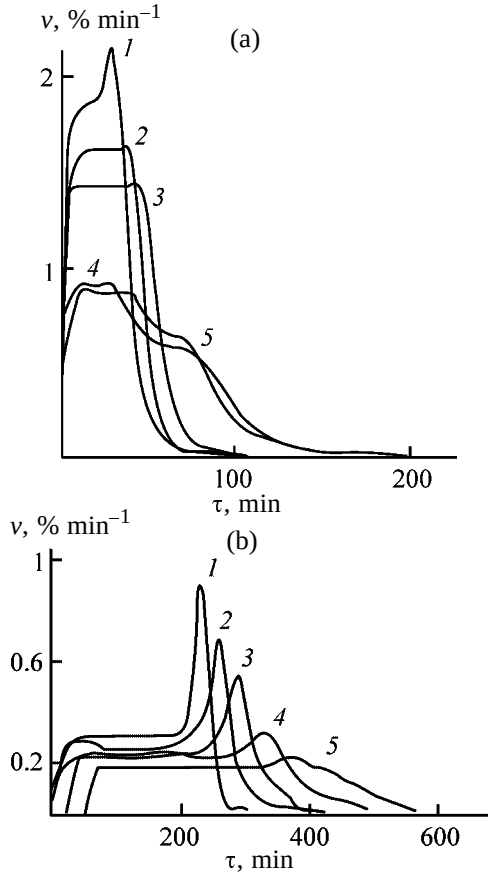

Fig. 1. Differential kinetic curves of styrene polymerization. Synthesis temperature, °C: (a) 100 and (b) 70; initiator: (a) 1.0 mol % BP and (b) 0.8 mol % AIBN; the same for Figs. 2 and 3. (*v*) Polymerization rate and (τ) time. Additive, mol %: (a) MNP, (*1*) 0, (*2*) 0.2, (*3*) 0.3, (*4*) 0.5, and (*5*) 0.8; (b) ND, (*1*) 0, (*2*) 0.008, (*3*) 0.08, (*4*) 0.16, and (*5*) 0.2.

number-average molecular weights of polystyrene prepared in the presence of the tested regulators uniformly grow with increasing styrene conversion. Without additives, under similar other conditions, the curve of M of the polymer vs. conversion is S-shaped, with uncontrollable growth of the molecular weight in the stage of the gel effect. Figures 2a and 2b show how the viscosity-average and number-average molecular weights of polystyrene prepared in the presence of MNP and PBN, respectively, vary with conversion.

Particular attention should be given to the polydispersity coefficients M_w/M_n of the synthesized polymers. In polymerization of styrene in the presence of MNP, the polydispersity coefficients do not change noticeably with conversion, amounting to 1.3–1.4 (see table, sample nos. 3–6). These values are somewhat higher than the similar characteristics of polystyrene prepared in the presence of TEMPO (~1.2) [5, 7]. The polydispersity coefficients of polystyrene prepared in

Molecular-weight characteristics of polystyrene

Sample no.	Additive, wt %	Conversion, %	$M_w \times 10^{-3}$	$M_n \times 10^{-3}$	M_w/M_n
		Initiator 1.0 mol % BP			
1	–	51	23	11	2.1
2	–	91	41	20	2.1
3	MNP, 0.8	17	26	18	1.4
4	〃	29	26	19	1.4
5	〃	50	27	20	1.3
6	〃	74	28	22	1.3
7	BPT, 0.08	26	19	14	1.4
8	〃	53	33	22	1.5
9	〃	60	34	23	1.5
10	〃	67	37	23	1.6
		Initiator 0.8 mol % AIBN			
11	PBN, 0.08	24	45	31	1.5
12	〃	84	246	77	3.2
13	〃	8	39	24	1.6
14	〃	16	39	26	1.5
15	〃	30	41	28	1.5
16	〃	56	53	34	1.5
17	〃	80	66	45	1.5
18	ND, 0.2	30	43	26	1.5
19	〃	53	53	35	1.5
20	〃	75	102	58	1.7

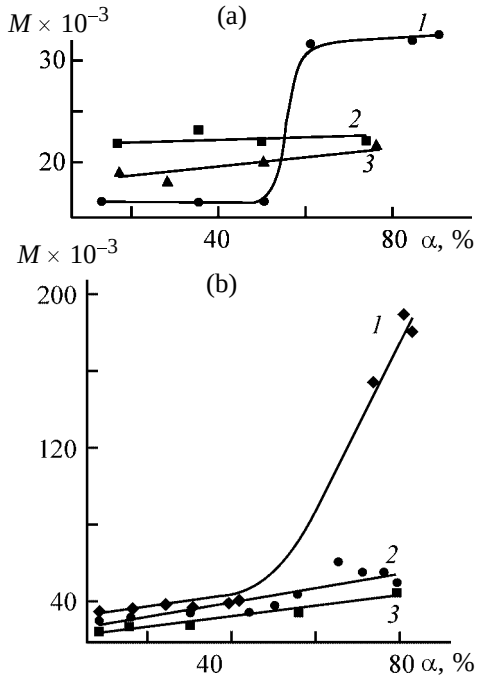

Fig. 2. (*1*, *2*) Viscosity-average and (*3*) number-average molecular weights *M* of polystyrene as functions of conversion α. (*1*) No regulator; (a) (*2*, *3*) 0.8 mol % MNP; (b) (*2*, *3*) 0.08 mol % PBN.

the presence of BPT, PBN, and ND are somewhat higher (1.4–1.6; see table, sample nos. 7–10, 13–17, and 18–20, respectively). Nevertheless, all these parameters are considerably lower than those of polystyrene prepared without additives in the presence of BP and AIBN initiators at 100 and 70°C, respectively (2.1 and 3.2; see table, sample nos. 1, 2, and 12).

The molecular-weight distribution (MWD) curves of polystyrene obtained at various conversions of the monomer in the presence of the above additives are unimodal; their maximum shifts toward higher molecular weights with increasing conversion (Figs. 3a, 3b). This pattern is typical of pseudoliving polymerization.

Thus, when styrene polymerization is performed in the presence of additives that are potential sources of stable radicals (MNP, BPT, PBN, ND), the main features of pseudoliving polymerization are observed: the lack of the gel effect, uniform increase in the molecular weight of the polymer, and shift of the unimodal MWD curves of polystyrene toward higher *M* with increasing conversion. The polymers have relatively low polydispersity coefficients. The polymerization time, compared to the process without addi-

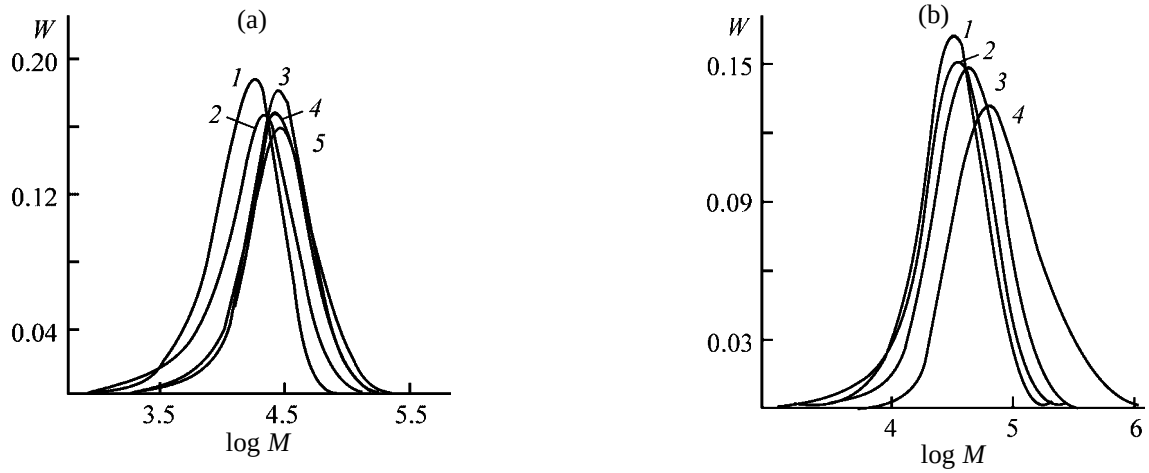

Fig. 3. MWD curves of polystyrene samples of various conversions: (*W*) wt fraction and (*M*) molecular weight. Regulator: (a) 0.5 mol % BPT and (b) 0.2 mol % ND. Conversion, %: (a) (*1*) 26.0, (*2*) 41.0, (*3*) 53.0, (*4*) 67.0, and (*5*) 60.0; (b) (*1*) 9.4, (*2*) 29.7, (*3*) 53.4, and (*4*) 75.1.

tives, increases insignificantly (by a factor of no more than 2).

Our experimental results, in combination with published data [18–24], suggest the following scheme of polymerization in the presence of the additives. Nitroso compounds and nitrones added to the polymerization system react with propagating radicals Pn$^{\bullet}$, generating stable nitroxyl spin adducts $^{\bullet}$X:

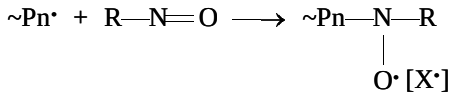

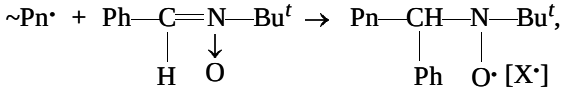

where R = *tert*-butyl and duryl.

Nitroxyl spin adducts, detected by ESR, react with propagating radicals by scheme (1), forming a labile R–X bond. After that, the chain propagation follows the traditional pattern of controlled radical polymerization in the presence of stable radicals [4–7, 18–20, 33].

The pattern of radical polymerization of styrene in the presence of BPT, which can also generate stable nitroxyl spin adducts directly in the polymerizing system [22], is similar to that described above for the synthesis of polymethyl methacrylate in the presence of this additive [23].

The somewhat higher polydispersity coefficients of polystyrene samples prepared in the presence of the above additives, as compared to the polymerization controlled by TEMPO, are probably due to the occurrence, along with the controlled process, of a common radical polymerization due to excess initiator, yielding the "dead" polymer by bimolecular termination.

CONCLUSION

Spin traps and oxytriazenes as sources of stable nitroxyl radicals effectively control chain propagation in styrene polymerization under the conditions maximally similar to those of the commercial process. The lower temperature of the controlled polymerization and relatively high polymerization rates are responsible for slightly higher polydispersity coefficients of the samples, compared to the process occurring in the living chain mode.

ACKNOWLEDGMENTS

The study was financially supported by the Russian Foundation for Basic Research (project no. 02-03-32 427).

REFERENCES

1. Georges, M.K., Veregin, R.P.N., Kazmaier, P.M., and Hamer, G.K., *Polym. Mater. Sci. Eng.*, 1993, vol. 68, pp. 6–9.
2. Smirnov, B.R., *Vysokomol. Soedin., Ser. A*, 1990, vol. 32, no. 3, pp. 583–589.
3. Otsu, T. and Matsumoto, A., *Adv. Polym. Sci.*, 1998, vol. 136, pp. 75–137.
4. Matyjaszewski, K., *Controlled/Living Radical Polymerization*, Oxford: Oxford Univ. Press, 2000.

5. Korolev, G.V. and Marchenko, A.P., *Usp. Khim.*, 2000, vol. 69, no. 5, pp. 447–475.
6. Grishin, D.F. and Semenycheva, L.L., *Usp. Khim.*, 2001, vol. 70, no. 5, pp. 486–510.
7. Zaremskii, M.Yu. and Golubev, V.B., *Vysokomol. Soedin.*, 2001, vol. 43, no. 9, pp. 1689–1728.
8. Georges, M.K., Veregin, R.P., Kazmaier, P.M., *et al.*, *Macromolecules*, 1994, vol. 27, no. 24, pp. 7228–7234.
9. Veregin, R.P.N., Odell, P.G., Michalak, L.M., and Georges, M.K., *Macromolecules*, 1996, vol. 29, no. 11, pp. 4161–4168.
10. Baldovi, M.V., Mohtad, N., and Scaiano, J.C., *Macromolecules*, 1996, vol. 29, no. 16, pp. 5497–5499.
11. Odell, P.G., Veregin, R.P.N., Michalak, L.M., and Georges, M.K., *Macromolecules*, 1997, vol. 30, no. 8, pp. 2232–2235.
12. Goto, M. and Fukuda, T., *Macromolecules*, 1997, vol. 30, no. 15, pp. 4272–4276.
13. Greszta, D. and Matyjaszewski, K., *J. Polym. Sci., Polym. Chem. Ed.*, 1997, vol. 35, no. 9, pp. 1857–1861.
14. Bon, S.A.F., Chambard, G., and German, A.L., *Macromolecules*, 1999, vol. 32, no. 25, pp. 8269–8271.
15. Veregin, R.P.N., Odell, P.G., Michalak, L.M., and Georges, M.K., *Macromolecules*, 1996, vol. 29, no. 8, pp. 2746–2754.
16. Miura, Y., Nakamura, N., and Taniguchi, I., *Macromolecules*, 2001, vol. 34, no. 3, pp. 447–455.
17. Han, C.H., Drache, M., Baethge, H., and Schmidt-Naace, G., *Macromol. Chem. Phys.*, 1999, vol. 200, no. 7, pp. 1779–1781.
18. Grishin, D.F., Semionicheva, L.L., and Koliakina, E.V., *Mendeleev Commun.*, 1999, no. 6, pp. 45–47.
19. Grishin, D.F., Semenycheva, L.L., and Kolyakina, E.V., *Vysokomol. Soedin., Ser. A*, 1999, vol. 40, no. 4, pp. 609–614.
20. Kolyakina, E.V., Grishin, D.F., and Semenycheva, L.L., *Vysokomol. Soedin., Ser. A*, 2001, vol. 43, no. 12, pp. 2092–2196.
21. Grishin, D.F., Semenycheva, L.L., and Kolyakina, E.V., *Zh. Prikl. Khim.*, 2001, vol. 74, no. 3, pp. 483–486.
22. Grishin, D.F., Moykin, A.A., Smirnova, E.P., *et al.*, *Mendeleev Commun.*, 2000, no. 5, pp. 152–154.
23. Grishin, D.F., Pavlovskaya, M.V., and Semenycheva, L.L., *Vysokomol. Soedin., Ser. A*, 2001, vol. 43, no. 11, pp. 1913–1917.
24. Grishin, D.F., Pavlovskaya, M.V., and Semenycheva, L.L., *Izv. Vyssh. Uchebn. Zaved., Khim. Khim. Tekhnol.*, 2001, vol. 44, no. 5, pp. 33–39.
25. Terabe, S. and Konaka, S., *J. Chem. Soc., Perkin Trans. 2*, 1972, no. 14, pp. 2163–2172.
26. Emmons, W.D., *J. Am. Chem. Soc.*, 1957, vol. 79, no. 5, pp. 5739–5744.
27. Dugar, S.M. and Sogani, N.C., *J. Indian Chem. Soc.*, 1966, vol. 43, no. 4, pp. 289–290.
28. *Organic Syntheses*, Blatt, A.H., Ed., New York: Wiley, 1946, 2nd ed., coll. vol. 2.
29. *Praktikum po khimii i fizike polimerov* (Practical Course of Polymer Chemistry and Physics), Moscow: Khimiya, 1990.
30. *Entsiklopediya polimerov* (Polymer Encyclopedia), Moscow: Sovetskaya Entsiklopediya, 1972, vol. 1.
31. Rafikov, S.R., Pavlov, S.A., and Tverdokhledova, I.I., *Metody opredeleniya molekulyarnykh vesov i polidispersnosti vysokomolekulyarnykh soedinenii* (Methods for Determining the Molecular Weights and Polydispersity of Macromolecular Compounds), Moscow: Khimiya, 1963.
32. Belen'kii, B.G. and Vilenchik, L.Z., *Khromatografiya polimerov* (Chromatography of Polymers), Moscow: Khimiya, 1978.
33. Mercier, C. le, Lutz, J.-F., and Margue, S., in *Controlled/Living Radical Polymerization*, Washington, DC: Am. Chem. Soc., 2000, ch. 8, pp. 109–122.
34. Zubarev, V.E., *Metod spinovykh lovushek* (Method of Spin Traps), Moscow: Mosk. Gos. Univ., 1984.

Russian Journal of Applied Chemistry, Vol. 75, No. 11, 2002, pp. 1873–1877. Translated from Zhurnal Prikladnoi Khimii, Vol. 75, No. 11, 2002, pp. 1910–1914.
Original Russian Text Copyright © 2002 by Selyanina, Makarevich, Tel'tevskaya, Afanas'eva, Selivanova.

MACROMOLECULAR CHEMISTRY AND POLYMERIC MATERIALS

Influence of Adsorption of Lignosulfonates on Kraft Lignin in the Presence of Tall Oil on Separation of Water–Tall Oil Emulsion

S. B. Selyanina, N. A. Makarevich, S. E. Tel'tevskaya, N. I. Afanas'eva, and N. V. Selivanova

Institute of Environmental Problems of the North, Ural Division, Russian Academy of Sciences, Arkhangelsk, Russia

Received July 3, 2001; in final form, March 2002

Abstract—The degree of hydrophilicity–oleophilicity of solid lignin recovered from cooking liquors of deciduous and coniferous wood at various pH and its influence on the aggregative stability of water–tall oil emulsion were estimated. The stabilizing effect of lignosulfonates on lignin suspension in aqueous electrolyte solution was studied. The values of absorption of lignosulfonates from aqueous solutions on kraft lignin were determined depending on the molecular weight of lignosulfonates and content of tall oil in the suspension.

Chemical treatment of plant materials in some cases involves formation of emulsions stabilized with a solid emulsifier. In particular, treatment of sulfate soap with an acid results in formation of a complex heterogeneous system oil–aqueous salt solution–lignin, which is an oil-in-water emulsion stabilized with solid lignin distributed at the interface in the form of a film preventing coalescence of emulsified oil droplets [1, 2].

In the practice of kraft cellulose production, coniferous and deciduous woods are usually processed in separate flows with the aim to produce cellulose of different quality. In so doing, the efficiency of recovery of sulfate soap and tall oil is different, which is apparently caused by the nature of lignin, the main component of spent cooking liquors, entrained into soap micelles with black liquor. Despite the fact that the optimization of these processes is a pressing problem in the pulp and paper industry, these aspects virtually were not considered in the literature. Therefore, in this work we studied one of the most important characteristics of kraft lignin as emulsion stabilizer: hydrophilic–oleophilic characteristics and adsorption capacity.

In the study, we used the lignin samples recovered by acidification of prederesined kraft black liquors of Solombal and Arkhangelsk pulp and paper combines (STsBK and ATsBK), in which coniferous and deciduous woods, respectively, predominate in the wood raw materials. After precipitation the lignin was washed with water on a filter cloth to neutral reaction, dried at 25–30°C, and ground to powder.

To characterize the recovered samples of lignins, we estimated their hydrophilic–oleophilic characteristics (Table 1) from the data obtained by the vacuum-static method from the adsorption of water vapor and a set of normal hydrocarbons on the lignin samples with subsequent evaluation of differential adsorption heats (with half-monolayer filling) [3].

For all these samples, the oleophilicity predominates over the hydrophilicity. However, the degrees of hydrophilicity and oleophilicity can be close (as, e.g., for sample no. 7) or can differ substantially (as, e.g., for sample no. 1 for which the degree of oleophilicity is 3.5 times greater than the degree of hydrophilicity). Table 1 reveals some correlation of hydrophilic–oleophilic characteristics of the recovered lignin samples with the type of wood raw materials. The balance of hydrophilic and oleophilic properties is characteristic of coniferous kraft lignin produced in cooking of pine wood, while the hydrophobic properties are clearly prevalent for lignins of deciduous wood (birch) and, to a greater extent, for spruce wood. This is apparently caused by saturation of these lignins with hydrogen bonds. The analysis of experimental data on the yield and composition of water–tall oil emulsion (Table 2) showed that the emulsion yield is affected by both the lignin origin and its content in sulfate soap, while the composition of the emulsion phase is predominantly governed by the lignin origin.

1070-4272/02/7511-1873$27.00 © 2002 MAIK "Nauka/Interperiodica"

Table 1. Characteristics of kraft lignin samples

Sample no.	Sampling site, predominant wood	Precipitation pH	Degree of oleophilicity	Degree of hydrophilicity	Classon lignin content, %
1	Coniferous flow of STsBK, spruce	3.0	0.78	0.22	88.1
2	" "	2.6	0.75	0.25	88.5
3	Deciduous flow of AtsBK, birch	2.5	0.70	0.30	90.2
4	" "	3.5	0.62	0.38	91.4
5	Coniferous flow of STsBK, spruce	3.2	0.60	0.40	89.7
6	Coniferous flow of STsBK, pine	2.5	0.58	0.42	91.9
7	" "	3.5	0.53	0.47	91.0

* The sample was subjected to hydrophilzation.

Table 2. Influence of lignin on formation of water–tall oil emulsion

Sample no.	Lignin content in sulfate soap*, %	Emulsion phase			
		yield, %	content, %		
			water	resinious matter	lignin
3	0.86	10.8	46.5	31.8	7.2
	1.12	19.7	32.3	37.3	7.2
	3.37	33.9	48.9	32.1	6.7
	5.36	64.8	27.0	54.1	7.9
	8.08	40.2	31.0	45.0	8.2
4	4.01	52.0	32.4	45.6	8.0
2	1.90	21.5	49.8	41.3	8.9
6	1.97	5.4	51.8	21.8	20.7
	3.62	11.4	39.8	39.8	20.6
	4.64	14.2	48.9	32.1	17.4
	6.40	18.9	38.8	37.1	17.1

* Recalculated to absolutely dry substance.

Based on the data presented in Tables 1 and 2, we can conclude that spruce and deciduous kraft lignins, being more hydrophobic, exhibit the affinity for the oil phase. This is responsible for their stronger stabilizing effect as compared to pine lignin. The hydrophilic–oleophilic characteristics of lignin also affect the phase ratio of the emulsion. In stabilization with deciduous kraft lignin, 31–54% of oil component remains in the emulsion, while in stabilization with coniferous lignin the oil fraction is somewhat lower (21–42%).

The positive effect of addition of lignosulfonates on production of tall oil was noted previously [4, 5]. In this case, the system behaved differently depending on the characteristics of the added agent [3]. Only high-polymeric fraction of lignosulfonates exerts a positive effect on the recovery of the oil phase, while nonfractionated and low-molecular-weight agents decrease the rate and efficiency of phase separation. At the same time, addition of any lignosulfonate sample to the system decreases the extent and rate of separation of the aqueous phase. It was also noted that addition of high-polymeric fraction of lignosulfonates exerts a positive effect only in the case of its addition to sulfate soap before acid treatment.

With the aim to elucidate the mechanism of the effect of lignosulfonates on the water–tall oil emulsion, we carried out a series of model experiments on the reaction of kraft lignins with fractionated and commercial lignosulfonates in aqueous medium.

As additives, we used commercial lignosulfonates (ILSs) of ATsBK and low- and high-molecular-weight fractions produced from them by separation on a polysulfonamide membrane (pressure 0.40 MPa, flow velocity 7.87×10^{-3} $m^3\,m^{-2}\,h^{-1}$, degree of selection

Table 3. Characteristics of lignosulfonates

Characteristic	Initial ILS	Fraction of ILS	
		I	II
Average molecular weight M_w	37 800	8400	73 000
Content of main substance,* %	80.1	68.2	86.9
Ash content,* %	15.3	25.7	9.4
Content of reducing substances,* %	4.6	6.1	3.7
Sulfur content in organosulfur compounds, %	7.3	7.3	4.5

* Recalculated to absolutely dry substance.

0.77, and retention coefficient 0.85) (Table 3). The gel chromatograms of these fractions in a buffer solution (pH 6.2) on Sephadex G-75 are shown in Fig. 1.

The molecular-weight distribution (MWD) of the commercial sample (Fig. 1, curve *1*) is clearly bimodal, while the fractions recovered from this sample are monomodal and correspond mainly to fairly well-resolved high- and low-molecular-weight peaks of the initial lignosulfonates. Along with gel chromatograms and the average molecular weights M_w, the efficiency of fractionation is indirectly confirmed by the contents of ash, reducing substances, and sulfur in organosulfur compounds (Table 3).

From the samples of air-dry lignin (Table 1) we prepared a 5% alkaline solution simulating black liquor of the industrial process and containing 20% of a mixture of sodium sulfate and sodium hydroxide whose ratio ensured the solution density of 1160 kg m^{-3} and pH 10.5. The samples were placed into cylinders and thermostated at 85 ± 1°C, and lignosulfonates were added. The mixtures were treated with sulfuric acid with vigorous stirring at pH 2.5.

Without lignosulfonates, lignin immediately formed a precipitate whose volume did not change in time. For all the lignin samples, on adding any of the studied samples of lignosulfonates both before and after acidification, a suspension stable for 3 days and more was formed. It may be suggested that, in the presence of lignosulfonates with various MWDs, the hydrophilic–oleophilic ratio of modified particles of kraft lignin in the polyelectrolyte solution varies noticeably, which results in stabilization of the suspension. The data obtained differ substantially from those observed in the above laboratory experiments close to the real processes. This suggests that hydrophobization of lignin with tall oil is of considerable importance in the reaction of kraft lignin with lignosulfonates.

To elucidate the possibility of variation of the hydrophilic–oleophilic ratio of lignin, we studied the adsorption of fractionated and industrial lignosulfonates on lignins, whose characteristics are listed in Table 1.

The amount of adsorbed lignosulfonates was determined from the difference in their concentrations in the solution before and after adsorption:

$$\Gamma = (c_0 - c_1)\frac{V}{m}, \quad (1)$$

where Γ is the amount of adsorbed lignosulfonates (kmol kg^{-1}); c_0, the initial concentration of lignosulfonates in the solution (kmol m^{-3}); c_1, the equilibrium concentration in the solution after adsorption (kmol m^{-3}); m, the weighed portion of the adsorbent (kg); and V, the volume of the solution of lignosulfonates (m^3).

The content of lignosulfonates in the solution was monitored by the surface tension technique [6], using the calibrating curve $\sigma = f(c)$ for the selected samples at a given temperature.

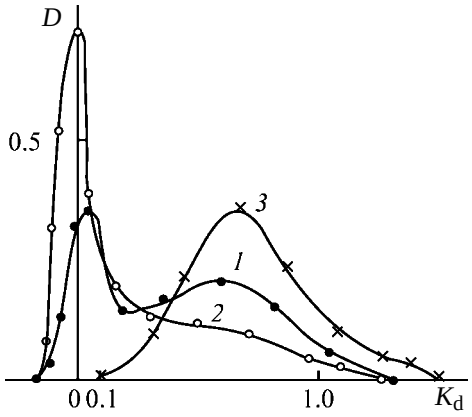

Fig. 1. Gel-chromatograms of lignosulfonates. (*D*) Optical density at λ = 280 nm and (K_d) distribution coefficient. (*1*) Industrial samples; fractions: (*2*) I and (3) II.

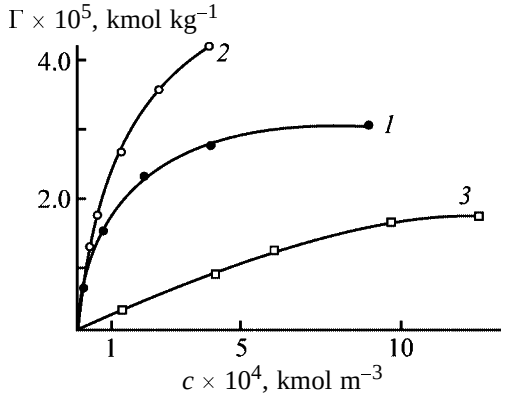

Fig. 2. Adsorption Γ on kraft lignin no. 3 as a function of concentration *c*: (*1*) commercial lignosulfonates (M_w = 37000); fraction: (*2*) I (M_w = 8400) and (*3*) II (M_w = 73000).

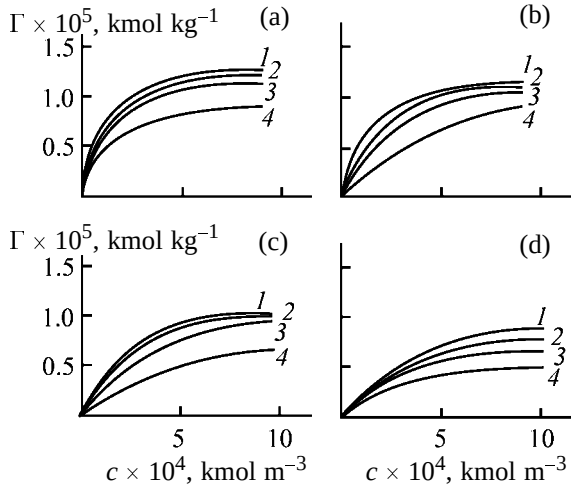

Fig. 3. Adsorption of lignosulfonates on kraft lignin Γ as a function of concentration *c* at pH 6.2: (a) before conditioning with tall oil; with conditioning at tall oil concentration of (b) 0.03, (c) 3, and (d) 30%. Kraft lignin sample no.: (*1*) 7, (*2*) 6, (*3*) 4, and (*4*) 3.

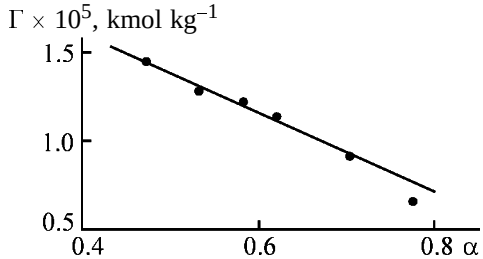

Fig. 4. Correlation between the degree of oleophilicity of kraft lignin α and the maximum adsorption of lignosulfonates on lignin Γ.

It follows from Fig. 2 that the adsorption on lignin no. 3 decreases with increasing molecular weight of lignosulfonates. Previous studies [7–11] showed an increase in the surface activity of lignosulfonates with increasing molecular weight. This is caused by the fact that high-molecular-weight lignosulfonates have more developed hydrophobic hydrocarbon part than low-molecular-weight lignosulfonates.

When dispersion of solid particles in the solution is considered in parallel with adsorption, it is characteristic [9] that dispersion of lignin suspension with lignosulfonates that have the highest molecular weight and surface activity begins with the first small additions of lignosulfonate and abruptly increases with their amount, reaching higher values in comparison with other samples. With respect to the ability of fractionated lignosolfonates to disperse a suspension, they can be ranked in the order corresponding to the increase in the molecular weight. This trend is well pronounced in adsorption on lignins with various degrees of oleophilicity.

Of the most interest for the industrial use is adsorption of industrial lignosulfonates on kraft lignin in the presence of the hydrophobic component of the emulsion layer, tall oil formed in decomposition of sulfate soap. Therefore, in further experiments we studied adsorption of commercial lignosulfonates on kraft lignin recovered at various pH from liquors formed in cooking of coniferous and deciduous wood (Table 1) before and after preconditioning of lignin suspension with tall oil of various concentrations.

In the absence of tall oil, the adsorption noticeably increases with increasing degree of hydrophilicity of kraft lignin (Fig. 3a). An increase of the amount of tall oil added to the suspension does not alter the shape of the adsorption isotherms (Figs. 3b–3d), but results in a significant decrease in adsorption of lignosulfonates on the lignin surface. Based on this fact, we can make a conclusion on additional hydrophobization of the lignin surface as a result of interaction with tall oil. This is also confirmed by the correlation between the degree of oleophilicity of the studied lignins and the maximum adsorption of lignosulfonates on these lignins (Fig. 4). This correlation shows how the lignin surface as an emulsion stabilizer is modified in the system tall oil–polyelectrolyte solution–lignin.

CONCLUSIONS

(1) Studies of the interphase interactions in the system tall oil–aqueous salt solution–lignin showed that the hydrophilic–oleophilic characteristics of lignin affect the stability and phase ratio of the emulsion: deciduous lignin, being more hydrophobic, exerts a stronger stabilizing effect than pine lignin.

(2) Addition of lignosulfonates with various molecular weight distributions noticeably affects the hydrophilic–oleophilic ratio of kraft lignin particles in the polyelectrolyte solution, which results in stabilization of the suspension.

REFERENCES

1. Selyanina, S.B., Afanas'ev, N.I., Bogomolov, B.D., and Yanglyaeva, N.Zh., in *Khimiya drevesiny i lesokhimiya: Tr. Komi Nachn. Tsentra Ural'sk. Otd. Ross. Akad. Nauk* (Wood Chemistry: Proc. Komi Sci. Center, Ural Division, Russian Acad. Sci.), Syktyvkar, 1997, pp. 126–132.
2. Selyanina, S.B., Bogolitsyn, K.G., and Yanglyaeva, N.Zh., *Lesn. Zh.*, 2000, no. 3, pp. 123–129.
3. Selyanina, S.B., Afanas'ev, N.I., and Makarevich, N.A., *Zh. Prikl. Khim.*, 2000, vol. 73, no. 12, pp. 1986–1991.
4. Lewis, N.G., Goring, D.A.J., and Wong, A., *Can. J. Chem.*, 1983, vol. 61, pp. 416–420.
5. Norman, H.S. and George, P., *Proc. Int. Tall Oil Symp.*, Imatra (Finland), June 7–9, 1983, pp. 110–130.
6. Afanas'ev, N.I., Telysheva, G.M., and Makarevich, N.A., *Khim. Drev.*, 1990, no. 1, pp. 20–26.
7. Afanas'ev, N.I., Structure of Macromolecules in Solutions and at the Phase Boundaries and Surface-Active Characteristics of Lignosulfonates, *Doctoral Dissertation*, St. Petersburg, 1996.
8. Tel'tevskaya, S.E., Formation of Surface-Active Characteristics of Lignosulfonates in Wood Delignification Processes and Their Control by Physicochemical Actions, *Cand. Sci. Dissertation*, St. Petersburg, 1996.
9. Afanas'ev, N.I., Telysheva, G.M., Makarevich, N.A., and Khrol, Yu.S., *Khim. Drev.*, 1990, no. 2, pp. 85–92.
10. Sapotnitskii, S.A., *Ispol'zovanie sul'fitnykh shchelokov* (The Use of Sulfite Liquors), Moscow: Lesn. Prom–st., 1981.
11. Chudakov, M.I., *Promyshlennoe ispol'zovanie lignina* (Industrial Use of Lignin), Moscow: Lesn. Prom–st., 1983.

Russian Journal of Applied Chemistry, Vol. 75, No. 11, 2002, pp. 1878–1882. Translated from Zhurnal Prikladnoi Khimii, Vol. 75, No. 11, 2002, pp. 1915–1919.
Original Russian Text Copyright © 2002 by Platonov, Polovetskaya, Proskuryakov, Shavyrina.

CHEMISTRY OF FOSSIL FUEL

Pyrolysis Kinetics of Phenols from Lignite Semicoking Tar

V. V. Platonov, O. S. Polovetskaya, V. A. Proskuryakov, and O. A. Shavyrina

Leo Tolstoy Tula State Pedagogical University, Tula, Russia
St. Petersburg State Technological Institute, St. Petersburg, Russia

Received January 28, 2002

Abstract—The features of pyrolysis of phenols from lignite semicoking tar were studied. The activation energy and order of the reactions of accumulation of methane, hydrogen, carbon monoxide and dioxide, naphthalene and its methyl homologs, phenols, and isomeric cresols and dimethylphenols were determined.

The goals of this work were to study the kinetic features of pyrolysis of phenols from lignite (near-Moscow fields) semicoking tar at 750–900°C, contact time of 0.5–6.0 s, and volume dilution with argon of 1 : 25, to determine the major pathways of pyrolysis, and to calculate the kinetic characteristics of accumulation of particular gaseous and liquid pyrolysis products. Pyrolysis of individual phenols has been extensively studied [1–21]; however, in some of these papers [1–7] data on the chemical group, qualitative, and quantitative component composition of the forming liquid products are virtually lacking, and no kinetic calculations are performed. To examine the feasibility of using the phenolic fraction of the lignite semicoking tar as a source of compounds whose production by other procedures is less profitable, it seemed interesting to study high-temperature pyrolysis of this fraction. Understanding of the behavior of this major (up to 40 wt %) component of the semicoking tar and knowledge of the kinetic parameters of accumulation of particular gaseous and liquid pyrolysis products are necessary for predicting the composition of "secondary" tars and for developing the mathematical model of tar pyrolysis as a whole.

Hypothetical structural formulas of compounds present in the phenolic fraction of lignite semicoking tar are shown in the scheme. According to [22–26], these include alicyclic (**1**–**7, 15, 24**), heterocyclic (**8**–**14, 16, 17, 26**), and aromatic (**17**–**23, 25**–**32**) compounds containing various alkyl and functional substituents. However, data on the kinetic features of high-temperature transformations of both individual phenols and phenolic fraction of the semicoking tar are virtually lacking.

In this connection, it is appropriate to study the kinetic features of high-tempertature pyrolysis of phenols from lignite semicoking tar and suggest possible pathways of formation of the identified liquid and gaseous products by thermal decomposition of particular components of phenols.

The kinetic parameters of accumulation of methane, hydrogen, carbon monoxide, carbon dioxide, and major liquid products are listed in the table.

Formation of methane follows a first-order equation; the activation energy E_a is 45.2 kJ mol^{-1}. The first order of the reaction is apparently due to the presence of various hydrocarbon substituents in the initial phenols which are cleaved to smaller fragments (and, finally, to methane) under the conditions of high pyrolysis temperatures and high concentrations of atomic hydrogen in the reaction zone.

Accumulation of hydrogen follows a 1.5-order equation; E_a = 66.1 kJ mol^{-1}.

Accumulation of CO follows a second-order equation; E_a = 42.8 kJ mol^{-1}. At lower temperatures, CO is formed by decomposition of quinoid rings and aromatic ketones; with increasing temperature, a growing contribution is made by processes involving pyrocarbon and water released in dehydration and pyrolysis:

$$C + H_2O \rightarrow CO + H_2, \quad (I)$$

$$C + CO_2 \rightarrow 2CO. \quad (II)$$

Thus, the overall reaction of CO accumulation is described by a second-order equation.

For the accumulation of CO_2, the reaction order is 1.5, and E_a = 81.8 kJ mol^{-1}. The noninteger reaction order is due to simultaneous occurrence of decarboxylation and reactions involving pyrocarbon:

$$C + 2H_2O \rightarrow CO_2 + 2H_2. \quad (III)$$

1070-4272/02/7511-1878$27.00 © 2002 MAIK "Nauka/Interperiodica"

Scheme

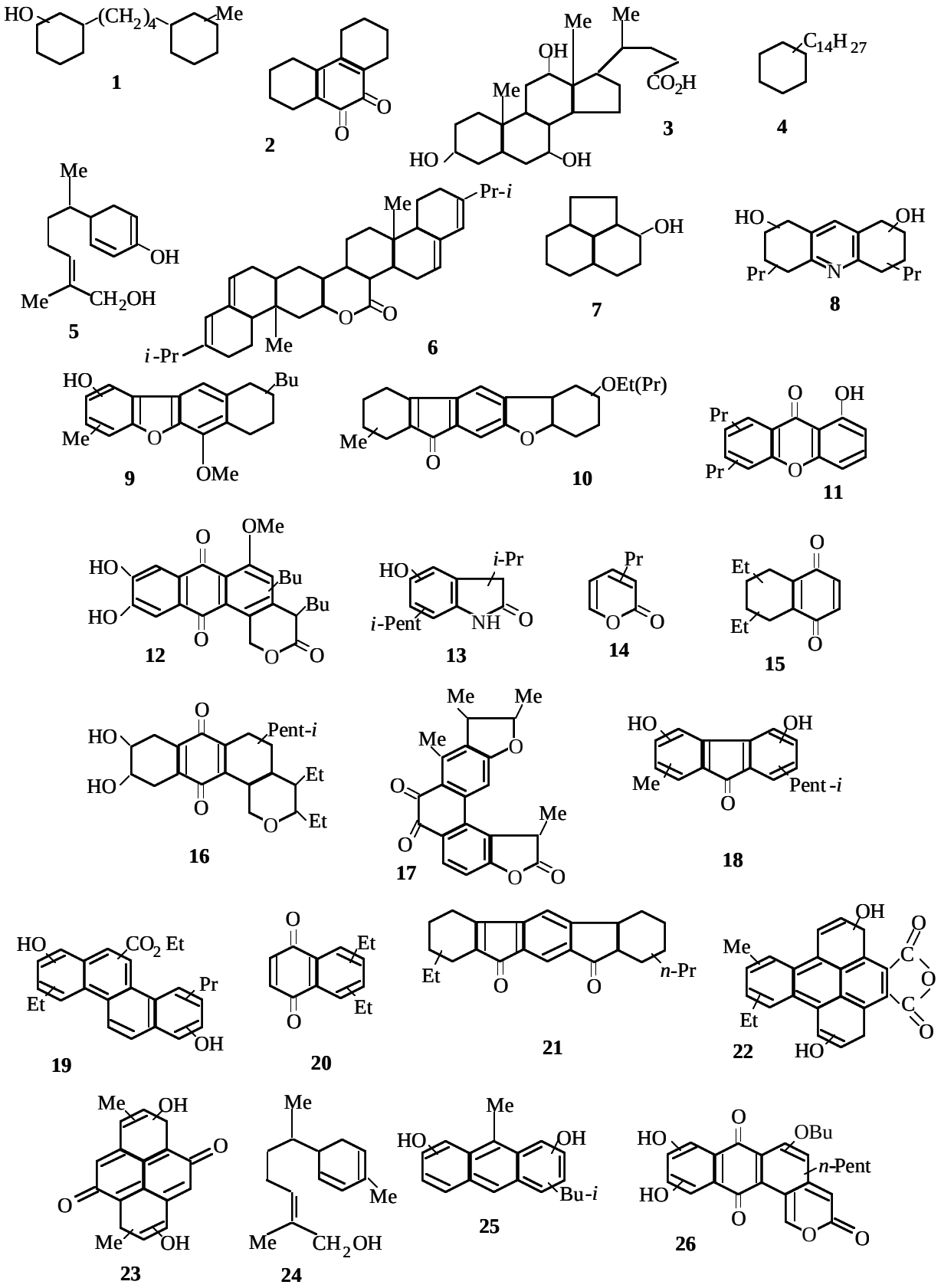
HO
(CH2)4
Me
1
O
O
2
Me
Me
OH
CO2H
Me
HO
OH
3
C14H27
4
Me
OH
Me
CH2OH
5
Me
Pr-i
O
O
i-Pr
Me
6
OH
7
HO
OH
Pr
N
Pr
8
HO
Bu
Me
O
OMe
9
OEt(Pr)
Me
O
O
10
O
OH
Pr
Pr
O
11
O
OMe
HO
Bu
HO
Bu
O
O
O
12
i-Pr
HO
i-Pent
NH
O
13
Pr
O
O
14
O
Et
Et
O
15
O
Pent-i
HO
Et
HO
O
Et
O
16
Me
Me
Me
O
O
Me
O
O
17
HO
OH
Me
Pent-i
O
18
HO
CO2 Et
Et
Pr
OH
19
O
Et
O
Et
20
Et
O
O
n-Pr
21
OH
O
Me
C
O
Et
C
O
HO
22
Me
OH
O
O
Me
OH
23
Me
Me
CH2OH
24
Me
HO
OH
Bu-i
25
O
OBu
HO
n-Pent
HO
O
O
26

Scheme (Contd.)

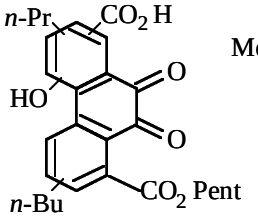

27

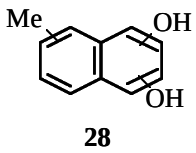

28

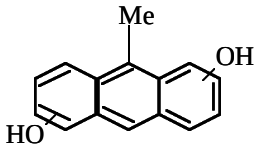

29

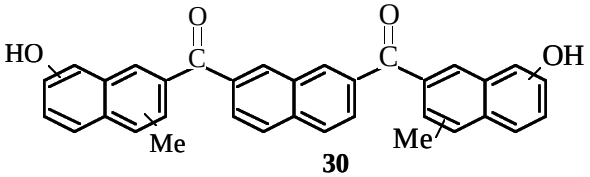

30

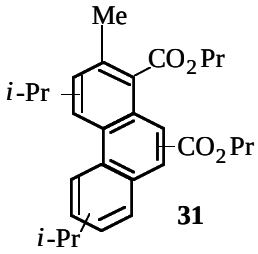

31

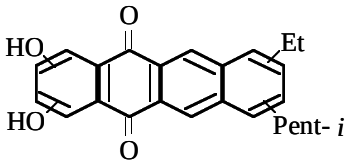

32

Accumulation of the liquid products is described by equations of orders 1 and 1.5. The first order of accumulation of particular components is due to the fact that the initial phenols contain compounds in which these components are structural fragments linked by carbonyl bridges or long hydrocarbon chains, unsubstituted or substituted with, e.g., phenolic and carboxy groups. Such bonds are the weakest and are cleaved first. Thus, these components are formed directly in pyrolysis of the initial phenols (1- and 2-methylnaphthalenes, *m*-cresol, 2,3-, 2,5-, and 3,4-dimethylphenols). The 1.5-order accumulation is characteristic of naphthalene, phenol, *o*- and *p*-cresols, and 2,6- and 3,5-dimethylphenols. These compounds, along with direct formation from the initial phenols, are products of cyclization, condensation, isomerization, and disproportionation; therefore, their accumulation is described by a more complex kinetic equation. The activation energy of accumulation is the highest for 1-methylnaphthalene (112 kJ mol^{-1}) and the lowest for 3,5-dimethylnaphthalene (19 kJ mol^{-1}). Among isomeric cresols, it is the highest for *o*-cresol (111 kJ mol^{-1}) and the lowest for *p*-cresol (47.2 kJ mol^{-1}).

Kinetic parameters of accumulation of particular gaseous and liquid pyrolysis products

Components	Reaction order	Equation for the rate constant k
Hydrogen	1.5	$4.39 \times 10^{-2} \exp(-66.1/RT)$
Methane	1.0	$6.43 \times 10^{-4} \exp(-45.2/RT)$
Carbon monoxide	2.0	$9.99 \times 10^{6} \exp(-42.8/RT)$
Carbon dioxide	1.5	$4.68 \times 10^{5} \exp(-81.8/RT)$
Naphthalene	1.5	$3.66 \exp(-67.4/RT)$
1-Methylnaphthalene	1.0	$5.73 \times 10^{4} \exp(-112/RT)$
2-Methylnaphthalene	1.0	$2.41 \times 10^{2} \exp(-62.2/RT)$
Phenol	1.5	$1.91 \times 10^{-2} \exp(-97.8/RT)$
o-Cresol	1.5	$1.98 \times 10^{8} \exp(-111/RT)$
m-Cresol	1.0	$1.56 \times 10^{2} \exp(-56.3/RT)$
p-Cresol	1.5	$1.24 \times 10^{5} \exp(-47.2/RT)$
2,6-Dimethylphenol	1.5	$1.01 \times 10^{5} \exp(-43.5/RT)$
2,5-Dimethylphenol	1.0	$8.92 \times 10^{1} \exp(-49.3/RT)$
2,3-Dimethylphenol	1.0	$4.87 \exp(-90.6/RT)$
3,4-Dimethylphenol	1.0	$6.32 \exp(-28.6/RT)$
3,5-Dimethylphenol	1.5	$6.07 \times 10^{3} \exp(-19.0/RT)$

As for isomeric dimethylphenols, the activation energies for 2,5- and 2,6-dimethylphenols are close (49.3 and 43.5 kJ mol^{-1}, respectively), but for 2,3-dimethylphenol E_a is substantially higher, 90.6 kJ mol^{-1}.

In the first stages of pyrolysis, the main reactions responsible for formation of gaseous and liquid pyrolysis products are decarbonylation (IV), decarboxylation (V), and dealkylation (VI).

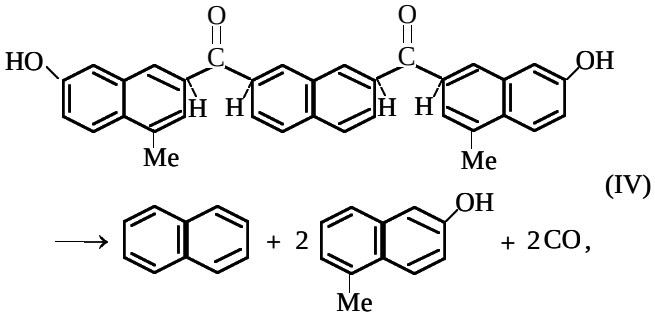

(IV)

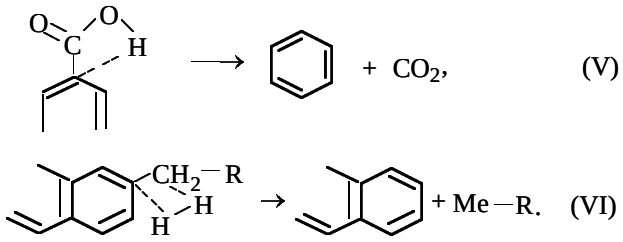

To confirm this assumption, we calculated for these reactions the activation energy, using the procedure in [27]. For example, for reaction (IV) E_a is 100.6 (taking into account release of 2 mol of CO), for (V), 121.5, and for (VI), 79.6 kJ mol^{-1}.

Specifically reactions (IV)–(VII) will occur first, determining the composition of pyrolysis products at low temperatures and short (0.5–1.5 s) contact times:

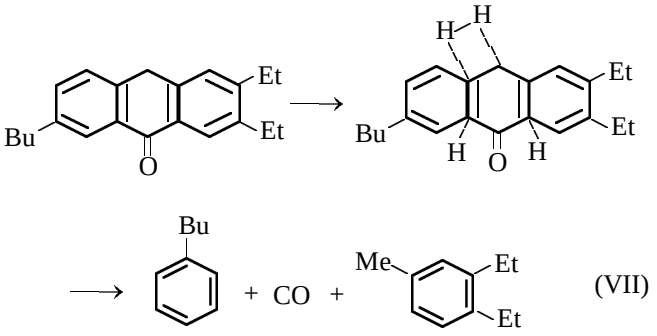

E_a = 146.7 kJ mol^{-1}.

As the pyrolysis conditions become more rigorous, the contribution of condensations and cyclizations increases:

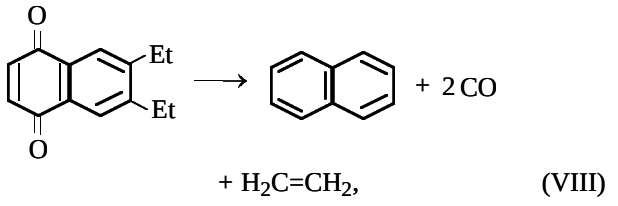

E_a = 280.7 kJ mol^{-1};

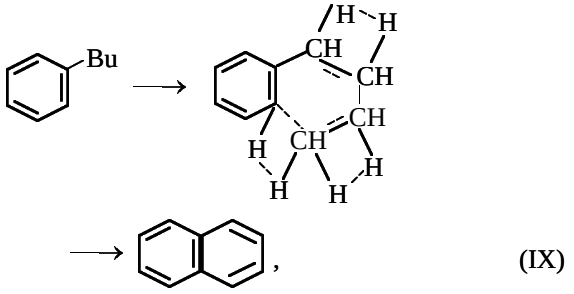

E_a = 632.7 kJ mol^{-1};

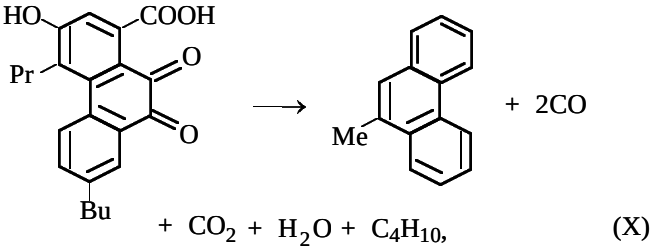

E_a = 972.1 kJ mol^{-1}.

The above calculations of E_a once again confirm the reaction sequence in pyrolysis of phenols: Less energy-consuming processes occur at lower temperatures and shorter (0.5–1.5 s) contact times, whereas under more rigorous conditions the contribution of reactions requiring more energy increases.

It should be noted that we are dealing with effective E_a of a rather complex process involving numerous branched successive and parallel reactions. According to the analysis results, phenols undergo both degradation and condensation to higher-molecular-weight products (neutral oxygen-containing compounds, asphaltenes). The final condensation product is pyrocarbon; its yield sharply increases in going to more rigorous pyrolysis conditions. Our special experiments (pyrolysis on pyrocarbon packing) confirmed the autocatalytic effect of pyrocarbon in pyrolysis.

The calculations show that homogeneous pyrolysis of phenols is a complex and multistage process, which is due to specific features of the chemical composition of the phenols and their degradation products.

CONCLUSIONS

(1) The kinetic features of pyrolysis of phenols from lignite (near-Moscow fields) semicoking tar were studied.

(2) The activation energies were calculated, and the reaction orders were determined for accumulation of methane, hydrogen, carbon monoxide and dioxide, naphthalene, 1- and 2-methylnaphthalenes, phenol, and isomeric cresols and dimethylphenols.

(3) Calculations of the activation energy by the additive scheme gave the results consistent with the bond energies in the activated complex. The sequence of reactions in pyrolysis of phenols was determined.

REFERENCES

1. Tishchenko, D.N., Foliadov, V.G., and Nosova, N.M., *Zh. Prikl. Khim.*, 1956, vol. 29, no. 9, pp. 1447–1449.

2. Muller, E., *J. Pr. Chem.*, 1898, vol. 38, no. 1, pp. 27–45.
3. Fischer, F. and Ehrhardt, U., *Gesamm. Abhandl. Kenntn. Kohle*, 1919, vol. 4, pp. 237–261.
4. Meyer, H. and Hoffmann, A., *Monatsh. Chem.*, 1917, vol. 38, pp. 343–346.
5. Kramers, A., *Brennstoff-Chemie*, 1877, vol. 189, p. 129.
6. Meyer, H. and Wesche, B., *Ber.*, 1917, vol. 50, pp. 441–445.
7. Jones, B.W. and Neuworth, M.B., *Ind. Eng. Chem.*, 1952, vol. 12, pp. 2772–2880.
8. Cypres, R., *Ann. Mines Belg.*, 1965, nos. 7–8, pp. 1091–1109.
9. Cypres, R., Braekmann, C., Bredael, P., and Einhorn, L., *Ann. Mines Belg.*, 1970, no. 9, pp. 1105–1113.
10. Yamasaki, Y., Kamai, T., and Higuchi, T., *J. Jpn. Petrol. Inst.*, 1971, vol. 14, no. 8, pp. 594–600.
11. Braekmann-Danheux, C. and Heyvaert, A., *Ann. Mines Belg.*, 1972, vol. 1, pp. 37–44.
12. Cypres, R. and Bettens, B., *Tetrahedron*, 1971, vol. 30, no. 10, pp. 1253–1260.
13. Delaunois, C. and Bettens, B., *Ann. Mines Belg.*, 1968, no. 5, pp. 633–641.
14. Kawese, T., Arai, H., Tominaga, H., and Kunugi, T., *J. Chem. Soc. Jpn., Ind. Chem. Sect.*, 1970, vol. 73, no. 5, pp. 959–964.
15. Platonov, V.V., Ivleva, L.N., and Prokof'ev, E.E., *Khim. Tverd. Topl.*, 1980, no. 2, pp. 138–147.
16. Platonov, V.V., Ivleva, L.N., Klyavina, O.A., and Prokof'ev, E.E., *Khim. Tverd. Topl.*, 1982, no. 5, pp. 89–99.
17. Platonov, V.V., Klyavina, O.A., Ivleva, L.N., and Prokof'ev, E.E., *Khim. Tverd. Topl.*, 1983, no. 2, pp. 138–144.
18. Platonov, V.V., Ivleva, L.N., Klyavina, O.A., and Prokof'ev, E.E., *Khim. Tverd. Topl.*, 1981, no. 5, pp. 84–94.
19. Platonov, V.V., Klyavina, O.A., Prokof'ev, E.E., and Ivleva, L.N., *Khim. Tverd. Topl.*, 1981, no. 6, pp. 96–103.
20. Platonov, V.V., Ivleva, L.N., and Klyavina, O.A., *Khim. Tverd. Topl.*, 1984, no. 3, pp. 105–114.
21. Platonov, V.V., Klyavina, O.A., and Ivleva, L.N., *Khim. Tverd. Topl.*, 1986, no. 5, pp. 75–84.
22. Platonov, V.V., Klyavina, O.A., Prokof'ev, E.E., and Ivleva, L.N., *Khim. Tverd. Topl.*, 1983, no. 4, pp. 144–150.
23. Platonov, V.V., Ivleva, L.N., Klyavina, O.A., and Tabolenko, N.V., *Khim. Tverd. Topl.*, 1985, no. 5, pp. 71–78.
24. Platonov, V.V., Ivleva, L.N., Klyavina, O.A., and Kanitskaya, L.V., *Khim. Tverd. Topl.*, 1989, no. 4, pp. 116–121.
25. Platonov, V.V., Ivleva, L.N., Klyavina, O.A., and Tikhonenko, N.I., Available from NIITEKhIM, Cherkassy, 1989.
26. Platonov, V.V., Proskuryakov, V.A., Manuel' Afonso, and Nechaeva, E.A., *Zh. Prikl. Khim.*, 1998, vol. 71, no. 10, pp. 1725–1728.
27. Moin, F.B., *Usp. Khim.*, 1967, vol. 36, no. 7, pp. 1223–1243.

Russian Journal of Applied Chemistry, Vol. 75, No. 11, 2002, pp. 1883–1884. Translated from Zhurnal Prikladnoi Khimii, Vol. 75, No. 11, 2002, pp. 1920–1921.
Original Russian Text Copyright © 2002 by Moiseeva, Kurylev, Pomerantsev, Tubolkin.

BRIEF COMMUNICATIONS

Catalyst for Melamine Production

I. D. Moiseeva, A. Yu. Kurylev, V. M. Pomerantsev, and A. F. Tubolkin

Novomoskovsk Institute, Mendeleev Russian University of Chemical Engineering, Novomoskovsk, Tula oblast, Russia

St. Petersburg State Technological Institute, St. Petersburg, Russia

Received February 5, 2002

Abstract—A novel electrolytic method for preparing the catalyst (active aluminum oxide) for melamine synthesis and a process for catalytic synthesis of melamine from urea are proposed.

Melamine (1,3,5-triamino-2,4,6-triazine) is a valuable precursor in production of plastics, lacquers, and adhesives exhibiting high mechanical strength, stability in hot water and in organic solvents, low electrical conductivity, and high thermal stability. These materials based on melamine–formaldehyde resin are widely used in various branches of industry [1, 2].

To synthesize melamine from urea, we developed a catalyst, active aluminum oxide with the specific surface of about 300–400 $m^2 g^{-1}$.

A goal of this work was to develop a low-waste procedure for preparing the catalyst, by ensuring stable conditions of granule formation and improved quality of the target product.

We improved a process for production of $Al(OH)_3$ and γ-Al_2O_3 to increase the melamine content in the target product from 80 to 96–98%. Initially we took commercial aluminum hydroxide with the specific surface area of 80–120 $m^2 g^{-1}$. Impurities present in it (up to 0.1 wt % Na_2O, 0.1 SiO_2, and 0.4 Fe_2O_3) adversely affected the quality of the γ-Al_2O_3 obtained (the melamine yield was about 80%). To remove them, commercial aluminum hydroxide was reprecipitated from chemically pure grade HNO_3, washed to remove ammonia, molded, dried, and calcined. The thus prepared γ-Al_2O_3 provided the melamine yield of up to 88.5% and had the specific surface area of 160–170 $m^2 g^{-1}$, which is insufficient for commercial production of melamine.

Nevertheless, the above study showed that purification of alumina increases the process selectivity. However, the above purification procedure is unacceptable, because the increase in the number of reprecipitation stages complicates the technology and increases the washwater amount. Therefore, we developed a method for preparing $Al(OH)_3$ from pure metallic aluminum by electrolytic precipitation. The precipitate was molded in grains by a sol–gel process and then was thermally treated to obtain granulated γ-Al_2O_3 [3].

Two electrodes (200 × 120 × 15-mm plates) made from metallic aluminum (99.9 wt % Al) were placed parallel to each other at a distance of 10–15 cm in a glass vessel filled with distilled water containing 2–4 wt % NH_4NO_3 as an electrolyte; dc electrolysis was performed at I = 27 A and U = 65 V.

A gel-like $Al(OH)_3$ precipitate was formed on the anode. The pulp was separated at the solid : liquid ratio of 1 : 8 by centrifuging, and a substance with the solid : liquid ratio of 1 : 4 and pH 7 was obtained. Concentrated chemically pure grade HCl was added to decrease pH to 3–4. A transparent thixotropic colloid of basic aluminum chloride (BAC) was thus obtained by the reaction [4]

$$2Al(OH)_3 + HCl \rightarrow Al_2(OH)_5Cl + H_2O \qquad (1)$$

with the Al_2O_3 content of 50 g dm^{-3}; it was aged at room temperature for 12–24 h.

A drop-oil method was used to mold granules. A molding mass was poured in a cone-shaped vessel and fed through a pipette 1.5 mm in diameter at a rate of 2–3 drops s^{-1} into a molder, a cylinder filled with a two-phase liquid (3–4-cm layer of kerosene to form drops and 25% aqueous solution of urea to form three-dimensional gel structure; the layer thick was sufficient for neutralization of granules for 3–4 min). In the first stage, granules were dried for 1 day in air. In the second stage, they were dried in a vacuum drier for 2–3 days at 40°C. Then the temperature was elevated at a 10 deg h^{-1} rate to 150°C, and at this tem-

1070-4272/02/7511-1883$27.00 © 2002 MAIK "Nauka/Interperiodica"

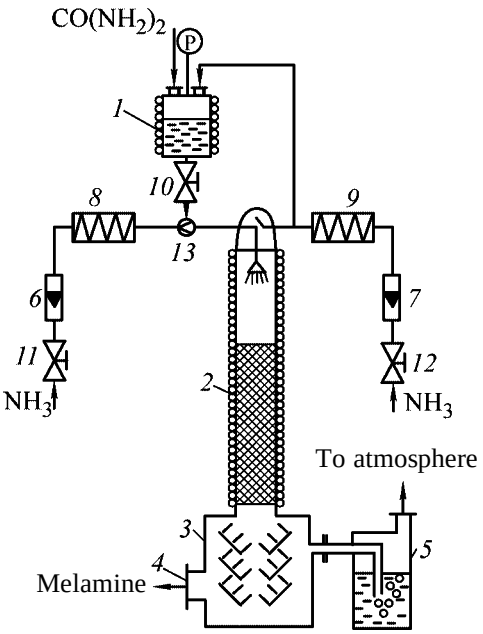

Scheme of the pilot setup for melamine production from urea: (*1*) melter, (*2*) catalytic reactor, (*3*) sublimer with packings for collecting product, (*4*) hatch for unloading the target product, (*5*) bubbler with ammonia water, (*6, 7*) rotameters, (*8, 9*) ammonia heaters, (*10–12*) valves, and (*13*) injector.

perature the granules were kept for 4 h. In the third stage, granules were calcined in a muffle furnace according to the following schedule: heating at a rate of 20 deg h^{-1} from 150 to 200°C, 50 deg h^{-1} from 200 to 500°C, 100 deg h^{-1} from 500 to 900°C; keeping at 900°C for 4 h; and gradual cooling and sampling. Production of the catalyst was tested in a pilot setup (see figure).[1]

The urea melt is fed from a melter *1* at 140–160°C under a pressure of 0.8 MPa into the reactor *2*. Ammonia heated to 350–500°C is also fed at the melt to gas wt ratio of 1 : (7–9). In the reactor, the melt is entrained with the gas and decomposes by the reaction

$$CO(NH_2)_2 \rightarrow HNCO + NH_3. \quad (2)$$

[1] The pilot setup was developed in Novomoskovsk Institute, Mendeleev Russian University of Chemical Engineering.

A mixture of cyanic acid and ammonia is fed to the catalyst bed, where melamine is formed by the reaction

$$6HNCO \rightarrow C_3H_6N_6 + 3CO_2 \quad (3)$$

at a pressure of 0.1–0.2 MPa.

The reaction products are sublimed in vessel *3* at 180–200°C. Melamine as a white finely dispersed powder is unloaded through hatch *4*. An NH_3 + CO gas mixture from the sublimer is bubbled through water in vessel *5*, where ammonia partially dissolves. The urea conversion amounts to 97–98%, and the yield of the target product is 98% [5].

CONCLUSION

The developed procedure for preparing granulated γ-Al_2O_3 provides high specific surface area of the catalyst (up to 300–400 $m^2\ g^{-1}$) and elevated selectivity with respect to the target product, melamine (yield 96–98%).

REFERENCES

1. Hermann, D.F., *Nitrogen*, 1973, no. 83, pp. 49–50.
2. Haines, W., *Nitrogen*, 1966, no. 40, pp. 32–34.
3. Moiseev, I.D.,, Kurylev, A.Yu., and Pomerantsev, V.M., Abstracts of Papers, *Konferentsiya molodykh uchenykh, Novomoskovskii institut Rossiiskogo khimiko-tekhnologicheskogo universiteta im. D.I.Mendeleeva* (Conf. of Young Scientists, Novomoskovsk Inst., Mendeleev Russian Univ. of Chemical Engineering), Novomoskovsk: NI RKhTU, 2001, pp. 200–201.
4. Sychev, M.M., *Neorganicheskie klei* (Inorganic Adhesives), Leningrad: Khimiya, 1974.
5. Moiseev. I.D., Kurylev, A.Yu., and Pomerantsev, V.M., Abstracts of Papers, *XIV Mezhdunarodnaya konferentsiya "Uspekhi v khimii i khimicheskoi tekhnologii"* (XIV Int. Conf. "Progress in Chemistry and Chemical Technology), Moscow: RKhTU, 2001, pp. 20–23.

Russian Journal of Applied Chemistry, Vol. 75, No. 11, 2002, pp. 1885–1886. Translated from Zhurnal Prikladnoi Khimii, Vol. 75, No. 11, 2002, pp. 1922–1923.
Original Russian Text Copyright © 2002 by Aronova, Ginak.

BRIEF COMMUNICATIONS

A Procedure for Isolating Desmotropic Forms of Tautomeric Compounds, with 5-Benzylidene-2-mercapto-Δ^2-thiazolin-4-one as Example

E. B. Aronova and A. I. Ginak

St. Petersburg State Technological Institute, St. Petersburg, Russia

Received March 29, 2002

Abstract—Reaction of aniline with a mixture of tautomes of 3-benzylidene-4-oxothiazolidine-2-thione, followed by treatment with hydrogen chloride, allowed isolation of the pure desmotropic form of this compound, 5-benzylidene-2-mercapto-Δ^2-thiazolin-4-one.

It is known that different tautomers of synthetic and natural biologically active substances exhibit different activity [1]; therefore, isolation of pure desmotropic forms is an urgent problem. However, this is often difficult and even impossible, because tautomeric transformations are reversible, with the position of the equilibrium depending on numerous factors: polarity and basicity of the medium, acid–base properties of tautomers, nature of substituents, ionic strength of solution, and, finally, thermodynamic characterisitcs of crystallization of desmotropic forms, since specifically the desmotropic form with the lower crystallization energy is isolated as a solid [2, 3]. Therefore, in most cases, the tautomeric equilibrium in crystallization is shifted toward one of the forms [4, 5], with the other form being detectable only in solution; this prevents studying its biological and physicochemical properties relevant to practical applications (in medicine, agriculture, and microelectronics).

Sometimes tautomers crystallize in two forms simultaneously; the crystals can be distinguished with a microscope [6, 7] and even separated manually, but this procedure is unsuitable for practice.

To develop an efficient procedure for isolating pure desmotropic forms, we chose 5-benzylidine-2-mercapto-Δ^2-thiazolin-4-one **IB** whose tautomerism and reactivity are well studied [8, 9].

It was shown previously that mercaptothiazolidine **IB** exists in equilibrium with its thione form, 5-benzylidene-4-oxothiazolidine-2-thione **IA**; these forms crystallize from solutions in a 1 : 0.55 ratio, respectively. The tautomers are weak bases with $pK_{a_{eff}}$ 9.34; the equilibrium is shifted toward less acidic form **IA** (the acidity gradient of the tautomers is 0.17). Potentiometric and conductometric studies [10] showed that the tautomers form stable salts with alkali metals and amines, existing in solutions as equilibrium mixtures of contact ion pairs and free ions. The degree of dissociation of the salts is higher in more polar solvents; in low-polarity solvents (dioxane, chloroform), the salts are nonconducting, i.e., they exist in the nondissociated form. This fact suggests the possibility of isolating the more acidic tautomeric form by the reaction with a base (e.g., $C_6H_5NH_2$) in a basic solvent; in this case, it can be expected that the base would react primarily with the more acidic form **IB** to form the corresponding salt. This suggestion was confirmed previously [11].

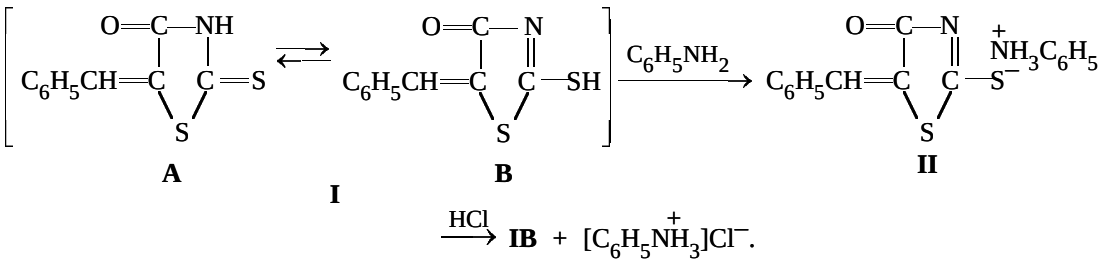

$\xrightarrow{HCl}$ **IB** + $[C_6H_5\overset{+}{N}H_3]Cl^-$.

1070-4272/02/7511-1885$27.00 © 2002 MAIK "Nauka/Interperiodica"

After solvent evaporation, chromatographically pure salt **II** is obtained. Its treatment with gaseous HCl yields a mixture of pure desmotropic form **IB** and amine hydrochloride; the latter can be quantitatively washed out with water. The composition and structure of **IB** were confirmed by elemental analysis and IR spectroscopy [12].

The acidity gradient of the tautomers can also be used for isolating one of the desmotropic forms by crystallization from a medium with appropriate pH. Indeed, according to Kabachnik [2], in media with pH ≤ pK_a the tautomeric equilibrium will be stabilized, with the more basic species forming an ion pair with the acid, which is solvated more strongly, and the more acidic species precipitating when the solubility is decreased. To check this assumption, we attempted to isolate the more acidic form **IB** from solutions with pH ≤ p$K_{a_{SH}}$. To do this, we added water to an acidified alcoholic solution of **I** (pH 7.5) to decrease the solubility; in the process, needle-shaped crystals of **IB** precipitated. Their composition and structure were confirmed by elemental analysis, IR spectroscopy [12, 13], mixing test, and TLC [14].

EXPERIMENTAL

The IR spectra were recorded on a UR-20 spectrometer.

TLC analysis was performed on standard Silufol-254 plates in the solvent system acetone : hexane : acetic acid, 1 : 2 : 0.01.

Compound **I** was prepared as described in [15] and purified by threefold recrystallization from ethanol; the product purity was checked by TLC (Al_2O_3).

Isolation of the thiol form. *a*. A 0.01-mol (2.21-g) portion of **I** was dissolved in 50 ml of aniline; the mixture was stirred for 10 min at room temperature and evaporated by half. Then dry HCl was passed for 30 min, 50 ml of chloroform was added, the mixture was evaporated to dryness, the solid residue was washed with 50 ml of water to remove aniline hydrochloride, and the precipitate was dried in a desiccator over phosphorus pentoxide. Yield 98%, mp 198°C. IR spectrum, ν, cm^{-1}: 1688 ($\nu_{C=O}$), 2515 ($\nu_{C=H}$), 860 (δ_{SH}).

Found, %: C 54.28, H 3.16, N 6.30, S 28.93.
$C_{16}H_{14}N_2OS_2$.
Calculated, %: C 54.30, H 3.17, N 6.33, S 28.96.

b. A 0.01-mol (2.21-g) portion of **I** was dissolved in 20 ml of ethanol, acetic acid was added to pH 7.5, the mixture was stirred for 20 min, the solution was evaporated by half, 20 ml of chloroform was added, and a small crystal of **I** was introduced. The precipitate that formed was filtered off, washed with water to neutral reaction, and dried in a desiccator over phosphorus pentoxide. Yield 97%, mp 198°C. The IR spectrum is identical to that of the sample prepared by method *a*.

Found, %: C 54.26, H 3.17, N 6.31, S 28.93.
$C_{16}H_{14}N_2OS_2$.
Calculated, %: C 54.30, H 3.17, N 6.33, S 28.96.

REFERENCES

1. Henichart, J.P., Houssin, R., Lablanche, B., *et al.*, *J. Heterocyclic Chem.*, 1977, vol. 14, no. 3, pp. 439–442.
2. Kabachnik, M.I., *Zh. Vses. Khim. O–va im. D.I. Mendeleeva*, 1962, vol. 7, no. 3, pp. 263–273.
3. Kitaigorodskii, A.I., *Molekulyarnye kristally* (Molecular Crystals), Moscow: Nauka, 1971.
4. Uner, M., Kovac, S., Martvon, A., and Jezek, M., *Chem. Zvesti*, 1978, vol. 32, no. 4, pp. 486–492.
5. Kamat, P.V., Laxmeshwar, N.B., and Datar, M.G., *J. Indian Chem. Soc.*, 1971, vol. 48, no. 2, pp. 199–203.
6. Boer, F.P., Turley, J.W., and Remoortere, F.P., *J. Chem. Soc., Chem. Commun.*, 1972, no. 9, pp. 573–574.
7. Rapi, G., Ginanneschi, M., and Belgodere, E., *J. Heterocyclic Chem.*, 1972, vol. 9, no. 2, pp. 285–292.
8. Ginak, A.I., V'yunov, K.A., and Sochilin, E.G., *Zh. Org. Khim.*, 1971, vol. 7, no. 7, pp. 1500–1506.
9. Ginak, A.I., V'yunov, K.A., and Ramsh, S.M., *Zh. Org. Khim.*, 1983, vol. 19, no. 1, pp. 212–215.
10. Sushchev, V.G., Ramsh, S.M., Ginak, A.I., and Sochilin, E.G., *Zh. Org. Khim.*, 1979, vol. 15, no. 8, pp. 1720–1723.
11. Ginak, A.I., V'yunov, K.A., and Sochilin, E.G., *Khim. Geterotsikl. Soedin.*, 1971, no. 3, pp. 858–859.
12. Lebedev, R.S., *Zh. Prikl. Spektrosk.*, 1971, vol. 15, no. 1, pp. 148–150.
13. V'yunov, K.A., Ginak, A.I., and Sochilin, E.G., *Zh. Prikl. Spektrosk.*, 1977, vol. 27, no. 6, pp. 1071–1077.
14. Ginak, A.I., V'yunov, K.A., and Sochilin, E.G., *Zh. Prikl. Khim.*, 1971, vol. 44, no. 9, pp. 2123–2126.
15. Brown, F.C., *Chem. Rev.*, 1961, vol. 61, no. 5, pp. 463–521.

Russian Journal of Applied Chemistry, Vol. 75, No. 11, 2002, pp. 1887–1888. Translated from Zhurnal Prikladnoi Khimii, Vol. 75, No. 11, 2002, pp. 1924–1925.
Original Russian Text Copyright © 2002 by the Editorial Board.

ANNIVERSARIES

Sergei Stepanovich Ivanchev (on 70th Anniversary of His Birthday)

On December 1, 2002, Sergei Stepanovich Ivanchev, one of the leading polymer scientists, doctor of chemical science, professor, corresponding member of the Russian Academy of Sciences, Honored Scientist and Technologist of the Russian Federation, winner of the Prize of the Council of Ministers of the USSR, awardee of the Academician Kargin Award, and director of the St. Petersburg Branch of the Boreskov Institute of Catalysis, Siberian Division, Russian Academy of Sciences, is 70.

S.S. Ivanchev started his scientific and pedagogical activities at Lvov State University and continued these activities at Mechnikov State University in Odessa, where he defended his doctoral dissertation and made a career, from docent, acting head of a chair, to dean of the chemical faculty. In the 1970s, Ivanchev headed a department of exploratory research, organized by him at Plastpolimer Okhta Research and Production Association (St. Petersburg), where he was the first deputy general director for research from 1981 till 1998. At the end of 1998, he organized a branch of the Boreskov Institute of Catalysis, presently headed by him.

Ivanchev's scientific interests are in radical oligomerization and polymerization in homogeneous and heterogeneous systems (including emulsion polymerization, polymerization filling, and processes used to obtain polymeric formulations) and in catalysis of polymerization and oligomerization.

He substantiated scientifically and implemented pathways for synthesis of new classes of polyfunctional components used to obtain oligomers and reactive polymers and polymer systems (initiators, emulsifiers, monomers, fillers, etc.). In studying the polymerization initiated by polyfunctional initiators, he suggested for the first time and proved the polymerization–recombination nature of macromolecule formation and revealed conditions for its implementation. He formulated and implemented procedures for obtaining new polymers with complex structure and improved properties. Under Ivanchev's supervision, new methods for obtaining new latex systems with controllable morphology for coatings with a wide variety of properties, and also a number of filled formulations

for vibration-absorbing polymer systems and formulations for ship-building, electronic, and automobile industries were developed. In the field of Ziegler catalysis Ivanchev developed and put into practice a catalyst for ethylene dimerization into butene and developed new catalysts for polymerization and copolymerization of ethylene, based on components that had not been used for such purposes.

Ivanchev is the author or co-author of three monographs: *Emul'sionnaya polymerizatsiya* (Emulsion Polymerization) (Khimiya, 1978), *Radikal'naya polimerizatsiya* (Radical Polymerization) (Khimiya, 1985), and *Reaktsii v polimernykh sistemakh* (Reactions in Polymer Systems) (Khimiya, 1987). The first of these was republished in the United States in 1981. He published more than 300 review papers and papers in scientific journals and received more than 200 patents and inventor's certificates. He is actively working with young scientists: he has trained 43 candidates and 8 doctors of science.

Under Ivanchev's supervision, the research center for technology of polymerization plastics, Plastpolimer Okhta Research and Production Association, was designed, built, and put into operation at Tomsk Petro-

1070-4272/02/7511-1887$27.00© 2002 MAIK "Nauka/Interperiodica"

chemical Combine, and a technology of ethylene dimerization into α-butene was developed and the corresponding installation were put into operation. He also supervised the development, in the framework of an intergovernmental agreement with GDR, of a technology for ethylene synthesis.

Sergei Stepanovich is an Honorary Chemist of the Russian Federation; Honored Engineer of St. Petersburg (2002); member of the Higher Qualification Committee of the Council of Ministers of, first, USSR and then Russia; member (for 12 years) of the Editorial Board of *Vysokomolekulyarnye Soedineniya* (Macromolecular Compounds) journal and Editorial Boards of *Uspekhi Khimii* (Advances in Chemistry) and *Zhurnal Prikladnoi Khimii* (Russian Journal of Applied Chemistry) journals. He is a member of the Scientific Council for Macromolecular Compounds at the Presidium of the Russian Academy of Sciences, Bureau of the Board of Directors of the Mendeleev Russian Chemical Society, and Scientific Council for Catalysts.

Ivanchev continues work on development of new postmetallocene catalysts for polymerization, improvement of the emulsion polymerization processes, control over the morphology of latex particles, synthesis of latexes with hollow particles, and modification of polyolefins, which was reflected in more than 30 publications in the last three years.

The Editorial Board and Editorial Office of *Zhurnal Prikladnoi Khimii* (Russian Journal of Applied Chemistry) heartily congratulate Sergei Stepanovich on his jubilee and wish him sound health and further success in his creative work.

Russian Journal of Applied Chemistry, Vol. 75, No. 11, 2002, pp. 1889–1892. Translated from Zhurnal Prikladnoi Khimii, Vol. 75, No. 11, 2002, pp. 1926–1929.
Original Russian Text Copyright © 2002 by Morachevskii.

HISTORY OF CHEMISTRY AND CHEMICAL TECHNOLOGY

Marcellin Berthelot (on 175th Anniversary of His Birthday)

Pierre Eugene Marcellin Berthelot ranks among the most prominent chemists of the second half of the XIX century and early XX century. The great number of his works include fundamental investigations in virtually all branches of chemistry of that time, original studies in physics, biology, history of science and art, archeology, philosophy, pedagogics, linguistics, ethics, and esthetics. Works of the French scientist much promoted the transformation of organic chemistry into a separate kind of science, stimulated the development of the most important fields of physical chemistry, and enriched the history of chemistry.

M. Berthelot was born on October 25, 1827, in Paris into a doctor's family. In 1846, he graduated from a lyceum, having demonstrated substantial learning capability both in natural sciences and in humanities. Berthelot was aided in his diverse scientific activities by his knowledge of foreign languages, including Grecian and Sanskrit. Soon after graduating from the lyceum, he passed an examination to obtain bachelor's degree in philosophy and history (es lettres) and in mathematics and natural sciences (es sciences). Following the example of his father, Berthelot started his higher education from medicine and simultaneously attended lectures in chemistry and physics at College de France. In 1849, he obtained a degree of licentiate in physical sciences. By that time, the final choice of the main direction of research had been made, and this was chemistry. Berthelot mentioned among his teachers chemists J.B. Dumas (1800–1884), A.J. Balard (1802–1876), and T.J. Pelouze (1807–1867), and especially a physicist H.V. Regnault (1810–1878). All of them were known scientists and members of the Paris Academy of Sciences. In 1849, Berthelot started to work at Pelouze's private chemical laboratory, and in 1851, he became an assistant at Balard's laboratory at College de France.

In 1854, Berthelot defended his doctoral dissertation. His study was concerned with the reaction of glycerol with acids and artificial synthesis of natural fats. In 1858, he passed examinations and became a first-class pharmacist.

In 1859–1864, Berthelot was a professor at Ecole de Pharmacie in Paris. In 1863, the scientist was elected a member of the Academy of Medicine. From 1865 till 1906, he was a professor at College de France. Professors of this institution are not bound by any curricula and are free from taking part in examinations. Every year a scientist chooses the subject of his lectures himself, commonly in correspondence with the field of science he is currently interested in. In 1869, by proposition of J. Liebig (1803–1873), a known chemist, Berthelot was elected a member of the Bavarian Academy of Sciences. In 1873, he became a member of the Paris Academy of Sciences in physics. By recommendation of a group of academicians, including A.M. Butlerov (1826–1880), Berthelot was elected in 1876 a foreign corresponding member of the St. Petersburg Academy of Sciences. In 1877, the London Royal Society elected him a foreign member. Beginning in 1889, Berthelot was a permanent secretary of the Paris Academy of

1070-4272/02/7511-1889$27.00 © 2002 MAIK "Nauka/Interperiodica"

Sciences; in the same year he was elected a member of the French Academy of Literature and Fine Arts.

Together with being engaged in intensive and diverse scientific activities, Berthelot held a number of high state posts, he became a general supervisor of higher education in 1876 and was a minister of popular schooling in 1886–1887 and foreign minister of France in 1895–1896.

Berthelot was elected an honorary member of the German chemical society in 1894 and an honorary member of the French chemical society in 1900; in 1866, 1875, 1882, 1889, and 1901 he was elected the president of the French chemical society.

A lot of the credit for the development of various branches of chemistry and chemical technology must go to Berthelot; he made the most prominent contribution to the development of organic synthesis. This is quite understandable since organic chemistry dominated the development of chemistry in the middle of the XIX century.

Voluminous literature has been concerned with Berthelot's life and scientific activities; his works have been studied in detail. A prominent contribution to studies of this kind performed in Russia was made by Yu.S. Musabekov (1910–1970), a known historian of chemistry [1, 2]. Rather detailed reminiscences about his French colleague were published by K.A. Timiryazev (1843–1920), an outstanding natural scientist [3] who was well-acquainted with Berthelot and worked at his laboratory (1868–1870). In 1927, a collection of articles was published in connection with the centennial anniversary of Berthelot's birthday. The collection presented evidence about scientist's life (D.P. Konovalov) and his works in thermal chemistry (I.A. Kablukov), technology of explosives (S.P. Vukolov), and history of chemistry (B.N. Menshutkin). Materials on Berthelot can be found in numerous reference publications [5–8].

Berthelot was the first to synthesize by original methods from elements and simple substances a great number of new and known natural compounds. Berthelot's contribution to the development of the synthetic direction in organic chemistry was analyzed in [9–11]. In 1853–1854, the scientist was dealing with synthesis of fats by heating glycerol with palmitic, stearic, and oleic acids in sealed ampules. Berthelot proved that the substances synthesized by him form the basis of animal and vegetable fats and are composed of a combination of three parts of acids and one part of glycerol, with liberation of three parts of water. In 1855, he synthesized ethanol from ethylene and water mixed with sulfuric acid, and later (1882) obtained formic acid from carbon monoxide and water in an alkaline medium. Already in 1861, Berthelot wrote a two-volume book *Organic Chemistry Based on Synthesis*, which made its author famous.

Much later, in a three-volume publication *Hydrocarbons, Experimental Investigations*, 1851–1901, Berthelot summarized the results of an enormous number of syntheses of hydrocarbons and their derivatives from simple substances or elements.

He synthesized acetylene from carbon and hydrogen in an arc furnace, and acetylene could then be converted into quite a number of compounds: benzene, styrene, naphthalene, anthracene, etc. Berthelot then passed from acetylene to ethylene, methane, and other compounds of the aliphatic series, to numerous oxygen- and nitrogen-containing substances. The part played by acetylene in classical Berthelot's syntheses and the influence exerted by works of the French scientist on the subsequent development of the chemistry of acetylene were analyzed in detail in [12]. Berthelot proposed a versatile method for reduction of organic compounds with hydrogen iodide. This technique had been widely used before the discovery of the catalytic hydrogenation method.

Together with problems of organic synthesis, Berthelot had been intensively studying for more than 40 years, beginning in 1865, thermal chemistry and was, together with a Russian scientist G.I. Hess (1802–1850) and Danish physical chemist J. Thomsen (1826–1909), one of its founders. As noted by Solov'ev [13], Berthelot published in the field of thermal chemistry 152 works of his own, and 63, together with his numerous disciples. In particular, V.F. Luginin (1834–1911), a Russian physical chemist who organized at Moscow University the first Russian calorimetric laboratory (1892), took part in Berthelot's calorimetric studies. Berthelot paid much attention to improvement of techniques for calorimetric measurements. The manual of thermal chemistry, written by him, was translated in Russia (Odessa, 1894). As far back as 1881, Berthelot was the first to design a calorimetric bomb for determining the heat of formation of organic compounds. The bomb later found wide use in thermochemical laboratories all over the world. The advance in calorimetric measurements was much promoted by the invention by H. Le-Chatelier (1850–1936) of the platinum–rhodium thermocouple.

The basic idea in Berthelot's works, and also in investigations by Hess and Thomsen, was the concept of the heat effect of a chemical reaction as a measure of affinity of the reactants. In the final form, Berthelot

formulated the principle of maximum work as follows (1875): "Any chemical transformation occurring without any influence of a foreign external energy tends to produce bodies or systems of bodies whose formation is accompanied by liberation of the maximum amount of heat." In the subsequent years, the appropriateness of application of the maximum work principle was discussed by quite a number of scientists [13–15]. In particular, D.I. Mendeleev wrote in the fourth edition of *Osnovy khimii* (Fundamentals of Chemistry) (St. Petersburg, 1881, part 1): "...Although the principle of maximum work can well be applied to experimental data in numerous cases, it can be considered neither firmly established nor being in agreement with the whole body of chemical evidence."

The development of chemical thermodynamics in the end of the XIX century affected Berthelot's views and, as noted in [15], this principle is already not dominant in the two-volume publication of the French scientist, *Thermal Chemistry, Quantities and Numerical Laws* (1897). A constructive criticism of the Berthelot–Thomsen principle can be found in works by A.L. Potylitsyn (1845–1905), a Russian chemist, Mendeleev's disciple [15, 16].

Berthelot also worked in the field of chemical kinetics. Together with L. Pean de Saint-Gilles, he studied the rates of the reversible esterification–saponification and demonstrated that, at any given instant of time, the rate of ester formation is proportional to a product of reactant masses and described mathematically the reaction of acetic acid with ethanol. Having mentioned the relatively slow course of reactions of this kind, the authors predetermined for decades their being chosen as model reactions in studying the main kinetic laws. Berthelot was one of the first to pay attention in his book *Studies of Chemical Mechanics* (1879) to the role of time in the course of chemical reactions. Experimental studies by Berthelot and Saint-Gilles, carried out in 1862–1863, preceded classical works in chemical kinetics, performed in 1864–1867 by Norwegian scientists C.M. Guldberg (1836–1902) and P. Waage (1833–1900).

A prominent place in Berthelot's investigations was occupied by inflammation and explosion. According to Berthelot, two kinds of waves are generated in explosion: blast wave and sound wave. Berthelot was concerned with problems of explosion and chemistry and technology of explosives till the end of his life. This aspect of the activities of the French scientist was considered in detail by Vukolov [4]. The results obtained by Berthelot in studying explosives and explosions have been used for military purposes and in mining.

Much attention was paid by Berthelot to methodological and scientific-historical problems. The philosophical concepts of the scientist were summarized in quite a number of monographs: *Science and Philosophy* (1886), *Science and Morals* (1887), *Science and Education* (1901), and *Science and Free Thinking* (1905), and also in his correspondence with E. Renan (1898). E. Renan (1823–1892), professor of ancient Oriental languages at College de France, author of the multivolume publication *History of the Origin of Christianity*, was on very friendly terms with Berthelot from his teens till the end of his life. Berthelot imagined the beginning of the XXI century as the time of unprecedented flourishing and leading role of chemistry. Simultaneously, he suggested evolution of means of transportation, energetics, and communication. Unfortunately, Berthelot's predictions, and in the first place those concerning the structure of society and its morals and manners, proved to be unrealizable.

In 1869, Berthelot visited, as a member of the French delegation, Egypt in connection with the opening of the Suez channel. This trip much stimulated Berthelot's interest in the ancient culture of this country, and also in alchemy and astronomy. He studied the composition of ancient coins, decoration articles, and arms. Berthelot wrote 10 volumes directly concerned with history of chemistry, and he can be rightfully considered one of founders of archeological chemistry.

Marcellin Berthelot died on March 18, 1907, at the age of 79, several hours after his wife passed away. He was buried in the Pantheon, near other outstanding sons of France. As an exception, his wife was buried nearby.

Academician N.N. Beketov (1827–1911), a prominent Russian physical chemist, spoke of his French colleague as follows: "Markings of his activities will remain indelible in the intellectual development of the mankind." W. Nernst (1864–1941), an outstanding German physicist and physical chemist and Nobel Prize winner, named Berthelot "...one of the most prominent scientists of all times." And this is no overstatement. The already mentioned Timiryazev's reminiscences were named "Lavoisier of the XIX Century (Marcellin Berthelot, 1927–1907)."

In 1927, the centennial anniversary of Marcellin Berthelot's birthday was celebrated in France. A rather

representative Russian delegation, headed by A.V. Lunacharskii (1875–1933), a known statesman and public figure, people's commissar of education of the Russian Soviet Federative Socialistic Republic, took part in the celebration. Reminiscences of this celebration were published by V.E. Tishchenko [17] and Kablukov [18], members of this delegation.

REFERENCES

1. Musabekov, Yu.S., *Marcellin Berthelot, 1827–1907*, Moscow: Nauka, 1965.
2. Musabekov, Yu.S., *Sb. Nauchn. Tr. Yaroslav. Tekhnol. Inst.*, 1972, vol. 22, no. 2, pp. 3–17.
3. Timiryazev, K.A., *Sochineniya* (Works), Moscow: Sel'khozgiz, 1939, vol. 8.
4. *M. Berthelot, 1827–1927, Sbornik statei* (M. Berthelot, 1827–1927, Coll. of Works), Leningrad: Izd. Akad. Nauk SSSR, 1927.
5. Blokh, M.A., *Biograficheskii spravochnik* (Biographic Book of Reference), Leningrad: Nauchnoe Khimiko-Tekhnol. Izd., 1929, vol. 1.
6. Musabekov, Yu.S. and Chernyak, A.Ya., *Vydayushchiesya khimiki mira: Bibliograficheskii ukazatel'* (Outstanding Chemists of the World: Biographic Guide), Moscow: Kniga, 1971.
7. Tuchs, G., Heinig, K., Kertscher, G., *et al*., *Biographien bedeutender Chemiker*, Berlin: Volk und Wissen Volkseigener Verlag, 1977.
8. Crosland, M.P., *Dictionary of Scientific Biography*, Gillespie, Ch.C., Ed., New York: Charles Scrilner's, 1980, vol. 1, pp. 63–72.
9. Giua, M., *Storia della Chimica*, Torino: Union Tipografico-Editrige Torinese, 1962.
10. Bykov, G.V., *Istoriya organicheskoi khimii: Otkrytie vazhneishikh organicheskikh soedinenii* (History of Organic Chemistry: Discovery of the Most Important Organic Compounds), Moscow: Nauka, 1978.
11. Nikulina, E.P., *Ocherki po istorii organicheskoi khimii* (Essays on the History of Organic Chemistry), Moscow: Nauka, 1977, pp. 21–63.
12. Shmulevich, L.A., *Glavy iz istorii organicheskoi khimii* (Selected Chapters of the History of Organic Chemistry), Moscow: Nauka, 1975, pp. 28–121.
13. Solov'ev, Yu.I., *Ocherki iz istorii fizicheskoi khimii* (Essays on the History of Physical Chemistry), Moscow: Nauka, 1964.
14. Kipnis, A.Ya., *Razvitie khimicheskoi termodinamiki v Rossii* (The Development of Chemical Thermodynamics in Russia), Moscow: Nauka, 1964.
15. *Istoriya ucheniya o khimicheskom protsesse: Vseobshchaya istoriya khimii* (History of the Concept of the Chemical Process: General History of Chemistry), Moscow: Nauka, 1981.
16. Solov'ev, Yu.I., *Istoriya khimii v Rossii* (History of Chemistry in Russia), Moscow: Nauka, 1985.
17. Tishchenko, V.E., *Zh. Prikl. Khim.*, 1928, vol. 1, no. 1, pp. 57–59.
18. Kablukov, I.A., *Nauch. Rabotn*., 1928, no. 1, pp. 67–75.

A. G. Morachevskii

Russian Journal of Applied Chemistry, Vol. 75, No. 11, 2002, pp. 1893–1894. Translated from Zhurnal Prikladnoi Khimii, Vol. 75, No. 11, 2002, pp. 1930–1931.
Original Russian Text Copyright © 2002 by Zaikov, Minsker.

INFORMATION

2nd International Conference on Polymer Modification, Degradation, and Stabilization

The 2nd International Conference on Polymer Modification, Degradation, and Stabilization (MoDeSt-2) was held from June 30 to July 4, 2002 in Budapest (Hungary).[1] The conference participants were more than 800 scientists from practically all the European Countries and also from the United States, Canada, Japan, China, Israel, and Brazil. The conference Chairman was Prof. Gy. Marosi (Hungary) and Co-chairman, Prof. Bela Pukanszky (Hungarian Academy of Sciences). The conference organizers were European Polymer Federation (EPF), Hungarian Academy of Sciences, and Polymer Degradation Discussion Group of the Macromolecular Group of the Royal Society of Chemistry, UK. The conference was held on the basis of the Budapest University of Technology and Economics (BUTE).

In the Opening session, Prof. Detrekoi (BUTE President), Prof. A.-C. Albertsson (EPF President), and Prof. F. La Mantia (MoDeSt-1 Chairman) outlined the topicality of the conference for fundamental and applied polymer research. The Conference Program included a plenary lecture and seven general lectures. The plenary lecture presented by W. Kaminsky was devoted to feedstock recycling of polymers by pyrolysis in a fluidized bed.

Seven general lectures covered the topical problems of the conference:

(1) W. Starnes: New Nonmetallic Additives for the Thermal Stabilization of PVC.

(2) F.E. Karasz: Electro-Optical Properties of Polymer Blends.

(3) F. La Mantia: Can Recycling Improve the Properties of Post-Consumer Plastic Materials?

(4) H. Höcker: Biomaterials—From Drug Release Systems to Surface Modified Implants with Enhanced Biocompatibility.

(5) G. Camino: Thermal Degradation and Combustion Behavior of Polymer–Layered Silicate Nanocomposites.

(6) M. Zrinyi: Smart Polymer Materials and Systems.

(7) N. Billingham: Surface Modification of Polyolefins by Migrating Additives.

Then the Conference was held in the form of a series of minisymposia on 6 dedicated topics. The first session (Thermal Degradation) covered 31 oral presentations. In this session, the problems of modeling random and end-chain scission (depolymerization), and of the use of modern instrumental methods, particularly ESR, for studying the kinetics and mechanisms of polymer thermal degradation were discussed. A special attention was paid to development and application of the chemiluminescence methods for studying thermooxidative degradation, and also of the isotopic methods including ^{18}O. Particular interest was aroused in the audience by the reports on "weak points" in the PVC structure sensitive to heating and thermal oxidation. A series of reports were devoted to natural and artificial aging of polymers and also to polymer degradation in the course of processing. The organizers, chairmen, and keynote lecturers in this section were K.S. Minsker, L. Rychla, F. Cataldo, J.E.J. Stagges, S. Seidler, J. Rychly, E. Pichett, N.C. Billingham, E. Foldes, B. Ivan, W. Habicher, A. Wegmann, D. Acierno, B. Balazs, S. Al-Malaika, M. Blazco, B. Pukanszky, and S. Schlick.

The second session (Aging, Irradiation, Stabilization) included 30 oral presentations on the problems of polymer aging, photo- and radiation degradation, and stabilization. A series of reports were devoted to the mechanisms of action of various types of stabilizers including new UV light absorbers and spatially hindered piperidines, synergism and antagonism with various chemical additives. Among the subjects of other reports were photodegradation of films and fibers, radiation-chemical and ozone-induced aging of polymers, and also development of methods for prediction of the lifetime of polymer goods. The organizers, chairmen, and keynote lecturers in this section were N.S. Allen, A.R. Horrocks, P. Staniek, M.P. Foulc, R. Todesco, C. Decker, J.L. Gardette, B. Mailhot, J. Pospisil, L. Audouin, W. Starnes, I. Stevenson, I. Rusznak, M. Stephan, Gy. Pokol, O. Figovsky, A. Vig, and L. Kravets.

The third session (Combustion and Fire Retard-

[1] MoDeSt-1 was held in September 2000 in Palermo (Italy).

1070-4272/02/7511-1893$27.00 © 2002 MAIK "Nauka/Interperiodica"

ance) included 32 lectures. Of primary concern were the problems of polymer burning and searching for the ways to decrease the flammability of polymer materials. Among the topics were changing halogen-containing fire retardants for non-halogen ones (particularly, nanocomposites), pyrolysis and degradation of polymers in burning, fire-retardant mechanisms, bloating and foaming in burning polymers, and development of new environmentally friendly fire retardants. The organizers, chairmen, and keynote lecturers in this section were T.R. Hull, J. Wang, M. Lewin, P. Anna, C.A. Wilkie, C. Jama, G. Camino, J.E.J. Staggs, S. Varma, I. Dekany, R. Kozlowsky, O. Grexa, S. Bourbigot, B. Schartel, P.R. Hornsby, and A. Kettrup.

The topic of the fourth session was Blends, Functionalization, and Reactive Processing (35 lectures). A particular attention was paid to cross-linking of polymer chains, control of the morphology of polymeric materials, modification of polymers by means of polymer-homologous transformation, phase transitions, and synthesis of special-purpose additives for polymers. The chairmen and keynote lecturers in this section were F.E. Karasz, A. Fainleib, R. Pfaendner, Gy. Bertalan, K. Ishizu, F. Fenouillot, J.E. Gerard, X. Xu, G. Ruggeri, Gy. Bunhegyi, B. Voit, J. Varga, A. Michel, E.V. Prut, T. Czigany, A. Murakami, M. van Duin, A. Toth, M. Zrinyi, and K.N. Chen.

The fifth session (Biodegradation, Biomaterials, Drug Release) included 28 oral presentations. Of primary concern were the problems of synthesis of biodegradable polymers, kinetics and mechanisms of their degradation in bioactive media, and performance of biodegradable materials for various purposes. A special emphasis was made on polyfunctional biomaterials, including their morphology, mechanical characteristics, and recycling. The chairmen and keynote lecturers in this section were H. Hocker, M. Zsuga, P.J. Lemstra, E. Csiszar, S. Slomkowsky, I. Tomka, A.J. Domb, J. Borza, J.E. Puskas, E. Polyanszky, R. Faust, S. Keki, J.P. Kennedy, S. Bronco, L. Costa, and K. Jacobson.

Finally, the sixth session (Recycling, Material and Energy Recovery) was devoted to recycling of post-consumer polymeric materials. The session covered 32 oral presentations. As the material and energy recovery methods, there were considered pyrolysis, hydrolysis, biodegradation of heterochain polymers, and recycling of polymers by, for example, reactive extrusion. The organizers, chairmen, and keynote lecturers in this section were U. Arena, W. Kaminsky, C. Papaspyrides, E. Takacs, A. Galeski, A. Jimenez, A. Okuwaki, J. Borda, P.J. Davis, T. Spychaj, J. Karger-Kocsis, Y. Sato, T. Czvikovszky, P. van Schijndel, F. La Mantia, I. Racz, J. Schoner, and E. Jakob.

Each of the minisymposia included poster presentations (a total of about 150 posters in all).

It was concluded that the problems discussed at the conference are topical from both the theoretical and practical standpoints. The next Conference (MoDeSt-3) is planned to be held in 2004.

G. E. Zaikov and K. S. Minsker

Russian Journal of Applied Chemistry, Vol. 75, No. 11, 2002, pp. 1895–1896. Translated from Zhurnal Prikladnoi Khimii, Vol. 75, No. 11, 2002, pp. 1932–1933.
Original Russian Text Copyright © 2002 by Morachevskii, Beloglazov.

BOOK REVIEWS

Naboichenko, S.S., Ni, L.P., Shneerson, Ya.M., and Chugaev, L.V., *Avtoklavnaya gidrometallurgiya tsvetnykh metallov* (Autoclave Hydrometallurgy of Nonferrous Metals)

Yekaterinburg: Ural'sk. Gos. Tekh. Univ.—Ural'sk. Politekh. Inst., 2002, 940 pp.

In recent decades, certain difficulties have been encountered in manufacture of a number of nonferrous metals. These difficulties are associated with deteriorating quality of raw materials, short supply of carbon fuels, and environmental problems. Also still important are mechanization and automation of industrial processes, possibility of remote control over these processes, and improvement of the safety of production. Of promise in solving these problems may be further extension of hydrometallurgical technologies and, in the first place, of their most intensive variety, autoclave processes (autoclave hydrometallurgy). The authors understand by the autoclave hydrometallurgy the processes employing hermetically sealed apparatus with intensive mass exchange at elevated temperature and pressure and those with the use of an external reaction gas.

The autoclave hydrometallurgy started to develop successfully in the second half of the XX century, when numerous publications and designs appeared, and a number of industrial installations of varied output capacity were constructed. The first book concerned with implementation of autoclave processes was the monograph *Avtoklavnye protsessy v tsvetnoi metallurgii* (Autoclave Processes in Nonferrous Metallurgy) (Maslenitskii, I.N., Dolivo-Dobrovol'skii, V.V., Dobrokhotov, G.N., *et al*., Moscow: Metallurgiya, 1969). During more than 30 years that have elapsed since that time, new results of investigations have accumulated and the scale of implementation of autoclave processes has increased, which required systematization, analysis, and generalization of the data obtained. In our opinion, the team of authors of the monograph, headed by S.S. Naboichenko, a corresponding member of the Russian Academy of Sciences, has successfully tackled with the problem.

The monograph considers physicochemical foundations of hydrometallurgical processes carried out at elevated temperatures and pressures and discusses their thermodynamics and kinetics. Examples of application of autoclave processes in manufacture of alumina, nickel, cobalt, zinc, copper, noble, and less-common metals are described. A special section is devoted to engineering implementation of the autoclave technologies.

The monograph comprises an introduction, twenty chapters grouped into five parts, and brief conclusion. Bibliography is given at the end of each chapter, with a total of about 1300 references to works by domestic and foreign authors given.

The introduction (pp. 10–29) contains evidence about a number of Russian scientists whose investigations much promoted the development of autoclave processes and application of high pressures in chemical technology. The introduction also discusses the history of development of autoclave processes at Russian plants and abroad.

The first part of the monograph (pp. 30–150, chapters 1–4) is concerned with specific features of equilibrium in a hydrothermal system including gas, solution, and solid. The first chapter considers general principles and concepts of the autoclave metallurgy. Typical solvents used in autoclave processes, reaction gases, oxidants, methods for preparing raw materials for autoclave leaching, various kinds of leaching of sulfide raw materials, and choice of optimal parameters of autoclave processes are discussed. The second chapter is concerned with thermodynamics of autoclave processes. Diagrams demonstrating the stability regions of separate compounds in metallurgical systems of interest for autoclave technologies are discussed. The third chapter contains data on solubility of oxygen and some other gases in aqueous solutions in a wide range of temperatures and pressures. The fourth chapter considers the influence exerted by a number of factors on the solubility of metal salts at elevated temperatures.

The second part of the book (pp. 151–318, chapters 5–8) covers a wide range of issues concerning dissolution of minerals, metals, and metal alloys under autoclave conditions. The fifth chapter is concerned with

1070-4272/02/7511-1895$27.00 © 2002 MAIK "Nauka/Interperiodica"

dissolution of chalcogenides, mainly sulfides, of quite a number of metals. The sixth chapter discusses side processes occurring in autoclave oxidation of sulfide concentrates. The seventh chapter is devoted to kinetics of dissolution of metals and alloys in various media. The eighth chapter discusses the kinetics and mechanism of dissolution of oxide minerals.

The third part of the monograph (pp. 319–670, chapters 9–14) considers processes of autoclave leaching in manufacture of alumina (chapter 9), metallurgy of nickel and cobalt (chapter 10), metallurgy of copper, zinc and lead, and noble metals (chapters 11–13), and processing of less-common-metal raw materials (chapter 14). The autoclave leaching, the leading operation in most of schemes for raw material processing, makes it possible to solve the whole set of technological problems.

The fourth part of the book (pp. 671–777, chapters 15 and 16) contains evidence concerning the autoclave precipitation of metals and their compounds. Chapter 15 considers autoclave methods for solution purification, which are based on hydrolysis of ions and precipitation of sulfides and end in formation of difficultly soluble compounds. Chapter 16 discusses the potentialities of the autoclave precipitation of metals.

The fifth part (pp. 778–935, chapters 17–20) is devoted to general engineering problems of autoclave hydrometallurgy. To these belong the apparatus implementation of autoclave processes (chapter 17), description of materials used in fabrication of autoclave apparatus (chapter 18), problems of safety in operation of autoclave installations (chapter 19), and mathematical modeling of autoclave processes (chapter 20).

The brief conclusion (pp. 936 and 937) points to advantages of autoclave processes and lists the most promising objects of their application. The authors also formulate the possible directions of improvement of the apparatus and technology of the autoclave hydrometallurgy.

The team of authors, comprising prominent specialists in autoclave processes, performed a vast amount of work, summarized and discussed numerous experimental studies and designs, and analyzed flowsheets and results of operation of industrial installations. However, it is impossible to envelop immensity. The book has a technological orientation, and this, probably, accounts for the fact that some sections of thermodynamic and electrochemical nature (e.g., chapter 2 and also paragraphs 3.2, 15.1, and 16.1) are presented without due clearness. Chapter 20 falls out of the general style of presentation. Probably, problems associated with modeling of autoclave processes should have been considered in more detail in a special-purpose monograph. The exceedingly brief description in the book of the models proposed raises too many questions.

The book is intended for engineers and research workers from plants and institutions concerned with problems of nonferrous metallurgy. Separate sections of the monograph may be of value for undergraduate students, masters, and postgraduate students specialized in nonferrous metallurgy or chemical technology.

A. G. Morachevskii and I. N. Beloglazov

Russian Journal of Applied Chemistry, Vol. 75, No. 12, 2002, pp. 1897–1902. Translated from Zhurnal Prikladnoi Khimii, Vol. 75, No. 12, 2002, pp. 1937–1942.
Original Russian Text Copyright © 2002 by Dorozhkin.

INORGANIC SYNTHESIS AND INDUSTRIAL INORGANIC CHEMISTRY

Solid-Phase Conversion of Nonstoichiometric Hydroxoapatite into Two-Phase Calcium Phosphate

S. V. Dorozhkin

Nicol Hall, Mechanical Engineering, Queen's University, Kingston, Canada

Received June 25, 2000

Abstract—Two-phase and nonstoichiometric hydroxoapatites were synthesized and studied by X-ray phase and chemical analyses and by IR spectroscopy. A probable mechanism of solid-phase conversion of nonstoichiometric hydroxoapatite into two-phase calcium phosphate was considered on the basis of the model proposed and calculations.

Two-phase calcium phosphate (TCP), consisting of stoichiometric hydroxoapatite (SHA) $Ca_{10}(PO_4)_6(OH)_2$ and β-modification of calcium orthophosphate $Ca_3(PO_4)_2$, is widely used as a biomaterial owing to its chemical similarity to bone tissue [1, 2]. TCP is commonly obtained by calcination of nonstoichiometric hydroxoapatite (NHA) $Ca_{10-x}(HPO_4)_x(PO_4)_{6-x}(OH)_{2-x}$ ($0 < x < 1$) at 1000–1200°C for 1–4 h [3, 4]. Upon calcination, NHA is converted into TCP, but the mechanism of this process has not been elucidated as yet.

It is known that X-ray patterns of TCP are similar to those of a mechanical mixture of SHA and β-$Ca_3(PO_4)_2$ (Fig. 1). Therefore, TCP can be regarded as a mixture of SHA and β-$Ca_3(PO_4)_2$ crystals. However, no reports of successful separation of these phases could be found in the literature. Thorough studies of TCP in a scanning electron microscope at the highest possible magnifications of up to 100 000 failed to reveal two phases, and, consequently, TCP consists of phases with very fine crystals. According to [5], substances with very small-sized (less than 20–30 nm) crystals are characterized by broadened diffraction peaks in X-ray patterns. Furthermore, it is known that the majority of solid substances have so-called mosaic (or granular) structure and consist of crystallites (or blocks) with average size of 50–100 nm [5].

The aforesaid has also been established for calcium phosphates. For example, a block structure characterized by three levels of hierarchy has been suggested for crystals of fluoroapatite $Ca_{10}(PO_4)_6F_2$ [6]. The following data concerning the relation between crystallite sizes and width of diffraction peaks of calcium phosphates have been found.

(1) Crystallites of NHA enamel are 130 × 30 nm in size, similar crystallites of bones and tooth dentine have dimensions of 25 × 3 and 20 × 4 nm, respectively. Therefore, diffraction peaks of enamel are nar-

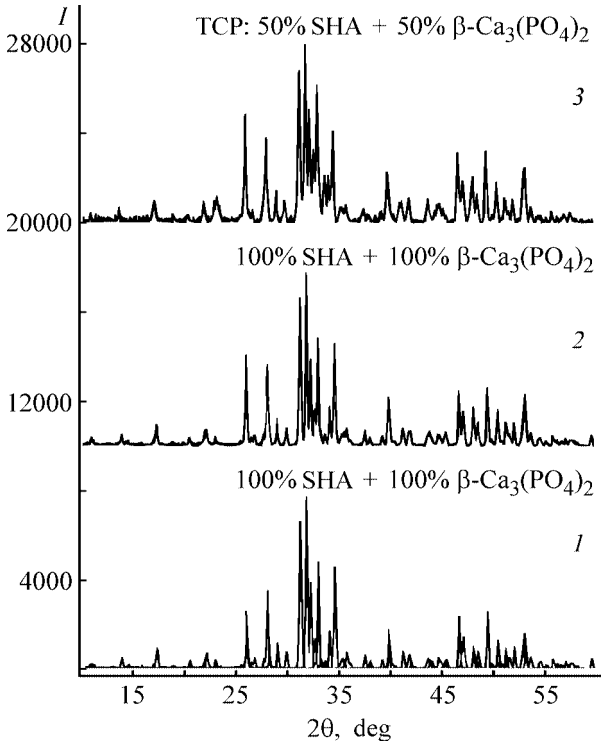

Fig. 1. X-ray patterns of calcium phosphates. (*I*) intensity and (2θ) Bragg angle; the same for Figs. 2 and 3. (*1*) Calcined SHA and β-$Ca_3(PO_4)_2$ (printed out together); (*2*) mathematical addition of X-ray patterns of calcined SHA and β-$Ca_3(PO_4)_2$; (*3*) doubled X-ray pattern of TCP composed of 50% SHA + 50% β-$Ca_3(PO_4)_2$. The intensities of all the TCP lines were doubled for convenience of their comparison with the X-ray patterns of calcined SHA and β-$Ca_3(PO_4)_2$.

1070-4272/02/7512-1897 $27.00 © 2002 MAIK "Nauka/Interperiodica"

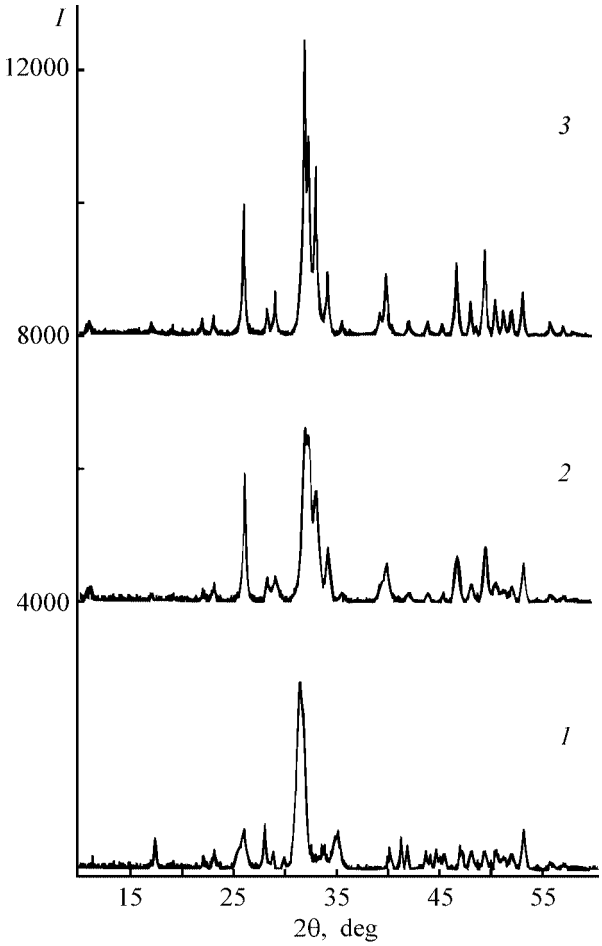

Fig. 2. X-ray patterns of uncalcined calcium phosphates. (*1*) $Ca_3(PO_4)_2$, (*2*) NHA, (*3*) SHA; the same for Fig. 4.

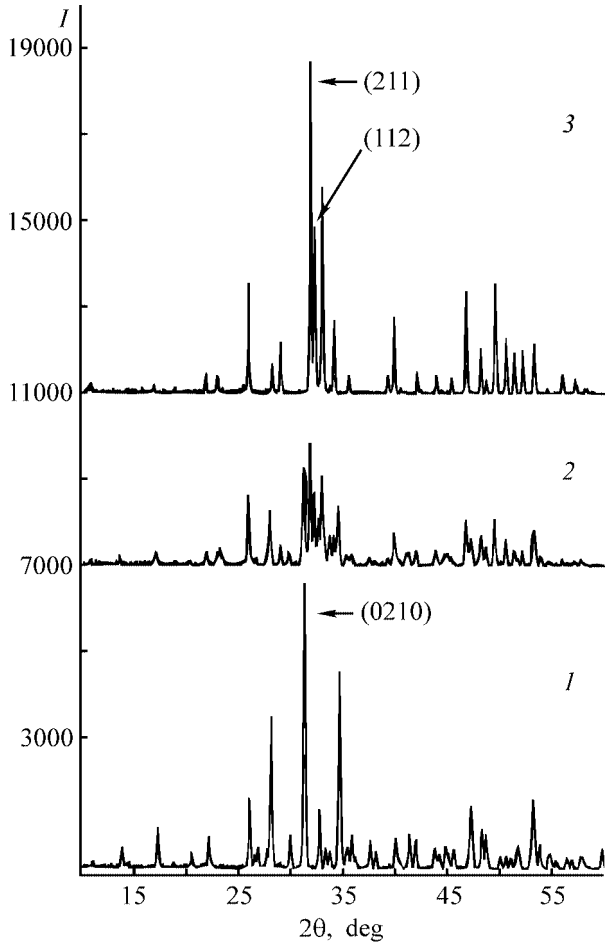

Fig. 3. X-ray patterns of calcined calcium phosphates. (*1*) β-$Ca_3(PO_4)_2$; (*2*) TCP consisting of 50% SHA + 50% β-$Ca_3(PO_4)_2$; (*3*) SHA; the same for Fig. 5. Peaks used to calculate the crystallite sizes are indicated.

row and intense, and the X-ray patterns of bone tissue and dentine have broad and low-intensity diffraction peaks, similar to X-ray patterns of amorphous substances [1].

(2) Coherent domains of size 50–60 nm, responsible for medium-width peaks in the X-ray patterns, have been found in natural fluoroapatite [7].

(3) X-ray patterns of SHA composed of 40–60-nm crystallites have broad low-intensity peaks, whereas X-ray patterns of SHA composed of 75-, 100-, and, especially, 130-nm crystallites have narrow and intense peaks [8, 9]. Even broader diffraction peaks have been detected in the case of SHA consisting of 20–50-nm crystallites [10].

(4) SHA calcined at 1200°C consists of crystallites 102 ± 2 nm in size, which is manifested in the presence of narrow and intense peaks in the X-ray patterns [11].

(5) A study of SHA, three types of bone tissue, and Endobone® biomaterial (Merck Biomaterial, Darmstadt, Germany) by X-ray phase analysis on a HASYLAB synchrotron (Hamburg) has shown that, depending on a selected crystallographic direction, the size of NHA crystallites in bone tissue is 8–23 nm, which is manifested as very broad diffraction peaks [12]. The SHA sample studied consisted of 22–34-nm crystallites characterized by rather broad, but narrower than in the case of NHA bone tissue, X-ray peaks. Only Endobone® (100% calcined SHA) gives intense and narrow diffraction peaks, since it consists of crystallites larger than 65 nm in size [12].

Thus, it may be suggested that the narrow and intense peaks of SHA and β-$Ca_3(PO_4)_2$, found in TCP (Fig. 1), indicate that TCP consists of two phases with crystallites (or blocks) of size 60 nm and larger. The aim of this study was to verify this assumption experimentally and to elucidate the mechanism of NHA conversion into TCP.

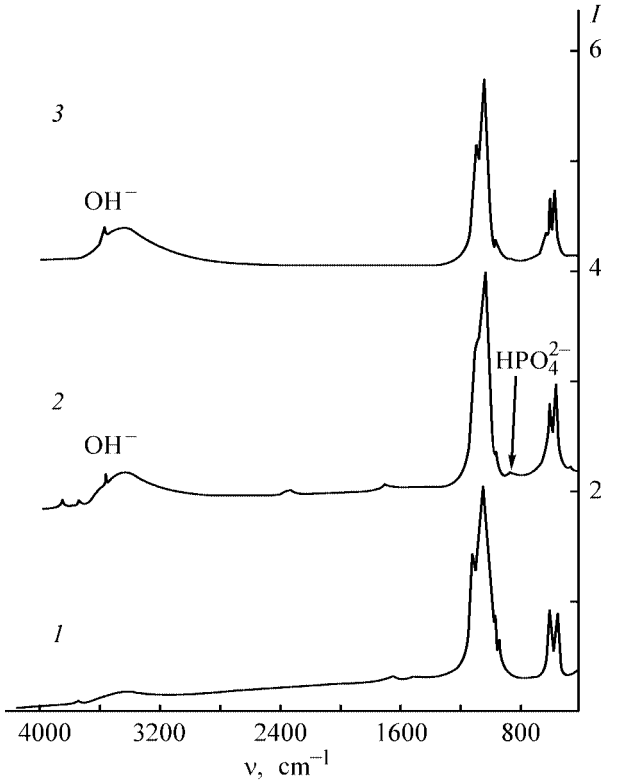

Fig. 4. IR spectra of uncalcined calcium phosphates. (*I*) intensity and (ν) wave number; the same for Fig. 5. Absorption bands of OH^- (3570 m^{-1}) and HPO_4^{2-} ions (875 cm^{-1}) are indicated.

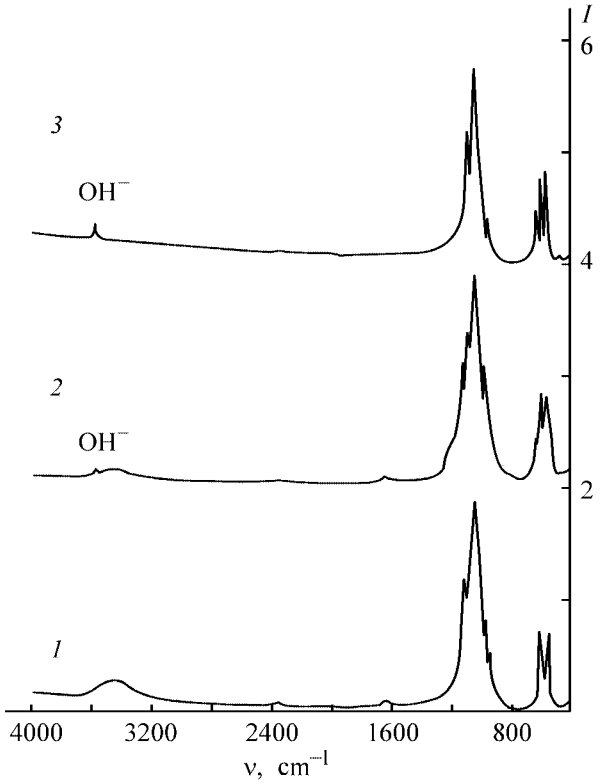

Fig. 5. IR spectra of calcined calcium phosphates. The absorption band of OH^- ion (3570 cm^{-1}) is indicated.

EXPERIMENTAL

TCP was synthesized by the method described in [3, 4, 11]. Chemically pure $CaHPO_4 \cdot 2H_2O$ and KOH were used as starting reagents. First, NHA was prepared by adding 36 g of solid KOH to 1 l of a $CaHPO_4 \cdot 2H_2O$ suspension (100 g l^{-1}) in distilled water. The suspension was heated to boiling and boiled for 4 h with constant stirring and pure nitrogen bubbled through. After cooling, the NHA precipitate was filtered off and washed with distilled water to absence of alkaline reaction with phenolphthalein. Then the precipitate was dried at 80°C for 24 h. To obtain TCP, the dry NHA precipitate was calcined at 1050°C for 4 h.

SHA and β-$Ca_3(PO_4)_2$ were prepared similarly, except that the amounts of KOH added were different. To obtain SHA, an excess amount of alkali (45 g KOH per 100 g of $CaHPO_4 \cdot 2H_2O$) is required, whereas for β-$Ca_3(PO_4)_2$, deficiency of alkali is necessary (31 g per 100 g of $CaHPO_4 \cdot 2H_2O$).

The chemical and phase composition of all the calcium phosphates prepared (whether calcined or not) was studied by X-ray phase analysis (XPA) (D8 Advance Bruker AXS diffractometer, 2θ angle variation range 10°–60°, Cu_{K_α} radiation), IR spectroscopy (1720X Perkin Elmer spectrometer) in the range 400–4000 cm^{-1}, and chemical analysis. In the last case, a 0.2-g weighed portion of calcium phosphate was dissolved in 10 ml of 0.5 M HCl, and the concentration of calcium (titration with Trilon B) and phosphate ions (photometric determination with ammonium molybdate) was determined by standard techniques [13].

XPA data for uncalcined and calcined calcium phosphates are shown in Figs. 2 and 3. As expected, diffraction peaks of calcined samples are more intense and narrower than similar peaks for uncalcined samples.

A similar conclusion about the width of absorption bands can be made on the basis of IR spectral data (Figs. 4 and 5). Moreover, the formation of TCP from NHA leads to disappearance of the characteristic absorption band of the HPO_4^{2-} ion (870 cm^{-1}) and to a decrease in the intensity of the absorption band of the OH^- ion (3570 cm^{-1}) [14].

Table 1. Average crystallite size τ calculated by formula (7)

Calcium phosphate	β,* deg	τ, nm
Uncalcined SHA	0.35	27
NHA	0.5	19
Uncalcined $Ca_3(PO_4)_2$	0.9	10
Calcined SHA	0.12	78
TCP: 50% SHA + 50% β-$Ca_3(PO_4)_2$	0.15	62
β-$Ca_3(PO_4)_2$	0.19	49

* Width of diffraction peaks in the range $2\theta = 31°–32°$ (it is in this range that most intense peaks are located in Figs. 2 and 3). In calculations by formula (7) these values should be expressed in radians.

Table 2. Time required for ions to diffuse over distance of 19 and 38 nm at 1000°C

Ion	Time, s	
	One crystallite (19 nm)	Two crystallites (38 nm)
OH^-	0.18	0.72
Ca^{2+}	3610 (~1 h)	14 400 (~4 h)
PO_4^{3-}	> 361 000 (> 4 days)	> 1 440 000 (>16 days)

The results of chemical analysis (molar ratio Ca/P) of all the calcium phosphates studied are presented below:

Calcium phosphate	Ca/P
Uncalcined SHA	1.66 ± 0.03
NHA	1.58 ± 0.03
Uncalcined $Ca_3(PO_4)_2$	1.49 ± 0.03
Calcined SHA	1.68 ± 0.02
TCP: 50% of SHA + 50% of β-$Ca_3(PO_4)_2$	1.59 ± 0.02
β-$Ca_3(PO_4)_2$	1.51 ± 0.02

The preparation of calcium phosphates is described by the following chemical reactions: (a) synthesis of SHA

$$10CaHPO_4 \cdot 2H_2O + 12KOH = Ca_{10}(PO_4)_6(OH)_2 + 4K_3PO_4 + 30H_2O, \quad (1)$$

(b) synthesis of $Ca_3(PO_4)_2$

$$3CaHPO_4 \cdot 2H_2O + 3KOH = Ca_3(PO_4)_2 + K_3PO_4 + 9H_2O, \quad (2)$$

(c) synthesis of NHA

$$CaHPO_4 \cdot 2H_2O + KOH \rightarrow Ca_{10-x}(HPO_4)_x(PO_4)_{6-x}(OH)_{2-x} + K_3PO_4 + H_2O, \quad (3)$$

where $0 < x < 1$.

In the case of $x = 0.5$, NHA is converted upon calcination into TCP consisting of 50% SHA and 50% β-$Ca_3(PO_4)_2$, and reaction (3) can be rewritten as

$$19CaHPO_4 \cdot 2H_2O + 21KOH = 2Ca_{9.5}(HPO_4)_{0.5}(PO_4)_{5.5}(OH)_{1.5} + 7K_3PO_4 + 56H_2O. \quad (4)$$

It is seen from the equations that the type of the final product is completely determined by the molar ratio of $CaHPO_4 \cdot 2H_2O$ and KOH being mixed.

The chemical reaction occurring in the course of calcination can only be written for NHA, whereas neither SHA nor $Ca_3(PO_4)_2$ undergo any chemical transformations in calcination (with only adsorbed water lost). The chemical transformation of NHA to TCP can be written as follows:

$$Ca_{10-x}(HPO_4)_x(PO_4)_{6-x}(OH)_{2-x} \rightarrow Ca_{10}(PO_4)_6(OH)_2 + \beta\text{-}Ca_3(PO_4)_2 + H_2O, \quad (5)$$

where $0 < x < 1$.

In the case of $x = 0.5$, NHA is converted upon calcination into TCP composed of 50% SHA and 50% β-$Ca_3(PO_4)_2$, and reaction (5) can be rewritten as follows:

$$2Ca_{9.5}(HPO_4)_{0.5}(PO_4)_{5.5}(OH)_{1.5} = Ca_{10}(PO_4)_6(OH)_2 + 3\beta\text{-}Ca_3(PO_4)_2 + H_2O. \quad (6)$$

The NHA structure has not been determined so far, mainly because of the inconstancy of its chemical composition. Nevertheless, chemical, spectroscopic, and X-ray studies of NHA give reason to maintain that, in all probability, NHA is SHA containing ionic vacancies at calcium and hydroxy sites and also a small number of protons in the form of HPO_4^{2-} ions [2]. In calcination, H^+ and OH^- ions present in the NHA crystal lattice diffuse and react to form water [reactions (5) and (6)] [1–4]. The formation of water is indirectly confirmed by IR spectral data. Comparison of NHA and TCP spectra (Figs. 4 and 5) shows that the intensity of the absorption band of the OH^- ion at 3570 cm^{-1} decreases and that of the absorption band of HPO_4^{2-} ion at 870 cm^{-1} disappears. In addition,

the IR spectral data point to an increase in the degree of ordering of calcium phosphates upon calcination. This follows from the fact that the absorption bands of phosphate groups at 500–600 and 950–1100 cm^{-1} become narrower and sharper [1, 2, 14].

According to the XPA data, calcination of calcium phosphates always results in upsizing of crystallites, which directly follows from the widths of diffraction peaks (Figs. 2 and 3). The average size of crystallites τ can be calculated by Scherrer's equation [15]:

$$\tau = K\lambda/(\beta \cos \theta). \quad (7)$$

Here β is the broadening (rad) of diffraction peaks, which is due to crystallites of small size; K, the form factor ($K \sim 0.9$ for most of substances [5]); λ = 1.54056 Å, the wavelength of Cu_{K_α} radiation; θ, the reflection angle corresponding to a diffraction peak.

The results of calculation by formula (7) are listed in Table 1.

It follows from Table 1 that, in the case of SHA and β-$Ca_3(PO_4)_2$, calcination only results in coarsening (agglomeration) of crystallites, without any change in their chemical composition. In the case of NHA, the agglomeration is complicated by chemical transformations resulting in the formation of new phases [reactions (5) and (6)]. Such transformations are impossible without ion diffusion, which can occur both in the bulk of the crystallites and along their boundaries.

Formally, SHA and $Ca_3(PO_4)_2$ are related by

$$3Ca_3(PO_4)_2 + Ca^{2+} + 2HO^- \rightleftarrows Ca_{10}(PO_4)_6(OH)_2. \quad (8)$$

In accordance with the calculated sizes of crystallites (Table 1), several small NHA crystallites transform upon calcination to a single large SHA or β-$Ca_3(PO_4)_2$ crystallite. This process is shown schematically in Fig. 6. In this case, calcium and hydroxy ions must diffuse over a distance approximately equal to the sizes of 1 or 2 small crystallites (19–38 nm). As follows from Eq. (8), phosphate ions are not involved in the diffusion. Now it is necessary to support these statements by calculations.

The numerical values of volume diffusion coefficients of ions in SHA at 1000°C are as follows ($cm^2\ s^{-1}$): OH^- 2×10^{-11}, Ca^{2+} 10^{-15}, and PO_4^{3-} $<10^{-17}$ [2]. Diffusion laws can be used to calculate the time required for these ions to diffuse over distances of 19 and 38 nm. The results of calculation are listed in Table 2. As seen from Table 2, calcination at 1050°C for 4 h is quite sufficient for diffusion of hydroxy and calcium ions over the distances specified, and, therefore, for NHA to be converted into TCP. The calculations demonstrate that phosphate ions virtually do not diffuse, and this is what was to be proved.

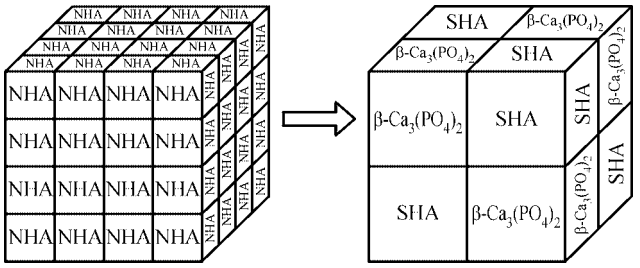

Fig. 6. Scheme of NHA conversion into TCP composed of 50% SHA + 50% β-$Ca_3(PO_4)_2$. The cubic structure is used for simplicity of drawing.

CONCLUSIONS

(1) Uncalcined and calcined calcium phosphates with varied initial Ca/P molar ratio were studied by IR spectroscopy, X-ray phase and chemical analyses. Published data indicating that no chemical transformations occur upon calcination of stoichiometric hydroxoapatite and $Ca_3(PO_4)_2$, whereas calcination of unstoichiometric hydroxoapatite results in its transformation to two-phase calcium phosphate, were confirmed. The sizes of crystallites of all the calcium phosphates studied were estimated on the basis of the widths of X-ray peaks, and a structure was suggested of two-phase calcium phosphate composed of stoichiometric hydroxoapatite and β-$Ca_3(PO_4)_2$ crystallites with average size about 62 nm. This value is in good agreement with the available published data.

(2) A mechanism of solid-phase conversion of nonstoichiometric hydroxoapatite into two-phase calcium phosphate was suggested. According to this mechanism, the transformation occurs via solid-phase diffusion of hydroxy and calcium ions over distances no longer than 38 nm. Phosphate ions virtually do not diffuse.

REFERENCES

1. LeGeros, R.Z., *Monographs in Oral Science*, Myers, H., Ed., Basel: S. Karger AG, 1991, vol. 15.
2. Elliott, J.C., *Studies in Inorganic Chemistry*, Amsterdam: Elsevier, 1994, vol. 18.
3. Bouler, J.M., Trecant, M., Delecrin, J., *et al.*, *J. Biomed. Mater. Res.*, 1996, vol. 32, no. 4, pp. 603–609.
4. Bouler, J.M., LeGeros, R.Z., and Daculsi, G., *J. Biomed. Mater. Res.*, 2000, vol. 51, no. 4, pp. 680–684.

5. Jenkins, R. and Snyder, R.L., *Chemical Analysis: A Series of Monographs on Analytical Chemistry and Its Application*, Wineforner, J.D., Ed., New York: John Willey, 1996, vol. 138.
6. Dorozhkin, S.V., *Neorg. Mater.*, 1993, vol. 29, no. 7, pp. 1021–1022.
7. Krivoputskaya, L.M., Zanin, Yu.N., and Grigor'eva, T.N., *Dokl. Akad. Nauk SSSR*, 1976, vol. 226, no. 5, pp. 1162–1165.
8. Zyman, Z., Weng, J., Liu, X., *et al.*, *Biomaterials*, 1994, vol. 15, no. 2, pp. 151–155.
9. Zyman, Z., Ivanov, I., Rochmistrov, D., *et al.*, *J. Biomed. Mater. Res.*, 2001, vol. 54, no. 2, pp. 256–263.
10. Tufekci, E., Brantley, W.A., Mitchel, J.C., *et al.*, *Int. J. Oral. Maxillofac. Implants*, 1999, vol. 14, no. 5, pp. 661–672.
11. Tas, A.C., Korkusuz, F., Timuçin, M., and Akkaç, N., *J. Mater. Sci. Mater. Med.*, 1997, vol. 8, no. 2, pp. 91–96.
12. Peters, F., Schwarz, K., and Epple, M., *Thermochim. Acta*, 2000, vol. 361, no. 1–2, pp. 131–138.
13. *Metody analiza fosfatnogo syr'ya, fosfornykh i kompleksnukh udobrenii, kormovykh fosfatov* (Methods for Analysis of Phosphate Raw Materials, Phosphate and Complex Fertilizers, Fodder Phosphates), Krotova, I.K., Ed., Moscow: Khimiya, 1975.
14. Chumaevskii, N.A., Orlovskii, V.P., Ezhova, Zh.A., *et al.*, *Zh. Neorg. Khim.*, 1992, vol. 37, no. 7, pp. 1455–1457.
15. Scherrer, P., *Nachr. Ges. Wiss. Göttingen Math.-Phys. Kl.*, 1918. Bd 2, no. 3, pp. 96–100.

Russian Journal of Applied Chemistry, Vol. 75, No. 12, 2002, pp. 1903–1906. Translated from Zhurnal Prikladnoi Khimii, Vol. 75, No. 12, 2002, pp. 1943–1946.
Original Russian Text Copyright © 2002 by Titova, Nikol'skaya, Buyanov, Suprun.

INORGANIC SYNTHESIS AND INDUSTRIAL INORGANIC CHEMISTRY

Methods for Concentration of Hydrogen Peroxide To Obtain It in Anhydrous Form

K. V. Titova, V. P. Nikol'skaya, V. V. Buyanov, and I. P. Suprun

Institute for Problems of Chemical Physics, Russian Academy of Sciences, Chernogolovka, Moscow oblast, Russia

Gosudarstvennyi Naucho-Issledovatel'skii Institut Biologicheskogo Priborostroeniya State Scientific Center, Moscow, Russia

Received February 11, 2002

Abstract—Methods for concentrating hydrogen peroxide and obtaining this compound in anhydrous form, based on removal or binding of water from the surface of solution in an open vessel or in a closed volume and also on binding of water directly in a H_2O_2 solution, are described.

Methods for concentration of aqueous solutions of hydrogen peroxide in order to raise its concentration up to 90–99% H_2O_2 markedly differ from methods for obtaining anhydrous H_2O_2, containing no other impurities, suitable for measuring physical parameters of hydrogen peroxide. In the first case, water is removed from aqueous solutions of H_2O_2 by ordinary distillation or rectification [1]. This is done at moderate temperatures and pressures of about 20 mm Hg. A large number of old investigations in this field had been devoted to concentration of diluted H_2O_2 solutions obtained from solid peroxides, mainly BaO_2 [2]. These studies are of only historical interest.

Anhydrous, high-purity hydrogen peroxide to be used in physical measurements or in single-crystal growth is commonly obtained by multiple freezing of the solid phase from concentrated (95–99%) solution [3]. This method involves considerable loss of hydrogen peroxide and low yield of the target product. Anhydrous hydrogen peroxide can be obtained by extraction from a concentrated solution with ether dehydrated with $CaCl_2$ or P_2O_5 [4]. It should be noted that the problem of obtaining anhydrous H_2O_2 of high purity remains topical until now. This is so since numerous physical properties of hydrogen peroxide, reported in the literature, have been determined by extrapolation to the anhydrous state of the system H_2O–H_2O_2 at high hydrogen peroxide concentrations.

All the above techniques for concentration of H_2O_2 solutions involve gross energy expenditure, loss of substance, and explosion hazard. It is known that microimpurities of many solids, catalysts for decomposition of hydrogen peroxide, favor fast or explosive decomposition of this compound upon heating. Explosive mixtures with hydrogen peroxide are also formed in a wide range of compositions by numerous organic substances used as solvents.

The authors made an attempt to develop safe and energy-saving methods for concentrating and obtaining anhydrous hydrogen peroxide. The methods developed are based on a fundamentally new technique, specifically, removal or binding of water from the surface of solutions of hydrogen peroxide or directly in its solution. The methods require no heating, design of rectification apparatus, or use of organic solvents.

EXPERIMENTAL

It is known [2] that, on keeping hydrogen peroxide solutions in open state, their concentration increases since the pressure of water vapor exceeds by more than an order of magnitude the vapor pressure of hydrogen peroxide (17.5 against 1.36 mm Hg at 20°C). However, account should be taken of the fact that, simultaneously with an increase in the concentration of hydrogen peroxide, its decomposition is possible under the catalytic action of the surface of a vessel used or because of the ingress of catalytic impurities into the solution from the air. No quantitative characteristics of the process of H_2O_2 concentration by water evaporation have been reported in the literature.

1070-4272/02/7512-1903 $27.00 © 2002 MAIK "Nauka/Interperiodica"

Table 1. Process of concentration of H_2O_2 (30%) solutions by natural evaporation of water

c_f H_2O_2,* %	Without airflow						Air flow velocity 0.5 m s^{-1}			
	h = 10 mm		h = 21 mm		h = 37 mm		h = 8 mm		h = 17 mm	
	τ, days	A, %	τ, days	A, %	τ, days	A, %	τ, days	A, %	τ, days	A, %
50	4.5	93.0	10.0	94.0	14.5	92.5	1.7	91.0	4.0	94.0
55	6.0	89.5	12.5	91.5	17.5	90.5	2.5	89.0	6.1	89.8
60	7.5	86.0	16.0	89.8	21.0	86.6	3.4	86.0	6.0	86.9
65	9.5	81.0	18.0	88.5	27.0	83.5	4.5	81.8	6.8	84.1
70	13.0	70.0	22.0	79.0	35.0	77.0	6.0	74.9	7.9	79.0

* c_f H_2O_2 is the final concentration of H_2O_2; the same for Table 2.

Previously, the concentration of hydrogen peroxide solutions by means of natural evaporation of water at room temperature and humidity has been studied. A relationship between the degree of concentration and loss of H_2O_2, on the one hand, and height of solution layer and air flow velocity over the solution, on the other, has been established [5]. Experiments have been carried out in a laboratory compartment with forced ventilation, with 30% H_2O_2 solutions. The solutions were placed in polymeric cuvettes and kept at 20°C in the absence of airflow over solution or at 0.5 m s^{-1} flow velocity. The air humidity was varied between 35 and 45%. Every 24 h the solutions were stirred and, after the intervals of time τ, indicated in Table 1, were weighed and analyzed for the content of hydrogen peroxide by permanganatometric titration to within ±0.1%.

It was found that keeping a 30% solution of H_2O_2 in an open state is accompanied by a considerable increase in H_2O_2 concentration without pronounced loss of H_2O_2 (Table 1). The time necessary for obtaining a sufficiently concentrated, e.g., 60% solution of H_2O_2 strongly depends on the height of the solution layer, being equal to 7.5, 16, and 21 days for h 10, 21, and 37 mm, respectively. The yield A (%) of hydrogen peroxide was calculated by the formula

$$A = (m_f c_f)/(m_s c_s) \times 100,$$

where m_s, m_f is the mass of the starting and final solutions (g); c_s, c_f is the concentration of the starting and final H_2O_2 solution (wt %), respectively.

The yield of H_2O_2 in the form of a 60% solution is (%) 86 for h = 10 mm, 90 for h = 21 mm, and 87 for h = 37 mm. Attempts to obtain more concentrated solutions by making the exposure longer failed because of a considerable increase in the rate of H_2O_2 evaporation. At a cuvette area of 73.5 cm^2 the output capacity of the process for obtaining a 60% solution was (g day^{-1}) 1.9 for h = 10 mm, 3.2 for h = 21 mm, and 3.4 for h = 37 mm. Thus, raising the height of the solution layer leads, on the one hand, to an increase in the time necessary for a prescribed temperature to be reached and, on the other, to a rise in output capacity, with the loss of hydrogen peroxide varying only slightly. With an air flow over solution, the process of H_2O_2 concentration is much faster: a 60% solution can be obtained in 3.5–6.0 days at a flow velocity of 0.5 m s^{-1}, depending on the layer height. In this case, the yield of H_2O_2 is 86–87%.

Table 2. Process of concentration of H_2O_2 solutions in a closed vessel over H_2SO_4

$V_{H_2O_2}$, ml	h, mm	c_f H_2O_2 (%) after indicated time τ, days				$A_{H_2O_2}$,* %
		1	3	5	7	
300	40	40.3	49.6	53.8	75.5	63.2
150	20	45.3	51.7	76.9	99.6	31.6
100	13	49.4	55.1	80.3	99.1	30.4
50	7	53.3	77.2	98.8	98.0	26.6
30	4	67.7	81.0	99.7	–	21.1

* At the highest concentration.

The process of concentration of hydrogen peroxide solutions in a closed vessel over a desiccant is much faster than that in the case of natural evaporation of water [6]. H_2O_2 solutions were kept in a desiccator over sulfuric acid. The acid volume was 560 ml; acid surface area, 75 cm^2; concentration of the starting H_2O_2 solution, 31.7%. The process of concentration occurs at both reduced and atmospheric pressure. Solutions of any concentration can be obtained, including nearly anhydrous solutions (Table 2). Both under natural evaporation of water and with its absorption from the gas phase over solution in a closed

volume, the time in which a prescribed concentration of hydrogen peroxide is reached depends on the thickness of the solution layer. A concentration close to 50% H_2O_2 is reached in 3 days at h = 20 and 40 mm and in 1 day at h = 13 mm. A concentration close to 99% H_2O_2 is reached in 7 days at h = 20 mm and 5 days at h = 4 mm. The loss of H_2O_2 grows with increasing time of exposure and concentration, to become 70–79% at H_2O_2 solution concentration of 98–99%. A single example of H_2O_2 concentration by a similar method has been reported in the literature: an 88% solution was obtained in a vacuum desiccator over H_2SO_4 in 3 days, with hydrogen peroxide loss of 19% [7]. The method developed in the present study is a convenient laboratory technique for obtaining minor amounts of highly concentrated solutions and anhydrous hydrogen peroxide.

To significant disadvantages of the method based on removal of water from the gas phase over an H_2O_2 solution belong pronounced loss of hydrogen peroxide and preservation of all impurities present in the starting solution in the preparations obtained. The method in which water is bound directly in solution is devoid of these disadvantages [8]. This technique yields H_2O_2 solutions of any concentration and anhydrous hydrogen peroxide of high purity. It employs anhydrous magnesium perchlorate, capable of binding water to give hydrates $Mg(ClO_4)_2 \cdot nH_2O$ (n = 2, 4, 6), as drying agent. Anhydrous magnesium perchlorate was obtained by dehydration of a dihydrate $Mg(ClO_4)_2 \cdot 2H_2O$ in a vacuum with temperature gradually raised from 20 to 220°C.

The device for concentration comprised a vessel for reagent mixing, connected to a trap and, further, to a pumping system. To a H_2O_2 solution cooled to 0°C was added, in a "dry" box, anhydrous magnesium perchlorate. In most cases, viscous solutions were obtained because of the high solubility of $Mg(ClO_4)_2$ in water [9] and in hydrogen peroxide [6]; suspensions were obtained when large amount of magnesium perchlorate was added to a 30% solution of H_2O_2. Hydrogen peroxide was separated from the mixture obtained by vacuum distillation at 20°C into a trap cooled to –196°C. A single treatment of a 30% H_2O_2 solution with magnesium perchlorate taken in a ratio $Mg(ClO_4)_2 : H_2O$ close to 1 : 6 [which corresponds to formation of magnesium perchlorate hexahydrate (Table 3)] can bind most part of water present in solution, with 81–82% hydrogen peroxide obtained by keeping in a vacuum.

Solutions with higher concentrations (93–94% H_2O_2) can be prepared with molar ratio $Mg(ClO_4)_2 : H_2O$ = (1.2–1.4) : 6. Introduction of a greater amount of magnesium perchlorate into a 30% solution of H_2O_2 is inexpedient since a thick inhomogeneous suspension is formed in this case, with the process of hydrogen peroxide evaporation decelerated dramatically. Raising the concentration of the starting solution to 46–73% H_2O_2 at a constant ratio of 1 : 6 between magnesium perchlorate and water contained in solution does not make higher the concentration of the final solution. Apparently, the forming magnesium perchlorate hexahydrate is partly dehydrated in vacuum evaporation of hydrogen peroxide. Finding its way into the trap, water liberated in the process makes the concentration of hydrogen peroxide lower.

Table 3. Final H_2O_2 concentration c_f in relation to the concentration c_s of the starting H_2O_2 solution and to the molar ratio $Mg(ClO_4)_2 : H_2O$

c_s H_2O_2, %	$Mg(ClO_4)_2 : H_2O$, mol : mol	c_f H_2O_2, %
29.9	1.05 : 6	80.8
30.2	1.07 : 6	82.0
30.2	1.25 : 6	94.4
31.4	1.40 : 6	93.3
45.8	1.00 : 6	90.9
72.8	1.00 : 6	94.2
76.6	1.40 : 4	95.6
76.7	1.70 : 4	97.5
78.5	1.20 : 2	100.0
87.2	1.20 : 2	100.0
95.9	1.00 : 2	100.0
96.0	1.10 : 2	100.0

To obtain a 95–98% H_2O_2 solution, it is necessary to use a 70% starting solution and introduce magnesium perchlorate in an amount corresponding to the ratio $Mg(ClO_4)_2 : H_2O$ = (1.4–1.7) : 4, which leads to formation of a mixture of magnesium perchlorate tetra- and dihydrate. Anhydrous hydrogen peroxide is formed upon treatment with magnesium perchlorate of a H_2O_2 solution with initial concentration of 80% and more at a molar ratio $Mg(ClO_4)_2 : H_2O$ = (1.0–1.2) : 2, which exceeds somewhat the ratio required for $Mg(ClO_4)_2$ dihydrate to be formed. In all experiments, the loss of H_2O_2 does not exceed 1%.

To determine the stability of H_2O_2 during storage of solutions obtained using various concentration methods in unstabilized form and stabilized with various stabilizing additives known for hydrogen peroxide, the solutions were placed in nonhermetically closed glass vessels and stored under identical conditions (20 + 2°C). After the intervals of time indicated

Table 4. Stability of H_2O_2 solutions obtained by removal or binding of water

Concentration method	$c_{H_2O_2}$, %	Stabilization technique	Loss of H_2O_2 (%) in indicated time, days		
			10	19	50
With air flow	65.1	–	3.1	6.7	9.1
		$Na_4P_2O_7$, 0.1%	2.6	4.1	6.5
		$Sn(OH)_4$, 0.3%	3.7	5.0	7.4
		Vacuum evaporation	0.7	2.6	2.7
Over H_2SO_4	99.6	–	1.6	3.6	7.0
		Vacuum evaporation	0.5	1.7	2.1
Introduction of $Mg(ClO_4)_2$	100	The same	0.0	0.3	1.6

in Table 4 came to an end, the content of hydrogen peroxide in the solutions was determined. The stability was evaluated as loss of H_2O_2 (%) relative to the content of hydrogen peroxide in an initial solution placed in storage.

The stability of hydrogen peroxide solutions obtained by water evaporation with air flow is satisfactory. The loss of H_2O_2 in storage in a glass vessel is 3% in 10 days and 9% in 50 days. Such solutions can be used without additional stabilization. Introduction of sodium diphosphate or tin(IV) hydroxide as stabilizing additives improves their stability only slightly. The loss of H_2O_2 is much lower in the case of vacuum distillation of the solutions at 20°C into a receiver cooled to –196°C. The same procedure markedly improves the stability of solutions obtained in a closed volume (Table 4). Anhydrous hydrogen peroxide obtained by dehydration with magnesium perchlorate is distinguished by high stability. With account of the catalytic action of the glass surface on hydrogen peroxide [10], solutions of this kind have higher stability when stored in polymeric vessels and can be used to measure physical parameters of hydrogen peroxide.

CONCLUSION

The methods developed for concentrating hydrogen peroxide and obtaining it in anhydrous form are based on (i) evaporation of water from the solution surface in an open vessel with and without air flow, (ii) keeping a solution in a closed vessel over dehydrating agent, and (iii) binding of water directly in the H_2O_2 solution with anhydrous magnesium perchlorate and separation of hydrogen peroxide by vacuum evaporation at 20°C.

REFERENCES

1. *Handbuch der praparativen anorganischen Chemie*, Bd. 1, *Unter Mitarb.*, von Baudler, M., Brauer, G., Feher, F., *et al.*, Stuttgart: Ferdinand Enke, 1975.
2. *Gmelins Handbuch der anorganischen Chemie*, Sauerstoff, S/N 3, Lfg 7, pp. 2156–2160.
3. Giguere, P.A., Liu, J.D., Dugdale, J.A., and Morrison, J.A., *Canad. J. Chem.*, 1954, vol. 32, no. 1, pp. 118–121.
4. Schmidt, M. and Bornmann, P., *Z. anorg. Chem.*, 1964, vol. 330, no. 2, pp. 309–311.
5. Titova, K.V., *Zh. Neorg. Khim.*, 1998, vol. 43, no. 11, pp. 1794–1795.
6. Titova, K.V., Nikol'skaya, V.P., and Buyanov, V.V., *Koordinatsionnye soedineniya peroksida vodoroda. Sintez, stroenie, svoistva, sporotsidnaya aktivnost', tekhnologiya i proizvodstvo dezinfitsiruyushchikh preparatov* (Coordination Compounds with Hydrogen Peroxide: Synthesis, Structure, Properties, Sporocide Activity, Technology, and Manufacture of Disinfecting Preparatins), Chernogolovka: Inst. Probl. Khim. Fiz. Ross. Akad. Nauk, 2000.
7. Kilpatrick, M.L., Reiff, O.M., and Rice, F.O., *J. Am. Chem. Soc.*, 1926, vol. 48, no. 11, pp. 3019–3021.
8. Titova, K.V., Kolmakova, E.I., and Rosolovskii, V.Ya., *Zh. Neorg. Khim.*, 1987, vol. 32, no. 11, pp. 2849–2850.
9. Willard, H.H. and Smith, G.F., *J. Am. Chem. Soc.*, 1923, vol. 45, no. 2, pp. 286–287.
10. Titova, K.V., Nikol'skaya, V.P., Buyanov, V.V., and Suprun, I.P., *Zh. Prikl. Khim.*, 2001, vol. 74, no. 6, pp. 886–890.

Russian Journal of Applied Chemistry, Vol. 75, No. 12, 2002, pp. 1907–1910. Translated from Zhurnal Prikladnoi Khimii, Vol. 75, No. 12, 2002, pp. 1947–1950.
Original Russian Text Copyright © 2002 by Belyaev, Eremin, Simanova, Evreinova.

INORGANIC SYNTHESIS AND INDUSTRIAL INORGANIC CHEMISTRY

Reactions of *trans*-$[OsO_2Cl_2L_2]$ (L = PPh_3, $AsPh_3$, $SbPh_3$) with Acetic Acid

A. N. Belyaev, A. V. Eremin, S. A. Simanova, and N. V. Evreinova

St. Petersburg State Technological Institute, St. Petersburg, Russia

Received November 15, 2001; in final form, September 2002

Abstract—The possibility of reactions between *trans*-$[OsO_2Cl_2L_2]$ (L = PPh_3, $AsPh_3$, $SbPh_3$) osmium(VI) complexes and glacial acetic acid to give osmium(IV) compounds of general formula $[Os_2(\mu\text{-}O)(\mu\text{-}O_2CCH_3)_2Cl_4(L)_2]$ was studied.

Dissolution of platinum-containing raw materials is a labor-consuming and ecologically unsafe process [1–4]. The creation of safer and less expensive technologies for breaking-down such concentrates and the closely related problem of analytical monitoring of the efficiency of raw material processing can be regarded as one of important lines of development of modern chemical technologies for recovery of platinum metals.

At present, one of ways to dissolve osmium-containing concentrates consists in their fusion with sodium disulfate, leaching of the melt, and its treatment with chlorine for distilling-off OsO_4, which is absorbed successively, first by HCl solutions with methanol and then by an alcoholic solution of NaOH. Heating the latter with NH_4Cl allows osmium to be precipitated as $[OsO_2Cl_2(NH_3)_2$ [4].

The development of alternative procedures for dissolving osmium-containing concentrates is based on replacement of highly aggressive solutions with ethanol–acetate mixtures [5]. However, this requires a detailed study of the behavior of *trans*-$[OsO_2Cl_2L_2]$ complexes with ligands L of varied nature in acetic acid media.

Boiling of *trans*-$[OsO_2X_2L_2]$ (X = Cl, Br; L = PPh_3, PEt_2Ph, or Py) in a RCOOH-$(RCOO)_2O$ (R = CH_3, C_2H_5) mixture is known [6, 7] to give binuclear osmium acetates with a $Os_2(\mu\text{-}O)$ core.

X-ray structural data [6, 7] suggest that the formation of a linear or bent binuclear Os–O–Os fragment is affected by the nature of ligand (L) in the starting mononuclear *trans*-$[OsO_2X_2L_2]$ (X = Cl, Br) compound. If L is PPh_3 or PEt_2Ph, then $[Os_2^{IV}(\mu\text{-}O)(\mu\text{-}O_2CCH_3)_2Cl_4(L)_2]$ (R = CH_3, C_2H_5; X = Cl, Br) complexes are formed with bent metal-containing $Os_2(\mu\text{-}O)$ core and bidentate coordination of two bridging acetate groups [6]. If L is Py, then $[(Py)_2Cl_2(CH_3COO)Os(\mu\text{-}O)Os(Py)_2Cl_3]$ compound with a linear $Os_2(\mu\text{-}O)$ core and only one monodentately coordinated acetate group is formed [7].

The present study is concerned with the influence exerted by the nature of ligand L in *trans*-$[OsO_2Cl_2L_2]$ on the formation and spectral characteristics of osmium acetates $[Os_2^{IV}(\mu\text{-}O)(\mu\text{-}O_2CCH_3)Cl_4(L)_2]$. PPh_3, $AsPh_3$, or $SbPh_3$ were selected as ligands L. Their choice was determined by the fact that, on the one hand, they behave as donors having a free electron pair and, on the other, they possess, unlike such a ligand as Py, free *d*-orbitals with rather low energies.

EXPERIMENTAL

The starting *trans*-$OsO_2Cl_2(PPh_3)_2$ was obtained using the procedure proposed in [8].

***trans*-$OsO_2Cl_2(AsPh_3)_2$.** A 2-g portion of OsO_4 was introduced into a mixture of 30 ml of ethanol and 5 ml of concentrated hydrochloric acid heated to approximately 90°C. Triphenylphosphine (4.5 g, or 14 mmol per 0.39 mmol of OsO_4) was dissolved in a minimal amount of boiling ethanol and poured into the first solution. The precipitated light beige complex was washed on a filter with ethanol and diethyl ether. Yield ~70%. IR spectrum, cm^{-1}: 471 s, 693 vs, 742 vs, 845 s, 1001 w, 1030 w, 1083 w, 1190 vs, 1460 s, 1510 w.

Found, %: Os 21.1; Cl 8.2.

$C_{36}H_{30}As_2Cl_2Os$.

Calculated, %: Os 21.0; Cl 7.8.

1070-4272/02/7512-1907 $27.00 © 2002 MAIK "Nauka/Interperiodica"

***trans*-$OsO_2Cl_2(SbPh_3)_2$.** The synthesis was similar to that of *trans*-$OsO_2Cl_2(AsPh_3)_2$. Owing to the low solubility of triphenylantimony in ethanol, the alcohol was replaced with an EtOH–Et_2O mixture (1 : 1 by volume). The precipitated light green complex was filtered off and carefully washed with ether, in which it is partially soluble. Slow evaporation of the filtrate gave an additional amount of the finely crystalline precipitate of the complex. Total yield ~80%. IR spectrum, cm^{-1}: 454 s, 683 vs, 729 vs, 836 s, 993 s, 1019 s, 1061 w, 1179 w, 1301 w, 1329 w, 1433 s, 1475 s, 1571 w, 1637 wide, 1871 wide.

Found, %: Os 18.9, Cl 7.2.

$C_{36}H_{30}Cl_2OsSb_2$.

Calculated, %: Os 19.0, Cl 7.1.

$[Os_2(\mu\text{-}O)(\mu\text{-}O_2CCH_3)_2(PPh_3)_2Cl_4]$ (I). A suspension of 1 g of *trans*-$[OsO_2(PPh_3)_2Cl_2]$ in 20 ml of glacial acetic acid was boiled until the starting complex dissolved completely. In the process, the colorless solution turned dark brown. The dry residue formed upon evaporation of the solution on an air bath was dissolved in 40 ml of chloroform and a minor amount of pentane or hexane was added to the resulting solution. The precipitated complex was filtered off, washed with ether, and kept in a desiccator over KOH to constant weight.[1] Yield ~95%. IR spectrum, cm^{-1}: 443 w, 523 vs, 619 w, 691 vs, 720 s, 744 s, 997 w, 1028 w, 1091 s, 1159 w, 1220 w, 1408 w, 1435 vs, 1482 s, 1697 wide, 2927 w, 2964 w, 3059 w, 3440 wide.

Found, %: Os 32.0, Cl 12.5.

$C_{40}H_{36}Cl_4O_5Os_2P_2$.

Calculated, %: Os 32.2, Cl 12.0.

$[Os_2(\mu\text{-}O)(\mu\text{-}O_2CCH_3)_2(AsPh_3)_2Cl_4]$ (II). The synthesis was similar to that of complex **I**. The yield of the dark brown complex was about 70%. IR spectrum, cm^{-1}: 472 s, 690 s, 740 s, 778 w, 860 wide, 1000 w, 1028 w, 1085 s, 1163 wide, 1187 wide, 1440 s, 1490 w, 1630 s, 3420 wide.

Found, %: Os 29.8, Cl 11.4.

$C_{40}H_{36}As_2Cl_4O_5Os_2$.

Calculated, %: Os 30.0, Cl 11.2.

[1] An X-ray structural analysis of a similar $[Os_2^{IV}(\mu\text{-}O)\cdot(\mu\text{-}O_2CCCl_2)_2Cl_4(PPh_3)_2]$ complex, obtained recently by the authors, confirmed the bent structure of the $Os_2(\mu\text{-}O)$ core and the presence of two bridging carboxylate ions.

Electronic absorption spectra of solutions of the complexes were recorded on an SF-56 spectrophotometer in the range 200–1100 nm in quartz cells with l = 1 cm. The IR spectra were recorded in the range 4000–400 cm^{-1} on a Nicolet FT-360 spectrophotometer in KBr pellets, and X-ray-photoelectron spectra (XPS), on a Perkin–Elmer PHI 5400 spectrophotometer with excitation by X-ray emission of Mg. Powdered samples were compacted with indium and placed, after preliminary evacuation of the chamber, on a manipulator cooled with liquid nitrogen. The working residual pressure in the spectrophotometer was 10^{-8} mm Hg.

The X-ray structural analysis was carried out on a SYNTEX P21 diffractometer with Cu_{K_α} emission (λ = 1.54178 Å) at 20 ± 1°C.

The experimental data obtained suggest that binuclear oxygen-bridged osmium acetates $[Os_2^{IV}(\mu\text{-}O)\cdot(\mu\text{-}O_2CCH_3)_2Cl_4(L)_2]$ (L = PPh_3 or $AsPh_3$) can be formed in the reaction of *trans*-$[OsO_2Cl_2L_2]$ with CH_3CO_2H in the absence of $(CH_3CO)_2O$, too. Heating of the *trans*-$[OsO_2Cl_2L_2]$ complexes with glacial acetic acid gives dark brown binuclear osmium(IV) compounds of general formula $[Os_2^{IV}(\mu\text{-}O)(\mu\text{-}O_2CCH_3)_2Cl_4(L)_2]$ in high yield. However, $[Os_2^{IV}(\mu\text{-}O)(\mu\text{-}O_2CCH_3)_2Cl_4(L)_2]$ complexes can only be isolated for L = PPh_3 (**I**) or $AsPh_3$ (**II**). According to XPS data, the Os ($4f7/2$) bond energies are 53.0 and 53.1 eV for complexes **I** and **II**, respectively, which corresponds to a formal oxidation state of osmium atoms in these compounds equal to +4, in good agreement with the data of [5].

Compounds **I** and **II** are stable in air, poorly soluble in water, ethanol, ether, and saturated hydrocarbons, but readily soluble in such solvents as chloroform, dichloromethane, or benzene.

The electronic absorption spectra of $[Os_2^{IV}(\mu\text{-}O)\cdot(\mu\text{-}O_2CCH_3)_2Cl_4(L)_2]$ solutions in chloroform contain absorption bands with λ_{max} = 456.0 nm (ε = 10134 l mol^{-1} cm^{-1}) for compound **I** and λ_{max} = 426.0 nm (ε = 7362 l mol^{-1} cm^{-1}), and a shoulder at 533.0 nm for complex **II** (Fig. 1). It is seen from Fig. 1 that the most intense band in the electronic absorption spectrum of complex **II**, which can be assigned to the $\pi^{unbonding} \rightarrow \pi^*$ transition within the $Os_2(\mu\text{-}O)$ [7], is shifted by 30 nm to higher energies. It is most likely that the shoulder in the low-energy region of the spectrum is related to charge transfer from the core to π^*-orbitals of $AsPh_3$.

The band related to the $\pi^{unbonding} \rightarrow \pi^*$ transition within the $Os_2(\mu\text{-}O)$ core shifts to higher energies

when osmium complexes react with $HClO_4$ (Fig. 2). The appearance of a shoulder with $\lambda_{max} \sim 580$ nm seems to be attributable to charge transfer from $d\pi$–$p\pi$ orbitals of the core to π^* orbitals of PPh_3. This process seems to be due to protonation of the bridging oxygen atom in the metal-containing core:

$$[Os_2^{IV}(\mu\text{-}O)(\mu\text{-}O_2CCH_3)_2Cl_4(L)_2] + H^+ \rightarrow [Os_2^{IV}(\mu\text{-}OH)(\mu\text{-}O_2CCH_3)_2Cl_4(L)_2]^+.$$

It is necessary to note that protonation of bridging oxygen atoms in similar binuclear ruthenium complexes $Ru_2(\mu\text{-}O)(\mu\text{-}O_2\text{-}CCH_3)_2^{2+}$ is well known [9, 10].

The study demonstrated that the formation of complexes **I** and **II** can be described by the scheme:

$$2[OsO_2Cl_2L_2] + 2RCO_2H \rightarrow [Os_2^{IV}(\mu\text{-}O)(\mu\text{-}O_2CR)_2Cl_4L_2] + 2O = L + H_2O,$$

where L = PPh_3 or $AsPh_3$.

The presence of triphenylphosphinoxide ($POPh_3$) or triphenylarsinoxide ($AsOPh_3$) in the reaction products is indicated by the results of elemental analysis and also by IR spectral data and melting points of these compounds, which are in good agreement with published data [11, 12].

Found for $PO(C_6H_5)_3$, %: P 11.0, C 78.1, H 5.0.
Calculated for $C_{18}H_{15}OP$, %: P 11.1, C 77.7, H 5.43.

IR spectrum, cm^{-1}: 420 w, 452 wide, 500 s, 542 s, 695 s, 722 vs, 759 s, 950 s, 998 w, 1030 s, 1077 s, 1123 s, 1195 ws ($\nu_{P=O}$), 1440 s, 1490 s, 1590 s; mp 156°C.

Found for $C_{18}H_{15}AsO$, %: C 67.0, H 3.2.
Calculated for $AsOC_{18}H_{15}$, %: C 67.1, H 4.7.

IR spectrum, cm^{-1}: 418 w, 461 s, 690 vs, 742 vs, 812 vs, 998 w, 1026 w, 1086 s (As=O), 1162 w, 1190 w, 1450 s, 1490 s; mp 184°C.

Triphenyldichloroantimony and a poorly soluble osmium-containing light brown compound are always formed in the reaction of *trans*-$[OsO_2Cl_2(SbPh_3)_2]$ with acetic acid. The composition of the osmium-containing product could not be determined; however, according to the elemental analysis it contains 59.2% Os and 16.4% C, and also trace amounts of chlorine. The Os : C ratio of about 1 : 4.4 shows that this product contains acetate ions $CH_3CO_2^-$. This is also indirectly confirmed by IR spectral data. Characteristic bands present in the frequency range 1400–1700 cm^{-1} are attributable to vibrations of acetate groups [8, 9, 11]. However, these bands are too broad and have too low intensity to be used in determining the coordination of the $CH_3CO_2^-$ ion.

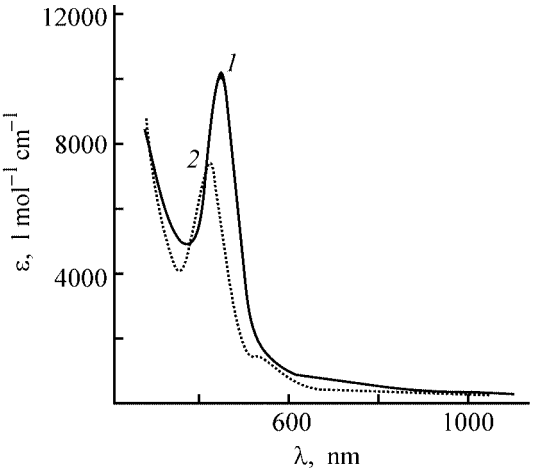

Fig. 1. Electronic absorption spectra of solutions of (*1*) $[Os_2(\mu\text{-}O)(\mu\text{-}O_2CCH_3)_2(PPh_3)_2Cl_4]$ and (*2*) $[Os_2(\mu\text{-}O)\cdot(\mu\text{-}O_2CCH_3)_2(AsPh_3)_2Cl_4]$ complexes in $CHCl_3$. (ε) extinction coefficient related to 1 mol of a complex and (λ) wavelength.

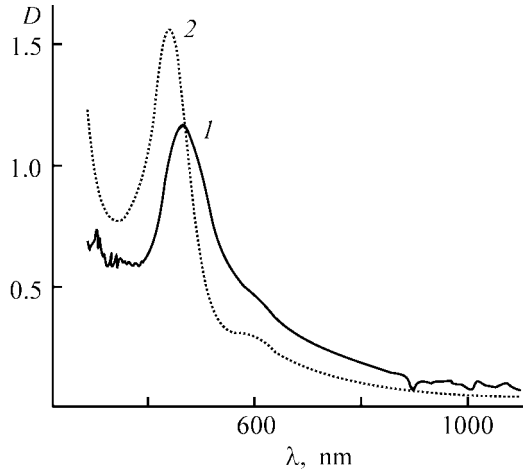

Fig. 2. Electronic absorption spectra of acetonitrile solutions of (*1*) $[Os_2(\mu\text{-}O)(\mu\text{-}O_2CCH_3)_2(PPh_3)_2Cl_4]$ and (*2*) $[Os_2(\mu\text{-}OP)(\mu\text{-}O_2CCH_3)_2(AsPh_3)_2Cl_4]^+$ complexes. (*D*) optical density and (λ) wavelength.

The formation of $SbCl_2Ph_3$ is confirmed by the elemental and X-ray analyses[2] (Fig. 3).

Crystallographic data for $SbCl_2Ph_3$: the complex is crystallized from ether as colorless needles characterized by the orthorhombic space group *Pbca*, a = 13.122(2) Å, α = 90°, b = 23.885(3) Å, β = 90°,

[2] The X-ray structure analysis was carried out at the Karpov Physicochemical Institute (Moscow).

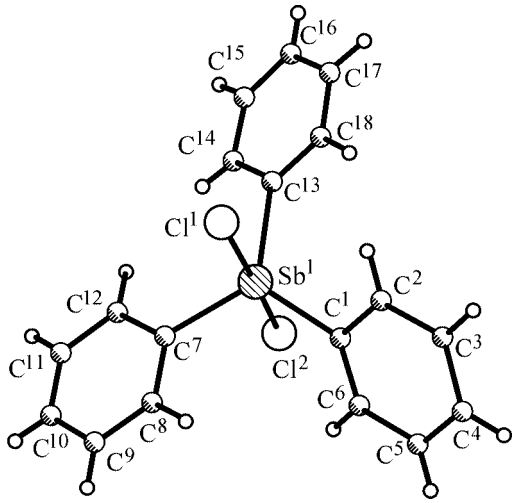

Fig. 3. Structure of $SbCl_2Ph_3$.

c = 43.823(8) Å, γ = 90°, V = 13735(4) Å^3, z = 16, R = 0.0353.

Found for $SbCl_2(C_6H_5)_3$, %: Cl 16.5, C 51.0, H 3.3. Calculated for $C_{18}H_{15}Cl_2Sb$, %: Cl 16.72, C 50.99, H 3.57.

IR spectrum, cm^{-1}: 450 vs, 681 s, 727 s, 993 wide, 1018 w, 1055 w, 1430 s, 1480 s.

Since the starting *trans*-$[OsO_2Cl_2(SbPh_3)_2]$ complex is isolated from the reaction mixture containing hydrochloric acid, it is unlikely that its reaction with acetic acid may lead to an intramolecular redox reaction yielding $SbCl_2Ph_3$. Presumably, the first stage of the reaction between *trans*-$[OsO_2Cl_2(SbPh_3)_2]$ and acetic acid results in an unstable binuclear osmium acetate $[Os_2^{IV}(\mu\text{-}O)(\mu\text{-}O_2CCH_3)_2Cl_4(SbPh_3)_2]$, which further decomposes to give $SbCl_2Ph_3$ and an osmium-containing compound, possibly of polymer composition.

In conclusion, it should be noted that the ionization energies I (eV) of ligands L increase in the order 7.85 (PPh_3) < 8.03 ($AsPh_3$) < 8.08 ($SbPh_3$). However, small differences between these energies suggest that the ligands have similar donor–acceptor properties. Therefore, it is most probable that the instability of the $[Os_2^{IV}(\mu\text{-}O)(\mu\text{-}O_2CCH_3)_2Cl_4(SbPh_3)_2]$ complex is caused by steric effects: $SbPh_3$ is larger in size than PPh_3 or $AsPh_3$.

CONCLUSIONS

(1) Binuclear oxygen-bridged osmium acetates $[Os_2^{IV}(\mu\text{-}O)(\mu\text{-}O_2CCH_3)_2Cl_4(L)_2]$ (L = PPh_3 or $AsPh_3$) can be formed in high yield (95 to 70%) in the reaction of *trans*-$[OsO_2Cl_2L_2]$ complexes with glacial acetic acid.

(2) In glacial acetic acid, *trans*-$[OsO_2Cl_2(SbPh_3)_2]$ undergoes an intramolecular redox conversion to $SbCl_2Ph_3$.

(3) It is suggested that the increase in the size of ligands L in the order $SbPh_3$ > $AsPh_3$ > PPh_3 is one of the main reasons for the decrease in the stability of oxygen-bridged osmium acetates $[Os_2^{IV}(\mu\text{-}O)\cdot(\mu\text{-}O_2CCH_3)_2Cl_4(L)_2]$ in acetic acid medium.

ACKNOWLEDGMENTS

The study was supported financially by the Russian Foundation for Basic Research (grant nos. 00-03-32659 and 01-03-06119) and by the program of the Ministry of Education of the Russian Federation "Research in Higher School in the Field of Chemistry and Chemical Products" (Section 003).

REFERENCES

1. Maslenitskii, I.N., Chugaev, L.V., Borbat, V.F., *et al.*, *Metallurgiya blagorodnykh metallov* (Metallurgy of Noble Metals), Moscow: Metallurgiya, 1987.
2. *Blagorodnye metally: Spravochnoe izdanie* (Noble Metals: Reference Book), Savitskii, E.M., Ed., Moscow: Metallurgiya, 1984.
3. Lavrov, A.A., Gorbatov, L.D., Tarakanov, R.G., *et al.*, Abstracts of Papers, *XVII Vsesoyuznoe Chernyaevskoe soveshchanie po khimii, analizu i tekhnologii platinovykh metallov* (XVII All-Union Chernyaev Symp. on Chemistry, Analysis, and Technology of Platinum Metals), Moscow, 2001, p. 256.
4. Livingstone, S.E., *The Chemistry of Ruthenium, Rhodium, Palladium, Osmium, Iridium and Platinum*, Oxford: Pergamon, 1973.
5. Danilova, F.I., Munina, V.M., Simanova, S.A., *et al.*, Abstracts of Papers, *XIV Vsesoyuznoe Chernyaevskoe soveshchanie po khimii, analizu i tekhnologii platinovykh metallov* (XIV All-Union Chernyaev Symp. on Chemistry, Analysis, and Technology of Platinum Metals), Novosibirsk, 1990, vol. 2, p. 76.
6. Armstrong, J.E., Robinson, W.R., and Walton, R.A., *Inorg. Chem.*, 1983, vol. 22, no. 9, pp. 1301–1306.
7. Imbe, Y., Umakoshi, K., Matsunami, C., and Sasaki, Y., *Inorg. Chem.*, 1995, vol. 34, no. 4, pp. 813–820.
8. Salmon, D.J. and Waltom, R.A., *Inorg. Chem.*, 1978, vol. 17, no. 9, pp. 2379–2382.
9. Neubold, P., Weighard, K., Nuber, B., and Wiess, J., *Inorg. Chem.*, 1989, vol. 28, no. 3, pp. 459–467.
10. Valli, M., Miyata, S., Wakita, H., *et al.*, *Inorg. Chem.*, 1997, vol. 36, no. 21, pp. 4622–4626.
11. Nakamoto, K., *Infrared Spectra of Inorganic and Coordination Compounds*, New York: Wiley, 1963.
12. Chichibabin, A.E., *Osnovnye nachala organicheskoi khimii* (Fundamentals of Organic Chemistry), Moscow: Gos. Nauch.-Tekhn. Izd. (GONTI), 1958.
13. Distefano, G., Pignataro, S., Szepes, L., and Borrossay, J., *J. Organometall. Chem.*, 1975, vol. 102, pp. 313–316.

Russian Journal of Applied Chemistry, Vol. 75, No. 12, 2002, pp. 1911–1915. Translated from Zhurnal Prikladnoi Khimii, Vol. 75, No. 12, 2002, pp. 1951–1954.
Original Russian Text Copyright © 2002 by Feoktistova, Sapozhnikov, Aleksandrova, Medvedeva, Grishchenko.

INORGANIC SYNTHESIS AND INDUSTRIAL INORGANIC CHEMISTRY

X-ray Study of Iron-containing Derivatives of Arabinogalactan

L. P. Feoktistova, A. N. Sapozhnikov, G. P. Aleksandrova, S. A. Medvedeva, and L. A. Grishchenko

Irkutsk Institute of Geochemistry, Siberian Division, Russian Academy of Sciences, Irkutsk, Russia

Irkutsk Institute of Chemistry, Siberian Division, Russian Academy of Sciences, Irkutsk, Russia

Received November 27, 2001; in final form, August 2002

Abstract—Iron-containing derivatives of arabinogalactan (ferroarabinogalactans) were subjected to X-ray diffraction analysis to determine the form and structure of bound iron. Crystal lattice parameters a of the iron-containing phase were measured and the average crystallite size was determined.

The problem of obtaining new iron-containing medicinal preparations is rather acute because of the wide occurrence of iron-deficiency anemia in the population. A promising way to create iron-containing preparations is to incorporate iron compounds into a polymer carrier [1]. As a carrier of this kind was used arabinogalactan distinguished from other polysaccharides by good water solubility and membranotropic properties. The concept of synthesis consisted in that a water-soluble iron-containing preparation should be created and delivered into a cell.

It is known that reaction of aqueous solutions of iron(II, III) salts with alkalis yields difficultly soluble hydrated iron(II, III) oxides. This reaction with a mixture of Fe^{3+} and Fe^{2+} salts in the presence of arabinogalactan has been used to obtain previously unknown iron derivatives of arabinogalactan, ferroarabinogalactans [2]. All ferroarabinogalactans are well soluble in water (up to 50%), whereas standard samples of the oxides FeO, Fe_2O_3, and Fe_3O_4 are water-insoluble. The characteristic viscosity of 1% aqueous solutions of the samples is 0.052–0.054 dl g^{-1}, which is close to the characteristic viscosity of the starting arabinogalactan (0.058 dl g^{-1}). This confirms that the reaction performed [2] yields hydrophilic and water-soluble kind of ferrites.

In order to establish the form and structure of bound iron, iron-containing derivatives of arabinogalactan were subjected to X-ray diffraction analysis in the present study.

EXPERIMENTAL

The starting arabinogalactan was isolated from an aqueous extract of larch wood and purified by reprecipitation into alcohol. Iron-containing polymers were synthesized as follows: aqueous solutions of iron salts ($FeSO_4 \cdot 4H_2O$ and $FeCl_3 \cdot 5H_2O$, sample nos. 1 and 2; $FeCl_3 \cdot 5H_2O$, sample no. 3) with iron content of 0.22–1.25 mmol were added to a concentrated (50%) aqueous solution of arabinogalactan under vigorous stirring and allowed to stay at room temperature for 15 min (all samples). Further, the resulting mixture was treated with 30% ammonium hydroxide to pH of reaction medium, 10–12. The mixture obtained was boiled on a water bath for 15 min and filtered, and ferroarabinogalactans was precipitated with alcohol.

The content of iron in the preparations obtained was found spectrophotometrically on an SF-26 instrument, with Trilon B as complexing agent, and by atomic-absorption analysis: 3.53% (sample no. 1), 5.01% (sample no. 2), and 4.50% (sample no. 3).

The X-ray analysis was carried out on a DRON-3.0 diffractometer with Cu_{K_α} (Ni filter) and $Fe_{K_{\alpha,\beta}}$ radiation, set of slits (2, 8 mm, Soller slit 1.5°, and 0.25 mm), scanning rate of 1 (phase analysis) and 0.25 deg min^{-1} (determination of parameters and halfwidths of reflections). The phase analysis was performed with Cu_{K_α} radiation, and the position and halfwidth of the (311) line was measured with $Fe_{K_{\alpha,\beta}}$ radiation. The lattice parameter was determined by the internal standard method for the (311) reflection, with quartz (a =

1070-4272/02/7512-1911 $27.00 © 2002 MAIK "Nauka/Interperiodica"

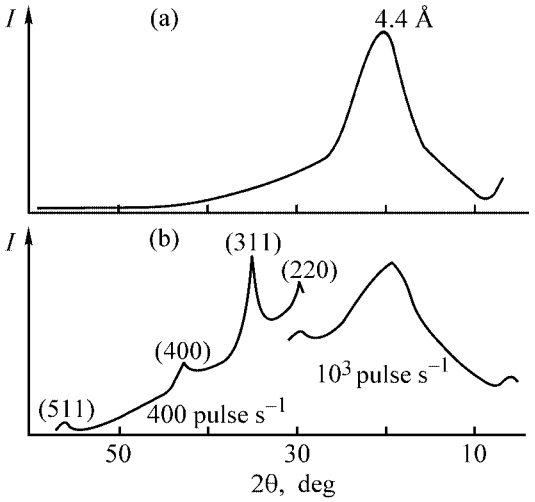

Fig. 1. Fragments of X-ray diffraction patterns of (a) starting arabinogalactan and (b) ferroarabinogalactan with 3.53% iron (sample no. 1). Cu_{K_α} radiation. (*I*) Intensity and (2θ) Bragg angle; the same for Fig. 2.

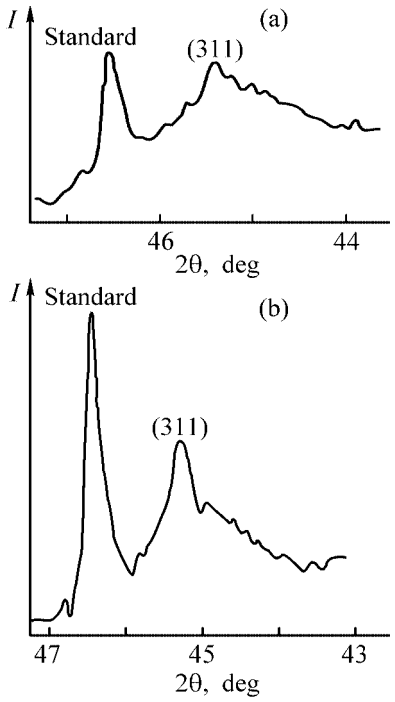

Fig. 2. Fragments of X-ray diffraction patterns of ferroarabinogalactan with iron content of (a) 3.53% (sample no. 1) and (b) 5.01% (sample no. 2) with internal standard (quartz), demonstrating changes in the profile and position of the (311) line. $Fe_{K_{\alpha,\beta}}$ radiation.

4.9126, b = 5.4044 Å) as standard. A correction for instrumental broadening of reflections was introduced using reflections from magnetite as reference.[1]

[1] As standard was used magnetite synthesized at the laboratory of experimental geochemistry, Institute of Geochemistry, Siberian Division, Russian Academy of Sciences.

Natural hemicelluloses may exist as amorphous or crystalline aggregates, with the forms and their ratio being individual for different types of polysaccharides. For example, xylan can be obtained in the crystalline form as hexagonal plates; galactoglucomannans are amorphous, but may contain fibrillar regions of molecule ordering [3]. It was of interest to find out what type of structure, crystalline or amorphous, is characteristic of arabinogalactan. For this purpose, an X-ray diffraction pattern of the starting arabinogalactan preparation isolated from larch wood was measured [2]. The X-ray diffraction pattern demonstrates in the range of angles 2θ = 8–40° an intense halo with peak intensity at d = 44 Å. No other reflections in the range of angles 2θ = 8–60° (Cu_{K_α}) are observed. This indicates that arabinogalactan is amorphous (Fig. 1a).

There exist several anhydrous iron oxides, occurring in nature as various minerals: hematite α-Fe_2O_3 (high-temperature form), maghemite γ-Fe_2O_3 (low-temperature form), magnetite Fe_3O_4, wustite FeO, and a number of ferrihydrites (which may be either crystalline or amorphous) [4].

Incorporation of iron into an arabinogalactan molecule changes the X-ray diffraction patterns of ferroarabinogalactan nos. 1 and 2 (Figs. 1b, 2a, and 2b). For example, several broad weak lines are observed on the background of a broad reflection from arabinogalactan in the range of angles 2θ = 28–75° (Cu_{K_α}), with the peak intensity of reflection from arabinogalactan remaining in the same position, at d = 4.4 Å.

X-ray diffraction data for sample nos. 1 and 2 are listed in the table. It can be seen that the interplanar spacings and line intensity distributions for sample nos. 1 and 2 are in good agreement with the X-ray diffraction pattern of magnetite (PDF, 19-629) and main lines of maghemite (PDF, 24-81). This confirms that iron is present in sample nos. 1 and 2 as magnetite and(or) maghemite.

Among important structural parameters are lattice constants. Magnetite is characterized by cubic symmetry, space group F*d3n*, and crystal structure of inverted spinel with lattice constant a = 8.396 Å (PDF, 19-629). Maghemite, having a structure of magnetite, differs from the latter in that only 21 1/3 out of 24 crystallographic positions of the metal are occupied, which leads to a decrease in a to 8.350 Å [5, PDF, 24-81]. Its X-ray diffraction pattern contains additional lines, absent in the case of minerals belonging to the spinel group. However, these lines are weak and cannot be seen in X-ray diffraction patterns of finely dispersed samples. In this case, the X-ray diffraction

X-ray diffraction data for ferroarabinogalactans in comparison with reference data for magnetite and maghemite

Sample no. 1		Sample no. 2		Magnetite (PDF, 19-629), a = 8.396 Å			Maghemite (PDF, 24-81), a = 8.350 Å		
d, Å	I	d, Å	I	d, Å	I	hkl	d, Å	I	hkl
							5.90	2	110
4.4		4.4		4.85	8	111	4.82	5	111
							4.18	1	200
							3.73	5	210
							3.41	2	211
2.95	2	2.94	3	2.967	30	220	2.95	34	220
							2.78	19	221
							2.64	–	310
2.52	10	2.52	10	2.532	100	311	2.52	100	311
				2.424	8	222	2.41	1	222
							2.32	6	320
							2.23	1	321
2.09	1	2.08	2	2.099	20	400	2.08	24	400
							1.87	1	420
				1.715	10	422	1.70	2	422
1.61	1	1.60	2	1.616	30	511	1.61	33	511, 333
							1.55	1	432, 520
							1.53	1	521
1.48	1	1.48	3	1.485	40	440	1.48	53	440

pattern corresponds to that of magnetite, differing from it in only somewhat smaller interplanar spacings. In addition, phases of intermediate composition exist between magnetite and maghemite [5]. Studying these compounds, Basta [5] revealed a linear composition dependence of the lattice constant a, which enables evaluation of the Fe(II) to Fe(III) ratio from the lattice constant.

The lattice constant a was determined by the internal standard method for the preparations obtained. Only the (311) line was used in calculations, since the weak diffraction pattern and strongly broadened lines give no way of using lines at large angles 2θ, the accuracy of determining the lattice constant a being poor in this case. The position of the line was measured at 1/2 I for sample no. 1 and at 1/2 I and 2/3 I for sample no. 2, the profile of the (311) line being asymmetric in the latter case. The following values were obtained: $a = 8.39 \pm 0.01$ Å for sample no. 1 and $a = 8.36 \pm 0.01$ (with line position measured at half maximum) and $a = 8.346 \pm 0.007$ Å (with line position measured at 2/3 maximum) for sample no. 2. According to the plot of composition against lattice constant [5], the composition of sample no. 1 is close to that of magnetite. With account of the measurement error, the content of γ-Fe_2O_3 in its structure does not exceed 20–30%. Sample no. 2 is close in composition to maghemite, with a = 8.36 Å corresponding to approximately 80% γ-Fe_2O_3, and a = 8.350 Å characteristic of 100% γ-Fe_2O_3.

The information furnished by the X-ray diffraction pattern is not restricted to only the lattice metric. It is known that small dimensions of coherence domains, structural defects, presence of microstrains, and measurement conditions cause broadening of diffraction lines [6–8]. The existing analytical methods for revealing and evaluating the effect of one or another factor on the linewidth require precision measurements. However, even linewidths can yield, without any analysis of line profiles, a certain information about the fine structure of crystals. For example, presence of structural defects leads to broadening of only part of lines. Presence of microstrains causes broadening that is wavelength-independent, but depends on reflection indices; in addition, the linewidth is the larger at the same microstrain, the greater the absolute value of the angle θ [8, 9]. Line broadening associated with small dimensions of coherence domains, contrariwise, depends on the radiation wavelength, but is independent of reflection indices, and all lines are broadened to the same extent with account taken of the correction for radiation nonmonochromaticity.

The particle size, which can be determined from the broadening of X-ray diffraction lines, is limited to approximately the range from 10 to 10^3 Å [6–8]. The instrumental broadening of diffraction lines is taken into account in the simplest way, with the use of a standard. In the case when the line broadening is associated with only particle sizes, the average dimension of the coherence domains is calculated by the formula [7, 9]

$$L = 0.94\,\lambda / \left[(\sqrt{B_0^2 - B^2})\cos\theta\right],$$

where L is the particle size; λ, the wavelength; B_0, the line halfwidth for a sample under study (rad); B, the line halfwidth for the standard (rad).

The diffraction pattern of sample no. 2 made it possible to measure the halfwidths of (311), (220), and (440) reflections. The following 2θ values were obtained (deg): B_0 (220) = 1.08 ± 0.10, B_0 (311) = 1.00 ± 0.10, B_0 (440) = 1.15 ± 0.10. The halfwidth of the (311) line of standard magnetite, measured under the experimental conditions, is $(0.20 \pm 0.05)°$ (2θ). It can be seen from the data obtained that, within the experimental error, all lines are broadened to the same extent, irrespective of reflection indices and the absolute value of θ. Consequently, the main contribution to line broadening comes, in the case in question, from the small size of coherence domains. This made it possible to calculate L by the above formula. In addition, it is seen that the instrumental broadening is comparable with the measurement error. Therefore, it is unimportant in the given case whether magnetite or maghemite is used as a standard, since the differences between B_0 for standard lines is far less than the error in measurements of line halfwidths for the samples under study. For sample no. 1, only the halfwidth of the (311) reflection could be measured, the intensities of other lines being too low. However, with account of the nature of the object and of the method by which it is obtained, it may be assumed that the reason for line broadening is the same, specifically, the small size of coherent domains.

The (311) reflection was used to obtain the particle size $L \approx 160$–170 Å for sample no. 1 containing 3.53% iron, and $L \approx 250$ Å for sample no. 2 containing 5.01% iron. In addition, the profile of the (311) line for sample no. 2 was found to be somewhat asymmetric, looking like superposition of a wide and a narrow lines. This can be attributed to the presence in the sample of groups of crystallites with large and small average dimensions of coherent domains. The formation of phases with different crystal structures and of crystals with different sizes can be accounted for by dependence of crystal growth in aqueous solutions of iron salts and(or) suspensions of iron hydroxide on the process conditions.

The diffraction pattern of sample no. 3 contains only a halo of arabinogalactan, with lines of the iron-containing phase absent and no shift of the peak of reflection from arabinogalactan observed. This may mean that particles of the iron-containing phase are smaller in size than 10 Å or the phase is amorphous. This phase was identified as "ferrihydrite" on the basis of the results obtained in [10]. In the authors' opinion, ferrihydrite is characterized by empirical composition $Fe_2O_3 \cdot 1.8H_2O$. Iron in ferrihydrite is amorphous and exists in the form of δ-FeOOH and γ-FeOOH.

On the basis of the results of X-ray analysis performed in the present study, an assumption can be made that, similarly to dextranferrites [11], the ferroarabinogalactans synthesized are microspheroids with nuclei composed of either iron oxides with crystal structure of magnetite (maghemite), or amorphous ferrihydrites coated with a layer of arabinogalactan molecules.

CONCLUSIONS

(1) The starting natural polysaccharide arabinogalactan exists in the amorphous state, and preparations of ferroarabinogalactans have two-phase amorphous-crystalline structure.

(2) Iron is incorporated into ferroarabinogalactans in the form of an analogue of minerals of the magnetite-maghemite series or as ferrihydrite. The lattice constant a of the iron-containing phase varies within the range 8.35–8.39 Å, and the average size of crystallites, within 160–250 Å.

REFERENCES

1. Bendikene, V., Yuodka, B., and Kazlauskas, R.M., *Prikl. Biokhim. Mikrobiol.*, 1995, vol. 31, no. 4, pp. 393–399.
2. Aleksandrova, G.P., Medvedeva, S.A., Grishchenko, L.A., and Tyukavkina, N.A., Abstracts of Papers, *Vserossiiskaya konferentsiya "Khimiya i tekhnologiya rastitel'nykh veshchestv"* (All-Russia Conf. "Chemistry and Technology of Vegetal Substances"), Syktyvkar, 2000, p. 17.
3. Dudkin, M.S., Gromov, V.S., Vedernikov, N.A., *et al.*, *Gemitsellyulozy* (Hemicelluloses), Riga: Zinatne, 1991.

4. *Mineraly: Spravochnik* (Minerals: Reference Book), Moscow: Khimiya, 1967, vol. 2.
5. Basta, E.Z., *Economic Geology*, 1959, vol. 54, pp. 698–719.
6. Mirkin, L.I., *Spravochnik po rentgenostrukturnomu analizu polikristallov* (Handbook of X-ray Structural Analysis of Polycrystals), Moscow: Khimiya, 1961.
7. Umanskii, Ya.S., *Rentgenografiya metallov i poluprovodnikov* (X-ray Diffraction Analysis of Metals and Semiconductors), Moscow: 1969.
8. Lipson, H. and Steeple, H., *Interpretation of X-ray powder diffraction patterns*, London: Macmillan, 1970.
9. Gorelik, S.S., Rastorguev, L.N., and Skakov, Yu.A., *Rentgenograficheskii i elektronograficheskii analiz metallov* (X-ray and Electron Diffraction Analysis of Metals), Moscow: 1963.
10. Bagautdinova, R.R., Tolchev, A.V., Kleshchev, D.G., and Pervushin, V.Yu., *Zh. Prikl. Khim.*, 1999, vol. 72, no. 10, pp. 1588–1592.
11. Brusentsov, N.A., Gogosov, V.V., and Lukashevich, N.V., *Khim. Farm. Zh.*, 1996, no. 10, pp. 48–53.

Russian Journal of Applied Chemistry, Vol. 75, No. 12, 2002, pp. 1916–1919. Translated from Zhurnal Prikladnoi Khimii, Vol. 75, No. 12, 2002, pp. 1955–1958.
Original Russian Text Copyright © 2002 by Trusov, Trusova, Shchukina.

PHYSICOCHEMICAL STUDIES OF SYSTEMS AND PROCESSES

Thermodynamic Determination of the Most Probable Route of High-Temperature Formation of β-Spodumene in Lithium–Alumina–Silica Mixtures

N. V. Trusov, Yu. D. Trusova, and L. P. Shchukina

Kharkovskii Politekhnicheskii Institut National Technical University, Kharkov, Ukraine

Received March 5, 1999; in final form, September 2002

Abstract—The equilibrium composition of β-spodumene formed in high-temperature synthesis from lithium carbonate, metakaolinite, and silica was calculated thermodynamically. The extents of the thermodynamically possible reactions were determined in the range 400–1600K.

Studies of crystallization of a multiphase mixture from a heat-treated glaze glass required that the order of crystallization of separate phases should be determined, and, in the case of simultaneous phase formation, the conditions for formation of the maximal amount of β-spodumene $Li_2Al_2Si_4O_8$, responsible for the heat stability of the final complex of phases, should be elucidated. In particular, it was of certain interest to find the most energetically advantageous route β-$Li_2O \cdot Al_2O_3 \cdot 4SiO_2$ formation from lithium carbonate, metakaolinate $Al_2Si_2O_7$, β-SiO_2. This could provide a scientifically substantiated tool for optimization of the β-$Li_2O \cdot Al_2O_3 \cdot 4SiO_2$ production by the most thermodynamically probable route.

First, the thermodynamic parameters of thermal decomposition of the starting reagents

$$Li_2CO_3 = Li_2O + CO_2, \quad (1)$$

$$Al_2Si_2O_7 = \alpha\text{-}Al_2O_3 + 2\beta\text{-}SiO_2, \quad (2)$$

and of the reaction between them, resulting in the formation of the final product

$$Li_2CO_3 + 2Al_2Si_2O_7 = \beta\text{-}Li_2Al_2Si_4O_{12} + \alpha\text{-}Al_2O_3 + CO_2, \quad (3)$$

were determined.

The temperature dependence of the Gibbs energy in reactions (1)–(3) is illustrated in Table 1. The standard thermodynamic data for the reactants were taken from [1–8].

It follows from Table 1 that all the three reactions are highly probable thermodynamically. However, despite the predominance of reaction (3), which has the minimal ΔG_T^0 values in the temperature range studied, this gives no way of maintaining that β-spodumene is obtained by direct interaction, rather than via oxides preliminarily formed by reactions (1) and (2), the more so as the subsequent interaction of the oxides by the overall reaction

$$Li_2O + \alpha\text{-}Al_2O_3 + 4\beta\text{-}SiO_2 = \beta\text{-}Li_2Al_2Si_4O_{12} \quad (4)$$

is thermodynamically possible up to 1200 K. Therefore, it was necessary to calculate the equilibrium composition formed in parallel-consecutive reactions (1)–(3) [9]. Only calculations of this kind make it possible to determine the extent of all the reactions under consideration.

A graphical interpretation of the results of calculations, concerning the extent of reaction (3) on the background of the other two reactions, demonstrated that only reaction (3) proceeds at low temperature (600K). By contrast, β-spodumene is not formed by the reaction of lithium carbonate with metakaolinite at 1600 K. Varying simultaneously both the parameters (reaction temperature and initial molar ratio $Al_2Si_2O_7$: Li_2CO_3) within the range from minimal to maximal values leads to a complicated variation of the extent of β-spodumene formation by reaction (3).

Thus, the results of preliminary calculations show that the formation of the target product both by direct reaction between the reactants and via overall reac-

1070-4272/02/7512-1916 $27.00 © 2002 MAIK "Nauka/Interperiodica"

tion (4), which reflects the so-called oxide mechanism, cannot be ruled out. The latter assumption is confirmed by several facts.

First, if account is taken of only reaction (3), it is difficult to explain the experimental fact that, for β-spodumene to be formed, the starting raw mixture must contain silicon dioxide [10]. Second, there is no reasonable explanation for the presence of such highly active component as lithium oxide in the equilibrium mixture, which follows from the calculations of equilibrium composition formed in reactions (1)–(3).

Thus, it is impossible to solve the problem at hand without considering the thermodynamic possibility of occurrence of the reactions by the so-called oxide mechanism. Therefore, reactions between oxides in the Li_2O–Al_2O_3–SiO_2 system were studied. The system was divided into three binary systems: Li_2O–Al_2O_3, Li_2O–SiO_2, and Al_2O_3–SiO_2. The Gibbs energies were determined for each of the reactions resulting in the formation of the known binary oxides [10]:

$$Li_2O + \alpha\text{-}Al_2O_3 = Li_2Al_2O_4, \quad (5)$$

$$Li_2O + 5\alpha\text{-}Al_2O_3 = Li_2Al_{10}O_{16}, \quad (6)$$

$$Li_2O + \beta\text{-}SiO_2 = Li_2SiO_3, \quad (7)$$

$$Li_2O + 2\beta\text{-}SiO_2 = Li_2Si_2O_5, \quad (8)$$

$$2Li_2O + \beta\text{-}SiO_2 = Li_4SiO_4, \quad (9)$$

$$\alpha\text{-}Al_2O_3 + \beta\text{-}SiO_2 = Al_2SiO_5, \quad (10)$$

$$\alpha\text{-}Al_2O_3 + 2\beta\text{-}SiO_2 = Al_2Si_2O_7, \quad (11)$$

$$3\alpha\text{-}Al_2O_3 + 2\beta\text{-}SiO_2 = Al_6Si_2O_{13}. \quad (12)$$

It is necessary to note that only the last of three aluminum silicate modifications (andalusite, kyanite, and sillimanite) was considered, since it is its structure that is characterized by the strongest aluminum-oxygen bond [11], which forms a basis for further interactions yielding aluminosilicates.

The results of calculations are listed in Table 1, which shows that only reactions (7)–(9) are thermodynamically possible within the entire temperature range under consideration (400–1600 K). Reactions (5) and (11) do not occur, and the other reactions occur selectively, since the Gibbs energy changes its sign within this temperature range.

A system analysis of the reactions of newly formed compounds ($Li_2Al_{10}O_{16}$, Li_2SiO_3, $Li_2Si_2O_5$, Li_4SiO_4, Al_2SiO_5, and $Al_6Si_2O_{13}$) with an excess amount of oxides (Li_2O, α-Al_2O_3, and β-SiO_2), which yield β-spodumene and constitute the second stage of the oxide mechanism, revealed the following reactions:

Table 1. Gibbs energies of reactions (1)–(3) and (5)–(29) at different temperatures

Reaction	ΔG_T^0 (kJ) at indicated temperature, K		
	400	1000	1600
(1)	–194.5	–810.1	–1386.6
(2)	–282.8	–277.9	–271.3
(3)	–920.8	–1565.2	–1789.1
(5)	+993.4	+902.0	+852.2
(6)	–156.0	–101.2	+35.8
(7)	–143.5	–129.3	–105.6
(8)	–105.7	–82.9	–37.4
(9)	–211.5	–227.0	–259.9
(10)	–4.8	–0.8	+3.2
(11)	+282.8	+277.9	+271.3
(12)	+10.5	–4.5	–18.5
(13)	–4.5	+36.1	+104.2
(14)	+4542.8	+4161.1	+3935.4
(15)	+14.5	+39.4	+91.4
(16)	–25.5	+45.0	+141.3
(17)	+413.4	+452.0	+562.5
(18)	+274.7	+323.5	+453.7
(19)	–2.8	+66.6	+236.0
(20)	+1129.3	+1087.1	+1066.6
(21)	+50.9	+100.8	+214.9
(22)	–87.8	–27.7	+106.0
(23)	–45.3	+19.5	+171.9
(24)	+1862.8	+1745.7	+1772.7
(25)	–65.3	+22.3	+196.0
(26)	+685.6	+843.0	+1179.6
(27)	+478.8	+616.8	+916.5
(28)	–141.5	–61.8	+127.2
(29)	–181.5	–56.2	+177.1

$$Li_2Al_{10}O_{16} + 4\beta\text{-}SiO_2 = \beta\text{-}Li_2Al_2Si_4O_{12} + 4\alpha\text{-}Al_2O_3, \quad (13)$$

$$Li_2Al_{10}O_{16} + 4Li_2SiO_3 = \beta\text{-}Li_2Al_2Si_4O_{12} + 4Li_2Al_2O_4, \quad (14)$$

$$Li_2Al_{10}O_{16} + 4Al_2SiO_5 = \beta\text{-}Li_2Al_2Si_4O_{12} + 8\alpha\text{-}Al_2O_3, \quad (15)$$

$$Li_2Al_{10}O_{16} + 2Al_6Si_2O_{13} = \beta\text{-}Li_2Al_2Si_4O_{12} + 10\alpha\text{-}Al_2O_3, \quad (16)$$

Table 2. Phase composition of equilibrium mixtures at varied composition of starting mixture ($Li_2CO_{3\,in}$ = 1 mol, T = 1000 K)

Reactant content, mol		Composition of equilibrium mixture, mol %								
$Al_2Si_2O_7$	β-SiO_2	β-SiO_2	α-Al_2O_3	Al_2SiO_5	$Al_6Si_2O_{13}$	$Li_2Al_{10}O_{16}$	Li_2SiO_3	$Li_2Si_2O_5$	Li_4SiO_4	β-$Li_2Al_2Si_4O_{12}$
2.0	0	33.69	11.07	14.02	2.36	4.93	5.48	3.96	1.20	22.58
1.8	0.4	37.00	8.06	16.50	1.90	3.86	4.09	2.80	3.44	22.35
1.6	0.8	41.98	6.86	12.91	1.25	3.72	3.81	3.28	3.51	22.67
1.4	1.2	48.39	6.47	7.32	0.78	3.60	3.58	3.59	3.58	22.69
1.2	1.6	54.27	4.01	3.51	0.26	3.65	3.65	3.65	3.65	23.35
1.0	2.0	58.04	2.41	2.81	0.09	2.80	4.21	4.22	4.12	21.32

$$4Li_2SiO_3 + \alpha\text{-}Al_2O_3 = \beta\text{-}Li_2Al_2Si_4O_{12} + 3Li_2O, \quad (17)$$

$$3Li_2SiO_3 + Al_2SiO_5 = \beta\text{-}Li_2Al_2Si_4O_{12} + 2Li_2O, \quad (18)$$

$$Li_2SiO_3 + 3Al_2SiO_5 = \beta\text{-}Li_2Al_2Si_4O_{12} + 2\alpha\text{-}Al_2O_3, \quad (19)$$

$$2Li_2SiO_3 + 2Al_2SiO_5 = \beta\text{-}Li_2Al_2Si_4O_{12} + Li_2Al_2O_4, \quad (20)$$

$$2Li_2Si_2O_5 + \alpha\text{-}Al_2SiO_3 = \beta\text{-}Li_2Al_2Si_4O_{12} + Li_2O, \quad (21)$$

$$2Li_2Si_2O_5 + Al_2SiO_5 = \beta\text{-}Li_2Al_2Si_4O_{12} + Li_2SiO_3, \quad (22)$$

$$Li_2Si_2O_5 + 2Al_2SiO_5 = \beta\text{-}Li_2Al_2Si_4O_{12} + \alpha\text{-}Al_2O_3, \quad (23)$$

$$2Li_2SiO_5 + 2Al_2SiO_5 = \beta\text{-}Li_2Al_2Si_4O_{12} + Li_2Al_2Si_4O_8, \quad (24)$$

$$Li_2Si_2O_5 + Al_6Si_2O_{13} = \beta\text{-}Li_2Al_2Si_4O_{12} + 2\alpha\text{-}Al_2O_3, \quad (25)$$

$$4Li_4SiO_4 + \alpha\text{-}Al_2O_3 = \beta\text{-}Li_2Al_2Si_4O_{12} + 7Li_2O, \quad (26)$$

$$3Li_4SiO_4 + Al_2SiO_5 = \beta\text{-}Li_2Al_2Si_4O_{12} + 5Li_2O, \quad (27)$$

$$4Al_2SiO_5 + Li_2O = \beta\text{-}Li_2Al_2Si_4O_{12} + 3\alpha\text{-}Al_2O_3, \quad (28)$$

$$2Al_6Si_2O_{13} + Li_2O = \beta\text{-}Li_2Al_2Si_4O_{12} + 5\alpha\text{-}Al_2O_3. \quad (29)$$

The Gibbs energies for these reactions at various temperatures are given in Table 1.

It can be seen that reactions (14), (15), (17), (18), (20), (21), (24), (26), and (27) are thermodynamically impossible within the entire temperature range under study. Other reactions occur selectively, i.e., their thermodynamic probability is temperature-dependent.

Even if the consideration is restricted to the base temperature (for which 1000K was taken), then, with account of the data of Table 1, 12 reactions for which $\Delta G_T^0 < 0$ should be considered in order to elucidate the mechanism of β-spodumene formation. Obviously, it is impossible to determine the extent of each reaction on the background of other reactions from a single Gibbs energy. Therefore, the equilibrium composition formed in the simultaneous parallel-consecutive course of all the above-mentioned reactions was calculated. The composition of the starting mixture, whose stoichiometry ensures β-spodumene formation (1 mol at the minimum) was selected as the variable parameter. The results obtained are listed in Table 2. In the entire range of variation of this parameter, Li_2CO_3, Li_2O, and $Li_2Si_2O_7$ are absent from the equilibrium mixture, and, therefore, these compounds are not listed in Table 2.

It is noteworthy that all the components of the equilibrium mixture fall into two groups: (a) compounds whose molar content exceeds 10% at least at a single temperature (β-SiO_2, α-Al_2O_3, Al_2SiO_5 and β-$Li_2Al_2Si_4O_{12}$) and (b) other compounds whose content does not exceed 6%. It is significant that the yield of β-spodumene depends on the initial mixture composition only slightly, whereas the equilibrium content of β-SiO_2 decreases by almost a factor of 2; the amount of Al_2SiO_5 aluminum silicate shows a small extremum at $Al_2Si_2O_{7\,in}$ = 1.8 and $\beta\text{-}SiO_{2\,in}$ = 0.4 mol.

Interesting conclusions can be reached in analysis of how the extent of the reactions under consideration depends on the initial composition of the stock. Thermodynamic calculations demonstrated that the distribution of lithium carbonate among reactions (1) and (3) is independent of the stock composition and constitutes about 0.5 of that possible theoretically. At the same time, the extent of reaction (2) increases linearly from 0 to 1. The extents of the other reactions do not exceed 0.15, but it is these reactions that determine the content of β-spodumene in the equilibrium mixture of the products.

CONCLUSION

A thermodynamic analysis of 29 stoichiometric reactions between lithium carbonate, metakaolinite, and silica, with the subsequent formation of β-spodumene, revealed 12 reactions to be taken into account in calculating the equilibrium composition. The molar content of β-$Li_2Al_2Si_4O_{12}$ in the equilibrium mixture of reaction products was found to be virtually independent of the composition of the starting stock mixture if its stoichiometry ensures formation of at least 1 mol of β-spodumene.

REFERENCES

1. Babushkin, V.I., Matveev, G.M., and Mchedlov-Petrosyan, O.P., *Termodinamika silikatov* (Thermodynamics of Silicates), Moscow: Gosstroiizdat (GSI), 1962.
2. *Termodinamicheskie svoiistva neorganicheskikh veshchestv* (Thermodynamic Characteristics on Inorganic Substances), Zefirov, A.P., Ed., Moscow: Atomizdat, 1965.
3. Karapet'yants, M.Kh. and Karapet'yants, M.L., *Osnovnye termodinamicheskie konstanty neorganicheskikh i organicheskikh vehhestv* (Main Thermodynamic Constants of Inorganic and Organic Substances), Moscow: Khimiya, 1968.
4. Berezhnoi, A.S., *Mnogokomponentnye sistemy okislov* (Multicomponent Oxide Systems), Kiev: Naukova Dumka, 1970.
5. Karapet'yants, M.Kh., *Khimicheskaya termodinamika* (Chemical Thermodynamics), Moscow: Khimiya, 1970.
6. Kireev, V.A., *Metody prakticheskikh raschetov v termodinamike khimicheskikh reaktsii* (Methods for Practical Calculations in Thermodynamics of Chemical Reactions), Moscow: Khimiya, 1970.
7. Ryabin, V.A., Ostroumova, M.A., and Svit, T.F., *Termodinamicheskie svojjstva vehhestv* (Thermodynamic Properties of Substances), Leningrad: Khimiya, 1977.
8. *Termodinamicheskie svoiistva individual'nykh veshchestv* (Thermodynamic Properties of Individual Substances), Glushko, V.P., Ed., Moscow: Nauka, 1978.
9. Trusov, N.V., *Zh. Prikl. Khim.*, 1998, vol. 71, no. 4. pp. 556–559.
10. Bobkova, N.M., *Fizicheskaja khimija silikatov i tugoplavkikh soedinenii* (Physical Chemistry of Silicates and Refractory Compounds), Moscow: Vysshaya Shkola, 1984.
11. Strelov, K.K. and Mamykin, P.S., *Tekhnologiya Ogneuporov* (Technology of Refractories), Moscow: Metallurgiya, 1978.

Russian Journal of Applied Chemistry, Vol. 75, No. 12, 2002, pp. 1920–1924. Translated from Zhurnal Prikladnoi Khimii, Vol. 75, No. 12, 2002, pp. 1959–1962.
Original Russian Text Copyright © 2002 by Pak, Nepomnyashchii, Burkat, Mal'kova.

PHYSICOCHEMICAL STUDIES OF SYSTEMS AND PROCESSES

Diffusion of Aqueous Solutions of $CoCl_2$, $Co(NO_3)_2$, and $Cu(NO_3)_2$ in Porous Glass Membranes

V. N. Pak, A. B. Nepomnyashchii, T. M. Burkat, and S. V. Mal'kova

Hertzen Russian State Pedagogical University, St. Petersburg, Russia

Received January 24, 2002

Abstract—Diffusion coefficients of $CoCl_2$, $Co(NO_3)_2$, and $Cu(NO_3)_2$ salts, characterizing permeation of their aqueous solutions across glass membranes with predominant pore radius in the range from 70 to 4.5 nm are determined. With pores in the membranes becoming narrower, the diffusion mobility of the electrolytes decreases.

The possibility and efficiency of membrane purification of liquids and separation of solution components are determined by the diffusion coefficients D of substances in the corresponding porous media [1, 2]. It is known that, in the case of finely porous hydrophilic membranes, diffusion transport of a number of substances, including electrolytes, is characterized by lower D values, compared with diffusion in aqueous solutions [1–5]. This is due to the influence of pore walls, determining the formation of an electrical double layer, possibility of sorption, and specific properties of the near-wall layers of the liquid. The joint influence of the above factors makes difficult interpretation of diffusion processes and hinders prognostication of properties of particular systems. For example, the general concept that a decrease in pore radius r_p in a hydrophilic membrane must make smaller the diffusion coefficient of substances in it seems to be nearly obvious. Nevertheless, the importance and type of a D–r_p dependence can only be determined experimentally, and its analytical form has not been established for any particular system. A study [5] of NaCl diffusion in porous glasses demonstrated, in particular, that the expected decrease in D is weakly pronounced in a wide range of pore radii, being markedly manifested only at $r_p \leq 15$ nm. This fact was tentatively accounted for in terms of the structural-geometric model of the system constituted by a membrane and a pore solution.

Proceeding with previous investigations [5], the present study analyzes the diffusion transport of aqueous solutions of $CoCl_2$, $Co(NO_3)_2$, and $Cu(NO_3)_2$ in porous-glass membranes in order to determine the analytical dependence D–r_p. The existance of Co^{2+} and Cu^{2+} ions in aqueous solutions of the chosen salts in the form of stable aqua complexes, possibility of their direct photometric determination [6], and low adsorption on the silica surface in an acid medium [7], much simplify the formulation and solution of the problem, making it possible to distinguish the pore radius of membranes as the main potential factor exerting influence on the diffusion coefficient.

EXPERIMENTAL

Porous-glass membranes were fabricated in the form of thin (1-mm) disks 25 mm in diameter. The parameters of the porous structure of the membranes (see table) were preset by varying the modes of preliminary thermal treatment and conditions of subse-

Pore radius r_p and porosity δ of glass membranes and diffusion coefficients D of aqueous solutions of salts in the membranes

r_p, nm	δ, $cm^3\ cm^{-3}$	$D \times 10^6$, $cm^2\ s^{-1}$		
		$CoCl_2$	$Co(NO_3)_2$	$Cu(NO_3)_2$
4.5	0.265	1.70	1.59	1.78
6	0.345	2.19	2.18	2.06
9	0.350	3.37	3.05	2.50
13	0.580	4.12	3.69	2.84
32	0.513	5.40	4.94	3.43
45	0.426	5.90	5.40	3.60
70	0.569	6.43	5.74	3.84

1070-4272/02/7512-1920 $27.00 © 2002 MAIK "Nauka/Interperiodica"

quent leaching (and, in some cases, additional alkaline etching) of DV-1 sodium borosilicate glass [8–10]. The predominant pore radii r_p were found from the hysteresis loop parameters of water adsorption isotherms or from the gas permeability of the membranes by the Deryagin method, and the porosity δ, by triple weighing [10, 11]. In studying the diffusion, the membranes were fixed between two cells, with twice-distilled water poured into one of these (receiver), and an aqueous solution of a salt (with concentration of 0.1–0.5 M), into the other (feeding cell). The dynamics of the diffusion process was judged from the results of direct photometric determination of the amount of ions that passed into the receiver cell: Co^{2+} at a wavelength λ_{max} = 510 nm, and Cu^{2+} at λ_{max} = 800 nm [6]. In all cases, the profiles of absorption bands of solutions from the receiving and feeding cells were preserved, which indicates that the form of existence of cations remains invariable in the course of experiments carried out with temperature maintained constant at 25°C and continuous stirring of the solutions. It was established preliminarily that the difference between levels of liquid in the cells within 10–20 mm has virtually no effect on the rate of diffusion, which indicates that hydrostatic and osmotic pressures are not manifested in the experiments. A steady flow across the membranes was established after a certain delay, whose duration depended on the solution concentration and porous structure parameters r_p and δ. In special-purpose experiments, the membranes were preliminarily saturated with the working solution and then a receiving cell was connected. In these cases, a steady-state diffusion process, whose rate was the same as that in experiments without preliminary filling of the membranes, was attained already in 5–10 min.

Linear dependences of the amounts Q of substances transferred across the membranes on time τ give the diffusion rate as $dQ/d\tau$; a typical family of Q–τ straight lines is shown in Fig. 1. The first Fick law was considered to be valid for the stationary process. According to this law, the diffusion flux across the membrane is represented as

$$dQ/d\tau = Ds\delta\Delta c/h, \quad (1)$$

where D is the diffusion coefficient; $s\delta$, the free cross-section of a membrane, equal to its geometrical area with correction for the porosity δ (see table); $\Delta c/h$, the difference between the solution concentrations before and after a membrane of thickness h.

Since the solution concentration in the receiving cell, c_{out}, was much lower that that in the feeding

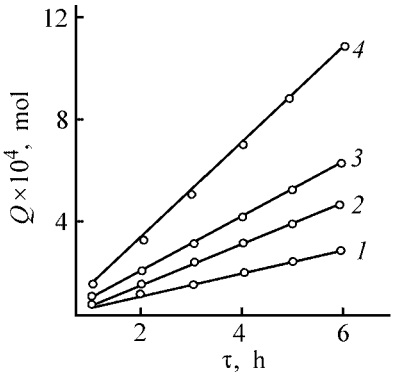

Fig. 1. Amount Q of $CoCl_2$ transferred across the membrane with pore radius r_p = 70 nm vs. time τ. Solution concentration (M): (*1*) 0.10, (*2*) 0.16, (*3*) 0.25, and (*4*) 0.50.

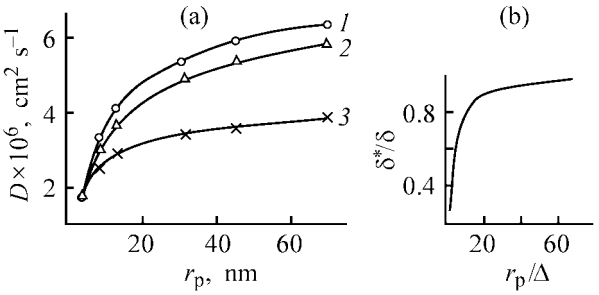

Fig. 2. (a) Diffusion coefficient D of (*1*) $CoCl_2$, (*2*) $Co(NO_3)_2$, and (*3*) $Cu(NO_3)_2$ in porous-glass membranes vs. pore radius r_p and (b) result of modeling of the system constituted by porous glass and pore solution on the basis of the structural-geometric approach. For explanations see text.

cell, c_{in}, in all experiments, the gradient was taken to be

$$\Delta c/h \simeq (c_{in} - c_{out})/h \simeq c_{in}/h. \quad (2)$$

A calculation of the diffusion coefficients from experimental data in accordance with Eqs. (1) and (2) demonstrated the lack of any regular variation of D in the salt concentration range 0.1–0.5 M, in agreement with the known fact of weak variation of D with concentration in aqueous solutions of electrolyte solutions [12, 13]. Correspondingly, the table lists averaged values of the diffusion coefficients, and Fig. 2 shows their graphical dependence on the pore radius of the membranes. A lower mobility of $Cu(NO_3)_2$, compared with that of cobalt(II) salts, is observed in a wide range of r_p, and a slight, but clearly noticeable decrease in D on passing from $CoCl_2$ to $Co(NO_3)_2$. The deficiency in reliable data on diffusion in solutions gives no way of comparing the coefficients obtained with the corresponding "bulk" values. However,

analysis of the data available for aqueous solutions of 1 : 1 electrolytes makes it possible to state with confidence that a systematic decrease in D values for nitrates, compared with those for chlorides of the same cations, is observed [12, 13].

As for the ratio of the diffusion coefficients in porous-glass membranes and in solutions, the run of the D–r_p dependences suggests that, even at large pore radii $r_p \geq 70$ nm, the mobility of ions within pores remains somewhat lower than that in free solution. With increasing r_p, the tendency for D to grow becomes increasingly less pronounced, which corresponds to weakening effect of the surface. However, at a distance of even tens of nanometers from pore walls the solutions still experiences their influence, which is indicated by the recorded increase in D (see table and Fig. 2). A decrease in the radii of membrane channels in the nanometer range results in that the diffusion coefficients of the salts studied fall considerably and, simultaneously, approach one another. It is not improbable that this is to a certain extent determined by an increase in tortuosity of narrow pores, which, when taken into account, may lead to higher h values in Eqs. (1) and (2). It is known [3, 14] that the tortuosity factor η depends on the method by which a porous glass is obtained; it is important that even in the case of pores with radii close to the smallest possible value, it exceeds unity only slightly ($\chi = 1.38$ at $r_p \approx 3$ nm [3]). It may be assumed that correction to the calculated D values is not very important in comparison with their pronounced variation between the membranes studied (see table).

The result obtained is apparently due to hindered diffusion of ions in the boundary layers of solutions in the membranes, changed with respect to the bulk. It is rather difficult to specify this general thesis, although it is clear that it is based on water structuring by the silica surface, which sets a limit on the mobility of hydrated ions. A transformation of the network of intermolecular hydrogen bonds under the action of surface forces predetermines, in particular, an increase in the viscosity of the boundary layers [1, 15–17]. There is good reason to believe that bound water is characterized by lowered dissolving ability [17, 18]. One of the reasons is a dramatic (caused by mobility restriction) decrease in its dielectric constant [19], with the result that it is less favorable energetically for ions dissolved in water to be in the boundary layer of water. All the aforesaid has to do with the decrease in the diffusion coefficient, observed in small-radius pores. In this context, the general appearance of the D–r_p dependences determined can be described, to a first approximation, in terms of the structural-geometric approach [5]. The limited involvement of the pore solution in diffusion will be modeled with a volume of a hypothetical near-wall layer of thickness Δ, entirely excluded from the transport process. With this assumption made, the effective pore space δ^* involved in diffusion can be determined, together with its fraction relative to the total porosity δ of the membrane. The total porosity is defined as the ratio of the pore volume V_p to the geometrical volume V of the membrane. The approximation of a cylindrical structure of pores in the porous glass gives for a flat disk of radius R, thickness h, and n pores on its cross section, the following

$$\delta = V_p/V = \frac{n(\pi r_p^2 h)}{\pi R^2 h} = \frac{n r_p^2}{R^2}, \quad (3)$$

$$\delta^* = n(r_p - \Delta)^2/R^2, \quad (4)$$

$$\delta^*/\delta = (r_p - \Delta)^2/r_p^2. \quad (5)$$

The dependence of the function (5) on the dimensionless parameter r_p/Δ, shown in Fig. 2, represents the general features of the experimentally established behavior of D, reflecting the manifestation of the structural-geometric factor in the series of the porous-glass membranes. The fraction of the free diffusion space of pores, δ^*/δ, decreases dramatically as their radius becomes comparable with Δ ($\delta^*/\delta \to 0$ at $r_p \to \Delta$); extrapolation to large radii gives $\delta^*/\delta \to 1$ at $r_p \to \infty$.

Despite the general agreement with experiment, the approach in question cannot be regarded as satisfactory. It is the assumption of a layer excluded from diffusion that is the weak point of the model, and attempts to evaluate its effective thickness [5] presumably have no strict physical meaning. Indeed, the structure-sensitive properties of water remain changed at a large distance from the silica surface [1, 15–19], exceeding the pore size of the membranes studied. In all probability, this is also valid in the case of aqueous solutions, whose properties must vary continuously with increasing distance from the surface, which corresponds to the type of variation of the diffusion coefficients in a wide range of pore radii of silica membranes (Fig. 2).

Thus, it seems important to determine the analytical approximation to the experimentally established D–r_p dependences. With the disjoining pressure considered to be a generalizing characteristic of the extent to which the properties of thin layers of liquids deviate from the bulk properties [1, 15–17], account will be taken of its exponential dependence on dimen-

sion parameters. This makes it possible to suggest, in the given case, a simple form

$$D = D_0 \exp(-K_p/r_p), \quad (6)$$

where D_0 is the diffusion coefficient in free solution, and K_p is the dimension constant.

In this case, the necessary physically grounded conditions are satisfied: $D \to D_0$ at $r_p \to \infty$ and $D \to 0$ at $r_p \to 0$. Figure 3 shows a good agreement between the experimental results and the exponential dependence (6); processing of the results by the least-squares method gives the following estimates for the parameters D_0 and K_p of Eq. (6):

Salt solution	$CoCl_2$	$Co(NO_3)_2$	$Cu(NO_3)_2$
$D_0 \times 10^6$, $cm^2\ s^{-1}$	6.78	6.09	3.89
K_p, nm	6.41	6.11	3.68

The dimension constants K_p obtained are characteristic, i.e., reflect the extent to which the silica surface affects the structure and properties of a particular solution. For example, it may presumably be assumed that the $Cu(NO_3)_2$ solution is structured by membrane pore walls to a much lesser extent (by a factor of ~1.7) than the $Co(NO_3)_2$ solution. This gives reason to believe that copper(II) cations cause stronger structuring of water, compared with cobalt(II) cations, and thereby partly "neutralize" the influence of the silica surface. In accordance with Eq. (6), the physical meaning of K_p is reduced to the observance of the rule: $D = 0.368 D_0$ at $r_p = K_p$. This means that the diffusion coefficient in pores of glass membranes with radius equal to the dimension constant K_p is approximately 2.7 times less than the "bulk" value.

The diffusion coefficients determined in a mesoporous membrane with r_p = 70 nm for three electrolytes constitute 94–99% of the D_0 values obtained by extrapolation $r_p \to \infty$. Thus, the concept of a compact near-wall layer of solution, which is totally or in part excluded from diffusion, should be considered incorrect. The structuring of the solutions studied by the silica surface, actually affecting the diffusion mobility of ions, decreases exponentially away from the wall and extends to layers with thickness of approximately 70 nm. The observance of the dependence (6) means, in addition, that even reducing the pore radius of porous-glass membranes to the maximum possible extent (limited by experimental capabilities), to $r_p \approx$ 1 nm, will not allow separation of water from dissolved salts "in a single run." The diffusion coefficient of, e.g., $Cu(NO_3)_2$, will be equal in this case to a finite value of about 10^{-7} $cm^2\ s^{-1}$.

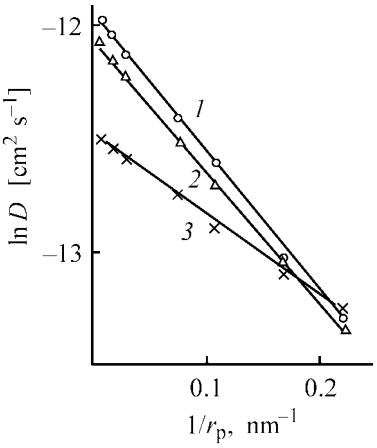

Fig. 3. Results obtained in measurements of diffusion of aqueous solutions of (*1*) $CoCl_2$, (*2*) $Co(NO_3)_2$, and (*3*) $Cu(NO_3)_2$ in porous glass and processed in accordance with Eq. (6). (*D*) Diffusion coefficient and (r_p) radius of pores in membranes.

CONCLUSIONS

(1) A study of transport of aqueous solutions of $CoCl_2$, $Co(NO_3)_2$, and $Cu(NO_3)_2$ across glass membranes revealed a substantial (by a factor of 2–4) decrease in the diffusion coefficients of salts with pore radii in porous glasses decreasing from 70 to 4.5 nm.

(2) The inadequacy of interpretation of the behavior of systems in terms of their structural-geometric models and concepts that a near-wall layer of solution is excluded from the diffusion process was demonstrated.

(3) It was established that the exponential dependence (6) fits experimental data. The following rule was formulated: The dimension constant characterizing the extent to which the silica surface affects the structure and properties of the pore solution is equal to the pore radius of a glass membrane in which the diffusion coefficient of the solute is approximately 2.7 times smaller than that in free solution.

(4) The structuring influence of the silica surface on the diffusion mobility of aqueous electrolyte solutions was shown to extend over an average boundary layer thickness of about 70 nm.

REFERENCES

1. Churaev, N.V., *Fizikokhimiya protsessov massoperenosa v poristykh sredakh* (Physical Chemistry of Mass-Transfer Processes in Porous Media), Moscow: Khimiya, 1990.
2. Nikolaev, N.I., *Diffuziya v membranakh* (Diffusion in Membranes), Moscow: Khimiya, 1980.

3. Antropova, T.V., Tsyganova, T.A., and Krylova, N.L., *Fiz. Khim. Stekla*, 1990, vol. 16, no. 5, pp. 732–737.
4. Mazurin, O.V. and Antropova, T.V., *Fiz. Khim. Stekla*, 1986, vol. 12, no. 4, pp. 507–510.
5. Voloshina, O.S., Burkat, T.M., and Pak, V.N., *Zh. Fiz. Khim.*, 2000, vol. 74, no. 6, pp. 1099–1102.
6. Lever, A.B.P., *Inorganic Electronic Spectroscopy*, Amsterdam: Elsevier, 1984.
7. Pak, V.N., Tikhomirova, I.Yu., Burkat, T.M., and Lobov, B.I., *Zh. Fiz. Khim.*, 1999, vol. 73, no. 11, pp. 2024–2028.
8. Mazurin, O.V., Roskova, G.P., Aver'yanov, V.N., and Antropova, T.V., *Dvukhfaznye stekla: struktura, svoistva, primenenie* (Two-Phase Glasses: Structure, Properties, and Use), Leningrad: Nauka, 1991.
9. Roskova, G.P. and Tsekhomskaya, T.S., *Fiz. Khim. Stekla*, 1981, vol. 7, no. 5, pp. 513–534.
10. Burkat, T.M. and Dobychin, D.P., *Fiz. Khim. Stekla*, 1992, vol. 18, no. 5, pp. 129–140.
11. Deryagin, B.V., *Dokl. Akad. Nauk SSSR*, 1946, vol. 53, no. 3, pp. 627–631.
12. *Spravochnik khimika* (Chemist's Reference Book), Nikol'skii, B.P., Ed., vol. 3, Moscow: Khimiya, 1964.
13. Robinson, R.A. and Stokes, R.H., *Electrolyte Solutions. The Measurement and Interpretation of Conductance, Chemical Potential and Diffusion in Solutions of Simple Electrolytes* (Second Edition), London: Butterworths, 1959.
14. Krylova, N.L., Antropova, T.V., Sidorova, M.P., and Ermakova, L.E., *Kolloid. Zh.*, 1992, vol. 54, no. 1, pp. 86–91.
15. Lashnev, V.I., Sobolev, V.D., and Churaev, N.V., *Teor. Osn. Khim. Tekhnol.*, 1976, vol. 10, no. 6, pp. 926–932.
16. Kiseleva, O.A., Sobolev, V.M., Starov, V.M., and Churaev, N.V., *Kolloid. Zh.*, 1979, vol. 41, no. 2, pp. 926–931.
17. Deryagin, B.V., Churaev, N.V., Ovcharenko, F.D., *et al.*, *Voda v dispersnykh sistemakh* (Water in Dispersed Systems), Moscow: Khimiya, 1989.
18. Dumanskii, A.V., *Liofil'nost' dispersnykh sistem* (Liophilic Nature of Dispersed Systems), Kiev: Akad. Nauk USSR, 1960.
19. Chelidze, T.L., Derevyanko, A.I., and Kurilenko, O.D., *Elektricheskaya spektroskopiya geterogennykh sistem* (Electrical Spectroscopy of Heterogeneous Systems), Kiev: Naukova Dumka, 1977.

Russian Journal of Applied Chemistry, Vol. 75, No. 12, 2002, pp. 1925–1930. Translated from Zhurnal Prikladnoi Khimii, Vol. 75, No. 12, 2002, pp. 1963–1067.
Original Russian Text Copyright © 2002 by Ya. Naziev, Shakhverdiev, Gasanov, Dzh. Naziev.

PHYSICOCHEMICAL STUDIES OF SYSTEMS AND PROCESSES

P–V–T Dependence for Methanol Solutions with Aromatic Hydrocarbons

Ya. M. Naziev, A. N. Shakhverdiev, V. G. Gasanov, and Dzh. Ya. Naziev

Azerbaijani Technical University, Baku, Azerbaijan
Azerbaijani State Academy of Oil, Baku, Azerbaijan

Received January 24, 2002

Abstract—The density of binary solutions methanol–*para*-xylene, methanol–*ortho*-xylene, and methanol–*meta*-xylene was measured on an installation for hydrostatic weighing in relation to pressure, temperature, and concentration. The experimental results are generalized using the equation of state.

Density is one of the most important physicochemical characteristics related to the structure of a substance. The thermal properties of binary solutions of methanol with aromatic hydrocarbons attract attention of not only researchers in various fields of science, but also engineers and designers in chemical, petrochemical, food, medical, and other industries. Studying the properties of these solutions is also of scientific interest for modernization of the theory of solutions.

An analysis of published data demonstrated that there is sufficient body of data on density of pure methanol and *para*-, *meta*-, and *ortho*-xylenes [1, 2], whereas for methanol–*para*-xylene, methanol–*ortho*-xylene, and methanol–*meta*-xylene solutions no data of this kind are available in the literature.

In this context, we studied experimentally the *P–V–T* dependence for these binary solutions in liquid phase at temperatures of 290–500 K in the pressure range 0.1–58.9 MPa at 25 wt % intervals.

The choice of the given systems is governed by the fact that the molecules of these substances contain even numbers of carbon atoms, have about the same ring structure, and, as shown by optical studies, these hydrocarbons and their solutions are characterized by intermolecular interaction varying with temperature, pressure, and concentration.

We chose the method of hydrostatic weighing for the experimental study. The piezometer used to determine the density of liquids operates on the principle that a solid submerged in a liquid experiences a buoyancy force, which depends on the density of a medium under study. Having determined the buoyancy force acting on the float (whose volume is known) and the mass of the float in empty space and in liquid, we can calculate the density of the medium [3, 4].

This method was proposed in [5, 6]. The experimental setup for measuring the *P–V–T* dependence for liquids is based on a variation of the hydrostatic weighing technique, which ensures high measurement accuracy and is comparatively simple in preparing for experiment and carrying out the procedure itself. In order to improve the sensitivity and to use heavier floats, the integrated circuit in the electronic servo system was replaced [7, 8].

Based on analysis of calibration data for elements of the suspension system, we obtained the following volumes and masses of the suspension system: m = 8.9650 g, V_f = 3.1212 cm^3, V_c = 0.2647 cm^3, V_t = 3.1212 cm^3, where subscript "f" corresponds to the float; "c" to core; "t" to thread. The measurement was done with maximum error of 0.1% in the entire range of parameters of state.

The purity of the substances studied was determined using a Tsvet chromatograph to be 99.87% for methanol and 99.96–99.98 wt % for *para*-, *meta*-, and *ortho*-xylenes.

Having determined on VLA-200g-M analytical balance to within 10^{-7} kg the mass of each component necessary for obtaining the required concentration of mixtures, we mixed the components in quartz vessels.

1070-4272/02/7512-1925 $27.00 © 2002 MAIK "Nauka/Interperiodica"

The experimental temperature was measured with a standard PTS-10 platinum resistance thermometer with an accuracy of 0.01°C (thermometer parameters: R_0 = 10.1792 Ω, R_{100}/R_0 = 1.3940).

As controls were used densities of *n*-heptane and benzene, measured at temperatures of 290–520 K in the pressure range 0.1–58.9 MPa with temperature and pressure steps of, respectively, 20–25 K and 5–10 MPa. The measurement results demonstrated good agreement with the most reliable published data [4, 9], with discrepancy not exceeding 0.05%.

The experimental data on the density of methanol–*meta*-xylene, methanol–*ortho*-xylene, and methanol–*para*-xylene systems are listed in Table 1. A detailed analysis of the concentration dependence of *P*–*V*–*T*-data for all of the systems studied demonstrates that the concentration dependence of density deviates from the additivity line and changes with temperature and pressure.

In practice, empirical and semiempirical equations of state are widely used to compile tabulated data. The procedure for constructing equations of this kind assumes the existence of a sufficient body of high-precision experimental data, which is not always the case.

Analysis of our experimental data shows that, for all of the substances studied, the equation of state, proposed in [10], is valid:

$$\rho^4 = A + BP^{0.5} + CP, \quad (1)$$

where P is the pressure (MPa), ρ is the density of a substance (g cm^{-3}), and A, B, C are coefficients dependent on temperature T (K).

The coefficients A, B, C were determined for each isotherm by the least-squares method and described analytically as

$$A = \sum_{i=0}^{3} a_i T^i, \quad B = \sum_{i=0}^{3} b_i T^i, \quad C = \sum_{i=0}^{3} c_i T^i. \quad (2)$$

Table 1. Density of methanol–*meta*-xylene, methanol–*ortho*-xylene, and methanol–*para*-xylene binary systems

T, K	Density (g cm^{-3}) at indicated pressure *P*, MPa							
	0.1	5.0	9.9	19.7	29.5	39.3	49.1	58.9
Methanol, 25%–*para*-xylene, 75%								
292.65	844.0	848.1	852.4	859.7	866.2	872.0	877.7	883.2
314.15	824.6	829.1	833.6	842.0	849.6	856.4	862.5	868.3
338.15		807.3	812.1	821.2	830.1	837.7	844.4	851.3
361.65		785.0	790.4	801.0	810.9	819.6	826.6	834.0
383.15		763.0	769.0	782.0	793.0	802.4	810.0	818.0
406.65		737.0	745.4	761.0	773.4	784.1	792.5	801.2
431.35		705.0	717.5	736.5	750.8	763.1	772.4	781.8
458.65		666.0	682.0	705.0	722.2	737.0	748.7	758.8
477.35		640.0	657.0	683.0	703.3	719.0	732.5	744.0
496.65		602.4	622.0	653.6	676.0	694.0	710.0	724.0
Methanol, 50%–*para*-xylene, 50%								
293.15	826.2	830.9	835.3	843.0	850.0	856.4	862.2	867.5
312.55	808.7	813.0	817.6	826.0	833.9	841.0	847.5	853.3
333.16		795.2	800.0	808.8	817.6	825.3	832.2	838.8
355.45		774.0	779.3	789.7	799.0	807.7	815.0	822.0
374.35		753.0	760.0	772.6	782.6	792.0	800.2	807.4
393.16		731.0	739.4	754.0	765.5	775.6	784.7	792.3
416.25		700.0	711.6	729.2	743.5	755.0	765.2	773.9
434.16		673.0	686.5	708.0	725.0	738.0	749.1	758.5
455.28		639.6	655.0	681.5	700.9	716.6	729.0	740.2
476.16		595.0	620.0	651.4	674.4	691.6	707.2	720.4
497.16		538.0	581.0	622.0	647.0	667.3	685.0	700.8

Table 1. (Contd.)

T, K	Density (g cm^{-3}) at indicated pressure *P*, MPa							
	0.1	5.0	9.9	19.7	29.5	39.3	49.1	58.9
Methanol, 75%–*para*-xylene, 25%								
292.65	811.3	816.0	820.6	828.4	835.3	842.0	847.7	853.6
312.19	793.9	798.5	803.1	811.4	819.4	826.8	833.2	839.3
331.05		781.0	785.9	794.8	803.9	811.6	818.7	825.4
354.36		757.6	763.5	773.5	783.5	792.4	800.3	807.0
375.25		734.3	742.0	753.0	764.6	774.0	783.0	790.0
396.05		708.8	718.0	731.1	744.8	754.6	765.1	773.0
414.18		684.0	694.4	711.0	727.0	737.7	749.2	758.1
435.45		650.4	665.4	686.0	703.6	717.1	729.4	740.4
455.06		615.0	635.7	661.0	680.8	696.0	710.4	723.0
477.17		578.4	604.0	637.0	659.1	677.0	693.4	706.8
497.06		503.0	557.1	605.0	631.5	651.6	671.4	686.4
Methanol, 25%–*ortho*-xylene, 75%								
291.65	858.7	862.0	865.8	872.4	879.4	885.1	891.2	896.6
312.25	841.4	845.0	849.1	856.5	863.6	870.0	876.2	881.8
333.56		827.0	831.8	840.0	847.1	854.4	861.0	867.0
352.15		809.8	815.6	824.4	832.4	840.3	847.3	853.8
372.05		790.2	796.4	807.3	816.5	825.0	832.6	839.3
390.38		771.2	778.5	791.5	801.8	811.1	819.0	826.0
414.74		744.2	753.0	768.8	781.2	791.6	800.0	808.0
435.17		717.4	728.0	747.0	761.8	773.2	782.5	791.7
453.15		692.0	704.7	726.2	743.0	756.0	766.2	776.0
475.34		657.2	672.0	698.3	717.8	733.4	746.0	756.6
498.05		613.0	635.8	668.0	689.5	707.8	721.7	773.0
Methanol, 50%–*ortho*-xylene, 50%								
292.2	837.6	841.3	844.8	852.2	859.0	865.3	871.2	876.6
312.05	820.0	824.2	828.2	836.0	843.2	850.1	856.6	862.2
332.16		806.5	811.6	820.0	827.6	835.1	841.8	847.7
353.65		785.8	791.7	801.6	810.2	818.4	825.6	832.0
374.35		763.1	770.1	782.2	792.3	801.4	809.1	816.2
393.19		741.0	749.2	763.9	775.2	785.6	793.9	801.1
415.25		711.9	722.8	740.9	754.0	766.0	775.4	783.2
434.18		684.0	697.7	718.4	734.3	747.2	757.9	767.2
456.28		648.3	665.2	690.4	709.6	724.2	736.1	748.0
474.3		612.0	635.3	665.2	687.3	704.4	717.9	731.8
497.06		553.0	598.4	632.7	658.0	677.8	695.1	711.2
Methanol, 75%–*ortho*-xylene, 25%								
292.65	816.4	820.6	824.8	833.0	840.0	846.6	852.6	857.9
314.54	797.6	802.2	806.4	814.6	822.4	829.8	836.5	842.5
335.2		783.4	788.0	796.6	805.0	813.4	820.3	827.0
353.16		764.6	770.4	780.0	789.1	798.1	806.0	813.4
373.05		742.2	749.0	760.4	771.0	780.8	789.4	797.1

Table 1. (Contd.)

T, K	Density (g cm^{-3}) at indicated pressure *P*, MPa							
	0.1	5.0	9.9	19.7	29.5	39.3	49.1	58.9
Methanol, 75%–*ortho*-xylene, 25%								
394.24		715.9	724.6	738.8	751.0	762.0	771.2	779.6
412.56		690.0	700.4	718.0	731.8	743.7	753.2	762.8
433.55		658.5	674.0	694.2	710.8	724.0	734.4	745.2
454.46		622.0	644.0	667.8	686.7	701.7	714.3	726.7
475.05		577.4	607.2	639.4	661.0	680.0	694.3	706.8
496.65		499.0	564.0	609.0	634.5	655.8	674.0	689.5
Methanol, 25%–*meta*-xylene, 75%								
292.2	845.2	849.6	853.5	861.1	867.8	873.7	879.0	884.4
312.05	829.6	833.8	838.0	845.8	852.8	859.8	865.6	871.3
332.16		817.7	822.0	830.0	838.0	845.5	852.1	858.0
353.65		799.0	803.8	812.9	822.0	830.0	837.3	843.4
374.35		778.0	783.7	794.8	805.0	813.5	821.4	828.0
393.19		757.0	765.0	778.1	789.4	798.3	806.9	813.7
415.25		730.0	744.0	757.0	770.0	779.8	788.6	796.1
434.18		704.0	717.0	736.2	750.8	762.5	771.9	780.0
456.28		675.5	686.0	709.5	728.2	741.3	752.0	768.0
474.3		644.6	659.0	685.8	707.6	723.0	735.5	745.0
497.06		605.3	624.1	654.7	679.2	698.9	713.7	724.7
Methanol, 50%–*meta*-xylene, 50%								
291.65	829.3	833.8	837.8	845.3	852.2	858.2	863.7	869.0
312.25	811.8	816.5	820.8	829.1	836.6	843.4	849.6	855.5
333.56		798.6	803.4	812.5	820.4	828.0	834.8	841.0
352.15		780.0	785.0	795.1	804.6	813.0	820.4	826.9
372.05		758.7	764.8	777.0	787.7	796.6	804.7	811.8
390.38		737.0	745.0	760.0	772.0	781.1	790.0	797.3
414.74		705.0	716.0	734.3	748.7	759.0	768.8	777.5
435.17		674.0	687.4	709.0	726.0	738.4	749.3	758.6
453.15		644.0	660.0	686.0	705.0	720.0	731.8	742.0
475.34		600.4	623.0	654.8	678.0	694.7	708.8	720.0
498.05		537.6	578.0	621.0	648.4	667.2	685.0	698.8
Methanol, 75%–*meta*-xylene, 25%								
293.15	811.6	816.0	820.0	828.0	835.0	841.4	847.7	852.8
314.54	793.4	798.0	802.1	810.3	818.3	825.5	831.6	838.3
335.2		778.7	783.1	792.4	800.4	809.3	816.6	823.5
353.16		760.8	766.0	776.8	785.6	794.8	802.4	810.0
373.06		738.5	745.5	757.4	767.9	777.8	786.0	794.2
485.24		712.6	721.4	735.6	748.4	758.6	767.6	776.2
412.56		686.0	697.0	715.0	729.4	739.6	749.8	759.5
433.55		654.5	668.5	691.1	708.0	718.9	730.9	741.0
454.46		619.2	636.4	663.8	683.0	697.2	710.6	722.0
475.05		573.3	600.4	634.8	656.6	674.1	690.0	702.3
496.65		495.0	552.0	603.8	630.7	651.0	669.6	683.0

Table 2. Coefficients of Eq. (2) for methanol–*meta*-xylene, methanol–*ortho*-xylene, and methanol–*para*-xylene systems

i	a_i	b_i	c_i
	Methanol, 25%–*meta*-xylene, 75%		
0	–0.6057578	0.7293074	-5.6537804×10^{-2}
1	1.179961×10^{-2}	-5.935732×10^{-3}	4.756782×10^{-4}
2	-3.649564×10^{-5}	1.5741602×10^{-5}	-1.271587×10^{-6}
3	3.129067×10^{-8}	-1.342362×10^{-8}	1.100052×10^{-9}
	Methanol, 50%–*meta*-xylene, 50%		
0	0.3265963	0.2213183	-2.004268×10^{-2}
1	3.72394×10^{-3}	-1.776661×10^{-3}	1.721292×10^{-4}
2	-1.438186×10^{-5}	4.537733×10^{-6}	-4.410843×10^{-7}
3	1.138355×10^{-8}	-3.503952×10^{-9}	3.5317009×10^{-10}
	Methanol, 75%–*meta*-xylene, 25%		
0	1.293416	–1167966	4.998021×10^{-3}
1	-4.606804×10^{-3}	1.031825×10^{-3}	-3.586691×10^{-5}
2	8.2750101×10^{-6}	-3.153691×10^{-6}	1.292419×10^{-7}
3	-8.660322×10^{-9}	3.412062×10^{-9}	-1.615239×10^{-10}
	Methanol, 25%–*para*-xylene, 75%		
0	-4.899846×10^{-3}	0.5918644	-5.012723×10^{-2}
1	7.156115×10^{-3}	-4.833614×10^{-3}	4.206022×10^{-4}
2	-2.497689×10^{-5}	1.287828×10^{-5}	-1.118544×10^{-6}
3	2.204741×10^{-8}	-1.103521×10^{-8}	9.648399×10^{-10}
	Methanol, 50%–*para*-xylene, 50%		
0	0.6497322	0.1471604	-8.287553×10^{-3}
1	1.233099×10^{-3}	-1.199893×10^{-3}	8.137668×10^{-5}
2	-8.279427×10^{-6}	3.087876×10^{-6}	-2.129725×10^{-7}
3	6.589197×10^{-9}	-2.335932×10^{-9}	1.677235×10^{-10}
	Methanol, 75%–*para*-xylene, 25%		
0	6.209584×10^{-2}	–0.3470884	-3.519363×10^{-2}
1	5.559211×10^{-3}	2.867024×10^{-3}	2.994688×10^{-4}
2	-1.947774×10^{-5}	-7.934511×10^{-6}	-7.942276×10^{-7}
3	1.636409×10^{-8}	7.471935×10^{-9}	6.788492×10^{-10}
	Methanol, 25%–*ortho*-xylene, 75%		
0	0.7912022	0.1337729	-3.074075×10^{-3}
1	1.077998×10^{-3}	-1.224019×10^{-3}	5.2159006×10^{-5}
2	-8.856259×10^{-6}	3.495846×10^{-6}	-1.677734×10^{-7}
3	7.731478×10^{-9}	-2.978231×10^{-9}	1.549457×10^{-10}
	Methanol, 50%–*ortho*-xylene, 50%		
0	0.6875726	8.168647×10^{-2}	-1.218396×10^{-3}
1	1.344951×10^{-3}	-7.894602×10^{-4}	3.629956×10^{-5}
2	-9.093657×10^{-6}	2.293909×10^{-6}	-1.240529×10^{-7}
3	7.538094×10^{-9}	-1.865638×10^{-9}	1.141339×10^{-10}
	Methanol, 75%–*ortho*-xylene, 25%		
0	1.675606	–0.2876951	2.572509×10^{-2}
1	-7.548444×10^{-3}	2.406451×10^{-3}	-2.012461×10^{-4}
2	1.589379×10^{-5}	-6.789705×10^{-6}	5.635003×10^{-7}
3	-1.517035×10^{-8}	6.560636×10^{-9}	-5.349648×10^{-10}

Values of a_i, b_i, c_i are listed in Table 2.

Equation (1) describes, with account of dependences (2), the whole array of experimental data with average error of 0.1–0.2%.

REFERENCES

1. Naziev, Ya.M. and Gasanov, V.G., *Probl. Energ.*, Baku, 2001, no. 2, pp. 57–60.
2. Mamedov, A.M. and Akhundov, T.S., *Tablitsy termodinamicheskikh svoistv gazov i zhidkostei. Vypusk 5. Uglevodorody aromaticheskogo ryada* (Tabulated Thermodynamic Properties of Gases and Liquids, issue 5, Hydrocarbons of the Aromatic Series), Moscow: Izd. Standartov, 1978.
3. Ekhlakov, A.D. and Rodionov, K.P., *Fiz. Met. Metalloved.*, 1960, vol. 9, no. 6, pp. 932–935.
4. Mirinskii, D.S., *125 let MVTU: Termodinamicheskie voprosy teplotekhniki* (To 125th Anniversary of Foundation of Moscow Higher Technical College: Thermodynamic Problems of Heating Engineering), Moscow: Mashgiz, 1955, pp. 30–49.
5. Golubev, I.F., *Nauchnye trudy GIAP* (Sci. Works of GIAP), Moscow, 1957, issue 7, pp. 47–61.
6. Golubev, I.F. and Dobrovol'skii, O.A., *Gaz. Prom–st.*, 1964, no. 5, pp. 43–48.
7. Gasanov, V.G., Density of Binary Mixtures of Higher Hydrocarbons at Various Parameters of State, *Cand. Sci. Dissertation*, Baku, 1994.
8. Gasanov, V.G. and Naziev, Dzh.Ya., *AzTU: Uch. Zap.*, 1999, vol. 8, no. 1, part 2, pp. 137–141.
9. Gasanov, G.T. Naziev, Dzh.Ya., and Gasanov, V.G., *Probl. Energ.*, Baku, 2000, no. 2, pp. 50–53.
10. Naziev, Dzh.Ya. and Gasanov, V.G., *Zh. Prikl. Khim.*, 1995, vol. 68, no. 2, pp. 210–213.

Russian Journal of Applied Chemistry, Vol. 75, No. 12, 2002, pp. 1931–1934. Translated from Zhurnal Prikladnoi Khimii, Vol. 75, No. 12, 2002, pp. 1968–1971.
Original Russian Text Copyright © 2002 by Sladkov, Kokhatskaya.

PHYSICOCHEMICAL STUDIES OF SYSTEMS AND PROCESSES

Boiling Point of Tetraethyllead

I. B. Sladkov and M. S. Kokhatskaya

St. Petersburg State Polytechnic University, St. Petersburg, Russia

Received January 22, 2001; in final form, May 2002

Abstract—In view of the pronounced inconsistency of published data on the boiling point of tetraethyllead, its value was determined by several independent calculation procedures. Simultaneously, data on the molar volume of liquid tetraethyllead at the boiling point, lacking in the literature, were obtained.

The fields of practical application of tetraethyllead $Pb(C_2H_5)_4$ (TEL), which are rather diverse, are described in virtually the only Russia's monograph on TEL by Korshak and Kolesnikov [1]. References to later studies concerned with synthesis and use of TEL can be found in the monograph by Morachevskii and co-workers [2].

However, reliable data on such a fundamental constant of TEL as its boiling point are still lacking. This is largely determined by the impossibility of direct experimental determination of the boiling point because of the decomposition of TEL at temperatures close to its boiling point.

The present study was aimed to obtain missing data with the use of a number of independent calculation techniques. This task can be accomplished because experimental data on critical parameters are available for TEL. This allows application of methods developed on the basis of the theory of thermodynamic similarity, distinguished by high reliability of prognostication of physicochemical properties.

The experimental data on the physicochemical properties of TEL, available in the literature, give no way of producing an unambiguous answer to the question of its boiling point. For example, data on the boiling point can be obtained using the saturated vapor pressure (Table 1), but this gives rather contradictory results. In [9], the boiling point of TEL was given as 473 K, with the range 471–475 K reported in [10].

It can be seen that the information presented is rather contradictory: according to different sources, the boiling point of TEL is within 448.7–475 K. This is the probable reason why no evidence on the boiling point of TEL can be found in a fundamental reference book of thermodynamic properties of substances [11].

In the present study, the boiling point of TEL was determined as follows. The calculation procedure 1 is based on the temperature dependence of the density of the liquid. According to published data [12], the temperature dependence of the density (g cm^{-3}) of the liquid phase of TEL is described by the equation

Table 1. Boiling point of $Pb(C_2H_5)_4$, calculated from saturated vapor pressures

Temperature series of TEL saturated vapor pressure P, mm Hg	ΔT, K	Reference	T_b, K
$\log P = -2960/T + 9.4262$	351–423	[3]	452.2
$\log P = -2938/T + 9.428$	273–343	[4]	448.7
$\log P = -2908.43/T + 9.34286$	350–440	[5]	450.1
$\log P = -2535.84/T + 8.2724$	373–473	[6]	470.3
$\log P = -2899/T + 9.314$	350–450	[7]	450.6
$\log P = -2832/T + 9.122$	348–450	[7]	453.8
$\log P = -2184.6/(T - 43.2) + 8.1547$	345–455	[7]	457.4
$\ln P = -2063/(T - 43.2) + 11.576$	360–450	[8]	460.6
$\ln P = -1686/(T - 73.2) + 10.96355$	360–450	[8]	462.6

1070-4272/02/7512-1931 $27.00 © 2002 MAIK "Nauka/Interperiodica"

Table 2. Physicochemical properties of alkyl compounds of Si, Ge, Sn, and Pb [8]

Substance no.	Substance	Π, $J^{1/4}\ cm^{5/2}\ mol^{-1}$	T_b, K	V_b	V_{cr}	$K_1 = V_b/\Pi$	$K_2 = V_{cr}/V_b$
				$cm^3\ mol^{-1}$			
1	$Si(CH_3)_4$	4.70	300.1	138.3	361.0	29.43	2.61
2	$Si(C_2H_5)_4$	7.46	426.8	215.5	585.0	28.89	2.71
3	$Ge(CH_3)_4$	4.89	316.6	142.4	380.0	29.12	2.67
4	$Ge(C_2H_5)_4$	7.65	436.6	220.4	596.2	28.81	2.72
5	$Sn(CH_3)_4$	5.16	350.6	148.3	400.0	28.74	2.70
6	$Sn(C_2H_5)_4$	7.92	451.4	228.7	–	28.88	–
7	$Pb(CH_3)_4$	5.41	382.9	150.8	398.5	29.34	2.58
8	$Pb(C_2H_5)_4$	8.17	–	–	636	–	–

$$\rho = 2.118 - 0.00163T. \quad (1)$$

This temperature series was obtained up to 453 K, a temperature which is, presumably, rather close to the standard boiling point. From relation (1) follows that

$$T_b = (2.118 - \rho_b)/0.00163, \quad (2)$$

where ρ_b is the density of the liquid at its boiling point, which can be calculated from the corresponding molar volume ($\rho_b = M/V_b$).

Since data on the molar volume of liquid TEL at the boiling point are lacking, this volume was calculated using the following approximate relations

$$V_b = K_1\Pi, \quad (3)$$

$$V_b = V_{cr}/K_2, \quad (4)$$

where Π is the parachor; V_{cr}, the critical volume; K_1 and K_2, constants calculated from the properties of substances of the same type.

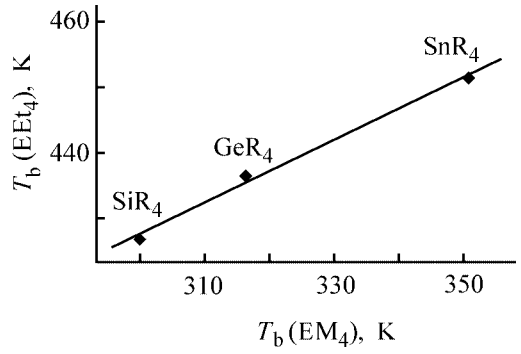

Fig. 1. Variation of the boiling point T_b in the series of ethyl and methyl compounds of Si, Ge, and Sn.

Calculation of the parachor for alkyl compounds was considered in detail in [13].

As substances of the same type were chosen alkyl compounds of elements belonging to Group IV of the periodic table, for which experimental values of the critical volume and the volume of the liquid at the boiling point are known [12, 14] (Table 2). The data listed in Table 2 were used to find the coefficients K_1 and K_2, equal to 29.05 and 2.66, respectively. Further, Eqs. (3) and (4) were applied to calculate the molar volume of TEL, which gave fairly consistent values of this parameter, 237.4 and 238.7 $cm^3\ mol^{-1}$.

Averaging of the data obtained gives the molar volume of liquid TEL at the boiling point of 238.1 $cm^3\ mol^{-1}$, which corresponds to ρ_b = 1.358 $g\ cm^{-3}$. Substitution of this value into Eq. (2) gives the boiling point of TEL, equal to 466.3 K.

The calculation procedure 2 is based on the Watson formula [15]

$$T_b = (T_b/T_{cr})\exp[2.77V_b^{0.18}/(T_b/T_{cr}) - 2.94]/V_b^{0.18}. \quad (5)$$

Substitution into formula (5) of the thus obtained molar volume of TEL liquid at the boiling point (238.1 $cm^3\ mol^{-1}$) and of its critical temperature (655 K [8]) yields a value T_b(TEL) = 466.8 K.

In the following stage of the study, the boiling point of TEL was determined using the method of comparative calculation, according to which a change in two properties in a single series of one-type substances or a single property in two series of one-type substances is described by a linear relation [16]. The existence of a linear relation was first verified by plotting the corresponding curve, with subsequent processing of the data by the least-squares method. The necessary experimental data are listed in Table 2.

Table 3. Verification of the reliability of the calculation procedure used to find the boiling point parameters

Substance	T_b, K		Δ, %	V_b, cm^3 mol^{-1}		Δ, %
	calculation	experiment		calculation	experiment	
$Si(C_2H_5)_4$	426.5	426.8	0.3	218.3	215.5	1.3
$Ge(C_2H_5)_4$	438.1	436.6	0.5	223.8	220.4	1.5
$Sn(C_2H_5)_4$	450.0	451.4	0.6	230.1	228.7	0.6

The following techniques were used in the present study for comparative calculation of the boiling point of TEL: procedure 3, based on comparison of boiling points in series of methyl and ethyl compounds of Si, Ge, and Sn (Fig. 1, correlation factor of the linear dependence R = 0.9968, rms error S = ±0.2%); procedure 4, comparing the boiling point and the parachor in a series of ethyl compounds of Si, Ge, and Sn (Fig. 2, R = 0.9997, S = ±0.1%); procedure 5, based on comparison of the quantity $\Pi^{3/2}/T_b^{1/2}$ and the critical volume in the series of methyl and ethyl compounds of Si and Ge, and also those of methyl compounds of Sn and Pb (Fig. 3, R = 0.9749, S = ±1.8%).

The results obtained in determining the boiling point of TEL by different methods are presented below:

Calculation technique	1	2	3	4	5
T_b, K	466.3	466.8	467.1	464.7	465.7
Average	466.1 K				

The boiling points obtained are in good agreement with one another and fall into the range established on the basis of experimental data on saturated vapor pressure. It may be assumed that averaging of the values obtained in this study will give a boiling point of TEL, close to the most reliable value of this parameter for $Pb(C_2H_5)_4$. This averaged value is 466.1 K.

Substitution of the thus obtained boiling point of TEL into Eq. (1) describing the temperature dependence of the density of the liquid yields the molar volume of the liquid at the boiling point (238.1 cm^3 mol^{-1}), coinciding with the value found above by other methods. This confirms once more the reliability of the molar volume of liquid TEL at the boiling point.

To confirm the reliability of the boiling point and molar volume at this temperature, the technique described above was applied to the closest analogues of TEL: $Si(C_2H_5)_4$, $Ge(C_2H_5)_4$, and $Sn(C_2H_5)_4$, for which experimental data on these properties are available in the literature (Table 2). The calculation results obtained, listed in Table 3, indicate the high reliability of the method used.

CONCLUSIONS

(1) T_b = 466.1 K and V_b = 238.1 cm^3 mol^{-1} were found using a number of independent calculation procedures.

(2) The good agreement between the results obtained using different methods and verification of the technique employed in the present study on compounds of the same type confirm the reliability of the data obtained.

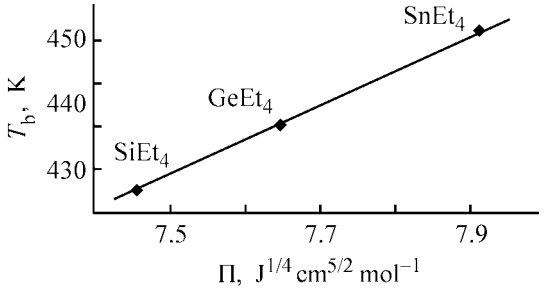

Fig. 2. Boiling point T_b vs. the parachor Π in the series of ethyl compounds of Si, Ge, and Sn.

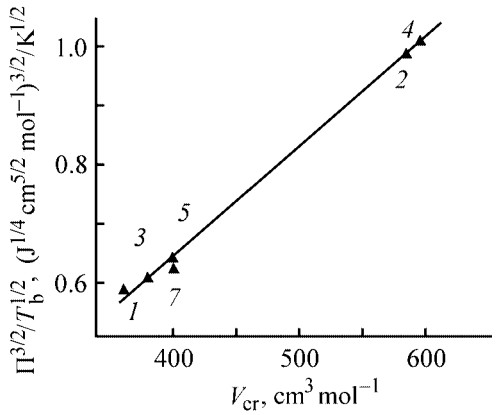

Fig. 3. $\Pi^{3/2}/T_b^{1/2}$ vs. critical volume V_{cr} in the series of ethyl and methyl compounds of Si, Ge, Sn, and Pb. *Digits at points* correspond to compound numbers in Table 2.

REFERENCES

1. Korshak, V.V. and Kolesnikov, G.S., *Tetraetilsvinets* (Tetraethyllead), Moscow: Goskhimizdat, 1946.
2. Morachevskii, A.G., Shesterkin, I.A., Busse-Machukas, V.B., *et al.*, *Natrii* (Sodium), St. Petersburg: Khimiya, 1992.
3. Buckler, E.J. and Norrish, R.G., *J. Chem. Soc.*, 1936, pp. 1567–1570.
4. Jones, W.D. and Evanc, D.P., *J. Chem. Soc.*, 1935, pp. 39–41.
5. Stull, D.R., *Ind. Eng. Chem.*, 1947, vol. 39, no. 3, pp. 517–540.
6. Zorin, A.D., Kut'in, A.M., and Kuznetsova, T.V., *Zh. Fiz. Khim.*, 1985, vol. 59, no. 1, pp. 154–158.
7. Kut'in, A.M., Zorin, A.D., and Kuznetsova, T.V., *Poluchenie i analiz chistykh veshchestv* (Preparation and Analysis of Pure Substances), Nizhni Novgorod: Nizhegorodskii Gos. Univ., 1990, pp. 3–8.
8. Rummens, F.H.A. and Rajan, S., *Canad. J. Chem. Eng.*, 1979, vol. 57, no. 6, pp. 349–354.
9. Kamlet, M.J., Doherty, R.M., and Taft, R.W., *J. Am. Chem. Soc.*, 1984, vol. 106, no. 5, pp. 1205–1213.
10. Kaufman, H.C., *Handbook of Organometallic Compounds*, New York: VNCI, 1961.
11. *Termicheskie konstanty veshchestv: Spravochnik* (Thermal Constants of Substances: Reference Book), Glushko, V.P., Ed., Moscow: Akad. Nauk SSSR, 1970, issue 4.
12. Sladkov, I.B., *Zh. Prikl. Khim.*, 2000, vol. 73, no. 5, pp. 727–732.
13. Sladkov, I.B., *Zh. Prikl. Khim.*, 1999, vol. 72, no. 8, pp. 1266–1272.
14. Sladkov, I.B., *Zh. Prikl. Khim.*, 2001, vol. 74, no. 11, pp. 1748–1752.
15. Reid, R.G. and Sherwood, T.K., *The Properties of Gases and Liquids*, New York: McGraw-Hill, 1966.
16. Morachevskii, A.G. and Sladkov, I.B., *Fiziko-khimicheskie svoistva molekulyarnykh neorganicheskikh soedinenii* (Physicochemical Properties of Molecular Inorganic Compounds), St. Petersburg: Khimiya, 1996.

Russian Journal of Applied Chemistry, Vol. 75, No. 12, 2002, pp. 1935–1938. Translated from Zhurnal Prikladnoi Khimii, Vol. 75, No. 12, 2002, pp. 1972–1975.
Original Russian Text Copyright © 2002 by Krasnoperova, Sytnik, Yukhno, Bezuglaya, Lyapunov.

PHYSICOCHEMICAL STUDIES OF SYSTEMS AND PROCESSES

Relationships in Dissolution and Solvation of Miconazole Nitrate in Binary and Ternary Solvents Based on Polyethylene Glycol-400

A. P. Krasnoperova, O. Yu. Sytnik, G. D. Yukhno, E. P. Bezuglaya, and N. P. Lyapunov

Karazin National University, Kharkov, Ukraine

State Scientific Center of Medicinals, Kharkov, Ukraine

Received July 3, 2002

Abstract—The solubility of 1-[2,4-dichloro-β-(2,4-dichlorobenzyloxy)phenethyl]imidazole nitrate (miconazole nitrate) $C_{18}H_{14}Cl_4N_2O \cdot HNO_3$ in binary mixtures 1,2-propylene glycol–polyethelene glycol-400 and in ternary mixtures of these glycols with water at 293.15 K was studied. The correlation between the miconazole nitrate solubility and the dielectric constant of the solvents was discussed. The deviations of the miconazole nitrate solubility from additivity throughout the composition range of mixed solvents were calculated.

Imidazole derivatives are heterocyclic nitrogen-containing biologically active compounds widely used in modern pharmacology. Synthesis in solutions and development of the compositions of medicinals based on imidazole derivatives require knowledge of the solubility of these compounds in multicomponent solvents.

It is known that imidazole derivatives form with "rigid" acids complexes involving "pyridine"-type nitrogen atoms [1–3]. Among such compounds is 1-[2,4-dichloro-β-(2,4-dichlorobenzyloxy)phenethyl]imidazole nitrate (miconazole nitrate) used as microbiocide and fungicide

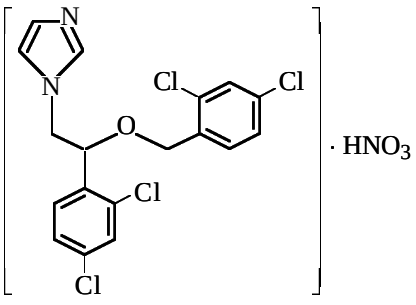

In this communication, we report on a study of the solubility of miconazole nitrate in a binary solvent, 1,2-propylene glycol–polyethylene glycol with the molecular weight 400 (1,2-PG–PEG-400), and in a ternary solvent, H_2O–1,2PG : PEG-400 (90 : 10 mol %), in the entire concentration range at 293.15 K.

EXPERIMENTAL

Mixed solvents, 1,2-PG – PEG-400 and H_2O – (1,2-PG – PEG-400), were prepared gravimetrically. To this end, we used double-distilled water, PEG-400 (Merck, Germany), and 1,2-PG preliminarily purified by double vacuum distillation [4]. The quality of 1,2-PG and PEG-400 was checked by measuring their density [$\rho^{25°C}$ (1,2-PG) = 1.0328 and $\rho^{25°C}$ (PEG-400) = 1.1250 kg m^{-3}] and dielectric constant [$\varepsilon^{25°C}$ (1,2-PG) = 29.0 and $\varepsilon^{25°C}$ (PEG-400) = 13.9]. Prior to being used, miconazole nitrate was dried at 105°C for 2 h, and its purity was checked by measuring the melting point (mp 454 K) and also chromatographically.

The solubility of miconazole nitrate was studied isothermally. To this end, an excess amount of the salt was placed in vessels with ground-glass stoppers, poured over with an appropriate solvent, and kept in a thermostat (temperature maintained constant to within 0.1 K) until the thermodynamic equilibrium was established. The saturation time was estimated experimentally to be 100 to 300 h, depending on the content of the nonaqueous component. The attainment of the thermodynamic equilibrium in miconazole nitrate solutions was judged from the invariance of the miconazole nitrate concentration in experiments with several successively taken samples. The concentration

1070-4272/02/7512-1935 $27.00 © 2002 MAIK "Nauka/Interperiodica"

Solubility L of miconazole nitrate in 1,2-PG–PEG-400 and H_2O–(1,2-PG : PEG-400) mixtures at 293.15 K

1,2-PG–PEG-400 system		H_2O–(1,2-PG : PEG-400) system	
x, mole fraction	$L \times 10^2$, M	x, mole fraction	$L \times 10^2$, M
0.000	1.31	0.000	0.029
0.048	2.10	0.008	0.048
0.113	2.98	0.017	0.070
0.208	3.03	0.040	0.100
0.307	2.99	0.057	0.129
0.417	2.79	0.092	0.204
0.482	2.72	0.125	0.275
0.582	2.68	0.177	0.428
0.903	2.36	0.245	0.660
1.000	2.13	0.343	1.00
		0.586	1.78
		0.702	2.14
		0.887	2.67
		1.000	2.98

* (x) Content of PEG-400 in the 1,2-PG–PEG-400 system and that of nonaqueous solvent in H_2O–(1,2-PG–PEG-400) system.

of the saturated solutions was determined by the spectral method. The optical density was measured on a Hitachi U3210 spectrophotometer in the UV spectral range at 280 nm. To this end, 2 ml of a transparent solution was diluted with ethanol to 100 ml so that the optical densities were within 0.3–0.7. Each solubility value was an average of those obtained in 3–4 runs. The maximal relative error in determining the solubility was 3% at a confidence level of 0.95. The results obtained are listed in the table.

Our data show that the solubility of miconazole nitrate varies widely depending on the solvent composition being a nonlinear function of the composition of mixed solvents.

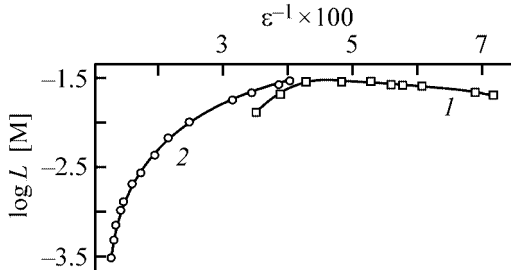

Fig. 1. Variation of $\log L$ of miconazole nitrate with the dielectric constant ε of (*1*) 1,2-PG–PEG-400 and (*2*) H_2O–(1,2-PG–PEG-400) systems at 293.15 K.

Izmailov *et al.* [5, 6] found that the solubility of substances in solvents of identical chemical nature is described by the equation

$$\log L = A + (\beta'\mu - \beta) \cdot 1/\varepsilon. \quad (1)$$

Here, L is the solubility, M; β' and β are empirical constants, μ is the dipole moment of the solvent, and ε is the dielectric constant of the solvent.

Equation (1) suggests that the solubility of miconazole nitrate in water must exceed that in PEG-400 and 1,2-PG, since the dielectric constant of water ($\varepsilon^{20°C} = 80.1$) significantly exceeds those of PEG-400 ($\varepsilon^{20°C} = 14.4$) and 1,2-PG ($\varepsilon^{20°C} = 30.8$). At the same time, the solubility of miconazole nitrate in these solvents varies in the reverse order: $L_{\text{PEG-400}} > L_{\text{1,2-PG}} > L_{H_2O}$. Hence, it is the specific solvation, rather than the dielectric constant, that governs the miconazole nitrate solubility.

A lower solubility of miconazole nitrate in water, compared to nonaqueous solvents, is typical of salts containing bulky hydrophobic ions. Bulky asymmetric hydrophobic ions exhibit a "structure-forming" effect in aqueous solutions by increasing the energies of the hydrogen bonds between the surrounding water molecules [7], thus hindering dissolution.

The higher solubility of miconazole nitrate in the studied glycols, compared to water, may also be due to the specific interactions between the π electrons of the phenyl groups of miconazole nitrate and hydrogen atoms in the solvents [8] and to the influence of the universal solvation via dipole–dipole and dispersion interactions [9].

Also, Eq. (1) suggests that, in contrast to the systems under study, the logarithm of the electrolyte solubility in mixed solvents with the same chemical nature depends linearly the reciprocal of the dielectric constant (Fig. 1). This once again confirms the leading role played by specific interactions in the systems studied.

The table shows that the solubility of miconazole nitrate in the 1,2-PG–PEG-400 binary solvent has a maximum at ~20 mol % PEG-400. This maximum can be attributed to the conformational changes in PEG-400 molecules, resulting from an increase in the content of 1,2-PG in the mixed solvent.

The conformation of the PEG chains, both in individual state and in solutions, has been studied extensively [10–14]. However, there is no consensus regarding the molecular structure of PEG. X-ray dif-

fraction studies [10] showed that the oxyethylene chain has a tortuous, rather than linear, structure. Beginning with nine oxyethylene groups (PEG-400), the tortuous chain forms a helix, and, with the number of units growing further, it can fold into a coil. Thus, steric hindrances in straight PEG-400 can make the oxyethyl groups insufficiently accessible to interactions with the substance being dissolved, and their interaction is accompanied by extra energy expenditure required for helix transformation. The interaction between the oxyethyl groups in PEG-400 and hydroxy groups in 1,2-PEG, evidently, results in helix unfolding. This makes the oxyethyl groups in PEG more easily accessible to miconazole nitrate solvation, which is responsible for the appearance of a solubility maximum.

We calculated the deviations of the solubility of miconazole nitrate from additivity throughout the composition range of the binary and ternary solvents by the formula [5]

$$L^E = L_{\text{exp}} - \Sigma L_i x_i. \quad (2)$$

Here, L^E is the deviation of the solubility from additivity; L_{exp} and L_i are the solubilities of miconazole nitrate in a mixed solvent and in straight ith solvent, respectively; and x_i is the mole fraction of ith straight solvent in a mixed solvent.

As seen from Fig. 2, the isotherm of deviations of the solubility from additivity in the 1,2-PG–PEG-400 system passes through a maximum at ~20 mol % PEG-400 in the mixture. The deviation exceeds 10%, which suggests that the solubility of miconazole nitrate is significantly influenced by the intermolecular interactions in the binary solvent.

In contrast to the binary solvent, the isotherm of deviations in the ternary solvent is more complex. With minor additions of the nonaqueous solvent to water, the solubility deviations are negative, and in the region rich in the nonaqueous solvent, positive. This suggests that the solubility of miconazole nitrate is affected by complex interactions in the mixed solvent H_2O–(1,2-PG–PEG-400). Numerous publications [11, 12, 16–19] suggest that minor additions of nonaqueous components to water are responsible for phenomena competing with dissolution of the third component. Physicochemical analysis and solubility studies with inert gases in the mixed solvent H_2O–1,2-PG showed [17, 18] that the methyl radical in 1,2-PG increases the hydrogen bonding energy in water, thus stabilizing the water structure. At the same time, in the H_2O–PEG-400 system with about 10 mol % PEG-400, oxonium compounds are formed

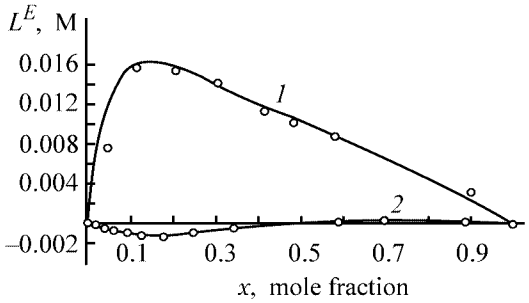

Fig. 2. Deviations of the solubility of miconazole nitrate from additivity, L^E, in (*1*) 1,2-PG–PEG-400 and (*2*) H_2O–1,2-PG–PEG-400 systems at 293.15 K. (x) Mole fraction of PEG-400 in 1,2-PG–PEG-400 system and the total mole fraction of the nonaqueous components in the H_2O–1,2-PG–PEG-400 system.

[19] via interaction of ether bridges in PEG with water molecules. This allows an assumption that, with minor additions of the nonaqueous solvent 1,2-PG–PEG-400 to water, both processes occur, and their competing influence is responsible for negative deviations of the solubility of miconazole nitrate from additivity.

CONCLUSION

Analysis of the correlation between the solubility of miconazole nitrate and the composition of a mixed solvent, dielectric constant, and deviations of the solubility from additivity showed that the solubility of miconazole nitrate is primarily determined by the specific interactions in the solvents under study and by conformational transformations in polyethylene glycol-400 molecules.

REFERENCES

1. Khamaganova, L.D., Baikalova, L.V., Domnina, E.S., and Gol'shtein, I.P., *Koord. Khim.*, 1993, vol. 19, no. 9, pp. 736–741.
2. Khoshtariya, D.E. and Berzenishvili, N.O., *Zh. Fiz. Khim.*, 1989, vol. 63, no. 4, pp. 966–970.
3. Koryagin, Yu.S., Shormanov, V.A., and Krestov, G.A., *Koord. Khim.*, 1985, vol. 11, no. 8, pp. 1046–1049.
4. Weissberger, A. and Proscauer, E.S., *Organic Solvents. Physical Properties and Methods of Purification*, Riddick, J.A., and Toops, E.E., Eds., New York: Interscience, 1955.
5. Izmailov, N.A., *Elektrokhimiya rastvorov* (Solution Electrochemistry), Moscow: Khimiya, 1966.
6. Izmailov, N.A. and Chernyi, V.S., *Tr. Komiss. Anal. Khim.*, 1958, vol. 9, pp. 44–49.

7. Johnson, D.A., *Some Thermodynamic Aspects of Inorganic Chemistry*, Cambridge: Cambridge Univ., 1982.
8. Krestov, G.A., Afanas'ev, V.N. and Agafonov, A.V., *Kompleksoobrazovanie v nevodnykh rastvorakh* (Complexing in Nonaqueous Solutions), Moscow: Nauka, 1989.
9. Krestov, G.A., Novoselov, I.P., Perelygin, I.S., *et el.*, *Ionnaya sol'vatatsiya* (Ionic Solvation), Moscow: Nauka, 1987.
10. Dyment, O.N., Kazanskii, K.S., and Miroshnikov, A.M., *Glikoli i drugie proizvodnye okisei etilena i propilena* (Glycols and Other Derivatives of Ethylene and Propylene Oxides), Moscow: Khimiya, 1976.
11. Toryanik, A.I., *Zh. Strukt. Khim.*, 1984, vol. 25, no. 3, pp. 49–53.
12. Zinchenko, I.D., Mank, V.V., Moiseev, V.A., and Ovcharenko, F.D., *Kolloidn. Zh.*, 1977, vol. 38, no. 1, pp. 44–49.
13. Johnson, J.A., Saboungi, M.-L., Price, D.L., *et al.*, *J. Chem. Phys.*, 1998, vol. 109, no. 16, pp. 7005–7010.
14. Fuson, M.M., Harser, K.H., and Ediger, M.D., *Macromolecules*, 1997, vol. 30, pp. 5714–5720.
15. Lilich, L.S., Mogilev, M.E., and Chernykh, L.V., *Zh. Strukt. Khim.*, 1967, vol. 8, no. 2, pp. 200–204.
16. Shinyashiki, Naoki, Sudo, Seiichi, Abe, Wataru, and Yagihara, Shin, *J. Chem. Phys.*, 1998, vol. 109, no. 22, pp. 9843–9847.
17. Chistyakov, Yu.V. and Egorova, I.V., in *Termodinamika i stroenie rastvorov: Mezhvuzovskii sbornik* (Solution Thermodynamics and Structure: Intercollegiate Coll.), Ivanovo, 1979, pp. 51–56.
18. Chistyakov, Yu.V., Egorova, I.V., Krestov, G.A., and Karaseva, E.A., *Zh. Strukt. Khim.*, 1980, vol. 21, no. 5, pp. 86–90.
19. Krasnoperova, A.P., *Vestn. Khar'kov. Univ., Khimiya*, 1998, no. 420, no. 2, pp. 178–181.

Russian Journal of Applied Chemistry, Vol. 75, No. 12, 2002, pp. 1939–1944. Translated from Zhurnal Prikladnoi Khimii, Vol. 75, No. 12, 2002, pp. 1976–1981.
Original Russian Text Copyright © 2002 by Blokhin, Maiorov, Kopyrin, Taushkanov.

SORPTION AND ION-EXCHANGE PROCESSES

Acid–Base Properties and Structural Features of Composite Ion Exchangers Based on KU-23 and KM-2p Cation Exchangers and Hydrated Zirconium Oxide

A. A. Blokhin, D. Yu. Maiorov, A. A. Kopyrin, and V. P. Taushkanov

St. Petersburg State Technological Institute, St. Petersburg, Russia

Received, May 23, 2002

Abstract—A method for introduction of hydrated zirconium oxide into macroporous cation exchangers KU-23 and KM-2p and the acid–base properties and structural features of the composite ion exchangers are described.

In contrast to anion-exchange resins, hydrated oxides (HOs) of multicharge metal ions exhibit increased selectivity with respect to certain oxygen-containing anions: phosphate, arsenate, and silicate [1–3]. Therefore, HOs show promise as sorbents for removal of their trace amounts from salt solutions. Unfortunately, inorganic ion exchangers, including HOs, are not commercially available because of difficulties encountered in their preparation in the form of mechanically strong spherical granules. A way to solve the problem of obtaining inorganic ion exchangers with satisfactory performance is to introduce them into an appropriate mechanically strong support and to use such a combined ion exchanger. Ion-exchange resins with porous structure are convenient supports for HOs. In [4, 5], we described methods for preparing composite ion exchangers consisting of macroporous KU-23 and KM-2p cation exchangers and hydrated zirconium oxide (HZO), one of the most efficient HO-based ion exchangers, and reported certain data on their ion-exchange properties.

In this study, we considered data on acid–base properties of the above composite ion exchangers, their pore structure, and distribution of the inorganic component in a sorbent.

EXPERIMENTAL

Commercial granulated macroporous sulfonic cation exchanger KU-23 and carboxylic cation exchanger KM-2p were used as supports. The cation exchangers were pretreated by the standard method [6]. Hydrated zirconium oxide was prepared by precipitation of hydroxide gel from 1 M zirconium nitrate solution with aqueous ammonia (pH 9.0–9.5). The gel was aged for 24 h, and the precipitate was separated from the mother liquor, washed with water by decantation, filtered, again washed with water, dried in air at 80°C, crushed, and sized. The 0.2–0.5-mm fraction was taken. The composite ion exchangers were prepared under dynamic conditions by saturation of cation exchangers with Zr(IV) from 0.1 M solution of zirconium nitrate at pH 1.0–1.2, washing with water, treatment with 1 M aqueous ammonia, and washing with water to remove excess ammonia [4, 5]. The composite ion exchangers thus obtained were unloaded from the column and dried in air at room temperature.

We prepared several batches of the composite ion exchangers on the basis of KU-23 and KM-2p cation exchagers and HZO. The scatter in the HZO content between different batches of the composite sorbents prepared with the same support was within 4.5 rel.% (Table 1), which indicates good reproducibility of the preparation procedure. Samples of the KU-23–HZO

Table 1. Composition of combined ion exchangers

Batch no.	ZrO_2 content (%) in indicated ion-exchange resin	
	KU-23	KM-2p
1	28.7	21.9
2	29.2	23.0
3	27.8	22.4
4	28.5	–
5	29.4	–
Average	28.7	22.4

1070-4272/02/7512-1939 $27.00 © 2002 MAIK "Nauka/Interperiodica"

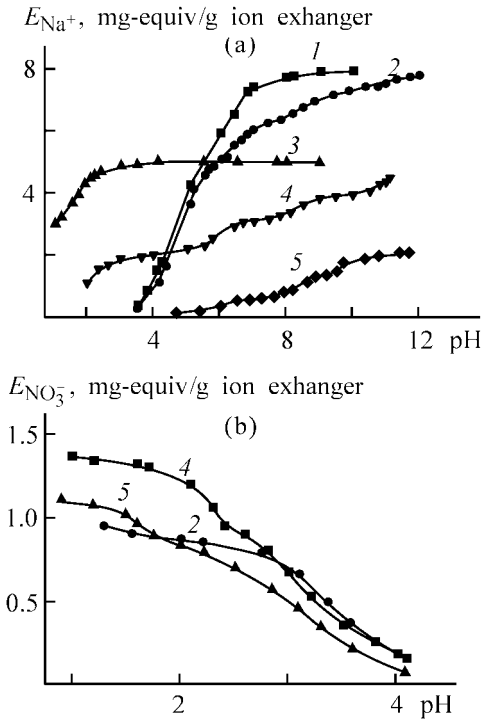

Fig. 1. Curves of potentiometric titration of ion exchangers with (a) 0.1 M NaOH in 2 M $NaNO_3$ solution and (b) 0.1 M HNO_3 in 2 M $NaNO_3$ solution. (E_{Na^+}, $E_{NO_3^-}$) Ion exchanger capacities with respect to Na^+ and NO_3^-, respectively. Ion exchanger: (*1*) KM-2p, (*2*) KM-2p–HZO, (*3*) KU-23, (*4*) KU-23–HZO, and (*5*) HZO.

and KM-2p–HZO ion exchangers contained 29.0 and 22.5 wt % ZrO_2, respectively.

Before potentiometric titration (method of separate samples), the ion exchangers were transformed into the H form (titrated with NaOH solution) by treatment with 0.1 M HNO_3 or into the deprotonated form (titrated with HNO_3 solution) by treatment with 0.1 M NaOH, followed by washing with distilled water to neutral reaction. The pretreated ion exchangers were contacted under static conditions with solutions of NaOH or HNO_3 of various concentrations in the presence of a supporting electrolyte, 2 M $NaNO_3$. The contact time was 8–10 days.

The average size of prevailing pores and the specific surface area of the swollen ion exchangers were determined by small-angle X-ray scattering (SXS) [7, 8]. The intensity of SXS was measured within the range of angles 2–17' on a Kratky camera "Anton Paar" setup. The specific surface area of dried ion exchangers was determined by thermal desorption of argon [9]. The pore volume was estimated by adsorption of cyclohexane and toluene vapors [10]. The IR spectra of ion exchangers in a KBr matrix were recorded on a UR-20 spectrophotometer. An electron microscopic study of ion exchangers was performed on an REM-100U scanning electron microscope at an electron-accelerating voltage of 30 kV. The X-ray analysis of composite ion exchangers containing HZO was performed with characteristic zirconium radiation on a VDAR attachment to the electron microscope. The chemical stability of ion exchangers was estimated as the extent to which Zr(IV) passes into the solution at contact with solutions of various compositions. The Zr(IV) concentration in solution was determined photocolorimetrically with Alizarin Red S [11]. The Zr(IV) detection limit was 1 mg l^{-1}. The ZrO_2 content in the composite ion exchangers was determined gravimetrically after ashing at 800–850°C.

The curves of the potentiometric titration of KU-23–HZO, KM-2p–HZO, KU-23, KM-2p, and granulated HZO are shown in Fig. 1. Four inflections are observed in curves of KU-23–HZO and KM-2p–HZO titration with NaOH, corresponding to four stages of dissociation of functional groups by the acid mechanism. In the curve of HZO titration, there are three such inflections. The first inflection in the titration curves of composite ion exchangers corresponds to dissociation of functional groups of the support, and the other three inflections, to dissociation of OH groups of HZO by the acid mechanism. The exchange capacity of all the composite ion exchangers, corresponding to the first stage of dissociation of HZO OH groups by the acid mechanism, is virtually equal to that of the second stage of the dissociation. Because the capacities of ion exchangers corresponding to the first and second stages of dissociation of HZO OH groups are equal, we can identify these groups as $=Zr(OH)_2$, with the following dissociation scheme:

$$=Zr(OH)_2 + Na^+ \rightleftarrows =ZrO_2HNa + H^+, \quad (1)$$

$$=ZrO_2HNa + Na^+ \rightleftarrows =ZrO_2Na_2 + H^+. \quad (2)$$

The third inflection corresponds, most likely, to dissociation of isolated =Zr–OH groups. The titration curves of KU-23–HZO and HZO with HNO_3 exhibit a single inflection, whereas in the titration curve of KM-2p–HZO, clear inflections are absent. The anion-exchange power of the composite ion exchangers is due to dissociation of the HZO OH groups by the base mechanism only, since the supports (cation exchangers) have no anion exchange power. In principle, in titration of HZO with HNO_3, the isolated =Zr–OH groups must dissociate first, since this dissociation is facilitated as compared to that of $=Zr(OH)_2$ group. Inflections corresponding to particular steps of dissociation of $=Zr(OH)_2$ do not appear in the titration curves. Probably, the constants of the first and second steps

Table 2. Acid–base properties of ion exchangers

Ion exchanger	Acid mechanism				Base mechanism	
	pK of support	pK_1	pK_2	pK_3	pK_1	pK_2
KU-23	1.03 ±	–	–	–	–	–
KU-23–HZO	1.73 ± 0.08	6.49 ± 0.22	8.30 ± 0.16	11.50 ± 0.09	10.50 ± 0.14	12 ± 0.05
KM-2p	4.85 ± 0.05	–	–	–	–	–
KM-2p–HZO	4.88 ± 0.08	6.33 ± 0.27	8.83 ± 0.18	11.08 ± 0.29	10.67 ± 0.39	–
HZO	–	6.03 ± 0.31	8.12 ± 0.27	10.7 ± 0.15	10.95 ± 0.36	12.47 ± 0.31

Table 3. Capacity of ion exchangers

Ion exchanger	Capacity for NaOH			Capacity for HNO_3	
	mg-equiv/g ion exchanger	mg-equiv/mmol ZrO_2^*	mg-equiv/g support*	mg-equiv/g ion exchanger	mg-equiv/mmol ZrO_2
KU-23	5.00	–	5.00	–	–
KU-23–HZO	4.50	1.03	2.00	1.40	0.57
KM-2p	7.90	–	7.90	–	–
KM-2p–HZO	7.75	1.50	5.00	1.05	0.57
HZO	2.20	0.35	–	1.00	0.14

* The cation-exchange capacity due to HZO and support was calculated from the potentiometric titration curves.

of dissociation of this group are similar. The concentration constants of dissociation of ion exchangers by the acid and base mechanisms, calculated by least-squares fitting of the titration curves are listed in Table 2; the data on ion exchanger capacities are presented in Table 3.

The difference between the cation exchange capacity of composite sorbents and the capacity caused by dissociation of functional groups (sulfo or carboxy) of the support (i.e., the capacity corresponding to the first step in the titration curve) is the cation-exchange capacity of HZO incorporated in the sorbent. It follows from Table 3, that HZO belonging to KU-23–HZO has cation exchange capacity approximately three times, and that incorporated in KM-2p–HZO, four times higher than neat HZO (recalculated to ZrO_2). The anion-exchange capacity of the inorganic part of the composite ion exchangers is about four times the capacity of granulated HZO.

The difference in the cation and anion-exchange capacities of granulated and supported HZO is probably caused by better accessibility of the latter to ions being exchanged. In granulated HZO, only Zr atoms containing free OH groups are active. They are situated on the HZO surface, including the pore surface. A substantial fraction of Zr atoms are incorporated in the three-dimensional matrix. These atoms are bound with one another by oxide and hydroxide bridges and have no free (terminal) hydroxy groups. In HZO incorporated in the ion-exchange resin granules, the fraction of such a "ballast" must be smaller, which causes its higher ion-exchange power. It should be noted that the capacity of composite ion exchangers per unit mass of the supports for the first stage of the titration curves (corresponding to dissociation of functional groups of the support) is substantially lower than the capacity of the starting cation-exchange resins. This fact suggests that, after treatment of Zr(IV)-saturated cation exchangers with an ammonia solution, not all zirconium ions undergo complete hydrolysis, and part of them remain bound to functional groups of cation exchangers, which is confirmed by the IR spectra (Fig. 2). The spectra of both KU-23–HZO in the H^+ form and the support in the H^+ form (Fig. 2a) contain a broad band at 1140–1230 cm^{-1} with three peaks assigned to antisymmetric stretching vibrations of protonated sulfo groups, whereas the bands at 1370 and 920 cm^{-1} are absent. These bands are also absent in the spectrum of the support in the NH_4^+

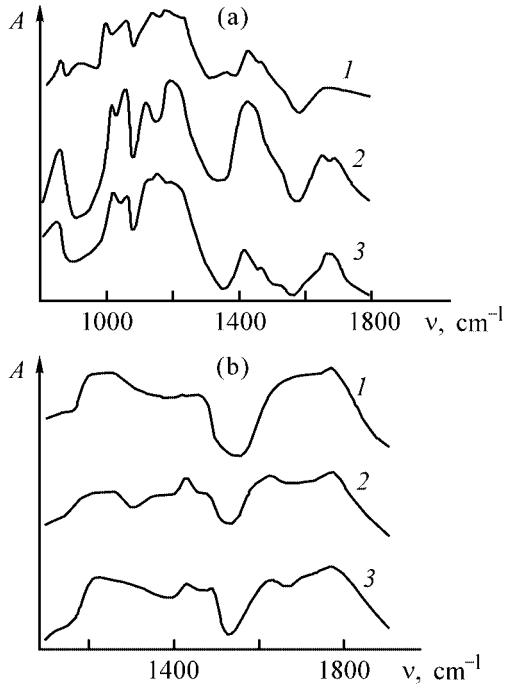

Fig. 2. IR spectra: (a) KU-23 cation exchanger in the (*1*) H^+ and (*2*) NH_4^+ form (*3*) KU-23–HZO in the H^+ form; (b) KM-2p in the (*1*) H^+ and (*2*) NH_4^+ form and (*3*) KM-2p–HZO in the H^+ form. (*A*) Absorption and (ν) wave number.

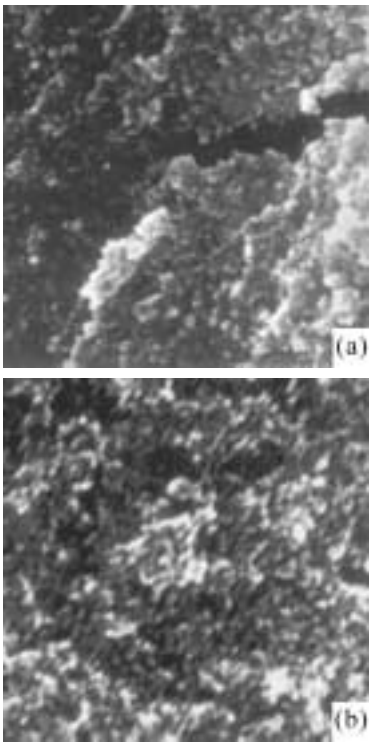

Fig. 3. Cross-sectional electron micrographs of grains for (a) KU-23 and (b) KU-23–HZO (29 wt % ZrO_2). Magnification 10 000.

form. The first of them belongs to symmetrical stretching vibrations of the S=O bond in the $–SO_3H$ group, and the second, to stretching vibrations of the S–OH bond [12]. The spectrum of KM-2p–HZO in the H^+ form (Fig. 2b) contains, along with the band at 1760 cm^{-1} belonging to stretching vibrations of the protonated –COOH group, also the bands at 1620 and 1420 cm^{-1} belonging to antisymmetric and symmetrical stretching vibrations of the carboxylate ion, respectively. This indicates that, after treatment of composite ion exchangers with HCl (conversion into the H^+ form), part of functional groups of the support remain in the ionized form, which may be caused by preservation of the bond between SO_3H or COOH groups and hydrolyzed Zr(IV). At the same time, part of functional groups of the cation exchangers can be shielded with HZO particles.

The properties of ion exchangers (e.g., sorption kinetics) are determined not only by their sorption capacity but also by the pore structure. Introduction of HZO into the granules of macroporous cation exchangers may be accompanied by transformation of the support pore structure. However, as follows from Table 4, HZO introduced into KU-23 macroporous

Table 4. Characteristics of ion exchangers pore structure

Ion exchanger	R^*_{min}	R^*_{max}	S_{sp} ($m^2\ g^{-1}$) of ion exchangers		Pore volume V, $cm^3\ g^{-1}$		
	Å		dry	swollen*	total	microporous	mesa- and macroporous
KU-23	134	312	5.0	2.5	0.154	0.014	0.14
KU-23–HZO	127	350	38.0	31.0	0.518	0.067	0.451
KM-2p	–	–	4.5	–	0.096	0.014	0.082
KM-2p–HZO	–	–	22.0	–	0.340	0.054	0.286
HZO	46	64	40.0	33.5	0.190	–	–

* Parameters of pores and specific surface area of swollen ion-exchangers as determined by SXS.

cation exchanger does not decrease the effective radius of the support pores. This shows that HZO exists in the cation exchanger as finely dispersed inclusions. The specific surface area of the combined ion exchangers, both dry and swollen, and the total pore volume are larger than those in the support, which may be due to the own porous structure of HZO inside the ion exchanger granules and to an increase in the rigidity of resins after introduction of HZO into the support (the specific volume of dry combined ion exchangers is larger, and that of swollen ion exchangers, substantially smaller than that of the supports).

The virtually equal sizes of predominant pores in KU-23 and in the composite sorbent KU-23–HZO indirectly indicates that HZO introduced into the cation exchanger granules occurs in them in the finely dispersed state. Nevertheless, it was interesting to obtain direct information on the size of HZO particles and their depth distribution in the granules by electron microscopy. Cross-sectional electron micrographs of KU-23 and KU-23–HZO grains are shown in Fig. 3. No significant differences between them are seen. Taking into consideration the magnification, we can suggest that the composite ion exchanger contains no HZO particles of size larger than 100 nm. Figure 4 shows the results of X-ray microanalysis of a cross-section of a KU-23–HZO grain in the characteristic zirconium X-ray radiation. As seen, HZO is distributed in the depth of the ion exchanger grain fairly uniformly.

We also performed experiments to assess the chemical stability of composite ion exchangers. It was found that, in 1–2 M NaOH, 6 M NH_4NO_3, 6 M NH_4NO_3 + 3 M NH_3, and dilute solutions of HNO_3 (up to 0.5 M), both unsupported HZO and supported HZO are fairly stable. To estimate the mechanical wash-out of HZO from composite ion exchangers, distilled water was pumped through a column packed with KU-23–HZO (20–30 sp. vols.) at a linear velocity of 400–500 cm min^{-1}. Then, the ion-exchanger and water passed (after evaporation and acidification to dissolve the HZO particles that could be washed out from the composite ion exchanger) were analyzed. No zirconium was detected in the filtrate. Thus, the combined ion exchangers based on cation-exchange resins and HZO are fairly stable with respect to chemical and mechanical (under conditions of strong hydrodynamic load) impacts.

CONCLUSIONS

(1) The method proposed for introduction of HZO into macroporous cation exchangers KU-23 and KM-2p allows preparation of composite ion exchangers with stable content of the mineral constituent.

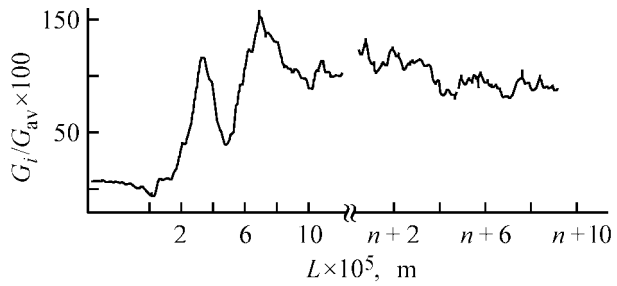

Fig. 4. Depth distribution of HZO in KU-23–HZO grains. (G_i) Running HZO concentration in the ion exchanger phase at a distance L from the grain surface of KU-23–HZO and (G_{av}) average HZO concentration in the ion exchanger phase. $L = 0 \ldots n \ldots (n + 10) \times 10^{-5}$ m.

(2) HZO is uniformly distributed throughout the depth of grains of the composite ion exchanger based on KU-23; particles of hydrated zirconium oxide with size exceeding 100 nm are absent.

(3) In the composite ion exchangers, hydrated zirconium oxide has greater ion-exchange power than neat HZO; part of functional groups of the support do not participate in the ion exchange.

ACKNOWLEDGMENTS

The authors thank V.K. Lavrent'ev and E.A. Ivanova for recording the IR and SXS spectra and V.V. Emelin for electron-microscopic study and X-ray microanalysis of ion exchangers.

REFERENCES

1. Fuller, M.J., *Chromatogr. Rev.*, 1971, no. 14, pp. 45–76.
2. Vesely, V. and Pekarek, V., *Talanta*, 1972, vol. 19, no. 3, pp. 219–262.
3. Vol'khin, V.V., Egorov, Yu.V., Belinskaya, F.A., *et al.*, *Ionnyi obmen* (Ion Exchange), Moscow: Nauka, 1981, pp. 25–44.
4. Maiorov, D.Yu., Blokhin, A.A., Taushkanov, V.P., and Solodukhin, S.S., *Poluchenie i izuchenie ionoobmennykh svoistv kompozitsionnogo sorbenta na osnove kationita KU-23 i gidratirovannogo oksida tsirkoniya* (Preparation and Study of Ion-Exchange Properties of a Composite Sorbent Based on KU-23 Cation Exchanger and Hydrated Zirconium Oxide), Available from VINITI, November 28, 1989, no. 7109-V89.
5. Maiorov, D.Yu., Blokhin, A.A., and Taushkanov, V.P., *Poluchenie i izuchenie ionoobmennykh svoistv kom-*

pozitsionnykh ionitov na osnove gidratirovannogo oksida tsirkoniya i kationitov KM-2p i KMD (Preparation and Study of Ion-Exchange Properties of Composite Ion Exchangers Based on Hydrated Zirconium Oxide and Cation Exchangers KM-2p and KMD), Available from VINITI, March 29, 1990, no. 1495-V90.

6. Marhol, M., *Ion Exchangers in Analytical Chemistry. Their Properties and Use in Inorganic Chemistry*, Prague: Academia, 1982.
7. Plavnik, G.M., *Kristallografiya*, 1985, vol. 30, no. 6, pp. 1064–1071.
8. Glatter, O. and Kratky, O., *Small-Angle X-ray Scattering*, New York: Academic, 1982.
9. Kuyapova, N.E. and Karnaukhov, A.G., *Opredelenie udel'noi poverkhnosti poroshkov metodom teplovoi desorbtsii gazov* (Determination of Specific Surface Area of Powders by Thermal Desorption of Gases), Novosibirsk: Inst. Kataliza, 1968.
10. Lyustgarten, E.I., Li, V.P., Pashkov, A.B., *et al.*, *Plast. Massy*, 1964, no. 5, pp. 79.
11. Elinson, S.V. and Petrov, K.I., *Tsirkonii, khimicheskie i fizicheskie metody analiza* (Zirconium, Chemical and Physical Methods of Analysis), Moscow: Khimiya, 1960.
12. Bellamy, L.J., *Advances in Infrared Group Frequencies*, London: Methuen, 1968.

Russian Journal of Applied Chemistry, Vol. 75, No. 12, 2002, pp. 1945–1950. Translated from Zhurnal Prikladnoi Khimii, Vol. 75, No. 12, 2002, pp. 1982–1987.
Original Russian Text Copyright © 2002 by Blokhin, Maiorov, Kopyrin, Taushkanov.

SORPTION AND ION-EXCHANGE PROCESSES

Purification of Ammonium Molybdate and Tungstate Aqueous Solutions To Remove Phosphate, Arsenate, and Silicate Anions with a Composite Sorbent Based on KU-23 and KM-2p Cation Exchangers

A. A. Blokhin, D. Yu. Maiorov, A. A. Kopyrin, and V. P. Taushkanov

St. Petersburg State Technological Institute, St. Petersburg, Russia

Received May 23, 2002

Abstract—Selectivity sorption of phosphate, arsenate, and silicate anionic impurities from concentrated aqueous solutions of ammonium molybdate and tungstate by a composite sorbent consisting of macroporous KU-23 (or KM-2p) cation exchanger and hydrated zirconium oxide was studied.

It is known that phosphorus, arsenic, and silicon impurities deteriorate the properties of metallic molybdenum and tungsten [1–3]. These anionic impurities are distributed nonuniformly in the bulk of molybdenum and tungsten in the form of phosphide and silicide inclusions giving rise to structural strains increasing the brittleness of these refractory metals [2, 3].

Ammonium molybdate (AM) and tungstate (AT) used as starting compounds in production of metallic molybdenum and tungsten are recovered from weakly alkaline solutions. These solutions contain phosphorus, arsenic, and silicon impurities in the form of phosphate (HPO_4^{2-}), arsenate ($HAsO_4^{2-}$), and mononuclear and polymeric silicate anions [4]. One of the most efficient processes for purification of AM and AT solutions to remove phosphate, arsenate, and silicate impurities is based on treatment of solutions with hydrated multicharged metal oxides (HOs). There are two variations of this process. In the first of these, the impurities are coprecipitated and sorbed on HOs in the course of formation of these oxides [5–7]. In the second, the impurities are sorbed on a column packed with granulated HOs. The second version ensures more efficient purification of the solution to remove impurities because, in passing through a sorption column, the solution repeatedly contacts the sorbent. It has been reported previously that hydrated zirconium oxide (HZO), being one of the most efficient metal oxide ion exchangers, can be used as a component of a composite sorbent based on macroporous resin [8–10]. Certain properties of such composite sorbents and procedures for their preparation have been reported.

This study is concerned with purification of AM and AT aqueous solutions to remove phosphate, arsenate, and silicate impurities with a composite sorbent consisting of KU-23 (or KM-2p) cation exchanger and HZO.

EXPERIMENTAL

The composite sorbents and neat hydrated zirconium oxide were prepared by procedures reported in [8–10]. In sorption experiments, we used KU-23–HZO and KM-2p–HZO composite sorbents. The first of these consists of KU-23 cation exchanger and ZrO_2 (29.0 %) and the second, of KM-2p cation exchanger and ZrO_2 (22.5%). Granulated Fe(III) hydroxide (HIO) being the most available ion exchanger of the metal hydroxide type, and composite KU-23–HIO sorbent, consisting of KU-23 cation exchanger and Fe_2O_3 (13.5%), were also tested. Sorption was studied under both static and dynamic conditions. The ratio of the sorbent weight (g) to solution volume (ml) in static experiments was 1 : 1000. The contact time was 5–7 days. In dynamic experiments, the sorbents were fractionated and then packed in columns. The grain size of the air-dried composite sorbent and granulated zirconium and iron oxides was in the range 0.5–1 and 0.32–0.5 mm, respectively. These sorbents were loaded into identical fluoroplastic columns 10 mm in diam-

1070-4272/02/7512-1945 $27.00 © 2002 MAIK "Nauka/Interperiodica"

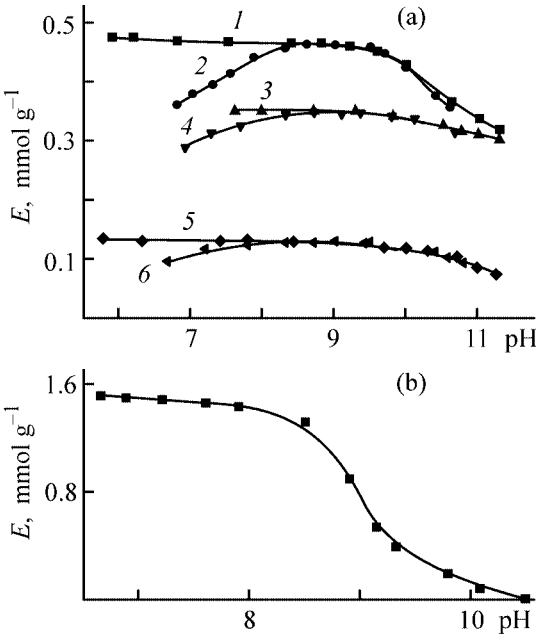

Fig. 1. (a) Sorption capacity E of KU-23–HZO for (*1*, *2*) phosphate, (*3*, *4*) silicate, (*5*, *6*) arsenate from (*1*, *3*, *5*) 2 M NH_4NO_3 and (*2*, *4*, *6*) 1M $(NH_4)_2MoO_4$ on KU-23–HZO vs. pH and (b) sorption E of molybenum(VI) from 1 M $(NH_4)_2MoO_4$ vs. pH. Initial concentration (mM): HPO_4^{2-} 4.8, $HSiO_4^{3-}$ 3.6, and $HAsO_4^{2-}$ 1.3.

eter. The cation exchanger bed height was 150 mm (ratio of the bed height to the column inner diameter $H : D = 15 : 1$). Molybdate and tungstate-containing solutions were passed through a column at a rate of one column volume per hour. Molybdenum(VI) and tungsten(VI) were determined gravimetrically or photocolorimetrically, depending on their content in solutions. Silicon(IV) and arsenic(V) were determined photocolorimetrically [11, 12]. pH was measured on an I-120 ionometer equipped with ESL-47-07 glass and EVP-AM-3 silver chloride electrodes. Phosphate anions were labeled with ^{32}P, and the specific β-activity of the isotope was measured on a KRK-1-01A setup equipped with a BDIB-01-1 counter and a PSO2-4 scaler.

It is known that hydrated zirconium and iron oxides exhibit high sorption power with respect to phosphate, arsenate, and silicate anions, which is due to formation of poorly soluble compounds in interaction of these anions with multicharged cations of the hydrated oxides [13–15]. At the same time, it is known that HOs efficiently sorb molybdate and tungstate anions [14, 15], which, present in solutions in microscopic amount, must interfere with their purification to remove phosphate, arsenate, and silicate anions. The state of molybdenum(VI) and tungsten(VI) in solutions, their affinity for ion-exchange resines, and, consequently, the extent to which anionic impurities affect sorption depend on the solution acidity. Solution acidity can also affect the anion-exchange sorption of the anionic impurities on HOs exhibiting weakly basic anion-exchange features. The state of phosphate, arsenate, and silicate impuritiesthemselves can also be influenced by acidity. Ammonium tungstate solutions are stable only at pH ≥ 9.6–9.7. In adjusting acidity of these solutions, pH must be not lower than these values but lower than ~10.5. Ammonium molybdate solutions are stable within a wider pH range. We studied the influence of pH on sorption of phosphate, arsenate, and silicate anions from AM solutions on composite sorbents containing HZO and HIO. To elucidate how anions of a macrocomponent affect the sorption of anionic impurities under consideration, we studied their sorption on HOs in the presence of NH_4NO_3 (2 M) at different pH. Ammonium nitrate was used in these experiments because nitrate anions are sorbed on HOs by the anion-exchange mechanism only.

Figure 1a shows typical patterns of sorption of the anionic impurities on the KU-23–HZO sorbent as influenced by pH. The pH dependence of sorption of these anions on other composite ion exchangers and also on neat HZO and HIO sorbents was found to be identical. These data show that phosphate, arsenate, and silicate anions are fairly well sorbed from AM solutions on KU-23–HZO within a wide pH range. The maximum sorption of these anions is reached at pH ~8.5–9.5. At higher and lower pH, their sorption on KU-23–HZO decreases.

We found that, in sorption on hydrated oxide sorbents of anionic impurities from solutions having the same ionic strength but free of molybdate ions, the pH dependence is different. In sorption of phosphate and arsenate anions from NH_4NO_3 solutions at pH (5.5–6.0)–9.5 and silicate anions within the pH range 7.5–9.5, sorption of these anionic impurities remains approximately constant or slightly decreases with increasing pH. At pH > 9.5, the decrease in sorption is more noticeable. Figure 1a shows that the right-hand parts of the sorption curves related to the similar anions and sorbents are identical, irrespective of the macrocomponent nature.

The decrease in sorption of the anionic impurities on KU-23–HZO, KM-2p–HZO, HZO, KU-23–HIO, and HIO with increasing pH is quite expected. This trend is caused by the fact that the sorbents used in our experiments are weakly basic anion exchangers whose sorption power decreases with increasing content of hydroxide ions in the solutions. Potentiometric titration of ion exchangers based on metal oxides shows [10] that they lose their capability to sorb an-

ions (e.g., nitrate anions) by the ion-exchange mechanism already at pH > 5. The high sorbability of phosphate, arsenate, and silicate anions on HOs from neutral and weakly alkaline solutions is consistent with the well-known fact that sorbents of this type exhibit high sorption power for multicharged anions. The noticeable decrease in sorption is only observed at pH > 9.5–10. The difference between the *E*-vs.-pH plots for anionic impurities in the presence and absence of molybdate anions at moderate pH is caused by sorption of molybdate ions on HOs (Fig. 1b). Hydrated metal oxides strongly sorb polymolybdate anions. In a 1 M molybdenum(VI) solution, the $Mo_7O_{24}^{6-}$ polymeric species are formed at pH < 7.5. It is possible that, in the bulk of the sorbents, these polymerized species are even formed at a lower acidity. With increasing pH, the fraction of $Mo_7O_{24}^{6-}$ species decreases, and, therefore, the sorption of molybdenum on the metal oxide sorbents decreases too. As a result, the sorption of phosphate, arsenate, and silicate anions grows with increasing pH, until the concentration of hydroxide anions becomes so high that they begin to displace anionic impurities from the sorbent.

Thus, in purification of AM solutions to remove anionic impurities with HZO- and HIO-containing composite sorbents, pH should be maintained within the range 8.5–9.5. Under these conditions, the sorption of anionic impurities changes only slightly in the presence of molybdenum(VI). This is demonstrated in Fig. 2 for the example of sorption of phosphate anions. Figure 2 shows that, in the presence of ammonium tungstate, which is stable at higher pH, sorption of phosphate decreases to a greater extent. With the AM concentration increasing from 0.1 to 2 M, sorption of phosphate anions decreases by 10–15%, and with the tungstate concentration increasing from 0.1 to 1M, sorption of phosphate anions decreases by 25–40%.

It was of interest to compare the sorption power of the composite sorbents and neat hydrated metal oxides contained in them. For this purpose, we obtained sorption isotherms of the anionic impurities on sorbents of both types (Fig. 3). These isotherms were constructed in the form of a plot of the sorption capacity *E* (mmol of anionic impurity/1 ml of sorbent) against the anionic impurity concentration in the solution (mM). The sorption capacity for anionic impurities was expressed in mmol/ml because this scale is the most frequently used in practice. Figure 3 shows that all of the sorbents tested, both composite and neat HZO and HIO, efficiently sorb phosphate, arsenate, and silicate impurities from concentrated solutions of ammonium molybdate and tungstate. The HZO-containing composite sorbents exhibit higher sorption power for anionic impurities than HIO-containing composite sorbents. Furthermore, the sorption capacity of HZO-containing composite sorbent for anionic impurities exceeds that of neat HZO in the whole range of equilibrium concentrations. The sorption power of neat HIO for the impurities is somewhat higher than that of KU-23–HZO composite ion exchanger. These data are consistent with the results on potentiometric titration of ion exchangers under consideration [10], which showed that HZO distributed throughout the bulk of macroporous cation exchangers has higher sorption power than neat HZO.

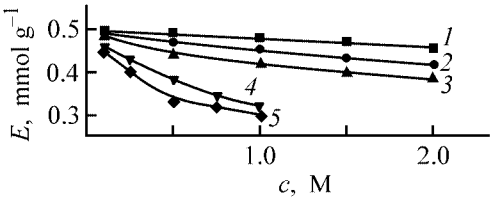

Fig. 2. Sorption capacity *E* for phosphate anions of (*1*, *4*) KU-23–HZO, (*2*) KM-2p–HZO, and (*3*, *5*) HZO vs. (*1*–*3*) the $(NH_4)_2MoO_4$ concentration in the solutions (*c*) at pH 8.7 ± 0.1 and (*4*, *5*) $(NH_4)_2WO_4$ concentration (*c*) at pH 9.7 ± 0.1.

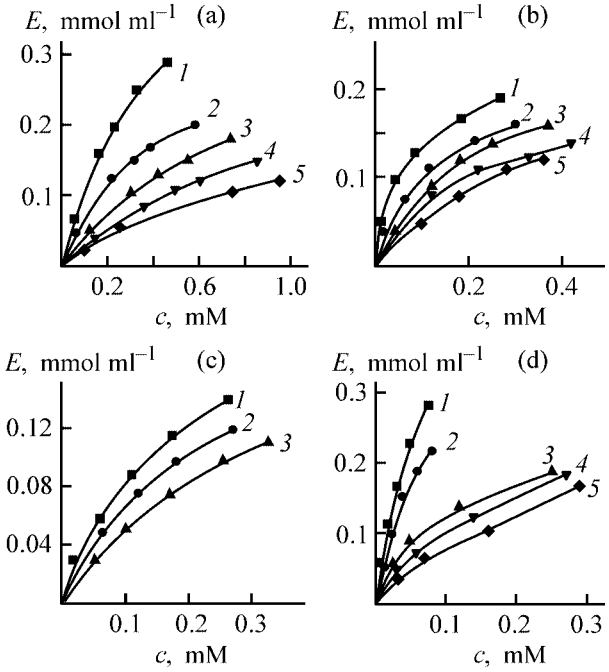

Fig. 3. Sorption isotherms of (a, b) phosphate, (c) arsenate, and (d) silicate anions (a, c, d) from 1.4 M $(NH_4)_2MoO_4$ at pH 8.9 ± 0.1 and (b) 0.7 M $(NH_4)_2WO_4$ at pH 9.7 ± 0.1 on (*1*) KU-23–HZO, (*2*) KM-2p–HZO, (*3*) granulated HZO, (*4*) HIO, and (*5*) KU-23–HIO sorbents. (*E*) Sorption capacity and (*c*) content of anionic impurities.

Purification of AM and AT solutions to remove anionic impurities under dynamic conditions

Ion exchanger	Anionic impurity	c^*, mg l^{-1}	K_{pur}^{**}	Sorption capacity, mg ml^{-1}	
				before breakthrough	total
$(NH_4)_2MoO_4$ solution					
HZO	HPO_4^{2-}	2.5	60	5.4	12.9
	$HAsO_4^{2-}$	2.5	40	3.2	7.0
	$HSiO_4^{3-}$	2.0	75	5.9	11.9
KM-2p–HZO	HPO_4^{2-}	1.5	100	12.3	16.8
	$HAsO_4^{2-}$	1.0	70	7.1	8.6
	$HSiO_4^{3-}$	1.5	100	12.9	20.8
KU-23–HZO	HPO_4^{2-}	1.5	100	13.8	17.6
	$HAsO_4^{2-}$	1.0	100	8.2	9.7
	$HSiO_4^{3-}$	1.5	100	13.0	15.6
HIO	HPO_4^{2-}	3.0	50	1.9	4.9
	$HSiO_4^{3-}$	2.0	75	2.1	4.4
KU-23–HIO	HPO_4^{2-}	2.0	75	2.4	4.1
	$HSiO_4^{3-}$	2.0	75	2.7	4.7
$(NH_4)WO_4$ solution					
HZO	HPO_4^{2-}	6.0	25	2.1	6.8
	$HSiO_4^{3-}$	3.0	50	2.8	8.1
KM-2p–HZO	HPO_4^{2-}	3.0	50	4.5	6.9
	$HSiO_4^{3-}$	3.0	50	6.3	9.2
KU-23–HZO	HPO_4^{2-}	3.0	50	4.8	7.5
	$HSiO_4^{3-}$	3.0	50	6.6	9.6

* (c) Content of anionic impurity in the eluate.

** (K_{pur}) Purification factor (ratio of the anionic impurity content in the initial solution to that in eluate).

In cotrast to zirconium hydroxide contained in the composite sorbents, zirconium atoms in a matrix of granulated HZO lack free hydroxide groups capable of exchanging anions or cations. We could expect that, with increasing surface area of granulated HZO, the number of its active sorbing sites and, hence, its sorption capacity must increase. Indeed, we found that, with the average HZO grain diameter decreasing from 0.75 to 0.1 mm, the sorption capacity of phosphate anions increases by a factor of 2.5. In these experiments, the sorbent was allowed to stand in a phosphate-containing solution for a long time (24 h) to exclude the kinetic effect on sorption. It was found that, for KU-23–HZO mesoporous composite sorbent in which HZO is uniformly distributed over the surface of cation exchanger pores, variation in the grain size and the corresponding variation in the surface area do not affect the sorption power.

The equilibrium sorption of phosphate impurities from 1 M AM and 2 M NH_4NO_3 on HZO, KU-23–HZO, and KM-2p–HZO was studied within the temperature range 0–60°C. We found that, with increasing temperature, the sorption of phosphate anions from both AM and NH_4NO_3 solutions becomes more pronounced, irrespective of the type of competing macrocomponent anions. The strengthening of sorption with increasing temperature shows that heat is consumed in this process, i.e., the enthalpy increases in sorption of phosphate. Therefore, the observed increase in sorption is due to the entropy factor.

We found that the sorption power of HZO-containing composite sorbent exceeds that of neat granulated HZO, irrespective of whether the sorption power of the composite sorbent is recalculated to zirconium oxide contained in the sorbent or to the total weight or volume of the composite sorbent. This experimental fact is somewhat unexpected if we take into account that the limiting cation and anion-exchange sorption capacity of zirconium oxide used in our experiments was typical of sorbents of this type [13–15]. Of course, we do not rule out the possibility that HZO used by us had lower sorption power than, e.g., the best sorbents of this type prepared by the sol–gel technique. However, we believe that this difference is mainly due to better kinetic characteristics of sorption on the composite sorbents as compared to granulated HZO, ensured by the developed porous structure of the cation-exchange matrix. This assumption is completely confirmed by the data on sorption kinetics of phosphate and arsenate anions from $(NH_4)_2MoO_4$ and NH_4NO_3 solutions, reported in [16]. The effective diffusion coefficients of anions in their sorption on HZO-containing composite sorbent are, on the average, an order of magnitude higher than those of neat HZO, and the corresponding activation energy of diffusion is lower by approximately a factor of 2 [16].

To quantitatively characterize the efficiency of purification of AM and AT solutions to remove anionic impurities with the composite sorbents (degree of purification, solution volume passed through a column till breakthrough of impurities, sorption capacity for impurities by the instant of breakthrough), the process should be studied in dynamic experiments. In these experiments, we used AM [c_{Mo} = 144 g l^{-1} (1.5 M); pH 8.7] and AT [c_{WO_3} = 174 g l^{-1} (0.75 M); pH 9.8] solutions prepared from ammonium para-

molybdate and tungstic acid of chemically pure grade, respectively. Anionic impurities were introduced into these solutions in the form of sodium silicate, disodium hydrogen phosphate, and disodium hydrogen arsenate in the following concentrations (mg l^{-1}): silicon and phosphorus 150, and arsenic 100. These anionic impurities were desorbed from the column with 2 M NaOH. The results of the desorption experiments are listed in the table and shown in Fig. 4. It is seen that the HZO- and HIO-containing composite sorbents, in spite of their larger grain size, sorb the anionic impurities more efficiently than neat granulated HZO and HIO and surpass the latter in the degree of purification, sorption capacity for impurities by the instant of breakthrough, total sorption capacity of anionic impurities under dynamic conditions, and easiness of desorption in sorbent regeneration. The reason for these advantages of the composite sorbents is their better kinetics features. We found that, on passing concentrated AM and AT solutions through a column packed with the composite sorbent, the content of anionic impurities in the eluate decreases by a factor of 50–100. Similarly to sorption of anionic impurities under static conditions, the HZO-containing composite sorbents exhibit better sorption characteristics in sorption under dynamic conditions than those containing HIO. The best purification of AT and AM solutions to remove anionic impurities was achieved with KU-23–HZO. This sorbent also surpasses the other sorbents in their sorption capacity for anionic impurities by the instant of breakthrough and in their total sorption capacity. The KM-2p–HZO sorbent is only slightly inferior to KU-23–HZO.

The possibility of reusing KU-23–HZO sorbent in the sorption-desorption cycles was studied by us in recovery of phosphate anions from AM solutions. The phosphate anions were desorbed with 2 M NaOH. The sodium anions were washed off from the sorbent with 2.5 M NH_4NO_3. We found that, after five sorption-desorption cycles, the purification factor and the sorption capacity for phosphate remained virtually unchanged.

KU-23–HZO and KU-23–HIO composite sorbents were successfully tested in large-scale laboratory experiments on purification of an AT-containing process solution to remove arsenic(V) impurities.[1]

KU-23–HZO was used in combination with ANKB-35 ampholyte and AN-106 anion exchanger for integrated purification of AM solutions to remove anionic impurities in preparation of several batches

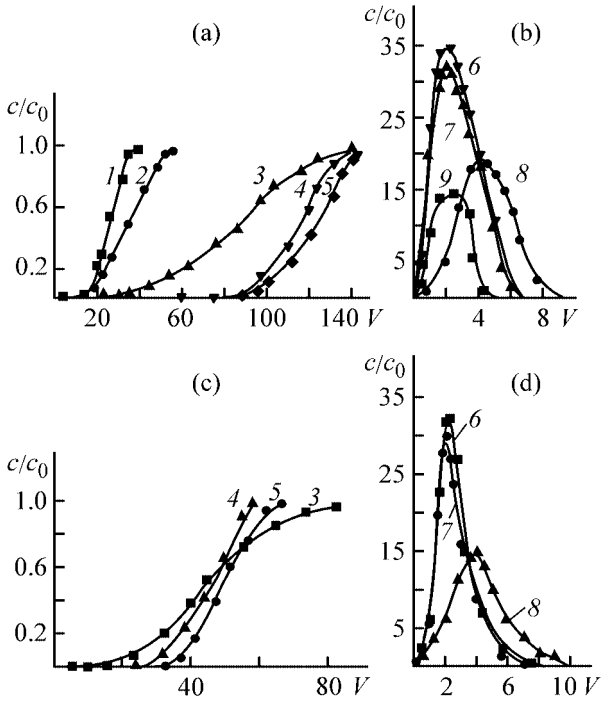

Fig. 4. Output sorption curves of phosphate anions from (a) 1.5 M $(NH_4)_2MoO_4$ and (c) 0.75 M $(NH)_4WO_4$ on (*1*) KU-23–HIO, (*2*) HIO, (*3*) HZO, (*4*) KM-2p–HZO, and (*5*) KU-23–HZO; output desorption curves of phosphate anions sorbed from (b) $(NH_4)_2MoO_4$ and (d) $(NH_4)WO_4$ solutions on (*6*) KU-23–HZO, (*7*) KM-2p–HZO, (*8*) HZO, and (*9*) KU-23–HIO. (c/c_0) ratio of phosphate anion concentration in the initial solution and eluate; (*V*) number of column volumes.

of high-purity ammonium paramolybdate. The silicon and arsenic content (phosphorus was not determined) in two batches of single-crystal molybdenum prepared from high-purity ammonium paramolybdate was less than 3×10^{-5} and 1×10^{-5} wt %, respectively, which is lower than their detection limits by mass spectrometry.[2]

CONCLUSION

Composite sorbents consisting of KU-23 or KU-2p cation exchanger and zirconium or iron hydrated oxide exhibit high selectivity with respect to phosphate, arsenate, and silicate anions in their sorption from concentrated ammonium molybdate and ammonium

[1] The tests were carried out at Uzbek combine for production of refractory and heat-resistant metals.

[2] Single-crystal molybdenum samples were prepared by G.L. Klimenko (Institute for Technological Problems of Microelectronics and Ultrapure Materials, Russian Academy of Sciences, Chernogolovka, Moscow oblast, Russia). Their mass-spectrometric analysis was carried out at the same institute.

tungstate aqueous solutions. These sorbents ensure purification of molybdate and tungstate to remove anionic impurities with purification factor of 50–100.

REFERENCES

1. Petrdlik, M., *Necistoty a Primesi ve Spekanych Kovech, in Pokroky Praskove Metalurgie*, no. 2, Praha: VUPM, 1966, pp. 1–77.
2. Devyatykh, G.G. and Burkhanov, G.S., *Vysokochistye tugoplavkie i redkie metally* (High Putity Refractory and Less-Common Metals), Moscow: Nauka, 1993.
3. Burkhanov, G.S., Vlasov, I.V., Kirillova, V.M., and Savitskii, E.M., *Izv. Akad. Nauk SSSR, Neorg. Mater.*, 1985, vol. 21, no. 8, pp. 1348–1351.
4. Myshlyaeva, L.V. and Krasnoshchekov, V.V., *Analiticheskaya khimiya kremniya* (Analytical Chemistry of Silicon), Moscow: Nauka, 1972.
5. Kunaev, A.M., Nerezov, V.M., and Dadabaev, A.Yu., *Novye protsessy v gidrometallurgii molibdena, vol'frama i reniya* (New Processes in Hydrometallurgy of Molybdenum, Tungsten, and Rhenium), Alma-Ata: Nauka, 1985.
6. Nerezov, V.M. and Popova, T.N., *Kompl. Ispol'z. Miner. Syr'ya*, 1985, no. 2, pp. 41–43.
7. USSR Inventor's Certificate, no. 454178.
8. Maiorov, D.Yu., Blokhin, A.A., Taushkanov, V.P., and Solodukhin, S.S., *Poluchenie i izuchenie ionoobmennykh svoistv kompozitsionnogo sorbenta na osnove kationita KU-23 i gidratirovannogo oksida tsirkoniya* (Preparation and Study of Ion-Exchange Features of a Composite Sorbent Consisting of KU-23 Cation Exchanger and Hydrated Zirconium Oxide), Available from VINITI, November 28, 1989, no. 7109-V89.
9. Maiorov, D.Yu., Blokhin, A.A., and Taushkanov, V.P., *Poluchenie i izuchenie ionoobmennykh svoistv kompozitsionnykh ionitov na osnove gidratirovannogo oksida tsirkoniya i kationitov KM-2p i KMD* (Preparation and Study of Ion-Exchange Features of Composite Ion Exchanger Consisting of Hydrated Zirconium Oxide and KM-2p and KMD Cation Exchangers). Available from VINITI, March 20, 1990, no. 1495-V90.
10. Blokhin, A.A., Maiorov, D.Yu., Kopyrin, A.A., and Taushkanov, V.P., *Zh. Prikl. Khim.*, 2002, vol. 75, no. 12, pp. 1976–1981.
11. Charlot, G., *Les Methods de la Chemie Analytique. Analyse quantitative Minerale*, Quatrieme Edition, Paris: Masson, 1961.
12. Busev, A.I., Tiptsova, V.G., and Ivanov, V.M., *Rukovodstvo po analiticheskoi khimii redkikh metallov* (Manual on Analytical Chemistry of Less-Common Metals), Moscow: Khimiya, 1978.
13. Fuller, M.J., *Chromatogr. Rev.*, 1971, no. 14, pp. 45–76.
14. Veseley, V. and Pekarek, V., *Talanta*, 1972, vol. 19, no. 3, pp. 219–262.
15. Vol'khin, V.V., Egorov, Yu.V., Belinskaya, F.A, *et al.*, *Ionnyi obmen* (Ion Exchange), Moscow: Nauka, 1981, pp. 25–44.
16. Maiorov, D.Yu., Blokhin, A.A., Taushkanov, V.P., and Timoshenko, K.N., *Khimiya i tekhnologiya redkikh i rasseyannykh elementov: Mezhvuzovskii sbornik nauchnykh trudov* (Chemistry and Technology of Less-Common and Trace Elements: Intercollegiate Collection of Scientific Works), Leningrad: Leningr. Technol. Inst. im. Lensoveta, 1989, pp. 164–170.

Russian Journal of Applied Chemistry, Vol. 75, No. 12, 2002, pp. 1951–1955. Translated from Zhurnal Prikladnoi Khimii, Vol. 75, No. 12, 2002, pp. 1988–1992.
Original Russian Text Copyright © 2002 by Dmitrieva, Bondaletov, Antonov, Chernov.

SORPTION AND ION-EXCHANGE PROCESSES

Adsorption of Hydrocarbons from Gas–Air Mixture on Polypropylene Stereoisomers

Z. T. Dmitrieva, V. G. Bondaletov, I. G. Antonov, and E. B. Chernov

Institute of Petrochemistry, Siberian Division, Russian Academy of Sciences, Tomsk, Russia

Received February 27, 2002

Abstract—Kinetics of absorption of a mixture of aliphatic, aromatic, and unsaturated hydrocarbons from the gas phase onto polypropylene containing 5, 18, and 40% atactic polymer in its molecular lattice was studied. The kinetic parameters, equilibrium constant, and Gibbs energy of adsorption–desorption of the hydrocarbons were determined by zero-, first-, and second-order optimization of the solution of the multiparameter equation. These parameters were correlated with the adsorbent composition and the number of sorption–desorption cycles.

To develop and improve industrial adsorption processes, new sorbents with high sorption capacity and selectivity are required. The main experimental efforts are aimed at overcome the internal diffusion hindering mass transfer in porous materials. Thermal treatment of graphite [1, 2] and silica gel [3], mechanical [4] and chemical [5, 6] deformation of internal surfaces of carbon materials, and chemical modification of silica [7, 8] were used for this purpose. The transport and functional properties of these sorbents can be changed, and adsorption and structural parameters of their surface, improved by varying duration and intensity of these treatments. The adsorption kinetics, rate of saturation of the sorption capacity, and relationship between the surface structure and the adsorption rate are of great importance for industrial processes, along with porosity (fractal dimensionality) of sorbents.

Previously we developed materials based on isotactic polypropylene with inclusions of an atactic polymer, to be used for sorption of hydrocarbons from gas–air flows. To improve the composition of the polymeric adsorbent, we studied the kinetics of cyclic adsorption and desorption of a mixture of aliphatic, aromatic, and unsaturated hydrocarbons from a gas–air mixture on the surface of polypropylene containing 5, 18, and 40 wt % atactic polymers (SP-5, SP-18, and SP-40, respectively).

EXPERIMENTAL

The adsorbents were prepared by suspension polymerization of propylene in heptane at 50–70°C in the presence of the MSC–$TiCl_3$–$Al(C_2H_5)_xCl_y$ catalytic system (MSC is a microspherical catalyst). The cocatalyst (ethylaluminum chloride) was prepared by mixing heptane solutions of AlC_3 and $Al(C_2H_5)_3$ in definite weight ratios. The polymers prepared in the presence of cocatalysts with Cl/Al weight ratio of 1.36, 1.24, and 1.18 contained 5, 18, and 40 wt %, respectively, atactic polypropylene (APP) in the molecular lattice of isotactic polypropylene (PP). As hydrocarbon mixture (HM) served a solvent used at Tomsk petrochemical plant in production of spherical catalysts for propylene polymerization. The solvent composition determined by GLC (solid phase Chromosorb P, liquid phase PFMS–4, carrier gas helium) is as follows, wt %: *n*-butane 0.03, 1-butene 0.02, 2-butene 0.01, isopentane 0.04, 1-pentene 0.01, 2-methylbutene 0.20, 2-methylpentene 0.04, 2-methylpentane 0.01, *n*-hexane 0.04, 2,2-dimethylbutane 0.38, 2-methyl-3-pentene 0.03, 2-methylhexane 8.75, 3-methylhexane 15.50, 2-hexene 1.12, cyclohexane 39.51, *n*-heptane 8.31, 2,3-dimethylhexane 1.11, heptene 0.46, benzene 19.93, *n*-octane 0.20, toluene 1.55, and *o*-xylene 2.76. Adsorption of HM from the gas–air mixture and regeneration of the adsorbent were performed on a unit consisting of a compressor, a Drechsel bottle, and a filter with continuous bed of the adsorbent. The gas–air flow was filtered through the sorbent bed. The flow rate of the gas–air flow was 6 $cm^3\ h^{-1}$. The weight of adsorbed and desorbed hydrocarbons was determined gravimetrically 15–20 min after attainment of equilibrium. Hydrocarbons adsorbed in the filter were desorbed with an air flow. The adsorption of hydrocarbons from the gas phase

1070–4272/02/7512–1951 $27.00 © 2002 MAIK "Nauka/Interperiodica"

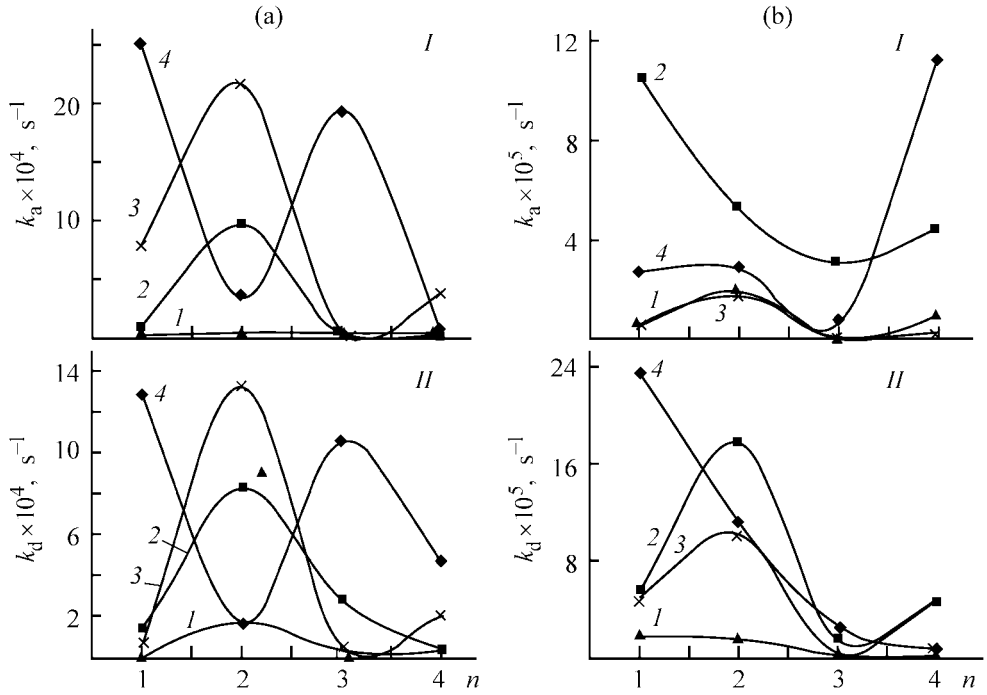

Fig. 1. Rate constants of (*I*) adsorption k_a and (*II*) desorption k_d of HM on (a) external and (b) internal surfaces of (*1*) SP-5, (*2*) SP-18, (*3*) PP, and (*4*) SP-40 adsorbents vs. the number of regeneration cycles *n*.

onto the surfaces of polypropylene (PP) and its stereoisomers (SP-5, SP-18, and SP-40) is an equilibrium nonlinear process described by the overall equation

$$\Delta m_\tau = \Delta m_1[1 - \exp(-k_1\tau)] + \Delta m_2[1 - \exp(-k_2\tau)], \quad (1)$$

where Δm_τ is the total weight of hydrocarbons adsorbed (g); Δm_1, the weight of hydrocarbons adsorbed on the external surface (sites of the first type) (g); Δm_2, the weight of hydrocarbons adsorbed on the internal surface (sites of the second type) (g); k_1, the rate constant of hydrocarbon adsorption on the external surface (s^{-1}); k_2, the rate constant of hydrocarbon adsorption on the internal surface (s^{-1}); τ, the sorption time (s) (independent variable).

Equation (1), containing five parameters, was solved by absolute optimization using OPTIM software. This method involves zero-order optimization by the Hook–Jeeves and Nelder–Mead procedures (direct calculation of the function being optimized), first-order optimization by generalized gradient procedure (calculation of the first derivative of the function being optimized), and second order optimization by the McCormick procedure (calculation of the first and second derivatives of the function being optimized) [9, 10].

The rate constants [k_a and k_d (s^{-1})], equilibrium constants (K_{eq}), and Gibbs energies (ΔG, kJ g^{-1} of sorbate) were calculated for four cycles of hydrocarbon adsorption–desorption on the external and internal surfaces of the sorbent by, respectively, Eq. (1) and the equations $K_{eq} = k_a/k_d$ and $\Delta G = -RT \ln K_{eq}$ with an accuracy of 0.1–0.3% (Fig. 1, 2).

The rate constants of sorption are close to those for a process controlled both kinetically and by diffusion, which is typical of spontaneous heterogeneous reactions. The rate constants of adsorption on the external surface are higher by 1–2 orders of magnitude than those of adsorption on the internal surface. The rate constants of equilibrium desorption from these polymer surfaces are close. The rate constants of HM desorption from the external surface of SP-18, determined in three cycles, are higher by approximately an order of magnitude than those of HM desorption from the internal surface. The total weight of hydrocarbons adsorbed in four cycles on the external polymer surface is higher than that on the internal surface. As the APP fraction in the PP structure increases, the rate constants of hydrocarbon adsorption–desorption on the external (sites of the first type) and internal (sites of the second type) surfaces grow (Figs. 1a, 1b). This behavior is the most pronounced for the sites of first type. The dependences of the rate of equilibrium sorption–desorption on both surfaces of all the

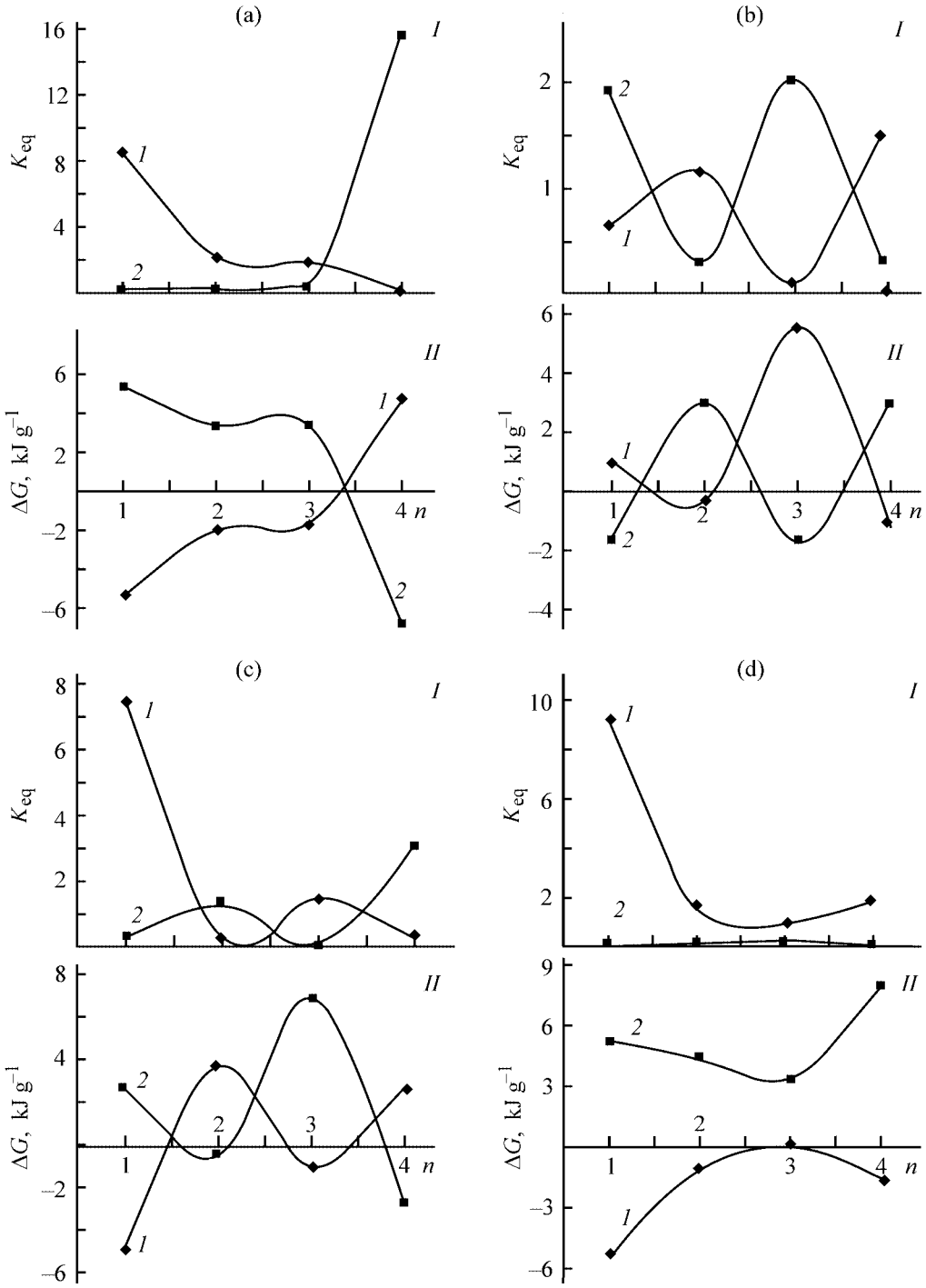

Fig. 2. (*I*) Equilibrium constants K_{eq} and (*II*) Gibbs energies ΔG of HM adsorption on (*1*) external and (*2*) internal surfaces of (a) SP-40, (b) SP-18, (c) SP-5, and (d) PP adsorbents vs. the number regeneration cycles *n*.

polymers examined on the number of the regeneration cycles pass through extrema. However, the shapes of these curves depend on the surface type and the polymer composition. The influence of the adsorbent composition and the number of sorption–desorption cycles on the sorption energy and the possibility of hydrocarbon sorption is illustrated by the dependence of the equilibrium constant and Gibbs energy of sorption, ΔG, on these parameters (Figs. 2a–2d). As seen from Fig. 2, the equilibrium constants of hydrocarbon sorption on the internal surface of SP-40 increase sharply after the third regeneration cycle and the Gibbs

Kinetic parameters of regeneration of the adsorbents at 293 K

Adsorbent	Cycle no.	Nonequilibrium desorption of hydrocarbons			
		$k_1 \times 10^5$, s^{-1}	m_1, %	$k_2 \times 10^5$, s^{-1}	m_2, %
SP-40	1	0.43	69.4	1.40	30.6
	2	0.57	68.9	1.72	31.1
	3	0.70	64.7	0.16	35.3
SP-18	1	0.22	63.1	0.53	36.9
	2	0.44	62.6	0.93	37.4
	3	0.60	57.1	1.20	42.9
SP-5	1	0.15	50.5	0.53	49.5
	2	0.34	42.9	0.58	57.1
	3	0.59	42.0	0.80	58.0
PP	1	0.16	45.0	1.0	55.0
	2	0.41	49.5	0.80	50.5
	3	0.37	52.9	0.72	47.1

energy of adsorption becomes negative. At the same time, the parameters of sorption on the external surface change in the opposite direction (Fig. 2a). As a result, sorption on the internal, rather than external (as in the case of the first, second, and third sorption desorption cycles) surface becomes more energetically favorable. The dependences of the equilibrium constants and the sign of the Gibbs energy of adsorption on both surfaces of SP-18 and SP-5 sorbents (with lower APP content) on the number of adsorption cycles show oscillatory behavior (Figs. 2b, 2c).

Such a behavior of the equilibrium constant and of the Gibbs energy of hydrocarbon adsorption on SP-18 and SP-5 is clearly due to instability of the surface structure of these polymers under sorption conditions. An unusual compensation effect is observed in cyclic adsorption on SP-18 and SP-5. Three regions with similar energy states coexist on both surfaces in the adsorbent–adsorbate system. The sorption at the intersections of the dependences of K_{eq} and ΔG on the number of regeneration cycles is hindered as if it would occur on sites the first type. Small values of $-\Delta G$ for HM sorption on SP-18 and SP-5 indicate

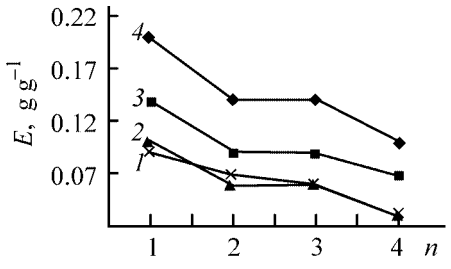

Fig. 3. Sorption capacity E of (*1*) PP, (*2*) SP-5, (*3*) SP-18, and (*4*) SP-40 vs. the number of regeneration cycles n of the adsorbent.

a negligible contribution of spontaneous adsorbent–adsorbate interactions to the sorption energy. The mechanism of HM sorption on PP differs fundamentally from that on SP-5, SP-18, and SP-40 (Fig. 2d). The energetically high absorption power of the external surface of PP remains constant in all the adsorption cycles. The structure of the PP surface, unlike that of SP-40 and especially SP-5 and CP-18, does not change during adsorption and desorption of hydrocarbons.

In contrast to the case of equilibrium adsorption of HM on PP, SP-5, SP-18, and SP-40, the dependence of the rate constants of nonequilibrium forced desorption of HM from the polymer surface on the number of desorption cycles is linear (see table). With increasing number of regeneration cycles, the kinetic parameters of equilibrium hydrocarbon adsorption on SP-18 and SP-40 (Figs. 1a, 2b) decrease and pass through extrema, whereas the rate constants of nonequilibrium forced desorption of HM from external (k_1) and internal (k_2) surfaces of these polymers increase linearly.

As the APP content in PP increases, the hydrocarbon desorption from the external surface increases, and that from the internal surface decreases. In each sorption–desorption cycle, hydrocarbon desorption from the external polymer surface decreases and that from the internal surface increases. Strongly sorbed hydrocarbons are accumulated on the internal surface (see table).

Thus, the mechanism of HM adsorption from the gas phase depends substantially on the APP content in the sorbent. Sorption of HM by polypropylene containing no APP in its molecular lattice is only enhanced on the external surface, whereas in the case of SP-5 and SP-18 the increase and decrease in sorption on external and internal surfaces alternate from cycle to cycle. In the case of SP-40, energetically favorable sorption on the external surface weakens after three cycles, whereas sorption on the internal surface strongly increases steeply in the fourth cycle. The dependence of K_{eq} and ΔG on the APP content and on the number of regeneration cycles indicates a gradual transformation of the heterogeneous process into a homogeneous process, i.e., mutual dissolution of hydrocarbons and gelatinous APP swollen in the PP structure after 3 sorption cycles on SP-40. Although HM sorption on the external PP surface is energetically favorable, the area of this surface is substantially smaller than that of the SP-40 surface. The influence of this parameter is clearly seen from the dependence of the sorption capacity (E) on the polymer composition and on the number of sorption–desorption cycles (Fig. 3). As the content of amorphous APP in the crys-

tal structure of PP increases, the sorption capacity of the adsorbent increases owing to an increase in its external surface area. The kinetic and thermodynamic parameters of equilibrium sorption of HM at 293 K on PP stereopolymers confirm the possibility of preparing adsorbents with required surface structure and surface area.

CONCLUSIONS

(1) Cyclic adsorption of a hydrocarbon mixture from the gas phase on the surface of polypropylene stereoisomers was studied. The sorption is an equilibrium and nonlinear process.

(2) To improve the sorbent composition, we determined the rate constants, equilibrium constants, and Gibbs energy of adsorption–desorption of a mixture of gaseous hydrocarbons on the external and internal surfaces of isotactic polypropylene containing 5, 18, and 40 wt % of atactic polymer in its molecular lattice.

(3) The rate constants of nonequilibrium desorption of hydrocarbons from the sorbents subjected to three equilibrium adsorption cycles were determined.

(4) The sorption capacity of the polymers for gaseous hydrocarbon increases with increasing content of the atactic polymer in polypropylene and decreases with increasing number of sorption–desorption cycles.

REFERENCES

1. Shoniya, N.K., Vlasenko, E.V., and Filatova, G.N., *Zh. Fiz. Khim.*, 1999, vol. 73, no. 12, pp. 2223–2227.
2. Yashkin, S.N., Svetlov, D.A., Kurbatov, S.V., and Buryak, A.K., *Izv. Ross. Akad. Nauk., Ser. Khim.*, 2000, no. 5, pp. 849–853.
3. Finite, I. and Bilinski, B., *J. Colloid Interface Sci.*, 1998, vol. 201, no. 2, pp. 180–185.
4. Demin, A.A. and Papukova, K.P., *Zh. Prikl. Khim.*, 2000, vol. 73, no. 5, pp. 844–846.
5. Morozova, A.A., *Zh. Fiz. Khim.*, 2000, vol. 74, no. 5, pp. 908–912.
6. Fomkin, A.A., Regent, N.I., and Sinitsyn, V.A., *Izv. Ross. Akad. Nauk, Ser. Khim.*, 2000, no. 6, pp. 1018–1021.
7. Roshchina, T.M., Shoniya, N.K., Kitaev, L.E., Gurevich, K.B., and Kaz'mina, A.A., *Zh. Fiz. Khim.*, 2000, vol. 74, no. 12, pp. 2221–2229.
8. Roshchina, T.M., Astakhov, L.A., Gurevich, K.B., and Lisichkin, G.V., *Zh. Fiz. Khim.*, 2000, vol. 74, no. 10, pp. 1839–1844.
9. Ostrovskii, G.M. and Berezhinskii, T.A., *Optimizatsiya khimiko-tekhnologicheskikh protsessov: Teoriya i praktika* (Optimization of Chemical Processes: Theory and Practice), Moscow: Khimiya, 1984.
10. Reklaitis, G.V., Rawintran, A., and Ragsdell, K.M., *Engineering Optimization. Methods and Applications*, New York: Willey, 1983.

Russian Journal of Applied Chemistry, Vol. 75, No. 12, 2002, pp. 1956–1959. Translated from Zhurnal Prikladnoi Khimii, Vol. 75, No. 12, 2002, pp. 1993–1996.
Original Russian Text Copyright © 2002 by Stavitskaya, Goba, Tsyba.

SORPTION AND ION-EXCHANGE PROCESSES

Comparison of Various Procedures for Regeneration of Activated Carbons Used for Recuperation of Ethyl Acetate

S. S. Stavitskaya, V. E. Goba, and N. N. Tsyba

Institute of Sorption and Endoecology Problems, Ukrainian National Academy of Sciences, Kiev, Ukraine

Received November 15, 2001; in final form, October 2002

Abstract—The efficiency of various procedures (chemical, thermal, and electrochemical) for regeneration of activated carbons used for recuperation of ethyl acetate was studied. For each procedure, the optimal conditions were determined for complete regeneration of the sorption capacity of activated carbons without significant structural changes. The possibility of eliminating the interfering catalytic effect of carbon in its concomitant oxidation in the course of operation, causing loss of the target product, was evaluated.

Activated carbons (ACs) are widely used for deep purification and drying of various gases and liquids, for treatment of gas mixtures to isolate individual components, and in recuperation for recovering valuable products from industrial exhaust gases and liquids. Sorbents used in continuous processes, along with high sorption capacity and selectivity with respect to the target product, should be easily regenerated. Activated carbons belong to such type of sorbents.

Due to the expanding areas of AC application [1] and short supply of carbon sorbents, their regeneration is a topical problem.

Along with high sorption capacity and mechanical strength, activated carbons used for recuperation of vapors of organic solvents (benzine, ethanol, ethyl acetate, etc.) should have low retention power.

One of the main stages in regeneration of organic solvents by ACs is recovery of the sorbed material, usually performed by steam treatment [2]; simultaneously, the pores of sorbent are cleared, i.e., the sorbent is regenerated. A recuperation installation operates in such a mode (sorption-steam treatment) during many cycles, but, in the course of time, the sorption capacity of ACs decreases, especially due to filling of the sorbent pores with impurities contained in the target product and unremovable by steam treatment. Such a spent material should be substituted with fresh sorbent or regenerated. Hence, development of procedures for treatment of the spent ACs, providing complete regeneration of their sorption capacity, is very important. Despite considerable amount of published data on this problem [3–8], development of simple and efficient procedures for regeneration of spent carbons is still urgent, because they can provide significant economy of the resources, prolong the operation life of the deficient sorbents, and decrease the amount of waste.

EXPERIMENTAL

In this study, we analyzed the physicochemical properties and structural characteristics of the initial and spent Sorbon (Austria) and AR-V (Ukraine) carbons used in recuperation of ethyl acetate (common solvent used, e.g., in production of adhesive tapes) and the possibility of regeneration of these carbons by various procedures. The efficiency of various procedures (chemical, thermal, and electrochemical) [5–9] for regeneration of activated carbons used for ethyl acetate recuperation was compared. After a large number of operation cycles, the AC sorption capacity decreases by a factor of 2.5–3, and its further operation in the sorption-steam regeneration mode, with the regeneration performed directly in an adsorber, becomes inefficient. The experimental data show that the main contaminants, which block pores and decrease the sorption capacity, are varnishes, pigments, and other high-molecular-weight compounds and some volatile products.

The following desorbing agents were used: water, 0.05–3.00 M HCl, 1.00–5.00 M H_2SO_4, 1–5% ammonia, ethanol, acetone, and various mixtures of these.

The elution regeneration was performed under static conditions on bringing a 20-g potion of activated carbon in contact with a desorbing solution (100 ml) for 24 h, with intermittent stirring. After the treatment, the solid was separated from the solution, washed

1070-4272/02/7512-1956 $27.00 © 2002 MAIK "Nauka/Interperiodica"

with water, and dried. Then, the degree of regeneration of the sorption capacity was determined by measuring the limiting sorption volume W_s for benzene and ethyl acetate vapor [2]. Under similar conditions, solutions of oxidants ($KMnO_4$ and H_2O_2 in an acid medium) for chemical breakdown of sorbed compounds were studied. We also studied the procedure for electrochemical regeneration, presented in [7], which involves treatment of spent carbon with a mixture of sulfuric acid and hydrogen peroxide (3.5 : 0.5 wt % ratio) at 80°C for 2 h at anodic current density of 40 A m^{-2}. The silver chloride reference electrode and platinum anode and cathode were used. We also performed common thermal regeneration of spent carbons in a CO_2 flow; for this purpose, AC was placed in a quartz reactor and heated to 400–900°C for 1–5 h.

The data on regeneration of the spent activated carbon of Sorbon type by various procedures are listed in Table 1. As seen, elution regeneration does not fully restore the sorption capacity of carbon. Even triple treatment with water at the room temperature is virtually inefficient. Desorption grows with increasing temperature, especially so in the case of boiling. The W_s value for C_6H_6 increases from 0.2 to 0.5 $cm^3\ g^{-1}$. The highest efficiency of carbon boiling in water, compared with steam treatment in absorbers, is probably due to stirring and to other physical factors. The sorbent pores are also cleaned after treatment with acids, alkalis, and organic solvents. These data are in agreement with the existing concepts and with published data on the properties of ACs contaminated with organic impurities. It should be noted that, in our case, no significant difference was found in regeneration performance between compounds of varied nature. In all cases, W_s for benzene and ethyl acetate are about the same. Some mixtures, especially ethanol–acetone and ethanol–acetone–ammonia, are more efficient than the individual compounds. However, in general, all the eluents studied give similar results (Table 1), and each of them can be used for regeneration of spent activated carbon. Hence, selection of an appropriate reagent is determined by local requirements taking into account the possibility of further use (utilization) of the recovered compounds and permissible amount of industrial wastes.

When there is no need in complete recovery of the sorbed compounds, oxidative degradation procedures with breakdown of these compounds and their profound oxidation may be preferable. For this purpose, we studied the effect of oxidants (hydrogen peroxide and potassium permanganate in acid media). As seen from Table 1, after such a treatment the sorption capacity of activated carbons is restored by 30–75%.

Table 1. Regeneration of Sorbon activated carbons by various procedures

Regenerating agent	W_s, $cm^3\ g^{-1}$	
	for benzene	for ethyl acetate
Carbon:		
initial	0.53	0.47
spent	0.11–0.22	0.1–0.2
Elution and chemical regeneration		
H_2O:		
20°C (triple treatment)	0.25	0.28
80°C	0.29	0.28
boiling for 3 h	0.44	0.32
HCl (0.05, 1, 2, 3 M)	0.33–0.44	0.40–0.43
H_2SO_4 (1, 2, 4 M)	0.30–0.44	0.40–0.42
$H_2SO_4 + H_2O_2$ (1 : 1, 1 : 2, 1 : 4, 2 : 1 wt %)	0.37–0.44	0.41–0.44
NH_4OH (1, 2, 3, 4, 5 wt %)	0.39–0.43	0.41–0.42
$KMnO_4$ (0.1, 0.5, 2, 6, 8, 10 wt %)	0.37–0.44	0.41–0.43
$C_2H_5OH + H_2O$ (15, 20, 40, 60, 90 wt %)	0.42–0.44	0.40–0.42
Acetone + H_2O (20, 40, 60, 80, 90 wt %)	0.39–0.43	0.40–0.42
Acetone + ethanol (1 : 1, 1 : 2, 1 : 3, 2 : 1)	0.40–0.50	0.41–0.45
Acetone + ethanol + NH_4OH (1 : 1 : 1, 1 : 1 : 2, 1 : 1 : 5)	0.40–0.50	0.41–0.45
Electrochemical regeneration		
$H_2SO_4 + H_2O_2$ + electrochemical treatment [7]	0.52–0.53	0.46–0.47
Thermal regeneration		
Treatment with CO_2 for 60 min at indicated temperature, °C:		
400	0.44	0.43
500	0.45	0.44
600	0.46	0.44
700	0.46	0.45
800	0.48	0.47
900	0.53	0.47

To increase the regeneration efficiency, combined procedures should be probably used. For example, the highest, nearly quantitative regeneration was found after treatment with hydrogen peroxide in a sulfuric acid solution, with subsequent electrochemical treatment according to the procedure given above and in [7]. The same result was attained after thermal treatment at high temperatures in a CO_2 flow, when

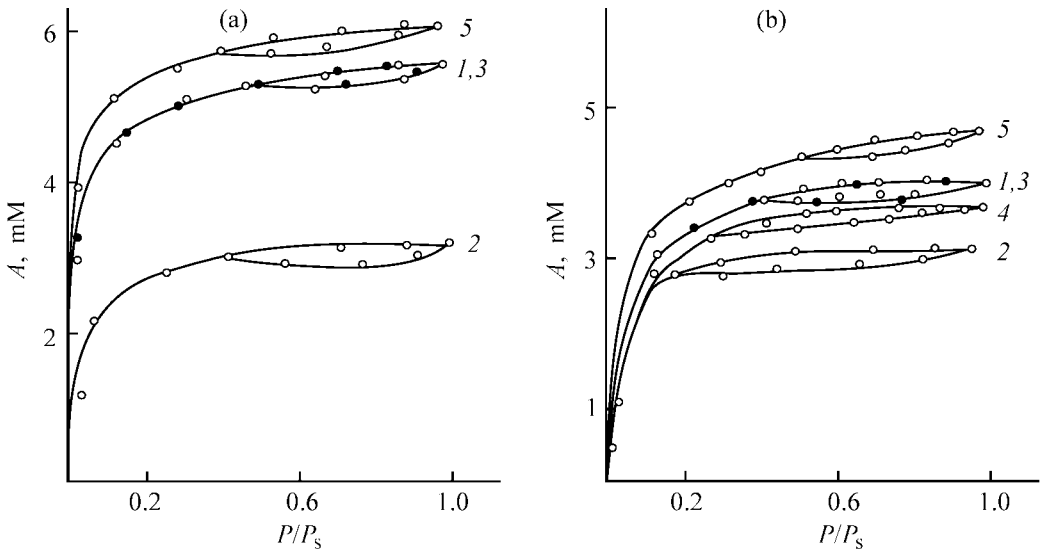

Fig. 1. Isotherms of sorption–desorption *A* of benzene on (a) Sorbon and (b) AR-V carbons: (*1*) initial carbons, (*2*) after regeneration with ethyl acetate, (*3*) after electrochemical treatment, and (*4, 5*) after thermal regeneration. (P/P_s) Relative pressure, where *P* is the equilibrium adsorbate pressure (mm Hg) and P_s is the pressure of the saturated adsorbate vapor (mm Hg). Thermal treatment conditions: (*4*) 440°C, 1 h; (*5*) 900°C, 5 h.

the sorbed compounds burned out (Table 1). We found in our experiments that the results of regeneration obtained for AR-V activated carbon are similar to those given in Table 1 for activated carbon of Sorbon type.

Using a vacuum-adsorption unit [2], we measured sorption–desorption isotherms of benzene on the initial, spent, and regenerated activated carbons to analyze possible changes in the structure of regenerated carbons (Figs. 1a, 1b). The isotherm of benzene sorption on the Sorbon activated carbon lies higher than that on AR-V carbon, indicating higher sorption capacity of this carbon, whereas the isotherms of the spent samples lie significantly lower. As seen, in some cases, the isotherms corresponding to the initial and regenerated samples are rather close, and, for high-temperature regeneration, the sorption capacity of regenerated carbons is even greater.

Comparison of the structural characteristics determined from these data (namely, total pore volume W_s, volume of micro- W_{mi} and mesopores W_{me}, and specific surface area S_{sp} [2]) shows that these values and their ratios vary only slightly, depending on the procedures and conditions of regeneration, indicating

Table 2. Structural characteristics of initial, spent, and regenerated activated carbons

Carbon	Regenerating agent	W_s	W_{mi}	W_{me}	S_{sp}, $m^2\ g^{-1}$
		$cm^3\ g^{-1}$			
Sorbon:					
initial	–	0.803	0.390	0.413	692
spent	–	0.428	0.208	0.220	182
	Steam, 120°C	0.513	0.228	0.285	253
	CO_2:				
	400°C, 5 h	0.689	0.450	0.239	478
	600°C, 0.5 h	0.561	0.347	0.214	351
	600°C, 5 h	0.824	0.319	0.505	548
	900°C, 1 h	0.888	0.519	0.369	695
	Electrochemical regeneration	0.795	0.375	0.420	678
AR-V:					
initial	–	0.481	0.261	0.220	360
spent	–	0.266	0.218	0.048	244
	Steam, 120°C	0.397	0.260	0.137	314
	CO_2:				
	400°C	0.490	0.280	0.210	367
	900°C	0.555	0.308	0.247	389

no profound structural changes (Table 2). Upon high-temperature treatment (800–900°C), the total pore volume and the volumes of micro- and mesopores slightly increase, whereas the specific surface area of activated carbons treated at these temperatures is nearly 2 times higher as compared to spent carbons. If such an increase in S_{sp} is undesirable, thermal treatment can be performed at lower temperature but for longer time (Fig. 1b; Tables 1, 2). As seen, high-temperature treatment of Sorbon and AR-V carbons at 900°C in a CO_2 atmosphere restores completely their sorption capacity. Moreover, such a treatment causes additional activation, improving the structural properties of the sorbents.

Our experimental data show that activated carbons, especially Sorbon carbon, are oxidized in prolonged operation, and the concentration of the surface acidic groups reaches 0.6–1.2 mg-equiv g^{-1}. These groups can catalyze ethyl acetate hydrolysis [10], causing its undesirable loss. To eliminate this reaction, we studied the possibilities of inhibition of the carbon sorbent oxidation. It was found [11] that preliminary treatment of the carbon surface with certain additives can strongly affect carbon oxidation. For this purpose, carbons were impregnated with solutions of magnesium or calcium sulfates of various concentrations. Then, the impregnated carbon was subjected to common oxidation with atmospheric oxygen at 400–450°C [11].[1]

It was found that unmodified carbons can be easily oxidized, i.e., become catalytically active, whereas the carbons impregnated with even insignificant amounts of calcium or magnesium salts are stable to oxidation under the similar conditions. Thus, preliminarily impregnation of activated carbon containing surface acidic groups with calcium or magnesium salts is advisable to eliminate their interfering catalytic effect in the course of ethyl acetate sorption.

[1] Selection of a procedure for regeneration of carbon sorbents strongly depends on its required performance characteristics. The cost of the installation for chemical regeneration is rather low as compared to that of thermal treatment. Certain losses in sorption capacity after chemical regeneration are outweighed by its relative simplicity. Thermal regeneration requires more complex equipment. In our opinion, electrochemical regeneration is rather efficient and promising.

CONCLUSIONS

(1) Oxidative degradation procedure for regeneration almost completely restores the sorption capacity of activated carbons used in recuperation, without significant structural changes. The resulting regenerated carbon can be used for recharging the absorbers for subsequent many-cycle operation with current steam regeneration.

(2) The experimental data obtained allow selection of most appropriate regeneration procedure for specific production.

(3) Optimal procedures of sorbent regeneration improve the performance characteristics of absorption installations, in particular, in production of adhesive tapes.

REFERENCES

1. Von Kinle, H. und Bader, E., *Aktivkohle und ihre industrielle Anwendung*, Stutgart: Enke 1980.
2. Kel'tsev, N.V., *Osnovy adsorbtsionnoi tekhniki* (Bases of Adsorption Techniques), Moscow: Khimiya, 1984.
3. Kunibe, S., *Kagaku Kodze*, 1985, vol. 19, no. 5, pp. 62–79.
4. Lukin, N.D. and Antsypovich, I.S., *Regeneratsiya adsorbentov* (Sorbent Regeneration), Leningrad: Khimiya, 1983.
5. Tarkovskaya, I.A., Tomashevskaya, A.N., Shvets, D.I., and Puzii, G.V., *Khimicheskaya, kataliticheskaya i radiatsionnaya regeneratsiya uglerodnykh sorbentov* (Chemical, Catalytic, and Radiation Regeneration of Carbon Sorbents), Chisinau: Shtiintsa, 1986.
6. Ternovoi, K.S., Puzii, G.V., Tarkovskaya, I.A., *et al.*, *Dopov. Akad. Nauk Ukr. RSR*, 1985, no. 11, pp. 76–79.
7. Tarkovskaya, I.A., Goba, V.E., Atamanyuk, V.Yu., *et al.*, *Khim. Tekhnol.*, 1991, no. 3, pp. 38–41.
8. USSR Inventor's Certificate, no. 1 528 728.
9. Slavinskii, A.S., Velikaya, L.P., Kirimova, A.M., and Baturin, G.A., *Khim. Tekhnol. Vody*, 1984, no. 6, pp. 509–511.
10. Stavitskaya, S.S., *Ukr. Khim. Zh.*, 1997, vol. 63, no. 7, pp. 27–36.
11. Tarkovskaya, I.A., *Okislennyi ugol'* (Oxidized Carbon), Kiev: Naukova Dumka, 1981.

Russian Journal of Applied Chemistry, Vol. 75, No. 12, 2002, pp. 1960–1964. Translated from Zhurnal Prikladnoi Khimii, Vol. 75, No. 12, 2002, pp. 1997–2001.
Original Russian Text Copyright © 2002 by Stavitskaya, Goba, Kartel'.

SORPTION AND ION-EXCHANGE PROCESSES

Preparation and Antimicrobial Properties of Chlorinated Carbon Materials

S. S. Stavitskaya, V. E. Goba, and N. T. Kartel'

Institute of Sorption and Endoecology Problems, Ukrainian National Academy of Sciences, Kiev, Ukraine

Received March 25, 2002

Abstract—Antimicrobial preparations based on anthracite and carbon fabric and prepared by chlorination were studied as influenced by the moisture content of sorbent, its bulk weight, chlorination temperature, etc.

Preparation of efficient antimicrobial materials based on solid sorbents, polymers, and fibrous materials is an urgent problem. Such materials can be obtained as granules, powders, pellets, plates, etc. They are especially important for local water treatment and can be used in development of new procedures for the water treatment which would be more progressive than the reagent water treatment, etc.

Materials of this kinds both bactericidal,[1] ensuring death of bacteria upon contact, and bacteriostatic, hindering growth and reproduction of bacteria, antimicrobial composites are based on cellulose and some other fibers, polymers, and activated carbons [1–3]. The antimicrobial efficiency is imparted either by impregnation of appropriate materials with active chemical preparations or by chemical modification of the preparation, introduction of appropriate functional groups, cations, or anions into the sorbent (fiber) skeleton or surface. In the latter case, stronger grafting of antimicrobial material to the support is achieved.

Various antimicrobial modifying agents (silver, copper, and mercury salts, antibiotics, heteroorganic compounds, etc.) have been studied [1]. It has been found that the antimicrobial activity is largely determined by the type of bonding between the modifying agent and support, the highest antimicrobial activity being typical of composites with ionic, labile covalent, or coordination bonding, whereas in the case of strong covalent bonding no antibacterial activity is observed.

The aim of this study was to prepare water disinfectants based on charcoal and other carbon materials (activated carbons, carbon fibers) and to evaluate their antimicrobial effectiveness. It should be noted that the antibacterial activity has been observed previously for pure activated carbons [2, 3], which is probably due to sorption of bacteria onto the developed sorbent surface. To improve the antibacterial effect, activated carbon or carbon fiber was impregnated with drugs (e.g., antibiotics) or some other appropriate compounds [2, 4]. Activated carbon with silver additives is used in the known domestic Rodnik unit for additional purification and disinfection of water, in mobile compact installations, and in special-purpose filters; activated carbons impregnated with silver and other antimicrobial additives are widely used for water treatment on airplanes and ships [2]. The possibility of preparing antimicrobial materials by chlorination of anthracite and other coals has also been studied. As known [5], chlorination is the most widely used procedure for water disinfection. The disinfection effect of chlorine is based on oxidation and breakdown of compounds in the photocytoplasm of bacteria, which causes their death. Water is often treated with gaseous chlorine or compounds containing active chlorine, e.g., chloride lime, hypochlorite, chloramine, etc. Thus, it is believed that the chlorine sorbed or grafted on the carbon surface, or possibly incorporated in the surface compounds or skeleton would also exhibit antimicrobial activity. No published data on biological (bactericidal, bacteriostatic) activity of chlorinated carbon materials could be found. At the same time,

[1] According to "Regulations concerning Protection of Surface Waters from Pollution," water in sources of potable and public water consumption must contain no pathogenic organisms, and wastewaters should be disinfected after treatment. The permissible content of Saprophyte and Escherichia coli in potable water must not exceed 100 bacteria ml^{-1} and 3 bacteria l^{-1}, respectively [GOST (State Standard) 2374–73 "Potable Water"].

1070-4272/02/7512-1960 $27.00 © 2002 MAIK "Nauka/Interperiodica"

Table 1. Preparation conditions of chlorinated carbon materials

Sample no.	Carbon sorbent	Weight gain, g g^{-1}
1	Air-dry anthracite chlorinated at room temperature	0.40
2	Anthracite preliminarily dried at 200°C for 1.5 h and chlorinated at room temperature	0.44
3	Sample no. 2 treated without air at 900°C for 20 min	Weight loss
4	Wet anthracite chlorinated at room temperature	0.37
5	Initial anthracite without chlorination	–
6	Air-dry BAU chlorinated at room temperature	0.27
7	BAU preliminarily dried at 200°C for 1 h and chlorinated at room temperature	0.37
8	Initial chlorinated anthracite (similar to sample no. 2) for dilution	0.38
	Mixture of sample no. 8 + initial anthracite in indicated ratios:	
9	3 : 1	–
10	2 : 1	–
11	1 : 1	–
	Air-dry DOU chlorinated at indicated temperature, °C:	
12	room	0.26
13	200	0.08
14	450	Weight loss
15	650	〃
16	Initial chlorinated activated anthracite for dilution	–
	Mixture of sample no. 16 + sample no. 5 in indicated ratios:	
17	1 : 2	–
18	1 : 3	–
19	Chlorinated sample no. 16 triple treated with distilled water (3 × 200 ml)	–
20	Carbon fabric chlorinated at room temperature	–

the high sorption capacity of activated carbons for chlorine is well known, and even during World War I these materials were used in respirators [2]. Moreover, it has been found [5] that the sorption capacity of carbon materials increases after their chlorination.

In our study, we analyzed for the first time activated anthracite; in our previous experiments we used charcoals commercial with varied surface nature, activated (BAU) and oxidized charcoal (DOU) [4], and AUT carbon fabric.

The chlorination was performed with gaseous chlorine obtained from a reaction of concentrated hydrochloric acid with crystalline potassium permanganate; in all the tests, 100 ml of HCl was added dropwise to 100 g of $KMnO_4$. The chlorine formed was passed through a carbon material (anthracite, charcoal, or fabric) placed in a standard vessel (column), when the experiment was performed at room temperature, or in a tubular reactor, when the experiments were performed on heating to 200–950°C with a furnace. The amount of carbon material was different for each treatment; it was determined by the reactor capacity and bulk weight of the material.

After being passed through a reactor, unchanged chlorine was fed into a vessel with ice-cooled 1 M NaOH. The amount of chlorine sorbed by the carbon material was evaluated from the difference of the concentrations of chlorine in the blank test (without carbon material) and after reaction with a weighed amount of a support. The initial concentration of chlorine was 0.62 mol l^{-1}; both weight and volume concentration of chlorine in the carbon material were estimated.

The time of chlorination varied because of the different reaction rates in each particular case; it was determined by the fact that equal amounts of chlorine were used in each experiment.

Along with chemical analysis, the increase in the coal weight after chlorination was also determined. These data were used only for tentative comparison of the results, because the increase in the material weight may be due to both sorbed chlorine and water vapor, especially when a preliminarily dried carbon material is used.

We prepared more than 20 samples of chlorinated carbons, with the type of carbon, sorbent moisture content (wet, air-dry, and dried at high temperature), and chlorination temperature (room, 200, 450, 650, and 950°C) varied. The preparation conditions of the samples are listed in Table 1.

Table 2. Sorption of chlorine, *A*, by activated anthracite and carbon fabric as influenced by experimental conditions (initial concentration of chlorine c_0 = 0.62 mol g^{-1})

Sample no.	Sample weight, g	c_{eq},* M	*A*		Sample no.	Sample weight, g	c_{eq},* M	*A*	
			mmol g^{-1}	mg g^{-1}				mmol g^{-1}	mg g^{-1}
1	62.8	0.08	8.6	305.3	13	40.9	0.02	14.7	521.8
2	60	0.1	10.1	358.6	14	41.4	0.006	14.8	525.4
4	60	0.14	9.93	352.5	15	40.5	0.004	15.2	539.9
8	64.2	0.08	9.03	320.6	20	45	0.49	2.88	102.2

* (c_{eq}) Equilibrium concentration of chlorine.

Table 3. Antimicrobial properties of chlorinated carbons

Sample no.*	Concentration of sorbed chlorine				Disinfecting effect at indicated carbon : water ratio		Chlorine smell
	mmol g^{-1}	mg g^{-1}	mmol ml^{-1}	mg ml^{-1}	50 mg : 100 ml	100 mg : 100 ml	
5	–	–	–	–	5	7	–
2	10.1	358.6	5.77	204.8	100	100	+
3	–	–	–	–	100	100	–
4	–	–	–	–	100	100	+
13	14.7	521.8	–	–	36	100	–
14	14.8	525.8	–	–	100	100	–
15	15.2	539.9	–	–	100	100	–
10	–	–	–	–	25	30	–
11	–	–	–	–	Inactive	Inactive	–
18	–	–	–	–	″	″	–
12	–	–	4.29	152.3	100	100	+
7	–	–	4.79	170.0	100	100	+
20	–	102.3	–	–	35	35	–

* Conditions of sample preparation are listed in Table 1.

The data on the sorption capacity for chlorine, recalculated to the weight and volume of the carbon material, are listed in Tables 2 and 3. As seen, sorption of chlorine is rather high, but depends strongly on the experimental conditions. The smallest sorption (102 mg g^{-1}) is observed for carbon fabric; anthracite samples exhibited high sorption capacity (*A* = 300–550 mg g^{-1}), similar results were recorded for commercial charcoals.

As seen from Table 2, the amount of sorbed chlorine increases, (from about 300 to 350 mg g^{-1}) with increasing treatment temperature, which indicates chemical interaction of chlorine with carbons, and the mechanism of such an interaction may be rather complex [6, 7]. Various processes (e.g., chemical sorption, substitution reactions, addition reactions, etc.) may proceed simultaneously; the composition of the carbon material and chemical nature of the surface can also affect the process.

Taking into account the possible use of chlorinated carbons as antimicrobial materials, we evaluated (even if approximately) the strength of chlorine binding in the samples of carbon materials prepared. For this purpose, we determined the amount of active chlorine easily removed from the surface with water (Table 4); 1-g sample was shaken with distilled water (100 ml) for 1.5 h , then the solid phase was filtered off, and the concentration of chlorine in the filtrate was determined [8]. In some cases, we used 0.1-g samples and 50-ml water portions (conditions similar to those when the antimicrobial activity was determined). It should be noted that the amount of chlorine desorbed

Table 4. Desorption of chlorine from chlorinated carbons (carbon sample m = 1 g, water portion V = 100 ml, contact time τ = 1.5 h)

Sample no.	Equilibrium concentration of chlorine after desorption c_{eq}		Sample no.	Equilibrium concentration of chlorine after desorption c_{eq}	
	mmol l^{-1}	mg ml^{-1}		mmol l^{-1}	mg ml^{-1}
2	1.52×10^{-4}	5.39	14	1.04×10^{-4}	3.69
3	4.0×10^{-5}	1.70	15	4.0×10^{-6}	0.14
4	1.42×10^{-4}	5.04	16	0.9×10^{-4}	3.20
7	0.0	0.0	16a*	1.16×10^{-4}	4.12
10	1.28×10^{-4}	4.54	17	8.00×10^{-6}	0.28
11	1.00×10^{-4}	3.55	18	2.00×10^{-6}	0.07
12	8.00×10^{-6}	0.28	20	0.0	0.0
13	1.52×10^{-4}	5.39			

* Carbon sample m = 0.1 g, V = 150 ml.

from samples of chlorinated charcoals (BAU, DOU) and carbon fabric is 10–20 times smaller compared to that in the case of chlorinated anthracite (Table 4).

Moreover, we determined in some cases the rate of chlorine desorption from the carbons (see figure); the desorption was effected by triple treatment of a sample with distilled water (3×200 ml).

Our results showed that, under such conditions, only insignificant amount of chlorine is desorbed; however, the resulting concentration of chlorine in the solution is comparable with that used in at common water treatment. Actually, the initial concentration of chlorine for efficient water disinfection is 1–10 mg l^{-1} [8], and after the reaction with bacteria and impurities, the residual concentration decreases to 0.3–0.5 mg l^{-1}.

As seen from the figure, most of weakly bound chlorine is removed after first treatment with water, and then its amount decreases fast.

We also studied mixed samples of carbon materials, in which a chlorinated sample was diluted with pure anthracite in various ratios to decrease their activity and amount of desorbed chlorine (sample nos. 10, 11, etc; Table 1), and a sample three times washed with distilled water (sample no. 19).

The antimicrobial activity was evaluated with respect to *E.coli* K12, because the coli-index (content of bacteria per liter of water) is a standard characteristic of the water quality [2, 8].[2]

Data on the antimicrobial properties of the samples studied are listed in Table 3. As seen, unmodified activated anthracite exhibits zero antimicrobial activity; a similar behavior is observed for carbon fabric. At the same time, almost all samples of chlorinated anthracite and charcoals possess strong disinfection activity. Dilution of chlorinated samples with straight anthracite decreases the recovery of available chlorine into water (Table 4) and completely eliminates antimicrobial activity (Table 3).

Correlation of the disinfection effect with the amount of the sorbed and desorbed weakly bound chlorine (Table 4) shows no direct dependence between these parameters. In our opinion, sample nos. 2, 4, 7, 12 cannot be used in practice because of the strong smell of chlorine.

Some samples, including those chlorinated at high temperatures (e.g., sample nos. 3, 15 and charcoals BAU and DOU), possess the strongest disinfection activity and liberate insignificant amount of chlorine into solution.

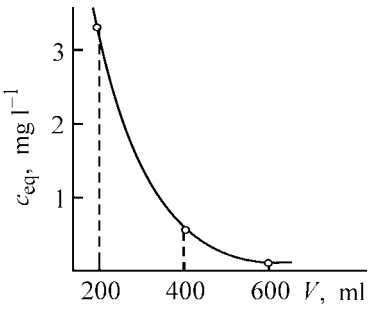

Chlorine desorption after triple treatment with water (3×200 ml) of anthracite sample no. 16; m = 15 g and τ = 15 min. (c_{eq}) Equilibrium chlorine concentration and (V) distilled water volume.

[2] These tests were performed at the Kiev Research Institute of General and Public Hygiene, Kiev, Ukraine.

CONCLUSIONS

(1) Chlorinated carbon materials are promising antimicrobial agents. Several samples with strongly bound chlorine were prepared, which possess high antimicrobial activity with respect to *E.coli* K12 (bacteria commonly used in evaluation of hygienic requirements); the amount of chlorine desorbed from these materials into water is close to that satisfying sanitary requirements to potable water (GOST 2874–54).

(2) In some cases, chlorinated anthracene and charcoals can be used to replace water treatment with gaseous chlorine, which is especially important in water treatment at remote installations; their use does not require any special equipment, the necessary concentrations can be easily obtained, etc. Some of chlorinated anthracite samples exhibit acceptable (with respect to sorption capacity, stability, energy consumption, cost, antimicrobial activity, etc.) properties.

REFERENCES

1. *Novye voloknistye sorbenty meditsinskogo naznacheniya* (New Fiber Medical-Purpose Sorbents), Ermolenko, I.N., Ed., Minsk: Nauka i Tekhnika, 1978.
2. Tarkovskaya, I.A., *Sto "professii" uglya* (A Hundred Jobs of Coal), Kiev: Naukova Dumka, 1983.
3. Von Kinle, H. and Bader, E., *Aktivkohle und ihre industrielle Anwendung*, Stutgart: Enke 1980.
4. Tarkovskaya, I.A., *Okislennyi ugol'* (Oxidized Carbon), Kiev: Naukova Dumka, 1981.
5. Hall, C.R. and Holmes, R.G., *Carbon*, 1993, vol. 31, no. 6, pp. 881–886.
6. Ermolenko, I.N., Lyubliner, T.M., and Gul'ko, N.V., *Elementoorganicheskie ugol'nye voloknistye materialy* (Heteroorganic Fibrous Carbon Materials), Minsk: Nauka i Tekhnika, 1982.
7. Ivin, V.D., Smirnov, E.P., Levit, R.M., *et al.*, *Zh. Prikl. Khim.*, 1980, vol. 53, no. 1, pp. 109–114.
8. Kul'skii, L.A., Levchenko, T.M., and Petrov, M.V., *Khimiya i mikrobiologiya vody* (Water Chemistry and Microbiology), Kiev: Vishcha Shkola, 1976.

Russian Journal of Applied Chemistry, Vol. 75, No. 12, 2002, pp. 1965–1967. Translated from Zhurnal Prikladnoi Khimii, Vol. 75, No. 12, 2002, pp. 2002–2004.
Original Russian Text Copyright © 2002 by Zarubitskii, Omel'chuk, Budnik, Melekhin.

APPLIED ELECTROCHEMISTRY AND CORROSION PROTECTION OF METALS

Cathodic Deposition of Copper–Indium Alloy from Trilonate–Tartrate Electrolyte

O. G. Zarubitskii, A. A. Omel'chuk, V. G. Budnik, and V. T. Melekhin

Vernadskii Institute of General and Inorganic Chemistry, National Academy of Sciences of Ukraine, Kiev, Ukraine

Received April 22, 2002

Abstract—The results obtained in studying the deposition of copper–indium alloys from a trilonate–tartrate electrolyte are presented. The conditions for joint discharge of copper and indium ions, the optimal composition of the electrolyte, and the electrolysis mode ensuring deposition of protective and decorative gold-colored coatings are determined.

It is known that the factors determining the possibility of joint electrochemical deposition of two metals at their certain ratio in the alloy are the following: equilibrium potentials of these metals and polarizations at discharge of the corresponding ions at the cathode from a given electrolyte, concentration ratio of ions of codeposited metals and their ability to form complex compounds, presence of surfactants in the electrolyte, overvoltage of hydrogen evolution at the alloy being deposited, electrolysis conditions (temperature, current density, stirring), etc.

The standard potentials of copper and indium (+0.337 and –0.34 V) differ to such an extent that mainly copper is deposited at the cathode from solutions of simple salts of these metals. With complex salts, e.g., trilonates or tartrates, used instead of simple salts, conditions can be chosen (modifier concentration, current density, electrolyzer potential, etc.), which ensure joint discharge of copper and indium ions.

It is known that Trilon B and potassium-sodium tartrate form with copper ions complex compounds $Na_2[CuR]$ (R is the acid residue of ethylenediaminetetraacetic acid) and $KNa[C_4O_6H_2Cu]$, whose instability constants are 1.38×10^{-19} and 7.3×10^{-20}, respectively [1]. The trilonate electrolyte enables electroplating of high-quality copper coatings. It has been established experimentally [2] that indium is mainly present in a solution of the Seignette salt, $NaK[C_4H_4O_6]$, in the form of an $In[C_4H_4O_6]^{2-}$ anion, whose instability constant is 3.2×10^{-8}.

Data on electroplating of copper, indium, and their alloys from a tartrate electrolyte were summarized in [3]. It was noted that the cathodic deposits obtained in this case contain a small amount of indium (up to 8%), have good antifriction properties, and their quality is high [3, 4].

This communication present the results obtained in studying the reduction of copper and indium ions from trilonate–tartrate electrolytes. The conditions for joint discharge of these metal ions, the optimal composition of the solution, and the electrolysis mode for electroplating of protective and decorative gold-colored coatings based on copper–indium alloys from the above complex electrolytes were determined.

EXPERIMENTAL

The reduction of copper(II) and indium(II) ions was studied by the potentiodynamic method in a YASE-1 standard electrochemical cell equipped with a magnetic stirrer. A copper plate served as the cathode. The anodes were fabricated from electrolytic copper or In-00 indium. The electrodes were polarized with a PI-50-1.1 potentiostat at 20–25°C. The potential sweep rate was 5×10^{-3} V s^{-1}. The cathode potential was recorded relative to a silver chloride reference electrode. Main components of the plating electrolyte (g l^{-1}): 32 NaOH, 25 Trilon B, 8 $CuSO_4 \cdot 5H_2O$, and 5 $In_2(SO_4)_3$. The content of the Seignette salt in the solution was varied within 0–320 g l^{-1}.

1070-4272/02/7512-1965 $27.00 © 2002 MAIK "Nauka/Interperiodica"

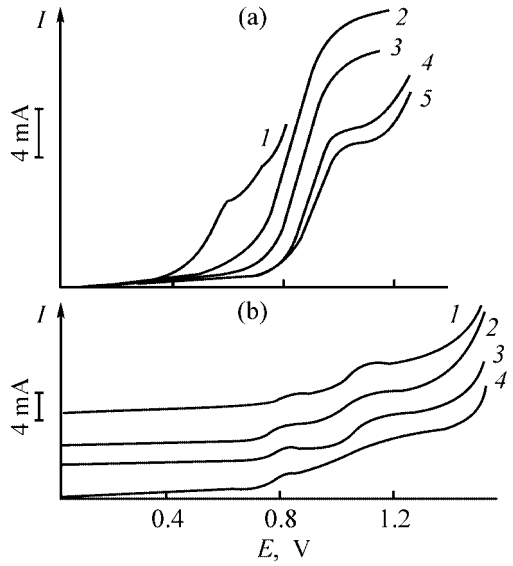

Fig. 1. Polarization curves for (a) copper and (b) indium deposition from electrolyte. (*I*) Current and (*E*) potential. $NaK[C_4H_4O_6]$ concentration (g l^{-1}): (*1*) 0.1, (*2*) 80, (*3*) 160, (*4*) 240, and (*5*) 320.

The voltammetric curves shown in Fig. 1a illustrate the cathodic reduction of copper ions. Curve *1* characterizes the discharge of trilonate complexes of this metal. A solution contained no indium sulfate and was agitated with a magnetic stirrer. It can be seen that the potential of copper reduction from the electrolyte of a given composition is 0.43 V.

Curves *2–5* in Fig. 1a were measured in a solution containing Seignette salt $NaK[C_4H_4O_6]$. It can be seen that the potential of copper reduction (0.68–0.8 V) shifts toward the electronegative region with increasing $NaK[C_4O_6H_4]$ concentration.

The polarization dependences measured in a solution containing (g l^{-1}): 5 $In_2(SO_4)_3$, 32 NaOH, 25 Trilon B, and 0–320 $NaK[C_4H_4O_6]$, are plotted in Fig. 1b. The data obtained suggest that tartrate complexes with indium(III) are less strong. The potential of indium reduction lies within 0.7–0.75 V. This range of potentials corresponds to joint deposition of copper and indium from a solution containing these metal ions and Trilon B and $NaK[C_4H_4O_6]$, simultaneously, as complexing agents.

Also, the influence of various factors on the quality of galvanic coatings was studied. The main parameter determining the color and quality of a deposit is the cathodic current density. Depending on its value, the color of the alloy deposited at the cathode varies from pinkish (at j_c = 0.05–0.2 A dm^{-2}) to golden-like (at j_c = 0.35–0.6 A dm^{-2}). Electrolysis at current densities exceeding 0.6 A dm^{-2} yielded a gray deposit turning darker in the course of time.

The anodic current density is also the important parameter of the process, which affects the deposit quality and the electrolyte efficiency. The dependence of the current efficiency by copper, η_a, on j_a is as follows:

j_a, A dm^{-2}	0.05	0.1	0.15	0.2	0.3
η_a, %	164	133.6	102	100.7	100.3
j_a, A dm^{-2}	0.4	0.5	0.6	0.8	1.0
η_a, %	100.7	42.5	7.7	1.9	0.73

At current densities in the range 0.15–0.40 A dm^{-2} the anodic current efficiency approaches 100%, which ensures stable dissolution of copper anodes. With j_a increasing further, η_a decreases drastically (to nearly zero). This indicates that, under these conditions of the electrolysis, the anode is virtually completely passivated and behaves as insoluble. At current densities lower than 0.15 A dm^{-2}, the current efficiency increases sharply. At j_a = 0.05 A dm^{-2}, η_a is as high as 164%, which points to formation of single-charged copper ions at the anode, which strongly affect the cathodic process. Galvanic coatings deposited under these conditions are matte pink, the anodes turn dark, and a red copper(I) oxide deposit is formed. According to the experimental data obtained, the optimal anodic current density is within 0.15–0.40 A dm^{-2}.

The $In_2(SO_4)_3$ concentration strongly affects the color and quality of a cathodic deposit. Under conditions of a stirred solution, the optimal $In_2(SO_4)_3$ concentration is within 2.5–5.0 g l^{-1}. Electrolysis of solutions containing more than 5 g l^{-1} of this salt yields are matte light yellow deposits. At $In_2(SO_4)_3$ concentration lower than 2.5 g l^{-1}, pinkish galvanic coatings are deposited on the cathode.

The concentration of $CuSO_4$ in the electrolyte affects the color of a cathodic deposit to a lesser extent; however, at concentrations lower than 8 g l^{-1}, the range of permissible cathodic current densities is narrowed to 0.1–0.2 A dm^{-2}, which makes the process unproductive. At $CuSO_4$ and $In_2(SO_4)_3$ concentrations higher than 12 and 3.5–5.0 g l^{-1}, respectively, the alloy deposited on the cathode has pink color.

The effect of $NaK[C_4H_4O_6]$ content in solution on joint deposition of copper–indium alloys was studied within the range 80–320 g l^{-1} of $NaK[C_4H_4O_6]$. It was found that at $NaK[C_4H_4O_6]$ concentrations lower than 100 g l^{-1}, a white deposit of basic indium salts was precipitated from the electrolyte. Raising the con-

centration of sodium-potassium tartrate to 160 g l^{-1} has no effect on the color and quality of the alloy deposited at the cathode. With the concentration of sodium-potassium tartrate increasing further, the range of current densities ensuring a prescribed coating composition and color becomes narrower.

The optimal Trilon B concentration, ensuring cathodic deposition of high-quality gold-colored coatings containing no less than 20% indium, is 25–30 g l^{-1}. Trilon B not only ensures joint discharge of indium and copper ions, but also hinders formation in the electrolyte of sparingly soluble compounds of these metals and concomitants, which appear in the course of prolonged electrolysis (e.g., as a result of exchange reactions between the support and the solution).

The NaOH concentration of 30–35 g l^{-1} leads to an electrolyte pH within 13.4–13.6 and ensures stability of indium compounds soluble in the electroyte. The pH of an electrolyte is the key parameter responsible for its stable operation and formation of a high-quality cathodic deposit.

It was found that the quality of a galvanic coating is largely dependent on the bulk current density. It was established that at a surface current density at the cathode, j_c = 0.5 A dm^{-2}, the bulk current density in a bath must not exceed 1.5–1.6 A l^{-1}. For the electrolyte to have higher electrical conductivity and throwing power, it must contain 15–30 g l^{-1} Na_2SO_4. Simultaneous introduction of glycerol (15–25 g l^{-1}) and gelatin (0.05–0.2 g l^{-1}) into the electrolyte ensures cathodic deposition of lustrous coatings.

The results of the study performed show that the optimal content of components in the electrolyte for deposition of lustrous gold-colored copper–indium alloy coatings is as follows (g l^{-1}): 8–12 $CuSO_4 \cdot 5H_2O$, 2.5–5.0 $In_2(SO_4)_3$, 100–160 $NaK[C_4H_4O_6] \cdot 4H_2O$, 25–30 Trilon B, 30–35 NaOH, 15–30 Na_2SO_4, 15–25 glycerol, and 0.05–0.2 gelatin.

Electrolysis mode: cathodic current density 0.4–0.6 A dm^{-2}, anodic current density 0.15–0.40 A dm^{-2}, temperature 20–25°C, and electrolyte pH 13.4–13.6. The electrolyte should be stirred during electroplating.

CONCLUSION

An electrolyte containing tartrate and trilonate complexes of indium and copper and ensuring formation of lustrous low-porosity gold-colored coatings strongly adherent to a carbon steel support was developed. The alloy deposited from the electrolyte contains 79–81% copper and 19–21% indium. The electrolyte is easy to prepare and stable during operation; it was tested in industrial conditions. It is recommended for deposition of protective decorative coatings.

REFERENCES

1. Yatsimirskii, K.B. and Vasil'ev, V.P., *Konstanty nestoikosti kompleksnykh soedinenii* (Instability Constants of Complex Compounds), Moscow: Akad. Nauk SSSR, 1959.
2. Savchenko, G.S. and Goncharov, E.V., *Zh. Neorg. Khim.*, 1959, vol. 4, pp. 1558–1567.
3. Bespal'ko, O.P. and Vdovenko, I.D., *Elektroosazhdenie metallov i splavov iz tartratnykh elektrolitov* (Electrodeposition of Metals and Alloys from Tartrate Electrolytes), Kiev: Naukova Dumka, 1971.
4. Bondar' V.V., Grinina, V.V., and Pavlov, V.N., *Itogi Nauki i Tekhniki. Elektrokhimiya* (Advances of Science and Technology, Electrochemistry) Moscow: VINITI, 1980, vol. 16, pp. 141–142, 155.

Russian Journal of Applied Chemistry, Vol. 75, No. 12, 2002, pp. 1968–1971. Translated from Zhurnal Prikladnoi Khimii, Vol. 75, No. 12, 2002, pp. 2005–2008.
Original Russian Text Copyright © 2002 by Nagirnyi, Apostolova, Baskevich, Shembel'.

APPLIED ELECTROCHEMISTRY AND CORROSION PROTECTION OF METALS

Anodic Deposition of Vanadium(V) Oxide from Solutions in the Presence of Nickel Ions

V. M. Nagirnyi, R. D. Apostolova, A. S. Baskevich, and E. M. Shembel'

Ukrainian State University of Chemical Engineering, Dnepropetrovsk, Ukraine

Received May 13, 2002

Abstract—The preparation conditions, properties of the deposits obtained, and the nature of anodic processes occurring in the course of electrolytic deposition of vanadium oxide in the presence of nickel ions from solutions of oxovanadium and nickel sulfates were studied.

Electrolytic deposition of vanadium(V) oxide from acid solutions (pH ~2.0) of oxovanadium sulfate and $NiSO_4$ is of interest for studying the possibility of joint anodic deposition of vanadium and nickel oxides to obtain the corresponding V–Ni oxide system. Complex vanadium–nickel oxide systems with enhanced electrochemical activity are formed by anodic deposition of vanadium oxide from solutions of oxovanadium sulfate in the presence of nickel ions [1]. It is also essential that, unlike vanadium oxide, which is deposited on the anode from oxovanadium sulfate solution with current efficiency of about 40% [2], anodic oxidation of nickel(II) under the standard conditions does not give nickel oxide by itself in quantitative yield. At the same time, such a reaction is permissible thermodynamically in accordance with the equation [3]

$$2Ni^{2+} + 3H_2O - 2e \rightarrow Ni_2O_3 + 6H^+,\ E^0 = 1.84\ V. \quad (1)$$

Therefore, it would be expected that, if anodic oxidation by reaction (1) occurs in parallel with of oxidation of oxovanadium ions

$$2VO^{2+} + 3H_2O - 2e \rightarrow V_2O_5 + 6H^+,\ E^0 = 1.84\ V, \quad (2)$$

then more favorable energy conditions can be attained, at which reaction (1) proceeds irreversibly to give the corresponding modifying phase in a mixed anodic product.

This study is concerned with the nature of the anodic processes occurring in the course of electrolytic deposition of vanadium(V) oxide in the presence of nickel ions and the conditions for preparation of anodic deposits with properties (outward appearance, surface micro- and macrostructure, compactness) and composition close to those prescribed.

As objects of study served mixed solutions of oxovanadium and nickel sulfates with total concentration of 40–45 g l^{-1} at concentration ratios (hereinafter, V : Ni) of 5 : 1, 3 : 1, 1 : 1, 1 : 3, and 1 : 5 (the first digits stand for the main component, i.e., oxovanadium sulfate, and the second, for the modifying component). The solutions were prepared from reagents of pure and analytically pure grade and distilled water. Prior to use, the solutions were subjected to additional electrolytic treatment to remove metal impurities. The electrolysis was performed in a 200-ml temperature-controlled glass cell. Deposits were obtained in the form of compact coatings on two sides of smooth plate-like $10 \times 10 \times 0.3$-mm anodes made of 12Kh18N9T steel. For X-ray structural analysis, 0.15–0.20-g dispersed deposits were obtained on a smooth plate of technical-grade titanium with $S_a : S_c$ ratio of 1 : 5. The tests were performed at 85°C and pH 1.9–2.2, which were chosen on the basis of data from [2, 4]. The efficiency of the anodic process was estimated from the deposition rate V_{dep} (mg cm^{-2} h^{-1}) and conventional current efficiency CE_{con} (%) by the anodic product, on the assumption that the whole useful current is spent for formation of V_2O_5 vanadium oxide [electrochemical equivalent 3.4 g $(A\ h^-)^1$]. This assumption is justified in this case, since nickel oxide Ni_2O_3 has nearly the same electrochemical equivalent [3.02 g $(A\ h)^{-1}$]. Despite the incorrectness of the quantity thus defined, CE_{con} shows how the anodic process varies with electrolysis conditions with better reliability. The amount of the "modifying" phase (wt %) in the anodic deposits was estimated by a simplified procedure consisting in dissolution of a deposit in a H_2O_2 solution, alkalinization with NaOH to pH 9.0, settling, and subsequent washing, drying, and weighing of the $Ni(OH)_2$ sediment formed, with

1070-4272/02/7512-1968 $27.00 © 2002 MAIK "Nauka/Interperiodica"

the result recalculated to Ni_2O_3. Polarization curves were measured in a U-shaped cell with a 12Kh18N9T steel anode (S_a = 1 cm^2, $S_a : S_c$ = 1 : 5) under the above electrolysis conditions at I_a = 0.5–50 mA cm^{-2}. The potentials were measured relative to a silver chloride reference electrode (E = +0.225 V) with a ShCh-4315 digital voltmeter and then recalculated to the hydrogen scale. The phase composition of the deposits was determined qualitatively and approximately evaluated quantitatively (for selected samples) by comparing X-ray diffraction data (DRON-2 diffractometer) with the standard case, using a calibration plot [5]. The surface microstructure and morphology of the deposits were studied on 1.5–2.5-μm-thick films, using a digital nanoscope.

Figure 1 shows the deposition rate V_{dep} and the conventional current efficiency CE_{con} (%) by the anodic product as functions of the current density in anodic deposition of vanadium oxide in the presence of nickel ions from the above solutions with varied V : Ni concentration ratio. At V : Ni ≥ 1 these dependences are characterized by a pronounced rise in the deposition rate in the range I_a = 5–10 mA cm^{-2}, a limiting plateau at higher current densities, and only slight variation of the deposition rate with the current density increasing further. The last kind of behavior is also observed at V : Ni < 1 in the V_{dep}–I_a dependences over nearly the entire range of the current densities studied. The CE_{con}–I_a dependences are characterized by a pronounced fall in the CE_{con} by the anodic product in the range I_a = 5–15 mA cm^{-2}, with its subsequent gradual decrease to a certain minimum value with increasing current density. It can be seen that the efficiency of the anodic process decreases markedly in the presence of nickel ions. Even at their relatively low concentration in solution (V : Ni = 5 : 1), V_{dep} and CE_{con} are lower by approximately a factor of 1.5 than the corresponding values for a "straight" oxovanadium sulfate solution under comparable electrolysis conditions. This points to considerable energy hindrance to the concurrent reaction (1) of nickel ion oxidation in the anodic process occurring together with reaction (2), which makes higher the rate of the simultaneous oxygen evolution. The rise in the relative concentration of nickel ions in solution is not accompanied by any pronounced increase in the rates of codeposition of the modifying component and formation of the corresponding phase in the anodic deposit. This is confirmed by the weak dependence of the deposit formation rate on current density at V : Ni < 1 and by its relatively high values at V : Ni = 1 : 1, which is possibly due to predominant vanadium oxide deposition in the entire range of current densities studied. The same conclusion follows from the dependence of the concentration of the modifying nickel oxide phase in the anodic deposit on the V : Ni ratio in solution (Fig. 2). Comparative estimate shows that, even at V : Ni = 1 : 5, the limiting content of nickel oxide in the anodic deposits does not exceed 20 wt % (in terms of Ni_2O_3). The current efficiency by the anodic product, corresponding to the above V : Ni ratio, is the lowest (2.5%), and the deposits obtained under the corresponding conditions have unstable composition and quality. Probably, this is due to disturbance of the ion balance in the near-electrode layer, caused by the increasing influence of concurrent redox reactions.

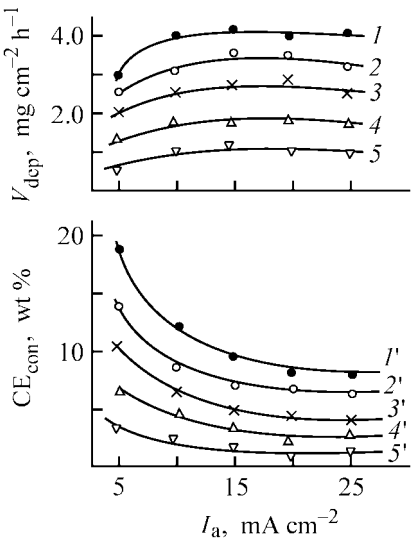

Fig. 1. Dependences of (*1*–*5*) deposition rate V_{dep} and (*1'*–*5'*) conventional current efficiency by the anodic product, CE_{con}, on the current density I_a in electrolysis of solutions of oxovanadium and nickel sulfates with total concentration of 40–45 g l^{-1}. Temperature 85°C, pH 2.0–2.2. V : Ni concentration ratio: (*1*, *1'*) 5 : 1, (*2*, *2'*) 3 : 1, (*3*, *3'*) 1 : 1, (*4*, *4'*) 1 : 3, and (*5*, *5'*) 1 : 5.

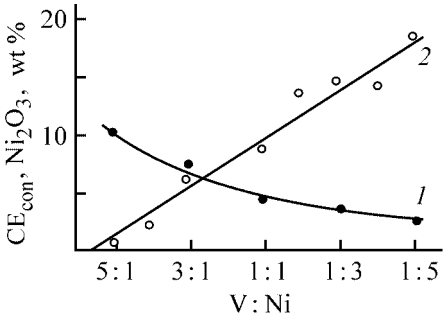

Fig. 2. Dependences of (*1*) conventional current efficiency by the anodic product, CE_{con}, and (*2*) the content of the Ni_2O_3 modifying phase in the anodic product on the ratio V : Ni of oxovanadium and nickel sulfate concentrations in electrolysis of solutions with total concentration of the sulfates of of 40–45 g l^{-1}. Temperature 85°C, pH 2.0–2.2, I_a = 10 mA cm^{-2}.

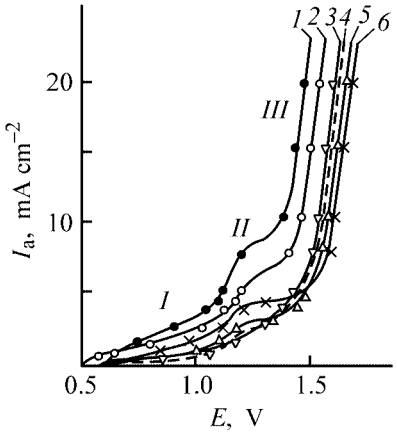

Fig. 3. I_a–E curve describing anodic deposition of vanadium oxide in the presence of nickel ions from solutions of oxovanadium and nickel sulfates. Temperature 85°C, pH 2.0, total sulfate concentration 40 g l^{-1}. V : Ni concentration ratio: (*1*) 5 : 1, (*2*) 3 : 1, (*3*) 0 : 1, (*4*) 1 : 5, (*5*) 1 : 3, and (*6*) 1 : 1.

The decrease in the rate of anodic deposit formation, occurring when the part played by the concurrent reaction (1) of nickel ion oxidation in the total anodic process becomes more pronounced, leads to higher rate of oxygen evolution, which markedly affects the kinetics of the anodic process. This is confirmed by analysis of the voltammetric I_a–E characteristics obtained for the processes studied at various V : Ni ratios in solution, whose appearance and relative positions are largely determined by the rate of jointly occurring discharge and oxygen evolution. The corresponding dependences are characterized by steplike curves with two ascending portions (*I*, *III*) and an intermediate portion (*II*) in between (Fig. 3). The only exception is curve *3* (Fig. 3) obtained in $NiSO_4$ solution, distinguished by a smooth transition from the lower gently sloping portion to the upper ascending portion. The lower portions of the curves (region *I*) are shifted with respect to one another toward more positive potentials in a sequence corresponding to increasing relative nickel ion concentration in solution. The same sequence is observed for the limiting current densities corresponding to the bends in the polarization curves (region *II*). The relative positions of the upper portions (region *III*) depends on the ratio of main component concentrations in solution (V : Ni) and corresponds to the above sequence of rise in the anodic potential at V : Ni > 1 (Fig. 3, curves *1*, *2*). At V : Ni ≤ 1 the corresponding portions of the curves are shifted toward positive potentials in the reverse order, starting from the curve describing the anodic polarization of nickel in pure $NiSO_4$ solution (Fig. 3, curves *3*–*6*).

The appearance and the relative positions of the curves (Fig. 3), considered with account of the above V_{dep}–I_a and CE_{con}–I_a dependences, suggest that their lower portions (region *I*) are due to predominant deposition of vanadium oxide and oxygen evolution at the anode. In this case, the overpotential of the total process grows with increasing nickel ion concentration in solution. The accumulation of nickel ions in the near-electrode layer hinders access of oxovanadium ions to anode, thus making lower the limiting current of their oxidation and enhancing the concentration polarization (region *II*). The relative positions of the upper ascending portions of the curves (region *III*) are determined by the ratio of the rates of the concurrent anodic reactions, i.e., oxidation of oxovanadium and nickel ions and oxygen discharge, which is established in solution at a given V : Ni ratio. At V : Ni > 1, the rate of nickel oxide deposition is close to zero because of the competing reactions of vanadium oxide deposition and oxygen evolution, which occur with lower energy expenditure. Nonetheless, the concurrent reaction of nickel oxidation decelerates the anodic process, thus enhancing the anodic polarization and leading to a shift of the corresponding portions of the curves to more positive potentials with increasing nickel ion concentration in solution (Fig. 3, curves *1*, *2*). At V : Ni ≤ 1, formation of nickel oxide and its codeposition with vanadium oxide become probable. However, this reaction is accompanied by a considerable deceleration of the total process and an increase in the anodic polarization (Fig. 3, curves *3*, *4*). This leads, at a still sufficient intensity of vanadium oxide deposition under the given conditions, to lower yield of the anodic product and higher rate of oxygen evolution. The latter grows with increasing nickel ion concentration in solution, which causes the corresponding decrease in the anodic potential because of the weaker screening of the anodic product by the forming film and the approach of the deposition conditions to those corresponding to oxygen evolution at the initial surface of the stainless steel anode. This conclusion is confirmed by the I_a–E dependence of the anodic polarization curve obtained in pure $NiSO_4$ solution (Fig. 3, curve *3*).

The formation of a complex binary oxide system during electrolysis of the mixed solutions studied is also confirmed by X-ray diffraction patterns of the anodic deposits obtained. The deposits formed under the optimal electrolysis conditions (85°C, pH 2.0, and I_a = 10 mA cm^{-2}) from solutions with V : Ni sulfate concentration ratios of 5 : 1, and 1 : 3 are systems, in which the V_2O_5 and NiV_3O_8 phases are identified (Figs. 4a, 4b). These phases are clearly resolved both

after drying at room temperature and after heat treatment in air at 300°C for 7–10 h. In this case, the deposits studied contain a single-phase compound of the NiV_3O_8 type. This compound is formed directly in the course of electrolysis and its content grows with increasing nickel ion concentration in solution (Fig. 4b). This may be a consequence of a complex multistage mechanism of formation of nickel oxide compounds at the anode, which undergo simultaneous structural and chemical interaction with vanadium oxide deposited in quantitative yield. Such a mechanism may be quite adequate if an assumption is made that NiV_3O_8 is a nonstoichiometric compound and can be, in principle, regarded as a structural formation of the $NiO \cdot VO_2 \cdot V_2O_5$ type, which reveals the relationship with the V–Ni oxide system formed in joint anodic deposition of vanadium and nickel oxides.

The surface microstructure and morphology of the deposits studied is to a certain extent dependent on the electrolysis conditions and the V : Ni ratio in solution. The deposits obtained at V : Ni = 5 : 1 have a rather developed surface and amorphous structure close to that typical of "pure" vanadium oxide. At the same time, already at V : Ni = 3 : 1, the deposits are more compact and the observed surface microstructure and microprofile confirm their crystalline structure characterized by disordered formation of chaotically oriented crystalline grains. At V : Ni ≤ 1, the anodic deposits have more ordered columnar crystalline structure, which shows that the concurrent reaction of nickel ion oxidation plays an important role in nucleation and formation of the V–Ni binary oxide system under the conditions studied. This is possibly related to the corresponding enhancement of the anodic polarization and to suppression of the random growth of vanadium oxide threads by the forming nickel oxide molecules.

Thus, the anodic deposition of vanadium oxide in the presence of nickel ions from mixed solutions of oxovanadium and nickel sulfates at a certain ratio of their concentrations and certain electrolysis parameters results in the formation of anodic deposits belonging to a complex binary oxide system V–Ni. This becomes possible owing to the fact that favorable energy conditions for quantitative transformation of nickel ion oxidation into a stage of nucleation and formation of the corresponding oxide are attained at a certain level of the anodic polarization.

CONCLUSION

It is established that, for anodic deposits to be obtained in the form of V–Ni binary systems containing 0.1–20 wt % modifying phase, the electrolysis should be performed in solutions of oxovanadium and nickel sulfates with a total concentration of 40–45 g l^{-1} at V : Ni concentration ratios of 3 : 1–1 : 3 at 80–85°C, pH 2.0–2.2, and I_a = 7.5–10 mA cm^{-2}. The maximum permissible concentration of nickel ions in solution (V : Ni = 1 : 3) is determined by the limiting conditions for electrolysis stability and by the sufficient current efficiency by the anodic product.

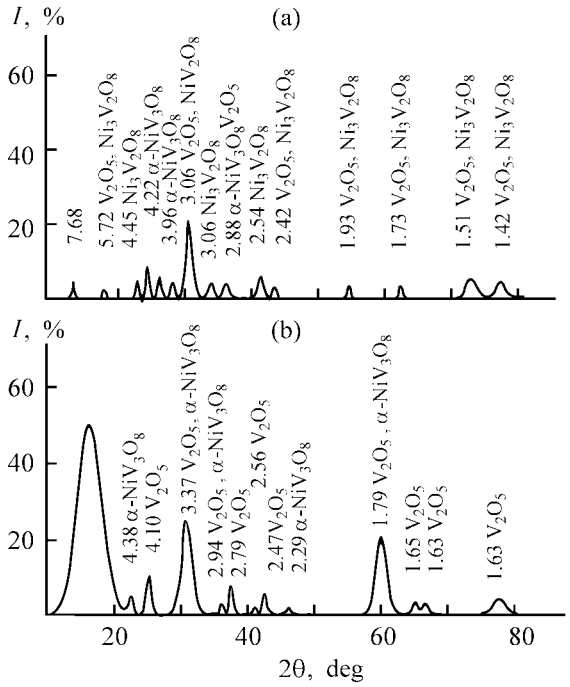

Fig. 4. X-ray diffraction patterns of anodic deposits obtained in electrolysis of solutions of oxovanadium and nickel sulfates with total concentration of 40–45 g l^{-1}. Temperature 85°C, pH 2.0, I_a = 10 mA cm^{-2}. (I) Intensity and (2θ) Bragg angle. V : Ni ratio: (a) 5 : 1 and (b) 1 : 3.

REFERENCES

1. Potiron, E., Le Gal La Salle, A., Verbaere, A., *et al., Joint Int. Meeting,* Honolulu, Havaii, October 17–22, 1999. p. 228.
2. Shembel', E.M., Nagirnyi, V.M., Apostolova, R.D., and Chaikovskaya, V.M., *Zh. Prikl. Khim.,* 2000, vol. 73, no. 3, pp. 409–412.
3. *Spravochnik po elektrokhimii* (Handbook of Electrochemistry), Sukhotin, A.M., Ed., Leningrad: Khimiya, 1986.
4. Yuichi, S., Takeru, N., Hiroaki, T., and Koichi, K., *J. Electrochem. Soc.*, 1999, vol. 138, no. 9, pp. L37–L39.
5. Mirkin, A.I., *Spravochnik po rentgenostrukturnomu analizu polikristallov* (Handbook of X-Ray Structural Analysis of Polycrystals), Moscow: Fizmatgiz, 1961.

Russian Journal of Applied Chemistry, Vol. 75, No. 12, 2002, pp. 1972–1978. Translated from Zhurnal Prikladnoi Khimii, Vol. 75, No. 12, 2002, pp. 2009–2015.
Original Russian Text Copyright © 2002 by Lukiyanchuk, Rudnev, Tyrina, Panin, Gordienko.

APPLIED ELECTROCHEMISTRY AND CORROSION PROTECTION OF METALS

Anodic-Spark Layers Formed on Aluminum Alloy in Tungstate-Borate Electrolytes

I. V. Lukiyanchuk, V. S. Rudnev, L. M. Tyrina, E. S. Panin, and P. S. Gordienko

Institute of Chemistry, Far-Eastern Division, Russian Academy of Sciences, Vladivostok, Russia

Received August 22, 2002

Abstract—The effect of sodium tungstate concentration in 0.4 M H_3BO_3 on the sparking voltage, thickness, and the phase and elemental composition of coatings formed on AMtsM aluminum alloy (~98% Al) by anodic-spark oxidation in a galvanostatic mode (i = 3 A dm^2) was studied.

The method of anodic-spark oxidation is commonly used to obtain coatings of various functional purposes: corrosion-resistant, heat-resistant, wear-resistant, etc. It was shown in [1, 2] that there exists a relationship between the formation of vanadium-phosphorus heteropolyoxo anions (HPA) in an aqueous solution and joint proportional incorporation of phosphorus and vanadium compounds into coatings formed on rectifying metals. The role of HPA consists in that it delivers necessary elements to the anode surface, which are then involved in high-temperature reactions at the anode. It is suggested that thermolysis of complexes contained in the deposit formed on the anode occurs in regions adjacent to electric breakdown channels, with only compounds and glass phases insoluble in the given electrolyte remaining in the coating. The number of presently known HPA is enormous: more than 65 elements can play the role of central elements in these anions [3, 4]. It is important to establish the relationship between the presence of HPA in an electrolyte and the composition of anodic-spark coatings formed on metals being treated in order to solve the problem of directed synthesis of coatings.

Tungstate-borate electrolytes are of interest because borotungstate HPA are formed in them at pH < 8, with the HPA hydrolyzed to borate and monotungstate anions at higher pH values [5].

The aim of the present study was to analyze the specific features of formation and composition of coatings formed on aluminum alloy in tungstate-borate electrolytes, including cases with pH higher and lower than this boundary value. It is noteworthy that the effect of the pH of borate, and the concentration of tungstate, electrolytes on the composition of anodic-spark coatings on aluminum alloy was studied preliminarily in [6, 7].

EXPERIMENTAL

The electrolytes were prepared from distilled water and the following reagents: $Na_2WO_4 \cdot 2H_2O$ and $(NH_4)_{10}[H_2W_{12}O_{42}] \cdot 10H_2O$ of analytically pure grade; H_3BO_3, $Na_2B_4O_7 \cdot 10H_2O$, $NaBO_2 \cdot 2H_2O$, H_2WO_4, and CH_3COOH of chemically pure grade. Potassium boroundetungstate $K_8[BW_{11}O_{39}H] \cdot 13H_2O$ was synthesized by a procedure described in [5]. Ammonium paratungstate was dissolved at 70°C. The electrolyte containing tungstic and boric acids and sodium tungstate was boiled for 1 h with stirring. All the other electrolytes were prepared by pouring solutions together at room temperature. The electrochemical cell employed and the pretreatment of aluminum samples have been described previously [6]. Oxide layers were formed on 40 × 10 × 1 mm AMtsM alloy samples in the galvanostatic mode at current densities of 3 A dm^{-2} in 10, 30, and 60 min. In the course of anodic-spark oxidation, the electrolyte temperature did not exceed 20°C. After treatment, samples with coatings were thoroughly washed with tap and distilled water and dried in air at room temperature.

The sparking voltage was evaluated from the appearance of the first visually observable sparks on the anode surface or by analysis of the forming curves $U = f(t)$ (from the onset of deviation from linearity of the time dependence of the voltage across the electrodes). As a measure of electrolyte development, Q^*, (C l^{-1}) was taken the quantity of electricity passed

1070-4272/02/7512-1972 $27.00 © 2002 MAIK "Nauka/Interperiodica"

Table 1. Phase composition of coatings formed in tungstate-borate electrolytes on AMtsM alloy

Electrolyte parameters						Phase composition of coatings*		
$c \times 10^{-2}$, M	B : W	initial		after anodization		1	2	3
		pH	æ × 10^3, S cm^{-1}	pH	æ × 10^3, S cm^{-1}			
1.3	30	6.63	1.46	6.80	1.52	α-Al_2O_3 + η-Al_2O_3	α-Al_2O_3 + η-Al_2O_3	α-Al_2O_3 + η-Al_2O_3
2.6	15	6.98	2.98	7.14	3.0	Al_2O_3 + WO_3	Al_2O_3	α-Al_2O_3 + Al_2O_3 + $WO_{2.9}$
4.0	10	7.35	4.22	7.38	4.4	Al_2O_3 + WO_3	Al_2O_3	Al_2O_3 + $WO_{2.9}$
5.7	7	7.35	6.10	7.50	6.50	WO_3	WO_3	WO_3
6.7	6	7.44	6.75	7.52	7.10	WO_3	WO_3	WO_3
7.0	5.74	7.55	7.3	7.60	7.5	WO_3	WO_3	WO_3 + Al_xWO_3
7.1	5.61	7.58	7.5	7.60	7.7	WO_3	WO_3 + $WO_{2.9}$	Al_xWO_3 + $Na_2W_2O_7$ + $Na_2W_4O_{13}$
7.2	5.5	7.59	7.7	7.62	7.8	Amorphous phase + WO_3	Amorphous phase + WO_3	$W_{20}O_{58}$ + $W_{18}O_{49}$ + ?$WO_{2.9}$ + $Na_2W_4O_{13}$
8.0	5	7.60	8.3	7.62	8.4	The same	The same	$H_{0.1}WO_3$ + $Na_2W_4O_{13}$ + ?$W_{20}O_{58}$
10.0	4	7.63	10.2	7.70	10.3	〃	〃	Amorphous phase + WO_3
13.3	3	7.97	12.8	7.97	13.3	〃	〃	The same
20.0	2	8.12	18.7	8.12	19.2	Amorphous phase + WO_3 + $WO_{2.9}$	〃	Amorphous phase + WO_3 + $WO_{2.9}$
40.0	1	8.47	33.0	8.48	34.0	Amorphous phase + trace amounts of WO_3	Amorphous phase + trace amounts of WO_3	Amorphous phase + trace amounts of WO_3

* Coatings formed in 10 min: (1) in undeveloped electrolyte ($Q^* = 0$), (2) in developed electrolyte ($Q^* = 1400$ C l^{-1}), and (3) in developed electrolyte ($Q^* \geq 1800$ C l^{-1}) in 30–60 min; æ is the electrical conductivity.

through the electrochemical cell before oxidation of a given electrode, normalized to the solution volume.

The phase composition of the coatings was studied by X-ray phase analysis on a DRON-2.0 diffractometer (Cu_{K_α} radiation). The elemental composition of the coatings was determined using a JEDE JXA-5A X-ray fluorescence analyzer. The content of boron in the coatings was evaluated using an EMAL-2 laser mass spectrometer. The film thickness was measured with an MBI-15 microscope in reflected light on cross-sections of a coating as an average of 10–15 measurements with accuracy of ±2 μm. ^{11}B NMR spectra of aqueous solutions were recorded on a Bruker WP-80SY high-resolution spectrometer at a frequency of 25.705 MHz. The chemical shifts are given relative to 0.1 M NH_4BF_4.

With increasing concentration of Na_2WO_4 in 0.4 M H_3BO_3 solution, there occurs a gradual increase in pH values and electrical conductivity of the solutions, (changes of these parameters in the course of anodization being small) (Table 1). The decrease in the acidity of the medium is accompanied by formation of various forms of borate anions, with an equilibrium that maintains the pH value established between them. Colloids of tungstic acids start to form in all of the electrolytes in question, and those of Heteropoly Blue, in electrolytes with Na_2WO_4 concentrations in the range from 0.05 to 0.1 M, already 1 min after the onset of sparking. It should be noted that, 30–60 min after termination of electrolysis, the solutions turn colorless because of the oxidation of Heteropoly Blue by atmospheric oxygen.

The plots describing how the sparking voltage and final forming voltage, and also the thickness and elemental composition of the coatings obtained, depend on the sodium tungstate concentration (Fig. 1) show three ranges of concentrations c (M): (*I*) 0.005–0.05 (pH < 7.35), (*II*) 0.057–0.067 (7.35 ≤ pH ≤ 7.44), and (*III*) 0.07–0.4 (pH ≥ 7.55). An assumption can be made on the basis of the data of [5] that the change in the parameters is due to presence of borotungstate HPA at pH < 7.5 and their hydrolysis at pH > 7.5. However, in accordance with the outward appearance (Fig. 2) and phase and elemental composition of the coatings, a transition range 0.07 < c < 0.072 M

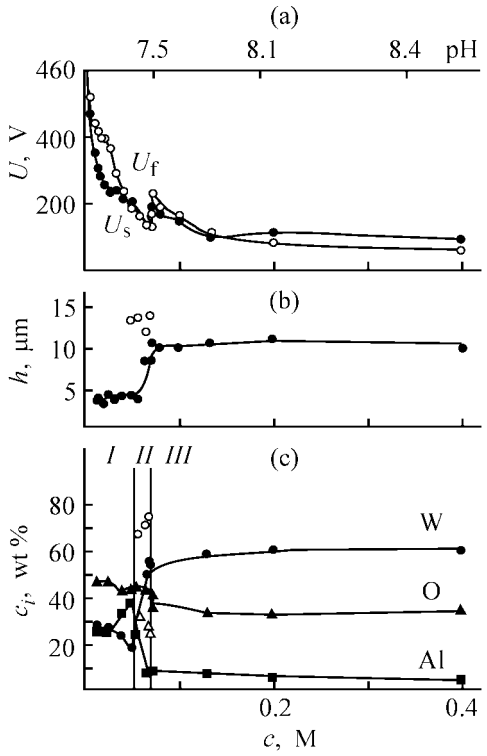

Fig. 1. (a) Sparking voltage U_s and final voltage U_f across the electrodes, (b) coating thickness, and (c) content of main elements in the coatings vs. concentration c of sodium tungstate in an electrolyte containing 0.4 M of H_3BO_3. Time of coating formation (min): (a, b) 10 and (c) 30. *Open symbols*: elemental composition and thickness of green coatings. The oxygen content was found from the difference.

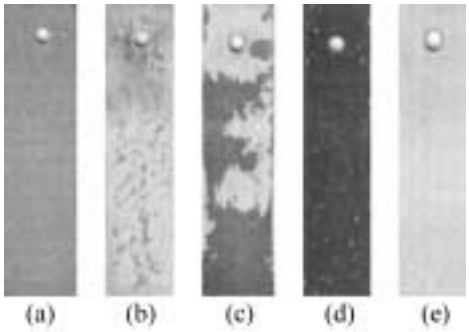

Fig. 2. Outward appearance of samples with coatings formed in tungstate-borate electrolytes in 10 min. Coating: (a) in range *I*, (b) in range *II*, (c) in transition range, (d) in range *III*, and (e) in 0.0091 M solution of $K_8[BW_{11}O_{39}H]$.

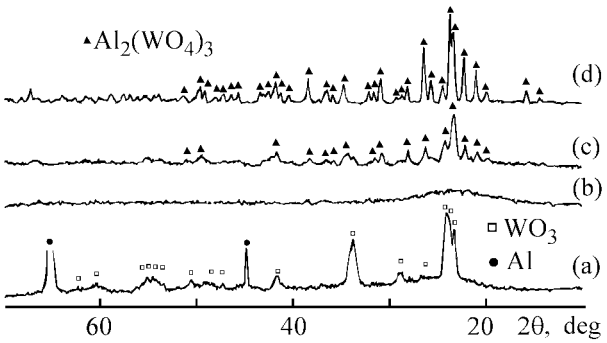

Fig. 3. X-ray diffraction patterns of (a) a sample with coating containing green islands and powders prepared from bluish black parts of the coatings (b) before and after annealing at (c) 760 and (d) 1000°C. Coatings formed in the course of 10 min in electrolyte no. 4. (2θ) Bragg angle.

(7.44 < pH < 7.55) should be additionally distinguished.

In range *I*, small islands of light green color, corresponding to tungsten oxides WO_3, are formed on the aluminum surface in undeveloped electrolytes ($Q^* < 45$ C l^{-1}) beginning with $c = 0.02$ M. They are formed by the mechanism of discharge propagation, following the spark front. Upon the development of the electrolyte, no WO_3 phase is formed, with thin (h = 3–4 μm) moire coatings appearing instead (Fig. 2a; dark gray and light gray islands are present). These coatings mainly contain aluminum oxides, predominantly in α and η modifications. At the same time, with the duration of anodic-spark oxidation increasing to 30–60 min, a $WO_{2.9}$ phase is crystallized. There is reason to believe that the existence of dark parts of the coatings is due to the presence of this phase. In range *I*, the content of tungsten in the coatings decreases, and that of aluminum increases, with growing Na_2WO_4 concentration.

In range *II*, the phase composition of the coatings is dependent on neither electrolyte development nor time of anodic-spark anodization. All the coatings are light green (Fig. 2b) and contain WO_3. The content of tungsten in the coatings is about 70 wt %, and that of aluminum does not exceed 0.4 wt %. The coating thickness grows with increasing oxidation time from 12–14 (10 min) to 60 μm (60 min).

In range *III*, bluish black layers of thickness ranging from 10 (10 min) to 30 μm (60 min) are formed, with raised green points of the WO_3 phase evenly distributed over the surface (Fig. 2d). The content of tungsten and aluminum in the bluish black layers is independent of the time of anodic-spark oxidation, being equal to, respectively, 45–60 and 4–8 wt %, with the Al/W ratio corresponding to aluminum tungstate. X-ray diffraction patterns of the green parts of the coating material and those of the coating material detached from the substrate contain an amorphous halo in the region characteristic of tungsten compounds. Upon annealing in air at 1000°C the powder changes its color from bluish black to white, and aluminum tungstate crystallizes in it (Fig. 3). XPA data indicate that, in addition to the amorphous

Table 2. Effect of the pH of electrolytes with total concentration of 0.4 M B(III) and 0.1 M W(VI) on the outward appearance and phase composition of coatings on aluminum

Electrolyte no.	Electrolyte parameters			Coating* parameters			
	composition, M	pH	æ × 10^3, S cm^{-1}	outward appearance		phase composition	
				1	2	1	2
1	0.4 H_3BO_3 + 0.0083 $(NH_4)_{10}[H_2W_{12}O_{42}]$	6.1	3.1	Green	Green	WO_3	WO_3
2	0.4 H_3BO_3 + 0.0042 $(NH_4)_{10}[H_2W_{12}O_{42}]$ + 0.05 Na_2WO_4	7.2	7.7	″	″	WO_3	WO_3
3	0.4 H_3BO_3 + 0.05 H_2WO_4 + 0.05 Na_2WO_4	7.4	5.5	″	″	WO_3	WO_3
4	0.4 H_3BO_3 + 0.1 Na_2WO_4	7.5	8.3	Bluish black with green inclusions	Green layer over black	Amorphous phase + WO_3	WO_3
5	0.2 H_3BO_3 + 0.05 $Na_2B_4O_7$ + 0.1 Na_2WO_4	8.6	15.3	The same	The same	The same	WO_3
6	0.1 $Na_2B_4O_7$ + 0.1 Na_2WO_4	9.6	20.0	Blue-gray	Bluish black	Amorphous phase	Al_2O_3 + $Al_2(WO_4)_3$ + $H_{0.33}WO_3$
7	0.4 $NaBO_2$ + 0.1 Na_2WO_4	11.0	25.0	Brown	Black	Al_2O_3	Al_2O_3 + ?$WO_{2.9}$

* Coatings formed in (1) 10 and (2) 60 min.

phase and WO_3, phases with W(V), such as tungsten bronzes $H_{0.1}WO_3$, $H_{0.33}WO_3$, Al_xWO_3 and nonstoichiometric oxides $WO_{2.9}$, $W_{20}O_{58}$, and $W_{18}O_{49}$, are possibly present in the initial coatings.

In the transition region (Fig. 2c), simultaneous formation of light green and dark blue-gray islands is observed. In this case, the green islands are formed by the mechanism of linear discharge following the spark front, whereas blue-gray layers are produced by uniform sparking on that part of the surface of the aluminum anode, which remained uncovered with green films.

Laser mass spectrometry enabled evaluation of the amount of boron in coatings obtained in electrolytes with sodium tungstate concentration $c \leq 0.1$ M. The content of boron is not too high (≤ 1 at.%, or 0.5 wt %). At the same time, coatings containing 1 to 9 at.% boron were obtained in the absence of sodium tungstate in borate electrolytes ($6.5 \leq pH \leq 10.2$) [6].

It is noteworthy that the manner in which the thickness and composition of coatings on aluminum depend on the concentration of Na_2WO_4 in electrolytes with and without boric acid [7] is about the same. In both cases, three ranges of Na_2WO_4 concentrations affecting the coating composition can be distinguished: ranges *I*, *II*, and *III*, in which, respectively, moire, green, and black layers are formed. The presence of H_3BO_3 leads to a shift of these concentration ranges, independence of the composition of coatings formed within range *II* from electrolyte development, and change in the coating color {the coatings turn bluish, instead of being green, which is possibly due to formation of compounds with W(V) [8]}. In addition, tungstate-borate electrolytes have, compared with tungstate electrolyte, lower pH value and possess buffer properties, which leads to formation of tungstic acid colloids. The existence of range *II* in tungstate solutions is due to the presence of isopolytungstates [7], and formation of borotungstates becomes possible in tungstate-borate electrolytes. Since the region of existence of borotungstate HPA is limited by the pH of the medium and concentrations of tungstate anions, the following may be assumed. In range *I*, the concentration of borotungstates in solution and their effect on coating formation are insignificant. In range *II*, their amount becomes sufficient for their predominant involvement in coating formation. In range *III*, the rise in pH leads to hydrolysis of borotungstate HPA to monotungstate and polyborate anions. The assumption that HPA are present in the electrolyte bulk is confirmed by the formation of Heteropoly Blue at Na_2WO_4 concentrations of 0.05 to 0.1 M ($7.35 \leq pH \cong 7.70$).

In order to additionally verify the effect of the electrolyte pH on the phase and elemental composition of coatings, solutions with constant total concentrations of boron (0.1 M) and tungsten (0.4 M) and varied pH value were prepared (Tables 2 and 3). The pH value

Table 3. Effect of the pH of electrolytes containing 0.4 M H_3BO_3, 0.1 M Na_2WO_4, and different concentrations of CH_3COOH on the phase composition of coatings on aluminum alloy

Electrolyte pH		Phase composition of coatings			Electrolyte pH		Phase composition of coatings		
initial	after anodization	1	2	3	initial	after anodization	1	2	3
7.00	8.06	$WO_{2.9}$	$WO_{2.9}$	$Al_2(WO_4)_3$	5.00	5.14	WO_3	$Al_2(WO_4)_3$	$Al_2(WO_4)_3$ + ?$Na_{0.28}WO_3$
6.50	7.05	$WO_{2.9}$	$WO_{2.9}$	$Al_2(WO_4)_3$					
6.00	6.5	$WO_{2.9}$	$WO_{2.9}$	$Al_2(WO_4)_3$ + ?$Na_{0.28}WO_3$	4.00	4.07	$WO_{2.9}$	$Al_2(WO_4)_3$ + ?$Na_{0.28}WO_3$	The same

* Coatings formed in 10 min: (1) in undeveloped electrolyte ($Q^* = 0$), (2) in developed electrolyte ($Q^* = 1400$ C l^{-1}), and (3) in developed electrolyte ($Q^* \geq 1800$ C l^{-1}) in 30–60 min.

was varied by using different borate and tungstate anions (Table 2) or by acidifying electrolyte no. 4 (Table 2) with an acetic acid solution (Table 3).

Analysis of the data in Fig. 4 and Table 2 reveals two ranges of the pH of "acetate-free" electrolytes differing in their effect on the thickness and composition of coatings. At pH ≤ 7.5, green WO_3-containing coatings of thickness 12–14 μm (10 min) are formed. In anodic-spark oxidation of aluminum in electrolyte no. 1 (Table 2), green layers are formed on the background of a gray film. At pH > 7.5, the character of sparking changes, it becomes finer and more uniform, with the coating becoming thinner, 5–8 μm (10 min), and the content of tungsten and aluminum in the coatings, respectively, decreasing and increasing. The number of green islands (WO_3 phase) on the surface of the amorphous layer decreases. At pH 11.0 no WO_3 phase is formed.

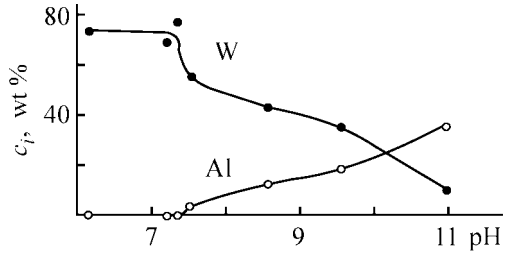

Fig. 4. Content c_i of main elements in coatings vs. pH of electrolytes containing 0.4 M B(III) and 0.1 M W(VI). Coatings formed in 10 min.

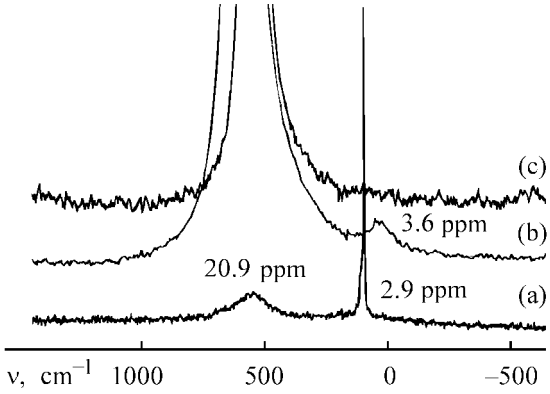

Fig. 5. ^{11}B NMR spectra of solutions containing B(III) and W(VI) in (a) 1 : 12 and (b, c) 4 : 1 ratios. Chemical shifts (ppm) refer to H_3BO_3 (20.9) and $[BW_{12}O_{40}]^{5-}$ (2.9 and 3.6) [3]. (ν) Frequency. (a) 0.2 M H_3BO_3 + 2.4 M Na_2WO_4 + HCl, pH 4; (b, c) electrolyte no. 1 (Table 2) pH 6.1 [(a) before and (c) after electrolysis).

It is noteworthy that, upon storage of electrolyte no. 1 for 1 month in a closed vessel, a precipitate is formed, which contains, according to XPA, $H_5[BW_{12}O_{40}] \cdot xH_2O$. After electrolysis, the precipitate formed in the electrolyte contains, in addition to borotungstic acid, products of its thermolysis, HBO_2 and WO_3. ^{11}B NMR spectra of solutions confirm the presence of a borododecatungstate peak in electrolyte no. 1 before electrolysis and a decrease in its intensity after electrolysis (Figs. 5b and 5c). In the other electrolytes (Tables 1–3), no ^{11}B NMR peaks characteristic of boron in tetrahedral environment are recorded, which is presumably due to hydrolysis of $[BW_{12}O_{40}]^{5-}$ at pH > 6.5. In the range 5 < pH < 8, the $[BW_{11}O_{39}H]^{8-}$ anion, characterized by a coordination intermediate between tetrahedral and triangular, is stable. It is noteworthy that coatings formed on aluminum alloy in a 0.0091 M $K_8[BW_{11}O_{39}H]$ solution [with W(VI) concentration equal to 0.1 M] are light green and contain the WO_3 phase (Fig. 2e).

Thus, there is reason to believe that borotungstic acids are formed as a result of acidification in the course of electrolysis in the near-anode region, and these acids decompose in the course of dehydration

to WO_3 [4]. It is noteworthy that the formation of ligt green coatings in a 0.0091 M $K_8[BW_{11}O_{39}H]$ solution is similar to that of oxide layers in vanadate-phosphate electrolytes [1, 2]. In both cases, nuclei of a new phase, which contains electrolyte components, precipitate after the onset of sparking. Further growth of coatings occurs via expansion of the region of the new phase, following the moving front of sparks at the perimeter of the nuclei.

Lowering the pH value by introducing acetic acid into a solution containing 0.4 M H_3BO_3 and 0.1 M Na_2WO_4 favors formation of intensely colored Heteropoly Blue on the cathode in the course of anodic-spark oxidation. The intensity of electrolyte coloration grows with decreasing pH, which indicates a rise in the concentration of borotungstate HPA. Formation of Heteropoly Blue in electrolysis of tungstate solutions containing 0.1 M Na_2WO_4 and acetic acid (pH 6) is only observed upon their boiling. At the same time, a decrease in the pH of tungstate-borate-acetate solutions affects neither the elemental composition nor the outward appearance of the coatings, which remain the same as in the case of an electrolyte containing no acetic acid (pH 7.6). The decrease in pH only favors crystallization of a $Al_2(WO_4)_3$ in the coatings (Table 3). The possible presence of the $?Na_{0.28}WO_3$ phase must be insignificant, since the content of sodium does not exceed 0.4 wt %.

It is known [9] that aluminum hydroxide has the lowest solubility in the pH range 6.5–7.5. Presence in an electrolyte of ions that can form soluble compounds or complexes with aluminum, including acetate ions, markedly raises the solubility of its oxide and hydroxide even in a neutral medium. As a result, first an amorphous phase and then $WO_{2.9}$ are formed on the surface of the anodic oxide film instead of tungsten(VI) oxide, whose formation is observed at the given pH values in the absence of acetate ions. At lower pH and longer anodic-spark oxidation, aluminum tungstate is formed.

In the absence of acetate ions in tungstate-borate electrolytes, the solubility of aluminum is controlled by the acidity of the medium. Aluminum ions are present in solution in the form of positively charged ions in an acid medium, and as negatively charged hydroxo complexes, in an alkaline medium. Thus, the coating formation involves both the elements contained in the initial components of the electrolyte and elements from an alloy being treated. It would be expected that, in neutral medium, aluminum ions from the electrolyte should be involved in the formation of anodic-spark layers to the minimum extent because of the low solubility of aluminum oxide and hydroxide, and just this is observed in range *II* (Fig. 1c) and at $6.1 < pH < 7.5$ (Table 2). The fact that the range of Na_2WO_4 concentrations (in 0.4 M H_3BO_3 solution) in which Heteropoly Blue is formed is wider than the range in which WO_3 is formed in the coatings confirms the assumption that the electrolyte pH affects not only HPA formation, but also the conditions of anode metal dissolution.

CONCLUSIONS

(1) Three ranges of Na_2WO_4 concentrations in 0.4 M H_3BO_3 solution, affecting the composition of anodic-spark layers on aluminum alloy, were established. In range *I*, thin layers mainly containing aluminum oxides are formed; in range *II*, solid layers containing WO_3 are produced; in range *III*, coatings are formed, which contain an amorphous phase approaching $Al_2(WO_4)_3$ in composition, with islands of the WO_3 phase uniformly distributed over its surface.

(2) At B : W = 4 : 1, solid WO_3 layers are formed on the surface of aluminum being anodized at $pH < 7.5$; at $pH > 7.5$ the content of aluminum in the coatings becomes higher, and that of tungsten, lower, and the coatings contain an amorphous phase and WO_3 in the form of islands.

(3) The data are obtained suggesting that the growth of WO_3 layers on the surface of the aluminum anode is related to formation in tungstate-borate electrolytes of borotungstate heteropolyoxo anions $[BW_{11}O_{39}H]^{8-}$ and(or) $[BW_{12}O_{40}]^{5-}$.

(4) It is shown that introduction of acetate ions chemically dissolving aluminum and its oxide into a borate-tungstate electrolyte favors crystallization of $WO_{2.9}$ and $Al_2(WO_4)_3$ phases.

(5) A correlation is observed between the influence of the electrolyte pH on the solubility of aluminum and its oxide and the phase and elemental composition of the anodic layers formed. At neutral pH values, when the solubility of Al_2O_3 is insignificant, the content of aluminum in coatings falls.

ACKNOWLEDGMENTS

The authors thank T.A. Kaidalova for performing X-ray analysis, N.A. Andenko for carrying out a number of experiments, V.V. Kon'shin for NMR studies of solutions, and A.S. Rudneva for mass-spectrometric analysis of coatings.

REFERENCES

1. Rudnev, V.S., Gordienko, P.S. Kon'shin, V.V., *et al.*, *Elektrokhimiya*, 1996, vol. 32, no. 10, pp. 1242–1246.
2. Gordienko, P.S. and Rudnev, V.S., *Elektrokhimicheskoe formirovanie pokrytii na alyuminii i ego splavakh pri potentsialakh iskreniya i proboya* (Electrochemical Formation of Coatings on Aluminum and Its Alloys at Sparking and Breakdown Potentials), Vladivostok: Dal'-nauka, 1999.
3. Pop, M.S., *Geteropoli- i izopolioksometallaty* (Heteropoly and Isopolyoxo Metallates), Novosibirsk: Nauka, 1990.
4. Maksimov, G.M., *Usp. Khim.*, 1995, vol. 64, no. 5, pp. 481–496.
5. Tézé, A., Michelon, M., and Hervé, G., *Inorg. Chem.*, 1997, vol. 36, pp. 505–509.
6. Lukiyanchuk, I.V., Rudnev, V.S., Kaidalova, T.A., *et al.*, *Zh. Prikl. Khim.*, 2000, vol. 73, no. 6, pp. 926–929.
7. Lukiyanchuk, I.V., Rudnev, V.S., Andenko, N.A., *et al.*, *Zh. Prikl. Khim.*, 2002, vol. 75, no. 4, pp. 587–592.
8. Remy, H., *Lehrbuch der anorganischen Chemie*, Bd 2, Leipzig: Akademische Verlagsgesellschaft, Geest and Portig K.-G., 1961.
9. Kul'skii, L.A., *Teoreticheskie osnovy i tekhnologiya konditsionirovaniya vody* (Theoretical Foundations and Technology of Water Treatment), Kiev: Naukova Dumka, 1980.

Russian Journal of Applied Chemistry, Vol. 75, No. 12, 2002, pp. 1979–1983. Translated from Zhurnal Prikladnoi Khimii, Vol. 75, No. 12, 2002, pp. 2016–2020.
Original Russian Text Copyright © 2002 by Shabalina, Erofeev, Minakova, Koval'.

CATALYSIS

Specific Features of Conjugate Conversion of Methanol and Propane–Butane Fraction on Pentasil

L. B. Shabalina, V. I. Erofeev, T. S. Minakova, and L. M. Koval'

Department of Scientific and Technical Development, Tomsk Petrochemical Plant, Joint-Stock Company, Tomsk, Russia
Tomsk State University, Tomsk, Russia

Received April 22, 2002

Abstract—The conversion of methanol and propane–butane fraction, taken separately and in combination, on Pentasil at 500–650°C was studied. The pathways and specific features of the occurring reactions were determined.

Today, one of the main processes for commercial production of lower olefins (ethylene, propylene) is pyrolysis of various straight-run oil fractions and oil distillates [1]. However, because of the short supply of petroleum raw materials, active efforts are made to develop processes for production of lower alkenes (C_2–C_4), arenes, motor fuels, and other valuable products from alternative raw materials: condensed gases, natural and casing-head gases. Utilization of natural and casing-head gases for chemical processing is impeded by the low reactivity of C_2–C_4 alkanes and, especially, of methane.

Of much promise in this context, is conjugate conversion of the propane–butane fraction (PBF) and methanol into lower olefins and arenes in the presence of high-silica catalysts like ZSM-5. Introduction into the reaction mixture of lower alkanes (C_2–C_4) and methanol in the presence of zeolite-containing catalysts allows the process to be performed at lower temperatures and without considerable heat effects, owing to conjugation of the endothermic cleavage of hydrocarbons and exothermic conversion of methanol [2].

The activity and selectivity of decationized high-silica zeolites (HSZs) in conversion of hydrocarbons are primarily governed by the composition of their framework and by the reaction conditions shifting the thermodynamic equilibrium toward formation of target products [3]. In conversion of methanol and C_2–C_4 alkanes on an HSZ, the primary products are lower olefins, which subsequently undergo dehydrocyclization and aromatization to give arenes; the yield of lower olefins can be increased by properly choosing the reaction conditions, modifying HSZ, etc.

In this study, we examined the influence of temperature, feed space velocity, methanol : PBF weight ratio, and time of Pentasil operation on its activity and selectivity in formation of C_2–C_4 olefins in the conjugate conversion of PBF and methanol.

EXPERIMENTAL

The initial samples of high-silica zeolites of the ZSM-5 type (silicate ratio 50) were prepared as described in [4]. The H form of the zeolite (H-HSZ) was prepared by decationization of the initial Na form (Na-HSZ) in 25% aqueous NH_4Cl, followed by thermolysis at 600°C for 8 h to remove ammonium ions. The residual content of Na_2O in H-HSZ did not exceed 0.05% (here and hereinafter, wt %). The degree of crystallinity of the zeolite sample, evaluated from the IR spectrum, was 93%.

The conversion of methanol and PBF, taken separately and in combination, was studied in a flow-through installation with fixed catalyst bed (reactor volume 3 cm^3) in the temperature range 450–700°C at atmospheric pressure. Methanol contained ≤0.02% water; the composition of PBF (%) was 0.9 ethane, 58.3 propane, 5.5 isobutane, and 35.3 butane.

The reaction mixture and products were analyzed by gas chromatography.

It is known that transformations of lower alkanes (C_2–C_4) on zeolite-containing catalysts start at temperatures above 500°C [3]; therefore, it was necessary to study transformations of methanol at these high temperatures.

Examination of the influence of temperature on the composition of products of methanol conversion on

1070-4272/02/7512-1979 $27.00 © 2002 MAIK "Nauka/Interperiodica"

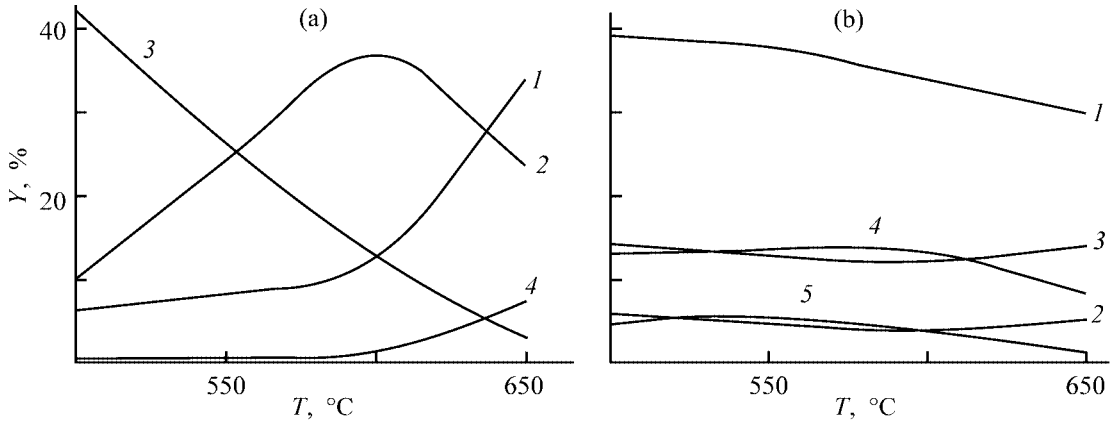

Fig. 1. Yields *Y* of methanol conversion products vs. temperature *T*. (a) (*1*) Methane, (*2*) C_2–C_4 olefins, (*3*) C_2–C_4 alkanes, and (*4*) CO; (b) (*1*) arenes, (*2*) benzene, (*3*) toluene, (*4*) xylenes, and (*5*) C_{9+} alkylbenzenes.

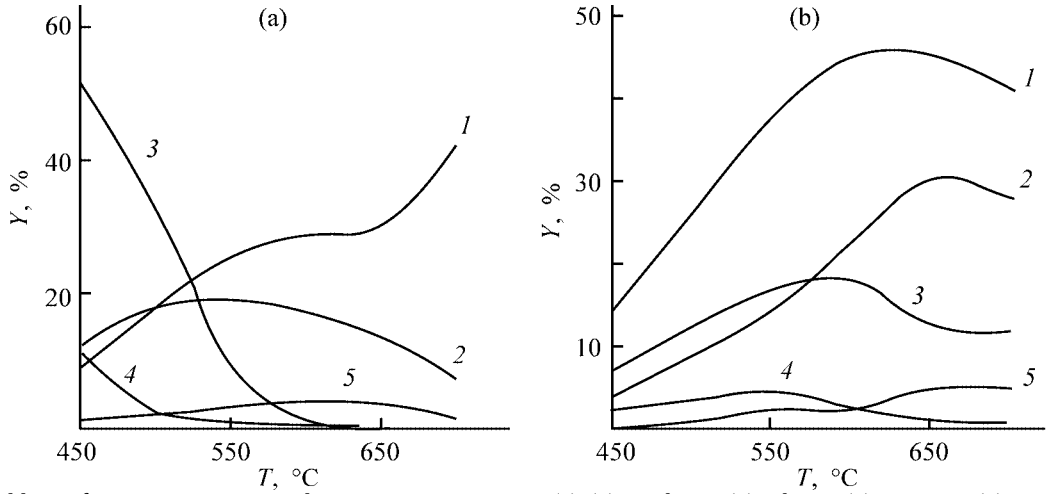

Fig. 2. Yields *Y* of PBF conversion products vs. temperature *T*. (a) (*1*) Methane, (*2*) ethane, (*3*) propane, (*4*) isomeric butanes, and (*5*) C_2–C_4 olefins; (b) (*1*) arenes, (*2*) benzene, (*3*) toluene, (*4*) xylene, and (*5*) naphthalenes.

HSZ at a space velocity of 2 h^{-1} showed that, with the temperature increasing from 500 to 650°C, the yields of CO and methane grow sharply, and the yield of C_2–C_4 olefins passes through a maximum at T_{max} = 600°C (Fig. 1a). The total yield of arenes in methanol conversion decreases monotonically with increasing temperature (Fig. 1b); the content of individual arenes varies insignificantly. The minimum (T_{min} = 600°C) in the temperature dependence of the benzene and toluene yields and the maximum (T_{max} = 550–600°C for the yields of xylenes and C_{9+} alkylbenzenes suggest the occurrence of dealkylation and disproportionation. The content of naphthalene in methanol conversion products was less than 0.5% at 500°C, and it also decreased with increasing temperature.

Transformations of propane in the presence of H-HSZ become noticeable at 500°C, i.e., at higher temperatures as compared to butanes (Fig. 2a). With the temperature increasing to 700°C, the content of PBF in the reaction mixture decreases drastically (to 0.3%). Nevertheless, the yield of C_2–C_4 olefins is low, as in conversion of methanol; their yield is the highest at 600°C. The high yield of arenes (up to 45%, Fig. 2b) indicates a high activity of Pentasil and high concentration on its surface of strong acid centers responsible for aromatization of alkenes. We should also note a high degree of methanation and high content of naphthalenes (up to 5%) in the liquid products. The shift of the reaction equilibrium toward formation of arenes may be due to plugging of zeolite channels and voids with coke deposits, which enhances the molecular-sieve properties of Pentasil [5]. The diffusion hindrance arising in the process shifts the reaction equilibrium toward formation of final products, specifically, arenes.

Thus, the increase in the CO yield with temperature in conversion of methanol and the high degree of methanation for both processes show that it is appropriate to perform conjugate conversion of PBF and methanol at temperatures above 650°C.

Table 1. Influence of temperature on the yield of hydrocarbons in conjugate conversion of methanol and PBF (weight ratio methanol : PBF 4 : 1)

Reaction products	Yield (%) at indicated temperature, °C			
	500	550	600	650
Gaseous:				
H_2	0.2	0.2	0.2	0.4
CO	0.4	0.4	2.1	7.5
methane	6.1	6.7	15.8	31.3
ethane	4.0	2.8	1.8	1.2
ethylene	3.7	9.0	14.3	10.8
propane	29.6	19.4	10.5	3.6
propylene	4.4	10.4	12.9	8.2
isobutane	10.4	7.1	1.9	0.7
butane	6.2	5.4	2.0	1.0
butenes	3.2	5.8	4.1	3.5
C_2–C_4 alkenes	11.3	25.2	31.3	22.5
Liquid:				
C_{5+} alkanes	0.6	0.7	0.3	Traces
C_{5+} alkenes	0.4	1.3	1.1	"
benzene	4.8	3.6	3.8	4.5
toluene	12.7	11.8	13.6	16.2
xylenes	9.6	11.7	12.9	10.4
C_{9+} arenes	3.3	3.3	2.6	0.6
arenes (total)	30.4	30.4	32.9	31.7
naphthalenes	0.4	0.2	0.1	<0.1

Table 2. Influence of the methanol : PBF weight ratio on the yield of hydrocarbons in conjugate conversion of methanol and PBF at 600°C

Reaction products	Yield (%) at indicated methanol : PBF weight ratio		
	2 : 1	4 : 1	6 : 1
Gaseous:			
methane	9.7	16.9	19.8
ethane	3.1	2.0	1.0
ethylene	13.7	14.4	13.5
propane	22.9	10.5	3.1
propylene	11.5	13.1	10.7
isobutane	2.5	2.1	2.4
butane	5.7	2.5	1.6
butenes	4.2	4.2	4.0
C_2–C_4 alkenes	29.4	31.5	28.2
Liquid:			
C_{5+} alkanes	0.1	0.3	0.9
C_{5+} alkenes	0.5	1.1	1.1
benzene	2.9	3.8	2.5
toluene	11.1	13.6	15.1
xylenes	9.1	12.9	21.0
C_{9+} arenes	1.7	2.6	3.1
arenes (total)	24.3	32.9	41.7
naphthalenes	0.1	0.1	0.2

Preliminary experiments in the presence of Na-HSZ showed that the initial activity of the nondecationized zeolite is fairly high, but after operation for 3 h the catalyst loses its activity. The products contain propane (~50%), butane (~25%), methane (~13%), and no more than 5% lower olefins.

The composition of products formed in conjugate conversion of methanol and PBF in the presence of H-HSZ is given in Table 1. The major products are lower alkanes, olefins, and arenes. As seen from Table 1, with the reaction temperature increasing from 500 to 650°C, the content of propane and isomeric butanes in the products decreases by approximately a factor of 4, i.e., the Pentasil activity grows with temperature. The yield of C_2–C_4 olefins on H-HSZ as a function of temperature passes through a maximum, reaching 31%. It should be noted that ethylene and propylene are formed in about the same amounts. Below 600°C, the yield of propylene is somewhat higher, whereas above 600°C the yield of ethylene increases owing to larger contribution of cracking reactions.

The conversion of separately taken PBF (Fig. 2b) is characterized by an increase in the yield of arenes (especially benzene) with temperature, whereas in conjugate conversion of methanol and PBF on H-HSZ, the temperature rise has no appreciable effect on the total yield of arenes. The fraction of C_6–C_8 arenes contains 3–4 times less benzene than toluene; with increasing temperature, the yields of toluene and xylenes grow. The decrease in the content of xylenes in the reaction products at 650°C and the increase in the content of benzene and toluene suggest that alkylaromatic hydrocarbons undergo dealkylation. A similar pattern is characteristic of conversion on Pentasil of methanol taken alone, which is attributed to the occurrence of the carbocation mechanism of arene formation [6].

The calculated and experimental data given in [2] show that the heat effect of the conjugate process is close to zero when methanol and decane are taken in a weight ratio of (1.5–2) : 1; in this case, the conversion of methanol and decane is virtually complete, and the yield of lower olefins is as high as 35–40%. Conversion of PBF requires high temperatures than cleavage of decane; therefore, we took higher weight ratios of methanol to PBF. The composition of products formed at methanol : PBF weight ratios of 2 : 1, 4 : 1, and 6 : 1 is given in Table 2. Experiments were per-

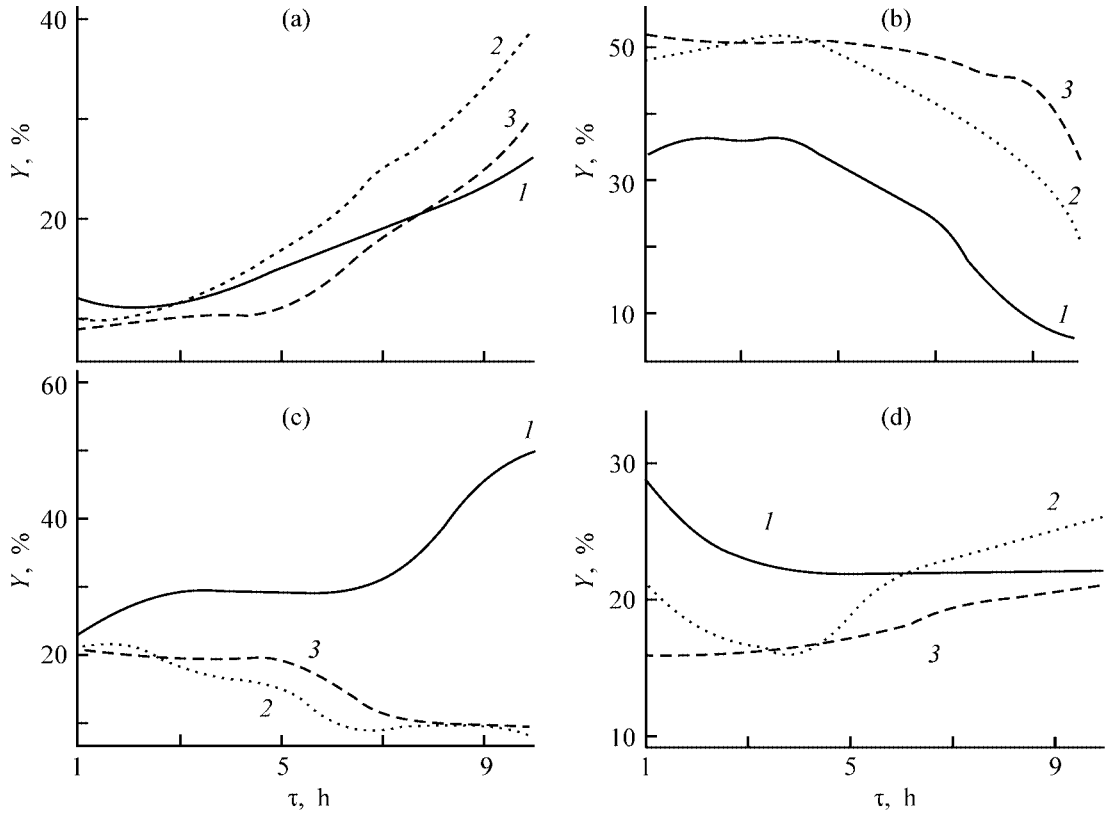

Fig. 3. Yields *Y* of products of conjugate conversion of methanol and PBF vs. time τ. Feed space velocity, h^{-1}: methanol 2 and PBF 200. *T* = 600°C. (a) Methane, (b) C_2–C_4 olefins, (c) C_2–C_4 alkanes, and (d) arenes. Yields: (*1*) before zeolite regeneration, (*2*) after first regeneration, and (*3*) after second regeneration.

formed at 600°C, since the yield of C_2–C_4 olefins is at a maximum at this temperature (Table 1) and the conversion of propane and isomeric butanes is fairly high. As seen from Table 2, the yield of methane grows with increasing content of methanol; hence, the contribution of methanol to methanation is higher under these conditions than that of PBF. The yield of olefins is the highest at methanol : PBF = 4 : 1; the yield of arenes grows with increasing content of methanol, mainly at the expense of formation of alkylsubstituted benzenes (toluene, xylenes, C_{9+} arenes).

It is known that, in conversion of methanol, the reaction equilibrium can be shifted toward formation of lower olefins by decreasing the partial pressure of methanol, for which purpose diluents are added [7]. In our system, on the one hand, methanol enhances the reactivity of lower alkanes, and, on the other, these alkanes act as diluents shifting the equilibrium toward formation of olefins. Therefore, the subsequent experiments were performed at 600°C and weight ratio methanol : PBF = 4 : 1.

Figure 3 illustrates the stability of H-HSZ functioning in conjugate conversion of methanol and PBF. Experiments showed that, in the first 10 h (before regeneration), the yield of C_2–C_4 olefins gradually decreases (Fig. 3b). The yield of methane increases by a factor of 2 in the course of the run (Fig. 3a); probably, gradual coking of the zeolite promotes additional methanation of coke [8]. One more evidence in favor of the gradual deactivation of the catalyst is the steady growth of the content of propane and isomeric butanes in the products (Fig. 3c, curve *1*).

The next 10-h run of the catalyst after regeneration is characterized by similar trends in the yield of lower olefins (Fig. 3b, curves *1*, *2*); however, the content of lower olefins in the reaction mixture increases, on the average, by 15%. The content of propane and isomeric butanes in the reaction products after 10-h run decreases, and the yield of arenes grows (Fig. 3d); that is, the catalyst activity remains high, but its selectivity with respect to formation of C_2–C_4 olefins decreases.

The second regeneration improves the stability of the catalyst functioning as compared to the first and second runs. These results can be accounted for by the influence exerted on zeolite by the water vapor released in methanol cleavage. Regeneration of the zeo-

lite at 550°C probably leads to escape of Al^{3+} ions from the zeolite lattice. Dealumination of the zeolite framework in the course of high-temperature treatment with water vapor decreases the total acidity of the zeolite, with replacement of strong acid centers with weaker centers [4, 9]. As a result, the zeolite selectivity changes: after Pentasil regeneration, the yield of olefins increases and the yield of arenes formed on strong Brønsted acid centers decreases.

CONCLUSIONS

(1) In conversion of methanol, the yields of CO and H_2 sharply grow with the temperature increasing from 500 to 650°C; the major contribution is made by dealkylation and disproportionation of alkylaromatic hydrocarbons.

(2) In conversion of the propane–butane fraction on Pentasil at 500°C and higher temperatures, the major products are aromatic hydrocarbons; methanation also occurs intensively. In conjugate conversion of methanol and propane–butane fraction on Pentasil, the major gaseous products are C_2–C_4 alkenes, and the major liquid products are arenes.

(3) In successive cycles of catalyst operation and regeneration, the yield of lower olefins increases, which is due to high-temperature effect on Pentasil of water formed in the process and to a decrease in the total acidity of the catalyst.

REFERENCES

1. Babash, S.E. and Mukhina, T.N., *Khim. Prom–st.*, 1998, no. 4, pp. 195–197.
2. Nowak, S., Günschel, H., Lantzsch, J., and Anders, K., *Neftekhimiya*, 1987, vol. 27, no. 6, pp. 736–749.
3. Minachev, Kh.M. and Dergachev, A.A., *Izv. Ross. Akad. Nauk, Ser. Khim.*, 1993, no. 6, pp. 1018–1028.
4. Vos'merikov, A.V. and Erofeev, V.I., *Zh. Prikl. Khim.*, 1993, vol. 66, no. 10, pp. 2277–2281.
5. Dejaifve, P., Gravelle, P.C., Vedrine, J.C., *et al.*, *J. Catal.*, 1981, vol. 70, no. 1, pp. 123–136.
6. Derouane, E.G., Nagy, J.B., Dejaifve, P., *et al.*, *J. Catal.*, 1978, vol. 53, no. 1, pp. 40–55.
7. US Patent 4025576.
8. Ryabov, Yu.V. and Erofeev, V.I., *Izv. Akad. Nauk SSSR, Ser. Khim.*, 1986, no. 9, pp. 1966–1970.
9. Ryabov, Yu.V., Korobitsyna, L.L., and Erofeev, V.I., *Zh. Fiz. Khim.*, 1987, vol. 61, no. 7, pp. 1817–1820.

Russian Journal of Applied Chemistry, Vol. 75, No. 12, 2002, pp. 1984–1989. Translated from Zhurnal Prikladnoi Khimii, Vol. 75, No. 12, 2002, pp. 2021–2025.
Original Russian Text Copyright © 2002 by R. Aliev, M. Aliev, A. Aliev.

PROCESSES AND EQUIPMENT OF CHEMICAL INDUSTRY

Continuous Selective Heating of the Dispersion Medium in a Unit Constituted by Heater and Mass-Exchange Apparatus

R. Z. Aliev, M. R. Aliev, and A. R. Aliev

Daghestan Research Institute of Viticulture and Processing Products, Mamedkala, Daghestan, Russia
Institute of Physics, Daghestan Scientific Center, Russian Academy of Sciences, Makhachkala, Daghestan, Russia

Received March 18, 2002

Abstract—A new method for heat exchange between dispersed flows and a unit for continuous selective heating, comprising a heater and a mass-exchange apparatus, was proposed. A mathematical model of the unit was developed for the cases of direct-flow and counterflow heaters. Analytical solutions to the model equations were obtained. The parameters affecting the result of continuous selective heating of the dispersion medium in the unit were determined.

Suspensions, gas-dispersed systems, or other dispersed systems are commonly heated by heat exchange in known apparatus with impermeable surface or in more complex apparatus with cleanable heat-exchange surface [1–3]. In apparatus of this kind, solid particles of material, contained in the dispersion medium, and the carrying continuous phase are subjected to a not-always-desirable identical direct action of the high-temperature heat-carrying agent.

For example, in the known thermochemical and power apparatus for thermal treatment of a flow of a gas-dispersed system containing pneumatically transported solid particles, both the gas and the particles themselves are subjected in the thermal treatment chamber to identical action of high temperature [1]. Dispersed particles or gas may undergo thermochemical decomposition or change irreversibly their properties. This may also occur in thermal treatment of a hydrodispersion, e.g., suspensions or sludges containing thermolabile phases, in fine chemical and foodstuff technologies, in which unacceptable overheating of solid particles of a product at the heat-exchange surface may affect its composition and quality [3].

Therefore, it is advisable to carry out, in some thermochemical, fine chemical, and foodstuff technologies, separate thermal treatment of the dispersed solid and continuous fluid or gas phases of the dispersion under conditions optimal for each phase. A technological scheme for such a treatment, e.g., for heating of the continuos phase of the dispersion involves three stages: separation of the dispersion into continuous and solid phases in a separator, transport of the solid phase from the separator to a mixer, heating of the continuous phase in a heat exchanger, and its mixing with the solid phase in the mixer. The multistage nature of this scheme and impossibility of performing the entire process in a continuous mode are apparent.

In the present study, we developed a process and a unit comprising a heater and a mass-exchange apparatus for continuous selective heating of the continuous phase of the dispersion on the basis of a new technique for mass exchange between dispersed flows across a convectively permeable surface, constructed a mathematical model of the process, and carried out calculations on its base.

We propose to use for selective heating of the continuous phase a continuous process according to which the separation of the dispersion into phases, the transport of the dispersed phase, and its mixing with the heated continuous phase are combined in the same continuous, valve-pulsatory mass-and-heat-exchange apparatus (VPMA) described in [4–6]. This method can be implemented in a unit (Fig. 1) comprising a heater (H) and VPMA (M) connected in a circuit with a circulatory pump. The VPMA contains two spaces *1* and *2*, separated by a porous semi-permeable partition *3*. The VPMA also includes a set

1070-4272/02/7512-1984 $27.00 © 2002 MAIK "Nauka/Interperiodica"

of valves *4–7*. The heater H contains a space for the continuous phase *8* being heated and for the heat-carrying agent *9*, separated by an impermeable partition *10*. The dispersion, containing the continuous phase being heated, with the initial temperature of the continuous phase equal to θ_L^{ini}, is delivered into channel *1* of VPMA through a valve *4*, and the heated continuous phase, coming out of the heater H, is delivered as a counterflow into the adjacent channel *2* through a valve *6* with temperature θ_L^{out}. The pulsatory system, including computer-controlled valves *4–7*, creates alternating pressure differences between the channels, with the result that the flows moving in VPMA repeatedly exchange portions of the continuous phase, without mixing their dispersed phases. In this case, counterflow convective mass-and-heat exchange results in that the cold continuous phase passes from channel *1* into channel *2*. The continuous phase being heated is delivered from channel *2* of VPMA through valve *5* with temperature θ_L^{in} to the inlet of the space *8* of the heater H. Hot heat-carrying agent with temperature θ_T^{in} is delivered to the inlet of the space *9* of the heater H. Heated continuous phase with temperature θ_L^{fin} is discharged, together with the dispersed phase, from channel *1* of VPMA through valve *7*.

The advantage of the given unit consists in that it enables continuous selective heating of the continuous phase of the dispersion. The dispersed phase does not penetrate into the heater and is not subjected to direct action of its hot wall.

The convective mass-and-heat exchange in VPMA was studied in [7–12].

The efficiency of a VPMA is characterized by the extent E of heat exchange, which is a constant parameter for a given VPMA [6, 9–12]. In the case in question, the parameter E is defined by:

$$E = \frac{\theta_L^{ini} - \theta_L^{fin}}{\theta_L^{ini} - \theta_L^{out}}. \quad (1)$$

Let us write down a heat balance equation for the VPMA:

$$\varepsilon\theta_L^{ini} + \theta_L^{out} = \varepsilon\theta_L^{fin} + \theta_L^{in}, \quad (2)$$

where ε is the porosity of the dispersion medium in the first channel of VPMA.

Equation (2) accounts for the fact that the volumetric flow rates in both channels of VPMA are the same. The heat balance for the heater can be represented as:

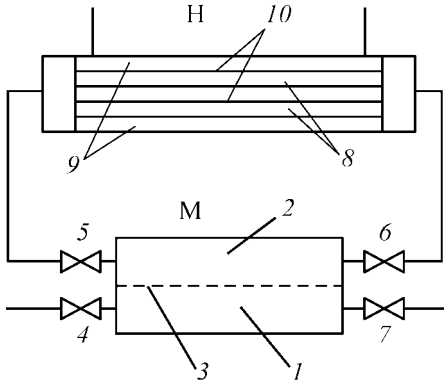

Fig. 1. Schematic of the unit comprising a heater H and mass-and-heat exchange apparatus M for permanent selective heating of the continuous phase of the dispersion: (*1*, *2*) channels of the mass-and-heat exchange apparatus, (*3*) permeable partition, (*4–7*) valves, (*8*) space for continuous phase being heated, (*9*) space for heat-carrying agent, and (*10*) impermeable partition.

$$|B|(\theta_L^{in} - \theta_L^{out}) + (\theta_T^{in} - \theta_T^{out}) = 0,$$

$$|B| = \frac{c_{pL}\rho_L|g_L|}{c_{pT}\rho_T g_T}, \quad (3)$$

where c_p is the specific heat under constant pressure, ρ is the density, the subscripts "L" and "T" make it possible to distinguish the continuous phase being heated and the heat carrying agent, the superscripts "in" and "out" refer to the inlet and outlet temperatures in the heater, and the superscripts "ini" and "fin" indicate the initial (at the unit inlet) and final (at the unit outlet) temperatures.

The volumetric flow rates of the continuous phase being heated, g_L, and of the heat-carrying agent, g_T, have the same signs for a direct-flow heater and opposite signs for a counterflow one. Equation (3) involves the absolute values of the volumetric flow rates.

Thus, six temperatures at the inlets and outlets of the VPMA and heater are related by three equations, (1)–(3). Having set three temperatures, we can determine the remaining three. Commonly, the following temperatures are known: temperature θ_L^{ini} of the continuous phase being heated, at the VPMA inlet (unit entry); temperature θ_T^{in} of the heat-carrying agent at the heater inlet; and temperature θ_L^{fin} of the continuous phase being heated, at the VMPA outlet (unit output). Then we can find from Eqs. (1)–(3) the temperatures θ_L^{in}, θ_L^{out}, and θ_T^{out}:

$$\theta_L^{out} = \theta_L^{ini} + \frac{1}{E}(\theta_L^{fin} - \theta_L^{ini}), \quad (4)$$

$$\theta_L^{in} = \theta_L^{ini} + \left(\frac{1}{E} - \varepsilon\right)(\theta_L^{fin} - \theta_L^{ini}), \quad (5)$$

$$\theta_T^{out} = \theta_T^{in} - \varepsilon|B|(\theta_L^{fin} - \theta_L^{ini}). \quad (6)$$

Thus, we find the temperatures of the continuous phase being heated and the heat-carrying agent at the inlets and outlets of the heater, which are necessary for a prescribed mode of unit operation. Further, we have to calculate the heater parameters ensuring the required temperatures of the continuous phase being heated and the heat-carrying agent.

Let us write the equation of convective heat exchange for the continuous phase (or heat-carrying agent) in the heater in the differential form [13]:

$$c_p\rho\left(\frac{\partial\theta}{\partial t} + \mathbf{w}\,\mathrm{grad}\,\theta\right) - \lambda\,\mathrm{div}(\mathrm{grad}\,\theta) = 0, \quad (7)$$

$$-\lambda\,\mathrm{grad}\,\theta = \alpha(\theta_w - \theta)\mathbf{e}, \quad (8)$$

where t is time; c_p, the specific heat at constant pressure; ρ, the density; $\theta = \theta(x, y, z, t)$, temperature; **w**, velocity; λ, the heat conductivity; θ_w, the temperature of the heat-exchange surface; α, the heat-transfer coefficient at heater walls; **e**, the unit vector of the external normal to the heater surface.

Equation (7) is a balance equation for the heat of the continuous phase, and Eq. (8) is the continuity equation for the flux of heat at the heater wall. Let us analyze the case when c_p, ρ, λ, and α can be considered temperature-independent. This assumption is commonly valid for a fluid, and, in the case of small variations of temperature and density, also for a gas.

Let us align the heater axis with the flow direction of the continuous medium being heated. We choose a small element of volume, $dV = s\,dx$, bounded by two closely spaced cross-sections s of the heater and a part of the lateral surface, $\pi_f\,dx$, between them. Here dx is the distance between the chosen cross-sections (infinitely small), and π_f is the perimeter of the cross-section s. Let us integrate Eq. (7) over the volume chosen, with account of the fact that, in the flow of the continuos phase along the heater, the velocity divergence of the continuous phase is zero, the flux of the velocity vector **w** across the lateral surface is zero, and the flux of heat across the lateral surface is determined by the condition (8). Dividing by the specific heat of the chosen volume, we obtain an equation for temperature averaged over the heater cross-section:

$$\frac{\partial\theta}{\partial t} + u\frac{\partial\theta}{\partial x} - \frac{\lambda}{c_p\rho}\frac{\partial^2\theta}{\partial x^2} - \frac{\alpha\pi_f}{c_p\rho s}(\theta_w - \theta) = 0, \quad (9)$$

where u is the x-component of the cross-section-average flow velocity of the continuous phase.

Let us now pass to dimensionless variables by the following rules:

$$T = \frac{ut}{l_0},\quad X = \frac{x}{l_0},\quad \Theta = \frac{\theta - \theta_L^{ini}}{\theta_T^{in} - \theta_L^{ini}}, \quad (10)$$

where l_0 is the heater length.

In a flow of the continuous phase along the heater, the following condition is commonly satisfied:

$$\frac{1}{\mathrm{Pe}} = \frac{\lambda}{c_p\rho u l_0} << 1. \quad (11)$$

With account of (11), Eq. (9) in dimensionless variables will take, for the steady-state case, the form:

$$\frac{\partial\Theta}{\partial X} - \frac{\alpha f}{c_p\rho g}(\Theta_w - \Theta) = 0, \quad (12)$$

where $g = us$ is the volumetric flow rate, and $f = \pi_f l_0$ is the total heat-exchange surface.

In the steady state, it follows from the heat flux continuity condition that:

$$\alpha_T(\theta_T - \theta_{wT}) = \frac{\lambda_w}{\delta_w}(\theta_{wT} - \theta_{wL})$$

$$= \alpha_L(\theta_{wL} - \theta_L) = K(\theta_T - \theta_L), \quad (13)$$

where θ_{wT} and θ_{wL} are the heater wall temperatures from the sides of, respectively, the heat-carrying agent and the continuous phase being heated; λ_w and δ_w are the heat conductivity and thickness of the heater wall; K is the coefficient of heat transfer between the flow of the heat-carrying agent and that of the continuous phase being heated.

Eliminating the wall temperatures θ_{wT} and θ_{wL} from Eq. (13), we obtain an expression for the heat-transfer coefficient:

$$\frac{1}{K} = \frac{1}{\alpha_T} + \frac{\delta_w}{\lambda_w} + \frac{1}{\alpha_L},$$

$$K = \frac{\alpha_T\alpha_L\lambda_w}{\alpha_T\lambda_w + \alpha_L\lambda_w + \alpha_T\delta_w}. \quad (14)$$

Then, having written Eq. (12) for the continuous phase being heated and for the heat-carrying agent, we obtain, with account of (13) and (14),

$$\frac{d\Theta_L}{dX} - A(\Theta_T - \Theta_L) = 0, \quad (15)$$

$$\frac{d\Theta_T}{dX} + AB(\Theta_T - \Theta_L) = 0, \quad (16)$$

$$A = \frac{K}{c_{pL}\rho_L g_L}, \quad B = \frac{c_{pL}\rho_L g_L}{c_{pT}\rho_T g_T}, \quad F(X) = \frac{\pi_f x}{f}. \quad (17)$$

For the direct flow, $g_L > 0$, $g_T > 0$, $A > 0$, and $B > 0$; for the counter flow, $g_L > 0$, $g_T < 0$, $A > 0$, and $B < 0$. Solutions to Eqs. (15) and (16) have the following form [13]:

$$\Theta_L(X) = \frac{\Theta_T(0) + B\Theta_L(0)}{1 + B} - \frac{1}{1 + B}[\Theta_T(0) - \Theta_L(0)]\exp[-A(1 + B)(X)], \quad (18)$$

$$\Theta_T(X) = \frac{\Theta_T(0) + B\Theta_L(0)}{1 + B} + \frac{B}{1 + B}[\Theta_T(0) - \Theta_L(0)]\exp[-A(1 + B)F(X)], \quad (19)$$

In a particular case, at $B = -1$

$$\Theta_L(X) = \Theta_L(0) + A[\Theta_T(0) - \Theta_L(0)]F(X), \quad (20)$$

$$\Theta_T(X) = \Theta_T(0) + A[\Theta_T(0) - \Theta_L(0)]F(X). \quad (21)$$

The heat balance equation (3) for the heater can be written in dimensionless form:

$$B[\Theta_L(0) - \Theta_L(1)] + \Theta_T(0) - \Theta_T(1) = 0. \quad (22)$$

From Eq. (18) we find the parameter A:

$$A = \frac{1}{1 + B}\ln\left[\frac{\Theta_T(0) - \Theta_L(0)}{\Theta_T(0) + B\Theta_L(0) - (1 + B)\Theta_L(1)}\right]. \quad (23)$$

With a knowledge of the dimensionless temperatures $\Theta_L(0)$, $\Theta_T(0)$, $\Theta_L(1)$, $\Theta_T(1)$, we can find the parameter A and the necessary heat-exchange surface area f from (23) and (17).

For a unit with a direct-flow heater ($B > 0$), we have

$$\Theta_L(0) = \Theta_L^{in}, \ \Theta_T(0) = \Theta_T^{in}, \quad \Theta_L(1) = \Theta_L^{out}, \ \Theta_T(1) = \Theta_T^{out}. \quad (24)$$

Then, we obtain from (23) with account of (4)–(6):

$$A = \frac{1}{1 + B}\ln\frac{E - (1 - \varepsilon E)\Theta_L^{fin}}{E - (1 + \varepsilon EB)\Theta_L^{fin}}. \quad (25)$$

From Eq. (25) follow the inequalities:

$$0 \le \Theta_L^{fin} \le \frac{E}{1 + \varepsilon E} \le \frac{E}{1 - \varepsilon E}. \quad (26)$$

Using (26), we can find the interval of possible values for one of the quantities ε, E, B, Θ_L^{fin}, if the other three are set. For example, at preset values of the parameters ε, E, and B, the maximum possible dimensionless temperature of the continuous phase being heated, at the outlet of a unit with direct-flow heater, can be calculated by the formula

$$\Theta_{L\,max}^{fin} = \frac{E}{1 + \varepsilon EB} \le E, \quad (27)$$

with the maximum only reached at $A \to \infty$.

For a unit with counterflow heater ($B < 0$), we have

$$\Theta_L(0) = \Theta_L^{in}, \ \Theta_T(0) = \Theta_T^{out}, \quad \Theta_L(0) = \Theta_L^{out}, \ \Theta_T(0) = \Theta_T^{in}. \quad (28)$$

Then we obtain from formulas (22) and (23), with account of (4)–(6),

$$A = \frac{1}{1 + B}\ln\left[\frac{1 + \left(\varepsilon + \varepsilon B - \frac{1}{E}\right)\Theta_L^{fin}}{1 - \frac{1}{E}\Theta_L^{fin}}\right]. \quad (29)$$

Using expression (29), we can find the limit at $B = -1$:

$$\lim_{B \to -1} A = \frac{\varepsilon E\Theta_L^{fin}}{E - \Theta_L^{fin}}. \quad (30)$$

Let us write the following possible intervals for the dimensionless temperature of the continuous phase being heated, at the outlet of a unit with a counterflow heater

$$0 \le \Theta_L^{fin} \le \Theta_{L\,max}^{fin}, \quad (31)$$

$$\Theta_{L\,max}^{fin} = \frac{E}{1 - \varepsilon E(1 + B)} \text{ at } 1 + B < 0, \quad (32)$$

$$\Theta_{L\,max}^{fin} = E \text{ at } 1 + B > 0, \quad (33)$$

with these maximum values only reached at $A \to \infty$.

Comparison of formula (27) with (32) and (33) shows that, all other conditions being the same,

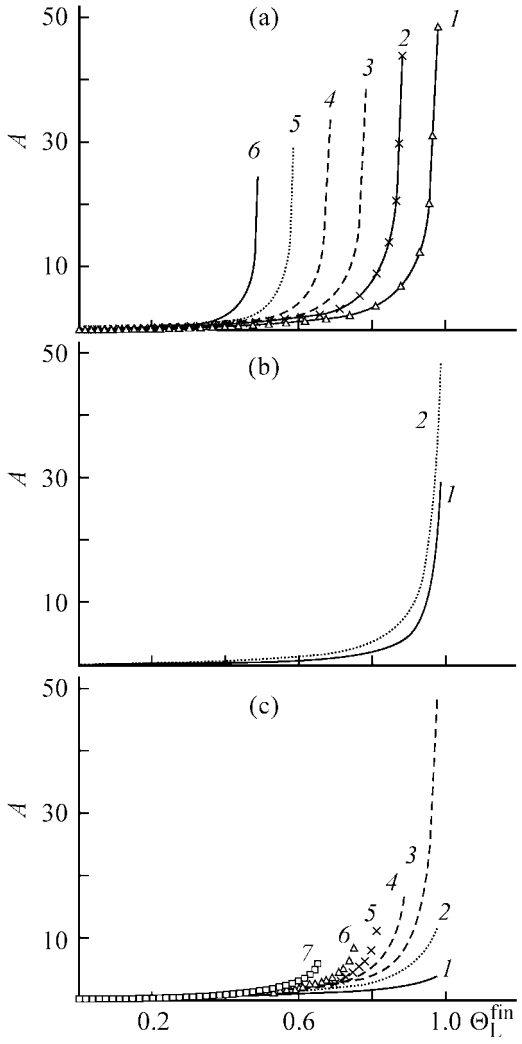

Fig. 2. Parameter A vs. preset dimensionless temperature Θ_L^{fin} of the continuous phase being heated, at the outlet of a unit with counterflow heater. (a) $\varepsilon = 1$, $B = -1$; (b) $E = 1$, $B = -1$; (c) $E = 1$, $\varepsilon = 1$. (a) Degree of heat exchange, E: (*1*) 1.0, (*2*) 0.9, (*3*) 0.8, (*4*) 0.7, (*5*) 0.6, and (*6*) 0.5. (b) Porosity: (*1*) 0.6 and (*2*) 1.0. (c) Parameter B: (*1*) 0, (*2*) 0.8, (*3*) 1.0, (*4*) 1.1, (*5*) 1.2, (*6*) 1.3, and (*7*) 1.5.

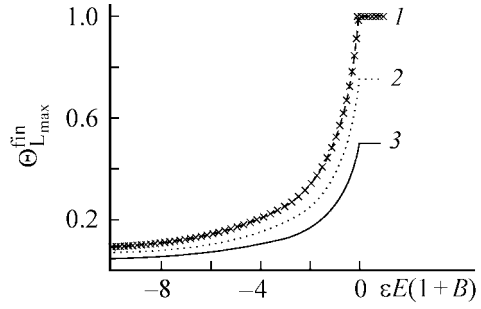

Fig. 3. Maximum dimensionless temperature of the continuous phase being heated, $\Theta_{L\,max}^{fin}$, at the outlet of a unit with counterflow heater vs. the product $\varepsilon E(1 + B)$. Degree of heat exchange E: (*1*) 1.0, (*2*) 0.75, and (*3*) 0.5.

the unit with counterflow heater is more efficient than that with a direct-flow heater. The efficiency of the unit can be characterized by the dimensionless temperature Θ_L^{fin}. The higher Θ_L^{fin}, the better the efficiency of the unit.

Let us calculate the final temperature of the dispersion medium in the outlet pipe of VPMA

$$\theta^{fin} = \frac{\varepsilon c_{pL}\rho_L\theta_L^{fin} - (1 + \varepsilon)c_p S\rho_S\theta_S^{ini}}{\varepsilon c_{pL}\rho_L - (1 + \varepsilon)c_p S\rho_S}, \qquad (34)$$

where the subscript "S" indicates the dispersed phase.

Figure 2 shows dependences of the parameter A on the preset dimensionless temperature Θ_L^{fin} of the continuous phase being heated, at the outlet of a unit with a counterflow heater, at different values of the degree E of heat exchange (Fig. 2a), porosity of the dispersion medium (Fig. 2b), and parameter B (Fig. 2c). Similar curves can also be calculated for a unit with directflow heater, using formula (25) with account of inequality (26).

With increasing absolute value of the parameter B and porosity ε of the dispersion medium and decreasing degree E of heat exchange, the value of the parameter A, necessary for prescribed Θ_L^{fin} to be obtained, grows. The increase in A at preset physical properties and flow rates of the continuous phase being heated and the heat-carrying agent means that the heat-exchange surface area, and, consequently, the heater length become greater.

It can be seen from Fig. 3 that the maximum dimensionless temperature of the continuous phase being heated, at the outlet of a unit with counterflow heater, calculated using formulas (32) and (33), decreases with increasing absolute value of $\varepsilon E(1 + B)$ and decreasing E.

CONCLUSIONS

(1) It was established that the process of continuous selective heating of the continuous phase of the dispersion in a unit comprising a heater and a mass-and-heat-exchange apparatus is affected by the following parameters: E, the degree of heat exchange in a valve-pulsatory mass-and-heat-exchange apparatus; ε, the porosity of the dispersion medium being heated; A, the ratio of the heat flux across the heat-exchange surface in the heater at unit temperature gradient to the specific heat of the continuous phase being heated, flowing through the heater in unit time; $|B|$, the ratio of the heat capacities of

the continuous phase being heated and the heat-carrying agent, flowing through the heater in unit time.

(2) It was found that, all other conditions being the same, a unit with counterflow heater has higher efficiency than that with direct-flow heater.

(3) It was established that the efficiency of the unit comprising a heater and a mass-and-heat-exchange apparatus is the higher, the greater E and A and the smaller ε and $|B|$.

REFERENCES

1. Gorbis, Z.R., *Teploobmen i gidromekhanika dispersnykh skvoznykh potokov* (Heat-Exchange and Hydromechanics of Through Dispersion Flows), Moscow: Energiya, 1970.
2. Kasatkin, A.G., *Osnovnye protsessy i apparaty khimicheskoi tekhnologii* (Basic Processes and Apparatus of Chemical Technology), Moscow: Khimiya, 1971.
3. Borchenkova, L.A., Leonov, I.T., and Fromzel', O.G., *Asepticheskoe konservirovanie geterogennykh produktov* (Aseptic Preserving of Heterogeneous Foodstuff Products), Moscow: TsNIITEIpishcheprom, 1984, issue 9.
4. USSR Inventor's Certificate, no. 1 091 018.
5. USSR Inventor's Certificate, no. 1 213 308.
6. Aliev, M.R., Aliev, R.Z., and Aliev, A.R., *Teor. Osn. Khim. Tekhnol.*, 2001, vol. 35, no. 3, pp. 288–297.
7. Aliev, M.R. and Aliev, R.Z., *Teor. Osn. Khim. Tekhnol.*, 1997, vol. 31, no. 1, pp. 102–104.
8. Aliev, M.R., Aliev, R.Z., and Aliev, A.R., *Teor. Osn. Khim. Tekhnol.*, 1999, vol. 33, no. 1, pp. 23–29.
9. Aliev, M.R., Aliev, R.Z., and Aliev, A.R., *Mat. Model.*, 1998, vol. 10, no. 7, pp. 48–60.
10. Aliev, R.Z., Aliev, M.R., and Aliev, A.R., *Khim. prom-st'*, 2000, no. 5, pp. 22–33.
11. Aliev, R.Z., Aliev, M.R., and Aliev, A.R., *Zh. Prikl. Khim.*, 2001, vol. 74, no. 12, pp. 2006–2012.
12. Aliev, A.R., Aliev, M.R., and Aliev, R.Z., *Teploenergetika*, 2002, vol. 49, no. 6, pp. 64–69.
13. Romankov, P.G. and Frolov, V.F., *Teploobmennye protsessy v khimicheskoi tekhnologii* (Heat-Exchange Processes in Chemical Technology), Leningrad: Khimiya, 1982.

Russian Journal of Applied Chemistry, Vol. 75, No. 12, 2002, pp. 1990–1992. Translated from Zhurnal Prikladnoi Khimii, Vol. 75, No. 12, 2002, pp. 2026–2028.
Original Russian Text Copyright © 2002 by Skokina, Voronchikhina.

ORGANIC SYNTHESIS AND INDUSTRIAL ORGANIC CHEMISTRY

Cleansing Action of Synergistic Mixtures of Surfactants in Pretreatment of Glass Fibers before Electroless Metal Plating

R. E. Skokina and L. I. Voronchikhina

Tver State University, Tver, Russia

Received January 8, 2002

Abstract—Cleansing action of synergistic mixtures of cationic and nonionic surfactants as influenced by their composition, temperature, and contact time is studied with the aim of developing detergents for pretreatment of thin glass fibers before electroless metal plating.

Applying thin (<1 μm) metallic (Cu, Ni, Co) coatings onto glass fibers by electroless metal plating solutions requires fiber surface pretreatment (degreasing), to remove paraffinic and dextrin-oil glass fiber sizers (the presence of such sizers on the fiber surface considerably decreases the wettability of glass fibers and the adhesion strength of coatings).

The procedure for fiber surface pretreatment largely controls extent the coating quality, adhesion to the support, continuity, and electrical conductivity (these characteristics are crucial in using metal-plated glass fibers in electronic countermeasure systems. There are two routine degreasing methods: treatment with organic solvents or special solutions and thermal treatment. Application of these traditional methods to thin (5–8 and 7–10 μm in diameter) glass fibers does not provide the desired result, since thermal treatment decreases the fiber strength (by up to 40%), and the use of chlorinated hydrocarbons requires their frequent regeneration to remove oils. Furthermore, these compounds are toxic, which makes necessary specially designed facilities.

Use of detergents containing phosphates, silicates, and alkali (commonly used in electroplating) also affects adversely the strength of thin glass fibers, since they have highly developed surface (compared to glass), failing faster in aggressive media. As a result, their strength decreases by 50–60% [1]. Therefore, the goal was to decrease the destructive effect of detergents on glass fibers in the course of their pretreatment before electroless metal plating. We studied synergistic mixtures of surfactants and recommended them for practical use in pretreatment of glass fibers before metal plating.

It is known that, on passing from individual surfactants to their mixtures, synergistic effects are often observed [2]. For example, the use of mixtures of surfactants with stepwise increasing polarity considerably improves removal of sizers. We found in the literature information on both synergistic and antagonistic effects of surfactant binary mixtures on such properties as micelle formation, solubility, cleansing action, etc. [3].

Widely used mixtures of ionic and nonionic surfactants demonstrate synergism in cleansing action [4, 5].

In this study, we used as cleaning fluids for pretreatment of glass fibers mixtures of cationic [cetyltriethylammonium bromide $C_{16}H_{33}N(C_2H_5)_3Br$, dodecyltriethylammonium bromide $C_{12}H_{25}N(C_2H_5)_3Br$, and decyltriethylammonium bromide $C_{10}H_{21}N(C_2H_5)_3Br$] and nonionic surfactants [Syntanol DS-10 (polyethylene glycol monoalkyl ether based on primary fatty alcohols, $C_nH_{2n+1}(C_2H_4O)_mH$, n = 10–18, m = 8–10) and OP-10 (polyethylene glycol monoalkylphenyl ether $C_nH_{2n+1}C_6H_4O(C_2H_4O)_mH$, n = 8–10, m = 10–12)]. We studied the effect of the detergent concentration and the degreasing temperature and time on the degreasing efficiency. The cleansing action (degree of degreasing) was estimated gravimetrically and also from the wetting angles of model glass surfaces pretreated by dressing. The detergent compositions were optimized by varying the surfactant mixture composition. The total surfactant content in the mixtures was constant (0.1 wt %). The cleansing action of synergistic mixtures as a function of their composition is illustrated in Fig. 1. In the $C_{16}H_{33}N(C_2H_5)_3Br$–DS-10 system, the maximal

1070-4272/02/7512-1990 $27.00 © 2002 MAIK "Nauka/Interperiodica"

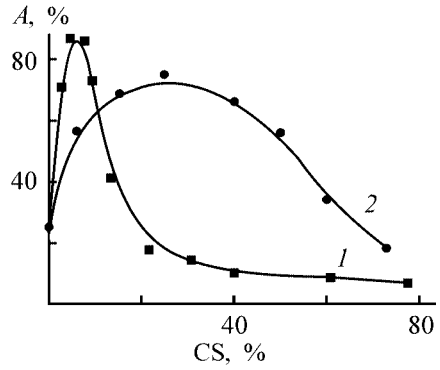

Fig. 1. Cleansing action *A* of synergistic mixtures vs. their composition. (CS) Fraction of the cationic surfactant in a mixture; the same for Fig. 4. Detergent: (*1*) $C_{16}H_{33}N(C_2H_5)_3Br$–DS-10 and (*2*) $C_{10}H_{21}N(C_2H_5)_3Br$–DS-10.

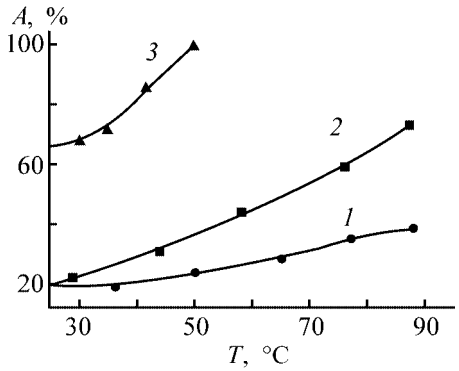

Fig. 3. Degree *A* of degreasing of the glass fiber surface vs. temperature *T*. Degreasing time 5 min. Detergent: (*1*) H_2O, (*2*) Syntanol DS-10, and (*3*) $C_{16}H_{33}N(C_2H_5)_3Br$–DS-10 (5 : 95).

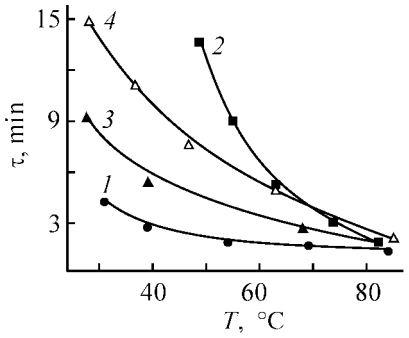

Fig. 2. Time of complete degreasing τ vs. temperature *T*. Detergent: (*1*) $C_{16}H_{33}N(C_2H_5)_3Br$–DS-10 (5 : 95), (*2*) Syntanol DS-10, (*3*) $C_{12}H_{25}N(C_2H_5)_3Br$–DS-10 (30 : 70), and (*4*) OP-10.

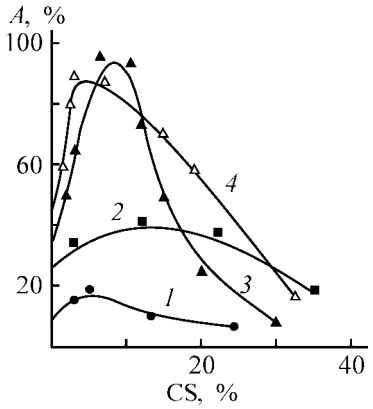

Fig. 4. Cleansing action *A* of $C_{16}H_{33}N(C_2H_5)_3Br$–DS-10 at various temperatures (°C): (*1*) 15, (*2*) 65, (*3*) 45, and (*4*) 35.

cleansing action is observed at a component ratio of 5 : 95. In the other systems, the maximum shifts toward higher concentrations of a cationic surfactant. In the system $C_{10}H_{21}N(C_2H_5)_3Br$–DS-10 it is observed at the 25 : 75 ratio (Fig. 1, curve *2*).

The results obtained show that the degreasing proceeds slowly at low temperatures, being accelerated on heating (Fig. 2), evidently, because of the increasing activity of the surfactants and decreasing viscosity of oils. Also, we observed the effect of the structure of a cationic surfactant on its degreasing efficiency: compounds with longer hydrocarbon chains (C_{16}) are more effective, which allows reduction of the degreasing time and temperature. At low temperatures the synergistic mixtures are more favorable, since the same degreasing effect is achieved at lower temperature (Fig. 3). The composition corresponding to the maximal cleansing action of the synergistic mixtures depends on temperature (Fig. 4). For the system $C_{16}H_{33}N(C_2H_5)_3Br$–DS-10 (5 : 95), the maximal cleansing action is observed at 35°C. The absolute maximum of the cleansing action in this system was observed for the composition 10 : 90 at 45°C. A study of how the cleansing action of a detergent depends on the liquor ratio showed that the synergistic mixtures are more efficient, whereas higher concentration of individual Syntanol DS-10 and OP-10 is required with increasing charge of fibers. However, addition of Syntanol above 0.1 wt % produces strong foaming (this is not the case with the synergistic mixtures).

There are several concepts of synergism in surfactant mixtures, their cleansing action, and other colloid-chemical properties. It is commonly accepted that the synergistic effect is associated with the formation of mixed micelles capable to sorb oil pollutants more effectively as compared to micelles formed with an individual surfactant [6]. In some cases, antagonism or synergism may be due to formation of heteroassociates [3] or interfacial adsorption of surfactants. It is known [7] that cationic surfactants demonstrate only

insignificant detergency; being adsorbed on negatively charged areas of the contaminated surface, they impart hydrophobic properties to it and impede wetting of the surface with water. At the same time, being a component of a synergistic mixture, a cationic surfactant facilitates adsorption of nonionic surfactants on the hydrophobized surface, decreasing the attraction between pollutant particles and the surface and also between separate pollutant particles. As a result, this facilitates detachment of the oil film from the fiber surface with the formation of an emulsion, i.e., the cleansing action of a detergent increases.

Finally, the results obtained on the synergistic mixtures of cationic and nonionic surfactants show that they can be recommended as components of cleaning solutions for pretreatment of glass fibers before electroless metal plating.

CONCLUSIONS

(1) Synergistic mixtures containing cationic surfactants with longer hydrocarbon chains ($C_{16}H_{33}$) demonstrate higher cleansing efficiency.

(2) In low-temperature degreasing of glass fibers, the cleansing action of synergistic mixtures of cationic and nonionic surfactants is considerably higher than that of individual components.

(3) Among the synergistic mixtures studied, the system $C_{16}H_{33}N(C_2H_5)_3Br$–DS-10 (5 : 95) demonstrates the highest cleansing effect in low-temperature degreasing of glass fibers.

REFERENCES

1. Levit, R.M., *Elektroprovodyashchie khimicheskie volokna* (Current-Conducting Chemical Fibers), Moscow: Khimiya, 1986.
2. Demchenko, P.A., *Zh. Vses. Khim. O–va*, 1966, vol. 11, no. 7, pp. 381–385.
3. Mitsevich, N.A., Dergacheva, L.A., Tugushi, L.A., *et al., Kolloidn. Zh.*, 1978, vol. 40, no. 3, pp. 557–558.
4. Rubingh, D.H. and Jones, T., *Ind. Eng. Chem.*, 1982, vol. 21, no. 2, pp. 176–182.
5. Lutsenko, V.A., Panich, R.M., and Korenkova, O.P., *Kolloidn. Zh.*, 1975, vol. 37, no. 1, pp. 181–184.
6. Verezhnikov, V.N., Kashlinskaya, P.S., and Garaeva, N.G., *Kolloidn. Zh.*, 1974, vol. 36, no. 3, pp. 535–536.
7. Täuber, T., *Tenside Detergents*, 1982, vol. 19, no. 3, pp. 151–154.

Russian Journal of Applied Chemistry, Vol. 75, No. 12, 2002, pp. 1993–1998. Translated from Zhurnal Prikladnoi Khimii, Vol. 75, No. 12, 2002, pp. 2029–2035.
Original Russian Text Copyright © 2002 by Men'shikova, Evseeva, Chekina, Peretolchin, Skurkis, Ivanchev.

MACROMOLECULAR CHEMISTRY AND POLYMERIC MATERIALS

Synthesis of Monodisperse Polymethyl Methacrylate Particles in Buffer Solutions under the Action of Carboxyl-Containing Initiator

A. Yu. Men'shikova, T. G. Evseeva, N. A. Chekina, M. V. Peretolchin, Yu. O. Skurkis, and S. S. Ivanchev

Institute of Macromolecular Compounds, Russian Academy of Sciences, St. Petersburg, Russia

Received March 29, 2002

Abstract—Influence exerted by salts with buffering action and by the initial pH of the reaction mixture on the polymerization kinetics, viscosity-average molecular weight, and amount and degree of surface carboxylation of polymethyl methacrylate particles formed in the course of emulsifier-free emulsion polymerization of methyl methacrylate initiated by 4,4'-azobis(4-cyanoisovaleric acid) was studied.

Synthesis of monodisperse polymethyl methacrylate (PMMA) particles with surface carboxy groups by emulsion polymerization of methyl methacrylate (MMA) with a carboxyl-containing azo initiator is complicated by partial hydrolysis of the monomer to methacrylic acid (MAA), which is especially pronounced at high initial pH of the reaction mixture [1]. In this case, MAA formed in the course of the synthesis copolymerizes with MMA, producing water-soluble oligomeric products and considerably reducing the size of the resulting particles. In this context, the method for directed control of the size of polymer particles by varying the initial pH of the reaction mixture, which provides good results in polymerization of styrene [2, 3], needs further modification in the case of MMA. The essence of the method indicated is that, in the course of polymerization, terminal carboxy groups of the initiator residues move toward the interface during formation of polymer-monomeric particles (PMPs). The surface charge formed as a result of ionization of these groups stabilizes PMPs through electrostatic repulsion.

Therefore, the degree of ionization of the initiator carboxy groups and carboxyl-containing styrene polymerization products strongly affects the size of the resulting particles, which allows its directed control by varying the initial pH of the reaction mixture. However, in the course of MMA polymerization started in an alkaline medium, the formation of MAA shifts pH to lower values, thus reducing the surface charge of PMPs and impairing the stability of the polymer dispersion. Furthermore, insertion of units of a carboxyl-containing comonomer into the oligomeric chains reduces their surface activity, thus changing the PMP formation conditions. To overcome these difficulties and to reveal factors controlling characteristics of the resulting PMMA particles, we studied the effect of salts, capable of stabilizing pH in weakly acidic or weakly alkaline medium, on the course of synthesis.

EXPERIMENTAL

Methyl methacrylate, isoamyl alcohol, and DMF were purified by distillation by the standard procedures. 4,4'-azobis(4-cyanoisovaleric acid) (CVA) was purified and characterized as in [1]. Suberic acid $HOOC(CH_2)_6COOH$ ("Ferak"), NaOH, HCl, NaCl,

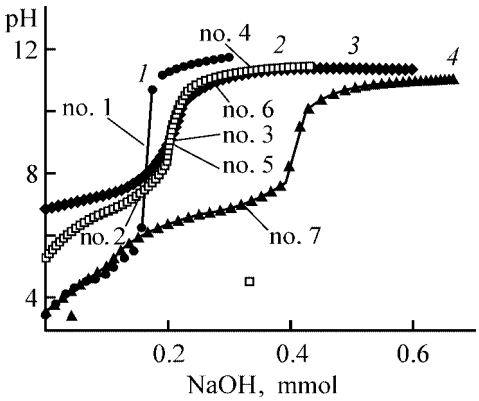

Fig. 1. Titration curves of the reaction mixture at 293 K. (NaOH) Amount of alkali consumed for titration. Salt concentration (M): (*1*) 0.02 M NaCl, (*2*) 0.01 M Na_2HPO_4, (*3*) 0.02 M Na_2HPO_4, and (*4*) 0.02 M KH_2PO_4. Nos. 1–7 correspond to run nos. in the table.

1070-4272/02/7512-1993 $27.00 © 2002 MAIK "Nauka/Interperiodica"

Effect of the salt composition of reaction mixtures on the steady-state polymerization rate of MMA r and characteristics of the resulting PMMA latexes

Run no.	Reaction mixture, M		pH_0	D, μm	S^*_{COOH}, μg-equiv m^{-2}	$r \times 10^5$, mol l^{-1} s^{-1}
	$c_{salt} \times 10^2$	$c_{NaOH} \times 10^2$				
1-0	–	1.21	5.51	0.63	2.36	2.16
2-0		1.37	8.25	0.60	1.31	1.47
3-0		1.60	11.08	0.39	0.96	1.54
1	NaCl, 2	1.37	9.01	0.7–0.8	–	1.58
2	Na_2HPO_4, 1	1.23	7.47	0.48	1.14	2.66
3		1.60	8.74	0.42	0.73	2.33
4		2.20	11.15	0.46	1.45	1.42
5	Na_2HPO_4, 2	1.60	9.10	0.73	1.41	1.17
6		2.20	10.95	0.48	1.22	1.11
7	KH_2PO_4, 2	2.29	6.93	0.72	0.99	1.08

* (S_{COOH}) Concentration of surface carboxy groups.

KH_2PO_4, and Na_2HPO_4 (analytically pure grade) were used without further purification. Double-distilled water was used as a dispersion medium.

The latexes were synthesized at 348 ± 1 K in the presence of 0.02 M NaCl or 0.01–0.02 M KH_2PO_4 or Na_2HPO_4 (initial pH 6.93–11.15) [1–3]. The amount of MMA in the reaction mixture was 10 wt %, and the CVA concentration, 7.14×10^{-3} M (2 wt % relative to MMA). The salt composition of the reaction mixtures is given in the table. The initial pH values of the reaction mixtures were determined by preliminary titration of the initiator [1] (run nos. are marked in Fig. 1). In the course of polymerization, samples of the reaction mixture were taken to determine the conversion of MMA, its surface tension, and current pH. The MMA concentration was determined by gas chromatography to within 5%, using isoamyl alcohol as internal reference. The surface tension at the interface between the reaction mixture and air was determined by the Du Noui method [4]. The pH was measured with a pH-121 instrument immediately after taking a sample and cooling it to 298 K.

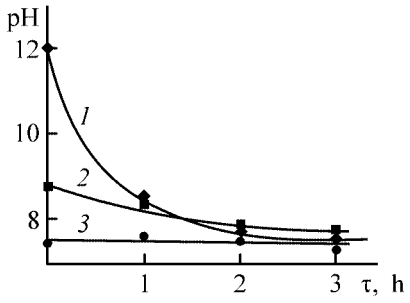

Fig. 2. pH of the reaction mixtures containing MMA, 0.01 M Na_2HPO_4, and suberic acid (instead of CVA) vs. the time τ at 348 K. pH_0: (*1*) 11.7, (*2*) 8.74, and (*3*) 7.47.

The diameter of latex particles D was found by electron microscopy (JEM 100 S, JEOL, Japan). After removal of water-soluble admixtures from latexes by centrifugation and redispersion in twice-distilled water, the surface carboxy groups were determined by conductometric titration [4]. The electrophoretic mobility of latex particles in 0.01 M NaCl was determined over a wide pH range (1.6–11.0) using the standard procedure [5]. The viscosity-average molecular weight (MW) of PMMA was found from the intrinsic viscosity measured at 20°C in DMF, using the Mark–Kuhn equation with $K = 1.73 \times 10^{-4}$ and $\alpha = 0.645$ [6].

The degree of MMA hydrolysis in synthesis of PMMA particles was estimated from data obtained with model reaction mixtures prepared with 0.01 M Na_2HPO_4, various amounts of NaOH, and suberic acid instead of CVA, to eliminate polymerization. pH was measured just after addition of MMA. Then the mixtures were allowed to stand at 348 K, and pH was measured at 3-h intervals (Fig. 2).

To study the effect of salt and pH value on CVA-initiated polymerization of MMA and characteristics of the resulting latex particles, we performed experiments with 0.01–0.02 M KH_2PO_4 and Na_2HPO_4, i.e., salts demonstrating buffer action in, respectively, weakly acidic and weakly alkaline solutions, and also with 0.02 M NaCl as an indifferent electrolyte, at varied initial pH of the reaction mixture. The compositions of the reaction mixtures and characteristics of

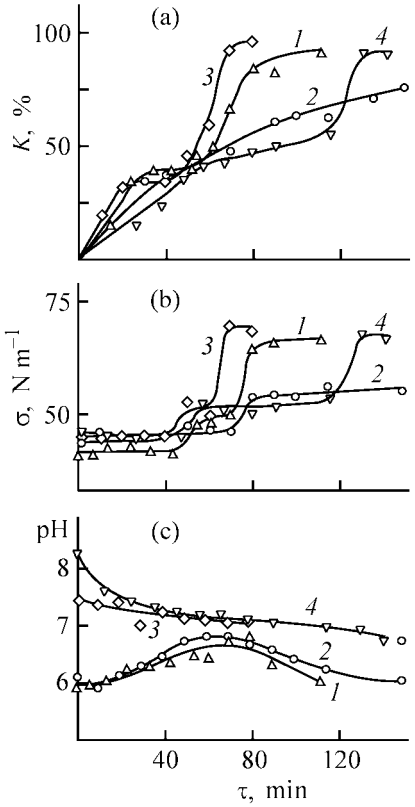

Fig. 3. Effect of salts on (a) MMA conversion *K*, (b) surface tension σ, and (c) pH. (τ) Time; the same for Fig. 4. (*1*) No salt, (*2*) 0.02 M NaCl, (*3*) 0.01 M Na_2HPO_4, and (*4*) 0.02 M KH_2PO_4. (*1–4*) Experiment nos. 1–0, 1, 2, and 7, respectively.

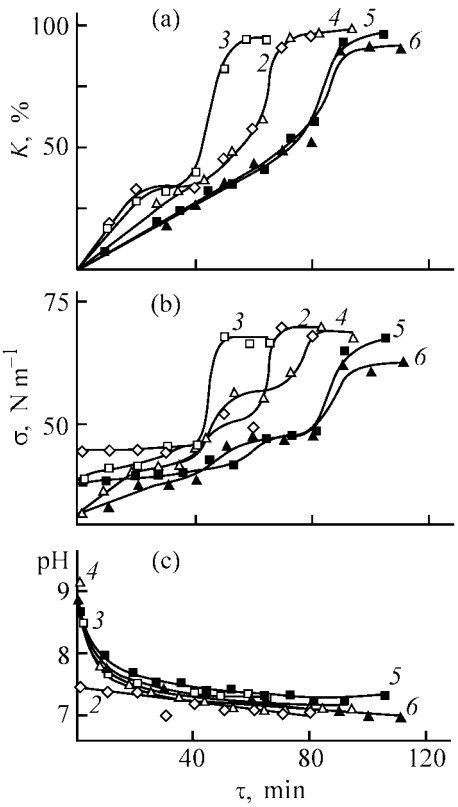

Fig. 4. Effects of Na_2HPO_4 and pH_0 on (a) MMA conversion *K*, (b) surface tension σ, and (c) pH. $NaHPO_4$ concentration (M): (*2–4*) 0.01 and (*5*, *6*) 0.02. (*2–6*) Experiment nos. 2–6, respectively.

latexes obtained in these experiments and also in the experiments conducted without salt additives [1] are listed in the table. Experiments with the model reaction mixtures revealed (Fig. 2) that, even with salt additives, the high initial pH values decrease considerably during the first hour, i.e., hydrolysis of MMA occurs and MAA appears in the mixture. Furthermore, it has been demonstrated previously in the experiments on polymerization of styrene that pH may change by virtue of the formation of a highly developed interfacial surface [2, 3]. Therefore, only data obtained in titration of the reaction mixtures at room temperature allow reliable determination of the amount of NaOH needed for setting the initial pHs (pH_0) corresponding to various fixed degrees of ionization of the initiator carboxy groups (note that, in the experimental pH range, the initiator is totally soluble in water).

The MMA conversion and the surface tension and pH of the reaction mixtures with or without salt additives are shown in Figs. 3 and 4 as functions of the polymerization time. An important factor in CVA-initiated emulsifier-free emulsion polymerization is the degree of ionization of the terminal carboxy groups in surface-active oligomers and of growing radicals formed in the aqueous phase (on approaching the critical length of the chain, they form primary particles). At low pH_0, these nuclei of the new phase are mainly formed from oligomers bearing terminal carboxy groups in the H form, since their surface activity is higher as compared to the ionized form [1]. In this case, pH of the reaction mixture increases somewhat, since part of the carboxy groups become incorporated in the bulk of the primary particles. By contrast, at high pH_0, pH decreases through neutralization of the alkali by the reaction with the carboxy groups on the highly developed surface of newly formed particles. As a result, pH corresponding to the onset of polymerization (Figs. 3c, 4c) differs from pH_0. In the next stage of aggregation of the primary particles and their saturation with MMA, the displacement of the Na^+ cations from PMPs to the more polar aqueous phase via substitution with H^+ may result in a certain increase in pH of the reaction mixture (Fig. 3c, curves *1, 2*). The decrease in pH in the final stage of the

synthesis may be due to slow diffusion of the terminal polar carboxy groups of the polymer from the bulk of PMPs to the interface, as demonstrated for CVA-initiated polymerization of styrene [2, 3]. However, in the case of MMA, its partial hydrolysis causes polymerization in the stage of PMP growth even in weakly acidic medium. By contrast, salt additives make it possible to keep pH within the weakly alkaline range throughout the polymerization (Fig. 3c, curves *3*–*5*).

Figure 3 shows the results obtained at the lowest pH_0 (corresponding to the initial part of the abrupt change in the CVA titration curve) with and without salt additives (KH_2PO_4 and $NaHPO_4$). With NaCl additive, pH_0 was found to be 9.01, which corresponds to the central part of the abrupt change in the CVA titration curve. However, it appeared that, despite higher pH_0, raising the ionic strength by adding an indifferent electrolyte, NaCl, leads to the formation of a large amount of coagulum and also to polydispersity of the latex. We also observed deceleration of the polymerization after 75% conversion of MMA was attained, whereas in the absence of NaCl, at the same pH_0, the conversion was above 90% [1]. By contrast, in the presence of KH_2PO_4 and Na_2HPO_4, the MMA conversion was above 90% (Figs. 3, 4). In this case, polymerization of MMA was accompanied by the gel effect, as under the salt-free conditions [1]. In the stage of the synthesis, when a gel effect was observed, the surface tension of the reaction mixture considerably increased too, suggesting that the monomer and oligomeric reaction products are incorporated into growing PMPs. By contrast, we observed no gel effect with NaCl, and the surface tension of the reaction mixture remained rather low throughout the synthesis. This suggests the presence of a large amount of oligomers in the aqueous phase, which could provide formation of new particles and, as a result, of polydisperse latex. Therefore, compared to NaCl, addition of KH_2PO_4 and $NaHPO_4$ ensures higher aggregative stability of PMMA particles in the course of synthesis, thus favoring formation of monodisperse latexes. This is a result of stabilization of the surface charge of growing PMPs by virtue of keeping the pH of the reaction mixture within the weakly alkaline range regardless of pH_0 (Figs. 2–4). This constitutes the significant difference of CVA-initiated polymerization of MMA in the presence of salts with buffering effect from salt-free polymerization, when pH drifts steadily toward the acidic region (by virtue of hydrolysis of the monomer), the more so with increasing pH_0 [1]. In the presence of NaCl, we also observed a decrease in pH to 5.7. In this case, the reduction in the surface charge on PMMA particles resulted in latex agglomeration, which decelerated the polymerization.

The nature of a salt also considerably influences the dependences of the MMA conversion and the surface tension and pH of the reaction mixture on the polymerization time, and also on the size of the resulting PMMA particles and the carboxy group concentration on their surface. For example, in the presence of $NaHPO_4$ (run no. 2), considerably smaller monodisperse particles are formed, as compared to those obtained with KH_2PO_4 (run no. 7). The more developed interfacial surface in smaller particles formed with Na_2HPO_4 causes, evidently, a higher steady-state polymerization rate (see table and Fig. 3). A study of CVA-initiated polymerization of MMA in initially weakly acidic (run nos. 7 and 1-0) or weakly alkaline medium (no. 2) revealed temporary deceleration of the process at intermediate degrees of MMA conversion (Fig. 3). This period goes on until the gel effect onsets; its duration increases with salt composition of the reaction mixture changing in the order—no salt < 0.01 M Na_2HPO_4 < 0.02 M KH_2PO_4. In this case, the surface tension of the reaction mixture changes in time parallel to the conversion trend. In the presence of Na_2HPO_4, the gel effect is observed on reaching 30% conversion of MMA, being considerably more pronounced than that in the case of a more acidic buffer, KH_2PO_4, when the gel effect takes place only at 50% conversion.

The decrease in the polymerization rate at intermediate degrees of MMA conversion is probably due to a decrease in lifetime of the radical in PMP, which may occur on attaining a sufficiently low pH of the reaction mixture (6.7–7.5) corresponding to a small surface charge of PMP. In this case, the terminal carboxy groups of the oligoradicals occur essentially in the H form too, which increases their surface activity and, evidently, the rate of their capture by PMPs. At low pH, PMPs can also capture oligomers formed in the aqueous phase, as demonstrated by a certain increase in the surface tension of the reaction mixtures (Fig. 3).

The viscosity-average molecular weight of PMMA obtained in weakly acidic and neutral media (Fig. 5b) is remarkably lower if the reaction is performed in the presence of buffer salts. Raising the ionic strength of the dispersion medium stimulates the surface activity of oligomers and oligoradicals, favoring their capture by PMP and recombination of the radicals in the particle. In this case, MW of the resulting polymer and the polymerization rate decrease, and the gel effect is observed later, being less pronounced.

Exhaustion of the monomer in the aqueous phase must decrease the rates of oligoradical formation and capture by the particles, which may again increase the lifetime of the radicals in PMPs. As a result, the abrupt increase in the surface tension of the reaction mixture (Figs. 3b, 4b) coincides in time with the onset of the gel effect (Figs. 3a, 4a).

With increasing pH_0 of the reaction mixture, the inflections in the conversion curves at intermediate conversions of MMA disappear (Fig. 4). With the pH_0 increasing to the values corresponding to the central part of the abrupt change in the titration curve of CVA, the MW of PMMA increases too (Figs. 1, 5). This is caused by an increase in the degree of ionization of carboxy groups on the PMP surface and in oligoradicals, which decreases their surface activity and, therefore, makes lower the rate of their capture by the particles. Even at high pH_0 of the reaction mixtures, the decrease in MW of PMMA obtained in the presence of the buffer salts is not so pronounced as without them (Fig. 5). The reason is that hydrolysis of the monomer is suppressed in buffered weakly alkaline solutions.

In polymerization of MMA in salt-free media, the size of the resulting latex particles, carboxy group concentration on their surface, and steady-state polymerization rate decrease with increasing pH [1]. By contrast, in the presence of 0.01 M Na_2HPO_4 (run nos. 2–4), variation of pH over the range 7.47–11.15 has no remarkable effect on the particle size (see table and Fig. 5a). At the same time, the rise in ionic strength with Na_2HPO_4 concentration increasing from 0.01 to 0.02 M at the initial pH of the reaction mixture lying in the weakly alkaline range leads to coarsening of the resulting latex particles and to a noticeable decrease in the steady-state polymerization rate (run nos. 3, 5). This is probably due to contraction of the diffuse part of the electrical double layer and formation of $COO^{-1}Na^{+}$ ion pairs on the surface, which reduces the effective surface charge of the primary particles and promotes their aggregation into coarser PMPs. However, in strongly alkaline media (run nos. 4, 6), we observed no remarkable coarsening of the particles with increasing Na_2HPO_4 concentration, while the steady-state polymerization rate decreased as before. Evidently, incorporation of the hydrophilic MAA units into the polymeric chains results in the formation of water-soluble oligomeric products additionally stabilizing PMPs. With pH_0 shifted to the strongly alkaline region, the carboxy group concentration on the surface of the resulting PMMA particles increases (Fig. 5a), while in the absence of the salt additions, the reverse trend is observed [1]. Presumably, ion pairing on the PMMA surface reduces the lateral repulsion between the ionized carboxy groups, which allows higher degree of carboxylation to be attained. In this case, removal of water-soluble admixtures after synthesis does not provide a considerable reduction in the degree of carboxylation of the particle surface. Therefore, in CVA-initiated emulsifier-free polymerization of MMA, introduction of appropriate buffer salts allows formation of monodisperse submicrometer latex particles and also variation of the carboxy group concentration on their surface.

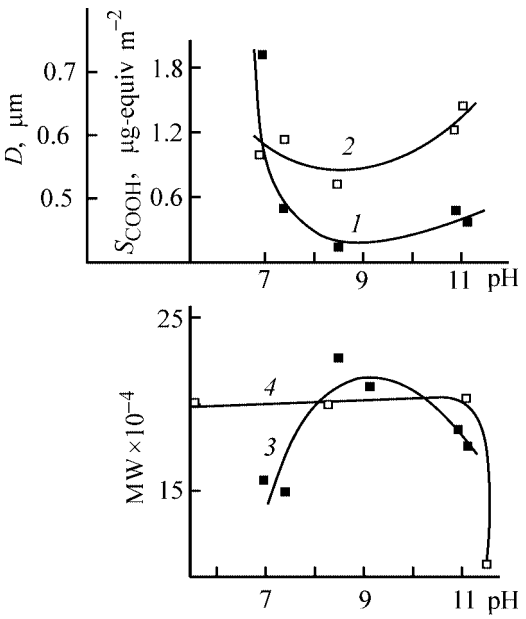

Fig. 5. (*1*) Particle size *D*, (*2*) concentration of the surface carboxy groups, S_{COOH}, and (*3*, *4*) viscosity-average molecular weight MW of PMMA in latex particles obtained with and without bufferring additives, respectively, vs. the initial pH of the reaction mixture.

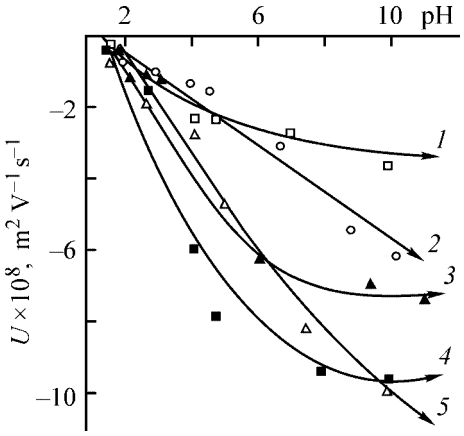

Fig. 6. Electrophoretic mobility of PMMA particles, *U*, in 0.01 M NaCl vs. pH. S_{COOH} (μg-equiv m^{-2}): (*1*) 0.73, (*2*) 0.96, (*3*) 1.05, (*4*) 1.41, and (*5*) 1.45.

A microelectrophoretic study of the surface electrical properties of PMMA particles obtained in the presence of buffer salt additions showed that their electrophoretic mobility *U* and, therefore, the surface charge grows both with increasing carboxy group concentration on the surface and with pH increasing, because of the rise in the degree of ionization of these groups (Fig. 6). Also, the electrophoretic mobility of the resulting PMMA particles exhibited the classical dependence on the ionic strength of the dispersion medium, i.e., decreased with increasing ionic strength as a result of compaction of the diffuse part of the electrical double layer. This points to a planar distribution of the carboxy groups and to weak conformational flexibility of the polymeric chains [7]. Therefore, the surface layer structure presumably remains unchanged when the salt composition of the dispersion medium is varied.

CONCLUSIONS

(1) In emulsifier-free emulsion polymerization of methyl methacrylate initiated by a carboxyl-containing azo initiator [4,4'-azobis(4-cyanoisovaleric acid)], addition of buffer salt (KH_2PO_4, $NaHPO_4$) eliminates the negative effect of hydrolysis of the monomer on the aggregative stability of the resulting polymethyl methacrylate particles.

(2) Raising the ionic strength of the reaction mixture by adding a buffer salt decreases the yield of water-soluble products of polymerization even at high initial pH and makes higher the yield of the polymer in the form of a monodisperse latex. Also, this leads to an increase in the size of PMMA particles formed in strongly alkaline medium and in the carboxy group concentration on their surface.

(3) A study of the surface electrical properties of the resulting latex particles demonstrated the possibility of controlling their surface charge over a wide range by varying the electrolytic composition and pH of the dispersion medium.

ACKNOWLEDGMENTS

The study was supported financially by the Russian Foundation for Basic Research (project no. 01-03-32 414).

REFERENCES

1. Men'shikova, A.Yu., Chekina, N.A., Ivanchev, S.S., *et al.*, *Vysokomol. Soedin., Ser. A*, 2001, vol. 43, no, 4, pp. 607–615.
2. Lishanskii, I.S., Men'shikova, A.Yu., Evseeva, T.G., *et al.*, *Vysokomol. Soedin., Ser. B*, 1991, vol. 33, no, 6, pp. 413–416.
3. Men'shikova, A.Yu., Evseeva, T.G., Shabsel's, B.M., *et al.*, *Kolloidn. Zh.*, 1997, vol. 59, no. 5, pp. 671–675.
4. *Praktikum po kolloidnoi khimii lateksov i PAV* (Practical Course of Colloid Chemistry of Latexes and Surfactants), Neiman, R.E., Ed., Moscow: Vysshaya Shkola, 1972.
5. Grigorov, O.N., Karpova, I.F., Kuz'mina, Z.P., *et al.*, *Rukovodstvo k prakticheskim zanyatiyam po kolloidnoi khimii* (Practical Guide on Colloid Chemistry), Moscow: Khimiya, 1964.
6. Reddi, C.R., *Polymer*, 1977, vol. 18, no. 1, pp. 32–36.
7. Shubin, V.E., Sidorova, M.P., Men'shikova, A.Yu., *et al.*, *Kolloidn. Zh.*, 1990, vol. 52, no. 5, pp. 935–941.

Russian Journal of Applied Chemistry, Vol. 75, No. 12, 2002, pp. 1999–2004. Translated from Zhurnal Prikladnoi Khimii, Vol. 75, No. 12, 2002, pp. 2036–2041.
Original Russian Text Copyright © 2002 by Artem'eva, Kostereva, Kukarkina, Praslova, Fedorova, Samarin, Sazanov, Sidorovich, Panov,. Kudryavtsev.

MACROMOLECULAR CHEMISTRY AND POLYMERIC MATERIALS

Preparation and Structure of Polyimides Derived from H Complexes of Benzophenonetetracarboxylic Acid with Diaminodiphenyl Ether

V. N. Artem'eva, T. A. Kostereva, N. V. Kukarkina, O. E. Praslova, G. N. Fedorova, V. P. Samarin, Yu. N. Sazanov, A. V. Sidorovich, Yu. N. Panov, and V. V. Kudryavtsev

Institute of Macromolecular Compounds, Russian Academy of Sciences, St. Petersburg, Russia

Received August 1, 2002

Abstract—The possibility of using H complexes of dialkyl dihydrogen 3,3',4,4'-benzophenonetetracarboxylates and 4,4'-diaminodiphenyl ether and of polyimides prepared therefrom as polyimide foam materials, carbon-reinforced plastics, and foam composites was examined.

A number of such polyimide composite materials as polyimide foams [1], binders for carbon-reinforced plastics [2], and foam composites [3] have been prepared from dialkyl esters of 3,3',4,4'-benzophenonetetracarboxylic acid (BZP) and 4,4'-diaminodiphenylmethane (DADPM). However, DADPM is cancerogenic. Therefore, an urgent task is to replace DADPM with environmentally safer 4,4'-diaminodiphenyl ether (DADPE). As a rule, such a replacement impairs the properties of polyimide materials. The goal of this study was to find why the properties of DADPE-derived polyimides get worse and how this drawback can be overcome. To this end, we studied the features of thermal cyclization of H complexes of BZP diesters with DADPE and analyzed the supramolecular structure of the resulting polyimides.

EXPERIMENTAL

Dimethyl and diethyl BZP esters (BZPMe and BZPEt, respectively) were prepared by refluxing 0.03 mol of BZP dianhydride [TU (Technical Specifications) TSR 2159–69, purified by refluxing in acetone, mp 225°C) in 50 ml of an appropriate alcohol (anhydrous or containing 10 vol % water). To prepare the H complexes, DADPE (purified by distillation at 1–3 mm Hg, mp 150°C) or an equimolar mixture of DADPE and *m*-phenylenediamine (mPDA, purified by distillation at 1–3 mm Hg from zinc dust, mp 63°C) was dissolved (in the case of the mixture, the components were added successively) at room temperature in an alcoholic solution containing an equimolar amount of BZP diester. The solid H complexes were obtained by evaporating the alcohol at 20–30°C/1–3 mm Hg.

Samples for DSC were prepared by heating H complexes for 1 h at 220°C.

The viscosity of melts of H complexes was measured on a PIRSP rheometer with a cone–plane working unit (angle at the cone apex 1°, cone diameter 40 mm, shear rate $\gamma = 2 \times 10^{-2}$ s^{-1}) at 95 and 105°C [4].

Thermal gravimetric analysis (DTA, DTG, TG) of H complexes was performed with a C derivatograph (MOM, Hungary) in a ceramic crucible (50-mg sample, heating rate 5 deg min^{-1}).

The melting point of polyimides was measured with a Boetius heating stage.

The DSC studies were performed with a DSM-2M scanning microcalorimeter; heating rate 16 deg min^{-1}, threshold sensitivity 0.04 mW.

X-ray diffraction patterns of the H complexes and polyimides formed therefrom were obtained with a DRON-2 diffractometer (Ni-filtered Cu radiation).

The H complexes are formed spontaneously in the course of mixing of the reactants (dialkyl dihydrogen arenetetracarboxylates and aromatic diamines) in alcohols; after isolation from solution and drying, they may have different supramolecular structures and be amorphous or crystalline [5]. The supramolecular structure of H complexes appreciably affects the vis-

1070-4272/02/7512-1999 $27.00 © 2002 MAIK "Nauka/Interperiodica"

Table 1. Initial viscosities η of melts of H complexes

Sample no.	H complex	Solvent	log η* [Pa s] at indicated temperature, °C	
			95	105
1	BZPMe · DADPE	CH_3OH	3.0	2.5
2			–	4.0
3	BZPEt · DADPE	C_2H_5OH	4.0	3.3
4			–	–
5	BZPMe · DADPE	$CH_3OH + H_2O$	–	5.0
6	BZPEt · DADPE	$C_2H_5OH + H_2O$	–	–
7	BZPMe–DADPE–mPDA	$CH_3OH + H_2O$	4.2	3.7
8	BZPMe–DADPE–mPDA	$C_2H_5OH + H_2O$	4.0	3.5

* The dash denotes no melting at the indicated temperature.

cosity of their melts. The more ordered the structure of H complexes, the higher the melt viscosity. In low-temperature impregnation of fibers to prepare prepregs of foam composites, it is desirable to use H complexes with low viscosity of the melt.

With DADPE, the viscosities of the melts of H complexes are considerably less reproducible as compared to the H complexes of DADPM; this fact may be responsible for problems arising when DADPM is replaced with DADPE. Let us take the H complexes with the highest and lowest viscosities of the melts and consider the differences in the structure and thermal behavior of these H complexes and of the polyimides therefrom.

Fig. 1. Diffraction patterns: (*1*) H complex BZPMe · DADPE, sample no. 1, initial; (*2*) the same, heated at 105°C for 20 min; (*3*) the same as 1, heated at 95°C for 90 min; and (*4*, *5*) final polyimides prepared from this H complex by heating at 220 and 275°C, respectively. (2θ) Bragg angle; the same for Fig. 2.

For analysis, we chose the H complexes obtained in methanol or ethanol with low viscosity of the melt, which is preserved for a long time at 95°C (sample nos. 1, 3) and the samples (nos. 2, 4) that do not melt at 95°C (Table 1).

Thermal treatment (220°C, 1 h) gives polyimides differing in the supramolecular structure. X-ray diffraction studies showed that the polyimides formed from sample nos. 2 and 4 are amorphous, and those formed from sample nos. 1 and 3, crystalline. The formation of the crystalline structure in sample nos. 1 and 3 was monitored in stages, from the initial H complex to the final polyimide, at various temperatures and times of heat treatment.

Naturally, the H complexes whose melts have low viscosity are amorphous (Figs. 1, 2, curves *1*). When a sample of the H complex BZPMe · DADPE is heated at 105°C for 20 min, a tendency toward formation of an ordered structure is revealed (Fig. 1, curve *2*). Heating at 95°C for 90 min gives a more ordered structure (Fig. 1, curve *3*). Previous rheological data for melts of H complexes suggest that, in the second case, the extent of imidization of the H complex is greater than in the first case despite the lower heating temperature [6]. Heating to 220°C yields a crystalline polyimide (Fig. 1, curve *4*).

Table 2. Temperature parameters of imidization and degradation of samples* and degree of imidization of polyimides

Sample no.	$T_{on.\ im}$ (TG)	$T_{max.\ im.\ rate\ 1}$ (DTG)	$T_{max.\ im.\ rate\ 2}$ (DTG)	$T_{com.\ im}$ (TG)	τ_0	$T_{max.\ degr}$ (DTA)	$T_{max.\ degr.\ rate}$ (DTG)	*i*, % TG
	°C							
1	121	133	216	249	351	470, 520, 604 (+) (–) (+)	475, 546	80
2	100	148	231	277	431	513 (+)	613	99
3	123	146	183	266	346	471, 527, 602 (+) (–) (+)	473, 544	86
4	121	155	210	261	448	522 (+)	595	90
5	106	139	228	265	414	515 (+)	600	93
6	121	154	233	280	473	522 (+)	606	90
7	116	144	225	260	480	518 (+)	596	99
8	117	154	227	265	475	520 (+)	587	98

* Temperatures of: ($T_{on.\ im}$) onset of imidization, ($T_{com.\ im}$) completion of imidization, (τ_0) onset of degradation, ($T_{max.\ im.\ rate}$) maximal imidization rate, ($T_{max.\ degr.\ rate}$) maximal degradation rate, and ($T_{max.\ degr}$) degradation peaks in DTA curves [(+) exothermic and (–) endothermic].

Similar structural changes were observed in heat treatment of the H complex BZPEt · DADPE (Fig. 2). Heating at 95°C for 1 h results in the appearance of weak reflections at 2θ ~22° and 25° (Fig. 2, curve *2*). Heating at 105°C for 30 min gives a more ordered structure (Fig. 2, curve *3*), and heating at 105°C for 1 h results in the appearance of well-defined peaks at 2θ ~19°, 23°, and 28° (Fig. 2, curve *4*). Thus, the sample structure becomes more perfect with the progress of imidization, and, finally, a crystalline polyimide is obtained (Fig. 2, curve *5*). By contrast, amorphous polyimides were obtained in all cases from crystalline H complexes [7].

Comparison of the positions of the main reflections in the diffraction patterns of BZPMe · DADPE (Fig. 1) and BZPEt · DADPE (Fig. 2) shows that the packing of polyimide chains in these samples (Fig. 1, curve *4*; Fig. 2, curve *5*) is about the same, with the structural motif being formed already in the course of heat treatment of the H complexes at 95–105°C.

Polyimide sample no. 1, heated to 220 or 275°C, has different crystal structures (Fig. 1, curves *4*, *5*), i.e., this sample exhibits polymorphism depending on the heat treatment temperature.

A thermal gravimetric analysis of H complexes revealed significant differences in behavior between sample nos. 1 and 3, compared to sample nos. 2 and 4, in all the stages from formation of the imide structure to degradation of the polyimide.

The DTG curves (Fig. 3) show that all the samples are characterized by two-step imidization with a slow second step; this is associated with the phase state of the substance: in the first step, imidization occurs in the melt, and in the second step, in the solid phase. For samples based on BZPMe (nos. 1, 2), according to the TG and DTA data, increase in the initial viscosity of the melts of the H complexes leads to extension of the temperature range of imidization and increase in the temperature of the maximal imidization rate. As a result, sample no. 2 transforms with almost 100% degree of imidization into a macromolecular polyimide exhibiting high heat resistance (Table 2). By contrast, at narrower temperature range

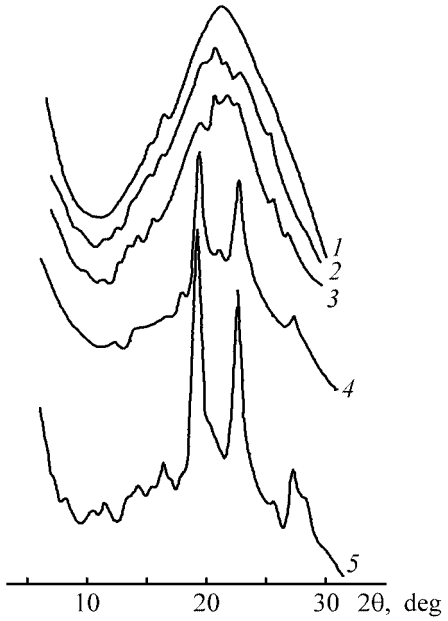

Fig. 2. Diffraction patterns: (*1*) H complex BZPEt · DADPE, sample no. 3, initial; (*2*) the same, heated at 95°C for 60 min; (*3*, *4*) the same as 1, heated at 105°C for 30 and 60 min, respectively; and (*5*) final polyimide prepared from this H complex by heating at 220°C.

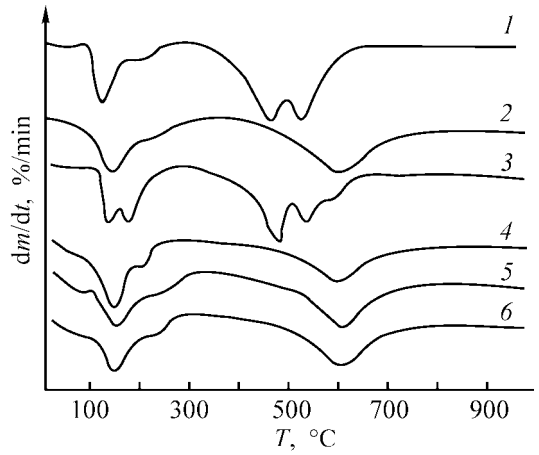

Fig. 3. DTG curves of H complexes: (*m*) weight, (*t*) time, and (*T*) temperature. *Curve nos*. are sample nos. in Table 1; the same for Fig. 4.

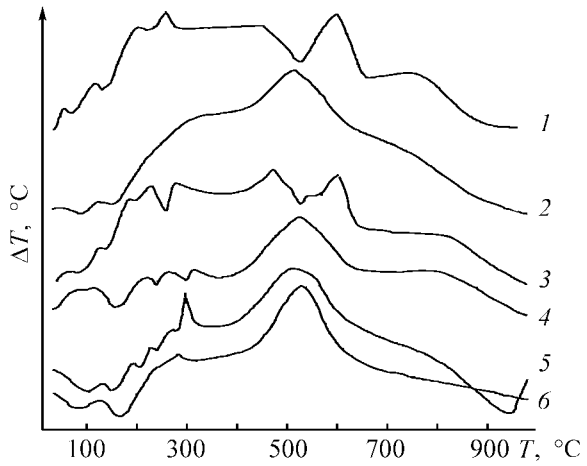

Fig. 4. DTA curves of H complexes. (*T*) Temperature; the same for Figs. 5 and 6.

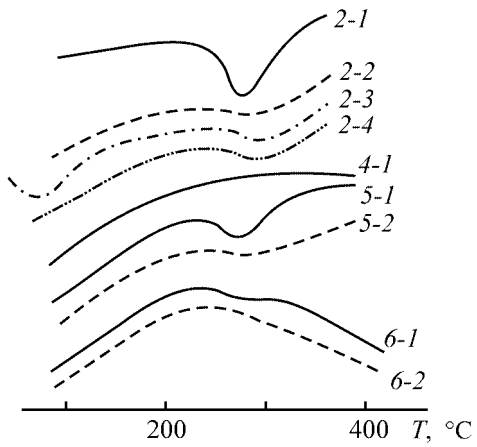

Fig. 5. DSC curves for samples of amorphous polyimides prepared by heating of H complexes at 220°C for 1 h. The first digit corresponds to sample no., and the second to (*1*) first scanning, (*2*) second scanning, (*3*) scanning after keeping for 24 h at 100% humidity, and (*4*) the same and second scanning.

of imidization and lower temperature of the maximal imidization rate (sample no. 1), imidization is incomplete (degree of imidization 80%), and a crystalline polyimide is obtained. Similar results were obtained with sample nos. 3 and 4, prepared in ethanol.

Sample nos. 1 and 3 have low τ_0 values because of the incomplete imidization; furthermore, their degradation occurs in two steps, which is untypical of polyimides of this chemical composition (Fig. 3, Table 2). The degradation rate and the rate of the corresponding weight loss are appreciably higher than those for sample nos. 2 and 4. The two steps of degradation of sample nos. 1 and 3 are also seen in the DTA curves (Fig. 4).

Usually, the onset of degradation of polyimides is accompanied by an exothermic reaction; this was, indeed, observed with sample nos. 2 and 4. By the moment when the degradation rate reaches a maximum, the exothermic reaction is virtually complete. The difference between $T_{\text{max. degr}}$ of the exothermic peak and $T_{\text{max. degr. rate}}$ is 80–100°C. The DTA and DTG curves of sample nos. 1 and 3 (Figs. 3, 4) show that the temperature of the first maximum of the exothermic reaction virtually coincides with the temperature of maximal degradation rate in the first step, instead of the ~100°C difference. This is followed by an endothermic reaction corresponding to partial damping of degradation. The second degradation step occurs again with an exothermic effect, with the maximum virtually reached when the degradation is complete. Apparently, in these cases, the mechanism of thermal degradation differs from that observed in sample nos. 2 and 4.

In the range 220–350°C, the DTA curves for all the samples (Fig. 4) exhibit endo- and/or exothermic peaks of various intensities, not accompanied by any weight loss. These peaks might be assigned to softening, melting, and/or crystallization (for exothermic peaks) of the samples. However, visual examination shows that only samples of low-molecular-weight polyimides nos. 1 and 3 melt in the range 250–280°C. The other samples undergo no apparent changes in their aggregative state.

To reveal the nature of endo- and exothermic peaks in the DTA curves in the range 220–350°C, we studied by DSC the polyimide samples obtained by heating H complexes to 220°C. The results we obtained are shown in Fig. 5. In the case of amorphous polyimide prepared from the H complex based on BZPEt (no. 4), no noticeable thermal effects are detected in the range 220– 300°C (Fig. 5, curve *4*). The amorphous polyimide prepared from the H complex based on BZPMe (no. 2) shows a broad endothermic peak

(Fig. 5, curve *2-1*); the weight loss upon scanning to 310°C is about 1%. In a repeated scan (Fig. 5, curve *2-2*), the endothermic effect almost disappears, and no weight loss is observed. After keeping a sample for a day in a 100% humid atmosphere, an endothermic peak appears at 90°C, with the weak endothermic peak at 280°C remaining virtually unchanged. The weight loss is exclusively due to removal of sorbed moisture. Therefore, the endothermic peak under consideration may be assigned to softening and structural transformations of the polyimide, which do not occur at 220°C [at this temperature in the isothermal mode (1 h), imidization is complete in contrast to dynamic TGA].

The DSC curves of samples of crystalline polyimides (nos. 1 and 3; Fig. 6) strongly differ from the curves of amorphous polyimide samples. With crystalline polyimides, the endo- and exothermic effects above 220°C are preserved in repeated scans (Fig. 6). However, the temperatures of the peak maxima change, which is due, according to the X-ray diffraction data, to structural ordering and to polymorphism. The DSC data confirm that these samples have definite melting points.

The discrepancies between the temperatures of the exo- and endothermic peaks in the DTA and DSC curves may be due to different thermal histories of the initial samples (preliminary heating at 220°C for 1 h before DSC measurements and dynamic heating of H complexes to obtain polyimide in DTA measurements) and different heating rates.

Thus, with DADPE-based H complexes having the lowest viscosity of the melt, imidization in the course of heat treatment is incomplete, and low-molecular-weight crystalline polyimides are obtained. Therefore, in synthesizing prepregs for polyimide foam composites, low viscosity of melts of H complexes should not be sought for, because this may result in formation of brittle low-molecular-weight systems.

In this context, we studied H complexes formed from BZP diesters and DADPE in alcohols containing 10% water (sample nos. 5, 6) or from BZP diesters and an equimolar mixture of two diamines: DADPE and *m*-phenylenediamine (Tables 1 and 2, Figs. 3–5, sample nos. 7 and 8).

The H complexes prepared in alcohols with addition of water have relatively high viscosity of the melt, which complicates prepreg formation, but they yield exclusively high-molecular-weight amorphous polyimides. With mixtures of diamines, the viscosity of melts of H complexes at 95 and 105°C decreases. Therefore, it can be recommended to prepare DADPE-based H complexes in aqueous alcohol with addition of a second diamine as a comonomer.

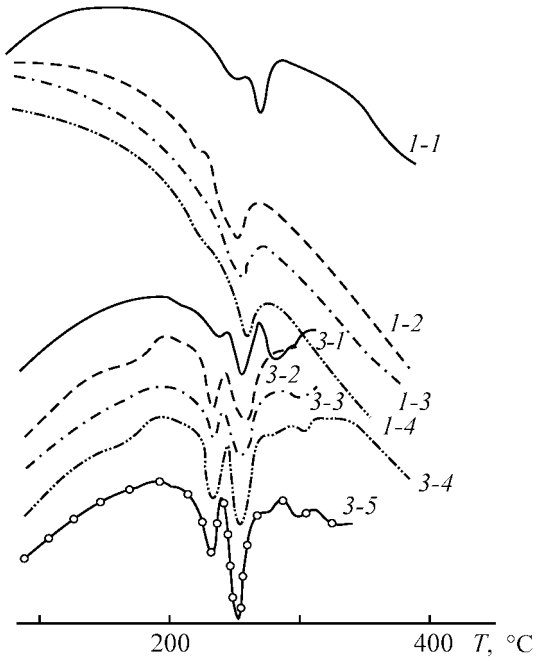

Fig. 6. DSC curves of samples of crystalline polyimides prepared by heating H complexes at 220°C for 1 h (repeated scans). *First digit*: H complex sample no.; *second digit*: number of scan.

CONCLUSIONS

(1) Factors impairing the performance characteristics of polyimides prepared from H complexes based on dialkyl dihydrogen 3,3',4,4'-benzophenonetetracarboxylates and 4,4'-diaminodiphenyl ether were revealed. These factors are associated with the crystallinity of the polymer, which determines the viscosity of the process melt.

(2) The main features of thermal imidization of H complexes based on dialkyl dihydrogen 3,3',4,4'-benzophenonetetracarboxylates and 4,4'-diaminodiphenyl ether, affecting the supramolecular structure of the forming polyimides, were determined.

(3) One of the components of the formulation for preparing a polyimide can be replaced with an environmentally safe product, 4,4'-diaminodiphenyl ether, provided that aqueous alcohols are used as solvents and 4,4'-diaminodiphenyl ether is taken as an equimolar mixture with another diamine (namely, *m*-phenylenediamine).

ACKNOWLEDGMENTS

The study was supported financially by the Russian Foundation for Basic Research (project no. 00-15-97297).

REFERENCES

1. US Patent 4296208.
2. Wilson, D., *Brit. Polym. J.*, 1988, vol. 20, no. 2, pp. 405–416.
3. RF Patent 2081134.
4. Vinogradov, G.V., Malkin, A.Ya., Plotnikova, E.P., *et al.*, *Vysokomol. Soedin., Ser. A*, 1978, vol. 20, no. 2, pp. 226–230.
5. Artem'eva, V.N., Baklagina, Yu.G., Kukarkina, N.V., *et al.*, *Zh. Prikl. Khim.*, 2002, vol. 75, no. 7, pp. 1155–1158.
6. USSR Inventor's Certificate, no. 798585.
7. Kostereva, T.A., Artem'eva, V.N., Kukarkina, N.V., *et al.*, *Zh. Prikl. Khim.*, 2001, vol. 74, no. 9, pp. 1533–1536.

Russian Journal of Applied Chemistry, Vol. 75, No. 12, 2002, pp. 2005–2008. Translated from Zhurnal Prikladnoi Khimii, Vol. 75, No. 12, 2002, pp. 2042–2045.
Original Russian Text Copyright © 2002 by Maizlish, Shaposhnikov, Zhukova.

MACROMOLECULAR CHEMISTRY AND POLYMERIC MATERIALS

Copper Tetra-4-Carboxyphthalocyanine as a Chemical Additive and Dye for Composites and Polycaproamide

V. E. Maizlish, G. P. Shaposhnikov, and Z. N. Zhukova

Ivanovo State Chemical Engineering University, Ivanovo, Russia

Received April 10, 2002

Abstract—Copper tetra-4-carboxyphthalocyanine was studied as a chemical additive and dye for a polymeric binder of fibrous composites and polycaproamide.

To make phthalocyanines (PC) soluble in aqueous alkaline solutions, carboxy and sulfonic groups are introduced into their structure. However, the solubility of carboxyphthalocyanines has been poorly studied. These compounds can be used in various fields of science and technology as dyes, catalysts for various reactions, photosensitizers for photodynamic cancer therapy, etc. [1–9]. Carboxyphthalocyanines are precursors for preparing thermally stable polymers and various phthalocyanine derivatives [10–20]. Copper tetra-4-carboxyphthalocyanine was studied as a component of a polymeric binder for composites and as a dye for polycaproamide (PCA).

Fibrous composites (FCs) have been recently regarded as a separate class of structural materials. They compete with conventional structural materials, such as metals, ceramics, and fiber glasses, and are widely used in various branches of science and industry [21].

Carbon fibers and high-strength high-modulus organic fibers composed of various linear aromatic polymers (SVM and ARMOS [21]), which show the most promise in this respect, are used to reinforce the composites.

Epoxy resins are used as curable polymeric matrices for organic plastics, being are one of the best binders for most of FCs [22]. This is due to the following: the adhesion of epoxy resins to many fillers, reinforcing components, and supports is high; the wide variety of available resins and curing agents allows preparation of materials with widely diverse properties under conditions meeting industrial requirements; no water and volatile compounds are formed in reaction of epoxy resins and curing agents, and shrinkage in the course of this process is lower than that in curing of phenol and polyester resins; cured epoxy resins are chemically stable and exhibit good insulating properties.

To further increase the production of FCss, their strength and resistance to light and heat should be improved. In addition, special demands are imposed on refractoriness of these materials and fire safety of articles therefrom.

A mixture of epoxy-4,4-isopropylidenediphenol and bromine-containing resins and a curing agent (a mixture of phenol-formaldehyde resin with aminophenol) is used as a binder for fireproof plastics [23].

In this study, we used ED-20 epoxy-4,4-isopropylidenediphenol resin [GOST (State Standard) 10487–84], AREM-2-20 epoxy-alkylresorcinol resin [TU (Technical Specification) 28.309.101–87] and Oksilin-6 epoxychloroaliphatic resin (TU 6-02-1376–87). SF 341A phenol-formaldehyde resin served as curing agent, and copper tetra-4-carboxyphthalocyanine $CuPc(4\text{-}COOH)_4$, as an additive to the polymeric binder [24]. Copper tetra-4-carboxyphthalocyanine enhances the heat resistance, with the refractoriness of the composite being preserved. In the presence of this compound, introduction of the bromine-containing epoxy resin used in the known procedure [23] is not required, which simplifies preparation of the composites.

The temperature of 0.8% weight loss by the modified binder based on ED-20 with and without $CuPc(4\text{-}COOH)_4$ is 258 and 265°C; fast weight loss is observed at 343.5 and 364.6°C, respectively.

The resistance of the coloration of SVM fiber and ARMOS containing $CuPc(4\text{-}COOH)_4$ to water, soap-sodium carbonate solution, organic solvents, UV radiation and daylight is evaluated as 5 points.

1070-4272/02/7512-2005 $27.00 © 2002 MAIK "Nauka/Interperiodica"

Properties of PCA

Property	Dye content, wt %	
	0.10	0.25
η_{rel}	2.38 ± 0.02	2.30 ± 0.01
Molecular weight	15600 ± 200	14700 ± 100
Content (wt %) of:		
LMWC*	10.13 ± 0.37	10.86 ± 0.21
caprolactam	7.53 ± 0.15	7.40 ± 0.28
mp, K	486 ± 1.0	482.5 ± 0.5

* LMWC denotes low-molecular-weight compounds.

The heat resistance of SMV fiber with and without CuPc(4-COOH)$_4$ additive is characterized by the following parameters:

Elongation, %	1.00/0.95
Preservation of elongation, %	71.4/95.0
Preservation of strength, %	82.05/97.7

The time of complete combustion of SVM fiber, ARMOS, and carbon fiber with/without CuPc(4-COOH)$_4$ is 5.4/10.3, 12/17, and 25/28 s, respectively.

Thus, introduction of the Pc in the composition of oligomeric binder improves the elastic, strength, thermal, and other properties of microplastics prepared from epoxy binders and reinforcing fiber, which extends the range of application of these FCs. Probably, in the presence of CuPc(4-COOH)$_4$ exhibiting mesomorphic properties [25], a more extended interface with improved structure is formed between the reinforcing filler and the polymeric matrix. In addition, in this case, blue-green composites with enhanced performances were prepared using SVM and ARMOS.

Among heterochain synthetic fibers, those based on caproamide polymers and copolymers (PCA) are of special interest. The world production of these fibers increases steadily. Having good consumer properties, these fibers are, however, difficultly colored. Preparation of colored and heat-resistant filaments and fibers is a topical problem. For the color of a composite to be most resistant to external effects, covalent bonds between the dye and polymer should be formed. Formation of these bonds is possible in the step of the polymer synthesis. Production of colored polymers is a kind of dyeing in the bulk and has all advantages of this process. In this case, the dye affects the process of fiber formation negligibly, the dye consumption decreases, and the resistance of the color to external effects is at a maximum.

Introduction of CuPc(4-COOH)$_4$ as a dye allowed us to abandon the use of acetic, benzoic, and adipic acids as chain-terminating agents. In addition, it is known that copper carboxyphthalocyanines are used to dye polyamides in the bulk.

We prepared PCA blocks with intense and uniform blue color. This color does not change after reprecipitation from sulfuric acid and 85% formic acid solutions, as well as after treatment with soap-sodium carbonate solutions, which indicates the formation of relatively strong chemical bonds between the phthalocyanine and the polymer.

The parameters of these polymers, listed in the table, meet the requirements to fiber-forming PCAs [26]. The fact that some macroheterocyclic compounds structurally similar to Pc are used as thermal and light stabilizers of PCAs suggests that the fibers prepared in the presence of CuPc(4-COOH)$_4$ must be resistant to heat and light [27].

EXPERIMENTAL

The tests of copper tetra-4-carboxyphthalocyanine as a chemical additive to a polymeric binder for composites were performed as follows. To prepare a polymeric binder, the epoxy resin, SF 341A phenol-formaldehyde resin, and copper tetra-4-carboxyphthalocyanine, taken in (95–105) : (65–75) : (0.9–1.1) weight ratio, were dissolved in 1 : 1 alcoholic–acetone mixture to obtain a 50% solution. The reinforcing fiber was impregnated with this solution on a bench impregnation unit and was air-dried for 15 min. The resulting composite was cured at 70°C for 30 min, 100°C for 60 min, 130°C for 60min, and 160°C for 120 min.

The heat resistance was estimated form the temperature of 0.8% weight loss, determined from TG curves.

Also, to evaluate the heat resistance, the samples were kept at 200°C for 12 h in a furnace. Then the strength and elongation were measured on a PM30-1 dynamometer at a clamping length of 10 cm and stretching rate of 300 mm min^{-1}.

The refractoriness was determined by the VIAM procedure in accordance with OST (Branch Standard) 190094–79.

To estimate the resistance of the composite coloration to external effects, the samples were treated with

cold and hot (100°C) water for 1 h, a solution of 5 g l^{-1} soap and 3 g l^{-1} sodium carbonate for 1.5 h, or organic solvents (acetone, 1 : 1 acetone–alcohol, DMF, DMSO), or were exposed to UV radiation of a PRK mercury lamp for 10 h or to daylight.

Polycaproamide. Caprolactam was polymerized in glass ampules in a special thermostat [28] maintaining temperature constant with an accuracy of ±0.3°C. A mixture of caprolactam with a definite amount of copper tetra-4-carboxyphthalocyanine and water was melted at 80°C, thoroughly stirred, and cast in thick-walled test tubes. The tubes were cooled with an ice-sodium chloride mixture, evacuated to a residual pressure of 66 Pa, and sealed. After the reaction was complete, the polymer obtained was cut in thin chips and analyzed.

Unreacted caprolactam was determined by vacuum sublimation. A weighted portion of PCA (0.2000 ± 0.0002 g) was placed in an open weighing bottle, dried in a vacuum desiccator over P_2O_5 at room temperature, and then sublimed at 150 ± 2°C for 150 min at a residual pressure of 66 Pa. The caprolactam content was determined from the weight loss after sublimation.

To determine the LMWC content, predried PCA (1 g) was poured over with distilled water (60 ml) and refluxed for 2 h with water replaced after 1 h. The polymer was filtered off and dried at 70°C under atmospheric pressure and for 6 h under reduced pressure (~66 Pa). The LMWC content was determined from the weight loss after extraction.

The relative viscosity η_{rel} of a polymer solution [1 g of the polymer in 100 ml of concentrated H_2SO_4 (ρ = 1.83 g cm^{-3})] was determined on a VPZh-2 viscometer at 20.00 ± 0.05°C.

The molecular weight was calculated by the equation

$$M = 113P_{av},$$

where P_{av} is the average degree of polymerization; 113 is the molecular weight of the polymer unit, $P_{av} = 100(\eta_{rel} - 1)$.

CONCLUSION

Fibrous composites with intense blue color and enhanced performance were prepared using a polymeric binder with copper tetra-4-carboxyphthalocyanine additive. Introduction of this complex allowed us to abandon conventional chain-terminating agents (carboxylic acids) in the polymerization.

REFERENCES

1. *The Chemistry of Synthetic Dyes*, Venkataraman, K., Ed., New York: Academic, 1971. Translated under the title *Khimiya sinteticheskikh krasitelei*, Leningrad: Khimiya, 1977, vol. 5, ch. 4, pp. 211–250.
2. Gaspard, S., Verdaguer, M., and Violy, R., *C.R. Acad. Sci. Paris, Ser. C*, 1972, vol. 275, no. 11, p. 573.
3. Shirai, H., Maruyama, A., Takano, J., *et al., Macromol. Chem.*, 1980, vol. 181, no. 3, pp. 565–573.
4. Achar, B.N., Fohlen, G.M., Parker, J.A., and Keshavayya, J., *Indian J. Chem.*, 1998, vol. 27A, pp. 411–416.
5. Kobayashi, N., Shirai, H., and Hojo, N., *J. Polym. Sci., Part C: Polym. Lett.*, 1989, vol. 27, pp. 191–195.
6. Ichinohe, T., Miyajima, M., Noguchi, Y., *et al., J. Porphyrins Phthalocyanines*, 1998, vol. 2, no. 2, pp. 101–106.
7. Spiller, W., Kliesch, H., Wohrle, D., *et al., J. Porphyrins Phthalocyanines*, 1998, vol. 2, no. 2, pp. 145–158.
8. Kalija, O.L., Lykyanets, E.A., and Vorozhtzov, G.N., *ICCP, Dijon (France)*, June 25–30, 2000, p. 243.
9. Borisenkova, S.A., Batanova, E.A., Solovyova, L.I., and Kaliya, O.L., *ICCP, Dijon (France)*, June 25–30, 2000, p. 359.
10. Iton, H., Kondo, S., Masuda, E., *et al., Makromol. Chem., Rapid Commun.*, 1986, vol. 7, pp. 585–589.
11. Fujiki, M., Tabei, H., and Kurihara, T., *J. Phys. Chem.*, 1988, vol. 92, no. 5, pp. 1281–1285.
12. Ogawa, K., Kinoshita, S., Yonehara, H., *et al., J. Chem. Soc., Chem. Commun.*, 1989, pp. 477–479.
13. Iton, H., Koyama, T., and Hanabusa, K., *J. Chem. Soc., Dalton Trans.*, 1989, pp. 1543–1546.
14. Kobayashi, N., Nisshiyama, Y., Ohya, T., and Sato, M., *J. Chem. Soc., Chem. Commun.*, 1987, pp. 390–392.
15. Dulog, L. and Gittinger, A., *Mol. Cryst. Liq. Cryst.*, 1992, vol. 213, pp. 31–42.
16. Albouy, P.A., *J. Phys. Chem.*, 1994, vol. 98, no. 34, pp. 8543–8548.
17. Valli, L., Rella, R., Tepore, A., and Zocco, A., *Mat. Sci. Eng. C-Biomimetic Mat. Sens. Syst.*, 1998, vol. 5, no. 3–4, pp. 243–250.
18. Jin, C.S. and Shim, Y.B., *Bul. Kor. Chem. Soc.*, 1999, vol. 20, no. 3, pp. 381–383.
19. Rella, R. Serra, A., Siciliano, P., *et al., Supramol. Sci.*, 1997, vol. 4, nos. 3–4, pp. 461–464.
20. Rella, R., Siciliano, P., Manno, D., *et al., Sensors*

Actuators. B: Chem., 1997, vol. 44, nos. 1–3, pp. 585–589.

21. *Armiruyushchie khimicheskie volokna dlya kompozitsionnykh materialov* (Reinforcing Chemical Fibers for Composites), Kudryavtsev, G.I., Ed., Moscow: Khimiya, 1992.
22. *Handbook of Composites*, Lubin, G., Ed., New York: Van Nostrand Reinhold, 1982.
23. USSR Inventor's Certificate, no. 730753.
24. RF Patent 2148598.
25. Usol'tseva, N.V., *Liotropnye zhidkie kristally: khimiya i nadmolekulyarnaya struktura* (Lyotropic Liquid Crystals: Chemistry and Supramolecular Structure), Ivanovo: Ivanov. Gos. Univ., 1994.
26. Mizerovskii, L.N., Theoretical Foundations of Modern Production of Fiber-Forming Polycaproamide, *Doctoral Dissertation*, Kazan, 1983.
27. Smirnov, R.P., Kharitonov, V.M., and Smirnov, L.N., *Tr. Ivanov. Khim.-Tekhnol. Inst.*, 1972, no. 14, pp. 111–116.
28. Bazarov, Yu.M., Paikachev, Yu.S., and Mizerovskii, L.N., *Izv. Vyssh. Uchebn. Zaved., Khim. Khim. Tekhnol.*, 1972, vol. 15. no. 11, pp. 1758–1760.

Russian Journal of Applied Chemistry, Vol. 75, No. 12, 2002, pp. 2009–2013. Translated from Zhurnal Prikladnoi Khimii, Vol. 75, No. 12, 2002, pp. 2046–2050.
Original Russian Text Copyright © 2002 by Goncharik, Mozheiko.

MACROMOLECULAR CHEMISTRY AND POLYMERIC MATERIALS

Influence of Inorganic Electrolytes on the Stability and Structural and Rheological Properties of Emulsions Based on Rapeseed Oil

I. I. Goncharik and F. F. Mozheiko

Institute of General and Inorganic Chemistry, National Academy of Sciences of Belarus, Minsk, Belarus

Received May 14, 2002

Abstract—Formation conditions and structural and rheological properties were studied for emulsions based on rapeseed oil in the presence of aqueous solutions of sodium, potassium, and calcium chlorides and of sodium carbonate and sodium hydroxide.

At present, many branches of industry, such as paint-and-varnish, food, soap, and lubricant manufacturing, etc., utilize vegetable (linseed, hempseed, sunflowerseed, etc.) oils. In recent years, wide application has been enjoyed by rapeseed oil and emulsions on its base. Published data suggest that the formation conditions and structural and rheological properties of rapeseed oil emulsions, as well as the phase transformations in microemulsions and the influence of inorganic electrolytes on these properties, have been studied inadequately.

EXPERIMENTAL

We studied rapeseed oil containing, wt %: fat oils 38.1–45.3, essential oil 0.11–1.16, raw protein 25.0–29.8, P_2O_5 2.6, and other components [1]. The emulsions were prepared by the procedure from [1]. After a 15-min dispersing, a portion of the resulting emulsion was placed in calibrated test tubes, and the phase separation in the systems under study was monitored visually. As the measure of stability served the ratio (in per cent) of the volume of the separated aqueous or oil phase to that of the entire initially prepared emulsion. The remaining emulsion was used for structural and rheological, and electrical-conductivity studies. The structural and rheological properties of the emulsions were studied on a Rheotest 2 rotation viscometer in a coaxial-cylinder system at strain rates within 3.0–1312 s^{-1}. Based on the measured data, we calculated for each rate gradient D_r by standard procedures [2] the shear stress τ_r and the effective viscosity η. The procedure of studying the equilibrium shear stress as a function of the strain rate yielded full rheological curves.

First, we studied the emulsion formation in a system formed by water and rapeseed oil. We found that, whatever its concentration, rapeseed oil is able to forming emulsions in water without introdution of any emulsifying agent into the system (Table 1). The role of the emulsifying agent is, presumably, played by the impurities contained in rapeseed oil, such as phosphatides, soluble proteins, dyes, etc., as well as by oil hydrolysis products (in particular, monoglycerides), which are active emulsifiers [3]. The stability of the resulting emulsions varies with the oil phase concentration in the system. It was shown that, with increasing oil phase content, the emulsion stability increases to a maximum and then decreases. For example, the highest stability is observed at rapeseed oil concentrations of 50–60 wt %. Evidently, at these concentrations the adsorption layer at the liquid–liquid interface gets saturated with the emulsifier molecules, which is responsible for the high emulsion stability.

Table 1. Type, stability, and structural and rheological properties of rapeseed oil emulsions vs. the rapeseed oil concentration $c_{r.o.}$

$c_{r.o.}$, wt %	η, Pa s	æ, S cm^{-1}	P_{c2}, Pa	Emulsion type	Degradability, %	
					1 h	1 day
25	0.051	1.1×10^{-4}	11	1	66	66
50	0.052	7.4×10^{-4}	31	1	20	32
60	1.043	6.7×10^{-7}	80	2	6	16
75	0.520	1.3×10^{-7}	60	2	40	80
90	0.520	1.3×10^{-7}	80	2	70	Phase separation
100	0.208	1.3×10^{-7}	15	2	–	–

1070-4272/02/7512-2009 $27.00 © 2002 MAIK "Nauka/Interperiodica"

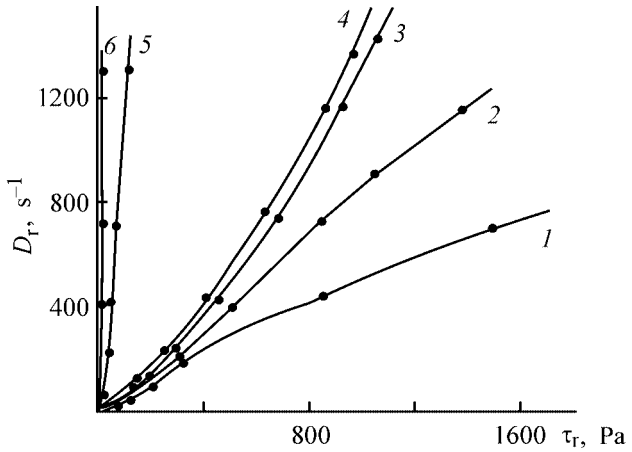

Fig. 1. Rheological flow curves of rapeseed oil-based emulsions at different rapeseed oil concentrations. (D_r) Velocity gradient and (τ_r) shear rate; the same for Fig. 2. Rapeseed oil content, wt %: (*1*) 60, (*2*) 75, (*3*) 90, (*4*) 100, (*5*) 50, and (*6*) 25.

Further increase in the rapeseed oil concentration in the system favors coalescence of the particles, which leads to emulsion breakdown. For example, at a rapeseed oil content of 75 and 90 wt % the resulting emulsions are characterized by significantly lower stability. They begin to break down already within 10–20 min, while at concentrations of 50–60 wt % only 32–16% breaks down even within 24 h.

Figure 1 shows how the structural and rheological properties of rapeseed oil emulsions vary with the oil concentration. It is seen that both individual rapeseed oil and emulsions on its base are structured liquid-like systems belonging to non-Newtonian liquids. For weakly structured liquids, the initial straight-line portion of the plot is typically short and virtually unidentifiable. With further increase in D_r and τ_r, the plots for these parameters get nonlinear. At the ultimate shear stress P_{c2} the system structure degrades completely. Our studies showed that, with increasing oil phase concentration, the emulsion structure gets somewhat stronger, as evidenced by an increase in the rheological characteristics P_{c2} and η. These parameters reach their maximal values, 80 Pa and 1.043 Pa s, respectively, with 60 wt % rapeseed oil in the system. With the rapeseed oil concentration increasing to 90 wt %, these parameters decrease to 80 Pa and 0.520 Pa s, respectively, thus evidencing a poorer structure strength.

Since many emulsification processes occur in the presence of inorganic electrolytes, it was of interest to elucidate how these electrolytes affect the stability and structural and rheological properties of the systems prepared from rapeseed oil. As known, inorganic electrolytes themselfes do not act as emulsion stabilizers because of the insufficient adsorption of their ions on the nonpolar hydrocarbon–water interface. However, in the presence of emulsifiers, the interphase activity of inorganic electrolytes may increase, thus making higher the packing density of the molecules in the surface layer at the liquid–liquid interface. Upon introduction of inorganic additions, the electrical double layer is compressed, the degree of hydration of the surfactant molecules decreases, and the structure of the solvent is modified. All this will affect the emulsion stability. In this study, we used sodium, potassium, and calcium chlorides, as well as sodium carbonate and sodium hydroxide [4, 5]. Our results (Tables 2, 3) suggest that the emulsion stability is determined by both the salt nature and concentration.

Table 2. Influence of the concentration *c* of sodium, potassium, and calcium chlorides on the stability of rapeseed oil emulsions (Rapeseed oil content 75 wt %)

$c \times 10^2$, M	Emulsion degradabilty, %				$c \times 10^2$, M	Emulsion degradabilty, %				$c \times 10^2$, M	Emulsion degradabilty, %			
	1 h	4 h	7 h	1 day		1 h	4 h	7 h	1 day		1 h	4 h	7 h	1 day
–	16	21	30	PS*	KCl electrolyte					$CaCl_2$ electrolyte				
NaCl electrolyte					0.03	0	0	0	33.0	0.01	0	0	0	16.6
					0.05	0	0	0	29.0	0.09	3	3	22	PS
0.02	0	0	0	16	0.50	0	0	7	36.0	0.18	8	30	53	″
0.30	0	0	0	33	1.00	0	0	10	PS	0.90	18	40	PS	–
1.40	0	0	16	33	3.20	4	12	50	″	5.00	70	PS	–	–
4.00	41	49	58	PS	12.00	4	15	60	″	11.00	PS	–	–	–
14.00	80	80	PS	–	24.00	70	75	PS	–					
					48.00	PS	–	–	–					

* Phase separation.

Table 3. Influence of the concentration c of sodium carbonate and sodium hydroxide on stability and structural and rheological properties of rapeseed oil-based emulsions (Rapeseed oil content 75 wt %)

$c \times 10^2$, M	æ, S cm^{-1}	P_{c2}, Pa	Emulsion type	Emulsion degradabilty, %				
				1 h	4 h	7 h	1 day	3 days
Sodium carbonate								
–	1.3×10^{-7}	66	2	17	22	29	Phase separation	–
0.8	1.2×10^{-5}	–	1	0	0	0	0	0
1.9	3.2×10^{-4}	–	1	0	0	0	0	0
4.7	6.3×10^{-4}	–	1	0	0	0	0	0
7.5	7.5×10^{-4}	80	1	0	0	0	0	0
9.4	13.3×10^{-4}	–	1	0	0	0	0	0
11.0	4.5×10^{-4}	120	1	0	0	0	0	0
15.0	4.2×10^{-4}	180	1	0	0	0	0	0
19.0	3.2×10^{-4}	120	1	0	0	0	0	0
23.0	1.3×10^{-7}	–	2	25	50	60	75	–
28.0	1.3×10^{-7}	–	2	30	60	70	Phase separation	–
34.0	1.3×10^{-7}	–	2	40	70	Phase separation	–	–
Sodium hydroxide								
0.2	8.0×10^{-4}	–	1	0	0	0	0	0
0.4	9.0×10^{-4}	240	1	0	0	0	0	0
2.5	3.0×10^{-4}	330	1	0	0	0	0	0
36.0	–	290	1	0	0	0	0	0
90.0	4.5×10^{-6}	–	2	0	0	0	0	0
120.0	1.3×10^{-7}	100	2	0	0	0	0	0
180.0	1.3×10^{-7}	90	2	0	0	0	0	0

Our studies of the influence of cations on the stability of the emulsions prepared showed that, at minor cation concentrations, the emulsion stability is enhanced owing to the formation of a more stable adsoption layer at the liquid–liquid interface. For example, with $(0.02–0.3) \times 10^{-2}$ and $(0.03–0.05) \times 10^{-2}$ M of sodium and potassium chlorides, respectively, introduced into the rapeseed oil–water system, the resulting emulsions remain stable within 7 h, whereas without these additives they undergo 16% phase separation within 1 h (Table 2). With increasing concentrations of these salts, the emulsifier salting-out from the interface tends to enhance, facilitating breakdown of the emulsion. For example, with (0.04–0.14) and (0.12–0.24) M of sodium and potassium chlorides, respectively, introduced into a system formed by rapeseed oil and water, the emulsions undergo 12–80% phase separation within 4 h. With 0.09×10^{-2} M $CaCl_2$ introduced, these emulsions begin to break down, and, with 0.11 M $CaCl_2$, they completely break down within 1 h. According to the capability to form stable emulsions, the cations studied can be arranged in the lyotropic series $Na^+ > K^+ > Ca^{2+}$.

Sodium carbonate and sodium hydroxide exert a much stronger stabilizing effect on the system formed by rapeseed oil and water than the chlorides studied by us. It should be noted that, in the case of sodium hydroxide and sodium carbonate, the emulsion stability can be retained for longer time at concentrations much exceeding those of the chlorides. For example, at NaOH and Na_2CO_3 concentrations as high as 1.2 and 0.19 M, the emulsions remain stable for 1–3 days, respectively, whereas with 0.04 M NaCl, the 41% phase separation occurs already within 1 h. Thus, according to the effect on the emulsion stability, the anions can be ranked in the order $OH^- > CO_3^{2-} > Cl^-$.

Figure 2 presents the rheological curves obtained for rapeseed oil emulsions with varied content of NaOH and Na_2CO_3. The plots of the strain rate vs. shear stress are typical of pseudoplastic liquids. As expected, minor concentrations of the electrolytes much improve the rheological properties of the emulsions, most prominently in the case of sodium hydroxide. With 0.004–0.36 M NaOH, the ultimate shear stress is 240–290 Pa (Table 3) against 66 Pa

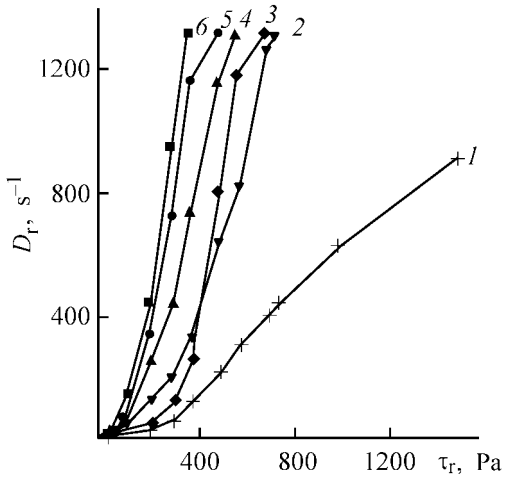

Fig. 2. Rheological flow curves for rapeseed oil emulsions (75 wt % rapeseed oil) at different concentrations of (*1–3*) NaOH and (*4–7*) Na_2CO_3 electrolytes. Electrolyte concentration, M: (*1*) 0.36, (*2*) 0.002, (*3*) 0.004, (*4*) 0.28, (*5*) 0.15, and (*6*) 0.075.

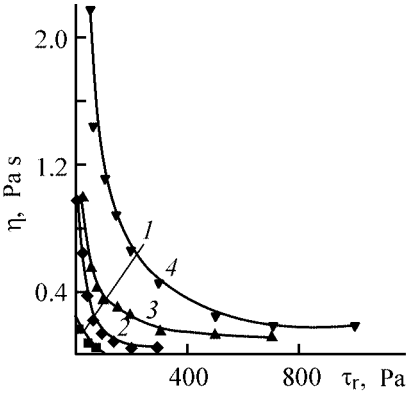

Fig. 3. Effective viscosity η, vs. shear stress τ_r, for rapeseed oil emulsions (75 wt % rapeseed oil) in the presence of (*2*) Na_2CO_3 and (*3*, *4*) NaOH. Electrolyte concentration, M: (*1*) 0, (*2*) 0.16, (*3*) 0.016, and (*4*) 0.36.

without NaOH. Na_2CO_3 tends to slightly decrease the ultimate shear stress P_{c2} to 80–180 Pa. With high concentrations of sodium hydroxide and carbonate (1.2–1.8 M), the structural and rheological properties decline dramatically, approaching those of the system formed by rapeseed oil and water. The ultimate shear stress in this case is 90–100 Pa.

An important characteristic of the structural and rheological properties of a system is its viscosity. Figure 3 shows the plots of the effective viscosity calculated from the flow rheograms against the shear stress for rapeseed oil emulsions containing inorganic electrolytes NaOH and Na_2CO_3. The $\eta = f(\tau_r)$ curves also suggest that these are non-Newtonian liquids, since their viscosity tends to decrease with increasing shear stress in the system. In this case, there is no region characterized by the highest Newtonian viscosity, where it is independent of the shear stress. The highest Newtonian viscosity of the system, probably, corresponds to very low shear stresses [6], which hinders measurements in view of the limited instrument capabilities. Our data suggest that, with NaOH (curves *3* and *4*) and Na_2CO_3 (curve *2*), both the initial and final viscosities increase relative to the emulsions without electrolytes. For example, with 0.36 and 0.16 M of sodium hydroxide and carbonate, respectively, the initial viscosities were equal to 2.0 and 1.1 Pa s, respectively, and the final viscosities, to 0.20 and 0.02 Pa s, the initial viscosity being 0.10, and the final, 0.01 Pa s, without electrolytes.

We identified the type of the resulting emulsions from the electrical conductivity. We found that formed by water, rapeseed oil, and potassium, sodium, and calcium chlorides yield type-2 (water-in-oil) emulsions, and those formed by water, rapeseed oil, and sodium carbonate or hydroxide, give both oil-in-water and water-in-oil emulsions (Tables 1 and 3). The electrical conductivity of the oil-in-water emulsions significantly exceeds that of the water-in-oil emulsions. With potassium, sodium, and calcium chlorides, it is independent of their concentrations, having a low value and remaining equal to that of rapeseed oil, i.e., 1.3×10^{-7} S cm^{-1}. In this case, the emulsifier dissolves in the oil phase, thus forming a type-2, i.e., water-in-oil, emulsion. With 0.2×10^{-2} and 0.8×10^{-2} M sodium hydroxide and sodium carbonate, the electrical conductivity increases to 8×10^{-4} and 1.2×10^{-5} S cm^{-1}, respectively, against 1.3×10^{-7} S cm^{-1} without additives. In this case, the phases invert. With further increase in the concentrations of these electrolytes, the specific electrical conductivity increases and only at 0.23 and 0.9 M Na_2CO_3 and NaOH, respectively, it declines to 1.3×10^{-7} S cm^{-1}, and the phases invert once again (Table 3). Evidently, with low concentrations of these electrolytes the emulsifier is accumulated at the interface and dissolves in the aqueous medium, thus forming type-1, i.e., oil-in water, emulsions. At high electrolyte concentrations, the emulsifier passes from the aqueous into the hydrocarbon phase, thus favoring formation of type-2 emulsions. In the system formed by water and rapeseed oil, with oil phase concentration of up to 60 wt %, type-1 emulsions are produced, and, with further increase in the oil phase concentration, type-2 emulsions (Table 1).

CONCLUSIONS

(1) Inorganic electrolytes introduced into a system formed by water and rapeseed oil modify its structural and rheological properties. The cation affects the emulsification of this system insignificantly, whereas the nature of the anion is of key importance.

(2) Sodium carbonate and sodium hydroxide affect the structural and rheological properties to a much extent than sodium, potassium, and calcium chlorides do. For example, introduction of sodium hydroxide or sodium carbonate into the system formed by water and rapeseed oil furnishes an opportunity of raising its thickening power, thus decreasing the amount of rapeseed oil to be spent for production of emulsions on this base and improving the quality of the structured dispersed systems.

(3) Phases invert under the action of inorganic electrolytes in the system formed by water and rapeseed oil: With alkali metal chlorides, type-2 emulsions are obtained in the system, and with sodium carbonate and hydroxide, both type-1 and type-2 emulsions, depending on the salt concentration.

REFERENCES

1. *Laboratornye raboty i zadachi po kolloidnoi khimii* (Laboratory Works and Problems on Colloidal Chemistry), Frolov, Yu.G. and Grodnenskii, A.S., Eds., Moscow: Khimiya, 1986.
2. Bibik, E.E., *Tekhnologiya dispersnykh sistem* (Dispersed System Technology), Leningrad: Leningr. Gos. Univ., 1981.
3. Golont, B.Ya. and Petrov, N.A., *Masloboin. Zhir. Prom–st.*, 1959, no. 2, pp. 16–19.
4. Dikhtievskaya, L.V. and Mozheiko, F.F., *Dokl. Nats. Akad. Nauk Belarusi*, 1999, vol. 43, no. 5, pp. 58–61.
5. Chistyakov, B.E. and Chernin, V.I., *Kolloidn. Zh.*, 1988, vol. 50, no. 1, pp. 187–190.
6. Filippova, A.G., Kirillova, L.G., Okhotina, N.A., *et al.*, *Kolloidn. Zh.*, 2000, vol. 62, no. 6, pp. 832–836.

Russian Journal of Applied Chemistry, Vol. 75, No. 12, 2002, pp. 2014–2020. Translated from Zhurnal Prikladnoi Khimii, Vol. 75, No. 12, 2002, pp. 2051–2057.
Original Russian Text Copyright © 2002 by Platonov, Kudrya, Proskuryakov.

CHEMISTRY OF FOSSIL FUEL

Homogeneous Pyrolysis of 1,4-Dimethoxynaphthalene

V. V. Platonov, A. N. Kudrya, and S. V. Proskuryakov

Lev Tolstoy Tula State Pedagogical University, Tula, Russia

St. Petersburg State Technological Institute, St. Petersburg, Russia

Received April 24, 2002

Abstract—Homogeneous pyrolysis of 1,4-dimethoxynaphthalene was studied. The yield and group composition of liquid products and the component compositions of the gaseous products and hydrocarbons were determined; the asphaltenes and neutral oxygen-containing compounds were characterized. The kinetic parameters were determined, and possible mechanisms suggested, for decomposition of 1,4-dimethoxynaphthalene with the formation of CH_4, H_2, CO, and CO_2.

The need to study high-temperature transformations of compounds of strictly definite classes and, especially, of individual components corresponding to fragments of the organic matter of various caustobioliths and making the major contribution to formation of liquid products was convincingly substantiated in [1–16].

The goal of this study was to analyze the features of homogeneous pyrolysis of 1,4-dimethoxynaphthalene (DMN), determine the group composition of liquid products and the component compositions of the gaseous products and hydrocarbons, characterize asphaltenes and neutral oxygen-containing compounds (NOCs), and calculate the kinetic parameters of decomposition of 1,4-DMN and formation of CH_4, H_2, CO, and CO_2.

Pyrolysis of 1,4-DMN was performed on an installation described in [17]; the group composition of the liquid products was determined according to [18].

Data on the material balance of 1,4-DMN pyrolysis (Table 1) show that the thermal stability of this compound is relatively low. As the pyrolysis temperature was increased from 700 to 800°C and the pyrolysis time, from 1.5 to 4.5 s, the yield of liquid products decreased from 53.4 to 17.3 wt %, yield of gaseous products increased from 24.7 to 37.4 wt %, and yield of pyrocarbon increased from 21.2 to 44.3 wt % (based on the feed). The content of "crude benzene" was low and did not exceed 2.6 wt % (800°C, 3 s), which is apparently due to the lack of a simple route from a system of two fused aromatic rings to mononuclear aromatic hydrocarbons.

It should be noted that variation of temperature at fixed pyrolysis time affects the product yields less strongly than variation of the pyrolysis time. For example, as the pyrolysis temperature is raised from 750 to 800°C, at fixed pyrolysis times of 1.5 and 4.5 s, the yield of liquid products decreases by 8.5 and 8.8 wt %, respectively, whereas an increase in the pyrolysis time from 1.5 to 4.5 s causes a decrease in the yield of liquid products by 19.9 and 20.2 wt %, respectively.

Table 1 shows that, in the initial steps of 1,4-DMN pyrolysis (1.5 s), CO makes a half of the gaseous pyrolysis products (54.0 vol % at 700°C and 50.1 vol % at 750°C). Methane and CO_2 are formed in comparable amounts. As the pyrolysis temperature and time are increased, the content of CO decreases from 54.0 to 36.4 vol %, with the yield of hydrogen growing by a factor of 5 (from 4.6 to 23.2 vol %). Hence, with increasing temperature and time of pyrolysis, the relative contribution of condensation processes, occurring in parallel with the degradation to CO, CO_2, and CH_4, increases. The condensation processes can be monitored by formation of hydrogen and pyrocarbon. The yield of ethene decreases from 11.2 (700°C, 1.5 s) to 0.9 vol % (800°C, 4.5 s). This is apparently due to its participation in condensations by the Diels–Alder mechanism, more active under more severe conditions.

The tendency of 1,4-DMN to undergo condensations is confirmed by the high yield of asphaltenes, varying from 33.5 to 61.6 wt % based on the liquid products. The asphaletene structures are insufficiently

1070-4272/02/7512-2014 $27.00 © 2002 MAIK "Nauka/Interperiodica"

Table 1. Material balance of 1,4-DMN pyrolysis

Pyrolysis product	Yield at indicated pyrolysis temperature, °C and time, s								
	700			750			800		
	1.5	3.0	4.5	1.5	3.0	4.5	1.5	3.0	4.5
Liquid products, wt % based on 1,4-DMN	53.4	41.5	35.0	46.0	35.0	26.1	37.5	24.9	17.3
Groups of compounds, wt % based on liquid products:									
phenols	20.5	16.3	2.8	14.2	3.0	1.8	3.0	2.4	1.3
hydrocarbons	5.5	13.5	22.7	11.2	25.2	36.4	16.2	33.7	42.2
neutral oxygen-containing compounds	9.5	6.2	3.7	6.6	4.7	2.2	5.2	3.9	1.4
asphaltenes	33.5	43.1	58.4	44.5	48.4	51.2	61.6	54.5	52.1
resinous substances	28.0	20.9	12.4	23.5	18.7	8.4	14.0	5.5	3.0
Pyrocarbon, wt % based on 1,4-DMN	21.2	26.5	30.0	24.8	30.5	36.7	28.1	37.2	44.3
Natural gas, wt % based on 1,4-DMN	24.7	31.0	33.5	28.2	33.2	35.5	3.1	35.3	37.4
Components of pyrolysis gas, vol %:									
H_2	4.6	7.2	9.4	11.2	16.0	18.9	15.0	17.3	23.2
CH_4	17.0	20.1	21.8	16.4	18.6	19.3	16.5	18.5	19.1
CO	54.0	50.1	49.2	50.1	44.3	42.8	44.1	40.6	36.4
CO_2	11.8	14.5	13.8	15.8	17.5	16.0	19.4	20.9	18.2
C_2H_4	11.2	6.6	5.2	6.0	2.4	1.3	2.7	1.7	0.9
Crude benzene, wt % based on 1,4-DMN	0.7	1.0	1.5	1.0	1.3	1.7	1.3	2.6	1.0

stable: With the pyrolysis time increasing from 1.5 to 4.5 s at 700–750°C, asphaltenes tend to accumulate, whereas at 800°C their relative content decreases from 61.6 to 52.1 wt %, with the yield of pyrocarbon growing simultaneously (Table 1).

The second most abundant group of liquid products is that of hydrocarbons. Their amount increases from 5.5 (700°C, 1.5 s) to 42.2 wt % (800°C, 4.5 s).

The yield of phenols is substantial only at 700 (1.5–3.0 s) and 750°C (1.5 s), amounting to 20.5, 16.3, and 14.2 wt %, respectively, but it decreases dramatically (to 1.3 wt %) at 800°C (4.5 s).

The content of NOCs, the main of which is unchanged 1,4-DMN, in liquid pyrolysis products is lower: Their yield decreases from 9.5 (700°C, 1.5 s) to 1.4 wt % (800°C, 4.5 s).

When studying thermochemical transformations of various compounds, it is important to obtain detailed data on the qualitative and quantitative composition of the products, in order to elucidate the main pyrolysis pathways, reveal its features, and find the best conditions for obtaining useful products in the highest yields.

The hydrocarbon fraction of liquid products of 1,4-DMN pyrolysis was studied by GLC. The yields of its components are listed in Table 2.

The major components of the hydrocarbon fraction are naphthalene, diphenyl, fluorene, and phenanthrene. The content of 2- and 1-methylnaphthalenes, pyrene, and chrysene is also high. A characteristic feature of the pyrolysis of 1,4-DMN is that the hydrocarbon fraction contains no anthracene.

The content of naphthalene, methylnaphthalenes, dimethylnaphthalenes, and acenaphthene decreases as the pyrolysis conditions are made more severe. At the same time, the content of more condensed components, such as phenanthrene, fluoranthene, pyrene, and chrysene, increases.

Table 2. Yields of components of the hydrocarbon fraction of liquid products formed in pyrolysis of 1,4-DMN

Hydrocarbon	Yield $c \times 10^2$ (wt %) based on the feed, at indicated pyrolysis temperature, °C and time, s								
	750			800			850		
	1.5	3.0	4.5	1.5	3.0	4.5	1.5	3.0	4.5
Naphthalene	48.46	117.66	150.96	104.07	151.70	106.94	78.98	93.98	53.30
2-Methylnaphthalene	8.81	14.57	17.48	10.30	12.35	12.30	7.90	9.23	5.84
1-Methylnaphthalene	20.85	36.42	45.29	22.67	26.46	22.71	16.40	15.10	5.84
Diphenyl	21.15	34.18	42.90	44.82	56.45	56.78	39.49	60.42	69.36
2,6- and 2,7-Dimethylnaphthalenes	3.82	5.60	5.56	3.09	7.06	5.68	3.65	4.20	3.65
2,3- and 1,5-Dimethylnaphthalenes	4.11	6.16	5.56	3.09	8.82	8.52	6.08	7.55	5.11
Acenaphthene	2.06	2.80	2.38	2.06	2.65	1.89	1.82	2.52	1.46
Fluorene	9.40	21.85	37.75	20.01	44.98	54.89	30.38	47.00	45.27
Phenanthrene	9.40	28.02	68.33	48.43	106.72	159.00	84.44	146.84	157.70
Fluoranthene	1.47	4.48	7.15	4.64	17.64	24.61	16.40	25.17	23.36
Pyrene	3.82	5.53	16.69	7.73	18.52	30.29	13.97	26.01	28.47
Chrysene	3.27	8.97	25.42	7.73	26.46	4.48	22.48	41.12	39.43

Table 3. Parameters of asphaltenes and neutral oxygen-containing compounds formed in pyrolysis of 1,4-DMN

T, °C	τ, s	Parameter
		Asphaltenes
700	4.5	*M* 226, C 91.60, H 5.69, O 2.71, DA 0.784, $C_{20.30}H_{12.16}O_{0.45}$, QG 0.73, AG 0.44, O_c 0.32, IN 0.21
750	1.5	*M* 250, C 92.20, H 5.65, O 2.15, DA 0.791, $C_{19.21}H_{14.12}O_{0.34}$, QG 1.07, AG 0.03, O_c 0.44, IN 0.13
	3.0	*M* 263, C 92.50, H 5.60, O 1.90, DA 0.797, $C_{20.27}H_{14.73}O_{0.31}$, QG 0.83, AG 0.24, O_c 0.27, IN 0.28
	4.5	*M* 291, C 92.90, H 5.54, O 1.56, DA 0.800, $C_{22.53}H_{16.12}O_{0.28}$, QG 0.47, AG 0.72, O_c 0.56, IN 0.14
800	1.5	*M* 271, C 93.00, H 5.50, O 1.50, DA 0.810, $C_{22.00}H_{19.91}O_{0.25}$, QG 0.61, AG 1.43, O_c 0.55, IN 0.29
	3.0	*M* 305, C 93.30, H 5.48, O 1.22, DA 0.810, $C_{23.71}H_{16.71}O_{0.23}$, QG 0.72, AG 0.56, O_c 0.23, IN 0.16
	4.5	*M* 326, C 94.20, H 5.44, O 0.36, DA 0.817, $C_{25.59}H_{17.72}O_{0.07}$, QG 0.33, AG 0.63, O_c 0.85, IN 0.42
		Neutral oxygen-containing compounds
700	4.5	*M* 181, QG 0.37, AG 0.33, O_c 0.33, IN 0.33
750	1.5	*M* 175, PG 0.07, QG 0.69, AG 0.69, O_c 0.25, IN 0.13
	3.0	*M* 200, PG 0.25, QG 0.43, AG 0.71, O_c 0.70, IN 0.17
	4.5	*M* 214, PG 0.14, QG 0.05, AG 0.85, O_c 0.36, IN 0.07

Note: (*M*) molecular weight; (C, H, O) content of carbon, hydrogen, and oxygen, respectively, wt % daf; (DA) degree of aromaticity, (PG) phenolic groups; (QG) quinoid groups; (AG) alkoxy groups; (O_c) oxygen in heterocycles; and (IN) iodine number, g-equiv mol^{-1}.

For asphaltenes, the molecular weight and elemental and quantitative functional compositions were determined (Table 3).

An increase in the molecular weight of asphaltenes from 250 to 326 in the examined range of parameters of 1,4-DMN pyrolysis indicates intensification of condensation processes. The high content of carbon (91.6–94.2%) and low content of hydrogen (5.44–5.65%) and oxygen (0.36–2.71%), in combination with the high molecular weight, point to the predominantly aromatic character and high degree of con-

densation of asphaltenes and to the relatively low content of oxygen-containing functional groups in them. The major functional groups of asphaltenes are alkoxy, quinoid, and oxygen-containing heterocyclic groups. The content of methoxy groups increases from 0.03 to 0.72 g-equiv mol^{-1} as the time of pyrolysis at 750°C is increased from 1.5 to 4.5 s. At 800°C and pyrolysis time of 3 s, their content reaches a maximum (1.56 g-equiv mol^{-1}) and then decreases to 0.63 g-equiv mol^{-1} at pyrolysis time of 1.5 s. This may be due to attack on the 1,4-DMN molecule by radical fragments generated in the initial stage of degradation, which results in incorporation of methoxy groups in asphaltene structures:

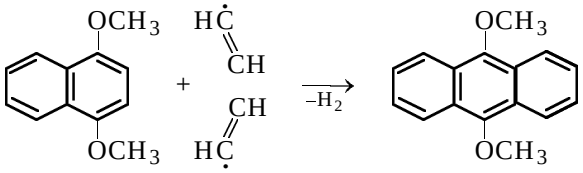

As the residence time of the feed in the heated zone is increased, methoxy groups have time to decompose not only in 1,4-DMN, but also in asphaltenes, and their content decreases.

The content of quinoid groups tends to gradually decrease, which is due to their very high lability. It is important that quinoid groups, identified previously in asphaltenes formed by pyrolysis of a number of phenols [1–9] were also detected in asphaltenes formed by pyrolysis of 1,4-DMN, with the phenolic hydroxy groups being absent.

In view of this fact, we can suggest the following scheme of accumulation of quionid groups in asphaltenes in 1,4-DMN pyrolysis:

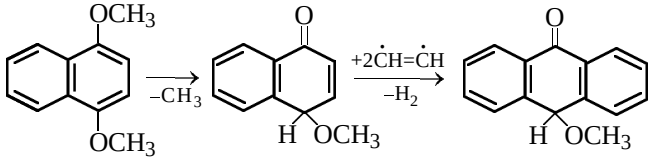

Heterocyclic oxygen can be formed as follows:

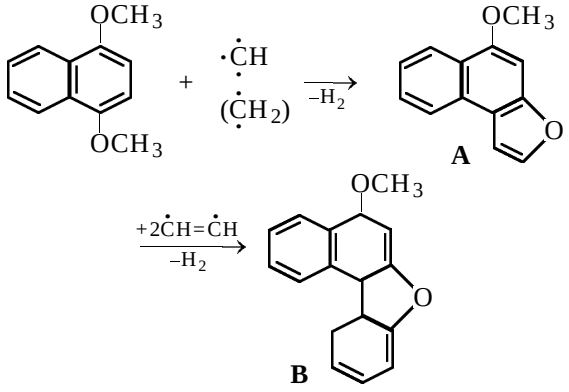

Table 4. Kinetic equations of overall decomposition of 1,4-DMN and formation of particular gaseous pyrolysis products*

Process	K
Overall decomposition of 1,4-DMN	$1.10 \times 10^7 \exp(-123\,186/RT)$
Formation of:	
H_2	$2.63 \times 10^4 \exp(-79\,191/RT)$
CH_4	$3.31 \times 10^6 \exp(-52\,794/RT)$
CO	$2.58 \times 10^7 \exp(-159\,639/RT)$
CO_2	$2.94 \times 10^7 \exp(-162\,153/RT)$
C_2H_4	$2.36 \times 10^7 \exp(-27\,654/RT)$

* Reaction order 1.5, except the formation of CO_2 (reaction order 2.0).

The minimum in the content of heterocyclic oxygen, attained in 3 s and followed by its growth (4.5 s), is apparently due to easy transformation of unstable heterocycles of type **A** into more condensed and more stable structures of type **B**. Naturally, this multistage process must take certain time; therefore, the highest content of heterocyclic oxygen is reached in 4.5 s.

As compared to asphaltenes, NOCs have lower molecular weight (175–236). Their characteristic feature is the presence of small amounts of phenolic hydroxy groups (0.07–0.25 g-equiv mol^{-1}), reaching a maximum in 3 s. This is apparently due to their formation by reduction of the quinoid groups under the conditions when the concentration of these groups becomes high; in addition, increased concentrations of hydrogen are detected:

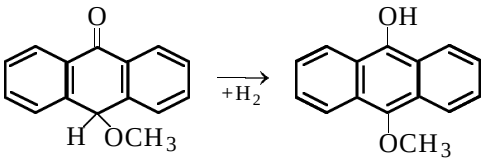

The content of the other functional groups is, on the whole, two times lower than that in asphaltenes.

The data on material balance, group composition, and component composition of the gaseous and liquid pyrolysis products were used to calculate the kinetic characteristics of the process (Table 4).

The overall decomposition of 1,4-DMN is described by an equation of the order of 1.5, with the activation energy E_a = 123.35 kJ mol^{-1}. The relatively low value of E_a of the overall decomposition process is apparently due to a significant contribution of radical reactions occurring with low energy barrier. The activation energy is considerably lower than that

of pyrolysis of naphthalene (278.64 kJ mol^{-1} [19]), α-naphthol (233.80 kJ mol^{-1} [7]), and 1,4-dimethylnaphthalene (159.09 kJ mol^{-1} [20]). Thus, methoxy groups destabilize the naphthalene core to a greater extent than phenolic hydroxyls and methyl groups do. The destabilizing effect of two methoxy groups is considerably stronger than that of a single methoxy group, so that E_a of 1,4-DMN decomposition is closer to that of 1,4-dimethylnaphthalene decomposition than to that of decomposition of compounds with a single functional group. The effect of oxygen atoms is stronger than that of methyl groups.

To elucidate the reaction mechanism and deduce the kinetic equations allowing control over formation of individual compounds with the use of an appropriate mathematical model of the process, it is of large interest to calculate the kinetic characteristics of particular pathways of the complex pyrolysis process.

Accumulation of CO follows a kinetic equation of order 1.5; E_a of this process is 159.64 kJ mol^{-1}. This activation barrier is two times lower compared to formation of CO from α-naphthol, which is probably due to a greater contribution of radical reactions to elimination of CO.

Transformation of 1,4-DMN into quinoid compounds must involve initiating demethylation. In this connection, we suggest the following scheme of CO formation. The first stage is initiation:

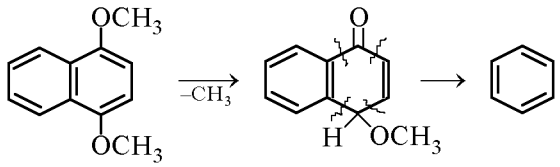

+ CO + $\dot{C}H{=}\dot{C}H$ + $H\dot{C}OCH_3$

This process generates a large number of radical products intensifying the cleavage of the 1,4-DMN molecule. The intermediate formation of the quinoid structure is confirmed by identification of quinoid groups in pyrolysis products, e.g., in asphaltenes and NOCs.

Second stage:

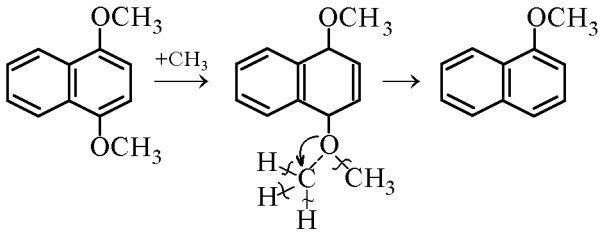

+ CO + CH_4 + H_2

A calculation of the theoretical E_a, assuming additivity of the bond energies in the activated complex [21], gave a value of 155.03 kJ mol^{-1}, in good agreement with the experimental value of 159.64 kJ mol^{-1}. This confirms the validity of the suggested scheme of the process. An additional evidence in favor of the presence of a second bimolecular initiating stage in the formation of CO is the reaction order of 1.5, since in the monomolecular cleavage of the ring in phenolic compounds it is equal to 1.0.

CO_2 formation is characterized by a similar activation energy (162.15 kJ mol^{-1}, Table 4), which suggest a kinetic relationship between these two processes, or similar mechanisms of formation of CO and CO_2. In this connection, we assume the following scheme: The first stage is initiation, similar to that in CO formation; the second stage is

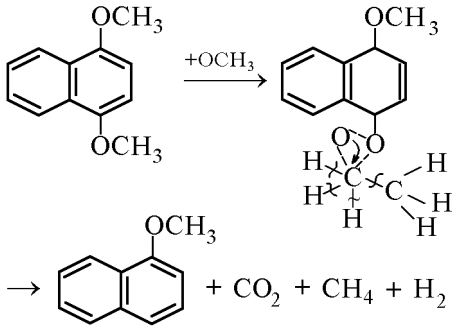

→ + CO_2 + CH_4 + H_2

The calculated activation energy of CO_2 formation is 159.22 kJ mol^{-1}, which is nicely consistent with the experimental value of 162.15 kJ mol^{-1}; this fact supports the mechanism suggested. For anisole, E_a of CO_2 formation is 206.15 kJ mol^{-1}, i.e., it is higher than that for 1,4-DMN [8]. This is a manifestation of the destabilizing effect of two methoxy groups.

The relatively low energy barrier of methane formation (E_a 52.79 kJ mol^{-1}) is most probably due to the radical recombination mechanism of its formation, from both demethylation products and radical fragments of cleaved aromatic rings. This process is described by a kinetic equation of order 1.5.

The above schemes of CO and CO_2 formation involve formation of methane as a by-product. A calculation of the effective activation energy of methane formation by the method of additivity of the bond energies in the activated complex gave a value of 56.57 kJ mol^{-1} (with account taken of the demethylation stage); the experimental value is 52.79 kJ mol^{-1}. This indicates that the actual mechanism of methane formation is similar to that suggested here, with the only difference that the contribution of the less energy-consuming demethylation process is somewhat higher

(in calculations, it was assumed to be equal to the contribution of the ring cleavage).

In the case of naphthalene and α-naphthol, the activation energy of methane formation is higher by almost a factor of 5 (E_a 239.67 and 256.85 kJ mol^{-1}, respectively), which reflects the fact that, for these compounds, the only pathway of methane formation is energy-consuming cleavage of the aromatic ring.

Ethene is formed with a still lower activation energy (E_a 27.65 kJ mol^{-1}); the reaction order is 1.5. This is facilitated by the presence of C_2 radical fragments (e.g., $\dot{C}H=\dot{C}H$) in the stage of initiation of ring cleavage with the formation of CO. The C_2 radical fragments recombine with hydrogen present in the reaction zone to give ethene:

$$\dot{C}H=\dot{C}H + H_2(2H) \longrightarrow CH_2=CH_2$$

Such radical recombination reactions have zero activation energy, which is consistent with the low activation energy of the overall process of ethene accumulation in the pyrolysis zone. The very low preexponential term, equal to 2.36, supports the presumed formation of ethene from radical fragments like $\dot{C}H=\dot{C}H$ or by recombination of methyl radicals, followed by dehydrogenation, since the probability of radical recombination under conditions of dilution with an inert gas (1 : 25 by volume, neglecting additional dilution with gaseous and vaporous pyrolysis products) is very low. As a result, the concentration of ethene is low in most cases, although, in principle, it could be high.

Hydrogen can be formed by a number of pathways, including condensation of the initial 1,4-DMN molecules and radical fragments from degradation processes. The hydrogen formation is satisfactorily described by a kinetic equation of order 1.5, with E_a = 79.19 kJ mol^{-1} (Table 4). For 1,4-dimethylnaphthalene, this value is higher by almost a factor of 2 (159.22 kJ mol^{-1}), and for α-naphthol [7] and naphthalene [19] it is still higher (269.84 and 349.87 kJ mol^{-1}, respectively), which is indicative of the large contribution of molecular condensation reactions for these compounds.

The activation energy of hydrogen formation from anisole, 98.88 kJ mol^{-1} [8], proved to be the closest to that of hydrogen formation from 1,4-DMN.

CONCLUSIONS

(1) The thermal stability of 1,4-dimethoxynaphthalene is relatively low; its noticeable decomposition starts at 700°C. The major liquid products are asphaltenes and hydrocarbons. The major gaseous product is CO.

(2) The hydrocarbon fraction consists of naphthalene, methyl- and dimethylnaphthalenes, phenanthrene, fluoranthene, pyrene, and chrysene. The molecular weight of asphaltenes varies within 250–326, and that of neutral oxygen-containing compounds, within 175–236. The main functional groups are quinoid, alkoxy, and oxygen-containing heterocyclic groups.

(3) The kinetic parameters of overall decomposition of 1,4-dimethylnaphthalene and formation of particular gaseous products were calculated; the mechanisms of formation of these products were suggested.

REFERENCES

1. Platonov, V.V., Ivleva, L.N., and Prokof'ev, E.E., *Khim. Tverd. Topl.*, 1980, no. 2, pp. 138–147.
2. Platonov, V.V., Ivleva, L.N., Klyavina, O.A., and Prokof'ev, E.E., *Khim. Tverd. Topl.*, 1982, no. 5, pp. 88–99.
3. Platonov, V.V., Klyavina, O.A., Ivleva, L.N., and Prokof'ev, E.E., *Khim. Tverd. Topl.*, 1982, no. 2, pp. 138–144.
4. Platonov, V.V., Ivleva, L.N., Klyavina, O.A., and Prokof'ev, E.E., *Khim. Tverd. Topl.*, 1981, no. 5, pp. 84–94.
5. Platonov, V.V., Klyavina, O.A., Prokof'ev, E.E., and Ivleva, L.N., *Khim. Tverd. Topl.*, 1981, no. 6, pp. 96–103.
6. Platonov, V.V., Ivleva, L.N., and Klyavina, O.A., *Khim. Tverd. Topl.*, 1984, no. 5, pp. 105–114.
7. Platonov, V.V., Proskuryakov, V.A., Ryl'tsova, S.V., and Popova, Yu.N., *Zh. Prikl. Khim.*, 2001, vol. 74, no. 6, pp. 1024–1028.
8. Platonov, V.V., Proskuryakov, V.A., Ryl'tsova, S.V., and Popova, Yu.N., *Zh. Prikl. Khim.*, 2001, vol. 74, no. 6, pp. 1018–1023.
9. Platonov, V.V., Proskuryakov, V.A., Rozental', D.A., *et al.*, *Zh. Prikl. Khim.*, 2001, vol. 74, no. 5, pp. 858–862.
10. Magaril, R.Z., *Mekhanizm i kinetika gomogennykh termicheskikh prevrashchenii uglevodorodov* (Mechanism and Kinetics of Homogeneous Thermal Transformations of Hydrocarbons), Moscow: Khimiya, 1970.
11. Hund, C.D. and Macon, A.R., *J. Am. Chem. Soc.*, 1962, vol. 84, no. 23, p. 1524.
12. Hund, C.D., *The Pyrolysis of Carbon Compounds: Am. Chem. Soc. Monograph*, New York, 1929.

13. Vypers, R., *Ann. Mines Belg.*, 1965, nos. 7–8, pp. 1091–1109.
14. Makoto, T., *Bull. Soc. Chem. Jpn.*, 1960, vol. 33, no. 6, pp. 801–808.
15. Badger, G.M. and Novotny, J., *J. Chem. Soc.*, 1961, no. 8, pp. 3400–3402.
16. Telicheev, M.D., *Zh. Prikl. Khim.*, 1939, vol. 12, no. 5, pp. 739–758.
17. Bunkina, N.A., Makarov, G.N., Bronshtein, A.P., and Platonov, V.V., *Koks Khim.*, 1975, no. 8, pp. 26–30.
18. Kamneva, A.I. and Korolev, Yu.G., *Laboratornyi praktikum po khimii topliva* (Laboratory Manual on Fuel Chemistry), Moscow: Mosk. Khimiko-Tekhnol. Inst. im. D.I. Mendeleeva, 1976.
19. Platonov, V.V., Klyavina, O.A., Ivleva, L.N., *et al.*, *Khim. Tverd. Topl.*, 1986, no. 5, pp. 75–84.
20. Platonov, V.V., Ivleva, L.N., and Klyavina, O.A., *Khim. Tverd. Topl.*, 1984, no. 3, pp. 105–114.
21. Moin, F.B., *Usp. Khim.*, 1967, vol. 36, no. 7, pp. 1223–1243.

Russian Journal of Applied Chemistry, Vol. 75, No. 12, 2002, pp. 2021–2026. Translated from Zhurnal Prikladnoi Khimii, Vol. 75, No. 12, 2002, pp. 2058–2063.
Original Russian Text Copyright © 2002 by Platonov, D. Nikolaev, Sakharovskii, Proskuryakov, S. Nikolaev.

CHEMISTRY OF FOSSIL FUEL

High-Resolution ^{1}H NMR Spectroscopy of Organic Matter of Carbonate-Chara Sapropel

V. V. Platonov, D. S. Nikolaev, V. G. Sakharovskii, V. A. Proskuryakov, and S. G. Nikolaev

Lev Tolstoy State Pedagogical University, Tula, Russia

Skryabin Institute of Biochemistry and Physiology of Microorganisms, Pushchino, Moscow oblast, Russia

St. Petersburg State Technological Institute, St. Petersburg, Russia

Received July 3, 2002

Abstract—The structural-group composition of samples of organic matter of Chara sapropel and *Characeae* algae was studied by ^{1}H NMR.

In investigation of bioliths, high-resolution NMR spectroscopy was first used by Schnitzer and Barton [1] to analyze the functional composition of soil humus extracts. This allowed identification of methyl, polymethylene, phenolic, and carboxy groups in soil humus. By now, a great body of information on fragmentary structure of organic fractions of lignites, soils, shale oils, and bottom sediments has been derived from the ^{1}H NMR spectra [2–4].

However, studies concerning structural organization of various fragments of organic matter (OM) of saprpels are fragmentary and devoted to humic acids (HAs) only [3].

The aim of this work was to study the features of structural-group composition of OM of carbonate-chara sapropel and its main precursor, *Characeae* algae, using high-resolution ^{1}H NMR spectroscopy.

EXPERIMENTAL

Carbonate-chara sapropel samples for OM studies were taken from Lake Bezdonka (Tula oblast) and *Characeae* algae used by local balneal institutions. To obtain comparative data, we recorded ^{1}H NMR spectra of HA samples recovered from valley peat of the Yakhroma deposit (Moscow oblast) and macrophyt sapropel from Lake Glubokoe (Republic of Tatarstan).

Dry samples of HAs, fulvic acids (FAs), and nonhydrolyzable residue, humin (H), were produced from preliminary decalcified sapropel [5]. A set of "free" humic substances (FHSs) was recovered by extraction of dry sapropel with a solution of deuterated alkali immediately before recording the spectrum.

The hexane and alcoholic samples of macroalga, *Chara contraria L.*, were produced by extraction of dry native mass in a Soxhlet apparatus. All the extracts were dried in a vacuum at a temperature not exceeding 40°C.

The ^{1}H NMR spectra were recorded on a WP-80SY NMR spectrometer (Bruker, Germany) operating at 80 MHz with proton decoupling.

Samples for the ^{1}H NMR study were prepared by dissolution in chloroform-*d* or in a solution of deuterated alkali in heavy water. The samples were subjected to additional deuteration. For this purpose, the solutions of the samples were dried in a vacuum on a water bath at a temperature of approximately 90°C to remove heavy water, with subsequent dissolution of the dry residue in heavy water. The chemical shifts in the ^{1}H NMR spectra were measured relative to the signals of the residual protons of deuterated solvents: δ 7.25 ppm for chloroform and δ 5.00 ppm for water at pH > 2.

The signals in the ^{1}H NMR spectra of the samples were assigned according to [6].

The average length of alkyl radicals in the samples was evaluated by analysis of the integral intensities of the ^{1}H NMR signals from methyl and methylene groups. The average branching of alkyl radicals was estimated from the relative content of methine groups. The content of methylene and methine groups was

1070-4272/02/7512-2021 $27.00 © 2002 MAIK "Nauka/Interperiodica"

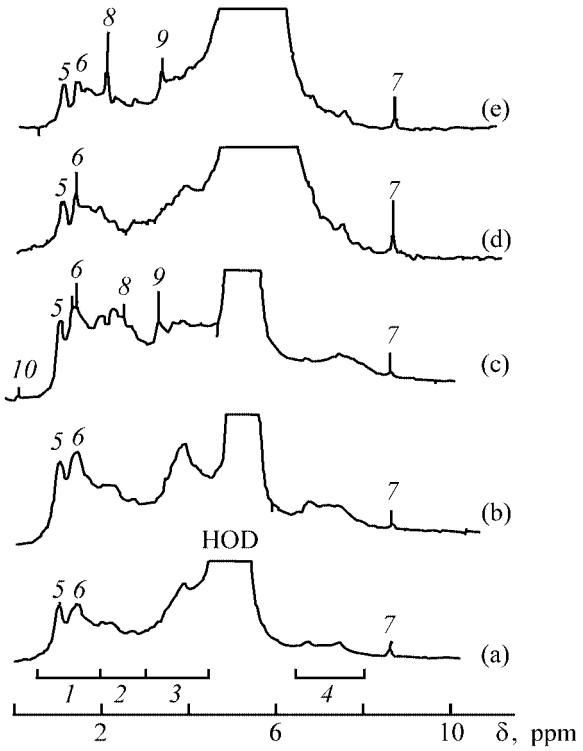

Fig. 1. ^{1}H NMR spectra of HSs of Chara sapropel of Lake Bezdonka. (δ) Chemical shift, the same for Figs. 2–4. (a) FHSs, (b) HA, (c) FA, (d) humin, and (e) humin after base hydrolysis. Assignment of proton signals in the spectra: (*1–4*) alkyl, carbonyl, polyols, and aromatic fragments, respectively; (*5*, *6*) methyl and methylene groups, respectively; (*7*) formyl group; (*8*) acyl methyl group; (*9*) *N*-methyl group; and (*10*) methyl group of silane.

calculated using the integral intensity of the signals from methyl groups as reference.

The samples of Chara sapropel are polyfunctional mixtures; therefore, for qualitative and quantitative comparative analysis, we used arbitrary division of the spectrum into ranges corresponding to the signals of the main proton-containing functional groups.

In particular, the spectrum range from 0.5 to 2.0 ppm was assigned to proton signals from the CH_3–, –CH_2–, and –CH= groups of the hydrocarbon radical. The range from 2.0 to 3.0 ppm was assigned to the proton signals from carbonyls (methyl, methylene, and methine groups in the α-position to the carbonyl carbon, i.e., ketones and carboxylic acids). The range from 3.0 to 4.5 ppm was assigned to the proton signals from polyols (methyl, methylene, and methine groups in the α-position to the OH group, i.e., alcohols and carbohydrates). The range from 4.0 to 6.0 ppm was assigned to the protons at double bonds, and the range from 6.0 to 8.0 ppm, to the protons of aromatic and heteroaromatic groups.

Ecosystematic studies of the deposit of sapropel in hand have shown [7] that its OM is produced under conditions of a medium strongly enriched in calcium ions (up to 400 mg l^{-1}) and unique type of the initial production of the pond, owing to predominant evolution of some species of *Characeae* algae, constituting 96.6% of OM and accumulating 95% of mineral substances of the lake ecosystem. In this case, the influence of terrigenous drainage on the lake ecosystem is at a minimum.

Hence follows that sapropel to be studied is of clearly pronounced carbonate-chara type, and the monodominant role of *Characeae* algae in the primary production and formation of the lake sediments makes it a convenient model object for studying the structure formation of OM of chara-type sapropels.[1]

The ^{1}H NMR spectra of humin samples (HSs) of Chara sapropel (Figs. 1a–1d) contain a set of broadened multiplets in the range 0.5–0.8 ppm and a singlet of formic acid at 8.6 ppm. The exception is the ^{1}H NMR spectrum of FA (Fig. 1c). In the range of FA spectrum characteristic of polyol protons, the signals show no pronounced polysaccharide pattern typical of other HSs. In addition, in the spectrum of FA narrow singlets were observed at 2.52 and 3.31 ppm against the background of broadened multiplets. These singlets were assigned to methyl groups of the acetate residue and *N*-methyl, respectively.

The functional composition of HSs of Chara sapropel from Lake Bezdonka according to ^{1}H NMR is presented in Table 1.

After boiling in strong alkali for 8 h, a narrow singlet appears at δ 2.08 ppm in the NMR spectrum of humin (Fig. 1e) on the background of broadened multiplets. This singlet is identified as the signal from the acetate methyl group. The appearance of an acetate group after severe alkaline treatment suggests that the sample contains *N*-acetylglucosamine, the main monomeric block of chitinic polyamino saccharides [9, 10].

This suggestion is confirmed by the appearance of a narrow singlet at δ 3.32 ppm in the ^{1}H NMR spectrum of the humin sample (Fig. 1b) after its severe alkaline treatment. This singlet was assigned to protons of the *N*-methyl group. This was also observed with the FA sample (Fig. 1b).

Hence follows that Chara sapropel contains chitinic polyamino saccharides. To prove more convincingly

[1] Vast resources of such Chara sapropels exist in Valdai, Issyk-Kul', Balkhash, and other lakes [8].

Table 1. Functional composition of Chara sapropel

Sample	Structure of aliphatic fragment	Relative content of stuctural fragments, %						
		aliphatic	carbonyl	polyols	aromatic	formyl	*N*-methyl	silane
FHA	$CH_3(CH_2)_3$–	26	20	45	8	0.6	0	0
FA	$CH_3(CH_2)_4$–	21	28	34	16	0.4	+	+
HA	$CH_3(CH_2)_4$–	27	19	36	17	0.4	0	0
H*	$CH_3(CH_2)_4$–	25	14	42	17	1.0	+	0

* Alkaline extract after boiling in concentrated alkali for 8 h.

this conclusion and also to obtain differential data on the structural organization of OM of Chara sapropel, we studied the functional composition of nonpolar (hexane) and polar (alcohol) extracts from sapropel in comparison with the composition of similar extracts from decalcified Chara.

According to the ^{1}H NMR spectrum (Fig. 2a), the hexane extract mainly consists of free unsaturated hydrocarbon of the hexadecene type.

It seems plausible that the source of this free hydrocarbon is chlorophyll, easily decomposing in an acidic or alkaline medium to phytol, chlorophyllin, and porphyrin core [9]. According to ^{1}H NMR analysis (Fig. 2b), the hexane extract from sapropel consists of free hydrocarbon, as in the case of Chara. However, the spectra of sapropel contain no clearly pronounced signals from protons at the double bond and protons of methylene groups in the α-position to the double bond in the range 1.8–2.3 ppm, present in the spectrum of the hexane extract of Chara (Fig. 2a). A relatively weak broadened multiplet observed in this range of the spectrum can be assigned to methylene groups at carbonyl, and the structure of the alkyl substituent as a whole, most likely, corresponds to the residue of hexylic acid (Fig. 2b).

This fact suggests that utilization of Chara to Chara sapropel is accompanied by degradation of free hydrocarbons (in particular, hexadecene) to hydrocarbons with lower molecular weight, proceeding by the exo mechanism.

According to the ^{1}H NMR spectrum (Fig. 3a), the polar extract from Chara consists of carbohydrates and bound hydrocarbons. A doublet of 1-α-proton of saccharide (δ 5.4 ppm) and a singlet in the region of δ 3.31 ppm, characteristic of *N*-methyl protons, suggest that the carbohydrate part of the polar extract from Chara is a polyaminosaccharide of the hyaluronic acid type, based on glucuronic acid and *N*-acetylglucosamine [1], or polyaminosaccharide of the chitin type with a monomeric unit incorporating glucosamine and its derivatives [9].

In biochemistry of algae, there are no published data on identity of polyaminosaccharides of *Characeae* algae. Only polysaccharides, starch and α-1,4-glucan, were described as reserve nutrients for *Characeae* algae [12]. These biopolymers occur in cells of many higher plants, algae, fungi, and bacteria in the form of polysaccharide exoskeleton [13].

As follows from the ^{1}H NMR spectra, the amino group of glucosamine in the Chara polysaccharide is methylated and/or acylated, and the carboxy or hy-

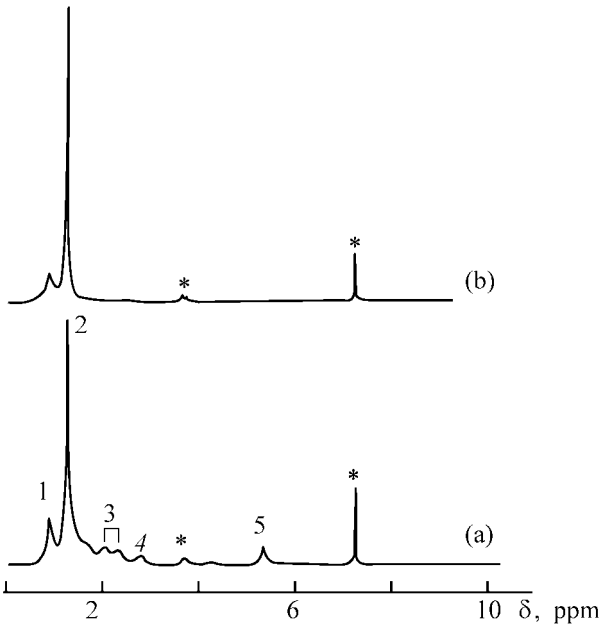

Fig. 2. ^{1}H NMR spectra of hexane extract from (a) Chara and (b) Chara sapropel of Lake Bezdonka. Assignment of proton signals in the spectra: (*1*, *2*) methyl and methylene groups, (*3*) methylene groups in the α-position to the double bond, (*4*) methylene groups in the α-position to carbonyl group, and (*5*) double bonds. The asterisks denote proton signals of the solvent and impurities in the solvent.

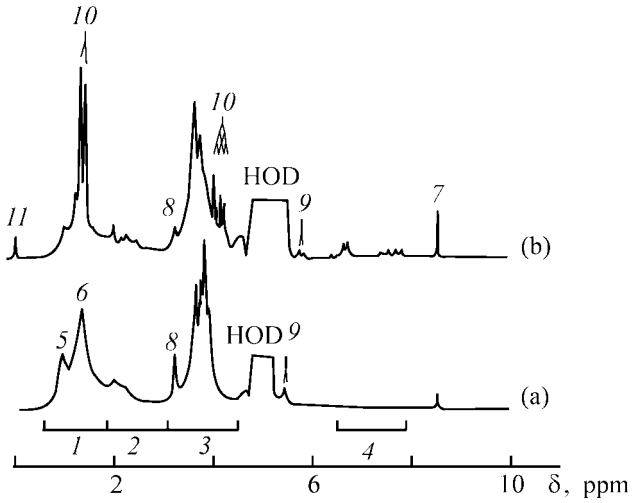

Fig. 3. ^{1}H NMR spectra of alcohol extracts from (a) Chara and (b) Chara sapropel of Lake Bezdonka. Assignment of proton signals in the spectra: (*1–4*) alkyl, carbonyl, polyols, and aromatic fragments, respectively; (*5*, *6*) methyl and methylene groups, respectively; (*7*) formyl group; (*8*) *N*-methyl; (*9*) α-H-1 residue of glucosides; (*10*) methyl and methylene groups of lactic acid; and (*11*) methyl groups of silane.

droxy group of glucuronic acid is probably alkylated, which follows from the structure of the alkyl radical of polar extract from Chara (Table 2). Based on these facts, we constructed a hypothetical structure of the polysaccharide skeleton of Chara:

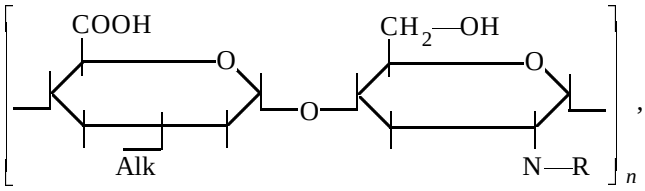

where R is H, CH_3, and $CO–CH_3$.

The calculated content of the functional groups of the structure suggested is as follows (%): alkyl 42, polyols (carbohydrates) 46, and *N*-methyl and/or *N*-acyl 12.

The content of the functional groups of the polar extract from Chara, established on the basis of the ^{1}H NMR spectra (Table 2), appears to be close to that obtained for the hypothetical structure, except for the content of the *N*-methyl fragment, which is apparently caused by its alkaline hydrolytic elimination in preparation of Chara samples.

As in the case of Chara, the alcoholic extract from sapropel mostly consists, according to the ^{1}H NMR data (Fig. 3b), of polysaccharides and bound hydrocarbons (Table 2). The presence of a doublet at 5.4 ppm and a singlet at 3.2 ppm suggests that the structures of polysaccharides in Chara and in sapropel are similar. Hence follows that, in utilization of Chara to Chara sapropel, the structure of polysaccharide undergoes no noticeable transformations. It is likely that the degree of transformation of the carbohydrate skeleton of Chara is governed by the molecular weight of polysaccharide.

The presence of structures of the *N*-acetylglucosamine type and Chara origin in the humin fraction and in polar extract of the sapropel under study allows us to prognosticate a high physiological activity of sapropel and its individual fractions [13].

Along with bound hydrocarbons and polysaccharide fragment, the alcohol extract from Chara sapropel contains lactic acid, an insignificant amount of aromatic groups, formate, and silane group linked to the polymer matrix.

The absence of lactic acid and aromatic fragments in the alcohol extract from Chara (Fig. 3a) suggests

Table 2. Structural-group composition of hexane and alcohol extracts from sapropel and *Characeae* algae

Structure fragments	Relative content, %			
	hexane extract		alcohol extract	
	Chara $C_{14}H_3OCH=CH$	sapropel $CH_3(CH_2)_4–$	Chara $CH_3(CH_2)_4–$	sapropel $CH_3(CH_2)_4–$
Aliphatic	96	93	39	35
Carbonyl	4	5	14	9
Polyols	0	0	35	49
Aromatic	0	0	0	3
N-Methyl	0	0	5	3
Formyl	0	0	1	1
–HC=CH–	+	0	0	0

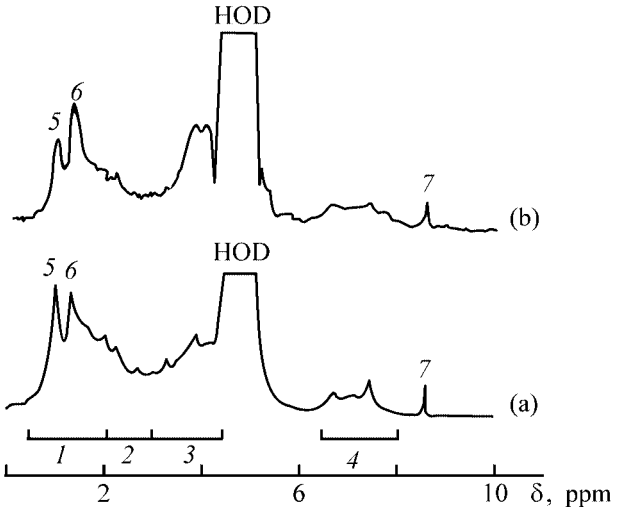

Fig. 4. ^{1}H NMR spectra of the HA samples of (a) macrophytic sapropel and (b) valley peat. Assignment of proton signals in the spectra: (*1–4*) alkyl, carbonyl, polyols, and aromatic fragments, respectively; (*5*, *6*) methyl and methylene groups, respectively; and (*7*) formyl group.

that these components are of secondary origin, i.e., they are exametabolites of microorganisms utilizing Chara.

It should be noted that the first conclusions concerning the structural organization of Chara and Chara sapropel are of limited nature, since the hexane and alcoholic extracts alone cannot reflect in full measure the overall structural organization of the substances in hand. A more detailed study of the structure of polysaccharide of *Characeae* algae and Chara sapropel requires appropriate experiments, which is the subject of our further work.

It is of interest to compare the functional compositions of Chara sapropel and bioliths of other nature. However, owing to the scarcity of data, this is only possible only for HAs of bioliths.

Data on fragmentary composition of HAs, obtained from the ^{1}H NMR spectra, are listed in Table 3 and shown in Fig. 4. For convenience of comparison, the functional groups of alkyl radicals and carbonyl-containing hydrocarbons are combined into aliphatic groups.

Table 3. Structural-group composition of HAs

Origin of HAs	Structural-group composition, %		
	aliphatic	polyols	aromatic
Chara sapropel	47	36	17
Macrophytic sapropel	58	29	13
Valley peat	49	38	11
South chernozem	66	11	23

Comparison of these formalized data shows that HAs of sapropels and peat are similar in the ratio of functional groups, being characterized by relatively high content of polyols (carbohydrates) and twice lower content of aromatic hydrocarbons.

The trend observed is accounted for by the fact that predominantly aquatic flora containing no lignin is the initial raw material for formation of these bioliths. This agrees with the conclusion about the secondary role of aromatic hydrocarbons and their derivatives in formation of Chara sapropel, made in this study.

In the case of HA samples recovered from chernozem, the opposite pattern is observed: relatively low content of the polyol fraction and a double amount of aromatic hydrocarbons. This is due to the nature of the surface plant materials forming soil humus containing lignin (phenolic derivative) [11].

Thus, analysis of the relative content of polyols and aromatic hydrocarbons in HA samples can be used to establish the origin of a biolith.

CONCLUSIONS

(1) The structural organization of Chara and Chara sapropel is based on polysaccharides of the type of hyaluronic acid or chitin, with the monomeric unit apparently incorporating glucuronic acid and derivatives of glucosamine. The amino group of glucosamine is methylated and/or acylated, and carboxy or hydroxy groups of glucuronic acid are apparently alkylated.

(2) Utilization of Chara to Chara sapropel is accompanied by degradation of unsaturated hydrocarbons of Chara to hydrocarbons with lower molecular weight, most likely by the exo mechanism.

(3) The structure of polysaccharide does not change significantly. Aromatic hydrocarbons and their derivatives (in particular, phenols) and also lactate found in the Chara sapropel are of secondary nature, being exo metabolites of microorganisms utilizing Chara.

(4) The relative content of the polyol fraction (carbohydrates) and aromatic hydrocarbons in the samples of humic acids of bioliths can be used for determining their origin.

REFERENCES

1. Schnitzer, M. and Barton, D.N., *Nature*, 1963, vol. 198, pp. 217–219.
2. Orlov, D.S., *Gumusovye kisloty pochv i obshchaya teoriya gumifikatsii* (Soil Humus Acids and General Theory of Humification), Moscow: Mosk. Gos. Univ., 1990.
3. Stepanov, A.A., Zharkova, L.V., and Stepanova, E., *Pochvoved.*, 1997, no. 2, pp. 173–177.
4. Lundermann, H.D., *Erdol Kohle, Erdgas, Petrochem. Verlin. Brenstoff-Chem.*, 1973, vol. 26, pp. 506–509.
5. Orlov, D.S. and Grishina, L.A., *Praktikum po khimii gumusa* (Manual on Humus Chemistry), Moscow: Mosk. Gos. Univ., 1981.
6. Bystrov, V.F. and Sakharovskii, V.G., *Zh. Vses. Khim. O–va*, 1971, vol. 16, no. 4, pp. 381–391.
7. Platonov, V.V., Nikolaev, D.S., Proskuryakov, V.A., *et al.*, *Geol. Vestn.*, 2002, no. 1, pp. 21–26.
8. Sviridenko, B.F., *Botan. Zh.*, 1993, vol. 78, no. 7, pp. 29–37.
9. Karrer, P., *Lehrbuch der Organischen Chemie*, Stuttgart: George Thieme, 1959.
10. Besednova, N.N., Ivanushko, L.A., Zvyagintseva, T.N., and Elyakova, L.A., *Antibiot. Khimioter.*, 2000, vol. 45, no. 2, pp. 37–43.
11. Vikha, I.V., Sakharovsky, V.G., Bystrov, V.F., and Khorlin, A.Ya., *Carbohydr. Res.*, 1972, vol. 25, pp. 143–152.
12. Senechkin, V.N., Sakharovskii, V.G., Il'chenko, V.Ya., and Akimenko, V.K., *Khim. Drev.*, 1986, no. 5, pp. 77–85.
13. South, G.R. and Whittick, A., *Introduction to Phycology*, Oxford: Blackwell, 1987.

Russian Journal of Applied Chemistry, Vol. 75, No. 12, 2002, pp. 2027–2028. Translated from Zhurnal Prikladnoi Khimii, Vol. 75, No. 12, 2002, pp. 2064–2065.
Original Russian Text Copyright © 2002 by Ban'kovskaya, Gorbatova, Sazonova, Ermolenko, Popov, Turoverov, Baranov, Gerasimov, Cheremisin

BRIEF COMMUNICATIONS

Refractory Materials Resistant to Quartz Glass in Vacuum at 1600–1700°C

I. B. Ban'kovskaya, G. N. Gorbatova, M. V. Sazonova, T. A. Ermolenko, S. A. Popov, P. K. Turoverov, B. P. Baranov, V. V. Gerasimov, and I. I. Cheremisin

Grebenshchikov Institute of Silicate Chemistry, Russian Academy of Sciences, St. Petersburg, Russia

Received January 28, 2002

Abstract—Graphite materials with coatings based on boron nitride and molybdenum disilicide were studied in order to find a way to prevent reaction of quartz glass with graphite members.

In quartz glass processing by extrusion, the equipment members are fabricated from finely dispersed MG graphite. The quality of extruded quartz glass articles, characterized by content of gas bubbles and capillaries, foreign inclusions, ribbing, and surface crystallization, depends on the intensity of the reaction between silica, SiO_2, and the forming graphite members at 1500–1750°C. Making this reaction slower is an important problem in manufacture of quartz glass tubes and rods. The reaction of silica with the graphite members occurs with intense gas evolution. The reaction products remaining within the closed space of the reactor are incorporated into the glass melt to form capillaries and bubbles in the articles. In addition, surface crystallization of the glass melt occurs under these conditions. As a result, extrusion is decelerated to the point of its complete stopping, and the quality of the article surface is deteriorated. The practice shows that the maximum permissible thickness of a cristobalite layer on the surface of an extruded quartz glass block must not exceed 350–450 μm.

Presently, a glass block is protected with a molybdenum sheath to prevent reaction of glass melt with graphite in the course of extrusion. To exclude the expensive molybdenum "shield" from the technological process, refractory materials that could prevent the reaction of the quartz glass melt with graphite members were selected.

Direct evidence concerning the behavior of refractories when in contact with quartz glass at temperatures of up to 1750°C in a vacuum is virtually lacking. The best materials, resistant to glass melts, were chosen on the basis of the available published data. These are materials based on zirconium, aluminum, hafnium, yttrium, and tin oxides, and also boron nitride and silicon oxynitride [1–6].

This study is concerned with the resistance of a quartz glass brought in contact with uncoated and coated graphite, and also with other materials, at 1600–1700°C in a vacuum. The equipment used gave no way of studying the effect of higher temperatures.

Quartz glass samples $1 \times 1 \times 0.5$ cm in size (or having the form of small pieces with flat surface) were

Results obtained with various materials brought in contact with a quartz glass at 1600–1700°C for 15 h in vacuum

Composition no.	Composition of coating on graphite	Thickness of cristobalite layer, μm	Loss of glass mass, %
1	Mo*	50	8
2	Graphite without coating	Lacking	40
3	SnO_2	Trace amounts	50
4	$ZrSiO_4$	25, only along perimeter	Not detected
5	$SiC–ZrSiO_4$	Trace amounts	50
6	$B_3Si–BN$	Lacking	30
7	BN	″	5
8	CeO_2	″	100
9	Y_2O_3	Trace amounts	50
10	HfO_2	150	70
11	$MoSi_2$	Lacking	10
12	$MoSi_2–TiSi_2–Mo$	″	10
13	$MoSi_2–HfO_2–SiO_2$	″	10

* Container material.

1070-4272/02/7512-2027 $27.00 © 2002 MAIK "Nauka/Interperiodica"

placed onto the surface of a material under study and introduced into a furnace in molybdenum sheet containers. After the test was complete, the samples were subjected to visual inspection. The percentage loss of the glass mass was estimated, and the degree of its crystallization was monitored.

The results obtained in tests with different materials brought in contact with quartz glass at 1700°C for 15 h in a vacuum are listed in the table.

Dense samples of composition Al_2O_3–SiO_2–$ZrSiO_4$ and Al_2O_3–SiO_2 were compacted into pellets and tested at 1600°C for 24 h in a vacuum when in contact with a quartz glass. After the test, the glass was found to be crystallized completely.

The results of the experiments indicate that graphite with a BN coating is a promising refractory material to be used in contact with a quartz glass at 1600–1700°C. Graphite with $MoSi_2$-based coatings (composition nos. 11–13 in the table) is also of interest. The material of the coating acts as a barrier between the glass and the graphite members.

CONCLUSION

The study performed showed that $MoSi_2$-based and BN coatings are promising for preventing the reaction between graphite members and quartz glass.

REFERENCES

1. Zhukovskaya, A.E., Strakhov, V.I., and Taras'yan, L.P., in: *Sbornik trudov Leningr. Tekhnol. Inst im. Lensoveta* (Coll. of Works of Lensovet Technological Institute), 1975, issues 1–2, pp. 62–65.
2. Bundschuh, K., Schuze, M., Muller, C., *et al.*, *J. Eur. Ceram. Soc.*, 1998, vol. 18, pp. 2389–2391.
3. Sil'vestrovich, T.S., Rublevskii, I.P., and Rykov, L.V., *Steklo Keram.*, 1978, no. 10, pp. 8–10.
4. Grosheva, V.M., Karpinos, D.M., and Pilipovskii, Yu.L., *Steklo Keram.*, 1970, no. 11, pp. 36–37.
5. Siging, W., and Yu-hua, V., *Trans. Nonferrous Metals Soc.*, China, 2000, vol. 10, no. 3, pp. 418–420.
6. Ejichi,A., Manabu,F., Kenichiro, M, and Kazuo, A., *Refractories*, 1986, vol. 38, no. 6, pp. 393–395.

Russian Journal of Applied Chemistry, Vol. 75, No. 12, 2002, pp. 2029–2030. Translated from Zhurnal Prikladnoi Khimii, Vol. 75, No. 12, 2002, pp. 2066–2067.
Original Russian Text Copyright © 2002 by Kazakov, Kazantsev, Malyshev.

BRIEF COMMUNICATIONS

Synthesis of New Sulfonic Acid Acrylamide Derivative from Acrylonitrile, Camphene, and Oleum

S. A. Kazakov, O. A. Kazantsev, and A. P. Malyshev

Dzerzhinsk Branch, Nizhnii Novgorod State Technical University, Dzerzhinsk, Nizhnii Novgorod oblast, Russia

Received June 28, 2002

Abstract—Synthesis of a new monomer, 2-acrylamido-7,7-dimethyl-1-sulfomethylbicyclo[2.2.1]heptane, is described.

Reaction of acrylonitrile with camphene in the presence of a sulfonating agent (oleum) yielded a new camphene derivative containing acrylamide and sulfonic acid moieties, 2-acrylamido-7,7-dimethyl-1-sulfomethylbicyclo[2.2.1]heptane **I**:

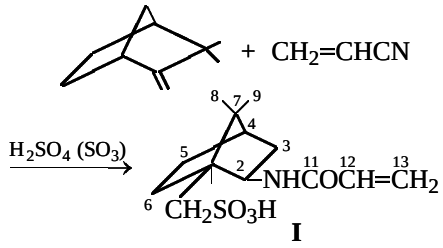

(1)

I

The initial reactant ratio, oleum concentration, and reaction temperature were chosen on the basis of published data on similar syntheses of *N*-substituted acrylamides, containing sulfo group, from other olefins [1, 2].

In the course of experiments, a precipitate formed. Product **I** can be purified by repeated washing of the crude precipitate with organic solvents (e.g., a mixture of acetone and chloroform) or by recrystallization from acetic acid. The second procedure affords the highest yield of **I**.

It is known [3] that acid-catalyzed transformations of camphene may be accompanied by its isomerization, yielding a large set of compounds. Comparison of the ^{13}C and ^{1}H NMR spectra of the purified product with the spectra of various camphene derivatives [3] allowed identification of this substance as pure **I**.

Analysis of the precipitate and mother liquor after the reaction revealed that, along with the main reaction, there occur the Ritter reaction yielding *N*-isobornylacrylamide **II** [Eq. (2)] and hydration of acrylonitrile to acrylamide [Eq. (3)]:

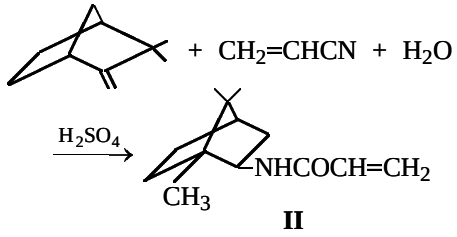

(2)

II

$$CH_2{=}CHCN + H_2O \xrightarrow{H_2SO_4} CH_2{=}CHCONH \quad (3)$$

The distribution of the products and unchanged reactants among the phases is illustrated in the table. It is seen that, when the reaction is performed at 40°C in the course of 6 h, the conversion of camphene reaches 93%, and the selectivity of its transformation into **I**, 47%; 88% of **I** occurs as precipitate.

Material balance of synthesis of **I**

Compound	Loaded		Obtained			
	g	mmol	precipitate		mother liquor	
			g	mmol	g	mmol
Camphene	10.0	73.5	0.7	5.1	–	–
Acrylonitrile	27.3	515	17.1	322	5.9	107
H_2SO_4	6.7	68.4	2.7	28.4	1.9	19.2
SO_3	1.0	12.1	–	–	–	
I	–	–	1.1	3.9	8.2	29.0
II	–	–	4.4	20.5	3.2	15.5
Acrylamide	–	–	0.9	12.2	0.4	5.5

1070-4272/02/7512-2029 $27.00 © 2002 MAIK "Nauka/Interperiodica"

EXPERIMENTAL

Syntheses were performed at 40°C in a temperature-controlled reactor equipped with a stirrer, a thermometer, and a reflux condenser. The initial molar ratio acrilonitrile : camphene : (H_2SO_4 + SO_3) was 1.0 : 7.0 : 1.2, and the oleum concentration, 15%.

Camphene was prepared according to [4]; its physicochemical characteristics were in agreement with published data.

In the reaction mixtures and isolated products, the concentrations of **I** and **II** were determined by liquid chromatography, the concentration of C=C bonds, by bromide–bromate titration, and the concentration of sulfo groups, by alkali titration. Liquid chromatography was performed on a Praha device equipped with a UV detector (λ = 254 nm) and a 150 × 3-mm glass column packed with Separon SCX C_{18}; eluent acetonitrile. The ^1H and ^{13}C NMR spectra were recorded on a Gemini-300 spectrometer (D_2O, internal reference DMSO). The IR spectrum was measured on a Specord M-80 spectrometer (KBr pellet).

Compound **I**. To a mixture of 27.3 g (0.515 mol) of acrylonitrile, 10 g (0.0735 mol) of camphene, and 0.1 g of hydroquinone, we added with stirring and cooling (temperature ≤10°C) 7.7 g of 15% oleum. The mixture was stirred for 6 h at 40°C. The precipitate was filtered off, recrystallized from acetic acid [1], and dried in a vacuum (40°C, 2 mm Hg) to constant weight. Yield 7.2 g (34.3%); white crystalline product readily soluble in water, lower alcohols, and DMSO and insoluble in nonpolar organic solvents.

Found, mg-equiv g^{-1}: C=C bonds 3.38, acid groups 3.62. Calculated, mg-equiv g^{-1}: C=C bonds 3.48, acid groups 3.48.

^1H NMR spectrum, δ, ppm: 5.90 s and 5.96 s (3H, CH_2=CH), 6.04–6.20 m (3H, CH=CH_2), 7.50–7.58 m (1H, NH), 3.80–3.88 m (2H, CH_2SO_3), 0.58 s and 0.75 s (3H, CH_3C), 0.90–1.80 m and 2.60–3.20 m (camphene core).

^{13}C NMR spectrum, δ_C, ppm: 48.98 (C^1) 49.81 (C^2), 38.95 (C^3), 44.42 (C^4), 26.74 (C^5), 32.91 (C^6), 48.54 (C^7), 19.75 (C^8), 19.60 (C^9), 55.75 (C^{10}), 130.40 (C^{11}), 55.86 (C^{12}), 127.00 (C^{13}).

Characteristic IR bands, ν, cm^{-1}: 1060 (SO_3H), 1165 (S=O), 1250 (amide III), 1590 (amide II), 1650 (C=C), 1720 (amide I).

CONCLUSION

2-Acrylamido-7,7-dimethyl-1-sulfomethylbicyclo-[2.2.1]heptane was prepared by reaction of acrylonitrile with camphene in the presence of a sulfonating agent (oleum); the by-products are acrylamide and *N*-isobornylacrylamide.

REFERENCES

1. Khalistova, I.D. and Podgornova, V.A., *Zh. Prikl. Khim.*, 1994, vol. 67, no. 8, pp. 1346–1350.
2. Kazakov, S.A., Kazantsev, O.A., Shirshin, K.V., and Danov, S.M., *Zh. Prikl. Khim.*, 1999, vol. 72, no. 7, pp. 1168–1171.
3. Fomenko, V.V., Korchagina, D.V., Yarovaya, O.I., *et al.*, *Zh. Org. Khim.*, 1999, vol. 35, no. 7, pp. 1031–1041.
4. Sasaki, T., Eguchi, S., and Oyobe, T., *Bull. Chem. Soc. Jpn.*, 1970, vol. 43, no. 4, pp. 1252–1254.

Russian Journal of Applied Chemistry, Vol. 75, No. 12, 2002, pp. 2031–2032. Translated from Zhurnal Prikladnoi Khimii, Vol. 75, No. 12, 2002, p. 2071.
Original Russian Text Copyright © 2002 by Morachevskii.

BOOK REVIEWS

Moiseev, G.K., Vyatkin, G.P., Barbin, N.N., and Kazantsev, G.F., *Primenenie termodinamicheskogo modelirovaniya dlya izucheniya vzaimodeistvii s uchastiem ionnykh rasplavov* (Thermodynamic Modeling in Studies of Interactions Involving Ionic Melts), Chelyabinsk, Yuzhn. Ural'sk. Gos. Univ., 2002, 165 pp.

Attention of readers is called to a monograph in which methods of thermodynamic modeling are applied to analysis of interactions occurring in systems containing ionic melts based on alkali metal carbonates and halides and more complex formulations. The general principles of thermodynamic modeling by means of the computer program used by the authors have been described in detail previously.

The book comprises a foreword, introduction, four chapters, conclusion, bibliography, and appendix. The foreword, having its own list of references (to 34 reports, mainly by the authors of the monograph), mentions the possibility of processing technological wastes containing heavy nonferrous metals and secondary raw materials (aluminum and aluminum alloy scrap, scrap lead from batteries) in ionic liquids, to which belong melts of halides, carbonates, and other oxygen-containing salts of, in the first place, alkali metals. A very brief introduction describes the software packages and databases used in thermodynamic modeling.

The first chapter (pp. 11–112) occupies the central place in the monograph, as regards its volume and nature of the problems discussed. It presents the results of thermodynamic modeling as applied to individual molten carbonates of alkali metals in the temperature range 1000–2000 K in various media (Ar, O_2, CO_2, CO). Also considered are mixtures of carbonates and more complex systems including compounds of lead and some other metals.

The second chapter (pp. 113–127) is devoted to more specific problems—possibility of synthesizing indium and gallium phosphides and gallium arsenide in complex ionic media. The authors carried out necessary thermodynamic calculations. As base melts served mixtures of metaphosphates, in one case, and those of sodium and potassium arsenates, in another.

The third chapter (pp. 128–136) applies the technique developed by the authors to evaluation of the content of cations in different oxidation states in molten halides. As specific objects of thermodynamic analysis served solutions of zirconium or titanium chloride in molten individual chlorides of sodium, potassium, or cesium in an atmosphere of argon.

The small fourth chapter (pp. 137–141) considers the interaction of silumin with ionic melts in the temperature range 300–1400 K under total pressure of 10^5 Pa in argon or in a model medium containing 20 wt % O_2 + 80 wt % Ar.

A number of important theoretical and practical problems related to ionic melts are discussed in the final part of the monograph (pp. 142–157). The authors, based on the models known for high-temperature phases of variable composition in liquid state, substantiate the validity of the model of "ideal solutions of interaction products," which is a variation of the model of ideal associated solutions, to thermodynamic analysis of complex systems. The main list of references (pp. 158–163) covers 90 reports, 30 of which belong to the authors of the monograph. An additional list includes references to 16 studies published in 2000–2002.

The book was written by known specialists in thermodynamic modeling and processing of secondary raw materials, working at the Southern-Ural State University (G.P. Vyatkin, corresponding member of the Russian Academy of Sciences), and Institutes of Metallurgy (G.K. Moiseev and G.F. Kazantsev) and

1070-4272/02/7512-2031 $27.00 © 2002 MAIK "Nauka/Interperiodica"

High-Temperature Electrochemistry (N.M. Barbin), Ural Division, Russian Academy of Sciences.

With the monograph, which is of interest and of use, highly appreciated, there is no escape from mentioning that it gives insufficient attention to comparison of the results of thermodynamic modeling with the data obtained in experimental studies of the systems and processes considered. Also, the atmosphere of argon is untypical of the technological practice and may hinder to a certain extent the use of the results of modeling in estimates and comparisons. The use of the model of ideal solutions of interaction products for describing some systems, e.g., Al–Si–Na–K solutions, can hardly be substantiated.

The monograph by G.K. Moiseev and co-authors may be of use for, in the first place, specialists in thermodynamic modeling of complex high- temperature systems.

A. G. Morachevskii

Russian Journal of Applied Chemistry, Vol. 75, No. 12, 2002, pp. 2033–2034. Translated from Zhurnal Prikladnoi Khimii, Vol. 75, No. 12, 2002, p. 2072.
Original Russian Text Copyright © 2002 by Morachevskii.

BOOK REVIEWS

Mel'nichenko, E.I., *Ftoridnaya pererabotka redkometal'nykh rud Dal'nego Vostoka* (Fluoride Processing of Rare-Metal Ores from the Far East), Vladivostok: Dal'nauka, 2002, 268 pp.

The widely diverse existing technologies for processing of rare-metal ores are based on complicated hydro- and pyrometallurgical operations and have disadvantages related to ecological safety. In the Russian Far East, there are rather large deposits of such rare metals as tungsten, titanium, and zirconium, but no processing of these raw materials is done in the region. The monograph by E.I. Mel'nichenko summarizes the results obtained in scientific studies of scheelite, baddeleyite, ilmenite, sphene, and rutile processing to obtain oxides of rare metals, and considers a number of other technological problems. The book comprises a foreword, ten chapters, and a list of references, common to the monograph.

The brief foreword (pp. 5 and 6) notes the advisability of using widely a common reagent, ammonium bifluoride (hydrofluoride), in processing of various rare-metal raw materials. This recommendation is largely based on the presence in Primorskii krai of unique deposits of fluor-spar.[1]

The first chapter (pp. 7–13) presents evidence concerning the mineral resources of the Far East. This region is a part of the so-called Pacific ore belt. Quite a number of minerals from Primor'ye govern the balance of mineral resources of the country.

The second chapter (pp. 14–25) discusses the use of fluorinating agents in metallurgical processes ("fluoride metallurgy"). The author emphasizes that ammonium hydrofluoride is a serious rival to fluorine and hydrogen fluoride in fluoride metallurgy.

The third chapter (pp. 26–71) is concerned with problems associated with processing of tungsten concentrates. It describes the existing industrial technologies for manufacture of tungsten and physicochemical foundations of methods used in processing of scheelite concentrates with NH_4HF_2. Much attention is given to properties of ammonium oxofluorotungstates and tungsten oxyfluorides.

The fourth (pp. 72–110) and fifth (pp. 111–169) chapters contain data on processing of zirconium and titanium concentrates, possibility of using ammonium hydrofluoride in technological processes, and properties of fluoride compounds of zirconium and titanium.

The sixth chapter (pp. 170–193) discusses the behavior of molybdenum and chromium oxides heated with NH_4HF_2. The seventh chapter (pp. 194–200) summarizes results of original investigations into processing of gold- and silver-containing ores with the use of the fluoride technology. The eighth chapter (pp. 201–213) describes to other promising fields of application of ammonium hydrochloride (dressing of the fluorite concentrate, production of biocides). The ninth chapter (pp. 214–221) is concerned with thermodynamic substantiation of the use of NH_4HF_2 for processing of rare-metal ores. The tenth chapter (pp. 222–244) presents rather useful evidence concerning the corrosion resistance of construction materials in various fluorine-containing media in a wide range of temperatures. Also, the stability of high-nickel steels, nickel-based alloys, and fluoroplastics of domestic manufacture is considered.

The list of references (pp. 245–261) covers 308 original studies, inventor's certificates, patents, and other sources. The highly informative list gives titles of journal articles. A large number of works cited in the list have been carried out with participation of the author of the monograph.

The book has technological orientation and clear and logical structure; it is devoted to solution of a specific important problem and is well written. Some critical remarks may concern, in our opinion, the ninth

[1] The resources of fluor-spar ores are considered in more detail by V.I. Saenko, V.P. Yushkevich, V.V. Korshunov, *et al.* (*Tsvet. Metal.*, 1999, nos. 8–9, pp. 33–38).

1070-4272/02/7512-2033 $27.00 © 2002 MAIK "Nauka/Interperiodica"

chapter whose unwarranted brevity gives rise to a number of questions. In particular, it would be well to give, irrespective of temperature, the aggregative state of substances involved in a reaction in those cases when it may vary.

The monograph was recommended for publication by the Scientific Council of the Institute of Chemistry, Far-Eastern Division, Russian Academy of Sciences, and published with support from the Russian Foundation for Basic Research and administration of Primorskii krai. The book will be undoubtedly of interest to a wide audience of specialists working in research and design institutions dealing with technology of processing of various rare-metal raw materials. The simplicity and clarity of presentation make it possible to recommend the book for use as a textbook for students specialized in the corresponding branches of chemical technology and metallurgy.

A. G. Morachevskii

Russian Journal of Applied Chemistry, Vol. 75, No. 12, 2002, p. 2035. Translated from Zhurnal Prikladnoi Khimii, Vol. 75, No. 12, 2002, p. 2073.
Original Russian Text Copyright © 2002 by Morachevskii.

BOOK REVIEWS

Yukhnin, Yu.M. and Mikhailov, Yu.I., *Khimiya vismutovykh soedinenii i materialov* (Chemistry of Bismuth Compounds and Materials), Novosibirsk: Sib. Otd. Ross. Akad. Nauk, 2001, 360 pp.

The keen interest in bismuth compounds and bismuth-containing materials is indicated by nearly simultaneous publication of two monographs, which have similar titles and well supplement each other.[1] The book by Yu.M. Yukhnin and Yu.I. Mikhailov pays much attention to chemistry of aqueous solutions of bismuth salts, hydrometallurgical operations involving compounds of bismuth, and properties of its salts. The book comprises five chapters and very brief introduction and conclusion.

The first chapter (pp. 5–22) considers the physical and chemical properties of bismuth, application fields of the metal and its compounds, and dynamics of prices on the world market. Probably, the authors used not quite consistent sources of information. According to Table 1.13, the world production of refined bismuth in 1993 was 4.39 thousand tons. At the same time, it is stated on page 15 that the world consumption of the metal in 1993 was 5.01 thousand tons. Such an excess of consumption over production is unlikely.

The second chapter (pp. 23–40) is concerned with chemistry of aqueous solutions of bismuth, hydrolysis of its ions, complexation, and effect of the anionic composition of solution on the stability of complex ions. According to the conventional concepts, the coordination number in formation of complex bismuth ions in aqueous solutions is 6, and the complexation reaction occurs in stages, with preliminary removal of water molecules from the first coordination sphere of the Bi^{3+} ion and formation of intraspheric complexes. At the same time, according to recent studies, formation of bismuth complexes with coordination number exceeding 6 is possible.

The third chapter (pp. 41–99) contains evidence concerning preparation of solutions of, mainly nitrate, bismuth salts and subsequent hydrometallurgical operations (hydrolytic precipitation, extractive recovery, ion-exchange processes) aimed to purify bismuth compounds.

The fourth chapter (pp. 100–235) describes chemical properties of the most widely occurring and frequently used bismuth compounds: oxides, nitrates, sulfates, perchlorates, chromates, carbonates, halides, and organobismuth compounds. In describing the properties of compounds, much attention is given to their structure and crystal-chemical characteristics.

The fifth chapter (pp. 236–354) analyzes publications of the last decade, concerned with chemical properties of various bismuth materials. Of particular interest among these materials are formulations with valuable electrical characteristics (superconductors; thermoelectric, magnetic, and optical materials; ferroelectrics; piezoelectrics), solid electrolytes with oxygen conduction, catalysts, light-sensitive materials, luminophores, pharmaceutical preparations, glasses and ceramics, and pigments.

Lists of references are given separately for each chapter of the monograph, with their total number equal to 1046. Particularly extensive is the list for the fifth chapter (521 references), with 95% of these published during the period from 1992 till 2000.

In the conclusion (pp. 355–357), the authors emphasize that the chemistry of bismuth materials has been successfully developing in the last 10–15 years in quite a number of directions. The monograph by Yukhin and Mikhailov is the most prominent summary of the chemical properties of bismuth, its compounds, and bismuth-containing materials. The informational value of the monograph is rather high.

The book is well written and contains a neatly presented graphical material. The monograph will be of interest for research workers and engineers engaged in studies or use of bismuth compounds or materials on their base.

A. G. Morachevskii

[1] The first of these: Denisov, V.M., Belousova, N.V., Moiseev, G.K., *et al.*, *Vismutsoderzhashchie materialy: stroenie i fiziko-khimicheskie svoistva* (Bismuth-containing Materials: Structure and Physicochemical Properties), Yekaterinburg: Ural'sk. Otd. Ross. Akad. Nauk, 2000, 526 pp.

1070-4272/02/7512-2035 $27.00 © 2002 MAIK "Nauka/Interperiodica"